



Behavior of S_x^{2-} Species in Molten Sodium Polysulfide

T. Yoshida and K. Nakajima

Toyota Central Research and Development Laboratories, Incorporated, Nagakute-cho, Aichi-Ken, Japan

ABSTRACT

An electrolytic cell having four electrodes, each separated by a β -alumina plate or a porous ceramic separator and impregnated with molten sodium polysulfide was constructed. The electrolysis was carried out between two of these two sets of electrodes, and the composition change of the melt in the test electrode was observed from the OCV change during the electrolysis. The results of this study strongly suggested that S_2^{2-} ions migrated preferentially as a carrier on the electrolysis and that they would exist in the equilibrium with S_4^{2-} or S_5^{2-} ions even in a melt with the composition of $Na_2S_{4.66}$. The S_4^{2-} or S_5^{2-} ions also seem to contribute to the charge transport as the depletion of S_2^{2-} ions in the melt, whereas Na^+ is considered not to take part in the charge transport. These phenomena characterize the determination of the distribution of sodium polysulfide in the porous current collector of the sodium sulfur battery.

Since sodium sulfur batteries are expected to have a high energy density of more than 150 W-hr/kg, a considerable number of research and development programs are exploring their applications for load leveling and transportation power source. The behavior of molten sodium polysulfide, Na_2S_x , in a charge-discharge reaction affects the performance of this type of battery, and much effort has been devoted to clarify the properties of the compound, the phase diagram of Na_2S_x (1, 2), and properties such as electrical conductivity (3), density (4), and sulfur activities (5). However, there seem to be few experimental studies on the behavior of molten sodium polysulfides as battery electrode.

The composition of molten sodium polysulfide is known to change ($Na_2S_5 \rightarrow Na_2S_4 \rightarrow Na_2S_3$) progressively during the discharge process. The termination of the reaction is ascribed to the formation of solid sodium polysulfide in the electrode.

The reaction distribution in a porous current collector of a sodium sulfur battery has been estimated (6-9) by applying a network model. However, the reaction distribution would not necessarily correspond with the resultant distribution of the composition, when S_x^{2-} ions formed during the reaction migrate through the current collector. Since the sulfur utilization would be determined by the resultant distribution of the composition, the effect of migration of S_x^{2-} species seems essential.

Cleaver and Davies (5) derived the Washburn number instead of the transference number to observe the activity of sulfur in molten sodium polysulfide. This number only defines the number of moles of sulfur per unit charge passing through a reference frame in the melt, where the frame is chosen so that sodium ion does not pass through it. However, the mutual migrations of Na^+ and S_x^{2-} species should be considered for a better understanding of the resultant distribution of the composition in the porous current collector.

Key words: sodium-sulfur battery, molten salt, sodium polysulfide, transference number.

From these considerations, the migration of S_x^{2-} species for an electrode which is taken as the frame of reference was observed with the composition change in the electrode, when an ionic current was passed through the melt.

Experimental

Figure 1(a) shows a schematic representation of a cell constructed for the present experiment. This cell consists of two flat β -alumina plates (1.0 mm thickness, 20 mm width, and 35 mm height), auxiliary electrodes denoted A and B, testing electrodes A' and B', and ceramic separators. A and B are made up of blocks of porous graphite and are mounted on the outsides of both β -alumina plates. The operating cross-sectional area of A and B is 25.0×20.0 mm² and the thickness is 10 mm. The area of A' and B' is equal to that of A and B, respectively. The thickness of A' and B' is taken to be 2.0 mm. The porosity of the graphite block measured by paraffin impregnation method is 46.0%.

Sodium reference electrodes, R_A and R_B , were inserted at 5 mm depth for A' and B', respectively. The sodium reference electrode was a half-cell of Na/ β -alumina which was made of α -alumina tube (100 mm length, 2 mm outer diameter, and 1 mm inner diameter) with a fine rod of β -alumina on the tip and filled with metallic sodium (10).

Ceramic separators with fine pores (average pore diameter: 2 μ m, porosity: ca. 30%, thickness: 2 mm) were arranged on the insides of both A' and B', respectively. SUS 304 wires (0.3 mm ϕ) were inserted for the potential and current lead of A' and B' between A' and B' and the ceramic separators. SUS 304 backing plates were used for A and B current lead.

The electrode assemblies were tightly surrounded with glass plates for the side walls and the bottom so as not to leave any clearance between the edge surfaces of the β -alumina plates, ceramic separators, and glass plates. The cell was installed in a Pyrex glass container equipped with a side tube as shown in Fig. 1(b).

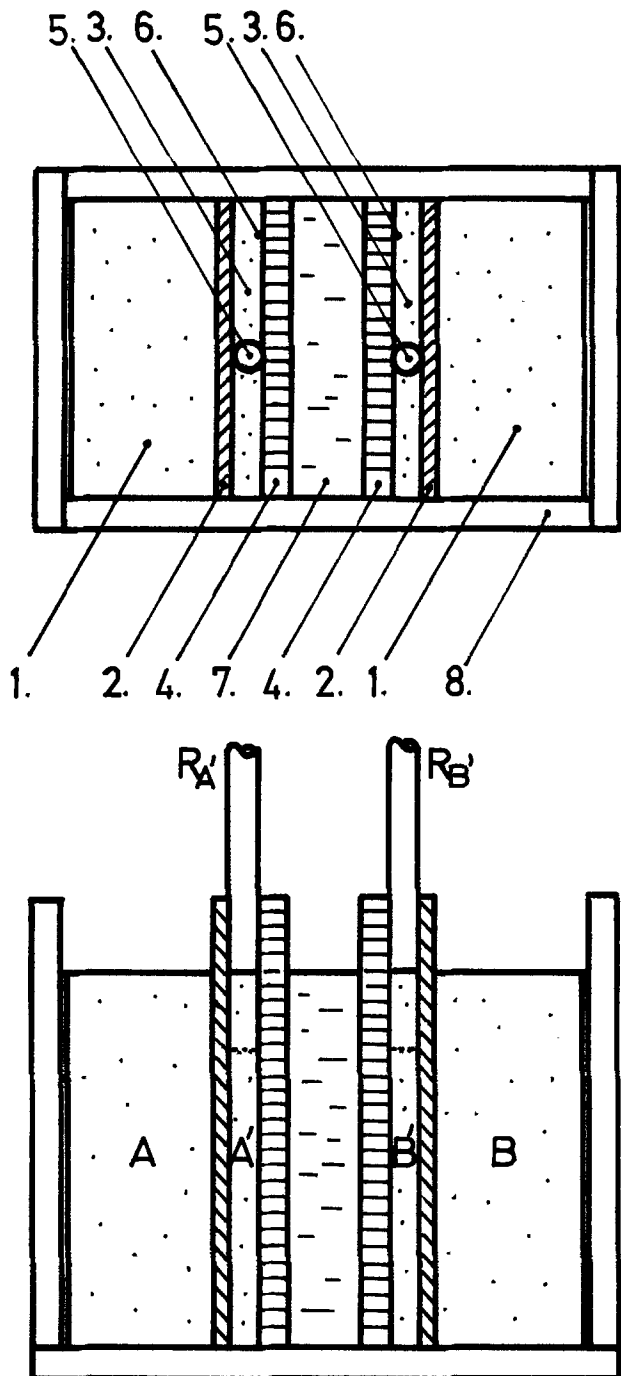


Fig. 1a. Construction of electrolytic cell. 1: Outer electrode, A or B, impregnated with molten Na_2S_x ; 2: β -alumina plate; 3: inner electrode, A' or B' impregnated with molten Na_2S_x ; 4: porous ceramic separator; 5: sodium reference electrode, R_A or R_B ; 6: lead for A' or B' (0.3 ϕ SUS 304); 7: molten Na_2S_x ; 8: glass plate.

Sodium polysulfide used in this experiment was prepared by the following method, which is substantially the one as reported by Selis (12). Two hundred gr. of CP grade crystalline $\text{Na}_2\text{S} \cdot 9\text{H}_2\text{O}$ was vacuum heated in a Pyrex glass container, being careful to increase the temperature gradually so as not to melt the crystal from room temperature to 200°C over 8 hr. In this procedure almost all of the combined water evaporated and white, porous grains of anhydride were obtained which kept the original shape of hydrate. Then the anhydride was maintained at 350°C and further vacuum dried overnight. The obtained anhydride was maintained at 200°C, 110 gr. of purified sulfur was added, and it was vacuum dried again for 24 hr. After this treatment, the temperature of the mixture was raised to 450°C for a few hours, then the melt of so-

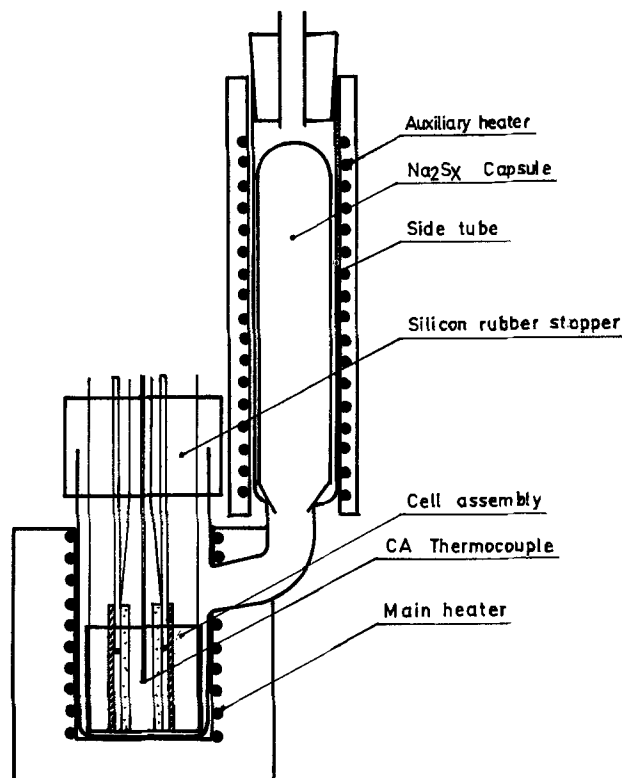


Fig. 1b. Cell container and auxiliary equipment

dium polysulfide was pipetted out into glass capsules, which were stocked in an airtight container.

The prepared capsule was put into the side tube of the cell, heated, and molten sodium-polysulfide was poured down into the cell from the capsule in an argon atmosphere at 300°C. In order to completely impregnate the pores of the electrodes with the molten sodium polysulfide, evacuations and pressurization between 1 Torr and 1 atm in the argon atmosphere were repeated several times. The surface level of molten sodium polysulfide after the impregnation was controlled so as to correspond with the upper surface of the electrodes, A, B, A', and B'.

The cell was maintained at $300 \pm 1^\circ\text{C}$ in a small electric furnace, and constant current electrolysis was carried out between A-A', A'-B', A-B, and A-B' by a galvanostat. During the electrolysis, the circuit was opened for 1 sec every 5 min and the differences from the initial open-circuit voltage were measured by a buffer amplifier with a voltage cancellation circuit and recorded with a 5 mV full scale pen recorder. Since the relationship between the OCV and the composition Na_2S_x is given by Gupta and Tischer (1), the following approximation equation obtained from this result was used in this experiment

$$x \text{ in } \text{Na}_2\text{S}_x = 10.93V - 17.521 \quad [1]$$

where V represents the OCV value (volts) vs. Na reference electrode. The range of applicability of Eq. [1] is $2.020 \leq V \leq 2.030$.

Theory—The Composition Change in Electrode A'

Consider the composition change of electrode A' which is placed on the inside of the β -alumina. Although an anodic or cathodic electrolysis of electrode A' against the other electrodes, A, B, or B', necessarily causes a composition change of sodium polysulfide contained in A', the composition of sodium polysulfide in A' also changes even in the electrolysis between A and B or A and B'. This composition change in A' has no charge transfer reaction in itself and is supposed to be caused by mutual migration of ionic species, Na^+ and S_2^{2-} , which consist of molten sodium polysulfide.

Thus the composition change in A' varies with the electrodes chosen in the electrolysis. In this experiment, the following treatments were derived for each electrolysis.

The constant current electrolysis between A and A'.—When a constant current electrolysis is conducted through β -alumina between A and A', it/F moles of Na^+ ion will be transported from A to A' as shown in Fig. 2(a) if A is the anode and A' the cathode. Assuming that there are no mass transfers by diffusion through the ceramic separator, the composition change of sodium polysulfide contained in A' is represented as

$$m \text{Na}_2\text{S}_{x_1} + (it/F)\text{Na}^+ + (it/F)e^- = m' \text{Na}_2\text{S}_{x_2} \quad [2]$$

Here, m and $\text{Na}_2\text{S}_{x_1}$ are the mole number of sodium polysulfide contained in A' and its composition before electrolysis, respectively; m' and $\text{Na}_2\text{S}_{x_2}$ are the mole number of sodium polysulfide and the composition also contained in A' after the electrolysis; moreover, i , t , and F are the current, electrolysis time, and Faraday constant, respectively. Hereafter, the same symbols are used in all equations for A'. From the material balance in Eq. [2], m' is eliminated and m is calculated as follows

$$m = itx_2/2F(x_1 - x_2) \quad [3]$$

Similarly, if A' is the anode and A the cathode

$$m = itx_2/2F(x_2 - x_1) \quad [3']$$

The constant current electrolysis between A' and B'.—When B' is chosen as the anode and A' the cathode in a constant current electrolysis, transfer of ionic species in the melt is considered to be as shown in Fig. 2(b). Just as before, if the mass transfers by diffusion through the ceramic separator are neglected, the composition change of sodium polysulfide in A' will be represented as

$$m \text{Na}_2\text{S}_{x_1} + \{(1 - \alpha)it/F\}\text{Na}^+ + (it/F)e^- = m' \text{Na}_2\text{S}_{x_2} + (\alpha it/2F)\text{S}_{x_2}^{2-} \quad [4]$$

From the material balance of Na^+ and $\text{S}_{x_2}^{2-}$ in Eq. [4], the transference number α of $\text{S}_{x_2}^{2-}$ for the electrode A' as the reference frame is calculated as

$$\alpha = \{x_2 - 2Fm(x_1 - x_2)/it\}/(x_2 - x) \quad [5]$$

Similarly, when A' is the anode and B' the cathode

$$\alpha = \{x_2 - 2Fm(x_2 - x_1)/it\}/(x_2 - x) \quad [5']$$

The constant current electrolysis between A and B.—The constant current electrolysis between A as the anode and B as the cathode leads to Na^+ ion transfers of it/F moles from A to A' and B' to B. These transfers of ionic species in the cell in this case are as shown in Fig. 2(c). If we assume again that there are no mass transfers by diffusion through the ceramic separator, the composition change of $\text{Na}_2\text{S}_{x_1}$ in A' will conform to the following equation

$$m \text{Na}_2\text{S}_{x_1} + (\beta it/F)\text{Na}^+ + (\beta it/2F)\text{S}_{x_2}^{2-} = m' \text{Na}_2\text{S}_{x_2} \quad [6]$$

The transference number β of $\text{S}_{x_2}^{2-}$ for A', when A' is taken as the frame of reference, is given by Eq. [7]

$$\beta = 2Fm(x_1 - x_2)/it(x_2 - x) \quad [7]$$

β also represents the ratio of Na^+ ion staying at A' when an amount of Na^+ ion is transferred into A' from A. In the case of B as the anode and A as the cathode, β is also expressed by Eq. [7].

Constant current electrolysis between A and B'.—The transfers of ionic species in the melt are considered to be as shown in Fig. 2(d), and the composition change in A' is represented by Eq. [6], which is the same as in the case of electrolysis between A and B. The transference number β for A' is also given by Eq. [7].

Results

Determination of the mole number m of sodium polysulfide contained in A'.—The electrode A' containing $\text{Na}_2\text{S}_{4.66}$ was electrolyzed against A in the constant current of 0.005A (1 mA/cm²). The measured OCV value of A' vs. the sodium reference electrode R_A changed linearly as shown in solid lines in Fig. 3. The value x in Na_2S_x was obtained from the OCV value using Eq. [1], then m (mole of $\text{Na}_2\text{S}_{4.66}$ contained in A') was calculated from Eq. [3] or [3']. The average value, $m = 3.9 \times 10^{-3}$ moles, was obtained from the results. The calculated m value considering the volume occupied by A' ($2.0 \times 20.0 \times 25.0$ mm³), the porosity of A' (46.8%), and the volume excluded by the sodium reference electrode was 4.3×10^{-3} moles¹ and corresponded with the measured value of m within a tolerance of about 10%. In this experiment, the value of 3.9×10^{-3} moles was used for m .

The transference number α for A' in the direct electrolysis of A'.—The OCV change of A' vs. R_A measured every 5 min was shown by the dotted line in Fig. 3 when the electrolysis was carried out between A' and B' in 0.005A (1 mA/cm²).

The transference number α of $\text{S}_{x_2}^{2-}$ species for A' taken as the frame of reference was calculated from Eq. [1] and [5] or [5'] based on the measured OCV values. The calculated results are given in Fig. 4, where α is plotted in the hyperbolic function of x . These curves in Fig. 4 only signify the mathematical relationship between α and x based on the results and contain regions which are not defined physically, such as $\alpha > 1$. These hyperbolic curves showed a characteristic inclination that passes through an α

¹ The value of 1.892 g/cm³ at 300°C (4) was used for the density of $\text{Na}_2\text{S}_{4.66}$.

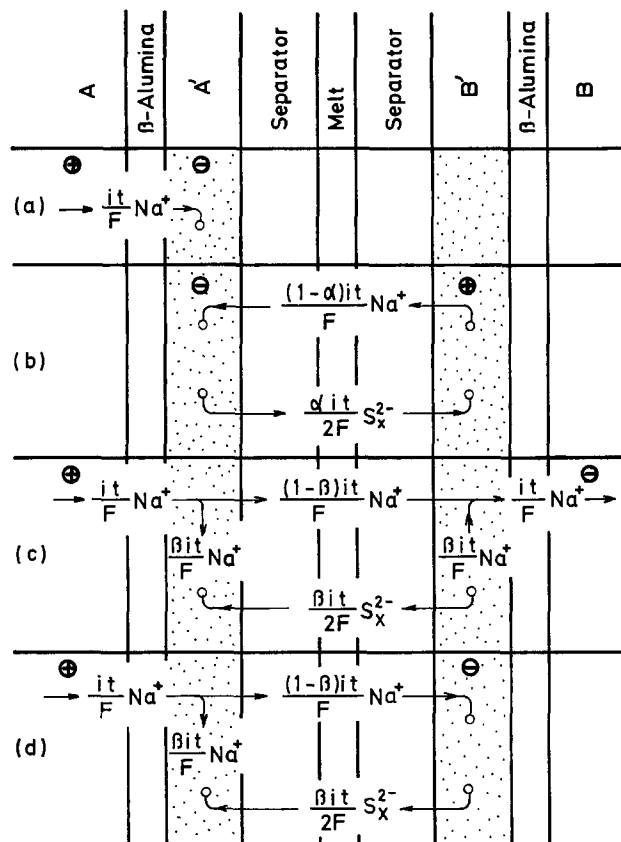


Fig. 2. Migration of ionic species in molten sodium polysulfide. (a) Electrolysis between A and A'; (b) electrolysis between A' and B'; (c) electrolysis between A and B; (d) electrolysis between A and B'.

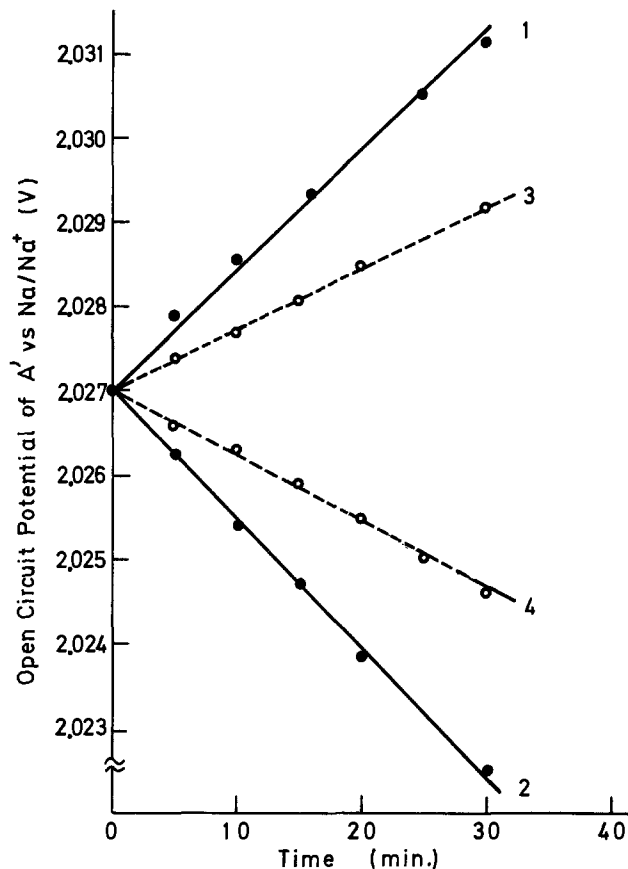


Fig. 3. Open-circuit potential change of A' in the direct electrolysis of A'. Solid line: electrolysis between A and A'; curve 1: A' anode, curve 2: A' cathode. Dotted line: electrolysis between A' and B'; curve 3: A' anode, curve 4: A' cathode.

value of about 1 in $x = 2$, irrespective of the polarity of A' or electrolysis time.

The transference number β for A'.—The measured OCV values of A' vs. R_A and B' vs. R_B , every 5 min when the constant current electrolysis of 0.005A was carried out between A the anode and B the cathode, are shown in Fig. 5. Figure 5 also shows the OCV change (dotted line) of A' where B is the anode and A the cathode. In this case, the changes of OCV values were larger at an early stage of the electrolysis and became smaller gradually with time. In particular, with the OCV of the electrode placed in the inner side of a cathode and separated by β -alumina (B' when B is the cathode, or A' when A is the cathode), little changed with the passage of time. The transference

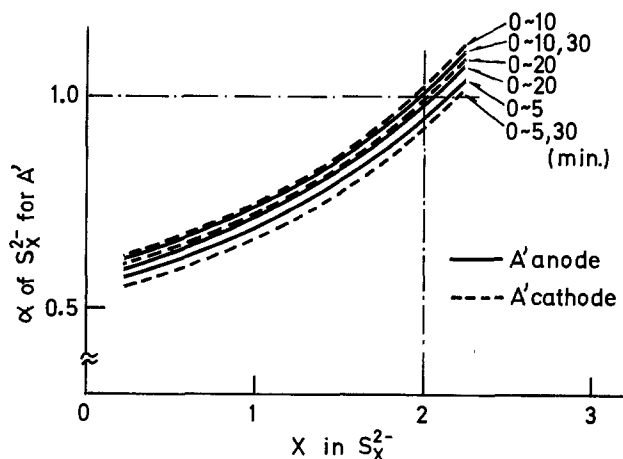


Fig. 4. Relation between transference number α of S_x^{2-} for A' and x in S_x^{2-} in electrolysis between A' and B'.

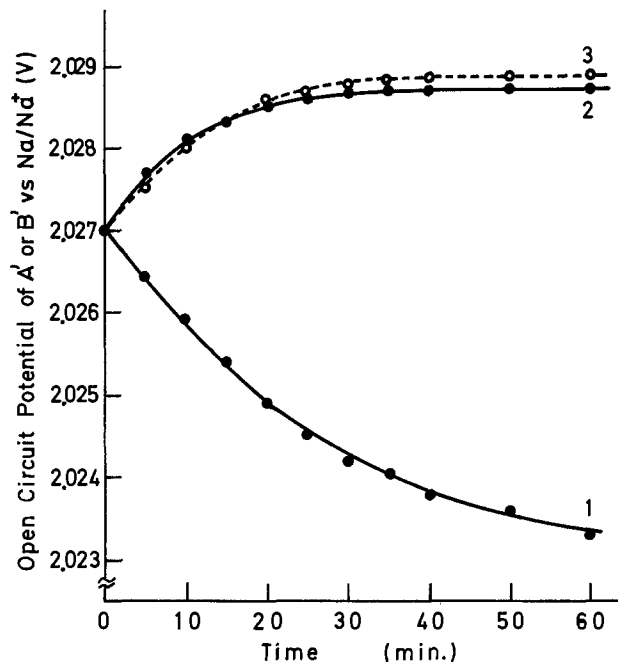


Fig. 5. Open-circuit potential change of A' or B' in electrolysis between A and B. Curve 1: A' potential in A anode and B cathode; curve 2: B' potential in A anode and B cathode; curve 3: A' potential in B anode and A cathode.

number β of S_x^{2-} species for A' taken as the frame of reference was calculated using Eq. [1] and [7]. These results are shown in Fig. 6 and Fig. 7 as the relation between β and x in Na_2S_x . The figures also

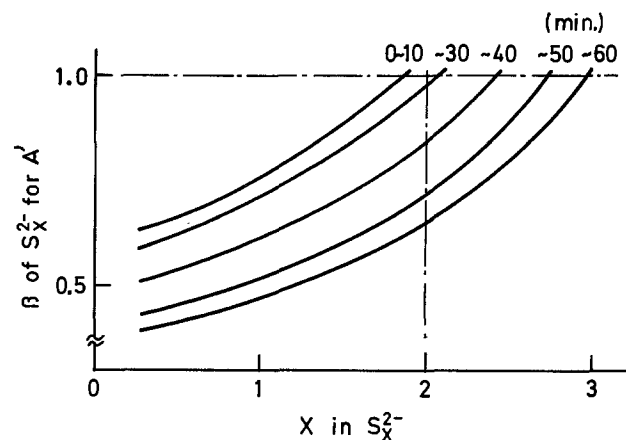


Fig. 6. Relation between transference number β of S_x^{2-} for A' and x in S_x^{2-} . Electrolysis between anode A and cathode B.

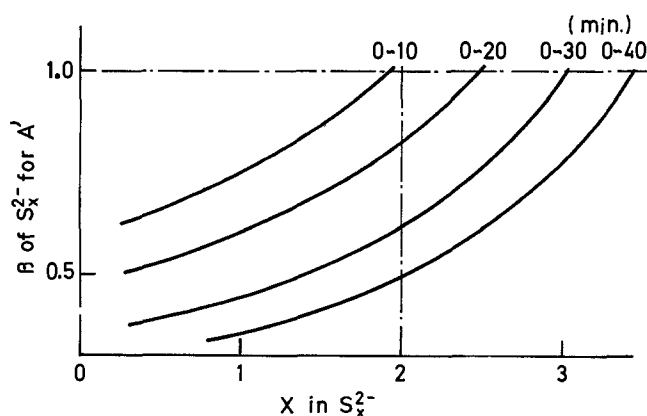


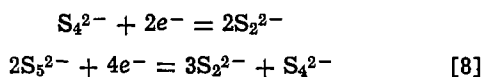
Fig. 7. Relation between transference number β of S_x^{2-} for A' and x in S_x^{2-} . Electrolysis between anode B and cathode A.

indicate the mathematical relationship between β and x based on the results as shown in the case of Fig. 4. Figure 6 represents the case when A is the anode and B the cathode, where hyperbolic curves pass through a β value of 1 in $x = 2$ at an early stage of the electrolysis and shift to the right side with time. Figure 7 represents the case when B is the anode and A the cathode and the tendency to shift of hyperbolic curve with time is more remarkable.

When electrolysis was conducted between A the anode and B' the cathode, relations between the transference number β of S_x^{2-} species for A' and x in S_x^{2-} are represented as in Fig. 8. Although the hyperbolic curves tend to shift towards the right side with time, the degree of shift is much smaller than when A is the anode and B the cathode as shown in Fig. 6.

Discussion

S_x^{2-} in molten sodium polysulfide consists mainly of S_2^{2-} , S_4^{2-} , S_5^{2-} , and some S_6^{2-} species (11). Consequently, the elimination of regions, $x < 2$ and $\alpha > 1$, from the curves in Fig. 4 leads to only one valid point, $x = 2$ and $\alpha = 1$. This result shows that Na^+ ions do not move to or from the electrode A' under the direct electrolysis of A' and B', and the composition change of sodium polysulfide contained in the electrode A' is determined only by the transfers of S_2^{2-} species in the melt. For example, when A' is the cathode, the following reactions would occur in the electrode (11)



and the S_2^{2-} ion produced in the reaction processes seems to move from A' to B' direction. When A' is the anode, S_2^{2-} ions brought from the B' side are oxidized at first at A' by the reverse reaction of Eq. [8].

On the other hand, when an electrolysis is conducted between A and B, the change in A' is not as simple as seen before. When A is the anode and B the cathode, OCV in B' is virtually unchanged after an electrolysis of 20 min, despite the fact that OCV in A' continues to decrease still more as shown in Fig. 5. Since the change of OCV for A' or B' placed on the inside of the cathode (the upper two curves in Fig. 5) is nearly the same in both cases, the behavior of S_x^{2-} species in B' in this case can be represented by the one shown for A' in Fig. 7. Thus, when A is the anode and B is the cathode, the behavior of A' and B' are explained by Fig. 6 and Fig. 7, respectively. In Fig. 6, if regions $x < 2$ and $\beta > 1$ are eliminated from the curves of 0 ~ 30 min, as in the direct electrolysis mentioned above, $\beta = 1$ in $x = 2$ becomes the only valid point. This means that S_2^{2-} species migrate to A' during this time to satisfy the condition of electroneutrality for Na^+ ions which are injected into A' from A continuously

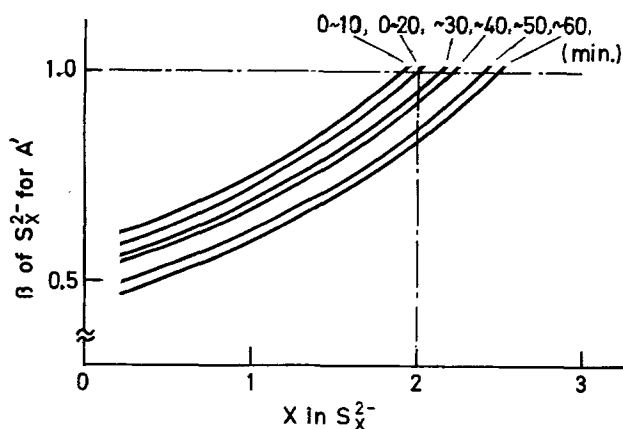


Fig. 8. Relation between transference number β of S_x^{2-} for A' and x in S_x^{2-} . Electrolysis between anode A and cathode B'.

through β -alumina. On the other side, the condition, $\beta = 1$ in $x = 2$ is fulfilled for no more than 0 ~ 10 min in B'. Still, the result in A' by which the charge carrier through A' to B' is S_x^{2-} for 10 ~ 30 min implies that curves in Fig. 7 and Fig. 6 are valid not only for $\beta = 1$ in $x = 2$ but also for $\beta = 1$ irrespective of x value, if $x \geq 2$. This means that the charge carrier in molten sodium polysulfide is only the sulfide ion, S_x^{2-} , and x values change with electrolytic conditions. The crossing point values of x with the straight line of $\beta = 1$ in Fig. 6 and Fig. 7 are depicted in Fig. 9 against electrolysis time.

As there is no charge transfer reaction between A' and B', S_2^{2-} ions that migrate from B' to A' are not a product of the cathodic reactions as shown in Eq. [8], but may have existed in an equilibrium with other species such as S_4^{2-} , S_5^{2-} in the melt. It is supposed that S_2^{2-} moves out from B' in the early electrolytic stage, and the gradual depletion of S_2^{2-} with time in B' causes the migration of larger sulfide ions in B'. The increase of x value with time in Fig. 9 would show the comigration of larger sulfide ions with S_2^{2-} , although the effect of diffusion by concentration gradients would not be negligible in the late stage of electrolysis. As for A', the period in which only S_2^{2-} ions flow into A' is much longer. This is attributed to the relatively large volume of the melt in the midst of the cell. But the gradual depletion of S_2^{2-} results with time, and comigration of larger sulfide ions also occurs.

On the contrary, the electrolysis between A as the anode and B' as the cathode gives a β - x relation for A' which distributes nearly around the hyperbolic curves of $\beta = 1$ in $x = 2$, and the change of x value with time in $\beta = 1$ in this case reveals that mainly S_2^{2-} ions migrate, as shown in Fig. 9. This is ascribed to the migration of S_2^{2-} ion produced by the cathodic reaction in B' to A'.

Conclusion

The migration behavior of ionic species in molten sodium polysulfide was investigated using a transport cell of four electrodes. S_2^{2-} ions migrate preferentially into the vicinity of β -alumina to fulfill the electroneutrality for Na^+ ions injected through the β -alumina. S_4^{2-} or S_5^{2-} ions also seemed to contribute to the migration as the depletion of S_2^{2-} ions in the melt, whereas Na^+ ions are considered not to take part in the charge transport. When S_2^{2-} ions are continuously produced by a cathodic reaction in another portion of

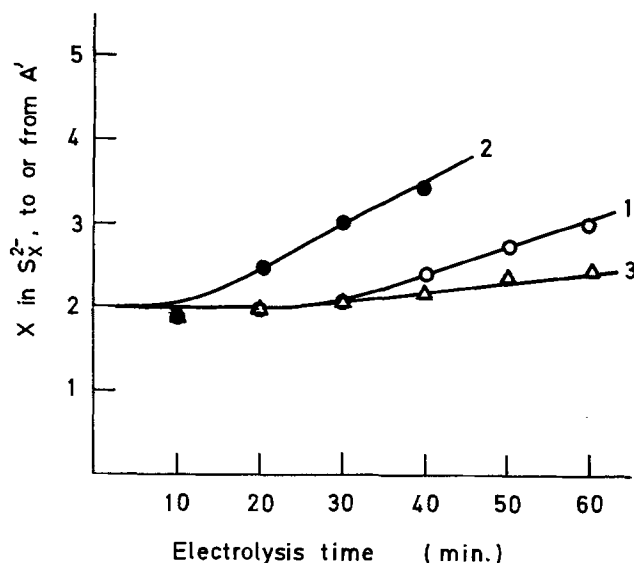


Fig. 9. x value of charge carrier, S_x^{2-} , to or from A'. curve 1: A anode and B cathode (from Fig. 6); curve 2: B anode and A cathode (from Fig. 7); curve 3: A anode and B' cathode (from Fig. 8).

the melt, the migration of S_2^{2-} ions towards Na^+ ions injected through β -alumina becomes more remarkable. This phenomenon would be responsible for the determination of the distribution of sodium polysulfide in the porous current collector of the sodium sulfur battery.

Manuscript submitted April 16, 1980; revised manuscript received Aug. 6, 1980.

Any discussion of this paper will appear in a Discussion Section to be published in the December 1981 JOURNAL. All discussions for the December 1981 Discussion Section should be submitted by Aug. 1, 1981.

Publication costs of this article were assisted by Toyota Central Research and Development Laboratories, Incorporated.

Ionic Conductivity and Thermoelectric Power of Pure and Al_2O_3 -Dispersed AgI

K. Shahi* and J. B. Wagner, Jr.*

Center for Solid State Science, Arizona State University, Tempe, Arizona 85281

ABSTRACT

Ionic and electronic conductivities, and thermoelectric power have been measured for AgI and AgI containing a dispersion of submicron size Al_2O_3 particles. While the dispersion of Al_2O_3 enhances the ionic conductivity significantly, it does not affect the electronic properties of the matrix. The enhancement is a strong function of the size and concentration of the dispersoid. Various models have been tested to account for the enhanced conduction. However, the complex behavior of the present results points out the need for more sophisticated theoretical models. Ionic conduction and thermoelectric power data suggest that the dispersed Al_2O_3 generates an excess of cation vacancies and thereby enhances the conductivity and suppresses the thermoelectric power of the matrix. The individual heats of transport of cation interstitials and vacancies have been estimated and compared to their respective migration energies.

As a result of intensive efforts in the past decade, many solid ionic conductors that exhibit conductivities in excess of $10^{-2} \Omega^{-1} \text{cm}^{-1}$ at ambient temperatures are now known. Most are stable intermediate compounds between two or more phases with one phase being silver (1) or copper (2) halides or chalcogenides. While the classical doping technique has long been used to increase ionic conductivity, particularly at low temperatures, such an enhancement has been limited to a factor of 2-20, though it has been most useful in the elucidation of ion-transport mechanisms in general.

Recently Liang (3), Liang *et al.* (4), Pack *et al.* (5), and Jow and Wagner (6) studied the effect of Al_2O_3 dispersion in LiI (3-5) and CuCl (6), respectively. These authors reported ionic conductivity enhancements by as much as 2 orders of magnitude. Based on x-ray powder diffraction results the conclusion was that the Al_2O_3 particles are insoluble (3) and hence the classical doping concept cannot be used to explain the enhancement in conductivity. The purpose of the present investigation is (i) to examine whether this effect is general and (ii) to test the various proposed mechanisms and/or to develop an adequate model.

Experimental

High purity AgI (99.999%) obtained from Apache Chemicals was used without further treatment. Al_2O_3

- ### REFERENCES
1. N. K. Gupta and R. P. Tischer, *This Journal*, **119**, 1033 (1972).
 2. D. G. Oei, *Inorg. Chem.*, **12**, 435 (1973).
 3. B. Cleaver, A. J. Davies, and M. D. Hames, *Electrochim. Acta*, **18**, 719 (1973).
 4. B. Cleaver and A. J. Davies, *ibid.*, **18**, 727 (1973).
 5. B. Cleaver and A. J. Davies, *ibid.*, **18**, 735 (1973).
 6. J. G. Gibson, *J. Appl. Electrochem.*, **4**, 125 (1974).
 7. Y. K. Kao and P. C. Wayner, Jr., *This Journal*, **124**, 230 (1977).
 8. M. W. Breiter and B. Dunn, *J. Appl. Electrochem.*, **9**, 291 (1979).
 9. M. P. J. Brennan, *Electrochim. Acta*, **24**, 473 (1979).
 10. T. Yoshida, K. Ninomiya, and T. Chiku, *Denki Kagaku*, **47**, 293 (1979).
 11. R. P. Tischer and F. A. Ludwig, "Advances in Electrochem. and Electrochem. Eng.," Vol 10, John Wiley and Sons, New York (1977).
 12. S. M. Selis, *Electrochim. Acta*, **15**, 1285 (1970).

(99.98%) of different reported particle sizes (0.06, 0.3, 1, 3, 8, and 15 μm) was obtained from Adolf Meller and was also used as received, and in certain experiments it was vacuum dried at $\sim 700^\circ\text{C}$ - 800°C for at least 12 hr prior to use. Appropriate amounts of AgI (mp 557°C) and Al_2O_3 were intimately mixed in an agate mortar and pestle, vacuum sealed in quartz tube, heated at 800°C for 6-8 hr, and then quenched to room temperature. When undried Al_2O_3 was directly used, the mixture was heated in a sealed quartz tube to a lower temperature ($< 600^\circ\text{C}$) to avoid any rupture of the quartz tube due to excessive water vapor pressure. The resultant material prepared by either method was pulverized and pelletized at pressures in the range 70,000-80,000 psi in a nickel-plated steel die. Each sample was annealed for 10-12 hr to relax any stresses and also to homogenize the charge carriers.

The temperature of the furnace was controlled to within $\pm 0.5^\circ\text{C}$ by a Thermac Controller (Series 6000) and measured by Chromel-Alumel thermocouple.

The total conductivity was measured using a cell, Ag|AgI (Al_2O_3) or AgI|Ag, and a GR 1608A impedance bridge in conjunction with GR 1310B oscillator and GR 1232-P2 preamplifier as the null detector. No appreciable frequency dependence was observed except at lower (near room) temperatures where the conductivity at 10 kHz was 5-7% higher than that at 1 kHz. The data reported in this paper are at 1 kHz. The inaccuracy below $1 \Omega^{-1} \text{cm}^{-1}$ was less than $\pm 5\%$.

The d-c polarization technique was used to measure the electronic conductivity using a cell, Ag|AgI (Al_2O_3)

* Electrochemical Society Active Member.

Key words: cations, conduction, thermoelectric power.

or AgI/graphite. In this experiment Keithley 2600 nV source was used as standard voltage source and the current in response to applied polarization potential was measured by measuring the voltage drop by means of Keithley 616 digital electrometer across a known standard resistor.

The thermoelectric power was measured using a sample holder similar to that used for conductivity measurements except the former has Pt-Pt-10% Rh thermocouples welded on the back of each Pt electrode (in contact with the Ag electrode) which are used to record the temperature of each side of the sample. The thermoelectric voltage (ΔV) induced by the small temperature difference (ΔT of the order of 10°C) was also measured by Keithley 616 digital electrometer with an input impedance of $>10^{14}\Omega$ at balance that ensures almost zero current through the specimen under examination. The thermoelectric power was calculated from the ratio $\Delta V/\Delta T$ and assigned the usual sign convention, i.e., it is positive if the hot end is positive.

In the following, the results on ionic conductivity are presented first followed by those on electronic conductivity and thermoelectric power.

Results and Discussion

Ionic Conductivity

Ionic conductivity vs. composition.—Figure 1 shows the total (a-c) conductivity of the AgI(Al_2O_3) system containing both dried and undried alumina particles of $0.06\ \mu\text{m}$ size as a function of the Al_2O_3 content at room temperature. This figure also shows the same results obtained for dried alumina particles of 0.3 and $8\ \mu\text{m}$ sizes. The conductivity of AgI(Al_2O_3) system initially increases with increasing Al_2O_3 content for both dried and undried, and for all sizes of Al_2O_3 particles. It reaches a maximum around 30 mole percent (m/o) Al_2O_3 content and then decreases. The dispersion of undried Al_2O_3 ($0.06\ \mu\text{m}$) leads to a relatively sharp maximum as well as to more enhancement than predried Al_2O_3 . This latter result indicates the possibility that the presence of adsorbed water on the Al_2O_3 might be playing an important role in the enhancement of conductivity.

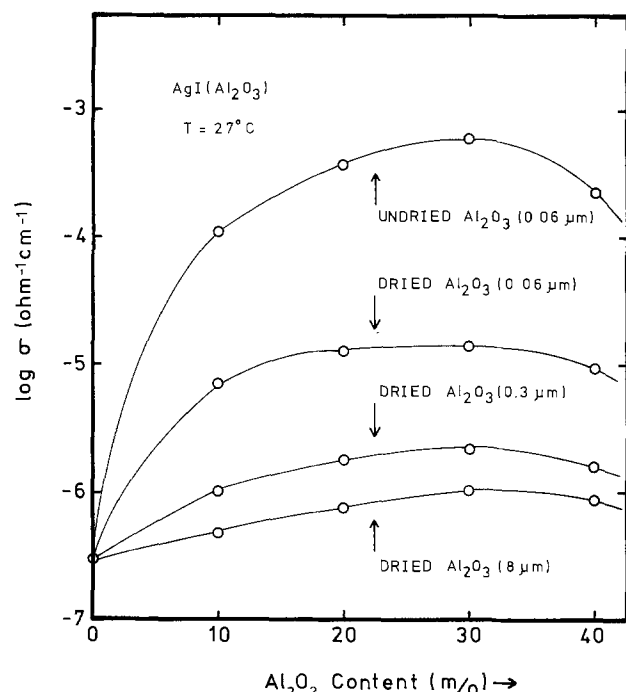


Fig. 1. Logarithm of total (a-c) conductivity of AgI(Al_2O_3) system as a function of the concentration of Al_2O_3 particles at room temperature. Measurements employ silver electrodes and a frequency of 1 kHz.

A maximum conductivity of $6 \times 10^{-4}\ \Omega^{-1}\ \text{cm}^{-1}$ was obtained for AgI containing 30 m/o undried Al_2O_3 ($0.06\ \mu\text{m}$) at room temperature.

Another point to be emphasized is that the conductivity enhancement is a strong function of the size of Al_2O_3 particles. Figure 1, for example, also shows the results of AgI(Al_2O_3) system containing the dried Al_2O_3 particles of 0.3 and $8\ \mu\text{m}$ sizes. Figure 2 further illustrates the dependence of conductivity of the AgI(Al_2O_3) system as function of the size of Al_2O_3 particles. Obviously the conductivity enhancement is larger for smaller particles. When Al_2O_3 particles as large as 8 or $15\ \mu\text{m}$ are used there is very little or practically no enhancement in conductivity.

Ionic conductivity vs. temperature.—Figure 3 shows the plot of $\log \sigma$ vs. $10^3/T$ for AgI and AgI containing a dispersion of dried and undried Al_2O_3 ($0.06\ \mu\text{m}$). A conductivity of $3 \times 10^{-7}\ \Omega^{-1}\ \text{cm}^{-1}$ at 25°C was obtained for pure AgI, and an overall activation energy of $0.56\ \text{eV}$ in the temperature range 300 – $400\ \text{K}$; these values are in good agreement with some of the previous findings on polycrystalline AgI and also close to single crystal values (1). The rather high conductivity and low activation energy reported by some researchers may have been due to the presence of impurities or γ -AgI in their samples and/or a lack of prolonged annealing of samples used in their experiments. We found the conductivity of freshly prepared samples of AgI decreased and activation energy increased considerably when the samples were annealed overnight at 70° – 80°C .

The addition of undried 30 m/o Al_2O_3 of $0.06\ \mu\text{m}$ size increased the conductivity by about 3 orders of magnitude, the room temperature value being $\sim 6 \times 10^{-4}\ \Omega^{-1}\ \text{cm}^{-1}$ as compared to $3 \times 10^{-7}\ \Omega^{-1}\ \text{cm}^{-1}$ for pure AgI. The enhancement in conductivity by the dispersion of Al_2O_3 is accompanied by a decrease in activation energy as is usual for most high conductivity solid electrolytes. Summarized in Table I are the conductivities and the related parameters for AgI and AgI(Al_2O_3).

The dispersion of predried Al_2O_3 (30 m/o, $0.06\ \mu\text{m}$) increased the conductivity by about a factor of 50. The larger enhancement caused by undried Al_2O_3 is not quite understood but seems to be related to the adsorbed moisture on the Al_2O_3 particles. Further

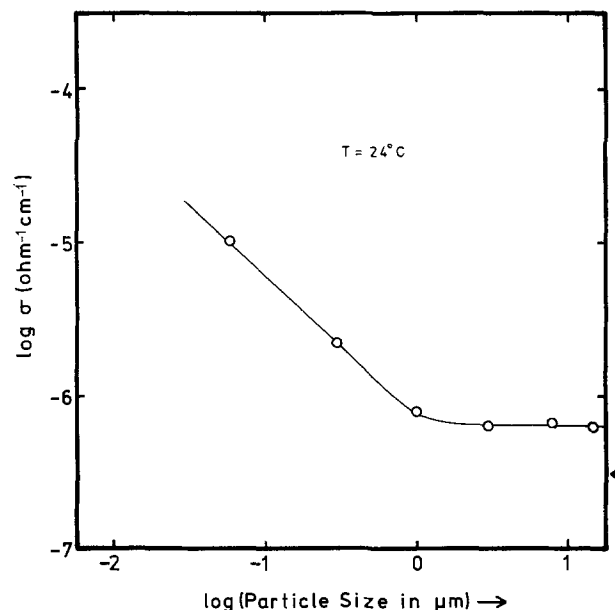


Fig. 2. Logarithm of conductivity of AgI containing 30 m/o dried Al_2O_3 at room temperature as a function of the logarithm of the size (in μm) of Al_2O_3 particles.

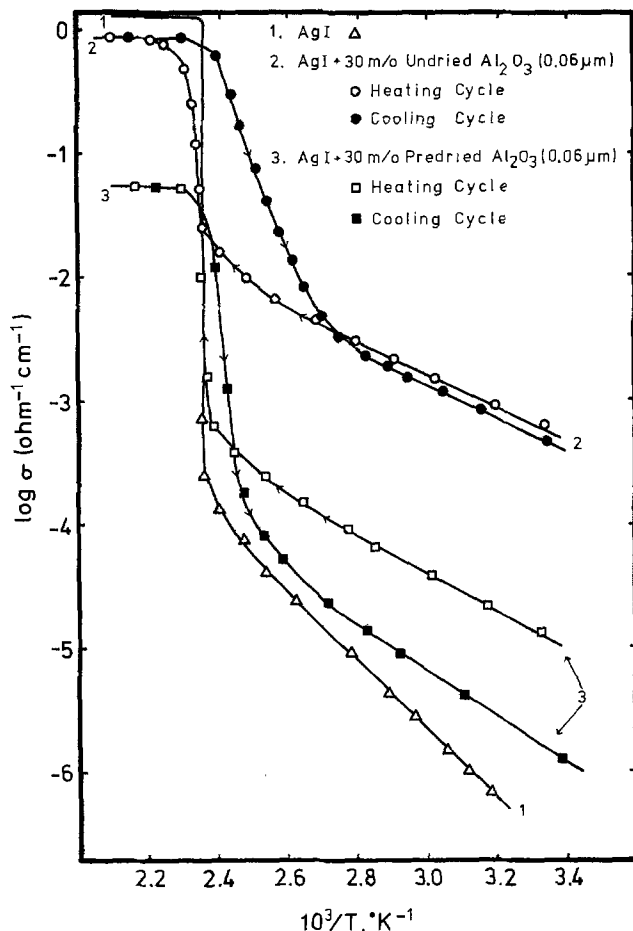


Fig. 3. Logarithm of conductivity of pure AgI and AgI + 30 m/o Al_2O_3 ($0.06 \mu\text{m}$), using both dried and undried Al_2O_3 , as a function of inverse absolute temperature.

experiments to quantify the effect of adsorbed water content on the conductivity enhancement are planned.

The activation energy of 0.31 eV for AgI + 30 m/o Al_2O_3 ($0.06 \mu\text{m}$) can be compared to the migration energies of Ag^+ interstitials (Δh_i^+) and Ag^+ vacancies (Δh_v^+) in β -AgI. According to one study on polycrystalline AgI (7) Δh_i^+ is ~ 0.14 eV which is much less than what is observed (0.31 eV) for AgI(Al_2O_3) system suggesting that Ag^+ interstitials are less likely to be a mechanism responsible for conduction in AgI(Al_2O_3). However, the other studies (8-10) on β -AgI reveal that Δh_i^+ and Δh_v^+ are quite comparable; Δh_i^+ is in the range 0.3 eV (8) to 0.4 eV (9) and Δh_v^+ amounts to 0.4 eV (8) to 0.5 eV (8, 10). Therefore, it is very difficult to deduce the type of charge carrier responsible for conduction in AgI(Al_2O_3) from these data.

Another interesting feature of Al_2O_3 dispersion is that it leads to a hysteresis in $\log \sigma$ vs. $10^3/T$ plot (see Fig. 3). When the temperature is cycled through the $\beta \rightarrow \alpha$ phase transition temperature (T_c) of AgI ($\sim 147^\circ\text{C}$), the σ decreased by a factor varying between 2 to 10 depending on the temperature, thermal

Table I. Electrical conductivity and activation energy in AgI and AgI(Al_2O_3)

| Material | σ ($\Omega^{-1} \text{cm}^{-1}$) at 25°C | Activation energy (eV) | Temperature range ($^\circ\text{C}$) |
|---|---|------------------------|--|
| AgI | 3×10^{-7} | 0.56 | 25-120 |
| AgI + 30 m/o undried Al_2O_3 ($0.06 \mu\text{m}$) | 6×10^{-4} | 0.26 | 15-110 |
| AgI + 30 m/o dried Al_2O_3 ($0.06 \mu\text{m}$) | 1.2×10^{-5} | 0.31 | 25-100 |

history of the sample, and the Al_2O_3 content. A common feature of these results is that the smaller the width of the hysteresis loop in the $\log \sigma$ vs. $1/T$ plot the larger is the difference in σ 's before and after cycling the temperature across T_c . It should be noted however that the σ of AgI with or without Al_2O_3 remained almost the same when temperature was cycled between room temperature and T_c .

Figure 4 compares the conductivity results for usual (cold pressed) pellets to that for hot-pressed (at 300°C) pellets, at different temperatures. A somewhat higher σ for the hot-pressed samples might be due to a better packing than that of the former but there is no significant difference between the two samples.

Neither in conductivity nor in thermoelectric power (to be discussed later) is the effect of Al_2O_3 dispersion pronounced in α -AgI. In general there is a drop in the σ whose magnitude, by and large, solely depends on the content of Al_2O_3 . Since at the present time these results do not seem promising technically, nor do they contribute significantly towards the understanding of the mechanism of transport in these dispersed solid electrolyte systems, they will not be discussed further.

Summary of the results.—Table II summarizes some of the characteristics of the AgI(Al_2O_3) and other systems reported thus far, viz. LiI(Al_2O_3) (3), CuCl(Al_2O_3) (11), and HgI₂(Al_2O_3) (12). The results of AgI(Al_2O_3) indicate a more complex behavior, e.g., "wet" Al_2O_3 appears more effective than dry ones and $\log \sigma$ vs. composition plot exhibits a rather flat maximum (Fig. 1) similar to that in HgI₂(Al_2O_3) but unlike those in CuCl(Al_2O_3) and LiI(Al_2O_3). In brief, the important features of all these Al_2O_3 -dispersed systems can be summarized as follows: (i) there is an enhancement in conductivity by a dispersion of sec-

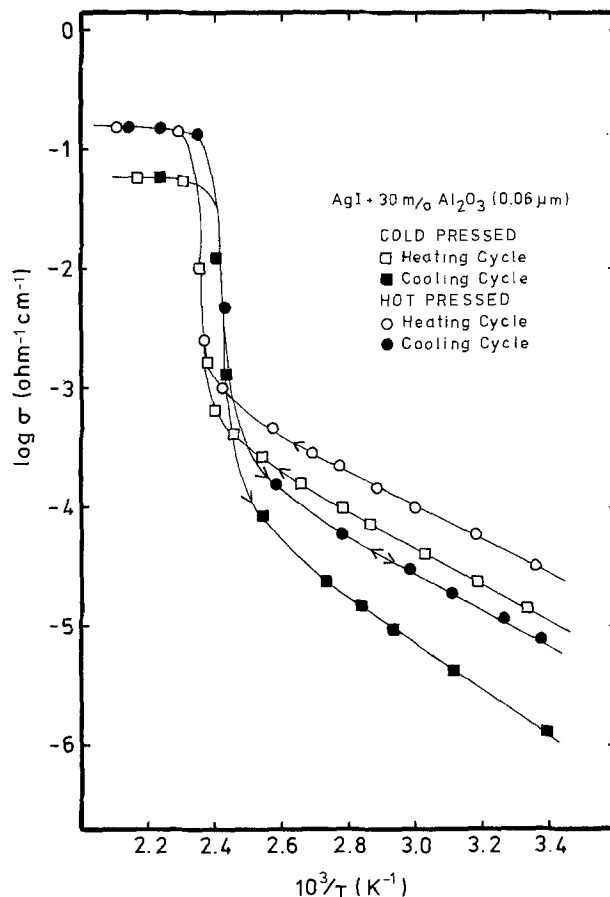


Fig. 4. Logarithm of conductivity of cold and hot (300°C) pressed pellets of AgI + 30 m/o dried Al_2O_3 ($0.06 \mu\text{m}$) as a function of inverse absolute temperature.

Table II. Some characteristics of solid electrolytes containing a dispersion of dried Al_2O_3

| Material | Size of Al_2O_3 (μm) | m/o Al_2O_3 for maximum enhancement | Temp. ($^\circ\text{C}$) | Maximum enhancement in conductivity by a factor of |
|------------------|---|---|----------------------------|--|
| AgI | 0.06 | 30 | 25 | ~ 50 (this work) |
| LiI | — | 40 | 25 | ≈ 50 (3) |
| CuCl | 0.06 | 10 | 60 | ~ 50 (11) |
| HgI_2^* | 0.06 | 30 | 203 | ~ 100 (12) |

* HgI_2 is not known to be solid electrolyte and the quoted value of the enhanced conductivity corresponds to the inclusion of undried Al_2O_3 .

ond phase (such as Al_2O_3); (ii) the larger enhancement is due to finer dispersoids; (iii) "wet" dispersoids cause a larger enhancement than dry ones; (iv) there is larger enhancement at lower temperatures where the intrinsic defect concentration is low compared to that generated by the dispersoids. This also implies a decrease in activation energy in the low temperature regime. However, the data on $\text{LiI}(\text{Al}_2\text{O}_3)$ (3) do not agree with others, i.e., the activation energies are the same with and without Al_2O_3 . (v) The occurrence of a rather flat maximum for some systems in the $\log \sigma$ vs. composition plot, seems to extend from 15 to 35 m/o Al_2O_3 in $\text{AgI}(\text{Al}_2\text{O}_3)$ and up to 80 m/o in $\text{HgI}_2(\text{Al}_2\text{O}_3)$, and (vi) the position of maximum for a particular system, e.g., $\text{AgI}(\text{Al}_2\text{O}_3)$, to be independent of the size of the dispersoids but a sensitive function of the matrix, for example, in $\text{CuCl}(\text{Al}_2\text{O}_3)$ the maximum occurs at 10 m/o, in $\text{AgI}(\text{Al}_2\text{O}_3)$ at 30 m/o, and in $\text{LiI}(\text{Al}_2\text{O}_3)$ at 40 m/o Al_2O_3 .

Discussion of models.—The electrical transport in multiphase systems has been fundamentally treated by Maxwell (13a) and Lord Rayleigh (13b). However, these models did not consider the possible existence of electrical double layer at the interfaces and thus, in turn, did not predict a higher conductivity for the mixed phases than for the pure single phase materials.

In 1972, Wagner (14) reconsidered the problem and, based on the fact that there can be a space charge layer at the interfaces, he derived an expression that predicted an enhanced electronic conduction in two-phase semiconductors, the enhancement being proportional to the volume fraction of the dispersoid and the square of the Debye length and inversely proportional to the square of the radius of the dispersoid.

Recently Jow and Wagner (6) derived a model for ionic conduction based on the fact that ultrafine dispersoids have some kind of charge at or near their surfaces. Due to formation of the double layer at the dispersoid/matrix interface, the defect concentration and hence conductivity, in the vicinity of the dispersoids differs from that in the bulk. They obtained the following expression

$$\Delta\sigma = 3 \sum_i e \mu_i \langle \Delta n_i \rangle \lambda \left(\frac{1}{r_1} \right) \left[\frac{V_v}{1 - V_v} \right] \quad [1]$$

where $\Delta\sigma$ is the change in conductivity of the matrix with the dispersoid relative to that of the bulk matrix, e the electronic charge, μ_i the mobility of the i th defect species, $\langle \Delta n_i \rangle$ the average excess density of defects within the space charge region, λ the space charge layer thickness (\sim Debye length), r_1 the radius (half the size) of the dispersoid, r_2 the distance between two dispersoids, and V_v the volume fraction of the dispersoid. This model predicts that the enhancement in σ is proportional to $(1/r_1)$ ($V_v/1 - V_v$) for the cases where $r_1 \ll r_2$ is satisfied.

Stoneham *et al.* (15) have extended Landauer's (16) effective medium model which assumes a high conductivity layer around each insulating particle, and shown that the enhanced conduction is possible if one assumes the layer to be of a few hundred angstroms thickness.

According to another (12) so-called interface-capacitor model which also involves the space charge layer between the dispersoid and matrix, the conductivity is given by

$$\sigma = \sigma_1(1 - V_v) + G \cdot S(1 - V_v)^2 + \sigma_2 V_v \quad [2]$$

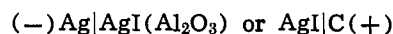
where σ , σ_1 and σ_2 are, respectively, the conductivities of the mixed phase, the first phase (or matrix), and the second phase (or dispersoid), S the surface area generated by the dispersoid per cm^3 , and G a factor which accounts for the number of excess charge per cm^3 .

All these models recognize in some way the existence of a "double layer" or "conducting layer" at the matrix-dispersoid interface and agree qualitatively in their predictions to some extent. While the model of Jow and Wagner (6) works well with respect to both accounting for enhanced conduction and predicting the correct temperature dependence, its applicability is limited to smaller concentrations of the dispersoid ($r_1 \ll r_2$). The latter two models (12, 15) also explain the "blocking effect" of the dispersoid at larger concentrations but these both lack in predicting the correct temperature dependence. For instance, the σ 's of CuCl and $\text{CuCl}(\text{Al}_2\text{O}_3)$ all fall around the same value at $T \geq 300^\circ\text{C}$.

In brief, the results on dispersed-systems point out the need for more sophisticated models capable of explaining the additional features such as (i) the larger effectiveness of "wet" dispersoid, (ii) the occurrence of flat maximum in some systems, e.g., $\text{AgI}(\text{Al}_2\text{O}_3)$, and (iii) the position of maximum which is a sensitive function of the matrix.

Electronic Conductivity

Since in many electrochemical applications it is desired that electronic conductivity be small (or preferably negligible) compared to the ionic part, a d-c polarization cell of the type



was constructed for this measurement. When a potential (V) less than the decomposition potential of the electrolyte is applied with positive polarity on the right side, the Ag^+ ions move initially from right to left side (toward Ag electrode). Since graphite is an inert (so-called blocking) electrode, there is no supply of Ag^+ ions and hence a depletion of Ag^+ ions results at the $\text{C}/\text{AgI}(\text{Al}_2\text{O}_3)$ interface. At steady state the potential gradient due to electric field is just balanced by that due to the chemical potential gradient and then the ionic current is zero. Under these conditions the current is solely due to diffusional flow of electrons or holes. Wagner (17) has shown that the steady-state current (I) is given by

$$I = I_e + I_h = \frac{kTA}{eL} \left[\sigma_e \left\{ 1 - \exp\left(-\frac{eV}{kT}\right) \right\} + \sigma_h \left\{ \exp\left(\frac{eV}{kT}\right) - 1 \right\} \right] \quad [3]$$

where σ is the conductivity and the subscripts e and h refer, respectively, to electrons and holes, L the length and A the area of the sample, k the Boltzmann constant, and V the polarization potential. When $eV \gg kT$, which is often satisfied except at very low polarization potentials and very high temperatures, the above expression simplifies to

$$I = I_e + I_h = \frac{kTA}{eL} \left[\sigma_e + \sigma_h \exp\left(\frac{eV}{kT}\right) \right] \quad [4]$$

Generally the conductivity due either to electrons or to holes is predominant, and hence we have

$$I \approx I_e = \frac{kTA}{eL} \sigma_e \quad (\text{when } \sigma_e \gg \sigma_h) \quad [5]$$

and

$$I \approx I_h = \frac{kTA}{eL} \sigma_h \exp\left(\frac{eV}{kT}\right) \quad (\text{when } \sigma_h \gg \sigma_e) \quad [6]$$

According to Eq. [5] the current is independent of V when electron conduction is dominant while in case of predominant hole conduction (Eq. [6]) the current varies exponentially with V . Thus in the former case, the limiting current can be used to obtain σ_e while in the latter case the slope of linear $\log I$ vs. V plot yields the σ_h .

The $\log I$ vs. V plot for the cell $\ominus \text{Ag} | \text{AgI}(\text{Al}_2\text{O}_3) | \text{C} \oplus$ at different temperatures is shown in Fig. 5, which suggests that the hole conduction is predominant in $\text{AgI}(\text{Al}_2\text{O}_3)$. We do not know of any polarization measurements on $\beta\text{-AgI}$, but there are results available for $\alpha\text{-AgI}$ ($T > 146^\circ\text{C}$) (18). $\alpha\text{-AgI}$ is known to be a p-type conductor. The electronic conductivity measurements on $\beta\text{-AgI}$ are now in progress. Preliminary results show that $\beta\text{-AgI}$ without Al_2O_3 is essentially a p-type conductor. Thus it can be concluded that dispersion of Al_2O_3 does not affect the nature of electron (hole) conductivity, nor does it significantly change its magnitude. The values of σ_h at different temperatures are given in Table III. When hole conduction is predominant, Eq. [6] predicts that $\log I$ vs. V plot will display slopes which are independent of any transport parameters related to the material studied. These slopes, $e/2.3026 kT$, which

Table III. Data obtained from polarization measurements on the cell $\ominus \text{Ag} | \text{AgI}(\text{dried-Al}_2\text{O}_3) | \text{C} \oplus$

| Temp. ($^\circ\text{C}$) | Hole conductivity ($\Omega^{-1} \text{cm}^{-1}$) | Slope of $\log I$ vs. V plot | |
|----------------------------|--|--------------------------------|----------------------|
| | | Theoretical (V^{-1}) | Expt'l. (V^{-1}) |
| 50 | 3.5×10^{-17} | 15.58 | 15.62 |
| 80 | 2.6×10^{-15} | 14.25 | 14.46 |
| 110 | 1.2×10^{-14} | 13.14 | 14.21 |
| 140 | 2.2×10^{-13} | 12.18 | 13.05 |

depend only on $1/T$ are compared with experimental slopes in Table III. The good agreement indicates that the polarization technique is quite successful in $\text{AgI}(\text{Al}_2\text{O}_3)$ system. The $\log \sigma_h$ vs. $10^3/T$ plot for $\text{AgI}(\text{Al}_2\text{O}_3)$ is shown in Fig. 6 and can be expressed by

$$\sigma_h = 13.3 \exp(-1.13 \text{ eV}/kT) \quad (300\text{-}420 \text{ K}) \quad [7]$$

Although the concentration of electron holes depends strongly on the concentration of silver (or of iodine), the concentrations of lattice defects do not and hence the activation energy of 1.13 eV may be identified as the activation energy for the migration of electron holes, Δh_h^* , plus the partial enthalpy of mixing of I_2 per molecule of AgI . In conclusion, while a dispersion of second phase such as Al_2O_3 enhances the ionic conductivity significantly, it does not affect the electronic transport properties, for instance the nature and magnitude of electron hole conductivity.

Thermoelectric Power

When a temperature gradient is applied across a solid, MX, containing lattice defects, owing to the increased concentration and increased jump frequency of the defects near hot end, a flow of defects from hot to cold region is set up. At steady state a voltage across the sample appears which directly reflects the

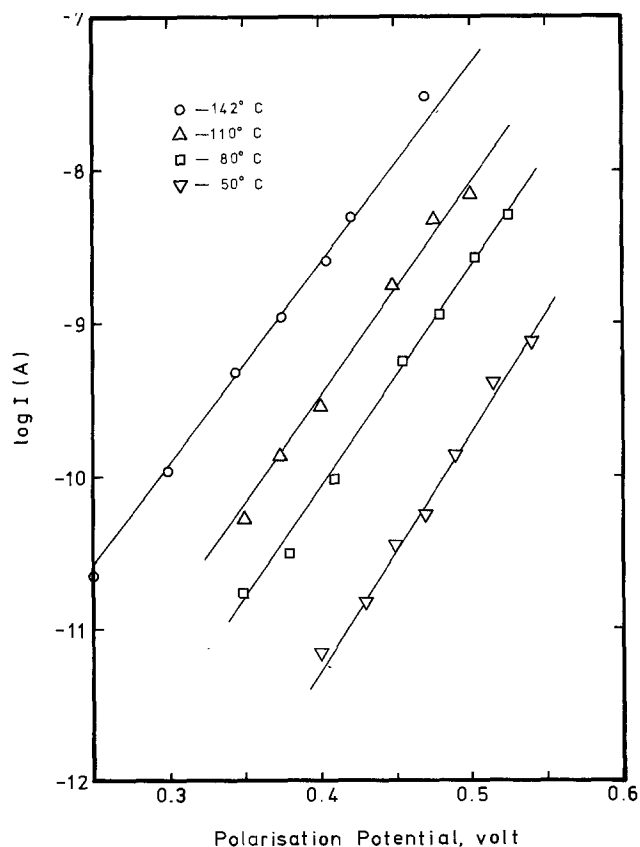


Fig. 5. Logarithm of steady-state current (I , A) in the asymmetric cell $(-)\text{Ag} | \text{AgI} + 30 \text{ m/o Al}_2\text{O}_3 (0.06 \mu\text{m}) | \text{C}(+)$ as a function of the applied polarization potential (V) at four different temperatures.

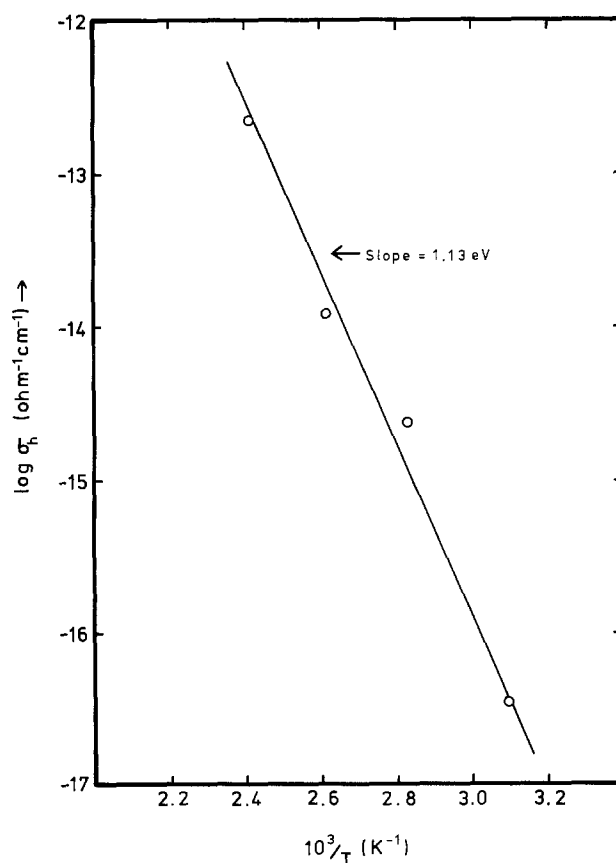


Fig. 6. Logarithm of electron hole conductivity (σ_h) of $\text{AgI} + 30 \text{ m/o dried Al}_2\text{O}_3 (0.06 \mu\text{m})$ equilibrated with silver as function of inverse absolute temperature.

sign of charge carriers in the system. Thus the thermoelectric power measurement is the most powerful tool for examining the nature of charge carriers in any system. In fact this measurement combined with the conductivity data has revealed a number of key features of solid electrolytes (1, 19) rarely disclosed by any other technique.

The homogeneous thermoelectric power (θ_{hom}) which arises due to a temperature gradient across the solid is given by (1, 20)

$$\theta_{\text{hom}} = \frac{1}{eT} \frac{(q_v^+ + h) - \phi q_i^+}{1 + \phi} - \frac{kT \text{ grad } n_i}{en_i \text{ grad } T} \quad [8]$$

for thermocells of the type (T)M|MX|M(T + ΔT), where q_i^+ and q_v^+ are the heats of transport of Ag^+ ion interstitials and vacancies, respectively, h the heat of formation of a pair of Schottky or Frenkel defects, ϕ the ratio of interstitial to vacancy mobility, k the Boltzmann constant, and n_i the concentration (number per cm^3) of each kind of defects and the other symbols have their usual meaning. The above equation states that the θ_{hom} is a direct function of $1/T$ provided other quantities are not strong functions of temperature.

However the situation gets complicated because of the heterogeneous thermoelectric power (θ_{het}) which arises as a result of temperature dependence of the contact potential between the electrode and electrolyte. For reversible thermocells using Ag electrodes it is given by (1, 20, 21)

$$\theta_{\text{het}} = \frac{k}{e} \ln \left(\frac{n_i}{N} \right) + \frac{kT \text{ grad } n_i}{en_i \text{ grad } T} + \frac{1}{e} S_{\text{Ag}^+ \text{Ag}} - \frac{1}{e} S_{\text{Ag}^+} \quad [9]$$

where N is the number of normal cation sites per cm^3 , S_{Ag^+} is the entropy of a silver ion in AgI or AgI(Al_2O_3) and $S_{\text{Ag}^+ \text{Ag}}$ is the entropy of a silver ion in silver metal. The latter can be approximated by the entropy of silver metal since the free electrons supposedly contribute very little to the total entropy. Thus approximate value of $S_{\text{Ag}^+ \text{Ag}}$ could be obtained, for example, from the free electron theory or from the thermionic emission experiments. However the molar entropy of the defects in solid electrolytes, S_{Ag^+} , is the most tedious quantity to determine either from theory or from experiments. The most straightforward way to determine these entropies of defect formation is from the detailed analysis of conductivity (or diffusion) measurements (22). However such an analysis yields only the sum of the entropies of the two complementary defects rather than individual molar entropies as these are not independent thermodynamic quantities. Several approximate methods have been used to separate these quantities and are reviewed (23, 24) elsewhere.

The total thermoelectric power (θ) is obtained on adding Eq. [8] and [9] which is not always too simple to yield defect parameters of interest. However there are some special cases of interest as indicated below.

Interstitial dominant conduction.—When cation interstitials are much more mobile than vacancies *viz.* $\phi \gg 1$, and their concentration is an exponential function of temperature, Eq. [8] reduces to a simpler form which, on adding to Eq. [9], gives

$$\theta = \frac{q_i^+ + \frac{1}{2}h}{eT} + \frac{1}{e} S_{\text{Ag}^+ \text{Ag}} - \frac{1}{e} S_{\text{Ag}^+} \quad [10]$$

Considering the sum $1/e(S_{\text{Ag}^+ \text{Ag}} - S_{\text{Ag}^+})$ to be small and independent of T as discussed elsewhere (1), Eq. [10] can be used to obtain q_i^+ from the slope of linear θ vs. $1/T$ plot provided the h is known from independent experiments such as conductivity or diffusion measurements.

Vacancy dominant conduction.—When cation vacancies are the only charge carriers *viz.* $\phi \ll 1$

and their concentration is almost independent of T , *e.g.*, in the extrinsic region, Eq. [8] and [9] reduce to simpler forms and their sum is given by

$$\theta = \frac{q_v^+}{eT} + \frac{k}{e} \ln \left(\frac{n_v}{N} \right) + \frac{1}{e} S_{\text{Ag}^+ \text{Ag}} - \frac{1}{e} S_{\text{Ag}^+} \quad [11]$$

Since n_v is independent of T , the last three terms could be considered as independent of T and then the slope of θ vs. $1/T$ plot can be used to obtain the q_v^+ .

Figure 7 shows the plot of θ vs. $10^3/T$ for AgI and AgI containing a dispersion of dried 30 m/o Al_2O_3 of 0.06 μm size with silver electrodes. For AgI, θ is large and negative which could be attributed to Ag^+ interstitials. The θ increases initially, attains a maximum around 80°C and then it decreases with increasing temperature which is in qualitative agreement with a recent measurement (25) of θ on β -AgI. The behavior at $T \geq 80^\circ\text{C}$, *viz.* decreasing θ with increasing temperature, is typical of solid electrolytes and is also in accord with theory. The behavior at $T \leq 80^\circ\text{C}$, *viz.* increasing thermal power with increasing T , is not well understood. However, the increasing θ from a less negative to a more negative value is attributable to increasing dominance of cation interstitials and consequently the maximum in θ vs. $1/T$ plot could be correlated to a switchover in the transport mechanism of β -AgI. It seems reasonable to consider that at near room temperature the conduction is dominated by Ag^+ vacancies while at $T \cong 80^\circ\text{C}$ it is the Ag^+ interstitials which are responsible for conduction. Such a switchover in the transport mechanism should be observable, in principle, in a $\log \sigma$ vs. $1/T$ plot. However our results (Fig. 3) do not reveal any change in slope perhaps because of the very small difference in the two migration energies (9), *viz.* Δh_i^+ (0.4 eV) and Δh_v^+ (0.5 eV). There are a number of other studies (1, 7-10) on pure and doped β -AgI. Most studies, particularly those on polycrystalline samples, do not yield more than one slope indicating no obvious change in the transport mechanism. Although a mere change in the slope of $\log \sigma$ vs. $1/T$ plot is not always an indication that more than one mechanisms are in operation. A more straightforward answer is provided

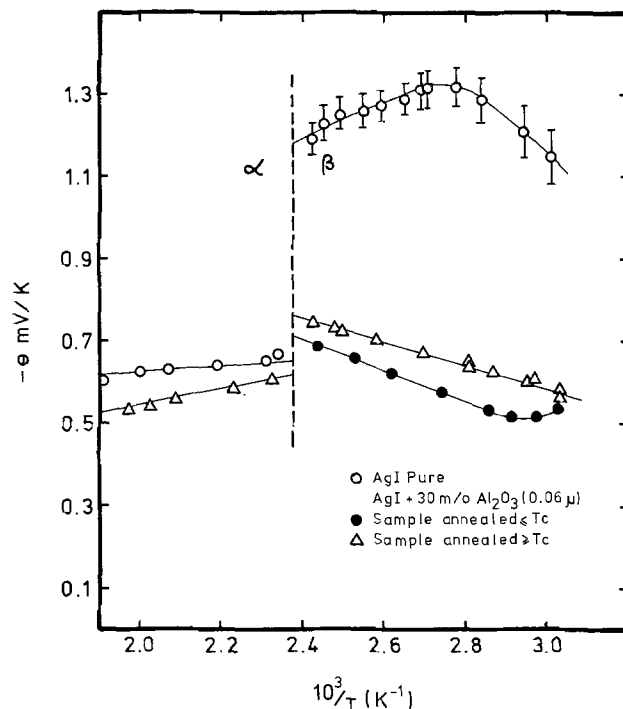


Fig. 7. Thermoelectric power (θ) of pure AgI and AgI containing 30 m/o dried Al_2O_3 of 0.06 μm size with reversible silver electrodes as a function of inverse absolute temperature.

by the conductivity data on pure and doped samples. While for AgCl and AgBr there exists a wealth of data, few conclusive studies exist on β -AgI. The main reason appears to lie in the fact that AgI is too reactive a solid to accommodate impurity atoms substitutionally. Intermediate compounds are formed instead, for instance, $\text{AgI} + \text{CdI}_2 \rightarrow \text{Ag}_2\text{CdI}_4$ (26, 27), $\text{AgI} + \text{Ag}_2\text{S} \rightarrow \text{Ag}_3\text{SI}$ (28). A part of the reason also seems to be the presence of the violent ($\beta \rightarrow \alpha$) phase transition at 147°C that prevents the growth of good crystals containing divalent impurities from the melt. Nevertheless, defect properties have been studied (8-10, 24) and it is generally agreed (1) that cationic Frenkel disorder prevails in β -AgI and that the Ag^+ vacancies are the dominant (8) charge carriers. At high temperature, the conduction is however solely attributed (8) to Ag^+ interstitials. While Govindacharyulu *et al.* (9) conclude that Ag^+ interstitials are the dominant charge carriers over the entire temperature range, our prediction based on thermoelectric power data precisely agrees with (8) and also with the latter (9) at higher temperatures (intrinsic region).

The θ of β -AgI in the vacancy dominant region (<80°C), see Fig. 7, is rather limited in range and involves large uncertainty and therefore it may not be used to obtain q_v^+ . However, the data at $T \geq 80^\circ\text{C}$ can be expressed by

$$-\theta = 0.43 \left(\frac{10^3}{T} \right) + 0.16 \text{ mV/K} \quad [12]$$

and can be used to calculate q_1^+ . Comparing Eq. [10] and [12], we get $q_1^+ + \frac{1}{2}h = 0.43 \text{ eV}$. Since h is reported to be 0.60, 0.64, and 0.68 eV, we obtain $q_1^+ = 0.11 \pm 0.02 \text{ eV}$, using the intermediate value of $h = 0.64 \text{ eV}$, which can be compared with the value of 0.06 eV obtained in a previous investigation (29).

The θ vs. $10^3/T$ plots for AgI containing 30 m/o Al_2O_3 are also shown in Fig. 7. The θ of the sample annealed below T_c is smaller than that annealed above T_c which is consistent with the conductivity data and may again be attributed to the changes in dispersoid distribution resulting from the phase transition of the matrix at 147°C. The net effect of dispersion is to decrease the magnitude of θ from a more negative (for pure β -AgI) to a less negative value. Recalling that negative charge carriers (Ag^+ vacancies) give rise to a positive θ , the above behavior is compatible with the increased dominance of Ag^+ ion vacancies in $\text{AgI}(\text{Al}_2\text{O}_3)$, i.e., with the hypothesis that dispersed Al_2O_3 generates excess silver ion vacancies and thereby enhances the σ and suppresses the θ . Moreover, the fact that θ vs. $1/T$ plot for $\text{AgI}(\text{Al}_2\text{O}_3)$ exhibits a negative slope, i.e., θ is increasing with increasing temperature, might be considered as well (compare Eq. [10] and [11]) an indication of the presence of excess cation vacancies. Also the concentration of these vacancies could be considered as almost independent of T as the thermally generated defects would form only a negligible fraction of the total defect concentration in low temperature regime. Under these circumstances the slope of the linear θ vs. $10^3/T$ plot that can be expressed by

$$-\theta = -0.28 \left(\frac{10^3}{T} \right) + 1.43 \text{ mV/K} \quad [13]$$

can be used to extract q_v^+ . Comparing Eq. [11] and [13], we get $q_v^+ = 0.28 \text{ eV}$. The heats of transport (q_1^+ and q_v^+) thus obtained are compared with their respective migration enthalpies in Table IV. These parameters for AgCl and AgBr are also quoted in the above table. The fair agreement between the two transport parameters, viz. the heat of transport and activation energy for isothermal migration, and their consistency with those in AgCl and AgBr provide further support to the model used in this paper.

Table IV. Heat of transport and activation energy for migration in AgI and their comparison with AgCl and AgBr (all energies are in eV)

| Solid | Δh_1^+ | q_1^+ | Δh_v^+ | q_v^+ | Ref. |
|-------|----------------|---------|----------------|---------|-----------|
| AgI | 0.14-0.4 | 0.11 | 0.31 | 0.28 | This work |
| AgCl | 0.15 | 0.18 | 0.30 | 0.31 | (30) |
| AgBr | 0.15 | 0.08 | 0.30 | 0.50 | (31) |

In summary, the studies so far indicate that the effect of Al_2O_3 -dispersion is quite general, and that it can be used to increase the ionic conductivity by orders of magnitude in a solid electrolyte without altering the electronic conductivity significantly. The existing models explain some of the features satisfactorily but the very complex behavior of the observed results points out to the need for more sophisticated theoretical models. The thermal power data suggests that dispersed Al_2O_3 introduces an excess of Ag^+ ion vacancies and thereby enhances the conductivity of the matrix.

Acknowledgment

This research was sponsored by the National Aeronautics and Space Administration (NASA) under the contract No. NAS8-32937.

Manuscript submitted Dec. 14, 1979; revised manuscript received ca. Aug. 8, 1980.

Any discussion of this paper will appear in a Discussion Section to be published in the December 1981 JOURNAL. All discussions for the December 1981 Discussion Section should be submitted by Aug. 1, 1981.

Publication costs of this article were assisted by Arizona State University.

REFERENCES

1. K. Shahi, *Phys. Status Solidi A*, **41**, 11 (1977).
2. T. Matsui and J. B. Wagner, Jr., in "Solid Electrolytes," P. Hagenmuller and W. Van Gool, Editors, p. 237, Academic Press, New York (1978).
3. C. C. Liang, *This Journal*, **120**, 1289 (1973). See also the U.S. Pat. 3,713,897 (1973).
4. C. C. Liang, A. V. Joshi, and N. E. Hamilton, *J. Appl. Electrochem.*, **8**, 445 (1978).
5. S. Pack, B. B. Owens, and J. B. Wagner, Jr., *This Journal*, **127**, 2177 (1980).
6. T. Jow, Ph.D. Thesis, Northwestern University (1977); T. Jow and J. B. Wagner, *This Journal*, **126**, 1963 (1979).
7. K. H. Lieser, *Z. Phys. Chem. (N.F.)*, **9**, 302 (1956); *ibid.*, **2**, 238 (1954).
8. G. Cochran and N. H. Fletcher, *J. Phys. Chem. Solids*, **32**, 2557 (1971).
9. P. A. Govindacharyulu, D. N. Bose, and S. K. Suri, *ibid.*, **39**, 961 (1978).
10. J. Schoonman and R. A. Huggins, *ibid.*, **36**, 815 (1975).
11. M. R. W. Chang, K. Shahi, and J. B. Wagner, Jr., Paper 367 presented at The Electrochemical Society Meeting, Boston, Massachusetts, May 6-11, 1979.
12. S. Pack, Paper 133 presented at The Electrochemical Society Meeting, Los Angeles, California, Oct. 14-19, 1979.
13. (a) J. C. Maxwell, "A Treatise on Electricity and Magnetism," 2nd ed., Vol. 1, p. 435, Clarendon Press, Oxford (1881); (b) Lord Rayleigh, *Philos. Mag.*, (5) **34**, 481 (1892).
14. C. Wagner, *J. Phys. Chem. Solids*, **33**, 1051 (1972).
15. A. M. Stoneham, E. Wade, and J. A. Kilner, *Mater. Res. Bull.*, **14**, 661 (1979).
16. R. Landauer, *J. Appl. Phys.*, **23**, 779 (1952).
17. C. Wagner, in "Proc. 7th meeting Int. Comm. Electrochem. Thermodynamics and Kinetics," p. 361, Lindau, Butterworth, London (1957).
18. J. Mizusaki, K. Fueki, and T. Mukaibo, *Bull. Chem. Soc. Jpn.*, **51**, 694 (1978).

19. S. M. Girvin, *J. Solid State Chem.*, **25**, 65 (1978).
20. R. E. Howard and A. B. Lidiard, *Philos. Mag.*, **2**, 1462 (1957).
21. A. R. Allnatt and P. W. M. Jacobs, *Proc. R. Soc. London, Ser. A*, **260**, 350 (1961).
22. S. Chandra and J. Rolfe, *Can. J. Phys.*, **48**, 397 (1970).
23. A. R. Allnatt and A. V. Chadwick, *Chem. Rev.*, **67**, 681 (1967).
24. J. Dupuy, in "Physics of Electrolytes," Vol. 2, J. Hladik, Editor, p. 669, Academic Press, London (1972).
25. G. Nogami, *J. Phys. Chem. Solids*, **41**, 205 (1980).
26. H. Hoshino and M. Shimoji, *J. Phys. Chem. Solids*, **35**, 321 (1974).
27. Y. Otsubo, A. Nitta, M. Kancko, Y. Iwata, and A. Veki, *Kogyo Kagaku Zasshi*, **69**, 1716 (1966).
28. B. Reuter and K. Hardel, *Naturwissenschaften* **48**, 161 (1961).
29. K. Shahi and S. Chandra, *Z. Naturforsch., Teil. A*, **30**, 1055 (1975).
30. J. Corish and P. W. M. Jacobs, *J. Phys. Chem.*, **6**, 57 (1973).
31. E. Haga, *J. Phys. Soc. Jpn.*, **13**, 1090 (1958).

LiB(CH₃)₄-Dioxolane Electrolyte in Rechargeable Li/TiS₂ Cells

Lawrence P. Klemann* and Gerald H. Newman*

Exxon Research and Engineering Company, Corporate Research Laboratories, Linden, New Jersey 07036

ABSTRACT

LiB(CH₃)₄ is an example of a large class of boron complex anion salts which are very soluble and highly conductive in dioxolane. Solutions of LiB(CH₃)₄ have been investigated as electrolytes in Li-TiS₂ cells. At room temperature such cells have been operated as rechargeable energy storage devices which are capable of continuous discharge (5 mA/cm²) and charge (1.25 mA/cm²) cycling. While solutions of LiB(CH₃)₄-dioxolane appear stable over long periods, contact with TiS₂ results in anion oxidation with concomitant formation of Li_xTiS₂ ($x < 1$). The oxidation products are gases whose apparent rate of generation is proportional to the concentrations of solute and TiS₂. The product distribution depends on whether LiB(CH₃)₄-dioxolane solution contacts TiS₂ alone, or in a Li-TiS₂ cell. The electrolyte-cathode reaction is thought to involve transient methyl radicals which are formed during a concerted process involving anion oxidation and TiS₂ lithiation.

The discovery in our laboratories of the reversible intercalation of lithium into titanium disulfide (1) spurred investigations into other components of advanced battery systems. Extensive research into lithium alloy (2) and pure lithium anodes and organic electrolytes led to the development of a rechargeable, ambient temperature Li-TiS₂ cell with a lithium perchlorate electrolyte (3, 4). However this electrolyte, due to its explosion hazard (4), posed unacceptable risks for further system development and a safe replacement for the perchlorate salt was sought.

In our search for an alternate organic electrolyte, dioxolane, by virtue of its high kinetic stability toward alkali metals (a feature considered essential for efficient operation of a rechargeable lithium electrode) was retained. As the likelihood of encountering a suitable replacement solute from the stocks of commercially available lithium salts seemed increasingly remote, a different approach was chosen. We reasoned that a desirable set of electrolyte properties was intimately related to fundamental properties of the anion (i.e., spatial shape, ion-pairing tendencies, charge to size ratio, charge delocalization, oxidation potential, etc.). If one had adequate synthetic freedom to modify anion structure and thereby affect these fundamental properties, a proper balance of bulk electrolyte properties would be achievable by design.

The potential scope for anion structure modification is unsurpassed in a complex (multicomponent) anion, and a particularly rich synthetic chemistry for lithium tetraorganoborate salts has been well documented (5-7). A straightforward synthetic access to these salts and evidence for their favorable ion-pair dissociation (8) relative to LiClO₄ in dilute ether solutions (9)

prompted our choice of borate salts as a launching point for this investigation. Lithium tetramethylborate whose tetrahedral symmetry and ionic dimensions (10) closely resemble those of LiClO₄ (11) was one of first model solutes whose ionic properties were examined in detail.

Experimental

Dioxolane (Burdick and Jackson) was distilled from sodium benzophenone ketyl under N₂. Low halide methyl lithium was supplied by LITHCOA. BF₃·etherate (Ventron) was distilled before use. CH₃MgBr (Aldrich), butyllithium, and tributylborane (Ventron) were used to prepare LiB(CH₃)₄ and LiB(C₄H₉)₄ in accordance with published procedures (12, 13). Both borate salts were isolated free of solvent by means of vacuum drying. The dimethoxyethane (DME) solvate of LiB(CH₃)₄ was prepared by dissolving the salt in DME followed by vacuum evaporation. TiS₂ was used either as the dry powder or admixed with approximately 10 weight percent Teflon binder for cathode construction. Cathodes were prepared by pressing the TiS₂-Teflon mixture into 6.5 cm² tantalum Distex® screens which had ~8 cm long tabs for electrical connection. Anodes were prepared by pressing 6.5 cm² sections of 20 mil lithium foil (Foote) onto carbon fiber supports or tantalum Distex® screens. Cells consisted of a cathode sandwiched between two lithium electrodes; polypropylene mat and microporous polypropylene separators were placed between the electrodes. The cells were inserted into polypropylene bags and electrode alignment was maintained by means of small clamps. About 5 ml of electrolyte was added to the bag and the cell assembly was mounted upright in a glass test vessel which had a ground glass joint (for sealing) and glass sealed metal through-puts (for electrical connection to the cell electrodes). Cell test-

* Electrochemical Society Active Member.

Key words: anion, battery, discharge, organic, oxidation.

ing was accomplished using Propel automatic battery cycling equipment. Unless otherwise specified, cycling was done at constant current to preset voltage cutoff limits.

NMR spectra were recorded on a Varian A-60 spectrometer and chemical shifts are reported in parts per million (ppm) vs. tetramethylsilane (TMS) reference (internal or external as indicated). Specific resistivities were measured in a Vacuum Atmospheres N₂ drybox at room temperature with a Barnstead Model PM-70CB Bridge (1000 Hz a.c.) and a Yellow Springs Instrument Company dip cell (cell constant 1/cm).

The gas containment jar (14) used to study LiB(CH₃)₄ decomposition consisted of a large tube (~1.5 in. diam × ~6 in. long) with a 45/50 standard taper male joint at the upper end (cf. Fig. 7). At the bottom, a U-tube (~8 mm OD) was attached which had sufficient length so as to allow about one-half of the volume of the large tube to be filled with mercury before equal heads of mercury inside and outside of the large tube were achieved. Above the level of the mercury inside the large tube, indentations which protruded into the tube provided support for a small (~20 ml) cup used to contain the sample. Samples in specific experiments were DME·LiB(CH₃)₄-dioxolane solutions alone or in contact with one of four substrates: TiS₂, LiTiS₂, Li, and a Li-TiS₂ cell. After loading the sample, the upper portion of the jar was closed by means of a cap made with a 45/50 standard taper female joint. During closing, in a helium dry box, mercury was displaced so as to maintain the sample at 1 atm. The jar and its contents generally equilibrated rapidly to the 28°C test temperature with additional mercury displacement. Once thermally equilibrated, production of volatile products could be followed by weighing the mercury which had been displaced out the top of the U-tube. Mercury displaced was usually monitored as a function of time.

To sample the gas generated and trapped in the upper portion of the jar, a short length of polyethylene tubing (~1.5 mm OD) was inserted down the U-tube and finally up into the gas space above mercury level. The flow of gas through the tube was controlled by connecting the accessible end of the polyethylene tube to a Hamilton miniature metering valve which was in turn attached to a syringe needle which penetrated the rubber septum of an evacuated, 50 ml side arm flask. As the gas sample was withdrawn the mercury level in the U-tube dropped and additional mercury was added to the U-tube by means of a hypodermic syringe. Once transferred, gases contained in the 50 ml storage flask were sampled through a Fischer-Porter valve into a CEC-103 mass spectrometer for qualitative and quantitative analysis.

Results

In agreement with the literature (12), solid samples of lithium tetramethylborate did not show visual evidence for reactivity with dry air. On the other hand, solvent free samples of LiB(C₄H₉)₄ prepared for comparison with lithium tetramethylborate were found to be pyrophoric under similar conditions of exposure (13).

Dioxolane solutions of lithium tetramethylborate were characterized by proton NMR which showed the methyl proton resonance as a quartet ($J_{BH} = 3.7$ Hz) centered 0.7 ppm upfield of external tetramethylsilane reference (Fig. 1, curve A). No changes in the position, appearance, or relative intensities of the anion or the solvent proton resonances were evident in samples that had been sealed and stored for up to 14 months. Neither were any new proton resonances observed in these samples (Fig. 1, curve B). Dissolution of approximately equal molar amounts of LiB(CH₃)₄ and methyl-lithium in excess dioxolane produced an exothermic reaction with vigorous CH₄ evolution. Subsequent NMR analysis of the resulting cloudy solution

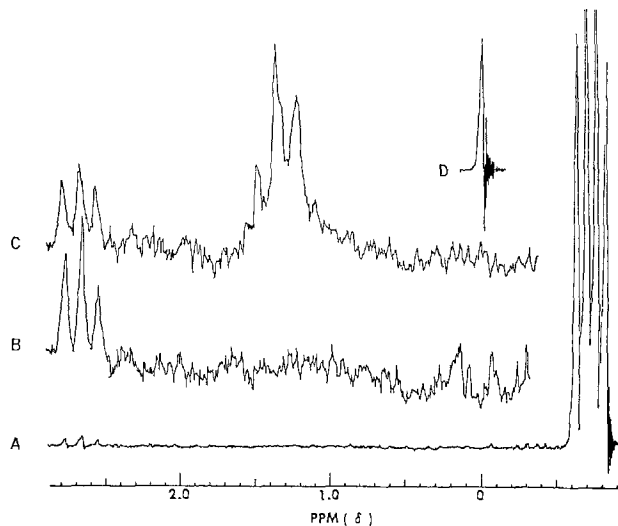


Fig. 1. ¹H NMR spectra in dioxolane: curve a, methyl quartet for LiB(CH₃)₄; curve b, high gain scan of 14 month old LiB(CH₃)₄ sample; curve c, high gain scan of CH₃Li-LiB(CH₃)₄ mixture; curve d, external TMS reference.

revealed a complex pattern of new proton resonances between 1.1 and 1.6 ppm (Fig. 1, curve C). The chemical shift positions of the dioxolane protons were sensitive to the concentration of dissolved tetramethylborate. Figure 2 demonstrates that the dioxolane proton resonances are shifted downfield as the concentration of LiB(CH₃)₄ increases.

The solubilities of LiB(CH₃)₄ and LiB(C₄H₉)₄ in dioxolane are approximately 3m. Resistivity measurements made on dioxolane solutions of these salts reveal that the specific resistance is a function both of the particular anion as well as the concentration of solute (cf. Fig. 3). At comparable concentrations, solutions of LiB(CH₃)₄ exhibit a lower specific resistance than LiB(C₄H₉)₄. The increase in specific resistance which is evident at higher solute concentrations is more pronounced in the case of lithium tetrabutylborate.

A dioxolane solution approximately 2.5m in LiB(CH₃)₄ concentration was employed as the electrolyte in an Li-TiS₂ cell which was discharged at 2.5

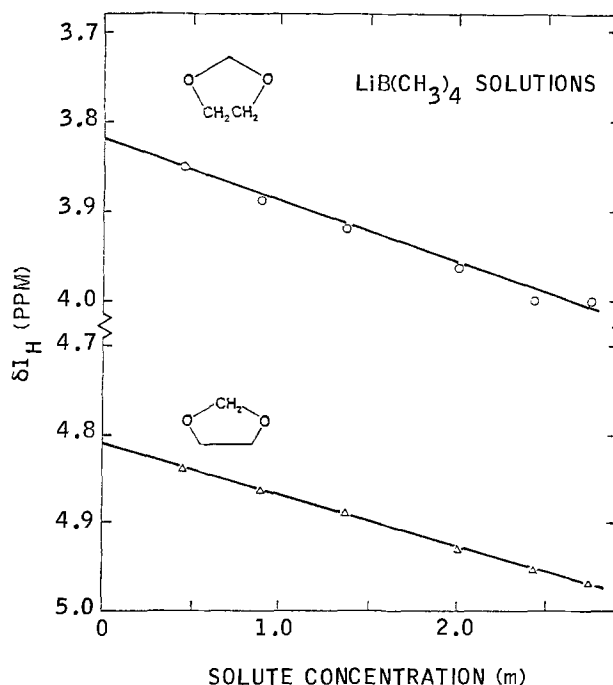


Fig. 2. Effect of LiB(CH₃)₄ concentration on dioxolane proton chemical shifts.

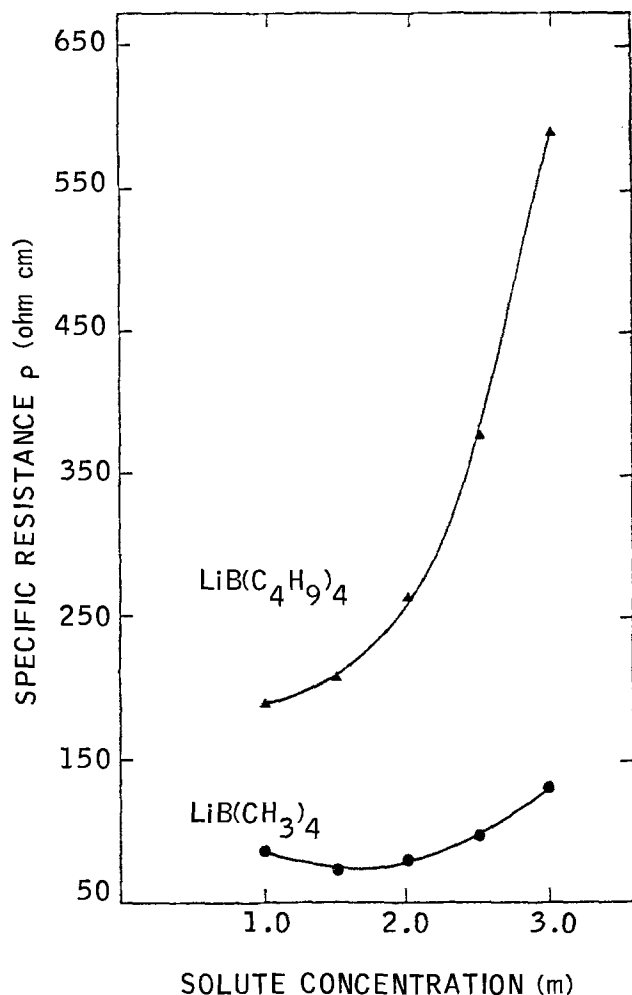


Fig. 3. Specific resistance of LiBR₄ salts in dioxolane

mA/cm². At 105 sec intervals a 15 sec 10 mA/cm² pulse was drawn. The curves in Fig. 4 record the dynamic cell emf (in volts) observed during this mode of discharge. Nearly 90% of the theoretical TiS₂ capacity was actually realized before the cell cutoff voltage was reached. The long term cycling results obtained with another Li-TiS₂ cell containing ~1.5m LiB(CH₃)₄-dioxolane electrolyte are given in Fig. 5. The figure shows the percentage of the theoretical cathode capacity (which was available for discharge on each cycle at 5.0 mA/cm²) plotted as a function of cycle number. Following each discharge this cell was charged at 1.25 mA/cm². After the initial rapid loss in TiS₂ utilization which occurred in the first nine discharge/charge cycles, the discharge capacity decreased in an essentially linear manner at less than 0.3% per

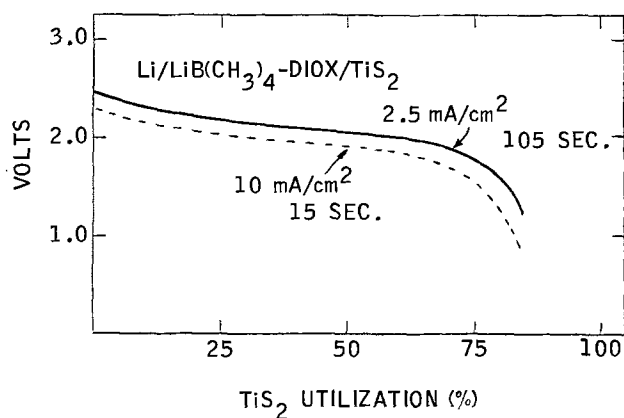


Fig. 4. Pulsed discharge of Li-TiS₂ cell in LiB(CH₃)₄-dioxolane electrolyte.

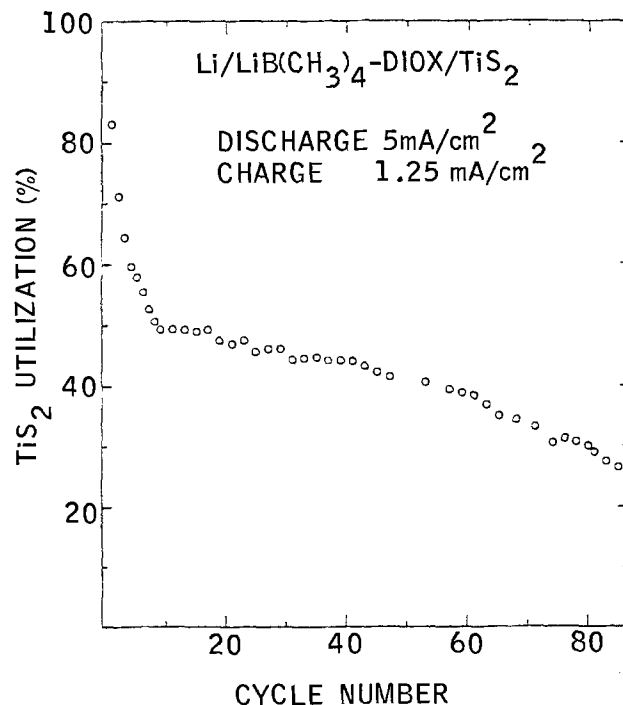


Fig. 5. Charge-discharge cycling of Li-TiS₂ cell in LiB(CH₃)₄-dioxolane electrolyte.

cycle. Cycling was terminated after 85 cycles at which point 4 A-hr of discharge capacity had been accumulated with the 105 mA-hr TiS₂ cathode and the ~600 mA-hr lithium anode. Another cell was assembled and its open-circuit voltage (OCV) was monitored as a function of time. As shown in Fig. 6, the OCV of this cell, after an initial fairly rapid decrease, asymptotically approached an equilibrium value of about 1.98V.

Dioxolane solutions of LiB(CH₃)₄ or DME·LiB(CH₃)₄ undergo slow decomposition in the presence of various substrates. Application of the apparatus (14) shown in Fig. 7 allowed investigation of the LiB(CH₃)₄ decomposition reaction which was responsible for the decrease in cell OCV. The major hydrocarbon products from LiB(CH₃)₄ decomposition were gases, specifically, trimethylboron, methane, ethane, and ethylene in the approximate proportions shown in Table I. Extensive LiB(CH₃)₄ decomposition occurred only in the presence of titanium disulfide and concomitantly produced partially lithiated TiS₂. As is shown in the table a very small amount of CH₄ was generated when a solution of LiB(CH₃)₄ was contacted with

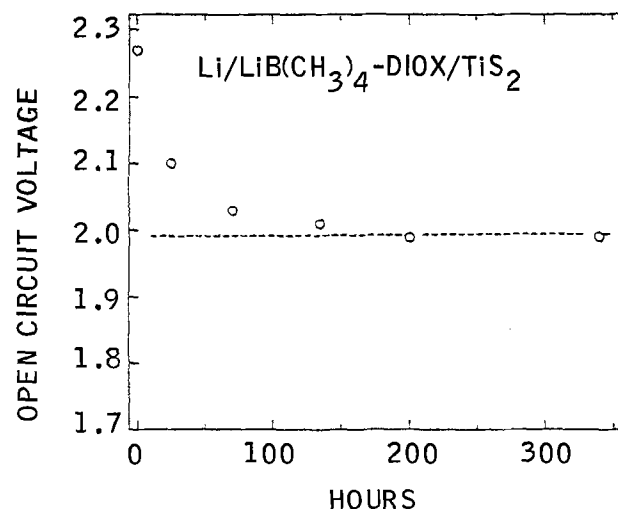


Fig. 6. Open-circuit voltage of Li-TiS₂ cell

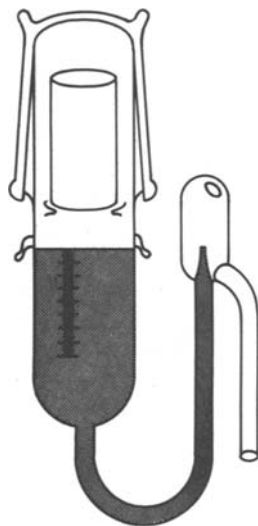


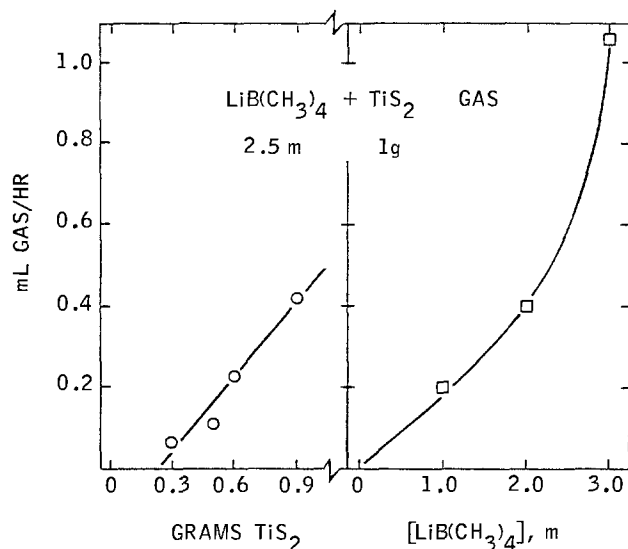
Fig. 7. Gas containment jar

LiTiS_2 . In contact with TiS_2 which was formulated as the cathode of an Li-TiS_2 cell, the $\text{LiB}(\text{CH}_3)_4$ solution gave rise to ethylene along with a different distribution of $\text{B}(\text{CH}_3)_3$, CH_4 , and C_2H_6 compared with the case of powdered TiS_2 . In the presence of a metallic lithium substrate alone, CH_4 and ethylene were observed. As shown in Fig. 8 the apparent rate of production of volatile hydrocarbon products from the reaction between $\text{LiB}(\text{CH}_3)_4$ and TiS_2 is a function of the weight of TiS_2 substrate (at constant concentration of tetramethylborate), and $\text{LiB}(\text{CH}_3)_4$ concentration (at a fixed weight of TiS_2).

Discussion

From the results of single crystal x-ray crystallographic investigations of $\text{LiB}(\text{CH}_3)_4$ (10) and LiClO_4 (11), the similarities in anion symmetry and steric size for these two lithium salts are clearly recognizable. Our interest in investigating the possible existence of less obvious parallels in the solution properties of these salts prompted a detailed examination of $\text{LiB}(\text{CH}_3)_4$ in dioxolane.

Since dioxolane, a cyclic five-membered ring containing an acetal functional group, polymerizes in the presence of Lewis acids (15), the question whether dissociation of the $\text{B}(\text{CH}_3)_4^-$ anion occurs and can thereby generate solvent incompatible reagents was raised. Proton NMR was used to periodically monitor dioxolane solutions of $\text{LiB}(\text{CH}_3)_4$ (external TMS) which had been stored at room temperature for up to 14 months. No change was apparent in the chemical shift (-0.7 ppm) or the intensity of the anion $-\text{CH}_3$ resonance (Fig. 1, curve A), or in the dioxolane resonances (not shown). A significant observation was the fact that no new proton resonances appeared between 0-2 ppm during the extended period of time over which the sample was monitored even when this region was scanned at an approximately 20-fold gain in signal intensity (Fig. 2, curve B; the apparent triplet

Fig. 8. Effect of TiS_2 weight and $\text{LiB}(\text{CH}_3)_4$ concentration on apparent rate of gas generation.

at ~ 2.6 ppm is a ^{13}C satellite of the higher field dioxolane resonance). The importance of this negative finding became evident when the NMR spectrum of a mixture of $\text{LiB}(\text{CH}_3)_4$ and methyl lithium in dioxolane was obtained. This mixture had given rise to an exothermic reaction and CH_4 evolution. The high gain NMR spectrum of the resulting solution contained new peaks between 1.1-1.6 ppm (Fig. 1, curve C). While we have not characterized the material responsible for this complex resonance pattern, we believe it to be the soluble product(s) from a reaction between CH_3Li and dioxolane. This proton resonance between 1.1-1.6 ppm serves then as a fingerprint for dioxolane solutions which have been in contact with methyl lithium. From the absence of this fingerprint in the aged dioxolane solution of $\text{LiB}(\text{CH}_3)_4$ we infer that the $\text{B}(\text{CH}_3)_4^-$ anion does not spontaneously dissociate to $\text{B}(\text{CH}_3)_3$ and CH_3Li in dioxolane. Reported chemical evidence for the integrity of the tetramethylborate anion in ether (16) is consistent with this conclusion.

Relative to internal TMS reference, the proton chemical shift of the $\text{B}(\text{CH}_3)_4^-$ anion remained invariant in dioxolane over an $\text{LiB}(\text{CH}_3)_4$ concentration range of ~ 0.47 -2.75m. This was not the case for the singlet resonances of the dioxolane protons. The data presented in Fig. 2 shows that dioxolane proton resonances are shifted progressively downfield as the concentration of $\text{LiB}(\text{CH}_3)_4$ increases. Similar downfield shifts for the α - CH_2 protons in tetrahydrofuran (THF) solutions of LiClO_4 have been reported (17, 18) and have been attributed to a polarizing effect of the Li^+ cation on the C-H bonds adjacent to oxygen in the donor solvent.

The high solubility of $\text{LiB}(\text{CH}_3)_4$ in dioxolane enabled a-c resistivity measurements to be made on solutions over a wide range of solute concentrations. The results, presented in Fig. 3, reveal a resistivity minimum around 1.7m for $\text{LiB}(\text{CH}_3)_4$ in dioxolane. The resistivity value ($\sim 75 \Omega \text{ cm}$) at the minimum is actually less than was found for an equivalent concentration of LiClO_4 in dioxolane. As the concentration of $\text{LiB}(\text{CH}_3)_4$ in dioxolane increases above 1.7m, the solution resistivity rises. As shown in Fig. 3, this increase in resistivity is much more pronounced in dioxolane solutions of $\text{LiB}(\text{C}_4\text{H}_9)_4$ at high concentrations. It is obvious that the solution resistivity is a function of the relative size of the tetraalkylborate anion; however, a more detailed interpretation of these apparent differences must be deferred until more is known about fundamental solution properties such as ion-pair association and quadrupole formation, etc.

Table I. Decomposition studies on dioxolane solutions of $\text{DME} \cdot \text{LiB}(\text{CH}_3)_4$

| Substrate | Normalized volume percent* | | | | Σ |
|------------------------|----------------------------|---------------|------------------------|------------------------|----------|
| | $\text{B}(\text{CH}_3)_3$ | CH_4 | C_2H_6 | C_2H_4 | |
| TiS_2 | 38 | 13 | 20 | — | 71 |
| LiTiS_2 | — | 5 | — | — | 5 |
| Li-TiS_2 cell | 1 | 4 | 27 | 9 | 41 |
| Li | — | 1 | — | 1 | 2 |

* Normalized $v/o = [v/o \text{ product gas}] / [v/o \text{ helium}] (\times 100)$.

The parallels in electrolyte properties for dioxolane solutions of LiClO₄ and LiB(CH₃)₄ again became apparent when the latter solute was investigated in Li-TiS₂ cells. Using a dioxolane solution containing approximately 2.5M LiB(CH₃)₄ in a limited electrolyte configuration Li-TiS₂ cell, a pulsed discharge was performed to evaluate the high rate current carrying capability of the electrolyte. The pulsed discharge consisted of a base 2.5 mA/cm² current that was interrupted at 105 sec intervals by the imposition of a 15 sec, 10 mA/cm² current pulse. The base load-pulse sequence was repeated until the predetermined cell cutoff voltage was reached. The results (Fig. 4) show that nearly 90% of the theoretical TiS₂ capacity was available using this pulsed discharge technique. The solid curve tracks the total cell voltage during the 2.5 mA/cm² base load, while the broken curve records the cell voltage during the 10 mA/cm² pulse. Cell resistance losses during the pulse account for the ~200 mV drop in total cell voltage (difference between the solid and broken curves in Fig. 4). This magnitude of increased cell polarization during periods of high current drain, and the overall cell performance closely parallel the results reported for Li-TiS₂ cells containing LiClO₄-dioxolane (3, 4).

Also analogous to results reported (4) for Li-TiS₂ cells containing LiClO₄ electrolyte is our finding that repetitive charge-discharge cycling of Li-TiS₂ cells can be achieved in LiB(CH₃)₄-dioxolane. The results of one such experiment are presented in Fig. 5. As can be seen in Fig. 5, after the ninth discharge, the percentage of the theoretical amount of TiS₂ available for discharge at 5 mA/cm² (following each recharge at 1.25 mA/cm²) showed a nominal incremental decrease of about 0.3% per cycle. Over 85 complete cycles, 4 A-hr of discharge capacity had been realized from a cell constructed with a 105 mA-hr TiS₂ cathode and an anode which contained ~600 mA-hr of lithium. After termination of cycling, a visual examination of the anode revealed the presence of metallic lithium beneath a layer of porous material. This observation strongly suggests that considerably less than 600 mA-hr of Li was actually involved in the successive plating-stripping cycles.

Monitoring of the open-circuit voltage (OCV) of a freshly prepared Li-TiS₂ cell containing LiB(CH₃)₄-dioxolane revealed that this parameter changed with time. Specifically, as is shown in Fig. 6, the OCV dropped over 200 hr reaching an equilibrium value of ~1.98V. That this drop in OCV was the result of spontaneous discharge was confirmed by the identification of partially lithiated TiS₂ in the final cathode material. Using published voltage-composition data (19) and our equilibrium OCV value, the final stoichiometry of Li_{0.8}TiS₂ is indicated for the spontaneous redox reaction.

The agent responsible for the partial reduction of the titanium disulfide is the B(CH₃)₄⁻ anion whose corresponding oxidation products were gases. The TiS₂ + LiB(CH₃)₄ reaction was investigated in detail using the apparatus pictured in Fig. 7. The rate of production of hydrocarbon products was monitored by following the weight of mercury displaced from this apparatus as a function of time, and these results are given in Fig. 8. These experiments demonstrated that the apparent rate of the decomposition reaction is a function of the LiB(CH₃)₄ concentration as well as weight of TiS₂ substrate used. The presence or absence of a stoichiometric amount of DME relative to LiB(CH₃)₄ did not affect either the apparent rate of decomposition or the distribution of volatile products.

The gaseous decomposition products collected from the gas generation apparatus were characterized and analyzed quantitatively by mass spectrometry. The data, obtained for a powdered TiS₂ substrate as well as for samples of LiTiS₂, Li metal, and an Li-TiS₂ cell, are summarized in Table I.

In Table I the normalized volume percent (v/o) for each component was derived by dividing the observed v/o by the v/o He background. Extensive decomposition occurs when LiB(CH₃)₄-dioxolane contacts TiS₂, whereas with fully lithiated TiS₂, decomposition is virtually negligible. When LiB(CH₃)₄ reacts with TiS₂ alone three volatile products, (CH₃)₃B, methane, and ethane, are formed; the relative amounts of these three products change when the layered dichalcogenide is configured as the cathode of an Li-TiS₂ cell and in this case ethylene is also observed. The decrease in (CH₃)₃B seen in the Li-TiS₂ cell experiment is particularly dramatic compared with the experiment with TiS₂ alone. While it is tempting to invoke a redistribution reaction between (CH₃)₃B and Li to give LiB(CH₃)₄ and a boron residue as an explanation for this finding we have no independent evidence to support such a reaction pathway. In the control experiment with a metallic lithium substrate alone, the LiB(CH₃)₄-dioxolane solution produced traces of methane and ethylene.

Observation of C₂ hydrocarbon products, particularly ethane ((CH₃)₂CH₂), from a reaction between TiS₂ and LiB(CH₃)₄ suggests a mechanistic pathway whereby methyl fragments, probably ·CH₃ radicals, dimerize. That such dimerization is a fate of short-lived hydrocarbon radicals generated under such conditions was postulated by Dines (20) who studied n-C₈H₁₈ formation from the reaction between TiS₂ and CH₃CH₂CH₂CH₂-Li⁺. Since we find no evidence for B(CH₃)₄⁻ dissociation in dioxolane (*loc. cit.*) to give trimethylboron and CH₃⁻ Li⁺, we prefer to picture ·CH₃ radicals arising from B(CH₃)₄⁻ oxidation at a TiS₂ surface with simultaneous intercalation of Li⁺ ion into the layered compound. Once generated, the methyl radicals either dimerize or abstract ·H from solvent to give CH₃CH₃ or CH₄, respectively.

Conclusions

Dioxolane solutions of LiB(CH₃)₄ appear to be stable indefinitely at room temperature. These solutions are highly conductive and show utility as electrolytes in ambient temperature, rechargeable, lithium battery systems wherein a high rate of current drain is a desirable feature. However the oxidation potential of the B(CH₃)₄⁻ anion renders it reactive toward TiS₂ and long duration contact with this layered compound produces (CH₃)₃B, CH₄, and CH₃CH₃. Due to this reactivity, LiB(CH₃)₄ is not ideally suited for long term use as an electrolyte in Li-TiS₂ cells. Nevertheless, the feasibility of its successful application in cells with potentials below about 2.0V is certainly not precluded.

Acknowledgments

The authors gratefully acknowledge and express sincere appreciation for the skilled experimental assistance provided by Mrs. P. L. Williams and Ms. J. E. Serrano during the course of this work.

Manuscript submitted March 19, 1980; revised manuscript received Aug. 4, 1980. This was Paper 21 presented at the Los Angeles, California, Meeting of the Society, Oct. 14-19, 1979.

Any discussion of this paper will appear in a Discussion Section to be published in the December 1981 JOURNAL. All discussions for the December 1981 Discussion Section should be submitted by Aug. 1, 1981.

Publication costs of this article were assisted by Exxon Research and Engineering Company.

REFERENCES

1. M. S. Whittingham, *J. Chem. Soc. Chem. Commun.*, 328, (1974); M. S. Whittingham, *This Journal*, 123, 315 (1976).
2. B. M. L. Rao, R. W. Francis, and H. A. Christopher, *ibid.*, 124, 1490 (1977).
3. L. H. Gaines, R. W. Francis, G. H. Newman, and

- B. M. L. Rao, in "11th Intersociety Energy Conversion and Engineering Conference (1976), Extended Abstracts," pp. 418-423 (1976).
4. G. H. Newman, R. W. Francis, L. H. Gaines, and B. M. L. Rao, *This Journal*, **127**, 2025 (1980).
 5. M. F. Lappert, *Chem. Rev.*, **56**, 1035 (1956).
 6. E. L. Muetterties, Editor, "The Chemistry of Boron and its Compounds," pp. 443-582, John Wiley and Sons, Inc., New York (1967).
 7. E. Negishi, *J. Organomet. Chem.*, **108**, 281 (1976).
 8. D. N. Bhattacharyya, C. L. Lee, J. Smid, and M. Szwarc, *J. Phys. Chem.*, **69**, 608 (1965).
 9. P. Jagodzinski and S. Petrucci, *ibid.*, **78**, 917 (1974).
 10. W. E. Rhine, G. Stucky, and S. W. Peterson, *J. Am. Chem. Soc.*, **97**, 6405 (1975).
 11. A. Sequeira, I. Bernal, I. D. Brown, and R. Faggi-ani, *Acta Crystallogr. B*, **31**, 1735 (1975).
 12. D. T. Hurd, *J. Org. Chem.*, **13**, 711 (1948).
 13. R. Damico, *ibid.*, **29**, 1971 (1964).
 14. J. C. Cessna, *Corrosion*, **27**, 244 (1971).
 15. W. K. Busfield, R. M. Lee, and D. Merigold, *Die Macromolek. Chem.*, **156**, 183 (1972).
 16. E. C. Ashby, L. C. Chao, and J. Laemmle, *J. Org. Chem.*, **39**, 3258 (1974).
 17. D. Nicholls and M. Szwarc, *J. Phys. Chem.*, **71**, 2727 (1967).
 18. E. C. Ashby, F. R. Dobbs, and H. P. Hopkins, Jr., *J. Am. Chem. Soc.*, **95**, 2823 (1973).
 19. A. H. Thompson, *Phys. Rev. Lett.*, **40**, 1511 (1978).
 20. M. B. Dines, *Mater. Res. Bull.*, **10**, 287 (1975).

Investigation of Factors Affecting Performance of the Iron-Redox Battery

L. W. Hruska*

Diamond Shamrock Corporation, Painesville, Ohio 44077

and R. F. Savinell*

Department of Chemical Engineering, University of Akron, Akron, Ohio 44325

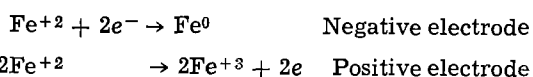
ABSTRACT

The iron-redox battery is a low power density energy storage device that may be attractive for applications such as load leveling and solar energy storage. During the charge cycle of this battery, the ferrous ion from an aqueous chloride electrolyte plates onto the negative electrode and is oxidized to ferric ion at the positive electrode. A solid graphite or titanium plate can be used for the iron electrode while a high specific area material is necessary for the redox electrode. A 100 cm² single cell with a microporous plastic separator has been cycled at a current density of 60 mA/cm² at 60°C. The cell was capable of storing and discharging energy at a round trip current efficiency of 90% and an energy efficiency of 50%, with a maximum discharge power density of 50 mW/cm². The largest voltage losses occurred at the iron electrode and to a lesser extent at the redox electrode. Factors affecting voltaic and coulombic losses including electrolyte composition and temperature, cell separators, electrode materials, and electrolyte additives have been studied and the results reported.

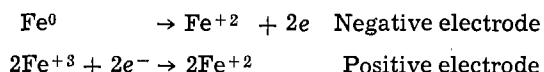
Several electrochemical energy storage batteries are under development for bulk energy storage (1, 2). These batteries are often characterized by their low power density, but are attractive as stationary storage devices for load leveling and solar applications because of their potentially low cost. One such battery which has undergone rapid development over the past several years is the redox battery (3-6). In the redox battery, both the products and reactants of electrolysis are soluble salts. In order to prevent chemical shorting and irreversible loss of reactants, a highly efficient anion permeable membrane separator must be employed. An alternative method of preventing the irreversible loss of reactants is through utilization of a reactant couple which involves three different valence states of a single metallic element. One such device is the iron-redox battery (Fe⁰/Fe⁺²/Fe⁺³), which is the subject of this paper.

The half-cell reactions for the iron-redox battery can be expressed as follows:

Charge



Discharge



Electrochemically, this battery can be viewed as a hybrid of more common battery types. The negative or iron electrode utilizes plating and dissolution of iron as a solid plate, similar to Zn/Cl₂ or Fe/Ni batteries. The positive electrode, however, uses a carbon structure to oxidize and reduce iron cations which remain in solution. Ideally, upon complete discharge, the battery would be brought to its initial state with ferrous ion as the only active cation in the system. Other advantages of the iron-redox battery include: low temperature aqueous electrolytes with inexpensive reactants that are readily available in large quantities; the use of inexpensive materials of construction; the use of electrodes which are not subject to shape change or dendrites; the distinction of being the least hazardous of any advanced battery system.

A disadvantage with the iron-redox battery is its inherently low cell voltage (1.21V as compared to 2.12V for Zn/Cl₂ and 1.98V for Pb/acid) which tends to limit the power density and efficiency of the battery. The actual operational characteristics of the battery must be measured experimentally. Develop-

* Electrochemical Society Active Member.

Key words: membrane, separators, energy storage.

mental work on an iron-redox battery has been reported previously (7, 8), but data on factors controlling energy efficiency and on cell operation are limited.

The results obtained in this experimental study indicate the energy levels that can be obtained from the iron-redox battery and identify factors which limit its performance.

Experimental

The studies reported herein were primarily experimental. Separators and electrode materials were commercial, readily available items. The salts were all of reagent grade and deionized water was used for electrolyte makeup.

The electrolyte resistivity measurements were taken with a standard H-type conductivity cell with platinized platinum electrodes (cell constant of 0.1). The cell was immersed in a temperature bath and the resistance was measured with a Beckman Instruments a-c bridge operating at a frequency of 1000 Hz.

Daily cycle tests were performed in a 100 cm² rectangular acrylic laboratory cell. Each half-cell was equipped with electrolyte inlet and outlet manifolds and viton O-rings were used for sealing. Chlorided silver wires were employed as reference electrodes. The electrolyte circuit is depicted schematically in Fig. 1. All components of the test system were made of polypropylene, PVC, or glass.

Results and Discussion

Electrolyte properties.—The primary ionic reactants of the iron-redox battery are the ferric and ferrous ions. Since these reactants are soluble in aqueous solution their salts serve as the battery electrolyte. In order to operate a cell at high voltaic efficiency the electrolyte resistivity must be maintained as low as possible. For this reason we chose the chloride salts of iron as our solute (the chloride salts will also have greater charge carrying capacity per gram of salt as compared to other salts such as sulfates or nitrates). An examination of solution conductivity data is useful for identifying a promising concentration range for cell operation. Measured resistivity data for both ferric and ferrous chloride solutions at 18°C are given as a function of concentration in Fig. 2. The data agree with published data (9). The useful concentration range can be established from these data as ca. 100–500 gpl of iron chloride. At lower concentrations the charge carrying density becomes too low and concentration polarizations become too high. At high concentrations the forces related to interionic attraction predominate and ionic mobility decreases. By knowing the workable concentration range, the minimum volume of electrolyte for a given coulombic capacity of the battery can be estimated.

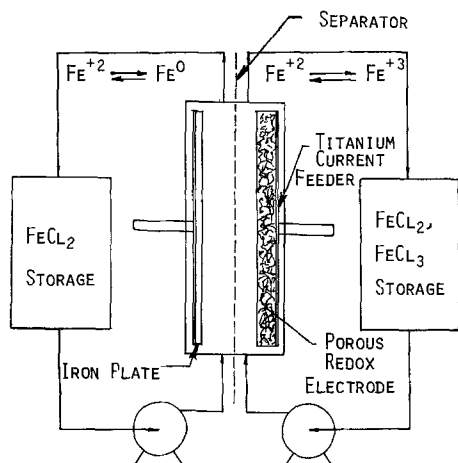


Fig. 1. Schematic of iron-redox laboratory cell and electrolyte circuit.

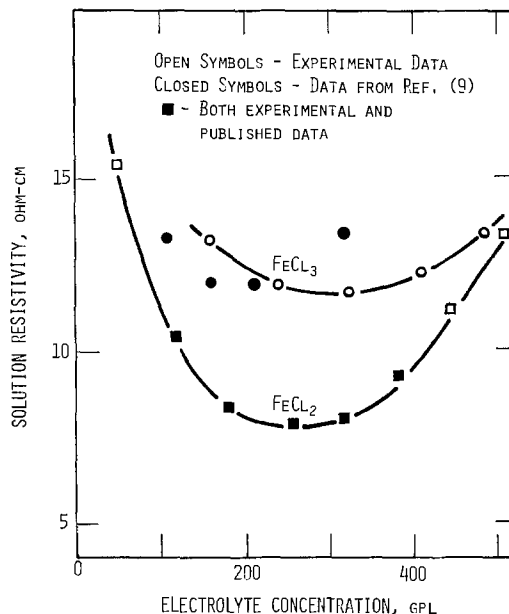


Fig. 2. Measured and published resistivity data of iron chloride aqueous solutions at 18°C.

For example, considering an initial concentration of both catholyte and anolyte to be 500 gpl ferrous chloride and after full charge there is 50 gpl ferrous chloride remaining in the anolyte, the charge density of the battery is 63.5 A-hr/liter.

As will be shown later, pH control is essential in order to maintain a high faradaic efficiency and good plating morphology. Since parasitic reactions in this battery do result in an alteration of the electrolyte pH, it is quite important to use an electrolyte having a pH response that is moderate and not abrupt when the concentration is perturbed. We have found the ferrous chloride electrolyte to be well behaved as demonstrated by the data reported in Fig. 3.

In order to reduce voltaic losses, an indifferent but conductive solute can be added to the electrolyte. The resistivities of a 250 gpl ferrous chloride electrolyte with additions of several indifferent solutes are shown in Fig. 4. The top curve is for the addition of calcium chloride. Although this additive is common in iron plating baths, it has no advantage as a conductivity

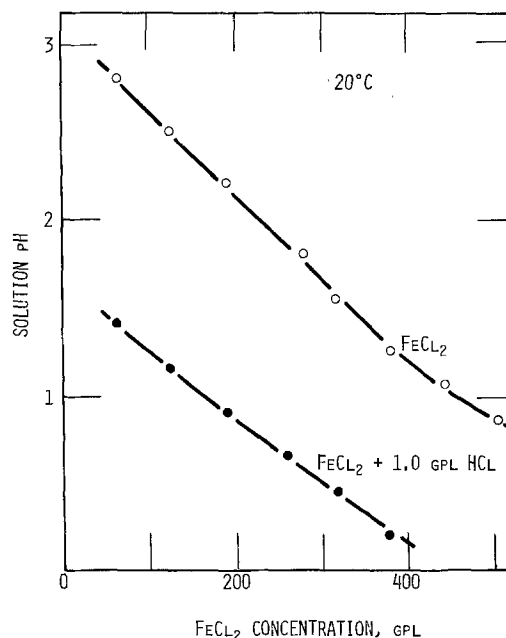


Fig. 3. Measured pH of ferrous chloride solutions at 20°C

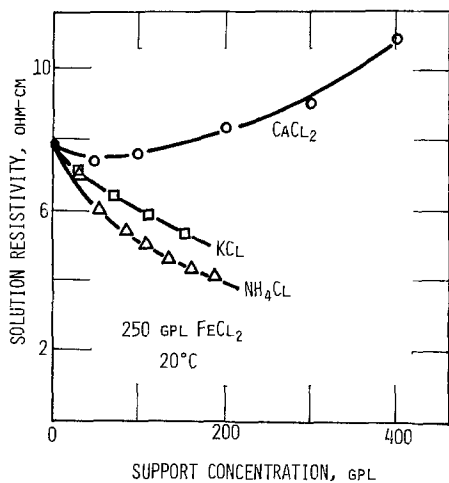


Fig. 4. Measured effect of supporting electrolyte on the resistivity of a 250 gpl ferrous chloride aqueous solution at 20°C.

support. The addition of sodium or potassium chloride, however, lowers the resistivity significantly. One difficulty found with using a sodium or potassium chloride additive was the poor quality and nonadherence of the iron plate deposited from electrolytes having these salt additives.

The most effective conductivity support tested was ammonium chloride. The addition of 3.5 moles of ammonium chloride to a liter containing 2.0 moles ferrous chloride (nearly saturated solution) will reduce the electrolyte's resistivity from 7.8 to 4.0 Ω -cm at 20°C. Further testing has shown that good quality iron plates can be obtained in the presence of ammonium chloride additives. In fact, the iron deposit had very little tendency to dendrite, powder, crater, peel-off, or exhibit the other problems that are generally associated with many of the metallic plates used for battery applications. A further reduction in resistivity of the ferrous-ammonium chloride solution can be achieved at elevated temperatures. This effect is shown in Fig. 5. The resistivity of 4 Ω -cm at 20°C can be reduced to 2 Ω -cm at 77°C. For a cell with a 2 mm gap operating at a current density of 60 mA/cm², this represents an overall voltaic loss of 4% (as compared to 16% at 20°C with no addition of indifferent electrolyte). The ferrous chloride/ammonium chloride electrolyte was chosen for further battery studies.

Cell separators.—At the fully discharged state iron is not in metallic form and the ferrous concentration is at its maximum (perhaps 500 gpl FeCl₂ and 50 gpl FeCl₃). During charge, ferrous ion is oxidized at the

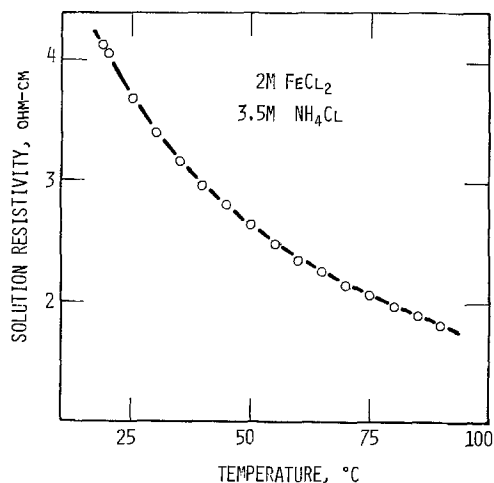
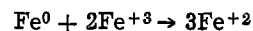


Fig. 5. Measured temperature dependence of the resistivity of a 2M FeCl₂/3.5M NH₄Cl aqueous solution.

anode to produce the ferric ion. Simultaneously, at the cathode the ferrous ion is reduced to metallic iron. The ferric ion produced at the anode is then capable of reacting directly with the iron plate according to the chemical reaction



This reaction is limited by mass transport of the ferric ion to the electrode surface and can be a primary source of coulombic efficiency loss (other losses are discussed in later sections). The current efficiency (based on iron plate) when discharging an unseparated cell was found to be about 60%. This corresponds to the level of efficiency loss that would be expected from mass transfer control of the above reaction (see Table I).

In order to reduce the coulombic efficiency loss caused by the oxidation of the iron plate, microporous materials were evaluated as cell separators. Ferric ion diffusion data and membrane resistivity data are presented in Fig. 6 and 7 for two commercial materials. Using these data, calculations were made on the expected performance of these separators in cell operation. The Celgard® separator (Celanese Corporation)

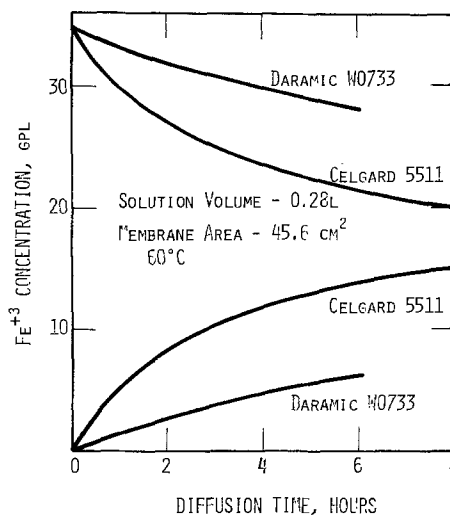


Fig. 6. Measurements of ferric ion transport rate across two commercial microporous separators using a well-stirred membrane cell.

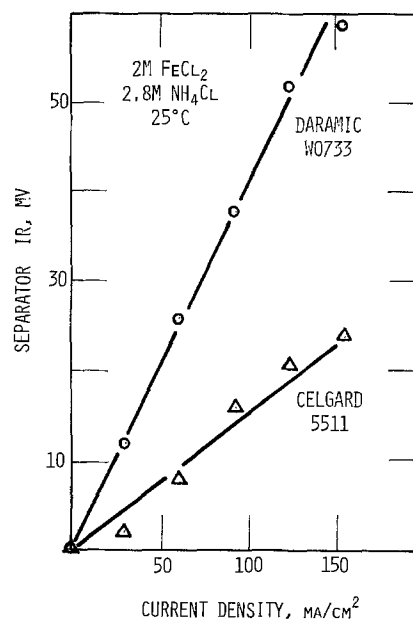


Fig. 7. Measured IR drop across two commercial microporous separators.

Table I. Porous separator performance at 60 mA/cm² utilizing diffusion and resistivity data of Fig. 6 and 7

| | i_{corr}^* (mA/cm ²) | $CE_c =$ $I_c - i_{corr}$ | $CE_D = I_D /$ $I_D + i_{corr}$ | $CE_t =$ $CE_c \times CE_D$ | Separator thickness (mm) | Pore size (μ m) | Resistivity (Ω -cm ²) | IR_{loss} (mV) |
|----------------|---------------------------------------|------------------------------|------------------------------------|--------------------------------|--------------------------------|-------------------------|--|---------------------|
| No separator | 29.0 | 0.52 | 0.67 | 0.35 | — | — | 0 | 0 |
| Celgard** 5511 | 14.6 | 0.76 | 0.80 | 0.61 | 0.20 | 0.04 | 0.155 | 9.3 |
| Daramic† W0733 | 1.94 | 0.97 | 0.97 | 0.94 | 0.58 | 0.05 | 0.41 | 24.6 |

* This value was calculated using Fick's law of simple diffusion ($N = -DC_B/\delta$) and assuming an electrolyte linear velocity of 2 cm/sec, electrode length of 7 cm, a diffusion coefficient of 10^{-5} cm²/sec, a membrane gap of 0.1 cm, and a change of ferric ion concentration during charge from 0 to 127 gpl.

** Porous polypropylene material manufactured by Celanese Corporation.

† Porous polyethylene based material manufactured by W. R. Grace Corporation.

CE_c = charge coulombic efficiency; CE_D = discharge coulombic efficiency.

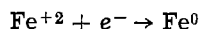
I_c = charge current; I_D = discharge current.

i_{corr} = calculated diffusion controlled corrosion current.

offers some improvement in coulombic efficiency. On the other hand, the Daramic® separator (W. R. Grace Corporation) should limit the ferric ion diffusional loss to about 3% for both charge and discharge modes of operation. Daily operation of laboratory size (100 cm²) redox cells with the Daramic separators gave coulombic efficiencies of 93%-96% during charge and 90% during discharge. The chemical resistances of both Celgard and Daramic separators in iron electrolytes were excellent at pH = 0.

Studies on electrode polarizations (which are reported later in this paper) indicate the optimum catholyte (on charge) to have a pH of 3-4 while the anolyte must be kept at or below a pH of approximately 1.0 to maintain stability of the ferric ion. In order to maintain a pH difference of this magnitude across the cell, a highly efficient anion permeable membrane must be used as the separator. Two commercial membranes were evaluated in this study: Neosepta ACH-45T (Tokuyama Soda Company, Limited) and Selamion® DMV (Asahi Glass Company Limited). Both of these membranes had an initial resistivity of approximately 7 Ω -cm² in a ferric-ferrous chloride solution (420 mV loss at 60 mA/cm²). Upon evaluation in laboratory cells, the membranes discolored giving evidence of deterioration and the resistivity of the membrane increased significantly. The increased resistivity is attributed to FeCl₄⁻ fouling and is not an uncommon phenomena among anion membranes (2, 3, 10). In spite of the poor voltaic performance of the membrane, the overall coulombic efficiency was found to be exceptionally good (CE ~ 96%).

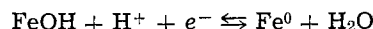
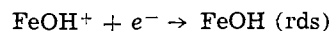
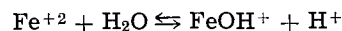
Characteristics of the iron electrode.—Electrode polarization.—During cell charging the ferrous ion is reduced at the iron electrode



The plating reaction is carried out on a nonreactive substrate. In this way complete discharges eliminate shape change of iron plate, limited cycle life, etc. Both titanium and graphite are suitable substrates and have been utilized in laboratory cell studies. Although both of these materials are resistant to corrosion and good iron plate morphology has been obtained on both of them, they do suffer from degradation if polarized anodically to a great extent (as during overdischarge). Graphite will anodically corrode excessively at higher pH's (pH 3-4) (11) while bare titanium will dissolve anodically at sufficiently positive potentials. A titanium substrate used in our laboratory cell had experienced massive pitting during an overdischarge. One of the positive aspects of utilizing graphite as a substrate is the low cost. On the other hand, titanium is more conductive and is weldable (for bus bar connections), thus capable of higher loads for a given level of substrate/bus bar voltage loss.

The polarization curves (steady state) of the iron electrode in 250 gpl FeCl₂/150 gpl NH₄Cl are given

in Fig. 8. Although the data reported are for a titanium substrate, similar data were obtained for the Fe⁺²/Fe⁰ reaction on a graphite substrate. With a nominal current density of 60 mA/cm², at 90°C and pH = 1, the cathodic and anodic polarizations are 95 and 135 mV, respectively. This represents a voltaic efficiency for the iron electrode of 70%. The iron electrode polarization can be decreased by adjusting the electrolyte pH to higher values. For example, at the same conditions as above but with a pH = 3, the voltaic efficiency would be 83%. The pH dependence of the electrode polarization is in agreement with the following reaction mechanism as put forth in the literature (12)



Finally, as would be expected, the electrode polarization was found to be temperature sensitive (see Fig. 8). For example, reducing the electrolyte temperature from 70° to 60°C will decrease the voltaic efficiency to 75% (at 60 mA/cm², pH = 3.7).

Plating current efficiency.—The coulombic efficiency of the iron-redox battery is controlled by reactions at the iron plate (the ferric/ferrous redox reaction is nearly 100% efficient). One source of efficiency loss is the reaction of ferric ion with the iron plate

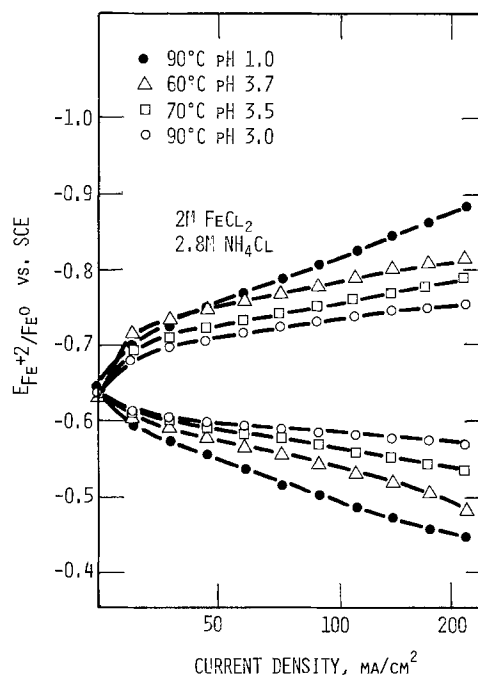
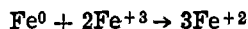
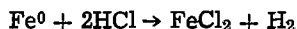


Fig. 8. Measured polarization of an iron electrode on a titanium substrate.



This reaction has been discussed earlier and can be minimized by the use of a suitable microporous separator.

A second source of coulombic efficiency loss can be represented by the following reaction



Chemical corrosion of this type results in hydrogen gassing which has been confirmed by analysis of gases above electrolyte storage bottles. A lowered coulombic efficiency has been measured even when the cell was at open circuit. It is therefore desirable to minimize the rate of this reaction. Studies in our laboratory have shown the above reaction to have a corrosion rate strongly dependent on electrolyte pH and on plate composition (*i.e.*, additives in the plate).

The pH effect on chemical corrosion is demonstrated by the results presented in Fig. 9. According to these results the desired electrolyte pH should be greater than pH 1-1.5. (Note: the higher pH electrolyte also contributes to more favorable polarizations of the iron electrode.) On the other hand, in order to prevent the formation of insoluble ferric oxides and hydroxides, the electrolyte must be kept below pH = 1.5. Since protons are highly mobile, the electrolyte pH must be similar on both sides of the cell. Consequently, chemical corrosion can be minimized by altering the composition and morphology of the iron plate (open-circuit corrosion can be avoided by draining the cell of electrolyte, a feature of the iron-redox battery system).

It is well known that small quantities of metal ions in the electrolyte will affect the properties of the iron plate. Tests have shown that some additives result in iron with a lower corrosion rate in acidified ferrous chloride solution. The measured corrosion rates of samples plated from solutions containing 0.01-10.0 gpl of several metal ion additives along with a standard base rate for pure electrolytic iron are presented in Fig. 10. Three of the metal ion additives reported (Zn, Mn, Cr) have electroplating potentials more

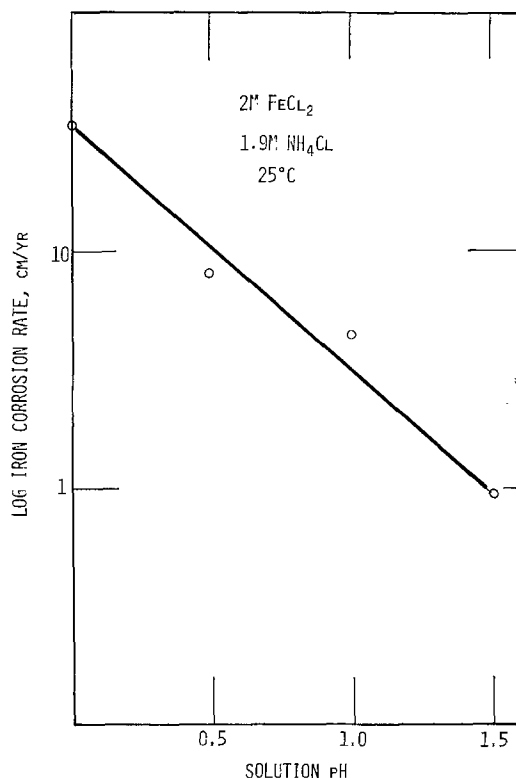


Fig. 9. Measured dependence of electrolytic iron corrosion rate on solution pH.

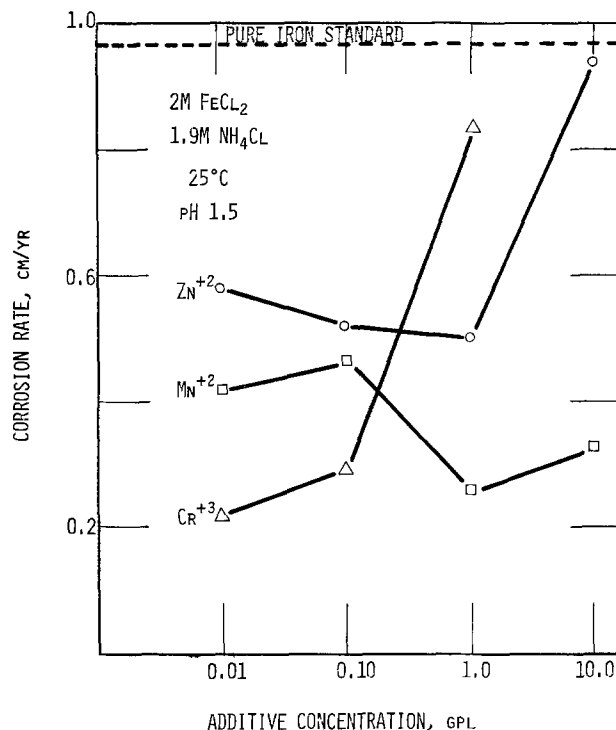
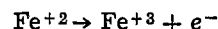


Fig. 10. Measured corrosion rate for iron samples plated from solutions containing metal ion additives.

cathodic than iron. When added to the plating bath, all were generally effective in reducing the corrosion rate as measured by weight loss. Four other metal ion additives tested, cobalt, nickel, cadmium, and lead, have plating potentials less cathodic than iron and were generally ineffective in reducing the chemical corrosion mechanism. One exception was a 1 gpl nickel ion addition which resulted in an iron dissolution rate 91% lower than the standard. However, this beneficial effect was not present at the lower concentrations, and chemical analysis of the plating solutions showed the nickel ion to be present at a much higher concentration in the plate than in the initial solution. This concentrating effect would remove the nickel ion from the electrolyte at the start of plating, leaving an ineffectively low concentration of nickel ion in the electrolyte. Consequently, nickel cannot be considered a good additive.

Characteristics of the redox electrode.—In a single cell, counter to the iron electrode is the ferrous/ferric redox electrode. The reaction at this electrode can be written as follows (during charge)



This reaction has been selected previously for application in Fe/Ti and Fe/Cr redox batteries and its polarization has been shown to be small (13-15). One of these studies (15) used a rotating disk electrode of edge-on pyrolytic graphite and has shown the reaction mechanism in $\text{FeCl}_3/3\text{M HCl}$ to be by simple electron transfer. Of course, in order to minimize unfavorable diffusional effects, a high surface area porous electrode must be used.

In Fig. 11, a comparison between smooth graphite and porous carbon electrodes is shown for the oxidation of ferrous ion in the $\text{FeCl}_2/\text{NH}_4\text{Cl}$ electrolyte. Although the single electrode potentials are not reported, the beneficial effect that the porous electrode has on the ferrous ion oxidation is demonstrated. This is especially true at lower temperatures and higher current densities.

A polarization curve of the ferrous-ferric reaction on porous carbon, during charge, is given in Fig. 12. Although not reported, the Fe^{+3} reduction curve is

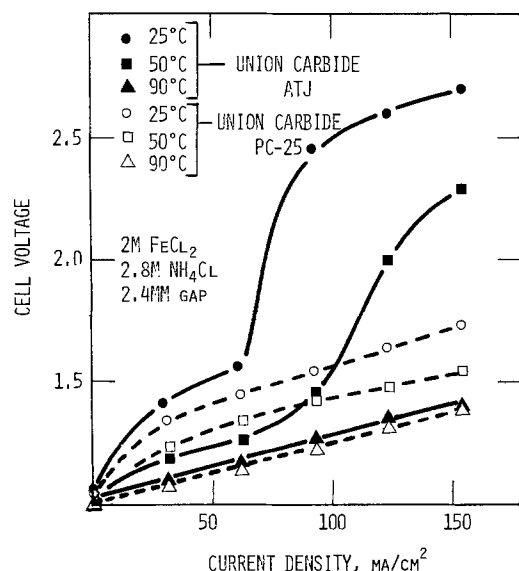


Fig. 11. Comparison of measured charge voltage between laboratory cells having a smooth graphite redox electrode (Union Carbide ATJ) and one having a porous carbon redox electrode (Union Carbide PC-25).

symmetrical when a clean electrode is used. Some other observations made during our studies may be worth mentioning at this time. For instance, the voltaic efficiency of the ferrous/ferric electrode was greatest on a fresh carbon surface. Oxides accumulating on the electrode surface quickly deteriorated the voltage performance of this electrode. These oxides precipitated when solution pH became greater than 1.5 and they have been identified as mixed oxides and hydroxides, noncrystalline, and primarily of ferric ion. The solution pH would increase because of proton discharge at the iron cathode during charge and because of air oxidation. The second factor was eliminated by sealing the electrolyte tanks and nitrogen blanketing. The activity of the electrode could be restored to its original state by applying an acid wash.

Unlike the graphite electrode for the zinc/chloride battery (16), the surface activity of the electrode in this system was not important and no activation procedures were required. Poor electrode performance was noted for the ferrous ion oxidation when Fe^{+2} concentration dropped below 50 gpl. A reticulated vitreous carbon showed acceptable activity although it had poor electronic conductivity. A ruthenized porous titanium electrode also showed good activity and has a very conductive substrate.

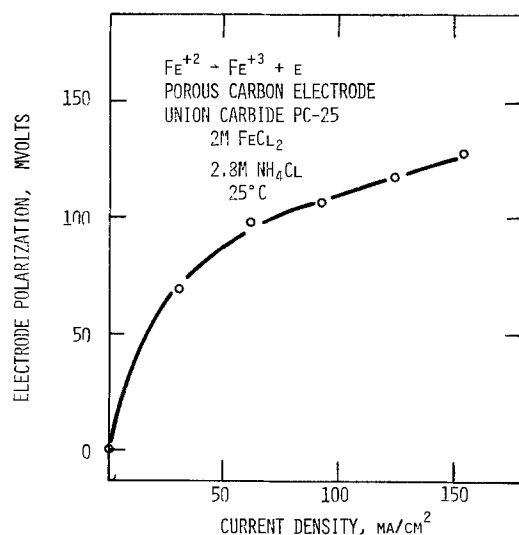


Fig. 12. Measured polarization of ferrous ion oxidation at a porous carbon electrode.

The coulombic efficiency of the ferrous/ferric couple was always measured to be near 100%; that is, no side reactions (O_2 or Cl_2 evolution during charge) were observed. The only coulombic loss was due to ferric ion migration through the separator. The high coulombic efficiency of the ferrous/ferric reaction coupled with the competing proton reaction at the iron electrode lead to an accumulation of ferric ion. This charge/discharge imbalance causes operational problems of a battery and is discussed in the next section.

Daily cycle performance.—In order to measure the actual current and energy efficiencies of an iron-redox cell, daily cycling operation is necessary. Cycle tests were performed in our laboratory with a 100 cm^2 cell and using a catholyte and anolyte volume of 2 liters each. Generally the cell was charged for 3 hr then discharged until a lower limit of zero volts was reached. Both the charging and the discharging were at constant current density of 60 mA/cm^2 . During cell cycling, solution pH ($\text{pH} = 1$) and temperature (60°C) were held constant.

A graph showing the current and energy efficiencies for 57 cycles is shown in Fig. 13. It is obvious that cell performance is highly variable from one cycle to the next, not attributable to any intentional change in operating parameters. The major changes that were made during this period are given in Table II. The effects from many of these changes have already been discussed. Current efficiencies of 80%–90% could be routinely obtained but the best energy efficiency was around 50%. The low energy efficiency then, of course, was due to the poor voltaic efficiency (55% at best).

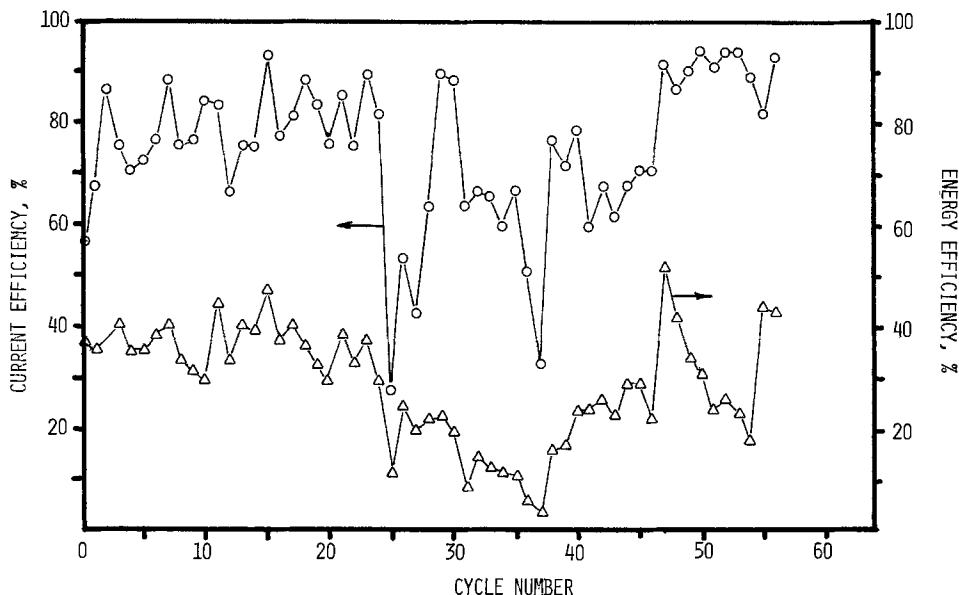
Measurements with silver/silver chloride reference electrodes identified the source of electrode polarizations that occurred during cell cycling. A typical voltage breakdown at the start of cell cycling is given in Fig. 14. As can be seen, during charge 50% of the voltage loss is due to the iron electrode, 27% due to the redox electrode, and 14% due to the separator resistance. During the first cycle the voltage loss across the Daramic separator was about 50–60 mV. This polarization increased rapidly to about 120 mV shortly thereafter. The increase in diaphragm resistivity has been attributed to $\text{Fe}(\text{OH})_2$ blockage of the separator pores. The conductivity of the separator could be returned to its original state by applying an acid wash. Eventually, a thicker (2.4 mm) Daramic sep-

Table II. Notes on iron-redox cell cycle tests

| Cycle number | Coulombic efficiency (%) | Energy efficiency (%) | Action taken prior to cycle |
|--------------|--------------------------|-----------------------|---|
| 1 | 58 | 36 | Separator, Celgard 5511 |
| 5 | 70 | 35 | New separator, Daramic W0733 |
| 6 | 72 | 35 | FeCl_2 addition |
| 11 | 84 | 29 | FeCl_2 addition |
| 12 | 83 | 44 | Cell drained of electrolyte and acid washed |
| 17 | 77 | 37 | FeCl_2 addition |
| 21 | 75 | 29 | Cell drained of electrolyte and acid washed, flow rate increased to 40 cm/sec |
| 22 | 85 | 38 | Flow rate decreased to original value |
| 27 | 53 | 24 | Water addition |
| 29 | 63 | 21 | Cell drained of electrolyte, solutions replaced |
| 35 | 59 | 11 | Electrolytes filtered to remove oxides |
| 39 | 76 | 15 | New separator, electrodes, and solutions |
| 42 | 59 | 23 | New redox electrode, reticulated vitreous carbon |

Electrolyte: $\text{FeCl}_2/\text{NH}_4\text{Cl}$ (2M/2.8M). Redox electrode: PC-25. Temperature: 60°C . Iron electrode substrate: titanium sheet. Current density: 60 mA/cm^2 . Electrolyte flow rate: 10 cm/sec . Acid additions: required almost daily to maintain pH of 1.

Fig. 13. Measured efficiency during cycling of a 100 cm² iron-redox cell. Details of operating conditions are given in Table II.



arator with a ribbed structure was evaluated and found to have a longer life (greater than 20 cycles).

The largest voltage loss is caused by the polarization at the iron electrode. This polarization may be reduced by adjusting the electrolyte pH to higher values. We attempted to maintain a pH differential in laboratory cells by using an anion selective membrane separator. But, as discussed previously, the separators quickly fouled. The fouling problem may be avoided in the future by incorporating recent advances in membrane technology from the NASA redox program (2).

The second most significant voltage loss was at the redox electrode. Although not large initially, the polarization increased during cell operation. The loss of electrode performance was associated with a passivating film accumulating on the electrode surface. As stated earlier, electrode performance was restored by applying an acid wash.

The operating cycle of 100%-83% depth of discharge in these tests do not represent a practical operating cycle such as 90%-10% depth of discharge. However, it was sufficient to note the occurrence of electrolyte imbalance and further charging only would compound the problem at this time. The electrolyte imbalance is brought about by proton reduction (during charge) which in turn affects electrolyte pH and causes an accumulation of ferric ion. As a result, hydrochloric acid and ferrous chloride had to be routinely added to the electrolyte. Later in the pro-

gram (at about 100 cycles) two metal ion additives were evaluated in the cell after obtaining the results from the iron corrosion tests. The zinc ion caused a reduction in observed current efficiency to 70% as compared to the usual 90%. Although not confirmed at this time, we speculate the zinc addition caused a shift to more negative potentials of the iron plating reaction and, consequently, increased the significance of the proton reduction reaction. The addition of manganese ion improved battery operation substantially. Although no increase in current efficiency was obvious, the electrolyte pH remained stable thus eliminating the need for acid addition.

Conclusions

An iron-redox single cell, at 60°C and using a microporous plastic separator, has been shown to be capable of storing and discharging energy at a round trip current efficiency of 90% and energy efficiency of 50%. A discharge power density of 50 mW/cm² has been obtained.

Several factors affecting the cell performance have been investigated. A ferrous-ammonium chloride electrolyte was found to be a highly conductive medium capable of yielding good quality electrolytic iron plate. Both titanium and graphite were found to be suitable substrates for iron plating. The largest voltage loss observed occurred at the iron electrode for both charge and discharge. Attempts at lowering this polarization by maintaining a pH differential across the cell with commercial anion membranes were unsuccessful because of membrane fouling. To a lesser extent, but not inconsequential, was the polarization at the high specific area porous redox electrode. The addition of small amounts of manganese ion was beneficial to cell performance in that ferrous chloride and acid additions during cycle tests become unnecessary.

Acknowledgment

The financial support for this project was received from Diamond Shamrock Corporation. Technical discussions with Jack Bennett and Nick Fatica and experimental assistance provided by P. J. Palmer were invaluable and greatly appreciated.

Manuscript submitted July 8, 1980; revised manuscript received Aug. 25, 1980.

Any discussion of this paper will appear in a Discussion Section to be published in the December 1981 JOURNAL. All discussions for the December 1981 Discussion Section should be submitted by Aug. 1, 1981.

Publication costs of this article were assisted by the University of Akron and the Diamond Shamrock Corporation.

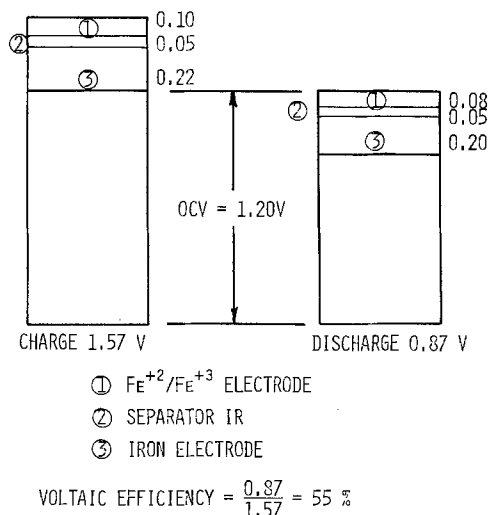


Fig. 14. Measured voltage breakdown for the initial cycle of a 100 cm² laboratory cell at 60 mA/cm², 60°C, and pH = 1.

REFERENCES

1. "Energy Storage," J. Berkowitz and H. Silverman, Editors, The Electrochemical Society, Soft-bound Proceedings Series, Princeton, N.J. (1976).
2. "Proceedings of the 14th Intersociety Energy Conversion Engineering Conferences," Boston, Massachusetts, Aug. 5-10, 1979, American Chemical Society, Washington, D.C. (1979).
3. L. H. Thaller, NASA Technical Memorandum TM-79186, 1979; also in Ref. (2), Vol. 1, p. 715.
4. L. H. Thaller, U.S. Pat. 3,996,064 (1976).
5. L. H. Thaller, Abstract 85, p. 229, The Electrochemical Society Extended Abstracts, Atlanta, Georgia, Oct. 9-14, 1977.
6. R. F. Savinell, C. C. Liu, R. T. Galasco, S. H. Chiang, and J. F. Coetzee, *This Journal*, **126**, 357 (1979).
7. R. Zito, U.S. Pat. 3,719,526 (1973).
8. R. Zito and C. M. Harman, Presented at Department of Energy Second Annual Battery and Electrochemical Technology Conference, Arlington, Va., June 5-7, 1978.
9. E. W. Washburn, "International Critical Tables of Numerical Data, Physics, Chemistry and Technology," Vol. 6, pp. 229-233. Published for National Research Council by McGraw-Hill, New York (1929).
10. R. F. Savinell, Ph.D. Dissertation, University of Pittsburgh, Pittsburgh, Pa. (1977).
11. J. S. Sconce, "Chlorine: Its Manufacture, Properties and Uses," ACS Monograph, pp. 81-166, Reinhold Publishing Corp., New York (1962).
12. J. O'M. Bockris and A. K. N. Reddy, "Modern Electrochemistry," Vol. 2, p. 1091, Plenum Publishing Corp., New York (1970).
13. J. Giner, L. Swette, and K. Cahil, NASA CR-134705, 1976. (Available through NTIS, Springfield, Va.).
14. M. A. Reid and R. F. Gahn, NASA Technical Memorandum TM X-73669 (1977).
15. R. O. Miller, NASA Technical Memorandum TM-73716 (1977).
16. P. C. Symons, Report EM-711, pp. 2.2-2.17 (1978). (Available from Electric Power Research Institute, Palo Alto, Cal.).

The Effect of Zirconium on the Cyclic Oxidation of NiCrAl Alloys

C. A. Barrett, A. S. Khan,¹ and C. E. Lowell*

NASA-Lewis Research Center, Cleveland, Ohio 44135

ABSTRACT

Cyclic oxidation tests of Ni-(9-20)Cr-(15-30)Al- x Zr alloys were carried out at 1100° and 1200°C in static air. In these alloys the concentration of zirconium varied from 0 to 0.63 atomic percent (a/o). The phases found in the cast alloys were γ , γ' , β , and α . The oxidized surfaces were characterized by metallography, XRD, and electron microscopy. Although the alloys were basically alumina/nickel aluminate formers, the zirconium-containing alloys also formed small amounts of ZrO₂. The metallographic and electron microscopic examination of oxidized surfaces revealed significant aluminum oxide(s) penetration. The depth of attack and the degree of oxide penetration, however, strongly depended on the zirconium content of the alloy. The zirconium-free alloy had massive penetration of aluminum oxide(s). Small amounts of zirconium led to minimal penetration. However, as the zirconium content increased, the oxide penetration again became more pronounced. All of the weight change ($\Delta W/A$)-time data were fitted to the parabolic oxidation model: $\Delta W/A = k_1^{1/2}t^{1/2} - k_2t$ where $k_1^{1/2}$ represents the rate of scale formation and k_2 the rate of oxide spalling. The Zr-containing alloys had relatively good cyclic oxidation resistance as a result of intraoxide spalling at low rates. The Zr-free alloys had relatively poor cyclic oxidation resistance due to massive alumina spalling to bare metal, which resulted in a shift to NiO-controlled oxidation and even greater rates of attack. The derived parameters K_a (which equals $k_1^{1/2} + 10k_2$) and W_m (metal consumption) which indicate the degree of total oxidation attack were also estimated as a function of zirconium content. All four parameters showed minimums in the range of 0.03 to about 0.20 a/o zirconium. Further addition of zirconium beyond 0.20 resulted in increased values of $k_1^{1/2}$, K_a , k_2 , and W_m . Alloys with zirconium contents between 0.03 and 0.20 a/o seemed to have the best cyclic oxidation resistance over the range of compositions tested, while oxidation resistance was essentially independent of Cr and Al content over the compositional range evaluated for these alloys.

The improvement of the oxidation resistance of alloys by the addition of reactive elements such as Y, Si, etc. has been known for several years (1-8). However, the mechanism by which these elements improve oxidation resistance has not yet been satisfactorily explained. In this respect several mechanisms have been proposed assuming that the added elements produce beneficial effects due to some interaction either at the alloy-oxide interface, in the oxide layer, or in the matrix. Pettit and co-workers (7, 8, 11) pro-

posed that the internal rare earth oxide which is formed during oxidation mechanically keys the external oxide to the alloy and also prevents void formation at the alloy-oxide interface. Allam *et al.* make a similar case for oxide adhesion by pegging in the CoCrAl system(s). Their work indicated not only an improved adhesion of the scale by the addition of Y or Hf, but also made a case for an optimum concentration of these elements below 1 weight percent (w/o). On the other hand, in a recent paper Golightly *et al.* (9) proposed that the addition of rare earth elements prevents oxide formation within the existing oxide layer, probably by altering the outward diffusion of aluminum. Subsequent oxide growth occurs at the alloy-oxide interface forming an adherent scale.

* Electrochemical Society Active Member.

¹ Present address: Pratt & Whitney Aircraft, West Palm Beach, Florida 33402.

Key words: scale adhesion, oxide spalling, Al₂O₃ formation, oxidation attack parameters.

The subject of oxide adhesion by small additions of rare earth or other reactive elements has also been treated extensively by Wright (10). However, no theory yet developed accounts for all of the observations.

Earlier work at this laboratory showed the beneficial effects of small amounts of Zr for Ni-Cr-Al alloys in the general range [9-20 atomic percent (a/o) Cr, 15-30 a/o Al] (12, 13), and a paper on the effect of zirconium on the isothermal oxidation of Ni-Cr-Al alloys has recently been published (14). This work showed that Zr additions resulted in a minimum in the parabolic scaling constant of Ni-14Cr-24Al alloys. Just as important as the effect of Zr was the drastic reduction in spalling at the end of the tests. While some oxide penetration was noted, it was concluded that "pegging" was not the mechanism of improved adhesion, but rather a reduction in void formation at the oxide/metal interface and an improved oxide/metal bond. The present paper describes the effect of Zr on the cyclic oxidation behavior of this class of Ni-Cr-Al alloys. This paper attempts to relate cyclic oxidation resistance with zirconium content. It is hoped that the study will provide additional information on the mechanism of oxide adhesion by tramp elements. The relatively large solubility of zirconium in the alloy permitted evaluation of oxidation properties without intermetallic compound formation which would have led to segregation of the zirconium.

Materials

The alloys investigated are mainly in the $\beta + \gamma/\gamma'$ regions of the Ni-Cr-Al phase diagram (15), and Fig. 1 shows a general map of the alloys tested. In the as-cast condition some nonequilibrium α -Cr was detected. This phase was not present in the oxidized samples. The thermal history and chemical composition of many of the alloys have been described in previous publications (12, 13) and are presented in Table I for reference. In the present paper the general compositions of the alloys studied are expressed as Ni-14Cr-24Al- x Zr (a/o) for convenience during description, while Table I lists the actual composition of each alloy. The zirconium content varied from 0 to 0.63 a/o (1.10 w/o Zr). In several alloys, zirconium was added as an element during induction melting, while the rest of the alloys picked up zirconium from the zirconia crucible used in melting. Besides chemical analysis, the phases present in the alloys were characterized by SEM, optical microscopy, and energy dispersive analysis. In Ref. (14) an elemental x-ray micrograph was obtained for zirconium and showed a uniform distri-

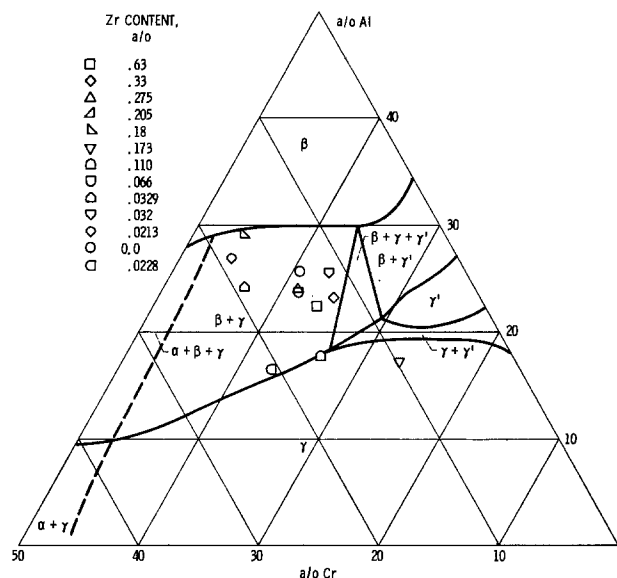


Fig. 1. Map of test alloys. Ni-Cr-Al, 1100°-1200°C

bution of zirconium in the matrix. Therefore, the zirconium content of the alloys studied was thought to be below its solubility limit.

Procedure

Experimental.—The Ni-14Cr-24Al- x Zr alloys were cyclically oxidized at 1100° and 1200°C. The experimental apparatus which has been described elsewhere (16) is shown in Fig. 2 and is briefly outlined here. Six samples were suspended individually in alumina furnace tubes. The suspended specimens were automatically raised and lowered by pneumatic cylinders controlled by reset timers. As the samples were raised, individually shielded cups automatically slid under the samples to catch the oxide spall. Each coupon used for oxidation was $22 \times 10 \times 2$ mm with a small hole drilled in one end for wire suspension in the furnace. Samples were cleaned ultrasonically in alcohol before testing. Each cycle consisted of 1 hr heating and a minimum of 20 min cooling. Samples were periodically weighed throughout the test and data obtained were used to generate specific weight change *vs.* time curves. The samples were also examined by x-ray diffraction periodically to identify the oxides formed. The oxide scales were characterized by metallography and were analyzed by electron microprobe.

Table I. Chemical composition of Ni-Cr-Al alloys with melt history and Zr levels for alloys tested in cyclic oxidation at 1100° and 1200°C for basic $Al_2O_3/NiAl_2O_4$ scale formers

| Zr (a/o) | Cr (a/o) | Al (a/o) | Melt history | Method of Zr pickup | Ht. No. |
|----------|----------|----------|---|-------------------------------|----------|
| 0.63 | 14.01 | 22.34 | Scratch induction melt, ZrO_2 crucible | Held extra long crucible | 5(A) |
| 0.33 | 12.30 | 23.17 | Induction remelt, Al_2O_3 crucible | Alloy addition to master heat | M-3 |
| 0.275 | 14.68 | 24.00 | Arc melted Cu mold | Alloy addition | JS |
| 0.205 | 12.44 | 22.72 | Scratch induction melt, ZrO_2 crucible | Std. melt. random pickup | 2B orig. |
| 0.18 | 16.81 | 29.19 | Scratch induction melt, ZrO_2 crucible | Std. melt, random pickup | 5B orig. |
| 0.173 | 9.73 | 17.18 | Scratch induction melt, ZrO_2 crucible | Std. melt, random pickup | 9 orig. |
| 0.110 | 15.98 | 17.54 | Scratch induction melt, ZrO_2 crucible | Std. melt, random pickup | 1 orig. |
| 0.066 | 14.35 | 23.65 | Scratch induction melt, ZrO_2 crucible | Std. melt, random pickup | 5A orig. |
| 0.0329 | 19.15 | 24.16 | Scratch induction melt, ZrO_2 crucible | Std. melt, random pickup | 6A orig. |
| 0.032 | 11.50 | 25.58 | Scratch induction melt, ZrO_2 crucible | Std. melt, random pickup | 2A orig. |
| 0.0228 | 20.84 | 16.52 | Scratch induction melt, ZrO_2 crucible | Std. melt, random pickup | 8B orig. |
| 0.0213 | 18.87 | 26.99 | Scratch induction melt, ZrO_2 crucible | Std. melt, random pickup | 8A orig. |
| 0.0 | 13.89 | 25.14 | Master ingot, Certified Alloys, Inc. | No Zr in ingot | 5C orig. |

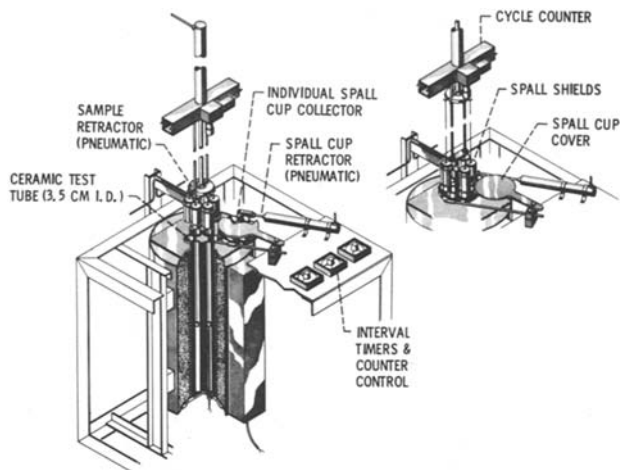


Fig. 2. Multitube automatic high temperature cyclic oxidation test rig. (a, left) Samples at test temperature. (b, right) Samples cooled to ambient temperature.

Treatment of experimental data.—In previous reports from this laboratory cyclic oxidation attack has been estimated by two parameters, K_a and W_m , both of which can be derived from sample weight change/time data. First the specific weight change data are regression fitted to the approximate parilinear equation

$$\Delta W/A = k_1^{1/2} t^{1/2} - k_2 t \pm \sigma \quad [1]$$

where $\Delta W/A$ is the specific weight change at any time t , A is the area of the specimen, $k_1^{1/2}$ and k_2 are the growth and spalling constants respectively, and σ is the standard error of estimate.

The attack parameter is then defined as

$$K_a = (k_1^{1/2} + 10 k_2) \quad [2]$$

where the coefficient 10 was derived empirically [Ref. (12)]. As K_a increases, oxidation resistance decreases. W_m , on the other hand, is the total specific amount of metal converted to oxide up to any time regardless of whether all or part of the oxide is retained or has spalled and/or vaporized. W_m can be estimated directly from weight change data only when no spalling and/or vaporization has occurred in the oxidation process (i.e., parabolic oxidation). Otherwise W_m must be inferred from the mass balance equation for any time t

$$W_m = W_r - \Delta W/A \quad [3]$$

where W_m is the specific amount of metal consumed and W_r the specific amount of oxide retained and $\Delta W/A$ the specific weight change at any time. If parilinear kinetics are assumed, Eq. [3] has been solved in terms of specific weight change/time values and set up as a computer program termed COREST to handle conventional oxidation data as input [Ref. (17)]. The relationship between K_a and W_m is linear for values derived from the same weight change data with W_m shifted because it increases with time [Ref. (12)].

It should be reemphasized that W_m should be a universal measure of corrosion attack always a positive value and always monotonically increasing as time increases and environmental factors become more severe. No matter how complicated the actual kinetics, W_m estimates are required to fully satisfy any particular oxidation model. This has the additional advantage that the W_m can also be measured directly based on thickness change and alloy depletion.

Results and Discussion

Characterization of oxides.—Retained oxide and spalled oxides obtained at 1100° and 1200°C during

cyclic oxidation of Ni-14Cr-24Al- x Zr were identified by XRD and the results are shown in Table II. All alloys formed predominantly alumina and nickel aluminate ($\alpha_0 = 8.05$ -8.10Å) scales. Zirconium-containing alloys also produced small amounts of ZrO_2 (both cubic and monoclinic form). The Zr-free alloy spalled to bare metal during cooling, resulting in accelerated metal loss. This profuse spalling depleted Al from the Zr-free alloys and led to the formation of less protective NiO with a further acceleration of metal loss. On the other hand, the zirconium-containing alloys, which spalled only at the outer parts of the oxide, retained the basic alumina/aluminate scale after prolonged cycling. An exception was the case of the higher zirconium content alloys which formed some NiO at high temperature. For example, at 1200°C the alloys containing 0.33 and 0.63 a/o Zr spalled extensively, although not to bare metal, and produced considerable amounts of NiO on the surface.

This behavior is consistent with that expected from isothermal oxidation (14). The extensive bare metal spalling of Zr-free alloys at the conclusion of the isothermal testing also occurs with repeated cycles [see also (18)]. Similarly, the lesser oxide spalling tendency of the Zr-containing alloys also persisted and resulted, for the most part, in substantially reduced metal loss.

Metallography.—Figures 3 and 4 contain photomicrographs of several of the alloys, which span the range of zirconium contents, after 200 cycles at both 1200° and 1100°C, respectively. One of the most striking features of these microstructures is oxide penetration into the metal. All of the alloys containing zirconium displayed this oxide penetration as a feathery oxide, largely Al_2O_3 . This is consistent with the isothermal work previously cited (14). The extent of this attack is proportional to the extent of metal loss which is, in turn, proportional to the zirconium level. However, oxide penetration was also found in the cyclic testing of the Zr-free alloy, which is not consistent with isothermal testing (14). This penetration was by massive oxide globules, largely Al_2O_3 . This penetration undoubtedly contributes to the extensive loss of metal caused by the massive spalling to bare metal associated with this type of "pure" Ni-Cr-Al or Ni-Al alloy (18).

Kinetic data.—The specific weight change data are plotted in Fig. 5 and 6 at 1200° and 1100°C, for selected alloys over the range of Zr levels. In general, the alloys gained weight initially as the weight of oxygen consumed in forming the oxide layer was greater than the oxide weight lost by spalling. At longer times, especially at 1200°C the spalling rate overtook the oxygen pick up rate, and the net specific weight vs. time slope decreased and ultimately became negative. Eventually, the net weight of the sample became negative. This behavior is typical of such tests, e.g., Ref. (12) and (16). In contrast, the alloys containing no Zr started with a nearly constant, negative slope since the massive spalling greatly exceeded the oxygen weight gain.

Regression analysis was performed on all test data fitted to Eq. [1] and the results are presented in Table III. In general, the R^2 values are quite high, showing that a parilinear model is a reasonable approach to analyzing the data. The 0.0 a/o Zr samples were also fitted to the parilinear model equation even though the weight loss was massive. The apparent $k_1^{1/2}$ and k_2 values were extremely large and represent a different class of alloys, i.e., bare metal oxide spallers with strong NiO formation.

The values (exclusive of the 0.0 a/o Zr data) for $k_1^{1/2}$, k_2 , K_a , and W_m were then individually fitted to second-degree polynomial equations at 1200° and 1100°C by multiple linear regression as a function of Zr content and plotted in Fig. 7-11 and listed in Tables IIIa and IIIb. An evaluation of the R^2 values of these equations shows that most of the total variability can

Table II. Observed phases at various Zr levels of Ni-Cr-Al- γ/γ' - β alloys after 200 1-hr cycles at 1100° and 1200°C

| Zr content (a/o) | 1100°C | | 1200°C | |
|---------------------|--|--|---|---|
| | Surface ^a | Spall ^b | Surface ^a | Spall ^b |
| 0.63 | Al ₂ O ₃ 8.05 spinel ^d Ni S.S. ZrO ₂ (mono.) ZrO ₂ (cubic) | NiO (s) Al ₂ O ₃ (s) 8.30 spinel (w) ^e 8.05 spinel (w) Cr ₂ O ₃ (w) Unknown d—1.96 2.17 | NiO ^c 8.10 spinel 8.25 spinel Al ₂ O ₃ Cr ₂ O ₃ ZrO ₂ Ni S.S. | NiO (s) ^c Al ₂ O ₃ (s) 8.10 spinel (m) 8.30 spinel (w) Cr ₂ O ₃ (vw) ZrO ₂ -mono. (vw) |
| 0.33 | Al ₂ O ₃ 8.05 spinel ZrO ₂ (mono.) ZrO ₂ (cubic) Ni S.S. | No significant spall after 200 hr | 8.10 spinel Al ₂ O ₃ Cr ₂ O ₃ NiO ZrO ₂ Ni S.S. | 8.05 spinel (s) Al ₂ O ₃ (s) NiO (w) ZrO ₂ -cubic (w) ZrO ₂ -mono. (w) Unknown spinel (vw) |
| 0.066 | Al ₂ O ₃ 8.05 spinel Ni S.S. Ni ₃ Al (?) ZrO ₂ Unknown d—1.96 2.17 | No significant spall after 200 hr | Al ₂ O ₃ 8.05 spinel Ni S.S. Ni ₃ Al possible | No significant spall after 200 hr |
| 0.0 | Cr ₂ O ₃ 8.10 spinel Al ₂ O ₃ Ni S.S. | Al ₂ O ₃ (s) NiO (m) 8.30 spinel (w) 8.10 spinel (w) Cr ₂ O ₃ (w) | NiO 8.10 spinel Al ₂ O ₃ 8.20 spinel Cr ₂ O ₃ Ni S.S. | NiO (s) Al ₂ O ₃ (w) 8.10 spinel (w) 8.30 spinel (w) Cr ₂ O ₃ (w) |

^a Listed in decreasing order of intensity of surface phases.

^b (s) strong, (m) medium, (w) weak, and (vw) very weak powder intensities.

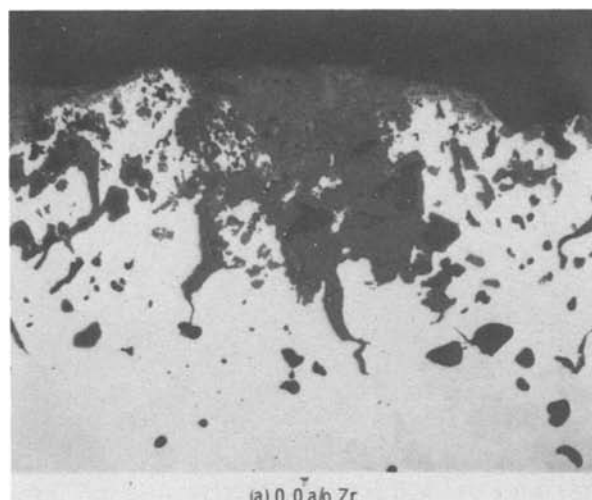
^c Sample cracked and removed from test after 190 hr/cycles.

^d NiAl₂O₄ spinel — a_0 , 8.05 to 8.20 Å [Ref. (16)].

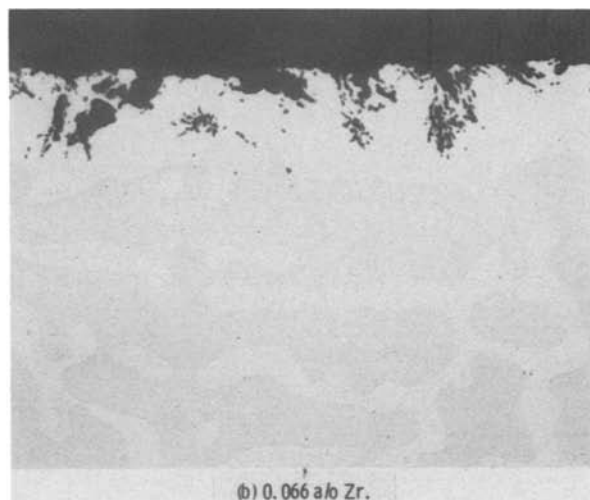
^e Chromite spinels — a_0 , >8.25 Å [Ref. (16)].

be explained by differences in the Zr content. A similar fit with Cr and Al levels showed a much lower level of explained variation. This implies that over this range

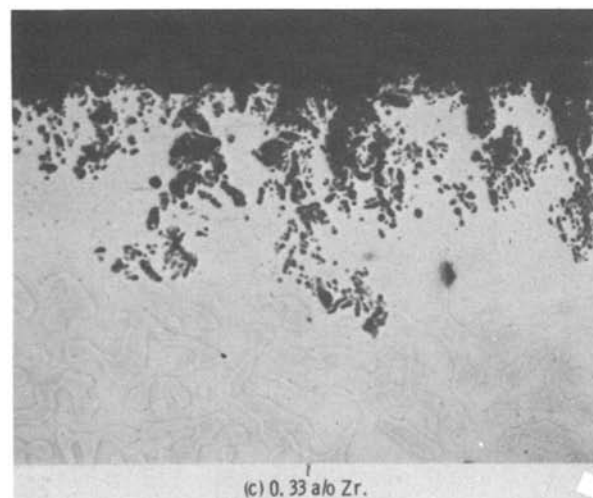
of compositions the variation in Cr/Al levels are at most second- or third-order effects. The open circles represent the data used to derive the vector line esti-



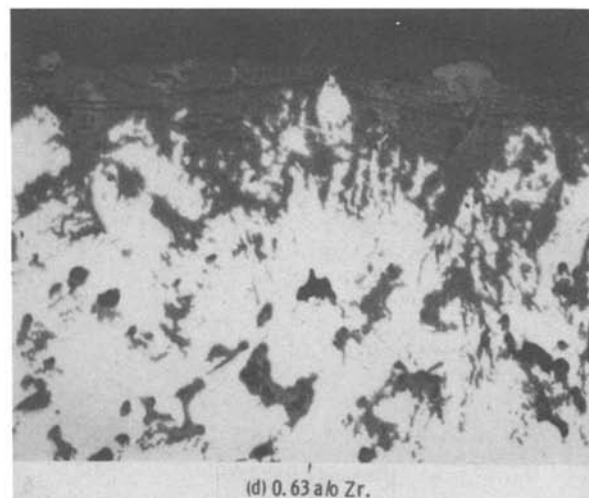
(a) 0.0 a/o Zr.



(b) 0.066 a/o Zr.



(c) 0.33 a/o Zr.



(d) 0.63 a/o Zr.

Fig. 3. Selected Ni-Cr-Al alloys at 1200°C in static air after 200 1-hr cycles with 0.0, 0.066, 0.33, and 0.63 a/o zirconium content; magnification 250 \times .

Table IIIa. Cyclic oxidation constants,^a 1200°C

| | Zirconium content (a/o) | Fit time (hr) | Square root of oxide growth constant, $k_1^{1/2}$ (mg · cm ⁻² · hr ^{-1/2}) | Oxide spalling constant, k_2 (mg · cm ⁻² · hr ⁻¹) | Coefficient of determination, ^b R ² | Standard error of estimate, σ (mg · cm ⁻²) | Attack parameter, ^c K _a | Specific amount of metal consumed in total oxidation process up to a given time, ^d W _m (mg · cm ⁻²) | |
|----|-------------------------|---------------|---|--|---|---|---|---|--------|
| | | | | | | | | 200 hr | 500 hr |
| 1 | 0.63 | 175 | 5.806 | 0.5983 | 0.860 | 5.69 | 11.788 | 187.7 | 344.3 |
| 2 | 0.33 | 200 | 1.105 | 0.1247 | 0.992 | 0.43 | 2.352 | 36.81 | 68.67 |
| 3 | 0.205 | 200 | 0.483 | 0.0340 | 0.968 | 0.21 | 0.823 | 14.16 | 24.64 |
| 4 | 0.18 | 200 | 0.657 | 0.335 | 0.991 | 0.29 | 0.992 | 18.53 | 31.31 |
| 5 | 0.173 | 200 | 0.269 | 0.0250 | 0.770 | 0.37 | 0.519 | 8.47 | 15.29 |
| 6 | 0.173 | 200 | 0.214 | 0.0195 | 0.859 | 0.21 | 0.409 | 6.72 | 12.08 |
| 7 | 0.110 | 200 | 0.280 | 0.0361 | 0.996 | 0.11 | 0.641 | 9.79 | 18.75 |
| 8 | 0.110 | 200 | 0.191 | 0.0329 | 0.998 | 0.10 | 0.520 | 7.57 | 15.51 |
| 9 | 0.110 | 200 | 0.296 | 0.0345 | 0.992 | 0.13 | 0.641 | 9.98 | 18.72 |
| 10 | 0.066 | 200 | 0.297 | 0.0223 | 0.993 | 0.06 | 0.520 | 8.81 | 15.44 |
| 11 | 0.066 | 200 | 0.286 | 0.0263 | 0.992 | 0.06 | 0.549 | 8.99 | 16.21 |
| 12 | 0.066 | 200 | 0.293 | 0.0241 | 0.991 | 0.06 | 0.534 | 9.03 | 16.02 |
| 13 | 0.066 | 200 | 0.228 | 0.0218 | 0.985 | 0.07 | 0.446 | 7.23 | 13.11 |
| 14 | 0.0329 | 200 | 0.187 | 0.0271 | 0.997 | 0.06 | 0.457 | 6.84 | 13.44 |
| 15 | 0.032 | 200 | 0.283 | 0.0273 | 0.926 | 0.06 | 0.556 | 9.02 | 16.63 |
| 16 | 0.032 | 200 | 0.333 | 0.0469 | 0.998 | 0.10 | 0.803 | 12.06 | 23.55 |
| 17 | 0.032 | 200 | 0.160 | 0.0418 | 0.999 | 0.12 | 0.578 | 8.33 | 18.69 |
| 18 | 0.032 | 200 | 0.354 | 0.0510 | 0.999 | 0.11 | 0.864 | 12.91 | 25.33 |
| 19 | 0.032 | 200 | 0.104 | 0.0402 | 0.999 | 0.14 | 0.506 | 7.60 | 18.03 |
| 20 | 0.0213 | 200 | 0.240 | 0.0227 | 0.974 | 0.10 | 0.468 | 7.62 | 13.79 |
| 21 | 0.0213 | 200 | 0.147 | 0.0280 | 0.994 | 0.04 | 0.427 | 6.17 | 12.93 |
| 22 | 0.0213 | 200 | 0.189 | 0.0235 | 0.999 | 0.04 | 0.424 | 6.52 | 12.40 |
| 23 | 0.0213 | 200 | 0.179 | 0.0273 | 0.990 | 0.04 | 0.452 | 6.69 | 13.31 |
| 24 | 0.0 | 200 | 9.649 | 1.6887 | 0.974 | 18.23 | 26.536 | 629.4 | 1143.0 |
| 25 | 0.275* | 200 | 1.071 | 0.0432 | 0.986 | 0.74 | 1.503 | 19.70 | 33.53 |

^a Model equation: $\Delta W/A = k_1^{1/2}t^{1/2} - k_2t \pm \sigma$ from multiple linear regression.

^b Ratio of explained variability to total variability.

^c K_a is defined as $(k_1^{1/2} + 10 k_2)$ [Ref. (12)].

^d Estimated from COREST [Ref. (17)] using gravimetric data input, based on NiAl₂O₃ scale control except for 0.0 Zr sample which controls with NiO scale.

* Check run (see Fig. 7 to 10).

Table IIIb. Cyclic oxidation constants,^a 1100°C

| | Zirconium content (a/o) | Fit time (hr) | Square root of oxide growth constant, $k_1^{1/2}$ (mg · cm ⁻² · hr ^{-1/2}) | Oxide spalling constant, k_2 (mg · cm ⁻² · hr ⁻¹) | Coefficient of determination, ^b R ² | Standard error of estimate, σ (mg · cm ⁻²) | Attack parameter, ^c K _a | Specific amount of metal consumed in total oxidation process up to a given time, ^d W _m (mg · cm ⁻²) | |
|----|-------------------------|---------------|---|--|---|---|---|---|--------|
| | | | | | | | | 200 hr | 500 hr |
| 1 | 0.63 | 1000 | 0.5495 | 0.02128 | 0.893 | 1.00 | 0.7623 | 15.28 | 25.39 |
| 2 | 0.33 | 500 | 0.1988 | 0.00216 | 0.998 | 0.24 | 0.2204 | 5.09 | 8.15 |
| 3 | 0.205 | 500 | 0.1315 | 0.00643 | 0.980 | 0.08 | 0.1958 | 3.79 | 6.38 |
| 4 | 0.173 | 500 | 0.0960 | 0.00432 | 0.987 | 0.05 | 0.1392 | 2.64 | 4.42 |
| 5 | 0.173 | 500 | 0.1136 | 0.00524 | 0.977 | 0.08 | 0.1659 | 3.30 | 5.53 |
| 6 | 0.110 | 500 | 0.0893 | 0.00510 | 0.978 | 0.05 | 0.1403 | 2.62 | 4.48 |
| 7 | 0.110 | 500 | 0.0960 | 0.00559 | 0.991 | 0.04 | 0.1519 | 2.80 | 4.78 |
| 8 | 0.110 | 500 | 0.0788 | 0.00413 | 0.977 | 0.05 | 0.1201 | 2.23 | 3.78 |
| 9 | 0.066 | 500 | 0.0996 | 0.00219 | 0.998 | 0.04 | 0.1215 | 2.62 | 4.26 |
| 10 | 0.066 | 500 | 0.1101 | 0.00203 | 0.998 | 0.05 | 0.1304 | 2.88 | 4.65 |
| 11 | 0.066 | 500 | 0.1079 | 0.00222 | 0.997 | 0.05 | 0.1301 | 2.82 | 4.57 |
| 12 | 0.0329 | 500 | 0.0850 | 0.00523 | 0.982 | 0.05 | 0.1373 | 2.51 | 4.31 |
| 13 | 0.0329 | 500 | 0.0891 | 0.00596 | 0.972 | 0.09 | 0.1487 | 2.67 | 4.61 |
| 14 | 0.0329 | 500 | 0.0734 | 0.00412 | 0.988 | 0.06 | 0.1146 | 2.14 | 3.64 |
| 15 | 0.032 | 500 | 0.1036 | 0.00823 | 0.972 | 0.12 | 0.1859 | 3.21 | 5.66 |
| 16 | 0.032 | 500 | 0.0882 | 0.00816 | 0.995 | 0.06 | 0.1698 | 2.84 | 5.12 |
| 17 | 0.032 | 500 | 0.1063 | 0.00734 | 0.981 | 0.08 | 0.1797 | 3.19 | 5.53 |
| 18 | 0.0213 | 500 | 0.0631 | 0.00591 | 0.983 | 0.08 | 0.1222 | 2.04 | 3.69 |
| 19 | 0.0213 | 500 | 0.0695 | 0.00689 | 0.982 | 0.07 | 0.1384 | 2.28 | 4.16 |
| 20 | 0.0 | 700 | 4.5831 | 0.51361 | 0.950 | 20.21 | 9.719 | 277.1 | 476.0 |
| 21 | 0.275* | 200 | 0.1807 | ~0.0 | 0.999 | 0.08 | 0.181 | 4.57 | 7.27 |

^a Model equation: $\Delta W/A = k_1^{1/2}t^{1/2} - k_2t \pm \sigma$ from multiple linear regression.

^b Ratio of explained variability to total variability.

^c K_a is defined as $(k_1^{1/2} + 10 k_2)$ [Ref. (12)].

^d Estimated from COREST [Ref. (17)] using gravimetric data input, based on NiAl₂O₃ scale control except for 0.0 Zr sample(s) where NiO scale controls.

* Check run (see Fig. 7 to 10).

mate shown in the plot. The dark circle point represents an alloy that was run later to test how well the estimated life predicts results for other Zr levels. The closeness of the shaded point to the predicted value for the various parameters lends confidence to this approach. It should be reemphasized the 0.0 a/o Zr data points were not included in the curve fits since they represent a different class of oxide formers and spallers.

Figure 7 is a plot of $k_1^{1/2}$ vs. Zr. The growth constant increases monotonically with Zr after a large discontinuous drop from the 0.0 a/o Zr level at 1200°C and the same type of behavior was observed at 1100°C. This increase in growth constant with Zr content is consistent with an effect observed during isothermal oxidation in Ref. (14). However, the increased scaling

rate primarily results in increased oxide penetration rather than increased scale thickness. During cyclic oxidation the situation is complicated by the accelerating effects of spalling which can in turn lead to the formation of different oxides, e.g., NiO, which may be less protective and lead to an even greater metal loss rate and correspondingly higher growth constants.

Likewise, a plot of k_2 , the spalling constant (Fig. 8) shows similar results. There is a drastic reduction in the spalling constant as the Zr level goes from 0 to about 0.06 a/o where it reaches a minimum, rises slowly at first, and then increases rapidly. The initial rapid decrease in spalling as the Zr content increases from 0 to about 0.06 a/o appears to be the result of a strengthening of the oxide-metal bond which prevents spalling to bare metal. The cause of the gradual in-

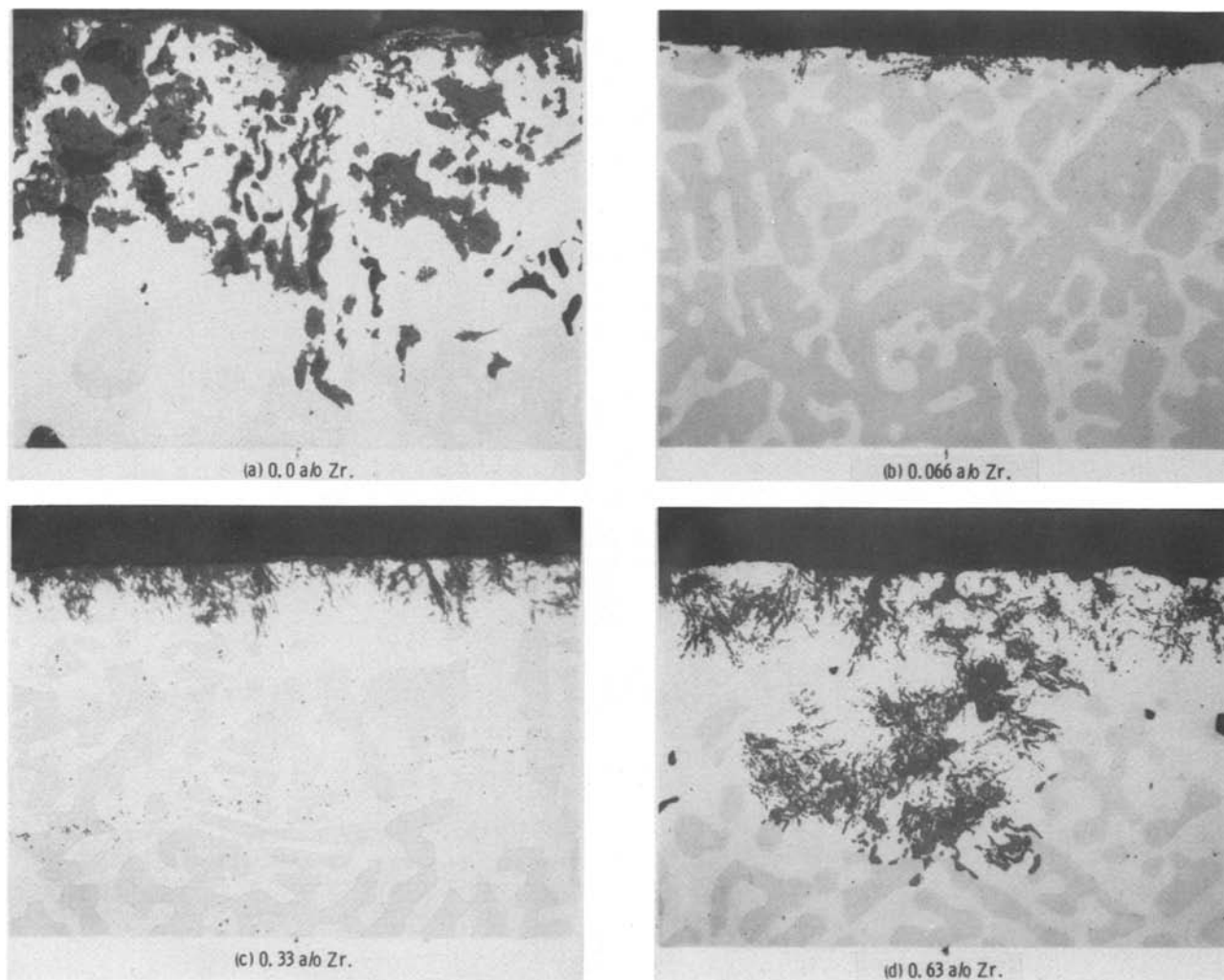


Fig. 4. Selected Ni-Cr-Al alloys at 1100°C in static air after 200 1-hr cycles with 0.0, 0.066, 0.33, and 0.63 a/o zirconium content; magnification 250 \times .

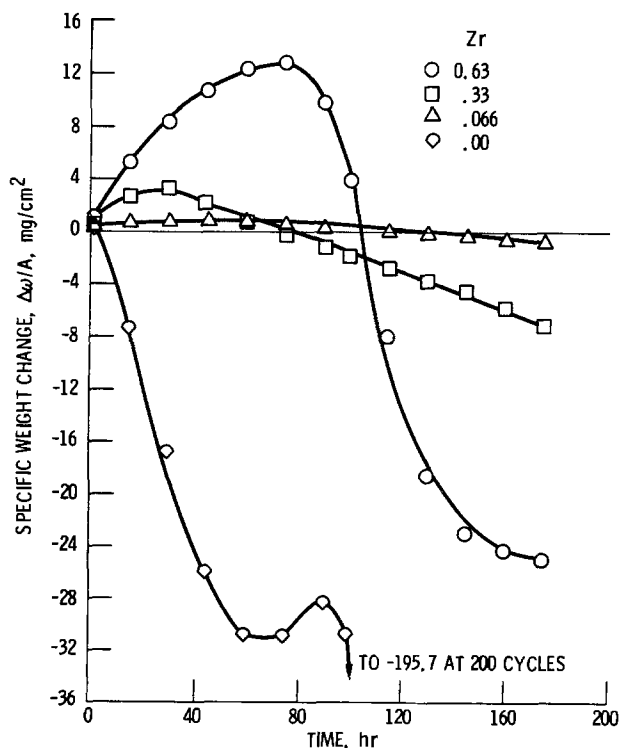


Fig. 5. Effect of Zr on cyclic oxidation of some NiCrAl alloys at 1200°C.

crease with increasing Zr is unclear. Perhaps Zr in solution in the alumina scale has increasingly damaging effects on the mechanical properties of the scale. Or the combination of spalling and high growth rates results in the formation of more spall-prone oxides, e.g., NiO.

To assess a combined effect of oxide growth and spalling, Fig. 9 and 10 should be evaluated. These curves show K_a at 1200° and 1100°C and W_m at 1200°C for 500 hr and 1100°C for 200 hr. W_m is the parameter directly measuring total oxidation attack. The shapes of the W_m curves are similar to the K_a vs. Zr data in that they have minimums in the range of 0.03-0.20 a/o

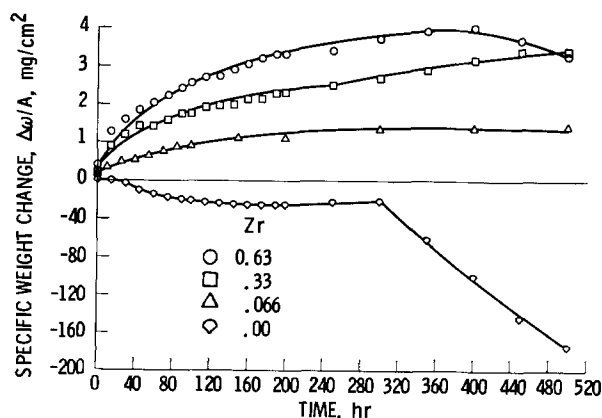


Fig. 6. Effect of Zr on cyclic oxidation of some NiCrAl alloys at 1100°C.

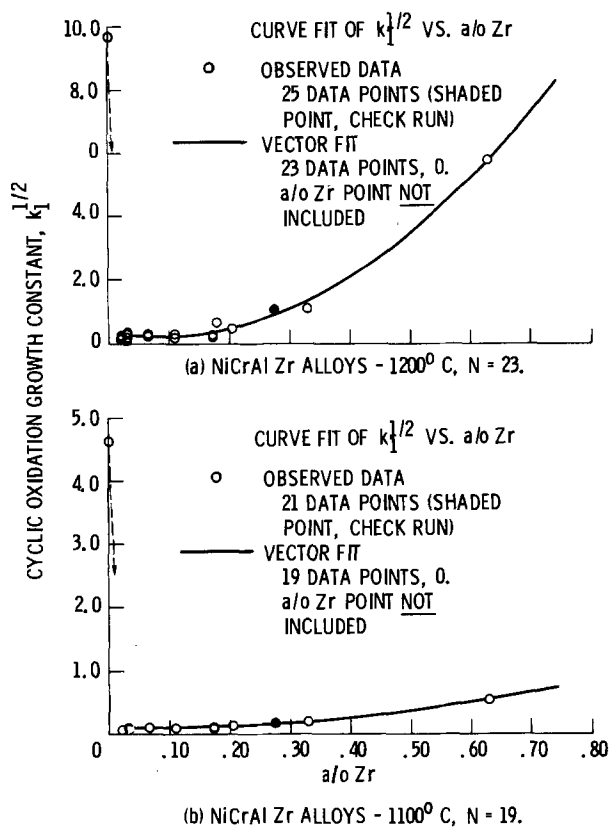


Fig. 7. Derived $k_1^{1/2}$ scale growth constants as a function of a/o Zr in $\gamma/\gamma' + \beta$ -NiCrAl alloys tested in cyclic oxidation at 1200° and 1100°C in static air for 1 hr exposure cycles. $k_1^{1/2}$ values from: $\Delta\omega/A = k_1^{1/2}t^{1/2} - k_2t$ fits.

Zr. As shown in Ref. (12), the relationship of K_a to $k_1^{1/2}$ and k_2 is useful only if W_m is linear in K_a . This relationship was tested and the results plotted in Fig. 11. Since the slopes of $\log(W_m)_T$ vs. $\log K_a$ are essentially unity, K_a may be used to scale the degree of cyclic oxidation attack of these alloys. This emphasizes the spalling mechanism's overriding effect in cyclic oxidation degradation.

Summary of Results

The results obtained during the cyclic oxidation of Ni-(9-20)Cr(15-30)Al- x Zr alloys at 1200° and 1100°C are summarized below:

1. The addition of Zr at concentrations between 0.03 and 0.20 a/o gives optimum cyclic oxidation resistance to NiCrAl alloys.

2. The Zr-free alloys spalled to bare metal during cycling. The addition of zirconium significantly decreased spalling to some critical Zr content of the alloys near 0.066 a/o. The spalling increased gradually with further addition of zirconium above this level. Additions of Zr also changed the nature of spalling, i.e., from spalling at the oxide/metal interface to intra-oxide spalling.

3. $\Delta W/A$ vs. time data for all the alloys were fitted with good correlation to a parabolic model. The derived growth and spalling constants showed strong dependence on the zirconium content of the alloys.

4. A number of kinetic parameters, $k_1^{1/2}$, k_2 , K_a , and W_m , were estimated as a second-degree function of Zr content of the alloys at both 1200° and 1100°C. They all showed minimums ranging from 0.03 to about 0.20 a/o Zr above which they increased with Zr content. Most of the variation of the various parameters could be explained by changes in Zr level alone. Comparable fits based on Cr and Al levels indicated the Cr and Al level effects were minimal.

5. Metallography of the oxidized samples showed some oxide penetration. The amount and type of oxide

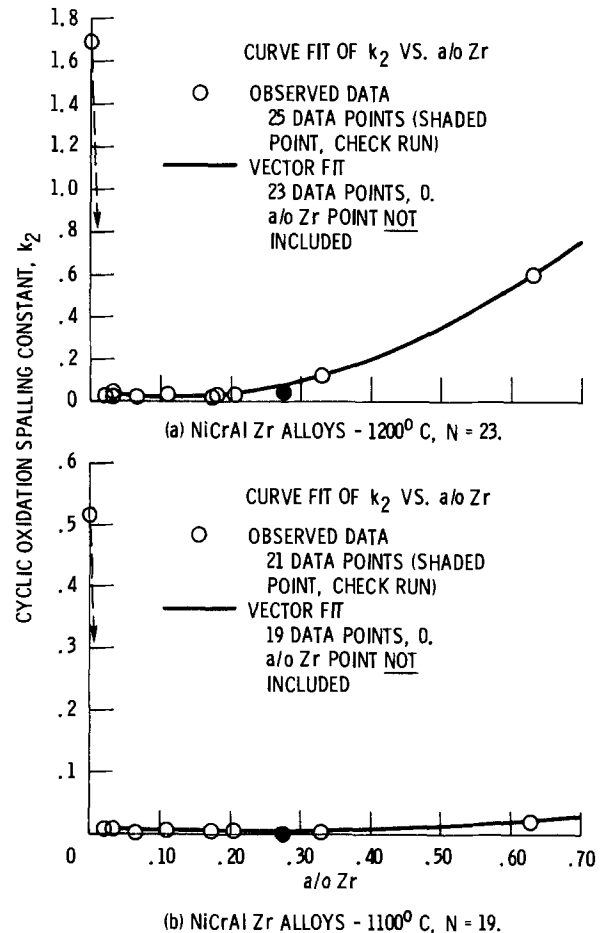


Fig. 8. Derived k_2 scale spalling constant as a function of a/o Zr in $\gamma/\gamma' + \beta$ -NiCrAl alloys tested in cyclic oxidation at 1200° and 1100°C in static air for 1 hr exposure cycles. k_2 values from: $\Delta\omega/A = k_1^{1/2}t^{1/2} - k_2t$ regression fits.

penetration strongly depended on the zirconium content of the alloys. The addition of zirconium significantly decreased the penetration up to about 0.066 a/o. Above this, penetration increased with the Zr content.

6. The alloys studied are basically alumina/ NiAl_2O_4 spinel formers. The zirconium-containing alloys also produced small amounts of ZrO_2 (both cubic and monoclinic form). After prolonged cyclic attack NiO tends to form on the less resistant alloys.

Concluding Remarks

This study confirmed that small additions of Zr to NiCrAl alloys can have a beneficial effect on their cyclic oxidation resistance. While the exact mechanism of such an effect remains unclear, the Zr (similar to Y, etc.) improves the oxide-metal bond so that spalling no longer takes place at the oxide-metal interface, but instead occurs within the oxide. At low Zr levels this results in a marked reduction in metal consumption. However, at higher Zr levels spalling, while still an intra-oxide failure, increases gradually. But even at the highest Zr level studied the metal consumption rates are still well below those of the pure alloy. How this increase occurs needs further investigation, but may be related to changes in the mechanical properties of the oxide. The optimum Zr content for maximum cyclic oxidation resistance was found to be between 0.03 and 0.20 a/o Zr.

Manuscript submitted April 8, 1980; revised manuscript received Aug. 1, 1980.

Any discussion of this paper will appear in a Discussion Section to be published in the December 1981 JOURNAL. All discussions for the December 1981 Discussion Section should be submitted by Aug. 1, 1981.

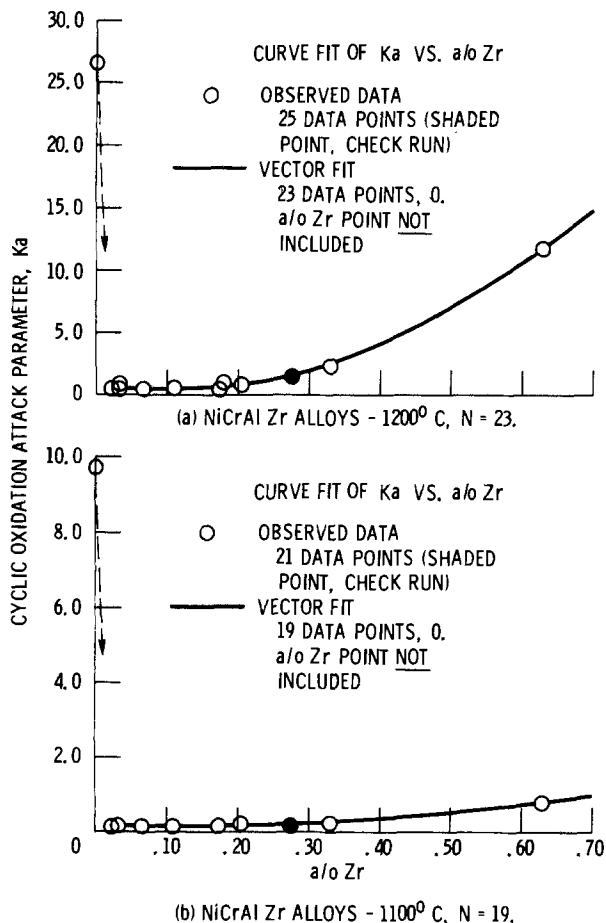


Fig. 9. Derived K_a oxidation attack parameter as a function of a/o Zr in $\gamma/\gamma' + \beta$ -NiCrAl alloys tested in cyclic oxidation at 1200° and 1100° C in static air for 1 hr exposure cycles. $K_a = (k_1^{1/2} + 10k_2)$ where $k_1^{1/2}$ and k_2 from $\Delta\omega/A = k_1^{1/2}t^{1/2} - k_2t$ regression fits.

Publication costs of this article were assisted by NASA-Lewis Research Center.

REFERENCES

- W. Hessenbruck, "Metallen und Legierungen für Hohe Temperaturen," Part 1, J. Springer, Berlin (1940).
- B. Lustman, *Trans. AIME*, **188**, 99 (1950).
- E. J. Felten, *This Journal*, **108**, 490 (1961).
- C. S. Wukusick and J. F. Collins, *Mater. Res. Stand.*, **4**, 637 (1964).
- I. M. Allam, D. P. Whittle, and J. Stringer, *Oxid. Metals*, **12**, 35 (1978).
- J. Stringer, *Metals Rev.*, **11**, 113 (1966).
- J. K. Tien and F. S. Pettit, *Metall. Trans.*, **3**, 1587 (1972).
- C. S. Giggins, B. H. Kear, F. S. Pettit, and J. K. Tien, *ibid.*, **5**, 1685 (1974).
- F. A. Golightly, F. H. Stott, and G. C. Wood, *Oxid. Metals*, **10**, 163 (1976).
- I. G. Wright, Metals and Ceramic Information Center, Battelle Columbus Labs, Ohio, MCIC-72-07 (1972).
- C. S. Giggins and F. S. Pettit, Pratt & Whitney Aircraft, East Hartford, Conn., PWA-5042 (1974).
- C. A. Barrett and C. E. Lowell, NASA TN D-8255 (1976).
- G. J. Santoro and C. A. Barrett, *This Journal*, **125**, 271 (1978).
- A. S. Khan, C. E. Lowell, and C. A. Barrett, *This Journal*, **127**, 670 (1980).
- A. Taylor and R. W. Floyd, *Inst. Metals J.*, **81**, 451 (1952-1953).
- C. A. Barrett and C. E. Lowell, *Oxid. Metals*, **9**, No. 4 (1975).
- C. A. Barrett and A. F. Presler, NASA TN D-8132 (1976).
- J. L. Smialek, *Metall. Trans.*, **9A**, 309 (1978).

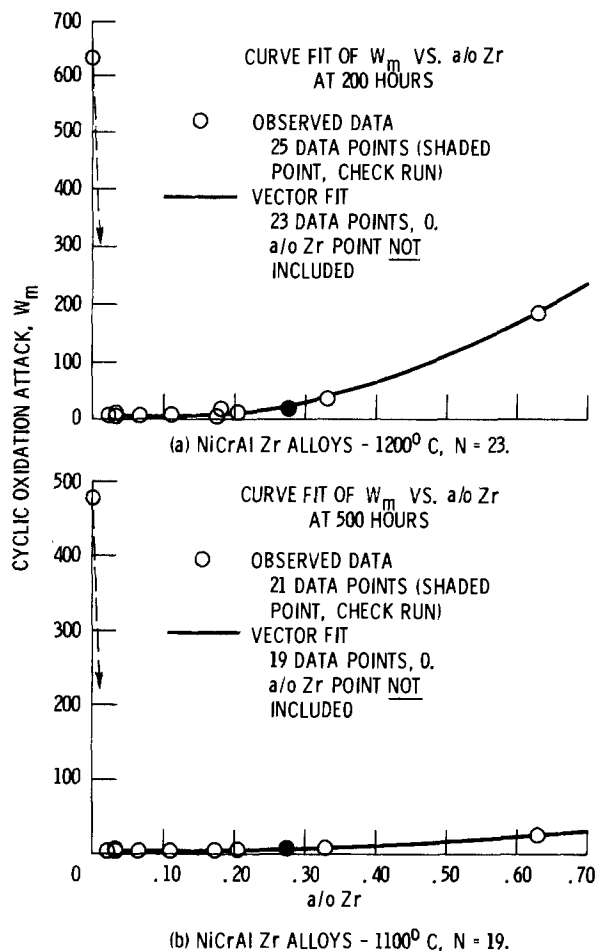


Fig. 10. Estimate of W_m , specific amount of metal consumed as a function of a/o Zr in $\gamma/\gamma' + \beta$ -NiCrAl alloys tested in cyclic oxidation at 1200° and 1100° C in static air for 1 hr exposure cycles. Estimates based on parabolic kinetics analysis, COREST [Ref. (17)].

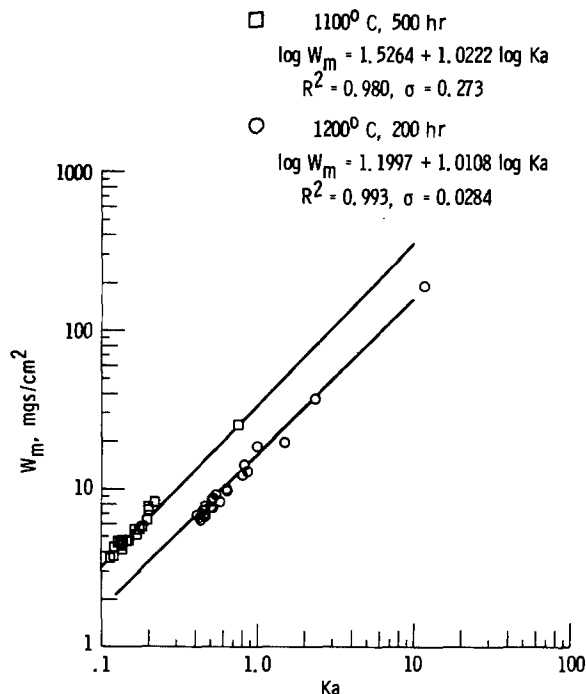


Fig. 11. Relationship of the metal consumed estimate, W_m , to the attack parameter K_a , for $NiAl_2O_4$ forming alloys at 1100° and 1200° C in cyclic oxidation for 500 and 200 hr, respectively. K_a is $(k_1^{1/2} + 10k_2)$ derived from a regression fit of gravimetric data to: $\Delta\omega/A = k_1^{1/2}t^{1/2} - k_2t$ and W_m is derived from the mass balance equation $W_m = W_r - \Delta\omega/A$ using COREST to analyze parabolic kinetics [Ref. (17)].

The Electrochemical Behavior of Scratched Iron Surfaces in Aqueous Solutions

G. T. Burstein* and D. H. Davies

Department of Metallurgy and Materials Science, University of Cambridge, Cambridge, CB2 3QZ, England

ABSTRACT

A technique involving rapid scratching of rotating disk electrodes under potential control is presented and used to examine rapid reaction steps in the anodic behavior of iron in aqueous solutions of pH 0-14. Both anodic and cathodic reaction rates are greatly accelerated during scratching; current densities of up to $\sim 10 \text{ A cm}^{-2}$ of bare metal surface were observed. The results obey Tafel's law and demonstrate the formation of an adsorbed layer of FeOH by: (i) $\text{Fe} + \text{H}_2\text{O} \rightleftharpoons \text{Fe} \cdot \text{H}_2\text{O}_{\text{ads}}$, followed by (ii) $\text{Fe} \cdot \text{H}_2\text{O}_{\text{ads}} \rightarrow \text{FeOH}_{\text{ads}} + \text{H}^+ + e^-$ for $\text{pH} < 7$, or (iii) $\text{Fe} \cdot \text{H}_2\text{O}_{\text{ads}} \rightleftharpoons \text{Fe} \cdot \text{OH}^-_{\text{ads}} + \text{H}^+$, and (iv) $\text{Fe} \cdot \text{OH}^-_{\text{ads}} \rightarrow \text{FeOH}_{\text{ads}} + e^-$ for $\text{pH} > 7$. The layer of adsorbed FeOH is formed at potentials negative with respect to the reversible potentials for oxide formation and exists on the surface during steady-state anodic oxidation of Fe and during cathodic reduction of H^+ from solution. The results are discussed in terms of the mechanism of steady-state dissolution of Fe.

The technique of investigating the electrochemical mechanisms of a bare metal surface reactions in solution by scratching a specimen while it is held under potential control has received little attention since its inception. Measurements of bare surface corrosion potentials on Al made by cutting a lacquered electrode with a ruby stylus (1, 2) showed that the metal adopts a very low potential on cutting; the potential then rises owing to the evolution of hydrogen followed by repassivation. Later work on evaporated Al films (3) confirmed that this behavior is a feature of a bare Al surface and does not arise from stress or heating effects during cutting and subsequent relaxation or cooling. Similar measurements have been made on a large number of metals by high speed drilling with a dentist's drill-bit (4). It was concluded that several metals such as Fe, Co, and Ni have bare surface exchange current densities orders of magnitude greater than those obtained by steady-state techniques. Schwabe *et al.* (5-7) and Tomashov *et al.* (8) used a carborundum disk to scour potentiostatically controlled specimens of Fe, Ni, and stainless steel in aqueous solutions. They showed that the current densities were considerably larger than those observed during steady-state voltammetry. Polarization of scraped Al was performed by Hagyard *et al.* (2). The results agree with more recent work using a scratched rotating disk electrode of Al-7 weight percent Mg (9), showing the first step in the oxidation process to be loss of a single electron to produce Al(I) as an intermediate in both dissolution and passivation. Hydrogen evolution was also found to be greatly accelerated on the bare metal surface. Beck *et al.* (10-12) used a rotating ring scraped disk electrode to show that some Ti(III) is produced during anodic oxidation of Ti.

A large amount of work dealing with the kinetics of the anodic dissolution of Fe in aqueous solutions has been published. Tafel behavior has been observed in a variety of electrolytes with steady-state slopes ranging from 30 to 100 mV depending on the content of the solution and the experimental conditions (13). Mechanisms involving two single electron transfer steps have been proposed by Kabanov *et al.* (14), Bockris *et al.* (15), and Kelly (13). All three mechanisms involve formation of adsorbed FeOH in a rapid electron transfer step with subsequent oxidation of this intermediate as the rate-determining step. Heusler

(16) also proposes rapid formation of adsorbed FeOH as a step in the dissolution reaction, but in his mechanism FeOH acts as a catalyst for a rate-determining two-electron transfer reaction between Fe and OH^- .

No direct evidence has, however, been provided for the formation or existence of FeOH and attempts to describe its formation have been speculative. In this paper we describe the electrochemical behavior of scratched Fe electrodes, showing how the technique elucidates reactions of a bare Fe surface with isolation of the rapid first oxidative step in the anodic dissolution and passivation process.

Experimental

All chemicals were of analytical grade except $\text{K}_2\text{B}_4\text{O}_7 \cdot 4\text{H}_2\text{O}$ which was laboratory grade. Electrolytes were made with doubly distilled water and were deoxygenated with purified nitrogen prior to and during experiments. Rotating disk electrodes were made from deoxidized, high purity iron (supplied by British Iron and Steel Research Association) (C 0.006%, Si 0.001%, S 0.0066%, Al 0.004%, O 0.0017%, N 0.0016%, Mn <0.005%). The metal was spark-cut into disks (diameter 8 mm), cleaned, and mounted into Perspex holders with Araldite. The electrodes were ground to a 1200 grit finish, ultrasonically cleaned, and washed thoroughly in doubly distilled water.

The scratched rotating disk assembly was described by Lees and Hoar (17) and Ford *et al.* (9). It consists of a belt-driven electrode rotated by a d-c motor; rotation rates ω , of up to 200 Hz could be achieved, although the results reported in this paper were taken at 100 Hz. A circular platinum counter-electrode of diameter 50 mm was mounted symmetrically about 60 mm below the working electrode. A small hole cut through the center of the counterelectrode allowed a Luggin capillary to emerge through it from the bottom of the cell. The capillary tip of internal diameter $\sim 1 \text{ mm}$ was positioned $\sim 40 \text{ mm}$ from the working electrode surface, this distance being employed to allow easy access of the scratching stylus. In terms of ohmic resistance measurements of the electrolyte this probe distance is effectively infinity and is consequently easily reproducible. The scratching stylus consisted of a glass-cutter's diamond tool whose steel shank was liberally and completely coated with Araldite. The diamond tool was mounted onto a Perspex arm which was free to rotate about a horizontal axis through the cell. An electromagnet mounted outside the cell attracted a steel bolt which

* Electrochemical Society Active Member.

Key words: rotating disk electrodes, steady-state dissolution of iron.

was screwed into the top of the arm: this held the stylus away from the working electrode surface at a distance of 1-2 mm. On breaking the electromagnet circuit the inertia of the arm allowed the stylus to swing upward, striking the working electrode surface with a tracking weight of $\sim 2g$, then bouncing away when it was again picked up by the reactivated electromagnet. The diamond thus caused a scratch on the rotating metal surface with a contact time of up to ~ 1.8 msec (although generally 1.0 msec), generating a bare metal surface at a rate of 1.6 msec^{-1} , the radius of curvature of the scratch being typically 2 mm. The scratch appeared as an arc of $\sim 1.5 \mu\text{m}$ depth, $30 \mu\text{m}$ width, and ~ 1.6 mm length; its area was therefore $\sim 0.1\%$ of the total working electrode area. Because of the small depth to width ratio of the scratch the cross-sectional curvature was ignored for calculation of the scratch area.

Specimens were held at constant potential with a fast response potentiostat (Wenking Type OPA 69, response time $< 1 \mu\text{sec}$) until a steady-state current density on the electrode as a whole was achieved. The stylus was then released and the current transient arising from the resulting scratch captured in a transient recorder (Datalab Type DL 905), which was triggered either from the electromagnet circuit or from the current transient itself. All transients showed a rise in current (either anodic or cathodic depending on potential) for the period of stylus contact, followed by a decay when the stylus fell away. The direction of flow of current on the scratch was not necessarily the same as that flowing on the remaining electrode surface. The current rise was linear for most of its length (see below), but tailed at the beginning and end. This tailing is due to the changing scratch width when the stylus makes or breaks contact with the electrode and constitutes an insignificant fraction of the total scratch length. Tailing at the top of the transient can also occur because of significant repassivation of the scratch during stylus contact. Experiments were carried out at $298 \pm 2 \text{ K}$.

The current density on the bare surface, i_s , was determined from the gradient of the linear rising part of the current transient by the formula

$$i_s = \frac{1}{2\pi r \omega y} \frac{dI}{dt}$$

where dI is the change in the total current in time dt , r is the radius of the scratch (i.e., its distance from the center of rotation), ω is the rotation rate (Hz), and y is the width of the scratch. Where tailing occurred on the rising part of the transient the maximum slope dI/dt was used to determine i_s since this gives the fastest rate of reaction of the scratch and therefore the most bare surface.

Potentials were measured with respect to a saturated calomel or saturated $\text{Hg}/\text{Hg}_2\text{SO}_4/\text{K}_2\text{SO}_4$ reference electrode and are presented on the normal hydrogen scale. Where necessary, corrections have been made for the liquid junction potential between the working and reference electrolytes by the formula of Henderson (18) and for the ohmic potential drop due to the steady-state base current density (i.e., that current flowing from the disk as a whole) by the formula of Newman (19).

The ohmic potential drop in the electrolyte due to the current from the scratch could not readily be measured because of the nature of the transient electrochemical response of the scratch itself. Instead, the scratch situation was simulated using the edge of a foil electrode made of copper in the following way (20). A sheet of copper foil was mounted edge-on into Araldite to form a rotating disk with the edge of the foil forming the actual electrode and the Araldite forming the rest of the disk. The ohmic po-

tential drop to this electrode was then measured by applying a double galvanostatic pulse and measuring the transient potential response using a similar cell geometry to that described above for scratching experiments. To ensure that the measured potential change was indeed ohmic the height of the first current pulse was varied while that of the second pulse (used to determine the ohmic resistance) was held constant. Thus pulsing first from 0 to 1 mA and then directly to 2 mA gave a similar resistance as pulsing first from 0 to 9 mA and then directly to 10 mA. Similarly the measured resistance was independent of the height of the second pulse itself. In this way values of the ohmic resistance were determined as a function of foil length, foil width, and solution conductivity, allowing values representing the dimensions of the scratches to be interpolated. The results agree well with a theoretical solution to the problem full details of which will be presented elsewhere (20).

Results

A typical graph of the bare surface current density i_s is shown in Fig. 1 as a function of potential. This type of graph is referred to as a "bare surface polarization curve" (even though the surface may not be fully bare at all potentials). The bare surface polarization curve lies at current densities which are orders of magnitude greater than those of the steady-state polarization curve (also shown in Fig. 1 for the same electrolyte). Both the anodic and cathodic regions of i_s are shown, with the mixed potential E_{ms} of the bare surface at -860 mV (NHE). This value is more negative than that for the steady-state curve [$E_m = -615 \text{ mV}$ (NHE)]. The large acceleration of both the anodic and cathodic reactions on scratching was found for all electrolytes. Figures 2 and 3 show

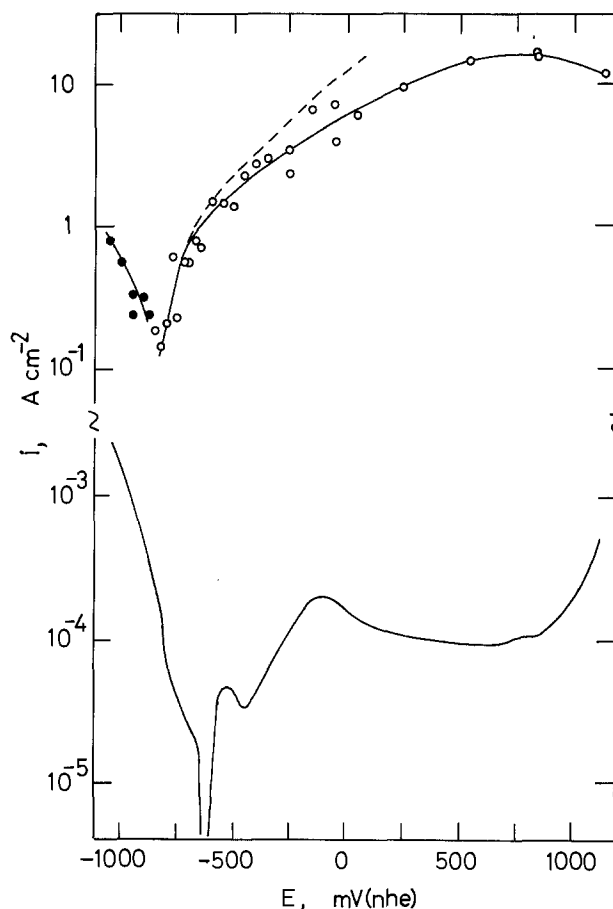


Fig. 1. Steady-state (lower) and bare surface (upper) polarization curves for Fe in $1.0M \text{ K}_2\text{CO}_3$, pH 11.6. Steady-state curve swept at 15 mV sec^{-1} . \circ , anodic; \bullet , cathodic. Broken line shows ohmic potential correction for the scratch surface.

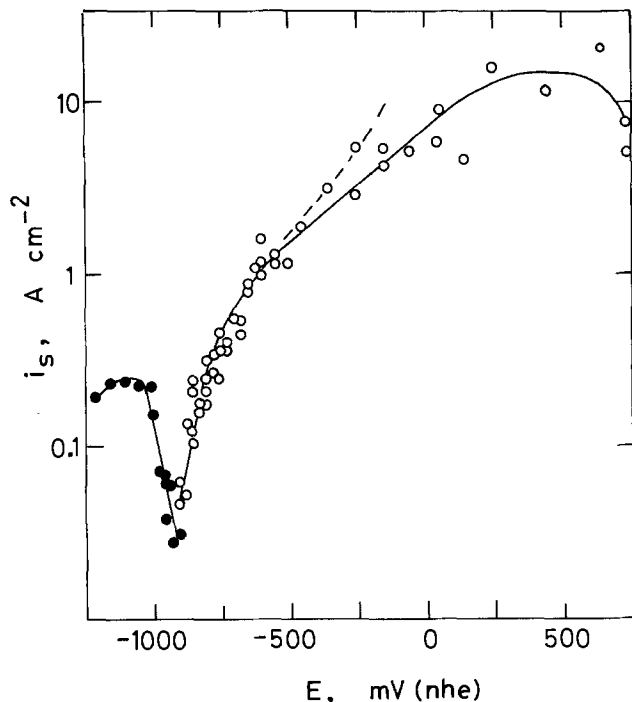


Fig. 2. Bare surface polarization curve for Fe in 1.0M KOH, pH 14. \circ , anodic; \bullet , cathodic. Broken line shows ohmic potential correction for the scratch surface.

bare surface polarization curves in 1.0M KOH, pH 14 and in 1.0M H_2SO_4 , pH 0, respectively. Similar trends are shown; the current density increases in both the anodic and cathodic directions from E_{ms} . For H_2SO_4 the potential range is restricted because of the high base currents at higher anodic and cathodic potentials, which obscure the current transient due to scratching. There is an effect of pH, with E_{ms} lying at more negative values for higher pH. This is shown for an intermediate pH range in Fig. 4 for acetate (pH 4.9), borate (pH 7.6), and bicarbonate (pH 9.8) solutions.

All bare surface polarization curves show a linear Tafel region over approximately 1-2 orders of magnitude in i_s from E_{ms} in the anodic direction. The Tafel parameters are presented in Table I for each electrolyte. Anodic Tafel slopes are all in the range 121 ± 15 mV, the error bar representing the maximum deviation from this value. Owing to the scatter in the experimental points on the bare surface polarization curves the Tafel slope for each curve was measured by linear regression successively over a progressively increasing potential range: those presented in Table I were those which showed the highest correlation coefficient with the data points.

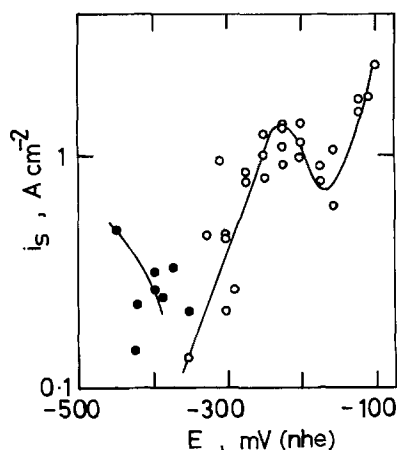


Fig. 3. Bare surface polarization curve for Fe in 1.0M H_2SO_4 , pH 0. \circ , anodic; \bullet , cathodic.

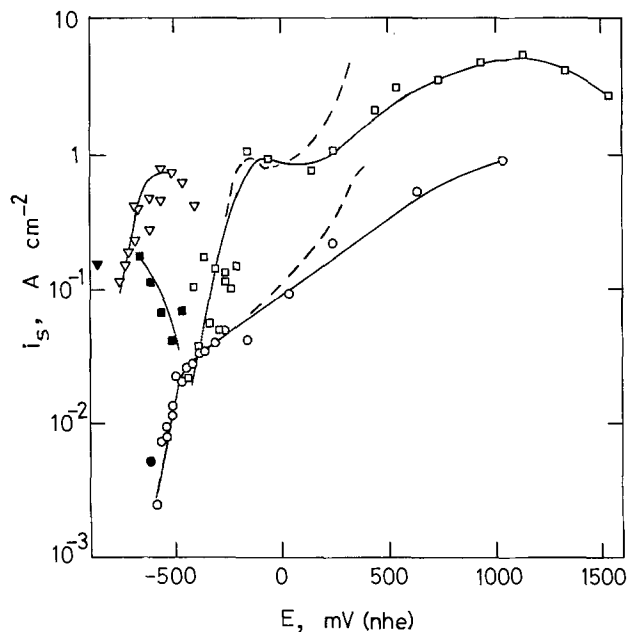


Fig. 4. Bare surface polarization curves for Fe in: 0.5M H_3BO_3 , 0.05M $\text{K}_2\text{B}_4\text{O}_7$, pH 7.6 (\circ , \bullet); 0.75M HOAc, 0.75M NaOAc, pH 4.9 (\square , \blacksquare); 0.5M KHCO_3 , 0.5M K_2CO_3 , pH 9.8 (∇ , \blacktriangledown). White points anodic, black points cathodic. Broken lines show ohmic potential corrections for the scratch surfaces.

Corrections for the ohmic resistance of the electrolyte arising from the current density on the scratch were made to all anodic bare surface polarization curves using the values obtained by the method described above. These corrections are shown as the broken lines in Fig. 1-5. In every case the anodic Tafel region is unaffected by such corrections, although at current densities higher than the Tafel regions significant corrections are observed. Thus, for example in Fig. 2 at an anodic scratch current density of 300 mA cm^{-2} (representing the highest point of Tafel linearity), the ohmic potential drop due to the scratch is 8 mV, whereas at 10 A cm^{-2} the value is 267 mV. In no case does this ohmic potential correction enable the linear Tafel region to be extended to higher anodic current densities.

The effects of bicarbonate anions were investigated by comparing bare surface polarization curves in bicarbonate and borate electrolytes of the same pH (8.8), and this is shown in Fig. 5. The linear Tafel region is extended to higher potentials in the bicarbonate, but does not accelerate the Tafel region itself. Thus the Tafel regions in the two electrolytes are common. Part of this difference arises, of course, from the different ohmic resistances of the two electrolytes. However, that determined for the bicarbonate electrolyte (145Ω) is only 0.27 of that determined for the borate electrolyte (547Ω), and this difference is insufficient to account for the order of magnitude difference in the maximum current density in the Tafel region (300 and 25 mA cm^{-2} , respectively).

Table I. Parameters for the anodic behavior of scratched iron electrodes in various electrolytes

| Electrolyte | pH | E_{ms} [mV (NHE)] | $\partial E/\partial \log i_s$ (anodic) (mV) | i_0 (C cm^{-2}) |
|--|------|---------------------------|--|---------------------------------|
| 1.0M H_2SO_4 | 0 | -365 | 114 | 98 |
| 0.75M HOAc, 0.75M NaOAc | 4.9 | -445 | 128 | 61 |
| 0.5M H_3BO_3 , 0.05M $\text{K}_2\text{B}_4\text{O}_7$ | 7.6 | -545 | 109 | 15 |
| 0.32M H_3BO_3 , 0.19M $\text{K}_2\text{B}_4\text{O}_7$ | 8.8 | -705 | 112 | 11 |
| 0.75M KHCO_3 , 0.05M K_2CO_3 | 8.8 | -705 | 112 | 69 |
| 0.5M KHCO_3 , 0.5M K_2CO_3 | 9.8 | -765 | 132 | 117 |
| 1.0M K_2CO_3 | 11.6 | -865 | 124 | 108 |
| 1.0M KOH | 14.0 | -920 | 136 | 149 |

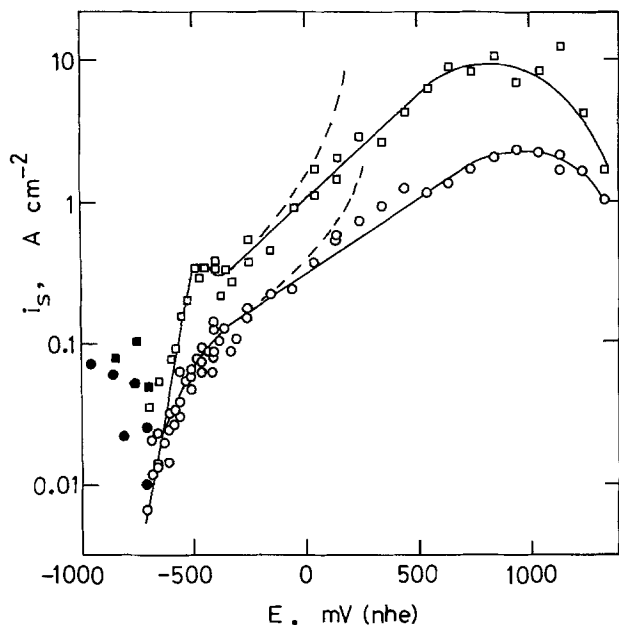


Fig. 5. Bare surface polarization curves for Fe at pH 8.8. 0.32M H_3BO_3 , 0.19M $\text{K}_2\text{B}_4\text{O}_7$ (\circ , \bullet); 0.75M KHCO_3 , 0.05M K_2CO_3 (\square , \blacksquare). White points anodic, black points cathodic. Broken lines show ohmic potential corrections for scratch surfaces.

At potentials more anodic than the linear Tafel regions all bare surface polarization curves tend toward higher values of $\partial E/\partial \log i_s$, becoming almost independent of E at high potentials.

Values of E vs. pH at constant i_s were measured at $i_s = 100 \text{ mA cm}^{-2}$. This current density lies in the linear Tafel region for all electrolytes except those containing borate for which the Tafel regions were extrapolated to 100 mA cm^{-2} . The values are shown in Fig. 6. They give $\partial E/\partial \text{pH} = 0$ for $\text{pH} < 7$, $\partial E/\partial \text{pH} = -114 \text{ mV}$ for $7 < \text{pH} < 11.7$, and $\partial E/\partial \text{pH} = 0$ for $\text{pH} > 11.7$.

Cathodic scratch transients, representing reduction of hydrogen ions or water on the scratch surface, showed very large scatter. Values of i_s as a function of E in the cathodic region were therefore in general difficult to quantify. Figure 2 shows a linear Tafel

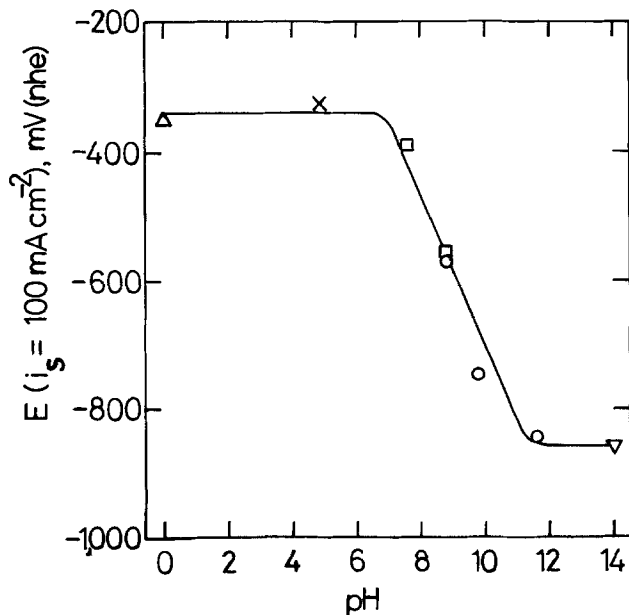
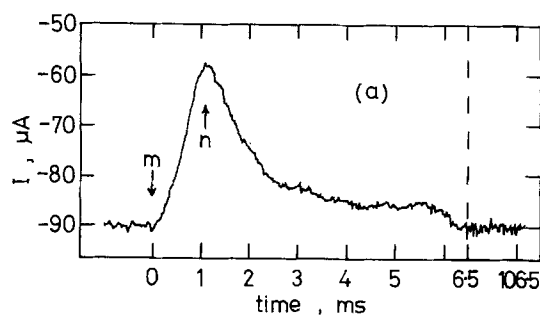


Fig. 6. Dependence of potential at constant anodic current density ($i_s = 100 \text{ mA cm}^{-2}$) on pH. ∇ , H_2SO_4 ; \times , HOAc , NaOAc ; \square , H_3BO_3 , $\text{K}_2\text{B}_4\text{O}_7$; \circ , KHCO_3 , K_2CO_3 ; ∇ , KOH .

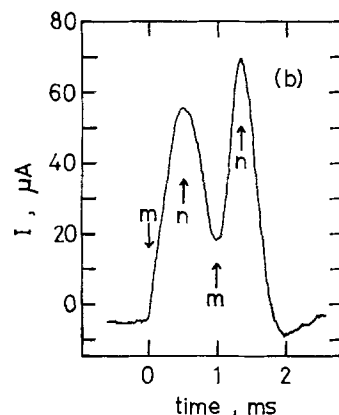
region in the hydrogen evolution reaction with a Tafel slope of -116 mV . The potential range over which the cathodic process could be detected was small since the currents on the electrode as a whole quickly become quite large with increasing overpotential: large base currents tend to obscure the small transients arising from the scratch.

Three types of anodic current transient are depicted in Fig. 7. Type A scratches were observed within the Tafel regions, type B scratches at the upper potential limits of the Tafel regions, and type C scratches only at potentials higher than the Tafel regions. Some idea of the origins of these three basic types of scratches may be obtained by considering the value of q_p which represents the charge density that has flowed from the scratch at the time that the stylus leaves the surface. Transients of type A were obtained where $q_p \ll 100 \mu\text{C cm}^{-2}$; those of type B gave $q_p \sim 100 \mu\text{C cm}^{-2}$; those of type C gave $q_p \gg 100 \mu\text{C cm}^{-2}$. Values of q_p for the top of each Tafel region are shown in Table I.

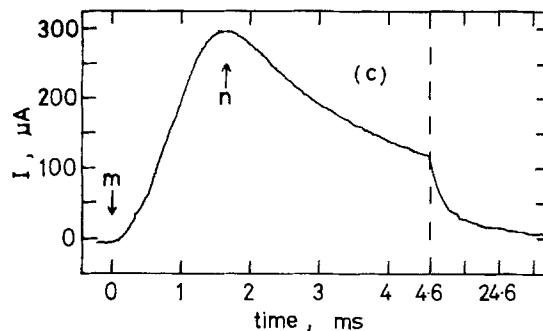
In some instances the rising current on the transient showed two or three small peaks or points of inflection separated by times of $< 1 \text{ msec}$. This is probably due to a stick-slip type of scratching process, where the



a. 0.75M KHCO_3 , 0.05M K_2CO_3 , pH 8.8, $E = -655 \text{ mV}$. Type A



b. 1.0M K_2CO_3 , pH 11.6, $E = -805 \text{ mV}$. Type B



c. 0.75M KHCO_3 , 0.05M K_2CO_3 , pH 8.8, $E = -155 \text{ mV}$. Type C

Fig. 7. Typical current transients due to scratching. m, scratching commences; n, scratching complete. Broken lines indicate change in time scale.

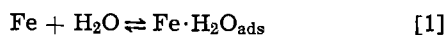
debris may pile up in front of the stylus to a sufficient extent for the stylus to have to jump over the pile before continuing the scratch. However, microscopic examination of the scratch scars showed little evidence of this. Similarly there was very little debris piled up at the sides of the scars and none at the ends. While the exact mode of machining of this type is still under investigation, it appears that the metal is removed in very small pieces rather than in long strips since no strips of debris were found in the cell after experiments. As such, the added area of bare metal caused by the still-electrically coupled debris in front of the stylus during scratching is small. It is worth noting, however, that much of the scatter in the results probably arises from variation in scratch width and depth during a run (giving scatter in the scratch area) as well as from pile-up of debris.

The bare surface current densities were unaffected by electrode rotation rate ω (and therefore scratching rate) for 200 Hz $> \omega >$ 16.7 Hz. Rotation rates less than 16.7 Hz generally gave current transients too small to quantify while for $\omega >$ 150 Hz visible turbulence occurred. The work presented here was performed at 100 Hz.

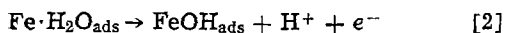
Discussion

Comparison of the values of E_{ms} shown in Table I with the equilibrium potentials for oxide formation given by Pourbaix (21) shows that in the intermediate pH range Fe oxidizes anodically below the minimum theoretical potential for oxide formation. Bearing in mind that the total charge passed from the scratch $q_t > 2q_p$ (q_p represents only that fraction passing during stylus contact) then, with the exception of the two borate electrolytes, the charge densities shown in Table I are too large for i_s to be controlled solely by nonfaradaic double layer charging processes. For the two borate electrolytes the top of the Tafel regions are probably controlled by the ohmic resistance of the electrolytes, as was indicated by the fact that no type B transients were observed. In other words for the borate electrolytes $q_t \gg 2q_p$. The charge densities clearly must contain a nonfaradaic double layer component; nevertheless the bare surface current densities are controlled by charge transfer electrochemical reactions. In the anodic Tafel region which exists in all electrolytes (see Table I) the charge transfer reaction is the first oxidative step in the total dissolution (or passivation) of Fe.

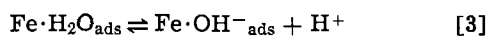
The initial step must be the adsorption of water onto the fresh metal surface which proceeds rapidly to completion immediately behind the stylus



Reaction [1] is followed by one of two mechanisms as follows



or



By considering the coverage of adsorbed water to be complete, and the coverage of FeOH to be small, reaction [2] gives

$$i_s = Fk_2 \exp \left[\frac{\beta FE}{RT} \right] \quad [5]$$

and $\partial E/\partial \log i_s = 118$ mV, $\partial E/\partial \text{pH} = 0$ for $\beta = 0.5$. Reaction [3] forms a rapid equilibrium prior to reaction [4], with

$$K_3 = \theta[\text{H}^+]/(1 - \theta) \quad [6]$$

where θ is the coverage of adsorbed OH^- , and

$$i_s = Fk_4\theta \exp \left[\frac{\beta FE}{RT} \right] \quad [7]$$

provided the coverage of the oxidized product FeOH

is not large. In practice, because of the scatter in the results, this means a coverage of FeOH of $< \sim 0.5$. For $\theta \rightarrow 0$, $\theta[\text{H}^+] \rightarrow K_3$ (from Eq. [6]), whence

$$i_s = Fk_4K_3[\text{H}^+]^{-1} \exp \left[\frac{\beta FE}{RT} \right] \quad [8]$$

and $\partial E/\partial \log i_s = 118$ mV, $\partial E/\partial \text{pH} = -118$ mV for $\beta = 0.5$. For $\theta \rightarrow 1$, Eq. [7] gives

$$i_s = Fk_4 \exp \left[\frac{\beta FE}{RT} \right] \quad [9]$$

and $\partial E/\partial \log i_s = 118$ mV, $\partial E/\partial \text{pH} = 0$ for $\beta = 0.5$. In the above equations K_j and k_j are the equilibrium and rate constants, respectively, for reaction j . It should be noted that $\theta = 1$ does not necessarily define a complete monolayer of adsorbed OH^- (which would imply enormous lateral repulsion between adjacent adsorbed ions), but rather the coverage beyond which the anodic reaction can no longer be accelerated.

Three regions of anodic behavior are observed from Fig. 6 (and Table 1), all in excellent agreement with the equations above. Between pH 0 and 7, Eq. [5] controls the bare surface reaction rate, and reaction [2] (pH independent) is rate controlling. For $7 < \text{pH} < 11.7$ the scheme represented by reactions [3] and [4] controls the reaction rate, with $\theta \rightarrow 0$; the rate is given by Eq. [8], which is first order in pH. For $\text{pH} > 11.7$, $\theta \rightarrow 1$ and Eq. [9] (pH independent) is rate determining. In practice, of course, there must be a continuous change through the $\text{pH} = 11.7$ region controlled by the Langmuir isotherm given in Eq. [6], which would cover 1 to 2 units of pH, for which

$$i_s = Fk_4K_3([\text{H}^+] + K_3)^{-1} \exp \left[\frac{\beta FE}{RT} \right] \quad [10]$$

The following points should be realized in the above mechanisms. (i) Reaction [1] must proceed rapidly and to completion. In this sense the term "bare surface" actually applies to that surface on which reaction [1] has already occurred. If this were not the case a void would form on the metal surface immediately behind the stylus and render that part of the scratch surface electrochemically inactive. (ii) Reactions [3] and [4] must proceed through OH^- adsorbed by rapid equilibration on the surface (reaction [3]). A reaction of the type $\text{Fe} + \text{OH}^-_{\text{aq}} \rightleftharpoons \text{Fe} \cdot \text{OH}^-_{\text{ads}}$ would have a diffusion-controlled rate given by $i = FD\Delta c/\delta$, where D is the diffusion coefficient of OH^- and δ the diffusion layer thickness. For $\text{pH} = 7$ and $\delta = 10^{-3}$ cm, $i \approx 10^{-5}$ A cm $^{-2}$, which is far less than the observed bare surface current densities. (iii) In the Tafel regions the coverage of adsorbed FeOH which is formed during scratching must be sufficiently low to be ignored for the purposes of the kinetic treatment of the mechanisms above. In this connection it is to be noted that the maximum charge densities which flow from the surface, q_p , are all less than that required to oxidize a monolayer of Fe. One would expect the charge required to oxidize a monolayer of Fe to FeOH to be around 200 $\mu\text{C cm}^{-2}$, depending on which crystal orientations are exposed by scratching. Bearing in mind that (i) the surface density of Fe in FeOH is unknown, but probably less than that in the substrate and (ii) the roughness factor of the surface is unknown, but probably between 1.5 and 2 (22), the maximum values of q_p shown in Table I are all significantly less than one monolayer of FeOH. These values are observed at the upper potential limit of the Tafel regions; at lower potentials q_p (given approximately by $0.5 i_{s,c} t_c$, where t_c is the contact time of the stylus) is also lower. At potentials below the steady-state reversible potentials reactions [2] and [4] must of course cease when the coverage of FeOH reaches one monolayer.

The upper limit of Tafel linearity can be controlled by a number of factors. (i) A significant ohmic potential drop in the electrolyte occurs at higher bare surface current densities: thus the borate electrolytes show low values of q_p (see Table I) and do not show type B transients (see Fig. 7b). It is, however, significant in this respect that correction of the polarization curves for the ohmic potential drop does not extend the Tafel lines to higher potentials (see Fig. 1-5). (ii) A significant coverage of FeOH during scratching would cause the rate of reactions [2] and [4] to decrease. At higher potentials where the values of q_p are large (see Fig. 7c) the values of i_s are not true bare surface current densities. (iii) Above the steady-state reversible potential for Fe(II) formation partial coverage of a thicker film containing Fe(II) can also occur during scratching. In either case (ii) or (iii) the true bare surface current density above the Tafel region is actually greater than that shown in Fig. 1-5, but the rate of scratching cannot outrun the rate of reaction. However, some bare surface must always exist during scratching. The rate of scratching would have to be increased enormously in order to extend the range of linear Tafel behavior to significantly higher potentials. This has been noted previously (4) during studies of open-circuit scrape potentials.

Of the several mechanisms proposed for the steady-state anodic dissolution of Fe (13-16), most have involved either reactions [2] or [4] as initial electron transfer steps in the process. This arises from steady-state Tafel parameters that have previously been observed, which range upward from 30 mV. Despite the diversity of previous results there seems to be general agreement that steady-state measurements involve subsequent reactions as rate determining and that these reactions are preceded by a single electron transfer step which is fast. The above results support these theories and establish the kinetics of the first step; subsequent steps are slow compared with the rate of bare surface reaction from the scratched electrode, as demonstrated by the high current densities in Fig. 1-5. The fact that the scratched iron electrode reacts anodically below its equilibrium potentials also indicates that some early oxidation step is occurring, a reaction which has a reversible potential more negative than those quoted by Pourbaix (21) for the iron oxides. A similar effect has been observed for the anodic behavior of scratched silver electrodes (22); in this case the reversible potential for the reaction of Ag to form a monolayer of adsorbed AgOH was isolated. In the present work the reversible potential for FeOH formation cannot be found since it lies in the region obscured by the accelerated hydrogen discharge reaction. These first electrochemical steps shown by reactions [1]-[4] are followed by the slower steps measured in the steady state, in which FeOH on the surface is oxidized to Fe(II) in solution or as a surface film. It should be noted that reactions [1]-[4] are precursor reactions to both dissolution and passivation and that a high coverage of FeOH occurs. Whereas dissolution occurs exclusively through these reactions (in the absence of electroactive anions), passivation occurs by oxidation of the FeOH layer to produce a thicker film of some higher oxide of Fe. Once this passive film is formed, the FeOH layer is no longer in contact with the electrolyte solution. In this case it may remain as an interfacing layer between the metal and the film, or it may be entirely oxidized and disappear. The thickening of the passive film may therefore not necessarily require the formation of the precursor FeOH.

Interference by the accelerated hydrogen discharge reaction on the scratched surface prevents measurement of E_o and hence i_o (reversible potential and exchange current density, respectively) for reactions [2] and [4]. Nevertheless, the fact that these reactions

occur at very low potentials means that the adsorbed FeOH species must exist on the metal at potentials where Fe(II) can be reduced from solution. The adsorbed layer must thus be an intermediate in low overpotential electroreduction of Fe(II) and H^+ from solution. Scratching of Fe at potentials in the cathodic regions shown in Fig. 1-5 shows greatly accelerated H^+ reduction current densities, with a Tafel slope (at pH 14) of 116 mV. The reaction involved is probably the reduction of a proton, *viz.*, $H_3O^+ + e^- \rightarrow H + H_2O$, but now it occurs on the bare metal surface instead of a surface covered by a layer of FeOH, which exists during steady-state hydrogen evolution. It would be expected that below the reversible potential for FeOH formation cathodic reduction processes would not be significantly accelerated by using scratched metal electrodes. For Fe these potentials are inaccessible because of the large proton reduction current densities which occur on the remaining unscratched area of the electrode.

It is of some consequence that the anodic transfer coefficients, β , for reactions [2] and [4] do not differ significantly from 0.5, despite the high current densities of up to 1 A cm^{-2} which emanate from the scratched surface (see Fig. 1-5). It is possible that the exchange current densities for these reactions are high and the anodic Tafel regions shown in Fig. 1-5 for the scratched surfaces do not represent very high overpotentials [in agreement with the conclusions of Andersen *et al.* (4)].

While some difference in ohmic potential drop occurs between borate and bicarbonate electrolytes of similar pH, this difference is insufficient to account quantitatively for the extension of the linear Tafel range by bicarbonate, as shown in Fig. 5. Bicarbonate does not affect the rate of bare surface reaction, but does appear to hold the surface bare for a longer period of time. In another paper we have shown (23) that HCO_3^- forms soluble complexes with Fe(II) and thus strongly affects the steady-state anodic dissolution and passivation of Fe. The effects in the scratching experiments are probably to accelerate the oxidation of FeOH to dissolved Fe(II), thereby allowing more charge to flow before the surface becomes covered by FeOH. Other anions may affect the actual bare surface reaction itself (*e.g.*, chloride) and these are presented in another paper (24).

It has been shown that rapid scratching of electrodes under potentiostatic control enables fast steps in electrode reactions to be elucidated. Whereas potentiostatic pulse experiments also measure fast reaction steps, the case of the anodic behavior of Fe could not be revealed by pulse measurements since cathodization of the metal prior to the anodic pulse either produces hydrogen which can then be oxidized, or does not reduce the FeOH layer. Further, potentiostatic pulse experiments are particularly susceptible to impurities adsorbed on the electrode surface. In scratching experiments trace impurities from the electrolyte are not important, and those arising from preparation of the metal surface are scratched away. It has been suggested earlier (4) from open-circuit scraping experiments on some metals that inhibiting films or layers of molecules occur on active metals like Fe, such that the slow step in the metal oxidation reaction in aqueous solution is not the transfer of an ion into solution from the bare metal surface. The present results confirm the existence of such a film (FeOH) on Fe and demonstrate the suitability of the scratching technique to elucidate the kinetics of its formation.

Conclusions

1. The scratching of metals under potentiostatic control can reveal the presence of intermediates in electrode reactions, and elucidate the kinetics of fast electron transfer processes.

2. Anodic and cathodic reactions on Fe are greatly accelerated when the metal is scratched to remove surface films.

3. The kinetics of the first oxidative step in the anodic dissolution and passivation of Fe over the pH range 0-14 follows Tafel's law with a single electron transfer. For $pH < 7$ reaction [2] occurs, and the process is independent of pH. For $pH > 7$ the reaction occurs by Eq. [3] and [4], with first-order kinetics in OH^- in the pH range 7-11.7 and zero order for $pH > 11.7$.

4. The formation of FeOH by reactions [2], [3], and [4] occurs at potentials below the thermodynamic reversible potentials for equilibrium film formation. The FeOH layer is an intermediate in the anodic dissolution and passivation of Fe and is also an intermediate in the cathodic reduction of H^+ and Fe^{2+} from solution, since it exists at potentials where each of these processes can occur.

5. Deviation from linear Tafel behavior in the anodic bare surface polarization curve results from rapid partial repassivation or from the ohmic potential drop in the electrolyte.

Acknowledgment

We are grateful to the Ernst Oppenheimer Fund for the financial support of D.H.D.

Manuscript submitted Oct. 19, 1979; revised manuscript received July 8, 1980. This was Paper 221 presented at the Los Angeles, California, Meeting of the Society, Oct. 14-19, 1979.

Any discussion of this paper will appear in a Discussion Section to be published in the December 1981 JOURNAL. All discussions for the December 1981 Discussion Section should be submitted by Aug. 1, 1981.

REFERENCES

1. T. Hagyard and J. R. Williams, *Trans. Faraday Soc.*, **57**, 2288 (1961).
2. T. Hagyard and W. B. Earl, *This Journal*, **114**, 694 (1967).
3. T. Hagyard, W. B. Earl, K. J. Kirkpatrick, and I. G. Watson, *ibid.*, **113**, 962 (1966).
4. T. N. Andersen, J. L. Anderson, and H. Eyring, *J. Phys. Chem.*, **73**, 3562 (1969).
5. K. Schwabe, *Z. Phys. Chem.*, **205**, 304 (1955).
6. K. Schwabe, *ibid.*, **214**, 6 (1960).
7. E. Kunze and K. Schwabe, *Corros. Sci.*, **4**, 109 (1964).
8. N. D. Tomashov and L. P. Vershinina, *Electrochim. Acta*, **15**, 501 (1970).
9. F. P. Ford, G. T. Burstein, and T. P. Hoar, *This Journal*, **127**, 1325 (1980).
10. T. R. Beck, *Electrochim. Acta*, **18**, 807 (1973).
11. T. R. Beck, *ibid.*, **18**, 815 (1973).
12. T. R. Beck, *Corrosion*, **30**, 408 (1974).
13. E. J. Kelly, *This Journal*, **112**, 124 (1965).
14. B. Kabanov, R. Burstein, and A. Frumkin, *Discuss. Faraday Soc.*, **1**, 259 (1947).
15. J. O'M. Bockris, D. Drazic, and A. R. Despic, *Electrochim. Acta*, **4**, 325 (1961).
16. K. E. Heusler, *Z. Elektrochem.*, **62**, 582 (1958).
17. D. J. Lees and T. P. Hoar, *Corros. Sci.*, In press.
18. D. J. G. Ives and G. J. Janz, "Reference Electrodes," p. 54, Academic Press, New York (1961).
19. J. Newman, *This Journal*, **113**, 501 (1966).
20. H. J. Pearson, G. T. Burstein, and R. C. Newman, Submitted to *This Journal*.
21. M. Pourbaix, "Atlas of Electrochemical Equilibria in Aqueous Solutions," p. 307, Pergamon, London (1966).
22. G. T. Burstein and R. C. Newman, *Electrochim. Acta*, **25**, 1009 (1980).
23. D. H. Davies and G. T. Burstein, *Corrosion*, **36**, 416 (1980).
24. G. T. Burstein and D. H. Davies, *Corros. Sci.*, In press.

Use of Activity Coefficients to Calculate the Equilibrium Conditions within a Localized Corrosion Cell on Iron

E. McCafferty*

Naval Research Laboratory, Washington, D.C. 20375

ABSTRACT

The equilibrium electrochemical conditions within a localized corrosion cell on iron have been calculated using activity coefficients to take into account the high ionic concentrations which occur within the occluded corrosion cell. The calculations utilize Pourbaix's model that the stable solid phases within a corrosion pit, crevice, or stress-corrosion crack are Fe, Fe_3O_4 , and $FeCl_2 \cdot 4H_2O$. The calculated equilibrium conditions are: $E = -0.385V$ vs. NHE, $pH = 5.2$, $[Fe^{++}] = 4.5$ moles/liter, and $[Cl^-] = 9.0$ moles/liter. If the occluded corrosion cell is limited to atmospheric pressure conditions, the internal conditions are calculated to be: $E = -0.281V$ vs. NHE, $pH = 4.8$, $[Fe^{++}] = 4.5$ moles/liter, and $[Cl^-] = 9.0$ moles/liter. With both sets of results, the internal pH is only slightly higher and the electrode potential slightly more negative than in the original Pourbaix calculations. Thus, the calculated results support the basic ideas first proposed by Pourbaix.

Pitting, crevice corrosion, stress-corrosion cracking, and other forms of localized corrosion all develop a local electrolyte of different chemical composition than the bulk solution. These compositional differences, in-

cluding changes in local pH, arise due to a limited mass transport from the "occluded corrosion cell" (1).

A guide as to the equilibrium conditions within such "occluded corrosion cells" for iron has been given by the thermodynamic calculations of Pourbaix (2). Pourbaix has suggested that the internal electrolyte within an occluded corrosion cell on iron is highly concen-

* Electrochemical Society Active Member.

Key words: iron, localized corrosion, thermodynamics, activity coefficients.

trated in both Fe^{++} and Cl^- ions. The proposed solid phases are $\text{FeCl}_2 \cdot 4\text{H}_2\text{O}$ and Fe_3O_4 , existing as deposits on the iron substrate. Based on thermodynamic data, and as a first approximation, Pourbaix has calculated the equilibrium conditions within localized corrosion cells involving iron to be

$$\left. \begin{aligned} E &= -0.368\text{V vs. NHE} \\ \text{pH} &= 4.80 \\ [\text{Cl}^-] &= 556 \text{ moles/liter} \\ [\text{Fe}^{++}] &= 278 \text{ moles/liter} \end{aligned} \right\} [1]$$

These calculations predict concentrations of Fe^{++} and Cl^- which are enormously high and far in excess of the solubility (4.5 moles/liter) of ferrous chloride. This particular result seems to be generally overlooked. This is probably because of the agreement between calculated and experimental values of E and pH , as has been reported for a number of different types and instances of localized corrosion of iron (3-9), see Table I. Nevertheless, the calculated equilibrium values of internal E and local pH are directly related to the concentrations of Fe^{++} and Cl^- . In the strictest sense then, an overestimation of the concentrations of Fe^{++} and Cl^- must impart some error to the calculation of the local pH and internal electrode potential.

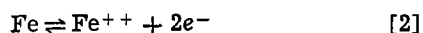
Pourbaix has suggested that the high calculated values of Fe^{++} and Cl^- arise from the failure of dilute solution approximations to hold in more concentrated solutions. The purpose of this communication is to recalculate the equilibrium conditions for occluded corrosion cells on iron making two modifications. The first is the use of activity coefficients in the treatment of the concentrated electrolyte. Secondly, account is taken that one of the solid phases is $\text{FeCl}_2 \cdot 4\text{H}_2\text{O}$ rather than the anhydrous salt. Pourbaix's calculations have utilized thermodynamic data for the anhydrous salt FeCl_2 rather than for the hydrate $\text{FeCl}_2 \cdot 4\text{H}_2\text{O}$.

When these modifications are made, the resulting calculated values of $[\text{Fe}^{++}]$ and $[\text{Cl}^-]$ are those of an aqueous solution saturated in ferrous chloride. The revised calculated pH value is slightly higher, and the revised calculated electrode potential slightly more negative than the Pourbaix results. However, the present calculations support the basic features of the model as proposed by Pourbaix.

In addition, calculations are also made assuming that the surface oxide formed within the localized cell, rather than being magnetite, is each of the following: $\text{Fe}(\text{OH})_2$, $\alpha\text{-FeOOH}$, $\gamma\text{-FeOOH}$, $\alpha\text{-Fe}_2\text{O}_3$, or $\gamma\text{-Fe}_2\text{O}_3$.

Analysis and Calculations

Pourbaix's model.—When there is a lack of oxygen, as within occluded corrosion cells (10, 11), the overall iron dissolution reaction is



The preponderance of ferrous ions (rather than ferric ions) within occluded corrosion cells on iron has been demonstrated for crevice corrosion by several investi-

Table I. Some experimental observations of the internal pH and electrode potential in the localized corrosion of iron

| Type of localized corrosion | Investigator(s) | pH | E vs. NHE |
|-----------------------------|---------------------------|------------|----------------|
| Pitting | Butler <i>et al.</i> (3) | 2.0 | -0.35 to -0.48 |
| | Suzuki <i>et al.</i> (4) | 4.7 (70°C) | — |
| Crevice corrosion | Bogar and Fujii (5) | 4.7 | — |
| | McCafferty (6, 7) | 4.5-5.0 | -0.40 to -0.45 |
| Stress corrosion cracking | Brown <i>et al.</i> * (8) | 3.8 | — |
| | Smith <i>et al.</i> † (9) | 3.5-3.9 | -0.32 to -0.36 |

* 0.45 C steel.

† 4340 steel; values for freely corroding conditions.

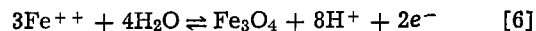
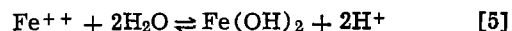
gators (5, 12, 13) and for stress-corrosion cracking by Brown and co-workers (8). At equilibrium, Eq. [2] is described by

$$E = E^\circ + \frac{2.303 RT}{2F} \log a_{\text{Fe}^{++}}$$

or

$$E = -0.440 + 0.0295 \log a_{\text{Fe}^{++}} \quad [3]$$

Ferrous ions then hydrolyze with acidification, according to several possible reactions (12, 14)



In the absence of oxygen, the thermodynamically favored corrosion product is Fe_3O_4 (14, 15). The presence of magnetite has been observed experimentally in several studies which simulated occluded cell corrosion through the use of scaled-up macro-facsimile cells (14, 16, 17). In addition, the corrosion products within crevices on 304 stainless steel in seawater were found to be black with no indication of red rust (12). For Eq. [6]

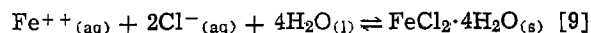
$$E = 0.980 + 0.2364 \log a_{\text{H}^+} - 0.0886 \log a_{\text{Fe}^{++}} - 0.1182 \log a_{\text{H}_2\text{O}} \quad [7]$$

It should be noted that the term in $a_{\text{H}_2\text{O}}$ is necessary for concentrated solutions, although this term vanishes for dilute solutions, where the activity of water is unity.

With the buildup of Fe^{++} and H^+ ions within the confined local electrolyte, Cl^- ions migrate into the occluded cell to preserve charge neutrality. That is, $\Sigma c_i z_i = 0$, or in terms of molalities

$$2m_{\text{Fe}^{++}} + m_{\text{H}^+} = m_{\text{Cl}^-} \quad [8]$$

The resulting increased local concentration of ferrous chloride is limited by the reaction



The solid phase in equilibrium with a bulk saturated solution of ferrous chloride at 25°C is the hydrate $\text{FeCl}_2 \cdot 4\text{H}_2\text{O}$ (18). The existence of this solid phase within the confined local electrolyte, as proposed by Pourbaix, has been verified by the macro-facsimile cell studies of Fujii (17) and Sathler and Van Muylder (14).

Equilibrium calculations.—The need for using ion activities rather than concentrations is seen in Fig. 1, which shows activity coefficients for aqueous solutions of the transition metal chlorides (19-21). As seen in Fig. 1, the mean molal activity coefficient for ferrous chloride is greater than unity for concentrations above 2.5m.

For the ferrous chloride 2:1 electrolyte

$$a = a_{\text{Fe}^{++}} + a_{\text{Cl}^-} = a_{\pm}^3 \quad [10]$$

The relationship between the ionic activities and activity coefficients is $a_{\text{Fe}^{++}} = \gamma_+ m_{\text{Fe}^{++}} = \gamma_+ m$, and $a_{\text{Cl}^-} = \gamma_- m_{\text{Cl}^-} = 2\gamma_- m$, where m is the molal concentration of ferrous chloride. Thus

$$a_{\pm}^3 = 4m^3\gamma_+\gamma_-^2$$

or

$$a_{\pm}^3 = 4(m\gamma_{\pm})^3 \quad [11]$$

where γ_{\pm} is the mean molal activity coefficient for the 2:1 electrolyte and is given by $\gamma_{\pm}^3 = \gamma_+\gamma_-^2$.

The equilibrium constant for Eq. [9] is

$$K_{\text{eq}} = \frac{1}{a_{\text{Fe}^{++}} + a_{\text{Cl}^-}^2 a_{\text{H}_2\text{O}}^4} \quad [12]$$

with

$$\Delta G^\circ = -2.303 RT \log K_{\text{eq}} \quad [13]$$

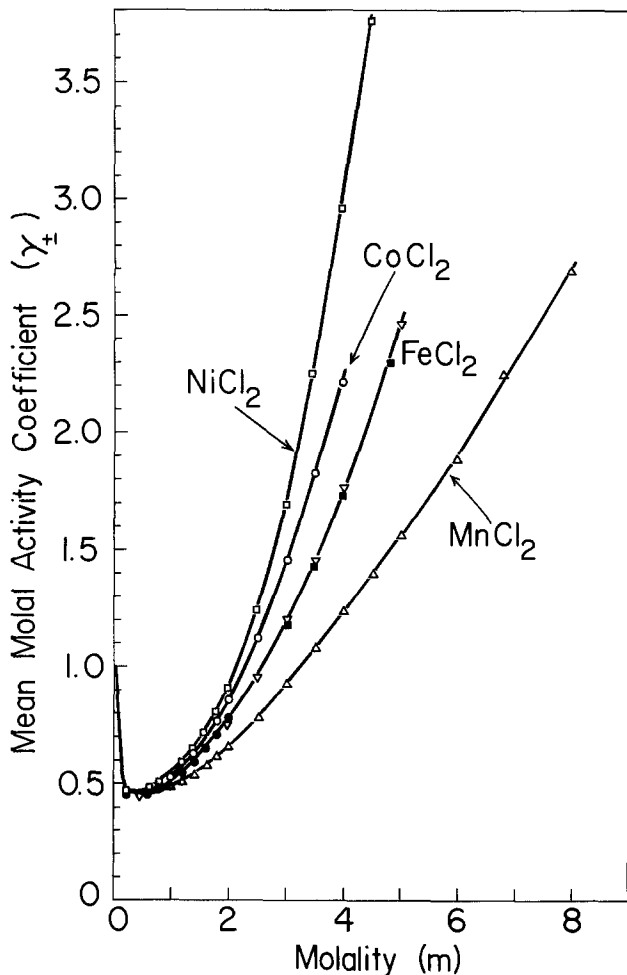


Fig. 1. Activity coefficients for aqueous solutions of the transition metal chlorides. Data for FeCl_2 are from: ● Stokes (19), ▽ Kangro and Groeneveld (20), ■ Susarev et al. (21). All other data are from Stokes (19).

where

$$\Delta G^\circ = \Delta G^\circ_f(\text{FeCl}_2 \cdot 4\text{H}_2\text{O}_{(s)}) - \Delta G^\circ_f(\text{Fe}^{++}_{(aq)}) - 2\Delta G^\circ_f(\text{Cl}^-_{(aq)}) - 4\Delta G^\circ_f(\text{H}_2\text{O}_{(l)}) \quad [14]$$

where $\Delta G^\circ_f(i)$ is the standard free energy of formation (per mole) of the i th ion or compound. Using the appropriate values listed in Table II, Eq. [12]-[14] combine to give

$$\frac{1}{a_{\text{Fe}^{++}} + a_{\text{Cl}^-} - 2a_{\text{H}_2\text{O}}^4} = 10^{-3.0521} \quad [15]$$

Equations [3], [7], and [15] combine to give

$$a_{\text{H}^+} = (2.370 \times 10^{-6}) (a_{\text{Fe}^{++}})^{0.375} (a_{\text{Cl}^-})^{-0.250} \quad [16]$$

Using Eq. [16] and the definition of single-ion activity coefficients in Eq. [8] gives

$$2a_{\text{Fe}^{++}} \left\{ \frac{1}{\gamma_{\text{Fe}^{++}}} + \frac{1}{\gamma_{\text{H}^+}} \right\} [(1.185 \times 10^{-6}) (a_{\text{Fe}^{++}})^{-0.625} (a_{\text{Cl}^-})^{-0.250}] = \frac{a_{\text{Cl}^-}}{\gamma_{\text{Cl}^-}} \quad [17]$$

As is well known, individual ionic activity coefficients cannot be measured but can be calculated at low concentrations. Recently Bates and co-workers (23, 24) have derived a method for calculating individual ionic coefficients in concentrated solutions. Their results for a variety of chlorides suggest that as a first approximation, the order of activity coefficient for Fe^{++} and H^+ can be taken to be the same. That is, $0(\gamma_{\text{Fe}^{++}}) = 0(\gamma_{\text{H}^+})$. Also

Table II. Standard free energies of formation at 25°C

| Species | ΔG°_f (kcal/mole) | Source |
|--|--------------------------------|---------------------|
| $\text{Fe}^{++}(\text{aq.})$ | -20.30 | Pourbaix (22) |
| $\text{Cl}^-(\text{aq.})$ | -31.35 | Pourbaix (22) |
| $\text{H}_2\text{O}(l)$ | -56.690 | Pourbaix (22) |
| $\text{FeCl}_2 \cdot 4\text{H}_2\text{O}(s)$ | -305.6 | Susarev et al. (21) |
| $\text{Fe}(\text{OH})_2(s)$ | -116.3 | Wagman et al. (28) |
| $\alpha\text{-Fe}_2\text{O}_3(s)$ | -177.4 | Pourbaix (30) |
| $\gamma\text{-Fe}_2\text{O}_3(s)$ | -169.466 | Pourbaix (30) |

$$1 \gg (1.185 \times 10^{-6}) (a_{\text{Fe}^{++}})^{-0.625} (a_{\text{Cl}^-})^{-0.250}$$

so that Eq. [17] reduces to

$$2 \frac{a_{\text{Fe}^{++}}}{\gamma_{\text{Fe}^{++}}} \cong \frac{a_{\text{Cl}^-}}{\gamma_{\text{Cl}^-}} \quad [18]$$

or, $2m_{\text{Fe}^{++}} \cong m_{\text{Cl}^-}$. Thus, the electrolyte in the occluded corrosion cell is essentially ferrous chloride (with lesser amounts of hydrogen ion).

The factor $a_{\text{Fe}^{++}} + a_{\text{Cl}^-}$ in Eq. [15] can thus be replaced by a_{\pm}^3 , the mean molal activity of ferrous chloride. The activity of water in aqueous ferrous chloride solutions has been determined from vapor pressure measurements (20, 21). The water activity varies from unity for the dilute electrolyte to 0.59 for saturated ferrous chloride. The water activity is shown in Fig. 2 as a function of the mean activity a_{\pm} of the electrolyte. For concentrations of ferrous chloride greater than 2m, the following empirical least squares relationship holds

$$a_{\text{H}_2\text{O}} = -0.2977 \log a_{\pm} + 0.9863 \quad [19]$$

Equations [15], [10], and [19] combine to give

$$f(a_{\pm}) = a_{\pm}^3 [-0.2977 \log(a_{\pm}) + 0.9863]^4 = 1127 \quad [20]$$

Equation [20] can be solved graphically for a_{\pm} . From Fig. 3, the solution is $a_{\pm} = 20.8$. Use of this value in Eq. [11] gives $m_{\gamma_{\pm}} = 13.11$. Figure 4 shows Fig. 1 replotted as $m_{\gamma_{\pm}}$ vs. m for ferrous chloride. The product $m_{\gamma_{\pm}} = 13.11$ corresponds to a ferrous chloride concentration of 5.15m (and to $\gamma_{\pm} = 2.55$). From the density data of Ionen and Kozhakova (25), a 5.15m solution of ferrous chloride corresponds to a molal concentration of 4.5 moles/liter.

To calculate the electrode potential and pH using Eq. [3] and [16], it is first necessary to calculate single ion activities for the Fe^{++} and Cl^- ions. As noted earlier, Bates and co-workers (23, 24) have developed a method for calculating individual ionic activities in concentrated solutions. Their method is based on the Stokes and Robinson (26) hydration theory for calculating mean activity coefficients in concentrated solutions. According to Stokes and Robinson

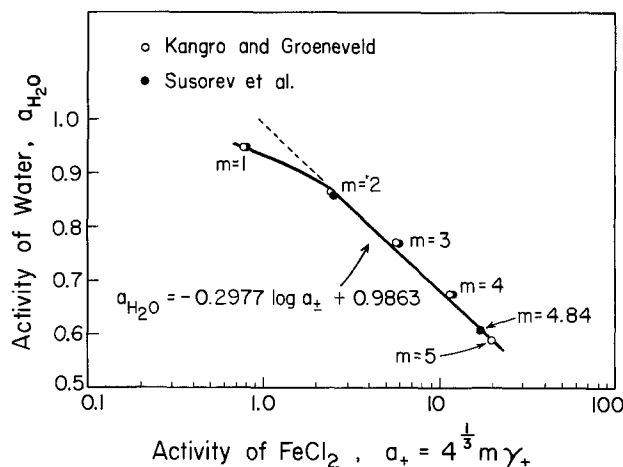


Fig. 2. Activity of water in ferrous chloride solutions

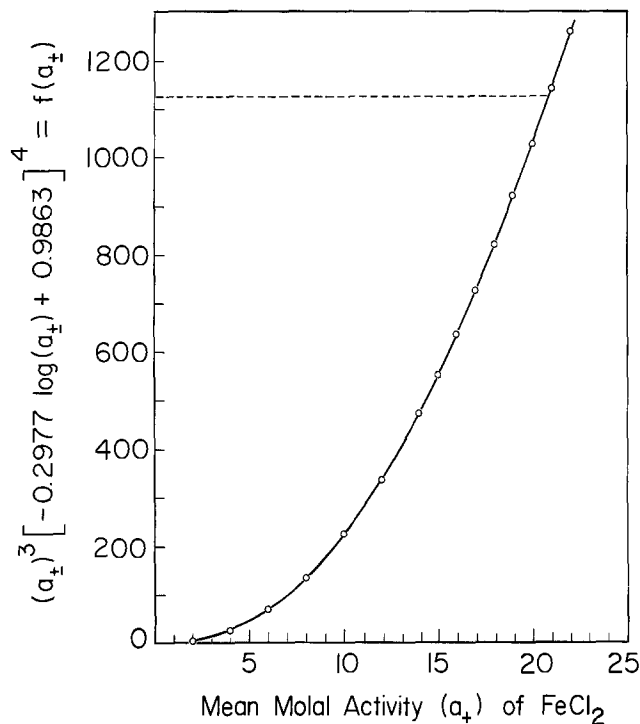


Fig. 3. Graphical solution of Eq. [20]. The solution to $f(a_{\pm}) = 1127$ is: $a_{\pm} = 20.8$.

$$\log \gamma_{\pm} = -\frac{0.5092|z_1 z_2| \sqrt{\mu}}{1 + 0.3286 \bar{a} \sqrt{\mu}} - \frac{h}{\nu} \log a_{\text{H}_2\text{O}} - \log [1 - 0.018(h - \nu)m] \quad [21]$$

where z_1 and z_2 are the valencies, μ the ionic strength in molality units, ν the number of ions per molecule (3 for FeCl_2), and \bar{a} and h are two adjustable parameters related to the ion size and hydration, respectively. Using $\bar{a} = 4.8$ and $h = 12$ for FeCl_2 , Stokes and Robinson obtained good agreement between calculated and measured values of γ_{\pm} for concentrations

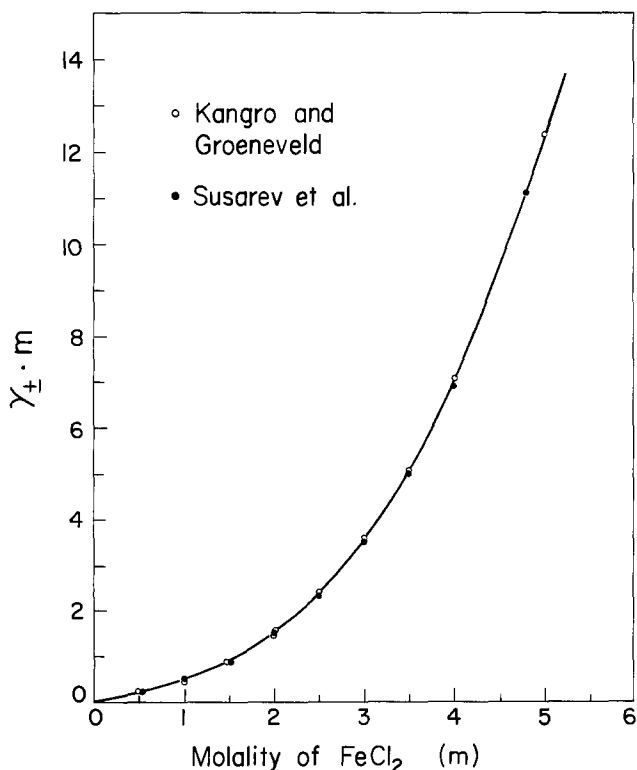


Fig. 4. Data in Fig. 1 for FeCl_2 replotted as $m\gamma_{\pm}$ vs. m

up to about 2m. As noted by these authors, at higher concentrations the "hydration number" h must decrease due to increased competition between neighboring ions for available water molecules. Figure 5 shows the concentration dependence of h which enables Eq. [21] to hold over the entire concentration range for FeCl_2 solutions.

Assuming that $h = 0$ for the chloride ion, Bates and co-workers developed the following equations for a bi-univalent electrolyte, such as ferrous chloride

$$\log \gamma_{\text{M}^{2+}} = 2 \log \gamma_{\pm} - \frac{h}{3} \log a_{\text{H}_2\text{O}} + \log [1 + 0.018(3 - h)m] \quad [22]$$

$$2 \log \gamma_{\text{Cl}^-} = \log \gamma_{\pm} + \frac{h}{3} \log a_{\text{H}_2\text{O}} - \log [1 + 0.018(3 - h)m] \quad [23]$$

The solution to Eq. [20], as cited earlier, is: $a_{\pm} = 20.8$, $m = 5.15$, and $\gamma_{\pm} = 2.55$. From Fig. 5, the Stokes and Robinson hydration number corresponding to $m = 5.15$ is $h = 8.5$. From Eq. [15] or Eq. [19], $a_{\text{H}_2\text{O}} = 0.594$. Using these data in Eq. [22] and [23] gives: $\gamma_{\text{Fe}^{2+}} = 13.941$ and $\gamma_{\text{Cl}^-} = 1.091$. Also, $a_{\text{Fe}^{2+}} = m \gamma_{\text{Fe}^{2+}}$ and $a_{\text{Cl}^-} = 2m \gamma_{\text{Cl}^-}$ yields: $a_{\text{Fe}^{2+}} = 71.80$ and $a_{\text{Cl}^-} = 11.24$. Use of these activities in Eq. [16] and [3] gives the pH of the occluded corrosion cell as 5.2 and the electrode potential as -0.385V vs. NHE.

The calculated results for the occluded corrosion cell on iron are summarized in Table III. Comparison of these calculated results with Eq. [1] shows that the calculated value of the internal pH is slightly higher than the Pourbaix result (5.2 compared to 4.8). Also, the calculated electrode potential is slightly more negative (-0.385 compared to -0.368). However, the present calculations predict more realistic concentrations of dissolved Fe^{2+} and Cl^- ions.

These calculated results apply to equilibrium and not to those stages of localized corrosion when there are concentration gradients within or ionic migration across the crevice, crack, or pit. Thus, these calculations describe the localized cell at times beyond the initiation stage and well into the propagation stage. For the crevice corrosion of iron and steels for example, the observation of constant internal electrode potentials with time (6, 10, 27) is an indication of the approach to the steady state.

Atmospheric pressure model.—Figure 6 illustrates the equilibria considered in the previous section. The diagram is essentially the same as that given earlier by Pourbaix (2). The only difference is that Fig. 6 is based on the present results: $a_{\text{Fe}^{2+}} = 71.80$ and $a_{\text{H}_2\text{O}} = 0.594$. The equilibrium conditions (as calculated above) lie below the "a" line for hydrogen

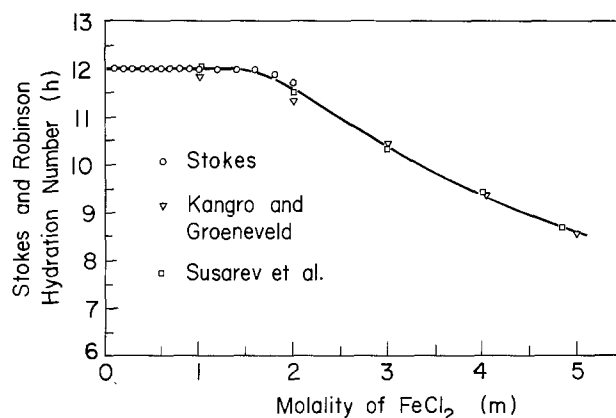
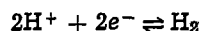


Fig. 5. Calculated values for the Stokes and Robinson hydration number h for aqueous solutions of FeCl_2 . (Sources of experimental data used in Eq. [21] are indicated on the figure.)

Table III. Summary of calculated and experimental results for the occluded corrosion cell on iron

| Equilibrium model | Atmospheric pressure model | | | | |
|---------------------|----------------------------|-----------------|-----------------|-----------------|------------------------------|
| | Present calculations | Calculations | | Experimental | |
| | | Present results | Pourbaix (2) | Fujii (17) | Sathler and Van Muylder (14) |
| <i>E</i> vs. NHE | -0.385 | -0.281 | -0.254 | -0.332 | -0.330 |
| pH | 5.2 | 4.8 | 4.3 | 3.8 | 3.8 |
| [Fe ²⁺] | 4.5 moles/liter | 4.5 moles/liter | 276 moles/liter | 4.2 moles/liter | 4.6 moles/liter |
| [Cl ⁻] | 9.0 moles/liter | 9.0 moles/liter | 552 moles/liter | 8.4 moles/liter | 9.2 moles/liter |

evolution



Thus, hydrogen evolution can occur within the occluded corrosion cell, and at equilibrium, the pressure of hydrogen given by

$$E = 0.000 - 0.0591 \text{ pH} - 0.02955 \log p_{\text{H}_2} \quad [24]$$

is $p_{\text{H}_2} = 400$ atm for the conditions $E = -0.385\text{V}$ and $\text{pH} = 5.2$.

If the pressure of hydrogen gas within the occluded corrosion cell is restricted to 1 atm, then the equilibrium conditions are given by the intersection of line 26 with line "a" rather than with line 23. That is, simultaneous solution of Eq. [7], [8], [15], and [24] ($p_{\text{H}_2} = 1$ atm) gives the results: $E = -0.281\text{V}$ vs. NHE, $\text{pH} = 4.8$, and the concentration of ferrous chloride equals 4.5 moles/liter. These results are summarized in Table III, which also lists the experimental results from the macro-facsimile cell studies of Fujii (17) and Sathler and Van Muylder (14).

Calculations based on Fe(OH)₂.—The above calculations assume that the thermodynamically favored oxide (Fe₃O₄) is formed on the iron surface within the localized corrosion cell. If instead, the formation of Fe(OH)₂ is considered, as in Eq. [5], then

$$\frac{a_{\text{H}^+}^2}{a_{\text{Fe}^{2+}} + a_{\text{H}_2\text{O}}^2} = K_5 \quad [25]$$

From the free energy of formation data listed in Table II, K_5 is calculated to be 1.774×10^{-13} . Equations [25], [3], [8], and [15], in conjunction with the single-ion activity coefficient calculations in Eq. [22] and [23] give the results: $\text{pH} = 5.7$, $E = -0.385\text{V}$ vs. NHE, $[\text{Fe}^{2+}] = 4.5$ moles/liter, and $[\text{Cl}^-] = 9.0$ moles/liter.

Calculations based on ferric oxyhydroxides or oxides.—It is well known that corrosion products formed in natural environments contain oxyhydroxides, usually α -FeOOH or γ -FeOOH (29). Although occluded corrosion cells are low in oxygen content, the formation of hydrated ferric oxides might occur through the hydrolysis reactions



or

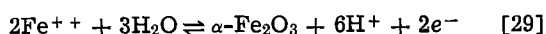


In each case

$$E = E^\circ + 0.1773 \log a_{\text{H}^+} - 0.0591 \log a_{\text{Fe}^{2+}} - 0.1182 \log a_{\text{H}_2\text{O}} \quad [28]$$

where $E^\circ = 0.655$ for α -FeOOH and 0.919 for γ -FeOOH (29). Solution of Eq. [28], [3], [8], and [15] again using the Bates single-ion activity coefficients gives: $\text{pH} = 5.4$ for α -FeOOH and 6.9 for γ -FeOOH. For both cases, $E = -0.385\text{V}$ vs. NHE, $[\text{Fe}^{2+}] = 4.5$ moles/liter, and $[\text{Cl}^-] = 9.0$ moles/liter.

If the ferric oxides are not hydrated



or



then

$$E = E^\circ + 0.1773 \log a_{\text{H}^+} - 0.0591 \log a_{\text{Fe}^{2+}} - 0.08865 \log a_{\text{H}_2\text{O}} \quad [31]$$

Based on the free energies of formation listed in Table II, $E^\circ = 0.721$ for α -Fe₂O₃ and 0.893 for γ -Fe₂O₃. With Eq. [31] in place of Eq. [28], the pH within the occluded corrosion cell is calculated to be 5.7 based on an α -Fe₂O₃ layer and 6.7 based on a γ -Fe₂O₃ layer. For both cases, the calculated electrode potential is -0.385V vs. NHE with $[\text{Fe}^{2+}] = 4.5$ moles/liter and $[\text{Cl}^-] = 9.0$ moles/liter.

Discussion

The available experimental evidence indicates that magnetite is the stable oxide phase formed within localized corrosion cells on iron. The occurrence of magnetite was shown by Sathler and Van Muylder in their macrofacsimile cell studies (14). Moreover, if it is assumed that the stable oxide phase is ferrous hydroxide or one of the ferric oxides or oxyhydroxides (instead of magnetite), then the calculated pH's are substantially higher than those observed in various experimental studies (3-9) or in the scaled up macrofacsimile cells (14,17).

Table III summarizes the present calculations based on the Pourbaix model of a magnetite-covered iron surface in contact with a concentrated solution of acidified ferrous chloride. Results are given for both

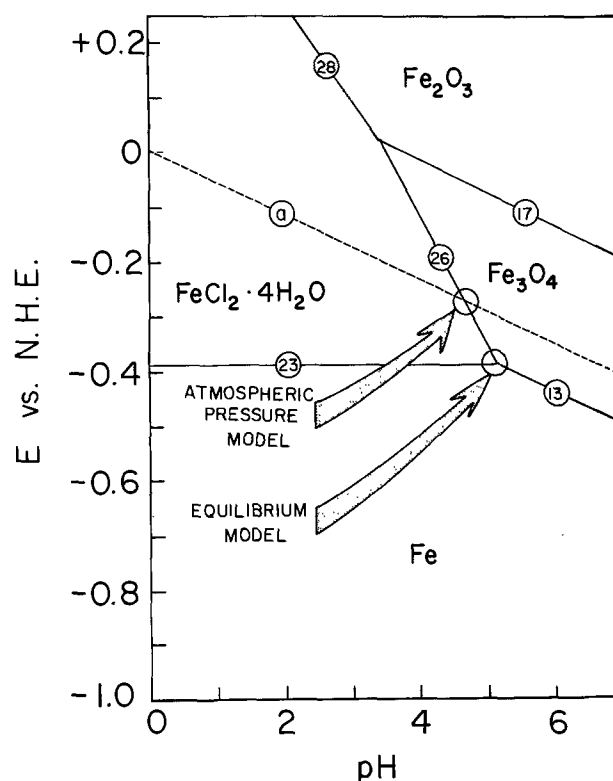


Fig. 6. Equilibrium diagram for an occluded corrosion cell on iron. After Pourbaix (2). The encircled numbers correspond to reactions given in Ref. (22).

the equilibrium model and for the case where the localized cell is maintained under 1 atm pressure of hydrogen gas. In both instances, the calculated local pH is slightly higher and the calculated internal potential slightly more negative than in the original Pourbaix calculations. But these are minor differences; the main difference is in the results for the concentrations of Fe^{++} and Cl^- .

Table III also gives the experimental results from the macro-facsimile cell studies of Fujii (17) and Sathler and Van Muylder (14). Fujii immersed an iron electrode in a simulated pit consisting of a deaerated saturated solution of FeCl_2 mixed with excess $\text{FeCl}_2 \cdot 4\text{H}_2\text{O}$, magnetite, and powdered iron. Sathler and Van Muylder used a deaerated saturated solution of $\text{FeCl}_2 \cdot 4\text{H}_2\text{O}$, which also contained iron powder. Table III shows that the electrode potential of iron in these synthetic occluded corrosion cells is closer to the present results than to Pourbaix's calculated value. The reverse is true with the pH comparisons.

The present calculations also predict that the internal electrolyte is saturated in ferrous chloride. A direct comparison with the concentrations of Fe^{++} and Cl^- in the experimental macro-cells cannot be made, of course, because the macro-cell electrolytes were intentionally made up to saturation in these two ions. However, recent studies on the solution chemistry within corrosion pits on stainless steels have established that the local electrolytes are concentrated in both Fe^{++} and Cl^- ions. Chloride concentrations of 3-6N (4) and 3-12N (31) have been reported. Ferrous ion concentrations of 2-4N have been observed, accompanied by Cr^{+++} concentrations of about 1N (4). Although these studies were made on stainless steels, rather than on pure iron, the evidence is that the local electrolyte is concentrated in the metallic cation and in chloride ion, as predicted by Pourbaix and supported by the present calculations.

It should be emphasized that the present calculations apply to localized corrosion processes on pure unalloyed iron. Various experimental studies have shown that the internal pH is much lower for the localized corrosion of stainless steels, due to the hydrolysis of certain alloying elements, especially Cr^{+++} (4, 5, 12).

Summary

1. The equilibrium electrochemical conditions within a localized corrosion cell on pure iron have been calculated using the thermodynamics of concentrated aqueous solutions.

2. The internal pH is calculated to be between 4.8 and 5.2, and the electrode potential of internal iron to be between -0.280 and -0.385V vs. NHE. (Both pH and E depend on the pressure of hydrogen within the occluded cell.)

3. The composition of the internal electrolyte is calculated to be saturated in FeCl_2 ; i.e., 4.5 moles/liter Fe^{++} and 9.0 moles/liter Cl^- .

4. The calculated internal pH is slightly higher and the electrode potential slightly more negative than in the original Pourbaix calculations. In general, the present calculations support the Pourbaix model of the iron occluded corrosion cell.

Manuscript submitted Aug. 13, 1979; revised manuscript received Aug. 5, 1980.

Any discussion of this paper will appear in a Discussion Section to be published in the December 1981 JOURNAL. All discussions for the December 1981 Discussion Section should be submitted by Aug. 1, 1981.

Publication costs of this article were assisted by the Naval Research Laboratory.

REFERENCES

1. B. F. Brown, *Corrosion*, **26**, 249 (1970).
2. M. Pourbaix in "Localized Corrosion," p. 12, NACE, Houston, Texas (1974).
3. G. Butler, P. Stretton, and J. G. Beynon, *Br. Corros. J.*, **7**, 168 (1972).
4. T. Suzuki, M. Yamabe, and Y. Kitamura, *Corrosion*, **29**, 18 (1973).
5. F. D. Bogar and C. T. Fujii, "Solution Chemistry in Crevices on Fe-Cr Binary Alloys," NRL Report 7690, Washington, DC (1974).
6. E. McCafferty, *This Journal*, **126**, 385 (1979).
7. E. McCafferty, "Corrosion of Iron in Crevices," NRL Report 7781, Washington, DC (1974).
8. B. F. Brown, C. T. Fujii, and E. P. Dahlberg, *This Journal*, **116**, 218 (1969).
9. J. A. Smith, M. H. Peterson, and B. F. Brown, *Corrosion*, **26**, 539 (1970).
10. I. L. Rosenfeld and I. K. Marshakov, *ibid.*, **20**, 115t (1964).
11. I. B. Ulanovskii and Yu. M. Korovin, *J. Appl. Chem., USSR*, **35**, 1683 (1962).
12. M. H. Peterson, T. J. Lennox, Jr., and R. E. Groover, *Mater. Protect.*, **9**, 23 (1970).
13. B. E. Wilde and E. Williams, *Electrochim. Acta*, **16**, 1971 (1971).
14. L. Sathler and J. Van Muylder, *Rapp. Tech. CEBELCOR*, RT. 224, Dec. 1974.
15. U. R. Evans, "The Corrosion and Oxidation of Metals," p. 91, Edward Arnold, London (1960).
16. A. Pourbaix, *Corrosion*, **27**, 449 (1971).
17. C. T. Fujii, *Rapp. Tech. CEBELCOR*, RT. 213, Jan. 1974.
18. W. F. Linke and A. Seidell, "Solubilities of Inorganic and Metal-Organic Compounds," Vol. 1, p. 1013, D. Van Nostrand, Princeton, N.J. (1958).
19. R. H. Stokes, *Trans. Faraday Soc.*, **44**, 295 (1948).
20. W. Kangro and A. Groeneveld, *Z. Phys. Chem., N.F.*, **32**, 110 (1962).
21. M. P. Susarev, L. I. Gorelik, A. M. Toikka, R. V. Lyzlova, and Yu. L. Ponomarev, *J. Appl. Chem. USSR*, **49**, 1086 (1976).
22. M. Pourbaix, "Atlas of Electrochemical Equilibria in Aqueous Solutions," Pergamon Press, Oxford (1966).
23. R. G. Bates, B. R. Staples, and R. A. Robinson, *Anal. Chem.*, **42**, 867 (1970).
24. R. G. Bates and R. A. Robinson, *Pure Appl. Chem.*, **37**, 575 (1974).
25. M. V. Ionen and A. A. Kozhakova, *J. Appl. Chem. USSR*, **46**, 865 (1973).
26. R. H. Stokes and R. A. Robinson, *J. Am. Chem. Soc.*, **70**, 1870 (1948).
27. G. Karlberg and G. Wranglen, **11**, 499 (1971).
28. D. D. Wagman, W. H. Evans, V. B. Parker, I. Halow, S. M. Bailey, and R. H. Schumm, "Selected Values of Chemical Thermodynamic Properties," NBS Technical Note 270-4, Washington, D.C., May 1969.
29. T. Misawa, *Corros. Sci.*, **13**, 659 (1973).
30. M. Pourbaix, in "Passivity and its Breakdown on Iron and Iron Base Alloys," R. W. Staehle and H. Okada, Editors, p. 27, NACE, Houston (1976).
31. J. Mankowski and Z. Sklarska-Smialowska, *Corros. Sci.*, **15**, 493 (1975).

Effect of Plating Parameters on Electrodeposited NiFe

Jean Horkans*

IBM, Thomas J. Watson Research Center, Yorktown Heights, New York 10562

ABSTRACT

Films of NiFe alloys were deposited under galvanostatic conditions from solutions containing no stress-relieving additives and no surfactants. The composition of the films and the deposition efficiency were determined as a function of current density, pH, the identity of the anion (SO_4^{2-} or Cl^-), and the boric acid content of the solution. The Fe content is lower in deposits from chloride solution than from sulfate solution and is increased by the addition of H_3BO_3 . The efficiency increases with increasing current density and increasing pH, is higher in deposits from chloride solution, and is little affected by H_3BO_3 . The observations are interpreted in terms of suppression of Ni deposition by a surface iron hydroxide precipitated when the local surface pH rises during deposition. The way in which the solution components and conditions of deposition influence the formation of this hydroxide determines their effect on deposit properties. Increasing current density causes greater hydroxide precipitation and thus increases the Fe content of the film up to the point where ionic diffusion in the hydroxide limits the rate of Fe deposition. Chloride ion forms a weak complex with Fe^{2+} and thereby limits hydroxide formation, lowering the percentage Fe in the deposits. Boric acid has its greatest effect under conditions where hydroxide formation is most extensive. It does not act as a buffer, but apparently adsorbs on the hydroxide-covered surface.

The composition and properties of electrodeposited NiFe alloys are known (1) to be highly dependent on the composition of the solution from which they are plated and the conditions of deposition. Variables which are significant in the deposition process include mass transport conditions, current density, temperature, and variation in concentration of all of the solution components (including pH). A large number of deposit properties, including composition, magnetic properties, and metallurgical properties, depend on these plating variables, but the interdependence is not yet well understood.

Strong evidence exists that the simultaneous evolution of H_2 during deposition is a dominant factor in determining the composition and properties of NiFe alloys. This is a system which displays the phenomenon of anomalous codeposition (2), i.e., the less noble metal, Fe, appears at unexpectedly high concentration in the deposit. Although several explanations of this phenomenon exist [see, e.g., (3)], the one which is most consistent with the observations is the model of Dahms and Croll (4, 5). These authors note that H_2 evolution during deposition will cause a local pH rise near the electrode surface. This surface elevation in pH has been measured for Ni deposition (6) and deposition of NiFe (7). Dahms and Croll hypothesize that the high local pH can cause precipitation of $\text{Fe}(\text{OH})_2$ on the electrode surface. Such hydroxide precipitation has been shown (4) to impede the discharge of other metal ions, and thus suppresses the rate of Ni deposition in the alloy.

A recent paper (8) from this laboratory reported on an investigation of the role in NiFe deposition of two important factors, the nature of the anion and the presence of boric acid, H_3BO_3 , in solution. Boric acid was investigated because of its common use in Ni and NiFe plating. There is a persistent lore [e.g., (9)] that H_3BO_3 serves as a buffer to oppose the pH rise caused by H_2 evolution. Because H_2 evolution plays such an important role in NiFe deposition, the influence of these two solution components on H^+ reduction from solutions containing no Ni^{2+} or Fe^{2+} was also studied. The nature of the anion influences both metal discharge and H_2 evolution. It was found that limiting currents for H^+ reduction were lower in NaCl solutions than in

Na_2SO_4 solutions at the same pH; this was attributed to different diffusion coefficients for H^+ in the two solutions. Overpotentials for reduction of Ni^{2+} and Fe^{2+} are lower in Cl^- than SO_4^{2-} solution, probably due to catalysis through a Cl^- bridge between the electrode and the metal ion. Boric acid was shown not to have a significant buffering effect either during H_2 evolution from NaCl and Na_2SO_4 solutions or during metal deposition. While having little effect on the current-potential behavior in Ni^{2+} and Fe^{2+} solution, it greatly influences the appearance of the deposit. It was proposed that H_3BO_3 influences deposition through adsorption on the electrode surface.

The present work expands on the earlier investigation. The composition of NiFe films and the efficiency of deposition have been measured as a function of current density, pH, anion (SO_4^{2-} or Cl^-), and the presence of H_3BO_3 in solution. The results are interpreted in terms of the theory of Dahms and Croll (4, 5).

Experimental

The NiFe films were deposited at constant current density under conditions of controlled mass transport (using a rotating disk electrode). The cathode was a 3.18 cm (1.25 in.) diam disk of Corning 0211 glass. On this was evaporated 200Å of Nb (as an adhesion layer) followed by 2000Å of Au. This wafer was contacted and mounted on the shaft of a Pine Instruments rotating disk in the manner shown in Fig. 1. A strip of Au foil was wrapped around the wafer to contact the edge of the evaporated film. The foil on the back side was pressed against the stainless steel disk by a Teflon holder, which also served to mask the contact from the solution. The exposed area of the cathode was 2.91 cm^2 .

The hydrodynamic characteristics of this rotating disk assembly were compared with those of a 0.7 cm diam Ni disk in a straight Teflon cylinder (i.e., a disk not modified by the wafer holder). Limiting currents on an Ni electrode were measured in alkaline ferrocyanide-ferricyanide solution. Ferrocyanide oxidation in both cases showed a dependence of limiting current on the square root of rotation rate which is linear and extrapolates through (0, 0). The results were the same within experimental error for the two electrodes.

Rotation rate was controlled with a Pine Instruments ASR speed control. The effect of mass transport was

* Electrochemical Society Active Member.

Key words: alloy, current efficiency, electrodeposition.

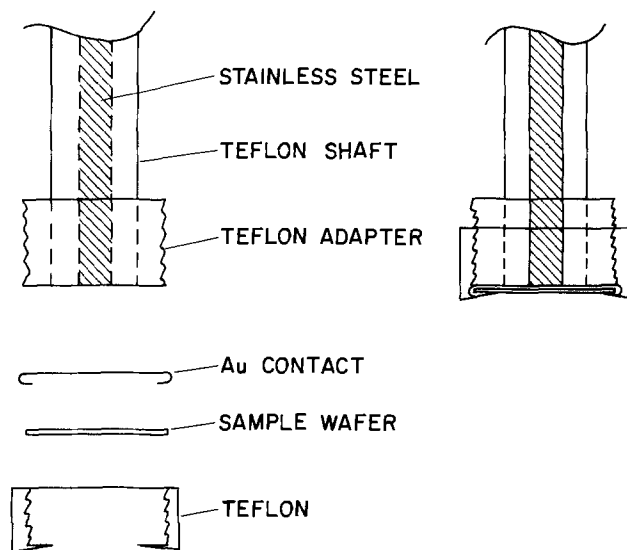


Fig. 1. Method of mounting a 1.25 in. diam wafer in the rotating disk assembly. Left side shows the components; right side shows the assembled system. All films in this study were deposited at 200 rpm.

not investigated. A single rotation speed of 200 rpm was used. This was found (10) to give approximately the same rate of mass transport to the surface as the paddle cell (11) used in this laboratory for NiFe deposition.

Solutions of eight different compositions were studied, as shown in Table I. The concentrations of Ni^{2+} and Fe^{2+} were kept constant at 0.50M and 0.01M, respectively; the metal salts were either sulfates or chlorides. Films were deposited from solutions containing either no H_3BO_3 or 0.40M H_3BO_3 . Two pH values, 2.0 and 3.0, were investigated. In each of these solutions, films were deposited at 1, 2, 5, 10, and 20 mA/cm^2 .

The current was controlled with an Electronic Measurements Model C621 constant current supply. A Koslow Model 541 coulometer was used to monitor the amount of charge passed during deposition. Knowledge of total charge allowed calculation of the current efficiency after analysis of the total deposited Ni and Fe. The NiFe films were dissolved from the substrate in a small amount of concentrated HNO_3 , diluted to volume, and analyzed by atomic absorption spectroscopy.

Results

The film composition and deposition efficiency are shown in Table II and represented graphically in Fig. 2-5.

Composition.—The Fe content of the film goes through a maximum as a function of current density (Fig. 2 and 3). At pH 3.0 (Fig. 2), this maximum occurs between 2 and 5 mA/cm^2 . There are not sufficient data in this current range to determine precisely the location of the peak; the apparent shifts in peak position in Fig. 2 may not be significant. At pH 2.0

Table I. Compositions of the solutions studied

| Solution | NiSO_4 (M) | NiCl_2 (M) | FeSO_4 (M) | FeCl_2 (M) | H_3BO_3 (M) | pH |
|----------|------------------------|------------------------|------------------------|------------------------|--------------------------------|-----|
| 1 | 0.50 | — | 0.01 | — | — | 3.0 |
| 2 | 0.50 | — | 0.01 | — | 0.40 | 3.0 |
| 3 | — | 0.50 | — | 0.01 | — | 3.0 |
| 4 | — | 0.50 | — | 0.01 | 0.40 | 3.0 |
| 5 | 0.50 | — | 0.01 | — | — | 2.0 |
| 6 | 0.50 | — | 0.01 | — | 0.40 | 2.0 |
| 7 | — | 0.50 | — | 0.01 | — | 2.0 |
| 8 | — | 0.50 | — | 0.01 | 0.40 | 2.0 |

(Fig. 3), the maximum occurs at higher current density and is broader than at pH 3.0. As at pH 3.0, the precise location of the peak at pH 2.0 is not known, but it is $\sim 10 \text{ mA/cm}^2$.

Deposition from SO_4^{2-} solution results in a larger proportion of Fe in the film than deposition from Cl^- . This is true at both pH values and in the presence and absence of H_3BO_3 .

The effect of H_3BO_3 on composition depends on pH. At pH 3.0, addition of H_3BO_3 leads to a large increase in Fe content of deposits from both SO_4^{2-} and Cl^-

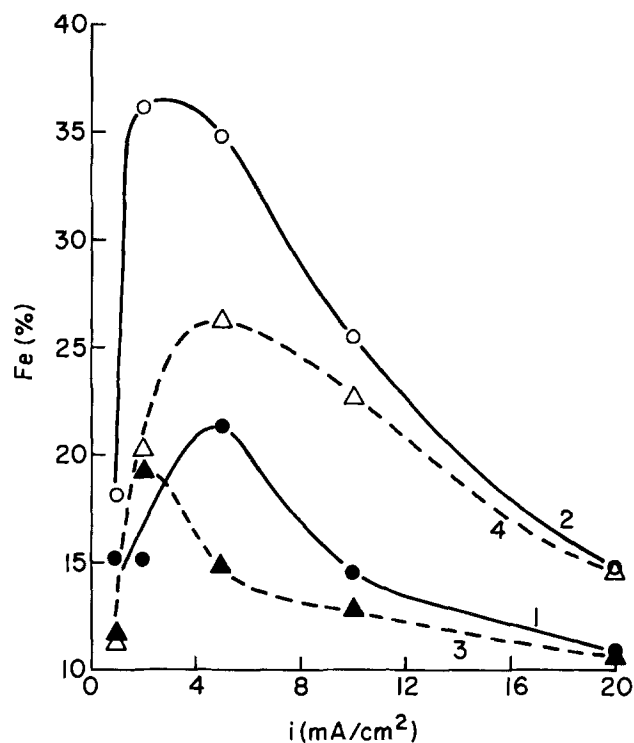


Fig. 2. Dependence of film composition on current density in various pH 3.0 solutions: 1, ●; 2, ○; 3, ▲; 4, △. Solution key is given in Table I.

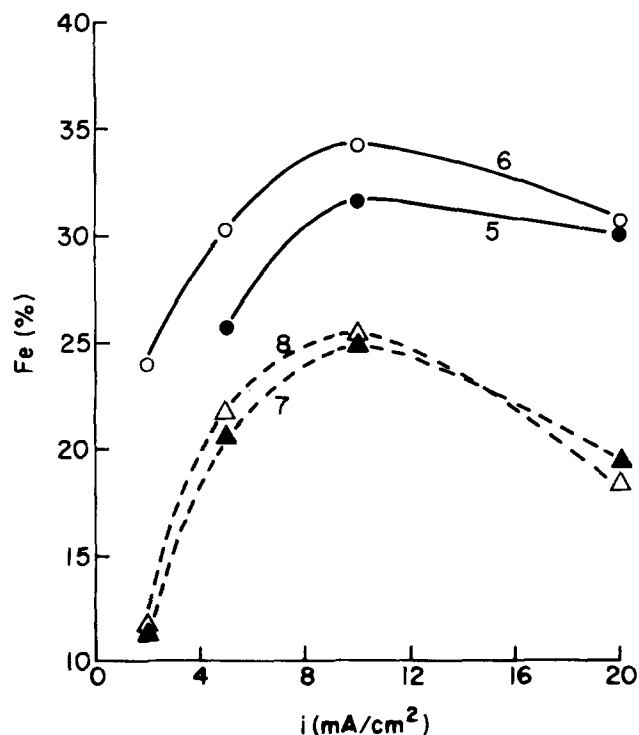


Fig. 3. Same as Fig. 2 for pH 2.0 solutions: 5, ●; 6, ○; 7, ▲; 8, △. Solution key is given in Table I.

Table II. Composition and efficiency of deposition of NiFe under various conditions

| Solution | i (mA/cm ²) | Fe (%) | Efficiency (%) | i_{H_2} (mA/cm ²) | i_{Ni} (mA/cm ²) | i_{Fe} (mA/cm ²) | Appearance |
|----------|------------------------------|--------|------------------------------|------------------------------------|-----------------------------------|-----------------------------------|---------------------|
| 1 | 1 | 15.3 | 18.6 | 0.81 | 0.16 | 0.03 | Bright |
| | 2 | 15.2 | 40.0 | 0.80 | 1.02 | 0.18 | Bright, pinholes |
| | 5 | 22.4 | 69.0 | 1.55 | 2.68 | 0.77 | Bright, spirals |
| | 10 | 14.6 | 83.4 | 1.66 | 7.12 | 1.22 | Spirals |
| | 20 | 10.9 | 83.2 | 3.36 | 14.82 | 1.82 | Spirals, dark |
| 2 | 1 | 18.1 | 16.7 | 0.83 | 0.14 | 0.03 | Bright |
| | 2 | 36.1 | 39.5 | 1.21 | 0.51 | 0.29 | Bright |
| | 5 | 34.8 | 68.9 | 1.56 | 2.24 | 1.20 | Bright |
| | 10 | 25.5 | 80.6 | 1.94 | 6.00 | 2.06 | Slightly hazy |
| | 20 | 14.8 | 85.2 | 2.95 | 14.52 | 2.52 | Slightly hazy |
| 3 | 1 | 11.6 | 56.4 | 0.44 | 0.50 | 0.07 | Bright |
| | 2 | 19.2 | 72.6 | 0.55 | 1.17 | 0.28 | Bright |
| | 5 | 14.8 | 83.3 | 0.84 | 3.55 | 0.62 | Dark, spirals |
| | 10 | 12.9 | 87.2 | 1.28 | 7.60 | 1.12 | Dark, spirals |
| | 20 | 10.7 | Powdery, nonadherent deposit | | | | Dark, spirals |
| 4 | 1 | 11.3 | 57.0 | 0.43 | 0.51 | 0.06 | Slightly dark |
| | 2 | 20.2 | 71.3 | 0.57 | 1.14 | 0.29 | Bright |
| | 5 | 26.3 | 82.9 | 0.85 | 3.06 | 1.09 | Bright |
| | 10 | 22.7 | 89.3 | 1.07 | 6.91 | 2.02 | Bright |
| | 20 | 14.6 | 94.1 | 1.18 | 16.08 | 2.74 | Bright |
| 5 | 1 | — | 0.7 | 0.99 | 0.00 | 0.00 | No deposit |
| | 2 | — | 0.8 | 1.98 | 0.01 | 0.01 | No deposit |
| | 5 | 25.7 | 7.7 | 4.61 | 0.29 | 0.10 | Bright |
| | 10 | 31.6 | 10.1 | 8.99 | 0.69 | 0.32 | Bright, pinholes |
| | 20 | 30.0 | 22.2 | 15.55 | 3.11 | 1.34 | Bright, pinholes |
| 6 | 1 | — | 1.7 | 0.98 | 0.01 | 0.00 | No deposit |
| | 2 | 24.0 | 5.0 | 1.90 | 0.08 | 0.02 | Bright, pinholes |
| | 5 | 30.3 | 6.8 | 4.66 | 0.24 | 0.10 | Bright, pinholes |
| | 10 | 34.2 | 10.2 | 8.98 | 0.67 | 0.35 | Bright, pinholes |
| | 20 | 30.6 | 24.8 | 15.05 | 3.44 | 1.51 | Bright, pinholes |
| 7 | 1 | — | 5.5 | 0.94 | 0.05 | 0.00 | Almost no deposit |
| | 2 | 11.4 | 41.3 | 1.17 | 0.73 | 0.09 | Bright |
| | 5 | 20.6 | 52.2 | 2.39 | 2.07 | 0.54 | Bright |
| | 10 | 24.9 | 60.1 | 3.99 | 4.51 | 1.50 | Bright, black spots |
| | 20 | 19.1 | 73.2 | 5.35 | 11.84 | 2.80 | Bright, black spots |
| 8 | 1 | — | 4.3 | 0.96 | 0.04 | 0.00 | Almost no deposit |
| | 2 | 11.8 | 36.5 | 1.27 | 0.64 | 0.09 | Bright |
| | 5 | 21.7 | 47.7 | 2.62 | 1.87 | 0.52 | Bright |
| | 10 | 25.4 | 56.4 | 4.36 | 4.21 | 1.43 | Bright |
| | 20 | 18.3 | 71.2 | 5.76 | 11.64 | 2.60 | Bright |

solution. This effect also occurs in SO_4^{2-} solutions at pH 2.0, but it is less pronounced. In pH 2.0 Cl^- solutions, H_3BO_3 has little effect on composition.

The effect of pH on composition is complicated. At current densities above 10 mA/cm², (i.e., above the current density of the peak Fe content at either pH), the Fe content is always appreciably higher in deposits from the pH 2.0 than from the pH 3.0 solution. Generally, however, the pH 3.0 solution gives the higher Fe content at lower current densities. (This is indeterminate for the SO_4^{2-} solution containing no H_3BO_3 , since at pH 2.0, no deposit is obtained below 5 mA/cm².)

Efficiency.—The efficiency of deposition shows the expected increase with increasing current density and increasing pH (Fig. 4 and 5).

Deposition from Cl^- solution occurs with higher efficiency than deposition from SO_4^{2-} solution, the difference between the two being larger at pH 2.0. Deposits can be obtained from Cl^- solutions under conditions (low i , low pH) where no deposition occurs from SO_4^{2-} solutions.

The effect of H_3BO_3 on current efficiency is small. In pH 3.0 SO_4^{2-} or Cl^- solutions, the efficiency is nearly independent of H_3BO_3 . In pH 2.0 solutions, the effect of H_3BO_3 varies with anion. Boric acid increases efficiency at 1 and 2 mA/cm² in SO_4^{2-} solutions, but has little effect at higher current densities. In Cl^- solutions, H_3BO_3 results in a small decrease in efficiency over the entire current range studied.

Appearance.—The appearance of the films also varies considerably with the conditions of deposition (Table II). The appearance tends to deteriorate with increas-

ing current density, although in some solutions films of good appearance can be obtained over the entire range examined. Appearance is slightly better in deposits from Cl^- than in those from SO_4^{2-} solutions.

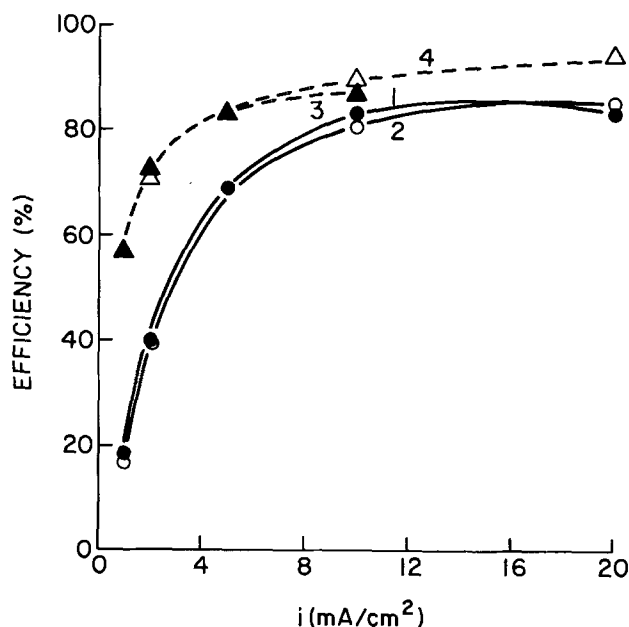


Fig. 4. Dependence of deposition efficiency on current density in various pH 3.0 solutions: 1, ●; 2, ○; 3, ▲; 4, △. Solution key is given in Table I.

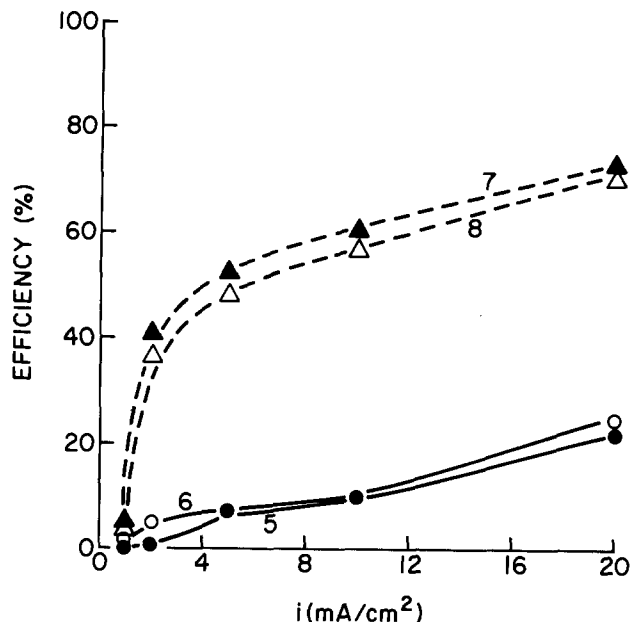


Fig. 5. Same as Fig. 4 for pH 2.0 solutions: 5, ●; 6, ○; 7, ▲; 8, △. Solution key is given in Table I.

For a pH 3.0 solution containing no H_3BO_3 , deposits at current densities of 5 mA/cm² or greater are dark to black and show spirals marking the pattern of solution flow over the surface of the electrode. The spirals are not seen at pH 2.0, but films obtained from the low pH solution tend to have pinholes or dark spots.

Addition of H_3BO_3 markedly improves the appearance of deposits from both SO_4^{2-} and Cl^- solution, at both pH values (the effect being stronger at pH 3.0), and at all current densities. A typical illustration is given in Fig. 6. The dark spirals occurring in the absence of H_3BO_3 are completely eliminated in its presence.

Discussion

All of the deposits, at all current densities examined and at both pH values, show the phenomenon of anomalous codeposition; the Fe content is unexpectedly high.¹ If the data are interpreted in terms of the theory of Dahms and Croll (4, 5), this result is consistent with observations (7) of measurable surface pH rises even at the lowest current densities used.

The maximum in percentage Fe vs. current density is related to the relative importance of mass transport control and activation control of the various species undergoing electroreduction reactions.² At low i , where the surface pH rise is small, little iron hydroxide forms and the Ni content of the film is relatively high. Increasing i results in a larger pH rise, and thus the Fe content of the film increases. Since at any given total current the surface pH is always lower in the pH 2.0 than in the pH 3.0 solution, the Fe content rises

¹ If the Fe:Ni ratio in the deposit were the same as the $\text{Fe}^{2+}:\text{Ni}^{2+}$ ratio in solution, the film would contain <2% Fe.

² The limiting currents for Fe^{2+} reduction and H_2 evolution in this solution are not known but can be estimated from other work. Horkans (8) found that limiting currents for H^+ reduction were lower in NaCl solutions than in Na_2SO_4 solutions at the same pH; this was attributed to different diffusion coefficients for H^+ in the two solutions. Under the conditions of the present study, the H^+ limiting currents were 8 mA/cm² for NaCl and 27 mA/cm² for Na_2SO_4 at pH 2.0. At pH 3.0, the limiting currents were a factor of 10 lower. Diffusivities in the nickel-iron solutions may differ from those in solutions containing only Na^+ cations, but these numbers can be used as a guide. The diffusivity of Fe^{2+} is less than that of H^+ by a factor of ~ 10 (12), and the Fe diffusion limiting current should thus be about half that of H_2 . As the solutions of the present study do not contain supporting electrolyte, it might be argued that migration is an important mode of mass transport and thus limiting currents will be higher than the diffusion limitation. However, the total current density is a very small fraction of the sum of the limiting currents for Ni, Fe, and H_2 . The excess of Ni^{2+} present serves to increase the conductivity of the solution and to cause migration to be a less important mode of mass transport than diffusion. Hence, migration effects are not expected to lead to major error in the interpretation.

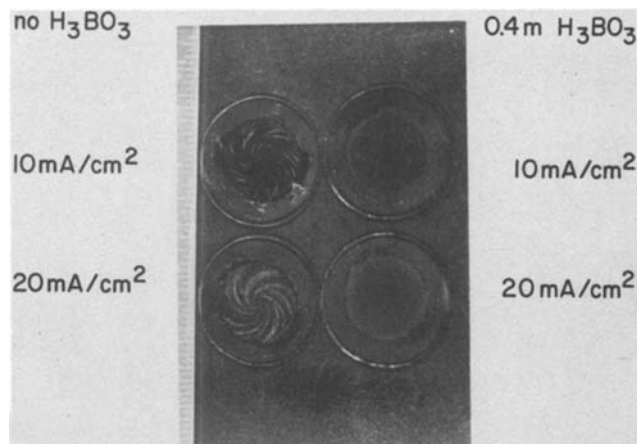


Fig. 6. Effect of H_3BO_3 on the appearance of NiFe deposited from 0.50M NiCl_2 , 0.01M FeCl_2 , pH 3.0, (solutions 3 and 4). Only the center portion of the wafer was exposed to the solution.

more slowly as a function of i at the lower pH. At higher current densities, the proportion of Fe in the film decreases. Examination of Table II shows that the partial Fe current at the peak is well below its diffusion-limiting current, and thus the decrease in percentage Fe with i is not due solely to mass transport limitation of Fe^{2+} in solution. The hypothesis that Fe(II) discharge takes place through the hydroxide leads to the conclusion that the decrease in percentage Fe at higher current densities is caused by rate limitation due to slow ionic diffusion in the Fe(OH)_2 .

Two factors work together to cause a higher deposition efficiency in Cl^- than in SO_4^{2-} solution. The Cl^- ion catalyzes the discharge of the metal ion (8). However, the observed effects (especially at pH 2.0) are too large to be explained by this alone. The explanation must involve a difference in diffusivities of H^+ in the two solutions similar to that observed (8) in NaCl and Na_2SO_4 solutions. A lower H_2 limiting current in Cl^- than in SO_4^{2-} solution would result in the observed higher efficiency in the Cl^- solution.

The anion also markedly affects the Fe content of the deposits; the percentage Fe is smaller when depositing from Cl^- than from SO_4^{2-} solutions. This suggests that Cl^- ion hinders the formation of surface iron hydroxides through weak complexation of Fe^{2+} (13).

Boric acid, which has only small effects on the current-potential dependence of an Ni electrode in these solutions (8), nonetheless has a large effect on film composition. Its effects are not those predicted for a buffer. A buffer, by maintaining a low surface pH and providing a reservoir of readily available H^+ ions, would be expected to lead to a less anomalous deposit and to decrease the efficiency of the deposition process. Instead, the deposit is generally more anomalous (i.e., the Fe content is higher) in films deposited from solutions containing H_3BO_3 . Boric acid has a stronger effect on composition under conditions where the formation of surface iron hydroxides is more extensive, that is at higher pH and in SO_4^{2-} solutions. The H_3BO_3 molecule may adsorb more readily on the hydroxide covered surface than on the bare metal. The effects of H_3BO_3 on the efficiency of NiFe deposition are somewhat different than those on deposition of unalloyed Ni (8). In the case of Ni, addition of H_3BO_3 to pH 2.0 solutions causes a small increase in efficiency in SO_4^{2-} solutions and a larger efficiency increase for Cl^- solutions. The different effect of H_3BO_3 in Ni and NiFe systems is apparently due to an interaction of H_3BO_3 with surface iron hydroxide.

Boric acid is extremely important to the appearance of electrodeposited NiFe. It extends the current den-

sity range over which good quality deposits can be obtained, eliminating the "burned" appearance and the dark spirals at higher currents. The influence of H_3BO_3 on appearance is presumably also related to its adsorption on the hydroxide.

The formation of spiral patterns during deposition on a rotating disk has been discussed by Hill *et al.* (14) and Pleskov and Filinovskii (15). They claim that even submicroscopic protrusions and depressions on the surface can cause wakes which result in the observed spirals. In the present investigation, the arms of the spiral appear to originate in small macroscopic protrusions on the surface. The formation of these protrusions occurs in conjunction with a "burned" deposit and is probably associated with the inclusion of oxides or hydroxides. Such inclusions are less favorable at low pH, and thus the spiral patterns are not observed at pH 2.0. The pinholes which occur at pH 2.0 are due to blocking of the surface by H_2 bubbles.

The evidence concerning the role of H_3BO_3 remains incomplete. Its influence on composition and efficiency appears to rule out a buffering role. It strongly affects both appearance and composition of NiFe deposits, but the effect on efficiency is small. Neither the present analysis of composition nor the earlier linear potential sweep measurements, however, is adequate for determining the mechanism through which H_3BO_3 influences the deposition process. The hypothesis that it adsorbs on hydroxide-covered surfaces is consistent with the data, but remains to be confirmed experimentally.

Conclusions

The results of the present investigation are generally consistent with the theory of Dahms and Croll (4, 5) concerning the mechanism of anomalous codeposition of Ni and Fe. The high Fe content of the alloys is apparently caused by inhibition of Ni^{2+} discharge by surface $Fe(OH)_2$ precipitated when H_2 evolution causes the local surface pH to rise. Factors which affect H_2 evolution and hydroxide precipitation thus influence the composition and properties of the deposit.

The deposit properties are strongly dependent on current density. Appearance degrades and efficiency increases with increasing current density. The Fe content of the NiFe films shows a maximum as a function of current density. This peak results from the simultaneous interaction of several factors. Increased H_2 evolution causes increased surface alkalization, leading to greater formation of iron hydroxides and the inhibition of Ni deposition. At sufficiently high currents, however, ionic diffusion in the hydroxide becomes rate limiting for Fe deposition and the Fe content of the films drops.

A decrease in pH generally causes a decrease in efficiency and an improvement in appearance. The decrease in efficiency is due to the larger $[H^+]$ at low pH. Appearance improves because less hydroxide is incorporated in the deposit at low pH. The maximum in the percentage Fe *vs.* *i* dependence occurs at higher *i* for lower pH since, at a given current density, the surface pH is lower in this case.

The anion affects the deposition efficiency and the composition of the deposit. The data suggest that Cl^- hinders the formation of a surface iron hydroxide,

resulting in a lower Fe content in deposits from Cl^- solution than from SO_4^{2-} solution. The better appearance of deposits from chloride solution is probably also related to chloride's hindering surface hydroxide formation. Efficiency is higher in Cl^- solutions, apparently due to a lower H_2 limiting current in these solutions.

Addition of H_3BO_3 causes an increase in the Fe content of the deposits and does not greatly affect efficiency; neither result would be expected of a buffer. It greatly alters the appearance of deposits and extends the range of current densities over which good quality deposits may be obtained. Boric acid has the strongest effects under conditions where surface iron hydroxides are expected to form; evidence suggests that H_3BO_3 adsorbs on the hydroxide-covered surface.

Acknowledgments

The author is indebted to R. E. Acosta and L. T. Romankiw for useful discussions concerning this work. The evaporated samples were provided by B. J. Stoeber.

Manuscript submitted April 28, 1980; revised manuscript received July 21, 1980. This was Paper 512 presented at the St. Louis, Missouri, Meeting of the Society, May 11-16, 1980.

Any discussion of this paper will appear in a Discussion Section to be published in the December 1981 JOURNAL. All discussions for the December 1981 Discussion Section should be submitted by Aug. 1, 1981.

Publication costs of this article were assisted by IBM Corporation.

REFERENCES

1. L. T. Romankiw, J. V. Powers, and E. E. Castellani, Paper 152 presented at The Electrochemical Society Meeting, Pittsburgh, Pennsylvania, October 15-20, 1978.
2. A. Brenner, "Electrodeposition of Alloys," Vol. I, pp. 77, 84, Academic Press, New York (1963).
3. M. J. Nicol and H. I. Philip, *J. Electroanal. Chem. Interfacial Electrochem.*, **70**, 233 (1976).
4. H. Dahms, *J. Electroanal. Chem.*, **8**, 5 (1964).
5. H. Dahms and I. M. Croll, *This Journal*, **112**, 771 (1965).
6. J. Matulis and R. Slizys, *Electrochim. Acta*, **9**, 1177 (1964).
7. L. T. Romankiw and L. Miu, Unpublished data.
8. J. Horkans, *This Journal*, **126**, 1861 (1979).
9. A. H. DuRose, *Plating*, **64** (8), 52 (Aug., 1977).
10. R. E. Acosta, Private communication.
11. L. T. Romankiw, R. E. Acosta, and J. V. Powers, Paper 287 presented at The Electrochemical Society Meeting, Atlanta, Georgia, October 9-14, 1977.
12. A. C. Riddiford, in "Advances in Electrochemistry and Electrochemical Engineering," Vol. 4, P. Delahay, Editor, p. 89, Interscience, New York (1966).
13. "Stability Constants," p. 280, The Chemical Society, London (1964).
14. M. R. H. Hill, G. T. Rogers, and K. J. Taylor, *J. Electroanal. Chem. Interfacial Electrochem.*, **96**, 87 (1979).
15. Yu. V. Pleskov and V. Yu. Filinovskii, "The Rotating Disk Electrode," p. 51, Consultants Bureau, New York (1976).

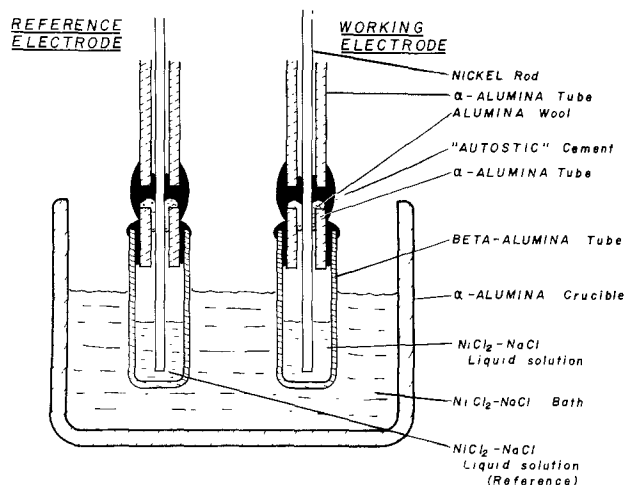


Fig. 1. Experimental apparatus

wires rapidly became embrittled due to grain boundary attack by the salt vapor.

The outer crucible containing the salt bath was 5 cm in diameter and 8 cm high. The entire assembly was maintained under purified argon in a vertical resistance-heated tube furnace fitted with a grounded metal sheath to eliminate induced emf's. Temperatures were measured with a Chromel-Alumel thermocouple immersed in a tube in the outer bath, and were controlled to $\pm 1^\circ\text{C}$.

No attack on the Autostic cement by the salt vapor was evident after several days of operation at up to 1000°C .

Results

Emf's were measured with various compositions of the melt in the working electrode compartment and with the mole fraction of NiCl_2 in the reference electrode compartment held constant at $X_{\text{NiCl}_2} = 0.1589 \pm 0.0005$. Emf's were stable to ± 0.2 mV over several days and after several heating and cooling cycles. If the cells were polarized for several seconds in either direction the emf returned to within 0.1 mV of its former value within a few seconds after the polarization was terminated.

Results are shown in Table I for emf's at 1073, 1173, and 1273 K. Each value shown is the average of at least two measurements made at the same temperature ($\pm 1^\circ$) before and after a thermal cycle. These values always agreed within ± 0.2 mV except at high values of X_{NiCl_2} where the reproducibility was only ± 1 mV. Hence, the last two entries in Table I for $X_{\text{NiCl}_2} > 0.5$ are reported only to the nearest millivolt. Because of this observed lower reproducibility at high concentrations of NiCl_2 and because the phase diagram limits measurements to higher temperatures at high NiCl_2 concentrations (the melting point of NiCl_2 being

1303 K), no values are reported for X_{NiCl_2} greater than 0.6.

Calculation of thermodynamic properties.—The Gibbs-Duhem equation at constant temperature may be written as follows

$$X_{\text{NaCl}} dg_{\text{NaCl}}^E + X_{\text{NiCl}_2} dg_{\text{NiCl}_2}^E = 0 \quad [3]$$

where g_{NaCl}^E and $g_{\text{NiCl}_2}^E$ are the partial molar excess free energies of NaCl and NiCl_2 . This equation may be rearranged to give

$$dg_{\text{NaCl}}^E = \frac{X_{\text{NiCl}_2}}{1 + X_{\text{NiCl}_2}} (2dg_{\text{NaCl}}^E - dg_{\text{NiCl}_2}^E) \quad [4]$$

Now, Eq. [2] may be written as

$$2FE = RT \ln(X_{\text{NaCl}}^2/X_{\text{NiCl}_2})^{II} + (2g_{\text{NaCl}}^E - g_{\text{NiCl}_2}^E)^{II} + RT \ln(a_{\text{NiCl}_2}/a_{\text{NaCl}}^2)^I \quad [5]$$

The term $RT \ln(a_{\text{NiCl}_2}/a_{\text{NaCl}}^2)^I$ contains the unknown activities in the reference electrode compartment. However, this term is, of course, independent of the composition in the working electrode compartment and hence drops out when the derivative is taken. Differentiating Eq. [5] and substituting into Eq. [4] we obtain

$$dg_{\text{NaCl}}^E = \frac{X_{\text{NiCl}_2}}{1 + X_{\text{NiCl}_2}} d(2FE - RT \ln(X_{\text{NaCl}}^2/X_{\text{NiCl}_2})) \quad [6]$$

where the compositions refer to the working electrode compartment. Equation [6] may be integrated with the lower limit taken at $X_{\text{NiCl}_2} = 0$ where $g_{\text{NaCl}}^E = 0$ to give

$$g_{\text{NaCl}}^E = \int_{X_{\text{NiCl}_2}=0}^{X_{\text{NiCl}_2}} \frac{X_{\text{NiCl}_2}}{1 + X_{\text{NiCl}_2}} d(2FE - RT \ln(X_{\text{NaCl}}^2/X_{\text{NiCl}_2})) \quad [7]$$

In this way, g_{NaCl}^E can be calculated. It is not necessary to know the voltage of the reference electrode. It is only necessary that it be constant.

In Fig. 2 is a plot of $X_{\text{NiCl}_2}/(1 + X_{\text{NiCl}_2})$ vs. $(2FE - RT \ln(X_{\text{NaCl}}^2/X_{\text{NiCl}_2}))$ at 1073 K. A smooth curve is obtained which is easily integrated. Plots at 1173 and 1273 K gave similar curves. These were integrated graphically to give the values of g_{NaCl}^E listed in Table I. A plot of g_{NaCl}^E vs. X_{NiCl_2} at 1073 K is shown in Fig. 3. A smooth curve can be drawn through all the points except the last two points at high X_{NiCl_2} . The plots of g_{NaCl}^E at 1173 and 1273 K are similarly smooth.

Substitution of the calculated values of g_{NaCl}^E back into Eq. [5] will then permit $g_{\text{NiCl}_2}^E$ to be calculated provided that the value of $a_{\text{NiCl}_2}^I$ in the reference electrode compartment is known. Hamby and Scott (2) have measured a_{NiCl_2} in NaCl- NiCl_2 melts using a formation cell with Ni and Cl_2 electrodes. With the value of Hamby and Scott for $a_{\text{NiCl}_2}^I$ at $X_{\text{NiCl}_2} = 0.1589$ in

Table I. Experimental results

| $X_{\text{NiCl}_2}^{II}$ | E (mV) | | | g_{NaCl}^E (j/mole) | | | $g_{\text{NiCl}_2}^E$ (j/mole) | | | S_{NaCl}^E (j/mole-K) | Δh_{NaCl} (j/mole) |
|--------------------------|--------|--------|--------|------------------------------|--------|--------|--------------------------------|----------|----------|--------------------------------|-----------------------------------|
| | 1073 K | 1173 K | 1273 K | 1073 K | 1173 K | 1273 K | 1073 K | 1173 K | 1273 K | | |
| 0.0210 | 157.0 | 170.1 | 180 | 0 | 0 | 0 | -34060 | -34520 | -35150 | 0 | 0 |
| 0.0492 | 107.4 | 114.2 | 119.2 | -35 | -40 | -40 | -32890 | -32970 | -32430 | 0.03 | -10 |
| 0.0774 | 76.7 | 80.5 | 84.6 | -115 | -125 | -125 | -31670 | -31630 | -31510 | 0.05 | -60 |
| 0.0944 | 57.0 | 59.8 | 63.2 | -250 | -275 | -270 | -30250 | -30040 | -29960 | 0.10 | -150 |
| 0.1589* | 0.0 | 0.0 | 0.0 | -820 | -835 | -825 | -26320** | -26070** | -25940** | 0.03 | -800 |
| 0.2031 | -35.5 | -40.6 | -45.0 | -1465 | -1465 | -1550 | -23810 | -22970 | -22510 | 0.43 | -990 |
| 0.2515 | -74.8 | -79.1 | -83.4 | -2220 | -2260 | -2300 | -20880 | -20420 | -20150 | 0.40 | -1790 |
| 0.3066 | -124.4 | -131.9 | -137.9 | -3640 | -3725 | -3765 | -17030 | -16610 | -16320 | 0.63 | -2980 |
| 0.3406 | -157.5 | -166.5 | -173.3 | -4750 | -4600 | -4435 | -14900 | -14850 | -14850 | -1.58 | -6440 |
| 0.3497 | -166.1 | -168.5 | -170.5 | -5020 | -4855 | -4645 | -14360 | -12450 | -14480 | -1.88 | -7040 |
| 0.3965 | -217.9 | -222.0 | -225.9 | -7100 | -6945 | -6695 | -10880 | -10900 | -10500 | -2.03 | -9290 |
| 0.5093 | -317 | -324 | -324 | -11215 | -11005 | -10920 | -5820 | -5820 | -5770 | -1.48 | -12780 |
| 0.5970 | -421 | -432 | -442 | -16445 | -16360 | -16235 | -1170 | -1000 | -960 | -1.05 | -17580 |

* $X_{\text{NiCl}_2}^I = 0.1589$ in reference electrode compartment.

** Values of $g_{\text{NiCl}_2}^E$ for the reference electrode from Ref. (2).

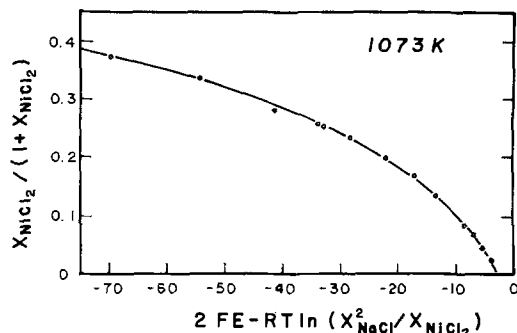


Fig. 2. Plot of experimental results at 1073 K such as to permit g_{NaCl}^E to be calculated by integration of Eq. [7].

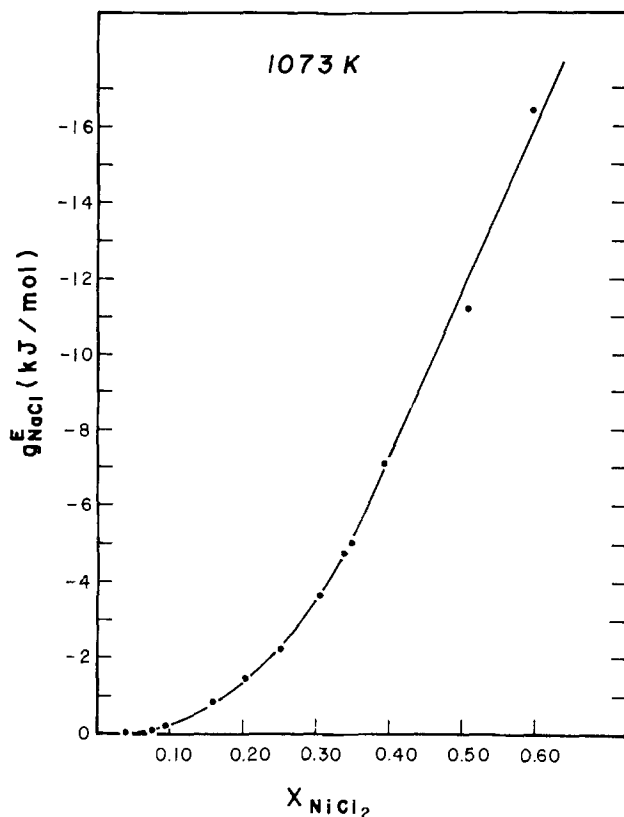


Fig. 3. Partial molar excess free energy of NaCl in NaCl-NiCl₂ melts at 1073 K.

the reference electrode compartment, $g_{\text{NiCl}_2}^E$ was calculated from Eq. [5]. Results are shown in Table I. In Fig. 4, $g_{\text{NiCl}_2}^E$ at 1073 K from Table I is compared with the measurements of Hamby and Scott. Similarly good agreement is also obtained at 1173 and 1273 K.

If measurements had been made over to $X_{\text{NiCl}_2} = 1$, then an equation similar to Eq. [5] could have been written to permit $g_{\text{NiCl}_2}^E$ to be calculated without the necessity of knowing the activities in the reference electrode compartment. Since this was not the case, however, the present results permit only the partial properties of NaCl to be calculated completely independently of any other measurements.

Activities of NaCl and NiCl₂ at 1073 K are plotted in Fig. 5. The values of g_{NaCl}^E in Table I were expressed as linear functions of temperature by a least squares regression analysis. Only very slight deviations from linearity were observed, and these were not systematic but random. Hence, the partial molar entropy and excess entropy of NaCl are quite constant over the temperature range 1073-1273 K. These were calculated from the equation

$$g_{\text{NaCl}}^E = \Delta h_{\text{NaCl}} - Ts_{\text{NaCl}}^E \quad [8]$$

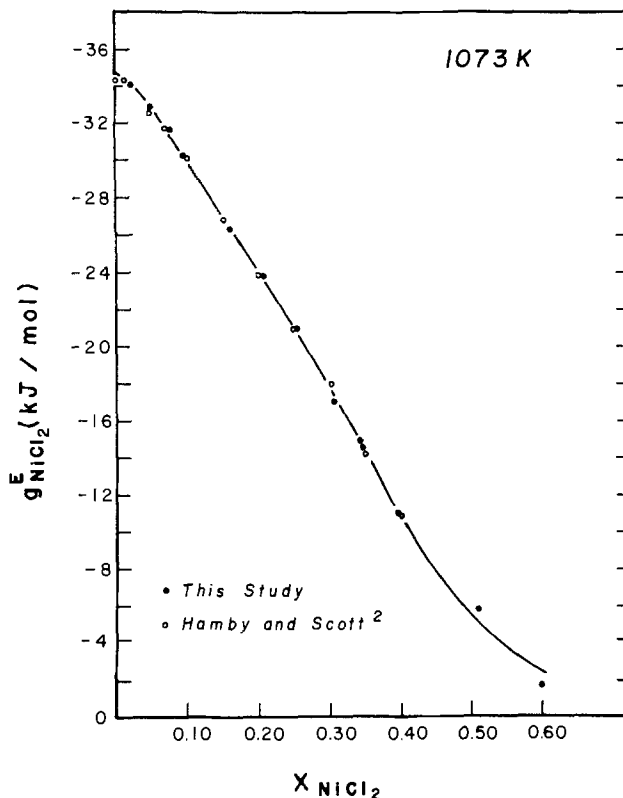


Fig. 4. Partial molar excess free energy of NiCl₂ in NaCl-NiCl₂ melts at 1073 K.

Results are listed in Table I and are plotted in Fig. 6 and 7.

Papatheodorou and Kleppa (3) have measured the enthalpy of mixing of NaCl-NiCl₂ solutions by solid-liquid mixing experiments at 810°C. They fitted their measured integral enthalpy of mixing to a series expansion in the mole fractions. From their equation the partial molar enthalpy of NaCl was calculated and is also plotted in Fig. 6. Very good agreement with the present results is obtained.

Stability of beta-alumina in the chloride melts.—After several days in the NaCl-NiCl₂ melt, the beta-alumina tubes were removed and examined. A very thin blue-green layer was observed on the inner and outer surfaces of the tubes which were in contact with the melt. When the tubes were broken it was observed that the interior of the beta-alumina was white. After

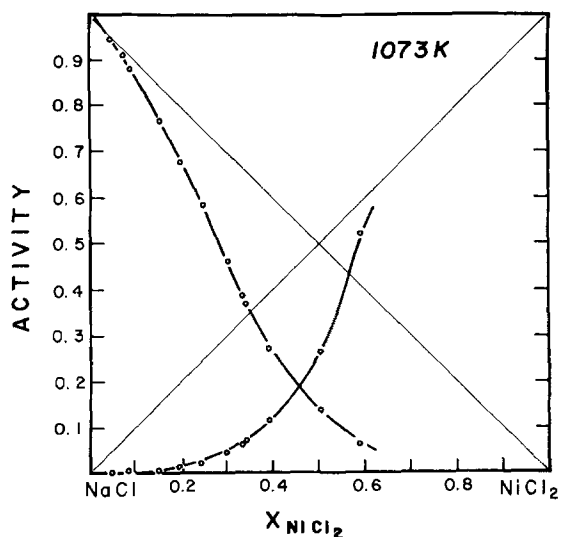


Fig. 5. Activities of NaCl and NiCl₂ in NaCl-NiCl₂ melts at 1073 K.

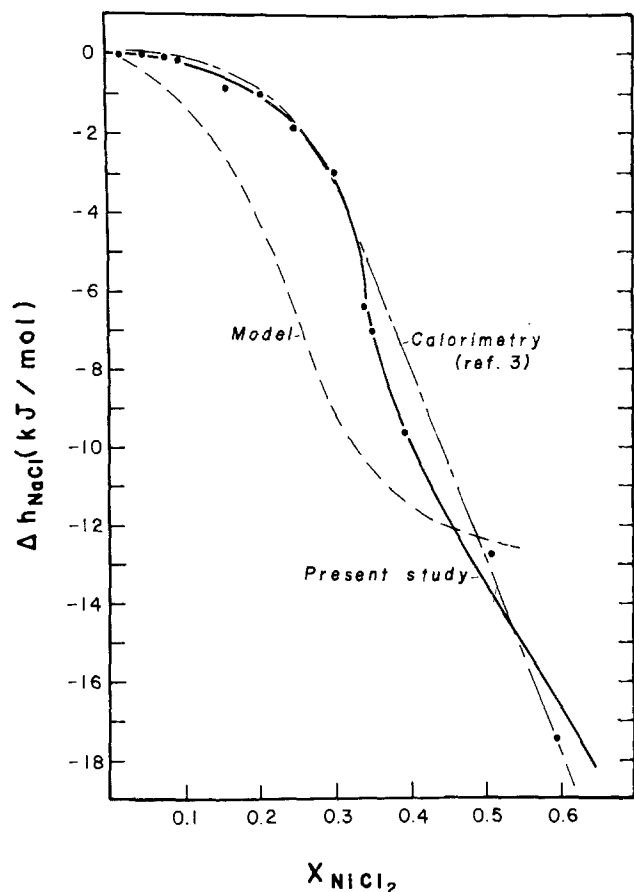
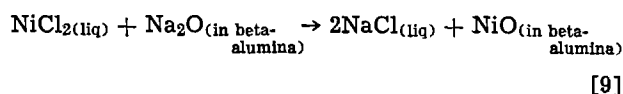


Fig. 6. Partial molar enthalpy of mixing of NaCl in NaCl-NiCl₂ melts.

the blue-green surface layer was removed, chemical analysis of the tubes showed no detectable nickel content.

A source of experimental error which must be considered is the exchange reaction



At 1200 K, ΔG° for reaction [9] is -375 kJ (4). The activity of Na₂O in beta-alumina is approximately 10^{-12} at 1200 K (5). This is not low enough to counteract the very negative ΔG° , and so beta-alumina should be thermodynamically unstable in the NaCl-NiCl₂ melts. (Although, for melts dilute in NaCl it is just possible within the various experimental error

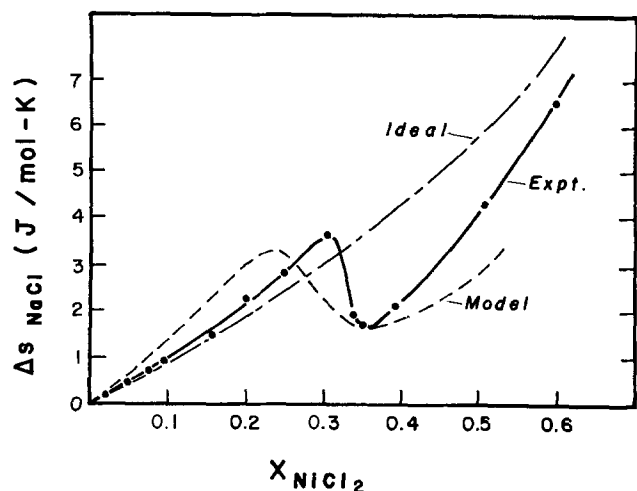


Fig. 7. Partial molar entropy of mixing of NaCl in NaCl-NiCl₂ melts.

limits that ΔG of the exchange reaction could be positive.) However, the mobility of Ni²⁺ ions in beta-alumina would be expected to be many orders of magnitude lower than that of the Na⁺ ions. Yao and Kummer (6) found that many divalent ions could enter the structure of beta-alumina, but that these ions diffuse only very slowly. Hence, if the exchange reaction proceeds with Ni²⁺ diffusion, it may occur so slowly that the cell emf is still effectively given by Eq. [2].

If, on the other hand, the Ni²⁺ does not enter the beta-alumina but, instead, if a layer of pure NiO forms on the surface, then the beta-alumina will become impoverished in Na₂O near its surface such that a surface layer of alpha-alumina will form, greatly retarding further reaction by hindering sodium transport. Whatever the exact reason, the stability and reproducibility of the experimental results together with the excellent agreement with previous studies show that the exchange reaction is not a problem in this system and that the open-circuit emf is given by Eq. [2]. The blue-green surface layer indicates that the exchange reaction has occurred, but only to a very limited extent. The absence of any nickel within the solid electrolyte indicates that no nickel transport has occurred. The aforementioned diminished reproducibility when $X_{\text{NiCl}_2} > 0.5$ may be due to interference from the exchange reaction which would become more pronounced at higher NiCl₂ concentrations.

Coulometric titration.—It was decided to attempt to vary the composition in the working electrode compartment by coulometric titration. This technique was found earlier (7) to work very well in concentration cells containing Na-Sn alloys, the beta-alumina permitting the transport only of Na⁺ ions.

Accordingly, a Ni wire was placed in the outer NaCl-NiCl₂ bath (see Fig. 1) and a fixed current of 96.4 mA was passed between this wire and the working electrode for measured periods of time with the aid of a Sargent-Welch Model IV Coulometric Current Source. Under the assumption that only Na⁺ ions can cross the beta-alumina, the composition of the working electrode compartment could be calculated after each passage of current.

However, when cell emf's were measured after the passage of current they did not correspond to those in Table I. When the beta-alumina tubes were removed and cracked open, they were found to be blue-green right through. Analysis of a tube through which 28 meq of charge had been passed showed it to contain 1.8 weight percent nickel. Rough calculations show that this means that between 1% and 10% of the current was carried by nickel ions.

Thus, the coulometric titration was unsuccessful since nickel entered the beta-alumina. This is surprising in view of the aforementioned observation that upon open circuit the Ni²⁺ does not penetrate the solid electrolyte and in view of Yao and Kummer's (6) observation of very low diffusivities in beta-alumina. If the mobility of Ni²⁺ in beta-alumina is so low, why is so much Ni²⁺ transported upon passage of current? A possible explanation is that the thermodynamic equilibrium favors the formation of nickel beta-alumina at the surface, so that a large fraction of the mobile cation sites at the surface are always occupied by nickel ions. The nickel ions are not sufficiently mobile to diffuse into the beta alumina upon open circuit, but when a potential is applied they are forced to enter. Flinn and Stern (8) observed a similar effect in the case of beta-alumina in NaCl-ZnCl₂ melts. No zinc entered the beta-alumina upon open circuit, but when current was passed their cell resistance rose very sharply. This behavior of beta-alumina in divalent halide melts merits further study.

The coulometric titration was repeated, but this time the outer bath contained only pure NaCl and current was passed only in the direction such as to cause Na⁺ ions to pass through the beta-alumina from the pure

NaCl bath into the working electrode compartment. After each passage of 2000 meq the current was interrupted and the open-circuit emf was measured. It required only about 5 sec for equilibrium to be established after the polarization was terminated. In this way the composition of the working electrode compartment was varied by 27 mole percent. (The total mass of salt in the working electrode compartment was approximately 5g.) Results at 1173 K are shown in Table II where comparison is made with the previous results from Table I. Very good agreement is obtained until X_{NiCl_2} has been reduced from 0.38 to about 0.25. Thereafter, upon further titration, the emf's measured in the titration experiment deviated more and more from the previous results. The direction of the deviation was the same as that of the polarization and was the same as that which was observed when the outer bath contained NiCl_2 as well as NaCl. The explanation is most likely as follows. As the titration proceeds, Ni^{2+} ions enter the outer bath from the Ni electrode to replace the Na^+ ions which have gone through the beta-alumina. Hence, the concentration of NiCl_2 in the outer bath builds up and eventually these Ni^{2+} ions start to enter the beta-alumina.

Discussion

The rapid decrease in Δh_{NaCl} near $X_{\text{NiCl}_2} = 1/3$ in Fig. 6 and the anomaly in Δs_{NaCl} in Fig. 7 near the same composition are indicative of a stabilization and structural ordering of the melt around $X_{\text{NiCl}_2} = 1/3$ which is the composition represented by Na_2NiCl_4 . (The shape of the partial entropy curve in Fig. 7 corresponds to an integral curve with a minimum near $X_{\text{NiCl}_2} = 1/3$.) This type of behavior has been observed in a large number of other AX-MX_2 systems (where A = alkali, X = halogen, and M = divalent metal). See, for example, Ref. (9).

A simple "discrete complex anion model" has been suggested (9) for these systems. The existence of NiCl_4^{2-} complex anions is proposed. These anions are in equilibrium with Ni^{2+} and Cl^- ions in the melt



A parameter α is defined which gives the fraction of total nickel existing in the NiCl_4^{2-} complexes. The entropy of the melt is then written as a function of α by assuming an ideal Temkin solution of Ni^{2+} and Na^+ cations on the cation sublattice and of Cl^- and NiCl_4^{2-} anions on the anion sublattice. The enthalpy of mixing is assumed to arise from the formation of complexes according to Eq. [10]. Hence, the enthalpy can also be written as a function of the degree of complexing α as well as of two adjustable parameters b_1 and b_2 which give the energy change of reaction [10] as a function of composition. The parameter α is then determined by minimizing the free energy: $d\Delta G/d\alpha = 0$. Details

Table II. Results of coulometric titration at 1173 K

| | X_{NiCl_2} | E (mV) | E (mV) from previous results |
|--------------------|---------------------|----------|--------------------------------|
| Start of titration | 0.3800 | -199.7 | -199.4 |
| | 0.3563 | -176.3 | (-174.3)* |
| | 0.3340 | -153.7 | (-152.5)* |
| | 0.3120 | -132.4 | -132.0 |
| | 0.2907 | -112.25 | -112.3 |
| | 0.2703 | -93.25 | -93.7 |
| | 0.2504 | -74.85 | -76.6 |
| | 0.2311 | -57.35 | -59.7 |
| | 0.2124 | -40.75 | -44.3 |
| | 0.1943 | -24.6 | -30.1 |
| | 0.1767 | -9.2 | -15.7 |
| | 0.1596 | +6.3 | -0.3 |
| | 0.1431 | +21.1 | +12.9 |
| | 0.1269 | +36.7 | +26.4 |
| | 0.1113 | +52.4 | +41.9 |
| | End of titration | | |

* These values are placed in parentheses because it is difficult to interpolate the experimental emf's accurately in the composition region near $X_{\text{NiCl}_2} = 1/3$ where s^E and Δh vary rapidly.

are given in Ref. (9). Plots of Δh_{NaCl} and of Δs_{NaCl} calculated via this model with $b_1 = -62.5$ kJ and $b_2 = 0$ are shown in Fig. 6 and 7. These values of b_1 and b_2 were chosen to give the best "by eye" fit to the experimental curves, but with consideration given to the values of b_1 and b_2 required for many other $\text{MCl}_2\text{-ACl}$ systems as discussed in Ref. (9). [The values originally suggested in Ref. (9) for this system were $b_1 = -58.5$ kJ and $b_2 = +2.0$ kJ which give virtually identical results to those obtained with the present values.] It is seen that the model predicts the shapes of the curves, but that the anomaly in Δs_{NaCl} as well as the rapid drop in Δh_{NaCl} are predicted to occur at lower values of X_{NiCl_2} than are observed. Were the calculations to be repeated with assumption of NiCl_3^- complexes rather than NiCl_4^{2-} , the anomalies would occur near $X_{\text{NiCl}_2} = 0.5$. This would give very poor agreement with the measured values. Possibly some NiCl_3^- complexes are formed along with the NiCl_4^{2-} complexes. This is equivalent to saying that there is a preferred coordination of chlorine around nickel which is slightly less than 4.

Conclusions

Beta-alumina solid electrolytes can be used to measure the thermodynamic properties of NaCl-NiCl₂ melts in the temperature range 800°-1000°C. The use of beta-alumina tubes, sealed in the hot zone, permitted separate gas-tight electrode compartments to be realized and eliminated all problems of volatilization. Very stable reversible emf's were obtained. The cells are of very low polarizability. Entropies and enthalpies could be calculated with good accuracy from the temperature dependence of these emf's.

Although the emf of the cell at any given melt composition gives only a ratio of activities in the melt, integration of the Gibbs-Duhem equation permits the individual activities to be determined as long as measurements have been made for compositions over to the pure component in question.

The beta-alumina was attacked to only a negligible extent by the NiCl_2 melts and no Ni^{2+} entered the solid electrolyte at open circuit. However, when current was passed the Ni^{2+} rapidly entered the beta-alumina. It is proposed that the presence of Ni^{2+} in the beta-alumina blocks the transport of Na^+ ions. This observation may have practical consequences for the use of beta-alumina in electrochemical devices. If divalent ions are present as impurities, even in small quantities, they may accumulate with time and poison the beta-alumina.

It is possible, nevertheless, to vary the composition of the fused salt under study by coulometric titration provided the titration is made from a bath containing only NaCl. The fact that the composition can be precisely varied *in situ* by several mole percent will decrease the time required to study a system.

The results for the enthalpy and entropy of the NaCl-NiCl₂ solutions indicate a stabilization and structural ordering of the melts near a NiCl_2 mole fraction of 1/3.

Acknowledgments

The authors wish to thank Mr. J. Desrochers for his valuable assistance in making the beta-alumina tubes. One of the authors (R.R.) was supported by a France-Québec Fellowship. This work was financed by the National Research Council of Canada.

Manuscript submitted Oct. 26, 1979; revised manuscript received Aug. 6, 1980.

Any discussion of this paper will appear in a Discussion Section to be published in the December 1981 JOURNAL. All discussions for the December 1981 Discussion Section should be submitted by Aug. 1, 1981.

Publication costs of this article were assisted by the National Research Council of Canada.

REFERENCES

1. M. Rivier and A. D. Pelton, *Ceram. Bull.*, **57**, 183 (1978).

2. D. G. Hamby and A. Scott, *This Journal*, **115**, 704 (1968).
3. G. N. Papatheodorou and O. J. Kleppa, *J. Inorg. Nucl. Chem.*, **32**, 889 (1970).
4. C. E. Wicks and F. E. Block, "Thermodynamic Properties of 65 Elements—Their Oxides, Halides, Carbides and Nitrides," U.S. Bur. Mines Bull., No. 605 (1963).
5. A. Dubreuil, Master's Dissertation, Ecole Polytechnique, Montreal (1978). Submitted to *This Journal*.
6. Y.-F. Y. Yao and J. T. Kummer, *J. Inorg. Nucl. Chem.*, **29**, 2453 (1967).
7. M. Rivier and A. D. Pelton, *This Journal*, **125**, 1377 (1978).
8. D. R. Flinn and K. H. Stern, *ibid.*, **123**, 978 (1976).
9. A. D. Pelton, *Can. J. Chem.*, **49**, 3919 (1971); A. D. Pelton and W. T. Thompson, *ibid.*, **48**, 1585 (1970).

Diffusion-Controlled Polarization of Pt, Ag, and Au Electrodes with Doped Ceria Electrolyte

Da Yu Wang* and A. S. Nowick*

Henry Krumb School of Mines, Columbia University, New York, New York 10027

ABSTRACT

The nature of electrode polarization, previously investigated for Pt paste electrodes, is now studied for Pt foil, Ag and Au paste, and Ag foil electrodes. The current interruption method with a reference electrode is employed in the temperature range 500°-800°C under O₂-Ar gas mixtures. Electrode structures are also examined by optical and electron microscopy. The principal experimental feature is that the Butler-Volmer equation is obeyed with cathodic and anodic transfer coefficients of 1/2 and 3/2, respectively, and an effective exchange current which varies as the 3/8 power of p_{O_2} . Also, transient decay curves are much slower than for the pure charge transfer mechanism. These features can be interpreted in terms of a model in which charge transfer takes place in the two-phase region between electrode and electrolyte, but where the rate is controlled by interfacial diffusion of oxygen atoms along the electrode, except when the electrode particles are extremely small. For extreme cases of diffusion limitation, the adatom concentration over most of the two-phase region becomes so low that electrolyte reduction takes place. The resulting appreciable electronic contribution can be treated in terms of the Wagner polarization-cell theory.

This is the fourth of a series of papers dealing with electrode polarization in high temperature cells that involve oxygen transport. In the previous papers (1-3) use was made of a current interruption method in combination with a reference electrode to study the nature of electrode processes occurring at Pt paste electrodes (composed of fine Pt particles) on a doped ceria electrolyte. With this method, it is possible to determine separately the anodic and cathodic overpotentials as well as the ohmic polarization of the electrolyte. Steady-state measurements were reported in (1) and both transient and a-c measurements in (2). These studies showed that electrode polarization is controlled by a charge transfer (or "activation") mechanism. Study of the exchange current as a function of p_{O_2} (oxygen partial pressure) and temperature showed that oxygen for the charge transfer process is supplied from adsorbed atoms on the Pt electrode surface which obey the Langmuir isotherm. The fraction of adsorbed sites, θ , is found to be large at low temperatures and small at high temperatures, giving rise to a charge transfer rate that switches over from a $p_{O_2}^{-1/4}$ to a $p_{O_2}^{+1/4}$ dependence in these two ranges, respectively. Observations of the electrodes were also made by scanning electron microscopy to show the changes in microstructure that occur during aging.

At high overpotential or low p_{O_2} , limiting-current behavior was observed at the cathode. For even higher overpotentials, it was shown (3) that reduction takes place at the cathode and electrons are directly injected into the electrolyte. The steady-state behavior associated with this reduction phenomenon has been ex-

plained in terms of the Wagner polarization-cell model, while the transient behavior was interpreted in terms of diffusion of electrons from the cathode to other regions of the electrolyte.

In the previous papers, little was said about the region between the electrode and electrolyte where the charge transfer process takes place. These electrochemically active sites might be located in the three-phase region (electrode-gas-electrolyte) or in the more extensive two-phase region (electrode-electrolyte). In the literature the two-phase region is generally preferred (4, 5) because, otherwise, extremely high local ionic current densities would be required. However, this has never been established conclusively.

If the reaction takes place in the two-phase region, oxygen atoms must diffuse laterally inward along the interface from the three-phase region. This is particularly true for Pt electrodes since oxygen solubility and diffusivity in the bulk are extremely small (6). The concentration of oxygen in the two-phase region will then depend on the interfacial diffusion rate as well as on the local charge-transfer exchange rate. The relative ratio of these two rates can be modified by varying the particle sizes of the electrode. Thus, different electrode morphologies should give rise to different overall polarization behavior.

In the present study, we first examine the cathodic and anodic polarization of Pt foil electrodes using the current interruption method. The results are quite different from those of the previous Pt paste electrodes and are interpreted in terms of a model in which the reaction occurs over the two-phase region, with oxygen diffusing along the electrode from the three-phase region. The theory is similar to that of Wills (7, 8) who dealt with a surface diffusion problem in

* Electrochemical Society Active Member.

Key words: ceramics, fuel cell, chemisorption, Tafel slope.

a system consisting of a liquid aqueous electrolyte, a metal electrode, and a gas.

Morphologically, silver and gold electrodes are similar to platinum, and one would therefore expect to be able to interpret polarization phenomena in cells employing Ag and Au electrodes in a similar way. The present work explores such systems and shows the similarities and differences as compared to Pt.

Theory

When current passes through an oxygen-ion conducting electrolyte, oxygen atoms and electrons must be exchanged between the electrolyte and the ambient gas by way of the metal electrode. Generally the rate of diffusion through the bulk of the metal electrode is so small that only diffusion which proceeds along the interface between the electrode and the electrolyte is important for maintaining the supply of oxygen. Therefore, a concentration gradient may be built up on this interface. Such a gradient depends on the local rate of the charge transfer reaction which, in turn, is dependent on the local concentration of the reactants $C(u, v)$ (or the adatom concentration) where u, v are coordinates in the interface. The total current per unit area, I , will be the integral over the plane of the local current density, $I_w(u, v)$

$$I = \frac{1}{A} \iint I_w(u, v) du dv \quad [1]$$

where the subscript w denotes the direction perpendicular locally to the (uv) plane and A is the area. The function $I_w(u, v)$ is proportional to the local rate of the charge transfer reaction and is given for high temperatures or $\theta \ll 1$ (θ being the fraction of available surface active sites on the electrode that are occupied by chemisorbed oxygen adatoms), as (1)

$$I_w(u, v) = I_0 \{ \exp[\alpha_a e \eta(u, v)/kT] - [C(u, v)/C_0] \exp[-\alpha_c e \eta(u, v)/kT] \} \quad [2]$$

where I_0 is the exchange current, e is the electronic charge, $\eta(u, v)$ is the overpotential, α_a and α_c are the anodic and cathodic charge transfer coefficients (here $\alpha_a = \alpha_c = 1$), C_0 is the equilibrium concentration of oxygen adatoms, and kT has the usual meaning. Generally, the metal surface is an equipotential so that the overpotential $\eta(u, v)$ can be taken as constant. Accordingly, only the function $C(u, v)$ must be known in order to carry out the integration of Eq. [1]. For mass conservation, $C(u, v)$ must satisfy the continuity equation

$$D \nabla^2 C(u, v) + I_w(u, v)/2e = 0 \quad [3]$$

where D is the interfacial diffusion coefficient of oxygen and the total number of transferred charges per reactant is assumed to be equal to 2. We will consider two possible boundary conditions for Eq. [3], either

$$C(u, v)|_B = C_0 \quad [4]$$

or

$$D \nabla C(u, v)|_B = \gamma(C_0 - C_B) \quad [5]$$

where B stands for the boundary (i.e., the three-phase periphery) of the metal-electrolyte interface region and γ is a constant. The first condition assumes that thermal equilibrium between gas and chemisorbed adatoms is maintained on the boundary. Alternatively, the second condition assumes that, on the boundary, the interfacial diffusion rate of chemisorbed adatoms is proportional to the difference between the actual concentration and the thermal-equilibrium concentration; it is just this condition that gives rise to limiting-current type behavior (1).

For simplicity we consider an electrode with the geometry shown in Fig. 1 (with concentration independent coordinate v and boundaries at $u = \pm L$). For

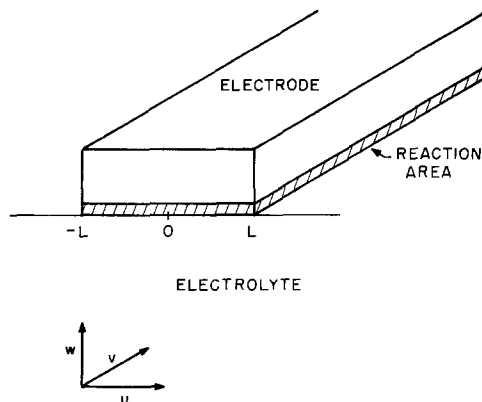


Fig. 1. Schematic diagram of an electrode particle of simple geometry on an electrolyte.

this case, the solution of Eq. [3] for the first boundary condition, Eq. [4], is

$$C(u)/C_0 = [1 - \exp(2e\eta/kT)] [\cosh(Gu/L)/\cosh G] + \exp(2e\eta/kT) \quad [6]$$

where

$$G \equiv Q \exp(-e\eta/2kT) \quad [7]$$

and

$$Q \equiv [I_0 L^2 / 2eDC_0]^{1/2} \quad [8]$$

The total current per unit area of electrode is then

$$I = (I_0/Q) [\exp(3e\eta/2kT) - \exp(-e\eta/2kT)] \tanh G \quad [9]$$

The quantity Q defined by Eq. [8] is a measure of the relative ratio of the charge exchange rate and the interfacial diffusion rate. If the latter is much greater than the former, we have $Q \ll 1$. In this case, $\tanh G \cong G$ in Eq. [9] and that equation becomes

$$I = I_0 [\exp(e\eta/kT) - \exp(-e\eta/kT)] \quad [10]$$

which is the same as Eq. [2] with $C(u, v) = C_0$. Therefore, under these conditions, the interfacial diffusion has no effect on the total current. Alternatively, if the diffusion rate is much smaller than the exchange rate, or $Q \gg 1$, the \tanh function will then equal unity and Eq. [9] becomes

$$I = (I_0/Q) [\exp(3e\eta/2kT) - \exp(-e\eta/2kT)] \quad [11]$$

Comparing Eq. [11] and [10], we find that both are of the Butler-Volmer form except that in Eq. [11] I_0 , α_a , and α_c take on new (primed) values

$$I_0' = I_0/Q \quad [12]$$

$$\alpha_a' = 3/2 \quad [13]$$

$$\alpha_c' = 1/2 \quad [14]$$

At low $|\eta|$ ($\ll kT/e$), Eq. [11] can be linearized to obtain

$$I = I_0'(2e\eta/kT) \quad [15]$$

Thus, at low $|\eta|$ the electrode polarization is ohmic, while at large $|\eta|$ a plot of $\ln |I|$ vs. $|\eta|$ gives a Tafel slope of $(3e/2kT)$ at the anode and $(e/2kT)$ at the cathode.

In Fig. 2, Eq. [9] is plotted as $\log(I/I_0)$ vs. η for various values of Q . We see that for $Q < 0.4$ Eq. [10] is a good approximation, while for $Q > 4$ Eq. [11] suffices.

At high temperature and/or low p_{O_2} , where $\theta \ll 1$, according to the previous study (1), $I_0 \propto p_{O_2}^{1/4}$ and $C_0 \propto p_{O_2}^{1/2}$. Substituting these results into Eq. [8] and [12], we find that I_0' should have the following p_{O_2} dependence

$$I_0' \propto p_{O_2}^{3/4} \quad [16]$$

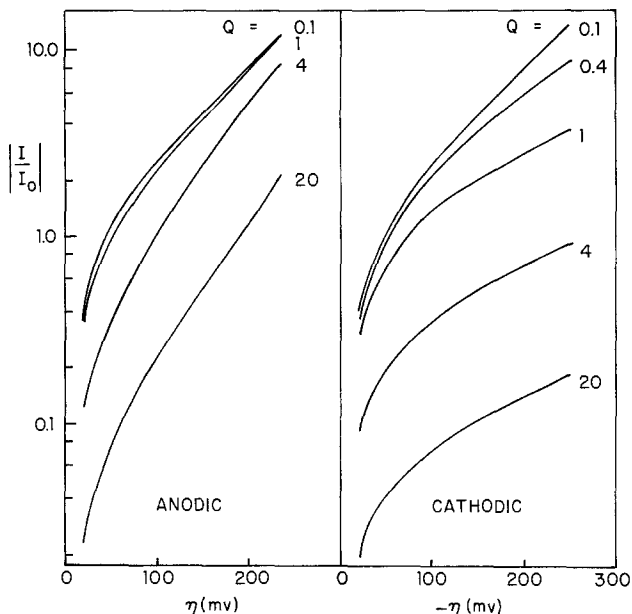


Fig. 2. Plot of $\log I/I_0$ vs. η (both cathodic and anodic) as calculated from Eq. [9] for different values of Q at a temperature of 800°C .

Alternatively, we may choose Eq. [5] as the boundary condition instead of Eq. [4]. Following a procedure similar to the one above, we obtain for the total current density

$$I = (I_0/Q) \{ [\exp(3e\eta/2kT) - \exp(-e\eta/2kT)] / [(DG/\gamma L) + \coth G] \} \quad [17]$$

For $Q \ll 1$, this equation becomes

$$I = [\exp(e\eta/kT) - \exp(-e\eta/kT)] / [I_0^{-1} + \exp(-e\eta/kT)/I_1] \quad [18]$$

where I_1 is defined as

$$I_1 = 2e\gamma C_0/L \quad [19]$$

which is the general form for the current when there is a limiting current density I_1 (1). For $Q \gg 1$, Eq. [17] becomes

$$I = [\exp(3e\eta/2kT) - \exp(-e\eta/2kT)] / [Q/I_0 + \exp(-e\eta/2kT)/I_1] \quad [20]$$

Comparing Eq. [19] and [20], we find that both take the same form, if for the interfacial-diffusion controlled case (Eq. [20]) we let I_0 , α_a , and α_c be replaced by new (primed) values, exactly as given in Eq. [12]-[14].

Equation [20] can be linearized for $e|\eta| \ll kT$ and becomes

$$I = I_0''(2e\eta/kT) \quad [21]$$

where

$$I_0'' = I_0'I_1/(I_0' + I_1) \quad [22]$$

The above derivation, Eq. [6]-[22], can be generalized for other geometrical shapes of the electrodes. The solutions for diffusion-limited behavior should be similar to Eq. [11] and [20], except that Q will then involve different geometrical parameters.

Experimental Methods

Doped ceria electrolytes and platinum paste electrodes were prepared as described previously (1). The arrangement for the current interruption method is also described in Ref. (1)-(3), as are the sample chamber and gases used (O_2 -Ar mixtures).

The platinum foil electrodes utilized platinum foil $12.7 \mu\text{m}$ thick and of 99.99% purity. An unfluxed Pt paste (Engelhard 6926) was first brushed on the surface of the electrolyte, onto which the Pt foil was

pressed under an alumina disk weighing 23g. This combination was fired at 950°C for 7 days (denoted electrode A) or at 1500°C for 4 hr in an argon atmosphere (denoted electrode B).

Silver electrodes generally were prepared by painting flexible silver coating (Engelhard No. 16) on the electrolyte, then firing at 600°C in open air for 2 hr. Silver foil ($127 \mu\text{m}$ thick, 99.99% purity) was rolled down to $50.8 \mu\text{m}$, after which it was lightly etched in cold 30% HNO_3 to eliminate any possible surface contamination. It was then rinsed in distilled water and finally in acetone. Silver foil electrodes were prepared by first brushing the surface of the electrolyte with silver paste (Engelhard No. 16), then pressing the foil on it with a 23g alumina disk, and finally, firing at 700°C for 8 hr.

Gold electrodes were prepared by brushing gold paste (Engelhard A-2123) onto the surface of the electrolyte and firing at 800°C in open air for 4 hr. The average thickness of paste electrodes (silver and gold) is estimated by weighing the samples with and without the electrodes. The difference in weight was then divided by the density of the metal and nominal electrode area. Generally the average thickness ranges from 1.0 to $1.8 \mu\text{m}$.

After the electrical experiments were completed, some samples were cut into small pieces ($<0.6 \times 0.8 \text{ cm}^2$) and placed into a JEM-100C electron microscope for electrode surface scanning at a magnification of $1000\times$. Platinum foil and silver foil electrodes were also examined by an optical microscope at a magnification of $778\times$; in this way the entire sample could be examined without being destroyed.

Results

It was previously demonstrated (1) that for chemisorption of oxygen on Pt, θ becomes rather high at the lower temperatures (with $\theta = 1/2$ at $p_{\text{O}_2} = 0.94 \times 10^{-3}$ atm and $T = 550^\circ\text{C}$). In the present study of Pt-foil electrodes, the temperature was limited to values near 800°C so as to keep $\theta \ll 1$.

Two platinum foil electrodes (A and B) which were prepared differently (see Experimental Methods) were tested, and typical results are shown in Fig. 3. The

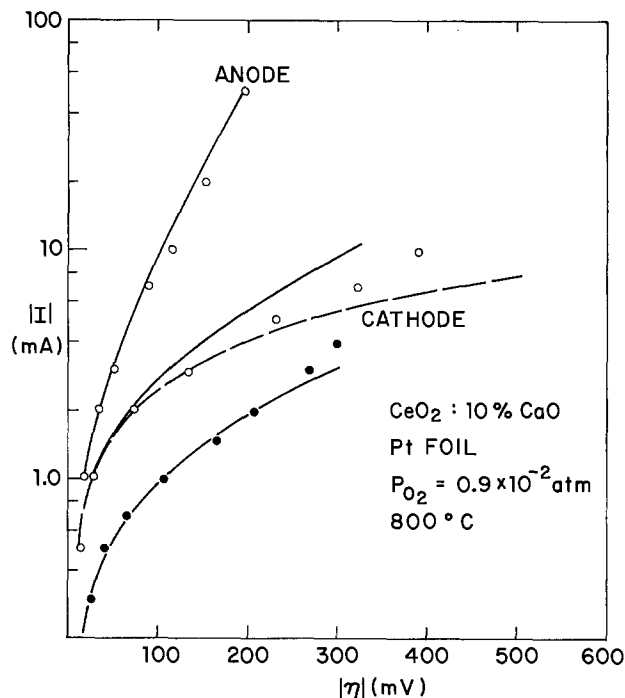


Fig. 3. Anodic and cathodic polarization curves for the two Pt foil electrodes at 800°C . Open circles are for electrode A and filled circles for electrode B. Solid lines and dashed lines are, respectively, the fits to Eq. [11] and [20].

anodic results could always be fitted to Eq. [11], in which the one adjustable parameter (I_0') was obtained from the linear range (where $|\eta| \ll kT$) by utilizing Eq. [15]. (For clarity, the anodic results for electrode B are omitted in Fig. 3.) The cathodic data were fitted either in the same way (solid curves) or to Eq. [20] (dashed curve), which involves I_1 as a second parameter. For electrode A this second fitting is more satisfactory, indicating the need to include a limiting current. Using previously published values of I_0 [(1), Fig. 13] and Eq. [12], values of Q of 9.5 and 26 are obtained for electrodes A and B, respectively.

Results for the p_{O_2} -dependence of I_0' for both foil electrodes are given in Fig. 4. The two solid lines are drawn with the slope of 3/8, in agreement with Eq. [16]. The reproducibility of the data is good, in contrast to those for the Pt paste electrodes where changes could be produced by high applied currents (1). No time-dependent effects were detected in the present range of temperature and p_{O_2} .

The observed polarization of silver paste electrodes can also be described by Eq. [11] or [20]. Typical results are given in Fig. 5, where both anodic and cathodic data are presented and fitted to Eq. [11]. The circled numbers mark the values of overpotentials at which transient behavior is studied, as given in Fig. 6. Comparison with Ref. (2) shows that the overpotentials decay very slowly in this case, clearly suggesting that activation polarization is not the rate-controlling process.

Results for the p_{O_2} -dependence of I_0' for the Ag electrodes are given in Fig. 7 in the temperature range between 700° and 500°C. The solid lines in this log-log plot are drawn with a slope of 3/8. It is clear from Fig. 7 that the same power-law dependence of I_0' on p_{O_2} is obeyed over the entire temperature range, in contrast to the results for Pt paste electrodes (1). The temperature dependence of I_0' at constant p_{O_2} is given in Fig. 8 along with data for other paste electrodes. The straight line drawn through the Ag data in this plot gives an activation energy of 1.1 eV.

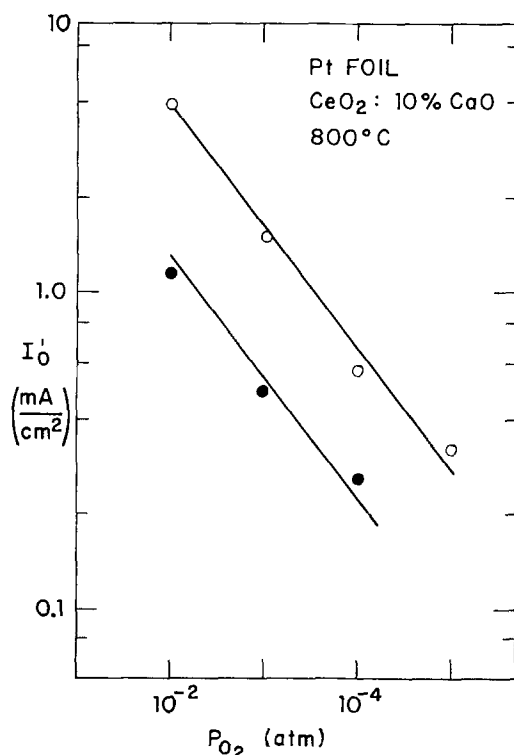


Fig. 4. Dependence of I_0' on p_{O_2} for the two Pt foil electrodes. Open and filled circles are for electrodes A and B, respectively. The straight lines are both drawn with slope of 3/8.

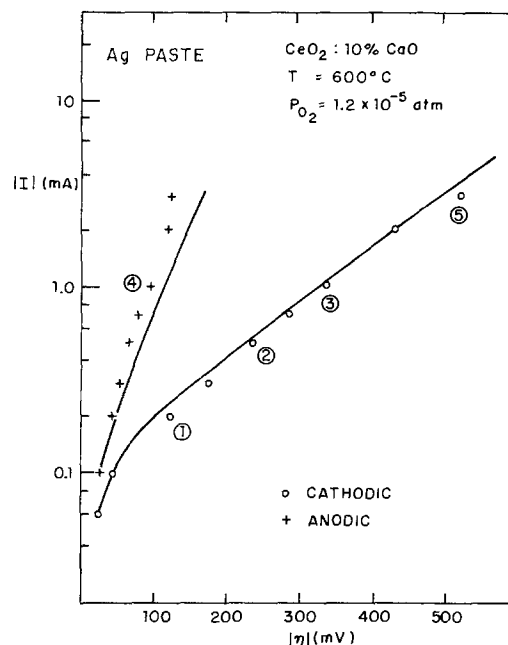


Fig. 5. Anodic and cathodic polarization curves for Ag paste electrode at 600°C. Solid lines are the fits to Eq. [11]. Circles mark the overpotentials at which the transient data of Fig. 6 are obtained.

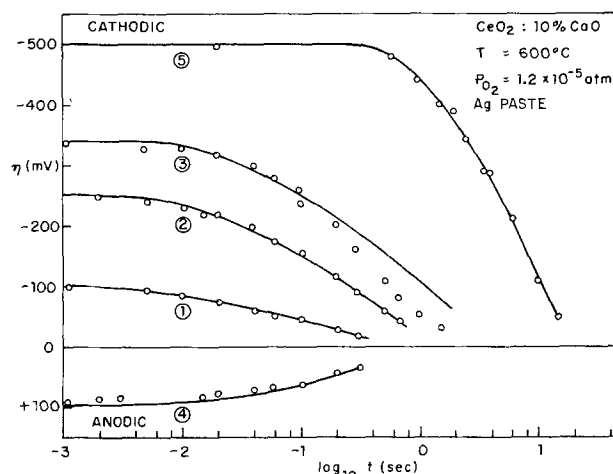


Fig. 6. Decay of cathodic and anodic overpotentials with time corresponding to the five points marked on Fig. 5.

Silver foil electrodes give results similar to the silver paste except that, at the cathode, limiting current effects are more prevalent in the case of the foil. Figure 9 shows a typical result, with the anodic data fitted to Eq. [11] and the cathodic data to Eq. [20]. The quantity I_0' is similar in magnitude to that for silver paste electrodes. At low overpotentials ($<kT/e$) the polarization again shows linear behavior in accordance with Eq. [15] and [21].

In Fig. 10, I_0' and I_1 are plotted as functions of temperature; I_0' is found to have an activation energy of 1.1 eV, the same as that of the Ag paste electrodes. In the case of I_1 , as well as I_0'' (not shown), a straight line is not obtained over this range. These same data, when plotted vs. p_{O_2} at constant temperature show that $I_0' \propto p_{O_2}^{3/8}$ in agreement with the results for Ag paste electrode (Fig. 7), while I_0'' and I_1 show roughly $p_{O_2}^n$ behavior with $n = 1/2$ and 1, respectively.

The polarization of gold paste electrode can also be described by Eq. [11]. The p_{O_2} -dependence of I_0' at 785°C is shown in Fig. 11, where the solid line is again drawn with a slope of 3/8; however, there is a deviation from this power law at low p_{O_2} . The tem-

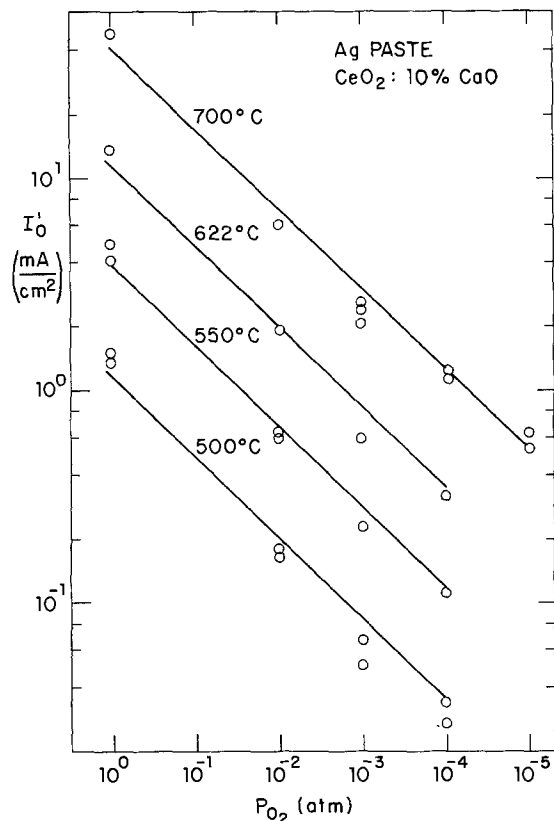


Fig. 7. Variation of I_0' with p_{O_2} for Ag paste electrodes at various temperatures. The straight lines are all drawn with slope of 3/8.

perature dependence of I_0' is given in Fig. 8 (open circles) for two different p_{O_2} ; in both cases the slope corresponds to an activation energy of 1.69 eV.

At sufficiently low p_{O_2} , we find that the entire range of the cathodic polarization cannot be fitted very well by either Eq. [11] or [20]. A typical example for an Ag foil electrode at 735°C is given in Fig. 12. The open circles are the data and the solid line A is the fit of Eq. [20]. The solid circles give the difference of current $\Delta|I|$ between the measured values and line A. The plot of this difference as $\log \Delta|I|$ vs. $|\eta|$ shows a linear region of slope $2.3e/kT$. For Pt foil electrodes, similar behavior has also been observed, an example of which is given in Fig. 13 for a temperature of 600°C. The open circles represent the data and line A is the best fit of Eq. [11]. Again, the difference of current between the data and line A gives a slope of $2.3e/kT$.

Finally, we present results of scanning electron microscope and optical microscope examination of the various electrodes in order to relate the structures to the polarization behavior.

Figure 14(a) shows a freshly prepared platinum paste electrode without flux. The sizes of particles are the same as for the electrode with flux (1). Since this electrode is freshly prepared, the coarsening effect which we have reported previously has not taken place, and the width of Pt particles is around 1 μm . Figure 14(e) shows platinum foil electrode B. There are many pores, both along the grain boundary and inside the grains, which expose the electrolyte to the ambient gas; therefore, this electrode will not function as an oxygen-blocking electrode, as one might otherwise have expected.

Figure 14(b) shows the fresh silver paste electrode heated only to 500°C, while Fig. 14(c) represents the same electrode after heating to 700°C showing that sintering has taken place. Both of these Ag paste electrodes show considerably larger particles than the Pt electrode of Fig. 14(a). In Fig. 14(f), the silver foil electrode is shown. Again, we see that along the grain boundary and inside the grain there are many pores which expose the electrolyte to the am-

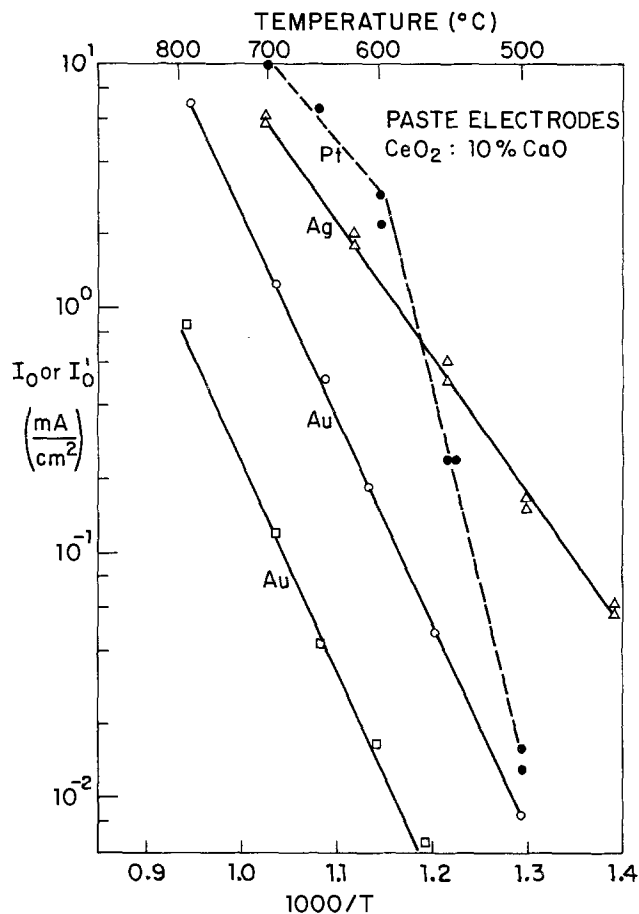


Fig. 8. Variation of I_0' (or I_0 , for Pt paste) with reciprocal absolute temperature for the various paste electrodes. All data are taken at $p_{O_2} = 0.9 \times 10^{-2}$ atm except for the lowest curve (squares) which was taken at 1.2×10^{-5} atm.

bient gas. Finally, Fig. 14(d) shows the gold paste electrode. The particles are larger than those of platinum paste and comparable to those of the silver paste electrodes.

Examining the dendrite-like structure of the metal paste electrodes [Fig. 14(a)-(d)], we conclude that morphologically Fig. 1 provides a reasonable approximation to the actual structure. On the other hand, for

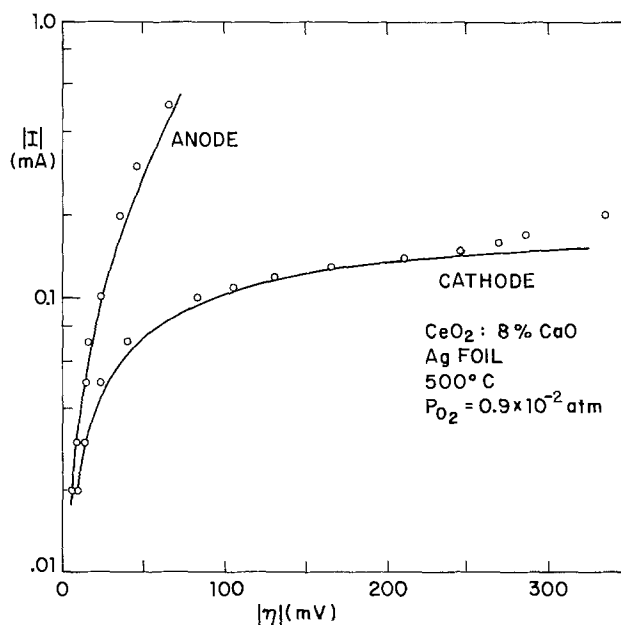


Fig. 9. Polarization curves for Ag foil electrodes at 500°C. The anodic data is fitted to Eq. [11] and the cathodic to Eq. [20].

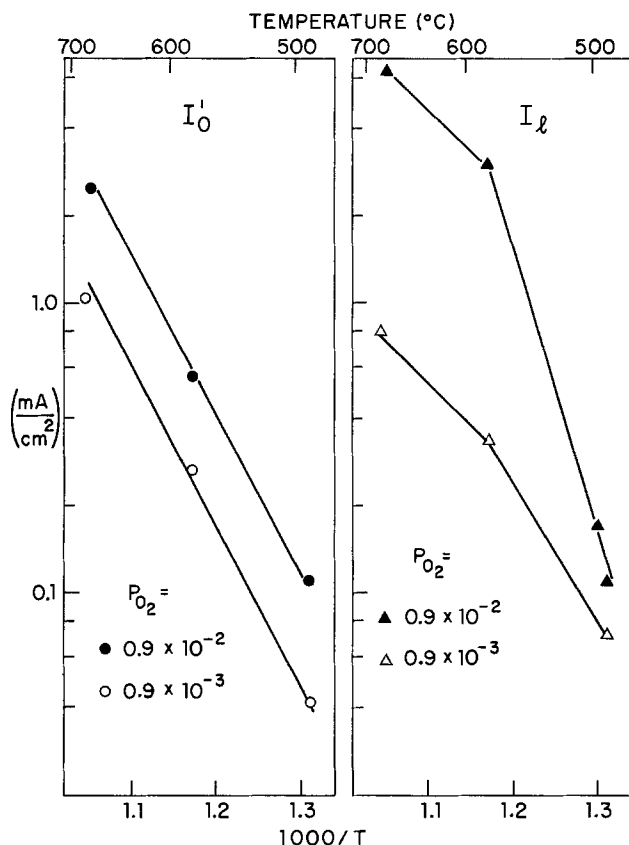


Fig. 10. Variation of I_0' and I_l with $1000/T$ for Ag foil electrodes at two values of p_{O_2} .

the foil electrodes [Fig. 14(e) and (f)], Fig. 1 is a poor representation; rather, a grid-like geometry would provide a better representation.

Discussion

Pt electrodes.—An important result of the present work is the clear demonstration that, for platinum foil electrodes, polarization at both the anode and the cathode is controlled by interfacial diffusion. The verification of this statement follows from the observation that the Butler-Volmer equation is obeyed with $\alpha_a' = 3/2$, $\alpha_c' = 1/2$, and $I_0' \propto p_{O_2}^{3/8}$, in agreement with the

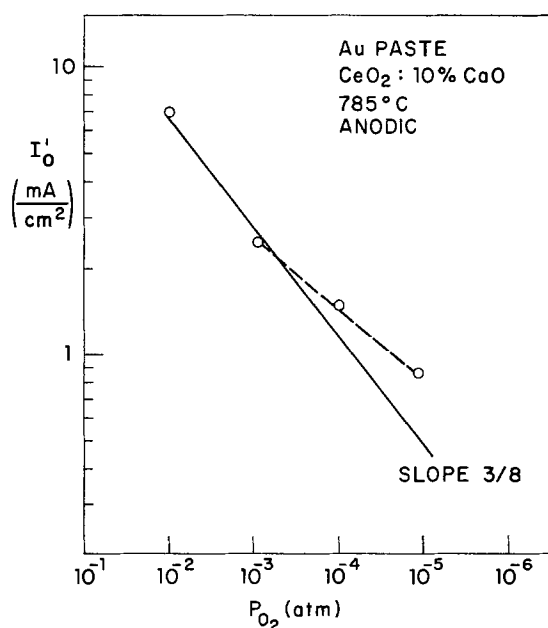


Fig. 11. Variation of I_0' with p_{O_2} for Au paste electrode at 785°C . The solid line is drawn with slope of $3/8$.

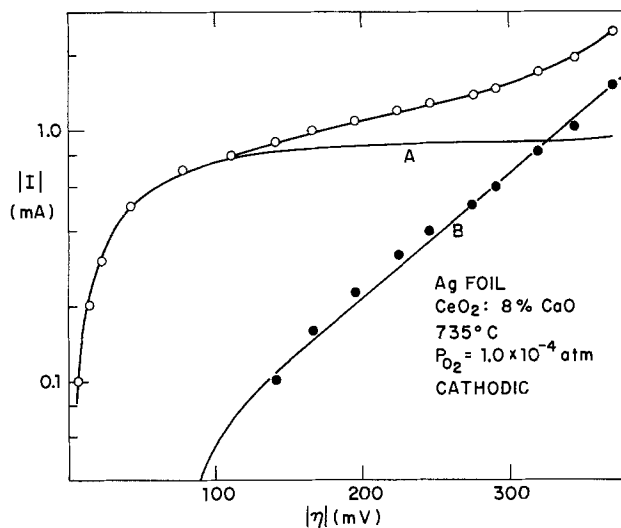


Fig. 12. Cathodic polarization curve for Ag foil electrode at 735°C and $p_{O_2} = 10^{-4}$ atm (open circles). Line A is the fit to Eq. [20]. Filled circles are obtained by subtracting line A from the data. Line B is obtained from Eq. [24] with E replaced by $|\eta|$.

theory (see Eq. [13], [14], and [16]), in contrast to the previous result (1) that under charge-transfer process control, platinum paste electrodes show $\alpha_a = \alpha_c = 1$ and $I_0 \propto p_{O_2}^{1/4}$.

Next we discuss the quantity Q . Based on Eq. [8], it involves the exchange current I_0 , oxygen adatom concentration C_0 , interfacial diffusivity D , and the geometrical parameter L . Values of I_0 and C_0 are available from the previous study (1), while microscopic observations of the electrodes (as in Fig. 14) give the magnitudes of L . Lewis and Gomer (9) have measured the surface diffusion rate of oxygen on (100)- and (111)-oriented Pt field emitters and expressed the results as

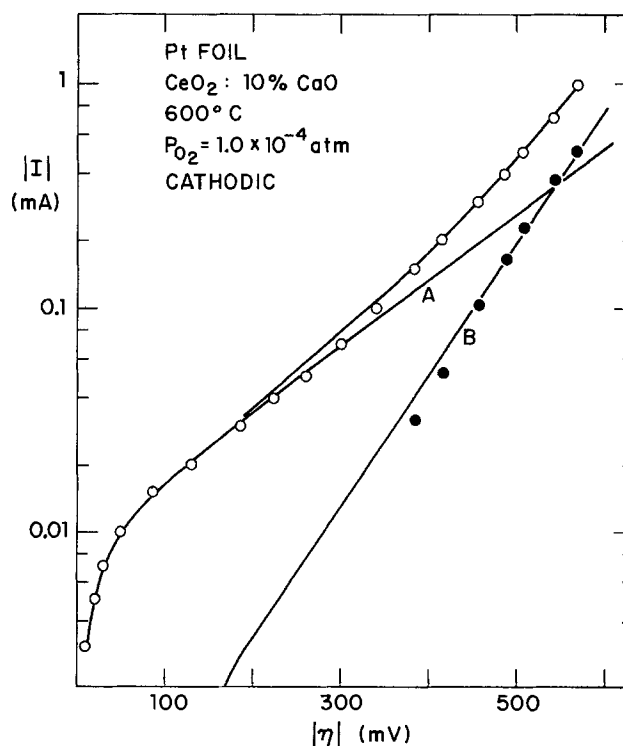


Fig. 13. Cathodic polarization curve for Pt foil electrode B at 600°C and $p_{O_2} = 10^{-4}$ atm (open circles). Line A is the fit to Eq. [11]. Filled circles and line B are as in Fig. 12.

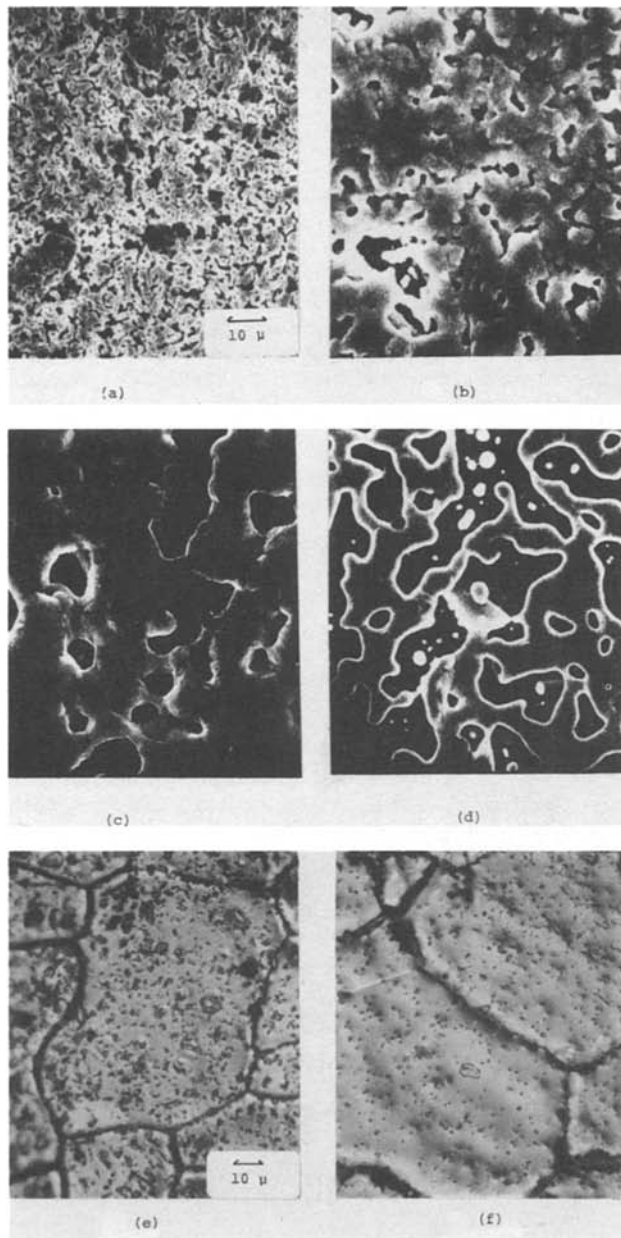


Fig. 14. Surface scanning electron micrographs (magnification $1000\times$) of various paste electrodes: (a) Pt (without flux), (b) Ag, freshly prepared and heated to 500°C , (c) Ag, after several cycles of measurement up to 700°C , (d) Au. Optical micrographs (magnification $735\times$) of foil electrodes: (e) Pt, electrode B and (f) Ag.

$$D = a^2\nu \exp(\Delta S/k) \exp(-E_d/kT) \quad [23]$$

with $a = 3A$, $\Delta S = 17 \text{ eu}$, $\nu = 10^{12} \text{ sec}^{-1}$, and $E_d = 1.48 \text{ eV}$, for temperatures above 500 K and with low oxygen adsorption ($\theta \ll 1$). In the absence of better information, we tentatively use Eq. [23] for the interfacial diffusion coefficient. With all of this data, we are able to estimate values of Q for Pt electrodes. Table I lists the calculated values of Q for the various p_{O_2} employed here, for $T = 800^\circ\text{C}$ and $L = 1 \mu\text{m}$. (Since Q is linearly proportional to L , the Q value for a given p_{O_2} and another value of L can easily be obtained.)

From Fig. 2, we see that, in order to have a pure charge transfer process, the value of Q must be less than unity. Referring to Table I, this means the Pt particles should not be larger than $0.2 \mu\text{m}$ (or $L \leq 0.1 \mu\text{m}$). The width of platinum particles of a freshly prepared electrode, as determined by SEM, is $\sim 1 \mu\text{m}$ [Fig. 14(a)]. However, considering the curvature of the Pt particles and the surface roughness of the electrolyte, it is reasonable to expect that the actual

Table I. Values of Q for Pt electrodes calculated from Eq. [8] for $T = 800^\circ\text{C}$ and $L = 1 \mu\text{m}$. [D is obtained from Ref. (9) and i_0 and C_0 from Ref. (1)].

| p_{O_2} (atm) | Q |
|------------------------|-----|
| 0.92×10^{-2} | 9.5 |
| 0.94×10^{-2} | 13 |
| 1.0×10^{-2} | 17 |
| 1.2×10^{-2} | 22 |

contact between the particles and the electrolyte involves a smaller value of L . It is thus understandable why freshly prepared Pt-paste electrodes give polarization behavior characteristic of the simple charge transfer process (1). For Pt foil electrode A (which had a relatively low heat-treatment temperature), it is probably the Pt paste between foil and the electrolyte, and not the foil itself, which controls the polarization. Previous results (1) have demonstrated that a heat-treatment like the one used in the preparation of electrode A can cause the Pt particles to coarsen by a factor of 3 ($1 \rightarrow 3 \mu\text{m}$). In addition, the placing of a weight on top of the Pt foil during firing can only have served to enlarge the actual contact area. Taking $2L = 3 \mu\text{m}$ (for $p_{\text{O}_2} = 0.92 \times 10^{-2} \text{ atm}$) gives $Q = 14$, in reasonable agreement with the actual value of 9.5. Figure 2 shows that such a Q value is well into the range where interfacial diffusion controls the polarization. For Pt foil electrode B we believe, based on Fig. 14(e), that actual contact between electrolyte and Pt foil has been established; therefore the Pt foil plays the major role. Figure 14(e) shows that pores in the foil have an average separation $\sim 5 \mu\text{m}$; using Table I this corresponds to $Q \cong 24$, in good agreement with the actual value of 26.

There is reason to question whether oxygen adatoms can diffuse into the interface region between electrode and electrolyte and, if so, whether the diffusivity is the same as that measured for oxygen over the free and clean surface of a Pt crystal. It appears reasonable to expect that, as long as there is no strong chemical bonding between the platinum and the electrolyte, oxygen adatoms should have no difficulty in diffusing along the interface, and with a diffusivity that is similar (at least in order of magnitude) to that for the free surface. That bonding is indeed very weak between Pt and doped CeO_2 is supported by the fact that the unfluxed Pt paste electrode can easily be rubbed off with the finger tips.

Multilayer oxide films can be grown on the surface of high purity polycrystalline Pt under appropriate temperatures and oxygen pressures. If this had occurred in the present experiments, it would be the platinum oxides that act as the electrode, not the platinum. A recent study (10) which establishes the dissociation pressure-temperature relationship between Pt oxide and Pt shows, however, that within the present experimental range of p_{O_2} and T no Pt oxide layer will form. This is also consistent with our observation that the electrode polarization is reproducible and not time dependent.

Ag electrodes.—The solubility and diffusivity of oxygen in solid silver is relatively high (11). Assuming that the outer surface layer of the silver is always saturated with an equilibrium concentration of chemisorbed oxygen and that the diffusion of the oxygen from this saturated layer through the body of the silver is the rate-limiting step, one can calculate limiting currents, I_l , for cases such as those given by Fig. 5 and 9. The values obtained are consistently at least one order of magnitude too small. It is therefore reasonable to conclude that bulk diffusion cannot be the rate-controlling step. In fact, silver paste electrodes behave like platinum foil electrodes in that the anodic and cathodic polarizations can be described by the

Butler-Volmer equations with $\alpha_a' = 3/2$ and $\alpha_c' = 1/2$, I_0' has a 3/8 power dependence on p_{O_2} , and the overpotentials decay slowly (see Fig. 6). [If the polarization were of the activated type, η should decay to zero within 10^{-4} sec (2).] Therefore, we conclude that for Ag electrodes, polarization is also controlled by interfacial diffusion.

Oxygen chemisorption on the surface of silver single crystals has been widely studied (12-14). It has been shown that oxygen adsorbs on the surface and dissociates into oxygen atoms, similarly to the case of platinum, although the equilibrium adatom concentration is lower. Thus, for example, on the silver (110) face, $\theta = 1/2$ is obtained at 500 K and $p_{O_2} = 10 \times 10^{-4}$ Torr (11); assuming that adsorption obeys the Langmuir equation, we calculate that $\theta = 1/2$ at $T = 500^\circ\text{C}$ for $p_{O_2} = 1.6$ atm. Such estimates show that, within the present experimental ranges of temperature and p_{O_2} , θ is always less than $1/2$. This explains why there is no change of slope in the isothermal plot of I_0' vs. p_{O_2} for silver electrodes, while there is a sharp change for platinum paste electrodes (see Fig. 8).

Both Ag paste and Ag foil give not only the same p_{O_2} - and temperature-dependence of I_0' , but also the same magnitude of I_0' . This is probably because of the many pores that exist in the silver foil [see Fig. 14(f)], which expose the electrolyte to the ambient gas.

Tannenberger *et al.* (15) have studied silver paste electrodes with a doped zirconia electrolyte using a current-interruption method. This method differs from the present one only in that it did not use a reference electrode, and therefore they measured the total overpotential, $\eta_t = (\eta_a - \eta_c)$, instead of η_a and η_c separately. In their work, ohmic behavior was observed in the range below 300 mV. At 811°C and air atmosphere their data yield $I_0' = 76$ mA/cm². By adding the present cathodic and anodic polarizations for Ag paste electrodes and extrapolating the data to their experimental conditions, a linear range for η_t up to 300 mV was found, as well as a value of I_0' of 85 mA/cm². This agreement between these two diverse studies is most satisfactory.

The results for the limiting current density, I_1 , reported in Fig. 10 show that the behavior of this quantity is more complex than that of I_0' and indicates that different mechanisms may be involved at high and at low temperatures. In previous work on Pt paste electrodes (1), we also found that the quantity I_1 was more difficult to control or reproduce than the exchange current I_0 . Since the quantity I_0'' obtained from the ohmic range involves both I_0' and I_1 , (see Eq. [21] and [22]), we must conclude that, until there is better control and understanding of the limiting-current behavior, measurements of I_0'' (or of the resistance in the ohmic range) are not as meaningful as one might have hoped. In support of this statement, it is noteworthy that measurements of ohmic resistance with Ag electrodes by a-c or d-c methods have yielded no distinct p_{O_2} dependence or activation energy (16-18).

Au electrodes.—Gold is one of the least active metals in chemisorption; none of the common adsorbates, including oxygen, have been found to chemisorb at room temperature (19). At high temperatures, substantial evidence is available for the existence of chemisorption at moderate p_{O_2} ($> 10^{-5}$ atm) but not at low p_{O_2} ($\sim 10^{-8}$ atm) (20-23). For the present experimental range of temperature and p_{O_2} , there is no doubt that some chemisorption of oxygen occurs on the gold paste electrodes, although to a lesser extent than for silver and platinum ($\theta_{Au} < \theta_{Ag} < \theta_{Pt}$).

The polarization behavior of Au paste electrodes is sufficiently similar to that of silver paste and platinum foil electrodes as to lead to the conclusion that, also in this case, it is controlled by surface diffusion. However, the departure, at low p_{O_2} , from a slope of $3/8$ (Fig. 11) is not understood.

In Fig. 8, we have collected data for I_0' of Au and Ag and I_0 of Pt paste electrodes for comparison. The fact that the activation energies are different for various metals supports the present model that the controlling diffusion process occurs on the metal surface, rather than, say, on the electrolyte. It is also noteworthy that the relatively high activation energy (1.69 eV) of gold electrodes serves to bring the magnitude of I_0' close to that for Pt and Ag electrodes at high temperatures (800°C - 1000°C).¹

Reduction phenomenon.—The departure from the fitted curves at high $|\eta|$ in Fig. 12 and 13, is very interesting and can be explained with the help of the present model. Using Eq. [6], we plot in Fig. 15, the relative surface concentration of oxygen $C(u)/C_0$ as a function of the relative distance u/L on a log-log scale for various cathodic overpotentials at $T = 700^\circ\text{C}$. As clearly shown in this figure, the concentration gradient is significant only at the periphery ($u/L \approx 1$); further, the larger Q (or $|\eta|$) the more extreme is this effect. Over most of the electrode area $C(u)/C_0$ is nearly constant. Equation [3] shows that in such regions there will be almost no ionic current. Physically, what happens is that almost all of the oxygen adatoms leaving the edge are immediately drawn into the electrolyte because of the relatively high local charge transfer rate. The rest of the area is then left without a supply of reactants, forming a so-called ionically blocking electrode.

According to Wagner's polarization theory (24), an electronic current will flow as a result of reduction of the electrolyte adjacent to an ionically blocking cathode to give an electronic current I^e of

$$I^e = I_0^e [1 - \exp(-eE/kT)] \quad [24]$$

where I_0^e is a constant and E is the total emf across the sample. This equation follows under the assumptions that there is no ohmic polarization from electrode leads

¹ This fact can have practical significance in that it suggests that Au (or Au alloy) paste may be useful for high temperature electrodes in a range ($\geq 800^\circ\text{C}$) where Ag is not suitable because of its high vapor pressure and Pt because of the difficulty in producing adhesion.

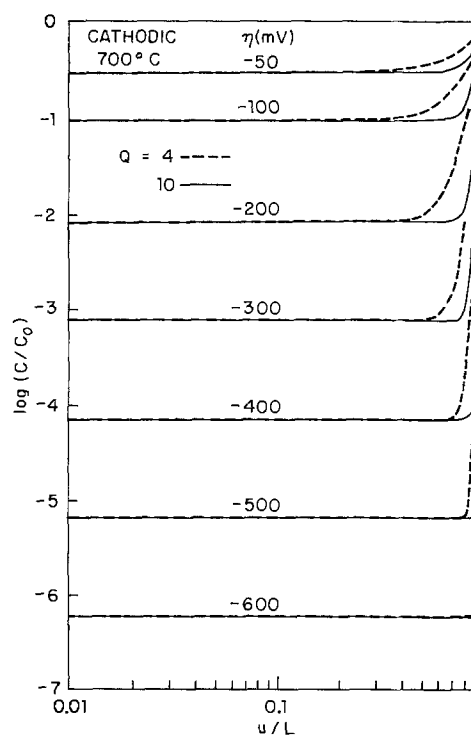


Fig. 15. Dependence of (C/C_0) on the fractional distance from center of the electrode at 700°C for various cathodic overpotentials, as calculated from Eq. [6] for $Q = 4$ and 10 (dashed and solid curves, respectively).

or electrolyte and that the anode is reversible to the conducting ion. In a previous study (3), we have shown that for the case of incomplete blocking at the cathode and $\eta_a \neq 0$, Eq. [24] remains valid but with E replaced by $|\eta|_c$, which is measurable using the current interruption method with the help of a reference electrode.

Under the conditions shown in Fig. 15, the current is, therefore, ionic in the peripheral region while over the rest of the electrode it is predominantly electronic, and the total current should be the sum of both. The electronic current is given by Eq. [24] with E replaced by $|\eta|_c$. Thus, at high $|\eta|_c$ ($|\eta|_c > kT$), a slope of $2.3e/kT$ is predicted for the plot of $\log I^e$ vs. $|\eta|_c$, in agreement with the observations in Fig. 12 and 13.

Another consequence of Fig. 15 is that, since the ionic current is only concentrated in the peripheral region, the electrolyte polarization is of the constriction type. Indeed, constriction polarization has been observed in the work of Tannenberger *et al.* (15) with silver paste electrodes. By varying the thickness of an yttria-stabilized zirconia electrolyte, they found a residual resistance which they attributed to the fact that the electrodes are active only on discrete spots, although they had no further explanation.

Conclusions

1. The charge transfer reaction takes place in the two-phase region between the metal electrode and the oxygen-ion conducting electrolyte. For most electrodes, the rate of this reaction is limited by diffusion of oxygen atoms on the metal surface along the electrode-electrolyte interface, a mechanism often neglected when the totality of possibilities is considered (25). Only if the electrode particle dimension ($2L$) is small enough, as in the case of freshly prepared Pt paste electrodes, have we observed the pure charge transfer mechanism.

2. If the rate of surface diffusion is lower than the local rate of charge transfer, ionic current will flow predominantly near the three-phase (gas-electrode-electrolyte) region. In that case, the central area of the electrode particle becomes initially blocking and electrons may be injected into the electrolyte. The Wagner polarization-cell theory can then be used to describe the behavior.

Acknowledgments

This work was supported by the U.S. Department of Energy under Contract ER 78-S-02-4693.

Manuscript submitted March 13, 1980; revised manuscript received Aug. 6, 1980. This was Paper 3 presented at the Boston, Massachusetts, Meeting of the Society, May 6-11, 1979.

Any discussion of this paper will appear in a Discussion Section to be published in the December 1981 JOURNAL. All discussions for the December 1981 Discussion Section should be submitted by Aug. 1, 1981.

Publication costs of this article were assisted by the Department of Energy.

REFERENCES

1. Da Yu Wang and A. S. Nowick, *This Journal*, **126**, 1155 (1979).
2. Da Yu Wang and A. S. Nowick, *ibid.*, **126**, 1166 (1979).
3. Da Yu Wang and A. S. Nowick, *ibid.*, **127**, 113 (1980).
4. D. O. Raleigh, *Adv. Electroanal. Chem.*, **6**, 88 (1973).
5. J. Vedel, in "Electrode Processes in Solid State Ionics," M. Kleitz and J. Dupuy, Editors, p. 223, D. Reidel Publishing Co., Dordrecht-Holland (1976).
6. L. R. Velho and R. W. Bartlett, *Metall. Trans.*, **3**, 65 (1976).
7. F. G. Will, *This Journal*, **110**, 145 (1963).
8. F. G. Will, *ibid.*, **110**, 152 (1963).
9. R. Lewis and R. Gomer, *Surf. Sci.*, **12**, 157 (1968).
10. R. J. Berry, *ibid.*, **76**, 415 (1978).
11. T. A. Ramanarayanan and R. A. Rapp, *Metall. Trans.*, **3**, 3239 (1972).
12. H. Albers, W. J. J. Van del Wal, O. L. J. Gijzeman, and G. A. Bootsma, *Surf. Sci.*, **77**, 1 (1978).
13. G. Rovida, *J. Phys. Chem.*, **80**, 150 (1976).
14. M. M. P. Janssen, J. Moolhuysen, and W. M. H. Sachtler, *Surf. Sci.*, **44**, 553 (1974).
15. H. Tannenberger and H. Siegert, in "Fuel Cell Systems-II," R. F. Gould, Editor, p. 281, Advances in Chem. Series 90, American Chemical Society, Washington (1967).
16. E. Schouler, M. Kleitz, and C. Deportes, *J. Chim. Phys.*, **70** [6], 35 (1973).
17. P. Fabry and M. Kleitz, *J. Electroanal. Chem. Interfacial Electrochem.*, **57**, 165 (1974).
18. E. Schouler and M. Kleitz, *ibid.*, **64**, 135 (1975).
19. M. A. Chesters and G. A. Somorjai, *Surf. Sci.*, **52**, 21 (1975).
20. I. S. Sazonova and N. P. Keier, *Kinetics and Catalysis*, **6**, 390 (1965).
21. N. V. Kul'kova and L. L. Levchenko, *ibid.*, **6**, 688 (1965).
22. P. C. Richardson and D. R. Rossington, *J. Catal.*, **20**, 420 (1971).
23. D. D. Eley and P. B. Moore, *Surf. Sci.*, **76**, L599 (1978).
24. C. Wagner, in "Proceedings of Seventh Meeting of International Committee of Electrochemistry, Thermodynamics and Kinetics (CITCE) Lindau 1955," p. 361, Butterworths, London (1957).
25. S. Pizzini, in "Fast Ion Transport in Solids," W. van Gool, Editor, p. 461, North-Holland, Amsterdam (1973).

Bubble Effects on the Terminal Voltage of a Vertical Cell with Perforated Electrodes

Fumio Hine* and Koichi Murakami¹

Nagoya Institute of Technology, Nagoya 466, Japan

ABSTRACT

Effect of bubbles on terminal voltage, solution *IR*-drop, and overvoltage in a vertical cell with perforated electrode were investigated. Cell voltage was minimized by use of properly designed perforated electrode. Reduction of the surface area of such machined electrodes is an important disadvantage. With the experimental results obtained, an optimum was estimated to be in the range of 5-15% perforation depending on the current and the rate of gas evolution.

Vertical cells equipped with a pair of plate electrodes are a common style of electrolyzers such as found in water electrolysis cells and diaphragm-type chlorine cells. Such electrolyzers liberate gases at the electrodes, and the gas bubbles disperse in the electrolyte resulting in large solution *IR*-drops. Some bubbles may adhere or cover the electrode surface, in which case the overvoltage rises due to a significant increase of the actual current density. Such difficulties with gas bubbles must be minimized to save energy for the electrolytic process considered.

We have shown in a previous paper that circulation of electrolytic solution between two electrodes is of great importance for reducing the bubble effects in a vertical cell equipped with flat plate electrodes (1). For example, a solution downcomer was provided for this purpose.

Perforated electrodes employed in practical cells are useful to remove electrolytic gas bubbles quickly from the electrolysis zone to the back side. The dimensionally stable anodes (DSA) in modern diaphragm cells consisting of titanium mesh allow the mixture of chlorine gas and brine to pass through toward the inside space of the box-type electrode. Journé and Louvar have published a paper on the effectiveness of the gas-diverting electrodes of various shapes, which enable the diversion of the electrolytic gas bubbles to the back side of the electrode (2).

This paper deals with the effectiveness of the perforated electrodes on reducing the terminal voltage of vertical cells in which gas evolution takes place. Complicated patterns of the solution flow containing gas bubbles were observed. The electric resistivity of the gas-solution mixture and the overvoltage on the working electrode were measured. The current distribution along the vertical electrode was also studied.

As reference for discussion, results previously obtained for three types of vertical cells with a pair of nonperforated plate electrodes arranged in parallel for blocked convection, for natural circulation, and for pumped circulation, were used [see Fig. 2 in Ref. (1)].

Experimental Procedure

The flowsheet and the electrolytic cell employed were essentially the same as of the previous work with flat plate electrodes (1). That is, a vertical Lucite resin cell, 1m high, had a flat plate counterelectrode made of 304 stainless steel (SS) in parallel with a perforated plate test electrode, also SS, of 3 cm wide, 89 cm long, and 3 mm thick. The total area of perforation of the test electrode was varied in the range 0-60%. In the preliminary experiment, the hole diameter was changed from 3 to 8 mm, but had almost no effect on

the experimental results obtained, whereas the percent perforation was an important factor. Therefore, most experiments were conducted with test electrodes having 3 mm diam holes.

The test electrode was sectioned into ten segments to determine the current distribution. Each electrode segment had a shunt, of which one side was connected with a common copper bus bar.

Three pairs of the Luggin-Haber probes connected with respective reference electrodes consisting of Hg/HgO were provided at 8, 44, and 80 cm above the cell bottom to obtain the solution *IR*-drops at those respective points. The potential drop of the Luggin-to-electrode was also measured, and was referred to the polarization potential.

Caustic soda solutions, 0.5N and 2.0N NaOH, were electrolyzed, thus oxygen and hydrogen were liberated from the anode and the cathode, respectively, and those gases mixed together because there was no separator between the two electrodes. Caustic soda solution was circulated between the back-side space of the counter-electrode and the electrolyte reservoir to keep the solution temperature constant at 40°C. Its pumped circulation did not affect the gas-solution mixture in the electrolysis zone.

The electrode gap was varied in the range 3-25 mm, and the back-side space behind the test electrode was also changed from 0 to 30 mm.

The current density in this paper was based on the plain electrode. Therefore, the actual current density is about twice of the nominal value in the case of 50% perforation, for example.

Electrolysis was conducted up to 100A of total current, in which case the current density was 37.4 A/dm² on a test electrode of 3 × 89 cm² superficial area. In some cases, however, electrolysis was carried out with a part of the sectioned electrode to confirm the effect of the electrode height on the current distribution on a vertical electrode. For this purpose, some segments located at the bottom, the center, and the top were employed.

The voltage drops of the Luggin-to-Luggin and of the Luggin-to-electrode (referred to the solution *IR*-drop and the polarization potential, respectively) were measured to obtain the voltage balance through the cell. The terminal voltage was also measured. The Luggin probes were arranged from the back side of the electrode at those respective points to avoid turbulence of solution flow. Although the tip of the probe was located close to the electrode surface, the potential difference of Luggin-to-electrode contained some ohmic voltage drops along with the overvoltage.

Results and Discussion

The flow pattern of solution in a vertical cell during electrolysis was complicated, and affected greatly by the current density or the total current. Drawing A

* Electrochemical Society Active Member.

¹ Present address: The Japan Carlit Company Research Laboratory, Sibukawa, Japan.

Key words: electrolytic gas bubbles, electrolyte resistivity, cell voltage, current distribution, perforated electrodes.

in Fig. 1 illustrates a sketch of the flow pattern in a cell operated at 100A. The gas-solution mixtures passed through the perforated electrode all the way around, the back-side space was crowded, and complicated flow occurred. A part of the solution was recirculated through the holes at the bottom to the electrolysis zone. At low currents, such as 5A or at about 2 A/dm², gases liberated at the lower part of the electrode rose along the electrode and did not escape to the back-side space at the bottom. Those mixtures accumulated to pass through the holes of the electrode at a certain height, say 40 cm. The solution free of gas bubbles at the bottom of the back-side space was, of course, clear. The level at which the gas-solution mixture in the electrolysis zone diverted to the back side of the working electrode was related to the current up to 30A or ca. 10 A/dm² as shown in Fig. 1(B), but it remained almost constant at about 10 cm at higher currents. Also the level was dependent on the inter-electrode gap, i.e., the level became low in narrow channels due to the increase of gas void fraction even at the same current density. The flow pattern was almost independent of the percent perforation of the electrode in the range more than 10%.

Figure 2 shows the resistivity vs. current density curves at the top (80 cm above the cell bottom), the center (44 cm), and at the bottom (8 cm) in a cell equipped with a 20% perforated electrode positioned 10 mm away from the counterelectrode (the open points). The ordinate is the reduced resistivity ρ/ρ_0 , where ρ and ρ_0 are the resistivity of electrolytic solution with and without gas bubbles, respectively, and the abscissa is the local current density at the respective points.

Since the solution at the cell bottom is free of bubbles, the reduced resistivity is nearly unity over the wide range of current density. On the other hand, the resistivity increases with increasing current density at the center and the top of cell. The resistivity has a linear relationship with the current density at those points whereas the slope differs because of different fraction of gas void.

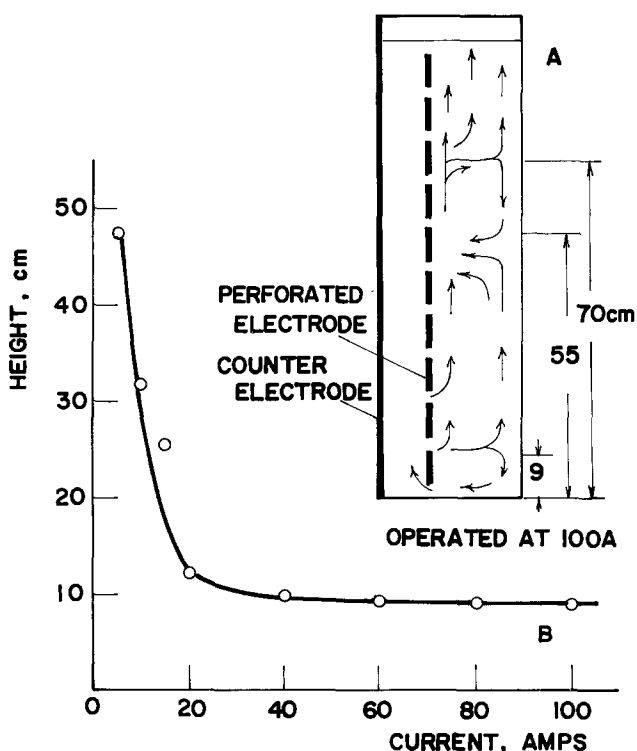


Fig. 1. Flow pattern of gas-solution mixture in a cell operated at 100A (A), and the lowest height for passing two-phase mixture as a function of current (B). Electrode gap = 1.1 cm; back-side space = 2.2 cm; electrolyte = 2N NaOH at 40°C.

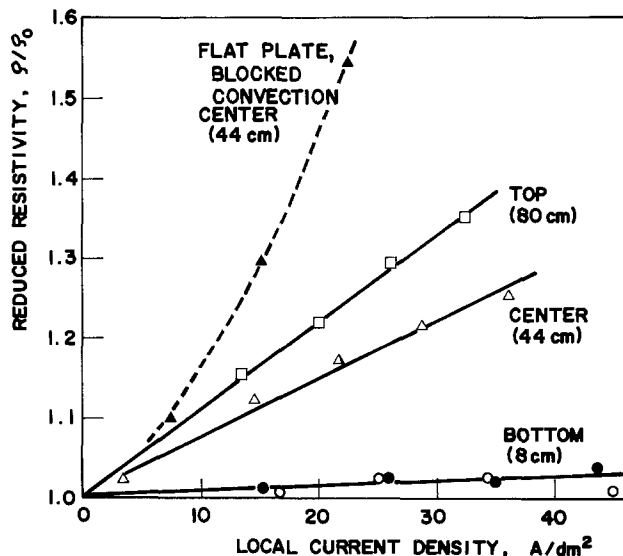


Fig. 2. Reduced resistivity vs. local current density curves at the top, the center, and the bottom of cell. Electrode gap = 1.9 cm; electrolyte = 2N NaOH at 40°C.

The experimental results obtained with a flat plate electrode under blocked convection are plotted as reference, shown by the closed points. No difference between the two cases can be found at the cell bottom, but the resistivity in a cell having a nonperforated electrode increases greatly with increasing current density at the center of cell (the dotted line). This tendency is more significant at the upper part of cell due to accumulation of electrolytic gas bubbles. The resistivity can be reduced considerably by solution circulation as described previously (1).

Variation of the resistivity causes the current distribution along the vertical electrode as shown in Fig. 3. The ordinate is the reduced height, x/h , where x is the distance from the bottom and h is the total height. The abscissa is the reduced current density, i_x/i_a , where the subscripts x and a refer to local and average, respectively. Drawing A illustrates the effect of the total current or the average current density. It is clear that the current distribution becomes uniform when the current density decreases because of the small volume of gas bubbles. The current density at a 40-50% height is about equal to the average value in all cases.

Figure 3B shows the current density vs. height curves obtained with the perforated electrodes of different sizes and locations. The test electrode had ten segments of equal size. Of these, three, five, and seven segments were employed as the working electrode to determine the effect of size. The location of the working surface was also changed: the top, the center, and the bottom of the cell. Although the plots fluctuated somewhat, we

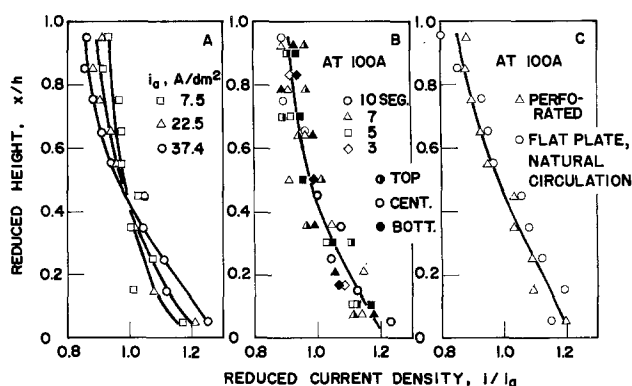


Fig. 3. Current distribution on the electrode as a function of the average current density (A), the electrode size and location (B), and the type of electrode (C). Electrode gap = 1.9 cm; electrolyte = 0.5N NaOH at 40°C.

considered that there was no significant effect of the electrode size and of the location on the i_x/i_a vs. x/h curve. Consequently, the current distribution on a tall electrode is relatively uniform in comparison to that on a short electrode.

Figure 3C shows the i_x/i_a vs. x/h curve for a perforated electrode operated at 100A compared to a flat plate electrode under natural circulation. The current distribution in both cases is almost the same. This is reasonable because the local current density is a function of the dimensionless height, $X = x/h$ (3)

$$i_x/i_a = 8(K + 2)^2 / (K + 4)(KX + 2)^2 \quad [1]$$

Although the gas effect parameter K contains many factors, it is in the range of 0.2-0.7, depending on the gas void fraction in the electrolysis zone, over the wide range of experiments (1). In the present case with the perforated electrode, electrolytic gases pass through the holes to the back-side space resulting in low gas void fraction. On the other hand, the electrolytic solution leaving excessive gas bubbles at the cell top with a flat plate under natural circulation through the downcomer provided at the back side of the electrode. The gas void fraction and the solution resistivity in both cases were confirmed to be about the same all the way along the electrode.

In a cell having a pair of flat plate electrodes operating under blocked convection, the local current density along the electrode varies greatly and the current distribution depends on the electrode gap at high current densities. In narrow channels less than 1 cm gap, the gas-solution mixture was slug flow, and the potentials to be measured fluctuated.

The current distribution with the perforated electrode is relatively uniform especially in narrow channels, and is a weak function of the electrode gap.

At small currents such as 20A or 7.6 A/dm² of the average current density, there is no significant difference of the current distribution between the flat plate electrode and the perforated electrode, and, of course, the current density along the electrode is uniform.

Drawing B in Fig. 4 shows the solution resistivity in the electrolysis zone as a function of the electrode gap. With a pair of the flat plate electrodes under blocked convection, the resistivity increases largely when the gap decreases. In a case of natural circulation, on the other hand, the solution resistivity is small except in narrow channels less than 7 mm in gap, and is a weak function of the electrode gap because the flow velocity of gas-solution mixture increases with decrease of the electrode gap, that is, the resistivity depends on the flow velocity (1, 4).

The solution resistivity in the electrolytic cell having a perforated electrode is kept low even if the electrode gap is small, say 3 mm.

The terminal voltage reflects this phenomenon as shown in Fig. 4A. The terminal voltage of a cell with a perforated electrode is a linear function of the electrode gap even in a narrow channel at high current densities. On the contrary, the voltage of the cell with a flat plate under natural convection rises greatly when the electrode gap becomes smaller than 5 mm.

However, it is important that the terminal voltage of the cell with a flat plate electrode is slightly lower compared to that of the perforated electrode when the electrode gap is larger than 10 mm. This is reasonable because the surface area of the perforated plate employed is 20% less than that of the flat plate of the same outside geometry. Therefore, this causes an increase in the solution IR-drop in a cell with perforated electrodes. Also the increase in overvoltage due to reduction of the surface area would be a factor.

Figure 5 illustrates that the solution resistivity decreases significantly when the perforation area increases from 0 to 10% as shown in Fig. 5C, but remains almost constant thereafter.

The overvoltage at 100A or 37.4 A/dm² is recorded to be a minimum in the range 5-15% of the perforation

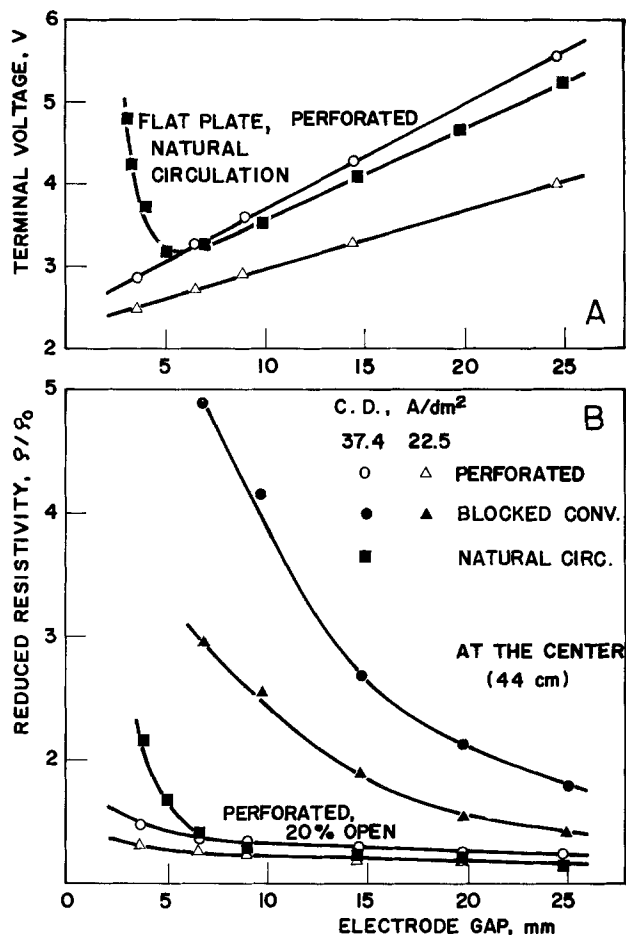


Fig. 4. Terminal voltage and solution resistivity as functions of the electrode gap. Back-side space = 1.2 cm; electrolyte = 2N NaOH at 40°C.

area (drawing B), but increases with increasing percent perforation.

According to the previous study on the current distribution in an electrolytic cell equipped with a pair of the flat plate electrodes in parallel, the ratio of the electrode-to-cell wall gap to the inter-electrode gap is an important factor on the current distribution and the total current under a given terminal voltage, that is, the larger the ratio the larger the current on the back side of electrode (5). With this concept, the effectiveness of the back-side area of the perforated electrode, also of the side wall of the holes, increases with decrease of the electrode gap. Since the current density decreases, the overvoltage is reduced slightly in a narrow channel.

Consequently, the terminal voltage depends on the percent perforation as shown in Fig. 5A. The voltage with a flat plate electrode (0% open) is very high because of a large fraction of gas void, but it decreases significantly with increasing area of holes. The terminal voltage becomes minimum in the perforation range 5-15% at 100A for example, and it rises gradually with increasing percent perforation because of excessive reduction of the electrode surface by machining. It was not significant, but the optimum point of perforation was dependent on the operating conditions, especially the current, *i.e.*, the larger the current the more the perforation.

Increase of the resistivity in the perforated electrode itself is also a factor of the terminal voltage if the percent perforation is large. The resistance of the electrode did not change significantly up to 15% perforation at about 3 mΩ for the longitudinal direction of the plate (89 cm), but it increased gradually with an increase in perforation area. At 55%, for example, the resistance was 9 mΩ.

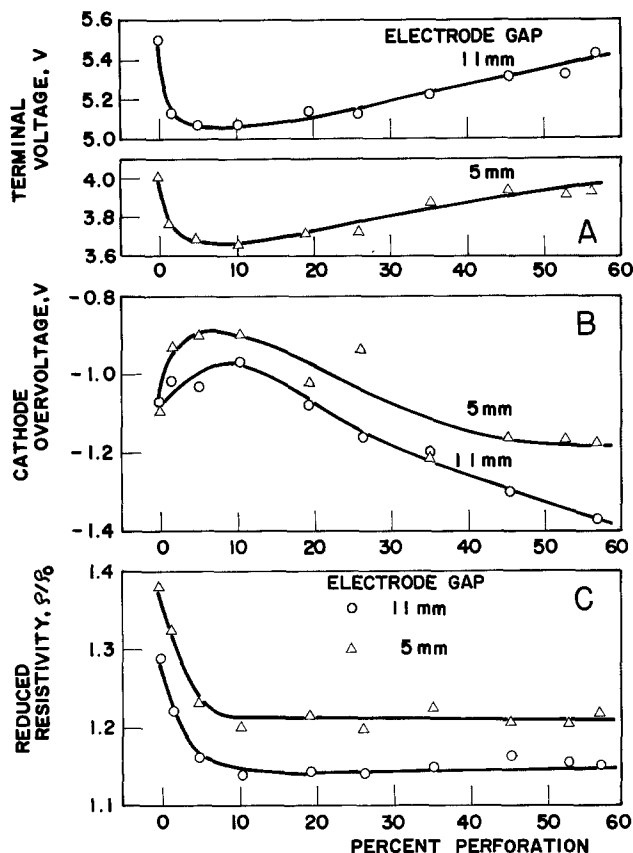


Fig. 5. Terminal voltage, cathode overvoltage, and solution resistivity as functions of the percent perforation of electrode. Back-side space = 2.2 cm; electrolyte = 0.5N NaOH at 40°C; total current = 100A.

Experimental results described that the back-side space could be minimized to be 3-5 mm thick, no large space was required in a cell with the perforated electrode, compared to 12-15 mm thick of the downcomer in a cell operated under natural circulation [see Ref. (1)].

Those experiments were conducted with NaOH solutions of 0.5N and 2.0N, and showed essentially the same results in both solutions.

Oxygen and hydrogen were liberated at the anode and the cathode, respectively, and those gases were mixed because there was no separator between two electrodes as stated above. It is obvious that the size of bubbles and their separation from the electrolytic solution are different for oxygen and hydrogen (6). In alkali solution, hydrogen bubbles were very small in size, and hence the gas void fraction was large in comparison with oxygen. Thus the lack of a separator makes an investigation unrealistic from the viewpoint of the industrial cells. However, the bubble effects in the electrolytic cell, especially the increase of the solution resistivity depends on the gas void fraction, but is almost independent of gas and the cell configuration (1). For one Faraday passed, 1/4 mole O₂ plus 1/2 mole H₂ were evolved, so that the experimental data in Fig. 2 and 3, for example, overrated the effects of gas void in comparison to a practical cell equipped with a separator in which either hydrogen or oxygen may evolve at the working electrode.

The gas void fraction increases with increasing distance from bottom to top in a vertical cell. It causes an increase in the cell voltage at a given current or an average current density, or a reduction in the total current at a given cell voltage. We will calculate a simple case as example. The cell height is h , the width is a , and the depth (the electrode gap) is b . The solution resistivity varies continuously from ρ_0 at the cell bottom to ρ_h at the top. The terminal voltage V_T consists of the decomposition voltage, the overvoltages at

the anode and the cathode, and the solution IR -drop. The terminal voltage may also contain the IR -drop through the separator in some cases. Of these, only the solution IR -drop is assumed to vary with the height due to the gas void.

The current I_x at a cross section of $a \cdot dx$ at height x , at which the resistivity of the electrolyte-gas mixture is ρ_x , is represented by Eq. [2]

$$dI_x = \frac{a V_T}{b} \frac{dx}{\rho_x} \quad [2]$$

Therefore, the total current I is

$$I = \frac{a V_T}{b} \int_0^h \frac{dx}{\rho_x} \quad [3]$$

For simplicity, we may assume a linear distribution of the resistivity of the electrolyte-gas mixture along the vertical cell

$$\rho_x = \rho_0 + (\rho_0 - \rho_h) x/h \quad [4]$$

From Eq. [3] and [4]

$$I = \frac{a V_T h}{b \rho_0} \frac{\ln k}{k - 1} \quad [5]$$

$$i_a = I/a h \quad [6]$$

$$V_T = i_a b \rho_0 \frac{k - 1}{\ln k} \quad [7]$$

where

$$k = \rho_h/\rho_0 \quad [8]$$

and

$$F = \frac{\ln k}{k - 1} \quad [9]$$

We may call k the resistivity ratio, and F is the current road factor. It is evident from Eq. [5] that the total current may decrease greatly when the resistivity ratio increases at a given terminal voltage. The electrolytic solution at the cell bottom is almost free of bubble as shown in Fig. 2. On the other hand, the reduced resistivity at the top of the cell equipped with a pair of the flat plate electrodes was 2.0 or more at 30 A/dm². From Eq. [5], the total current becomes as low as 70% of the cell free from gas bubble. More exact evaluation can be carried out if ρ_x is given as a real function instead of a simple assumption such as shown in Eq. [4].

Ibl and his co-workers have described a relationship between the solution conductivity and the gas void fraction (7). They measured the resistivity of the gas solution mixture directly with a conductivity probe. Gas was sent to the measurement cell from the frit, but was not generated by electrolysis. However, the technique might be useful for determining the resistivity of the solution containing electrolytic gas bubbles as a function of the height in the vertical cell.

For example, an estimated terminal voltage of the membrane-type chlor-alkali cell operated at 30 A/dm² and 80°C is about 2.9V, if the overvoltage and the solution IR -drop are assumed to be freed of bubble, compared to 3.9V of an experimental cell. A 1V difference is the unwanted bubble effects, that is, the voltage drop due to the bubble effects is surprisingly a quarter of the terminal voltage. It is a reason why we need to purge electrolytic gas bubbles from the interelectrode gap. Of the effectiveness of the gas-diverting electrodes in various types, such as mesh and expanded metal, there is no doubt. But a comparison of the performance of such materials is somewhat difficult and care must be taken. The detailed experiments with those electrodes under well-designed configuration and conditions of electrolytic cell must be conducted for the purpose.

In conclusion, bubble effects on the terminal voltage and its components such as the solution IR -drop and the overvoltage in a vertical cell equipped with the

perforated electrode were investigated. The flow pattern of gas-solution mixture in a cell was complicated. It depended on the electrolytic current, but was almost independent of the perforation in the range more than 10%.

The reduced resistivity of a gas-solution mixture in a cell with the perforated electrode was a weak function of the electrode gap, but it increased with increasing distance from the cell bottom due to accumulation of bubbles depending on the depth. The terminal voltage of a cell with the perforated electrode was a linear function of the electrode gap in a wide range whereas the voltage of a narrow cell with the flat plate electrode rose with a decrease of the electrode gap less than 7 mm. However, reduction of the surface area by machining becomes a penalty of the perforated electrode when disengagement of gases from the solution is easy in wide channels. A desirable size of the gap between the perforated electrode and the counterelectrode was estimated to be 5-10 mm (see Fig. 4A).

Since the gas void fraction in the electrolysis zone in a cell using the perforated electrode is low compared to cells having the solid plate electrode, the current distribution along the perforated electrode is relatively uniform, and is similar to that in a well-designed cell under natural circulation.

The perforation area is also an important factor for reducing the cell voltage and its components. The solution resistivity was almost independent of the perforation area more than 10%, while it increased quickly when the open area was insufficient for escape of gas-solution mixture. The overvoltage decreased with increase of perforation up to 10% because of reducing the surface coverage of the working electrode with gas bubbles. On the other hand, the overvoltage increased when the working area became small by machining. Consequently, a minimum cell voltage could be ob-

tained by the perforated electrode in the range 5-15% open.

It was clarified that only a small compartment such as 5 mm thick of the back side of the electrode was required to provide the space for disengagement of gases from the electrolytic solution so as to keep the cell voltage low.

Acknowledgment

The study has been conducted under the financial support of Japan Soda Industry Association and Grant-in-Aid for Developmental Scientific Research, The Ministry of Education, Science and Culture, No. 485,203.

Manuscript submitted April 8, 1980; revised manuscript received July 23, 1980. This was Paper 385 presented at the St. Louis, Missouri, Meeting of the Society, May 6-11, 1980.

Any discussion of this paper will appear in a Discussion Section to be published in the December 1981 JOURNAL. All discussions for the December 1981 Discussion Section should be submitted by Aug. 1, 1981.

Publication costs of this article were assisted by Fumio Hine.

REFERENCES

1. F. Hine and K. Murakami, *This Journal*, **127**, 292 (1980).
2. J. Jorné and J. F. Louvar, *ibid.*, **127**, 298 (1980).
3. C. W. Tobias, *ibid.*, **106**, 833 (1959).
4. F. Hine, M. Yasuda, R. Nakamura, and T. Noda, *ibid.*, **122**, 1185 (1975).
5. F. Hine, S. Yoshizawa, and S. Okada, *ibid.*, **103**, 186 (1956).
6. F. Hine and T. Sugimoto, Paper 459 presented at The Electrochemical Society Meeting, Seattle, Washington, May 21-26, 1978.
7. L. Sigrist, O. Dossenbach, and N. Ibl, *J. Appl. Electrochem.*, **10**, 223 (1980).

An Electrochemical Model for Oxide Growth on Zircaloy-2

N. Ramasubramanian*

Atomic Energy of Canada Limited, Materials Science Branch,
Chalk River Nuclear Laboratories, Chalk River, Ontario, Canada K0J 1J0

ABSTRACT

The kinetics of Zircaloy-2 oxidation were followed at 573 K in oxygen-free steam and dry air. At various stages during the oxidation polarization measurements were made in molten alkali nitrates and nitrite at 573 K. These measurements provided a comparison of the ionic conductivity of the zirconia and the electrical conductivity of the oxide on the intermetallics, grown in steam and air with those of the oxides grown in the molten salts. A model is proposed for thermal oxide growth on Zircaloy-2. During oxidation in steam, protons are conducted in the adsorbed water phase and reduced by the electron transport occurring at the conducting intermetallic sites. Thus, the oxidation behavior is similar to that in the molten salts, where nitronium and nitrosonium ions are reduced to complete the oxidation. The low rates of oxidation observed in air are attributed to a high resistance for the surface conduction of electrons, and the absence of a conduction and reduction step involving cationic species. Therefore, the rest potential is not lowered as effectively as that during oxidation in steam and the molten salts, in spite of the electron conduction at the intermetallic sites. The molten salts are suitable media for studying, in general, the mechanism of oxide growth on Zircaloy-2; the information obtained is relevant either directly or indirectly.

It is known that the metal-oxide interface, during oxide growth on zirconium and Zircaloy-2, is at a negative potential relative to the oxide-oxidation medium interface. This is demonstrated by the oxidation

studies in various media, such as aqueous electrolyte solutions (1, 2), oxygen (3, 4), molten salt (5-7), and steam (8). The attainment of this negative rest potential is determined by the relative ease of transport of oxygen ions and electrons through the growing oxide. An electrochemical interpretation of the kinetics

* Electrochemical Society Active Member.

Key words: fused salts, polarization, charge, transport.

of oxide growth is therefore based on the ionic and electronic conductivities of the growing oxide and their variations, if any, with the oxide growth.

When oxidizing in air, oxygen, or steam, the poor conductivity of the oxidation medium makes the use of an auxiliary electrode, contacting the oxide surface, a necessary requirement for electrochemical measurements. Such *in situ* measurements have been reported using evaporated or sputtered platinum layers (4, 8) and lithium-doped nickel oxide powder (3). In these types of experiments difficulties in interpreting the data were usually associated with an ill-defined contact area and the unknown factor of the influence of the contacting electrode on the oxidation itself.

It was shown that molten alkali nitrates and nitrites are convenient and suitable media for studying the mechanism of oxide growth on zirconium and Zircaloy-2 when the oxidation is also carried out in the molten salt (7). Unlike the evaporated metal and powdered semiconducting contacts, the contact area in the molten salt was well defined. We were, therefore, interested in extending the electrochemical polarization measurements in the molten salt to study the oxidation behavior of zirconium alloys in steam and air. In the study reported here, we have oxidized Zircaloy-2 in steam and air at 573 K and carried out polarization measurements at 573 K in the molten nitrite and nitrates at various stages during the oxidation. A model for thermal oxide growth on Zircaloy-2, which is essentially Cox's model (9) modified to account for the observed dependence of oxidation rate on the medium of oxidation in the early stages, is proposed.

Experimental

The molten salt baths used, and the procedures for sample preparation and polarization measurements following oxidation have been described elsewhere (7). All oxidation and polarization were carried out at 573 K. Samples, paddle-shaped and ≈ 8 cm² in area, were oxidized in oxygen-free steam at atmospheric pressure and dry air. In the closed steam loop, presence of air was avoided by flushing with argon before start-up and keeping it bubbling through the condensed water which returned to the boiler. At various times during the oxidation, the samples were withdrawn, weighed, polarized successively in molten KNO₃-NaNO₃, NaNO₂-NaNO₃-KNO₃, and NaNO₂, weighed again, and returned to their appropriate medium (steam loop or furnace) for further oxidation. Prior to polarization, sufficient time, usually half an hour, was allowed for the attainment of steady potential following immersion of the oxidized sample in the molten salt. The potentials are quoted relative to an Ag/Ag⁺ (0.07M in NaNO₃-KNO₃) reference. Only weight gain measurements were made with some control samples.

Results

Oxidation of Zircaloy-2 in steam and polarization in the molten nitrates and nitrite.—The rates of oxidation in steam at atmospheric pressure were generally faster than those in the molten nitrates and nitrite and dry air. The results are shown in Fig. 1 where the data obtained in the molten salts and dry air are included for the sake of comparison. After a period of oxidation in steam, when the samples were polarized in the three molten salt baths in turn, the changes in the weight gain caused by the polarizations were quite small. They decreased from ≈ 0.3 mg/dm² in the initial stages, 28 hr oxidation, to nondetectable amounts towards the final stages, 700 hr, of oxidation.

A set of polarization curves, obtained subsequent to a 28 hr oxidation in steam, is shown in Fig. 2. The anodic portions showed well-defined plateaus which were spaced fairly closely to each other, within a range of 1-2 μ A. However, the cathodic portions showed large differences; the resistance to the cathodic

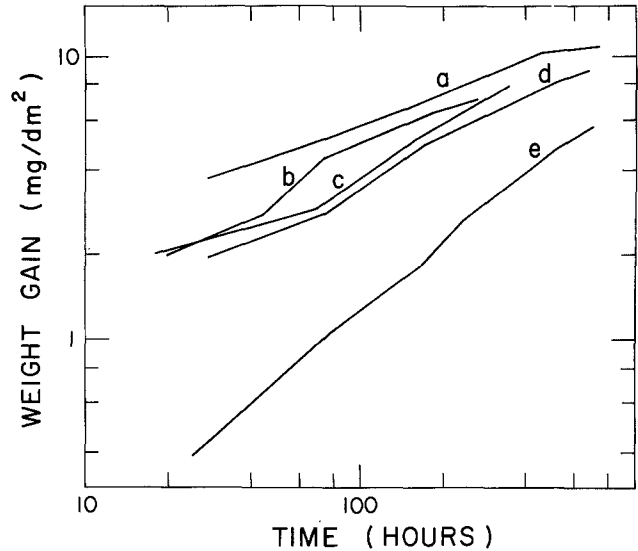


Fig. 1. Kinetics of oxidation of Zircaloy-2 at 573 K in: curve a, oxygen-free steam at atmospheric pressure; curve b, molten sodium nitrite; curve c, molten NaNO₂-NaNO₃-KNO₃; curve d, molten NaNO₃-KNO₃; and curve e, dry air.

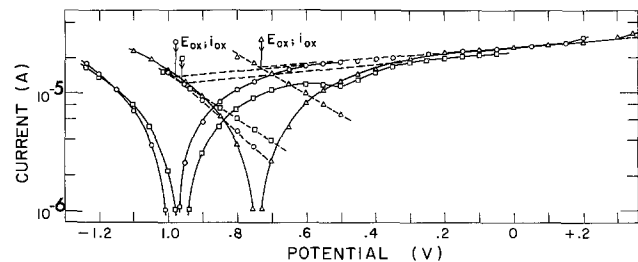


Fig. 2. Polarization curves traced at 573 K in Δ , binary nitrates; \circ , ternary nitrates-nitrite; and \square , sodium nitrite. Zircaloy-2 sample, oxidized 28 hr in steam at 573 K, had a weight gain of 3.8 mg/dm². Solid curves obtained experimentally, dashed curves obtained from analysis; E_{OX} — rest potential and i_{OX} — oxidation current.

current was much higher in the nitrite and ternary melts than in the binary melt. The oxidation currents (*i.e.*, the currents at the rest potentials on the extrapolated anodic plateaus) corresponded reasonably well with the rate of oxidation obtained from the kinetic data. Nearly identical oxidation currents were obtained by extrapolating the anodic plateaus in the linear plots of polarization current against applied potentials. Similar results were obtained from polarization measurements carried out after various periods of oxidation in steam. The cathodic portions of the polarization curves traced in the nitrite and ternary melts showed negative resistance regions; in the nitrite melt these were associated with a large shift by about 0.25V in the rest potential towards anodic values.

In Fig. 3(a), the rates of oxidation calculated from the oxidation currents and the kinetic data obtained in steam are compared at a series of weight gains. The agreement between the two sets of data is not as good as that reported previously for Zircaloy-2 when both the oxidation and polarization were done in the same melt (7). The differences between the rates calculated from the polarization data in the three melts, at any weight gain, were more than the differences between the polarization derived rate in one melt and the kinetic rate. However, all the data showed the same trend of a decreasing rate with increase in weight gain. The oxygen ionic conductance of zirconia, at any oxide thickness, was calculated as the ratio of the oxidation current, obtained from the polarization data, to the anodic shift in the rest potential from the immersion potential. Immersion

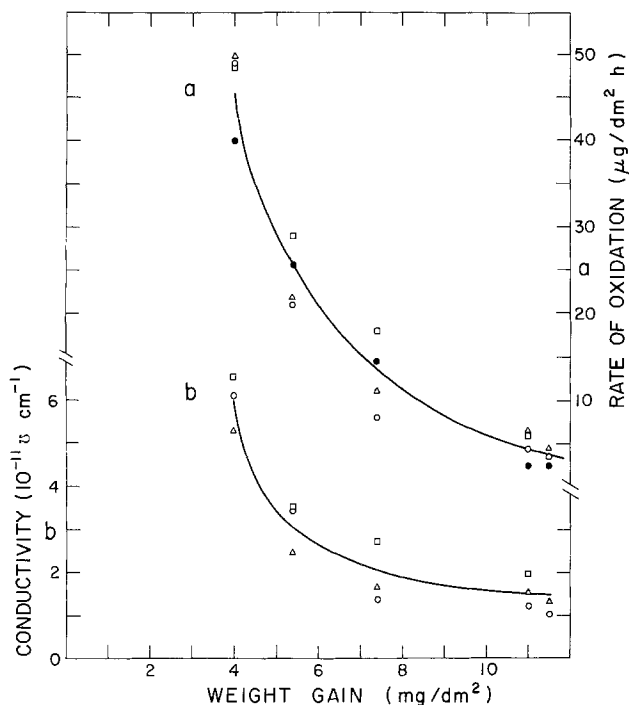


Fig. 3. Zircaloy-2 oxidized in steam at 573 K and polarized in the molten salts at the same temperature. Curve a, comparison of the oxidation rates obtained from the kinetic and polarization data. Polarization data from Δ , binary; \circ , ternary; and \square , nitrite melts; \bullet , kinetic data. Curve b, variation of the ionic conductivity with the weight gained; symbols refer to the same melts as in curve a.

potentials for Zircaloy-2 in the three melts at 573 K have already been reported (7); they varied from $-1.8V$ in the binary and ternary melts to $-1.6V$ in the nitrite. The ionic conductivities calculated are shown in Fig. 3(b) as a function of weight gain. The behavior is quite similar to that of the rate of oxidation shown in Fig. 3(a) and of the ionic conductivity of the oxide grown in the sodium nitrite melt reported elsewhere (7).

The variation of the resistance to cathodic current flow with time of oxidation is shown in Fig. 4. In the binary and ternary melts a systematic increase in the resistance was observed and the rest potentials were steady at ≈ -0.7 and $-0.85V$ during most of the oxidation. The rest potentials obtained in the three melts are listed in Table I. When the results were compared with the oxides grown in the molten salts (7) the steam-grown films were found to be more resistive.

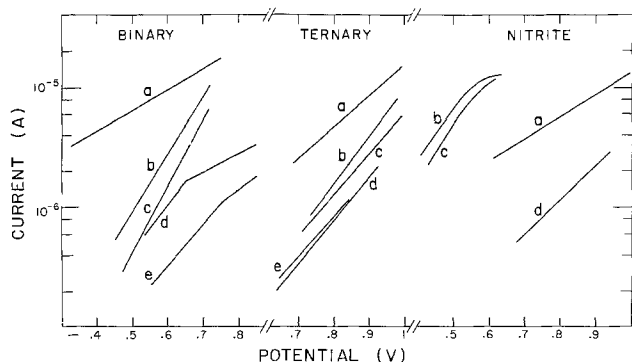


Fig. 4. Variation of the resistance to cathodic current flow at 573 K in the three molten salt baths with time of oxidation of Zircaloy-2 in steam at 573 K. Time of oxidation in hours: curve a, 28; curve b, 76; curve c, 172; curve d, 530; and curve e, 670.

Table I. Variation of the negative values of the rest potentials, obtained at 573 K in the three melts, with the time of oxidation of Zircaloy-2 in steam and dry air at 573 K

| Time of oxidation (hr) | Oxidation in steam | | | Oxidation in dry air | | |
|------------------------|-------------------------|---------|---------|-------------------------|---------|---------|
| | Rest potentials (volts) | | | Rest potentials (volts) | | |
| | Binary | Ternary | Nitrite | Binary | Ternary | Nitrite |
| 28 | 0.73 | 0.97 | 0.96 | 0.93 | 1.21 | 0.60 |
| 76 | 0.67 | 0.93 | 0.53 | 0.70 | 1.08 | 0.57 |
| 172 | 0.66 | 0.86 | 0.50 | 0.70 | 0.98 | 0.53 |
| 316 | | | | 0.61 | 0.97 | 0.52 |
| 503 | 0.70 | 0.85 | 0.86 | 0.61 | 0.95 | 0.49 |
| 670 | 0.79 | 0.83 | | 0.53 | 0.62 | |

Oxidation of Zircaloy-2 in dry air and polarization measurements in molten nitrates and nitrite.—The rate of oxidation in dry air was much slower than those in the molten salts and steam. When the samples were polarized in the molten salts the resulting changes in the weight gain were very considerable, especially in the initial stages. These changes are shown in Fig. 5 where the kinetics of oxidation in dry air of a control sample are compared with those of another sample on which intermittent polarizations in the molten salts were carried out. The changes in the weight gain as a result of these immersions and polarizations in the melts are shown by the dashed portions. In the initial stages the weight gained during one set of polarizations, i.e., in a total time of 5 hr of immersion and polarization in the three melts, was as much as that gained in 30 hr of oxidation in air. In the first 200 hr the weight gained as a result of three sets of immersions and polarizations, lasting nearly 18 hr, was more than half of the total weight gained.

In Fig. 6, the results are plotted on linear scales and the transfers made, from the dry air to the molten salts for polarization measurements and vice versa for continuing the oxidation in dry air, are shown by the horizontal dashed lines and are listed in alphabetical order. The direction of the arrows identifies the transfer made. The data for the control samples oxidized in air and the molten salts are shown by the solid curves; the curve for the latter is the average of the weights gained in the three melts. The data for the sample oxidized in air and polarized in the melts at various times during the oxidation are shown by the solid circles. When a transfer was made, e.g., from the air to the molten salts, the location corre-

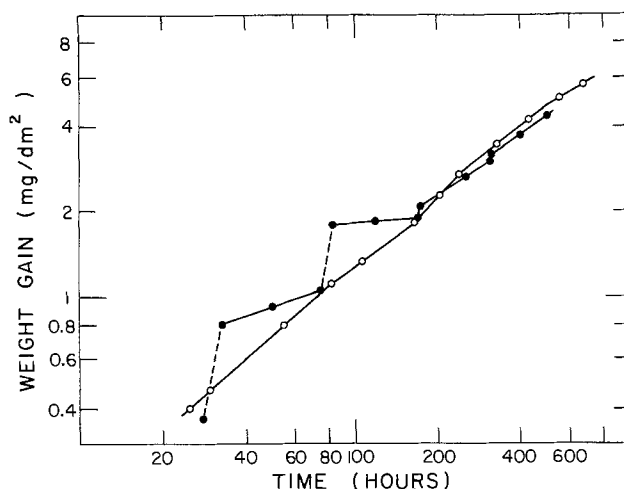


Fig. 5. Effect of immersion in the molten salts on the weight gained by Zircaloy-2 during oxidation in dry air at 573 K. \circ , control sample oxidized without immersion in the molten salts and \bullet , sample oxidized with intermittent immersions in the molten salts at 573 K for polarizations. Solid curves—weight gained in air and dashed curves—weight gained in the salts.

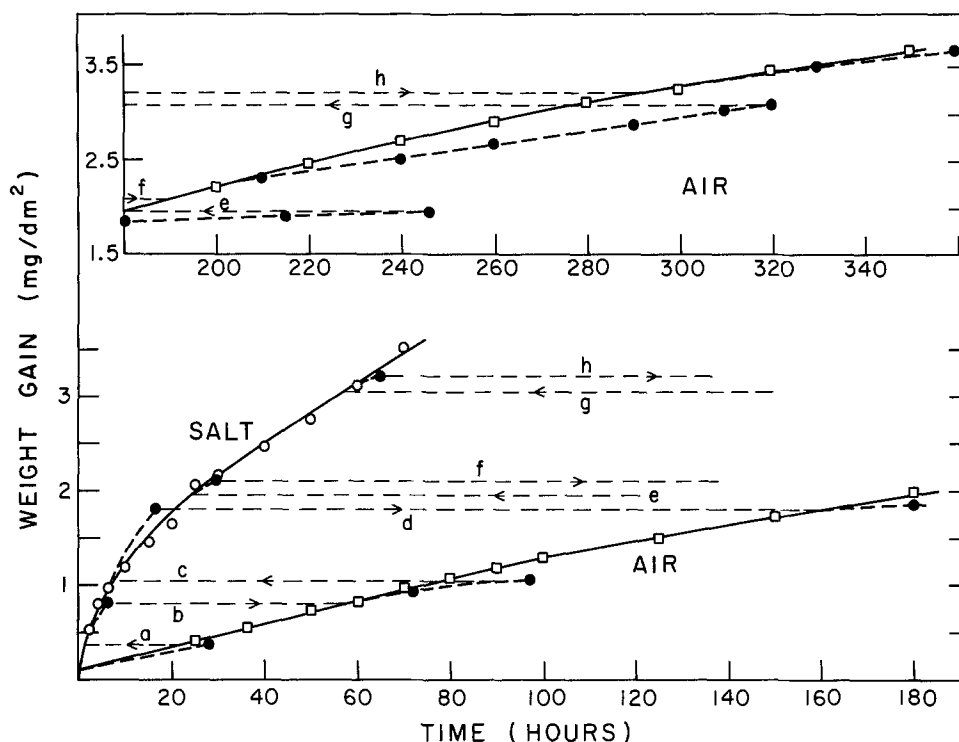


Fig. 6. Oxidation occurring, in the molten salts, during the polarization measurements on a Zircaloy-2 sample oxidized in dry air. Comparison of the kinetics of oxidation with those of the control samples oxidizing only in air or the molten salts. \circ , control oxidizing in the molten salts at 573 K; average of the weights gained in the three melts; \square , control oxidizing in dry air at 573 K; and \bullet , oxidized in dry air at 573 K and polarized in the three melts at 573 K. a, c, e, and g—transfers to the salts and b, d, f, and h—transfers to dry air.

ponding to the weight gain at the time of transfer is identified on the oxidation curve of the control sample in the melts and further weight gain is plotted from this location. A similar procedure is followed when the sample was returned to the air for further oxidation. It is readily seen that in all the transfers, excepting d, the kinetics of oxidation of the sample in air and the molten salts follow closely the kinetics of oxidation of the control samples in the respective medium. Therefore, the oxidation behavior of a sample oxidized both in dry air and in the molten salts, the latter resulting from the polarization measurements, is the same as that of an oxide of equivalent thickness growing only in air or the molten salts.

In order to separate the contributions to the weight gain changes in the melts caused by the immersion from those caused by anodic polarization, the following types of measurements were carried out with pairs of samples oxidized in dry air for various times. When a pair of samples oxidized for the same length of time was immersed in a melt, one of the pair was left unpolarized while the other was polarized to give current-voltage data. The changes in the weights gained by both were compared at the end of the experiment. When the initial weight gain in air was ≈ 0.4 mg/dm², immersion in the molten salt alone was responsible for $\approx 80\%$ of the increase in weight gain and anodic oxidation (resulting from the polarization) contributed to the remaining 20% increase. However, the latter decreased to $\leq 10\%$ at a total weight gain of ≈ 1 mg/dm² and was negligibly small at higher weight gains.

A set of polarization curves in the three melts following a 28 hr oxidation in air is shown in Fig. 7. The anodic plateaus were well defined and placed one below the other in the same order as the polarizations; the spread amongst the plateaus was about 10 μ A. With increasing oxidation, the anodic plateaus were still well defined, but the spread amongst them decreased to 1-2 μ A. The negative values of the rest potentials varied as sodium nitrite < binary nitrates < ternary nitrates and nitrite; these are listed in Table I. Negative resistance regions were observed in the cathodic portions of the polarization curves traced in the two nitrite-containing melts.

When the anodic plateaus were extrapolated, the oxidation currents obtained at the rest potentials were

too high to correspond to the rates of oxidation in air calculated from the kinetic data. However, the oxidation currents from the polarization data agreed well with the changes in the weight gain resulting from immersion and polarization in the melts, i.e., with the rates evaluated from the dashed portions in Fig. 5. These rates were also found to be comparable to the rates obtained in molten salt oxidation (7).

The results are shown in Fig. 8(a) where the rates of oxidation calculated from the polarizations, the oxidation kinetics in air, and the weight gain changes due to immersion in the melts are compared at different weight gains. Because the weight gain changed considerably due to immersion in the salt, the total weight gained by the sample at the end of a polarization step, rather than that due to oxidation in air, was used in plotting the data. At any weight gain the difference between the rates, calculated from the polarization data obtained in the ternary eutectic and the sodium nitrite melt, was rather large. In Fig. 8(b) the variation of the ionic conductivity of the oxide with the weight gain is shown. The conductivities and their variation in behavior were found to be similar to those reported for oxides grown in the three melts (7). When the results from the polarization data are compared the rate of oxidation decreased initially, up to a weight gain of ≈ 2.5 mg/dm², and the ionic conductivity stayed

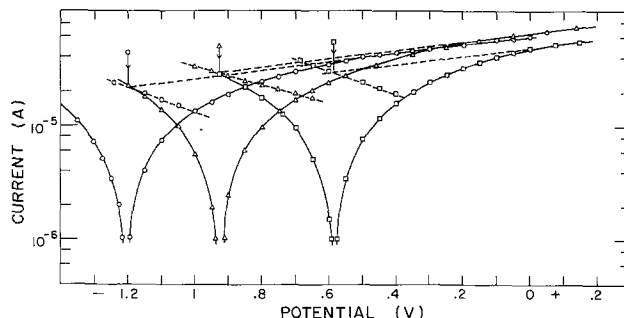


Fig. 7. Polarization curves traced at 573 K in Δ , binary nitrates; \circ , ternary nitrates-nitrite; and \square , sodium nitrite. Zircaloy-2 sample oxidized 28 hr in air at 573 K. Solid curves obtained experimentally, dashed curves obtained from analysis; arrows locate rest potentials and oxidation currents.

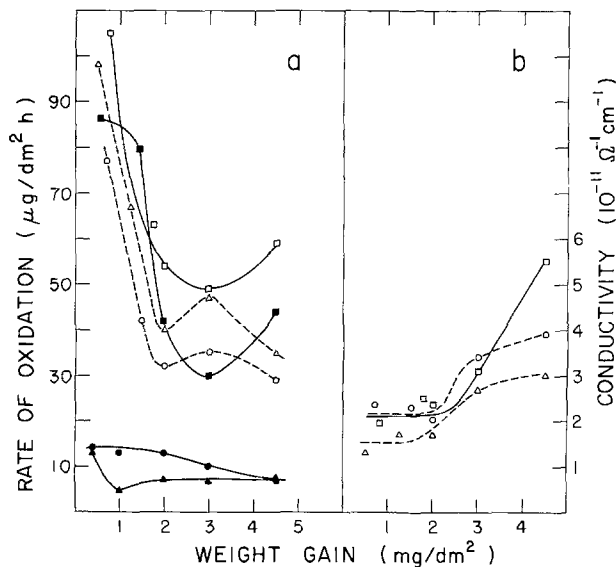


Fig. 8. Zircaloy-2 oxidized in dry air at 573 K and polarized in the three melts at the same temperature. (a) Comparison of the rates of oxidation calculated from the polarization with those obtained from the kinetic data in air and the weight gained in the salt. Polarization data: Δ , binary nitrates; \circ , ternary nitrates-nitrite; and \square , sodium nitrite. Kinetic data in air: \bullet , nonpolarized sample and \blacktriangle , sample intermittently polarized in the three melts. \blacksquare , rate from the weight gained due to immersion in the salt. (b) Variation of the ionic conductivity with the weight gained; symbols refer to the same melts as in (a).

nearly steady at $2 \times 10^{-11} \Omega^{-1} \text{cm}^{-1}$. With further increase in weight gain the rate of oxidation and the ionic conductivity increased; in the case of the binary and ternary melts the rate of oxidation showed a maximum and this corresponded to an inflection in the conductivity curve.

The resistance to cathodic current flow as a function of weight gain is shown in Fig. 9. The rest potential decreased with increasing oxidation; the resistance in the three melts varied as sodium nitrite < binary nitrates < ternary nitrate-nitrite. At comparable weight gains, the air-grown films were found to be more conducting than films grown in steam and less conducting than films grown in the molten salts (7).

Discussion

Anodic and cathodic processes during thermal oxide growth on Zircaloy-2.—In a discussion about the relation between the type of rate law obeyed, during the thermal oxidation of zirconium and Zircaloy-2 at 473–573 K, and the oxide thickness it was concluded that the anodic process is controlled by a field dependent rate-determining process within the oxide film and that the weak field approximation of the equation usually employed for anodic oxide growth is applicable (1). This was confirmed by the results

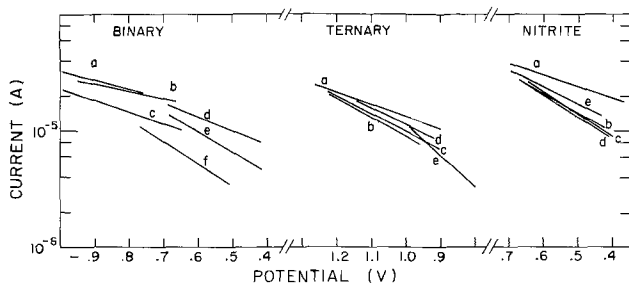


Fig. 9. Variation of the resistance to cathodic current flow at 573 K in the three molten salt baths with time of oxidation of Zircaloy-2 in air at 573 K. Time of oxidation in hours: a, 28; b, 76; c, 172; d, 316; e, 503; and f, 670.

obtained in the oxidation and polarization experiments in the molten salts at 573 K; it was shown that the potentials corresponding to the linear anodic plateaus in the polarization curves were essentially across the zirconium oxide and the anodic process of oxygen ion transport was determined by the ionic conductivity of the oxide (7).

Bacarella and Sutton had interpreted the cathodic process on the basis of a dual barrier model; the zirconium oxide was assumed to be a semiconductor having an electron transfer coefficient close to unity; a part of the potential drop was considered to be across this oxide barrier and the remaining at the oxide-solution interface controlling a charge transfer reaction (1). However, it has recently been shown that when the zirconia thickness is less than the average size of the intermetallic precipitates in the alloy, the electron transport, completing the oxidation, occurs predominantly at the oxidized zirconium-iron intermetallic precipitates (5, 6). The composition of the oxides grown on these second phase precipitates and its variation with the temperature and extent of oxidation have not been investigated in detail. In addition, the cathodic portions of the analyzed polarization curves generally showed two "Tafel" regions; the data could also be fitted to, sometimes better than a Tafel relation, a Schottky type of emission process. The variation of the resistance to cathodic current flow with increasing oxidation was found to depend on the medium in which the alloy was oxidized. Therefore, in the absence of definitive experimental evidence, of the fit of the data to a single type of electron transport mechanism, the cathodic process is simply considered to be determined by the conductivity of the oxide grown on the second phase intermetallic precipitates.

Oxidized Zircaloy-2 sample immersed in molten alkali nitrates, nitrites, and their eutectics.—The reactions occurring in molten alkali nitrates, nitrites, and their eutectics and their relevance to the mechanism of oxide growth on Zircaloy-2 in these melts have been discussed elsewhere (7). The oxide thicknesses investigated in the present study are well below $1 \mu\text{m}$ (equivalent weight gain is $\approx 15 \text{ mg}/\text{dm}^2$), the average size of the intermetallics. Therefore, irrespective of which medium the alloy was oxidized in, when it is immersed in the molten salt it can be expected to acquire a rest potential determined by the ionic conductivity of the zirconia and the electronic conductivity of the oxide grown on the intermetallic precipitates. The kinetics of oxidation of a Zircaloy-2 sample, oxidized in steam or aqueous solutions or molten salts and intermittently polarized in the molten salts, is found to be nearly identical to that of a control sample which had not been polarized. It can be concluded therefore, that immersion and polarization in the molten salts are not affecting the conduction properties of the zirconia and the oxide on the intermetallic precipitates and information on these oxide conductivities can be obtained from the polarization data. This is the basis for exploring the possibility of using molten alkali nitrates and nitrites as polarization media for studying oxide growth in other media such as air and steam.

However, the reactions on the alloy and the intermetallics at the oxide-molten salt interface would be different from those that occurred at the oxide-oxidation medium interface during the oxidation. Therefore, the polarization data obtained in the molten salts might correspond more closely to the oxidation behavior of a preoxidized sample in the salt than to the previous history of oxidation in another medium. But, apart from these differences (due to the different interfacial reactions at the oxide surface during oxidation and polarization) the data obtained in the molten salts should provide information on the variation of the oxide conductivities with increase in oxidation,

and a comparison amongst the oxides grown in various media. Such information is important in interpreting the mechanism of oxide growth.

Oxidation in steam.—Following a period of oxidation in steam, when a sample was polarized in the three melts it was observed that the anodic plateaus in the polarization curves were quite close to each other. As the plateaus are identified with the oxygen ionic transport in the zirconia (7, 9) this observation indicates that the ionic conductivity of the zirconia had remained the same during the polarization. But there were variations in the values of the ionic conductivity calculated, at any weight gain, as shown in Fig. 3(b). These might be due to small differences in the measured anodic currents resulting from the repeated polarizations within a short time and to some extent also due to the slightly different values of the measured immersion potentials used for the three melts. Unlike the ionic currents, the cathodic reduction currents in the three melts showed large variations indicating that the resistance of the same oxide film, grown in steam on the intermetallics, was different in the three melts. The interpretation is that the surface reactions involved and their current-voltage characteristics are different in the three melts; *viz.*, reduction of NO_2^+ in the binary nitrates, NO^+ in the nitrite, and possibly both of these species in the ternary nitrate-nitrite melt.

Thus, when the results from the polarization curves are correlated with the reactions occurring during the oxidation in steam, the ion transport can be expected to be in better agreement than the electron transport. The ion transport, determined by the conductivity along the crystallite boundaries, occurs through the same oxide during oxidation in steam and polarization in the three melts. The ionic conductivities shown in Fig. 3(b) are thus characteristic of the oxide grown in steam and the same as those that existed during the oxidation. The electron transport, on the other hand, is not only related to different reactions in the three melts during polarization but is also associated with a completely different reaction, the reduction of protons to hydrogen, during the oxidation in steam. Thus, the different rest potentials and oxidation currents measured in the three melts (subsequent to a period of oxidation in steam) and the differences in the oxidation rates calculated from the polarization data in the three melts and the kinetic data in steam (at a weight gain) are to be attributed mainly to the different cathodic reduction reactions. For the same reason the rest potential during the oxidation in steam would have been different from those observed during polarization.

In spite of only a reasonable agreement between the rates of oxidation calculated from the polarization and kinetic data, it can be stated that the polarization data do reflect changes in the ionic conductivity of the oxide grown in steam and also changes in the rate of oxidation in steam with the weight gain. The same trend is seen in the rates of oxidation derived from the kinetics as is seen in the calculated ionic conductivities [*cf.* Fig. 3(a)]. The ionic conductivity of the steam grown oxide (as revealed by polarization) is slightly higher than but close to that of the oxide grown in the nitrite melt (7). The kinetics of oxidation in steam are faster than in the molten salts to begin with, but at a weight gain $>4 \text{ mg/dm}^2$ the kinetics become comparable to those in the nitrite melt. This similarity between oxidation in steam and molten sodium nitrite might be attributed to a higher water content in the nitrite melt (present as an impurity) than in the binary and ternary eutectics (7). However, a high ionic conductivity for the oxide grown in steam is revealed by polarization in all the three melts. The similarity to oxidation in the nitrite melt then suggests that the current-voltage characteristics of the cathodic reduction of protons to hydrogen during steam oxidation are similar to

those of the reduction reactions occurring in the nitrite melt. Therefore, it can be concluded that molten alkali nitrates, nitrites, and their eutectics, in general, are suitable polarization media for studying the oxide growth on Zircaloy-2 in steam.

Oxidation in dry air.—The behavior of samples oxidized in dry air, when immersed in the molten salts, was very different from that of the steam-oxidized samples in that considerable additional oxidation occurred in the salt. The kinetic and polarization characteristics of this additional oxidation are seen to be nearly the same as those of an oxide of equivalent thickness grown in the molten salts. Therefore, it has to be concluded that the ionic conductivity of the zirconia and the electronic conductivity of the oxide on the intermetallics grown in air are not very different from those of the oxides grown in the molten salts. This is confirmed by the ionic conductivities and the resistances to cathodic current flow calculated from the polarization data.

There was no agreement between the rates of oxidation calculated from the polarization and kinetic data at any weight gain; the rates derived from the polarization data, however, corresponded to the additional oxidation occurring in the melts. The variation in the rates of oxidation, calculated from the polarization data obtained in the three melts, could also be related to the resistance of the oxide on the intermetallics to the cathodic current and the rest potentials. In the ternary melt the latter were high and the oxidation rate was low; in the nitrite melt, the resistance and the rest potentials were low and the oxidation rate was high. Therefore, the behavior of the air-grown oxide in the molten salts represents the oxidation occurring in the salt during immersion rather than the previous history of air oxidation. The polarization data are, therefore, not relevant to air oxidation.

The near linearity of the oxidation rate in the initial stages, of the control sample, suggests that the oxidation in dry air is controlled by a surface reaction. Similar low and near linear rates were observed in the case of samples oxidized in air and polarized intermittently in the molten salts. These results indicate that in spite of the electrical conduction properties of the oxides grown in air and/or the molten salts being basically the same the oxidation in dry air proceeds at a slower rate. As will be discussed later, this is to be attributed to a basic change in the mechanism related to the conduction properties of the oxide surface. Therefore, inferences regarding oxide growth in air could be drawn by comparing the polarization behavior of the oxide with those grown in steam and the molten salts.

Model for thermal oxide growth on Zircaloy-2.—The kinetics of oxidation in steam, though resulting in a faster rate of oxidation than in the molten salts, are seen to be close to those in the nitrite melt at weight gains $\geq 4 \text{ mg/dm}^2$. The mechanism of oxide growth in steam is, therefore, likely to bear some analogy to that in the molten salts (7). As the oxygen ions for the oxidation have to come from the water molecules the cathodic reaction completing the oxidation has to be the reduction of protons. The mechanism, generally proposed, for oxidation in aqueous electrolyte solutions is the reduction of water to hydroxyl ions (mostly localized at the intermetallic sites) and the reaction of a pair of hydroxyl ions from the solution on the zirconia surface producing oxygen ions and water (2). If the same scheme is to be applied for oxidation in steam, the hydroxyl ions produced at the intermetallic sites have to be transported by surface conduction to reaction areas on the zirconia. But the mobility of protons is considered to be generally faster than that of the hydroxyl ions (10); and during the initial stages of oxide growth in steam and aqueous solutions a considerable fraction of the hydrogen re-

leased is absorbed by the alloy (9). Therefore, equally well the oxygen ions could be extracted from the adsorbed water by the anion vacancy emerging on the zirconia surface and the protons released transported to the intermetallic sites and/or the alloy-oxide interface for reduction.

The model for oxide growth is the same as that proposed by Cox (9) and adapted for oxidation in molten salts (7). Oxygen ions, produced by a dissociation step, are transported along the zirconia crystallite boundaries by diffusion and the protons, transported by surface conduction, are reduced at the intermetallic sites. This latter reaction is analogous to the reduction of NO_2^+ and NO^+ during oxidation in the molten salts. The electronic conductivity of the doped oxide grown on the intermetallics maintains the rest potential at moderately low negative values. When the polarization data obtained in the molten nitrite are compared, the resistance of the oxide on the intermetallics grown in steam is higher than that grown in the molten nitrite. But the ionic conductivity of the zirconia grown in steam is higher than that grown in the nitrite; the compensating effect due to the ionic conductivity leads to faster oxidation in steam compared to that in the molten nitrite.

When the kinetics of oxidation in steam, molten salts, and air are compared the characteristics of the last are seen to be very different from those of the first two. The rate in air is about an order of magnitude less than that in the molten salts at a low weight gain of $\approx 1 \text{ mg/dm}^2$ and is about four times less than those in steam and molten salts at high weight gains up to $\approx 5 \text{ mg/dm}^2$. It is almost linear up to a weight gain of $\approx 2 \text{ mg/dm}^2$. When the air-oxidized sample is immersed in the molten salts, it oxidizes at an increased rate corresponding to the rate of oxidation of a control sample oxidizing in the melts. However, the rate returns to low values, similar to those of a control sample oxidizing in air, when further oxidation is continued in air. Therefore, there is a basic change in the mechanism of oxidation when a sample is transferred from dry air to molten salt and vice versa.

The transport of oxygen ions along crystallite boundaries, is nearly the same in various oxidation media due to nucleation and crystallite growth occurring at the alloy-oxide interface (9). The zirconia crystallites are reported to occupy almost 100% of the oxide volume by the time a thickness of $\approx 0.2 \mu\text{m}$ is reached. Therefore, major changes in the ionic conductivity of the oxide, imparted by the oxidation medium and associated with crystallite size, impurity incorporation, and surface structures, can be expected to occur during the initial stages of thin film growth. It is observed (c.f. Fig. 8) that the ionic conductivity of the air-grown oxide, subsequent to immersions and polarizations in the molten salts, and its variation with the total weight gained are comparable to those of the oxides grown in the molten salts (7). Therefore, the different oxidation behavior observed in dry air and the molten salts is not associated with the oxygen ion conduction in the growing zirconia. The cathodic step in air oxidation is the reduction of oxygen and this reaction has to occur on the zirconia surface near an emerging anion vacancy. The electrons could be transported from the intermetallics by conduction along the p-levels of the chemisorbed oxygen. This surface conduction and/or the reduction of oxygen must be then rate limiting.

Moreover, during oxidation in dry air, conduction and reduction of a cationic species are not involved. Therefore, lowering of the resistance of the alloy-oxide composite may not be as effective as that during oxidation in steam and the molten salts and consequently the rest potential could be highly negative. The rest potential at which the ionic current is equivalent to the rate of oxidation in air can be estimated

as $\sim -1.6\text{V}$ from the extrapolated anodic plateaus in the polarization curves. Such a highly negative rest potential, combined with a low rate of oxide growth, can be expected to contribute to a bulk electron current through the zirconia. In the initial stages, when the oxide is a few hundred angstroms thick, this might be an emission current, which may become space charge limited with increase in oxide thickness. The contribution from these bulk currents would, however, decrease with increasing weight gain.

Dawson *et al.* reported that the oxidation behavior of chemically polished Zircaloy-2 in oxygen at 573-633 K was complex (11). A change from a near linear to a near parabolic rate is also observed in the present study. Such variations can be interpreted as a reflection of the changes occurring in the electron transport. Initially the rate is linear due to the limited rate of oxygen reduction at the surface determined by the bulk emission current. The rate then decreases due to the buildup of electronic space charge which affects both the ionic and electronic transport and changes again at a higher oxide thickness when the bulk electron current is negligible and localized transport at the intermetallics combined with the surface conduction becomes limiting. When the air-oxidized sample is immersed in the molten salt for polarization the situation is changed completely. The reduction of nitronium and/or nitrosonium ions facilitated by the electron transport at the intermetallics, moves the rest potential to low negative values and any space charge or surface resistance effect on the oxidation rate is minimized; the alloy oxidizes at a rate near to that expected for an oxide of equal thickness in the molten salt.

In their model, Brown and Walton (2) proposed a surface barrier in addition to the growing oxide film barrier for the anodic current. This surface barrier was supposed to control an ionic reaction, not necessarily a rate-determining step, such as dehydroxylation in their experiments. It is seen from the results reported here that the role played by a surface barrier, if it exists, is a very minor one in the oxidation of Zircaloy-2. The interfacial reactions at the oxide-oxidizing medium are all different in different media. But in all media the rate of oxidation is determined by a combination of factors, such as ionic conductivity of the zirconia, electronic conductivity of the oxide on intermetallics, reduction of cationic species in the medium, and the bulk electronic conductivity of zirconia. The surface conduction properties of the zirconia associated with the reduction reactions play a more major role, than a surface barrier, in determining the oxidation of Zircaloy-2. In a similar manner, it cannot be said that either the ion transport or the electron transport is rate controlling (3); because ionic and electronic transport are occurring through different oxide systems, obey different current-voltage relations, and have to be coupled. It can be stated, however, that the anodic half of the oxidation (the oxygen ion transport) is less affected by changes in oxidation medium than the cathodic half. This effect is most evident when oxidation in a conducting medium is compared with that in a nonconducting medium.

Conclusions

Polarization measurements in molten alkali nitrates, nitrites, and their eutectics, on Zircaloy-2 samples oxidized in steam or dry air provide information on the variation of the ionic conductivity of zirconia and the electronic conductivity of the oxide grown on the intermetallics with increasing oxidation. The anodic part of the polarization data is directly relevant to the oxygen ion transport occurring during the oxidation; whereas the cathodic part of the polarization data has no direct correlation to the reduction reactions occurring during the oxidation. Thus, the differences in the oxidation rates calculated from the

polarization and kinetic data arise mainly from the different cathodic reactions involved.

A model for thermal oxide growth at $\leq 1 \mu\text{m}$ in thickness is proposed, based on the kinetic and polarization data.

1. When oxidizing in steam, the reduction of the protons released is assisted by their surface conduction in the adsorbed water phase on the zirconia surface and the electron transport at the intermetallic sites. Therefore, the rest potential stays at low negative values and the oxidation proceeds at a fast rate comparable to that in the molten salts.

2. In dry air, the oxidation proceeds at a much slower rate than in steam and the molten salts. The electrical conduction properties of the oxides grown in air, however, are similar to those of the oxides grown in the molten salts. Therefore, the low rates of oxidation in air are attributed to a highly negative rest potential on the alloy brought about by a high resistance for the surface conduction of electrons and the absence of a reduction step involving cationic species. The rate of oxidation, initially linear, is controlled by the reduction of oxygen at the surface; then the rate changes due to the buildup of an electronic space charge in the oxide and control by the combination of electron conductivity at the intermetallics and surface conduction.

Acknowledgments

The author wishes to acknowledge the many helpful discussions he had with Dr. B. Cox and the assistance offered by Mr. V. C. Ling in sample preparation.

Manuscript submitted Jan. 5, 1980; revised manuscript received May 20, 1980. This was Paper 63 pre-

sented at the Seattle, Washington, Meeting of the Society, May 21-26, 1978.

Any discussion of this paper will appear in a Discussion Section to be published in the December 1981 JOURNAL. All discussions for the December 1981 Discussion Section should be submitted by Aug. 1, 1981.

Publication costs of this article were assisted by Atomic Energy of Canada Limited.

REFERENCES

1. A. L. Bacarella and A. L. Sutton, *This Journal*, **112**, 546 (1965).
2. M. L. Brown and G. N. Walton, *J. Nucl. Mater.*, **66**, 44 (1977).
3. D. H. Bradhurst, J. E. Draley, and C. J. Van Drunen, *This Journal*, **112**, 1171 (1965).
4. J. H. Eriksen and K. Haufler, *Z. Phys. Chem. N.F.*, **59**, 332 (1968).
5. B. Cox, *J. Nucl. Mater.*, **31**, 48 (1969).
6. N. Ramasubramanian, *ibid.*, **55**, 134 (1975).
7. N. Ramasubramanian, *This Journal*, **127**, 2566 (1980).
8. A. W. Urquhart, D. A. Vermilyea, and W. A. Rocco, *ibid.*, **125**, 199 (1978).
9. B. Cox, in "Advances in Corrosion Science and Technology," Vol. 5, M. G. Fontana and R. W. Staehle, Editors, pp. 301-311 and 343-361, Plenum Press, New York (1976).
10. G. C. Pimentel and A. L. McClellan, "The Hydrogen Bond," p. 31 and 253, W. H. Freeman and Company, San Francisco, California (1960).
11. J. K. Dawson, U. C. Baugh, and J. F. White, in "Zirconium and Its Alloys," J. P. Pemsler, E. C. W. Perryman, and W. W. Smeltzer, Editors, p. 137, The Electrochemical Society Softbound Proceedings Series, New York (1966).

High Oxygen Ion Conduction in Sintered Oxides of the $\text{Bi}_2\text{O}_3\text{-Dy}_2\text{O}_3$ System

M. J. Verkerk and A. J. Burggraaf

Department of Inorganic Materials Science, Twente University of Technology, 7500 AE Enschede, The Netherlands

ABSTRACT

The phase diagram of the $\text{Bi}_2\text{O}_3\text{-Dy}_2\text{O}_3$ system was investigated. A monophasic fcc structure was stabilized for samples containing 28.5-50.0 mole percent (m/o) Dy_2O_3 . Above and below this concentration range polyphasic regions appear. The fcc phase showed high oxygen ion conduction. The ionic transference number is equal to one for specimens containing 28.5-40.0 m/o Dy_2O_3 , whereas an electronic component is introduced at low temperatures for specimens containing 50.0 m/o Dy_2O_3 . The conductivity of $(\text{Bi}_2\text{O}_3)_{0.715}(\text{Dy}_2\text{O}_3)_{0.285}$ is $0.71 \Omega^{-1}\text{m}^{-1}$ and $14.4 \Omega^{-1}\text{m}^{-1}$ at 773 and 973 K, respectively. Relations were found between the ionic radius, the conductivity, and the minimum concentration of lanthanide necessary to stabilize the fcc phase. It is concluded that the highest ionic conductivity will be found in the system $\text{Bi}_2\text{O}_3\text{-Er}_2\text{O}_3$ or $\text{Bi}_2\text{O}_3\text{-Tm}_2\text{O}_3$. From a study of relations between the activation energy, $\log \sigma_0$ and the composition it is concluded that two conductivity mechanisms play a role.

Recently Harwig investigated the electrical and structural properties of Bi_2O_3 (1-5). At room temperature the monoclinic α -phase is stable and the conductivity is predominantly electronic. On heating to 1002 K the oxide transforms to the face centered cubic (fcc) δ -phase, which is stable up to the melting point at 1097 K. In the δ -phase the electrical conductivity is about $100 \Omega^{-1}\text{m}^{-1}$ and varies little with temperature. The ionic transport number is equal to one (6). On cooling this highly conductive phase may be extended to

Key words: ionic conductor, solid electrolyte, bismuth oxide, lanthanide oxide, phase relations.

923 K, where it transforms into the tetragonal β -phase or to 912 K where it transforms into the body-centered cubic (bcc) γ -phase. These phase transformations are accompanied by sudden volume changes which cause deterioration of the mechanical properties of the material. The conductivity in the β - and γ -phase is mainly ionic and about three orders of magnitude lower than in the δ -phase.

The temperature range at which this material can be used as a solid electrolyte can be extended by substituting Bi_2O_3 . The region of highly ionic conductive δ -phase can be extended to room temperature by intro-

duction of 17.5-45 m/o Er_2O_3 (7,8), 25-43 m/o Y_2O_3 (9), 35-50 m/o Gd_2O_3 (10), 25 m/o WO_3 (11), 15-25 m/o Nb_2O_5 and 18-25 m/o Ta_2O_5 (12). The highest ionic conductivity is found in the system Bi_2O_3 - Er_2O_3 . The conductivity of $[\text{Bi}_2\text{O}_3]_{0.80}(\text{Er}_2\text{O}_3)_{0.20}$ is 2.3 and 37 $\Omega^{-1}\text{m}^{-1}$ at 773 and 973 K, respectively (7).

Oxygen ion conductors based on bismuth sesquioxide are substantially more conductive than the stabilized zirconias. In the temperature range 773-973 K the conductivity of $(\text{Bi}_2\text{O}_3)_{0.80}(\text{Er}_2\text{O}_3)_{0.20}$ is about 50-100 times higher than the conductivity of $(\text{ZrO}_2)_{0.915}(\text{Y}_2\text{O}_3)_{0.085}$.

Because of the relative ease of reduction at higher temperatures (6, 13, 14), the bismuth sesquioxide-based materials are not suitable for fuel cell applications. Their application will be limited to oxygen pumps [e.g., for oxygen-enrichment (15)] or electrolyte for "second generation" oxygen sensors [e.g., the device developed by Heyne (16, 17)]. The "second generation" oxygen sensor is used for automotive control and operates in the lean air/fuel ratio region, e.g., an oxygen-rich exhaust gas (1-10% O_2). The sensor produces a feedback signal to keep the gas mixture fed to the motor oxygen rich. So all the fuel is burned and most pollutants can be removed catalytically (16, 18, 19).

The occurrence of the cubic phase (fcc) in the Bi_2O_3 - Dy_2O_3 system is reported for $3\text{Bi}_2\text{O}_3 \cdot \text{Dy}_2\text{O}_3$ by Datta and Meehan (20) and for $\text{Bi}_2\text{O}_3 \cdot \text{Dy}_2\text{O}_3$ by Nasanova *et al.* (21). The fcc phase in comparable binary compounds exhibits high oxygen ion conduction over a wide temperature range. Therefore, the authors have investigated the phase diagram and the conductivity of the Bi_2O_3 - Dy_2O_3 system.

The investigations are a part of our studies on a number of Bi_2O_3 - Ln_2O_3 compositions. Phenomenological relations between the ionic radius of the lanthanide; the structure, and the conductivity are given. Some predictions about high ionic conductivity in stabilized Bi_2O_3 are made.

Experimental

Preparation and analysis of the specimens.— Bi_2O_3 (Merck, very pure) and Dy_2O_3 (Serva, 99.9%) were thoroughly mixed and pre-fired at 1020-1120 K for 16 hr, finely ground and isostatically pressed at about 40 MPa, sintered in air for 45 hr, and cooled down ($1/2$ K min^{-1}) to room temperature. The sintering temperature was raised as the content of Dy_2O_3 was increased, see Table I. Prefiring and sintering were performed in platinum crucibles.

After the synthesis the composition of the samples was checked with x-ray fluorescence. The accuracy is 0.1% absolute. The specimens were analyzed for small amounts of aluminum and silicon. The procedure is described elsewhere (7, 22). The detection limits of these analyses are 0.005 weight percent (w/o) Al and 0.001 w/o Si.

The crystal structures of the specimens were identified by a Philips PW 1370 diffractometer. $\text{Cu K}\alpha$ radiation was used with a Ni filter. The lattice parameters were calculated from diffraction angles in the 60° - 120° (2 θ) region, obtained at a scanning speed of $1/4^\circ \text{min}^{-1}$ using $\text{Pb}(\text{NO}_3)_2$ as the internal standard. High temperature x-ray experiments were performed with a Guinier-Simon camera (heating rate: 5 K hr^{-1}). The ceramic structures of polished and ther-

mally etched samples were investigated with the scanning electron microscope (SEM) Type JEOL JSM U3. Differential thermal analysis (DTA) measurements were performed with a du Pont 990 Thermal Analyser, heating rate: 10 or 15 K min^{-1} . The densities of the samples were measured at 298 K by the Archimedes method using mercury.

Measurement of the ionic conductivity.—The electrical conductivity was measured at a frequency of 10 kHz. The ionic transference number was measured by the emf of an oxygen gas concentration cell. Details of these measurements are described elsewhere (7).

Results

Samples prepared.—The densities of the specimens after sintering were 92-94% of the theoretical density, see Table I. The average grain size of the samples is about 30 μm . The ceramic structure of a specimen is shown in Fig. 1. On this photograph it can be seen that the grain growth in this system is very fast even at temperatures of 1273 K. The grain boundaries move so fast that they become curved and pores are isolated within the grains. This implies that higher final densities are difficult to obtain without controlling grain growth.

The color of the specimens was yellow/orange for low percentages of Dy_2O_3 and dark brown for high percentages.

The difference between the calculated composition and the composition measured by x-ray fluorescence was 2.0% absolute or less. Concentrations of silicon and aluminum impurities are lower than 0.002 and 0.03 w/o, respectively.

Structural aspects.—Table II gives a survey of the existing structures if the specimens are subjected to different heat-treatments. In the "quenching" procedure the samples were suddenly removed from the furnace and cooled down to room temperature by natural convection, with the result that the high temperature structure could be retained. Lower temperature phases are occasionally achieved by cooling down very slowly ($1/2$ K min^{-1}) or by annealing at a suitable temperature.

The sample containing 5 m/o Dy_2O_3 has a tetragonal structure. The high temperature structure is cubic (fcc) as determined by the High Temperature Guinier technique (HTG). The transition temperature is 913 K, see Table III. If this sample is annealed, minor concentrations of other phases appear. This was also

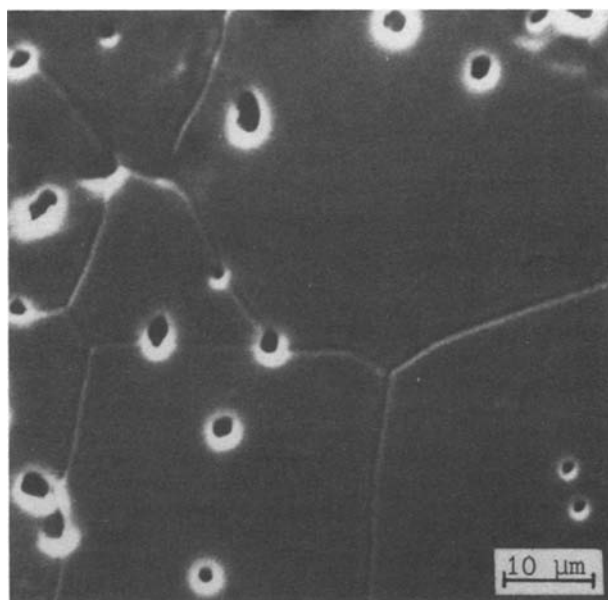


Fig. 1. The ceramic microstructure of $(\text{Bi}_2\text{O}_3)_{0.65}(\text{Dy}_2\text{O}_3)_{0.35}$

Table I. Sintering temperature and density

| x in $(\text{Bi}_2\text{O}_3)_{1-x}(\text{Dy}_2\text{O}_3)_x$ | Temperature (K) | Density* (%) |
|---|-----------------|--------------|
| 0.05-0.10 | 1073 | |
| 0.15-0.25 | 1173 | |
| 0.28-0.35 | 1273 | 92 |
| 0.40-0.50 | 1373 | 94 |
| 0.60 | 1373 | |

* Density is given as a percentage of the theoretical density based on defect fluorite-type lattice.

Table II. Survey of the structural information of the $\text{Bi}_2\text{O}_3\text{-Dy}_2\text{O}_3$ system

| x in $(\text{Bi}_2\text{O}_3)_{1-x}(\text{Dy}_2\text{O}_3)_x$ | Temperature treatment | | | |
|---|-------------------------------------|--|---------------------------|--------------------------------|
| | "Quenched" at sintering temperature | Cooled down by $\frac{1}{2}$ K min^{-1} | Annealing temperature (K) | Annealed for 350 hr |
| 0.05 | β^* | β | 823 | $\beta + \frac{\alpha + e}{2}$ |
| 0.10 | δ | $\delta + \frac{e + \delta}{2}$ | 823 | $\alpha + \delta + e$ |
| 0.15 | δ | $e + \delta$ | 903 | $e + \alpha$ |
| 0.20 | δ | $e + \delta$ | 973 | $e + \delta$ |
| 0.25 | δ | δ | 973 | $e + \delta$ |
| 0.28 ^b -0.50 | δ | δ | 973 | δ |
| 0.60 | $\delta + \theta^{**}$ | $\delta + \theta$ | | |

* The β -phase has a tetragonal structure.

** In this table θ denotes the unknown structure.

† In this table e denotes the rhombohedral structure.

‡ The underlined structures appear in minor concentrations.

observed in the $\text{Bi}_2\text{O}_3\text{-Er}_2\text{O}_3$ system (7). Possibly the tetragonal solid solution phase is stable at higher temperatures (*i.e.*, between 823-913 K) whereas at lower temperatures the solid solution exists over a narrower range of composition and ultimately only one tetragonal compound exists. It is suggested that this is the case in the $\text{Bi}_2\text{O}_3\text{-Y}_2\text{O}_3$ system (20).

The high temperature structure of the sample containing 10-25 m/o Dy_2O_3 is cubic (fcc). This can be concluded from the quenching experiments and was checked by HTG. The low temperature structure is rhombohedral, as can be seen from the samples cooled down by $1/2$ K min^{-1} as well as from the annealing experiments. The annealing experiments indicate that the rhombohedral solid solution is found from about 15 m/o Dy_2O_3 to 25 m/o Dy_2O_3 . After annealing for 2000 hr at 880 K the structure of the specimen containing 25 m/o Dy_2O_3 was $\approx 95\%$ rhombohedral. Table III shows the transition temperature of the rhombohedral structure to the cubic structure measured by DTA.

The equilibrium monophasic fcc structure was observed at low temperatures for samples containing 28.5-50.0 m/o Dy_2O_3 . These results do not agree with the observations of Datta and Meehan (20) who reported the existence of the fcc phase for $3\text{Bi}_2\text{O}_3 \cdot \text{Dy}_2\text{O}_3$ at low temperatures. It is very likely that these authors reported the nonequilibrium high temperature structure. Possibly contamination by the porcelain or silica crucibles used for the synthesis of the materials may play a role. The observations of the fcc phase for $\text{Bi}_2\text{O}_3 \cdot \text{Dy}_2\text{O}_3$ by Nasonova *et al.* (21) is confirmed.

As shown in Fig. 2 we see that in the whole range of the stabilized fcc phase (28.5-50 m/o Dy_2O_3) and in the range where the high temperature fcc phase can be retained by quenching (10-25 m/o Dy_2O_3) the lattice constant decreases linearly with an increasing Dy_2O_3 content, *i.e.*, Vegard's rule holds.

The specimen containing 60 m/o Dy_2O_3 shows an fcc phase and an unknown phase. Attempts to determine the composition of the two phases with the EDAX unit of the SEM failed because the size of the separate phases was too small compared to that of the analyzed area ($0.5\text{-}1 \mu\text{m}^2$). The deviation of the lattice constant of the fcc phase, see Fig. 2, cannot be explained.

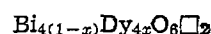
Table III. Transition temperatures measured by DTA in the heating-up direction*

| x in $(\text{Bi}_2\text{O}_3)_{1-x}(\text{Dy}_2\text{O}_3)_x$ | Transition | Temperature (K) |
|---|------------------------|-----------------|
| 0.05 | $\beta \rightarrow e$ | 913 |
| 0.10 | $e \rightarrow \delta$ | 848 |
| 0.15 | $e \rightarrow \delta$ | 946 |
| 0.20 | $e \rightarrow \delta$ | 989 |
| 0.25† | $e \rightarrow \delta$ | 1018 |

* Measured on samples cooled down by $\frac{1}{2}$ K min^{-1} from sintering temperature.

† Measured on the annealed sample (2000 hr at 880 K).

The theoretical densities can be calculated from the measured lattice constants assuming several defect models and can be compared with the observed densities. These defect models are extensively described and discussed in Ref. (7) and will not be repeated here. It appears that the system $\text{Bi}_2\text{O}_3\text{-Dy}_2\text{O}_3$ shows the same features as reported for $\text{Bi}_2\text{O}_3\text{-Er}_2\text{O}_3$ (7). So we conclude that all cations occupy their normal sites in the fluorite structure and that there are two vacancies in a unit cell, *i.e.*



Conductivity of the sintered specimens.—The conductivity of the sintered $\text{Bi}_2\text{O}_3\text{-Dy}_2\text{O}_3$ samples measured in air is shown in Fig. 3 and 4. In Fig. 4 the conductivity of pure Bi_2O_3 [after Takahashi *et al.* (6)] is given as a reference material. Table IV summarizes the values of the activation energies E_a and the pre-exponential terms σ_0 for the Arrhenius plots of the conductivity, while the deviation is given in the 90% reliability interval.

Figure 3 gives the conductivity of the cubic and rhombohedral structures of $(\text{Bi}_2\text{O}_3)_{0.75}(\text{Dy}_2\text{O}_3)_{0.25}$. Below 1018 K the cubic phase is unstable but can exist metastable because the transformation is too slow in order to take place during the rapidly performed conductivity measurements, see Table II. For the rhombohedral specimen these is a change in the activation energy at about 780 K. Possibly this may be correlated with a change in the ordering of oxygen in the lattice, as proposed for the cubic samples (see below). At 1010 ± 15 K there is a sudden increase in the conductivity. According to the HTG experiments this increase is caused by the structural change from the rhombohedral to fcc phase. The transformation temperature corresponds with the DTA data, see Table III. In the Arrhenius plot of the cubic sample

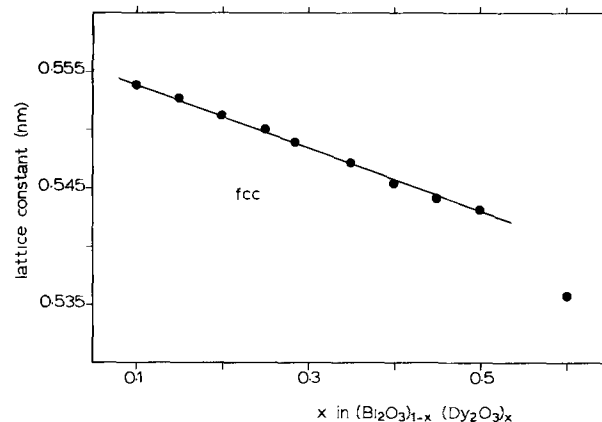


Fig. 2. Lattice constant of the fcc phase of the specimens cooled from the sintering temperature to room temperature by $1/2$ K min^{-1} . (For $x = 0.1\text{-}0.2$ the specimens were quenched.)

Table IV. Activation energies and pre-exponential terms for the Arrhenius plots of the conductivity

| x in $(\text{Bi}_2\text{O}_3)_{1-x}(\text{Dy}_2\text{O}_3)_x$ | Temperature range (K) | $\log \sigma_0$ ($\Omega^{-1}\text{m}^{-1}$) | E_a (kJ mole $^{-1}$) |
|---|-----------------------|--|--------------------------|
| 0.25 (rhomb) | 600-780 | 5.3 ± 0.2 | 97 ± 3 |
| | 780-1000 | 4.4 ± 0.1 | 85 ± 2 |
| 0.25 (cubic) | 600-870 | 7.2 ± 0.2 | 104 ± 3 |
| | 870-1060 | 5.0 ± 0.2 | 66 ± 4 |
| 0.28 ^s | 600-870 | 7.17 ± 0.04 | 108 ± 1 |
| | 870-1140 | 5.1 ± 0.1 | 73 ± 3 |
| 0.35 | 600-950 | 6.33 ± 0.05 | 101 ± 1 |
| | 950-1140 | 4.8 ± 0.1 | 73 ± 2 |
| 0.40 | 600-1050 | 6.34 ± 0.06 | 107 ± 1 |
| | 600-1050 | 6.4 ± 0.4 | 112 ± 6 |
| 0.50 | 600-1050 | 5.9 ± 0.1 | 109 ± 2 |
| | 600-1050 | 5.1 ± 0.1 | 112 ± 2 |

there is a change in the activation energy at about 870 K, this is discussed below.

The structure and the dimensions of the lattices of these phases are very different and the influence on the conductivity is striking. The volume of the rhombohedral and cubic unit cells is 0.123 and 0.166 nm³, respectively. The cubic lattice is "blown up" compared with the rhombohedral one. Therefore a flat potential profile along the transport path between oxygen ion lattice sites can be expected and rapid transport can occur in the cubic lattice, as suggested for other systems by Huggins (23).

Figure 4 gives the Arrhenius plots of the conductivity of the cubic specimens containing 0.25-0.60 m/o Dy₂O₃. The samples containing 0.25-0.35 m/o Dy₂O₃ show a knee in the Arrhenius plot at about 870-950 K. The changes in the activation energies and the pre-exponential terms are given in Table IV. Present authors (7) correlated this knee to a change in the lattice constant, probably caused by changes in the ordering of oxygen in the lattice. The increase of the lattice constant for (Bi₂O₃)_{0.80}(Er₂O₃)_{0.20} was confirmed by the Simon camera and is in the order of 1.5%. However, for the samples containing Dy₂O₃ no in-

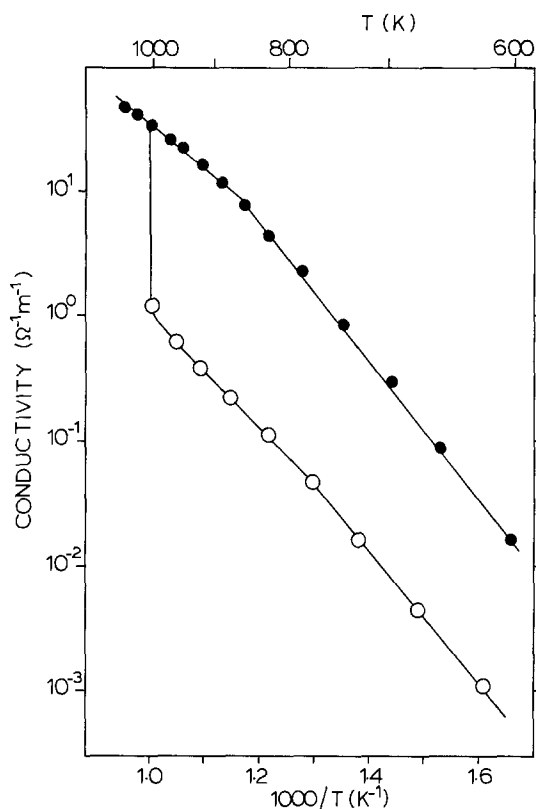


Fig. 3. Conductivity of $(\text{Bi}_2\text{O}_3)_{0.75}(\text{Dy}_2\text{O}_3)_{0.25}$ in air. ●, Cubic structure; ○, rhombohedral structure. The specimen with the rhombohedral structure could only be measured in the heating-up direction (see text).

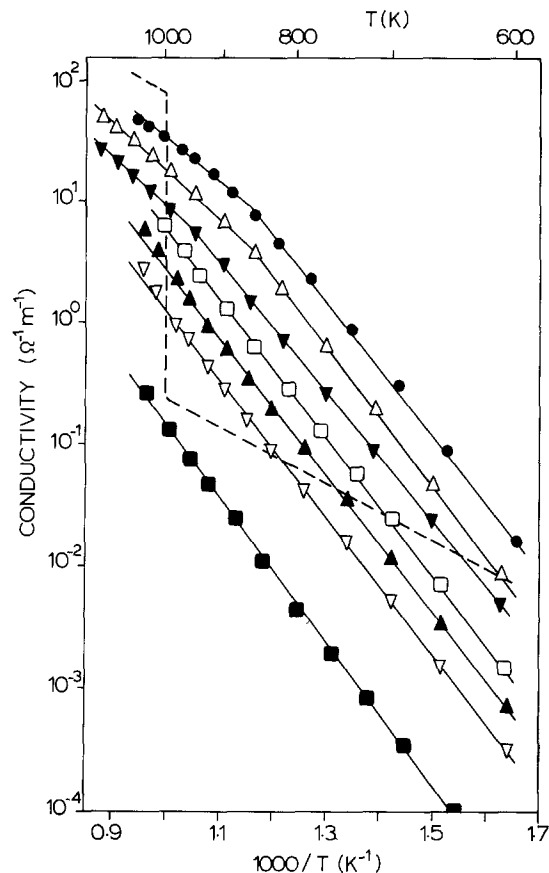


Fig. 4. Conductivity of $(\text{Bi}_2\text{O}_3)_{1-x}(\text{Dy}_2\text{O}_3)_x$ in air. ●, $x = 0.25$ (fcc); △, $x = 0.285$; ▼, $x = 0.35$; □, $x = 0.40$; ▲, $x = 0.45$; ▽, $x = 0.50$; ■, $x = 0.60$. The broken line represents the conductivity of pure Bi₂O₃ in the heating-up direction.

crease in the lattice constant could be measured with HTG. We conclude that the change in activation energy and the change in $\log \sigma_0$ is caused by a minor change in the structure which is not always accompanied by a measurable change in the unit cell volume.

The best oxygen ionic conductor in this system is found in the material with the composition $(\text{Bi}_2\text{O}_3)_{0.715}(\text{Dy}_2\text{O}_3)_{0.285}$. The conductivity at 773 and 973 K is 0.71 and 14.4 $\Omega^{-1}\text{m}^{-1}$, respectively. This is about three times lower than the conductivity of $(\text{Bi}_2\text{O}_3)_{0.80}(\text{Er}_2\text{O}_3)_{0.20}$ (7) and more than ten times higher than the conductivity of $(\text{ZrO}_2)_{0.195}(\text{Y}_2\text{O}_3)_{0.088}$ at the same temperatures.

The ionic transference number.—The ionic transference number was measured with an oxygen gas concentration cell under the condition of $P'_{\text{O}_2} = 0.21$ atm and $P''_{\text{O}_2} = 1.00$ atm. The ratio of the measured emf to the theoretical emf is given in Table V.

For $(\text{Bi}_2\text{O}_3)_{1-x}(\text{Dy}_2\text{O}_3)_x$ with $x = 0.25-0.40$ the ionic transference number is approximately one, therefore the conductivity in the range 1-100% O₂ can be almost wholly attributed to oxygen ions [this work, (27), (31)]. It may be remembered that the deviation of

Table V. Ratios of the measured emf E to the theoretical value E_0 of the following cell:

O₂ (0.21 atm), Pt | $(\text{Bi}_2\text{O}_3)_{1-x}(\text{Dy}_2\text{O}_3)_x$ | Pt, O₂ (1 atm) at different temperatures

| x in $(\text{Bi}_2\text{O}_3)_{1-x}(\text{Dy}_2\text{O}_3)_x$ | E/E_0 | | | | | |
|---|---------|-------|-------|-------|--------|--------|
| | 823 K | 873 K | 923 K | 973 K | 1023 K | 1073 K |
| 0.25 | — | 0.93 | 0.96 | 0.97 | 0.98 | 0.98 |
| 0.28 ^s | 0.94 | 1.00 | 0.98 | 0.98 | 0.98 | 0.98 |
| 0.40 | 0.95 | 0.97 | 0.99 | 1.00 | 1.01 | 1.00 |
| 0.50 | — | 0.85 | 0.99 | 0.94 | 0.95 | 0.95 |
| 0.60 | 0.42 | 0.47 | 0.54 | 0.61 | 0.69 | 0.72 |

the ionic transference number measured by oxygen concentration cells is about 5%. Additional experiments are necessary to determine the (small) contribution of the electronic conductivity. The sample containing 50 m/o Dy_2O_3 had an electronic component at low temperatures ($T < 900$ K). For the sample containing 60 m/o Dy_2O_3 an electronic component was measured for all temperatures. Because the ionic transference number for the monophasic fcc samples coexisting with the second phase is approximately one, the electrical conductivity has to be ascribed to the second phase. In this temperature range and at these oxygen partial pressures pure Dy_2O_3 is an electronic conductor (24). Possibly the unknown phase is Dy_2O_3 rich.

Discussion

The results of this study were combined with literature data of the following systems: $\text{Bi}_2\text{O}_3\text{-Er}_2\text{O}_3$ (7, 8), $\text{Bi}_2\text{O}_3\text{-Y}_2\text{O}_3$ (9), $\text{Bi}_2\text{O}_3\text{-Gd}_2\text{O}_3$ (10), and $\text{Bi}_2\text{O}_3\text{-Yb}_2\text{O}_3$ (25). Our attention is directed to two subjects, first, the optimization of the conductivity in sintered oxides of the $\text{Bi}_2\text{O}_3\text{-Ln}_2\text{O}_3$ system and, second, some considerations concerning the defect structure.

The optimization of the conductivity.—The conditions leading to an optimal conductivity of sintered oxides of the $\text{Bi}_2\text{O}_3\text{-Ln}_2\text{O}_3$ system were investigated concerning several aspects. These are, first, the influence of the ionic radius on the conductivity, second, the influence of the composition on the conductivity, and third, the influence of the ionic radius on the minimum substituent concentration necessary to stabilize the fcc phase.

Figure 5 gives the conductivity of bismuth sesquioxide stabilized by several lanthanides as a function of the ionic radius of the substituent. The ionic radii are based on $r(\text{VI}\text{O}^{2-}) = 0.140$ nm, coordination number VIII, as given by Shannon and Prewitt (26). The conductivity increases slightly with increasing ionic radius. No precise data about the lattice constants for some of the compositions are known. However, there is a linear relation between the ionic radius of the substituent and the lattice constant, as shown by Cahen (27), and thus there is a linear relation between the conductivity and the lattice constant. There is too little precise data known up till now to analyze this relation further in terms of relationships between the lattice constant and $\log \sigma_0$ respectively E_a .

We propose that it may be ascribed to a change in E_a . Assuming the same defect structure for all substituents at $x = 0.35$ the amount of vacancies is constant, so $\log \sigma_0$ will also be constant. Increasing the ionic radius of the substituent will cause an increase in the lattice constant. This may cause a decrease in the contributions of the local strain components during the passage of oxygen ions through the lattice, which

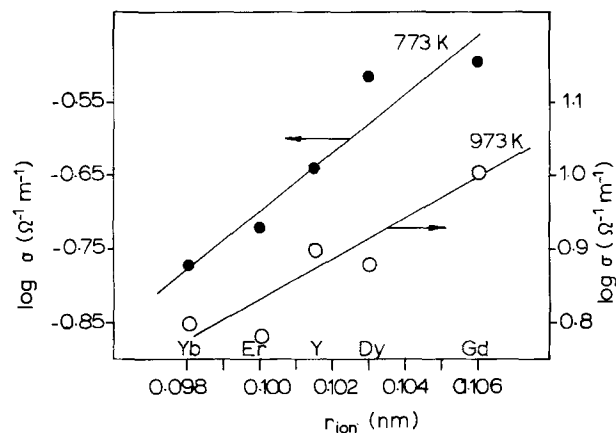


Fig. 5. The logarithm of the conductivity of $(\text{Bi}_2\text{O}_3)_{0.65}(\text{Ln}_2\text{O}_3)_{0.35}$ vs. the ionic radius of the substituent Ln^{3+} at 737 K (closed circles) and at 973 K (open circles).

leads to a decrease in the activation energy. This explanation agrees with the observation that the slope of the $\log \sigma$ vs. r_{ion} relation at 773 K is larger than that at 973 K. This hypothesis is confirmed in a related system. Kubo and Obayashi (28) showed that in $\text{Ce}_{1-x}\text{Ln}_x\text{O}_{2-x/2}$ for $x = 0.30$ the activation energy decreases with increasing ionic radius of the lanthanide.

In Fig. 6 the oxygen ion conductivity in the $\text{Bi}_2\text{O}_3\text{-Dy}_2\text{O}_3$ system is plotted against the Dy_2O_3 content at different temperatures. The conductivity of $(\text{Bi}_2\text{O}_3)_{0.80}(\text{Er}_2\text{O}_3)_{0.20}$ (7) is given as a reference. In the fcc solid solution phase field the conductivity decreases linearly with the composition. For $x = 0.60$ there is a negative deviation from this linear relation. This is due to the second phase. The deviation at $x = 0.25$ is caused by a structural phase transformation. The conductivity of the metastable fcc phase at $x = 0.25$ satisfies this linear relation as shown in Fig. 6. It should be noted that a linear relation between conductivity and concentration holds at temperatures above and below the observed knee in the Arrhenius plot. A linear relation in the fcc solid solution phase field is also found for Bi_2O_3 stabilized with Er_2O_3 (7), Y_2O_3 (9), and Gd_2O_3 (10).

From the Fig. 5 and 6 it is clear that the highest ionic conductivity will be found for large ions and low substituent percentages. As will be shown, these are contradictory requirements. Attention should be paid to the influence of the ionic radius of the Ln^{3+} ion on the minimum substituent concentration ($x_{\text{min.}}$) necessary to stabilize the fcc structure at room temperature. The correlation between the ionic radius and $x_{\text{min.}}$ is given in Fig. 7. It should be noted that the minimum concentrations given in (9, 10) for Gd_2O_3 and Y_2O_3 may be too low. Present work and (7) show that high temperature structures may be easily retained at low temperatures. So the cooling procedures applied in (9, 10) to determine the phase boundary of the fcc structure may not be sufficient to produce the "equilibrium" phase boundary. Figure 7 shows that there is a minimum in this curve at $r_{\text{ion.}} = 0.100$ nm (Er^{3+}). In literature there are no data about $x_{\text{min.}}$ for $\text{Ln} = \text{Tm}^{3+}$ ($r_{\text{ion.}} = 0.099$ nm). So it is possible that $x_{\text{min.}}$ for Tm^{3+} is somewhat lower than for Er^{3+} .

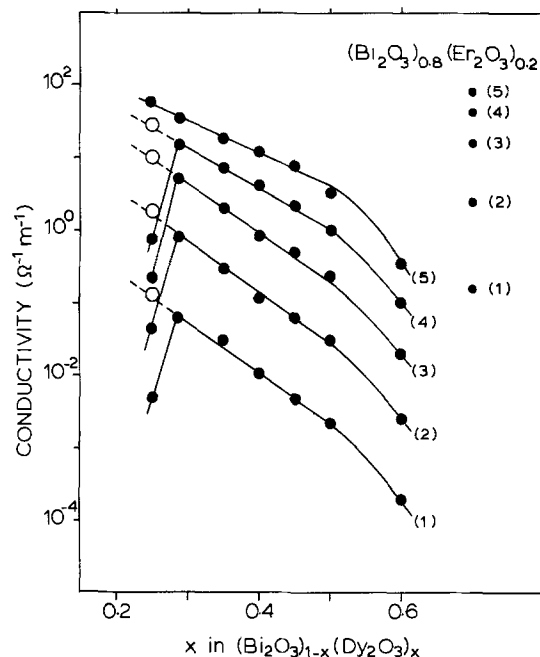


Fig. 6. Conductivity vs. composition at different temperatures. At the right the conductivity of $(\text{Bi}_2\text{O}_3)_{0.80}(\text{Er}_2\text{O}_3)_{0.20}$ is given as a reference. Curve 1, 673 K; curve 2, 773 K; curve 3, 873 K; curve 4, 973 K; curve 5, 1073 K. (The open circles represent the conductivity of the metastable fcc phase.)

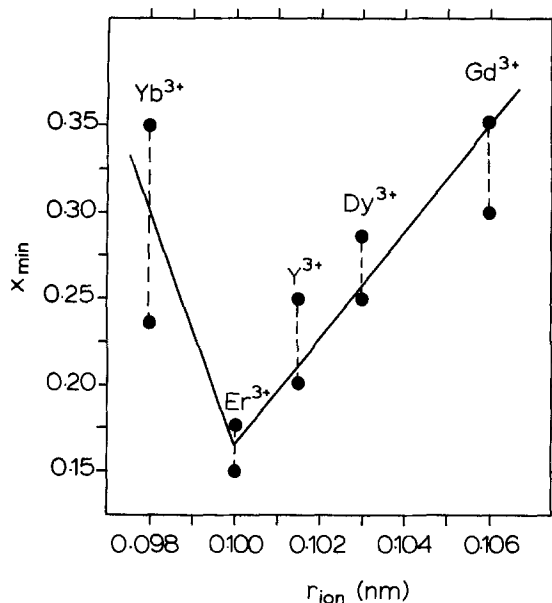


Fig. 7. X_{min} vs. the ionic radius (r_{ion}) of the substituent

The shape of the curve may be qualitatively explained in the following way. We assume that stabilization of the (very open) high temperature structure occurs at a certain contraction of this structure by the substituent. If the difference between the ionic radii of Bi^{3+} (0.111 nm) and the substituted M^{3+} is large, this will result in a large distortion in the host lattice and a small amount of substituent is necessary for supplying the energy required to stabilize the fcc phase, i.e., for Er^{3+} . Reversely, a small difference between the ionic radii needs a large amount of substituent to supply the energy to stabilize the fcc phase, i.e., for Gd^{3+} . For too large differences between the ionic radii of the Ln^{3+} ion and the Bi^{3+} ion the fcc phase becomes disfavored. At this stage we do not understand the stabilization of the fcc phase at higher concentration of Yb^{3+} , i.e., a substituent with a relatively large difference in ionic radius with respect to Bi^{3+} .

From Fig. 5 we can conclude that the fcc structure will also be stabilized at low temperatures for $Ln = Tm$ ($r_{ion} = 0.099$ nm), $Ln = Ho$ ($r_{ion} = 0.102$ nm), $Ln = Tb$ ($r_{ion} = 0.104$ nm), and possibly for $Ln = Sm$ ($r_{ion} = 0.102$ nm). The x_{min} values for these substituents are predicted in this figure.

This discussion allows us to make some predictions about optimization of the ionic conductivity of Bi_2O_3 stabilized by lanthanides. There are two contradictory tendencies. First, the ionic conductivity increases with increasing ionic radius (Fig. 5). Second, x_{min} increases with increasing ionic radius (Fig. 7) and a high x_{min} value results in a low conductivity (Fig. 6). However, the influence of the ionic radius on the conductivity is smaller than the influence of the Ln_2O_3 content. Therefore the optimization of the conductivity is only possible by lowering x_{min} . Figure 7 shows that there is a minimum in the x_{min} vs. r_{ion} plot at 0.098 nm $< r_{ion} < 0.105$ nm. The ions Er^{3+} ($r_{ion} = 0.100$ nm) and Tm^{3+} ($r_{ion} = 0.099$ nm) fall within this range. The highest conductivity occurs at the lowest x_{min} , as shown in Fig. 8. We conclude that the highest ionic conductivity will be found for Bi_2O_3 stabilized by Er_2O_3 or Tm_2O_3 .

If the conductivity above the knee could be stabilized at low temperature, a further optimization of the conductivity could be achieved. As shown below, the knee is correlated with an ordering process in the oxygen lattice. Therefore it is not very likely that the high temperature conductivity can be stabilized at lower temperatures.

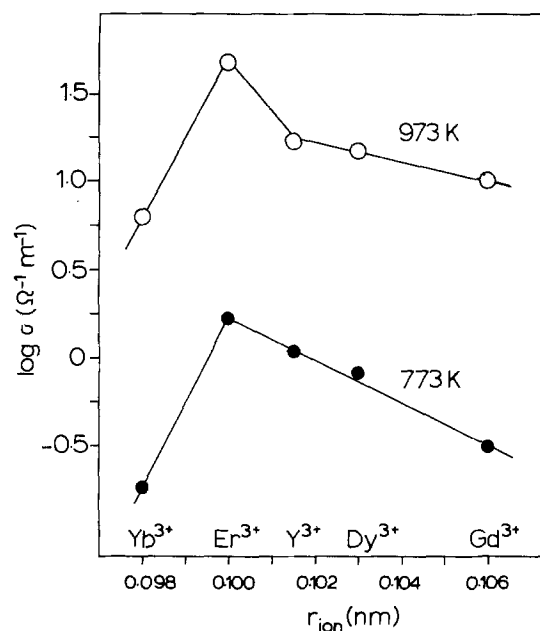


Fig. 8. The conductivity of $(Bi_2O_3)_{1-x}(Ln_2O_3)_x$ for x is the upper boundary of X_{min} vs. the ionic radius of the substituted Ln^{3+} at 773 K (closed circles) and at 973 K (open circles).

Defect structure.—As pointed out before the knee in the Arrhenius plot cannot simply be ascribed to a change in the lattice constant, but has to be ascribed to a change in the defect structure. At about the same temperature a knee in the Arrhenius plot is reported for Bi_2O_3 stabilized with Er_2O_3 (7), Y_2O_3 (9), and Gd_2O_3 (10), for yttria-stabilized zirconia (29, 30) and for lanthanide-doped ceria (28).

From this work and the results mentioned in literature (7, 9, 10) we searched for relations between the activation energy, $\log \sigma_0$, and the lanthanide content. For reasons of clarity the data are separately given for temperatures below 820 K and above 900 K. The results are given in Fig. 9 and 10. It appears that there are two different dependences, which can be related to different defect structures.

Above 900 K for the samples showing a knee in the Arrhenius plot the activation energy increases with increasing x whereas $\log \sigma_0$ is independent of x . The values of the activation energy and $\log \sigma_0$, extrapolated to $x = 0$, come very close to the values of δ - Bi_2O_3 . This suggests a disordered oxygen lattice analog to pure δ - Bi_2O_3 (4).

For the samples showing no knee in the Arrhenius plot, it appears that the activation energy is independent of x and $\log \sigma_0$ decreases linearly with increasing x . The same holds below 820 K for the samples showing a knee in the Arrhenius plot. These relations suggest that in this region the composition and therefore the lattice constant have no significant influence on the thermal activated passage of oxygen ions through the lattice, whereas the composition has a strong influence on $\log \sigma_0$. The hypothesis is put that in this region the oxygen ions are ordered. The concentration of the mobile oxygen ions strongly decreases with increasing lanthanide content.

This hypothesis is supported by neutron diffraction studies at room temperature by the present authors on $(Bi_2O_3)_{0.80}(Er_2O_3)_{0.20}$ which show a peak in the diffuse background, which can be correlated with a short distance ordering of oxygen ions. Further neutron diffraction studies are now being performed and will be correlated with a detailed description of the conductivity mechanism.

Conclusions

High oxygen ion conduction is found in the system Bi_2O_3 - Dy_2O_3 . The fcc phase can be stabilized by 28.5-50.0 m/o Dy_2O_3 . For the samples containing 28.5-40.0

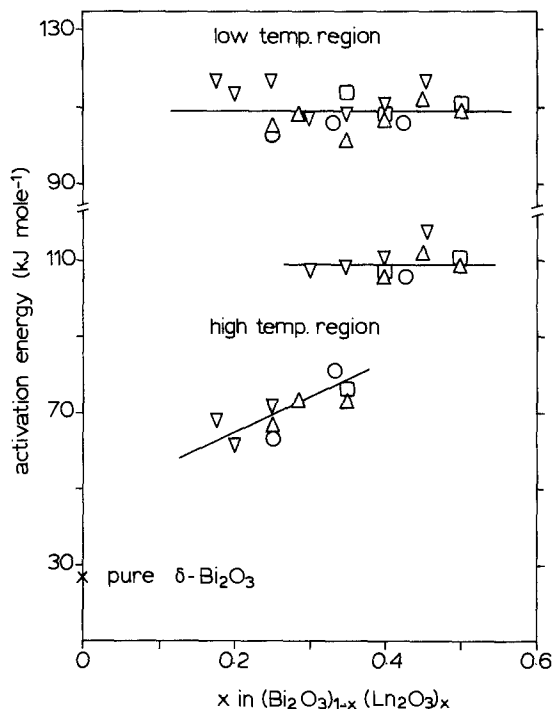


Fig. 9. The activation energy of the conductivity for the low temperature region (<820 K) and for the high temperature region (>900 K) as a function of the composition for several substituents. O, Ln = Y; □, Ln = Gd; △, Ln = Dy; ▽, Ln = Er.

m/o Dy_2O_3 the ionic transference number is one over the whole temperature range investigated, whereas for the sample containing 50.0 m/o Dy_2O_3 an electronic component is introduced at low temperatures. The conductivity of the most desirable composition in this system, i.e., $(\text{Bi}_2\text{O}_3)_{0.715}(\text{Dy}_2\text{O}_3)_{0.285}$, is about three times lower than the conductivity of the best oxygen ion conductor reported for Bi_2O_3 -based solid solutions.

It is concluded that the lowest percentage of lanthanide necessary to stabilize the fcc phase is found for Er_2O_3 or Tm_2O_3 .

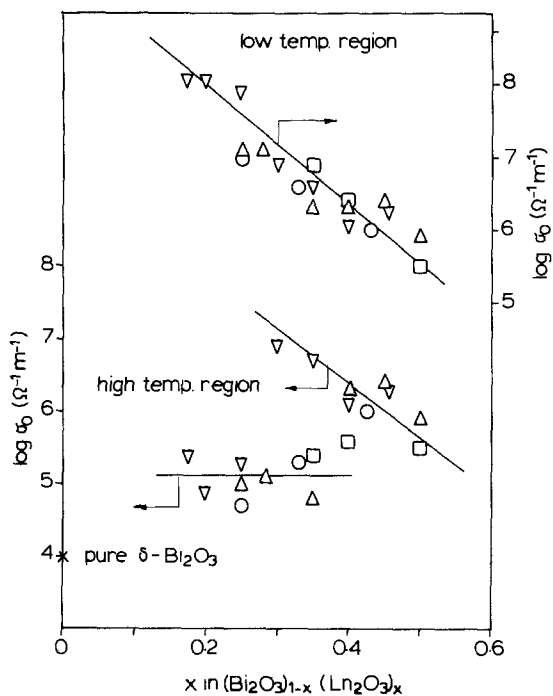


Fig. 10. The $\log \sigma_0$ of the conductivity for the low temperature region (<820 K) and for the high temperature region (>900 K) as a function of the composition for several substituents. O, Ln = Y; □, Ln = Gd; △, Ln = Dy; ▽, Ln = Er.

The influence of the ionic radius on the conductivity is smaller than the influence of the lanthanide content. Therefore it is concluded that the highest ionic conductivity based on Bi_2O_3 will be found in the systems Bi_2O_5 - Er_2O_3 or Bi_2O_3 - Tm_2O_3 . The knee in the Arrhenius plot of the conductivity of several specimens is ascribed to a change in the defect structure.

Acknowledgments

Dr. K. Keizer is thanked for performing some preliminary experiments in this system. We would like to express our appreciation to Mrs. A. van Pelt, Mr. J. Boeysma, and Mr. Th. van Dam for their experimental assistance. Financial assistance from Philips N.V. (Elcoma) is gratefully acknowledged.

Manuscript submitted March 4, 1980; revised manuscript received Aug. 7, 1980.

Any discussion of this paper will appear in a Discussion Section to be published in the December 1981 JOURNAL. All discussions for the December 1981 Discussion Section should be submitted by Aug. 1, 1980.

Publication costs of this article were assisted by the Twente University of Technology.

REFERENCES

- H. A. Harwig, Thesis, State University Utrecht (1977).
- H. A. Harwig and A. G. Gerards, *Thermochim. Acta*, **28**, 121 (1979).
- H. A. Harwig and A. G. Gerards, *J. Solid State Chem.*, **26**, 265 (1978).
- H. A. Harwig, *Z. Anorg. Allg. Chem.*, **444**, 151 (1978).
- H. A. Harwig and J. W. Weenk, *ibid.*, **444**, 167 (1978).
- T. Takahashi, H. Iwahara, and Y. Nagai, *J. Appl. Electrochem.*, **2**, 97 (1972).
- M. J. Verkerk, K. Keizer, and A. J. Burggraaf, *ibid.*, **10**, 81 (1980).
- K. Keizer, M. J. Verkerk, and A. J. Burggraaf, *Ceramurgia Int.*, **5**, 143 (1979).
- T. Takahashi, H. Iwahara, and T. Arao, *J. Appl. Electrochem.*, **5**, 187 (1975).
- T. Takahashi, T. Esaka, and H. Iwahara, *ibid.*, **5**, 197 (1975).
- T. Takahashi and H. Iwahara, *ibid.*, **3**, 65 (1973).
- T. Takahashi, H. Iwahara, and T. Esaka, *This Journal*, **124**, 1563 (1977).
- T. Takahashi, T. Esaka, and H. Iwahara, *J. Appl. Electrochem.*, **7**, 299 (1977).
- M. J. Verkerk and A. J. Burggraaf, Accepted for publication in *J. Appl. Electrochem.*
- K. W. Browall, Paper 467 presented at The Electrochemical Society Meeting, Seattle, Washington, May 21-26, 1978.
- L. Heyne, in "Measurement of Oxygen," H. Degn et al., Editors, Elsevier, Amsterdam, Oxford, New York (1976).
- L. Heyne, N. M. Beekmans, P. J. Poolman, and R. K. Eijnthoven, Dutch Pat. Appl. 7,309,537 (1973).
- R. L. Klimisch and J. M. Komarmy, in "The Catalytic Chemistry of Nitrogen Oxides," R. L. Klimisch and J. G. Larson, Editors, Plenum Press, New York (1975).
- R. Zechall and G. Baumann, *Motortech. Z.*, **34**, 7 (1977).
- R. K. Datta and J. P. Meehan, *Z. Anorg. Allg. Chem.*, **383**, 328 (1971).
- S. N. Nazonova, V. V. Serebrennikov, and G. A. Narnov, *Russ. J. Inorg. Chem.*, **18**, 1244 (1973).
- H. Kruidhof, *Anal. Chim. Acta*, **99**, 193 (1978).
- R. A. Huggins and A. Rabenau, *Mater. Res. Bull.*, **13**, 1315 (1978).
- V. B. Tare and H. Schmalzried, *Z. Phys. Chem. N.F.*, **43**, 30 (1964).
- M. J. Verkerk, Unpublished work.
- R. D. Shannon and C. T. Prewitt, *Acta Crystallogr., Sect. B*, **25**, 925 (1969).
- H. T. Cahen, Thesis, State University Utrecht

- (1980).
 28. T. Kudo and H. Obayashi, *This Journal*, **122**, 142 (1975).
 29. J. E. Bauerle and J. Hrzio, *J. Phys. Chem. Solids*, **30**, 565 (1969).
 30. E. Schouler, Thesis, Grenoble (1979).
 31. T. Takahashi, T. Esaka, and H. Iwahara, *J. Appl. Electrochem.*, **7**, 303 (1977).

Diffusion-Limited Charge Transport at Platinum Electrodes on Doped CeO₂

D. Braunshtein, D. S. Tannhauser,* and I. Riess

Department of Physics, Technion, Israel Institute of Technology, Haifa, Israel

ABSTRACT

We have measured the d-c and a-c properties of platinum paste electrodes on samples of the solid electrolyte (CeO₂)_{0.9}(Gd₂O₃)_{0.1} in the temperature range 700°-900°C and the oxygen pressure range $1 \cong P_{O_2} \cong 10^{-4}$ atm. The d-c measurements showed that the current through the system saturated at a value proportional to the oxygen pressure and that the cathode (the electrode where oxygen enters) limits the current. We explain the limitation by a gas diffusion mechanism, which adds a small term to the dynamic resistance of the sample. The dynamic resistance is mainly determined by the resistivity of the electrolyte together with the current constriction at the triple line gas-electrolyte-electrode. A-C measurements gave impedance plots with the shape of a quarter circle, pointing to a diffusion process. We propose as model that part of the oxygen molecules arriving at the triple line is ionized directly and enters the electrolyte, and a second part diffuses as atoms along the interface electrolyte-electrode before being ionized. This model explains the observed quarter circle as well as the impedances measured for $\omega = 0$ and for $\omega = \infty$.

It is well known that electrode impedance plays an important role in the overall impedance of high temperature fuel cells. A large number of papers treat the subject phenomenologically but only a few try to understand the subject in microscopic detail. Some authors measured d-c properties and proposed a detailed model (1-3), other measured also a-c properties but did not analyze the results microscopically (4-7).

In the present paper we report on d-c and a-c properties of platinum electrodes on gadolinia-doped ceria, combined with scanning electron microscope studies of these electrodes. We then present a detailed model for the processes involved.

Very recently two papers by Wang and Nowick (8, 9) reported on a-c and d-c measurements on the same system. We believe that the differences between the results of their work and ours is due to the structure of the electrodes and we shall come back to this in the discussion.

Sample and Electrode Preparation

The starting material for the electrolyte was prepared by coprecipitation of oxalates of cerium and gadolinium and calcination at 1000°C to obtain (CeO₂)_{0.9}(Gd₂O₃)_{0.1}. The powder was then pressed at 2000 bar (2×10^8 Nt/m²) and sintered at 1700°C for 3 hr.

The shape after sintering was a round cylinder 40 mm long and 11 mm across. Pellet-shaped samples about 1 mm thick were cut with a diamond saw from this cylinder. Some additional samples were prepared directly as pellets and sintered under similar conditions. Platinum electrodes were prepared by spreading a thin layer of platinum paste (Engelhard 6082), heating to 900°C at 100°C/hr, and cooling to room temperature in 1 hr. Scanning electron microscope (SEM) pictures confirm that the heating rate is crucial for the electrode resistance: if the rate is too fast (less than a few hours to 900°C) the platinum tends to form sepa-

rate islands. This was found to increase the impedance of the sample. Figure 1 shows an SEM picture of a Pt-paste electrode heated slowly; it is seen that the platinum grains are connected and do not form separate islands.

The platinum covered surface S_{Pt} equals about 70% of the visual gross electrode area S_E , which is 0.64 cm². The cross section of the sample, S_0 , is 1.13 cm². The typical width of the interconnected platinum islands in Fig. 1 is 2 μm.

We observed also that the surface condition of the sample influences strongly the two-point resistance of the sample. For electrodes prepared on the surface of sintered pellets (the SEM picture of such a surface is shown in Fig. 2) the two-point resistance was a few hundred ohms at 800°C, much higher than the 2.2Ω calculated from the bulk conductivity with the assumption of ideal electrodes (see below). If the surface of the sample was roughened with sandpaper, the

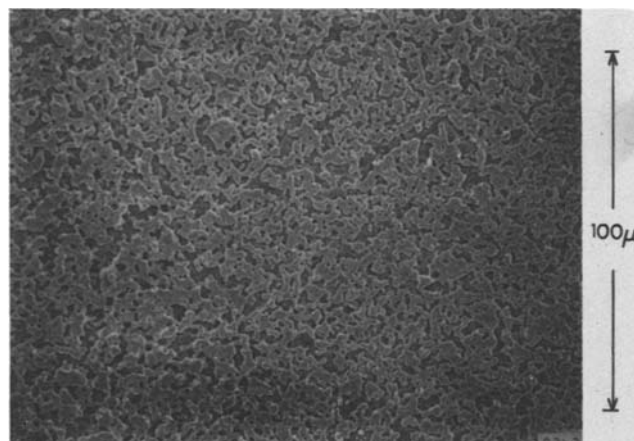


Fig. 1. SEM picture of Pt-paste electrode right after preparation. The lighter areas are platinum.

* Electrochemical Society Active Member.

Key words: fuel cell, solid electrolyte, interface impedance.

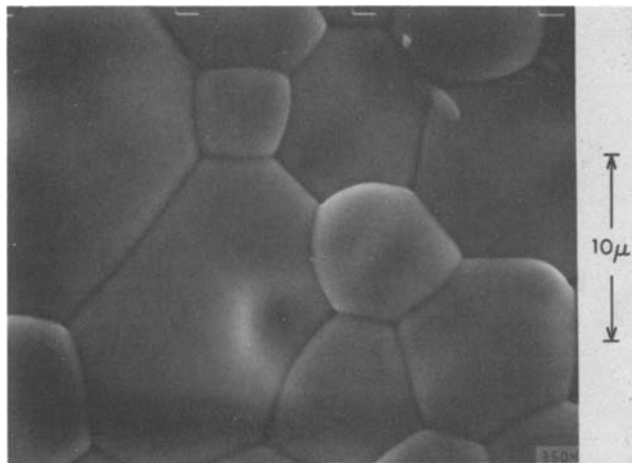


Fig. 2. SEM picture of the surface of a $(\text{CeO}_2)_{0.9}(\text{Gd}_2\text{O}_3)_{0.1}$ sample after sintering.

resistance dropped considerably. The surfaces cut by a diamond saw (see Fig. 3) were naturally rough and gave a two-point resistance of only $\sim 14\Omega$ at 800°C in pure oxygen. Most of the measurements reported in this paper were taken on one sample, 1.4 mm thick, but other samples gave very similar results. It is known that the structure of the platinum electrodes coarsens under heat-treatment (8). Our measurements were taken after the sample had been for a few days at the working temperature; the structure of the electrodes was then presumably coarser than that of the freshly prepared electrode shown in Fig. 1.

Experimental Procedure

The four-point van der Pauw method (10) was used to measure the specific conductivity of the electrolyte. In order to avoid polarization effects the measurements were made with low frequency a.c. (22 Hz).

The sample holder used for two-point measurements has been described previously (11). It permits measurements with two different atmospheres at the two electrodes. I - V curves with an external voltage applied were drawn by an X-Y recorder and the dynamic resistance of the system at zero current, $R_0 = dV/dI$, was measured from the slope of the curve.

The complex impedance of the system was measured in the frequency range 1 Hz to 50 kHz, using the circuit shown in Fig. 4.

Measurements were performed in the temperature range $700^\circ \leq T \leq 900^\circ\text{C}$, and oxygen partial pressure range $10^{-4} \leq P_{\text{O}_2} \leq 1$ atm. Ar- O_2 mixtures were used to obtain low oxygen pressures, which were measured by a commercial instrument (Thermox I).

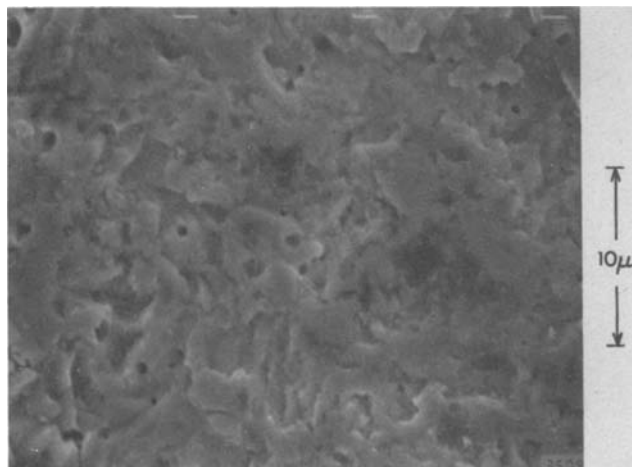


Fig. 3. SEM picture of the surface of a $(\text{CeO}_2)_{0.9}(\text{Gd}_2\text{O}_3)_{0.1}$ sample cut by a diamond saw.

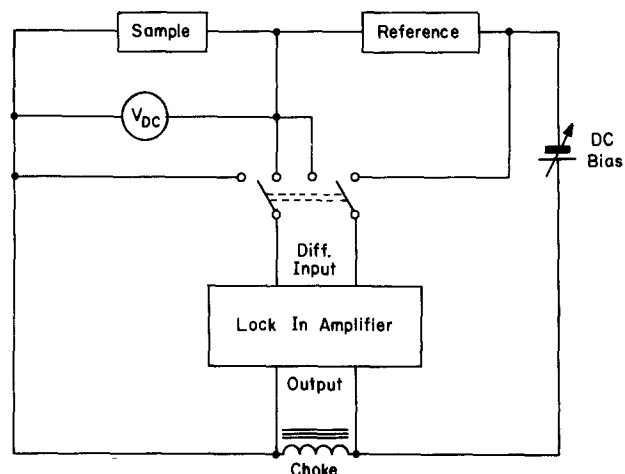


Fig. 4. Circuit for measuring the complex impedance of a sample with d-c bias. The lock-in amplifier supplies the alternating current and measures the alternating voltage; the choke serves as shunt for d.c.

Results

D-C measurements.—In Fig. 5 we present I - V curves for various oxygen pressures. For the symmetrical cells used the shape of the curves was the same for both current directions, and we observed, in common with other workers (3, 4, 8), a tendency towards current limitation. The limiting current, defined as the value where the I - V curve begins to deviate from a straight line, was proportional to the oxygen pressure, as shown in Fig. 6.

The bulk conductivity of the electrolyte was measured and found to be independent of the current. The nonlinear behavior of the system EEE (electrode-electrolyte-electrode) is therefore attributed to the electrodes.

In order to check which electrode limits the current, the I - V characteristic of a cell with different atmospheres at the two electrodes was measured (see Fig. 7). In this cell current limitation occurs when oxygen enters the electrolyte from the low oxygen pressure side. Since it is seen from Fig. 5 that in pure oxygen the limiting current is much larger than in an (Ar, O_2) mixture we conclude that the cathode (the electrode where oxygen enters) is responsible for the current limitation. This conclusion was confirmed by measurements on a cell with electrodes differing in size. The ratio of the areas was 2:1, and the limiting current was twice as large when the oxygen entered the sample through the large electrode as in the reverse case. Our conclusion that the cathode causes the current limitation through the sample agrees with that of other workers (1-3).

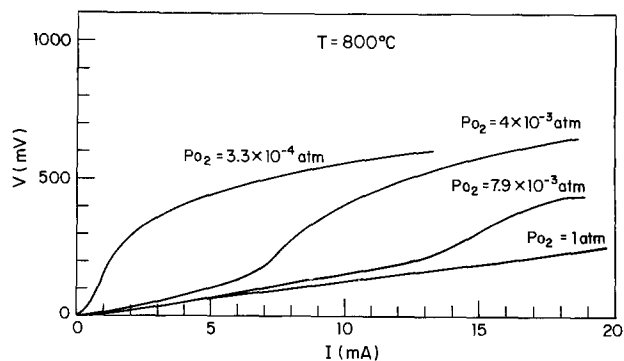


Fig. 5. I - V characteristics of a $(\text{CeO}_2)_{0.9}(\text{Gd}_2\text{O}_3)_{0.1}$ sample with Pt-paste electrodes at various oxygen pressures.

$$V = IR - \frac{kT}{4q} \ln \frac{C_s}{C_o} \quad [1]$$

Here C_s and C_o are volume concentrations of oxygen at the surface of the cell and in the undisturbed atmosphere. R is the resistance of the electrolyte. In Eq. [1] we have assumed that \bar{t}_1 (the average ionic transport number in the sample) equals one, and have also neglected the diffusive part of the ionic current (12). These are good approximations for our range of oxygen pressures and our highly doped samples in which the vacancy concentration is practically constant. We have also neglected any concentration gradient of oxygen at the anode.

Since we expect $C_o - C_s$ to be linearly dependent on the current in the form $C_o - C_s = KI$, we can write

$$V = IR - \frac{kT}{4q} \ln \left(1 - \frac{KI}{C_o} \right) \quad [2]$$

and current limitation will occur when the second term diverges. The limiting current will be $I_1 = C_o/K$ and since $C_o = P_{O_2}/kT$, we get the observed $I_1 \propto P_{O_2}$ behavior. Equation [2] can now be written

$$V = IR - \frac{kT}{4q} \ln \left(1 - \frac{I}{I_1} \right) \quad [3]$$

a form which has been mentioned before in the literature (3). For $I \ll I_1$ we get the dynamic resistance R_o

$$R_o = \frac{dV}{dI_{I=0}} = R + \frac{kT}{4q} \frac{1}{I_1} \quad [4]$$

i.e., for small currents the diffusion term adds a constant contribution to the overall resistance of the cell.

From the observed values of I_1 we calculate the second term in Eq. [4] to be about 4Ω at $P_{O_2} = 4 \times 10^{-3}$ atm and 800°C , and smaller for higher pressures. Since the total measured dynamic resistance R_o is 11Ω at pressures $\geq 10^{-3}$ atm, we conclude that in this pressure range the major part of R_o is the resistance of the electrolyte. If we assume that the whole platinized area of the electrode determines the current geometry we calculate from Eq. [A-4] of Appendix A, with $S_{Pt} = 0.45 \text{ cm}^2$, $S_o = 1.13 \text{ cm}^2$, $\sigma = 0.089 \Omega^{-1} \text{ cm}^{-1}$, and $l = 1.4 \text{ mm}$, a bulk resistance R_b of 2.2Ω , much smaller than the observed R_o . Let us assume however more realistically that the reaction between free oxygen, electrolyte, and electrons is restricted to a narrow strip along the triple line gas-electrolyte-electrode, the width of the strip being δ and its area S_{TL} . The resistance is then dominated by a constriction effect and will be called R_c . From the SEM picture of the electrode (Fig. 1) we estimate the length of the triple line as $L = 5 \times 10^3 \text{ cm}$. If we assume that $\delta = 10\text{\AA}$ we get $S_{TL} = \delta L = 5 \times 10^{-4} \text{ cm}^2$. Equation [A-4] of Appendix A gives now $R_c = 23\Omega$, about twice the experimental $R_o = 11\Omega$. The calculated constriction effect, which increases the resistance by a factor ten, depends only logarithmically on the width of the triple line, so that the assumption of $\delta = 10\text{\AA}$ is not critical. The agreement between R_c and R_o can be considered satisfactory in view of the geometrical approximations involved. It is supported by the equal temperature dependence of $1/R_o$ and σ , shown in Fig. 10.

The increase of R_o seen at $P_{O_2} < 10^{-3}$ atm in Fig. 5 can be explained through the inverse dependence of the second term of Eq. [4] on I_1 and thus on P_{O_2} . This term becomes dominant at low pressures.

The further rise of current after saturation seen in Fig. 5 is presumably connected to reduction of the electrolyte, as discussed by Casselton for ZrO_2 (13).

We have arrived therefore at the reasonable picture that the oxygen transport goes by gas diffusion to the triple line and from there as ionic current through a resistance determined by constriction effects.

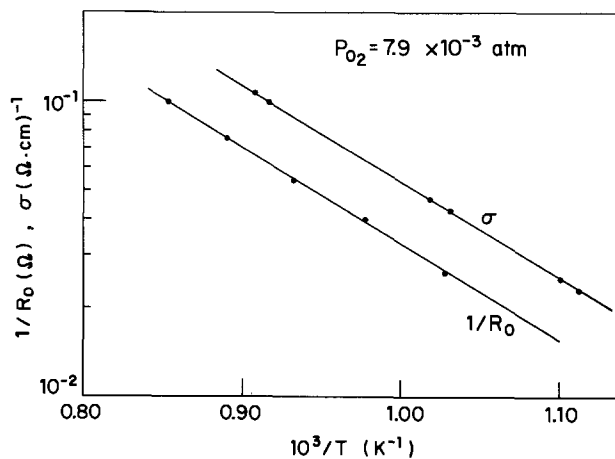


Fig. 10. The dynamic conductance $1/R_o$ together with the bulk conductivity of a $(\text{CeO}_2)_{0.9}(\text{Gd}_2\text{O}_3)_{0.1}$ sample vs. $1/T$ at $P_{O_2} = 7.9 \times 10^{-3}$ atm.

It is interesting to consider a more detailed picture for the diffusion process. If we assume a cylindrical diffusion geometry around the triple line with one-quarter of all directions being allowed, it can easily be shown that I_1 is given by

$$\frac{I_1}{P_{O_2}} = \frac{KqD}{kT \ln(\delta/r)} \quad [5]$$

Here D is the gas diffusion coefficient of oxygen, r the distance beyond which $C = C_o$, i.e., the gas is undisturbed by the cell, and K is a constant of order one. Using $D = 0.2 \times 10^{-4} \text{ m}^2/\text{sec}$ and $I_1/P_{O_2} = 1.43 \times 10^{-5} \text{ Am}^2/\text{N}$ (see Fig. 6) we get $\delta/r = 10^{-6}$. Our assumed $\delta = 10\text{\AA}$ implies therefore $r = 10^{-3}\text{m}$ which is a reasonable order of magnitude.

We considered also the possibility that the current limitation is caused not by diffusion in the gas phase but by the kinetic limitation of the number of oxygen molecules impinging on the triple line. From such a model one can calculate directly that the width of the triple line involved in the limiting current is 1\AA . Since however the mean-free path in air is only 100\AA it is unlikely that this is the limiting mechanism.

We saw that the gas diffusion term is a small part of the total dynamic resistance. In a-c measurements this diffusion process would appear as a finite Warburg resistance, which we shall discuss in detail below.

A-C results.—The quarter circle observed in our measurements points mathematically to a diffusive process with a resistive process in parallel (14). The gas diffusion process which we have discussed above cannot serve as explanation because (i) there is no conceivable resistive process in parallel with it and (ii) the contribution of the diffusion term to the d-c resistance is small, therefore the short-circuiting of the gas diffusion impedance at higher frequencies would change the total impedance by much less than the observed effect. We therefore neglect for the moment the impedance of the gas diffusion process and propose the following model, which uses an interface diffusion process, to explain the results.

The oxygen molecules which arrive from the gas at the triple line are adsorbed and dissociate into two atoms. We now assume that charge is transported through the sample by two parallel modes of transport (see Fig. 11). In one mode the reaction $\text{O} + 2e^- + \text{V}_o \rightarrow \text{O}_o$ occurs directly on the triple line, i.e., oxygen ions (transported by oxygen vacancies) penetrate the SE directly from this line. In the second mode the oxygen atoms diffuse along the interface electrode-electrolyte and the above reaction occurs on the interface. Schematically this can be written

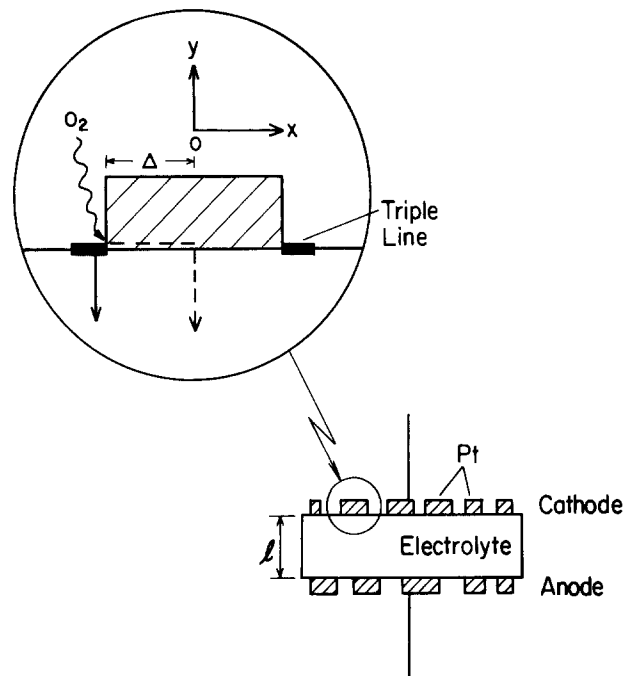
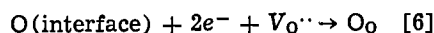
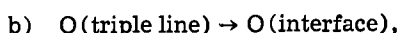
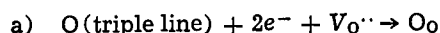
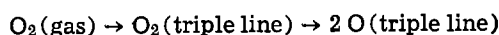


Fig. 11. Schematic cross section of a sample with Pt-paste electrodes. The diffusive mode of oxygen transport from the triple line into the electrolyte is shown by a broken line, the direct penetration mode by a full line.



The diffusion mode is connected with a finite diffusion path length, Δ , of about $1 \mu\text{m}$, given by the size of the platinum islands (see Fig. 11), but we shall see that in our system the parameters are such that one can treat Δ as infinite.

In order to calculate the impedance of the diffusion mode we choose the origin $x = 0$ in the middle of a platinum island, as shown in Fig. 11, and assume that oxygen reacts with vacancies only at this point of the interface rather than over the whole area. This idealization makes our model quasi-one-dimensional and therefore more amenable to calculation. We also assume for simplicity that only one electrode contributes to the impedance. It can be shown that the results are essentially the same if both electrodes contribute.

An external voltage is applied between the two electrodes. The interface concentration c_0 of oxygen atoms at the triple line c_0 is constant; while the interface concentration at $x = 0$ varies with time, $c = c(0, t)$. The applied voltage is connected with the potential difference $\Delta\phi$ in the electrolyte by

$$V = \Delta\phi - \frac{kT}{2q} \ln \frac{c(0, t)}{c_0} \quad [7]$$

which is essentially the same as Eq. [1]. (Here we have assumed that the effective P_{O_2} is proportional to the square of the interface concentration of oxygen atoms). The impedance is therefore

$$Z_D = \frac{V}{I_D} = \frac{\Delta\phi}{I_D} - \frac{kT}{2qI_D} \ln \frac{c(0, t)}{c_0} \quad [8]$$

where I_D is the part of the external current transported by the diffusion mode.

Continuity at $x = 0$ demands that the ionic current flowing from this point into the electrolyte should be the equivalent of the particle current I_a flowing by

diffusion along the interface EE and be equal also to I_D

$$I_1 = 2qI_a|_{x=0} = I_D \quad [9]$$

The particle current according to Fick's law is

$$I_a = -D_s L \frac{dc}{dx} \quad [10]$$

Here D_s is the surface diffusion coefficient and L the length of the triple line, which defines the cross section of the diffusion path.

We use for the first term of Eq. [8] the bulk resistance R_b of the electrolyte, which was calculated before. This calculation of R_b deviates from the one-dimensional model which we introduced above, but is a more realistic approximation.

To calculate the second term of Eq. [8] we assume that c changes only slightly around the value c_0 . This will be valid for small currents

$$c(x, t) = c_0[1 + \epsilon(x, t)]; \quad |\epsilon| \ll 1 \quad [11]$$

The concentration c obeys the diffusion equation

$$\frac{\partial c}{\partial t} = D_s \frac{\partial^2 c}{\partial x^2} \quad [12]$$

Substitution of [11] into [12] gives

$$\frac{\partial \epsilon}{\partial t} = D_s \frac{\partial^2 \epsilon}{\partial x^2} \quad [13]$$

We are looking for a solution of Eq. [13] of the form

$$\epsilon(x, t) = \epsilon_0 e^{j(\omega t + u'x)} \quad [14]$$

By substitution of [14] into [13] we get for $u'(\omega)$

$$u' = \pm \sqrt{\frac{\omega}{2D_s}} (1 - j) \equiv \pm u \quad [15]$$

The general solution of [12] is therefore

$$c = c_0[1 + \epsilon_0' e^{j(\omega t - ux)} + \epsilon_0 e^{j(\omega t + ux)}] \quad [16]$$

and with the boundary condition

$$c(-\Delta, t) = c_0[1 + \epsilon_0' e^{j(\omega t + u\Delta)} + \epsilon_0 e^{j(\omega t - u\Delta)}] = c_0 \quad [17]$$

we get

$$\epsilon_0' = -\epsilon_0 e^{-2ju\Delta} \quad [18]$$

From Eq. [16] we obtain

$$\ln \frac{c(0, t)}{c_0} = \ln [1 + (\epsilon_0' + \epsilon_0) e^{j\omega t}] \simeq (\epsilon_0' + \epsilon_0) e^{j\omega t} \quad [19]$$

while the current is given by

$$\frac{I_D}{2q} = I_a|_{x=0} = -D_s L \frac{\partial c}{\partial x} \Big|_{x=0} = D_s L c_0 j u (\epsilon_0' - \epsilon_0) e^{j\omega t} \quad [20]$$

We substitute Eq. [15], [19], and [20] into Eq. [8] and get for the impedance of the diffusion mode

$$Z_D = R_b + B\omega^{-1/2} (1 - j) \frac{\epsilon_0 + \epsilon_0'}{\epsilon_0 - \epsilon_0'} \quad [21]$$

where we have defined

$$B \equiv \frac{kT}{4q^2} \frac{1}{c_0 L \sqrt{2D_s}} \quad [22]$$

Using [15] and [18] this gives

$$Z_D = R_b + B\omega^{-1/2} (1 - j) \frac{1 - \exp[-\sqrt{2\omega/D_s}(1 + j)\Delta]}{1 + \exp[-\sqrt{2\omega/D_s}(1 + j)\Delta]} = R_b + Z_{\text{WF}}(\text{int}) \quad [23]$$

$Z_{\text{WF}} \equiv B\omega^{-1/2}(1 - j)$, known as Warburg impedance, is

the diffusional impedance for an infinite diffusion path (14). Its electrical analog is an infinite transmission line of distributed R-C links. We have therefore called the second term in Eq. [23] $Z_{Wf}(int)$; it is the impedance of the finite interface diffusion path, represented mathematically by a finite transmission line shorted at the end. The frequency dependence of $Z_{Wf}(int)$ is seen in Fig. 13(a), and it is easy to show that $Z_{Wf}^0(int) = B\Delta\sqrt{2/D_s}$. Equation [23] implies that for $\sqrt{\omega/D_s}\Delta \gg 1$ $Z_{Wf}(int) \approx Z_W$, i.e., the diffusion path length Δ is effectively infinite.

The total impedance of the sample is represented by the equivalent circuit shown in Fig. 12, where we have now added R_c in parallel to Z_D , R_c being again the (real) resistance for the current entering the SE directly through the triple line. $Z_{Wf}(gas)$ represents the gas diffusion process; its frequency dependence should be that of $Z_{Wf}(int)$ and is also given by Fig. 13(a). Since we have seen that its contribution is small compared to R_c even at $\omega = 0$, and since its absolute value decreases for higher frequencies, we will neglect it for the moment in the discussion.

The complex impedance of the circuit of Fig. 12 is shown in Fig. 13 for various values of $R_b/Z_{Wf}^0(int)$ and $R_c/Z_{Wf}^0(int)$. We see that if and only if

$$Z_{Wf}^0(int) \gg R_b, R_c \quad [24]$$

does the curve, which is given by

$$Z = \left[\frac{1}{R_c} + \frac{1}{R_b + Z_{Wf}(int)} \right]^{-1} \quad [25]$$

have the experimentally observed shape of a quarter circle. Its end points are then $Z^0 = R_c$ and $Z^\infty = R_b R_c / (R_b + R_c)$. We shall show in Appendix B that [24] implies that diffusion can be neglected for $\omega < 4D_s/\Delta^2$. Since for higher frequencies $Z_{Wf}(int) \approx Z_W$ it follows that the diffusion path is effectively infinite at any frequency and that $Z_{Wf}(int)$ in Fig. 12 and Eq. [25] can be replaced by Z_W .

The expression $R_b R_c / (R_b + R_c)$ for Z^∞ is formal only because the resistances R_c and R_b shown in the equivalent circuit of Fig. 12 are physically not in parallel. From the suggested model it follows that when $\omega = 0$, diffusion can be neglected, i.e., $Z^0 = R_c$, as demanded by Eq. [25]. But when $\omega = \infty$ the active areas of both cathode and anode are S_{Pt} , the surface covered by platinum. Therefore Z^∞ should equal R_b rather than $R_b R_c / (R_b + R_c)$. Since in our case $R_b < R_c$, the difference between the two expressions for Z^∞ is small. The measured values of R_o are in good agreement with the calculated R_b (e.g., R_b at 800°C is 2.2Ω, R_o is 3Ω) and are also independent of P_{O_2} as required by the fact that σ is independent of P_{O_2} in the range of our measurements. The activation energy of the measured R_o is smaller than that of R_b , the discrepancy is probably a result of the approximations involved in our one-dimensional model.

The inequality [24] determines an upper limit for D_s , given by

$$Z_{Wf}^0(int) = B\Delta\sqrt{\frac{2}{D_s}} = \frac{kT\Delta}{4q^2c_oLD_s} \gg R_b, R_c \quad [26]$$

For our samples $R_c > R_b$. We take the measured values of $\Delta = 1 \mu\text{m}$, $L = 5 \times 10^3 \text{ cm}$, substitute for R_c the measured $R_o = 11\Omega$ and for $c_o \sim 10^{14} \text{ cm}^{-2}$ (corresponding to a monoatomic layer of oxygen) and ob-

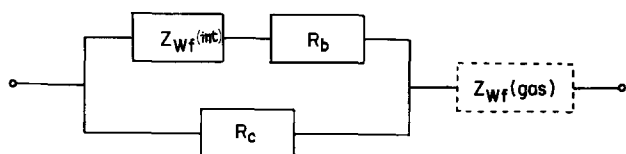


Fig. 12. Equivalent circuit for the model shown in Fig. 11

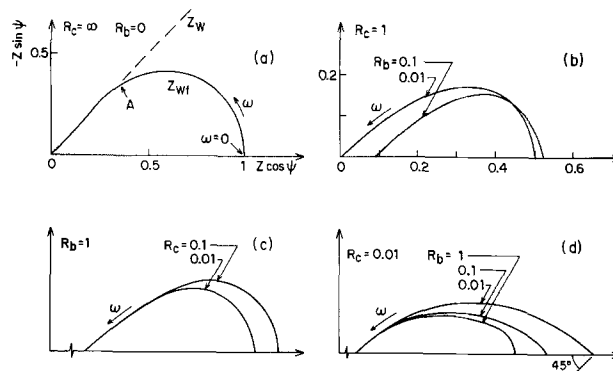


Fig. 13. Complex impedance of the circuit shown in Fig. 12, with various values of R_b and R_c . In all cases $Z_{Wf}^0(int) = 1$. Curve (a) shows Z_{Wf} , the impedance of a finite diffusion path. The curves in (c) and (d) are normalized and shifted to emphasize their shape, their scale is of no significance. $Z_{Wf}(gas)$ is taken as zero.

tain that at 800°C $D_s \ll 10^{-5} \text{ cm}^2/\text{sec}$, which is a reasonable upper limit.

Figure 13(a) shows incidentally that a finite impedance at $\omega = 0$ can also be explained on the basis of a finite diffusion path without any resistance in parallel, but the shape of the curve would then be very different from the observed quarter circle.

The gas diffusion impedance, $Z_{Wf}(gas)$, which we neglected in the present discussion, can be expected to become more important at lower oxygen pressures. The reason is that the constant B defined by Eq. [22] is proportional to $P_{O_2}^{-1/2}$ for $Z_{Wf}(int)$ (because $c_o \propto P_{O_2}^{1/2}$), while the equivalent constant should be proportional to $P_{O_2}^{-1}$ for $Z_{Wf}(gas)$. Qualitatively we then expect a total impedance given by Eq. [25], i.e., a quarter circle, in series with a curve given by Fig. 13(a). The slope on the left end of the total impedance should stay 45° while that on the right end will be steeper. We found indeed some evidence for such an effect at low P_{O_2} , (See Fig. 8, insert).

Conclusions

We conclude that the limiting current is determined by gas diffusion to the triple line on the cathode side and that the small signal d-c resistance of the system EEE is governed by the constriction resistance associated with the small area of the triple line. This resistance reduces the efficiency of a fuel cell and should be eliminated as far as possible.

The a-c results are successfully explained by an interface diffusion mode of transport of oxygen ions which is in parallel with the above constriction resistance. This model predicts a complex impedance in the shape of a quarter circle and fits very well the experimental data. On the other hand the results of Wang and Nowick (9) did not show such clearly defined quarter circles. They found depression angles up to 26°, rather than the 45° corresponding to a quarter circle. It should be remembered that their experiments were done on freshly prepared platinum electrodes, while we made measurements after the electrodes had been held for a few days at temperature. The length and area of the triple line was therefore larger in their case, while the width of the platinum islands was smaller. These geometrical changes would mainly tend to reduce $Z_{Wf}(int)$, so that condition [24] may not be fulfilled anymore. We see from Fig. 13 parts (b) and (c) that in this case we could get curves which more or less resemble depressed circles. It seems very likely that diffusion played less of a role in the samples of Wang and Nowick than in ours. These authors do also mention that coarser electrodes lead to diffusion effects.

A very recent article by Franceschetti and Macdonald (15) derives in a much more general form the small signal response for electrode reactions limited by dif-

fusion through the electrode or along the interface electrode-electrolyte. The article is partly based on a diffusion model proposed by Wang (16) which is similar to the model used here, but does not include explicitly the direct penetration mode at the triple line.

Acknowledgment

This work was supported by a grant from the National Council of Research and Development, Israel, and the KFA, Julich, Germany.

Manuscript submitted April 24, 1980; revised manuscript received Aug. 11, 1980.

Any discussion of this paper will appear in a Discussion Section to be published in the December 1981 JOURNAL. All discussions for the December 1981 Discussion Section should be submitted by Aug. 1, 1981.

Publication costs of this article were assisted by Technion-Israel Institute of Technology.

APPENDIX A

The Resistance of a Sample with Electrodes of Different Sizes

We would like to derive an analytical formula describing approximately the resistance of a cylindrical sample shown in Fig. 14 which has two electrodes on the two flat surfaces. The electrodes are in the centers of the end planes. The cross section of the sample is S_0 and its height l .

For simplicity of calculation we shall assume that the sample is two-dimensional, so that the electrodes become lines of length S_a and S_b . We further approximate the current flow geometry as shown in Fig. 14. Here we have assumed that the current flows in straight lines, that the current density is a function of y only and that the ratio l_a/l_b is such that the current path length is minimized.

The last assumption gives immediately by simple geometrical calculations that

$$l_a = l \frac{S_0 - S_a}{2S_0 - S_a - S_b} \quad l_b = l \frac{S_0 - S_b}{2S_0 - S_a - S_b} \quad [\text{A-1}]$$

The resistance of the sample is that of two truncated pyramids with common base. For the upper pyramid we use the following easily derived formula

$$R_a = \frac{l_a}{\sigma} \frac{\ln(S_0/S_a)}{S_0 - S_a} \quad [\text{A-2}]$$

so that finally we get for the resistance of the sample

$$R = \frac{l}{\sigma} \frac{\ln(S_0^2/S_a S_b)}{2S_0 - S_a - S_b} \quad [\text{A-3}]$$

When $S_a = S_b$ we get

$$R = \frac{l}{\sigma} \frac{\ln(S_0/S_a)}{S_0 - S_a} \quad [\text{A-4}]$$

For our samples the electrodes are porous, i.e., made up of many connected small electrodes. We assume in

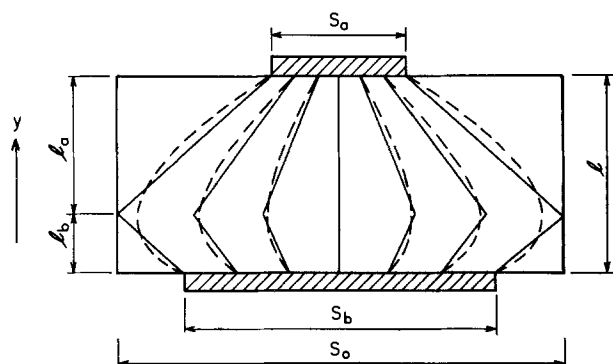


Fig. 14. Approximate distribution of current lines in a cylindrical sample with electrodes differing in size. The dotted lines show the real situation, the full lines are the basis of our approximate calculation and define the truncated pyramids mentioned in the text.

this case that the effective area is the sum of all the small ones.

APPENDIX B

Proof That the Condition $Z_{Wf}^0 \gg R_b, R_c$ Implies That Diffusion Does Not Play a Role for $\omega < 4D_s/\Delta^2$

The impedance diagram for Z_{Wf} , the diffusional impedance in the case of a finite diffusion path, is shown in Fig. 13(a). At the point A $\omega = 4D_s/\Delta^2 \equiv \omega_{cr}$. It is seen from the curve that for $\omega < \omega_{cr}$

$$Z_{Wf} = Z_{Wf}^0 [1 - \beta + j\gamma]; \quad 0 \leq \beta, \quad \gamma < 1/2 \quad [\text{B-1}]$$

The total impedance of the equivalent circuit is as before

$$Z = \frac{(Z_{Wf} + R_b)R_c}{Z_{Wf} + R_c + R_b} \quad [\text{B-2}]$$

and it follows from the condition $Z_{Wf}^0 \gg R_b, R_c$ and Eq. [B-1] that $Z \approx R_c$, i.e., the diffusion mode does not contribute to the impedance for $\omega < \omega_{cr}$.

LIST OF SYMBOLS

| | |
|----------------------|---|
| B | $kT/(4q^2c_0L\sqrt{2D_s})$ |
| C_0, C_s | concentration of oxygen molecules in the undisturbed gas and at the surface of the sample |
| c_0, c | concentration of oxygen atoms at the triple line and along the interface EE |
| D | diffusion coefficient of gaseous oxygen |
| D_s | diffusion coefficient for oxygen atoms on the interface EE |
| EE | electrode-electrolyte |
| EEE | electrode-electrolyte-electrode |
| I | total electric current |
| I_a | particle current |
| I_D | electric current transported by diffusion mode |
| I_1 | ionic current |
| I_l | limiting current |
| j | $\sqrt{-1}$ |
| k | Boltzmann constant |
| l | thickness of sample |
| L | length of triple line |
| O_0 | O^- ion on a normal lattice site |
| P_{O_2} | partial pressure of oxygen |
| q | absolute value of electronic charge |
| τ | thickness of disturbed gas layer |
| R_0 | measured dynamic resistance of system EEE |
| R_a | measured resistance for $\omega \rightarrow \infty$ |
| R_b | bulk resistance of electrolyte |
| R_c | constriction resistance |
| S_0 | cross section of sample |
| S_E | gross area of electrode |
| S_{Pt} | area of sample covered by platinum |
| S_{TL} | area of triple line |
| SE | solid electrolyte |
| \bar{t}_1 | average ionic transport number |
| T | absolute temperature |
| u | $\sqrt{\omega/2D_s} (1 - j)$ |
| V | applied voltage |
| $V_{O^{2-}}$ | doubly ionized oxygen vacancy |
| Z | impedance of system EEE |
| Z^0, Z^∞ | impedance at zero and infinite frequency |
| Z_D | impedance for diffusion mode of transport |
| Z_W | Warburg impedance |
| $Z_{Wf}(\text{int})$ | impedance of finite diffusion path along interface |
| $Z_{Wf}(\text{gas})$ | impedance of finite diffusion path in the gas phase |
| α | angle between radius of impedance diagram and abscissa |
| δ | width of triple line |
| Δ | average length of diffusion path for oxygen along the EE interface |
| σ | specific conductivity of the electrolyte |
| ω | angular frequency |
| ψ | phase of the impedance |
| $\Delta\phi$ | potential difference in the electrolyte |

REFERENCES

1. H. Yanagida, R. J. Brook, and F. A. Kroeger, *This Journal*, **117**, 593 (1970).

2. R. J. Brook, W. L. Pelzmann, and F. A. Kroeger, *ibid.*, **118**, 185 (1971).
3. T. H. Etsell and S. N. Flenglas, *ibid.*, **118**, 1890 (1971).
4. M. Kleitz, Thesis, Grenoble (1968), see also D. O. Raleigh, "Electroanalytical Chemistry," Vol. 6, p. 168, Marcel Dekker, New York (1973).
5. E. Schouler, G. Giroud, and M. Kleitz, *J. Chim. Phys.*, **9**, 1309 (1973).
6. E. Schouler and M. Kleitz, *J. Electroanal. Chem. Interfacial Electrochem.*, **64**, 135 (1975).
7. E. Schouler, M. Kleitz, and C. Deportes, *J. Chim. Phys.*, **6**, 923 (1973).
8. D. Y. Wang and A. S. Nowick, *This Journal*, **126**, 1155 (1979).
9. D. Y. Wang and A. S. Nowick, *ibid.*, **126**, 1166 (1979).
10. L. J. Van der Pauw, *Philips Res. Rept.*, **13**, 1 (1958).
11. D. Braunschtein and D. S. Tannhauser, *J. Phys. E.*, **12**, 921 (1979).
12. D. S. Tannhauser, *This Journal*, **125**, 1277 (1978).
13. R. E. W. Casselton, *J. Appl. Electrochem.*, **4**, 25 (1974).
14. J. E. Bauerle, *J. Phys. Chem. Solids*, **30**, 2657 (1969).
15. D. R. Franceschetti and J. R. Macdonald, *J. Electroanal. Chem. Interfacial Electrochem.*, **101**, 307 (1979).
16. D. Y. Wang, D. Eng. Sci. dissertation, Krumb School of Mines, Columbia University (1978).

Current Transients and Stress Corrosion Cracking in LiCl-KCl

William H. Smyrl

Sandia Laboratories, Albuquerque, New Mexico 87115

ABSTRACT

The current transients observed during crack propagation in titanium-8 aluminum-1 molybdenum-1 vanadium immersed in molten LiCl-KCl have been analyzed. The electrochemical events which cause the transients have been determined. The dominant event during the initial stages of cracking was anodic dissolution from the film-free crack walls. A film was then deposited on the walls which passivated the surface, causing a decrease in current density. The final stage involved thickening of the film. The analysis has revealed that anodic dissolution could not support the very fast crack extension described here (i.e., crack velocities greater than 10^{-3} cm/sec).

The stress corrosion cracking of the titanium alloy Ti-8% Al-1% Mo-1% V has been studied extensively in molten LiCl-KCl (1-3). These studies have shown that minor traces of H_2O (as OH^-), O_2 , H_2 , and H^- , do not influence cracking and are not acting as critical species. Model calculations have also indicated that minor components (such as OH^-) could not support cracking at the rates observed (up to 1 cm/sec) in the molten eutectic (4). These results were important for demonstrating that hydrogen embrittlement was not operative in this molten salt environment. The simple molten salt environment was important for assessing the importance of other crack extension mechanisms as well, as shown below.

The influence of electrical potential on crack growth rate has been investigated (3). The results and conclusions of that investigation (3) are briefly described here to aid in the introduction of the present study. Cracking was observed to occur at potentials from -1735 mV (the open-circuit potential in the absence of cracking) to -2235 mV (very cathodic conditions). Cracking was retarded by cathodic potentials, i.e., the crack extension was slower at more negative potentials. Investigations at more positive potentials caused gross dissolution of the entire specimen surface which precluded crack length measurements, but cracking did occur at these potentials as well. Increasing the concentration of Ti^{+2} did not change the crack growth rate at any potential. Also, the crack growth rate was too high by several orders of magnitude to be supported by the small anodic current densities observed in the tests. It was concluded that these results would not support an anodic dissolution mechanism. It was found that one could account for the potential dependence by assuming that Cl^- at the metal-solution interface would depend on the potential of the titanium alloy surface and that the crack extension rate was a function of the interfacial

concentration of Cl^- . These observations are summarized in Fig. 1. Cracking in the plateau region can be limited by fluid flow, as discussed earlier (5). Cl^- -induced cracking is the controlling mechanism down to low crack velocities and anodic potentials, where anodic dissolution becomes important as an extension mechanism.

The tentative assignment of control in these areas was given in (3). The present paper gives results for cracking in the plateau and Cl^- control region, i.e., for velocities between $\sim 10^{-3}$ cm/sec and the plateau velocity and for stress intensities as shown in Fig. 1. Each of the separate curves was measured at a constant potential. The most anodic potential is on the left, with more cathodic potentials progressing to the right. The curves are separated by 100 mV, and the left-most curve was taken at the corrosion potential (i.e., -1735 mV vs. 1M Pt^{+2}/Pt), i.e., zero net current to the specimen with no cracking in the pure melt. The potential of the right-most curve was -2235 mV, and the potential of zero charge on Ti for this melt was estimated (3) to be about $-2.35V$ vs. 1M Pt^{+2}/Pt . The background current on the specimens in this potential range was small and cathodic, due to the trace quantities of OH^- remaining in the melt. No cracking was observed at low crack velocities, i.e., below 10^{-3} cm/sec, for the four most cathodic potentials shown. That is to say, cracking was never observed to occur below 10^{-3} cm/sec for the most cathodic potentials. Observation at these potentials (i.e., -1935 to -2235 mV) was extended so that cracking at velocities greater than 10^{-7} cm/sec would have been observed, but cracking between 10^{-3} and 10^{-7} cm/sec was not observed. These observations and conclusions serve as a background for the present study.

It has been reported that an anodic current transient accompanies crack extension (2). This current transient has now been investigated as a function of potential, and analyzed, and the results are to be reported here. The investigation was conducted over the poten-

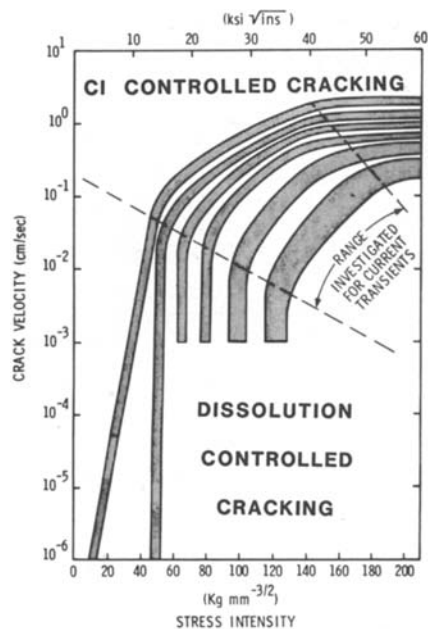


Fig. 1. Processes which control cracking of Ti-8Al-1Mo-1V in molten LiCl-KCl.

tial range of -1.7 to $-2.3V$ vs. $1M Pt^{+2}/Pt$.¹ The current and crack length were recorded simultaneously, so that the average current density on the crack walls could be calculated as cracking progressed. The analysis of the current density behavior both as a function of time and at different potentials has shown that the current transient was caused by three distinct processes: (i) anodic dissolution from film-free crack walls, followed by, (ii) nucleation and growth of a passivating film, which leads to, (iii) thickening of the film at the later stages of crack growth. The observation that cracking occurs with film-free crack walls implies that the brittle-film mechanism is not important for these molten salt experiments. Anodic dissolution does occur during cracking at some potentials, but is not important for the velocity ranges considered here. The anodic current transients do not support an anodic dissolution controlled cracking mechanism at high velocity.

Experimental

The molten salt, dry box, and electrochemical instrumentation have been discussed previously (3). The DCB specimen has been described as well (1, 4). The material was Ti-8% Al-1% Mo-1% V in a duplex-annealed heat-treatment which produces an $\alpha + \beta$ microstructure, with no precipitated α_2 (6, 7). The texture of the microstructure was such that the preferred cracking plane was oriented in a direction parallel to the rolling direction of the plate material, and specimens were cut from the plate so that the preferred cracking plane was along the length of the specimen. The thickness, B , of the specimens was 0.5 cm.

The specimens were stressed to a constant deflection. This resulted in crack extension at high stress intensities (and thus high crack velocities) in the beginning, with cracking at lower stress intensities as the crack propagated. The highest stress intensity was about 60 ksi (in.)^{1/2}, and it dropped to less than 10 for cracking at -1735 mV.

Crack extension was videotaped at 60 frames/sec. Frame by frame playback allowed determination of the high initial crack velocity (up to 1 cm/sec) with crack length resolution of <0.5 mm. The crack length data were synchronized with the current transient

¹Note: This couple is the standard reference for molten LiCl-KCl [cf. (12)].

results as described below and were used in the data analysis.

The block diagram of the experimental arrangement is shown in Fig. 2. The potentiostat controlled the potential of the specimen. Current from the potentiostat was monitored on the Biomation Waveform Recorder. The recorder had an analog-to-digital converter and a 4096 word memory. The dual time-base capability of the recorder was used, whereby an initial fast time base (A) was changed to a slower time base (B) by a front panel manual push-button. The current was monitored on time base A until cracking began and the current rose rapidly, and time base B was switched in. This allowed "pre-trigger" information to be preserved. The current transient had a fast rise time and slow decay which was easily resolved with the recorder operation as described.

A pulse was triggered by the manual time base switch on the Biomation and recorded simultaneously on the audio channel of the videotape. This pulse synchronized the crack length and current transient time bases.

Data from the waveform recorder was read out on either a strip-chart recorder or directly into the memory of an HP-9830 calculator.

Results and Discussion

The crack length increased with time [see Ref. (3) for a more complete description], initially at a constant rate (i.e., at a constant "plateau" velocity) and then at a decreasing rate at longer time and longer crack lengths.

A current transient measured on a strip chart recorder is shown in Fig. 3. The background current

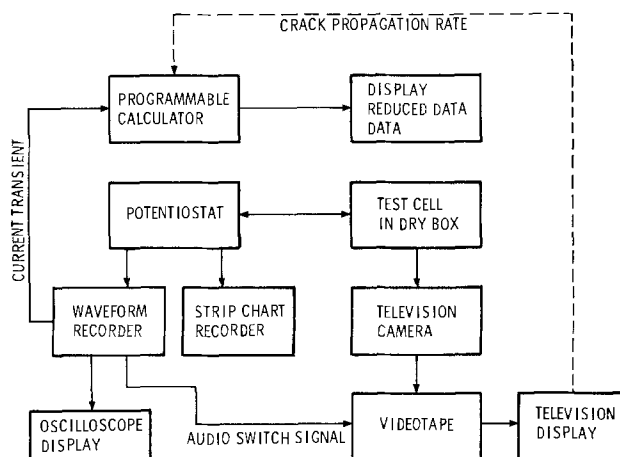


Fig. 2. Block diagram of experimental arrangement for monitoring crack propagation and current transients.

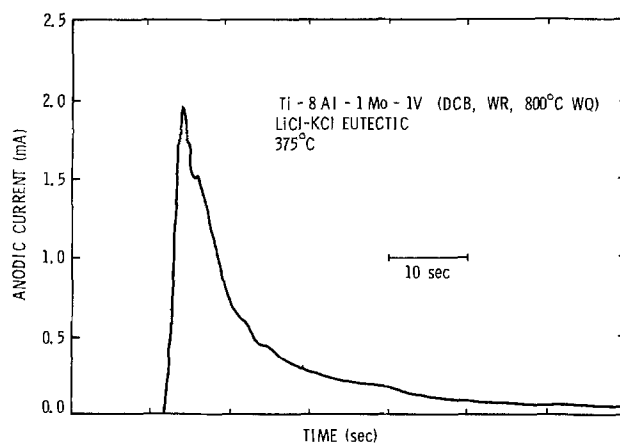


Fig. 3. Current transient measured during crack propagation at -1915 mV vs. $1M Pt^{+2}/Pt$.

before cracking was extremely small and cathodic, and the current transient was anodic. The total anodic charge passed during the cracking event was of the order of 10 mC and was dependent on potential. By synchronizing the time bases for crack length and current, it was possible to associate a particular crack length with a particular current level as shown in Fig. 4. The current in this figure was reconstructed from the Biomation Waveform Recorder data and was smoothed for the purpose of drawing the curve. This clearly revealed that the rising portion of the curve was resolved by using the dual-time base recording mode of the recorder.

The observed cracking and the current transient were always found to begin at the same time, within our resolution. The limit of resolution was in the crack length measurements. Crack length could be resolved to less than 0.5 mm, and for a crack velocity of the order of 1 cm/sec, the time resolution for the onset of cracking was therefore of the order of 0.05 sec. Time resolution for the current transient was always 0.005 sec or better.

Stirring the melt with no crack extension caused a cathodic current transient. Increasing the surface area would also cause a cathodic current transient for a cathodic background current. Therefore, neither stirring nor increasing the surface area could be responsible for the observed anodic current transient during crack propagation.

Since the background current was small, and stirring caused a cathodic transient, it was concluded that the anodic current transient was caused by electrochemical processes within the propagating crack. The average anodic current density from the crack walls was calculated for a typical experiment and is shown in Fig. 5. The crack wall area was calculated as twice the length of the crack multiplied by the specimen thickness. As might be anticipated from Fig. 4, the current density was constant for several seconds of crack life and then decreased at longer times at t^{-1} . This pattern was observed at all potentials, and it appears that an initial dissolution process from the crack wall was modified by the deposition of a passivating film at longer time.

Possible Current Transients

Before any further analysis of the results is discussed, it seems worthwhile to describe the current transients that might be expected for several simple processes. This is not meant to be an exhaustive survey of all possible transients, but rather a description of the transients that could be anticipated for processes that were known or were expected to occur during the tests. This is followed by a more complete analysis of the current density results.

Several current-time curves are shown in Fig. 6 that might be expected if the associated processes were to occur during cracking. In the upper left

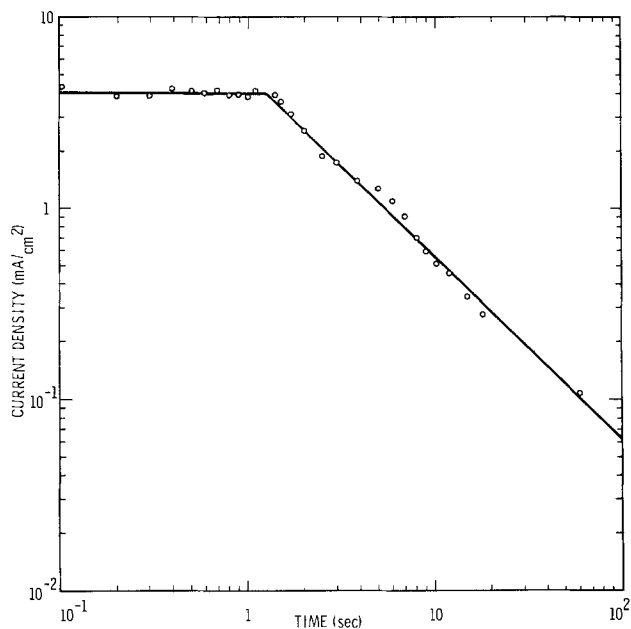


Fig. 5. Time dependence of current density on the crack walls

figure, the current necessary to charge the electrical double layer on the surface for increasing area is shown. This is analogous to the charging current to growing mercury drops, which is well known in polarography (8). Yeager *et al.* (11) have also recently given the relationship for the charging current to an ideally polarizable electrode at constant voltage with changing area as

$$I = VC \frac{dA}{dt}$$

Here, I is the current, V is the (constant) voltage, C is the differential double layer capacitance, and dA/dt is the change of area with time. For a crack propagating through a specimen of constant thickness

$$\frac{dA}{dt} = B \frac{dl}{dt} = B\bar{v}$$

where B is the plate thickness and \bar{v} is the velocity of crack extension. Therefore

$$I = VCB\bar{v}$$

and the current is proportional to the crack velocity. The curve is drawn schematically for a crack length-time dependence as shown in Fig. 4. The initial sharp jump of current (because the velocity jumps from zero to the plateau velocity) would be followed by a level portion (constant velocity) and finally a de-

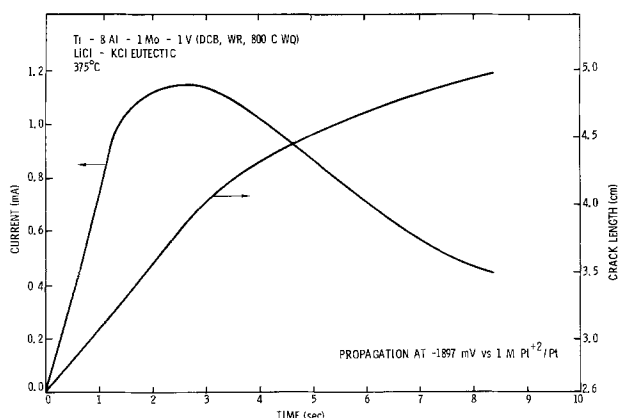


Fig. 4. Current transient and crack length as a function of time

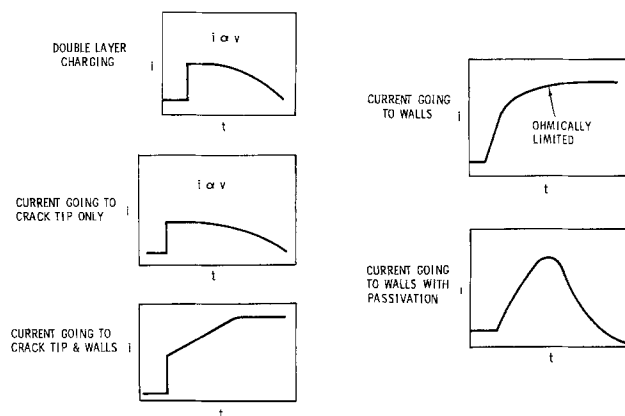


Fig. 6. Current transients expected for various processes

crease with time as the crack velocity decreased. Although this process does occur during cracking, the expected current for double layer charging is smaller than that observed in the anodic transients. For a nominal $25 \mu\text{F}/\text{cm}^2$ double layer capacitance, and a rate of change of crack area of $0.5 \text{ cm}^2/\text{sec}$ (i.e., a velocity of $1 \text{ cm}/\text{sec}$ multiplied by the 0.5 cm thickness of the specimen), the maximum charging current would be $12.5 \mu\text{A}$. This is more than two orders of magnitude lower than the observed current. The predicted initial jump of current from 0 (i.e., back-ground) to $12.5 \mu\text{A}$ was below the resolution of our measurements. It is concluded that the charging current was a negligible part of the observed current transient, except for the most cathodic potentials as discussed below.

In the middle figure on the left is shown the current transient expected if the anodic current were only from the crack tip and this represented the cause of crack extension. The current would again be proportional to the velocity of cracking as given by the relationship

$$I = nF \frac{\rho}{M} (B) (W) \bar{v}$$

where n = number equiv./mole for the reaction, taken as 2 in this example, F = Faraday constant, ρ = density of the metal, M = molecular weight, B = thickness of the specimen, W = width of the crack tip region dissolved, and \bar{v} = crack velocity. If one assumes the properties of metallic titanium, and the width of the zone equal to 1 atomic diameter (i.e., $3 \times 10^{-8} \text{ cm}$ for Ti), one calculates the maximum current to be $2.7 \times 10^{-4} \text{ A}$ with a current density of $1.8 \times 10^4 \text{ A}/\text{cm}^2$. This is about one order of magnitude lower than the observed current. One could increase the current an order of magnitude by increasing W by an order of magnitude and the current density over the dissolution zone, W , would remain constant, i.e., $1.8 \times 10^4 \text{ A}/\text{cm}^2$. There would be an initial jump in current to $2.7 \times 10^{-4} \text{ A}$ or higher, as the velocity jumps to the constant, plateau velocity of $\sim 1 \mu\text{m}/\text{sec}$. The current resolution was about 1%, and a current jump of $2.7 \times 10^{-4} \text{ A}$, or higher, could have been seen easily, but was not. Increasing the zone width, W , would only make the disagreement worse, and decreasing the width below an atomic diameter may not be credible. At any rate, the observed current transient did not match this transient in any way. It is concluded that attributing all the current to crack tip dissolution alone cannot be supported by the experimental data.

If the above process were superimposed on anodic dissolution from the crack walls, the curve on the lower left (Fig. 6) would be expected. The initial current "jump" would be due to the sudden increase in velocity, and the current from the crack tip would be the dominant factor in the total current at first. Current from the crack walls would become increasingly important as the crack grew and could be dominant at long times. The calculation made above of the magnitude of the initial current jump is relevant here as well. The absence of an initial current jump leads to the conclusion that anodic dissolution from the crack tip to cause crack extension was not a significant contribution to the current transient, even if one assumes that other processes were superimposed on it.

At this point in the discussion, it is worthwhile to emphasize what has just been concluded. The absence of an observed current jump at the beginning of cracking means that the crack tip dissolution current was too small to be resolved by our measurements, i.e., lower than 0.02 mA . This is smaller by an order of magnitude than the minimum current which was calculated above for crack propagation due only to anodic dissolution. In addition, the mag-

nitude of the current density (up to $1.8 \times 10^4 \text{ A}/\text{cm}^2$ for velocities of $1 \text{ cm}/\text{sec}$) for this mechanism is enormous. The largest current densities which can be accounted for in the present investigation (see below) is about $1\text{--}10 \text{ mA}/\text{cm}^2$. This is a discrepancy of 6-7 orders of magnitude. Large anodic current densities are observed in other electrochemical systems, for example, electrochemical machining, but only at high potentials. The present investigation has been carried out at low potentials (less than 1 V anodic of the equilibrium potential), potentials which appear to be too small to give such large current densities. One might alter the dissolution model to allow dissolution from a low density atomic plane, for example, which would lower the total current and the current density. The observed current transient would then be insensitive to such a process and could not be used to give any information about the crack extension (dissolution) mechanism. Nothing more will be said about this or other possible ways of developing a dissolution mechanism which does not conflict with the present current transient results. On the other hand, the point of view is adopted here that the crack tip behaves much as the rest of the crack walls, at least electrochemically, in this molten salt. Dissolution occurs from the tip and walls, but there is no enhancement of current density at the crack tip during the initial stages of crack extension. This is developed below and is shown to be consistent with all the experimental facts. There are no observations in molten LiCl-KCl which are contrary to this point of view. The current transients then do not reveal the mechanism for extension, but are the result of electrochemical reactions on the fresh crack walls which have been created by crack propagation.

Anodic dissolution from the crack walls (and tip) would be expected to give a current transient like that shown on the upper right of Fig. 6. The current would never decrease and would only level off if ohmic resistance became controlling or the crack stopped. The current density would be constant, for a constant potential, independent of crack length or area until the ohmic resistance became dominant. This does not match the observed transient overall, but the initial part of the measured current transient did have the constant current density feature.

Superimposing a passivation phenomena on the anodic dissolution process just discussed would lead to the curve shown on the bottom right (Fig. 6). The current in the beginning would be proportional to area (i.e., constant current density) but this would be modified by nucleation and growth of a passivating film. After the film grew to cover the total area, the current would be governed by transport through the film. This transient most nearly matches that observed and is used as the basis for the remainder of the analysis.

The conclusions which have been reached are: (i) the current transient was not caused by double layer charging, and (ii) there was no evidence to support anodic dissolution controlled cracking. In fact, the absence of an initial jump in current at the beginning of cracking is strong evidence that anodic dissolution from the crack tip made no major contribution to the current transient and probably did not control crack extension. The current transient can be simply modeled as three processes that are superimposed on one another: region I, anodic dissolution from film-free walls, modified by region II, nucleation and growth of a passivating film patch, followed by region III, increased film thickness. The remainder of the discussion is separated into three parts representing these three different regions of the current transient.

Anodic Dissolution Region (Region I)

The cracking has been investigated as a function of potential, and the associated current transients

recorded. The constant initial current density at the onset of cracking was found to be a function of potential as shown in Fig. 7. There is a break in the curve at a potential of about -2.06V vs. $1\text{M Pt}^{+2}/\text{Pt}$. At more negative potentials the measured current was very small as was the total crack growth (although the velocity was still high), and this caused an uncertainty that was as large as the calculated current density. The estimated current density at potentials more negative than -2.06V was about 0.2 mA/cm^2 and is shown because an anodic current was observed. Each point on Fig. 7 was from a complete run, and the scatter of data is the measure of variations of metallurgy from sample to sample.

As noted in the beginning the anodic dissolution of an unstressed Ti electrode, with normal air formed oxide coating, occurs at potentials more positive than about -1735 mV . Li deposition from the melt onto a Ti electrode begins to become significant at -2.750 mV , as determined in the course of this investigation. At potentials between -2750 and -1735 mV , the steady-state current is small, cathodic, and presumably due to the diffusion-limited reduction of residual OH^- impurity. The anodic transients of the present investigation were observed in this very negative potential region. Presumably, the oxide film suppresses any anodic reaction on the unstressed electrode until sufficiently anodic potentials are attained ($>1735\text{ mV}$) to break down the film.

Net anodic dissolution current would be expected from a film-free wall at potentials positive of the equilibrium potential calculated for the concentration of metal ion in the solution. Typical concentrations of Ti^{+2} in salt frozen and removed from the crack was about 10^{-5} molar (3). The reversible potential for Ti/Ti^{+2} for this concentration is -2.07V vs. $1\text{M Pt}^{+2}/\text{Pt}$. At potentials more positive than this, net anodic dissolution would occur. At more negative potentials, the current would be due to net reduction of Ti^{+2} , superimposed on double layer charging. The maximum diffusion-limited cathodic current for reduction of Ti^{+2} (10^{-5} molar) would be about 10^{-4} mA/cm^2 . The potential of zero charge (pzc) for Ti has been estimated (3) to be about -2.35V vs. $1\text{M Pt}^{+2}/\text{Pt}$. At potentials positive of the pzc, the charging current would be anodic and superimposed on the Ti^{+2} reduction current. The charging current density for a propagating crack was estimated above. In the plateau velocity region, the charging current density was calculated to be about $1.25 \times 10^{-5}\text{ A/cm}^2$. Therefore, the charging current in this region can be larger in magnitude than the Ti^{+2} reduction current.

The current density at potentials anodic of the equilibrium potential should be a linear function of the overpotential, i.e.,

$$i = \frac{i_o(\alpha_a + \alpha_c)F}{RT} \eta$$

If α_a and α_c are equal, the linear kinetic range should extend about 50 mV from the equilibrium potential with a slope of

$$\frac{di}{d\eta} = \frac{i_o(\alpha_a + \alpha_c)F}{RT} \quad (i \ll i_o)$$

Logarithmic Tafel behavior should be observed at large current densities (i.e., $i \gg i_o$). The data in Fig. 7 reveal that i vs. overpotential has linear behavior, but extends over a larger range than expected. This could be due to experimental uncertainty, but is more likely due to a partial cancellation of the non-linear current density overpotential behavior at the higher current densities by ohmic effects. The ohmic effects are discussed below.

The linear current density-potential curve was found to yield a value of $(\alpha_a + \alpha_c)i_o$ of 1.18 mA/cm^2

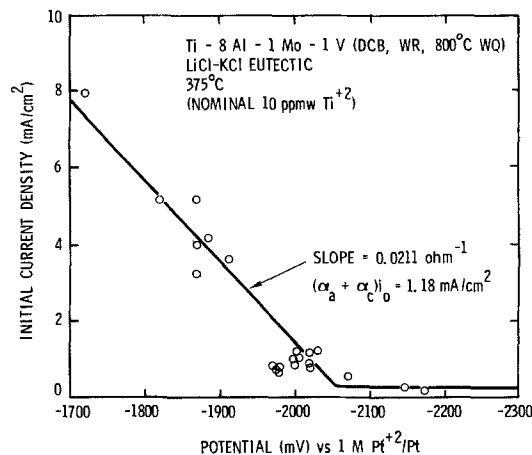


Fig. 7. Initial current density as a function of potential

where α_a and α_c are kinetic transfer coefficients for the anodic and cathodic reactions and i_o is the exchange current density. Assuming α_a and α_c are both 1, the exchange current density corrected to 1M Ti^{+2} was calculated to be 59 A/cm^2 . This is somewhat higher than the exchange current densities observed for other divalent metals in LiCl-KCl (7).

The anodic current density in the region negative of -2.07V is larger than the calculated double layer capacitance of $25\text{ }\mu\text{f/cm}^2$. In order to make the two comparable, the double layer capacitance would have to be increased by about an order of magnitude to $250\text{ }\mu\text{f/cm}^2$. On the other hand, the current density in this region is difficult to measure and could be in error by more than enough to accommodate the model. The transients in this region were quite small, and the total crack extension for an individual test was short and of the order of 4 mm . Both combine to give an error bar that would cover the proposed charging current. There are no other anodic processes that can be identified at this time, for the alloy in the melt, so double layer charging is adopted as a tentative model for the current transient at potentials more negative than -2.07V vs. $\text{Pt}/\text{Pt}^{+2}(1\text{M})$. Of course, it should also occur at more positive potentials but it is obscured by the anodic dissolution reaction in this region.

The model of the rising portion of the current transient (region I) as described above has assumed that the current density is uniformly distributed on the crack walls. This is appropriate for the situation where the current-voltage behavior is dominated by the interfacial electrode kinetics, and it is possible to demonstrate this quantitatively as follows. To estimate the potential and current distributions along the crack, the following model of the crack is adopted: (i) the crack is wedge shaped, and has a nominal 1° opening, although the crack angle will be included in the model as a parameter; (ii) the potential drop across the crack is negligible as compared to the potential variation down the crack length; and (iii) there is a single, anodic dissolution reaction on the crack walls. Figure 8 shows the crack model and the coordinate system used for the calculations. At any instant Laplace's equation for the potential may be written

$$\frac{\partial^2 \phi}{\partial r^2} + \frac{1}{r} \frac{\partial \phi}{\partial r} + \frac{1}{r^2} \frac{\partial^2 \phi}{\partial \theta^2} = 0$$

On the crack walls it is assumed that there is a single anodic reaction under linear polarization control, i.e.

$$\begin{aligned} i_{\theta=\theta_w} &= - \frac{(\alpha_a + \alpha_c)F i_o}{RT} (V - \phi) \\ &= - \frac{\kappa}{r} \frac{\partial \phi}{\partial \theta} \Big|_{\theta=\theta_w} \end{aligned}$$

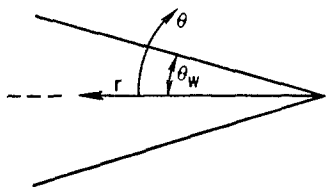


Fig. 8. Coordinate system for a wedge-shaped crack with the origin at the crack tip.

The other boundary condition on i_θ is that there is no current across $\theta = 0$ because of symmetry, i.e.

$$i_\theta|_{\theta=0} = 0 = -\frac{\kappa}{r} \frac{\partial \phi}{\partial \theta} \Big|_{\theta=0}$$

We assume that the predominant variation of potential is radial and that $\partial^2 \phi / \partial r^2$ may be approximated by

$$\frac{\partial^2 \phi}{\partial r^2} = \frac{\frac{\partial \phi}{\partial r} \Big|_{r=\delta} - \frac{\partial \phi}{\partial r} \Big|_{r=0}}{\delta} = \frac{1}{\delta} \frac{\partial \phi}{\partial r} \Big|_{r=\delta}$$

Hence

$$r \frac{\partial^2 \phi}{\partial r^2} + \frac{\partial \phi}{\partial r} + \frac{(\alpha_a + \alpha_c) F i_o}{\theta_w \kappa R T} (V - \phi) = 0$$

is to be solved subject to the boundary conditions $\phi = \phi_1$ at $r = \delta$ (crack length) and $\phi = \phi_0$ at $r = 0$ (crack tip). The solution is shown in Appendix I to be

$$\frac{(\phi_1 - \phi)}{(\phi_1 - V)} = \left\{ 1 - \left[\frac{I_o(Z\sqrt{\lambda})}{I_o(\sqrt{\lambda})} \right] \right\}$$

where

$$\lambda = \frac{4(\alpha_a + \alpha_c) F \delta i_o}{\theta_w \kappa R T}$$

$$Z = \left(\frac{r}{\delta} \right)^{1/2}$$

λ is an important parameter in determining the potential and current distributions in the crack. The significance of λ is discussed below.

The potential distribution down the crack is shown in Fig. 9, and Fig. 10 shows the total potential drop in the crack for cracks of different length. It is shown below that the potential drop down the crack is small for the molten salt system studied here and that the current distribution is nearly uniform.

The total current from the crack walls at any instant is found from

$$I_{\text{total}} = -2B \int_0^\delta i_\theta|_{\theta=\theta_w} dr$$

$$= \frac{2B\delta(\alpha_a + \alpha_c)i_o F}{RT} \left[\frac{2I_1(\sqrt{\lambda})}{\sqrt{\lambda} I_0(\sqrt{\lambda})} \right] (V - \phi_1)$$

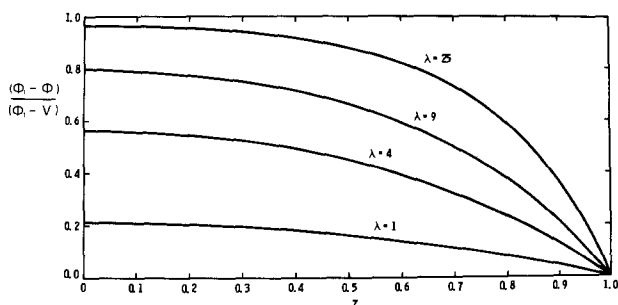


Fig. 9. Potential distribution in a crack for several values of the polarization parameter, λ .

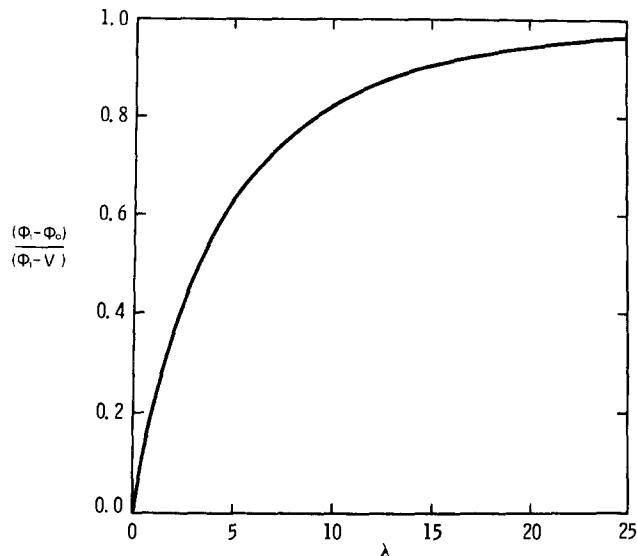


Fig. 10. Potential drop down the crack for cracks of different length.

and for small values of λ

$$I_{\text{total}} = 2B\delta(\alpha_a + \alpha_c) \frac{i_o F}{RT} \left[1 - \frac{\lambda}{8} \right] (V - \phi_1)$$

As expected, the average current density, $I_{\text{total}}/2B\delta$, retains a linear dependence on the applied potential. The slope of the current density-potential curve would be

$$\frac{(\alpha_a + \alpha_c) i_o F}{RT} \left[1 - \frac{\lambda}{8} \right]$$

and was found to be $0.0211 \Omega^{-1} \text{ cm}^{-2}$ from Fig. 7, assuming $\lambda/8$ was small. This calculation supports the basic idea that current density at the beginning of cracking (Fig. 7) is controlled by dissolution kinetics, with some ohmic contribution. The ohmic contribution causes the current distribution to be nonuniform (i.e., decreasing as the crack tip is approached).

The dimensionless polarization parameter for the crack, λ , measures the relative importance of kinetic vs. ohmic influences for the crack environment. Large values of λ are characteristic of ohmic domination and nonuniform current distribution. Small values of λ are appropriate for kinetically controlled dissolution and uniform current distribution down the crack. Factors favoring kinetic control are small exchange current densities, short cracks, large conductivities, and large crack angles. For a typical situation in the present investigation $(\alpha_a + \alpha_c) i_o F / RT = 0.0211 \Omega^{-1} \text{ cm}^2$, $\delta = 0.5 \text{ cm}$ (equal to the specimen thickness), $\kappa = 1.2 \Omega^{-1} \text{ cm}^{-1}$, $\theta_w = 2\pi/360$ (for a 1° crack), $\lambda = 2.0$. The current distribution as a function of λ can be calculated, and from Appendix I

$$\frac{i|_{r=0} - i|_{r=\delta}}{i_{\text{avg}}} = \frac{\Delta i}{i_{\text{avg}}} = \frac{[I_0(\sqrt{\lambda}) - 1]\sqrt{\lambda}}{2I_1(\sqrt{\lambda})}$$

and for small values of λ

$$\frac{\Delta i}{i_{\text{avg}}} = \frac{\lambda}{4} = \frac{(\alpha_a + \alpha_c) i_o F \delta}{RT \kappa \theta_w}$$

Thus, for the calculated value of λ from above

$$\lambda = 2$$

$$\frac{\Delta i}{i_{\text{avg}}} = 0.5$$

and the current density will deviate about the average value by approximately 50%. This is not a large effect, and it would be even smaller for cracks of shorter

length. For these same conditions the potential drop down the crack (see also Fig. 10) would be calculated from

$$(\phi_o - V)I_o(\sqrt{\lambda}) = (\phi_i - V)$$

At the conditions

$$\lambda \approx 2 \\ (V - \phi_i) = 50 \text{ mV}$$

then the potential drop is calculated as

$$\phi_o - \phi_i \approx 17 \text{ mV}$$

The potential drop would be smaller for shorter cracks (see Fig. 10) or larger crack angles.

The model described above is appropriate for cracks whose length is less than the thickness of the specimen. Said another way, the treatment is appropriate for that part of the crack (measuring from the crack tip) which is less than the specimen thickness. At larger lengths, the crack opening is sufficient to cause the current and potential distributions to be rather uniform on the outer crack walls for the molten salt system. The model may be applied to other systems where the walls are film free and a single anodic dissolution occurs on the crack walls.

The model is an instantaneous picture of the electrochemistry within the crack. The time dependence is implicitly included in the dependence of the crack length on time. Separating out the time dependence in this way is legitimate where the relaxation of the current and potential distributions occur on a much faster time scale (10-100 μsec) than the rise time of the current transients (seconds) caused by crack propagation. Since the current and crack length have the same time dependence, the current density would be constant. This correctly models the experimental results.

Film Nucleation and Growth (Region II)

According to the last section, crack propagation would cause the total current to continue to increase and the current density would remain constant until the crack became long enough for ohmic limitations to become important. The current would never decrease unless some other process interfered. The current was observed to decrease in the stress corrosion tests, and it is proposed that it was caused by the deposition of a film which passivated the surface. This section discusses the model of nucleation and growth of the film. The details of the mathematical derivation are in Appendix II.

Vermilyea (9) has discussed a simple model of nucleation and growth of a film. The film patches would "throttle" the anodic dissolution reaction discussed in the previous section. As coverage of the surface approached completion, the total current would have a time dependence given by the passivating reaction. However, the total current would continue to be dominated by the anodic dissolution reaction if the film were insulating and only a small amount of current would go to form the film.

We adopt the approximation that the current to form the film and the current through the film are both much smaller than the current for anodic dissolution from the bare areas of the surface. The total anodic dissolution current density should be a function of time as (see Appendix II)

$$i_t = i_b \exp(-t/\tau)$$

By plotting $-\ln i$ vs. t one should obtain a straight line over the time period of nucleation and growth of the film. In Fig. 11 this plot is shown for a typical current transient. Before $t = 1$ sec, there was no appreciable contribution from film growth, probably because the solubility limit had not been exceeded. Dissolution between patches was dominant from t

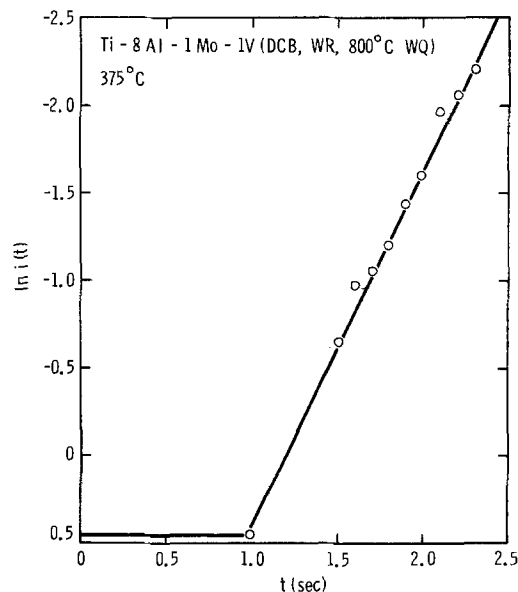


Fig. 11. Drop in current density due to precipitation of passivating layer.

= 1 to $t = 2.5$ sec as evidenced by the linear curve. At about 2.5 sec, deviations from the straight line could be observed, and this was interpreted as the region where the small film growth current became appreciable, i.e., as complete coverage of the crack wall was approached.

The slope of the curve in Fig. 11 was found to be relatively independent of potential for our tests which were conducted over the range -1750 to -2050 mV (vs. 1M Pt^{2+}/Pt). The slope gave a decay constant which varied from 0.38 to 0.71 sec with an average value of 0.59 sec. From Appendix II, the decay constant was shown to be related to the current density, i_b , before nucleation by

$$\tau = ZF\rho\Delta/Mi_b$$

For the initial current density of 5.6 mA/cm^2 at -1800 mV, for example, the thickness of the film (calculated as TiO) would be

$$\Delta = 2.2 \times 10^{-7} \text{ cm}$$

From the slope of the curve in Fig. 11, the fractional surface coverage may be calculated (see Appendix II), and is shown in Table I. Zero time was taken as $t = 1$ sec on Fig. 11. Therefore the surface approaches complete coverage at times between 1.5 and 2 sec (above 2.5 sec on Fig. 11). This should cause deviations from the linear behavior shown in Fig. 11, as the current in bare areas becomes comparable to the current on the passive areas.

Identification of the film as TiO is somewhat arbitrary because no direct measurements of film properties were made. The solubility of TiCl_2 in LiCl-KCl is too high for it to have been precipitated on the surface.² There are small quantities of O^{2-} and OH^- in the melt even though the tests were conducted in

² Solutions of TiCl_2 of over 10^{-3} molar have been made in this laboratory.

Table I

| Time (sec) | f |
|------------|------|
| 0 | 0 |
| 0.14 | 0.25 |
| 0.35 | 0.5 |
| 0.69 | 0.75 |
| 1.15 | 0.9 |
| 1.5 | 0.95 |

a dry box. It is proposed that the impurity level of O^{2-} was sufficient to give precipitation of TiO on the surface. No more definite identification of the film will be attempted until more information has been obtained.

Growth of a Thicker Film (Region III)

The third and final stage of the current transient observed during cracking obeyed a $1/t$ decay as shown in Fig. 12. Curves of current density vs. $1/t$ were also linear in this region. The slope varied from 3.1 to 6.3 for different tests, with an average of 4.54×10^{-3} C/cm².

The time dependence is consistent with a high field conduction mechanism [see, e.g., Vetter (10)] for thickening of a passive film under potentiostatic conditions. The thickness of the film, Δ , would be expected to have a logarithmic time dependence as (10)

$$\frac{1}{\Delta} = a - b \ln t, \text{ with } b = 1/(\beta\Delta\phi)$$

Here, β is the kinetic constant and $\Delta\phi$ is the (constant) potential drop across the film. The slope of the current density vs. $1/t$ curve should be approximately

$$\frac{ZF\beta\Delta\phi}{M}$$

where

$$\beta = \alpha ZFa/RT$$

and all the symbols have been identified except α = transfer coefficient, taken as 0.5 and a = jump distance [see (10)] = $\sim 3 \times 10^{-8}$ cm. Using the parameters for TiO , the slope was calculated from this expression to be 8×10^{-3} C/cm². This is considered to be in adequate agreement with the experimental results which were $3.1\text{--}6.3 \times 10^{-3}$ C/cm².

The film thickness in region II was found to be independent of potential. This suggests that the slope of the i vs. $1/t$ curve in region III should have an exponential dependence on applied potential, but our data scattered too much to draw any definite conclusions at this point.

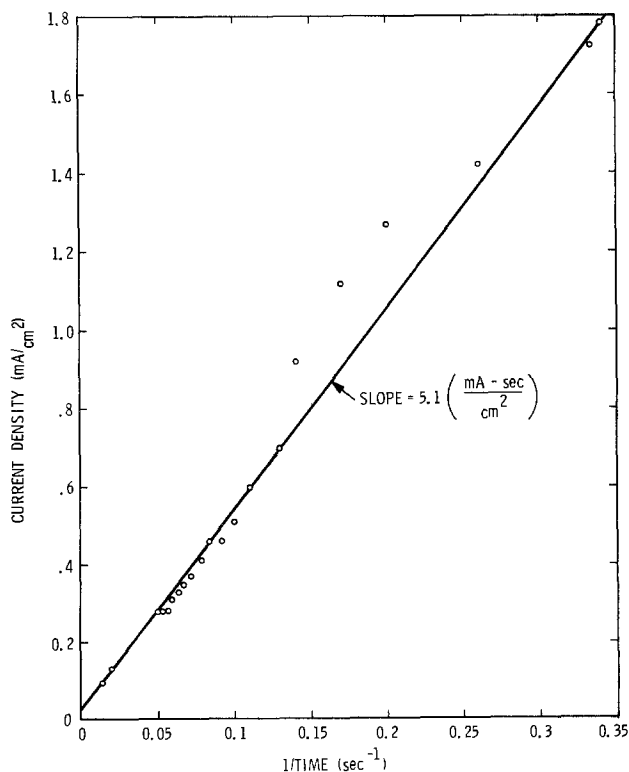


Fig. 12. Decay of current density at long times

Conclusions and Summary

The model which has been presented here accounts for the macroscopic features of the current-time behavior during crack propagation. The anodic dissolution reaction was rather uniformly distributed on the crack walls in the initial stage, and there was no indication that preferential anodic dissolution occurred at the crack tip. The crack walls were free of any film before region II. The film which was nucleated and grown during region II passivated the surface and the current-time behavior reflected the dominant source of current as that which came from the film-free surface. Deviations from this pattern occurred at longer times when the film covered the surface. Current through the film was the dominant source at still longer times where the film grew thicker by a high-field kinetic mechanism.

The dominant effect of potential was in region I. This influence was found to be consistent with linear dissolution kinetics. Data in the other two stages varied enough that the expected potential dependence could not be confirmed.

It is proposed that the events which have been described here occurred along with cracking in this simple environment, but were not responsible for cracking. That is, there has been no necessity to assume anything remarkable about the crack tip. None of the behavior could be ascribed to crack tip events.

Two of the possible mechanisms for crack propagation are eliminated by the model of events adopted here. The anodic dissolution mechanism requires preferential crack tip dissolution in order for a sharp crack to propagate, and none of the observations were consistent with this. In addition, current densities on the order of $10^3\text{--}10^5$ A/cm² would be required to propagate cracks at the velocities observed here, and this seems unreasonable for the low voltage conditions of the tests. A brittle-film mechanism which requires a passivating film on the crack walls appears to be eliminated by the behavior in region I. All the events in region I occurred on film-free walls.

At times longer than those described here (i.e., lower velocities) and at more positive potentials, crack extension could involve anodic dissolution as previously described (3). This may be consistent with the onset of intergranular cracking at low velocities (3). However, current transients have not been measured under such conditions. It should be emphasized that the present treatment is only intended to describe electrochemical events in the crack tip during the initial stages of cracking at high velocities and high stress intensities.

The molten salt environment has made it possible to eliminate from consideration several possible cracking mechanisms. The properties of the eutectic have allowed the separation of controlling parameters, so that each could be studied independently. The simple chemical nature of the environment was the most important property for defining critical processes at the crack tip. The success of the present study suggests that simple environments should be used for other mechanistic studies of stress corrosion cracking. An extension of the present study which is underway is the cracking of stainless steels in molten $AlCl_3\text{--}NaCl$. The relative importance of hydrogen embrittlement and Cl^- cracking in the austenitic (e.g., 21-6-9 and 22-13-5) and ferritic (e.g., 430) stainless steels will be determined.

Having eliminated several mechanisms, we have Cl^- -induced cracking as a remaining possibility. It is more of an idea than a model and has never been made quantitative. It is simply the idea that adsorption (e.g., Cl^-) onto a surface would weaken substrate lattice bonds so that mechanical failure would occur at reduced stress levels. Many questions about such a process remain unanswered, such as why the crack surface morphology changes from dimpled

(mechanical overload) to brittle cleavage (molten salt stress corrosion cracking) if simple adsorption is the mechanism. These unanswered questions suggest that more study is needed to definitively attribute the cracking to such a mechanism. This is to be the aim of the steel study mentioned above.

In summary, the anodic current transients observed in LiCl-KCl were caused by stress corrosion cracking of titanium-8% aluminum-1% molybdenum-1% vanadium. The transients could be broken into three stages as in Fig. 13. In region I, anodic dissolution occurred from film-free walls by linear kinetics. Nucleation and growth of a film (taken to be TiO here) dominated the behavior in region II. Growth of a thicker film caused the current decay shown in region III. None of these events are responsible for the stress corrosion cracking, but occur on the crack walls exposed by crack extension. The behavior may be consistent with crack extension induced by chloride ion (3).

Acknowledgment

This work was supported by the U.S. Department of Energy.

Manuscript submitted Sept. 18, 1978; revised manuscript received Aug. 14, 1980.

Any discussion of this paper will appear in a Discussion Section to be published in the December 1981 JOURNAL. All discussions for the December 1981 Discussion Section should be submitted by Aug. 1, 1981.

Publication costs of this article were assisted by Sandia Laboratories.

APPENDIX I

Potential Distribution in a Crack

The potential drop within the crack is to be determined by solving

$$r \frac{d^2\phi}{dr^2} + \frac{d\phi}{dr} - \frac{(\alpha_a + \alpha_c) i_o F}{RT\kappa\theta_w} [\phi - V] = 0$$

Let

$$\theta = \phi - V$$

$$Z = (r/\delta)^{1/2}$$

and this yields

$$\frac{d^2\theta}{dZ^2} + \frac{1}{Z} \frac{d\theta}{dZ} - \frac{4(\alpha_a + \alpha_c) i_o F \delta}{RT\kappa\theta_w} \theta = 0$$

Let

$$\lambda = \frac{4(\alpha_a + \alpha_c) i_o F \delta}{RT\kappa\theta_w}$$

to obtain

$$\frac{d}{dZ} \left(Z \frac{d\theta}{dZ} \right) - \lambda Z \theta = 0$$

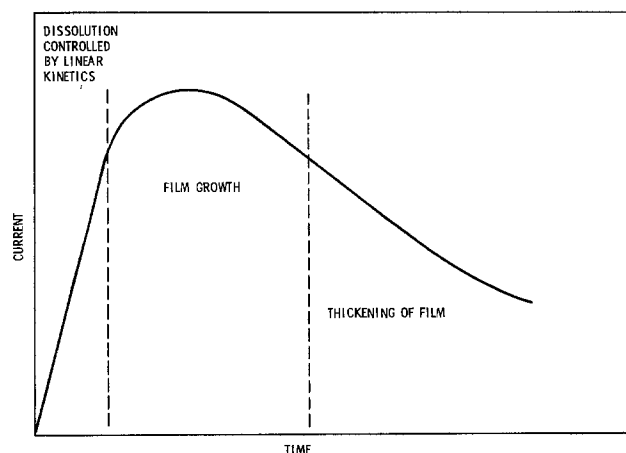


Fig. 13. Summary of processes which occur during a current transient caused by stress corrosion cracking.

The solution may be expressed in terms of Bessel functions as

$$\theta = C_1 I_0(Z\sqrt{\lambda}) + C_2 K_0(Z\sqrt{\lambda})$$

The boundary conditions

$$\theta = \phi_0 - V \quad (\text{finite}) \quad \text{at } Z = 0$$

$$\theta = \phi_1 - V \quad \text{at } Z = 1$$

gives

$$C_2 = 0$$

$$C_1 = (\phi_0 - V) = \frac{(\phi_1 - V)}{I_0(\lambda)}$$

and

$$\theta = \phi - V = (\phi_1 - V) \frac{I_0(Z\sqrt{\lambda})}{I_0(\sqrt{\lambda})}$$

The total current may be calculated now, and

$$I_{\text{current}} = -2B \int_0^\delta i_\theta|_{\theta=\theta_w} d\tau$$

$$= \frac{4B(\alpha_a + \alpha_c) i_o F \delta}{RT} \int_0^1 \theta Z dZ$$

$$= \frac{4B(\alpha_a + \alpha_c) i_o F \delta}{RT\sqrt{\lambda}} \left[\frac{I_1(\sqrt{\lambda})}{I_0(\sqrt{\lambda})} \right] (\phi_1 - V)$$

As

$$\lambda \rightarrow 0$$

$$I_1 \rightarrow \sqrt{\lambda}$$

$$I_0 \rightarrow 1$$

and

$$I_{\text{total current}} = \frac{2B(\alpha_a + \alpha_c) i_o F \delta}{RT} \left[1 - \frac{\lambda}{8} \right] (V - \phi_1)$$

Current distribution down the crack is nearly uniform for small values of λ as measured by

$$\frac{i|_{\theta=\theta_w} - i|_{\theta=\theta_w}}{r=0 \quad r=\delta} = \frac{(I_0(\sqrt{\lambda}) - 1)\sqrt{\lambda}}{2I_1(\sqrt{\lambda})}$$

For small values of λ this becomes

$$\frac{i|_{\theta=\theta_w} - i|_{\theta=\theta_w}}{r=0 \quad r=\delta} = \frac{(\alpha_a + \alpha_c) i_o F \delta}{RT\kappa\theta_w}$$

The above derivation of the potential and current distributions assumed a narrow crack, thick specimen (thickness, B, \gg the crack length, δ), and quasi-steady state. These results would thus be applicable at any instant and do not give the time dependence. The current would have the same time dependence as the crack length, and the current density would be independent of time.

APPENDIX II

Nucleation of a Passivating Film

Dissolution of a metal may be throttled by a passivating film that forms on the surface when the solubility of the solid is exceeded. The current density on the free surface will be constant at constant potential. The total current to a given surface area will be composed of the current density to the free surface, plus the current to the edges of passivating patches, plus the current to the surface of the patch to increase its thickness. If we assume that the dominant current is the dissolution current on the film-free surface, that the current to thicken the patches is negligible, and that the current to nucleate and grow a patch is important only to change the area covered by the film, the total current density is

$$i_t = i_b(1 - f)$$

Here, f is the fraction of the surface covered by the passivating solid and i_r is the current density to the film-free surface. The time dependence of the total current density will be that of the area fraction f , i.e., i_t will change with time only because f changes.

Once the solubility limit is exceeded and a film begins to precipitate, the rate of deposition of a constant thickness film will cause the fraction of surface covered to change as

$$\frac{df}{dt} = i_t M / ZF\rho\Delta$$

The first equation may be substituted into the second, and integration yields

$$i_t = i_b \exp(-t/\tau)$$

where the decay constant τ is given by

$$\tau = ZF\rho\Delta/i_b M$$

and Z = number equiv./mole, taken to be 2 here, F = Faraday constant, ρ = density of the solid, Δ = thickness of the film, i_b = constant current density to the film-free surface, and M = molecular weight of the film solid.

The surface is half covered at

$$i_t = 0.5 i_b$$

or

$$t/\tau = 0.693$$

REFERENCES

- H. L. Logan, in "Fundamental Aspects of Stress Corrosion Cracking," R. W. Staehle, A. J. Forty, and D. van Rooyen, Editors, NACE, Houston, Texas (1969).
- W. H. Smyrl and M. J. Blackburn, *Corrosion*, **31**, 370 (1975).
- W. Smyrl, in "Molten Salts," J. P. Pemsler, J. Braunstein, K. Nobe, D. R. Morris, and N. E. Richards, Editors, The Electrochemical Society Softbound Proceedings Series, Princeton, N.J. (1976).
- W. H. Smyrl and J. Newman, *This Journal*, **121**, 1000 (1974).
- M. J. Blackburn, J. A. Feeney, and T. R. Beck, in "Advances in Corrosion Science and Engineering," Vol. 3, M. R. Fontana and R. W. Staehle, Editors, Plenum Press, New York (1973).
- M. J. Blackburn, W. H. Smyrl, and J. A. Feeney, in "Stress Corrosion Cracking in High Strength Steels and in Titanium and Aluminum Alloys," B. F. Brown, Editor, U.S. Government Printing Office, Washington, D.C. (1972).
- A. D. Graves, G. J. Hills, and D. Inman, in "Advances in Electrochemistry and Electrochemical Engineering," Vol. 4, P. Delahay, Editor, Interscience, New York (1966).
- J. Newman, "Electrochemical Systems," Prentice-Hall, Englewood Cliffs, N.J. (1973).
- D. A. Vermilyea, in "Advances in Electrochemistry and Electrochemical Engineering," Vol. 3, C. W. Tobias, Editor, Interscience, New York (1965).
- K. J. Vetter, "Electrochemical Kinetics," Academic Press, New York (1967).
- E. Yeager and J. Kuta, in "Physical Chemistry: An Advanced Treatise," Vol. IXA, H. Eyring, Editor, Academic Press, New York (1970).
- J. A. Plambeck, in "Encyclopedia of Electrochemistry of the Elements," Vol. X, A. J. Bard, Editor, Marcel Dekker, New York (1976).

Technical Notes



A Seawater Battery Based upon the Sulfuryl Chloride/Magnesium Couple

K. A. Klinedinst* and F. G. Murphy*

GTE Laboratories, Incorporated, Waltham, Massachusetts 02154

In the continuing search for the optimum energy source for the propulsion of underwater vehicles, the "seawater" battery has established a unique position (1-4). The silver chloride/magnesium couple utilizes seawater as both the electrolyte and the cooling medium for high power applications. One concept to extend the operating life of the seawater battery (while maintaining maximum power density) involves the use of a liquid oxyhalide reactant as in the zinc/chromic acid cell (5-7). In this battery, the stored concentrated chromic acid and sulfuric acid are injected into the incoming seawater as needed.

The use of a liquid oxyhalide cathodic reactant in a seawater battery has recently been suggested (8). This note describes the initial experimental work performed to evaluate the feasibility and potential of seawater batteries containing magnesium or magnesium alloy anodes and liquid oxyhalide cathodic reactants. In this battery, the liquid oxyhalide flows through and is reduced upon an inert porous carbon cathode. The products of the cathodic half-cell reaction along with any unreduced oxyhalide then pass into the seawater electrolyte which flows between the carbon and magnesium

electrodes. The consequent acid enrichment of the seawater serves to keep the products of the anodic half-cell reaction in solution.

Experimental

The experimental cell was made almost entirely of PTFE. It consisted of two parts: the body and the cap (as shown in Fig. 1). The body of the cell was made from two pieces of cylindrical PTFE stock joined together to make an L-shaped unit. A hole was drilled

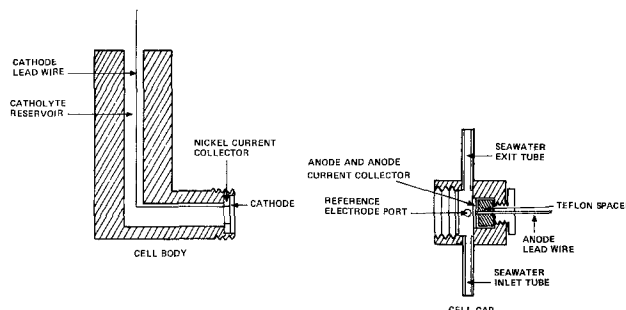


Fig. 1. Experimental cell schematic

* Electrochemical Society Active Member.

Key words: battery, magnesium, seawater, sulfuryl chloride.

through the body to serve as a reservoir for the liquid oxyhalide. A nickel washer (welded to a nickel lead wire) served as the cathode current collector. The porous cathode (a mixture of carbon black and PTFE pressed onto a nickel metal screen) was pressed onto this nickel washer when the cell cap was fastened to the body by means of screw threads machined into the PTFE parts. Thus, during the operation of the cell, the liquid reactant could flow from the reservoir through the porous cathode.

The cell cap was a more complicated assembly. The magnesium or magnesium alloy anode was pressed against a nickel current collector by means of a stainless steel ring. The nickel lead wire (welded to the anode current collector) exited the cell through a hole drilled into a PTFE plug which screwed into the end of the cap. Two stainless steel tubes extended from opposite ends of a cap diameter and were used to transfer the "seawater" (3.5% NaCl dissolved in distilled water) into and out of the cell. (The seawater flowed between the two electrodes in the assembled cell at a rate of about 1 ml/sec.) The Ag/AgCl reference electrode (AgCl electrochemically formed upon the surface of a silver wire) passed into the cell via a third opening in the cap (at right angles to the two stainless steel tubes).

Once the cathode and anode were positioned within the cell body and cap, respectively, the two cell parts were screwed together. However, a thin PTFE washer was placed within the cap just before the parts were joined to insulate the two electrodes from each other. The electrode spacing (about 0.635 mm) was determined by the combined thicknesses of this PTFE washer and the stainless steel ring by which the anode was positioned within the cell cap. The exposed electrode area was 0.8 cm².

Once the seawater had begun flowing through the cell, the test was initiated by filling the oxyhalide reservoir. In every experiment, the cell voltage, the anodic half-cell potential, and the cathodic half-cell potential (relative to the Ag/AgCl reference electrode) were simultaneously recorded during each measurement interval by the use of a multichannel recording voltmeter. Two types of measurements were made: current and potential *vs.* time on constant load, and current *vs.* potential under initial discharge conditions. The initial condition performance data were obtained in two ways: either by the application of constant load pulses (in which case the current was calculated from the voltage on load) or by the application of galvanostatic pulses. The half-cell polarization curves were corrected for solution IR losses using standard techniques.

Results and Discussion

Of the liquid cathode reactants that have been used in lithium anode cells, sulfur chloride (SO₂Cl₂) and thionyl chloride (SOCl₂) have yielded the highest cell voltages (9). Therefore, these two compounds were chosen as the liquid oxyhalides to be examined as seawater battery cathode reactants. Both pure magnesium and MTA (a magnesium alloy containing 7% Ti and 5% Al) were considered as possible anode materials.

Initially, seawater cells were assembled with MTA as the anode material and with SO₂Cl₂ and SOCl₂ as the cathode reactants. The open-circuit voltages of the MTA/SO₂Cl₂ and MTA/SOCl₂ cells were 2.83V and 2.50V, respectively. It was noted that the difference between the two open-circuit voltages (0.33V) is nearly the same as the difference between the open-circuit voltages of the Li/SO₂Cl₂ and Li/SOCl₂ cells (0.35V). The two seawater cells were then discharged across constant 100Ω loads resulting in a discharge current density of about 20 mA/cm². Again, the MTA/SOCl₂ cell voltage was about 0.3V below that of the MTA/SO₂Cl₂ cell, the latter quantity being about 2.3V. Since even lower cell voltages are to be expected with other liquid oxyhalide reactants (*e.g.*, POCl₃), SO₂Cl₂ is

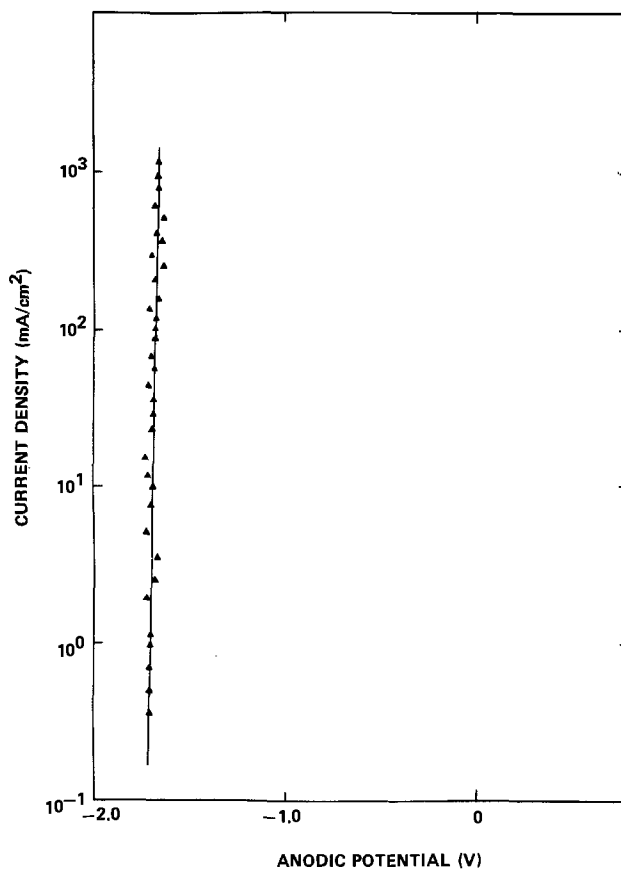


Fig. 2. Anodic polarization curve (vs. Ag/AgCl reference)

clearly the preferred cathode reactant for the Mg anode seawater battery.

Then, two seawater cells were assembled with SO₂Cl₂ as the cathode reactant and with pure Mg and MTA as

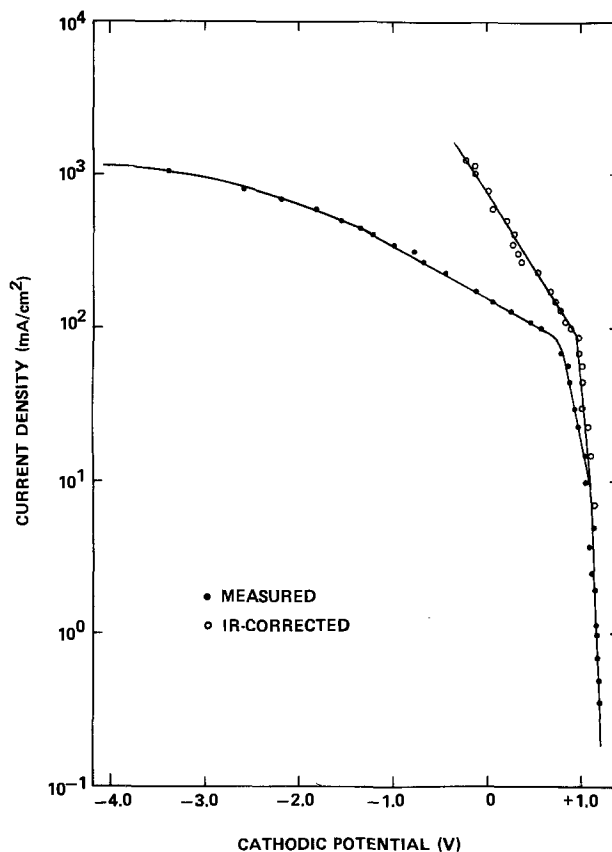


Fig. 3. Cathodic polarization curve (vs. Ag/AgCl reference)

the anode materials. With the pure Mg anode, the open-circuit voltage was about 0.14V below that obtained with the MTA anode. A similar voltage differential was observed when the two cells were discharged across constant 100 Ω loads. Therefore, MTA was chosen as the anode material to be used in all of the subsequent experiments.

Initial performance data were then obtained for the MTA/SO₂Cl₂ seawater cell by the application of both the constant load and galvanostatic pulse techniques described above (using the Ag/AgCl reference electrode). The results obtained with the two measurement techniques were essentially identical. Thus, only the results of the galvanostatic pulse measurements will be described here.

The anodic half-cell polarization curve is shown in Fig. 2. (Because of the positioning of the Ag/AgCl reference electrode within the cell cavity, negligible solution IR losses were encountered between the anode and the reference electrode.) The data demonstrate that the MTA anode operates with very little polariza-

tion. In fact, the anodic potential only decreases by about 50 mV as the current density is raised by over three orders of magnitude.

The measured and IR-corrected cathodic half-cell polarization curves are shown in Fig. 3. In contrast to the anodic half-cell results, the SO₂Cl₂ cathode is observed to suffer considerable polarization, particularly at current densities greater than about 100 mA/cm². The IR-free full cell polarization curve is shown in Fig. 4.

Summary and Conclusions

The feasibility of a new seawater battery system comprising a magnesium or magnesium alloy anode and a liquid oxyhalide cathodic reactant has been demonstrated experimentally. SO₂Cl₂ has been found to be the preferred cathodic reactant. Tests have shown that the magnesium anode operates with very little polarization, virtually all of the cell polarization occurring at the cathode. Continuing work will seek to identify the process or processes responsible for the observed cathodic polarization.

Acknowledgments

The authors wish to thank Miss Mary McLaughlin for her assistance in the experimental work and the U.S. Naval Underwater Systems Center, Newport, Rhode Island for their support of this work under contract No. N00140-77-C-6767. In particular, the assistance and advice of Dr. Peter Hirshler is gratefully acknowledged.

Manuscript submitted March 17, 1980; revised manuscript received July 25, 1980.

Any discussion of this paper will appear in a Discussion Section to be published in the December 1981 JOURNAL. All discussions for the December 1981 Discussion Section should be submitted by Aug. 1, 1981.

Publication costs of this article were assisted by GTE Laboratories, Incorporated.

REFERENCES

1. National Defense Research Committee, Final Report on Seawater Batteries, Bell Telephone Laboratories, Inc., New York (1945).
2. J. B. Mullen and P. L. Howard, *Trans. Electrochem. Soc.*, **90**, 529 (1946).
3. E. H. Lawson, U.S. Pat. 2,428,850 (1947); L. H. Harriess, U.S. Pat. 2,543,166 (1951).
4. I. C. Blake, *This Journal*, **99**, 202C (1952).
5. G. Pistoia and B. Scrosati, *ibid.*, **117**, 644 (1970).
6. H. A. Barbian and R. E. McNulty, *Trans. Electrochem. Soc.*, **91**, 106 (1947).
7. A. S. Berchielli and R. F. Chireau, Paper 71, presented at The Electrochemical Society Meeting, Las Vegas, Nevada, Oct. 17-22, 1976.
8. F. G. Murphy, U.S. Pat. 4,063,006 (1977).
9. J. J. Auborn, R. D. Bezman, K. W. French, A. Heller, and S. I. Lieberman, in "Proceedings of the 26th Power Sources Symposium," p. 45, Atlantic City, New Jersey (1974).

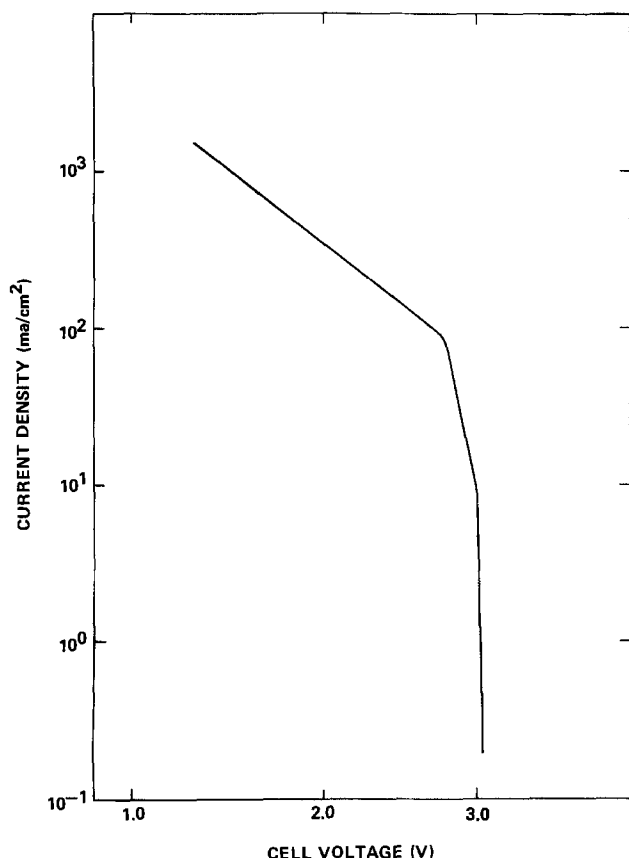


Fig. 4. Cell polarization curve

Heat of Transport of Superionic Conducting Glass 2AgI · Ag₂MoO₄

Tsutomu Minami, Katsunori Matsuda, and Masami Tanaka

Department of Applied Chemistry, University of Osaka Prefecture, Sakai-Shi, Osaka-Fu 591, Japan

Superionic conductors have attracted attention from the viewpoint of technological applications, such as solid-state batteries (1), electrochromic displays (2), and so on. There are two types in AgI-based superionic conductors; crystalline and glassy ones. The latter

Key words: heat of transport, superionic conductor, solid electrolyte, glassy electrolyte, ionic transport.

ones, or superionic conducting glasses, have several advantages compared to crystalline ones; higher conductivities (3, 4), isotropic properties, and ease of thin film formation.

In crystalline superionic conductors the activation energy for conduction, E_{σ} , is reported to be experimentally equal to the heat of transport, q^* , which is

the anode materials. With the pure Mg anode, the open-circuit voltage was about 0.14V below that obtained with the MTA anode. A similar voltage differential was observed when the two cells were discharged across constant 100 Ω loads. Therefore, MTA was chosen as the anode material to be used in all of the subsequent experiments.

Initial performance data were then obtained for the MTA/SO₂Cl₂ seawater cell by the application of both the constant load and galvanostatic pulse techniques described above (using the Ag/AgCl reference electrode). The results obtained with the two measurement techniques were essentially identical. Thus, only the results of the galvanostatic pulse measurements will be described here.

The anodic half-cell polarization curve is shown in Fig. 2. (Because of the positioning of the Ag/AgCl reference electrode within the cell cavity, negligible solution IR losses were encountered between the anode and the reference electrode.) The data demonstrate that the MTA anode operates with very little polariza-

tion. In fact, the anodic potential only decreases by about 50 mV as the current density is raised by over three orders of magnitude.

The measured and IR-corrected cathodic half-cell polarization curves are shown in Fig. 3. In contrast to the anodic half-cell results, the SO₂Cl₂ cathode is observed to suffer considerable polarization, particularly at current densities greater than about 100 mA/cm². The IR-free full cell polarization curve is shown in Fig. 4.

Summary and Conclusions

The feasibility of a new seawater battery system comprising a magnesium or magnesium alloy anode and a liquid oxyhalide cathodic reactant has been demonstrated experimentally. SO₂Cl₂ has been found to be the preferred cathodic reactant. Tests have shown that the magnesium anode operates with very little polarization, virtually all of the cell polarization occurring at the cathode. Continuing work will seek to identify the process or processes responsible for the observed cathodic polarization.

Acknowledgments

The authors wish to thank Miss Mary McLaughlin for her assistance in the experimental work and the U.S. Naval Underwater Systems Center, Newport, Rhode Island for their support of this work under contract No. N00140-77-C-6767. In particular, the assistance and advice of Dr. Peter Hirshler is gratefully acknowledged.

Manuscript submitted March 17, 1980; revised manuscript received July 25, 1980.

Any discussion of this paper will appear in a Discussion Section to be published in the December 1981 JOURNAL. All discussions for the December 1981 Discussion Section should be submitted by Aug. 1, 1981.

Publication costs of this article were assisted by GTE Laboratories, Incorporated.

REFERENCES

1. National Defense Research Committee, Final Report on Seawater Batteries, Bell Telephone Laboratories, Inc., New York (1945).
2. J. B. Mullen and P. L. Howard, *Trans. Electrochem. Soc.*, **90**, 529 (1946).
3. E. H. Lawson, U.S. Pat. 2,428,850 (1947); L. H. Harriess, U.S. Pat. 2,543,166 (1951).
4. I. C. Blake, *This Journal*, **99**, 202C (1952).
5. G. Pistoia and B. Scrosati, *ibid.*, **117**, 644 (1970).
6. H. A. Barbian and R. E. McNulty, *Trans. Electrochem. Soc.*, **91**, 106 (1947).
7. A. S. Berchielli and R. F. Chireau, Paper 71, presented at The Electrochemical Society Meeting, Las Vegas, Nevada, Oct. 17-22, 1976.
8. F. G. Murphy, U.S. Pat. 4,063,006 (1977).
9. J. J. Auborn, R. D. Bezman, K. W. French, A. Heller, and S. I. Lieberman, in "Proceedings of the 26th Power Sources Symposium," p. 45, Atlantic City, New Jersey (1974).

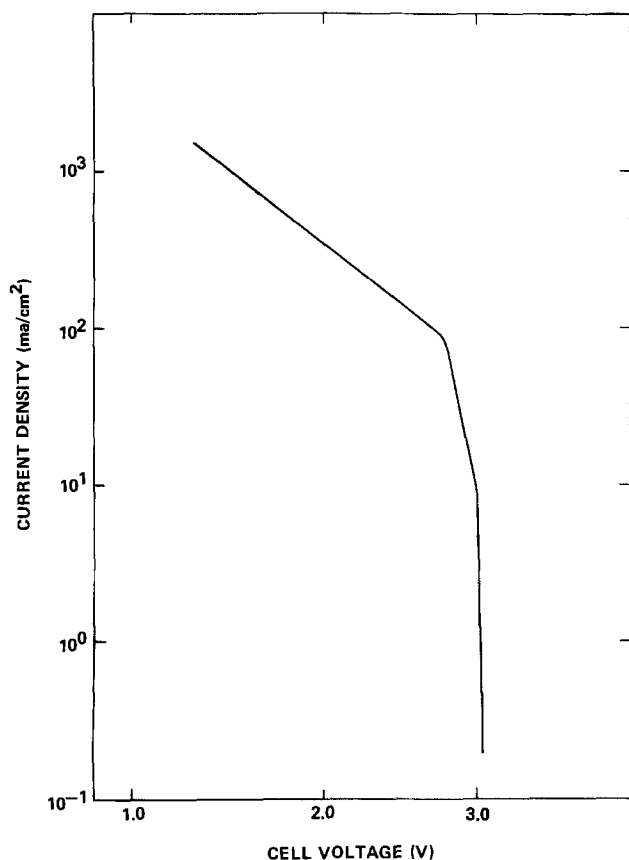


Fig. 4. Cell polarization curve

Heat of Transport of Superionic Conducting Glass 2AgI · Ag₂MoO₄

Tsutomu Minami, Katsunori Matsuda, and Masami Tanaka

Department of Applied Chemistry, University of Osaka Prefecture, Sakai-Shi, Osaka-Fu 591, Japan

Superionic conductors have attracted attention from the viewpoint of technological applications, such as solid-state batteries (1), electrochromic displays (2), and so on. There are two types in AgI-based superionic conductors; crystalline and glassy ones. The latter

Key words: heat of transport, superionic conductor, solid electrolyte, glassy electrolyte, ionic transport.

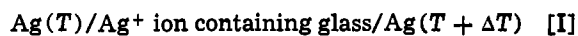
ones, or superionic conducting glasses, have several advantages compared to crystalline ones; higher conductivities (3, 4), isotropic properties, and ease of thin film formation.

In crystalline superionic conductors the activation energy for conduction, E_{σ} , is reported to be experimentally equal to the heat of transport, q^* , which is

determined from the temperature dependence of thermoelectric power, and several papers are presented to discuss the ionic transport mechanism of the conductors based on such equality between E_σ and q^* (5-9).

We have found, however, that there is an appreciable difference between E_σ and q^* in superionic conducting glass $2\text{AgI}\cdot\text{Ag}_2\text{MoO}_4$ (mole ratio), which shows the ionic conductivity as high as $4 \times 10^{-3} \Omega^{-1} \text{cm}^{-1}$ at room temperature and the transport number of unity of silver ions (3, 10). In the present note q^* of the glass $2\text{AgI}\cdot\text{Ag}_2\text{MoO}_4$ is compared with E_σ reported previously (10). The appreciable difference between these values must give a clue to reveal the transport mechanism in the glass.

The thermoelectric power was measured by using the cell shown in Fig. 1; the cell can schematically be shown as



Chamber 1 in the figure was sunk in a low temperature ethyl alcohol-Dry Ice bath cooled with a cooler (Neslab, Cryocool Model cc-80II) after it was filled with dry nitrogen gas. The temperature of the sample was monitored with the thermocouple 8 and regulated with a PID temperature controller connected to furnace 2 so as to achieve no temperature difference between the top and bottom surfaces of the sample at a given temperature. After keeping the sample at that temperature for at least 30 min, the upper heater 3 was gradually heated with d.c. to generate the temperature gradient in the sample. The thermoelectric voltage ΔV caused by the temperature difference ΔT , smaller than 2 K, was recorded on an X-Y recorder C. The thermoelectric power θ was determined from the slope on the recorder as defined by

$$\Delta V = \theta \cdot \Delta T \quad [1]$$

The sign convention that θ is positive if the hot end shows higher potential is followed in this paper. The impedance of the amplifier A was $10^7 \Omega$ and that of B was higher than $10^{14} \Omega$. The measurements were repeated at least 5 times at each temperature.

The glass preparation technique has been described elsewhere (10). Two types of samples were used for

the thermoelectric power measurement, similar to the conductivity measurement: bulk glass and pressed pellet of pulverized glass. The pellet contained voids of about 4.5%.

Figure 2 shows the temperature dependence of θ ; circles are for bulk glass and triangles for pellet. A very small difference is observed between bulk and pellet. The thermoelectric power θ was expressed by

$$\theta = -\frac{q^*}{T} + H \quad [2]$$

where q^* is so called the heat of transport of silver ions and H is a constant. The equation of the straight lines was determined by the least squares as

$$\theta(\text{mV/K}) = -(0.067 \pm 0.006) \frac{10^3}{T} - (0.23 \pm 0.02) \quad [3]$$

for bulk glass and

$$\theta(\text{mV/K}) = -(0.059 \pm 0.006) \frac{10^3}{T} - (0.27 \pm 0.02) \quad [4]$$

for pellet.

Table I summarizes q^* and θ_{25} (thermoelectric power at 25°C), together with E_σ and σ_{25} (conductivity at 25°C) for comparison (10). As evident from the table the discrepancy in properties is very small between bulk and pellet, indicating that the bulk diffusion instead of surface or boundary diffusion controls the migration of Ag^+ ions. The value of q^* is appreciably smaller than E_σ , in contrast to the crystalline superionic conductors (5-9). It is also worth noting that q^* of the present glass is very close to that of $\alpha\text{-AgI}$ (1.20 kcal/mole) (7). According to Girvin (8, 9) q^* is equal to the static barrier height for ion hopping and the difference between E_σ and q^* is explained in terms of the phonon coupling.

It has been reported that the present glass is composed of Ag^+ , I^- , and MoO_4^{2-} ions and some Ag^+ ions show strong partial covalency with oxide ions in MoO_4^{2-} tetrahedra (11). The fact that q^* of the glass is nearly equal to that of $\alpha\text{-AgI}$ must imply that Ag^+ ions contributing to the ionic conduction interact electrostatically with I^- ions only and thus a part of Ag^+ ions in glass take part in the ionic conduction; this result is consistent with the deduction given in the pre-

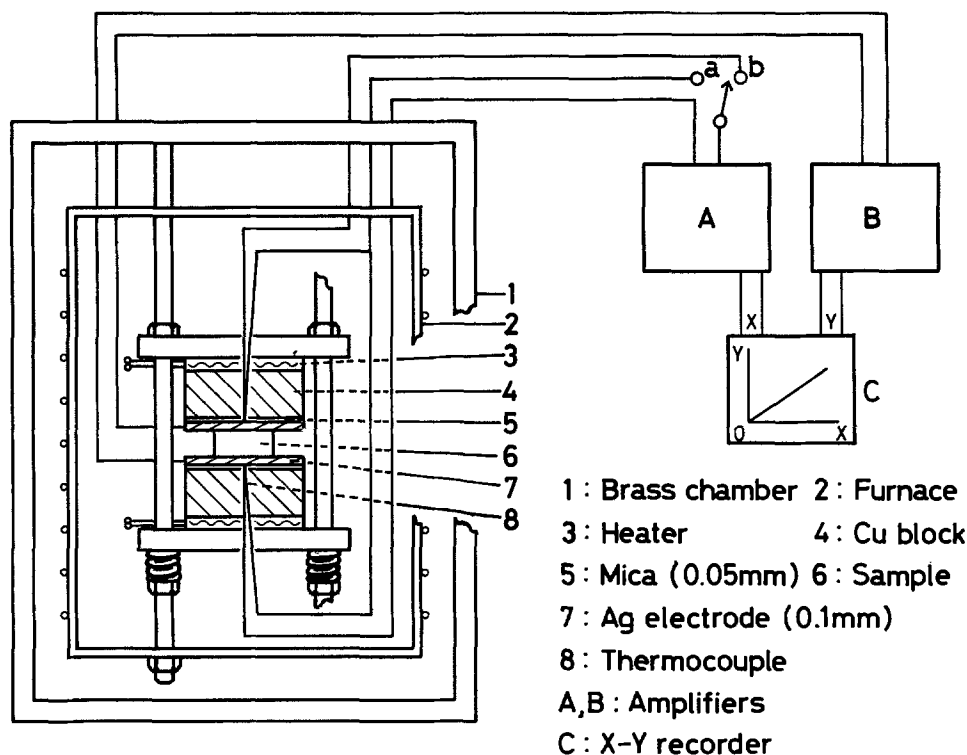


Fig. 1. Schematic diagram of the cell for the measurement of thermoelectric power.

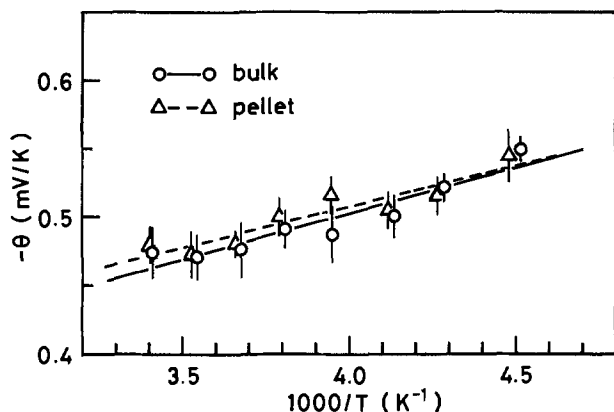


Fig. 2. Temperature dependence of thermoelectric power of glass 2AgI · Ag₂MoO₄ (mole ratio).

vious paper (10). Much detailed study is under progress on the heat of transport and the ion transport mechanism of superionic conducting glasses, and will be published elsewhere in the future.

Table I. Some parameters for ion transport in superionic conducting glass 2AgI · Ag₂MoO₄ (mole ratio)

| | q^* (kcal/ mole) | θ_{25} (mV/K) | E_{σ}^a (kcal/ mole) | σ_{25}^a ($\Omega^{-1} \text{cm}^{-1}$) |
|------------|--------------------------|-------------------------|-----------------------------------|---|
| Bulk glass | 1.6 | -0.45 ₀ | 5.5 | 4.0×10^{-3} |
| Pellet | 1.4 | -0.46 ₀ | 5.7 | 2.9×10^{-3} |

^a The activation energy for conduction, E_{σ} , and the conductivity at 25°C, σ_{25} (10). The values of E_{σ} were determined by $\sigma = \sigma_0 \exp(-E_{\sigma}/RT)$.

Acknowledgment

The authors wish to thank Dr. N. Tohge for his helpful advice in the thermoelectric power measurement. This work was supported by a Grant-in-Aid for Developmental Scientific Research from the Ministry of Education of Japan and by the Asahi Glass Foundation for Contribution to Industrial Technology.

Manuscript received May 2, 1980.

Any discussion of this paper will appear in a Discussion Section to be published in the December 1981 JOURNAL. All discussions for the December 1981 Discussion Section should be submitted by Aug. 1, 1981.

Publication costs of this article were assisted by the University of Osaka Prefecture.

REFERENCES

1. T. Minami, T. Katsuda, and M. Tanaka, *This Journal*, **127**, 1308 (1980).
2. M. Green, W. C. Smith, and J. A. Weiner, *Thin Solid Films*, **38**, 89 (1976).
3. T. Minami, H. Nambu, and M. Tanaka, *J. Am. Ceram. Soc.*, **60**, 467 (1977).
4. T. Minami, Y. Takuma, and M. Tanaka, *This Journal*, **124**, 1659 (1977).
5. T. Takahashi, O. Yamamoto, and E. Nomura, *Denki Kagaku*, **38**, 360 (1970).
6. M. J. Rice and W. L. Roth, *J. Solid State Chem.*, **4**, 294 (1972).
7. K. Shahi, *Phys. Status Solidi, A*, **41**, 11 (1977).
8. S. M. Girvin, *J. Solid State Chem.*, **25**, 65 (1978).
9. S. M. Girvin, Extended Abstract (#1.6) of the 2nd International Meeting on Solid Electrolytes, St. Andrew, Scotland (1978).
10. T. Minami and M. Tanaka, *J. Solid State Chem.*, **32**, 51 (1980).
11. T. Minami, T. Katsuda, and M. Tanaka, *J. Non-Cryst. Solids*, **29**, 389 (1978).



Acceleration of Plasma Etch Rate Caused by Alkaline Residues

T. Makino, H. Nakamura, and M. Asano¹

*Nippon Telegraph and Telephone Public Corporation,
 Musashino Electrical Communication Laboratory, Tokyo 180, Japan*

ABSTRACT

Effects of positive resist developer processing on plasma etching characteristics are described. The etch rate of polycrystalline silicon was measured with and without positive resist developer processing using a barrel-type plasma etching system and $\text{CF}_4 + 5\% \text{O}_2$ as an etching gas. A considerably accelerated etch rate was observed for polycrystalline silicon with residues of positive resist developer. The acceleration is attributed to NaOH residues adhered on the surface, which act as catalytic agents. The residual KOH also accelerates the etch rate of polycrystalline silicon.

Plasma etching has become a promising technique for delineation of patterns in polycrystalline Si (poly-Si), Si_3N_4 , and SiO_2 during the manufacture of integrated circuits. Particularly for poly-Si, plasma etching takes the place of a wet process with HF-HNO_3 solution since it is simpler, more economical, and capable of automatic operation. Using CF_4 or $\text{CF}_4 + \text{O}_2$ as an etching gas, pressure dependences or rf power dependences of etch rate are widely examined (1-3) in addition to the influence of impurity doping in poly-Si (4). In order to improve the controllability or repeatability, effects of various parameters in the photolithographic process should also be investigated. Zellej has reported (5) that organic residues associated with a negative resist developer sequence can exert a major influence on plasma etch rate and uniformity of Si_3N_4 . It is also concluded that the use of a positive resist is the best solution to the problem by avoiding the troublesome residues altogether. However the result was limited to Si_3N_4 and the details of the positive develop process, such as components of the developer, were not clearly described. There are two types of developing solution for positive resist; one is a nonmetal developer and the other contains alkaline metal compounds. The former is inferior in resolution of fine pattern delineation, although it avoids alkaline metal contamination.

This paper describes, for the first time, effects of positive resist developer processing on plasma etching characteristics of boron (B) doped poly-Si. Here an AZ developer was used as a positive resist developer. AZ developer residues result in a considerably faster etch rate than is experienced with virgin wafers and in considerably poorer etch uniformity and repeatability. The enhancement is attributed to NaOH adhered on the poly-Si surface during the photolithographic process, which acts as a catalytic agent. The residual KOH also accelerates the etch rate of poly-Si. In addition, it is found that the etch rate of poly-Si in CF_4 (5% O_2) decreases with B concentration, a result

which is contrary to the case of phosphorus doping (4).

Experimental Procedure

The rf plasma unit (IPC-2005T, manufactured by International Plasma Corporation) was used in this study. In this type of apparatus, an aluminum tunnel was inserted into the quartz chamber, so that the etch process consisted of the chemical reaction of neutral free radicals with the wafers. On loading the wafers into the chamber, it was evacuated to 0.01 Torr and then filled with nitrogen to a pressure of 0.5 Torr. RF power (13.56 MHz, 400W) was applied to raise the wafer temperature up to 50°C. The chamber was reevacuated and the etchant gas of CF_4 (5% O_2 as a minor constituent) was introduced, while maintaining at a pressure of 0.5 Torr. RF power of 100W was applied and the plasma was excited for a given time. The temperature of the wafers was 50° ~ 70°C during plasma etching.

Boron-doped poly-Si films were obtained on SiO_2 from an $\text{SiH}_4\text{-BCl}_3\text{-H}_2$ mixture at 600°C in an air-cooled radiation-heated horizontal reactor. Boron concentrations ranged from $2 \times 10^{19} \sim 3 \times 10^{21} \text{ cm}^{-3}$. Here B concentrations were measured using methylene blue colorimetric analysis (6), where the poly-Si films covered with CVD SiO_2 0.1 μm in thickness were entirely oxidized in a wet oxygen ambient followed by dissolution in HF aq. solution. The details of this procedure were described in a previous paper (7).

The etched thickness of poly-Si was measured by two methods; (i) Tallysurf measurement using a painted resist as a mask, and (ii) reflectometer (Nanospec AFT, manufactured by Nanometrics Incorporated) readings.

As the positive developer process, an AZ developer manufactured by Shipley Company Incorporated was employed. NaOH or KOH solutions were also used in order to investigate etch rate enhancement.

The surface contamination of the poly-Si was measured by x-ray photoelectron spectroscopy (XPS). The photoelectron spectra were obtained with a PHI Model 590 photoelectron spectrometer manufactured by Physical Electronics Industries, Incorporated using $\text{MgK}\alpha$ excitation. The typical residual pressure in this

¹ Present address: Nippon Telecommunication Engineering Company, Tokyo 180, Japan.

Key words: plasma etching, polycrystalline silicon, adhesive alkali, accelerated rates.

ISSN

system was in the 10^{-9} Torr range. In order to obtain depth profiles, Ar sputtering was done with a beam current of 25 mA and a beam voltage of 1 kV, at a pressure of 5×10^{-5} Torr.

Results and Discussion

Intrinsic etch rate of B-doped poly-Si.—First, the etch rate of B-doped poly-Si was measured without photolithographic treatment. Figure 1 shows the etched thickness of B-doped poly-Si vs. etch time with B concentration as a parameter, where the poly-Si was etched almost linearly with etch time. It is found that the etch rate decreases with B concentration, from 3200 Å/min for undoped to 480 Å/min for 3×10^{21} cm^{-3} B-doped poly-Si. The similar decrease of etch rate was also observed in B ion implanted poly-Si. The boron concentration dependence of etch rate is contrary to the P doping case (4) as well as B concentration dependence of growth rate (8).

Impurity dependence of plasma etch rate seems to be correlated to surface potential of poly-Si, as well as impurity dependence of growth rate (9). In the case of poly-Si growth using SiH_4 with B_2H_6 or PH_3 as a dopant gas, the surface potential during the growth is maintained to be positive or negative because of electron deficiency or excessiveness relative to intrinsic silicon, respectively. Naturally a similar surface potential should be maintained during plasma etching. A change in the surface potential affects the adsorption rate of SiH_4 or desorption rate of SiF_4 and/or reaction velocity at the surface. First let us consider the effects of surface potential on adsorption or desorption rate. From a chemical point of view, SiH_4 (SiF_4) gas has the partial ionic Si^+-H^- (9, 11) (Si^+-F^-) bond resulting in making SiH_4 (SiF_4) a molecule with four negative charged hydrogen (fluorine) atoms surrounding a positive charged atom in the center. Therefore it is thought that the enhanced growth rate with B doping is due to positive surface potential which attracts SiH_4 molecules and the reduced growth rate with P doping to negative surface potential. In a case of plasma etching of poly Si, the etching process can be described as follows (2): $\text{Si} + 4\text{F} \rightarrow \text{SiF}_4 \uparrow$. The positive surface potential of B-doped poly-Si is thought to attract and retard the reduction of SiF_4 molecules from the surface, which therefore results in a decrease in plasma etch rate with B concentration.

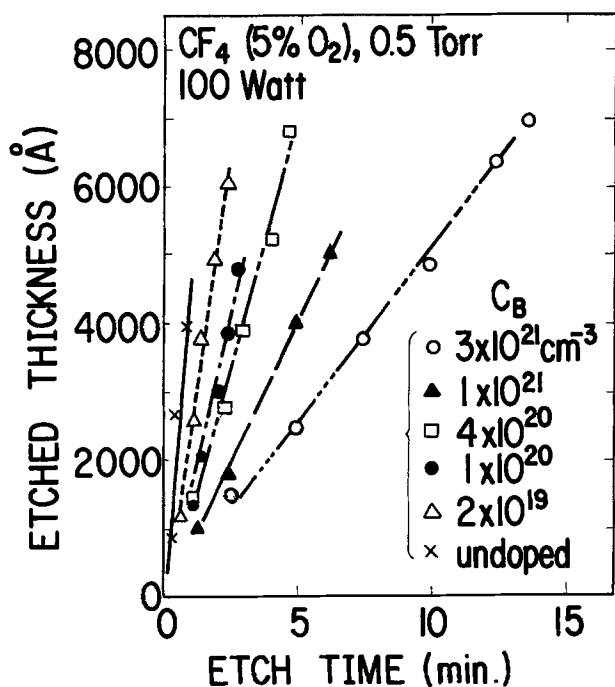


Fig. 1. Etched thickness of poly-Si vs. etch time, with B concentration as a parameter.

As for reaction velocity, it is thought that surface potential undoubtedly plays an essential role before decomposition or chemical reaction. A change in the surface potential affects interaction of the reactant F atom with the surface, probably resulting in larger reaction rate.

Effects of developing sequence on etching characteristics.—A long subsequent rinse of wafers with water after development occasionally results in lifting of the resist patterns of IC's. This limits the rinse time and gives rise to residues of the developer on the surface of the wafer.

Etched thickness was measured on the poly-Si which was dipped in an AZ developer and rinsed for 1 min in DI (deionized) water. The results are shown in Fig. 2. Linear relationships between etched thickness and etch time are also observed, as well as for virgin poly-Si. Figure 3 summarizes intrinsic and accelerated etch rate of B-doped poly-Si. Extremely accelerated etch rates are found in the "dipped" poly-Si. Particularly for heavily B-doped specimens, the relative etch rate with and without the developing sequence is very large compared with the undoped one. It is noted that the resist itself, not used in the developing sequence, was not interacting with the plasma to influence etch rate. The accelerated etch rate is independent of B concentration, the result of which will be discussed in the next section in connection with the mechanism. With increasing rinse time in DI water, the enhanced effect is eliminated (Fig. 4). A 10 min rinse brings performance in line with the intrinsic etch rate already established in Fig. 1. That is, the etch rate is actually accelerated by the presence of the residues, with the fainter traces apparently exerting the influence. The uniformity of etch rate appears to be related to the uniformity of distribution of the trace residues.

It is noted that the residues are so insignificant when it comes to conventional wet processing that they exert absolutely no influence whatsoever on the normal etching process, such as $\text{HF}-\text{HNO}_3$ solution.

Behavior of alkaline residues during plasma etch.—Since it is known that the AZ developer contains NaOH as a major component, (13), etch rates of poly-Si were measured after dipping NaOH solution with various concentration. Here spinning of wafers

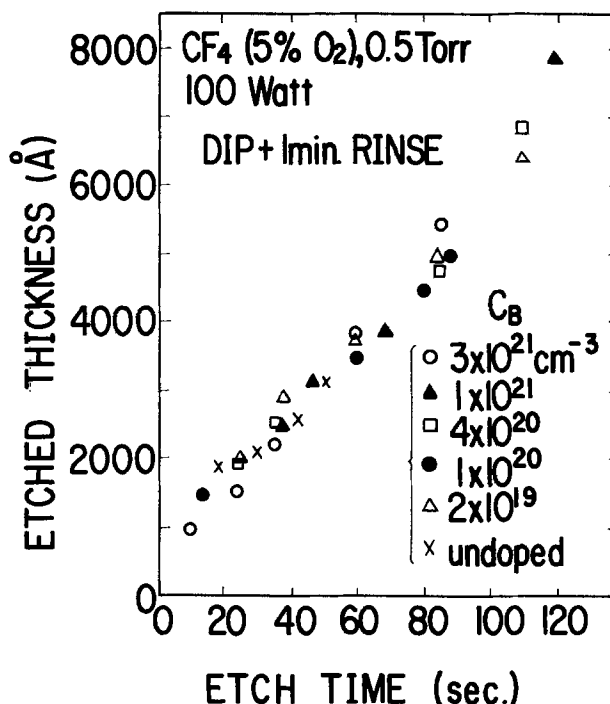


Fig. 2. Etched thickness of dipped poly-Si vs. etch time

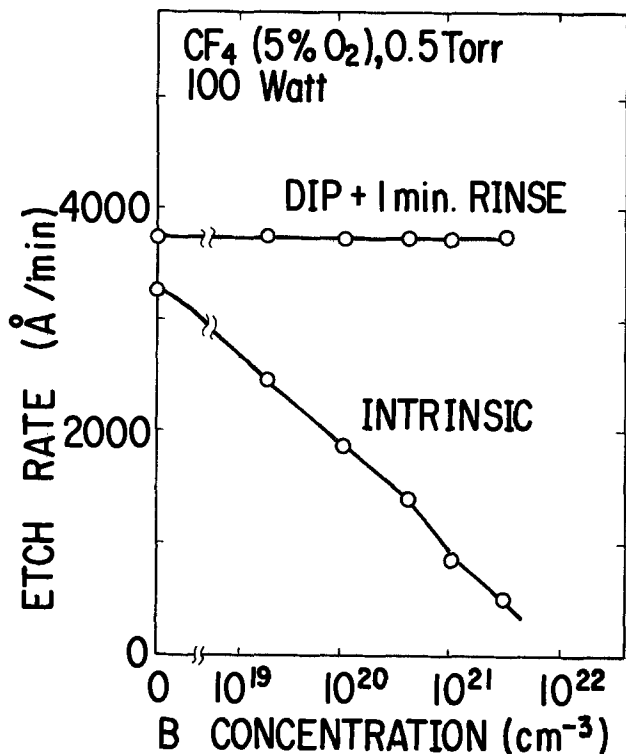


Fig. 3. Intrinsic and accelerated etch rate of poly-Si as a function of B concentration.

followed the dipping. Figure 5 shows the relationships between the etch rate of poly-Si and the pH of the NaOH solution. The enhancement of the etch rate was observed with increasing NaOH concentration in the solution. With increasing concentration, the uniformity of etch rate becomes poor, which is related to the poor uniformity of NaOH distribution adhered on the poly-Si surface. A similar enhancement is also observed in the case of "dipping" in KOH solution as shown in Fig. 4. Therefore it can be concluded that alkaline residues such as NaOH or KOH on the poly-Si surface are responsible for enhancement of the etch rate.

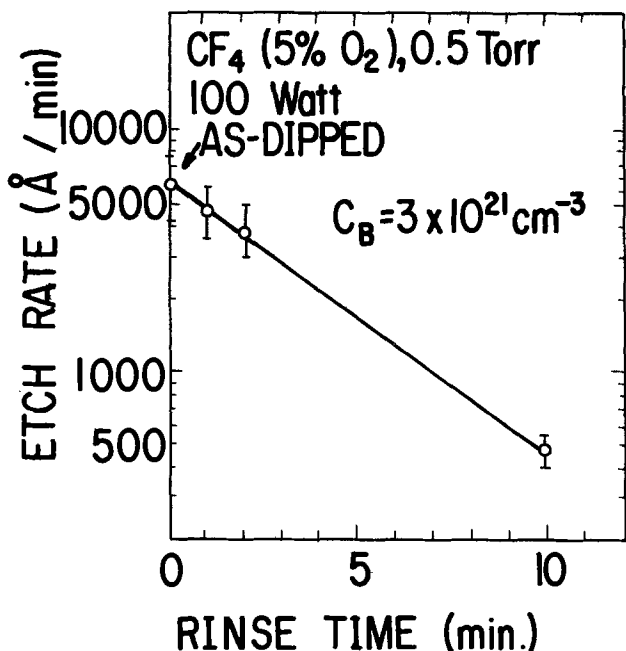


Fig. 4. Dependence of etch rate on rinse time after dipping in an AZ developer.

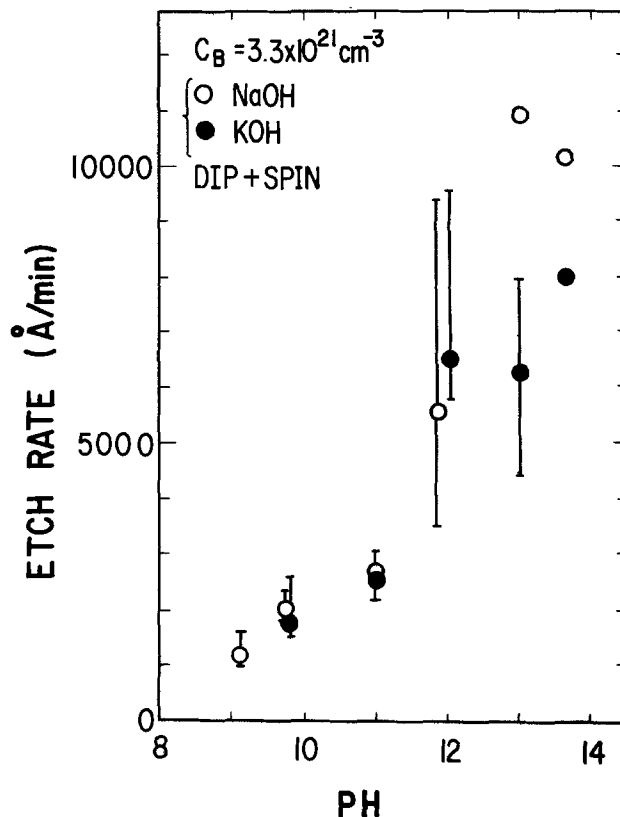


Fig. 5. Dependence of etch rate on pH of dipping NaOH or KOH.

XPS measurements were done in order to confirm that residual NaOH exists on the poly-Si surface. Figure 6 shows an Na 1s photoelectron spectrum, which is relatively easy to detect, from the poly-Si surface: for

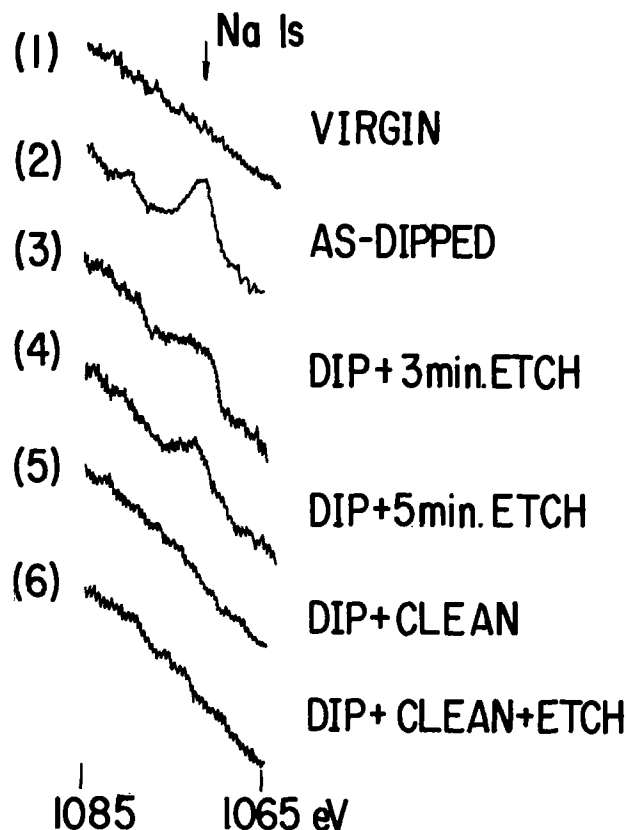


Fig. 6. XPS spectra of poly-Si ($C_B = 3 \times 10^{21} \text{ cm}^{-3}$) surface with various treatment.

(1) virgin, (2) as-dipped, (3) dip + 3 min plasma-etched, (4) dip + 5 min plasma-etched, (5) dip + cleaned, and (6) dip + clean + 10 min plasma-etched poly-Si. The dipping was done in NaOH solution with a pH of 9.2 followed by spinning. Using an $H_2SO_4 + H_2O_2$ mixture, the wafers were cleaned after the dipping. Residual Na was observed both for as-dipped and for the 3 and 5 min plasma-etched poly-Si surface, which indicates that NaOH remains on the poly-Si surface even during plasma etching. It is thought that adhered NaOH acts as a catalytic agent to accelerate the etch rate.

The depth profile of adhesive Na is shown in Fig. 7; intensity of Na 1s emission vs. sputtering time for the poly-Si, as-dipped, and dip + 3 min plasma-etched poly-Si, where 1 min sputtering corresponds to 10Å sputtering of a single Si wafer. Adhesive Na is near the surface of the as-dipped poly-Si, probably within 50Å estimating from the sputter time. Even for plasma-etched poly-Si, Na exists only near the surface, although it distributes twice as deep as for as-dipped poly-Si. The total amount of Na is almost constant-independent of plasma etch time. Therefore it is confirmed that adhesive alkali acts as a catalytic agent to accelerate etch rate and that the acceleration is not a bulk effect.

It is of interest that the intrinsic etch rate decreases with B concentration and the accelerated etch rate is independent of B concentration, as shown in Fig. 3. A specific mechanism by which the etch rate can be accelerated is as yet not clear, but some general comments can be made. As mentioned before, a decrease in the intrinsic etch rate with B concentration is corre-

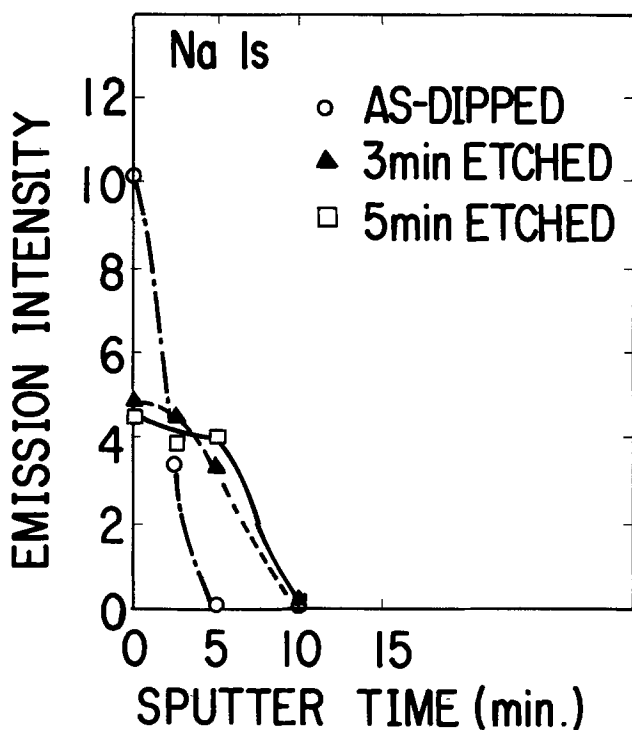


Fig. 7. Depth profile of Na 1s emission intensity

lated to a change in the surface potential of B-doped poly-Si. Similarly it is thought that P doping exerts the surface potential negative, which results in an increase in etch rate with P concentration (4). According to these explanations, it seems that the poly-Si surface changes to negative, independent of B concentration owing to excess OH^- species similar to an SiO_2 surface (14, 15) or owing to an electric double layer such as $Na^+ OH^-$ having the negative end towards the vacuum. The negative surface potential allows SiF_4 molecules to desorb easily from the poly-Si surface. Another possibility is that the interaction of the reactant F atom with silicon at the surface is accelerated owing to a change in the surface potential.

Cleaning in an $H_2O_2-H_2SO_4$ mixture after the dipping can eliminate both the adhesive alkali and the etch rate enhancement. There are other methods available to clean the surface of wafers. Sufficient rinsing in DI water or a dilute acid dip also can accomplish the elimination of the enhancement, which results in the intrinsic etch rate. Since there is no method available to obtain a uniformly adhered surface, providing a residue-free surface by the method mentioned above is necessary in order to obtain improved uniformity and reproducibility of etch rate from run to run.

Acknowledgment

The authors would like to thank Mr. H. Ikawa for helpful discussions and encouragement during the course of this work. We are indebted to Mr. Y. Watanabe for the XPS measurement.

Manuscript submitted April 24, 1980; revised manuscript received July 16, 1980.

Any discussion of this paper will appear in a Discussion Section to be published in the December 1981 JOURNAL. All discussions for the December 1981 Discussion Section should be submitted by Aug. 1, 1981.

Publication costs of this article were assisted by Nippon Telegraph and Telephone Public Corporation.

REFERENCES

1. R. L. Bersin, *Solid-State Technol.* (May 31, 1976).
2. K. Jinno, Y. Matsumoto, and S. Inomata, *Denki Kagaku*, **44**, 205 (1976).
3. H. Abe, Y. Sonobe, and T. Enomoto; *Jpn. J. Appl. Phys.*, **12**, 154 (1973).
4. K. Jinno, H. Konoshita, and Y. Matsumoto, *This Journal*, **125**, 827 (1978).
5. A. Zelle, SPIE, 174, Developments in Semiconductor Microlithography IV (1979).
6. L. Ducret, *Anal. Chim. Acta.*, **17**, 213 (1957).
7. T. Makino and H. Nakamura, Submitted to *Solid-State Electron.*
8. F. C. Eversteyn and B. H. Put, *This Journal*, **121**, 106 (1973).
9. C.-A. Chang, *ibid.*, **123**, 1245 (1976).
10. F. G. Allen and G. W. Gobeli, *Phys. Rev.*, **127**, 150 (1962).
11. F. A. Cotton and G. Wilkinson, "Advanced Inorganic Chemistry," p. 446, John Wiley and Sons, New York (1966).
12. C. J. Mogab, *This Journal*, **124**, 1262 (1977).
13. T. Nakayama and H. Nakane, *Oyo Buturi*, **43**, 483 (1974).
14. A. A. Bergh, *This Journal*, **112**, 457 (1965).
15. E. A. Taft, *ibid.*, **118**, 1985 (1971).

Studies of the Growth and Oxidation of Metal-Silicides Using Radioactive ^{31}Si as Tracer

R. Pretorius

Southern Universities Nuclear Institute, Faure 7131, South Africa

ABSTRACT

Radioactive ^{31}Si marker experiments show that the metal is the diffusing species during Ni_2Si and Pt_2Si formation, whereas both Pd and Si diffuse during Pd_2Si growth. The formation of CrSi_2 on Pd_2Si was also investigated. At low temperatures (480°C) silicon was found to be primarily transported directly from the Si(100) substrate by grain boundary and/or interstitial diffusion through the Pd_2Si layer. At higher temperatures substitutional (vacancy) diffusion of silicon started to be predominant, until at temperatures of about 650°C complete intermixing between radioactive and nonradioactive Si took place between the Pd_2Si and Cr_2Si layers. Tracer studies of the steam oxidation of CoSi_2 indicate that silicon diffuses through the CoSi_2 layer by a substitutional (vacancy) mechanism during SiO_2 formation. The measured activity profile in the SiO_2 layer shows that growth takes place at the $\text{CoSi}_2/\text{SiO}_2$ interface and that oxygen is the diffusion species through the SiO_2 layer.

A more comprehensive understanding of the inter-diffusion and reaction between components of thin film structures can be obtained by using suitable tracers of the relevant atomic species. Stable or radioactive isotopes are the most suitable for such purposes as their physical and chemical properties are identical to those of the element which is to be traced. The three main questions, which are to be answered in such investigations are, what is the diffusing species, what is its rate of diffusion, and by what mechanism does it diffuse?

A suitable tracer for studying thin film structures used in silicon semiconductor technology, is radioactive ^{31}Si , which can be formed during irradiation of natural silicon in a nuclear reactor, by the reaction $^{30}\text{Si}(n, \gamma)^{31}\text{Si}$. Although ^{30}Si only has a natural abundance of 3.1 atom percent (a/o) and notwithstanding its low thermal neutron cross section of 0.10 barns, sufficient ^{31}Si radioactivity is formed for its practical use as a tracer. Silicon-31 can be readily measured, as it decays with a half-life of 2.62 hr by the emission of beta-particles (maximum energy = 1.48 MeV) for 99.93% of its disintegrations.

To carry out such tracer experiments, it is necessary to create certain regions in the structure where the silicon atoms are radioactive and other regions where they are not. This can usually be achieved by a proper choice of experimental procedure and conditions during the preparation of the thin film structure. By measuring the position or radioactivity profile of the tracer before and after annealing, information about the diffusing species, as well as the rate and mechanism of diffusion may be obtained.

In this paper a review is given of the use of radioactive ^{31}Si as tracer for studying the formation and oxidation of metal-silicides. Some new results are also reported.

Experimental

Thin film structures were prepared by electron beam evaporation onto single crystal silicon substrates (about 1 cm^2 in size) at pressures of about 5×10^{-7} Torr. Sequential depositions were carried out by using a multiple hearth. Before the evaporation of radioactive silicon, care was taken to first wash it in organic solvents, followed by etching in an $\text{HF}:\text{HNO}_3$ solution, in order to remove any possible interfering radioactivity due to surface contamination which could have taken place prior to irradiation in the nuclear reactor.

Key words: thin films, diffusion, mechanism, marker.

Samples were annealed in a vacuum tube furnace at pressures below 1×10^{-6} Torr, and for the oxidation studies, heated at temperatures between 800° and 1000°C , in a tube furnace through which steam flowed at atmospheric pressure. The position or activity profile of the radioactive ^{31}Si in the sample, was determined by a combination of chemical or ion beam etching, radioactivity measurement, and Rutherford back-scattering.

Results and Discussion

Silicide formation and silicon self-diffusion.—Identification of the dominant diffusing species and its diffusion mechanism is crucial to a fuller understanding of silicide growth. Implanted noble gas markers such as Xe and Ar have been fruitfully used as diffusion markers in thin film studies (1-4), but unfortunately they do have some inherent disadvantages: (i) the introduction of foreign atoms into the system could affect the kinetics and mechanism of silicide formation; (ii) radiation damage introduced during marker implantation may also influence silicide formation and should first be removed by appropriate annealing; (iii) solubility effects could cause dragging of the marker at the interface, thereby giving erroneous results; (iv) the choice of marker elements and of silicides which can be studied is restricted because backscattered particles from the marker must be distinguishable from those particles scattered from silicon and metal atoms; and (v) the technique only gives information about mass movement past the marker: no information is obtained about the mechanism of the diffusion process. Other approaches to identifying the diffusing species during silicide formation have been the deposition of a thin discontinuous inert metal layer on the silicon surface followed by the deposition of the silicide forming metal (5), measurement of the relative movement of the interface between two different silicide phases (6), and the use of a metal marker having similar physical and chemical properties to that of the metal in the metal-silicide to be studied (7, 8).

We have used radioactive ^{31}Si as a marker for studying Ni_2Si , Pd_2Si , and Pt_2Si formation (9, 10). In this approach a few hundred angstrom of radioactive silicon is first deposited onto the silicon substrate, followed immediately by the deposition of a few thousand angstrom of the metal. When the sample is heated a silicide is first formed with the radioactive silicon. Upon further silicide formation (see Fig. 1) this band of radioactive silicide can move to the

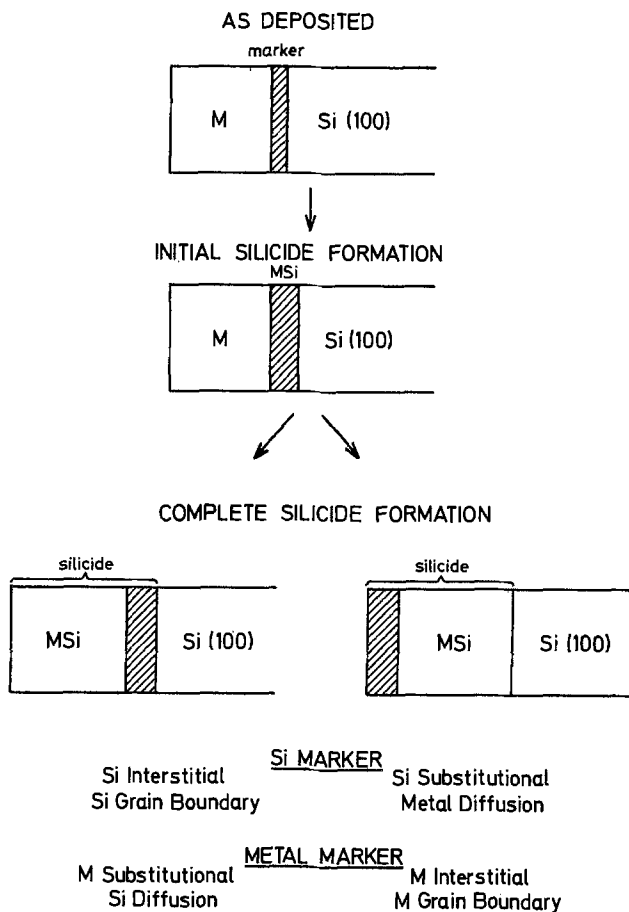


Fig. 1. Schematic diagram showing how radioactive silicon or a radioactive metal marker can be used to determine the diffusing species and mechanism during metal silicide formation.

surface of the sample if silicide formation takes place by diffusion of the metal or by silicon substitutional (vacancy) diffusion. However, if the band of radioactive silicide stays at the silicon substrate interface it can be concluded that silicon diffuses by interstitial and/or grain-boundary diffusion. Apart from these two limiting cases the marker could be located somewhere in the middle of the silicide layer, if silicide formation takes place by interstitial or grain boundary diffusion of both the metal and silicon atoms, the exact position depending on the relative diffusion rates of both species. The information obtained when using a stable or radioactive isotope of the metal as marker is also indicated in Fig. 1. It can be seen that a unique answer regarding the identity of the diffusing species and its mechanism of diffusion is obtained when using both metal and silicon markers, the only exception being the case where the silicon marker is at the surface and the metal marker at the silicon/silicide interface. It should also be pointed out that this approach cannot distinguish between grain boundary and interstitial diffusion.

The ^{31}Si activity profiles for Ni_2Si , Pd_2Si , and PtSi formation are given in Fig. 2. The calculated activity profile at the silicon substrate interface immediately after initial silicide formation is also shown (dashed lines). The movement of the activity to the surface of the Ni_2Si and PtSi samples indicates that the metal is the diffusing species or that Si diffuses substitutionally during Ni_2Si formation and first phase formation of Pd_2Si . For Pd_2Si one can deduce that diffusion of both Pd and Si atoms probably occurred during silicide formation in order to obtain a maximum activity somewhere near the middle of the silicide.

It is interesting to note that the activity profiles for PtSi and Ni_2Si are still in a well-defined band, although Ni_2Si shows some broadening. The sharp-

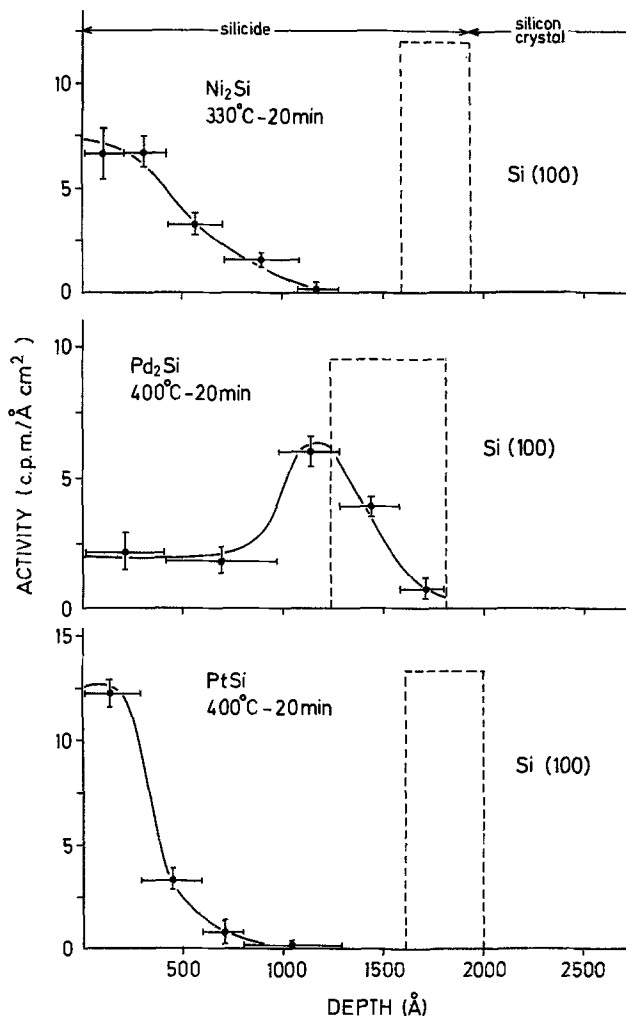


Fig. 2. Silicon-31 activity profiles, measured after complete silicide formation. Calculated activity profile after initial silicide formation is also shown (dashed line). From Ref. (10).

ness of the PtSi and Ni_2Si profiles indicate that the mobility of silicon in these silicides is very low, thereby providing further evidence that the metal is the diffusing element during their formation. It is also interesting to note that the Pd_2Si has an activity tail right to the surface of the sample (Fig. 2). In our discussion of the movement of the initial band of radioactive marker (see Fig. 1) we have only taken into consideration atomic diffusion in solids, by "pure" interstitial or grain boundary diffusion or "pure" substitutional (vacancy) diffusion. There are, however, other diffusion mechanisms, which should also be taken into account (11). We thus believe that not only the general displacement of the initial band of radioactivity is important, but that the whole shape of the activity profile should be considered.

The results we have obtained for Ni_2Si and Pd_2Si formation are consistent with measurements using implanted noble gas markers (1, 2). Our results for Pt_2Si formation do, however, differ from those obtained by other techniques which indicate that both Pt and Si diffuse during silicide formation (6).

If the silicide is heated to still higher temperatures, the mobility of the Si atoms increases and the band of radioactivity (Fig. 3, top) starts to spread out in the silicide due to self-diffusion of the silicon atoms. After heating the sample for 20 min at 570°C the activity for both PtSi and Pd_2Si spreads out completely due to complete mixing of radioactive and nonradioactive silicon atoms (Fig. 3, bottom). By careful measurement of the activity profile as a function of time or temperature, the self-diffusion coefficient and activation coefficients for silicon diffusion in metal-

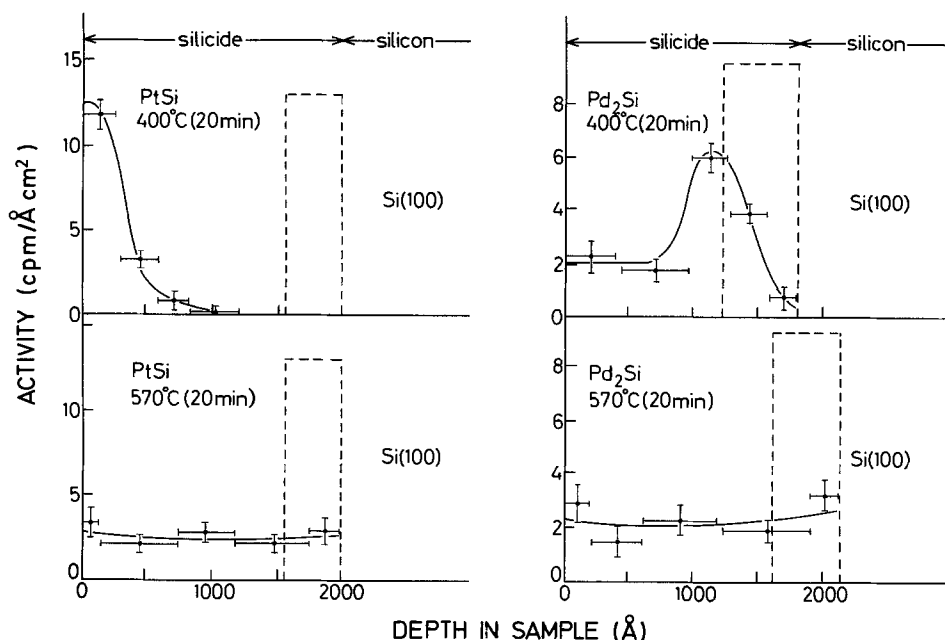


Fig. 3. Activity profiles measured in PtSi and Pd₂Si. Due to the high mobility of silicon in these silicides at 570°C, the radioactive ³¹Si has spread out and complete mixing between radioactive and nonradioactive silicon has taken place.

silicides can be determined. Such measurements are now in progress.

CrSi₂ formation on Pd₂Si.—When CrSi₂ is formed on Pd₂Si it is of interest to know whether silicon is supplied for such growth from the silicide layer or directly from the single crystal silicon substrate. We have investigated this problem by using radioactive silicon-31 to mark the Pd₂Si layer. By determining whether radioactive silicon atoms are incorporated into the CrSi₂ layer during its growth one can obtain information on the mechanism of the CrSi₂ growth.

In Fig. 4, Rutherford backscattering spectra for CrSi₂ formation on Pd₂Si are shown. When the as-deposited virgin sample [Fig. 4(a)] is heated at 400°C for 5 min the Pd reacts with the radioactive amorphous silicon above it and with the Si(100) substrate to form Pd₂Si. It can be seen [Fig. 4(b)] that all the radioactive silicon marker is consumed during Pd₂Si formation and that the Cr signal remains unchanged indicating that no CrSi₂ forms at this temperature. However, upon heating at higher temperatures, CrSi₂ forms on the surface of the sample as can be deduced from the appearance of the silicon signal from CrSi₂ at the surface position [Fig. 4(c)]. After complete CrSi₂ formation, the CrSi₂ surface layer was selectively removed by etching the sample in dilute HF (20%), which attacks CrSi₂ but not Pd₂Si or silicon. Because HF forms gaseous SiF₄ with the silicon in CrSi₂ the activity in the etchant solution could not be measured and the silicon radioactivity left in the Pd₂Si layer was thus determined by measuring the activity in the sample before and after removal of the CrSi₂ layer.

In Fig. 5 the percentage of the activity left in the Pd₂Si layer after CrSi₂ formation is plotted as a function of CrSi₂ (*D*-value) thickness. From the activity profile in Pd₂Si (Fig. 2) the percentage activity left in the Pd₂Si layer during CrSi₂ growth was calculated (see curve A in Fig. 5) for the case in which silicon is supplied by substitutional (vacancy) diffusion through the Pd₂Si layer. During this type of diffusion, the silicon in the Pd₂Si layer is effectively displaced from the bottom upwards by nonradioactive silicon atoms entering from the single crystal silicon substrate, and as would be expected, all the radioactive silicon atoms are displaced from the Pd₂Si layer for *D* = 1. In practice this would happen at a value slightly higher than *D* = 1 owing to the statistical nature of diffusion. Thus silicon atoms supplied from the substrate in effect "push" the radioactive silicon from the Pd₂Si into the growing CrSi₂. This would be similar to the mechanism found for silicon diffusion through Pd₂Si during solid-phase epitaxial growth of

silicon in the Si(100)/Pd₂Si/Si (amorphous) system (12).

At temperatures higher than about 570°C, the self-diffusion rate of silicon in Pd₂Si is so high that complete intermixing of radioactive and nonradioactive silicon atoms in the Pd₂Si layer takes place within 20 min (see Fig. 3). It is clear that, for CrSi₂ formation on Pd₂Si at such temperatures, all the radioactivity in the Pd₂Si layer can never be removed during substitutional diffusion of silicon, regardless of the thickness of the CrSi₂ layer. Curve B in Fig. 5 was calcu-

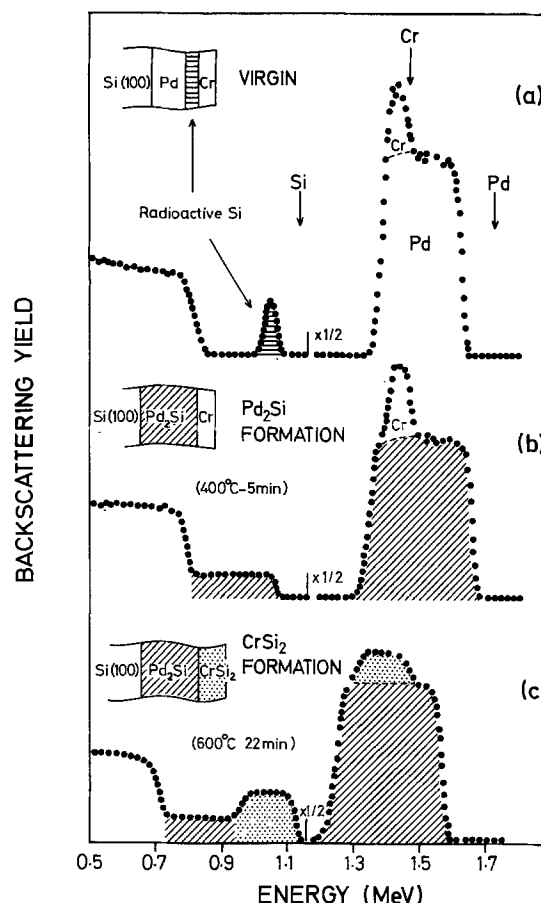


Fig. 4. Rutherford backscattering (2 MeV alpha's) showing CrSi₂ growth on Pd₂Si. Vertical arrows indicate energy of alpha particles scattered from surface.

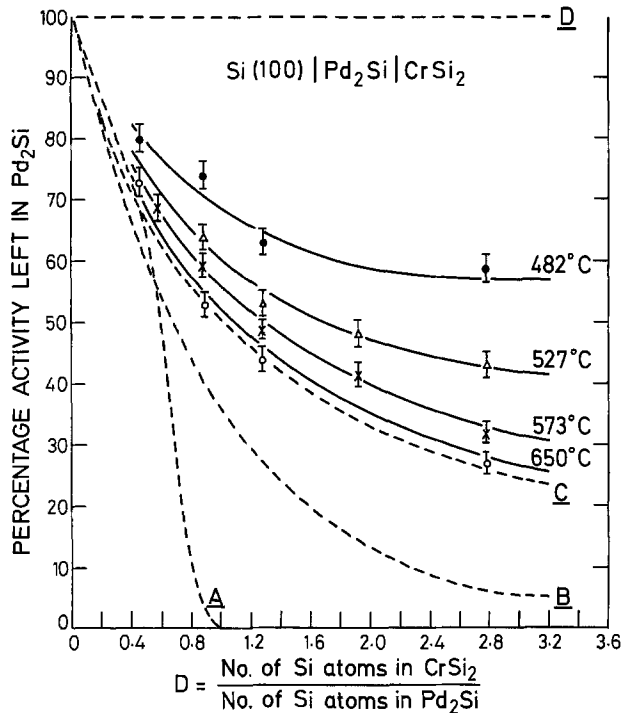


Fig. 5. Percentage ^{31}Si radioactivity left in Pd_2Si layer after CrSi_2 formation, as a function of CrSi_2 thickness (D -value). A, B, C, and D are calculated curves as described in text.

lated for conditions such that complete equilibrium is immediately obtained between radioactive silicon atoms in the Pd_2Si layer and nonradioactive silicon atoms entering from the single crystal substrate. As the CrSi_2 layer grows, the percentage activity in the Pd_2Si layer decreases exponentially with D , and curve B is given by

$$\% \text{ activity} = 100 \exp - D \quad [1]$$

Curve C is calculated for the case in which silicon self-diffusion is very high in both the Pd_2Si and CrSi_2 layers. In this case complete intermixing between radioactive and nonradioactive silicon atoms takes place throughout both silicide layers. The relationship between the percentage activity left in the Pd_2Si layer and D is then given by

$$\% \text{ activity} = 100 / (1 + D) \quad [2]$$

Another possible mechanism of supplying silicon to the growing CrSi_2 layer would be by grain boundary or "pure" interstitial (no interaction with Si atoms in the Pd_2Si lattice) diffusion of nonradioactive Si atoms directly from the single crystal substrate. In this case no radioactive silicon atoms will be incorporated into the CrSi_2 layer (see curve D in Fig. 5). From Fig. 5 it can be seen that our measurements are located between cases C and D, which indicates that the silicon for CrSi_2 growth is being supplied from both the single crystal substrate and the Pd_2Si layer.

The most striking feature of the data is that the supply of silicon for CrSi_2 growth comes in part directly from the silicon substrate without interaction or exchange with the silicon atoms in the Pd_2Si layer. For $D = 1$, about 50-75% of the silicon is supplied directly from the silicon substrate without exchange. We believe that grain boundary and/or interstitial diffusion is the most likely mechanism for this supply.

As the CrSi_2 formation temperature is increased, the amount of radioactive silicon left in the Pd_2Si layer decreases, showing that there is more exchange between the radioactive silicon and the silicon atoms from the substrate during passage through the silicide layers. It is not possible for the silicide to act as a

static lattice; instead the Pd_2Si bonds will be broken and reformed at the temperature of CrSi_2 formation. Curves A, B and C in Fig. 5 apply to such a bond-breaking diffusion mechanism. However, in the case of curves B and C, the self-diffusion rate of silicon is much higher than the growth rate of CrSi_2 .

We conclude, therefore that the silicon is primarily transported directly from the substrate by grain boundary and/or interstitial diffusion. At higher temperatures there is more exchange between this silicon and the radioactive silicon atoms present in the palladium silicide layer, so that in effect, silicon is supplied from both the substrate and the underlying Pd_2Si layer. At still higher temperatures our results begin to indicate a complete intermixing of radioactive and nonradioactive silicon between the CrSi_2 and Pd_2Si layers (see curve C in Fig. 5).

The investigation of CrSi_2 growth on Pd_2Si and PtSi , by using radioactive ^{31}Si as a marker, is described in greater detail elsewhere (13).

Oxidation of CoSi_2 .—There is much interest in the oxidation of silicon and metal silicides as the formed SiO_2 layers can act as electrical insulators in thin film semiconductor devices. We have studied the steam oxidation of CoSi_2 and have used radioactive ^{31}Si to obtain more information about the oxidation mechanism.

Figure 6 shows the Rutherford backscattering spectra of the as-deposited virgin sample, silicide formation at 800°C for 10 min and the spectrum of the sample after oxidation in steam at 1000°C for 30 min. The thickness of the formed SiO_2 layer was determined in three ways: (i) measurement of the width of the oxygen signal; (ii) measurement of the width of the step due to silicon in the SiO_2 ; and (iii) determining the shift

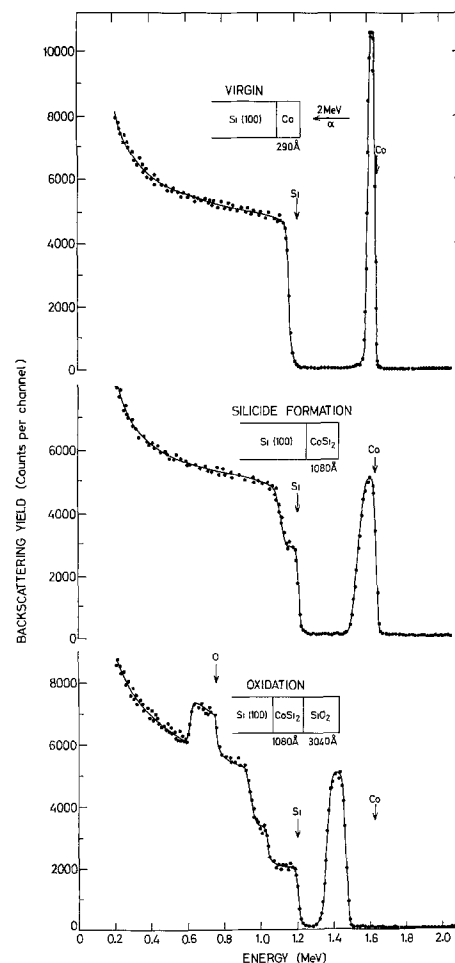


Fig. 6. Backscattering spectra showing CoSi_2 formation (800°C) and atmospheric steam oxidation at 1000°C for 30 min.

of the front edge of the Co signal with respect to its surface position. These measurements show that the thickness of the SiO_2 layer is proportional to the square root of time, thereby indicating that the oxidation process is diffusion limited.

Radioactive tracer experiments were carried out in a similar way as that described for the study of CrSi_2 growth on Pd_2Si . The CoSi_2 was marked with ^{31}Si , by first evaporating a few hundred angstrom of radioactive silicon onto the Si (100) substrate. After silicide formation in a vacuum furnace, oxidation of the CoSi_2 took place at 1000°C in steam at atmospheric pressure. Because both CoSi_2 and SiO_2 are soluble in HF, rf ion-beam sputtering was used to selectively remove the SiO_2 layer. The percentage ^{31}Si activity left in the CoSi_2 layer was determined by measuring the radioactivity in the sample before and after sputtering.

In Fig. 7 the percentage of the activity left in the CoSi_2 layer after SiO_2 formation is plotted as a function of SiO_2 (D -value) thickness, where the D value again refers to the ratio of the number of Si atoms in the SiO_2 layer to that in the CoSi_2 layer. Curves A, B, C, and D have been theoretically calculated for different modes of silicon transport through the CoSi_2 layer, and have the same meaning as previously described, namely: A—substitutional (vacancy) diffusion, B—substitutional (vacancy) diffusion, high self-diffusion of silicon in the CoSi_2 , low self-diffusion of silicon in SiO_2 ; C—substitutional (vacancy) diffusion, high self-diffusion in both CoSi_2 and SiO_2 layers; D—interstitial and/or grain boundary diffusion of Si through the CoSi_2 layer.

It is clear from Fig. 7 that our results at 1000°C approach case B very closely, which is in contrast to the CrSi_2 growth on Pd_2Si where curve C is approached at high temperatures.

Activity profiles were also measured in the SiO_2 layer itself. From these results we can see (Fig. 8) that the highest concentration of radioactive ^{31}Si is at the surface of the sample and that the activity decreases exponentially as one moves towards the

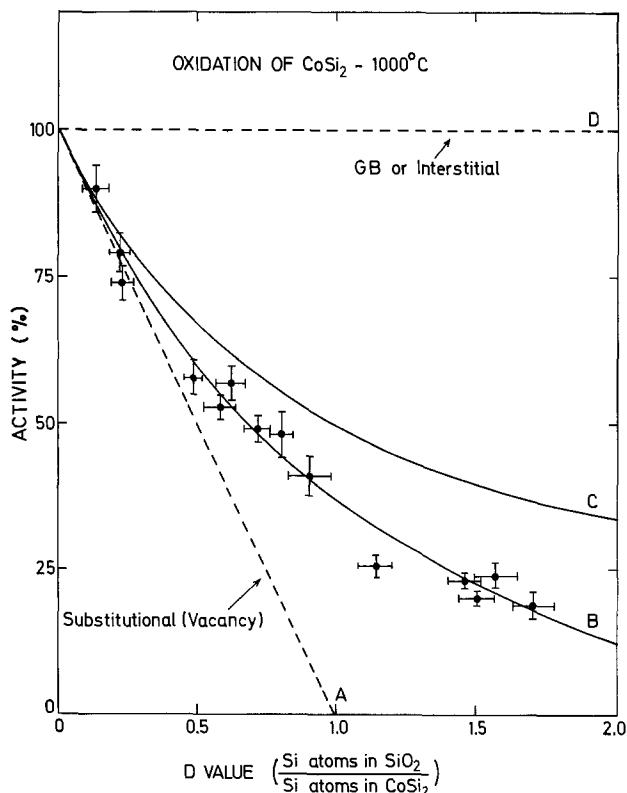


Fig. 7. Percentage ^{31}Si activity left in CoSi_2 layer as a function of SiO_2 thickness (D -value). A, B, C, and D are calculated curves for different diffusion mechanisms.

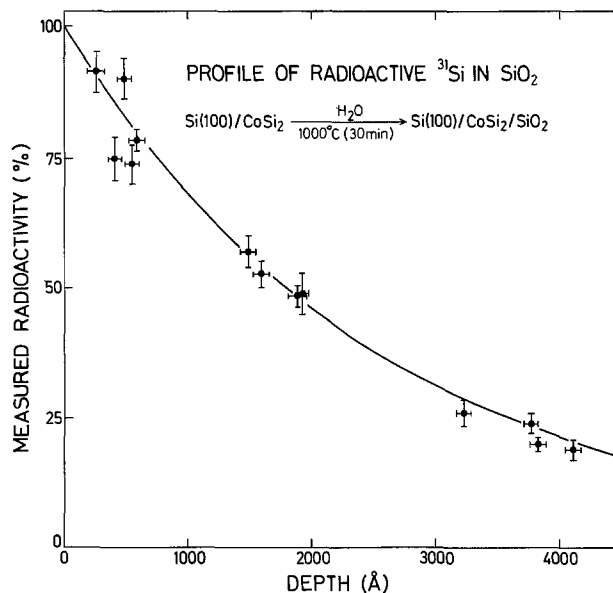


Fig. 8. Radioactivity profile in formed SiO_2 layer on CoSi_2 . Profile was determined by a combination of ion-beam etching, activity measurement, and Rutherford backscattering.

$\text{CoSi}_2/\text{SiO}_2$ interface. Such an activity profile can only be obtained if three conditions are fulfilled: (i) high silicon self-diffusion at 1000°C in the CoSi_2 layer—this has already been proved to be the case (see Fig. 7). (ii) Very low silicon self-diffusion in the SiO_2 layer. Once the radioactive silicon originating from the CoSi_2 layer is bound to form SiO_2 it becomes completely immobile and its activity concentration gives a record of the activity concentration in the CoSi_2 layer at that specific moment. (iii) Oxygen is the diffusing species through the growing SiO_2 layer and growth takes place at the $\text{CoSi}_2/\text{SiO}_2$ interface. If silicon was the diffusing species through the SiO_2 layer, growth would have taken place on the surface of the sample. The highest ^{31}Si concentration would then have been at the $\text{CoSi}_2/\text{SiO}_2$ interface, decreasing exponentially towards the sample surface.

This work is published in greater detail, elsewhere (14).

Summary and Conclusion

Processes such as silicide formation, silicon self-diffusion, and silicide oxidation usually take place at temperatures well below the melting points of the various components in thin layered structures and thus involve atomic motion in the solid state. We have shown that radioactive ^{31}Si can be successfully used as a tracer to study the motion of silicon in such systems.

Radioactive silicon when used as a marker can give information about the moving species and its mechanism of diffusion during metal-silicide formation. The main disadvantage of the technique is that the radioactive Si is not an immobile marker and only gives a unique answer when silicon is the diffusing species. For silicides where the metal is the moving species a radioactive metal marker should be used, or additional information should be obtained from other marker techniques such as implanted noble gas markers. Also, for silicides which form at high temperature the self-diffusion of silicon in the silicide may be so large that the radioactive silicon marker may spread throughout the silicide layer, thereby losing its usefulness as a marker. The radioactive silicon marker technique does however have the advantage that no foreign atoms are introduced into the system, thereby eliminating erroneous results from interface dragging. Furthermore, it can be applied to all metal silicides and is the only marker technique which can give direct information about the diffusion

mechanism. For Ni_2Si and Pt_2Si formation we have found that the metal is the diffusing species, whereas both Pd and Si diffuse during Pd_2Si formation.

The growth of CrSi_2 on Pd_2Si has been studied by marking the silicon atoms in the Pd_2Si layer with radioactive ^{31}Si . At low temperatures (480°C) we find that silicon is primarily transported directly from the Si (100) substrate through the Pd_2Si layer by grain boundary and/or interstitial diffusion. As the temperature at which CrSi_2 is formed increases, more exchange occurs between the radioactive silicon atoms in the Pd_2Si layer and the nonradioactive silicon atoms from the substrate, indicating that a substitutional (vacancy) diffusion mechanism of Si through the Pd_2Si starts to dominate. At 650°C our data suggest that complete intermixing of radioactive and nonradioactive silicon takes place between the Pd_2Si and CrSi_2 layers.

A similar approach was used to study the steam oxidation of CoSi_2 at 1000°C . In this case the silicon atoms in the CoSi_2 layer were marked with radioactive ^{31}Si . By using ion-beam sputtering the radioactivity profile in the formed SiO_2 layer could also be measured. These measurements show that silicon is transported through the CoSi_2 layer mainly by a substitutional (vacancy) mechanism. Growth was found to take place at the $\text{CoSi}_2/\text{SiO}_2$ interface by oxygen diffusion through the growing SiO_2 layer. These results also show that the silicon atoms have a very low self-diffusion coefficient in the SiO_2 layer and a very high self-diffusion coefficient in the CoSi_2 layer, at 1000°C .

One of the biggest advantages of using radioactive ^{31}Si as a marker is the fact that it has a very convenient half-life of 2.62 hr. Enough radioactivity is available for measurement, for up to 15 hr after the activation of silicon in a nuclear reactor. This is usually long enough to complete most of the experiments of the type described. Because of its relatively short half-life, all the ^{31}Si activity decays almost completely after about 2 days, thereby minimizing the radiation hazards usually associated with the use of radioactive tracers. Also, because of the very low penetration of beta-particles it is easy to shield the ^{31}Si radioactivity thereby further reducing radiation hazards due to exposure. Although ^{31}Si also has a gamma-ray of 1.26 MeV, it is very weak, as it is only emitted for 0.07% of the ^{31}Si disintegrations. The beta-particle (max β^- energy = 1.48 MeV) emitted by ^{31}Si can be readily measured with relatively simple and inexpensive beta-counting equipment and because of the very high purity of semiconductor silicon, no interfering activities are found during neutron activation. Interfering activities due to surface contamination do, however, have to be removed after activation.

Radioactive ^{31}Si has nuclear properties which lends itself readily to use as a tracer. When used in conjunction with a depth-sensitive analytical probe such

as Rutherford backscattering, much valuable information can be obtained about thin film systems used in silicon semiconductor technology.

Acknowledgments

A large part of the work reported here was carried out during a one year period as a visiting associate at the California Institute of Technology. Special thanks are thus due to my colleagues at Caltech, in particular to S. S. Lau, Z. L. Liau, J. W. Mayer, M.-A. Nicolet, J. O. Olowolafe, and C. Ramiller, who all contributed substantially to the work discussed here. The contribution and assistance of A. Botha and W. Strydom of the Southern Universities Nuclear Institute and C. Comrie of the University of Cape Town is also gratefully acknowledged. The financial assistance obtained from the South African Council for Scientific and Industrial Research and the South African Atomic Energy Board is gratefully acknowledged.

Manuscript submitted April 3, 1980; revised manuscript received July 29, 1980. This was Paper 389 presented at the Los Angeles, California, Meeting of the Society, Oct. 14-19, 1979.

Any discussion of this paper will appear in a Discussion Section to be published in the December 1981 JOURNAL. All discussions for the December 1981 Discussion Section should be submitted by Aug. 1, 1981.

REFERENCES

1. W. K. Chu, H. Kraütle, J. W. Mayer, H. Müller, M.-A. Nicolet, and K. N. Tu, *Appl. Phys. Lett.*, **25**, 454 (1974).
2. K. N. Tu, W. K. Chu, and J. W. Mayer, *Thin Solid Films*, **25**, 403 (1975).
3. S. S. Lau, J. S. Feng, J. O. Olowolafe, and M.-A. Nicolet, *ibid.*, **25**, 415 (1975).
4. W. K. Chu, S. S. Lau, J. W. Mayer, H. Müller, and K. N. Tu, *ibid.*, **25**, 393 (1975).
5. G. J. van Gurp, D. Sigurd, and W. F. van der Weg, *Appl. Phys. Lett.*, **29**, 159 (1976).
6. J. M. Poate and T. C. Tisone, *ibid.*, **24**, 391 (1974).
7. J. Baglin, F. d'Heurle, and S. Petersson, *ibid.*, **33**, 289 (1978).
8. S. Petersson, J. Baglin, W. Hammer, F. d'Heurle, J. de Sousa Pires, I. Ohdomari, P. Tove, and K. N. Tu, *J. Appl. Phys.* Submitted for publication.
9. R. Pretorius, C. L. Ramiller, S. S. Lau, and M.-A. Nicolet, *Appl. Phys. Lett.*, **30**, 501 (1977).
10. R. Pretorius, C. L. Ramiller, and M.-A. Nicolet, *Nucl. Inst. Meth.*, **149**, 629 (1978).
11. P. G. Shewmon, "Diffusion in Solids," p. 43, McGraw-Hill, New York (1963).
12. R. Pretorius, Z. L. Liau, S. S. Lau, and M.-A. Nicolet, *Appl. Phys. Lett.*, **29**, 598 (1976).
13. R. Pretorius, J. O. Olowolafe, and J. W. Mayer, *Philos. Mag.*, **37**, 327 (1978).
14. R. Pretorius, W. Strydom, C. Comrie, and J. W. Mayer, *Phys. Rev.*, **22**, 1885 (1980).

The Detection of Structural Defects in Indium Phosphide by Electrochemical Etching

C. R. Elliott and J. C. Regnault

Post Office Research Centre, Martlesham Heath, Ipswich IP5 7RE, England

ABSTRACT

Two new etching procedures for InP are described; one for damage removal with retention of surface flatness, and the other for high resolution defect delineation. A comparison of the defect etching with transmission x-ray topography is given. Studies of wafers from Sn, S, and Fe-doped InP ingots are reported. The new procedures have revealed a variety of defects.

This paper describes electrochemical replication and defect etching techniques for single crystal n-type and semi-insulating indium phosphide and some results of their application to ingot material. Indium phosphide is assuming increasing importance both as an electronic device material and as a substrate for lattice matched GaInAs and GaInAsP epitaxial layers for optoelectronic devices. In the first case defects in InP will directly affect device performance and in the second case they may also affect the epitaxial growth. A comparison of electrochemical etching with chemical etching and other defect revealing techniques has been given recently (1). Chemical defect etching of InP has been reported in a number of recent publications (2-5). Here we consider the application of an electrochemical etching procedure similar to that of Faktor and Stevenson for GaAs (6); the advantages of which include high resolution, sensitivity to optoelectrically active defects and minimal material removal, the latter making it applicable to submicron layers. The electrolytes used for GaAs are not suitable for InP and for this material new specific procedures had to be developed. The successful outcome of this work is illustrated by the results obtained with ingot material.

Experimental

Single crystal (100) cut slices of InP were obtained from a number of sources and were conventionally polished using solutions of bromine in methanol (7). Residual damage left by the polishing process was removed, prior to defect revealing. This was achieved by continuous electrochemical etching, in the presence of a thick anodic oxide, at constant voltage. The technique is similar to that developed for GaAs by Faktor and Stevenson (6) and extended by the present authors (8). (It was shown that such a process can remove material smoothly, while retaining the initial surface topography).

Removal of about 5 μm of InP left a smooth, damage-free surface. Establishment of a suitable oxide film, about 100 nm thick, is critically dependent upon electrolyte composition. We empirically investigated a number of electrolytes for best results. Dilute phosphoric acid, sodium phosphate solutions from pH 4 to pH 12, 2M potassium hydroxide, ammonium hydroxide pH 11, 1M acetic acid and 1M citric acid were found unsatisfactory. 14M orthophosphoric acid (analytical reagent grade) was found acceptable. Figure 1 is a schematic diagram of the anodization cell. With a constant 40V applied across the cell and rotation of the sample anode at 100 rpm, the steady-state dissolution rate was controlled by varying the bath temperature between 4° and 30°C. When a predetermined amount of material had been removed, the oxide film was dissolved by a short immersion in either 2N hydrochloric or 2N nitric acid.

Key words: anodization, etching, defects, indium phosphide.

The electrochemical defect etching was carried out in similar apparatus, using 0.5N hydrochloric acid. (This medium chemically attacks InP at room temperature, but the rate of attack is 10^{-2} $\mu\text{m/hr}$, which is insignificant in relation to the duration of the experiment.) The potential of the strongly illuminated anode relative to a saturated calomel electrode was monitored during etching, after initial adjustment to yield a current density of 400 $\mu\text{A/cm}^2$. In most cases an average of 0.3 μm of material was removed. The etched specimens were then examined microscopically using Nomarski interference contrast.

Results and Discussion

The variation of current density with electrolyte temperature for etching in the presence of an anodic oxide is shown in Fig. 2. Corresponding material removal rates, determined from weight loss experiments, ranged from 0.5 to 5 $\mu\text{m/hr}$. Measured faradaic yields averaged nine electrons per unit of formula weight, but were not precisely reproducible. Clearly this yield is not accounted for by simple conversion of InP to oxides, since the highest yield to be expected would be eight, corresponding with the overall reaction $2\text{InP} + 16e^+ \rightarrow \text{In}_2\text{O}_3 + \text{P}_2\text{O}_5$. Furthermore, the anodic oxide appears to contain lower oxides of phosphorus (it evolves a volatile product with phosphine-like odor on standing at room temperature). The discrepancy is probably due to parasitic electrochemical reactions at the oxide-electrolyte interface, in view of the well-established electronic conductivity of In_2O_3 based

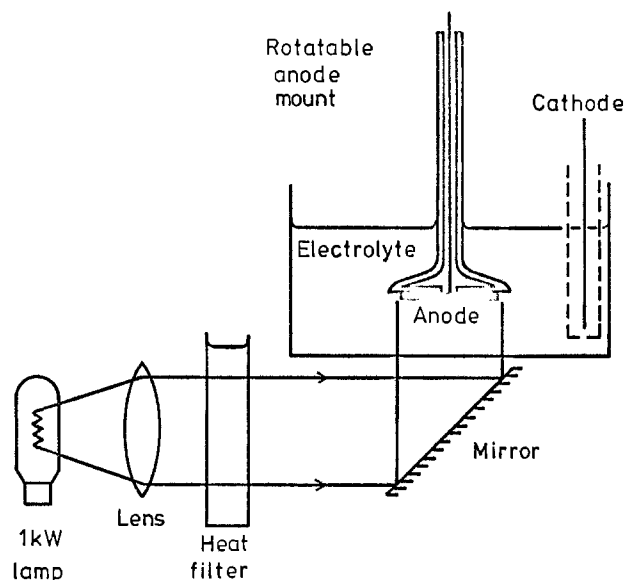


Fig. 1. Anodization cell for n-type semiconductors. The cooling coil for temperature control has been omitted for clarity.

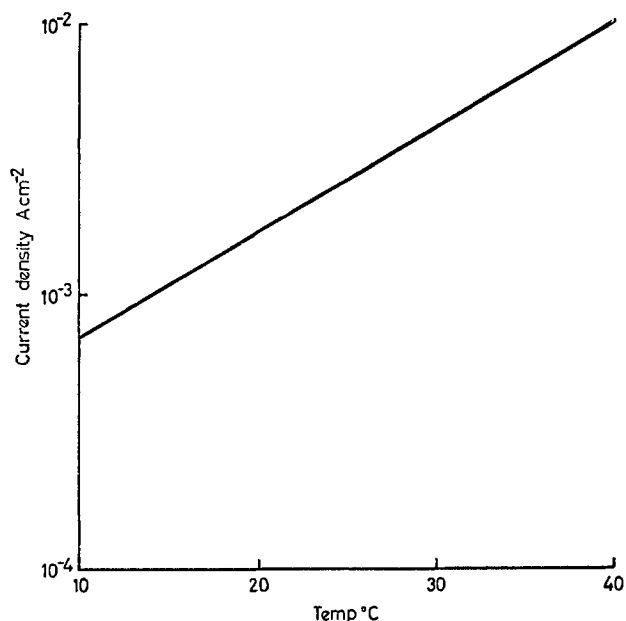


Fig. 2. The variation of the steady-state anodic current with temperature of concentrated phosphoric acid electrolyte.

systems (9, 10). No attempts to eliminate or minimize this problem were made in this work, although the accuracy of control of material removal is dependent upon the reproducibility of the faradaic yield.

Interference contrast micrographs of a typical bromine-methanol polished surface before and after anodic removal of 20 μm of material are shown in Fig. 3. Only a small decrease in surface smoothness is apparent after the anodization.

In order to determine the optimum anodic conditions for revealing defects the anodic polarization characteristics of damage-free n-type InP were investigated. Figure 4 shows the variation of anodic (reverse biased) overpotential with current density for two n-type samples in 0.5M hydrochloric acid, under conditions of strong, 0.4 Wcm^{-2} , broadband (tungsten halogen) illumination. Photopotentials of -370 mV were observed with this level of illumination. The conditions chosen for defect-sensitive etching ($400 \mu\text{A cm}^{-2}$) are two orders of magnitude below the photosaturation current. The corresponding overpotential is close to the range chosen by Faktor and Stevenson (6) for GaAs (250-300 mV anodic). In the latter case the illumination level was lower, so that the photosaturation current was not much greater than the minimum required to give a useful etch rate. Since their photosaturation currents were somewhat dependent upon majority carrier concentration, it was necessary for them to define an anodic overpotential rather than a current density in order to avoid operating in the photosaturation region (where the sensitivity to defects is low).

Figure 5 is a typical interference contrast micrograph taken after anodic removal of approximately $\frac{1}{4} \mu\text{m}$ of

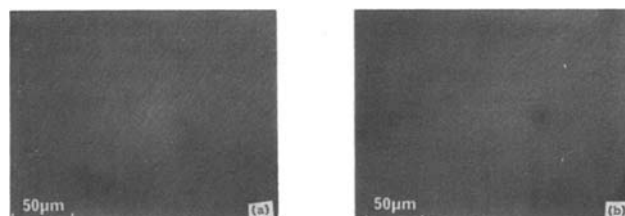


Fig. 3. Nomarski interference contrast micrographs of (a) a typical chemo-mechanically polished InP (100) surface, and (b) the same after removing 20 μm by anodization in H_3PO_4 .

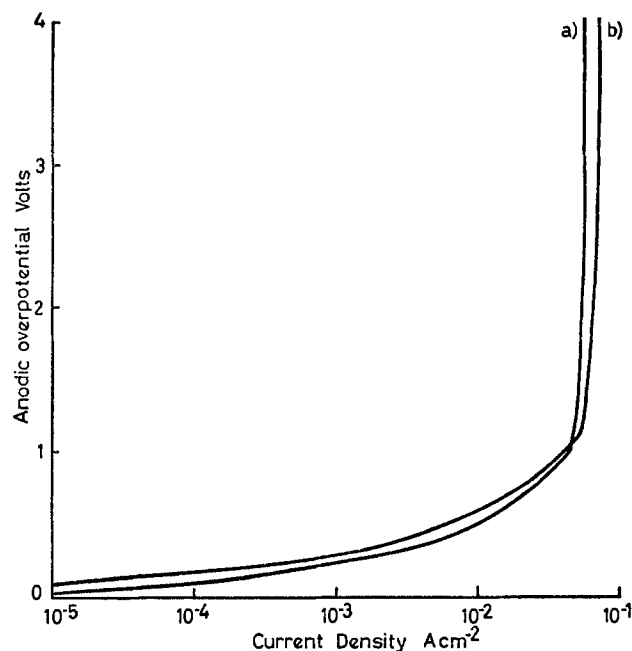


Fig. 4. The anodic, reverse bias, characteristics of two n-type InP wafers in 0.5M HCl. (a) $N_D - N_A = 1.5 \cdot 10^{16} \text{ cm}^{-3}$; (b) $N_D - N_A = 2.0 \cdot 10^{18} \text{ cm}^{-3}$.

material under defect-sensitive conditions. The material was Czochralski grown, nominally undoped InP and (100) cut. The sharply-defined etch features are raised above the general level of the surface.

Defects delineated show no crystal orientated effects normally associated with the production of etch pits at defects. The very high resolution of the technique can be seen clearly from the series of micrographs in Fig. 6, where the sample was again Czochralski grown and (100) cut, but Sn-doped with a carrier concentration of $3.3 \times 10^{18} \text{ cm}^{-3}$. The density of defect clusters is $2 \times 10^4 \text{ cm}^{-2}$, the majority of these being of the type shown in Fig. 6(c). Further investigation of Sn-doped InP from two sources showed similar defects in most ingots. Figure 7(a) is a 220 transmission x-ray topograph of similar material, taken with copper radiation. This same area was then electrochemically etched to remove approximately 0.3 μm of material from the surface. Figure 7(b) is an optical micrograph of the etched area. Each of the defect clusters, which appear as white spots in the micrograph, corresponds with a feature (black spot) in the x-ray topograph. This can be confirmed with an overlay prepared from

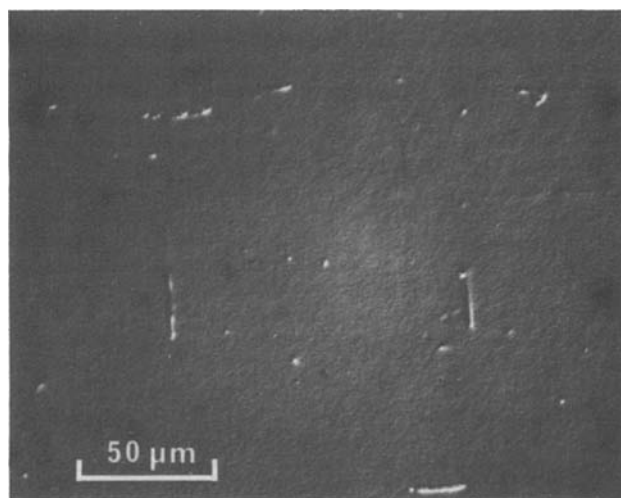


Fig. 5. Nomarski interference contrast micrograph of an InP (100) surface after etching off 0.25 μm of material under defect-sensitive conditions.

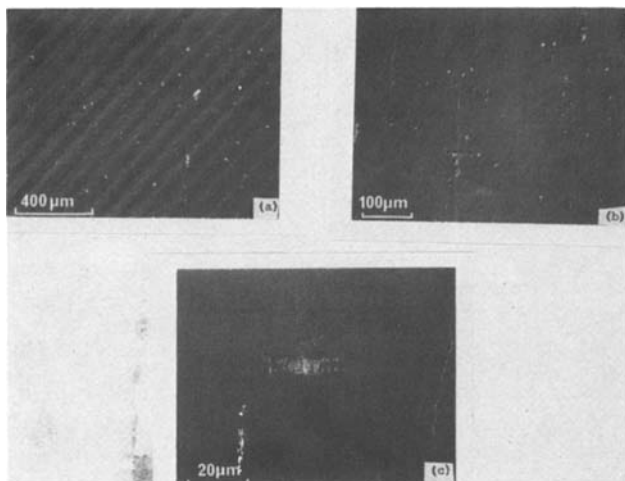


Fig. 6. Nomarski interference contrast micrographs, at increasing magnifications, of an InP (100) surface after defect etching. InP doped with Sn to $3.3 \cdot 10^{18} \text{ cm}^{-3}$.

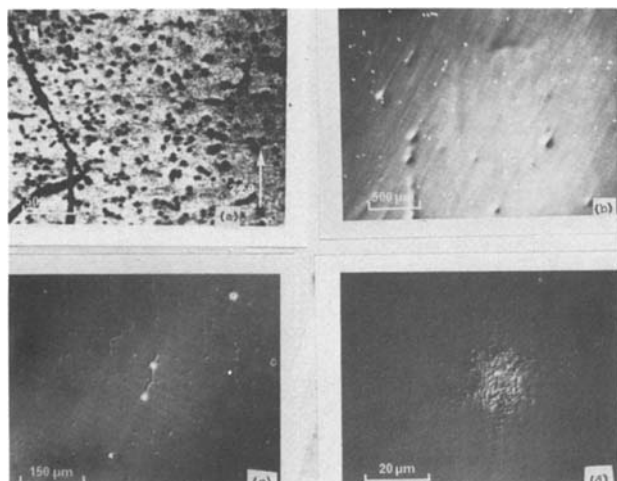


Fig. 7. (a) Transmission x-ray topograph of InP:Sn; (b) surface area of (a) after defect etching; (c) selected area from (b), showing dislocations and defect clusters; (d) single defect cluster.

Fig. 7(b), if allowance is made for the small geometrical distortion of the topograph, due to the Bragg angle used. However, there are six times as many features visible in the topograph as there are on the etched surface. The defect clusters average $20 \mu\text{m}$ in diameter [Fig. 7(d)] and are approximately spherically symmetrical. This was confirmed by etching a (110) cleavage face perpendicular to (100). Therefore, although the etching only images defects within the $0.3 \mu\text{m}$ layer removed, it effectively samples a volume of material approaching $40 \mu\text{m}$ in thickness. As the transmission topograph images defects in the full $200 \mu\text{m}$ thickness of the sample, a ratio of six to one in the number of defects seen is to be expected. Figures 7(c) and (d) are higher magnification micrographs of a selected area of the same sample. Figure 7(c) shows many defects, the total density being $4 \times 10^4 \text{ cm}^{-2}$. The highest magnification Fig. 7(d) shows that the defect clusters extend over an area of $400 \mu\text{m}^2$ in the $0.3 \mu\text{m}$ section taken. Because the very fine detail within the defect cluster is not resolved by optical microscopy a carbon replica of the etched surface was taken. Examination of the replica in a transmission electron microscope showed the cluster to be made up of many small dislocations as can be seen in Fig. 8. Because of the very high x-ray contrast obtained at these defects they are assumed to be associated with precipitates or inclusions. A similar x-ray topograph has been reported recently (11).

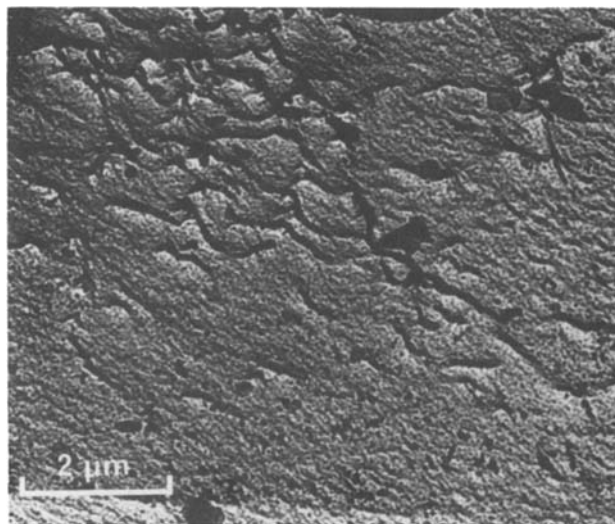


Fig. 8. Transmission electron micrograph of Pt/C shadowed replica taken from the area of Fig. 7(d). Shadowing angle $\tan^{-1} 1/2$.

Some defect etching has been performed on highly sulfur-doped (typically $8 \times 10^{18} \text{ cm}^{-3}$) InP. Whereas GaAs of similarly high doping level has been found to contain microdefects (12), the defect etching of complete InP wafers has revealed only growth striations, Fig. 9. The absence of dislocations in this material was confirmed by x-ray transmission topography. We would, however, caution that electrochemical defect etching of such highly doped n-InP has not been attempted previously and that assessment of this material is still incomplete.

Turning to Fe-doped semi-insulating InP, Fig. 10 shows a typical (100) surface after removal of $0.5 \mu\text{m}$ of material under defect-sensitive conditions. Good defect delineation with high resolution was obtained, as with n-type samples, despite the dark bulk resistivity of the material being $10^9 \Omega \text{ cm}$. Detailed studies of semi-insulating semiconductor materials will be reported on in a further paper (13).

Conclusion

Electrochemical etching has been shown to produce sharp delineation of defects in InP, with a large useful range of magnifications spanning the gap between those of x-ray topography and transmission electron microscopy. Good correlation between transmission

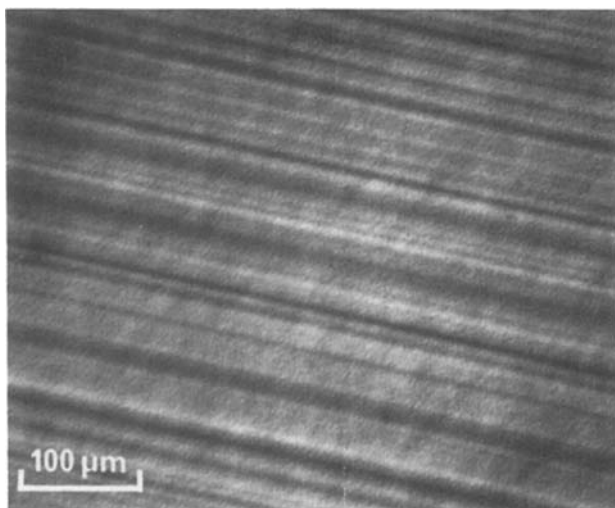


Fig. 9. Nomarski interference contrast micrograph of (100) surface of n^+ InP:S, after defect etching, showing only growth striae.

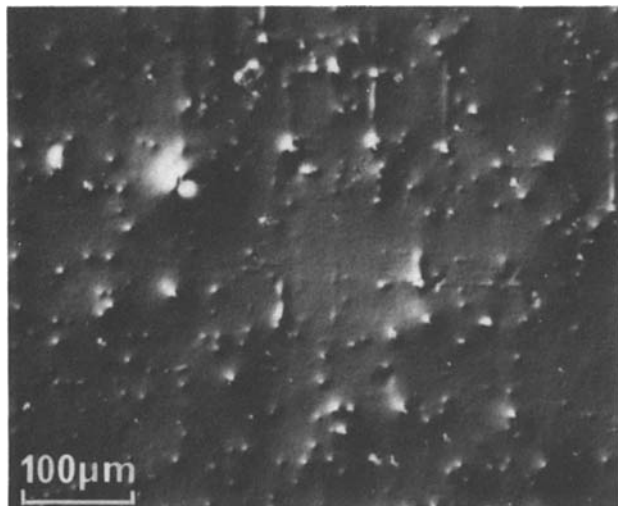


Fig. 10. Nomarski interference contrast micrograph of (100) surface of InP:Fe, after defect etching.

x-ray topography and electrochemical etching was obtained and defect clusters have been shown in great detail. The high sensitivity of the electrochemical etching technique, which only requires a very small amount of material removal, makes the technique ideally suitable for the investigation of defects in thin epitaxial InP layers. As the technique is not restricted to small areas, whole boat-grown or Czochralski-pulled slices may be investigated to carry out defect studies in conjunction with crystal growth.

Anodic thinning, in the presence of an oxide film, may have other applications where damage-free smooth surfaces are required. However, unlike the case of GaAs and GaSb (8) electronic conductivity in the oxide layer gives rise to irrational faradaic yields and precludes the method being used for very precise thinning.

This work is now being extended to cover $\text{Ga}_x\text{In}_{1-x}\text{As}$ and $\text{Ga}_x\text{In}_{1-x}\text{As}_y\text{P}_{1-y}$ ternary and quaternary alloys.

Acknowledgments

We are grateful to M. M. Faktor for much advice and encouragement, to Mrs. M. A. G. Halliwell for the x-ray topograph, to G. A. Antypass for providing some of the material studied, and for the cooperation of colleagues at the Post Office Research Centre. Acknowledgment is made to the Director of Research of the British Post Office for permission to publish this paper.

Manuscript submitted April 24, 1980; revised manuscript received July 23, 1980.

Any discussion of this paper will appear in a Discussion Section to be published in the December 1981 JOURNAL. All discussions for the December 1981 Discussion Section should be submitted by Aug. 1, 1981.

Publication costs of this article were assisted by the Post Office Research Centre.

REFERENCES

1. M. M. Faktor, T. Ambridge, C. R. Elliott, and J. C. Regnault, in "Current Topics in Materials Science," Vol. 6, p. 1, North Holland (1980).
2. R. C. Clarke, D. S. Robertson, and A. W. Vere, *J. Mater. Sci.*, **8**, 1349 (1973).
3. A. Huber and N. T. Linh, *J. Cryst. Growth*, **29**, 80 (1975).
4. K. Arita, T. Kusonski, S. Komiya, and T. Kotani, *J. Cryst. Growth*, **46**, 783 (1979).
5. E. A. Thiel and R. L. Barnes, *This Journal*, **126**, 1272 (1979).
6. M. M. Faktor and J. L. Stevenson, *ibid.*, **125**, 621 (1978).
7. C. S. Fuller and H. W. Allison, *ibid.*, **109**, 880 (1962).
8. C. R. Elliott and J. C. Regnault, *ibid.*, **127**, 1557 (1980).
9. S. Kulaszewicz, I. Lasocka, and C. Z. Michalski, *Thin Solid Films*, **55**, 283 (1978).
10. C. Wagner, *J. Phys. Chem. Solids*, **33**, 1051 (1972).
11. G. H. Olsen and H. Kressel, *Electron Lett.*, **15**, 141 (1979).
12. R. M. Redstall, J. C. Regnault, and J. L. Stevenson, in "Semiconductor Characterization Techniques," P. A. Barnes and G. A. Rozgonyi, Editors, p. 296, The Electrochemical Society Softbound Proceedings Series, Princeton, N.J. (1978).
13. C. R. Elliott and J. C. Regnault, To be published (1980).

A Model for Electrochromic Tungstic Oxide Microstructure and Degradation

Thomas C. Arnoldussen*¹

General Motors Research Laboratories, Electronics Department, Warren, Michigan 48090

ABSTRACT

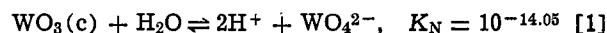
Despite much investigation of the electrochromic (EC) coloration process in WO₃ films, such displays have not yet become commercially viable because of limited useful device life. Device degradation occurs by WO₃ film dissolution on the shelf and erosion during cycling. Water plays a crucial role in both efficient coloring/bleaching and in film degradation. To better understand the degradation process and the role of water, dissolution of EC WO₃ films in aqueous media was studied. The results strongly suggest that EC films formed by evaporation are amorphous molecular solids consisting of trimeric W₃O₉ molecules bound weakly to each other through water-bridge, hydrogen, and van der Waal's bonding. The nature of this microstructure is responsible for the high solubility. Films subjected to ion bombardment show decreased dissolution rates as well as decreased electrochromism and, while amorphous, are believed to have a random network rather than molecular microstructure.

The chief problem to be overcome before electrochromic displays can be commercially viable is the short device life. Degradation of WO₃-acid electrolyte ECD's is associated with film dissolution on the shelf and erosion during cycling. Aqueous acid cells show superior performance from the standpoint of response speed, however, water is a primary culprit in shortening lifetimes through WO₃ dissolution. Nevertheless, Knowles and Hersh have shown (1) that some water must be incorporated in the WO₃ film, even in so-called "aprotic" devices to obtain any electrochromic coloration. Others have studied WO₃ in aprotic solvents but have not systematically analyzed their films for water content as have Knowles and Hersh. The need to better understand the role of water in electrochromism, the interaction of H₂O and WO₃, and the mechanism of ECD degradation have motivated the work presented here. Study of WO₃ dissolution is a proper starting point and provides several key insights into the nature of electrochromic films and the electrochromic process. Others (2, 3) have reported data on dissolution rates of EC WO₃ films in various solvents, but have not related the high observed rates to a detailed physical mechanism or to the nature of the film itself.

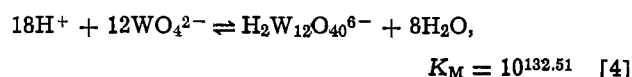
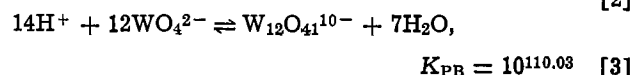
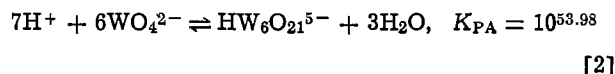
Amorphous WO₃ Film Dissolution (Aqueous)

Theoretical.—The thermodynamic equilibrium between crystalline WO₃ and water predicts that WO₃ dissolves by hydrolysis to form normal tungstate ions, WO₄²⁻, plus 2H⁺. The solubility at 25°C is 1.3 × 10⁻⁵ moles/liter in a neutral starting solution and decreases exponentially with decreasing pH. The presence of other species of tungstate ions is negligible. According to this result, a crystalline film 1 cm² in area exposed to 1 cm³ water should saturate the solution after only 4.0 nm of film has dissolved. In an acid environment of pH ~1-2 such as used in EC devices, much less than one molecule-layer would dissolve. By comparison, an EC film which is amorphous and usually deposited by evaporation (0.5-1.0 μm thick) dissolves comparatively fast and completely, even in the small volumes of low pH solutions used in EC devices. We expect the somewhat higher free energy of an amorphous film to drive dissolution more strongly, but unless WO₄²⁻ ions precipitate from solution elsewhere as WO₃ · nH₂O or are converted to metastable polytungstate ions, saturation should ensue and dissolution cease.

Experimental observation during film dissolution indicates no evidence of reprecipitation as WO₃ particles for amorphous films dissolving completely in small volumes of DI water or acid solutions. This strongly suggests that amorphous WO₃ forms polytungstate anions (such as the metatungstate ion which is very stable even in strong acids) (3) upon dissolution. Dissolved WO₃ concentration can reach values far above that expected to produce precipitation. Only many days after a film has been dissolved, or upon extreme concentration of the solution by solvent evaporation, are precipitate particles observed. Crystalline WO₃ dissolves as normal tungstate (WO₄²⁻) ions according to the hydrolysis reaction



Tungstate ions are also known to agglomerate in acid solution to form polymeric anions (4) according to



where the polyanions formed in Eq. [2]-[4] are called paratungstate A, paratungstate B, and metatungstate, and the various *K*'s are molar equilibrium constants at 25°C. Pseudo-metatungstate (HW₆O₂₀³⁻) may also be formed. When crystalline WO₃ is allowed to dissolve in an aqueous medium, each of these species can form. The H⁺ concentration (C_H) is given by the charge balance

$$\begin{aligned} (C_H - C_{\text{H}^+}) - (C_{\text{OH}^-} - C_{\text{OH}^0}) \\ = 2C_N + 5C_{PA} + 10C_{PB} + 6C_M \quad [5] \end{aligned}$$

where the *C*'s denote molar concentrations of the ions noted in Eq. [1]-[4].

C_{OH} is the hydroxyl ion concentration and C_H⁰ and C_{OH}⁰ refer to the H⁺ and OH⁻ concentrations of the initial solvent before WO₃ dissolution has occurred. For dissolution in DI water, which is neutral-to-weakly acid, the C_{OH} and C_{OH}⁰ terms may be ignored. The total molar concentration of dissolved WO₃, C_w, is given by the mass balance

$$C_w = C_N + 6C_{PA} + 12C_{PB} + 12C_M \quad [6]$$

* Electrochemical Society Active Member.

¹ Present address: IBM, San Jose, California 95193.

Key words: electrochromic tungstic oxide, dissolution.

Equations [5] and [6] apply regardless of whether the solubility limit has been reached. Equation [5] applies only for dissolution of an oxide, not a tungstate salt, while Eq. [6] pertains to dissolved oxides or salts. The solubility of crystalline WO_3 may be determined using Eq. [5] and [6] in conjunction with the equilibrium mass action relations derived from Eq. [1]-[4]. Doing this, one finds that the solubility of crystalline WO_3 in water is 1.30×10^{-5} moles/liter and the pH attained at saturation is 4.58, corresponding to essentially all the dissolved WO_3 in the form of normal WO_4^{2-} ions. The author verified this pH and solubility experimentally.

A similar quasi-equilibrium analysis for dissolving amorphous WO_3 is unsuitable. This would require (i) that the kinetics of reprecipitation elsewhere as crystalline WO_3 be so slow as to be ignored for the time periods of interest, (ii) that the detailed mechanism of dissolution be the same as for crystalline WO_3 shown in Eq. [1], and (iii) that a dynamic microscopic quasi-equilibrium between the amorphous WO_3 surface and the solution tungstates exists. Experimental observation suggests that condition (i) may be met, but there is no evidence to justify assuming that conditions (ii) and (iii) hold.

Therefore we cannot predict the solubility of an amorphous WO_3 film. In fact, we cannot even say whether quasi-equilibrium solubility is a tenable concept for amorphous WO_3 . However, we would expect the solution equilibria expressed by Eq. [2]-[4] to be obeyed regardless of the particular dissolution kinetics and thermodynamics. This permits us to use an indirect approach to investigate amorphous WO_3 dissolution, yet draw some important conclusions.

If we assume various values of dissolved WO_3 concentrations, C_w , then by means of Eq. [2]-[6] we can calculate the pH achieved as a result of dissolution and the distribution of tungsten among the various tungstate and polytungstate species when solution quasi-equilibrium is reached. The result of such a calculation is shown in Fig. 1, showing the quasi-equilibrium curves for pH and tungsten: (free) proton ratio as a function of C_w for dissolution in neutral water. The

tungsten:proton ratio is a convenient representation of the distribution of tungsten among the various polytungstate species since this ratio is uniquely determined by the equilibrium distribution. For example, if all the tungsten were in the form of WO_4^{2-} ions, this ratio would be 1:2; if all were in the form of $\text{H}_2\text{W}_{12}\text{O}_{40}^{2-}$, this ratio would be 2:1.

Chemical processes generally do not proceed immediately to equilibrium (particularly true for the reactions considered here). If amorphous WO_3 dissolution proceeds as crystalline WO_3 , one WO_3 unit at a time hydrolyzing to form one WO_4^{2-} ion plus two free H^+ , we would expect that during and for sometime after dissolution, the pH and $C_w:(C_H - C_{OH})$ ratio would be lower than the values given by the quasi-equilibrium curves of Fig. 1. There would be an excess of lower order species (monomeric ions) and free protons. During equilibration, the excess acidity would induce polymerization of the normal tungstate ions, thereby consuming protons and raising the pH and the $C_w:(C_H - C_{OH})$ ratio. On the other hand, if after dissolving an amorphous film in water we found the measured pH and $C_w:(C_H - C_{OH})$ ratio to fall on the high side of the quasi-equilibrium curves, we would be forced to conclude that the amorphous WO_3 entered solution directly in a polymerized form with equilibration proceeding in the direction of depolymerization.

Experimental

With these theoretical considerations in mind, the following experiment was performed. A $0.70 \mu\text{m}$ thick WO_3 film was evaporated onto an unheated glass substrate from a Ta boat. The film area was 2.5 cm^2 . This film was placed in 40 ml DI water (pH = 6.15, slight acidity due to dissolved CO_2 presumably) and allowed to dissolve. When dissolution was complete, the pH was measured to be 4.35. This was lower than the 4.58 value predicted and measured for crystalline WO_3 . This solution was then titrated back to neutrality while monitoring the pH. A pH = 11.65 NaOH titrant was used. The solution was constantly stirred and 5 min elapsed between each addition of NaOH and the pH measurement. The titration curve is shown in Fig. 2.

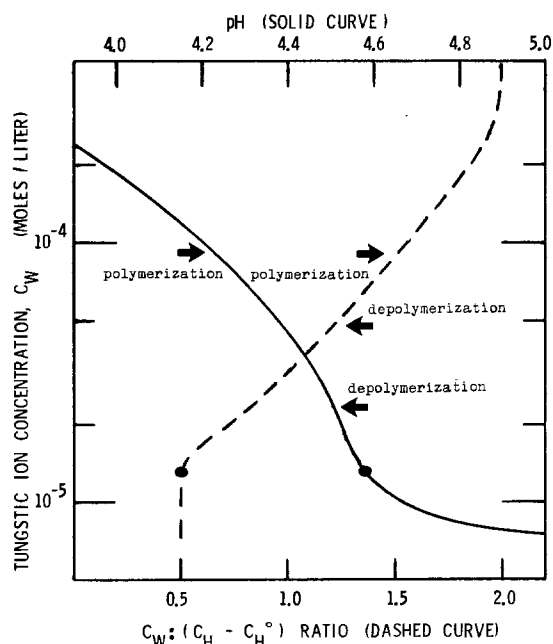


Fig. 1. Calculated quasi-equilibrium curves for pH and tungsten: free proton ratio, assuming various amounts of WO_3 to be dissolved by neutral H_2O . Measured values falling to the left or right of these curves imply equilibration occurs by polymerization or depolymerization, respectively. Dots on lower portions of curves correspond to crystalline WO_3 .

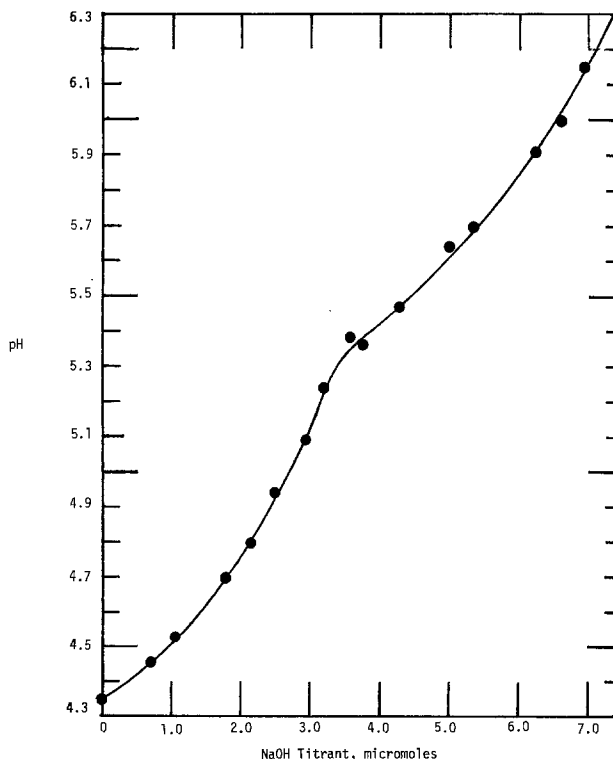


Fig. 2. Titration curve for amorphous WO_3 film dissolved in 40 ml DI water. Film was 2.5 cm^2 and $0.70 \mu\text{m}$ thick.

The features of interest here are the initial pH of the dissolved film solution, the quantity of NaOH added to return the pH to that of the DI water (pH = 6.15), and the appearance of a cusp at about 3.4×10^{-8} moles NaOH. From the initial pH = 4.35 of the dissolved film solution and the pH of the starting DI water, we calculate the H^+ concentration due to WO_3 film dissolution is $C_H - C^0_H = 4.40 \times 10^{-5}$ moles/liter. The cusp is characteristic of a depolymerization process induced by raising the pH.

At the point where the pH has been restored to that of the DI water used to dissolve the film, virtually all the WO_3 in solution may be assumed to be in the form of WO_4^{2-} ions and we have essentially a Na_2WO_4 salt solution. The quantity of NaOH needed to reach this point, $C_{Na} = 1.74 \times 10^{-4}$ moles/liter, gives the total concentration of tungsten ions in solution: $C_W = C_{Na}/2 = 8.71 \times 10^{-5}$ moles/liter. The ratio $C_W:(C_H - C^0_H)$ is 1.98:1. This is essentially the ratio (2:1) expected if WO_3 goes into solution from the amorphous film as metatungstate ions, $6H^+ + H_2W_{12}O_{40}^{6-}$. Pseudo-metatungstate, $3H^+ + HW_6O_{20}^{3-}$, could also be the species formed since the tungsten/proton ratio is likewise 2:1.

The important result here is that both the pH and the tungsten:free proton ratio resulting from the dissolution of this amorphous evaporated WO_3 film fall significantly to the high side of the quasi-equilibrium curves shown in Fig. 1. The amount of normal tungstate (WO_4^{2-}) present is less than 3% of that needed to maintain equilibrium with the metatungstate. Clearly, we must infer that the film dissolves not as WO_4^{2-} which subsequently polymerizes, but as 6- or 12-mer ions or as unstable 3-mer ions which quickly form metatungstate or pseudo-metatungstate. Any reactions going on in solution must be in the direction of depolymerization.

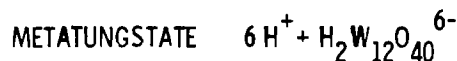
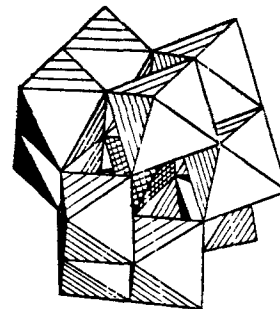
The titration results also allow us to calculate the film density from the measured C_W and film thickness and area. We obtain 1.20×10^{22} tungsten ions/cm³ or 4.62 g/cm³ assuming stoichiometric WO_3 free of water. Evaporated WO_3 has been reported (5) to contain as much as 0.5 H_2O per WO_3 which would increase the mass density to 4.80 g/cm³. These values compare with densities ~ 5 g/cm³ reported by Randin (2) using another technique.

Proposed Structural Model

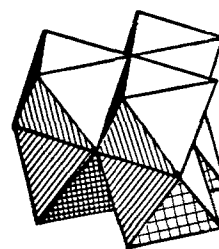
One clue to understanding the high solubility of evaporated amorphous WO_3 and the peculiar way in which it dissolves directly as polytungstate ions is seen by examining the proposed structures of metatungstate and pseudo-metatungstate ions, shown in Fig. 3. The basic building block of polytungstate ions is a trigonal unit consisting of three edge-sharing WO_3 octahedra. The metatungstate ion (Fig. 3a) is formed by four such trigonal units tetrahedrally coordinated, sharing corners, about a central tetrahedral void containing two trapped protons (3). Similarly, a pseudo-metatungstate ion (Fig. 3b) may be formed by two such trigonal units sharing faces with one proton trapped in the central bi-pyramidal void.

This tendency to form trigonal or trimeric units reappears in numerous WO_3 related substances. Various forms of crystalline tungsten bronzes and solid tungstate salts also contain trigonally oriented octahedra forming low symmetry structures with 3, 5, and 6 member rings. Hashimoto *et al.* have shown that near sublimation temperature WO_3 forms a hexagonal phase (6). And the vapor generated by subliming WO_3 has been shown (7) to consist chiefly of trimeric W_3O_9 molecules as schematically shown in Fig. 4a. Such trigonal clustering may be attributed to formation of delocalized molecular orbitals within the three member ring stabilizing the structure.

The demise of an evaporated amorphous WO_3 film by dissolution as clusters of trigonal units provides



(a)



(b)

Fig. 3. (a). Metatungstate ion composed of four tetrahedrally oriented trigonal units sharing corners with two protons in the center cage. Each trigonal unit consists of three edge-sharing WO_3 octahedra (4). (b). Pseudo-metatungstate ion is composed of two trigonal units sharing faces with one proton in the center bi-pyramidal void.

one clue to understanding the degradation process. The second important clue is obtained by examining the manner in which such a film is formed during vapor condensation.

As mentioned, the vapor generated by subliming WO_3 consists chiefly of trimeric W_3O_9 molecules illustrated in Fig. 4a. There is also a strong tendency for WO_3 to carry water of hydration, two possible forms of hydrated trimers being shown in Fig. 4b and 4c. When trimeric molecules are deposited at a high rate on low temperature substrates, such as in EC film deposition, it is probable that they remain more or less intact, bonding together weakly through van der Waal's forces or through water-bridge hydrogen bonding. Such phenomena have been observed in evaporation of elemental species such as sulfur and selenium and compounds such as As_2O_3 . Evaporating As_2O_3 generates As_4O_6 vapor molecules which upon condensation form the metastable As_4O_6 molecular solid arsenolite (8, 9). Due to the relative stability of molecules exhibiting such associative tendencies, some activation energy is needed to dissociate them into the simplest molecular units before the lower energy network structure can form.

We expect the situation to be similar in EC film deposition, where insufficient thermal activation energy is available to dissociate trimers into monomers

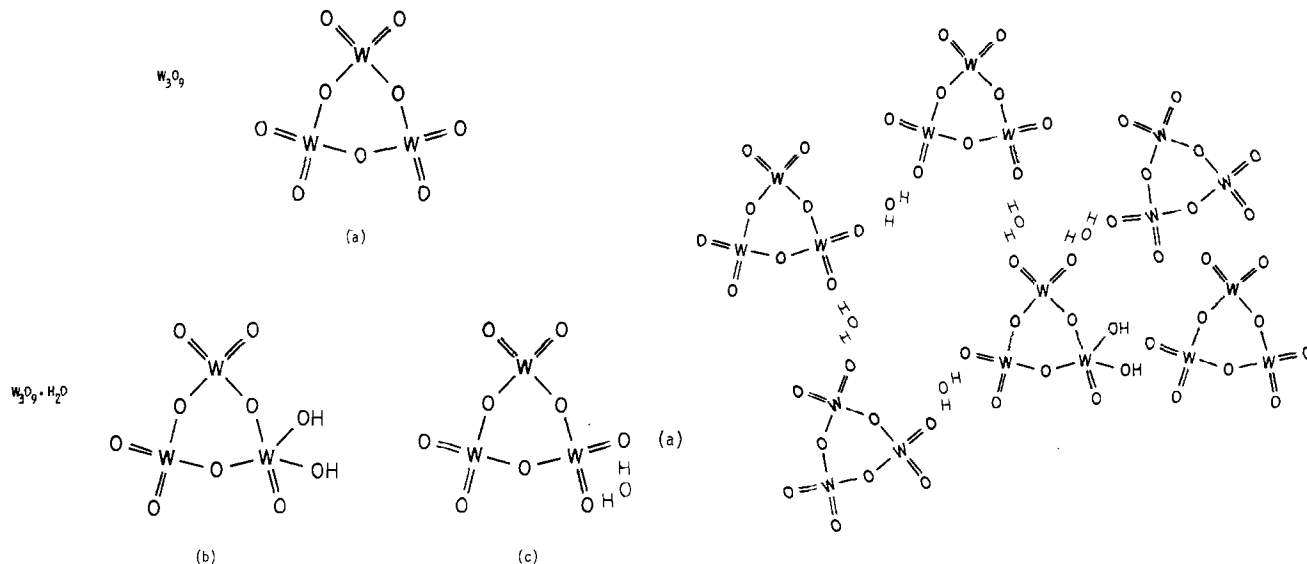


Fig. 4. (a). Schematic representation of W_3O_9 trimeric vapor molecule. (b) and (c). Two possible forms of monohydrated W_3O_9 molecule.

or to break the outer oxygen double bonds which is a precondition to network formation. Moreover, water of hydration, located at outer oxygens of the trimer, will further inhibit W-O-W cross bonding and network formation. Any inter-trimer bonding which does occur is likely to be weakened by lattice distortions inherent in an amorphous structure, while intratrimer bonding should remain strong and largely unaffected by the disordered arrangement of trimeric units.

The picture that evolves is that an evaporated amorphous WO_3 film, as-deposited, resembles an amorphous molecular solid, rather than an amorphous random network structure, comprised of trimeric units bound weakly to one another such as depicted in Fig. 5. It is easy to imagine that when such a film is placed in an aqueous solution such trimers hydrolyze directly to the trigonal building blocks of polytungstate ions, without forming monomeric WO_4^{2-} ions as an intermediate step. This would account not only for the high solubility of such films, but also for the observation that they dissolve directly as polymeric ions. Trigonal ions carrying high coulombic charge can lower their free energy by agglomerating to form larger clusters of lower charge such as the metatungstate ion. This may occur on the dissolving surface or immediately after entering solution.

Film Restructuring

If evaporated amorphous WO_3 films are molecular solids as proposed then, if by some means one could break double bonds, perhaps even dissociate trimers, rebonding with neighboring molecules could occur to form a lower free energy network structure. Such a film should exhibit a decreased solubility compared to the as-deposited film. Raising the average lattice temperature (energy) by heating, as in recrystallization, is one way of dissociating the trimers. In this case, all the molecules are raised to an activated state simultaneously and can, therefore, undergo a cooperative rearrangement to form a crystalline network with considerable long range order. This would provide no further insight, since we already know that crystalline WO_3 has low solubility.

One can also induce lattice restructuring without crystallization by bombarding the sample with particles of sufficient energy. The activation energy thus provided is absorbed discontinuously in space and time without raising the average lattice temperature significantly. Crystallization would be inhibited because, at any given time, only individual molecules or very

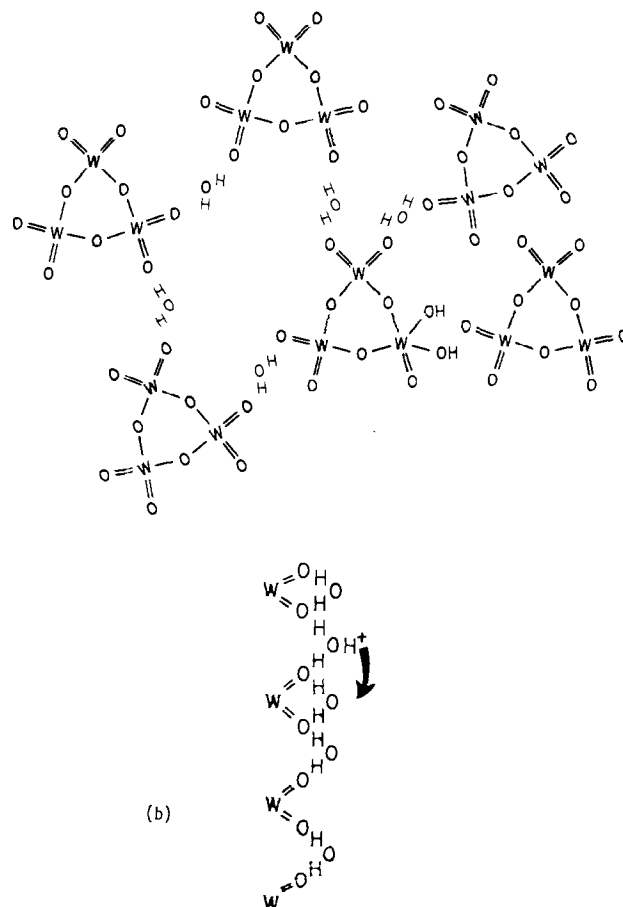


Fig. 5. (a). Representation of EC film as an amorphous molecular solid composed of W_3O_9 trimers banded together by water-bridge, hydrogen, and van der Waal's bonding. (b). Example of water molecule chain which can form giving rise to high proton mobility by H_3O^+ rotation and proton transfer to adjacent H_2O .

localized regions are in an activated state. Only short range restructuring or relaxation is expected. Amorphous WO_3 films were bombarded by implanting $10^{15}/cm^2$, 70 keV oxygen ions into the film. Primary energy transfer is by ion collisions with the lattice to a depth of 100-150 nm and secondary transfer is by high energy phonon or photon excitation ("thermal spikes") generated by collisions. The incident ion power was ~ 4 mW/cm² and the temperature rise was small, well below the recrystallization temperature of $\sim 345^\circ C$ (5).

Figure 6 shows an x-ray diffraction pattern obtained by using a rotating nanogram diffraction camera and particles of the bombarded film scraped from the substrate. Only amorphous-like halos are seen. One extends from about 0.24-0.48 nm and another faint halo is centered near 0.18 nm. These correspond to nearest W-W and W-O distances, respectively.

Such bombarded films, despite the implantation of oxygen, were slightly reduced as evidenced by a very slight bluish cast. A several hour postbake in air at $130^\circ C$ (well below crystallization temperature) was sufficient to reoxidize the films to a transparent yellow. Virgin films used as control samples were given this same baking procedure to guarantee that any differences in film properties were due to the ion bombardment rather than thermal treatment.

As hypothesized, the bombarded films showed over an order of magnitude decrease in dissolution rate in neutral water compared to unbombarded films. They remained more soluble than crystalline WO_3 , as might be expected for an amorphous structure. In aqueous acid solutions, bombarded films showed no evidence of significant dissolution even after many weeks in the

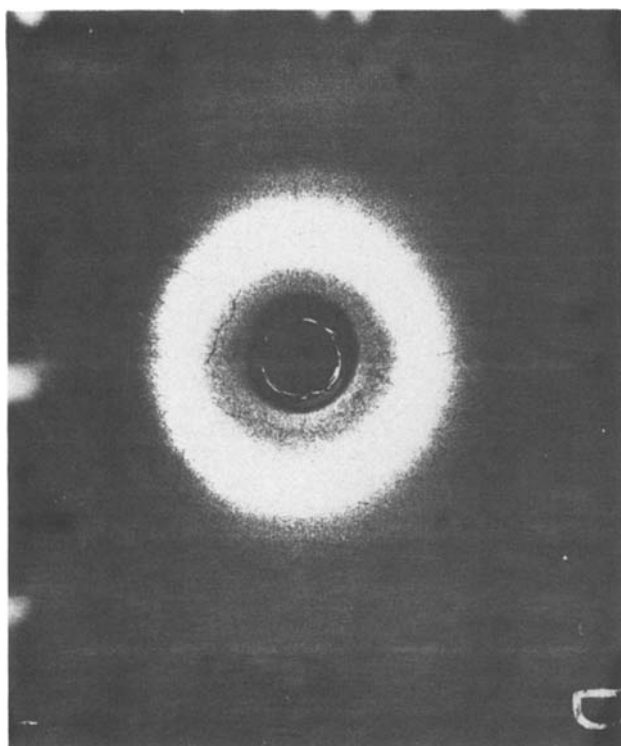


Fig. 6. Nanogram powder diffraction pattern for $10^{15}/\text{cm}^2$ 70 keV oxygen ion implanted WO_3 film. Pattern appears amorphous.

solvent, whereas virgin films dissolve within one to several days. This dramatic change in solubility is strong evidence of a change in local bonding and microstructure, and it suggests that WO_3 may indeed exist in two distinct amorphous forms: an amorphous molecular solid and an amorphous random network. In addition to the solubility change, ion bombardment produces the additional effect of destroying (or greatly decreasing) the electrochromism.

Electrochromic WO_3 films were also subjected to low energy ion/electron bombardment in an rf glow discharge chamber used for photoresist ashing (~ 13 Pa O_2 , 13.56 MHz, 75W rf power capacitively coupled into a cylindrical chamber 7.6 cm in diameter and 15 cm deep with 50Ω impedance). Again, little heating occurred. Unlike the ion implantation bombardment, the electron/ion energies were only of order 10 eV. Similar decrease in solubility was observed for such low energy bombardment. While it has not been ruled out, chemical oxidation effects are not believed to be responsible for the solubility change. The low energy bombarded films showed no signs of reduction, as did the high energy implanted films (bluish cast), and may in fact have undergone some additional oxidation. Yet both types of bombardment produced the same solubility and colorability change.

Colorability of these bombarded films was checked by the indium wire/ H_2SO_4 technique (10). This involves placing an acid droplet on the film and touching an In wire to the surface through the droplet. In dissolves as In^{3+} and the excess electrons on the wire are injected into the film. 3H^+ are displaced from solution by the In^{3+} , entering the film to neutralize the injected electrons. The coloration spreads from the In contact radially (see Fig. 7a).

In the case of low energy bombardment, the colorability through the surface decreases rapidly during the first 5-10 min of bombardment, but lateral "color bleeding" from an adjacent unbombarded region remains possible until 20-30 min of bombardment have elapsed. This suggests a restructuring process which begins at the upper surface and migrates to the sub-

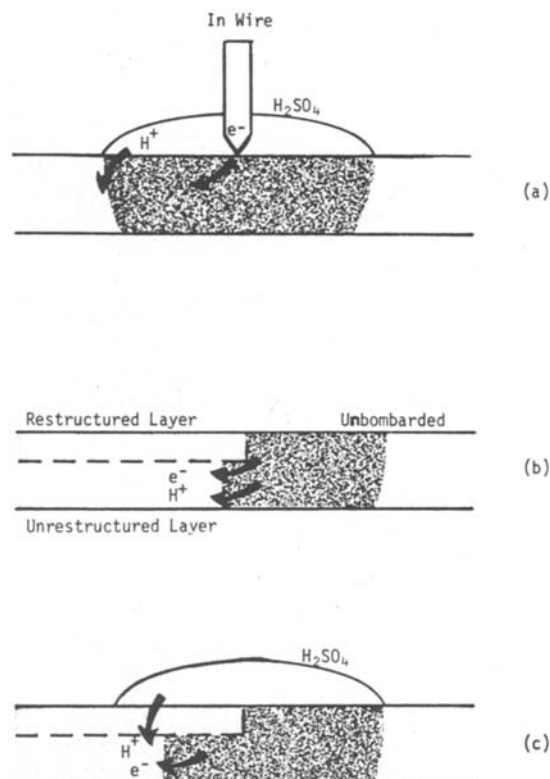


Fig. 7. (a). In wire/ H_2SO_4 film coloration technique (10). In dissolves as In^{3+} causing $3e^- + 3\text{H}^+$ to be injected into the film. (b). Left portion of film partially restructured (upper layer) by ion bombardment. Right side colored by In/ H_2SO_4 , rinsed, and dried. Color bleeds slowly into region beneath restructured layer by lateral proton controlled $e^- + \text{H}^+$ diffusion. (c). Same as (b) but acid overlaps two regions. Color bleeds rapidly into region beneath restructured layer by lateral electron diffusion plus proton flow through restructured layer.

strate with continued bombardment. (X-ray diffraction was done on 30 min bombarded films.)

In the coloration tests on samples bombarded for 5-10 min, if an unbombarded region is colored up to the boundary with a bombarded region and the sample is rinsed and dried, diffusion of color into the bombarded region is slow (~ 0.1 mm in $\frac{1}{2}$ hr). If the acid droplet is not removed and overlaps the two regions, color diffusion is rapid (~ 0.5 mm/sec). These observations are essentially the same as for an unbombarded film, slow color diffusion in the absence and fast diffusion in the presence of an electrolyte. The difference is that an unbombarded film colors by direct contact of the In wire (through an acid) to the film surface, while the bombarded film does not. Moreover, an unbombarded film, so colored, can be bleached thoroughly by heating in air at 135°C for 15-30 min. A bombarded film, colored by bleeding from an unbombarded region, does not bleach even after days of heating in air.

These results may be interpreted as follows. Low energy bombardment restructures the upper portion of the film, leaving the lower portion unchanged (for bombarding times $\lesssim 10$ min). Color bleeds from an unbombarded region into the deeper layer of the bombarded region. In the absence of an electrolyte on the surface, this proceeds by lateral diffusion of electrons and protons from the unbombarded region and is proton diffusion controlled. See Fig. 7b. In the presence of the acid on the surface, the fast color diffusion must be interpreted as lateral diffusion of electrons from the unbombarded region coupled with proton diffusion through the bombarded surface to neutralize the electrons (10). See Fig. 7c. The high speed of color diffusion cannot be explained by lateral proton diffusion.

The inability to color the bombarded region directly by in wire contact, the fast lateral bleeding, and the inability to bleach such a region, once colored by lateral bleeding, implies that the bombarded, restructured layer is still proton permeable, but is blocking to electron transport. The restructuring strengthens the overall bonding (evidenced by decreased solubility) without significantly diminishing the fast proton transport. But it apparently does inhibit electron injection or transport, or induces noncoloring trapping states.

These bombardment studies suggest two important concepts which are worth further investigation: (i) It may be proper to speak of not one amorphous state for WO_3 , but two: one being closer to a molecular solid, the other a random network. Only the former is electrochromic. (ii) Lattice porosity and incorporated H_2O giving high proton mobility may be necessary but insufficient to produce rapid electrochromic response. The electronic states produced by a particular structure are of critical importance to electrochromic response.

Nonaqueous Solvents

It is apparent that EC device shelf degradation in aqueous electrolytes is caused by polytungstate formation. The much lower solubility of EC films in organic solvents may be understood in terms of solvent ionizability, solvent molecule size, and the nature of the solute ion formed. Dissolution is favorable when W-O-W bonds are broken in such a way that the bonds remain saturated. Water is a particularly good solvent because its small size permits it to attack a W-O-W bond and form two saturated W-OH HO-W bonds with a small local distortion of the lattice. Upon going into solution, $(\text{WO}_3)_n$ combines with water to form the compact tungstate and polytungstate ion structures. On the other hand, solvents which are not ionizable show little if any action on WO_3 films. Alcohols and glycols with one or more OH radical may ionize to form $\text{R}^+ + \text{OH}^-$ or $\text{RO}^- + \text{H}^+$ but are poor solvents for WO_3 films because (i) they do not ionize as readily as water, (ii) their molecular size is too bulky to penetrate the lattice without severe lattice distortion, and (iii) the R^+ and RO^- radicals are too bulky to form compact or complex polytungstate ions in solution. Dissolution in these solvents is likely to be limited to molecular species or simple monomeric ions. Solubility should be low in either case. When an electrolyte, such as H_2SO_4 , is added to a nonaqueous solvent, an additional dissolution mechanism may be operative, namely, formation of electrolyte anion- WO_3 complexes. This is further discussed in the next section.

Cycling Degradation

EC device cycling degradation in aqueous and nonaqueous acid electrolytes occurs by an erosion process, probably similar to dissolution, but enhanced by the voltage drive. Film thinning during cycling has been measured by optical interference techniques (2). In aqueous electrolytes, the quiescent dissolution process occurs by polytungstate ion formation and diffusion into the electrolyte. Intuitively, one might expect that it is the nonequilibrium nature of the color/bleach process which leads to cycling degradation. However, nonequilibrium by itself does not imply degradation. A more detailed model is needed. In the literature it has frequently been suggested that cycling degradation may be due to such things as impurities or "irreversible side reactions." Having delineated the nature of quiescent dissolution of electrochromic WO_3 films in the present work, we propose the following intrinsic mechanism of cycling degradation.

In the bleached or moderately colored quiescent state, the electrode potentials are such that the Helmholtz double layer probably has the following struc-

ture. The inner layer consists of (i) a monolayer of chemisorbed H_2O forming a surface layer of tungstic-oxide-hydroxide which is anionic in nature; (ii) just beyond the surface is a layer of predominantly electrolyte anions plus polytungstate anions. The outer layer is chiefly $\text{H}_2\text{O} + \text{H}_3\text{O}^+ +$ protons with hydration shells of six or more water molecules. During the coloration cycle, electrolyte and polytungstate anions are driven away from the surface by the applied voltage, while hydrated protons are driven toward it. During this disturbance of the Helmholtz double layer, the depletion of polytungstate anions leads to the removal of tungstic oxide-hydroxide surface molecules to replenish polytungstate anions in the double layer. At the same time, the hydrated protons shed much, if not all, of their water of hydration upon entering the WO_3 surface, leaving an abundance of bond-breaking water molecules in the surface region and inner Helmholtz layer, further promoting dissolution.

While the current carried by the negative tungstate ions leaving the surface may be a small fraction of the proton current, over thousands of cycles it is sufficient to completely erode the film. This voltage-enhanced dissolution would account for the device cycle life decreasing with increased switching speed (higher voltage drive, greater anion depletion, and greater disturbance of the double layer structure) and with increased final point coloration (increased total charge driven per cycle). We expect and, in fact, observe that fast switching to a low contrast state produces more degradation per cycle than slow switching to a high contrast state.

Voltage-enhanced dissolution in nonaqueous electrolytes may occur by one of the following mechanisms. Dissolution by tungstate ion formation requires an oxygen donor species such as H_2O . If there were no dissolved oxygen or trace water in the electrolyte/solvent, and if neither the electrolyte nor solvent dissociate or electrolyze to donate oxygen, tungstate ions cannot form by interaction with the electrolyte. H_2O incorporated in the WO_3 during deposition could, however, contribute to tungstate formation. The $\text{H}_2\text{O}:\text{WO}_3$ ratio can be as high as 1:2 in evaporated films (5) while to form metatungstic acid only 1:3 is needed. Thus, the water incorporated in the film, apparently necessary to achieve high cation mobility (1), may be a self-contained cause of cycling degradation. In addition to this, WO_3 could enter solution by forming a complex with electrolyte anions. Phosphoric acid is known to form complexes with WO_3 . To a lesser extent, sulfuric acid may do likewise.

Electrolyte anions are attracted to the surface in the bleached state, and during dynamic bleaching this anion activity is further enhanced. Anions such as SO_4^{2-} may bond to surface molecules forming negative complexes which are swept into solution during coloration. Simple complexes like $[(\text{WO}_3)(\text{SO}_4^{2-})]^{2-}$ or polymeric complexes like $[(\text{SO}_4^{2-}) \cdot (\text{WO}_3)_9 \cdot \text{H}^+ \cdot (\text{W}_3\text{O}_9) \cdot (\text{SO}_4^{2-})]^{3-}$ could form. Another possibility is a metatungstate isomorph in which SO_6 octahedra are incorporated in place of some WO_3 , such as $[\text{H}_2^+(\text{WO}_3)_8 \cdot (\text{SO}_4^{2-})_4]^{6-}$.

Conclusion

Aqueous dissolution and titration results indicate that amorphous WO_3 films (as-deposited) dissolve to form metatungstate or pseudo-metatungstate ions. Moreover, evidence indicates that complex 3-, 6-, or 12-mer ions enter solution directly from the dissolving surface. These results, together with the fact that associative vapor molecules tend to form molecular or semimolecular solids upon condensation, strongly suggest that as-deposited WO_3 films are composed chiefly of trimeric clusters weakly bound to one another. The very open microstructure that would result, along with water-bridge bonds between mole-

cules, can account for the high proton mobilities observed in EC films, but also for the unfortunate rapid dissolution and cycling erosion.

Analysis of evaporated films subjected to oxygen ion bombardment suggests two concepts which may be important to electrochromic development. (i) There may exist two distinct amorphous structures, one closer to a molecular solid, the other closer to a random network structure. (ii) The restructured (network) film shows decreased colorability, not because it is less permeable to proton flow but because electron injection or transport is inhibited, or noncoloring trapping states are introduced. Further study of bombardment restructuring may provide key information about the effect of microstructure on EC performance.

Cycling erosion can be understood as a natural extension of the dissolution process—voltage enhanced dissolution. Neither impurity side reactions nor any fundamental irreversibility in the proton injection/extraction process need be postulated. In nonaqueous systems, both quiescent dissolution and cycling erosion are slowed because of (i) low ionizability and large size of organic molecules such as glycerine and (ii) inhibited tungstate ion formation. In these systems, degradation may result from formation of negative complexes with electrolyte anions or from tungstate formation due to H₂O incorporated in the film.

The molecular solid model presented here for electrochromic films may prove to be a fruitful avenue for understanding the nature of coloration in these films. The intervalence transfer model proposed by Crandall and Faughnan (11) may be given physical interpretation by relating phenomenological configuration coordinates to, say, instantaneous configuration of water-bridged W₃O₉ molecules. This would be similar to coloration in charge transfer complexes in solution. Bridging water bonds may be important not only for proton transfer but for electron transfer as well.

Acknowledgments

I wish to thank B. MacIver for performing the ion implants and F. A. Forster, J. Johnson, and D. Eddy for their assistance in the x-ray diffraction studies.

Manuscript submitted Jan. 21, 1980; revised manuscript received July 23, 1980.

Any discussion of this paper will appear in a Discussion Section to be published in the December 1981 JOURNAL. All discussions for the December 1981 Discussion Section should be submitted by Aug. 1, 1981.

Publication costs of this article were assisted by General Motors Research Laboratories.

REFERENCES

1. T. J. Knowles, H. N. Hersh, and W. Kramer, in 19th Electronic Materials Conference of AIME, Cornell, N.Y. (1977).
2. J. P. Randin, in *Ibid.*
3. T. B. Reddy and E. A. Battistelli, in *Ibid.*
4. "Comprehensive Inorganic Chemistry," Vol. 4, A. F. Trotman-Dickenson, Executive Editor, chap. 51, Pergamon Press, England, (1973).
5. H. R. Zeller and H. U. Beyeler, *Appl. Phys.*, **13**, 231 (1977).
6. H. Hashimoto, T. Naiki, M. Mannami, and K. Fujita, in "Structure and Properties of Thin Films," C. A. Neugebauer, Editor, p. 71, John Wiley & Sons, Inc., (1959).
7. J. Berkowitz, W. A. Chupka, and M. G. Inghram, *J. Chem. Phys.*, **27**, 85 (1957).
8. W. Hirschwald and I. N. Stranski, in "Condensation and Evaporation of Solids," E. Rutner, Editor, Gordon and Breach, New York (1964).
9. G. M. Rosenblatt, in "Treatise on Solid State Chemistry," Vol. 6A, Surfaces I, N. B. Hannay, Editor, p. 233, Plenum Press, New York (1976).
10. R. S. Crandall and B. W. Faughnan, *Appl. Phys. Lett.*, **26**, 120 (1975).
11. B. W. Faughnan, R. S. Crandall, and P. M. Heyman, *RCA Rev.*, **36**, 1977 (1975).

SF₆, a Preferable Etchant for Plasma Etching Silicon

K. M. Eisele*

Fraunhofer-Institut für Angewandte Festkörperphysik, D-7800 Freiburg, West Germany

ABSTRACT

SF₆ is a far more selective etchant for silicon than CF₄ + O₂ when excited to a plasma discharge. This applies to good advantage in parallel plate reactors where under given conditions of rf power and pressure the etch ratio of silicon to SiO₂ is 30:1 but with CF₄ only 7:1. In contrast to the deposition of carbon in a CF₄ process sulfur has not been found on a silicon surface etched in SF₆. The selectivity of an SF₆ etching process cannot be shifted sufficiently in favor of SiO₂ by adding hydrogen, it can also not be increased much in favor of silicon by adding oxygen. The reaction product is SiF₄. No other silicon compound than SiF₃⁺ appeared in the mass spectrum. 1% SF₆ in argon achieves etch rates of more than 100 nm/min with moderate rf energy. SF₆ is also a useful etchant for Si₃N₄ with etch rates of 100 nm/min.

The etching of polysilicon by means of a CF₄ plasma has almost become a standard process in the manufacture of integrated circuits (1). The polysilicon deposited on an SiO₂ layer serves as gate electrode and for interconnections between the active elements, resistors, and bonding pads. The etch rate of a CF₄ + 4% O₂ gas mixture excited to a plasma discharge in a tunnel reactor is selective in favor of silicon over SiO₂ with a ratio of 30:1 (1, 2) so that the SiO₂ is little affected when the time necessary to etch the silicon layer is exceeded by a marginal amount.

Structures of micrometer width are preferably etched in a parallel plate reactor because the anisotropic etching of such a system achieves better definition, less underetching, and better profile control than can be obtained in a tunnel system. Unfortunately, in a parallel plate system the etch ratio Si:SiO₂ is reduced to 7:1 and therefore not any longer sufficiently selective.

This fact has given incentive to look for other etchants. Based on earlier experiences in thermally etching silicon surfaces *in situ* before epitaxial growth with SF₆ (3), this gas seemed suitable for trials in plasma etching (10). SF₆ is not inflammable and not toxic.

* Electrochemical Society Active Member.
Key words: plasma etching, silicon, SF₆, selectivity.

Even in low concentrations it is a powerful etchant for silicon and reacts almost negligibly with SiO_2 .

Experimental

The parallel plate reactor consisted of two rectangular water-cooled stainless steel plates with an area of 600 cm^2 spaced 6 cm apart. Either plate could be made cathode by connecting it to an rf-voltage supply while the other plate was grounded or left floating. This configuration permitted to realize any desired bias condition. The etch gas emerged from a diffusor pipe with suitably spaced holes, flowed across the short dimension of the rectangle and was pumped out through a long horizontal slit in the vacuum manifold at the rear (Fig. 1). The gas flow was electronically metered and controlled. The pressure was measured by a special rf protected thermocouple gauge and a capacitive manometer. By optical observation the plasma filled the space between the plates uniformly. A mass spectrometer was connected to a narrow sampling tube. A roots blower and a two stage vane pump permitted vacua of 10^{-3} mbar which could be adjusted to the etching pressure by a diaphragm valve. The etch depth was determined with a stylus at a step on the surface, produced by a photoresist edge during the plasma process.

Anode Coupled Etching

Undiluted SF_6 produced etch rates 10-15 times higher than $\text{CF}_4 + 4\% \text{ O}_2$ under the same conditions of rf-voltage and pressure, (rf = $1000 \text{ V}_{\text{dtp}}$, 0.23 mb, 50 sccm SF_6 , anode coupled). With reduced rf power we began to systematically dilute the SF_6 with argon. The results are shown in Fig. 2, where for a constant total gas flow of 20 sccm the fraction of SF_6 was decreased down to 1%. Even at this high degree of dilution the etch rate was still at least that of an undiluted $\text{CF}_4 + \text{O}_2$ etch. There are also a few etch rates for SiO_2 entered in that graph, all below $0.013 \mu\text{m}/\text{min}$ so that the objective of a high selectivity in favor of sili-

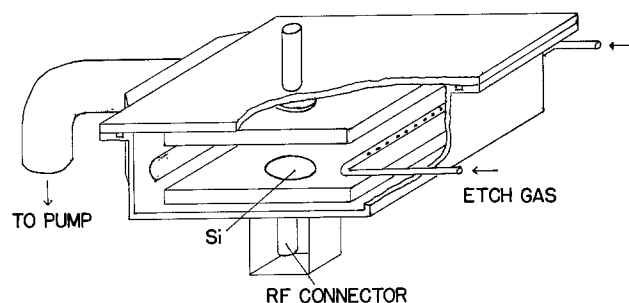


Fig. 1. Etch reactor, showing the gas flow across the electrode

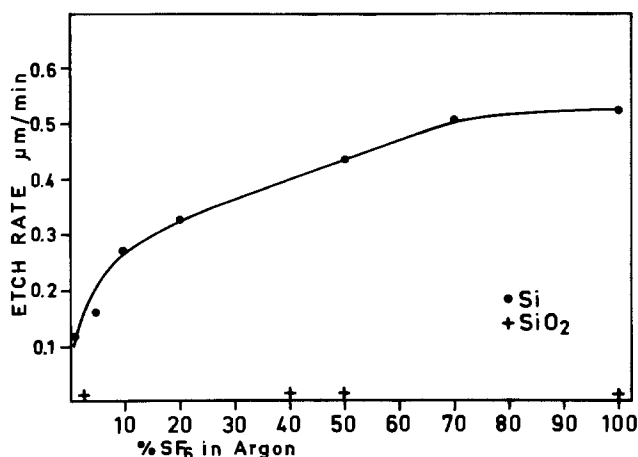


Fig. 2. Etch rate of silicon and SiO_2 in a plasma, anode coupled, when the part of SF_6 in argon increases from 1 to 100% at a total gas flow of 20 sccm. Pressure 0.26 mbar, $0.16 \text{ W}/\text{cm}^2$.

con over SiO_2 was obtained with a ratio of at least 30:1.

In etch processes using CF_4 , carbon atoms are set free which may deposit on the silicon surface and impede the attack by the fluorine. This deposition of carbon is suppressed by oxygen which converts it into volatile CO_2 and in consequence raises the etch rate considerably (4, 5). Similarly we expected sulfur to appear on the surface of the silicon in an SF_6 plasma. If this analogy existed between sulfur and carbon a spontaneous increase in etch rate should also obtain in an SF_6 plasma when oxygen is added. Figure 2 shows the result of such an experiment with both SF_6 and CF_4 . Oxygen causes a moderate increase in etch rate with SF_6 while with CF_4 the increase is fivefold. We can conclude that if sulfur is on the surface of the silicon, it does not shield against the attack of the fluorine.

The influence of hydrogen added to CF_4 on the etch rate of silicon is a means of steering the selectivity in favor of SiO_2 by suppressing the attack on silicon.

The large amount of fluorine in the SF_6 molecule and the absence of any polymerization moderates the influence of hydrogen to a 10-20% decrease in etch rate. Figure 3 presents this dependence for the smaller percentage of hydrogen where at 20% there seems to be a slight increase. But when the dilution is continued the etch rate will drop faster than with argon, which means it is not just a dilution but a reaction.

It is now obvious that the selectivity of etching only silicon and not SiO_2 is very high and cannot be shifted sufficiently either way by adding oxygen or hydrogen. The selectivity does not depend on the fluorine to sulfur ratio in contrast to CF_4 processes where the F to C ratio is all important (6, 7).

Cathode Coupled Etching

The same measurements were also made in a cathode coupled configuration. Here higher etch rates are achieved because of the more intense activation of the surface by ions. But the same dependence of the etch rate on the admixture of H_2 and O_2 was observed (Fig. 3 and 4). The selectivity is, however, dependent on the pressure. In Fig. 5 the etch rates of Si and SiO_2 are plotted against SF_6 pressure in the reactor. For higher pressure the mean-free path decreases and with it the plasma potential and in consequence the ion bombardment of the surface. This reduces the etch rate of SiO_2 where the activation of the surface by ions is necessary for achieving high etch rates.

The Surface

Occasionally the etched surface was not smooth. On such wafers the etch rate had been unusually high, but also with considerable variations across the wafer. This caused serious difficulties in the earlier stages of the experiments. This effect could be traced to a catalytic action caused by residues from the photoresist

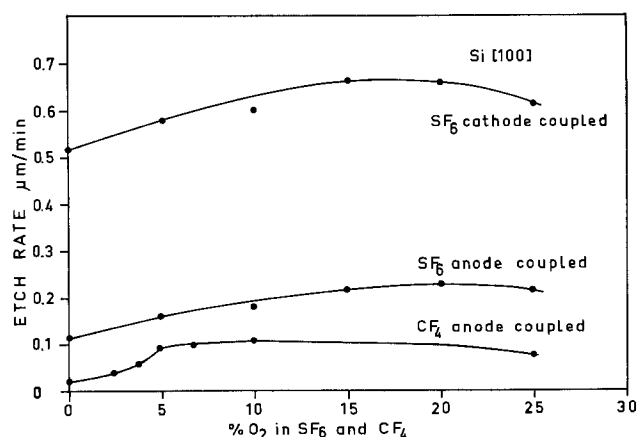


Fig. 3. Etch rate of silicon in SF_6 and CF_4 plasma when oxygen is added. Total gas flow 20 sccm; pressure 0.22 mbar, $0.16 \text{ W}/\text{cm}^2$.

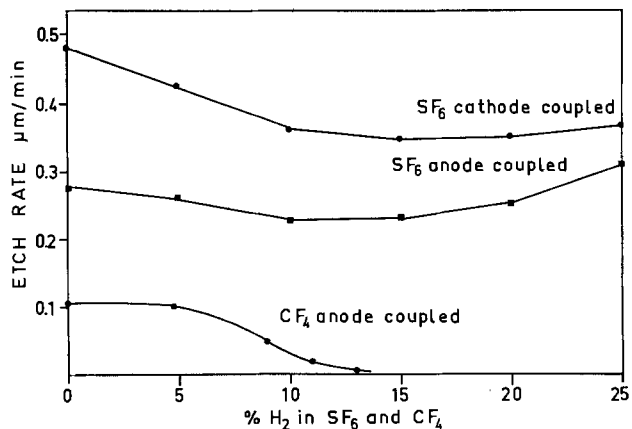


Fig. 4. Etch rate of silicon in SF₆ and CF₄ plasma when hydrogen is added. Total gas flow 20 sccm; pressure 0.22 mbar, 0.16 W/cm².

process although the surface appeared clean by inspection even with a microscope. After the wafer was immersed in a 10% HF solution the surface remained perfectly smooth in the process, the etch rate became uniform on a single wafer and from wafer to wafer, but was distinctly less than obtained on wafers that had not been dipped in the HF solution but etched simultaneously. Untreated surfaces sometimes had etched four times deeper than the pretreated ones. This effect was later also found with other etchants, for instance with NF₃. The suspicion is justified that this phenomenon is also present with CF₄, but not easily observed because the etch rates are considerably lower. When SF₆ was used in dilution the overetching was not apparent without special attention.

The crucial question for a semiconductor device application of SF₆ is whether sulfur is deposited on the silicon surface in an SF₆ plasma. XPS analysis was performed on etched and not etched silicon. There was never any sulfur detected. Surprisingly the oxygen and carbon lines increased in intensity on etched samples although no oxygen or carbon containing gas was knowingly admitted to the reactor. Figure 6 shows an XPS spectrum of an SF₆ etched silicon surface. The minimum detectable level of sulfur is 0.07 of a monolayer. Figure 7 shows the energy range around the S2s line, with high resolution.

Mass-Spectroscopic Analysis

When the plasma is switched on without silicon present in the reactor some compounds appear associated with oxygen SO, SOF, SOF₂ which are synthesized in the plasma. When silicon is being etched the only reaction product is SiF₄ observed as SiF₃⁺. The height of its mass peak appears at the expense of SF₃⁺ which reduces sometimes below that of the SiF₃⁺. This close relation between the two mass signals induces speculation about a direct exchange between sulfur and silicon because the SF⁺ and SF₂⁺ peaks remain

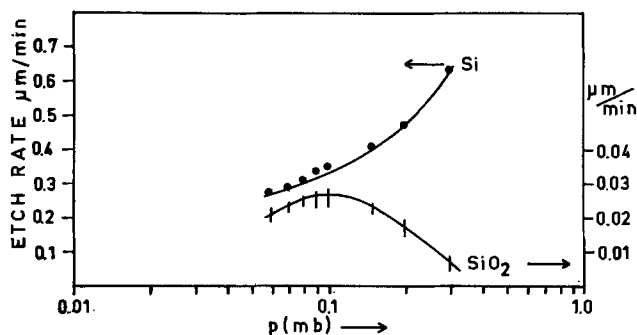


Fig. 5. Etch rate of silicon and SiO₂ in dependence of SF₆ pressure, 0.16 W/cm², cathode coupled.

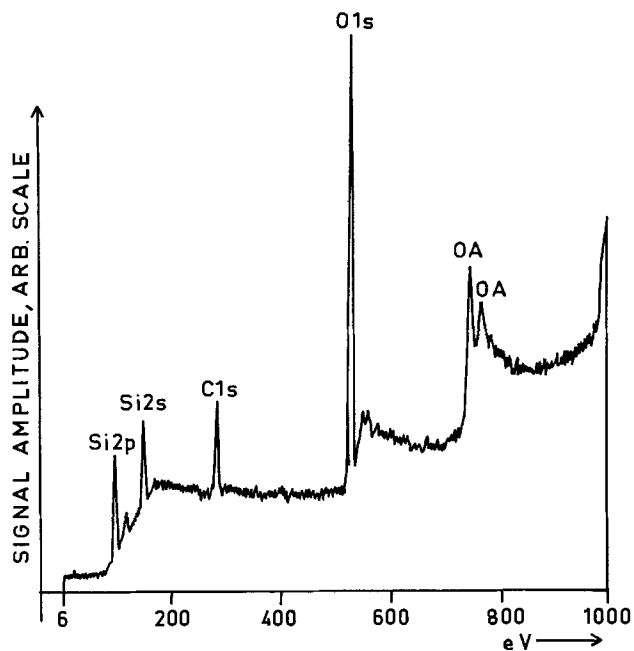


Fig. 6. XPS spectrum of silicon surface etched in SF₆

unchanged. SF₄⁺ also reduces, but this peak being much smaller to begin with, its contribution is not as obvious. SF₅⁺ seems to change little although it is the largest peak. Recently a mass spectroscopic examination of this process has been published (8) where also an increase in SiF₃ signal concurs with a corresponding decrease in the SF₃ signal. Those measurements were obtained at a much higher power density such as is usually applied in sputter processes. These power levels were not reached in this work here. Therefore, a detailed comparison is not possible.

When the silicon is covered by thermal oxide and is anode coupled then the signal of SiF₃⁺ rises barely above the background due to the very low etch rate. Cathode coupled, however, the etch rate is higher and therefore a moderate but distinct signal at 85 amu is recorded. At the same time the sulfuroxyfluorides SO₂F, SO₂F₂, and SOF₃ appear. The peaks of SO₂F and SO₂F₂ can also arise from S₂F and S₂F₂. But as the latter were not present without the SiO₂ in the reactor, only the first assumed identity is acceptable. There are small peaks at 164 and 186 amu which have previously been identified as siliconoxyfluorides Si₂O₂F₄ and Si₂O₂F₆ (9). But these complex compounds have negligible importance in the process.

Because of the absence of carbon, the SF₆ plasma does not have the ambiguity that all mass peaks attributable to silicon could also arise from CO-combinations, because of the same mass, e.g., SiF₂ and COF₂.

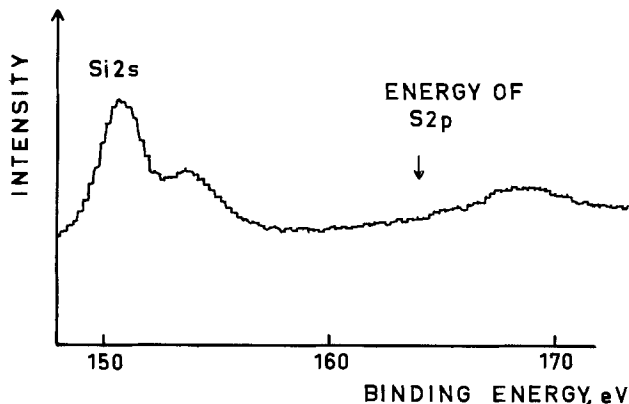


Fig. 7. XPS measurement at the S2s energy level

SF₆ in a Barrel Reactor

Commercially available barrel reactors are in widespread use in the semiconductor industry. Therefore it was considered useful to investigate the etching effect of SF₆ in such a reactor configuration. The etch rates for silicon were higher by a factor 2-3 than previously found with CF₄. At the same time the attack on SiO₂ was immeasurably small. The effects of adding oxygen or hydrogen were the same as in the parallel plate reactor. At more than 50% hydrogen the etch rate falls off considerably as the fluorine is being pumped off as HF. The selectivity in favor of silicon over SiO₂ was 200:1 without aiming for optimum conditions. Exceeding the time in etching a polysilicon structure becomes thus meaningless. Although CF₄ achieves adequate etching in a barrel reactor, the improvement introduced by SF₆ deserves consideration.

The Etching of Silicon Nitride

SF₆ is also a useful etchant for silicon nitride, especially as an alternative when CF₄ does not achieve a good surface. This applies for instance when nitride is used as a passivation layer on already metallized devices and contact holes have to be cut through the nitride. In this case SF₆ leaves a shiny surface suitable for bonding. With 0.2 W/cm² rf power density in an anode coupled setup, 0.25 mbar pressure and 20 sccm SF₆ flow, 80-100 nm/min of silicon nitride can be etched. The same conditions but cathode coupled do not achieve an appreciable higher etch rate yet the selectivity with respect to SiO₂ is diminished. Nitride etching is not influenced by small percentages (<20%) of hydrogen added to the SF₆ and also not by oxygen and nitrogen. There is a small increase in etch rate with pressure. In this respect the nitride behaves like the silicon and not like the oxide in Fig. 4. It means that activation of the surface by ion bombardment is not a significant condition for etching nitride.

Conclusion

For plasma etching silicon, SF₆ is a unique etching gas. It requires no oxygen to achieve high etch rates

with outstanding selectivity. It is economical and leaves a clean smooth surface with no danger of depositing any layers on the wafer. It should therefore find wide application in the manufacture of semiconductor devices.

Acknowledgments

The author gratefully acknowledges the contribution of Dr. H.-J. Richter and P. Meisen and the assistance of Mrs. E. Olander and P. Hofmann. This work was supported by the Ministry of Research and Development of the Federal Republic of Germany.

Manuscript submitted Feb. 21, 1980; revised manuscript received July 28, 1980.

Any discussion of this paper will appear in a Discussion Section to be published in the December 1981 JOURNAL. All discussions for the December 1981 Discussion Section should be submitted by Aug. 1, 1981.

Publication costs of this article were assisted by Fraunhofer-Institut für Angewandte Festkörperphysik.

REFERENCES

1. R. G. Poulsen, *J. Vac. Sci. Technol.*, **14**, 266 (1977).
2. R. L. Bersin, *Solid-State Technol.*, **31**, May 1976.
3. P. Rai-Choudhury, *This Journal*, **118**, 266 (1971).
4. Y. Horiike and M. Shibagaki, *Jpn. J. Appl. Phys. Suppl.*, **45**, 13 (1976).
5. W. R. Harshbarger, T. A. Miller, P. Norton, and R. A. Porter, *Appl. Spectrosc.*, **31**, 201 (1977).
6. R. A. H. Heinecke, *Solid-State Electron.*, **18**, 1146 (1975).
7. J. W. Coburn and E. Kay, *IBM J. Res. Dev.*, **23**, 33 (1979).
8. J. J. Wagner and W. W. Brandt, in "Proceed. 4th Intern. Symposium on Plasma Chem," p. 120, Zurich (1979).
9. C. I. M. Beenakker and R. P. J. Van de Poll, *ibid*, p. 125.
10. R. A. Gdula, Paper 608 presented at The Electrochemical Society Meeting, Los Angeles, California, Oct. 14-19, 1979. This paper appeared after the work reported here was completed, and could therefore not be considered.

Secondary Ion Mass Spectrometric Analysis of Cobalt-Hardened Gold Electroplate Surfaces

Rudolf Schubert

Bell Laboratories, Columbus, Ohio 43213

ABSTRACT

In Co-hardened Au electroplate, the Co will diffuse to the surface with time, where it can form an insulating film. It is of interest to know the chemical form of this surface Co on electrical connectors. Secondary ion mass spectrometry is used to distinguish Co, CoO, Co₃O₄, and cobalt hydroxides in less than full monolayer quantities on impure surfaces. This distinction of compounds is made by comparing the positive and negative secondary ion spectra of Au electroplate with standard samples. Both Ar and O₂ are used for the primary beam. Spectra are compared from before and after UHV bakeout. It is shown that electroplated Au samples have different Co compounds on their surface depending upon the sample histories. For Co-hardened Au electroplate heat-treated at 150°C in air, the surface Co is in the form of CoO and Co. When heat-treated at 200°C in air, the surface Co appears to be in the form of a cobalt hydroxide. Numerous other surface species are also identified and discussed.

Cobalt is a component used in many alloys to influence specific properties of these alloys. In the electronics industry, Co is added to electroplating bath

Key words: SIMS, cobalt oxides, hard gold, electrical connectors.

solutions to improve the mechanical hardness characteristics of electroplated Au surfaces (1). A side effect of the Co included in the Au electroplate is that, with time and temperature, it diffuses to the surface and can cause high contact resistance upon oxidation in air.

Cobalt metal oxidation has been extensively studied and reviewed (2, 3). Three different oxides form (CoO , Co_3O_4 , and Co_2O_3) and are stable under various conditions. Formation is a function of temperature and gas environment except for Co_2O_3 , which does not form by dry oxidation (2). The normal oxide formation can be expected to be altered when the Co is in/on a complicated, impure Au electrodeposit. Bulk Au electroplate impurities were first shown to include complicated, organic compounds by wet chemistry (4). The exact nature of these bulk complexes is still uncertain even after sophisticated analyses by Mössbauer spectroscopy (5-7). The majority of the Co is metallically substituted in the matrix (7). However, whatever the nature of these complexes, ($\beta\text{-CoOOH}$) (6), or ($\text{Co}(\text{CN})_6^{-3}$) (7), they will have to disassociate before being able to diffuse to the surface where they are of interest for their electrical contact resistance.

Recently, Auger electron spectroscopy (AES) (8, 9) and x-ray photoelectron spectroscopy (XPS) (10) have been used to evaluate Co diffusion constants in Co-hardened Au electroplate. That work has pointed to a variety of possible surface compounds: CoO , CoOOH , and K_2O . Compounds with C, N, S, Na, and Cl have been neglected although these elements are also present on the surfaces (8, 10).

Secondary ion mass spectrometry (SIMS) used in the static mode is ideal for a qualitative chemical surface analysis (11-14). Static SIMS uses sufficiently low primary ion beam densities ($\sim 10^{11}$ ions/sec-cm² = 16 nA/cm²) such that less than 10% of a monolayer of the surface is destroyed through sputtering during an analysis. Chemical analysis is achieved by comparing the unknown spectrum to spectra of standards.

This paper reports on the surface analysis of Co-hardened Au electroplate before and after heat-treatments at $\leq 200^\circ\text{C}$ in laboratory air. Standard SIMS spectra of Co foil, CoO , and Co_3O_4 powders were used for comparison. Both positive and negative SIMS spectra are used for analysis. Qualitative interpretation of the Au electroplate spectra indicate varying amounts of hydrocarbons (HC), halogens, alkalies, sulfur, cyanogens, Co, and oxides. The source of these elements and compounds is attributed to the electroplating process.

Apparatus and Sample Preparation

The apparatus in which the SIMS measurements were made is a stainless steel, ion pumped, ultrahigh vacuum system with a 12 in. bell jar. Typically, the system background pressure is 3×10^{-9} Torr before a 225°C , 8 hr bakeout and 1×10^{-10} Torr after a bakeout. A monopole mass spectrometer continuously monitors the background residual gases. Primary residual gases are H_2 , CO , H_2O , CH_4 , and inert gases. This is typical of an ultrahigh vacuum system. The system and SIMS apparatus have been described and shown in detail previously (15, 16).

Briefly, the SIMS equipment consists of an ion gun, quadrupole mass filter (QMS), and a cylindrical mirror energy prefilter (CMA). The hot filament ion gun is differentially pumped with a liquid nitrogen trapped hydrocarbon oil diffusion pump to reduce the inert gas load on the ion pump when using an Ar ion beam. Other primary ion beams, such as oxygen, can also be generated but with a reduction in filament life. Primary ion beam currents can be varied between 1-400 nA with a beam half-width variable from 300 μm to ~ 1 cm. The CMA filters out higher energy (>10 eV) secondary ions and neutral species. Both positive and negative ion spectra can be measured in the QMS which has an electron multiplier detector. With a 10 nA primary ion beam, typical background counting rates are <1 sec⁻¹.

A pure Co standard (99.9%) was cut ($0.5 \times 1 \times 0.025$ cm) from commercial (MRC Corporation) foil. CoO and Co_3O_4 samples were prepared from commercial (Alfa-Ventron) technical grade powders. X-ray diffraction analysis of the CoO and Co_3O_4 powders showed only CoO and Co_3O_4 lines, respectively. The powders were spread between two pieces of Ag foil which had been previously ultrasonically cleaned in methanol. The sandwich was then compressed to ~ 100 psi. Excess oxide powder was tapped off after the two foils had been gently separated. Similar Co oxide samples were also made on Sn backed, electroplated soft Au foils to check for substrate effects. Co_2O_3 was not available commercially and since it does not form by dry oxidation (17), it will not be considered in this paper. Immediately prior to insertion in the vacuum system, all samples were ultrasonically cleaned in CH_3OH .

Co-hardened, electroplated Au samples were plated on OFHC Cu to a thickness of 25 microns. A standard commercial (Autronex-CI), citrate buffered, plating solution was used at low current densities. The source of Au and Co was $\text{KAu}(\text{CN})_2$ and CoSO_4 , respectively. Samples similar to these have been described previously (6-8). Cohen *et al.* (7) have shown that bulk impurities are similar over a range of plating currents, Co concentration, and bath age. Co concentration in the films was 0.26 weight percent (w/o) as determined by atomic absorption analysis. Three histories of Au samples were analyzed: (i) after plating without a heat-treatment, (ii) after 150°C in air for 2000 hr, and (iii) after 200°C in air for 120 hr. All samples were ultrasonically cleaned in CH_3OH before the heat-treatment and before vacuum insertion.

Analysis Procedure and Results

Six different types of samples were mounted on a carousel for sequential analysis under the same analysis conditions. Typical sample groupings were Co foil, CoO and Co_3O_4 on Ag foil, and Au sample types (i), (ii), and (iii). Analyses were made before and after bakeout of the vacuum system. All analyses were made such that for an assumed sputtering yield of unity, less than a monolayer of material was sputtered, i.e., the product of ion beam current and analysis time produced an ion dosage of $<10^{15}$ primary ions/cm². This insured that when after-UHV-bakeout analyses were made, the original surfaces had not been destroyed by the prebakeout analyses.

Figure 1 shows the positive secondary ion (PSI) spectrum (log relative intensity vs. amu) from the pure Co foil sample before the system had been baked

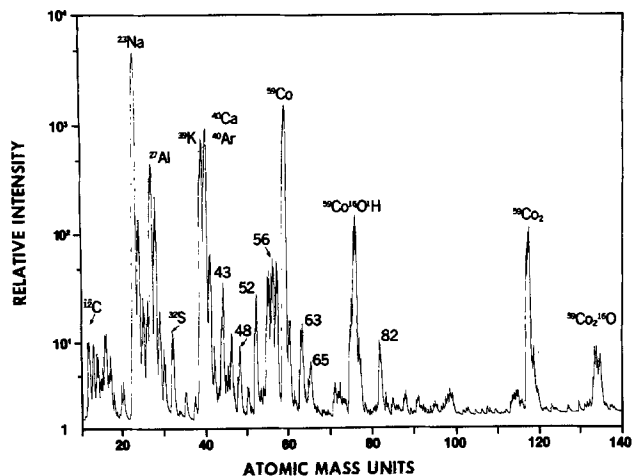


Fig. 1. PSI spectrum of Co metal foil using a 2 keV Ar^+ primary beam of density 1.5×10^{12} sec⁻¹ cm⁻². The sample has been ultrasonically cleaned in CH_3OH and the system background pressure = 3×10^{-9} Torr. Unlabeled peaks are due primarily to hydrocarbons.

and when it was at a background pressure of 3×10^{-9} Torr. In addition to those impurities labeled, many other peaks are seen and attributed mostly to elemental oxides and to organic surface impurities, i.e., CH_x , C_2H_y , etc. (which are typical of nonvacuum-baked samples which have been exposed to air). In the negative secondary ion (NSI) spectrum, one finds oxides, F, S, Cl and more fragmented organic ions than in the PSI spectrum. The NSI spectrum for Co foil is not shown but is similar to the spectra for the cobalt oxides discussed below. After bakeout of the vacuum system, the Co foil SIMS spectra change considerably. Figure 2 shows a reduction of most impurities in the PSI spectrum. Low mass hydrocarbons increase but high mass ones decrease which is normal for samples that have been through a UHV-bakeout procedure. The mass peaks at amu 113 and 115 increase and are attributed to In diffusing out of the bulk. Also note the substantial reduction of cobalt oxide.

NSI spectra of the two cobalt oxides, CoO and Co_3O_4 pressed into Ag foil samples which have not been baked are shown in Fig. 3 and 4, respectively. The samples show various levels of elemental impurities and hydrocarbons. The primary NSI mass peaks of interest are Co^- at amu 59, CoO^- at 75 amu, and CoO_2^- at 91 amu. The cobalt oxide powder samples pressed into soft Au plated Sn have comparable NSI relative intensities and are not shown. For PSI spectra, the peaks involved in the fragmentation patterns are Co^+ at amu 59, CoO^+ at amu 75, Co_2^+ at amu 118, and Co_2O^+ at amu 134. These spectra are not shown since they are similar to the CoO oxide in the unbaked Co foil shown in Fig. 1 but with more intense oxide peaks. Furthermore, none of the oxides studied showed any significant differences in their PSI fragmentation patterns. Table I lists the normalized relative intensities of fragmentation pattern peaks of both PSI and NSI spectra for the studied cobalt oxides and Co foil after UHV bakeout. Cobalt oxide samples showed no significant differences due to the UHV bakeout with regards to the oxide fragmentation pattern.

PSI and NSI spectra of Co-hardened electroplated Au samples were also recorded. The normalized relative intensities of the relevant Co mass peaks are also listed in Table I. Figure 5 illustrates a typical PSI spectrum of the Co-hardened Au electroplate reference sample (i) (no heat-treatment). The PSI and NSI spectra of sample (iii) are shown in Fig. 6 and 7, respectively.

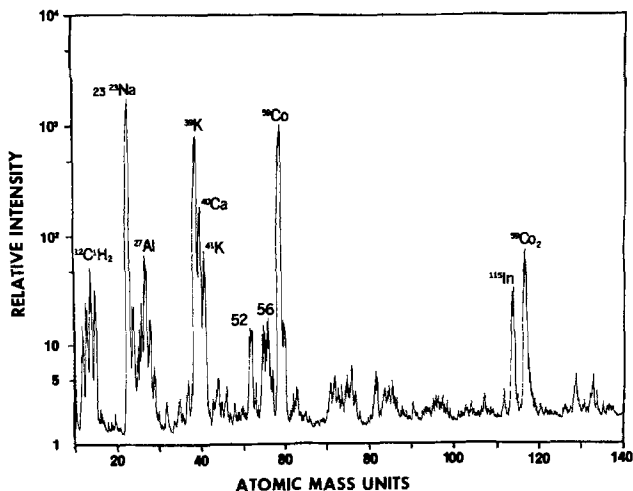


Fig. 2. PSI spectrum similar to Fig. 1 except that the system and sample have been baked in high vacuum at 225°C for 8 hr. Base pressure = 1×10^{-10} Torr. The In is believed to be a bulk impurity which has diffused to the surface during bakeout.

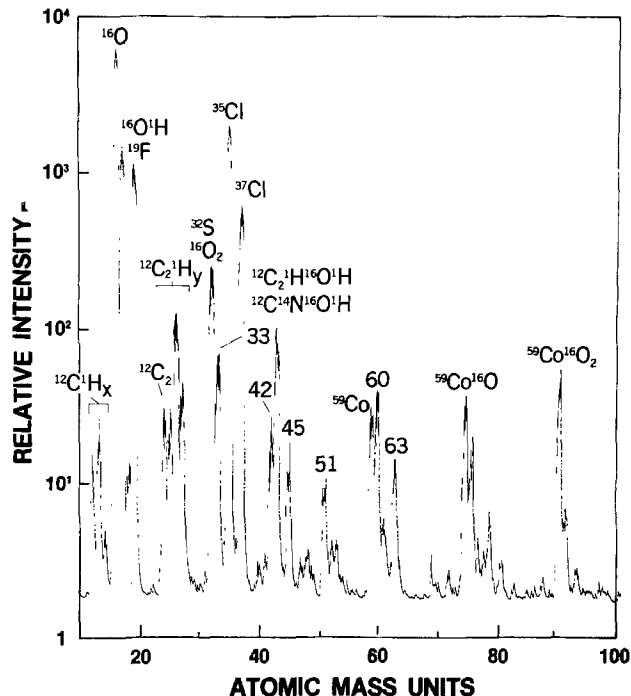


Fig. 3. NSI spectrum of CoO powder pressed onto an Ag foil and ultrasonically cleaned in CH_3OH . The primary Ar^+ beam density is $2 \times 10^{12} \text{ sec}^{-1} \text{ cm}^{-2}$. The ions at amu 60 and 63 are unrelated to Co.

The primary purpose of this experiment was to determine by SIMS the surface Co oxide compounds in Co-hardened Au electroplated OFHC Cu. As can be seen in the spectra shown in Fig. 6 and 7, the heat-treated Au sample (iii) is even more contaminated than the standard powder samples discussed above. Tompkins (8) and Thomas and Sharma (10) using Auger electron spectroscopy and concurrent sputtering, have shown that the surface impurity and oxide layers are only tens of angstroms thick. It has also been shown that cyanide and hydrocarbon complexes extend throughout the Co-hardened, Au plating (6, 7, 23-25). Thus, the surface impurities are not

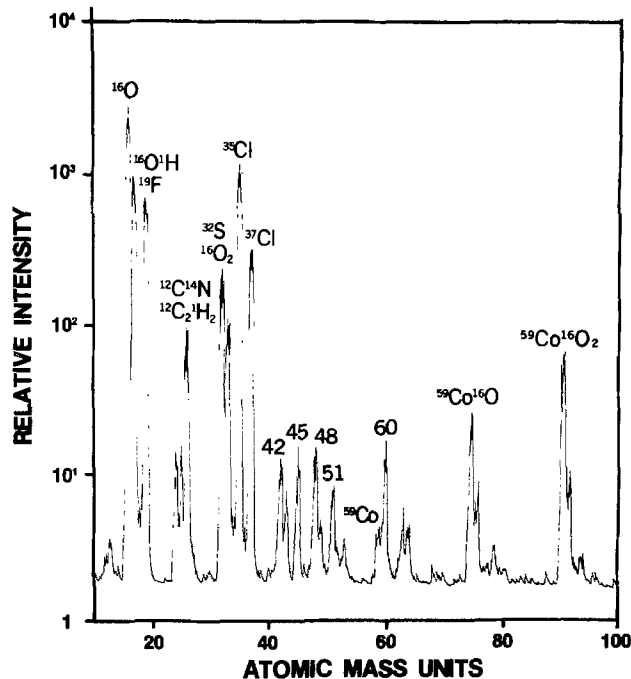


Fig. 4. NSI spectrum of Co_3O_4 recorded with conditions similar to Fig. 3.

Table I. Fragmentation patterns of PSI and NSI of cobalt and cobalt oxides

| Sample | Pos./Neg. | Relative intensities | | | | |
|---------------------------------------|-----------|----------------------|-------------------------------|---------------------------------|--------------------|---------------------------------|
| | | ^{59}Co | $^{59}\text{Co}^{16}\text{O}$ | $^{59}\text{Co}^{16}\text{O}_2$ | $^{59}\text{Co}_2$ | $^{59}\text{Co}_2^{16}\text{O}$ |
| Co foil | P | 100 | 0.5 | — | 6.9 | 0.4 |
| CoO powder | N | 100 | — | — | — | — |
| | P | 100 | 1.1 | — | 1.2 | 1.0 |
| | P | 50 | 66 | 100 | — | — |
| Co ₃ O ₄ powder | P | 100 | 0.8 | — | 2.5 | 0.9 |
| | N | 7 | 40 | 100 | — | — |
| | P | 100 | • | — | • | — |
| Au (i) No heat-treatment | P | • | • | • | • | • |
| Au (ii) 150°C, 2000 hr in air | P | 100 | 0.5 | — | 1.0 | 0.2 |
| | N | 100 | 49 | 71 | — | — |
| | P | 100 | 0.4 | — | 0.7 | 0.1 |
| Au (iii) 200°C, 120 hr in air | P | 100 | — | — | — | — |
| | N | 0.9 | 100 | 92 | — | — |

* Intensities after UHV bakeout are <10 counts/sec with primary beam densities of $\sim 2 \times 10^{12}$ Ar⁺/(sec-cm²) which precludes listing an accurate fragmentation pattern.

readily cleaned off without also removing the Co oxides of interest. However, from the discussion below it will be indicated that the contamination does not affect the Co oxide fragmentation pattern.

Discussion

It is apparent that the surfaces being analyzed have various impurities on them. It is also well known that electronegative and electropositive elements and compounds dramatically increase or decrease the PSI and NSI yields (16, 18-20), respectively. For example, if one exposes clean Fe-Cr alloys to either CO or C₆H₆, the PSI yield of Fe and Cr increases uniformly by approximately a factor of 100 (21). Oxygen adsorption will increase the PSI yield by >1000, but nonuniformly for the two elements (13). However, the ratio of the fragmentation pattern peaks for a given element does not change [similar results have been reported for Cu and CuO (19) and Si (22)].

In this paper we are concerned with the effects of impurities and oxygen on Co on the Au surface and their effect on the SIMS fragmentation patterns. Comparison of Fig. 1 and 2 show that the PSI Co oxide yield from the Co foil surface has become smaller by more than a factor of 20 due to the surface impurity desorption occurring during bakeout of the vacuum system. Other surface impurities, such as Al and Ca have also been reduced substantially. Indium, at mass 113 and 115, has diffused from the bulk to the surface. Low mass hydrocarbons (HC) have increased while

higher mass HC have decreased. After system bakeout CH₄ is a prime residual gas and probably is responsible for a substantial portion of the PSI intensity increases at amu's 12-16. Although Na and K decrease during bakeout, their remaining high PSI intensity is misleading. Both have PSI yields ~ 100 times higher than Co and both are trace elements in the primary ion beam from the hot filament gun. However, the ratio of Co⁺/Co₂⁺ is unchanged at 14.5 after all the surface impurity changes and reductions. One concludes that the fragmentation pattern for Co does not change with surface impurity adsorption.¹

From Fig. 1 to 4 and Table I it is obvious that Co can be distinguished from cobalt oxides. Distinction of the oxides from one another is not so obvious in the PSI spectra of the powdered samples (not shown) in which only small differences in fragmentation patterns are seen. The smaller peaks, CoO⁺ and CoO₂⁺, are essentially equal with a small signal to noise ratio. $^{59}\text{Co}^+$ is always the main peak. In the NSI spectra, the fragmentation patterns are unambiguous when comparing the Co⁻, CoO⁻, and CoO₂⁻ peaks. Thus, from the ratios of Co⁻/CoO₂⁻, which are 0.5 and 0.07 for CoO and Co₃O₄, respectively, one can separately identify the two oxides.

The Au electroplated sample which has not been heat-treated in air shows only minimal contamination. One sees the alkalis predominantly, traces of other

¹ As a further check on the effects of oxygen on the fragmentation pattern, a primary O₂ ion beam, as opposed to an Ar ion beam, was also used on all the standard samples. No changes were observed in either the Co metal or oxide fragmentation ratios.

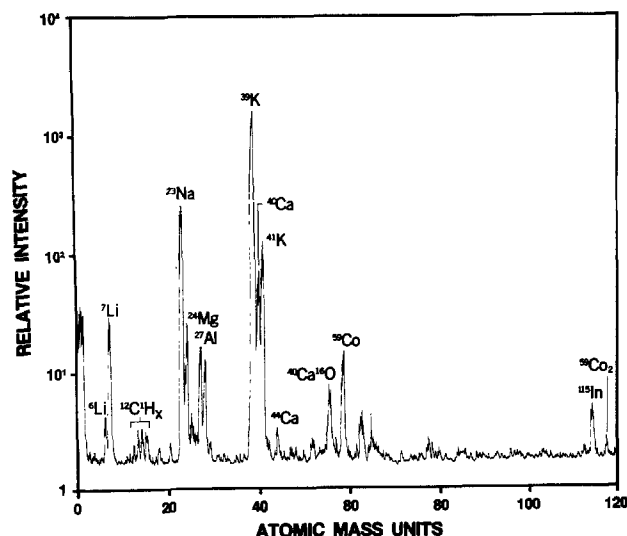


Fig. 5. PSI spectrum of Co-hardened Au electroplated OFHC Cu after UHV bakeout. The sample was inserted directly into the vacuum system following an ultrasonic CH₃OH rinse after plating. Primary Ar⁺ beam density was 3×10^{12} sec⁻¹ cm⁻².

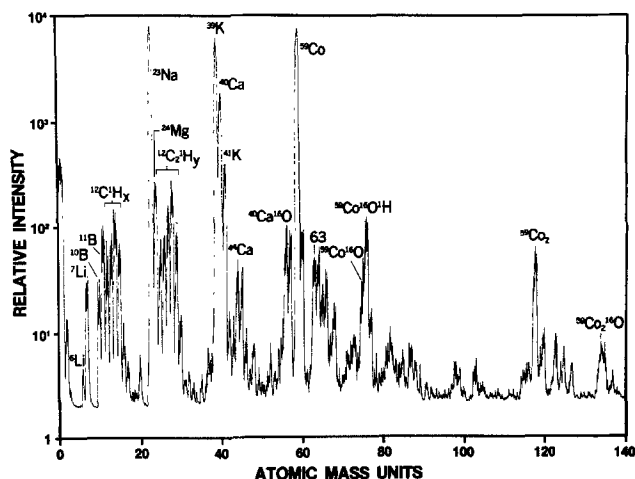


Fig. 6. PSI spectra of a Co-hardened Au electroplated OFHC Cu. After electrodeposition the sample was baked in laboratory air for 120 hr at 200°C, then ultrasonically cleaned in CH₃OH before insertion in the vacuum system. Ar⁺ beam density was 3×10^{12} sec⁻¹ cm⁻². Unlabeled peaks are due primarily to hydrocarbons.

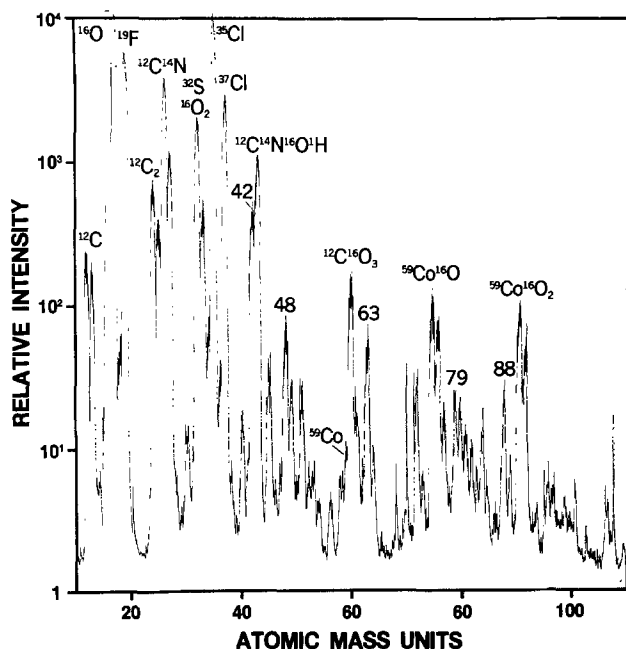


Fig. 7. NSI spectrum of sample shown in Fig. 6. Primary ion beam was similar to the data in Fig. 6.

electropositive elements, and small amounts of Co as shown in Fig. 5. This data was recorded at the same sensitivity level as the data in Fig. 6. If one assumes that the SIMS signal originates from the topmost monolayer of atoms only, then there is less than 1 atomic percent (a/o) of Co and 1 a/o of alkalis present on that surface.

Co-hardened Au electroplate sample (ii) data (spectra not shown) can be interpreted, with respect to surface Co, from the data listed in Table I. Taking the NSI contributions at amu 75 (CoO^-) and amu 91 (CoO_2^-) to be due to CoO then the contribution of CoO to the amu 59 (Co^-) signal is 35 units (relative intensity). Assuming equal NSI yields (primary ions in/secondary ions out) for Co and CoO, the calculated value of Co is then $65/(155 + 65)$ or approximately 30 a/o Co with the concurrent value of 70 a/o for CoO. These values are in agreement with Ref. (10). Other surface impurities will be discussed below.

Inspection of both the PSI and NSI data in Table I and Fig. 6 and 7 indicates that the cobalt oxide in the Co-hardened Au electroplate sample (iii) is not Co, CoO, Co_3O_4 , or a combination thereof. The fragmentation pattern ratios of amu's 59/76 or 59/91 do not fit the standard samples. The ratio of $\text{CoO}_2^-/\text{CoO}_2\text{H}^-$ is 6 and 8.5 for the CoO (Fig. 3) and Co_3O_4 (Fig. 4) standards, respectively. For the unknown this ratio is only 1.5. Similar numbers apply to the $\text{CoO}^-/\text{CoOH}^-$ ratio. This four to sixfold increase in hydroxide signal implies a proportionally greater amount of hydroxide than the standard and that it is strongly bonded, since it has survived a UHV bakeout. This is further substantiated by the large O^- and OH^- peaks which are off scale in Fig. 7. Thus, one concludes that the surface Co is really a form of cobalt hydroxide after a 200°C -120 hr heat-treatment in laboratory air. This is in agreement with the work of Leidheiser *et al.* (6), who claimed the bulk Co was complexed as $\beta\text{-CoOOH}$. Other surface analysis reports on Co-hardened Au electroplate are not in conflict with this conclusion since with AES (8, 10) hydrogen cannot be detected and after the ESCA analysis (10) its presence on the surface was debated.

Hydrocarbons are present in significant amounts on all the samples except the Co foil and unheat-treated Au after UHV bakeout. HC are typically seen at amu's 12-15 (CH_2), amu's 24-27 (C_2H_2), amu's 36-39 (C_3H_2),

etc. in both PSI and NSI spectra (11, 21). For the powder samples, HC cannot be eliminated since as one sputters into the "clean" interior of a granule, new exterior surfaces are being exposed from surrounding granules. Figures 6 and 7 show the richest HC spectra. In addition to the labeled HC, it is expected that most of the lower intensity unlabeled peaks are also due to HC. At this point it would be too speculative to attempt an identification due to the myriad possibilities and not having standards available.

Numerous other compounds and complexes are purported to be in the bulk or on the surface of the electroplate depending on which publication one reads and what technique that author used. CN complexes are expected due to the electroplating bath. CN^- is seen at amu 26 in Fig. 7 where it dominates the C_2H_2^- ion. The NSI at amu 42 and 43 are due primarily to CNO^- and CNOH^- , respectively. The presence of CoCN complexes on the surface should produce a strong peak at amu 85 in the NSI spectrum. Since a negative amu 85 ion was not observed one concludes that CoCN complexes were not present on the surface. KO and KCN surface complexes also appear doubtful since they appear in neither the PSI nor NSI spectra although the possibility exists that they are only sputtered as neutrals. Thus it appears that large chemically bound complexes are not readily found on the surface of Co-hardened Au electroplate either before or after heat-treatment in air.

Summary

Static SIMS surface analysis has been shown capable of distinguishing Co, CoO, and Co_3O_4 standard samples. The technique has demonstrated that an unheat-treated, Co-hardened Au electroplate surface is relatively clean with predominantly metallic surface impurities of K and Co. For Au electroplate heat-treated at 150°C in laboratory air, the primary surface constituents are CoO, Co, and K. At heat-treatment temperatures of 200°C these surfaces produce complex PSI and NSI spectra and are highly contaminated. A partial listing of contaminants include hydrocarbons, hydroxides, Na, K, Ca, Co, CoOOH , CN, S, and Cl. CoCN, KO, and KCN complexes are believed not to be present on surfaces in substantial quantities.

Manuscript submitted June 9, 1980; revised manuscript received July 31, 1980.

Any discussion of this paper will appear in a Discussion Section to be published in the December 1981 JOURNAL. All discussions for the December 1981 Discussion Section should be submitted by Aug. 1, 1981.

REFERENCES

1. M. Antler, in "Gold Plating Technology", F. H. Reid and W. Goldie, Editors, pp. 478-494, Electrochemical Publishers Ltd., Ayr, Scotland (1974).
2. E. A. Gulbransen and K. F. Andrew, *This Journal*, **98**, 241 (1951).
3. K. Hauffe, "Oxidation of Metals," pp. 194-201, Plenum Press, New York (1965).
4. G. B. Munier, *Plating*, **56**, 1151 (1969).
5. Y. Okinaka and S. Nakahara, *This Journal*, **123**, 1284 (1976).
6. H. Leidheiser, Jr., A. Vértes, M. L. Varsányi, and I. Czako-Nagy, *ibid.*, **126**, 391 (1979).
7. R. L. Cohen, F. B. Koch, L. N. Schoenberg, and K. W. West, *ibid.*, **126**, 1608 (1979).
8. H. G. Tompkins, *ibid.*, **122**, 983 (1975).
9. J. H. Thomas III, *ibid.*, **125**, 898 (1978).
10. J. H. Thomas III and S. P. Sharma, *ibid.*, **126**, 445 (1979).
11. A. Benninghoven, *Surf. Sci.*, **35**, 427 (1973).
12. H. W. Werner, H. A. M. DeGrefte, and J. VanDenBerg, "Ion Surface Interactions, Sputtering, and Related Phenomena," Gordon and Breach Sci. Pub., New York (1973); Alternate reference is: *Radiat. Phys.*, **18** and **19** (1973).
13. R. Schubert, *J. Vac. Sci. Technol.*, **12**, 505 (1975).

14. R. Schubert, *This Journal*, **125**, 1215 (1978).
15. R. Schubert and J. C. Tracy, *Rev. Sci. Instrum.*, **44**, 487 (1973).
16. R. Schubert, *J. Vac. Sci. Technol.*, **11**, 903 (1974).
17. M. LeBlanc and E. Mobins, *Z. Phys. Chem.*, **142**, 151 (1929).
18. A. Benninghoven, *Surf. Sci.*, **53**, 596 (1975).
19. H. W. Werner, in "Advances in Applied Spectroscopy," Vol 7A, E. Grove, Editor, p. 239, Plenum Press, New York (1969).
20. J. A. McHugh, in "Methods of Surface Analysis," A. W. Czanderna, Editor, pp. 232-233, Elsevier Sci. Pub. Co., New York (1975).
21. R. Schubert, unpublished.
22. J. M. Morabito and R. K. Lewis, in "Methods of Surface Analysis," A. W. Czanderna, Editor, p. 289, Elsevier Sci. Pub. Co., New York (1975).
23. G. B. Munier, *Plating*, **56**, 1151 (1969).
24. L. Holt and J. Stanyer, *Trans. Inst. Met. Finish.*, **50**, 24 (1972).
25. E. Raub, C. J. Raub, A. Knödler, and H. P. Wiehl, *Werkst. Korros.*, **23**, 643 (1972).

A Review of Depreciative Color Center Phenomena in Lamp Phosphors

John M. Flaherty*

GTE Products Corporation, Lighting Group, Danvers, Massachusetts 01923

ABSTRACT

A review of the role played by color centers in the deterioration of lumen output of lamp phosphors with special attention to the halophosphates is presented. Color center dynamics in halophosphates result in a rapid degradation in phosphor brightness within minutes after the beginning of lamp life. An examination of the extent and rapidity of this effect is reviewed. Unirradiated spectral characteristics of halophosphates are dependent on growth stoichiometry. Radiatively induced spectral absorptions are dependent on the relative intensity of Hg u.v. components and crystal deformation and show thermal and optical bleaching effects. A dynamical model of color centers in halophosphates is extracted from the literature that explains the essential experimental dependencies. Related color center effects in phosphors including defect generation considerations for long-term brightness deterioration are also presented.

The various phenomena which contribute, each in its own degree, to the depreciation in fluorescent lamp performance are often quite complicated. One such phenomenon is due to color center dynamics occurring in the phosphor. A review of the role played by color centers in the deterioration of lumen output of phosphors with special attention to the halophosphates is presented with subsequent generalizations on defect considerations for lamp phosphors.

Ever present in solids are defects. Defects are categorized (1, 2) as point defects and extended defects, the latter considered as sizable aggregates of point defects that together constitute dislocations, voids, or bubbles. Typical examples of point defects are host interstitials or vacancies which are termed intrinsic defects and impurities, an extrinsic defect; a small complex or cluster of these simple defects is also considered a point defect.

Solids whose bonds are predominantly ionic present bandgaps sufficiently wide that these defects and/or their charge modifications often exhibit absorption structure in the u.v., visible, or infrared and are collectively termed "color centers."

High u.v. irradiation may induce new and/or significantly increased color center absorption in the u.v. and visible regions especially. This signals generation, modifications, and interactions of and between defects. Often defect interactions which tend to bring about a diminution of these induced absorptions and their associated defects are initiated by less energetic u.v. and visible radiation as well as thermal treatments. All defects and their interactions occurring in a solid will here be regarded as constituting the defect system of the solid.

The ideal lamp phosphor should absorb and convert all of the u.v. of the lamp discharge to the appropriate

visible emission with quantum efficiency of at least unity. In order that all of this visible emission should escape the phosphor layer, the phosphor host lattice must present an energy bandgap sufficiently wide to pass all visible electromagnetic radiation (≥ 3.5 eV). Most phosphors are constituted of a nonfluorescing host lattice into which specific impurities are purposely doped in order to absorb the u.v. of the discharge and emit it as visible radiation. The absorption and emission processes may be accomplished by a single type of impurity in which case it is called an activator or they may be accomplished separately, be unlike impurities whereby an absorber (called the sensitizer) transfers its excitation energy to the emitter (the activator) by some energy transfer process (3). If only the activator or sensitizer, hereafter together constituting the activator system of the solid, is to absorb the u.v. radiation, then the bandgap of the host lattice must pass the u.v. of the discharge additionally. For an Hg discharge this corresponds to a bandgap of ≥ 6.8 eV. The activator system may also be composed, at least in part, of host ions and/or ion complexes. In this case the u.v. is generally absorbed by the host whereby all excitation is ideally transferred to the activator which subsequently emits in the visible.

The defect system can undermine the aforementioned intent of the ideal phosphor, thus lowering its efficiency in essentially three ways as symbolized in Fig. 1. In process 1 the defect system may compete with the activator system for the exciting radiation. Visible absorption caused by defects can reduce activator emission before it is able to escape the phosphor layer in 2. Additionally, entities of the defect system may be intimately connected with or in communication with those of the activator system resulting in a direct nonradiative transfer of excitation energy from the activator system to the defect system. This loss is symbolized by process 3. The relative importance of these

* Electrochemical Society Active Member.

Key words: defects, luminescence, ultraviolet, stoichiometry.

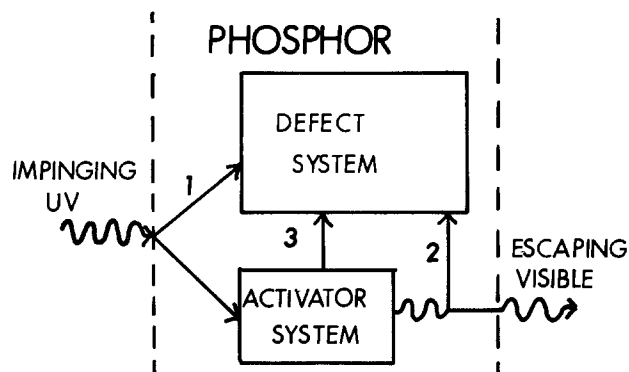


Fig. 1. Schematic of energy loss processes to the defect system of a phosphor.

three loss processes is dependent on the particular phosphor at hand.

Many lamp phosphors show color center absorptions with resulting brightness degradations (4, 5), but none have been analyzed so thoroughly as the halophosphates. Calcium halophosphate, the predominantly used commercial phosphor in fluorescent lamps, shows significant depreciation in brightness under Hg u.v. radiation comprised of the 185 and 254 nm components. A review of the results of the many investigations in the literature on this depreciative effect is of interest for a general understanding of this important phosphor as well as a fruitful example of the typical effects that can occur in other phosphors.

Calcium Halophosphate Depreciation Due to Color Centers

First, the extent and rapidity of this effect will be presented. After a look at the relevant structural aspects of the halophosphates and their probable sites for impurity inclusion, I will examine the experimental results associated with high u.v. radiation correlated with crystal preparation conditions. On the basis of experimental findings, a model of color center dynamics in this phosphor, chosen from the literature, is presented which explains the experimental dependencies and behaviors as well as revealing the deleterious workings of unwanted defects.

General lumen dependencies.—There occurs a rapid deterioration in the lumen output of a halophosphate lamp within ~ 10 min of lamp life after which time this deterioration onslaught saturates resulting in $\sim 10\%$ lumen loss, $3/4$ of which is attributed to overall phosphor efficiency degradation brought on by Hg u.v. irradiation. This lumen loss is depicted in Fig. 2. This short-term depreciation behavior common to various phosphors (5) is generally characterized as exhibiting an initial onslaught of depreciation, the effect of which more or less quickly reaches a saturation level as shown by the dotted line in Fig. 2. This saturation level is defined relatively and more correctly represents

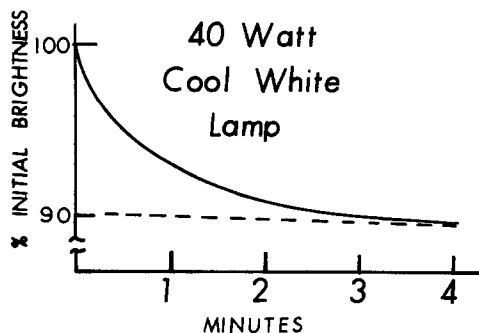


Fig. 2. Typical short-term lumen depreciation of a 40W cool white lamp. Dotted line represents short-term saturation level.

a time domain of a considerably slower depreciation rate.

With regard to the Hg u.v. irradiation of the phosphor, Singleton and Suchow (6) showed that the extent of the depreciation at the saturation level is dependent only on the ratio of the intensity of 185 to 254 nm radiation; the extent being more severe for an increased intensity ratio of the 185 to 254. Moreover, the rate at which the saturation level is attained for a fixed intensity ratio increases with increasing total intensity of radiation.

When the intensity ratio is held fixed the amount of brightness loss is reduced for increased Sb concentration (5, 7). Increasing the concentration of Mn increases the severity of the saturation level (5), but only in the presence of an oxygen-containing atmosphere, otherwise the saturation is independent (7) of Mn concentration. Vrenken *et al.* (8) illustrated the reduction in short term lumen depreciation as the Cd concentration is increased. Figure 3 shows the short-term time dependence of this effect in a 40W cool white lamp. The time dependence of the short-term depreciation can be fitted to a sum of three exponential terms of the same form as in the Butler-Lowry maintenance equation; however, the time constants are, of course, very short. The total short-term depreciation effect is accomplished in ~ 6 min. Incorporation of nonemitting elements other than Cd can also reduce lumen depreciation (5, 9), but not as effectively as Cd. Cs (10) was found to improve initial brightness as well as maintenance. Apple (11) showed that a halophosphate rapidly quenched from 1150°C will show less short-term lumen loss than one that was slowly cooled.

Short-term brightness loss can be recovered completely after annealing the sample to 500°C (8, 12). Approximately 50% recovery takes place if the sample is irradiated by 254 nm radiation alone (6, 8, 12). Visible radiation is much less effective in the recovery process than the 254 nm radiation (10).

Any defect system model describing the interactions taking place within the phosphor should explain these effects.

Halophosphate structure and dopant sites.—Calcium fluorophosphate forms in the hexagonal fluorapatite structure, space group $C6_3/m$, with two molecules of $\text{Ca}_5(\text{PO}_4)_3\text{F}$ per unit cell (13-15). Figure 4(a) shows the manner in which the crystal is constituted. Each of the large circles in the upper portion represents the group of ions shown below. The plane of the large circles is the mirror plane. These planes are stacked upon each other with the ions in the circle of each successive plane rotated by 60 degrees. The Ca(I) ions are situated between the planes. The dashed rhombus outlines the unit cell containing 42 atoms. The fluorine ions at the center of the circles sit directly above each other as more planes are added on. These fluorine ions follow the direction of the crystal axis and constitute

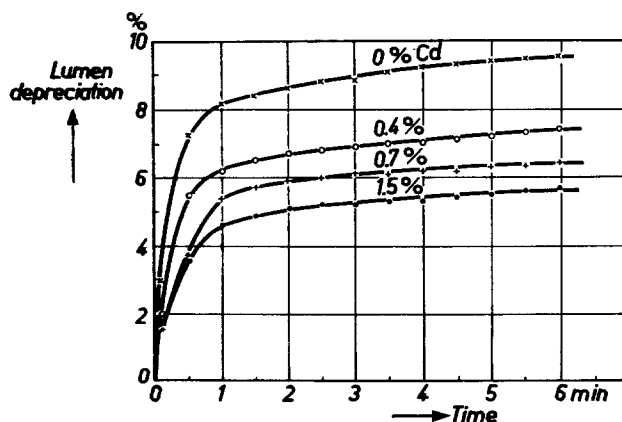


Fig. 3. Lumen depreciation in 40W cool white fluorescent lamps with increasing cadmium percentage as a function of time. After Vrenken *et al.* (8).

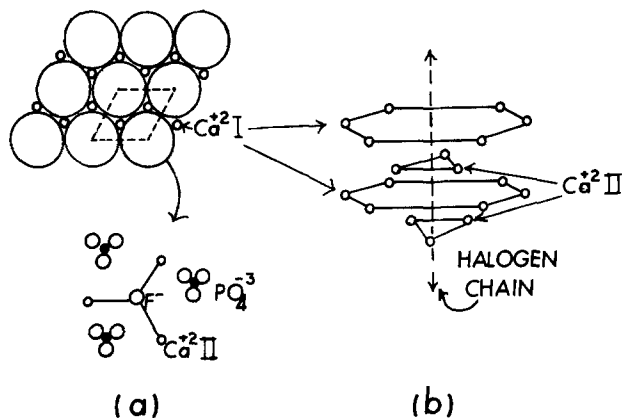


Fig. 4. (a) Diagram of fluorapatite structure. Each circle represents the group of atoms shown below. The circles constitute a plane perpendicular to the *c*-axis. The Ca(I) ions are behind the plane of the circles and the dashed rhombus outlines the unit cell. (b) Diagram illustrating the orientation of the halogen chain in the apatite structure devoid of phosphorus and oxygen atoms.

by themselves a one-dimensional chain of fluorine ions. The distance between these chains is 9.37Å while the distance between the fluorines of a given chain is 3.44Å. Figure 4(b) illustrates the chain environment devoid of the phosphate groups. The fluorine chain will play a significant role in the defect system in this phosphor.

Calcium enters the lattice as Ca²⁺ (p⁶ configuration) in two inequivalent sites labeled Ca(I) and Ca(II) with relative abundance of 2 to 3, respectively. The Ca(II) sites reside at the apexes of an equilateral triangle centered on the fluorine and are in good communication with the chain, whereas the Ca(I) sites are more isolated.

Calcium chlorophosphate (16, 17) is a hexagonal chlorapatite above 212°C but monoclinic below this temperature. The Cl ion (radius = 1.81Å) is larger than the F ion (radius = 1.33Å). This causes a slight expansion of the lattice with the Cl ions displaced slightly above and below the would-be F position. If at least 36% of the halogens in the mixed chlorofluorophosphate are fluorines, then the halophosphate remains at all temperatures in the hexagonal apatite structure (18).

All impurities appear to occupy the calcium sites (19). Sb substitutes in the lattice as Sb³⁺. Its s² configuration, leaving it nonparamagnetic, makes it uncertain as to its occupation position. By charge compensation arguments (20) it is assumed to occupy the Ca(II) site with an oxygen substituting for the neighboring fluorine ion. Dale (21) has some experimental evidence suggesting the substitution of Sb for phosphorus. It will be assumed in this report that Sb resides in the Ca(II) site, however, the model and conclusions would not be substantially altered if Sb actually does substitute for phosphorus.

Manganese goes into the lattice as Mn²⁺ (3d⁵ configuration). It can occupy either the Ca(I) or Ca(II) sites and several investigations (22-24) have attempted to determine the relative proportionment of manganese among these calcium sites. At very low concentrations Mn preferentially occupies the Ca(II) sites, but as the Mn concentration increases, preference to occupying the Ca(I) sites dominates (25). At normal concentrations (1%) approximately 65% of the Mn resides in the Ca(I) sites which are termed Mn(I). Extensive (20, 23, 25-27) optical and ESR investigations show several modifications to the site symmetry and, therefore, fluorescence characteristic of Mn in Ca(II) sites, likewise termed Mn(II). These modified Mn(II) sites are symbolized as Mn(Cl), Mn(Sb), Mn(IIm) and refer to the Mn ion in the Ca(II) site that is closely neighbored by a Cl ion, Sb ion, and oxygen-vacancy complex, respectively.

Cd goes into the lattice as Cd²⁺. Since it is essentially the same size as the Ca²⁺ ion, it is assumed to fit into both calcium sites.

Spectral characteristics.—It is the purpose of this section to introduce those spectral properties of halophosphate crystals which are most pertinent to the color center depreciation dynamics addressed in a later section.

Unirradiated characteristics.—The bandedge of halophosphates occurs at wavelengths shorter than 160 nm corresponding to forbidden energy gaps of >8 eV (15). Nevertheless, absorption can occur in the 250 and 185 nm regions of unactivated and unirradiated samples and has prompted several studies (15, 17, 28). Variouso crystals of fluorapatite were grown (see Fig. 5) with melts of varying degrees from stoichiometry (29). The dependencies of these absorptions on melt conditions relate to their identification with imperfections. The absorption band peaked at 250 nm is attributed (26) to a complex consisting of an oxygen substitution sandwiched by two vacancies along the fluorine chain termed the "X center." The absorption in the 185 nm region is attributed to another defect somewhat similar to, but distinct from, the X center and is termed the "Y center." The strength of the X center absorption present in the crystal is quite strongly dependent on melt conditions (see Fig. 6) An excess in CaF₂ reduces the amount of X centers formed whereas a slight excess of CaCO₃ greatly increases X center formation. Obviously, if a low concentration of X centers is desirable in the resulting apatite, the melt should be excess in CaF₂ and deficient in CaCO₃.

The amount of overall X band absorption, and therefore the number of X centers, decreases with increasing temperature (29). The X band absorption, though, eventually returns to its initial value when the crystal is brought back to room temperature implying a reformation of X centers. The Y center exhibits the same dependencies as the X center, but to a much smaller degree, suggesting that it is a more stable defect complex than the X center.

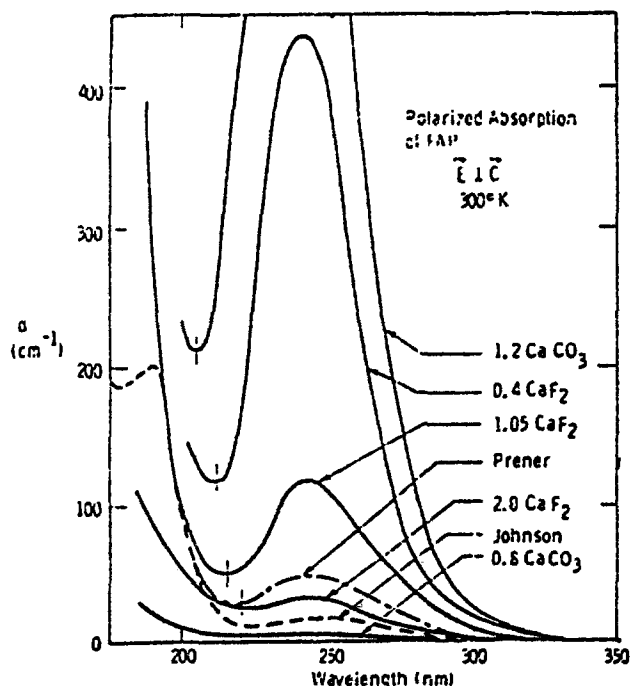


Fig. 5. Absorption of fluorapatite (FAP) in the 185 and 254 nm regions at 300 K. The curves are labeled to indicate the stoichiometry of the melt from which each crystal was grown. 1.2 CaCO₃, for instance, means that this melt was stoichiometric except for CaCO₃ which was 1.2 times the stoichiometric value. After Warren (29).

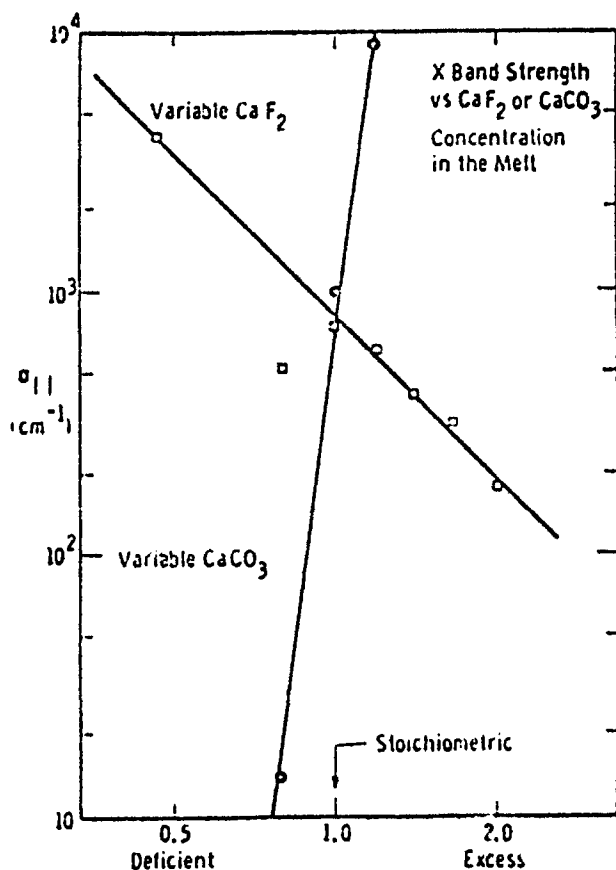


Fig. 6. Dependence of the X band absorption on stoichiometry of the melt. After Warren (29).

The inclusion of Mn and Sb suppresses the X center absorption. Apparently, there occurs a gettering phenomenon whereby some of the oxygen-vacancy complexes are gettered by some Mn(II) sites resulting in a modified Mn site called Mn(II_m).

Figure 7 shows a typical fluorescence spectrum (7) of fluorophosphate doubly activated by Sb and Mn. The absorption spectrum [from Ref. (30)] of Sb in a single crystal of fluorophosphate is presented in Fig. 8. It is important to note for later consideration that the absorption at 185 nm is stronger than at 254 nm. In the presence of an Hg discharge the vast amount of Mn is excited by energy transfer from Sb because of the preponderance of Sb absorption in the region of the Hg emissions and the efficiency of the Sb-Mn transfer process (15, 31).

Cd absorbs below 200 nm. Figure 9 shows a diffuse reflection spectrum of Ca, Cd chlorofluorophosphate for several dopant levels of Cd. Cd does not fluoresce

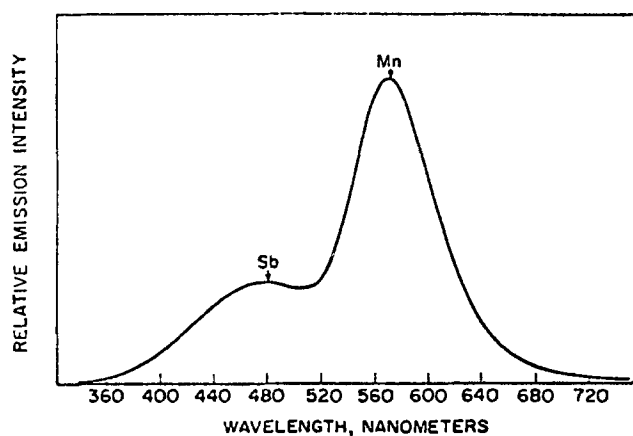


Fig. 7. Fluorescence spectrum of $\text{Ca}_{0.72}\text{Mn}_{0.18}(\text{SbO})_{0.07}\text{F}_{1.92}(\text{PO}_4)_6$ excited by 254 nm radiation. After Parodi (7).

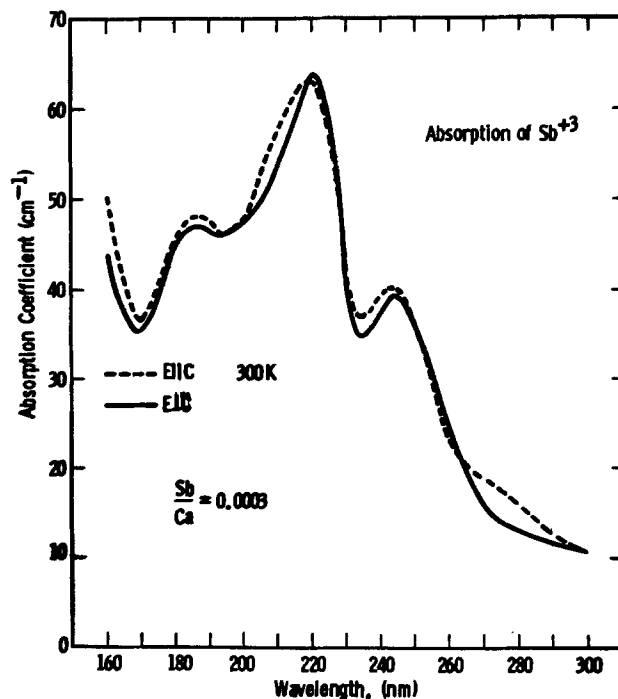


Fig. 8. The absorption of a single crystal of calcium fluorophosphate containing 0.03 atomic percent antimony. After Warren *et al.* (30).

in the visible and essentially nonradiatively degrades its excitation energy. In phosphate lattices which are heavily doped with Cd or with complete replacement of Ca by Cd, there is efficient Cd to Mn energy transfer occurring. However, it is presumed that in the normal halophosphates employed in lighting, such a transfer process is of negligible contribution.

The incorporation of Cs into the unactivated fluorochlorophosphate actually increases the reflectivity of the host lattice (10). A comparison of the reflectivities of the host matrix, Cs-doped and a standard (no Cd) Sb, Mn-activated halophosphate is presented from Ref. (10) in Fig. 10.

Irradiated halophosphates.—Hg u.v. irradiation induces many absorptions throughout the visible and u.v. as well as a variety of ESR spectra (6, 12, 16, 29, 30, 32-34) in the halophosphates. This coloration occurs in fluoro, chloro, and all proportions of chlorofluorophosphates with only unessential variations in the shapes and peak positions of the induced absorption bands and are therefore associated with defects or color centers common to the halophosphate structure. Mechanical grinding increases the number of defects present in the halophosphate as well as the propensity

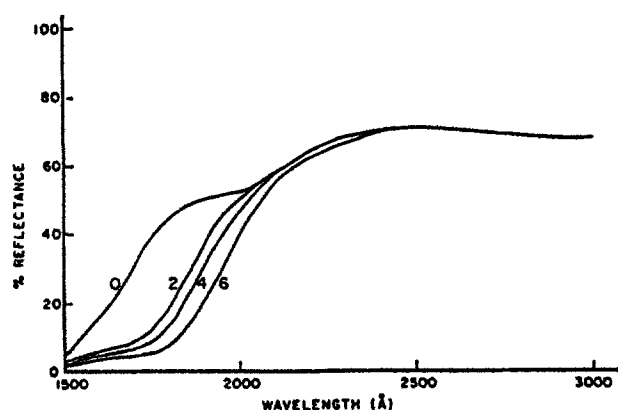


Fig. 9. Diffuse reflectance of Ca, Cd chlorofluorophosphate. Numbers indicate atom percent Cd added in place of Ca. After Apple (11).

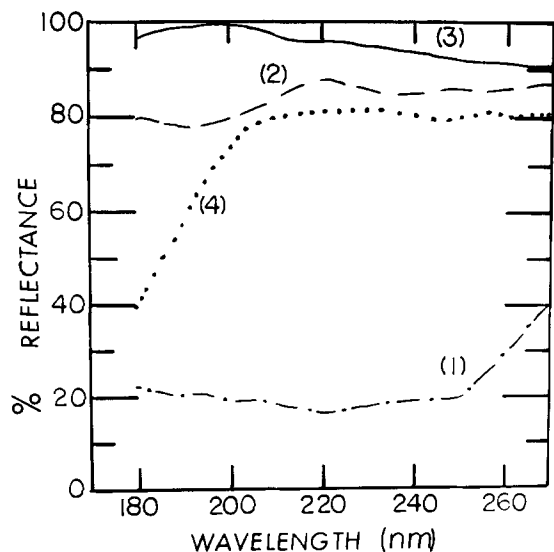


Fig. 10. Diffuse reflection spectra of several halophosphate samples of different dopants. Curve 1, typically activated 4200 K phosphor: $\text{Ca}_{9.5}\text{Sb}_{0.1}\text{Mn}_{0.2}(\text{PO}_4)_6(\text{F}_{0.9}\text{Cl}_{0.1})_2$; curve 2, unactivated halophosphate: $\text{Ca}_{9.8}(\text{PO}_4)_6(\text{F}_{0.9}\text{Cl}_{0.1})_2$; curve 3, unactivated halophosphate with Cs as an additive: $\text{Ca}_{9.7}\text{Cs}_{0.1}(\text{PO}_4)_6(\text{F}_{0.9}\text{Cl}_{0.1})_2$; curve 4, unactivated halophosphate with Cd as an additive: $\text{Ca}_{9.7}\text{Cd}_{0.1}(\text{PO}_4)_6(\text{F}_{0.9}\text{Cl}_{0.1})_2$. After Narita *et al.* (10).

to generate new defects under continued exposure to x-rays (36, 37).

Of specific importance is an induced absorption (29) occurring in the 254 nm region due to the u.v. irradiation of Hg at 185 nm. This induced absorption should be distinguished from the aforementioned "ingrown" X center absorption in the region of 254 nm which can be suppressed by melt conditions and activator inclusions. Narita *et al.* (10) showed that the proclivity of the 185 nm irradiation to induce 254 nm absorption is reduced in proportion to the extent of the absorption introduced at 185 nm by metal additives to the halophosphate.

A measurable decrease in the relative fluorescence and concentration of paramagnetic manganese ions following high u.v. irradiation was found by Skreblyukov *et al.* (38).

Temperature annealing of the u.v. irradiated halophosphate leads to a complete restoration of the concentration of paramagnetic manganese ions, the recovery of phosphor brightness, and to a complete bleaching of all induced absorptions (38). Thermoluminescence however, accompanies the thermal treatment only for activated halophosphate (6) and is composed of the characteristic emissions of Sb^{3+} and Mn^{2+} (38, 40).

Radiational treatment by 254 nm and visible radiation of samples that have been irradiated by 185 nm u.v. shows a bleaching of the induced absorptions (6), especially of the 254 nm induced absorption. However, bleaching with visible light is in no way as effective as 254 nm radiation (10). Radiational bleaching does not bring about the complete recovery of phosphor brightness that a 500°C thermal bleaching affords.

In summarizing the essential radiation dependencies above, it is seen that sample irradiation of 185 nm Hg emission is in part absorbed by a "primitive" defect termed the Y center which is present in the virgin phosphor. Such irradiation induces a defect (color center) absorption in the region of 254 nm which can also bleach out under 254 nm Hg irradiation. The relevant defect absorption locations are presented in Fig. 11. The absorptions are labeled according to Ref. (29, 30). The top of the figure presents regions of absorption in the unactivated and unirradiated halophosphate. Identified are the absorptions due to the X and Y centers which are not induced by high u.v. irradiation, but are ingrown defects. No attempt is made to pre-

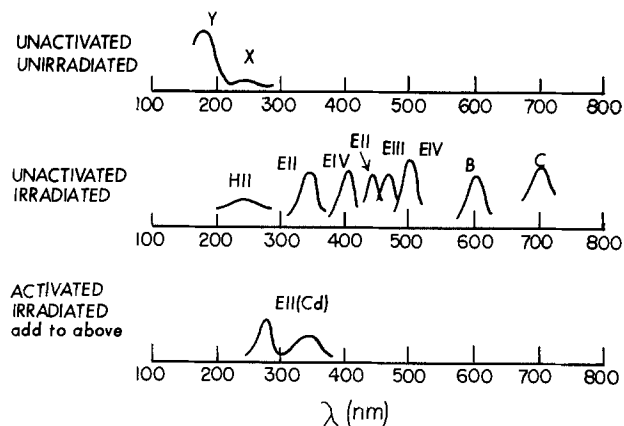


Fig. 11. Schematic of some of the defect absorptions occurring before and after u.v. irradiation in unactivated and activated Ca fluorophosphate. It is the intent here to show only the relevant spectral positions of these color center absorptions and not any absolute or relative (even among the defects) absorption strength.

sent the absolute or relative strengths of the absorptions in these figures; only the positions of certain particular absorptions are relevant to the proposed dynamics discussed presently. The middle spectrum presents the general locations of the many absorptions that are induced by high energy irradiation of the unactivated halophosphates. These absorptions are taken from Ref. (12, 14, 29, 30, 32). They were induced by high energy irradiations from 185 nm of Hg, x-rays, and those associated with the tesla coil.

When the halophosphates are activated by Sb, Mn, and Cd, two new induced absorption bands appear under high u.v. excitation in addition to those that occur in the unactivated phosphor. For clarity, these two bands are shown alone in the lower part of the figure. They are labeled EII(Cd), the reason to be explained in the next section. The induced absorption in the region of 250 nm labeled H(II) should be noticed.

In addition to the spectral evaluation of these absorption bands induced by high u.v. irradiation, extensive electron spin resonance (ESR) investigations were performed (16, 26, 29, 30, 32, 35). There occurred a good amount of ESR spectra that was induced by high u.v. irradiation.

A particular advantage of ESR spectral studies is that the spectra are highly dependent on the symmetry of the entities producing the spectra. As a result, given a particular ESR spectrum, a fairly probable symmetry for the entity can be surmised which is extremely propitious to the identification of the defect responsible for the ESR spectrum.

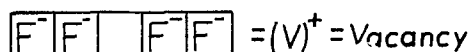
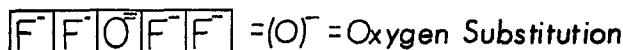
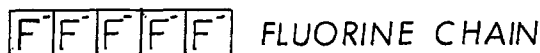
The various ESR and optical spectra were closely correlated under u.v. irradiation processes and subsequent temperature variations and thermal and radiational bleaching treatments. Through these correlations various defects were identified along with particular dependencies and interactions with other identified defects. The defects are often referred to as "color centers," and it is their specific definition and interactions with which I will be concerned in the next section.

Defect interaction model.—The identification of all the defects are not unique and discrepancies do occur among different papers. All concur, though, that the defects are constituted of vacancies, oxygen substitutions, or combinations thereof along the halogen chain in various charge states. The defect model proposed in this section is taken from Warren (29) and Warren *et al.* (30) since these papers carried through most completely an analysis of the overall phosphor depreciation effects. It was initiated by Piper, Kravitz, and Swank (32).

Identification and definitions of defects in unactivated calcium fluorapatite.—According to conditions associ-

ated with the growth process there will occur to a greater or lesser extent two primitive defects in the fluorapatite lattice. They are (i) the oxygen anion substitutions for fluorine anions and (ii) fluorine vacancies.

In Fig. 4 it was noted that the fluorine anions constituted one-dimensional chains running along the crystal axis. The two primitive defects occur consequently on the fluorine chain structure. Below is shown a string of blocks symbolizing the fluorine chain. Di-



rectly underneath this chain is shown two fluorine chains in which a fluorine ion has been replaced by an oxygen anion and a vacancy, respectively. To the right of these chains is the notation used to symbolize the corresponding defect: O for oxygen and V for vacancy. The superscript outside of the parenthesis designates the effective charge associated with the defect relative to the perfect fluorine chain.

Groupings or clusters of these primitive defects can occur. Two defects are symbolized below

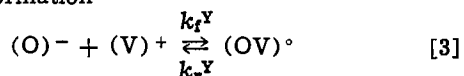


The $(OV)^{\circ}$ represents a neutral complex defect formed by the combining of the two, presumably attractive, primitive defects. This defect tends to be fairly stable. The $(VOV)^+$ complex defect is formed as symbolized and is less stable than the $(OV)^{\circ}$ complex. Apparently, no other clustering affords sufficient stability to be considered to exist leaving only these four defects present in the unirradiated halophosphate crystal.

Table I gives the four defects listed and named along with their absorption characteristic for easy reference.

Defects can reappportionate their relative abundance in accordance with a mass action law if there is sufficient mobility among themselves to afford their interaction. Although the oxygens are considered relatively immobile here, vacancy mobility is sufficient to allow any reapportionment.

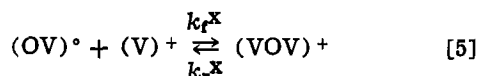
To examine this point, it is noted that the equation for Y center formation



gives an equilibrium concentration ratio for the defects

$$\frac{[(O)^-] [(V)^+]}{[(OV)^{\circ}]} = K_1 = \frac{k_f^Y}{k_r^Y} \quad [4]$$

Likewise in X center formation, the equation



gives

$$\frac{[(OV)^{\circ}] [(V)^+]}{[(VOV)^+]} = \frac{k_f^X}{k_r^X} = K_2 \quad [6]$$

Table I. Defects in the unirradiated, unactivated halophosphate

| Name | Defect | Optical absorption (nm) |
|-----------|----------------|-------------------------|
| Oxygen | $(O)^-$ | None |
| F vacancy | $(V)^+$ | None |
| Y center | $(OV)^{\circ}$ | ~185 |
| X center | $(VOV)^+$ | ~250 |

which is further converted to

$$\frac{[(O)^-] [(V)^+]^2}{[(VOV)^+]} = K = K_1 K_2 \quad [7]$$

Equation [7] shows that since $K_2 < 1$ and because of the quadratic dependence in the numerator, high oxygen and vacancy inclusions will cause more than proportionately higher concentrations (dominance) of X centers. Similarly, Eq. [4] shows that Y center concentration should be favored at lower oxygen vacancy concentrations. Such a behavior was elucidated by Warren (29) through monitoring the relative number of u.v. induced defects arising from samples variously prepared to emphasize different concentrations of the primitive defects. This analysis is also in agreement with the reduction of X center absorption under increasing temperature; as temperature is increased, the equilibrium constants K_1 increase which favors the reduction of the more complex defects.

Under high u.v. excitation these defects (or centers as they are also called) are converted to "modified centers." The essential modification of the four centers is that they can either (i) lose an electron in which case the resulting center is classified as an H center (H implies trapped hole) or (ii) gain an electron in which case the resulting defect is classified as an E center (E implying excess electron). The source or sink, as the case may be, for the electrons is simply another defect center. Therefore, under irradiation, defects are swapping electrons resulting in their own modification as well as that of other defects. Many of these modified defects have their own associated absorption bands which clearly have been induced through creation of the modified defects by high u.v. excitations. These modified centers are referred to as "color centers." Some of the H and E centers that occur under high u.v. excitation are listed in Table II along with their construction, evolution, and comments (note: e = electron, h = hole, P = permutation). E and H centers can be destroyed by converting into each other or reverting to one of the four original defects under certain radiations or heating of the crystal (i.e., radiational and thermal bleaching treatments). These processes will be enlarged upon presently.

Defect dynamics in unactivated crystals.—The defect dynamics are initiated by the 185 component of the Hg radiation. Absorption of the 185 nm radiation by the Y center causes it to lose an electron to the conduction band resulting in itself being converted to an H(I) center. This H(I) center may either remain so or with a 50% probability dissociate into an H(II) center and a vacancy which thermally moves off.

The electron that has been freed to the conduction band will be subsequently trapped by a defect located somewhere else in the crystal to produce an excess electron center (an E center). The defects which are available to trap this electron are simply the four centers; a vacancy, an oxygen substitution, an X center, and a Y center. The oxygen center, presenting an effective negative charge, would presumably repel the conduction electron and thus contribute no cross sec-

Table II. Relevant u.v. induced defects*

| Name | Defect | Evolution | Comment |
|---------------------------|-------------------|--------------------|---------------------|
| H centers (hole trap) | | | |
| H(I) | $= (OV)^+$ | $(OV)^{\circ} + h$ | |
| H(II) | $= (O)^{\circ}$ | $(O)^- + h$ | absorbs ~250 nm |
| E centers (electron trap) | | | |
| E(I) | $= (VOV)^{\circ}$ | $(VOV)^+ + e$ | |
| E(II) | $= (V)^{\circ}$ | $(V)^+ + e$ | absorbs 360, 450 nm |
| E(III) | $= (OVV)^{\circ}$ | $P(VOV)^+ + e$ | |
| E(IV) | $= (OV)^-$ | $(OV)^{\circ} + e$ | |
| B | $= (OVV)^-$ | $P(VOV)^+ + 2e$ | |

* h = hole, e = electron, P = permutation.

tion to the capture. The other three defects can be converted to their respective E centers, namely, E(II), E(I), and E(IV). The relative occurrence of these three trapping processes is a function of the crystal growth conditions according to the mass action argument. E(I) and E(IV) thermally decompose, each to an E(II) center and, respectively, to a Y center and an oxygen substitution afforded by the presumed mobility of the E(II) center.

The action of the 254 nm radiation tends to reverse this resulting E(II) production of the 185 nm radiation through its absorption by the H(II) center which resulted from thermal decomposition of the ionized Y center. Upon this absorption the H(II) center releases a hole to the valence band as it reverts to a simple oxygen substitution. The released hole is then trapped by an E(II) center causing it to revert to a simple vacancy. This is the presumed process of radiational bleaching. The vacancy can combine with the oxygen substitution to become a Y center.

Increased mobility of the E(II) centers under increasing temperatures allows them to annihilate with H(II) centers, thus creating Y centers again. This process accounts for part of the thermal bleaching.

The annihilation processes result in the replenishment of the Y centers which again causes the regeneration of E(II) centers. Obviously, there will exist some steady-state number of E(II) and H(II) centers which will evolve whose number is dependent upon the ratio of 185 to 250 nm radiation penetrating into the phosphor.

Dynamics of activated halophosphates.—The processes just enumerated appear in large measure to be taking place in activated halophosphates. The influence of the dopants does not alter the essential character of the processes, but modifies somewhat the conditions and parameters attendant to the processes. These influences of the dopants Mn^{2+} , Sb^{3+} , Cd^{2+} , and Cs^+ are summarized below.

The presence of Mn does not decidedly affect the defect dynamics mentioned above. There is some (5, 38, 39) oxidation of Mn but this appears to be minor, most likely a surface effect. Nevertheless, oxidized Mn will reduce brightness and possibly supply electrons to other defect entities.

Sb presents two effects in conjunction with the defect system. First, it absorbs both Hg u.v. components with the 185 nm component more strongly absorbed than the 254. This allows Sb, under increased concentration, to compete more favorably with Y and H(II) absorptions and to cause a reduction of the 185 to 250 nm intensity ratio within the phosphor which favors less H(II) absorption and a lower steady-state number of E(II) and H(II) centers. Second, Sb is believed (30) to moderately trap an E(II) center residing on a neighboring chain. Such a trapped E(II) center may (30) quench an excited Sb through an $Sb \rightarrow E(II)$ energy transfer process. The fact that Sb emission appears in thermoluminescence (38) may suggest a change in the oxidation state (41) of some Sb due to the interaction with a u.v. induced defect. Nevertheless, a significant loss in Sb excitation energy is presumed degraded by an induced defect interaction. The net result of these effects is that increased Sb concentration should reduce the severity of lumen depreciation consistent with the experimental observations.

Cd also presents two effects similar to those of Sb. First, by its absorption of 185 nm radiation it reduces the ratio of 185 to 254 nm radiation affording a smaller steady-state number of induced color centers to rob Sb excitation energy. Second, it strongly traps an E(II) center [termed EII(Cd)] again reducing the possibility that an E(II) center may directly rob excitation energy from Sb.

Incorporation of Cs rather than Cd in an activated halophosphate system actually increases the initial light output relative to a Cd or non-Cd halophosphate phosphor. This is due to the fact that the presence of

Cs increases the transparency at 254 nm of the unactivated halophosphate matrix so that the activator system when incorporated can more efficiently compete for the exciting radiation (10). Cs, however, does not present any absorption in the 185 nm region that would offset induced absorption at 254 nm. In light of this, the smaller brightness depreciation of the Cs containing phosphor compared even to the Cd containing phosphor is surprising and is attributed to a Cs fluxing action in the ignition process to produce a more defect-free phosphor (10). It may also be that the Cs presence inhibits the direct color center interactions with excited Sb that degrade the excitation energy since Cs can reside close to Sb as a charge compensator. Last, the u.v. induced absorption throughout the visible are generally considered of negligible importance in the loss of halophosphate brightness (10, 30).

Figure 12 (analogous to Fig. 1) symbolizes the essential loss processes. As mentioned, process 2 is assumed negligible with perhaps process 3 accounting for the most severe loss, yet it is triggered by the existence of process 1.

The defect dynamics considered so far explain the short-term depreciation in halophosphates in terms of the number density of primitive defects present in the virgin phosphor. The saturation level of the short-term depreciation in Fig. 2, as stated earlier, represents a much slower rate of depreciation. The contribution of color center or defect phenomena to this long-term phosphor depreciation in a lamp environment is not known. Certainly processes which would continually increase the defect number density of the phosphor over the long term would cause a progressive depreciation in lumen output. Such processes will be elaborated upon in the next section.

Other Defect Examples and Considerations of Short- and Long-Term Defect Mechanisms

Defects that can occur in phosphor-type solids in the lamp environment may be delineated into three broad classes:

1. The electronic class: no ionic defects are formed; just the electronic state of existing defects are changed as charge is moved around by photons inducing and bleaching color centers.

2. Photochemical class: new or additional atom or ionic defects are formed by a series of reactions beginning with a photoexcited electron.

3. Diffusional class: new defects are formed under precipitation, aggregation, or evaporation at extended defect locations or through external penetration of the phosphor by impurities.

The first class corresponds to a short-term adjustment of u.v. induced defects to the type and number density of ingrown defects. The latter two classes address the longer term generation and evolution of primitive defects. It is to these generative defects that the induced defects of class I adjust more or less quickly throughout lamp life.

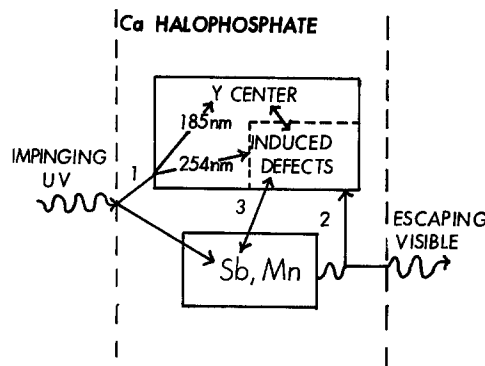


Fig. 12. Schematic of energy loss processes to the defect system of calcium halophosphate.

The ingrown and short-term induced defect dynamics of the halophosphates are a good example of the electronic class phenomena. The color center literature is abundant with other examples of this class. Under no guise of completeness or comprehensive analysis, a look at several other examples in oxidic lattices is of interest as important to lamp phosphors before consideration of generative defect processes of classes 2 and 3.

Reiterating, it can be said that the phosphor depreciation attributed to defect structures arises from (i) their possible absorption of u.v. excitation energy, (ii) visible absorption, and (iii) the fact that their presence can create an energetic environment which can capture and degrade energy from excited entities of the activator system. Impurities and intrinsic host defects are generally intimately connected and the very presence of impurities can necessitate the presence of intrinsic defects. Two major influences on the nature of this connection are growth stoichiometry and charge compensation mechanisms. Some examples of these influences are given below.

The impurities that go into the matrix may be intentional, such as entities of the activator system, or unintentional and undesired. Unwanted doping by transitional metal ions of numerous oxides have been detected and shown to be a promoting factor of color center phenomena as for example, LiNbO_3 (42, 43), CaWO_3 (44, 45), and Al_2O_3 (46). This is due to oxide lattices often having a high incorporation coefficient for transition metal ions (47, 48). Electron transfer between cation impurities or a cation impurity and a defect is considered (49) to occur most easily with the increased covalency of the oxide compounds. This, along with the easy valence state changes of transition metal ions, can lead to a tendency for multiple interimpurity charge compensation schemes (50, 51). Iron and manganese impurities substituting in trivalent cation positions may compensate as Fe^{3+} and Mn^{3+} or as Fe^{2+} - Mn^{4+} (48, 50) local pairs. In metal vanadates the VO_4^{-3} sublattice may trap an electron forming a VO_4^{-4} complex from easily oxidized impurity cations (52). So those impurity cations which have easily changed oxidation states, including some of the rare earths (53, 54), will afford a high probability of bringing about a variety of induced defects that may interfere with phosphor activation.

It was seen that growth stoichiometry affects defect density in halophosphates. Likewise CaWO_4 whose luminescence centers are the WO_4^{-2} complexes must be prepared with an excess of WO_3 due to its volatility. This excess can give rise to WO_3 defect centers in the CaWO_4 lattice (55).

The deformation of phosphors under milling can introduce lattice distortions that result in the generation of defects. For the case of halophosphate, the brightness of luminescence decreases by as much as 15%-20% according to the time of grinding which increases the dislocation density from 10^8 to 10^{10} cm^{-2} (36).

Since impurities will be present, charge compensation must occur and, therefore, intrinsic lattice defects are always present. The nature of the lattice, specifically with regard to anion and cation size, will often determine the manner of its natural tendency to charge compensate through intrinsic defect generation. Realization that some natural mechanism may be particularly injurious to efficient operation of an activator system allows possible alternative, less injurious compensation mechanisms to be introduced. As an example, trivalent impurity cations in MgO are charge compensated by positive ion vacancies (56). Such a defect, appearing negative in the lattice, can trap holes causing the lattice to more easily supply possible unwanted reducing electrons to activator entities. Generally it can be said that if something is a hole (electron) trap, it creates a tendency for something else to be an electron (hole) trap. To avoid an activator from gaining or losing an electron in such a tendency-provoking de-

fect environment, a compensating impurity may be introduced that, in a noninjurious way, fully absorbs the effect of the tendency. Easily oxidized impurities are hole traps while those easily reduced are electron traps.

Some activator systems may be particularly sensitive to a specific type of intrinsic defect. An alternative compensation scheme that suppresses the injurious intrinsic defect can restore the efficiency of the activator system. An example of such a circumstance (57) is $\text{SrAl}_{12}\text{O}_{19}:\text{Eu}^{2+}$. In aluminates, inter Eu^{2+} energy transfer under increasing Eu concentration allows the excitation energy to be transported over increasingly larger distances through the lattice before luminescence can occur. The transfer is so good that lattice defects where a nonradiative transfer can occur governs the quantum efficiency even at low Eu concentrations. Strontium aluminate: Eu^{2+} with addition of a small amount of Mg^{2+} ions incorporated at Al^{3+} sites is strongly quenched owing to the creation of oxygen vacancies that offset the reduction of positive charge in the lattice. The oxygen vacancies injurious to Eu^{2+} efficiency can be prevented by adding equal quantities of La^{3+} ions with Mg^{2+} which allows the efficiency of $\text{SrAl}_{12}\text{O}_{19}:\text{Eu}^{2+}$ to be maintained (57).

Bunch (58) showed a Mollwo-Ivey relation between peak color center (oxygen vacancy type) absorption energy and average oxygen ion spacing in several oxides of group II and group III metals. The absorption energy increases as the average oxygen spacing decreases. Such a relation can assist in predicting the deleteriousness of a specific defect according to the approach of the defect's resonance energy with that of an activator's in different oxide host lattices.

Long-term brightness depreciation due to color center phenomena arises from the generative defect processes under the photochemical and diffusional classes. The general conditions promoting such processes are considered now. The strength by which an atom is bound in its position in a solid has a profound effect on the damage that can occur in the solid under radiation. The atoms in ionic solids are bound to their positions by the electrostatic binding energy

$$\text{Electrostatic binding energy} = \frac{A(Ze)^2}{r^2}$$

where the ionic charges are $\pm Ze$, r is the nearest neighbor distance, and A is the Madelung constant (~ 1.6 - 1.8). The electrostatic binding energy for alkali halides ($Z = 1$) are from 6 to 10 eV whereas that for the alkaline earth oxides ($Z = 2$) is 30 to 40 eV. The higher binding energy of the alkaline earth oxides is of course responsible for the hardness and refractory nature of MgO compared to NaCl, but also for the fact that MgO is quite resistant to radiational damage unlike NaCl. The electronic excitations of alkali halides brought on by u.v. radiation have energies of 5-10 eV, which is sufficient to create defects since the atomic binding energies have the same range. In the alkaline earth oxides, on the other hand, the electronic excitations are still only 5-10 eV and clearly far less able to cause atomic displacements against 30-40 eV binding energies (2).

In the less homogeneous lattices of phosphors the local binding energy is the yardstick by which to measure propensity to radiation damage. Local binding energy will be quite sensitive to the local structure. A phosphor's ability to resist longer term color center depreciation is strongly dependent on its points of weak local structure where defect generating ionic displacements can occur more easily. Displacements can be driven by aggregation processes, gradient diffusions, or through the continual polarization stresses brought on by u.v. maintained induced defects. The last refers to a photochemical process. Typically, under u.v. excitation a self-trapped electron or hole may occur, possibly in response to hole or electron trap impurities. The lattice structure in the region of the

self-trapped entity may be sufficiently weak to give in to the local distortion of the self-trapped entity by local atomic rearrangements resulting in vacancy and/or interstitial creation (59, 60). Tamatani (49) has ascribed the severe and irreversible depreciation of the $K\beta$ - $Al_2O_3:Eu^{2+}$ phosphor to permanent defects caused by ion and/or vacancy diffusion instigated by a self-trapped electron. He states that the potassium and oxygen ions are loosely bound in the mirror plane between the spinel layers of aluminum and oxygen ions in the $K\beta$ - Al_2O_3 lattice. Loosely bound ions near flaws or extended defects can also be precursors to new defect formation.

Loss of surface fluorine from halophosphates would allow new vacancies to diffuse into the phosphor adding to the defect populations. Last, phosphors that most easily permit Hg ions to diffuse into them should be degraded somewhat by either the direct presence of the Hg or the various other defects that its presence generates.

The processes due to color centers which lead to brightness depreciation in phosphors can be quite subtle and complicated as evidenced by the above examples. The design of phosphors resistant to color center effects will require judicious choice of additives to offset the color center interactions as well as minimizing as much as possible the primitive defects from which color centers are born.

Manuscript submitted May 22, 1980; revised manuscript received Aug. 4, 1980. This was Paper 212 presented at the St. Louis, Missouri, Meeting of the Society, May 11-16, 1980.

Any discussion of this paper will appear in a Discussion Section to be published in the December 1981 JOURNAL. All discussions for the December 1981 Discussion Section should be submitted by Aug. 1, 1981.

Publication costs of this article were assisted by GTE Products Corporation.

REFERENCES

1. P. D. Townsend, *Nature*, **258**, 293 (1975).
2. W. A. Sibley and D. Pooley, "A Treatise of Material Science and Technology," Vol. 74, p. 45, Academic Press, New York (1974).
3. D. L. Dexter, *J. Chem. Phys.*, **21**, 836 (1953).
4. G. T. Bauer, *This Journal*, **115**, 1178 (1968).
5. E. F. Apple, and J. D. Aicher, Proceedings of the International Conference on Luminescence, 1966, Budapest, p. 2013.
6. J. H. Singleton and L. Suchow, *This Journal*, **110**, 36 (1963).
7. J. A. Parodi, *J. Lumin.*, **9**, 315 (1974).
8. L. E. Vrenken, J. H. DeVette, and R. W. Van Der Wolf, *Illumin. Eng. J.*, **59**, 59 (1964).
9. A. Wachtel, *This Journal*, **105**, 256 (1974).
10. K. Narita and N. Tsuda, *Bull. Chem. Soc. Jpn.*, **48**, 2047 (1975).
11. E. F. Apple, *This Journal*, **110**, 374 (1963).
12. R. K. Swank, *Phys. Rev.*, **135**, A266 (1964).
13. St. Naray-Szabo, *Z. Kristallogr.*, **75**, 387 (1930).
14. L. Suchow, *This Journal*, **108**, 847 (1961).
15. P. D. Johnson, *ibid.*, **108**, 159 (1961).
16. D. I. M. Knotterus, A. Lanjou, and H. W. den Hartog, *Phys. Status Solidi*, **41**, 95 (1977).
17. J. S. Prener, *This Journal*, **114**, 77 (1967).
18. F. M. Ryan and F. M. Vodoklys, *ibid.*, **118**, 1819 (1971).
19. T. S. Davis, E. R. Kreidler, J. A. Parodi, and T. F. Soules, *J. Lumin.*, **4**, 48 (1971).
20. J. G. Rabatin, G. R. Gillooly, and J. W. Hunter, *This Journal*, **114**, 956 (1967).
21. E. A. Dale, Private communication.
22. P. H. Kasai, *J. Phys. Chem.*, **66**, 674 (1962).
23. W. W. Piper, *J. Lumin.*, **1**, 2, 669 (1970).
24. W. W. Piper and J. S. Prener, *Phys. Rev. B*, **6**, 2547 (1972).
25. R. W. Warren, *ibid.*, **2**, 4383 (1970).
26. F. M. Ryan, R. C. Ohlmann, J. Murphy, R. Mazelsky, G. R. Wagner, and R. W. Warren, *ibid.*, **2**, 2341 (1970).
27. F. M. Ryan and F. M. Vodoklys, *This Journal*, **118**, 814 (1971).
28. J. S. Prener, W. W. Piper, and R. M. Chrenko, *J. Phys. Chem. Solids*, **30**, 1465 (1969).
29. R. W. Warren, *Phys. Rev. B*, **6**, 4679 (1972).
30. R. W. Warren, F. M. Ryan, R. H. Hopkins, and T. Van Broekhoven, *This Journal*, **122**, 752 (1975).
31. T. F. Soules, R. L. Bateman, P. A. Hewes, and E. R. Kreidler, *Phys. Rev. B*, **7**, 1657 (1973).
32. W. W. Piper, L. C. Kravitz, and R. K. Swank, *Phys. Rev.*, **138**, A1802 (1965).
33. P. D. Johnson, *J. Appl. Phys.*, **32**, 127 (1961).
34. D. I. M. Knotterus, H. W. den Hartog, and W. Van der Lugt, *Phys. Status Solidi A*, **13**, 505 (1972).
35. B. Segall, G. W. Ludwig, H. H. Woodbury, and P. D. Johnson, *Phys. Rev.*, **128**, 76 (1962).
36. L. N. Aleksandrov, V. D. Zolotov, and U. S. Mordyuk, *Inorg. Mater.*, **12**, 1639 (1976).
37. G. T. Bauer, *This Journal*, **123**, 79 (1976).
38. A. E. Skreblyukov, T. I. Morozova, E. R. Il'mas, V. D. Zolotov, P. Mordyuk, and V. S. Mordyuk, *Zh. Prikl. Spektrosk.*, **21**, 347 (1974).
39. J. Rudolph, *Osram Tech. J.*, **10**, 141 (1969).
40. A. E. Skreblyukov, T. I. Morozova, V. D. Zolotov, T. P. Mordyuk, and R. S. Zhuravleva, *Zh. Prikl. Spektrosk.*, **22**, 883 (1975).
41. W. A. Weyl, "Coloured Glasses," p. 507, Dawson's of Pall Mall Pub., London (1959).
42. E. G. Valyashko, L. N. Roshkovich, and V. A. Timoshenkov, *Opt. Spectrosk.*, **24**, 637 (1968).
43. W. Philips, J. J. Amodei, and D. L. Stachler, *RCA Rev.*, **33**, 94 (1972).
44. D. G. Gronemeyer and M. W. Beaubien, *J. Appl. Phys.*, **35**, 1779 (1964).
45. D. G. Gronemeyer and M. W. Beaubien, *ibid.*, **36**, 3414 (1965).
46. S. Geschwind, P. Kisluik, M. P. Klein, J. P. Remeika, and D. L. Wood, Proceedings of International Conference on Paramagnetic Resonance, Jerusalem, 1962.
47. H. Bernhardt, *Phys. Status Solidi A*, **31**, 365 (1975).
48. H. Bernhardt, *ibid.*, **37**, 445 (1976).
49. M. Tamatani, *Jpn. J. Appl. Phys.*, **13**, 957 (1974).
50. L. Riseberg and M. J. Weber, *Solid State Commun.*, **9**, 791 (1971).
51. K. Mori, *Phys. Status Solidi*, **42**, 375 (1977).
52. M. Ya. Khodos, A. A. Foliev, and B. V. Shul'gin, *Inorg. Mater.*, **10**, 1658 (1974).
53. G. N. Pirogova, V. E. Kritskaya, N. A. Anisimov, and L. G. Dem'yashkina, *Inorg. Mater.*, **11**, 1812 (1975).
54. S. Kh. Batygov, B. I. Denker, V. F. Kalabukhova, V. A. Myzina, and V. V. Osiko, *ibid.*, **12**, 1057 (1974).
55. H. A. Koehler and C. Kikuchi, *Phys. Status Solidi*, **43**, 423 (1977).
56. A. E. Hughes and B. Henderson, "Point Defects in Solids," p. 381, Plenum Press, New York (1972).
57. J. L. Sommerdijk and A. L. N. Stevels, *Philips Tech. Rev.*, **37**, 221 (1977).
58. J. M. Bunch, *Phys. Rev. B*, **16**, 724 (1977).
59. J. M. Ortega, *ibid.*, **19**, 3222 (1979).
60. A. M. Stoneham, *Adv. Phys.*, **28**, 457 (1979).

An Experimental Proof of Radiative Recombination Mechanisms of Electron-Hole Pairs at Activator Ions

Lyuji Ozawa*¹

Zenith Radio Corporation, Glenview, Illinois 60025

ABSTRACT

It has been shown that the concentration dependence curve of activator luminescence provides us with a powerful tool in studying cathodoluminescence. The experimental results reveal the excitation mechanisms of activator ions by irradiation of electron beam on phosphor crystals; two excitation mechanisms should be considered: (i) direct excitation by incident electrons, including internally generated secondary electrons; and (ii) indirect excitation through the mobile electron and holes generated by incident electrons. The experimental results also suggest a possible model that (iii) radiative recombination of electron-hole pairs only occurs at the activator ions showing two valences at the ordinary conditions, and (iv) the type of radiative recombination process at the activator ions is determined by the type of carrier which is first trapped.

It is generally observed that under ionized radiation, many inorganic crystals emit characteristic luminescence in the visible spectral region (1) caused by the chemical impurities (i.e., activator ions); different crystals exhibit different luminescence efficiencies with the same activator ions. The variation in luminescence efficiencies, however, has been believed to be due to a difference in the probability of energy transfer from radiation-induced carriers of either charge (or excited host lattice) to the activator ions. In this report, we shall try to clarify experimentally these mechanisms of activator ions by incident electrons.

Electron beam irradiation of crystals creates equal amount of electrons and holes (EH's) i.e., radiation-induced carriers, as well as exciting lattice ions in the volume V_d where the incident electrons have penetrated. Hence, there are three possible modes of excitation of activator ions: (i) direct excitation by incident electrons, including internally generated secondary electrons; (ii) indirect excitation by EH's (i.e., radiative recombination of EH's); and (iii) some combination of the two. Even though quite different excitation mechanisms are involved, an ambiguity arises because the activator ions emit the same characteristic luminescence. We, thus, cannot distinguish the difference between the excitation mechanisms from the luminescence spectrum alone. It has recently been shown (2) that the concentration dependence (CD) curve of activator luminescence provides us with a powerful tool for better understanding of the excitation mechanisms of activator ions by incident electrons (10 keV). The type of the excitation mechanisms can be determined from the CD curves. This is explained for the CD curves illustrated in Fig. 1. Before the explanation of the CD curve, however, we must discuss the luminescence intensity measurements on the phosphor crystals.

Luminescence Intensity Measurements

In the study of luminescence intensities from phosphor crystals on the screen, we usually measure time-averaged luminescence intensities $\langle I \rangle$ which are proportional to the number of quanta emitted from the excited activator ions in unit time, on the assumption that each excited activator ion in the crystal emits a photon and returns to ground state. The activator ions are excited as a consequence of the action of the exciting energy carriers to activator ions in the crystals on

the screen in unit time. Thus, $\langle I \rangle$ (number of photons/sec/volume) from the phosphor crystals on the screen is expressed as a form of the volume integral in unit time. The phosphor screen is usually large e.g., 1 cm² compared with the crystal size (e.g., phosphor crystals are usually about 10 μ m). In such a screen, the excitation of activator ions only occurs in the crystals in the first layer of the irradiation side because the penetration depth of the incident electrons (10 keV) is about 0.4 μ m (3), and EH's are never transferred to other crystals [the crystal is covered with the surface recombination center of EH's (4)]. When the size of electron beam on the screen is kept constant for all measurements (it is usually so), $\langle I \rangle$ is proportional to the number of the excited activator ions in the finite volume V in the crystals arranged in the first layer on the fixed screen area (i.e., cross-sectional area of electron beam) in unit time. Hence, $\langle I \rangle$ is proportional to a result of the volume integral of the action of the exciting energy carriers to activator ions in V and in unit time, which is expressed as

$$\langle I \rangle = k_1 \int_0^t \int_V NJ \, dv \, dt \quad [1]$$

where N is the number of activator ions in V , J is the number of exciting energy carriers having entered (or generated) in V , and k_1 is constant. (In contrast, the measurement results of many physical properties are given by a form of the differential; e.g., optical absorption, conductivity, lifetime of the excited state, and others.) For studying $\langle I \rangle$, we must take account of the volume integral, not the differential.

There are two ways of obtaining the solution of Eq. [1]: (i) a mathematical solution and (ii) a qualitative approach. In this study, we have taken the qualitative approach on the assumption that $\langle I \rangle$ (substantially the number N^* of the excited activator ions per unit time) is proportional to the number of the possible combinations of activator ions and exciting energy carriers in V and in unit time. This study is a first step for increasing the better understanding $\langle I \rangle$ from the phosphor crystals. The results of this study, therefore, will give a macroscopic (instead of microscopic) picture of the excitation mechanisms of activator ions by electron beam irradiation on phosphor crystals.

The chemical analysis usually informs us that the activator ions are uniformly distributed in the crystal, and the activator ions never move out of their positions under the ordinary cathode-ray excitation conditions. For the excitation of activator ions, the activator ions must be visited (or sampled) by the exciting energy

* Electrochemical Society Active Member.

¹ Present address: Matsushita Electric Industrial Company, Limited, Material Research Laboratory, Osaka, Japan.

Key words: luminescence, phosphor, concentration dependence curve.

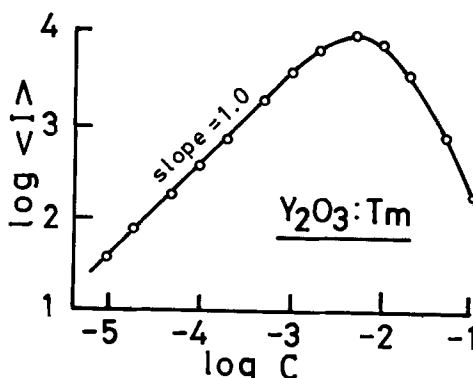
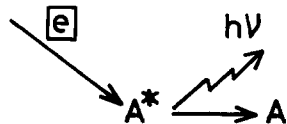
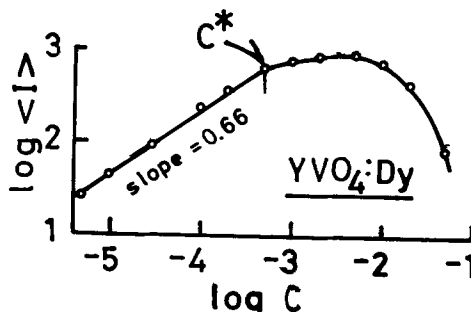
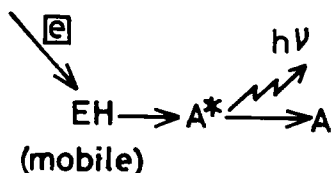
(A) direct excitation(B) excitation by mobile EH

Fig. 1. Difference in concentration dependence curves with types of excitation mechanisms of activator ions by incident electrons. (A) Curve for directly excited activator luminescence which exhibits no crystal size effect and has unity slope. (B) Curve for activator luminescence arising from recombination of mobile carriers; the curve discontinues at C_D^* which exhibits crystal size effect due to migration of mobile carriers.

carriers (e.g., photons and/or electrons) which are travelling in the crystal. Consequently, the different travelling mode of the carriers results in the different sampling (i.e., excitation mode) of the activator ions. In order to discuss the CD curve of $\langle I \rangle$ shown in Fig. 1, thus, we know about the travelling modes of the incident electrons and EH's in the phosphor crystals.

CD Curve for Directly Excited Activator Luminescence

When the crystal is irradiated by electron beam, a large part of the incident electrons penetrate into the crystal and the residuals are ejected from the crystal surface (5) (i.e., backscattered primary electrons due to the elastic scattering with the ions arranged in the surface layers of the crystal). The penetrating electrons lose their energy by elastic and inelastic collisions with the lattice ions along the electron trajectories, generating x-ray, Auger electrons, secondary electrons, electron-hole pairs, and phonons. The electron trajectories in the crystal can be computed by using Monte Carlo technique (6) with single and/or multiple scattering models (7, 8). The profile of the calculated electron trajectories (6-10) are qualitatively confirmed with the observation by Ehrenberg and Frank (11), who have used microphotographs of cathodoluminescence from CaWO_4 , KI, and plastic. This indicates the incident electrons are randomly scattered (travelling) in the penetration volume. The lattice ions are excited not only by the incident electrons but also by the secondary electrons generated internally. Bohm and Pine (12) proposed a model that the secondary electrons and scattered incident electrons form the electron gas plasma in the crystal, and the lattice ions are excited with the electron-plasmon interaction to produce another secondary electron of the energy smaller than that of the previous one, i.e., the cascade model. Quinn (13) gave an equation to calculate the mean-free path of the plasma electrons in various energies; according to his equation, the mean-free path is about 10Å for 1 keV electrons and about 100Å for 10 keV electrons. Hence, only the secondary electrons generated in the surface volume in depth smaller than the mean-free path can escape from the crystal surface, giving rise to Auger electrons and true secondary electrons which can be collected in front of the crystal; both are now used for studying the surface physics of

the crystal. (Auger electrons which are characterized by the elements are used for the identification of the elements in the surface volume and true secondary electrons are used as a signal source in the scanning electron microscope.) The existence of the plasmon in the crystal may be proved by analyzing both the true secondary electrons collected in front of the crystal and the values of the energy loss of the incident electrons in the crystal. Amelio (14) calculated the theoretical distribution of the true secondary electrons, which were in agreement with the experimental results, for Cu metal and Si semiconductor based on the electron-plasmon interaction (dominant) plus electron-electron interaction. Both theory and experiments of the energy loss of the incident electrons show that the values for Si, Ge, ZnS, PbS, SiO_2 , MgO, and others are explained by the electron-plasmon interaction (15). These results are probably enough to draw a conclusion that the lattice ions in the crystals are predominantly excited by the electron-plasmon interaction. If the activator ions in the crystal are excited with the plasmons (i.e., incident electrons and internally generated secondary electrons), the excitation of activator ions is limited in the volume where the plasmons are contained. Since the mean-free path of the plasma electrons (less than 100Å) is negligibly small as compared with the penetration depth of the incident electrons (0.4 μm for 10 keV), the volume V for direct excitation of the activator ions by the plasmons is, as a first order, approximated to the volume V_d defined by the penetration depth of the incident electrons and cross-sectional area of the incident electron beam on the screen which is constant for the measurements of $\langle I \rangle$. The total surface area of the crystals arranged in the first layer on the fixed screen area is not only a constant but is also independent of the crystal size (16). Consequently, V_d is independent of the crystal size of phosphors and is a constant for a given cathode-ray voltage (the crystal size greater than the penetration depth). Since the incident electrons are randomly scattered (travelling) in V_d , it may be said that in some time interval, the plasmons are randomly distributed in V_d , so that the random mixing of activator ions N and the plasmons J in V_d and in unit time can be considered. It follows that the excitation of activator ions by the plasmons is comparable with the random sam-

pling of N by J in V_d and in unit time. If both N and J are large (it is always so), the outcome of the random sampling (corresponding to N^*) in V_d in unit time is proportional to the number of possible combinations of N and J , which is given by

$$N^* = k_2 \frac{N! J!}{(N-1)!(J-1)!} = k_2 N J \quad [2]$$

where k_2 is constant. This leads to a linear dependence of $\langle I \rangle$ on both N and J . Under the given excitation conditions (e.g., J is constant), $\langle I \rangle$ is linear with the activator concentration in the range where self-concentration quenching is negligible, and the normalized CD curves of $\langle I \rangle$ should exhibit no difference due to the crystal size (V_d remains a constant even if the crystal size is changed). Furthermore, the scattering of the plasmons in V_d is possibly independent of the irradiation time of the electron beam at the ordinary conditions of the cathodoluminescence study, so that the CD curve of $\langle I \rangle$ shows no dependence on the excitation duration (i.e., the pulse width effect). Therefore, if the activator ions are only excited directly by the incident electrons (and internally generated secondary electrons), the normalized CD curves will be the same for pulsed and continuous (d-c) excitations, and the CD curves, plotted on logarithmic basis of the activator luminescence, will have unity slope in the low activator concentration range and exhibit no crystal size effect. This is the case for Tm^{+3} luminescence in $\text{Y}_2\text{O}_3:\text{Tm}$ as shown in Fig. 1(A); the CD curve of Tm^{+3} luminescence exhibits no crystal size effect and no pulse width effect, and the curve has unity slope in the low activator concentration range.

CD Curve for Indirectly Excited Activator Luminescence

The plasma electrons also produce EH's which have the long mean-free path (12). If the activator ions are excited by these EH's (i.e., radiative recombination of EH's at activator ions), the excitation of the activator ions occurs in the effective volume V_e (greater than V_d) in which the EH's are present.

We assume that EH's can move out from the volume in which they are created and disappear by one or more recombination mechanisms (radiative or nonradiative) at the intrinsic and extrinsic recombination centers, which may be host atoms and surface and internal recombination centers, respectively. Since no bandgap luminescence has ever been observed with the phosphor crystals, EH's must disappear at surface and internal recombination centers. It is known empirically that the formation of surface recombination centers depends largely on preparation conditions (4); for crystal prepared under well-controlled conditions (this is true for phosphor crystals), it is assumed that the rate of surface recombination of EH's is constant. Hence the recombination rate of EH's depends solely on the presence of internal recombination centers. There are two types of internal recombination centers to be considered: chemical impurities, including activator ions; and lattice imperfections (e.g., vacancies, dislocations, grain boundaries, and interstitials). It has been shown in our previous work (17) that lattice imperfections do not influence the internal recombination of EH's in Y_2O_3 . This is likely to be true for other phosphors. If so, the migration of EH's generally depends on the activator concentration when 99.9999% pure material is used.

We assume that the migration of an EH terminates on the first visit to an unexcited activator ion; the average migration distance L of EH's in the crystal increases as activator concentration decreases. It follows that there are two activator concentration regions in which L is limited by (i) crystal size ϕ_M (i.e., $L = \phi_M$) and by (ii) activator concentration (i.e., $L < \phi_M$). Because the excitation of activator ions by EH's occurs

in the crystals arranged in the first layer on the fixed phosphor screen area, the CD curve of $\langle I \rangle$ should be inflected (i.e., have a discontinuity in the curve) at the activator concentration C^* corresponding to $L = \phi_M$. Therefore, the value of C^* of the CD curve of $\langle I \rangle$ shows the crystal size effect; the value of C^* decreases as the crystal size increases. In the concentration region below C^* , the effective volume will be limited by the total volume V_ϕ of the crystals involved which is a constant. Under this condition, the number of excited activator ions per unit time will be proportional to the number of EH's created in unit time and also to the number of activator ions N_ϕ in V_ϕ . At concentration greater than C^* , the effective volume is smaller than V_ϕ and decreases as C increases. Therefore, the number of activator ions involved in the excitation is no longer equal to N_ϕ but instead is related to the number of activator ions N_e in the effective volume V_e which shrinks with increasing activator concentration (even as ϕ_M remains constant). Consequently, the CD curve of $\langle I \rangle$ has two characteristic slopes depending on the activator concentration while the value of C^* depends on crystal size. The experimental CD curves of $\langle I \rangle$ for many efficient cathodoluminescent phosphors, indeed, have two slopes and the value of C^* exhibits the crystal size effect (3, 17, 18), showing that the activator luminescence arises from the radiative recombination of mobile EH's; however, the interpretation of the experimental value of C^* and the slopes is complicated by the facts that the value of C^* for some phosphors (e.g., $\text{Y}_2\text{O}_2\text{S}:\text{Eu}$) differs greatly with the excitation mode (e.g., d-c and pulse excitations), even if the crystal size is the same. Figure 2 shows the CD curves of $\text{Y}_2\text{O}_2\text{S}:\text{Eu}$ ($\phi_M = 3 \mu\text{m}$) under d-c and pulse (2 μsec) electron beam irradiation; the value of C_p^* , for pulse excitation, is 1×10^{-4} whereas the value of C_D^* , for d-c excitation, is 2×10^{-3} (20 times greater). C_D^* depends on crystal size, activator concentration, and excitation intensity, for which the experimental equation can be expressed as

$$C_D^* = \frac{k_3}{\phi_M} \quad [3]$$

where k_3 is a constant relating to the excitation intensity; k_3 increasing with the excitation intensity. On the other hand, C_p^* does not depend on excitation intensity in the range studied (peak beam density smaller than $10 \mu\text{A}/\text{cm}^2$) and can be expressed as

$$C_p^* = \frac{k_4}{\phi_M} \quad [4]$$

where $k_4 = 3 \times 10^{-8}$ cm. Furthermore, the slopes below the inflection points are unit for pulse excitation

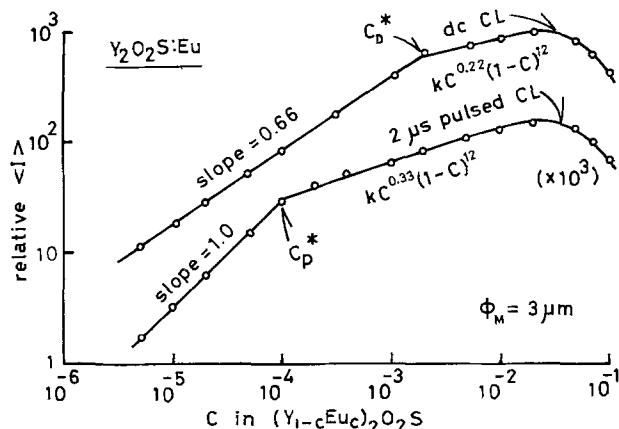


Fig. 2. Concentration dependence curves of Eu^{+3} (5D_0 luminescence) of $\text{Y}_2\text{O}_2\text{S}:\text{Eu}$ ($\phi_M = 3 \mu\text{m}$) under irradiation of continuous (d-c) and pulsed electron beam.

and 0.66 (sublinear) for d-c excitation. These results strongly suggest that the excitation of activator ions by EH's is not simply expressed by the random sampling by the EH's, and that the EH's probably do not migrate randomly on cation lattice sites even if there is no externally applied field on the crystals. Further study on the motion of EH's will prove to be an interesting subject.

Although we do not clarify the ambiguities of C_D^* , C_p^* , and slopes of the CD curves in this study, it is sure that under the given d-c excitation conditions, the CD curve of $\langle I \rangle$ certainly has two slopes depending on the activator concentration which the value of C_D^* is changed with the crystal size (2, 18) according to Eq. [3], showing that the activator luminescence arises from the radiative recombination of mobile EH's (the activator ions are not excited directly). Thus, if the activator ions are excited by mobile EH's (i.e., if radiative recombination of mobile EH's occurs at activator ions) the CD of $\langle I \rangle$ under d-c excitation differs significantly from the curve for directly excited activator luminescence; the curve should have two slopes which inflected at C_D^* and the value of C_D^* exhibits a crystal size effect (due to the migration of EH's). This is a case for Dy^{+3} luminescence in $YVO_4:Dy$ as shown in Fig. 1(B).

We use, as a new tool, these distinguishable differences between direct excitation and excitation by mobile EH's seen in the CD curve of cathodoluminescence to study further the excitation mechanisms of the activator ions by incident electrons.

It should be noted that if the concentration quenching mechanisms are involved in the range of C_D^* , the inflection of the CD curves, eventually the crystal size effect, is vague. This is a case of the CD curve of $ZnS:Cu$ (or Ag) and of the 5D_1 and 5D_2 Eu^{+3} luminescence (19). The inflection point at C_D^* is also vague if the phosphor crystals have a wide distribution in size. We do not use these CD curves in this study.

Results and Discussion

The present study was made with Y_2O_3 , YVO_4 , and Y_2O_2S crystals activated with eight rare earth elements (Pr, Sm, Eu, Tb, Dy, Ho, Er, and Tm) which emit line luminescence in the visible spectral region (20). The trivalent rare earth (RE^{+3}) activator ions are quite suitable for this purpose for the following reasons: first, each RE^{+3} emits its characteristic, easily identifiable, luminescence spectrum; second, RE^{+3} and Y^{+3} compounds form solid-solution over a wide range; and third, under the ordinary conditions, some RE's show two valences (e.g. RE^{+3} and RE^{+2} or Re^{+3} and RE^{+4}) while others exhibit one valence (RE^{+3}).

The results indicate that two modes of excitation of activator ions should be considered for ordinary cathodoluminescence study; direct excitation and indirect excitation through mobile EH's. If the activator ions are excited by the mobile EH's the number of directly excited activator ions is negligibly small as compared with the number of EH's (substantially the number of the activator ions excited by EH's in the crystals). It follows that direct excitation results in weak cathodoluminescence and the radiative recombination of mobile EH's at activator ions results in high efficiency. Thus, we may explain the major difference in efficiency of the same RE^{+3} in different host crystals, as will be described below.

Figure 3(A) shows the CD curves for Eu^{+3} luminescence (${}^5D_0 \rightarrow {}^7F_2$) in $Y_2O_3:Eu$ and $Y_2O_2S:Eu$ under the continuous (d-c) irradiation of electron beam (10 keV, $0.2 \mu A/cm^2$); in both crystals the Eu^{+3} are excited by mobile EH's. In contrast, Fig. 3(B) shows the CD curves for Pr^{+3} luminescence from $Y_2O_3:Pr$ (${}^3P_0 \rightarrow {}^3H_6$) (21) and $Y_2O_2S:Pr$ (${}^3P_0 \rightarrow {}^3H_4$) (22), respectively; there is a direct excitation of Pr^{+3} in Y_2O_3 , and Pr^{+3} is excited by mobile EH's in Y_2O_2S . The results obtained are summarized in Table I. It is inferred that

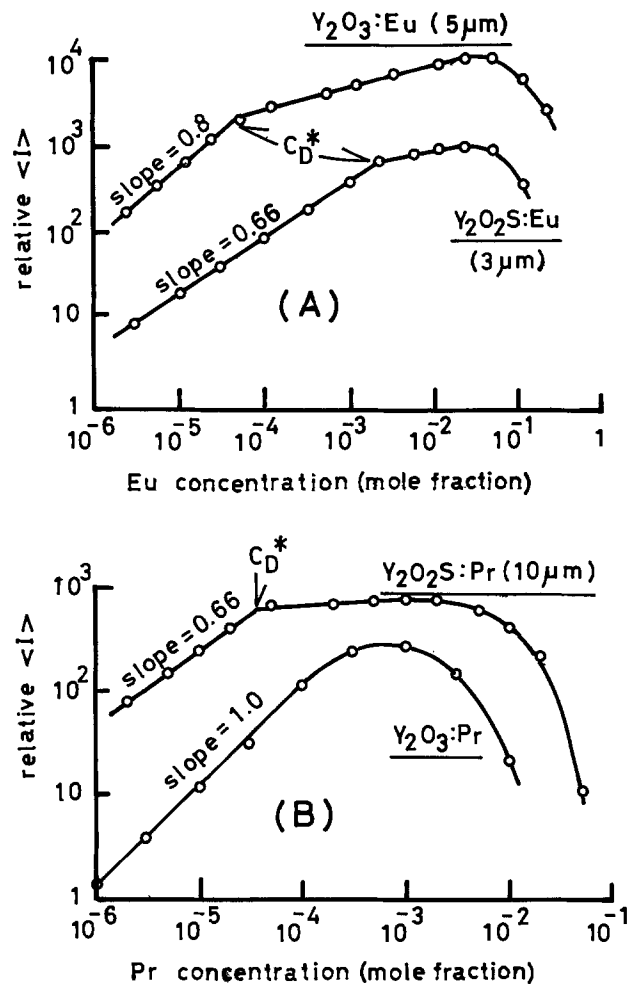


Fig. 3. Concentration dependence curves of Eu^{+3} and Pr^{+3} under continuous irradiation of electron beam. (A) Curve for $Y_2O_3:Eu$ ($\phi_M = 5 \mu m$) and $Y_2O_2S:Eu$ ($\phi_M = 3 \mu m$). (B) Curves for $Y_2O_3:Pr$ and $Y_2O_2S:Pr$ ($\phi_M = 10 \mu m$).

trivalent RE ions which can also be divalent (23) (i.e., Eu, Sm, and Dy) are excited by EH's in Y_2O_3 , YVO_4 and Y_2O_2S . The trivalent RE ions which can also be tetravalent (23) (i.e., Tb and Pr) are excited by EH's in Y_2O_2S . The RE ions are not excited by EH's in Y_2O_3 and YVO_4 (they are excited directly); the sulfur ion rather than the crystal structure is probably responsible for their excitation in Y_2O_2S . This is confirmed for Tb in La_2O_3 and La_2O_2S (both host crystals having the same crystal structure, hexagonal with D_{3d}^5 space group). There is direct excitation of Tb^{+3} in La_2O_3 and Tb^{+3} is excited by EH's in La_2O_2S . [These results may explain why Cu (and Ag) activator ions which show two valences (+1 and +2) form the recombination centers for EH's in ZnS , but not in ZnO . It will be interesting to further the experiments on this

Table I. Experimental results on the excitation mechanisms of rare earth activator ions in Y_2O_3 , YVO_4 , and Y_2O_2S by incident electron beam

| Activator ions | Crystals | | |
|--|----------|---------|-----------|
| | Y_2O_3 | YVO_4 | Y_2O_2S |
| Eu, Dy, and Sm (RE^{+3} and RE^{+2}) | RC | RC | RC |
| Tb and Pr (RE^{+3} and RE^{+4}) | direct | direct | RC |
| Ho, Er, and Tm (RE^{+3}) | direct | direct | direct |

RC: recombination centers of electrons and holes
direct: direct excitation by incident electrons

point.) RE ions which exhibit only one valence RE^{+3} at the ordinary conditions (i.e., Er, Ho, and Tm) do not form recombination centers (they are excited directly) in the crystals studied. Thus, the recombination of EH's occurs at impurities showing two valences at the ordinary conditions. These results suggest that the recombination of EH's in the rare earth phosphors, which have many direct excitation lines in the spectral region of the energy smaller than the bandgap energy of host crystals, is probably independent of the location of impurity states in the bandgap of the host crystal as has been previously considered (24).

From the above results (Table I), one may propose a model of a recombination mechanism of EH's at activator ions. Using RE ions as an example, we shall explain this model (Fig. 4). In the crystals, the RE ion, which shows the trivalent and divalent traps first as electrons and is converted to RE^{+2} , producing a negatively charged local field. A hole is attracted to this region and is captured by the RE^{+2} to form the excited state of RE^{+3} (RE^{+3*}). The excited RE^{+3*} , after remaining some time in its excited state, emits a photon (luminescence) and returns to the ground state to repeat the excitation process with another EH [Fig. 4(A)]. In the crystal containing sulfur, the RE^{+3} , which shows RE^{+3} and RE^{+4} , can first trap a hole (probably from the sulfur ion), and the RE^{+3} is converted to RE^{+4} , producing a positively charged local field. This RE^{+4} then captures the electron to form RE^{+3*} . The RE^{+3*} returns to the ground state after emitting a photon [Fig. 4(B)]. These models suggest that the type of carrier which is first trapped determines the type of recombination process at the activator ions. The first trapped carrier in Y_2O_3 and YVO_4 crystals is an electron, and in Y_2O_2S crystal, it is either an electron or a hole (depending on the impurities).

As a concluding remark, the usefulness of the concentration dependence curve of the activator luminescence has been demonstrated. Under irradiation of electron beam on phosphor crystals, two excitation mechanisms of the activator ions should be considered; direct excitation by electron beam and the excitation through the mobile electrons and holes generated by incident electrons (i.e., radiative recombination of the

electron-hole pairs). The experimental results of the rare earth activators suggest a possible model that the radiative recombination of electron-hole pairs only occurs at the activator ions showing two valences. It should be noted that the results of the concentration dependence curves of the activator cathodoluminescence only give a macroscopic picture and do not allow the drawing of a microscopic picture of the excitation of activator ions, e.g., whether resonance energy transfer and other Auger type process are involved. I feel that the theoretical consideration and further experiments by other techniques are necessary to prove the precise and microscopic picture of the excitation mechanisms of the activator ions by electron-hole pairs. I hope the experimental results of this study may suggest some ideas for the further study.

Manuscript submitted Aug. 6, 1979; revised manuscript received July 23, 1980. This was Paper 342 presented at the Seattle, Washington, Meeting of the Society, May 21-26, 1978.

Any discussion of this paper will appear in a Discussion Section to be published in the December 1981 JOURNAL. All discussions for the December 1981 Discussion Section should be submitted by Aug. 1, 1981.

Publication costs of this article were assisted by Tektronix, Incorporated.

REFERENCES

1. F. A. Kroger, "Some Aspects of the Luminescence of Solids," Elsevier Publishing Co., New York (1948); H. W. Leverenz, "An Introduction to Luminescence of Solids," Dover Publications, Inc., New York (1968).
2. L. Ozawa and H. N. Hersh, *Phys. Rev. Lett.*, **36**, 683 (1976).
3. J. R. Young, *Phys. Rev.*, **24**, 292 (1955); J. S. Prener, *This Journal*, **122**, 1516 (1975).
4. "Surface Physics of Phosphors and Semiconductors," C. C. Scott and C. E. Reed, Editors, Academic Press, New York (1968); G. Gergely, *J. Phys. Chem. Solids*, **17**, 112 (1960).
5. C. F. F. Garlick, "Luminescence of Inorganic Solids," P. Goldberg, Editor, p. 685, Academic Press, New York (1966).
6. "X-ray Optics and Mineralysis," P. Descams and J. Philibert, Editors, pp. 112 and 127, Hermann,

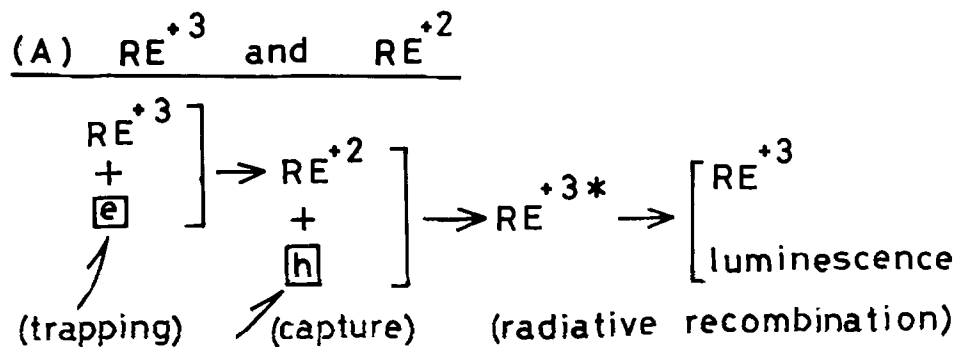
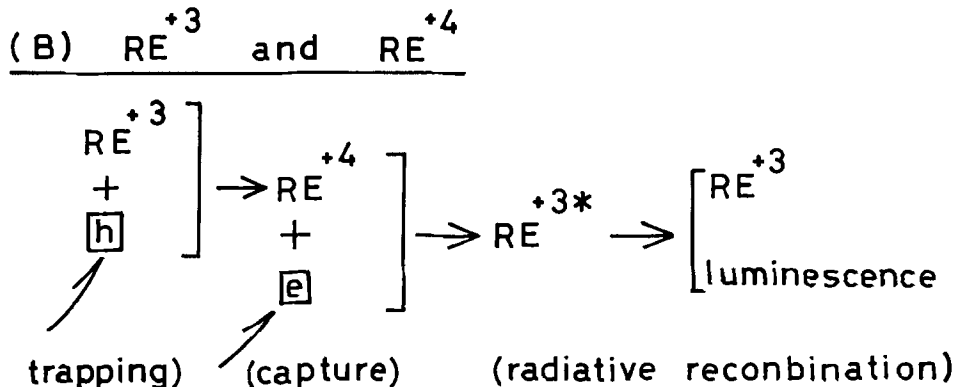


Fig. 4. Recombination mechanisms of electrons and hole at (A) rare earth ions showing trivalent and divalent, and (B) rare earth ions showing trivalent and tetravalent.



- Paris (1966).
7. L. Remier, *Optik*, **27**, 86 (1968).
 8. H. W. Lewis, *Phys. Rev.*, **78**, 526 (1950).
 9. K. Murata, T. Matsukawa, and R. Shimizu, *Jpn. J. Appl. Phys.*, **10**, 678 (1971).
 10. R. Shimizu, T. Ikuta, and K. Murata, *J. Appl. Phys.*, **43**, 4233 (1972).
 11. W. Ehrenberg and J. Frank, *Proc. Phys. Soc., B*, **66**, 1057 (1953).
 12. D. Bohm and D. Pine, *Phys. Rev.*, **92**, 609 (1953).
 13. J. J. Quinn, *ibid.*, **126**, 1453 (1962).
 14. G. F. Amelio, *J. Vac. Sci. Technol.*, **7**, 593 (1970).
 15. Y. Nakai, *Butsuri (Bull. Jpn. Phys. Soc.)*, **26**, 486 (1971) (in Japanese).
 16. L. Ozawa and H. N. Hersh, *This Journal*, **121**, 894 (1974).
 17. L. Ozawa and H. N. Hersh, *ibid.*, **124**, 420 (1977).
 18. L. Ozawa, *Phys. Rev. B*, **17**, 3434 (1978).
 19. L. Ozawa, *This Journal*, **126**, 106 (1979).
 20. G. H. Dieke, "Spectra and Energy Levels of Rare Earth Ions in Crystals," Interscience Publishers, New York (1968).
 21. L. Ozawa and T. Toryu, *Anal. Chem.*, **40**, 187 (1968).
 22. L. Ozawa and P. M. Jaffe, *This Journal*, **117**, 1297 (1970).
 23. C. P. Shinha, "Complexes of the Rare Earths," Pergamon, New York (1966).
 24. A. Rose, *Phys. Rev.*, **87**, 322 (1955).

Effect of Diffusion-Induced Dislocations on Antimony Diffusion into Silicon

Sung Hae Song and Tatsuya Niimi

Department of Electrical Engineering, Keio University, Hiyosh, Yokohama 223, Japan

ABSTRACT

The diffusion of antimony atoms into silicon was performed under the following conditions: diffusion temperatures 1150° and 1050°C, surface concentrations of antimony atom 4.5×10^{19} and $5.0 \times 10^{18}/\text{cm}^2$, using antimony-doped oxides as the diffusant source. The distribution of the diffusant in silicon deviated from the well-known erf curve when the diffusion was carried out for a longer time at the higher diffusion temperature and the higher surface concentration of antimony. In that case, the diffusion coefficient of antimony was determined by the Boltzmann-Matano method. It showed a considerable dependence on the local concentration of antimony and was interpreted in terms of the generation of diffusion-induced dislocations and the excess vacancies introduced from the surface during the diffusion.

Many investigators reported on the anomalous diffusion of phosphorus and boron into silicon, which was observed when the diffusion was carried out from a high concentration source (1-4), and on the effect of diffusion-induced dislocations on their diffusion coefficients (5, 6). It was proposed that these dislocations might explain the anomalous diffusion, because the generation of excess vacancies due to their climbing motion was supposed to be responsible for the marked enhancement of the diffusion and the emitter-push effect (7, 8).

On the other hand, the retardation effect of phosphorus atoms observed when they were diffused into silicon at very high concentration was related to the formation of diffusion-induced dislocations (9, 10). In this case, the effect could be explained by assuming that the excess vacancies generated when phosphorus atoms were diffused would be absorbed by the dislocations (11).

The generation of diffusion-induced dislocations is generally considered due to the stress induced by diffusion, which depends both on the size of a diffused atom and on its concentration (5, 12). As for phosphorus and boron atoms, referred to above, they have smaller atomic radii than silicon.

In this paper, it is reported that antimony, which has a larger atomic radius than silicon, was diffused into silicon using the doped oxide source. Comparing the diffusion coefficient of antimony, which was dependent on its local concentration, with the densities of diffusion-induced dislocations generated, their effect on the diffusion is discussed.

Experimental

Silicon substrates used were (111) oriented p-type single crystal wafers of resistivity $1 \sim 3 \Omega\text{cm}$, mechani-

cally and chemically polished, and had low dislocation densities ($<5 \times 10^2/\text{cm}^2$). The wafers were etched in dilute HF solution and then rinsed in deionized water. The condition of the preparation of antimony-doped silicon dioxide deposited on the substrates as a diffusant source and the method of measuring the antimony concentration in the substrates were the same as previously reported (13). The diffusion of antimony into silicon was performed in nitrogen atmosphere under the conditions listed in Table I, in which the data for four typical cases are shown. The diffusion was performed, maintaining the surface concentration of antimony at values indicated in Table I.

The junction depths formed in the substrates were measured by using the interferometer after the substrates were angle-lapped with 2 degrees and then chemically etched with the mixture of 30 cm³ HF and a drop HNO₃. They were also measured by another method using anodic oxidation (13). The junction depths measured by two different methods agreed with

Table I. Diffusion conditions of antimony into silicon and observed results of the generation of diffusion-induced dislocations. "Yes" means that the generation of diffusion-induced dislocations was observed and "No", not observed, under the specified condition

| Case | I | II | III | IV |
|--|---------------------------------------|----------------------------------|---|----------------------------------|
| Diffusion temperature (°C) | 1150 (abr. H) | 1050 (abr. L) | 1150 (abr. H) | 1050 (abr. L) |
| Surface concentration of antimony ($/\text{cm}^2$) | 5.0×10^{18} (abr. l) | 5.0×10^{18} (abr. l) | 4.5×10^{19} (abr. h) | 4.5×10^{19} (abr. h) |
| | 0.5 No 1.0 No | 8.0 No 15.0 No | 0.5 No 1.0 Yes | 8.0 No 15.0 Yes |
| Diffusion time (hr) | 2.0 No 4.5 No 9.0 No 18.0 No | 24.8 No 46.5 No 77.0 No | 2.0 Yes 4.5 Yes 9.0 Yes 18.0 Yes | 25.0 Yes 47.5 Yes |

Key words: diffusion, dislocations, antimony

each other. The diffusion-induced dislocations could be observed near the surface of the substrates by repeating the Sirtl etching (14) successively.

Results and Discussion

Figure 1 shows typical concentration profiles of antimony, which were obtained for case I in Table I. They were taken at diffusion time, 0.5, 2.0, and 4.5 hr. The intrinsic carrier concentration n_i in silicon at the diffusion temperature is $2.1 \times 10^{19}/\text{cm}^3$, therefore, the local concentration of diffused antimony atoms in the substrate was kept less than the intrinsic carrier concentration during the diffusion. The junction depth corresponds to the three points on the abscissa, where the Sb concentration is equal to the substrate concentration of $1.0 \times 10^{16}/\text{cm}^3$. Each of the full lines shows a theoretical erfc curve. These were drawn so as to pass through the two points, one of which was a junction depth on the abscissa and the other, the surface concentration on the ordinate, which were given by the experimental condition. They show a comparatively good agreement with plots by measurements.

The concentration profiles of antimony obtained for case II in Table I turned out, like case I, to agree with erfc curves, so they are omitted from the text.

Figure 2 shows the results obtained for case III in Table I. In the figure, the concentration profiles, corresponding to diffusion time, 0.5, 2.0, and 4.5 hr, are given. Three plots on the abscissa show the junction depths, respectively. They are, in this case, at the concentration $1.0 \times 10^{17}/\text{cm}^3$. The profile for a shorter diffusion time (0.5 hr) agreed well with an erfc curve,

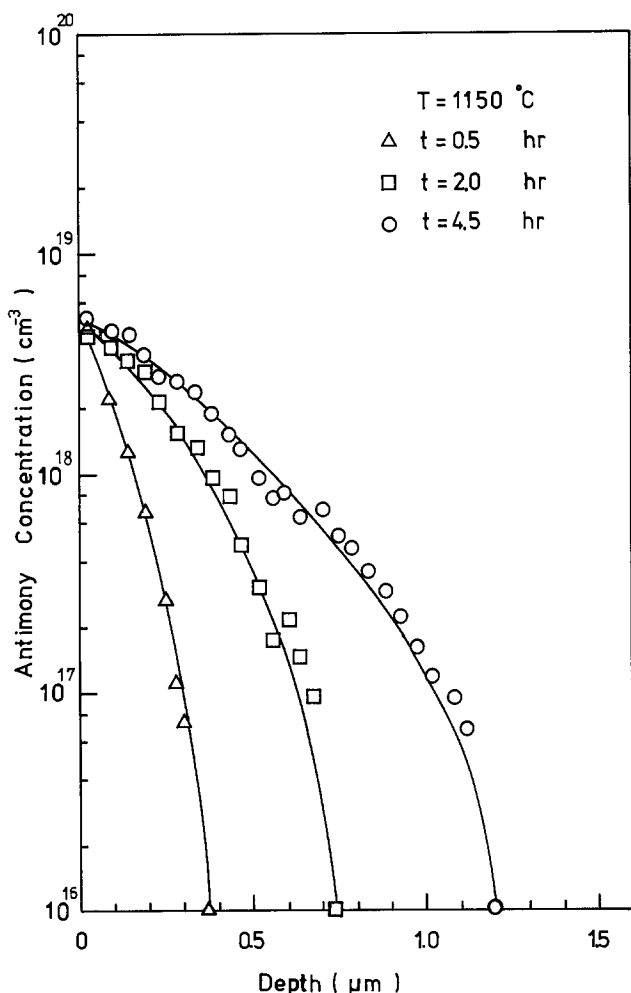


Fig. 1. Profiles of antimony concentration obtained for case I in Table I. Marks Δ , \square , and \circ show the concentrations measured after diffusion was carried out for 0.5, 2.0, and 4.5 hr, respectively. The full lines are theoretical erfc curves drawn as described in the text.

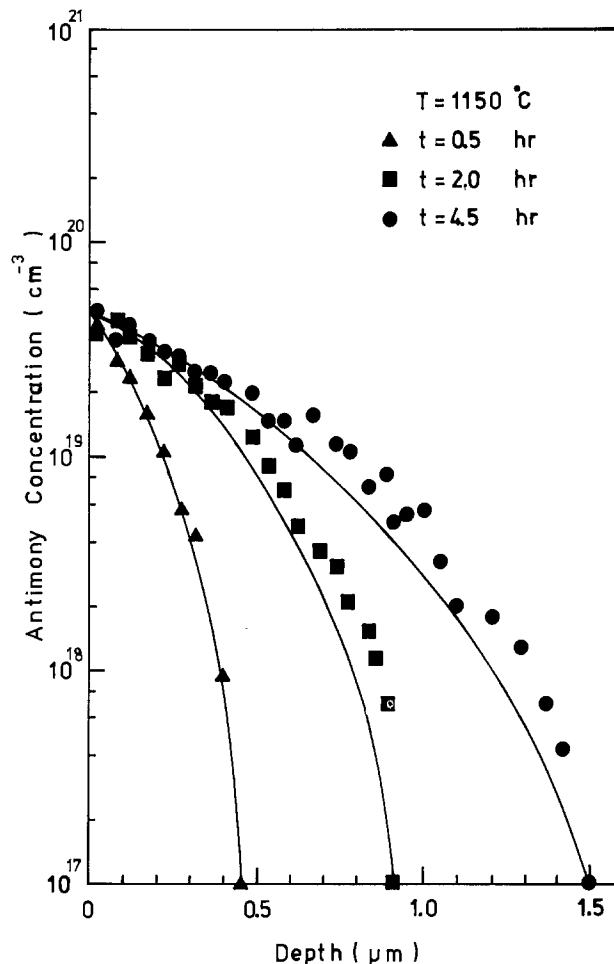


Fig. 2. Profiles of antimony concentration obtained for case III in Table I. Marks Δ , \square , and \circ show the concentrations measured for the diffusion times, 0.5, 2.0, and 4.5 hr, respectively. The full lines are theoretical erfc curves drawn as in Fig. 1.

drawn the same way as in Fig. 1, but the profiles for diffusion time longer than 2.0 hr did not.

The concentration profiles obtained for the case IV in Table I had similar characteristics as those given in Fig. 2, showing that the profiles for longer diffusion time deviated from the theoretical curve.

The solid solubility of antimony atoms into silicon, according to Trumbore (15), is $6.0 \times 10^{19}/\text{cm}^3$ at the temperature 1150°C and $4.5 \times 10^{19}/\text{cm}^3$ at 1050°C . Therefore, the higher surface concentration adopted in this study is roughly equal to the solubility limit of antimony into silicon at the diffusion temperatures.

Figure 3 shows an example of the relationship between diffusion time and dislocation densities generated on the surface of silicon substrates into which antimony was diffused with the condition, case III in Table I. They were measured by counting the number of etch pits on the surface from which the doped oxide had been removed by chemical etching. The vertical spreads of dislocation densities correspond to their measured maximal and minimal values. They have a tendency to be saturated as diffusion time becomes longer. The dislocation densities obtained at diffusion time longer than 4.5 hr could not be determined accurately, because the etch pits were piled up on the wafer. The saturated dislocation densities, $1.0 \sim 3.0 \times 10^9/\text{cm}^2$, extended deeply from the surface into about half a distance of the junction depth. The observed results about the generation of diffusion-induced dislocations are listed in Table I, including the above. Whenever dislocations were generated, the concentration profile of diffused antimony atoms deviated from an erfc curve and when dislocations were not generated, the diffusion profile followed an erfc curve. From the results, it is

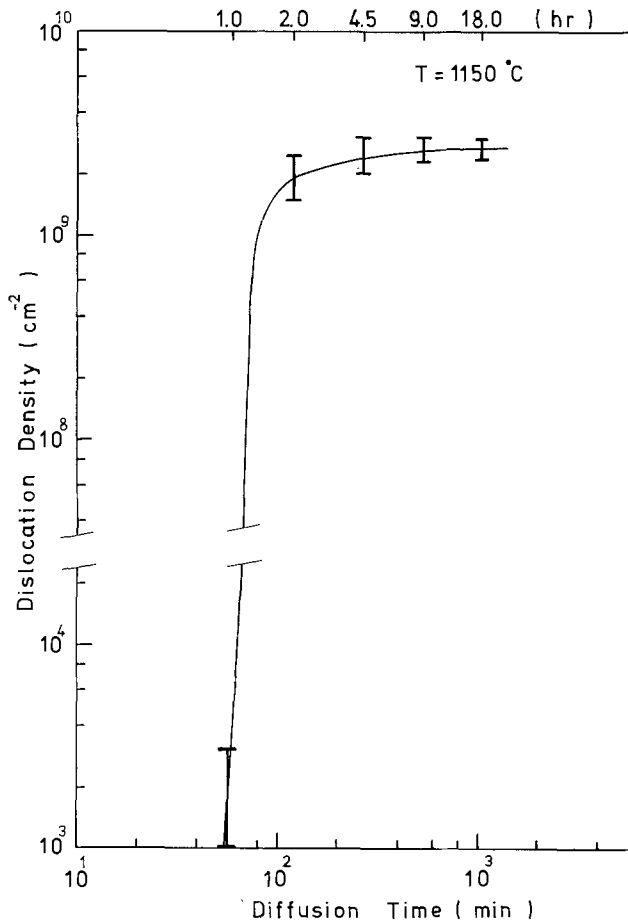


Fig. 3. A relationship between the densities of diffusion-induced dislocations and diffusion time. The diffusion condition is given in case III in Table I.

concluded that the generation of diffusion-induced dislocations depends mainly on the concentration of diffused antimony atoms.

Figure 4 shows the relationship between the measured junction depths and the diffusion times, which were obtained under the diffusion conditions given in Table I. Four lines, labeled (a), (b), (c), and (d), correspond to the diffusion conditions, case I, II, III, and IV in Table I, respectively. Lines (a) and (b) have a slope 1/2, but lines (c) and (d) have a steeper slope than either line (a) or (b). Under the diffusion conditions that lines (c) and (d) were taken, the generation of diffusion-induced dislocations was observed in the substrates after diffusion was carried out, except for the two diffusion conditions labeled P and Q in the figure, where no dislocations were observed. From the slopes of the lines, it is observed that the diffusion represented by line (c) or (d) is enhanced, compared with the case of line (a) or (b). It was reported that the diffusion coefficients of antimony in silicon depended on the surface concentration and that they increased with increased concentration (13). Therefore, if we draw broken lines (a') and (b') parallel to lines (a) and (b) through the points P and Q, the difference between (a') and (a) or the difference between (b') and (b) may be ascribed to the enhancement of diffusion due to the surface concentration of antimony and the difference between (c) and (a') or the difference between (d) and (b'), due to the enhancement of diffusion caused by the generation of diffusion-induced dislocations. It should be noted that the difference between lines (c) and (a') or between lines (d) and (b') increased with increase in diffusion time.

In order to find out a relation between the density of diffusion-induced dislocations and the diffusion coefficient of antimony, the diffusion coefficient was deter-

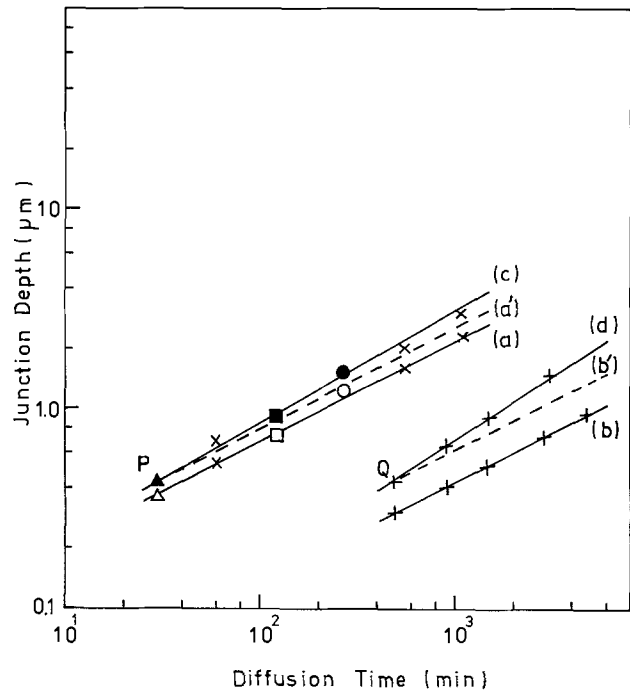


Fig. 4. Relations between the junction depths and the diffusion times. Lines (a), (b), (c), and (d) are drawn, corresponding to the diffusion conditions, case I, II, III, and IV in Table I, respectively.

mined from Fig. 1 and 2, where the measured concentration profiles of antimony could be well fitted with an erfc curve, respectively, except the two cases, in which the diffusions were carried out under the conditions, *i.e.*, diffusion temperature 1150°C, surface concentration of antimony $4.5 \times 10^{19}/\text{cm}^3$, and diffusion time 2.0 and 4.5 hr. When the profile could be well fitted with an erfc curve, a value of the parameter D , which was used to represent the erfc curve, $\text{erfc}(x/\sqrt{Dt})$, was adopted as a diffusion coefficient of antimony. When it could not be, the Boltzmann-Matano method (16) was adopted to determine the diffusion coefficient as a function of local antimony concentrations. To ensure the applicability of the method to the cases stated above, the two profiles in Fig. 2 were transformed to those in Fig. 5, in which the representation of the abscissa was changed from x in Fig. 2 to x/\sqrt{t} in Fig. 5. The two concentration profile curves in Fig. 2 may be considered to be bundled roughly along a broken curve in Fig. 5, showing that the two concentration profile curves in Fig. 2 could be represented by a single parameter of x/\sqrt{t} only. This is considered reasonable because the conditions in the substrates, which would affect the diffusion coefficient, must not be so much different when the two diffusions were carried out. This manifests indirectly the validity of applying the Boltzmann-Matano analysis to the above cases.

The values of the diffusion coefficient of antimony, thus determined, are given in Fig. 6, together with those obtained by the experiments at the diffusion temperature 1050°C. The diffusion conditions and the explanations of symbols used in the figure are summarized in Table II. First, the diffusion coefficient of antimony determined by the experiments, in which the surface concentration of antimony was maintained at $5.0 \times 10^{18}/\text{cm}^3$ during the diffusion, is described. This is expressed as D_1^H or D_1^L in Table II or in Fig. 6. As is clearly shown in Fig. 6, these were constant over the whole range where antimony atoms were diffused, and irrespective of their local concentration. In this case, the concentration of the diffused atoms was, in all cases, lower than the intrinsic carrier concentration in silicon at the diffusion temperature, 1150° or 1050°C. However,

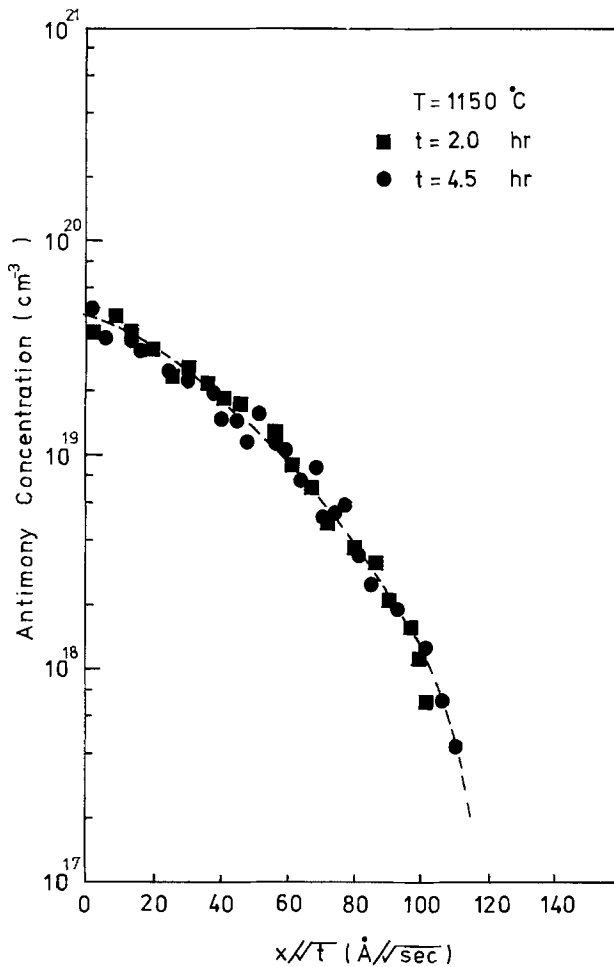


Fig. 5. Concentration profile vs. x/\sqrt{t}

the values of D_1^H or D_1^L do not agree with Ghoshtagore's intrinsic diffusion coefficient (2.4×10^{-14} cm²/sec at 1150°C or 2.6×10^{-15} cm²/sec at 1050°C) (17), which was determined by extrapolating his experimental result to the diffusion temperature in the authors' case. This difference must be due to the different methods of diffusion used in the experiments (13).

Next, we will describe the diffusion coefficients determined by the experiments with the higher surface concentration 4.5×10^{19} /cm³. For example, in the case of the diffusion temperature 1150°C, these are shown as $D_h^{H4.5}$, $D_h^{H2.0}$, and $D_h^{H0.5}$ in Fig. 6. These values are always larger than D_1^H over the whole range of antimony concentration examined. Moreover, the difference between $D_h^{H4.5}$ or $D_h^{H2.0}$ and D_1^H can be considered to be divided into two parts, the difference between $D_h^{H0.5}$ and D_1^H and that between $D_h^{H4.5}$ or $D_h^{H2.0}$ and $D_h^{H0.5}$. Though $D_h^{H4.5}$ and $D_h^{H2.0}$ correspond to the diffusion coefficients determined at different diffusion time, 4.5 and 2.0 hr, they could not clearly be

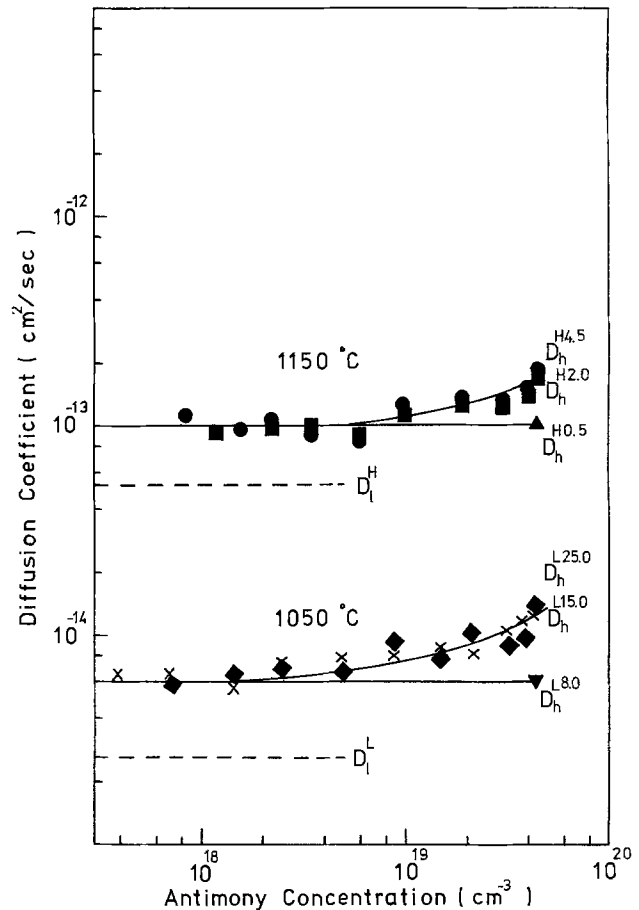


Fig. 6. Diffusion coefficient of antimony vs. local antimony concentration in the substrates. Diffusion conditions and the explanations of the symbols are given in Table II.

discriminated in this experiment. In spite of the determination at the higher surface concentration, $D_h^{H0.5}$ turned out constant over the whole range of antimony concentration, but $D_h^{H4.5}$ and $D_h^{H2.0}$ were constant only in the range of lower concentration, and increased with increase in the concentration.

Next, we will discuss the difference between $D_h^{H0.5}$ and D_1^H . Referring to Tables I and II, it must be pointed out that in the substrates used to determine $D_h^{H0.5}$ or D_1^H , there could be observed no dislocations after the diffusions had been performed. Therefore, we would like to ascribe the difference to the different densities of excess vacancies in the substrates, into which the antimony might be introduced from the surface with the use of the oxide sources containing different densities of diffusant (18, 19). As for the effect of the excess vacancies, the junction depth shown in Fig. 4 must be affected by them and, for example, the difference between lines (a') and (a) may be ascribed to this effect.

Table II. List of diffusion conditions in Fig. 6 and the explanations of the symbols used. Diffusion constants D_1^H and D_1^L obtained under specified conditions were constant, respectively. Also, $D_h^{H0.5}$ and $D_h^{L8.0}$ were constant, but $D_h^{H4.5}$, $D_h^{H2.0}$, $D_h^{L25.0}$, and $D_h^{L15.0}$ were dependent on the local concentration of antimony

| Diffusion temperature (°C) | 1150 (H) | 1050 (L) | 1150 (H) | 1050 (L) |
|---|---|---|---|--|
| Surface concentration of antimony (/cm ³) | 5.0×10^{18} (l) | 5.0×10^{18} (l) | 4.5×10^{19} (h) | 4.5×10^{19} (h) |
| Diffusion time (hr), mark and symbols | 0.5 } D_1^H 1.0 } 2.0 } 4.5 } 9.0 } 18.0 } | 8.0 } D_1^L 15.0 } 24.8 } 46.5 } 77.0 } | 0.5 ▲ $D_h^{H0.5}$ 1.0 ● $D_h^{H2.0}$ 2.0 ■ $D_h^{H4.5}$ 4.5 ● $D_h^{H4.5}$ 9.0 — 18.0 — | 8.0 ▼ $D_h^{L8.0}$ 15.0 ◆ $D_h^{L15.0}$ 25.0 × $D_h^{L25.0}$ 47.5 — |

Next, we will consider the difference between $D_h^{H4.5}$ (or $D_h^{H2.0}$) and $D_h^{H0.5}$. They are nearly the same in the range of the lower concentration of antimony, but become different as the concentration becomes increased. As already shown in Fig. 3, in the substrates which was used for the determination of $D_h^{H4.5}$ (or $D_h^{H2.0}$), the diffusion-induced dislocations were observed after the diffusion had been performed. Then, the difference between $D_h^{H4.5}$ (or $D_h^{H2.0}$) and $D_h^{H0.5}$ may be considered due to the appearance of the diffusion-induced dislocations. Their appearance must enhance the diffusion of antimony. About the enhancement of diffusion due to dislocations, a pipe diffusion model (20) or a dislocation short-circuit model (21) has been proposed.

The same circumstances as stated above may be applied to explain the similar behavior among the diffusion constants, $D_h^{L25.0}$, $D_h^{L15.0}$, and $D_h^{L8.0}$, which were obtained by the experiments with the higher surface concentration at the lower diffusion temperature, listed in Table II.

Moreover, the appearance of diffusion-induced dislocations could be thought to be responsible for the difference between lines (c) and (a') in Fig. 4, referring to the junction depths formed by the diffusion, or the difference between lines (d) and (b'). Some explanations about this point are already given in the previous paragraph.

Conclusion

Antimony atoms were diffused into p-type silicon substrates, using a doped oxide as a diffusant source under the conditions, diffusion temperatures 1150° and 1050°C, and the surface concentrations of antimony 4.5×10^{19} and $5.0 \times 10^{18}/\text{cm}^2$.

When the diffusion was performed for a longer diffusion time with the higher surface concentration, a profile representing the concentration of antimony vs. diffusion depth might deviate from an erfc curve. In that case, the diffusion coefficient of antimony was determined using the Boltzmann-Matano method, for which the integral was calculated numerically by the computer program. Differences between the diffusion coefficients obtained with the higher and lower surface

concentration were analyzed and could be explained qualitatively in terms of diffusion-induced dislocations and the introduction of excess vacancies into the substrate. From the results it has been concluded that the diffusion-induced dislocations will enhance the diffusion of antimony into silicon.

Manuscript submitted Jan. 2, 1980; revised manuscript received July 1, 1980.

Any discussion of this paper will appear in a Discussion Section to be published in the December 1981 JOURNAL. All discussions for the December 1981 Discussion Section should be submitted by Aug. 1, 1981.

Publication costs of this article were assisted by Keio University.

REFERENCES

1. E. Tannenbaum, *Solid-State Electron.*, **2**, 123 (1961).
2. I. M. Mackintosh, *This Journal*, **109**, 392 (1962).
3. S. Maekawa and T. Oshida, *J. Phys. Soc. Jpn.*, **19**, 253 (1964).
4. K. H. Nicholas, *Solid-State Electron.*, **9**, 35 (1966).
5. S. Prussin, *J. Appl. Phys.*, **32**, 1876 (1961).
6. J. E. Lawrence, *This Journal*, **113**, 819 (1966).
7. J. J. Parker, *J. Appl. Phys.*, **38**, 3475 (1961).
8. S. M. Hu and T. H. Yeh, *ibid.*, **40**, 4615 (1969).
9. M. C. Duffy, F. Barson, J. M. Fairfield, and G. H. Schwuttke, *This Journal*, **115**, 84 (1968).
10. M. Yoshida and S. Kanamori, *Jpn. J. Appl. Phys.*, **9**, 338 (1970).
11. S. Matsumoto, E. Arai, H. Nakamura, and T. Niimi, *Jpn. J. Appl. Phys.*, **16**, 1177 (1977).
12. J. E. Lawrence, *J. Appl. Phys.*, **37**, 4106 (1966).
13. S. H. Song, S. Matsumoto, and T. Niimi, *Jpn. J. Appl. Phys.*, **18**, 2181 (1979).
14. E. Sirtl and A. Adler, *Z. Metallkd.*, **52**, 529 (1961).
15. F. A. Trumbore, *Bell Syst. Tech. J.*, **39**, 205 (1960).
16. C. Matano, *Jpn. J. Phys.*, **8**, 109 (1933).
17. R. N. Ghoshtagore, *Phys. Rev. B*, **3**, 389 (1971).
18. M. Yoshida, E. Arai, H. Nakamura and Y. Terunuma, *J. Appl. Phys.*, **45**, 1498 (1974).
19. S. Matsumoto, E. Arai, H. Nakamura, and T. Niimi, *Jpn. J. Appl. Phys.*, **14**, 1665 (1975).
20. D. Turnbull and R. E. Hoffman, *Acta Metall.*, **2**, 419 (1954).
21. A. L. Ruoff and R. W. Balluffi, *J. Appl. Phys.*, **34**, 1848 (1963).

Preparation of Carbon-Free GaAs Surfaces: AES and RHEED Analysis

A. Munoz-Yague, J. Piqueras,¹ and N. Fabre

Laboratoire d'Automatique et d'Analyse des Systèmes
du Centre National de la Recherche Scientifique, 31400 Toulouse, France

ABSTRACT

Chemical polishing using an $\text{H}_2\text{SO}_4:\text{H}_2\text{O}_2:\text{H}_2\text{O}$ system and thermal treatments in vacuum to obtain clean GaAs surfaces have been systematically studied for {100} and {111} surfaces. The behavior of these surfaces as far as oxidation and carbon adsorption are concerned has been found to depend on both conductivity type and crystal orientation. The results presented for {100} n- and p-type and semi-insulating material show that it is possible to obtain carbon-free surfaces, covered by a thin oxide layer which protects the semiconductor surface against contamination. A subsequent thermal treatment around 550°C under vacuum permits elimination of the oxide and achieves atomically clean, crystalline and ordered surfaces, which has been confirmed by AES and RHEED analysis.

The preparation of a clean semiconductor surface is among the critical steps in the manufacture of Schottky and ohmic contacts, as well as in epitaxy or

photocathode manufacture. The surface should be free of oxides and adsorbed impurities to ensure an intimate contact between the substrate and the deposited layer. The aim of this work is to study a reliable procedure to clean GaAs substrates intended for molecular beam epitaxy.

¹Permanent address: Laboratorio de Semiconductores, IFES (CSIC-UAM), Cantoblanco, Madrid, Spain.
Key words: semiconductor, etching, oxidation, epitaxy.

The ease in obtaining such a clean surface depends on its chemical activity which is, as is well known, high for most semiconductors. Carbon and other chemical impurities are easily adsorbed from the ambient and the cleaning solvents. Moreover, an unavoidable thin and inhomogeneous oxide layer is formed during or just after the last chemical treatment. In the case of gallium arsenide, if the remaining oxide is etched away with HCl or HF, the surface exhibits a high reactivity and, in addition to the usual C and O contaminants, traces of other impurities such as Cl, S, Ca, N, etc. can be observed (1). Carbon cannot be removed by thermal treatments unless temperatures above 600°C are used (2). This can also be achieved by long time bombardment with argon ions followed by annealing at around 500°C (3). These methods are not appropriate, the first because it requires temperatures above the limit of congruent evaporation of the components, and the second because it involves the creation of a large density of defects. In addition, if the carbon contamination is great enough both treatments lead to faceting of the {100} (2) and $\bar{1}\bar{1}\bar{1}$ surfaces (3). Moreover, in the case of molecular beam epitaxy, carbon contamination affects both crystal growth and layer morphology, and it should be avoided.

Arsenic and gallium oxides decompose around 370°C and 570°C, respectively, (3) which offers a possibility for obtaining a clean GaAs surface under vacuum: indeed, if a thin homogeneous oxide layer could be obtained at the end of the chemical processing, impurity adsorption while pumping down would be avoided and the oxide layer could then be eliminated later on by an appropriate thermal treatment. Surface passivation by chemical etching was pointed out by Cho and Arthur (4) and Cho and Tracy (5), using a Br:CH₃OH solution and deionized water rinsing.

For our purpose, anodic oxidation of GaAs and oxidation by pure oxidants such as H₂O₂ or HNO₃ will not be considered since it is difficult to obtain homogeneous oxide layers of small thickness (~10Å) by these methods and also because thicker oxides are difficult to evaporate. In contrast, chemical treatments with systems such as Br:CH₃OH; H₂SO₄:H₂O₂:H₂O; HNO₃:HF; HNaO:H₂O₂ lead to slightly oxidized GaAs surfaces (2, 4, 6, 7).

The results reported up to now only concern <100> oriented semi-insulating Cr-doped (2) and n-type Si-doped (6) GaAs substrates. The results of a systematic study on n-type, p-type, and semi-insulating GaAs substrates oriented in the <100>, [111], and $\bar{1}\bar{1}\bar{1}$ directions are detailed here. The polishing solution used is H₂SO₄:H₂O₂:H₂O, which appears to be the most suitable etch for surface preparation (2, 6, 7). The analysis was done by Auger electron spectroscopy (AES) and reflected high energy diffraction (RHEED).

Experimental Procedure

The main specifications of the samples used in our study are given in Table I. After mechanochemical polishing, they were degreased in trichloroethylene (boiling), acetone (boiling), ethanol (60°C), and deionized water (60°C). Then, the samples were immersed in HCl in order to remove the remaining inhomogeneous oxide layer and finally etched with an H₂SO₄:H₂O₂:H₂O solution, of different proportions depending on the type and orientation of the sample.

The etching solution was always freshly prepared and stirred in an ultrasonic bath. The violent stirring

was introduced in order to ensure a more reproducible oxidizing activity of the solution. The etching was performed at 70°C, and sometimes an additional 30 Klux white light illumination was used.

Just after etch the samples were rinsed and inserted in an ultrahigh vacuum molecular beam epitaxy (MBE) system. The substrate was mounted on an Mo substrate holder that incorporates a heating filament and a thermocouple for temperature measurements; thermal contact between substrate and Mo was ensured by In.

A vacuum interlock system allowed pressures down to 10⁻⁸ Torr to be reached in 30 min; the pressure limit was 10⁻¹⁰ Torr and no hydrocarbon residuals were detected in the mass spectrum obtained with a quadrupole mass spectrometer.

The vacuum chamber was provided with a cylindrical mirror analyzer (CMA), Auger spectrometer (RIBER OPC 105) and a 5 keV glancing angle electron diffraction apparatus. The analyses were made in accordance with the following sequence: RHEED and AES at room temperature, AES during the slow and progressive increase in temperature, and AES and RHEED observation at the final temperature of the thermal treatment.

Experimental Results

No traces of cleaning products or impurities other than C and O were detected, and care was taken to avoid electron-induced adsorption or desorption. The most significant results are given in Tables II and III, in which the proportions of the polishing solution and the conditions of the etch are indicated for faces {100} and {111}, respectively. AES results are presented in the form of peak amplitudes relative to the Ga amplitude. The peaks retained in the $dN(E)/dE$ spectra are:

| | |
|---------|-----------------------|
| 272 eV | KLL transition for C |
| 510 eV | KLL transition for O |
| 1070 eV | LMM transition for Ga |
| 1228 eV | LMM transition for As |

{100} Faces.—After chemical polishing all the samples showed a mirrorlike aspect and only some minor features were observed when contrast microscopy was used. As far as the chemical state of the surface is concerned, the behavior of each conductivity type was different: the oxide coverage for the same polishing solution (3:1:1) was larger for n-type than for p-type, being the lowest for semi-insulating substrates (see Fig. 1). As a general result, it must be pointed out that the carbon contamination increases as the detected oxide coverage decreases. Also it should be mentioned that for a given substrate, an increase in the oxide coverage causes a lowering of the carbon contamination.

In the case of n-type substrates, a carbon-free surface can be prepared with a 3:1:1 solution; to obtain the same result on p-type substrates, the oxidizing activity of the solution has to be increased. A good result was obtained with a 2:1:1 solution. As far as semi-insulating substrates are concerned, the latter ratio was not yet sufficient to avoid carbon adsorption. Nevertheless, a further increase in the concentration of the oxidizing agent results in more difficult control of the etching process and some surface roughness showed up, although the aspect remained mirrorlike. It was found that a 2:1:1 solution under illumination of about 30 Klux was appropriate and led to a carbon-free surface of semi-insulating substrate.

Once these analyses at room temperature were completed, the substrate temperature was increased step by step, and after each one the Auger spectrum was recorded. At about 400°C, a slight reduction of the oxygen peak was observed, probably due to the decomposition of arsenic oxides. To completely remove the oxygen, it was necessary to reach temperatures

Table I. Specifications of the GaAs substrates used in this work

| Substrate | Face | Dopant | Dopant concentration (cm ⁻³) |
|-----------|-----------------------------------|--------|--|
| 1 | {100} | Te | 5.2 × 10 ¹⁷ |
| 2 | {100} | Zn | 2.2 × 10 ¹⁸ |
| 3 | {100} | Cr | $\rho = 10^7 \Omega \cdot \text{cm}$ |
| 4 | (111) ($\bar{1}\bar{1}\bar{1}$) | Sn | 5 × 10 ¹⁷ |

Table II. Results obtained for {100} GaAs surfaces

| Substrate | GaAs:Te {100} | | | GaAs:Zn {100} | | | GaAs:Cr {100} | | |
|---|-----------------------|------|-------|-----------------------|------|-------|-------------------------------------|------|-------|
| Polishing solution H ₂ SO ₄ :H ₂ O ₂ :H ₂ O | 3:1:1 ~70°C, 1 min | | | 2:1:1 ~70°C, 2 min | | | 2:1:1 ~70°C, 2 min, illumination | | |
| AES | C/Ga | O/Ga | As/Ga | C/Ga | O/Ga | As/Ga | C/Ga | O/Ga | As/Ga |
| Before heat-treatment | 0 | 1,58 | 0,91 | 0 | 1,41 | 0,81 | 0 | 2,34 | 0,76 |
| Maximum temperature of the thermal treatment | 530°C | | | 583°C | | | 560°C | | |
| After heat-treatment | 0 | 0 | 0,69 | 0 | 0 | 0,77 | 0 | 0 | 0,74 |

Table III. Results obtained for (111) and (111) GaAs surfaces

| Substrate | GaAs:Sn (111) | | | GaAs:Sn (111) | | |
|---|-----------------------|------|-------|-----------------------|------|-------|
| Polishing solution H ₂ SO ₄ :H ₂ O ₂ :H ₂ O | 3:1:1 ~70°C, 2 min | | | 2:1:1 ~70°C, 2 min | | |
| AES | C/Ga | O/Ga | As/Ga | C/Ga | O/Ga | As/Ga |
| Before heat-treatment | 0,18 | 1,23 | 1,09 | 0,11 | 0,96 | 0,66 |
| Maximum temperature of the thermal treatment | 540°C | | | 530°C | | |
| After heat-treatment | 0 | 0 | 0,91 | 0,07 | 0 | 0,64 |

around 550°C, slightly lower than those reported by Laurence *et al.* (2).

Figure 2 shows Auger spectra obtained before and after the thermal treatment. The removal of the oxide layer is rather fast: once the critical temperature is reached the oxygen peak suddenly disappears (see

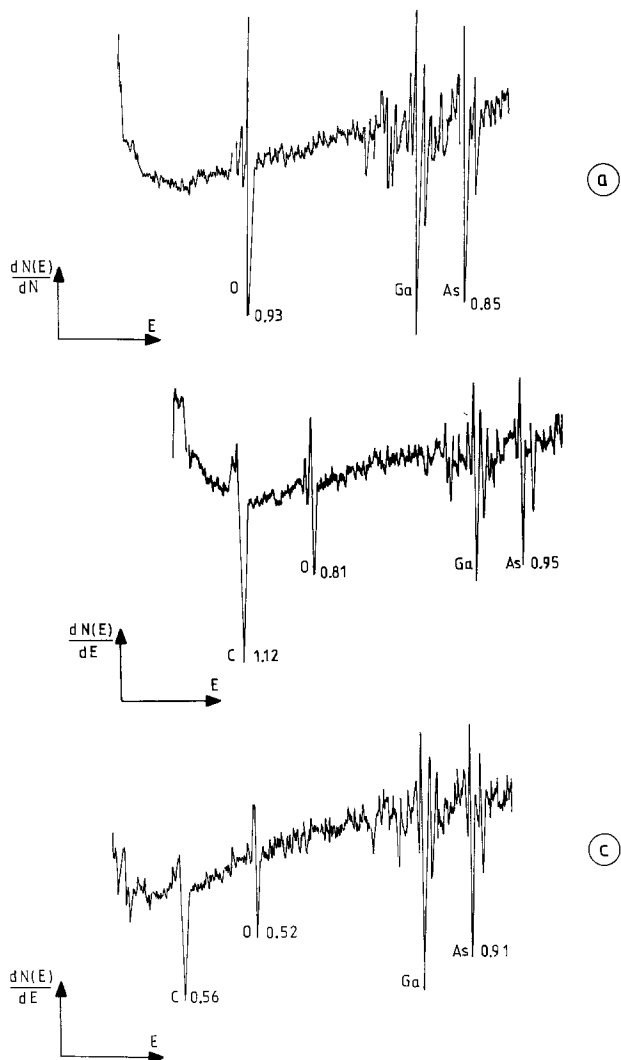


Fig. 1. Auger spectra of {100} GaAs surfaces etched with H₂SO₄:H₂O₂:H₂O (3:1:1) for three different kind of samples: (a) n-type, (b) p-type, and (c) semi-insulating chromium doped.

Fig. 3). After overnight storage in the vacuum chamber, at a pressure lower than 10⁻⁹ Torr no appreciable contamination of the surface was observed. At this point, the surface coverage by any impurity was less than 1% monolayer (detection limit of the CMA). From the chemical point of view, such a surface is

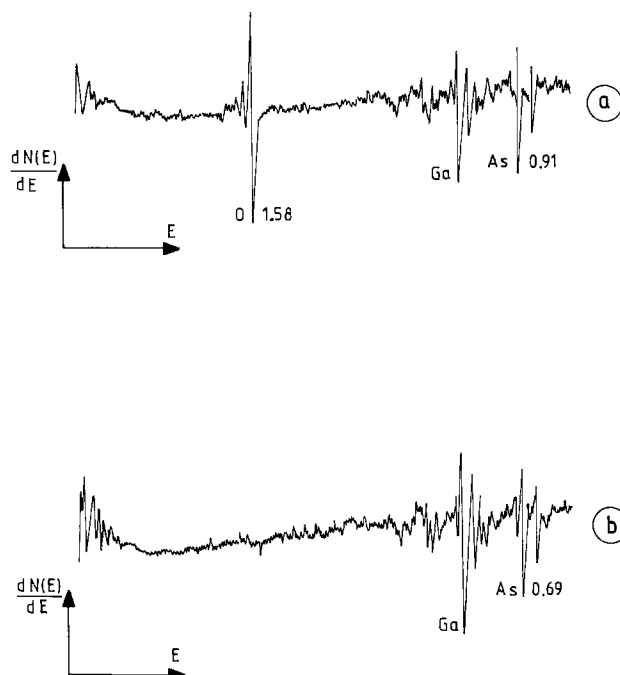


Fig. 2. Auger spectra of {100} n-type GaAs surfaces etched with H₂SO₄:H₂O₂:H₂O (3:1:1) (a) at room temperature and (b) at ~530°C.

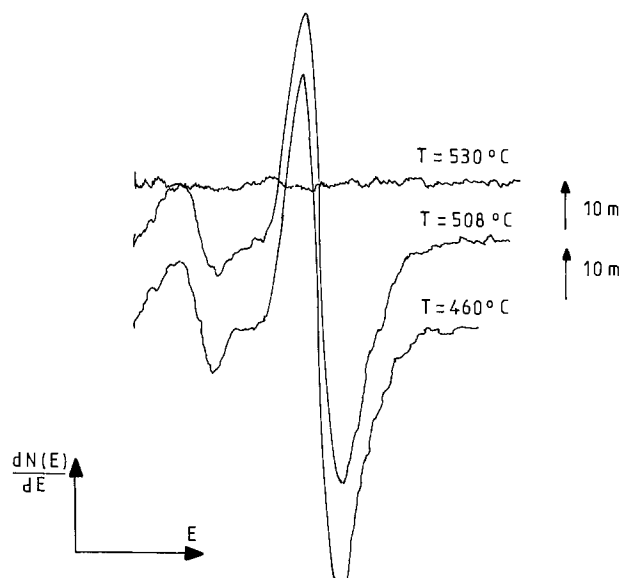


Fig. 3. Oxygen Auger peak obtained at three different temperatures for n-type GaAs {100} surface.

capable of fulfilling the requirements of the different device manufacturing processes mentioned above.

The electron diffraction diagram of the sample before the thermal treatment shows a fairly diffuse spotty pattern because of the presence of an adsorbed layer (see Fig. 4a). At the end of the thermal treatment, the diffraction image consisted of rods showing a weak amplitude modulation. The surface roughness can be estimated to be in the 10^2\AA range.

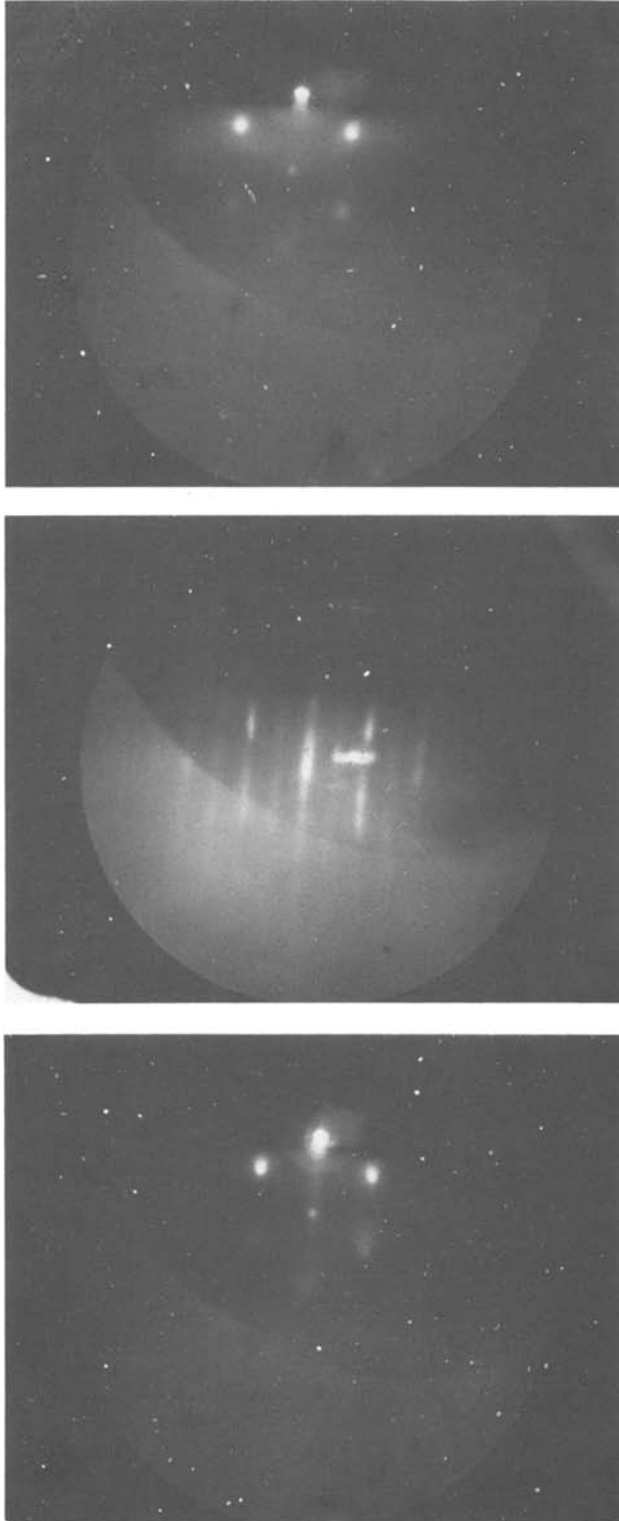


Fig. 4. RHEED diagrams obtained (a, top) at room temperature, (b, center) at the end of thermal treatment with an As flux impinging on the surface, and (c, bottom) at 620°C when after O disappearance a certain amount of C remains at the surface. 5 keV $[110]$ azimuth.

Under As_4 flux (arsenic pressure $\sim 10^{-6}$ Torr) provided by an evaporation cell, the clean surface exhibited surface reconstruction. Figure 4b shows a diagram observed in the $[110]$ azimuth, which corresponds to either the $C(2 \times 8)$ or the (2×4) surface structures, already observed in molecular beam epitaxy studies.

If, once the oxide layer has been removed a noticeable amount of adsorbed carbon remains on the GaAs surface, a further increase of the temperature would not fully desorb the carbon, and the undesirable result obtained was faceting, as shown in Fig. 4c. The pattern consists of elongated spots tilted with respect to the streak direction of the smooth surface, corresponding to facets which were found to be parallel to the planes (411) by Laurence *et al.* (2).

(111) and $(\bar{1}\bar{1}\bar{1})$ Faces.—As is well known the (111) and $(\bar{1}\bar{1}\bar{1})$ GaAs faces are not equivalent: the $[111]$ direction can be considered to consist of double GaAs layers "weakly" bound between them; one of the faces will be As-rich ($\bar{1}\bar{1}\bar{1}$), and the other will be Ga-rich (111). This fact gives rise to substantial differences between both faces in the mechanochemical as well as in the chemical polishing: the Ga face showed a roughness in the micrometer range while for the As face the final aspect was comparable to that of the $\{100\}$ substrates.

The best results obtained for these faces are summarized in Table III. The difficulty in obtaining a free carbon surface at the end of the chemical polishing must be noted. Moreover a remarkable difference with $\{100\}$ surfaces was found: an increase in the relative concentration of the oxidizing agent gave rise to an enhancement of the oxygen peak amplitude, but did not cause an appreciable lowering of the carbon peak amplitude, as illustrated in Fig. 5. This is valid for both faces, even though the As-rich appeared to oxidize more easily than the Ga-rich.

As was the case for $\{100\}$ surfaces, the oxide removal was obtained around 550°C , but a small quantity of carbon sometimes remained on the surface. An overnight storage in the vacuum chamber at a pressure

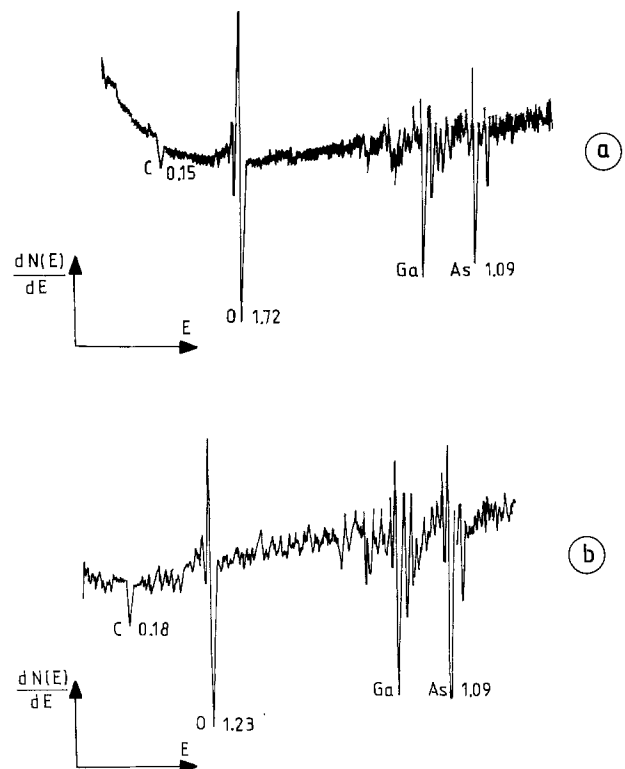


Fig. 5. Auger spectra of $(\bar{1}\bar{1}\bar{1})$ GaAs surfaces prepared with $\text{H}_2\text{SO}_4:\text{H}_2\text{O}_2:\text{H}_2\text{O}$; (a) 2:1:1 and (b) 3:1:1.

$<5 \cdot 10^{-10}$ Torr gave rise to a significant enhancement of the C and O peaks. The oxygen could again be eliminated by heating, but carbon remained and a further increase in temperature caused the faceting of the surface. In the case of the (111) face, if this situation is not reached, a surface reconstruction can be obtained even in the absence of As or Ga fluxes; Fig. 6 shows the $2\times$ structure observed, which corresponds to a Ga-stabilized surface.

Discussion and Conclusion

It has been found that for {100} surfaces, n-type GaAs is more easily oxidized than p-type or semi-insulating material. This is not surprising if we consider the electrochemical aspects of the oxidation process which involve a loss of electrons from GaAs; indeed, both Ga and As are less electronegative than oxygen (8). This loss may occur via the conduction band in n-type material whereas it would take place via the valence band in p-type samples. Furthermore the electron supply is a diffusion-dominated process; thus it should be expected that the reaction occurs more easily in n-type than in p-type material. According to this, and if we deal with semi-insulating material, the activity of the oxidation process should still be lower. This difficulty was overcome with the aid of the carriers generated by strong illumination.

For n-type GaAs we also observed that as far as ease of oxidation is concerned, the different surfaces can be ordered: {100} > $(\bar{1}\bar{1}\bar{1})$ > (111). The difference between {100} and the last two surfaces can be explained by (i) the different configuration of the dangling bonds in the two cases (9, 10), and (ii) the higher density of dangling bonds in the {100} case. Also, on the basis of the same atomistic model, $(\bar{1}\bar{1}\bar{1})$ would be more easily oxidized than (111) since in the latter case there are no dangling electrons on the surface Ga atoms. (11).

The carbon contamination after the chemical polishing or after UHV storage was also different for these surfaces: C adsorbed more easily on $(\bar{1}\bar{1}\bar{1})$ and (111) faces than on the {100} face. This could be explained by considering that the (111) face is Ga-rich and that the $(\bar{1}\bar{1}\bar{1})$ surface was probably also partially covered by Ga (the As-stabilized structure was never observed in this study). Then, if Ga exhibits higher chemical activity than As as far as C is concerned, the $(\bar{1}\bar{1}\bar{1})$ and (111) faces will show higher carbon adsorption than {100} faces. This hypothesis is sustained by the fact

that the electronegativity difference is higher for the Ga-C bond (0.9 eV) than for the As-C one (0.5 eV) (8).

In all cases, the removal of the oxide layer was practically instantaneous, in contrast with the values often reported for the duration of thermal treatment (10-30 min). Also, the oxide removal was completed at around 550°C, which implies its being almost entirely Ga₂O₃. This agrees with the mechanism proposed for anodic oxidation and with the experimental observations of Chang *et al.* (1): gallium oxide formation and As pile-up at the GaAs oxide interface. This excess of As was not troublesome in our case because it was removed during thermal treatment; this can be checked in Tables II and III: the As-to-Ga ratio decreases in all cases and, for example, for the {100} cases, it approaches the value reported for the As-stabilized surface (9).

In conclusion, the presented results show that it is possible to prepare by chemical polishing, GaAs surfaces presenting a mirrorlike aspect with no traces of chemical agents and almost completely covered by a thin oxide layer which passivates the semiconductor. This layer can be easily removed by thermal treatment in ultrahigh vacuum giving a C- and O-free GaAs surface of negligible roughness, atomically clean, and ordered. The results obtained show that $\langle 100 \rangle$ oriented surfaces should be more suitable for technological applications from the point of view of cleanliness and stability.

Finally, it must be emphasized that the reproducibility of the results of the suggested preparation procedures was checked with good results and that these procedures are now being currently used in our MBE system. Indeed this reproducibility of the result allowed this study to progress, and in almost all the cases treated carbon-free surfaces were obtained by varying the etch proportions.

Acknowledgments

We acknowledge the technical assistance of L. Amat, and thank D. Esteve and J. Buxo for their continued encouragement in the completion of this work.

Manuscript submitted Feb. 4, 1980; revised manuscript received July 24, 1980.

Any discussion of this paper will appear in a Discussion Section to be published in the December 1981 JOURNAL. All discussions for the December 1981 Discussion Section should be submitted by Aug. 1, 1981.

Publication costs of this article were assisted by the Laboratoire d'Automatique et d'Analyse des Systèmes du Centre National de la Recherche Scientifique.

REFERENCES

1. C. C. Chang, P. H. Citrin, and B. Schwartz, *J. Vac. Sci. Technol.*, **14**, 943 (1977).
2. G. Laurence, F. Simondet, and P. Saget, *Appl. Phys.*, **19**, 63 (1979).
3. A. Trueba, E. Munoz, and J. Piqueras, *Solid State Commun.*, **15**, 199 (1974).
4. A. Y. Cho and J. R. Arthur, *Prog. Solid State Chem.*, **10**, 157 (1975).
5. A. Y. Cho and J. C. Tracy, U.S. Pat. 3,969,164 (1976).
6. T. Oda and T. Sugano, *Jpn. J. Appl. Phys.*, **15**, 1317 (1976).
7. I. Shiota, K. Motoya, T. Ohmi, N. Miyamoto, and J. Nishizawa, *This Journal*, **124**, 155 (1977).
8. L. Pauling, "The Nature of the Chemical Bond," 3rd ed., p. 93, Cornell University Press (1960).
9. A. Y. Cho, *J. Appl. Phys.*, **47**, 7, 2841 (1976).
10. A. Y. Cho and I. Hayashi, *Solid State Electron.*, **14**, 125 (1971).
11. H. C. Gatos, in "Crystal Growth and Characterization," R. Ueda and J. B. Mullin, Editors, p. 407, North Holland Publishing Co., Amsterdam (1975).

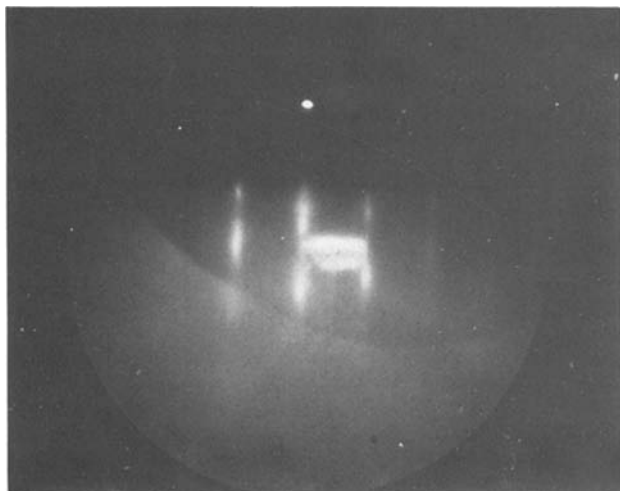


Fig. 6. RHEED diagram of (111) GaAs surface after O and C removal.

Growth Mechanisms of Silicon Crystallites Grown on Top of a Metal-Coated Graphite Substrate

W. J. P. van Enckevort and M. W. M. Graef

R.I.M. Laboratory of Solid State Chemistry, Faculty of Science,
Catholic University, Toernooiveld, Nijmegen, The Netherlands

ABSTRACT

Microscopic *in situ* observations and *a posteriori* surface topography by means of optical and scanning electron microscopy have been carried out in order to study the growth of large-grain polycrystalline silicon films from the gas phase onto a graphite substrate coated with a liquid layer of tin or aluminum. In the present study, only the initial stages of the process, where crystal growth is governed by vapor-liquid-solid mechanisms, are considered. For the growth of the crystallites in the polycrystalline layers, which occur in two morphological forms, *viz.*, needles and platelets, two different mechanisms could be identified: (i) a twin plane reentrant edge (TPRE) mechanism, leading to a fast lengthwise growth of needles and a fast sidewise growth of platelets; and (ii) a nucleation mechanism, accounting for a slow thickness growth of the needles and a slow expansion of the platelike crystals. On the upper surfaces of some needles and platelets a capricious surface pattern (always in conjunction with the occurrence of some solidified metal droplets) could be identified, which could be interpreted in terms of a two-dimensional VLS growth mechanism.

The interest in the preparation of photovoltaic silicon solar cells via inexpensive processes has resulted in the publication of a variety of studies dealing with the growth of silicon onto nonsilicon substrates, particularly graphite (1-4). One of the main problems in the chemical vapor deposition (CVD) of silicon onto foreign substrates is the poor crystallinity of the grown layers. It was found that the crystallinity could be enhanced by means of coating the graphite with liquid tin, prior to the deposition of silicon (5). In this CVDOLL process (chemical vapor deposition on liquid layers) the purpose was to grow large-grain polycrystalline silicon layers on top of graphite substrates. The deposition of silicon onto graphite plates, coated with a 10 μm thick molten tin film, resulted in the growth of polycrystalline films having a mean grain size exceeding 100 μm , which is a requirement for satisfactory solar cell operation (typical conditions: 0.75% SiHCl_3 and 1.0% HCl in H_2 ambient; surface temperature 1500 K). The formation of large grains is evidently associated with the presence of a liquid film that influences the nucleation and growth of silicon. Although it was assumed that the presence of liquid tin (or, alternatively, liquid aluminum) (i) reduces the density of the silicon nuclei, and (ii) feeds the growing crystals from a solution of silicon in the solvent (6), a detailed investigation into the nature of this growth process has not yet been carried out.

The purpose of the present studies was to characterize the growth mechanism for the growth of silicon on a liquid-metal coated substrate. This was done by the analysis of the polycrystalline silicon deposits by means of scanning electron microscopy and optical microscopy.

Experimental

Preparation of samples.—The growth process was carried out in a conventional horizontal epitaxial quartz reactor tube, provided with water cooling and rf heating. Trichlorosilane was used as a silicon source, hydrogen chloride as an etching agent, and hydrogen as a carrier gas. The substrates were graphite plates, coated with pyrolytic graphite, and with dimensions $2.0 \times 2.5 \times 0.1 \text{ cm}^3$, placed on a graphite susceptor.

Key words: polycrystalline silicon, vapor liquid-solid growth, twin plane reentrant edge mechanism.

Tin or aluminum were deposited onto these graphite plates via sublimation *in vacuo* prior to the deposition of silicon. The thickness of the metal layer amounted to 10 μm . The substrate temperature during growth was kept at 1500 K.

The formation of a liquid metal layer was brought about as follows (6): upon melting, the metal contracted to droplets, due to its high surface tension. The surface tension could be reduced by dissolving silicon into the droplets. This was done by an injection of several pulses of 0.75% SiHCl_3 in H_2 , each one lasting about 10 sec. This caused the droplets to spread out over the graphite, eventually forming a continuous liquid layer.

The growth of silicon on tin-coated graphite was initiated by the continuous addition of 0.75% SiHCl_3 /1% HCl , which resulted in the formation of silicon needles and platelets. Simultaneously, the tin was evaporated due to the etching activity of HCl . After completion of the evaporation of tin, the growth process continued in a way essentially comparable to conventional CVD of polycrystalline silicon layers [cf., for instance, Ref. (7)].

The growth of silicon on aluminum-coated graphite was carried out by (i) dissolving silicon into liquid aluminum [forming a 70 atomic percent (a/o) $\text{Si}/30$ a/o Al liquid mixture at 1500 K], and (ii) the removal of aluminum by the addition of HCl to the gas phase, causing silicon needles to grow from a supersaturated solution. This process was described by Graef and Monkowski (8).

For the purpose of this work it was necessary to interrupt the growth process before the evaporation of the liquid metal was completed, since the grain boundaries had not yet developed during this stage, and thus the crystallites could be studied separately.

Observational techniques.—The growth of silicon needles and platelets from solution could be studied *in situ* by means of a binocular microscope placed over an epitaxial reactor tube provided with a quartz window.

A more refined study of these crystallites was performed by means of optical reflection differential interference contrast microscopy in order to reveal low contrast surface patterns. In order to obtain a three-dimensional view at higher magnifications a

scanning electron microscope (SEM) was used. Most of the microscopic observations were carried out on as-grown samples. However, some SEM observations

were realized on samples which were etched during 2 hr in a solution 50 volume percent (v/o) concentrated $\text{HNO}_3/50$ v/o H_2O in order to remove residual

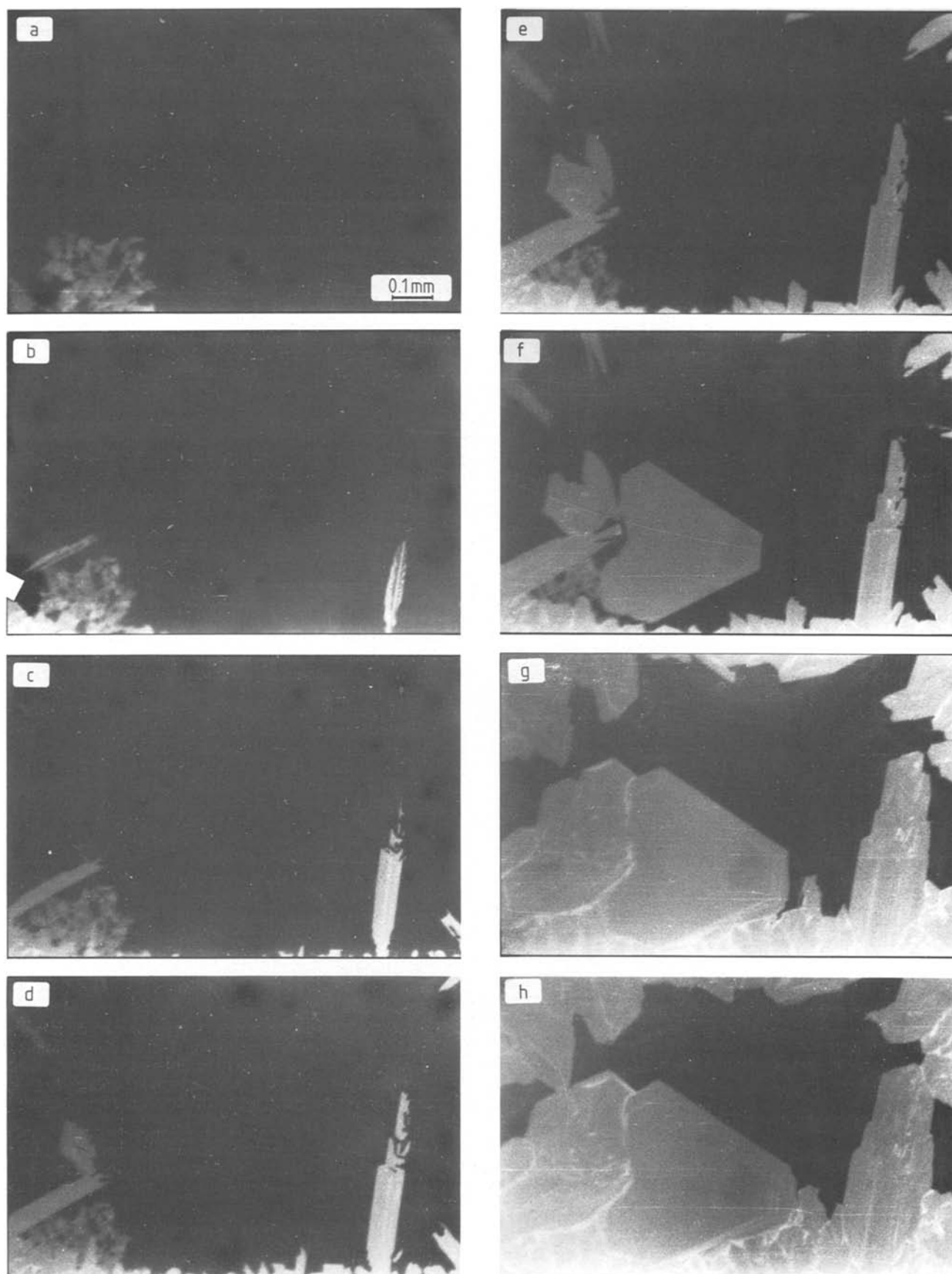


Fig. 1. Successive stages of the growth of silicon crystallites on tin-coated graphite. The addition of 0.75% SiHCl_3 and 1% HCl started at $t = 0$. Light regions: silicon; dark regions: tin. a. $t = 1'00''$; b. $t = 1'20''$; c. $t = 2'30''$; d. $t = 3'00''$; e. $t = 4'30''$; f. $t = 4'45''$; g. $t = 6'00''$; h. $t = 8'40''$.

droplets of tin or aluminum. This etching was carried out in order to reveal the areas of the silicon crystallites that had been covered by solidified metal. For studying the perfection of the crystals and to reveal stacking faults and twin planes, Sirtl etching (9) was applied.

The Growth of Needles and Platelets

The growth of silicon needles and platelets was observed to be typically associated with the presence of liquid metal droplets on top of the graphite substrate. These crystallites could be studied both during their formation, and *a posteriori*. In order to study the growth mechanism of needles and plates, investigations were made on the morphology of large crystallites that were grown on isolated droplets.

In situ observations.—Figure 1 shows a sequence of micrographs that was made during the deposition of silicon onto tin-coated graphite substrate. It can be observed that the initial growth of needles (e.g., Fig. 1, a and b) and plates (Fig. 1, e and f) proceeds very rapidly, but after a short time, the rapid growth stops, after which the crystallites grow in all directions at a much slower rate. It was estimated that the initial growth rate of the needles lengthwise was more than 60 times larger than the thickness growth rate. The initial expansion velocity of the platelets was of about the same order of magnitude as the needle propagation rate. This observation permits the conclusion that two growth mechanisms are operative: one for the rapid growth and one for the slow growth.

Needle growth.—Characteristics.—The growth of needles is characterized by the following features:

1. The growth of needle-shaped crystallites always starts on the edge of a liquid droplet, and the growth continues in a direction more or less toward the center of the droplet. Figure 2 gives a survey of a group of needles grown from liquid aluminum, whereas Fig. 3 shows silicon needles that were grown from a liquid tin droplet.

2. The upper surfaces of the needles are curved, while the lower ones are in contact with the graphite substrate. For the Sn/Si system the morphology of the needles could be elucidated by the removal of the solidified tin using a 1:1 HNO₃/H₂O etchant, which does not affect the silicon needles and the graphite. Figure 4 shows a typical large needle in the Sn/Si system. The profile of the upper surface is determined by the curvature of the droplet (Fig. 4a and d). This is similar to the way in which the external shape of cylindrical or rectangular crystals is determined by the shape of the meniscus in the case of Czochralski (10) or edge-defined film-fed growth (11). Figure 4b shows that the bottom side of the needle follows the morphology of the graphite substrate.

Both features, *viz.*, the fact that the top surfaces of the needles are determined by the gas-liquid interface and the fact that the bottom surfaces are determined by the substrate, have also been observed clearly in the Si/Al system. Furthermore, it was found that the upper and lower surfaces of the needles are no crystallographic faces in general.

3. The top surfaces of the needles, both in the Si/Sn and in the Si/Al system exhibit a reentrant corner (Fig. 4c and Fig. 5). Associated with a reentrant corner, a group of twin planes running parallel to the needle axis may always be observed (Fig. 4 and 5). These twin planes can be recognized by means of SEM, but particularly by means of differential interference contrast microscopy. The twin planes may be revealed more clearly by slight etching, e.g., by gas phase etching using HCl (Fig. 6a, for Si/Al) or by Sirtl etching (Fig. 6b).

It appears that the needle axis and consequently the twin planes always run parallel to one of the sides of the stacking fault triangles that were created by

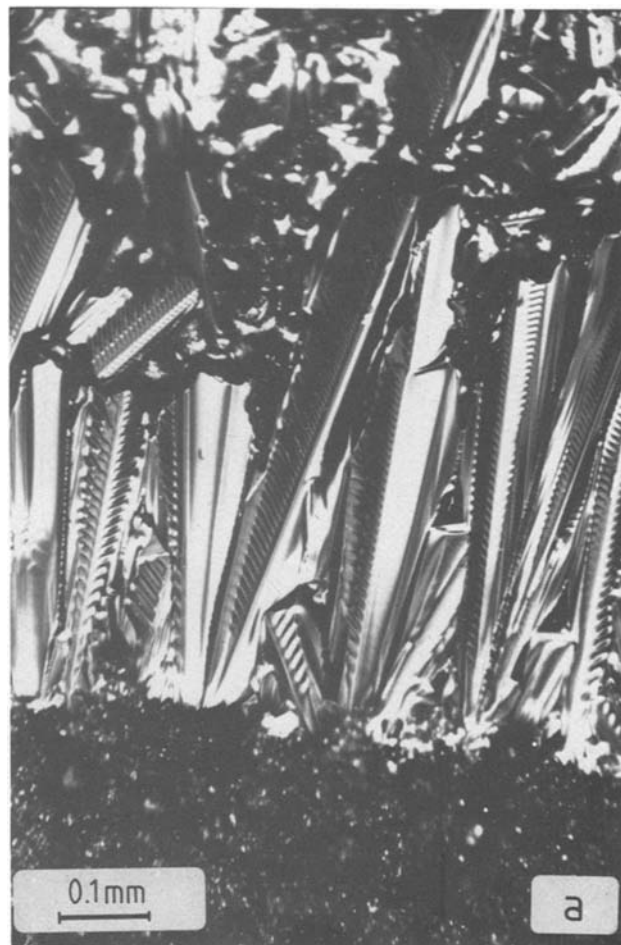


Fig. 2. Silicon needles grown on graphite coated with liquid aluminum. Differential interference contrast micrograph showing that the growth of the needles starts at the edge of the liquid droplet.

the deposition of epitaxial silicon layers onto the needles (12) (Fig. 6b). This indicates that the twin lines always run parallel to a {111} plane. Also, the twin planes are virtually always parallel to the lateral faces of the needles. These faces constitute {111} planes, being the only stable F-face for the growth

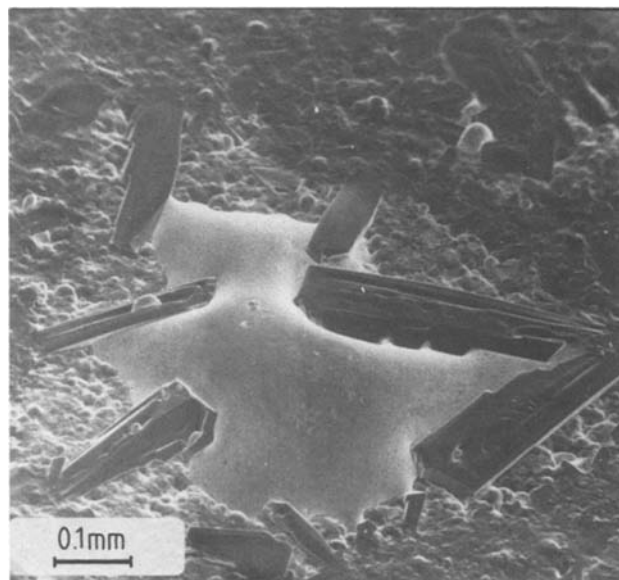


Fig. 3. Silicon needles (dark) grown from a liquid tin droplet (light). The growth of the needles starts at the edge of the droplet (SEM micrograph).

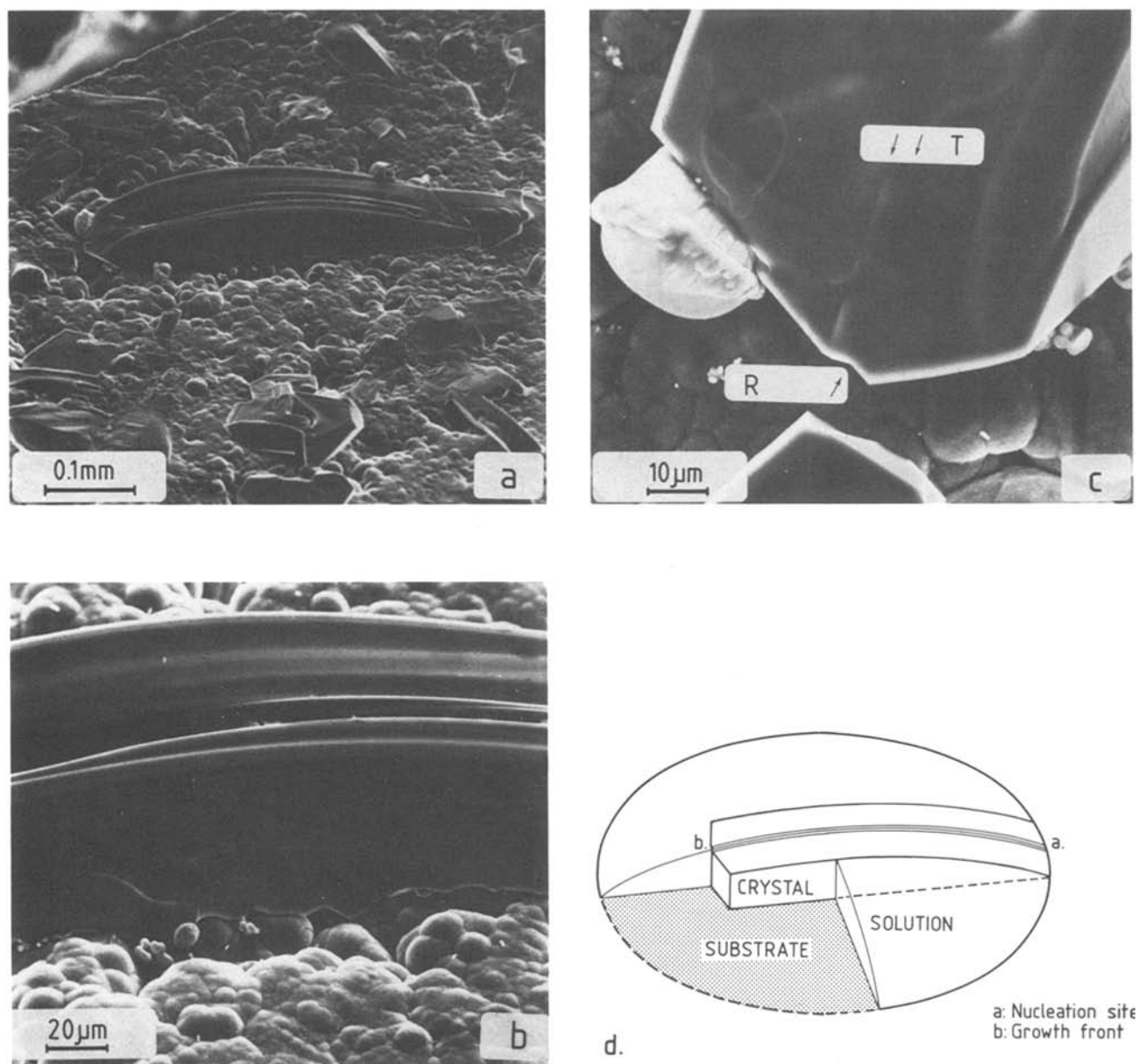


Fig. 4. SEM micrographs showing a typical large needle grown in the Si/Sn system. The tin has been removed by chemical etching. a. Overall view: the profile of the upper surface of the needle is determined by the curvature of the droplet. b. Detail of (a): the lower surface of the needle is in close contact with the substrate. c. Detail of the needle in (a): the top surface shows a reentrant corner (R) and some twinning lines (T) running parallel to the needle axis. d. Schematic representation of the characteristic features of needle growth.

of silicon from the metal melt (13). Hence it can be concluded that the twinning is of the type $\{111\}$ normal twin (the twin axis $\langle 111 \rangle$ is normal to the $\{111\}$ composition plane). This type of twinning is the most common one that occurs in the diamond lattice (14) (Fig. 7).

The growth mechanism that accounts for the generation of steps at a twin plane reentrant edge (TPRE) has been extensively studied both theoretically (15-17) and experimentally (18-21) for germanium, silicon, and diamond. The easy nucleation at a reentrant corner explains the high growth rate of the needles; Bennett and Longini (18) have been able to grow germanium crystals at a rate of 15 cm/min using TPRE growth.

The rate-determining step in this VLS mechanism is unknown in the present case; it is possible that the growth is limited by surface kinetics, volume diffusion, or heat transport.

It was shown by Wagner (19) and by Hamilton and Seidensticker (15) that at least two twin planes are required for a continued reentrant edge growth mechanism. As a matter of fact, on virtually all needles

two or more twin planes could be discerned; the separation was sometimes less than $0.5 \mu\text{m}$.

Growth history of the needles.—The growth process of the silicon needles can be summarized as follows (cf. Fig. 8):

1. The growth starts in the vicinity of the edges of the liquid droplets. Some of the microcrystals (having a size of a few microns) that are formed contain two or more parallel $\{111\}$ twins. If these twins are directed toward the liquid, the formation of needles will start (Fig. 8a).

2. Needle growth (Fig. 8b): the TPRE-defined needle growth takes place at a very high rate (roughly $1000 \mu\text{m}/\text{sec}$) and stops suddenly. In the Si/Al system the needle growth is stopped only by collision against other needles (cf. Fig. 2), but in the Si/Sn system, the needle growth often stops without an evident reason (this might be due to poisoning of the reentrant corner, or exhaustion of the solution due to the poor solubility of Si in Sn, 2 a/o at 1500 K). In principle, the needle size in the Al/Si system is unlimited (needles having a length up to 10 mm have been grown); the top and bottom surfaces are deter-

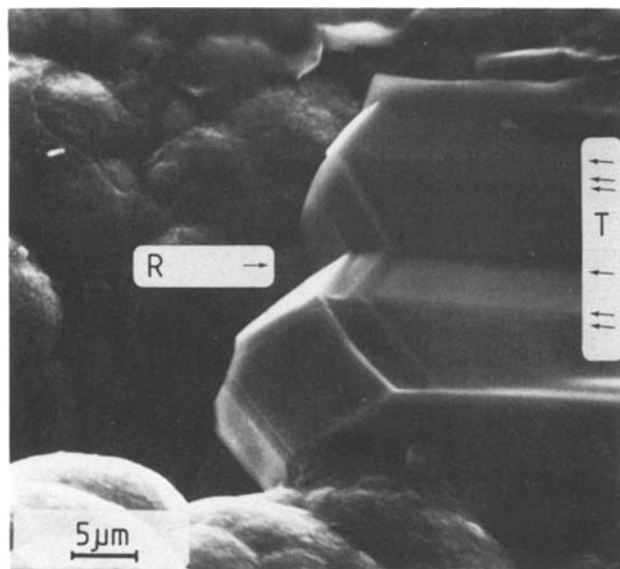


Fig. 5. Reentrant corner (R) and twinning lines (T) on the top surface of a silicon needle grown in the Si/Sn system (SEM micrograph).

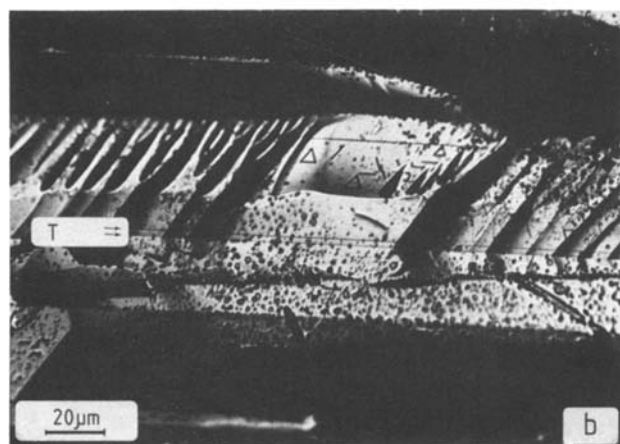
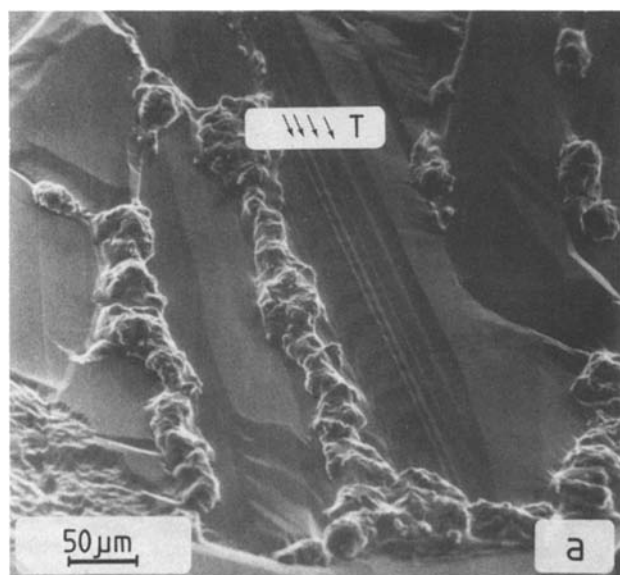


Fig. 6. Twinning lines (T) on silicon needles, revealed by etching. a. Silicon needle grown in the Si/Al system, etched by gaseous HCl at 1500 K (SEM micrograph). b. Silicon needle grown in the Si/Al system, etched by Sirtl solution, and showing stacking fault triangles. The twinning lines run parallel to one of the sides of the triangles (optical micrograph).

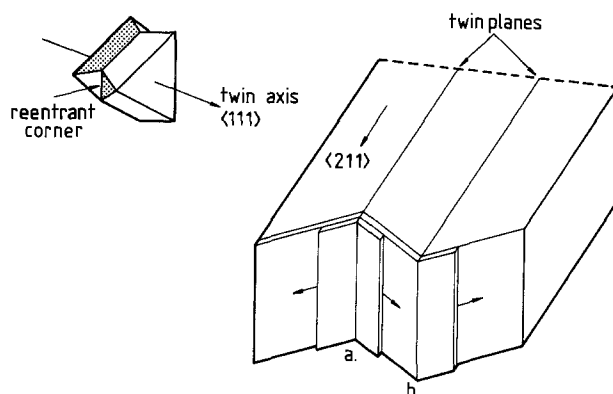


Fig. 7. Schematic representation of the twin plane reentrant edge growth mechanism at the tip of silicon needles.

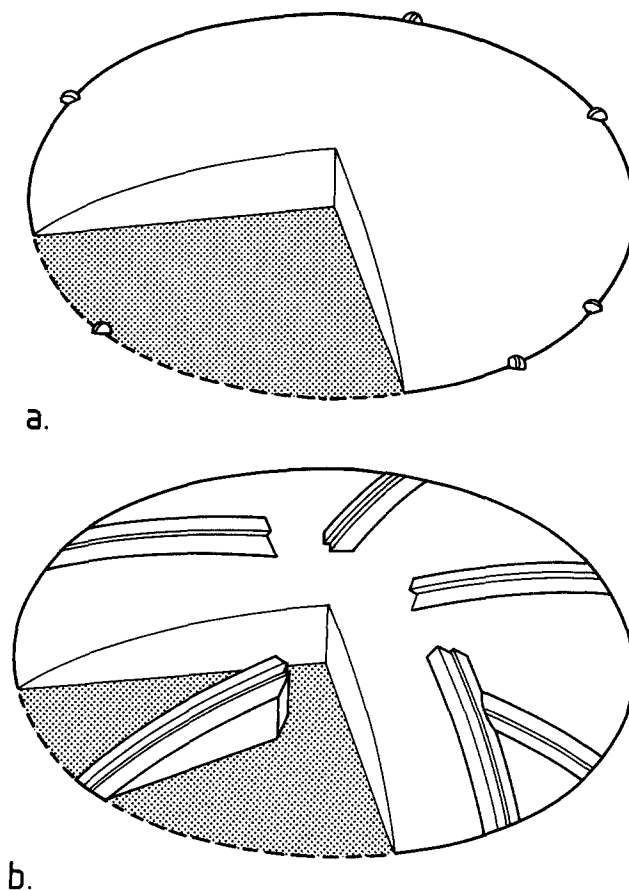


Fig. 8. Growth history of silicon needles. a. Nucleation on the edges of a droplet. b. Needle growth by a TPRE growth mechanism, followed by two-dimensional nucleation.

mined by the shape of the aluminum liquid and by the substrate, respectively.

3. Thickness growth: subsequently, the growth of the needles in the directions perpendicular to the silicon-liquid interfaces starts. Here, the growth rate is less than 1/60 of the TPRE growth. From this sharp decrease in growth rate, it can be concluded that for the thickness growth, the surface kinetics constitute the rate-determining step in the process. Very probably, this growth process is determined by a nucleation mechanism. This is indicated by the fact that the TPRE mechanism only occurs if no spiral growth mechanism is operative (17). It is well known that VLS growth can result in the formation of highly perfect crystals (22, 23). The defects that were revealed by Sirtl etchant were typically twins, stacking faults, and many point defects (the latter were presumably created due to tin inclusions, or after growth).

Only in a few cases dislocations or dislocation arrays (which might have been formed during cooling) have been found. The relatively low dislocation density is in agreement with the assumed nucleation mechanism.

Platelet growth.—Characteristics.—The growth of platelets is characterized by the following features:

1. The platelets usually originate in the liquid metal (homogeneous nucleation; Fig. 1e and f) and subsequently grow rapidly over the liquid surface via a VLS mechanism. In some cases platelets were observed to originate from the edge of a droplet (Fig. 9). Platelet growth was found to occur only in the Si/Sn system, and not in the Si/Al system.

2. The platelets always exhibit a hexagonal shape (Fig. 1f and Fig. 9), so it can be concluded that the top and bottom surfaces are usually $\{111\}$ crystal faces. However, since the curved surface of the liquid determines the upper surface of the platelet (analogous to the morphology of needles), this surface can be slightly curved. The bottoms of the platelets are usually not in contact with the substrate; in some cases a movement of platelets over the liquid surface has been observed.

3. Sirtl etching and surface topography did not reveal any twinning lines (intersection lines of a twin plane with a crystal face) on the upper surfaces of the platelets originating from a central point to the corners. Careful observation, however, revealed the presence of twinning lines and associated reentrant corners on the narrow side faces of the $\{111\}$ plates (Fig. 10). These lines were parallel to the $\{111\}$ surface.

This indicates that the growth of platelets is governed by two or more twin planes parallel to the $\{111\}$ surface. Thus, the growth of platelets proceeds via the TPRES mechanism that is also responsible for the growth of needles, as described by Faust and John (20) and Wagner (19). The growth mechanism has been pictured schematically in Fig. 10b.

Growth history of the platelets.—The growth process of the platelets can be summarized as follows (Fig. 11):

1. Probably, homogeneous nucleation in the liquid metal is responsible for the formation of platelets. Alternatively, nucleation may be initiated at the liquid-vapor interface (which might be explained by the existence of a concentration gradient in the liquid metal). Nucleation at the liquid metal-substrate interface is improbable, since after etching of the solidified

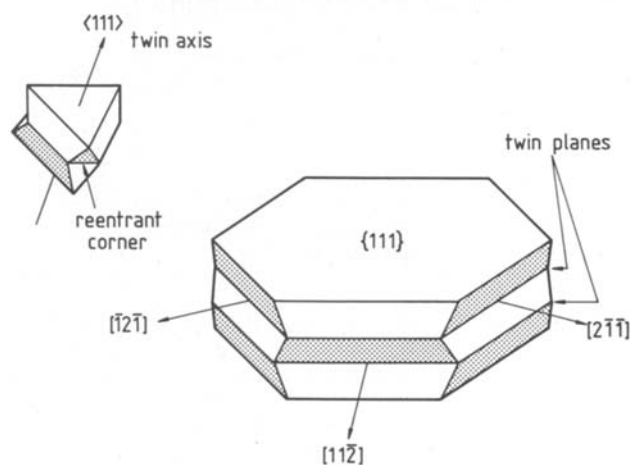
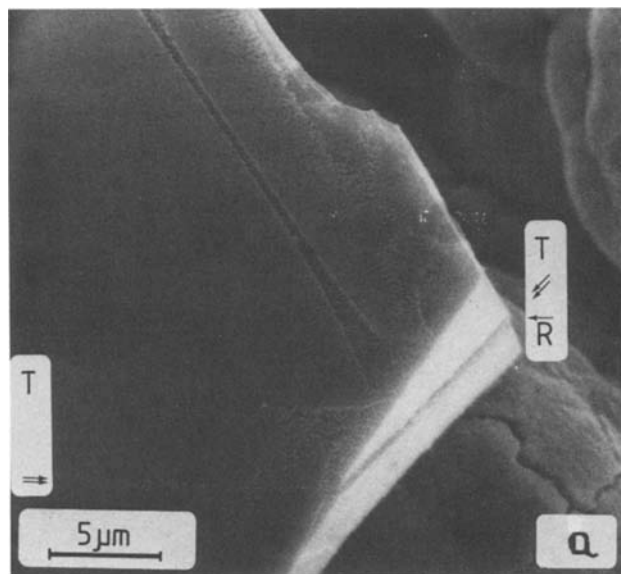


Fig. 10. Twin lines (T) and reentrant corners (R) on the narrow side faces of silicon platelets grown on a tin droplet. a. Twinning line on a side face of a platelet, revealed by Sirtl etching (SEM micrograph). b. Schematic representation of a TPRES grown platelet.

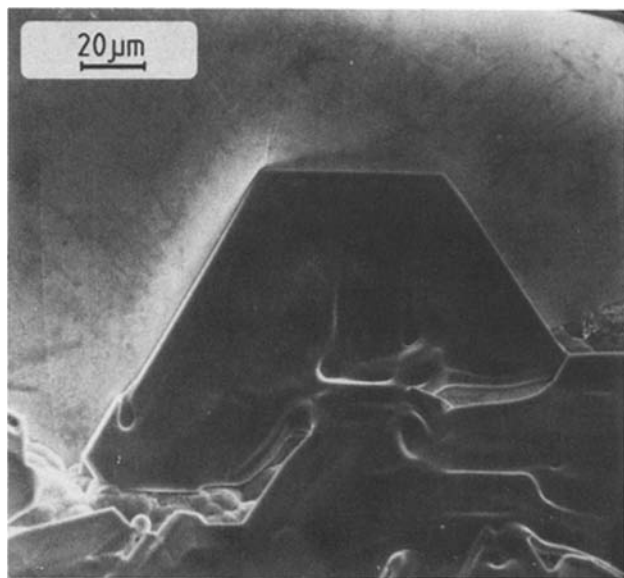


Fig. 9. Silicon platelet, nucleated on the edge of a tin droplet (SEM micrograph).

metal no traces of silicon on the graphite could be detected. In some cases heterogeneous nucleation on the graphite on the edge of a droplet caused the formation of platelets; in this case the twin planes run parallel to the liquid surface.

In the case of homogeneous nucleation inside the liquid, a microcrystal migrates to the liquid surface (due to its small density compared with that of tin), where the platelet adjusts itself to the surface (*i.e.*, the twin planes become directed parallel to the surface). Any other geometry will result in the growth of needles.

2. Subsequently, a rapid lateral growth of the platelets takes place. Since the curvature of the droplet determines the curvature of the crystal top surface, the platelet will be slightly bent. As a consequence of this bending, after some time the twin planes will come out at the top surface instead of at the side facets, and lose contact with the liquid (Fig. 11b). Then, the growth rate decreases suddenly (Fig. 1f). On the upper surface of some platelets twin lines have indeed been found, running parallel to the edges.

3. If there are no twinning lines left on the side faces of the platelets (and consequently the reentrant corners are no longer operative), the subsequent growth continues via a nucleation mechanism. This is the slow growth (about 1/60 times the TPRES growth rate) that has been observed after the rapid growth

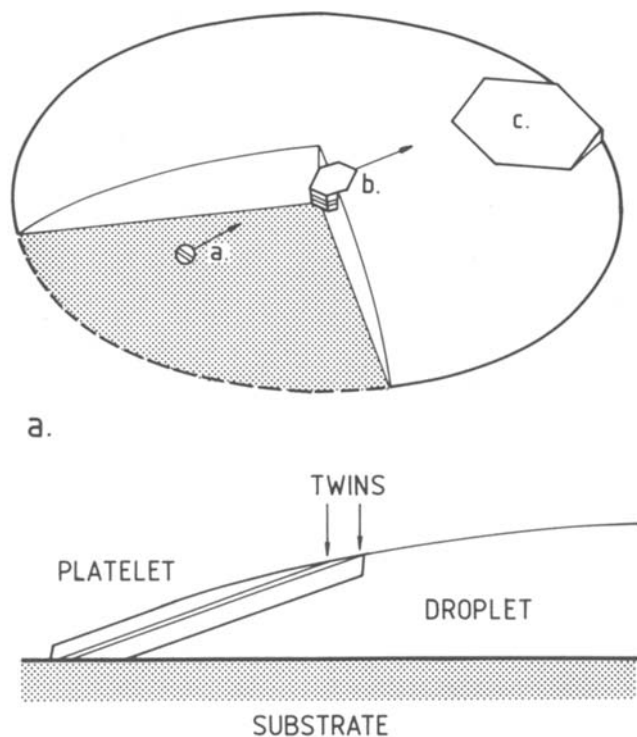


Fig. 11. Growth history of silicon platelets. a. Nucleation and TPRE growth of a platelet. b. Cross section showing that the twin planes lose contact with the liquid.

(Fig. 1g and h). The arguments for the assumption that this growth is governed by a nucleation mechanism, and that the surface process is the rate-determining step, are similar to the reasons given for the growth via nucleation for needles.

Two-dimensional VLS Growth

In some cases it was observed that some small tin droplets remained present on the top surfaces of the needles and platelets. Here the crystal surface always exhibited a very complicated pattern in which these few isolated tin droplets could be detected (see Fig. 12a). These patterns can be understood in terms of a two-dimensional VLS growth mechanism and are similar to the ones that have been observed on ice by Kobayashi (24) (however, in the present case there is no repeatable process for the formation of multiple terraces) and on CuGaS_2 by van Enckevort *et al.* (25). This two-dimensional VLS growth mechanism for the advancement of a macrostep has been outlined schematically in Fig. 12b. The growth of such a step is governed by the presence of a liquid tin front, which accelerates the process via a VLS mechanism. The observed solidified tin droplets are the remnants of these liquid "frills" at the edges of the macrosteps.

Conclusions

Silicon crystallites that resulted from the isothermal growth of silicon by means of chemical vapor deposition onto a graphite substrate coated with a liquid metal have been analyzed. It was found that the initial growth of the crystallites proceeds via a VLS mechanism. Two stages in this growth process could be discerned:

1. A rapid growth of needles and platelets according to the twin plane reentrant corner (TPRE) mechanism: the twin planes that are responsible for this mechanism run parallel to the needle axis in the case of needles and parallel to the surface in the case of platelets. There is no essential difference between the growth of needles and platelets. The distinction in morphology is determined by geometrical factors.

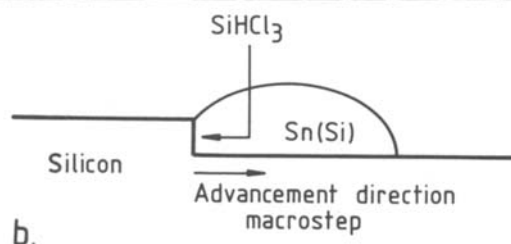
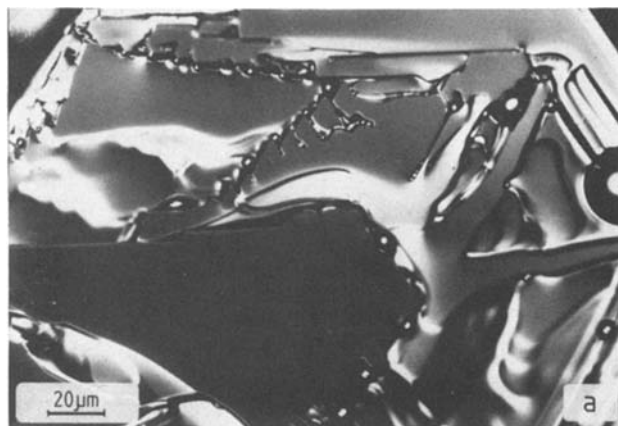


Fig. 12. Two-dimensional VLS growth of silicon in the Si/Sn system. a. Differential interference contrast micrograph showing an irregular surface pattern caused by two-dimensional VLS growth on the upper surface of a silicon platelet. Various solidified tin droplets are present. b. Schematic cross section showing a liquid "frill" at the edge of an advancing step.

2. A slow growth via a nucleation mechanism: in the case of needles this process is observed as the thickness growth perpendicular to the needle axis. In the case of platelets it is observed as a slow lateral growth of the platelets if the twinning lines are no longer in contact with the liquid. Crystallites without twin planes have not been observed. This is caused by the overgrowth of these slow-growing clusters by crystallites possessing two or more parallel twin planes. Two-dimensional VLS growth has been observed on the upper surfaces of needles and platelets. The velocity of macrosteps appeared to be influenced considerably by the presence of a liquid metal frill at the step front. From the fact that even for higher supersaturations growth of the $\{111\}$ faces of silicon and germanium from the melt or metallic solution is strongly accelerated by the occurrence of a TPRE mechanism as compared to two-dimensional nucleation, it can be concluded that the standard temperature θ [for definition of θ , see Ref. (26) and (27)] of these systems is far below the roughening transition point as was determined by Monte Carlo simulation (27). In a forthcoming paper (28), in which a comparison will be made between the Monte Carlo simulation results and growth experiments of $\{111\}$ Si and Ge from the liquid phase, special attention will be paid to the relation between the parameters, which rule the simulations (such as θ), and experimentally known values. A closer investigation into the thermodynamic and kinetic phenomena that are associated with the described growth process may lead to an augmented knowledge of the growth of thin large-grain polycrystalline silicon layers onto nonsilicon substrates, and enable the preparation of inexpensive materials for photovoltaic solar cell fabrication.

Acknowledgments

The authors wish to thank H. A. v. d. Linden and Ing. A. W. Dicke for their help in making the SEM photographs. They also want to thank Prof. Dr. P. Bennema, Prof. Dr. J. Bloem, and Dr. L. J. Giling for stimulating discussions and for their kind interest in the present study. W. J. P. van Enckevort acknowl-

edges the support of The Netherlands Foundation for Pure Research (ZWO/SON), whereas M. W. M. Graef acknowledges the Commission of the European Communities for an EC grant Contract No. 442-78-2 ESN.

Manuscript submitted March 28, 1980; revised manuscript received July 29, 1980.

Any discussion of this paper will appear in a Discussion Section to be published in the December 1981 JOURNAL. All discussions for the December 1981 Discussion Section should be submitted by Aug. 1, 1981.

Publication costs of this article were assisted by Catholic University.

REFERENCES

1. T. L. Chu, H. C. Mollenkopf, and S. S. Chu, *This Journal*, **123**, 106 (1976).
2. C. Belouet, J. Hervo, R. Martres, Ngo-Tich Phuoc, and M. Pertus, Proceedings of the XIIth IEEE Photovoltaic Specialists Conference, Washington, D.C., p. 131 (1978).
3. C.-A. Chang and W. J. Siekhaus, *J. Appl. Phys.*, **46**, 3402 (1975).
4. T. F. Cizek, G. H. Schwuttke, and K. H. Yang, *J. Cryst. Growth*, **46**, 527 (1979).
5. M. W. M. Graef, L. J. Giling, and J. Bloem, *J. Appl. Phys.*, **48**, 3937 (1977).
6. J. Bloem, L. J. Giling, M. W. M. Graef, and H. H. C. de Moor, Proceedings of the 2nd E.C. Photovoltaic Solar Energy Conference, Berlin p. 759 (1979).
7. C. H. J. van den Brekel and J. Bloem, *Philips Res. Rep.*, **32**, 134 (1977).
8. M. W. M. Graef and J. R. Monkowski, To be published.
9. E. Sirtl and A. Adler, *Z. Metallk.*, **52**, 529 (1961).
10. W. Bardsley, F. C. Frank, G. W. Green, and D. T. J. Hurle, *J. Cryst. Growth*, **23**, 341 (1974).
11. T. Surek, C. B. Hari Rao, J. C. Swartz, and L. C. Garone, *This Journal*, **124**, 112 (1977).
12. B. H. Berry, in "Fundamentals of Silicon Integrated Device Technology," Vol. 1, R. M. Burger and R. P. Donovan, Editors, p. 434, Prentice-Hall Inc., Englewood Cliffs, N.J. (1967).
13. J. W. Faust, A. Sagar, and H. F. John, *This Journal*, **109**, 824 (1962).
14. G. A. Wolff, *Am. Mineral.*, **41**, 60 (1956).
15. D. R. Hamilton and R. G. Seidensticker, *J. Appl. Phys.*, **31**, 1165 (1960).
16. A. A. Davydov and V. N. Maslov, *Soviet Phys.-Cryst.*, **9**, 393 (1965).
17. M. Kitamura, S. Hosoya, and I. Sunagawa, *J. Cryst. Growth*, **47**, 93 (1979).
18. A. I. Bennett and R. L. Longini, *Phys. Rev.*, **116**, 53 (1959).
19. R. S. Wagner, *Acta Metall.*, **8**, 57 (1960).
20. J. W. Faust and H. F. John, *J. Phys. Chem. Solids*, **25**, 1407 (1964).
21. C. Lemaignan and Y. Malmejac, *J. Cryst. Growth*, **46**, 771 (1979).
22. E. I. Givargizov, in "Current Topics in Materials Science," Vol. 1. E. Kaldis, Editor, p. 79, North-Holland Publishing Co. (1978).
23. B. J. Baliga, *This Journal*, **125**, 598 (1978).
24. T. Kobayashi, *J. Cryst. Growth*, **26**, 6 (1974).
25. W. J. P. van Enkevort, H. Binsma, and G. Staarink, *ibid.*, To be published.
26. J. P. van der Eerden, P. Bennema, and T. A. Cherepanova, "Prog. Crystal Growth and Charact.," Vol. 1, p. 219, Pergamon, Oxford (1978).
27. W. J. P. van Enkevort and J. P. van der Eerden, *J. Cryst. Growth*, **47**, 501 (1979).
28. W. J. P. van Enkevort, P. Bennema, and L. J. Giling, Work in progress.

Boron Autodoping during Silicon Liquid Phase Epitaxy

B. Jayant Baliga

General Electric Company, Corporate Research and Development, Schenectady, New York 12345

ABSTRACT

The occurrence of boron autodoping phenomena during the growth of silicon layers from the liquid phase (tin melt) is described. Autodoping has been observed to occur in this epitaxial growth process whenever meltback of the substrate occurs prior to epitaxial growth. Measurements of lateral autodoping show that the boron injected into the melt due to substrate meltback is rapidly dispersed in the melt. However, by preventing meltback with supersaturation of the melt prior to the introduction of the substrate into the melt, autodoping can be eliminated, thus allowing the achievement of abrupt doping profiles between the substrate and the epitaxial layer, and also allowing the fabrication of closely spaced, buried, boron-diffused regions for device applications.

Many silicon devices, such as bipolar integrated circuits, microwave IMPATT and PIN diodes, high speed varactors, and high frequency discrete transistors, require the growth of epitaxial layers on heavily-doped substrates with an abrupt transition in the doping between the substrate and the epitaxial layer. The silicon layers have conventionally been grown by vapor phase epitaxial growth techniques. In this process, two phenomena that prevent the achievement of an abrupt interface are the out-diffusion of the dopant from the substrate into the epitaxial layer during the high temperature epitaxial growth, and autodoping effects. In general, autodoping can be defined as the transport of dopants from the substrate into the epitaxial layer via the gas phase. Since auto-

doping degrades the abruptness in the transition between the doping of the substrate and the epitaxial layer and also increases the background doping concentration in the epitaxial layers, many studies have been conducted in order to minimize autodoping effects during silicon vapor phase epitaxial growth (1-4). These studies have shown that autodoping during vapor phase epitaxial growth arises primarily from (i) dopant outgassing into the vapor phase prior to the commencement of epitaxial growth, (ii) dopant evaporation from the back surface of the wafer during epitaxial growth, and (iii) dopant introduction into the gas phase due to substrate etching by halides during epitaxial growth. Based upon these mechanisms reduction in the autodoping during vapor phase epitaxy has been achieved by (i) lowering the epitaxial growth temperature, (ii) sealing the back surface

Key words: silicon epitaxy, autodoping, liquid phase epitaxy, meltback.

of the substrates with silicon dioxide, silicon nitride, or polycrystalline silicon, (iii) performing the epitaxial growth in the absence of halides by using silane as the source, and (iv) lowering the pressure in the reactor during epitaxial growth so as to reduce the partial pressure of the dopant impurities during deposition. In addition, two step epitaxial growth procedures have been developed to reduce autodoping effects (2, 3). Although all of these techniques have been successful in reducing the autodoping, they have not been able to eliminate the problem altogether. This is particularly noticeable when epitaxial growth is conducted over localized diffusions of dopants into the substrates, as is necessary, for example, during the fabrication of integrated circuits. In this case, autodoping causes the lateral transport of the dopant from the diffused area which results in severe distortion of the geometry of the diffused buried layer (5). Further, in the case of devices requiring closely spaced diffused buried layers such as field-controlled devices (6, 7), lateral autodoping can result in the formation of a connecting layer which prevents the desired isolation between these buried regions. The fabrication of these devices by vapor phase epitaxy, consequently, requires compensation of the autodoping by the addition of dopants in the gas phase. This approach is difficult to pursue in practice because of the need to achieve low epitaxial doping concentrations in the presence of strong autodoping effects.

This paper discusses autodoping phenomena observed during the growth of silicon layers by using liquid phase epitaxy. It is demonstrated here that autodoping effects can be completely eliminated by performing the epitaxial growth from the liquid phase. However, autodoping can occur even during silicon liquid phase epitaxial growth if care is not taken to prevent substrate meltback prior to epitaxial growth. In addition, the results of lateral autodoping studies are reported here for the case of boron-diffused regions in n-type silicon substrates. On the basis of these studies, growth conditions have been established which allow the fabrication of closely spaced boron diffused fingers buried under an n-type epitaxial layer. This new epitaxial growth technology has allowed the fabrication of high voltage field-controlled thyristors (8).

Epitaxial Growth Technique

The silicon epitaxial growth technique utilized in this study was based upon using liquid tin as the medium for the epitaxial growth. Tin was chosen as the solvent for the silicon because it is an element that lies in the fourth column of the periodic table of elements. Thus, the incorporation of the tin in the epitaxial layers was not expected to introduce either shallow dopant levels or deep lying recombination levels in the silicon energy gap. This has been confirmed by the fact that, although more than 10^{19} atoms per cm^3 of tin have been detected in the epitaxial layers by electron microprobe analysis, layers could be grown with n-type background doping levels between 5×10^{15} and 1×10^{16} per cm^3 with high minority carrier recombination lifetimes (greater than 10 μsec). In addition, the solubility of silicon in tin at relatively low temperatures (900°-950°C) is sufficient for the growth of even thick (50-100 micron) epitaxial layers.

The growth of the epitaxial layers was conducted in a hydrogen ambient by using the dipping technique. Studies of the growth of epitaxial layers conducted under slow cooling, as well as steady-state conditions using supersaturation, have demonstrated the capability for growing specular films with growth rates in the range of 0.1-1 micron per minute (9-11). In order to grow n-type epitaxial layers, the tin melt was first saturated with 100 $\Omega\text{-cm}$, phosphorus-doped silicon wafers. The saturation was conducted while periodically monitoring the weight of the saturation wafers and was terminated when no further loss in the weight

of the saturation wafers could be detected. In order to study the influence of both undersaturation and supersaturation, epitaxial growths were conducted on substrates which were introduced into the melt at temperatures above and below the saturation temperature. In each case, the epitaxial growth was induced by reducing the temperature of the furnace at controlled cooling rates ranging from 0.1° to 7°C/min. After epitaxial growth, the substrates were withdrawn from the melt and any excess tin attached to them was removed in aqua regia.

Autodoping Experiments

Heavily-doped substrates.—The first set of autodoping experiments were conducted with 0.01 $\Omega\text{-cm}$, boron-doped, (111) $\pm 1/2^\circ$ oriented silicon wafers. Epitaxial layers were grown on these substrates with the melt undersaturated and supersaturated by 5°C prior to the introduction of the substrates into the melt. The doping profile in the epitaxial layer was then measured by using the ASR100 spreading resistance measurement system. The profiles are shown in Fig. 1. It can be seen that when the melt is undersaturated, a p-type interface layer with a graded doping concentration profile is observed at the interface between the epitaxial layer and the substrate. The nature of this doping profile has been analyzed and the p-type layer shown to arise from meltback of the substrate prior to epitaxial growth (12). If the melt is undersaturated when the substrate is introduced into it, part of the substrate is dissolved and the boron in that portion of the substrate is injected into the melt. This boron is subsequently incorporated into the epitaxial layer forming an exponentially graded p-type interface. This phenomena is, thus, similar to the autodoping observed in the case of vapor phase epitaxy and leads to a nonabrupt doping profile at the interface between the epitaxial layer and the substrate. In contrast, when the melt is supersaturated prior to the introduction of the substrate into the melt, no meltback can occur and an abrupt doping transition is observed at the interface between the epitaxial layer and the substrate as shown in Fig. 1b. Consequently, these experiments show that although autodoping can occur during silicon liquid phase epitaxy, it can be completely suppressed by supersaturation of the melt prior to the introduction of the substrates into the melt.

Boron-diffused substrates.—As stated in the introduction, one of the problems encountered during vapor phase epitaxy is the occurrence of lateral autodoping effects. This has been found to be particularly severe in the case of boron diffusions in n-type silicon substrates. Experiments were, therefore, conducted to study lateral autodoping effects during liquid phase epitaxy. For these experiments, boron diffusions were performed over a portion of 40 $\Omega\text{-cm}$, phosphorus-doped silicon wafers using thermally grown silicon dioxide as a mask. After stripping the oxide on the wafer surface, n-type epitaxial layers were grown with an undersaturation of 5°C to determine the extent of the lateral autodoping. As illustrated in Fig. 2, if the boron injected into the melt due to meltback is localized to the diffused region, the lateral autodoping should be limited to a portion close to the diffused region. In contrast, if the boron injected into the melt is rapidly dispersed, the lateral autodoping should extend across the entire surface of the wafer.

To measure the lateral autodoping, spreading resistance measurements were made at the diffused portion of the wafer and at various distances from the edge of the diffused region as illustrated in Fig. 3 and 4. In the case shown in Fig. 3, only a part of the diffused layer was etched away by meltback as can be seen in the profile taken at the diffused region. The profiles taken at various distances from the edge of

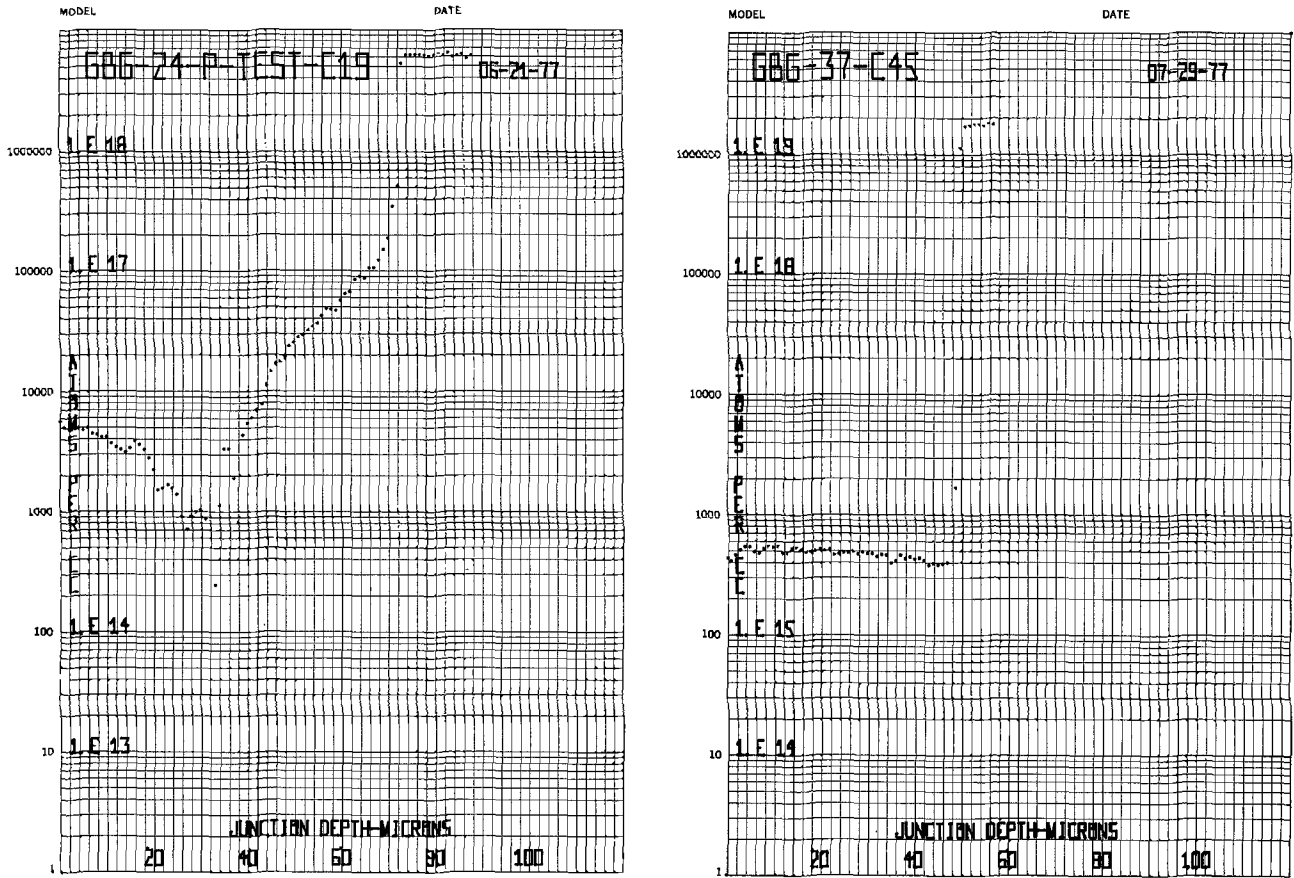


Fig. 1. Impurity distribution profiles of epitaxial layers grown on heavily boron doped substrates with (a, left) 5° undersaturation of the melt and (b, right) 5° supersaturation of the melt before epitaxial growth.

LATERAL AUTODOPING

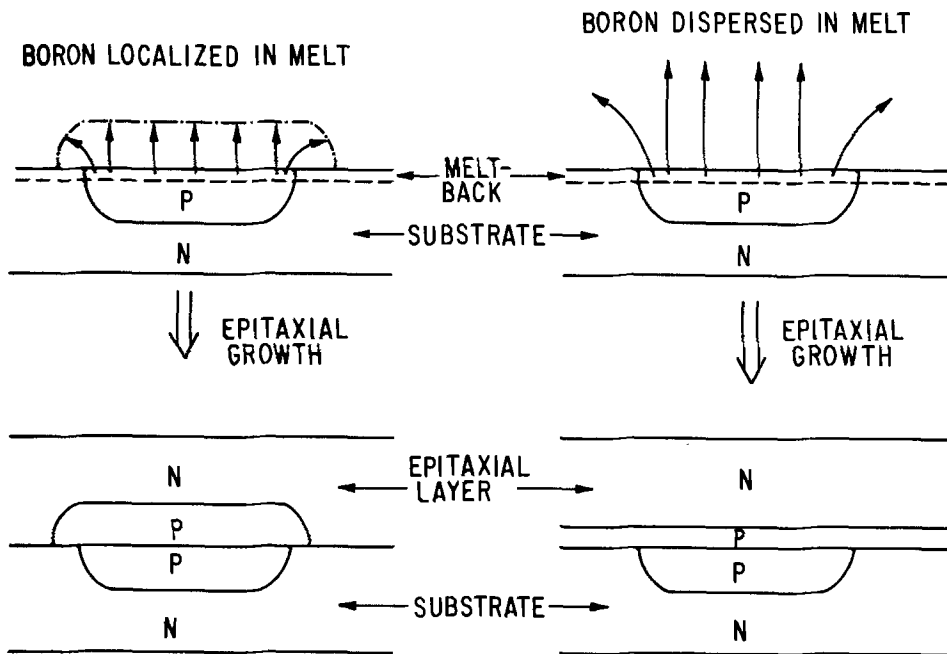
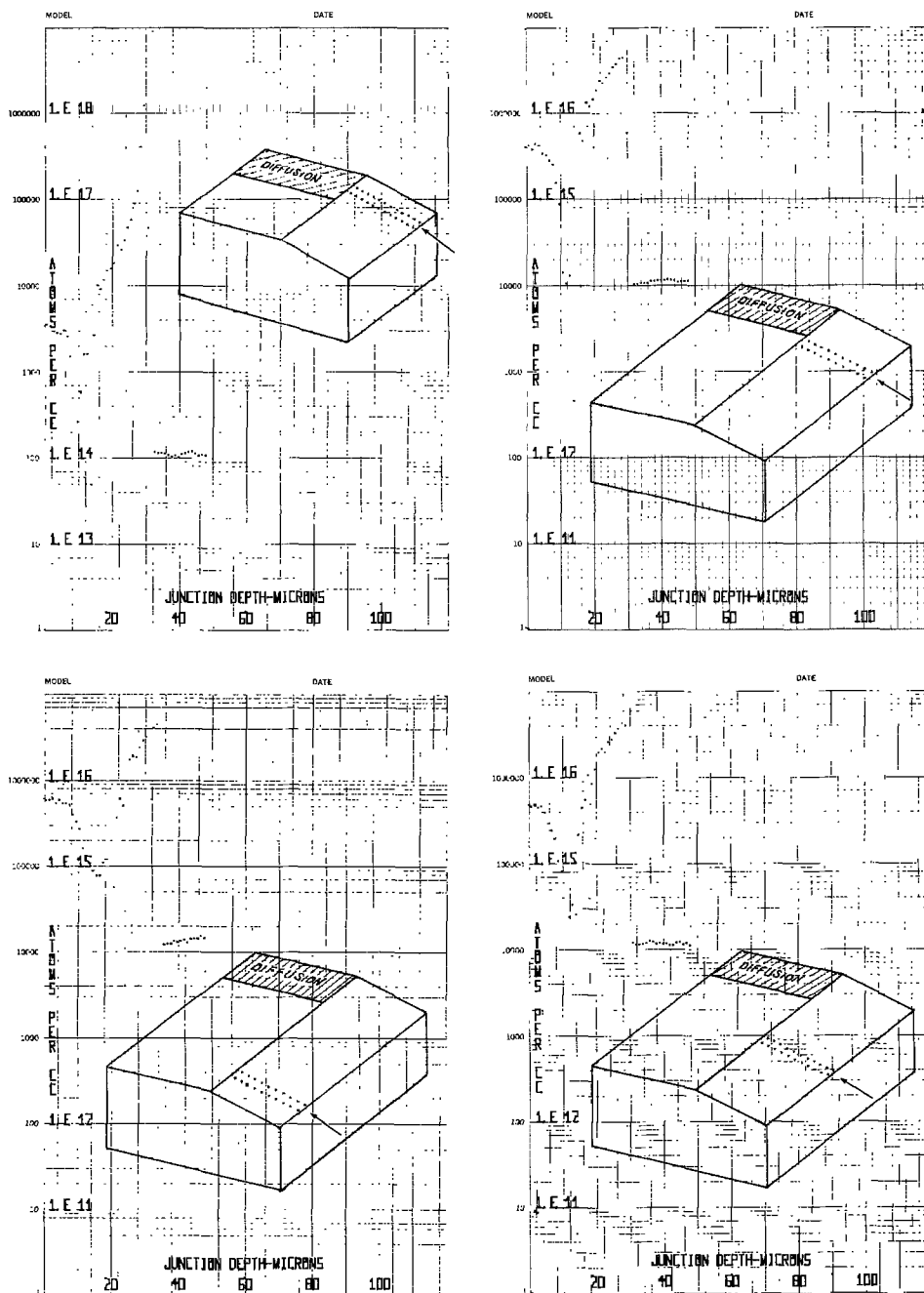


Fig. 2. Schematic illustration of lateral autodoping which occurs when the boron injected into the melt due to meltback is localized or dispersed in the melt.

the diffused region are also shown in Fig. 3. It can be seen that a p-type layer is observed at all distances from the edge of the diffused layer. (The maximum distance from the edge of the diffused region that was profiled was 1 in.) This p-type layer has the same peak doping concentration and width at all the profiled locations within the limits of experimental error. From this observation it can be

concluded that the boron injected into the melt must be rapidly dispersed throughout the melt during epitaxial growth. Another example of this can be seen in Fig. 4. In this case, the meltback was sufficient to completely dissolve the boron diffused region prior to epitaxial growth. As a result the p-type layer formed at the interface between the substrate and the epitaxial layer has the same doping profile and

Fig. 3. Impurity distribution profiles taken at four locations on a wafer with boron diffusion at one end and an epitaxial layer grown with partial meltback of the diffused region prior to epitaxial growth.



thickness across the entire wafer. The results of these lateral autodoping studies, thus, indicate that to prevent lateral autodoping it is imperative to prevent meltback of the substrate prior to epitaxial growth by careful supersaturation of the melt.

Conclusions

Autodoping phenomena during silicon liquid phase epitaxy have been studied for the cases of boron-doped substrates and boron diffused layers in n-type substrates. It has been determined that autodoping can also occur during silicon liquid phase epitaxy if any meltback of the substrate occurs prior to epitaxial growth. In the case of localized boron diffused regions, it has been found that the lateral autodoping extends uniformly across the entire wafer surface indicating that the boron injected into the melt from the diffused regions due to meltback is rapidly dispersed throughout the melt. It can, therefore, be concluded that in order to eliminate autodoping during silicon liquid phase epitaxy it is essential to prevent any meltback of the substrate by supersaturation of the melt prior

to the introduction of the substrate. With supersaturation of the melt, the liquid phase epitaxial growth technique is capable of completely eliminating boron autodoping effects. This has allowed the fabrication of epitaxial layers with abrupt doping transitions between the epitaxial layer and heavily-doped substrates, and the fabrication of closely spaced, buried, boron diffusion regions in n-type substrates (13).

Acknowledgments

The author wishes to acknowledge the technical assistance received from G. Gidley during epitaxial growth and B. Hatch during spreading resistance measurements.

Manuscript submitted April 17, 1980; revised manuscript received July 25, 1980. This was Paper 157 presented at the Boston, Massachusetts, Meeting of the Society, May 6-11, 1979.

Any discussion of this paper will appear in a Discussion Section to be published in the December 1981 JOURNAL. All discussions for the December 1981 Discussion Section should be submitted by Aug. 1, 1981.

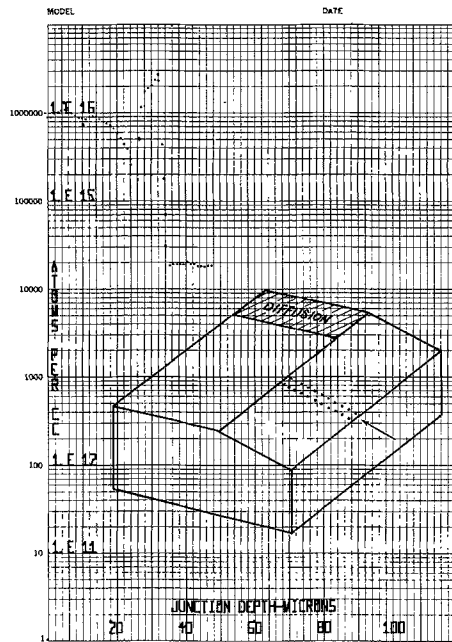
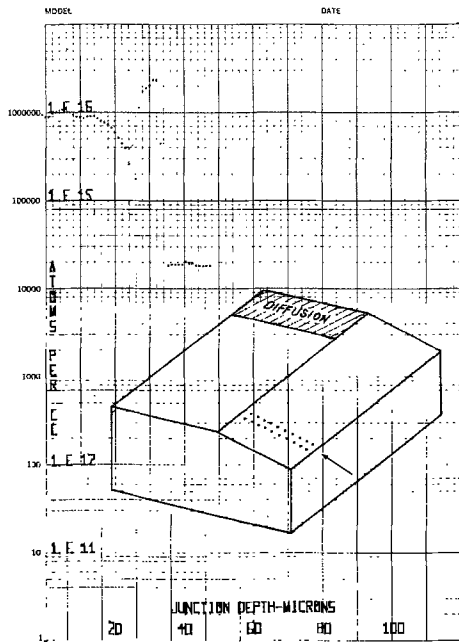
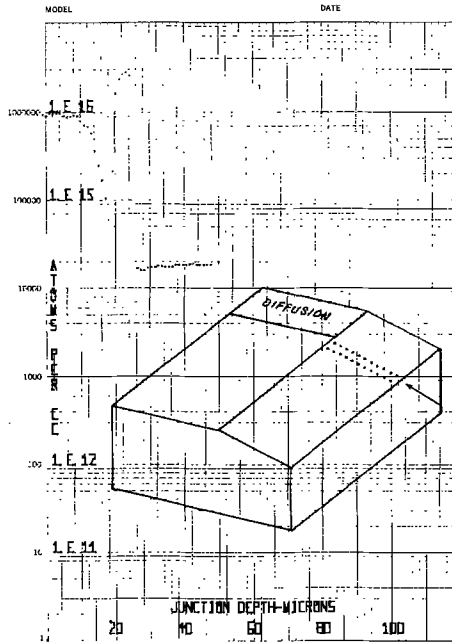
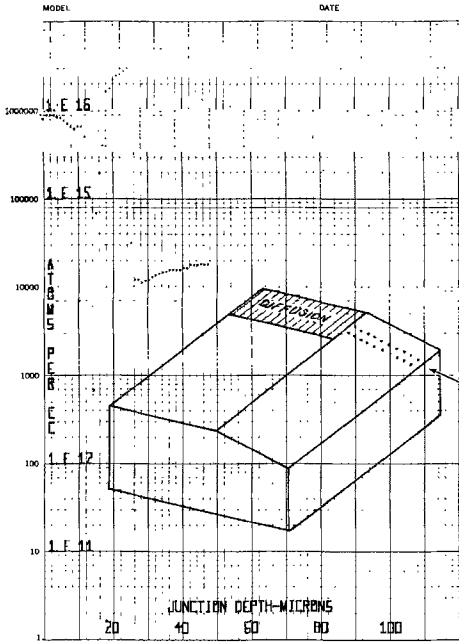


Fig. 4. Impurity distribution profiles taken at four locations on a wafer with boron diffusion at one end and an epitaxial layer grown with complete meltback of the diffused region prior to epitaxial growth.

Publication costs of this article were assisted by General Electric Company.

REFERENCES

1. C. O. Bozler, *This Journal*, **122**, 1705 (1975).
2. D. C. Gupta and R. Yee, *ibid.*, **116**, 1561 (1969).
3. T. Ishii, K. Takahashi, A. Kondo, and K. Shirahata, *ibid.*, **122**, 1523 (1975).
4. G. Skelly and A. C. Adams, *ibid.*, **120**, 116 (1973).
5. G. R. Srinivasan, Paper 191 presented at The Electrochemical Society Meeting, Philadelphia, Pennsylvania, May 8-13, 1977.
6. J. I. Nishizawa, T. Terasaki, and J. Shibata, *IEEE Trans. Electron Devices*, **ed-22**, 185 (1975).
7. R. Barandon and P. Laurenceau, *Electron. Lett.*, **12**, 486 (1976).
8. B. J. Baliga, Device Research Conf., Paper WP-B7, *IEEE Trans. Electron Devices*, **ed-26**, 1858 (1979).
9. B. J. Baliga, *This Journal*, **124**, 1627 (1977).
10. B. J. Baliga, *J. Cryst. Growth*, **41**, 199 (1977).
11. B. J. Baliga, *This Journal*, **125**, 598 (1978).
12. B. J. Baliga, *ibid.*, **126**, 138 (1979).
13. B. J. Baliga, *Appl. Phys. Lett.*, **34**, 789 (1979); *ibid.*, **35**, 647 (1979).

Resolution Limits of PMMA Resist for Exposure with 50 kV Electrons

Alec N. Broers

IBM, T. J. Watson Research Center, Yorktown Heights, New York 10598

ABSTRACT

An electron beam with a diameter below 1 nm has been used to measure the resolution of PMMA. Test patterns are written in 30 nm thick PMMA layers coated onto 60 nm thick Si_3N_4 membrane substrates. Both lateral scattering of electrons in the resist and backscattering from the substrate are negligible for these samples. Preliminary results obtained with 50 kV electrons are presented in this paper. The test patterns contain nominal linewidths down to 4.4 nm. The exposure distribution is determined by measuring the exposure dose needed to open up lines with widths smaller than the width of the distribution. Samples are examined in the scanning transmission microscope mode using the same beam used to write the patterns. The width [standard deviation (σ) assuming a normal distribution] of the exposure distribution has been measured to be between 11 and 14 nm. This spread function makes it possible to resolve lines on 45 nm centers in these very thin resist layers. Spreading is assumed to be set by straggling of low energy secondary electrons into the resist although effects that may be attributable to the finite molecular size of the PMMA have also been observed. It is pointed out that thin film substrates are not essential to obtain linewidths of 50 nm. Resolution and contrast on thick substrates are discussed and compared with the resolution and contrast obtainable with light optical systems.

Since the original publication of Haller, Hatzakis, and Srinivasan (1), polymethyl methacrylate (PMMA) has been used as the standard resist for high resolution electron beam fabrication. The exposure dosage for PMMA (5×10^{-5} - 2×10^{-4} C/cm²) is too high for many semiconductor direct exposure applications, but, to the extent that it has been measured, its resolution is unsurpassed by other resists. Operational devices with dimensions of 0.15 μm (2) and metal structures as small as 60 nm (3) have been fabricated on bulk substrates (substrates thick compared to the electron penetration distance), and 25 nm lines have been resolved on substrates thin compared to the electron penetration distance (4). In addition to PMMA's use with electron beams, exposure with 4.5 nm x-rays has yielded features of 17.5 nm (5) and exposure with ions has produced linewidths below 100 nm (6).

The resolution that can be obtained in an electron resist layer is usually determined by lateral scattering of electrons in the resist layer and by electron backscattering from the underlying substrate. In order to measure the resolution in the absence of significant electron scattering we have used 50 kV electrons to expose very thin (~ 30 nm) layers of PMMA supported on thin (~ 60 nm) Si_3N_4 membrane substrates. Under these conditions, resolution becomes effectively limited only by the basic physical processes involved in breaking the bonds in the methacrylate polymer. The probability that lateral scattering of electrons will be significant can be estimated from the theoretical and experimental data of Misell (7), if it is assumed that scattering in PMMA is similar to that in carbon. Such an estimation shows that in passing through a 50 nm thick carbon film, less than 1% of 50 kV electrons will be scattered through angles equal to or exceeding the convergence angle of the electron beam (10^{-2} radian). Lateral scattering effects in a 30 nm thick PMMA layer should therefore be negligible. Backscattering from the Si_3N_4 substrate can be estimated by calculating the probability of Rutherford scattering events through angles greater than 90° . Data presented by Wells (8) indicate that there is only a 10^{-3} probability that a 50 kV electron will be backscattered from a 60 nm thick film of atomic num-

ber 12. Therefore, backscattering from the Si_3N_4 substrate should also be negligible.

The minimum energy required to break bonds in PMMA can be estimated to be 5 eV from the wavelength of the "softest" u.v. radiation capable of exposing the resist (9). With electrons, it is proposed that exposure is effected predominantly by low energy secondary electrons because the cross section of these electrons for bond scission will be very much greater than the cross section of the high energy primaries. The secondaries can be excited at a distance from the path of the high energy primaries and they can travel further into the resist before their energy is fully dissipated. The overall distance the secondaries travel blurs the pattern and determines the ultimate resolution of the resist exposure process. Measurements of the secondary electron yield from thin dielectric layers indicate that the range of low energy secondary electrons in dielectrics is several tens of nanometers (10). The measurements on PMMA presented here in general confirm this deduction.

Sample Preparation

The membrane substrates were fabricated by selectively etching holes through the silicon of Si_3N_4 coated silicon wafers. An anisotropic silicon etch was used to etch the holes (11). The etch stops at the Si- Si_3N_4 interface and leaves the Si_3N_4 membrane covering the holes. The holes were generally about $100 \times 100 \mu\text{m}$. We used 30 and 60 nm thick membranes, however, the 30 nm membranes were generally too fragile to be practicable; almost half of them broke during processing. Because no loss in resolution was observed with the 60 nm membranes (this is expected from electron backscattering data), they were used for most experiments. Very few cases of breakage were encountered with the thicker membranes.

After window fabrication, the silicon wafers were diced into chips 2.6×1 mm. For electron beam exposure and subsequent examination in the scanning transmission electron microscopy (STEM) mode, the chips were mounted in a sample holder designed for standard 3 mm diam electron microscope grids. Each chip contained two windows.

Resist was coated onto the membrane substrates using a conventional spin-coater. The samples were held with a vacuum chuck designed to avoid the application of atmospheric pressure across the membranes. Very dilute resist (1:50, 2010 PMMA:chlorobenzene) and relatively slow spinning rates (2000-3000 rpm) were used to produce resist layers with thicknesses between 30 and 100 nm. As discussed below precise measurement of resist thickness was made from STEM images of the developed samples after shadowing the samples with a thin layer of metal. Resist thickness was uniform to better than 10 nm over the window areas. Resist layers were baked at 160°C for 1 hr to remove residual solvent.

In order to provide detail on the sample for focusing, a 5 nm thick PdAu layer was vapor deposited onto the underneath of the membrane. Structure in this layer provided high contrast in the bright field STEM image and made it easy to determine that the beam diameter was less than 1 nm. The number of primaries backscattered from this layer is less than 1 in 500 (8), and few low energy secondaries formed at the PdAu/Si₃N₄ interface will penetrate the Si₃N₄ membrane to the resist. The PdAu layer should therefore have little effect on resist exposure.

Image spreading due to the finite angular width of the beam was about 2 nm (resist thickness 30 nm, substrate thickness 60 nm, beam half-angle 10⁻² radian) assuming that the beam was focused accurately on the bottom of the Si₃N₄ membrane. The AuPd layer had sufficient conductivity to avoid sample charging during exposure.

Exposure

Patterns were written in an STEM (12) with an electron beam diameter of less than 1 nm. The patterns were written under the control of a flying spot scanner. The exact nominal exposed linewidths were measured from the video signal produced by the STEM bright field detector. The linewidth is given by the width of the "beam-on" pulses on the video signal. This method eliminated any errors that might have arisen due to the finite resolution of the flying spot scanner. In practice the linewidths scaled very closely with the actual mask dimensions.

Beam current was measured using a Faraday cup located below the sample. Beam current had to be kept at a level of about 2×10^{-12} A because of the small area of the pattern and the relatively slow scan rate of the STEM system (minimum frame time of 10 sec). The pattern was typically $2.5 \times 2.5 \mu\text{m}$ for a minimum nominal linewidth of about 2.5 nm.

Before each pattern was exposed, the beam was offset to an area adjacent to the exposed area and the beam focused on the PdAu layer underneath the membrane. The sample was mechanically moved approximately 20 μm between exposure sites. The vertical accuracy of the sample stage was such that adjustment of focus after movement was unnecessary in the majority of cases.

Samples were developed for about 50 sec with the standard PMMA developer; one part methyl isobutyl ketone to three parts of isopyl alcohol. Our measurements indicated that the developer dissolved the unexposed resist at a rate of about 25 nm/min so the initial resist thickness was approximately 20 nm thicker than that measured for the developed patterns.

After development, 5 nm of AuPd was vapor deposited onto the top of the resist at an incidence angle of 45°. This metal layer clearly outlined the resist pattern, and the shadow length was an accurate measure of the resist thickness.

Determination of Exposure Distribution

The test pattern used in these experiments is shown in Fig. 1. The pattern was written at a size that yielded a minimum nominal linewidth of 4.4 nm.

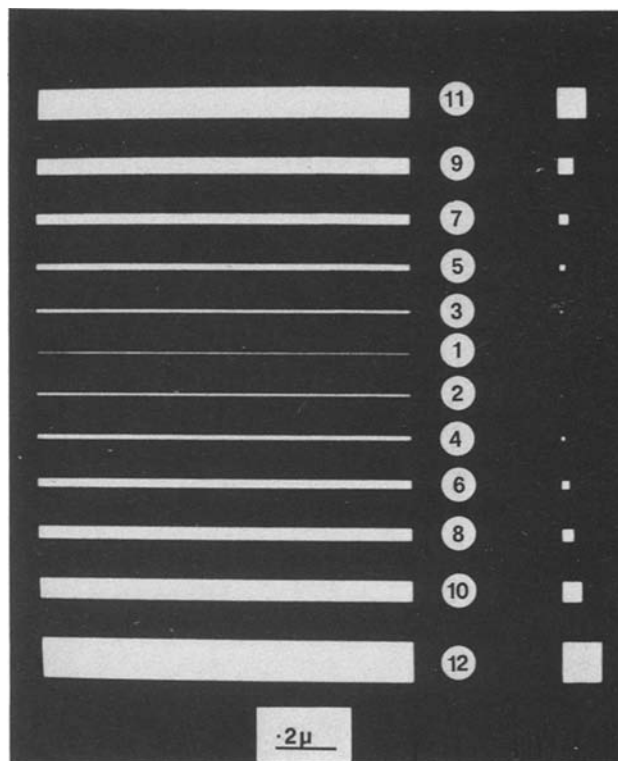


Fig. 1. Pattern used to evaluate exposure distribution in PMMA. Nominal linewidths in the exposed patterns were as follows: 1, 4.4 nm; 2, 7.5 nm; 3, 11 nm; 4, 14 nm; 5, 20 nm; 6, 26 nm; 7, 33 nm; 8, 38 nm; 9, 53 nm; 10, 62 nm; 11, 96 nm; 12, 120 nm.

The broadest line was about 120 nm wide. Eleven different exposure times were used for each experimental run. The shortest time gave an exposure dose which was below that needed to open up the largest shapes. The longest time was such that the resist developed through in the site of the narrowest line.

If the exposure distribution is Gaussian, then using the "reciprocity principle" of Chang (13), the exposure dose (Q_w) received at the center of an infinitely long rectangle of width w can be shown to be given by

$$Q_w = Q_0 \operatorname{erf}(w/2\sigma)$$

where Q_0 is the exposure dosage in the center of an infinitely large shape and σ is the standard deviation of the distribution.

Figure 2 is a bright field STEM micrograph of the test pattern exposed at a dose slightly greater than that needed to open large shapes. The standard deviation (σ) of the exposure distribution was calculated from patterns of this type exposed at progressively greater doses. σ was calculated from the nominal linewidth (w) of the narrowest line that had developed through to the substrate, and the ratio of the exposure dosage for the given test exposure to the exposure dosage needed to develop through to the substrate in the sites of the large shapes (Q_w/Q_0). If the distribution is truly Gaussian, then the same σ will be found for each of the test exposures. In practice, this was not the case. Heavier exposures, in which narrower lines had developed through to the substrate, in general yielded σ values higher than those deduced from lower exposure doses. In a series of five separate experiments, the average values of σ varied from 11 to 14 nm. The resist thickness was about 30 nm. The fractional exposures received for different linewidths are plotted in Fig. 3. The fractional exposure was determined from the exposure times needed to open up different linewidths. For example, it took about five times longer to open the 5 nm nominal linewidth line than it did to open the large shapes. Figure 3 also

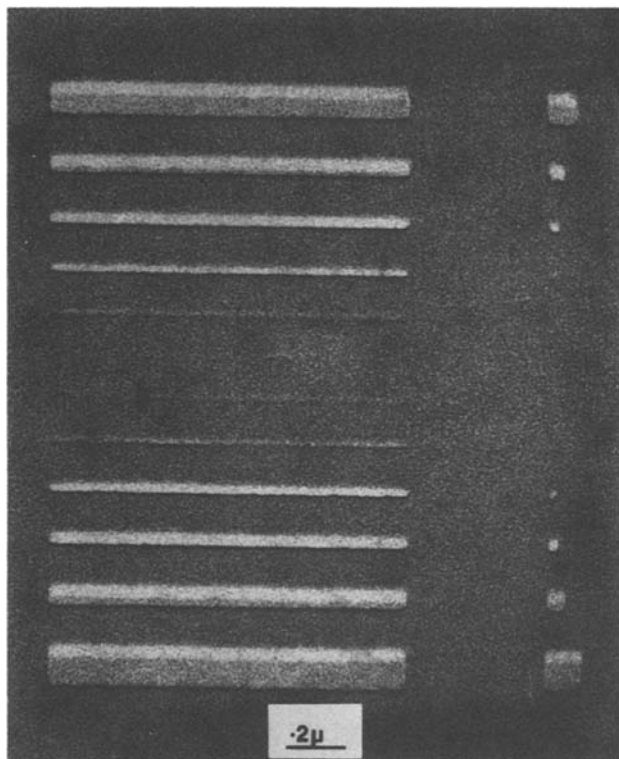


Fig. 2. Bright field STEM micrograph of test pattern exposed at a level slightly greater than that necessary to open up shapes that are large, compared to the width of the exposure distribution. Narrowest line that has opened up in this case is 20 nm wide. Electron beam used to write the pattern was smaller than that used to obtain this micrograph. Detail resolved in the AuPd coatings at higher magnification shows that the beam diameter is less than 1 nm. Sample is shadowed at 45° with AuPd to reveal resist thickness.

shows the fractional exposure that would be obtained with a resist with a Gaussian distribution ($\sigma = 12.5$ nm). An additional experiment in which identical exposures were made on three different resist thicknesses (50, 80, and 100 nm) showed that, as expected from electron scattering data, there was no significant dependence on resist thickness for thicknesses below 100 nm.

The narrowest line that opened up at the dose required to open up the large shapes ($\sim 3 \times 10^{-4}$ C/cm²) was between 20 and 25 nm wide (line 5 and line 6). In practice the developed lines were close to their nominal width. As the exposure dose was

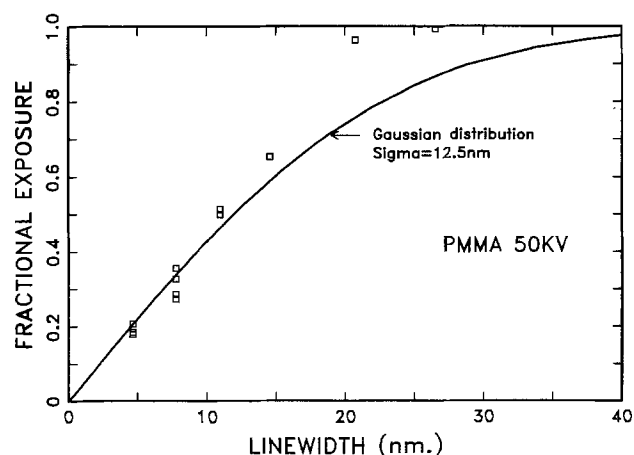


Fig. 3. Fractional exposure received at the center of isolated lines of various widths for PMMA exposed on a thin substrate with 50 kV electrons. Curve shows case for a Gaussian exposure distribution with $\sigma = 12.5$ nm.

increased to open the narrower lines, the linewidth of the wider lines increased. The rate of increase can also be used to estimate the σ of the spread function in the resist, however, this will not be discussed here.

If exposure is due to low energy secondary electrons alone, and the excitation of secondaries is isotropic and random, it would appear reasonable for the distribution to be Gaussian. The deviation observed could be the result of a dependence of development rate on linewidth. Development may be slower for narrower lines because the lines become comparable in size to the molecular size of the PMMA and slow the development process.

If the exposure distribution is Gaussian, then the ratio of the exposure dose received at the center of a line (Q_1) to the exposure dose received at the center of a space (Q_s) for an array of infinitely long parallel lines with equal linewidth and spacing is given by

$$\frac{Q_1}{Q_s} = \frac{\text{erf } S/4 + \sum_{n=1}^{n=m} [\text{erf}(4n+1)S/4 - \text{erf}(4n-1)S/4]}{\sum_{n=1}^{n=m} [\text{erf}(4n-1)S/4 - \text{erf}(4n-3)S/4]}$$

where s is the center to center spacing between the lines, and m = the number of lines taken in account on either side of the line under consideration. It is also useful to define what we shall call the resist contrast function (RCF), K , where

$$K = \frac{Q_1 - Q_s}{Q_1 + Q_s}$$

This definition is similar to that of the modulation transfer function (MTF) for an optical system except that for the optical case the pattern distribution is generally assumed to be sinusoidal rather than the square wave we have assumed for the electron beam resist case. Figure 4 shows the RCF for a resist that exhibits a Gaussian exposure distribution. For a thin substrate, 60% contrast ($K = 0.6$) corresponds to a spatial frequency (ν) of $0.28 \sigma^{-1}$. If it is assumed that the distribution for PMMA is Gaussian and that $\sigma = 12.5$ nm, then 60% contrast is obtained for $\nu = 0.28 \div 12 \times 10^{-7} = 2.24 \times 10^5$ lines/cm (44.6 nm center to center spacing). As already discussed, it is assumed that the electron beam diameter is zero and that lateral electron scattering in the resist is negligible.

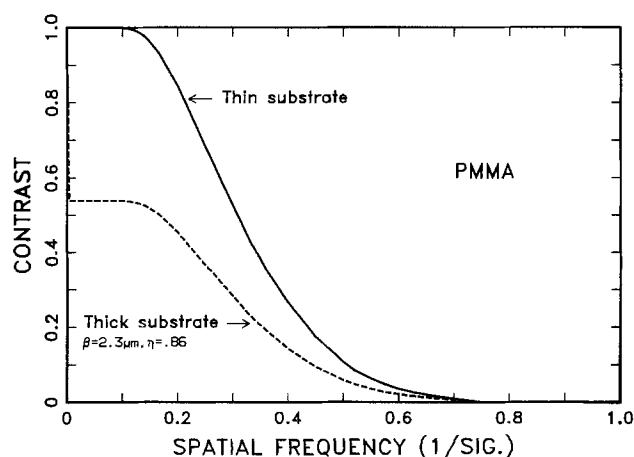


Fig. 4. Resist contrast function (RCF) for a resist with a Gaussian exposure distribution. Thick substrate curve assumes that the width of the backscattered distribution \gg that of the resist exposure distribution, and that the total backscattered exposure contribution is 0.86 times that of the incoming beam.

60% is the order of contrast normally required for adequate definition in a developed resist pattern. Broers, Harper, and Molzen (4) reported a minimum center to center spacing of 50 nm for a 110 nm thick PMMA layer on top of a 20 nm layer of AuPd on an Si_3N_4 membrane. This is in good agreement with the results reported here. The RCF for a thick substrate shown in Fig. 4 is discussed in the next section.

Resolution with Thick Substrates and with Optical Systems

On thick substrates, both backscattered and primary electrons produce secondaries and contribute to resist exposure. It has been found that exposure by the backscattered electrons can be approximated by a Gaussian distribution with a standard deviation of several microns. The total exposure contribution of the backscattered electrons is approximately equal to that of the primary electrons. Several workers have modeled and measured the parameters associated with backscattering from targets of different materials and thicknesses [e.g., Ref. (14-18)]. We shall assume that for silicon, the standard deviation of the distribution is $2.3 \mu\text{m}$, and the total exposure due to backscattered electrons is 0.86 times that of the primaries (19). According to these parameters, the backscattered contribution to an isolated line 25 nm wide on a silicon substrate is $0.86 Q_0 \text{erf}(0.025/4.6) = 0.004 Q_0$, where Q_0 is the incident dosage. The contribution is, therefore, so small that it can be ignored. This is the case for an isolated shape that is very small compared to the area from which backscattered electrons re-emerge from the sample. For an array of such shapes that covers an area that approaches, or is greater than, the area from which the backscattered electrons emerge, then backscattering becomes significant and gives rise to the well-known proximity effect (13). The dotted curve in Fig. 4 shows what happens to the RCF in this case. In the example shown, it is assumed that $\sigma_{\text{backscattered}} = 184 \times \sigma_{\text{resist}}$ ($\sigma_{\text{backscattered}} = 2.3 \mu\text{m}$, $\sigma_{\text{resist}} = 12.5 \text{ nm}$), and that the total backscattered contribution is η times the contribution of the primary beam, where $\eta = 0.86$ (silicon substrate). The maximum contrast is 0.54 under these conditions.

Figure 5 shows the resist contrast functions for PMMA plotted against linewidth. Again it is assumed that the pattern consists of an infinite array of equal lines and spaces. The contrast for a light optical system with a numerical aperture (NA) = 0.41 and operating wavelength (λ) = 405 nm is also shown. The dotted version of the optical curve shows the

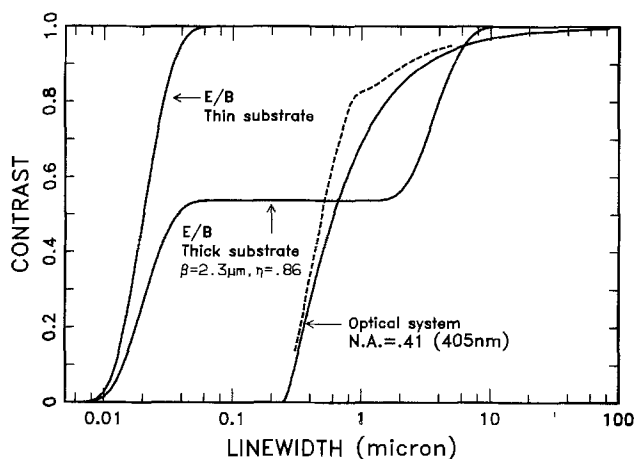


Fig. 5. Contrast vs. linewidth for electron beam exposure of thin PMMA on a thin substrate, electron beam exposure of thin PMMA on a thick silicon substrate and for an optical system with NA = 0.41 and $\lambda = 405 \text{ nm}$ (dotted curve shows contrast for optical system when target has a square wave distribution). Contrast is calculated for an infinite array of equal lines and spaces.

contrast for a square-wave target (20) rather than a sinusoidal target. Several observations can be made from Fig. 5:

1. For electron beam (50 kV) exposure of PMMA on a thin substrate, 60% contrast is obtained for a linewidth of 22.3 nm.

2. For the thick silicon substrate, the electron beam RCF for PMMA is essentially flat from 50 nm to $2 \mu\text{m}$, meaning that it should be no more difficult to produce 50 nm lines and spaces than it is to produce $2 \mu\text{m}$ lines and spaces. As before, this assumes that resolution is not limited by the electron optical system or by lateral electron scattering in the resist (i. e., the resist must be very thin). Proximity correction will probably have to be used in most cases. The algorithms used for computing proximity corrections will depend on the ratio of the size of the pattern elements to the width of the backscattered distribution. For very small pattern features, proximity correction may be easier because it may be possible to treat the backscattered contribution as a uniform background. For intermediate dimensions, it may be adequate to use the average exposed area in regions surrounding each pattern element, rather than to take individual pattern elements, and even partial elements, into account as is done for $1 \mu\text{m}$ dimensions.

3. On the thick silicon substrate, 54% contrast is reached for a linewidth of 50 nm, whereas on the thin substrate, 54% contrast is reached at 20 nm. In other words, minimum lines 2.5 times smaller should be obtained on the thin substrate.

4. The 0.41 NA optical system has higher contrast than the electron beam on a thick substrate for linewidths above about $0.5 \mu\text{m}$. At $1.25 \mu\text{m}$ linewidth, the contrast of the optical system is 85% compared to 54% for the electron beam. It is important to realize, however, that the exposure transition at the boundary between a line and a space can be sharper for the electron beam case than it is for an optical system even when the nominal contrast is lower. This is illustrated in Fig. 6 which simply compares the exposure profiles of four lines and three spaces for an optical system with 85% contrast, and for an ideal electron beam system with 54% contrast.

All of the preceding discussion relates to the contrast obtained for an infinite array of lines and spaces. When the total pattern area is small compared to the area from which the backscattered electrons emerge, resolution on bulk substrates should be as good as that on thin membranes. This is the case for

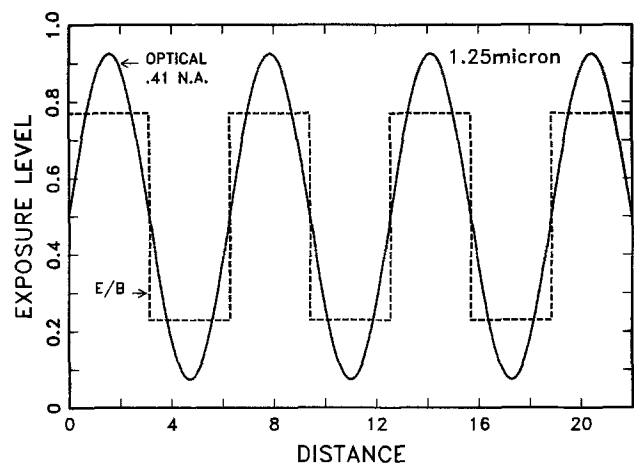


Fig. 6. Exposure distribution for an ideal electron beam system exposing thin resist on a thick substrate (contrast 54%), compared to exposure distribution for an optical system with 85% contrast. In the electron beam case, the transition between line and space is sharp, but there is an overall background exposure due to the backscattered electrons.

several of the experimental structures and devices built to date, for example, nanobridges (21) and SQUIDS (22). These devices were fabricated using contamination resist and thin substrates, however it would seem quite possible to make them using PMMA on thick substrates. In support of this, lines of 40 nm have recently been produced on a thick substrate using a high contrast double layer resist process (23).

A significant practical disadvantage of samples on bulk substrates is that they have to be examined in the conventional surface SEM with relatively low contrast and resolution. When the samples are on thin membranes, they can be examined by transmission electron microscopy with much higher contrast and resolution. This is particularly important for structures smaller than about 20 nm in size where we have had difficulty with the SEM in examining resist patterns, in knowing whether samples were completely etched, or even in knowing whether the films from which the structures were fabricated were continuous.

Acknowledgment

The author would like to acknowledge and thank W. Molzen and J. Speidell for preparation of the Si_3N_4 membrane substrates, and M. Hatzakis, W. Grobman, C. D. Cullum, and F. Hohn for fruitful discussions.

Manuscript received May 12, 1980.

Any discussion of this paper will appear in a Discussion Section to be published in the December 1981 JOURNAL. All discussions for the December 1981 Discussion Section should be submitted by Aug. 1, 1981.

Publication costs of this article were assisted by IBM Corporation.

REFERENCES

1. I. Haller, M. Hatzakis, and R. Srinivasan, *IBM J. Res. Develop.*, **12**, 251 (1968).
2. E. G. Lean and A. N. Broers, *Microwave J.*, **13**, 97 (1970).
3. A. F. Mayadas and R. B. Laibowitz, *Phys. Rev. Lett.*, **28**, 156 (1972).
4. A. N. Broers, J. M. E. Harper, and W. Molzen, *Appl. Phys. Lett.*, **33**, 392 (1978).
5. D. C. Flanders, *ibid.*, **36**, 93 (1980).
6. R. Seliger, J. W. Ward, V. Wang, and R. L. Kubena, *ibid.*, To be published.
7. D. L. Misell, *Adv. Electron. Electron Phys.*, **32**, 63 (1973).
8. O. C. Wells, "Scanning Electron Microscopy," chap. 3, McGraw-Hill, New York (1974).
9. B. J. Lin, *J. Vac. Sci. Technol.*, **12**, 1317 (1975).
10. H. Seiler, *Z. Angew. Phys.*, **22**, 249 (1967).
11. W. W. Molzen, A. N. Broers, J. J. Cuomo, J. M. E. Harper, and R. B. Laibowitz, *J. Vac. Sci. Technol.*, **16**, 269 (1974).
12. A. N. Broers, *Appl. Phys. Lett.*, **22**, 610 (1973); *J. Vac. Sci. Technol.*, **10**, 979 (1973).
13. T. H. P. Chang, *J. Vac. Sci. Technol.*, **12**, 1271 (1975).
14. F. Jones and M. Hatzakis, in "8th International Conference on Electron and Ion Beam Science and Technology," R. Bakish, Editor, p. 256, The Electrochemical Society Softbound Proceedings Series, Princeton, N.J. (1978).
15. M. Parikh and D. F. Kyser, in "8th International Conference on Electron and Ion Beam Science and Technology," R. Bakish, Editor, p. 371, The Electrochemical Society Softbound Proceedings Series, Princeton, N.J. (1978).
16. J. S. Greeneich, *J. Vac. Sci. Technol.*, **16**, 1749 (1979).
17. N. Aizaki, *ibid.*, **16**, 1726 (1979).
18. I. Adesida, R. Shimizu, and T. E. Everhart, *ibid.*, **16**, 1743 (1979).
19. W. D. Grobman and A. J. Speth, in "8th International Conference on Electron and Ion Beam Science and Technology," R. Bakish, Editor, p. 276, The Electrochemical Society Softbound Proceedings Series, Princeton, N.J. (1978).
20. W. J. Smith, quoted in "Handbook of Optics," p. 2-35, W. G. Driscoll, Editor, McGraw-Hill, New York (1978).
21. R. B. Laibowitz, A. N. Broers, J. T. C. Yeh, and J. M. Viggiano, *Appl. Phys. Lett.*, **35**, 891 (1979).
22. R. Voss, R. B. Laibowitz, and A. N. Broers, Submitted to *Phys. Rev. Lett.*
23. R. E. Howard, E. L. Hu, L. D. Jackel, P. Grabbe, and D. M. Tennant, *Appl. Phys. Lett.*, **36**, 592 (1980).

Subthreshold Degradation in MNOS Technology

P. K. Chaudhari¹

IBM Corporation, Poughkeepsie, New York 12602

ABSTRACT

A film of Si_3N_4 deposited on thermally grown SiO_2 was studied to determine the subthreshold voltage stability. Long-term reliability results have indicated the presence of more than one mechanism causing the subthreshold degradation. The two mechanisms are identified as electron tunneling and lateral migration of the ions along the surface of the device. The relevant experimental results have confirmed the sources of these mechanisms to be: (i) polyoxide-nitride interface for electrons, and (ii) metal-nitride interface and/or a cavity at the edge of the device gate for ions.

A major instability and hence reliability concern in an insulated-gate field effect transistor (IGFET) technology is the threshold voltage shift. Many of the current applications of MOS and related devices depend critically upon current flowing in the device in the normally off or subthreshold region of operation. As the gate-to-source voltage is reduced below the conventional threshold voltage, channel current does not suddenly drop to zero. Rather it diminishes approximately exponentially with decreasing gate voltage, making I_D - V_G characteristics very sensitive to any small variations in the gate voltage. Therefore a slight

departure in the subthreshold region of I_D - V_G behavior will be a serious reliability concern for the design circuitry, with stringent low current restrictions (low picoampere range) such as dynamic memory arrays. For several years, Si_3N_4 films have been the subject of extensive studies. The objectives of these studies were to eliminate the instabilities of MOS devices due to contamination of Na ions (1) and to enhance gate reliability. Recently DeSimone *et al.* of IBM (2) announced a dynamic memory using MNOS FET technology. It has been found that MNOS structures exhibited a new type of instability, electronic in origin (3), causing a conventional threshold shift (4). However, nothing has been reported about the subthresh-

¹ Present address: IBM Corporation, 91102 Essonnes, France.
Key words: oxide-nitride dielectric, MNOS FET, subthreshold leakage mechanism.

old degradation of these MNOS FET devices. Therefore MIS structures consisting of a film of Si₃N₄ deposited on thermally grown SiO₂ were studied to determine the subthreshold voltage stability. In this paper, we first describe the fabrication of MNOS FET devices and provide details of measurements. Then the results of the subthreshold voltage degradation are analyzed with the development of a physical model. Next, consistent with the experimental results, the sources of the degradation mechanism are discussed, followed by concluding remarks.

Experimental

A number of experimental MNOS FET devices were fabricated using p-type 1-2 Ω cm silicon wafers. The first step in the process is the deposition of arsenosilicate glass film, which acts as a dopant for the source and drain regions. The first masking operation defines a window in this initial oxide for source and drain formation. After the diffusion of arsenic from this glass film to form source and drain regions, the film is stripped off and gate oxide is grown immediately after cleaning. Immediately following thermal oxidation, silicon nitride is deposited on SiO₂ by decomposition of silane in ammonia. The physical and electrical properties of Si₃N₄ films have been found to vary with the deposition conditions such as NH₃/SiH₄ ratio and the deposition temperature. As the Si₃N₄ film is a part of the gate dielectric in this study, the requirement was to have the lowest electrical conductivity films and high dielectric constant. Such an ideal insulator film was obtained when Si₃N₄ was chemically deposited at 925°C using a ratio of NH₃/SiH₄ of 150:1 by volume, with H₂ as a carrier gas. The deposition rate was approximately 10 nm/min. The dielectric constant of the film was 7.0 and the etch rate in 5:1 buffered etch was 6 nm/min at 50°C. Transmission electron microscopic examination did not reveal any evidence of crystallinity and were found to be essentially amorphous. Si₃N₄ films thus fabricated were used in this study. In order to make an n-channel technology practical for dynamic storage applications, a field shield can be used to prevent high leakage due to depletion or inversion of the p-type silicon wafer (5). Therefore, the p-type polysilicon layer was chemically vapor-deposited on top of SiO₂ and Si₃N₄ dual dielectric. The oxide-nitride insulator forms the gate dielectric and the insulator which separates the field shield from the substrate. The field shield is then removed from the gate region and is oxidized in steam at 1050°C to reduce the possibility of shorting between the field shield and the gate. The thickness of the polyoxide is about 300 nm. After opening the contact holes through this polyoxide and cleaning the gate region, metal gate is deposited and is subtractively etched. The final process is the postmetal anneal in forming gas at 400°C for 20 min to minimize the surface states at the Si/SiO₂ interface. Conventional photolithography was used throughout the fabrication. A cross section of the device thus fabricated is shown in Fig. 1. The high frequency (1 MHz) MNOS C-V technique was used to measure the maximum capacitance, C_{max}, with a control wafer. The equivalent gate dielectric thickness, t_{eq}, was determined from

$$t_{eq} = t_{ox} + \frac{t_n \epsilon_{ox}}{\epsilon_n} = \epsilon_{ox} \epsilon_0 A_c / C_{max} \quad [1]$$

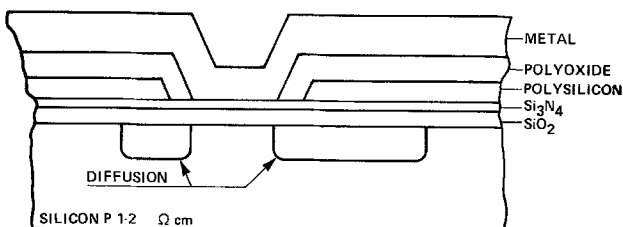


Fig. 1. MNOS FET device process profile

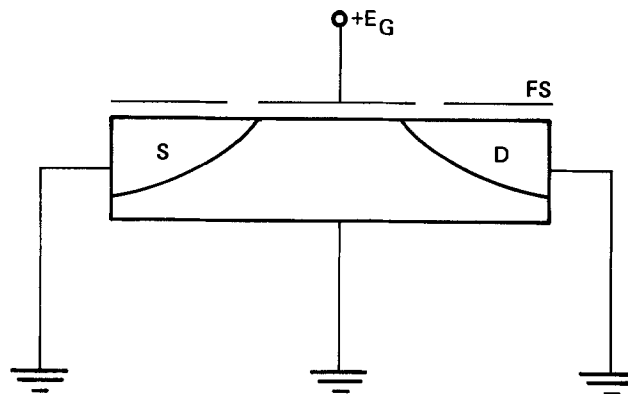
where t_{ox} is the oxide thickness, t_n is the nitride thickness, ε_{ox} and ε_n are the dielectric constants of the oxide and nitride, respectively, and A_c is the capacitor area. The equivalent dielectric thickness, t_{eq}, was 45 ± 3 nm. Mobile ion contamination, checked with a control wafer by the high temperature quasistatic technique (6), was found to be consistently less than 5 × 10¹⁰ cm⁻².

The aging experiments were performed in the following manner. Devices were stress aged in standard configuration, as shown in Fig. 2, at various voltages and temperatures. Forty to 70 devices were stressed in each stress cell. After a given period at elevated temperature, the devices were cooled to room temperature with the bias applied, subthreshold voltage readouts (I_D-V_G at V_s = -0.5V) were taken using automatic tester. A typical I_D-V_G relationship at time zero (i.e., before the device is stress aged) is shown in Fig. 3. As expected, the device turns off as the gate voltage is decreased. The device design specification in this region generally calls for a slope of ≤ 80-90 mV per decade at room ambient. On stressing, the I_D-V_G relationship for a device susceptible to the subthreshold leakage is also shown in Fig. 3, now the slope in the subthreshold region >> 80-90 mV/decade. Clearly this is not acceptable behavior, as the device is no longer an enhancement device. Therefore, the value of the stress voltage threshold at which the subthreshold begins to appear is important and should be high enough so that over the lifetime of the device there is no significant parasitic leakage. For the purpose of analysis of the results of this parasitic leakage (or subthreshold voltage shift), a failure criterion used was when the value of I_D measured at V_G = 0.5V < 350 Pa. For subthreshold degradation characterization, another suitable criterion used was a value ΔV_{eff} measured at I_D = 50 nA.

Results and Discussion

Using the failure criteria mentioned above, Fig. 4 shows a typical behavior of failure F, due to subthreshold degradation, as a function of time plotted on a linear scale. The curve is seen to follow an exponential law quite well, which can be described as

$$F = 1 - \exp(-t/\theta) \quad [2]$$



STRESS MATRIX

| FIELD/ V/CM | TEMP | 85°C | 125°C | 165°C |
|------------------------|------|------|-------|-------|
| 2.44 x 10 ⁶ | | | X | |
| 3.11 x 10 ⁶ | | | X | |
| 3.80 x 10 ⁶ | | X | X | X |

X = SAMPLES

Fig. 2. Standard stress configuration for subthreshold stability

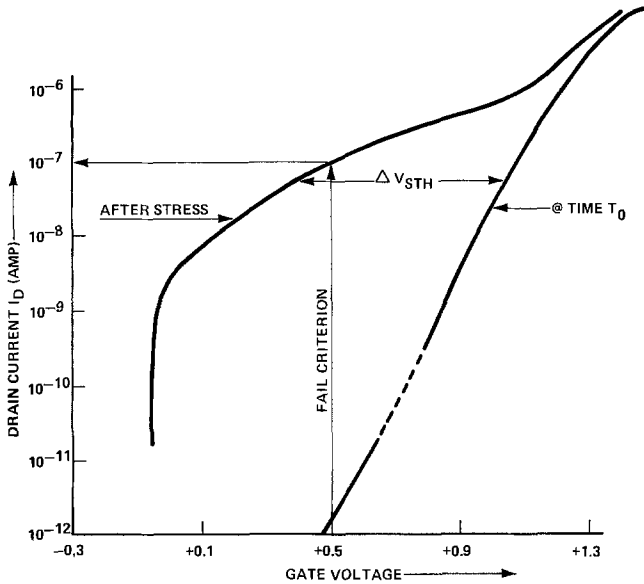


Fig. 3. Typical plot of subthreshold characteristics for MNOS FET.

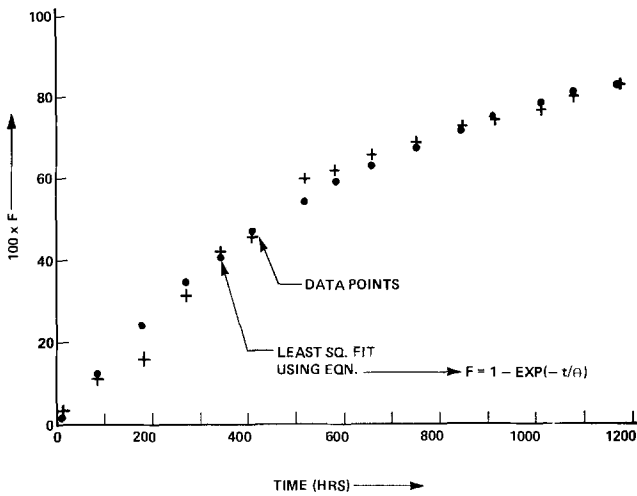


Fig. 4. Subthreshold degradation failure, F , as a function of stress time (standard stress at 85°C , $3.5 \times 10^6 \text{ V/cm}$).

where t is the time to fail and θ is the mean time to fail ($\text{MTTF} \rightarrow \theta$), a function of stress field and temperature. Functional dependence of θ on stress field E is shown in Fig. 5.

The curves A and B in Fig. 5 represent the results accumulated at two different time periods. The curve B does indicate the improvement over the curve A. The

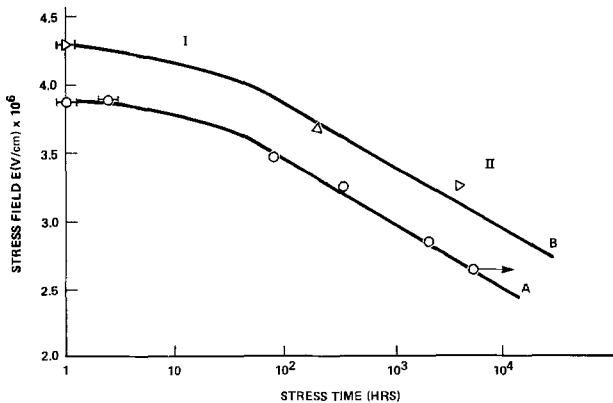


Fig. 5. Subthreshold failure characteristics mean time to fail vs. stress voltage.

only difference in these curves is that the polyox deposition temperature was 50°C higher in the curve B than in the curve A device process. However, it is evident that the mechanism causing the subthreshold degradation remains the same in both cases. The improvement due to higher polyox temperature (i.e., higher field for the onset of subthreshold leakage) is consistent with the proposed mechanism to be discussed below. From Fig. 5, the following salient features of the subthreshold failure characteristics are observed.

1. At fields $> 3.5 \times 10^6 \text{ V/cm}$, $\theta - E$ behavior is very sensitive to the stress field and does not follow the linear relationship, as is evident in the field range of $2.5 \times 10^6 < E < 3.5 \times 10^6 \text{ V/cm}$. This behavior is more clearly demonstrated with the combined short-term and long-term stress data shown in Fig. 6.

2. At low fields $< 2.5 \times 10^6 \text{ V/cm}$, the trend seems to indicate that the mechanism causing the failure is either minimal or insignificant. This point is elaborated later.

Physical Model

From Fig. 5 and 6, it is evident that the experimental data at high fields is below the linear region, i.e., θ tends to be small in going from region II to region I. Therefore, this observed behavior is successfully explained if the degradation mechanism is assumed to consist of two mechanisms as discussed below.

Region I.—Electronic and ionic, with electronic component dominant. In this region the presence of electronic component is positively demonstrated with the fact that the subthreshold degradation is seen to exist at liquid nitrogen (LN_2) temperature as shown in Fig. 7. Ionic drift cannot be possible at such a low temperature. Now the tunneling is well characterized by the current-field relationship, given by

$$I_{\text{STH}} \sim CE^2 \exp - B/E \quad [3]$$

where C and B are constants. Subthreshold leakage behavior observed in region I obeys this law very well, as shown in Fig. 8. Therefore the results lead to the conclusion that the subthreshold at high fields (i.e., in

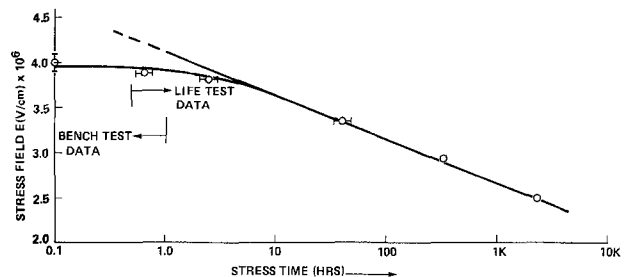


Fig. 6. Subthreshold failure characteristics time to fail as a function of stress field (standard stress of 120°C).

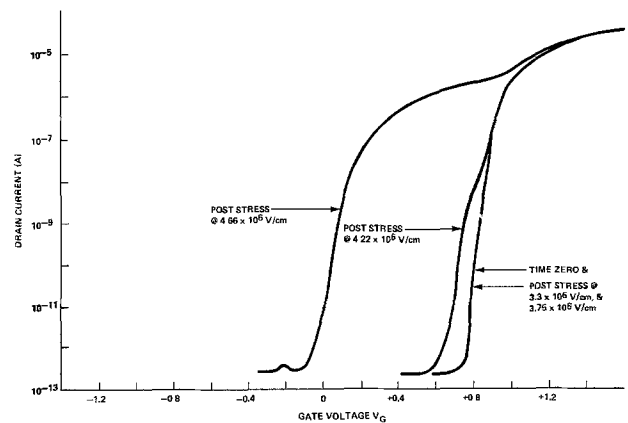


Fig. 7. Subthreshold leakage characteristics as a function of field (standard stress at LN_2).

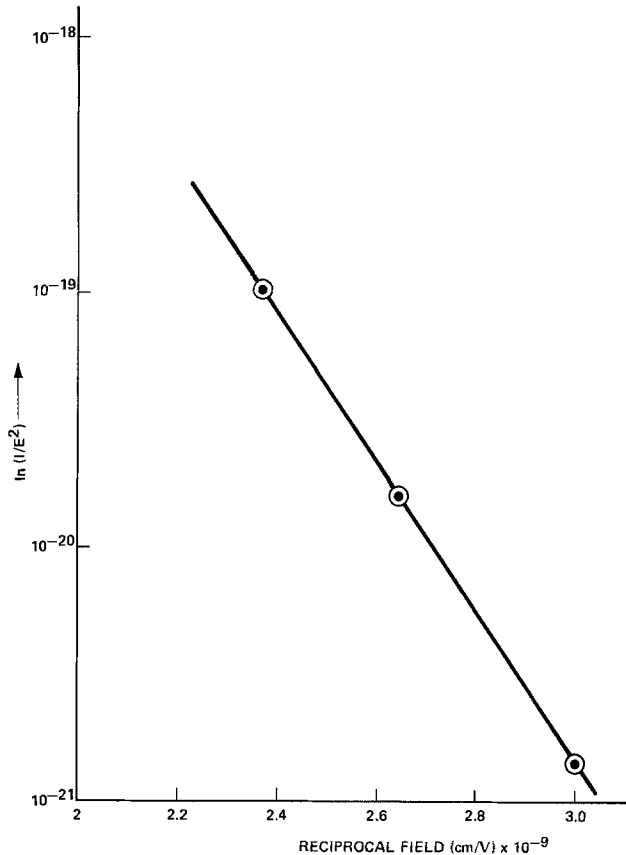


Fig. 8. Subthreshold leakage current, I_{STH} , as a function of stress field (standard stress at LN₂).

region I) is largely due to electron tunneling and ion drift, to be described below.

Region II.—Ionic drift. The field required for tunneling is generally $4-5 \times 10^6$ V/cm. Hence, as the field becomes low (i.e., $< 4 \times 10^6$ V/cm), a phenomenon other than electronic injection must be present. That phenomenon, the ionic drift, will now be established. There are two key characteristic features of the ionic drift-related instability (ΔV_{STH}).

1. $\Delta V_{STH} \sim t^{1/2} \exp -H/KT$, where t is the stress time, H is the activation energy, K is the Boltzmann constant, and T is the temperature in degrees Kelvin.

2. ΔV_{STH} recovers completely if the devices are shorted at stress temperature or are subjected to a negative bias-temperature stress aging.

Data shown in Fig. 9 and 10 does indeed confirm the characteristic features 1 and 2 observed in MNOS FET devices. These results clearly support the fact that the ionic drift most probably is the dominant mechanism for the subthreshold degradation in region II. Absence of electronic mechanism is also evidenced from the data of Fig. 9 and 10. The presence of ionic component in region I should not be ruled out, due to the field and temperature dependence. However, because of the exponential nature of the field dependence, the tunneling and hence electronic component would be dominant.

Sources of Subthreshold Degradation

From the practical point of view, the knowledge of the sources of origin causing the subthreshold degradation is of vital importance. Hence, with the help of the experimental facts, we will establish the sources of this problem mechanism.

Electron injection source.—Open-gated MNOS device consists of exposed nitride around the gate sides, with polyox-nitride interface absent under the gate region. Under positive bias stressing, these devices show no subthreshold degradation at LN₂, as shown in Fig. 11, while the devices having polyox-nitride interface under

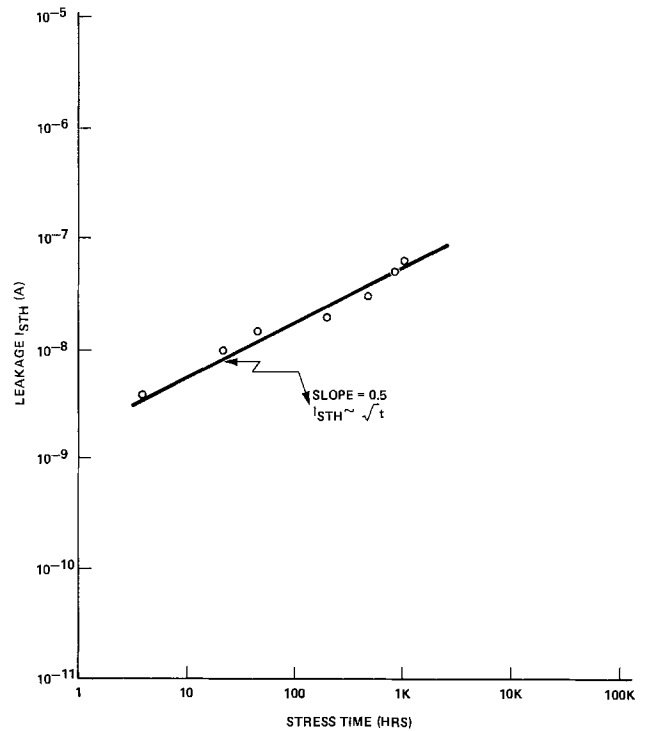


Fig. 9. Subthreshold leakage current, I_{STH} , as a function of stress time (standard stress at 165°C/2.66 $\times 10^6$ V/cm, I_{STH} measured at $V_G = 0.5V$).

the gate region show subthreshold degradation at LN₂ as discussed above in reference to Fig. 7. Electron injection from the thermal oxide-nitride interface cannot be possible as it contradicts the charge transport. Furthermore, thermal ox-nitride structures subjected to poly and polyox process cycles show instability, while the same samples not subjected to poly and polyox process were found to be quite stable. These observations clearly support the proposition that the

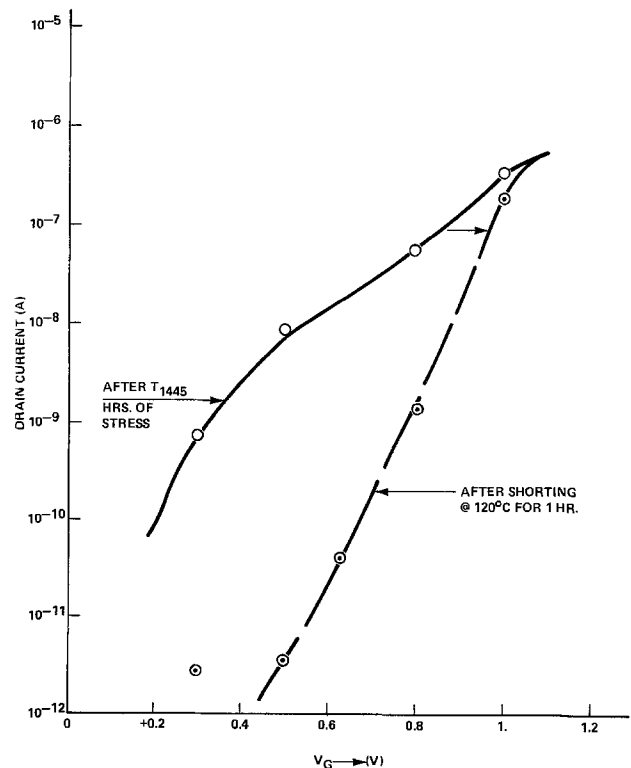


Fig. 10. Effect of baking on subthreshold shift (standard stress at 120°C/3.4 $\times 10^6$ V/cm).

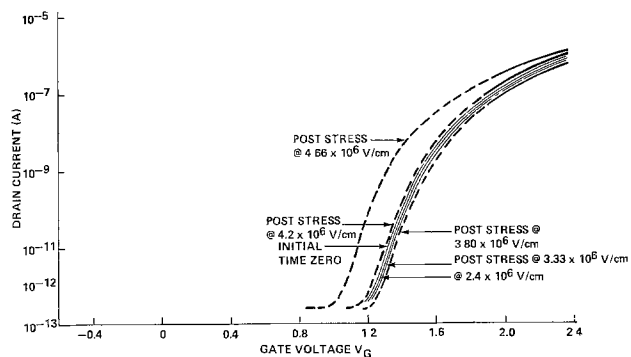


Fig. 11. Subthreshold leakage behavior at LN₂, open-gated MNOS FET device (standard stress).

seat of the electrons which cause subthreshold degradation via tunneling under high lateral field as discussed below is the interface between the polyox and nitride under the gate region. Data of Fig. 5 is consistent with this proposition, because polyox deposition at high temperature improves polyox-interface integrity. Therefore, curve B requires higher field for the onset of the subthreshold degradation.

Ionic drift source.—It is shown above that the ionic drift also causes the subthreshold degradation. Two-dimensional analysis indicates that the field at the edge of the device is the same within 50 nm along the horizontal and vertical directions (7). As the Si₃N₄ acts as a barrier to the ionic motion in the vertical direction, ionic drift will cause a subthreshold degradation only if we assume a lateral motion of these ions in the presence of a lateral field. Snow *et al.* (8) reported a $\sim t^{1/2}$ dependence for the Na⁺ transport through thermally grown SiO₂ films, deliberately contaminated in aqueous NaCl solutions. This time dependence can be attributed also to temperature-field induced emission of ions from trapping centers located near the metal-nitride interface at the edge of the gate. The field dependence of the ion transport process is also consistent with a trapping model (low field end of Fig. 5). Such a transport process is thermally activated with an activation energy found in the present case $\sim 0.45 \pm 0.05$ (see Fig. 12). The value obtained in the linear region of Fig. 5 was $\sim 0.55 \pm 0.05$, which agrees quite well with this bench data. This value is about the same for hydrogen (proton) ions in SiO₂ (9). The activation

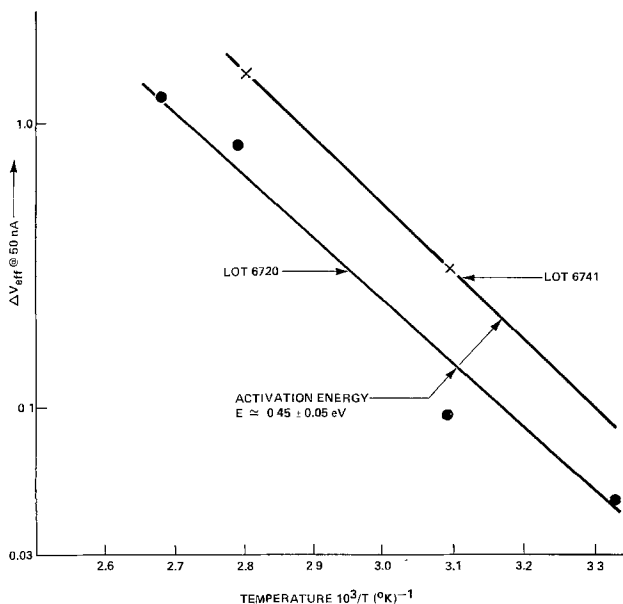


Fig. 12. Subthreshold shift as a function of reciprocal of temperature (standard stress at 3.1×10^6 V/cm for 10 min).

energy for Na⁺ in SiO₂ is about 1.0 eV (8, 10, 11). The mobile ion contamination in the lots studied here was consistently less than 5×10^{10} cm⁻², which cannot explain the degree of degradation observed. Therefore the charges causing the subthreshold degradation are most likely hydrogen ions (protons). The source of these ions is presumably the traps N-H, Si-H which are invariably present in chemically vapor-deposited Si₃N₄ films (12, 13). However, if there is any cavity or void left during poly and polyox processing, contamination like photoresist residue, wet chemicals, or moisture remaining during gate cleaning prior to metallization could be trapped, thereby causing a severe subthreshold degradation. Physical analysis has indeed confirmed the presence of a void in the polyox edge.

The deterministic evidence of the ionic source in the presence of such a fault region is clearly established when a lift-off process is used for gate metallurgy. Results of subthreshold degradation using lift-off and no-lift-off processed devices are shown in Fig. 13. The data clearly demonstrate that the source of the ions is the contamination trapped at the polyox corner at the metal-nitride edge of the gate region and/or the trapped ions at the metal-nitride interface. It was often found that certain lots showed subthreshold degradation, while physical analysis did not detect the presence of a void. In such a case, the trapped ions at the metal-nitride interface (*i.e.*, N-H, Si-H traps) is the only source that can explain the subthreshold degradation.

Thus, consistent with the analysis of the results, the subthreshold degradation is correctly described by a two-mechanism model as shown schematically in Fig. 14, *i.e.*, the accumulation of the positive charge at the edge of the metal gate which images into silicon to create an inversion and thus causing the subthreshold

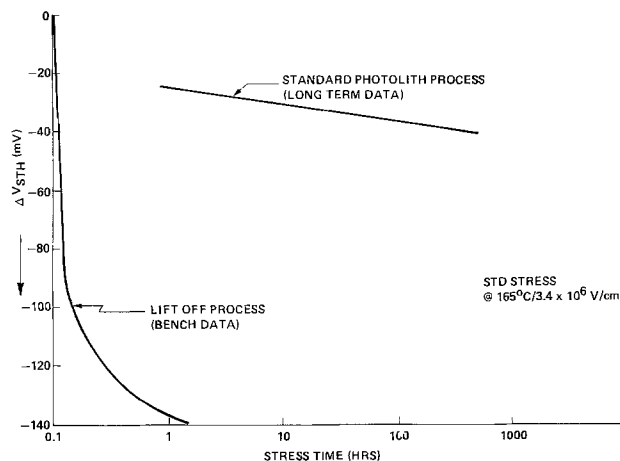


Fig. 13. Subthreshold degradation lift-off vs. standard photolith process.

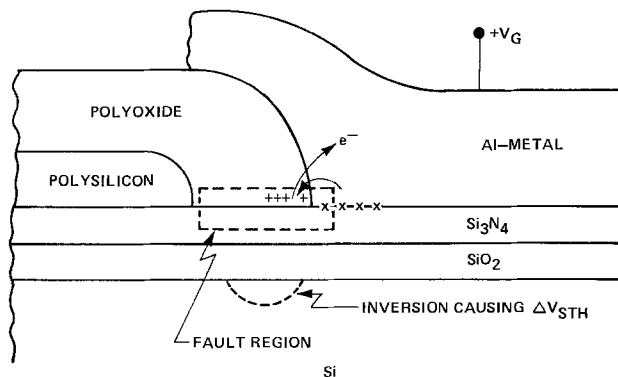


Fig. 14. Schematic showing the subthreshold degradation mechanism model.

leakage to occur by way of enhancement in the drain current. The accumulation of this positive charge is due to the surface ion migration away from the edge of the metal gate into the polyox-nitride interface and the electron tunneling from the polyox-nitride interface into the metal gate, especially at high fields of $\approx 3.5 \times 10^6$ V/cm. The mechanisms occur because of the presence of lateral field.

Conclusion

Long-term and short-term reliability data for sub-threshold degradation of MNOS FET devices is analyzed. Consistent with the results, a two-mechanism model is shown to correctly describe the observed sub-threshold degradation. These two mechanisms are identified as electron tunneling and surface ion migration in the presence of a lateral field. Electron injection is shown to occur from the polyox-nitride interface under the edge of the device, while the source of the ions is found to be wet chemicals, moisture trapped at the polyox edge, and/or ions trapped at the metal-nitride interface.

Acknowledgment

The author is grateful to Bernard Laflam for making many painstaking measurements and to Shakkir A. Abbas, Michael Potter, and Jane Howard for allowing the use of low temperature data. Thanks are also due to Dr. Abbas, Dr. Joseph Franz, Dr. Donald Kerr, Dr. Arup Bhattacharyya, and Dr. Wendall Noble for valuable discussions.

Manuscript submitted June 9, 1980; revised manuscript received Aug. 17, 1980.

Any discussion of this paper will appear in a Discussion Section to be published in the December 1981 JOURNAL. All discussions for the December 1981 Discussion Section should be submitted by Aug. 1, 1981.

Publication costs of this article were assisted by IBM Corporation.

REFERENCES

1. M. Greico, F. Worthing, and B. Schwartz, *This Journal*, **115**, 525 (1968).
2. R. R. DeSimone, N. M. Donofrio, B. L. Flur, R. H. Kruggel, H. H. Leung, and R. Schnadt, Paper presented at the 1979 IEEE Intl. Solid St. Ckts. Conference, San Francisco, California, Feb. 1979.
3. D. Frohman-Bentchkowsky and M. Lenzinger, *J. Appl. Phys.*, **40**, 3307 (1969).
4. P. K. Chaudhari, *This Journal*, **125**, 1657 (1978).
5. R. C. Dockerty, S. A. Abbas, and C. A. Barile, *IEEE Trans. Electron Devices*, **ed-22**, 33 (1975).
6. M. Kuhn, *Solid State Electron.*, **13**, 873 (1970).
7. P. Cottrel, Private communication.
8. E. H. Snow, B. Deal, and C. T. Sah, *J. Appl. Phys.*, **36**, 1664 (1965).
9. E. H. Nicollian and C. N. Berglund, *ibid.*, **42**, 5654 (1971).
10. S. R. Hofstein, *IEEE Trans. Electron Devices*, **ed-13**, 222 (1966).
11. J. M. Eldridge and D. R. Kerr, *This Journal*, **118**, 986 (1971).
12. R. Gereth and W. Scherber, *ibid.*, **120**, 446 (1973).
13. H. J. Stein and H. A. R. Wegener, *ibid.*, **124**, 908 (1970).

Suppression of Mobile Ion Related Instability in Mo-Gate MOS Structures

Tadatoshi Nozaki and Hidekazu Okabayashi

Nippon Electric Company, Limited, Central Research Laboratories, Miyazaki, Takatsu-ku, Kawasaki, Japan

ABSTRACT

Electrical instability in Mo-gate devices, caused by the presence of mobile ions, has been successfully prevented by depositing phosphosilicate glass (PSG) film on Mo-gate metal and carrying out high temperature annealing after PSG film deposition. It is concluded that mobile ions were gettered into PSG film along the perimeter of Mo-gate metal after lateral diffusion of mobile ions at the metal-oxide interface. The rate-limiting step was PSG film gettering reaction, which was expressed by a first-order reaction. Reaction velocity constant activation energy was 1.3 ~ 1.6 eV. Mo-gate MOSFET's, having good stability in short term BT stressing, were fabricated with satisfactory reproducibility.

Recently, applications of Mo film as a gate material in MOSLSI's have been reported (1-4). Mo film offers several advantages as a gate material in comparison with conventional poly-Si. Mo film has about 100 times lower resistivity, compared with poly-Si, and has smaller grain size resulting in easiness in fine pattern formation. Therefore, high speed and high density MOSLSI's are promising.

In Mo-gate MOS devices, however, it is not easy to establish stable characteristics for the metal-oxide interface, especially in suppression of mobile ion related instability. The Mo-gate fabrication process, including preevaporation step before Mo film deposition and washing wafers in H_3PO_4 solution, was reported as a method of obtaining mobile ion contamination-free devices (5). However, this process is rather complex.

Key words: molybdenum, MOSFET, mobile ion, gettering, phosphosilicate glass.

Recently, the effect of annealing in H_2/N_2 mixture gas on mobile ion contamination reduction was reported (4). However, details of this effect are not well known. MNOS structure was used to stabilize threshold voltage (2), since silicon nitride film has a blocking effect against mobile ions. Mo-gate structures with gate oxide having a passivation effect, such as phosphorus-diffused gate oxide (6) or HCl oxidized gate oxide (7, 8), will be considered. However, in these structures, it is difficult to reproducibly form a thin gate oxide film a few hundred Angstrom thick while maintaining good reliability at the metal-oxide interface and maintaining the passivation effect. Mo/poly-Si layered structure gate was investigated (9) in order to obtain the same stable gate-oxide interface properties as a poly-Si gate.

During this work, the new procedure for mobile ion gettering in Mo-gate MOS devices was developed. It was found that high temperature annealing after PSG

film deposition on Mo-gate metal had a pronounced effect on reduction in mobile ion related instability. The mechanism of this PSG annealing effect was examined with changing annealing time and temperature using MOS diodes having different areas. Mo-gate MOSFET's fabricated with the PSG annealing process were evaluated by positive BT stressing test.

Experimental

Mo-gate MOS structures were made using thermally grown 400Å thick silicon dioxide film and 3000Å thick sputtered Mo film on p-type silicon substrates of 2 ~ 3 Ωcm resistivity. In the case of diodes, the Mo film was annealed at temperatures ranging between 800° and 1100°C before overcoating film deposition on Mo-gate metal. In the case of FET, the Mo film was annealed at 1000°C in order to ensure flatband voltage saturated value (5) and implanted As atom electrical activation to form source and drain region. Mo film annealing was accomplished in nitrogen atmosphere without any Mo film surface oxidation. CVD SiO₂ or PSG film was used as an overcoating film on Mo-gate metal. After SiO₂ or PSG film deposition, high temperature annealing in nitrogen atmosphere was carried out for almost all devices, in order to examine the effect of the high temperature annealing on mobile ion related flatband or threshold voltage instability.

BT stress tests were made in order to examine mobile ion related instability of flatband voltage. Gate bias was mainly 2 or 4V. Temperature and time were 200°C and 30 min, respectively. Flatband voltage was measured by high frequency C-V method.

Results and Discussion

PSG annealing effect on flatband voltage instability under positive BT stressing.—A large amount of flatband voltage (V_{FB}) shift in the negative direction was observed for Mo-gate MOS diodes under positive BT stressing. Figure 1 shows the amount of V_{FB} shift ($|\Delta V_{FB}|$) for diodes fabricated with changing Mo film annealing temperature at 800°, 900°, 1000°, and 1100°C. Almost constant 2 ~ 4 V $|\Delta V_{FB}|$ values were observed. V_{FB} recovers to its initial bias value, if the diode is heated with zero or negative bias after positive BT stressing. These large V_{FB} shifts may be due to mobile ion migration from the metal-oxide interface to the silicon-oxide interface, as was reported by Yanagawa *et al.* (5). Considering negligibly small V_{FB} shift under neg-

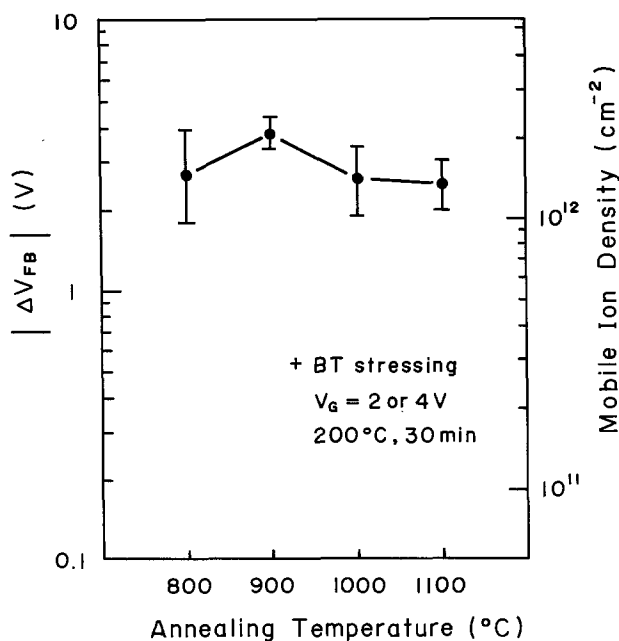


Fig. 1. $|\Delta V_{FB}|$ and mobile ion density vs. Mo film annealing temperature for diodes fabricated without PSG annealing.

ative BT stressing, mobile ion density was estimated from these $|\Delta V_{FB}|$ values to be approximately 1 ~ 3 × 10¹² cm⁻².

It was found that a large amount of V_{FB} shift could be avoided by depositing PSG film on Mo-gate metal and carrying out high temperature annealing after PSG film deposition. Figure 2 shows the results of positive BT stress tests on diodes having PSG overcoating film with different phosphorus content, together with the results of diodes having SiO₂ overcoating film. High temperature annealing at 1000°C for 10 or 30 min was carried out after PSG or SiO₂ overcoating film deposition for all devices, except one. SiO₂ overcoating film shows no stabilization effect, even though high temperature annealing at 1000°C was carried out. In the case of annealing for 10 min, poor stabilization effect was observed for PSG film with about 1 weight percent (w/o) phosphorus content. However, good stabilization effect was obtained for more than 2 w/o phosphorus content, showing minimum $|\Delta V_{FB}|$ constant value for higher phosphorus content. When annealing was carried out for 30 min, good stabilization effect was obtained, even for PSG film with about 1 w/o phosphorus content, and V_{FB} shift was negligibly small for more than 2 w/o phosphorus content. In the experiments described hereafter, PSG film with about 4 w/o phosphorus content was used. Diodes fabricated with PSG annealing at 1000°C for 10 min had 0.03 ~ 0.1V V_{FB} shift, which corresponds to 2 ~ 5 × 10¹⁰ cm⁻² mobile ion density. In the case of annealing for 30 min, the remaining V_{FB} shift was less than 0.01V, corresponding to less than 5 × 10⁹ cm⁻² mobile ion density. However, these remaining V_{FB} shifts were found to be dependent on diode area, as described in the next section. In this section, circular diode with 180 μm radius was used.

PSG annealing effect was found to be quite sensitive to annealing temperature. Figure 3 shows the results of positive BT stress tests on diodes fabricated with annealing at 800°, 900°, and 1000°C for 10 min. 1 ~ 2 × 10¹² cm⁻² mobile ion density was observed for annealing at 800°C, which is almost the same as that of diodes fabricated without PSG annealing. PSG annealing effect was observed for annealing at 900°C and good stabilization effect was obtained, as in the results in Fig. 2, for annealing at 1000°C.

Mechanism of mobile ion related instability suppression by PSG annealing.—Although the mobile ion contaminant is not definite at present, sodium may be responsible, as in the paper reported by Yanagawa *et al.* (5), where the coincidence of activation energy of V_{FB} change in the Mo-gate structures measured by BT stressing with that of sodium ions was reported. Kerr *et al.* (6) reported Al-gate MOS device stabilization by forming a phosphosilicate layer on the gate

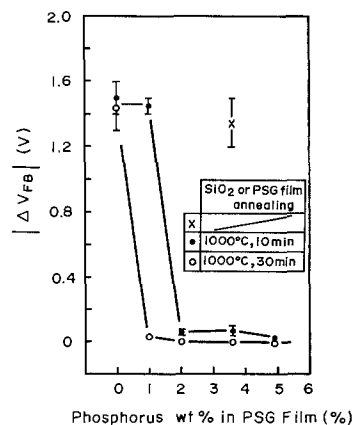


Fig. 2. $|\Delta V_{FB}|$ vs. phosphorus w/o in PSG film for diodes fabricated with and without annealing.

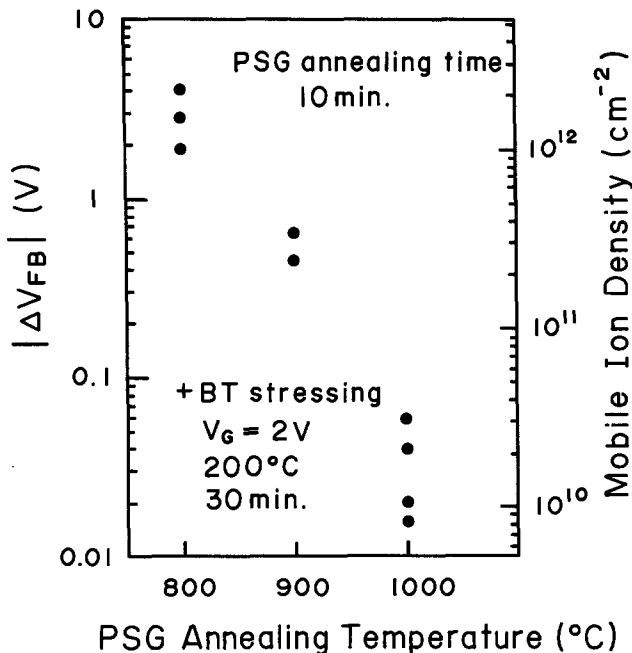


Fig. 3. $|\Delta V_{FB}|$ and mobile ion density vs. PSG annealing temperature.

oxide surface prior to metallization. Yon *et al.* (10) reported sodium ion accumulation in a phosphosilicate layer formed by phosphorus diffusion into a gate oxide film, which was heavily contaminated with NaCl. Considering these studies, the present results suggest that sodium ions are gettered during high temperature annealing into PSG overcoating film or gettered into a phosphosilicate layer, which might be formed on a gate oxide layer resulted from phosphorus diffusion from PSG overcoating film, since SiO₂ overcoating film showed no stabilization effect, as shown in Fig. 2.

Figure 4 shows the results of positive BT stressing on three kinds of diodes having different areas. The sodium ion contamination level was almost the same for these three kinds of diodes fabricated without PSG annealing. However, diode area dependence of PSG annealing stabilization effect was observed, as in the results in Fig. 4. Some amount of sodium ion density re-

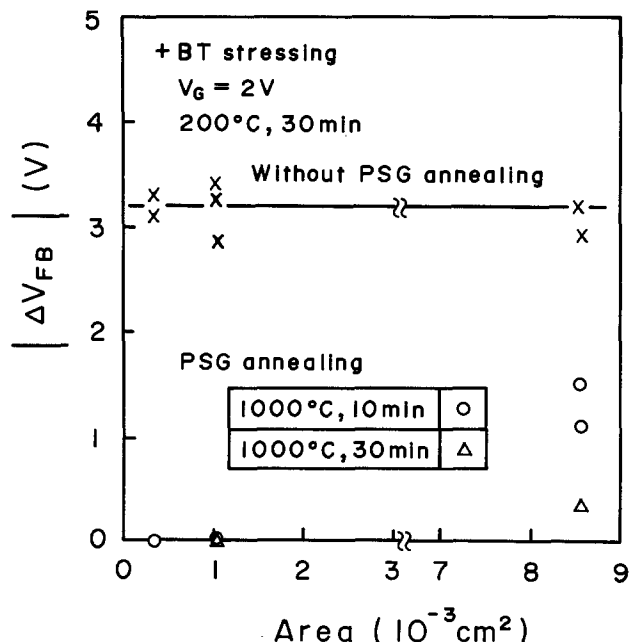


Fig. 4. BT stressing results on three kinds of diodes having different areas.

mained for the diode having the largest area, in contrast to negligible sodium ion density for the other two diodes.

PSG film gettering of sodium ions after sodium ion diffusion through Mo-gate metal or phosphorus diffusion into Mo-gate metal from PSG film, resulting in the formation of a phosphosilicate layer at the metal-oxide interface, can be ruled out for the mechanism of PSG annealing stabilization effect, because of difficulty in explaining the diode area dependence of this effect. Therefore, it is adequate to consider lateral diffusion of phosphorus or sodium ions.

As mentioned in the previous section, V_{FB} shift was negligibly small for diodes having 180 μm radius after PSG annealing at 1000°C for 30 min. If a phosphosilicate layer is formed by the phosphorus lateral diffusion, diffusion length will be the same diode radius order of 180 μm . Thus, the phosphorus lateral diffusion coefficient is estimated to be about 2×10^{-7} cm²/sec, which is approximately 10¹⁰ larger than phosphorus diffusion coefficient in bulk SiO₂ (11). This value is anomalously large, even though the enhancement of phosphorus diffusion at the metal-oxide interface occurs. Therefore, phosphorus lateral diffusion need not be taken into consideration and PSG film gettering along the perimeter of Mo-gate metal after sodium lateral diffusion can be considered as a mechanism. In this case, a considerable rate-limiting step is sodium ion lateral diffusion or PSG film gettering reaction of sodium ion. As shown in Fig. 3, for diodes having 180 μm radius, PSG film stabilization effect was not observed for PSG annealing at 800°C for 10 min. For this PSG annealing condition sodium diffusion length is estimated to be about 1000 μm using sodium diffusion coefficient of about 2×10^{-5} cm²/sec at 800°C, which was extrapolated from the diffusion coefficient at temperatures lower than 300°C (12, 13), assuming 1.4 eV (12-14) as an activation energy. This diffusion length is much larger than the 180 μm diode radius. Thus, the PSG film gettering reaction is considered to be a rate-limiting step.

Figure 5 shows the PSG annealing time dependence of $|\Delta V_{FB}|$ with changing PSG annealing temperature from 800° to 1100°C for square diodes with 880 μm sides.

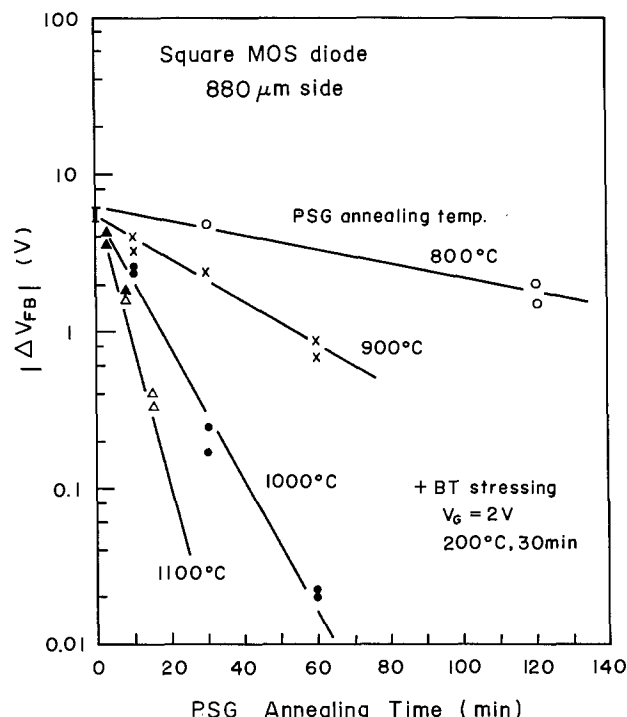


Fig. 5. $|\Delta V_{FB}|$ vs. PSG annealing time with PSG annealing temperature ranging from 800° to 1100°C.

Mobile ion density N decreases exponentially with PSG annealing time, as in the behavior of $|\Delta V_{FB}|$, since $N = C_o \cdot |\Delta V_{FB}|/q$, where q is an electronic charge and C_o is a gate-oxide capacitance per unit area. Thus, PSG gettering reaction is expressed to be a first-order reaction, such as

$$-dN/dt \propto N \quad [1]$$

As mentioned before, PSG film gettering reaction takes place only along the perimeter of Mo-gate metal. Therefore, Eq. [1] must be modified to

$$-dN/dt = kNL/A \quad [2]$$

where A , L , and k are diode area, perimeter, and reaction velocity constant, respectively. From Eq. [2], N can be expressed as the following equation

$$N = N_o \exp(-kLt/A) \quad [3]$$

where N_o is mobile ion density for diodes fabricated without PSG annealing. It is clear, from Eq. [3], that N at fixed PSG annealing condition increases with increasing diode area, since L/A is, for example, proportional to $(\text{radius})^{-1}$ for circular diodes. Equation [3] is rewritten as

$$[\ln(N_o/N)]^{-1} = r/(2kt) \quad [4]$$

for circular diodes with radius r . This relationship agrees with experimental results, which are shown in Fig. 6.

The reaction velocity constant at each PSG annealing temperature was obtained from the slope of the straight lines in Fig. 5 for square MOS diodes. For circular MOS diodes, reaction velocity constant was obtained from the slope of the straight lines in Fig. 6 and also from results similar to that in Fig. 5. The resultant reaction velocity constant plot as a function of $1/T$ is shown in Fig. 7. In obtaining the reaction velocity constant, a geometric perimeter was used. However, the effective perimeter, where PSG film gettering of sodium ions takes place, is considered to be smaller than geometric perimeter for square diodes. This leads to larger reaction velocity constant than that in Fig. 7 for square diodes. 1.3 ~ 1.6 eV activation energy was obtained for PSG film gettering reaction.

Short term positive BT stressing to MOSFET fabricated with PSG annealing.—Figure 8 shows the results of short term positive BT stress tests with from 2 to 16V gate voltage for FET's fabricated with PSG annealing process. In the case of FET, PSG annealing at 1000°C for 10 min was enough to prevent mobile ion related threshold voltage instability, since gate area is very small, as compared with diodes. It is clear in Fig.

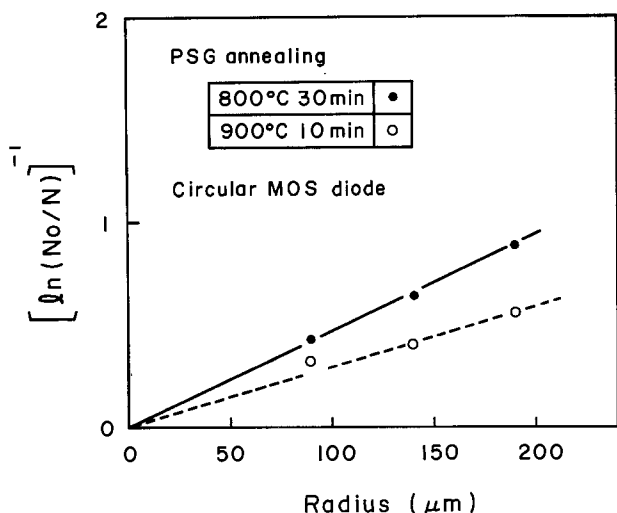


Fig. 6. $[\ln(N_o/N)]^{-1}$ vs. radius for circular MOS diodes

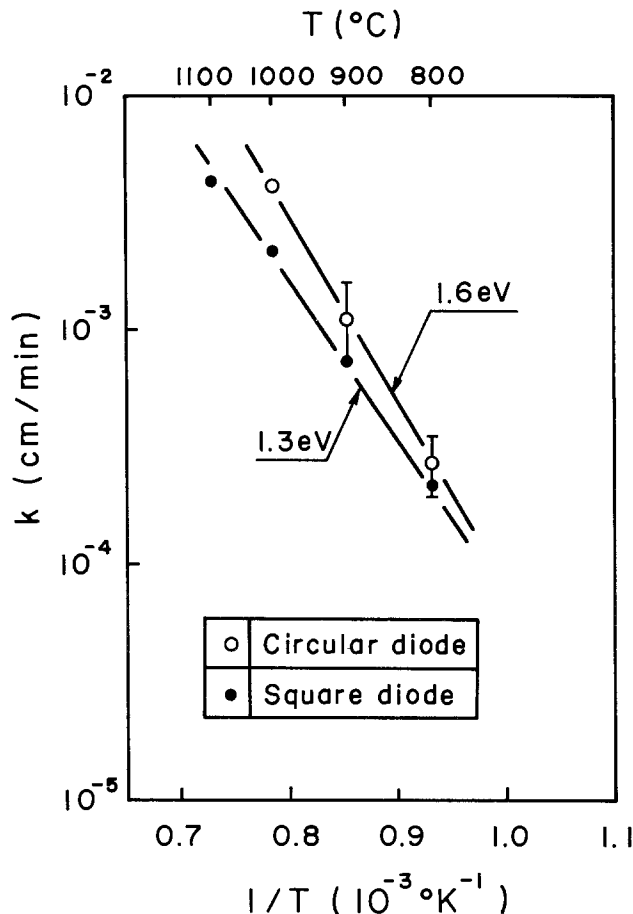


Fig. 7. PSG annealing temperature dependence of reaction velocity constant k .

8 that FET's fabricated in several lots show good stability in threshold voltage.

Summary

Mo-gate MOS devices fabrication process was investigated to suppress mobile ion related instability. By performing high temperature annealing after PSG film deposition on Mo-gate metal, mobile ion related instability has been successfully suppressed. The newly developed mobile ion gettering technology is expected to play an important role in fabrication of stable Mo-gate MOS devices in large scale production. A detailed summary of this study is as follows.

1. In order to ensure suppression of mobile ion related instability, PSG annealing temperature at 1000°C and phosphorus content of more than 2 w/o in PSG film were needed.
2. PSG film gettering reaction of mobile ions occurs along the perimeter of Mo-gate metal after lateral diffusion of mobile ions at the metal-oxide interface.
3. Rate-limiting step was PSG film gettering reaction, which was expressed by a first-order reaction.

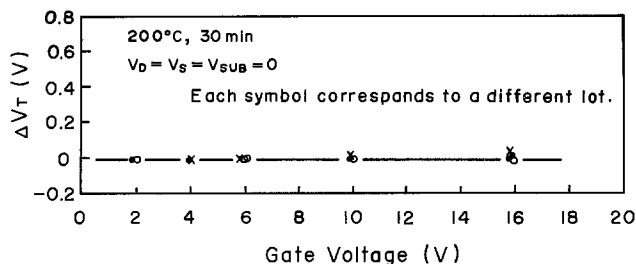


Fig. 8. Threshold voltage shifts (ΔV_T) vs. gate voltage in positive BT stressing.

Activation energy of reaction velocity constant was found to be 1.3 ~ 1.6 eV.

4. Mo-gate MOSFET's, having good stability in short term BT stressing, were fabricated with satisfactory reproducibility.

Acknowledgment

The authors would like to express their thanks to Drs. D. Shinoda and H. Muta for their encouragement, to Dr. K. Higuchi for helpful discussions, and to Mr. I. Nagashima and Mr. C. Takekawa for device fabrication.

Manuscript submitted Feb. 22, 1980; revised manuscript received July 28, 1980.

Any discussion of this paper will appear in a Discussion Section to be published in the December 1981 JOURNAL. All discussions for the December 1981 Discussion Section should be submitted by Aug. 1, 1981.

Publication costs of this article were assisted by Nippon Electric Company, Limited.

REFERENCES

- M. Kondo, T. Mano, F. Yanagawa, K. Kikuchi, T. Amazawa, K. Kiuchi, N. Ieda, and H. Yoshimura, *IEEE J. Solid-State Circuits*, **sc-13**, 611 (1978).
- T. Ohgishi, A. Doi, T. Akiyama, and N. Enomoto, *ibid.*, **sc-13**, 355 (1978).
- H. Ishikawa, M. Yamamoto, T. Nakamura, N. Toyokura, F. Yanagawa, K. Kiuchi, and M. Kondo, *IEDM Tech. Digest*, p. 358 (1979).
- F. Yanagawa, K. Kiuchi, T. Hosoya, T. Tsuchiya, T. Amazawa, and T. Mano, *ibid.*, p. 362 (1979).
- F. Yanagawa, T. Amazawa, and H. Oikawa, Proc. 10th Conf. Solid-State Devices, Tokyo, 1978; *Jpn. J. Appl. Phys. Suppl.*, **18**, 237 (1979).
- D. R. Kerr, J. S. Logan, P. J. Burkhardt, and W. A. Pliskin, *IBM J. Res. Dev.*, **8**, 376 (1964).
- A. Rohatgi, S. R. Butler, and F. J. Feigl, *This Journal*, **126**, 149 (1979).
- J. Monkowski, J. Stach, and R. E. Tressler, *ibid.*, **126**, 1129 (1979).
- M. Koyanagi, T. Hayashida, N. Yamamoto, and N. Hashimoto, Abstract 153, p. 409, The Electrochemical Society Extended Abstracts, Boston, Mass., May 6-11, 1979.
- E. Yon, W. H. Ko, and A. B. Kuper, *IEEE Trans. Electron Devices*, **ed-13**, 276 (1966).
- R. N. Ghoshtagore, *Solid-State Electron.*, **18**, 399 (1975).
- A. E. Owen and R. W. Douglas, *J. Soc. Glass Technol.*, **43**, 159 (1959).
- Y. Komiya, Y. Tarui, and K. Nagai, *Bull. Electro-techn. Lab.*, **30**, 34 (1966) (in Japanese).
- E. H. Snow, A. S. Grove, B. E. Deal, and C. T. Sah, *J. Appl. Phys.*, **36**, 1664 (1965).

Silicon by Sodium Reduction of Silicon Tetrafluoride

A. Sanjurjo,* L. Nanis,* K. Sancier, R. Bartlett, and V. Kapur*

SRI International, Menlo Park, California 94025

ABSTRACT

High purity silicon can be prepared from the reaction of Na with SiF₄ to form Si and NaF. The SiF₄ is obtained from inexpensive H₂SiF₆ by precipitation and decomposition of Na₂SiF₆. Concentrations of B and P are each in the 0.1 ppm wt range in the product Si, separated from NaF by aqueous leaching.

Silicon is an important material in modern semiconductor technology and is finding increased use in solar cells for the photovoltaic generation of electricity. Each application presents special requirements for the purity of the silicon. Certain elements (Ti, Zr, Mo, V, Cr, Fe) have been found to be detrimental to the operation of silicon solar cells by acting as recombination traps when present in concentrations of as little as 0.01-1 ppba (1, 2). Low cost silicon of high purity is needed to foster the continued development of solar photovoltaic systems. With today's technology, approximately 20% of the total cost for the manufacture of a solar cell is ascribed to the silicon material produced by the conventional hydrogen reduction of chlorosilanes. It has been estimated (3) that the cost of silicon must be reduced from its present level of at least \$70/kg to about \$14/kg (in 1980 dollars) to achieve acceptance for use in solar photovoltaic panels. We have developed a process that offers a pathway to an industrial method that satisfies this cost requirement. The starting material is fluosilicic acid, H₂SiF₆, a low cost waste by-product of the phosphate fertilizer industry (4). SiF₄ gas is prepared from H₂SiF₆ and is reacted with sodium metal to produce a mixed reaction product consisting of Si and NaF. Aqueous leaching is used to separate NaF from granular Si.

The SiF₄-Na Process

The overall process consists of three major steps: step 1, precipitation of Na₂SiF₆, followed by SiF₄ gen-

eration; step 2, Na reduction of SiF₄; and step 3, separation of Si from the Si-NaF mixture. A flow diagram of the process steps is shown in Fig. 1. The sequence of reactions is described below.

Generation of SiF₄ (step 1).—Fluosilicic acid (H₂SiF₆) of commercial grade [23 weight percent (w/o)] was used directly as received without purification or special treatment. Sodium fluosilicate, Na₂SiF₆, was precipitated by adding solid sodium fluoride directly to the as-received H₂SiF₆. The mixture was stirred overnight at room temperature in a polypropylene tank. The supernatant liquid, containing mostly HF and some H₂SiF₆, was decanted, and the Na₂SiF₆ precipitate was filtered on a plastic Buchner funnel. The fluosilicate was washed with cold distilled water to remove HF and H₂SiF₆ and dried in an oven at 200°C. A minimum yield of 92% was obtained for 1 kg batches of pure Na₂SiF₆ as determined by x-ray diffraction. The product Na₂SiF₆ is a nonhygroscopic white powder that is very stable at room temperature and thus provides an excellent means for storing the silicon source before it is decomposed to SiF₄.

As SiF₄ is needed, the Na₂SiF₆ can be thermally decomposed (Fig. 1) at 650°C in a graphite-lined, gas-tight stainless steel retort. In separate experiments, it was determined that SiF₄ gas at a pressure of 0.4 atm is in equilibrium at 650°C with solid Na₂SiF₆ and NaF. Accordingly, gaseous SiF₄ evolved at 650°C was condensed as a white solid in a storage cylinder cooled by liquid nitrogen, attached to the retort. The SiF₄ gas was allowed to expand by warming of the storage cylinder

* Electrochemical Society Active Member.

Key words: silicon, solar cells, sodium, silicon tetrafluoride.

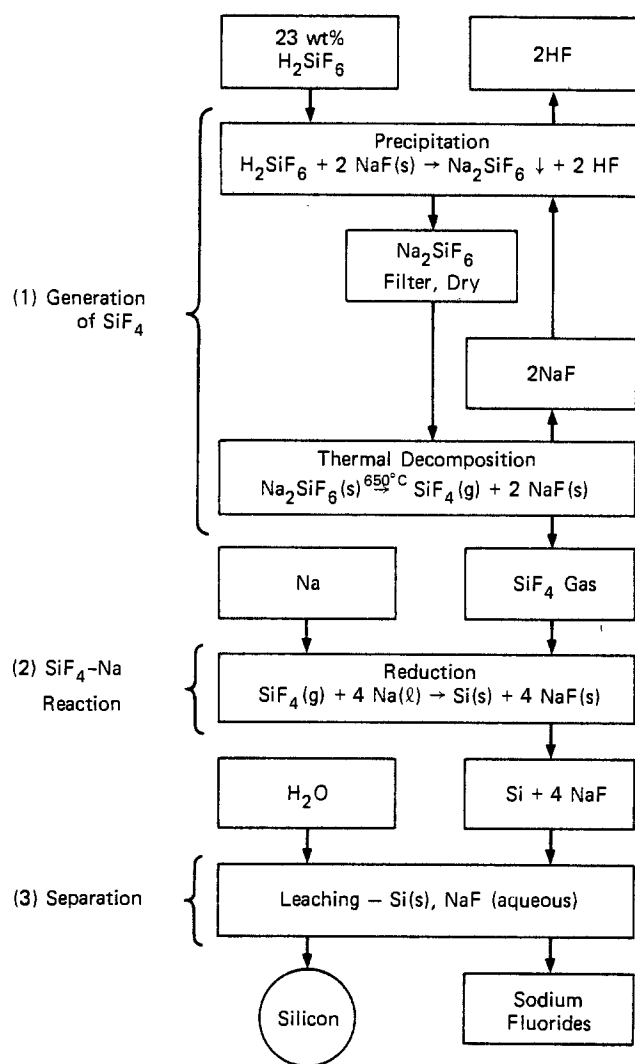


Fig. 1. Three-step method for silicon production

to room temperature and was fed into the reactor as needed. SiF_4 gas prepared in this manner was determined by mass spectrometric analysis to be more pure than commercial grade SiF_4 , as shown in Table I. Ions formed from the sample gas were identified from the observed mass numbers, isotopic distribution, and threshold appearance potentials. The detection limit was better than 0.005%. Positively identified gaseous impurities are listed in Table I; no metallic impurities were detected. Peaks corresponding to B compounds, such as BF_3 , were specially checked, but none were found.

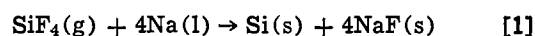
Although the SiF_4 produced from H_2SiF_6 had less impurity, the commercial grade SiF_4 was also used for experimental convenience. The possible presence of metallic impurities in commercial SiF_4 was determined by bubbling the gas through high purity H_2O and heating the resulting slurry with an excess of HF to drive off Si as SiF_4 . The final clear solution was then analyzed by plasma emission spectroscopy (PES). The

Table I. Mass spectrometric analysis of SiF_4

| Ion | SiF_4 prepared at SRI from H_2SiF_6 (%) | SiF_4 commercial (%) |
|-------------------------------------|--|-------------------------------|
| SiF_3^+ | 96.9 | 93.6 |
| Si_2OF_6^+ | 3.04 | 4.24 |
| SiOF_2^+ | — | 1.79 |
| CCl_3^+ | — | 0.159 |
| SO_2F_2^+ | 0.076 | 0.098 |
| $\text{Si}_2\text{O}_2\text{F}_4^+$ | — | 0.081 |
| SO_2^+ | — | 0.035 |

results are listed in Table II, together with PES analysis of the waste by-product H_2SiF_6 and the NaF used to precipitate Na_2SiF_6 (step 1, Fig. 1). Comparison of the first two columns of Table II with column three shows that the concentrations of some elements, e.g., Li, B, V, Mn, Co, K, and Cu, were unchanged by precipitation of Na_2SiF_6 , whereas the elements Mg, Ca, Al, P, As, and Mo were diminished by a factor of 5-10. Some elements were concentrated into the Na_2SiF_6 , namely Cr, Fe, and Ni. The fourth column in Table II is representative of the impurity content to be found in SiF_4 gas prepared on a commercial scale. The low content of P is of special significance for both semiconductor and solar cell applications. Elements known to reduce solar cell efficiency (V, Cr, Fe, Mo) are uniformly low in commercial grade SiF_4 . Only Mn, As, and Al are of comparable concentrations in both Na_2SiF_6 and SiF_4 at the 1 ppm or less level.

SiF₄-Na reaction (step 2).—The central operation of the pure Si process (step 2, Fig. 1) is the reduction of SiF_4 by Na according to the reaction



Although this reaction is thermodynamically favored at room temperature ($\Delta G^\circ_{298\text{K}} = -146$ kcal/mole Si), it has been found experimentally that Na has to be heated to about 150°C before any appreciable reaction can be observed. Once the reacting has been initiated, the released heat ($\Delta H^\circ_{298\text{K}} = -164$ kcal/mole Si) raises the temperature of the reaction Na, which in turn increases the reaction rate. Under adiabatic conditions, a temperature of 2200 K is predicted for reaction [1] with the stoichiometric quantities of SiF_4 and Na. In practical reactors, rapid consumption of gaseous SiF_4 produces a pressure decrease. The kinetic behavior of reaction [1] is complex because of the interplay of several factors, e.g., pressure of SiF_4 , vaporization of Na, local temperature, porosity of two solid products, and transport of SiF_4 and Na vapor through the product crust that forms on the liquid Na.

Although only preliminary studies have been made of the kinetics, the general features of reaction [1] have been surveyed. In a series of experiments to estimate reaction temperatures, 5g of Na were loaded in a Ni crucible (3 cm ID, 4 cm high) and heated in SiF_4 initially at 1 atm pressure. The Na surface tarnished at around 130°C , with the formation of a thin brown film. As the temperature increased, the color of the surface film gradually changed from light brown to brown and finally to almost black. The SiF_4 -Na reaction became rapid at $160^\circ \pm 10^\circ\text{C}$ and liberated a large amount of heat, as indicated by a sudden rise in re-

Table II. Plasma emission spectroscopy analysis, parts per million (wt)

| Element | H_2SiF_6^a | NaF^b | Na_2SiF_6 | SiF_4^c |
|---------|----------------------------|----------------|---------------------------|------------------|
| Li | 0.1 | — | 0.2 | 0.01 |
| Na | 460 | — | — | 1.8 |
| K | 9.0 | — | 8.0 | 0.3 |
| Mg | 55 | — | 6.4 | 2.3 |
| Ca | 110 | 10 | 18 | 1.6 |
| B | 1.0 | — | 0.8 | <0.01 |
| Al | 8.0 | <2.5 | 1.3 | 1.2 |
| P | 33 | — | 5 | 0.08 |
| As | 8.8 | — | 0.2 | 0.28 |
| V | 0.3 | <5 | 0.3 | <0.01 |
| Cr | 0.8 | <3.5 | 8.8 | <0.01 |
| Mn | 0.2 | <4 | 0.4 | 0.16 |
| Fe | 13 | >7 | 38 | 0.04 |
| Co | 0.54 | — | 0.7 | <0.01 |
| Ni | 1.17 | <8 | 4.2 | <0.01 |
| Cu | 0.12 | <4 | 0.6 | <0.01 |
| Zn | 1.4 | — | 1 | <0.01 |
| Pb | 14.5 | — | 5 | 0.03 |
| Mo | 11 | — | 1.0 | <0.01 |

^a 23 w/o waste by-product of phosphate fertilizer production.

^b Emission spectroscopy.

^c Commercial grade.

^d Major line.

action temperature. As shown in Fig. 2, the pressure in the reactor typically decreased slightly until the temperature increased sharply, with an associated rapid decrease in SiF_4 pressure. The reaction lasts for several seconds only. For SiF_4 pressures below 0.3 atm, the reaction mass was observed to glow at a dull red heat. For higher pressure, a characteristic flame was observed. The shortest reaction time (20 sec) and the highest temperatures (about 1400°C) were obtained when the initial pressure of SiF_4 was around 1 atm. In addition, complete consumption of Na was obtained for 1 atm SiF_4 . When scale-up of this reaction was attempted by loading larger amounts of Na, it was found that as the depth of the Na pool increased, the amount of Na remaining unreacted also increased. The product formed a crust on top of the Na surface, building a diffusion barrier for the reactants. As the barrier thickness increased, the reaction slowed and eventually stopped.

On the basis of preliminary studies of the parameters that affect reaction [1], a system was developed that is capable of producing Si at the rate of 0.5 kg/hr in a batch mode. The reactor is shown schematically in Fig. 3. The upper section of the Na dispenser is coated internally with epoxy resin on all Pyrex glass surfaces that may contact Na.

Sodium chips were prepared by feeding 225g blocks of sodium (6 cm diam rod, cut longitudinally) into a food processor using a blanket of argon to minimize contact with atmospheric oxygen and moisture. While Na chips were being introduced into the top of the storage chamber of the dispenser (2 kg capacity), dry argon flowed up through the chamber. The Na chips were transferred from the storage chamber to the reactor by means of a horizontal "hoe" mechanism. Downward flow of Na chips in the storage chamber was aided by agitation of the vertical rod.

The lower section of the reactor was made of Inconel (20 cm diam, 90 cm high) and was fitted with a sheet nickel liner (18 cm diam, 60 cm high) and an inner liner of sheet Grafoil (18 cm diam, 90 cm high). The outside of the Inconel reactor was wrapped with four sets of heavy duty electrical heating tapes (rated for use to 800°C), which were covered with Kaowool insulation (1.3 cm thick). The top of the Inconel reactor and the flanges that connect to the Pyrex Na dispensing section were water cooled.

In operating the reactor, the system was first evacuated, then filled with SiF_4 gas to a pressure of about 1

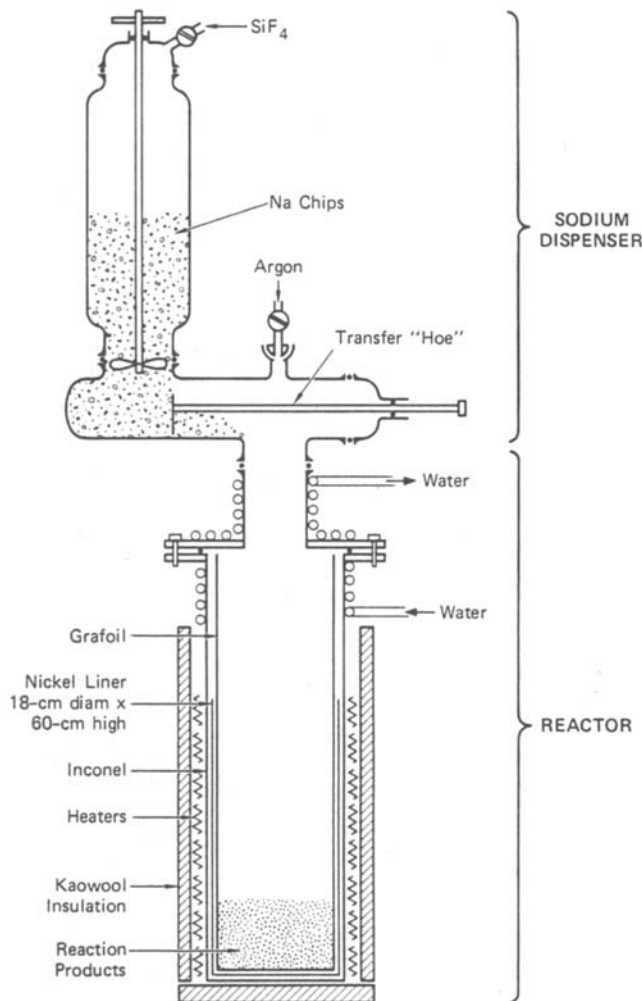


Fig. 3. Schematic of 18 cm diam Inconel reactor

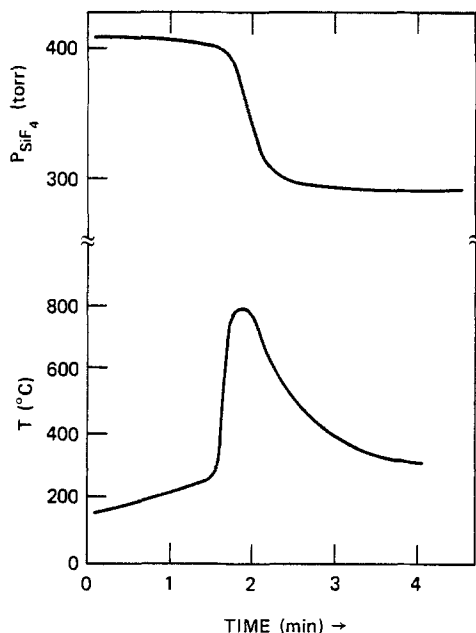


Fig. 2. SiF_4 -Na reaction: pressure and temperature profiles

atm. Reaction was initiated as soon as Na chips were dropped to the bottom of the reactor, which was preheated to 400°C . Reaction was sustained by manually adding Na chips at a rate sufficient to maintain a given SiF_4 flow rate, as indicated by an electronic flowmeter. The maximum flow rate used was 380 liters SiF_4/hr , corresponding to an addition rate of about 1.4 kg Na/hr and a production rate of 0.5 kg Si/hr. During the operation of the Inconel reactor, the temperature of the reactor walls in the region of the reaction products rose to $600^\circ\text{--}650^\circ\text{C}$, as indicated by external thermocouples. The temperature of the nickel liner reached the melting temperature of NaF (998°C), indicated by molten NaF observed on the outside of the nickel liner near seams as the reaction zone progressed upward.

After each SiF_4 -Na run was completed, the reaction products completely occupied the cylindrical space inside the Ni-Grafoil liner. The reaction products were pulverized with plastic equipment, and routine checks were made for the presence of unreacted Na by acid titration. An important parameter regulating the rate and extent of the reaction is the surface-to-volume ratio of the Na feed. For the 18 cm diam Inconel reactor, no unreacted Na was observed in the reaction products even for the highest Na addition rate used (1.4 kg/hr) when the Na chips had a surface to volume ratio of about 20 cm^{-1} .

The relative amounts of Si, NaF, and Na_2SiF_6 were conveniently determined by x-ray diffraction using standard mixtures. The weight fraction of Na_2SiF_6 was determined from the ratio of the peak intensities of Na_2SiF_6 and KCl reference additive. The method is rapid and accurate to about $\pm 5\%$. The presence of Na_2SiF_6 was also cross-checked by thermogravimetry.

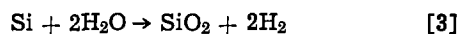
The presence of Na_2SiF_6 in the reaction product mixture is an indication of possible side reaction according to



which is the reverse of the decomposition reaction used for SiF_4 generation in step 1 (Fig. 1) of the overall process.

When the reactor walls are kept above 600°C , the formation of by-product Na_2SiF_6 was less than 2 w/o.

Separation (step 3).—The reaction product obtained by the SiF_4 -Na reaction [1] is a porous, brown mass. This intimate mixture of NaF and Si is readily separated by aqueous leaching. The Si product obtained after leaching is a brown crystalline powder with particle sizes ranging from submicrometers up to $150\ \mu\text{m}$. Some of the various morphological forms observed in this powder are shown in Fig. 4. Leaching is performed using 1.0N HCl in a polypropylene container, although other acids such as H_2SO_4 , CH_3COOH , and HF are equally effective. The acid normality can vary in the range 0.1-1.0N without affecting the leaching process, which may be monitored by measuring the F^- and Na^+ concentrations in the leachant using ion selective electrodes. When the F^- concentration is about 10^{-5} mole/liter, leaching is stopped. The acidification of the leach solution is a precautionary measure to prevent increase in local pH due to reaction of H_2O with Na, which could, in turn, result in Si loss by oxidation according to the reaction



It has been determined (6) experimentally that during leaching in 1N acid, Si can be oxidized at an initial rate of 15 weight percent per hour. The rate of oxidation increases with increased F^- ion concentration in solutions

with pH in the range of -0.8 to 10. The contact time may be minimized by using forced filtration, which yields a 98% complete recovery of Si. Differences in leaching rate due to particle size of the products, temperature of the leaching bath, and amount of stirring were found to be important only during the first minutes of leaching.

Purity of Silicon

Several analytical methods have been used to characterize the very low levels of impurity elements in the silicon leached from the products of SiF_4 -Na reaction [1]. Generally, each of the methods is used at the limit of resolution for several elements. For comparison, a reference sample of high purity Si was analyzed in a similar manner to provide a check of spurious readings caused by sample preparation, background effects, and instrumental limitations. The reference material was commercial polycrystalline semiconductor grade Si with resistivity greater than $1 \times 10^5\ \Omega\ \text{cm}$.

In Table III, the uncertainty in the methods of emission spectroscopy and spark source mass spectrometry has been taken into account by selecting representative average concentrations based on several analyses. A range is indicated for (Fe, Cr, and Cu) where wide variations occur because of its importance, phosphorous was also determined by a wet chemical colorimetric method (5).

Discussion

The process sequence shown in Fig. 1 was selected because of the inherent simplicity of the steps and their independent and combined suitability for scale-up. Some purification occurs during precipitation (step 1, Fig. 1) for Mg, Ca, Al, P, and As due to the high solubility of their fluosilicates and fluosalts. Some concentration takes place for Cr, Fe, and Ni, and this effect

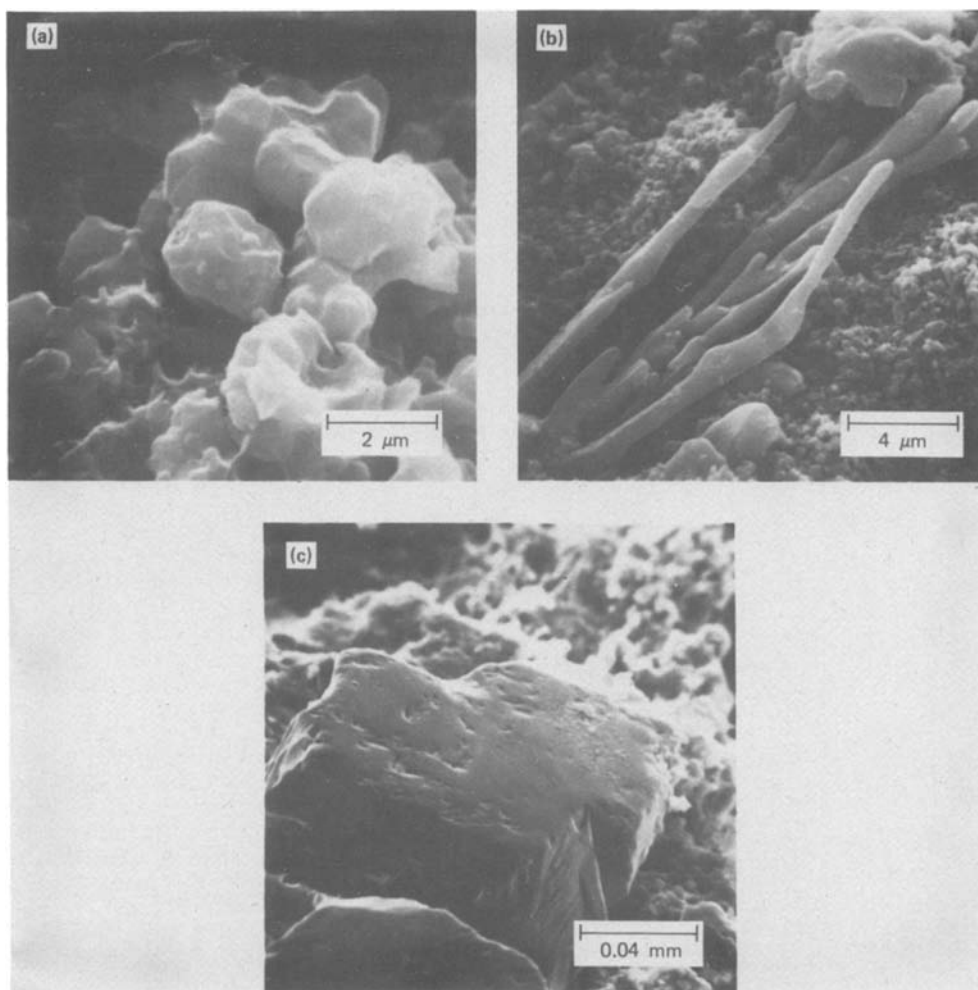


Fig. 4. Morphologies of Si produced in the SiF_4 -Na reaction: (a) fine powder, (b) branches, (c) cubes.

Table III. Representative silicon impurity content, parts per million (wt)

| Element | SRI Si ^a | Semiconductor Si |
|---------|-------------------------|------------------|
| B | 0.1 | 0.1 |
| P | 0.2 (0.09) ^b | 0.3 |
| As | ^c | ^c |
| Al | 0.8 | 0.4 |
| Ga | 0.06 | 0.1 |
| Ti | 2.0 | 0.2 |
| Zr | 0.01 | <0.3 |
| Mo | 0.3 | ^c |
| V | 0.04 | <0.3 |
| Cr | <3.5 ^d | 0.8 |
| Mn | 0.1 | ^c |
| Fe | <7 ^d | <0.3 |
| Co | 0.5 | 0.5 |
| Ni | 2.0 | 4 |
| Cu | <4 ^d | 0.2 |
| Zn | 0.01 | 15 |
| F | 0.1 | <0.1 |
| Na | 1.0 | 9.0 |
| K | 0.01 | <0.1 |
| Ca | 1.0 | 0.1 |
| Mg | 0.1 | ^c |

^a Polycrystalline silicon for single crystal growth.

^b Wet chemical analysis.

^c Not observed.

^d Emission spectroscopy; all others, spark source mass spectrometry.

may be due to coprecipitation of these elements as fluorides since their fluosilicates are very soluble. From Table II, it is clear that most of the purification is accomplished as a result of the thermal decomposition in step 1 (Fig. 1). Most transition metal fluorides are very stable condensed phases at 650°C, the temperature of decomposition in step 1 (Fig. 1) and, therefore, will stay in the solid. In addition, volatile fluorides formed during the decomposition of fluosalts such as Na₂TiF₆ and Na₂ZrF₆ will condense upon cooling of the SiF₄ gas stream from step 1. The condensed material is then removed from the gas mainstream by in-line fume particle filtration. Mass spectrometry did not detect the presence of any metallic or dopant impurity (Table I) in either the SRI produced gas or in the commercial SiF₄ gas. The analysis done on the SiF₄ by passing the gas through high purity water was based on the hypothesis that fluoride impurities should be hydrolyzed and/or trapped in the SiO₂ formed. The results listed in Table II show that the level of metal impurities in the resulting SiO₂ is so low that, for practical purposes, the SiF₄ can be considered free of metallic impurities.

The Na feed, reactor materials, and possible contamination of the product during handling remain as possible sources of impurities in the Si.

The impurities in Na can be divided roughly into three types according to their tendency to react with SiF₄, as classified by the free energy of reaction. The first type of impurity includes aluminum and elements from the groups IA, IIA, and IIIB. The free energy of reaction of SiF₄ with these impurities ranges from -100 to -200 kcal/mole SiF₄ at room temperature and from -50 to -100 kcal/mole SiF₄ at 1500 K. It is expected, therefore, that even when these impurities are present at the ppm level, they will react with the SiF₄ to form the corresponding fluorides. Subsequently, the fluorides will be dissolved preferentially in the NaF phase. The second type of impurity includes transition metals such as Mo, W, Fe, Co, Ni, and Cu, and the elements P, As, and Sb. These elements exhibit positive free energies of reaction in excess of 100 kcal/mole SiF₄ and are not expected to react with SiF₄. However it is an experimental fact that the silicon resulting from the SiF₄-Na reaction contains amounts of Fe, Ni, and Cr in proportion to the concentration of these elements in the Na feed. The mechanism by which these metals are transferred to the silicon has not yet been studied. In any case, the concentration of Fe, Cr, Ni, and also Ti can be decreased by a factor of about 10⁴-10⁶ for single-pass directional solidification or the

Czochralski crystal-pulling procedures used presently for solar cell manufacture. At the resulting levels, these elements would not be detrimental to solar cell performance (1). Boron represents a third type of impurity. The free energy of reaction of this element with SiF₄ is positive but small (5-20 kcal/mole SiF₄ for temperatures up to 1500 K); therefore, some partial reaction can be expected and B will be distributed between the NaF and Si phases. It is noted that the levels of the dopant elements, B, P, and As in SRI silicon are the same as in the semiconductor silicon used as reference. Since it is convenient to have dopant levels as low as possible to permit flexibility in subsequent doping procedures for semiconductor and solar cell applications, the low B and P content (Table III) of Si produced by the SRI process is of advantage. The possibility of contamination from the reactor materials was minimized by the use of Ni and Grafoil liners (Fig. 3) that completely contained the reaction products and avoided contact or impurity transfer with the reactor walls. The Ni liner served merely as a mechanical retainer for the Grafoil sheet and did not contact the solid mixed reaction product. Both Ni and Inconel were selected for use in the reactor (Fig. 3) because of their stability in the presence of fluoride compounds.

Contamination during handling was, after the Na feed, probably the second most important source of impurity pick up. Airborne dust could have contacted the products either during their removal from the reactor or during sampling. Furthermore, although electronic grade acid and deionized water were used for leaching the NaF, the large volume of liquid used could have contributed to the accumulation of impurity in the silicon. Finally, although the purity of the silicon produced by the SiF₄-Na reaction is appropriate for solar cell manufacture, it is expected that by prepurification of the commercial grade Na used and by avoiding contamination during handling, semiconductor grade silicon could be produced.

Conclusion

We have shown experimentally that high purity Si can be prepared as a powder using the inexpensive starting materials H₂SiF₆ and Na. Favorable thermodynamics of the reduction step, easily controlled kinetics, and abundant availability of inexpensive starting materials make this method attractive. Of special interest for semiconductor applications are the low concentrations of B and P impurities in the product Si. The Si produced by the SiF₄-Na reaction, if purified further by directional solidification, should be a low cost material suitable for the manufacture of solar cells.

Acknowledgments

The authors thank Dr. D. Hildenbrand, Dr. K. Lau, and Dr. R. Kleinschmidt for mass spectroscopy work, E. Farley for x-ray work, R. Weaver, S. Leach, S. Westphal, and G. Craig for their cooperation, and Dr. R. Lutwack and Dr. R. Rhein for their comments and suggestions. This work was performed for the Jet Propulsion Laboratory, California Institute of Technology, and was sponsored by the U.S. Department of Energy under Contract DOE/JPL-954471 by agreement with NASA.

Manuscript submitted Feb. 12, 1979; revised manuscript received July 21, 1980.

Any discussion of this paper will appear in a Discussion Section to be published in the December 1981 JOURNAL. All discussions for the December 1981 Discussion Section should be submitted by Aug. 1, 1981.

Publication costs of this article were assisted by SRI International.

REFERENCES

1. R. H. Hopkins, R. G. Seidenstecker, J. R. Davis, P. Rai-Choudhury, P. D. Blais, and J. R. McCormick,

- J. Cryst. Growth*, **42**, 493 (1977).
 2. J. W. Chem, A. G. Milnes, and A. Rohatgi, *Solid-State Electron.*, **22**, 801 (1979).
 3. Proceedings of the 10th LSA Project Integration Meeting, August 16-17, 1978, JPL Document 5101-86, p. 2-3.

4. H. E. Balke *et al.*, Report of Investigation No. RI 7502, U. S. Bureau of Mines (April 1971).
 5. Balazs Analytical Laboratory, Mountain View, California.
 6. K. M. Saucier and V. K. Kapur, *This Journal*, **127**, 1849 (1980).

Surface Conversion for Antisticking to Reduce Patterning Defects in Photolithography

Toshiharu Matsuzawa, Hiroshi Yanazawa, and Norikazu Hashimoto

Hitachi Limited, Central Research Laboratory, Kokubunji, Tokyo 185, Japan

and Hiromitsu Mishimagi

Hitachi Limited, Device Development Center, Kodaira, Tokyo 187, Japan

ABSTRACT

After an exhaustive reevaluation of the contact printing processes, photoresist sticking to the photomask surface is identified as the principal cause of patterning defects and a preventive measure is developed. This process, called surface conversion for antisticking (SURCAS), facilitates a reduction in defect density by about one-fourth compared to conventional contact printing. This technique opens the way for improvement of current LSI fabrication, and moreover should be useful in ultrafine pattern lithography down to 1 μm in the near future.

Photolithographic technology has been successively improved and has dominantly contributed to an increase in LSI packing density by almost a factor of two every year over the last decade. On the other hand, it has also been shown (1, 2) that low device yield is mainly due to patterning defects formed in photolithography. Presently, LSI's with lines and spacings of 3 μm or less are just going into commercial production. When positive photoresists, instead of negative ones, are used in combination with a contact printer, it seems rather easy to delineate 1 μm fine patterns. However, patterning defects due to fragility of the base resin itself have appeared as the most serious problem. Therefore, a new technique to reduce patterning defects is urgently needed to fully utilize the high resolution of positive photoresists for LSI fabrication. In the last several years, great progress has been made by using a 1:1 projection aligner in yield improvement. Still, its resolution limit is recognized to be about 2 μm .

In this work, the contact printing process is reexamined in detail focusing on patterning defects. The investigation has revealed that sticking of photoresist pieces on photomask surfaces is the dominant contributor. This photomask to photoresist adhesion phenomenon is analyzed based on the dry adhesion mechanism reported earlier (3). And finally, a novel technique to effectively prevent sticking, *i.e.*, surface conversion for antisticking (SURCAS), is developed.

Theoretical Treatment

It has become a matter of common knowledge that photoresist to substrate adhesion is improved by surface conversion of substrate wafers with organic compounds such as HMDS.¹

Our experiments revealed an inconsistent phenomenon; when the same conversion treatment is applied to a photomask surface, photoresist to photomask adhesion is drastically weakened. This inconsistency is solved by two different adhesion mechanisms, dry and wet adhesion (3).

Key words: photolithography, contact printing, patterning defects, adhesion, surface conversion.

¹ Hexamethyldisilazane: $(\text{CH}_3)_3\text{SiNHSi}(\text{CH}_3)_3$

Since there is no liquid in the contact printing process, adhesion in photomask-photoresist-substrate system is analyzed according to the dry adhesion mechanism as outlined below. Adhesion between two materials, *i.e.*, photomask to photoresist and photoresist to substrate wafer, is evaluated by dispersion interaction as follows

$$W_{a(\text{MR})} = 2(\gamma_{\text{M}}^{\text{d}}\gamma_{\text{R}}^{\text{d}}) \quad [1]$$

$$W_{a(\text{MR})} = 2(\gamma_{\text{R}}^{\text{d}}\gamma_{\text{S}}^{\text{d}}) \quad [2]$$

where the suffixes M, R, and S denote the photomask, photoresist, and substrate wafer respectively, W_a is the work of adhesion indicating the affinity between two materials denoted by suffixes, and γ^{d} is the dispersion component of surface free energy. Since adhesion increases with W_a , the photoresist will stick to the photomask rather than the substrate when

$$W_{a(\text{MR})} > W_{a(\text{RS})} \quad [3]$$

Substituting formulas [1] and [2] into [3] produces

$$\gamma_{\text{M}}^{\text{d}} > \gamma_{\text{S}}^{\text{d}} \quad [4]$$

Consequently, to prevent the photoresist sticking, $\gamma_{\text{M}}^{\text{d}}$ must be smaller than $\gamma_{\text{S}}^{\text{d}}$.

The values of γ^{d} were evaluated for various materials commonly used in the semiconductor industry, as shown in Fig. 1. The most important point is that a conventional chromium mask washed with organic solvents shows a higher γ^{d} value than any other substrate material. Thus, photoresist sticking can be expected with the above consideration. On the other hand, γ^{d} of the SURCAS mask is the lowest, indicating a low adherence to photoresist.

Experimental

Wafer inspection.—Two series of wafer inspection tests were carried out with each object. The first series was to classify the patterning defects in conventional processes. The second was for yield comparison with and without SURCAS. In the first series, 20 wafers, each including 80 chips of 9 mm² die, are processed

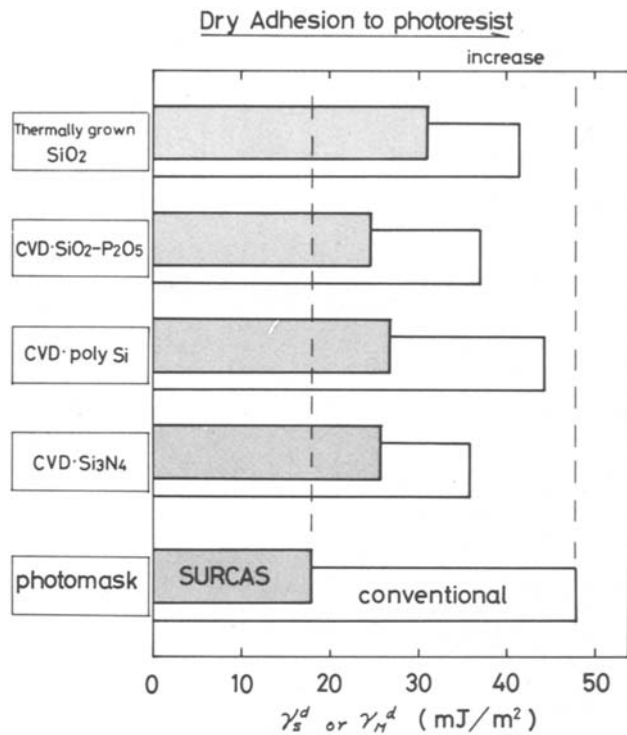
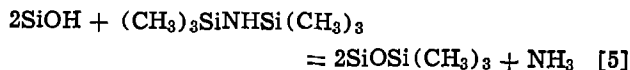


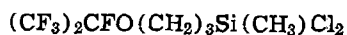
Fig. 1. Measured γ^d values for various substrate materials and photomask. Clear and shaded column of each material indicate surfaces before and after conversion treatment, respectively.

under standard MOS fabrication, including six lithography steps. A positive photoresist Shipley's AZ1350J, chromium hard surface mask, and Cobilt's contact printer AF 2800H were used. Wafers were inspected just after the four lithography steps by optical microscope. In normal inspection, 100 \times magnification is sufficient and, when needed, 1000 \times magnification permits detection of defects as small as 0.5 micron. For yield comparison 15 and 30 mm² dies were examined in the second series. Wafers were processed under same conditions except for photomask pretreatments.

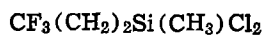
Surface conversion.—As reported earlier (4), an SiO₂ surface is converted into hydrophobic nature through the following reaction with HMDS



where SiOH denotes surface silanol group on SiO₂ film. Since HMDS reactivity with SiO₂ surface is extremely high compared to the alcohols, the above reaction is completed by exposing the SiO₂ to HMDS vapor at about 100°C for several minutes. Furthermore, at our laboratory, more effective conversion agents were found. These are silane derivatives with the following fluorocarbon chain



Heptafluoroisopropoxypropylmethylchlorosilane (7F-silane in abbreviation)



Trifluoropropylmethylchlorosilane (3F-silane in abbreviation). These F-silane compounds were also so reactive that the SiO₂ surface could be converted by exposure to their vapors.

Characterization of converted surface.—As mentioned, photomask-photoresist and photoresist-substrate adhesion can be accurately evaluated by the dispersion component of their surface free energy γ^d . This parameter was controlled through the surface conversion technique and estimated by measuring the

contact angle of iodomethylene, CH₂I₂, according to Fowkes' theory (5). Contact angles were measured by the sessile drop method using a goniomicroscope.

Dry adhesion test.—The procedure of the dry adhesion test is illustrated in Fig. 2. Silicon wafers of 3 in. diam were oxidized in steam oxygen at 1100°C to 1 μ m thickness. Then, various surface conversion treatments were applied to control the γ_S^d of SiO₂. The SiO₂ film was selectively etched to form 900 islands of 1 mm² die throughout the wafer by conventional photolithography. After the photoresist was removed, other photoresist patterns, 32 μ m square and 1 μ m thick, were formed. At the same time, photomasks were also prepared through various hydrophobic conversions. Then, the wafer and the photomask were pressed on to each other using a contact printer for 5 min. After removal of the photomask, the wafer was inspected to count the number of removed photoresist patterns, i.e., N^{dry} , under an optical microscope. In this work, N^{dry} counting was restricted to the tops of SiO₂ islands where it is considered better.

Results and Discussion

Classification of patterning defects.—Although wafer inspection with an optical microscope is painstaking work, it is nevertheless one of the most effective ways of classifying and determining the cause of patterning defects. In this report, inspected defects were divided into the following five categories according to shape, color, clarity, or opaqueness, etc. Elemental analyses by microprobe were also helpful in some cases.

Dust.—Despite stringent efforts to minimize dust, it remains as one of the main defect components. Some typical examples of dusts detected in this work are as follows: stainless steel dust from the planetary hot plates of chemical vapor deposition apparatus; hillocks and clusters formed in vacuum evaporation of metal films; some clear pieces from plastic wafer cassettes used in the rotary dryer; and so-called dust from ambient, oven, mask aligner etc.

Sticking.—Photoresist pieces stick on the photomask surface. A birds-eye view of a photomask surface pro-

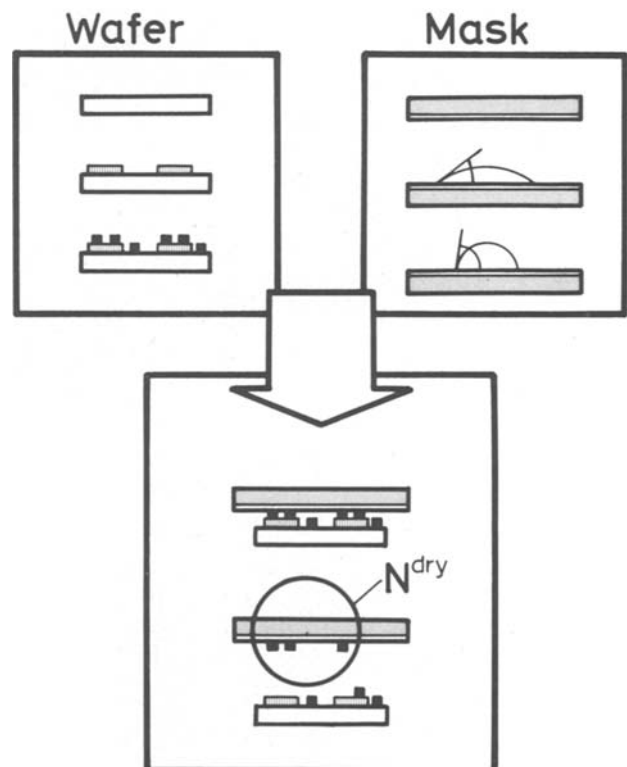


Fig. 2. Procedure of dry adhesion test

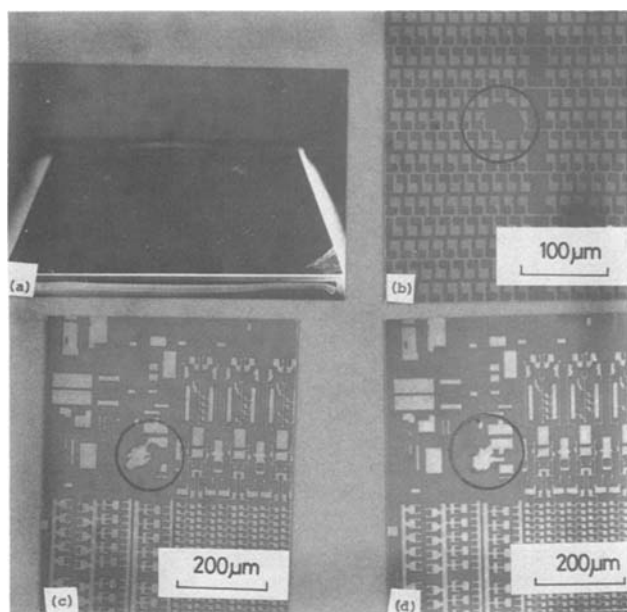


Fig. 3. Typical examples of inspected patterning defects. (a) Photoresist pieces stuck to photomask surface; (b) sticking results as patterning defect on the wafer where photoresist is stripped off; (c) and (d) stuck photoresist pieces interrupt exposure resulting in photoresist residues of similar shape at similar locations on different two wafers.

cessed with eight wafers using contact printer is shown in Fig. 3(a). In this photograph, a nonpatterned mask plate is used to expose the stuck photoresist pieces in the inclined light. These stuck photoresist pieces result in wafer defects such as shown in Fig. 3(b).

Exposure interruption.—The stuck photoresist pieces cause other kinds of patterning defects on the wafer as shown in Fig. 3(c) and (d). Two wafers, which were successively processed, are shown with similar resist patterns formed at similar locations on both wafers. These patterns are due to exposure interruption by the stuck photoresist pieces.

Mask defects.—Even when chromium hard surface mask are used, damage to the photomask is inevitable because soda-lime glass hardness is less than that of Si or Si_3N_4 . Mask defects will also interrupt exposure and result in defects similar to those mentioned above.

Others.—Patterning defects not classified into the preceding four categories and those thought to be the result of special accidents are included in this category, e.g., mechanical damage due to handling, patterning faults due to droplets of developer.

Patterning defects are distributed among the five causes as summarized in Table I. As mentioned above, since exposure interruption originates from sticking, it

Table I. Classification of inspected patterning defects

| Category | Lithography steps | | | | Total share (%) |
|---------------------------|-------------------|----|----|---|-----------------|
| | 1 | 2 | 3 | 4 | |
| (1) dust | 1 | 5 | 10 | 8 | 27 |
| (2) sticking | 15 | 7 | 7 | 1 | 22 |
| (3) exposure interruption | 4 | 12 | 5 | 3 | 27 |
| (4) mask defect | 4 | 0 | 0 | 7 | 12 |
| (5) others | 4 | 3 | 1 | 2 | 11 |

can be seen as causing up to 50% of patterning defects in conventional contact prints. This conclusion leads us to the development of SURCAS to prevent photoresist sticking.

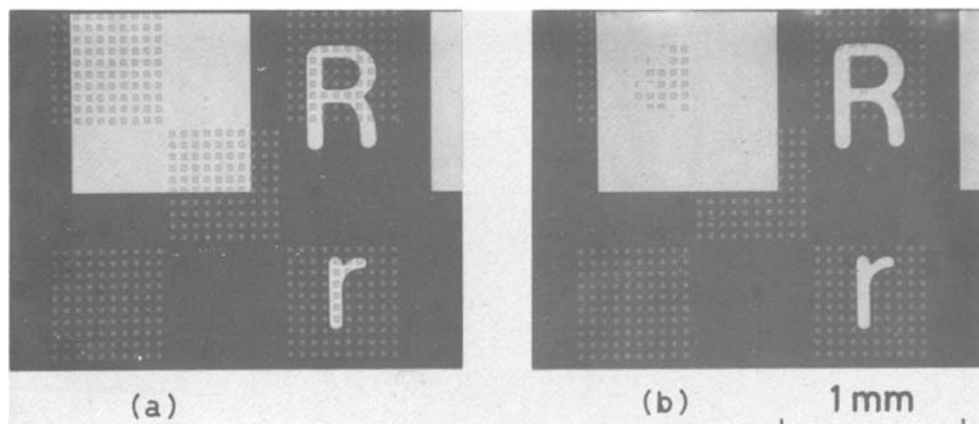
Results of dry adhesion test.—One example of a wafer put through the dry adhesion test is demonstrated in Fig. 4. Photoresist patterns of $32\ \mu\text{m}$ square on a wafer before (a) and after (b) contact with photomask. In these photographs, 1 mm white squares and letters (R and r) are delineated in SiO_2 film of $1\ \mu\text{m}$ thickness, the remaining part is Si substrate. Obviously, the photoresist patterns on the SiO_2 islands are favorably diminished, in this case 80%, whereas almost all patterns stay on the portion of the wafer outside the islands. The SiO_2 islands seem to serve our purpose by making photomask-wafer contact better at this address. However, after examining all addresses on the wafer, it is seen that N^{dry} tends to disperse, and in extreme cases no pattern was removed from the island. This fact indicates that the wafer comes in contact with photomask in a different manner from point to point. Though the contact printer is not a sufficient apparatus from the standpoint of a modeling experiment, it was adequate to relate our modeling concept to practical production processes. Considering those experimental difficulties, at least 70 addresses were examined and average value was taken as N^{dry} for each wafer. The relationship between the sticking frequency, N^{dry} in percent and the dry adhesion factor f^{dry} is shown in Fig. 5. This factor is defined as the ratio of the work adhesion mentioned above

$$f^{\text{dry}} = W_{\text{a(MR)}}/W_{\text{a(RS)}} = (\gamma_{\text{M}^{\text{d}}}/\gamma_{\text{S}^{\text{d}}})^{1/2} \quad [6]$$

From the definition, photoresist patterns are expected to stick to the photomask when f^{dry} exceeds unity. This premise is completely confirmed by the results shown in Fig. 5. Here, the negative photoresist OMR 83, the commercial product of Tokyo Ohka, was also tested in addition to positive AZ1350J. The fact that the above results fit for both polymers, poly(*cis*-isoprene) and phenol-novolak, respectively, indicates the broad applicability of our adhesion model.

Yield comparison with and without SURCAS.—Accumulated defect densities are plotted against the number of photolithographic steps in Fig. 6. Two series of wafer inspection results on 30 and $15\ \text{mm}^2$ dies are shown as circles and squares, respectively.

Fig. 4. Photoresist patterns on a wafer before (a) and after (b) contact with photomask. White squares and letters are delineated in SiO_2 film of $1\ \mu\text{m}$ thickness, the remaining part is Si substrate.



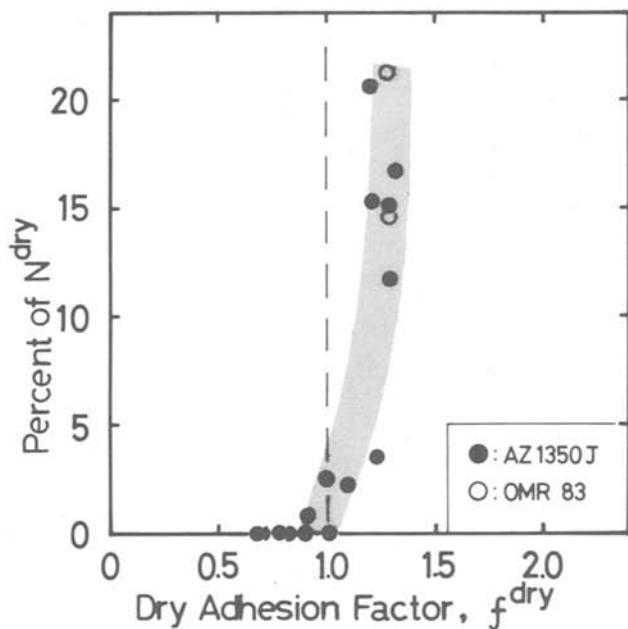


Fig. 5. Relationships between the number of stuck photoresist patterns, N^{dry} in percent, and dry adhesion factor f^{dry} .

The black and white symbols correspond to processes with and without SURCAS. Every defect density is normalized by die area for comparison.

A dramatic improvement in reducing defect density, almost to one-fourth at the final stage, is clearly apparent from this figure. In this wafer inspection, photoresist sticking is principally observed on the tops of the substrate steps as expected from the results of the dry adhesion test. It is also noteworthy that the remarkable increase during lithography steps 4 and 5 is mainly caused by dust introduced in the chemical vapor deposition process. Considering that patterning defects are affected by the various factors, dispersion in the inspected data within the same process is not unexpected.

The utility of contact printing using a positive photoresist combined with the SURCAS mask is demonstrated. The process enables delineation of ultrafine pattern down to $1\ \mu\text{m}$ at fairly low defect densities. Dust remains as main contributor to patterning defects.

Acknowledgments

The authors would like to express their appreciation to Kikuo Douta, Masahiko Tsujita, and Michie Morita

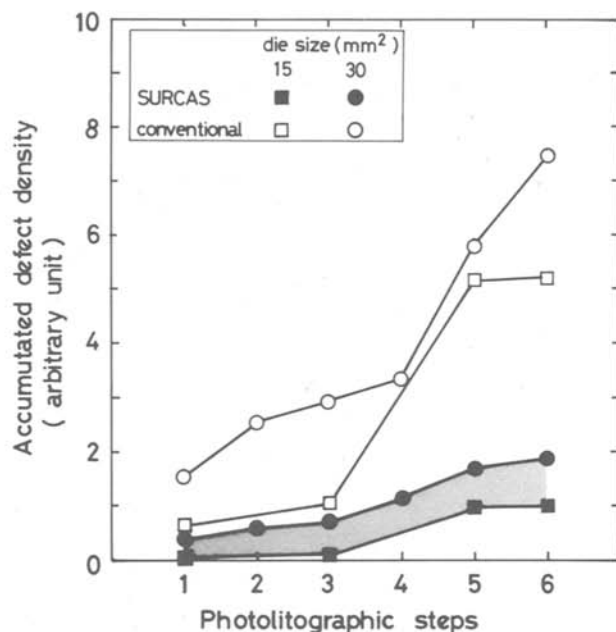


Fig. 6. Yield comparison with and without SURCAS inspected on 30 and 15 mm² dies.

for their assistance in wafer inspection. They are also deeply appreciative to Dr. Ichiro Miwa for his encouragement throughout this work.

Manuscript submitted May 1, 1979; revised manuscript received July 31, 1980.

Any discussion of this paper will appear in a Discussion Section to be published in the December 1981 JOURNAL. All discussions for the December 1981 Discussion Section should be submitted by Aug. 1, 1981.

Publication costs of this article were assisted by Hitachi Limited.

REFERENCES

1. D. L. Flowers, *This Journal*, **124**, 1608 (1977).
2. C. A. Deckert and D. A. Peters, in "Proceedings of Kodak Microelectronics Seminar," p. 14, Interface '77 (1977).
3. H. Yanazawa, T. Matsuzawa, and N. Hashimoto, in "Proceedings of Kodak Microelectronics Seminar," p. 153, Interface '77 (1977).
4. H. Yanazawa, H. Utsugi, N. Hashimoto, and M. Ashikawa, *Jpn. J. Appl. Phys. Suppl. No. 2, Part 1*, 753 (1974).
5. F. M. Fowkes, *Ind. Eng. Chem.*, **56**, 40 (1964).

Heavy Ion Nuclear Tracks—An Emerging Technology

R. Spohr

Gesellschaft für Schwerionenforschung mbH, D-6100 Darmstadt 11, Germany

ABSTRACT

Nuclear tracks are a logical extrapolation of the principles of cloud and bubble chamber onto solids. Besides their well-known application in particle detection, in solids a completely new aspect arises, the generation of extremely fine permanent tracks, which can be transformed into open channels. Nuclear tracks are therefore a unique single-particle structuring tool. Applications comprise (i) single hole membranes for particle counting and sizing, (ii) manufacture of microfilters with very uniform hole sizes, (iii) modification of magneto-optic materials for application in display memories, and (iv) micro-machining of surfaces.

One measure for the rapid pace of technological advancement is the steady refinement of our machining tools. If we extrapolate the existing trend from mechanical machining to particle beam scribing, a single particle technique appears as the ultimate approach for the shaping and machining of solid surfaces. The nuclear track technique (1) is actually such a tool, now at the verge of being applied in practice. In contrast to photon and electron lithography, in which only the interaction of many particles is capable of generating a permanent material change, in the track process the information on number, nuclear charge, energy, and direction of single particles is maintained. Nuclear tracks are thus capable to produce holes of uniform size, length, and angle of inclination. Beyond the production of discrete holes, the technique in a more general sense can be applied for the shaping of almost any material, either directly or using replica techniques.

One necessary requirement for a systematic study of nuclear tracks as a single-particle microstructuring tool has been the advent of powerful heavy ion accelerators. Such a facility is the accelerator UNILAC (2) at GSI Darmstadt. At GSI nuclear tracks can be generated with defined beam isotope, areal dose, range, and angle of incidence in virtually any material (3). In the following, four starting points for a practical utilization of tracks in technology are described.

Single Hole Membranes

In medical diagnostics the characterization and sorting of single living cells steadily gains in importance. This field is now established under the name "flow cytometry and sorting." Its goal of identifying individual cells is achieved using a capillary that reduces the observed volume to a fine cylinder containing only one cell at a time. The passage of a cell through this cylinder is registered either optically or electrically. Up to now, cell counters and sorters with capillaries down to about 10 μm have been used, whereby typical values, however, ranged around 100 μm .

In 1977, it became possible for the first time to generate at will a single nuclear track at a specified site of an elsewhere completely virgin solid body (4). This method for convenient production of single hole membranes developed at GSI works as follows.

The ion beam is defocused to a width, so that on the average only very few particles pass through a small beam-defining aperture per second. Once an ion has passed the aperture it penetrates through the track-sensitive virgin foil and is registered in an electronic particle detector. As soon as it is registered, the accelerator beam is shut off. Through etching of the foil a single hole is obtained which corresponds to the passage of exactly one single particle (cf. Fig. 1). Using a target inlet system for rapid replacement of the irradiated foil by a virgin foil, in this way a considerable

number of single hole membranes for test purposes has been generated at GSI.

The nuclear track technique enables the manufacture of channels as small as 10 nm and as large as 100 μm in diameter, controlled by the time of development. Foils more than 100 μm thick have been perforated up to now at GSI. The actual shape of the etched channel is defined by the sensitivity of the material, given by the ratio of track etching to general (bulk) etching v_t/v_g at a given specific energy loss $\Delta E/\Delta x$ of the penetrating ion. Track etching v_t can be more than thousand times faster than general etching v_g . This enables the manufacture of almost cylindrical cones which for prolonged etching transform into cylinders.

In blood rheology single hole membranes of 5 μm hole diam have been successfully applied for rigidity measurements of individual red blood cells (approximate diameter 8 μm) (4-6). Observed parameter is the passage time of the red blood cell, defined by the plastic deformation of the cell membrane from an oblate to a prolate shape. At present, GSI is the only facility capable of manufacturing single hole membranes with diameters smaller than 10 μm in membranes of sufficient thickness. This unique single particle application clarifies the concept of the nuclear track technique as a single-particle structuring tool.

Microfilters

Conventional filter materials as fibrous felts or open-porous foams are defined in their properties by several

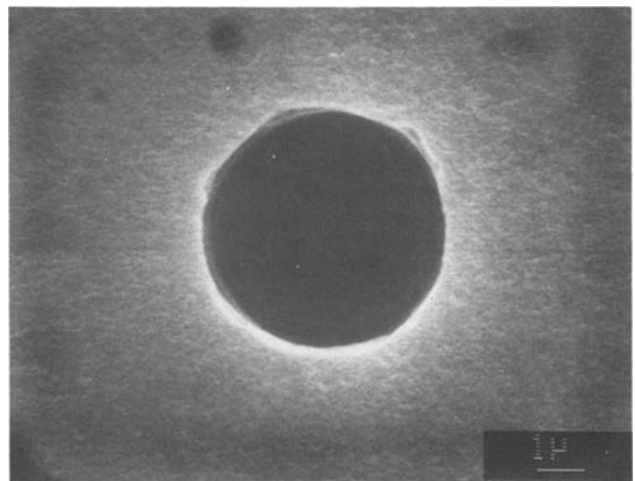


Fig. 1. Single hole for use in single hole cell counting apparatus (4-6). Hole diameter 5.0 μm , hole length 45 μm . Material: 50 μm thick Hostaphan BN 50 (Kalle, Wiesbaden, FRG). Irradiation: One single ^{136}Xe ion of 4.7 MeV/nucleon. Development: 70 min in 1/3 6n NaOH + 1/3 H_2O + 1/3 methanol at 40°C. Observation: Scanning electron microscope.

Key words: heavy ions, nuclear tracks, lithography, microfilters.

parameters, which are from each other dependent, parameters as temperature, concentration of various ingredients, and environmental factors. Particles suspended in the liquid are following intricate paths within the filter and finally are retained in the volume of the filter. The filter transmission function is broad and not well suited for classification of microscopic particles.

In contrast hereto, nuclear track filters (Fig. 2) are determined by very few parameters, which are practically independent from each other and can be precisely adapted to the required transmission properties of the filter (7): (i) each individual ion generates exactly one nuclear track, therefore, it is easy to adjust the throughput conductivity of the filter which is proportional to the number of holes; (ii) hole diameter increases linearly with the time of development, therefore, it is easy to adapt the hole size to the actual critical particle size; and finally, (iii) hole length corresponds to the thickness of the irradiated foil. Therefore, the total filter selectivity corresponds directly to the selectivity of the single hole.

Due to the statistical distribution of the original nuclear tracks on the filter surface, multiple holes of larger cross section occur. This leads to a mutual dependence of two of the originally independent parameters: hole size and areal density of tracks. The influence of multiple holes on filter properties has been investigated in computer simulation using square holes (8) and compared with image analysis of etched nuclear tracks in mica (9). An upper limit for the transmission of particles of given size is given by the "areal transmission function" T_s (Fig. 3). Only at very high "nominal porosity" P (defined as the product of areal track density, N , and single hole area, S_1), uncommon to conventional filters, the influence of multiple holes on transmission properties becomes important. For thick filters this influence can be minimized using irradiations under different angles.

Nuclear track filters using fission fragments from a nuclear reactor have been available since 1972.¹ This has been the first example of a commercial use of single atomic particles as a structuring tool. At GSI, heavy ions up to ten times the range of fission fragments are available at present, making possible nuclear track filters with a hundredfold increased mechanical strength. In addition, the applied ion beam technology

¹ Nuclepore Corporation, Pleasanton, California 94566.

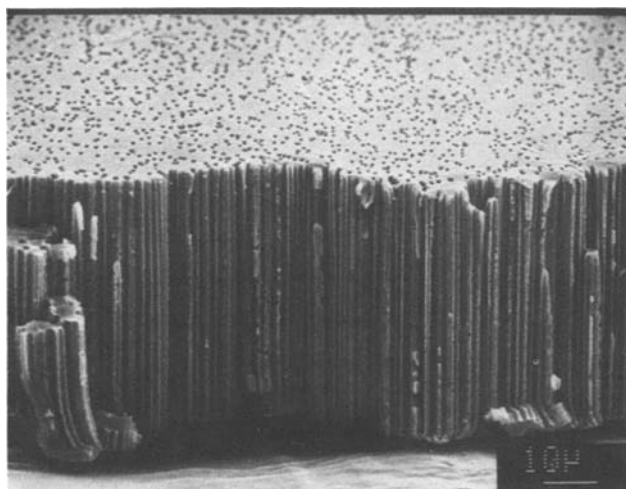


Fig. 2. Nuclear track filter manufactured with high energy heavy ions. Hole diameter $0.7 \mu\text{m}$, hole length $49 \mu\text{m}$. Material: $50 \mu\text{m}$ thick Hostaphan BN 50 (Kalle, Wiesbaden, FRG). Irradiation: $1.6 \times 10^7 \text{ cm}^{-2}$ ^{136}Xe ions of 4.7 MeV/nucleon . Development: $42 \text{ hr } 99\% \text{ In NaOH} + 1\% \text{ Tickopur R33}$ (Brinkmann Instrumentenbau GmbH, Mannheim, FRG) at 40°C . Observation: scanning electron microscope.

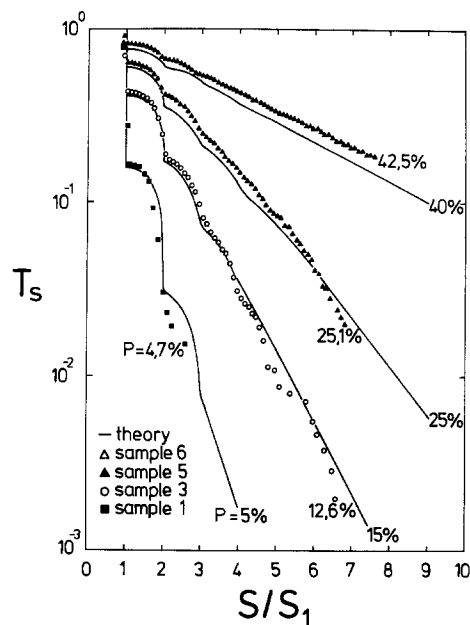


Fig. 3. Areal transmission function T_s , defined as fraction of holes with larger area than S , representing an upper limit for the actual transmission function. Points: image analysis (9). Lines: computer simulation (8).

enables the manufacture of almost parallel hole arrays (cf. Fig. 2).

Magneto-Optic Garnets

Iron garnets are a group of materials that were originally conceived and developed for use in bubble memories, where high domain wall mobility is a prerequisite. More recently, Philips Research Laboratory in Hamburg became interested in applying the same group of materials as an optical storage. In order to avoid cross-talk between neighboring storage cells, the magneto-optically active iron garnet film was subdivided into a regular array of discrete islands, each island representing a logical "1" or a "0", depending on its magnetization.

Another way to obtain a stable optical memory from the original high mobility garnet material was opened by heavy ion irradiation of an otherwise unstructured iron garnet film. Thereby, nuclear tracks act as very efficient pinning centers (Fig. 4), drastically reducing the originally high domain wall mobility by more than

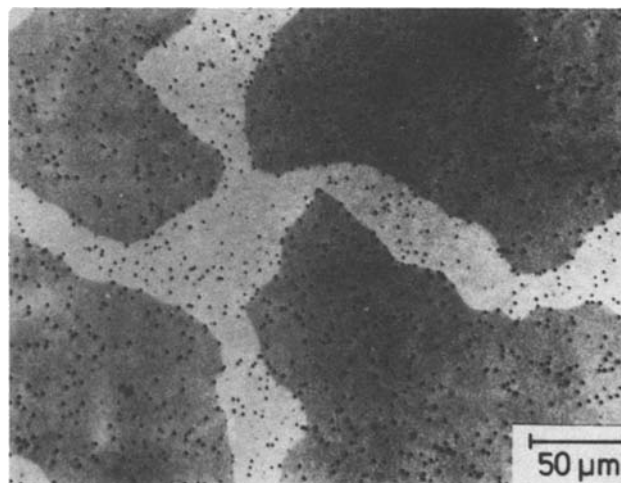


Fig. 4. Pinning of magnetic domain walls by etched nuclear tracks. Material: epitaxial $(\text{Gd}, \text{Bi})_3(\text{Fe}, \text{Ga})_5\text{O}_{12}$ garnet film. Irradiation: $3 \times 10^6 \text{ cm}^{-2}$ Xe ions of 1.4 MeV/nucleon . Development: $3 \text{ hr } 1/3 \text{ HNO}_3 + 1/3 \text{ CH}_3\text{COOH} + 1/3 \text{ H}_2\text{O}$ at 80°C . Observation: light microscope, Faraday contrast using polarized light.

a factor 100 (10-14). The pinning effect resides in the interaction of magnetically deactivated latent tracks with the domain walls, whereby each trapping process dissipates wall energy in the form of heat. Thus, on the average, the coercivity of domain wall movement is increased. Irradiated films can therefore carry much finer domain pattern than virgin films. Information densities of several hundred kilobits per cm^2 have been achieved up to now. An important aspect of such a modified magneto-optic storage material is that, due to the high optical contrast, memory and display can be realized in one and the same device. This reduces unnecessary shuffling back and forth of information between memory and display in a computer application.

Heavy Ion Lithography

In solid-state technology more and more components have to be compressed onto smaller and smaller areas. Maintaining simultaneously critical cross sections of conductors becomes a major problem in planar technology using light, u.v., x-rays, or electrons. Thereby, high lateral resolution is no longer a sufficient condition. Much more stress has to be placed on obtaining better control over depth profiling. Great efforts are undertaken, using, e.g., multiple layers of materials, to enlarge the planar technology concept into depth. However, any further progress will depend very essentially on the capability of the applied technique to generate a laterally well-defined activated zone that extends down to the desired depth.

For this purpose, heavy ion nuclear tracks appear to be an almost ideally suited tool (15, 16). In contrast to other techniques using photons or electrons, heavy particles possess a momentum and energy concentration that is several orders of magnitude higher. Only heavy particles are subject to a quasi-continuous energy loss on their trajectory and thus, come to a hold at a nicely defined depth. Range straggling of individual heavy ions can be of the order of only a few percent. In contrast hereto, for photons and electrons an equivalent term for "range" can only be defined rather arbitrarily as a gross property of many particles, via the exponential law of extinction. Every individual heavy ion thus creates a submicron size pencil of sensitized resist along its path, that can be used as a resolution element. The diameter of the latent track is around 10 nm which can be considered as the ultimate resolution limit (present experimental resolution limit is around 50 nm). Individual particle beam scribing may attain this ultimate limit in the future.

At GSI, a shadow casting technique (15, 16) has been developed, using low energy heavy ions from a 300 kV accelerator. Figure 5 shows the obtained deep structures with steep edges and a smooth bottom. Negligible mask scattering is observed in this micrograph. Also, due to the much smaller radiation damage in metals (higher atomic mobility) it should be possible to make many replicas of one metal mask in this way. Sputtering thereby should be a negligible effect, due to the small dose accumulated over many exposures. In the case of Fig. 5 the resist layer was thicker than the ion range. Even prolonged etching showed no measurable influence on structuring depth in this experiment. This proves the capability of the applied technique to sensitize a defined volume down to a well-defined depth. Depth resolution of the order of a few percent should be possible. In many cases a more precise definition may be achieved by termination of the etch attack, in a track or etch insensitive buried layer or substrate.

Application of heavy particles to lithography has another inherent advantage over x-rays and electrons. Due to the very high specific energy loss of heavy ions in solid matter (often more than 10 keV/nm) not only conventional resist materials can be sensitized but equally well an almost unlimited number of different materials. For example, the resist coating step in

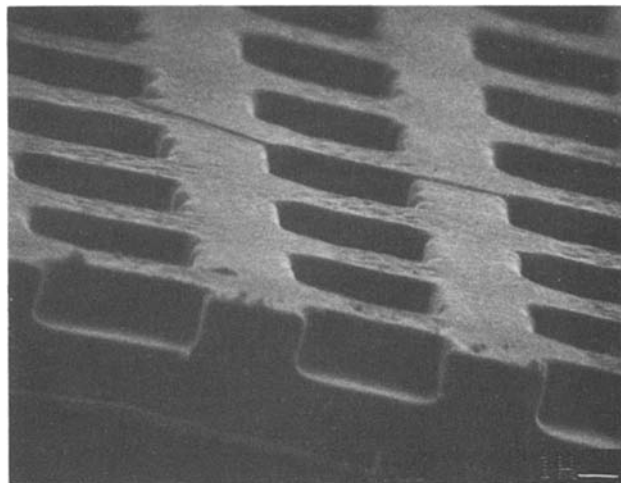


Fig. 5. Heavy ion lithogram of metal mask (courtesy P. Tischer, Siemens AG, Munich, Germany) inscribed into high resolution photoresist. Material: polymethyl methacrylate (PMMA) layer on silicon substrate (courtesy P. Tischer, Siemens AG, Munich, Germany). Irradiation: 3×10^{12} argon ions per cm^2 at 720 keV particle energy. Distance between metal mask and photoresist was approximately 1 mm. Development: 10 min methyl isobutyl keton plus isopropanol 1:3. Observation: scanning electron micrograph of cross section.

silicon technology can be replaced by a much simpler oxidizing step leading to a "resist" (passivation) layer of much better defined thickness. Even pure silicon can be track-sensitized using heavy ion irradiation and transforming the inscribed information into structure during a later selective etching process (Fig. 6). In this case, however, range and lateral resolution are dominated by nuclear stopping, yielding a quite rough bottom of the etched troughs due to multiple scattering and recoils atoms.

A final virtue of heavy ions as a structuring tool in comparison to x-ray sources resides in the existence of very bright ion sources. Parallel heavy ion beams of high intensity can be achieved using conventional ion optical systems. Heavy ion lithography can be directly applied to small accelerators and low energy implanters. At 1 mA beam current a sample throughput of $1 \text{ m}^2/\text{sec}$ can be achieved.

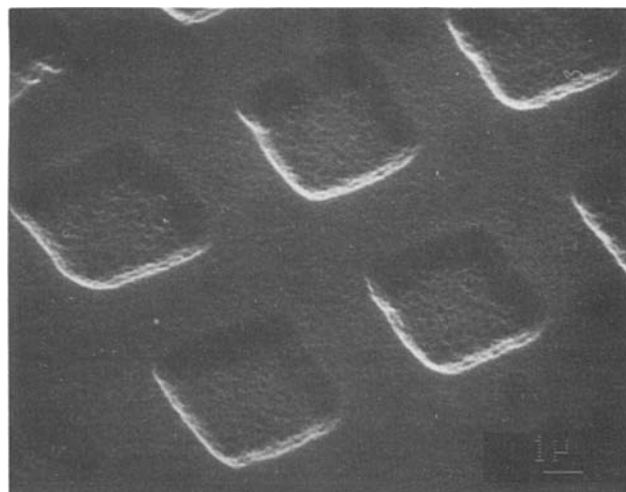


Fig. 6. Bare silicon—a resist material for heavy ion lithography. Mask (courtesy P. Tischer, Siemens AG, Munich, Germany): self-supporting metal mask. Resist (courtesy P. Tischer, Siemens AG, Munich, Germany): bare silicon, (111) orientation. Irradiation: 7×10^{13} argon ions per cm^2 720 keV particle energy. The distance between the mask and the silicon was approximately 1 mm. Development: 10 sec Sirtl etch ($\text{CrO}_3\text{-HF-H}_2\text{O}$), a dislocation sensitive etching medium. Observation: scanning electron microscopy.

Manuscript submitted March 24, 1980; revised manuscript received July 31, 1980.

Any discussion of this paper will appear in a Discussion Section to be published in the December 1981 JOURNAL. All discussions for the December 1981 Discussion Section should be submitted by Aug. 1, 1981.

Publication costs of this article were assisted by Gesellschaft für Schwerionenforschung mbH.

REFERENCES

1. R. L. Fleischer, P. B. Price, and R. M. Walker, "Nuclear Tracks in Solids. Principles and Applications," Univ. of Calif. Press, Berkeley (1975).
2. N. Angert and C. Schmelzer, *Kerntechnik*, **19**, 57 (1977).
3. R. Spohr, *Nucl. Tracks*, **4**, 101 (1980).
4. H. Kieseewetter, K. Mussler, H. Schmid-Schönbein, B. Genswürger, and R. Spohr, "Messung der Verformbarkeit roter Blutzellen mit Hilfe einer Einlochmembran," GSI Annual Report 1977, p. 141.
5. H. Kieseewetter, K. Mussler, P. Teitel, U. Dauer, H. Schmid-Schönbein, and R. Spohr, "New Methods for the Measurement of Red Cell Deformation Ability," Symposium on Blood Rheology, Glasgow, Sept. 27-28, 1979.
6. H. Kieseewetter, U. Dauer, K. Mussler, H. Schmid-Schönbein, and R. Spohr, "Rigidity Measurements in Individual Red Cells," Hemorheology et Pathologie Symposium European, Nancy, Oct. 1979.
7. C. Riedel and R. Spohr, *Ber. Bunsenges. Phys. Chem.*, **83**, 1165 (1979).
8. C. Riedel and R. Spohr, *Radiat. Eff.*, **42**, 69 (1979).
9. C. Riedel and R. Spohr, *ibid.*, **46**, 23 (1980).
10. J.-P. Krumme, I. Bartels, B. Strocka, K. Witter, C. Schmelzer, and R. Spohr, *J. Appl. Phys.*, **48**, 5191 (1977).
11. H. Heitmann, C. Fritzsche, P. Hansen, J.-P. Krumme, R. Spohr, and K. Witter, *J. Magn. Magn. Mater.*, **7**, 40 (1978).
12. P. Hansen and H. Heitmann, *Phys. Rev. Lett.*, **43**, 1444 (1979).
13. H. Heitmann, P. Hansen, K. Witter, and R. Spohr, *J. Magn. Magn. Mater.*, **10**, 97 (1979).
14. B. Strocka, G. Bartels, and R. Spohr, *Appl. Phys.*, **21**, 141 (1980).
15. B. E. Fischer and R. Spohr, *Nucl. Instr. Meth.*, **168**, 241 (1980).
16. B. E. Fischer and R. Spohr, "Heavy Ion Lithography," Contribution to "Microcircuit Engineering '79 — Microstructure Fabrication," Sept. 25-27, 1979, RWTH Aachen; Proceedings: Inst. of Semiconductor Electronics, pp. 349-357 (1979).

Auger Electron Spectroscopic Study of Oxidation of Zirconium

Gopala N. Krishnan, Bernard J. Wood, and Daniel Cubicciotti*¹

SRI International, Menlo Park, California 94025

ABSTRACT

The uptake of oxygen on the surface of an initially clean zirconium crystal was observed by means of Auger electron spectroscopy (AES). This technique permitted measurement of both rate of growth of surface oxygen and the chemical state of the oxygen. Experiments were performed in the temperature range 773-1008 K with oxygen pressures from 1.9×10^{-4} to 7.2×10^{-3} Pa. Under these conditions, the rate of diffusion of oxygen into the metal bulk becomes significant and determines the extent of the chemisorption regime. At the higher temperatures, the chemisorption regime extends to long exposure periods, whereas at the lower temperature, an oxide is rapidly formed. The observed linear rate of oxygen uptake after the appearance of the surface oxide may be caused by oxygen diffusing through an oxide layer of constant thickness and subsequently dissolving in the bulk metal underneath. This oxide layer is estimated to be about 1 nm thick.

In recent studies (1-3) of the reaction of zirconium with oxygen at low pressures (10^{-4} - 10^{-1} Pa)² and at elevated temperatures ($T > 775$ K), it was demonstrated that the oxygen uptake rate follows a linear rate law for a substantial length of time. After extended periods of exposure, especially at higher pressures, when there has been ample opportunity for the formation of an oxide scale layer, oxygen uptake can be described by a parabolic rate law. Previous investigators have hypothesized that, in the linear rate regime, oxygen uptake is controlled either by arrival rate of oxygen molecules to the surface or by diffusion of oxygen adspecies through a "thin layer" of oxide on the surface (2). However, no quantitative information is available on the nature of the rate of formation, or the thickness of such an oxide layer. Auger electron spectroscopy (AES) was used to characterize the initial stages of oxidation of zirconium under clean surface, ultrahigh vacuum conditions. For applications where the oxygen gettering quality of zirconium is of interest, the results of this study will permit one to define the conditions of temperature and oxygen pressure that

favor bulk dissolution of oxygen in contrast to oxide film (scale) formation.

Experimental Program

Approach.—The use of AES to study initial stages of gas-metal interactions has been well documented (4). In this technique, the emission of Auger electrons is stimulated by the bombardment of the specimen with a high energy (3 kV) electron beam. The emitted Auger electrons are energy analyzed to provide a spectrum of peaks whose positions on the energy scale identify the elemental components on the specimen surface. AES is a highly surface-selective analytical technique because of the limited escape depths of Auger electrons. For electron energies ranging from 50 to 500 eV, the range of interest in this study, the escape depth of electrons varies between 0.5 to 1 nm (5), which is equivalent to two to four atomic layers; hence, components in the bulk metal below this depth will not be detected by AES.

The concentration of a particular elemental component in the near-surface atomic layers of a specimen determines the amplitudes of the peaks in its Auger spectrum. But the proportionality factor relating concentration to peak amplitude, frequently referred to as the Auger yield, is a complex quantity that cannot be precisely evaluated from first principles (4). However,

* Electrochemical Society Active Member.

¹ Present address: Electric Power Research Institute, Palo Alto, California 94304.

² 1 Pa $\cong 1 \times 10^{-5}$ atm $\cong 7.5 \times 10^{-3}$ Torr.

Key words: chemisorption, kinetics, metals.

changes in concentration of a component can be followed with good precision by measuring the growth or decay of an Auger peak. Thus, we observed the adsorption of oxygen on the zirconium surface by measuring the amplitude of the oxygen Auger peak at 510 eV.

Apparatus and materials.—All experiments were conducted in an ultrahigh vacuum system capable of attaining 10^{-8} Pa base pressure. The AES analyses were performed with a Varian cylindrical mirror analyzer with an integral electron gun. The incident electron beam was ~ 100 μm in diameter at the specimen, and it was normally operated at 3000 eV and 5 μA . The total pressure in the system was measured with an ionization gauge, and the partial pressures of gaseous components were determined with a quadrupole mass spectrometer. A rastered, 3 keV argon gun was used to clean the specimen surface. The arrangement of the various components with respect to the specimen is shown in Fig. 1.

Measurements were made on a "Marz grade" zirconium crystal, containing ~ 100 ppm oxygen impurity obtained from Materials Research Corporation. This specimen was a disk, spark cut from a 0.63 cm diam rod that was nominally a single crystal. However, x-ray diffraction and metallographic observations revealed that the rod consisted of several large grains. After sequential mechanical and chemical polishing, seven large grains could be delineated on the face of the 1 mm thick specimen; thus, the average diameter of each grain was about 250 times greater than the AES electron beam diameter. To avoid problems associated with grain boundary impurities of oxygen transport the AES beam was focused onto the center of a large grain. The specimen was heated by radiation from a tungsten filament situated beneath it (Fig. 1), and the average temperature was measured with an iron-constantan thermocouple spot-welded to the edge of the disk.

Oxygen (Linde UHP grade, 99.99% O_2) was admitted to the vacuum chamber through a calibrated stainless steel capillary tube (75 cm long by 0.017 cm ID). The mass flow rate of gas into the chamber could be precisely controlled and measured, independent of the pressure in the chamber, by adjusting the oxygen pressure at the upstream end of the capillary tube. The downstream (outlet) end of the capillary tube pointed at the specimen surface from a distance of about 0.2 cm. On the basis of mass spectroscopic measurements of mass flux as a function of radial distance from the center line of the capillary tube, it was estimated that about 70% of the gas molecules emanating from the tube impinged on the specimen surface.

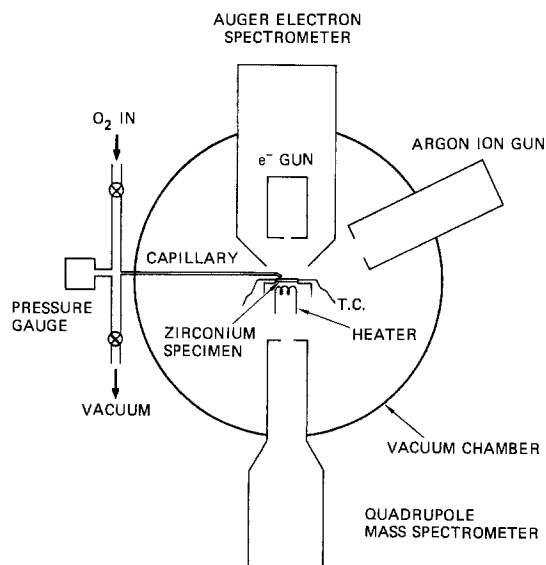


Fig. 1. Schematic diagram of apparatus

Procedure.—The only detectable impurity on the zirconium crystal surface following cleaning by argon ion bombardment at 1000 K was a trace of oxygen. In the vacuum chamber at 10^{-7} Pa, the surface of the specimen remained clean indefinitely at temperatures above 900 K. At lower temperatures, oxygen accumulated on the surface. The observed rate of accumulation was too fast to be due to adsorption from the gaseous environment in the vacuum chamber ($P_{\text{O}_2} \approx 10^{-9}$ Pa); hence, it was concluded that dissolved oxygen diffused from the bulk to the surface while the crystal was cooling.

Due to the relatively massive size of the crystal and its poor thermal contact with any heat sink, the specimen could not be quenched from a high temperature to give an oxygen-free surface at temperatures less than 750 K. Consequently, oxygen uptake rate measurements on the zirconium crystal were made only at temperature in the range 750-1050 K.

After the specimens were cleaned by Argon ion bombardment at 1000 K, the temperature was shifted to the desired level for the experiment by adjusting the power input to the heater. When the specimen temperature became stable (typically within 120 sec), the capillary inlet valve was opened enough to establish a steady flow of oxygen at a desired level. An equivalent, average, steady-state pressure, P_{O_2} , of oxygen at the specimen surface was calculated from the known mass flow rate, \dot{m} , of oxygen through the capillary tube using the following equation derived from the kinetic theory of gases (6)

$$\alpha \dot{m}/A = P_{\text{O}_2} \bar{c}/4RT$$

where \bar{c} is the mean molecular velocity at the gas temperature, T , R is the gas constant, A is the exposed geometric surface area of the specimen, and α is the fraction of incoming molecules that strike the specimen. Oxygen flux distribution as a function of lateral position of a specimen with respect to the nozzle was measured with the mass spectrometer using a movable aperture. From this measurement the fraction, α , was found to be 0.7 for our specimen geometry. Specimen temperatures and oxygen pressures used in these experiments are summarized in Table I.

Auger spectra over the energy range 60-560 eV were recorded every 30 sec on an oscillographic chart recorder (Beckman Dynograph, Type RS). Rate data were obtained from this chart by measuring the AES peak height as a function of elapsed time. At longer intervals, the Auger spectrum of the specimen surface was recorded more slowly in order to obtain higher resolution of the Auger peaks.

Results

Auger spectra.—The observed peaks in our experimental study are associated with particular Auger transitions (7) as shown in Table II. Figure 2 is a representative sequence of Auger spectra obtained during exposure of a specimen to oxygen at a constant temperature. Besides the obvious increase in the oxygen peak (510 eV) height, there are other features to be noted. The three zirconium peaks that involve valence band electrons (127, 147, and 175 eV) decrease in amplitude with increasing oxygen coverage. At some point during oxygen exposure, a new zirconium Auger peak appears and begins to grow in height. This peak

Table I. Summary of experimental conditions

| Specimen temperature (K) | O_2 flow rate (molec $\text{sec}^{-1} \times 10^{-14}$) | Equivalent O_2 pressure, P (Pa $\times 10^3$) | Maximum exposure duration (sec) |
|--------------------------|---|---|---------------------------------|
| 773 | 9.3 | 1.0 | 900 |
| 853 | 10.2 | 0.97 | 1100 |
| 933 | 6.4 | 0.57 | 2500 |
| 933 | 64 | 7.2 | 2500 |
| 963 | 33 | 2.7 | 2000 |
| 1008 | 40 | 3.6 | 3000 |

Table II. Auger electron energies in Zr-O₂ system

| Element | Transition* | Auger energy in | |
|---------|--|-----------------|------------|
| | | Metal | Oxide film |
| Zr | M ₅ N ₁ N _{2,3} | 92 | 88 |
| | M ₅ N _{2,3} N _{2,3} | 117 | 113 |
| | M ₄ N ₅ V | 127 | 120 |
| | M ₄ N _{2,3} N _{4,5} | 147 | 140 |
| | M ₅ N _{4,5} N _{4,5} | 175 | 167 |
| O† | K L ₁ L ₁ | — | 475 |
| | K L ₁ L ₂ | — | 490 |
| | K L ₂ L ₂ | — | 510 |

* Reference (7).

† No line shift was observed for the oxygen lines.

can be interpreted as a 7 eV shift to lower energy of the 147 eV peak. Similar shifts appear for the 175 and 127 eV peaks. Such peak shifts are indicative of a change in the chemical state of the zirconium atoms in the specimen surface region. Similar Auger peak shifts during oxide formation have been reported in the case of nickel (8), silicon (9), molybdenum (10), iron (11), and aluminum (12).

In contrast to this behavior, the Auger peaks (92 and 117 eV) arising exclusively from core level transitions are less profoundly affected by oxygen uptake. These peaks exhibit a modest shift of about 4 eV during oxide formation. This smaller shift attests to the fact that the core level electrons are less affected than the valence level electrons by the chemical environment.

More interestingly, the amplitudes of the core level Auger transition peaks (92 and 117 eV) do not change appreciably during oxygen uptake. In fact, within the precision of our experimental measurements, the 92 eV peak showed little change during the entire range of oxygen coverage studied in this investigation. This insensitivity of the zirconium core level peaks to the presence of oxygen was confirmed by obtaining an Auger spectrum of ZrO₂. In the oxide, the peaks involving valence band electrons are attenuated considerably relative to the peaks involving core levels only. Thus the ratio of Zr(M₅N₁N_{2,3})/Zr(M₄N_{2,3}N_{4,5}) is 0.17 in the pure metal and ~ 1 in the oxide.

Surface oxygen growth.—Figure 3 illustrates the surface oxygen coverage on Zr crystal as a function of oxygen exposure. Note that the surface coverage at 933 K is independent of oxygen pressure when the coverage is plotted as a function of oxygen exposure. Since exposure is defined as the product of oxygen pressure and exposure time, the above observation indicates that the surface coverage is linearly proportional to the oxygen pressure.

The variation in surface oxygen coverage on the zirconium specimens is displayed as a function of oxygen exposure and of temperature in Fig. 3. The abscissa of Fig. 3 is expanded in Fig. 4 to resolve the shape of

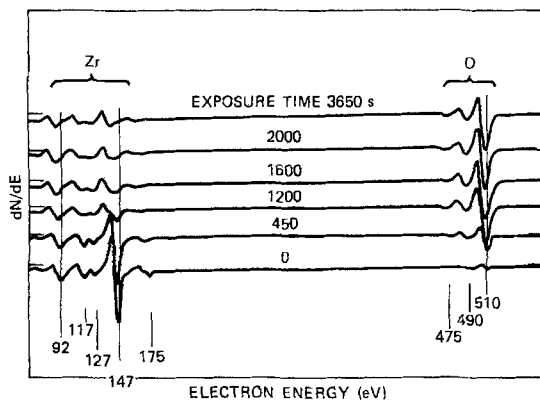


Fig. 2. Changes in Auger spectra of zirconium crystal during exposure to oxygen. $T_{Zr} = 963$ K. $P_{O_2} = 2.5 \times 10^{-3}$ Pa.

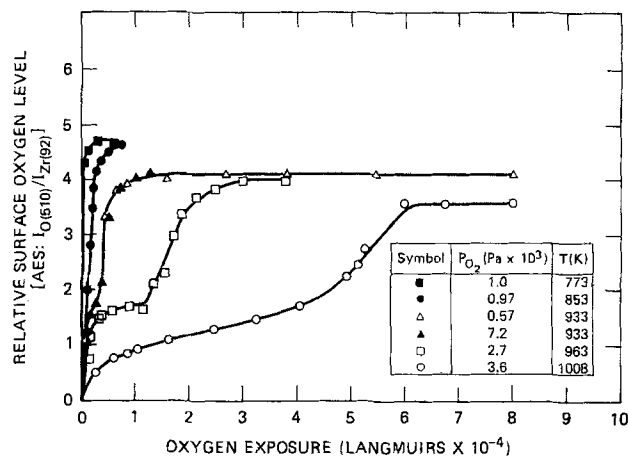


Fig. 3. Oxygen uptake on zirconium crystal as a function of temperature and oxygen exposure. (1 Langmuir = 1.33×10^{-4} Pa · sec.)

the curves at small values of exposure. Since the Zr (92 eV) peak height is shown to be insensitive to the presence of oxygen, we have used it as a normalizing factor to compensate for changes in incident electron beam current, electron multiplier gain, and the like.

The surface oxygen uptake curves indicate four distinct sequential stages in the accumulation of oxygen on the zirconium surface: stage 1, an initial period of rapid oxygen accumulation; stage 2, a region of slow increase in oxygen level; stage 3, a second period of further rapid oxygen accumulation; and stage 4, a constant coverage region. The rate at which oxygen accumulates on the surface decreases with increasing temperatures during stages 1 and 3. Stage 2, the slow growth regime, appears to be of negligible duration at 773 K but extends to longer exposure periods at higher temperatures. The final steady-state level of surface coverage attained on the crystal specimen in stage 4 reaches a lower value as the temperature of the specimen increases.

During stage 3, energy shifts in the zirconium AES peaks are observed, indicating the beginning of chemical changes on the surface. As mentioned earlier, these peak shifts are likely due to the formation and growth of a condensed phase of a zirconium oxide. Hence, the uptake of oxygen by a zirconium surface appears to be a sequential process in which initial chemisorption is followed by nucleation and growth

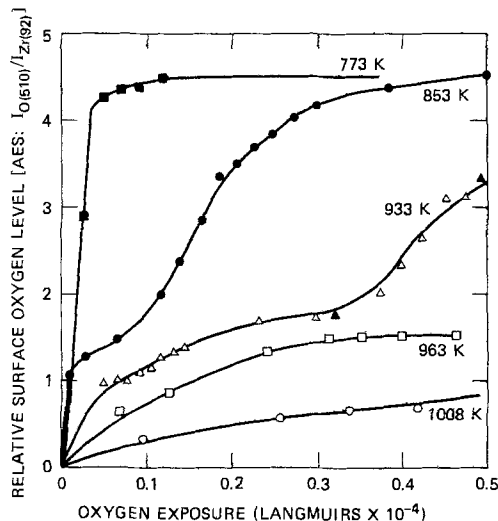


Fig. 4. Oxygen uptake on zirconium crystal as a function of temperature and oxygen exposure, expanded scale. See legend in Fig. 3 for symbols.

of an oxide phase. The experimental curves indicate that formation of the oxide phase is favored by lower temperatures and by higher oxygen pressures. Conversely, the chemisorption regime is extended at higher temperatures and at lower oxygen pressures.

Mass spectrometric measurements.—The residual oxygen partial pressure in the specimen chamber was monitored concurrently with the AES measurements. Entering oxygen molecules that do not adsorb or react irreversibly on the zirconium specimen surface are pumped out of the chamber. Thus a mass balance in oxygen is described by the following equation

$$r_{Zr} = \dot{m} - SP_{O_2}$$

where \dot{m} is the mass flow rate of oxygen into the chamber through the capillary tube, r_{Zr} is the rate of oxygen uptake by the zirconium specimen, and S is the pumping speed of the vacuum system for oxygen. In our experiments, \dot{m} is calculated from the observed pressure at the inlet of the capillary tube, the measured conductance of the tube, and P_{O_2} , which is monitored by the mass spectrometer. Thus, if S is known, values for r_{Zr} can be calculated. Pumping speed was evaluated by measuring the steady-state oxygen partial pressure in the chamber with the zirconium specimen absent, over a range of values of \dot{m} . The pumping speed was found to vary from 600 liters sec^{-1} at $\dot{m} = 2.7 \times 10^{-2}$ Pa liters sec^{-1} to 900 liters sec^{-1} at $\dot{m} = 4 \times 10^{-3}$ Pa liters sec^{-1} . The precision of this measurement was relatively poor because S exhibited some dependence on the chamber pressure and also on the immediate history of the system (it increased, for example, when titanium was freshly deposited in the sublimation pump). However, over most of the range of pressure variation observed in one kinetic experiment, the pumping speed was found to be reasonably constant ($\pm 25\%$).

The curves shown in Fig. 5 illustrate the change in oxygen pressure that occurs during exposure of the zirconium specimen to a constant flux of the gas. The scale on the abscissa in Fig. 5 is identical to that in Fig. 3, so that changes in P_{O_2} can be compared directly with the amount of oxygen observed on the crystal surface by AES. The oxygen partial pressure in the chamber increases monotonically with increasing exposure until it reaches a steady-state value (Fig. 5). There is no discontinuity in the rate of in-

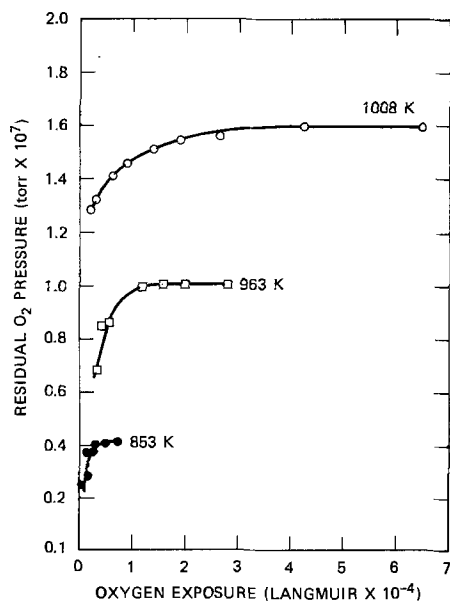


Fig. 5. Variation of P_{O_2} as a function of oxygen exposure at various temperatures.

crease of oxygen pressure corresponding to the first plateau in the rate of growth of oxygen on the zirconium surface (compare the respective curves in Fig. 3 and 5). This observation, that r_{Zr} exhibits a finite value in a region where the oxygen surface coverage is nearly constant, indicates that oxygen must be diffusing into the crystal as rapidly as it chemisorbs. At longer exposures, both surface coverage and P_{O_2} become constant. Based on the estimated values of S and the measured values of P_{O_2} , oxygen is still diffusing into the zirconium crystal but at a much lower rate. The steady-state rate of oxygen uptake was estimated to vary from $0.7 \pm 0.3 \times 10^{20}$ molec $\text{cm}^{-2} \text{sec}^{-1} \text{Torr}^{-1}$ at 930 K to $1.6 \pm 0.3 \times 10^{20}$ molec $\text{cm}^{-2} \text{sec}^{-1} \text{Torr}^{-1}$ at 1050 K with an apparent activation energy of $+9 \pm 4$ kcal mole^{-1} . It is this regime, undoubtedly, in which the linear oxygen uptake rates were observed by Nagasaka *et al.* (1). Where the experimental conditions overlap, our values of oxygen uptake rates are about an order of magnitude greater than these reported by these investigations. However, within the precision of our measurements and of the estimate of our pumping speed, this agreement is reasonable.

Dissolution of surface oxide.—After a steady-state P_{O_2} and a constant surface coverage are attained, interruption of the supply of oxygen to the crystal causes the surface oxygen level to gradually decrease. During this surface decay, the oxygen partial pressure in the chamber does not increase, an indication that the surface oxygen is disappearing by diffusion into the bulk of the crystal. The decrease in the normalized surface oxygen AES peak height is plotted as a function of time in Fig. 6. It is evident that the rate of diminution in surface oxygen depends on the temperature and on the previous oxygen exposure. After an initial rapid loss of surface oxygen, subsequent loss rates are very slow; that is, approximately 8 hr at 963 K were required to attain a nearly zero oxygen coverage. Note that the extent of surface oxygen coverage attained after the initial rapid loss appears to correspond to the steady-state chemisorption level (stage 2) observed during oxygen exposure. In view of the great affinity of Zr (bulk) for oxygen, the longevity of this oxygen adstate is remarkable.

Discussion

The oxygen surface accumulation is a function of oxygen exposure. The rate decreases with increasing temperature. However, the total rate of oxygen uptake calculated from the mass spectrometric data indicates that the total rate increases at higher temperature. The disparate behavior between AES and mass spectrometric data is due to the diffusion of oxygen into the bulk of the zirconium crystal. Zirconium metal can dissolve up to 28.6 atomic percent of oxygen, and the rate of diffusion of oxygen in zirconium metal becomes significant above 773 K (13). The initial rate

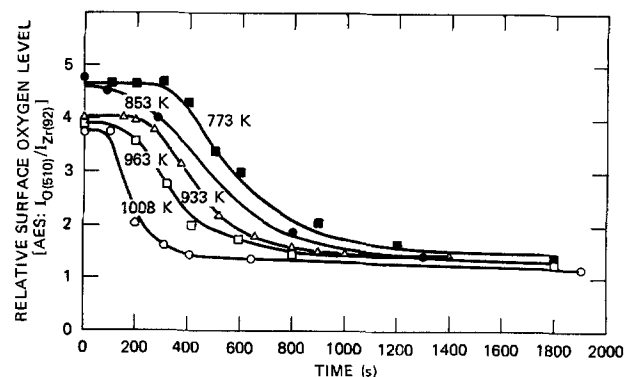


Fig. 6. Dissolution of surface oxygen at various temperatures

of surface coverage as measured by AES is plotted against inverse temperature in Fig. 7, and a negative activation energy of $-44 \text{ kcal mole}^{-1}$ is obtained. Indeed, this value is identical but opposite in sign to the activation energy reported for the diffusion of oxygen in zirconium metal (13). The total uptake of oxygen includes both surface accumulation and dissolution in the bulk. Thus, as the temperature increases, the rate of dissolution also increases thereby decreasing the surface coverage at any given oxygen exposure.

Since the rate of diffusion is proportional to the concentration gradient between the surface and the bulk, the diffusive flux would be low at the start of the exposure while oxygen accumulates on the surface. As the coverage increases, the amount of surface oxygen is determined by the dynamic competition between the adsorption rate of oxygen on the surface and by the rate of diffusion of oxygen into the bulk of the crystal. As the surface sites become filled with oxygen, the surface accumulation rate decreases and the total uptake rate is then determined essentially by the rate of diffusion into the crystal.

As the concentration of oxygen in the surface layers reaches a critical value, the AES oxygen peak height begins to increase. During this growth period (stage 3) the zirconium Auger peaks shift to lower energy indicating the formation of a condensed oxide layer. The characteristic shape of the kinetic curves (coverage *vs.* exposure) and the Auger energy shifts, taken together, give strong support to the hypothesis that in this region an oxide layer nucleates and grows. At this stage, the oxygen uptake rate is governed by the rate of the oxide growth and by the rate of diffusion of oxygen into the bulk.

When the surface is covered with the oxide layer, the oxygen uptake rate becomes limited by the diffusion of oxygen through the oxide into the metal. The rate of diffusion of oxygen in the oxide is significantly lower than in the metal (14), and thus the oxygen uptake rate decreases. In this region (stage 4) both the surface coverage as measured by AES and the uptake rate as calculated from oxygen partial pressure is constant. Even though the precision of the total oxygen uptake measurement is poor in this study, it is clear that the oxide layer is dynamic and that a steady-state condition exists between the oxygen arrival rate from the gas phase and the rate of diffusion into the crystal. In the absence of gaseous oxygen, the oxide layer dissolves into the metal.

The conditions of temperature and oxygen pressure used in this study overlap those used by Nagasaka *et al.* (1). Under these conditions an oxide layer would be formed in less than a few minutes. The reported linear oxygen uptake rate at higher exposure suggests that the oxide layer has a nearly constant thickness with steady-state diffusion of oxygen through the

oxide governing the rate of oxygen uptake. Similar considerations apply to the data reported by Dechamps and Lehr (2). Indeed the existence of a thin oxide layer was postulated earlier by Dechamps and Lehr (2). The present AES study confirms the existence of such an oxide layer and permits us to determine its thickness.

At the highest coverage of oxygen recorded in this study the Auger peaks corresponding to metallic zirconium are still evident in the spectra, suggesting that the thickness of the oxide layer is approximately 1 nm (10Å), the escape depth of Auger electrons with a kinetic energy of 150 eV. The AES oxygen peak height attained during the final steady-state condition decreases with increasing temperature (Fig. 3); thus, the thickness of the oxide layer could become even smaller as the temperature increases.

According to Nagasaka *et al.* (2), the activation energy associated with the linear oxygen uptake rate is about $10 \text{ kcal mole}^{-1}$, and our results tend to agree with that value. However, this value is rather small in comparison to the activation energy of $56 \text{ kcal mole}^{-1}$ reported for diffusion of oxygen in zirconium oxide (14). This discrepancy may be due to the nature of the oxide layer formed initially on the metal under the conditions employed. In fact, the activation energy for oxygen diffusion in oxide scales formed on metallic zirconium is substantially lower ($\sim 29 \text{ kcal mole}^{-1}$) (14). The initial oxide layer may have a high defect concentration and, according to Kofstad (15), the oxide may be a p-conductor, a mixed ionic/electronic conductor, or an n-conductor, depending on the stoichiometry and the impurity level. The studies conducted by Bradhurst *et al.* (16) and by Lightstone and Pemsler (17) have shown that the rate of ionic transport in the oxide is appreciable and that the growth of the oxide layer is controlled by the rate of transport of electronic defects. The transport of electrons have a rather low activation energy of $2\text{-}3 \text{ kcal mole}^{-1}$. In a mixed kinetic regime in which ionic and electronic transport controls the oxygen diffusion, the activation energy required may be comparable to the observed value.

An alternative scheme to explain the observed activation energy involves the adsorption of oxygen on the oxide surface and subsequent diffusion. The rate of adsorption decreases with increasing temperature while the rate of diffusion increases. Thus in a mixed kinetic regime, the combined effect of these two rates will result in a modest apparent activation energy as observed.

Conclusions

The initial stage of oxidation of a clean zirconium surface proceeds first as a chemisorption process followed by nucleation and growth of an oxide layer. At temperatures above 773 K, the rate of diffusion of oxygen into the bulk becomes significant and governs the extent of the chemisorption regime. At higher temperatures, the chemisorption regime extends to long exposure periods, whereas at low temperatures, an oxide is formed rapidly. The observed linear rate of oxygen uptake after the appearance of the surface oxide may be due to diffusion of oxygen through an oxide layer of constant thickness. This oxide layer formed at very low oxygen pressures is estimated to be approximately 1 nm thick.

Acknowledgment

This research was supported by the Office of Basic Energy Science of the U.S. Department of Energy under Contract EY-76-S-03-1339.

Manuscript submitted April 10, 1980; revised manuscript received July 1, 1980.

Any discussion of this paper will appear in a Discussion Section to be published in the December 1981 JOURNAL. All discussions for the December 1981 Discussion Section should be submitted by Aug. 1, 1981.

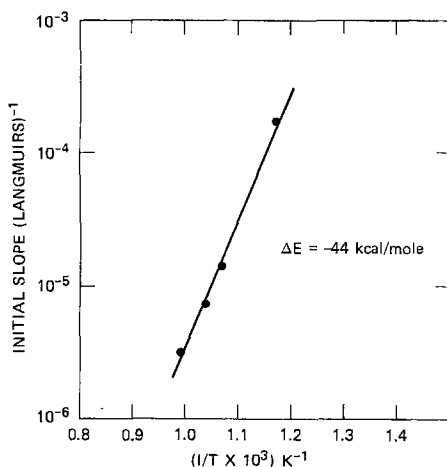


Fig. 7. Variation of initial rate with temperature

Publication costs of this article were assisted by SRI International.

REFERENCES

- M. Nagasaka, E. Udeya, and T. Yamashina, *Vacuum*, **23**, (2), 51 (1973).
- M. DeChamps and P. Lehr, *C. R. Acad. Sci. (Paris)*, **C270**, 1933 (1970).
- G. Horz and M. Hammel, *J. Nucl. Mater.*, **55**, 284 (1975).
- C. C. Chang, in "Characterization of Solid Surfaces," P. F. Kane and G. B. Larrabee, Editors, p. 537, Plenum Press, New York (1974).
- T. A. Carlson, "Photoelectron and Auger Spectroscopy," p. 264, Plenum Press, New York (1975).
- S. Dushman, "Scientific Foundations of Vacuum Techniques," p. 17, John Wiley and Sons, Inc., New York (1958).
- Y. E. Strausser and J. J. Uebbing, "Chart of Auger Electron Energies," Varian Associates, Palo Alto, Calif. (1971).
- A. M. Horgan and I. Dalins, *Surf. Sci.*, **36**, 526 (1973).
- P. H. Holloway, *ibid.*, **54**, 506 (1976).
- J. W. Haas, J. T. Grant, and G. J. Dooley III, *J. Appl. Phys.*, **43**, 1853 (1972).
- G. Ertl and S. Wandelt, *Surf. Sci.*, **50**, 479 (1975).
- Y. E. Strausser and J. H. Johannessen, *J. Vac. Sci. Technol.*, **13**, 48 (1976).
- I. G. Ritchie and A. Atrens, *J. Nucl. Mater.*, **67**, 254 (1977).
- P. Kofstad, "Nonstoichiometry, Diffusion and Electrical Conductivity in Binary Metal Oxides," pp. 158-159, Wiley-Interscience, Inc., New York (1972).
- P. Kofstad, *Corrosion NACE*, **24**, 379 (1961).
- D. H. Bradhurst, J. E. Draley, and C. J. Van Drunen, *This Journal*, **112**, 1171 (1965).
- J. B. Lightstone and J. Pemsler, Symposium on Mass Transport in Oxides, National Bureau of Standards, October 1967, NBS Special Publication 296 (August 1968).

Thermodynamics of Vaporization of ZrI_4 in the Univariant Region: Zirconium Monoiodide/Zirconium

Daniel Cubicciotti* and K. H. Lau

SRI International, Menlo Park, California 94025

ABSTRACT

The pressures of gaseous ZrI_4 over solid zirconium iodides in the composition range ZrI to Zr were measured by a torsion-effusion method. A univariant region was observed between solids of composition $ZrI_{1.05}$ and Zr for which the pressure of gaseous ZrI_4 was represented by the equation

$$\text{Log}_{10} P(\text{atm}) = (12.83 \pm 0.1) - (13,200 \pm 100)/T$$

These results extend literature information on the thermodynamics of vaporization in the ZrI_4/Zr region of the Zr -I system.

The chemistry of the zirconium-iodine system is intimately involved in the mechanism of iodine-induced stress corrosion cracking of zirconium alloys (1, 2). We have been investigating the thermodynamics to improve understanding of the chemistry of the system. The thermodynamic properties of the gaseous zirconium iodides are reported in Ref. (3). We have studied the vaporization of gaseous ZrI_4 from the solids to evaluate the thermodynamic properties of the solid phases. The vapor pressure of pure, solid ZrI_4 is given in Ref. (4). In a recent paper (5), the partial pressures of gaseous ZrI_4 in equilibrium with substoichiometric solid zirconium iodides in the composition range $ZrI_{2.4}$ to $ZrI_{1.0}$ were determined by the torsion-effusion method. This technique requires no knowledge of vapor composition to evaluate total vapor pressure. Simultaneous mass loss and effusion rate measurements confirmed that the vapor contained only gaseous ZrI_4 , and the measurements gave average molecular weight values within experimental error of the value of ZrI_4 gas. A univariant region was found between the solids $ZrI_{1.9}$ and $ZrI_{1.3}$, and the equilibrium pressures of gaseous ZrI_4 were derived. Between $ZrI_{1.3}$ and $ZrI_{1.0}$ the vapor pressure decreased as effusion proceeded at constant temperature, indicating that a single phase solid solution region existed in this range.

The part of the zirconium-iodine system most relevant to the stress corrosion cracking problem is the region that includes zirconium metal. In this paper we report the vaporization of ZrI_4 from the two-solid-

phase region that involves zirconium metal and the lowest iodide, approximately ZrI .

The principle of the method we used is described in Ref. (5). A sample of solid zirconium iodide (of composition approximately $ZrI_{1.2}$) was heated in a torsion-effusion gravimetric system so that gaseous ZrI_4 was released. The pressure of the gas was measured from the torque of the cell. The composition of the solid was monitored through its weight change. As ZrI_4 evaporated, the average composition of the residual solid changed, becoming richer in zirconium. The results are given below.

Experimental Materials

The $ZrI_{1.2}$ samples loaded in the graphite effusion cells were prepared as follows: the starting material was $ZrI_{2.4}$ prepared as described earlier (5). A weighed amount of $ZrI_{2.4}$ was loaded in a graphite crucible and sealed under high vacuum into a 20 cm long by 1.6 cm diam fused silica tube. The tube was placed in a two-zone tilted furnace. The lower 8 cm of the tube containing the sample was heated to 425°C. The upper 4 cm was kept at 140°C so that ZrI_4 vaporized from the sample condensed there, thereby maintaining a ZrI_4 vapor pressure of about 2×10^{-7} atm. The tube was heated in this temperature gradient for three weeks and was then transferred to a dry box under an atmosphere of argon. The tube was cracked in the center and a lump of reddish brown ZrI_4 product was collected from the upper end and weighed to obtain an estimate of the composition of the solid residue. The sample in the graphite crucible was a black, granular material.

* Electrochemical Society Active Member.

Key words: sublimation, free energy, inorganic, pressure.

Two samples were prepared; part of each was used for chemical and x-ray diffraction analyses. The rest was loaded into the effusion cells, one sample into cell A, the other into cell B. Titration with silver ion to an iodide electrode end point showed the composition of the starting material was $ZrI_{1.2 \pm 0.1}$ for cell A and $ZrI_{1.1 \pm 0.1}$ for cell B. These starting compositions were in good agreement with the total mass lost by the cells in the vaporization study, during which all the iodide was evaporated from the cell (see below). Table I gives the lines observed in a powder pattern taken on a portion of the sample placed in cell A. We believe the pattern represents the phase ZrI but the stoichiometry may differ somewhat.

Vapor Pressure Measurement

Vapor pressures were measured by the torsion-effusion method. The apparatus, the sample loading procedures, and other details of this method were described in our earlier publications (4, 5). Two series of vapor pressure measurements were made with graphite effusion cells labeled cell A (0.047 cm orifice diameter) and cell B (0.0803 cm orifice diameter). These are the same two cells used in our earlier work (4, 5) and described in detail there (3).

Results

The results of the measurements are listed in Table II. The data are presented in the chronological order in which they were obtained. The pressure (column 2) was calculated from the measured angular displacement of the torsion effusion cell at each temperature. The molecular weight of the effusing gas (column 3) was calculated from the pressure and the rate of mass loss of the cell. The composition of the solid (column 4) was calculated from the initial sample weight and the total mass loss incurred by the sample, assuming the vapor lost was gaseous ZrI_4 . The last column of the table, P_{obs}/P_{calc} , gives the ratio of the measured pressure divided by the pressure calculated from one of the equations that represents the univariant region for the given cell, namely, Eq. [1] or [2] below.

The molecular weights observed (column 3) were in the range 579-637, which is within the experimental error of the method for ZrI_4 gas—namely, 599. Vapor in equilibrium with zirconium metal under these conditions can be shown to contain essentially ZrI_4 , with only traces of lower valent gas (3). Thus the gas was

Table I. X-ray powder pattern* of sample used in cell A

| dA | 100 I/I ₁ |
|------|----------------------|
| 8.6 | 25 |
| 4.32 | 30 |
| 3.84 | 35 |
| 3.62 | 35 |
| 3.48 | 10 |
| 3.31 | 100 |
| 3.02 | 5 |
| 2.91 | 5 |
| 2.88 | 5 |
| 2.77 | 3 |
| 2.70 | 5 |
| 2.58 | 25 |
| 2.44 | 50 |
| 2.26 | 50 |
| 2.17 | 60 |
| 2.04 | 5 |
| 1.94 | 3 |
| 1.92 | 3 |
| 1.89 | 5 |
| 1.82 | 20 |
| 1.73 | 10 |
| 1.66 | 15 |
| 1.61 | 10 |
| 1.53 | 5 |
| 1.48 | 10 |
| 1.44 | 10 |
| 1.39 | 5 |
| 1.37 | 5 |
| 1.30 | 25 |
| 1.27 | 5 |
| 1.26 | 5 |

* Obtained with a 2 in. diam camera and $CuK\alpha$ radiation.

presumed to be pure ZrI_4 in all these measurements.

The pressures observed for cell A over the range of composition of the solid in the cell of $ZrI_{1.07}$ to $ZrI_{0.57}$ could be represented, within $\pm 3\%$, by a single equation independent of composition, as follows

$$\log_{10} P(\text{atm}) = (12.26 \pm 0.10) - (13,080 \pm 80)/T \quad (745-980 \text{ K}) \quad [1]$$

The pressures observed for cell B over the composition range $ZrI_{1.05}$ to $ZrI_{0.65}$ could also be represented by an equation independent of composition, as follows

$$\log_{10} P(\text{atm}) = (11.75 \pm 0.11) - (13,010 \pm 90)/T \quad (730-722 \text{ K}) \quad [2]$$

The uncertainty given in each equation is a standard deviation derived in a least squares treatment. The data are shown graphically in Fig. 1.

As part of our investigation (5) of ZrI_4 pressure in the solid composition range $ZrI_{2.4}$ to $ZrI_{1.3}$ we made some preliminary measurements at lower stoichiometries. Those measurements showed evidence for univariant behavior at compositions below about ZrI. Because of the small amount of sample remaining in the cells at compositions below ZrI (since the initial composition was $ZrI_{2.4}$), we were not sure of the reliability of the results and did not publish them at that time. The pressures observed in those experiments were found to be in good accord with the present data measured on samples of initial composition $ZrI_{1.2}$. The values found as part of the Ref. (5) measurements were as follows for cell A

$$\log_{10} P(\text{atm}) = (11.92 \pm 0.4) - (12,850 \pm 290)/T \quad (740-780 \text{ K}) \quad [3]$$

These values in cell A were observed over the range of compositions of $ZrI_{0.97}$ to $ZrI_{0.89}$. At lower stoichiometries the measured pressures were smaller. For cell B the results were represented by

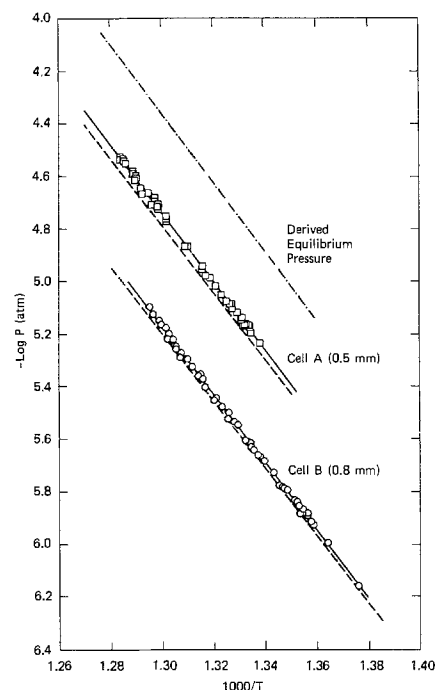


Fig. 1. Vapor pressures of ZrI_4 in the univariant region of the system between ZrI and Zr. Data points represent values from Table II and solid lines are least squares equations [1] and [2]. Dashed lines are results obtained earlier and work represented by Eq. [3] and [4]. Dot-dash line gives equilibrium pressures obtained by extrapolation to zero orifice area.

Table II. Results of torsion-effusion, mass loss measurements in the $ZrI_{1.2}$ to Zr region

| Temperature K | Pressure of ZrI_4 atm $\times 10^{-6}$ | Molecular weight of gas | Composition of solid, x of ZrI_x | $\frac{P_{obs}}{P_{calc}}$ | Temperature K | Pressure of ZrI_4 atm $\times 10^{-6}$ | Molecular weight of gas | Composition of solid, x of ZrI_x | $\frac{P_{obs}}{P_{calc}}$ |
|-------------------------------|--|-------------------------------|--|----------------------------|-------------------------------|--|-------------------------------|--|----------------------------|
| Cell A (0.5 mm diam orifices) | | | | | Cell B (0.8 mm diam orifices) | | | | |
| 736.2 | 2.12 | | 1.14 | 0.67 | 726.4 | 0.68 | | 1.05 | 0.99 |
| 763.7 | 9.10 | | 1.12 | 0.77 | 759.1 | 3.94 | 589 | 0.98 | 0.97 |
| 769.4 | 15.63 | 637 | 1.10 | 0.85 | 740.1 | 1.48 | | | 1.01 |
| 780.5 | 29.12 | 628 | 1.08 | 0.93 | 754.1 | 3.06 | | | 0.98 |
| | | | | | 749.3 | 2.34 | | | 0.97 |
| 771.6 | 19.42 | | 1.07 | 0.95 | 738.8 | 1.31 | | | 0.96 |
| 750.9 | 6.92 | 609 | 1.06 | 0.99 | 743.2 | 1.67 | | | 0.96 |
| 755.8 | 8.81 | | | 0.97 | 765.7 | 5.62 | | | |
| 763.9 | 13.47 | | | | 762.3 | 4.72 | | | 0.99 |
| 772.8 | 21.35 | | | | 769.7 | 7.10 | | | |
| 754.0 | 8.17 | | 1.04 | 0.98 | 767.3 | 6.24 | | | 1.02 |
| 770.5 | 18.89 | | | | 755.4 | 3.37 | | | |
| 768.2 | 16.75 | | | | 759.7 | 4.24 | | | |
| 778.7 | 29.43 | | | 1.00 | 736.2 | 1.18 | | | |
| 777.3 | 27.56 | 618 | | | 747.1 | 2.14 | | | |
| 753.8 | 8.21 | | | | 738.4 | 1.32 | | | 0.99 |
| 756.6 | 9.57 | | | | 742.9 | 1.63 | | | |
| 769.8 | 18.82 | | | | 756.8 | 3.60 | | | |
| 768.3 | 17.42 | | 0.98 | 1.00 | 754.1 | 3.14 | | | |
| 750.2 | 6.92 | 599 | | 1.02 | 763.0 | 5.04 | | | |
| 758.0 | 10.31 | | | | 760.3 | 4.41 | | | |
| 772.1 | 21.53 | | | 1.02 | 751.7 | 2.82 | | | 1.03 |
| 770.2 | 19.32 | | | | 765.2 | 5.68 | 579 585 | | |
| 777.9 | 29.08 | | | | 771.8 | 8.05 | | | |
| 755.1 | 9.13 | 601 | | | 768.1 | 6.64 | | 0.92 | 1.03 |
| 749.4 | 6.79 | | | | 733.1 | 1.02 | | | |
| 751.3 | 7.06 | | | 0.99 | 744.4 | 1.87 | | | |
| 771.0 | 20.69 | | | | 736.4 | 1.22 | | | |
| 749.2 | 6.62 | | | | 740.2 | 1.48 | | | |
| 752.1 | 7.58 | | | | 755.5 | 3.38 | | | |
| 763.3 | 13.58 | | | 1.01 | 752.9 | 2.91 | 591 | | |
| 759.9 | 11.41 | | | | 763.2 | 5.05 | | | 1.01 |
| 775.7 | 25.61 | | | | 749.6 | 2.45 | | | |
| 774.7 | 24.71 | | | | 746.4 | 2.07 | | | |
| 777.6 | 28.57 | | | | 741.7 | 1.62 | | | |
| 751.0 | 7.19 | | | 1.02 | 766.2 | 5.69 | 587 | | |
| 768.0 | 17.21 | | | | 764.9 | 5.31 | | | |
| 770.5 | 19.59 | | 0.90 | 1.00 | 771.4 | 7.53 | | | |
| 747.2 | 5.77 | | | | 753.0 | 2.89 | 584 | 0.85 | 0.99 |
| 754.0 | 8.26 | | | 1.00 | 750.0 | 2.45 | | | |
| 750.7 | 6.83 | | | | 738.8 | 1.38 | | | |
| 775.7 | 25.31 | | | | 757.2 | 3.53 | | | |
| 775.0 | 24.39 | | | | 754.1 | 2.99 | | | |
| 778.1 | 28.55 | | | | 738.8 | 1.35 | | | 0.99 |
| 771.1 | 19.79 | | | 0.99 | 742.7 | 1.64 | | | |
| 753.5 | 7.94 | | | | 767.7 | 5.93 | | 0.77 | 0.95 |
| 759.7 | 10.97 | | | | 764.9 | 5.11 | | 0.65 | |
| 758.9 | 10.37 | | | 0.84 | | | | | |
| 749.2 | 6.32 | | | 0.99 | 774.5 | 6.44 | | 0.57 | 0.73 |
| 754.8 | 8.40 | | | | 773.4 | 5.63 | 579 | | |
| 752.9 | 7.51 | | | | 773.5 | 4.28 | 577 | 0.33 | 0.51 |
| 775.5 | 24.51 | | | | 773.5 | 1.75 | | 0.07 | 0.21 |
| 774.0 | 22.59 | | | | 773.5 | 0.36 | | 0.03 | 0.04 |
| 778.6 | 28.65 | | 0.80 | 0.98 | | | | | |
| 775.6 | 24.45 | | 0.57 | 0.97 | | | | | |
| | | | | | | | | | |
| 775.5 | 22.83 | | 0.56 | 0.91 | | | | | |
| 775.7 | 21.80 | | 0.46 | 0.86 | | | | | |
| 776.7 | 19.31 | | 0.28 | 0.72 | | | | | |
| 776.0 | 9.98 | | 0.18 | 0.39 | | | | | |
| 773.9 | 5.13 | | 0.15 | 0.22 | | | | | |
| 869.7 | 5.45 | 604 | 0.08 | 0.003 | | | | | |
| 897.4 | 10.56 | 580 | 0.04 | | | | | | |
| 928.8 | 10.16 | | 0.01 | 0.001 | | | | | |

$$\log_{10} P(\text{atm}) = (11.38 \pm 0.2) - (12,750 \pm 130)/T$$

$$(740-780 \text{ K}) \quad [4]$$

These values in cell B were observed over the composition range $ZrI_{0.96}$ to $ZrI_{0.53}$. At lower stoichiometries the pressures were smaller than Eq. [4]. These results are shown in Fig. 1 as dashed lines. The values of Eq. [3] (cell A) are about 10% smaller than Eq. [1], and those of Eq. [4] (cell B) are about 6% smaller than Eq. [2]. The data represented by Eq. [3] and [4] were considered to be less accurate than those of Eq. [1] and [2] and so were not used further.

The differences between the values obtained in cell A and cell B were assumed to be due to the usual influence of effusion orifice size on apparent calculated pressure. The effect of orifice size on the measured pressure was treated by the Whitman-Motzfeldt method (4), which indicates that the reciprocal of measured pressure is expected to vary linearly with effective orifice area. For the cells used in the present work the effective orifice areas were 0.125 mm^2 for cell A and 0.478 mm^2 for cell B. The equilibrium pressures derived by extrapolation of the reciprocals of the pressures measured in cells A and B vs. their effective orifice areas are represented by the dot-dash line in Fig.

1. An equation representing those equilibrium pressures for the univariant composition region of the present work is

$$\log_{10} P_{eq}(\text{atm}) = (12.83 \pm 0.1) - (13,200 \pm 100)/T$$

$$(720-790 \text{ K}) \quad [5]$$

When the composition of the solid dropped below $ZrI_{0.57}$ in cell A and $ZrI_{0.65}$ in cell B, the measured pressures fell below the values anticipated from Eq. [1] and [2], respectively. That effect can be noted from the values given in the last column of Table II, which represents the ratios of the measured pressures (of ZrI_4) divided by the values calculated from Eq. [1] or [2], respectively, for cell A or B. The ratios are shown graphically as a function of composition in Fig. 2. The solid remaining in cell A after the series of pressure measurements reported in Table II was analyzed and found to correspond to an I/Zr ratio of 0.003. An x-ray powder diffraction pattern of that material showed only lines corresponding to alpha zirconium.

The ratios in Fig. 2 depart from unity in a fairly smooth fashion. We interpret this behavior to indicate that no new phase was being formed, and that the deviation from unity resulted from depletion of the

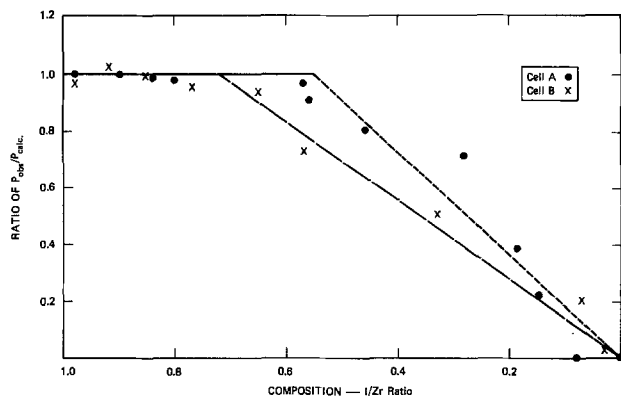
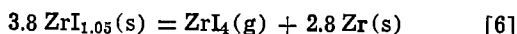


Fig. 2. Ratio of measured pressure to value calculated from Eq. [1] (for cell A) or Eq. [2] (for cell B) as a function of composition of solid remaining in cell. Dots and crosses represent cell A and cell B data, respectively.

samples in the cells. The fact that the cell B ratios fell off at lower I/Zr stoichiometries was in keeping with that interpretation.

To corroborate the above result, a sample of $ZrI_{2.4}$ in a graphite crucible was heated for 45 days at $475^\circ C$ in a sealed glass bulb with one end of the bulb maintained at about $50^\circ C$. During the heating period, ZrI_4 vaporized from the sample and condensed in the cold end of the bulb. The sample remaining in the crucible was analyzed and found to be $ZrI_{0.1}$. An x-ray powder pattern of that material showed lines mainly corresponding to alpha zirconium. The remaining lines were the same as the x-ray pattern for ZrI given in Table I, and the overall intensity was about one-tenth that of the alpha zirconium pattern. That result indicates that the equilibrium phases present for the overall composition $ZrI_{0.1}$ were ZrI and alpha Zr .

The upper composition limit for the univariant region corresponding to the pressures given in Eq. [5] was evaluated as follows. In Ref. (5) there was evidence for a new univariant region starting between $I/Zr = 1.03$ and 0.96 [see Table III of Ref. (5)]. The present results (Table II) indicate that the univariant region extends to I/Zr of about 1.05. (We do not understand why for cell A the observed pressures were smaller than the univariant values for I/Zr greater than 1.05. We presume that was due to some kinetic phenomenon in the cell—possibly some surface barrier on the sample which later was disrupted.) Therefore, the chemical reaction corresponding to the pressures of Eq. [5] is



The enthalpy change derived from Eq. [5] for reaction [6] is 60.4 ± 0.5 kcal/mole.

Figure 3 indicates our assessment of the vaporization thermodynamics for the zirconium iodides; the assessment combines our earlier results with the present data. Zirconium tetraiodide is the predominant vapor species, and the partial pressure of ZrI_4 as a function of composition of the solid is shown in the upper curve. The horizontal segments of the curve correspond to univariant regions, that is, regions in which two solids exist in equilibrium with the vapor (ZrI_4). The non-horizontal portions represent regions of solid solution that have approximately the stoichiometries of the tetraiodide, triiodide, diiodide, monoiodide, and are also indicated on the diagram. The enthalpies of vaporiza-

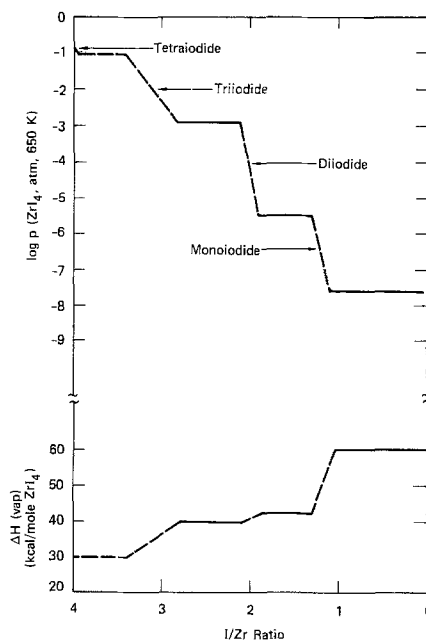


Fig. 3. Thermodynamics of vaporization as a function of composition in the Zr-I system. Upper curve, pressure of ZrI_4 at 650 K ; lower curve, enthalpies of vaporization reactions per mole of ZrI_4 . Dashed lines indicate regions of estimated data.

tion per mole of ZrI_4 gas are presented in the lower curve of Fig. 3. The enthalpies of vaporization became greater the smaller the I/Zr ratio of the solid, which indicates that the removal of ZrI_4 from the solid becomes energetically more difficult as the composition decreases in iodide.

Acknowledgments

This research was supported by the Office of Basic Energy Science of the U.S. Department of Energy under Contract EY-76-S-03-1339. We are grateful to D. R. Knittel for some of the experimental work, to A. C. Scott for preparation of the samples, and to Eldon Farley for x-ray diffraction patterns.

Manuscript submitted April 10, 1980; revised manuscript received July 31, 1980.

Any discussion of this paper will appear in a Discussion Section to be published in the December 1981 JOURNAL. All discussions for the December 1981 Discussion Section should be submitted by Aug. 1, 1981.

Publication costs of this article were assisted by SRI International.

REFERENCES

1. B. Cox and J. C. Wood, in "Corrosion Problems in Energy Conservation and Generation," C. S. Tedmon, Jr., Editor, p. 275, The Electrochemical Society Softbound Proceedings Series, New York (1974).
2. J. H. Schemel and T. P. Papazoglou, Editors, "Zirconium in the Nuclear Industry," ASTM Special Technical Publication 681, pp. 229-321, Am. Soc. Test. Mat., Philadelphia, Pa. (1979).
3. P. D. Kleinschmidt, D. Cubicciotti, and D. L. Hildenbrand, *This Journal*, **125**, 1543 (1978).
4. D. Cubicciotti, K. H. Lau, and M. J. Ferrante, *ibid.*, **125**, 972 (1978).
5. D. Cubicciotti and K. H. Lau, *ibid.*, **126**, 771 (1979).

Subband Gap Response of TiO_2 and SrTiO_3 Photoelectrodes

M. A. Butler*

Sandia National Laboratories, Albuquerque, New Mexico 87185

M. Abramovich,* F. Decker,* and J. F. Juliao**

UNICAMP, Instituto de Fisica, Campinas, SP, Brazil

ABSTRACT

The response of TiO_2 and SrTiO_3 photoelectrodes to subband gap light has been explored as a function of numerous variables, including intensity and wavelength of light, applied potential, temperature, and electrolyte composition. The photoresponse is shown to be linear with light intensity, to depend on the square root of the applied potential, to occur only for $h\nu \gtrsim 2.2$ eV, and to be independent of temperature and electrolyte composition. These results suggest a bulk excitation process involving impurity and defect-related states in the gaps of these semiconductors. A qualitative model is presented to account for the main features of this excitation process and to provide a basis for suggesting future experiments.

The development of the photoelectrochemical, energy conversion field (1) has proceeded to the point where details of the charge transfer process at the semiconductor-electrolyte interface are now of considerable interest (2). In particular, the role that surface states might play in this process has received considerable attention. Unfortunately, evidence for the importance of surface states has been primarily of an indirect nature. In an attempt to obtain more direct evidence for surface states several groups have explored the excitation of photoelectrodes by subband gap light (3). Some of these results have been presented as evidence for surface states in TiO_2 (4-5).

In this paper we present evidence of a subband gap excitation process for TiO_2 and SrTiO_3 which involves bulk rather than surface states. It is shown that the potential dependence of the photoresponse defines the nature of the excitation process and will allow a distinction between bulk and surface states. A model is presented which describes this excitation process and explains the dependence of the photoresponse on the wavelength of the light and its intensity.

Experimental Results

Measurements of the subband gap photoresponse were made using a conventional three electrode electrochemical cell where the TiO_2 or SrTiO_3 was the working electrode and a saturated calomel electrode (SCE) was the reference electrode. A platinum foil was used as the counterelectrode. The potential was controlled using a potentiostat patterned after a previously published design (6). The electrolytes were prepared using commercial reagents. The samples were cut from a boule obtained from Materials Research Company, polished using $\frac{1}{4}$ μm diamond paste, and reduced in hydrogen under various conditions as indicated in the figure captions. Contact was made using In-Ga alloy.

The light source was an Oriel 1000W xenon lamp with a single pass SPEX monochromator which provided about 1 mW/cm² incident on the sample. The light was chopped using a PAR Model 191 chopper at 5 Hz and then passed through a filter to remove stray light components. This filtering is of crucial importance since the subband gap response we are looking for is orders of magnitude smaller than the above-bandgap response. Thus a small amount of stray u.v. light can give an erroneous response. The best filter was a Pyrex glass plate combined with an unreduced, 2 mm

thick slice of the semiconductor being studied. The efficiency of this filter was checked by looking for a photoresponse above the bandedge. Since the observed response was significantly less than the observed subband gap response we can be confident that the filtering was adequate. Erroneous signals due to stray u.v. light were observed without this filtering.

The signal was detected using a PAR lock-in amplifier on the output of the potentiostat. Typical results for TiO_2 and SrTiO_3 are shown in Fig. 1 and 2, respectively. These spectra are not corrected for light intensity and thus they show structure around 470 nm which is due to structure in the lamp spectrum. In a sense, this is very useful since it proves that the photoresponse is due to excitation by subband gap light. While these spectra were taken using chopped light, the photocurrent was also observed using d-c techniques to insure that the a-c measurements did not represent a transient phenomenon such as a-c photoconductivity. These spectra come from a steady-state phenomenon and have the same sign as the photocurrent observed

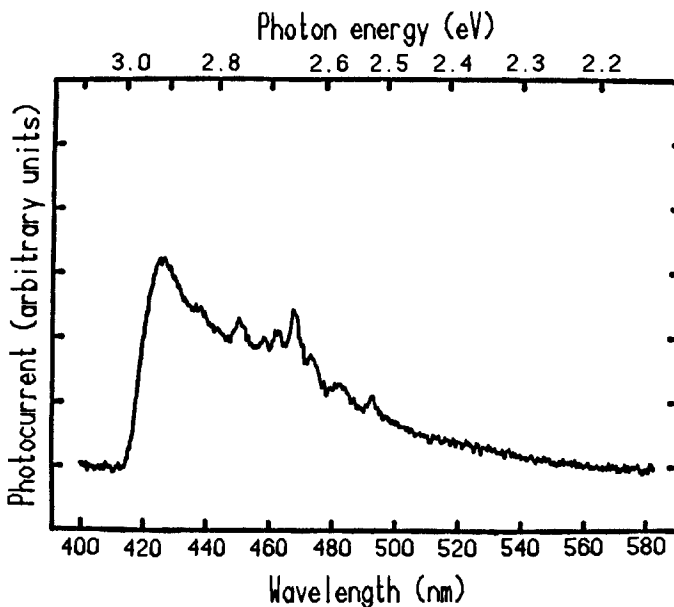


Fig. 1. The subband gap photoresponse of a TiO_2 sample in 1M KOH and at 0V (SCE). The sample was cut \perp to the C-axis and reduced at 700°C for 30 min in a 10% H_2 -90% N_2 atmosphere. The cutoff at short wavelengths is due to the optical filter cutting of the light source.

* Electrochemical Society Active Member.
** Electrochemical Society Student Member.

Key words: defects, semiconductor, spectra.

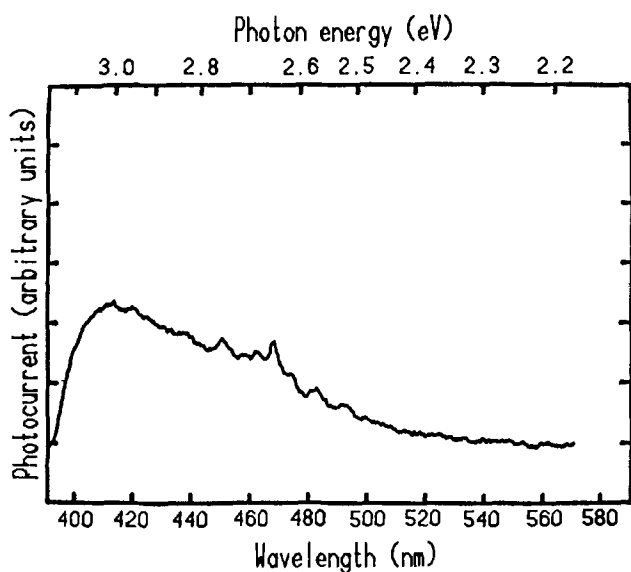


Fig. 2. The subband gap photoresponse of an SrTiO₃ sample in 1M KOH and at $-0.14V$ (SCE). The sample was reduced in vacuum at $800^{\circ}C$ for 2 hr. The cutoff at short wavelengths is due to the optical filter cutting of the light source.

with above-bandgap illumination (*i.e.*, these are anodic photocurrents). Typical quantum efficiencies for this subband gap excitation process are $\lesssim 10^{-5}$.

Note that these photocurrents occur under anodic bias which is the normal operating potential range for photoanodes in a photoelectrochemical cell. This is to be contrasted with the subband gap response observed in TiO₂ at cathodic bias (5) and subsequently explained as a photothermal effect (7). We have explored the potential behavior and the results are shown in Fig. 3 and 4 for TiO₂ and SrTiO₃, respectively. The behavior is identical to that observed for illumination just above the bandgap. This is the first hint that perhaps what we are observing arises from a "bulk" process rather than from excitation of surface states.

Another useful parameter to vary in exploring this subband gap photoresponse is the intensity of incident light. These results are shown for TiO₂ using our normal light source and neutral density filters in Fig. 5. Within experimental error the photocurrent depends linearly on light intensity. To explore the behavior at higher light intensities, the 4880Å line of an argon ion laser was used. The results for SrTiO₃ are shown on a log-log plot in Fig. 6. The relationship is linear over three orders of magnitude and has not saturated at power densities of 200 mW/cm^2 .

Several other variables were also explored for their possible effect on the subband gap photoresponse. In addition to the data shown which was taken in 1M KOH, other electrolytes were tried which spanned the complete range of pH from strong acid to strong base. No significant effect of electrolyte was noted other than changes in the potential dependence due to the shifting flatband potential. The electrolytes were saturated with various gases including O₂, N₂, and Ar. However, no changes in the subband gap photoresponse were observed. The temperature of the electrochemical cell was raised $30^{\circ}C$ above ambient temperature but no effect on the photoresponse was observed.

These results then pose the problem as to the origin of the subband gap photoresponse, whether it is a bulk or surface effect, and the mechanism for this process.

Discussion

The important clue to the nature of the subband gap photoresponse comes from the potential behavior. Figures 3 and 4 show that the square of the photocurrent depends linearly on potential and extrapolates to zero

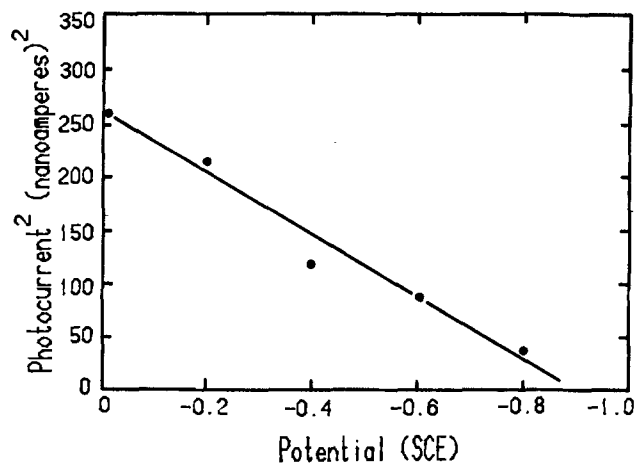


Fig. 3. The potential dependence of the subband gap photoresponse of TiO₂ in 1M KOH and for $h\nu = 2.95 \text{ eV}$. Note that the photocurrent disappears at the flatband potential.

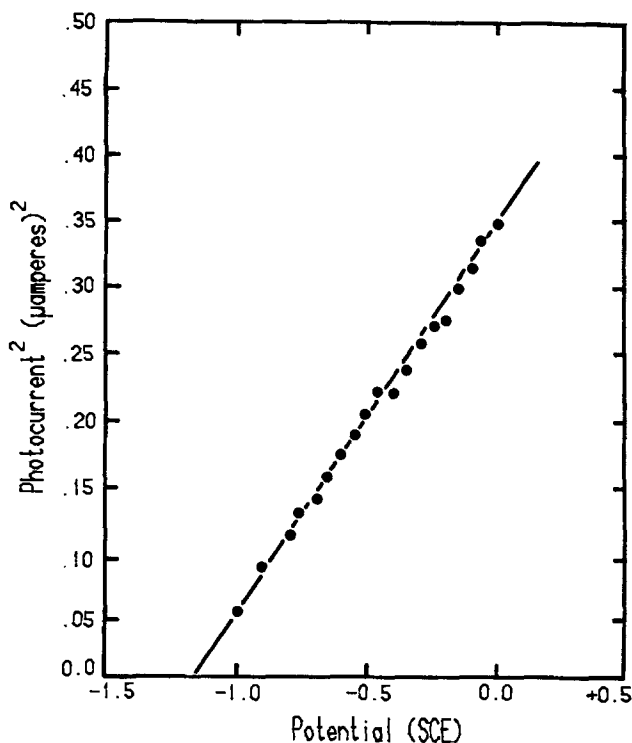


Fig. 4. The potential dependence of the subband gap photoresponse of SrTiO₃ in 1M KOH using the 4880Å (2.54 eV) argon ion laser line at 100 mW intensity. Note that the photocurrent disappears at the flatband potential.

at the flatband potential. Analysis of the response of the Schottky junction at the semiconductor-electrolyte interface has shown that the photocurrent density due to above-bandgap illumination may be expressed as (8)

$$J' = e\phi_0 \left[1 - \frac{e^{-\alpha W}}{1 + \alpha L} \right] \quad [1]$$

where e is the electronic charge, ϕ_0 is the incident photon flux, α is the optical absorption coefficient, W is the depletion layer thickness, and L is the minority carrier diffusion length. For subband gap illumination the absorption coefficient is small, thus $\alpha W \ll 1$ and $\alpha L \ll 1$. We also know that for a lightly reduced electrode such as we are using in these experiments $W \gg L$. Then we may expand the exponential and ignore the diffusion term so that

$$J \simeq e\phi_0\alpha W \quad [2]$$

Thus the photocurrent is linearly related to depletion

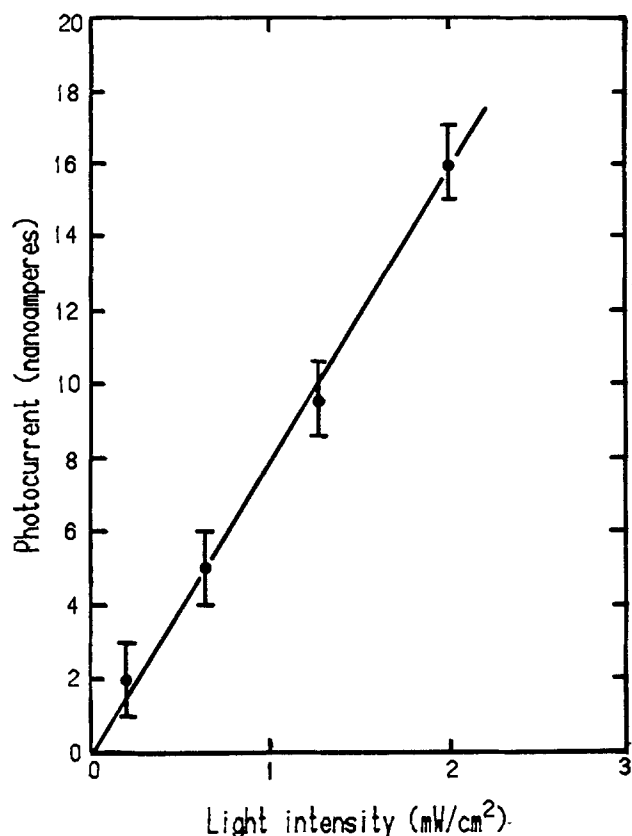


Fig. 5. The linear relationship between incident light intensity and subband gap photocurrent for TiO_2 in 1M KOH at 0V (SCE) just below the bandedge (2.95 eV).

layer thickness. Since (8)

$$W = W_0(V - V_{\text{FB}})^{1/2} \quad [3]$$

where V is the applied potential, V_{FB} is the flatband potential, and W_0 is a constant depending on the properties of the semiconductor, we expect that, for a bulk process which occurs uniformly throughout the depletion layer region, the square of the photocurrent should depend linearly on applied potential and extrapolate to zero at the flatband potential. While this relationship is usually not obeyed at small band bending (9, 10), this is exactly what we observe. We believe that the use of an I^2 vs. V plot and the relatively high noise level obscures this region of expected deviation. This result shows that the observed subband gap response is a bulk phenomenon occurring throughout the depletion layer. For surface state excitation we would not expect this square root dependence on applied potential. Thus the potential dependence of the photocurrent is a means of distinguishing between bulk excitation processes and surface state excitation processes.

The next question to address is the nature of the bulk excitation process and whether a consistent model can be constructed which will explain the dependence of the photoresponse on wavelength and intensity of light. Since the photocurrent is a d-c effect, the subband gap response probably involves a two-step process such as shown in Fig. 7. This seems to be necessary, since it is difficult to envision sufficient impurity level conduction to sustain the relatively large photocurrents observed with laser illumination without seeing saturation effects. The other possibility would be a two-step process in which one of the steps is a thermally assisted process. Again it is unlikely that the linear relationship between photocurrent and light intensity shown in Fig. 6 would be possible under these conditions. In addition we observed no dependence of the photocurrent on temperature. Thus we believe that the excita-

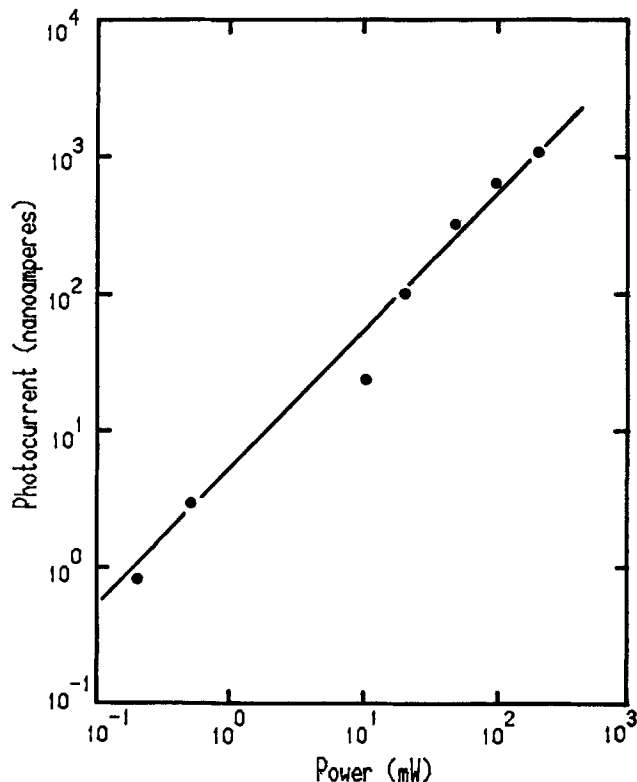


Fig. 6. The linear relationship shown on a log-log plot between incident light intensity and subband gap photocurrent for SrTiO_3 in 1M KOH at 0V (SCE) measured using the 4880Å (2.54 eV) line of an argon ion laser. The solid line shows linear behavior over three orders of magnitude and to power densities larger than 200 mW/cm^2 .

tion mechanism is a two-step process where both steps are photoexcitations and the intermediate state is an impurity or defect-related midgap state.

For a two-photon excitation process where there is no real intermediate state, there would be a quadratic dependence of the photocurrent on light intensity. However, for a two-photon process with a real intermediate state the effective transition rate W_{eff} can be shown using simple rate equations (11) to be

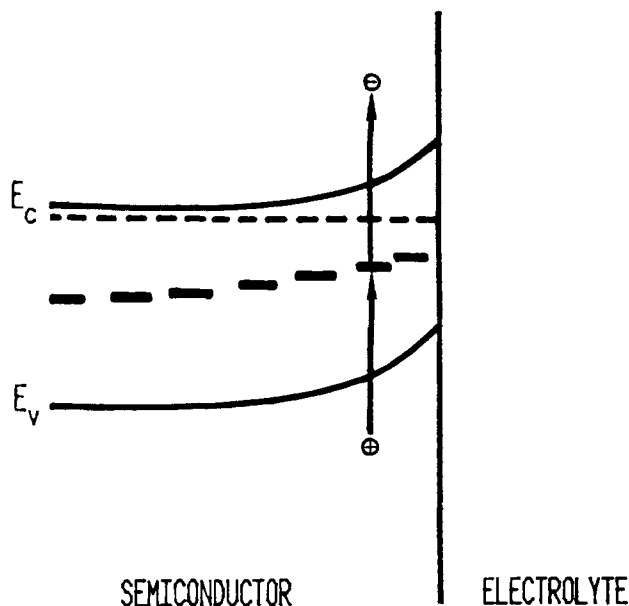


Fig. 7. The two-step excitation process envisioned for the subband gap photoresponse of TiO_2 and SrTiO_3 . Depending on the particular example there may be a distribution of midgap states.

$$W_{\text{eff}} = \frac{W_{12}W_{23}}{W_{12} + W_{23}} \quad [4]$$

where W_{12} is the transition rate from valence band to intermediate state and W_{23} is the transition rate from the intermediate state to the conduction band. Since both W_{12} and W_{23} depend linearly on light intensity, W_{eff} will also depend linearly on light intensity. This simple picture of course ignores spontaneous relaxation of the photoexcited electrons (W_{21}). This seems justified since it explains the linear dependence of photocurrent on light intensity.

The spectral dependence of the subband gap response is somewhat more difficult to explain than the intensity dependence, since many factors such as transition matrix elements and the energy distribution of the intermediate states are not known. Thus we are going to assume a plausible, simplified model to explore the general features of the behavior that is to be expected. Following arguments made for discussing optical absorption in semiconductors (12), we assume parabolic conduction and valence bands and that the transition matrix element is independent of photon energy. Furthermore, since the interband transitions in the materials of interest are known to be indirect (13), we will assume that the momentum k is not conserved. Then we are making primarily density of states arguments as to the spectral dependence of the photoexcitation process. The effective transition rate is then given by

$$W_{\text{eff}}(h\nu) = \int_{-(h\nu - E_g/2)}^{(h\nu - E_g/2)} f(x) W_{\text{eff}}(x, h\nu) dx \quad [5]$$

where x is the energy of the intermediate state shown in Fig. 7 measured from the center of the gap and $f(x)$ is the energy distribution of these midgap states. The limits of the integral insure that energy is conserved in the photoexcitation process. The individual transition rates in this two-step process may be written

$$W_{12} = M_{12} (h\nu - E_g/2 - x)^{1/2} \quad [6]$$

and

$$W_{23} = M_{23} (h\nu - E_g/2 + x)^{1/2} \quad [7]$$

where M_{12} and M_{23} are constants which include the transition matrix elements, and other factors independent of x and $h\nu$. If we use the full expression for the effective transition rate, Eq. [3], then the integral, while simple to evaluate numerically, will not clearly display the qualitative features of the model. Thus we again simplify by assuming $W_{12} \ll W_{23}$. Since $M_{12} \approx M_{23}$, this assumption is reasonable if the dominant midgap states are closer to the conduction band than the valence band. Then the frequency dependent factor determines the important rate constant and Eq. [4] becomes

$$W_{\text{eff}}(h\nu) \approx M_{12} \int_{-(h\nu - E_g/2)}^{(h\nu - E_g/2)} f(x) (h\nu - E_g/2 - x)^{1/2} dx \quad [8]$$

Consistent with the above approximation we will assume a uniform continuum of midgap states extending to an energy E_0 below the conduction bandedge. This limits the integral in Eq. [7] so that we have

$$W_{\text{eff}}(h\nu) \approx M_{12} \int_{(E_g/2 - E_0)}^{(h\nu - E_g/2)} (h\nu - E_g/2 - x)^{1/2} dx \quad [9]$$

Or the effective transition rate in this greatly simplified model is given by

$$W_{\text{eff}}(h\nu) \approx \frac{2}{3} M_{12} [h\nu - (E_g - E_0)]^{3/2} \quad [10]$$

Thus we expect that the quantum efficiency to the 2/3 power should be linear in photon energy and the intercept, $(E_g - E_0)$, defines the edge of the bulk defect state distribution. In the other extreme, where a con-

tinuum of midgap states extend from the valence band to an energy E_0 above the valence band, $W_{12} \gg W_{23}$. Integrating in this limit yields the same expression for W_{eff} except that M_{12} is replaced by M_{23} in Eq. [10]. A single dominant discrete state in the gap of energy E_0 would give

$$W_{\text{eff}}(h\nu) \approx [h\nu - (E_g - E_0)]^{1/2} \quad [11]$$

a square root dependence on photon energy. Naturally more complex distributions of intermediate states $f(x)$ would result in other forms for the effective transition rate $W_{\text{eff}}(h\nu)$.

While the model presented is overly simplified, it is instructive to compare it with the data we have for TiO_2 and SrTiO_3 . Figures 8 and 9 show a plot of the quantum efficiency to the 2/3 power vs. photon energy for TiO_2 and SrTiO_3 , respectively. The rather good linear dependence exhibited by the data suggests that the model with a continuum of midgap states extending E_0 from a bandedge is not an unreasonable description of the data. While there is no *a priori* reason to assume that the midgap states extend down from the conduction band rather than up from the valence band, a distribution of defect-related shallow traps have been observed to extend ~ 0.8 eV below the conduction bandedge (14) in TiO_2 . The 0.8 eV agrees rather well with the intercept shown in Fig. 8. The similarity in physical and chemical properties of TiO_2 and SrTiO_3 suggests

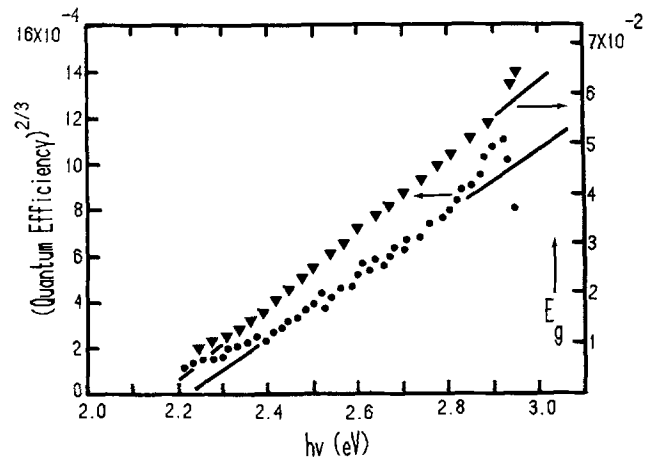


Fig. 8. Quantum efficiency to the 2/3 power vs. photon energy for TiO_2 . The dots are for the undoped TiO_2 data shown in Fig. 1, while the triangles are Cr-doped TiO_2 data taken from Ref. (12). The straight line behavior is expected for the model discussed in the text.

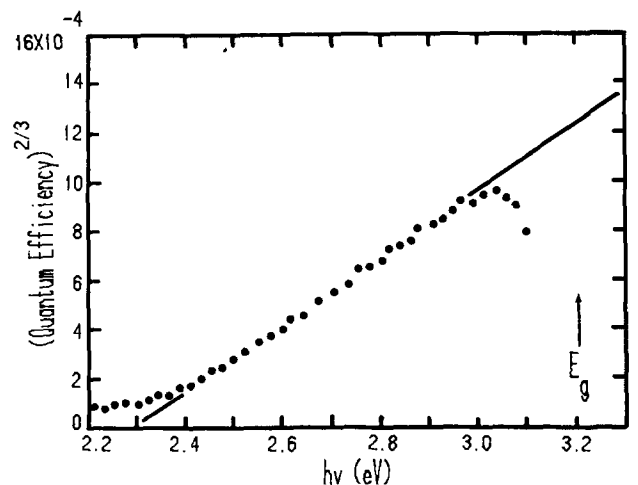


Fig. 9. Quantum efficiency to the 2/3 power vs. photon energy for the SrTiO_3 data shown in Fig. 2. The straight line behavior is expected for the model discussed in the text.

that a similar behavior for SrTiO_3 is not unreasonable. The tailing of the data exhibited below 2.4 eV is due to the noise level and poor baseline location. The peak around 2.9 eV in TiO_2 could come from a nonuniform distribution of states in the gap. This is an area that needs further exploration.

The model described above is unfortunately not unique. The same photon energy dependence can be obtained by assuming the two-step model with a single discrete intermediate state at an energy E_0 from a bandedge and that each transition is a forbidden direct transition (12). This model would lead to the same $3/2$ power dependence of W_{eff} on photon energy. However, the known distribution of midgap states (14) tends to favor our initial model for interpretation of the data.

Intentional doping of TiO_2 to extend the photoresponse to energies below E_g has been explored and found to show some promise (15). However, the mechanism for this effect has not been defined. In Fig. 8 we show the extended photoresponse of Cr-doped TiO_2 (15) plotted as the quantum efficiency to the $2/3$ power. The striking linear dependence and the similar intercept for this much stronger subband gap response suggests a similarity in mechanism for the Cr-doped TiO_2 and the ostensibly undoped samples. Since the intercept does not seem to correlate with the position of the Cr acceptor levels in TiO_2 (15), we would like to propose another interpretation of this data. Substitutional doping of TiO_2 with Cr requires the generation of charge compensating defects. We suggest that these defects are the same defects responsible for the subband gap response in both the Cr-doped and undoped samples of TiO_2 . Furthermore, the two-step model described in this paper is applicable to both kinds of samples. This interpretation would explain the spectral dependence of the data, both the power law and the intercept, and also remove the requirement for significant impurity band conduction in these samples.

Conclusions

The results of this paper clearly show that subband gap excitation of semiconducting photoelectrodes is possible by a bulk mechanism. This bulk excitation process may be distinguished from surface state excitation by the dependence of the photoresponse on electrode potential. A linear dependence of the photocurrent squared on potential with an intercept at the flat-band potential, implies a uniform excitation process throughout the depletion layer, *i.e.*, a bulk process. The simplified model presented, involving transitions to states in the gap, is capable of explaining qualitatively the dependence of the photocurrent on light intensity and wavelength. However, our lack of knowledge about the distribution of midgap states puts the model on a very tentative footing. A brief examination of the extended spectral response in Cr-doped TiO_2 suggests that the same model is applicable in these samples. It is proposed that the relevant midgap states arise from charge compensating defects generated by the Cr doping process.

These results in both the Cr-doped and undoped TiO_2 samples suggest further doping experiments with impurities which produce known states in the TiO_2 bandgap. Such experiments are necessary to test the validity of the proposed model and to explore some of the detailed aspects such as type of transition and the validity of the assumptions of the model.

Acknowledgments

One of us (MAB) is grateful to the Instituto de Física, UNICAMP, for its hospitality during a visit when this work was initiated, and to the Organization of American States for financial support during the visit. We thank Dr. J. H. Nicola for assistance with the argon ion laser experiments. Work at Sandia was supported by the Materials Science Program, Division of Basic Energy Sciences, U.S. Department of Energy under Contract DE-ACO4-76-DP00789 and work at UNICAMP was supported through grants from FAPESP, FINEP, and PICD.

Manuscript submitted May 19, 1980; revised manuscript received July 22, 1980. This was Paper 643 presented at the Los Angeles, California, Meeting of the Society, Oct. 14-19, 1979.

Any discussion of this paper will appear in a Discussion Section to be published in the December 1981 JOURNAL. All discussions for the December 1981 Discussion Section should be submitted by Aug. 1, 1981.

Publication costs of this article were assisted by Sandia National Laboratories.

REFERENCES

- Several reviews have recently been written on this subject including: M. A. Butler and D. S. Ginley, *J. Mater. Sci.*, **15**, 1 (1980) and A. J. Nozik, *An. Rev. Phys. Chem.*, **29**, 189 (1978).
- R. H. Wilson, *CRC Crit. Rev.*, In press.
- J. G. Mavroides and D. F. Kolesar, *J. Vac. Sci. Technol.*, **15**, 538 (1978).
- D. Laser and S. Gottesfeld, *This Journal*, **126**, 475 (1979).
- H. Morisaki, M. Hariya, and K. Yazawa, *Appl. Phys. Lett.*, **30**, 7 (1977).
- D. D. MacDonald, "Transient Techniques in Electrochemistry," p. 32, Plenum, New York (1977).
- F. Decker, J. F. Juliaio, and M. Abramovich, *Appl. Phys. Lett.*, **35**, 397 (1979).
- M. A. Butler, *J. Appl. Phys.*, **48**, 1914 (1977).
- R. H. Wilson, *J. Appl. Phys.*, **48**, 4292 (1977).
- J. Reichman, *Appl. Phys. Lett.*, **36**, 574 (1980).
- C. Kittel, "Elementary Statistical Physics," Part 3, Wiley, New York (1958).
- J. I. Pankove, "Optical Processes in Semiconductors," Chap. 3, Dover, New York (1971).
- F. P. Koffyberg, K. Dwight, and A. Wold, *Solid State Commun.*, **30**, 433 (1979).
- A. K. Ghosh, F. G. Wakim, and R. R. Addiss, *Phys. Rev.*, **184**, 979 (1969).
- A. K. Ghosh and H. P. Maruska, *This Journal*, **124**, 1516 (1977).

Surface Stability Studies on Some CRT Phosphors

S. Sinharoy, A. S. Manocha, and F. M. Ryan*

Westinghouse R&D Center, Pittsburgh, Pennsylvania 15235

Recently developed techniques of surface analysis (1-3), such as Auger electron spectroscopy (AES), electron spectroscopy for chemical analysis (ESCA), secondary ion mass spectrometry (SIMS), and ion scattering spectroscopy (ISS) etc., have found widespread application in the electronic, chemical, and metallurgical industries. The purpose of the present study was to demonstrate the usefulness of one of these techniques, namely ESCA, in the study of surface composition of phosphors, as well as the chemical stability of these phosphors under ion bombardment. This chemical stability is of particular interest in applications where phosphors are subjected to ion impact such as in plasma discharge displays.

ESCA was chosen in preference to the other common techniques mentioned above for the following reasons: (i) the primary excitation in ESCA is caused by soft x-rays rather than electrons or ions, thereby providing a nondestructive analytical tool for sensitive surfaces; (ii) surface charging effects are not as severe as in the other techniques and can be corrected very easily, thus providing a distinct advantage in the analysis of samples that are electrically nonconducting; (iii) it is a surface sensitive ($\sim 50\text{\AA}$) technique, and it provides information about the elemental composition (down to a level of 0.1 atomic percent) at the surface. Although the other techniques are slightly more surface sensitive and some of them (SIMS, ISS) can detect elements present to a much lower level, ESCA provides information over a larger sampling area of the surface. This is an advantage for the type of studies reported here. (iv) It provides information about the chemical bonding states of the elements detected on the surface. In this respect, the other techniques are not nearly as efficient.

There are also some disadvantages inherent in the ESCA technique. For example, (i) data acquisition process is very slow and (ii) meaningful data cannot be acquired simultaneously while the sample surface is being sputter-etched with inert gas ions.

In this particular case, the advantages of using ESCA far outweighed the disadvantages, mainly because of the nature of the samples and the type of information desired.

Experimental

Eight different types of CRT phosphor in powder form were obtained from various commercial sources for analysis. The phosphor types were the following: (i) YO₂ red, Y₂O₃:Eu; (ii) red YVO₄:Eu; (iii) Y(VO₄)_{1/2}(PO₄)_{1/2}:Eu³⁺; (iv) CaWO₄:Pb; (v) Y₂O₂S:Eu³⁺; (vi) P-22 green, ZnCdS:(Ag); (vii) P-22 blue, ZnS:(Ag); and (viii) P-22 red, CdS:(Ag).

ESCA analysis of the phosphor samples were performed in a GCA-McPherson/36 photoelectron spectrometer, using a magnesium anode as the source of primary x-rays (1253.6 eV). Some of the powders were analyzed in the form of pellets and the others on indium foil. In the latter case, the larger crystals

were ground in a wig-1-bug, the powder sprinkled between two indium foils and pressed to 1 ton/in.² for 1 min. The samples were mounted on a carousel sample holder. The pressure in the experimental chamber was in the low 10⁻⁹ Torr range. The chamber was equipped with an ion gun for sputter etching of the samples. The sputter rate was estimated to be approximately 5 Å/min. By alternating argon ion sputtering with ESCA measurements, it was possible to determine the composition and chemical state as a function of depth in each sample.

Results

Two types of spectra were plotted for each of the phosphor samples. The first was a 1000 eV "survey scan" to identify the various elements present on the surface. The second type consisted of high resolution spectra of lines corresponding to core level transitions of elements of interest. Both types of spectra were plotted before sputtering, and after various stages of sputtering. All binding energy values reported in this paper have been corrected for charging effects following the procedure of Wagner *et al.* (4), by making the carbon 1s line due to the adventitious hydrocarbon contaminant appear at 284.6 eV. The 1000 eV survey scans of all the phosphors show the presence of the common hydrocarbon and oxygen contaminants from the atmosphere. No special mention of these two contaminants will be made in the following. The results obtained in the various phosphors are presented and discussed below.

Y₂O₃:Eu.—A survey scan of this phosphor, shown in Fig. 1, reveals the presence of silicon as the only contaminant detected on the surface. The activator (Eu) concentration was below the level of detection of the spectrometer. High resolution spectra of the Y3d and O1s lines of the as-received and sputter-etched surfaces are shown in Fig. 2. It is clear that with the progress of sputtering, the impurity oxygen de-

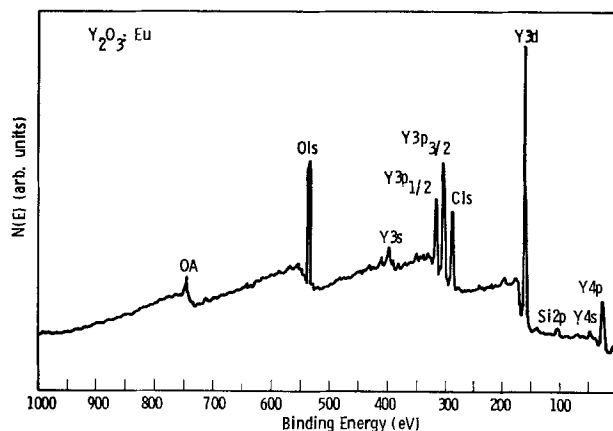


Fig. 1. Survey scan of Y₂O₃:Eu

* Electrochemical Society Active Member.

Key words: inorganic, cathodoluminescence, ESCA.

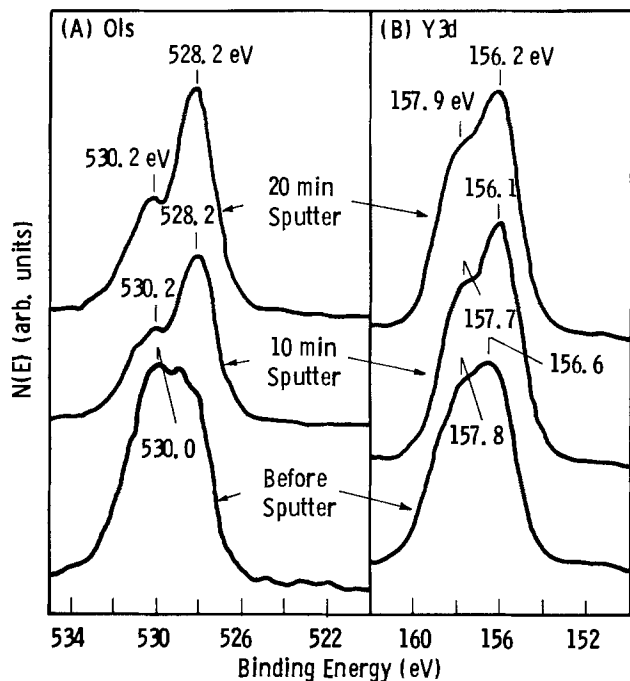


Fig. 2. High resolution O1s and Y3d lines of $Y_2O_3:Eu$ as received, after 10 min sputter and after 20 min sputter.

creases, resulting in the gradual decrease of the 530.1 eV component of the O1s line, and a slight improvement in the resolution of Y3d_{5/2,3/2} and Y3d_{3/2} peaks. There were no significant changes in the peak positions after 20 min of sputtering, indicating that $Y_2O_3:Eu$ is quite stable chemically under argon ion bombardment.

$YVO_4:Eu$.—Silicon was again the only contaminant detected on the phosphor surface. The high resolution spectra of the Y3d_{5/2,3/2}, O1s, and V2p_{3/2} lines after various periods of sputtering are shown in Fig. 3. The most significant change was observed in the V2p_{3/2} peak which shifted gradually to lower binding energies after 10 and 20 min sputtering. The binding energy shift, which was accompanied by a gradual broadening of the peak, was 1.9 eV after 20 min sputtering. The shift to lower binding energies is indicative of the transformation of vanadium to a lower oxidation state (4). However, the broadening would indicate that the transformation is not complete after 20 min sputtering.

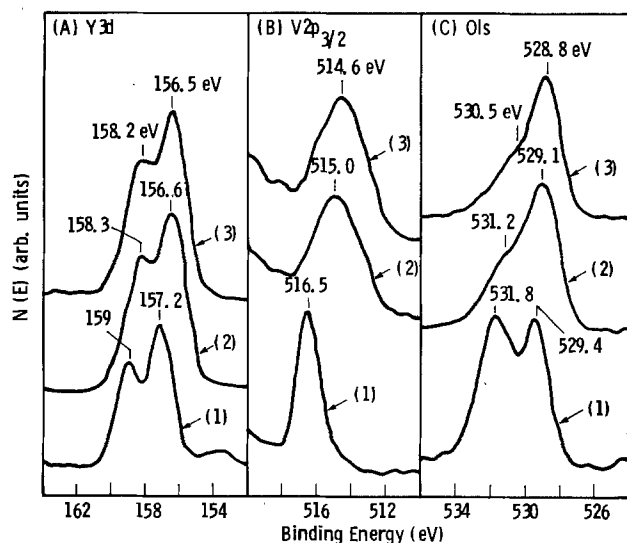


Fig. 3. High resolution Y3d, O1s, and V2p_{3/2} lines of $YVO_4:Eu$; curve (1) as received, curve (2) after 10 min sputter, and curve (3) after 20 min sputter.

Vanadium is thus present in a mixed oxidation state after 20 min of ion bombardment, the transformation being of the form $V^{V} \rightarrow V^{V} + V^{IV}$, the likely reduction process being $YVVO_4 \rightarrow Y_2V_2^{IV}O_7$. The Y3d_{5/2} and O1s peaks showed much smaller shifts in the B.E. after 20 min of argon ion bombardment. The binding energy 528.8 eV of O1s must be representative of oxygen in VO_4^{3-} and $V_2O_7^{6-}$ states.

$Y(VO_4)_{1/2}(PO_4)_{1/2}:Eu^{+3}$.—The survey spectrum of this phosphor did not indicate the presence of any impurities on the surface. The behavior under argon ion bombardment was quite similar to that of the vanadate phosphor. This is illustrated in Fig. 4, where the high resolution spectra of Y3d_{5/2,3/2}, P2p, O1s, and V2p_{3/2} lines of $Y(VO_4)_{1/2}(PO_4)_{1/2}$ have been plotted after various periods of sputtering. Both the P2p and V2p_{3/2} peaks undergo a gradual shift in the binding energy to lower energies, accompanied by a broadening of the peaks. As in the case of the vanadate phosphor, the shifts can be attributed to transformation of phosphorus and vanadium to lower oxidation states, the broadening being due to the presence of mixed oxidation states. As can be seen from Fig. 4, the trend towards reduction to lower oxidation states was continuing after 20 min argon ion bombardment. This is evidenced by the appearance of a new shoulder at 131.8 eV in case of P2p and continuing development of the shoulder at 514.3 eV in case of the V2p_{3/2} peak.

$CaWO_4:Pb$.—The survey spectrum of this phosphor, shown in Fig. 5, reveals the presence of a significant

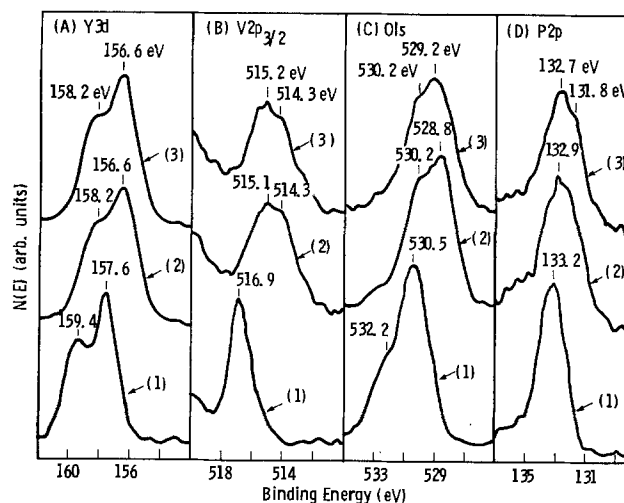


Fig. 4. High resolution Y3d, O1s, V2p_{3/2}, and P2p lines of $Y(VO_4)_{1/2}(PO_4)_{1/2}:Eu^{+3}$. Curve (1) as received, curve (2) after 10 min sputter, and curve (3) after 20 min sputter.

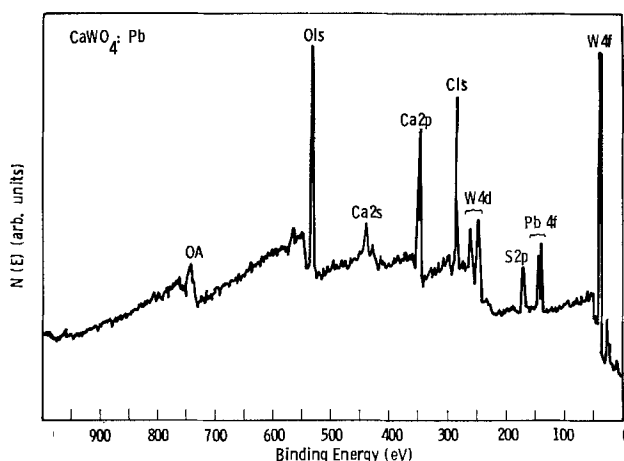


Fig. 5. Survey scan of $CaWO_4:Pb$

amount of lead on the surface, suggesting an enhancement of activator concentration at the surface region. The lead was present in the form of PbO^4 . There was also a significant amount of sulfur contaminant at the surface. After 10 min of argon ion bombardment, the Pb concentration fell below the level of detection. High resolution spectra of the $W4f_{7/2,5/2}$, $Ca2p_{3/2}$, and $O1s$ photoelectron transitions are shown in Fig. 6. Notice the splitting of the $W4f$ peak, indicating partial reduction of the tungsten in $CaWO_4$ to metallic tungsten (4). The small shift accompanied by some broadening of the $Ca2p_{3/2}$ peak indicates (4) the conversion of $CaWO_4$ to a mixture of CaO and $CaWO_4$. The partial reduction of $CaWO_4$ to W and CaO under argon ion bombardment might have taken place through intermediate metastable $CaWO_3$.

The sulfide phosphors ($ZnCdS:Ag$, $ZnS:Ag$, $CdS:Ag$, and $Y_2O_2S:Eu^{+3}$).—A small amount of silicon contaminant in the form of SiO_2 was detected in all sulfide phosphors studied. The activator amount was below the level of detection. The binding energies and widths of the $S2p$, $Cd3d_{5/2}$, and $Y3d_{5/2}$ photoelectron peaks and the zinc Auger peak of these phosphors remained unchanged after up to 20 min of argon ion bombardment, attesting to their chemical stability. The spectra corresponding to $S2p$, $Cd3d_{5/2}$, and zinc Auger lines from $ZnCdS$, ZnS , and CdS phosphors are shown in Fig. 7. In case of Y_2O_2S (Fig. 8), the $Y3d_{5/2}$ peak appeared in an altered form because of interference with the $S2p$ photoelectron peak. Sulfur in this phosphor had to be detected on the basis of the $S2s$ photoelectron peak, which had a much lower intensity compared to the $S2p$ peak. A measurement of the peak heights corresponding to the main elements in all the sulfide phosphors yielded information about the relative abundance of sulfur at various depths from the surface after sputtering. An examination of the results listed in Table I reveals that $ZnCdS$ and CdS are deficient in sulfur at the surface, relative to the bulk down to about 100Å. In case of ZnS and Y_2O_2S , the reverse appeared to be true. The reason for choosing the zinc Auger line in preference to a photoelectron peak in the results discussed above is the fact that for zinc, the Auger line is known (5) to be more sensitive to changes in the chemical environment.

Discussion

On the basis of the ESCA results presented in the previous section, the following conclusions can be made for the phosphors studied.

(i) Silicon is the principal surface contaminant in most of the phosphors examined. Probable sources of the silicon contamination are from the quartz used

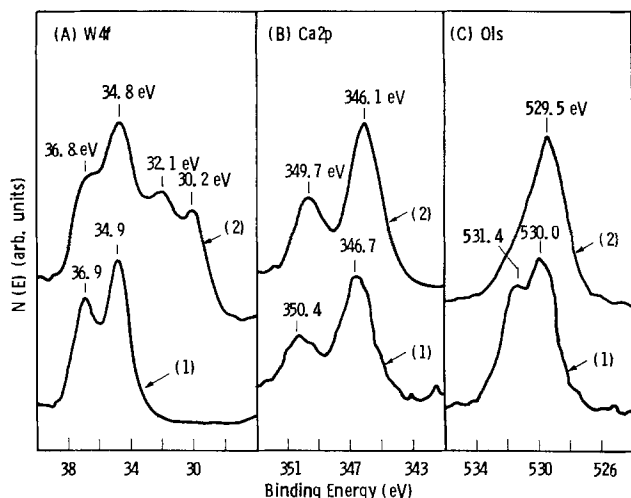


Fig. 6. High resolution $W4f$, $Ca2p$, and $O1s$ lines of $CaWO_4:Pb$. Curve (1) as received and curve (2) after 10 min sputter.

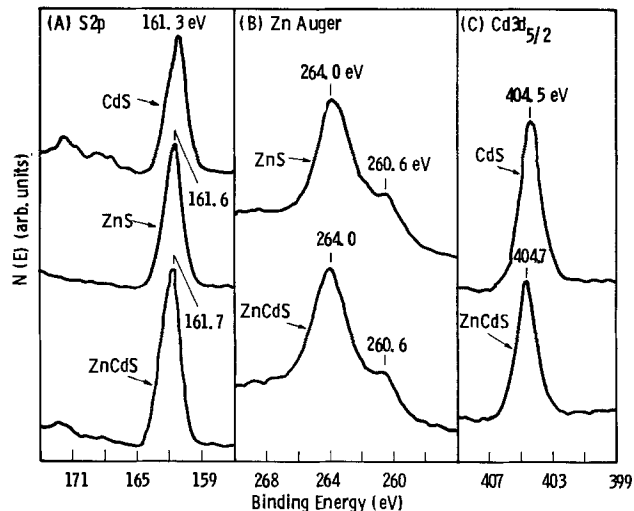


Fig. 7. High resolution $S2p$, $Cd3d_{5/2}$, and Zn Auger lines of $ZnCdS$: (Ag or Cu), ZnS : (Ag or Cu), and CdS : (Ag or Cu).

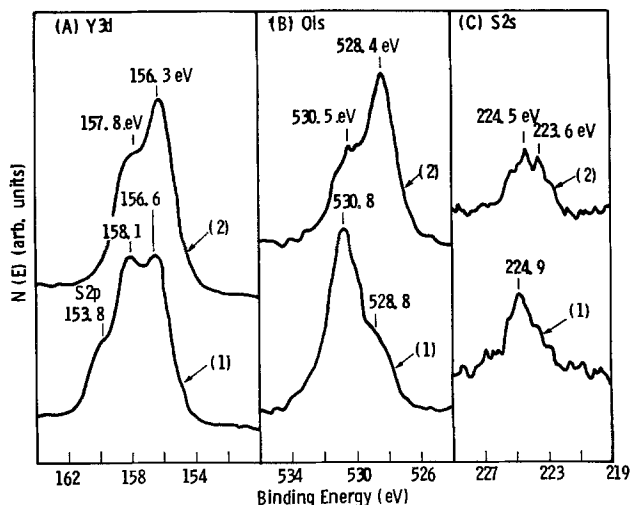


Fig. 8. High resolution $Y3d$, $O1s$, and $S2s$ lines of $Y_2O_2S:Eu^{+3}$. Curve (1) as received and curve (2) after 10 min sputter.

during preparation or from the "silicizing" used with some commercial phosphors. There was a significant amount of sulfur in the tungstate phosphor studied.

(ii) The calcium tungstate has a higher concentration of the activator (Pb) at the surface, compared to the bulk. The activator concentration in all the other phosphors (including the bulk activator concentration in calcium tungstate) is below the level of detection by ESCA. Migration of lead to the surface has also been observed (6) in glasses, where trace levels of Pb appear as percent levels on the surface.

(iii) The vanadate, vanadate-phosphate, and the tungstate phosphors reduce to lower oxidation states as a result of ion bombardment, whereas the oxide and the sulfide phosphors are chemically stable under ion bombardment for a limited time (up to 20 min). We have not studied the long-term stability of these phosphors under ion bombardment.

The present study deals with argon ions of 10 keV energy. These ions are normally used for sputter etchings and their advantage lies in penetrating the entire sampling depth. Smaller ions and electrons of the same energy are expected to have less damaging effects. Knowledge about the nature of the target material is very essential, e.g., SiO_2 powder shows (7) higher stability than SiO_2 films obtained on oxidation of silicon wafers.

Table I. Relative change in sulfur content at various depths from the surface in the sulfide phosphors

| Phosphor | ZnS | | ZnCdS | | CdS | | Y ₂ O ₃ S (Sample 1) | | Y ₂ O ₃ S (Sample 2) | |
|---|------|------|-------|------|------|------|--|------|--|------|
| | 0 | 2 | 13 | 0 | 10 | 20 | 0 | 10 | 0 | 10 |
| Sputter time (min) | 0.55 | 0.51 | 0.50 | 0.64 | 0.69 | 0.79 | 1.31 | 2.17 | — | — |
| ESCA peak height ratio S _{2p} /ZnA | — | — | — | 0.38 | 0.49 | 0.54 | 0.19 | 0.24 | — | — |
| ESCA peak height ratio S _{2p} /Cd3d _{5/2} | — | — | — | — | — | — | — | — | 0.07 | 0.03 |
| ESCA peak height ratio S _{2s} /Y3d _{5/2} | — | — | — | — | — | — | — | — | 0.07 | 0.03 |

Often times, reduction of a higher oxide to the elemental stage requires large amounts of energy, e.g., W in tungstate to the metallic state. In such cases, reduction proceeds via intermediate, stable or metastable states. The extent to which the different states may appear is a function of the fate of the released species. For instance the released species may recombine with the reduced species. In an extreme case, Storp and Holm (7) observed the formation of nitrates on reduction of nitrites.

Also, carbonates easily decompose under argon ions. In a closed system they may act as a source of oxygen for oxidation and carbon for reduction. The extent of reduction and the amount of various species as observed in our studies is therefore only a small step in understanding the nature of various processes that may be occurring in real systems. Our studies do however indicate that under similar conditions, the oxides and sulfides of the materials studied here are more stable towards ion-induced damage than the vanadates, phosphates and tungstates.

(iv) ZnCdS and CdS phosphors were found to be sulfur deficient at the surface compared to a depth of about 100Å from the surface. The reverse is true for ZnS and Y₂O₃S phosphors.

In this study we have shown that the surface composition of these phosphors can differ greatly from the bulk. This difference extends only a small distance into the bulk (~100Å) so that it comprises less than 1% of the phosphor particle volume and its presence cannot be inferred from bulk analysis. ESCA studies, coupled with ion sputtering, have proven to be ideally suited for studying such surface layers.

Summary

There are two significant results that we have obtained from these studies. One is that many phosphors lack chemical stability under ion impact, making them unlikely candidates for ion excited phosphor display panels. The second result is that many commercially important cathode ray phosphors possess an outer layer of differing composition. One can speculate that the presence of this outer layer may play

an important role in the functioning of the phosphor, particularly at high current densities. The saturation and loss of efficiency of cathode-ray phosphors at high current densities can be caused by diffusion of excitation energy to the surface of the phosphor where nonradiative recombination can occur. The presence of a second phase region, extending in an appreciable distance from the surface, will certainly affect this process. It is conceivable that this outer layer could tend to repel diffusing electron or holes away from the surface by means of a charge layer or by an increase in the bandgap energy near the surface. Further ESCA studies, coupled with saturation and efficiency measurements, should be capable of determining if such processes do indeed exist.

Manuscript received July 16, 1980. This was Paper 214 presented at the St. Louis, Missouri, Meeting of the Society, May 11-16, 1980.

Any discussion of this paper will appear in a Discussion Section to be published in the December 1981 JOURNAL. All discussions for the December 1981 Discussion Section should be submitted by Aug. 1, 1981.

Publication costs of this article were assisted by Westinghouse Electric Corporation.

REFERENCES

1. A. W. Czanderna, Editor, "Methods of Surface Analysis," Elsevier, Amsterdam (1975).
2. P. F. Kane and G. R. Larrabee, Editors, "Characterization of Solid Surfaces," Plenum Press, New York (1974).
3. L. Fiermans, J. Vennik, and W. Dekeyser, Editors, "Electron and Ion Spectroscopy of Solids," Plenum Press, New York (1978).
4. C. D. Wagner, W. H. Riggs, L. E. Davis, J. F. Moulder, and G. E. Muilenberg, Editors, "Handbook of X-Ray Photoelectron Spectroscopy," Perkin-Elmer Corporation, Eden Prairie, Minn. (1979).
5. C. D. Wagner, L. H. Gale, and R. H. Raymond, *Anal. Chem.*, **51**, 466 (1979).
6. A. S. Manocha, Unpublished results.
7. S. Storp and R. Holm, *J. Electron Spectros. Relat. Phenom.*, **16**, 183 (1979).

Luminescence in the SrO-Li₂O-P₂O₅:Mn, Ce System

A. Wachtel*

Westinghouse R&D Center, Pittsburgh, Pennsylvania 15235

Koelmans and Cox (1) reported the luminescence of (Sr, M)₃(PO₄)₂:Sn²⁺ where M is an ion such as Mg, Ca, Zn, Cd, Al which promotes the formation of the βCa₃(PO₄)₂ structure in Sr₃(PO₄)₂. They also have shown that the Mn emission in βSr₃(PO₄)₂:Mn, Sn²⁺ is relatively narrow and centered near 615 nm. Kroeger (2) sensitized Ca₃(PO₄)₂:Mn and Sr₃(PO₄)₂:Mn with Ce³⁺ and Froelich (3) charge-compensated Ce³⁺ in (Ca, Sr)₃(PO₄)₂:Mn, Ce with Li or Na.

During attempts to find an inexpensive replacement for Y₂O₃:Eu³⁺ in "Ultralume" (red + green +

blue emitting) fluorescent lamps, recent studies in this laboratory concerned Mn + Ce activated compositions along the Sr₃(PO₄)₂-Li₃PO₄ join. A small amount of Al (~0.09 Al per 2P) as well as the usual small excess of P₂O₅ was also found advantageous.

Phosphors were prepared by firing the mixed phosphates, carbonates, or oxides in air for 1 hr, followed by NH₃ for 2 hr. Firing temperatures depended on the composition and the oxidation state of the activators. It was interesting to note that for maximum red fluorescence intensity, the temperature had to be chosen so as to obtain hard rather than friable products. In optimized compositions firing temperatures ty-

* Electrochemical Society Active Member.
Key words: inorganic, visible, fluorescence.

pically ranged from 820° to 850°C. 254 nm excited fluorescence was measured through filters to isolate the red (Mn^{2+}) and u.v. (Ce^{3+}) bands and are reported in arbitrary units which are not comparable with each other.

The total Li content of the compositions between $M_3^{2+}(PO_4)_2$ and Li_3PO_4 included the charge compensation scheme $2Sr^{2+} = M^{3+} + Li^+$ so that a small amount of the Li remained part of the M^{2+} component. Compositions along the join therefore contained

$$Sr = 3 - Mn - 2(Ce + Al) - x$$

$$Li = (Ce + Al) + 2x$$

where $0 \leq x \leq 3 - Mn - 2M^{3+}$.

Figure 1 shows the relative fluorescence of phosphors as a function of x . It can be seen that between $x = 0.5$ and 1 ($SrLiPO_4$), both emissions, i.e., overall efficiency, decrease. Below $x = 0.5$ and above $x = 1$, Ce^{3+} emission increases while the Mn^{2+} emission decreases (energy transfer decreases); no independent measurements of overall efficiency were taken. It is clear, however, that maximum red fluorescence obtains approximately midway between the ideal compositions $Sr_3(PO_4)_2$ and $SrLiPO_4$.

X-ray powder diffraction analyses of phosphor powders with $x = 0, 0.533$, and 1 showed no significant differences, despite the fact that $Sr_3(PO_4)_2$ and $SrLiPO_4$ (4) have different structures. In all cases, reflections due to α and β $Sr_3(PO_4)_2$ (the latter predominating) were found. (Lines due to $SrLiPO_4$ as well as several weaker lines which could not be indexed were also noted.) Table I shows the data obtained for $x = 0.533$ where the lines assigned to β $Sr_3(PO_4)_2$ are based on published analyses of $(Ca, Sr)_3(PO_4)_2$ with allowances made for lattice contraction due to Mn, Al, and Li. The complexity of the pattern is consistent with earlier observations by Koelmans and Cox (1). They stated that $Sr_3(PO_4)_2$ containing additives which promote the β $Ca_3(PO_4)_2$ modification, displays a highly distorted structure if fired at high temperatures. Annealing at 600°C for 1 hr which caused a 10% reduction in fluorescence intensity had no effect on the pattern, neither did washing in dilute HCl which dissolves most of the Li_3PO_4 without significant change in fluorescence.

Figure 2 shows luminescence as a function of Mn and Ce. As one may expect, energy transfer from Ce to Mn increases rapidly with Mn concentration up to the optimum, after which it levels off. Measurements of quantum efficiency for compositions with $x = 0.53$, $Mn = 0.17$, and $Ce = 0.08-0.935$ range between 0.8 and 1.0. However, absorption of 254 nm is relatively

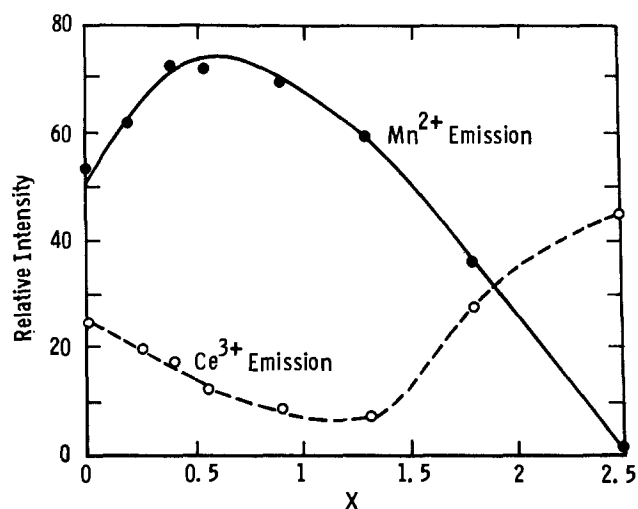


Fig. 1. 254 nm excited fluorescence of $Sr_{2.495-x}Mn_{0.131}Ce_{0.0935}Al_{0.0935}Li_{0.187+2x}P_{2.08}O_{8.2}$.

Table I. X-ray powder diffraction pattern obtained for the composition shown in Fig. 3 ($x = 0.533$)

| Assignment | d | I | Assignment | d | I |
|---------------------------|-------|-----|-------------------|-------|----|
| | 7.375 | 6 | | 2.704 | 9 |
| β | 6.712 | 8 | β | 2.682 | 6 |
| α | 6.578 | 3 | $\beta, SrLiPO_4$ | 2.657 | 62 |
| β | 5.310 | 32 | | 2.606 | 12 |
| β | 4.478 | 9 | | 2.554 | 3 |
| α | 4.366 | 2 | α | 2.530 | 3 |
| | 4.168 | 2 | | 2.463 | 4 |
| | 4.111 | 2 | | 2.402 | 2 |
| | 3.981 | 6 | | 2.378 | 2 |
| $SrLiPO_4$ | 3.837 | 4 | | 2.282 | 3 |
| α, β | 3.623 | 29 | $SrLiPO_4$ | 2.240 | 14 |
| β | 3.434 | 22 | α, β | 2.193 | 10 |
| | 3.411 | 25 | | 2.083 | 15 |
| β | 3.361 | 12 | | 2.065 | 11 |
| | 3.330 | 9 | | 2.047 | 13 |
| β | 3.278 | 30 | α, β | 2.006 | 2 |
| | 3.183 | 4 | $\beta, SrLiPO_4$ | 1.987 | 24 |
| | 3.127 | 5 | | 1.939 | 12 |
| β | 3.065 | 13 | | 1.924 | 5 |
| $\alpha, \beta, SrLiPO_4$ | 2.993 | 100 | | 1.920 | 7 |
| | 2.900 | 4 | | 1.861 | 9 |
| β | 2.840 | 8 | | 1.848 | 6 |
| β | 2.778 | 6 | α | 1.832 | 4 |
| | | | | 1.812 | 28 |

Notes: α = similar to α $Sr_3(PO_4)_2$ —hexagonal—but with contracted lattice. β = based on β $(Sr, Ca)_3(PO_4)_2$ (6) data but with contracted lattice. $SrLiPO_4$ = see Ref. (4). Additional lines were found only in rare instances.

weak and does not exceed 0.9 even for 5-30 μm particles which were freed of fines by DTPA¹ washing and elutriation.

Figure 3 shows the emission and reflectance spectra of an optimized phosphor. The Mn emission band shows a half-width of 72 nm and its shape and position is identical to that of $\beta(Sr, Al)_2(PO_4)_2:Mn, Sn^{2+}$. Its intensity is about 1.3 times as high, but in contrast to the Sn-sensitized species, the Ce^{3+} has a greater tendency to oxidize on heating in air. The SPD is also the same at least between $x = 0$ and 1. In this connection, it should be noted that essentially the same Mn emission is reported for $SrLiPO_4:Mn, Cu^+$ (4) and $\beta(Sr, Al)_3(PO_4)_2:Mn, Cu^+$ (5). Thus, we cannot distinguish the presence of $SrLiPO_4$ in our phos-

¹ Diethylenetriaminepentaacetic acid diammonium salt.

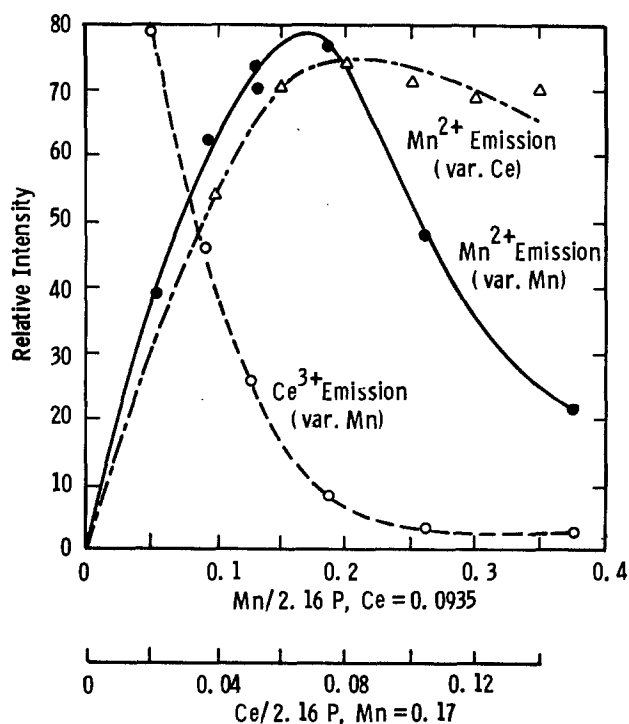


Fig. 2. 254 nm excited fluorescence of $Sr_{2.094-y}Mn_yCe_{0.0935}Al_{0.0935}Li_{1.253}P_{2.16}O_{8.4}$ (upper abscissa) and of $Sr_{2.11-2z}Mn_{0.17}Ce_zAl_{0.0935}Li_{1.16+z}P_{2.16}O_{8.4}$ (lower abscissa).

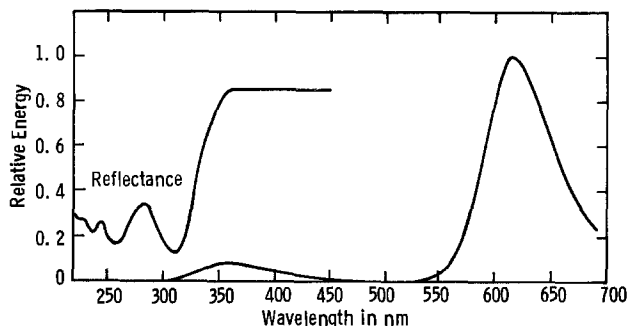


Fig. 3. Reflectance and 254 nm excited emission of $\text{Sr}_{1.923}\text{Mn}_{0.17}\text{-Ce}_{0.0935}\text{Al}_{0.0935}\text{Li}_{1.253}\text{P}_{2.16}\text{O}_{8.4}$.

phors from $\beta\text{Sr}_3(\text{PO}_4)_2$ on the basis of emission spectra.

Unfortunately, our x-ray patterns give no additional information concerning the presence of SrLiPO_4 . The patterns vary little over this composition range despite the fact that one might expect to see an increase of intensity of lines due to SrLiPO_4 as the proportion of Li_3PO_4 in the mixture is increased. In particular the second strongest line of the compound SrLiPO_4 , $d = 2.501\text{\AA}$, is missing from the pattern, and other lines which can be attributed to SrLiPO_4 lie close to lines for α and $\beta\text{Sr}_3(\text{PO}_4)_2$ (Table I). Several unindexed lines also remain in the pattern. Thus we cannot distinguish from our data whether Li_3PO_4 (i) enters a glassy phase during firing which cannot be detected by x-ray diffraction, (ii) enters into an unidentified phase which produces the unindexed lines in our pattern, or (iii) the reaction between Li_3PO_4 and $\text{Sr}_3(\text{PO}_4)_2$ proceeds so slowly that no significant amount of SrLiPO_4 formed during the firing process we used.

The important finding of the present study is the observation that there exists a multi-phase mixture along the $\beta\text{Sr}_3(\text{PO}_4)_2\text{-SrLiPO}_4$ join in which Mn fluorescence is sensitized by Ce^{3+} more efficiently than at either end, and also more efficiently than by Sn^{2+} . Based on present data, we feel that the present phosphor consists of $\beta\text{Sr}_3(\text{PO}_4)_2\text{:Ce}^{3+}$, Mn^{2+} and contains Li-bearing phases which act as fluxes.

Acknowledgment

The writer wishes to thank Mr. E. P. Metz for phosphor synthesis and measurements, Drs. W. Lehmann and W. A. Thornton for their help in obtaining spectral measurements, and Mr. R. Kuznicki for x-ray powder diffraction analyses.

Manuscript submitted May 15, 1980; revised manuscript received July 30, 1980.

Any discussion of this paper will appear in a Discussion Section to be published in the December 1981 JOURNAL. All discussions for the December 1981 Discussion Section should be submitted by Aug. 1, 1981.

Publication costs of this article were assisted by Westinghouse Electric Corporation.

REFERENCES

1. H. Koelmans and A. P. M. Cox, *This Journal*, **104**, 442 (1957).
2. F. A. Kroeger, *Physica*, **15**, 801 (1949).
3. H. C. Froelich, *This Journal*, **98**, 400 (1951).
4. W. L. Wanmaker and H. L. Spier, *ibid.*, **109**, 109 (1962).
5. W. L. Wanmaker and C. Bakker, *ibid.*, **106**, 1027 (1959).
6. J. F. Sarver, M. V. Hoffman, and F. A. Hummel, *ibid.*, **108**, 1103 (1961).

Suppression of Thermal Damage in InP Substrates in InGaAs Vapor Phase Epitaxy

Yoshiharu Yamauchi and Nobuhiko Susa

*Nippon Telegraph and Telephone Public Corporation,
Musashino Electrical Communication Laboratory, Musashino-shi, Tokyo, 180, Japan*

Photodiodes made from III-V compound semiconductors have been studied to cover the 1-1.7 μm wavelength region, where silica fibers have low material dispersion (1) and low loss characteristics (2). InGaAs crystal lattice-matched to InP is a suitable material, having sensitivity over this whole wavelength region. Low carrier density semiconductor crystals are desired in order to obtain uniform and reliable avalanche multiplication (3-5). In nonavalanche photodiodes, low carrier concentration is also favorable to low reverse bias voltage operation with low dark current (6) and small capacitance (7-9). Low diode capacitance is also beneficial for high speed response. Vapor phase epitaxy (VPE) is beneficial in obtaining a low carrier density layer. Low carrier concentration and high mobility InGaAs layers (10) can be grown without as much difficulty as the long time In melt heat-treatment (7, 11) encountered in liquid-phase epitaxy (LPE).

In growing high quality InGaAs or InGaAsP layers by VPE, it is important to start crystal growth after material gas flow reaches steady state (10, 12-14).

Key words: photodiode, VPE, crystal.

The authors have devised a quartz slide boat for this purpose (10). Thermal damage to the InP substrates caused by high phosphorus vapor pressure is suppressed by introducing PH_3 (15) or Ar (16) gas into the ambient H_2 gas. In LPE, the damaged surface is etched off by the In melt before growth (17). It has been reported that, in InGaAsP VPE growth, PH_3 gas flowing over the InP substrate is also effective in preventing substrate damage while waiting to establish steady-state gas flow (12-14). The PH_3 gas, however, affects the growth of InGaAs and InGaAsP with low P composition, resulting in lattice mismatch. Experimental results are reported in this letter to the effect that InP thermal damage and the PH_3 contamination in InGaAs layer can be suppressed in the VPE process by using the substrate holder with sliding cover (10).

The substrate holder made of quartz is shown in Fig. 1. The space to contain the substrate is small, only $25 \times 25 \times 1 \text{ mm}^3$, in order to minimize PH_3 gas contamination. Substrates are initially covered with a quartz sliding plate until steady-state gas flow is attained. The cover is slid off to expose the substrate surface for InGaAs deposition. The crystal growth equipment has been reported previously (10, 18).

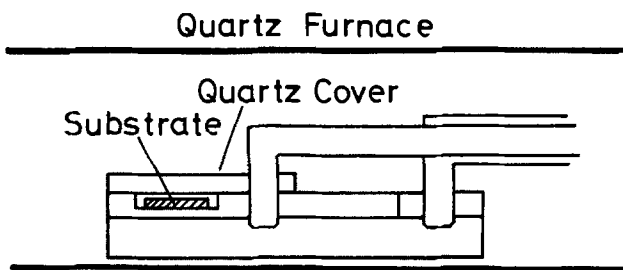


Fig. 1. Schematic view of substrate holder and cover

The InP substrate is mounted on the holder and is inserted into a reaction tube. In a palladium-purified hydrogen atmosphere, the substrate is heated to 730°C. Hydrogen chloride gas, which is obtained by the thermal decomposition of AsCl_3 at 850°C, flows over In and Ga melts. The H_2 carrier gas flow rates passing through AsCl_3 bubblers (16°C for In and 0°C for Ga) are 150 and 55 cm^3/min for the In and Ga melts, respectively. The 4% AsH_3/H_2 gas has a flow rate of 50 cm^3/min . Steady-state gas flow is obtained in about 30 min. InGaAs crystal growth is started by opening the holder cover and exposing the substrate surface to the gas flow.

In order to study the effect of the ambient gas on substrate surface quality, InP crystal heat-treatment experiments were carried out. Substrates mounted in the holder were exposed to temperature of 730°C for 1 hr, which is longer than the time required to establish steady-state gas flow in typical crystal growth procedure. Effects of the sliding cover and PH_3 gas content in hydrogen gas were studied, as shown in the left column in Fig. 2. Iron-doped InP substrates oriented, along (100) and (111)B were etched with

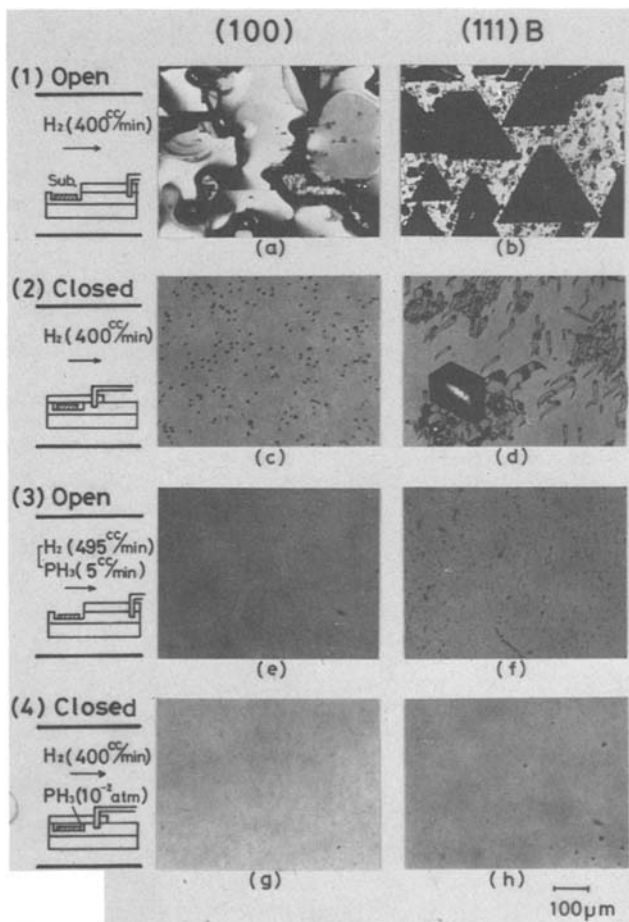


Fig. 2. Phase-contrast photomicrographs of the (100) and (111)B InP surfaces after exposure to various ambient gases at 730°C.

2.5% bromine methanol. Hydrogen gas flowing at 400 cm^3/min rate was used as the ambient gas. In addition, 5% PH_3 gas mixed with H_2 was introduced to the ambient. The PH_3 gas partial pressure was kept at 1×10^{-2} atmosphere pressure, which is higher than the PH_3 equilibrium pressure over In-P liquidus (19). Gas flow rates were measured with mass flow controllers. The substrate mounted in the holder with sliding cover was inserted into the furnace at room temperature and hydrogen ambient gas was flowed for purge. The temperature was then raised to 730°C in about 10 min.

When samples were exposed to the high temperature with the cover opened, as shown in Fig. 2(1), the (100) and (111)B surfaces suffered by severe thermal damage and In droplets appeared, as shown in Fig. 2(a) and (b). Tadpole shapes were observed on the (111)B faces, as previously reported (20), and triangular etching patterns, reported on (111)A face (20), were simultaneously found on the (111)B faces. When the sliding cover is closed, as shown in Fig. 2(2), the substrates shown in Fig. 2(c) and (d) were not as seriously damaged, as those shown in Fig. 2(a) and (b). This is because the phosphorus partial pressure established by initial evaporation suppresses further decomposition. These results show that the cover on the holder effectively seals the substrate. When the ambient gas contains PH_3 , as shown in Fig. 2(3), thermal deterioration is not present, as shown in Fig. 2(e) and (f). The undesired deposition shown in Fig. 2(f), however, was sometimes observed, probably due to Ga, In, and/or AsH_3 used for InGaAs growth. In Fig. 2(4), H_2 and PH_3 gas mixture flows at room temperature and the holder cover is closed. The ambient gas is then switched to pure H_2 . The substrate cell, in which PH_3 gas is sealed, is then heated to 730°C for 1 hr. The substrates after this heat-treatment show no thermal damage, as shown in Fig. 2(g) and (h). This treatment is useful in preventing the deposition shown in Fig. 2(f), as well as in preventing thermal damage. Similar experiments were carried out by using sulfur-doped InP substrates, yielding the same results as in Fig. 2.

InGaAs crystal growth was carried out after the steady-state gas flow was established. The substrate is in the H_2 and PH_3 ambient delivered in Fig. 2(4) and is then exposed to the stationary gas flow. Crystal thickness of 2.5 μm is obtained after 20 min growth. The layer was studied by electron probe microanalysis (EPMA) and Auger analysis, whose phosphorus detection limits are 1×10^{19} and $1 \times 10^{20} \text{ cm}^{-3}$, respectively. No traces of phosphorus atoms were detected, to the 10^{19} cm^{-3} concentration accuracy, on the InGaAs surface by the EPMA method. Auger measurements of a 3° angle polished sample are shown in Fig. 3. The acceleration voltage was 10 kV and the electron probe diameter less than 1 μm . The P concentration profile de-

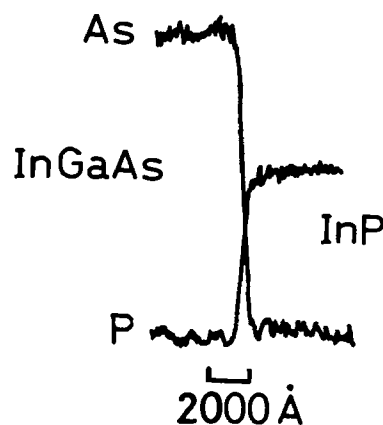


Fig. 3. Composition profile of InGaAs/InP layer by Auger analysis

creases rapidly in the InGaAs layer, and no PH_3 contamination in the layer was observed in this analysis either.

The double crystal x-ray diffraction rocking curve for this layer is shown in Fig. 4. The lines correspond to (400) plane reflection of the Cu-K α 1 line in InP and InGaAs. The InGaAs layer has a lattice constant slightly larger than that of InP due to the deviation of Ga and In compositions from the matching condition, not because of phosphorus atom contamination. Lattice mismatch $\Delta a/a$ is 0.002. Full widths at half maximum for the InGaAs layer and the InP substrate are 45 and

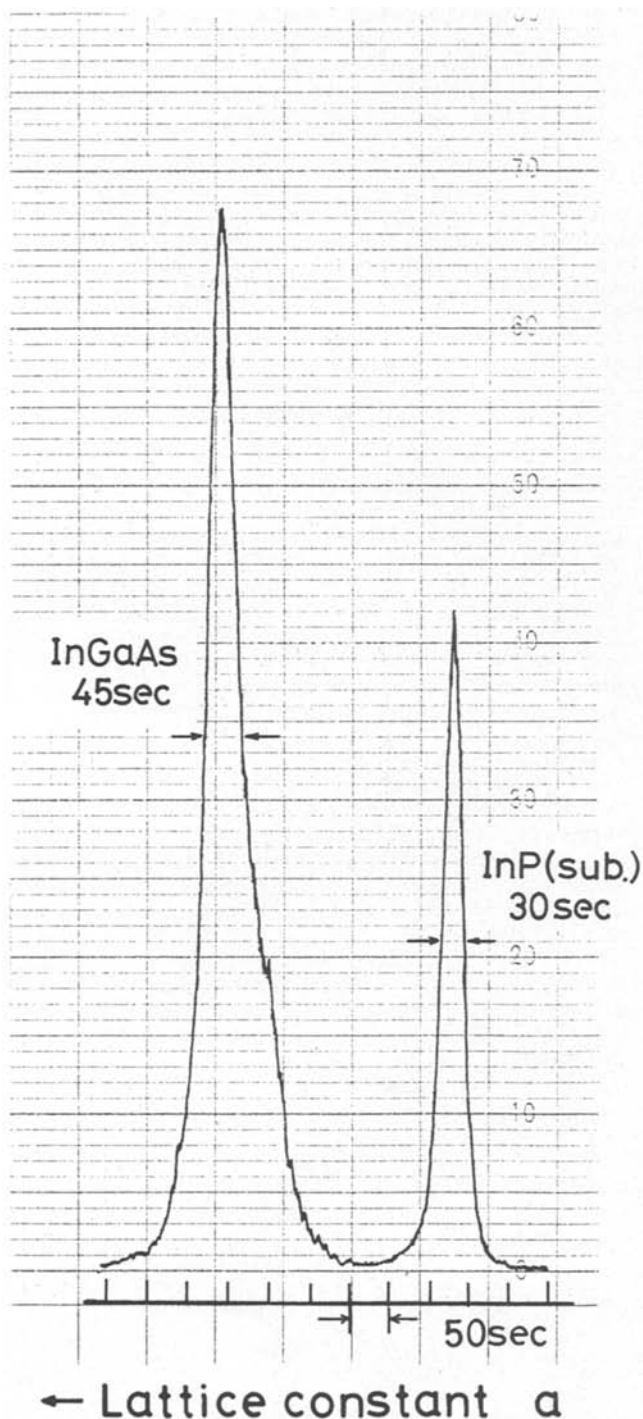


Fig. 4. X-ray double crystal rocking curve of InGaAs/InP layer

30 sec, respectively. The small shoulder, noted at the small lattice constant side tail of the InGaAs line, seems to be caused by gas composition fluctuation during the growth process, or residual PH_3 gas contained in the substrate holder cell, which causes a shift to a smaller lattice constant (21). Since the Auger measurement showed no trace of phosphorus in the InGaAs layer, and the holder cell size is only 0.63 cm³, the effect of PH_3 contamination is considered to be small.

In conclusion, the (100) and (111)B InP substrate thermal damage can be suppressed at 730°C by using a substrate holder with a sliding cover filled with PH_3 gas in InGaAs VPE. The holder is confirmed to be useful to minimize the PH_3 contamination in the VPE InGaAs growth by EPMA, Auger analysis, and double crystal x-ray rocking curve.

Acknowledgment

The authors would like to thank Dr. T. Kimura and Dr. H. Kanbe for encouragement and useful discussions, and H. Takaoka for Auger analysis measurement.

Manuscript submitted May 8, 1980; revised manuscript received Aug. 6, 1980.

Any discussion of this paper will appear in a Discussion Section to be published in the December 1981 JOURNAL. All discussions for the December 1981 Discussion Section should be submitted by Aug. 1, 1981.

Publication costs of this article were assisted by Nippon Telegraph and Telephone Public Corporation.

REFERENCES

- H. Tsuchiya and N. Imoto, *Electron Lett.*, **15**, 476 (1979).
- T. Miya, T. Terunuma, T. Hosaka, and T. Miyashita, *Electron. Lett.*, **15**, 106 (1979).
- Y. Takanashi, M. Kawashima, and Y. Horikoshi, *Jpn. J. Appl. Phys.*, **19**, 693 (1980).
- H. Ando, H. Kanbe, M. Ito, and T. Kaneda, *ibid.*, **19**, L277 (1980).
- S. R. Forrest, M. Didomenico, Jr., R. G. Smith, and H. J. Stocker, Topical Meeting on Integrated and Guided-Wave Optics, January 28-30, 1980, PD-1, Inciine Village, Nevada.
- T. P. Lee, C. A. Burrus, and A. G. Dentai, *IEEE J. Quantum. Electron.*, **qe-15**, 92 (1980).
- C. A. Burrus, A. G. Dentai, and T. P. Lee, *Electron. Lett.*, **15**, 655 (1979).
- R. F. Leheny, R. E. Nahory, and M. A. Pollack, *ibid.*, **15**, 713 (1979).
- N. Susa, Y. Yamauchi, and H. Kanbe, *IEEE J. Quantum. Electronics*, **qe-16**, 542 (1980).
- N. Susa, Y. Yamauchi, H. Ando, and H. Kanbe, *Jpn. J. Appl. Phys.*, **19**, L17 (1980).
- K. T. Ip, L. F. Eastman, and V. L. Wrich, *Electron. Lett.*, **13**, 682 (1977).
- G. H. Olsen and M. Ettenberg, in "Crystal Growth 2," C. H. L. Goodman, Editor, p. 1, Plenum Press, New York (1978).
- H. Enda, *Jpn. J. Appl. Phys.*, **18**, 2167 (1979).
- T. Mizutani, M. Yoshida, A. Usui, H. Watanabe, T. Yuasa, and I. Hayashi, *Jpn. J. Appl. Phys.*, **19**, L113 (1980).
- W. Y. Lum and A. R. Clawson, *J. Appl. Phys.*, **50**, 5296 (1979).
- K. Pak and T. Nishinaga, *Jpn. J. Appl. Phys.*, **18**, 1857 (1979).
- V. Wrich, G. J. Scilla, and L. F. Eastman, *Electron. Lett.*, **12**, 395 (1976).
- H. Kanbe, Y. Yamauchi, and N. Susa, *Appl. Phys. Lett.*, **35**, 603 (1979).
- M. B. Panish and J. R. Arthu, *J. Chem. Thermodyn.*, **2**, 299 (1970).
- K. Pak, T. Nishinaga, and S. Uchiyama, *Jpn. J. Appl. Phys.*, **14**, 1613 (1975).
- R. L. Moon, G. A. Antypas, and L. W. James, *J. Electron. Mater.*, **3**, 635 (1974).

Addition Rule for Patterned and Nonpatterned Hardenings in Dichromated-PVA Coatings

W. H. Fonger

RCA Laboratories, Princeton, New Jersey 08540

Dichromated-PVA photoresist is used to make phosphor and black-matrix dot or line patterns in color television picture tubes. The details of this application are reviewed in Morrell *et al.* (1); see especially Sections 3.1.1, 5.1, 5.2.1, 5.3.5, and 5.5. The photochemistry of dichromated colloids, including PVA, is reviewed in Chapter 2 of Kosar (2). Both books give many references.

The hardenings (PVA cross-linkings) of dichromated PVA coatings are often the combined result of patterned and nonpatterned hardenings. Patterned hardenings arise from light exposures through masks. Non-patterned hardenings arise from flood exposures or from coating dark hardenings (no light). We address the measurement of both hardening components for PVA clear-resist coatings. The analysis is handled in the approximation that all hardenings (PVA cross-linkings) increase linearly in time and that the transition to threshold hardening, the hardening level that just resists development, is very sharp.

The clear-resist case occurs for the black-matrix deposition (1). However, we are concerned here more with the general study of coating light and dark hardening, and envisioned experimental conditions are much more variable than in matrix deposition. The exposure light can be directed toward or through the glass substrate; the pattern mask can be q-spaced or contact; the pattern can have any desired shape; mask and flood exposures can utilize different wavelengths, etc. We generally consider fairly thin coatings so that the photohardening is not very graded from coating top to bottom. However, the only real requirement is that a point of threshold hardening can be properly read and rated for exposure, and it is possible to work with some hardening grading through the coating.

The simplest case is where the patterned hardening is digitalized in a large-area step or checkerboard pattern, as illustrated in Fig. 1. The numbers in the checkerboard squares give the units of patterned exposure time. The hatched area shows the portion of the coating that survived development. In the case illustrated, 9-10 units of patterned exposure time were needed to give threshold hardening. Calling this patterned exposure time t_p and the time for nonpatterned hardening t_n , the equation (addition rule) describing coating hardening at the hardening threshold is

$$\frac{t_p}{\tau_p} + \frac{t_n}{\tau_n} = 1 \quad [1]$$

where τ_p is the time for threshold patterned hardening for no nonpatterned hardening, and τ_n is the time for threshold nonpatterned hardening for no patterned hardening. The constants τ_p , τ_n are characteristic constants of the coating.

To measure the coating times τ_p , τ_n experimentally, one needs two coatings 1, 2 with different applied non-patterned hardening times t_{n1} , t_{n2} , and, therefore, different observed patterned exposure times t_{p1} , t_{p2} to bring the coating to threshold hardening. Using the addition rule [1], one then has two linear equations in the two unknowns $1/\tau_p$, $1/\tau_n$

$$\frac{t_{p1}}{\tau_p} + \frac{t_{n1}}{\tau_n} = 1, \quad \frac{t_{p2}}{\tau_p} + \frac{t_{n2}}{\tau_n} = 1 \quad [2]$$

which can be solved for these unknowns.

For the more complicated case of dot (or line) exposures using a television shadowmask, the patterned hardening is a continuously decreasing function of the dot-diameter coordinate D (or of the line-width co-

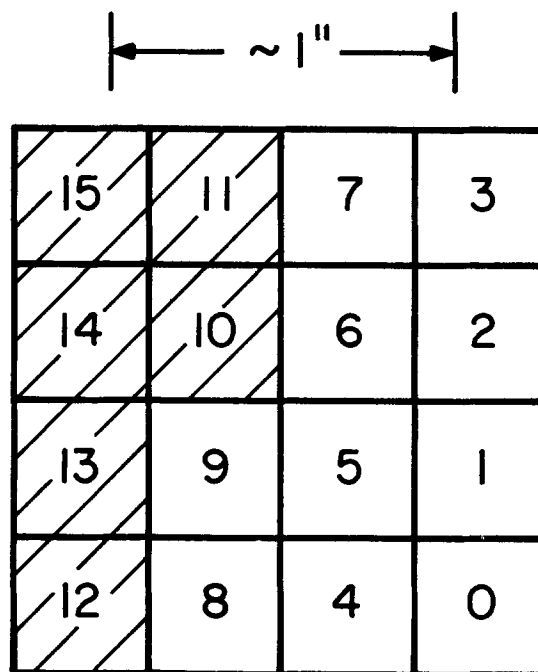


Fig. 1. Checkerboard pattern for light exposures. The integer in each square gives the units of exposure time.

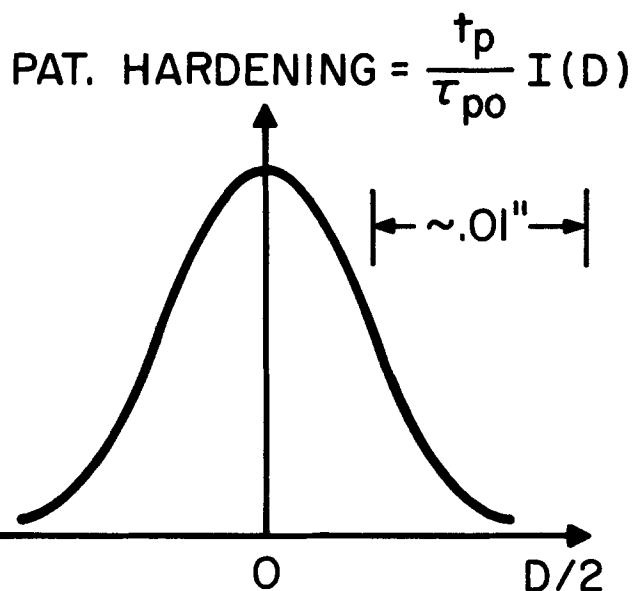


Fig. 2. Profile of patterned hardening beyond each mask hole. $I(D)$ is the normalized light shape function.

Key words: dichromated PVA, TV-screen deposition, photohardening.

ordinate W) due to the light penumbra developed between the mask and coating. See Fig. 2. In this figure, t_p is the mask-exposure time, the coating constant τ_{po} is the mask-exposure time needed to harden dots of some arbitrary standard diameter D_o with no nonpatterned hardening, and $I(D)$ is the shape function of the patterned light intensity at the coating, normalized to unity at $D = D_o$.

For combined shadowmask and nonpatterned hardenings, the addition rule analogous to Eq. [1] is

$$\frac{t_p}{\tau_{po}} I(D) + \frac{t_n}{\tau_n} = 1 \quad [3]$$

where t_n and τ_n have the same meanings as in Eq. [1], and D is the developed-dot diameter.

If a resist with negligible nonpatterned hardening ($t_n/\tau_n \ll 1$) is available, the light shape function $I(D)$ vs. D can be measured experimentally using Eq. [3] which then reduces to

$$I(D) = \frac{\tau_{po}}{t_p(D)} \quad [4]$$

Here $t_p(D)$ is the measured mask-exposure time for dots of diameter D . We assume hereafter that the shape function $I(D)$ has been measured and is known.

The constants τ_{po} , τ_n of an "unknown" coating can be determined using Eq. [3]. One uses two coatings with different nonpatterned hardening times t_{n1} , t_{n2} and superimposed mask-exposure times t_{p1} , t_{p2} which give developed dots of observed diameters D_1 , D_2 , respectively. One then has the two linear equations

$$\frac{t_{p1}}{\tau_{po}} I(D_1) + \frac{t_{n1}}{\tau_n} = 1, \quad \frac{t_{p2}}{\tau_{po}} I(D_2) + \frac{t_{n2}}{\tau_n} = 1 \quad [5]$$

which can be solved for the unknowns $1/\tau_{po}$, $1/\tau_n$.

We have used the methods underlying Eq. [1] and [3] to obtain the characteristic constants of unknown coatings. The method using Eq. [1] is simpler because

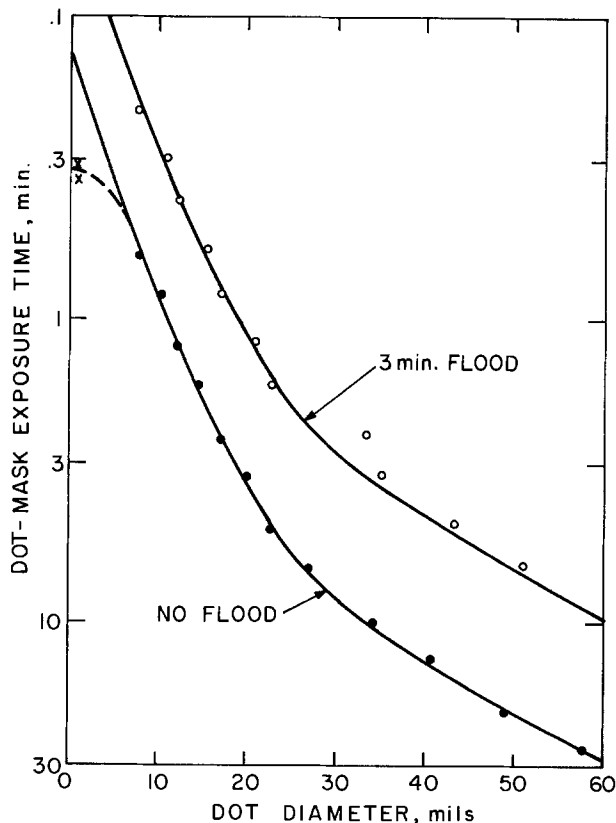


Fig. 3. Dot-mask exposure time vs. dot diameter with and without a superimposed flood exposure. This plot is drawn in the form $1/t_p$ vs. D which directly portrays the shape function $I(D)$.

it avoids both the light shape function $I(D)$ and microscope measurements.

The addition rules [1] and [3] will handle any case of combined light and dark hardening. Two special cases of rule [3] are of interest. We consider first the case where the nonpatterned hardening time t_n is held constant while the mask-exposure time t_p is varied. Equation [3] can then be written

$$\frac{t_p(D)}{\tau_{po}} = \frac{\alpha}{I(D)} \quad [6]$$

where α is the constant $\alpha = 1 - t_n/\tau_n$. Equation [6] shows that $t_p(D)$ is inversely proportional to the light shape function $I(D)$, just as it was in the Eq. [4] case for no nonpatterned hardening. That is, the function t_p vs. D (mask-exposure time vs. developed dot diameter) has the same shape with or without a superimposed constant nonpatterned hardening.

Figure 3 shows a measured example of this case. The measured shapes $t_p(D)$ are seen to be the same for no nonpatterned hardening and for a nonpatterned hardening for which t_n/τ_n was approximately 2/3. In this example, the nonpatterned hardening was provided by Hg 436 m μ floodlight. This light is weakly absorbed in dichromated-PVA coatings and gave uniform nonpatterned hardening vs. coating depth. The mask exposures used Hg 365 m μ light. The dot mask had 3 out of every 4 of its mask holes blocked so that the period between mask holes was double the normal size. Dot diameters up to 60 mils could therefore be used before adjacent dots overlapped.

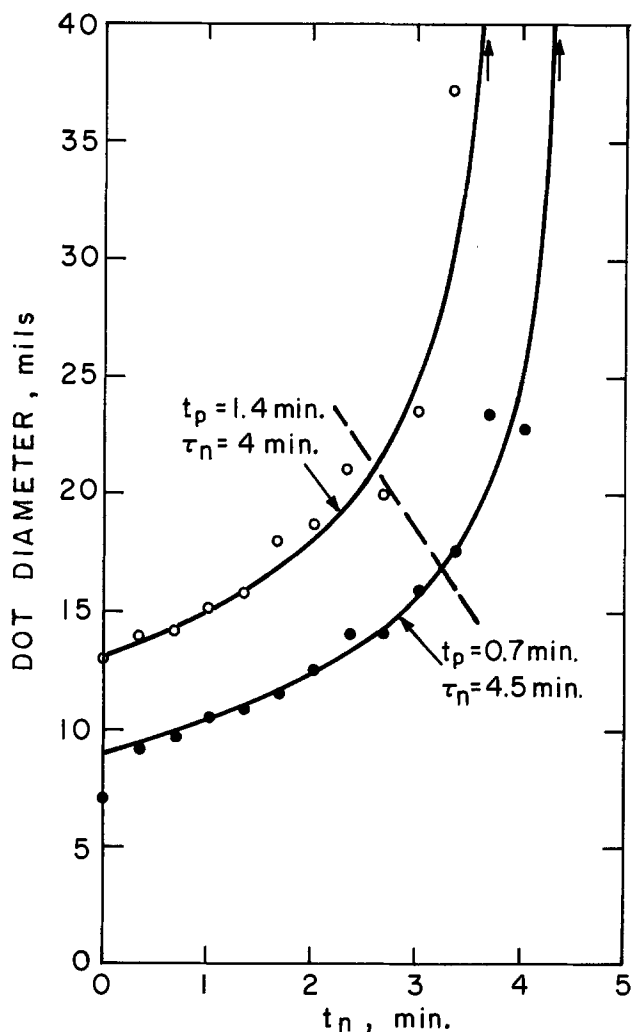


Fig. 4. Dot sizes when a variable flood exposure t_n was superimposed on fixed dot-mask exposures t_p . The curves through the data points were calculated from the shape function $I(D)$ in Fig. 3.

Figure 3 was purposely drawn in the form $1/t_p$ vs. D to directly portray the light shape function $I(D)$. This plot is in contrast to the more normal plot of D vs. t_p which displays the growth of dot diameter D with increasing mask-exposure time.

We consider finally the case where the mask-exposure time t_p is held constant while the nonpatterned hardening time t_n is varied. Equation [3] is then usefully written in the form

$$I(D) = \frac{\tau_{po}}{t_p} \left(1 - \frac{t_n}{\tau_n} \right) \quad [7]$$

We assume that τ_{po} , τ_n , and the shape function $I(D)$ are known, t_p is given, and t_n is varied. As t_n is varied, the right-hand side of Eq. [7] gives the numerical value of $I(D)$, and, from the known shape-function I vs. D , the expected dot diameter D can then be read off.

Figure 4 shows examples of measured (data points) and calculated (smooth curves) dot diameters D vs. the nonpatterned hardening time t_n . The exposure mask was the same dot mask used for the Fig. 3 measurements, and the shape function $I(D)$ used in the calculations is that shown in Fig. 3. All data in Fig. 4 were taken on two coatings. One was mask-exposed with Hg 365 m μ light with $t_p = 0.7$ min, the other with $t_p = 1.4$ min. The various nonpatterned hardening times t_n were obtained by superimposing on the dot exposures flood exposures with Hg 436 m μ light in a large-area checkerboard pattern. The flood-exposure times in the various checkerboard squares provided the various t_n abscissa values in the figure.

As $t_n \rightarrow \tau_n$, the developed dot diameter increases catastrophically, and the coating becomes undevelopable. This region (to the upper right of the dashed curve in Fig. 4) is readily recognized in practice and avoided. In the region to the lower left of the dashed line, the developed dots look innocently as if no nonpatterned hardening occurred. However, the coating photosensitivity to mask exposures would be seriously overestimated if the underlying nonpatterned hardening were ignored. In practice, underlying nonpatterned hardenings come from flood exposures and from coating dark hardenings.

Since the catastrophic increase of dot diameter with t_n is so sensitive to τ_n , the two τ_n values in Fig. 4 (4 and 4.5 min) were separately chosen empirically for best fit of the theory to the data points.

Manuscript submitted March 7, 1980; revised manuscript received July 21, 1980. This was Paper 222 presented at the St. Louis, Missouri, Meeting of the Society, May 11-16, 1980.

Any discussion of this paper will appear in a Discussion Section to be published in the December 1981 JOURNAL. All discussions for the December 1981 Discussion Section should be submitted by Aug. 1, 1980.

Publication costs of this article were assisted by RCA Laboratories.

REFERENCES

1. A. M. Morrell, H. B. Law, E. G. Ramberg, and E. W. Herold, "Color Television Picture Tubes," Academic Press, New York (1974).
2. J. Kosar, "Light-Sensitive Systems," Wiley, New York (1965).

Damage-Free Polishing of Polycrystalline Silicon

B. L. Sopori, T. Nilsson, and M. McClure

Motorola Incorporated, Semiconductor Group, Phoenix, Arizona 85008

Recently there has been considerable interest in using polycrystalline silicon for solar cells. Although cells of about 10% efficiency can be fabricated on polycrystalline silicon substrates, it is expected that higher efficiencies can be obtained if some of the grain-boundary effects, which limit the cell performance, are well understood and, thereby, subject to moderation. Much of this investigative work to study photovoltaic mechanisms at grain boundaries involves electro-optical techniques. For this purpose, it is necessary to polish the surface of a polycrystalline silicon sample such that surface damage and profile variations, in particular at the grain boundaries, can be minimized. This paper reports a polishing technique which yields a damage-free polished surface with grain-to-grain surface height variation, δ , less than 0.05 μm . A method for monitoring surface damage due to polishing in order to optimize the polishing conditions is also described.

The problems associated with polishing polycrystalline silicon can be generalized as follows: (i) both chemical and mechanical (using fine grit) polishing result in steps at the grain boundaries due to different removal rates for various grain orientations; (ii) mechanical polishing results in surface damage giving rise to a high surface recombination velocity (which has deleterious effects on solar cell performance and complicates the interpretation of measurement data); (iii) chemical polishing/etching generally causes "grooving" at the grain boundaries due to the fact

that the etch rate at grain boundaries is often higher than that of the grains. From these considerations it is clear that polishing to minimize surface damage and δ requires a sequence of mechanical polish followed by chemical/mechanical polish. The chemical/mechanical polishing should be done just long enough to remove the surface damage from mechanical polishing. We have tried several mechanical and chemical/mechanical polishing procedures and describe the one that gave best results.

Procedure and Results

Polycrystalline silicon samples that were polished had sawn and etched surfaces. These wafers have considerable surface roughness and their grain structure is clearly visible, as is shown in Fig. 1. Various grains show up due to variations in reflectivity caused by changing grain inclination with respect to the incident light. Wafers were first lapped with alumina powder (typical grit size $\sim 30 \mu\text{m}$) using a felt pad¹ for about 30 min. The lapped sample exhibits a grayish appearance and no grains are visible under normal visual inspection. A heavy surface damage was evidenced by a lack of surface photovoltage signal due to high surface recombination velocity (1).

Samples were then polished with oil-based diamond (typical grit size $\sim 2 \mu\text{m}$) while gradually reducing pressure from 5 to 2 psi and maintained at this value for 2 min. Diamond polishing removed much of the lapping damage, there is still residual surface stress

¹ A laboratory-type machine with single spindle and rocking arm was used for all polishing steps.



Fig. 1. Photograph of a polycrystalline wafer before polishing. Size: $2.5 \times 2.5 \text{ cm}^2$.

which must be removed. This is done by a chemical/mechanical polish using Nalcoag slurry, Type 2350.²

To optimize polishing conditions, as discussed earlier, surface photovoltage technique has been used to monitor the degree of surface damage based on the fact that the surface voltage signal developed across the sample is a function of surface recombination velocity (1).

Reduction in surface damage by chemical/mechanical polishing was compared by polishing the samples for short intervals of time and measuring its photovoltage. Light intensity and the gap between top electrode and sample surface were held constant throughout all measurements. Variation of photo-signal at 10 sec intervals of polishing time is shown in Fig. 2. The solid circles show this signal variation. The decreased signal after 60 sec of polish was felt to be caused by insufficient flow of Nalcoag during polishing since repeating the experiment on another wafer yielded the signal value shown by the triangle. Saturation of signal occurs after about 60 sec of polishing, implying the surface to be free from damage.

² Nalcoag is a colloidal silica slurry manufactured by Nalco Chemical Company.

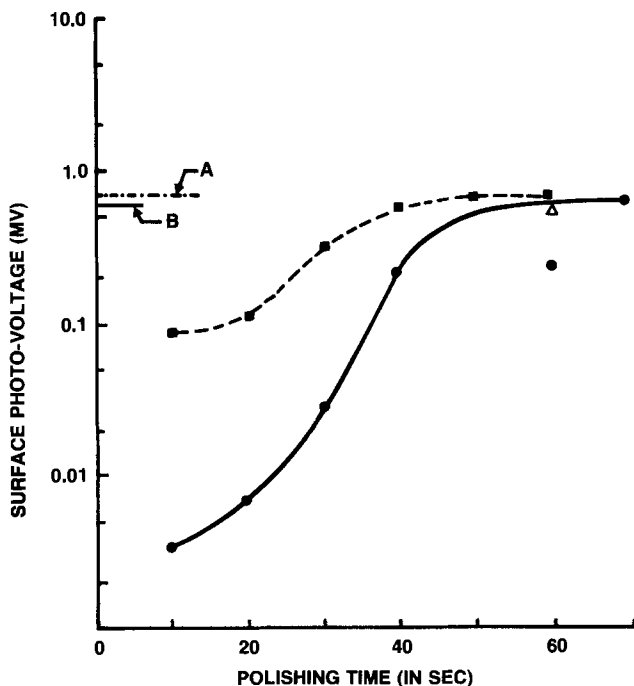


Fig. 2. Amplitude of SPV signal vs. polishing time for Wacker Silso polycrystalline silicon. Constant light intensity and optical beam size ($\lambda = 1.0 \mu\text{m}$).

In order to compare (qualitatively) the residual surface damage after lapping and diamond polishing with that of diamond polishing alone, the above sample (after Nalcoag polish) was given a diamond polish followed by repolishing with Nalcoag for 10 sec intervals and remeasuring the SPV signal. These data are shown by squares in Fig. 2. Residual damage from diamond polishing alone was much less than when the sample was lapped prior to diamond polish. Furthermore, the signal saturation occurred after only 40 sec of total polishing time. The two lines A and B in Fig. 2 indicate the signal levels obtained from two samples which were first Nalcoag polished and then etched using two different etchants. Since these samples were not mechanically polished, these signal levels correspond to damage-free surfaces lending support that the saturation signal level implies a damage-free surface.

The procedure was used to polish polycrystalline silicon wafers to a smoothness, δ_{max} , of less than $0.05 \mu\text{m}$ with negligible (or no) surface damage. This is clearly seen from Fig. 3 which is a surface profile trace of a polished Wacker polycrystalline silicon wafer. A Nomarski photograph of a part of the polished surface is given in Fig. 4. Although the photographed region has many grain boundaries, only a few are visible in Fig. 4. A Dektak trace (accompanying the photograph) across the most prominent grain shows the height variation to be $0.03 \mu\text{m}$. An interference photograph of a part of the surface, taken under sodium light ($\lambda = 0.513 \mu\text{m}$) is shown in Fig. 5.

The polishing procedure described above was established following several variations in mechanical and chemical/mechanical polishing sequences. Table I summarizes some essential features of these. It should be emphasized that procedures a, b, and c in Table I, lead to a steady-state grain-to-grain height variation (i.e., δ does not change if the polishing is continued past

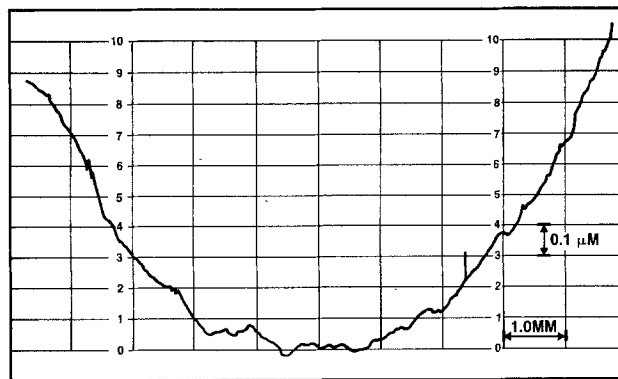


Fig. 3. Dektak trace of the surface profile of a polished Wacker polycrystalline silicon sample.

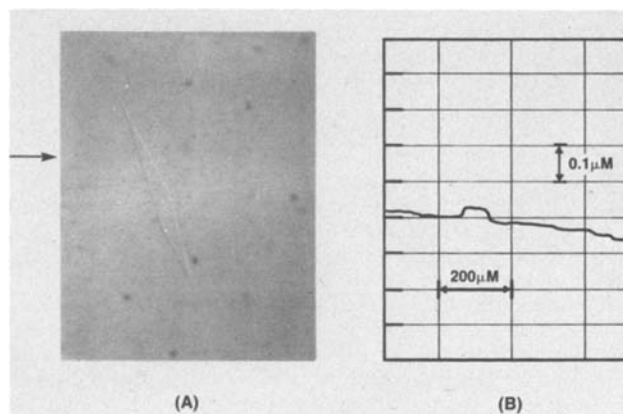


Fig. 4. (A) Nomarski photograph of a polished wafer, magnification = 50. (B) Dektak trace across the prominent grain (along the arrow in A).

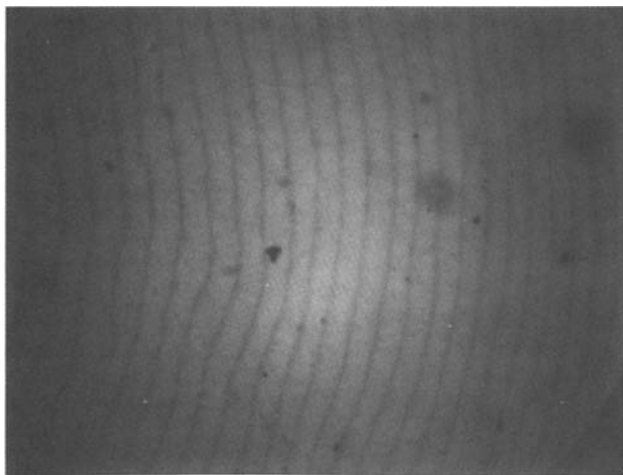


Fig. 5. Interferogram of a polished section of a polycrystalline silicon wafer.

an initial period of rapid variation). Results of chemically polishing the samples in two different etchants are also given in Table I for comparison. These etchants are often used for silicon surface preparation.

We have also found Nalcoag polishing to be a very attractive technique for wafer thinning. Figure 7 shows a plot of thickness removed vs. polishing time for two pressures. It is seen that removal rates are comparable

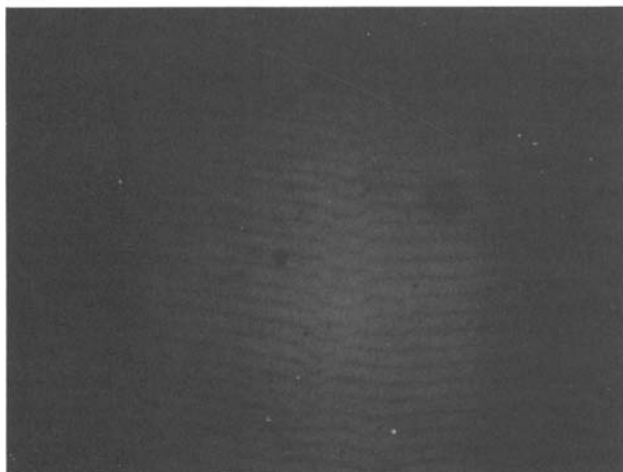
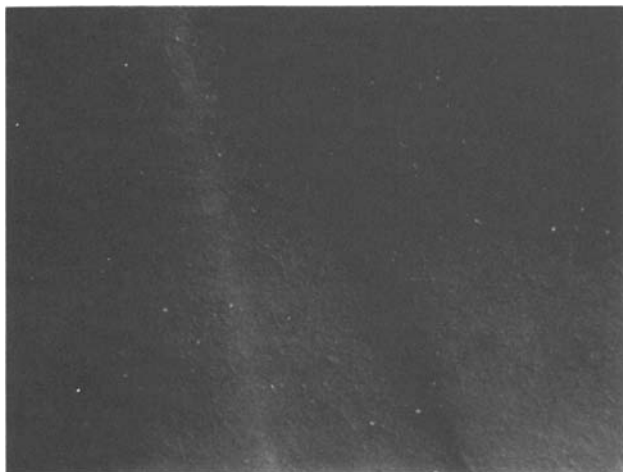


Fig. 6. (a, top) Nomarski photograph of a grain shows that damage introduced by lapping (as pits) is not completely removed by a chem mech polish for 4 min. A gentle taper at the grain boundary is clearly seen. Magnification $400\times$. (b, bottom) Low magnification ($10\times$) interference pattern of the grain in Fig. 6(a).

NALCOAG THINNING

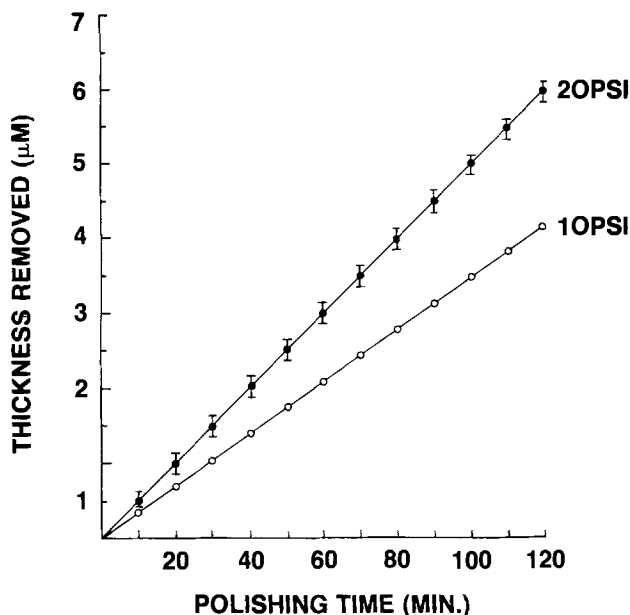


Fig. 7. Plot of thickness removed vs. polishing time during Nalcoag thinning.

to that of lapping. In addition, Nalcoag polishing allows better control for these wafers. Using Nalcoag thinning and the polishing techniques described in this paper we have been able to parallel polish RTR silicon ribbons down to a thickness of $28.1\ \mu\text{m}$ for the measurement of absorption coefficients at wavelengths down to $0.7\ \mu\text{m}$ (2).

Applications

The polishing of polycrystalline silicon is necessary for a variety of important electrical and optical characterization techniques. Some of these are: (i) focused laser scanning to determine local variations in photo-response and to evaluate some effects of grain boundaries; (ii) material thinning and polishing for measurement of optical constants such as reflection and absorption coefficients, and to determine microscopic stresses by infrared birefringence; (iii) planar defect characterization for delineating various types of defects using chemical etchants; (iv) angle lapping for a variety of characterizations such as variation of defects in the bulk, junction depth measurements (at and away from grain boundaries), and a variety of other measurements (e.g., potential probing) which require signal pick-off from the surface.

Summary

The Nalcoag polishing technique for polycrystalline silicon resulted in a grain-to-grain surface height variation of $\delta < 0.05\ \mu\text{m}$. The slope of the surface profile at grain boundaries is very gentle, and no "grooving" at grain boundaries has been observed. These properties are very important for probing grain boundaries, electrically and/or optically, along the sample surface. SPV monitoring showed the extent of surface damage to be minimal. This polishing/monitor technique has also facilitated other evaluation methods such as measurement of absorption coefficient for wavelengths near the bandedge, spectroscopic measurements of impurities like oxygen, and defect delineation by chemical etching.

Acknowledgments

The authors wish to thank Dr. M. Coleman and Mr. J. Parsons for many fruitful discussions with them re-

Table I. Summary of the results of some other polishing procedures

| Polishing method | δ_{\max} (μm) | $\langle\delta\rangle$ (μm) | Comments |
|--|-----------------------------------|--|---|
| a. Mechanical polish Final grit size = 0.05 μm Pad: Micro-cloth | 1.2 | 0.3 | (i) Grain boundaries have smooth taper (ii) Severe surface damage indicated by very low SPV signal |
| b. Lapping + Nalcoag Pressure 10 psi Pressure 20 psi | 1.2 0.4 | 0.5 0.25 | (i) δ attains steady-state value after about 4 min of polish with Nalcoag (ii) Lapping damage is not removed in 4 min (see Fig. 6) (iii) Grain boundaries show gentle taper (iv) Damage-free surface after 15 min polish with Nalcoag (v) Useful for sample thinning (i) Leaves shallow scratches (ii) Residual surface damage |
| c. Lapping + diamond | 0.2 | 0.1 | |
| d. Chemical polish HNO ₃ :HF:CH ₃ COOH 5:1:1 HNO ₃ :HF:Br:CH ₃ COOH | 4 4 | 1.5 ~2 | |

garding this work. This work was supported in part by DOE under the Contract AC-01-79ET-23104.

Manuscript submitted March 13, 1980; revised manuscript received June 20, 1980.

Any discussion of this paper will appear in a Discussion Section to be published in the December 1981

JOURNAL. All discussions for the December 1981 Discussion Section should be submitted by Aug. 1, 1981.

REFERENCES

1. A. M. Goodman, *J. Appl. Phys.*, **32**, 2550 (1961).
2. B. L. Sopori and R. W. Gurtler, "Properties of Laser/Electron Beam Crystallized Silicon Ribbons," Paper ThQ2 presented at Opt. Society Meeting, Rochester, New York, Oct. 1979.

Erratum

In the paper "Properties of Thin Polyimide Films" by L. B. Rothman which appeared on pp. 2216-2220 in the October 1980 JOURNAL, Vol. 127, No. 10 footnote one to Table I on page 2216 should read "NMP: n-methylpyrrolidinone." Also Figure 8(c) caption on page 2219 should read "after 645 hr $K = 5.12$ g/mm."

In addition the last sentence before the Conclusion section on page 2220 should read "Annealing the metal at 350°C in nitrogen before test improves the Al to polyimide adhesion, resulting in a peel factor of approximately 10 g/mm after the stress cycle."



The Influence of Promoter Elements in Acidic Sulfate Solutions on Hydrogen Absorption in Titanium

Z. A. Foroulis*

Exxon Research and Engineering Company, Florham Park, New Jersey 07932

It is well known that certain elements, particularly those of Group VA and VIA of the periodic table, can markedly increase the entry of hydrogen into iron and carbon steel during cathodic polarization. Elements which produce this effect are known in the literature (1, 2) as "promoters." Several papers have been published in the literature dealing with the influence of promoter elements on the rate of hydrogen absorption in iron and carbon steel (3-6). However, information on the role of these elements on the rate of hydrogen absorption in titanium is not available. This brief communication presents experimental data which show that promoter elements such as P, As, S and Sb have a rather pronounced effect on the rate of hydrogen absorption in titanium in acidic sulfate solutions under conditions of cathodic polarization.

EXPERIMENTAL

The material used in this study was commercially pure titanium (ASTM B265-72 Grade 2) of the following analysis (0.025% C, 0.06% Fe, 0.021% N, 0.005% H, 0.15% O₂). The titanium electrodes were small rectangles with dimensions 1 x 1 x 0.3 cm. All sides of the electrodes were exposed in the test solution. The electrode assembly in which only glass and teflon, besides the electrode, came in contact with the electrolyte, as well as the cell design, were similar to those described previously (7). Constant current for the cathodic charging experiments was drawn from a constant voltage power source through a variable resistance. The electrode surface was polished with 6/0 emery paper, rinsed with toluene and acetone and pickled with HF (14% HF) to remove the air formed oxide film. No measurable hydrogen absorption was detected as a result of surface

etching. The test solution was 0.1 N H₂SO₄ (pH = 1.2) with and without the addition of equal molar concentrations (3.1 x 10⁻³ M/l) of sulfur, phosphorous, arsenic and antimony which were added in the test solution as Na₂S, Na₄P₂O₇, NaAsO₂ and potassium antimony tartrate K(SbO) C₄H₄O₆ respectively. Charging solutions were prepared from distilled water and reagent grade chemicals. The cathodic charging experiments were carried out at 10 ma/cm² for 24 hours at 93°C. After cathodic charging, the hydrogen content of the titanium electrodes was determined by the hot extraction method at 1400°C (8). Several electrodes, after charging were also polished metallographically in cross section, etched with an HF-HNO₃-lactic acid reagent (9) and the morphology of the hydride layer was examined with an optical microscope.

RESULTS AND DISCUSSION

The Ti-H system forms an interesting contrast to the well known Fe-H system in at least two respects. First, in the Fe-H system, the affinity between metal and hydrogen is only slight; they form no chemical compounds and the hydrogen dissolves in the metal in comparatively small concentrations. In the titanium-hydrogen system, on the other hand, the mutual affinity is great, a chemical compound, titanium hydride (TiH₂) is formed and the hydrogen dissolves in the metal in relatively large quantities.

The second major difference between titanium and iron is that titanium in air or when immersed in most aqueous solutions at open circuit potential forms a stable "passive" film which is probably a thin TiO₂ film (10-11). This oxide film, when present, may act as a barrier to hydrogen pickup.

To eliminate the presence of an oxide surface film on titanium during the cathodic hydrogen charging experiments, the titanium electrodes, after pickling with HF to remove the air-formed oxide film, were kept in an inert

* Electrochemical Society Active Member.

Key Words: Hydrogen Absorption, Titanium, Promoter Elements.

atmosphere and immediately upon immersion in test solution were cathodically polarized at 10 ma/cm^2 while the charging solution was maintained at 93°C . The test solutions were acidic sulfate solutions $\text{pH} = 1.2$ with and without equal molar concentration of the promoter elements. During cathodic charging

Table I. Potential of Titanium Electrode Cathodically Polarized at 10 ma/cm^2 at 93°C in $0.1 \text{ N H}_2\text{SO}_4$

| Solution | Potential V (SCE) |
|---|----------------------|
| $0.1 \text{ N H}_2\text{SO}_4$ | -0.93 |
| $0.1 \text{ N H}_2\text{SO}_4 +$ $3.1 \times 10^{-3} \text{ M/l Na}_2\text{S}$ | -1.12 |
| $0.1 \text{ N H}_2\text{SO}_4 +$ $3.1 \times 10^{-3} \text{ M/l Na}_4\text{P}_2\text{O}_7$ | -1.15 |
| $0.1 \text{ N H}_2\text{SO}_4 +$ $3.1 \times 10^{-3} \text{ M/l NaAsO}_2$ | -1.0 |
| $0.1 \text{ N H}_2\text{SO}_4 +$ $3.1 \times 10^{-3} \text{ M/l K(SbO) C}_4\text{H}_4\text{O}_6$ | -0.92 |

at 10 ma/cm^2 , the electrochemical potential of titanium as shown in the table was in the range of -0.9 to -1.15 V (SCE) . In this potential region in acidic sulfate solutions ($\text{pH} = 1.2$), titanium oxides are not stable thermodynamically (12). It is, therefore, reasonable to assume that during the cathodic charging experiments, the bare titanium metal surface was exposed in the test electrolyte.

Figure 1 shows the titanium hydride (TiH_2) layer formed in titanium cathodically polarized at 10 ma/cm^2 for 24 hours in $0.1 \text{ N H}_2\text{SO}_4$ ($\text{pH} = 1.2$), at 93°C . This is typical of the morphology of the titanium hydride layer produced by cathodic charging in acidic sulfate solutions with and without the addition of the promoter elements. After prolonged exposure, diffusion of hydrogen and formation of titanium hydride thin plates far deep into the metal structure were also detectable. The effect of different promoter elements on the rate of hydrogen absorption in titanium cathodically polarized at 10 ma/cm^2 at 93°C is shown in Figure 2. The promoter elements were added as Na_2S , $\text{Na}_4\text{P}_2\text{O}_7$, NaAsO_2 , and $\text{K(SbO)C}_4\text{H}_4\text{O}_6$. These compounds were complete soluble and had no effect on the pH of the $0.1 \text{ N H}_2\text{SO}_4$ solution.

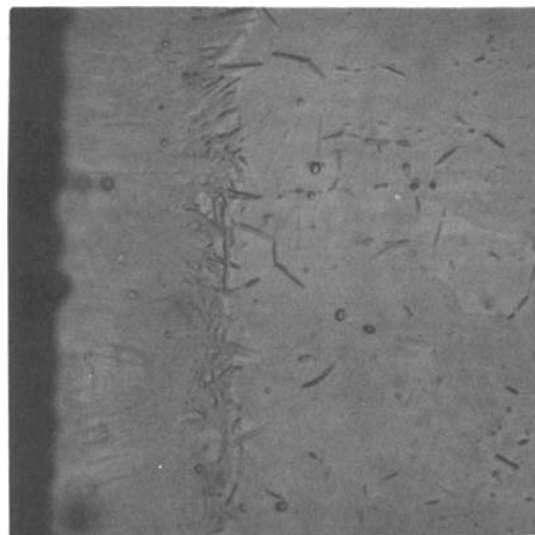


Figure 1. Morphology of Titanium Hydride Formed in Titanium Cathodically Polarized at 10 ma/cm^2 in $0.1 \text{ N H}_2\text{SO}_4$, 93°C .

The nature of the ionic species containing the promoter element which are present in the solution are likely to be SO_4^{2-} , SH^- , $\text{P}_2\text{O}_7^{4-}$, AsO_2^- and SbO_2^- respectively. The data shown in Figure 2 demonstrate the pronounced effect of SH^- , $\text{P}_2\text{O}_7^{4-}$ and to a lesser extent of AsO_2^- on the rate of hydrogen absorption in titanium cathodically polarized at 10 ma/cm^2 , 93°C in $0.1 \text{ N H}_2\text{SO}_4$. The effect of $\text{K(SbO) C}_4\text{H}_4\text{O}_6$ (which is likely to produce SbO_2^- in solution) on the hydrogen absorption rate was not as pronounced.

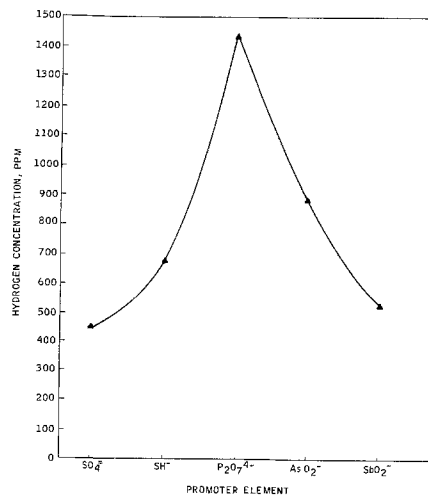


Figure 2. The Effect of Promoter Elements on Hydrogen Absorption in Titanium Cathodically Polarized at 10 ma/cm^2 in $0.1 \text{ N H}_2\text{SO}_4$ ($\text{pH} = 1.2$), 93°C .

As indicated previously, it is reasonable to assume that during the cathodic charging experiments, the bare titanium metal surface was exposed in the electrolytic solution. It is also reasonable to assume that the promoter element containing compounds exert their influence on increasing the rate of hydrogen uptake, by adsorbing on the titanium metal surface. However, the molecular species containing the promoter element which adsorb on the metal surface and the mechanism of their action in enhancing the rate of hydrogen absorption is not known. It is possible that the adsorbed promoter species increase the Ti-H bond on the metal surface and this increases the coverage of adsorbed atomic hydrogen which thereby increases the permeation rate. Other explanations such as formation of hydride of the promoter element during polarization as an essential process of hydrogen entry in titanium must also be considered. Additional work in this area is clearly required before a definitive mechanistic explanation of the role of promoter elements on hydrogen absorption in titanium can be advanced.

REFERENCES

- (1) W. Bankloh and G. Zimmermann, Arch. Eisenhüttenwes., 9, 459 (1936).
- (2) M. Smialowska and Z. Szklarska-Smialowski, Bull. Acad. Pol. Sci., CL, III, 2, 73 (1954).
- (3) V. Kuznetsov and V. Frolov, Zh. phisikl. khim. Mosk., 32, 582 (1962).
- (4) A. E. Shuetz and W. D. Robertson, Corrosion, 13, 437t (1957).
- (5) J. O. M. Bockris, J. McBreen and L. Nanis, J. Electroch. Soc. 112, 1025 (1965).
- (6) R. B. McCright and R. W. Staehle, J. Electroch. Soc., 121, 609 (1974).
- (7) Z. A. Foroulis, J. Electroch. Soc., 113 532 (1966).
- (8) "Methods for Analysis of Metals and Metals Bearing Ores," ASTM Book of Standards, Part 12, 1978 Edition, Specification E-146, p. 129.
- (9) Metals Handbook (ASM, 8th Edition), Volume 7, p. 342.
- (10) Z. A. Foroulis, Werkstoffe u. Korrosion, 30, 477 (1979).
- (11) E. E. Rider, V. I. Orchareuko, V. Y. Dudarev and V. M. Nowakovskii, Protect. of Metals, 11, 170 (1975).
- (12) M. Pourbaix, "Atlas of Electrochemical Equilibria in Aqueous Solutions," Pergamon Press, New York, NY (1966).

Manuscript received May 27, 1980.

Publication costs of this article were assisted by Exxon Research and Engineering Company.

Semiconductor Electrodes

XXXV. Slurry Electrodes Based on Semiconductor Powder Suspensions

Wendell W. Dunn**, Yoshihiro Aikawa, and Allen J. Bard*

Department of Chemistry, University of Texas at Austin, Austin, Texas 78712

Irradiated suspensions of semiconductor powders, e.g., TiO_2 , have been employed in such heterogeneous photo processes as the oxidation of cyanide, the decomposition of carboxylic acids, and the deposition of metals. Details about these and other reactions are given in recent reviews (1-3). The mechanism proposed for these processes is based on the formation of an electron-hole (e^-h^+) pair at the particle surface upon absorption of light of energy greater than the semiconductor band-gap. The particle then behaves as a short-circuited cell with both oxidation and reduction taking place at the particle surface. Recent measurements of the electrophoretic mobility of TiO_2 powder have demonstrated that in solution, the surface charge on the particle under illumination is more negative than that measured in the dark (4). Moreover, this negative charge persists for at least 10-15 minutes after the irradiation stops. These results suggest that when the holes are scavenged by an oxidation process, electron density builds up on the particle surface. We report here that this excess charge can be collected on an inert electrode to produce an anodic current flow.

Thus, semiconductor powder suspensions (e.g., TiO_2 , WO_3 , CdS) can behave as electrodes ("slurry electrodes") in the same manner as the

single crystal and polycrystalline semiconductor materials currently being investigated. Measurements involving such slurry electrodes are of use not only for the characterization of the powders but may also have practical applications in photoelectrochemical cells.

In a typical experiment, a suspension of n- TiO_2 particles in 0.02 M HCl was deaerated for 24 hours prior to measurements. A Pt foil (area $\sim 3 \text{ cm}^2$), polished with Al_2O_3 and cleaned in boiling HNO_3 , was used as the collector electrode. Electrochemical measurements were conducted in a Pyrex H-cell, with the compartments separated by a fine-porosity glass frit. One compartment contained the deaerated TiO_2 suspension while the other compartment contained a Pt counter electrode and 0.02 M HCl with a low oxygen concentration to support a current flow. A 2500 W xenon lamp, operated at 1600 W, was used for illumination. A Pyrex water bath approximately 15 cm in diameter was placed in front of the electrochemical cell to remove IR radiation.

A negligible current flowed between the two half-cells in the dark under short circuit conditions. When the TiO_2 suspension was irradiated, a cathodic current transient appeared; the current quickly became anodic and finally attained a steady anodic current

*Electrochemical Society *Active,
**Student Member. Key words: photoelectricity, photoanode, solar energy.

level (Fig. 1b). When the light beam was interrupted, an anodic transient appeared and the anodic current decayed to zero. In a control experiment in the absence of the suspension under otherwise identical conditions, only very small current responses appeared under illumination (Fig. 1a). The behavior of the TiO₂ suspension can be interpreted based on the model for photoprocesses at the particle surface (Fig. 2). The photoproduced hole rapidly forms a hydroxyl radical that reacts in a following reaction to produce oxygen (5). In the absence of oxidants in solution, electrons accumulate at the powder surface. While proton reduction is a possible process, this reaction is apparently slow at an uncatalyzed TiO₂ surface. The direction of current flow depends upon the relative rates of electron transfer between the collector electrode and the particle. Initially a cathodic current, probably representing reduction of OH[•], is observed. However the accumulation of electrons and the subsequent reaction of [•]OH leads to a net anodic current. A quantitative treatment of the model of Fig. 2, to be described elsewhere, leads to current-time (i-t) curves resembling the experimental ones. Evidence in favor of such a model is the finding that addition of oxygen to the suspension quenches the anodic photocurrent, and produces only a brief cathodic transient and a small cathodic steady state current, since the photogenerated electrons react with O₂. Similarly the anodic current with platinized TiO₂ is much smaller, because Pt catalyzes the proton reduction reaction. Finally the addition of acetate causes a decrease or elimination of the cathodic transient and an increase in the anodic current, because the preferential oxidation of acetate at the powder produces methyl radical which undergoes a very rapid reaction (6), so

that electron transfer to this species does not occur.

Similar behavior is observed with other semiconductor powders. The i-t curves with WO₃ powder in sulfate solutions (pH 1.8) are similar to those of TiO₂ (Fig. 1c). For a CdS suspension in a sulfate medium, however, no cathodic transient is observed and the current rises in an anodic direction and then decays to a steady value (Fig. 1d). In this case the photogenerated holes lead to decomposition of the semiconductor

$$\text{CdS} + 2\text{h}^+ \rightarrow \text{Cd}^{2+} + \text{S} \quad [1]$$

and the sulfur so produced is not reducible. The addition of Na₂SO₃ (10⁻⁵ M) which retards this decomposition reaction (8) caused no significant change in the photoresponse.

Electrochemical studies of semiconductor slurries in the dark and under illumination appear promising. The determination of photocurrent as a function of the wavelength of the irradiating light can provide information about the band gap energy and, perhaps the existence of energy levels within the gap, with the powder immersed in the reaction medium. Moreover the effect of solution conditions on the photoresponse can provide information about relative reaction rates at the particle surface. Although the magnitudes of the photocurrents generated with the slurry electrodes are small compared to single crystal and some polycrystalline film electrodes under similar irradiation intensities, they may find some practical application. They are potentially very inexpensive and easy to construct and replace. Regenerative (photovoltaic) and storage (photoelectrosynthetic) cells employing slurry electrodes are possible and are currently under investigation in this laboratory.

Acknowledgment.— The support of this research by the National Science Foundation (CHE 8000682) and the Robert A. Welch Foundation is gratefully acknowledged.

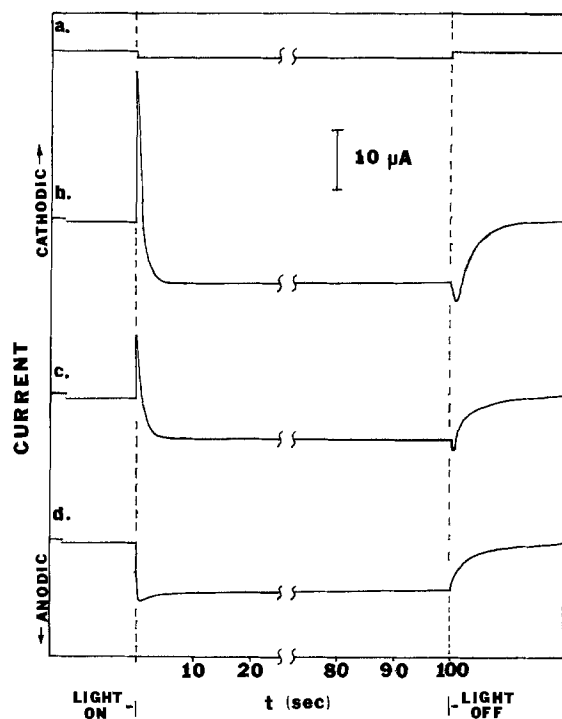


Fig. 1. Current-time responses under and following irradiation with xenon lamp. (a) Pt electrode alone in 0.02 M HCl; (b) suspension of 25 mg TiO_2 in 40 ml 0.02 M HCl; (c) 25 mg WO_3 in 40 ml 6.7 mM Na_2SO_4 (pH 1.8); (d) 30 mg CdS in 40 ml 6.7 mM Na_2SO_4 (pH 5).

Manuscript received Sept. 9, 1980.

Publication costs of this article were assisted by the University of Texas.

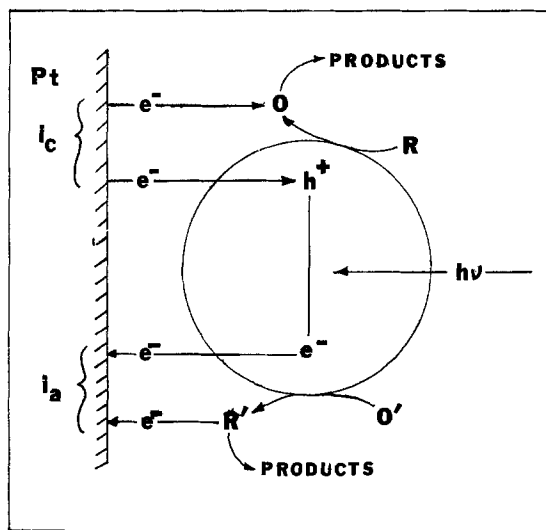


Fig. 2. Model of process at particle surface. R represents a solution reductant (e.g. H_2O , CH_3CO_2^-) and O' a solution oxidant (e.g. O_2).

REFERENCES

1. A.J. Bard, *Science*, **207**, 139 (1980).
2. A.J. Bard, *J. Photochem.*, **10**, 59 (1979).
3. M. Formenti and S.J. Teichner, *Spec. Periodical Repts. (The Chem. Soc., London)*, **2**, 1979, Chap. 4.
4. W.W. Dunn, Y. Aikawa, and A.J. Bard, manuscript in preparation.
5. C.D. Jaeger and A.J. Bard, *J. Phys. Chem.*, **83**, 3146 (1979).
6. B. Kraeutler, C.D. Jaeger, and A.J. Bard, *J. Am. Chem. Soc.*, **100**, 4903 (1978).
7. B. Kraeutler and A.J. Bard, *Nouv. J. Chim.*, **3**, 31 (1979).
8. T. Inoue, T. Watanabe, A. Fujishima, K. Honda, and K. Kohayakawa, *J. Electrochem. Soc.*, **124**, 719 (1977).

Edge Acuity Improvement by Spectral Filtration in the Deep U.V.

A. W. McCullough

The Perkin-Elmer Corporation, Norwalk, Connecticut 06856

It has previously been shown that shorter wavelength exposure can increase the modulation transfer function⁽¹⁾ and consequently the effective resolution⁽²⁾ of a projection mask aligner. This paper addresses the issue of edge acuity under these conditions.

A F/3 projection mask aligner was modified for exposure in the 275 nm to 325 nm region and used to expose one micron of Shipley AZ-2400 resist with standard processing conditions. The silicon substrate had 720 nm of wet grown oxide on it.

Figure 1a shows scanning electron micrographs of 1.5 micron features, of a mask of nominally equal lines and spaces, with two conditions of partial coherence (S). The edge acuity, that is the measured angle of the resist with respect to the substrate, is $\theta = 48^\circ$ for $S = 0.86$ and $\theta = 53^\circ$ for $S = 0.52$. In both cases the angle is too small for adequate linewidth control.

A high pass filter was used to reduce the exposure bandwidth to the range 300 nm to 325 nm. The motivation is illustrated in Figure 2 which shows the transmission of one micron of unexposed AZ-2400 resist as a function of wavelength. The strong absorption below 300 nm is characteristic of the Novalac resin contained in most commercial positive resists. Also shown is the bandwidth of the exposure tool and the transmission of the UBK-7 glass that was used as the filter.

It can be seen that there is considerable actinic light at shorter wave-

Key words: edge acuity, photoresist, deep UV

lengths than the resist absorption edge. Most of this light is absorbed in the resist leading to loss of resist thickness and poor edge acuity. The UBK-7 filter obviates this effect. The results using this high-pass filter are shown in Figure 1b. Here $\theta = 57^\circ$ for $S = 0.86$ and $\theta = 70^\circ$ for $S = 0.52$. These results are a notable improvement and indicate good lithographic performance. Additional experiments were performed with a filter consisting of AZ-2400 on a quartz plate. The results were similar but the organic coating deteriorated rapidly under the intense UV exposure.

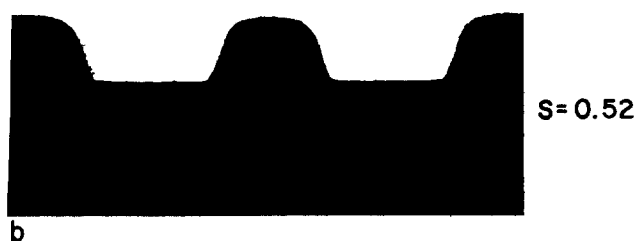
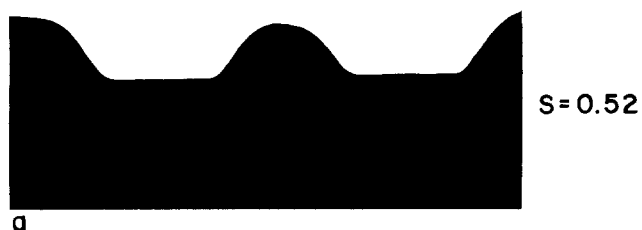
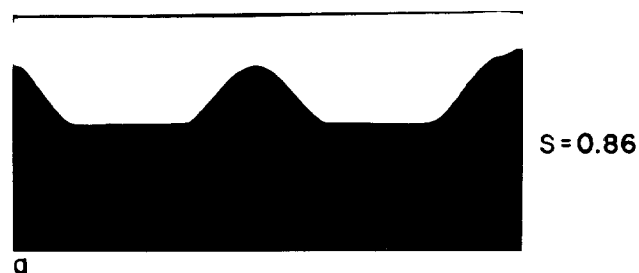
Exposure times were 20 sec without the high-pass filter and 30 sec with UBK-7. Experiments are in progress to optimize the filter in order to minimize the increase in exposure time. Different resists may require their own matched filter for optimum results. Similar experiments conducted in the near UV (350 nm to 440 nm range) showed an insignificant improvement in the slope angle as the exposure bandwidth was changed within this range. This would be expected because the Novalac resin has very low absorption in this range and the absorption of the photo active compound does not exhibit such large variations in this range as does the resin in the 280 to 320 nm range.

ACKNOWLEDGEMENTS

The SEM photographs were prepared by A. Venditti and useful discussions were held with M. King.

REFERENCES

1. Michael C. King. IEEE Transactions on Electron Devices, ED-26(4), 711-6 (April 1979)
2. J.H. Bruning. J. Vac. Sci. Technology, 16(6), 1925-8 (Nov/Dec 1979)



→ | ← 0.5 μm

Fig. 1. SEM edge profiles with filter
a, Quartz: b, UBK-7
Two values of the partial
coherence S .

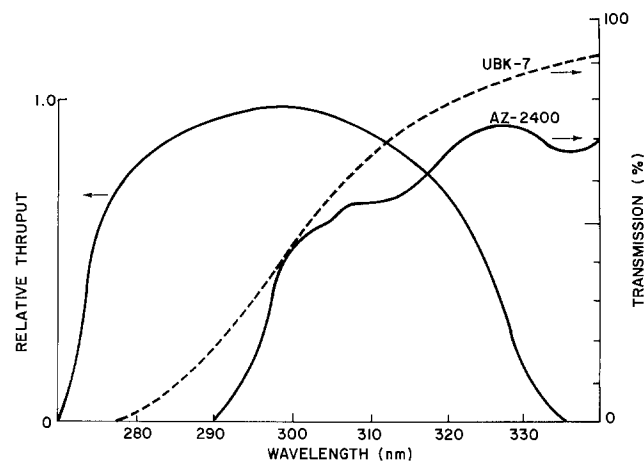


Fig. 2. Pass band of projection aligner;
Transmission of UBK-7 and AZ2400
resist layer.

Manuscript submitted May 30, 1980;
revised manuscript received Sept. 24, 1980.

Publication costs of this article
were assisted by Perkin-Elmer.

Zn Diffusion in GaAlAsSb and GaSb

R. Chin and H. D. Law

Rockwell International/Electronics Research Center, Thousand Oaks, California 91360

The demonstration of both optical sources (1) and detectors (2,3) in the GaAlAsSb-GaSb system at long wavelength ($1.0 \mu\text{m} < \lambda < 1.8 \mu\text{m}$) has stimulated further interest in this particular alloy system for optical communication purposes. For numerous optical devices in other III-V alloy systems, Zn diffusions have shown to be invaluable for device fabrication. In heterojunction structures, it is requisite that the diffusion rate of the impurity (Zn) be known for the different composition materials comprising the heterostructure. If the p-n junction must be placed within a narrow region such as the active region of a double heterojunction laser, this information is indispensable.

In this article, we describe the diffusion rate for GaAlAsSb and GaSb. In addition, the effect of antimony overpressure upon the regularity (planar p-n junction) of the p-n junction is shown to be important.

The GaSb material of this work is doped at $3-5 \times 10^{17} \text{ cm}^{-3}$ with Te, while the $\text{Ga}_{1-x}\text{Al}_x\text{As}_{1-y}\text{Sb}_y$ ($x \sim 0.3$; $y \sim 0.97$) is doped at $6-8 \times 10^{16} \text{ cm}^{-3}$ also with Te. Lattice matching of the GaAlAsSb epitaxial layer is aided by the addition of a small amount of arsenic. Since this amount of arsenic in the solid is minor, the GaAlAsSb will hereafter be referred to as GaAlSb. Although the doping of the GaSb and GaAlSb differs by a small amount, from other work (5) the gradient of the impurity is extremely large at the p-n junction. Therefore, the difference in doping will not lead to any appreciable error in comparisons of diffusion rate between the two materials. The diffusions of this work were performed at a temperature of 520°C . Although this temperature is low relative to zinc diffusions carried out in other III-V systems (e.g., GaAlAs-GaAs), it is still high for the antimonide system given that GaSb melts at approximately 712°C . The diffusion source consisted of Zn in Ga at 7 atomic percent. This is similar to the type of

source used by Rezek et al. (4). The samples were sealed in an ampoule evacuated to $\sim 10^{-6}$ torr. A small amount of pure antimony was also placed in the ampoule prior to seal off. This resulted in planar junctions which were not possible otherwise under the same conditions. A typical diffusion into GaAlSb is shown in Fig. 1. The p-n junction location in the GaSb and GaAlSb as well as the heterojunction between the GaAlSb and GaSb were revealed in cross section with a $\text{H}_2\text{O}:\text{KOH}:\text{K}_3\text{Fe}(\text{CN})_6$ 20:1:1 etch. The junction depth was ascertained with a Nomarski contrast optical microscope.

The p-n junction depths as a function of the square root of diffusion time for the $\text{Ga}_{0.7}\text{Al}_{0.3}\text{Sb}$ and GaSb are shown in Fig. 2. As is evident in the figure, the diffusion rate for the aluminum bearing alloy is approximately >1.6 times higher than for the GaSb. It is expected that the difference between diffusion rates of the two materials would be more pronounced as the diffusion temperature is increased for a given diffusion time (6). In addition, a break in the diffusion depth vs. time curve occurs at a depth of approximately one micron for both the GaAlSb and GaSb. A similar effect has been observed in GaP (7). This was attributed to the introduction of dislocations. The dislocations affect either the substitutional to interstitial impurity ratio or change the diffusion coefficients (D_i ; D_s), depending on the nature of the dislocations. The same effect is probably operative in the antimonide compounds. The net result is to enhance the diffusion rate. This is shown by the greater slope after a diffusion depth of $\sim 1 \mu\text{m}$ is exceeded. The higher rate of diffusion of zinc in the ternary over that of the binary is similar to that found for all Ga-Al compounds with an As or P anion. The diffusion concentration profile is not expected to follow a complementary error distribution owing to the concentration dependence of the distribution coefficient.

In conclusion, it has been found that Zn diffusion in GaAlSb-GaSb system is similar to other Ga-Al compounds with other anions such as As or P. In addition, much lower diffusion temperatures are required in this lower bandgap material. It has also been found that an antimony overpressure results in more planar p-n junctions.

ACKNOWLEDGEMENTS

The authors are grateful to P. D. Dapkus for valuable discussions, and to C. S. Hong for use of equipment and Y. Z. Liu for critical review of the manuscript. This work has been supported in part by the Air Force Systems Command, Hascomb Air Force Base, under Contract No. F19628-79-C-0143.

REFERENCES

1. Ya. A. Aarik, L. M. Dolginov, A. E. Drakin, L. V. Druzhinina, P. G. Eliseev, P. A. Lyuk, B. N. Sverdlov, V. A. Skripkin, and Ya. F. Friedentkhal, *Sov. J. Quant. Elect.*, **10**, 50, (1980).
2. H. D. Law, L. R. Tomasetta, K. Nakano, and J. S. Harris, *Appl. Phys. Lett.*, **33**, 416 (1978).
3. R. Chin, H. D. Law, K. Nakano, and R. A. Milano, *Appl. Phys. Lett.*, **37**, 550 (1980).
4. E. A. Rezek, P. D. Wright, and N. Holonyak, Jr., *Solid State Elec.*, **21**, 525 (1978).
5. L. L. Chang, and G. L. Pearson, *Appl. Phys.*, **25**, 374 (1964).
6. A. Flat, A. E. Milnes, and D. L. Feucht, *Solid State Elec.*, **20**, 1024 (1977).
7. S. F. Nygren, and G. L. Pearson, *J. Electrochem. Soc.*, **116**, 648 (1969).



Fig. 1 Cleaved and stained cross section of a Zn diffused GaAlSb-GaSb sample. A) denotes the p-n junction location in the GaAlSb and B) denotes the GaAlSb-GaSb heterojunction interface.

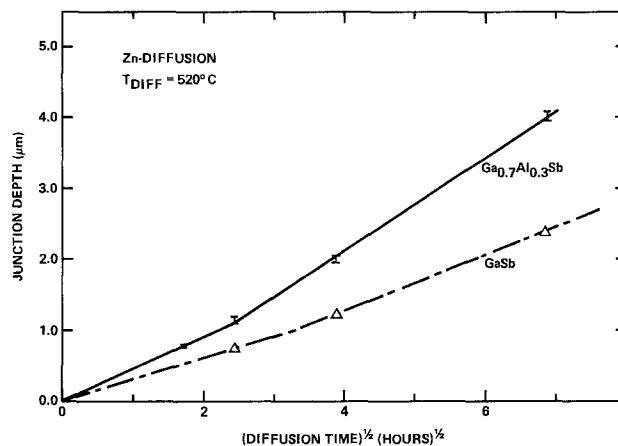


Fig. 2 P-N junction depth vs. (diffusion time)^{1/2} plot for Zn diffusions into GaAlSb and GaSb. A comparison between the diffusions into the two materials clearly shows that the diffusion rate of Zn in GaAlSb is higher than that of GaSb.

Manuscript submitted Sept. 8, 1980;
revised manuscript received Sept. 30, 1980.

Publication costs of this article were assisted by Rockwell International.

Electrochemical Inactivation of Marine Bacteria

H. P. Dhar and J. O'M. Bockris*

Department of Chemistry, Texas A&M University, College Station, Texas 77843

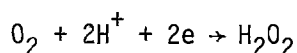
and D. H. Lewis

Department of Veterinary Microbiology, Texas A&M University, College Station, Texas 77843

Previous methods used to control microbial fouling have had limited success (1,2,3,4). One approach involved electrochemical evolution of Cl_2 in the bulk of the solution (4). Power requirements and Cl_2 concentrations of this method are, however, impractically large. Other electrochemical approaches have involved the cathodic evolution of H_2 , which, although partially successful, causes the region near the interface to become alkaline and encourages the development of other deposits (5,6).

The present report concerns the bactericidal properties of H_2O_2 , which is formed from dissolved O_2 present in an electrolyte at low power densities on the metal surface. Direct observations of bacterial activity of *Vibrio Anguillarum*, a marine species of bacteria were made in a cell constructed of transparent conducting SnO_2 glass, using dark field and phase contrast microscopic techniques. The cell used involved a transparent Nafion cationic membrane #425 to separate the anode and cathode compartments. The dimensions of each compartment were 3 cm X 2 cm X 0.02 cm. 400X magnification (3.10^{-6} m depth of field) allowed observation of the cathode surface, while eliminating transfer of anodically produced Cl_2 . In addition to direct observations, assessment of bacterial viability was made by diluting and culturing aliquots from each compartment (7).

The current-density/potential relation for the reaction



revealed that H_2O_2 formation would occur in 30% NaCl at approximately -0.3 V on the Normal Hydrogen Electrode (NHE) scale at a current density of around 100 mA m^{-2} .

*Electrochemical Society Active Member

Key Words: Microbial fouling, hydrogen peroxide, tin oxide glass

Trivial calculation shows that, at 10% current efficiency of the experimentally obtained value of $5 \cdot 10^{-6} \text{ amp cm}^{-2}$, the region of 0.02 cm near the surface has an H_2O_2 concentration of around $5 \cdot 10^{-6} \text{ mole l}^{-1}$. Bacterial viability as a function of H_2O_2 concentrations was determined in separate experiments. The results are presented in Table I.

TABLE I: VIABILITY OF *VIBRIO ANGUILLARUM* AT VARIOUS H_2O_2 CONCENTRATIONS

| H_2O_2 Concentration (mole l^{-1}) | Bacteria Concentration (number/ml) |
|---|---------------------------------------|
| 10^{-8} | 10^3 |
| 10^{-7} | $3 \cdot 10^2$ |
| 10^{-6} | 10^1 |
| 10^{-5} | 4 |
| 10^{-4} | 1 |
| 10^{-3} | 1 |

It can be seen that a concentration $5 \cdot 10^{-6} \text{ mole l}^{-1}$ of H_2O_2 would reduce the bacterial concentration about 33 times. The electrode surface itself would be likely, therefore, to be toxic to *Vibrio Anguillarum*.

The pH of the electrolyte used would have been near 7 before any effects of electrolysis. A change of pH near the electrode would be due to the concentration of H^+ ions near the cathode which combine with O_2 to produce H_2O_2 . Taking 1% current efficiency for the production of H_2O_2 , the concentration of H^+ near 0.02 cm of the electrode was calculated (Ficks Law) to be $4 \cdot 10^{-7} \text{ mole l}^{-1}$. Thus, a pH range of 6 to 7 is expected near the cathode and such a range is not unfavorable for bacterial existence (8).

A potentiostat was used to bring the SnO_2 cathode to the H_2O_2 -producing potential, and after introduction of bacteria at about 10^7 ml^{-1} in the cell the following direct assessments of the bacterial viability were made: (i) Some change in the motility

of the bacteria was observed immediately, upon achieving this potential and (ii) After five minutes, approximately half the observed bacteria ceased movement; after ten minutes no movement was observable. The data presented in Figure 1 represents bacterial viability as a function of time during the production of H_2O_2 in the cathode and Cl_2 in the anode compartments, as determined by the serial dilution counting method (7). In the visual experiments above, orders of magnitude more bacteria were used than in those where bacteria were counted by the serial dilution technique (7). The half life values of approximately one minute in the anode compartment and two minutes in the cathode compartment (Fig. 1) suggests that H_2O_2 is less bactericidal than Cl_2 . However, the H_2O_2 arises at a surface relatively cathodic and hence, less likely to corrode than one evolving Cl_2 .

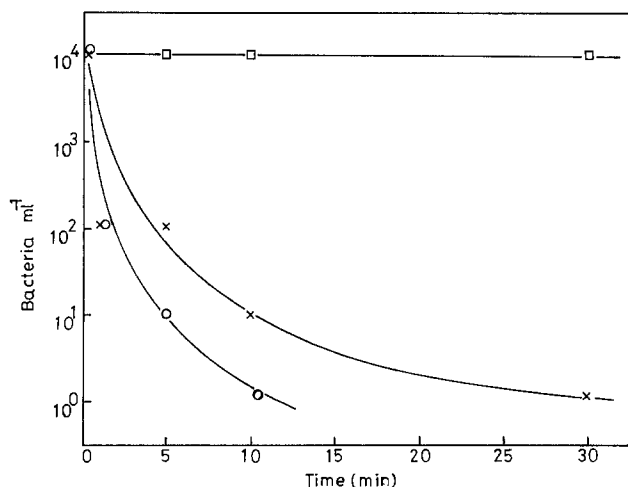


Fig. 1. Bacteria concentration v. time of experiment. □, blank, no potential being applied; × and ○, cathode and anode compartment results, respectively. Thickness of each compartment, 0.02 cm. Cathode potential -0.36V (NHE); cell potential 1.95V; current density 5.10^{-2} amp m^{-2} .

The bacterial concentrations presented in Figure 1 refer to those in the cathode and anode compartments. To obtain results more relevant to the conditions near the surface, four cells were fabricated so that distances between the plates were varied. Figure 2 presents data of bacterial viability (number of bacteria still living) versus time after applying potentials appropriate for the formation of H_2O_2 on the cathode in each of these cells.

At a constant time, the number of bacteria in the cell decreases with decreasing

cell thickness indicating that in a thinner cell, bacteria come into contact with a higher concentration of H_2O_2 , and thus die quicker than would have been possible in a thicker cell.

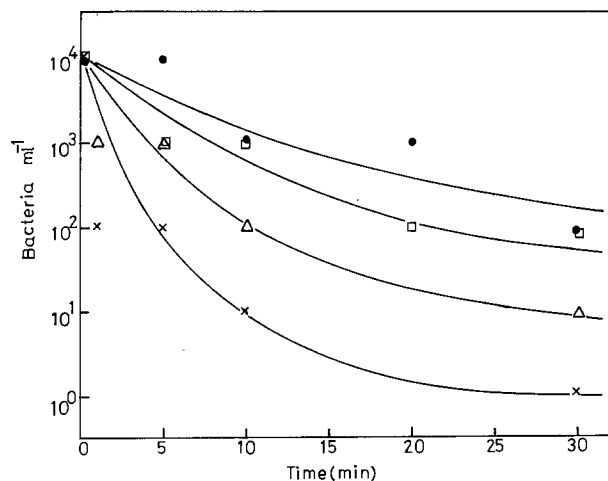


Fig. 2. Bacteria concentration v. time of experiment in cells of varying thickness: 0.15 cm (●), 0.09 cm (□), 0.06 cm (△), and 0.02 cm (×). Cathode potential -0.36 V (NHE). Current density 5.10^{-2} amp m^{-2} .

The bacterial half life revealed by reading from Figure 2 as a function of cell thickness yields data presented in Figure 3. The extrapolated zero thickness value from Figure 3 gives half life value of 30 ± 3 seconds near the electrode surface. This value was obtained through least square analysis of the data. The half life value should not be identified with concentration of bacteria on the surface.

The relevance of the present work to technological situations arises from the small power used and the possibility that device development to intermittent application of the H_2O_2 potential formation range would suffice to reduce greatly the growth of bacterial layers.

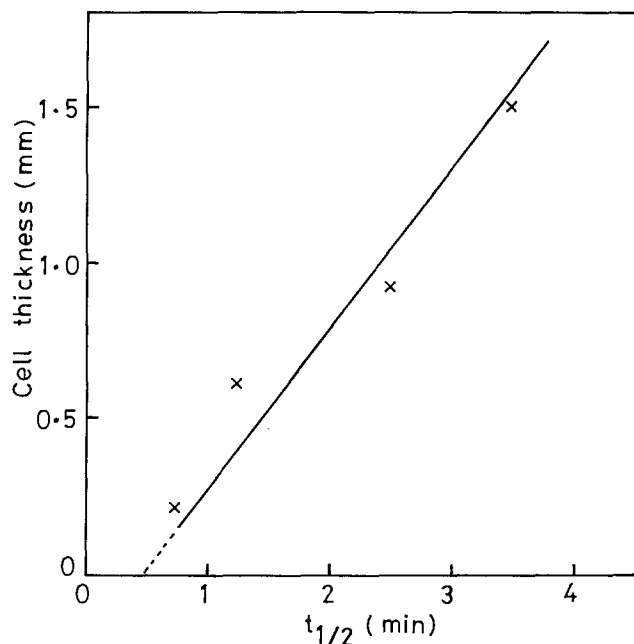


Fig. 3. Cell thickness v. half lifetime of bacteria.

ACKNOWLEDGMENTS

We thank Dr. J. Huff of the Department of Veterinary Microbiology of Texas A&M University for some discussions. We acknowledge financial support from the Texas A&M University Sea Grant College Program, supported by the National Oceanic and Atmospheric Administration Office of Sea Grant, Department of Commerce, under Grant #NA79AA-D-00127.

REFERENCES

1. L. D. Perrigo and G. A. Jensen. Proc. 4th Ann. Conf. on OTEC, Univ. New Orleans, March 1977, pp. VII 3-VII 10.
2. A. W. Conn, M. S. Rice and D. Hagel. Proc. 4th Ann. Conf. on OTEC, Univ. New Orleans, March 1977, pp. VII 11-VII 14.
3. E. D. Nübel. Proc. 4th Ann. Conf. on OTEC, Univ. New Orleans, March 1977, pp. VII 61-VII 63.
4. J. A. Fava and D. L. Thomas. Ocean. Engng., 5, 269 (1978).
5. E. S. Castle. Ind. & Eng. Chem., 43, 901 (1951).
6. E. Littauer and D. M. Jennings. Proc. 2nd Int. Cong. on Marine Corrosion and Fouling, Athens, 1968, pp. 527-536.

7. M. Frobisher, R. Hinsdill, K. Crabtree and C. Goodheart. "Fundamentals of Microbiology," W. B. Sanders Pub., 1974, p. 136.
8. S. C. Daniels, p. 19 in Adsorption of Microorganisms to Surfaces. Eds. G. Bitton and K. C. Marshall. John Wiley & Sons, 1980.

Manuscript submitted July 28, 1980; revised manuscript received Oct. 6, 1980.

Publication costs of this article were assisted by Texas A&M University.



Conductivities in Thionyl Chloride

Mark Salomon*

*U.S. Army Electronics Technology and Devices Laboratory (ERADCOM),
 Power Sources Division, Fort Monmouth, New Jersey 07703*

ABSTRACT

Conductivity measurements in thionyl chloride are reported for dilute solutions of AlCl_3 , LiAlCl_4 , and the tetrapropylammonium (Pr_4N) salts Pr_4NCl , Pr_4NClO_4 , $\text{Pr}_4\text{NAlCl}_4$. The data for electrolyte solutions having concentrations in the range of ~ 0.01 to 1×10^{-5} mole dm^{-3} were fitted empirically to an equation of the Fuoss-Hsia type. In all cases except for AlCl_3 ion pair formation was found to be extensive. AlCl_3 solutions in thionyl chloride appear to be complex possibly owing to the formation of complex species such as Al_2Cl_6 and Al_2Cl_7^- . The effect of ionic strength on the solubility of LiCl is discussed.

In addition to the interesting general solvent properties of thionyl chloride (1), this solvent has received considerable attention as a cathode depolarizer in primary lithium batteries (2, 3). A number of important physico-chemical properties of electrolytic solutions have been reported (1, 4) including the conductivities of LiAlCl_4 solutions (4). In the present paper, the conductivities of dilute solutions (between 0.01 and 1×10^{-5} mole dm^{-3}) of various salts including LiAlCl_4 are reported and analyzed in accordance with an ion pairing model. The dielectric constants and densities of the pure solvent over a small temperature range are also reported.

Experimental

Chemicals.—Purified LiAlCl_4 was supplied by W. K. Behl of this laboratory and was purified as described previously (3). Fluka purris AlCl_3 was sublimed in vacuum and transferred to a dry box while under vacuum. Tetrapropylammonium perchlorate (Pr_4NClO_4) was recrystallized from distilled water, and Pr_4NCl was precipitated from an acetone/ether mixture: both salts were dried in a vacuum at 60°C and stored in the dry box. AR grade LiCl was dried at 110°C and stored in the dry box. Tetrapropylammonium tetrachloroaluminate, $\text{Pr}_4\text{NAlCl}_4$, was prepared in the dry box by mixing stoichiometric quantities of AlCl_3 and Pr_4NCl followed by addition of the solvent. SOCl_2 (MC/B best grade) was refluxed with P_2O_5 at room temperature for 24–48 hr before distillation: the middle 2/3 of the colorless distillate was retained for use. A Vacuum Atmospheres Corporation dry box with an argon atmosphere was used in this work.

Dielectric constant measurements.—The static dielectric constants at 15° , 25° , and 35°C were measured by the comparison method (5). The cell, which utilized Type 304 stainless steel, consisted of concentric steel electrodes threaded onto a Teflon base which also formed part of a water jacket. The cell capacitances were measured at 1 MHz by a substitution method with a General Radio 1606-B bridge and 722-D and 1422-ME precision capacitors. The cell constants were deter-

mined from measurements with air, benzene, and tetrahydrofuran. The cell was filled with SOCl_2 in the dry box, sealed with a Teflon stopper, and removed to the laboratory for capacitance measurements at 15° , 25° , and $35^\circ \pm 0.1^\circ\text{C}$.

Conductivity measurements.—These measurements were carried out at $25^\circ \pm 0.03^\circ\text{C}$ (uncalibrated thermometer) at 1 kHz using a General Radio 1608-A impedance bridge. Yellow Springs Instrument Company Type 3402 conductivity cells were modified to permit sealing with a 10/20 ST Pyrex stopper, and to permit immersion in a thermostated water bath. Smooth Pt electrodes were used, and the two cells modified for this work had cell constants of the order of 0.1 cm^{-1} . The cell constants were determined with dilute KCl solutions. All solutions were prepared in the dry box at room temperature (22° – 26°C), the cells filled and sealed, and removed into the laboratory for the measurements. Solutions were prepared on a volume basis, and corrections to 25°C were made utilizing results from dilatometric measurements on the pure solvent, and in several cases for dilute salt solutions. The error in concentration using solvent densities rather than solution densities is negligible. The major factors influencing the accuracies of the conductivities were the weighing of salts in the dry box ($\pm 0.04\%$) and the determination of final volumes ($\pm 0.2\%$): the accuracy in the reported concentrations is therefore $\pm 0.3\%$. Due to the use of smooth Pt electrodes and associated instrumentation, the overall accuracy in the molar conductivities is no better than $\pm 3\%$.

Results and Data Analyses

The static dielectric constants at 15° , 25° , and 35°C are, respectively, 9.65, 9.23, and 8.77D. These results were fitted by least squares to the following smoothing equation

$$\epsilon/D = -3.88 + 3903/(T/K) \quad [1]$$

For the densities of pure SOCl_2 , dilatometric measurements at 15° , 20° , 25° , and 35°C were fitted by least squares to the following smoothing equation

$$d/\text{kg } m^{-3} = 1.6284 - 0.00191(t - 25) \quad [2]$$

* Electrochemical Society Active Member.
 Key words: battery, conductance, dissociation, solubility.

EST

The experimental conductivity data for LiAlCl_4 , AlCl_3 , Pr_4NClO_4 , Pr_4NCl , $\text{Pr}_4\text{NAlCl}_4$ (Δ) were calculated from the electrolytic conductivities, κ , after correcting for the solvent conductance: at 25°C the electrolytic conductivity of the solvent is $\kappa(\text{SOCl}_2) = 5 \times 10^{-9} \text{ S cm}^{-1}$ (6). The conductivity data were analyzed using the following equation (7)

$$\Lambda = \Lambda^\infty - S(\alpha c)^{1/2} + E(\alpha c) \ln(\alpha c) + J_1(\alpha c) + J_2(\alpha c)^{3/2} - \Delta \alpha c y_{\pm}^2 / (K_D^\circ y_n) \quad [3]$$

The Onsager and Fuoss-Onsager constants S and E were calculated using the present value for the dielectric constant of SOCl_2 and a value of 0.626 cp for the viscosity at 25°C (6). The remaining terms in Eq. [3] are defined as follows: α is the degree of dissociation of the neutral ion pair; c is the total molar concentration of the salt; Λ^∞ is the molar conductivity at infinite dilution; y_{\pm} is the mean molar activity coefficient and y_n is the activity coefficient for the neutral ion pair; J_1 and J_2 are constants which were evaluated empirically by least squares; and K_D° is the dissociation constant for the ion pair defined by

$$K_D^\circ = \alpha^2 c y_{\pm}^2 / [(1 - \alpha) y_n] \quad [4]$$

Initial attempts to evaluate activity coefficients by emf measurements on cells without transport failed. In spite of reports (1b) that metals such as Ag, Ni, Mo respond thermodynamically to Cl^- , attempts to utilize these electrodes in various combinations, and in combinations with Li and Ag, AgCl electrodes, lead to irreproducible results. The mean molar activity coefficients were therefore calculated from the Davies equation (8)

$$\log y_{\pm} = -A I^{1/2} / [1 + I^{1/2}] + 0.3AI \quad [5]$$

where I is the ionic strength,¹ and A is the Debye-Hückel factor. At the present time the only justification for the use of Eq. [5] for SOCl_2 solutions is that the Davies equation has previously been successfully used in aprotic solvents of varying dielectric constants (9, 10). Since SOCl_2 has a low dielectric constant, it is anticipated that salting out coefficients would be significantly more important than in aqueous solutions, and in the present calculations, it is assumed that the activity coefficient for the neutral ion pair is given by

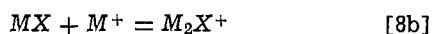
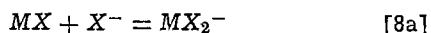
$$\log y_n = 0.3AI \quad [6]$$

For the concentrations employed in the present study, the y_n values as calculated from this equation are close to unity and have a small effect on the magnitudes of K_D° and Λ^∞ . Equation [6] was incorporated into the present calculations.

Equation [3] was solved by evaluating J_1 and J_2 by least squares (11). Both K_D° and Λ^∞ were varied until the error σ_Λ was minimized. σ_Λ is defined by

$$\sigma_\Lambda = \{ \sum (\Delta_{\text{obs}} - \Delta_{\text{calc}})^2 / (N - 3) \}^{1/2} \quad [7]$$

where N is the number of data points in each experiment. The results are summarized in Table VI, and the associated results for α and y have been included in Tables I-V. Two, or three at the most, data points for concentrations of the order of 0.1 mole dm^{-3} are not reported in the tables. The reason these points were omitted from the present analyses is that their inclusion gave rise to abnormally large σ_Λ values which is undoubtedly due to the formation of triple ions according to (4, 6)



The conductivity data for the binary $\text{AlCl}_3\text{-SOCl}_2$ system could not be analyzed by the present method, and the possible reasons for this are discussed below.

¹ For 1:1 electrolytes, $I = \alpha c$.

Table I.* The $\text{LiAlCl}_4\text{-SOCl}_2$ system at 25°C

| $10^4 c$ | Λ | α | y_{\pm} | y_n |
|----------|-----------|----------|-----------|-------|
| 93.68 | 7.28 | 0.147 | 0.357 | 1.012 |
| 61.00 | 7.76 | 0.152 | 0.427 | 1.008 |
| 38.15 | 9.52 | 0.165 | 0.494 | 1.006 |
| 14.80 | 12.37 | 0.209 | 0.606 | 1.003 |
| 11.58 | 13.97 | 0.225 | 0.631 | 1.002 |
| 10.72 | 14.42 | 0.230 | 0.639 | 1.002 |
| 7.806 | 16.38 | 0.253 | 0.669 | 1.002 |
| 6.134 | 17.49 | 0.273 | 0.690 | 1.001 |

* In Tables I-V, the experimental data are $c/\text{mole dm}^{-3}$ and $\Lambda/S\text{-cm}^2 \text{ mole}^{-1}$. The quantities α , y_{\pm} , and y_n were calculated as described in the text.

Table II. The $\text{AlCl}_3\text{-SOCl}_2$ system at 25°C

| $10^4 c$ | Λ |
|----------|-----------|
| 68.87 | 0.49 |
| 22.19 | 1.27 |
| 11.58 | 2.21 |
| 5.89 | 4.13 |

Table III. The $(\text{C}_8\text{H}_7)_4\text{NClO}_4\text{-SOCl}_2$ system at 25°C

| $10^4 c$ | Λ | α | y_{\pm} | y_n |
|----------|-----------|----------|-----------|-------|
| 14.23 | 25.71 | 0.310 | 0.552 | 1.004 |
| 8.223 | 30.70 | 0.353 | 0.616 | 1.003 |
| 7.110 | 32.34 | 0.367 | 0.631 | 1.002 |
| 4.106 | 38.67 | 0.424 | 0.686 | 1.002 |
| 3.510 | 39.93 | 0.442 | 0.700 | 1.001 |
| 2.085 | 48.18 | 0.506 | 0.744 | 1.001 |
| 1.066 | 57.85 | 0.599 | 0.794 | 1.001 |
| 0.640 | 67.30 | 0.671 | 0.828 | 1.000 |
| 0.510 | 68.56 | 0.703 | 0.841 | 1.000 |
| 0.258 | 80.59 | 0.792 | 0.877 | 1.000 |

Table IV. The $(\text{C}_8\text{H}_7)_4\text{NCl-SOCl}_2$ system at 25°C

| $10^4 c$ | Λ | α | y_{\pm} | y_n |
|----------|-----------|----------|-----------|-------|
| 29.69 | 35.15 | 0.463 | 0.357 | 1.012 |
| 15.27 | 40.83 | 0.485 | 0.466 | 1.006 |
| 7.907 | 48.06 | 0.533 | 0.559 | 1.004 |
| 4.916 | 53.12 | 0.580 | 0.618 | 1.002 |
| 2.321 | 63.64 | 0.665 | 0.701 | 1.001 |
| 1.840 | 64.96 | 0.692 | 0.723 | 1.001 |
| 0.968 | 76.28 | 0.768 | 0.780 | 1.001 |
| 0.481 | 84.45 | 0.843 | 0.832 | 1.000 |

Table V. The $(\text{C}_8\text{H}_7)_4\text{NAlCl}_4\text{-SOCl}_2$ system at 25°C

| $10^4 c$ | Λ | α | y_{\pm} | y_n |
|----------|-----------|----------|-----------|-------|
| 29.22 | 23.97 | 0.369 | 0.400 | 1.009 |
| 19.23 | 25.07 | 0.385 | 0.465 | 1.006 |
| 11.46 | 31.08 | 0.419 | 0.538 | 1.005 |
| 5.864 | 37.72 | 0.481 | 0.620 | 1.002 |
| 2.899 | 45.94 | 0.561 | 0.694 | 1.001 |
| 1.727 | 52.09 | 0.627 | 0.742 | 1.001 |
| 1.154 | 59.67 | 0.680 | 0.775 | 1.001 |
| 0.721 | 65.97 | 0.741 | 0.810 | 1.000 |

An attempt was also made to evaluate the solubility of LiCl , c_{satd} , in the pure solvent. The solubility is given by

$$c_{\text{satd}} = [\text{LiCl}]_{\text{sln}} + [\text{Li}^+] \quad [9a]$$

and in terms of equilibrium constants

$$c_{\text{satd}} = K_{\text{so}}^\circ / (K_D^\circ y_n) + (K_{\text{so}}^\circ)^{1/2} / y_{\pm} \quad [9b]$$

where K_{so}° is the thermodynamic solubility product constant for LiCl . $[\text{Li}^+]$ can be calculated from the electrolytic conductivity of a saturated LiCl solution, and c_{satd} is obtained from Eq. [9b]. SOCl_2 was saturated with LiCl in the dry box at 22°-26°C for 72 hr with occasional shaking. Storage of these solutions for more than 7 days results in slight decomposition which is indicated by the appearance of a light green color. The conductivity cell containing excess solid LiCl was filled in the dry box, removed to the laboratory, and

Table VI.* Results of analyses based on Eq. [3]

| Salt | J_1 | $-J_2$ | $\Lambda^\infty (\sigma)$ | $10^5 K^{\circ}_D (\sigma)$ | σ_A |
|------------------------------------|---------------------|---------------------|---------------------------|-----------------------------|------------|
| LiAlCl ₄ | 7.649×10^4 | 3.531×10^5 | 75.5 (1.7) | 3.0 (0.1) | 0.28 |
| Pr ₄ NClO ₄ | 1.015×10^5 | 2.142×10^5 | 106.2 (1.2) | 6.0 (0.2) | 0.72 |
| Pr ₄ NCl | 1.302×10^5 | 9.768×10^5 | 106.6 (1.3) | 15.0 (0.6) | 0.82 |
| Pr ₄ NAiCl ₄ | 8.411×10^4 | 8.149×10^4 | 97.0 (2.0) | 10.0 (0.5) | 0.88 |

* All data are for 25°C. Λ^∞ units are $S \text{ cm}^2 \text{ mole}^{-1}$, and K°_D units are mole dm^{-3} .

placed in the water bath at about 33°C for 10 min. Reducing the temperature to 25°C and measuring the conductivity gave an electrolytic conductivity for the solution of $\kappa(\text{sln}) = 1.65 \times 10^{-7} S \text{ cm}^{-1}$; correcting for the electrolytic conductivity of the solvent, $\kappa(\text{LiCl}) = 1.60 \times 10^{-7} S \text{ cm}^{-1}$. The concentration of dissociated LiCl, c' (note $c' = [\text{Li}^+]$), was calculated from the Onsager equation

$$1000\kappa(\text{LiCl})/c' = [\Lambda^\infty - S(c')^{1/2}]/[1 + y_{\pm}^2 c'/(K^{\circ}_D y_n)] \quad [10]$$

$\Lambda^\infty(\text{LiCl})$ is obtained from the data in Table VI, i.e., $\Lambda^\infty(\text{LiCl}) = \Lambda^\infty(\text{LiAlCl}_4) + \Lambda^\infty(\text{Pr}_4\text{NCl}) - \Lambda^\infty(\text{Pr}_4\text{NAiCl}_4) = 85.1 S \text{ cm}^2 \text{ mole}^{-1}$. Since at high dilutions α values are generally quite large (i.e., ≈ 0.9), K°_D is rather insensitive to the final c_{satd} and it is found that c_{satd} is almost constant (within experimental error) from $K^{\circ}_D = 0.1$ to $1 \times 10^{-5} \text{ mole dm}^{-3}$. Values of $K^{\circ}_D = 1 \times 10^{-6} \text{ mole dm}^{-3}$ or smaller results in significantly increasing c_{satd} values. In light of the smallest K°_D value of $3 \times 10^{-5} \text{ mole dm}^{-3}$ for LiAlCl₄ found in the present work, and the value of $K^{\circ}_D = 1 \times 10^{-5} \text{ mole dm}^{-3}$ for $(\text{CH}_3)_4\text{NOC}_6\text{H}_2(\text{NO}_2)_3$ (picrate) reported by Beronius and Brändström (15) in water saturated methylene chloride ($\epsilon = 9.53D$), the present assumed value of $K^{\circ}_D(\text{LiCl}) = 1 \times 10^{-5}$ in SOCl_2 seems a reasonable lower estimate. Solving for c' by an iterative method, the following are obtained (note $K^{\circ}_{s0} = (\alpha c_{\text{satd}} y_{\pm})^2$)

$$c_{\text{satd}} = 2.2 \times 10^{-6} \text{ mole dm}^{-3} \text{ and}$$

$$K^{\circ}_{s0} = 3.3 \times 10^{-12} \text{ mole}^2 \text{ dm}^{-12}$$

Discussion and Conclusions

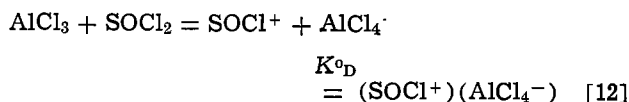
The data in Table VI demonstrate that the salts studied are all highly associated. The only other study on ion association by conductivity methods is that of Venkatesetty and Ebner (4) in which values of $\Lambda^\infty = 16.5 S \text{ cm}^2 \text{ mole}^{-1}$ and $K^{\circ}_D = 1.61 \times 10^{-3} \text{ mole dm}^{-3}$ were reported. They analyzed conductivity data from a simplified form of the Fuoss-Shedlovsky equation (12), and neglected to include activity coefficients. These authors also report $K_3/\Lambda_3^\infty = 1.21 \times 10^{-3} \text{ dm}^3 S^{-1} \text{ cm}^{-2}$. By means of Walden's rule, Λ_3^∞ for the triple ion can be estimated from $\Lambda^\infty(\text{LiAlCl}_4)/3$: using the present value for $\Lambda^\infty(\text{LiAlCl}_4)$, the molar conductivity for the triple ions given in Eq. [8] at infinite dilution is $25.8 S \text{ cm}^2 \text{ mole}^{-1}$ which gives a value of $0.03 \text{ mole}^{-1} \text{ dm}^3$ for the triple ion formation constant K_3 . Since the conductivity data of Venkatesetty and Ebner appear (only graphical data are given in their paper) similar to the present data, the differences in our results for Λ^∞ and K°_D must be due to the method of treatment of the data. For $K_D < 10^{-3}$, the Fuoss-Shedlovsky plots become insensitive to Λ^∞ , and the K_D values are even more uncertain (7, 13). In addition, the neglect of activity coefficients is not justified (the Debye-Hückel "A" factor = $12.64 \text{ mole}^{-1/2} \text{ dm}^{3/2}$ at 25°C). The major problem encountered in the present work involves the estimation of activity coefficients. In a previous study (11), it was found that the empirical solution of Eq. [3] using Eq. [4]-[6] can reproduce previously published Λ^∞ and K°_D values for K°_D ranging from 1 to $1 \times 10^{-5} \text{ mole dm}^{-3}$, and in solvents having dielectric constants ranging from 78.3D (water) to 9.53D (83

mass% p-dioxane in water). Generally, the analysis of the conductivity equation [3] by more elaborate methods (7) employs the following relation for the activity coefficients

$$\log y_{\pm} = -A(\alpha c)^{1/2}/[1 + BR(\alpha c)^{1/2}] \quad [11]$$

The activity coefficients listed in Tables I-V can be reproduced by Eq. [11] by taking values of the ion association distance, R , around 0.4 nm. However if R is equated (14) to the Bjerrum critical distance q ($q = z^2 e^2 / (2\epsilon kT) = 3.0 \text{ nm}$ for 1:1 electrolytes in SOCl_2 at 25°C), then the calculated activity coefficients differ significantly from those given in Tables I-V, e.g., for concentrations of the order of $0.01 \text{ mole dm}^{-3}$, Eq. [11] results in y_{\pm} values about twice as great as those calculated from Eq. [5], and this difference decreases to around 10% at concentrations of the order of $1 \times 10^{-4} \text{ mole dm}^{-3}$.

The analysis of the conductivity data for AlCl₃ solutions in terms of the simple dissolution reaction



was not successful, i.e., σ_A values were generally large and insensitive to values of K°_D . This inability to fit the data to this simple dissolution mechanism is attributed to both the experimental error and to the probability that dissolution is more complex and involves such species as Al_2Cl_6 , Al_2Cl_7^- , etc.

The solubility of LiCl in SOCl_2 plays an important role in the stability of lithium- SOCl_2 primary batteries (2). The solubility for the binary system is described by Eq. [9b], and in the presence of an excess of "neutral" electrolyte, i.e., one which does not yield Cl^- or Li^+ ions, the solubility is given to a good approximation by

$$c_{\text{satd}} = (K^{\circ}_{s0})^{1/2}/y_{\pm} \quad [13]$$

Equation [13] demonstrates the need for reliable activity coefficient data at high concentrations of the neutral salt. For example if Eq. [5] is used to approximate y_{\pm} at higher concentrations, the solubility of LiCl reaches a maximum of $0.005 \text{ mole dm}^{-3}$ at ionic strengths of around 0.4-0.5 mole dm^{-3} ; this is three orders of magnitude greater than the solubility in the binary system. In solutions containing a large excess of a salt which yields a common ion, say LiAlCl₄, the solubility of LiCl is given approximately by

$$c_{\text{satd}} = K^{\circ}_{s0}/\{y_{\pm}^2[\text{Li}^+]\} \quad [14]$$

In highly concentrated LiAlCl₄ solutions, say 1.5 mole dm^{-3} , c_{satd} will still be significantly larger than it would be in the pure binary system because $[\text{Li}^+]$ will be small as the major species in solution are the ion pair and the triplet Li_2Cl^+ . Taking $K_3 \approx 0.03 \text{ mole}^{-1} \text{ dm}^3$, the concentration of Li_2Cl^+ is about 0.3 mole dm^{-3} , and by Eq. [14], the solubility of LiCl should increase significantly.

Manuscript submitted June 9, 1980; revised manuscript received Aug. 29, 1980.

Any discussion of this paper will appear in a Discussion Section to be published in the December 1981

JOURNAL. All discussions for the December 1981 Discussion Section should be submitted by Aug. 1, 1981.

Publication costs of this article were assisted by the U.S. Army Electronics Technology and Devices Laboratory (ERADCOM).

REFERENCES

- (a) H. Spandau and E. Brunneck, *Z. Anorg. Chem.*, **270**, 201 (1952).
(b) H. Spandau and E. Brunneck, *ibid.*, **278**, 197 (1955).
- J. J. Auborn, K. W. French, S. I. Lieberman, V. K. Shah, and A. Heller, *This Journal*, **120**, 1613 (1973).
- W. K. Behl, J. A. Christopoulos, M. Ramirez, and S. Gilman, *ibid.*, **120**, 1619 (1973).
- H. V. Venkatesetty and W. B. Ebner, Paper presented at the 29th Power Sources Conference, Atlantic City, NJ, June 1980.
- L. Hartshorn and P. A. Oliver, *Proc. R. Soc. London Ser. A*, **123**, 664 (1929).
- D. L. Chua, Personal communication.
- R. Fernandez-Prini, in "Physical Chemistry of Organic Solvent Systems," Chap. 5.1, A. K. Covington and T. Dickinson, Editors, Plenum Press, London (1973).
- C. W. Davies, "Ion Association," Butterworths, London (1962).
- R. Alexander, A. J. Parker, J. H. Sharp, and W. E. Waghorne, *J. Am. Chem. Soc.*, **94**, 1148 (1972).
- M. Salomon, *J. Phys. Chem.*, **79**, 2000 (1975).
- M. Salomon, To be published.
- R. M. Fuoss and T. Shedlovsky, *J. Am. Chem. Soc.*, **71**, 1496 (1949).
- C. B. Monk, "Electrolytic Dissociation," Academic Press, London (1961).
- J.-C. Justice, *J. Chim. Phys.*, **65**, 353 (1968).
- P. Beronius and A. Brändström, *Acta Chem. Scand.*, **A30**, 687 (1976).

Effect of Discharge Current Density on Structure of the Lead Negative Plate

C. P. Wales, S. M. Caulder,¹ and A. C. Simon¹

Naval Research Laboratory, Washington, DC 20375

ABSTRACT

To help understand how the high current demands of an electric vehicle might affect the electrode microstructure and performance of lead-acid batteries, experiments were run wherein commercial negative plates were given 26 cycles of deep discharge at current densities of either 18, 125, 500, or 2000 A/m². Sections of the plates were removed after cycles 1, 6, 16, and 26 and carefully examined by light and electron microscopy, image analysis, and surface area analysis to determine how the electrode active material composition and structure changed with cycling at the different current densities. Electrochemical performance was monitored by measuring plate capacity and electrode potential as a function of current density and number of cycles. The size of the PbSO₄ crystals in the discharged plates decreased roughly in correspondence to the decrease in plate capacity produced by the increasing current densities. This suggests passivation as the cause for loss of capacity, since passivation is accepted as becoming more critical as PbSO₄ crystal size decreases. The shapes of the electrode polarization curves indicate, however, that limited electrolyte diffusion rates and lessened contact of active material crystals, the result of the porosity that develops with cycling, may also be acting to reduce plate capacity.

The present revival of interest in electric vehicles has raised questions as to the effect that the power demands of such vehicles would have on the microstructure of the lead-acid battery. Since electric vehicle applications will at times require high discharge rates, it was of interest to determine what differences in microstructure are produced by different rates of discharge.

As a first stage of this investigation the effect of different rates of discharge on the negative electrode was investigated. The microstructure of the negative plate of the lead-acid battery has been studied by a number of investigators but little effort has been made to determine the effect that various discharge currents have on the microstructure. Hughel and Hammer examined the structure of the constituents used in plates, and the active material structure before formation and after completing the forming charge (1). Hattori *et al.* examined a small area of the surface of a miniature negative plate (2). The surface of their formed plate contained smooth particles about the size shown by Hughel and Hammer (1) and also included some dendritic clumps of platelets. After a discharge and re-

charge these platelets aggregated into larger clumps. Pierson *et al.* showed that the surface of a negative plate was not typical of the bulk of the active material in the interior (3). Since Hattori *et al.* examined only the plate surface, this may explain why they found no differences between plates with and without expanders (2), while others reported that expanders have a strong effect on structure (1, 3-5). Weininger (6) found a greatly different structure for a formed negative plate than has been generally reported.

Negative plates require an expander for satisfactory life. When no additives are present the lead forms into large single crystals during the initial charge (4). These large particles cannot be completely converted to PbSO₄ during discharge, and result in a plate having low cycle life (5). The presence of lignin, an expander often added to the negative plate together with BaSO₄, yields a formed plate containing smaller and less complex dendritic Pb crystals than would be obtained without lignin (3, 4). Plates with both lignin and BaSO₄ give a much improved cycle life, and the lead forms into small rod-like particles that have a greatly increased surface area (4, 5).

In the present work commercial plates were cycled using four low to very high discharge rates. The struc-

¹International Lead Zinc Research Associate at Naval Research Laboratory.

Key words: particles, electrode, discharge, growth.

tural changes that occurred in the active material were studied mainly with the scanning electron microscope and with the light microscope, aided by an image analyzer.

Experimental

The negative and positive plates in this work were commercial plates of the type used in automotive batteries. The negative plates contained expander. The grids contained a Pb alloy with a 4% Sb content. The negative plates were $144 \times 122 \times 1.4$ mm, not including the tabs. The active material had not been formed. Before a negative plate was put in use, seven equal areas were outlined by removing some of the active material pellets to expose the grid members surrounding these seven areas. This treatment facilitated later removal of seven samples of equal size from a cycled wet plate. About 48.5g of unformed active material remained after removing the pellets. This was 64% of the amount originally present. Later, when a sample was to be taken, it was easy to cut the bare grid members and remove a sample without unduly disturbing the remaining active material.

Each cell contained one of these negative plates, two positive plates, a polyethylene separator between each positive and the negative, and an Hg/Hg₂SO₄ reference electrode. There was no pressure on the plates. Two pieces of sheet plastic were placed parallel to the plates, filling most of the empty space inside the cell case. Removal of the plastic allowed easy withdrawal and replacement of the negative plate. The cell contained 410-420 ml of electrolyte. The cell potential, the potential between the reference electrode and the negative plate, and the current were recorded using a strip chart recorder.

The two positive plates had a much greater capacity than the negative plate and were formed separately. Instead of using fresh positive plates for each cell, often a cell contained used positive plates taken from an earlier cell; no difference in negative plate behavior was observed. Negative plates form better in a more concentrated acid than the dilute H₂SO₄ often used for positive plates (7-9). The negative plates were formed in 1.200 sp gr H₂SO₄ at 40 A/m² apparent area (both sides) for 20 hr at room temperature. At the end of the forming charge the acid was adjusted to about 1.255 sp gr. The specific gravity at the end of charge was maintained at 1.250-1.260 during the cycling, except for one cell that was cycled in 1.190 sp gr H₂SO₄.

Discharge currents were chosen to give negative plate current densities of 18, 125, 500, or 2000 A/m² apparent area. Discharges at these four rates lasted approximately 20 hr, 2.5 hr, 0.5 hr, and 5 min, respectively, using final cell potentials of 1.8, 1.75, 1.5, and 1.0V. All discharges of a particular negative plate were done at the same current density to see the effect of repeated use of that discharge rate. Currents were lowered after each sample was removed, so that current densities remained constant on the negative plate. Capacity discharges were done at cycles 1-6, 16, and 26. All other discharges were ended after removing 80% of negative plate capacity, with capacity taken to be the value obtained in the most recent complete discharge. The cycling was done at room temperature (19°-25°C).

The negative plates were charged at a current density of 31.25 A/m² for all cycles except the forming charge. Charges were ended about 1 hr after the negative plate potential dropped sharply and strong gassing began.

Samples cut from the negative plates were washed in distilled water which was boiled and cooled immediately before use to exclude dissolved CO₂ or O₂. This was especially necessary for samples removed from formed plates, where the Pb is very reactive. After 1-2 hr of washing, the samples were dried for

about 1 hr under a slow flow of argon in a vacuum desiccator maintained at 100°-110°C.

The negative active material was examined by several methods. Direct examination of the fractured cross sections was made using an AMR Model 1000 scanning electron microscope. Portions of plates were impregnated with plastic, cut into cross sections, polished, and examined by optical microscopy. The approximate proportions of Pb, PbSO₄, and void space in representative cross sections were determined at 1350 \times or 2700 \times magnification using an Imanco Quantimet 720 image analyzer. The BET surface area of the active material was determined using a Micromeritics Model 2205 surface area analyzer. The active material was broken into pieces smaller than 5 mm to fit into the sample tube of the analyzer and was degassed 40 min at 200°C. Degassing temperature was not critical, with 150° and 250°C giving the same results as 200°C.

Results and Discussion

The capacity of the negative plates slowly declined with cycling (Fig. 1). Corrections for loss of active materials when a sample was cut from a plate are included in Fig. 1. These corrections assumed that the capacities of all samples were equal, but this was only approximately true since all active material pellets did not have exactly the same size. Therefore, the removal of samples at cycles 1, 6, and 16 could cause some error in the capacities calculated for the following cycles. This may be the cause of some vertical displacements of values in Fig. 1. The capacity decline averaged 0.7% per cycle for discharges at 125-2000 A/m², and 0.3% per cycle at 18 A/m².

The effect of discharge rate and cycling on the negative plate potential is shown in Fig. 2. Polarization of the active material increased when current density was increased. This was indicated by the lowered potential during the first half of a discharge, and by a decrease in the amount of discharge that was obtained before potential began to fall rapidly. Discharges between cycles 1 and 26 gave potentials intermediate between those shown in Fig. 2. Potentials during the main part of a discharge were relatively constant in the early cycles, but discharge potentials tended to decline continually after a negative plate had been cycled repeatedly.

The structure of the active material varied according to the cycling treatment used. The following descriptions refer to the active material in fractured cross sections of negative plates. It was noted that the structure of the surface of a plate was often not representative of the bulk of the active material. This agreed with the results of Pierson *et al.* (3).

Formed plates.—Most of the active material consisted of small Pb particles 2-5 μ m in size at the end of the forming charge (Fig. 3). The particles resembled un-

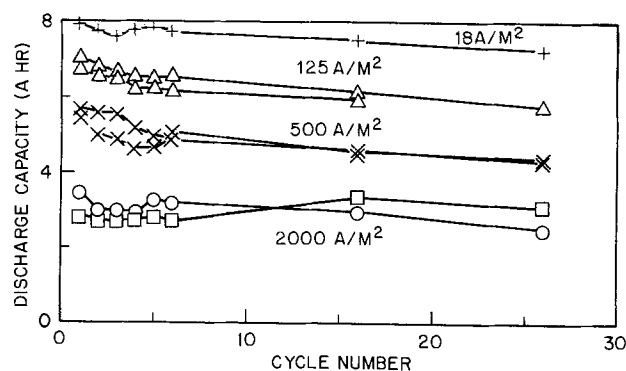


Fig. 1. The results of capacity discharges of negative plates. Discharge rates are given on the curves. Discharges in 1.190 sp gr H₂SO₄ at 2000 A/m² are shown by the squares. All other discharges were done in 1.260 sp gr H₂SO₄.

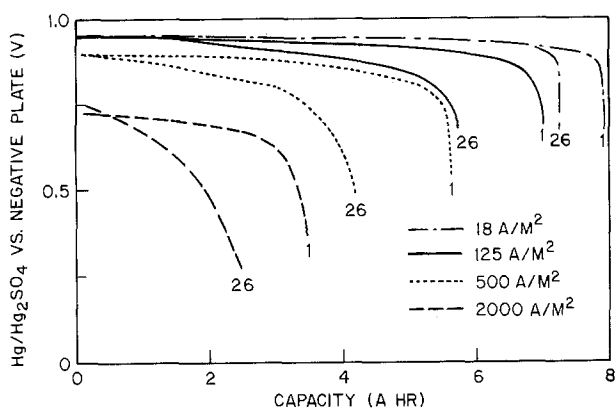


Fig. 2. Discharge potentials measured between the Hg/Hg₂SO₄ reference electrode and the negative plate. Potentials are shown for cycles 1 and 26 at four rates of discharge. The discharge current density used for the negative plate at cycle 1 was repeated in all subsequent cycles.

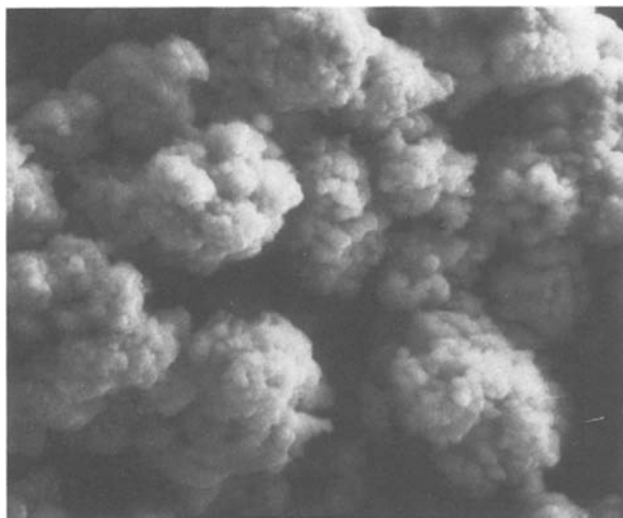


Fig. 3. Lead particles in the negative active material at the end of the forming charge. Magnification 5000 \times .

even clumps of small, irregular spheres. This shape was believed to result from dendritic growth, but the expander in the active material inhibited Pb from growing in the usual dendritic branches (3, 4). The active material also contained some PbSO₄ crystals and small amounts of symmetric clumps of short needles, believed to be Pb. The needle-like crystals were only found at the end of the forming charge. These crystals may be related to platelets reported to have been found among smooth Pb particles in negative plates after the forming charge. These platelets subsequently dissolved preferentially during discharge (2).

Hughel and Hammer (1) showed a negative plate at the end of the forming charge. Their formed plates consisted of particles that were smoother and about half the size of those shown in Fig. 3. The structural difference may result from differences in the manufacturing process or formation conditions.

Discharges at 18 A/m².—At the end of cycle 1 discharge at 18 A/m², the 20 hr rate, most of the active material consisted of PbSO₄ crystals about 2-7 μ m in size, although many particles fell outside this range. The PbSO₄ resembled that present after one discharge at 125 A/m² (Fig. 4), except the particles were about 1 μ m larger when using 18 A/m². Discharged plates showed only a slow change in structure with cycling. Large PbSO₄ crystals were found more frequently as the cycling progressed. At cycle 26 over half of the active material consisted of crystals in the 3-8 μ m

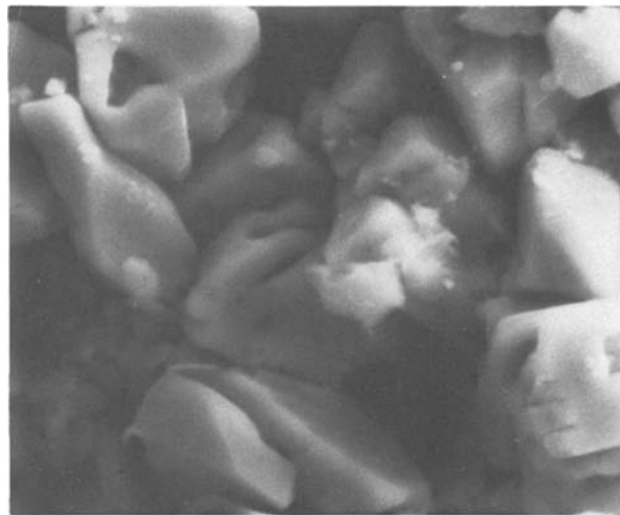


Fig. 4. Crystals of PbSO₄ in the negative plate at the end of cycle 1 discharge at 125 A/m², the 2.5 hr rate. Magnification 5000 \times .

range, although many crystals had grown to 10-20 μ m and some were only 0.5-2 μ m. The Pb in a charged plate was never completely converted to PbSO₄ during a discharge. The quantity of Pb present at the end of a discharge increased with cycling.

Discharges at 125 A/m².—Most PbSO₄ crystals were about 2-5 μ m in size after cycle 1 discharge at 125 A/m², the 2.5 hr rate (Fig. 4), although many particles were as small as 1 μ m or as large as 7 μ m. The PbSO₄ crystals often contained holes. It was again found that crystal size slowly increased with cycling. At cycle 26 the PbSO₄ crystals were up to 10-15 μ m in size, although many still were 2-5 μ m. The structure shown in Fig. 4 is much the same as given by Weininger (6) after a negative plate had been given 163 cycles at 60 A/m².

Discharges at 500 A/m².—In general, a typical PbSO₄ particle was only half as large when it developed at 500 A/m², the 0.5 hr rate, as it was at 125 A/m². The most common PbSO₄ crystal size fell in the range 0.5-3 μ m at cycles 1, 6, and 16, although the amount of PbSO₄ having a size greater than this gradually increased. Many particles up to 5 μ m were present at cycle 16.

A large number of small Pb particles remained at the end of these discharges, with their size generally under 1 μ m. Optical microscopy of the polished cross sections of a plate indicated that a higher proportion of Pb remained at the end of a discharge than one would assume judging only by the results of scanning electron microscopy. Much of the Pb was surrounded by PbSO₄ and was not visible when broken pieces of a plate were examined by SEM. The cross sections also gave a better idea of the way that porosity increased with cycling.

Discharges at 2000 A/m².—Most PbSO₄ crystals in the negative active material were between 0.4 and 2 μ m after one discharge at 2000 A/m², the 5 min rate (Fig. 5). Some crystals were as small as 0.2 μ m or as large as 4 μ m. These crystals that were produced at 2000 A/m² were noticeably smaller than those that developed at 500 A/m², and much smaller than those that developed at 18 or 125 A/m² (Fig. 4). Average PbSO₄ crystal size tended to increase as the plate was cycled. Crystals in the 2-5 μ m size range had become common at cycle 16, although most PbSO₄ crystals were still smaller than 2 μ m. A large proportion of the active material was still in the charged form of metallic Pb at the end of a discharge at 2000 A/m², since this

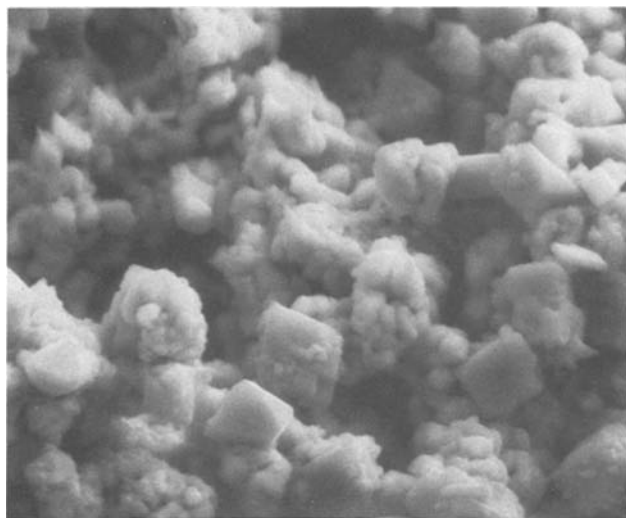


Fig. 5. Crystals of PbSO_4 at the end of cycle 1 discharge at 2000 A/m^2 , the 5 min rate. Compare with Fig. 4 to see the effect of discharge rate. Magnification $5000\times$.

rate gave much less discharge capacity than the other discharge rates.

Charged plates.—The type of irregular Pb surface present after the forming charge (Fig. 3) was never found in cycled active material. After the first discharge, all subsequent charges gave Pb particles that were smoother than those obtained in the forming charge. Typical Pb particles after cycle 6 charge were $1\text{--}3 \mu\text{m}$ in size when the active material had been discharged at $18\text{--}500 \text{ A/m}^2$. These particles were quite irregular in shape, with surface features rounded rather than angular, and they often contained hollows or caves. As cycling continued there was no great change in the appearance of the charged active material, although when using discharges of 18 or 125 A/m^2 the size of the Pb clumps had increased to $1\text{--}4 \mu\text{m}$ at the end of cycle 27 charge and the surface was a little smoother (Fig. 6).

The Pb often contained holes of $0.2\text{--}1 \mu\text{m}$ diam, corresponding to the holes found in some PbSO_4 particles at the end of discharges. Although the Pb did not usually take the angular shapes of PbSO_4 crystals, it did keep enough of the shape that a large hole in a PbSO_4 crystal could be maintained. Lead particles with angular shapes were found most often when using 18 A/m^2 as the discharge rate, the rate producing the largest PbSO_4 crystals. The electrolyte space between

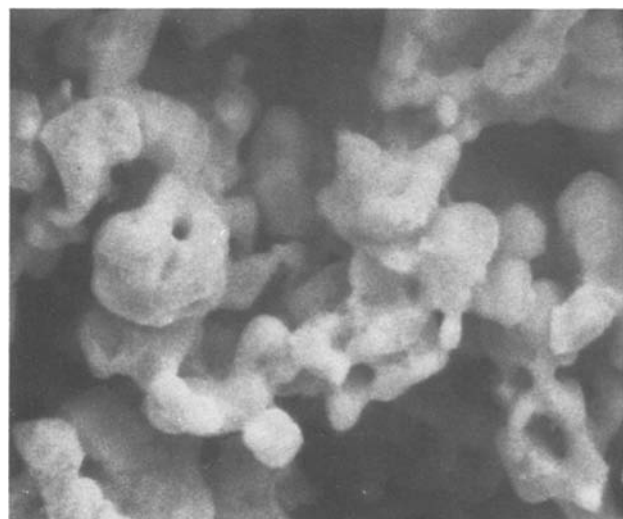


Fig. 6. Lead particles at the end of cycle 27 charge of a negative plate always discharged at 125 A/m^2 . Magnification $5000\times$.

particles gradually increased as the plate was cycled and became thicker or expanded.

When all discharges were done at 2000 A/m^2 , much of the Pb in the charged active material consisted of irregular clumps of small, rounded particles (Fig. 7). The small size of the Pb was the result of the particles developing from small PbSO_4 crystals such as those shown in Fig. 5. As the cycling continued, there was some tendency for these Pb clumps to grow together and become a little smoother.

Scattered crystals of PbSO_4 were often found among the Pb in a charged plate. In some places large patches of PbSO_4 remained. The amount of PbSO_4 in the charged plates increased with cycling. The size of typical PbSO_4 crystals remaining at the end of cycle 27 charge was $5\text{--}10 \mu\text{m}$ for a plate always discharged at 125 A/m^2 and $7\text{--}15 \mu\text{m}$ for a plate always discharged at 18 A/m^2 . The disappearance of most of the smaller PbSO_4 crystals during a charge indicates that these are more easily reduced to Pb than are the large crystals.

Acid concentration.—All results reported up to this point were with H_2SO_4 that was about 1.260 sp gr at the end of a charge. Since the test cells contained excess electrolyte, acid concentration did not decrease as greatly during discharges as it does in cells having the usual configuration. The results in the test cell could differ greatly from results in a typical lead-acid battery if a lower acid concentration at the end of a discharge has a strong effect on morphology.

In order to see the effect of a more dilute acid, one negative plate was cycled in $1.190 \text{ sp gr H}_2\text{SO}_4$ using 2000 A/m^2 as the discharge current. This is the approximate acid concentration for an automotive starting battery that is half discharged and would be closer to the average concentration in a typical battery during discharge. When the results in 1.190 sp gr were compared to the results in 1.260 sp gr , there was no significant difference in the appearance or size of PbSO_4 at the end of discharges nor of Pb at the end of charges. Thus the change in acid concentration did not have a strong effect on morphology and the results in the test cell were comparable to results in a typical lead-acid battery. The most noticeable effect was that discharge capacity in the first six cycles was a little lower in $1.190 \text{ H}_2\text{SO}_4$ (Fig. 1). This capacity difference may not be significant, since Fig. 1 shows that two plates cycled in $1.260 \text{ H}_2\text{SO}_4$ could give as much variation. According to the results of Gillibrand and Lomax (10) capacity should increase as H_2SO_4 concentration decreases.

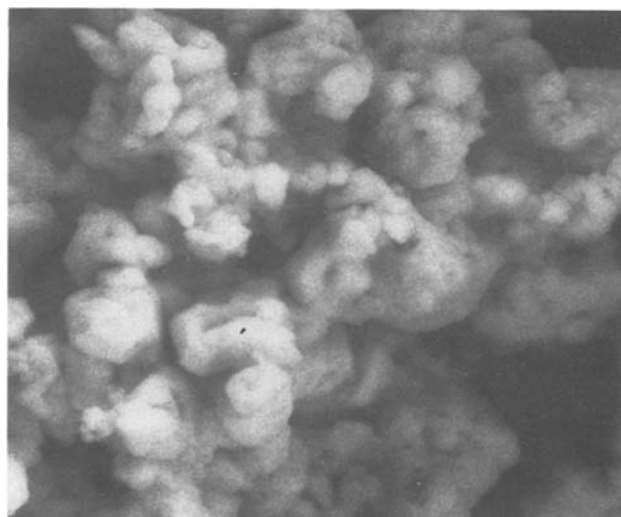


Fig. 7. Lead particles at the end of cycle 16 charge. This negative plate was always discharged at 2000 A/m^2 . Compare with Fig. 6 to see how discharge rate affects structure of charged active material. Magnification $5000\times$.

Surface area.—The active material had too low a surface area to give high reproducibility with the Micromeritics surface area analyzer. Table I gives results from cycled negative active material. Most values in Table I are averages of four measurements. Repeated measurements of the same sample often varied by as much as 10% from the average of these measurements. Five to nine measurements were made of the few samples with the highest variation. At least 16 measurements were made before reporting a value below $0.1 \text{ m}^2/\text{g}$. Since measurement accuracy decreased greatly as surface area decreased, values reported in Table I as being under $0.1 \text{ m}^2/\text{g}$ should only be regarded as an indication that surface area was low.

The results in the top half of Table I show that surface area of discharged negative active material increased as discharge current density increased. This agrees with the results of microscopic examination given above where the average crystal size of PbSO_4 decreased as current density increased (see Fig. 4 and 5). No significant change in surface area was detected after repeated cycling at any of these rates.

The unformed negative active material had a surface area of $0.82 \text{ m}^2/\text{g}$. Surface area dropped to $0.23 \text{ m}^2/\text{g}$ at the end of the forming charge at $40 \text{ A}/\text{m}^2$ in $1.200 \text{ sp gr H}_2\text{SO}_4$. Although the four discharge rates produced different surface areas, these differences became somewhat obscured by the time a charge had been completed, since all recharges were made using the same $31.25 \text{ A}/\text{m}^2$ current density. The low surface area produced by discharges at 18 or $125 \text{ A}/\text{m}^2$ resulted in a low surface area for charges that followed these rates (Table I). The sample taken at cycle 16 charge when all discharges were done at $125 \text{ A}/\text{m}^2$ apparently was not representative of the active material. The value of $0.39 \text{ m}^2/\text{g}$ was unacceptably large compared to all other samples of charged plates. None of the other recharged samples had surface areas quite as large as the $0.23 \text{ m}^2/\text{g}$ observed after the forming charge. This agrees with the observation given above that a recharged plate contained smoother Pb particles than had been obtained in the forming charge.

The values for surface area reported in the literature seem to depend somewhat on the measurement method. A dye adsorption method gave $0.3 \text{ m}^2/\text{g}$ for a charged negative (11). The BET method gave $0.3\text{--}0.5 \text{ m}^2/\text{g}$ in a study of the effect of several expanders, and surface area decreased a little with cycling (12). Other work found that the BET surface area remained fairly constant at values between 0.3 and $0.4 \text{ m}^2/\text{g}$ during the life of a battery (13). A radioactive method of measuring surface area agreed there was little change with cycling but gave much lower values, reporting a gradual decrease from $0.06 \text{ m}^2/\text{g}$ at cycle 10 to $0.05 \text{ m}^2/\text{g}$ at cycle 100 (14). The present work confirmed that surface area did not change appreciably with cycling, but found values a little lower than those usually reported.

Porosity.—As the negative plates were cycled an increasing number of large voids appeared in the active material and the plates gradually expanded. At

the end of cycling the plates were about 30–50% thicker than the original size. Since the active material softened considerably during the cycling, it gradually became easier for active material to be deformed by the hydrogen bubbles that formed during a charge (5). Expansion of the negative plates would have been more limited if the plates had been under some pressure, as usually occurs in a tightly packed cell case, and fewer large voids would have formed.

The image analyzer was used to determine porosity of the negative active material. The values given in Table II are averages of 15–25 measurements of void space made during a continuous series of adjoining views at $1350\times$ magnification in steps about 0.086 mm wide extending from one surface of a plate to the opposite surface. The number of views increased as a plate gradually became thicker when cycled. Areas were chosen that did not include the large voids that had developed. Porosity increased as the plate expanded, since the amount of active material per unit of volume decreased.

Although the two plates that were examined at the end of forming charges (Table II, cycle 1) had been treated similarly, the active material of one gave 43% and the other 48% porosity. This suggests that the difference between porosity of the various charged plates may be partly due to differences in the original plates, as well as being an effect of discharge current density.

Discharged plates showed less porosity than charged plates. This was caused by the PbSO_4 that formed during a discharge occupying a larger volume than the Pb in a charged plate. Since more PbSO_4 formed during the slower discharges, porosity of discharged active material decreased as discharge current decreased.

Active material composition.—The image analyzer was used to obtain values for composition of the negative active material. A magnification of $2700\times$ was used after discharges at $2000 \text{ A}/\text{m}^2$ because of the large number of small particles present. Magnification was $1350\times$ for discharges at all other rates. The composition values shown in Fig. 8 are averages of 15–35 measurements made in a continuous series from one surface to the other. Different areas of a plate usually showed large variations in composition. Therefore, the values in Fig. 8 could differ by several percent if the measurements had been made in different areas.

Another source of uncertainty was caused by the shades of lightness or darkness of the three phases (Pb, PbSO_4 , and void spaces) in the active material not differing sufficiently. One could not choose thresholds between these shades and be certain that the image analyzer would detect all of one phase while not detecting any part of another phase. Although the absolute values were uncertain, the trends in Fig. 8 were believed to be significant since the same threshold settings were used for a series of samples, and all results should be biased in the same direction.

The amount of PbSO_4 that formed during a discharge decreased as current density increased (Fig. 8), since discharges gave decreasing capacity at higher currents. Figure 8 also shows that the amount of PbSO_4 present in a discharged plate decreased slowly with cycling.

Table I. BET specific surface areas of the negative active material, given in m^2/g . Values under 0.1 are dubious

| Condition | Discharge rate (A/m^2) | Cycle | | | |
|------------|--|-------|------|------|------|
| | | 1 | 6 | 16 | 26 |
| Discharged | 18 | 0.02 | 0.11 | 0.03 | 0.00 |
| Discharged | 125 | 0.16 | 0.14 | 0.18 | 0.17 |
| Discharged | 500 | 0.18 | 0.20 | 0.20 | — |
| Discharged | 2000 | 0.25 | 0.24 | 0.26 | — |
| Charged | 18 | — | 0.11 | 0.19 | 0.13 |
| Charged | 125 | — | 0.18 | 0.39 | 0.16 |
| Charged | 500 | — | 0.21 | 0.21 | 0.21 |
| Charged | 2000 | — | 0.21 | 0.19 | 0.20 |

Table II. Porosity of negative active material (%)

| Condition | Cycle | Discharge rate (A/cm^2) | | | |
|------------|-------|---|-----|-----|------|
| | | 18 | 125 | 500 | 2000 |
| Charged | 1 | — | 43 | 48 | — |
| Charged | 6 | 46 | 48 | 52 | 52 |
| Charged | 16 | 49 | 55 | 54 | 56 |
| Charged | 26 | 51 | 52 | 56 | 57 |
| Discharged | 1 | 24 | 31 | 37 | 43 |
| Discharged | 6 | 35 | 39 | 46 | 44 |
| Discharged | 16 | 44 | 48 | 54 | 49 |
| Discharged | 26 | 52 | — | — | — |

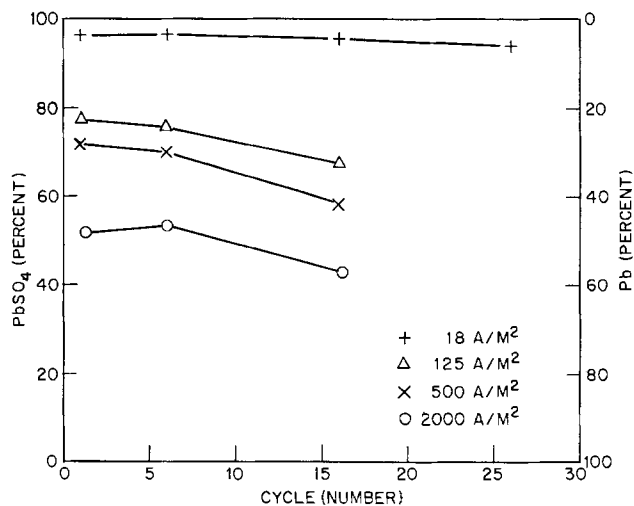


Fig. 8. Composition of negative active material at the end of discharges at 18, 125, 500, or 2000 A/m². The plates were recharged at 31.25 A/m². Composition was measured with an image analyzer.

The opposite effect occurred in charged plates. At the end of the forming charge (cycle 1) the active material was close to 100% Pb. Samples of active material examined after cycle 26 charge contained 1-10% PbSO₄. These changes in charged and discharged plates that occur with cycling may be caused by a gradual worsening of contact within the active material, isolating some active material from the electrochemical reactions. A gradual decrease in surface area could also bring about similar changes but surface area did not change with cycling (Table I).

Although random areas of high or low PbSO₄ concentration were common in the active material, there was no significant difference between the average of PbSO₄ concentrations measured in areas near the surface and average concentration in the center of plates discharged at 18-500 A/m². This agrees with the results of Panesar and Portscher, who reported an even distribution of PbSO₄ after discharges at 15-300 A/m² for negative plates 1.5 mm thick (15). Their plates were approximately the same thickness as the plates in the present work.

Measurements made at the end of cycle 1 and 6 discharges at 2000 A/m² indicated that the PbSO₄ concentration was usually a little higher near the plate surfaces than it was near the center. Figure 9 shows the smoothed results of 28-35 consecutive measurements in steps 43×10^{-6} m wide extending from one plate surface to the other surface. A rapid discharge does not allow sufficient time for much additional H₂SO₄ to diffuse into the plate interior after depletion of acid that was present when the discharge began. As the plate gradually expanded with cycling more acid became available in the interior, and an increased PbSO₄ concentration near the surface was less evident. Measurements at cycle 16 showed a fairly random distribution of PbSO₄ with little difference between plate surface and center. Panesar and Portscher measured PbSO₄ distribution after a discharge at 1800 A/m² (15). Their results show the center of a plate having only about 55% as much PbSO₄ as the surface areas, a much greater difference than the small variations shown in Fig. 9. Whether or not PbSO₄ is highly concentrated at the surfaces after a rapid discharge is probably greatly affected by plate structure. Variation among plates of different manufacturers is to be expected.

Summary and Conclusions

It is commonly accepted that passivation is increased as the size of the crystals forming the passivating barrier decreases. In the present case the change in capacity roughly corresponds to the change in crystal size of the lead sulfate in the range of current densities

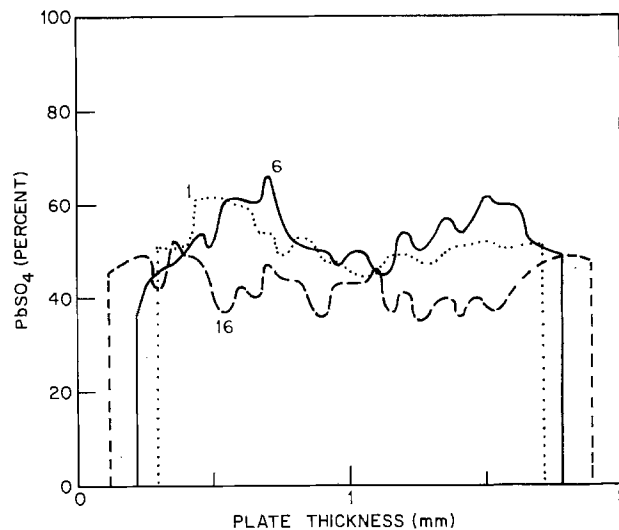


Fig. 9. Distribution of PbSO₄ at cycles 1, 6, and 16 in a negative plate that was always discharged at 2000 A/m². The plates are centered at 1 mm on the thickness scale.

studied (Fig. 1). The fact that the lead sulfate was evenly distributed from surface to center of the electrode (Fig. 9) also suggests that passivation rather than diffusion might have been the limiting factor in determining the available capacity.

On the other hand, the effects noted on the negative plate potential with increasing current density indicate that the diffusion rate was a factor. While the knee in the polarization curve might be indicative of passivation, the change in the initial portion of the curve at different current densities must be the result of limiting diffusion rates (Fig. 2). The change in the polarization curve between the 1st and 26th cycles indicates the introduction of another resistive factor, probably reduced contact areas between the crystals as a result of the repeated cycling.

Reduced contact area would also appear to be a logical consequence of the increased porosity noted as cycling progressed. This increased porosity was probably a result of using a lignin derivative and BaSO₄ in the formulation of the commercial plates that were used. This expander material also prevented an increased size differential for the lead sulfate crystals at the different current densities employed.

Acknowledgment

This work was supported by the U.S. Department of Energy's Applied Battery and Electrochemical Research Project under interagency agreement EC-76-A-31-1003. On behalf of two of the authors thanks are extended to the International Lead Zinc Research Organization, Incorporated for their support, and for permission to participate in this investigation.

Manuscript submitted June 20, 1980; revised manuscript received Sept. 17, 1980.

Any discussion of this paper will appear in a Discussion Section to be published in the December 1981 JOURNAL. All discussions for the December 1981 Discussion Section should be submitted by Aug. 1, 1981.

Publication costs of this article were assisted by the Naval Research Laboratory.

REFERENCES

1. T. J. Hughel and R. H. Hammer, "Power Sources 3," D. H. Collins, Editor, p. 35, Oriel Press, Newcastle Upon Tyne, England (1971).
2. S. Hattori, M. Yamaura, M. Kohno, Y. Ohtani, M. Yamane, and H. Nakashima, "Power Sources 5," D. H. Collins, Editor, p. 139, Academic Press Inc., New York (1975).
3. J. R. Pierson, P. Gurlusky, A. C. Simon, and S. M.

- Caulder, *This Journal*, **117**, 1463 (1970).
4. A. C. Simon, S. M. Caulder, P. J. Gurlusky, and J. R. Pierson, *Electrochim. Acta*, **19**, 739 (1974).
 5. A. C. Simon, S. M. Caulder, P. J. Gurlusky, and J. R. Pierson, *This Journal*, **121**, 463 (1974).
 6. J. W. Weininger, *This Journal*, **121**, 1454 (1974).
 7. E. Y. Weissman, in "Batteries," Vol. 2, K. V. Kor-desch, Editor, p. 130, Marcel Dekker, New York (1977).
 8. H. Bode, "Lead-Acid Batteries," p. 274-275, John Wiley & Sons, New York (1977).
 9. A. C. Simon and R. L. Jones, *This Journal*, **109**, 760 (1962).
 10. M. I. Gillibrand and G. R. Lomax, *Electrochim. Acta*, **11**, 281 (1966).
 11. T. I. Popova and B. N. Kabanov, *Zh. Prikl. Khim.*, **32**, 326 (1959).
 12. B. K. Mahato, *This Journal*, **124**, 1663 (1977).
 13. J. Nees and W. Bundy as reported by E. Wil-lihganz in "Advances in Electrochemistry and Electrochemical Engineering," Vol. 8, C. W. Tobias, Editor, p. 232, John Wiley & Sons, New York (1971).
 14. M. F. Skalozubov, *Zh. Prikl. Khim.*, **35**, 1812 (1962).
 15. H. S. Panesar and V. Portscher, *Metalloberfl.*, **26**, 252 (1972).

Cobalt and Nickel Cations as Corrosion Inhibitors for Galvanized Steel

Henry Leidheiser, Jr.* and Ichiro Suzuki¹

Center for Surface and Coatings Research, Lehigh University, Bethlehem, Pennsylvania 18015

ABSTRACT

Gravimetric measurements on galvanized steel and cathodic polarization curves indicate that corrosion of zinc in 3% NaCl is inhibited by a low concentration of cobalt ions in solution or by simple predipping of the zinc in 0.05 or 0.1M solutions of CoCl₂. Corrosion inhibition is also obtained when zinc is predipped in a nickel acetate solution and nickel ions are present in the NaCl solution. The corrosion inhibition is attributed to the introduction of electron traps (cobalt or nickel atoms) in the oxide on the surface of zinc which lead to inhibition of the cathodic reaction, $\text{H}_2\text{O} + \frac{1}{2} \text{O}_2 + 2e^- = 2\text{OH}^-$. When the concentration of elemental cobalt or nickel in or on the oxide becomes too great, the cathodic reaction, $2\text{H}^+ + 2e^- = \text{H}_2$, is catalyzed and corrosion activation occurs.

Galvanized steel (a coating of zinc on a steel substrate) is a very effective corrosion protective system under atmospheric exposure conditions. The zinc corrodes at a relatively low rate and it provides galvanic protection to the steel substrate at points where the steel is exposed. Longer system lifetimes would be possible if the zinc corroded at a lower rate under those conditions where the steel was not exposed. It has been pointed out previously (1) that greater system lifetimes should be possible if the oxide film on the surface of the zinc could be made a less effective catalyst for the cathodic reaction, $\text{H}_2\text{O} + \frac{1}{2} \text{O}_2 + 2e^- = 2\text{OH}^-$. The purpose of the present study was to seek effective inhibitors for the cathodic reaction on zinc. The experiments have been very successful and this article outlines the inhibiting properties of cobalt and nickel cations and gives a tentative interpretation of the corrosion inhibiting mechanism.

Attention was focused on cobalt and nickel ions as inhibitors on the basis of a preliminary screening using zinc cathodic polarization curves obtained in aerated 3% NaCl solution to which various cations were added. The decision to focus initially on cobalt was reinforced by the fact that a recently introduced commercial electrogalvanized steel contains a small concentration of cobalt and the claim has been made that the corrosion rate was greatly decreased (2, 3). Cobalt and nickel species are also constituents in proprietary commercial pretreatment baths used for developing corrosion resistance at the paint/metal interface. A parallel study of the chemical state of cobalt in electrogalvanized steel (4) provided additional background and incentive for the present study. The addition of nickel to electrogalvanized steel is also claimed to reduce the corrosion rate of zinc (5-9).

* Electrochemical Society Active Member.

¹ Present address: Department of Chemistry, University of Tokyo, Tokyo, Japan.

Key words: corrosion, inhibition, cobalt, nickel, galvanized steel.

Experimental Procedure

Corrosion rate measurements were carried out on the galvanized steel samples described in Table I. All of the reported measurements made with cobalt and nickel ions were carried out with sample L-6 since there was available a large supply of this material. The thickness of the zinc coating was also great enough that the chances of exposing the steel substrate during polishing were less. Another advantage of the L-6 samples was the 70% (0001) orientation, a representative value for many lots of hot-dipped galvanized steel. Orientation determinations were made by the method previously described by Kim and Leidheiser (11). A sufficient number of experiments was carried out with different samples of galvanized steel to be confident that the results apply generally, although the degree of the corrosion inhibition may be a function of the composition of the zinc coating. No specific experiments to explore this variable were conducted.

The majority of cathodic polarization curves was determined on single crystals of 99.999% pure zinc cut to expose the (0001) plane. The zinc crystals were ob-

Table I. Galvanized steel samples used in this study

| Sample designation | % (0001) orientation | Zinc coating thickness (μm) | Steel substrate thickness (μm) | Average zinc grain size (mm) |
|--------------------|----------------------|-----------------------------|--------------------------------|------------------------------|
| S10-9 | 98% | 14 | 400 | 0.5 |
| S10-6 | 90% | 19 | 400 | 0.6 |
| S10-7 | 80% | 16 | 400 | 2.9 |
| S10-1 | 75% | 17 | 400 | 3.6 |
| S10-2 | 70% | 17 | 400 | 1.5 |
| T-25 | 70% | 28 | 445 | 2.0 |
| L-6 | 70% | 28 | 545 | 1.3 |
| Q-5 | 65% | 26 | 420 | 1.7 |
| Q-3 | 60% | 20 | 490 | 1.1 |
| T-22 | 50% | 21 | 570 | 2.9 |

tained from Prof. Robert Pond of Johns Hopkins University in the form of cylindrical rods and were cut in the form of disks with surfaces parallel to the (0001) plane.

The galvanized steel samples used in the corrosion experiments were smoothed with No. 400 and No. 600 emery papers, followed by high-gloss polishing with alumina powders of 1 and 0.6 μm size. One side of the galvanized steel and all edges were covered with a vinyl adhesive tape and the exposed zinc was 20 cm^2 in area. Two samples were exposed to 200 ml of liquid in each reaction vessel. The panels were placed horizontally on the bottom of the vessel such that the liquid was 4.5 cm in depth. At the conclusion of the experiment, the panels were carefully abraded with a soft brush to remove any adhering corrosion product.

The polarization curves were determined on mechanically polished zinc single crystals. They were polished in much the same manner as the galvanized steel samples except that the final polishing step used diamond powder in place of the alumina. The crystals were mounted in an epoxy resin manufactured by the Woodhill Permatex Company and were used in the mounted condition.

Cathodic polarization curves were determined by manually increasing the potential at a rate of 20 mV/min. The counterelectrode was graphite and the cell was constructed with a fritted glass membrane in order to separate the solution and the cathode from any oxygen generated at the anode.

In some of the experiments, the zinc samples were preimmersed in solutions of cobalt chloride or nickel acetate. After immersion in the cobalt or nickel ion solutions, the zinc was heated at 80° for approximately 2 hr before immersion in the sodium chloride test medium. The effects of cobalt and nickel apparently were not dependent upon this heat-treatment since similar results were obtained on zinc that was simply dried in air before immersion in the sodium chloride test solution. The pH's of the cobalt and nickel ion solutions were as follows: CoCl_2 solutions: 1M, 4.0; 0.5M, 4.35; 0.1M, 4.65; 0.05M, 5.05; 0.01M, 5.60; Ni acetate solutions: 0.5M, 6.05; 0.1M, 6.70; 0.05M, 6.80; 0.01M, 6.70; 0.005M, 6.45.

Experimental Results

The corrosion rates of many different samples of galvanized steel were determined in 3% sodium chloride and 3% sodium sulfate solutions under the standard procedure described. Representative data are summarized in Table II. It will be noted that the corrosion rates of the 10 different samples were approximately the same, averaging 0.34 $\text{mg}/\text{cm}^2/\text{day}$ in the 3% NaCl and 0.28 $\text{mg}/\text{cm}^2/\text{day}$ in the 3% Na_2SO_4 . Typical cathodic polarization curves for a zinc single crystal in the absence and presence of stirring are given in Fig. 1 and a comparison of polarization curves obtained in aerated and deaerated solutions is given in Fig. 2. The method of generating the polarization curves in the aerated and deaerated solutions was slightly different in that the aerated curve was obtained in a quiescent

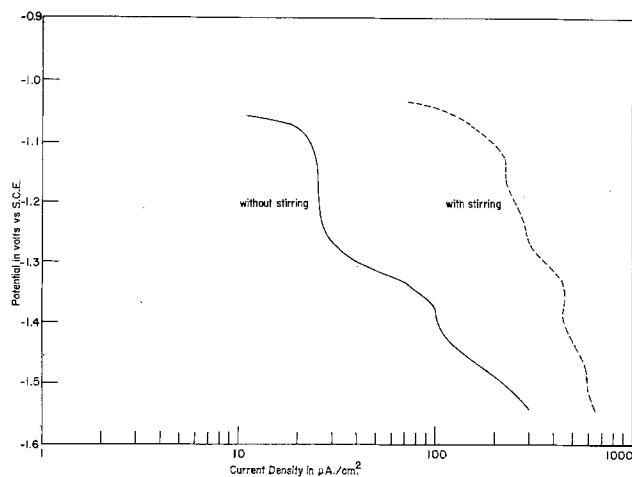


Fig. 1. Typical polarization curves for zinc in 3% NaCl solution in the absence and presence of stirring.

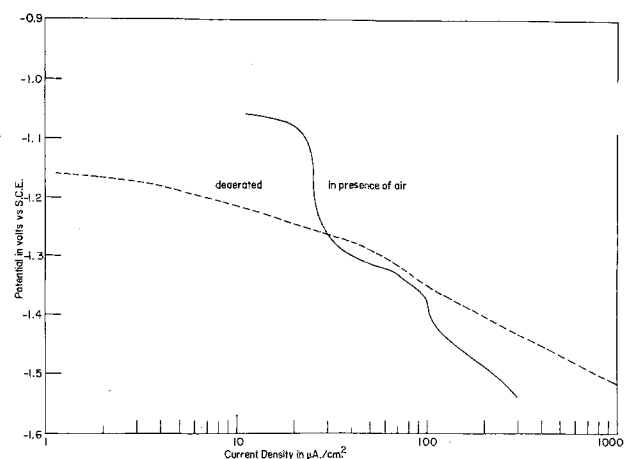


Fig. 2. Typical polarization curves for zinc in 3% NaCl solution in the absence and presence of air.

solution and the deaerated curve was obtained in a solution which was slightly agitated by the passage of a stream of nitrogen through a porous thimble. This difference in procedure probably accounts for the higher current density at the more negative potentials in the case of the curves obtained in the aerated solutions. As described in more detail later, these data suggest that the rate-controlling step in the corrosion of zinc under these conditions is the cathodic reaction, $\text{H}_2\text{O} + \frac{1}{2} \text{O}_2 + 2e^- = 2\text{OH}^-$. The rate of corrosion of galvanized steel samples in deaerated solutions of 3% NaCl was 0.01 $\text{mg}/\text{cm}^2/\text{day}$ indicating that a small fraction (about 3%) of the total corrosion was a consequence of the alternate cathodic reaction, $2\text{H}^+ + 2e^- = \text{H}_2$.

A survey was made of the effect of various ions added to the NaCl solution on the corrosion rate of galvanized steel using both gravimetric measurements and cathodic polarization curves. The ions that were surveyed included barium, cadmium, cobalt, lead, manganese, nickel, tin, and strontium. As a result of this survey, cobalt and nickel were selected for intensive study. The experiments with cobalt and nickel will be described separately because of the slightly different approaches used.

Cobalt ions as inhibitors.—Cathodic polarization curves are given in Fig. 3 for zinc single crystal samples that were dipped in various concentrations of CoCl_2 solution for 30 sec, washed in a stream of water, dried in air at 80°C for approximately 2 hr, and the polarization curve then determined in 3% sodium chloride solution. It will be noted that the cathodic current was significantly lower at potentials of -1.06 to -1.2V

Table II. Rates of corrosion of galvanized steel samples in 24 hr period in solutions open to the air

| Sample designation | Corrosion rate in $\text{mg}/\text{cm}^2/\text{day}$ | |
|--------------------|--|-----------------------------|
| | 3% NaCl | 3% Na_2SO_4 |
| S10-9 | 0.31 | 0.28 |
| S10-6 | 0.29 | 0.28 |
| S10-7 | 0.34 | 0.28 |
| S10-1 | 0.35 | 0.27 |
| S10-2 | 0.35 | 0.30 |
| T-25 | 0.36 | — |
| L-6 | 0.33 | — |
| Q-5 | 0.36 | 0.27 |
| Q-3 | 0.33 | 0.29 |
| T-22 | 0.34 | 0.30 |
| Average | 0.34 | 0.28 |

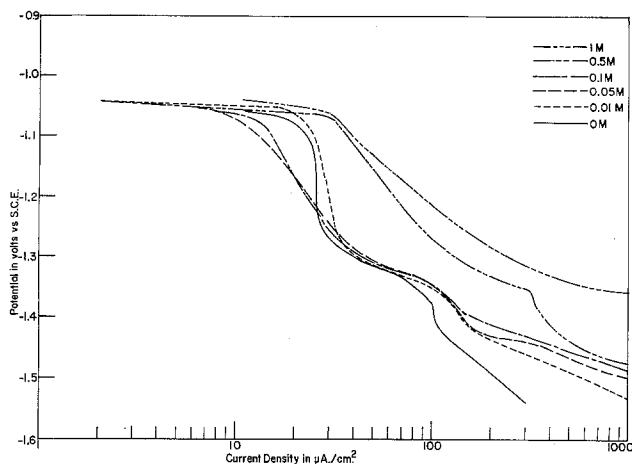


Fig. 3. Cathodic polarization curves for zinc single crystals immersed in 3% NaCl solution. Zinc samples were immersed for 30 sec in cobalt chloride solutions prior to determining the polarization curves. See text for details.

for the samples that were dipped in 0.05M and 0.1M CoCl_2 solutions prior to obtaining the cathodic polarization curve. At potentials more negative than -1.3V the cathodic current was greater than the blank for all the CoCl_2 concentrations from 0.01 to 1M.

Figure 4 summarizes corrosion rate data for galvanized steel and gives the cathodic current at -1.10V for zinc single crystal samples that were predipped in cobalt chloride solutions. The gravimetric data and the cathodic polarization current data are complementary and indicate that a low corrosion rate is obtained when zinc is predipped in solutions of 0.05 and 0.1M CoCl_2 prior to immersion in the NaCl solution. Figure 5 gives corrosion rate and cathodic polarization current data for zinc materials predipped in 0.1M CoCl_2 for various periods of time before immersion in the 3% NaCl. As seen in Fig. 5 the two types of data give parallel results and the optimum time of predipping in the CoCl_2 solution is 30 sec.

The results of a series of experiments carried out in deaerated 3% NaCl are given in Fig. 6, where it will be noted that the corrosion rate and cathodic corrosion current at -1.15V increase with increase in concentration of CoCl_2 in the solution in which the zinc samples are predipped. At the two higher concentrations, 0.5 and 1.0M, the surface exhibited blackening that sug-

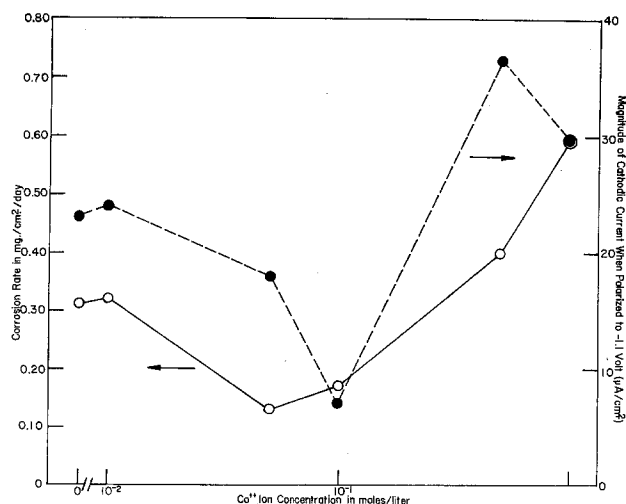


Fig. 4. The corrosion of galvanized steel (solid curve) and cathodic polarization current at -1.10V vs. SCE of zinc single crystal (dashed curve) after dipping in cobalt chloride solutions of different concentrations for 30 sec followed by immersion in aerated 3% NaCl solution. Note similarity in shape of curves.

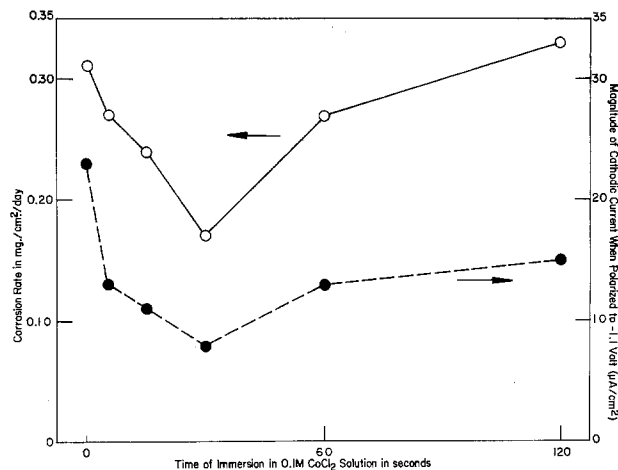


Fig. 5. The corrosion of galvanized steel (solid curve) and cathodic polarization current at -1.10V vs. SCE of zinc single crystal (dashed curve) after dipping in 0.1M CoCl_2 solution for different times prior to immersion in 3% NaCl solution. Note similarity in shape of curves.

gested the formation of metallic cobalt on the surface. No blackening was observed at the lower CoCl_2 concentrations. Cathodic polarization curves obtained in deaerated solution are summarized in Fig. 7.

A few experiments were also carried out in which galvanized steel was exposed to 3% NaCl solution which contained additions of CoCl_2 such that the Co^{++} ion concentration was in the range of 10^{-5} to 10^{-2}M . In these experiments there was no predipping of the zinc in Co^{++} -containing solutions; the cobalt was present only in the corrosion test medium. Results of these experiments are summarized in Fig. 8 where it will be noted that slight corrosion inhibition was obtained at 10^{-5} and 10^{-4}M concentrations of Co^{++} and strong activation of corrosion was obtained at 10^{-3} and 10^{-2}M concentrations of Co^{++} . At the higher concentrations a black coating, which appeared to be finely divided metallic cobalt, formed on the surface.

Samples of zinc dipped for 30 sec in cobalt chloride solutions of 0.01, 0.05, 0.1, 0.5, and 1.0M were examined by x-ray photoelectron spectroscopy (XPS). Elemental cobalt is characterized by two peaks representing binding energies of 778 and 793 eV whereas CoO is characterized by 4 peaks with binding energies of 780.0 and 795.5 eV plus two satellite peaks at 787 and 804 eV. In all cases the predominant spectrum of the unspattered surface was that characteristic of a cobalt

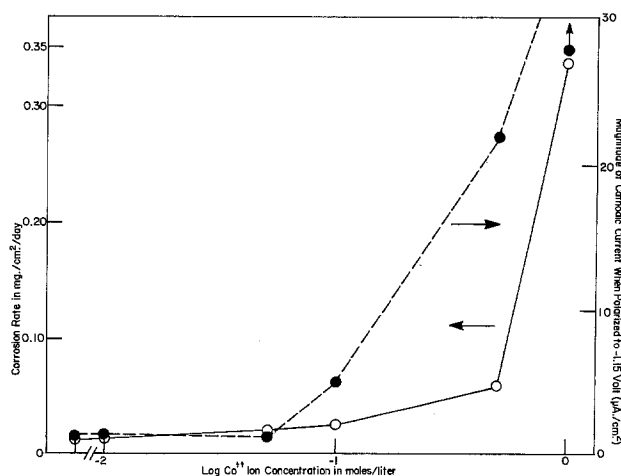


Fig. 6. The corrosion of galvanized steel (solid curve) and cathodic polarization current at -1.15V vs. SCE of zinc single crystal (dashed curve) after dipping in cobalt chloride solutions of different concentrations for 30 sec followed by immersion in deaerated 3% NaCl solution. Note similarity in shape of curves.

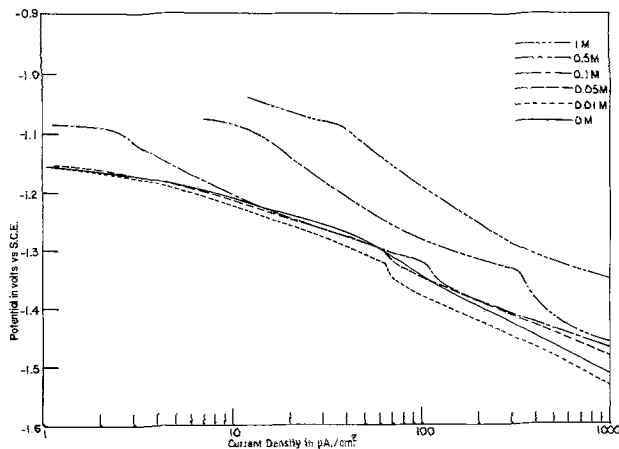


Fig. 7. Cathodic polarization curves for zinc single crystals immersed in deaerated 3% NaCl solutions. Zinc samples were immersed for 30 sec in cobalt chloride solutions prior to determining the polarization curves. See text for details.

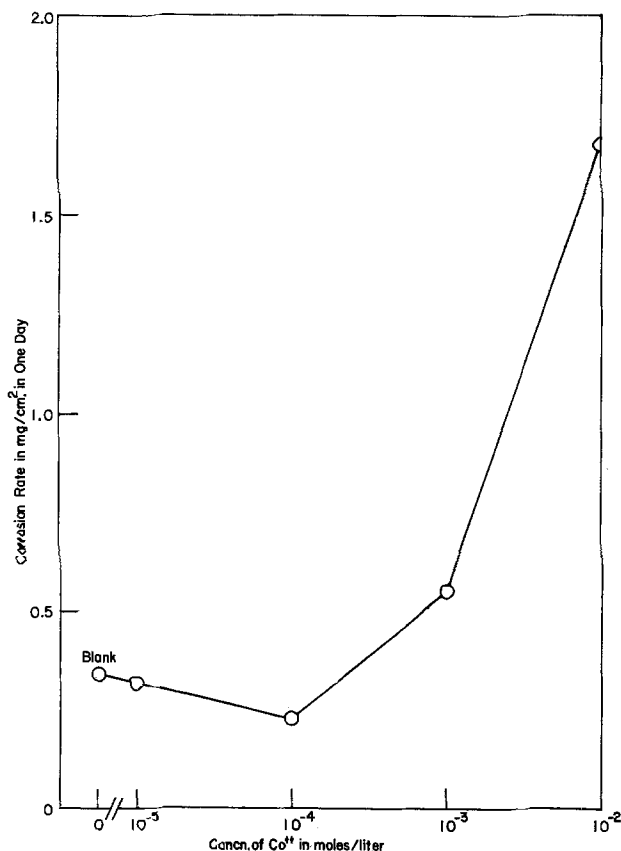


Fig. 8. The corrosion rate of galvanized steel samples in 3% NaCl solution containing different concentrations of cobalt chloride. Note corrosion inhibition at low Co^{++} concentrations and corrosion acceleration at high Co^{++} concentrations.

oxide, probably CoO (12). Sputtering of the superficial oxide resulted in the formation of a spectrum consisting of both ionic cobalt and elemental cobalt (13). Examples of the spectra are shown in Fig. 9 and 10. Figure 9A is a spectrum of the sample dipped in 0.05M CoCl_2 . The two major peaks ($2p_{3/2}$ and $2p_{1/2}$) approximate those characteristic of CoO and the two minor peaks are the so-called "shake-out" satellite peaks. After sputtering away the surface layer, the spectrum shows elemental cobalt as a major component and ionic cobalt as a second component (Fig. 9B). In the case of the most concentrated solution, the major component is elemental cobalt after sputtering etching but ionic cobalt can also be seen (Fig. 10B). After a

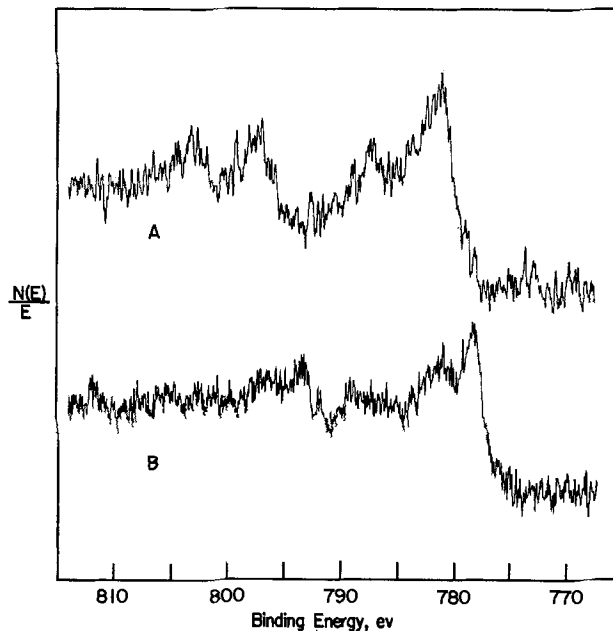


Fig. 9. XPS spectra of zinc single crystal that had been dipped in 0.05M CoCl_2 for 30 sec and dried at 80°C . Top spectrum (A) is before sputtering and bottom spectrum (B) is after superficial sputtering. Note the increase in intensity of the elemental cobalt peaks at 778 and 793 eV after sputtering.

second sputtering, the ionic cobalt decreased to a very low level and the total spectrum was largely due to elemental cobalt as seen in Fig. 10C.

Qualitative information concerning the amount of cobalt present on the surface of zinc after exposure to cobalt chloride solutions was obtained using Auger spectroscopy. The spectra were obtained over an energy range of 0-1200 eV and the ratios of the amounts of zinc, cobalt, and oxygen in the surface region were obtained approximately from measurements of peak-to-peak values. Data for oxygen/cobalt ratios are given in Fig. 11 and data for zinc/cobalt ratios are given in Fig. 12 as a function of the cobalt chloride concentration in the pretreatment solution. These data along with the XPS data of the type shown in Fig. 9 and 10 indicate that the cobalt concentration in the zinc oxide increased with increasing cobalt concentration in the pretreatment solution. The oxygen/cobalt ratio and the zinc/cobalt ratio also both decrease with increase in the cobalt concentration in the pretreatment solution.

Nickel ions as inhibitors.—Experiments similar to those carried out with cobalt were executed with nickel ions. Galvanized steel panels were dipped in solutions of nickel acetate ranging in concentration from 0.005 to 0.5M for 60 sec, the surface was washed in a stream of water, the panels were heated at 80°C for 1-2 hr, and they were then immersed in 3% NaCl solution open to the air for 24 hr. The data, summarized in Table III, indicate that there was no significant corrosion inhibition at any concentration and slight corrosion activation at an Ni^{++} ion concentration of 0.5M. These results were very puzzling in view of the fact that the cathodic polarization curves, shown in Fig. 13, suggested that corrosion inhibition of the same order of magnitude as with cobalt was to be expected. The major difference between corrosion rates determined gravimetrically and those estimated qualitatively from the cathodic polarization curves is the time of exposure of the sample to the corrosive medium. The polarization curve data were obtained on samples that were exposed to the test medium, at the low overvoltages, for less than 1 hr, while the gravimetric measurements were obtained on samples exposed for 24 hr or more. When this fact was recognized, it suggested that the nickel was probably rapidly leached out of the oxide

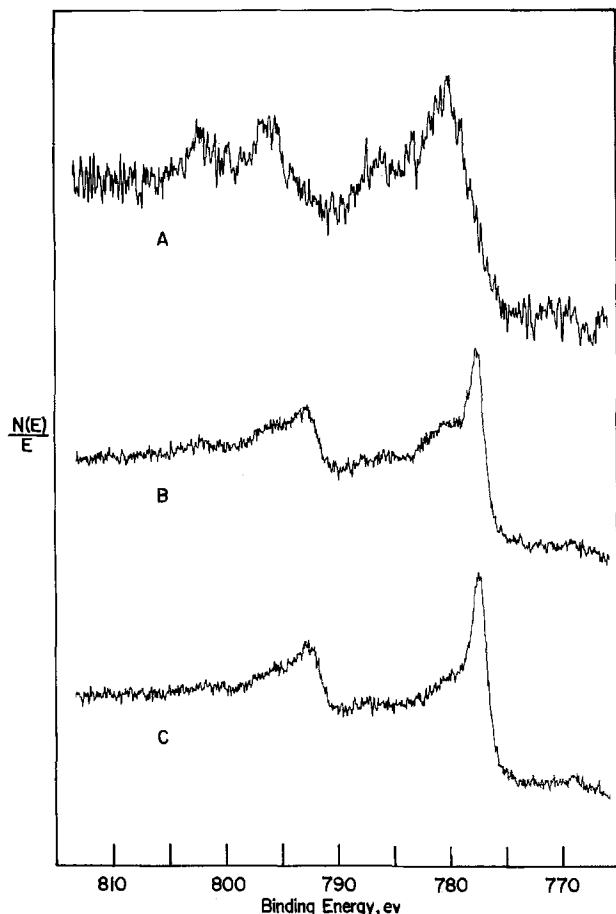


Fig. 10. XPS spectra of zinc single crystal that had been dipped in 1M CoCl_2 for 30 sec and dried at 80°C . Top spectrum (A) is before sputtering, middle spectrum (B) is after superficial sputtering, and bottom spectrum (C) is after a second sputtering. Top spectrum is largely characteristic of CoO while the bottom two spectra indicate elemental cobalt as the major constituent.

coating on the zinc. The following experiments were then performed.

The galvanized steel panels were dipped in 0.01M nickel acetate solution for 15 sec, washed in a stream of water, dried in a warm air stream, and weighed. They were then immersed in 3% NaCl solution containing nickel ion concentrations of 0.0001, 0.0005, and 0.001M and exposed for 24 hr. Results are summarized in Table IV. It is apparent that good corrosion inhibition was obtained in the case of predipping in the nickel acetate solution and exposing to the 3% NaCl solution which contained 0.0005M Ni^{++} .

Discussion

The major experimental facts resulting from this study may be summarized as follows.

1. Predipping zinc in solutions of cobalt salts of the proper concentration for 15-60 sec results in a lower corrosion rate in 3% sodium chloride solution. The

Table III. The corrosion rate of galvanized steel samples in 3% NaCl exposed to air after pre-exposure for 1 min to solutions of nickel acetate

| Concentration of nickel acetate solution | Corrosion rate during 24 hr exposure |
|--|---|
| Blank—dipped in zinc acetate | 0.31 $\text{mg}/\text{cm}^2/\text{day}$ |
| 0.005M | 0.35 |
| 0.01 | 0.33 |
| 0.05 | 0.39 |
| 0.1 | 0.32 |
| 0.5 | 0.43 |

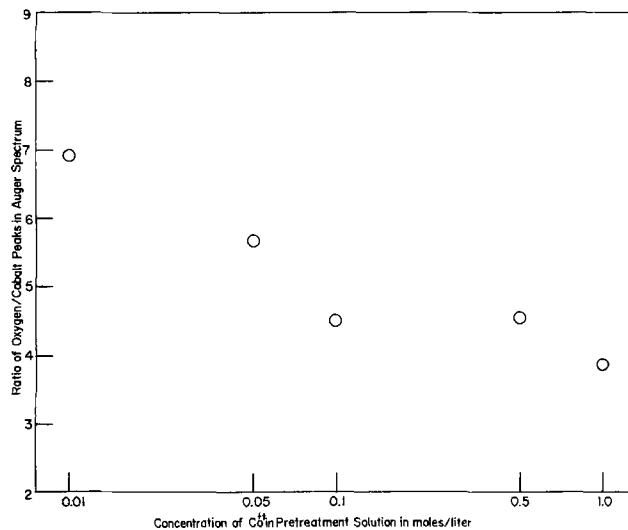


Fig. 11. Relative amounts of oxygen and cobalt in surface region of zinc single crystals after dipping in different concentrations of CoCl_2 solution for 30 sec. Ratios of oxygen/cobalt are relative peak-to-peak values for characteristic emissions in Auger spectrum.

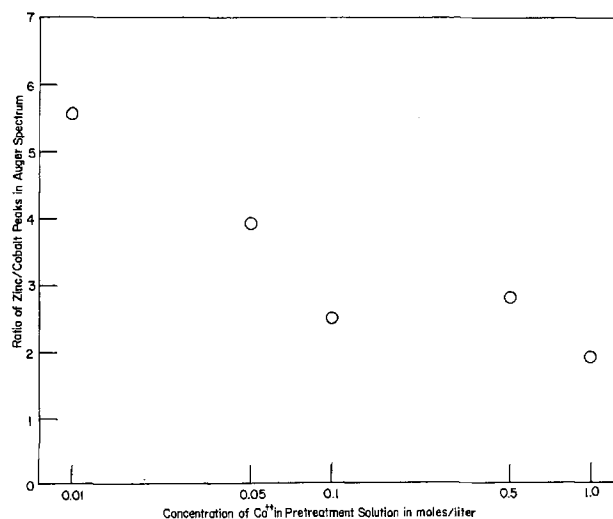


Fig. 12. Relative amounts of zinc and cobalt in surface region of zinc single crystals after dipping in different concentrations of CoCl_2 solution for 30 sec. Ratios of zinc/cobalt are relative peak-to-peak values for characteristic emissions in Auger spectrum.

corrosion inhibiting effects last for a minimum of 2 days.

2. Cobalt ions at low concentrations are corrosion inhibitors for zinc in 3% NaCl .

3. Cathodic polarization curves of zinc previously exposed to low concentrations of cobalt or nickel ions indicate inhibition at low cathodic overvoltages and activation at high cathodic overvoltages.

4. Predipping zinc in concentrated solutions of cobalt chloride leads to corrosion activation in both aerated and deaerated solutions of NaCl .

Table IV. The corrosion rate of galvanized steel samples in air-exposed 3% NaCl solution containing different concentrations of nickel acetate. Samples were pre-exposed to 0.01M nickel acetate solution for 15 sec before immersion in the NaCl solution

| Ni^{++} ion concentration in NaCl solution | Corrosion rate during 24 hr exposure |
|--|---|
| 0 | 0.33 $\text{mg}/\text{cm}^2/\text{day}$ |
| 0.0001 | 0.16 |
| 0.0005 | 0.026 |
| 0.001 | 0.23 |

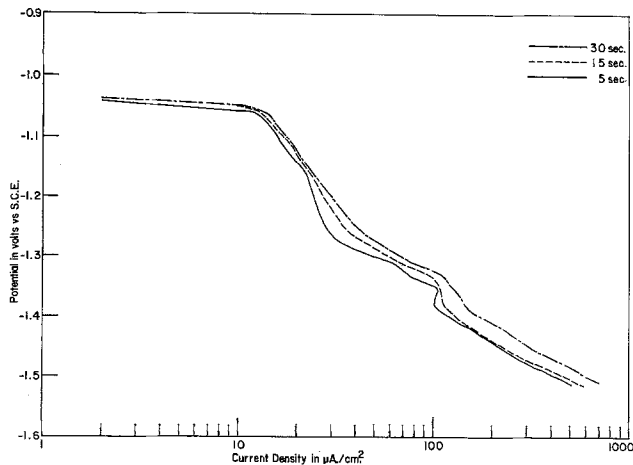


Fig. 13. Cathodic polarization curves for galvanized steel samples immersed in 0.05M nickel acetate solutions for 5, 15, and 30 sec before polarization in 3% NaCl solutions.

5. Dipping zinc into 1.0M CoCl_2 solution leads to a significant amount of elemental cobalt on the surface. Dipping zinc into 0.05M CoCl_2 solution leads to the formation of minor amounts of cobalt in both the ionic and elemental form.

6. Predipping zinc in solutions of nickel acetate does not result in long-term corrosion inhibition.

7. Predipping zinc in solutions of nickel acetate, followed by immersion in NaCl solutions containing low concentrations of nickel ions, leads to a high degree of corrosion inhibition.

It is the purpose of the remarks that follow to explain these results.

The majority of the experiments reported herein were carried out in 3% sodium chloride solution and it must be recognized that the conclusions made herein apply to this electrolyte. However, sodium chloride is utilized as a test medium in many accelerated tests and there is a body of practical experience that suggests that the behavior of materials in a sodium chloride environment can be generalized to apply to many types of atmospheric exposure. It is believed that the conclusions drawn below should apply in many different environments.

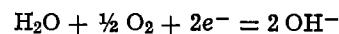
Experiments reported previously (1) have shown that an oxide (or hydrated oxide) coating forms on zinc when immersed in sodium chloride solution open to the air. This oxide coating becomes approximately 50Å thick after 1-2 min immersion and develops a steady-state film thickness of the order of 75-150Å in about 5 min. The oxide is reducible as shown by a reduction peak at approximately -1.3V . The exact values obtained for the rate of growth of the oxide, the steady-state film thickness, and the potential at which the reduction peak occurs are all a function of particular lots of galvanized steel.

Predipping galvanized steel in an aqueous solution containing cobalt ions results in the incorporation of cobalt in, or on, the oxide which is present on the surface of the zinc. The chemical nature of the cobalt was ascertained from the XPS spectra. All samples that had been predipped in cobalt chloride solutions exhibited a spectrum characteristic of CoO. Superficial sputtering caused the majority of the ionic spectrum to disappear in the case of samples dipped in the more concentrated solutions. Presumably the CoO spectrum was largely a consequence of reaction of the metallic cobalt with air during the period between removal from the CoCl_2 solution and insertion into the spectrometer. In the case of samples immersed in the lower concentration solutions, such as 0.05M CoCl_2 , the spectrum after sputtering was characteristic of a mixture of divalent cobalt and elemental cobalt, as shown for example in Fig. 9. The concentration of cobalt at the

surface was relatively low as indicated by the noisy nature of the spectrum.

It is concluded that predipping of the zinc in solutions containing high concentrations of Co^{++} (0.5 and 1.0M) leads to the formation of a large amount of elemental cobalt on the surface. This conclusion from the XPS studies is in agreement with the data shown in Fig. 3 and 4 where the surface is very active for the cathodic reaction. At the lower concentrations of Co^{++} in the pretreatment solutions, it appears that the cobalt is present in or on the surface of the zinc oxide in both the elemental and ionic form. This conclusion must be considered tentative since the analytical procedure itself may cause valence changes in the cobalt on the surface.

The corrosion rate data summarized in Table II, the large effect of stirring on the current density of the plateau in the cathodic polarization curve, and the negligible rate of corrosion of zinc in deaerated NaCl all lead to the conclusion that the cathodic reaction in aerated solutions includes oxygen and is in all probability



This reaction is the dominant cathodic reaction, but the corrosion rate in deaerated solution (Fig. 6) suggests that the competing cathodic reaction, $2\text{H}^+ + 2e^- = \text{H}_2$, accounts for approximately 3% of the total cathodic reaction. Although no study was undertaken, it is likely that the relative ratio of these two cathodic reactions is a function of the impurity content and perhaps crystallographic nature of the zinc.

The surface of a typical galvanized steel is a very effective catalyst for the water-oxygen reaction under the conditions used in these experiments and the rate is determined by concentration polarization, either the rate at which oxygen reaches the surface or the rate at which the OH^- ions can diffuse away from the surface. This conclusion is borne out by the fact that stirring has a great effect on the cathodic polarization curve (Fig. 1) and that the corrosion rates of a number of galvanized steel samples were approximately the same as shown by the data in Table II. It thus appears that the corrosion rate of galvanized steel is limited by a diffusion process in the aqueous phase and is not limited by the availability of electrons for the cathodic reaction.

The proposed mechanism for corrosion inhibition by cobalt ions will now be given. It is suggested that during the predipping process in cobalt chloride solution, the oxide (or hydrated oxide) film on zinc grows by the mechanism outlined schematically in Fig. 14. The anodic reaction, $\text{Zn} - 2e^- = \text{Zn}^{++}$, occurs at the zinc/oxide interface and the cathodic reaction, $\text{H}_2\text{O} + \frac{1}{2} \text{O}_2 + 2e^- = 2 \text{OH}^-$, occurs at the oxide/solution interface. The oxide thickness at the surface of the zinc reaches a steady-state value determined by the balance between the rate of formation of the oxide (or hydrated oxide) and the rate of dissolution of the oxide in the medium. So long as the concentration of zinc in the chloride solution does not exceed the solubility limit, there is no precipitation of hydroxide and the oxide maintains a steady-state thickness of the order of 100Å. It is through this oxide that the corro-

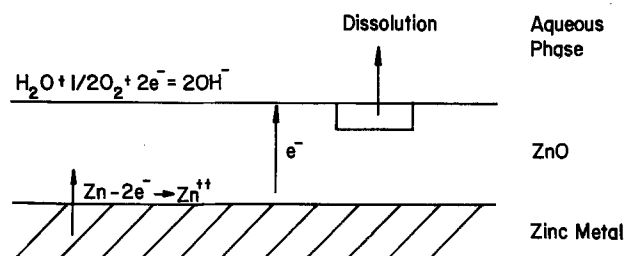
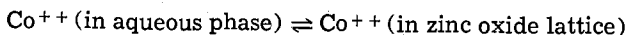


Fig. 14. Schematic representation of the corrosion of zinc in NaCl solution through an oxide film on the surface.

sion process occurs and it is on the surface of the oxide that the cathodic reaction occurs. When the solubility limit of the zinc corrosion product is exceeded, a dynamic process develops in which the corrosion product precipitates at one site and dissolves at another site. The precipitate which forms on the zinc surface may act as a diffusion barrier for species in solution, but presumably it plays no significant role in controlling reactions that occur through the compact oxide present on the zinc surface.

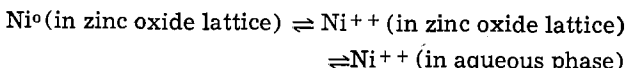
When the zinc samples are dipped in the cobalt chloride solutions, it is proposed that a portion of the total cathodic current that occurs may be represented by the reaction, $\text{Co}^{++} + 2e^- = \text{Co}$, and that uncharged cobalt atoms are incorporated in the oxide. It is also probable that a certain amount of ionic exchange occurs and that cobalt ions are also incorporated into the oxide by this mechanism. Some of these ionic species may later be converted to elemental cobalt during the corrosion process ($\text{Zn} - 2e^- = \text{Zn}^{++}$) as the companion cathodic reaction, $\text{Co}^{++} (\text{in oxide}) + 2e^- = \text{Co} (\text{in oxide})$. This latter reaction is viewed as the electron trapping reaction. In the presence of a sufficient number of trapping sites, the anodic reaction ($\text{Zn} = \text{Zn}^{++} + 2e^-$) is inhibited because of an excess of Zn^{++} ions in the oxide. Cobalt, at the proper concentration in the zinc oxide lattice, thus reduces the flux of electrons through the oxide to supply charges for the cathodic reaction. At high cobalt concentrations in or on the surface of the oxide, the elemental cobalt aggregates sufficiently to form metallic cobalt in contact with metallic zinc which then serves as an effective catalyst for the competing cathodic reaction, $2\text{H}^+ + 2e^- = \text{H}_2$.

The fact that the corrosion inhibitive effects are long-lived in the case of cobalt is probably because the equilibrium, $\text{Co}^{++} (\text{in zinc oxide lattice}) + 2e^- \rightleftharpoons \text{Co}^0 (\text{in zinc oxide lattice})$, is shifted strongly to the right such that there are few cobalt ions available to enter the aqueous phase. Cobalt remains in the zinc oxide lattice during the corrosion reaction and it continues to serve as an electron trap. The reaction



is also shifted very strongly to the right. The net effect is that cobalt atoms remain in the zinc oxide lattice and are not leached out during the corrosion process.

The situation with nickel is different from that of cobalt in that the cathodic polarization curve (taken immediately after immersion in the test electrolyte) indicates corrosion inhibition and the weight loss measurements indicate no significant inhibition. The strong inhibition under those conditions where the zinc is predipped in the nickel acetate solution and the sodium chloride solution contains a low concentration of nickel ions, suggests that the equilibrium

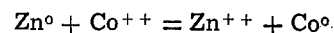


is shifted sufficiently to the right that the nickel ions are leached from the oxide during the corrosion reaction.

Support for the greater stability of Co^{++} ions in the zinc oxide lattice than Ni^{++} ions is found in the relative solubilities of the hydroxides in water. Cobalt hydroxide $[\text{Co}(\text{OH})_2]$ is soluble to the extent of 0.00032 g/liter in cold water, whereas nickel hydroxide $[\text{Ni}(\text{OH})_2]$ is 40 times more soluble with a solubility under similar conditions of 0.013 g/liter (14). The solubility data are for water solutions, whereas the corrosion experiments were carried out in 3% NaCl solution, so it is not known if the same relative solubilities apply in the chloride medium.

The cathodic polarization curves shown in Fig. 3 are consistent with all other observations made during the study. Samples dipped in a solution 0.01M in Co^{++} yielded a polarization curve at potentials more positive

than -1.35V very similar to that of the blank. Samples dipped in solutions 0.05M and 0.1M in Co^{++} showed lower cathodic currents than the blank at potentials slightly negative to the rest potential and higher cathodic currents at potentials more negative than -1.35V . The higher cathodic currents at potentials more negative than -1.35V are developed because the oxide film is reduced at this potential and the cobalt present in the oxide remains on the surface of the zinc in the metallic form. The greater catalytic activity of cobalt, as compared to zinc, for the hydrogen evolution reaction results in a higher cathodic current. At potentials more negative than -1.35V the cathodic current increases with increase in concentration of the cobalt chloride solution in which the predipping occurred. Samples dipped in 0.5M and 1.0M CoCl_2 gave higher cathodic currents over the entire range of potentials, a result consistent with the fact that the reaction



occurred to such an extent that large amounts of metallic cobalt were present on the zinc surface after predipping. The blackened appearance of the surface and the XPS data support this conclusion.

An alternate explanation of the corrosion inhibition by cobalt and nickel ions which must be considered is the following. Let us assume that the zinc oxide is an excellent catalyst for the cathodic reaction, $\text{H}_2\text{O} + \frac{1}{2}\text{O}_2 + 2e^- = 2\text{OH}^-$, and metallic cobalt is a good catalyst for the cathodic reaction, $2\text{H}^+ + 2e^- = \text{H}_2$. The cathodic activity of the surface is then the total of (i) the activity for the hydroxyl generation reaction times the surface area fraction of zinc oxide exposed and (ii) the activity for the hydrogen evolution reaction times the surface area fraction of metallic cobalt exposed. If the polarization curves for these two reactions on these two different substrates are greatly different, it might be reasonably expected that the measured polarization curve would have a range of shapes such as those shown in Fig. 3 depending upon the relative area ratios. We discard this alternate explanation for the following reasons.

1. It is not likely that alloying zinc with cobalt at concentrations of the order of 0.2% would lead to corrosion inhibition as has been proven experimentally
- (2). If the cobalt was active as a catalyst, it would be expected to concentrate at the surface of the zinc as corrosion occurred and the corrosion reaction would be activated after a time, rather than deactivated.

2. Nickel is rapidly leached from the oxide film and it is hard to conceive that sufficient nickel would remain on the zinc surface in the metallic form to provide corrosion inhibition by the alternate explanation in the case of zinc-nickel alloys, which have been shown by others (5-9) to have corrosion protective properties.

3. The data for deaerated solutions summarized in Fig. 6 indicate that metallic cobalt only becomes a significant catalyst for the hydrogen evolution reaction in the case of dipping in solutions of 0.5 and 1.0M CoCl_2 . Thus, significant amounts of cobalt are required on the surface before the hydrogen evolution reaction is vigorously catalyzed.

A simple calculation indicates that corrosion inhibition by cobalt results from the presence of very few cobalt atoms. The Auger data summarized in Fig. 12 indicate that the cobalt concentration on the surface of a sample dipped in 0.05M CoCl_2 solution is not great relative to that of zinc. The surface appearance gives no indication of metallic cobalt. If we assume that the oxide layer is of the order of 30 atom layers in thickness and that there are approximately 10^{15} metallic atoms per cm^2 per layer, the total number of metal atoms in or on the oxide would be of the order of 12×10^{17} metallic atoms for 40 cm^2 area (2 samples of 20 cm^2 each). If half of the metal atoms are cobalt, there are 6×10^{17} cobalt atoms.

The least soluble cobalt species in the sodium chloride solution would be expected to be $\text{Co}(\text{OH})_2$ or $\text{Co}(\text{OH})_3$, the solubility of both of which is given as 0.00032 g/liter since in aerated solution the stable species in the case of high-surface-area hydroxide would be expected to be the trivalent form. For a liquid volume of 200 cm^3 , as used in these experiments, the total number of soluble cobalt ions can be calculated to be 6×10^{17} ions.

Although these numbers are very crude, they do show that only a limited number of cobalt atoms would be expected to exist on the surface of zinc in NaCl solution under conditions where the zinc was pre-dipped in a solution of 0.01M CoCl_2 . Since the zinc oxide is continually being generated by the corrosion reaction, it is extremely unlikely that metallic cobalt could occupy a significant fraction of the surface during the 24 or 48 hr duration of the corrosion experiment.

The suggested interpretation of the corrosion inhibition by cobalt and nickel opens up an entirely new approach to corrosion control for galvanized steel. Any means whereby the catalytic activity of the surface oxide on zinc can be poisoned for the cathodic reactions offers hope for reducing the corrosion rate of zinc. The ideal poison would be one that is effective against both the water-oxygen reaction and the hydrogen evolution reaction. Such poisons might be electron traps within the oxide, as hypothesized for cobalt and nickel, or they might be trapping sites developed by adsorption of a species from the solution.

A recent survey (15) has described the various ways in which metallic cations may serve as corrosion inhibitors. The present study, which has shown the inhibition of zinc corrosion by cobalt and nickel, bears some resemblance to the effect of cobalt on the corrosion of lead anodes in sulfuric acid (16). Both types of corrosion inhibition apparently result because the metal cation enters an oxide film on the surface of the metal and changes its electrical properties. The inhibition of anodic lead corrosion by cobalt is accompanied by a reduction in the overvoltage for the oxygen evolution reaction on lead (17). Cobalt appears to play its role by entering the PbO_2 film on the surface of lead and increasing the predominance of the anodic reaction, $2\text{OH}^- = \text{H}_2\text{O} + \frac{1}{2}\text{O}_2 + 2e^-$, over the undesirable reaction, $\text{Pb} - 2e^- = \text{Pb}^{++}$.

Acknowledgment

This research has been supported jointly by the American Iron and Steel Institute and the International

Lead Zinc Research Organization. We are grateful for this support. We are also grateful to Prof. G. W. Simmons who carried out the Auger and XPS studies and advised on the interpretation of the data.

Manuscript submitted May 15, 1980; revised manuscript received Sept. 16, 1980.

Any discussion of this paper will appear in a Discussion Section to be published in the December 1981 JOURNAL. All discussions for the December 1981 Discussion Section should be submitted by Aug. 1, 1981.

Publication costs of this article were assisted by Lehigh University.

REFERENCES

1. H. Leidheiser, Jr. and I. Suzuki, *Corrosion*, **36**, 701 (1980).
2. T. Adaniya, *Sheet Metal Ind.*, **55**, 73 (1978).
3. T. Adaniya and M. Ohmura, *Metal*, **31**, 1100 (1977).
4. H. Leidheiser, Jr., A. Vértes, M. L. Varsányi, and I. Suzuki, Abstracts of Proceedings of Mössbauer Symposium, American Chemical Society Meeting, Houston, Texas, March 1980.
5. L. F. Williams, *Corrosion Australasia*, **1976**, 6 (1976).
6. E. E. Kravtsov, V. D. Ovcharenko, and A. R. Zagainyi, *Tekhnol. Organ. Proizvod.*, **11**, 53 (1974).
7. Yawata Iron and Steel, French Pat. 1,581,111 (1968).
8. Wheeling Pittsburgh Steel, U.S. Pat. 3,558,442 (1969).
9. M. Kurachi, K. Fujiwara, and T. Tanaka, *Proc. Congr. Int. Union Electrodeposition Surf. Finishing, Basel*, 152 (1972).
10. S. R. Rajogopalan, *Met. Finish.*, **70**, No. 12, 52 (1972).
11. D. K. Kim and H. Leidheiser, Jr., *Metall. Trans. B*, **9**, 581 (1979).
12. T. J. Chuang, C. R. Brundle, and D. W. Rice, *Surf. Sci.*, **59**, 413 (1976).
13. C. D. Wagner, W. M. Riggs, L. E. Davis, J. F. Moulder, and G. E. Mullenberg, "Handbook of X-Ray Photoelectron Spectroscopy," Perkin-Elmer Corp. (1979).
14. "Handbook of Chemistry and Physics," Robert C. Weast, Editor, CRC Press, Cleveland, Ohio.
15. H. Leidheiser, Jr., *Corrosion*, **36**, 339 (1980).
16. P. G. Balakrishnan, R. Janakiraman, R. K. Galgali, R. V. Vasudeva Rao, and H. V. K. Udupa, *J. Electrochem. Soc. India*, **27**, 115 (1978).
17. M. Rey, P. Coheur, and H. Herbiet, *Trans. Electrochem. Soc.*, **73**, 315 (1938).

Redox Potential Measurements in High Temperature Aqueous Systems

Digby D. Macdonald,^{*1} Arthur C. Scott, and Paul Wentrcek

SRI International, Materials Research Laboratory, Menlo Park, California 94025

ABSTRACT

Redox potential measurements on platinum and Type 304 stainless steel in equilibrium (H_2 or O_2) and nonequilibrium ($H_2 + O_2$) boric acid/lithium hydroxide solutions at 275°C are reported. For equilibrium systems containing hydrogen, good agreement was obtained between the measured potentials on platinum and calculated equilibrium potentials for pH (275°C) = 5.49, 5.60, and 8.02. For highly basic systems (0.1M LiOH), however, the observed potentials tended to be more positive than the calculated values; the difference was probably due to trace amounts of oxygen remaining in the system. In oxygenated equilibrium systems, good agreement was found between the observed and calculated potentials for the 0.1M LiOH solution for $[O_2] \leq 7$ ppm, but the observed potentials tended to be less positive than the calculated values for more acidic solutions and for lower oxygen concentrations. Steady-state measurement on nonequilibrium ($H_2 + O_2$) boric acid solutions at 275°C showed that the redox potential on platinum becomes more negative as the ratio $[H_2]/[O_2]$ increases. Transient studies on nonequilibrium ($H_2 + O_2$) boric acid solution revealed that the redox potential can vary over a wide range on cycling the relative concentrations of oxygen and hydrogen. The experimental findings are interpreted in terms of mixed potential model from which numerical simulations have reproduced the essential features of the data.

Considerable interest has arisen in recent years on the properties of high temperature aqueous solutions (100°-300°C) because of their use as heat transport media in many power generating systems. For example, extensive work on the electrochemical behavior of metals and alloys in this hostile environment has been reported over the last decade (1), particularly with reference to corrosion processes. Ion hydrolysis and acid/base dissociation phenomena have also been studied (2-7) using concentration cells for precise acidity measurements at temperatures as high as 300°C. Also, considerable progress has been made in the development of a reliable pH electrode for the long-term monitoring of high temperature aqueous systems (8-13). Some of this latter work (13) is part of a more extensive effort in this laboratory to develop electrochemical probes for monitoring the chemical properties of aqueous heat transport systems in electrical energy producing facilities.

Because corrosion processes and many oxide dissolution phenomena involve a change in oxidation state of one or more components, it is necessary, from a purely thermodynamic viewpoint, to specify or control the redox state if the chemistry of the system is to be fully understood. In practical power generating systems this normally involves the continuous or periodic injection of reducing agents (e.g., H_2 , N_2H_4) or oxidizing agents (e.g., O_2 , H_2O_2) into the high temperature environment. However, the effective control of the redox state of a system requires a means for the continuous monitoring of the redox potential. Experimental studies aimed at developing suitable probes have been reported (14). However, the theoretical basis for the redox potential is not well established and the relationship between the measured potential and the composition of the system is poorly understood.

In this study, we report redox potential measurements carried out on platinum and Type 304 stainless steel electrodes in boric acid/lithium hydroxide solutions at a temperature of 275°C (548 K). The potential measurements were made in systems containing oxy-

gen, hydrogen, and nonequilibrium mixtures of these components. A theoretical analysis of the redox potential is presented and used to interpret the experimental data.

Experimental

Apparatus.—The high temperature recirculating loop used for these studies is described elsewhere (15). Briefly, boric acid/lithium hydroxide buffer solutions were pumped from a reservoir through a preheater and into the measurement cell using a positive displacement diaphragm pump. The exiting solution was heat-exchanged with the input, cooled in a second heat exchanger, and then discharged back to the reservoir via a pressure control valve. The pressure in the circuit was set at 75.3 kPa (1100 psig) to maintain a single (liquid) phase within the loop. Both the preheater and the measurement cell were thermostatted with electrical heaters and controllers. Adjustment of these heaters permitted the cell temperature to be controlled to within ± 2 K at temperatures as high as 548 K (275°C). The solution flow rate could be varied between 0 and 5 ml sec⁻¹ by changing the stroke of the pump. Because the volume of the loop (excluding the reservoir) was 2.5 liters, the time required to completely replace the solution is estimated to be 2-3 hr for the flow rate (1 ml sec⁻¹) employed here. The reservoir contained facilities for continuously sparging the solution with oxygen, hydrogen, or mixtures of these gases. Gas concentrations in the solution were computed using the appropriate Henry's law coefficient. The calculated oxygen concentration was confirmed ($\pm 10\%$) by direct measurement using a dissolved oxygen analyzer (Delta Scientific Model 2210).

Details of the measurement cell used in this work are given in Fig. 1. The main body of the cell was machined from Type 316 stainless steel, and contained ports for the entrance and exit of the solution, a CONAX lead-through for the platinum and Type 304 stainless steel bead electrodes (~ 2 mm diam), and the reference electrode. The bead electrodes were always placed in the same, reproducible, position with respect to both the fluid stream and the reference electrode liquid junction. Reproducible placement with respect to the fluid flow was considered to be necessary, because theory predicts (see Discussion) that the redox

* Electrochemical Society Active Member.

¹ Department of Metallurgical Engineering, The Ohio State University, Columbus, Ohio 43210.

Key words: redox potential, high temperature aqueous solution, oxygen electrode reaction, hydrogen electrode reaction.

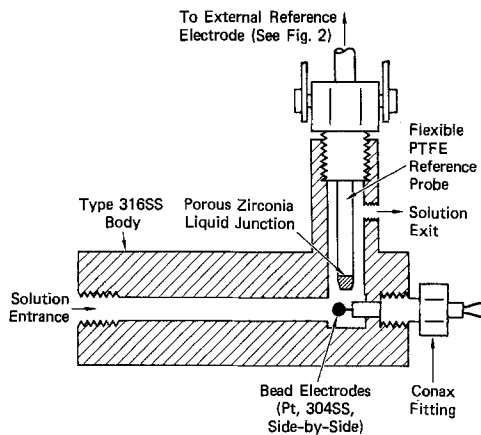


Fig. 1. Cell for the measurement of redox potential in high temperature $B(OH)_3/LiOH$ buffer solutions.

potential will be a function of the mass transfer coefficients for the various electroactive components in the system.

A major problem in any study of this kind is choosing a suitable reference electrode against which the potential of the indicator electrode can be measured. The problems encountered with the traditional internal reference electrodes have been reviewed by Macdonald (16). In this work, we employed a pressure balanced external reference electrode of the type recently described by Macdonald, Scott, and Wentzcek (17). The design of this reference electrode is shown in Fig. 2; details of the construction and operation of the electrode are given in the original publication (17). Briefly, the external $Ag/AgCl$ electrode was calibrated against an identical internal electrode in various KCl solutions ranging in concentration from $0.005 \text{ mole kg}^{-1}$ to $0.505 \text{ mole kg}^{-1}$. Thermodynamic analyses then permitted evaluation of the correction parameters, $\Delta E_{SHE}(T) - \Delta E_{obs}(T)$, where $\Delta E_{obs}(T)$ is the observed potential of the bead electrode against the external reference electrode, and $\Delta E_{SHE}(T)$ is the corresponding potential vs. the hypothetical standard hydrogen electrode (SHE) at the system temperature. Analysis of the reference electrode with an internal KCl solution of concentration $0.102 \text{ mole kg}^{-1}$ showed that the correction term for $T = 275^\circ\text{C}$ is -0.001V (17). Therefore, within the precision of the measurements ($\pm 5 \text{ mV}$), the observed

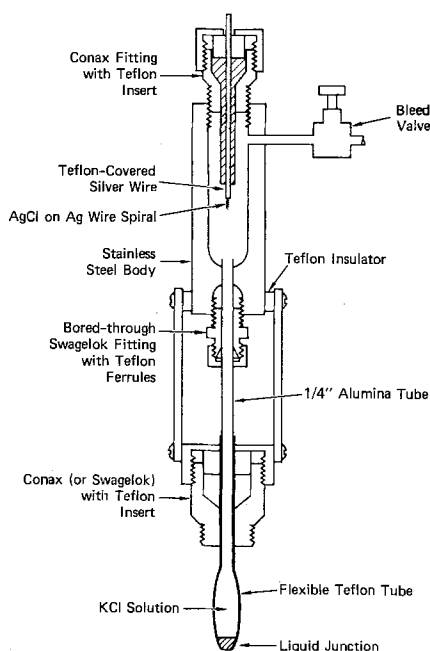


Fig. 2. Reference electrode assembly

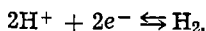
potentials at $275^\circ \pm 2^\circ\text{C}$ can be assumed to refer to the thermodynamically well-defined standard hydrogen electrode scale.

Method.—After assembly of the apparatus, the system was pressurized to 75.3 kPa (1100 psig), and the reservoir purged of oxygen using high purity nitrogen for at least 10 hr while the solution was circulated around the high pressure loop. The temperature was then increased to $275^\circ \pm 2^\circ\text{C}$ by adjusting the inputs to both the preheater and the cell heater. Once the cell temperature was stable, the reservoir was sparged with the desired gas or mixture of gases. The redox potential was then measured using a battery-powered electrometer with input impedance $> 10^{14}\Omega$. The electrometer output was connected to a strip-chart recorder for continuous monitoring of the potential.

Three sets of experiments were carried out: (i) equilibrium studies using oxygenated and hydrogenated solutions separately, (ii) nonequilibrium studies in which the solution was sparged with mixtures of hydrogen and oxygen and the potential recorded until a steady-state response was obtained, and (iii) transient experiments in which the system was cycled between oxygenated and hydrogenated states. The experiments were carried out in various boric acid and boric acid/lithium hydroxide solutions. The pH of each solution at 275°C was calculated as described previously (13).

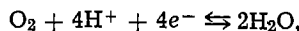
Results and Discussion

Equilibrium studies.—Typical plots of the potential of a platinum electrode vs. the concentration of hydrogen and oxygen in solution as a function of pH are shown in Fig. 3 and 4, respectively. The equilibrium potentials also plotted in these figures were calculated from the composition of the solution assuming that the potential-determining reactions for the hydrogenated and oxygenated systems are



$$E_{H^+/H_2} = -(2.303RT/2F) \log p_{H_2} - (2.303RT/F)pH \quad [1]$$

and



$$E_{O_2/H_2O} = E^\circ + (2.303RT/4F) \log P_{O_2} - (2.303RT/F)pH \quad [2]$$

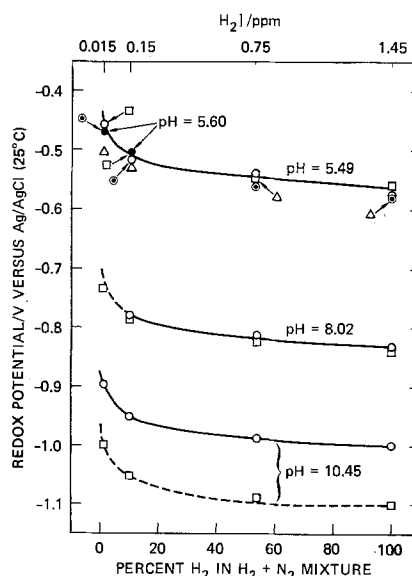


Fig. 3. Equilibrium potential at 275°C vs. concentration of hydrogen in 0.1m boric acid ($pH = 5.49$), 0.01m boric acid ($pH = 5.60$), 0.01m boric acid + 0.001m $LiOH$ ($pH = 8.02$), and 0.1m $LiOH$ ($pH = 10.45$). Data points: \circ —Pt, experimental. \triangle —Type 304 stainless steel. \square —calculated ($pH = 5.49, 8.02, 10.45$). \ominus — $pH = 5.60$, for the reaction $2H^+ + 2e^- = H_2$.

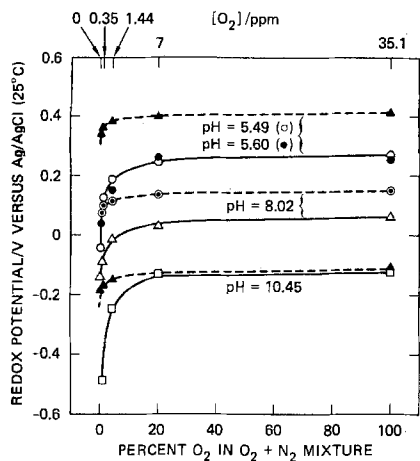


Fig. 4. Equilibrium potential at 275°C vs. concentration of oxygen for a platinum electrode in boric acid/LiOH buffer solutions (see Fig. 3 for compositions). Data points: \circ , \bullet , Δ , \square —experimental. \blacktriangle —calculated for the reaction $O_2 + 4H^+ + 4e^- = 2H_2O$.

Hypothetical partial pressures of hydrogen and oxygen in the high temperature zone can be calculated from the known concentrations of these solutes in the reservoir at 25°C and the Henry's law coefficients at 275°C. For a solute concentration in the reservoir at 25°C of x parts per million (ppm), the equivalent partial pressure at the operating temperature is

$$p_i = x_i/1000 M_i B_{275,i} \quad (i = H_2, O_2) \quad [3]$$

where M_i is the solute molecular weight and $B_{275,i}$ is the Henry's law coefficient at 275°C (18). Substitution of Eq. [3] into Eq. [1] and [2] therefore yields

$$E_{H^+/H_2} = 0.0408 - 0.0544 \log x - 0.10875 \text{ pH} \quad [4]$$

$$E_{O_2/H_2O} = 0.9857 + 0.272 \log x - 0.10875 \text{ pH} \quad [5]$$

The data plotted in Fig. 3 show that for hydrogenated systems the observed redox potential for platinum and Type 304 stainless steel (pH = 5.49 only) is in excellent agreement with the calculated values for the three lowest pH values (5.49, 5.60, 8.02). However, the experimental data at the highest pH (10.45) do not agree with the theoretical values; the experimental values are approximately 100 mV more positive than the potentials calculated using Eq. [4]. Conversely, experimental and theoretical data plotted in Fig. 4 for the oxygenated systems show reasonable agreement at the highest pH, particularly for high oxygen concentration ($[O_2] \geq 7$ ppm), but progressively poorer agreement is found as the acidity of the solution increases. At low oxygen concentrations the observed potentials tend to be less positive than the calculated values by an amount that increases with decreasing concentration.

The generally good agreement found between the observed and calculated data for the three most acidic hydrogenated systems illustrates the precision that can be obtained in potential measurements using external pressure balanced reference electrodes. For this reason we do not believe that the discrepancy between experiment and theory found in the most highly basic solution (pH = 10.45) is due to a malfunction of the reference electrode. Nor do we believe that it is due to any uncertainty in the calculated pH, even though the association constant for Li^+ and OH^- is not well established, particularly at elevated temperatures. If a significant error in the calculated pH did exist, it is unlikely that close agreement would have been found between the calculated and observed potentials for oxygenated systems at pH = 10.45 and $[O_2] \geq 7$ ppm (Fig. 4). The discrepancy between the calculated and experimental data at high pH in the hydrogen-containing solutions presumably arises from kinetic factors and/or more probably from contamination of the sys-

tem with other electroactive species, particularly oxygen.

The generally poor agreement found between the observed and calculated potentials for oxygenated solutions at low oxygen concentrations and pH is not surprising in view of previous work on the oxygen electrode reaction. For example, Hoare (19) points out that in oxygenated systems platinum is not inert and the metal surface reacts with the environment to form platinum oxides. The observed potential may therefore refer to a mixed potential which arises from the simultaneous operation of anodic (e.g., Pt oxidation) and cathodic (oxygen reduction) reactions at the surface. This theory predicts that the observed potential will be less positive than the equilibrium potential for the oxygen electrode, as observed. Also, the observed potential should lie closest to the equilibrium potential for that partial process with the highest exchange current density; that is, closest to the equilibrium potential for the most reversible reaction. The data plotted in Fig. 4 show that progressively better agreement between the theoretical and observed potentials is obtained as the pH increases from 5.49 to 10.45. This behavior indicates that the oxygen electrode reaction becomes more reversible compared with the anodic reaction on platinum as the pH increases.

Steady-state nonequilibrium studies.—Many industrial systems that utilize high temperature aqueous solutions operate under nonequilibrium conditions as far as the oxygen and hydrogen contents of the fluid are concerned. For example, in Boiling Water (Nuclear) Reactors (BWR's), nonequilibrium concentrations of oxygen and hydrogen are produced in-core due to the radiolysis of water. These nonequilibrium concentrations persist into out-of-core areas, so that any realistic study of the redox potential in this environment must consider kinetic as well as equilibrium factors.

Typical steady-state redox potentials observed on platinum in nonequilibrium high temperature (275°C) boric acid/lithium hydroxide solutions are summarized in Fig. 5 as a function of the relative amounts of oxygen and hydrogen in the fluid. At all pH values, the redox potential becomes more negative as the ratio

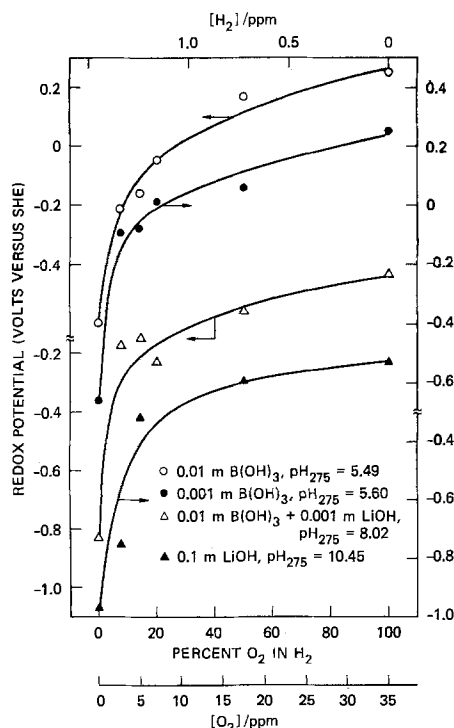


Fig. 5. Steady-state redox potentials for platinum as a function of composition for nonequilibrium systems containing oxygen and hydrogen at 275°C.

$[H_2]/[O_2]$ increases. However, the data were not sufficiently reproducible or stable, particularly at the highest pH, to ascertain the composition dependence of the redox potential quantitatively.

The poor reproducibility of these data could be due to reaction of the electroactive components (O_2 , H_2) in the high temperature zone, so that the actual concentrations sensed by the redox probe are considerably lower than those established in the reservoir and hence those used for the plotting of Fig. 5. A more probable explanation is that the system is inherently unstable for kinetic reasons over the composition range of interest due to the approximate equality of the limiting currents for the oxidation of hydrogen and the reduction of oxygen. This latter explanation is supported by the theoretical work described later in this paper.

Transient experiments.—The most important application of redox potentiometry in industrial systems is expected to be for the monitoring of aggressive environments such as aqueous solutions at elevated temperatures. Few industrial systems operate in a steady state; for example, the levels of both oxygen and hydrogen in BWR heat transport circuits vary with the power output of the core, temperature, and with time upon start-up and shut-down. Accordingly, considerable interest exists in defining the redox potential response under transient conditions in which the relative concentrations of hydrogen and oxygen are cycled over a wide range. In the present work these transient experiments were carried out using platinum redox probes only. Also, the concentration of hydrogen in solution in the high temperature ($275^\circ C$) zone was monitored continuously using the palladium resistance probe that is described in another publication (20).

A typical plot of redox potential *vs.* time for an experiment in which the reservoir was sparged cyclically with various mixtures of hydrogen and oxygen is shown as the lower curve in Fig. 6. Also plotted in this figure (upper curve) is the output of the palladium resistance hydrogen monitor. This output is proportional to the resistance of a palladium wire sensing element and has been processed to compensate for small temperature fluctuations in the experimental apparatus. Since the monitor output is nearly linear with hydrogen concentration, the value for V_c may be taken as an approximate measure of the hydrogen content of the high temperature aqueous solution (0-1.45 ppm).

Prior to recording the segment of data shown in Fig. 6, the system had been exposed to 100% hydrogen for 22 hr. Injection of 9% O_2 in H_2 caused the redox potential to increase rapidly to a maximum after 2-3 hr. This response time corresponds to the estimated mass transfer time of the loop, and it is not considered to be an indication of the performance of the probe itself.

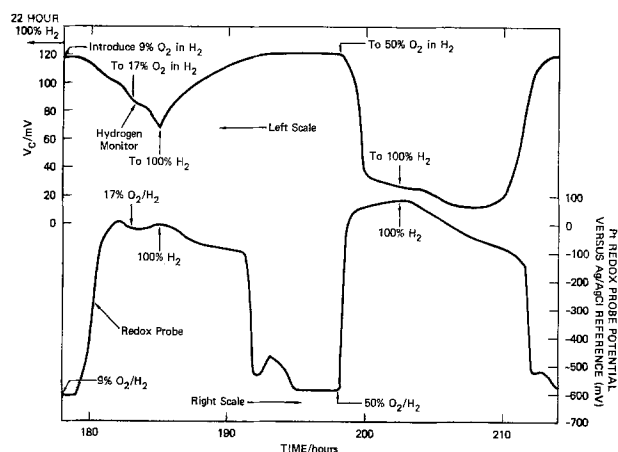


Fig. 6. Response of hydrogen monitor (upper curve) and redox probe (lower curve) to hydrogen and oxygen in 0.1M boric acid at $275^\circ C$.

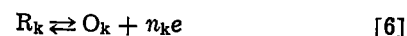
Injection of a slightly higher oxygen level (17% O_2 in H_2) causes a further small upward response in the redox potential. Subsequently, injection of 100% hydrogen into the system caused the potential at first to shift slowly in the negative direction, followed by a rapid change to a value that is close to the equilibrium value for the H^+/H_2 reaction. A similar response is observed during the second cycle.

Comparison of the two curves in Fig. 6 shows clearly that the transient response of the redox probe is closely associated with the relative concentrations of hydrogen and oxygen in the fluid. For example, good coincidence is observed between the increase in hydrogen concentration (decrease in $[O_2]$) and the shift in the redox potential to more negative values. Similarly, the decrease in the hydrogen concentration (increasing $[O_2]$) is in excellent fidelity with the rapid rise in the redox potential.

In many experiments, a small maximum was observed in the redox potential on sparging the solution with hydrogen after prior exposure to oxygen. It is probable that this maximum arises from the reduction of surface platinum oxide phases. We consider this to be indirect evidence in support of the mixed potential hypothesis for the discrepancy between the observed and calculated potentials for the oxygen electrode reaction in this environment.

Mixed potential model.—The close correspondence between the redox potential and composition suggests that the electrochemistry of the system may be modeled using mixed potential theory.

In the mixed potential model developed here, we assume that the electrochemical reactions involved occur uniformly across the active surface, that each reaction may involve varying degrees of charge and mass transfer control, and that each reaction is characterized by a set of parameters which include the exchange current density, transfer coefficients, equilibrium potential, and limiting currents for the forward and reverse directions. In this analysis, we limit the model to two simultaneous electrochemical reactions of the type



where R and O are reduced and oxidized species, respectively, and $k = 1, 2$. Consideration of both charge transfer and mass transfer shows (21) that the generalized current-voltage expression for reaction [6] can be written in the form

$$i_k = i_{o,k} \left\{ \left(\frac{i_{l,f,k} - i_k}{i_{l,f,k}} \right) \exp(a_k n_k) - \left(\frac{i_{l,r,k} - i_k}{i_{l,r,k}} \right) \exp(-b_k n_k) \right\} \quad [7]$$

where $i_{o,k}$ is the exchange current density

$$i_{o,k} = i^{\circ}_{o,k} (C_{O,k})^{\alpha_k} (C_{R,k})^{\beta_k} \quad [8]$$

$i^{\circ}_{o,k}$ is the standard exchange current density, $C_{O,k}$ and $C_{R,k}$ are the bulk solution concentrations of O_k and R_k , respectively, and α_k and β_k are the transfer coefficients for the forward and reverse directions. The constants a_k and b_k are equal to $\alpha_k n F / RT$ and $\beta_k n F / RT$, respectively. The limiting currents for the forward and reverse reactions are designated by $i_{l,f,k}$ and $i_{l,r,k}$; the latter quantity being negative.

Rearrangement of Eq. [7] yields an expression for the current i_k

$$i_k = \omega_k \{ \exp[a_k(E - E_{e,k})] - \exp[-b_k(E - E_{e,k})] \} / \{ x_k + y_k \exp[a_k(E - E_{e,k})] - z_k \exp[-b_k(E - E_{e,k})] \} \quad [9]$$

where

$$\omega_k = i_{o,k} i_{l,f,k} i_{l,r,k} \quad [10]$$

$$x_k = i_{l,f,k} i_{l,r,k} \quad [11]$$

$$y_k = i_{o,k} i_{l,r,k} \quad [12]$$

$$z_k = i_{o,k} i_{l,f,k} \quad [13]$$

and $E_{e,k}$ is the equilibrium potential for reaction [6] under the prevailing conditions

$$E_{e,k} = E^{\circ}_{e,k} - \frac{RT}{n_k F} \ln \left\{ \frac{\gamma_{R,k} C_{R,k}^b}{\gamma_{O,k} C_{O,k}^b} \right\} \quad [14]$$

$E^{\circ}_{e,k}$ is the standard potential, and $\gamma_{R,k}$ and $\gamma_{O,k}$ are activity coefficients for the reduced and oxidized species, respectively.

For an electrically isolated surface upon which $k = 1, 2, \dots, n$ reactions of type [6] are taking place, the mixed potential, E_m , is determined by the zero total current condition

$$Y(E) = \sum_{k=1}^h i_k \cdot A_k = 0 \quad [15]$$

where A_k is the local area on which the k th reaction occurs. In this analysis we have invoked the uniform accessibility condition so that $A_{\text{electrode}} = A_k$ and Eq. [15] therefore reduces to

$$Y(E) = \sum_{k=1}^h i_k = 0 \quad [16]$$

The more general expression, Eq. [15], permits galvanic effects to be taken into account. In both cases, the problem reduces to one of finding a value for the potential which satisfies the zero total current condition as expressed by Eq. [15] or [16].

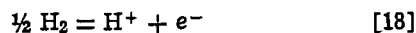
The solution to Eq. [16] is most easily determined using the Newton-Raphson iterative technique. In this method, an improved approximation for the mixed or redox potential, $E_{m,j}$, is obtained from

$$E_{m,j} = E_{m,j-1} - Y(E_{m,j-1})/Y'(E_{m,j-1}) \quad [17]$$

where j is the iteration number, and Y' is the first derivative of Eq. [16] with respect to potential. The iteration is continued until the desired level of precision is obtained. Alternatively, E_m may be estimated directly by plotting the current function $Y(E)$ vs. po-

tential; E_m being that potential at which $Y(E) = 0$. Both methods have been used in this study.

Because the experimental work reported in this paper was restricted to systems containing oxygen and hydrogen only, the two following reactions are considered in this analysis



Both reactions are written in the oxidation sense to emphasize that the forward (anodic) current is considered to be positive, whereas the reverse (cathodic) current is negative. No attempt was made to include the oxidation of platinum in the analysis, since insufficient data are available on the thermodynamic and kinetic parameters involved.

After an extensive search of the literature it was evident that few data are available for the kinetic parameters for reactions [18] and [19] at 275°C. Accordingly, no particular attempt was made in this study to reproduce the experimental data. Instead, the redox potential was calculated for a range of environmental and kinetic parameters so that trends in the experimental data could be identified. The input data for the numerical simulations are summarized below and in Tables I and II.

As noted above, insufficient data are available in the literature for α , β , and i°_o for the two reactions of interest. For the H^+/H_2 reaction we have adopted values of $\alpha = 0.43$, $\beta = 1$, $i^{\circ}_o = 4 \times 10^7 \text{ A cm}^{-2}$; and for the $\text{O}_2/\text{H}_2\text{O}$ reactions values of $\alpha = 0.375$, $\beta = 0.125$, and $i^{\circ}_o = 0.2 \times 10^{-3} \text{ A cm}^{-2}$ were assumed. The transfer coefficients are among those listed by Bockris and Reddy (22) for these two reactions under ambient conditions. The i°_o values yield exchange current densities (i_o) for the H^+/H_2 and $\text{O}_2/\text{H}_2\text{O}$ reactions at $\text{pH} = 5$ and for $[\text{H}_2] = 2.2 \times 10^{-7} \text{ mole cm}^{-3}$ and $[\text{O}_2] = 3.1 \times 10^{-10} \text{ mole cm}^{-3}$ of $0.8 \times 10^{-3} \text{ A cm}^{-2}$ and $0.12 \times 10^{-6} \text{ A cm}^{-2}$, respectively. These values are typical of those expected for these reactions under the conditions of interest. Limiting current for the two reactions

$$i_l = nFDC/\delta \quad [20]$$

where δ is the diffusion layer thickness, were calculated

Table I. Equilibrium potentials* for the H_2/H^+ couple as a function of pH and dissolved hydrogen concentration at 275°C

| pH | C_{H_2} (mole cm^{-3}) | | | | | | | |
|----|---|----------------------|----------------------|----------------------|----------------------|----------------------|----------------------|----------------------|
| | 4.4×10^{-10} | 2.2×10^{-9} | 4.4×10^{-9} | 2.2×10^{-8} | 4.4×10^{-8} | 1.1×10^{-7} | 2.2×10^{-7} | 4.4×10^{-7} |
| 5 | -0.337 | -0.375 | -0.391 | -0.429 | -0.446 | -0.467 | -0.484 | -0.500 |
| 6 | -0.446 | -0.484 | -0.500 | -0.538 | -0.555 | -0.576 | -0.593 | -0.609 |
| 7 | -0.554 | -0.592 | -0.608 | -0.646 | -0.663 | -0.684 | -0.701 | -0.717 |
| 8 | -0.663 | -0.701 | -0.717 | -0.755 | -0.772 | -0.793 | -0.810 | -0.826 |
| 9 | -0.772 | -0.810 | -0.826 | -0.864 | -0.881 | -0.902 | -0.919 | -0.935 |
| 10 | -0.881 | -0.919 | -0.935 | -0.973 | -0.990 | -1.011 | -1.028 | -1.044 |

* All potentials vs. SHE at 275°C.

Table II. Equilibrium potentials* for the $\text{O}_2/\text{H}_2\text{O}$ couple as a function of pH and dissolved oxygen concentration at 275°C

| pH | C_{O_2} (mole cm^{-3}) | | | | | |
|----|---|-------------------------|------------------------|------------------------|------------------------|------------------------|
| | 3.125×10^{-11} | 3.125×10^{-10} | 3.125×10^{-9} | 3.125×10^{-8} | 3.125×10^{-7} | 3.125×10^{-6} |
| 5 | 0.352 | 0.379 | 0.406 | 0.433 | 0.460 | 0.487 |
| 6 | 0.243 | 0.270 | 0.297 | 0.324 | 0.351 | 0.378 |
| 7 | 0.135 | 0.162 | 0.189 | 0.216 | 0.243 | 0.270 |
| 8 | 0.026 | 0.053 | 0.080 | 0.107 | 0.134 | 0.161 |
| 9 | -0.083 | -0.056 | -0.029 | -0.002 | 0.025 | 0.052 |
| 10 | -0.192 | -0.165 | -0.138 | -0.111 | -0.084 | -0.057 |

* All potentials vs. SHE at 275°C.

assuming that $D_{H_2} = D_{O_2} = 5 \times 10^{-5} \text{ cm}^2 \text{ sec}^{-1}$, $D_{H^+} = 5 \times 10^{-4} \text{ cm}^2 \text{ sec}^{-1}$, and $\delta = 10^{-2} \text{ cm}$.

Four sets of numerical simulations were carried out (Table III), each intended to determine the response of the redox potential to systematic variations in a single system parameter. The variables of interest include: pH (set A), $[H_2]$ — low $[O_2]$ (set B), $[H_2]$ — high $[O_2]$ (set C), and $[O_2]$ — low $[H_2]$ (set D). Set A is divided into three subsets; A(1) — high $[H_2]$, low $[O_2]$; A(2) — low $[H_2]$, high $[O_2]$; and A(3) — med $[H_2]$, med $[O_2]$. Appropriate nuclear technologies to which these cases and sets B, C, and D refer are also indicated in Table III. Typical current-voltage curves for the simultaneous oxidation of hydrogen and the reduction of oxygen at an inert electrode are shown in Fig. 7. The total current ($I = i_1 + i_2$) is also plotted, and the intercept at which $I = 0$ defines the mixed potential (E_m) for the system. In the case shown, the mixed potential is dominated by the hydrogen electrode reaction with the reduction of oxygen being under mass transfer control.

The effect of pH on the calculated redox potential for the three subsets A(1), A(2), and A(3) is shown in Fig. 8. The redox potentials for low $[H_2]$ — $[O_2]$ [A(2)] and med $[H_2]$ — med $[O_2]$ [A(3)] are predicted to exhibit the same pH dependencies as the equilibrium potential. For the first case (A(1), high $[H_2]$ — low $[O_2]$) a small deviation from the equilibrium potential pH dependence is predicted; the deviation is, however, small (10 mV) over the five pH units considered in the simulation.

The predicted variation of redox potential, E_m , with the relative concentrations of hydrogen and oxygen in solution is shown in Fig. 9 for cases B, C, and D listed in Table III. The equilibrium potentials for the hydrogen and oxygen electrode reactions for all three cases are also plotted for comparison. For case B, in which $[H_2] \gg [O_2]$, the redox potential behavior is dominated by the hydrogen electrode reaction and the dependence of E_m on composition closely follows that for the equilibrium potential $E_{e,1}$. These calculations suggest that, under typical operating conditions for PWR primary coolant circuits, redox potential measurements, at least on platinum, will be of little value for indicating the presence of small nonequilibrium concentrations of oxygen in the fluid. However, the assumption of a higher oxygen concentration (1.0 ppm vs. 0.001 ppm) yields curve C, which exhibits a sharp transition from a response that is dominated by the oxygen electrode reaction for low $[H_2]/[O_2]$ ratios to one that is determined by the hydrogen electrode reaction for hydrogen-rich systems. A similar behavior is predicted for case D (low $[H_2]$ -varying $[O_2]$) which was intended to simulate start-up and operating conditions in BWR's. Indig and co-workers (14) have observed large redox potential swings on start-up and shut-down of

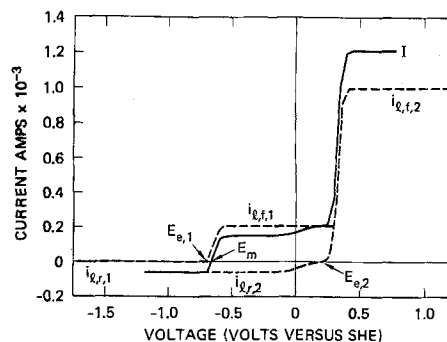


Fig. 7. Current-voltage curves for the simultaneous oxidation of hydrogen and reduction of oxygen at a platinum electrode. Reaction 1, $H_2 \rightleftharpoons 2H^+ + 2e^-$. Reaction 2, $2H_2O \rightleftharpoons O_2 + 4H^+ + 4e^-$. $[H_2] = 2.2 \times 10^{-7} \text{ mole cm}^{-3}$, $[O_2] = 3.125 \times 10^{-8} \text{ mole cm}^{-3}$, $pH = 7$, $E_{e,1} = 0.701V \text{ vs. SHE}$, $E_{e,2} = 0.216V \text{ vs. SHE}$. The total current $I = i_1 + i_2$.

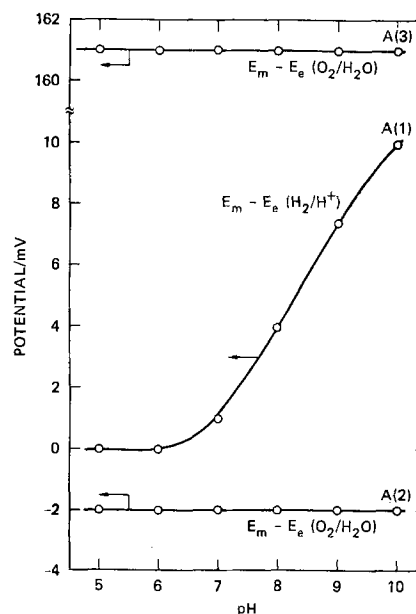


Fig. 8. Effect of pH on the simulated redox potential relative to the equilibrium potentials for the H^+/H_2 and O_2/H_2O reactions. The numerals identifying the curves are as given in Table III.

an operating boiling water reactor apparently due to large changes in oxygen concentration, in agreement with the predictions reported here.

The origin of the sudden shift in the redox potential on changing the composition of the system can be seen by examining the data plotted in Fig. 7. Because both

Table III. Concentrations of oxygen and hydrogen used for the numerical simulation of the redox potential

| Simulation number | $[H_2]$ mole cm^{-3} (ppm) | $[O_2]$ mole cm^{-3} (ppm) | pH | Appropriate nuclear technology |
|--|-------------------------------------|-------------------------------------|------|--------------------------------|
| A. Effect of pH | | | | |
| (1) High $[H_2]$ -low $[O_2]$ | 2.2×10^{-7} (0.44) | 3.125×10^{-11} (0.001) | 5-10 | PWR* |
| (2) Low $[H_2]$ -high $[O_2]$ | 4.4×10^{-10} (0.00088) | 3.125×10^{-7} (10.0) | 5-10 | BWR** start-up |
| (3) Med $[H_2]$ -med $[O_2]$ | 4.4×10^{-9} (0.0088) | 3.125×10^{-9} (0.1) | 5-10 | BWR operating |
| B. Effect of $[H_2]$ | | | | |
| | 4.4×10^{-10} (0.00088) | 3.125×10^{-11} (0.001) | 7 | PWR operating |
| | 2.2×10^{-7} (0.44) | | | |
| C. Effect of $[H_2]$ | | | | |
| | 4.4×10^{-10} (0.00088) | 3.125×10^{-8} (1.0) | 7 | PWR high oxygen |
| | 4.4×10^{-7} (0.88) | | | |
| D. Effect of $[O_2]$ | | | | |
| | 4.4×10^{-10} (0.00088) | 3.125×10^{-11} (0.001) | 5 | BWR start-up/operating |
| | | 3.125×10^{-7} (10.0) | | |

* Designates pressurized water reactor.

** Designates boiling water reactor.

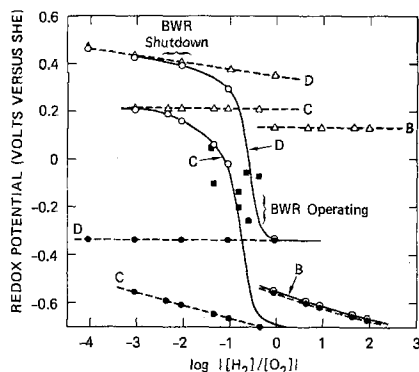


Fig. 9. Simulated redox potential E_m (○), vs. composition curves for sets B, C, D listed in Table III. ●—equilibrium potentials $E_{e,1}$ for the H^+/H_2 reaction; △—equilibrium potentials $E_{e,2}$ for the O_2/H_2O reaction; ■—experimental data (see text).

reactions exhibit mass transfer control over most of the potential region between $E_{e,1}$ and $E_{e,2}$, it is evident that if $i_{l,r,1} > i_{l,r,2}$ then $E_m \rightarrow E_{e,1}$; that is, the redox response is dominated by the hydrogen electrode reaction. On the other hand, for $i_{l,r,1} \ll i_{l,r,2}$, $E_m \rightarrow E_{e,2}$, and the redox potential tends to mimic the oxygen electrode behavior. In the intermediate region where $i_{l,r,1} \approx i_{l,r,2}$ the system is unstable in that a small change in either of the limiting currents (and hence concentration) will cause a large shift in potential.

Because the sparging of a dissolved gas from a fluid is expected to be a first-order kinetic process, then to a first approximation it is expected that $\log \{ [H_2]/[O_2] \}$ will be roughly proportional to time. Accordingly, it is expected that the form of the experimental redox potential vs. time curve (Fig. 6) will show qualitative similarities to the calculated curves plotted in Fig. 9. Comparison of the two sets of data shows that this is indeed the case. For example, theory predicts (Fig. 9) that sparging of a hydrogen-containing system with oxygen will cause the redox potential to first increase rapidly with time, followed by a more gradual change towards the equilibrium potential for the oxygen electrode reaction. On the other hand, sparging of an oxygenated solution with hydrogen is expected to have the reverse effect; a relatively slow change with time is first predicted for E_m , followed by a sharp drop to the equilibrium potential for the hydrogen electrode reaction, as observed.

Finally it is of interest to compare (semiquantitatively) the observed redox potentials with the calculated values. In carrying out this comparison, we have adjusted the potential scales for the experimental data at pH = 5.49 and 8.02 to pH = 7 by subtracting and adding, respectively, the amount $(2.303 RT/F) \Delta pH$ to the experimental values. The experimental conditions under which the steady-state redox potential measurements were made most closely correspond to those for case C, Table III. In spite of the considerable scatter in the experimental data, reasonable agreement between theory and experiment is observed.

Summary and Conclusions

Redox potential measurements in boric acid/lithium hydroxide solutions at 275°C in the presence of equilibrium and nonequilibrium amounts of oxygen and hydrogen have shown that:

1. Platinum adopts the equilibrium potential for the hydrogen electrode reaction in hydrogen-containing solutions of pH 5.49–8.02. In a more basic solution (0.1M LiOH), the observed potentials were less negative than those predicted from theory, probably due to contamination by oxygen.

2. In oxygenated solutions, the observed potential of a platinum electrode was found to be in good agreement with the predicted equilibrium value only in the highly basic solution (0.1M LiOH), and then only for

$[O_2] \geq 7$ ppm. Under all other conditions, the observed potentials were less positive than the predicted values.

3. In steady-state, nonequilibrium systems containing both hydrogen and oxygen, the redox potential becomes more negative as the ratio $[H_2]/[O_2]$ increases.

4. Transient studies on nonequilibrium systems showed that the redox potential swings over a wide range on cyclically sparging the solution with oxygen and hydrogen. Comparison of the redox probe response with that for a hydrogen monitor revealed a high fidelity between the observed potential and the concentration of hydrogen in solution.

5. Extensive numerical simulations of the redox potential for nonequilibrium oxygen- and hydrogen-containing solutions have shown that the observed data can be understood using a mixed potential model which assumes that the potential-determining reactions are the simultaneous oxidation of hydrogen and reduction of oxygen at the electrode surface.

Acknowledgments

The authors wish to thank the Electric Power Research Institute, Palo Alto, California, Dr. T. O. Passell, Project Manager, for financial support of this work under Contract No. RP-1168-1.

Manuscript submitted March 12, 1980; revised manuscript received Sept. 22, 1980.

Any discussion of this paper will appear in a Discussion Section to be published in the December 1981 JOURNAL. All discussions for the December 1981 Discussion Section should be submitted by Aug. 1, 1981.

Publication costs of this article were assisted by SRI International.

REFERENCES

1. D. D. Macdonald, in "Modern Aspects of Electrochemistry," Vol. 11, B. E. Conway and J. O'M. Bockris, Editors, Plenum Press, New York (1975).
2. R. E. Mesmer, C. F. Baes, and F. H. Sweeton, *J. Phys. Chem.*, **74**, 1937 (1970); *Inorg. Chem.*, **11**, 537 (1972).
3. R. E. Mesmer and C. F. Baes, *Inorg. Chem.*, **10**, 2290 (1971).
4. R. E. Mesmer and C. F. Baes, *J. Solution Chem.*, **3**, 307 (1974).
5. D. D. Macdonald, P. Butler, and D. Owen, *Can. J. Chem.*, **51**, 2590 (1973).
6. D. D. Macdonald, P. Butler, and D. Owen, *J. Phys. Chem.*, **77**, 2474 (1973).
7. D. D. Macdonald and D. Owen, *Can. J. Chem.*, **51**, 2747 (1973).
8. J. V. Dobson, M. N. Dagless, and H. R. Thirsk, *J. Chem. Soc. Faraday Trans.*, **1**, **68**, 749 (1972).
9. J. V. Dobson, M. N. Dagless, and H. R. Thirsk, *ibid.*, **68**, 764 (1972).
10. L. Niedrach, *Science*, **207**, 1200 (1980).
11. J. V. Dobson, B. R. Chapman, and H. R. Thirsk, in "High Temperature High Pressure Electrochemistry in Aqueous Solutions," R. W. Staehle, D. de G. Jones, and J. E. Slater, Editors, p. 341, National Association of Corrosion Engineers, Houston, NACE-4 (1976).
12. J. V. Dobson, *J. Electroanal. Chem. Interfacial Electrochem.*, **35**, 129 (1972).
13. D. D. Macdonald, P. R. Wentreck, and A. C. Scott, *This Journal*, **127**, 1745 (1980).
14. M. E. Indig, J. E. Weber, and A. D. Miller, *Corrosion*, **34**, 3 (1978); M. E. Indig and A. R. McIlree, *ibid.*, **35**, 288 (1979).
15. D. D. Macdonald, A. C. Scott, P. R. Wentreck, and M. C. H. McKubre, "Monitoring Techniques for pH, Hydrogen, and Redox Potential in Nuclear Reactor Circuits," Final Report, Electric Power Research Inst., Palo Alto, California, Contract No. RP 1168-1 (1979).
16. D. D. Macdonald, *Corrosion*, **34**, 75 (1978).
17. D. D. Macdonald, A. C. Scott, and P. Wentreck, *This Journal*, **126**, 908 (1979).
18. G. B. Naumov, B. N. Ryzhenko, and I. L. Khodakovskiy, "Handbook of Thermodynamic Data," USGS Transl. USGS-WRD-74-001 (1974).

19. J. P. Hoare, in "Advances in Electrochem. and Electrochem. Eng.," Vol. 6, P. Delahay and C. W. Tobias, Editors, p. 201, Interscience, New York (1967).
20. D. D. Macdonald, M. C. H. McKubre, A. C. Scott, and P. R. Wentreck, *J. Nucl. Energy*, Submitted for publication (1979).
21. D. D. Macdonald, "Transient Techniques in Electrochemistry," Plenum Press, New York (1977).
22. J. O'M. Bockris and A. K. N. Reddy, "Modern Electrochemistry," Vol. 2, Plenum Press, New York (1973).

Reaction Model for Iron Dissolution Studied by Electrode Impedance

I. Experimental Results and Reaction Model

Michel Keddad, Oscar Rosa Mattos, and Hisasi Takenouti

Groupe de Recherche No. 4 du CNRS "Physique des Liquides et Electrochimie," associé à l'Université Pierre et Marie Curie, 75230 Paris Cedex 05, France

ABSTRACT

Steady-state polarization curves and electrode impedances were measured during the dissolution of iron in 1M Na₂SO₄ solution acidified by the addition of 1M H₂SO₄. These experiments were performed within very wide pH (0-5), current density (up to 0.1 A · cm⁻²), and frequency (10⁻³-10⁵ Hz) ranges. Three time constants, in addition to the high-frequency capacitive loop attributed to the double layer capacity and the charge transfer resistance, were observed before the onset of the passivation process. The experimental results were quantitatively interpreted by computer simulation on the basis of a reaction model including three dissolution paths. At low current densities, the dissolution path, which can be related to the consecutive mechanism, controls the overall rate. At higher current densities, a self-catalytic path, implying a ferrous intermediate, determines the overall current. Another self-catalytic path, with monovalent iron, plays an important role in the electrode impedance and the prepassivation process although its contribution to the current is not prevalent at any pH.

Bonhoeffer and co-workers strove to establish the mechanism of iron dissolution in acidic medium and proposed, for the first time, reaction models implying reaction intermediate species (1-4). According to Heusler, the dissolution of iron takes place in two steps coupled by monovalent iron (model I) (4)

Model I



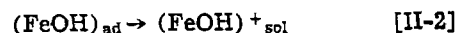
The subscripts "ad" and "sol" indicate, respectively, the species adsorbed at the electrode surface and that dissolved in the solution bulk. (FeOH)⁺_{sol} decomposes in the solution bulk into hydrated Fe²⁺ and OH⁻. The reaction step [I-2] does not consume the intermediate species (FeOH)_{ad}; thus at steady state, step [I-1] remains in equilibrium. This reaction mechanism was proposed in order to interpret the following three experimental observations: (i) The slope of the steady-state polarization curve, usually called Tafel slope, $d(\log J)/dE$, is equal to 0.03V. (ii) The transient Tafel slope obtained from the maximum potential E_{tr} following the stepwise current change, $d(\log J)/dE_{\text{tr}}$, is equal to 0.06V. (iii) The reaction order with respect to OH⁻ ion concentration, $d(\log J)/dpH$, is equal to two.

A few years later, Bockris and co-workers (5-7) repeated the experiments made by Heusler and found somewhat different results, namely, (i) The steady-state Tafel slope is equal to 0.04V. (ii) The reaction order with respect to OH⁻ concentration is equal to unity.

Key words: adsorption, metals, passivity.

They examined several reaction models, including model I and proposed the reaction model constituted by two consecutive steps (5)

Model II



Step [II-2] is considered slow and limits the overall reaction rate whereas the first step is in pseudo-equilibrium. The occurrence of a pseudo-equilibrium reaction implies an electrode potential close to its thermodynamic equilibrium potential and its reaction rate very fast compared to that of step [II-2]. Bockris and co-workers considered these situations satisfied by the open-circuit corrosion potential (6).

In both cases, similar hypotheses were considered in order to transcribe the reaction models into mathematical expressions.

1. The reaction rate of the elementary step K_1 follows the Tafel law

$$K_1 = K_{0,1} \exp\left(\frac{z\alpha_1 FE}{RT}\right) \quad [1]$$

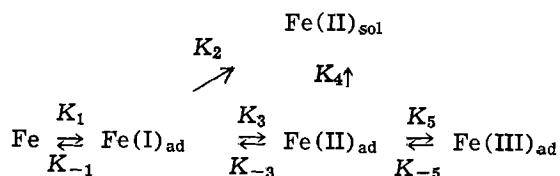
where $K_{0,1}$ is the reaction rate at $E = 0$ determined with respect to the equilibrium potential or to any reference electrode, z the number of electrons implied in the elementary step, α_1 the transfer coefficient corresponding to the fraction of energy supplied by the electrical field in forward reaction. For the inverse reaction, $\alpha_{-1} = 1 - \alpha_1$. F , R , and T have their usual meaning.

2. α is considered to be equal to 0.5.

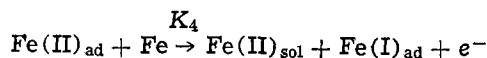
3. All reactions occur on the whole surface area.

Since then, much work has been done to verify these two reaction mechanisms (8-11). The steady-state Tafel slope is, very often, found to be equal or close to 0.04V, thus model II is, nowadays, generally considered as confirmed. However, in certain cases, the Tafel slope was very different from the two previous values and was measured between 0.029 and 0.1V (12-14). Later on, when the measurements were extended to potential values far from the corrosion potential, near which earlier work was constrained, more complicated behaviors were found. Lorenz and co-workers (15-18) investigated iron dissolution up to the onset of the passivation process in weakly acidified sulfate media (pH 4-5). They proposed the reaction model implying two dissolution paths and trivalent passivation species which can be represented schematically by

Model III



where the K_4 reaction can be written explicitly by



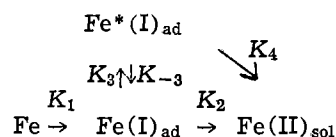
The dissolution path through the K_2 reaction is identical to that of model II. The reactions relating to K_1/K_{-1} and to K_3/K_{-3} are in pseudoequilibrium and thus they are very fast compared to K_2 and K_4 reactions over the whole potential range considered. Using hypotheses 1 and 2 given above and introducing instead of 3 the surface coverage by intermediate species which follows the Langmuir-type isotherm, they succeeded in simulating by computer the experimental steady-state polarization curves.

It is now generally accepted that elucidating an intricate reaction mechanism by means of steady-state techniques alone is an extremely difficult task. Selective criteria for mechanisms have to be elaborated on the basis of Tafel slopes by using highly questionable and strongly restrictive assumptions. In fact, the steady-state approach provides too little information in comparison with the complexity of the process under investigation.

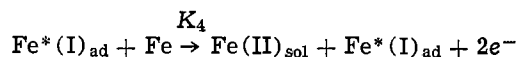
In our Laboratory, the electrode kinetics study based on electrode impedance measurements over a very wide frequency range (typically 10^{-3} - 10^5 Hz) has been developed and applied to dissolution-passivation processes as well as to electrodeposition of various metals (19-24). Epelboin and Keddou (25) showed experimentally that the electrode impedance, measured between 10^{-2} and 10^4 Hz during iron dissolution in acidic sulfate media, reveals an inductive behavior. By means of the rotating disk electrode and correction of the ohmic drop due to solution resistance, the measurements were spread over a wide range of current densities compared to earlier works. The electrode impedance was calculated on the basis of model II according to the formalism developed by Gerischer and Mehl (26) for the hydrogen evolution reaction. It was found that both steady-state polarization curves and electrode impedance measurements could only be interpreted by assuming a large degree of irreversibility of the first step and also values of α_1 and α_2 different from 0.5.

Later, the electrode impedance was measured at even higher current densities and more accurately than in earlier experiments. The electrode impedance revealed two inductive loops. These new results were interpreted by introducing into model II a parallel dissolution path (27), different from model III

Model IV



The K_4 reaction is such that



Although, according to Bechet *et al.* (27) the K_4 reaction is under the influence of sulfate anions, this reaction path can be related to model I. In fact, $\text{Fe}^*(\text{I})_{\text{ad}}$ is the dissolution intermediate species and, at the same time, plays a catalytic role in this reaction. We call this kind of reaction a "self-catalytic reaction."

Recently, with very careful experiments, it was found that the impedance diagrams reveal three inductive loops under certain experimental conditions (28). The presence of three time constants in addition to the high-frequency capacitive loop were also found by Schweikert (29).

The aim of this paper is twofold: first, to present the results of electrode impedance measurements performed within a wide range of experimental conditions: pH (0-5), current density up to $0.1 \text{ A} \cdot \text{cm}^{-2}$, and full frequency range, and second, to describe a reaction model which interprets quantitatively these experimental results. In Part II of this paper, the hypotheses used to transcribe the reaction models into mathematical expressions are examined in detail. Since experimental results showed three time constants in addition to the high-frequency capacitive loop, it is supposed that there are three adsorbed species. Forty different reaction schemes were established as the whole set of prospective models. In Part II, the reason for which only one reaction scheme was retained will be shown.

Experimental and Numerical Procedures

The experimental conditions were described elsewhere (28). The current is practically free of mass transfer effects in the range of current densities examined in this work.

Based on the reaction model and using the hypotheses described below, the mathematical expressions were established. Then by setting the numerical value of the kinetic constants, the steady-state polarization curve was numerically simulated. Some parameters were very sensitive for this calculation, but many of them were not. Once the calculated polarization curve was considered sufficiently close to the experimental curve, the electrode impedance was calculated about various steady-state polarization points. The kinetic parameters were modified manually after each calculation, up to the run which gives results in sufficiently good agreement with the experimental results. No fitting program for adjusting kinetic parameters was used. It is found that double precision (64 bits) was necessary for the calculation of the electrode impedance, although the mathematical expressions were simplified as far as possible. During the simulation calculation, it was found very difficult to establish other sets of kinetic parameters, and the rate constants change reasonably with the solution pH, but it is not possible to ascertain that the values given in the results were the only possible set.

Experimental Results and Discussion

Steady-state polarization curves.—In Fig. 1, the steady-state polarization curves obtained for different pH's are shown. The points on these curves indicate the polarization condition at which the electrode impedance measurements were performed, *i.e.*, during the measurements which last *ca.* 1.5 hr, the current remains constant except a few percent variation. In the following, only some will be shown which illustrate typi-

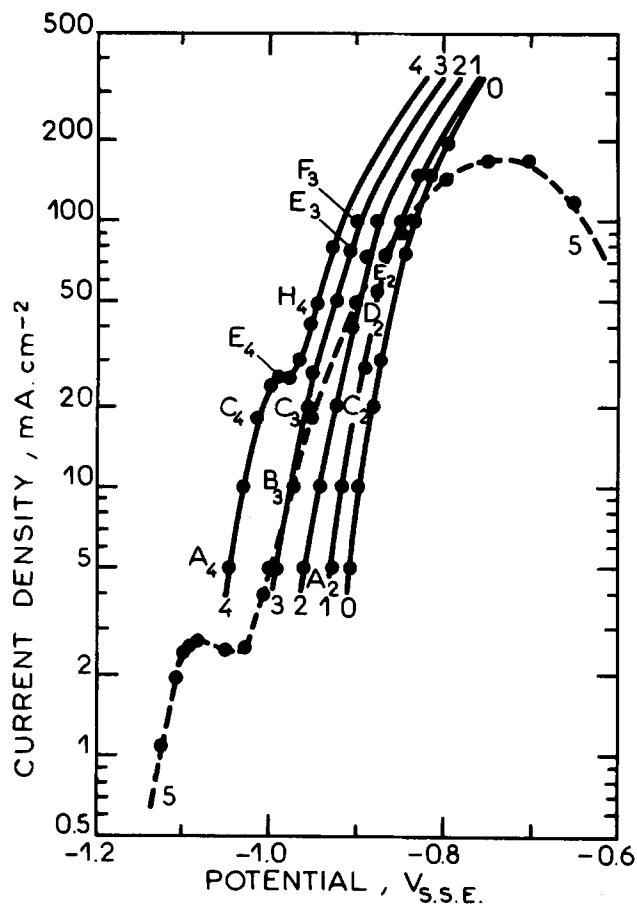


Fig. 1. Steady-state polarization curves; Fe (Johnson-Motthey) disk electrode; diameter = 3 mm; rotation speed = 1600 rev · min⁻¹; mixture in various proportion of 1M Na₂SO₄ and 1M H₂SO₄; 25° ± 0.2°C; deoxygenated by Ar. Solution pH: curve 0, pH = 0; curve 1, pH = 1.0; curve 2, pH = 2.0; curve 3, pH = 2.6; curve 4, pH = 4.0; and curve 5, pH = 5.0. The electrolyte resistance for the actual electrode (3 mm in diameter) was: pH 0, 4.3Ω; pH 1, 14Ω; pH 2, 15Ω; pH 2.6, 15Ω; pH 4, 16Ω; pH 5, 17Ω.

cal features of the impedance diagram and its change with potential and pH. On this figure, it can be seen that the dissolution current is greater for a given potential when the solution pH increases except for the pH 5 solution. In low pH solutions, the curves bend at high current densities in agreement with our previous results (25, 27). The experimental reaction order with respect to OH⁻ concentration is ca. 0.7 in the low current density range and ca. 0.3 in the high current density range when the potential E is measured against an SSE (Hg, Hg₂SO₄ sat. K₂SO₄) reference electrode. It is worth noting that the potential difference between SSE and SCE (KCl saturated calomel electrode) reference electrodes depends on the solution pH. The experiments were performed with SSE and all results are referred to this electrode.

The curve obtained in the pH 5 solution showed two current maxima. The current maximum located at a less anodic potential ($E = -1.09V$) will be called maximum I and the domain preceding this maximum will be called the active dissolution domain and that corresponding to subsequent current decrease up to the current minimum will be called the prepassivation domain. The further current increase corresponds to the prepassive dissolution and finally beyond current maximum II ($E = -0.75V$) the passivation process sets in. These labelings (30) were used for the sake of simplicity. Similar results were reported for weakly acidic media (15-18), but in contrast to (29), two maxima were obtained in the steady-state polarization curve. Two current maxima for the polarization curve of iron

dissolution were also reported in different acid media (18, 31, 32).

A current arrest observed in the pH 4 solution near -1.0V is, as will be shown more clearly by the impedance measurements, closely related to the prepassivation process observed in the pH 5 solution. It can be seen that the shoulder current corresponding to maximum I for the pH 5 solutions is about ten times greater. No current arrest or shoulder is observed in the polarization curves obtained in a more acidic solution (pH ≤ 3). In these solutions, the current maximum is limited by convective diffusion (not shown in Fig. 1) and the limiting current is proportional to the square root of the rotation speed of the disk electrode. The transition from activity to passivity occurs by a steep current change under a voltage regulation (33, 34).

Electrode impedance.—Figure 2 shows the impedance diagrams obtained for the pH 0 solution at various polarization points: hydrogen evolution domain (K), open-circuit corrosion potential (A₀), and anodic dissolution (B₀-F₀). The steady-state conditions at which the impedance measurements were performed are marked by the corresponding letter in the polarization curve given on the same figure.

The diagram K was measured at the potential 0.06V cathodic to the open-circuit corrosion potential and shows only one capacitive loop. For pure iron, almost the entire surface is covered by adsorbed hydrogen, which is probably the reason why the relaxation of this coverage cannot be seen by the impedance (23). The electrode remained practically undamaged and retained its bright appearance after a 24 hr immersion at this potential. Besides, the inductive loop relating to dissolution was not seen, i.e., the hydrogen adsorption hinders considerably the metal dissolution process. It was also noticed that the steady-state current was reached only after a 20 hr polarization at constant potential, indicating that interaction between iron and hydrogen is a very slow process. This slow current change was observed in the cathodic domain and at potentials very slightly anodic to the open-circuit corrosion potential. These observations were interpreted by the blocking nature of a strongly bonded adsorbed hydrogen (35). In the anodic range for instance $J > 2$ mA · cm⁻² in the pH 0 solution, where no blocking nature of hydrogen is observed, the current reaches a steady state within 10 min.

At the open-circuit corrosion potential, the surface coverage by hydrogen is still close to unity for pure iron. This is the reason why diagram A₀ shows only one inductive loop. The desorption of hydrogen occurs

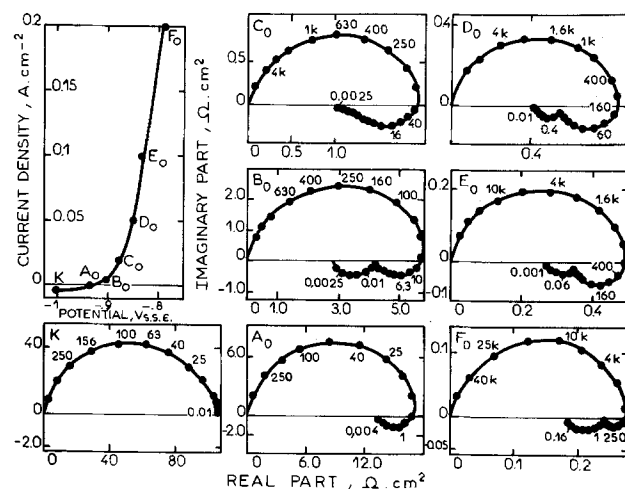


Fig. 2. Impedance diagrams in pH 0 solution. Polarization points about which the impedance was measured are marked on the polarization curve by corresponding letter. Parameter is frequency in Hz.

at potentials considerably anodic to the open-circuit corrosion potential. This slow process can be seen in the hysteresis cycle exhibited by the polarization curves when measured by the voltage sweep method (23). During the potential-increasing sweep, the hydrogen desorption cannot reach its steady state and the metal dissolution takes place on a smaller surface area than its steady-state value. Hydrogen desorption will be complete only at high anodic potentials. During the reverse sweep, the hydrogen coverage becomes significant only when the electrode potential becomes very cathodic and iron dissolution takes place over almost the entire surface area. When certain organic inhibitors, such as an acetylenic alcohol, is added to the electrolyte, the hysteresis loop is enlarged (36). On the other hand, the steady-state plot does not show the hysteresis and the current value is independent of the direction of voltage sweep. In the impedance diagram, the adsorption-desorption of hydrogen is detected by the inductive loop in the lowest frequency domain as shown in diagrams B₀ and C₀ (36, 37).

Thus the Tafel slope determined at low current densities is under the influence of both the iron dissolution process and the adsorption-desorption of hydrogen. In this range, the potential-decreasing sweep gives roughly the Tafel slope related only to the dissolution process on a hydrogen-free surface and values close to 0.06V. The Tafel slope can also be roughly evaluated by the R_p' value corresponding to the extrapolation toward the low frequency limit of the higher-frequency inductive loop, i.e., at a frequency high enough to have a constant hydrogen coverage. If, locally, the polarization curve follows the Tafel law whose slope is B , the product of R_p' times the current J gives

$$B = \ln 10 \times R_p' \cdot J \quad [2]$$

Diagrams B₀ and C₀ give the B value close to 0.06V. This dynamic value can be related to the transient Tafel slope determined by Heusler (4).

It can be concluded that low values of the Tafel slope (0.03-0.04V) observed in the low current density range arise clearly from a potential-dependent hydrogen coverage and must not be used for mechanistic purposes and particularly as a proof for a first step at equilibrium. This result illustrates the advantage of a-c techniques compared to steady-state experiments for discriminating between various contributions in the electrode process.

At high current densities (diagrams D₀, E₀, and F₀), two inductive loops can also be observed in impedance diagrams in agreement with our previous measurements (27). The origin of the lower-frequency loop is different from that observed at low current densities, which is no longer detected at current densities greater than 0.02 A · cm⁻². At higher current densities, no hydrogen adsorption takes place. It can also be remarked that the characteristic frequency, corresponding to the top of the low-frequency inductive loop, is ten to one hundred times greater than that observed by the relaxation of hydrogen coverage. The lower-frequency inductive loop is actually related to the iron dissolution process.

Impedance diagrams plotted in the pH 1 solution were very similar to those measured in the pH 0 solution. It can nevertheless be remarked that the characteristic frequencies of two inductive loops decrease for a given current density as the pH increases. In Fig. 3, the impedance diagrams relating to the pH 2 solution are shown. Diagrams A₂ and C₂ are very close to those observed in strongly acidic media though similar diagrams were observed at current densities about ten times greater compared to those in the pH 0 solution. On the other hand, at higher current densities (diagrams D₂ and E₂) three inductive loops can clearly be seen. None of them originates in the adsorption-desorption of hydrogen; thus they are all to be attributed to

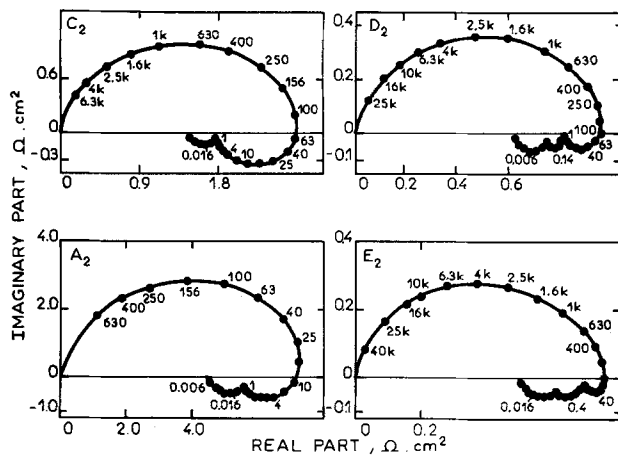


Fig. 3. Impedance diagrams in pH 2 solution. Polarization points marked on curve 2 in Fig. 1.

the iron dissolution process. The presence of three time constants is reported by (29) even in a strongly acid medium.

Again, in the pH 2.6 solution (Fig. 4), and with the experimental conditions examined here, only two time constants, in addition to the high-frequency capacitive loop, can be seen. If the characteristic frequencies are compared to those of the pH 2 solution, the relaxation process corresponding to the lowest and highest frequencies in the pH 2 solution are visible in the pH 2.6 solution. The comparison of diagrams C₃ and E₃ reveals that the lower-frequency inductive loop (diagram C₃) transforms into a capacitive loop when the anodic potential increases. The diameter of this capacitive loop becomes considerably greater when the potential becomes further anodic (diagram F₃).

In Fig. 5, the impedance diagrams relative to the pH 4 solution are shown. Diagrams A₄ and C₄ are very similar to diagrams C₃ and E₃, respectively. The transformation of the lower-frequency inductive loop into the capacitive one takes place at lower current density when the solution pH increases. In the pH 4 solution, the shoulder on the polarization curve was observed. Diagram E₄ is obtained at a potential very close to this shoulder potential. The low-frequency capacitive branch shows a very high value of the zero-frequency limit of the electrode impedance corresponding to the slope of the polarization curve almost parallel to the voltage axis. In the potential range more anodic to that related to the high-frequency capacitive loop, are revealed by two capacitive and one inductive loops, as seen in diagram H₄.

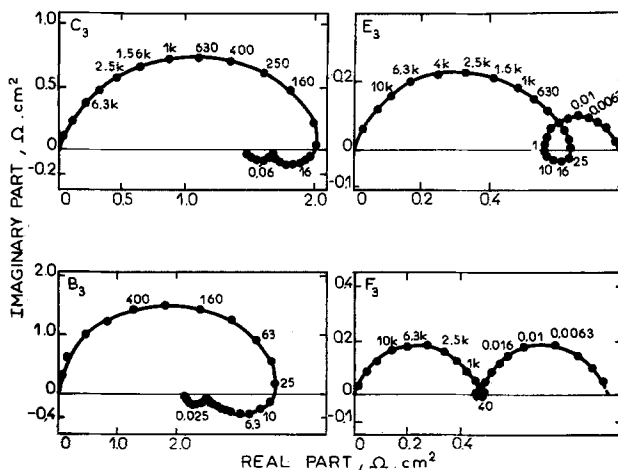


Fig. 4. Impedance diagrams in pH 2.6 solution. Polarization points marked on curve 3 in Fig. 1.

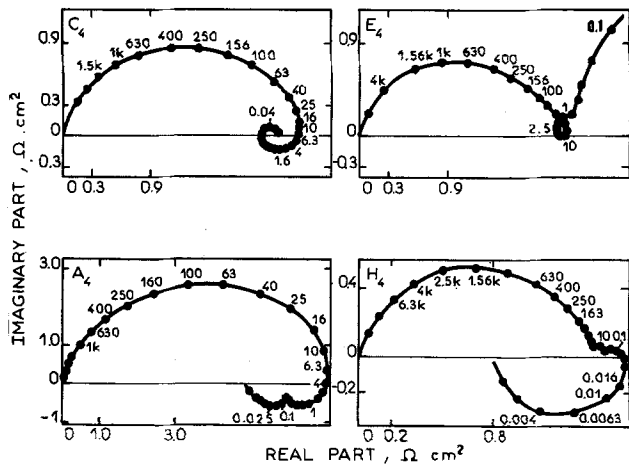


Fig. 5. Impedance diagrams in pH 4 solution. Polarization points marked on curve 4 in Fig. 1.

The impedance diagrams obtained in the pH 5 solution are shown in Fig. 6. Diagram D₅ is obtained in the active dissolution domain. This diagram is very similar to those observed in a more acidic solution. The low-frequency capacitive loop observed in diagram D₅ is directly related to the prepassivation process as indicated in diagram E₅. From these results, it can be corroborated that the current shoulder observed in the pH 4 solution is actually related to the prepassivation process because the low-frequency capacitive branch of diagram E₄ is compared to the capacitive branch leading to the negative polarization resistance (limit of the zero frequency of the electrode impedance which is equal to the slope of the steady-state polarization curve). Diagram F₅, obtained in the polarization corresponding to the prepassive dissolution domain, is very similar to diagram H₄ (Fig. 5) obtained at the potential more anodic to the current shoulder. A relatively large capacitive loop observed in diagram F₃ (Fig. 4) in the pH 2.6 solution may indicate that the transition to prepassive dissolution is taking place at rather high current density ($J > 0.1 \text{ A} \cdot \text{cm}^{-2}$) even in this solution, without showing any current maximum or current shoulder. Diagrams H₄ and F₅ show also that the capacitive loop leading to the prepassivation process transforms again into the inductive loop when the polarization points are reached in the prepassive dissolution domain. Since the passivation process can only appear as a capacitive loop (38), this transformation seems to indicate that the species leading to the prepassivation process progressively vanishes in the prepassive dissolution range. This observation was found

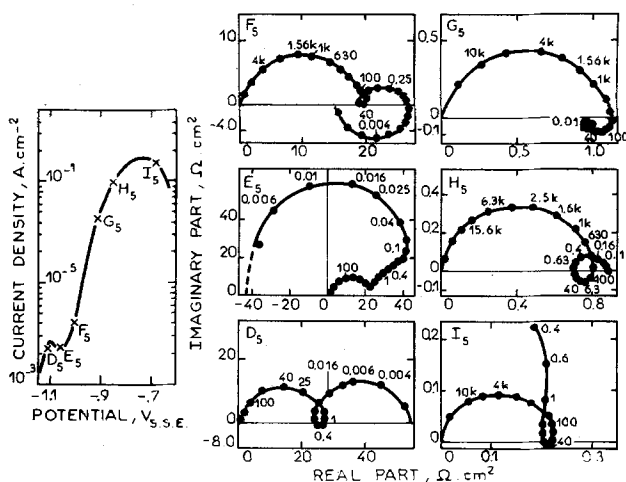


Fig. 6. Impedance diagrams in pH 5 solution. Polarization points marked on curve a.

later to be very crucial for the choice of the reaction model (see Part II).

When the potential becomes very anodic, $E \approx -0.95\text{V}$, all relaxation phenomena disappear in the impedance diagram and only one capacitive loop at the high-frequency range was observed. At a more anodic potential, approaching maximum II, two time constants, in addition to the high-frequency capacitive loop, are again observed. One of them reveals itself as a capacitive loop and is related to the passivation process as can be seen on diagrams H₅ and I₅.

The high-frequency capacitive loop is attributed to the double layer capacity in parallel with the charge-transfer resistance R_t . The product of R_t times the d-c current J indicates the change of the reaction path as will be shown later. In fact, the $R_t \cdot J$ value, which is close to 0.04V in the active dissolution domain, increases with the electrode potential and reaches about 0.08V in the prepassive dissolution domain. The increase of the $R_t \cdot J$ value is observed even in the pH 0 solution, which actually indicates that the change of dissolution paths is also taking place in a strongly acidic solution even though the steady-state polarization curve hardly reveals any such phenomenon.

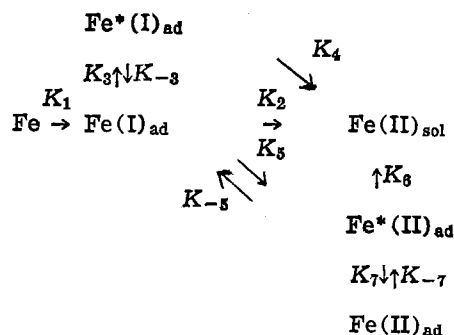
It seems useful to summarize the main experimental results:

1. Impedance diagrams of iron dissolution reveal, under certain experimental conditions, three time constants in addition to that related to the double layer capacity-charge transfer resistance before the onset of the passivation process.
2. In pH 2 solution, these three time constants are revealed by three inductive loops.
3. They are all clearly observed at the beginning of the prepassive dissolution domain. Under other conditions, with the iron specimen used here, only two time constants were observed clearly.
4. The prepassivation process, clearly observed in the pH 5 solution, can be seen as a current shoulder in the pH 4 solution. Only the impedance measurements performed at relatively high current densities (diagram F₃ in Fig. 4) indicate the existence of this process in the pH 2.6 solution.
5. The species leading to the prepassivation process seems to decrease its surface coverage again when the polarization potential attains the prepassive dissolution domain.
6. The current density at which the change of dissolution paths occurs depends on the solution pH. The more acidic the solution, the greater the current density at which this change takes place.
7. The measurements of the $R_t \cdot J$ value show the change of the reaction paths even in a very acidic solution. The steady-state polarization curve hardly reveals such a change.

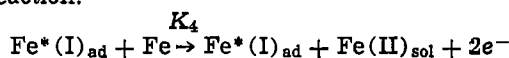
Results of Calculation

Reaction model.—As will be shown in Part II, among all of the schematic configurations of reaction paths implying three intermediate species, only one model is able to interpret the set of experimental results

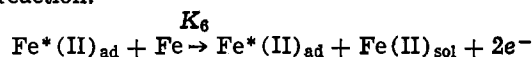
Model V



K_4 reaction:



K_6 reaction:



As can be seen, this reaction model stems from model III by introducing a third dissolution path. The reactions relating to K_4 and to K_6 are both self-catalytic and no consumption of $\text{Fe}^*(\text{I})_{\text{ad}}$ and $\text{Fe}^*(\text{II})_{\text{ad}}$ takes place. The reason for such a process is explained in detail in Part II, but essentially this assumption allows one to make the time constant of the corresponding relaxation process independent of the d-c current flux. The passivation process, K_7/K_{-7} path, forms a bivalent passivation species. In fact, the formation of the $\text{Fe}(\text{III})$ passive species becomes significant only at potentials very close to the Flade potential, and the main part of the current decrease in the passivation process is due to the $\text{Fe}(\text{II})$ coverage (39). In this paper, nevertheless, the main interest is focused on the iron dissolution process. In the model examined in Part II, the passivation process accounted for by the K_7/K_{-7} path will be omitted since we are interested only in the mechanism of iron dissolution. However in the pH 5 solution, this passivation can no longer be ignored. It can also be seen that the reaction scheme includes three dissolution paths, K_2 , K_4 , and K_6 . The K_1 reaction is considered to be irreversible according to our previous investigations (25, 27, 37). The reactions relating K_3/K_{-3} , K_5/K_{-5} , and K_7/K_{-7} are reversible but not necessarily in pseudo-equilibrium, i.e., the reaction rate of these reactions is not necessarily very high compared to others (see Part II). Neither the role of OH^- ion is *a priori* considered nor the chemical nature of the intermediate species. Conclusions will be drawn only from the pH dependence of the kinetic parameters as they result from the numerical simulation.

Equation setup.—The reaction scheme given above will be transcribed into the series of mathematical expressions using a certain number of hypotheses. They are identical to those used in previous works and are summarized in the following:

1. The elementary steps obey the Tafel law.
2. The Tafel coefficient α is any value between 0 and 1 and is independent of potential.
3. The intermediate species occupies the fraction θ of the electrode surface and the adsorption-desorption follows the Langmuir-type isotherm law. θ_1 indicates the fraction of the surface covered by $\text{Fe}(\text{I})_{\text{ad}}$, θ_2 by $\text{Fe}^*(\text{I})_{\text{ad}}$, θ_3 by $\text{Fe}^*(\text{II})_{\text{ad}}$, and θ_4 by the passivating species $\text{Fe}(\text{II})_{\text{ad}}$. No overlapping of these coverages is considered thus $\theta_1 + \theta_2 + \theta_3 + \theta_4 < 1$. The so-called chemical reaction step, implying no electron transfer, may be potential dependent (see Part II).

Based on these hypotheses, the charge balance gives the current flowing through the electrode interface

$$\frac{J}{F} = K_1 \Sigma + (K_2 + K_5) \theta_1 + 2K_4 \theta_2 + (2K_6 - K_{-5}) \theta_3 \quad [3]$$

where $\Sigma = 1 - \theta_1 - \theta_2 - \theta_3 - \theta_4$, K is the potential-dependent parameter, and θ is the potential- and time-dependent parameter. Since J is expressed in $\text{A} \cdot \text{cm}^{-2}$, K implies implicitly the concentration expressed in $\text{mole} \cdot \text{cm}^{-2}$. The mass balance of the adsorbed species allows one to express the time dependence of θ through differential equations

$$\beta_1 \frac{d\theta_1}{dt} = K_1 \Sigma - (K_2 + K_3 + K_5) \theta_1 + K_{-3} \theta_2 + K_{-5} \theta_3 \quad [4]$$

$$\beta_2 \frac{d\theta_2}{dt} = K_3 \theta_1 - K_{-3} \theta_2 \quad [5]$$

$$\beta_3 \frac{d\theta_3}{dt} = K_5 \theta_1 - (K_{-5} + K_7) \theta_3 + K_{-7} \theta_4 \quad [6]$$

$$\beta_4 \frac{d\theta_4}{dt} = K_7 \theta_3 - K_{-7} \theta_4 \quad [7]$$

β is the constant linking the fraction of the surface θ and the surface concentration of adsorbed species expressed in $\text{mole} \cdot \text{cm}^{-2}$. β_i values are considered to be equal to 10^{-8} ($\text{mole} \cdot \text{cm}^{-2}$) which corresponds to about one monolayer for the case of one intermediate bonding to one surface metal atom. K_4 and K_6 do not intervene in the mass balance because the related reactions neither produce nor consume the intermediate species.

Steady state.—The steady state is characterized by the constancy of the surface coverage with time, i.e., $d\theta/dt \equiv 0$. Putting this condition into Eq. [4]–[7], the steady-state value of θ can be calculated

$$\bar{\theta}_1 = \frac{K_1 K_{-3} K_{-5} K_{-7}}{D}; \quad \bar{\theta}_2 = \frac{K_1 K_3 K_{-5} K_{-7}}{D};$$

$$\bar{\theta}_3 = \frac{K_1 K_{-3} K_5 K_{-7}}{D}$$

and

$$\bar{\theta}_4 = \frac{K_1 K_{-3} K_5 K_7}{D}$$

where

$$D = K_1 K_{-3} K_5 K_7 + [K_1 \{K_3 K_{-5} + K_{-3} (K_5 + K_{-5})\} + K_2 K_{-3} K_{-5}] K_{-7} \quad [8]$$

By using the steady-state expressions of Eq. [4]–[7], the steady-state current can be expressed by

$$\frac{\bar{J}}{F} = 2(K_2 \bar{\theta}_1 + K_4 \bar{\theta}_2 + K_6 \bar{\theta}_3) \quad [9]$$

The steady-state polarization curve thus can be computer simulated according to Eq. [8] and [9] with suitable values of $K_{0,i}$ and $b_i (= \alpha_i F/RT)$.

Faradaic impedance.—The electrode impedance is defined by perturbing the electrode interface with a small signal. About the d-c potential \bar{E} , a sine wave potential change δE of small amplitude $|\delta E|$ will be superimposed. If its frequency is f (Hz), its angular frequency ω is equal to $2\pi f$, then

$$\delta E = |\delta E| \exp(j\omega t), \quad j = \sqrt{-1}$$

This potential change prompts the variation of J , (δJ), of the same frequency about its steady-state value \bar{J} . The faradaic impedance Z_F can be calculated by the Taylor expansion of Eq. [3] limited to the first order

$$\frac{1}{Z_F} = \frac{1}{R_t} - F \left\{ (K_1 - K_2 - K_5) \frac{d\theta_1}{dE} + (K_1 - 2K_4) \frac{d\theta_2}{dE} + (K_1 + K_{-5} - 2K_6) \frac{d\theta_3}{dE} + K_1 \frac{d\theta_4}{dE} \right\}$$

where

$$\frac{1}{R_t} = F[(b_1 + b_2) K_2 \bar{\theta}_1 + 2b_4 K_4 \bar{\theta}_2 + \{(b_5 + b_{-5}) K_{-5} + 2b_6 K_6\} \bar{\theta}_3] \quad [10]$$

R_t is the charge-transfer resistance corresponding to the high-frequency limit of the faradaic impedance at which θ can no longer follow the potential change, i.e., $d\theta/dE = 0$. If K_{-5} is small, the charge transfer resistance is closely correlated to the steady-state current given in Eq. [9]. In other words, if one of the reaction paths is very fast compared to others, for instance $K_2 \theta_1$,

the product of R_t by the current \bar{J} is constant, for instance equal to $2/(b_1 + b_2)$ (25). When there is a change in the reaction path, for instance to the K_4 path, the $R_t \cdot \bar{J}$ value approaches $1/b_4$ continuously. The change of the $R_t \cdot \bar{J}$ value corresponds thus to the change of reaction path.

Z_F can be calculated if $d\theta/dE$ is determined, which contains implicitly the relaxation of θ due to the potential perturbation. This term can be derived from Eq. [4]-[7]. With a sine wave potential change, θ changes also in a sine wave of the same frequency. Thus $d\theta/dt = j\omega\delta\theta$ and then

$$X_1 = Z_1 \frac{d\theta_1}{dE} + (K_1 - K_{-3}) \frac{d\theta_2}{dE} + (K_1 - K_{-5}) \frac{d\theta_3}{dE} + K_1 \frac{d\theta_4}{dE}$$

where

$$X_1 = (b_1 - b_2)K_2\bar{\theta}_1 - (b_3 + b_{-3})K_{-3}\bar{\theta}_2 - (b_5 + b_{-5})K_{-5}\bar{\theta}_3$$

$$Z_1 = K_1 + K_2 + K_3 + K_5 + j\omega\beta_1 \quad [11]$$

$$X_2 = -K_3 \frac{d\theta_1}{dE} + Z_2 \frac{d\theta_2}{dE}$$

where

$$X_2 = (b_3 + b_{-3})K_{-3}\bar{\theta}_2$$

and

$$Z_2 = K_{-3} + j\omega\beta_2 \quad [12]$$

$$X_3 = -K_5 \frac{d\theta_1}{dE} + Z_3 \frac{d\theta_3}{dE} - K_{-7} \frac{d\theta_4}{dE}$$

where

$$X_3 = \{(b_5 + b_{-5})K_{-5} + (b_5 - b_7)K_7\}\bar{\theta}_3 - (b_5 + b_{-7})K_{-7}\bar{\theta}_4$$

and

$$Z_3 = K_{-5} + K_7 + j\omega\beta_3 \quad [13]$$

$$X_4 = -K_7 \frac{d\theta_3}{dE} + Z_4 \frac{d\theta_4}{dE}$$

where

$$X_4 = (b_7 + b_{-7})K_{-7}\bar{\theta}_4$$

and

$$Z_4 = K_{-7} + j\omega\beta_4 \quad [14]$$

Once $K_{0,i}$ and b_i are determined, Eq. [11]-[14] allow calculation of $d\theta_i/dE$, and substituting these values into Eq. [10], the faradaic impedance is obtained. Setting the double layer capacitance C_{dl} in parallel with Z_F , the electrode impedance is numerically simulated. The value of C_{dl} is considered to be equal to $100 \mu\text{F}\cdot\text{cm}^{-2}$ independent of the electrode potential, though a slight dependency was observed experimentally.

Calculation results.—Since in the pH 5 solution, the prepassivation process was clearly observed and also since the impedance diagrams were plotted throughout the polarization curve, the experimental results from

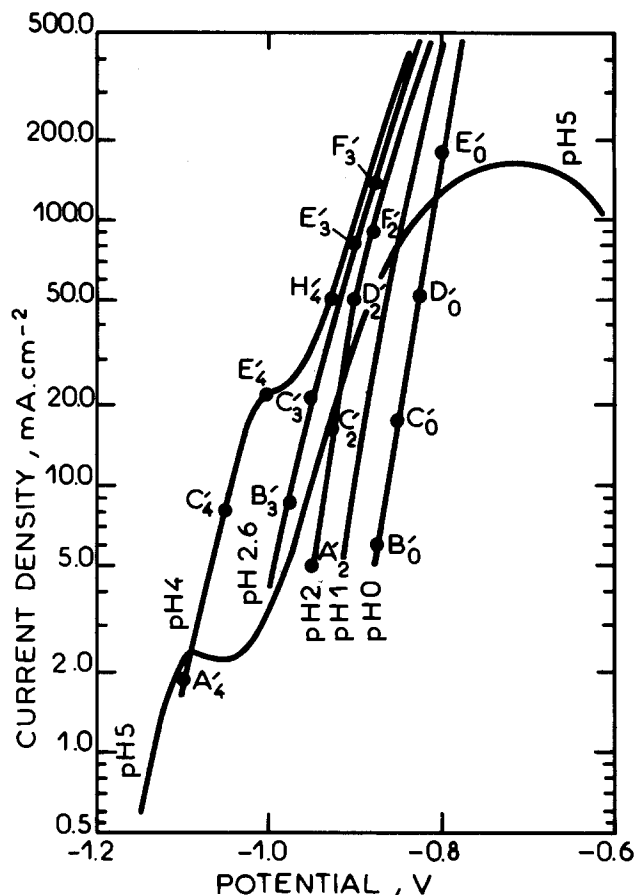


Fig. 7. Simulated polarization curves; rate constants are shown in Tables I and II. Corresponding solution pH is marked near the curve.

this solution are first numerically simulated. The kinetic constants that gave satisfactory results are shown in Table I.

The results relative to other pH solutions are also computer simulated. To perform this, one attempts to reproduce the experimental results by keeping the b_1 value independent of pH and by modifying the least number of $K_{0,i}$ values. We tried to change the rate constant $K_{0,i}$ monotonically with respect to the solution pH. The reaction order for each process is not introduced *a priori*. The $K_{0,i}$ values used for the simulation calculation are summarized in Table II.

The results of the simulation calculation of the steady-state polarization curves are shown in Fig. 7. The simulated impedance diagrams for the solutions of different pH are shown in Fig. 8-12. These figures will be compared to the experimental results shown in Fig. 1-6. The steady-state polarization curves obtained by the simulation calculation are similar to the experimental curves, except the bending observed experimentally at high current densities is ignored in simulation curves. This is the price to be paid for better agreement of the impedance diagrams. The model reflects

Table I. Kinetic constants used for the simulation calculations in model V in the pH 5 solution

| K_1 | | K_2 | | K_3 | | K_{-3} | | K_4 | |
|----------------------|-------|----------------------|----------|----------------------|-------|-----------------------|----------|-----------------------|----------|
| $K_{0,1}$ | b_1 | $K_{0,2}$ | b_2 | $K_{0,3}$ | b_3 | $K_{0,-3}$ | b_{-3} | $K_{0,4}$ | b_4 |
| 4.0×10^{10} | 38.4 | 8.0×10^{-4} | 7 | 1.5×10^{-9} | 0 | 2.6×10^{-10} | 20 | 1.2×10^{-7} | 33 |
| K_5 | | K_{-5} | | K_6 | | K_7 | | K_{-7} | |
| $K_{0,5}$ | b_4 | $K_{0,-5}$ | b_{-5} | $K_{0,6}$ | b_6 | $K_{0,7}$ | b_7 | $K_{0,-7}$ | b_{-7} |
| 4.0×10^9 | 35.4 | 5.2×10^{-9} | 3 | 5.0×10^2 | 23 | 4.0×10^{-9} | 0 | 4.0×10^{-10} | 27 |

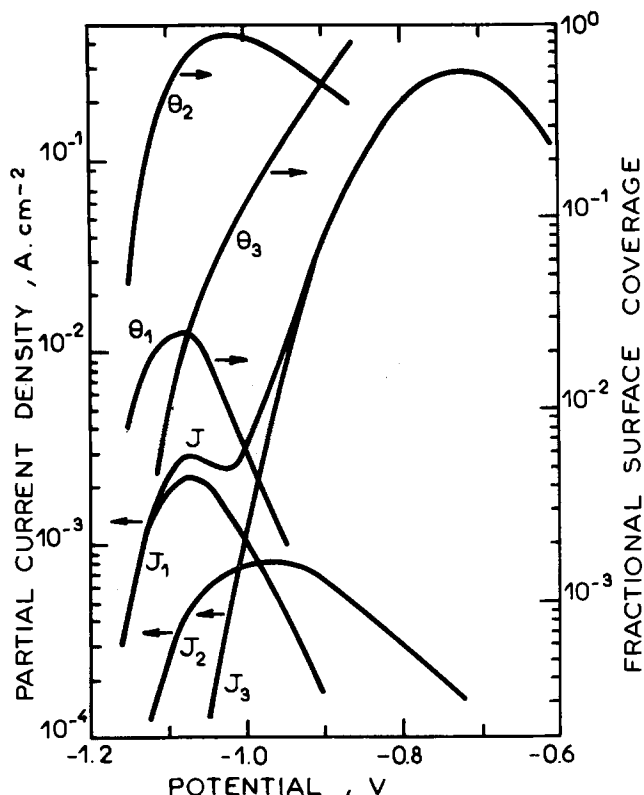


Fig. 13. Contribution of partial currents for the overall current J . Simulation calculation for the pH 5 solution. J_1 the current through K_2 reaction, J_2 and J_3 are, respectively, the current through K_4 and K_6 reaction. Change of surface coverage with respect to potential. θ_1 is the fractional surface coverage by Fe(I)_{ad} , θ_2 by $\text{Fe}^*(\text{I})_{\text{ad}}$, and θ_3 by $\text{Fe}^*(\text{II})_{\text{ad}}$.

lution. It can be seen that at very low anodic potential in the active dissolution domain, the metal dissolves through the K_2 reaction path (J_1). On the other hand, prepassive dissolution is almost entirely limited by the K_6 dissolution path (J_3). In this way, the model proposed by Lorenz *et al.* (15-18) is verified in the corresponding pH medium. However, the decrease of θ_1 , consequently the prepassivation process, is due to the increase of θ_2 , the surface coverage by $\text{Fe}^*(\text{I})_{\text{ad}}$. The current minimum is coincident to the maximum of θ_2 which will be gradually replaced by $\text{Fe}^*(\text{II})_{\text{ad}}$ coverage. The dissolution through K_4 reaction (J_2) contributes to the current minimum not too much pronounced in agreement with the experiments.

Figure 14 shows the contribution of different dissolution paths on the overall current for the pH 2 solution. It can be seen that the K_2 dissolution path controls in the low current density domain, whereas the K_6 dissolution path determines the overall current at high current densities. The K_4 dissolution path is the fastest process within the narrow domain in which three inductive loops were clearly observed. The comparison of Fig. 13 and 14 shows that the contribution of J_1 , J_2 , and J_3 with respect to the potential is relatively similar and the approach of J_1 and J_3 curves is the main cause for not observing maximum I.

In models III and IV, the influence of sulfate ion concentration is suggested, respectively, in the K_5/K_{-5} and in the K_4 reaction. In this paper, the overall sulfate concentration was kept constant and the effect of HSO_4^- and SO_4^{2-} was not examined.

Conclusion

The experimental results covering a very wide range of current density, solution pH value, and frequency allowed the establishment of the reaction model of iron dissolution in acidic sulfate media. The simulation calculations are performed by computer for the reaction

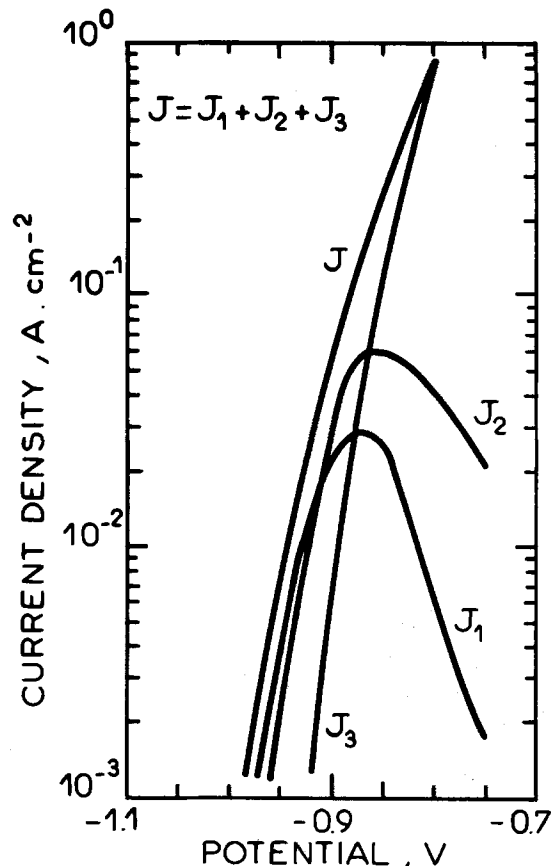


Fig. 14. Contribution of partial current for the overall current. Simulation calculation for pH 2 solution. J_1 , J_2 , and J_3 see Fig. 13.

model implying three dissolution paths using several hypotheses previously used in this Laboratory. Three intermediate species, corresponding to three dissolution paths, are revealed under capacitive or inductive loops. The calculated impedances correspond well to those obtained by experiment. The pH dependence of the different reactions are examined on the basis of the experimental results. The model proposed here is limited to the current density range where mass transfer does not affect the reaction rate.

Acknowledgment

This paper in two parts is dedicated to the memory of the late Dr. I. Epelboin who died during the last stages of this work. This paper constitutes a part of O.R.M.'s Thesis to be submitted to the Université Pierre et Marie Curie.

Manuscript submitted July 16, 1980; revised manuscript received Sept. 19, 1980. This was Paper 262 presented at the Los Angeles, California, Meeting of the Society, Oct. 14-19, 1979.

Any discussion of this paper will appear in a Discussion Section to be published in the December 1981 JOURNAL. All discussions for the December 1981 Discussion Section should be submitted by Aug. 1, 1981.

Publication costs of this article were assisted by the Centre National de la Recherche Scientifique (CNRS).

REFERENCES

1. K. F. Bonhoeffer and W. Jena, *Z. Elektrochem.*, **55**, 151 (1951).
2. K. F. Bonhoeffer and K. E. Heusler, *Z. Phys. Chem. N.F.*, **8**, 390 (1958).
3. K. F. Bonhoeffer and K. E. Heusler, *Z. Elektrochem.*, **61**, 122 (1957).
4. K. E. Heusler, *ibid.*, **62**, 582 (1958).
5. J. O'M. Bockris, D. Drazic, and A. R. Despic, *Electrochim. Acta*, **4**, 326 (1961).
6. J. O'M. Bockris and H. Kita, *This Journal*, **108**, 676 (1961).
7. J. O'M. Bockris and D. Drazic, *ibid.*, **7**, 293 (1962).

8. F. Hilbert, Y. Miyoshi, G. Eichkorn, and W. J. Lorenz, *ibid.*, **118**, 1919 (1971).
9. F. Hilbert, Y. Miyoshi, G. Eichkorn, and W. J. Lorenz, *ibid.*, **118**, 1927 (1971).
10. E. J. Kelly, *ibid.*, **112**, 124 (1965).
11. J. Podesta and A. J. Arvia, *Electrochim. Acta*, **10**, 159 (1965).
12. G. Okamoto, M. Nagayama, and N. Sato, "Proceedings of 8th Meeting of CITCE, Madrid," p. 72, Butterworth, London (1958).
13. A. C. Makrides, *This Journal*, **107**, 869 (1960).
14. S. Barnartt, *ibid.*, **119**, 812 (1972).
15. D. Geana, A. A. El Miligy, and W. J. Lorenz, *Corros. Sci.*, **13**, 505 (1973).
16. D. Geana, A. A. El Miligy, and W. J. Lorenz, *ibid.*, **14**, 657 (1974).
17. A. A. El Miligy, D. Geana, and W. J. Lorenz, *Electrochim. Acta*, **20**, 273 (1975).
18. J. Bessone, L. Karakaya, P. Lorbeer, and W. J. Lorenz, *ibid.*, **22**, 1147 (1977).
19. I. Epelboin, M. Ksouri, and R. Wiart, *J. Electroanal. Chem. Interfacial Electrochem.*, **65**, 373 (1975).
20. C. Cachet, I. Epelboin, M. Keddarn, and R. Wiart, *ibid.*, **100**, 745 (1979).
21. C. Deslouis, I. Epelboin, C. Gabrielli, and B. Tribollet, *ibid.*, **82**, 251 (1977).
22. M. Keddarn, Z. Stoyanov, and H. Takenouti, *J. Appl. Electrochem.*, **7**, 539 (1977).
23. I. Epelboin, Ph. Morel, and H. Takenouti, *This Journal*, **118**, 1282 (1971).
24. I. Epelboin, M. Keddarn, and H. Takenouti, *J. Appl. Electrochem.*, **2**, 71 (1972).
25. I. Epelboin and M. Keddarn, *This Journal*, **117**, 1052 (1970).
26. H. Gerischer and W. Mehl, *Z. Elektrochem.*, **59**, 1049 (1955).
27. B. Bechet, I. Epelboin, and M. Keddarn, *J. Electroanal. Chem. Interfacial Electrochem.*, **76**, 129 (1977).
28. I. Epelboin, M. Keddarn, O. R. Mattos, and H. Takenouti, *Corros. Sci.*, **19**, 1105 (1979).
29. H. Schweikert, Doctoral Thesis, University of Karlsruhe (1978); H. Schweikert, W. J. Lorenz, and H. Friedburg, *This Journal*, **127**, 1693 (1980).
30. M. Keddarn, O. R. Mattos, and H. Takenouti, 29th Meeting of International Society of Electrochemistry, Budapest 1978, *Extended Abstracts*, **2**, 945.
31. H. Nord and G. Bech-Nielsen, *Electrochim. Acta*, **16**, 849 (1971).
32. W. Allgaier and K. E. Heusler, *Z. Phys. Chem. N.F.*, **98**, 161 (1975).
33. I. Epelboin, C. Gabrielli, M. Keddarn, J. C. Lestrade, and H. Takenouti, *This Journal*, **119**, 1632 (1972).
34. I. Epelboin, C. Gabrielli, M. Keddarn, and H. Takenouti, in "Comprehensive Treatise on Electrochemistry," J. O'M. Bockris, B. E. Conway, and E. B. Yeager, Editors, Vol. 10, Submitted.
35. A. Caprani, I. Epelboin, Ph. Morel, and H. Takenouti, 4th European Symposium on Corrosion Inhibitors, Ferrara 1975, *Proceedings*, **III**, 517 (1975).
36. I. Epelboin, M. Keddarn, and H. Takenouti, 3rd European Symposium on Corrosion Inhibitors, Ferrara, 1971; *Annali. Univ. Ferrara N.S., Sez. V*, p. 237 (1971).
37. M. Keddarn and H. Takenouti, *C.R. Acad. Sci. Paris, Ser. C*, **270**, 283 (1970).
38. I. Epelboin, M. Keddarn, O. R. Mattos, and H. Takenouti, 7th International Congress on Metallic Corrosion, Rio de Janeiro, 1978, *Proceedings*, p. 1977, Abraco, Rio de Janeiro (1979).
39. M. Baddi, C. Gabrielli, M. Keddarn, and H. Takenouti, in "Passivity of Metals," R. P. Frankenthal and J. Kruger, Editors, p. 625, The Electrochemical Society Softbound Proceedings Series, Princeton, N.J. (1978).

Reaction Model for Iron Dissolution Studied by Electrode Impedance

II. Determination of the Reaction Model

Michel Keddarn, Oscar Rosa Mattos, and Hisasi Takenouti

*Groupe de Recherche No. 4 du CNRS "Physique des Liquides et Electrochimie,"
associé à l'Université Pierre et Marie Curie, 75230 Paris Cedex 05, France*

ABSTRACT

The electrode impedance determined experimentally shows a certain number of time constants as capacitive or inductive features. These impedances arise from various processes occurring at or near the electrode interface, such as charge transfer, adsorption-desorption of reaction intermediate species, changes of the roughness factor, changes of the number of active sites or of volume concentration in the vicinity of the electrode, etc. The origins of impedances are examined on the basis of experimental results given in Part I. Then, hypotheses describing reaction rates, such as the Tafel law, reaction reversibility, and the adsorption isotherm law, are analyzed in order to translate reasonably the reaction models into mathematical expressions. With hypotheses retained, it is concluded that the experimental results should be interpreted by a model including three adsorbed reaction intermediate species. Forty possible reaction schemes, as the complete set of prospective models, were written and examined according to both steady-state polarization curves and electrode impedances. The appearance of two current maxima implies at least two dissolution paths in the reaction models and allowed us to eliminate 10 of the 40 reaction schemes. On the other hand, the appearance of inductive impedance was found to constitute a very selective criterion. Only one model, given in Part I, was found to simulate suitably the whole set of experimental results.

In Part I (1), the experimental results of the steady-state polarization curves and the electrode impedance

Key words: capacitance, electrode kinetics, inductance, surface relaxation, transfer coefficient.

measurements performed over wide ranges of pH and current density were shown. These results were interpreted quantitatively on the basis of the reaction model. In this paper, the reasons for which this model

is selected from 40, corresponding to the complete set of possible prospective reaction schemes, is described. But first, critical examinations are made of various hypotheses by which reaction models are translated into mathematical expressions. When the electrode kinetics are analyzed by a crude method, even with unduly restrictive hypotheses, the results are interpreted on the basis of a model. For instance, a steady-state polarization curve indicates only the overall reaction rate which depends on the slowest reaction path for a series process or on the fastest reaction path for a parallel process. Thus the hypotheses regarding other processes may have little influence on a calculated polarization curve. On the other hand, with hypotheses that allow too much flexibility in mathematical expressions, numerous models may explain the same results.

The electrode impedance contains varied information, in particular, on intermediate reaction steps. Even if they cannot sensitively affect the overall reaction rate, their contribution cannot, very often, be neglected in the electrode impedance. Since many impedance diagrams are plotted along with steady-state polarization curves, the number of results that should be taken into consideration for comparison of the models and experiments increases considerably. Furthermore, as was shown elsewhere (2), the electrode impedance behaves as an inductance or as a capacitance according to rather well-determined analytical conditions. With hypotheses that restrict the possibility of quantitative exploitation of any tested model, satisfactory agreements between experimental results and those drawn from a model become difficult or impossible to realize. It can also be noticed that the experimental conditions at which the iron dissolution was performed in this study are unusually wide: the H^+ concentration was spread over five orders of magnitude and the current densities changed by more than two orders. More realistic hypotheses have to be taken into consideration.

Examinations of Hypotheses

Origins of the electrode impedance.—The different origins of the electrode impedance were examined with mathematical models by Grahame (3). But in all of these models, the electrode impedance appears only as a capacitive feature. It can also be noticed that the transcription of a reaction model into a set of mathematical expressions is not very easy with the formalism used in this paper. In 1955, Gerischer and Mehl (4) established that the relaxation of surface coverage by an adsorbed intermediate species is able to cause a capacitive as well as an inductive faradaic impedance. This formalism was used by Epelboin and Keddam (5) to interpret quantitatively the results of impedance measurements during iron dissolution in acidic sulfate media.

Since then, the electrode impedance of various electrochemical interfaces of greater complexity during anodic as well as cathodic processes were largely interpreted on the basis of this concept. However, this is not the only possible origin of the electrode impedance: it is well known that mass transport, if it intervenes in the overall reaction rate, contributes to the electrode impedance (6). In passivity, the growth of the oxide film gives rise to a capacitive or inductive impedance (7). But the experiments on iron dissolution examined in this paper were performed under such conditions that these processes did not need to be taken into account.

If the electrode surface area is dependent on potential and on time through the roughness factor or the number of active sites N^* , these phenomena interfere in the electrode kinetics and will appear in the electrode impedance. Bignold and Fleischmann (8) also discussed origins of the time constant observed during iron dissolution, and they considered the pit-shaped relaxation: when iron dissolves, conical pits are formed on the surface. The number of pits is determined by the

number of dislocations and thus constant, but the pit form is potential dependent. In other words, the roughness factor is considered as a time and potential-dependent parameter. By considering the overlapping of conical pits, they concluded that the relaxation time constant is reciprocally proportional to the current.

In the case of electrodeposition, the short period current transient was interpreted by the formation of crystal nuclei and their growth (9, 10). But this model cannot describe the steady state and the related impedance since no equation of mass balance is proposed for the time dependence of N^* . This type of model was reformulated, very recently, in our Laboratory, (11) for successfully describing the electrodeposition of silver in order to express the impedance as a step-line propagation of the crystallite. Lorenz and Schweikert (12) considered the potential and time dependence of the number of active sites without any physicochemical model. The expression of dN^*/dt in the case of dissolution cannot be compared to the formation of crystal nuclei; thus calling it negative deposition does not resolve the problem physically.

The time constants observed in the electrode impedance, whatever their origin, are interpreted by the relaxation phenomenon of "sites." If these sites are metal atoms bonded with a chemical species and if they are taking part in the reaction, the adsorption of intermediate species is inferred. The relaxation time constant is thus dependent on the chemistry of the interface. If these sites are specific points on the metal surface, in particular crystallographic imperfections, the active sites may be considered. The relaxation time constants will be essentially determined by the metal specimen itself. Heusler used successively both concepts for the same iron electrode (13-15). Numerous observations concerning the influence of potential, of solution pH, and of the addition of alloying elements such as Cr (16), indicate that the change of chemical nature of the parameter determines the time constants observed in the electrode impedance. Thus, it can be reasonably assumed that, in the case of iron dissolution, the origin of the time constants, except that related to the high-frequency capacitive loop, is due to the relaxation of surface coverages by reaction intermediate species. Since this relaxation rate is essentially dependent on the formation and the consumption of intermediate species, the hypotheses which will be used to express reaction rates in mathematical form have to be examined in detail. The main hypotheses concern the potential dependence and reversibility of the reaction rate and an adsorption isotherm law. These three points are examined in this order in the following.

Potential dependence of reaction rate.—It is generally admitted that the reaction rate follows with respect to the potential the so called Tafel law (17, 18)

$$K = K_0 \exp \left(\frac{z\alpha F}{RT} E \right) \quad [1]$$

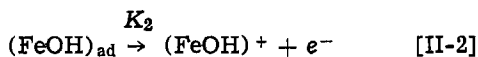
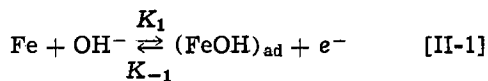
The value of α has been found to be 0.5 for the hydrogen evolution reaction on various metals (19), and this value is widely assumed to be valid for any other electrochemical process. However, from the view point of theory, α may have any value between 0 and 1 (20, 21) and may be potential dependent (22, 23).

Though the potential range considered in this work is very wide, the Tafel law ($\alpha = \text{constant}$) can be considered as a reasonably restrictive approximation.

When the solution pH is changed, the chemical nature of intermediate species may be modified. Thus α could be considered to be pH dependent especially when a very wide range of pH is investigated.

Reversibility of reaction.—In early works on iron dissolution, the electrode kinetics were examined in the potential range near its thermodynamic equilibrium

potential (24-26). Notice that the model proposed in (24) concerns both dissolution and electrodeposition of iron. This model (model II) is recalled here



Step [II-1] is considered to be in pseudo-equilibrium, i.e., the reaction is reversible and very fast compared to step [II-2]. Thus, $K_{-1} \gg K_2$. This situation is assumed to be realized in the region of the open-circuit corrosion potential (25).

There is no doubt that at the equilibrium potential all steps are in equilibrium. However, when the electrode potential is removed from this potential, the reaction becomes irreversible. This has been disregarded in previous works (27-30). At the onset of the passivation process, the difference from the equilibrium potential reaches ca. 1V. Considering that pseudo-equilibrium is maintained for such an overpotential seems unrealistic. The maximum current observed in this solution is limited by mass transfer even at the rotation speed of the disk electrode equal to 6000 rev · mn⁻¹, and was 2.6 A · cm⁻². If a pseudo-equilibrium were assumed for an intermediate step, its exchange current density would be greater than a few tens of A · cm⁻². This value is far greater than that known for any fast system of Red-Ox reaction (31).

Let us examine now the consequence of a pseudo-equilibrium reaction on the electrode impedance. Model II is used as an example. Considering that the Langmuir-type isotherm law is valid (32) (see the following paragraph), the charge balance due to model II can be written by

$$\frac{J}{F} = (1 - \theta)K_1 - (K_{-1} - K_2)\theta \quad [2]$$

The Taylor expansion of Eq. [2] limited to the first-order term leads to the expression for the faradaic impedance Z_F

$$\frac{1}{Z_F} = \frac{dJ}{dE} = \frac{1}{R_t} - F(K_1 + K_{-1} - K_2) \frac{d\theta}{dE} \quad [3]$$

R_t is the charge transfer resistance corresponding to $(\partial J / \partial E)_\theta$, i.e., the resistance value when any θ change is frozen, and can be calculated by

$$\frac{1}{R_t} = \left\{ (b_1 + b_2) + (b_1 + b_{-1}) \frac{K_{-1}}{K_2} \right\} \frac{J}{2} \quad [4]$$

The pseudo-equilibrium for the first step corresponds to $K_{-1} \gg K_2$, thus $(K_1 + K_{-1} - K_2) > 0$. Since θ is a potential increasing function, $d\theta/dE > 0$, Z_F appears always as capacitive (2) and a so-called "pseudo-capacitance" is observed (25). The capacitance value depends on θ . The pseudo-capacitance is maximum at $\theta = 0.5$ and has the value of ca. 10 mF for $\beta = 10^{-8}$ (mole · cm⁻²). For $\theta = 0.1$, the capacitance is equal to 3 mF for the same β value.

Experimentally, such a high capacitive value is not obtained in the high-frequency capacitive loop if the metal is of sufficient purity and the surface remains bright during the dissolution. Furthermore, if the high-frequency capacitive loop includes the pseudo-capacitance, two time constants should be seen. Experimentally, though, the high-frequency capacitive loop cannot be represented by a true R-C circuit and a frequency distribution can be observed (5). None of the results allowed us to ascertain the presence of two distinct time constants.

If the first step is irreversible, K_{-1} is very small and Eq. [4] leads to

$$R_t \cdot J = \frac{2}{b_1 + b_2} (K_{-1} \ll K_2) \quad [5]$$

Thus the $R_t \cdot J$ value is independent of current. The minimum value of $R_t \cdot J$ can be calculated when $\alpha_1 = \alpha_2 = 1$ and is equal to 0.026V. Experimentally, the diameter of the high-frequency loop multiplied by the current yields a value close to 0.04V and remains constant up to medium current densities (5, 33). Thus the diameter of this loop may reasonably be attributed to the transfer resistance. The parallel capacitance, determined at the top of the loop, is ca. 100 $\mu\text{F} \cdot \text{cm}^{-2}$ and may reasonably be considered as the double layer capacitance. The high-frequency capacitive loop is thus considered to be due to the transfer resistance and the double layer capacitance.

Adsorption isotherm.—The simplest adsorption isotherm at appreciable θ values is the Langmuir type. The reaction rate K is assumed independent of θ , thus the rates of formation or of consumption k of a species concerned can be written by

$$k = k_1(1 - \theta) \quad \text{or} \quad k_- = k_{-1}\theta \quad [6]$$

Strictly speaking, Eq. [6] is considered valid for $\theta < 0.2$ or $\theta > 0.8$ and a more elaborate isotherm might be taken into consideration at intermediate θ values. It may be expected that by using a more elaborate isotherm, complicated results can be interpreted on the basis of simple models, at least for steady-state polarization curves (34, 35). No matter how elaborate is the isotherm, it does not give rise to an additional time constant. The number of processes to be considered is determined by experiment. On the other hand, mathematical resolution of the model becomes difficult and increases the number of parameters to be adjusted. Therefore, as a first approximation, the Langmuir-type isotherm is assumed. Since this isotherm is a rather crude model, it may affect a fine quantitative analysis (36). If the experiments cannot be simulated suitably, other isotherm will be considered.

The hypotheses which are used in this work are summarized in the following:

1. The high frequency capacitive loop is due to the double layer capacity and the transfer resistance.
2. The time constants observed in addition to hypothesis 1 are due to the surface coverage relaxation of reaction intermediate species.
3. The elementary steps obey the Tafel law. Tafel coefficient b values between 0 and 38.4V⁻¹ correspond to α values equal to 0 and 1, respectively, for a one-electron transfer.
4. The adsorption-desorption of intermediate species follows the Langmuir-type isotherm.
5. The reaction may be reversible but not necessarily in pseudo-equilibrium.

Criteria for Model Determination

Tafel slope measurements constitute one of the main criteria for the determination of the reaction mechanism. For instance, Lorenz *et al.* (37) found that the Tafel slope changed from 0.04 to 0.03V when the iron specimen was subjected to a severe mechanical deformation. This variation was interpreted by the change of the reaction model from model II to model I. However, with the hypotheses retained in this paper, such a consideration is no longer possible.

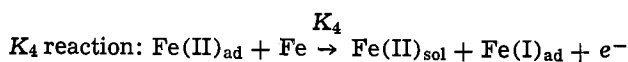
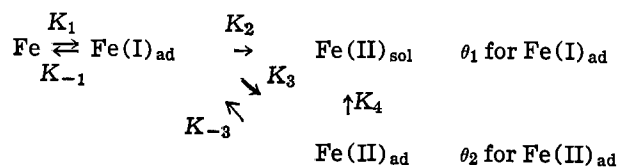
According to the hypotheses given above and assuming that the first step of model II is irreversible, model I has a Tafel slope smaller than 0.06V and model II greater than this value. On the polarization curves shown in Fig. 1 of Part I, it is seen that the Tafel slope, in the current density range where most work has been performed, is significantly smaller than 0.06V. This is true even when the current density is determined from weight loss measurements and no contribution of cathodic current is included (38). This result

may be interpreted in favor of model I. However, the impedance diagram B_0 (see Fig. 2 in Part I) shows clearly two inductive loops, which is in contradiction with model I. Both models I and II predict only one time constant corresponding to the relaxation of $(\text{FeOH})_{\text{ad}}$. As was shown in Part I, the lower frequency inductive loop is due to the relaxation of surface coverage by hydrogen. The Tafel slope without the influence of hydrogen coverage is close to 0.06V, but this measurement cannot be used as the criterion for determination of the reaction model. The model will be examined in terms of both the polarization curves and the impedance diagrams obtained at various potentials.

Analysis of Models Including Two Intermediates

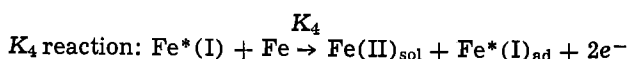
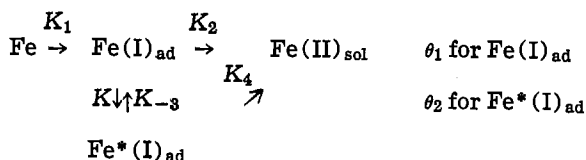
Since three time constants in addition to the high-frequency capacitive loop due to the double layer are observed in impedance diagrams, the iron dissolution model has to include at least three intermediate species. Before discussing the three-intermediate reaction model, it seems useful to examine two reaction models proposed in the literature. One was proposed by Lorenz *et al.* (27-30) on the basis of polarization curves obtained in weakly acidic media:

Model III



The other model was proposed by Bechet *et al.* (33) on the basis of steady-state polarization curves and impedance measurements in strongly to mildly acidic media:

Model IV



These two models are relatively similar and both have two dissolution paths. The K_2 dissolution path can be related to model II. The main difference between these two models are:

1. The K_1 reaction is considered to be in pseudo-equilibrium in model III and irreversible in model IV. Model III explains the 0.04V Tafel slope according to hypotheses discarded in this work.

2. In the K_4 reaction, both models imply the participation of an adjacent Fe, but model IV is a self-catalytic process and produces two electrons. On the other hand, model III is a noncatalytic and mono-electronic process. The two-electron transfer reaction is less likely to occur from the viewpoint of theoretical physical chemistry but seems intimately related to a catalytic reaction (13).

3. The intermediate species for the K_4 dissolution path is bivalent in model III and monovalent in model IV. Thus their formation implies one electron in model III and no electron transfer in model IV. This difference appears in the electrode impedance, as seen below.

Using the expressions of charge and mass balances, the steady-state current can be expressed by the same equation for both models

$$\bar{J} = 2F(K_2\theta_1 + K_4\theta_2) \quad [7]$$

On the other hand, the expressions for the faradaic impedance Z_F differ for the two models. For model III

$$\frac{1}{Z_F} = \frac{1}{R_t} - F \left\{ (K_1 + K_{-1} - K_2 - K_3) \frac{d\theta_1}{dE} + (K_1 + K_{-3} - K_4) \frac{d\theta_2}{dE} \right\} \quad [8]$$

where

$$\frac{1}{R_t} = F \{ (b_1 + b_{-1})K_{-1}\bar{\theta}_1 + (b_1 + b_2)K_2\bar{\theta}_1 + (b_3 + b_{-3})K_{-3}\bar{\theta}_2 + (b_3 + b_4)K_4\bar{\theta}_2 \} \quad [9]$$

and for model IV

$$\frac{1}{Z_F} = \frac{1}{R_t} - F \left\{ (K_1 - K_2) \frac{d\theta_1}{dE} + (K_1 - 2K_4) \frac{d\theta_2}{dE} \right\} \quad [10]$$

where

$$\frac{1}{R_t} = F \{ (b_1 + b_2)K_2\bar{\theta}_1 + 2b_4K_4\bar{\theta}_2 \} \quad [11]$$

Comparing Eq. [7] and [11], it can be seen for model IV that the product of R_t times \bar{J} is equal to $2/(b_1 + b_2)$ when the metal dissolves through the K_2 path ($K_2\theta_1 \gg K_4\theta_2$) and equals $1/b_4$ through the K_4 path. The change of the $R_t \cdot \bar{J}$ value indicates thus the change of dissolution path. Besides, if $(b_1 + b_2) > 2b_4$, the increase of the $R_t \cdot \bar{J}$ value, observed experimentally (33), can be explained in the reaction model. On the other hand, in model III (Eq. [9]), even if the K_1/K_{-1} reaction is considered to be irreversible, the change of the $R_t \cdot \bar{J}$ value is not so simply related to the change of the reaction path. At relatively low anodic potentials, both $d\theta_1/dE$ and $d\theta_2/dE$ may be positive in both models. If the terms related to these values in Eq. [8] and [10] are negative, the faradaic impedance may appear as two inductive loops (2). In other words, if the pseudo-equilibrium reaction (K_1/K_{-1}) is no longer retained, model III can also explain, under certain conditions, the appearance of inductive faradaic impedance.

Models Including Three Adsorbed Intermediates

An Fe(III) species does not intervene in the dissolution range (29) and appears only at potentials close to the Flade potential (39). Therefore, the three reaction intermediates that will be taken into consideration are mono- or bivalent species. The dissolution process through model II is kept in all reaction schemes according to the examination of models and of hypotheses made above. The first step [II-1] may be reversible, but as was shown in our previous works (5, 33) the contribution of the backward reaction is negligibly small. For the sake of simplicity, different models are examined assuming a nonreversible first step. Introducing the slow backward reaction in the first step does not essentially change the results. It was found during preliminary work that no fundamental difference can be detected between models in which intermediate species are directly formed from the metal atom and those involving branching from Fe(I). This latter case was retained because it leads to simpler mathematical expressions. According to schematic forms, reaction schemes can be divided into three groups. Reaction schemes differ from one another by interactions between intermediate species, and consequently the expressions for charge and mass balance are different for each reaction scheme. But each elementary step is not explicit and may be written in many ways. Though a self-catalytic reaction intervenes in the expression of mass balance, this type of reaction is also considered.

Table I shows the reaction schemes in which all intermediate species are monovalent. Eight different

Table I. Reaction schemes with three monovalent intermediates

| Schemes | Eliminated | Schemes | Eliminated |
|--|------------|--|------------|
| 1-A $\begin{array}{c} \text{Fe}^*(\text{I}) \\ \updownarrow \\ \text{Fe} \rightarrow \text{Fe}(\text{I}) \rightarrow \text{Fe}(\text{II})_{\text{sol}} \\ \updownarrow \\ \text{Fe}^\dagger(\text{I}) \end{array}$ | A | 1-B $\begin{array}{c} \text{Fe}^*(\text{I}) \\ \updownarrow \\ \text{Fe} \rightarrow \text{Fe}(\text{I}) \rightarrow \text{Fe}(\text{II})_{\text{sol}} \\ \updownarrow \\ \text{Fe}^\dagger(\text{I}) \end{array}$ | B |
| 1-C $\begin{array}{c} \text{Fe}^*(\text{I}) \\ \updownarrow \\ \text{Fe} \rightarrow \text{Fe}(\text{I}) \rightarrow \text{Fe}(\text{II})_{\text{sol}} \\ \updownarrow \nearrow \\ \text{Fe}^\dagger(\text{I}) \end{array}$ | B | 1-D $\begin{array}{c} \text{Fe}^*(\text{I}) \\ \updownarrow \\ \text{Fe} \rightarrow \text{Fe}(\text{I}) \rightarrow \text{Fe}(\text{II})_{\text{sol}} \\ \updownarrow \nearrow \\ \text{Fe}^\dagger(\text{I}) \end{array}$ | C |
| 1-E $\begin{array}{c} \text{Fe} \rightarrow \text{Fe}(\text{I}) \rightarrow \text{Fe}(\text{II})_{\text{sol}} \\ \updownarrow \\ \text{Fe}^*(\text{I}) \\ \updownarrow \\ \text{Fe}^\dagger(\text{I}) \end{array}$ | A | 1-F $\begin{array}{c} \text{Fe} \rightarrow \text{Fe}(\text{I}) \rightarrow \text{Fe}(\text{II})_{\text{sol}} \\ \updownarrow \\ \text{Fe}^*(\text{I}) \nearrow \\ \updownarrow \\ \text{Fe}^\dagger(\text{I}) \end{array}$ | B |
| 1-G $\begin{array}{c} \text{Fe} \rightarrow \text{Fe}(\text{I}) \rightarrow \text{Fe}(\text{II})_{\text{sol}} \\ \updownarrow \\ \text{Fe}^*(\text{I}) \\ \updownarrow \nearrow \\ \text{Fe}^\dagger(\text{I}) \end{array}$ | B | 1-H $\begin{array}{c} \text{Fe} \xrightarrow{1} \text{Fe}(\text{I}) \xrightarrow{2} \text{Fe}(\text{II}) \\ \updownarrow \nearrow \\ \text{Fe}^*(\text{I}) \\ \updownarrow \nearrow \\ \text{Fe}^\dagger(\text{I}) \end{array}$ | C |

schemes can be constructed. If the two intermediate species formed from Fe(I) are both bivalent, they are classified in group 2. Sixteen different schemes were considered and are given in Table II. The last group is formed by two monovalent and one bivalent intermediate species. Sixteen schemes can also be written, as seen in Table III. It must be emphasized that these models are restricted to a minimal degree of complexity with respect to the data of impedance measurements.

Comparison of Models and Experiments

The selected models have to describe, using the hypotheses retained above, the maximum number of experimental results given in Part I. It is found that a certain number of prospective models can be ruled out

by examining their mathematical structure analytically, without making a numerical simulation.

Analytical Examination of Models

Polarization curve having two current maxima.—In the pH 5 solution, the steady-state polarization curve exhibited two current maxima. As was shown in (29) and in agreement with Bech-Nielsen (35), such a curve can only be explained by reaction models including at least two dissolution paths. Thus 10 models having only one dissolution path were eliminated from the models shown in Tables I-III (marked "A").

Three inductive loops.—Three inductive loops were observed simultaneously in certain diagrams in mildly acidic solution and with medium current densities (dia-

Table II. Reaction schemes with 1 mono- and 2-divalent intermediates

| Schemes | Eliminated | Schemes | Eliminated |
|--|------------|---|------------|
| 2-A $\begin{array}{c} \text{Fe} \rightarrow \text{Fe}(\text{I}) \xrightarrow{\nearrow} \text{Fe}^*(\text{II}) \\ \xrightarrow{\searrow} \text{Fe}(\text{II})_{\text{sol}} \\ \xrightarrow{\nearrow} \text{Fe}^\dagger(\text{II}) \end{array}$ | A | 2-B $\begin{array}{c} \text{Fe} \rightarrow \text{Fe}(\text{I}) \rightarrow \text{Fe}(\text{II})_{\text{sol}} \\ \nearrow \text{Fe}^*(\text{II}) \\ \searrow \text{Fe}^\dagger(\text{II}) \end{array}$ | B |
| 2-C $\begin{array}{c} \text{Fe} \rightarrow \text{Fe}(\text{I}) \xrightarrow{\nearrow} \text{Fe}^*(\text{II}) \\ \xrightarrow{\searrow} \text{Fe}(\text{II})_{\text{sol}} \\ \xrightarrow{\nearrow} \text{Fe}^\dagger(\text{II}) \end{array}$ | B | 2-D $\begin{array}{c} \text{Fe} \rightarrow \text{Fe}(\text{I}) \rightarrow \text{Fe}(\text{II})_{\text{sol}} \\ \nearrow \text{Fe}^*(\text{II}) \\ \searrow \text{Fe}^\dagger(\text{II}) \end{array}$ | C |
| 2-E $\begin{array}{c} \text{Fe} \rightarrow \text{Fe}(\text{I}) \xrightarrow{\nearrow} \text{Fe}(\text{II})_{\text{sol}} \\ \xrightarrow{\searrow} \text{Fe}^*(\text{II}) \\ \xrightarrow{\nearrow} \text{Fe}^\dagger(\text{II}) \end{array}$ | A | 2-F $\begin{array}{c} \text{Fe} \rightarrow \text{Fe}(\text{I}) \rightarrow \text{Fe}(\text{II})_{\text{sol}} \\ \nearrow \text{Fe}^*(\text{II}) \\ \searrow \text{Fe}^\dagger(\text{II}) \end{array}$ | B |
| 2-G $\begin{array}{c} \text{Fe} \rightarrow \text{Fe}(\text{I}) \xrightarrow{\nearrow} \text{Fe}(\text{II})_{\text{sol}} \\ \xrightarrow{\searrow} \text{Fe}^*(\text{II}) \\ \xrightarrow{\nearrow} \text{Fe}^\dagger(\text{II}) \end{array}$ | B | 2-H $\begin{array}{c} \text{Fe} \rightarrow \text{Fe}(\text{I}) \rightarrow \text{Fe}(\text{II})_{\text{sol}} \\ \nearrow \text{Fe}^*(\text{II}) \\ \searrow \text{Fe}^\dagger(\text{II}) \end{array}$ | |
| 2-I $\begin{array}{c} \text{Fe} \rightarrow \text{Fe}(\text{I}) \rightarrow \text{Fe}(\text{II})_{\text{sol}} \\ \nearrow \text{Fe}^*(\text{II}) \\ \searrow \text{Fe}^\dagger(\text{II}) \end{array}$ | A | 2-J $\begin{array}{c} \text{Fe} \rightarrow \text{Fe}(\text{I}) \rightarrow \text{Fe}(\text{II})_{\text{sol}} \\ \nearrow \text{Fe}^*(\text{II}) \\ \searrow \text{Fe}^\dagger(\text{II}) \end{array}$ | B |
| 2-K $\begin{array}{c} \text{Fe} \rightarrow \text{Fe}(\text{I}) \rightarrow \text{Fe}(\text{II})_{\text{sol}} \\ \nearrow \text{Fe}^*(\text{II}) \\ \searrow \text{Fe}^\dagger(\text{II}) \end{array}$ | B | 2-L $\begin{array}{c} \text{Fe} \rightarrow \text{Fe}(\text{I}) \rightarrow \text{Fe}(\text{II})_{\text{sol}} \\ \nearrow \text{Fe}^*(\text{II}) \\ \searrow \text{Fe}^\dagger(\text{II}) \end{array}$ | |
| 2-M $\begin{array}{c} \text{Fe} \rightarrow \text{Fe}(\text{I}) \rightarrow \text{Fe}(\text{II})_{\text{sol}} \\ \nearrow \text{Fe}^*(\text{II}) \\ \searrow \text{Fe}^\dagger(\text{II}) \end{array}$ | A | 2-N $\begin{array}{c} \text{Fe} \rightarrow \text{Fe}(\text{I}) \rightarrow \text{Fe}(\text{II})_{\text{sol}} \\ \nearrow \text{Fe}^*(\text{II}) \\ \searrow \text{Fe}^\dagger(\text{II}) \end{array}$ | B |
| 2-O $\begin{array}{c} \text{Fe} \rightarrow \text{Fe}(\text{I}) \rightarrow \text{Fe}(\text{II})_{\text{sol}} \\ \nearrow \text{Fe}^*(\text{II}) \\ \searrow \text{Fe}^\dagger(\text{II}) \end{array}$ | B | 2-P $\begin{array}{c} \text{Fe} \xrightarrow{1} \text{Fe}(\text{I}) \xrightarrow{2} \text{Fe}(\text{II})_{\text{sol}} \\ \nearrow \text{Fe}^*(\text{II}) \\ \searrow \text{Fe}^\dagger(\text{II}) \end{array}$ | C |

Table III. Reaction schemes with 2 mono- and 1-divalent intermediates

| Schemes | Eliminated | Schemes | Eliminated | | |
|---------|---|---------|------------|---|---|
| 3-A | $\begin{array}{c} \text{Fe}^*(\text{I}) \\ \uparrow \downarrow \\ \text{Fe} \rightarrow \text{Fe}(\text{I}) \rightarrow \text{Fe}(\text{II})_{\text{sol}} \\ \rightleftharpoons \text{Fe}^*(\text{II}) \end{array}$ | A | 3-B | $\begin{array}{c} \text{Fe}^*(\text{I}) \\ \uparrow \downarrow \\ \text{Fe} \rightarrow \text{Fe}(\text{I}) \rightarrow \text{Fe}(\text{II})_{\text{sol}} \\ \rightleftharpoons \text{Fe}^*(\text{II}) \end{array}$ | B |
| 3-C | $\begin{array}{c} \text{Fe}^*(\text{I}) \\ \uparrow \downarrow \\ \text{Fe} \rightarrow \text{Fe}(\text{I}) \rightarrow \text{Fe}(\text{II})_{\text{sol}} \\ \rightleftharpoons \text{Fe}^*(\text{II}) \end{array}$ | B | 3-D | $\begin{array}{c} \text{Fe}^*(\text{I}) \\ \uparrow \downarrow \\ \text{Fe} \rightarrow \text{Fe}(\text{I}) \rightarrow \text{Fe}(\text{II})_{\text{sol}} \\ \rightleftharpoons \text{Fe}^*(\text{II}) \end{array}$ | |
| 3-E | $\begin{array}{c} \text{Fe} \rightarrow \text{Fe}(\text{I}) \rightarrow \text{Fe}(\text{II})_{\text{sol}} \\ \uparrow \downarrow \\ \text{Fe}^*(\text{I}) \rightleftharpoons \text{Fe}^*(\text{II}) \end{array}$ | A | 3-F | $\begin{array}{c} \text{Fe} \rightarrow \text{Fe}(\text{I}) \rightarrow \text{Fe}(\text{II})_{\text{sol}} \\ \uparrow \downarrow \\ \text{Fe}^*(\text{I}) \rightleftharpoons \text{Fe}^*(\text{II}) \end{array}$ | B |
| 3-G | $\begin{array}{c} \text{Fe} \rightarrow \text{Fe}(\text{I}) \rightarrow \text{Fe}(\text{II})_{\text{sol}} \\ \uparrow \downarrow \\ \text{Fe}^*(\text{I}) \rightleftharpoons \text{Fe}^*(\text{II}) \end{array}$ | | 3-H | $\begin{array}{c} \text{Fe} \rightarrow \text{Fe}(\text{I}) \rightarrow \text{Fe}(\text{II})_{\text{sol}} \\ \uparrow \downarrow \\ \text{Fe}^*(\text{I}) \rightleftharpoons \text{Fe}^*(\text{II}) \end{array}$ | |
| 3-I | $\begin{array}{c} \text{Fe} \rightarrow \text{Fe}(\text{I}) \rightleftharpoons \text{Fe}(\text{II})_{\text{sol}} \\ \uparrow \downarrow \\ \text{Fe}^*(\text{I}) \rightleftharpoons \text{Fe}^*(\text{II}) \end{array}$ | A | 3-J | $\begin{array}{c} \text{Fe} \rightarrow \text{Fe}(\text{I}) \rightleftharpoons \text{Fe}(\text{II})_{\text{sol}} \\ \uparrow \downarrow \\ \text{Fe}^*(\text{I}) \rightleftharpoons \text{Fe}^*(\text{II}) \end{array}$ | B |
| 3-K | $\begin{array}{c} \text{Fe} \rightarrow \text{Fe}(\text{I}) \rightleftharpoons \text{Fe}(\text{II})_{\text{sol}} \\ \uparrow \downarrow \\ \text{Fe}^*(\text{I}) \rightleftharpoons \text{Fe}^*(\text{II}) \end{array}$ | B | 3-L | $\begin{array}{c} \text{Fe} \rightarrow \text{Fe}(\text{I}) \rightleftharpoons \text{Fe}(\text{II})_{\text{sol}} \\ \uparrow \downarrow \\ \text{Fe}^*(\text{I}) \rightleftharpoons \text{Fe}^*(\text{II}) \end{array}$ | |
| 3-M | $\begin{array}{c} \text{Fe} \rightarrow \text{Fe}(\text{I}) \rightleftharpoons \text{Fe}(\text{II})_{\text{sol}} \\ \uparrow \downarrow \\ \text{Fe}^*(\text{I}) \rightleftharpoons \text{Fe}^*(\text{II}) \end{array}$ | A | 3-N | $\begin{array}{c} \text{Fe} \rightarrow \text{Fe}(\text{I}) \rightleftharpoons \text{Fe}(\text{II})_{\text{sol}} \\ \uparrow \downarrow \\ \text{Fe}^*(\text{I}) \rightleftharpoons \text{Fe}^*(\text{II}) \end{array}$ | B |
| 3-O | $\begin{array}{c} \text{Fe} \rightarrow \text{Fe}(\text{I}) \rightleftharpoons \text{Fe}(\text{II})_{\text{sol}} \\ \uparrow \downarrow \\ \text{Fe}^*(\text{I}) \rightleftharpoons \text{Fe}^*(\text{II}) \end{array}$ | | 3-P | $\begin{array}{c} \text{Fe} \rightarrow \text{Fe}(\text{I}) \rightleftharpoons \text{Fe}(\text{II})_{\text{sol}} \\ \uparrow \downarrow \\ \text{Fe}^*(\text{I}) \rightleftharpoons \text{Fe}^*(\text{II}) \end{array}$ | |

grams D_2 and E_2 in Fig. 3 of Part I). Similar considerations to that for models including two intermediate species can be made here. From the expression of the charge balance, the electrode impedance can be written in general form such that

$$\frac{1}{Z_F} = \frac{1}{R_t} - F \left(p \frac{d\theta_1}{dE} + q \frac{d\theta_2}{dE} + r \frac{d\theta_3}{dE} \right) \quad [12]$$

$d\theta/dE$ will be positive in the low potential range where most of the electrode surface is bare and the increase of θ_1 is not disturbed by other coverages. In order that three inductive loops be observed, p , q , and r must be negative (2). The charge balance of the remaining schemes was written down and the Taylor expansion limited to first order was made. It is found that an inductive impedance can only appear when an intermediate species dissolves as $\text{Fe}(\text{II})_{\text{sol}}$ (18). Models that cannot show three inductive loops simultaneously are marked by B on Tables I-III.

Impedance diagrams E_5 and F_5 (see Fig. 6 in Part I).—These diagrams showed the peculiar nature of the species intervening in the prepassivation process. In fact, the capacitive loop observed in diagram E_5 at the lowest frequency range transforms into an inductive loop near the current minimum. A process giving rise to this loop has appeared as an inductive loop at potentials less anodic to maximum I as seen in diagrams A_4 and C_4 (Fig. 5 of Part I). This change from an inductive to a capacitive loop cannot be interpreted by the change of sign in q or r in Eq. [13], $d\theta_1/dE$ being attributed to the inductive loop observed at the highest frequency range. The change from a capacitive to an inductive loop near the current minimum may be interpreted by the change of sign in $d\theta_2/dE$ or $d\theta_3/dE$. That is to say, a species which leads to the prepassivation process by an increase of the surface coverage decreases when the prepassive dissolution process sets in. On the other hand, the capacitive loop observed at about 0.4 Hz remains capacitive. Therefore, relationships such as $(d\theta_2/dE) \times (d\theta_3/dE) < 0$ will be satisfied in the prepassivation dissolution domain.

With the steady-state relationship, the following relation can be written for schemes 1-D, 1-H, 2-D, and 2-P

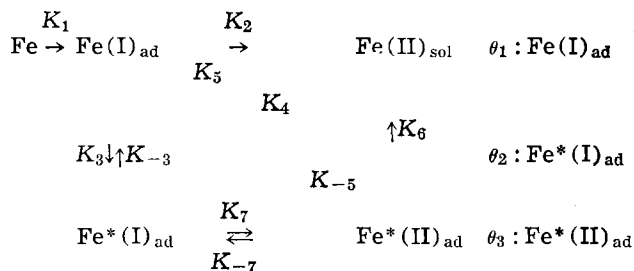
$$\theta_2 = \frac{K_3 K_{-7}}{K_{-3} K_7} \theta_3 = \bar{\theta}_3 K \cdot \exp \{ (b_3 + b_{-3} - b_7 - b_{-7}) E \} \quad [13]$$

Step i is marked in schemes 1-H and 2-P. Thus the product $\theta_2 \cdot \theta_3$ is a monotonic function with respect to the potential and $(d\theta_2/dE) \times (d\theta_3/dE) > 0$. These models cannot illustrate the change of the diagram shapes such as from E_5 to F_5 . These reaction schemes are marked by "C" in Table I-III.

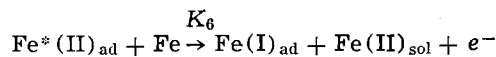
Examination of these three points allowed us to eliminate analytically 32 schemes from 40. The remaining eight schemes will be examined by numerical simulation.

Simulation Calculation

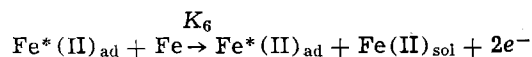
Reaction scheme 3-P corresponds to the general form of group 3. The other schemes can be discussed by considering certain reaction rates to be equal to zero. Let us recall scheme 3-P



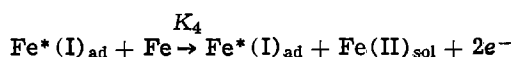
For K_6 reaction, two different cases are considered: for case 1 as proposed in (29)



and for case 2 as a self-catalytic reaction



Although two cases were also considered for the K_4 reaction, only the case of a self-catalytic reaction is given here for the sake of simplicity



The expression for the charge balance can be written as

$$\frac{J}{F} = K_1 \Sigma + (K_2 + K_5) \theta_1 + (2K_4 + K_7) \theta_2 - \{K_{-5} + K_{-7} - (2 - \rho) K_6\} \theta_3 \quad [14]$$

where $\rho = 1$ for case 1 and $\rho = 0$ for case 2 in reaction K_6 .

From expressions for the mass balance of these three intermediate species, the steady-state values of the surface coverage can be calculated and one obtains

$$\frac{\bar{J}}{F} = 2(K_2 \bar{\theta}_1 + K_4 \bar{\theta}_2 + K_6 \bar{\theta}_3) \quad [15]$$

The electrode impedance can be expressed from Eq. [14]

$$\frac{1}{Z_F} = \frac{1}{R_t} - F \left\{ (K_1 - K_2 - K_5) \frac{d\theta_1}{dE} + (K_1 - 2K_4 - K_7) \frac{d\theta_2}{dE} + (K_1 + K_{-5} + K_{-7} - (2 - \rho) K_6) \frac{d\theta_3}{dE} \right\}$$

where

$$\frac{1}{R_t} = F \{ (b_1 + b_2) K_2 \bar{\theta}_1 + b_5 K_5 \bar{\theta}_1 + (2b_4 K_4 + b_7 K_7) \bar{\theta}_2 + (b_{-5} K_{-5} + (2 - \rho) b_6 K_6 + b_{-7} K_{-7}) \bar{\theta}_3 \} \quad [16]$$

$d\theta/dE$ can be derived from the mass balance expression

$$X_1 = Z_1 \frac{d\theta_1}{dE} + (K_1 - K_{-3}) \frac{d\theta_2}{dE} + (K_1 - K_{-5} - \rho K_6) \frac{d\theta_3}{dE}$$

$$X_1 = \{ (b_1 - b_2) K_2 - b_3 K_3 - b_5 K_5 \} \bar{\theta}_1 - b_{-3} K_{-3} \bar{\theta}_2 - (b_{-5} K_{-5} - \rho b_6 K_6) \bar{\theta}_3$$

$$Z_1 = K_1 + K_2 + K_3 + K_5 + j\omega\beta_1 \quad [17]$$

$$X_2 = -K_3 \frac{d\theta_1}{dE} + Z_2 \frac{d\theta_2}{dE} - K_{-7} \frac{d\theta_3}{dE}$$

$$X_2 = \{ (b_3 + b_{-3}) K_{-3} + (b_3 - b_7) K_7 \} \bar{\theta}_2 - (b_7 + b_{-7}) K_{-7} \bar{\theta}_3$$

$$Z_2 = K_{-3} + K_7 + j\omega\beta_2 \quad [18]$$

$$X_3 = -K_5 \frac{d\theta_1}{dE} - K_7 \frac{d\theta_2}{dE} + Z_3 \frac{d\theta_3}{dE}$$

$$X_3 = (-b_5 + b_7) K_7 \bar{\theta}_2 + \{ (b_5 + b_{-5}) K_{-5} + (b_5 + b_{-7}) K_{-7} + \rho (b_5 - b_6) K_6 \} \bar{\theta}_3$$

$$Z_3 = K_{-5} + K_{-7} + \rho K_6 + j\omega\beta_3 \quad [19]$$

Equations [17]-[19] allow one to calculate the $d\theta/dE$ values for three intermediate species. By introducing these values into Eq. [16], the faradaic impedance can be obtained.

Model 3-P includes ten rate constants K_i , and since K_i is expressed by two potential-independent parameters, $K_{o,i}$ (mole·cm⁻²·sec⁻¹) and b_i (V⁻¹), 20 parameters will be adjusted for the simulation calculation. The β values are considered to be equal to 10⁻⁸ (mole·cm⁻²) (5), corresponding to one intermediate species bonded to one metal atom of the electrode surface. Impedance diagrams were calculated by considering that the overall impedance Z contains the contri-

bution of the double layer capacitance in parallel with the faradaic impedance Z_F

$$\frac{1}{Z} = \frac{1}{Z_F} + j\omega C_{dl}; \quad C_{dl} = 10^{-4} \text{ (F·cm}^{-2}\text{)} \quad [20]$$

As an example, Fig. 1 shows the steady-state polarization curves calculated on the basis of scheme 3-G, i.e., $K_4 = K_5 = K_{-5} = 0$. This example was calculated with $\rho = 1$. The agreement between the experimental and the calculated curves is very satisfactory. When the dissolution is determined by the K_6 path, the overall reaction rate is controlled by the smallest of K_3 , K_6 , and K_7 . Thus the bending of curves at high current densities was easily simulated.

On the other hand, the electrode impedance is somewhat difficult to simulate with the reaction corresponding to $\rho = 1$ both in shape and in frequency. The time constants τ of the relaxation phenomena are determined by expressions of Z_i . Since $\tau = 1/\omega$, one obtains from Eq. [17]-[19]

$$\frac{1}{\tau_1} = \frac{K_1 + K_2 + K_3 + K_5}{\beta_1}; \quad \frac{1}{\tau_2} = \frac{K_{-3} + K_7}{\beta_2};$$

$$\frac{1}{\tau_3} = \frac{\rho K_6 + K_{-7}}{\beta_3} \quad [21]$$

For the Fe*(II)_{ad} relaxation, the following relationship can be derived

$$\frac{1}{\tau_3} > \frac{K_6}{\beta_3} = \frac{\bar{J}}{2F\beta_3\theta_3} = \frac{\bar{J}}{2 \cdot 10^{-3} \cdot \bar{\theta}_3} > \frac{\bar{J}}{2 \cdot 10^{-3}} \quad [22]$$

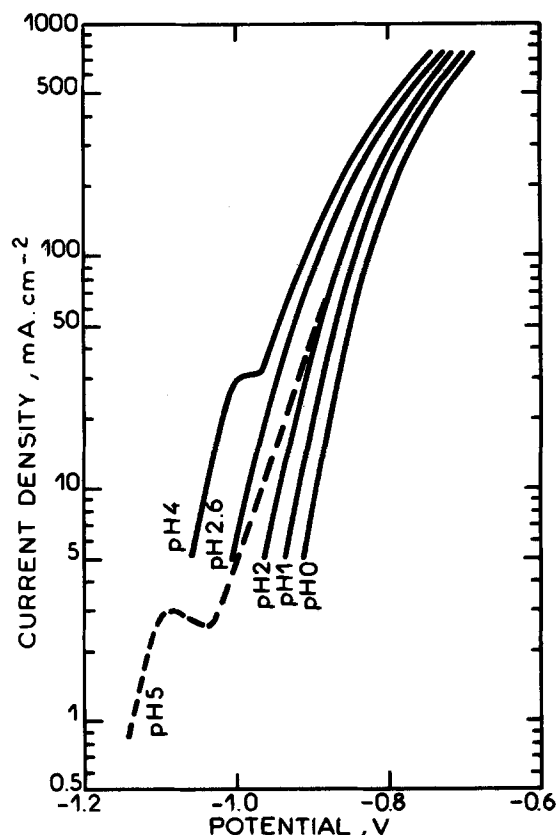
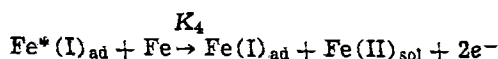


Fig. 1. Simulated polarization curves for various pH values according to reaction scheme 3-G. The K_6 reaction is nonself-catalytic. Reaction rates for the pH 5, solution are: $K_1^* = 4 \cdot 10^{10} \exp(38.4E)$; $K_2 = 8 \cdot 10^{-4} \exp(7E)$; $K_3^* = 1 \cdot 10^7 \exp(29E)$; $K_{-3} = 1.5 \cdot 10^{-8}$; $K_6^* = 2.3 \cdot 10^2 \exp(23E)$; $K_7 = 1.4 \exp(16.4E)$; and $K_{-7} = 8.4 \cdot 10^{-18} \exp(22E)$. * indicates the pH dependent parameter.

Equation [22] shows that the relaxation time constant τ_3 is smaller than $(2 \cdot 10^{-3})/\bar{J}$, i.e., the characteristic frequency in Hz for this relaxation process (top of the loop) is greater than $\bar{J}/(1.2 \cdot 10^{-2})$. With the experimental current \bar{J} , the calculated characteristic frequency is too high compared to that observed experimentally. Strictly speaking, this characteristic frequency is related to the electrode admittance and a slight difference is expected when using the impedance diagrams. If the self-catalytic reaction ($\rho = 0$) is considered, $\tau_3 = \beta_3/K_7$. The current and the relaxation time constants are separated and the simulation calculation may show satisfactory results. This consideration is also true for the K_4 reaction. In fact, as mentioned above, this process was considered self-catalytic for the sake of simplicity in Eq. [14]-[19]. If the K_4 reaction were written for instance as



the same analysis as the $\text{Fe}^*(\text{II})_{\text{ad}}$ relaxation shows that this reaction yields too small relaxation time constants compared to the experimental results if satisfactory polarization curves are simulated. However, with a self-catalytic reaction, the overall reaction rate is no longer limited by the slowest step in a series reaction, $K_3 - K_7 - K_6$, and the simulated polarization curves no longer bend at high current densities.

In Fig. 2, the impedance diagrams calculated at the foot of the prepassive dissolution domain are shown. The impedance at the lowest frequency range is capacitive instead of inductive (cf. diagram F_5). If steady-state polarization curves and other impedance diagrams were suitably simulated, this loop will remain capacitive even when numerical parameters are changed. This was found also true for models 2-H, 2-L, 3-G, 3-H, 3-L, 3-O, and 3-P. Only scheme 3-D allowed simulating the whole set of experimental results, except the bending of polarization curves at high current densities. It was impossible for us to rule out these seven models analytically. Nevertheless, it can be remarked that scheme 3-D is the only model having no direct interaction between two intermediate species $\text{Fe}^*(\text{I})_{\text{ad}}$ and $\text{Fe}^*(\text{II})_{\text{ad}}$. The results of numerical simulation and the value of parameters were given in Part I.

As was stated previously, the reaction steps considered in the model are of a minimal degree of complexity to interpret the experimental results obtained in this work. For instance, a two-electron transfer process is likely to take place through at least two steps. However if one of the steps is fast and reversible, the time constant cannot be observed experimentally. Furthermore, if the surface coverage by our intermedi-

ate species is small, the pseudocapacitance may be of the same order of magnitude or smaller than the double layer capacity. Therefore no experimental proof for this first step can be obtained by impedance measurements.

The reaction steps given for the K_6 path are an example of the simplest expression but different from the K_2 path. What we can verify by experiment is the reaction scheme and not the individual chemical steps. In particular, only the introduction of a self-catalytic process allows the separation of time constant and current flow.

In the simulation calculation, it was found that even the simulation of the steady-state curve needs the potential dependence of the so-called chemical process. Sato and co-worker (40) assumed that the dissolution of metal hydroxide is potential dependent and that $\alpha_+ + \alpha_-$ is equal to unity. On the other hand, if the reaction occurs through multiple steps and the rate-determining step is different for the forward and for the backward processes, $\alpha_+ + \alpha_-$ is no longer unity (41).

From the 40 schemes examined, ten were eliminated by steady-state polarization curves (A), 18 by the impossibility of interpreting three inductive loops (B), and 11 schemes were eliminated because they cannot predict diagrams such as H_4 and F_5 . Since the ten models eliminated by polarization curves also cannot explain three inductive loops, the usefulness of electrode impedances for comparison of models and experiment is clearly demonstrated. Only one model covering wide experimental conditions is retained using reasonable hypotheses.

Bending of the polarization curves at high current densities was not simulated with the reaction model selected. This may be interpreted in different ways: another process begins to occur, the Langmuir adsorption isotherm is no longer valid, or the Tafel law is no longer valid. Since impedance diagrams cannot be plotted with sufficient accuracy at these current densities, it is not possible to examine these assumptions at present.

Conclusion

Fundamental hypotheses of electrode kinetics allowing transcription of the reaction models into mathematical expressions were critically examined. The experimental impedance diagrams showed one high-frequency capacitive arc and three time constant at lower frequencies appearing as inductive or capacitive loops. They are attributed in the models, respectively, to the double layer capacitance in parallel with the transfer resistance and to the relaxation of three reaction intermediates.

Provided that the dissolution mechanism through two consecutive steps implying adsorbed $\text{Fe}(\text{I})$ remains valid, two adsorbed intermediate species could be introduced. Then, 40 different reaction schemes were constructed as the complete set of prospective combinations. It is worth noting that, since individual reactions can be differentiated in reaction schemes, a fairly large number of models must be tested. The examination of steady-state polarization curves allowed us to rule out only ten schemes. On the other hand, the analysis of impedance enabled us to select only one reaction model. The procedure developed in this work may be applied to other electrochemical interfaces.

Acknowledgments

O. Rosa Mattos thanks the Brazilian CNPq and MIC for his scholarships. The authors are indebted to Miss F. Haubert for her assistance in the elaboration of computer programs. The authors are sincerely grateful to the reviewer whose pertinent remarks allowed them to improve the text.

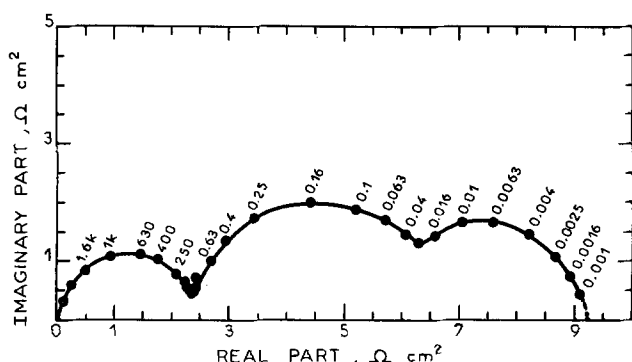


Fig. 2. Simulated impedance diagram. $E = -1.0\text{V}$ and $J = 4 \text{ mA} \cdot \text{cm}^{-2}$ in the prepassive dissolution domain in pH 5 solution. Reaction scheme 3-G, the K_6 reaction being self-catalytic. The reaction rates are equal to those given in Fig. 1 $\beta_i = 1 \cdot 10^{-8} \text{ mole} \cdot \text{cm}^{-2}$ and $C_{\text{dl}} = 1 \cdot 10^{-4} \text{ F} \cdot \text{cm}^{-2}$.

Manuscript submitted July 16, 1980; revised manuscript received Sept. 19, 1980. This was Paper 262 presented at the Los Angeles, California, Meeting of the Society, Oct. 14-19, 1979.

Any discussion of this paper will appear in a Discussion Section to be published in the December 1981 JOURNAL. All discussions for the December 1981 Discussion Section should be submitted by Aug. 1, 1981.

LIST OF SYMBOLS

| | |
|-----------------|---|
| ad | subscript for adsorbed species |
| B | Tafel slope (V) |
| b | Tafel coefficient (ln 10)/B (V ⁻¹) |
| C _{dl} | double layer capacitance (F·cm ⁻²) |
| C | capacitance (F) |
| E | electrode potential (V) |
| F | Faraday constant (A·sec) |
| J | current density (A·cm ⁻²) |
| \bar{J} | steady-state value of J (A·cm ⁻²) |
| K ₁ | forward reaction rate for step i (mole·sec ⁻¹) |
| K ₋₁ | backward reaction rate for step i (mole·sec ⁻¹) |
| N* | number of active sites |
| R | gas constant (J·deg ⁻¹) |
| R _t | charge transfer resistance (Ω) |
| sol | subscript for species in solution bulk |
| T | absolute temperature (deg) |
| Z | overall electrode impedance (Ω) |
| Z _F | faradaic impedance for unit surface (Ω·cm ²) |
| α | transfer coefficient |
| β | constant linking θ and surface concentration (mole·cm ⁻²) |
| θ | fractional surface coverage |
| $\bar{\theta}$ | steady-state value of θ |
| Σ | fractional bare surface area, 1 - Σθ _i |
| τ | relaxation time constant (sec) |
| ω | angular frequency (rad·sec ⁻¹) |

REFERENCES

- M. Keddam, O. R. Mattos, and H. Takenouti, *This Journal*, **128**, 257 (1981).
- I. Epelboin, M. Keddam, O. R. Mattos, and H. Takenouti, 7th International Congress on Metallic Corrosion, Rio de Janeiro, October 1978; *Proceedings*, p. 1977, Abraco, Rio de Janeiro (1979).
- D. C. Grahame, *This Journal*, **99**, 370C (1952).
- H. Gerischer and W. Mehl, *Z. Elektrochem.*, **59**, 1049 (1955).
- I. Epelboin and M. Keddam, *This Journal*, **117**, 1052 (1970).
- C. Deslouis, I. Epelboin, M. Keddam, and J. C. Lestrade, *J. Electroanal. Chem. Interfacial Electrochem.*, **28**, 57 (1970).
- M. Keddam, P. Mirebeau, and H. Takenouti, Abstract 262, p. 275, The Electrochemical Society Extended Abstracts, Los Angeles, California, Oct. 14-19, 1979.
- G. J. Bignold and M. Fleischmann, *Electrochim. Acta*, **19**, 363 (1974).
- M. Fleischmann and H. R. Thirsk, in "Advances in Electrochemistry and Electrochemical Engineering," Vol. 3, P. Delahay, Editor, p. 123, Interscience, New York (1963).
- J. A. Harrison and H. R. Thirsk, in "Electroanalytical Chemistry," Vol. 5, A. J. Bard, Editor, p. 67, Marcel Dekker, New York (1971).
- C. Cachet, I. Epelboin, M. Keddam, and R. Wiart, *J. Electroanal. Chem. Interfacial Electrochem.*, **100**, 745 (1979).
- W. J. Lorenz and H. Schweikert, 1st International Fischer Symposium, Karlsruhe, October 1979.
- K. E. Heusler, *Z. Elektrochem.*, **62**, 582 (1958).
- W. Allgaier and K. E. Heusler, *Z. Phys. Chem. N.F.*, **98**, 161 (1975).
- W. Allgaier and K. E. Heusler, *J. Appl. Electrochem.*, **9**, 155 (1979).
- I. Epelboin, M. Keddam, O. R. Mattos, and H. Takenouti, *Corros. Sci.*, **19**, 1105 (1979).
- J. Tafel, *Z. Physik. Chem.*, **34**, 187 (1900).
- J. A. V. Butler, *Trans. Faraday Soc.*, **19**, 734 (1924).
- T. Erdey-Gruz and M. Volmer, *Z. Physik. Chem.*, **A150**, 203 (1930).
- R. A. Marcus, in "Special Topics in Electrochemistry," P. A. Rock, Editor, p. 180, Elsevier, Amsterdam (1977).
- H. H. Bauer, *J. Electroanal. Chem. Interfacial Electrochem.*, **16**, 419 (1968).
- J. M. Saveant and T. Tessier, *ibid.*, **65**, 57 (1975).
- K. Matsuda and R. Tamamushi, *ibid.*, **100**, 831 (1979).
- J. O'M. Bockris, D. Drazic, and A. R. Despic, *Electrochim. Acta*, **4**, 326 (1961).
- J. O'M. Bockris and H. Kita, *This Journal*, **108**, 676 (1961).
- J. O'M. Bockris and D. Drazic, *Electrochim. Acta*, **7**, 293 (1962).
- D. Geana, A. A. El Miligy, and W. J. Lorenz, *Corros. Sci.*, **13**, 505 (1973).
- D. Geana, A. A. El Miligy, and W. J. Lorenz, *ibid.*, **14**, 657 (1974).
- A. A. El Miligy, D. Geana, and W. J. Lorenz, *Electrochim. Acta*, **20**, 273 (1975).
- J. Bessone, L. Karakaya, P. Lorbeer, and W. J. Lorenz, *ibid.*, **22**, 1147 (1977).
- R. Tamamushi, "Kinetic Parameters of Electrode Reactions of Metallic Compounds," IUPAC Additional Publication, Butterworths, London (1975).
- E. J. Kelly, *This Journal*, **112**, 124 (1965).
- B. Bechet, I. Epelboin, and M. Keddam, *J. Electroanal. Chem. Interfacial Electrochem.*, **76**, 129 (1977).
- W. J. Lorenz and J. R. Vilche, *Corros. Sci.*, **12**, 785 (1972).
- G. Bech-Nielsen, *Electrochim. Acta*, **21**, 627 (1976).
- D. D. Macdonald, "Transient Techniques in Electrochemistry," p. 303, Plenum Press, New York (1977).
- F. Hilbert, Y. Miyoshi, G. Eichkorn, and W. J. Lorenz, *This Journal*, **118**, 1919, 1927 (1971).
- I. Epelboin, M. Keddam, and H. Takenouti, 3rd European Symposium on Corrosion Inhibitors, Ferrara, 1971; *Annali. Univ. Ferrara. N.S., Sez V*, p. 237 (1970).
- M. Baddi, C. Gabrielli, M. Keddam, and H. Takenouti, in "Passivity of Metals," R. P. Frankenthal and J. Kruger, Editors, p. 625, The Electrochemical Society Softbound Proceedings Series, Princeton, N.J. (1978).
- M. Seo and N. Sato, *Boshoku Gijutsu*, **24**, 399 (1975).
- M. W. Breiter, "Electrochemical Process in Fuel Cells," pp. 29-31, Springer-Verlag, Berlin (1969).

Atmospheric Corrosion of Copper and Silver

D. W. Rice,* P. Peterson, E. B. Rigby, P. B. P. Phipps, R. J. Cappell, and R. Tremoureaux

IBM Corporation, General Products Division, San Jose, California 95193

ABSTRACT

The corrosion rate of copper in laboratory tests is shown to be a sensitive function of relative humidity, sulfur dioxide, hydrogen sulfide, ozone, hydrogen chloride, and chlorine concentrations. Observed indoor corrosion rates obey log normal statistics over the field population of this study. Also, the observed indoor rates correlate reasonably well with the measured reduced sulfur concentrations (H_2S , S_8). The corrosion rate of silver is shown not to be humidity dependent. Hydrogen sulfide, ozone, chlorine, and hydrogen chloride concentrations substantially influence its corrosion rate. The observed indoor rates obey log normal statistics and correlate well with the reduced sulfur gas concentration. In contrast to copper, where indoor rates are 1% of outdoor values, silver often corrodes faster indoors than outdoors. Its sensitivity to sulfur gases and insensitivity to relative humidity is proposed as a plausible explanation for these findings. It is proposed that metallic silver is stable in polluted acidic atmospheric environments and therefore is the dominant surface species while Cu_2O is present on the surface of copper. The thermochemistry and kinetics of these two surfaces will control the stability of silver and copper, respectively, in the presence of pollutants.

Copper and silver are important functional materials. They are widely used in industrial, commercial, and home environments. Found in their native state approximately 6000 years ago, they are considered noble metals. Corrosion of both copper and silver, a common problem, can be aesthetically beautiful and frustratingly complex.

Atmospheric corrosion of copper has been studied extensively. Reviews by Leidheiser (1) and Rozenfeld (2), among others (3-5), provide the reader with a historical perspective. The majority of these studies focused attention on outdoor urban corrosion. The atmospheric corrosion process is more complex than high temperature oxidation, where theories exist that explain reasonably well the observed rates (6). No such theory exists for atmospheric corrosion, although attempts have been made to correlate observed outdoor rates to sulfate and relative humidity levels (7). Water vapor, sulfur dioxide, and hydrogen sulfide have been shown to influence the rate of copper corrosion (8-10).

Silver has been cited as a classical example of a material that decays by a diffusion-controlled process at either the atmosphere-product interface or in the corrosion product itself (11). Its propensity to tarnish is well recognized by scientists and homemakers alike. Sulfur gases are the dominant reactive pollutants (10, 12); however, some reference is given to humidity and chlorine-containing gases as accelerators of corrosion (13, 14).

The purpose of this paper is to add to the understanding of both copper and silver atmospheric corrosion, with particular emphasis given to the corrosion response in indoor environments. We develop the quantitative rate dependence on relative humidity and pollutant concentrations in synthetic laboratory environments that are not grossly accelerated. The results of an indoor test site program in the United States are also presented and compared to published indoor and outdoor data. The observed rates are correlated to pollutant and relative humidity measurements made concurrently. This paper is the last in a series that has addressed cobalt corrosion (15), nickel corrosion (16), the role of water in atmospheric corrosion (17), and indoor atmospheric corrosion (18).

Experiment

Copper and silver coupons, both greater than 99.999% pure, were exposed to either laboratory syn-

thesized test environments or indoor field test sites. The total corroding area was 12.9 cm². The samples were generally cleaned by a sequence of hot xylene, isopropanol, and deionized water immersions. As-received metals corroded at the same rate as the cleaned samples; therefore, the above procedure was not found to be critical, but good practice. The coupon weight increase to the nearest microgram was measured as a function of time in either the laboratory or field environments.

The weighing accuracy for the laboratory test samples was $\pm 0.16 \mu\text{g}/\text{cm}^2$. This resulted in a 16% weighing error for the lowest total weight changes measured, $1 \mu\text{g}/\text{cm}^2$, and a 0.03% error for the highest weight changes measured. The weighing accuracy for the field samples was $\pm 0.39 \mu\text{g}/\text{cm}^2$. This was equivalent to a 16% error in the lowest weight changes recorded and 0.3% in the highest weight changes.

The laboratory tests were performed in chamber environments synthesized from purified humid air containing predetermined trace quantities of sulfur dioxide (SO_2), nitrogen dioxide (NO_2), hydrogen sulfide (H_2S), chlorine (Cl_2), hydrogen chloride (HCl), ammonia (NH_3), and ozone (O_3).

Figure 1 is a schematic of one of the laboratory test systems used in this study. In this particular example, two chambers run simultaneously from the same cylinder tank farm and analytic equipment, one for general humidity variation and the other for pollutant variations.

The purity of the compressed-air supply was found to be very important to insure reproducibility of the corrosion rate results. Purification was accomplished by a reverse coalescent filter in series with activated charcoal and particle filters. These filters removed oil mist, pollutants and oil vapors, and residual particles, respectively. This combination allowed comparatively high flow rates, 50-500 liters/min, while maintaining the background inorganic pollutant concentrations equal to or less than $0.9 \mu\text{g}/\text{m}^3$ for SO_2 , $0.1 \mu\text{g}/\text{m}^3$ for NO_2 , $0.006 \mu\text{g}/\text{m}^3$ for H_2S (S_8), $0.05 \mu\text{g}/\text{m}^3$ for Cl_2 (HCl), $0.1 \mu\text{g}/\text{m}^3$ for NH_3 , and $1 \mu\text{g}/\text{m}^3$ for O_3 . The most common problems we encountered in cleaning the air were high concentrations of NO_x , O_3 , and oil vapors passing through the filter system. The first two are typically high in our local urban California environment; the oil vapor comes from the compressor.

The purified air was proportioned so that some would pass over a thermostatically controlled kettle containing deionized water for humidification. Humid-

* Electrochemical Society Active Member.
Key words: pollution, failure, reliability, sulfidation, environment.

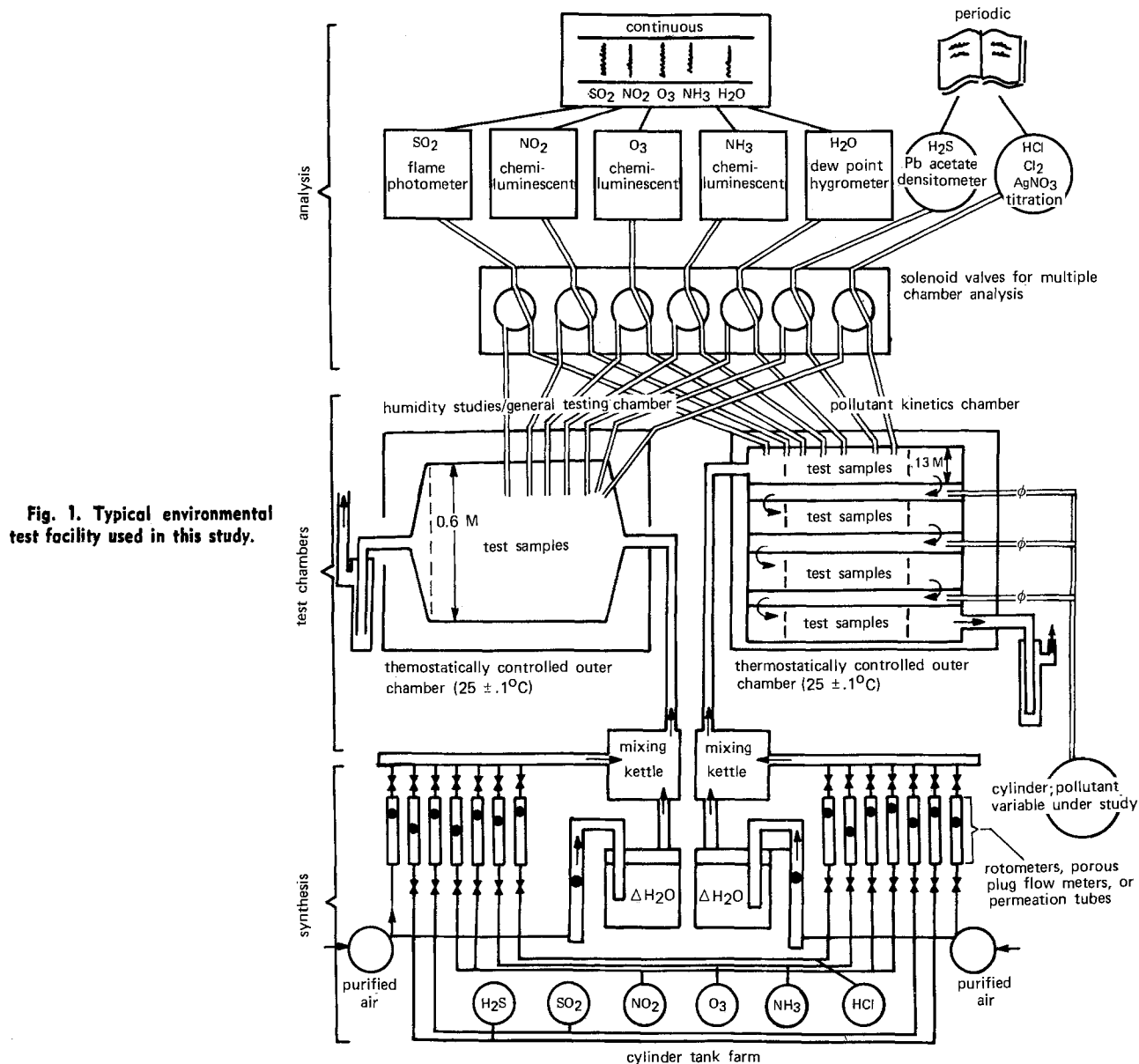


Fig. 1. Typical environmental test facility used in this study.

ity control could be maintained at $\pm 3\%$ (25°C) up to 80% relative humidity. The relative humidity was routinely measured by the dew point method (19); however, the wet and dry bulb technique was used as a cross check. This was necessary because the laboratory environments would slowly condense species such as sulfuric acid on the gold reflecting surface and yield incorrect humidity values.

Pollutants were added to the dry ($< 5\%$ RH) purified air by one of three methods: permeation tubes (20), rotameters from 0.1% by volume pollutant in a high purity N_2 cylinder, and porous plug flowmeters (21) from 1% by volume pollutant in high purity N_2 cylinders. All three methods were acceptable for short-term tests of the order of two weeks, but the porous plug flowmeters were the most reliable over long periods and not restricted to certain pollutants. Rotameters required constant attention. Reliable permeation tubes are only available for a limited number of pollutants. SO_2 , H_2S , and Cl_2 permeation tubes were found satisfactory for our short-term tests. Our objective was to control pollutants to $\pm 10\%$ of the desired concentration.

The pollutant-containing dry air was premixed with the humid air before entry into the chambers. The construction materials of the gas-handling system downstream from the metering valves was Pyrex glass, Plexiglas, and Teflon. These materials eliminated system failures due to corrosion and minimized adsorption losses of the pollutants that are common to other

construction materials. The atmospheric exchange rate varied from 3/min for the larger chambers to 6/min for the smaller chambers.

The dependence of corrosion rate on pollutant concentration was measured in special multiple compartment Plexiglas chambers that permitted up to five different concentrations by serial addition of the pollutant being studied (Fig. 1). All other pollutants and relative humidity were fixed at the input levels. This proved a very efficient and simple way to obtain significant quantities of data. This technique minimized problems associated with chamber reproducibility.

The pollutant concentrations were measured near the samples by the techniques summarized in Table I. The acidic chlorine gases, HCl , and Cl_2 , as well as H_2S , could not be measured continuously because of the low concentrations. Integrating methods were developed for these gases. The actual choice of inorganic pollutants for this study was based on either reported problems associated with the pollutant or its presence at high levels in urban atmospheres. Graedel and Schwartz have reviewed both pollutants and problems (29). The pollutant concentrations in the laboratory tests were chosen to be similar to urban levels but at the 99%-99.9% upper end of the distribution function. Table I summarizes the rationale for pollutant selection and typical ranges in indoor and outdoor environments.

The field site tests were performed in specially designed flow control modules that pulled the ambient

Table I. Inorganic pollutants used in this study, typical indoor and outdoor ranges, analytic methods, and rationale for selection

| Pollutant gas | Typical outdoor range ($\mu\text{g}/\text{m}^3$) (18, 29) | Typical indoor range ($\mu\text{g}/\text{m}^3$) (18) | Analytic methods | Rationale for selection |
|------------------|---|--|--|---|
| SO ₂ | 3-185 | 1-40 | Flame photometric, (continuous) (22), West Gaeke (23) (periodic) | Major pollutant, known to attack many metals. Forms acidic surface |
| NO ₂ | 20-160 | 3-60 | Chemiluminescence, (continuous) (24), Saltzman (periodic) (25) | Major pollutant, known to attack Co, Ni, and Fe (18) |
| H ₂ S | 1-36 | 0.2-1 | Lead acetate tape sampler with prefilter (periodic) (26) | Stress corrosion accelerator, known to attack Cu and Ag |
| O ₃ | 10-90 | 7-65 | Chemiluminescence (continuous) (27) | Major pollutant, degrades polymers and accelerates oxidation of H ₂ S, NO ₂ , and SO ₂ |
| HCl | 0.3-5 | 0.08-0.3 | O-tolidine densitometry (periodic), AgNO ₃ titration (periodic) | Destabilizes passive films by lattice impregnation and acid dissolution |
| Cl ₂ | Less than 5% of HCl levels except where local Cl ₂ source exists | 0.004-0.015 | Same as above | Same as above |
| NH ₃ | 6-12 | 10-150 | Chemiluminescence (continuous) (28) | Major pollutant, forms complexes with Cu and Ag, forms basic surface |

indoor air over the samples at 2.5 m/sec parallel to the surface. The location and characteristics of the eight indoor test sites in this study are given in Table II. Samples were returned after 6, 12, and 18 month exposure and reweighed after removing benzene soluble organic deposits. These organic deposits generally were only 10%-20% of the inorganic weight gain; however, for a few samples they were comparable. Pollutant and humidity measurements were concurrently measured at six of the eight sites. This data has been summarized previously, as has the high resolution x-ray photoelectron spectroscopic analysis of the corrosion product on the samples returned after 18 months (18).

Results and Discussion

Relative humidity.—The corrosion rate, r , dependence on relative humidity, RH, for both copper and silver in two complex test environments are shown in Fig. 2. Pollutant concentrations in these tests are listed in Table III. The rates are the initial linear rate constants. These were chosen because the total weights are more representative of the field measurements. These rates will generally overestimate the amount of weight increase for long test times; however, the same general dependence on atmospheric variables will be observed. Figure 3 shows representative weight gain vs. time curves at various relative humidities for copper.

The difference between copper and silver is remarkable. The corrosion rate of copper is strongly dependent on relative humidity. The approximate equation relating rate and relative humidity is $r = 0.042 \exp 4.6RH$ for environment A with a correlation coefficient equal to 0.97. Environment B results in a rate that is more sensitive to RH. These results are generally in agreement with the work of Vernon (8) and others (1-5) at higher pollutant concentrations. Corrosion rates could be measured over the entire range of RH's studied. There was no "critical humidity" in an absolute sense. At high SO₂ concentrations or in SO₂ environments only, where equilibrium with sulfate surface products

Table II. Field site physical characteristics

| Site | Location | Outdoor environment | Air conditioned |
|------|--------------------------|---------------------|-----------------|
| 1 | Los Angeles, CA | Urban | Yes |
| 2 | Chicago, IL | Urban | Yes |
| 3 | Manhattan, New York City | Urban | Yes |
| 4 | Houston, TX | Industrial/rural | Yes |
| 5 | North Indiana | Industrial | Yes |
| 6 | South Carolina | Industrial | Yes |
| 7 | New Jersey | Industrial | No |
| 8 | New Jersey | Industrial | No |

Table III. Composition of the complex accelerated laboratory test environments. ($T = 25^\circ\text{C}$, $v = 0.36 \text{ M/sec}$)

| Pollutant | Concentration ($\mu\text{g}/\text{m}^3$) | |
|------------------|--|---------------|
| | Environment A | Environment B |
| SO ₂ | 810 | 860 |
| NO ₂ | 940 | 990 |
| O ₃ | 334 | 0 |
| NH ₃ | 0 | 0 |
| Cl ₂ | 8.6 | 8.4 |
| HCl | 0 | 16.8 |
| H ₂ S | 21 | 54 |

or condensed sulfuric acid controls the amount of adsorbed water, the idea of a critical humidity may be useful. For complex environments, care must be taken in using the critical humidity concept without a precise understanding of the corrosion products. The atmospheric corrosion mechanism for copper is electrochemical with the water-pollutant chemistry providing the medium for ionic mobility and surface product dissolution. There are many surface reactions that are thermodynamically favorable for copper oxidation.

Silver, unlike copper, shows no significant rate dependence on relative humidity, $r = 0.37 \exp 0.13RH$, in these complex environments. This is evidence that aqueous electrochemical intermediates have different roles in the mechanism of silver and copper corrosion.

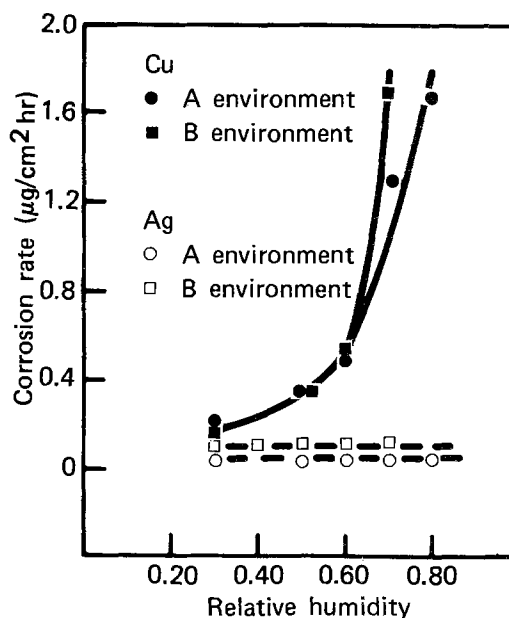


Fig. 2. Corrosion rate of copper and silver vs. relative humidity in two test environments.

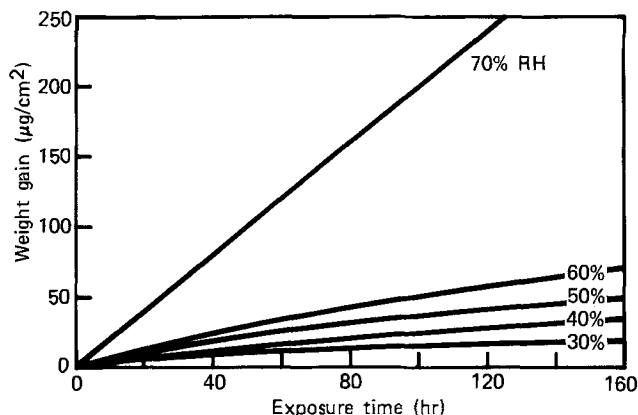


Fig. 3. Weight gain vs. environment B test exposure time for copper at various percentage relative humidities.

Direct chemical attack of silver metal by sulfur or H_2S is a plausible explanation of the observed results. We use the lack of a rate dependence on relative humidity to explain the similarity between its indoor and outdoor corrosion rates. These results contradict reported silver corrosion rate models that assume a relative humidity dependence (13-14).

Pollutants.—A series of tests was performed at 70% RH (25.0°C) with a single pollutant as the controlled variable either in the absence of other pollutants or with other pollutants present. The purpose of the tests was at minimum to yield engineering information about each pollutant and hopefully some insight into mechanisms. A summary of the rate data at various pollutant concentrations is given in Table IV for both metals. We will discuss each pollutant and its influence on the corrosion rate.

Sulfur dioxide.—Sulfur dioxide is a common pollutant produced by fossil fuel combustion. It has been studied from both a health and corrosion point of view.

A great deal of effort and money has been expended to reduce its urban concentration. It is readily soluble in water and reacts with it to form sulfurous acid. Further oxidation yields sulfuric acid. The mean outdoor urban site SO_2 concentration was $17.6 \mu g/cm^3$ for 840 monitoring stations reported by the U.S. Environmental Protection Agency in 1975 (30). Significantly higher values can be experienced on the average at a few sites or for short periods of time at any given site. The mean indoor concentration of SO_2 is $12.2 \mu g/m^3$ (18). The reader is referred to reviews on the atmospheric chemistry of SO_2 for background information (31).

Sulfur dioxide is known to increase the rate of copper corrosion at higher RH's (8). The mechanism is still an issue. Vernon (8), as well as the authors (15, 16), propose that SO_2 influences the local anodic pH sufficiently to cause increased oxide dissolution and, hence, an increase in corrosion rate. Sulfurous acid would be the dominant acid species on the surface because it is simply formed by reacting with one water molecule. Rozenfeld has proposed that SO_2 enhances the rate by depolarizing the cathodic region of the surface (2).

The equilibrium of gaseous SO_2 with liquid water and sulfurous acid yields a pH between 3 and 4 for the partial pressures in this study. The condensate of test environment A had a pH = 3.75. If sulfuric acid was the resultant product, which is thermodynamically favorable, the pH would be extremely low and very corrosive. Some metals do indeed catalyze the formation of sulfuric acid (32).

The copper and silver corrosion rate dependence on SO_2 partial pressure is shown in Fig. 4. The rate was measured in environments containing SO_2 as the only pollutant and in environments containing the background levels of environment A in Table III. The rates measured under these two conditions are labeled S and M, respectively. The rates, r , were fit to an equation of the form $r = AC^n$ where A and n are constants and C is the pollutant concentration.

Table IV. Summary of copper and silver corrosion rates, in $\mu g/cm^2$ hr, at various pollutant concentrations. C is the pollutant concentration in $\mu g/cm^3$, while Cu and Ag are used to identify the rates for copper and silver, respectively. n and A are the coefficients in the expression $r = AC^n$ for each pollutant. C.C. is the correlation coefficient which represents the quality of the data fit to the analytic expression.

| | | | | | | | | | |
|-----------------|----|--------|--------|--------|-------|-------|-------|---------|-------|
| SO_2^* | C | 0 | 39 | 118 | 786 | 1415 | n | A | C.C. |
| | Cu | 0.56 | 0.87 | 1.08 | 2.62 | 2.76 | 0.36 | 0.22 | 0.99 |
| | Ag | 0.061 | 0.054 | 0.058 | 0.056 | 0.059 | 0.015 | 0.052 | 0.65 |
| SO_2^{**} | C | 50 | 152 | 299 | | | n | A | C.C. |
| | Cu | 0.0042 | 0.0063 | 0.0075 | | | 0.33 | 0.001 | 0.996 |
| | Ag | 0.0029 | 0.0032 | 0.0039 | | | 0.16 | 0.0015 | 0.95 |
| H_2S^* | C | 0 | 7.9 | 20 | 66 | 328 | n | A | C.C. |
| | Cu | 0.77 | 1.24 | 1.68 | 1.88 | 4.08 | 0.30 | 0.63 | 0.97 |
| | Ag | 0.104 | 0.060 | 0.085 | 0.143 | 0.462 | 0.55 | 0.017 | 0.99 |
| H_2S^{**} | C | 2.62 | 6.50 | 14.4 | | | n | A | C.C. |
| | Cu | 0.0026 | 0.0032 | 0.013 | | | 0.93 | 0.00087 | 0.90 |
| | Ag | 0.015 | 0.017 | 0.019 | | | 0.14 | 0.013 | 0.999 |
| H_2S^\dagger | C | 4.42 | 11.5 | 22.4 | | | n | A | C.C. |
| | Cu | 0.039 | 0.050 | 0.071 | | | 0.36 | 0.022 | 0.98 |
| | Ag | 0.0042 | 0.0071 | 0.0079 | | | 0.40 | 0.0024 | 0.97 |
| Cl_2^* | C | 0 | 87 | 29 | 116 | 290 | n | A | C.C. |
| | Cu | 1.26 | 1.21 | 1.43 | 1.22 | 1.27 | 0 | 1.29 | 0 |
| | Ag | 0.052 | 0.057 | 0.049 | 0.073 | 0.097 | 0.17 | 0.035 | 0.85 |
| Cl_2^{**} | C | 7.83 | 16.5 | 25.2 | | | n | A | C.C. |
| | Cu | 0.113 | 0.166 | 0.244 | | | 0.64 | 0.029 | 0.99 |
| | Ag | 0.015 | 0.029 | 0.050 | | | 1.01 | 0.0018 | 0.994 |
| Cl_2^\ddagger | C | 70 | 11.9 | 20.3 | | | n | A | C.C. |
| | Cu | 0.060 | 0.15 | 0.216 | | | 1.20 | 0.0063 | 0.97 |
| | Ag | 0.011 | 0.021 | 0.022 | | | 0.65 | 0.0034 | 0.89 |
| HCl^{**} | C | 2.47 | 4.93 | 7.40 | | | n | A | C.C. |
| | Cu | 0.065 | 0.10 | 0.13 | | | 0.63 | 0.037 | 0.999 |
| | Ag | 0.019 | 0.021 | 0.023 | | | 0.17 | 0.016 | 0.993 |
| NO_2^* | C | 0 | 26 | 102 | 376 | 1316 | n | A | C.C. |
| | Cu | 1.15 | 1.18 | 1.41 | 1.46 | 1.78 | 0.097 | 0.87 | 0.97 |
| | Ag | 0.069 | 0.068 | 0.080 | 0.057 | 0.067 | -0.03 | 0.079 | 0.36 |
| O_3^* | C | 0 | 27 | 98 | 330 | 980 | n | A | C.C. |
| | Cu | 0.26 | 0.47 | 0.75 | 1.62 | 1.15 | 0.29 | 0.20 | 0.85 |
| | Ag | 0.054 | 0.050 | 0.057 | 0.058 | 0.163 | 0.29 | 0.016 | 0.82 |
| NH_3^* | C | 0 | 2.1 | 6.7 | 35 | 139 | n | A | C.C. |
| | Cu | 1.59 | 1.99 | 1.77 | 1.75 | 1.48 | -0.06 | 2.67 | 0.94 |
| | Ag | 0.041 | 0.032 | 0.040 | 0.289 | 0.710 | 0.8 | 0.014 | 0.985 |

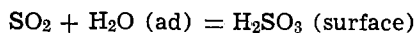
* The reference background environment was A in Table III.

** No other pollutants were present.

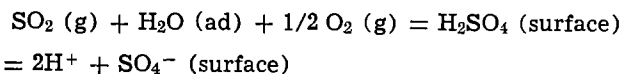
† HCl gas was present at $1.46 \mu g/m^3$.

‡ SO_2 gas was present at $47 \mu g/m^3$.

For copper, the exponent for both environments was close to 0.35. The correlation coefficients were equal to or greater than 0.99. A value of ± 1 is a perfect fit while zero indicates no correlation. In this case, the equation is an excellent approximation of the data. If we assume, as we have proposed earlier (15, 16), that SO_2 controls the surface pH and, hence, oxide stability (dissolution) by the reaction



then we would expect $n = 0.5$. For Co and Ni, this is the case; however, for Cu the reaction is more complex. It is clearly less sensitive to SO_2 concentration changes. One possible explanation is that copper catalyzes the formation of sulfuric acid



which is a much stronger acid; $pK_{\text{H}_2\text{SO}_4} = -3, +1.9$ and $pK_{\text{H}_2\text{SO}_3} = 1.8, 7.2$. The equilibrium concentration of hydrogen ions from the above equation is

$$[\text{H}^+] = P_{\text{SO}_2}^{1/3} P_{\text{O}_2}^{1/6} a_{\text{H}_2\text{O}}^{1/3} K^{1/3}$$

At fixed P_{O_2} and $a_{\text{H}_2\text{O}}$, the rate will depend on $P_{\text{SO}_2}^{0.33}$ if we assume that the corrosion rate is linear in the concentration of hydrogen ions (33). Even if the surface were saturated in CuSO_4 , the SO_4^- concentration would not suppress the ionization of H_2SO_4 significantly and the $P_{\text{SO}_2}^{0.33}$ dependence would be predicted. This clearly implies that the dissolution rate of a surface oxide, such as Cu_2O , controls the overall copper corrosion rate.

Silver showed comparative insensitivity to SO_2 . In the complex environment $n = 0.015$ while in the simple SO_2 environment $n = 0.16$. Reaction of silver with SO_2 to form concurrently sulfide and oxide is not thermodynamically favorable, $\Delta G^\circ = +57$ kcal/mole. The production of a sulfate is, however, feasible, $\Delta G^\circ = -4$ kcal/mole. The rationalization of the magnitude of n is not clear. The observation that silver corrosion is insensitive to SO_2 is consistent with its resistance to dilute sulfuric acid. Copper will corrode forming Cu^{++} in dilute sulfuric acid that contains oxygen. It is also important to note that for both metals, the more complex environment showed significantly higher rates at a fixed SO_2 concentration. This demonstrates that other pollutants act either synergistically or individually to enhance the rates, a fact that is repeatedly demonstrated in the remaining sections of this paper.

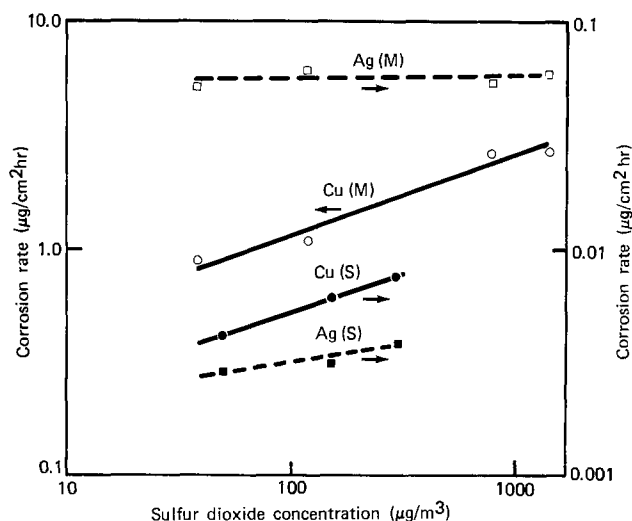


Fig. 4. Corrosion rate of copper and silver vs. sulfur dioxide concentration (70% RH, $T = 25^\circ\text{C}$). Arrows indicate appropriate scale. S and M refer to SO_2 only and the more complex reference environment A (Table III), respectively.

It is interesting to compare this behavior of the metals in atmospheric corrosion with their chemistry in bulk aqueous solutions. In neutral air-saturated solutions, the surface of copper will be covered with a layer of Cu_2O with a comparatively thin CuO layer at the solution interface. Silver will be immune from corrosion in this neutral environment.

If SO_2 is introduced, the pH will fall. The CuO will dissolve exposing Cu_2O . This compound will remain comparatively stable and protect copper until the pH reaches 3-4 where significant dissolution will begin. In the presence of other atmospheric species which complex Cu^+ or form compounds, such as CuCl , the protection is less good kinetically. In the case of silver, the metal is thermodynamically stable with respect to Ag^+ at lower pH. Presentation of a sulfiding species at the Ag surface will result in sulfidation. Attack by chloride-containing species and complexing agent can also be facilitated by the presence of metallic silver. The difference in the surface of the two metals due to the different solubility of the oxides will profoundly affect the kinetics of metal oxidation and of the depolarization reaction which is probably oxygen reduction.

Hydrogen sulfide.—Hydrogen sulfide is produced by fossil fuel combustion, vegetation decay, and geological activity. It is slightly soluble in water and forms a weak acid. It causes sulfiding of both copper and silver in the presence of oxygen. It can be oxidized by species like O_2 and Cl_2 to free sulfur, a reactive form of sulfur. Typical H_2S concentrations in urban areas are $1 \mu\text{g}/\text{m}^3$ (18); however, significantly higher concentrations have been reported in some urban areas where local sources such as paper mills exist (8, 29, 34). Indoor concentrations are not significantly less than outdoor levels.

Figure 5 shows the copper and silver corrosion rates vs. the H_2S partial pressure in three different reference conditions: M, the complex environment A in Table III, S, the H_2S pollutant only environment, and HCl, an environment with HCl at $1.46 \mu\text{g}/\text{m}^3$. The corrosion rates of both metals are significantly influenced by the H_2S partial pressure. Copper exhibits a monotonic increase in rate when going from a simple to a complex environment. The values of n are 0.9, 0.4, and 0.3 for the S, HCl, and M environments, respectively. The

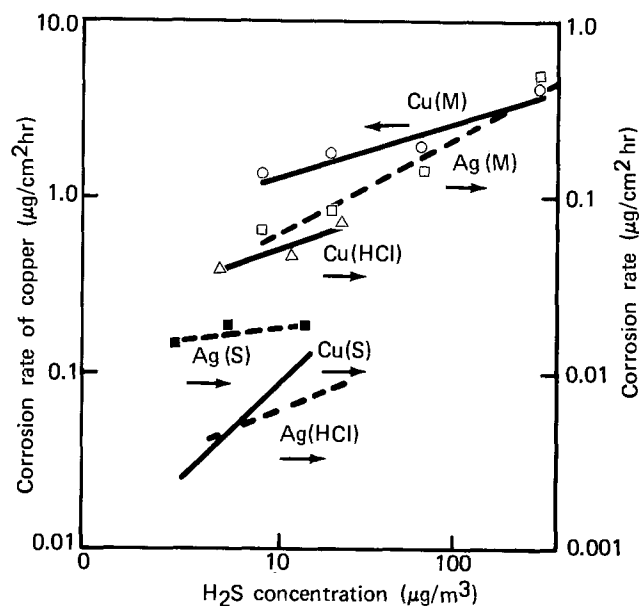


Fig. 5. Corrosion rate of copper and silver vs. hydrogen sulfide concentration. M is the multipollutant environment A, S is the single pollutant environment, HCl is the environment with the HCl concentration fixed at $1.45 \mu\text{g}/\text{m}^3$ with no other pollutants except H_2S . The arrows identify the appropriate scales (RH = 70%, $T = 25^\circ\text{C}$).

mechanism of corrosion must change significantly as indicated by these comparatively large changes in n . The rate dependence in the simple environment can be explained by a controlling surface process such as diffusion of H_2S to the surface or oxidation of H_2S by O_2 to a reactive sulfur species accompanied by a rapid diffusion process in the developing corrosion product. Either of these rate-controlling processes results in a linear dependence of surface active concentration on H_2S . This states that $n = 1$ which is close to the observed value of 0.9. The corrosion product in the polluted H_2S environment is Cu_2S and adds plausibility to a simple sulfiding process. Application of Wagner's model (35) will not explain the sulfiding rate dependence on H_2S . It would yield a less sensitive dependence on H_2S .

The more complex test environment, M, results in a less sensitive function of rate on H_2S concentration $n = 0.3$. The corrosion products are more complex consisting of hydroxide, oxide, sulfate, and chloride combinations with little, if any, sulfide. Hydrogen sulfide must then enhance the rate of corrosion by a far more complex process. In an independent experiment a strong positive synergism of H_2S ($1335 \mu\text{g}/\text{m}^3$) and SO_2 ($2980 \mu\text{g}/\text{m}^3$) was demonstrated on the rate of copper corrosion with a resultant $CuSO_4 \cdot 5H_2O$ product. No sulfides were detected. The H_2S may catalyze the oxidation of copper followed by rapid sulfurous acid attack. These are purely speculative mechanisms and more detailed experiments are needed to test the hypothesis.

Silver, in contrast to copper, shows the lowest corrosion in the HCl-containing reference environment, followed by the simple H_2S and complex reference conditions. The presence of an $AgCl$ surface product may inhibit sulfidation. The exponent n for silver is 0.14, 0.4, and 0.55 for the S, HCl, and M environments, respectively. The corrosion product in environment A (M) at the highest H_2S level tested, $328 \mu\text{g}/\text{m}^3$, as measured by XPS was Ag_2S with trace quantities of hydroxide and sulfate. Chlorides were detected, in addition to the above products, when this environment had H_2S at the lower concentration of $20 \mu\text{g}/\text{m}^3$.

The mechanism of silver sulfidation in the H_2S environment is different than copper. It would be tempting to propose that the Wagner model fits the data. This is, however, not the case, because, first, the kinetics were linear at each H_2S concentration as shown in Fig. 6 and, second, a simple defect diffusion model would predict $n = 0.25$ if the equilibrium concentration of cation vacancies controlled the rate.

Acidic chlorine gases.—The acidic chlorine gases considered in this study are HCl and Cl_2 . These are produced in urban environments by fossil fuel combustion, synthetic product incineration, purification of water, and salt spray interaction with secondary photochemical pollutants. Typical levels in urban environments range from 0.1 to $5 \mu\text{g}/\text{m}^3$, although very little data has been published (29). Hydrogen chloride is estimated to be the dominant acidic chlorine gas in the environment (36). HCl is highly soluble in water. The presence of Cl^- is a known accelerator of electrochemical corrosion for many materials. The pH of a solution in equilibrium with $4 \mu\text{g}/\text{m}^3$ of HCl gas is approximately 1. This is a typical concentration for our test and at the upper bound of observed values in urban environments. The equilibrium pH for $4 \mu\text{g}/\text{m}^3$ of Cl_2 is 5.

Figure 7 summarizes the silver and copper corrosion-rate dependence on Cl_2 in a mixed reference environment, and singly polluted environments containing either HCl or Cl_2 . Copper rates increase significantly with an increase in HCl and Cl_2 partial pressures in the single polluted environments. The rate depends on the 0.63 power of the pollutant pressure. In the complex environment M, little influence is observed. The presence of a high concentration of SO_2 and H_2S may dominate the process. Clearly, SO_2 will result in a

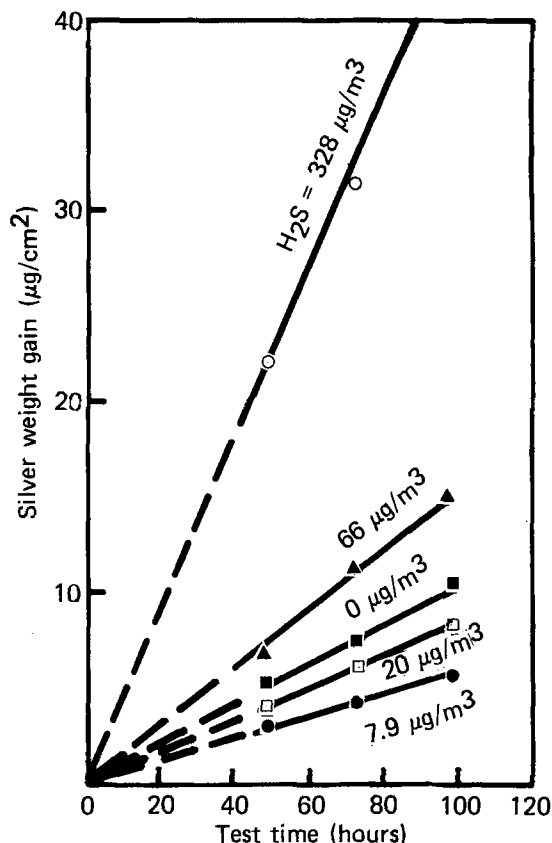


Fig. 6. Weight gain of silver vs. test time for various H_2S concentrations in environment A (Table III).

much lower surface pH and mask the influence of Cl_2 . Silver is most sensitive to Cl_2 alone, showing an exponent in the rate dependence on P_{Cl_2} of 1.01. The other two environments had an exponent equal to 0.17.

Nitrogen dioxide.—Nitrogen dioxide is a secondary pollutant of photochemical smog and is also produced in combustion processes. It is typically found at a concentration of $44 \mu\text{g}/\text{m}^3$ in urban centers (37). Its direct or acidic contribution to corrosion problems has not been reported; however, nitrate particles formed in the

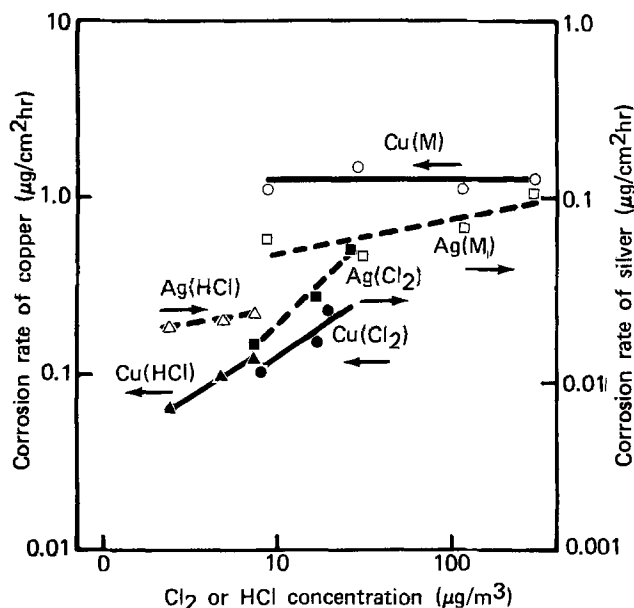


Fig. 7. Corrosion rate of copper and silver vs. Cl_2 or HCl concentrations. M, environment A (Table III) with variable Cl_2 , Cl_2 is the single pollutant in the environment, HCl is the single pollutant in the environment. The arrows identify the appropriate scale (RH = 70%, $T = 25^\circ\text{C}$).

atmosphere have caused electric contact failures (38). Nitrogen dioxide is a precursor to nitrous and nitric acid, but the kinetics are slow.

Neither copper nor silver corrosion rate was significantly affected by an increase of NO_2 levels in the test environment A over the concentration range 0-1316 $\mu\text{g}/\text{m}^3$.

Ozone.—Ozone, O_3 , is produced in photochemical processes as well as by natural and anthropogenic electrical discharges. Urban concentrations are generally in the range of 10-115 $\mu\text{g}/\text{m}^3$ (39). It is well recognized that ozone attacks carbon double bonds and degrades rubber. The influence of ozone on metals has not been well documented. It may directly influence the rate of oxidation; however, pure oxygen oxidation is not generally considered a problem in urban materials corrosion.

The corrosion rate dependence of copper and silver on ozone partial pressure in the multipolluted environment A is shown in Fig. 8. The corrosion of both metals is significantly influenced by ozone. This may be explained for silver as an increased oxidation of H_2S to form sulfur which reacts readily with Ag. Recall that silver corrosion is very sensitive to H_2S . For copper, ozone may, in addition to the above mechanism, enhance oxidation of SO_2 to SO_3 , followed by the formation of sulfuric acid on the copper surface, a reactive acid in the presence of oxygen.

Photoelectron spectroscopy of the high level O_3 corroded silver surface shows equal amounts of both sulfate and sulfide which supports the argument that the O_3 can enhance the oxidation of SO_2 .

Ammonia.—Ammonia is produced by decaying vegetation, as well as by many anthropogenic sources. It is found at typical levels of 6-12 $\mu\text{g}/\text{m}^3$ in urban areas (40). Ammonia complexes of copper and silver are common. This ability to complex may cause significant acceleration in the corrosion of these metals. The pH of aqueous solutions in equilibrium with the NH_3 partial pressures in this study are very basic.

Figure 8 shows copper and silver corrosion rates vs. ammonia concentration in the complex multipolluted environment. The rate of copper corrosion is inhibited while silver shows a significant weight increase. The NH_3 must act to increase the pH on copper surfaces rather than accelerate the dissolution rate by complex formation. Analysis of the white corrosion product on silver showed ammonium chloride with significant quantities of silver. Silver was a good catalyst for the ammonia and chlorine reaction to form solid NH_4Cl . This is a thermodynamically favorable reaction at the chamber conditions where NH_3 was present. For example, at 9 $\mu\text{g}/\text{m}^3$ of HCl, the NH_3 vapor pressure in equilibrium with NH_4Cl (s) is 16 $\mu\text{g}/\text{m}^3$. At pressures higher than this, we expect NH_4Cl precipitation. Table IV indicates that for an NH_3 concentration between 6

and 35 $\mu\text{g}/\text{m}^3$ the NH_4Cl precipitation begins in good agreement with the above calculations.

Indoor corrosion.—Extensive work has been directed to understand the magnitude and mechanism of copper corrosion in outdoor urban and marine environments. The American Society for Testing Materials has coordinated much of the work on the North American Continent and summarized the researchers' work in a multitude of publications (41-45). Guttman and Sereda have made an attempt to correlate observed rates with atmospheric parameters (7). Sulfur dioxide (sulfate particles) and water vapor (time of wetness) were the most important parameters; however, the correlation was not great. The outdoor corrosion of silver is not well documented but is recognized as a problem.

The indoor corrosion of materials has received less attention, because in most applications it is an insignificant problem. This is not, however, the case for the electronics industry. The integrity of microconductors, contacts, cables, semiconductors, and memories is an integral and important consideration for reliability in indoor environments. We will compare the indoor corrosion rates of copper and silver with the extensive outdoor data. Furthermore, we will correlate the observed indoor rates to a given pollutant, reduced sulfur.

Table V summarizes the indoor copper rates in this study (the first eight sites), other reported indoor rates, and outdoor rates. The rates are reported as weight gain per square centimeter per hour. We had in some cases to convert the other researchers' rates, obtained by cathodic reduction or weight loss measurements, to weight gain by either use of the reported products or by an estimate of the products. Table VI is a similar summary for silver.

All of the indoor data were used to fit to a log normal distribution function over the 35 sites for copper and 25 sites for silver. The statistical summary is given in Table VII. This includes the rate at various cumulative percentages of the population, the standard geometric deviation, correlation coefficient, and sample size. A similar analysis is reported for the outdoor data in Table VII.

Examination of these results demonstrates that the log normal distribution is a good fit of the data. Also, copper is shown to corrode indoors at approximately 0.01 the rate outdoors, while silver corrodes more rapidly indoors than outdoors by a factor of two or three. We propose that silver's comparative insensitivity to relative humidity accounts for the similarity in indoor and outdoor rates. The presence of indoor sources of H_2S and S_3 may account for the higher indoor levels. The corrosion rate of copper shows a much more pronounced humidity dependence and, hence, upper extremes of outdoor humidity will cause it to corrode significantly faster than indoors.

The pollutant measurements, as well as the relative humidity for six of the eight indoor sites in this study, have been summarized in a previous report (18). The reduced sulfur concentration, which consists of the sum of H_2S and free sulfur, was the best indicator of the indoor environmental severity toward both copper and silver. For example, if we combine our copper data with that of Vernon (8), the resulting rate in $\mu\text{g}/\text{cm}^2\text{hr}$ vs. reduced sulfur concentration in $\mu\text{g}/\text{m}^3$ is

$$r = 0.00211 [S_x] + 0.00054$$

with a correlation coefficient equal to 0.995. Figure 9 shows the results. For silver the equation is

$$r = 0.00423 [S_x]^{0.33}$$

with a correlation coefficient equal to 0.91. Both of these equations must be regarded as empirical fits. Examination of the laboratory data would clearly indicate that many pollutants are operative and circumstances may occur that make reduced sulfur an insignificant pollutant.

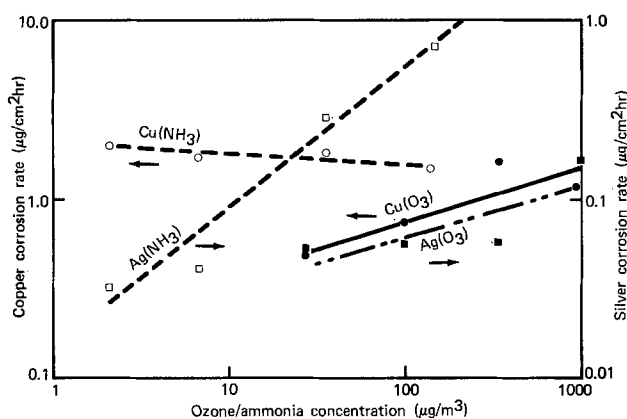


Fig. 8. Copper and silver corrosion rate vs. ozone and ammonia concentrations (RH = 70%, $T = 25^\circ\text{C}$, reference environment A).

Table V. Copper atmospheric corrosion rates
(All corrosion rates were converted to weight gain)

| Location | Type of environment | Corrosion rate ($\mu\text{g}/\text{cm}^2 \text{ hr} \times 10^4$) | Method* | Ref. |
|----------------------------|---------------------------|--|---------|------|
| Indoor | | | | |
| Los Angeles, CA | Air conditioned-comp. rm. | 13.9 | WG | (18) |
| Chicago, IL | Air conditioned-comp. rm. | 15.3 | WG | (18) |
| New York, NY | Air conditioned-comp. rm. | 20.3 | WG | (18) |
| Houston, TX | Air conditioned-comp. rm. | 5.49 | WG | (18) |
| Northern Indiana | Air conditioned-comp. rm. | 42.6 | WG | (18) |
| South Carolina | Air conditioned-comp. rm. | 94.1 | WG | (18) |
| New Jersey | Industrial work area | 29.2 | WG | (18) |
| New Jersey | Industrial work area | 62.7 | WG | (18) |
| New York, NY | Urban indoor-no A.C. | 17.2 | WG | (10) |
| New York, NY | Urban indoor-no A.C. | 18.4 | WG | (10) |
| Buffalo, NY | Urban indoor-no A.C. | 10.7 | WG | (10) |
| Buffalo, NY | Urban indoor-no A.C. | 8.92 | WG | (10) |
| Pittsburgh, PA | Urban indoor-no A.C. | 32.4 | WG | (10) |
| Pittsburgh, PA | Urban indoor-no A.C. | 11.6 | WG | (10) |
| Pittsburgh, PA | Urban indoor-no A.C. | 7.14 | WG | (10) |
| Pittsburgh, PA | Urban indoor-no A.C. | 10.4 | WG | (10) |
| Cincinnati, OH | Urban indoor-no A.C. | 21.2 | WG | (10) |
| Covington, KY | Urban indoor-no A.C. | 11.9 | WG | (10) |
| St. Louis, MO | Urban indoor-no A.C. | 13.1 | WG | (10) |
| Rockaway, NY | Rural indoor-no A.C. | 10.1 | WG | (10) |
| New York, NY | Urban indoor-enclosed | 6.54 | WG | (10) |
| Asbury Park, NJ | Marine indoor-no A.C. | 15 | WG | (10) |
| Cleveland, OH | Office | 4.98 | CD | (14) |
| Houston, TX | Office | 5.63 | CD | (14) |
| New York, NY | Office | 4.73 | CD | (14) |
| Los Angeles, CA | Office | 4.06 | CD | (14) |
| Borrego Sp., CA | Office | 3.38 | CD | (14) |
| Cleveland, OH | Basement | 7.08 | CD | (14) |
| S. Kensington, London, UK | Basement | 83.2 | WG | (8) |
| S. Kensington, London, UK | Roof | 78.6 | WG | (8) |
| South West London, UK | Home | 113.3 | WG | (8) |
| New York, NY | Air conditioned-comp. rm. | 4.7 | CD | (46) |
| New Jersey | Industrial chemical | 22.5 | CD | (46) |
| New Jersey | Industrial oil ref. | 8.0 | CD | (46) |
| Alabama | Industrial paper | 137.6 | CD | (46) |
| Outdoor | | | | |
| Cardington, U.K. | Rural | 1810 | WG | (9) |
| Bournville, U.K. | Suburban | 4230 | WG | (9) |
| Wakefield, U.K. | Industrial | 4540 | WG | (9) |
| Birmingham, U.K. | Urban | 13280 | WG | (9) |
| South Park, U.K. | Marine | 4400 | WG | (9) |
| Cleveland, OH | Urban/industrial | 1450 | WL | (7) |
| Ottawa, Canada | Urban | 1290 | WL | (7) |
| South Bend, PA | Rural | 1810 | WL | (7) |
| Trail, BC, Canada | Industrial | 2100 | WL | (7) |
| Kure Beach, NC | Marine | 2960 | WL | (7) |
| Kure Beach, NC | Marine | 3190 | WL | (7) |
| Altoona, PA | Industrial | 1400 | WL | (47) |
| New York, NY | Industrial | 1300 | WL | (47) |
| Sandy Hook, NJ | Marine | 798 | WL | (47) |
| Lajolla, CA | Marine | 1470 | WL | (47) |
| Keynest, FL | Marine | 600 | WL | (47) |
| State College, PA | Rural | 450 | WL | (47) |
| Phoenix, AZ | Rural | 80 | WL | (47) |
| Mandapan Camp, India | — | 7990 | WL | (48) |
| New Haven, CT | Industrial | 1110 | WL | (49) |
| Brooklyn, NY | Urban | 1970 | WL | (49) |
| Daytona Beach, FL | Marine | 2480 | WL | (49) |
| Prahly, Czechoslovakia | Industrial | 2910 | WL | (50) |
| Kapisty, Czechoslovakia | Industrial | 7200 | WL | (50) |
| Milesovka, Czechoslovakia | Industrial | 2170 | WL | (50) |
| Bystrany, Czechoslovakia | Industrial | 3120 | WL | (50) |
| Cinovic, Czechoslovakia | Industrial | 2240 | WL | (50) |
| Hamr, Czechoslovakia | Industrial | 3290 | WL | (50) |
| Dubji, Czechoslovakia | Industrial | 2830 | WL | (50) |
| Trebenice, Czechoslovakia | Industrial | 2450 | WL | (50) |
| Borislav, Czechoslovakia | Industrial | 2790 | WL | (50) |
| Vysluni, Czechoslovakia | Industrial | 2200 | WL | (50) |
| Hjezd, Czechoslovakia | Industrial | 3830 | WL | (50) |
| Petipsy, Czechoslovakia | Industrial | 2450 | WL | (50) |
| Medenec, Czechoslovakia | Industrial | 2700 | WL | (50) |
| Teplice, Czechoslovakia | Industrial | 3030 | WL | (50) |
| Most, Czechoslovakia | Industrial | 4160 | WL | (50) |
| Andelka, Czechoslovakia | Industrial | 1710 | WL | (50) |
| Nove Mesto, Czechoslovakia | Industrial | 1540 | WL | (50) |
| Hejnice, Czechoslovakia | Industrial | 1500 | WL | (50) |
| Frydlant, Czechoslovakia | Industrial | 1750 | WL | (50) |
| S. Kensington, Ld, UK | Urban | 3190 | WG | (8) |

* WG = weight gain, CD = cathodic reduction, WL = weight loss.

Summary

Copper corrosion rate is shown to be a sensitive function of relative humidity in a complex test environment, while silver is insensitive. The rate of copper corrosion is influenced by SO_2 , H_2S , Cl_2 , HCl ,

and O_3 concentrations. Silver's rate depends on H_2S , Cl_2 , HCl , and O_3 concentrations. The indoor corrosion rates of both metals are comparable and fit log normal statistics over the population size studied. Silver corrodes faster indoors than outdoors, while copper cor-

Table VI. Silver atmospheric corrosion rates (weight gain)

| Location | Type of environment | Corrosion rate ($\mu\text{g}/\text{cm}^2 \text{ hr} \times 10^4$) | Method* | Ref. |
|---------------------------|------------------------|--|---------|------|
| Indoor | | | | |
| Los Angeles, CA | Computer office-A.C. | 30.7 | WG | (18) |
| Chicago, IL | Computer office-A.C. | 23.9 | WG | (18) |
| New York, NY | Computer office-A.C. | 36.6 | WG | (18) |
| Houston, TX | Computer office-A.C. | 30.0 | WG | (18) |
| Northern Indiana | Computer office-A.C. | 37.5 | WG | (18) |
| South Carolina | Computer office-A.C. | 73.4 | WG | (18) |
| New Jersey | Industrial work area | 28.0 | WG | (18) |
| New Jersey | Industrial work area | 53.5 | WG | (18) |
| New York, NY | Computer office | 8.47 | CD | (46) |
| Los Angeles, CA | Computer office | 19.1 | CD | (46) |
| New Jersey | Chemical work area | 10.7 | CD | (46) |
| New Jersey | 0.1 Refinery work area | 23.0 | CD | (46) |
| Cleveland, OH | Industrial | 2.8 | CD | (14) |
| New York, NY | Urban indoor-no A.C. | 32 | WG | (10) |
| New York, NY | Urban indoor-no A.C. | 59 | WG | (10) |
| Buffalo, NY | Urban indoor-no A.C. | 34 | WG | (10) |
| Buffalo, NY | Urban indoor-no A.C. | 36 | WG | (10) |
| Pittsburgh, PA | Urban indoor-no A.C. | 31 | WG | (10) |
| Pittsburgh, PA | Urban indoor-no A.C. | 43 | WG | (10) |
| Pittsburgh, PA | Urban indoor-no A.C. | 39 | WG | (10) |
| Pittsburgh, PA | Urban indoor-no A.C. | 42 | WG | (10) |
| Cincinnati, OH | Urban indoor-no A.C. | 23 | WG | (10) |
| Covington, KY | Urban indoor-no A.C. | 28 | WG | (10) |
| St. Louis, MO | Urban indoor-no A.C. | 41 | WG | (10) |
| Rockaway, NY | Rural indoor-no A.C. | 9.5 | WG | (10) |
| Outdoor | | | | |
| Artesia, NM | Oil fields | 127 | CD | (51) |
| Borego Sp., CA | Desert | 3.70 | CD | (51) |
| Cleveland, OH | Urban/industrial | 18.6 | CD | (51) |
| Columbus, OH | Suburban | 3.29 | CD | (51) |
| Houston, TX | Urban/industrial | 41.2 | CD | (51) |
| Jersey City, NJ | Urban/industrial | 8.05 | CD | (51) |
| Kure Beach, NC | Marine | 9.71 | CD | (51) |
| Los Angeles, CA | Urban | 9.53 | CD | (51) |
| New York, NY | Urban | 8.00 | CD | (51) |
| St. Louis, MO, U.S.A.—103 | Urban | 9.98 | CD | (34) |
| St. Louis, MO, U.S.A.—105 | Urban | 8.38 | CD | (34) |
| St. Louis, MO, U.S.A.—106 | Urban | 6.75 | CD | (34) |
| St. Louis, MO, U.S.A.—108 | Urban | 19.20 | CD | (34) |
| St. Louis, MO, U.S.A.—112 | Urban | 6.72 | CD | (34) |
| St. Louis, MO, U.S.A.—115 | Urban | 10.9 | CD | (34) |
| St. Louis, MO, U.S.A.—118 | Urban | 8.14 | CD | (34) |
| St. Louis, MO, U.S.A.—120 | Urban | 8.19 | CD | (34) |
| St. Louis, MO, U.S.A.—122 | Urban | 10.8 | CD | (34) |

* WG = weight gain, CD = cathodic reduction.

rodes significantly faster outdoors. The indoor rates of both metals correlate well with the reduced sulfur pollutant concentration.

Acknowledgments

We thank D. Ramsey, J. Fazio, and I. Rodriguez for the weight gain measurements; F. Wagner and F. Lieu for the field support logistics; and the many dedicated researchers that have measured corrosion rates in both indoor and outdoor use environments.

Manuscript submitted May 21, 1980; revised manuscript received Sept. 19, 1980.

Any discussion of this paper will appear in a Discussion Section to be published in the December 1981

Table VII. Statistical summary of indoor and outdoor copper and silver atmospheric corrosion

| | Copper rates ($\mu\text{g}/\text{cm}^2 \text{ hr}$) | | Silver rates ($\mu\text{g}/\text{cm}^2 \text{ hr}$) | |
|--|--|---------|--|----------|
| | Indoor | Outdoor | Indoor | Outdoor |
| Cumulative % of the population | | | | |
| 10 | 0.00042 | 0.0766 | 0.00113 | 0.000387 |
| 30 | 0.00091 | 0.140 | 0.00188 | 0.000710 |
| 50 | 0.00156 | 0.213 | 0.00267 | 0.00108 |
| 80 | 0.00370 | 0.419 | 0.00471 | 0.00212 |
| 90 | 0.00583 | 0.597 | 0.00633 | 0.00301 |
| 95 | 0.00848 | 0.799 | 0.00809 | 0.00402 |
| 99 | 0.0171 | 1.379 | 0.0129 | 0.00694 |
| $\sigma = \frac{\ln r_{84.1} - \ln r_{15.9}}{2}$ | 1.030 | 0.801 | 0.673 | 0.799 |
| Correlation coefficient | 0.97 | 0.93 | 0.92 | 0.90 |
| Sample size | 35 | 41 | 25 | 18 |

JOURNAL. All discussions for the December 1981 Discussion Section should be submitted by Aug. 1, 1981.

Publication costs of this article were assisted by IBM Corporation.

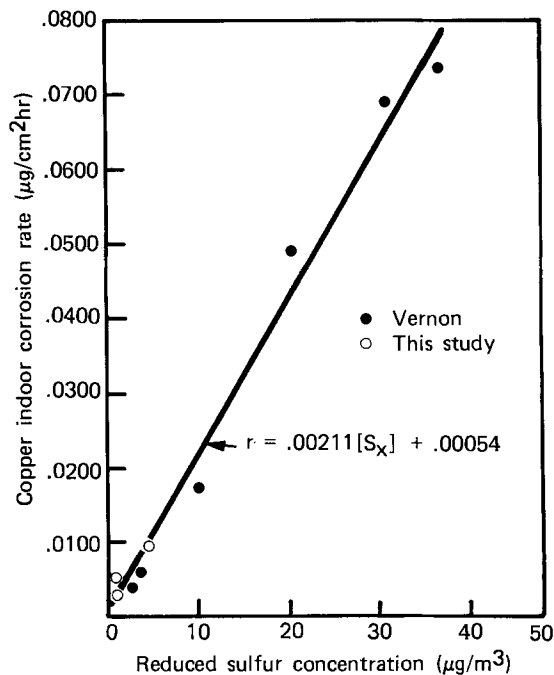


Fig. 9. Indoor corrosion rate of copper vs. reduced sulfur concentration.

REFERENCES

1. H. Leidheiser, "The Corrosion of Copper, Tin, and Their Alloys," John Wiley & Sons, Inc., New York (1974).
2. I. L. Rozenfeld, "Atmospheric Corrosion of Metals," NACE, Houston, Texas (1972).
3. L. L. Shreir, "Corrosion," 2nd ed., Newnes, Butterworths, London (1976).
4. H. H. Uhlig, "The Corrosion Handbook," John Wiley & Sons, Inc., New York (1948).
5. P. N. Aziz and H. P. Godard, *Corrosion*, **15**, 529 (1959).
6. C. Wagner and K. Grunewald, *Z. Phys. Chem.*, **B40**, 455 (1938).
7. H. Guttman and P. J. Sereda, ASTM Stp. No. 435, 326-59 (1968).
8. W. H. J. Vernon, *Trans. Faraday Soc.*, **23**, 113 (1921); **23**, 162 (1927); **27**, 264 (1931); **29**, 35 (1933); **31**, 1668 (1935).
9. J. C. Hudson, *ibid.*, **25**, 177 (1929).
10. W. E. Campbell and H. P. Thomas, Holm Conference Proceedings, pp. 233-265 (1968).
11. S. Mrowec, in "High Temperature Metallic Corrosion of Sulfur and Its Compounds," Z. A. Foroulis, Editor, pp. 55-109, The Electrochemical Society Softbound Proceedings Series, Princeton, N.J. (1970).
12. W. H. Abbott, *IEEE Trans. Parts, Hybrids, Packag.*, **php-10**, 24 (1974).
13. J. A. Lorenzen, Institute of Environmental Sciences Proceedings, pp. 110-114 (1971).
14. S. P. Sharma, *This Journal*, **125**, 2005 (1978).
15. D. W. Rice, P. B. P. Phipps, and R. Tremoureaux, *ibid.*, **126**, 1459 (1979).
16. D. W. Rice, P. B. P. Phipps, and R. Tremoureaux, *ibid.*, **127**, 563 (1980).
17. P. B. P. Phipps and D. W. Rice, "The Chemistry of Corrosion," pp. 235-261, ACS Publication, Washington, D.C. (1979).
18. D. W. Rice, R. J. Cappell, W. Kinsolving, and J. J. Laskowski, *This Journal*, **127**, 891 (1980).
19. R. G. Wylie, D. K. Davies, and W. A. Caw, in "Humidity and Moisture," Editor-in-Chief, A. Wexler, Vol. 1, R. E. Ruskin, Editor, pp. 125-134, Reinhold Publishing Corp., New York (1965).
20. A. E. O. Keefe and G. C. Ortman, *Anal. Chem.*, **38**, 760 (1966).
21. B. E. Saltzman and A. F. Wartburg, *ibid.*, **37**, 1261 (1965).
22. R. K. Stevens, A. E. O'Keefe, and G. C. Ortman, *Environ. Sci. Tech.*, **3**, 652 (1969).
23. P. W. West and G. C. Gaeke, *Anal. Chem.*, **28**, 1961 (1956).
24. A. Fontijn, A. J. Sabadell, and R. J. Ronco, *ibid.*, **42**, 575 (1970).
25. B. E. Saltzman, *ibid.*, **26**, 1949 (1954).
26. C. G. T. Prince, *J. Appl. Chem.*, **5**, 364 (1955).
27. J. A. Hodgeson, K. S. Krost, A. E. O'Keefe, and R. K. Stevens, *Anal. Chem.*, **42** (14), 1795 (1970).
28. J. E. Sigsby, *J. Environmental Sci.*, **7** (1), 51 (1973).
29. T. E. Graedel and N. Schwartz, *Mater. Performance*, **17** (1977).
30. Air Quality Data, 1975 Statistics, EPA-450-2-77-002, 109 (1979).
31. J. O. Nriagu, "Sulfur In The Environment," John Wiley & Sons, Inc., New York (1978).
32. C. E. Junge and T. Ryan, *Quart. J. Roy. Meteorol. Soc.*, **84**, 46 (1958).
33. D. A. Vermilyea, *This Journal*, **113**, 1067 (1966).
34. F. Mansfeld, Regional Air Pollution Study, AMC 7010.112 AR, 32 (1977).
35. C. Wagner, *Z. Phys. Chem.*, **B21**, 25 (1933).
36. "Chlorine and Hydrogen Chloride," EPA-600/1-76-020, National Technical Information Service, PB-253 196, 388 (1976).
37. Air Quality Data, 1975 Statistics, EPA 450-2-77-002, 155 (1977).
38. H. W. Hermance, C. A. Russel, E. S. Bauer, T. F. Egan, H. V. Wadlow, *Environmental Sci. Tech.*, **5**, 781 (1971).
39. Air Quality Data, 1973 Annual Statistics, Publication EPA-450/2-74-015, Research Triangle Park, N.C. (1974).
40. C. E. Junge, "Air Chemistry and Radio Activity," Academic Press, New York (1963).
41. "Atmospheric Factors Affecting the Corrosion of Engineering Metals," S. K. Coburn, Editor, ASTM-STP 646 (1978).
42. "Corrosion In Natural Environments," ASTM-STP 558 (1974).
43. "Galvanic and Pitting Corrosion—Field and Laboratory Studies," ASTM-STP 576 (1976).
44. Metal Corrosion In The Atmosphere," ASTM-STP 435 (1968).
45. "Atmospheric Corrosion of Nonferrous Metals," ASTM-STP 175 (1956).
46. R. V. Chiarenzelli, *IEEE Trans. Parts, Mater. Packag.*, **pmp-3**, 89 (1967).
47. A. W. Tracy, ASTM-STP 175, 67 (1955).
48. K. S. Rajagopalan, M. Sundaram, and P. L. Annamalai, *Corrosion*, **15**, 631 (1959).
49. R. S. Herman and A. P. Castillo, ASTM-STP 558, 82-96 (1974).
50. D. Knotkova-Cermakova, B. Bosek, and J. Vlckova, ASTM-STP 558, 52-72 (1974).
51. F. E. Bader, Personal communication.

Inclusions in Electroplated Additive-Free Hard Gold

S. Nakahara* and Y. Okinaka*

Bell Laboratories, Murray Hill, New Jersey 07974

ABSTRACT

Hard gold deposits plated from an additive-free phosphate bath have been analyzed for codeposited inclusions using transmission electron microscopy. Electron diffraction analyses of residues obtained from aqua regia dissolution of the gold deposits and those collected from the surface of thermally aged deposits showed that these residues consist of aurous cyanide (AuCN). These results and other electrochemical evidences suggest that AuCN is codeposited in additive-free hard gold, bringing about a grain refining effect and the resulting increase in hardness.

Hard gold deposits for electronics applications are generally electroplated from baths containing $\text{KAu}(\text{CN})_2$, a citrate or phosphate buffer, and a hard-

ening agent such as a cobalt salt. Recently, it was found that the inclusion of cobalt in the gold at concentrations above a certain limit may cause the formation of a highly resistive, cobalt-containing surface film (CoO) when the gold is aged at moderately high temperatures ($\sim 150^\circ\text{C}$) (1). As a practical solution to this

* Electrochemical Society Active Member.
Key words: electrodeposition, transmission electron microscopy, electron diffraction.

problem it has been suggested to replace the cobalt-hardened gold (CoHG) with an additive-free hard gold (AFHG) for certain applications (2).

The plating of AFHG was first described by Reinheimer (3), who obtained hard gold deposits by operating at low temperatures ($\sim 25^\circ\text{C}$) the conventional citrate or phosphate bath which normally yields soft gold at elevated temperatures ($\sim 70^\circ\text{C}$). He also observed that the increase in hardness with decreasing plating temperature is accompanied by a corresponding increase in carbon content of the deposit. Subsequently, we carried out a transmission electron microscope (TEM) study of various hard gold deposits (4), and found that AFHG contains a high density of small nonmetallic objects. The present study was undertaken to identify these inclusions and to obtain an understanding of the mechanism of codeposition and the role that the codeposited material might play in determining the structure and properties of AFHG. It is shown that AFHG contains aurous cyanide (AuCN), which is known to form a polymeric structure with infinite linear chains (5, 6). This finding is consistent with the recently proposed mechanism of cathodic gold deposition from $\text{Au}(\text{CN})_2^-$, which involves the formation of AuCN as an adsorbed intermediate (7-11).

Experimental

Plating procedure.—The AFHG deposits examined in this work were plated from a phosphate bath with the following composition: $\text{KAu}(\text{CN})_2$ 44 g/liter, KH_2PO_4 100 g/liter, KOH 28 g/liter, pH 7.0. The plating was carried out at 40°C using the previously described experimental setup (12) involving a stainless steel rotating cylinder cathode and a concentric anode. The cathode, 2 cm in diameter and 2.1 cm in height, was tightly wrapped with a substrate, which was a sheet of copper, $2.1 \times 6.5 \times 0.005$ cm, coated with a thin flash of gold strike. The anode was made of titanium, and it was coated with an active layer consisting of RuO_2 and TiO_2 (12). The inner diameter of the anode measured 2.9 cm. The cathode was rotated at 3600 rpm to obtain a turbulent flow condition which allowed high speed plating at a current density of 250 mA/cm^2 (12).

Specimen preparation.—The copper substrate was first dissolved off the gold deposit ($\sim 25 \mu\text{m}$) in 1:1 HNO_3 . TEM specimens for direct observation of inclusions were prepared by electropolishing the gold in a mixture of 25 ml ethyl alcohol, 25 ml glycerin, and 50 ml concentrated HCl (4).

The residue obtained upon dissolution of the AFHG deposit in aqua regia was collected on a TEM specimen grid after thorough washing in distilled water. In this procedure the aqua regia had to be replaced by distilled water immediately after complete dissolution of the gold because the residue dissolved rather rapidly in aqua regia. It was noted that the amount of this residue was considerably less than that obtained from a CoHG deposit. The latter was first discovered by Munier (13) and called "polymer," which more recently was identified as cobaltous cyanocobaltate, $\text{Co}_3[\text{Co}(\text{CN})_6]_2 \cdot x\text{H}_2\text{O}$ (14). This "polymer" is stable in aqua regia unlike the residue from the AFHG.

The surface residue formed on a thermally aged (150°C , 1 week) AFHG deposit was collected on a small piece of knife edge using the scraping technique described previously (15). The knife edge was directly mounted on a specimen holder for TEM observation.

Transmission electron microscopy.—TEM micrographs were taken with a JEM-200 electron microscope operated at 200 kV. The defocus imaging technique (16) was used for direct observation of nonmetallic inclusions in gold deposits.

Experimental Results

Direct observation.—A TEM micrograph of an AFHG film taken in the under-focused condition [Δf (defocus distance) = $-3.9 \mu\text{m}$] is shown in Fig. 1. Nonmetallic

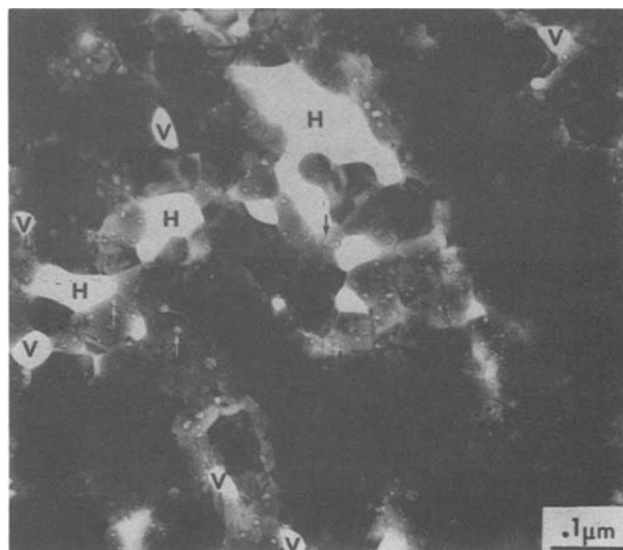


Fig. 1. TEM micrograph of electropolished AFHG, showing nonmetallic objects (black and white arrows), voids (denoted by a symbol V), and holes (marked by H). White arrows indicate inclusions inside the deposit, whereas black arrows show objects lying on the surface. The micrograph was taken in slightly underfocused condition in order to reveal the images of inclusions.

objects are seen in this micrograph mostly as small white circles surrounded by black rings (marked by white arrows), while some are seen with an opposite contrast as black circles surrounded by white rings (marked by black arrows). These small image features result from phase contrast, and therefore these objects are sometimes called "phase objects" (17). It can be easily shown from the previously described image analysis based upon geometric optics (18) that the black circles in Fig. 1 are due to objects situated on the specimen surfaces, whereas the white circles are images resulting from objects located inside the specimen. As shown previously (19), the image size measured from under-focused micrographs closely corresponds to the true size of phase objects in the range of about 20-50 Å. The micrograph of Fig. 1 shows that approximately 80% of the phase objects measure 20-55 Å in diameter, the remainder measuring up to 200 Å. The population density was $\sim 1 \times 10^{17}/\text{cm}^3$, and the volume ratio was estimated to be 1.3 to 1.9%, assuming the phase objects to be spherical and taking measurements in the regions of thicknesses ranging from 500 to 750 Å. A close examination of the micrograph shows that the phase objects are located both within the grains and at grain boundaries. In spite of the presence of these phase objects, the electron diffraction pattern obtained with the gold film did not show any detectable diffraction lines other than those due to gold metal.

It is also seen from Fig. 1 that the size of gold grains ranges from ~ 250 to 750 Å , which is somewhat larger than that of a typical CoHG (225-275 Å) (4) but considerably smaller than the grain size of soft gold deposits [typically 1-2 μm (20)]. Generally, when TEM specimens are prepared by electrothinning, holes surrounded by thin tapered edges are produced. The large holes denoted by H in Fig. 1 are seen to have this feature. On the other hand, the small faceted holes denoted by V are not surrounded by such tapered edges, and their size and shape resemble those of individual grains. Based on these observations, it may be assumed that these small holes are voids produced during film growth. The significance of this assumption will be discussed in a later section.

Residue from aqua regia dissolution.—A TEM micrograph obtained with the residue from aqua regia dissolution is shown in Fig. 2a, and the corresponding electron diffraction pattern in Fig. 2b. It is seen that the residue consists of extremely small crystals (25-

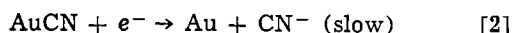
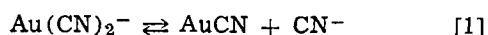
30Å) with poor crystallinity. The analysis of the diffraction pattern shows that the material is AuCN (Table I). It was noted that this material is stable to electron beam irradiation as opposed to the similar aqua regia residue obtained from a cobalt-hardened gold, which was observed to decompose in a few seconds in the electron microscope.

Surface residue.—Figures 3a and 3b show a TEM micrograph obtained with the residue collected from the surface of a thermally aged (150°C, 1 week) deposit and the corresponding electron diffraction pattern. The residue is seen as well-developed needle-shaped crystals 100-300Å thick. No such residue was obtained from the surface of as-deposited gold. The analysis of the diffraction pattern also showed that the crystals are AuCN (Table I). The relatively large discrepancy for the largest d-spacing is attributed to an experimental error.

Discussion

Existence of AuCN in deposits.—Reinheimer (3) studied the carbon inclusion in gold deposits plated from additive-free baths as a function of various plating parameters. He unequivocally showed that the carbon results from the inclusion of a cathodically formed product, and considered these compounds as the most likely source of carbon: KCN, AuCN, KAu(CN)₂, and HCN. For cobalt-hardened gold deposits, Raub, Knödler, and Lendvay (21) also considered the possibility of the inclusion of AuCN among other compounds as a source of carbon. Subsequently, Cohen, West, and Antler (22) made a Mössbauer spectroscopic study of cobalt-hardened gold, and reported that the deposit contained no detectable AuCN, KAu(CN)₂, or KAu(CN)₄. The detection limit for AuCN by this technique was ~2 mole percent (m/o) of the total Au. The analysis of AFHG plated under the conditions of the present experiment showed the presence of 0.055 weight percent (w/o) of carbon (2), which corresponds to 0.90 m/o as AuCN if all of the carbon is assumed to be present in this form. Thus, Mössbauer spectroscopy would not detect the AuCN in AFHG. Based on these considerations in conjunction with the results of analysis of aqua regia residue and surface residue, it is postulated that AuCN is codeposited in AFHG.

Mechanism of AuCN codeposition.—The mechanism of gold deposition from Au(CN)₂⁻ has been studied by many investigators in recent years. All agree that a chemical step precedes the charge transfer step but disagree in detailed description of the chemical step. Harrison and Thompson (8), using a potentiostatic linear sweep technique, found that the reduction of Au(CN)₂⁻ to be first order in cyanide, and proposed that AuCN is the reducible species



Beltowska-Brzezinska and Dutkiewicz (9) determined the dependence of exchange current on con-

Table I. Electron diffraction analysis of aqua regia and surface residues in AFHG

| Aqua regia residue | | Surface residue | | AuCN* | |
|-----------------------------|------------|-----------------------------|------------|--------------------|------------------------------------|
| <i>d</i> _{obs} (Å) | Inten-sity | <i>d</i> _{obs} (Å) | Inten-sity | <i>d</i> (Å) (hkl) | <i>I</i> / <i>I</i> _{max} |
| 5.06 | S | 4.90 | S | 5.08 (001) | 100 |
| 2.95 | S | 2.90 | S | 2.941 (100) | 100 |
| 2.50 | M | 2.58 | S | 2.542 (101, 002) | 70 |
| 1.88 | S | 1.93 | S | 1.921 (102) | 25 |
| 1.71 | M | 1.71 | M | 1.693 (003, 110) | 25 |
| 1.46 | M | 1.47 | M | 1.470 (200) | 10 |

S = strong; M = medium.

* Joint committee powder diffraction standard, formerly ASTM diffraction file 11-307.

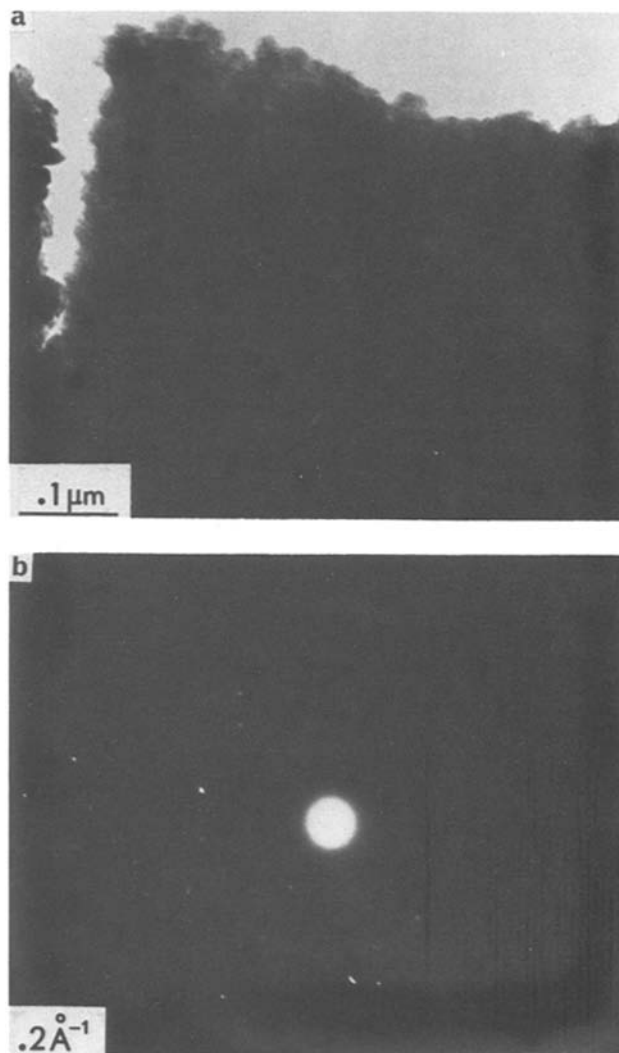
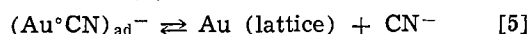
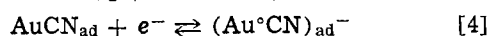


Fig. 2. Structure of aqua regia residue from AFHG. The image of the residue (a) and its electron diffraction pattern (b). Note details around edges in (a).

centrations and arrived at the same conclusion as above. MacArthur (7) carried out a cyclic voltammetric study and found evidence for the adsorption of AuCN intermediate at low overpotentials. Eisenmann (10) concluded from his kinetic studies of the deposition systems of soft as well as hard gold that the reaction proceeds via a common mechanism involving adsorption equilibria preceding and following the electron transfer step



McIntyre and Peck (11) observed a distinct cathodic prewave in their potential scan experiment, which they consider may be attributed to the reduction of an insoluble film of AuCN. These mechanistic evidences are consistent with our experimental results indicating that AuCN is incorporated in the gold deposit.

It was found by Reinheimer (3) that the carbon content of AFHG is strongly temperature dependent, and soft gold plated at 70°C contains only ~0.001 w/o C as compared to ~0.055 w/o for AFHG. From this result it is clear that soft gold contains essentially no AuCN. A TEM observation of soft gold also did not show any evidence of nonmetallic inclusions (19). This result can be understood if the adsorption of AuCN is involved because the coverage by an adsorbed species decreases exponentially as temperature is increased through an adsorption isotherm (23).

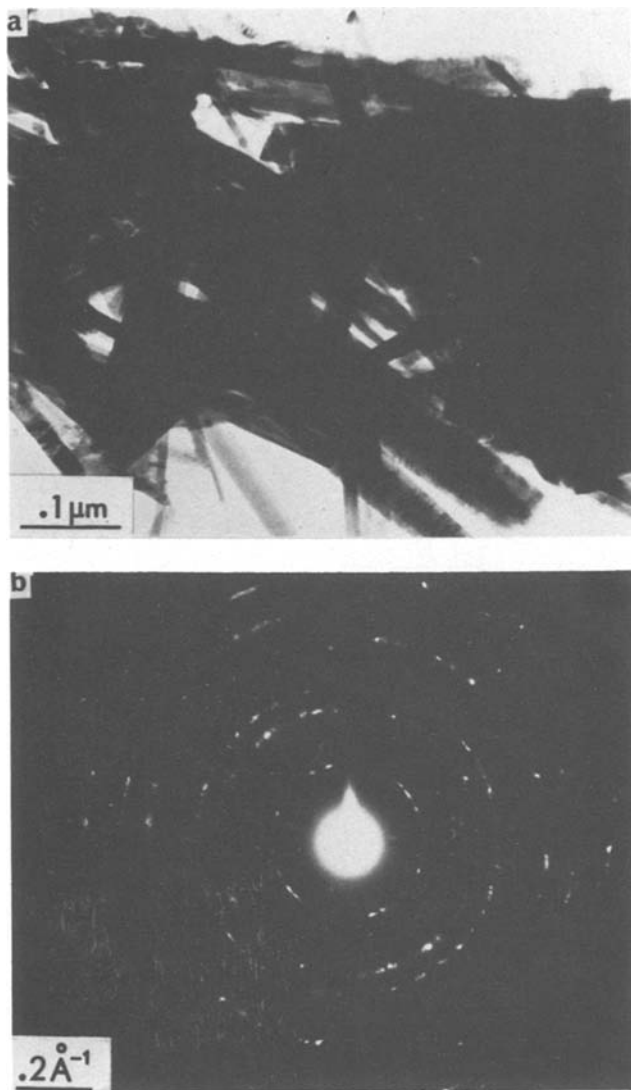
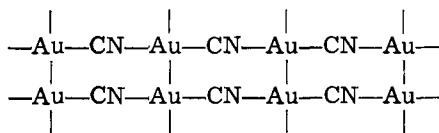


Fig. 3. Structure of surface residue obtained from thermally aged AFHG. The image of the surface residue (a) and its electron diffraction pattern (b).

AuCN as phase object.—As stated in the preceding section, the volume occupied by the phase object in the specimen amounts to 1.3-1.9%. If it is assumed that these objects are AuCN with a bulk density of 7.12 g/cm³, the carbon content of the specimen corresponding to the AuCN can be calculated to be 0.032 ± 0.006 w/o. Thus, under these assumptions the phase object accounts for approximately 50-70% of total carbon content (0.055 w/o). It appears that two or more sources of carbon exist in AFHG; a similar conclusion has been reached recently for CoHG (14).

The structure of AuCN is known to be polymeric with infinite linear chains arranged in parallel (5, 6)



As noted previously, the size of AuCN crystallites in the aqua regia residue was 25-30Å while the majority of phase objects measured 25-50Å. This similarity in size suggests that the phase objects are, in fact, AuCN crystallites, and they coagulate to form the residue upon dissolution of gold in aqua regia. From the known lattice constants (hexagonal, $a = 3.40\text{Å}$, $c = 5.09\text{Å}$) (6) it can be estimated that each crystallite consists of 5-10 unit cells. The observation of the needle-shaped crystals on the surface of thermally aged de-

posit shows that the small crystallites segregate on the surface to grow in the direction of c-axis upon heating.

It has been found that the density of AFHG determined by the gravimetric method using a specific gravity bottle is equal to 17.40 ± 0.10 g/cm³, as compared to 19.3 g/cm³ for pure bulk gold (2). A simple calculation using the volume percent of the phase object and the density of AuCN shows that the incorporation of AuCN as the phase object accounts for a decrease in density from 19.3 g/cm³ only to 19.1 g/cm³. It appears that the considerably lower density observed is due to the presence of voids. This interpretation is based on the following measurements and calculations. A TEM micrograph taken at a low magnification (20,000 \times) yielded $\sim 1 \times 10^{15}$ /cm³ for the population density of voids and 300-650Å for the range of void diameter. Using these values and estimated film thicknesses (750-1000Å), the ratio of the volume occupied by the voids to the film volume can be calculated as 8-14%. These values yield film densities ranging from 16.3 to 17.4 g/cm³ in good agreement with the observed density.¹

Role of AuCN.—Hard gold electrodeposits are generally obtained by the addition of small amounts of metal ions such as Co²⁺ or Ni²⁺. These ions are known to codeposit with gold in at least two different forms, cyano-complex and substitutional alloy (14, 25, 26). The increased hardness is primarily due to the grain refining effect (27) which is brought about by the codeposited cyano-complex (4, 14). Similarly, the codeposited AuCN appears to play the role of a grain refining agent for AFHG either by promoting the nucleation of gold or by inhibiting the growth of gold grains or both.

As was described in a previous communication, the contact resistance stability on thermal aging of AFHG is superior to that of CoHG (2). However, a small increase in contact resistance was found to occur upon heating AFHG at >100°C. The results described indicate that this increase is due to the surface segregation of AuCN at elevated temperatures.

Summary and Conclusion

A transmission electron microscope study of electroplated additive-free hard gold indicated that AuCN is codeposited as an impurity. Electrochemical evidences found in the literature suggest that this compound, which is formed as an adsorbed intermediate during the reduction of Au(CN)₂⁻, is incorporated in the gold deposit. The amount of AuCN estimated from the volume density of phase objects observed by TEM shows that about 50-70% of the total carbon found by chemical analysis of AFHG can be accounted for by AuCN. The AuCN appears to be present in AFHG as crystallites, each consisting of 5-10 unit cells, within gold grains as well as at grain boundaries. The incorporation of AuCN can explain the decreased grain size, increased hardness, and small contact resistance instability of additive-free hard gold.

Manuscript submitted April 17, 1980; revised manuscript received Aug. 8, 1980.

Any discussion of this paper will appear in a Discussion Section to be published in the December 1981 JOURNAL. All discussions for the December 1981 Discussion Section should be submitted by Aug. 1, 1981.

Publication costs of this article were assisted by Bell Laboratories.

¹ The density of CoHG is also known to be low (17.3-17.8 g/cm³) (24). A TEM examination of this type of gold showed that voids similar to individual grains in size and shape (~250Å) are distributed randomly. As in the case of AFHG, the volume of these voids appears to account for the decreased density of CoHG.

REFERENCES

- J. H. Thomas III and S. P. Sharma, *This Journal*, **126**, 445 (1979).
- F. B. Koch, Y. Okinaka, C. Wolowodiuk, and D. R.

- Blessington, *Plating*, **67**, 50 (1980); *ibid.*, **67**, 43 (1980).
3. H. A. Reinheimer, *This Journal*, **121**, 490 (1974).
 4. Y. Okinaka and S. Nakahara, *ibid.*, **123**, 1284 (1976).
 5. C. S. Gibson, *Proc. R. Soc. Ser. A*, **173**, 160 (1939).
 6. H. Zhdanov and E. Shugam, *Acta Physicochim. URSS*, **20**, 253 (1945).
 7. D. M. MacArthur, *This Journal*, **119**, 672 (1972).
 8. J. A. Harrison and J. Thompson, *J. Electroanal. Chem. Interfacial Electrochem.*, **40**, 113 (1972).
 9. M. Beltowska-Brzezinska, E. Dutkiewicz, and W. Lawicki, *ibid.*, **99**, 341 (1979).
 10. E. T. Eisenmann, *This Journal*, **125**, 717 (1978).
 11. J. D. E. McIntyre and W. F. Peck, Jr., *ibid.*, **123**, 1800 (1976).
 12. Y. Okinaka and C. Wolowodiuk, *ibid.*, **128**, 288 (1981).
 13. G. B. Munier, *Plating*, **56**, 1151 (1969).
 14. Y. Okinaka, F. B. Koch, C. Wolowodiuk, and D. R. Blessington, *This Journal*, **125**, 1745 (1978).
 15. S. Nakahara, *Thin Solid Films*, **67**, 73 (1980).
 16. S. Nakahara and Y. Okinaka, in "Properties of Electrodeposits—Their Measurement and Significance," R. Sard, H. Leidheiser, Jr., and F. Ogburn, Editors, Chap. 3, The Electrochemical Society Softbound Symposium Series, Princeton, N.J. (1975).
 17. L. Albert, R. Schneider, and H. Fischer, *Z. Naturforsch., Teil A*, **19**, 1120 (1964).
 18. S. Nakahara, *This Journal*, **126**, 1123 (1979).
 19. S. Nakahara, D. M. Maher, and A. G. Cullis, in "Proc. 6th Eur. Congr. on Electron Microscopy, Jerusalem, Israel, Vol. 1, p. 85, TAL International, Jerusalem (1976).
 20. J. D. E. McIntyre, S. Nakahara, and W. F. Peck, Paper 293 presented at The Electrochemical Society Meeting, Atlanta, Georgia, October 9-14, 1977.
 21. C. J. Raub, A. Knödler, and J. Lendray, *Plating*, **63**, 35 (January 1976).
 22. R. L. Cohen, K. W. West, and M. Antler, *This Journal*, **124**, 342 (1977).
 23. See, for example, "Electrosorption" E. Gileadi, Editor, Plenum Press, New York (1967).
 24. R. Duva and D. G. Foulke, *Plating*, **55**, 1056 (1968).
 25. H. Leidheiser, Jr., A. Vértes, M. L. Varsányi, and I. Czakó-Nagy, *This Journal*, **126**, 391 (1979).
 26. R. L. Cohen, F. B. Koch, L. N. Schoenberg, and K. W. West, *ibid.*, **126**, 1608 (1979).
 27. C. C. Lo, J. A. Augis, and M. R. Pinnel, *J. Appl. Phys.*, **50**, 6887 (1979).

Cyanaurate(III) Formation and Its Effect on Current Efficiency in Gold Plating

Y. Okinaka* and C. Wolowodiuk

Bell Laboratories, Murray Hill, New Jersey 07974

ABSTRACT

The cyanaurate(III) ion has been found to form and accumulate in acidic or neutral gold plating baths containing cyanaurate(I) as the source of gold. This trivalent gold species brings about a decrease in plating current efficiency because its reduction to gold metal requires three faradays per mole, whereas only one faraday is consumed to reduce one mole of Au(I). The accumulation of Au(III) should therefore be minimized to produce gold deposits with a thickness unaffected by bath age. This paper describes various methods for achieving this objective, which include the use of the so-called "dimensionally stable anode" and a technique of chemically reducing Au(III) to Au(I).

Thickness control in gold plating has become increasingly important in recent years because of the necessity for saving gold by plating only a minimal thickness required for specific applications. Since deposit thickness is directly proportional to plating current efficiency, it is important to have knowledge of factors affecting the latter. It is recognized that the current efficiency of both soft and hard gold plating from acidic or neutral cyanaurate(I) baths tends to decrease with increasing extent of bath use, and generally extrinsic contaminants are believed to be responsible for the efficiency deterioration.

During the course of our recent work to develop a polarographic method for analyzing gold plating solutions (1), significant amounts of cyanaurate(III) ions, $\text{Au}(\text{CN})_4^-$, were found in extensively used production baths. It has been established that this species is produced as a result of a reaction at the anode, generally platinum or platinized titanium, and that it is, at least partly, responsible for the decrease in plating current efficiency because of the greater quantity of electricity required to reduce Au(III) than Au(I).

In the present work, the relationship between current efficiency, Au(III) content, and bath age has been

studied, and methods for minimizing the formation and accumulation of Au(III) have been investigated.

Experimental

Plating Solutions

Results obtained with two different types of plating solutions are described in this paper: a conventional cobalt-containing hard gold bath (denoted as CoHG) and a high speed, additive-free hard gold bath (AFHG) (2). Make-up compositions and optimum operating conditions of these baths are listed in Table I. During the bath aging experiments, the plating solutions were analyzed for total gold and Au(III) and for Co^{2+} using, respectively, the polarographic and colorimetric methods described previously (1), and the total gold and cobalt concentrations were maintained within approximately $\pm 10\%$ by periodic addition of appropriate salts. The pH was kept constant within ± 0.1 unit by adding citric phosphoric acids for CoHG and AFHG baths, respectively.

Apparatus

CoHG.—A jacketed glass plating cell containing 300 ml of the CoHG plating solution was used. A rigid flat anode (platinum unless noted otherwise) measuring 3.8×3.8 cm was placed vertically at the center of the cell, and two copper sheets with the same dimensions plated

* Electrochemical Society Active Member.
Key words: cyanaurate(III), gold plating, current efficiency, dimensionally stable anode, hydrazine.

Table I. Bath compositions and operating conditions

| Ion | Form of salt added | CoHG | AFHG |
|----------------------------------|---|-----------------------|------------------------|
| Au(CN) ₂ ⁻ | KAu(CN) ₂ | 8.2 g/liter as Au | 30 g/liter as Au |
| Co ²⁺ | CoSO ₄ | 100 ppm as Co | — |
| Citrate | K ₃ C ₆ H ₅ O ₇ · H ₂ O and C ₆ H ₅ O ₇ · H ₂ O | 0.52M | — |
| Phosphate | KH ₂ PO ₄ and KOH | — | 1.23M |
| Condition | | | |
| pH | | 4.0 | 7.0 |
| Temp. | | 32°C | 40°C |
| Current | | 10 mA/cm ² | 250 mA/cm ² |
| Agitation | | Mild | Vigorous |

with strike gold were immersed on both sides of the anode with cathode-to-anode separation of about 3.2 cm. The solution temperature was maintained at 32°C by circulating constant-temperature water. Mild agitation was provided with a magnetic stirrer.

AFHG.—A rotating cylinder electrode system with a stationary, concentric cylindrical anode (Fig. 1) was used to plate AFHG at high speed. The substrate was a sheet of copper, 2.1 × 6.5 × 0.005 cm, coated with a thin flash of gold strike. It tightly wrapped the stainless steel portion of the rotating cathode as illustrated in Fig. 1. The ends of the substrate were folded into the vertical narrow groove, and a small Teflon key made to fit snugly into the groove was inserted to hold the substrate securely in place. The rotating cathode was fabricated by first attaching a short piece of stainless steel rod (1 cm in radius and 2.1 cm in height) to a rotating disk electrode core purchased from Pine Instruments Company, Grove City, Pennsylvania (Cat. No. DT-101-AA), followed by potting in epoxy resin and machining. This cathode design allowed quick, easy installation and removal of the substrate. The cylindrical anode had an inner radius of 1.46 cm, and was placed on a Teflon support in a glass plating cell. The volume of the plating solution was 1 liter. The solution temperature was maintained at 40°C by circulating it with a pump through an external heat exchanger.

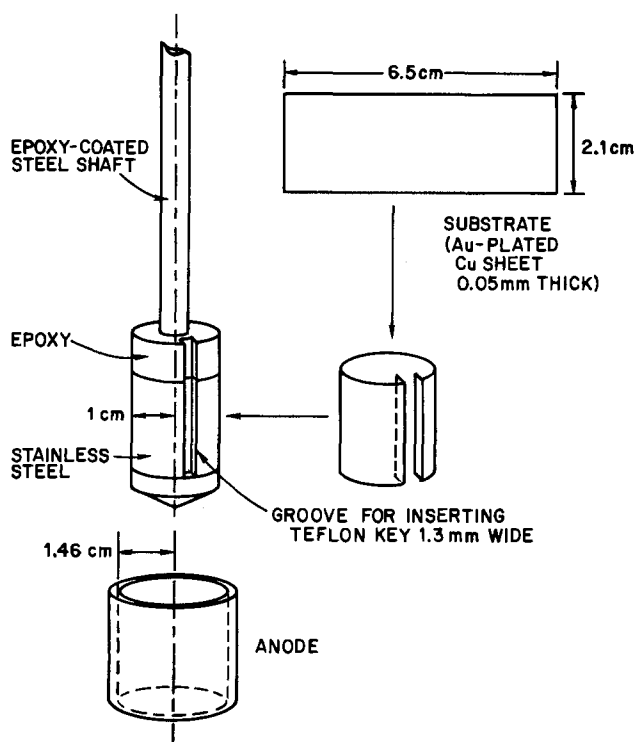


Fig. 1. Rotating cylinder electrode with demountable film substrate.

The cathode was rotated at 3600 rpm, which was well above the critical speed (822 ppm)¹ necessary to obtain turbulent flow. This high rotation speed was necessary to obtain hard, bright deposits at the plating rate (typically a minimum of 2.54 μm in 16 sec) required for practical high speed plating, for example, in continuous strip plating of electrical connector terminals.

Experimental Results

Current Efficiency, Bath Age, and Au(III) Content

CoHG.—Many actual production baths, including both citrate-based and organophosphonate-based baths, were analyzed for Au(III) and found to contain up to 25% of total gold in the form of Au(III). In the laboratory aging experiment carried out at 300 mA (~10 mA/cm² at both anode and cathode) with the apparatus described in the preceding section, the rate of accumulation of Au(III) was quite slow; for example, after ten bath turnovers² the Au(III) content was only about 5% of the total gold. In order to facilitate the study of the effect of Au(III) content on plating current efficiency, it was necessary to age the bath under accelerated conditions. It was found that Au(III) accumulates much more rapidly if plating is performed with a high initial gold concentration without cobalt present and the solution is subsequently heated (see Discussion section). Thus, a citrate buffer containing KAu(CN)₂ only (20.5 g/liter as Au) was first electrolyzed continuously at 32°C and 300 mA for 3 hr, and then the solution was heated at 60°C for 1 hr. The analysis of the resulting solution showed that the total gold concentration decreased to 8 g/liter, and that the Au(III) content amounted to 24% of the total gold. CoHG baths containing different amounts of Au(III) were prepared by diluting the above solution with the citrate buffer and adjusting the concentrations of total gold and cobalt to 8.2 g/liter and 100 ppm by adding KAu(CN)₂ and CoSO₄, respectively. Plating current efficiencies of these baths were measured at the cathode current density of 10 mA/cm² at 32°C with mild agitation. The results are shown in Table II. A significant decrease in plating current efficiency is seen with increasing Au(III) content. The "calculated efficiency" was obtained by multiplying the initial current efficiency observed in the absence of Au(III) by the theoretical fraction of initial current efficiency, which was calculated by taking account of the difference in number of electrons involved in reducing Au(I) and Au(III)

Fraction of initial current efficiency

$$= \frac{[\text{Au(I)}] + [\text{Au(III)}]}{[\text{Au(I)}] + 3[\text{Au(III)}]} = \frac{1}{1 + 2x} \quad [1]$$

where x is the Au(III) content of the bath expressed by

$$x = \frac{[\text{Au(III)}]}{[\text{Au(I)}] + [\text{Au(III)}]} \quad [2]$$

¹ For this electrode system the critical Reynolds number at which the transition from laminar to turbulent flow occurs is given by (3) $Re(\text{crit.}) = (\tau_0 - \tau_1)r_1\omega\nu^{-1} = 3960$, where τ_0 is the inner radius of the anode, r_1 the radius of the rotating cylinder electrode, ω the angular rotation speed, and ν the kinematic viscosity. With $\tau_0 = 1.46$ cm, $r_1 = 1.00$ cm, $\nu = 10^{-2}$ cm² · sec⁻¹, the above $Re(\text{crit.})$ value can be achieved when $\omega = 86.1$ rad/sec = 822 rpm.

² A bath turnover is defined as completed when the amount of gold initially present has been plated out and this amount of gold replenished.

Table II. Effect of Au(III) on plating current efficiency of CoHG bath (10 mA/cm², 32°C)

| Au(III)/total Au, % | Current efficiency, % | |
|------------------------|-----------------------|------------|
| | Observed | Calculated |
| 0 | 40.0 | (40.0) |
| 6.1 | 34.5 | 35.7 |
| 10.7 | 32.1 | 32.9 |
| 24.0 | 29.8 | 27.0 |

The good agreement between the observed and calculated efficiencies implies that the decrease in current efficiency brought about by Au(III) can indeed be accounted for by the greater number of electrons required to reduce Au(III) than Au(I).

AFHG.—In the high speed AFHG system the Au(III) buildup and accompanying current efficiency deterioration occurs more rapidly as the bath is aged. Results obtained with the platinum anode are represented by curves 1 and 1' in Fig. 2, in which changes in current efficiency and Au(III) content are plotted against the total weight of gold plated out from 1 liter of the plating solution and the number of bath turnovers. The cathodic current density used in this experiment was in the range of 230–300 mA/cm², while the corresponding current density at the platinum anode was 150–200 mA/cm². It is seen that the initial efficiency of greater than 90% decreased to only about 50% after four bath turnovers, during which the Au(III) content of the bath increased to almost 25%.³

From the results obtained with both CoHG and AFHG baths, it is clear that if plating current efficiency is desired to be maintained on the level of 90% of the initial efficiency, Au(III) content should not be allowed to exceed about 5% of total gold. In the case of CoHG this Au(III) level was reached after about 10 bath turnovers, whereas for AFHG it took only two-thirds of a turnover. Although the rate of Au(III) accumulation is likely to be controllable to some extent, for example, by increasing the anode area to decrease the anodic current density, it is clearly desirable to establish a method to compensate for the Au(III) effect, or to minimize or eliminate the formation and accumulation of Au(III).

Methods of Controlling Deposit Thickness

Adjustment of plating parameters.—The most obvious method of maintaining the deposit thickness con-

³ Theoretically, the minimum efficiency achievable should correspond to 33.3% of the initial efficiency, which should occur when all Au(I) is converted into Au(III), i.e., when $x = 1$ in Eq. (1).

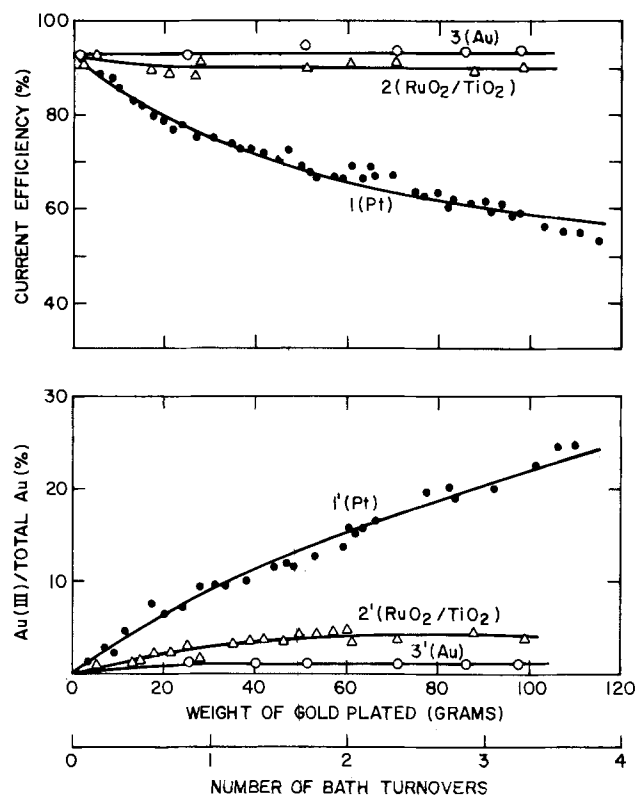


Fig. 2. Variation of plating efficiency and Au(III) content with bath age (AFHG bath). (Curves 1, 1': Pt anode; curves 2, 2': RuO₂/TiO₂ anode; curves 3, 3': Au anode.)

stant with changing current efficiency is to adjust either the plating current or the plating time. A general relationship between current efficiency and Au(III) content can be calculated as already explained for CoHG (Table II). Figure 3 shows this relationship, where the ordinate is the fraction of initial current efficiency, or the ratio of current efficiency at a given Au(III) content to that in its absence. The curve was calculated from Eq. [1], and the points are experimental. The agreement is considered to be fair. This relationship is valid for both CoHG and AFHG baths (and for any other gold plating baths), and can be used for adjusting plating current or time based on the results of total gold and Au(III) analyses.

This approach is simple but suffers from certain limitations. For example, the current adjustment method results in a continuous increase in current density at the anode, which in turn is expected to accelerate the accumulation of Au(III) and hence the plating efficiency deterioration. The method relying on the adjustment of plating time is applicable to batch plating, but not to continuous strip plating in which the substrate travels at a fixed speed.

Use of other anodes.—It was found that the Au(III) accumulation and accompanying current efficiency deterioration can be decreased significantly by replacing the platinum anode with an anode of the type often called "dimensionally stable anode" (DSA®), which is now widely used for chlorine production (4). This electrode, which is made typically by coating a titanium metal base with a mixture of RuO₂ and TiO₂, has anodic overvoltages considerably lower than platinum does for the evolution of chlorine (4) as well as oxygen (5). The initial study was carried out with CoHG bath using a RuO₂/TiO₂ anode obtained from Magneto-Chemie B.V., Schiedam, The Netherlands. During eleven bath turnovers, no detectable amount (<0.2%) of Au(III) was found, whereas with platinum 5.4% of Au(III) was found at the conclusion of the experiment performed under identical conditions. It was noted in these experiments that the yellow discoloration usually observed with CoHG baths operated with platinum anodes was much less intense for the solution aged with the RuO₂/TiO₂ anode. This appears to indicate that citrate ions are more stable at this anode.

The anode used with high speed AFHG bath was prepared using the procedure described by Janssen *et al.* (6). The results of the aging experiment carried out with this anode in AFHG bath are compared in Fig. 2 (curves 2 and 2') with those obtained with other anodes. The Au(III) concentration never exceeded

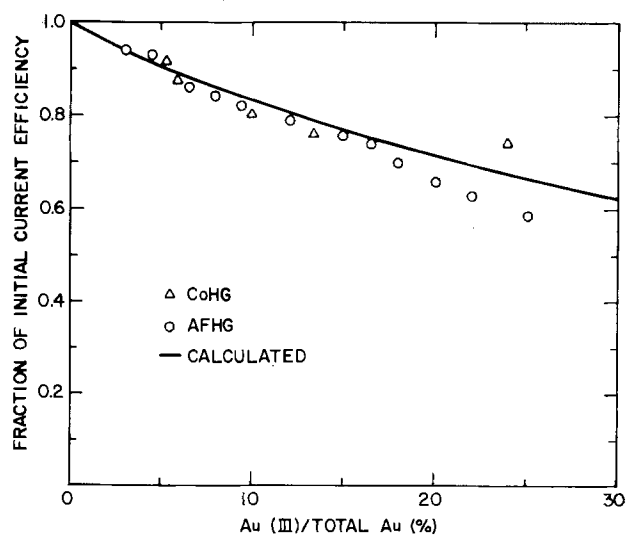


Fig. 3. Relationship between fraction of initial current efficiency and Au(III) content. (Points are experimental, line is calculated.)

~5% of total gold, and the efficiency remained greater than 89% (as compared to the initial efficiency of 93%) over the period of four bath turnovers. It is recognized that "dimensionally stable anodes" have a limited life as does platinized titanium depending on electrolysis conditions, coating composition, and the method of preparation. Results of our investigation concerning the life of anodes under the conditions of gold plating will be described elsewhere (7).

It was found that a gold anode also brings about the same beneficial effect. The level of Au(III) accumulation was even lower than that observed with the $\text{RuO}_2/\text{TiO}_2$ anode, and the current efficiency remained essentially unchanged at the initial level (curves 3 and 3', Fig. 2). The reason why the gold anode works is that gold dissolves preferentially over the oxidation of Au(I) to Au(III). Under the conditions of high speed plating, the concentration of free cyanide becomes quite high because of its rapid formation at the cathode. It was actually found that the gold anode loses its weight quite rapidly. Under our experimental conditions the rate of anode dissolution was such that a 0.38 mm (0.015 in.) thick anode would not last more than 100 hr of continuous plating. For this reason, a gold anode is not likely to be practical.

Chemical reduction.—Many common reducing agents are capable of reducing cyanoaurate(III) to cyanoaurate(I), but for the present application it is important to choose one which does not leave undesirable reaction products after treatment. Hydrazine was selected here for this reason (see Discussion section).

A CoHG bath, 100 ml, containing 20% of total gold in the form of Au(III) was treated with 0.25 ml of 85% hydrazine hydrate ($\text{N}_2\text{H}_4 \cdot \text{H}_2\text{O}$) at 75°C for 4 hr. Then, additional 0.25 ml of hydrazine was added, and heating was continued for 4 more hours. This treatment reduced about 90% of the Au(III) to Au(I). The initial current efficiency of this bath was 29%, which improved to 40% upon hydrazine treatment. No apparent difference was noted on the deposits from the hydrazine-treated bath and from the fresh bath. The addition of large excess hydrazine, e.g., 2 ml, greatly accelerated the reaction; however, the plating done after this treatment yielded discolored deposits.

The AFHG bath aged with platinum anode was also treated with hydrazine and the aging experiment continued. The hydrazine treatment-plating cycle was repeated several times under various treatment conditions. An optimum set of conditions found was to add about an equimolar amount of hydrazine hydrate and heat the bath at 75°–80°C for 1–3 hr depending on Au(III) content of the bath. When the Au(III) content was high (>15%), it was necessary to repeat the treatment in order to bring it down to <2%. The decrease in Au(III) concentration upon hydrazine treatment and the accompanying recovery of current efficiency are illustrated in Fig. 4.

Active carbon treatment.—Carbon treatment is conventionally carried out for removing organic contaminants. It was found that this treatment also removes Au(III) effectively. Active carbon (Darco Red Label), 0.25g, was added in 10 ml of a CoHG bath containing 14% of total gold in the form of Au(III), and the mixture heated at 90°C for 30 min. This treatment removed approximately 80% of the Au(III). However, about 29% of Au(I) was also lost. The loss of gold by carbon treatment is generally known, and for this reason this purification procedure should preferably be avoided. It is also known that carbon treatment does bring about a recovery of plating current efficiency. The experimental result described above shows that it is, at least partly, due to the removal of Au(III).

Discussion

Mechanism of Au(III) formation.—No detailed study has been carried out to establish the mechanism of the

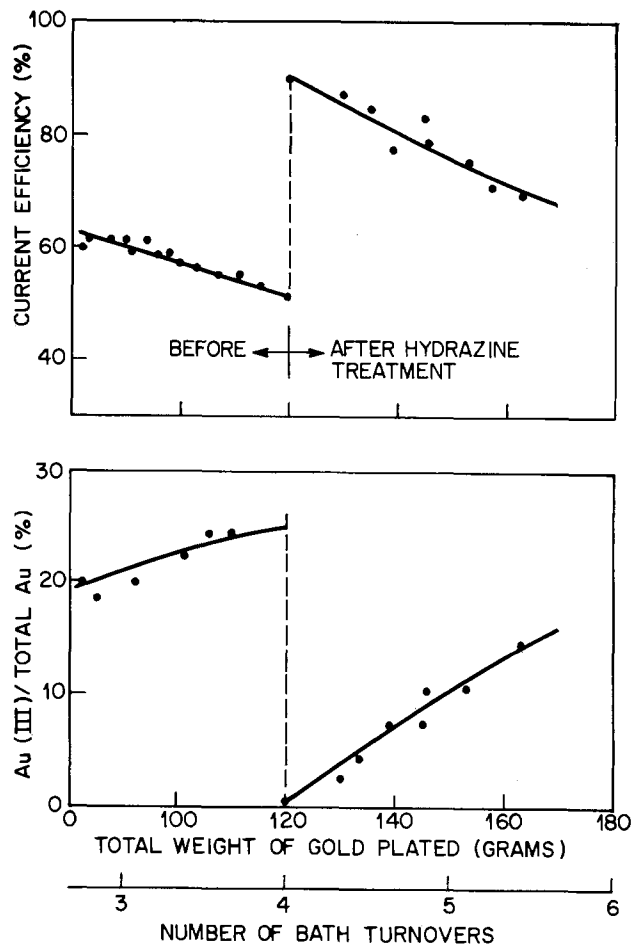


Fig. 4. Recovery of plating current efficiency and Au(III) content upon hydrazine treatment of aged AFHG bath.

formation of $\text{Au}(\text{CN})_4^-$. However, the following experimental observations should be noted: (i) A laboratory-aged CoHG bath was analyzed for $\text{Au}(\text{CN})_4^-$ by the polarographic method immediately after termination of electrolysis for 3 hr at 32°C and after heating in boiling water for 1 hr. The height of the Au(III) wave found after heating was nearly twice that observed before heating. (This post-heating effect was used for the accelerated aging described in the Experimental section.) It was also noted that the wave height increased significantly when a freshly electrolyzed CoHG bath was allowed to stand overnight at room temperature. (ii) Electrolysis of a fresh CoHG bath was carried out in an H-type cell in which cathode and anode compartments are separated by a sintered glass disk. A platinum sheet was used as the anode, while the cathode was a copper sheet. After electrolysis, the solution in each compartment was analyzed polarographically. Only the solution in the anode compartment showed the presence of Au(III). These two experimental results indicate that $\text{Au}(\text{CN})_4^-$ forms as a result of a slow homogeneous chemical reaction involving an intermediate species produced at the anode. The identity of this intermediate has not been established.

Effect of anode material.—In order to obtain some insight into the mechanism of the effect of anode material on Au(III) formation, polarization measurements were made at 32°C for CoHG bath as well as for the citrate buffer without gold and cobalt present. Results obtained with platinum and $\text{RuO}_2/\text{TiO}_2$ anodes are compared in Fig. 5. In both solutions potentials were higher in the plating solution than in the buffer. It is also seen that the potential ranges for the $\text{RuO}_2/\text{TiO}_2$ anode are about 0.5V lower than those for platinum in both solutions over the entire current range investigated. Quali-

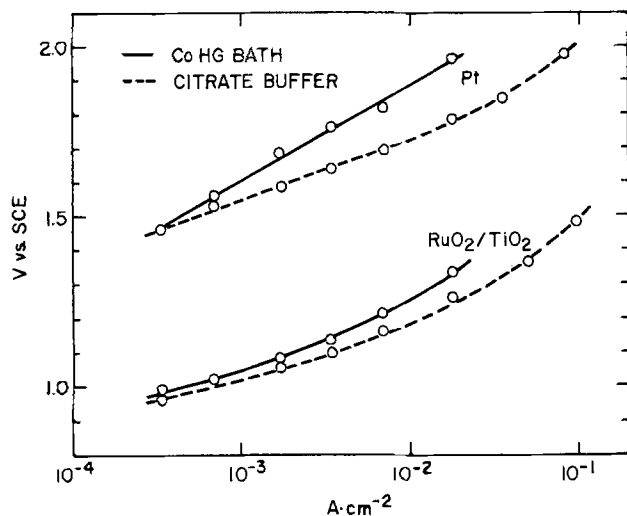
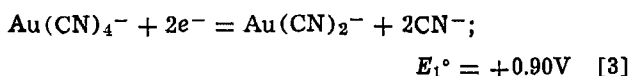
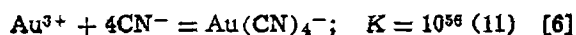
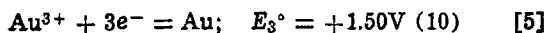
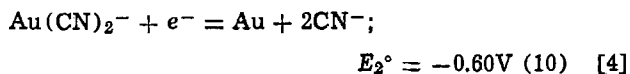


Fig. 5. Polarization curves for Pt and $\text{RuO}_2/\text{TiO}_2$ anodes in CoHG bath and in pH 4 citrate buffer at 32°C.

tatively, these results are expected from the known polarization behavior in strongly acidic solutions (8, 9). Because of the lack of identity of the reaction intermediate, no mechanistic interpretation can be offered for the observed anode effect on Au(III) formation. However, it is of interest to compare the potential ranges for the two electrodes with the equilibrium potential of the Au(III)/Au(I) couple



Since the standard potential E_1° was not found in the literature, it was calculated from the following values

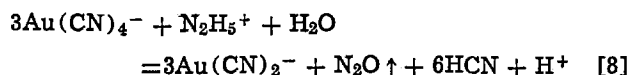
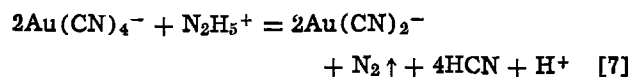


Furthermore, using $K = 1.62 \times 10^9$ (12) for the stability constant of HCN, the equilibrium potential for a typical plating solution with pH = 4 containing 0.04M $\text{Au}(\text{CN})_2^-$, 0.0004M $\text{Au}(\text{CN})_4^-$ [1% of Au(I)], and 0.01M free cyanide (a typical concentration of HCN plus CN^-) was calculated from E_1° to be equal to +1.26V (or +1.02V vs. SCE). An increase in the ratio of Au(III) to Au(I) by a factor of 10 (to 10%) shifts the potential by 0.03V in the positive direction. Comparison of these equilibrium potentials with the polarization curves in Fig. 5 shows that the oxidation of $\text{Au}(\text{CN})_2^-$ to $\text{Au}(\text{CN})_4^-$ is possible at both platinum and $\text{RuO}_2/\text{TiO}_2$ at practical current densities ($>10^{-2}$ A/cm²). The faster accumulation of Au(III) observed with the platinum anode may be anticipated from the higher potential at this anode. A further discussion of this subject will be given in a subsequent paper dealing with the behavior of various other anode materials (7).

The oxygen evolution at ruthenium metal was found to take place at potentials which are lower by additional 0.1-0.2V than at the $\text{RuO}_2/\text{TiO}_2$ anode. An experiment with a ruthenium-plated platinum electrode showed, however, that ruthenium metal dissolves significantly at current densities greater than ~ 30 mA/cm².

Reaction with hydrazine.—The reaction between hydrazine and Au(III) accompanies the evolution of colorless gas. From this fact and a comparison of E° values for the $\text{Au}(\text{CN})_4^-/\text{Au}(\text{CN})_2^-$ couple (reaction [3]) and various half-reactions of hydrazine (10), the

overall reaction is likely to be either or both of the following two reactions



where N_2H_5^+ is the protonated form of hydrazine which is predominant in the pH range under consideration [$\text{N}_2\text{H}_5^+ = \text{N}_2\text{H}_4 + \text{H}^+$, $K = 1.02 \times 10^{-8}$ (10)]. By using relevant thermodynamic data (10), the ΔG° values for reactions [7] and [8] have been calculated to be -154 and -138 kcal, respectively. The very large values reflect the combined effect of the strong oxidizing power of $\text{Au}(\text{CN})_4^-$ and the large numbers of electrons involved in these reactions (4 for [7] and 6 for [8]).

In order to obtain insight into the mechanism of these reactions, a kinetic study was carried out by following the disappearance of Au(III) after the addition of large excess hydrazine. The conventional first-order plot shown in Fig. 6 was obtained at 40°, 50°, and 60°C with an AFHG bath containing a total gold concentration of 30.5 g/liter (0.155M) and an initial Au(III) content of 13.9% (0.0215M). Concentrated hydrazine (85% $\text{N}_2\text{H}_4 \cdot \text{H}_2\text{O}$) was added to make the initial concentration equal to 0.215M. It is seen that the linear relationship holds only after about 7 min. A similar set of curves was obtained at 60°C with three different hydrazine concentrations as shown in Fig. 7. The slopes of these curves are approximately proportional to hydrazine concentration. Higher order analyses did not yield consistent results at different temperatures and hydrazine concentrations. Thus, the initial deviation from linearity appears to indicate the presence of some mechanistic complications which become less significant with increasing reaction time. For the linear range, the above results lead to the conclusion that the overall reaction consists of multiple steps including a rate-determining step which is first order with respect to both

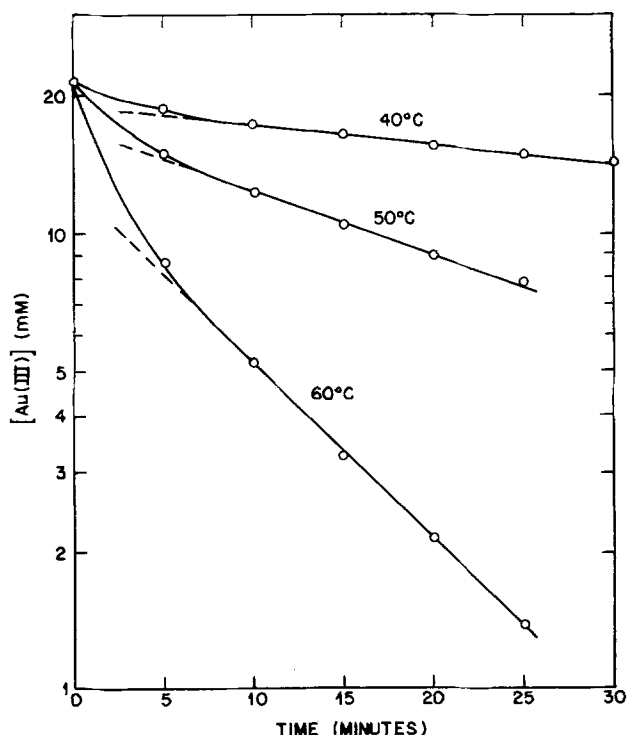


Fig. 6. Semi-logarithmic plot of Au(III) concentration against time after addition of excess hydrazine at different temperatures. (AFHG bath; total Au, 0.155M; initial Au(III), 0.0215M; hydrazine, 0.215M).

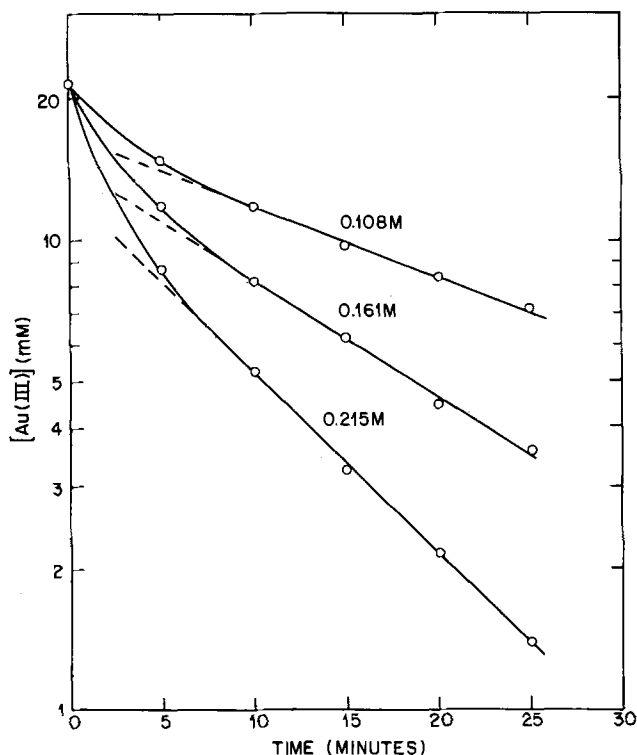
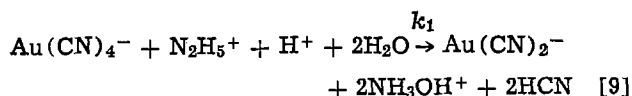
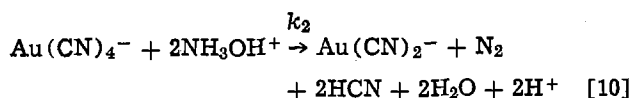


Fig. 7. Semi-logarithmic plot of Au(III) concentration against time after addition of different amounts of hydrazine at 60°C. (Same bath as for Fig. 6.)

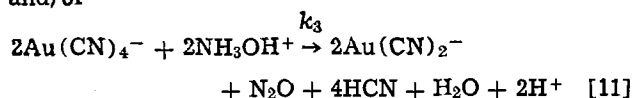
Au(III) and hydrazine. It is likely then that hydroxylamine is formed as an intermediate



This reaction is followed by



and/or



This type of reaction sequence is known to be encountered fairly often [e.g., "consecutive, competitive second-order reaction" (13)], and it can be shown readily that under the conditions of constant $[\text{H}^+]$ (buffer), constant $[\text{N}_2\text{H}_5^+]$ (large excess), and $k_1 \ll k_2$ and/or k_3 , the reaction becomes first order with respect to $[\text{Au(CN)}_4^-]$. The last condition has been verified experimentally; namely, the disappearance rate of Au(III) observed with hydroxylamine (added as hydrochloride) as the reducing agent was at least an order of magnitude faster than that found with hydrazine.⁴ The Arrhenius plot shown in Fig. 8 was obtained for the pseudo first-order rate constants calculated from the slope of linear portion of the curves in Fig. 6. The activation energy was found to be equal to 10.2 kcal mole⁻¹.

Finally, it should be noted that hydrazine has been described in the literature as an additive for gold plating baths. It is said to harden electroplated gold (14) presumably due to its influence on grain size (15). In addition, Winters (16) showed that hydrazine acts as an "oxygen scavenger" and increases the current effi-

⁴Hydroxylamine would be preferred to hydrazine for this reason. However, the former is available only in the form of salts, such as hydrochloride or sulfate, which would introduce unwanted anions into the bath.

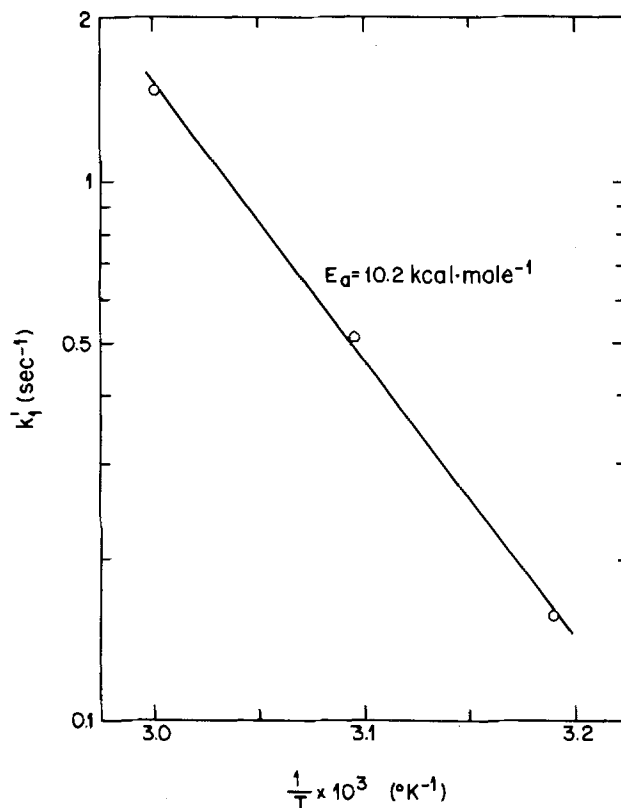


Fig. 8. Arrhenius plot derived from Fig. 6

ciency of soft gold plating. Presumably, a similar effect is expected for hard gold plating, but the discoloration of deposits by excess hydrazine noted previously precludes its use for this purpose.

Summary and Conclusions

1. Cyanoaurate(III) ions form and accumulate in acidic or neutral gold plating baths with platinum anodes as the baths are aged. The accumulation of the Au(III) species leads to a significant decrease in plating current efficiency.

2. Methods based on adjusting plating current or time to maintain a constant deposit thickness with steadily decreasing plating efficiency are not always applicable. As a simple and more general approach, it is recommended to replace the platinum anode with a low polarization anode such as the so-called "dimensionally stable anode." Although this electrode does not completely prevent the formation of Au(III), it is possible to maintain the Au(III) concentration at a level low enough to obtain a current efficiency greater than 90% of the initial level.

3. Hydrazine is useful for reducing Au(III) to Au(I) without forming undesirable reaction by-products.

4. Treatment with active carbon removes the Au(III) species, but this method suffers from the disadvantage that significant amounts of Au(I) are also removed.

Finally, it should be remembered that the current efficiency of hard gold plating is influenced by many other variables besides Au(III). Concentrations of Au(I), Co^{2+} , pH, temperature, agitation conditions, and impurities all affect the current efficiency. Therefore, it is important to control these variables as well as Au(III) concentration in order to maintain a stable current efficiency and to produce a constant deposit thickness.

Acknowledgment

We are grateful to A. Heller for his advice in obtaining the initial sample of RuO_2 -based dimensionally stable anode from Magneto-Chemie B.V., and to B. Miller for supplying the ruthenium-plated platinum electrode.

Manuscript submitted May 30, 1980; revised manuscript received Sept. 23, 1980. This was Paper 168 presented at the Pittsburgh, Pennsylvania, Meeting of the Society, Oct. 15-20, 1978.

Any discussion of this paper will appear in a Discussion Section to be published in the December 1981 JOURNAL. All discussions for the December 1981 Discussion Section should be submitted by Aug. 1, 1981.

Publication costs of this article were assisted by Bell Laboratories.

REFERENCES

1. Y. Okinaka and C. Wolowodiuk, *Plating Surf. Finish.*, **66**, 9, 50 (Sept. 1979).
2. F. B. Koch, Y. Okinaka, C. Wolowodiuk, and D. R. Blessington, *ibid.*, **67** (6), 50 (1980); **67** (7), 43 (1980).
3. J. Newman, "Electrochemical Systems," Chap. 1 and 17, Prentice-Hall, Englewood Cliffs, N.J. (1973).
4. G. Bianchi, V. DeNora, P. Gallone, and A. Nidola, South African Patent 68/7482 (1968); U.S. Pat. 3,616,445 (1971).
5. D. Gralizzioli, F. Tantardini, and S. Trasatti, *J. Appl. Electrochem.*, **4**, 57 (1974).
6. L. J. J. Janssen, L. M. C. Starmans, J. G. Visser, and S. Barendrecht, *Electrochim. Acta*, **22**, 1093 (1977).
7. C. G. Smith and Y. Okinaka, To be published.
8. A. Damjanovic, in "Modern Aspects of Electrochemistry, Number 5," J. O'M. Bockris and B. E. Conway, Editors, Chap. 5, Plenum Press, New York (1969).
9. G. Lodi, E. Sivieri, A. de Battisti, and S. Trasatti, *J. Appl. Electrochem.*, **8**, 135 (1978).
10. W. M. Latimer, "Oxidation Potentials," 2nd ed., Chap. 11, Prentice-Hall, Englewood Cliffs, N.J. (1952).
11. L. G. Sillén and A. E. Martell, "Stability Constants of Metal-Ion Complexes," Special Publication No. 17, The Chemical Society, London, p. 111 (1964).
12. R. M. Smith and A. E. Martell, "Critical Stability Constants, Vol. 4: Inorganic Complexes," Plenum Press, New York (1976).
13. See, for example, A. A. Frost and R. G. Pearson, "Kinetics and Mechanism," Chap. 8, John Wiley and Sons, New York (1953).
14. R. Duva and D. G. Foulke, U.S. Pat. 3,156,634 (1964).
15. D. G. Foulke, in "Gold Plating Technology," F. H. Reid and W. Goldie, Editors, Chap. 6, Electrochemical Publications Ltd., Ayr, Scotland (1974).
16. E. D. Winters, *Plating*, **59**, 231 (1972).

Steady-State Characteristics of Oxygen Concentration Cell Sensors Subjected to Nonequilibrium Gas Mixtures

J. E. Anderson and Y. B. Graves

Ford Motor Company, Chemistry Department, Research Staff, Dearborn, Michigan 48121

ABSTRACT

Oxygen sensors, based on membrane concentration cells, are to be used in a feedback control system on automobiles. For proper control function, the sensors should develop voltages corresponding to equilibrium oxygen partial pressures in engine exhaust, even when substantial deviations from chemical equilibrium actually exist in the bulk exhaust stream. This is accomplished through use of catalytic electrodes that are supposed to equilibrate local oxygen concentrations at the membrane surface and measure the emf developed across the concentration cell. This paper explores physicochemical factors influencing the emf across concentration cell oxygen sensors in the presence of surface reactions that are not necessarily in chemical equilibrium. Specifically, we report an isothermal kinetic analysis linking emf to (i) mass transfer between the bulk gas and boundary layers; (ii) adsorption, desorption, and chemical reaction on the catalyst/electrode surface. With nonequilibrium bulk gas mixtures, our analysis indicates that cell emf corresponds to equilibrium oxygen partial pressures when two restrictions are met: (i) mass transfer between bulk gas and surface boundary layers is slow relative to the rate of surface reactions; (ii) the reactant gases have identical mass transfer coefficients. Experimental studies of ZrO₂ oxygen sensors with platinum catalyst/electrodes are also reported. Voltage/composition curves for O₂/alkane systems deviate substantially from those calculated for chemical equilibrium. This reflects a relatively poor platinum catalytic efficiency for alkane oxidation. Following recent work by Takeuchi *et al.*, a "mass transfer shift" of voltage/composition curves was observed at 600°C with the O₂/H₂ and the O₂/D₂ systems. This result, which follows from our kinetic analysis, reflects the substantially different mass transfer coefficients of the reactant gases. In a second set of experiments, gas mixtures were equilibrated chemically before reaching the sensor by passing them over a secondary platinum catalyst. Stoichiometric voltage/composition curves were obtained under these conditions.

Oxygen sensors are being developed for engine control systems on automobiles (1-3). The basic concept involves sensing oxygen partial pressures in engine

Key words: solid electrolyte, gas electrode, control systems, kinetics.

exhaust, then using this information to control the air-to-fuel ratio entering the engine. In this way, engine efficiency is optimized while exhaust emissions are controlled.

Sensors based on oxygen concentration cells have been extensively investigated for this control operation.

These devices employ a solid-state oxygen-ion conducting electrolyte separating (i) an oxygen reference gas (air) from (ii) a gas of unknown oxygen concentration (engine exhaust). Sensor operation is based on the Nernst equation

$$\Delta V = - \left(\frac{RT}{4F} \right) \ln (P_{O_2}/P_{O_2}') \quad [1]$$

which relates the emf across the electrolyte, ΔV , to oxygen partial pressures in the two gases, P_{O_2} and P_{O_2}' . The most commonly used sensor consists of a Y_2O_3 -doped ZrO_2 electrolyte with platinum electrodes on both surfaces.

Control system strategy is based on sensing an oxygen partial pressure corresponding to chemical equilibrium in the exhaust stream. Meaningful air-to-fuel adjustments can then be made. It is well known, however, that the oxygen partial pressure in engine exhaust does not correspond to chemical equilibrium. Oxygen is present as one component of a nonequilibrium gas mixture containing products of incomplete combustion. Other important components include CO, CO_2 , H_2 , H_2O , NO, NO_2 , N_2 , and a variety of hydrocarbons and hydrocarbon derivatives.

Sensor electrodes are made from catalytic metals in order to circumvent this difficulty. The electrodes serve two functions. First, they catalyze oxidation reactions and equilibrate local oxygen concentrations; second, they monitor the emf developed across the concentration cell.

The present research explores physicochemical factors influencing sensor emf in the presence of nonequilibrium gas mixtures. Specifically, we develop an isothermal kinetic analysis linking sensor emf to the processes of mass transport, adsorption, desorption, and chemical reaction. Experimental studies relating sensor voltage to catalytic efficiency are also reported.

There has been relatively little previous research directed at the emf across concentration cells in the presence of nonequilibrium gas mixtures. Fleming (4, 5) presented an analysis where oxygen and carbon monoxide are assumed to be in chemical equilibrium at a fictive temperature that characterizes surface catalytic efficiency. Fleming's work does not treat surface boundary layers. Later, Takeuchi *et al.* (6) showed experimentally that boundary phenomena are crucial in producing sensor voltages corresponding to oxygen equilibrium in the bulk gas. This important finding is amplified and extended in the present work through kinetic analysis and experimental results. Etsell and Flengas (7) published definitive studies of ZrO_2 sensors in the presence of equilibrium oxygen partial pressures. Questions of gas adsorption and surface reactions on ZrO_2 oxygen fuel cells have also been explored (8). Haaland (9) has recently reported studies of O_2 sensors with non-catalytic surface electrodes.

The oxygen-ion conducting electrolyte (e.g., ZrO_2) plays a passive role in the present analysis: all internal electrochemical processes are idealized and cell emf becomes a convenient monitor of the surface processes that are the primary focus of the present work. This oversimplification both contrasts and complements simplifications made in previous studies of similar cells, where nonelectrochemical surface processes are idealized and internal electrochemistry is examined (8). Clearly, the experimental situation lies somewhere between these extreme views.

Kinetic Analysis

This analysis concerns the cell configuration shown in Fig. 1. We consider three regions on each side of an oxygen-ion conducting electrolyte: (i) a bulk gas region; (ii) a gaseous boundary layer; and (iii) the electrode/catalyst surface. Kinetic expressions, given below, describe both chemical reaction on the electrode/catalyst surface and mass transfer between adjacent regions.

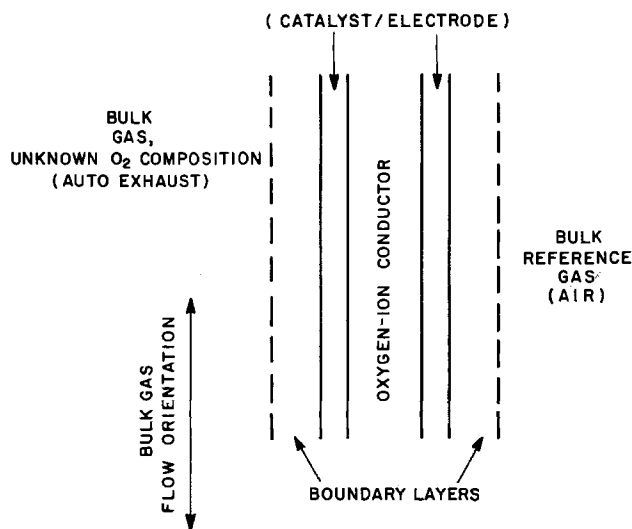


Fig. 1. Schematic drawing of oxygen concentration cell sensor showing the regions considered in the kinetic model: bulk gas region; gaseous boundary layer; electrode/catalyst surface.

The analysis is framed in terms of the reaction $O_2 + 2CO \rightleftharpoons 2CO_2$, which is of primary importance in sensor/exhaust applications. The same physical principles are, *mutatis mutandis*, directly applicable to other surface reactions.

Six coupled, nonlinear differential equations are involved:

Surface reactions

$$d\theta_A/dt = -2k_2\theta_A^2 + 2k_A A_1\theta_v^2 - k_R\theta_A\theta_B + k_D\theta_C\theta_v \quad [2]$$

$$d\theta_B/dt = -k_4\theta_B + k_B B_1\theta_v - k_R\theta_A\theta_B + k_D\theta_C\theta_v \quad [3]$$

$$d\theta_C/dt = -k_6\theta_C + k_C C_1\theta_v + k_R\theta_A\theta_B - k_D\theta_C\theta_v \quad [4]$$

Boundary layer reactions

$$dA_1/dt = -k_1(A_1 - A_g) - k_A A_1\theta_v^2 + k_2\theta_A^2 \quad [5]$$

$$dB_1/dt = -k_3(B_1 - B_g) - k_B B_1\theta_v + k_4\theta_B \quad [6]$$

$$dC_1/dt = -k_5(C_1 - C_g) - k_C C_1\theta_v + k_6\theta_C \quad [7]$$

The following variables appear in Eq. [2]-[7]: A_1 , B_1 , and C_1 are the partial pressures of O_2 , CO, and CO_2 in the boundary layer; θ_A , θ_B , and θ_C are the fractional surface coverages of atomic oxygen, CO, and CO_2 , respectively; θ_v , the fractional surface coverage of vacancies, is related to the others by $\theta_A + \theta_B + \theta_C + \theta_v = 1$. Rate constants k_1 , k_3 , and k_5 describe mass transfer of O_2 , CO, and CO_2 between the bulk gas and the boundary layer. k_A , k_B , and k_C describe adsorption of these gases from the boundary layer onto the catalyst surface. k_2 , k_4 , and k_6 characterize the corresponding desorption processes. k_R is the rate constant for the surface reaction $\theta_A + \theta_B \rightarrow \theta_C + \theta_v$; k_D is the rate constant for the reverse of this surface reaction. Input parameters are the partial pressures of O_2 , CO, and CO_2 in the bulk gas region; they are denoted A_g , B_g , and C_g .

The above expressions describe isothermal Langmuir-type adsorption/desorption kinetics (10). The oxygen-carbon monoxide reaction is assumed to occur exclusively on the catalyst/electrode surface via the Langmuir-Hinshelwood mechanism. This kinetic scheme is admittedly arbitrary. Simplifications have been introduced including an assumption of isothermal conditions. It should be noted that many particulars of carbon monoxide surface oxidation at atmospheric gas pressures remain unresolved despite extensive study (10-14). Although arbitrary and simplified for the present purpose, the kinetics described in Eq. [2]-[7] are in qualitative agreement with existing experimental observations.

The various rate constants are related to K_{eq} , the equilibrium constant for the O_2 -CO- CO_2 system, by

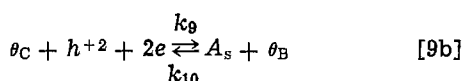
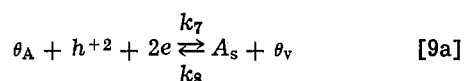
$$K_{\text{eq}} = \frac{(O_2)^{1/2} (CO)}{(CO_2)} = \frac{k_4 k_C k_D}{k_6 k_B k_R} \sqrt{\frac{k_2}{k_A}} \quad [8]$$

Equation [8] is readily obtained by applying detailed balance constraints to all adsorption/desorption processes and to the surface reaction.

K_{eq} is of order 10^{-10} atm^{1/2} or less for the O₂-CO-CO₂ system at temperatures below 1000 K (15). The back reaction, $2CO_2 \rightarrow 2CO + O_2$, is often neglected in catalytic studies for this reason. It must be included here if one is to compute proper limiting voltages when the bulk gas is rich in CO; i.e., when the bulk gas contains less than a stoichiometric amount of oxygen.

Cell EMF and Surface Concentrations

This section relates cell emf to surface concentrations on the catalyst/electrodes. It presumes that surface concentrations are determined by adsorption, desorption, and chemical reaction between un-ionized species; i.e., that cell emf is a convenient measure of surface concentrations governed by nonelectrochemical processes. Following Etsell and Flengas (8), two potential-determining reactions are considered



In the above equations, h^{+2} and A_s are surface concentrations of doubly charged oxygen ion vacancies and of oxygen atoms in the electrolyte. Under steady-state conditions with no external current, reaction rate theory gives

$$(k_7 \theta_A + k_9 \theta_C) h^{+2} e^{-F\phi/RT} = (k_8 \theta_v + k_{10} \theta_B) A_s e^{F\phi/RT} \quad [10a]$$

or

$$\frac{2F\phi}{RT} = \ln \left\{ \frac{k_7}{k_8} \left(\frac{\theta_A/\theta_v + (k_9/k_7)(\theta_C/\theta_v)}{1 + (k_{10}/k_8)(\theta_B/\theta_v)} \right) \frac{h^{+2}}{A_s} \right\} \quad [10b]$$

for the emf difference between electrolyte and an electrode exposed to O₂, CO, and CO₂. The reference electrode is exposed to air, and similar arguments lead to

$$\frac{2F\phi'}{RT} = \ln \left\{ \left(\frac{k_7}{k_8} \right) \left(\frac{\theta_A}{\theta_v} \right)' \left(\frac{h^{+2}}{A_s} \right) \right\} \quad [11]$$

since N₂ adsorption is vanishingly small. Making the usual assumption that (h^{+2}/A_s) is uniform across the electrolyte, the cell emf becomes

$$\Delta V = -\frac{RT}{2F} \ln \left\{ \left(\frac{\theta_A/\theta_v + (k_9/k_7)(\theta_C/\theta_v)}{1 + (k_{10}/k_8)(\theta_B/\theta_v)} \right) \left(\frac{\theta_v}{\theta_A} \right)' \right\} \quad [12a]$$

This reduces to

$$\Delta V = -\frac{RT}{2F} \ln \{ (\theta_A/\theta_v) (\theta_v/\theta_A)' \} \quad [12b]$$

for the case of an oxygen concentration cell with no external CO or CO₂. Equation [12b] is readily obtained from Eq. [1] for this case by application of Langmuir statistics. Note that strongly adsorbed nonreactive gases have no effect on ΔV . Such gases strongly reduce absolute values of θ_A and θ_v but not the (θ_A/θ_v) ratio under Langmuir adsorption/desorption statistics.

The mixed potential governed by Eq. [9a] and [9b] is reflected in the terms $(k_9/k_7)(\theta_C/\theta_v)$ and $(k_{10}/k_8)(\theta_B/\theta_v)$. Both terms are set equal to zero in the numerical results presented in the next section. This sim-

plification does not change qualitative conclusions to be drawn from the analysis in any substantial way, and it would be easy to include these terms in the analysis if we knew what their relative magnitude was experimentally. Clearly neglecting these terms has largest quantitative effect when excess CO is present.

We now rewrite Eq. [2]-[4] for steady-state conditions in terms of three new variables $\gamma_A \equiv (\theta_A/\theta_v)$, $\gamma_B \equiv (\theta_B/\theta_v)$, and $\gamma_C \equiv (\theta_C/\theta_v)$

$$2(k_A A_1 - k_2 \gamma_A^2) - k_R \gamma_A \gamma_B + k_D \gamma_C = 0 \quad [13]$$

$$S(k_B B_1 - k_4 \gamma_B) - k_R \gamma_A \gamma_B + k_D \gamma_C = 0 \quad [14]$$

$$S(k_C C_1 - k_6 \gamma_C) + k_R \gamma_A \gamma_B - k_D \gamma_C = 0 \quad [15]$$

where

$$S \equiv (1 + \gamma_A + \gamma_B + \gamma_C) \quad [16]$$

Addition of Eq. [12] and Eq. [15], etc. gives (in the same notation)

$$A_1 = A_g - (k_R \gamma_A \gamma_B - k_D \gamma_C) / (2k_1 S^2) \quad [17]$$

$$B_1 = B_g - (k_R \gamma_A \gamma_B - k_D \gamma_C) / (k_3 S^2) \quad [18]$$

$$C_1 = C_g + (k_R \gamma_A \gamma_B - k_D \gamma_C) / (k_5 S^2) \quad [19]$$

The simultaneous Eq. [13]-[19] can be solved numerically with specified input partial pressures while varying rate constants for adsorption, desorption, mass transfer, and chemical reaction. We used a two-dimensional version of Newton's method with γ_A and $(\gamma_B + \gamma_C)$ as parameters. The six variables are then determined by combinations of Eq. [13]-[19]. Concentration cell voltages are obtained from Eq. [12] once γ_A is known. Assuming that no oxygen reactions occur on the reference side of the cell, $\gamma_A' = (A_g' k_A / k_2)^{1/2}$.

Numerical Results

Figures 2-5 show calculated cell voltage, ΔV , plotted as a function of $(O_2/CO) = A_g/B_g$, the ratio of partial pressures in the bulk gas region. In all cases, bulk gas compositions do not correspond to chemical equilibrium. The parameters $T = 600^\circ\text{C}$, $A_g' = 2 \times 10^4$ Pa (0.2 atm), $K_{\text{eq}} = 5 \times 10^{-13}$ atm^{1/2} were used in generating the numerical results (15).

The data presented in Fig. 2-3 presume rapid mass transfer between the bulk gas and boundary layer, such that $A_1 \approx A_g$, $B_1 \approx B_g$, $C_1 \approx C_g$. The influence of bulk

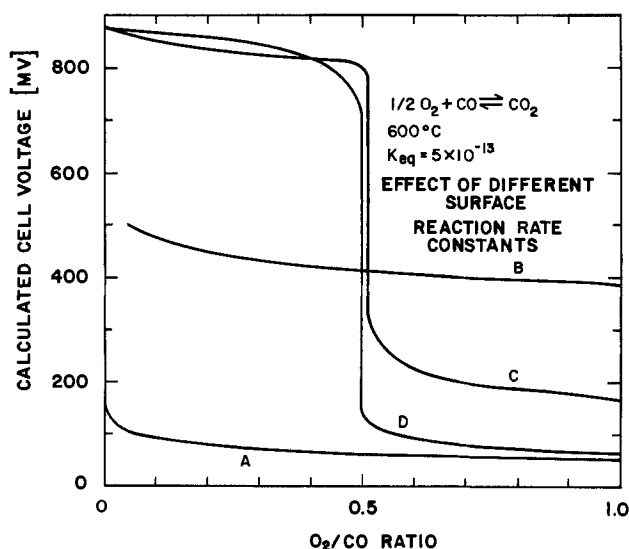


Fig. 2. Calculated cell voltage vs. bulk gas O₂/CO ratio with $B_g = 0.1$. Rapid mass transfer assumed, such that $A_1 \approx A_g$, $B_1 \approx B_g$, $C_1 \approx C_g$. Rate constants are $k_A = k_B = 100$, $k_C = 0.1$, $k_2 = k_4 = 0.001$, $k_6 = 1000$. In curve A, $k_R = 0.00001 = 5k_D$. In curve B, $k_B = 1 = 5k_D$. In curve C, $k_R = 1000 = 5k_D$. Curve D corresponds to chemical equilibrium. Similar trends, from curve A toward curve D, are seen with other input parameters as the surface reaction rate is increased.

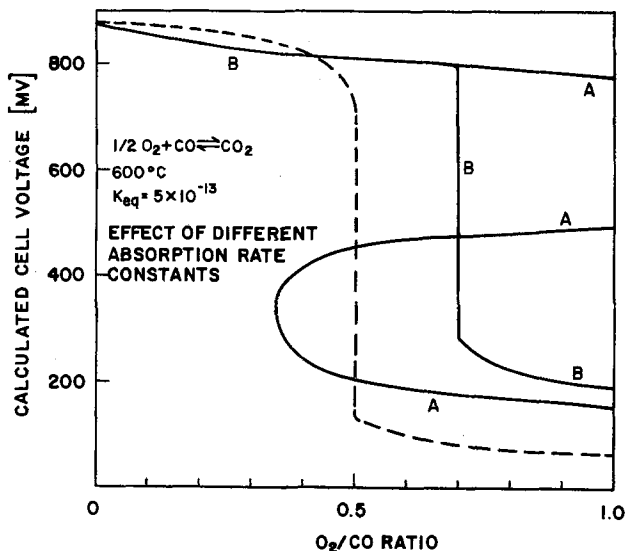


Fig. 3. Calculated cell voltage vs. bulk gas O₂/CO ratio with B_g = 0.1. Rapid mass transfer assumed. Rate constants are k_R = 1000 = 5k_D, k_c = 0.1, k₆ = 1000, k₂ = k₄ = 0.001. In curve A, k_A = 1.5k_B = 150. In curve B, k_A = 0.75k_B = 75. Dashed line shows equilibrium curve.

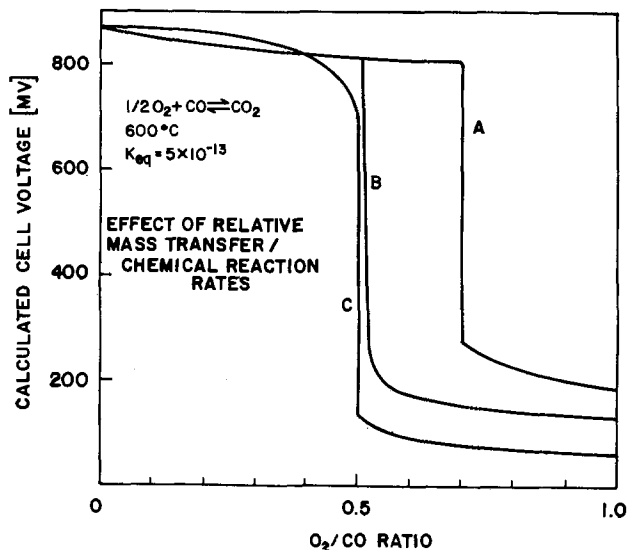


Fig. 4. Calculated cell voltage vs. bulk gas O₂/CO ratio with B_g = 0.1. Rate constants are k_R = 5k_D = 1000, k_c = 0.1, k₆ = 1000, k₂ = k₄ = 0.001, k_A = 0.75k_B. Curve A corresponds to fast mass transfer: k₁ = k₃ = k₅ = 10⁶; curve B, to an intermediate mass transfer rate: k₁ = k₃ = k₅ = 1; curve C to slow mass transfer: k₁ = k₃ = k₅ = 1 × 10⁻⁴.

gas/boundary layer mass transfer rates is illustrated in Fig. 4-5.

Adsorption of oxygen and carbon monoxide, from the boundary layer onto the catalyst surface, is presumed to occur at identical rates in the data presented in Fig. 2; e.g., k_A = k_B. Curves A-C, where the surface reaction is presumed to occur at progressively faster rates, are to be compared with curve D, which corresponds to each bulk gas composition at chemical equilibrium. Curve A assumes a surface where both gases are adsorbed but no reaction occurs (k_R = k_D = 0). An enormous change in equilibrium oxygen partial pressure, caused by the chemical reaction, produces the voltage step at stoichiometry in the equilibrium curve D. If no reaction occurs, as assumed here, the voltage-composition curve A corresponds to an oxygen concentration cell. Curve B assumes a reaction rate constant k_R comparable to adsorption/desorption rate constants. The limiting voltage at high A_g/B_g ratio corresponds to

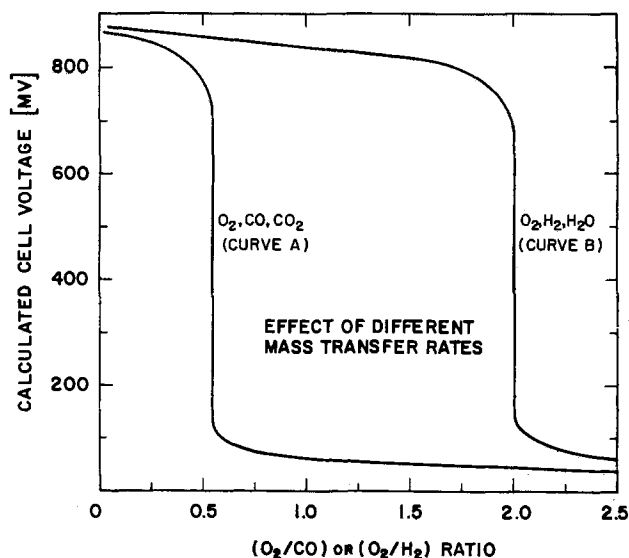


Fig. 5. Calculated cell voltage vs. bulk gas O₂/CO and O₂/H₂ ratios. Bulk CO and H₂ values of 0.1 atm assumed. Slow mass transfer in both curves. In curve A (for CO), k₁ = 0.94k₃ = 1.17k₅. In curve B (for H₂), k₁ = 0.25k₃ = 0.75k₅.

$$\gamma_A = \left(\frac{2k_A k_4}{k_B k_R} \right) \left(\frac{A_g}{B_g} \right) \quad [20]$$

which follows from $\gamma_B \approx (k_B B_g / k_4)$, $2k_A A_g \approx k_R \gamma_A \gamma_B$. Note that these voltages extend beyond the voltage limits calculated for (i) no chemical reaction and (ii) chemical equilibrium. This result cannot be interpreted by quasi-equilibrium concentration cell arguments, since these arguments require oxygen partial pressures between A_g (no reaction) and (A_g - 0.5 B_g) (complete irreversible reaction). This situation is caused by the rate of surface reaction being competitive with the rate of oxygen desorption; together these processes generate smaller (θ_A / θ_v) values than those resulting from adsorption/desorption alone.

Figure 2, curve C assumes a surface reaction rate faster than the rates of CO/O₂ adsorption/desorption. This situation best approximates equilibrium behavior, curve D. Deviations between Fig. 2, curve C and curve D persist both above and below stoichiometry.

Figure 3 illustrates the role of relative gas adsorption rates in a situation where the rate of surface reaction is faster than either adsorption process. Here voltage-composition curves shift along the (A_g/B_g) axis such that the voltage step occurs where A_g = 0.5 (K_B/K_A) B_g. This result was obtained previously by Fleming (5) from consideration of a different kinetic model.

Our numerical calculations frequently produced two steady-state solutions for one set of input parameters; e.g., Fig. 3, curve A. One of these solutions corresponds to high fractional surface coverage by oxygen; the other, to high surface coverage by carbon monoxide. Multiple steady states are well known in both experimental and theoretical studies of surface CO oxidation. They result from autoinhibitory features of Langmuir-Hinshelwood kinetics. The reader is referred to a recent review by Sheintuch and Schmitz (16) for a discussion of this phenomenon.

The numerical data presented thus far assume rapid mass transfer between bulk gas and boundary layers. Even with this restriction, there are seven adjustable rate constants. With judicious selection of relative k values, it is possible to produce a variety of voltage-composition curves in addition to those illustrated in Fig. 2-3. This serves to illustrate an important result: When the bulk gases are not in chemical equilibrium, there is no reason to expect oxygen concentration cell emf to reflect equilibrium oxygen partial pressures.

It turns out, however, that isothermal concentration cell emf corresponds to equilibrium oxygen partial pressures in a nonequilibrium bulk gas mixture when two conditions are met: (i) bulk gas/boundary layer mass transfer is slow, and (ii) the reactant gases have identical mass transfer rates.

Figure 4 contains some of the most important results of this analysis. Curve A is identical to Fig. 3, curve B, corresponding to rapid mass transfer with dissimilar adsorption rates. Note that the voltage step is shifted from stoichiometry. Figure 4, curves B and C assume progressively slower mass transfer. With slow mass transfer, (i) voltage-composition curves approach those calculated for chemical equilibrium of the bulk gases, and (ii) calculated gas partial pressures in the boundary layer match chemical equilibrium values for each bulk gas composition. This is a general result, independent of relative rates of adsorption, desorption, and surface reaction.

Figure 5 illustrates another important point. It demonstrates that voltage-composition curves shift under slow mass transfer conditions when the reactant gases have different mass transfer coefficients. Under isothermal/isobaric conditions, kinetic theory (Graham's law) predicts that mass transfer coefficients vary as $M^{-1/2}$, where M is the gas molecular weight. Similar variations of mass transfer coefficients in gas mixtures have been derived (17). CO and O₂ have approximately equal molecular weights, and mass transfer differences are expected to be slight under slow mass transfer conditions. On the other hand, Graham's law argues for a large effect in the H₂-O₂-H₂O system. This is shown in Fig. 5, curve B.

Finally, it should be noted that boundary layer partial pressures can be approximated by chemical equilibrium under slow mass transfer conditions; e.g.

$$(A_1)^{1/2}(B_1) = K_{eq}(C_1) \quad [21]$$

Mass balance constraints require $2k_1(A_g - A_1) = k_3(B_1 - B_g) = -k_5(C_1 - C_g)$. Together, these relations lead to a cubic equation for A_1 . The corresponding γ_A and ΔV can be obtained from $\gamma_A = (A_1 k_A / k_2)^{1/2}$, that is, by assuming the surface reactions are in dynamic equilibrium.

Experimental

Our experimental apparatus consisted of a gas flow system passing through a tube furnace. The homemade concentration cell sensor contained platinum electrodes on the inner and outer surfaces of an 8% Y₂O₃-doped ZrO₂ tube. The external electrode, in contact with nonequilibrium gas mixtures, was sputtered onto the closed tube tip and had a geometric surface area of approximately 0.25 cm². The inner electrode was in contact with air. Thin platinum wires connected the electrodes to a high-impedance voltmeter. Gas mixtures were prepared using Matheson Series 8240 Mass Flow Controllers. A thermocouple attached to the inner air/electrode surface measured cell temperature. Tests with a thermocouple mounted on the outer surface indicated a temperature difference less than 10°C.

Figure 6 compares experimental voltage/composition curves for gas mixtures in N₂. The λ scale is used as the abscissa, where λ is defined as the experimental O₂/reactant mole ratio divided by the corresponding mole ratio at stoichiometry. The experimental voltage step in the O₂/CO system occurs at $\lambda = 1$, as anticipated for two reactant gases with a mass ratio of 0.875 in contact with an efficient catalyst surface. These results are independent of flow rates past the sensor surface ranging between 130 and 520 cm/sec. The voltage steps in the O₂/H₂ and the O₂/D₂ systems are shifted from $\lambda = 1$ in the direction predicted by mass transport analysis when the reactant gases differ by 16 and 8 in mass, respectively. Since H₂ and D₂ have virtually identical reaction characteristics, the difference between the O₂/H₂ and the O₂/D₂ voltage/composition curves is unambigu-

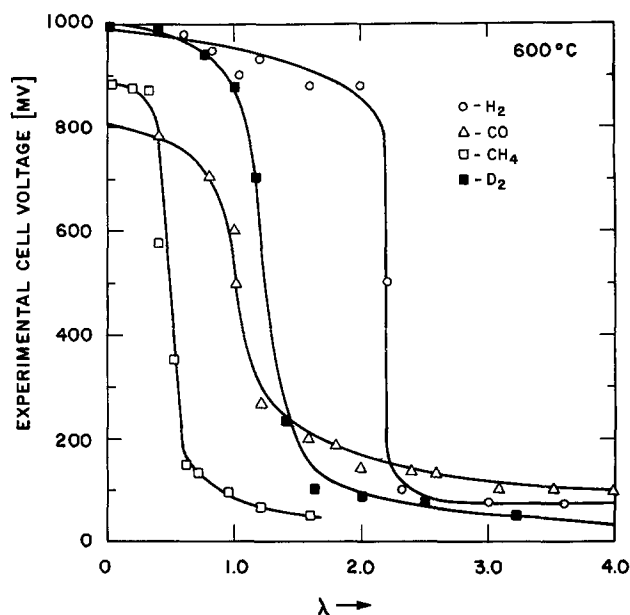


Fig. 6. Experimental cell voltage vs. λ , the ratio of reactant gas partial pressures. H₂, D₂, CO, and CH₄ partial pressures maintained at 0.02 atm and O₂ partial pressure varied.

ous experimental evidence for a mass transfer shift. Similar shifts were reported previously by Takeuchi *et al.* (6), who found voltage steps at $\lambda = 4$ and $\lambda = 2$ for the O₂/H₂/N₂ and the O₂/D₂/N₂ systems at 400°C. The earlier data is in total agreement with mass transfer concepts. Our experiments indicate a less dramatic shift; e.g., to $\lambda = 2.2$ for O₂/H₂. The magnitude of the shift is sensitive to the flow rate past the sensor. Consequently, we feel that variations in sensor design and fabrication, rather than temperature effects, are responsible for differences between the present results and those of Takeuchi.

The voltage step in the O₂/CH₄ system occurs near $\lambda = 0.5$. This is typical of experimental results (not shown) on other O₂/alkane systems (O₂/C₂H₆, O₂/C₃H₈, O₂/C₄H₁₀) and reflects the relative inefficiency of alkane oxidation over platinum catalysts (18). Some experiments with reactant gas mixtures containing both CO and CH₄ were performed. The voltage step moves systematically from that found in the O₂/CH₄ system to that found in the O₂/CO system as the CO/CH₄ ratio is increased.

In other experiments, a secondary catalyst was used to equilibrate gas mixtures before they reached the sensor. High surface area platinum supported on Al₂O₃ was used at an operating temperature of approximately 600°C. A three-way stopcock routed the gas flow to the sensor by either of two alternate paths: one path passed over the secondary catalyst; the other led directly to the sensor. Using this arrangement, we were able to explore the effects of gas pre-equilibration under highly controlled experimental conditions. Typical results are shown in Fig. 7. Voltage steps that occur either above or below stoichiometry with unequilibrated gas mixtures occur at $\lambda = 1$ after passing over the secondary catalyst. As expected, stoichiometric behavior can be modified if high flow rates are used and the catalyst no longer has sufficient time to equilibrate the gas mixtures.

Discussion

The main results of the present analysis include (i) relating concentration cell emf to catalyst/electrode surface concentrations under nonequilibrium conditions; (ii) expressing a catalytic analysis in terms of cell emf; and (iii) using the results of this analysis to assess the influence of mass transport, adsorption, desorption, and surface reaction upon sensor emf. Many conclusions drawn from this analysis appear in the

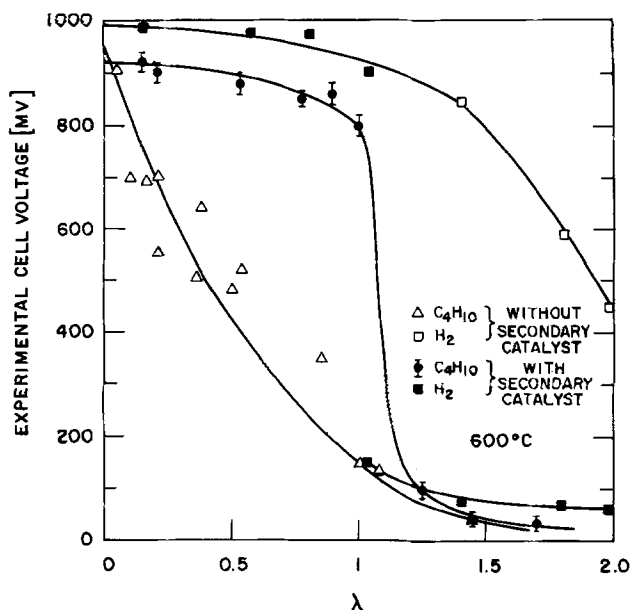


Fig. 7. Experimental cell voltage vs. λ , the ratio of reactant gas partial pressures. Deviations of the voltage step from stoichiometry are observed without pre-equilibration over a secondary catalyst. Pre-equilibration produces a transition at stoichiometry.

catalyst literature; previously they have not been expressed in terms of emf across a concentration cell.

It would appear that an ideal steady-state oxygen concentration cell sensor has a mass transfer rate much smaller than the rate of surface reaction; i.e., it has a small Thiele modulus (19). It is well known that heterogeneous catalysts typically exhibit small Thiele moduli at high temperatures; this follows directly from the higher activation energies for chemical reactions relative to the activation energy for mass transfer. The converse of this argument implies some lower temperature where mass transfer rates and surface reaction rates become comparable: this temperature varies with the catalyst, gas concentrations, and the reaction involved. This may explain experimental observations that concentration cell sensors operate best at high temperatures ($T > 500^\circ\text{C}$) where mass transfer is expected to be rate limiting. Internal electrochemical factors, such as electrode polarization and high electrolyte impedance, also influence low temperature sensor behavior (20). These factors lie beyond the scope of the present research.

At constant temperature, it is possible to move from mass transport limited kinetics to reaction limited kinetics by decreasing the concentration of the reactants, since the effective Thiele modulus is concentration dependent. This conclusion, which follows directly from the concentration dependence of the chemical reaction rate, may produce nonideal sensor characteristics at low reactant gas concentrations.

Criteria for an ideal sensor are modified when dynamic response characteristics are considered. With a small Thiele modulus, the sensor response rate to a change in bulk gas composition is proportional to the mass transfer rate. Consequently, an ideal steady-state cell with a slow mass transfer rate may be impractical because of poor response characteristics.

Pre-equilibration of gas mixtures before they reach the sensor is a useful way to circumvent difficulties connected with relative kinetic/mass transfer rates. Indeed, secondary catalysts are commonly used for this purpose in commercial laboratory instruments. It is to be noted, however, that pre-equilibration is not always feasible when large gas volumes and high flow rates are involved.

It is reasonable to inquire how strongly the conclusions of the present analysis depend on specifics in the

assumed kinetic scheme. The most important model-dependent element involves use of Langmuir-Hinshelwood kinetics. This mechanism is known to produce multiple steady-state solutions for surface concentrations with certain choices of input parameters. There is some experimental evidence that multiple steady states occur on the surface of oxygen sensors; notably the experiments of Hetrick and Logothetis (21) on ZrO_2 and TiO_2 , and the studies of Dauchot and Van Cakenberghe (22) on Schottky diodes. Multiple steady states provide a convenient explanation of experimental observations of voltage hysteresis in response to bulk gas composition changes, but this remains a subject for further study. Alternate reaction mechanisms (e.g., Eley-Rideal kinetics) also predict that slow mass transfer is necessary to produce quasi-equilibrium oxygen partial pressures in the boundary layer.

Ideal concentration cell sensors produce a sharp voltage step at stoichiometry in O_2 /reactant gas mixtures. Frequently, experimental (nonideal) sensors exhibit a broadened voltage transition that occurs over a range of compositions near stoichiometry (c.f. the data for the O_2/C_4H_{10} system in Fig. 7). As noted by Fleming (5), there is strong experimental evidence that the broadened transition is related to loss of catalytic activity by the sensor. Our analysis predicts some broadening of the voltage step at stoichiometry when (i) surface adsorption/desorption rates are much faster than mass transport rates, and (ii) mass transport rates are faster than surface reaction rates. However, calculated voltage transitions are sharper than those seen experimentally.

Turning to the experimental results, observation of a "mass transfer shift" in the O_2/H_2 and O_2/D_2 systems is of considerable interest. Under isothermal/isobaric conditions, it should occur even with extremely high activity catalytic surfaces and displace cell voltage from chemical equilibrium values. Explanation of this finding by the kinetic theory of gases involves independent diffusive transport of components in a gas mixture. As Jackson (23) points out, independent transport arguments cannot be extended indefinitely since they lead to pressure differences in the system that are relieved by convective processes that couple the transport of all component gases. Convective transport is augmented in the present case by thermal gradients between the bulk gas and boundary layer that are produced by exothermal chemical reactions. Our experiments confirm earlier results of Takeuchi *et al.* (6) that "mass transfer shifts" exist. However, our data suggest that the magnitude of the shifts is less extensive than those indicated by Takeuchi's experiments and by simple theory.

Finally, it should be noted that one must use caution in drawing parallels between (i) sensor characteristics with respect to pairs of reactants in a flow system (e.g., O_2/CO or O_2/H_2), and (ii) sensor behavior relative to the plethora of chemical species present in engine exhaust. While identical physicochemical principles hold in both cases, the varied interactions present in multi-component systems can severely modify experimental results.

Acknowledgments

We are grateful to M. Bettman, R. H. Hammerle, R. E. Hetrick, J. W. Kress, J. T. Kummer, E. M. Logothetis, N. Otto, and H. Wroblowa for fruitful discussions of both the experimental and analytical results reported in this paper.

Manuscript submitted July 1, 1980; revised manuscript received Aug. 22, 1980.

Any discussion of this paper will appear in a Discussion Section to be published in the December 1981 JOURNAL. All discussions for the December 1981 Discussion Section should be submitted by Aug. 1, 1981.

Publication costs of this article were assisted by the Ford Motor Company.

REFERENCES

1. D. S. Eddy, *IEEE Trans. Vehicle Tech.*, **4**, 125 (1974) provides a good overview of oxygen concentration cell sensors as applied to automobiles. The basic idea goes back much farther, to C. Wagner's pioneering studies of oxygen diffusion and reaction in metals: cf. C. Wagner, *Naturwissenschaften*, **31**, 265 (1943); *Z. Phys. Chem.*, **B21**, 25 (1933).
2. T. H. Etsell and S. N. Flengas, *Chem. Rev.*, **70**, 339 (1970).
3. B. Kraus, *Bosch Techn. Ber.*, **6**, 136 (1978).
4. W. J. Fleming, *SAE Trans.*, No. 770400 (1978); *SAE Trans.*, No. 800020 (1980).
5. W. J. Fleming, *This Journal*, **124**, 21 (1977).
6. T. Takeuchi, K. Saji, and I. Igarashi, Abstract 74, p. 196, The Electrochemical Society Extended Abstracts, Pittsburgh, Pa., Oct. 15-20, 1978.
7. T. H. Etsell and S. N. Flengas, *Metall. Trans.*, **3**, 27 (1972).
8. T. H. Etsell and S. N. Flengas, *This Journal*, **118**, 1890 (1971).
9. D. M. Haaland, *ibid.*, **127**, 796 (1980).
10. I. Langmuir, *Trans. Faraday Soc.*, **17**, 621 (1922).
11. Y. Nishiyama and H. Wise, *J. Catal.*, **32**, 50 (1974).
12. H. P. Bonzel and R. Ku, *Surf. Sci.*, **33**, 91 (1972).
13. W. L. Winterbottom, *ibid.*, **37**, 195 (1973).
14. C. A. Pikiros and D. Luss, *Chem. Eng. Sci.*, **32**, 191 (1977).
15. D. D. Wagman, J. E. Kilpatrick, W. J. Taylor, K. S. Pitzer, and F. D. Rossini, *J. Res. Natl. Bur. Standards*, **34**, 143 (1945).
16. M. Sheintuch and R. A. Schmitz, *Catal. Rev.-Sci. Eng.*, **15**, 107 (1977).
17. Cf., J. O. Hirschfelder, C. F. Curtis, and R. B. Bird, "Molecular Theory of Gases and Liquids," John Wiley & Sons, Inc., New York (1954).
18. C. F. Cullis, D. E. Keene, and D. L. Trimm, *J. Catal.*, **19**, 378 (1970).
19. E. W. Thiele, *Ind. Eng. Chem.*, **31**, 916 (1939).
20. See, for example, L. Heyne, in "Fast-Ion Transport in Solids," W. Van Gool, Editor, North Holland, Amsterdam (1973).
21. E. M. Logothetis and R. E. Hetrick, *Appl. Phys. Lett.*, **34**, 117 (1979); *Solid State Commun.*, **31**, 167 (1979).
22. J. P. Dauchot and J. Van Cakenberghe, *Nature*, **246**, 61 (1973); *Jpn. J. Appl. Phys.*, Suppl. 2, Pt. 2, p. 533 (1974). See also R. Dagonnier and J. Nuyts, *J. Chem. Phys.*, **65**, 2061 (1976).
23. R. Jackson, "Transport in Porous Catalysts," Chap. 10, 11, Elsevier, Amsterdam (1977).

Surface Changes during A.C. Etching of Aluminum

Christopher K. Dyer¹ and Robert S. Alwitt

United Chemi-Con, Incorporated, 3000 Dundee Road, Northbrook, Illinois 60062

ABSTRACT

Electrochemical etching of Al with alternating current produces a high density of cubic etch pits covered with a film of oxide or hydroxide. Micrographs of the metal and film structures are presented and a model is proposed to explain the observations. Calculations demonstrate the feasibility of film deposition from acid solution when a high cathodic current density is applied. A critical feature is that the high aluminum salt concentration near the metal surface hinders proton mobility.

Electrochemical etching with alternating current is used to obtain a high surface area on Al foil for electrolytic capacitor electrodes and also to obtain a roughened surface suitable for aluminum lithographic plates. A-c etching is characterized by a uniform depth of roughened metal and by the presence of a film of oxide or hydroxide within this etched layer. This film is presumed to deposit because of the increase in local pH caused by the cathodic half-cycle (1). The tunnel structures that dominate the appearance of Al etched with direct current in chloride solutions at high temperature (2, 3) are not seen with a-c etching.

Although a-c etching has been used commercially for over 25 years it has not been discussed in the scientific literature except for a recent paper which presented evidence for the deposited film (1). The present work shows the appearance and development of the etch structure and accompanying film under a limited set of experimental conditions. Calculations demonstrate the feasibility of film deposition from acid solution when a high cathodic current density (C.D.) is applied.

Experimental

99.99% Al foil was mounted and masked on a glass slide with epoxy resin (Shell 828 plus TETA). After the resin on the specimen had been cured at 65°C, the specimen was immersed in 1N NaOH at room temperature for 10 min and then thoroughly washed with

distilled water. Etching was done with 5 Hz sinusoidal current supplied from a potentiostat operating in the galvanostatic mode and coupled to a signal generator. The specimen was immersed in 1M HCl at 60°C and an rms current of 700 mA/cm² was applied, using graphite counterelectrodes, for a time calculated to give an anodic charge up to 25 C/cm².

After a-c etching, the specimen was immediately removed from the cell, washed in distilled water, and dried with methanol. Some specimens had no further treatment so only the film deposited during etching was on the surface. With other specimens, an anodic oxide film was grown in 40% ammonium pentaborate in ethylene glycol at room temperature. Then the etched area was cut from the specimen, peeled from the epoxy resin backing, and the Al metal was dissolved in warm 10% Br₂/methanol. The remaining oxide flakes, after sputter-coating with gold, were examined in a scanning electron microscope.

Results and Interpretation

The "Etch film."—When an a-c etched foil is immersed in Br₂/MeOH a fragile film remains after all the metal has been dissolved. This shall be called the "etch film." The film is probably a hydroxide, possibly in combination with amorphous oxide, since the film loses weight upon heating but shows no crystalline structure by electron diffraction. The etch film is obviously insoluble in 1M HCl at 60°C during the time of an experiment (15 sec) and was still present after much longer etches (10 min). An orthogonol view of

¹Present address: Bell Laboratories, Murray Hill, New Jersey 07974.

Key words: films, capacitor, diffusion, dissolution.

this film from the etchant side (Fig. 1) shows many interconnected cubic pits. Figures 1 and 2 show cubic "shadows" under the outer film surface, some of which are aligned with uncovered pits. This suggests that the outer film was undercut, presumably by dissolution of metal, and in some places the outer film separated from the surface while in other places it remained as a "cap." A view from the side of the flake in Fig. 3 shows the structure of the film from the metal side (in the lower two-thirds of the field of view) as well as the etchant side (top one-third of the field). It is seen that the etch film replicates the interior of the cubic pits on the metal surface. The thickness of the etch film seems to vary from place to place; in Fig. 2 where the film has broken and peeled back it is less than 50 nm.

Etch film + anodic oxide.—Figures 4 and 5 show the oxide after a 5 C/cm^2 etch charge followed by anodization to 100V. From Fig. 5 it is possible to deduce the method by which an additional pit grows onto an existing cubic pit. In the lower half of Fig. 5 are two views of a double cube structure, one above the other, with walls approximately 150 nm thick (the anodic film) and an internal ledge which is much thinner. This ledge was presumably not in contact with metal during anodization since it is much less than 150 nm thick. It is probably the remains of an etch film that covered the base of the upper cube before the start of dissolution that formed the lower pit.

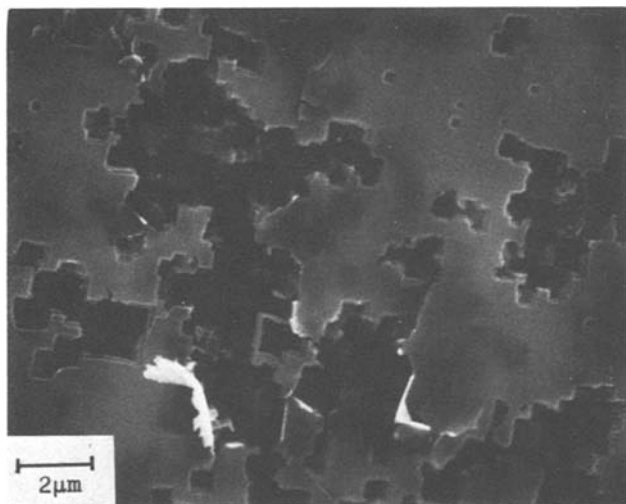


Fig. 1. Etch film from etchant side (not anodized). Conditions: 5 C/cm^2 , 5 Hz (0° tilt).

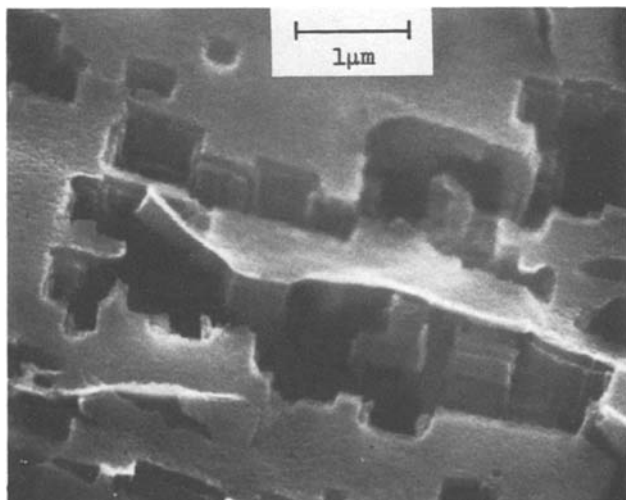


Fig. 2. As Fig. 1 but 60° tilt

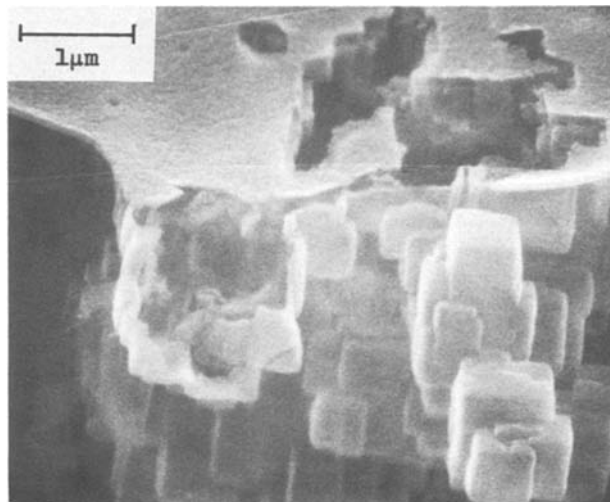


Fig. 3. Etch film showing pit shape from metal side and original surface (not anodized). Same conditions as Fig. 1 (60° tilt).

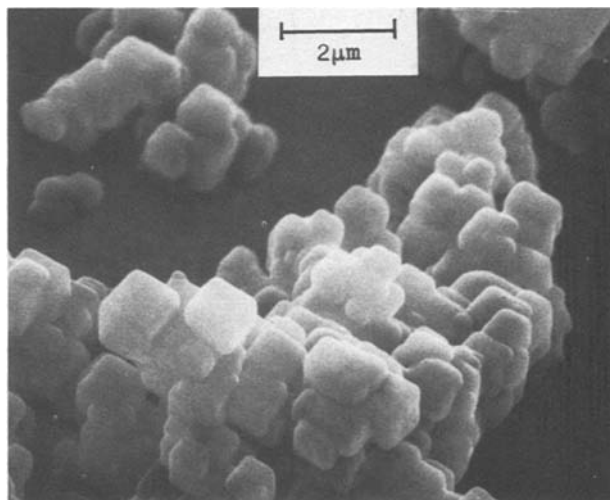


Fig. 4. View from metal side after anodization to 100V. Same conditions as Fig. 1 (45° tilt).

A sequence that could give rise to the observed double cube morphology is shown schematically in Fig. 6. A single cubic etch pit is shown with walls covered by an etch film that deposited during the cathodic half-cycle immediately following pit formation. At the pit base, a second pit initiates at a weak point in the etch film followed by orthogonal expansion underneath the film. The new pit undercuts the preexisting etch film and grows until the end of the anodic half-cycle. During the next cathodic half-cycle this metal

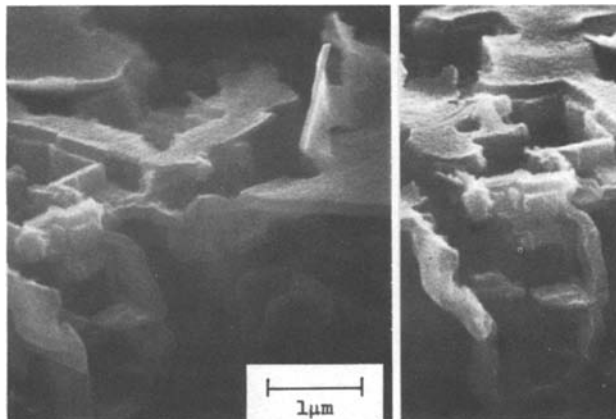


Fig. 5. As Fig. 4 but 60° tilt, different views

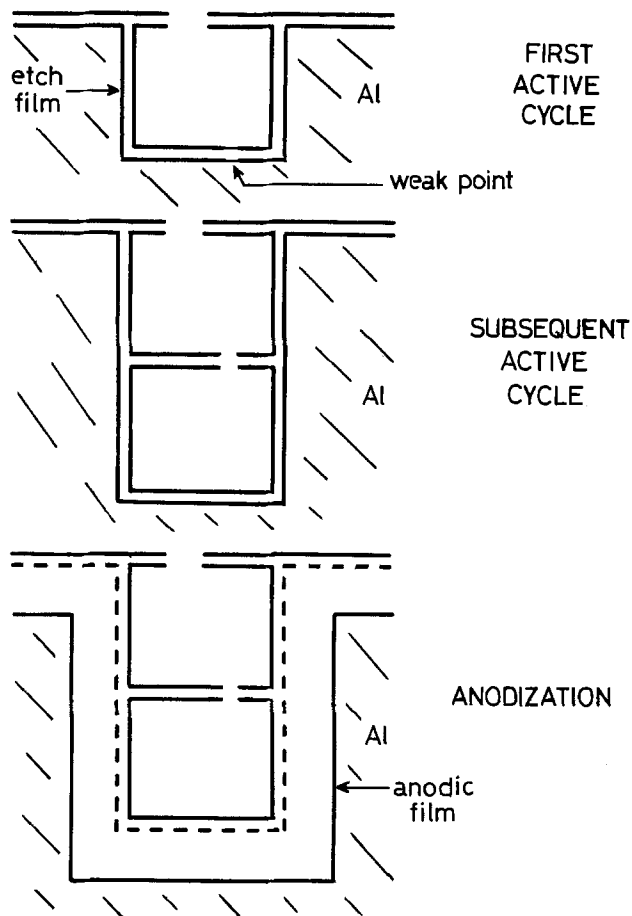


Fig. 6. Schematic diagram of cube-by-cube pit propagation

surface becomes covered with etch film, thus completing the sequence. Repeated sequences of this kind involving weak points in the etch film on different pit faces would give rise to multidirectional cube-by-cube pit propagation (Fig. 4).

The effect of frequency supports the idea that each cubic etch pit is formed during only one anodic half-cycle. Figure 7 shows smaller etch cubes formed at 10 Hz than at 5 Hz. The rms C.D. was the same in both cases but the charge per cycle at 5 Hz was twice that at 10 Hz.

The above model of pit propagation seems to apply also to the larger merged cube structures seen in Fig. 4 since random sections through these structures show

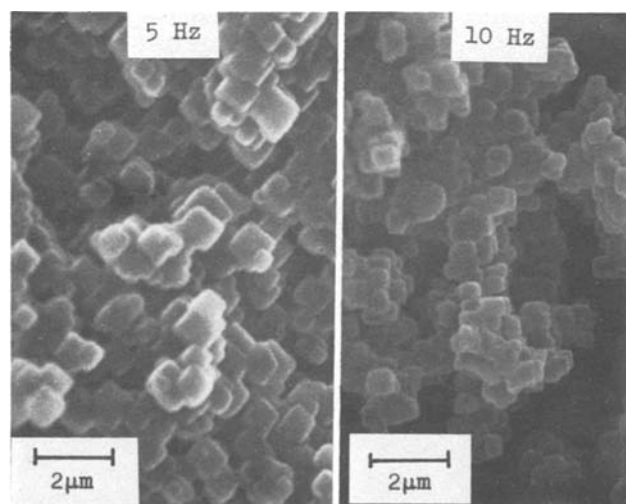


Fig. 7. Structure after 5 Hz (left) and 10 Hz (right) etch; both at 400 mA/cm², 25 C/cm². Anodization to 100V, metal side (0° tilt).

an internal network of walls and ledges. Figures 8 and 9 are sections through an etch film + 150V anodic film after a 10 C/cm² etch. At the lower right of these micrographs (particularly Fig. 9) is the anodically formed portion of the film which must have been in contact with metal since it is now ~200 nm thick. Elsewhere are seen much thinner films in cubic relationships to each other which are most probably undercut etch film.

Further evidence in support of the model of cube by cube pit propagation in each anodic half-cycle comes from an etch done at two frequencies. A foil was etched for 5 C/cm² at 5 Hz and then for 1 C/cm² at 20 or 100 Hz. The replicas, from the metal side, are shown in Fig. 10. Application of a small charge at the higher frequency produced small additional cubes characteristic of the higher frequency and therefore independent of the previous etch morphology. The results were not affected by the time on open circuit between the low and higher frequency etches which was varied between 10⁻³ and 200 sec. A second etch at higher frequency is therefore a useful tool in identifying places where further pits can propagate, presumably at weak points in the etch film of the "mother cube." From the patterns of small cubes observed, weak points did not seem to be concentrated at edges or between "mother cubes" (Fig. 10b) and often there were clusters of small cubes (Fig. 10c) which indicated that nucleation and propagation continued preferentially on the freshly activated surfaces.

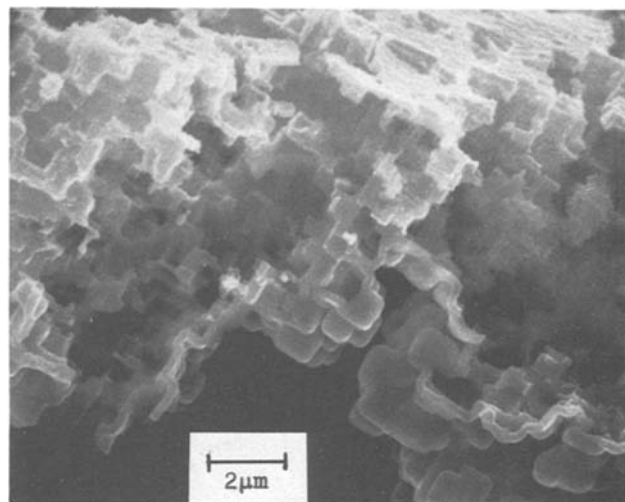


Fig. 8. Film section after 10 C/cm², 5 Hz etch then 150V anodization.

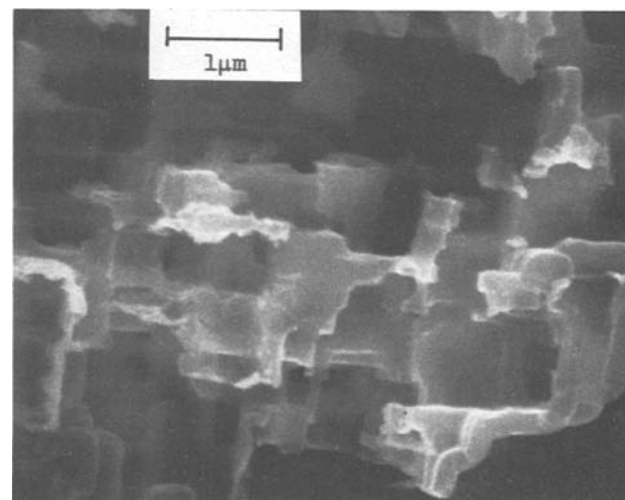


Fig. 9. As Fig. 8, higher magnification

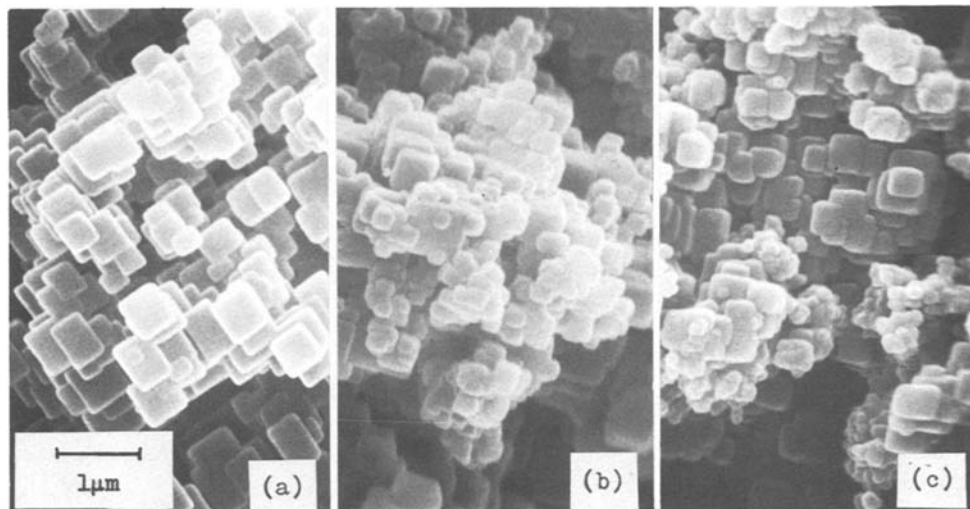


Fig. 10. Appearance of 2-frequency etch. (a) 5 Hz, 5 C/cm², (b) 5 Hz, 5 C/cm² + 20 Hz, 1 C/cm², (c) 5 Hz, 5 C/cm² + 100 Hz, 1 C/cm². Anodized to 60V, metal side. All at same magnification.

Typical values from the micrographs of cube side length (s) are plotted as a function of frequency in Fig. 11. For the conditions used in these experiments, it is found that $s \propto f^{-1/2}$.

Discussion

The formation of aluminum oxide in 1M HCl solution is unexpected, but the hydrogen evolution reaction during the cathodic half-cycle will certainly raise the pH close to the metal surface and, if the local Al³⁺ concentration is high enough, a precipitate might form. For example, at room temperature the pH of a saturated AlCl₃ solution is about 0.15 and increasing the pH to above 3 causes some Al(OH)₃ to precipitate. It must be determined if it is reasonable that such a pH increase could occur at the conditions used in these experiments, and if there is sufficient time during the cathodic half-cycle for film deposition.

Although a steady-state alternating current is applied to the electrode, the anodic and cathodic processes occur only on fresh surfaces at new positions for each cycle. To obtain an estimate of the time dependence of the pH increase we must consider only the time interval for a single cathodic half-cycle. The situation during the cathodic half-cycle can be approximated by a planar electrode to which is diffusing a species (H⁺) which reacts and disappears at the electrode surface at some time t . This problem has been considered at length by Bockris and Reddy (4) for a variety of conditions. The diffusion is described by Fick's second law

$$\frac{\partial C}{\partial t} = D \frac{\partial^2 C}{\partial x^2} \quad [1]$$

where C is the hydrogen ion concentration. If C_0 is the bulk concentration, suitable initial and boundary conditions are $C(t=0) = C_0$, $C(x \rightarrow \infty) = C_0$ at $t > 0$ where x is the distance from the surface. The rate of disappearance of H⁺ is given by the periodic flux, $J = J_{\max} \sin \omega t$, for the time interval $0 < t < \pi/\omega$. From the solution for a similar problem [p. 327 in (4)] we can directly give the solution for C_s , the time dependent surface concentration of H⁺

$$\frac{C_s}{C_0} = 1 - \frac{J_{\max}}{C_0(D\omega)^{1/2}} \sin\left(\omega t - \frac{\pi}{4}\right) \quad [2]$$

This shows that the surface concentration also varies sinusoidally, but lags the flux by a $\pi/4$ phase difference. This lag increases the response time for the change in surface pH.

The pH at which aluminum hydroxide deposition can occur depends on the local Al³⁺ concentration, but it must rise to at least pH 3. For the limiting case of deposition occurring when $C_s/C_0 \rightarrow 0$, a sufficient condition for deposition is

$$J_{\max}/C_0(D\omega)^{1/2} \geq 1 \quad [3]$$

since the value of the sine term in Eq. [2] is no greater than unity.

To obtain a value for J_{\max} requires an estimate of the specific C.D. during the cathodic half-cycle, which can be obtained from an estimate of the cathodic area. According to our model, the cathodic area is simply the surfaces of the freshly generated etch cubes from the previous anodic half-cycle. It is assumed that all etch cubes grow at the same rate and without impingement over the full anodic half-cycle, thus producing equal size cubes with side s . There will be created n cubes/cm²-cycle, each with a surface area of $5s^2$. We make use of the following relations

$$\text{charge/cm}^2\text{-half-cycle} = q = 2\sqrt{2}I/\omega \quad [4]$$

$$n = q/\text{charge-cube} = \frac{2\sqrt{2}M}{F\rho} - \frac{I}{s^3\omega} \quad [5]$$

$$i = I/5s^2n = \frac{F\rho}{10\sqrt{2}M} \cdot s\omega \quad [6]$$

$$J_{\max} = \sqrt{2}i/F = \frac{\rho}{10M} \cdot s\omega \quad [7]$$

In these equations I = nominal rms C.D., i = specific rms C.D., M = eq. wt., ρ = density of Al, F = Faraday.

Taking the results of 5 Hz, 0.7 A/cm² as an example, from the micrographs we estimate $s = 0.5 \mu\text{m}$. Using Eq. [5]-[7], $n = 2 \times 10^7$ cubes/cm², $i = 3$ A/cm², and $J_{\max} = 5 \times 10^{-5}$ eq./cm²-sec.

With this value of J_{\max} and $C_0 = 10^{-3}$ eq./cm³, Eq. [3] sets an upper limit for D at 8×10^{-5} cm²/sec. If H⁺ diffuses more rapidly than this, C_s will remain high enough so that precipitation cannot occur during the cathodic half-cycle. This value of D , at 60°C, is lower than reported values for protons in dilute solution, where transport occurs by a hopping mechanism. In these experiments the solutions are not dilute and the same mechanism for proton diffusion may not prevail. This must be examined in order to arrive at an estimate of D_{H^+} in the etch pit.

The apparent diffusion coefficient of H⁺ ions has been measured by polarography in supporting electrolytes of chloride salts at salt concentrations up to 3M (5). The value of D decreases with increasing [salt]/[acid] ratio and depends on the cation of the supporting electrolyte. In LiCl solutions the dependence on salt concentration is much stronger than in KCl or RbCl solutions. This difference is due to Li⁺ ions being more strongly solvated than K⁺ or Rb⁺ ions, so that at high salt concentration more water molecules are immobilized by the Li⁺ ions and not suitably oriented

Table I.

| C_{salt} (M) | $D_{H^+} \times 10^6 \text{ cm}^2/\text{sec}$ (25°C) | | | |
|-----------------------|--|-----------------|-----------------|------------------|
| | K ⁺ | Rb ⁺ | Li ⁺ | Al ³⁺ |
| 0 | 9.3 | 9.3 | 9.3 | 9.3 |
| 1.0 | 8.5 | 8.5 | 6.6 | — |
| 1.6 | — | 7.7 | — | — |
| 2.0 | 7.5 | — | 5.3 | — |
| Hydration number | 1.1 | 1.1 | 3.2 | 16 |

to contribute to proton conduction by the Grotthus hopping mechanism.

The "hydration number" is the effective number of water molecules attached to the ion as it moves through the solution. Hydration numbers calculated from the effect of solute on dielectric constant provide a measure of "irrotational binding" of water molecules to the ion (6). The ion hydration numbers calculated from the static dielectric constant (6) are listed in Table I, along with values of D_{H^+} determined polarographically for 10^{-2} M HCl at several chloride salt concentrations (5). Stastny and Strafelda (5) extrapolated to a D_{H^+} value of $3 \times 10^{-5} \text{ cm}^2/\text{sec}$ in 2M LiCl at very low HCl concentration, only one-third the value found in the absence of the salt.

A comparison of hydration numbers indicates that in AlCl_3 solutions five times as many water molecules would be immobilized as in LiCl solutions of the same molarity. The AlCl_3 content in the etch pits at the end of the anodic half-cycle is probably at least 1-2M. In 1M AlCl_3 30% of the water molecules would be immobilized. Under these conditions proton hopping could only occur to a very limited extent and H^+ diffusion would be mostly by conventional transport processes in the same manner as other ionic species. Thus, at 25°C the value of D_{H^+} would be expected to be close to $2 \times 10^{-5} \text{ cm}^2/\text{sec}$. The diffusion coefficient would be about $3 \times 10^{-5} \text{ cm}^2/\text{sec}$ at 60°C and using this value in Eq. [2], with the previously determined values for the other parameters, gives $t_0 = 5 \times 10^{-2} \text{ sec}$, where $t = t_0$ when $C_s/C_0 = 0$. Thus, t_0 is about 50% of the cathodic half-cycle time (t_c).

Since we observe $s \propto \omega^{-1/2}$ (see Fig. 11), it follows from Eq. [7] that $J_{\text{max}} \propto \omega^{1/2}$ and inspection of Eq. [2] shows that the pH increase occurs over a time interval such that $\omega t_0 = \text{constant}$. Because of this relationship, over the range 5-100 Hz the calculated t_0 remains at a constant fraction of the cathodic half-cycle time, $0.5t_c$. Because of the observed dependence of s on ω the calculated number of cubes per cycle increases with frequency. Since n depends on weak points in the etch film, this suggests that frequency influences the nature of the deposited etch film, making it more defective when the time for precipitation is shortened. Figure 10c indicates preferential pitting of 100 Hz cube walls.

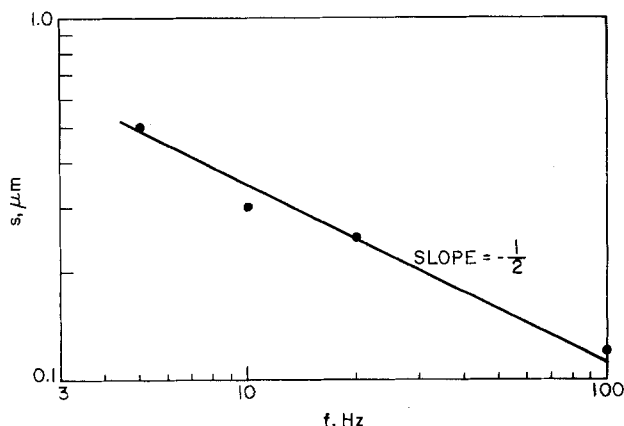


Fig. 11. Frequency dependence of cube side length

The total time for film deposition is the sum of the times for pH increase and for $\text{Al}(\text{OH})_3$ precipitation. This latter time interval can be estimated by solving Eq. [1] for Al ion diffusion to the hydroxide surface. C is now the aluminum ion concentration which we assume is uniform within the etch pit at the end of the pH increase. The initial condition and first boundary condition are then the same as used before: $C(t=0) = C_0$ and $C(x \rightarrow \infty) = C_0$, $t > 0$. When precipitation starts, the Al ion concentration at the surface drops to its saturation concentration at the surface pH. This will be more than an order of magnitude smaller than the bulk concentration so the second boundary condition is chosen as $C(x=0) = 0$, $t > 0$. This is a problem in unsteady diffusion analogous to the unsteady heat conduction problem of finding the temperature profile or total heat flux in a body initially at uniform temperature when one surface has an abrupt temperature change [e.g., see Ref. (7)]. The flux at the surface is

$$N \Big|_{x=0} = -D_{\text{Al}} \frac{\partial C}{\partial x} \Big|_{x=0} = \left(\frac{D_{\text{Al}}}{\pi t} \right)^{1/2} C_0 \quad [8]$$

Integrating the flux from $t = 0$ to $t = t$ gives the total amount of Al deposited as $\text{Al}(\text{OH})_3$

$$M_{\text{Al}} = \int_0^t C_0 \left(\frac{D_{\text{Al}}}{\pi t} \right)^{1/2} dt = 2C_0 \left(\frac{D_{\text{Al}} t}{\pi} \right)^{1/2} \quad [9]$$

Hence

$$t = \frac{\pi}{D_{\text{Al}}} \left(\frac{M_{\text{Al}}}{2C_0} \right)^2 \quad [10]$$

The thickest films were $\sim 50 \text{ nm}$ thick so assuming a composition of $\text{Al}(\text{OH})_3$ with a density of 2.5 g/cm^3 gives $M_{\text{Al}} \sim 2 \times 10^{-7} \text{ moles/cm}^2$. With $C_0 = 2 \times 10^{-3} \text{ moles/cm}^3$ and $D_{\text{Al}} = 3 \times 10^{-5} \text{ cm}^2/\text{sec}$, Eq. [10] gives the time for precipitation as $t = 3 \times 10^{-4} \text{ sec}$. At the highest frequency examined, 100 Hz, this is only 6% of the half-cycle time, much less than the time required for pH adjustment.

Thus, pH adjustment is the critical step in the deposition process. Although at 60°C the diffusion of H^+ is slow enough to permit film deposition, at some higher temperature D_{H^+} could become large enough to preclude deposition. No SEM observations were made of surfaces etched at elevated temperatures, but some data on the weight of etch film supports the importance of temperature. Specimens were etched in 1N HCl at 50 Hz, 400 mA/cm², 30 C/cm², and the weight of etch film was determined by difference after stripping the oxide in 5% H_3PO_4 -2% CrO_3 at 85°C. These average weights are given in Table II. The last column is an estimate of the specific area per square centimeter of projected area based on capacitance values of 20V anodic oxide films. The sharp decrease in surface area that accompanies the absence of etch film is further evidence of the key role of that film.

The inner surface (metal side) of the etch film is quite smooth compared with the outer surface (Fig. 2 and 3). It seems remarkable that a precipitated film could pack densely enough to replicate the surface, but another example of this is the deposition of pseudo-boehmite (8, 9) during the reaction of Al with hot water. The replicating etch film is precipitated, and not anodically grown, as evidenced by a cell voltage in the anodic half-cycle of only 6V, most of which is due to polarization at the two electrodes and the electrolyte resistance.

Another interesting feature of the etch film is that it formed over the whole of the original unpitted sur-

Table II.

| Temp (°C) | Film wt. ($\mu\text{g/cm}^2$) | Specific area |
|-----------|---------------------------------|---------------|
| 50 | 120 | 14 |
| 60 | 35 | 16 |
| 70 | 0 | 6 |

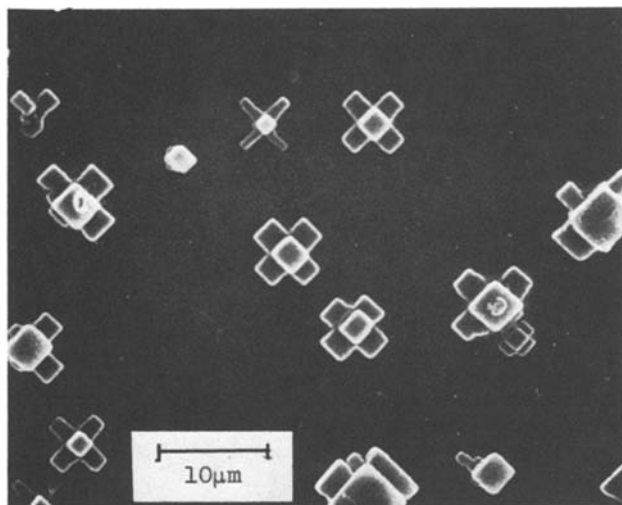


Fig. 12. 1 sec d-c etch at 1 A/cm² in 1M NaCl at 65°C

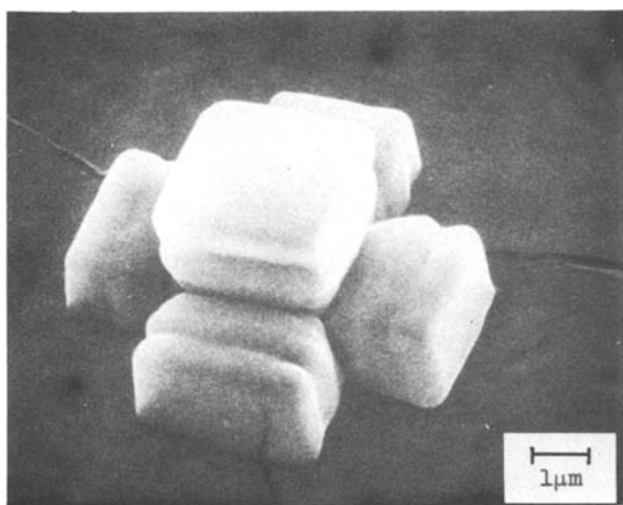


Fig. 13. 1 sec d-c etch at 1 A/cm² in 3M NaCl at 65°C

face (Fig. 1 and 2), so it appears that in the very earliest stages of the a-c etch uniform anodic dissolution and precipitation occurred before there was local attack with pit formation. This "pre-pitting" stage

was not studied but initial uniform precipitation may not be a general feature of a-c etching. The specific C.D. would be close to the nominal value so Eq. [3] would predict film formation only at low frequencies or low acid concentrations.

Although d-c etching of Al in acid or neutral chloride solutions produces a tunnel structure and no etch film, in the earliest stages of d-c etching, like a-c etching, a cube etch structure is formed (Fig. 12 and 13). The d-c etch in Fig. 12 and 13 corresponds to a single square-wave anodic half-cycle at 0.5 Hz, with no cathodic half-cycle. Although, like the a-c etch, a single cubic pit is formed first (Fig. 12) subsequent cubes seem to form only by propagation outward of the whole of each face of the first cube (Fig. 13) and not in the random way observed for a-c etching, where new cubes propagate from different points on the cube faces. This difference is consistent with the presence during a-c etching of a protective etch film containing weak points.

Manuscript submitted Jan. 2, 1980; revised manuscript received ca. Sept. 25, 1980.

Any discussion of this paper will appear in a Discussion Section to be published in the December 1981 JOURNAL. All discussions for the December 1981 Discussion Section should be submitted by Aug. 1, 1981.

Publication costs of this article were assisted by United Chemi-Con, Incorporated.

REFERENCES

1. G. E. Thompson and G. C. Wood, *Corros. Sci.*, **18**, 721 (1978).
2. N. F. Jackson, *Electrocomponent Sci. Technol.*, **2**, 33 (1975).
3. C. G. Dunn, R. B. Bolon, A. S. Alwan, and A. W. Stirling, *This Journal*, **118**, 381 (1971).
4. J. O'M. Bockris and A. K. N. Reddy, "Modern Electrochemistry," Vol. 1, pp. 317, ff., Plenum Press, New York (1973).
5. M. Stastny and F. Strafelda, *Coll. Czech. Chem. Commun.*, **34**, 168 (1969).
6. J. B. Hasted, "Aqueous Dielectrics," pp. 145, ff., Chapman and Hall, London (1973).
7. R. B. Bird, W. E. Stewart, and E. N. Lightfoot, "Transport Phenomena," p. 353, John Wiley & Sons, Inc., New York (1960).
8. W. Vedder and D. A. Vermilyea, *Trans. Faraday Soc.*, **65**, 561 (1969).
9. T. Kudo and R. S. Alwitt, *Electrochim. Acta*, **23**, 341 (1978).

Experimental Verification of a Simplified Model for Porous Electrode Electrochemical Reactors

Gilbert M. Brown and Franz A. Posey*

Oak Ridge National Laboratory, Chemistry Division, Oak Ridge, Tennessee 37830

ABSTRACT

A simplified, one-dimensional, macroscopic model for porous electrode reactors with forced convection was experimentally verified. The mass-transfer-limited reduction of ferricyanide ions was studied using porous graphite electrodes in a cell configuration having an upstream counterelectrode. Impedance characteristics of the electrode-electrolyte system were measured by the transient potentiostatic step method. An expression for the potential difference between upstream and downstream ends of an operating reactor was obtained based on the simplified macroscopic model. An experimental method was also developed for determining the efficiency of porous electrode systems from the variation of this potential difference with solution flow rate. In further work, new equations were derived that allow optimum linear flow rate and electrode length to be predicted for a porous electrode reactor operating at any desired efficiency. Predictions of a straight-pore model of porous electrodes are compared with those of the macroscopic model.

There has been a great deal of interest in recent years in the use of flow-through porous electrodes for the removal of metal ions and for other industrial electrochemical processes. Flow-through porous electrodes can provide a very large surface area per unit volume and also allow intimate contact of the electrode surface with the process stream. The minimum requirements for the scale-up of porous electrode electrochemical reactors to industrial demands are a knowledge of the collection efficiency (CE) for a single pass through the reactor and the potential drop in the solution-filled pores ($\Delta\phi_s$). The macroscopic model of porous electrode systems has been extensively developed, particularly by the groups of Newman and Alkire (1-4). Recent review articles (5, 6) have outlined the progress to date, although relatively few experimental tests of theoretical predictions have been made.

In this paper a simplified macroscopic model for the mass-transfer-limited reaction of a single species in a flow-through porous electrode reactor is considered for the case of a counterelectrode upstream of the porous electrode. The theoretical equations are presented in terms of the variables which are directly and conveniently measured by experiment. Detailed experimental tests of the model have been conducted, utilizing the reduction of $\text{Fe}(\text{CN})_6^{3-}$ at a commercially available porous graphite electrode material. Experimental procedures for evaluating the efficiency of porous electrodes are established. In this respect, our treatment resembles the semi-phenomenological treatment of Sioda (7-13). Equations have been derived to allow optimization of the electrode length and flow rate for a porous electrode at any desired efficiency, where the potential drop in solution and the concentration of the electroactive substance are variables.

The straight pore model (14) has not been developed as extensively as the macroscopic model. The former model differs from the latter in some detail, and the former will be briefly sketched out in an appendix. These two models will be compared, leading to the conclusion that the macroscopic model is preferred.

Theoretical

The porous electrodes to be treated in this work consist of a conducting matrix with electrolyte solution penetrating the void spaces of the electrode material. The conductivity of the matrix will be assumed to be

significantly higher than that of the solution-filled pores, so that any potential difference between the upstream and downstream faces of an operating porous electrode reactor will be attributed to the finite conductivity of the electrolyte phase. The macroscopic model treats the average properties of the electrode without a detailed description of the geometry of the pores. The porous electrode is assumed to be isotropic, and it is characterized by its porosity (void fraction, ϵ) and surface area per unit volume (a). The electrode configuration to be treated is the case of an upstream counterelectrode, with potentiostatic control of the front or upstream face of the porous electrode with respect to a reference electrode. A schematic diagram of a (hypothetical) pore is shown in Fig. 1 with the defined coordinate system and conventions for directions of (total) current flow from the electrode, superficial current density in the solution phase, superficial linear flow rate, and reactant flux at the interface between the pore wall and the solution (the convention of a positive anodic current is followed). The model is made one-dimensional by assuming that all quantities between the positions x and $x + dx$ in the electrode, which has the cross-sectional area A , are constant in any direction perpendicular to the flow. The distance from the front face of the electrode (x) is thus the only spatial variable; the total length of the electrode is denoted by L .

A simplified macroscopic model for the mass-transfer-limited reaction of a single species will be outlined, and this treatment follows closely the theoretical developments which have been presented in

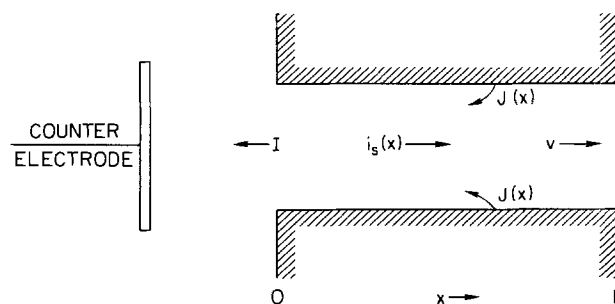


Fig. 1. Schematic diagram of idealized pore showing coordinate system and conventions for directions of total current (I), superficial current density in the solution phase ($i_s(x)$), superficial linear flow rate (v), and interfacial reactant flux ($J(x)$).

* Electrochemical Society Active Member.

Key words: current, convection, mass transport.

recent publications (1-6). The superficial current density in solution [$i_s(x)$, current per unit area of matrix plus pores] in the region between x and $x + dx$ varies according to the equation

$$\frac{di_s(x)}{dx} = nFaJ(x) \quad [1]$$

where n is the electron number of the interfacial reaction, F is Faraday's constant, and $J(x)$ is the flux of the reactant normal to the electrode surface. The local flux of reactant at the interface is related to the concentration of the reactant in solution by the equation

$$J(x) = k_m[C_o(x) - C(x)] \quad [2]$$

In Eq. [2], k_m is an average mass-transfer coefficient which is independent of position within the electrode, $C(x)$ is the position-dependent concentration of the reactant within the bulk of a pore, and $C_o(x)$ is the concentration at the pore wall. The treatment below (Eq. [6] ff.) applies to mass-transfer-limited electrochemical reactors in which the local overpotential is sufficient to drive the surface concentration, $C_o(x)$, essentially to zero. Generally, however, the potential in solution, $\phi_s(x)$, is described by Ohm's law within the pores, according to

$$i_s(x) = -\sigma_{\text{eff}} \frac{d\phi_s(x)}{dx} \quad [3]$$

where σ_{eff} is the effective conductivity of the solution phase. From Eq. [3] it follows that

$$\frac{di_s(x)}{dx} = -\sigma_{\text{eff}} \frac{d^2\phi_s(x)}{dx^2} = nFaJ(x) \quad [4]$$

The continuity or mass-balance equation within the porous electrode is

$$\frac{d[\epsilon C(x)]}{dt} = aJ(x) - v \frac{dC(x)}{dx} + D' \frac{d^2C(x)}{dx^2} \quad [5]$$

where v is superficial linear flow rate and D' is a diffusion coefficient (includes ϵ). The third term on the right side of Eq. [5] accounts for mass transfer within the porous electrode by diffusion and axial dispersion. The electrode material to be considered in this study has a moderately high surface area. At low flow rates the effects of diffusion become important, but at these flow rates the reactant is essentially completely consumed. At high flow rates the contribution to mass transport from diffusion is insignificant compared to that from forced convection. The transition from essentially complete conversion to significantly less than complete conversion occurs at a relatively high flow rate for the electrode material used in this study. Furthermore, the minimum Péclet number ~ 10 for the lowest flow rates used, so that the influence of axial dispersion on the apparent mass-transfer coefficient (6) is expected to be small over the range of flow rates of interest here. The diffusional term will therefore be omitted. Under steady-state conditions $d[\epsilon C(x)]/dt = 0$ and a solution of the resulting differential equation for $C(x)$, using the boundary condition $C(0) = C_b$, where C_b is the concentration of the electroactive species upstream of the porous electrode, is given by

$$C(x) = C_b \exp\left(-\frac{ak_mx}{v}\right) \quad [6]$$

Substitution of Eq. [2] (with $C_o(x) = 0$) and [6] into Eq. [1], followed by solution of the resulting differential equation with the boundary condition $i_s(L) = 0$, gives the result

$$i_s(x) = nFvC_b \left[\exp\left(-\frac{ak_mx}{v}\right) - \exp\left(-\frac{ak_mL}{v}\right) \right] \quad [7]$$

for a cathodic process. The total current from the reactor (I) appears at $x = 0$ (cf. Fig. 1), and by use of the definitions $I = -i_s(0)A$ and $U = vA$, where U is volume flow rate, it follows from Eq. [7] that

$$I = -nFUC_b \left[1 - \exp\left(-\frac{ak_mAL}{U}\right) \right] \quad [8]$$

for a cathodic process.

An explicit expression for the mass-transfer coefficient was derived by Wilson and Geonkopolis (15, 16) for a packed bed of spherical particles. Trainham and Newman (1) have proposed a different proportionality coefficient, and their recommendation has been followed, so that the mass-transfer coefficient is given by Eq. [9]

$$k_m = \frac{0.2574a^{2/3}D^{2/3}U^{1/3}}{\epsilon(1-\epsilon)^{2/3}A^{1/3}} \quad [9]$$

By combination of Eq. [8] and [9], an explicit expression for the current from a porous electrode reactor is therefore

$$I = -nFUC_b \left[1 - \exp\left(-\frac{0.2574a^{5/3}D^{2/3}A^{2/3}L}{\epsilon(1-\epsilon)^{2/3}U^{2/3}}\right) \right] \quad [10]$$

for a cathodic process. With long electrodes and/or low flow rates, Eq. [10] reduces to

$$I_{\text{max}} = -nFUC_b \quad [11]$$

which is Faraday's law for the maximum current from the reactor. The collection efficiency (CE) is defined by the relation

$$(CE) = \frac{I}{I_{\text{max}}} = 1 - \exp\left(-\frac{ak_mAL}{U}\right) \quad [12]$$

Use of (CE) or an analogous quantity as a measure of the efficiency of a porous electrode reactor was introduced by Gurevich and Bagotsky (17), Austin, Palasi, and Klimpel (18), and Sioda (19). Measurement of the total current from a porous electrode reactor as a function of flow rate is a convenient means of determining an important operating parameter of the reactor. Equation [10] can be rearranged, with use of Eq. [11], to

$$\ln \left[1 - \frac{I}{I_{\text{max}}} \right] = -\frac{P}{U^{2/3}} \quad [13]$$

where P is a constant for a given reactor length which is equal to

$$P = \frac{0.2574 a^{5/3} D^{2/3} A^{2/3} L}{\epsilon(1-\epsilon)^{2/3}} \quad [14]$$

Determination of an experimental value for P from the slope of a plot of $\ln [1 - I/I_{\text{max}}]$ vs. $U^{-2/3}$ thus provides the necessary information to calculate the (CE) of a reactor at any flow rate. This type of plot was employed by Coeuret (20) and by Gaunand, Hutin, and Coeuret (21). It is easily recognized that the effective reaction depth (x_o) within the porous electrode (i.e., the depth at which the reactant concentration is decreased by a factor of $1/e$) is given by

$$x_o = |C_b/C'(0)| = \frac{v}{ak_m} = \frac{U^{2/3}L}{P} \quad [15]$$

where the primed quantity denotes differentiation with respect to x . This definition of x_o was also used by Gurevich and Bagotsky (17) and by Newman and Tiedemann (5).

An expression for the potential in the solution phase is obtained by substituting Eq. [7] into Eq. [3]

$$\frac{d\phi_s(x)}{dx} = -\frac{nFUC_b}{\sigma_{\text{eff}}} \left[\exp\left(-\frac{ak_m x}{v}\right) - \exp\left(-\frac{ak_m L}{v}\right) \right] \quad [16]$$

Integration of Eq. [16] between the limits $x = 0$ and $x = L$ gives an equation for the potential difference between the upstream and downstream faces of the porous electrode

$$\frac{[\phi_s(0) - \phi_s(L)]}{nFvC_b} = \frac{1}{\sigma_{\text{eff}}} \left\{ \left(\frac{v}{ak_m} \right) \left[1 - \exp\left(-\frac{ak_m L}{v}\right) \right] - L \exp\left(-\frac{ak_m L}{v}\right) \right\} \quad [17]$$

This equation can also be obtained by setting D' (cf. Eq. [5]) equal to zero in an equation presented by Trainham and Newman (1). Equation [17] may be rewritten in terms of the volume flow rate and the maximum current from the reactor to give

$$\frac{|\Delta\phi_s|}{|I_{\text{max}}|} = R_s \left\{ \left(\frac{U}{ak_m AL} \right) \left[1 - \exp\left(-\frac{ak_m AL}{U}\right) \right] - \exp\left(-\frac{ak_m AL}{U}\right) \right\} \quad [18]$$

where $\Delta\phi_s = \phi_s(0) - \phi_s(L)$, and the resistance of the solution-filled pores is given by

$$R_s = \frac{L}{\sigma_{\text{eff}} A} \quad [19]$$

Various versions of Eq. [17] and [18] may be found in the works of Sioda (8, 9, 13), Bennion and Newman (22), and Gaunand, Hutin, and Coeuret (21).

Introduction of Eq. [9] for k_m into Eq. [18], with use of Eq. [14] for the parameter P , leads to the alternative form

$$\frac{|\Delta\phi_s|}{|I_{\text{max}}|} = R_s \left\{ \left(\frac{U^{2/3}}{P} \right) \left[1 - \exp\left(-\frac{P}{U^{2/3}}\right) \right] - \exp\left(-\frac{P}{U^{2/3}}\right) \right\} \quad [20]$$

At high flow rates the collection efficiency (CE) is small and Eq. [20] reduces to

$$\frac{|\Delta\phi_s|}{|I_{\text{max}}|} \sim \frac{R_s}{2} \cdot \frac{P}{U^{2/3}} \quad [21]$$

On the other hand, at flow rates where (CE) ~ 1 , Eq. [20] reduces to

$$\frac{|\Delta\phi_s|}{|I_{\text{max}}|} \sim R_s \cdot \frac{U^{2/3}}{P} \quad [22]$$

Equation [22] shows that a knowledge of the resistive impedance of the solution (R_s) together with information on the influence of flow rate upon the potential difference $\Delta\phi_s$, in the region where (CE) ~ 1 , will permit the parameter P to be calculated. By this means it is possible subsequently to calculate the flow-rate-dependent (CE) of the electrode at any flow rate by use of the relation

$$(CE) = 1 - \exp\left(-P/U^{2/3}\right) \quad [23]$$

which follows from Eq. [9], [12], and [14].

It is clear from the behavior of Eq. [21] and [22] with flow rate (U) that a plot of $|\Delta\phi_s|/|I_{\text{max}}|$ vs. $U^{2/3}$ will possess a maximum. Upon setting the derivative of the right side of Eq. [20] with respect to $U^{2/3}$ equal to zero, it follows that the maximum in the plot occurs when

$$\frac{P}{U^{2/3}} - \ln \left[1 + \left(\frac{P}{U^{2/3}} \right) + \left(\frac{P}{U^{2/3}} \right)^2 \right] = 0 \quad [24]$$

Numerical solution of Eq. [24] leads to the relation

$$P = 1.793 U_{\text{max}}^{2/3} \quad [25]$$

where U_{max} is the flow rate at which the maximum in the plot of $|\Delta\phi_s|/|I_{\text{max}}|$ vs. $U^{2/3}$ occurs. Furthermore, the value of $|\Delta\phi_s|/|I_{\text{max}}|$ at the maximum in the plot may also be used to obtain an independent estimate of R_s according to

$$R_s = 3.351 \left(\frac{|\Delta\phi_s|}{|I_{\text{max}}|} \right)_{\text{max}} \quad [26]$$

Consequently, all information needed for the rational design of porous electrode reactors of this type may be obtained from observations on the effect of flow rate upon the potential difference between the upstream and downstream faces of the reactor.

Experimental

Apparatus.—Porous electrodes were machined from a block of UCAR grade 45 porous graphite (23). A long cylinder (1.2 cm diam) was covered with heat-shrinkable polyolefin tubing. Individual electrode elements 0.25, 0.5, 1.0, and 2.0 cm in length were cut from this cylinder, thus ensuring uniform cross-sectional area and relatively homogeneous samples. The manufacturer specifies an average pore diameter of $\sim 60 \mu\text{m}$ and a nominal porosity of 0.48 for the porous graphite used in this study. The latter value represents both the micro- and macro-porosity of the material. As noted elsewhere (6), in a flow-through porous electrode it is the interfacial area which is accessible to the flow that is relevant. Consequently, we will use a value of 0.4 for the porosity accessible to flow, a value appropriate for random packing of spherical particles, as suggested by Newman and Tiedemann (6) and by the extensive measurements of Alkire *et al.* (24). The cylindrical electrodes were mounted in a Kel-F and Pyrex glass cell arrangement shown schematically in Fig. 2. This cell configuration is similar to that employed by Posey and Palko (25). The reference electrode (SCE) was located upstream of the porous electrode in a separate compartment containing the test solution which was bridged into the cell by the pointed capillary shown in Fig. 2. The tip of the reference electrode capillary terminated close to ($< 1 \text{ mm}$) the upstream end of the porous electrode. The counterelectrode (spectroscopic grade carbon rod) was also located upstream of the porous electrode in a compartment separated from the flowing stream by a glass frit; this arrangement prevented contamination of the test solution by counterelectrode reaction products. The potential of the front or upstream face of the porous electrode was controlled by a Princeton Applied Research Corporation Model 173D potentiostat with Model 176 current-to-voltage converter. Electrical contact to the porous graphite electrode was made by press fitting an 18-

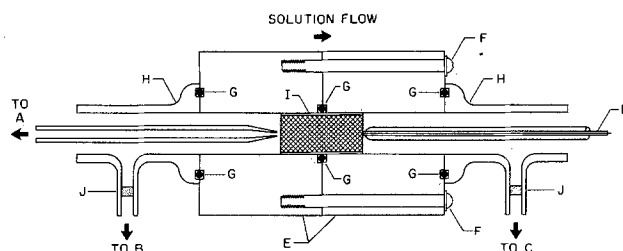


Fig. 2. Schematic diagram of cell assembly. A, upstream reference electrode (SCE); B, counterelectrode; C, downstream reference electrode (SCE); D, platinum contact rod (glass-covered); E, Kel-F cell body; F, assembly bolt; G, O-ring seal; H, glass tube with O-ring joint; I, porous graphite electrode inside heat-shrinkable tubing; J, glass frit.

gauge Pt wire, sealed in glass with ~ 1 mm exposed, to the downstream face of the electrode. Forced flow of solution (deoxygenated by sparging with argon) through the porous electrode was controlled with a Sage Instruments Model 375 peristaltic pump. The average volume flow rate was measured by noting the time required for collection of a known volume of the effluent.

Steady-state and transient current measurements were made in the conventional manner. The potential difference between the upstream and downstream faces of the porous electrode was measured by use of a second, downstream reference electrode (SCE). A battery-operated Keithley Model 602 electrometer, referenced to the ground of the PARC Model 173D potentiostat, served as a buffer amplifier for the downstream reference electrode. Steady-state measurements of the potential difference in solution between the upstream and downstream faces of the porous electrode ($\Delta\phi_s$) were measured from the differential voltage of the PARC Model 173D electrometer output and the Keithley Model 602 unity-gain output on a digital voltmeter. Transient measurements of $\Delta\phi_s$ were determined from photographs of the trace of a Tektronix Model 5115 storage oscilloscope. A Tektronix Model 5A19N differential amplifier plug-in unit was used to measure the voltage difference from the two electrometer outputs.

Procedure.—Solutions were prepared from reagent grade chemicals. Laboratory distilled water was further purified by passage through a Milli-Q purification system (Millipore Corporation) producing water with a conductivity of $\leq 8 \times 10^{-8} \Omega^{-1} \text{ cm}^{-1}$. All measurements were made in an electrolyte containing 1.0M KCl and 0.01M $\text{Na}_2\text{B}_4\text{O}_7$ (borax buffer, pH ~ 9). Solutions of $\text{K}_3\text{Fe}(\text{CN})_6$ were analyzed by coulometric methods. All solutions were degassed with a stream of argon before being pumped into the porous electrode apparatus. Observed values of the limiting current and of $\Delta\phi_s$ were considered to correspond to steady states after 3-4 electrode volumes of solution flow. The $\text{Fe}(\text{CN})_6^{3-}/\text{Fe}(\text{CN})_6^{4-}$ couple has an apparent "half-wave potential" at low flow rates and currents ($\Delta\phi_s < 10$ mV) of +0.22V vs. SCE. Steady-state measurements were made with the entire electrode maintained at potentials no more positive than ~ 0 V vs. SCE. The lowest concentration of $\text{Fe}(\text{CN})_6^{3-}$ employed in this study ($\sim 5 \times 10^{-4}\text{M}$) was dictated by a desire to make the residual current insignificant with respect to the Faradaic current. The highest flow rate ($\sim 0.7 \text{ cm}^3 \text{ sec}^{-1}$) was limited by the potential drop in the solution-filled pores and the necessity of keeping the entire electrode in the limiting-current region. At potentials of the upstream (controlled-potential) face more negative than -0.30V vs. SCE, the background current became too large to be neglected.

The impedance characteristics (C_T and R_s , cf. below) of the porous electrodes were measured by the potential step method (26) in the 1.0M KCl + 0.01M $\text{Na}_2\text{B}_4\text{O}_7$ electrolyte. A 50 or 100 mV potential step was applied to the upstream face of the porous electrode in the potential range +0.25 to +0.10V vs. SCE. The transient current data were analyzed as described below. All measurements were carried out at room temperature ($23^\circ \pm 2^\circ\text{C}$).

Results and Discussion

Determination of electrode impedance characteristics.—Theoretical aspects of the transient response of porous electrodes to a potential step have been discussed elsewhere (14, 26). The theory applies to charging of the double layer in the absence of a significant contribution to the current from Faradaic reactions, and it provides a convenient means of determining the effective resistance of a solution-filled porous electrode, a parameter that is needed for analysis or prediction of the behavior of a porous electrode

reactor. Although the transient current response to a potential step was derived by Posey and Morozumi (26), the plotting method used by Johnson and Newman (27) and by Tiedemann and Newman (28) is especially advantageous. In this method $I(t)\sqrt{t}$ is plotted against \sqrt{t} , where $I(t)$ is the total current at time t . Analysis shows that, for negligible resistance between the reference electrode and the upstream end of the porous electrode, this plot is described by

$$I(t)\sqrt{t} = \frac{2\eta_0\sqrt{\tau}}{R_s} \left\{ \sqrt{\frac{t}{\tau}} \sum_{k=0}^{\infty} \exp[-(k+1/2)^2\pi^2 t/\tau] \right\} \quad [27]$$

where η_0 is the change in the potential of the upstream end of the porous electrode, R_s (resistance of solution in pores of electrode) is given by Eq. [19], and $\tau = R_s C_T$ is a time constant. The total capacity of the porous electrode is given by

$$C_T = acAL \quad [28]$$

where c is the differential capacity per unit area and other quantities are defined above. For $t \ll \tau$, Eq. [27] reduces to

$$\lim_{t \rightarrow 0} [I(t)\sqrt{t}] = \frac{\eta_0}{\sqrt{\pi}} \cdot \frac{\sqrt{\tau}}{R_s} \sim [I(t)\sqrt{t}]_{\text{max}} \quad [29]$$

This result follows also from the equation of de Levie (14) for potentiostatic charging of the double layer of a semi-infinite porous electrode. In practice, as noted by Tiedemann and Newman (28), the quantity $I(t)\sqrt{t}$ cannot approach a constant at arbitrarily short times because of the finite resistance in the solution between the porous electrode and the reference electrode and any resistance associated with the leads and current collector. Instead a plateau or maximum is observed in the plot of $I(t)\sqrt{t}$ vs. \sqrt{t} . A plot of this type for a porous electrode with $L = 0.25$ cm is shown in Fig. 3; in this case of course no $\text{Fe}(\text{CN})_6^{3-}$ was present in the solution phase. The solid line in Fig. 3 follows Eq. [27]. The data points, taken from a photograph of the oscilloscope trace, lie below the line predicted by Eq.

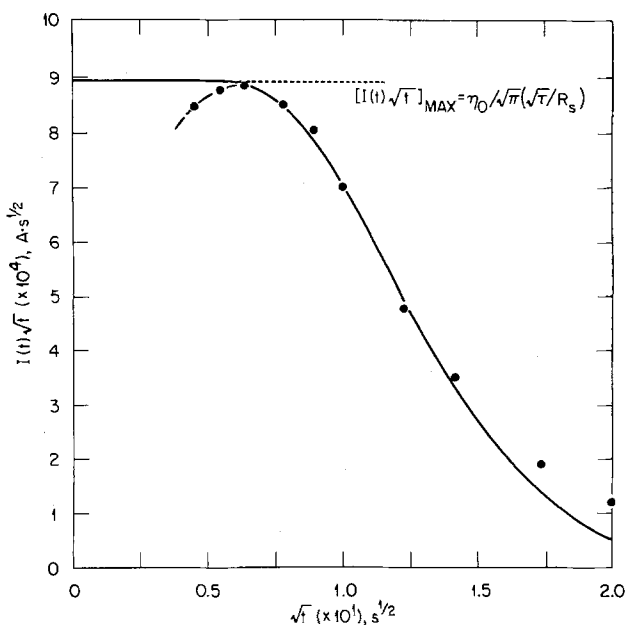


Fig. 3. Plot of $I(t)\sqrt{t}$ vs. \sqrt{t} for potential step. $|\eta_0| = 0.10\text{V}$ (+0.25 to +0.15V vs. SCE); $L = 0.25$ cm.

[27] or [29] at short times (cf. dashed line in Fig. 3) because of the resistive factor noted above.

If the resistance between the reference electrode and the porous electrode is not excessive (28), the value of the maximum or plateau observed in a plot like Fig. 3 will be a good measure of the quotient $\sqrt{\tau}/R_s$, as implied in Eq. [29] (cf. dotted line in Fig. 3). Furthermore, this type of plot may also be used to estimate τ from the data observed at times when the electrode capacity begins to saturate and $I(t)\sqrt{t}$ begins to decrease. Most of the data shown in Fig. 3 correspond to this case. It follows from Eq. [27] and [29] that the ratio of values of $I(t)\sqrt{t}$ to the maximum or plateau value is given by

$$\frac{[I(t)\sqrt{t}]}{[I(t)\sqrt{t}]_{\max}} = 2\sqrt{\pi} \left\{ \sqrt{\frac{t}{\tau}} \sum_{k=0}^{\infty} \exp[-(k + 1/2)^2 \pi^2 t/\tau] \right\} \quad [30]$$

Consequently each value of this ratio corresponds to a unique value of t/τ , so that use of Eq. [30] with any particular value of the ratio and the corresponding time leads to an estimate of τ . Values of the ratio defined by Eq. [30] along with corresponding values of t/τ are given in Table I.

Any number of estimates of τ may be obtained from a transient like that shown in Fig. 3. Obviously, consistency among separate estimates lends confidence to the procedure, but some deviation can be expected in practice because of the difficulty of removing traces of electroactive substances (e.g., dissolved oxygen) from the base electrolyte. The positive deviation of the data points in Fig. 3 for $\sqrt{t} > 0.15$ may be attributed to this cause.

Combination of values of $\sqrt{\tau}/R_s$ obtained by use of Eq. [29] with values of τ obtained by use of Eq. [30] leads to separate values of R_s and C_T for the four electrode lengths used in this study, and the results are shown in Fig. 4. As predicted by Eq. [19] and [28], both R_s and C_T are observed to depend linearly upon the length of the electrode. The lines in Fig. 4 are least-squares fits of the data forced through the origin. Use of Eq. [19] with the resistance data of Fig. 4 leads to $\sigma_{\text{eff}} = 2.1 \times 10^{-2} \Omega^{-1} \text{cm}^{-1}$. The deviation of this value from the bulk conductivity of 1.0M KCl ($\sigma_0 = 0.11 \Omega^{-1} \text{cm}^{-1}$ at 25°C) may be rationalized by use of the Bruggeman equation (29)

$$\sigma_{\text{eff}} = \sigma_0 \epsilon^{3/2} \quad [31]$$

where σ_0 is the bulk conductivity of the continuous liquid phase and ϵ is void fraction, as discussed by De La Rue and Tobias (30) and by Meredith and Tobias (31). For $\epsilon = 0.4$ and $\sigma_0 = 0.11 \Omega^{-1} \text{cm}^{-1}$, an estimate of $\sigma_{\text{eff}} \sim 2.8 \times 10^{-2} \Omega^{-1} \text{cm}^{-1}$ is obtained from Eq. [31]. This estimate is probably as consistent as can be expected with the quantity estimated from the data in Fig. 4 considering the uncertainty in ϵ and

Table I. Values of the function in Eq. [30]

| t/τ | $\sqrt{t/\tau}$ | $\frac{I(t)\sqrt{t}}{[I(t)\sqrt{t}]_{\max}}$ |
|----------|-----------------|--|
| 0.1 | 0.316 | 0.9999 |
| 0.2 | 0.447 | 0.9865 |
| 0.3 | 0.548 | 0.9287 |
| 0.4 | 0.632 | 0.8359 |
| 0.5 | 0.707 | 0.7300 |
| 0.6 | 0.775 | 0.6248 |
| 0.7 | 0.837 | 0.5273 |
| 0.8 | 0.894 | 0.4404 |
| 0.9 | 0.949 | 0.3650 |
| 1.0 | 1.000 | 0.3006 |
| 1.5 | 1.225 | 0.1072 |
| 2.0 | 1.414 | 0.0360 |

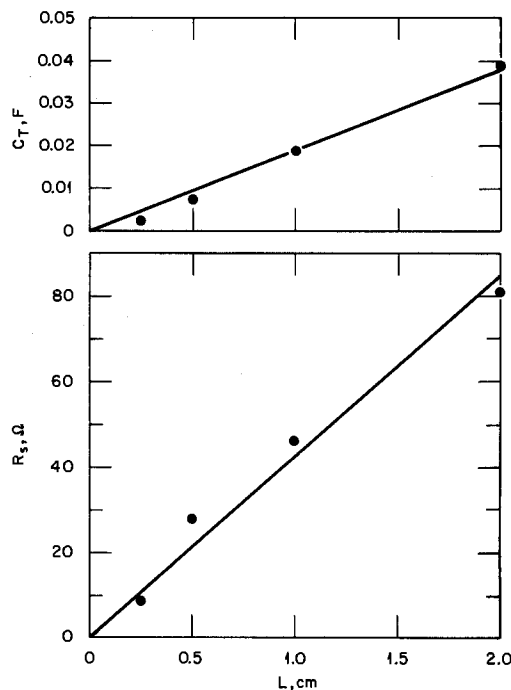


Fig. 4. R_s and C_T as a function of L

in the strict applicability of Eq. [31] to the present situation.

Use of Eq. [28] with the capacity data of Fig. 4 leads to $ca = 1.7 \times 10^{-2} \text{F cm}^{-3}$ for the double layer capacity per unit volume of the electrode material used here. Estimation of the area-to-volume ratio (a) from these data requires a knowledge of the differential capacity per unit area (c). Bauer, Spritzer, and Elving (32) observed approximately $50 \mu\text{F cm}^{-2}$ for the differential capacity of polished pyrolytic graphite in 0.5M KCl. More recently, Randin and Yeager (33) observed large differential capacities ($\sim 100 \mu\text{F cm}^{-2}$) for the edge orientation of stress-annealed pyrolytic graphite as determined by a-c measurements (1000 Hz), and even larger values could be estimated from voltammetry. A value of c greater than that observed for pyrolytic graphite in 0.5M KCl (32) seems reasonable since the material of this study is probably much more inhomogeneous than pyrolytic graphite, and it is known that surface roughness by itself plays a significant role in measurements of differential capacity by both a-c and pulse techniques, as shown by de Levie (34). If a value of $c \sim 100 \mu\text{F cm}^{-2}$ is assumed, then it follows that $a \sim 1.7 \times 10^2 \text{cm}^{-1}$. This value of a agrees well with that ($\sim 1.6 \times 10^2 \text{cm}^{-1}$) estimated from values of P determined from the variation of I or $\Delta\phi_s$ with U , as shown below. And in addition, microscopic examination of the individual grains comprising the porous electrode shows that the average particle diameter (D_p) is approximately $200 \mu\text{m}$. This value of D_p together with use of the well-known engineering formula $a = 6(1 - \epsilon)/D_p$ leads to the estimate $a \sim 1.8 \times 10^2 \text{cm}^{-1}$, in good agreement with the other estimates of a .

It was noted previously (26) that the ratio of the matrix resistance (R_m) to the solution resistance (R_s) may be estimated from observations on the transient response of a porous electrode to a potential step by use of the relation

$$\frac{R_m}{R_s} = \frac{\eta(L,0)}{\eta_0} \quad [32]$$

In Eq. [32] $\eta(L,0)$ is the sudden change in the potential of the downstream end of the porous electrode when the potential of the upstream end is changed by η_0 . For all electrode samples used in this work we

found that $R_m \leq 0.03 R_s$, in agreement with published data on matrix conductivity (23). This measurement also proved to be a convenient means of determining whether or not a good electrical contact had been obtained between the platinum contact rod and the porous graphite electrode.

Mass-transfer-limited current.—The simplified treatment of the macroscopic model predicts a linear relationship between current and flow rate (cf. Eq. [10] and [11]) in the flow regime in which (CE) is very near to unity. This is the observed relationship, as shown by the dashed line (unity slope) in the log-log plot of current vs. flow rate in Fig. 5. This type of plot has also been used by Sioda (7, 10, 19, 35-37), Alkire and Gracon (3), and Alkire and Ng (4). For short electrodes and/or high flow rates, Eq. [10] approaches the asymptotic limit of Eq. [33]. The flow rate required

$$I = - \frac{0.2574nFC_b a^{5/3} A^{2/3} D^{2/3} U^{1/3} L}{\epsilon(1-\epsilon)^{2/3}} \quad [33]$$

to observe this limit could not be achieved in these measurements before the potential drop in the pores becomes excessive, but the limit is being approached in Fig. 5 (these data were obtained on an electrode with $L = 0.25$ cm). The limiting behavior predicted by Eq. [33] has been observed in other studies of porous electrode systems (4, 38).

Equation [13] predicts that a plot of $\ln [1 - I/I_{\max}]$ vs. $U^{-2/3}$ will be linear with a zero intercept. Similar plots have been employed by Coeuret (20) and by Gaunand, Hutin, and Coeuret (21). Experimental data from three independent series of measurements carried out with different electrodes for which $L = 0.25$ cm are shown in Fig. 6. A linear regression analysis of these data leads to a slope of -0.48 with a correlation coefficient of 0.95 (cf. dashed line in Fig. 6). The intercept ($+0.06$) is sufficiently small to force a zero intercept. When analyzed in this manner the slope is -0.44 ± 0.05 , and this corresponds to the solid line in Fig. 6. These results show that, within experimental error, the data are described well by Eq. [13]. As noted in Eq. [15], the quantity $U^{2/3}L/P$ is the flow-rate-dependent effective reaction depth. Thus the parameter P , determined from the slope of the plot of Fig. 6, is an important experimental parameter which may be used to calculate (CE) for a given electrode material, electrode length, and flow rate. The solid line in Fig. 5 was calculated using $I = I_{\max} \cdot (CE)$ with Eq. [23] and a value of P determined by the procedure of Fig. 6; the agreement between calculated and experimental results is excellent. An analogous treatment of

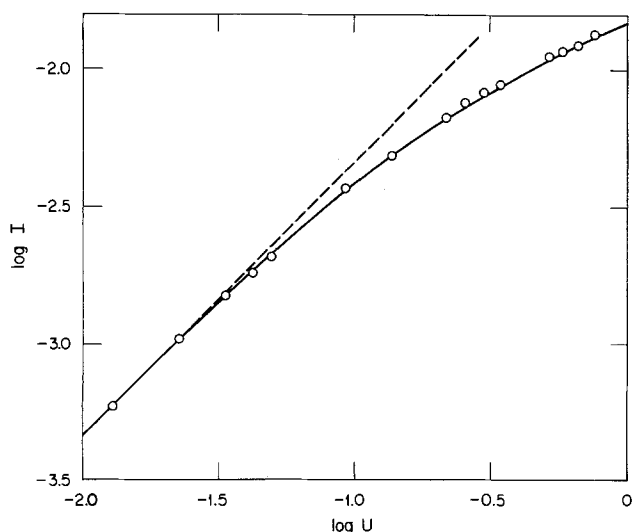


Fig. 5. Reduction of $4.8 \times 10^{-4} M$ $Fe(CN)_6^{3-}$ in porous graphite electrode; $L = 0.25$ cm.

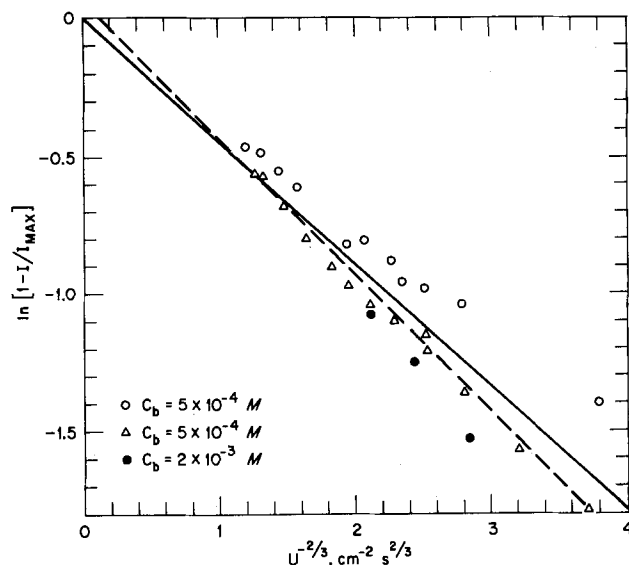


Fig. 6. Reduction of $Fe(CN)_6^{3-}$ in porous graphite electrode; $1.0 M$ $KCl + 0.01 M$ $Na_2B_4O_7$, $A = 1.13$ cm^2 , $L = 0.25$ cm.

data obtained with electrodes for which $L = 0.50$ cm led to $P = 1.0$. We were unable to achieve a high enough flow rate to observe that (CE) was significantly less than unity for electrodes with $L = 1.0$ and 2.0 cm, while maintaining the entire electrode in the potential region of mass transfer control. The method of data analysis used in this work is analogous to the double logarithmic plots used by Sioda (7, 10, 11, 36, 39, 40). Our treatment emphasizes determination of the parameter P whereas Sioda was interested in the power dependence of the limiting current on the flow rate.

The predictions of the simplified model may be compared with those of the more extended model of Trainham and Newman (1), which includes effects of axial diffusion and dispersion and of a simultaneous side reaction. Upon neglect of these factors their expression for the current reduces to Eq. [8]. Substitution of the appropriate parameters to describe the electrode material and conditions of this study into the expression of Trainham and Newman (1) shows that the current predicted by the extended model differs from that of Eq. [10] by less than 5%. This is taken to be evidence that the diffusional flux, at least to a first approximation, is an insignificant mode of mass transport for these electrodes and flow rates.

Potential drop in solution-filled porous electrodes.—It is important to develop a relationship for $|\Delta\phi_s| = |\phi_s(0) - \phi_s(L)|$ as a function of flow rate which will allow the parameters needed for design of a porous electrode reactor to be determined. Furthermore, as noted above, this potential difference itself is one of the important criteria that must be satisfied for optimum design of a porous electrode reactor.

The theoretical expression for the potential difference in solution is given by Eq. [20], which suggests use of a plot of $|\Delta\phi_s|/|I_{\max}|$ vs. $U^{2/3}$. Plots of experimental data for three different electrode lengths are shown in Fig. 7 and 8. In the flow regime where (CE) is near unity, the experimental data are described by Eq. [22]. The dashed lines in Fig. 7 and 8 are in good agreement with this relation. Consequently, it is possible to estimate a value of P from data of this type by use of a value of R_s obtained from analysis of the current transient of a porous electrode to a potential step, as noted above.

In all cases investigated, the experimental data points at the lowest flow rates did not follow the prediction of Eq. [22] as well as might have been desired. This positive deviation (cf. Fig. 8) cannot be accounted for by the simple model used in this analysis. How-

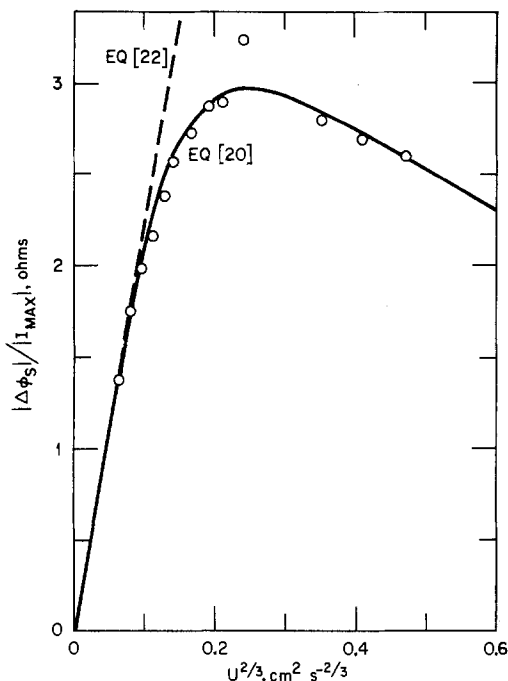


Fig. 7. Plot of $|\Delta\phi_s|/|I_{\max}|$ vs. $U^{2/3}$ for $L = 0.25$ cm. Solid line: Eq. [20] with $P = 0.45$ $\text{cm}^2 \text{sec}^{-2/3}$, $R_s = 10\Omega$; dashed line: Eq. [22].

ever, it is probably related to diffusion effects at the upstream face of the electrode. At low flow rates, all of the reactant is consumed near the upstream face of the electrode, i.e., the effective reaction depth is a very small percentage of the reactor length (cf. Eq. [15]). And even for $U = 0$ a finite current can be expected due to diffusion (and possible natural convection) of the reactant to the upstream face of the electrode (6), a process that is not treated here. In any event, this problem will not be serious in determination of the parameters needed for design of porous electrode reactors, and in addition one consideration for optimization of reactor design is to maximize the effective reaction depth, as described below.

At flow rates where (CE) is appreciably less than unity, it is clear from Eq. [20] that a plot of $|\Delta\phi_s|/|I_{\max}|$

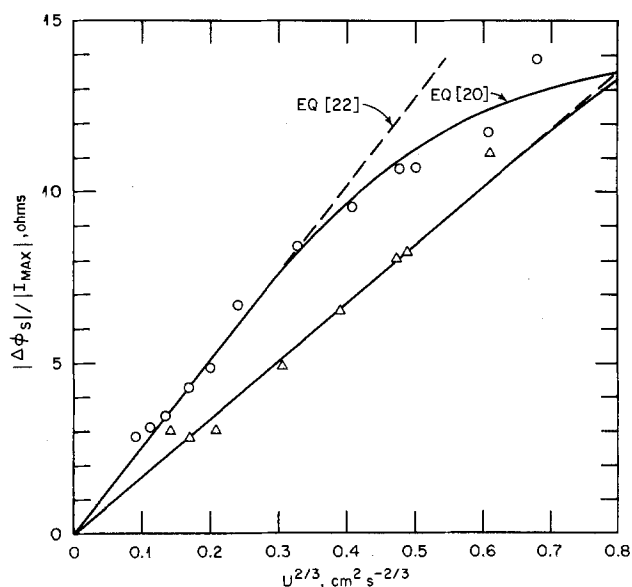


Fig. 8. Plot of $|\Delta\phi_s|/|I_{\max}|$ vs. $U^{2/3}$ for $L = 1.0$ and 2.0 cm. Circles: $L = 1.0$ cm, $P = 1.8$ $\text{cm}^2 \text{sec}^{-2/3}$, $R_s = 46\Omega$; solid line: Eq. [20]; dashed line: Eq. [22]. Triangles: $L = 2.0$ cm, $P = 4.8$ $\text{cm}^2 \text{sec}^{-2/3}$, $R_s = 81\Omega$; solid line: Eq. [20]; dashed line: Eq. [22].

vs. $U^{2/3}$ will possess a maximum (cf. Eq. [21] and [22]). This is illustrated by the data in Fig. 7. As noted above (cf. Eq. [25]), the parameter P may be calculated from the value of U at which the maximum occurs. In addition, the resistance of the solution within the porous electrode (R_s) may be calculated from the maximum value of $|\Delta\phi_s|/|I_{\max}|$ by use of Eq. [26]. Thus, under favorable conditions, two important parameters needed for design of a porous electrode reactor may be determined by measurement of the flow rate dependence of $\Delta\phi_s$. Unfortunately the maximum in a plot of $|\Delta\phi_s|/|I_{\max}|$ vs. $U^{2/3}$ is rather broad, and the difficulty of precise determination of its location may limit the usefulness of this method to some extent.

Sioda (8, 40) and Gaunand, Hutin, and Coeuret (21) have also investigated the potential difference between the upstream and downstream faces of a porous electrode reactor. Sioda (8, 40) chose to plot the ratio $|\Delta\phi_s|/|I|$ as a complex function of (CE) which can be obtained by rearrangement of Eq. [17], [18], or [20]. A similar plot was used by Gaunand, Hutin, and Coeuret (21). These plots only allowed a determination of the effective conductivity of the solution (σ_{eff}). The method of data analysis suggested above allows not only R_s , and thus σ_{eff} (cf. Eq. [19]), but also the important parameter P to be determined.

Values of the parameter P were calculated from both potential drop and current measurements for electrodes with $L = 0.25$ and 0.50 cm. Based upon current measurements, as discussed above, the calculated values of P were 0.44 and 1.05 $\text{cm}^2 \text{sec}^{-2/3}$. The values based upon measurements of $\Delta\phi_s$ were 0.45 and 0.90 $\text{cm}^2 \text{sec}^{-2/3}$, respectively. This good agreement between two measuring techniques also extends to determinations of R_s . Use of the maximum values of $|\Delta\phi_s|/|I_{\max}|$ for the 0.25 and 0.50 cm electrodes leads to $R_s = 10$ and 29Ω , respectively, in good agreement with the values estimated for the same electrodes by analysis of the current response to a potential step (cf. Fig. 4).

The good agreement of experimental data with theoretical predictions of the macroscopic model is taken to be evidence that Eq. [20] (or Eq. [17]) accurately describes the potential difference between the upstream and downstream faces of a porous electrode. Furthermore, the agreement between parameters calculated from current measurements and from potential measurements indicates the self-consistency of the macroscopic model. We were unable to use a flow rate high enough to observe a (CE) significantly different from unity for $L = 1.0$ and 2.0 cm without encountering excessively large $\Delta\phi_s$, so that P could not be estimated by use of Eq. [25] in these cases. However, P could be calculated for these cases by use of Eq. [22] and values of R_s estimated from the current response to a potential step (cf. Fig. 4). The values of P obtained in this manner were 1.8 and 4.8 $\text{cm}^2 \text{sec}^{-2/3}$ for $L = 1.0$ and 2.0 cm, respectively.

The parameter P is predicted by the macroscopic model to be a linear function of reactor length (cf. Eq. [14]). Values of P determined by the methods described above are shown plotted as a function of L in Fig. 9. The data for $L = 0.25, 0.50,$ and 1.0 cm show within experimental error a linear dependence upon L . From the slope of the line in Fig. 9, with use of $D = 7.63 \times 10^{-6}$ $\text{cm}^2 \text{sec}^{-1}$ for the diffusivity of $\text{Fe}(\text{CN})_6^{3-}$ in $1M$ KCl (41), it can be calculated that $a \sim 1.6 \times 10^2$ cm^{-1} . As noted above, this value of a agrees well with that estimated from the average particle diameter and also with the value estimated from the total capacity of the electrodes. The value of P for the electrode with $L = 2.0$ cm deviates markedly from the line that describes the other data in Fig. 9. The cause for this deviation is not known.

Comparison of macroscopic and straight pore models.—The two models that describe mass transport to the pore walls of a porous electrode differ not only in the

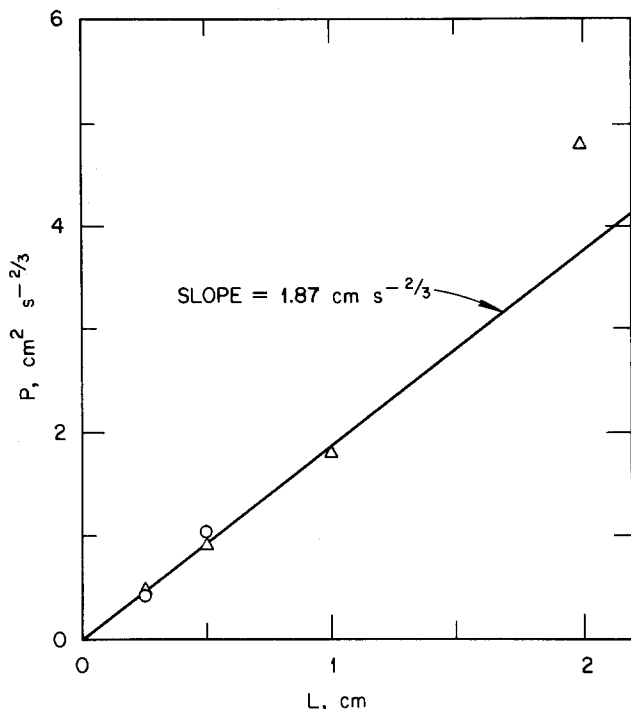


Fig. 9. Plot of the parameter P as a function of L . Circles: current measurements; triangles: potential measurements.

geometric description of the pores but also in the hydrodynamic description of flow. The straight pore model assumes that fully developed laminar flow takes place within the pores whereas the macroscopic model is based upon an average mass transfer coefficient which is independent of position. Theoretical predictions of total current (and thus collection efficiency) and potential difference based on the straight pore model are outlined briefly in the Appendix. It was shown above that the macroscopic model agrees well with experimental data. The two models are compared below using, as far as possible, the same parameters to describe the porous electrode system.

A plot of (CE) vs. $\log U$ for an electrode with $L = 0.25$ cm is shown in Fig. 10, which contains two different sets of experimental data on reduction of $\text{Fe}(\text{CN})_6^{3-}$. Plots of this type were used by Sioda (10, 42), Wroblowa and Razumney (43), Alkire and Gracon (3), and Alkire and Gould (44). The macroscopic model was fit to the data using Eq. [23] and the appropriate value of P from Fig. 9. The straight pore model was fit by choosing a value of the constant $a^2 D A L / \epsilon$ in Eq. [A-5] such that the two models coincide at high flow rates (cf. Eq. [33] and [A-7]). Nu-

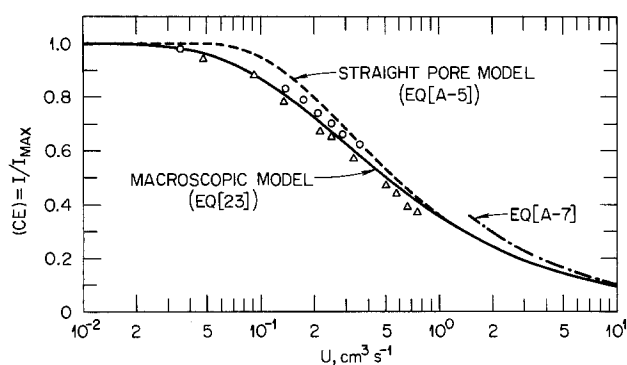


Fig. 10. Comparison of macroscopic and straight pore models: collection efficiency as a function of flow rate. Reduction of $5 \times 10^{-4} \text{M Fe}(\text{CN})_6^{3-}$; $L = 0.25$ cm. Macroscopic model: $P = 0.44 \text{ cm}^2 \text{ sec}^{-2/3}$. Straight pore model: $a^2 D A L / \epsilon = 3.85 \times 10^{-2} \text{ cm}^3 \text{ sec}^{-1}$.

merically the two models differ somewhat in the flow region from essentially complete conversion to $\sim 50\%$ conversion. Although the macroscopic model seems to fit these data a little better than the straight pore model, the scatter in the data precludes a clear distinction. An asymptotic solution valid at high flow rates (cf. Eq. [A-7]) is also shown in Fig. 10; this was obtained from the Lévêque solution to the mass transport problem (cf. Appendix) for $(CE) \sim 0$.

Consideration of the potential difference between the upstream and downstream faces of a porous electrode ($\Delta\phi_s$) provides a clear distinction between the two models. Figure 11 is a plot of $\log |\Delta\phi_s| / |I_{\text{max}}| R_s$ vs. $\log U$ for the two models using the same parameters as in Fig. 10. At low flow rates where (CE) is near unity the quantity $|\Delta\phi_s| / |I_{\text{max}}|$ varies directly with U for the straight pore model while for the macroscopic model this quantity varies with $U^{2/3}$, as may be seen by comparison of Eq. [22] and [A-8]. This same difference in dependence upon U is also exhibited by the effective reaction depth (cf. Eq. [15]). In addition the macroscopic model agrees well numerically with experimental data over the entire region of the maximum in Fig. 11. Although some improvement in fit with the straight pore model could be achieved by adjustment of the physical constants, the shape of the maximum predicted by this model for the log-log plot of Fig. 11 would not allow the close fit observed for the macroscopic model over a wide range of flow rates. From a mathematical standpoint the straight pore model is more complicated than the simplified macroscopic model (cf. Appendix). Consequently, use of the macroscopic model is preferable for analysis and design of porous electrode systems both for its convenience and because of its consistency with experimental results. However, there are electrode configurations for which the straight pore model might be a better approximation. Such an electrode consists of a bundle of parallel wires with longitudinal solution flow, a configuration which is similar to the brush electrode of de Levie (45).

Design considerations for porous electrode reactors.—The fundamental relationships needed to design a porous electrode electrochemical reactor are provided by Eq. [7] or [12] and [17]. Perhaps the most commonly used design criterion for a practical reactor arises as

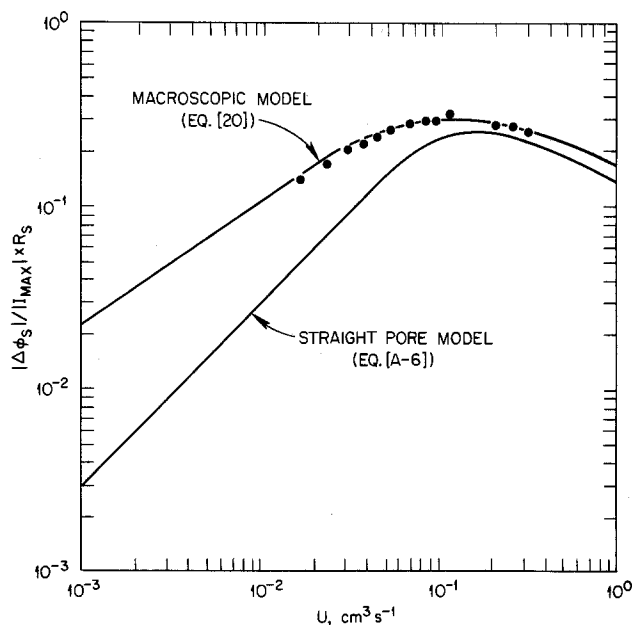


Fig. 11. Comparison of macroscopic and straight pore models: normalized potential drop as a function of flow rate. Reduction of $1.93 \times 10^{-3} \text{M Fe}(\text{CN})_6^{3-}$; $L = 0.25$ cm. Macroscopic model: $P = 0.44 \text{ cm}^2 \text{ sec}^{-2/3}$. Straight pore model: $a^2 D A L / \epsilon = 3.85 \times 10^{-2} \text{ cm}^3 \text{ sec}^{-1}$.

a result of a desire to keep the flow rate sufficiently low so that (CE) is near unity, and thus the reaction will be completed in a single pass. Equations [12] and [17], written in terms of superficial current density ($i_s(0)$) and superficial linear flow rate (v), become

$$(CE) = \frac{i_s(0)}{nFvC_b} = 1 - \exp\left(-\frac{ak_mL}{v}\right) \quad [34]$$

$$\frac{\Delta\phi_s}{nFvC_b} = \frac{L}{\sigma_{eff}} \left\{ \left(\frac{v}{ak_mL} \right) \left[1 - \exp\left(-\frac{ak_mL}{v}\right) \right] - \exp\left(-\frac{ak_mL}{v}\right) \right\} \quad [35]$$

The average mass transfer coefficient (k_m), written in terms of superficial linear flow rate, becomes (cf. Eq. [9])

$$k_m = \frac{0.2574}{\epsilon(1-\epsilon)^{2/3}} (aD)^{2/3} v^{1/3} \quad [36]$$

Equations [34] and [35] may be solved simultaneously, with use of Eq. [36], to give optimum values of v and L for any desired value of (CE) as a function of $\Delta\phi_s$, C_b , and the physical parameters that describe the electrode-electrolyte system.

It is convenient to introduce the parameter Q , defined by

$$Q = -\ln[1 - (CE)] = ak_mL/v = P/U^{2/3} \quad [37]$$

as a measure of the desired current or collection efficiency. Use of Q in Eq. [34] and [35] and solution for v and L lead to the following relations

$$v = 4.53 \times 10^{-4} \frac{(\sigma_{eff})^{3/5} a D^{2/5}}{\epsilon^{3/5} (1-\epsilon)^{2/5}} \left(\frac{\Delta\phi_s}{nC_b} \right)^{3/5} \frac{1}{[1 - (1+Q)\exp(-Q)]^{3/5}} \quad [38]$$

$$L = 2.29 \times 10^{-2} \frac{(\sigma_{eff})^{2/5} \epsilon^{3/5} (1-\epsilon)^{2/5}}{a D^{2/5}} \left(\frac{\Delta\phi_s}{nC_b} \right)^{2/5} \frac{Q}{[1 - (1+Q)\exp(-Q)]^{2/5}} \quad [39]$$

The required cross-sectional area of the reactor (A) may be calculated from the total volume flow rate (U) and the relation $A = U/v$. It is clear from Eq. [38] and [39] that the optimum reactor length and flow rate will depend on the allowable potential difference between the upstream and downstream faces of the electrode ($\Delta\phi_s$) and on the concentration of the electroactive species (C_b). The other quantities in Eq. [38] and [39] describe the properties of the electrode and the electrolyte and the desired (CE) . Bennion and Newman (22) and Newman and Tiedemann (5) discuss alternative relations that could be used for design and optimization of porous electrodes operating under limiting current conditions for $(CE) \sim 1$. Many other design considerations and a graphical method for estimation of v and L for situations where k_m differs from Eq. [9] or [36] are reviewed by Newman and Tiedemann (6).

These design equations can be used to estimate the appropriate physical size, linear flow rate, and cross-sectional area required for a typical industrial application. Two limiting cases are: (i) removal of trace metal ions from a flowing stream by electrodeposition, and (ii) electrosynthesis of a species soluble in aqueous solution. The properties of the porous graphite electrode material used in this study may be taken as fairly typical for many applications of interest. It has a relatively large average pore diameter ($\sim 60 \mu\text{m}$) to minimize pumping costs, and yet it retains a relatively large specific surface area ($> 10^2 \text{ cm}^{-1}$). Typi-

cal values which can be assigned to a , D , ϵ , and σ_{eff} are $1.7 \times 10^2 \text{ cm}^{-1}$, $1 \times 10^{-5} \text{ cm}^2 \text{ sec}^{-1}$, 0.4, and $0.05 \Omega^{-1} \text{ cm}^{-1}$, respectively. In addition, it will be assumed that an electrode assembly will be required to process $4.38 \times 10^2 \text{ cm}^3 \text{ sec}^{-1}$ (10,000 gal/day) to be economically feasible. In both cases it will be assumed that a potential difference of 0.5V is allowable between the upstream and downstream faces of the electrode and that $(CE) = 0.99$ so that $Q = 4.605$.

The reduction of Hg(II) in chlor-alkali process streams to Hg^0 at a concentration of approximately $2.5 \times 10^{-4} M$ ($\sim 50 \text{ ppm}$) is an application which has been considered previously (25). The optimum electrode length and linear flow rate, calculated from Eq. [38] and [39], are 2.3 cm and 1.1 cm sec^{-1} , respectively. Consequently the required volume flow rate demands use of a cross-sectional area $A \sim 400 \text{ cm}^2$. Thus a compact porous electrode device is capable of treating a large volume of liquid in applications of this type.

On the other hand, use of a porous electrode reactor for electrosynthesis, where a moderately high concentration of the electroactive substance is desirable, appears to be relatively inappropriate with the present configuration. For example, one might consider a redox process for which $nC_b = 0.5M$. It can be estimated from Eq. [38] and [39] that $L \sim 0.14 \text{ cm}$ and $v \sim 1.8 \times 10^{-2} \text{ cm sec}^{-1}$ for this application. Consequently the required cross-sectional area would be $A \sim 2.5 \times 10^4 \text{ cm}^2$, so that the physical dimensions of the reactor would need to be approximately 1.5m on a side by $\sim 1.5 \text{ mm}$ thick. These dimensions appear to be unrealistic for a practical device. However, a porous electrode cell might find application in electrosynthesis as a "polishing" device following prior treatment by a conventional flat plate electrochemical cell.

Conclusions and Summary

Equations have been derived, based upon a simplified macroscopic model, which allow optimum design parameters to be estimated for porous electrode reactors operating at any desired efficiency. The model has been verified experimentally by measurements of the limiting current and the potential difference between upstream and downstream faces of an operating reactor as a function of flow rate for a reaction under pure mass transfer control. Various methods are discussed for determining the efficiency and other parameters of a porous electrode reactor. A new method of data analysis has been proposed that is based entirely on measurements of the potential difference between upstream and downstream faces of a porous electrode. Based on the properties of the electrode material used in this study, the relative merits of the macroscopic model and the straight pore model have been compared. In addition, two typical industrial applications have been examined to delineate situations in which the use of a porous electrode reactor may be feasible.

Acknowledgment

Research sponsored by the Division of Materials Sciences, Office of Basic Energy Sciences, U.S. Department of Energy under Contract W-7405-eng-26 with the Union Carbide Corporation.

Manuscript submitted May 21, 1980; revised manuscript received Sept. 30, 1980. This was Paper 398 presented at the St. Louis, Missouri, Meeting of the Society, May 11-16, 1980.

Any discussion of this paper will appear in a Discussion Section to be published in the December 1981 JOURNAL. All discussions for the December 1981 Discussion Section should be submitted by Aug. 1, 1981.

Publication costs of this article were assisted by Oak Ridge National Laboratory.

APPENDIX

Straight pore model of porous electrodes.—The straight pore model assumes that the electrode consists

of a number of identical, straight, nonintersecting, cylindrical pores running the entire length of a conducting matrix (i.e., a bundle of capillaries). The problem involves accounting for the current from a single pore, and then multiplying by the total number of pores to obtain the total current. Current-potential relationships for a single pore in the absence of forced convection were reviewed by de Levie (14). An approximate solution for the mass-transfer limited current with forced convection was obtained by Posey and Nelson (38) by piecing together the asymptotic solutions for high flow rate and for low flow rate within a tubular electrode. The number of pores (N) was taken to be the cross-sectional area of voids divided by the cross-sectional area of a single pore, i.e., $N = \epsilon A / \pi R^2$, where R is pore radius.

More recently, Newman (46) has published an exact solution to the problem of mass transfer to the interior wall of a tube from a stream with fully developed laminar flow (the Graetz problem). The solution neglects axial diffusion as a mode of mass transport; this assumption is analogous to that used above in derivation of the simplified macroscopic model. The treatment should be valid for relatively long, narrow pores which can be thought of as constituting the porous electrodes of this study (radius $\sim 3 \times 10^{-3}$ cm; length $\geq 2.5 \times 10^{-1}$ cm). For the case of the limiting current (zero reactant concentration at wall), Newman presents an expression for the average concentration of reactant, $C_m(x)$, at the position x (cf. Eq. [6])

$$C_m(x) = C_b \sum_{k=1}^{\infty} M_k \exp(-\lambda_k^2 \pi D x / 2 U_1) \quad [\text{A-1}]$$

In this equation M_k and λ_k are the coefficients and eigenvalues for the solution of this Sturm-Liouville problem in convective diffusion, U_1 is the volume flow rate in the i^{th} tube or capillary, and other quantities are defined above. The first ten values of M_k and λ_k have been evaluated and tabulated by Newman (46). It follows that the (limiting) current from a single tube (I_i) of length L for a cathodic process is given by (cf. Eq. [8])

$$I_i = -n F U_1 C_b \left[1 - \sum_{k=1}^{\infty} M_k \exp(-\lambda_k^2 \pi D L / 2 U_1) \right] \quad [\text{A-2}]$$

The average current density in the solution phase for a single tube, $i_{s,i}(x)$, is given by (cf. Eq. [7] and [16])

$$\begin{aligned} i_{s,i}(x) &= \frac{n F U_1 C_b}{\pi R^2} \sum_{k=1}^{\infty} M_k [\exp(-\lambda_k^2 \pi D x / 2 U_1) \\ &\quad - \exp(-\lambda_k^2 \pi D L / 2 U_1)] \\ &= -\sigma_o \frac{d\phi_s(x)}{dx} \end{aligned} \quad [\text{A-3}]$$

In Eq. [A-3] $\phi_s(x)$ is the average potential in the solution phase at the point x and σ_o is the bulk conductivity of the solution as above. Equation [A-3] transforms into Eq. [A-2] when $x = 0$ since $\sum M_k = 1$ (46). Integration of Eq. [A-3] leads to an expression for the potential drop between upstream and downstream ends of the tube, $\Delta\phi_s = [\phi_s(0) - \phi_s(L)]$ (cf. Eq. [17])

$$\begin{aligned} \Delta\phi_s &= \frac{n F U_1 C_b}{\sigma_o \pi R^2} \sum_{k=1}^{\infty} M_k \left\{ \frac{2 U_1}{\lambda_k^2 \pi D} [1 - \exp(-\lambda_k^2 \pi D L / \right. \\ &\quad \left. 2 U_1)] - L \exp(-\lambda_k^2 \pi D L / 2 U_1) \right\} \end{aligned} \quad [\text{A-4}]$$

These relations may be put into forms that resemble the corresponding equations of the simplified macroscopic model. The flow rate for a single pore is related to the total flow rate by $U_1 = U/N$, where $N = \epsilon A / \pi R^2$ as above. The total current (I) is simply $I = N I_i$, the area-to-volume ratio (a) for a bundle of cylindrical capillaries is given by $a = 2\epsilon/R$, and the resistance

of the solution is $R_s = L/\sigma_o \epsilon A$. Then the total (limiting) current for the electrode is given by (cf. Eq. [10])

$$I = -n F U C_b \left[1 - \sum_{k=1}^{\infty} M_k \exp(-\lambda_k^2 a^2 D A L / 8 \epsilon U) \right] \quad [\text{A-5}]$$

And finally the potential drop is described by (cf. Eq. [20])

$$\begin{aligned} \frac{|\Delta\phi_s|}{|I_{\max}|} &= R_s \sum_{k=1}^{\infty} M_k \left\{ \frac{8 \epsilon U}{\lambda_k^2 a^2 D A L} \right. \\ &\quad \left. [1 - \exp(-\lambda_k^2 a^2 D A L / 8 \epsilon U)] \right. \\ &\quad \left. - \exp(-\lambda_k^2 a^2 D A L / 8 \epsilon U) \right\} \end{aligned} \quad [\text{A-6}]$$

For low flow rates the current approaches the asymptotic limit $I_{\max} = -n F U C_b$ (cf. Eq. [11]). For high flow rates $C_m(x) \sim C_b$ at all x and an asymptotic form for the current may be obtained from the Lévêque solution (46-48)

$$I \sim -1.017 n F C_b (a^2 D A L / \epsilon)^{2/3} U^{1/3} \quad [\text{A-7}]$$

Equation [A-7] is seen to be analogous to Eq. [33]. The potential drop at low flow rates is given approximately by

$$\frac{|\Delta\phi_s|}{|I_{\max}|} \sim 0.917 R_s (\epsilon U / a^2 D A L) \quad [\text{A-8}]$$

which may be compared with Eq. [22]. On the other hand, at high flow rates, the potential drop is described approximately by the relation

$$\frac{|\Delta\phi_s|}{|I_{\max}|} \sim 0.407 R_s (a^2 D A L / \epsilon U)^{2/3} \quad [\text{A-9}]$$

which was obtained from the Lévêque solution by the procedure used to derive Eq. [A-4]. Predictions of these relations for the behavior of the straight pore model are compared above with the predictions of the simplified macroscopic model.

LIST OF SYMBOLS

| | |
|--------------|--|
| a | specific interfacial area, cm^{-1} |
| A | cross-sectional area of electrode (matrix + solution), cm^2 |
| c | differential capacity per unit area, F cm^{-2} |
| C_b | concentration of electroactive species upstream of porous electrode, moles cm^{-3} |
| $C(x)$ | concentration of reactant in bulk of pore at the position x , moles cm^{-3} |
| $C_m(x)$ | average reactant concentration in straight pore at the position x (cf. Appendix), moles cm^{-3} |
| $C_o(x)$ | concentration of reactant at pore wall at the position x , moles cm^{-3} |
| C_T | total differential capacity of porous electrode (cf. Eq. [28]), F |
| (CE) | $= I/I_{\max}$, collection efficiency (cf. Eq. [12]) |
| D | diffusivity of electroactive species, $\text{cm}^2 \text{sec}^{-1}$ |
| D' | diffusion coefficient (cf. Eq. [5]), $\text{cm}^2 \text{sec}^{-1}$ |
| D_p | particle diameter, cm |
| e | base of Napierian logarithms (cf. discussion of Eq. [15]) |
| F | Faraday's constant, C eq^{-1} |
| $i_s(x)$ | superficial current density in solution (current per unit area of matrix plus pores), A cm^{-2} |
| $i_{s,i}(x)$ | average current density in solution phase of straight pore (cf. Appendix), A cm^{-2} |
| I | total current from electrode, A |
| I_i | current from single straight pore (cf. Appendix), A |
| I_{\max} | maximum current for $(CE) = 1$ (cf. Eq. [11]), A |
| $I(t)$ | total current at time t during transient response to potential step, A |
| $J(x)$ | local interfacial flux at the position x (cf. Eq. [2]), moles $\text{cm}^{-2} \text{sec}^{-1}$ |
| k | summation index |
| k_m | average mass transfer coefficient, cm sec^{-1} |

| | |
|-------|--|
| L | electrode length, cm |
| M_k | coefficients in solution to Graetz problem (cf. Appendix) |
| n | electron number of interfacial reaction |
| N | number of straight pores in electrode (cf. Appendix) |
| P | parameter defined by Eq. [14], $\text{cm}^2 \text{sec}^{-2/3}$ |
| Q | $= -\ln[1 - (CE)]$, efficiency parameter defined by Eq. [37] |
| R | radius of straight pore (cf. Appendix), cm |
| R_m | resistance of conducting matrix (cf. Eq. [32]), Ω |
| R_s | resistance of solution within porous electrode (cf. Eq. [19]), Ω |
| t | time, sec |
| U | volume flow rate, $\text{cm}^3 \text{sec}^{-1}$ |
| U_1 | volume flow rate in single straight pore (cf. Appendix), $\text{cm}^3 \text{sec}^{-1}$ |
| v | superficial linear flow rate, cm sec^{-1} |
| x | distance through porous electrode, cm |
| x_0 | effective reaction depth (cf. Eq. [15]), cm |

Greek Letters

| | |
|-----------------------|--|
| ϵ | void fraction or porosity |
| η_0 | potential step applied to upstream end of porous electrode; used in determination of impedance characteristics (cf. Eq. [27]), V |
| $\eta(L, 0)$ | sudden change in potential of downstream face of porous electrode corresponding to η_0 , V |
| λ_k | eigenvalues in solution to Graetz problem (cf. Appendix) |
| $\phi_s(x)$ | potential in solution phase at the position x , V |
| $\Delta\phi_s$ | potential difference between upstream and downstream faces of porous electrode, V |
| σ_{eff} | effective conductivity of solution phase, Ωcm^{-1} |
| σ_0 | bulk conductivity of solution, Ωcm^{-1} |
| τ | $= R_s C_T$, time constant for charging of double layer in porous electrodes, sec |

REFERENCES

- J. A. Trainham and J. Newman, *This Journal*, **124**, 1528 (1977).
- J. A. Trainham and J. Newman, *ibid.*, **125**, 58 (1978).
- R. Alkire and B. Gracon, *ibid.*, **122**, 1594 (1975).
- R. Alkire and P. K. Ng, *ibid.*, **124**, 1220 (1977).
- J. Newman and W. Tiedemann, *AIChE J.*, **21**, 25 (1975).
- J. S. Newman and W. Tiedemann, *Adv. Electrochem. Electrochem. Eng.*, **11**, 353 (1978).
- R. E. Sioda, *Electrochim. Acta*, **15**, 783 (1970).
- R. E. Sioda, *ibid.*, **16**, 1569 (1971).
- R. E. Sioda, *J. Electroanal. Chem. Interfacial Electrochem.*, **34**, 399 (1972).
- R. E. Sioda, *ibid.*, **34**, 411 (1972).
- R. E. Sioda, *Electrochim. Acta*, **17**, 1939 (1972).
- R. E. Sioda and T. Kambara, *J. Electroanal. Chem. Interfacial Electrochem.*, **38**, 51 (1972).
- R. E. Sioda, *ibid.*, **56**, 149 (1974).
- R. de Levie, *Adv. Electrochem. Electrochem. Eng.*, **6**, 329 (1967).
- C. J. Geonkopolis, "Mass Transport Phenomena," p. 296, Holt, Rinehart, and Winston, Inc., New York (1972).
- E. J. Wilson and C. J. Geonkopolis, *Ind. Eng. Chem. Fund.*, **5**, 9 (1966).
- I. G. Gurevich and V. S. Bagotsky, *Electrochim. Acta*, **9**, 115 (1964).
- L. G. Austin, P. Palasi, and R. R. Klimpel, "Fuel Cell Systems," *Advances in Chemistry Series*, No. 47, p. 35, American Chemical Society, Washington, D.C. (1965).
- R. E. Sioda, *Electrochim. Acta*, **13**, 375 (1968).
- F. Coeuret, *ibid.*, **21**, 185 (1976).
- A. Gaunand, D. Hutin, and F. Coeuret, *ibid.*, **22**, 93 (1977).
- D. N. Bennion and J. Newman, *J. Appl. Electrochem.*, **2**, 113 (1972).
- C. L. Mantell, "Carbon and Graphite Handbook," p. 434, Interscience, New York (1968).
- R. Alkire, B. Gracon, T. Grueter, J. Marek, and P. Blackburn, *This Journal*, **127**, 1085 (1980).
- F. A. Posey and A. A. Palko, "Ecology and Analysis of Trace Contaminants Prog. Rep. June 1972-Jan. 1973," ORNL-NSF-EATC-1, p. 367 (March 1973).
- F. A. Posey and T. Morozumi, *This Journal*, **113**, 176 (1966).
- A. M. Johnson and J. Newman, *ibid.*, **118**, 510 (1971).
- W. Tiedemann and J. Newman, *ibid.*, **122**, 70 (1975).
- D. A. G. Bruggeman, *Ann. Phys.*, **24**, 636 (1935).
- R. E. De La Rue and C. W. Tobias, *This Journal*, **106**, 827 (1959).
- R. E. Meredith and C. W. Tobias, *Adv. Electrochem. Electrochem. Eng.*, **2**, 15 (1962).
- H. H. Bauer, M. S. Spritzer, and P. J. Elving, *J. Electroanal. Chem. Interfacial Electrochem.*, **17**, 299 (1968).
- J.-P. Randin and E. Yeager, *ibid.*, **58**, 313 (1975).
- R. de Levie, *Electrochim. Acta*, **10**, 113 (1965).
- R. E. Sioda, *ibid.*, **13**, 1559 (1968).
- R. E. Sioda, *J. Appl. Electrochem.*, **5**, 221 (1975).
- R. E. Sioda, *ibid.*, **7**, 135 (1977).
- F. A. Posey and F. Nelson, "Water Research Program Biennial Progr. Rept. March 15, 1966-March 15, 1968, Reactions and Transport Phenomena at Surfaces," ORNL-TM-4099, p. 50 (March 1973).
- R. E. Sioda, *J. Electroanal. Chem. Interfacial Electrochem.*, **70**, 49 (1976).
- R. E. Sioda, *Electrochim. Acta*, **22**, 439 (1977).
- R. N. Adams, "Electrochemistry at Solid Electrodes," p. 219, Marcel Dekker, New York (1969).
- R. E. Sioda, *J. Appl. Electrochem.*, **8**, 297 (1978).
- H. S. Wroblowa and G. Razumney, *J. Electroanal. Chem. Interfacial Electrochem.*, **49**, 355 (1974).
- R. C. Alkire and R. M. Gould, *This Journal*, **127**, 605 (1980).
- R. de Levie, *Electrochim. Acta*, **9**, 1231 (1964).
- J. Newman, in "Electroanalytical Chemistry. A Series of Advances," Vol. 6, A. J. Bard, Editor, p. 187, Marcel Dekker, New York (1973).
- R. Alkire and A. A. Mirarefi, *This Journal*, **120**, 1507 (1973).
- R. Alkire and A. A. Mirarefi, *ibid.*, **124**, 1043 (1977).

Copper Recovery Using a Tumbled-Bed Electrochemical Reactor

Richard P. Tison

General Motors Research Laboratories, Electrochemistry Department, Warren, Michigan 48090

ABSTRACT

A tumbled-bed electrochemical reactor was described and shown to function well in reclaiming copper from a dilute acid copper system. A sound electrodeposit was obtained routinely and may be conducive to a stable and low maintenance industrial application. Graphs which approximately represent operating cost-capital cost trends have been presented and suggested as useful for future work in developing and comparing alternative waste treatment techniques.

Process waste waters generated at various manufacturing facilities often cause a twofold problem. They may have a toxic effect on the environment and their disposal causes a loss of much valuable material, not only in dissolved solids but in process water also. Waste treatment methods in current use often (i) detoxify inadequately, (ii) detoxify but generate undesirable by-products, creating a new waste disposal problem, or (iii) detoxify without materials recovery or water recycle. Current developments concerning both environmental considerations and the growing scarcity of natural resources provide an increasingly strong impetus for the development of more effective yet economical waste treatment technologies.

Electrochemical methods of treatment offer an intriguing alternative to conventional chemical methods in that waste waters may be treated without adding additional chemicals. Also, metals may be recovered in the metallic form, relatively pure and salable.

For dilute metal-bearing waste waters, three-dimensional conductive-bed electrodes are often considered, to provide extended surface area. The intention is to enhance the small electrochemical reaction rates anticipated with low metal ion concentrations. Descriptions of several types of bed electrodes may be found in the literature, including the packed bed (1-3), dynamic packed bed (4), fluidized bed (1, 5, 6), and vibrated bed (7, 8).

In this work we describe a tumbled-bed electrode, which is an adaptation of conventional barrel plating technology. By this technique a tumbling motion is imparted to a bed of conductive particles contained in a rotating barrel. A tumbled particulate-bed electrode has been described in a patent issued to McCoy *et al.* (9). While he suggested its use in electrowinning or refining processes, his application was in a battery. Inoue also used a tumbled-bed electrode, but his application was electrochemically deburring metal workpieces (10). Oehr (11) described the use of a barrel plater for waste treatment. He used the tumbled bed as an anode for cyanide oxidation. Kammel *et al.* (12) electroplated metals from dilute waste water by the employment of a tumbled-bed cathode. Their work was described in patent form, however, and little performance data was made available.

This present work describes the effectiveness for waste water treatment of a tumbled-bed electrochemical reactor. Copper recovery from a dilute acid copper system was used as the test case and serves as a representative of a number of toxic heavy metal waste waters which constitute a major waste handling problem.

Experimental

Apparatus and procedure.—The tumbled-bed electrochemical reactor concept is shown in Fig. 1. The

actual unit used in this work is shown in Fig. 2. It was made by reworking a commercially available miniature portab'e barrel plater. While one of the best geometries for industrial application of this concept may well involve an "open" rotating cylinder submerged in the waste water being treated in a fashion similar to conventional barrel plating, this initial work made use of an "internalized" design to facilitate controlled flow-through for single- and multiple-pass characterization studies. Thus, the porous cylinder was replaced by a sealed acrylic cylinder, 127 × 140 mm ID. Four acrylic blocks, 4 × 4 × 127 mm, were cemented to the interior walls, equally spaced around the periphery and parallel to the axis of rotation, to aid bed movement. All plumbing and electrical connections were made through two axial end-plate holes, as shown, and included a 3.1 mm diam lead (Pb) wire extending slightly below the axis as anode, two lead ball danglers, approximately 11 mm diam, which provided electrical feeds to the cathode bed, and solution inflow and outflow tubes. The cathode bed consisted of steel spheres, 4.5 mm diam, plated with 18 μm copper. The cylinder was loaded with 3.05 kg of copper-plated steel spheres

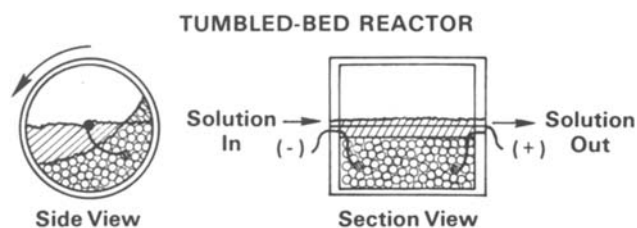


Fig. 1. Schematic of tumbled-bed electrochemical reactor. The waste water, cathode bed, and current feeders are shown in the approximate positions they assume during operation.

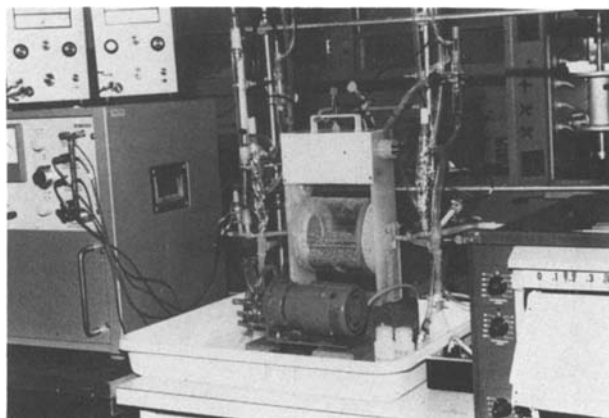


Fig. 2. Experimental setup for tumbled-bed work

Key words: metals, water, cathode, electrodeposition.

which took up approximately 35% of the cylinder's volume.

Simulated acid copper waste water was made up of various concentrations of reagent grade copper sulfate in 1M sulfuric acid using distilled water. This simulated waste water was then used without further purification. For multiple-pass studies, test solutions were pumped through the system using a tubing pump according to the scheme illustrated in Fig. 3. For once-through studies, spent solutions were returned to a second reservoir. All work was performed at room temperature and at a cylinder rotation speed of 9 rpm.

All runs were potentiostated via a saturated calomel reference electrode communicating with the inlet tube to the reactor. Copper concentrations were determined by use of a commercial cupric specific ion electrode calibrated daily by an atomic absorption spectrometer analysis of several samples withdrawn during each run. Current, overall voltage, and specific ion electrode potential were continuously recorded.

Polarization studies were obtained during single-pass runs by the "steady-state" method. For each multiple-pass run, a fresh 5 liter volume was continuously recirculated at constant cathode potential until all copper was depleted. Initial copper concentrations were approximately 1400 ppm. Each recirculatory run thus provided reactor performance data for a given potential over a range of concentration. Flow-through rates were also held constant at 550 ml/min except where otherwise specified. This rate corresponds to 58 turnovers/hr based on an experimentally determined 0.57 liter liquid capacity of the loaded cylinder. Approximately 3 hr per run were required to deplete the copper content in the waste water.

Calculations.—Data from the recirculatory runs were processed by a computer program which fit appropriate calibration equations to the cupric specific ion electrode data, and provided tabulations and plots of input data as well as several derived indices of reactor performance (see Appendix).

Reproducibility and sources of error.—As a test of reproducibility, one particular multiple-pass depletion run was performed three times. Experimental values for overall current efficiency, electrical energy yield, and volumetric reaction rate for each run over the range 300-10 ppm copper were calculated and compared. The maximum deviation from average of any of these performance indexes over the three runs was 15%.

After the reactor work was completed, a reanalysis of solution samples by atomic absorption was undertaken for iron. The analyses showed that iron had slowly built up in the recirculation solutions and may

have affected reactor performance. Final iron concentrations ranged from 81 ppm for the most rapid run (4 hr) to 177 ppm for the slowest runs (8 hr). This iron contamination apparently came from discontinuities in the copper plating on the steel spheres. These spheres were subsequently replaced by solid copper shot for further work (not yet reported). In the present work, however, an assessment of available data suggested that the iron dissolution was coupled partially with hydrogen evolution and partially with copper removal from the solution (cementation). Based on solution analyses, calculations indicate that the copper removal rates reported herein are only 3-7% larger in magnitude than would have occurred in the absence of the cementation effect.

Results and Discussion

Single-pass performance.—The flow of waste water through a reactor once-only for treatment is often advantageous as it is well suited to high production rates and involves minimum pumping requirements.

Polarization studies.—Figure 4 shows polarization curves for the tumbled-bed electrochemical reactor under single-pass conditions. It may be noted that each copper deposition curve exhibited an inflection but not a plateau before becoming obscured by the secondary hydrogen evolution reaction which dominated at large cathode polarizations. The absence of a mass transfer limiting current plateau sometimes associated with a "fast" electrochemical reaction such as this may be accounted for by several factors but perhaps the most significant is the following.

An increasing rather than constant (limiting) copper deposition current can result from a significant IR potential drop through the solution within the bed electrode causing the cathode reaction within the bed to be operating over a wide range of potential. Thus, as larger and larger negative potentials were applied to the cathode, more and more remote regions of this bed electrode would become active with a resultant increase in current, as was obtained experimentally. Unfortunately, this situation also eventually forces the most accessible areas of the bed electrode to potentials sufficiently negative to evolve hydrogen as well as deposit copper. Thus, performance of this reactor could be improved by suitable design changes to minimize these variations, e.g., a thinner bed (in the direction of current flow), additional counterelectrodes at

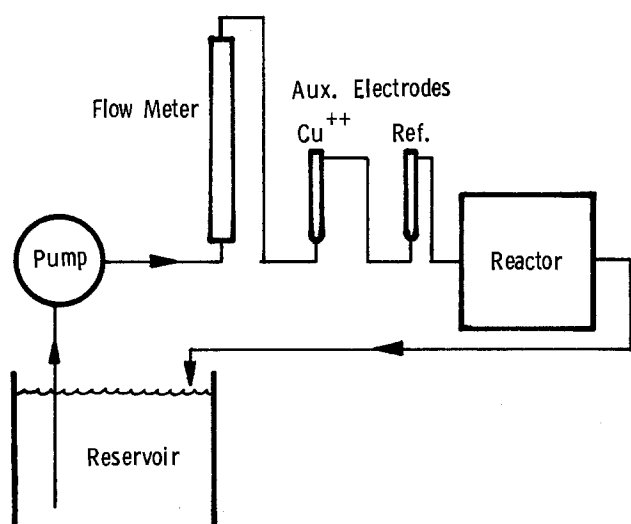


Fig. 3. Schematic diagram of the experimental system

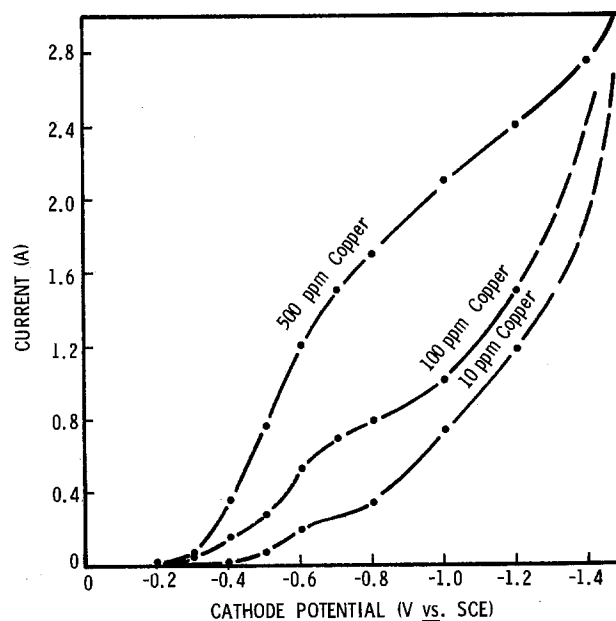


Fig. 4. Polarization studies of a tumbled-bed electrochemical reactor. Solution feed rate was 74 ml/min.

suitable positions throughout or surrounding the bed, greater solution conductivity, or greater bed porosity.

Effect of potential.—The effect of cathode potential on reactor performance may be seen in Fig. 5. Percent recovery increases with increasing cathode polarization. This increase is expected, especially since remote regions of the cathode bed apparently become productive at large polarizations as discussed earlier. Extreme polarizations contributed primarily to increased hydrogen gassing which tended to occur at the bed surface and therefore did not contribute greatly to increased rates of recovery.

Electrical energy yield and current efficiency, on the other hand, decrease with increasing cathode polarization. This is largely due to the increasing proportion of current and electrical energy being consumed by the hydrogen evolution side reaction, which becomes more prominent at large cathode polarizations. Obviously in selecting operating conditions for a practical application, a tradeoff must be made between operating costs and completeness of recovery in a single pass.

Effect of flow-through rate.—The influence of solution feed rate on a reactor performance is shown in Fig. 6. Percent recovery is enhanced by lower flow-through rates as would be expected due to the longer solution residence time involved. In this work, as much as 99.4% recovery was obtained. Again, improved performance in terms of percent recovery was obtained at the expense of higher operating costs as reflected by the electrical energy yield and current efficiency data. These performance indexes improve with higher flow rates and thus demonstrate one of the advantages of an alternate method of reactor operation which is described next.

Recirculatory performance.—A second method by which waste waters may be treated electrochemically is to allow the waste water to be recirculated through the reactor until satisfactory results are obtained. Recirculation involves greater pumping requirements, but the multiple pass and higher feed rates practical by this method often provide enhanced mass transport, more uniform concentrations throughout the reactor, and other inherent operational advantages, thus sometimes providing improved overall electrochemical performance.

Multiple-pass purification.—The gradual depletion of copper by recirculating a volume of waste water through the tumbled-bed electrochemical reactor is shown in Fig. 7. It is noted that decreased cathode potentials increase the speed of purification down to $-1.2V$, below which the rate of purification did not significantly change. (The test run at $-0.6V$ proceeded

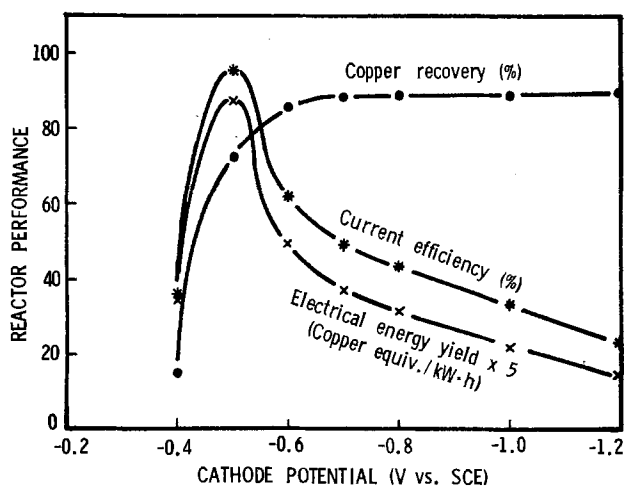


Fig. 5. Effect of cathode potential on single-pass reactor performance. Test solution contained 100 ppm copper. Solution feed rate was 74 ml/min.

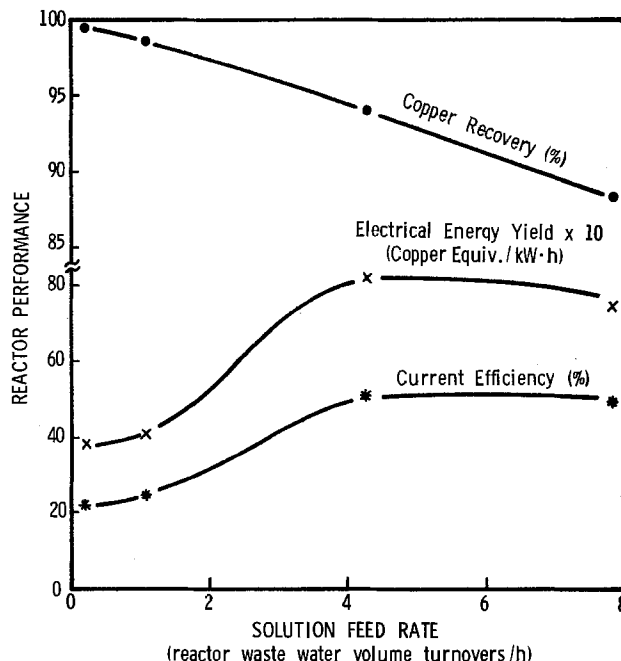


Fig. 6. Effect of feed rate on single-pass reactor performance. Test solution contained 100 ppm copper. Cathode potential was $-0.7V$.

so slowly that after 24 hr the starting concentration was reduced only slightly, and the run was terminated.)

Effect of potential.—Figure 8 shows trends in electrochemical performance over a range of cathode potentials. Volumetric reaction rate is seen to increase with increasing cathode polarization while electric energy yield and current efficiency decrease. Thus, in a manner similar to single-pass operation, tradeoffs between the performance indexes are seen to occur.

Effect of concentration.—Figure 9 provides a typical example of reactor performance over a range of inlet concentrations. The large falloff in performance with decreasing copper concentration is noted, and expected from theoretical considerations.

Lowest electrical energy yields and current efficiencies were observed when treating waste waters of lowest copper content. This is largely because nonproductive electrochemical reactions occur at the cathode as

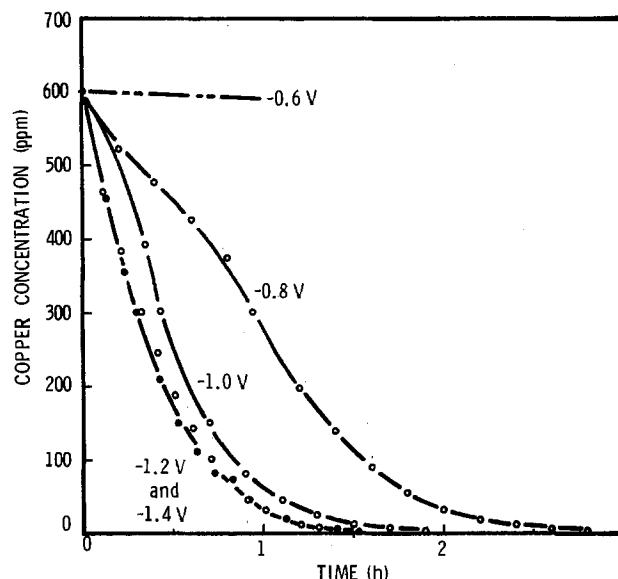


Fig. 7. Multiple-pass purification of acid copper waste waters with the tumbled bed. Five liters of solution were used for each run and recirculated at 58 turnovers/hr. Cathode potentials are listed.

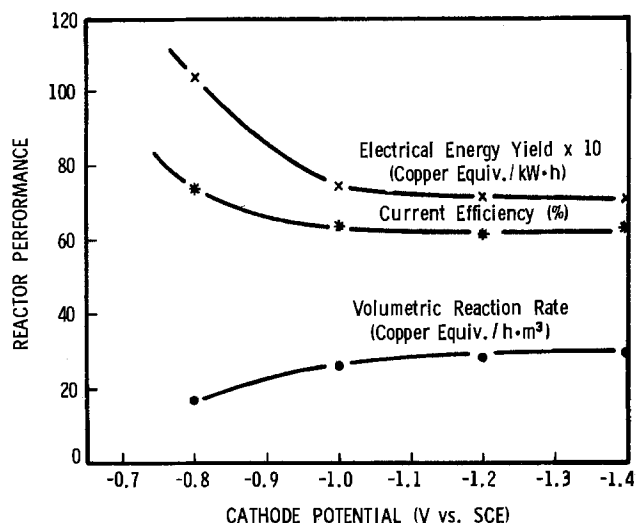


Fig. 8. Effect of cathode potential on multiple-pass reactor performance. Incoming solution contained 100 ppm copper. Rate of recirculation was 58 turnovers/hr.

well as copper deposition. These reactions likely include the reduction of dissolved oxygen as well as hydrogen ions, as the waste waters used in this work were not pretreated to remove dissolved oxygen, nor were the waste waters being treated kept isolated from the oxygen-generating anode. The resulting background current reduces both current efficiency and electrical energy yield during recovery efforts. This drain on performance becomes more significant at lower copper concentrations, where the copper deposition current is less, because the background current from these other reactions then makes up a larger fraction of the total current. This explains the observed trend.

Smaller reaction rates were also observed as copper concentrations decreased. A decrease in copper concentration in the bulk solution causes a decrease in the concentration gradient that can develop across the cathode boundary layer. This produces a decrease in diffusional transport of copper to the cathode surface which, in turn, results in a decrease in the limiting rate of the copper deposition reaction. For this reason, the diffusion-limiting rate for metal deposition from dilute solutions would be expected to be approximately proportional to concentration. This dependency was very much in evidence over the three-decade concentration range investigated in this work (Fig. 9).

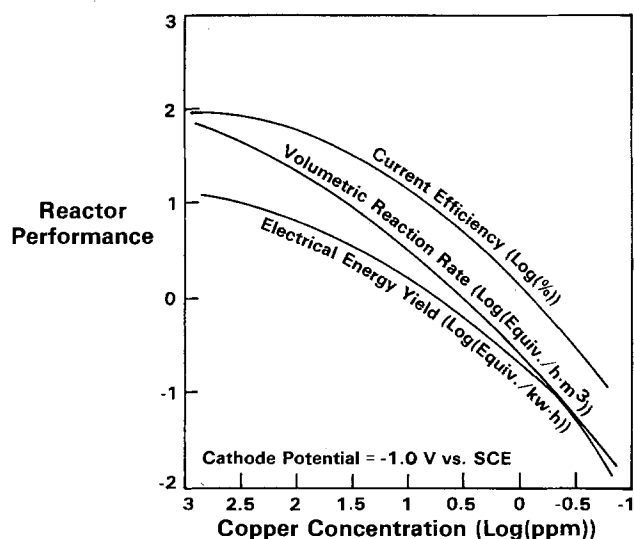


Fig. 9. Effect of copper concentration on multiple-pass reactor performance. Rate of recirculation was 58 turnovers/hr.

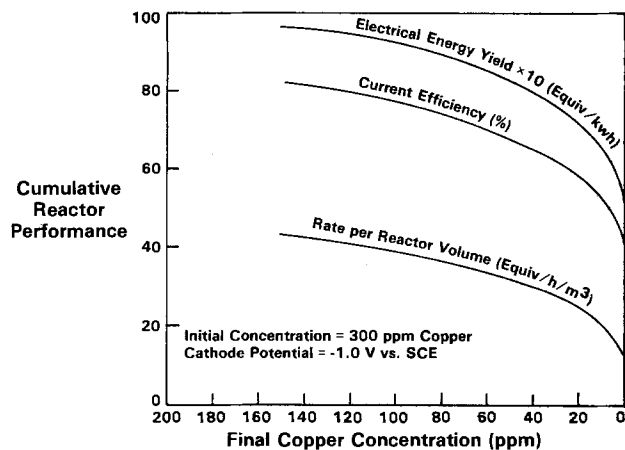


Fig. 10. Effect of degree of purification desired on overall reactor performance. Rate of recirculation was 58 turnovers/hr.

Overall reactor performance.—Resulting reactor performance during recirculatory operation will depend, of course, on the degree of purification one wishes to obtain. Figure 10 provides a typical example of how overall performance depends on the final concentration desired, when starting with a waste water containing 300 ppm copper. As shown in the plot, overall performance decreases as lower final concentrations are attained, with performance rapidly deteriorating below approximately 10 ppm as absolute purity is approached.

Method for making performance comparisons.—During this work the need for a procedure by which different modifications of the tumbled-bed reactor or alternate reactors could be compared on a sound economic basis became evident. An all-embracing, completely accurate assessment would be a formidable undertaking, not generally prudent at early stages of research and development efforts such as in this present work. We rather construct a useful approximation, selecting two appropriate engineering quantities, one that reflects operating costs and one that reflects capital costs. Drawing from available experimental performance data (in this study the family of constant potential plots, of which Fig. 9 is one example), these quantities are then plotted against each other, as in Fig. 11. In

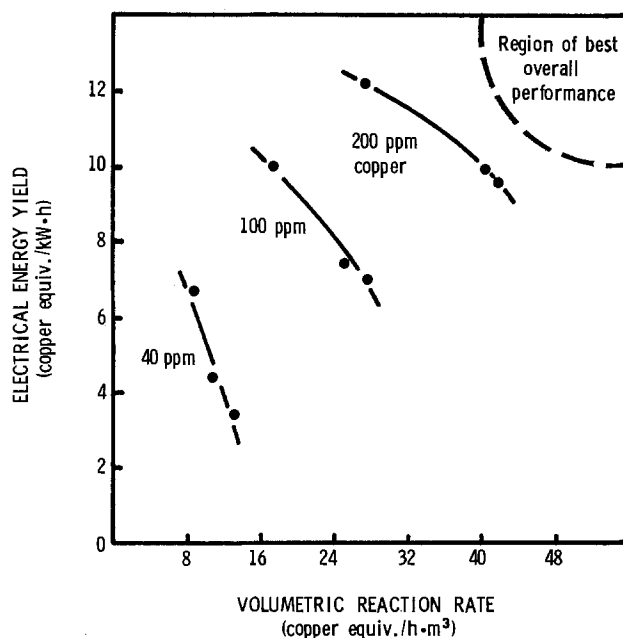


Fig. 11. Performance summary of the tumbled bed during multiple-pass operation. Concentrations of copper in the waste waters being treated are indicated. Rate of recirculation was 58 turnovers/hr.

this figure electrical energy yield (metal equiv./kW·hr) may be thought of as reflecting operating costs of the tumbled-bed electrochemical reactor as electrolytic power requirements have been considered a very substantial proportion of total operating costs in electrolytic processing of metals in aqueous solution (16-18). In a similar manner, volumetric reaction rate (metal equiv./m³·hr) may be thought of as reflecting capital costs which are generally related to reactor size and capacity (6, 14, 19, 20).

In applying and refining this assessment formalism, engineering quantities which indicate operating cost and capital cost trends must be judiciously selected based on the particular electrochemical reactors involved.

Referring to Fig. 11, the tumbled-bed is seen to be characterized by a gradual tradeoff relationship between electrical energy yield and volumetric reaction rate. Total performance improves with increasing copper concentrations in the waste water. While this type of plot was used in this present work to compare the tumbled-bed at different copper concentrations, it could also be used in a similar manner to compare different versions of the tumbled bed, or other similar reactors, with each other.

Deposit characteristics.—Figure 12 shows typical cathode bed surfaces from the tumbled-bed reactor after several runs. Cathode bed surfaces from a packed-bed electrochemical reactor studied in this laboratory are also shown for purposes of comparison. The packed-bed results were obtained using cathode bed material identical to that in the tumbled-bed and after having treated similar waste water solutions under similar conditions. After even a short-term test, deposits on the packed-bed were rough and unevenly distributed. Particularly, nonuniform deposits were obtained on circular areas (see Fig. 12) where the

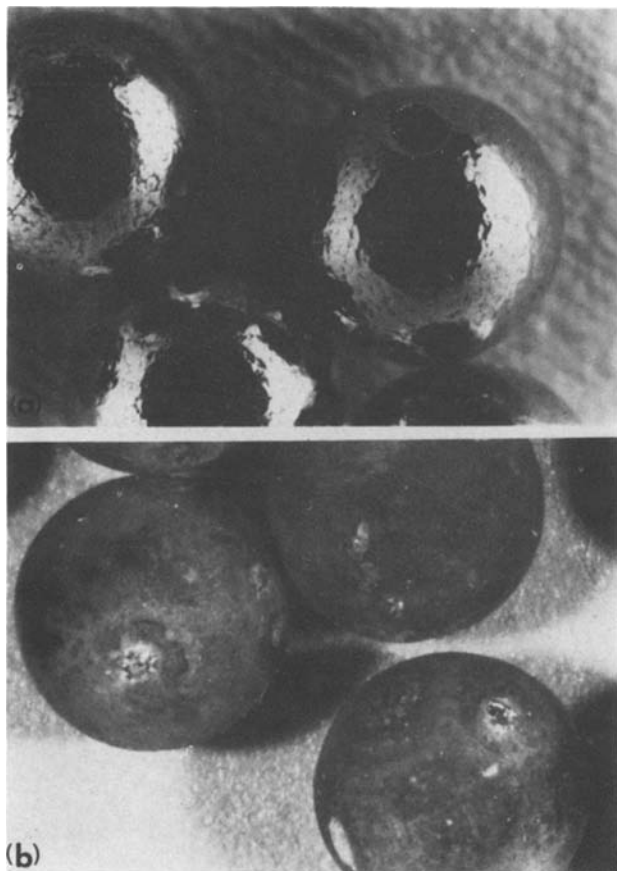


Fig. 12. Typical cathode bed surfaces from (a) a tumbled-bed electrochemical reactor and (b) a packed-bed electrochemical reactor after operation under similar conditions.

packed-bed particles were either in contact with each other or with the walls of the containing vessel.

One particularly pleasing observation made throughout this work with the tumbled-bed was that resulting deposits of reclaimed copper were smooth, bright, compact, adherent, and uniformly distributed over the entire cathode bed particle surfaces. (The only roughness observed was the "orange peel" texture initially present on the sphere surfaces.) This kind of deposit was obtained after extended operation, even under extreme operating conditions, such as during the simultaneous evolution of considerable hydrogen.

These contrasting deposit qualities are apparently the result of the impinging, burnishing, and redistributing action of the tumbling and cascading bed particles against each other and with the solution. This type of deposit would tend to eliminate certain problems reported with packed-bed electrochemical reactors (8, 13, 14) such as changes on the cathode surfaces with time, making optimum reactor control more difficult, electrical shorting by dendritic deposits, and interparticle bridging and nonuniformly distributed deposits, causing premature plugging of the cathode bed and premature regeneration requirements. Therefore, the tumbled-bed could presumably translate into a relatively simple, reliable, and low maintenance system for practical applications. Considering the purification of a typical plating rinse waste water containing 200 ppm copper, calculations show that even the small tumbled-bed reactor used in this investigation could handle 4300 liters (1100 gal.) of waste water before reaching a deposit loading of only 25% of the original bed particle volume.

Acknowledgment

The author is grateful to Russell A. Foust, Jr. for providing the computer program, Earl E. Williams for constructing the tumbled-bed reactor, and to Robert F. Paluch for analyzing the samples.

Manuscript submitted April 11, 1980; revised manuscript received ca. Sept. 5, 1980. This was Paper 406 presented at the St. Louis, Missouri, Meeting of the Society, May 11-16, 1980.

Any discussion of this paper will appear in a Discussion Section to be published in the December 1981 JOURNAL. All discussions for the December 1981 Discussion Section should be submitted by Aug. 1, 1981.

Publication costs of this article were assisted by General Motors Research Laboratories.

APPENDIX

Indexes of Reactor Performance

Current efficiency (%)

$$= \frac{\Delta C \times F \times v \times 2.778 \times 10^{-5}}{\Delta t \times I \times M}$$

Electrical energy yield (met. equiv./kW·hr)

$$= \frac{\Delta C \times v}{\Delta t \times I \times E \times M}$$

Volumetric reaction rate (met. equiv./m³·hr)

$$= \frac{\Delta C \times v \times 10^{-3}}{\Delta t \times V \times M}$$

where: C = copper concentration in solution (ppm); F = Faraday constant; v = total solution volume (liters); t = time (hr); I = current (A); M = metal equivalent weight (g); E = overall voltage (V); V = reactor volume (m³), defined as the internal volume of the rotating cylinder only.

REFERENCES

1. G. Kreysa, *Electrochim. Acta*, **23**, 1351 (1978).
2. A. K. P. Chu, M. Fleischmann, and G. J. Hills, *J. Appl. Electrochem.*, **4**, 323 (1974).
3. A. T. Kuhn and R. W. Houghton, *ibid.*, **4**, 69 (1974).
4. E. G. Gagnon and K. W. Mao, U.S. Pat. 3,966,571 (1976).
5. B. D. Barker and B. A. Plunkett, *Trans. Inst. Met.*

- Finish.*, **54**, 104 (1976).
6. G. van der Heiden, C. M. S. Raats, and H. F. Boon, *Chem. Ind.*, **13**, (July 1978).
 7. C. Yamauchi and H. Kametani, *ibid.*, **9**, 381 (1975).
 8. A. A. Wragg, *ibid.*, **8**, 334 (1975).
 9. L. R. McCoy and A. Heredy, U.S. Pat. 3,663,298 (1972).
 10. K. Inoue, U.S. Pat. 3,883,410 (1975).
 11. K. H. Oehr, Paper 579 presented at The Electrochemical Society Meeting, Seattle, Washington, May 21-26, 1978.
 12. R. Kammel and H. W. Lieber, U.S. Pat. 4,123,340 (1978).
 13. R. S. Wenger and D. N. Bennion, *J. Appl. Electrochem.*, **6**, 385 (1976).
 14. R. W. Houghton and A. T. Kuhn, *ibid.*, **4**, 173 (1974).
 15. A. T. Kuhn and R. W. Houghton, *Electrochim. Acta*, **19**, 733 (1974).
 16. R. G. Bautista and D. S. Flett, *AIChE Symp. Ser.*, **74**, No. 173, 146 (1978).
 17. C. L. Lopez-Caricedo, *Trans. Inst. Met. Finish.*, **54**, 112 (1976).
 18. N. Ibl, *Erzmetall*, No. 22, pp. B87-B98 (1969); as acquired from Overseas Activities Translation Service, O.A. Trans. 1078.
 19. T. R. Beck, in "Techniques of Electrochemistry," Vol. 3, E. Yeager and A. J. Salkind, Editors, p. 34, John Wiley & Sons, New York (1978).
 20. P. Gallone, *Electrochim. Acta*, **22**, 917 (1977).

Reduction of Benzene and Related Compounds in Aqueous Solution and Undivided Cells

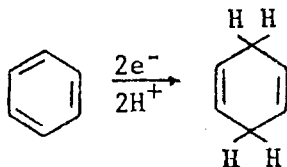
J. P. Coleman and J. H. Wagenknecht*

Monsanto Company, Corporate Research & Development Staff, St. Louis, Missouri 63166

ABSTRACT

Benzene and other aromatic compounds may be reduced to the 1,4-dihydroderivatives in an undivided cell using a dispersion of hydrocarbon and aqueous quaternary ammonium hydroxide. At optimum conditions benzene is converted to 1,4-cyclohexadiene at 90% selectivity with nearly quantitative current efficiency. A continuous reaction scheme for the benzene reduction is described.

The cathodic reduction of benzene to 1,4-cyclohexadiene (I), as an extension of the Birch (1) reaction, has been known for a long time. This reaction has been demonstrated in liquid ammonia (2)



I

amines (3-6), amides (7-8), ethers (9-17), and aqueous solution (18) with varying current efficiencies. All of the systems previously demonstrated have one or more features which make them unattractive as commercial processes.

The most substantial recent advance in this area was revealed in a patent (18) to Asahi Chemical Company and described the cathodic reduction of benzene and other aromatics in an aqueous emulsion with a quaternary ammonium salt as supporting electrolyte in a divided cell. We have substantiated their claims of high current efficiency and selectivity and later discovered conditions which allow this reaction to be carried out in an undivided cell. It is that study which led to a simplified method for synthesis of dihydroaromatics and an improved process for 1,4-cyclohexadiene that is described in this paper.

Experimental

The aromatic compounds that were reduced were reagent grade obtained commercially and used as received. Quaternary ammonium hydroxides were obtained from Southwestern Analytical Chemicals, In-

corporated, Fisher Scientific Company, or Monsanto Chemical Intermediates Company.

NMR spectra were obtained with a Varian T-60 NMR spectrometer. Mass spectra were obtained on a Varian MAT CH7A mass spectrometer. GC analyses (benzene reduction products) were obtained using a 6 ft \times 1/8 in. column packed with Carbowax 400 on Chromosorb P at 80°C isothermal. GC peak integration was performed by an Autolab System IVB integrator. A Lambda LP-412A-FM (up to 1A) or Sorensen DCR80-6B constant current/voltage power supply was used for the electrolyses.

Pure 1,4-cyclohexadiene used as a GC standard was obtained by distillation of several combined electrolysis products through a 3 ft heated, jacketed column packed with glass helices. A mixture of 50 ml benzene, 25 ml cyclohexene, 214 ml 1,4-cyclohexadiene, and 17 ml high boilers was distilled to give 140 ml of 99% purity 1,4-cyclohexadiene, bp 89°C. [The literature (19) reports 85.6°C, possibly low owing to the presence of benzene.] Figure 1 shows a plot of distillate composition vs. temperature for the early part of that distillation.

Batch reactions.—A large number of small batch reactions was carried out in the cell shown in Fig. 2 to examine the effects of variables. The cell was a 100 ml jacketed resin flask. When Hg was used as the cathode, 20 ml were added (20 cm² surface) and electrical contact was achieved via a Teflon tape-insulated copper wire. Mounted close to the Hg pool was a glass paddle stirrer. Good stirring was necessary to keep the aqueous and organic phases well mixed. The anode (steel tubing, Ni wire, metal plate, etc.) was mounted just above the stirrer paddles. The temperature was maintained by circulating water through the jacket from a temperature-controlled reservoir. A condenser was mounted on the cell, but some hydrocarbon was still carried away with the evolving O₂ and H₂. The cell was generally filled with 50 ml of aqueous quaternary am-

* Electrochemical Society Active Member.

Key words: electrochemical Birch reduction, aqueous solution, undivided cells, dihydroaromatics, 1,4-cyclohexadiene.

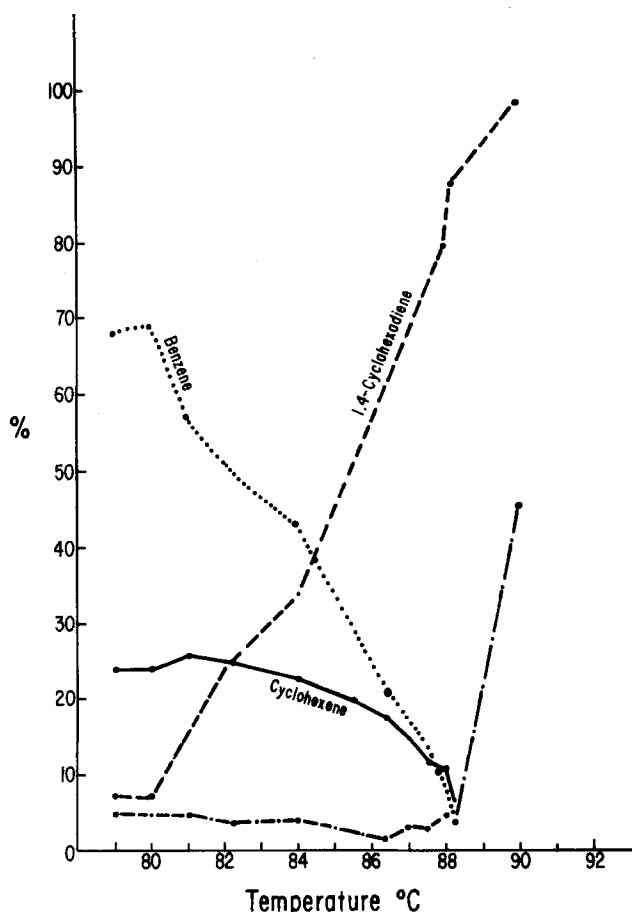


Fig. 1. Plot of the composition of distillate vs. temperature in the purification of 1,4-cyclohexadiene (— cyclohexene; benzene; - - - - 1,4-cyclohexadiene; - · - · distillate as a percentage of total sample).

monium hydroxide solution and 10 ml benzene (or other substrate).

Continuous electrolysis.—The cell apparatus is shown in Fig. 3 and 4. The system was filled with 150 ml 20% $\text{Bu}_4\text{N}^+\text{OH}^-$ and 25 ml benzene. The cell contained 135 ml Hg with a surface area of 80 cm^2 . The center post in the cell as 1.2 cm in diameter and the Hg pool 10 cm in diameter. The electrode gap was 4 mm. The solution was circulated through the system at about 2 liters/min with a centrifugal pump (Micro Pump Model 10-40-316). The temperature of the solution was held at 60°C via a heat exchanger. The electrolysis was started with a constant current of 2A requiring about 5V. The condenser above the electrolyte was cooled to 5°C with solvent circulated through a refrigerated bath (Neslab PCB-2). An Eagle Signal repeat-cycle timer was used to operate the reagent addition and sample recovery system. The system operated on a 1 hr cycle in which first a sample was removed and then 2 ml benzene and 1 ml of water were pumped into the solution.

Sample removal occurred as follows: under normal operation the N_2 valve was open and the vacuum valve and N_2 sidearm valve were closed. A small flow of N_2 kept the sidearm of the electrolysis reservoir empty. At the beginning of the sample period, the N_2 valve closed and the N_2 sidearm valve opened to the atmosphere. Electrolyte solution filled the side arm, and, since there was no agitation due to high flow rate, the organic phase formed a layer at the top. After 2 min, the vacuum valve opened and the organic layer was drawn into the product reservoir until the level fell below the end of the retrieval tube. After a few seconds, the vacuum and N_2 sidearm valves closed and the N_2 valve opened to resume normal operation. In this manner 48 ml of benzene were added to the system each day. An average of 30 ml of organic material were

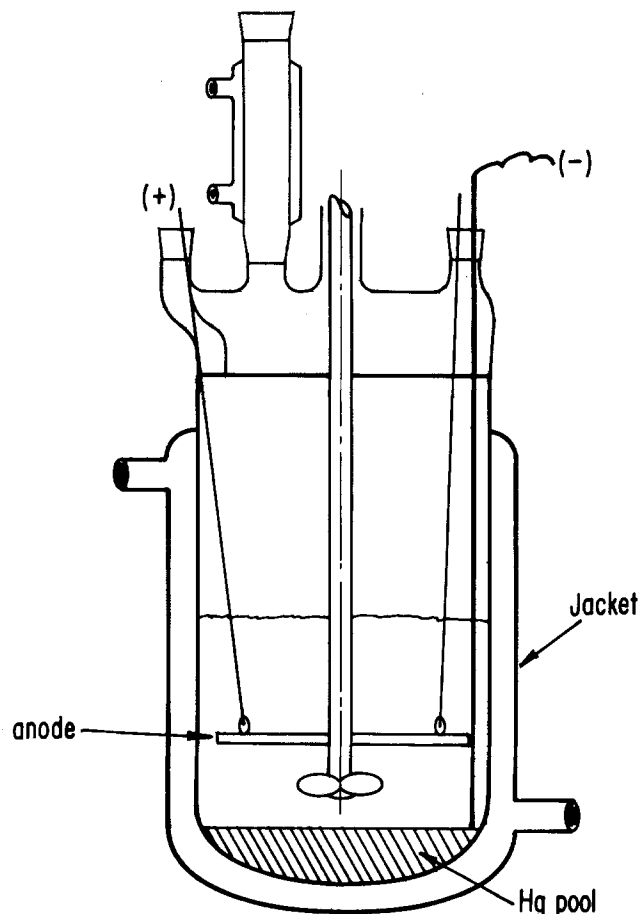


Fig. 2. Batch reaction cell

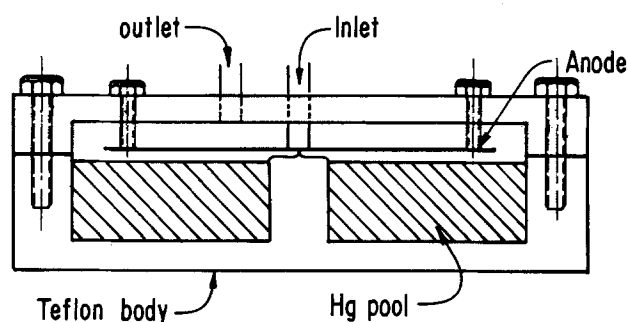


Fig. 3. Flow cell

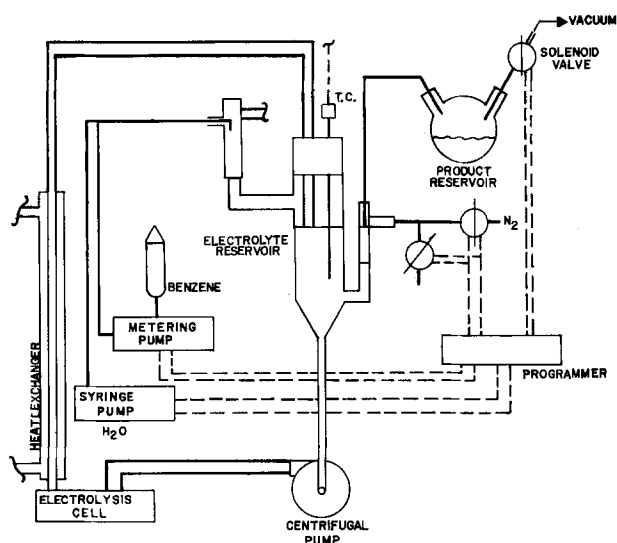


Fig. 4. Continuous electrolysis scheme

recovered each day; the remainder was lost, presumably by evaporation and migration through walls of the polyethylene tubing used for solution lines. Analysis of the daily product sample gave the following results

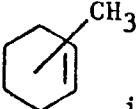
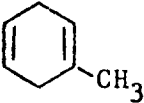
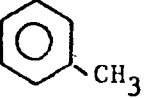
| Days of operation | % cyclohexene | % 1,4-cyclohexadiene | % benzene |
|-------------------|---------------|----------------------|-----------|
| 1 | 8.2 | 60.6 | 31.2 |
| 2 | 8.7 | 62.5 | 28.6 |
| 3 | 8.8 | 61.5 | 29.5 |
| 4 | 9.0 | 60.4 | 30.6 |
| 7 | 8.5 | 55.1 | 36.4 |

Assuming equivalent loss of all three components of the organic phase, the electrolysis operated at 38% current efficiency. That is less than obtained in batch-cell operation and may be due to less than optimum transport at the cathode because of improper cell-flow characteristics or contamination of the Hg surface by impurities in the system.

Electrolysis of toluene.—Into the cell shown in Fig. 2 was placed 25% aqueous tetrabutylammonium hydroxide solution and toluene (20g). The cathode was the mercury pool and the anode was a coil of 1/8 in. OD stainless steel tubing, 8 in. long, parallel to the pool and ca. 2 cm above it.

The solution was maintained at 60°C with vigorous stirring and electrolyzed at 1.0A for 20 hr.

The organic layer (15.82g) was separated and GC analysis showed

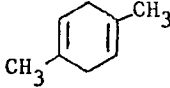

| | | |
|---|---------|--------------|
|  | isomers | 12% (area %) |
|  | | 74% |
|  | | 14% |

Structures were confirmed by NMR and GC-mass spectrometry.

Assuming equal loss of all three components, this represents current efficiencies of 43% to diene and 14% to methylcyclohexenes.

Electrolysis of p-xylene.—p-Xylene (20g) was reduced in the same way as toluene at 1.0A for 20.5 hr.

GC analysis of the product (14.25g) showed

| | | |
|---|----------------------|--------------|
|  | dimethylcyclohexenes | 68% (area %) |
| | | 13% |
|  | | 19% |

Assuming equal losses, this represents 34% current efficiency to diene and 12% to cyclohexenes.

4-Phenylbutyric acid electrolysis.—4-Phenylbutyric acid (8.4g, 0.05 mole) was dissolved in 28% aqueous tributylethylammonium hydroxide solution (41g) and stripped on the rotary evaporator to leave a yellow

oil. More 28% tributylethylammonium hydroxide solution (60 ml) was added and the homogeneous solution electrolyzed in the same way as p-xylene at 1.0A for 3 hr. The solution was cooled, filtered (to remove mercury), and acidified with concentrated HCl. The product was extracted into ether (2 × 100 ml) which was washed, dried (MgSO₄), and stripped to leave a yellow oil (7.65g).

A sample was silylated with "Regisil" and analyzed by GC (SP 2100, 140°) which showed 33% conversion to 4-(2,5-dihydrophenyl) butyric acid (current efficiency = 30%). Identification confirmed by NMR and GC-MS.

Electrolysis of biphenyl.—In a 1 liter jacketed resin pot fitted with overhead stirring, Hg pool cathode (95 cm²) and O₂-evolving DSA (TIR-2000, Diamond-Shamrock) (56 cm²) were placed 500 ml 10% Bu₄N⁺OH⁻ and 100g biphenyl. Hot water (60°C) was circulated through the jacket. A constant current of 4A was passed through the cell for 17 hr. The oil was removed from the cell, cooled to 0°C and filtered, giving 30g filtrate. The solid and 50g more biphenyl were added to the cell and the electrolysis continued for 33 hr. The cell was allowed to cool overnight after which some biphenyl had crystallized and precipitated to the bottom of the cell. The oil layer was removed, cooled to 0°C, and more biphenyl crystallized. The mixture was filtered, giving 50g of oil. The solid, 50g of fresh biphenyl and 54 ml water were returned to the cell and the electrolysis continued overnight. Another 50g of biphenyl were added and the electrolysis continued another day. The oil was then removed, cooled, and filtered, giving 69g of oil.

The first two oil samples were combined, mixed with 100 ml H₂O, and acidified with HCl. The oil was separated and dried over MgSO₄ and filtered, giving 74g of dry oil. The oil was distilled on a 3 ft glass helices-packed column at 0.2 mm Hg. A forecut of 2 ml was taken before the temperature reached 55°, then, 56g of material were collected. The distillate was redistilled on a spinning-band column at 2 mm Hg. After a small forecut, 36g were collected, boiling at 73°C. The distillate was analyzed by GC-mass spectroscopy and found to contain 21% phenylcyclohexane, 35% phenylcyclohexenes, 41% 1-phenyl-1,4-cyclohexadiene, and only a trace of biphenyl. The distillation pot contained more than 50% biphenyl.

Electrolysis of naphthalene.—In a 1 liter jacketed resin pot arranged as for the biphenyl reduction above were added 500 ml 15% Bu₄N⁺OH⁻ and 100g naphthalene. The cell was maintained at 80°C. The electrolysis was run for three days at 4A. The oil was removed, cooled to 0°C, and filtered. The filtrate was washed with water and dried over MgSO₄, giving 60 ml of dry oil. This was distilled on a spinning-band column at 4 mm. A small forecut was obtained and, then, 25g were collected at 75°C. GC analysis indicated it contained 16% 1,4,5,8-tetrahydronaphthalene, 16% naphthalene, and unidentified components. The pot from the distillation was treated with decolorizing carbon and filtered, giving 25g of oil containing 22% 1,4,5,8-tetrahydronaphthalene, 45% 1,4-dihydronaphthalene, 17% naphthalene, and unidentified components.

Results and Discussion

The reduction of benzene to 1,4-cyclohexadiene was studied in detail to optimize the yield and current efficiency. The goal of the study was to define conditions for a commercial process in an undivided cell in aqueous solution.

Initial studies were carried out in an undivided cell with a mercury cathode, quaternary ammonium ion (Bu₃EtN⁺), and benzene-water emulsions based on results of Asahi Chemical Company (18). In addition, the hydroxide form of the quaternary ammonium salt was used both to stabilize the steel (inexpensive) anode and to increase the hydrogen overpotential of

the cathode. It was found that the solution must be warm to obtain reasonable current efficiencies (Fig. 5). The warm (60°C) solution did give good current efficiencies even when most of the benzene had been converted to products (Fig. 6).

It was desirable from the standpoint of commercial cell design to have a solid cathode for this reaction, but none of the solid electrodes examined gave substantial current efficiencies for benzene reduction. Those cathode materials studied include glassy carbon, 75% Pb amalgam, 25% Cd amalgam, 3% Na amalgam (solid), Al, Wood's metal, Hg-coated Cu, Cd, Cu, Pb, and carbon.

In studies to examine alternative anodes for this reaction we were surprised to find that Pt and carbon anodes very efficiently converted 1,4-cyclohexadiene to benzene. An example is shown in Fig. 7. In that experiment a normal electrolysis in the cell shown in Fig. 2 was carried out for 4 hr using a steel anode. During that time about 20% of the benzene was converted to 1,4-cyclohexadiene. After 4 hr, the steel anode was replaced by a Pt anode after which the total conversion with time actually decreased, indicating that more benzene was being formed than consumed.

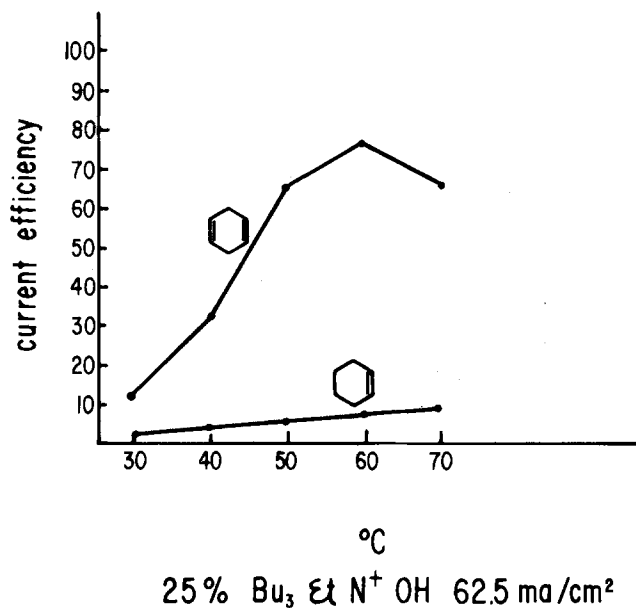


Fig. 5. Current efficiency for 1,4-cyclohexadiene formation vs. temperature.

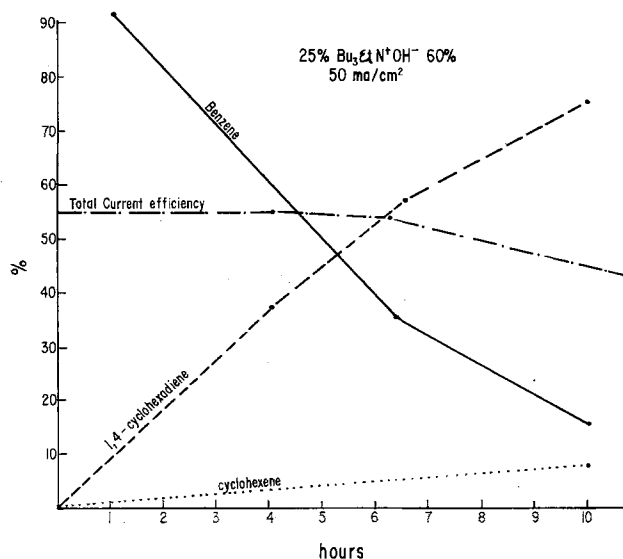


Fig. 6. Composition of the organic phase (and total current efficiency) vs. time.

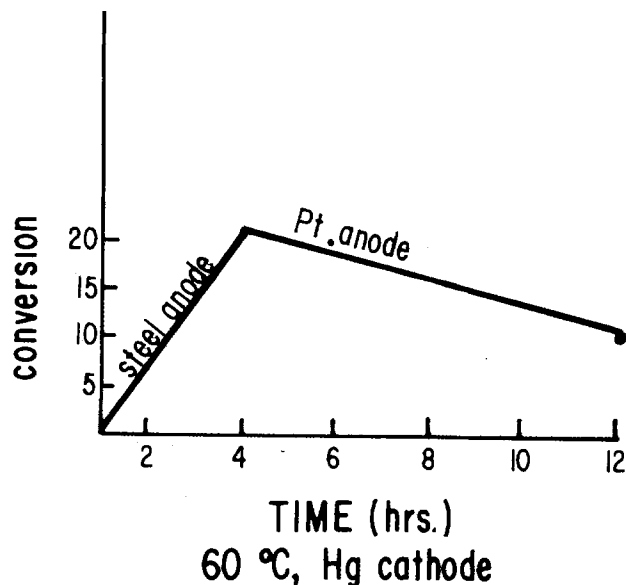


Fig. 7. Conversion of benzene to 1,4-cyclohexadiene with time using a steel and then Pt anode.

Ni and steel anodes were stable as long as the pH remained high (pH 13-14); however, lower pH led to anode corrosion. The O_2 -evolving DSA (TIR-2000) seems to be the best anode for the reaction although no long-term (weeks) lifetime studies were carried out.

In a survey of the effect of various quaternary ammonium ions on the current efficiency of the reaction it was found that under certain conditions $\text{Bu}_4\text{N}^+\text{OH}^-$ gave nearly quantitative current efficiencies for benzene reduction. A comparison of $\text{Bu}_4\text{N}^+\text{OH}^-$ and $\text{Bu}_3\text{EtN}^+\text{OH}^-$ is shown in Fig. 8. Good current efficiencies (>50%) could also be obtained using $\text{Pr}_4\text{N}^+\text{OH}^-$; however, $\text{Bu}_3\text{MeN}^+\text{OH}^-$ gave poor results (30% C.E.) and only traces of benzene reduction products were formed if $\text{Et}_4\text{N}^+\text{OH}^-$ or $\text{Me}_4\text{N}^+\text{OH}^-$ were used.

The concentration of quaternary ammonium hydroxide necessary for high current efficiency is surprisingly low. Even 2% $\text{Bu}_4\text{N}^+\text{OH}^-$ gives quite high (>90%) current efficiencies at low conversions; however, that drops off significantly as more benzene is converted to products (Fig. 9). With 20-25% $\text{Bu}_4\text{N}^+\text{OH}^-$ the current efficiency for benzene reduction is maintained at >90% even at 75% conversion.

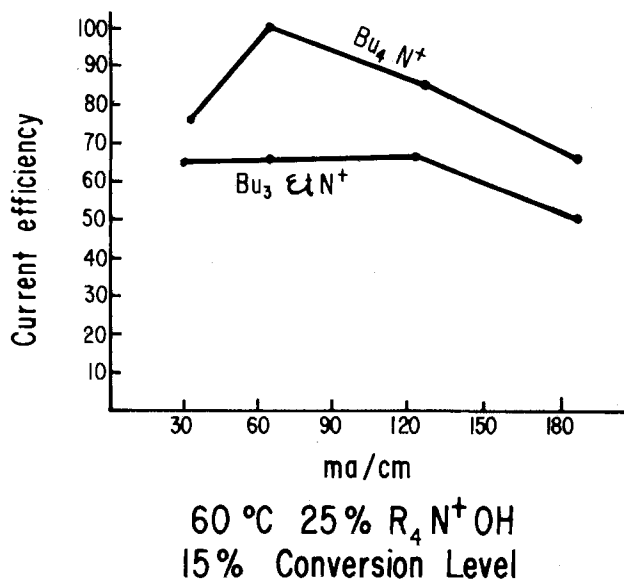


Fig. 8. Current efficiency for benzene reduction at varying current densities.

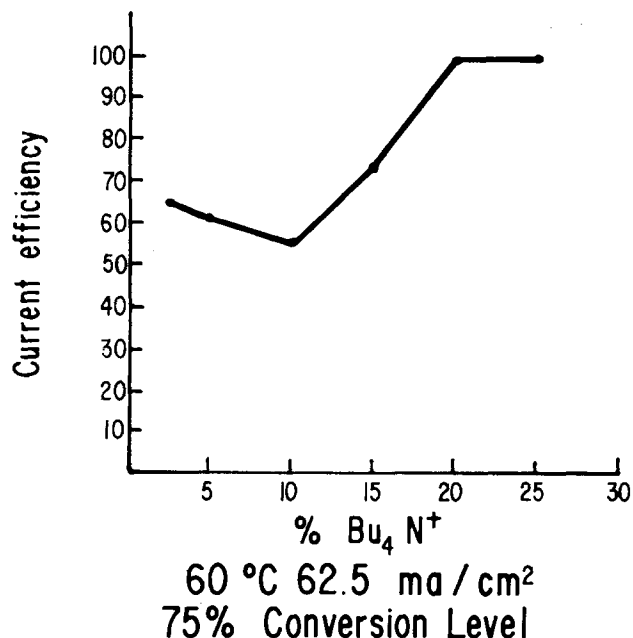


Fig. 9. Total current efficiency vs. Bu₄N⁺ concentration after 75% of the benzene is consumed.

Although the main aim of this study was to define a process for 1,4-cyclohexadiene production, a few other aromatic compounds were also examined but not optimized. Toluene and *p*-xylene give the expected dihydro-derivatives using these reaction conditions (see Experimental section). As a totally soluble substrate, 4-phenylbutyric acid was reduced to 4-(2,5-dihydrophenyl)butyric acid. Biphenyl gave a low yield of the 1,4-dihydro-derivative, whereas naphthalene was reduced predominantly to a mixture of 1,4-dihydronaphthalene and 1,4,5,8-tetrahydronaphthalene. The last two examples were carried out with sufficient heat to maintain the hydrocarbon in the molten state.

It is interesting to speculate about the first electron-transfer step to benzene in this reaction. The data suggest that the hydrocarbon is actually dissolved in the aqueous phase since the water-soluble example (4-phenylbutyrate) was reduced as well as toluene which is similar but not very soluble in the aqueous phase. If aqueous phase solubility is required, as suggested by the poor results obtained using small (Me₄N⁺, Et₄N⁺) quaternary ammonium ions, it is surprising that 2% Bu₄N⁺OH⁻ gives such good current efficiencies. However, with low Bu₄N⁺OH⁻ concentrations the current efficiency decreases as conversion increases, suggesting that benzene is extracted from the aqueous phase into the organic (predominantly, 1,4-cyclohexadiene) phase.

It may be that the aromatic substrate is dissolved in the predominantly organic layer of quaternary ammonium ions at the cathode surface, and it is irrelevant whether the organic molecules come from aqueous or organic phase in a well-stirred solution.

Direct electron transfer from cathode to benzene, toluene, or xylene seems unlikely in view of the large potential required for that step. Also, one would expect reduction at other high overvoltage cathode materials, such as lead and cadmium.

A mediated reduction involving reduced quaternary ammonium ion seems unlikely because one would expect to find large quantities of by-product amines and none were detected. Another mediated reduction scheme involves quaternary ammonium amalgam (20) which could transfer an electron to the aromatic hydrocarbon to initiate the reduction. In some reactions colloidal Hg is formed in the reaction which would be consistent with amalgam formation, separation from the cathode, and subsequent oxidation (by benzene).

Another argument for an amalgam mediated reduction is that only Hg gives significant current efficiencies for benzene reduction.

It is possible that solvated electrons are formed at or near the cathode surface and it is the solvated electrons that reduce the aromatic compound. The reactions appear very similar to those in which solvated electrons are, in fact, present (Na in NH₃).

Further work is required to answer the mechanistic questions.

To more nearly approximate a commercial process for the reduction of benzene to 1,4-cyclohexadiene it was necessary to devise a continuous reaction scheme involving a flow-through cell. Early attempts at construction of a flow cell having an Hg pool cathode led to rapid loss of Hg from the cell at quite low flow rates. Eventually, a cell was built (Fig. 3) which allowed a reasonable flow between anode and cathode without significant Hg loss from the cell.

In the cell shown in Fig. 3 the solution enters the center tube, flows radially out between cathode and anode, around and then behind the anode, and eventually out the exit port. Hg that separates from the cathode is carried up behind the anode where the solution velocity slows, allowing the Hg to drop to the back of the anode. The Hg droplets combine on the back surface of the anode and eventually drop back into the cathode.

This cell in combination with the components shown in Fig. 4 formed a continuous reaction system which operated for at least a week without interruption or operator interference (except to fill and empty reservoirs). A description of the system is given in the Experimental section.

Acknowledgment

The authors would like to thank K. F. Koncki for experimental assistance.

Manuscript submitted Aug. 18, 1980; revised manuscript received Sept. 27, 1980. This was Paper 434 presented at the St. Louis, Missouri, Meeting of the Society, May 11-16, 1980.

Any discussion of this paper will appear in a Discussion Section to be published in the December 1981 JOURNAL. All discussions for the December 1981 Discussion Section should be submitted by Aug. 1, 1981.

Publication costs of this article were assisted by Monsanto Company.

REFERENCES

1. A. J. Birch and G. S. Rao, "Advances in Organic Chemistry," Vol. 8, pp. 1-65, Wiley-Interscience, New York (1972).
2. E. C. French, U.S. Pat. 3,488,266 (1970); E. C. French and C. M. Starks, U.S. Pat. 3,493,477 (1970).
3. M. R. Rifi, in "Technique of Electro-organic Synthesis, Part II," N. L. Weinberg, Editor, pp. 216-218, Wiley-Interscience, New York (1975); W. J. Settinieri and L. D. McKeever, *ibid.*, pp. 400-403 and references therein.
4. J. S. Matthews, U.S. Pat. 3,684,669 (1972).
5. J. S. Matthews, U.S. Pat. 3,682,791 (1972).
6. J. S. Matthews, U.S. Pat. 3,682,794 (1972).
7. R. L. Hartranft, U.S. Pat. 3,492,207 (1970).
8. S. Asahaia, Jap. Pat. 72 40,786 (1972).
9. A. Misono and T. Osa, U.S. Pat. 3,485,726 (1969).
10. M. Fujii, Jap. Pat. 73 79,843 (1973).
11. M. Fujii, Jap. Pat. 73 79,844 (1973).
12. J. F. Connolly, U.S. Pat. 3,699,020 (1972).
13. J. F. Connolly, U.S. Pat. 4,022,673 (1977).
14. T. Hatayama, Jap. Pat. 74 47,740 (1974).
15. M. Fujii, Jap. Pat. 74 100,050 (1974).
16. M. Fujii, Jap. Pat. 74 56,952 (1974).
17. T. Hatayama, Jap. Pat. 74 41,192 (1974).
18. T. Hatayama, U.S. Pat. 3,700,572 (1973).
19. "Handbook of Chemistry and Physics," 58th Ed., p. C-260, CRC Press, Inc., Cleveland (1977).
20. L. Horner, "Organic Electrochemistry," M. M. Baizer, Editor, pp. 434, 435, Marcel Dekker, Inc., New York (1973).

Electron Transfer Reactions at Passive Tin Electrodes

S. Kapusta* and N. Hackerman**

Chemistry Department, Rice University, Houston, Texas 77001

ABSTRACT

The kinetics of charge transfer between passive tin electrodes and solutions of $\text{K}_3\text{Fe}(\text{CN})_6$ - $\text{K}_4\text{Fe}(\text{CN})_6$ have been studied in the pH range 7.5-10.0 and the temperature range 1°-50°C. The results have been analyzed on the basis of the quantum theories of electron transfer at oxide covered metal electrodes, and semi-quantitative agreement between theory and experiment was found. The electrochemical behavior of passive tin ranges from almost metallic, for very thin films, to that typical of n-type semiconductors, for thick films. Exchange current densities are, in all cases, much smaller than those measured on bare metal electrodes.

In a series of papers (1-3) we recently characterized the kinetics of growth and the semiconducting properties of passive films anodically grown on tin in borate buffer solutions. Both the thickness and the electronic properties of these films were found to be functions of the growing potential. A sharp distinction was seen between films grown at low potentials (below 1.7V *vs.* saturated calomel electrode), called thin films, and those grown at higher potentials. In both cases they were nonstoichiometric, having n-type conductivity due to an excess of tin cations. Measured flatband potentials were -0.25 and +0.5V at pH = 8.4 for thin and thick films, respectively. In both cases a dependence of -64 mV/pH was observed.

Donor concentrations could not be determined due to the frequency dispersion of the capacity data. However, using a value of $\epsilon = 10$ for the dielectric constant (*i.e.*, that corresponding to SnO_2), and the results obtained at high frequencies, the estimated donor concentrations ranged between 1×10^{19} and $1 \times 10^{21}/\text{cm}^3$, depending on the growing potential. The bandgap of these films could not be determined from optical measurements, because of the existence of an indirect transition at 2.55 eV. The bandgap is expected to be close to that of bulk SnO_2 (*i.e.*, 3.7 eV).

The kinetics of charge transfer across these films should reflect their semiconducting properties. It is well established that the rates of redox reactions at oxide covered metal electrodes are slower than at bare metal electrodes. The decrease in the rate constant depends strongly on film thickness, composition, and type of conductivity, as well as on the relative position of the rest potential of the redox couple and the flatband potential (4-8). According to the quantum mechanical theories of electron transfer (9-11) the main effect of very thin films (about 1 nm thick) is to increase the tunneling distance between the metal and the electrolyte (12). The tunnel probability decreases exponentially with the thickness of the barrier, and under normal conditions so does the exchange current (13).

For thicker films (several nm), on the other hand, direct tunneling from the metal cannot make a significant contribution to the overall current and these electrodes are expected to behave as semiconductor electrodes, with participation of electronic states inside the oxide in the electron transfer reactions. The boundary between both mechanisms (*i.e.*, direct tunneling from the metal and tunneling from states in the film) will depend on the electronic characteristics of both the film and the redox couple.

Although several studies of the electrochemical behavior of SnO_2 have been published [*e.g.*, (14-17)], only one of them was concerned with the semiconducting properties of passive tin (17). The kinetics of the $\text{Fe}(\text{CN})_6^{4/3-}$ redox couple was found to be slower than

on Pt under similar conditions, although no blocking of the oxidation reaction was observed as was the case for SnO_2 samples. The authors concluded that the thickness of the passive film (3 nm) was too low to show typical semiconductor behavior. More recently (18) passive tin was reported to be a very bad catalyst of the oxygen electroreduction reaction in alkaline solutions. The intrinsic complexity of this reaction, however, does not allow one to draw any conclusions on the rate of single electron transfer steps.

In the present work, we report on the kinetics of the $\text{K}_3\text{Fe}(\text{CN})_6$ - $\text{K}_4\text{Fe}(\text{CN})_6$ redox couple on passive tin electrodes in borate buffer solutions in the pH range 7.5-10.0, and for different thickness of the passive film. The results are analyzed on the basis of the quantum theories of charge transfer at oxide covered metal electrodes.

Experimental

Details of electrode preparation and film growth are given elsewhere (1-3). The redox system used was $\text{K}_3\text{Fe}(\text{CN})_6$ - $\text{K}_4\text{Fe}(\text{CN})_6$ dissolved in 0.2M borate buffer solutions of pH between 7.5 and 10.0. Films were grown for 16 hr at constant potential in pure borate buffer solutions, which were then replaced by deaerated redox solutions under nitrogen pressure. Solutions were continually deoxygenated by a stream of purified nitrogen. The temperature was maintained within 0.2°C of the chosen value (23°C unless otherwise stated) by means of a water thermostat.

Polarization curves were measured under steady-state conditions using a rotating disk electrode technique to eliminate diffusion effects by extrapolation to infinite rotation speed. Other details of the experimental setup have been given (1). Previous results indicate that the film thickness does not change (within $\pm 1\%$) during potentiostatic polarization for up to 1 hr at potentials lying between the growing potential and that of massive oxide reduction (about -1.0V *vs.* saturated calomel electrode). These conditions were satisfied during polarization measurements.

Since in many cases extrapolation of the anodic and cathodic Tafel regions to the redox potential yielded two different values of the exchange current density, i_0 , a linear polarization technique within ± 5 mV of the rest potential was used to determine i_0 (19). When no difference between the anodic and cathodic extrapolated values was observed, i_0 measured by linear polarization agreed with this single value.

All potentials are referred to the saturated calomel electrode (SCE) at the working temperature. All currents are expressed in terms of the projected electrode area (1 cm^2) without consideration for any roughness factor, estimated at about 2.

Results

The redox potential is rapidly established on passive tin electrodes, reaching a constant value equal to that measured on Pt (± 1 mV) within 5 min after intro-

* Electrochemical Society Active Member.

** Electrochemical Society Honorary Member.

Key words: passive tin, quantum theory, electron tunneling.

duction of the redox couple, for thin films, and within 1 hr for thick films. This behavior is usually observed on passive metal electrodes. Both types of films show a Nernstian behavior over at least 2 orders of concentration of the reduced and oxidized species (0.1-0.0025M). The redox potential does not depend appreciably on the redox couple concentration over that same range.

Steady-state current readings were obtained within 5 min (typically 30 sec) after imposing a potential step. These relatively slow transients can be attributed to a redistribution of charges in the film, since, as mentioned earlier, no changes in film thickness (determined by the cathodic reduction charge, Q_c) were observed. At least 5 different rotation speeds were used (between 600 and 3000 rpm) in order to extrapolate to infinite rotation speed.

Figure 1 shows typical polarization curves measured on tin electrodes passivated for 16 hr at 1.0, 1.4, 1.6, 1.8, 2.0, and 2.1V, after 1 hr of immersion in the redox electrolyte. Film thicknesses are expressed in terms of the reduction charge Q_c . A linear relationship between Q_c and film thickness d can be assumed. Considering a uniform film, we estimated that $Q_c = 2.4 \text{ mC/cm}^2$ corresponds to $d = 2.5 \text{ nm}$, and $Q_c = 20 \text{ mC/cm}^2$ to $d = 22 \text{ nm}$. Reflectometric results confirm both this estimate and the above assumption.

The exchange current density decreases continually with Q_c (i.e., d) over the whole range of growing potentials here considered, as is evident from the results in Fig. 2. The decrease in $\log i_0$ is approximately linear with Q_c for thin films, although it tends to a constant value for thick films. In all cases i_0 are much smaller than those measured on Pt under similar conditions i.e., about 0.1 A/cm^2 . As mentioned in the introduction, this result is expected on most passive electrodes, especially being n-type semiconductors.

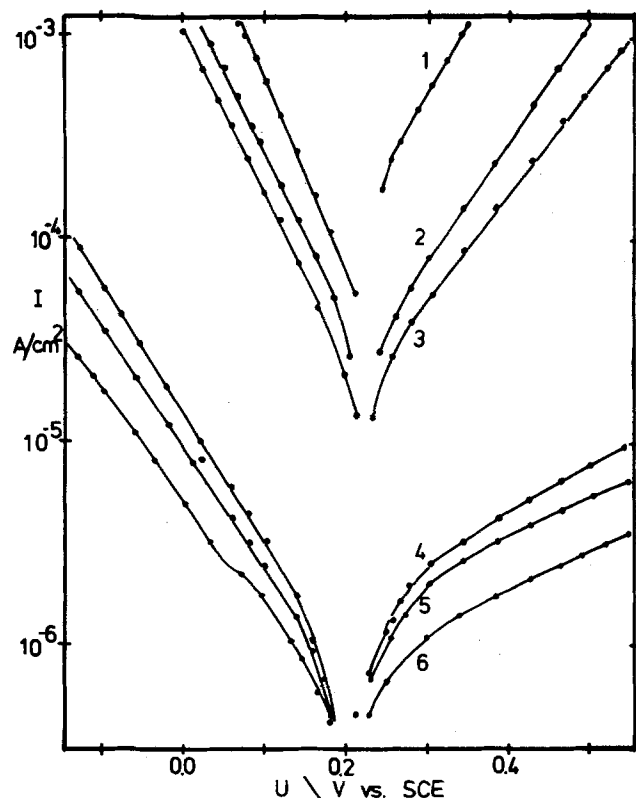


Fig. 1. Steady-state anodic and cathodic polarization curves measured on tin electrodes passivated for 16 hr at the following potentials: curve 1, 1.0V, $Q_c = 2.0 \text{ mC/cm}^2$; curve 2, 1.4V, $Q_c = 2.3 \text{ mC/cm}^2$; curve 3, 1.6V, $Q_c = 2.5 \text{ mC/cm}^2$; curve 4, 1.8V, $Q_c = 20 \text{ mC/cm}^2$; curve 5, 2.0V, $Q_c = 35 \text{ mC/cm}^2$; curve 6, 2.1V, $Q_c = 55 \text{ mC/cm}^2$. pH = 9.1. $T = 23^\circ\text{C}$. Redox potential, $U_r = 0.21 \text{ V vs. SCE}$. Redox couple concentration = 0.05M.

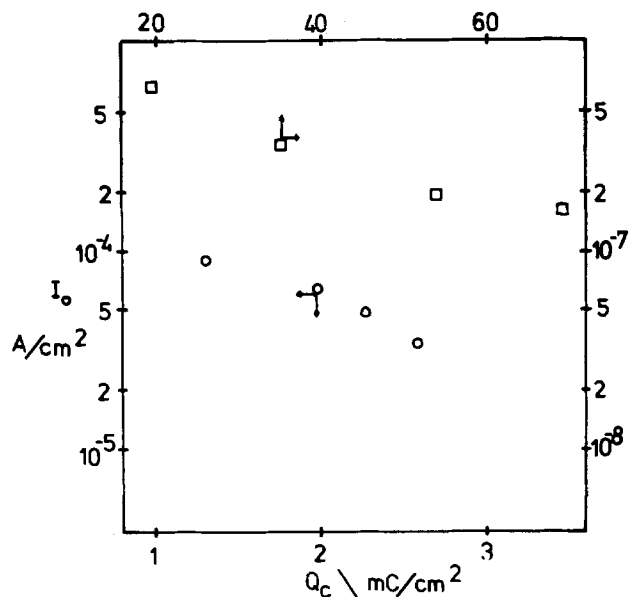


Fig. 2. Dependence of the exchange current density, i_0 , on cathodic reduction charge, Q_c , for thin (○) and thick (□) films. Same conditions as in Fig. 1.

Transfer coefficients for the cathodic Tafel regions, α_c , are close to 0.5 for thin films, and between 0.4 and 0.45 for thick films. Anodic transfer coefficients, α_a , on the other hand, decrease continually with Q_c , having a value of 0.45 for films grown at 1.0V ($Q_c = 2.0 \text{ mC/cm}^2$) but only 0.2 for films grown at 2.1V ($Q_c = 65 \text{ mC/cm}^2$). The blocking of the oxidation reaction is typical of n-type semiconductors, and these results reflect the increasing semiconducting properties of thicker films.

Extrapolation of the anodic and cathodic Tafel regions to the redox potential yields a single i_0 value for thin films, equal to that measured by linear polarization. For thick films, on the other hand, two different i_0 values are obtained from cathodic and anodic extrapolation. As a rule, i_0 anodic is larger than i_0 cathodic, although their relative magnitude depends on the pH value. A similar behavior has been reported for passive iron (20).

Figure 3 shows the Arrhenius plots obtained for two of the films in Fig. 1, i.e., those grown at 1.0 and 1.8V. The good linearity of the results indicates that activation energies are independent of temperature in the range here considered. Anodic and cathodic transfer coefficients were also found to be independent of tem-

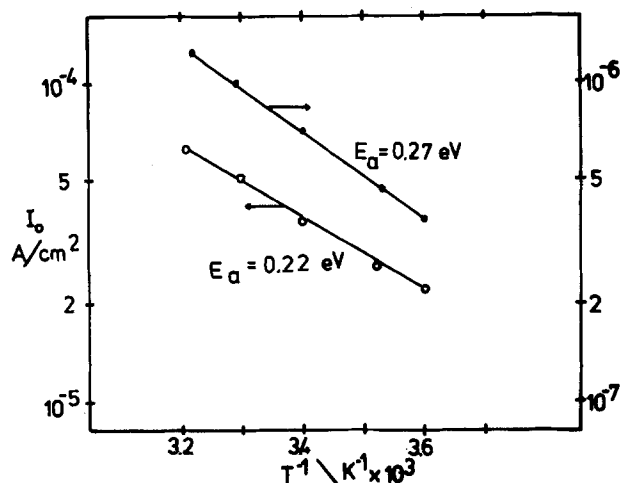


Fig. 3. Arrhenius plots of the exchange current density measured on films grown at 1.0V, $Q_c = 2.0 \text{ mC/cm}^2$ (lower line) and at 1.8V, $Q_c = 20 \text{ mC/cm}^2$ (upper line). Other conditions as in Fig. 1.

perature. Values of E_a ranging from 0.2 eV for films grown at 0.8V to 0.3 eV for films grown at 2.1V have been measured. The corresponding values are 0.19 eV on Au (21) and 0.17 eV on Pt (22). There is therefore a systematic dependence of E_a on Q_c , although no quantitative relationship could be derived.

Both the shape of the polarization curves and the values of the exchange currents measured on thick films depend on the solution pH, as is apparent from the results shown in Fig. 4. A small shoulder develops in the cathodic branch at the highest pH values and at potentials near the redox potential. The reaction order with respect to pH, defined as

$$\delta \log i_0 / \delta \text{pH}$$

is close to 0.5. The dependence of the exchange currents measured on thin films was much smaller, with a reaction order near zero.

Figure 5 shows the dependence of the exchange current measured on a thick film grown at 1.8V ($Q_c = 20 \text{ mC/cm}^2$) on the concentration of the redox couple. The reaction order is 1, as is also the case for thin films. For bare metal electrodes, the reaction order should be equal to the sum of the anodic and cathodic transfer coefficients. For this same electrode, $\alpha_a + \alpha_c = 0.7$. This result should again be attributed to the semiconducting properties of the film.

Discussion

Only the general concepts of the quantum theory of charge transfer in condensed media are given below, as far as they are needed in order to explain the experimental results.

Electron transfer proceeds by tunneling between occupied and unoccupied states of equal energy in the electrode and in the electrolyte. The transfer reaction is considered much faster than the thermal oscillations of the heavy particles. In the electrolyte the electronic states are localized at the reduced and oxidized species. The energy depends on the configuration of the re-

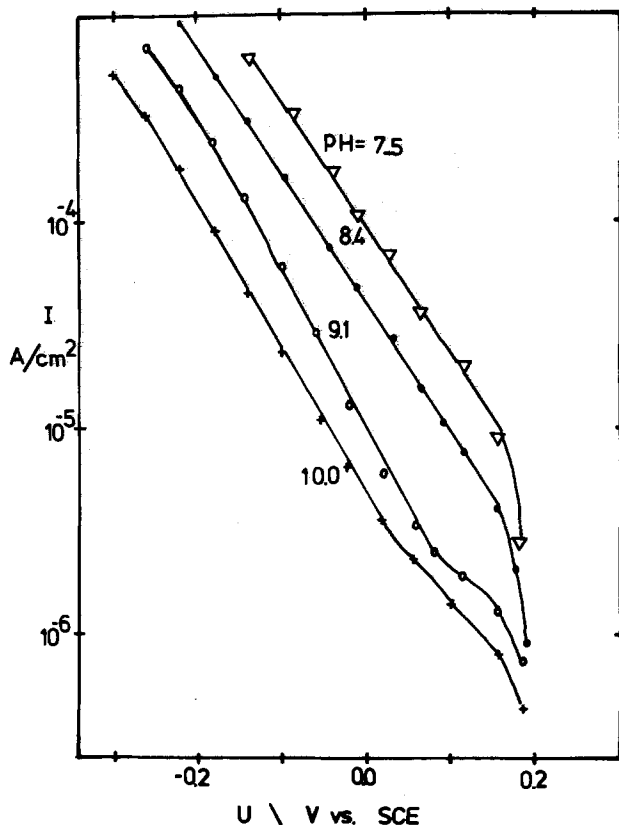


Fig. 4. pH dependence of the cathodic branch of the polarization curve, for a film grown at 1.9V for 16 hr, $Q_c = 30 \text{ mC/cm}^2$. Redox couple concentration = 0.05M. Temperature = 23°C.

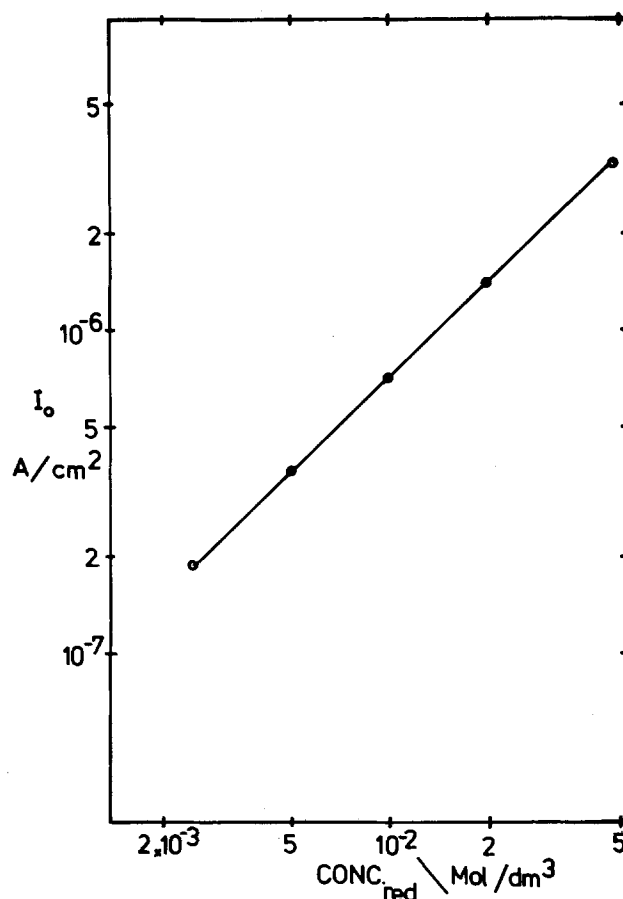


Fig. 5. Redox couple concentration dependence of the exchange current density measured on a film grown at 1.8V for 16 hr. Other conditions similar to those in Fig. 1. Note small change in ratio of reduced to oxidized form alters the quantities on the abscissa very slightly.

active complex. Thermal fluctuations produce a Gaussian distribution around the most probable state. Assuming for simplicity that the width of this Gaussian distribution is the same for the reduced and oxidized species, the Fermi energy $E_{F,el}$ at which occupied and empty states in the electrolyte have equal probability differs from the energy of the most probable state by a common reorganization energy, λ . The density of states function in the electrolyte is usually described by (14)

$$D_r = \exp - (E - E_{F,el} + \lambda)^2 / 4kT\lambda \quad [1]$$

$$D_o = \exp - (E - E_{F,el} - \lambda)^2 / 4kT\lambda \quad [2]$$

for the reduced and oxidized states, respectively. Here E is the energy.

The rates of electrochemical reactions are proportional to the total flux of reactive complex to the electrode, Zc_r ; to the tunneling probability, T ; and to the probability, $\rho(1-f)$, of finding unoccupied electronic states in the electrode and D_r , of finding occupied states in the electrolyte, for the anodic current, and vice versa for the cathodic current

$$J^+(E) = FZC_r\rho(1-f)D_rT \quad [3]$$

$$J^-(E) = FZC_o\rho(f)D_oT \quad [4]$$

where fluxes are given as the product of a velocity, Z , and the concentration, C . The measured current density can be written as the normalized integral of [3] and [4] at any energy level

$$J = 1/E_o \times \left[\int_0^\infty J^+(E) dE - \int_0^\infty J^-(E) dE \right]$$

[5]

Here E_o is the normalization constant.

In a metal electrode the probability of finding occupied states can be described by Fermi's distribution function

$$f(E) = [1 + \exp - (E - E_F)/kT]^{-1} \quad [6]$$

where E_F is the Fermi level of the metal. The probability of finding unoccupied states is then $1 - f(E)$. The maximum of $J(E)$ occurs at the Fermi level even under irreversible conditions, when

$$e\eta = E_{F,el} - E_F \quad [7]$$

η being the overvoltage. For $\eta \ll 2\lambda/e$ straight Tafel lines having transfer coefficients close to 0.5 are expected. The tunneling probability is high on bare metal electrodes ($T_0 \simeq 1$), independent of electrode potential. This probability decreases from T_0 to T if a film separates the metal from the electrolyte. The energy barrier assumes a trapezoidal shape due to the electric field inside the film. Therefore, T is usually given as

$$T = T_0 \exp [-4\pi d (2m^* \Delta E_b)^{1/2}/h] \quad [8]$$

Here d is the film thickness, m^* is the effective mass of the tunneling electrons, h is Planck's constant, and ΔE_b is the average barrier height. T decreases exponentially with d (11), as shown in Fig. 2. An order of magnitude for the barrier height can be calculated using the results of Fig. 2 for thin films, and an estimated value of 0.5 for m^* . The result (i.e., 0.2 eV) is reasonable for these type of films. Therefore, the experimental results obtained on thin films can be explained considering direct tunneling of electrons from the metal and through the oxide layer.

As the film thickens an additional current density due to electron exchange with electronic states in the oxide becomes important. For very thick films the current due to direct electron exchange with the metal becomes negligible, and electron transfer to and from the oxide predominates. The thickness at which the transition from one process to the other takes place will depend on the semiconducting properties of the film and on the nature of the redox couple. Assuming that the valence band does not significantly contribute to the observed C.D. (i.e., wide bandgap), electron tunneling proceeds to and from states in the conduction band below the surface. Both the height of the barrier and the tunneling distance depend on band bending and therefore on electrode potential and solution pH.

The tunneling probability can now be expressed as

$$T = T_0 \exp\{-8\pi/3h [m^* (E_c^s - E_c^b)^{1/2}] x\} \quad [9]$$

and the tunneling distance, x , as

$$x = (2/e) (\epsilon \epsilon_0/2N_d)^{1/2} [(E_c^s - E_c^b)^{1/2} - (E - E_c^b)^{1/2}] \quad [10]$$

where e is the electron charge, E_c^s and E_c^b are the energy of the conduction band of the oxide at the surface and in the bulk, respectively; N_d is the donor concentration; ϵ_0 is the permittivity of free space, and ϵ the dielectric constant of the film.

The total overvoltage, η , is composed of changes in the electrical potential inside the film, η_s , and in the Helmholtz layer, η_h .

$$\eta = \eta_s + \eta_h \quad [11]$$

It is therefore necessary to calculate η_s for any value of η . This is usually done following the procedure outlined in Ref. (6). The final expression for the current density is

$$j = j' \int_{E_c^b}^{E_c^s} \frac{\exp\{-r(E_c^s - E)^{1/2}[(E_c^s - E_c^b)^{1/2} - (E - E_c^b)^{1/2}]\}}{1 + \exp\{-(E - E_F)/kT\}} \exp\left\{-\frac{(E - E_{F,el} + \lambda)^2}{4kT\lambda}\right\} dE \\ - j' \int_{E_c^b}^{E_c^s} \frac{\exp\{-r(E_c^s - E)^{1/2}[(E_c^s - E_c^b)^{1/2} - (E - E_c^b)^{1/2}]\}}{1 + \exp\{+(E - E_F)/kT\}} \exp\left\{-\frac{(E - E_{F,el} - \lambda)^2}{4kT\lambda}\right\} dE \quad [12]$$

where

$$r = (16\pi/3he) (m^* \epsilon_0 \epsilon/N_d)^{1/2} \quad [13]$$

and J' is a constant containing all energy independent factors. The integration must be performed numerically, choosing an upper limit equal or greater than E_c^s .

Several assumptions are implicit in this derivation: (i) The contribution of electrons having a nonvanishing momentum parallel to the reaction interface has been neglected. In this way the 3-dimensional barrier could be approximated by a triangular cross-section barrier. (ii) The WKB-factor (Eq. [9]) is a good approximation to the tunneling probability only far from the flatband potential. (iii) Equation [10] does not consider the location of the donor level below the conduction band. For anodic films this level lies several tenths of eV below E_c and results in partial donor dissociation. This effect could however be partially compensated during calculation of η_s , and by the choice of E_F .

Schmickler (21) used an exact expression of the Poisson-Boltzmann equation in order to calculate the shape of the space charge barrier, i.e., $x(E)$. Although he considered E_c^b fixed and assumed that E_c^s changed with overvoltage η , the opposite convention seems more convenient, since E_c^s is usually fixed by external conditions (i.e., solution pH). Therefore (24)

$$x = L_d \int_v^{v_s} du/F(u) \quad [14]$$

where

$$v(x) = [E_c^b - E(x)]/kT \quad [15]$$

$$v_s = v(0) \quad [16]$$

$$F(v) = \sqrt{2} \{ (1 - g)(e^v - v - 1) + \ln [1 + (e^v - 1)g] - vg\}^{1/2} \quad [17]$$

$$g = [1 + \exp(E_d/kT)]^{-1} \quad [18]$$

E_d is the energy of the donor level with respect to the bottom of the conduction band in the bulk, E_c^b , and L_d is called the Debye length and is equal to $(2/e)(\epsilon \epsilon_0/2N_d)^{1/2}$.

The final expression of the C.D. is found introducing [14] instead of [10] for the tunneling distance. It is also possible to simplify this integral by noting that, from [14]

$$dE_c(x)/dx = -(kT/L_d)F(v) \quad [19]$$

It is not therefore necessary to calculate explicitly $x(E)$. The C.D. is then expressed as

$$j = j' \int_{E_c^b}^{E_c^s} \frac{\exp\left\{-\int_{x_1}^{x_2} [E_c(x) - E]^{1/2} dx\right\}}{1 + \exp[-(E - E_F)/kT]} \cdot \exp\left[\frac{-(E - E_{f,el} + E_\lambda)^2}{4kTE_\lambda}\right] dE \\ - j' \int_{E_c^b}^{E_c^s} \frac{\exp\left\{-\int_{x_1}^{x_2} [E_c(x) - E]^{1/2} dx\right\}}{1 + \exp[+(E - E_F)/kT]} \cdot \exp\left[\frac{-(E - E_{f,el} - E_\lambda)^2}{4kTE_\lambda}\right] dE \quad [20]$$

Equation [20] must be numerically integrated in order to obtain theoretical $J(E)$ curves. This can be done by substituting the integration terms by experimentally accessible quantities. Introducing the integration variable $y = E - E_c^b$, and calling U_r' the redox

potential with respect to the flatband potential, i.e., $U_r = U_r - U_{FB}$, then

$$\begin{aligned}
 E_{c^s} - E_{c^b} &= e(U_r + \eta) \\
 E - E_{F,el} &= e(y - \eta + E_d/2) \\
 E_{c^s} - E &= e(U_r + \eta - y) \\
 E - E_F &= e(y + E_d/2)
 \end{aligned}
 \quad [21]$$

Absolute values of J cannot be obtained because J' is unknown. Reliable values of N_d , U_{FB} , and ϵ for thick films on tin are also undetermined (2, 3). Therefore, an indirect approach was used, and the best values of these parameters were estimated from fitting of theoretical curves to the experimental results. Using $m^* = 0.5$ (2) and $\lambda = 1.2$ eV (25), the polarization curves shown in Fig. 6 and 7 have been obtained with the parameters indicated. A change of 60 mV/pH in U_{FB} was assumed (2).

The values of the film parameters obtained from the fitting procedure, i.e., $U_{FB} = -0.25$ V; $E_d = -0.5$ eV with respect to the conduction band; $\epsilon = 10$; and the range of N_d between 1.1×10^{20} and $3.3 \times 10^{19}/\text{cm}^3$, coincide fairly well with those given in the introduction for thin films. This result indicates that the differences observed in the electrical and photoelectrochemical properties between thin and thick films are not intrinsic, but can be attributed to the presence of discontinuities in the film or recombination centers, as postulated before (2, 3).

In any case the similarities between the theoretical calculations and the experimental results are mostly qualitative. Theory for instance predicts a stronger potential dependence of the cathodic branch of the polarization curves and weaker for the anodic branch. At the same time, the experimentally measured pH dependence of the current density is smaller than expected. The increase in activation energy with film thickness (i.e., decrease in donor concentration) can be at best explained only qualitatively. According to Schmickler (23) the maximum of the current distribution among the different electronic states is shifted towards higher values of the electronic energy with

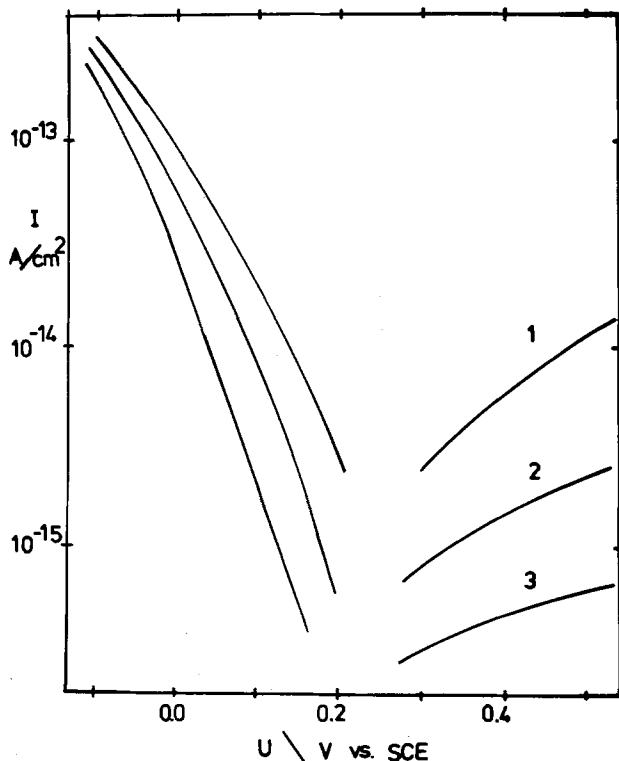


Fig. 6. Anodic and cathodic polarization curves calculated by numerical integration of Eq. [20], using the following parameters: pH = 9.1; $\epsilon = 10$; $U_{FB} = -0.25$ V; $U_r = 0.21$ V; $E_d = 0.5$ eV below the conduction band; $E_F = 0.25$ eV below the conduction band; and $N_d = 1 \times 10^{20}$; 2.5×10^{19} ; $3.3 \times 10^{19}/\text{cm}^3$.

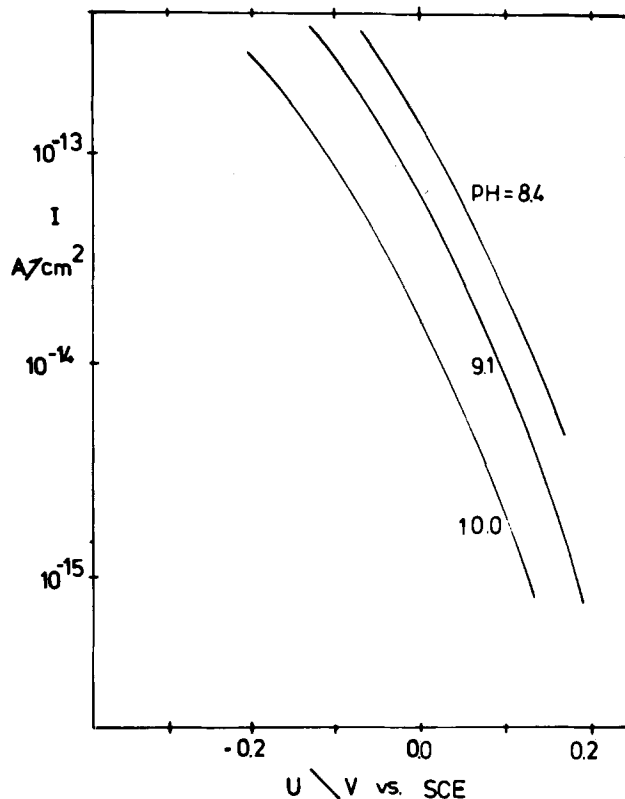


Fig. 7. Cathodic polarization curves calculated by numerical integration of Eq. [20], using the same parameters as in curve 2 in Fig. 6, and a change in U_{FB} of 60 mV/pH.

increasing Debye length, i.e., decreasing donor concentration, for thick films, and with increasing thickness for thin films where direct tunneling from the metal still makes an appreciable contribution. These effects are observed (Fig. 3), although a quantitative correlation with theory is not possible.

The differences in the i_0 values obtained by extrapolation of the anodic and cathodic Tafel regions for thick films is inconsistent with the present model. A possible explanation for this behavior is a resonance tunneling mechanism (23, 26) involving localized states within the bandgap of the film. The location of this resonance level, E_r , can in principle be determined from the difference between anodic, i_0^a , and cathodic, i_0^c , values of the exchange current density. Alternatively, it can also be determined from the increase in the activation energy of the redox reaction on passive electrodes with respect to bare metal electrodes (26). Defining

$$\Delta = kt (\ln i_0^c - i_0^a) \quad [22]$$

then

$$|\Delta| = |E_r|/kT \quad [23]$$

On the other hand, the activation energy measured on passive electrodes is

$$E_a = E_a^0 + e\eta_{FB}/2 + |E_r|/2 \quad [24]$$

where E_a^0 is the activation energy measured on bare metal electrodes, and η_{FB} the overvoltage at the flat-band potential.

Using the results shown in Fig. 1 for films grown at 2.0 V to calculate Δ , and a value of $E_a = 0.28$ eV for this same film, values of $E_r = 0.15$ to 0.2 eV below the conduction band have been calculated using Eq. [23] and [24], respectively. Further evidence for this resonance tunneling mechanism could not be obtained from the experimental results.

The contribution of other electron conduction mechanisms cannot be ruled out considering the above mentioned differences between theory and experiments. The effects of cracks in the passive film, or the presence of recombination centers or surface states, previ-

ously proposed to explain anomalous behavior of thick films, cannot be estimated from the present results.

Conclusions

The kinetics of charge transfer at passive tin electrodes can be explained on a semi-quantitative basis using the quantum mechanical theories developed for oxide covered metal electrodes. On thin films the main contribution to the measured current density arises from direct electron exchange between the metal and the redox electrolyte. The effect of the film is to increase the tunneling distance of electrons. Therefore, the exchange current decreases exponentially with film thickness. The activation energy increases continually from the value measured on Pt (0.17 eV), although a quantitative correlation, for instance between the increase in E_a and the barrier height, could not be obtained.

The behavior of thick films is similar to that of n-type semiconductor electrodes. Since in this case the direct tunneling contribution should be negligibly small, electronic states in the oxide participate in the exchange reaction and provide the main contribution to the total current. The effect of film thickness in this case is only secondary, and can be related to a decrease in the donor concentration. The activation energy also decreases with film thickness, although this can be attributed to an increase in the Debye length with decreasing donor concentration.

The experimental results, however, show some differences from the theoretical predictions, both in the magnitude of the anodic and cathodic Tafel slopes and in the pH dependence of the exchange current. At the same time, extrapolation of the anodic and cathodic Tafel regions to the rest potential yields different values of the exchange current. This later effect could be caused by a resonance tunneling phenomenon, involving localized states within the bandgap of the oxide. No conclusive evidence for this process was obtained.

The parameters describing the semiconducting properties of the thick films (i.e., U_{FB} , N_d , and ϵ) obtained from fitting the theoretically calculated polarization curves to the experimental results coincide fairly well with those estimated for thin films. This indicates that the difference between both types of films might be due only to the presence of imperfections in the thick films. The effect of these imperfections (e.g., cracks, recombination centers, or surface states) on the electrical and photoelectrochemical response of the electrodes has already been shown. Their participation in electron transfer reactions, however, is difficult to estimate.

Acknowledgments

The support of this research by the Robert A. Welch Foundation of Houston, Texas, is gratefully acknowledged. The authors would also like to thank Dr. Mark Wilhelm and Dr. Kyung Suk Yun for helpful suggestions and discussions.

Manuscript received July 3, 1980.

Any discussion of this paper will appear in a Discussion Section to be published in the December 1981 JOURNAL. All discussions for the December 1981 Discussion Section should be submitted by Aug. 1, 1981.

Publication costs of this article were assisted by Rice University.

REFERENCES

1. S. Kapusta and N. Hackerman, *Electrochim. Acta*, **25**, 1625 (1980).
2. S. Kapusta and N. Hackerman, *ibid.*, **25**, 949 (1980).
3. S. Kapusta and N. Hackerman, *ibid.*, **25**, 1001 (1980).
4. A. C. Makrides, *This Journal*, **111**, 392 (1964).
5. R. V. Moshtev, *Electrochim. Acta*, **16**, 2039 (1971).
6. K. E. Heusler and K. S. Yun, *ibid.*, **22**, 977 (1977).
7. J. W. Schultze, in "Passivity of Metals," R. P. Frankenthal and J. Kruger, Editors, p. 82, The Electrochemical Society Inc., Princeton, N.J. (1978).
8. R. Memming, in "Electroanalytical Chemistry," Vol. 11, A. J. Bard, Editor, Marcel Dekker, New York (1979).
9. H. Gerischer, in "Adv. Electrochemistry Electrochem. Engineering," Vol. 1, P. Delahay and C. W. Tobias, Editors, p. 139, Interscience, New York (1961).
10. R. A. Marcus, *Ann. Rev. Phys. Chem.*, **15**, 155 (1964).
11. V. G. Levich, in "Physical Chemistry, an Advanced Treaty," Vol. 9B, H. Eyring, D. Henderson, and W. Jorst, Editors, p. 985, Academic Press, New York (1970).
12. J. W. Schultze and K. J. Vetter, *Electrochim. Acta*, **18**, 889 (1973).
13. W. Schmickler, *J. Electroanal. Chem. Interfacial Electrochem.*, **84**, 203 (1977).
14. F. Möllers and R. Memming, *Ber. Bunsenges. Phys. Chem.*, **76**, 469, 475 (1972).
15. H. A. Laitinen, C. A. Vincent, and T. M. Bednarski, *This Journal*, **115**, 1024 (1968).
16. D. Elliot, D. E. Zellner, and H. A. Laitinen, *ibid.*, **117**, 1343 (1970).
17. O. G. Deryagina and E. N. Paleolog, *Elektrokhimiya*, **5**, 315 (1968).
18. E. Calvo, Ph.D. Thesis, University of La Plata, Argentina (1979).
19. P. Delahay, "Double Layer and Electrode Kinetics," Interscience, New York (1965).
20. J. W. Schultze and U. Stimming, *Z. Phys. Chem. NF*, **98**, 285 (1975).
21. P. Bindra, H. Gerischer, and L. M. Peter, *J. Electroanal. Chem. Interfacial Electrochem.*, **57**, 435 (1974).
22. J. Jordan, *Anal. Chem.*, **27**, 1708 (1955).
23. W. Schmickler, *Ber. Bunsenges. Phys. Chem.*, **82**, 477 (1978).
24. A. Many, Y. Goldstein, and N. B. Grover, "Semiconductor Surfaces," Amsterdam (1965).
25. J. M. Hale, in "Reactions of Molecules at Electrodes," N. S. Hush, Editor, Interscience, London (1971).
26. W. Schmickler, *J. Electroanal. Chem. Interfacial Electrochem.*, **82**, 65 (1977).

Spectroelectrochemical Study of the Formation of the Radical Cation and Dication of Perylene in Molten Antimony(III) Chloride

Morten Sørlye,¹ G. Pedro Smith, V. E. Norvell,² Gleb Mamantov,^{*3,4} and Leon N. Klatt⁴

Oak Ridge National Laboratory, Chemistry Division, Oak Ridge, Tennessee 37830

ABSTRACT

The oxidation of perylene (PeH) in aprotic melts containing primarily SbCl_3 was studied spectroelectrochemically. In molten SbCl_3 containing 0.038m CsCl at 100°C , PeH is oxidized at 0.26V relative to the SbCl_3/Sb , saturated CsCl reference electrode to form a stable solution of the radical cation $\text{PeH}^{\cdot+}$. The optical absorption spectrum (500-900 nm) of this cation has five maxima with the highest at 545 nm ($\epsilon = 4.2 \times 10^4$). In molten SbCl_3 containing 0.079m AlCl_3 at 100°C PeH is spontaneously oxidized to $\text{PeH}^{\cdot+}$ by reduction of SbCl_3 . In this melt electrochemical oxidation of $\text{PeH}^{\cdot+}$ to form the dication PeH^{2+} at 100°C occurs at 0.97V relative to the SbCl_3/Sb , saturated CsCl reference electrode. The optical absorption spectrum (400-800 nm) of PeH^{2+} consists of two overlapping bands with a peak at 533 nm ($\epsilon = 3.7 \times 10^4$).

Polycyclic aromatic hydrocarbons ArH are often soluble (1) in molten SbCl_3 ⁵ and can be oxidized chemically or electrochemically to form their radical cations $\text{ArH}^{\cdot+}$ (5-7). Many of these cations are quite stable in SbCl_3 , in spite of the elevated temperature, and some have been characterized by electron spin resonance (ESR) spectra at high resolution (8, 9). For three arenes, perylene PeH, 9,10-diphenylanthracene, and coronene, electrochemical studies (6) indicated that the radical cation in SbCl_3 could be oxidized further to form what was presumed to be the arene dication ArH^{2+} , and the visible absorption spectrum of the presumed perylene dication PeH^{2+} was subsequently published. However this absorption spectrum is quite different from that for PeH^{2+} prepared in superacid media, where the cation has been identified by its proton NMR spectrum (11, 12).

As part of a study of arene cations in molten SbCl_3 we have developed an electrochemical cell in which potentiometric, coulometric, and spectrometric methods may be used in concert to generate and characterize species formed by arene oxidation. The present paper describes the application of this cell to a clarification of the species formed by the oxidation of perylene and its radical cation.

Experimental

Materials.—Antimony(III) chloride (from three vendors, viz.: Ultrapure grade from Ventron Alfa Products; 99.0% min. from Mallinckrodt; and 99.0% min. from Matheson, Coleman, and Bell) was further purified by sublimation, distillation, and when very high purity material was needed, by repeated zone refining.

Aluminum chloride was made by reacting 99.9999% Al metal with semiconductor-grade HCl according to a procedure previously described (13). Potassium chloride and cesium chloride (both Suprapur grade, E. Merck, Darmstadt) were further purified by purging the molten salts with HCl(g) and then Ar.

Antimony metal (99.99%, Bradley Mining Company) was vacuum cast into 3 mm diam single crystals that were drilled and threaded to serve as electrodes.

* Electrochemical Society Active Member.

¹ Visiting scientist from the University of Tennessee, Knoxville, Tennessee.

² Graduate student, University of Tennessee, Knoxville, Tennessee.

³ Department of Chemistry, University of Tennessee, Knoxville, Tennessee.

⁴ Analytical Chemistry Division.

Key words: visible spectra, coulometry, voltammetry, AlCl_3 , CsCl , KCl .

⁵ mp, 73°C (2); bp, 223°C (3); crit. pt., 521°C (4).

Perylene (99+%, Gold Label from Aldrich Chemical Company) was either used without purification or, for purposes of spectrometric measurements, was recrystallized from toluene.

Instrumentation.—Differential pulse polarography and cyclic voltammetry experiments were performed with a Princeton Applied Research Model 174A Polarographic Analyzer, and coulometric measurements with a Model 173 Potentiostat/Galvanostat equipped with a Model 179 Digital Coulometer. A Hewlett-Packard Model 7045A X-Y recorder was used for data display.

Absorption spectra were measured with a Tektronix Model J20 silicon-vidicon rapid-scan spectrometer controlled by a Digital Equipment Corporation PDP-8/I minicomputer. A detailed description of the spectrophotometer and computerized data sampling and processing has been published (14). A Heath Company Model EU-701-50 tungsten/deuterium source served as the light source.

A resistance furnace made from Pyrex tubing and Ni/Cr heating wire was used. In order to minimize convection in the optical cell during the experiments, a thermal gradient kept the lower end of the cell at a temperature $2^\circ\text{--}5^\circ\text{C}$ lower than the rest. The furnace temperature was controlled by a Leeds and Northrup Series 80 3-action D.A.T. Controller in connection with a calibrated AZAR module and a Speedomax H recorder. During spectrometric measurements a furnace was used that had side arms to allow the light beam to pass.

Electro-optical cell.—The electrolytic cell (Fig. 1a) was made of Pyrex glass with a silica spectrometric cell fused to the lower end. Electrodes were inserted through threaded glass joints equipped with Teflon bushings and FETFE O-ring seals (Ace Glass). There was room for six joints on top of each cell, one central and five others spaced around it. Not all are shown in Fig. 1a. The usual electrode arrangement consisted of two working electrodes, one counterelectrode, one reference electrode, and one optical electrode. The sixth joint was used for evacuation of the cell. The temperature of the electrolyte was monitored with a thermocouple placed in a well fused to the top of the cell.

The working electrodes were made either of vitreous carbon (supplied by IMC Industry Group) or Pt wire, whereas the counterelectrode was fabricated from Pt foil. Electrode wires were sealed with vacuum-tight, standard tungsten/Pyrex seals. In most experiments

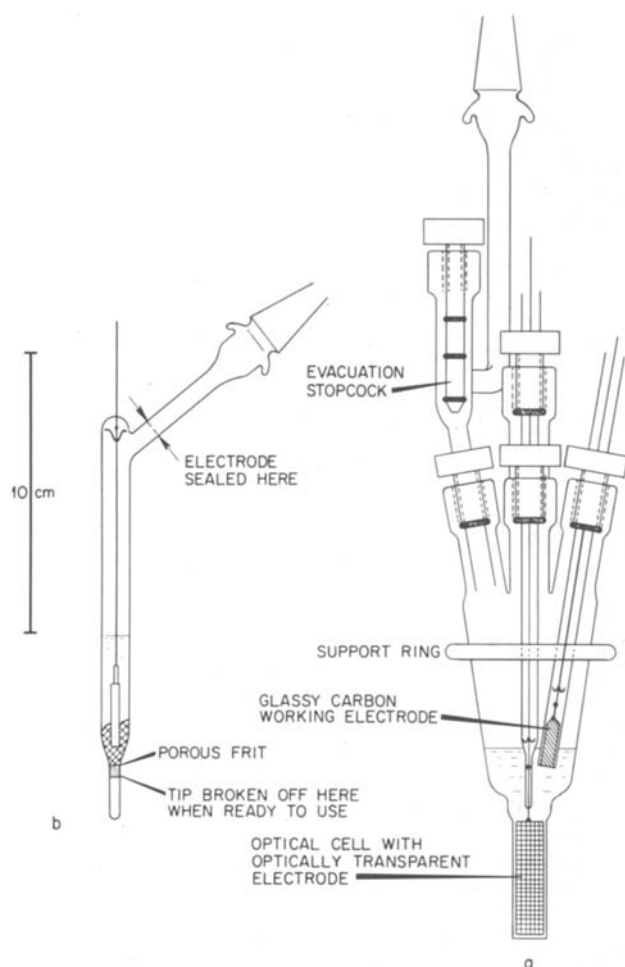


Fig. 1. (a) Electro-optical cell. Only two electrodes and an evacuation stopcock are shown for clarity. (b) Reference electrode.

the cell contained both a glassy carbon and a Pt working electrode.

Optically transmitting electrodes (OTE), which also were used in coulometric measurements, were made either from reticulated vitreous carbon (RVC, a glassy carbon foam from Fluorocarbon Company) or from Pt-wire screen. The RVC material was sliced into thin plates which fitted into the optical cells (1-2 cm path length). The characteristics of the vitreous carbon OTE have previously been described (15).

Reference electrode.—The reference electrode (Fig. 1b) was built to fit the bushings on top of the cell. The active electrode was a rod of Sb metal that was drilled and threaded on one end. At Pt pin, screwed into this end, provided good electrical contact. Electrical contact with the main electrolyte was through a porous alumina frit (Radiometer Copenhagen). As shown in Fig. 1b, this frit was sealed into a small, closed tube so that the electrode could be sealed under vacuum after it was filled with the salt. Then, the salt was melted and allowed to soak the frit so that when it resolidified, it formed a gas-tight plug. The closed tube over the frit was broken off just prior to first usage and thereafter the electrode could be used repeatedly.

The electrolyte in the Sb(III)/Sb reference electrode was SbCl_3 saturated with solid $\text{Cs}_3\text{Sb}_2\text{Cl}_9$ present in excess. This compound is the equilibrium solid phase when excess CsCl is added to molten SbCl_3 at temperatures within the range of interest here, $70^\circ\text{--}200^\circ\text{C}$ (16). We prepared $\text{Cs}_3\text{Sb}_2\text{Cl}_9$ by fusing stoichiometric amounts of SbCl_3 and CsCl together in a thick-walled silica ampul. The alternative procedure of trying to equilibrate solid CsCl with molten SbCl_3 was unsatisfactory because the rate at which CsCl reacted to form

the equilibrium compound was very slow even at temperatures near the melting point of $\text{Cs}_3\text{Sb}_2\text{Cl}_9$. The electrode described here is designated SbCl_3/Sb , sat. CsCl.

Note that the corresponding electrodes made with KCl or RbCl would not be satisfactory over the temperature range of interest here because in the KCl- SbCl_3 system the solid phase in equilibrium with molten SbCl_3 changes from KShCl_4 to $\text{K}_3\text{Sb}_2\text{Cl}_9$ at 110°C (17) while in the RbCl- SbCl_3 system a similar change occurs at 125°C (18). Phase diagrams are not available for the LiCl- SbCl_3 and NaCl- SbCl_3 systems.

Experimental procedure.—All inorganic salts were handled in an Ar-atmosphere glove box with H_2O and O_2 content kept constantly below 1 ppm. Perylene was weighed on a microbalance outside the glove box since it was neither hygroscopic nor air sensitive.

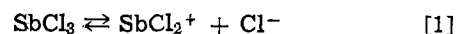
The cell was evacuated prior to each experiment and closed off by means of a bakeable, Teflon high-vacuum valve. Fusion of the electrolyte took place in the furnace. When all of the electrolyte was molten, it was necessary to expel liquid from the optical electrode compartment and refill from the main body of liquid several times in order to ensure complete mixing. Liquid cannot be poured out of the optical electrode compartment because the narrow space is filled with electrode grid and holds liquid like a sponge. Therefore, liquid was expelled by vapors of electrolyte boiled in the compartment with a hot-air gun.

Concentration units.—Molal concentrations (m) used here are calculated as moles of solute per kilogram of SbCl_3 .

Results and Discussion

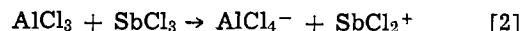
Solvent characterization.—Prior studies (6, 19-22) of the chemical and electrochemical properties of molten SbCl_3 that relate to the present investigation are summarized by the following, widely used model.⁶ SbCl_3 , a

molecular liquid, is assumed to be slightly ionized



where SbCl_2^+ is a Lewis acid and Cl^- is a base.

Aluminum chloride is a very strong Cl^- acceptor and reacts with SbCl_3



where AlCl_4^- in SbCl_3 is neither a Cl^- donor nor acceptor. Alkali metal chlorides MCl, on the other hand, separate into their constituent ions, M^+ and Cl^- , and are strong Cl^- donors. When MCl and AlCl_3 are both present, neutralization, the reverse of Eq. [1], occurs leaving M^+ and AlCl_4^- as spectator ions. We shall refer to a melt as neutral if $[\text{Cl}^-] = [\text{SbCl}_2^+]$, as basic if $[\text{Cl}^-] > [\text{SbCl}_2^+]$, and as acidic if $[\text{Cl}^-] < [\text{SbCl}_2^+]$.

Typical background cyclic voltammograms obtained in our research at a glassy carbon electrode at 100°C are shown in Fig. 2. The curve in Fig. 2a is for 0.038m CsCl ($\sim 0.1\text{M}$), a basic melt, while Fig. 2b is the background sweep for 0.077m AlCl_3 ($\sim 0.1\text{M}$), an acidic melt. The available potential range is quite close to that which Bauer and co-workers (7) reported for the SbCl_3 -KCl and SbCl_3 - AlCl_3 systems at 99°C with a Sb(III)/Sb, sat. KCl reference electrode.

The lower potential limit corresponds to the reduction of SbCl_3 to the metal



while the upper limit corresponds to oxidation to the pentachloride (6)



⁶ There is evidence (23, 24) that the structural entities responsible for Lewis acid-base chemistry in SbCl_3 melts are more complex than those postulated in this model. Nevertheless, the model is quite useful for purposes of correlating many important facts about the acid-base chemistry and at present there is no better model available.

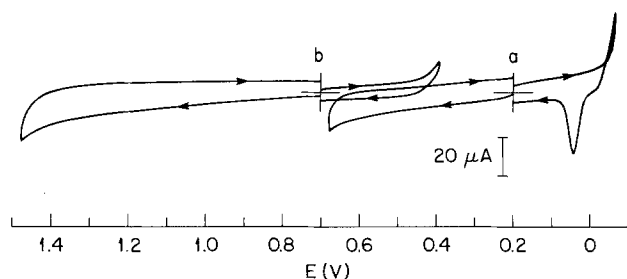


Fig. 2. Background cyclic voltammograms at a glassy carbon working electrode at 100°C. Sweep rate was 200 mV sec⁻¹. Electrode area was 0.071 cm². Melts were (a) 0.038m CsCl in SbCl₃ and (b) 0.077m AlCl₃ in SbCl₃.

Because of the role of Cl⁻ in these reactions, the solvent becomes more oxidizing and also more difficult to oxidize as the system progresses from basic to acidic. It is conventional to measure relative acidity in chloride melts in terms of $pCl = -\log [Cl^-]$. Thus, the potentials of the couples Sb(III)/Sb and Sb(V)/Sb(III) increase with increasing pCl .

In our work both Pt and glassy carbon working electrodes were used, but glassy carbon was found to be the most suitable. The available potential range with a Pt electrode was considerably smaller (~0.2V) because the reduction of SbCl₃ to antimony metal took place at a more positive potential than the theoretical value, probably because of Sb-Pt alloy formation (25) at the electrode.

The curves in Fig. 2 are smooth and featureless except for a peak that is caused by reoxidation of reduced antimony metal near the cathodic potential limit in the basic melt (Fig. 2a). Deposition of Sb on the glassy carbon surface took place at a small overpotential. This can be seen from the loop the curve makes and crosses itself; the stripping of Sb metal took place at a more anodic potential than that at which it was deposited.

Electrochemical oxidation of perylene.—Typical cyclic voltammograms of 1.60×10^{-3} m perylene in SbCl₃ are shown in Fig. 3. Here Fig. 3a was obtained in the basic 0.038m CsCl melt while Fig. 3b shows voltammograms of perylene in the acidic 0.079m AlCl₃ melt. All curves were obtained at 100°C at a glassy carbon working electrode. Sweep rates were 20, 50, 100, and 200 mV sec⁻¹, respectively.

There is one well-defined oxidation wave for each solution with an equally well-defined reduction wave on the return sweep. The separation between the two oxidation waves is 0.72V, which is close to that ob-

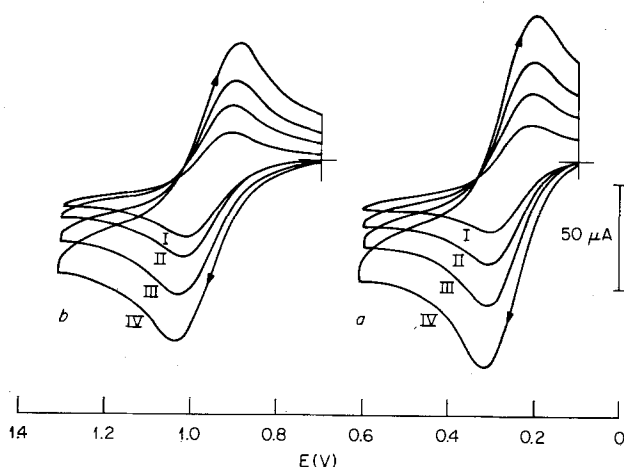
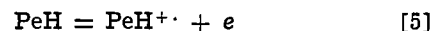


Fig. 3. Cyclic voltammograms at a glassy carbon working electrode in 1.60×10^{-3} m perylene at 100°C. Sweep rates were (I) 20 mV sec⁻¹, (II) 50 mV sec⁻¹, (III) 100 mV sec⁻¹, and (IV) 200 mV sec⁻¹. Electrode area was 0.071 cm². Solvents were (a) 0.038m CsCl in SbCl₃ and (b) 0.079m AlCl₃ in SbCl₃.

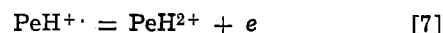
served by Bauer and co-workers (7) in SbCl₃-KCl and SbCl₃-AlCl₃ melts. As we shall demonstrate below with spectroscopic and additional electrochemical data, the neutral perylene molecule is stable in the basic melt and the oxidation wave is due to the formation of the perylene radical cation PeH^{•+} thus



In the acidic melt perylene is chemically oxidized to form a stable solution of PeH^{•+} in the following way (9)



For this system the oxidation wave represents the oxidation of PeH^{•+} to the perylene dication PeH²⁺ thus



In both the basic and acidic melts the perylene concentration was nearly equal but the two waves were not completely similar, as illustrated for the highest scan-rates in Fig. 3. Both the height and the slope of the oxidation wave in the acidic melt have somewhat lower values than in the basic solvent. By using Nicholson's (26, 27) method (with correction for the charging current) we found that within experimental error the cathodic to anodic current ratios were unity in the basic system whereas a tendency toward lower ratios with decreasing scan rates was found in the acidic melt (Table I). This might indicate that there is a slow follow-up reaction in the acidic melt which makes less PeH²⁺ available for reduction at slow scan rates.

The half-wave potentials, $E_{1/2}$, were calculated from the anodic half-peak potentials

$$E_{1/2} = E_{p/2} + 1.09 RT/nF \quad [8]$$

under the assumption that charge transfer is a one-electron reversible process. The results are listed in Table I.

Differential pulse polarograms obtained in the same melts are shown in Fig. 4. We found two well-defined, symmetric peaks that correspond to the formation of the radical cation, shown in Fig. 4a, and the dication, shown in Fig. 4b. A shoulder obtained at low anodic potential in Fig. 4b was probably due to the oxidation of a minor impurity.

The relation between the peak potential, E_p , for differential pulse polarography and the half-wave potential may be expressed as (28)

$$E_{1/2} = E_p + \Delta E/2 \quad [9]$$

where ΔE is the pulse amplitude. By using a small pulse amplitude, $\Delta E \leq 10$ mV, the correction term was reduced until it approached the uncertainty with which the peak potential could be read from the graph. The half-wave potentials derived from Eq. [9] are 0.26 and 0.97V for the oxidation to PeH^{•+} and PeH²⁺, respectively. The values correspond to those calculated from cyclic voltammetry (Table I).

The use of platinum working electrodes gave identical peak potentials, but side reactions appeared to take

Table I. Experimental and calculated parameters from cyclic voltammetry in SbCl₃ solvents at 100°C

| | ν (mV sec ⁻¹) | i_{pc}/i_{pa} * | E_p (V) | $E_{p/2}$ (V) | $E_{1/2}$ (V) |
|--|-------------------------------|-------------------|-------------------|-------------------|---------------|
| Oxidation to radical cation in basic 0.038m CsCl | 20 | 0.94 | 0.30 ₇ | 0.22 ₂ | 0.26 |
| | 50 | 0.99 | 0.31 ₀ | 0.22 ₄ | 0.26 |
| | 100 | 0.99 | 0.31 ₁ | 0.22 ₂ | 0.26 |
| | 200 | 1.00 | 0.31 ₇ | 0.22 ₇ | 0.26 |
| Oxidation to dication in acidic 0.079m AlCl ₃ | 20 | 0.58 | 1.01 ₈ | 0.92 ₅ | 0.96 |
| | 50 | 0.81 | 1.02 ₅ | 0.93 ₁ | 0.97 |
| | 100 | 0.90 | 1.03 ₃ | 0.93 ₃ | 0.97 |
| | 200 | 0.94 | 1.04 ₀ | 0.93 ₅ | 0.97 |

* i_{pc} and i_{pa} are cathodic and anodic peak currents, respectively.

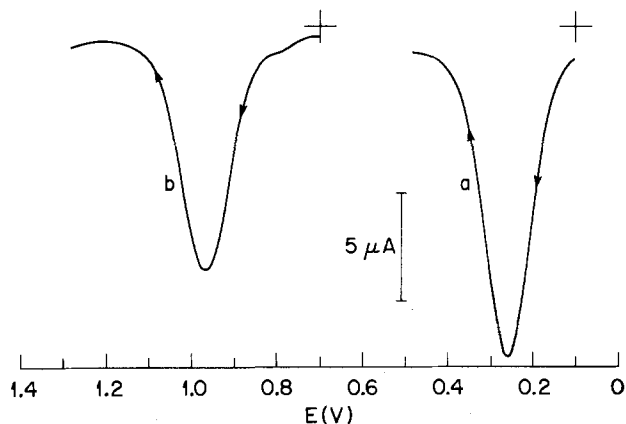


Fig. 4. Differential pulse polarogram at a glassy carbon working electrode in 1.60×10^{-3} M perylene at 100°C . Sweep rate was 2 mV sec^{-1} and pulse amplitude was 10 mV . Electrode area was 0.071 cm^2 . Solvents were (a) 0.038 M CsCl in SbCl_3 and (b) 0.079 M AlCl_3 in SbCl_3 .

place more readily on the metal surface and often resulted in additional oxidation waves. Also platinum electrodes were not as durable as those made of glassy carbon. We found it difficult to avoid a small amount of alloying by Sb that decreased the reproducibility of the electrodes upon reuse. This effect was probably due to surface defects that resulted from oxidation of Sb during cleaning.

Thin-layer coulometry.—An exhaustive electrolysis of the substrate in the optical cell may easily be carried out provided that mass transport due to convection between the electrolysis compartment and the bulk melt is eliminated or made very small. Figure 5a shows a coulogram obtained when $355 \mu\text{l}$ of SbCl_3 containing 7.75×10^{-4} M perylene and 0.38 M ($\sim 1 \text{ M}$) KCl was electrolyzed at a Pt screen electrode. The potential was switched from $+0.10$ to $+0.50 \text{ V}$ followed by switching back to $+0.10 \text{ V}$ after $\sim 1900 \text{ sec}$ elapsed time as shown in Fig. 5a, where the curve gives the net charge Q added to the system. When electrolysis started, there was a rapid increase in Q . Then, after about 1400 sec , Q leveled off as the current went to zero. This showed that all perylene in the electrolysis chamber had been oxidized to its radical cation. When the potential was switched back to $+0.1 \text{ V}$ the reverse reaction occurred

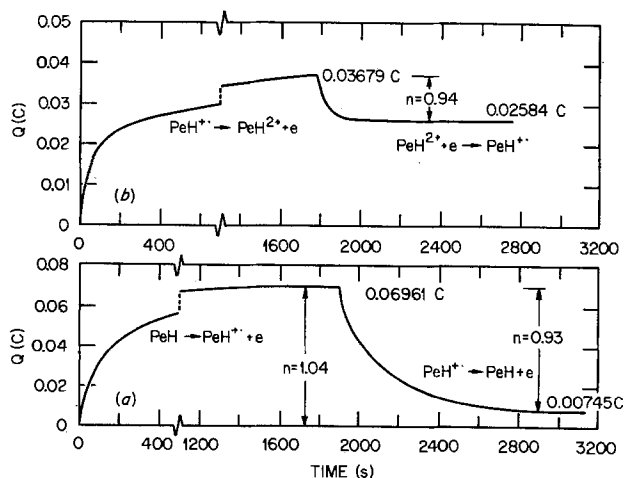


Fig. 5. (a) Thin layer coulogram of 7.75×10^{-4} M perylene in 0.38 M KCl at 100°C . Potential was switched from $+0.10$ to $+0.50 \text{ V}$ at start of curve and back to $+0.10 \text{ V}$ after $\sim 1900 \text{ sec}$. Electrolyte volume was $355 \mu\text{l}$. Electrode was Pt screen. (b) Thin-layer coulogram of 1.37×10^{-4} M perylene in 0.76 M AlCl_3 at 125°C . Potential was switched from $+0.69$ to $+1.15 \text{ V}$ at start of curve and back to $+0.69 \text{ V}$ after $\sim 1800 \text{ sec}$. Electrolyte volume was $380 \mu\text{l}$. Electrode was glassy carbon.

in which the radical cations were reduced to neutral molecules at the electrode. As the current flowed in the opposite direction, Q decreased and finally reached a steady, nonzero value. This value is due to both the diffusion of radical cations out of the cell during electrolysis and to their decomposition into nonreducible species. The formal number of electrons n for the oxidation step was 1.04 and for the reverse reduction was 0.93 .

The reason for substituting KCl for CsCl in the coulometric study was the following: a fairly substantial electrolyte concentration was necessary in order to keep the conductivity high enough to allow electrolysis to take place throughout the optical cell rather than just near the top of the cell. Our procedure was to begin with a basic melt and make various measurements including coulometry, then add a known excess of AlCl_3 and again make various measurements, this time on an acidic solution. When this was done with CsCl at the concentration level necessary for good conductivity, subsequent addition of excess AlCl_3 caused precipitation of solid CsAlCl_4 . This trouble was not encountered with KCl . We note that in going from CsCl solutions to KCl solutions the oxidation potential of perylene was shifted by only 30 mV , from 0.26 V in 0.038 M CsCl to 0.29 V in 0.38 M KCl at 100°C .

As previously discussed the second oxidation step to form the dication (Eq. [7]) appeared to be followed by a reaction on the electrode. Electrolysis of $380 \mu\text{l}$ of 1.37×10^{-4} M perylene in an acidic melt containing 0.76 M AlCl_3 gave no horizontal plateau within $\sim 1800 \text{ sec}$ that would have been indicative of an exhaustive electrolysis (Fig. 5b). (This electrolysis was done at a glassy carbon electrode at $+1.15 \text{ V}$ and 125°C .) On the contrary, the net charge added to the system at this time showed a much larger Q than the theoretical quantity for a one-electron oxidation according to Eq. [7].

When the potential was switched back to $+0.69 \text{ V}$ an exhaustive reduction of the generated dication took place and the charge Q corresponded to the formal number of 0.94 electrons for the reduction step.

The oxidation potential of the Sb(V)/Sb(III) couple is close to the applied potential in this acidic melt and only the presence of a considerable overpotential (5, 6) made it possible to extend the electrochemical window to the value shown in Fig. 2. Therefore, the excess charge consumed during the oxidation process was most probably due to an irreversible reaction involving Sb(V) .

Absorption spectra of perylene cations.—Figure 6 shows absorption spectra of perylene radical cations recorded during electrolysis of a solution containing 5.83×10^{-5} M perylene and 0.38 M KCl at a Pt screen electrode at 100°C . Spectrum I is the background prior to electrolysis and the other spectra display successive increases in radical cation concentration for successively longer electrolysis times up to 600 sec . The ϵ values for $\text{PeH}^{\cdot+}$ in the basic melt (Table II) were calculated from the known concentrations of the substrate based on the assumption of complete oxidation to PeH^+ after 600 sec . These radical cation spectra have five absorption bands in the range $500\text{--}900 \text{ nm}$. As shown in Table II the wavelengths and molar absorptivity of the band maxima agree well with prior measurements of the perylene radical cation spectrum in molten SbCl_3 (10, 29) and in other solvents (30, 31).

The spectra in Fig. 6 increase in intensity in a mathematically monotonous way at all wavelengths and thus give no evidence for the formation of more than one species. However, when electrolysis was carried beyond 600 sec , new bands appeared at wavelengths longer than 740 nm while the intense radical cation band at 546 nm decreased in intensity and its peak shifted toward longer wavelengths. The shift in existing bands and the appearance of new ones are probably due to the formation of arenium ions and condensation products as have been observed (34, 35) when other

Table II. Spectral characteristics of the perylene radical cation in various solvents

| Solvent | Band I | | Band II | | Band III | | Band IV | | Band V | |
|---|----------------|---|----------------|---|----------------|---|----------------|---|----------------|---|
| | λ (nm) | ϵ (Lmol ⁻¹ cm ⁻¹) | λ (nm) | ϵ (Lmol ⁻¹ cm ⁻¹) | λ (nm) | ϵ (Lmol ⁻¹ cm ⁻¹) | λ (nm) | ϵ (Lmol ⁻¹ cm ⁻¹) | λ (nm) | ϵ (Lmol ⁻¹ cm ⁻¹) |
| H ₂ SO ₄ , 25°C (30) | 538 | 55,600 | 650 | 5100 | 675 | 4800 | 707 | 5200 | 733 | 7200 |
| H ₂ SO ₄ , 25°C (31) | 540 | ~52,000 | | | | | | | 735 | ~6500 |
| Chlorobenzene-SbCl ₅ , 25°C (31) | 559 | ~50,000 | | | | | | | 745 | ~7500 |
| SbCl ₅ -O ₂ 80°C (29) | 554 | 52,500 | | | | | | | | |
| SbCl ₅ (presumably with AlCl ₃), 99°C (10) | 545 | | | | | | | | | |
| SbCl ₅ -KCl, 100°C (this work)* | 546 | 42,700 | 648 | 6100 | 672 | 5700 | 704 | 5600 | 732 | 7700 |
| SbCl ₅ -AlCl ₃ , 135°C (this work) | 544 | 41,400 | 646 | 6800 | 676 | 5400 | 708 | 5500 | 736 | 7100 |

* Electrochemically oxidized.

arenes were chemically oxidized in SbCl₅-AlCl₃ melts. However, in the case of PeH⁺ these follow-up reactions were much slower than those previously reported, a result that probably depends in part on the low concentration of PeH⁺ in our experiments as well as the relatively high stability of PeH⁺.

According to prior investigations (6, 7, 9) perylene is chemically oxidized in acidic melts by the reaction given in Eq. [6]. Accordingly, when we prepared a melt containing 6.38×10^{-5} m perylene and 0.77m AlCl₃ in SbCl₅, the absorption spectrum prior to electrolysis was that of PeH⁺ as shown in Fig. 7a. The molar absorptivities of the band maxima of this chemically generated PeH⁺ (Table II) are quite close to those we obtained for electrolytically generated PeH⁺. This fact provides independent evidence that electrolysis after 600 sec was virtually complete.

When the acidic melt was electrochemically oxidized until absorption due to PeH⁺ was gone, we obtained the spectrum shown in Fig. 7b. This spectrum was recorded after an electrolysis time of 600 sec at an anodic potential of +1.30V. Similar results were obtained at a glassy carbon optical electrode, and repeated oxidation-reduction-oxidation of the perylene ions showed no significant change in absorption values for PeH²⁺ after its formation was completed. Upon monitoring the spectrum of the electrogenerated dication over a period of 900 sec (open cell circuit), we found no significant decay. These results from the spectroscopic and coulometric experiments in the acidic melt do not appear to be fully consistent with the cyclic voltammetric results. This discrepancy might, however, be due to the different concentrations of perylene in these experiments, which differ by about one order of

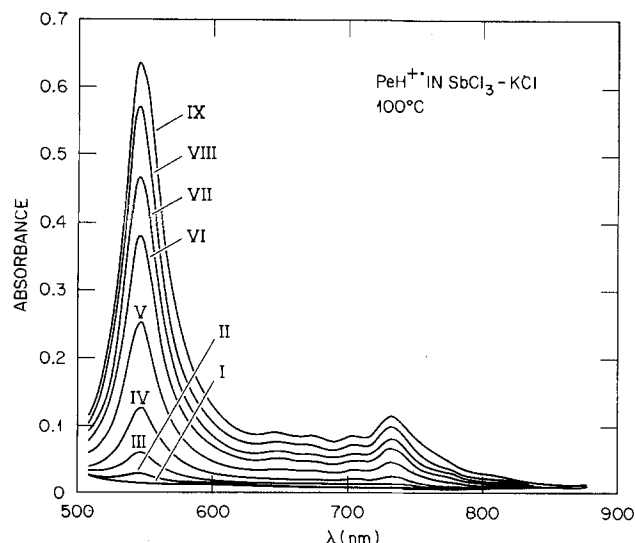


Fig. 6. Spectra of perylene radical cation generated at +0.55V in 5.83×10^{-5} m perylene in 0.38m KCl at 100°C. Electrode was Pt screen in 1.0 mm optical cell. Spectra were recorded during electrolysis. Electrolysis time (I) background (molecular perylene in the solvent), (II) 10 sec, (III) 20 sec, (IV) 50 sec, (V) 100 sec, (VI) 150 sec, (VII) 200 sec, (VIII) 300 sec, and (IX) 600 sec.

Table III. Spectral characteristics of the perylene dication in various solvents

| Solvent | Band I | | Band II | |
|--|----------------|---|----------------|---|
| | λ (nm) | ϵ (Lmol ⁻¹ cm ⁻¹) | λ (nm) | ϵ (Lmol ⁻¹ cm ⁻¹) |
| Oleum (12) | | | 517 | |
| SbF ₅ -SO ₂ ClF (or FSO ₃ H) (11) | 315 | ~20,000 | 512 | ~50,000 |
| SbCl ₅ -AlCl ₃ , 135°C (this work)* | | | 533 | 36,500 |

* Electrochemically oxidized.

magnitude. An optimal substrate concentration for cyclic voltammetry is too high for spectroscopic work in a 1 mm optical cell because of the very high absorptivity of the perylene cation.

The molar absorptivity value given in Table III is calculated on the basis of a total conversion to PeH²⁺ in the electrode compartment.

The spectrum of the species shown in Fig. 7b is quite different from that which Bauer and co-workers (10) reported for the dication formed by electrolysis of PeH⁺ in SbCl₅-AlCl₃, but it is quite similar to that previously reported for PeH²⁺ in superacid media (11, 12) where its identity was established by proton-NMR spectroscopy (11). We believe that Bauer and co-workers did prepare PeH²⁺ because the $E_{1/2}$ value they found agrees with ours, but this dication must have subsequently reacted prior to the time the spectrum was measured. It is interesting that the spectrum they reported as being that of PeH²⁺ is, in fact, rather like that of the perylenium ion, PeH₂⁺ (32, 33), which,

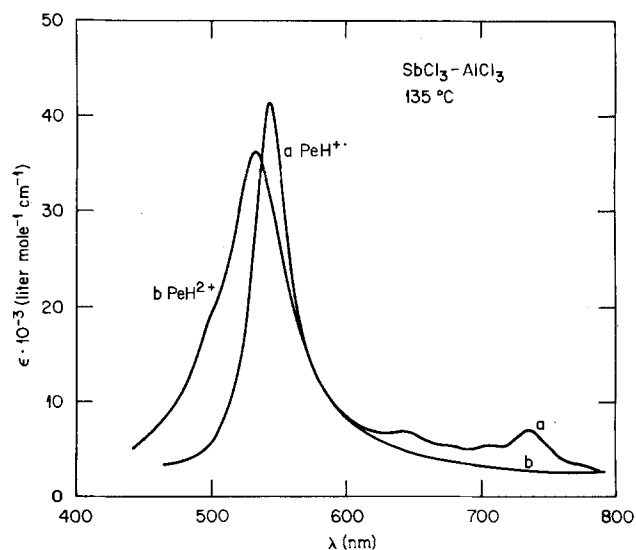


Fig. 7. Spectra of 6.38×10^{-5} m perylene in 0.77m AlCl₃ at 135°C. (a) Spectrum of perylene radical cation due to oxidation by the solvent. (b) Spectrum of perylene dication generated at +1.30V. Electrode was Pt screen in a 1.0 mm optical cell.

as we noted above, is also a likely product of the downstream reactions of PeH^+ .

Acknowledgment

This research was sponsored by the Division of Chemical Sciences, Office of Basic Energy Sciences, U.S. Department of Energy under Contract W-7405-eng-26 with the Union Carbide Corporation. We wish to thank L. O. Gilpatrick with help in purifying SbCl_3 . M. Sørli is grateful for financial assistance from Norges Teknisk-Naturvitenskapelige Forskningsråd and for a travel grant from Norges Almenvitenskapelige Forskningsråd.

Manuscript submitted March 14, 1980; revised manuscript received Sept. 10, 1980.

Any discussion of this paper will appear in a Discussion Section to be published in the December 1981 JOURNAL. All discussions for the December 1981 Discussion Section should be submitted by Aug. 1, 1981.

Publication costs of this article were assisted by Oak Ridge National Laboratory.

REFERENCES

- H.-H. Perkampus and E. Schönberger, *Z. Naturforsch. Teil B*, **31**, 475 (1976).
- G. B. Porter and E. C. Baughan, *J. Chem. Soc.*, 744 (1958).
- H. Oppermann, *Z. Anorg. Allg. Chem.*, **356**, 1 (1967).
- L. A. Nisel'son, V. V. Mogucheva, and T. D. Sokolova, *Russian J. Inorg. Chem.*, **10**, 320 (1965).
- D. Bauer, J.-P. Beck, and P. Texier, *C. R. Hebd. Seances Acad. Sci., Ser. C*, **266**, 1335 (1968).
- P. Texier, *Bull. Soc. Chim., Fr.*, 4315, 4716 (1968).
- D. Bauer, J.-P. Beck, and P. Texier, *Collect. Czech. Chem. Commun.*, **36**, 940 (1971).
- E. C. Baughan, T. P. Jones, and L. G. Stoodley, *Proc. Chem. Soc.*, 274 (1963).
- A. C. Buchanan, III, R. Livingston, A. S. Dworkin, and G. P. Smith, *J. Phys. Chem.*, **84**, 423 (1980).
- D. Bauer, C. Colin, and M. Caude, *Bull. Soc. Chim. Fr.*, 942 (1973).
- D. M. Brouwer and J. A. van Doorn, *Rec. Trav. Chim. Pays-Bas*, **91**, 1110 (1972).
- A. N. Sidorov, *Russian J. Phys. Chem.*, **48**, 926 (1974).
- N. J. Bjerrum, C. R. Boston, and G. P. Smith, *Inorg. Chem.*, **6**, 1162 (1967).
- L. N. Klatt, *J. Chromatogr. Sci.*, **17**, 225 (1979).
- V. E. Norvell and G. Mamantov, *Anal. Chem.*, **49**, 1470 (1977).
- V. G. Zyrjanov and E. S. Petrov, *Izv. Sib. Otd. Akad. Nauk SSSR, Ser. Khim. Nauk*, 31 (1972).
- V. G. Zyrjanov and E. S. Petrov, *ibid.*, 27 (1972).
- V. G. Zyrjanov and E. S. Petrov, *ibid.*, 119 (1976).
- G. Jander and K.-H. Swart, *Z. Anorg. Allg. Chem.*, **299**, 252 (1959); **301**, 54, 80 (1959).
- A. G. Davies and E. C. Baughan, *J. Chem. Soc.*, 1711 (1961).
- P. Texier and J. Desbarres, *C. R. Hebd. Seances Acad. Sci., Ser. C*, **266**, 503 (1968).
- D. Bauer and P. Texier, *ibid.*, **266**, 602 (1968).
- E. Johnson, A. H. Narten, W. E. Thiessen, and R. Triolo, *Faraday Discuss. Chem. Soc.*, **n66**, 287 (1978).
- R. Huglen, G. Mamantov, G. M. Begun, and G. P. Smith, *J. Raman Spec.*, **9**, 188 (1980).
- M. Hansen, "Constitution of Binary Alloys," 2nd ed., p. 1138, McGraw-Hill Book Co., New York (1958).
- R. S. Nicholson, *Anal. Chem.*, **38**, 1406 (1966).
- R. S. Nicholson and I. Shain, *ibid.*, **36**, 706 (1964).
- E. P. Parry and R. A. Osteryoung, *ibid.*, **37**, 1634 (1965).
- P. V. Johnson, *J. Chem. Soc. (A)*, 2856 (1971).
- K. Kimura, T. Yamazaki, and S. Katsumata, *J. Phys. Chem.*, **75**, 1768 (1971).
- H. Kuroda, T. Sakurai, and H. Akamatu, *Bull. Chem. Soc. Jpn.*, **39**, 1893 (1966).
- G. Dallinga, E. L. Mackor, and A. A. Verriijn Stuart, *Mol. Phys.*, **1**, 123 (1958).
- W. Ij. Aalbersberg, G. J. Hoijsink, E. L. Mackor, and W. P. Weijland, *J. Chem. Soc.*, 3049 (1959).
- A. C. Buchanan, III, A. S. Dworkin, J. Brynestad, L. O. Gilpatrick, M. L. Poutsma, and G. P. Smith, *J. Am. Chem. Soc.*, **101**, 5430 (1979).
- A. C. Buchanan, III, A. S. Dworkin, and G. P. Smith, *ibid.*, **102**, 5262 (1980).

Conductance Studies in Amide-Water Mixtures

V. Lithium and Cesium Bromides in Formamide-Water Mixtures at 25°C

Lal Bahadur and M. V. Ramanamurti

Department of Chemistry, Banaras Hindu University, Varanasi 221005, India

ABSTRACT

Conductance data for lithium and cesium bromides in formamide-water mixtures ($88 \leq D \leq 111$; $0.89 \leq \eta \leq 3.29$ cp) are reported at 25°C in the concentration range 0.01-0.10N. Solvent properties like density, viscosity, and dielectric constant are also reported at the same temperature. The conductance data have been analyzed by the Fuoss (1978) equation. Viscosities of the solvent mixtures show a slight negative deviation from ideal behavior without showing any maximum or minimum in the solvent composition-viscosity curve, indicating overall slightly less structured solvent mixtures than that expected from ideal behavior. The limiting equivalent conductance for each of the salts decreases with the increase of formamide content in the solvent mixtures over the whole range of the solvent composition, but the variation is not such that it can give a constant value for the Walden product. In any given solvent mixture $\Lambda_0(\text{CsBr}) > \Lambda_0(\text{LiBr})$. Both electrolytes were found to be practically completely ionized ($K_A < 4.0$) in all solvent mixtures studied. Although, a wide range of values of the distance parameter R was found to be acceptable for both the salts in each solvent mixture for fit to $\sigma \leq 1.1 \sigma_{\text{min}}$, best values ($\sigma = \sigma_{\text{min}}$) of R derived for CsBr were found to be almost constant ($2.18 \pm 0.19\text{\AA}$) in all solvent mixtures while no systematic trend was observed for LiBr.

In the first paper (1) of this series of investigations, the conductance data for Et_4NBr and Bu_4NBr in formamide-water mixtures were reported. In this communication little attention was paid to the variation of Walden product with solvent composition because Walden product was almost constant up to 50 mole percent (m/o) formamide in a solvent mixture. But later studies (2-4) in aqueous binary mixtures of other amides (DMF and DMA) showed quite systematic variation of the Walden product with a maximum at a solvent composition around 10 m/o amide for simple (2) as well as tetraalkylammonium salts (3, 4). Keeping these observations in view, previous results in formamide-water mixtures (1) were re-considered and it was interesting to note that if $\Lambda_0\eta$ values for Et_4NBr and Bu_4NBr in pure water (5) [$\Lambda_0\eta$ (Et_4NBr) = 0.986; $\Lambda_0\eta$ (Bu_4NBr) = 0.868] and in pure formamide (6) [$\Lambda_0\eta$ (Et_4NBr) = 0.931; $\Lambda_0\eta$ (Bu_4NBr) = 0.790] are incorporated in our results, a maximum in the Walden product becomes obvious at solvent composition around 70 m/o formamide for both the salts (Fig. 1). Since the existence of a maximum in the Walden product for tetraalkylammonium salts in DMA-water mixtures (3, 4) could successfully be attributed to hydrophobic dehydration of tetraalkylammonium ions due to presence of cosolvent (DMA), Fig. 1 clearly indicates that hydrophobic dehydration of Et_4N^+ and Bu_4N^+ by cosolvent (formamide) becomes effective only in the solvent composition region sufficiently rich in formamide, not in the water-rich region as was found in the case of disubstituted amide (DMA)-water mixtures (3, 4). Somsen and co-workers (7-9) also arrived at a similar conclusion in the case of formamide-water mixtures on the basis of their studies on enthalpies of tetraalkylammonium bromides in various amide-water mixtures. They observed that the presence of formamide reduces the ability of hydrophobic ions to promote the hydrogen-bonded structure in aqueous formamide containing more than 30 m/o formamide.

In view of these observations it was of interest to study a few simple salts also in formamide-water mixtures with particular attention to the trend of the

Key words: lithium bromide, cesium bromide, formamide-water mixture, conductance, Walden product.

Walden product with change in solvent composition. The present paper deals with the conductance data for LiBr and CsBr in formamide-water mixtures at 25°C along with the properties (density, viscosity, and dielectric constant) of the solvent mixtures.

Experimental

Water, KCl, and formamide used in present work were purified as described earlier (1). LiBr (E. Merck) and CsBr (L. R., Hopkin and Williams, London) were recrystallized from conductivity water and dried in a vacuum desiccator.

All experimental techniques and procedures for the measurements of viscosities and densities of the solvent mixtures and conductance of electrolyte solutions have been described earlier in detail (2).

Results and Discussion

Densities, viscosities, and dielectric constants of the solvent mixtures (formamide-water) at 25°C are re-

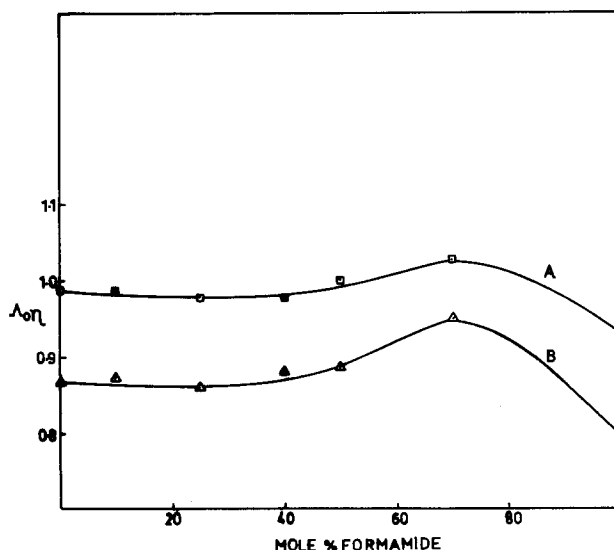


Fig. 1. Variation of Walden product with composition of the solvent mixtures. A, Et_4NBr ; B, Bu_4NBr .

Table I. Properties of the solvent mixtures (F-H₂O) at 25°C

| F (m/o) | D* | ρ (g/ml) | $\eta \times 10^2$ (cp) |
|---------|--------|---------------|-------------------------|
| 0 | 78.39 | 0.99707 | 0.8903 |
| 10 | 88.03 | 1.0276 | 0.9944 |
| 25 | 98.17 | 1.0597 | 1.1887 |
| 40 | 105.28 | 1.0808 | 1.4280 |
| 50 | 108.40 | 1.0919 | 1.6095 |
| 70 | 111.18 | 1.1108 | 2.1064 |
| 100 | 109.58 | 1.1292 | 3.2904 |

* Values taken from the literature [Ref. (10)].

ported in Table I. Dielectric constant data incorporated in this table have been taken from the literature (10). Equivalent conductance, Λ , of electrolyte solutions is given in Table II as a function of concentration, c , for both the electrolytes in solvent mixtures of different compositions.

For a given set of conductance data (c_j , Λ_j ; $j = 1, n$), the three adjustable parameters Λ_0 , K_A , and R were derived by solving the following three equations by successive approximations

$$\Lambda = \nu[\Lambda_0(1 + RX) + EL] \quad [1]$$

$$\nu = 1 - K_A c \nu^2 f^2 \quad [2]$$

$$\ln f = -\beta\kappa/2(1 + \kappa R) \quad [3]$$

Here R is cosphere diameter (11) and RX and EL are the relaxation and hydrodynamic terms, respectively. Other terms have their usual meanings. Expressions used for RX and EL were the same as those derived by Fuoss (12). Computational methods adopted here for the analysis of the conductance data were the same as those suggested by Fuoss and co-workers (11), and computer programs of Fuoss (1975) equations were used after the relevant portions of these programs corresponding to the expressions for RX and EL terms were modified according to new expressions (12) used for these two terms. Detailed description of the method of analysis has been given in our previous communication (3). Various parameters thus derived from the conductance data are summarized in Table III. Here it should be noted that Eq. [1] and [2] are the same as the Fuoss (1975) equation (11) except for the use of new expressions for RX and EL derived by Fuoss him-

self in his modified version (12) of the conductance-concentration relation. The introduction of the term α , as suggested by Fuoss (12), and consequently the replacement of ν by $[1 - \alpha(1 - \nu)]$ in Eq. [1] and K_A by $K_R/(1 - \alpha)$ in Eq. [2] seem to be redundant. Hence, these were avoided in our previous publications (3, 4) also. The reason for this is as follows: Fuoss in his recent publication (12) modified his previous equation (11) for the conductance-concentration relation in two ways. His first modification was the change in certain boundary conditions in the derivation of the expressions for the relaxation and hydrodynamic terms. This change resulted in different values of the coefficients of interpolation formulas for RX and EL as compared to the previous one (11). This change has been incorporated by us while using the equations for the analysis of the conductance data of present and previous studies (3, 4) also. His second modification was regarding ion pairs. According to this, all the ions for which center-to-center distance r is in the range $a \leq r \leq R$ are designated as diffusion pairs, with concentration $c(1 - \nu)$. All these ion pairs were considered as nonconducting in Fuoss' previous treatment (11), but in his recent publication (12) these diffusion pairs are divided into two subsets, dipolar pairs and virtual dipoles. It has been argued that only a fraction α of diffusion pairs [i.e., $c\alpha(1 - \nu)$] diffuse to contact to form nonconducting dipolar pairs (contact pairs, $r = a$), the rest of the diffusion pairs (virtual dipoles) taking part in conductance in addition to free ions. Thus, a fraction $[1 - \alpha(1 - \nu)]$ of the total ionic concentration takes part in conductance instead of ν as in previous treatment (11). The introduction of this new term α , therefore, resulted in the replacement of ν by $[1 - \alpha(1 - \nu)]$ in Eq. [1] and K_A by $K_R/(1 - \alpha)$ in Eq. [2]. But in our opinion, all of the ion pairs, if they are at all considered as paired, should be taken as nonconducting, otherwise if they are conducting there is no reason why they should be accounted as paired ions so far as conductance property is concerned. In addition to this, the distance parameter R introduced in the Fuoss (1975) equation is by definition "the average radius of the spheres containing partner ion for paired ions" and these ions are excluded from the population of free ions taking part in conductance. Since, this R value is derived from the experimentally observed

Table II. Conductance data in formamide-water system at 25°C

| Lithium bromide | | | | | | | | | |
|--|---|--|---|--|---|--|---|--|---|
| 10 ⁴ c/mole dm ⁻³ | Λ /Scm ² mole ⁻¹ | 10 ⁴ c/mole dm ⁻³ | Λ /Scm ² mole ⁻¹ | 10 ⁴ c/mole dm ⁻³ | Λ /Scm ² mole ⁻¹ | 10 ⁴ c/mole dm ⁻³ | Λ /Scm ² mole ⁻¹ | 10 ⁴ c/mole dm ⁻³ | Λ /Scm ² mole ⁻¹ |
| 10 m/oF | | 25 m/oF | | 40 m/oF | | 50 m/oF | | 70 m/oF | |
| 971.870 | 68.10 | 943.100 | 59.59 | 941.352 | 49.48 | 958.054 | 42.50 | 967.551 | 32.37 |
| 927.700 | 68.36 | 893.462 | 59.86 | 891.801 | 49.59 | 907.622 | 42.65 | 916.621 | 32.43 |
| 878.870 | 68.72 | 838.311 | 60.25 | 836.753 | 49.70 | 851.603 | 42.83 | 860.042 | 32.62 |
| 824.620 | 69.21 | 776.673 | 60.64 | 775.224 | 49.83 | 788.981 | 43.02 | 796.804 | 32.75 |
| 763.980 | 69.96 | 707.324 | 61.15 | 706.010 | 50.08 | 718.532 | 43.28 | 725.663 | 33.02 |
| 695.770 | 70.69 | 628.736 | 61.70 | 627.561 | 50.49 | 638.704 | 43.49 | 645.030 | 33.30 |
| 618.460 | 71.82 | 538.917 | 62.47 | 537.915 | 50.80 | 547.451 | 43.88 | 552.881 | 33.67 |
| 533.410 | 73.01 | 435.272 | 63.39 | 434.460 | 51.31 | 442.172 | 44.36 | 446.562 | 34.10 |
| 428.160 | 74.80 | 377.241 | 63.95 | 376.543 | 51.72 | 383.223 | 44.63 | 387.025 | 34.39 |
| 371.080 | 75.98 | 314.360 | 64.70 | 313.782 | 52.12 | 319.351 | 45.00 | 322.514 | 34.74 |
| 309.230 | 77.30 | 246.023 | 65.53 | 245.562 | 52.77 | 249.926 | 45.45 | 252.406 | 35.15 |
| 242.010 | 79.06 | 171.471 | 66.67 | 171.151 | 53.50 | 174.192 | 46.02 | 175.917 | 35.72 |
| 168.670 | 81.16 | — | — | — | — | — | — | — | — |
| Cesium bromide | | | | | | | | | |
| 10 ⁴ c/mole dm ⁻³ | Λ /Scm ² mole ⁻¹ | 10 ⁴ c/mole dm ⁻³ | Λ /Scm ² mole ⁻¹ | 10 ⁴ c/mole dm ⁻³ | Λ /Scm ² mole ⁻¹ | 10 ⁴ c/mole dm ⁻³ | Λ /Scm ² mole ⁻¹ | 10 ⁴ c/mole dm ⁻³ | Λ /Scm ² mole ⁻¹ |
| 10 m/oF | | 25 m/oF | | 40 m/oF | | 50 m/oF | | 70 m/oF | |
| 991.051 | 115.95 | 963.851 | 98.17 | 964.550 | 81.20 | 963.401 | 69.85 | 961.251 | 52.14 |
| 938.882 | 116.42 | 913.123 | 98.30 | 913.780 | 81.39 | 912.693 | 70.05 | 911.602 | 52.37 |
| 880.933 | 117.10 | 858.834 | 98.56 | 857.371 | 81.68 | 856.351 | 70.27 | 855.331 | 52.59 |
| 816.153 | 117.72 | 793.756 | 98.88 | 794.332 | 82.01 | 793.385 | 70.51 | 792.443 | 52.84 |
| 743.285 | 118.52 | 722.881 | 99.20 | 723.411 | 82.41 | 722.552 | 70.95 | 721.680 | 53.17 |
| 660.702 | 119.67 | 642.560 | 99.81 | 643.033 | 82.97 | 642.231 | 71.38 | 641.501 | 53.53 |
| 566.316 | 121.10 | 550.772 | 100.51 | 551.171 | 83.64 | 550.510 | 72.00 | 549.852 | 54.03 |
| 457.407 | 123.08 | 444.852 | 101.73 | 445.172 | 84.60 | 444.643 | 72.82 | 444.113 | 54.67 |
| 396.421 | 124.58 | 385.543 | 102.46 | 385.820 | 85.21 | 385.352 | 73.63 | 384.901 | 55.10 |
| 330.352 | 125.95 | 321.284 | 103.42 | 321.512 | 85.97 | 321.131 | 74.04 | 320.750 | 55.58 |
| 258.530 | 127.80 | 251.431 | 104.61 | 251.621 | 86.86 | 251.326 | 74.85 | 251.025 | 56.13 |
| 180.192 | 130.20 | 175.246 | 106.15 | 175.374 | 88.05 | 175.163 | 75.94 | 174.953 | 56.90 |

Table III. Conductance parameters

| Formamide (m/o) | D | Λ_0 | K_A | K_A^* (range) | R | R^* (range) | $\beta/2$ | σ (%) | Λ_{07} |
|-----------------|--------|-------------------|-------|-----------------|------|---------------|-----------|--------------|----------------|
| Lithium bromide | | | | | | | | | |
| 0 | 78.39 | 116.88 | — | — | — | — | — | — | 1.041 |
| 10 | 88.03 | 91.41 \pm 0.14 | 2.60 | 1.90-3.18 | 2.36 | 1.18-4.25 | 3.18 | 0.170 | 0.909 |
| 25 | 98.17 | 73.01 \pm 0.06 | 1.35 | 1.30-1.41 | 6.35 | 5.83-7.00 | 2.85 | 0.025 | 0.868 |
| 40 | 105.28 | 57.99 \pm 0.04 | 0.00 | 0.00-0.22 | 3.15 | 3.15-4.22 | 2.66 | 0.119 | 0.828 |
| 50 | 108.40 | 49.86 \pm 0.05 | 0.50 | 0.45-0.57 | 6.73 | 6.15-7.64 | 2.59 | 0.038 | 0.802 |
| 70 | 111.18 | 38.95 \pm 0.03 | 0.00 | 0.00-0.82 | 1.46 | 1.46-5.40 | 2.52 | 0.067 | 0.820 |
| 100 | 109.58 | 25.90 | — | — | — | — | — | — | 0.852 |
| Cesium bromide | | | | | | | | | |
| 0 | 78.39 | 155.37 | — | — | — | — | — | — | 1.383 |
| 10 | 88.03 | 141.69 \pm 0.16 | 1.20 | 0.74-1.64 | 1.99 | 1.10-3.45 | 3.18 | 0.128 | 1.409 |
| 25 | 98.17 | 113.24 \pm 0.22 | 0.30 | 0.00-0.74 | 2.20 | 1.33-4.45 | 2.85 | 0.225 | 1.346 |
| 40 | 105.28 | 93.96 \pm 0.08 | 0.40 | 0.08-0.70 | 2.15 | 1.12-3.77 | 2.66 | 0.100 | 1.342 |
| 50 | 108.40 | 81.07 \pm 0.10 | 0.50 | 0.00-0.86 | 2.37 | 0.70-4.72 | 2.59 | 0.145 | 1.305 |
| 70 | 111.18 | 60.80 \pm 0.02 | 0.50 | 0.26-0.74 | 2.08 | 1.20-3.37 | 2.52 | 0.031 | 1.281 |
| 100 | 109.58 | 30.60 | — | — | — | — | — | — | 1.007 |

* X (range) ($X = K_A$ or R) corresponds to $\sigma \leq 1.1 \sigma_{\min.}$ while others are best-fit values corresponding to $\sigma = \sigma_{\min.}$

values of conductance, it is obvious that this R includes only nonconducting ion pairs. Due to these reservations, the changes due to introduction of the term α have not been incorporated in Eq. [1] and [2] in the present work as well as in previous publications (3, 4).

The viscosity variation with composition of the solvent mixtures is represented in Fig. 2. As is clear from the figure, viscosity of this binary mixture increases monotonically with the increase of formamide content in the solvent mixture. No minimum or maximum was observed in the viscosity indicating total absence of structural enhancement of either of the components by the presence of the other in this binary mixture. However, the viscosity curve is slightly concave upward indicating a small negative deviation from the ideal behavior, contrary to dialkylated amide-water mixtures which show positive deviations (2-4). A similar difference between formamide-water and disubstituted amide-water mixtures has been observed in respect to other properties such as molar excess heat capacities (13); dielectric constants (10), and reorientational correlation times of the constituent molecules (14) of these binary mixtures. This negative deviation in viscosity of formamide-water mixtures shows the structure-breaking effect, although to a very small extent, of either of the components on the other one of

the solvent mixtures. Rohdewal and Moldner (10) proposed loose association between formamide and water molecules because according to their conclusion there is an association between amide and water molecules in general and the sign of the deviation depends on the strength of the hydrogen bond and ordering of the solvent dipoles. Rupley (15) has suggested that formamide molecules disrupt the structure of water, which was corroborated subsequently by Hinton and Ladner (16) on the basis of NMR shifts of water protons with increasing amount of formamide. Visser and Somsen (13) observed negative molar excess heat capacities for different solvent composition of this binary mixture, which indicated the structure-breaking effect of formamide on water.

In the light of these conclusions drawn by previous workers, coupled with the consideration of the present findings, it can be concluded that formamide molecules have a distinct influence on breaking the structure of water primarily, followed by the individual water molecules getting loosely associated with formamide molecules through hydrogen bonding, resulting in an overall slightly less structured solvent than that expected from an ideal behavior. Hydrogen bond energies in the case of

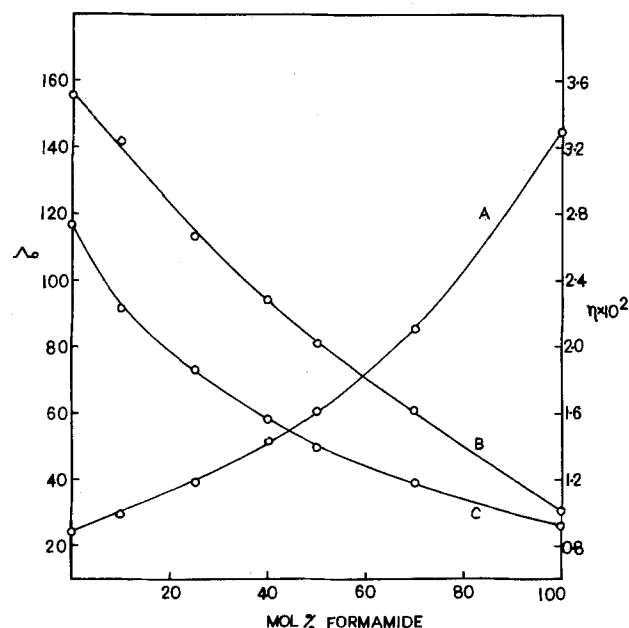
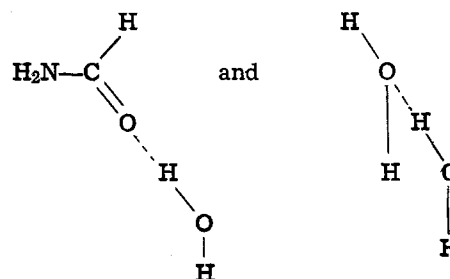


Fig. 2. Variation of viscosity of the solvent, η , and limiting equivalent conductance, Λ_0 , with composition of the solvent mixtures. A— η ; B— Λ_0 (CsBr); C— Λ_0 (LiBr).



are almost the same (17). This may be one of the reasons for higher compatibility of the two solvents.

The variation of limiting equivalent conductance, Λ_0 , with solvent composition for each of the salts studied is shown in Fig. 2. Values of Λ_0 for these salts in pure water (18) and in pure formamide (19) were taken from literature. As can be seen from Fig. 2, the limiting equivalent conductance decreases with the corresponding increase in the viscosity of the solvent mixture, but variation is not such that it can give a constant value of the Walden product, $\Lambda_0\eta$. In any given solvent mixture Λ_0 (CsBr) $>$ Λ_0 (LiBr), which can be attributed to the structure-forming effect of cations (Br^- being common anion). The predominant structure-breaking effect of Cs^+ is well known and this leads to greater mobility of Cs^+ . Correspondingly Li^+ , having a high surface charge density, is highly structure forming, thus resulting in less mobility.

For both the alkali bromides, the Walden product does not show constancy with the change in solvent composition (Fig. 3) showing appreciable ion-solvent interactions. The curve showing the variation of $\Lambda_{\infty}\eta$ with solvent composition is slightly concave downward for CsBr while it is concave upward (passing through a minimum) for LiBr. This difference is expected because Li^+ is a strong structure former while Cs^+ is a strong structure breaker. The trend in $\Lambda_{\infty}\eta$ with the increase of formamide content in the solvent mixture shows that ions are preferentially solvated with formamide resulting in smaller ionic mobility than that expected due to change in the solvent viscosity. In the water-rich solvent composition region this preferential solvation is more pronounced in the case of LiBr, resulting in a more sudden decrease in Walden product, than in the case of CsBr for which $\Lambda_{\infty}\eta$ decreases slightly. This is possibly because of the stronger structure-forming effect of Li^+ than Cs^+ . Now if we look into the trend in the formamide-rich region, the variations of $\Lambda_{\infty}\eta$ for these two salts are opposite to each other. $\Lambda_{\infty}\eta$ decreases in case of CsBr whereas it slightly increases for LiBr. This indicates that preferential solvation of CsBr with formamide is effective in the same direction with the increase of formamide content in solvent mixture right up to pure formamide and the sudden decrease in the highly formamide-rich region is possibly due to formamide molecules being larger than those of water. The ion solvated with formamide molecules will result in a larger mobile entity giving less mobility than the same ion solvated by even the same number of water molecules. In the case of LiBr the slight increase in $\Lambda_{\infty}\eta$ in the formamide-rich region (beyond 50 m/o formamide) after passing through a minimum clearly indicates that the mode of solvation in this case is different from that in the case of CsBr. In the light of Hemmes proposition (20) the minimum in $\Lambda_{\infty}\eta$ for LiBr indicates the existence of more than one type of solvated complex. However, it seems difficult to decide the actual modes of solvation in water-rich and formamide-rich solvent regions responsible for the reverse trend observed in $\Lambda_{\infty}\eta$ in these two regions. In addition to this, the free volume available between solvent molecules due to discrete structure of the solvent as proposed by Aprano and Fuoss (21) may be effective in the case of Li^+ because of its smaller size in comparison to the solvent

molecules and may be an additional factor for the non-constancy of $\Lambda_{\infty}\eta$.

While going through the literature, it was found that various reasons have been proposed from time to time to explain the variation of Walden product with the composition of mixed polar solvents. Attempts have been made by many workers to give the mathematical treatment to these physical reasons for the nonconstancy of Walden product, but no one has succeeded in establishing a single satisfactory relation between Walden product and solvent properties of mixed solvents which could explain quantitatively the observation made for the various types of systems. Zwanzig in his recent treatment (22) gave a relatively more accurate expression; however, this expression also could account only for the variation of Walden product with solvent composition, but fails to account for maximum and/or minimum in Walden product. The latest attempt claimed to be an improved version of Zwanzig's treatment (22) has been made by Hubbard and Onsager (23), but this treatment was still within the framework of continuum mechanics which has already been questioned (21). Furthermore, the Hubbard-Onsager equation was tested by Evans *et al.* (24) and some inconsistencies and marked deviations from experimental data have been shown, particularly for smaller ions for which theory was expected to be more accurate. Keeping all these in view, it can be concluded that specific ion-solvent interactions, which are rather difficult to account for theoretically, play an important role resulting in the variation of Walden product, and without giving due consideration to this effect it seems difficult to derive a theoretical expression to explain the observations successfully.

It can be seen from Table III that in all cases the association constants are almost negligible ($K_A < 4.0$) which shows that both salts are completely ionized practically in all the solvent mixtures studied. This is according to expectation because of the high dielectric constants of the solvent mixtures. It is general practice that if $K_A < 10$, numerical values of K_A are not taken seriously and electrolyte is considered to be completely ionized practically. However, recently Aprano *et al.* (25) attempted to find out the physical significance, rather than the mathematical parameter only, of an association constant even if it is less than 10, but could not arrive at any useful conclusion. Variation of R with reciprocal of the dielectric constant of the solvent mixtures is shown in Fig. 4. Dotted lines represent the variation of Bjerrum distance $\beta/2$. Perpendicular lines in this plot show the range of R values corresponding to $\sigma \leq 1.1\sigma_{\min.}$ (a realistic estimate which can reproduce the data within $1.1\sigma_{\min.}$) and circles correspond to the best values ($\sigma = \sigma_{\min.}$). It can be seen from Fig. 4 that the best-fit R values in the case of CsBr are almost constant ($2.18 \pm 0.19\text{\AA}$) throughout the solvent compositions, whereas no systematic trend was observed for LiBr. In spite of being unambiguously best values, these are too small in the case of CsBr to be physically meaningful. Since R is the measure of the extent of the influence of ionic charge in the solvent and consequently the extent of ionic association, R and K_A values are expected to decrease with the increase of dielectric constant of the solvent mixtures up to a certain limit where ionic association is almost negligible ($K \approx 0$) and R attains a minimum value. Beyond this dielectric constant of the solvent mixtures, no further decrease in R is expected with the increase of dielectric constant. On this basis, it can be said that in solvent mixtures of sufficiently high dielectric constants (lowest being ~ 88) studied in present work, small as well as almost constant values of R are expected throughout the solvent compositions. This expected constancy in R is supported by present results for CsBr as well as for tetraalkylammonium bromides studied previously (1) in the same solvent mixtures. Thus, the trend in R is in accordance with the expectation. However, the values of R , at least for CsBr, are

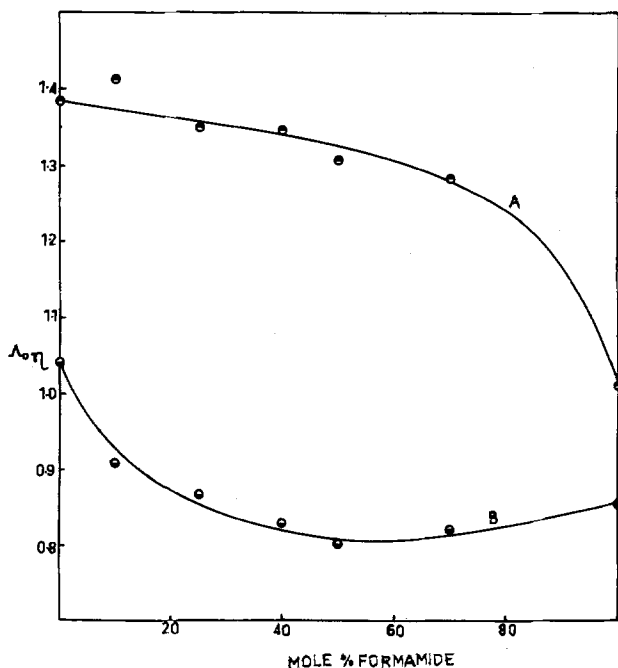


Fig. 3. Variation of Walden product with composition of the solvent mixtures. A, CsBr; B, LiBr.

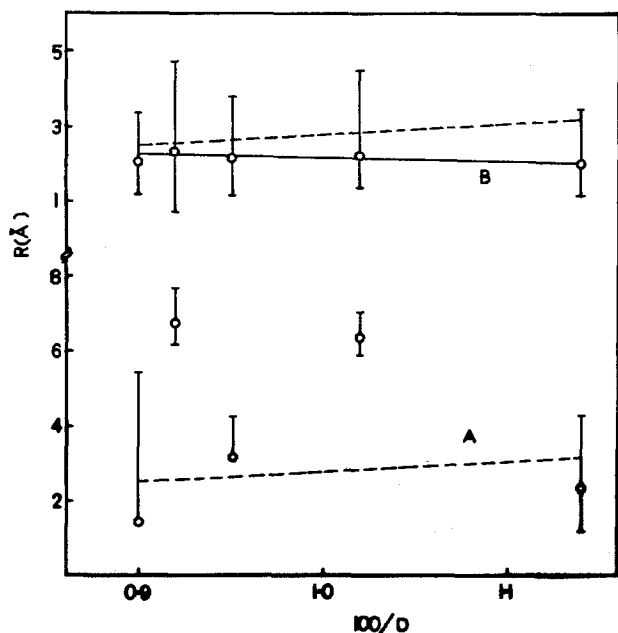


Fig. 4. Variation of pairing radius R with reciprocal of the dielectric constant of the solvent mixtures. A, LiBr; B, CsBr. Dotted lines represent $\beta/2$.

unreasonably small. Even in extreme case, the values of R should never be less than the lower limit, the sum of the crystallographic radii of the constituent ions of the electrolyte (3.64 Å for CsBr). Thus best-fit R values for CsBr are hardly acceptable. This makes it necessary to look for an alternative. From Fig. 4 and Table III, it is clear that wide ranges of R values can reproduce data equally well (within $1.1\sigma_{\min}$) so any value in that range can be accepted. Similar wide ranges of acceptable R values have been observed in our previous studies (3, 4) also. But this leads to another difficulty in assigning any definite value of R for a particular system, thus making it difficult to draw any definite conclusion on the basis of these R values. Also, wide ranges of acceptable R values observed in present as well as in previous works (3, 4) clearly indicate the insensitivity of goodness of fit to the parameter R of the model. The same has been noticed by Fuoss (12) also. Although, it has been mentioned in the paper by Fuoss (12) that data in dioxane-water mixtures for some electrolytes have been analyzed by Fuoss (1978) equation, but the variation of R with dielectric constant of the solvent mixture has not been given. No other papers we have come across analyzed the data by the same equation. So due to lack of literature data, it is not possible to make any correlation with our results and same is the reason for not being able to come to any definite conclusion at this stage about R values derived by using Fuoss (1978) equation.

Acknowledgments

The authors are indebted to Professor R. M. Fuoss of Yale University, U.S.A., for invaluable help in mak-

ing his computer programs available and to the computer center, Delhi University, for help in analyzing the data on an IBM 360 Computer. The authors' sincere thanks are due to Professor B. M. Shukla, Head, Department of Chemistry, Banaras Hindu University, for providing necessary facilities. Grateful thanks are also due to C.S.I.R., Government of India for granting a Junior Research Fellowship to one of the authors (Lal Bahadur) during this work.

Manuscript submitted Feb. 11, 1980; revised manuscript received ca. Aug. 8, 1980.

Any discussion of this paper will appear in a Discussion Section to be published in the December 1981 JOURNAL. All discussions for the December 1981 Discussion Section should be submitted by Aug. 1, 1981.

REFERENCES

1. M. V. Ramanamurti and Lal Bahadur, *Indian J. Chem.*, **14A**, 1015 (1976).
2. D. Singh, Lal Bahadur, and M. V. Ramanamurti, *J. Solution Chem.*, **6**, 703 (1977).
3. M. V. Ramanamurti and Lal Bahadur, *Electrochim. Acta*, **25**, 601 (1980).
4. Lal Bahadur and M. V. Ramanamurti, *J. Chem. Soc. Faraday Trans. I*, In press.
5. D. F. Evans and R. L. Kay, *J. Phys. Chem.*, **70**, 366 (1966).
6. J. Thomas and D. F. Evans, *ibid.*, **74**, 3812 (1970).
7. C. De Visser and G. Somsen, *J. Solution Chem.*, **3**, 847 (1974).
8. C. De Visser and G. Somsen, *J. Phys. Chem.*, **78**, 1719 (1974).
9. C. De Visser, W. J. M. Heuvelsland, and G. Somsen, *J. Solution Chem.*, **4**, 311 (1975).
10. P. Rohdewald and M. Moldner, *J. Phys. Chem.*, **77**, 373 (1973).
11. (a) R. M. Fuoss, *ibid.*, **79**, 525 (1975); (b) C. F. Mattina and R. M. Fuoss, *ibid.*, **79**, 1604 (1975).
12. (a) R. M. Fuoss, *Proc. Natl. Acad. Sci. U.S.A.*, **75**, 16 (1978); (b) R. M. Fuoss, *J. Phys. Chem.*, **82**, 2427 (1978).
13. C. De Visser and G. Somsen, *Z. Phys. Chem. (N.F.)*, **92**, 159 (1974).
14. H. Weingartner, M. Holz, and H. G. Hertz, *J. Solution Chem.*, **7**, 689 (1978).
15. J. A. Rupley, *J. Phys. Chem.*, **68**, 2002 (1964).
16. J. F. Hinton and K. H. Ladner, *J. Magn. Res.*, **6**, 586 (1972).
17. A. Johnson and P. A. Kollman, *J. Am. Chem. Soc.*, **94**, 6196 (1972).
18. (a) H. L. Hsia and R. M. Fuoss, *ibid.*, **90**, 3055 (1968); (b) T. L. Broadwater and R. L. Kay, *J. Phys. Chem.*, **74**, 3803 (1970).
19. R. C. Paul, J. P. Singla, D. S. Gill, and S. P. Narula, *Indian J. Chem.*, **9**, 981 (1971).
20. P. Hemmes, *J. Phys. Chem.*, **78**, 907 (1974).
21. A. D'Aprano and R. M. Fuoss, *J. Solution Chem.*, **4**, 175 (1975).
22. R. Zwanzig, *J. Chem. Phys.*, **52**, 362 (1970).
23. (a) J. Hubbard and L. Onsager, *ibid.*, **67**, 4850 (1978). (b) J. B. Hubbard, *ibid.*, **68**, 1649 (1978).
24. D. F. Evans, T. Tominaga, J. B. Hubbard, and P. G. Wolynes, *J. Phys. Chem.*, **83**, 2669 (1979).
25. A. D'Aprano, J. Komiyama, and R. M. Fuoss, *J. Solution Chem.*, **5**, 279 (1976).



The Application of Nb_2O_5 as a Cathode in Nonaqueous Lithium Cells

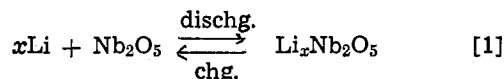
Benjamin Reichman* and Allen J. Bard*

Department of Chemistry, The University of Texas at Austin, Austin, Texas 78712

Materials that undergo intercalation or topochemical reactions with Li have been investigated actively in recent years as candidates for cathodes in nonaqueous cells (1-3). The desired properties for such materials include good conductivity, a high free energy of reaction with Li, and minimal structural change on reaction leading to the possibility of repeated charging and discharging of the electrodes without permanent changes or decomposition. Intercalation involves the interstitial introduction of Li into the host compound, such as with the layered compound TiS_2 (4, 5). The reaction of most other materials with Li is topochemical and involves larger structural modifications. For example, topochemical reactions occur with some transition metal oxides such as V_2O_5 (4, 6, 7), the layered MoO_3 (4, 8-11), TiO_2 (4, 7, 12), WO_3 (13, 14), and MnO_2 (9). We recently found that Li reacts with Nb_2O_5 , and that upon electrochemical reduction of Nb_2O_5 films on Nb metal in acetonitrile solutions containing LiClO_4 , a dark blue color appeared on the electrode surface (15). The blue color could be bleached upon oxidation and could be cycled repeatedly, thus suggesting possible application to electrochromic display devices (15). Similar experiments have been performed with sputtered and chemically vapor deposited Nb_2O_5 (16). We report here preliminary electrochemical studies of the cells Li/LiClO_4 (1M), propylene carbonate (PC)/ Nb_2O_5 . Measurements of the cell voltage as well as the stoichiometry of the $\text{Li}-\text{Nb}_2\text{O}_5$ reaction provided thermodynamic information about the reaction. The behavior of the system upon charging and discharging was also investigated.

Experimental

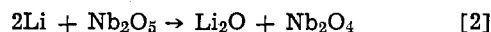
The Nb_2O_5 electrode was prepared by heating Nb metal to 550°C in air. By this treatment a white layer of Nb_2O_5 formed on the Nb metal. The amount of oxide was determined by weighing the sample before and after the thermal oxidation process. The electrical contact was made with a Cu wire attached with silver epoxy cement to the Nb substrate. The Li anode was Li wire of ~ 3 mm diam. The electrodes were assembled in a sealed cell which contained 1M LiClO_4 in propylene carbonate (PC) solution in a glove box under an He atmosphere. All electrochemical measurements were carried out with the cell in the glove box. The LiClO_4 PC solution was prepared in the glove box from $\text{LiClO}_4 \cdot \text{H}_2\text{O}$ (AR grade, G. F. Smith Company) which had been dried at 110°C under vacuum for three days. The PC was allowed to stand for four days over molecular sieves (4Å) and then was distilled twice under vacuum onto molecular sieves; the fraction collected at 65°C (vacuum 0.4 Torr) was used. The PC was then degassed by three freeze-pump-thaw cycles and was stored in the glove box over molecular sieves. The cell was discharged (see Eq. [1]) across a constant external



load resistance and its voltage was measured with a recorder through a voltage-follower circuit; the current was measured via a current-to-voltage converter to a recorder. The cell voltage as a function of x (where x is the $\text{Li}/\text{Nb}_2\text{O}_5$ mole ratio) was measured on discharge as follows: the cell was slowly discharged across a constant external load resistance (10 kΩ) and x was determined by integration of the current. The discharge process was interrupted at different stages and the open-circuit voltage was measured after the system reached equilibrium (several hours to one day). The cell was charged at constant current (0.1 mA) with a Princeton Applied Research (PAR) potentiostat, Model 173. The x-ray powder diffraction pattern was obtained with a Phillips Norelco x-ray diffractometer using $\text{Cu K}\alpha$ radiation.

Results and Discussion

The open-circuit voltage of a cell composed of an Nb_2O_5 (cathode) and Li (anode) as a function of x is shown in Fig. 1(a). The molar free energy, ΔG , involved in the cell reaction is also shown in the figure. The initial open-circuit voltage of the cell, 2.8V, was constant for at least two weeks to within $\pm 0.02\text{V}$ as was the cell voltage for other x values. The calculated emf for the reaction



is only 1.37V (based on the known values of ΔG° for Li_2O (-133.8 kcal/mole), Nb_2O_5 (-426.4 kcal/mole), and Nb_2O_4 (-355.8 kcal/mole) (17, 18). This is lower than the open-circuit voltage measured in any of the $\text{Li}/\text{Nb}_2\text{O}_5$ cells constructed. Thus the cell reaction is more probably the topochemical reaction of Eq. [1], as was suggested for V_2O_5 , MoO_3 , and TiO_2 (4, 8, 11, 12).

Upon increasing x , the cell voltage decreased at lower x values, but when x attained the value of ~ 0.4 it remained almost constant at $\sim 1.7\text{V}$ until $x \sim 1.5$. The constant cell voltage suggests equilibrium between two phases in this region. Prior to this region only a single phase of nonstoichiometric $\text{Li}_x\text{Nb}_2\text{O}_5$ exists as indicated by the decrease of the voltage with increase in x . The equilibrium existing between two different phases in the cathode material is also reflected in the discharge curve under load shown in Fig. 1(b). Again a sharp decrease in cell voltage is observed in the region of lower x values. The cell voltage then remains almost constant until the sharp decrease when x reaches 1.5. The sharp drop at $x \sim 1.5$ is probably caused by a sudden decrease in the diffusion coefficient of Li in the cathode material (1). For this experiment 0.02g Nb_2O_5 electrode material was used [in the form of a thin film (20)]. The time scale is indicated in the upper axis

* Electrochemical Society Active Member.
Key words: cathode, cell, emf.

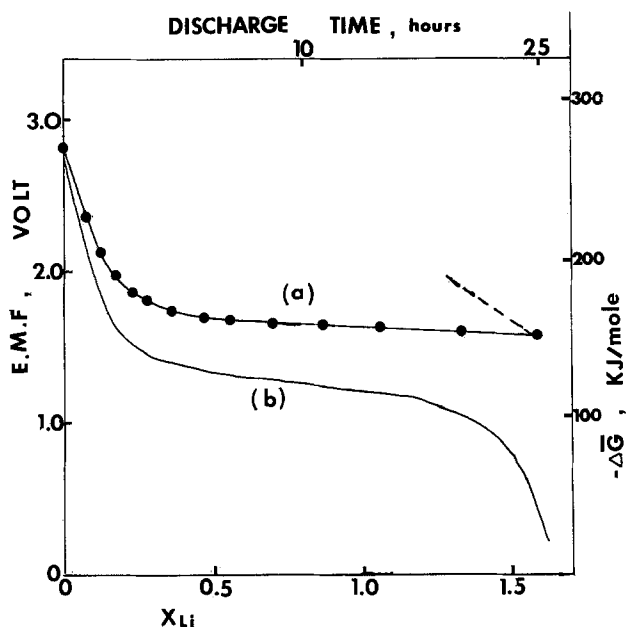


Fig. 1. Voltage of the cell $\text{Li}/1\text{M LiClO}_4$, propylene carbonate/ Nb_2O_5 as a function of x (moles Li discharged/mole Nb_2O_5): (a) open-circuit values during discharge of Nb_2O_5 (●) and recharge of $\text{Li}_x\text{Nb}_2\text{O}_5$ (---). The ΔG values related to these experiments are shown on the right ordinate; (b) cell voltages during discharge across a load resistance of 10 k Ω . 0.02g Nb_2O_5 formed on Nb by air oxidation was used in this experiment. The upper abscissa of the figure is the discharge time.

of Fig. 1; note that about 25 hr was required to complete the discharge at this load. Since saturation occurs only after reaction with ~ 1.5 equivalent of Li, the capacity of the $\text{Li}/\text{Nb}_2\text{O}_5$ cell is high (0.15 A-hr/g) and its theoretical energy density based on the initial open circuit (2.8V) is ~ 500 W-hr/kg; the more practical energy density based on the discharge curve shown in Fig. 1(b) is ~ 230 W-hr/kg. Values of x higher than 1.0 have also been found for other oxides like MoO_3 (7, 10) ($x = 1.5$), V_2O_5 (4, 7) ($x = 2$), and WO_{3-y} (14) ($x = 1.5$). The fact that a new phase of $\text{Li}_x\text{Nb}_2\text{O}_5$ is formed when the value of x increased over ~ 0.4 was also suggested by the x-ray diffraction patterns shown in Fig. 2. The x-ray pattern of the cathode material after charging to saturation ($x = 1.6$) [Fig. 2(b)] is different from that taken with the fresh electrode material [Fig. 2(a)]. The pattern of Fig. 2(a) is similar to the known one for Nb_2O_5 (19). Some of the x-ray peaks in the diffraction pattern of fresh cathode material are shifted with respect to those of the electrode material after complete discharge. Moreover some new peaks appear in the x-ray pattern of the discharged electrode. The peaks which appear at 28.2° , 63.4° , and 49.7° (Nb_2O_5 peaks) shift by about 1° to lower diffraction angles in the discharged electrode while the peaks at 36.3° and 42.5° (Nb_2O_5) in Fig. 2(a) are shifted by about 1.5° towards lower angles in 2(b). New peaks appear at 30° , 35° , 52° , 53° , 74.8° , and 78° . The shift in some diffraction angles of the original Nb_2O_5 can probably be attributed to some distortion in the structure of the Nb_2O_5 lattice as more Li is inserted into the lattice to form the nonstoichiometric $\text{Li}_x\text{Nb}_2\text{O}_5$, as is observed for Li_xTiS_2 (4). The new peaks which appear in Fig. 2(b) indicate formation of different phase, e.g., LiNb_2O_5 , which is the phase in equilibrium with the Nb_2O_5 . This compound is formed during the discharge of the cell in the region where the cell voltage plateau occurs.

Experiments were also carried out to study the reversibility of the cell. Upon charging the cell after complete discharge, only about 20% of the charge could be recovered; decomposition of the solvent started to take place at a charging voltage of $\sim 5\text{V}$

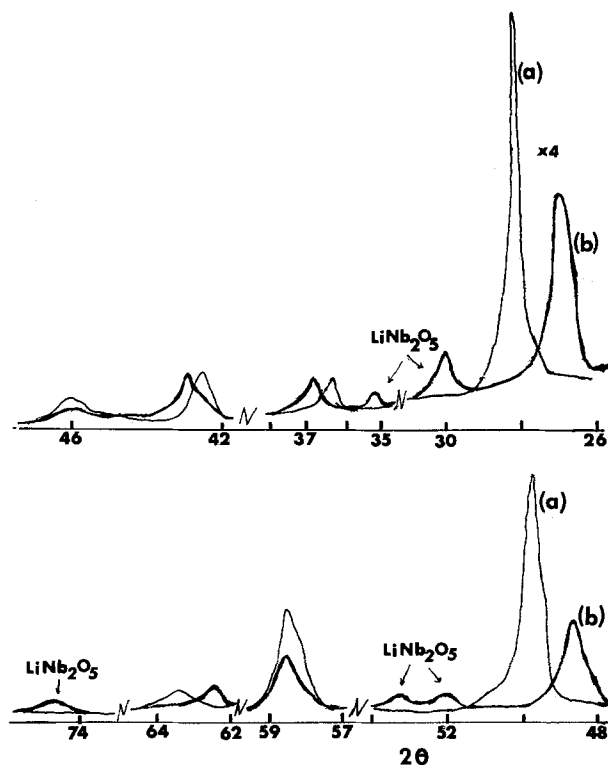


Fig. 2. X-ray diffraction pattern of (a) Nb_2O_5 electrode before discharge and (b) cathode material after complete discharge.

(applied charging current, 0.1 mA). The cell voltages (open circuit) as a function of x , measured during charging (broken line in Fig. 1) were different than those obtained during discharge. Upon further discharge-charge cycles the charge recovered in the charging cycles decreased further from cycle to cycle. The capacity lost is probably caused by the very low rate of oxidation of the LiNb_2O_5 phase which was formed during the discharge. Because of this low rate (high energy of activation for oxidation), higher voltages are needed for the charging process at reasonable current densities. However, the oxidation of the solvent itself occurs at voltages lower than that required to complete the oxidation of the electrode so that a loss of capacity is observed. This mechanism for capacity loss was clearly addressed by Wittingham (4) and others, and it usually occurs in cases where a new phase is formed during the discharge process. The oxidation of this phase probably involves a high activation energy and is very difficult to accomplish without decomposition of the solvent. This is in contrast to the highly reversible layered dichalcogenide cathodes, e.g., TiS_2 and others (1, 4), where no phase transition occurs during the discharge and where only a single nonstoichiometric compound Li_xTiS_2 is formed with only a slight change in the lattice structure. Note that in our experiments with Nb_2O_5 no attempt was made to optimize the properties of the active material. It has been previously shown that slight changes in the crystal structure, crystallite size, and method of preparation of cathode material can often improve significantly the cell performance, both in terms of capacity and reversibility (3, 12) as was found, for example, with V_6O_{13} (4, 21).

Conclusion

Li can be introduced in a topochemical reaction into Nb_2O_5 . Preliminary experiments show that a cell based on this reaction has a high open-circuit voltage (2.8V) and energy density. The reaction of the cell involves a phase transition in the cathode material, so that the cell voltage shows a plateau during discharge at $\sim 1.7\text{V}$. Only about 20% of the capacity can

be recovered upon recharge, however, and this poor reversibility of the cell will prevent its use as a secondary one. However, different methods of material preparation may lead to changes in the lattice structure of the cathode material to make it a more open one, which can accommodate Li ions and improve the cell reversibility.

Acknowledgment

The support of this research by grants from the National Science Foundation (CHE 7903729) and Texas Instruments is gratefully acknowledged.

Manuscript submitted June 9, 1980; revised manuscript received Sept. 22, 1980.

Any discussion of this paper will appear in a Discussion Section to be published in the December 1981 JOURNAL. All discussions for the December 1981 Discussion Section should be submitted by Aug. 1, 1981.

Publication costs of this article were assisted by the University of Texas at Austin.

REFERENCES

1. M. S. Whittingham, *Prog. Solid State Chem.*, **12**, 41 (1978).
2. M. S. Whittingham, *Chemtech.*, **9**, 766 (1979).
3. D. W. Murphy and P. A. Christian, *Science*, **205**, 651 (1979).
4. M. S. Whittingham, *This Journal*, **123**, 315 (1976).
5. M. S. Whittingham, *Science*, **192**, 1126 (1976).
6. C. R. Walk and J. S. Gore, Paper 27 presented at The Electrochemical Society Meeting, Toronto, Canada, May 11-16, 1976.
7. M. S. Whittingham and M. B. Dines, *This Journal*, **124**, 1387 (1977).
8. L. Campanella and G. Pistoia, *ibid.*, **118**, 1905 (1971).
9. F. W. Dampier, *ibid.*, **121**, 656 (1974).
10. N. Margalit, *ibid.*, **121**, 1461 (1974).
11. M. S. Whittingham, *ibid.*, **122**, 713 (1975).
12. T. Ohzuku, Z. Takehara, and S. Yoshizawa, *Electrochim. Acta*, **24**, 219 (1979).
13. S. K. Mohapatra and S. Wagner, *This Journal*, **125**, 1604 (1978).
14. M. Lazzari, G. Pistoia, and B. Scrosati, Paper 41 presented at The Electrochemical Society Meeting, Dallas, Texas, October 5-9, 1975.
15. B. Reichman and A. J. Bard, *This Journal*, **127**, 241 (1980).
16. T. Henning and A. J. Bard, Unpublished experiments, 1979-1980.
17. M. Pourbaix, "Atlas of Electrochemical Equilibria in Aqueous Solutions," Pergamon Press, Oxford (1966).
18. W. M. Latimer, "The Oxidation States of Elements and Their Potentials in Aqueous Solutions," Prentice-Hall, Inc., New York (1952).
19. X-ray Diffraction File, Search Manual, ASTM file No. 5-0352, L. G. Berry, Editor, PA, USA (1975).
20. (a) J. Broadhead and F. A. Trumbore, Paper 178 presented at The Electrochemical Society Meeting, Chicago, Illinois, May 13-18, 1973. (b) F. A. Trumbore and J. Broadhead, Paper 179 presented at The Electrochemical Society Meeting, Chicago, Illinois, May 13-18, 1973.
21. D. W. Murphy, P. A. Christian, F. J. Disalvo, and J. N. Carides, *This Journal*, **126**, 497 (1979).

Transport of Oxidant in Molten Na_2SO_4 in O_2 - SO_2 - SO_3 Environments

David A. Shores* and W. C. Fang**¹

General Electric Research and Development Center, Schenectady, New York 12301

In the Na_2SO_4 -induced hot corrosion of superalloys the main corrosion products are oxides and, to a lesser extent, sulfides. On susceptible alloys a small amount of salt can produce a relatively large quantity of corrosion products, demonstrating that the salt, for the most part, is not consumed by the corrosion reaction. Rather, oxidant is supplied by the gas phase. Thus, an important step in the overall hot corrosion reaction is the transport of oxidant through a layer of liquid salt. A knowledge of transport rates is needed to decide whether gradients of oxidants will exist in the salt film for a particular set of conditions. Oxidant gradients are a key part of the early theory of hot corrosion fluxing developed by Goebel and Pettit (1), and also of the recent theory of Rapp and Goto (2), that proposes a negative gradient of solubility of corrosion products as a criterion of sustained attack. The purpose of the present work was to identify which species would provide the predominant flux of oxidant through molten Na_2SO_4 in O_2 - SO_2 - SO_3 environments and to measure its diffusivity.

Transport rates of oxidant through Na_2SO_4 have been determined from the limiting cathodic current densities observed in polarization experiments. A three-electrode cell, shown schematically in Fig. 1, has been used with Pt (or Au) foil for the working and counter-electrodes and an Ag wire dipping into an Na_2SO_4 melt contained in a mullite tube as the reference electrode

(3). The Pt or Au foils were cemented (Aremco 552 cement) to the bottom of the crucible. The thickness of the salt was determined from the geometry of the cell, the amount of salt added, and the density of liquid Na_2SO_4 at temperature. Cathodic polarization runs were carried out with high purity Na_2SO_4 (99.999%) at 896°C with a scan rate of 0.33 mV/sec. Several runs

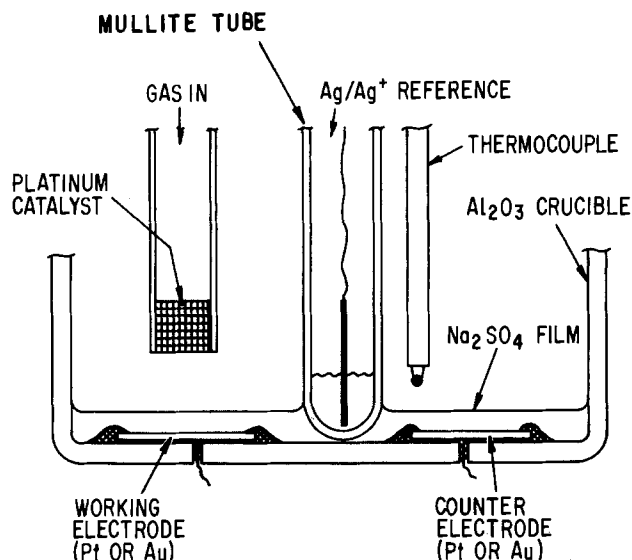


Fig. 1. Schematic diagram of experimental polarization cell

* Electrochemical Society Active Member.

** Electrochemical Society Student Member.

¹ Present address: Department of Metallurgical Engineering, Ohio State University, Columbus, Ohio 43210.

Key words: corrosion, alloy, salts.

were carried out in $O_2 + 0.15\%$ ($SO_2 + SO_3$) with salt thicknesses ranging from 0.022 to 0.24 cm. In addition, for a given salt thickness limiting currents were determined as a function of $P_{SO_3} + P_{O_2} \approx 1.0$ atm and as a function of $P_{SO_3} + P_{O_2}$ at $P_{SO_2} \approx 1.0$ atm. Because gas phase O_2 - SO_2 - SO_3 reactions are known to be slow, a Pt catalyst was placed in the gas inlet tube (shown in Fig. 1) to insure equilibration.

The shape of the polarization curves obtained from these experiments was typical of concentration polarization. The limiting current density increased as the thickness of the salt layer decreased. A plot of the limiting current density vs. $1/(\text{thickness})$ in $O_2 + 0.15\%$ ($SO_2 + SO_3$), as shown in Fig. 2, yielded a straight line, but with some scatter owing to the uncertainty in the determination of the salt thickness.

To help identify the predominant reduction reaction in an O_2 -rich environment containing small amounts of $SO_2 + SO_3$, a series of polarization runs at a given salt thickness was carried out in which the gaseous environment was varied. As shown in Fig. 3 the limiting current densities were found to increase linearly with increasing $P_{SO_3} + P_{SO_2}$ at constant P_{O_2} (≈ 1.0 atm). These data indicate that in the presence of SO_3 the reduction of O_2 is not the predominant reaction. In another series of runs with P_{SO_2} held constant at ≈ 1.0 atm the limiting current densities were found to increase linearly with $P_{SO_3} + P_{O_2}$ (Fig. 4). Thus, in the presence of SO_3 the reduction of SO_2 may also be ruled out as a predominant reaction. By this process of elimination the reduction of SO_3 , or as will be shown below, the reduction of a soluble species whose concentration is proportional to P_{SO_3} is proposed as the predominant reaction. Extrapolation of the limiting current data from Fig. 3 and 4 to $P_{SO_3} + P_{SO_2} = 0$ or $P_{SO_3} + P_{O_2} = 0$ yielded residual current densities that have been interpreted as due to the reduction of O_2 and SO_2 , respectively.

The limiting current density data have been further analyzed to obtain diffusion coefficients with the use of the well-known equation

$$D = i_l \delta / nFC \quad [1]$$

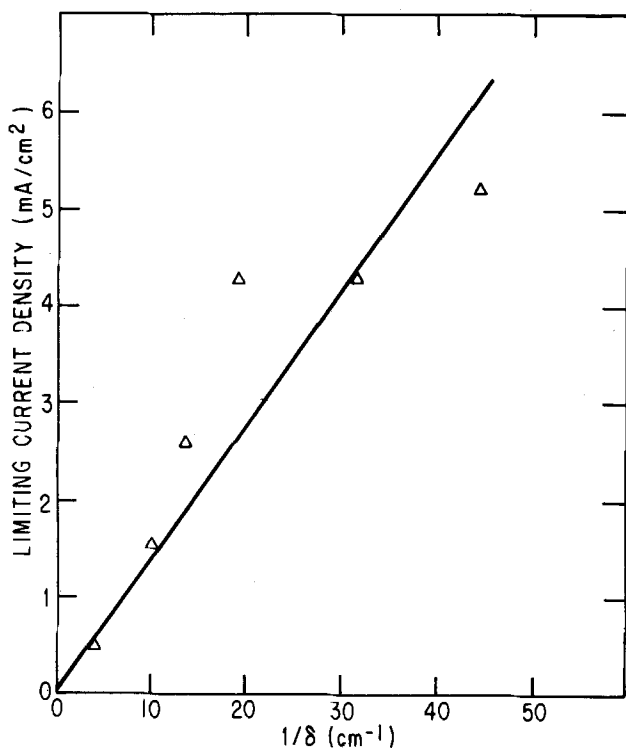


Fig. 2. Plot of limiting reduction current densities as a function of the reciprocal of the salt film thickness in $O_2 + 0.15\%$ ($SO_2 + SO_3$) at $896^\circ C$.

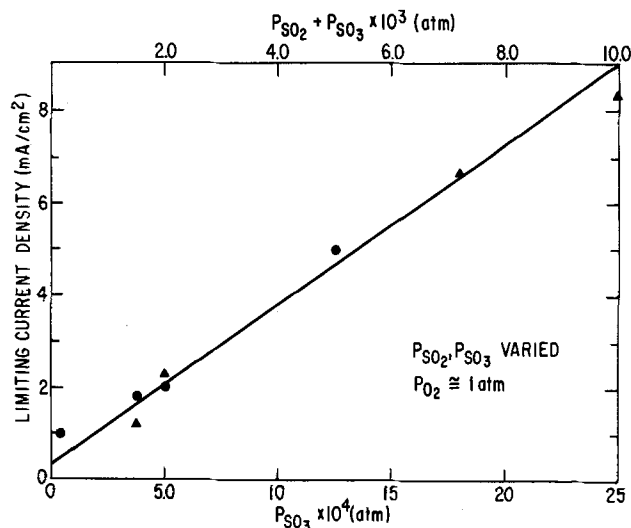
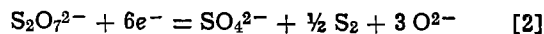


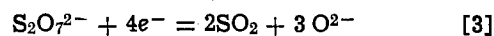
Fig. 3. Plot of limiting current densities as a function of P_{SO_3} from duplicate experiments with $P_{O_2} \approx 1$ atm at $896^\circ C$ with a salt thickness of 0.08 cm.

where i_l is the limiting current density, δ is the diffusion distance, n is the number of equivalents/mole, F is the Faraday constant, and C is the bulk concentration of the diffusing species. For most liquids diffusion coefficients lie in the range 10^{-4} cm²/sec. Inman (4) has quoted a value of $D_{SO_3} = 2 \times 10^{-4}$ cm²/sec in a chloride melt at $750^\circ C$. Although many reduction reactions in Na_2SO_4 are conceivable, it has been possible to eliminate some by showing that an unreasonable value of D would be required for the experimental data to be consistent with the above equation. Clearly, Na^+ and SO_4^{2-} are not being reduced under the present experimental conditions, because one would expect limiting current densities to be very high and not to be significantly influenced by the gas composition. In Table I are listed several reactions for the reduction of minority species. The solubilities of O_2 and SO_2 were obtained from the measurements of Andresen (5). The solubility of gaseous SO_3 is unknown, but it is unlikely to exceed that of SO_2 on the basis of its molecular diameter. The solubilities of Na_2SO_3 , $Na_2S_2O_7$, Na_2O_2 , and NaO_2 were calculated from thermodynamic stability data assuming ideal solution behavior (6-9).

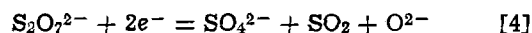
Table I shows that in an $O_2 + 0.15\%$ ($SO_2 + SO_3$) environment the reduction of SO_3 , SO_2 , SO_3^{2-} , O_2^{2-} , and O^{2-} can be ruled out as requiring unreasonably large values of D to be consistent with the experimental data.² On the other hand, the reduction of pyrosulfate ion provided a reasonable consistency with the experimental data. The concentration of pyrosulfate ions is proportional to P_{SO_3} . The reaction listed in Table I for the reduction of pyrosulfate ions is preferred over



on the grounds that dissolved S_2 (g) is an unlikely reaction product, since its solubility in Na_2SO_4 is expected to be extremely low. The reactions



and



also were rejected because the rates of these reactions would be limited by the rate of removal of the SO_2 product, if P_{SO_2} cannot exceed 1 atm at the reduction site. That SO_2 removal is not rate controlling in our experiments is demonstrated by the data in Fig. 3.

² The underlining implies dissolved gaseous species.

Table I. Diffusivities calculated from limiting reduction current densities in Na_2SO_4 in O_2 -0.15% ($\text{SO}_2 + \text{SO}_3$)

| Reaction | $i_1 \cdot \delta^*$ (A/cm) | C (mole/cm ³) | D (cm ² /sec) |
|---|--------------------------------|------------------------------|-----------------------------|
| $\text{O}_2 + 4e^- = 2 \text{O}^{2-}$ | $2.40 \times 10^{-5**}$ | 1.84×10^{-7} | 3.38×10^{-4} |
| $\text{SO}_2 + 6e^- = \text{S}^{2-} + 2 \text{O}^{2-}$ | 1.11×10^{-4} | 1.20×10^{-9} | 0.16 |
| $\text{SO}_3 + 2e^- = \text{SO}_2 + \text{O}^{2-}$ | 1.11×10^{-4} | $< 3.88 \times 10^{-10}$ | > 1.48 |
| $\text{S}_2\text{O}_7^{2-} + 8e^- = \text{SO}_4^{2-} + \text{S}^{2-} + 3 \text{O}^{2-}$ | 1.11×10^{-4} | 6.88×10^{-7} | 2.09×10^{-4} |
| $\text{SO}_4^{2-} + 6e^- = \text{S}^{2-} + 3 \text{O}^{2-}$ | 1.11×10^{-4} | 4.9×10^{-12} | 39 |
| $\text{O}_3 + 3e^- = 2 \text{O}^{2-}$ | 1.11×10^{-4} | $\sim 1 \times 10^{-11}$ | 33 |
| $\text{O}_2^{2-} + 2e^- = 2 \text{O}^{2-}$ | 1.11×10^{-4} | $\sim 4 \times 10^{-17}$ | 1.4×10^7 |

* The value of $i_1 \cdot \delta$ was obtained from the slope of the curve in Fig. 2.

** The proportion of i_1 due to oxygen reduction was estimated from Fig. 3 as the ratio of i_1 at $P_{\text{SO}_3} = 0$ to i_1 at $P_{\text{SO}_3} = 3.66 \times 10^{-4}$.

That is, upon increasing P_{SO_2} in the gas the SO_2 concentration gradient across the salt would decrease or, at the low P_{SO_2} levels in Fig. 3, remain essentially unchanged. Hence, if diffusion of SO_2 away from the electrode were rate controlling, i_1 would have decreased or remained essentially constant. In fact, i_1 increased as P_{SO_2} (and P_{SO_3}) increased.

The reduction of dissolved O_2 also yielded a reasonable value of D based on the value of i_1 extrapolated to $P_{\text{SO}_3 + \text{SO}_2} = 0$, $P_{\text{O}_2} = 1$ atm ($D_{\text{O}_2} = 3.4 \times 10^{-4}$ cm²/sec). (Measurements in pure O_2 were not consistent with these data. Since the salt is unbuffered in O_2 alone, its acidity, and hence the concentrations of minority species, can change radically during cathodic polarization experiments.) Similarly, a reasonable value of D_{SO_2} was obtained from i_1 at $P_{\text{SO}_3 + \text{O}_2} = 0$, $P_{\text{SO}_2} = 1$ atm from Fig. 4 ($D_{\text{SO}_2} \approx 1.6 \times 10^{-4}$ cm²/sec). The slopes of the curves in Fig. 3 and 4 also were found to be self-consistent. That is, $\delta(di_1/dP_{\text{SO}_3})$, obtained by differentiating Eq. [1] with respect to i_1 and C and taking $C \propto P_{\text{SO}_3}$, had about the same value for the data in Fig. 3 as in Fig. 4.

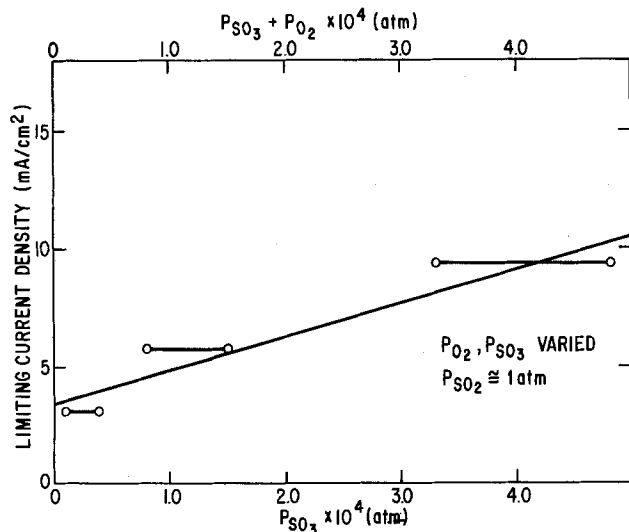


Fig. 4. Plot of limiting current densities as a function of P_{SO_3} with $P_{\text{SO}_2} \approx 1$ atm at 896°C with a salt thickness of 0.019 cm.

It is proposed that diffusion of pyrosulfate ion provides the predominant flux of oxidant through Na_2SO_4 in O_2 -rich environments containing more than a few hundred ppm of SO_3 . The diffusivity of $\text{S}_2\text{O}_7^{2-}$ has been estimated here as 2.1×10^{-4} cm²/sec at 896°C. Dissolved O_2 and SO_2 can also supply oxidant, but their contributions are limited by their very low solubilities in Na_2SO_4 . The actual contribution of each species will depend, of course, on the composition of the gas mixture. It is estimated that in $\text{O}_2 + 0.15\%$ ($\text{SO}_2 + \text{SO}_3$) the reduction of O_2 accounts for about 18% of the current and SO_2 for 0.1%.

Acknowledgment

The authors wish to acknowledge many helpful discussions with Dr. K. L. Luthra.

Manuscript submitted June 3, 1980; revised manuscript received ca. Sept. 15, 1980.

Any discussion of this paper will appear in a Discussion Section to be published in the December 1981 JOURNAL. All discussions for the December 1981 Discussion Section should be submitted by Aug. 1, 1981.

Publication costs of this article were assisted by General Electric Company.

REFERENCES

1. J. A. Goebel and F. S. Pettit, in "Metal-Slag-Gas Reactions and Processes," Z. A. Foroulis and W. W. Smeltzer, Editors, pp. 693-710, The Electrochemical Society Softbound Proceedings Series, Princeton, N.J. (1975).
2. R. A. Rapp and K. S. Goto, in "Proceedings of the Second International Symposium on Molten Salts," J. Braunstein, Editor, The Electrochemical Society, Princeton, N.J., To be published.
3. D. A. Shores and R. C. John, *J. Appl. Electrochem.*, **10**, 275 (1980).
4. D. Inman, in "Electromotive Force Measurements in High Temperature Systems," C. B. Alcock, Editor, p. 163, The Inst. of Mining and Metal, London, (1968).
5. R. E. Andresen, *This Journal*, **126**, 328 (1979).
6. W. W. Liang and J. F. Elliott, *ibid.*, **125**, 572 (1978).
7. JANAF Thermochemical Tables, 2nd ed. N.S.R.D.S.-NBS 37, U.S. Dept. of Commerce (1970).
8. L. P. Kostin, L. L. Pluzhnikov, and A. N. Ketov, *Russ. J. Phys. Chem.*, **49**, 1313 (1975).
9. I. Barin, O. Knacke, and O. Kubaschewski, "Thermochemical Properties of Inorganic Substances, Supplement," Springer-Verlag, Berlin (1977).

Generalization of the Boltzmann-Matano Method?

C. van Opdorp

Philips Research Laboratories, Eindhoven, The Netherlands

In a recent paper dealing with the diffusion of Cd in InAs, Kolodny and Shappir (1) presented a generalization of the Boltzmann-Matano (BM) method. The original, well-known method provides a means of evaluating an unknown dependence of a diffusion coefficient D on the concentration C of the diffusant from an experimentally determined concentration *vs.* depth (C - x) profile. The original method applies only if D is a function of C exclusively. In the generalization of Ref. (1), D is allowed to be an arbitrary function of C , x , and t .

In this paper it will be shown that the mentioned generalization of the BM method is incorrect. We restrict our critique of the paper of Ref. (1) to this confusing claim of generalization. In the same paper the authors have generated theoretical concentration profiles resembling the experimentally observed profiles by substituting a hypothetical dependence of D on C and x into Fick's second law. In principle this alternative heuristic approach of finding $D(C, x)$ is correct and basically independent of the validity of the BM generalization. The merits of this heuristic approach for the case in question lie outside the scope of the present paper.

The BM Method and the Impossibility of Generalization

Suppose one has a semi-infinite continuum into which diffusion of some species is performed subject to the conditions that the initial concentration in the continuum is everywhere equal to zero and at its surface the concentration is kept fixed at a constant value. Assume further that D is a function of C . Under these conditions the BM method provides a means of evaluating $D(C)$ from an experimentally determined C - x profile (2). The value of D at $C = C_1$ follows from the profile determined at $t = t_1$ by applying the formula (2)

$$D(C_1) = \frac{-1}{2t_1} \frac{\int_0^{C_1} x dC}{[dC/dx]_{C=C_1}} \quad [1]$$

The method applies only if D is a function of C exclusively. Experimentally one can verify whether this condition is fulfilled by checking invariance of the profile of C when plotted *vs.* x/\sqrt{t} for different values of the diffusion time t ; strictly speaking, this check should be performed for all values of x and t (3).

In the generalization of Ref. (1), D is allowed to be an arbitrary function of C , x , and t . The value of D at any given point (C_1, x_1, t_1) of this three-dimensional space was claimed to follow from an expression actually identical to the right-hand side of Eq. [1]

$$D(C_1, x_1, t_1) = -\frac{1}{2t_1} \frac{\int_0^{C_1} x dC}{[dC/dx]_{C=C_1}} \quad [2]$$

where again $C(x, t_1)$ is a known profile at time t_1 .

No derivation was presented for Eq. [2]. Actually generalization is impossible. This becomes evident if one follows the steps made in deriving the original BM formula of Eq. [1] (2). The essential step in de-

riying this equation consists of investigating the possibility of transforming the partial differential equation describing the diffusion process (*i.e.*, Fick's second law) to an ordinary differential equation. For this, one has to investigate the possibility of applying the Boltzmann transformation, *i.e.*, substitution of a single independent variable $\eta \equiv x/\sqrt{t}$ for the two variables x and t . If this can actually be accomplished, the resulting second-order ordinary differential equation is exact, *i.e.*, a first integral is obtainable by immediate integration (4). After that, rearrangement of this integral and re-introduction of x and t yield directly Eq. [1].

The crucial, obvious point in this whole procedure is that application of the Boltzmann transformation is indeed possible provided D is a function of C exclusively, whereas this is not possible if D is an arbitrary function of C , x , and t . This fact prohibits any generalization of the BM method as suggested in Ref. (1). Thus it is essentially impossible to reconstruct the field of local D values in the three-dimensional C - x - t space from applying Eq. [2] to (even an infinite set of) C - x profiles measured for different values of t .

A very simple example may serve to illustrate the serious consequences of improper application of the generalized expression given by Eq. [2]. Let D be a function of t only, *viz.* $D = D_0$ (constant) for $t \leq t_0$, and $D = 0$ for $t > t_0$. The resulting C - x profiles at different values t_1 for diffusion under the mentioned initial and boundary conditions are given by $C = C_0 \operatorname{erfc}(x/\sqrt{D_0 t_1})$ for $t \leq t_0$. For longer diffusion times the profile completely stagnates, so that $C = C_0 \operatorname{erfc}(x/\sqrt{D_0 t_0})$ for all $t_1 > t_0$. Application of Eq. [2] to the profiles for $t_1 \leq t_0$ and any value of C_1 yields the correct value $D(t_1 \leq t_0) = D_0$. Application to the profile(s) for $t_1 > t_0$, however, for any value of C_1 yields $D(t_1 > t_0) = D_0 t_0/t_1$ instead of the correct value $D(t_1 > t_0) = 0$.

Conclusion

Generalization of the Boltzmann-Matano method for evaluating a diffusion coefficient which depends not only on the concentration of the diffusant, but also on depth and time explicitly is impossible. Application of the incorrect generalized method of Ref. (1) may yield results which are seriously erroneous.

Manuscript submitted March 31, 1980; revised manuscript received Sept. 4, 1980.

Any discussion of this paper will appear in a Discussion Section to be published in the December 1981 JOURNAL. All discussions for the December 1981 Discussion Section should be submitted by Aug. 1, 1981.

Publication costs of this article were assisted by Philips Research Laboratories.

REFERENCES

1. A. Kolodny and J. Shappir, *This Journal*, **125**, 1530 (1978).
2. See, *e.g.*, J. Crank, "The Mathematics of Diffusion," pp. 230-232, Clarendon Press, Oxford (1975).
3. See, *e.g.*, B. Tuck, "Introduction to Diffusion in Semiconductors," p. 203, Peter Peregrinus Ltd., Stevenage (1974).
4. See, *e.g.*, E. L. Ince, "Integration of Ordinary Differential Equations," p. 73, Oliver and Boyd, London (1959).

Key words: diffusion, concentration, BM method.

High Precision Computer Controlled Electrocapillary Measurements

David M. Mohilner* and Takashi Kakiuchi¹

Department of Chemistry, Colorado State University, Fort Collins, Colorado 80523

In preparation for an investigation of the temperature dependence of organic electroadsorption in order to test a recently proposed theory (1), it was decided to try to improve the precision of our computer controlled capillary electrometer (2) over the precision we had already obtained (3) in 1976. The reason for attempting further improvement in precision is because it is known (4-6) that the temperature coefficient of interfacial tension is quite low. We have succeeded in improving the instrument so that it is now capable of measuring the interfacial tension with 95% confidence limits of ± 0.02 dyne cm^{-1} . The purpose of this note is to describe how this improvement was accomplished.

Experimental

14-bit A/D converter and new pressure transducer.—The previous best precision (3) of ± 0.1 dyne cm^{-1} represented a relative precision of about 1 part in 4000. This was approximately the same as the precision of the 12-bit A/D converter which was being used. We thought it was possible that an improvement might be made if we interfaced an A/D converter with more bits to the PDP-8/I computer which controls the electrocapillary measurements. Therefore we interfaced an Analog Devices ADC-1131K 14-bit A/D to the computer. Because the computer is only a 12-bit machine special hardware and software provisions were necessary. The hardware provision was an interface which can strobe the eleven most significant bits (plus sign) into the high order 12-bit mantissa word of the floating accumulator and the three least significant bits into the lower order mantissa word.² The software provision was to add a new routine to the vendor supplied floating point package to enable the computer to float a 14-bit number. This new routine, DFLOAT, was modeled on the vendor supplied FLOAT routine which floats an 11-bit number (plus sign) in the high order mantissa word of the floating accumulator. The only problems in adding the routine DFLOAT to the floating point package were caused by the necessary movement of several other floating routines within the code in order to collect the two or three spare words on each page of the package together onto one page so that there would be space for DFLOAT.³

The Lion pressure transducer which had been used previously was also replaced by a much more stable transducer based on a temperature compensated, unbonded, fully active strain gauge bridge, manufactured by Gould Incorporated, Measurements Systems Division, Oxnard, California. The new transducer system consists of a Model PL131TC transducer, a CON2 pressure adapter, a DC12 electrical disconnect, and a Model SC1105 power supply with bridge amplifier. In order to achieve even better stability the Gould bridge amplifier in the SC1105 was replaced with an Analog Devices Model 606M instrumentation amplifier which is connected to the analog input of the 14-bit A/D converter.

* Electrochemical Society Active Member.

¹ On leave from Department of Agricultural Chemistry, Kyoto University, Kyoto, Japan.

Key words: electrocapillary, interfacial tension, electroadsorption.

² Circuit diagrams of this interface will be supplied on request.

³ A listing of the modified floating point package will be supplied on request.

We found that with the 14-bit A/D converter and the new pressure transducer the precision of a measurement of the interfacial tension was improved. However it was not improved as much as would have been expected, i.e., 1 part in 16,000 which is the uncertainty of the least significant bit of a 14-bit A/D. We found that it was necessary to make several additional changes in the instrument to correct for sources of scatter in the data which had not been noticeable at the previous lower precision.

Improvement of the potential control.—On monitoring the long term reproducibility of the electrode potential with an accurate digital voltmeter (Fluke 8300A) it was found that there was a measurable scatter of tenths of a millivolt which could account for some of the scatter of the interfacial tension, especially at potentials far from the electrocapillary maximum. It was found that this scatter of electrode potential was due partly to the reproducibility of the 12-bit D/A converter which supplied the voltage signal to the potentiostat and partly to the stability of the operational amplifiers which were being used as the control amplifier and voltage follower in the potentiostat. The 12-bit D/A converter was replaced with an Analog Devices DAC-12QM ultrahigh stability 12-bit D/A. The control amplifier on the potentiostat was replaced with an Analog Devices Model 234L low noise-wideband chopper stabilized amplifier which has an extremely low drift ($0.1 \mu\text{V}/^\circ\text{C}$ and $1 \text{ pA}/^\circ\text{C}$). The voltage follower was replaced with an Analog Devices Model AD517L amplifier which is a laser trimmed precision IC amplifier which is recommended for ultrahigh stability as a unity gain voltage follower. These changes in the potential control circuitry have greatly improved the long term reproducibility of the electrode potential. The standard deviation of the drift of emf over a period of two months is now only about 0.1 mV.

Vibration control.—After the modifications just mentioned were introduced there still remained some scatter in the measurements. This scatter was traced to building vibrations. Therefore a Newport Research Corporation vibration free table was purchased (Research table top, Model RS-46-8 with support system Part No. XLB2A-24) and the cell was mounted on it. This last modification removed most of the remaining scatter from the data.

Mercury head.—At this stage the single most inaccurate part of the measurement remaining was the determination of the head of mercury which was read with a cathetometer calibrated to 0.01 mm. In order to minimize the frequency of necessary cathetometer readings the mercury reservoir which had an area of about 20 cm^2 was replaced with a much larger one having an area of 180 cm^2 . With this new reservoir it is now only necessary to read the head of mercury once every 2600 measurements of interfacial tensions. This means that one reading of the head of mercury remains valid for about ten 60 point electrocapillary curves, each of which is measured in triplicate.

Results and Discussion

After the modifications in the instrument described above had been installed, a critical test was performed to determine the 95% confidence limits of a triplicate

measurement of the interfacial tension at any electrode potential. This test was performed by measuring three times a 49 point electrocapillary curve for a 0.1M NaCl aqueous solution at 25°C. For each of these three measurements, a freshly prepared solution was used. Each of these electrocapillary curves was measured in triplicate. An Ag/AgCl reference electrode in the same solution was employed.⁴

In order to determine whether the precision of the measurements was independent of electrode potential, a statistical test for homogeneity of variance was performed. The variances at each emf were calculated for the three electrocapillary curves, i.e., nine measurements of the interfacial tension at each emf, and arranged in order of emf. Because the means at the different values of electrode potential are different, a generalized likelihood-ratio test is intractable (7). However, the theory of runs can be used to test the hypothesis that the observations have been drawn at random from a single population (8). We implemented a test for homogeneity of variance based on the theory of runs using the formulas for probability given (9) by Swed and Eisenhart. The result of this test was that indeed the variances at all of the different values of emf belonged to a single population. Therefore it was statistically permissible to pool the variance for all values of emf. The pooled variance was $3.96(10)^{-4}$ dyne² cm⁻² and the pooled standard deviation was $1.96(10)^{-2}$ dyne cm⁻¹. Therefore, using the t-table, the 95% confidence limits for any triplicate measurement of the interfacial tension is 0.02 dyne cm⁻¹ which represents a fivefold improvement in the precision of the instrument.

Figure 1 shows a typical triplicate measurement for an electrocapillary curve as recorded by the on-line plotter of the computer controlled capillary electrometer. It can be seen from this figure that the scatter of data with this improved instrument is smaller than the pen width on the plot. An idea of how much the instrument has been improved over the original version can be obtained by comparing this figure with Fig. 11 of Ref. (2).

Acknowledgment

This work was supported by the National Science Foundation under Grant No. CHE76-83432. Acknowledgment is also made to the donors of the Petroleum Research Fund, administered by the American Chemical Society for partial support of this research. This work constitutes a portion of the research in a collaborative international program on thermodynamic studies of the inner part of the electrical double layer supported in part by the North Atlantic Treaty Organization (NATO). We express our gratitude to the late Professor Patricia R. Mohilner, Department of Computer Science, Colorado State University who wrote the computer programs used in this study. We also thank Professor Paul W. Mielke, Department of Statistics and Professor Elliot R. Bernstein, Department of Chemistry, Colorado State University, for advice on the statistical analysis and on the selection of a vibration-free table.

⁴It was found that the glass sodium ion electrode which we had employed in our previous measurements (3) was not stable enough for use with the new level of precision.

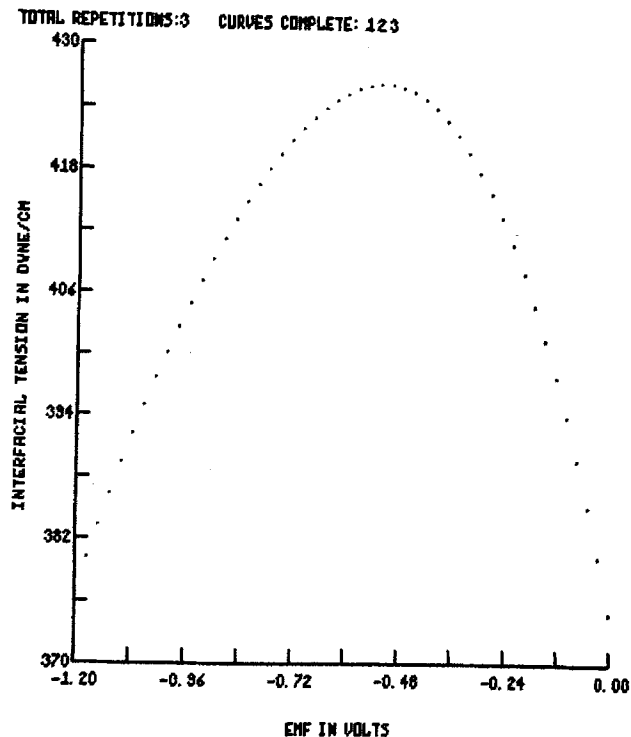


Fig. 1. Electrocapillary curve for mercury electrode in aqueous 0.1M NaCl at 25°C. Reference electrode: Ag/AgCl. This is the actual recording of the measurement in triplicate produced by the on-line plotter of the computer controlled capillary electrometer.

Manuscript submitted May 8, 1979; revised manuscript received Oct. 7, 1980.

Any discussion of this paper will appear in a Discussion Section to be published in the December 1981 JOURNAL. All discussions for the December 1981 Discussion Section should be submitted by Aug. 1, 1981.

Publication costs of this article were assisted by Petroleum Research Fund, American Chemical Society.

REFERENCES

1. D. M. Mohilner, H. Nakadomari, and P. R. Mohilner, *J. Phys. Chem.*, **81**, 244 (1977).
2. J. Lawrence and D. M. Mohilner, *This Journal*, **118**, 1596 (1971).
3. H. Nakadomari, D. M. Mohilner, and P. R. Mohilner, *J. Phys. Chem.*, **80**, 1761 (1976).
4. G. Gouy, *Ann. Chim. Phys.*, **9**, 75 (1906).
5. G. J. Hills and R. Payne, *Trans. Faraday Soc.*, **61**, 326 (1965).
6. R. G. Barradas and E. W. Herman, *J. Phys. Chem.*, **73**, 3619 (1969).
7. A. M. Mood, F. A. Graybill, and D. C. Boes, "Introduction to the Theory of Statistics," 3rd ed., p. 440, McGraw-Hill, New York (1974).
8. W. J. Dixon and F. J. Massey, Jr., "Introduction to Statistical Analysis," 3rd ed., p. 342, McGraw-Hill, New York (1969).
9. F. Swed and C. Eisenhart, *Ann. Math. Stat.*, **14**, 66 (1943).



Metallographic Aspects of the Corrosion of a Preoxidized Co-30 Cr Alloy in an H₂-H₂O-H₂S Atmosphere at 900°C

P. J. Hunt and K. N. Strafford

Newcastle upon Tyne Polytechnic, Newcastle upon Tyne NE1 8ST, England

ABSTRACT

The reaction at 900°C between preoxidized Co-30 Cr alloy samples and an H₂-H₂O-H₂S gas mixture has been studied from a metallographic viewpoint to allow comparison with the morphology and composition of the corrosion products formed on an unoxidized Co-30 Cr alloy exposed under the same test parameters. Preoxidation was carried out in an H₂-H₂O gas mixture in the temperature range 850°-1000°C. This binary gas mixture generated an oxidizing potential of between 3.5×10^{-21} atm (3.5×10^{-19} kN/m²) to 1.8×10^{-18} atm (1.8×10^{-16} kN/m²) resulting in the exclusive formation of a Cr₂O₃ layer on the alloy. On exposure at 900°C to the low oxidizing (2×10^{-19} atm, 2×10^{-17} kN/m²) and high sulfidizing (1×10^{-4} atm, 1×10^{-2} kN/m²) potentials generated in the ternary H₂-H₂O-H₂S gas, both oxide and sulfide species were formed. Samples which had been preoxidized at 850°C generally exhibited the formation of mainly Cr-sulfide rich regions above the preformed Cr₂O₃ scale; only isolated regions displayed the existence of thick mounds of a Co-rich sulfide. Samples preoxidized at 1000°C however yielded a greater density of rapidly growing Co-sulfide nodules on the surface of the alloy. Irrespective of the preoxidation temperature, subsurface oxidation and sulfidation additionally occurred. The alloy which had undergone no pretreatment developed a sulfide layer over the alloy surface, but in certain areas a continuous Cr₂O₃ layer formed beneath this exterior sulfide scale.

The current generation of commercially available heat-resistant stainless steels and cobalt and nickel base superalloys rely, for environmental protection, on the selective oxidation of chromium and/or aluminum to form a dense, compact, and adherent exterior oxide layer. However such conventional alloys were developed primarily for operation under highly oxidizing conditions such as those normally generated in power plants and gas turbine engines. In coal gasification or combustion process plants the metallic components are exposed at high temperatures to atmospheres of comparatively low oxygen and high sulfur activity. An analysis of the raw gas from a typical gasification step indicates oxygen and sulfur partial pressure of the order of 10^{-16} atm (10^{-14} kN/m²) and 10^{-5} atm (10^{-3} kN/m²), respectively (1).

Under certain conditions of operation the current generation of heat-resistant alloys are unable to form a protective oxide at the alloy-gas interface and unacceptably high rates of material degradation are observed (1, 2). Alternatively an oxide may form which is unable to prevent penetration of the oxide by sulfur and the subsequent formation of subsurface sulfides. In laboratory controlled experiments in sulfurous environments subsurface sulfidation has been regarded as a precursor of an accelerated rate of corrosion (3, 4).

Preliminary results from the first stage of a comprehensive investigation into the intrinsic capacity of preformed Cr₂O₃ oxide scales exposed to low oxidizing

and high sulfidizing potentials to prevent severe sulfidation of the underlying metallic components have already been reported (5). It was observed that samples of the Co-30 Cr alloy which had been preoxidized at 850°C displayed an incubation period before exhibiting an accelerated rate of attack, whereas alloy samples preoxidized at 1000°C corroded at an approximately linear rate from an early stage of the reaction. Irrespective of the preoxidation exposure time, samples preoxidized in the H₂-H₂O gas mixture at 850°C had gained only about 1 mg/cm² after 40 hr service at 900°C in the oxidizing-sulfidizing gas mixture whereas specimens preoxidized at 1000°C exhibited weight gains of approximately one order of magnitude greater (see Fig. 1). However, due to the accelerating form of the kinetics displayed by the alloy samples preoxidized at 850°C, these differences in reaction rates between preoxidized samples had narrowed considerably by the end of the various experimental runs. Unoxidized samples also corroded at an approximately linear rate when exposed to the H₂-H₂O-H₂S environment at 900°C. However, the preoxidized samples always corroded at a slower rate than the samples which had undergone no pretreatment. This paper describes the morphologies and compositions of the reaction products associated with these observed kinetic differences.

Experimental

The apparatus and experimental method associated with the exposure of the Co-30 Cr alloy in the equi-

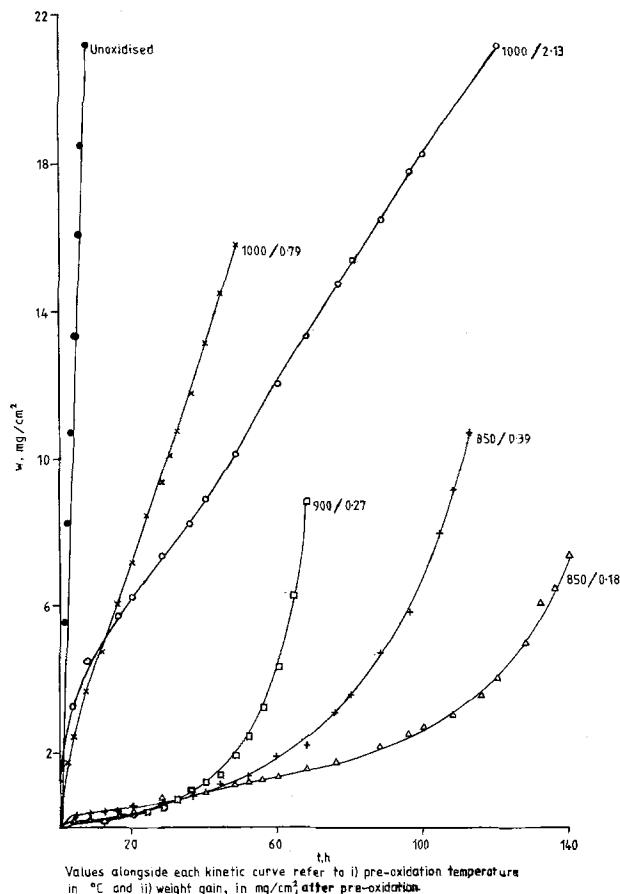


Fig. 1. The weight gain, as a function of exposure time, observed during the corrosion of various preoxidized samples of a Co-30 Cr alloy in an H₂-H₂O-H₂S atmosphere at 900°C.

librated H₂-H₂O-H₂S environment at 900°C have been described in detail elsewhere (5). The dimensions of a typical specimen were approximately 8 × 6 × 0.7 mm resulting in a surface area and weight of about 1.1 cm² and 200 mg, respectively. The preoxidation experiments were carried out in an H₂-H₂O gas mixture generated by bubbling hydrogen gas through dreschel bottles containing water maintained at 20°C. The main feature of this pretreatment assembly was a traveling furnace controlled by time clocks. After exposure periods of 24.33 to 290.33 hr, the oxidized samples were removed from the assembly and reweighed on a Stanton Balance, Model MCL, capable of reading to ± 0.02 mg.

A continuous corrosion monitoring technique was adopted with experiments undertaken in the H₂-H₂O-H₂S gas mixture. The balance/recorder arrangement was capable of reading changes in weight to ± 0.005 mg. In order to exclude corrosive gases from the balance a standard liquid seal technique was employed (5). The corroded samples, on removal from the test environment, were embedded in Scandiplast thermosetting resin and polished to a 1 μm finish prior to metallographic and energy dispersive x-ray analyses. Full details of the techniques of preparation and analysis have been given in another recent publication (6).

Results

In this section, the binary designations "CoS" and "CrS" are used as a convenient shorthand and are not intended to indicate a stoichiometric composition.

Co-30 Cr exposed to H₂-H₂O-H₂S environment: no preoxidation routine.—The exterior corrosion layer was of uneven thickness and, over parts of the alloy surface, was composed of mounds which were sometimes several hundred micrometers thick. It was clear from the globular appearance of the scale formed on

the alloy after exposure to the oxygen-sulfur environment at 900°C that in certain areas the reaction product had partially fused so that extreme softening or plastic flow of the mounds had occurred.

Figures 2a-c shows the S, Cr, and Co elemental traces across a severely corroded area. The corrosion product is structured into two distinct layers. The outer layer contained some cracks and large pores. However, it was more compact than the inner layer which contained numerous small pores and extended to the forefront of the subsurface degradation. Figures 2a-c show that the outer region of the outer layer was Co-sulfide, whereas the inner region of this layer was Cr-sulfide with some Co in solid solution. Cr-sulfide was also the predominant phase in the porous inner layer. No oxide was observed in regions which had undergone the most severe attack.

Over those areas of the Co-30 Cr alloy which had suffered less intensive corrosion than the areas described above, the external corrosion layer was also composed of sulfide phases (see Fig. 2d-f). This thin and irregular layer was principally Cr-sulfide containing some Co and in places the Cr-sulfide was surmounted by Co-sulfide regions, which displayed a lamellar structure characteristic of a eutectic phase mixture (Fig. 2g). At certain areas a Cr₂O₃ layer formed under the sulfide. Thus Fig. 2e and the region overlaid by a flag on Fig. 2g, h provide evidence for the existence of an apparently compact, though underlying, ragged oxide layer. At the forefront of the internal

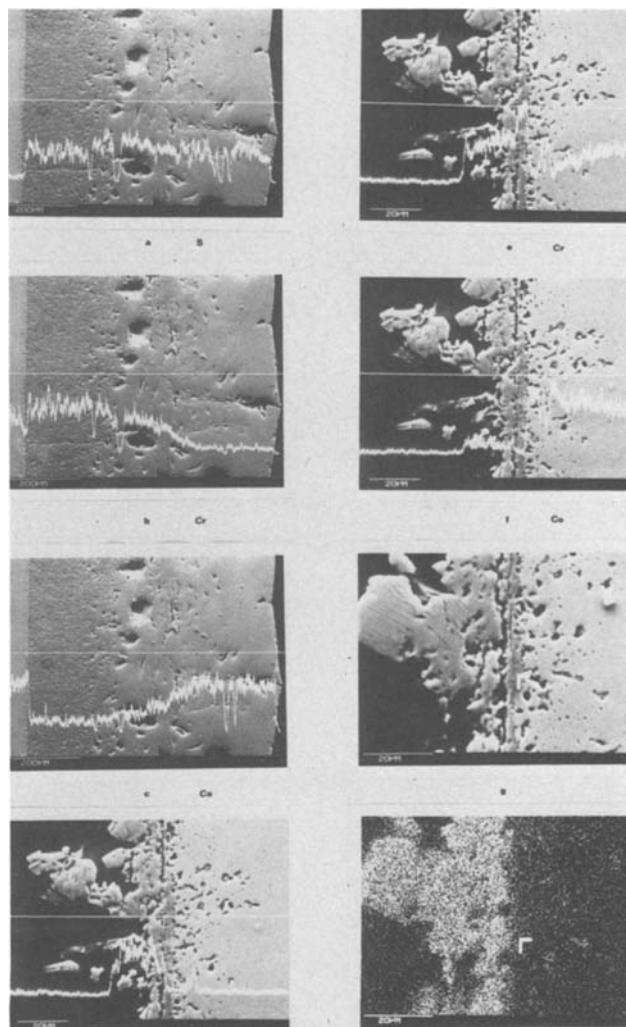


Fig. 2. Morphological features of corrosion relating to the exposure of a Co-30 Cr alloy for 7 hr in an H₂-H₂O-H₂S atmosphere at 900°C—electron and x-ray images, as indicated.

attack scattered and isolated Cr-sulfide particles were observed.

Cr-30 Cr exposed to the H_2 - H_2O - H_2S environment: preoxidized at $1000^\circ C$.—The preoxidation treatment was carried out for either 24.33 or 290.33 hr. After either treatment, some samples showed scale exfoliation. In order to minimize this problem the specimens were cooled slowly prior to removal from the pre-oxidation furnace. Only samples showing no exfoliation when examined at $120\times$ were used in the subsequent experiments in the oxygen-sulfur environment at $900^\circ C$. The rupture of the scale in small flakes occurred mainly at edges and to a lesser degree elsewhere (see Fig. 3a). All specimens displaying such spallation were excluded from the subsequent oxidation-sulfidation studies.

After exposure in the ternary environment mounds of a silver coloration had formed over parts of the alloy surface and these mounds had again been partially fused. These mounds of corrosion formed in a random distribution over much of the surface of the specimens but were definitely most thick and densely located along specimen edges and in areas neighboring the specimen suspension hole. In Fig. 3b an SEM photomicrograph shows a typical section of the corrosion products. It must be pointed out, however, that the mound shown in this figure had formed from an area of the specimen surface located adjacent to the oxide layer displayed. This applies also to Fig. 3c: here the mounds were composed of two morphologically distinct phases. Small Cr-sulfide mounds (Fig. 3d-f) were surmounted by areas principally rich in Co-sulfide. However there was also probably a degree of elemental interdistribution between the two mounds.

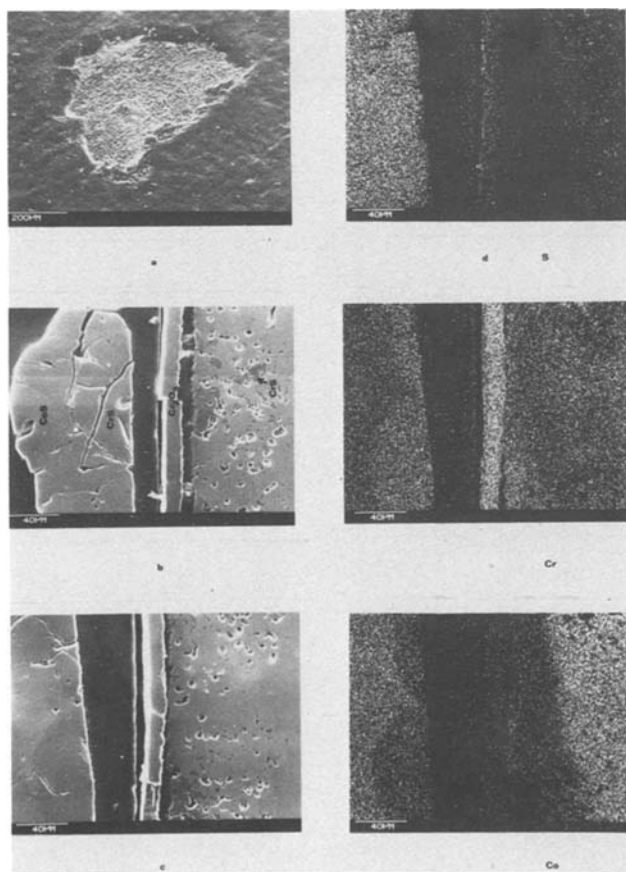


Fig. 3. (a) Electron image of the oxide formed on the surface of a Co-30 Cr alloy after exposure for 290.33 hr in an H_2 - H_2O atmosphere at $1000^\circ C$; (b-f) morphological features of corrosion relating to the exposure for 120 hr of a preoxidized Co-30 Cr alloy in an H_2 - H_2O - H_2S atmosphere at $900^\circ C$ —electron and x-ray images, as indicated; preoxidation conditions as above at (a).

The preformed oxide was exclusively Cr_2O_3 (Fig. 3e). Although compact and dense it had become detached from the underlying substrate and in places small cracks had appeared (Fig. 3b, c). In areas of the substrate adjacent to the oxide-alloy interface Cr_2O_3 oxide formation had occurred in localized regions with a degree of oxy-sulfide formation near the internal oxide-substrate boundaries. Again Cr-sulfide was the main internal corrosion product present as small clusters deep ($> 100 \mu m$) into the alloy.

The small grain size of the oxide formed after pre-oxidation for 24.33 hr at $1000^\circ C$ is shown in Fig. 4a. After exposure of these preoxidized samples to the ternary gas environment the corrosion products displayed the same general morphological and compositional aspects as described above. Thus, as shown in Fig. 4b, f, and g internal sulfidation was again evident.

Whereas the mound shown in Fig. 4b was composed of both Co-sulfide and Cr-sulfide (see Fig. 4c-e), Fig. 4f and g show mounds composed primarily of Cr-sulfide and Co-sulfide, respectively. It is of interest to compare the loss of integrity of the oxide when the outer sulfide mound was principally rich in Co. Figure 4g shows a segmented Cr-oxide layer whereas in Fig. 4f the Cr-sulfide mound has grown above an apparently compact and dense chromia layer.

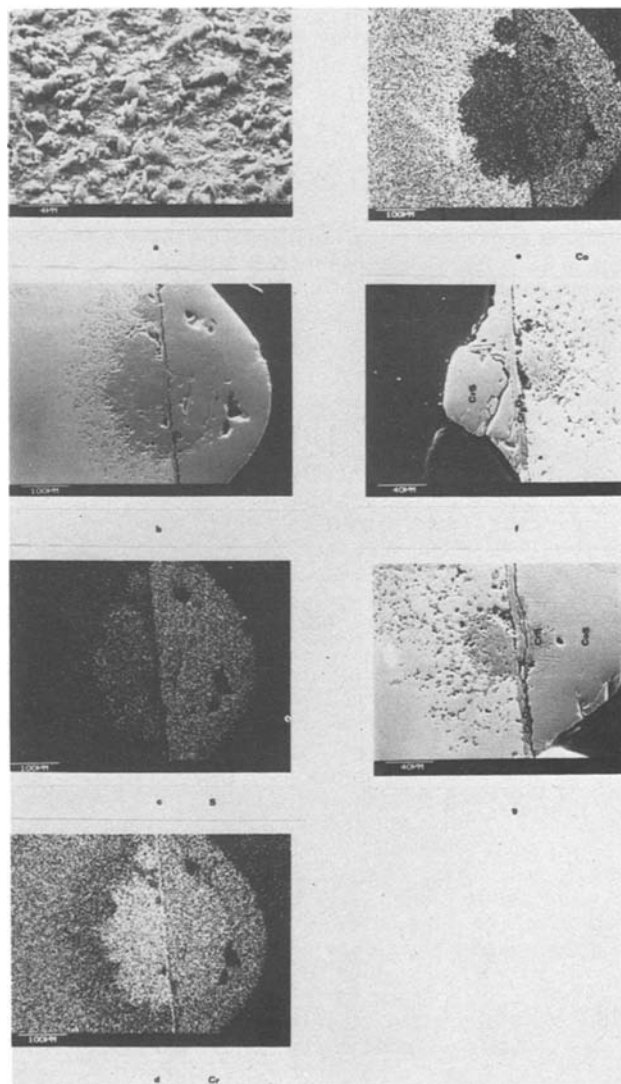


Fig. 4. (a) Electron image of the oxide formed on the surface of a Co-30 Cr alloy after exposure for 24.33 hr in an H_2 - H_2O atmosphere at $1000^\circ C$; (b-g) morphological features of corrosion relating to the exposure for 48 hr of a preoxidized Co-30 Cr alloy in an H_2 - H_2O - H_2S atmosphere at $900^\circ C$ —electron and x-ray images, as indicated; preoxidation conditions as above at (a).

Co-30 Cr exposed to the H₂-H₂O-H₂S environment: preoxidized at 850°C.—After preoxidation at 850°C the oxide formed on the surface of the Co-based binary alloy appeared to be completely adherent. Nevertheless as with samples preoxidized at 1000°C, the surface oxide on each alloy specimen was examined prior to exposure in the H₂-H₂O-H₂S gas assembly as described earlier. Energy dispersive x-ray analyses, carried out on sections of the oxide formed during the preoxidation treatment showed that the oxide was exclusively Cr₂O₃. The topography and grain size of the chromia layer is shown in Fig. 5a.

After exposure in the H₂-H₂O-H₂S environment at 900°C the surface of the preoxidized alloy was, in places, covered with nodules similar in composition, morphology, and location to those described in the preceding section relating to samples preoxidized at 1000°C. Thus the high temperature degradation was not uniformly distributed over the alloy surface. In

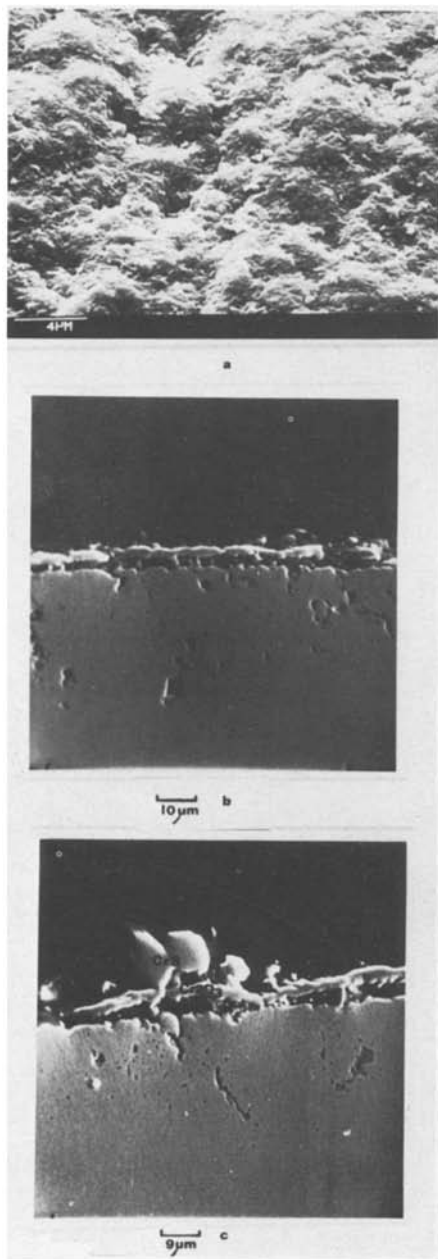


Fig. 5. (a) Electron images of the oxide formed on the surface of a Co-30 Cr alloy after exposure for 290.33 hr in an H₂-H₂O atmosphere at 850°C; (b, c) electron images of corrosion features relating to the exposure for 113 hr of a preoxidized Co-30 Cr alloy in an H₂-H₂O-H₂S atmosphere at 900°C; preoxidation exposure conditions as above at (a).

Fig. 5b a Cr₂O₃ scale, which had become separated from the underlying substrate and beneath which Cr-sulfide particles had formed, was the only surface corrosion product, whereas in Fig. 5c a Cr-sulfide phase had formed above the thin ballooned Cr₂O₃ layer. In this figure subsurface Cr-sulfidation is again noticeable and it is worthwhile mentioning that this internal degradation was evident below the Cr₂O₃ exterior layer even if this oxide had not been surmounted by a sulfide mound (Fig. 5b).

Other areas of the surface displayed more extensive sulfide corrosion products but apart from the relatively thick surface mounds most other corrosion products were lean in Co, being principally Cr-rich. Figures 6a-c show the formation of a compact Cr-sulfide mound. It is also apparent that the major part of the Cr₂O₃ layer beneath this sulfide mound is also compact. Co is again absent from both the internal and external corrosion species (Fig. 6d).

Discussion

The oxidizing potentials generated in the mixed and equilibrated H₂-H₂O environment at 850° and 1000°C were 3.5×10^{-21} atm (3.5×10^{-19} kN/m²) and 1.8×10^{-18} atm (1.8×10^{-16} kN/cm²), respectively. From a consideration of the Cr-O-S and Co-O-S phase stability diagrams set out in Fig. 7 it is clear that Cr₂O₃ would be expected to be the only stable phase to be formed on the surface of the alloy specimens. This was indeed verified by SEM and energy dispersive x-ray studies (see, for example, Fig. 3e). Thus the experiments carried out using preoxidized alloy samples gave information concerning the intrinsic capacity of preformed Cr₂O₃ layers to withstand severe material degradation when operating in a potentially aggressive oxygen-sulfur environment at 900°C. The oxygen and sulfur chemical potentials generated in the H₂-H₂O-H₂S atmosphere at this temperature were 2×10^{-19} atm (2×10^{-17} kN/m²) and 1×10^{-4} atm (1×10^{-2} kN/m²), respectively. This composition is represented by the symbol + in Fig. 7, where it can be seen that the stable phases to be formed on the surface of the Co-Cr alloy should be Cr₂O₃ and a Co-sulfide.

However from Fig. 2 it is seen that both Co and Cr-sulfides formed on the surface of the bare alloy in the ternary gas atmosphere and that, although Cr₂O₃ did indeed form, its location was always beneath an externally formed sulfide network (see Fig. 2e, g). Thus it would appear that the stable phases to be formed on the surface of the bare Co-30 Cr alloy were Cr-sulfide and Co-sulfide. The phase stability diagram shown in Fig. 7 has been constructed on the basis that the activities of the metal, oxide, and sulfide are unity. This results in the most restricted field of stability for each condensed phase (1). A decreased activity of sulfide (or oxide) reaction product enlarges the sulfide (or oxide) phase stability field. The fact that the Cr-sulfide contained some Co (see Fig. 2e and 2f) would result in the oxide-sulfide transition line marked ab on Fig. 7 moving to the right. This must, presumably, have been sufficient to ensure that the gas atmosphere would form Co and Cr-sulfide reaction products.

The partially fused nature of the surface corrosion product over certain areas of the alloy specimen after exposure in the oxygen-sulfur atmosphere can be accounted for by the formation of the Co-Co₄S₃ eutectic which forms at $\approx 880^\circ\text{C}$ (7). Thus in Fig. 2g and 4g a lamellar structure characteristic of a eutectic phase mixture is clearly evident. On metallographically scrutinizing these lamellae it was possible to discern that these Co-sulfide regions contained some metallic cobalt, formed as a result of the eutectoid reaction



which occurs at $\approx 790^\circ\text{C}$ (7).

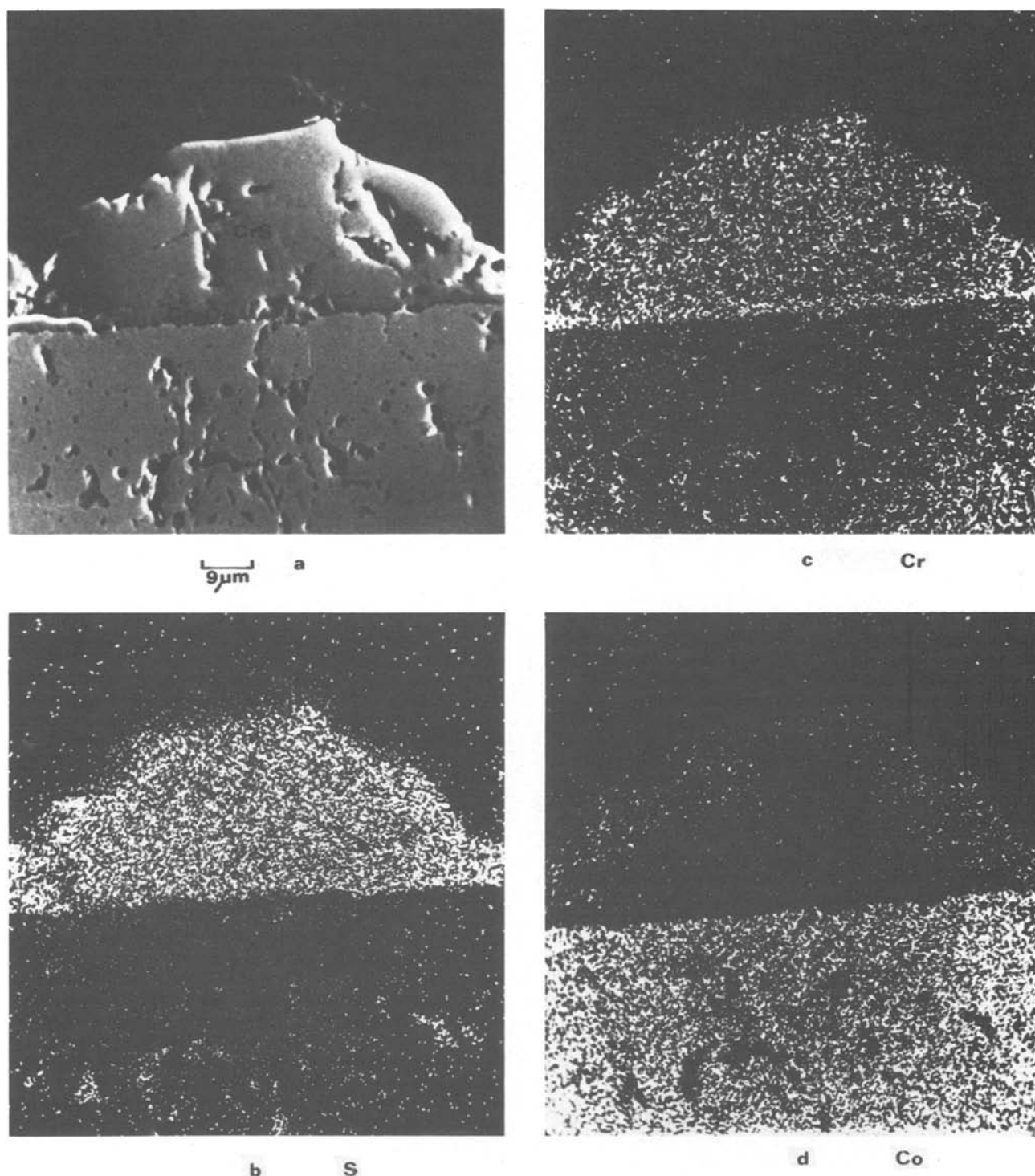


Fig. 6. Morphological features of corrosion relating to the exposure for 113 hr of a preoxidized Co-30 Cr alloy in an H_2 - H_2O - H_2S atmosphere at $900^\circ C$ —electron and x-ray images as indicated; preoxidation conditions—290.33 hr in an H_2 - H_2O atmosphere at $850^\circ C$.

On the Co-30 Cr alloy specimens which had been exposed to the ternary environment without any prior preoxidation routine, the corrosion product was mainly composed of sulfide, with a Cr_2O_3 subsurface layer being formed beneath this sulfide layer over certain areas (see Fig. 2d). Subsurface oxidation, as a phenomenological event, is akin to subsurface sulfidation occurring in a high oxidizing-low sulfidizing environment of which numerous examples have been reported in the literature (6). It was apparent that the external sulfide layer was relatively thin ($\approx 30 \mu m$) if there was an underlying compact Cr_2O_3 layer, in comparison with the thick ($\approx 600 \mu m$) layer formed when there had been no discernable oxide layer formation. Thus it must be concluded that the existence of a basal

barrier oxide layer restricted the outward diffusion of Co and Cr ions resulting in a thinner exterior sulfide layer.

Where there had been no discernable oxide formation, the morphology and composition of the external corrosion layer were similar to those reported in studies of the sulfidation of Co-Cr alloys (8, 9). Thus, in a solely sulfidizing environment, and irrespective of the exposure temperature, Biegun *et al.* (8) found that Co-based alloys containing approximately 30% Cr formed a multiphased scale with the outer layer consisting of a pure sulfide of the base metal and the inner layer composed of Cr-sulfide containing Co. It is also worthwhile noting that the irregular nature of the high temperature corrosive attack experienced by

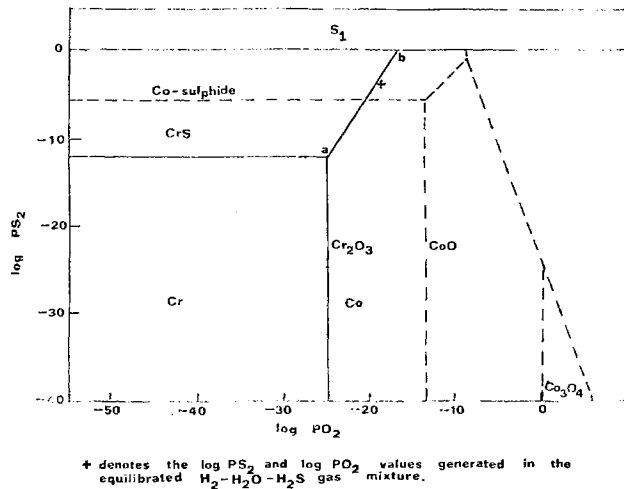


Fig. 7. Phase stability diagrams of the Cr-O-S and Co-O-S systems at 900°C (1173 K). All pO₂ and pS₂ values are in atmospheres.

this binary alloy after high temperature service in the oxygen-sulfur gas atmosphere has also been reported as a feature of the operation of Fe (1, 2, 10), Ni-(1), and Co(1)-based metallic materials in low oxygen-high sulfur activity atmospheres.

The observation that localized oxide exfoliation had occurred on the surface of certain alloy samples during cooling from the preoxidation temperature of 1000°C (but not 850°C) was indicative of the generation of severe internal stresses in the Cr₂O₃ scales. This is in agreement with the reported findings of Caplan *et al.* (11). Although it is reported in the literature that the scales formed after the high temperature oxidation of Co-(25-35%)Cr alloys almost invariably spall on cooling due to a phase change in the underlying alloy, it appears from this present work that the formation of relatively thin Cr₂O₃ oxide layers produced after preoxidation at 850°C may not result in a phase transformation. Thus the reduced Cr depletion associated with a thinner oxide layer may not have resulted in the formation of the fcc phase, which transforms to an hcp phase between 850°-700°C (7).

From the curves shown in Fig. 1, it is evident that preoxidation of the Co-30 Cr alloy conferred additional protection upon the alloy when exposed to the oxidizing-sulfidizing environment at 900°C. This effect of preoxidation is in agreement with the reported results of other independent investigators (2, 12). The observation of the formation of both Co and Cr-sulfides above the oxide barrier (which can be regarded as a marker) indicates that both Co and Cr were transported across the Cr₂O₃ layer. Perkins (1) has presented evidence for the outward diffusion of Fe, Mn, and Co ions across chromic oxide scales operating in atmospheres simulating typical coal gasification conditions. Thus, if Co ions can diffuse, via suitable short-circuit paths, to the surface of the Cr₂O₃ scale the formation of Co-sulfide will occur if the activity of Co is above the critical level required.

The alloy samples exposed to the O₂-S₂ environment after preoxidation at 850°C exhibited accelerated cor-

rosion kinetics after an incubation period. However even during the incubation period before the establishment of a manifestly accelerated rate of corrosion there was a small increase of weight indicative of some sulfide formation on the external surface at certain specific sites. Nevertheless the majority of the oxide surface was not surmounted by sulfide corrosion products at the end of the exposure period (compare Fig. 5b with 6a). The variable location of the external corrosion products tends to suggest that certain areas of the Cr₂O₃ oxide were more susceptible to outward cation transport.

Conclusions

A preformed layer of Cr₂O₃ improved the corrosion resistance of a Co-30 Cr alloy in an H₂-H₂O-H₂S atmosphere at 900°C. This beneficial effect, however, lasted for a limited period only.

Sulfide corrosion products then formed above the preformed Cr₂O₃ layer even though this oxide had been grown in a sulfur-free low oxidizing environment.

Acknowledgments

This work has been carried out with the support of the Science Research Council.

Manuscript submitted April 1, 1980; revised manuscript received Aug. 15, 1980.

Any discussion of this paper will appear in a Discussion Section to be published in the December 1981 JOURNAL. All discussions for the December 1981 Discussion Section should be submitted by Aug. 1, 1981.

REFERENCES

1. R. A. Perkins, Corrosion Chemistry in Low Oxygen Activity Atmospheres, Lockheed Research Laboratory, Annual Report LMSC-D562822, June 1977.
2. V. Nagarajan and A. V. Levy, Paper 49 presented at The Electrochemical Society Meeting, Seattle, Washington, May 21-26, 1978.
3. P. Kofstad and G. Akesson, *Oxid. Metals*, **13**, 57 (1979).
4. P. Singh and N. Birks, *ibid.*, **13**, 457 (1979).
5. P. J. Hunt and K. N. Strafford, "Environmental Degradation of High Temperature Materials," To be published by Chamelton Press Ltd., London (1980).
6. K. N. Strafford and P. J. Hunt, in "Materials and Coatings to Resist High Temperature Corrosion," D. R. Holmes and A. Rahmel, Editors, p. 39, Applied Science Publishers, London (1978).
7. M. Hansen, "Constitution of Binary Alloys," McGraw-Hill, New York (1958).
8. T. Biegun, A. Bruckman, and S. Mrowec, *Oxid. Metals*, **12**, 157 (1978).
9. S. Mrowec, in "Properties of High Temperature Alloys," Z. A. Foroulis and F. S. Pettit, Editors, p. 413, The Electrochemical Society Softbound Proceedings Series, Princeton, N.J. (1976).
10. F. H. Stott and S. Smith, Paper presented at International Conference on High Temperature Alloys held at Petten, Holland, October 1979, In press.
11. D. Caplan, A. Harvey, and M. Cohen, *Corros. Sci.*, **3**, 161 (1963).
12. G. Romeo and H. S. Spacil, "High Temperature Gas-Metal Reactions in Mixed Environments," S. A. Jansson and Z. A. Foroulis, Editors, p. 299, Boston (TMS-AIME) (1972).

Kinetic Study of Boron Tribromide Pyrolysis at Low Pressure

C. Combescure and B. Armas*

Laboratoire des Ultra-Réfractaires, C.N.R.S., B.P. No. 5, Odeillo 66120, Font-Romeu, France

and M. Alnot and B. Weber

Laboratoire Maurice Letort, L.A.R.I.G.S., C.N.R.S., B.P. No. 104, 54600 Villers-Nancy, France

ABSTRACT

We have studied the experimental growth rate of boron obtained by pyrolysis of BBr_3 under reduced pressure. Results are interpreted assuming that BBr_3 is adsorbed with dissociation on the boron surface, with no activation energy. Boron combines with the underlying lattice. Bromine is chemisorbed in the form of atoms. Bromine may either desorb in atomic form, or it may recombine and desorb in a molecular form or in the form of a bromide. The growth rate is a function of temperature and of surface coverage, hence of pressure. There is a good fit between the experimental results and the theoretical calculations. The deposition yield depends on the BBr_3 flow rate and on the pumping speed in the reactor.

Preparation of elementary boron by chemical vapor deposition has been frequently discussed, because this method allows one to obtain a very high purity product. Usually, boron halides (BCl_3 or BBr_3) are reduced by hydrogen at atmospheric pressure. Therefore, it is possible to prepare boron in large amounts in different allotropic forms, depending on the deposition temperature (1). However it is hard to make homogeneous deposits on pieces of complex shape by this process. On the other hand, coatings made under reduced pressure show a remarkable uniformity. This has induced us to study conditions of deposition by pyrolysis of BBr_3 under low pressure.

Thermodynamic Approximation

Although a chemical vapor deposition reactor, in particular a cold-wall reactor, does not behave like a system in thermodynamic equilibrium, we may assume that near the substrate there is a zone where chemical species are in thermodynamic equilibrium. The deposition field may then be computed. The boron-bromine system has been studied with a method of calculation based on minimization of the free energy of the system, taking material balance into account (2, 3).

The problem is easy to solve because only two elements are interacting. The number of possible species in the system is also limited. They are: Br_2 , Br , B , $\langle \text{B} \rangle$, BBr_3 , BBr_2 , BBr . Thermodynamic values necessary for the calculation are given in JANAF tables (4). At high temperature, all species are gaseous with the exception of boron.

We have plotted in Fig. 1 molar concentrations of products in equilibrium at different temperatures for one mole of gaseous BBr_3 at a total pressure of 7.7×10^{-2} Torr. Clearly, decomposition of BBr_3 occurs under reduced pressure, leading to the formation of solid boron.

At higher temperatures (i.e. > 1600 K) formation of boron is restricted by the formation of BBr . Nevertheless, the transformation yield of BBr_3 into elementary boron may exceed 95%.

One can also observe that the amounts of molecular bromine and of BBr_2 remain small and that gaseous boron may be neglected.

* Electrochemical Society Active Member.

Key words: low pressure vapor deposition (LPVD), boron, boron tribromide, kinetic model.

Experimental Study

The experimental study has been done in a cold-wall reactor (Fig. 2). The reaction chamber is a quartz tube 40 mm in diameter and 300 mm long. A BBr_3 evaporator made of Pyrex is immersed in an ice and water bath. A needle-valve allows one to regulate BBr_3 flow which is measured by a ball flowmeter.

In the reactor, a rotary pump maintains a pressure of about 1×10^{-2} Torr. The unreacted BBr_3 vapors and by-products of the deposition reaction are condensed in a liquid nitrogen trap located between the pump and the reactor. The substrate is a graphite cylinder, 16 mm in diameter and 8 mm thick and rf heated. It is possible to hang the substrate on the beam of an automatic microbalance, and the variation of weight may be followed continuously. Forces acting on the sample are: its weight, the electromagnetic force due to the induced currents from the magnetic field of the coil, and the upward thrust of the gaseous flow.

Archimedes's force on the sample can be neglected. The resultant of these three forces can be compensated by the re-equilibration force of the balance.

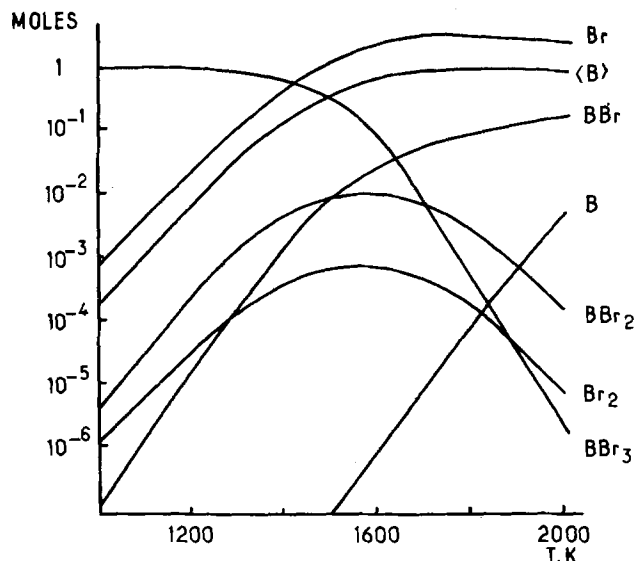


Fig. 1. Calculated compositions vs. temperature. Initial concentration: 1 mole of BBr_3 ; $P = 7.6 \cdot 10^{-2}$ Torr.

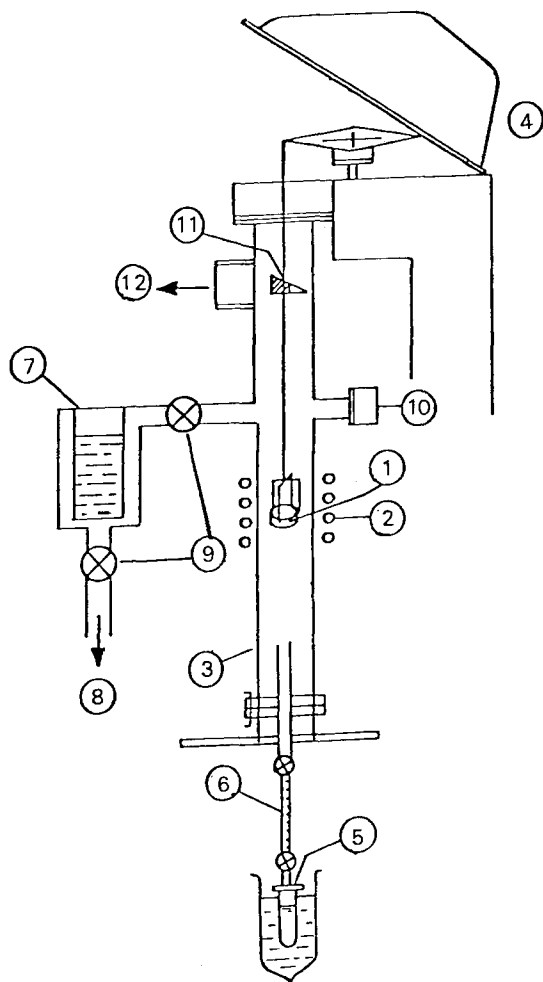


Fig. 2. CVD apparatus. 1, Sample; 2, induction coil; 3, silica tube; 4, balance; 5, BBr_3 evaporator; 6, flowmeter; 7, liquid nitrogen trap; 8, vacuum pump; 9, valve; 10, pressure sensor; 11, prism; 12, pyrometer.

The variation of this force will correspond to the variation of the weight of the sample assuming that other forces are constant. That is the case only if the temperature of the sample T , the gaseous flow Q , and the pressure P are constant. Thus, various experimental parameters must be varied stepwise. When all parameters are fixed, we obtain a record of the weight variation of the sample as a function of time. A derivative of this function gives the growth rate on a sample of a given area.

Since the deposit is thin, we may consider that the deposition area is constant. Series of runs with samples of various dimensions show that growth rate is proportional to the deposition area, all other parameters being equal. We can express the growth rate Vd as a function of weight change per unit area and per unit time. In practice, it is expressed in $\text{mg} \times \text{cm}^{-2} \times \text{hr}^{-1}$.

When substrate temperature, pressure, and flow of BBr_3 are constant, the increase in weight of the sample is a linear function of time. Therefore, growth rate is constant from the beginning of the deposition on graphite, whereas in the case of boron deposition on metallic substrates (Nb, Ta, W) a boronization of the underlying metal occurs (5), and the curve of weight increase *vs.* time is no longer linear but parabolic. We will only study boron deposition on a boron substrate; i.e., on a graphite cylinder previously covered with a boron layer, and we will not study the formation of the initial layers.

Keeping the pressure and BBr_3 flow constant, the substrate temperature was varied stepwise, and we obtained a series of straight line data that represents

weight gain *vs.* time. The slopes of these gave growth rates Vd at the corresponding temperatures.

First, the growth rate increases with substrate temperature T up to about 1700 K, beyond which it becomes quite steady.

We studied at constant temperature the growth rate *vs.* the pressure in the reactor and BBr_3 flow. Pressure can be varied without any significant change in the BBr_3 flow by varying the pumping speed of the gas, because the pressure in the evaporator (19 Torr) is higher than in the reactor ($P < 1 \cdot 10^{-1}$ Torr). On the other hand, if the BBr_3 flow is changed, the pumping speed must be modified in order to have a constant pressure in the reactor.

For fixed substrate temperature and BBr_3 flow, the growth rate increases *vs.* the pressure. For $T > 1700$ K the growth rate is proportional to the pressure (Fig. 3).

For fixed temperature and pressure, the growth rate is not dependent on the BBr_3 flow (Fig. 4). We deduce from these experimental results that the growth rate is only a function of the substrate temperature and the pressure in the reactor

$$Vd = f(T, P)$$

Only the β rhombohedral form of solid boron was obtained.

Interpretation

A kinetic model has been proposed to explain oxygenated (or halogenated) molecule-transition metal interactions (6). We have applied this model to the pyrolysis of BBr_3 at low pressure on a boron substrate.

The main assumptions of this model are as follows:

- (i) Adsorption of BBr_3 on the boron substrate is dissociative and nonactivated. Boron combines with the underlying lattice. Bromine is chemisorbed as atoms and may be desorbed in atomic or molecular form, or as boron bromide after reacting with boron surface atoms.
- (ii) Chemisorbed bromine is mobile at reaction temperatures.
- (iii) BBr_3 may not react with the adsorbed species (Eley-Rideal mechanism is excluded).

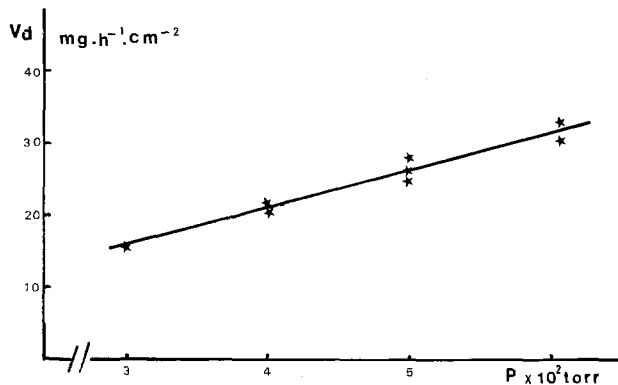


Fig. 3. Experimental growth rate *vs.* pressure. $T = 1720$ K; $Q_{\text{BBr}_3} = 4.18 \text{ g} \cdot \text{hr}^{-1}$.

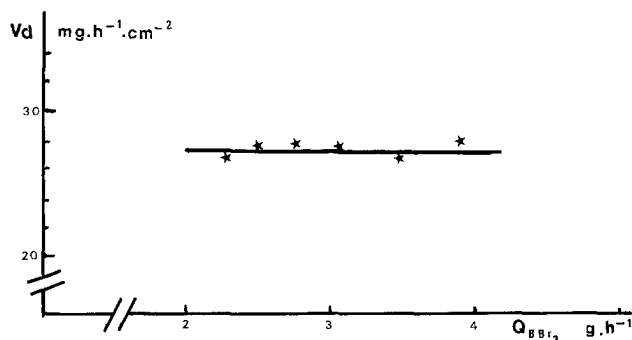
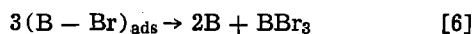
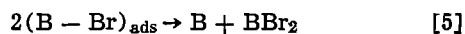
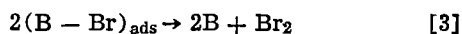
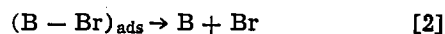
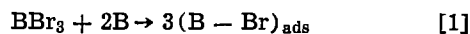


Fig. 4. Experimental growth rate *vs.* BBr_3 flow. $T = 1720$ K; $P = 5 \times 10^{-2}$ Torr.

The deposition mechanism can be described by the following reactions



Reactions [2] and [3], combined with reaction [1], lead to boron deposition, while reactions [4] and [5] involve boron attack. Reaction [6] induces neither deposit nor attack.

The flux of BBr_3 molecules which are adsorbed on the surface is

$$Z_{\text{ads}} = P_{\text{BBr}_3} \cdot (2\pi \cdot m_{\text{BBr}_3} \cdot kT_g)^{-1/2} \cdot b(\theta) \quad [I]$$

P_{BBr_3} is BBr_3 pressure in the reactor, T_g is the gas temperature (which is the wall temperature of the reactor, i.e., T_g is about 300 K), m_{BBr_3} is molecular weight of BBr_3 , and K is Boltzmann's constant. $b(\theta)$ represents the adsorption sticking probability which depends on the surface coverage θ of bromine.

Various desorption fluxes are

$$Z_{\text{Br}} = \nu_{\text{Br}} n_s \theta \exp\left(-\frac{x(\theta)}{RT}\right)$$

$$Z_{\text{Br}_2} = \nu_{\text{Br}_2} n_s^2 \theta^2 \exp\left(-\frac{2x(\theta) - D_{\text{Br}_2}}{RT}\right)$$

$$Z_{\text{BBr}} = \nu_{\text{BBr}} n_s \theta \exp\left(-\frac{x(\theta) + L_B - D_{\text{BBr}}}{RT}\right) \quad [II]$$

$$Z_{\text{BBr}_2} = \nu_{\text{BBr}_2} n_s^2 \theta^2 \exp\left(-\frac{2x(\theta) + L_B - D_{\text{BBr}_2}}{RT}\right)$$

$$Z_{\text{BBr}_3} = \nu_{\text{BBr}_3} n_s^3 \theta^3 \exp\left(-\frac{3x(\theta) + L_B - D_{\text{BBr}_3}}{RT}\right)$$

where ν represents pre-exponential factors, n_s the number of possible adsorption sites per area unit, $x(\theta)$ the heat of chemisorption of bromine atoms, L_B the heat of sublimation of boron, D_{Br_2} the heat of dissociation of molecular bromine, D_{BBr} , D_{BBr_2} , D_{BBr_3} the heats of dissociation of BBr , BBr_2 , BBr_3 into gaseous boron and bromine atoms at the substrate temperature T .

Under steady-state conditions, the material balance is

$$3Z_{\text{ads}} = Z_{\text{Br}} + 2Z_{\text{Br}_2} + Z_{\text{BBr}} + 2Z_{\text{BBr}_2} + 3Z_{\text{BBr}_3} \quad [III]$$

If Z_B is the flux of boron atoms deposited ($Z_B > 0$ corresponding to deposition of boron), the boron balance will be

$$Z_{\text{ads}} = Z_B + Z_{\text{BBr}_3} + Z_{\text{BBr}_2} + Z_{\text{BBr}} \quad [IV]$$

and

$$Z_B = 1/3 Z_{\text{Br}} + 2/3 Z_{\text{Br}_2} - 2/3 Z_{\text{BBr}} - 1/3 Z_{\text{BBr}_2} \quad [V]$$

Therefore boron's growth rate is not expressed in a simple form. Nevertheless, the previous thermodynamic study allows us to make several simplifications: (i) the BBr_2 and Br_2 fluxes are negligible in the entire range of temperature studied, (ii) at temperature $T > 1600$ K, the BBr_3 desorption flux is also negligible, and (iii) further, near $T = 1800$ K, the BBr flux is less than 10% of the Br flux; in this range Eq. [IV] just becomes

$$Z_{\text{ads}} = Z_B \quad [VI]$$

Experimental results and Eq. [I] allow us to calculate the sticking probability $b(\theta)$ of BBr_3 .

At very high temperature the growth rate approaches a constant value which means, as has been shown pre-

viously (6) and as we will confirm later, that surface coverage is small. So Eq. [I] and [VI] allow us to calculate easily the value of b for $\theta = 0$. The value we find is

$$b(\theta = 0) = 0.08$$

The other parameters ν and x cannot be determined easily. Therefore, we have proceeded to an optimization by the Rosenbrock method (7).

Equation [III] combined with Eq. [II] allows us to determine θ by successive approximations, then we calculate Z_{Br} and Z_{BBr} . Equation [V] then leads to a value for the growth rate for every experimental point. We have used the following thermodynamic data (4): $L_B = 132.8$ kcal/mole, $D_{\text{BBr}} = 103.5$ kcal/mole, $D_{\text{BBr}_2} = 258$ kcal/mole, and the value of $b(\theta = 0) = 0.08$ previously determined. The theoretical expression for $b(\theta)$ being unknown, we have used a cubic law $b(\theta) = b(\theta = 0)(1 - \theta)^3$ because it is necessary to have three superficial sites free to adsorb BBr_3 .

Optimization of other parameters (θ and x) has led to the following results: (i) the BBr_3 desorption flux is important only for the low temperature ($T \lesssim 1400$ K) range in which the experimental results are not very accurate, so it has not been possible to determine ν_{BBr_3} , (ii) the binding energy is independent of the surface coverage within the precision of the experiment. We have found that $x(\theta) = x(\theta = 0) = 65$ kcal/mole, and (iii) the order of magnitude of the pre-exponential factors are reasonable, $\nu_{\text{Br}} = 10^{23}$ and $\nu_{\text{BBr}} = 9 \times 10^{23}$.

Using all these values, we have calculated the curves of Fig. 5 and compared these curves with experimental data; the agreement is satisfactory. Nevertheless it should be observed that the number of optimized parameters is large and the only experimental result is the deposition rate. Hence it is not possible to obtain a set of parameters with good precision. To increase the accuracy, one would have to measure directly the Br , BBr , and BBr_3 fluxes and to determine their kinetic parameters.

Deposition Yield

We notice that the above interpretation of the experimental results does not need the BBr_3 flux through the reactor at any moment. The growth rate Vd will be determined only by the temperature of the substrate and the surface coverage, i.e., by the pressure.

In practice it is important to know the deposition yield Rd , i.e., the ratio of the boron deposited to the amount injected into the reactor in the form of BBr_3

$$Rd = (Vd \times S \times 250.5) / (Q_{\text{BBr}_3} \times 10.82)$$

where Q_{BBr_3} is the BBr_3 flow rate, S the deposition

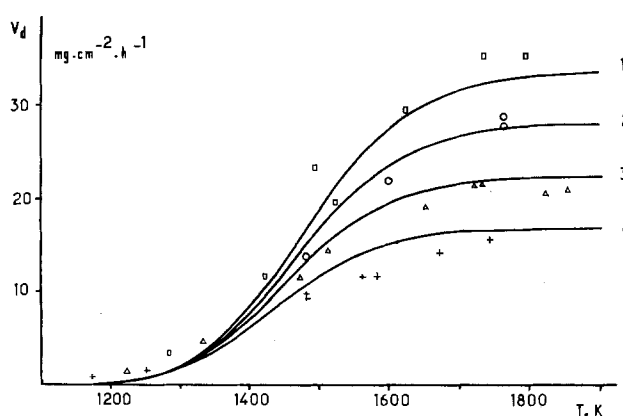


Fig. 5. Growth rate vs. substrate temperature. Experimental results: \square , $P = 6 \times 10^{-2}$ Torr; \circ , $P = 5 \times 10^{-2}$ Torr; \triangle , $P = 4 \times 10^{-2}$ Torr; $+$, $P = 3 \times 10^{-2}$ Torr. Calculated curves ($b(\theta = 0) = 0.08$): curve 1, $P = 6 \times 10^{-2}$ Torr; curve 2, $P = 5 \times 10^{-2}$ Torr; curve 3, $P = 4 \times 10^{-2}$ Torr; curve 4, $P = 3 \times 10^{-2}$ Torr.

area, and Vd the deposition rate. If Q_{BBr_3} is held constant, the yield Rd will increase with Vd or S . When the temperature is optimal Vd will increase with the pressure, i.e., with decreasing pumping speed. Rd will increase when the sticking probability increases.

It should be noticed that if Vd or S increase too much, Rd could be higher than 1, which is impossible. In this case, there is a consumption of BBr_3 greater than the flow and the steady-state conditions are no longer established. The BBr_3 partial pressure in the reactor will decrease until a new steady state is established. Then yield becomes maximum for these new conditions. We have obtained a yield $Rd = 0.89$ with an 8 cm^2 deposition area heated at $T = 1630 \text{ K}$, a 3.32 g/hr BBr_3 flow rate, and an initial total pressure of $1 \times 10^{-1} \text{ Torr}$. The growth rate was equal to 16 mg/hr/cm^2 , which corresponds to a BBr_3 partial pressure of $3 \times 10^{-2} \text{ Torr}$.

Conclusion

The kinetic model previously published (6) has been extended to BBr_3 pyrolysis at low pressure on a hot surface. We have determined the parameters determining the boron growth rate; these are the temperature and the surface coverage, therefore also the BBr_3 pressure. The reactor yield depends essentially on the BBr_3 flow and on the pumping speed that should be optimized as a function of deposition area.

Acknowledgment

The authors wish to thank the 'Centre d'Information de Thermodynamique Chimique Minérale' for the use of their thermodynamic computations.

Manuscript submitted Feb. 28, 1980; revised manuscript received Sept. 23, 1980. This was Paper 423 presented at the Los Angeles, California, Meeting of the Society, Oct. 14-19, 1979.

Any discussion of this paper will appear in a Discussion Section to be published in the December 1981 JOURNAL. All discussions for the December 1981 Discussion Section should be submitted by Aug. 1, 1981.

REFERENCES

1. P. Hagenmuller and R. Naslain, *Rev. Int. Htes Temp. Réfract.*, **2**, 225 (1965).
2. M. Ducarroir, M. Jaymes, C. Bernard, and Y. Deniel, *J. Less Common Met.*, **40**, 173 (1975).
3. C. Bernard, Y. Deniel, A. Jacquot, P. Vay, and M. Ducarroir, *ibid.*, **40**, 165 (1975).
4. JANAF Thermochemical Tables, 2nd ed. (1971).
5. B. Armas, *Rev. Int. Htes Temp. Réfract.*, **13**, 49 (1976).
6. B. Weber, J. L. Philippart, and A. Cassuto, *Surf. Sci.*, **52**, 311 (1975).
7. H. H. Rosenbrock and C. Storey, "Computational Technics for Chemical Engineers," Pergamon Press (1966).

A Negative-Working Plasma-Developed Photoresist

Gary N. Taylor,* Thomas M. Wolf, and Michael R. Goldrick

Bell Laboratories, Murray Hill, New Jersey 07974

ABSTRACT

Plasma-developed negative photoresists with good sensitivity and at least $1 \mu\text{m}$ resolution have been developed by the addition of quinone sensitizers such as phenanthrenequinone to a plasma-developed x-ray resist comprised of poly(2,3-dichloro-1-propyl acrylate) and N-vinyl carbazole. The sensitivity is optimum in the 290-350 nm range. Locking of the carbazole by cationic polymerization is presumably accomplished via cation radical intermediates produced upon quenching N-vinyl carbazole excited states with quinones that are excellent electron acceptors.

In a recent report (1) Taylor and Wolf described materials and a technique whereby patterns could be developed in negative x-ray resist by dry development using an oxygen plasma. An essential feature of this technique was the differential removal rates of resist in the imaged and nonimaged areas which allowed the shallow relief image obtained after fixing to be further enhanced to practically usable film thicknesses upon plasma development. The essential compositional elements which optimized sensitivity were found to be (i) an x-ray absorbing host polymer having a high removal rate in an oxygen plasma as best exemplified by poly(2,3-dichloro-1-propyl acrylate) DCPA and (ii) a moderately volatile aromatic monomer that is readily polymerized by ionizing radiation as best exemplified by N-vinyl carbazole NVC. Using an 81:19 mixture by weight of DCPA and NVC, submicrometer patterns were obtained upon exposure with low doses (4.5 mJ/cm^2) of $\text{Pd}_{L\alpha}$ x-rays at the 4.37\AA wavelength.

When these results were obtained it intrigued us as to whether such resists could be made sensitive to u.v. and visible radiation and thus be of use in more conventional photolithographic printing of high resolution negative resist patterns needed for VLSI device fab-

rication. The recent announcement by Motorola of a dry-developed photoresist (2) whose detailed structure was not given and a patent pertaining to this result (3) prompts us to report results obtained with monomer-polymer mixtures containing sensitizers which render them sensitive to u.v. and visible radiation.

Experimental

Poly(2,3-dichloro-1-propyl acrylate) was prepared as previously described (4). Its molecular parameters were $\bar{M}_w = 2.45 \times 10^6 \text{ g/mole}$, $P = \bar{M}_w/\bar{M}_n = 2.69$, $[\eta] = 1.95 \text{ dl/g}$ in ethyl acetate at 30°C . N-vinyl carbazole and hydroquinone dimethacrylate were used as received from Polysciences Incorporated and Monomer Polymer Labs, respectively. Sensitizers were obtained from Aldrich Chemical Company except for Irgacure 651 which was obtained from Ciba-Geigy Corporation. Wafers were coated by spinning from chlorobenzene solutions that had been filtered thru $0.45 \mu\text{m}$ pore membrane filters. These solutions were prepared by sequential dissolution of the polymer, monomer, and sensitizer, respectively, in the chlorobenzene.

Samples were exposed on a Kasper Model 2001 contact printer having standard optics. The mask and wafer were flushed with nitrogen in proximity prior to contact. Additional samples were exposed on a

* Electrochemical Society Active Member.

Key words: polymerization, quenching, x-ray.

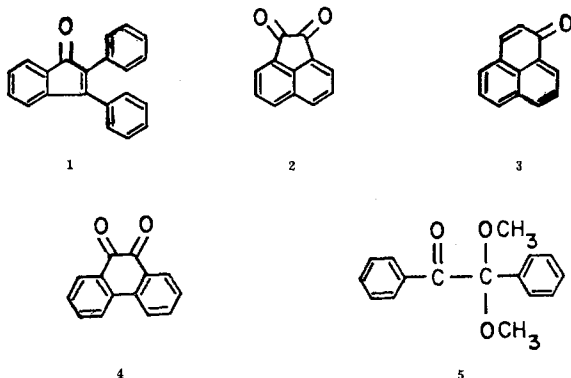
Perkin Elmer Model 120 projection printer and a Perkin Elmer Model 111 projection printer with the optics modified for exposure at 3100Å. After exposure the monomer not locked into the host polymer by irradiation was removed by treatment for 1 hr at 80°C and 0.1 Torr pressure. This afforded a relief image having greater thickness in the exposed regions but less than the initial thickness. Development was accomplished by treatment with an O₂ plasma in a Model 2005T-1813-SCA plasma etcher manufactured by the International Plasma Division of Dionics Incorporated. Operational parameters were: power = 100W, pressure = 0.55 Torr, and starting temperature = 35°C. Treatment was continued until the unexposed areas were completely removed. Sensitivity curves were obtained from step tablet and discrete exposures. Exposures using the step tablet always resulted in lower normalized film thickness through chrome areas of increasing optical density compared to discrete exposures of the equivalent dose. This indicated, that the sensitivity curves were flux dependent. Final evaluations were consequently conducted using discrete exposures of full wafers.

U.V. spectra were measured on a Cary 17 U.V.-visible spectrometer. Film thicknesses were measured on a Nanometrics, Incorporated Model 10-0174 Nano-Spec automatic film thickness gauge.

Results and Discussion

Two approaches were taken to try to sensitize the plasma-developed negative x-ray resists to u.v.-visible radiation. The first was use of sensitizers which generate radical species that initiate polymerization of acrylic and styrenic monomers thus locking them in the irradiated regions. The second approach was generation of cation radical intermediates by quenching suitable monomer or sensitizer excited states with either donor or acceptor quenchers. Best results were obtained with N-vinyl carbazole, a very good electron donor which is itself efficiently polymerized by cation radical species. These methods were recently reviewed by Ledwith and co-workers in 1974 (5) and 1975 (6), respectively.

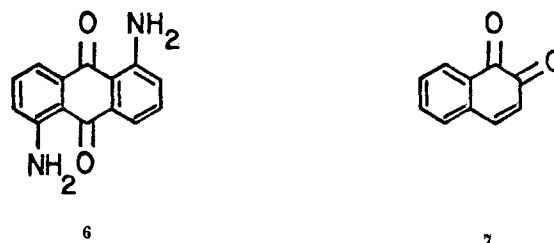
Five sensitizers were evaluated using DCPA as the host polymer and hydroquinone dimethacrylate as the polymerizable monomer. The sensitizers were 2,3-diphenylindenone (1), acenaphthenequinone (2), perinaphthenone (3), phenanthrenequinone (4), and Irgacure 651 (5). The first



four have moderate absorption in the u.v. and visible regions with ϵ ranging from 1000 to 5000 liters mole⁻¹ cm⁻¹ while Irgacure 651 is weakly absorbing at 3130 and 3660Å ($\epsilon = 150$ and 100 liters mole⁻¹ cm⁻¹ at these wavelengths, respectively). Using approximately 2.5 weight percent (w/o) of sensitizers 1-4 and 5.4 w/o of sensitizer 5 the results summarized in Table I were obtained using 1 μ m initial thickness films exposed for 4 min through a chrome step tablet mask. The least absorbing sensitizer, Irgacure 651, proved to be the most efficient sensitizer. Upon absorption of light it affords free radical species which initiate the

polymerization of acrylic monomers very efficiently. The two quinones, phenanthrenequinone and acenaphthenequinone were almost as effective as the Irgacure. Presumably, these sensitizers form free radical species by photoreduction of the reactive α -diketone groups to give a hemiketal radical by hydrogen abstraction presumably from the host polymer molecule. Monomer polymerization then ensues. The two eneones, perinaphthenone and 2,3-diphenylindenone, were less sensitive. The latter is very insensitive but highly absorbing. It may not undergo the facile photoreduction thought to provide initiating radical species because its lowest triplet state may be a π - π^* state rather than an n - π^* state which is more prone to undergo hydrogen abstraction (7). All of the combinations shown in Table I are less sensitive than the Kodak 747 negative photoresist which requires about 1 sec of exposure time.

The resolution of the resist mixtures listed in Table I was not optimized for the smallest features on the step tablet and mask because other formulations containing DCPA and N-vinyl carbazole offered improved sensitivity. Results for these materials are summarized in Table II. Typical sensitivity curves are given in Fig. 1. Two additional quinone sensitizers were studied. These were 1,5-diaminoanthroquinone (6) and 1,2-naphthoquinone (7).



All sensitizers resulted in highly sensitive negative resist materials with sensitivity comparable to that of conventional wet-developed negative resists and better than that of novolac-based positive photoresists. Phenanthrenequinone and acenaphthenequinone were the most efficient sensitizers. The photolocking mechanism which we suggest is outlined below (in Scheme 1) where Q represents the sensitizer quinone, N represents N-vinylcarbazole, and P represents polymerized N-vinylcarbazole. We believe that quenching of $^1N^*$ by the quinone is the dominant means of generating the radical cation which we feel is responsible for efficient polymerization of N. A less efficient means of generating N^+ is by quenching $^3Q^*$ with N. We presume this may be a less efficient process because the absorption of the quinone is much less than that of the N-vinylcarbazole in the short wavelength region. This is best visualized in the absorption spectra of various DCPA, NVC, and phenanthrenequinone films shown in Fig. 2. For example, at 334 nm and for 1 μ m thick films DCPA-NVC has OD = 0.53 compared to OD = 0.08 for DCPA-PQ. Here DCPA/NVC and DCPA/PQ values are 4.26 and 37.5, respectively. Thus, the quinones may not be sensitizers in the classical sense (reactions [10]-[12]) but probably sensitize primarily by quenching N-vinylcarbazole excited states.

Scheme 1

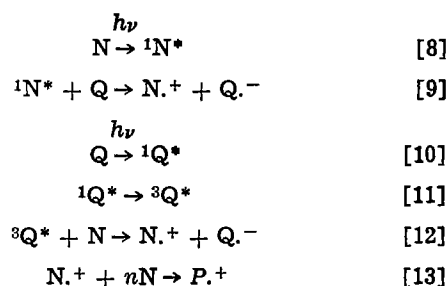


Table I. Sensitizers for plasma-developed photoresists containing HQDMA^{a,b}

| Sensitizer | ϵ (1 mole ⁻¹ cm ⁻¹) | | 405 nm | w/o Sensitizer | w/o DCPA | w/o HQDMA | $D^{0.15}$ (sec) ^c | γ^d |
|----------------------|---|--------|--------|----------------|----------|-----------|-------------------------------|------------|
| | 313 nm | 366 nm | | | | | | |
| Irgacure 651 | 149 | 98 | 0 | 5.4 | 80.9 | 13.7 | 20 | 0.22 |
| Phenanthrenequinone | 3500 | 1000 | 1300 | 2.4 | 85.4 | 12.1 | 24 | 0.19 |
| Acenaphthenequinone | — | — | — | 2.8 | 83.3 | 13.9 | 26 | 0.16 |
| Perinaphthenone | — | — | — | 2.8 | 83.3 | 13.9 | 34 | 0.23 |
| 2,3-Diphenylindenone | 4000 | 800 | 1500 | 2.8 | 83.3 | 13.9 | 240 | 0.58 |

^a Step tablet exposure for 4 min with variable transmittance regions used to obtain data for lower doses.

^b Final resist thicknesses obtained after fixing for 1 hr at 80°C and 0.1 Torr followed by O₂ plasma treatment to totally remove the unexposed regions.

^c $D^{0.15}$ is the dose required to give a normalized thickness of 0.15 after plasma development.

^d γ , the contrast, is the slope of the plot of normalized thickness vs. log dose.

Table II. Sensitizers for plasma-developed photoresists containing NVC^{a,b}

| Sensitizer | w/o Sensitizer | w/o DCPA | w/o NVC | $D^{0.20}$ (sec) ^c | γ^d |
|--------------------------|----------------|----------|---------|-------------------------------|------------|
| Phenanthrenequinone | 2.6 | 78.9 | 18.5 | 2.8 | 0.22 |
| Acenaphthenequinone | 2.6 | 78.9 | 18.5 | 3.7 | 0.32 |
| Irgacure 651 | 7.5 | 75.0 | 17.5 | 6.6 | 0.81 |
| Perinaphthenone | 2.6 | 78.9 | 18.5 | 7.8 | 0.56 |
| 1,5-Diaminoanthroquinone | 2.6 | 78.9 | 18.5 | 10.8 | 0.18 |
| 1,2-Naphthoquinone | 2.6 | 78.9 | 18.5 | 15.0 | 0.50 |

^a Step tablet exposure for 1 min with variable transmittance regions used to obtain data for lower doses.

^b Thickness obtained as previously described in Table I.

^c $D^{0.20}$ is the dose required to give a normalized thickness of 0.20 after plasma development.

^d γ , the contrast, is explained in Table I.



Except for the perinaphthenone and 1,2-naphthoquinone sensitizers these resists have very low contrast. Similar results were obtained for the compositions containing hydroquinone dimethacrylate except when 2,3-diphenylindenone was used as the sensitizer. However, we find, as Taylor and Wolf observed for the plasma-developed x-ray resists (1), that resolution is independent of the exposure dose. This results from the differential nature of the plasma development process in which the exposed regions are removed more slowly than the unexposed regions.

Since acenaphthenequinone is relatively insoluble in the DCPA-NVC mixture, we did not choose to try to optimize its effectiveness. Note in Fig. 1 that at exposure times greater than 7 sec and less than 30 sec

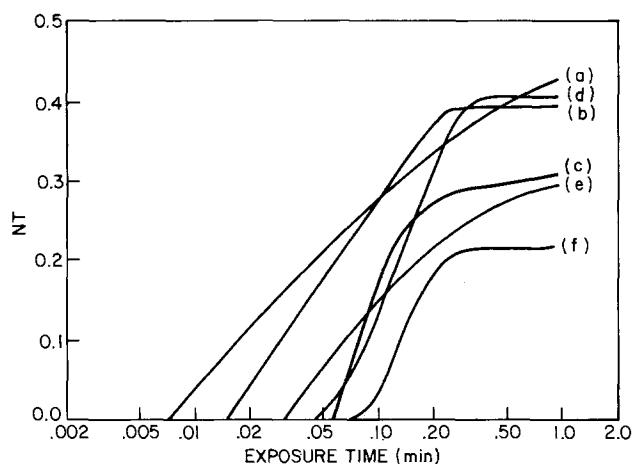


Fig. 1. Sensitivity curves for step tablet exposures of mixtures containing 78.9 parts DCPA, 18.4 parts N-vinyl carbazole, and 2.6 parts of the following sensitizers: curve (a), phenanthrenequinone; curve (b), acenaphthenequinone; curve (c), Irgacure 651; curve (d), perinaphthenone; curve (e), 1,5-diaminoanthroquinone; curve (f), 1,2-naphthoquinone. NT = normalized thickness.

acenaphthenequinone is a more effective sensitizer and thus could have offered the advantage of greater final thickness. Instead we chose to optimize formulations containing phenanthrenequinone sensitizer. Thus we studied the influence of composition, exposure conditions, and exposure mode on resist properties.

The data presented in Tables III and IV summarize the results of compositional changes in the DCPA-NVC-PQ formulation. Unfortunately, these results were obtained without flushing the wafer with a high enough flow of nitrogen (standard machine conditions were used) prior to contacting the mask and wafer. This allows residual dissolved oxygen to remain in the film and leads to higher contrast because the low dose exposures are quenched by O₂ to a greater extent than the high dose exposures. However, relative comparisons appear valid and two trends are evident. The first denoted by Table III is that excess sensitizer appears to act as a quencher. In these experiments the DCPA/NVC ratio was held constant at 4.29 while the sensitizer concentration was varied. Nearly optimum sensitivity was found at the intermediate 2.6 w/o concentration.

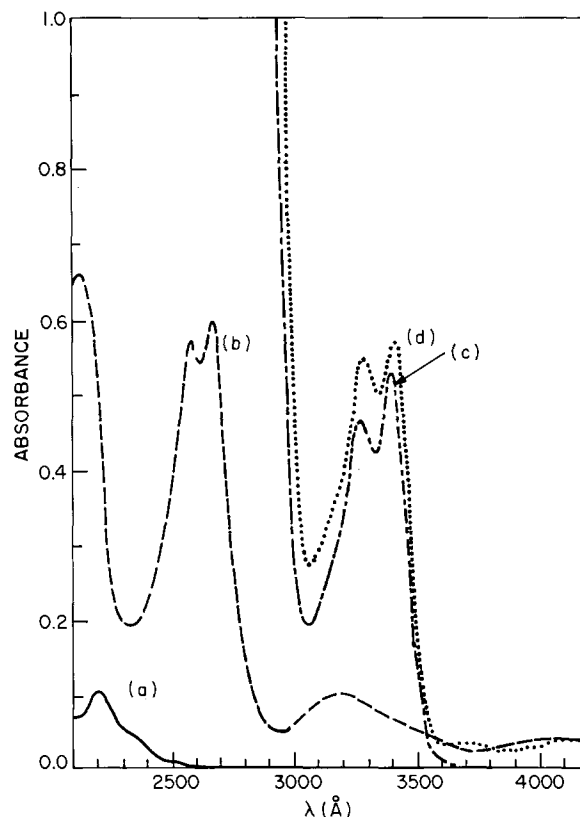


Fig. 2. Absorption spectra for 1 μ m thick films of curve (a), DCPA; curve (b), DCPA and 2.6 w/o phenanthrenequinone; curve (c) DCPA and 19 w/o N-vinyl carbazole; curve (d) 78.9 parts DCPA, 18.4 parts N-vinyl carbazole, and 2.6 parts phenanthrenequinone by weight.

Table III. Effect of sensitizer concentration on DCPA-NVC-PQ plasma-developed photoresist

| w/o DCPA | w/o NVC | w/o PQ | $D^{0.20}$ (sec) | γ |
|----------|---------|--------|------------------|----------|
| 79.8 | 18.6 | 1.5 | 14 | 0.42 |
| 78.9 | 18.4 | 2.6 | 9 | 0.66 |
| 76.9 | 17.9 | 5.1 | 14 | 0.59 |

Table IV. Effect of monomer concentration on DCPA-NVC-PQ plasma-developed photoresist

| w/o DCPA | w/o NVC | w/o PQ | $D^{0.20}$ (sec) | γ |
|----------|---------|--------|------------------|----------|
| 73.2 | 24.4 | 2.4 | 19 | 0.61 |
| 78.9 | 18.4 | 2.6 | 9 | 0.66 |
| 85.7 | 11.4 | 2.9 | 15 | 0.38 |

A second observation is that unlike the DCPA-NVC x-ray resist where sensitivity increased with increasing w/o NVC (1), the photosensitized samples show optimum sensitivity at an intermediate NVC concentration. This is indicated by comparing the results of the experiments listed in Table IV conducted at approximately 2.5 w/o sensitizer. From these results plotted as $D^{0.20}$ vs. w/o NVC and phenanthrenequinone, the composition for optimum sensitivity is predicted to contain approximately 80.0 w/o DCPA, 16.5 w/o NVC, and 3.5 w/o phenanthrenequinone.

The influence of exposure conditions has been mentioned in the previous section. A sufficient nitrogen flow is required to get reproducible results and to minimize exposure time. Comparison of adequate and inadequate nitrogen flushing of the mask-wafer sandwich prior to contact is presented in Fig. 3 which shows one sensitivity curve for each of these pretreatment conditions. Presumably, the residual oxygen in the inadequately flushed film b inhibits NVC polymerization at the lowest doses thus offering the advantage of higher contrast but adding the disadvantage of irreproducibility. We believe that failure to obtain short exposure times using the Perkin Elmer Model 120 printer with output primarily at 366, 405, and 435 nm is due to overwhelming O_2 quenching in the air atmosphere. The DCPA-PQ mixture is weakly absorbing at these wavelengths and moderately absorbing at 303, 313, and 334 nm where only weak lamp output is available. Short 23 sec exposure times have been obtained using the Perkin Elmer Micralign 111 with optics and filters modified to optimize exposure at the 303, 313, and 334 nm wavelengths. With these operat-

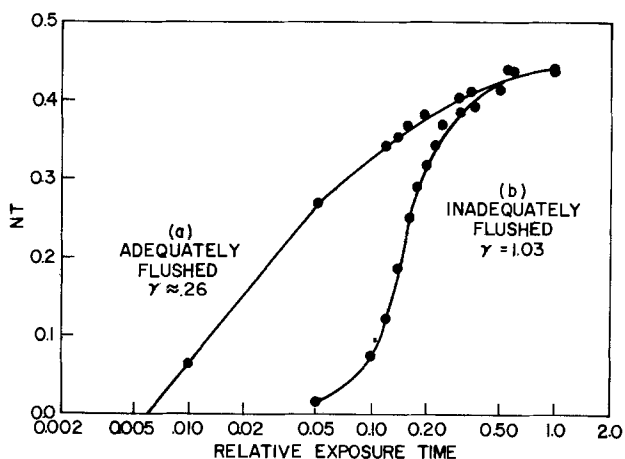


Fig. 3. Sensitivity curves for DCPA-NVC-PQ resist exposed with curve (a) adequate N_2 flushing; curve (b), inadequate N_2 flushing. NT = normalized thickness.

ing conditions the absorbed flux is apparently high enough to completely react all the O_2 present in the film as well as that which diffuses into the film during exposure.

Exposure mode is another factor which affects resist response. We mentioned previously that step tablet exposures made the resist appear less sensitive than it was when discrete exposures were conducted. This effect is best demonstrated by the sensitivity curves shown in Fig. 4. The resist was a 78.9, 18.4, and 2.6 part mixture by weight of DCPA, NVC, and phenanthrenequinone. For a constant normalized thickness of 0.2 the step tablet exposures gave varying exposure times of 4.7, 2.7, and 2.0 sec for total exposure times of 60, 30, and 15 sec, respectively. If discrete exposures were used, then for large features having $> 10 \mu m$ minimum dimensions, sensitivity curve a in Fig. 5 was obtained. Note that the contrast for this curve is 0.45, a much higher value than that for the 60 sec curve in Fig. 4 where $\gamma = 0.10$. Thus, to get a true sensitivity curve for these materials, discrete exposures must be used. Relative sensitivity data can be obtained from step tablet exposures. However, when resolution is the primary concern the discrete method must be used. Also included in Fig. 5 are sensitivity curves for Kodak 747 negative resist and Hunt HPR-204 positive resist. Both exhibit much higher contrast than the plasma-developed resist and require exposure times of 1.0 and 6.5 sec, respectively.

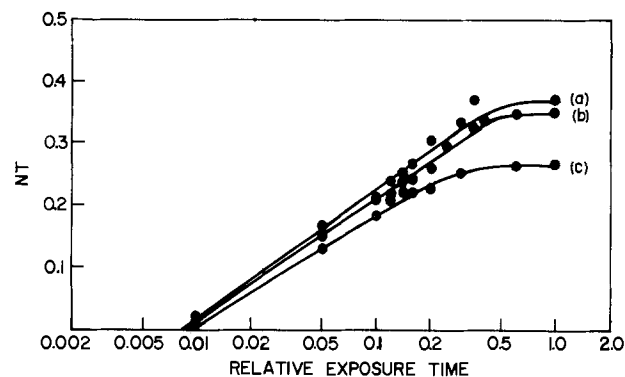


Fig. 4. Sensitivity curves for step tablet exposures of DCPA-NVC-PQ resist exposed for curve (a), 60 sec; curve (b), 30 sec; curve (c), 15 sec.

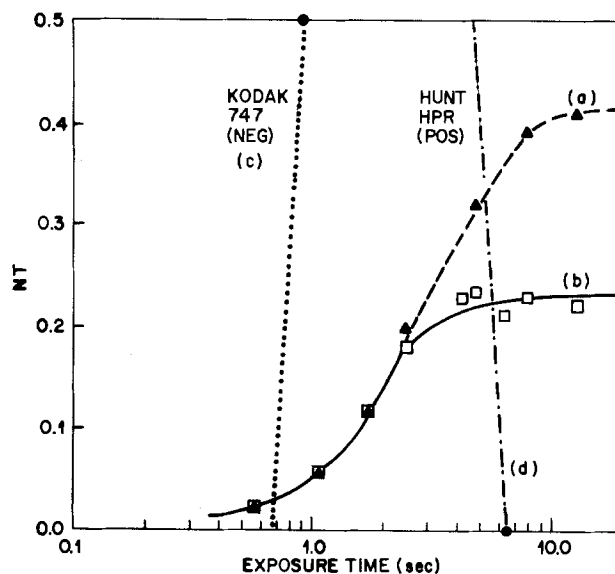


Fig. 5. Sensitivity curves for discrete exposures of DCPA-NVC-PQ resist showing the dependence on feature size: curve (a) features $> 10 \mu m$; curve (b), features $\geq 1 \mu m$. Curves (c) and (d) are for Kodak 747 negative resist and HPR-204 positive resist. The dark spots indicate the doses required for high resolution features.

The curves in Fig. 5 also reveal another important phenomenon. Curve (a) is the curve obtained when the thicknesses are measured for large features with minimum dimensions greater than $10 \mu\text{m}$. Unexposed regions contiguous to such regions have no residual resist remaining. However unexposed features having a minimum dimension $<10 \mu\text{m}$ are not completely cleared. The smallest features exhibit the worst deviations. If the smallest features on the mask ($\sim 1 \mu\text{m}$) are completely cleared, another sensitivity curve is obtained, curve (b) in Fig. 5. All features with dimensions $\geq 1.0 \mu\text{m}$ are well resolved for each point on curve (b). We believe the differences are due to diffraction effects even though the mask and wafer are presumably in contact. Exposures of a bowed wafer having proximity and contact exposures show even worse final resist thickness variations where the resist and mask are out of contact.

The effect on resolution by exposing for an exposure time longer than about 3 sec and plasma developing until only the large unexposed areas are cleared is shown in Fig. 6. The patterns were made by exposing for 10 sec (Fig. 6A) to give a $0.40 \mu\text{m}$ final thickness film, and 3 sec (Fig. 6B) to give a $0.21 \mu\text{m}$ final thickness film. Note that the image quality in 6A is fuzzy and that considerable resist remains in the $1 \mu\text{m}$ lines and spaces and the $2 \mu\text{m}$ contact windows which exhibit the worst diffraction effects. In Fig. 6B the features are much sharper and resolution appears to be about $1 \mu\text{m}$.

Better examples of the resolution of the plasma-developed photoresist are presented in Fig. 7. Here the $1 \mu\text{m}$ lines and spaces (Fig. 7a), the $2 \mu\text{m}$ contact windows (Fig. 7b), the isolated fine lines (Fig. 7c), and the isolated fine gaps (Fig. 7d) are all resolved at a final thickness of $0.24 \mu\text{m}$. The exposure time was 3 sec. High resolution patterns also were obtained on the modified Perkin Elmer at a 23 sec exposure time on the aperture 4 setting. Figure 8 shows examples of some of the patterns obtained. Exposure conditions and mask resolution were not optimum in these experiments. Better results might be obtained with more experimentation. Final resist thicknesses were $0.25 \mu\text{m}$.

Like the plasma-developed x-ray resist (1), the plasma-developed photoresist can only be used with trilevel processing (8) since flat surfaces are required. The DCPA-NVC-PQ mixture is quite resistant to conditions (CHF_3 reactive ion etching) used to etch the SiO_2 layer in the trilevel process (8). Typically,

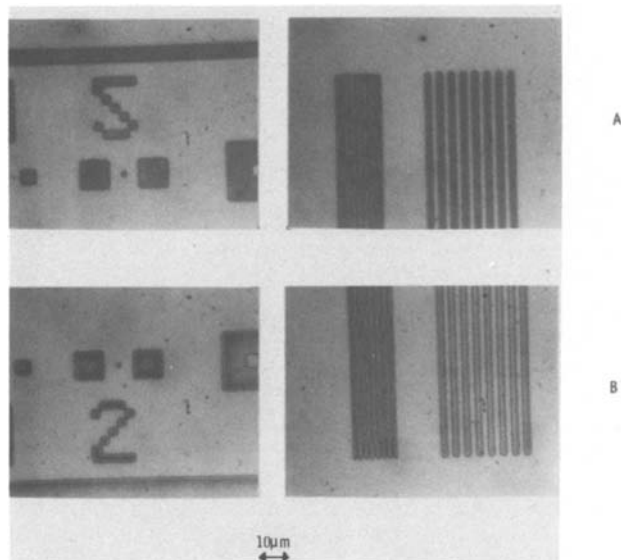


Fig. 6. Photomicrographs of contact exposures of 1 and $2 \mu\text{m}$ windows (left) and 1 and $2 \mu\text{m}$ lines and spaces in the DCPA-NVC-PQ resist exposed for (a) 10 sec, $0.40 \mu\text{m}$ thickness; (b) 3 sec, $0.21 \mu\text{m}$ thickness.

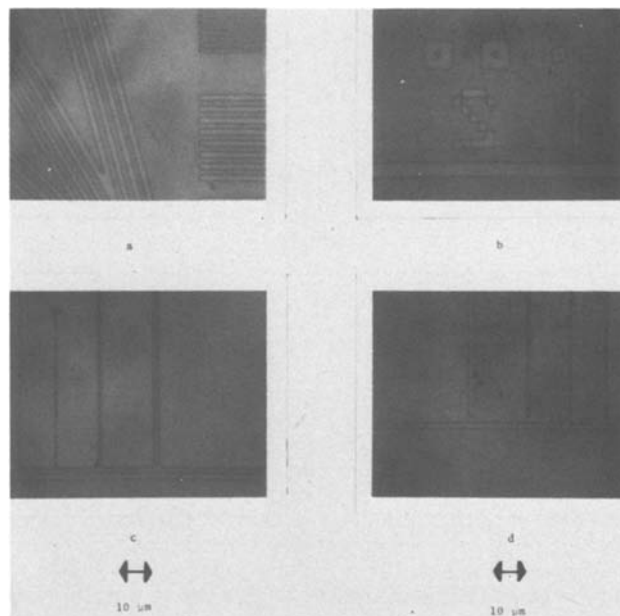


Fig. 7. Photomicrographs of $0.24 \mu\text{m}$ thick patterns in DCPA-NVC-PQ resist contact exposed for 3 sec (a) 1 and $2 \mu\text{m}$ lines and spaces and $2 \mu\text{m}$ oblique lines, (b) 1 and $2 \mu\text{m}$ windows, (c) 0.5, 1.0, and $2.0 \mu\text{m}$ isolated lines, (d) 0.5, 1.0, and $2.0 \mu\text{m}$ isolated gaps.

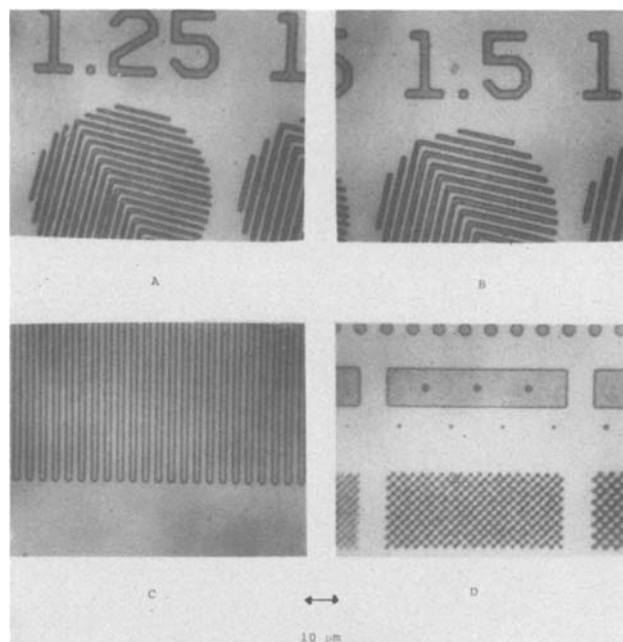
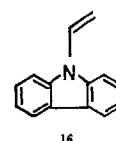
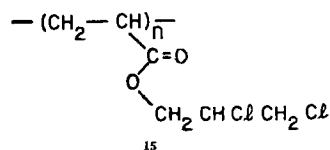


Fig. 8. Photomicrographs of $0.25 \mu\text{m}$ thick patterns in DCPA-NVC-PQ resist obtained by exposure with the Perkin Elmer 111 projection printer with optics modified for exposure at 3100 \AA . (A) $1.25 \mu\text{m}$ oblique lines, (B) $1.50 \mu\text{m}$ oblique lines, (C) $2 \mu\text{m}$ lines and spaces, (D) $1.25 \mu\text{m}$ contact windows. $1.0 \mu\text{m}$ and smaller features were not resolved. Exposure time was 23 sec.

$200\text{-}300 \text{ \AA}$ are lost when 1200 \AA of SiO_2 is removed by the RIE process.

Conclusions

The plasma-developed x-ray resist consisting of poly(2,3-dichloro-1-propyl acrylate) (15) and N-vinyl carbazole (16) has been sensitized to u.v. radiation by the addition



of quinone sensitizers. The most efficient sensitizer is phenanthrenequinone. The optimum composition contains 80.0 w/o DCPA, 16.5 w/o NVC, and 3.5 w/o phenanthrenequinone. With it 1 μm features can be printed in 0.23 μm final resist thickness with about one-half the exposure time required for HPR-204 positive photoresist. The resist is compatible with and can only be used with trilevel processing. It is sensitive primarily to the 3000-3400Å radiation of the u.v. spectrum. Resolution is sensitive to diffraction indicating a low modulation transfer function for this type of resist. However, high resolution features can still be obtained because of the differential development of exposed and unexposed regions during O_2 plasma processing.

Presently, this resist class offers no significant advantages over commercially available positive photoresists. Resolution is in fact probably somewhat higher for the latter. However, the resolution of plasma-developed photoresists is better than that of presently available negative photoresists. This is not a significant advantage since most high resolution photolithography is adequately accomplished using positive photoresists. The main advantages mentioned for the Motorola version (3) of the plasma-developed photoresist are that it is more cost effective and eliminates the need for the use of large volumes of potentially hazardous wet chemicals to develop and remove the resist patterns. These are important advantages. While plasma development avoids the use of wet chemicals, it does, however, require extensive capital investment in vacuum and plasma processing equipment which also must be safely exhausted. Throughput is less with presently available plasma processing units and uniformity of development can be a problem. In our opinion the foremost reasons for using plasma-developed resists are to obtain enhanced resolution and sensitivity. This makes such negative resists very attractive for x-ray lithography where resolution of highly sensitive re-

sists is limited by swelling during development to about 1 μm . Similar advantages are not as significant in photolithography at conventional wavelengths with the materials we have studied.

Manuscript submitted June 11, 1980; revised manuscript received Aug. 12, 1980.

Any discussion of this paper will appear in a Discussion Section to be published in the December 1981 JOURNAL. All discussions for the December 1981 Discussion Section should be submitted by Aug. 1, 1981.

Publication costs of this article were assisted by Bell Laboratories.

REFERENCES

1. G. N. Taylor and T. M. Wolf, *This Journal*, **127**, 2665 (1980).
2. "Electronics News," May 28, 1979, p. 99; "Semiconductor International," **2**, 6, 9 (1979); H. Hughes, W. Goodner, T. Wood, J. Smith, and J. Keller, Paper presented at the Regional Technical Conf., Mid-Hudson Section, Soc. Plast. Eng.; Oct. 10-12, 1979, Eilenville, New York; W. R. Goodner, T. E. Wood, H. G. Hughes, J. N. Smith, and J. V. Keller, "Proc. Kodak Microelect. Sem.," Oct. 25, 1979, New Orleans, Louisiana, pp. 51-59; J. N. Smith, H. G. Hughes, J. V. Keller, W. R. Goodner, and T. E. Wood, "Semiconductor International," **2**, 10, 41 (1979).
3. H. G. Hughes and J. V. Keller, *Ger. Offen.*, 2726813, Dec. 29, 1977.
4. G. N. Taylor, G. A. Coquin, and S. Somekh, *Polym. Eng. Sci.*, **17**, 420 (1977).
5. J. Hutchinson and A. Ledwith, *Fortschr. Hochpolym. Forschung*, **14**, 49 (1977).
6. R. A. Crellin and A. Ledwith, *Macromolecules*, **8**, 93 (1975).
7. For a discussion of the influence of the type of excited state on photoreduction see S. G. Cohen and J. I. Cohen, *J. Phys. Chem.*, **22**, 3782 (1968).
8. J. M. Moran and D. Maydan, *Bell System Tech. J.*, **58**, 1027 (1979).

Edge Profiles in the Plasma Etching of Polycrystalline Silicon

A. C. Adams* and C. D. Capio

Bell Laboratories, Murray Hill, New Jersey 07974

ABSTRACT

Five gas mixtures for plasma etching polycrystalline silicon films have been compared with emphasis on the edge profiles and the linewidth loss. The two isotropic etches, $\text{CF}_4\text{-O}_2$ and 1:1 $\text{C}_2\text{F}_6\text{-CF}_3\text{Cl}$ produce edge profiles that follow an arc of a circle and have line width losses that are nearly twice the thickness of polycrystalline silicon etched. In contrast the anisotropic etches, $\text{C}_2\text{F}_6\text{-Cl}_2$ and 4:1 $\text{C}_2\text{F}_6\text{-CF}_3\text{Cl}$ produce profiles that are nearly vertical and have line width losses that are dependent on the etch rate of the photoresist mask. Samples etched in CF_3Cl have circular profiles and have linewidth losses that are initially very small but increase rapidly as the samples are overetched. Measurements of the resist erosion rate indicate that the photoresist mask etches isotropically in $\text{C}_2\text{F}_6\text{-Cl}_2$ even though the polycrystalline silicon is etching anisotropically. Of the five etches examined, $\text{C}_2\text{F}_6\text{-Cl}_2$ is superior for etching very fine features.

Several processes for the plasma etching of polycrystalline silicon have been reported (1-5). The various etches differ in the degree of etching anisotropy, the etching selectivity over SiO_2 , the loss in feature size, and the sensitivity to loading effects. These effects become increasingly important in new

device technologies where gate oxides are very thin (300-500Å) and where submicron features must be etched. In addition, several papers discussing mechanisms of plasma etching have been published (6-11). It appears that the relative roles of ionic and neutral etching species and their relative lifetimes are important factors affecting the degree of etching anisotropy and the selectivity of various etchants (2, 12-15).

* Electrochemical Society Active Member.
Key words: etching, films, photoresist.

However, detailed comparisons of different plasma etching processes are not available. In this paper we report the etching of undoped and phosphorus-doped polycrystalline silicon with five different plasma etches, and compare the edge profiles and the losses in feature size.

Experimental

Samples are etched in a parallel-plate, radial-flow reactor that has been described previously (1). The etching conditions are summarized in Table I. Samples are prepared using standard processing techniques. The polycrystalline silicon (1.2 μm thick) is deposited at reduced pressure by decomposing silane at 640°C. The substrates are thermally oxidized silicon (0.4 μm of SiO_2 on 75 mm diam wafers). The polycrystalline silicon is doped with phosphorus subsequent to deposition using phosphorus tribromide at 1000°C for 25 min. The resistivity after doping is $1 \times 10^{-3} \Omega\text{-cm}$. The samples are baked (180°C, 45 min) and an adhesive layer of HMDS (hexamethyldisiloxane) is applied, followed by 1 μm of positive resist (HPR-204). The samples are then baked at 100°C for 20 min; the photoresist is exposed and developed; and, the samples given a final bake at 90°C for 30 min. Thick polycrystalline silicon (1.2 μm instead of the usual 0.3-0.5 μm) is used to improve the accuracies of the linewidth and the edge profile measurements. The underlying oxide is 0.4 μm thick (instead of 300-1000Å) to eliminate the possibility of etching through the oxide when samples are overetched for long times.

Edge profiles are measured by SEM cross sections at magnifications of 7000-12000 \times after cleaving the samples with the resist intact. Etch rates are determined by measuring the step height with a Taylor-Hobson Taly-step after removal of the photoresist. The etch rates have been checked using unpatterned wafers in separate experiments. Linewidths are measured for six features on each sample (the nominal feature sizes are 2, 3, 4, 5, 10, and 20 μm); each feature is measured at five places on the sample. The measurements are made optically at 1000 \times before plasma etching (to determine the feature sizes in the resist) and after etching (with the resist removed). The loss in linewidth is taken as the difference between the measurements. Etch times are chosen so samples are etched for approximately 25, 50, 75, 100, 125, 150, 200, and 300% of completion. Samples are etched singly, and loading effects have not been investigated. The $\text{CF}_4\text{-O}_2$ mixture is known to have large loading effects and the etch rate decreases as the area of etched material increases (9, 16). Loading effects for the four Cl containing etches are very small, and the use of single wafers should not affect the results (2, 3).

The process variables (power, pressure, and gas composition) have been previously adjusted for each of the gas mixtures to give optimum etching of the polycrystalline silicon. The five gas mixtures are compared using these optimum conditions (actual etching conditions) rather than trying to maintain constant process variables for all five gas mixtures. Independent experiments show that variations in the

pressure and power over the range indicated in Table I have almost no effect on the edge profiles, although the etch rates and sensitivities are affected.

The procedure for each sample is as follows: (i) the linewidths in the photoresist pattern are measured; (ii) the sample is etched; (iii) the sample is cleaved and examined by SEM to determine the edge profile; (iv) the photoresist is removed and the step height measured to determine the etch rate; and, (v) the linewidths in the etched pattern are measured and the line width losses calculated by difference.

Results

Etch rates.—The measured etch rates for P-doped and undoped polycrystalline silicon, for silicon dioxide, and for photoresist (HPR-204) are listed in Table II. The selectivities (the ratio of etch rates) are also given. The etch rates for silicon dioxide and for photoresist have been measured in separate experiments using unpatterned samples. The agreement between the measured rates in Table II and reported rates is good (2, 3). The selectivities over silicon dioxide are probably adequate for all five etches, especially if end-point detection is used to monitor the etching. The selectivity over photoresist is also adequate except for the $\text{C}_2\text{F}_6\text{-CF}_3\text{Cl}$ mixtures where the high resist etch rate contributes to the loss in feature size. This is a disadvantage when very fine features are being etched.

Edge profiles.—Edge profiles obtained from SEM cross sections at approximately 7000 \times are shown in Fig. 1 as a function of the amount of material etched. The profiles are shown with the resist still over the polycrystalline silicon. Representative SEM photographs are given in Fig. 2. The profiles in Fig. 1 and 2 show P-doped polycrystalline silicon; almost identical profiles are obtained for the undoped material. The profiles obtained with $\text{CF}_4\text{-O}_2$ and with 1:1 $\text{C}_2\text{F}_6\text{-CF}_3\text{Cl}$ indicate nearly isotropic etching; the profiles follow an arc of a circle with a radius nearly proportional to the etch time (17). In contrast, the profiles obtained with $\text{C}_2\text{F}_6\text{-Cl}_2$ and 4:1 $\text{C}_2\text{F}_6\text{-CF}_3\text{Cl}$ are nearly vertical with only a slight curvature at the bottom. As the etching proceeds a slight reverse taper develops for both gases. The profiles for these etching gases have a slight undercut at the resist edge. This undercut remains nearly constant as etching proceeds even though the resist is being etched away from the edges. A profile for 200% etching (100% overetch) is not shown in Fig. 1 for the 4:1 $\text{C}_2\text{F}_6\text{-CF}_3\text{Cl}$ gas because the photoresist is completely removed during the long etch time. The profile obtained from CF_3Cl follows a circular arc but the undercut is not as great as expected for isotropic etching; the etching in the vertical direction is greater than the lateral etching.

There are other features apparent in the profiles in Fig. 1. The relatively rapid etching of the photoresist with the $\text{C}_2\text{F}_6\text{-CF}_3\text{Cl}$ mixtures is indicated by the decrease in the resist thickness. Etching of the oxide is apparent for $\text{C}_2\text{F}_6\text{-Cl}_2$ and both $\text{C}_2\text{F}_6\text{-CF}_3\text{Cl}$ etches. This is expected since these gases have the lowest selectivity over silicon dioxide.

Table I. Etching conditions

| Etchant | Type | Gas composition | Power W | Pressure Torr |
|--|--------------|-----------------------------|---------|---------------|
| $\text{C}_2\text{F}_6\text{-Cl}_2$ | Anisotropic | 8% Cl_2 | 350 | 0.35 |
| $\text{C}_2\text{F}_6\text{-CF}_3\text{Cl}$ 1:1 | Isotropic | 50% CF_3Cl | 550 | 0.40 |
| $\text{C}_2\text{F}_6\text{-CF}_3\text{Cl}$ 4:1 | Anisotropic | 19% CF_3Cl | 550 | 0.40 |
| CF_3Cl | Intermediate | 100% CF_3Cl | 200 | 0.35 |
| $\text{CF}_4\text{-O}_2$ | Isotropic | 8% O_2 | 100 | 0.35 |

Electrode spacing: 3.1 cm
 Total gas flow: 200 sccm
 Wafer temperature: 25°-30°C
 Electrode area: 1250 cm^2

Table II. Etch rates and selectivities

| | CF_3Cl | $\text{C}_2\text{F}_6\text{-Cl}_2$ | $\text{CF}_4\text{-O}_2$ | $\text{C}_2\text{F}_6\text{-CF}_3\text{Cl}$ | $\text{C}_2\text{F}_6\text{-CF}_3\text{Cl}$ |
|--------------------------|------------------------|------------------------------------|--------------------------|---|---|
| Etch rates, Å/min | | | | 1:1 | 4:1 |
| P-poly | 800 | 570 | 1150 | 1590 | 820 |
| und-poly | 350 | 500 | 1050 | 980 | 700 |
| SiO_2 | 60 | 100 | 120 | 200 | 175 |
| Resist | 100 | 80 | 190 | 570 | 370 |
| Selectivity | | | | | |
| P-poly/ SiO_2 | 13 | 6 | 10 | 8 | 5 |
| P-poly/resist | 8 | 7 | 6 | 3 | 2 |
| und-poly/ SiO_2 | 6 | 5 | 9 | 5 | 4 |
| und-poly/resist | 4 | 6 | 6 | 2 | 2 |

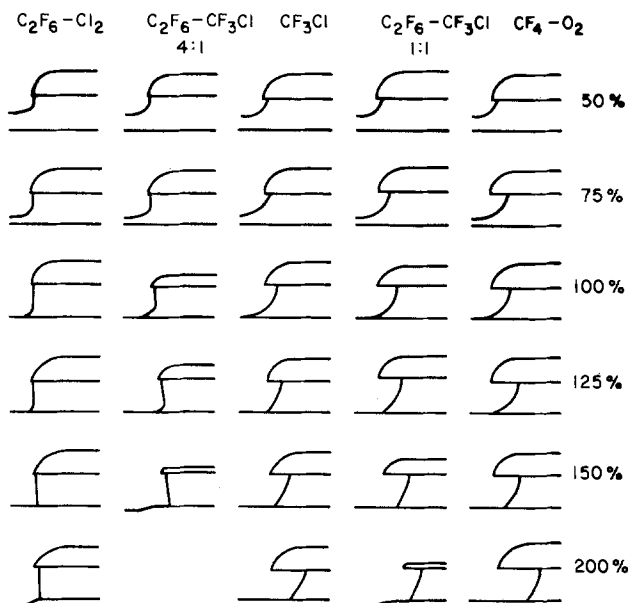


Fig. 1. Edge profiles at different stages of etching for five gas mixtures.

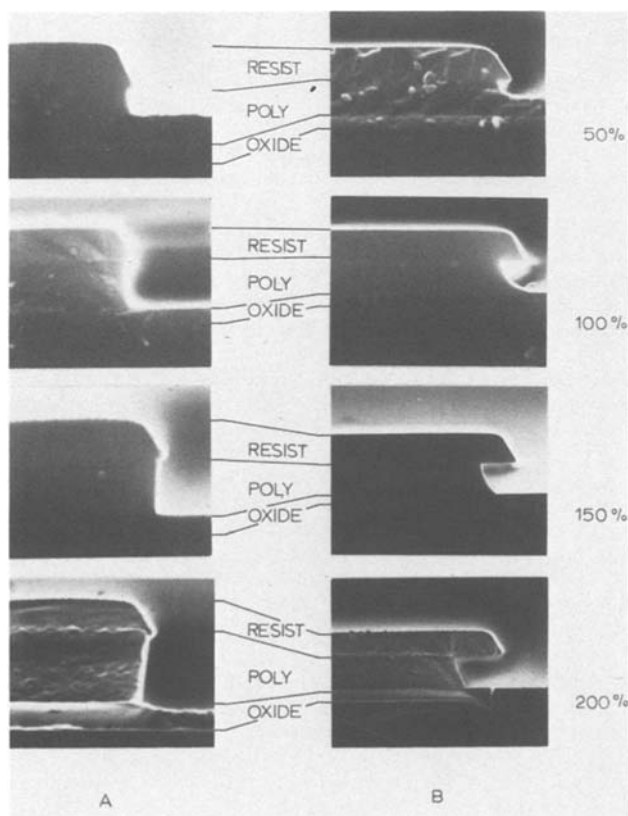


Fig. 2. SEM cross sections at different stages of etching for P-doped polycrystalline silicon etched with: (A) $C_2F_6-Cl_2$, (B) CF_4-O_2 .

A detailed model for anisotropic etching has been proposed (2). The anisotropy results from ion bombardment enhanced reactions of adsorbed species on the horizontal surfaces, with recombination of the etching species predominating on the vertical walls. Based on this model, the difference in edge profiles for the two $C_2F_6-CF_3Cl$ mixtures is caused mainly by differences in the rate of recombination. Sputtering is thought to have little or no contribution to the overall etch rate. This has been checked by using an argon plasma at the powers and pressures listed in Table I. No etching is observed; the detection limit is about 3 Å/min.

The edge profiles shown in Fig. 1 and 2 have been duplicated in other planar etchers (ranging in size from 35 to 61 cm diam). However, the results do not apply to tunnel etchers, where the anisotropic etches, $C_2F_6-Cl_2$ and 4:1 $C_2F_6-CF_3Cl$, have very slow etch rates, appear to etch isotropically, and do not etch reproducibly.

Linewidth loss.—The average loss in linewidth is shown as a function of the etching time (expressed as the amount of polycrystalline silicon that would have been etched) for each of the five gases in Fig. 3-7. The linewidth loss is independent of the feature size. The thickness etched is the actual amount for samples etched to less than completion ($1.2 \mu m$), and is calculated for greater times. The solid points are for undoped polycrystalline silicon; the open points are for P-doped samples. The dashed line is calculated for completely isotropic etching so the linewidth loss is twice the thickness of polycrystalline silicon etched. The solid lines are calculated for anisotropic etching of the polycrystalline silicon (etching only in the vertical direction with no component in the horizontal direction) assuming that the loss in linewidth is due entirely to erosion of the photoresist pattern (lateral etching of the photoresist). For this model, the slopes of the solid lines are given by $2E/R_p$, where E is the resist erosion rate and R_p is the etch rate of the polycrystalline silicon. For the calculated solid lines in Fig. 3-7, the resist erosion rate is assumed to be equal to the etch rate of the photoresist (given in Table II). A more exact discussion of resist erosion is given in the next section.

The calculated lines give good agreement for the anisotropic etches, $C_2F_6-Cl_2$ and 4:1 $C_2F_6-CF_3Cl$ (Fig. 3 and 4), and also for the two isotropic etches, 1:1 $C_2F_6-CF_3Cl$ and CF_4-O_2 (Fig. 6 and 7). The linewidth losses for samples etched with CF_3Cl are intermediate between the two lines (Fig. 5). For this case, the linewidth loss is best described by assuming anisotropic etching until completion (at $1.2 \mu m$) followed by isotropic etching. Although this model gives a good description of the linewidth loss data, it is not sup-

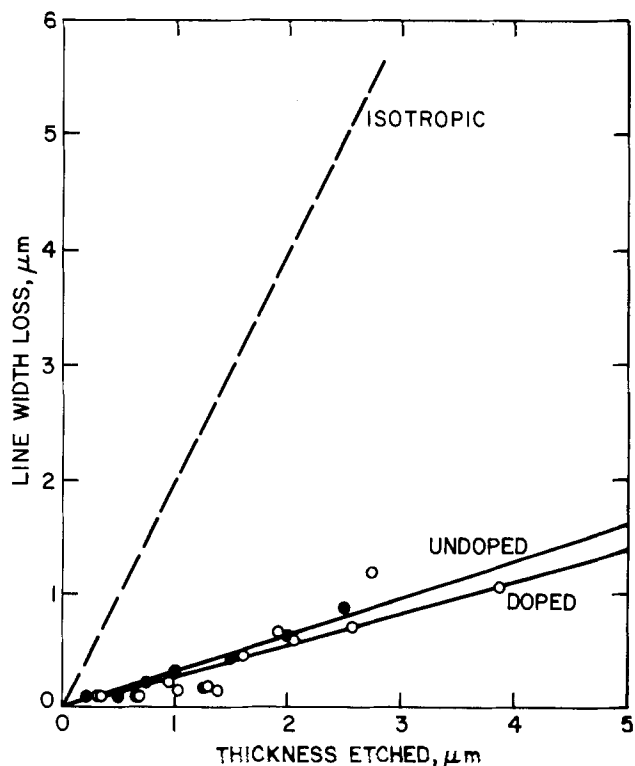


Fig. 3. Average linewidth loss vs. the thickness of silicon etched with $C_2F_6-Cl_2$.

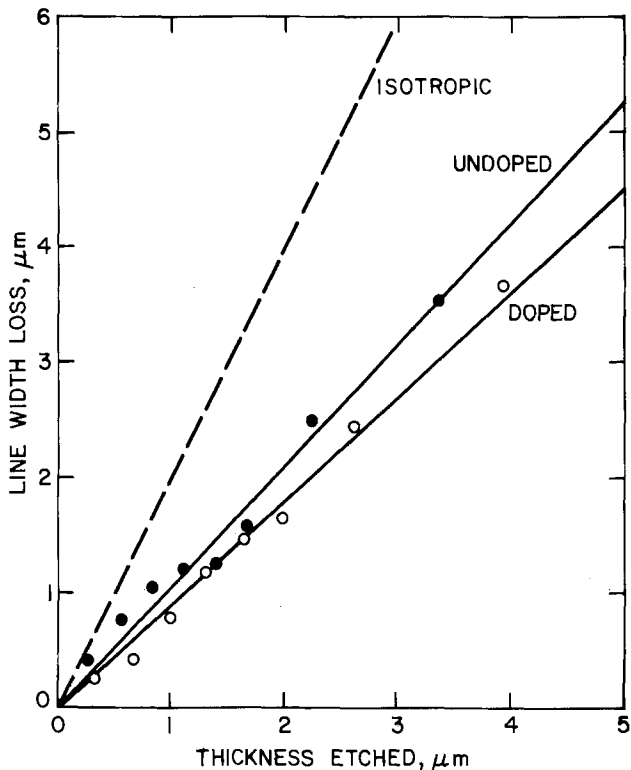


Fig. 4. Average linewidth loss vs. the thickness of silicon etched with 4:1 $C_2F_6-CF_3Cl$.

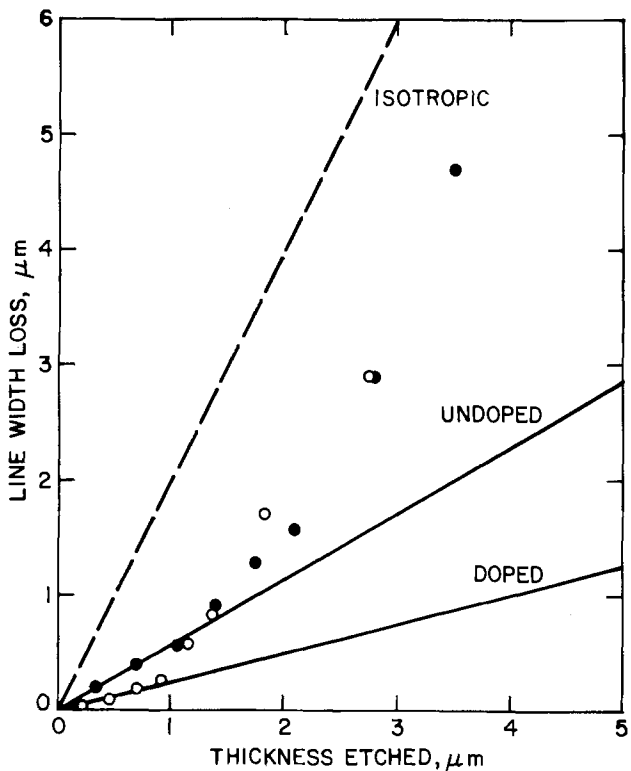


Fig. 5. Average linewidth loss vs. the thickness of silicon etched with CF_3Cl .

ported by the edge profiles shown in Fig. 1. In general, the loss in line width increases in the order: $C_2F_6-Cl_2 < CF_3Cl < 4:1 C_2F_6-CF_3Cl < 1:1 C_2F_6-CF_3Cl < CF_4-O_2$.

The data in Fig. 3-7 show the loss in linewidth for samples with the same thickness of polycrystalline silicon but etched for different times. The losses in linewidth for samples of different thicknesses (0.35, 0.60, and 1.2 μm) of polycrystalline silicon with all the

samples given a 25% overetch have been measured and compared with results calculated from Fig. 3-7. The agreement is good. The linewidth loss for 4:1 $C_2F_6-CF_3Cl$ is relatively large in spite of its being anisotropic because the photoresist is etching rapidly in this plasma.

A negative undercut (an increase in feature size) has been reported for silicon etched in a CF_4 plasma (18). The negative undercut decreases as etching

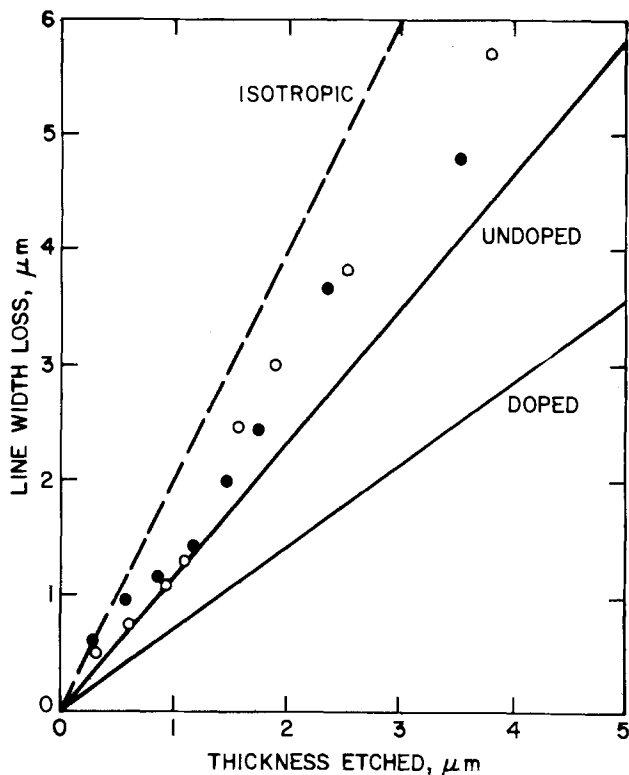


Fig. 6. Average linewidth loss vs. the thickness of silicon etched with 1:1 $C_2F_6-CF_3Cl$.

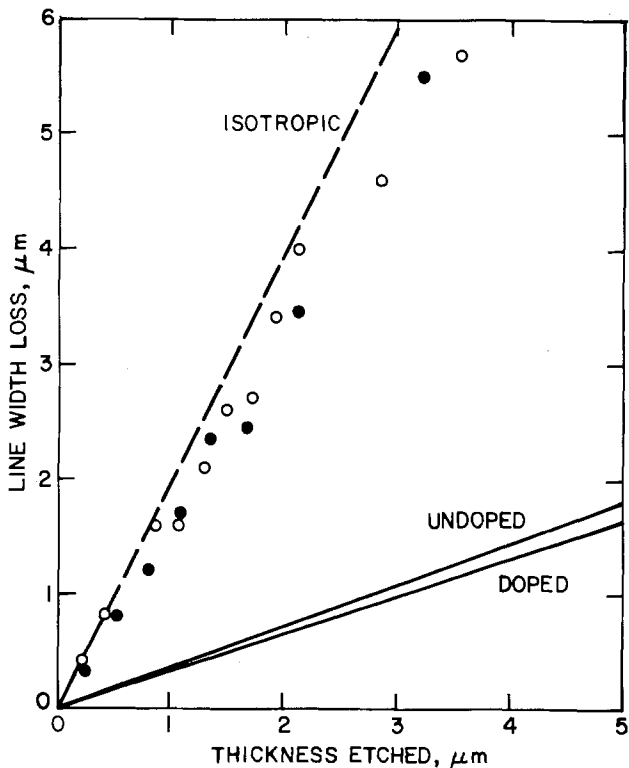


Fig. 7. Average linewidth loss vs. the thickness of silicon etched with CF_4-O_2 .

proceeds and eventually becomes positive (a decrease in feature size is a positive undercut). The overall effect gives an initial increase in feature size followed by a decrease or loss in size. This effect has not been observed for any of the five etchants. However, this phenomenon may explain the nonlinear loss in linewidth observed with CF_3Cl . The etching in this plasma may be nearly isotropic (as indicated by the edge profiles) but may be initially inhibited near the photoresist (as observed for the negative undercut) (18). The combined effect produces a small loss in linewidth during the initial etching followed by a more rapid loss as etching proceeds, as observed in Fig. 5.

Resist erosion.—Lateral etching of the photoresist pattern (resist erosion) depends on the angle made by the photoresist and on the nature of the photoresist etching (isotropic or anisotropic). For anisotropic etching of the photoresist (etching only in the vertical direction), the rate of resist erosion, E , is given by $R/\tan \theta$ where R is the etch rate of the photoresist and θ is the angle made by the photoresist edge. For isotropic etching of the photoresist (etching normal to the photoresist surface), the erosion rate is equal to $R/\sin \theta$. The rate of resist erosion divided by the resist etch rate is plotted in Fig. 8 as a function of the angle made by the resist profile. If the photoresist profile is vertical ($\theta = 90^\circ$), the erosion is zero for anisotropic etching of the resist and is equal to the resist etch rate for isotropic etching. As the angle decreases from 90° , the erosion increases until at small angles the erosion is nearly the same for both isotropic and anisotropic etching.

Experimental data showing resist erosion in a $\text{C}_2\text{F}_6\text{-Cl}_2$ plasma for three angles are also shown in Fig. 8. The angle is varied by using different bake temperatures after the photoresist is developed (the bake temperatures are 90° , 140° , and 210°C for angles of 60° , 45° , and 25°). The angles are measured from SEM cross sections. The rate of erosion is calculated from the slopes when the average linewidth loss is plotted against the thickness of polycrystalline silicon etched (Fig. 3). As already stated the slope is $2E/R_p$. This assumes that resist erosion is the only mechanism for the loss in linewidth. The solid point in Fig. 8 is obtained by measuring the resist erosion from the SEM cross sections. Although the data are not conclusive, there is an indication that the photoresist is

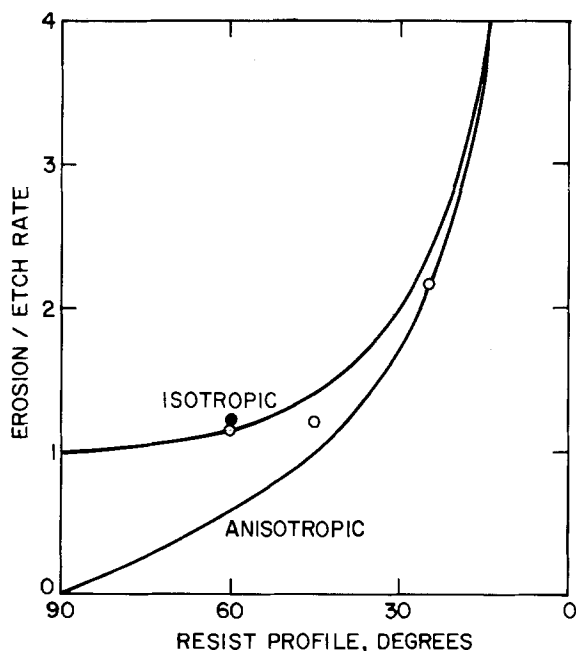


Fig. 8. The ratio of resist erosion to resist etch rate for different edge angles.

etching isotropically in the $\text{C}_2\text{F}_6\text{-Cl}_2$ plasma, even though the polycrystalline silicon is etching anisotropically.

Summary and Conclusions

Five different plasma etches for etching polycrystalline silicon have been compared. The loss in linewidth increases in the order $\text{C}_2\text{F}_6\text{-Cl}_2 < \text{CF}_3\text{Cl} < 4:1 \text{ C}_2\text{F}_6\text{-CF}_3\text{Cl} < 1:1 \text{ C}_2\text{F}_6\text{-CF}_3\text{Cl} < \text{CF}_4\text{-O}_2$. Examination of edge profiles as a function of etch time confirm that the $\text{C}_2\text{F}_6\text{-Cl}_2$ and $4:1 \text{ C}_2\text{F}_6\text{-CF}_3\text{Cl}$ etches are nearly anisotropic, and that the $1:1 \text{ C}_2\text{F}_6\text{-CF}_3\text{Cl}$ and $\text{CF}_4\text{-O}_2$ etches are nearly isotropic. Samples etched in CF_3Cl have profiles that appear to follow a circular arc but the lateral etching is less than expected for isotropic etching. As expected, the isotropic etches have a linewidth loss that is approximately twice the thickness of the polycrystalline silicon etched. In contrast, the linewidth loss for the anisotropic etches is determined by the erosion rate of the resist pattern. Samples etched in a CF_3Cl plasma have linewidth losses that are intermediate between isotropic and anisotropic etching. Initially the linewidth loss is small, but increases rapidly after samples are etched to completion. This nonlinear behavior of the linewidth loss may be related to the recently reported phenomenon of negative undercut (18). Of the five etches examined, $\text{C}_2\text{F}_6\text{-Cl}_2$ is superior for etching very fine feature sizes. Samples etched with this gas mixture have nearly vertical profiles and have very small losses in feature size.

Acknowledgments

The authors would like to thank J. E. McNulty for the step height measurements and for much of the plasma etching; E. I. Povilonis for help in processing the samples; and H. J. Levinstein, C. J. Mogab, and S. Broydo for many discussions.

Manuscript submitted March 13, 1980; revised manuscript received Aug. 19, 1980.

Any discussion of this paper will appear in a Discussion Section to be published in the December 1981 JOURNAL. All discussions for the December 1981 Discussion Section should be submitted by Aug. 1, 1981.

Publication costs of this article were assisted by Bell Laboratories.

REFERENCES

1. C. J. Mogab, A. C. Adams, and D. L. Flamm, *J. Appl. Phys.*, **49**, 3796 (1978).
2. C. J. Mogab and H. J. Levinstein, *J. Vac. Sci. Technol.*, **17**, 721 (1980).
3. W. R. Harshbarger and R. A. Porter, Private communication.
4. C. J. Mogab and W. R. Harshbarger, *Electronics*, **115**, 117 (1978).
5. G. C. Schwartz and P. M. Schaible, *J. Vac. Sci. Technol.*, **16**, 410 (1979).
6. J. W. Coburn, H. F. Winters, and T. J. Chuang, *J. Appl. Phys.*, **48**, 3532 (1977).
7. H. F. Winters, J. W. Coburn, and E. Kay, *ibid.*, **48**, 4973 (1977).
8. H. F. Winters, *ibid.*, **49**, 5165 (1978).
9. J. L. Mauer, J. S. Logan, L. B. Zielinski, and G. C. Schwartz, *J. Vac. Sci. Technol.*, **15**, 1734 (1978).
10. J. W. Coburn and E. Kay, *IBM J. Res. Develop.*, **23**, 33 (1979).
11. J. W. Coburn and H. F. Winters, *J. Vac. Sci. Technol.*, **16**, 391 (1979).
12. R. A. H. Heinecke, *Solid State Electron.*, **19**, 1039 (1976).
13. P. D. Parry and A. F. Rodde, *Solid State Technol.*, **22**, 125 (1979).
14. G. C. Schwartz, L. B. Rothman, and T. J. Schopen, *This Journal*, **126**, 464 (1979).
15. K. Suzuki, S. Okudaira, and I. Kanomata, *ibid.*, **126**, 1024 (1979).
16. C. J. Mogab, *ibid.*, **124**, 1262 (1977).
17. R. G. Brandes and R. H. Dudley, *ibid.*, **120**, 140 (1973).
18. H. Abe, *Jpn. J. Appl. Phys.*, **14**, 1825 (1975).

Progress in the Development of Solid-State Sulfate Detectors for Sulfur Oxides

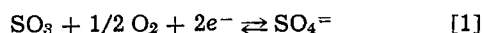
M. Gauthier,* R. Bellemare, and A. Bélanger*

Institut de recherche d'Hydro-Québec (IREQ), Varennes, Québec, J0L 2P0, Canada

ABSTRACT

The purpose of this article is to describe and analyze the performance of four different reference electrodes adapted for use in solid-state sulfate detectors for sulfur oxides: an electrode in which a calibrated gas circulates, an Ag/Ag⁺ electrode, an oxygen electrode using air as a reference and, finally, a thermal-decomposition type of electrode using an MSO₄-MO couple. The article also contains a description of a quartz detector for hot-gas analysis of SO₂-SO₃ mixtures and shows how the fact of replacing the platinum at the electrode by a less catalytic metal such as gold can lead to the specific detection of SO₃ in the presence of SO₂.

Previous work at IREQ has already shown that gaseous oxides, the major pollutants resulting from fossil-fuel combustion, can be measured potentiometrically using electrolytes containing oxyanions (1-3). Efforts so far have focused on the detection of the sulfur oxides SO₂ and SO₃. The reaction taking place at the triple-contact electrode SO₃ (g), O₂ (g), Pt/SO₄⁼ has been shown to correspond to the half-cell



Furthermore, with platinum, it has been observed that equilibrium is achieved rapidly between SO₂, O₂, and SO₃ in the vicinity of the electrode. The emf of the total sulfur oxide detector is given by the following equation

$$E = C_1 + \frac{RT}{2F} \ln(p_{\text{SO}_2})_{\text{in}} + \frac{RT}{2F} \ln p_{\text{O}_2} - \frac{RT}{2F} \ln(K + (p_{\text{O}_2})^{1/2}) \quad [2]$$

Two earlier papers (1, 2) presented the derivation of this equation and the symbols used, and described how in certain cases the emf expression can be made independent of the oxygen partial pressure. It was concluded from this that a total sulfur oxide detector is just as efficient for atmospheric-pollutant monitoring as for stack-gas analysis, where the oxygen partial pressure is not a constant.

The aim of this paper is to describe the latest improvements to the gas-circulation device developed at IREQ for the detection of atmospheric sulfur oxide pollutants. In view of the advantages this new detector offers for stack-gas analysis and the control of desulfurization processes, research efforts are still focusing on sulfur oxides. The results of various tests are presented in two sections, one related to the development of stable reference electrodes, the other to the study of gas-circulation electrodes operating both in equilibrium and in nonequilibrium conditions. In fact, the work reported in section two represents a first step towards the adaptation of the detector for hot-gas analysis of SO₂ and SO₃ mixtures and for the selective detection of SO₃ in the presence of SO₂.

Experimental

The preparation of the gas mixtures and the method of sintering the solid electrolytes were described in previous papers (1, 2) and remarks here will therefore be limited to pointing out that the K₂SO₄ electrolyte (mp 1063°C) is sufficiently plastic at the operating temperature of the detector to ensure a hermetic

seal of the various atmospheres in the device. The test setup used to study the SO₂-air mixtures is an alumina and stainless steel apparatus sealed with an organic resin, which was described in a previous publication (1). The photograph in Fig. 1 shows a two-compartment alumina cell together with details of the tip of the alumina tube and the platinum electrodes in contact with the potassium sulfate pellet. Adaptation of this type of detector for hot-gas analysis (SO₂ and SO₃) has led to the development of a quartz device based on an SiO₂ tube, Type 204, 6.5 mm OD, with 2-mm bores from General Electric, Willoughby, Ohio. The gas inlet and outlet, welded to the tube, are made of Pyrex glass and terminated in ball-and-socket joints lightly coated with silicon grease and

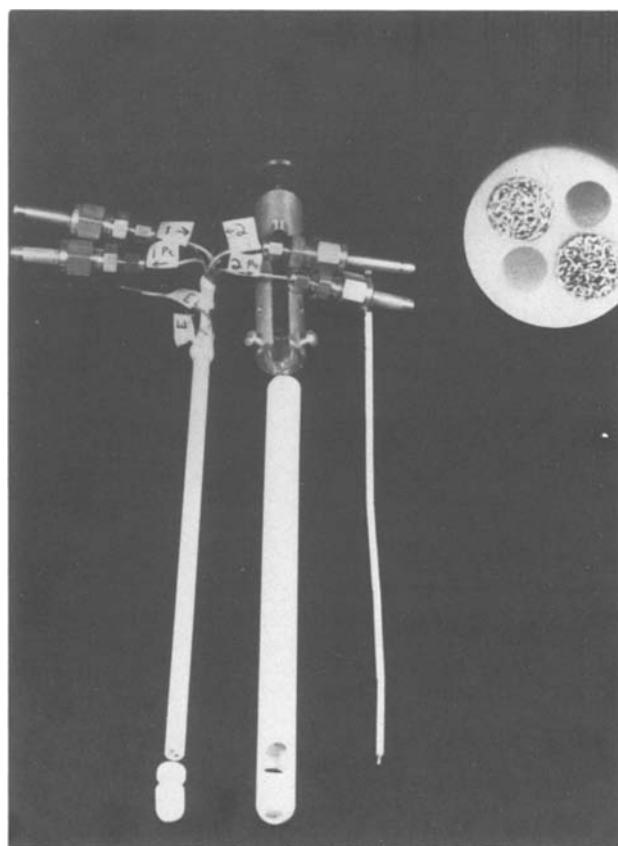
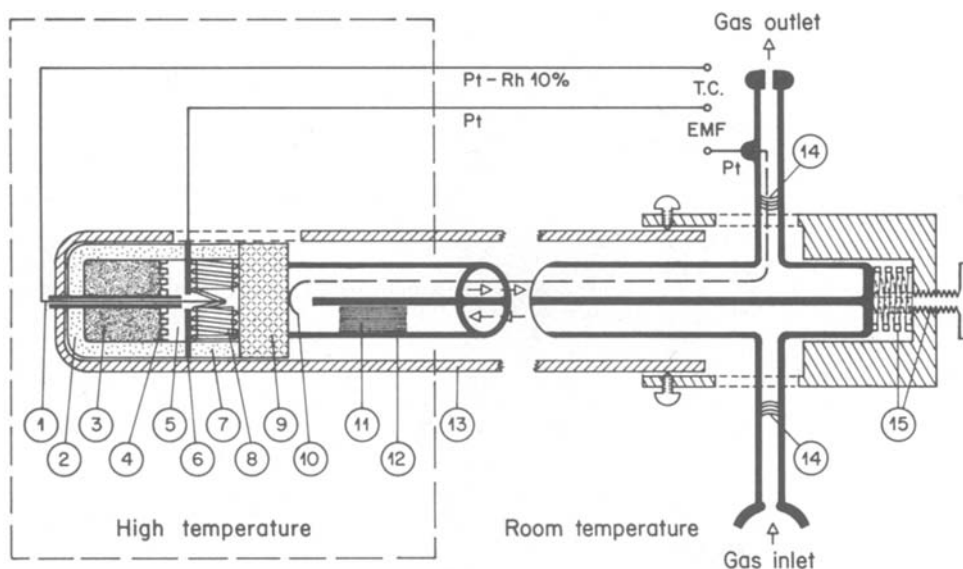


Fig. 1. Photograph of an alumina sensor comprising two gas-circulation electrodes. The close-up on the right shows details of the tip of the alumina tube where the platinum electrodes come into contact with the potassium sulfate pellet.

* Electrochemical Society Active Member.
Key words: solid electrolytes, sulfates, sulfur dioxide, sulfur trioxide, sensors, SO₂-SO₃ analysis.

Fig. 2. Schematic diagram of a quartz detector equipped with a thermal-decomposition type of reference electrode: 1. Pt/Pt-Rh 10% wire used as a thermocouple inside the reference electrode; 2. alumina crucible; 3. mixture of magnesium sulfate and oxide powders used as the thermal-decomposition reference electrode; 4. perforated alumina holder; 5. air atmosphere in equilibrium with 3; 6. deformable gold or platinum gasket; 7. external alumina ring to protect inner atmosphere; 8. internal alumina ring wound with platinum wire ensuring contact with the solid electrolyte; 9. potassium sulfate pellet; 10. platinum wire of the gas-circulation electrode; 11. precatalyst consisting of small alumina tubes platinized inside and outside; 12. two-bore quartz tube; 13. external alumina holder; 14. quartz-to-Pyrex seal; 15. mechanical device for pressure application and sealing.



gastight at 350°C. The platinum wire of the electrode in the gas outlet is welded with a special glass to ensure a good seal. With this setup the reference electrode must always be placed on the other side of the solid electrolyte. Figure 2 presents a schematic diagram of the quartz detector, equipped here with a thermal-decomposition type of reference electrode to be described later, while Fig. 3 shows the detector in its dismantled state on the right along with a simplified version on the left. In this simplified version, the wire forming the metal-electrolyte interface can be placed in position or removed freely, thus allowing replacement of the electrode metal during a test; small Viton O-ring joints are used in the gas outlet for adjusting the position of the wire of the gas-circulation electrode.

In all the tests described here, the gas is drawn by suction from the sample bag to the detector by means of a diaphragm pump. Care is taken to ensure that the pressure in the detector is close to atmospheric pressure; the flow rate is regulated by a control valve placed between the pump and the detector.

When SO_2 has to be converted into SO_3 upstream of the detector, an external catalyst is used consisting of 10 cm^3 of granular alumina platinized by the decomposition of chloroplatinic acid. Since the working temperature of the catalyst is 402°C, the gas feed-throughs connecting it to the detector are insulated and maintained at 350°C to avoid the risk of condensation of SO_3 or H_2SO_4 .

If a catalyst is used inside the apparatus near the measuring electrode, several platinized alumina tubes 0.85 mm OD and 2.5 cm long are placed in the gas inlet as shown in Fig. 2. An alternative method of establishing the platinum-electrolyte contact, which is particularly favorable to equilibrium of the gas constituent, is to use a platinum felt formed by compressing and annealing a mesh screen of platinum wire 0.08 mm OD, as illustrated in Fig. 1 and 4. In this method, complete equilibrium of the constituent gases (O_2 , SO_2 , and SO_3) is achieved, since only the small fraction of the gas that diffuses into the platinum felt escapes towards the electrode surface.

Results and Discussion

Study of the reference electrodes.—Four types of reference electrode were studied in terms of their stability over a number of weeks in comparison with a conventional gas-circulation electrode. This mea-

suring electrode was fed with SO_2 -in-air mixtures that were equilibrated in terms of SO_2 to SO_3 conversion by precatalyzing the mixture just before the gas reached the electrode.

The first reference electrode studied was the gas-circulation type identical to the measuring electrode. In fact, the detectors originally developed for the measurement of gaseous oxides were concentration cells of the type

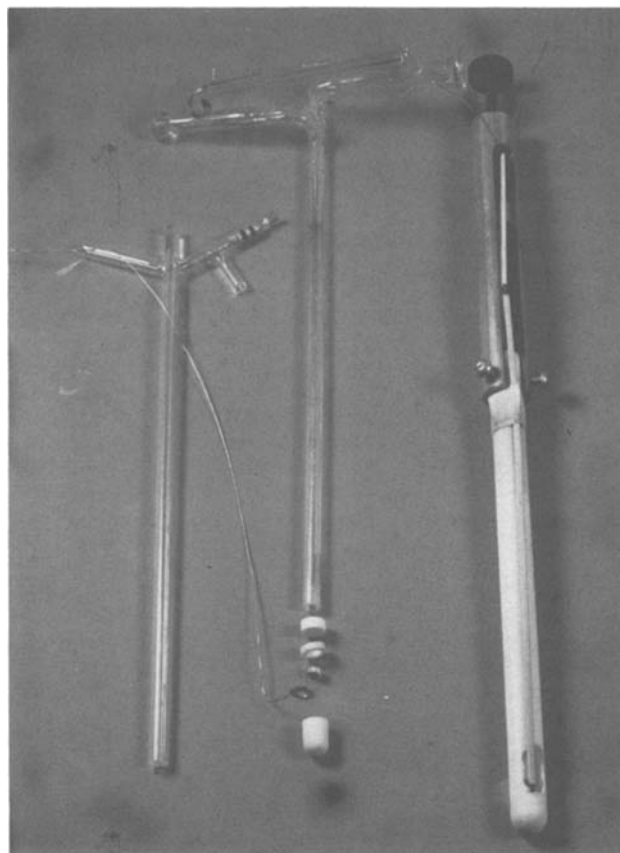


Fig. 3. Photograph of a quartz detector in the dismantled state (right). On the left is a simplified version of the quartz device in which small O-rings are provided to enable the electrode metal to be replaced during a test.

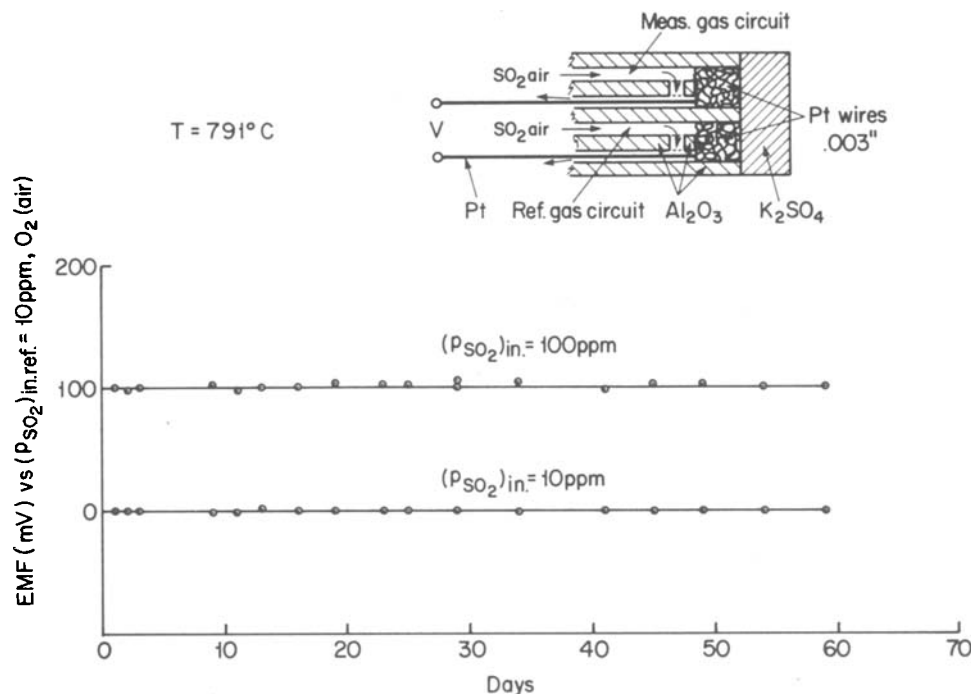
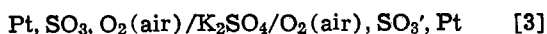


Fig. 4. Gas-circulation reference electrode: construction details of the electrodes and test results obtained over 60 days with $(p_{\text{SO}_2})_{\text{in.ref.}} = 10$ ppm in air.



where one of the two gases circulating at the electrodes was of known composition. The emf of this type of detector, used in air, is given by the simplified Nernst equation, as shown in our previous work (1)

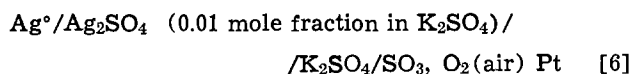
$$E = \frac{RT}{2F} \ln \left(\frac{p_{\text{SO}_2 \text{ in.}}}{p_{\text{SO}_2 \text{ in. ref.}}} \right) \quad [4]$$

The gas-circulation reference electrode seems very reliable and highly reproducible but it is cumbersome to use in a practical detector for pollutants, since it requires an external calibration source which periodically needs renewing. Despite this drawback, a study was made of its stability *vs.* time and it then served as a source of comparison for the other three reference electrodes. Every day for 60 days the reference gas, 10 ppm SO_2 in air, was first passed over the two electrodes simultaneously to check that the signal was at zero; a second gas, 100 ppm SO_2 in air, was then passed over the measuring electrode. The alumina test setup is illustrated in Fig. 1 with details of the electrodes provided in Fig. 4. The test results reported in the same Fig. 4 show that the 10 ppm signal offers excellent stability (± 1 mV) whereas for 100 ppm of SO_2 in air the signal fluctuates somewhat (± 6 mV) because of the poor reproducibility of the gas-mixture preparation method.

The second reference electrode studied was the Ag/Ag^+ type. Since Ag_2SO_4 is soluble in K_2SO_4 around the 0.01 mole fraction (1), this electrode can be adapted for solid oxyanions and is commonly used in aqueous or fused mediums. The emf of an SO_2 detector operating in air, for example, is expressed as follows

$$E = \text{Const.} - \frac{RT}{2F} \ln a_{\text{Ag}_2\text{SO}_4} + \frac{RT}{2F} \ln (p_{\text{SO}_2})_{\text{in.}} \quad [5]$$

The validity of this emf expression was established experimentally in an earlier work (1). A study of the stability *vs.* time of a detector corresponding to the following cell

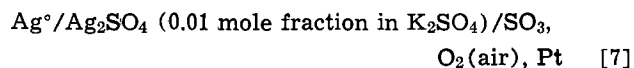


was conducted over a period of 53 days. The emf variations are plotted in Fig. 5 along with detailed

uses of the different electrodes tested, namely, two silver and one platinum. Two distinct types of behavior were observed in the signal (V_1) *vs.* time. The first was a rapid increase in potential during the first two days, which may be traced to a decrease in the silver ion activity at the silver electrode in contact with the solid solution. Since the potential (V_2) of the silver electrode in contact with pure K_2SO_4 simultaneously reflects an increase in silver ion activity, it was concluded that this is due to the rapid diffusion of silver ions through the entire electrolyte. Chemical analysis subsequently confirmed this. The second type of behavior was observed a few days later when the emf (V_1) began slowly but steadily to decrease. This may be attributed to the gradual formation of silver oxide as a solid solution in K_2SO_4 at the silver electrode in the presence of air, an explanation which was validated by a second test using a cell where the electrolyte was pure K_2SO_4 covered on its external face with metallic silver powder in contact with air (Fig. 6). The behavior of the signal reflects the presence of increasing silver ion activity over 48 days (Fig. 6). At the end of the test, the cationic fraction of the silver ions was determined by atomic absorption as 6.2×10^{-3} . Pure silver oxide alone is thermodynamically unstable under these conditions (4) but, as a solution in K_2SO_4 , the predictable activity of Ag_2O in equilibrium with air would be 8.8×10^{-3} .

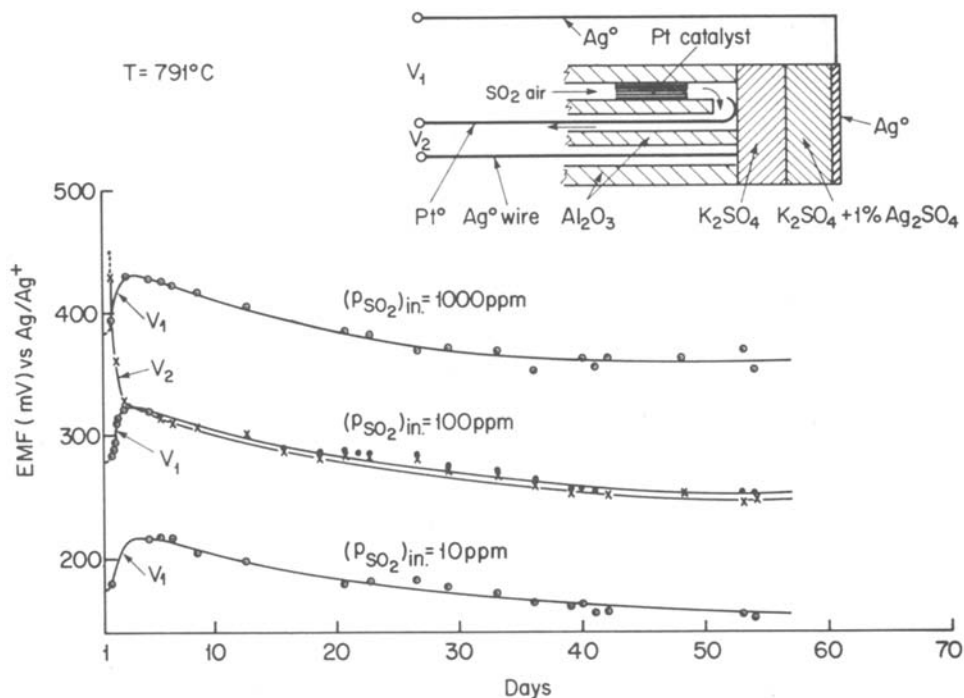
These results were in fairly good agreement with the atomic-absorption analysis after 48 days and were confirmed qualitatively by another independent test. Two pure K_2SO_4 pellets in the presence of powdered silver were kept for 14 days in an oven at 750°C , in air. Atomic-absorption analysis indicated silver ion concentrations of 1.2 and 1.1×10^{-3} cat. fract. in accordance with the silver oxide formation suggested by previous tests.

Finally, a third test with the silver electrode is described in Fig. 7 using the following type of cell



where the metallic silver was completely cut off from the ambient air. A silver rod, 0.5 mm OD, fusion-sealed in an alumina pellet, was protected from the air on one side by the K_2SO_4 electrolyte and, on the other, by a piece of annealed-platinum foil; pressure was then applied to press all these components one against the

Fig. 5. Ag/Ag⁺ reference electrode: construction details of the electrodes and test results obtained over 53 days at the measuring electrode with $(p_{\text{SO}_2})_{\text{in}} = 10, 100, \text{ and } 1000 \text{ ppm}$.



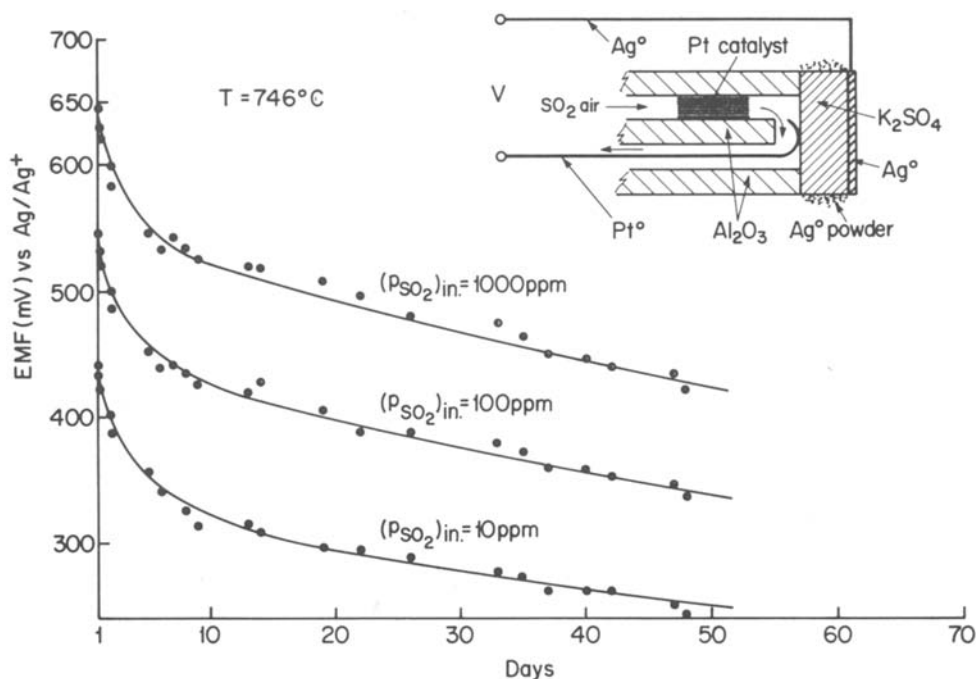
other. It was observed that the emf did not decrease as during the previous tests, but in fact rose slightly and seemed to stabilize after 30 days. This arrangement therefore seems to be an effective way of preventing the formation of Ag₂O, although the initial increase in emf remains difficult to explain. Silver sulfate is relatively stable in air and its equilibrium partial pressure of SO₃ in air at 800°C is in the order of 80 ppm (5); however, in solution at 0.01 mole fraction in K₂SO₄, its equilibrium partial pressure would be below the ppm level if activity should equal the mole fraction. This apparent stability of the solid solution Ag₂SO₄-K₂SO₄ was confirmed by the emf observed experimentally and it therefore cannot explain the initial rise in the emf, which could actually be due to losses by vaporization of Ag₂SO₄.

The silver electrode thus appears fairly stable in time, providing that certain precautions are taken, but its use should be limited to the analysis of gases relatively rich in oxygen because of the constant presence

of Ag⁺ ions at the platinum measuring electrode resulting from the rapid diffusion of the ions in the electrolyte. In order to illustrate this, tests were conducted on the performance of a detector with an Ag/Ag⁺ reference electrode at 750°C. No reduction of a gas containing 100 ppm of SO₂ was reduced to $p_{\text{O}_2} = 5 \times 10^{-4} \text{ atm}$. On the other hand, if an inert gas such as purified argon passed through the detector, the voltage dropped to zero and the detector did not resume its normal performance until it had operated for several minutes in air in the presence of sulfur oxide. This may be explained by the silver ion reduction near the electrode and the ensuing oxidation of the silver metal when the atmosphere becomes an oxidizing agent again. The Ag/Ag⁺ reference electrode should therefore never be used for other than the measurement of pollutants in ambient air.

A number of tests were performed in an attempt to use air as the reference gas with the juxtaposition of

Fig. 6. Emf variations measured between a gas-circulation electrode and a silver plate in contact with pure K₂SO₄.



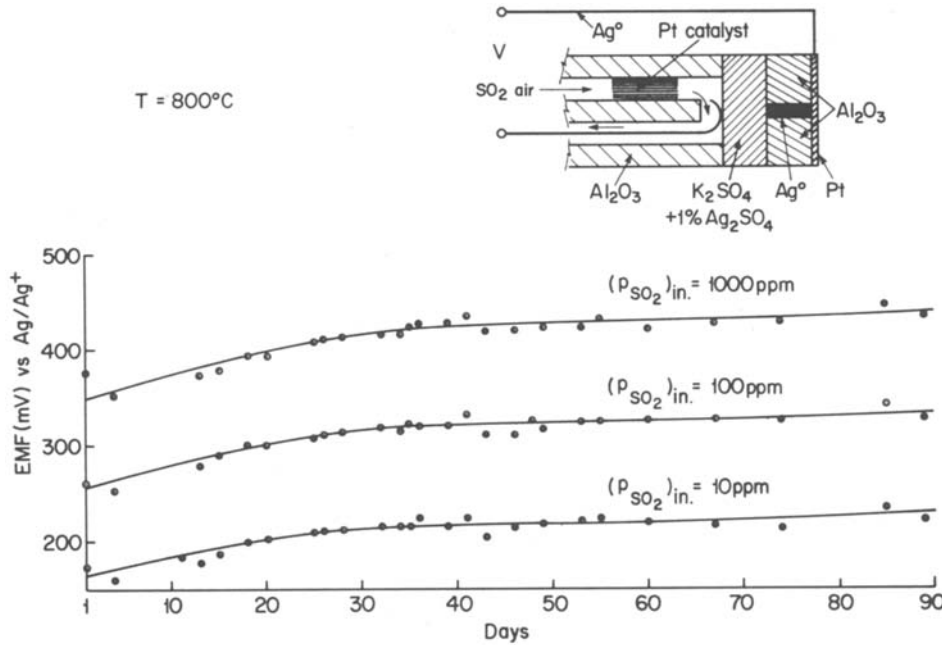
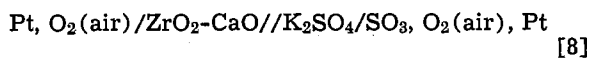


Fig. 7. Ag/Ag⁺ reference electrode in which the silver metal is protected from the ambient air.

two solid electrolytes, K₂SO₄ and ZrO₂-CaO. The following cell was used



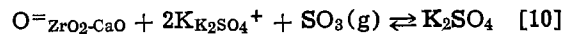
The resulting emf expression can be expressed as

$$E = \text{Const.} + \frac{RT}{2F} \ln (p_{\text{SO}_2})_{\text{in}}$$

where the constant includes the oxygen pressure ($-RT/4F \ln(p_{\text{O}_2})_{\text{ref}}$) of the reference electrode and the sulfate-zirconia junction potential, which is considered a constant.

The atmosphere surrounding the junction between the two solid electrolytes was sealed off from the ambient air by a gold O-ring as may be seen in Fig. 8. The emf signals observed experimentally over a period of 74 days are reported on the same figure. After the first few days the signals reached a constant value, the unmistakable shift observed after one month be-

ing the result of an uncontrolled variation in the oven temperature. An earlier duration test performed without controlling the atmosphere at the junction showed erratic emf fluctuations. This observation is in accordance with other studies performed at IREQ which have indicated that the sulfate-zirconia junction may involve an equilibrium such as



which depends on the composition of the gas phase (6).

Except for the unexpected variations in the detector temperature in the duration test, this type of reference electrode shows satisfactory results. However, the need to control the atmosphere at the junction calls for apparatus which, for the moment, is fairly complex to build.

The fourth type of reference electrode studied is somewhat similar to certain metal-oxide couples (e.g., Ni-NiO, Pd-PdO) developed as reference systems for stabilized zirconia-oxygen detectors (7, 8). A pow-

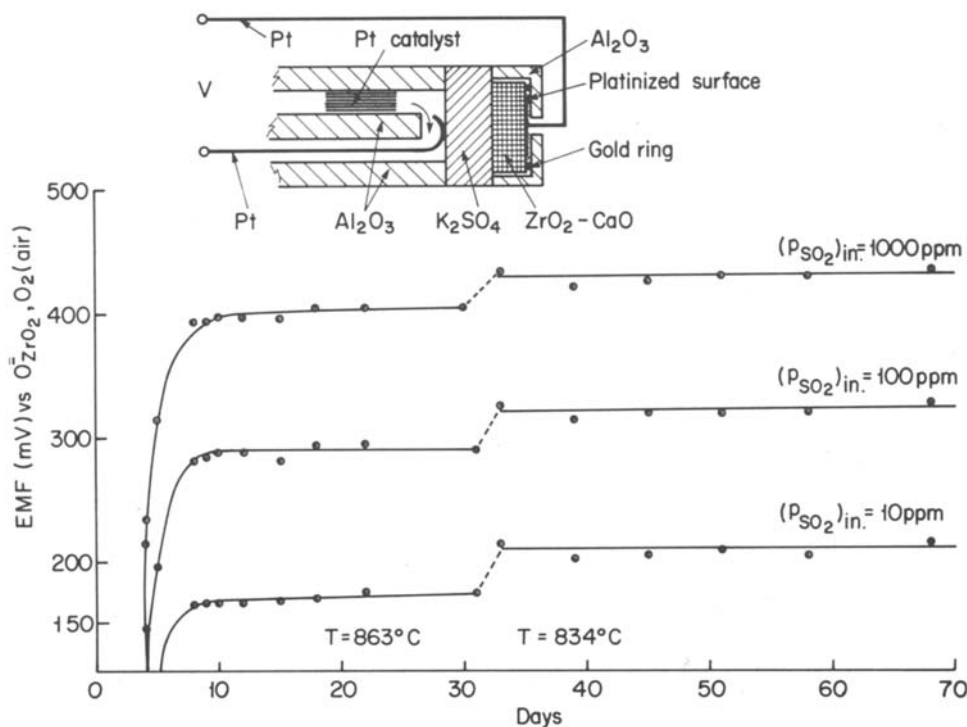
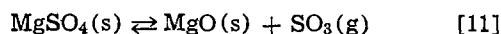


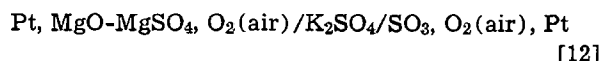
Fig. 8. Air reference electrode made by placing K₂SO₄ in contact with calcia-stabilized zirconia: construction details and results over 70 days.

dered metallic sulfate, which shows relatively thermal stability in air, is mixed with its oxide in order to fix a low sulfur oxide partial pressure at the detector operating temperature. The first system studied was $\text{MgSO}_4\text{-MgO}$. The chemical equilibrium reaction of this system was



with $K_2 = (p_{\text{SO}_3})$ as the equilibrium constant.

The whole electrochemical cell involved in the detector may be described as



In air, the sulfur trioxide in equilibrium with the solid mixture $\text{MgSO}_4\text{-MgO}$ is constant. If, in addition, the equilibrium between SO_3 , SO_2 , and O_2 is considered to be achieved rapidly, the emf corresponding to the electrochemical cell described above is expressed as

$$E = \frac{RT}{2F} \ln \frac{(p_{\text{SO}_2})_{\text{in}}}{K_2(1 + K/(0.21)^{1/2})}$$

The experimental setup corresponding to this electrochemical cell is shown schematically in Fig. 2 and 9. For this experiment the $\text{MgSO}_4\text{-MgO}$ mixture is placed in an alumina crucible open to the atmosphere through a small-diameter hole (0.05 mm), to ensure a constant total pressure of 1 atm. The electrode contact is obtained using a small alumina ring wound with platinum in contact with the K_2SO_4 pellet and inserted in another alumina ring which prevents direct contact of the electrode with ambient air (see details in the photograph in Fig. 3).

The results obtained over a three month period illustrate the stability of this type of reference electrode. The emf values observed experimentally (Fig. 9) are 30 mV higher than those calculated from the equilibrium constants culled from the literature (9). This was attributed to a temperature gradient between the inner crucible and the oven where the temperature reading was taken. Incidentally, the results of preliminary studies on the possibility of adapting these electrochemical cells for metallurgical applications (10) are in good accordance with calculated values for $\text{MgSO}_4\text{-MgO}$ (≈ 2 mV) with the temperature measured inside the crucible as illustrated in Fig. 2.

The slight drift observed in the emf over 90 days (≈ 23 mV) is largely explained by the temperature coefficient $(dE/dT)_{725^\circ\text{C}} = 1.5$ mV/ $^\circ\text{C}$ and by the differ-

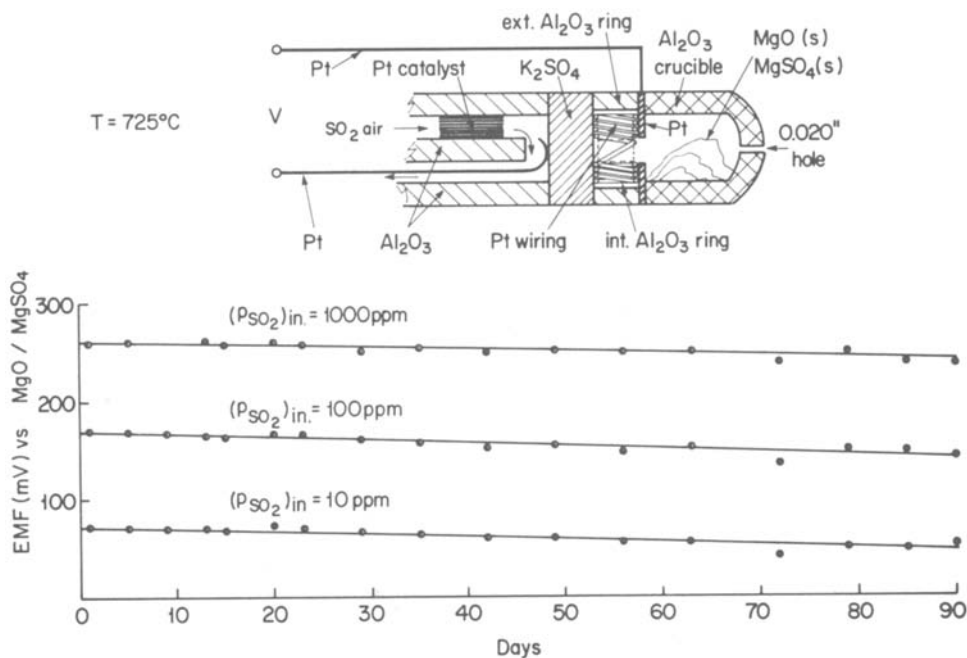
ence in temperature between initial and final measurements of 721° and 730°C , respectively. Moreover, x-ray examination before and after the test revealed no apparent modification of the sulfate-oxide mixture.

Another solid sulfate-oxide mixture, $\text{MnSO}_4\text{-Mn}_2\text{O}_3$, was studied at the lower temperature of 714°C using an experimental setup identical to the magnesium system. The results are presented in Fig. 10. The short lifespan of this system is probably due to a high sulfur oxide pressure ($\approx 10^{-8}$ atm). Furthermore, x-ray examination failed to indicate the presence of MnSO_4 at the end of the test. Hence this system appears better suited for lower detector operating temperatures whereas the magnesium mixture can operate at up to 900°C . Stringent control of the temperature guarantees the reliability and reproducibility of this thermal-decomposition type of electrode over extended periods of time. In addition, the reference-electrode potential could be adjusted by selecting the appropriate operating temperature and sulfate-oxide mixture. The use of a closed crucible to contain the powder mixture will eventually improve the lifespan of this promising type of reference electrode.

Study of the gas-circulation electrodes in equilibrium and nonequilibrium conditions.—Previous studies on sulfur oxide detectors have revealed that the active species at the electrode is SO_3 not SO_2 , and that the use of platinum for the metal electrode generally results in equilibrium between SO_2 , O_2 , and SO_3 , at least in the vicinity of the triple contact between the electrolyte, the metal, and the gas phase. One of the conclusions of recent work is that a platinum precatalyst is required in the gas inlet just before the electrode. The two types of precatalyst used for this purpose were described in the experimental section. Recourse to these catalysts resulted in close agreement between calculated and experimental values, as illustrated by the upper curve of Fig. 1. In previous work without a precatalyst, an increasing discrepancy was found between calculated and experimental values towards higher sulfur oxide concentrations as may be seen in Fig. 4 of Ref. (1). When equilibrium of the gas constituents prevails at the electrode, the sulfate-based detector can be used quite successfully for measuring either SO_2 or SO_3 or the two together ($\text{SO}_2 + \text{SO}_3$) when both oxides are present simultaneously.

In combustion-gas analysis, the sulfur oxide is mostly SO_2 , although occasionally a small percentage of the highly corrosive SO_3 is also observed. Consequently, a search was undertaken for an electrode metal that

Fig. 9. Thermal-decomposition type of reference electrode based on a mixture of MgSO_4 and MgO : construction details of the electrodes and test results over 90 days.



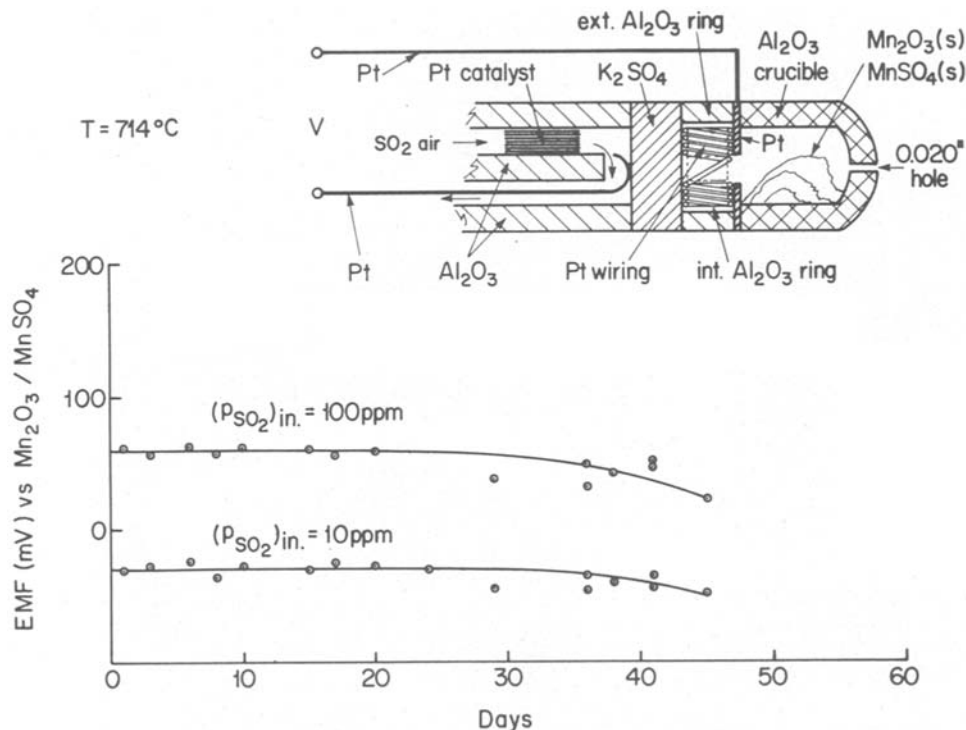


Fig. 10. Thermal-decomposition type of reference electrode based on a mixture of MnSO₄ and Mn₂O₃: construction details of the electrodes and test results over 45 days.

would not catalyze the equilibration of SO₂ with SO₃ so that SO₃ could be detected selectively. The quartz device with the removable electrode illustrated in Fig. 3 was used to test various metals in the same experimental conditions to assess their performance as electrode materials. For this purpose, the SO₂-in-air mixtures were first passed over a precatalyst placed in the vicinity of the electrode. As shown in Fig. 11, all the metals tested were electrochemically active in accordance with Eq. [1] except for iridium (not represented), which is erratic in its performance. A second test, reported on the same figure, was carried out by removing the precatalyst from the gas inlet to study the catalytic performance of these metals. For the same SO₂-in-air mixtures, palladium has a catalytic performance similar to that of platinum; however, gold and rhodium show very little response to the SO₂ content. Thus, there seems to be a possibility of optimizing certain experimental parameters—temperature, gas flow rate, geometry, etc., in order to measure SO₃ selectively in the presence of SO₂.

The last test to be described was performed with a quartz device adapted to the analysis of hot SO₃-bearing mixtures. The quartz gas-circulation circuit was identical to that shown in Fig. 2 except that the precatalyst was removed and an electrically insulated gold wire was used along with the platinum wire of the gas-circulation electrode. The aim of this test was to compare the two electrodes in the same conditions when the detector was supplied first with SO₂-in-air mixtures, then with hot SO₃-in-air mixtures. The latter were prepared on an external catalyst, described in the experimental section, that converts most of the SO₂ into SO₃ (≈99% at equilibrium at 402°C). As illustrated in Fig. 12, on platinum, the gas mixtures were at equilibrium at the electrode and the results are therefore identical, whether the gases entering the detector are SO₂-in-air or SO₃-in-air mixtures. On gold, the low catalytic activity of the metal was confirmed with the SO₂-in-air mixtures, particularly at high concentrations. On the other hand, with SO₃-in-air mixtures, the electrode responds to the proportion of SO₃ defined by the external catalyst at 402°C, at least when concentrations are high. To prevent the SO₃ from returning to equilibrium conditions as observed in Fig. 12, especially at low concentrations, the gas flow rate was increased to 200 cm³/min, which avoided a drop to the equilibrium potentials observed on platinum. However, the

external catalyst then seemed unable to ensure complete conversion of SO₂ into SO₃ and, although the curve is parallel to the curve predicted for SO₃ alone, it remains below it. Based on these preliminary tests, it was concluded that the quartz detector may be successfully adapted to hot-gas analysis and appears most interesting for the selective detection of SO₃, especially when gold is used at the electrode.

Since the preparation of this paper, more thorough studies of the specific determination of SO₃ in the presence of SO₂ have been undertaken by other researchers at IREQ which confirm the present results (11).

Conclusion

In this work, four types of reference electrodes were developed and compared with regard to their stability vs. time. Of these, the gas-circulation electrode seems to

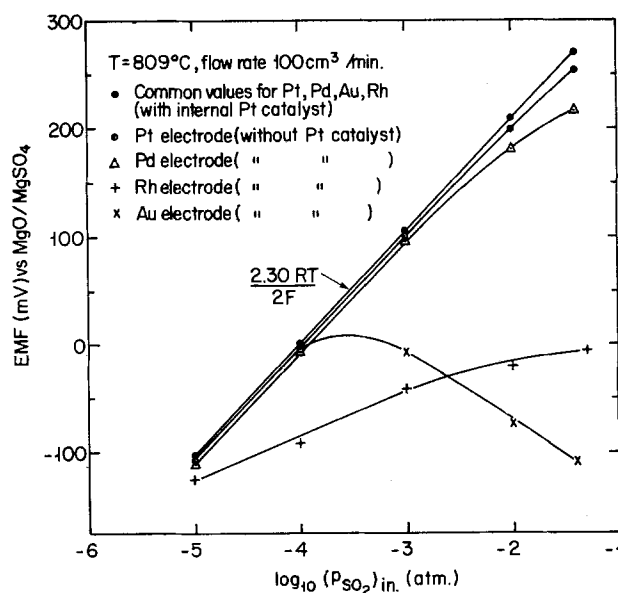


Fig. 11. Electrochemical and catalytic activities of four metal electrodes when several SO₂-in-air mixtures are precatalyzed in the gas inlet of the detector before reaching the electrode; the results of the same test repeated after removal of the precatalyst are also given in this figure.

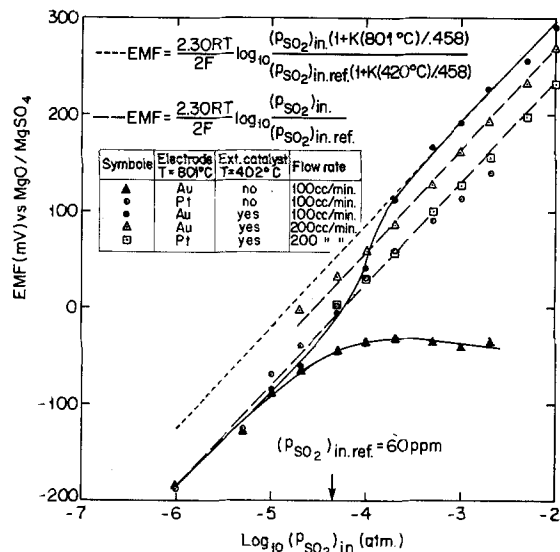


Fig. 12. Relative catalytic activities of Au and Pt electrodes with SO_2 -in-air and hot SO_3 -in-air gas mixtures; the dashed lines are the calculated values for complete nonequilibrium and complete equilibrium at the gas-circulation electrode, with the reference always considered to be at equilibrium at 801°C .

be the most stable and the most reliable, although in practice it is awkward and expensive to operate. The Ag/Ag^+ electrode, on the contrary, is easy to set up experimentally despite the fact that silver must be protected from air in order to maintain emf stability vs. time; in addition, the rapid diffusion of silver ions through the electrolyte precludes the use of these electrodes for the analysis of oxygen-lean gases. The air reference electrode with a sulfate/stabilized-zirconia junction provides satisfactory results but its elaborate experimental setup presents a drawback. Finally, the reference electrode based on the thermal decomposition of solid sulfate-oxide mixtures has a highly reproducible signal that is stable with respect to time, although the temperature needs to be particularly well controlled; its potential can be adjusted as required by selecting an appropriate sulfate-oxide system and temperature. This fourth type of electrode is still under investigation.

An attempt was also made, by adding a precatalyst upstream of the measuring electrode, to optimize the

equilibrium of the reacting species at the electrode when cell is to be used as a total sulfur oxide detector. Finally, demonstration of the weak catalytic activity of gold and rhodium with respect to the conversion of SO_2 to SO_3 led to the development of a quartz detector suitable for hot-gas analysis, which should eventually permit the selective measurement of SO_3 in the presence of SO_2 .

Acknowledgment

Thanks are due to Hydro-Québec for the financial support of this work through a research and development project at its research center IREQ.

Manuscript submitted Jan. 2, 1980; revised manuscript received ca. Sept. 19, 1980. This was Paper 103 presented at the Seattle, Washington, Meeting of the Society, May 21-26, 1978.

Any discussion of this paper will appear in a Discussion Section to be published in the December 1981 JOURNAL. All discussions for the December 1981 Discussion Section should be submitted by Aug. 1, 1981.

Publication costs of this article were assisted by the Institut de recherche d'Hydro-Québec (IREQ).

REFERENCES

1. M. Gauthier and A. Chamberland, *This Journal*, **124**, 1579 (1977).
2. M. Gauthier, A. Chamberland, A. Bélanger, and M. Poirier, *ibid.*, **124**, 1584 (1977).
3. A. Chamberland, M. Gauthier, and A. Bélanger, "4th Proc. Int. Clean Air Congr.," Paper No. 108, Tokyo (1977).
4. C. E. Wicks and F. E. Block, *US Bur. Mines Bull.* **605**, Wash. Govt. Print. Off. (1963).
5. H. H. Kellogg, *Trans. Metall. Soc. AIME*, **230**, 1622 (1964).
6. M. Gauthier, A. Bélanger, Y. Meas, and M. Kleitz, in "Solid Electrolytes," Chap. 29, P. Hagenmüller and W. Van Gool, Editors, Academic Press, New York (1978).
7. M. Sato and T. L. Wright, *Science*, **153**, 1103 (1966).
8. J. Fouletier, G. Vitter, and M. Kleitz, *J. Appl. Electrochem.*, **5**, 111 (1975).
9. J. M. Skeaf and A. W. Espelund, *Can. Met. Q.*, **12**, 445 (1973).
10. M. Gauthier and C. Bale, "Oxide-Sulfate Equilibria in the Mg, Ni and Mn Systems Measured by a Solid K_2SO_4 Concentration Cell," To be published in *Met. Trans.* (1981).
11. A. Bélanger and A. Chamberland, "Development of a Sulfur Trioxide Detector," Environment Canada, Report APCD 79-1, June 1979. Available from the authors.

Optical and Auger Microanalyses of Solder Adhesion Failures in Printed Circuit Boards

K. Kumar and A. Moscaritolo

The Charles Stark Draper Laboratory, Incorporated, Cambridge, Massachusetts 02139

ABSTRACT

Printed circuit boards used in electrical systems have shown solder separation from the copper wiring network with prolonged use at about 325 K (120°-130°F). Optical and Auger microanalyses of boards that have shown such failures have revealed the existence of discrete oxide particles in the form of an oxide layer at the separated interface. High temperature accelerated aging tests have shown that the time-dependent accumulation of the oxide particles at this interface results from rejection of the oxygen out of the reacted zone and into the intermetallic-matrix boundary with the continued growth of (low Pb-containing) Cu_xSn_y intermetallic compounds. (These compounds are formed as a consequence of the chemical reaction that occurs between the Pb-Sn solder and the underlying copper circuit.) Increased thermal activation leads to increased growth of the intermetallics, and this results in more oxygen exclusion from the reacted zone into the interface region (giving rise to a time-dependent accumulation of the oxide particles at this boundary). Eventually, these particles inhibit the solid-state diffusion reaction between copper and the Cu_xSn_y intermetallics and lead to the observed separation of the solder from the underlying copper. Experiments performed in this study have shown that the oxygen (giving rise to oxide-particle accumulation at the interface) is distributed throughout the bulk of the copper plating. Organic addition agents, codeposited with the copper during the formation of the copper wiring network, are probably acting as a source for the observed oxygen.

Printed circuit boards are used extensively in the electronics industry as components of larger-electrical assemblies. The printed circuit consists of a wiring network which is produced using a combination of photolithographic and plating and laminating techniques. Both electroless and electrodeposition procedures are used to fabricate these circuits. A layer of a preselected Pb-Sn solder composition is electrodeposited on top of the copper network. To achieve proper wetting of the copper by the solder material, a post-deposition fusion procedure is used. In one process, this consists of heating the entire assembly to about 480 K (410°F) for close to 15 sec. This results in phase segregation within the solder material and in chemical reaction between the solder and the copper circuit, thereby enhancing the integrity of the completed circuit through increased solder adhesion (due to the chemical forces that result from the solder-copper reaction).

A few of the printed circuit boards used in electronic systems at about 325 K (120°-130°F) have shown severe degradation of solder adhesion with prolonged use. This time-temperature dependence of solder layer separation in some of the printed circuits has been known to exist by the circuit industry for a reasonably long time (1). Past attempts at identifying the causes of these failures have met with only limited success (1-3). Our own experience with the use of these boards has shown that circuits obtained in 1977 from vendor A did not display solder adhesion failures. In contrast, samples procured from another vendor (B) in 1978 almost consistently showed this type of deterioration. In most instances, solder adhesion degradation was found to reach a level whereby the solder could be easily removed from the copper surface with a fine-edged X-acto blade with a minimum of effort. A detailed study was consequently initiated at this Laboratory to determine the causes of the observed dewetting of the solder. It was hoped that, as a result of such an investigation, further use of these materials could be qualified and also a determination made as to whether

newer (1979) material procured from vendor B could be used for future applications. Such an evaluation was deemed desirable in view of the manufacturer's claim that suitable modifications had been made in the processing procedures to produce a 1979-designated product that was superior to the 1978-designated product. This paper illustrates the nature of the problem and identifies the mechanism by which the observed solder separation has most probably occurred.

Experimental Procedure

Representative samples were mounted (with the copper-solder interface slightly inclined to the plane of polishing) at room temperature in a resin-containing cast and polished for metallographic examination. The selected angular tilt of the copper-solder assembly allowed amplification of the solder-copper interface, upon polishing, by a factor of ten. The samples were photographed, using optical microscopy, and analyzed using a Physical Electronics Auger system in the as-polished condition. The heat-treatments that were performed on several of the selected samples are described in detail in the next section.

Results and Discussions

The different features observed in microstructures which are typical of those observed in failed samples are shown in Fig. 1. As one traverses the solder-copper interface from the solder side to the copper side (that is from left to right), several layers are observed. The observed layers correspond to a two-phase solder region which contains a high concentration of the Pb-rich phase, two Cu_xSn_y intermetallic compounds (containing very low levels of Pb), and a region with a high concentration of oxide particles located between the Cu_3Sn intermetallic and the copper. The two intermetallic phases, Cu_3Sn and Cu_6Sn_5 , observed in this study have earlier been reported elsewhere (1). These correspond to the near-equilibrium phases predicted by the binary Cu-Sn phase diagram (4) indicating that the role of Pb in this ternary system is minimal. An Auger line scan for Pb (shown in Fig. 1), however, in-

Key words: oxide, intermetallics, solder separation, mechanism.

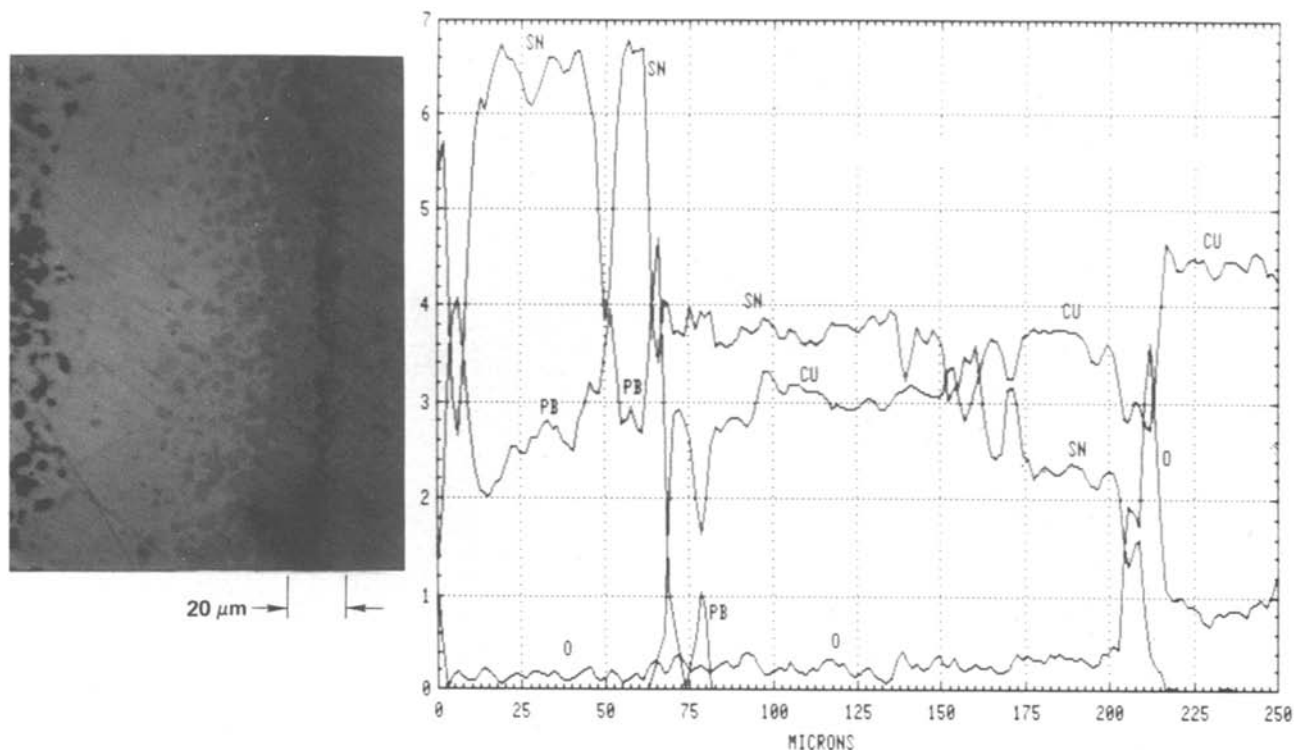


Fig. 1. Typical Cu-solder interface region in failed board. Photograph shows two Cu_xSn_y intermetallics and oxide presence at $\text{Cu}-\text{Cu}_3\text{Sn}$ boundary. Auger line scans were made across the entire interface region.

dicates that a small amount of Pb does exist in these phases, possibly in solid solution. [Details on Auger spectroscopy and interpretation of spectra can be obtained from Ref. (5).] All of the main features can be easily identified on the Auger line scans (also contained in Fig. 1) that were obtained on this sample. The strong intensity of the oxygen signal at the $\text{Cu}_3\text{Sn}-\text{Cu}$ boundary (in the Auger scan) clearly shows that the particles observed are indeed an oxygen-containing species that have collected at this interface. The presence of a two-phase zone with a high concentration of the Pb-rich phase (observed on the solder side of the micrograph as dark precipitates) was a direct consequence of the formation of the (low Pb-containing) $\text{Cu}-\text{Sn}$ intermetallic compounds between the solder material and the copper network. Formation of these intermetallics resulted in an exclusion of Pb from the reacted regions leading to an enrichment (in Pb) of the solder material close to the solder- Cu_6Sn_5 boundary. An Auger survey showed that the only elements which were consistently present in the several samples that were examined (in detectable quantities) were Cu, Pb, Sn, O, and C, all of which were expected.

Because of the known differences in the performance of the 1977 and 1978 circuit boards, typical samples representative of those years and one sample, designated as a 1979 product, were selected for further examination. Figure 2 shows the microstructure observed for the as-received condition of these circuit boards. The reacted zone was found to be considerably smaller in the 1977 sample compared to the 1978 and 1979 samples. This also accounted for the near absence of the Pb-rich zone in the 1977 sample in contrast to the 1978 and 1979 samples where its existence was clearly observed. Larger reaction zones mean more overall exclusion of Pb from the reacted area. One, therefore, expected an intense concentration of the Pb-rich phase at the solder-intermetallic boundary in the 1978 and 1979 samples in agreement with the observations. The differences in the extent of the reaction observed in samples obtained from the two vendors was partly explained by the differences in the solder-fusion procedures used by these vendors. Whereas

vendor A uses an infrared lamp to cause improved wetting of the copper by the solder, vendor B uses an oil bath in which the entire assembly is immersed. It is possible that the circuits are subjected to more thermal activation by oil immersion than is the case when they are exposed to infrared radiation. Differences in thermal activation can explain the differences in the extent of the reaction that was observed. The microstructures shown in Fig. 2 were found to be substantially free of the oxide layer that is known to exist at the copper- Cu_3Sn boundary in boards where separation of the solder is known to have occurred. It may be noted, however, that a few oxide particles were nevertheless found to be attached to the copper surface in the 1979 sample even in this condition.

Since the degradation in the solder-to-copper adhesion has been observed to be dependent on both time and temperature, samples of as-received boards were subjected to elevated temperature aging treatments in air (so as to accelerate the kinetics of the microstructure changes that are induced during actual service at lower temperatures). Effects related to sample-to-sample variations were avoided by sectioning the as-received boards in two, such that the as-received state of the individual boards could be examined on one piece while the other piece could be examined after it had been subjected to the desired heat-treatment. The microstructures observed for each of the as-received samples corresponded very closely to those shown in Fig. 2. The heat-treatment temperature was chosen as 438 K (165°C) and the samples were examined after 4, 75, and 264 hr of exposure. A gradual development of the oxygen-containing species, with increasing time, was observed in the 1978 and 1979 samples in contrast to the 1977 sample where none was observed. The sample microstructures obtained after the 264 hr treatment on these three samples are shown in Fig. 3. It is clear that the condition observed for the 1978 and 1979 type samples is most undesirable, since it ultimately results in solder separation from the copper network. That such a direct relationship exists between development of the oxygen-containing particles and degradation of solder adhesion was verified

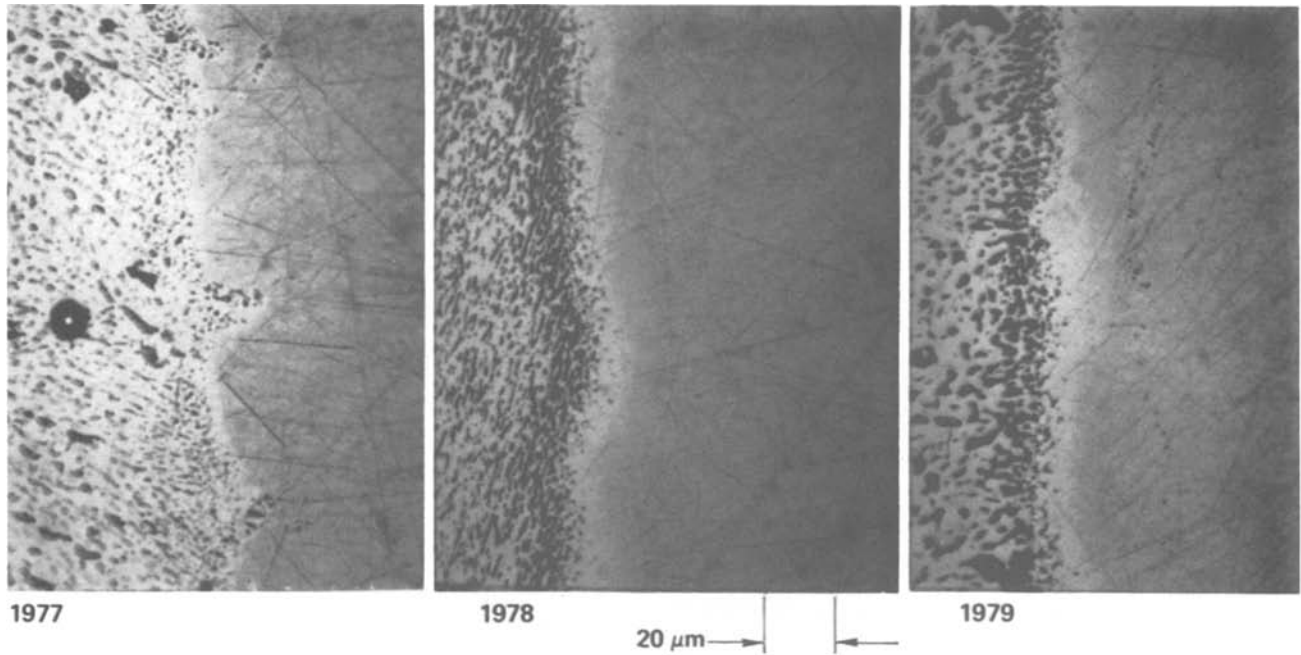


Fig. 2. As-received microstructures of 1977, 1978, and 1979 boards. Extremely narrow reaction zone with little enrichment of the Pb-rich phase in the neighboring solder region is observed in the 1977 sample compared to the 1978 and 1979 samples.

in separate experiments. These consisted of soldering individual wire leads to the printed wiring network prior to the 438 K treatment. After the thermal exposure the leads were pulled at known increasing loads until they separated from the circuit board. The decreasing value of load required to cause separation, and the increase in the amount of copper observed after separation (with increase in total thermal exposure), were considered a direct measure of the degradation in solder adhesion. It was determined that these correlated well with the accompanying changes in microstructure which showed a clear development of the oxygen-containing species in samples produced by vendor B.

Figure 4 contains an oxygen-line scan which was made across the copper-to-solder interface region in the 1978, 264 hr heat-treated sample. Unlike other line

scans that were made on similarly heat-treated samples, this one showed strong oxygen peaks on both sides of the Cu_xSn_y intermetallics; that is, at the $\text{Cu}-\text{Cu}_3\text{Sn}$ interface, and also at the (Pb-Sn solder)- Cu_6Sn_5 interface. Also, within the intermetallics themselves, a lower level of oxygen was detected than that which was found to exist in both the copper plating as well as in the Pb-Sn solder deposit. This observation clearly showed that the intermetallics rejected oxygen on both sides, as they grew, and this accumulated as oxides at both of the intermetallic-matrix interfaces. Oxide accumulation at the solder- Cu_6Sn_5 boundary could be a contributing factor to fractures at this interface that appeared in observations made earlier on similar metallic systems (2). The reasonably high level of oxygen in the solder area (of Fig. 4) was found to exist mostly as an oxide of Sn (as was interpreted from the close

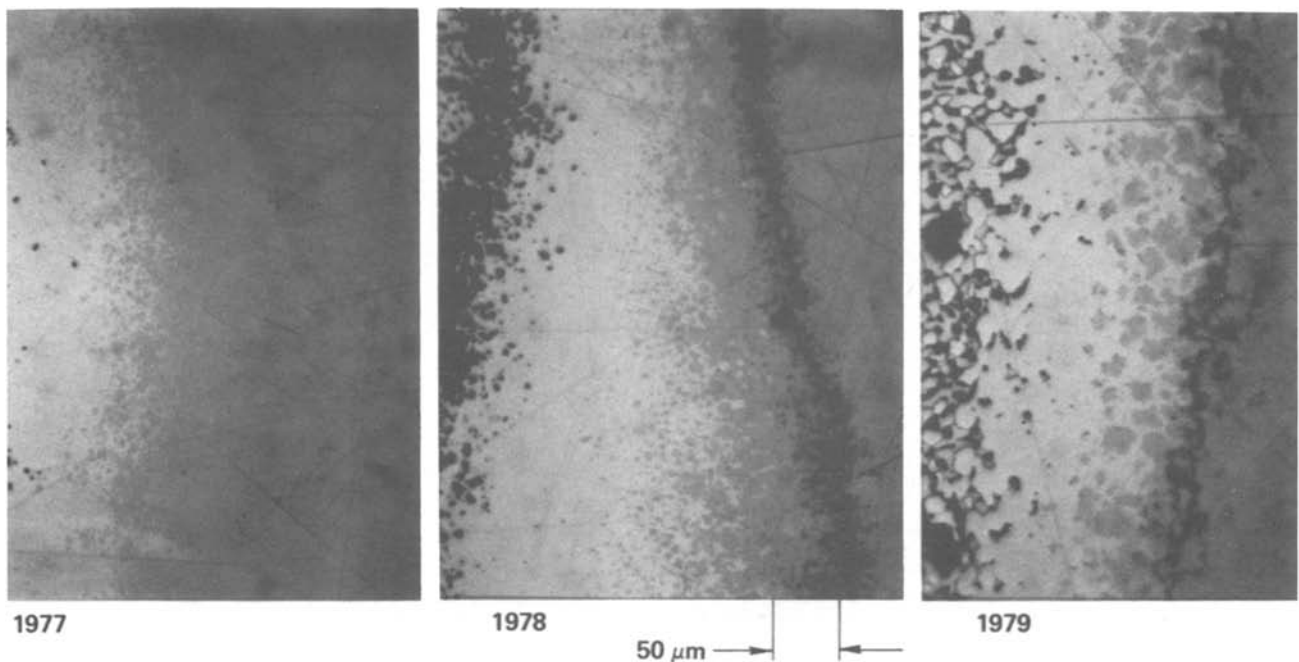


Fig. 3. Microstructures after 165°C, 264 hr air heat-treatment. Severe oxidation observed at Cu- Cu_3Sn boundary in 1978 and 1979 samples. None observed in 1977 sample.

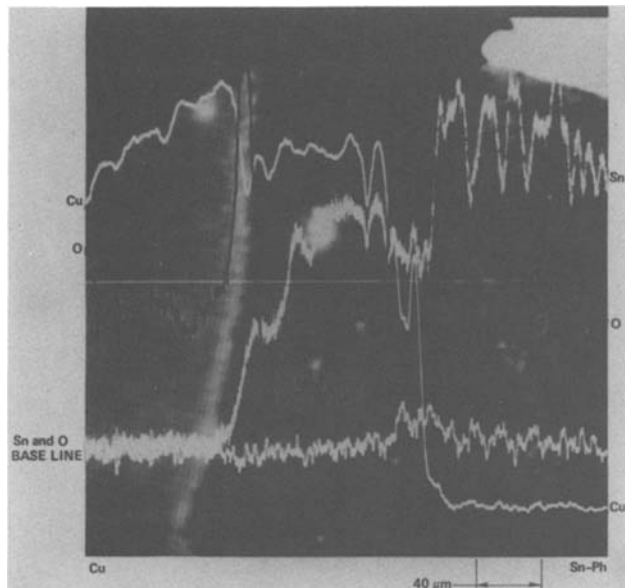


Fig. 4. Auger line scans across interface region in 1978 165°C, 264 hr air heat-treated sample. Oxygen peaks observed on both matrix-intermetallic interfaces.

correspondence between the Sn and the O Auger line scans in the solder region). A low level of oxygen within the intermetallics and the accumulation of an oxygen-containing species at the intermetallic-matrix boundaries clearly implies that oxygen present inside the solder will not migrate to the Cu-Cu₃Sn boundary and lead to the observed degradation of the adhesion at that interface. The source of oxygen must, therefore, be located on the copper side of the reacted assembly. The two sources that could conceivably give rise to the time-temperature accumulation of the oxide in failed samples are the environment (because all of the aging occurs in air) and the copper plating. If the oxygen contribution is from the copper plating, then the source of oxygen must be distributed reasonably uniformly throughout the thickness of the deposit. Surface oxidation of the copper plating, prior to solder deposition, cannot, by itself, account for the time-temperature dependence of oxide development at the interface. If surface oxidation of the copper were the

dominant contributor of the observed oxygen, the density of the oxide particles would not have significantly changed with increase in reaction time. The oxide particle concentration at the intermetallic-matrix interface, in such a circumstance, would have either remained constant (after all of the available oxygen was used up to form oxides in the very initial stages of the reaction), or even decreased because the intermetallics do show a finite, albeit low, oxygen solubility. Most of the oxygen contribution to the development of the oxide must, therefore, have originated either from the aging environment or from the bulk of the copper plating.

In order to further isolate the source of the oxygen (which leads to ultimate separation of the solder) an additional experiment was performed as part of this study. Sectioned samples, similar to those treated earlier in air, were obtained from the circuit boards and subjected to a 240 hr heat-treatment at 438 K (165°C) in an argon atmosphere. Figure 5 shows the microstructures that were obtained on the argon-treated samples. As with the air heat-treatments, formation of the oxide layer at the Cu-Cu₃Sn interface was observed in both the 1978 and the 1979 samples whereas none was observed in the 1977 sample. Development of the oxide layer from heat-treatment in an inert atmosphere clearly showed that the source of oxygen was located within the copper plating. Organic addition agents, codeposited with the copper during the plating process, are believed to be the contributing source for the oxygen which is detected at the interface (6). This view is indirectly supported by the observation that the 1977 sample (where the copper was deposited in a pyrophosphate bath) did not show development of the oxide, whereas the 1978 and 1979 samples (where copper deposition was performed in a copper sulfate bath) showed extensive oxide formation at the Cu-Cu₃Sn interface. The irregularly shaped, jagged Cu-Cu₃Sn interface observed for the 1977 sample in Fig. 2 is indicative of copper deposition with limited use of leveling (addition) agents. This contrasts sharply with the smooth matrix-intermetallic interfaces observed for the 1978 and 1979 samples which clearly suggest a greater role for the leveling agents in the copper sulfate bath. The reduced level of irregularity at the Cu-Cu₃Sn interface for the 1977 samples in Fig. 3 and 5 was believed to be related to effects resulting from extended high temperature ther-

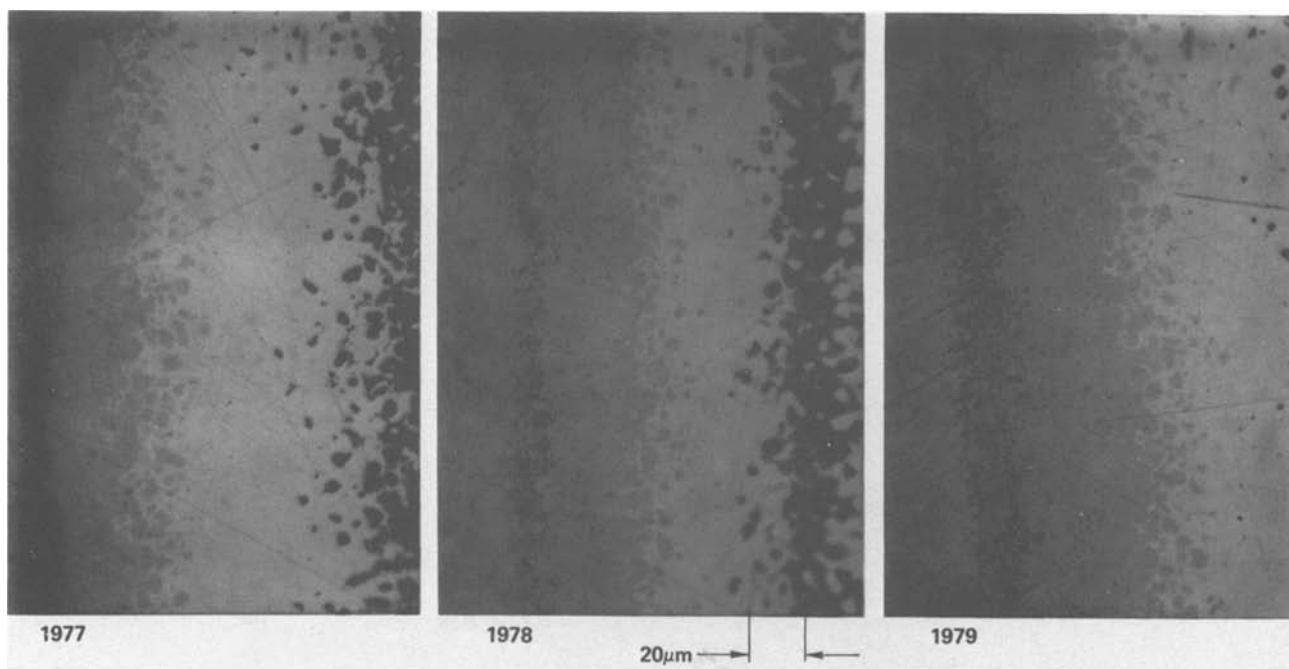


Fig. 5. Microstructures after 165°C, 240 hr argon heat-treatment. Oxide development similar to that observed in Fig. 3

mal exposure of the samples. It is possible that the treatments that were used resulted in decomposition of the organic addition agents and this may have permitted the development of a smoother Cu-Cu₃Sn interface with continued growth of the intermetallics. A bulk composition analysis, using Auger instrumentation, of the copper layer in the 1977, 1978, and 1979 samples indicated oxygen and carbon levels of about 3 to 5 atomic percent in the as-received condition for the 1978 and 1979 samples and an undetectable level of oxygen for the 1977 sample in agreement with the above interpretation of observed data. Carbon was not detected in the 1977 sample. All of this supported the view that organic addition agents might well be the source of the observed oxygen. These analyses were performed at a depth of about 1000Å to reflect actual bulk composition. (Depth profiles of the copper showed that the composition values stabilized after penetration by the Auger beam of a few hundred angstroms of thickness from the surface.) Examination of the composition after the 264 hr treatment in air (also at a depth of 1000Å) showed a much lower level of oxygen and almost no carbon in the 1978 and 1979 samples suggesting possible migration of these elements from regions close to the interface to the reacted zone under the influence of thermal activation.

Considerations such as solder composition, carbon contamination of the interface, and quality of the copper, can all, conceivably, to some extent, be expected to influence the rate of degradation of solder adhesion. Investigations at this Laboratory, however, suggest that the degradation mechanism itself will not be significantly altered by these several variations. The role of solder composition will be limited mainly to influencing the kinetics of growth of the various compounds and, therefore, to the accumulation rate of the oxygen-containing species. A detailed kinetics study showing the activation energy variations, for the several compounds, with changes in solder composition, is the subject of a separate publication (7). As for carbon contamination of the interface, this is expected to manifest itself in a manner similar to that observed for oxygen in this study. It may be noted, however, that even though almost equal amounts of carbon and oxygen were detected for the bulk composition of the as-received 1978 and 1979 boards, the distribution of these elements in the interface region was markedly different. Whereas oxygen was found to exist over the entire interface, where the oxygen-containing particles were distributed, high concentrations of carbon were detected only in a few discrete locations. This indicated that while carbon was also being rejected from the reaction zones in a manner similar to the oxygen (accounting for the observed buildup in concentration) its role in the observed degradation was minimal, albeit finite. The role of quality of the copper, however, is somewhat more complex.

In addition to solder separation occurring from buildup of occluded impurities, such as those discussed in this paper, microstructural details, in particular the grain size, can be expected to also influence the rate of solder separation. The kinetics of growth of the several compounds can be expected to be dependent on grain size variations especially if this is the slow stage in the overall growth process.

Conclusions

This study shows that every effort should be made to eliminate the source of oxygen in the copper plating to avoid solder-adhesion failures in printed circuit boards. There is reason to suspect that organic addition agents that are codeposited with copper are acting as sources of the observed oxygen. The oxygen accumulates as discrete oxide particles at the matrix-intermetallic boundaries because of oxygen exclusion from the reacted zone with the continued growth of the intermetallics. Increase in oxide-particle concentration leads to solder separation, possibly through inhibition of the solid-state diffusion reaction across the Cu-Cu₃Sn interface even while the diffusion reactions at the Cu₃Sn-Cu₆Sn₅ and the Cu₆Sn₅-(Pb-Sn) solder interfaces continue to proceed.

Acknowledgments

The authors wish to thank M. Seilonen for help in obtaining some of the Auger analyses and A. Lattanzi for continued encouragement of this effort. The keen interest of G. Ives in this activity is deeply appreciated.

Manuscript submitted June 3, 1980; revised manuscript received Aug. 29, 1980.

Any discussion of this paper will appear in a Discussion Section to be published in the December 1981 JOURNAL. All discussions for the December 1981 Discussion Section should be submitted by Aug. 1, 1981.

Publication costs of this article were assisted by The Charles Stark Draper Laboratory, Incorporated.

REFERENCES

1. E. Toledo, S. Bonis, J. Breen, and F. Oberin, *Circuits Manufacturing*, p. 64 (January 1970).
2. L. Zakraysek, in Proceedings of 11th Annual Reliability of Physics Conference, p. 6 (1973).
3. R. B. Keyson, Paper presented at 5th Contamination Control Seminar, Hughes Aircraft Company, El Segundo, California, October 1979.
4. "Metals Reference Book," 5th ed., C. J. Smithells, Editor, Butterworths (1976).
5. "Handbook of Auger Electron Spectroscopy," Physical Electronics Industries, (Perkin-Elmer) (1976).
6. T. Fulton, E. Toledo, and J. Breen, Tech. Report No. SR 70-4030, Raytheon Company, Equipment Division, January 1970 (Unpublished).
7. K. Kumar, A. Moscaritolo, and M. Brownawell, Unpublished.

Self-Aligned Aluminum Gate MOSFET's Fabricated by Laser Anneal

S. Iwamatsu¹ and M. Ogawa

VLSI Technology Research Association, Cooperative Laboratories,
4-1-1, Miyazaki, Takatsuku, Kawasaki, 213 Japan

ABSTRACT

Self-aligned aluminum gate MOSFET's have been fabricated by applying laser anneal technology. The threshold voltage and surface electron mobility were similar to the conventional silicon gate MOSFET's. But the low resistivity of gate and interconnection electrodes by aluminum is advantageous for high switching speed MOSLSI.

Most of the gate electrodes for self-aligned MOSFET's have been fabricated with silicon gate (1), molybdenum gate (2), molybdenum-silicide gate, and the other refractory metal gates. Silicon and refractory metal gates are advantageous because high temperature processes can be utilized after these gate materials are deposited and patterned. Aluminum gates have traditionally been fabricated after all high temperature processes are completed because of the low melting point of aluminum (660°C). Aluminum gates like Mo gates have low resistivity ($3 \times 10^{-6} \Omega\text{-cm}$ compared to $6 \times 10^{-6} \Omega\text{-cm}$ for Mo) which is advantageous for high speed MOSLSI circuits. Silicon gate has, on the other hand, a much higher resistivity ($10^{-3} \Omega\text{-cm}$). It is therefore desirable to develop self-aligned aluminum gate MOSFET's. In this paper, experimental results are reported for self-aligned aluminum gate SOS MOSFET's fabricated by laser anneal technology (3).

Figure 1 shows the fabrication sequence for self-aligned aluminum gate SOS MOSFET's by laser anneal technology. The wafers used in this study have 0.3 μm thickness undoped (100) single crystal films which are epitaxially grown on (1102) single crystal sapphire substrates. The silicon layer was first patterned to define silicon islands in a conventional manner. The patterning was accomplished with KOH aniso-

tropic etching. Then a 100 nm gate oxide was grown by dry oxidation at 1050°C. Next, a 300 nm aluminum layer was deposited by vacuum evaporation. The aluminum layer was patterned, using $\text{H}_3\text{PO}_4\text{-HAc-H}_2\text{O}$ solution etching, to form the gate electrodes and its connections. Phosphorus ion implantation was then applied to form the source and drain junctions, at the energy of 160 keV with a dose of $2.5 \times 10^{15} \text{cm}^{-2}$ and 80 keV with a dose of $2.5 \times 10^{15} \text{cm}^{-2}$. The next step was laser anneal on the top surface of the wafer to activate the ion implanted silicon layer. For the laser anneal, a 2 kHz pulsed and second harmonic generated YAG laser ($\lambda = 0.503 \mu\text{m}$) was used in an X-Y scanning system. The laser spot size was 100 μm^2 , the scan rate was 20 mm/sec, and the step size was 30 μm . The laser output power was chosen about 100 mW, so that the silicon layer was heated just below its melting point. In this step, the aluminum gate electrode was not melted by laser anneal in spite of its low melting point, because of its high reflectance of the laser light. In this step, the aluminum gates act as masks for source-drain ion implantations and laser anneal and perform self-aligned aluminum gate formation.

In the subsequent steps, silicon dioxide was chemically vapor deposited, and windows for the source, drain, and gate contacts were patterned and etched. Aluminum was deposited again over the entire surface which was patterned and etched to define the second interconnection plane. The final step was a 30 min sinter in H_2 at 450°C for minimizing the surface state densities to $5 \times 10^{10} \text{cm}^{-2}$ at the Si-SiO₂ interface and for performing the Si-Al contact alloy.

Devices with channel length of 2 to 40 μm were fabricated; the channel widths were 80 and 20 μm . A photograph of the self-aligned aluminum gate SOS MOSFET is shown in Fig. 2. The source-drain I-V characteristics of the device are shown in Fig. 3. The threshold voltage is -0.7V showing depletion mode operation, and surface electron mobility is 350 $\text{cm}^2/\text{V}\cdot\text{sec}$ at $V_0 = 0.1\text{V}$, $V_G = 2\text{V}$. These characteristics are similar to the conventional n-channel silicon gate SOS MOSFET's at nondoped 0.3 μm thick silicon layer. When an enhancement mode device is needed, it is possible to control the threshold voltage by applying the channel ion implantation and laser anneal to the silicon layer before the aluminum gate formation. Self-aligned aluminum gate MOSFET's technology is also useful for not only SOS MOSFET's but also bulk silicon MOSFET's.

The advantages of the self-aligned aluminum gate MOSFET's with laser anneal technology are: (i) low resistivity of gate and interconnection electrode by aluminum results in fabrication of high switching speed MOSLSI, and (ii) very low temperature process, except for thermal oxidation step, results in elimination of wafer warpage and minimum lateral

¹ Present address: Suwa Seiko Company, Limited, Suwa-gun, Nagano-ken, 399-02 Japan
Key words: laser anneal, VLSI, YAG laser, bulk silicon, SOS, ion implantation.

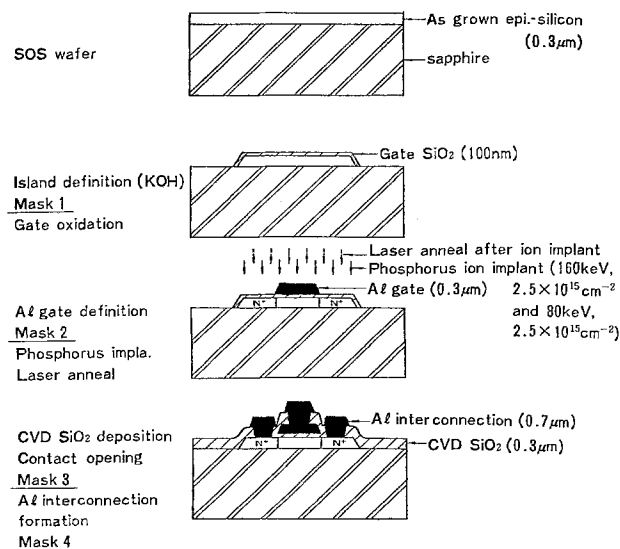


Fig. 1. Fabrication sequence for self-aligned aluminum gate MOSFET by laser anneal technology.

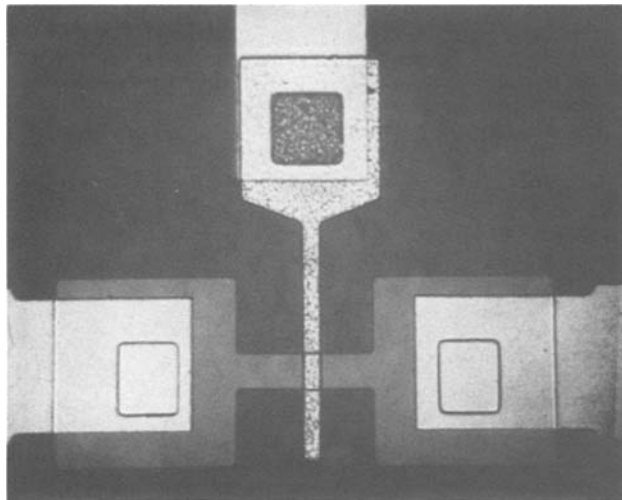


Fig. 2. Photograph of a self-aligned aluminum gate SOS MOSFET (channel length = 12 μm , channel width = 20 μm).

diffusion of source and drain junctions, results suitable for short channel MOS VLSI formation.

Manuscript submitted Oct. 20, 1979; revised manuscript received Feb. 28, 1980.

Any discussion of this paper will appear in a Discussion Section to be published in the December 1981 JOURNAL. All discussions for the December 1981 Discussion Section should be submitted by Aug. 1, 1981.

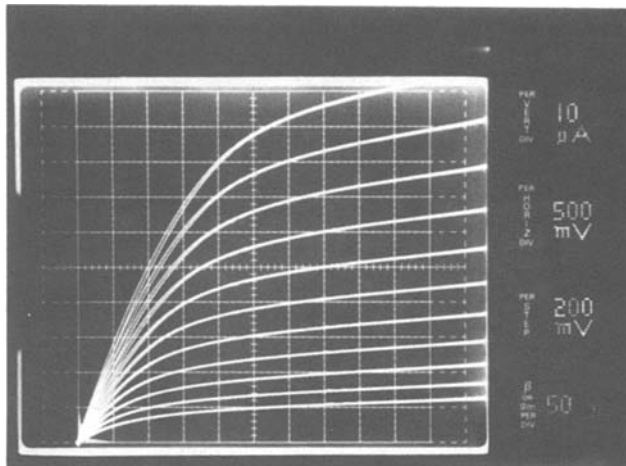


Fig. 3. Source-drain I - V characteristics of SOS MOSFET with $W = 20 \mu\text{m}$ and $L = 12 \mu\text{m}$.

Publication costs of this article were assisted by VLSI Technology Research Association.

REFERENCES

1. F. Faggin and T. Klein, *Solid-State Electron.*, **13**, 1125 (1970).
2. D. M. Brown, W. E. Engeler, M. Garfinkle, and P. V. Gray, *This Journal*, **115**, 847 (1968).
3. A. Gat and J. F. Gibbons, *Appl. Phys. Lett.*, **32**, 142 (1978).

Observation of Microtwinning in SOS by Scanning Electron Microscopy

M. L. Zorrilla Carfagnini¹ and J. Trilhe

C.E.A.-C.E.N.G., LETI/MEA 85 X, 38041 Grenoble Cedex, France

and M. Pitaval and P. Morin

Département de Physique des Matériaux, Université Claude Bernard Lyon 1, 69621 Villeurbanne, France

ABSTRACT

Microtwinning in silicon-on-sapphire (SOS) has been examined by a new technique. A crystallographic contrast on the sample surface is observed with a scanning electron microscope in the backscattered electron mode when a very bright source and a high pass energy filter is used. A modified Stereoscan MKIIa SEM with a field emission gun and an energy filter for backscattered electrons with a 200 eV window for a 45 kV primary beam has been used to study defect content in epitaxial SOS. Silicon layers thicknesses in the range of 0.1-1 μm were analyzed with a spatial resolution of 100Å.

This paper is concerned with an improved method for observing crystal defect content, it allows the determination of defect content in the surface region of thick samples without chemical etching or ion milling. We use an SEM in a special mode. The spatial resolution in the present experiments is 100Å. The depth explored beneath the surface is around 1000Å, so for a typical value of silicon epitaxial film thickness of (0.6 μm), we can obtain a defect content profile if we sequentially observe layers of varying thicknesses.

We briefly present here the fundamental of this technique and a description of the microscope used.

¹ Fellowship from CONICET, Republica Argentina.

Key words: silicon, sapphire, electron microscopy, defects.

We also discuss the results obtained for varying silicon film thicknesses in the range of 0.1-1 μm .

SEM Electron Channeling

A scanning electron microscope operating in the backscattered mode is sensitive to the relative orientation of the crystal with regard to the incident beam. A defect near the surface causes local bend of crystallographic planes and thus a local change in the backscattering current is observed. The anomalous absorption effect associated with Bragg reflection explains the contrasts observed (1).

Electron channeling patterns.—When a flat single crystal sample is observed at low magnification, bands

of contrast similar to Kikuchi lines in electron diffraction patterns are obtained. The symmetry of the pattern and its evolution when the specimen is tilted or rotated can be used to determine the crystallographic orientation of the sample. The origin of this contrast is explained qualitatively in Fig. 1.

When the electron probe scans the sample surface, the incident electron beam crosses the Bragg position for different sets of lattice planes. An anomalous electron absorption at Bragg angle θ_B produces variations in the backscattered electron current and consequently a contrast is obtained. A very flat surface is required to avoid a topographic contribution to contrast.

Crystal defect imaging.—At high magnification the variation of probe incidence angle can be neglected. When the incident beam is at the Bragg position for a set of lattice planes, a local bend of these planes, due to a crystal defect near the surface, produces an image contrast as shown in Fig. 2.

Required experimental conditions.—Crystal defect imaging needs a good compromise among the experimental parameters such as probe size, beam divergency, and electron beam current (1, 2). The probe size d must be smaller than the region where the lattice planes are perturbed. The divergency of the incident beam α must be smaller than the angular spread of the bent lattice planes. Thus it is necessary to work with a low illumination angle. In order to reveal the contrast pattern over the background noise the beam current I must be as high as possible.

These three parameters are related to the electron source brightness B by the equation

$$B = \frac{0.4I}{d^2\alpha^2}$$

Therefore a high brightness electron source is required (3). Patterns of reasonable contrast within standard exposure times are obtained with $B \approx 10^8$ A/cm² sec. Thus a field emission gun is needed.

For samples giving a weak contrast it is necessary to eliminate the influence of beam fluctuations on video signal electronically. Crystallographic contrast imaging being sensitive to crystal orientation, a goniometer stage has to be used. We use a high pass energy filter to collect the backscattered electrons which have lost ~ 100 eV energy so as to get a pattern of high contrast.

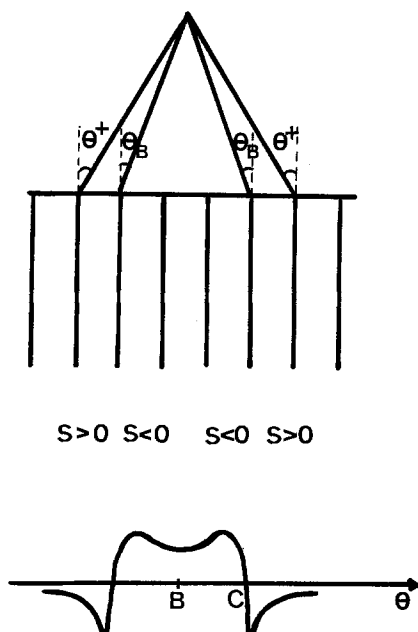


Fig. 1. Pseudo-Kikuchi pattern. Diagram illustrating the effect of the anomalous absorption at Bragg position and the formation of ECP.

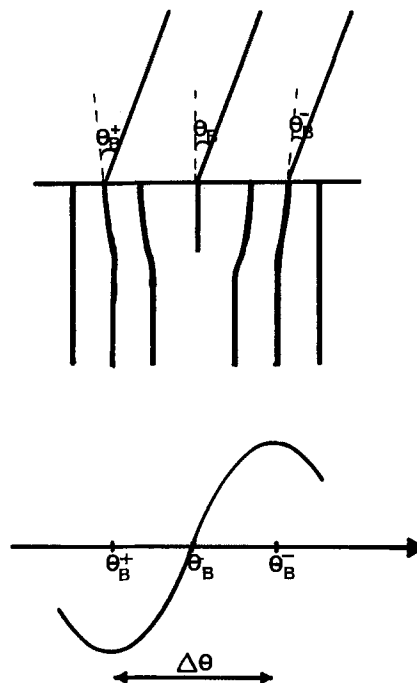


Fig. 2. Crystal defect imaging. At high magnification, a local bend of lattice planes produces an imaging contrast.

Experimental Arrangement

A schematic diagram of the microscope is shown in Fig. 3. The SEM is a Cambridge Stereoscan MKIIa with several modifications (4).

A field emission gun (5) differentially pumped (less than 10^{-10} Torr near the tip, 10^{-8} Torr in the intermediate chamber, and 10^{-5} Torr in the column) has been set up. Field emission instability is eliminated by an electronic attachment which divides the video signal by a signal proportional to the incident beam current (6).

The high pass energy filter is a spherical grid type. The transmission coefficient is 81% and its axis makes an angle of 117.5° with the primary beam (shown in Fig. 3). The detector is a scintillator light-pipe assembly. The energy resolution estimated is better than 100 eV for a 45 keV primary beam.

Diffracting conditions are determined by electron channeling patterns (ECP) recorded from a selected

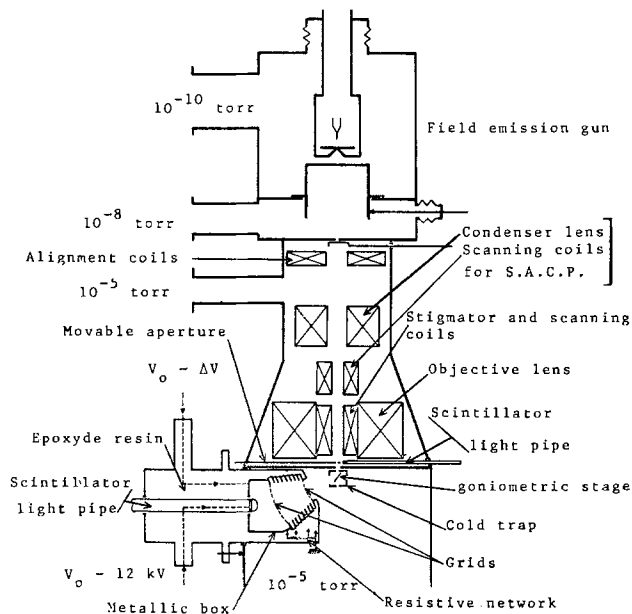


Fig. 3. Diagram of the scanning electron microscope

area (SACP) by the use of a rocking beam method. An extra set of coils near the cross-over of the gun, above the objective lens, allows the beam to be rocked around a point on the specimen surface.

The standard coils in the objective are not excited in this rocking mode. The objective diaphragm is removed in order to allow a $\pm 6^\circ$ deflection angle. The area analyzed in SACP has a diameter of at least 10 μm .

A goniometer stage of an EM Philips transmission electron microscope has been adapted to the specimen chamber. The mechanical shift associated with tilt adjustments of the goniometer is less than 0.5 μm .

In order to avoid contamination, which occurs during long-time observation on the same area, the specimen is surrounded by copper walls cooled with liquid nitrogen.

Experimental

(100) silicon was deposited from the vapor phase at 980° by the pyrolysis of silane in H_2 on (1012) CZ single crystal sapphire substrate. A growth rate of 2 $\mu\text{m}/\text{min}$ was used and silicon film thicknesses in the range 0.1-1 μm were investigated. Silicon quality was checked by double crystal x-ray rocking curves.

The SEM was operated at 45 keV and the back-scattered electrons were filtered with an energy filter window of 200 eV.

Results and Discussion

Figure 4 shows an electron channeling pattern obtained for an 8000 \AA thick silicon film. In all cases the flatness of the samples was sufficient to avoid a topographic contrast as evidenced by the good definition of the ECP.

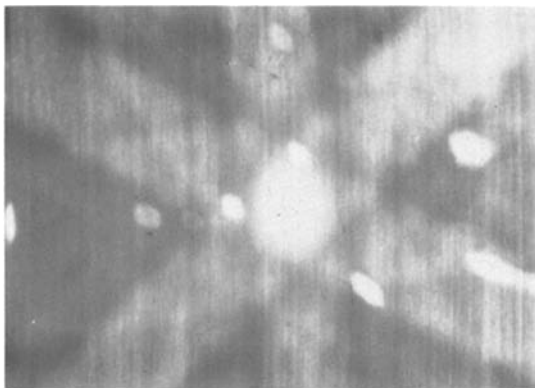
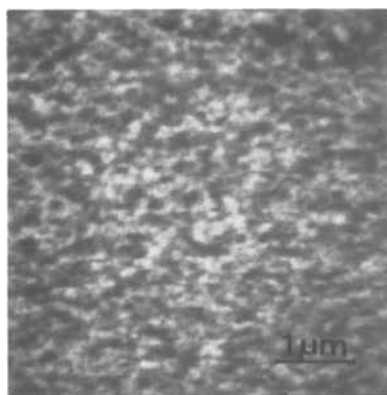
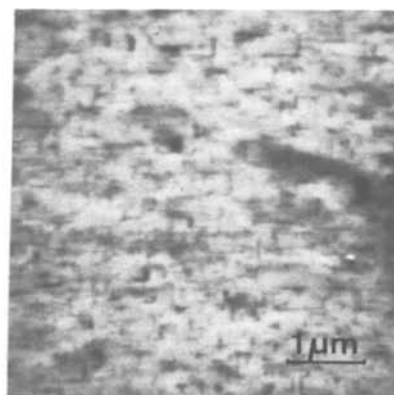


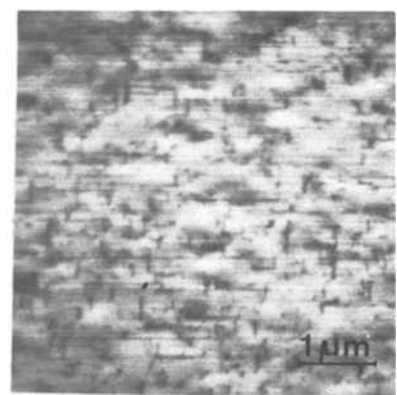
Fig. 4. ECP for 8000 \AA thick silicon film, showing [111] pole



2000 \AA



4000 \AA



6000 \AA

Fig. 5. ECI photographs of microtwins: (a) 2000 \AA , (b) 4000 \AA , (c) 6000 \AA thick (100) silicon layers. The [111] direction of the silicon is parallel to the incident beam.

Figure 5 shows the electron channeling image (ECI) obtained for three specimens with different silicon film thicknesses. These pictures were taken with the [111] silicon direction parallel to the incident beam. We can see a crystallographic contrast formed by two mutually perpendicular sets of black lines.

The contrast observed can be interpreted as the intersection of the microtwinning silicon planes {111} with (100) surface plane, that is along $\langle 110 \rangle$ directions.

We find that the density of microtwins increases for lower silicon film thickness. This result agrees with previous TEM observations (7). However for silicon film of thickness higher than 6000 \AA the density of defects is nearly constant, about $10^9/\text{cm}^2$. These results are comparable to those published by Inamura (8) for 1 μm silicon film thickness observed after chemical etching.

For silicon film thicknesses lower than 4000 \AA , counting of the defects is very difficult. Because of the small dimensions and the high density of defects we approach the limit of resolution of the method. The full width at half maximum (FWHM) of x-ray rocking-curves

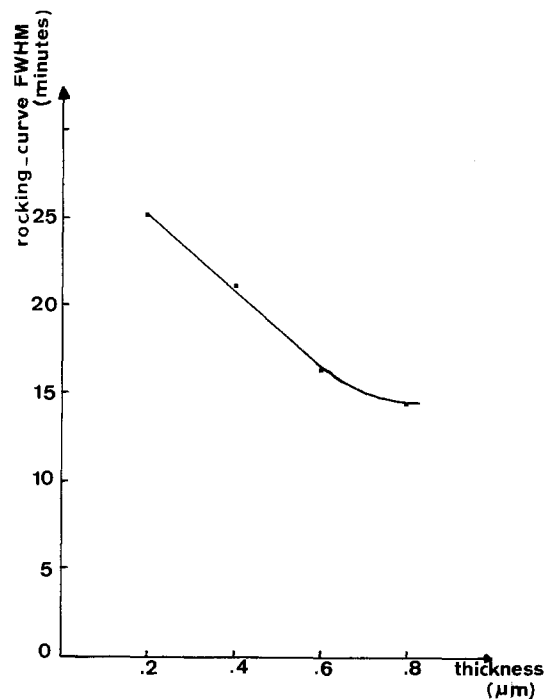


Fig. 6. Full width at half maximum (FWHM) of rocking curves vs. silicon film thickness.

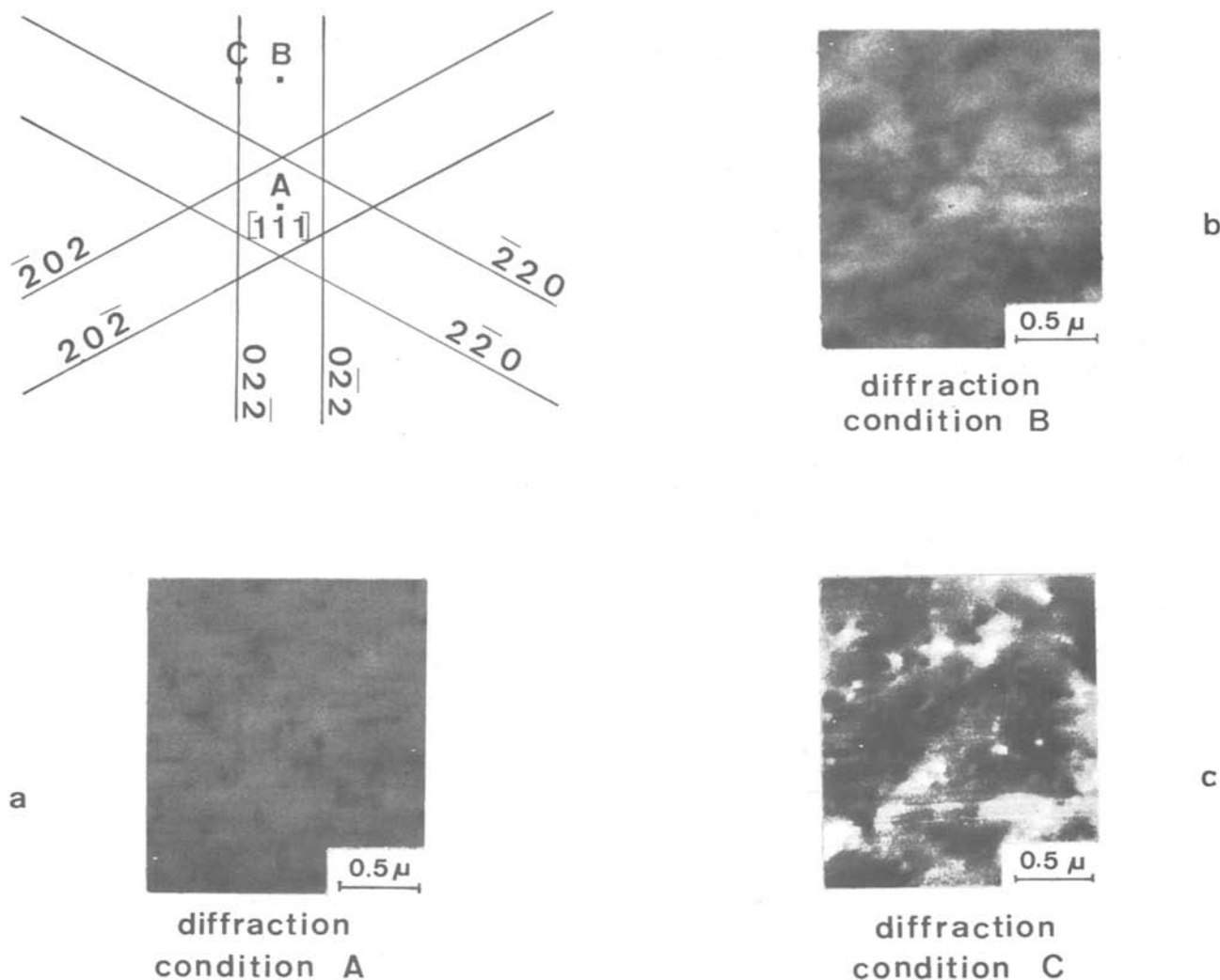


Fig. 7. ECI photographs of the same area of a 8000Å thick silicon film for different diffraction conditions

vs. silicon film thickness for these samples are plotted in Fig. 6. These values, proportional to the defect density in the epitaxial silicon volume, show the same decrease in defect density as ECI. Nevertheless the main interest of the ECI technique is that it affords the possibility of observing weak and strong lattice stresses.

There is a high dependence between the diffraction condition and the image contrast. Figure 7 shows the contrast obtained for the same region of the sample when different diffraction conditions are used. These results are for a silicon layer of 8000Å.

When the incident beam is oriented in A or B position (see Fig. 7) for an SACP mode there is little change in intensity when the incident angle varies (see Fig. 1b). Consequently if a contrast is seen, it is due to a strong stress or a disruption of the lattice [see Fig. 7 (a), (b)]. For incidence of the electrons corresponding to the diffraction condition C, that is very near to the Bragg condition, our method is very sensitive to weak lattice stresses; our crystal has been highly stressed and microtwinning is not seen any more as shown in Fig. 7 (c), for which a strong contrast is observed. We suppose that the black pits are due to the stress field of emerging dislocations.

Conclusion

We have presented a new method for SOS characterization. We believe that it can yield much information on crystal defects and stress field in silicon on sapphire epitaxial layers. This technique presents several advantages over others. No special sample preparation is needed either by chemical etch or by difficult ion milling as is necessary for TEM.

Electron channeling is complementary to the x-ray rocking curve technique as it reveals the nature of crystal defects which can be identified by observation of the surface layer (~1000Å).

Acknowledgment

We are grateful to Dr. M. Dupuy for fruitful discussions.

Manuscript submitted Dec. 28, 1979; revised manuscript received Aug. 21, 1980. This was part of Paper 567 presented at the Los Angeles, California, Meeting of the Society, Oct. 14-19, 1979.

Any discussion of this paper will appear in a Discussion Section to be published in the December 1981 JOURNAL. All discussions for the December 1981 Discussion Section should be submitted by Aug. 1, 1981.

Publication costs of this article were assisted by C.E.A.-C.E.N.G., LETI/MEA.

REFERENCES

1. G. Booker, A. Shan, M. Whelan, and P. Hirsch, *Philos. Mag.*, **16**, 1185 (1967).
2. M. Pitaval, P. Morin, J. Baudry, and G. Fontaine, *J. Phys.*, **37** (11), L 309 (1976).
3. D. R. Clarke and A. Howie, *Philos. Mag.*, **24**, 959 (1971).
4. P. Morin, M. Pitaval, D. Besnard, and G. Fontaine, *Philos. Mag.*, **A**, **40**, 4, 511 (1979).
5. S. Ranc, M. Pitaval, and G. Fontaine, *Surf. Sci.*, **57**, 667 (1976).
6. P. Morin, C. Rolland, M. Pitaval, and E. Vicario, *Rev. Phys. Appl.*, **13**, 39 (1978).
7. J. Trilhe, *This Journal*, **124**, 1299 (1977).
8. Y. Imamura, K. Daido, K. Mimageishi, and H. Nakamishi, *Jpn. J. Appl. Phys.*, **16**, Supplement 16-1, 547 (1977).

Pre- and Postepitaxial Gettering of Oxidation and Epitaxial Stacking Faults in Silicon

M. C. Chen¹ and V. J. Silvestri*

IBM T. J. Watson Research Center, Yorktown Heights, New York 10598

ABSTRACT

Certain gettering treatments on the back sides of wafers have been found to be effective in reducing stacking faults in Si bulk wafers. In this study results are reported for various back side, front side, and combined gettering processes on wafers used to receive epitaxial films. Focus in this investigation was on the effectiveness of gettering measures in removing defects in epitaxial films. Results of POCl_3 diffusion, Ar ion implantation (I/I), abrasion, and Si_3N_4 deposition as back-side treatments are reported as well as As I/I and boron diffusion front-side gettering effects. These treatments were employed either in the pre- or postepitaxial deposition mode. When used in the pre-epitaxial mode all of the back-side gettering techniques were found effective in reducing oxidation stacking faults (OSF) in epi films to levels of $\leq 10 \text{ cm}^{-2}$ as compared to nongettered levels of $100\text{-}1000 \text{ cm}^{-2}$. In the post-epi application, Ar I/I was found to give moderate reduction of OSF defects. The back-side gettering techniques combined with front-side gettering used in a pre-epitaxial mode reduces epitaxial type stacking faults (SFepi) significantly and eliminates oxidation stacking faults (OSF) in the epitaxial films. Counts of SFepi were not reduced using the back-side gettering alone. The two front-side procedures were, however, found to reduce both the OSF and SFepi types. The epitaxial films deposited on the As I/I surfaces showed a factor of ten reduction in SFepi defects and OSF types were reduced even more drastically. Boron diffusions in Si reduced OSF counts to nearly zero and SFepi faults by a factor of four over nongettered samples. Some effects of pre-epitaxial and postepitaxial oxidation treatments on stacking fault counts were also investigated. Results are also reported for effectiveness of stacking fault gettering relative to initial cleaning procedures used and stacking fault counts originating from substrates.

Good quality epitaxial films deposited on silicon are essential to achieve high yields in semiconductor device and integrated circuit fabrication. In practical applications, most often the epitaxial layer is grown at a point in the device processing sequence after a significant amount of high temperature treatment has occurred. This processing prior to epitaxy often includes an oxidation of the substrate with removal of the oxide just prior to the epitaxial deposition. Following film deposition, further high temperature treatment is often required before the final completion of devices or integrated circuits. All of this temperature cycling can result in increased density of defects in the epitaxial layer.

The defects which contribute to yield loss and anomalous device characteristics are classified as electrically active defects. Stacking faults and dislocation slip lines are two types of defects commonly included among the electrically active group. Their presence has been tied to excessively anomalous leakage in diodes (1), and they have been studied in relation to "pipes" in bipolar circuits (2-5). Two important kinds of stacking faults identified and studied in silicon epitaxial layers are the epitaxial stacking fault (SFepi) (6-8) and the oxidation-induced stacking fault (OSF) (1, 9, 10, 11). Since they are highly undesirable, various gettering techniques have been developed to help eliminate and suppress their densities in the starting silicon substrate material (6, 7, 12). The present work was specifically directed to studying the effects of gettering before and after epitaxial depositions and evaluate the effectiveness of the gettering procedures in reducing defects in the epitaxial films. Several decoration techniques were employed to detect the presence of SFepi and OSF type stacking faults and assess the effectiveness of the gettering procedures in films. In addition, observations are reported for epitaxial films deposited on arsenic ion implanted surfaces and

epitaxial films which had experienced heavy boron diffusions.

Experimental

The substrates used for the epitaxial depositions were polished (100) oriented 5.7 cm diam n-type and p-type silicon wafers. The wafers were 0.38 cm in thickness. The n-type wafers were generally phosphorus-doped ranging from 0.5 to 0.05 $\Omega\text{-cm}$ in resistivity. The p-type wafers, unless otherwise specified, were boron-doped with a nominal resistivity of 10 $\Omega\text{-cm}$. In most cases, when bulk n-type substrates were employed, they were first oxidized at 1000°C employing dry oxygen-water vapor-dry oxygen gases sequentially introduced which is referred to below as a dry-wet-dry (DWD) sequence. Generally the time involved 5 min for the dry oxygen steps. Most of the oxide, however, was grown during the steam cycle for a thickness of 6500Å (about 1 hr total oxidation time at 1100°C, or 2.5 hr at 1000°C). This oxide was then removed prior to epitaxial deposition. HCl gas was introduced during some oxidations. These cases will be specifically noted.

The epitaxial films were deposited by the hydrogen reduction of silicon tetrachloride (SiCl_4) at 1050°C using an AMC-1200 reactor. The epitaxial layers were deposited in blanket fashion to thicknesses of 8 μm on the n-type substrates and to 1.5 μm thicknesses on the n^+ subcollector patterned p-type wafers, respectively. The deposition rates for both thicknesses were 0.1 $\mu\text{m}/\text{min}$. Only n-type epitaxial films were deposited. AsH_3 was used as a dopant source. The film resistivities ranged from 0.1 to 1 $\Omega\text{-cm}$. A standard cleaning employing NH_4OH and HCl in combination with H_2O_2 was generally used along with a final 50:50 HF: H_2O exposure just prior to epitaxy.

The epitaxial film defects were decorated using Wright etch (16) and examined using a Nomarski-interference microscope. Decoration and detection of the electrically active defects was accomplished using

* Electrochemical Society Active Member.

¹ Present address: Department of Electronics Engineering, National Chiao Tung University, Hsinchu, Taiwan, China.

Key words: gettering, wafer, films.

an anodic etching technique (13) in which the n-type epitaxial film surface is exposed to a dilute HF solution (used as the electrolyte) while a voltage is applied to the substrate wafer which acts as the anode. A platinum wire in the solution acts as the cathode. Conditions used for anodic etching varied. In general, an HF concentration of 5% was employed. An applied voltage of 2V was generally used for the 1.5 μm epi films and 10V for the 8 μm epi films; 10-60 sec were typical times employed for anodic exposure.

Gettering measures were introduced both before (pre-epi) and after (post-epi) epitaxial depositions. Four back-side gettering measures specified below were evaluated. All these measures, whether used in a pre-epi or post-epi gettering mode, were restricted to one-half of the back side of the substrate wafers to allow for easy comparison. The back-side gettering techniques employed were: (i) Ar ion implant: Ar 350 keV, $5 \times 10^{15} \text{ cm}^{-2}$ dose, anneal 20 min 1000°C in N_2 ; (ii) POCl_3 -diffusion: 870°C 15' deposition, 20' O_2 -3 hr 40' N_2 , 1000°C drive-in; (iii) Si_3N_4 process: CVD Si_3N_4 ~5000Å on back side, 1100°C 2 hr Ar anneal; (iv) abrasion gettering. Although better gettering has been reported for Si substrates using higher temperature-time POCl_3 treatments, we chose to evaluate a 1000°C drive-in, since this was a more compatible process for our epitaxial films. The flow chart describing experimental pre-epitaxial gettering sequences is given in Fig. 1. Following back-side gettering, samples could either be given a pre-epitaxial oxidation and go directly in for epitaxial film deposition. For each gettering experiment a number of wafers were included which received a blanket front-side As I/I in addition to the back-side gettering. Following film deposition, defects were decorated using Wright etch and anodic etching for revealing SFepi type defects. A postepitaxial oxidation of the films was used to induce OSF type defects prior to decorating. The postepitaxial gettering process employed the following sequence: (i) epitaxial deposition, (ii) back-side gettering (either POCl_3 or Ar I/I), (iii) postepitaxial oxidation and Wright etch. Only OSF type defects were evaluated for the postepitaxial case. In addition to evaluating the above back-side gettering techniques in a postepitaxial mode, epitaxial films were deposited directly on surfaces which had received As I/I, or subsequent to deposition, were diffused with boron. These "front-side gettering" procedure details are as follows: As I/I (50

keV, $1.5 \times 10^{16} \text{ cm}^{-2}$ dose) followed by a drive-in oxidation from 1000° to 1100°C. The oxide formed was stripped just prior to epitaxial growth. The boron diffusions into the epi films used BN source wafers. The diffusion was performed through oxide openings into the n-type epitaxial film at a temperature of 1050°C for 65 min.

In order to facilitate observations and data gathering on the gettered *vs.* nongettered surface sectors, just prior to defect decoration, wafer surfaces were patterned using a metal mask. The mask consisted of circular holes (32 mils in diameter) on 100 mil centers. These holes were arranged in rectangular patterns which defined and covered five basic areas of the wafer surface. The areas covered on wafers are shown schematically in subsequent data description as rectangular shapes in Fig. 5, 6, and 7 and represent areas where defect counts were taken. To decorate the wafer, Al was evaporated through this mask to form an Al dot pattern on the Si surface. With the Al acting as a mask the exposed Si surfaces were then etched using reactive ion etching (RIE) to a depth of 600-1000Å. Other RIE masking techniques were also employed to produce surface steps in some cases. The steps formed in the Si from RIE etching were found to be retained during Wright etching and anodization. The mapped surfaces enabled us to (i) trace accurately particular etch figure changes through Wright etching and anodization, (ii) examine defect counts in boron diffused areas, and (iii) reduce the microscopic counting of defects necessary to determine a good statistical density for wafer areas.

Results and Discussion

Epitaxial Stacking Faults (SFepi) and Pre-epi gettering

The epitaxial stacking fault defect is believed to originate at the substrate-epi interface and propagate from this site during the epitaxial deposition. A typical SFepi as delineated by 20 sec Wright etch is shown in Fig. 2. The epitaxial film in Fig. 2 is 8 μm thick and the SFepi measures 13 μm on a side.

On epitaxial layers typically deposited on 0.05-0.5 $\Omega\text{-cm}$ n-type substrates which are nongettered, SFepi defects range in density from 30 to 60 cm^{-2} (Table I). The various gettering measures listed in the table when performed on the back side of substrate wafers in the pre-epi mode seemed to have little effect on the subsequent formation of SFepi faults. The numbers shown in the table give the typical SFepi densities observed on a number of wafers for each gettering procedure. For the Si_3N_4 case a definite increase was

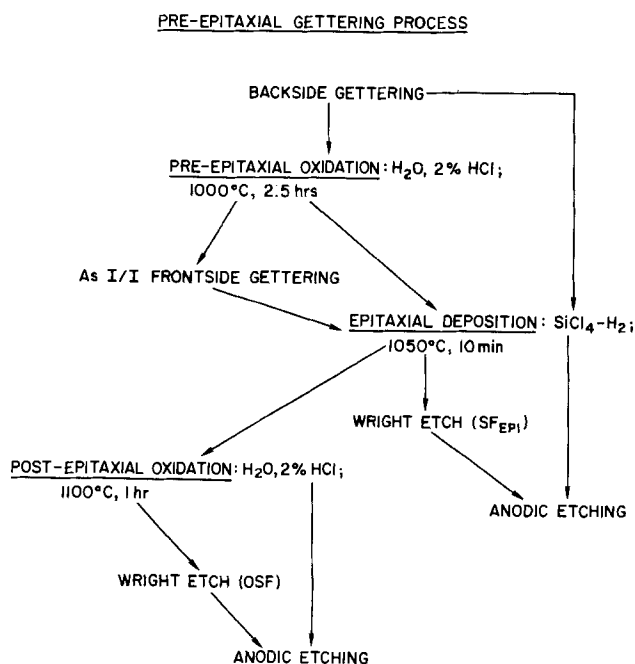


Fig. 1. Pre-epitaxial gettering process

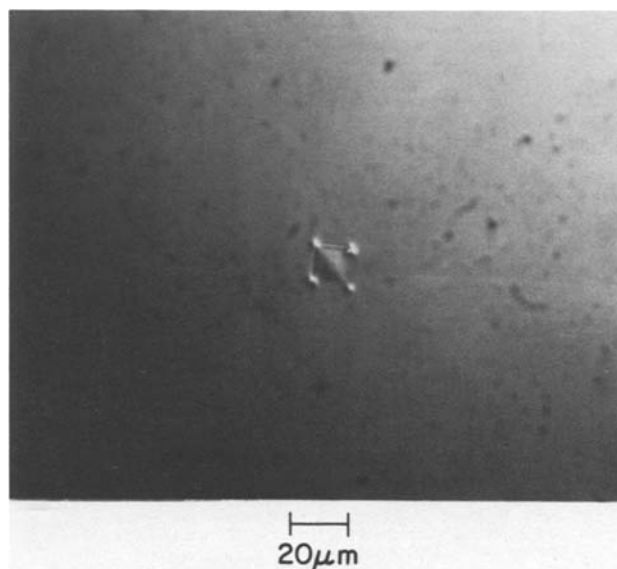


Fig. 2. Typical SFepi after 20 sec Wright etch

Table I. Pre-epitaxial gettering (SFepi)

| Gettering | SFepi density (cm ⁻²) (back side only) | SFepi density (cm ⁻²) (back side + As I/I front side) |
|--------------------------------|---|---|
| Nongettered | 30-60 | |
| POCl ₃ | 46 | 4 |
| Ar I/I | 49 | 4 |
| Si ₃ N ₄ | 87 | 35 |

noted overall. Since this gettering procedure caused significant wafer warpage, the higher SFepi counts may have been induced because of the substrate distortion.

The samples which had received both the back-side gettering plus the As I/I front-side gettering showed an outstanding decrease in SFepi (Table I). The only exception to the very low counts in SFepi for the front and back treated samples can again be noted for the Si₃N₄ sample. Even here, however, a moderate improvement is noted.

The SFepi are electrically active defects. If an anodic etch exposure of 10V for 30 sec in 5% HF was applied to an 8 μm epi-film a typical decoration as is shown in Fig. 3 is obtained. The large etch artifact indicates that intensive anodic etching occurs at SFepi sites. Generally, about 90% of the SFepi sites initially indicated using Wright etch were further decorated anodically using similar anodic etching conditions. Presumably this 90% of SFepi defects contain precipitates along the partial dislocations making them electrically active and result in artifact formation with anodic etching.

Oxidation-Induced Stacking Faults (OSF) and Gettering Measures

Oxidation-induced stacking faults (OSF) are produced on the surface of epitaxial layers when an epi-layer receives a high temperature steam oxidation treatment. Typical OSF structures are shown in Fig. 4. These OSF's occur even when the epitaxial films are deposited on substrates which in themselves do not exhibit OSF formation for similar oxidation treatments. The OSF densities can vary over the deposited epitaxial films. Typical densities ranged from 100 to 1000 cm⁻² for an oxidation of 1100°C for 1 hr with 2% HCl.

The various back-side gettering measures included in the OSF studies were Ar ion implantation, POCl₃ diffusion, Si₃N₄ application, and abrasion. With respect to the wafer processing sequence, the back-side get-

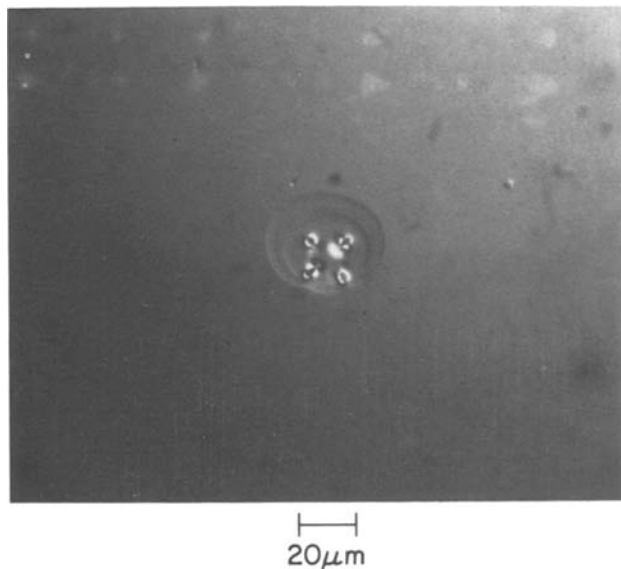


Fig. 3. Typical SFepi artifact after anodic etch, 10V, 30 sec, 5% HF.

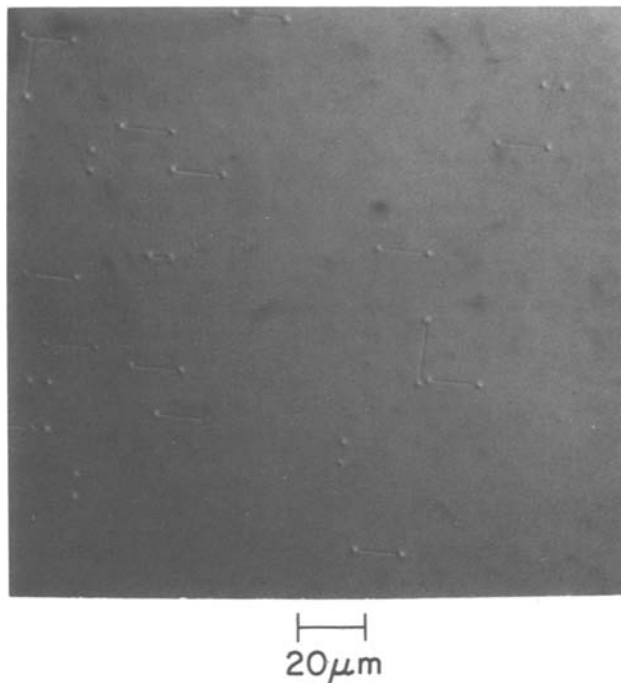


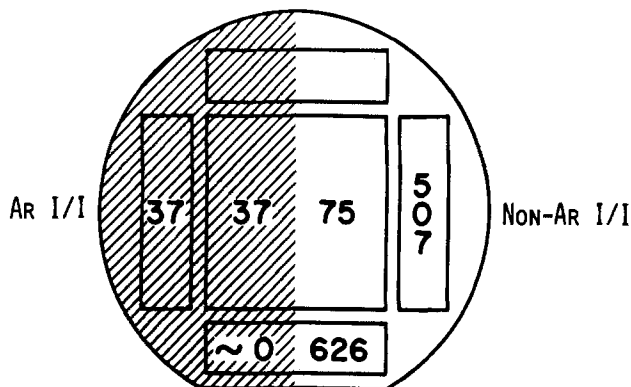
Fig. 4. Typical OSF revealed with 1 min Wright etch in epitaxial films.

tering measures were applied in both modes: pre-epi and post-epi. Dependent on the experiment, the processing could include a high temperature pre-epi oxidation treatment just prior to epitaxial growth. Following epitaxial growth all films were post-epi oxidized and etched for the OSF inspection. In all cases, except for the abrasion gettering experiment and otherwise specifically noted, the pre-epi and the post-epi oxidation conditions were [1000°C, DWD, 2.5 hr, 2% HCl] and [1100°C, DWD, 1 hr, 2% HCl], respectively. The pre-epi and post-epi gettering results for OSF defects follow below.

Pre-epi gettering of OSF.—With the Ar I/I, POCl₃, Si₃N₄, or abrasion gettering OSF's counts were observed to show reduced counts over the entire surface of the epitaxial layers even though the gettering had been applied to only one-half of the wafer back side. With the exception of abrasion gettering the OSF stacking fault densities found were very low (≤ 10 cm⁻²) as compared to separate wafers with no gettering (100-1000 cm⁻²) in Table II. In combination with As I/I on the front side the above back-side gettering reduced defects to nearly zero. In view of the higher OSF densities observed on the nongettered epi-wafers, coupled with an estimated 1-2 cm total diffusion length of the interstitial sites, it is probable that all the gettering measures are working to some extent over the whole wafer even when applied to only half. On wafer edges where defect counts are always higher, careful inspections were made (approximately within 0.37 cm from the edge). For these higher count areas, clear demarcations between gettered and nongettered halves of the wafers were more easily observed. This is shown most clearly for the Ar I/I

Table II. Pre-epitaxial gettering (OSF)

| Gettering | OSF density (cm ⁻²) |
|----------------------------------|---------------------------------|
| Nongettered | 100-1000 |
| Argon I/I | ≤ 10 c |
| POCl ₃ | ≤ 10 c |
| Si ₃ N ₄ | ≤ 10 c |
| Abrasion | ≤ 30 c |
| Back side + As I/I front side | ~ 0 |

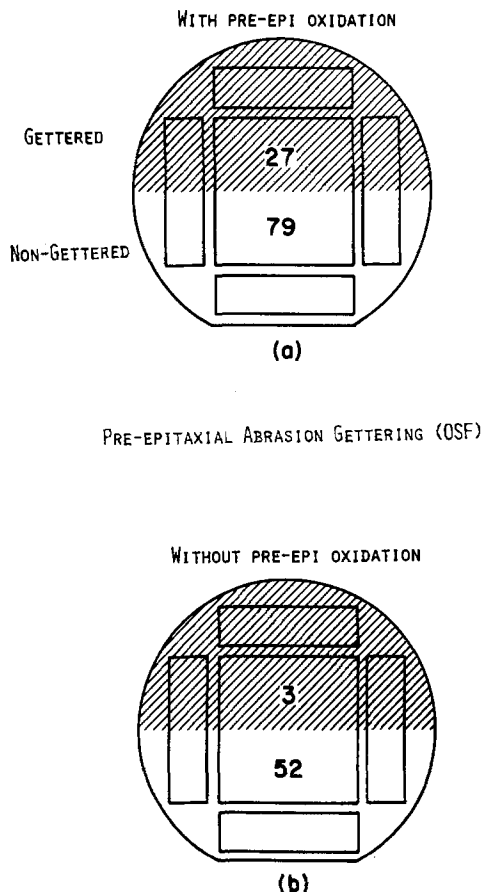


PRE-EPITAXIAL AR I/I GETTERING (OSF)

Fig. 5. Typical pre-epi Ar I/I gettering wafer count

case in Fig. 5. The POCl_3 and Si_3N_4 gettered wafers did not show as clear a demarcation between gettered and nongettered halves even in these edge regions.

The abrasion gettered samples in the OSF studies received a somewhat different process treatment. The treatment eliminated the normal pre-epi cleaning and employed only the final HF etch prior to epitaxy. In addition some wafers received a pre-epitaxial oxidation while others did not. These modified procedures were expected to introduce higher OSF densities in the samples. Figure 6 shows the results for two abrasion gettered epi-wafers. Epi-wafer 6(a) had received a pre-epi oxidation treatment, while 6(b) had not. Gettering is obvious for both cases with a slightly higher overall density of OSF's occurring in the sam-



PRE-EPITAXIAL ABRASION GETTERING (OSF)

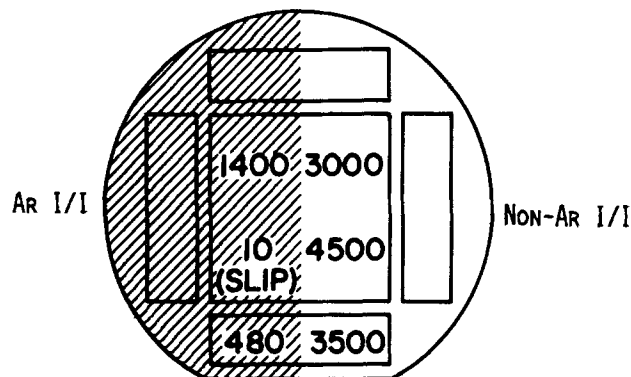
Fig. 6. Typical pre-epi abrasion gettered wafer defect count: (a) with pre-epi oxidation, (b) with no pre-epi oxidation.

ple having pre-epi oxidation. It should be noted in Fig. 1 (process sequence) that the back-side gettering precedes the pre-epitaxial oxidations. It is believed that during this oxidation-heating step the effectiveness of the gettering region was diminished making it less effective during the subsequent epitaxial deposition. Substrate gettering would be expected to occur during the pre-epi oxidation. The defect count in Fig. 6(b) shows more effective gettering without pre-epi oxidation consistent with the above. This suggests that gettering in the pre-epitaxial mode should be introduced just before the epitaxial deposition.

Post-epi gettering of OSF.—Back-side post-epi gettering by Ar I/I and POCl_3 diffusion of substrates with deposited epitaxial films in place was investigated. In both cases, a pre-epi oxidation was performed on the substrates, i.e., 1000°C DWD 2.5 hr, 2% HCl, prior to epi. The post-epi oxidation following back-side gettering was at 1100°C for 2 hr in steam with no HCl. In addition, the substrate wafers received only a final HF cleaning just prior to epitaxial deposition. Following the post-epi oxidation to induce OSF's in the epi the oxide was stripped and the wafers Wright etched to reveal the stacking faults. As might be expected, a much higher OSF count was generally observed (Fig. 7). In the post-epi gettering (Ar I/I), wafers having very high OSF defect densities ($> 10^5 \text{ cm}^{-2}$) displayed no obvious distinction between the gettered and nongettered halves in so far as defect counts. This was probably due to our inability to see distinctions and count at the very highest densities. However, a moderate gettering effect was readily observed on wafers where "poor" cleaning had introduced a medium-high OSF density ($\sim 3000 \text{ cm}^{-2}$) as shown in the Fig. 7. The very low local OSF density of 10 cm^{-2} appearing in Fig. 7 on the gettered side is not attributed necessarily to the Ar I/I since this local area was found to contain many slip dislocation lines which can absorb OSF's locally. The post-epi POCl_3 back-side diffusion gettering procedure did not seem effective in reducing OSF defect counts for the conditions employed.

Front-side Gettering

Arsenic I/I gettering.—The front-side As I/I procedure described earlier virtually eliminates oxidation stacking faults in epitaxial films deposited over the implanted regions. An example of such deposits over an n^+ As I/I region in a p^- substrate is shown in Fig. 8. The application of anodic etch to such epi surfaces shows greatly reduced decoration and etch artifacts over the n^+ implanted regions when compared to the p^- region.



POST-EPITAXIAL AR I/I GETTERING (OSF)

Fig. 7. Typical wafer defect counts for post-epi Ar I/I gettered samples.

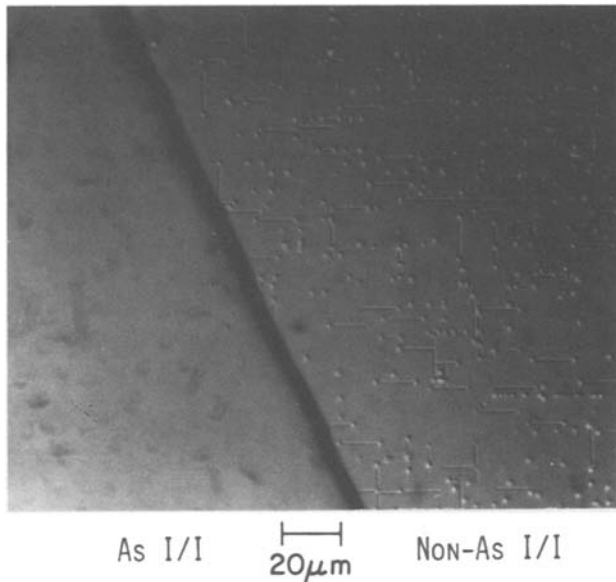


Fig. 8. Wright etch OSF decoration of epi surfaces having n^+ As I/I implanted regions.

Hillock-type defects, which will be discussed in greater detail further below, were found in both n^+ and p^- regions at similar densities [Fig. 9(a)]. These surface features appeared following Wright etching. Figure 9(b) shows the identical region in 9(a) photographed after it had been anodized. It is obvious that only some of the surface hillock features decorate anodically. Those that decorate appear as paired structures orthogonally oriented which can be seen with close examination of Fig. 9(a) in the p^- region.

Stacking fault reduction by boron diffusion.—Boron was diffused into $8 \mu\text{m}$ n -type epitaxial layers through

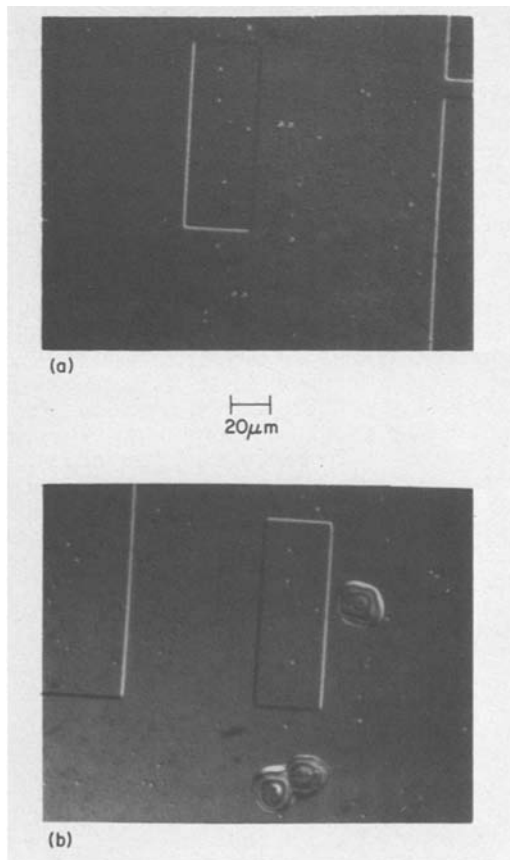


Fig. 9. Decorated hillock and OSF defects on As I/I subcollector structures: (a) after Wright etch, (b) after anodic decoration.

an oxide mask as described in the experimental section in forming p - n junction diodes. The diffusions resulted in p - n junction depths of $1.4 \mu\text{m}$ with very sharp concentration profiles at the junction. Prior to boron diffusion, the epitaxial films had been steam oxidized at 1100°C to generate $13 \mu\text{m}$ long oxidation stacking faults. The characteristic leakage current of the diodes at 15V reverse bias was in the order of 10^{-12}A for a 35 mils dot size diode. This is several orders of magnitude lower than reported values on diodes known to contain OSF's (1). Reactive ion etching, with the Al contacts in place as a mask, was used to mark the diode regions. They could then be readily located and examined for defects after the aluminum contacts were removed. A 1 min Wright etch was performed on the wafers such that approximately $0.6 \mu\text{m}$ of the silicon was removed from the surfaces. This etch depth exposed surfaces both within and outside the diode area about halfway into the diode volume from the p - n junction. Oxidation stacking faults were observed in large numbers on the surface outside the boron-diffused diode areas, but no stacking faults were observed within the boron-diffused region [Fig. 10(a)]. Following this the wafer was further Wright etched for an additional 2 min to remove a total of $1.8 \mu\text{m}$ of the original surface. This procedure exposed regions below the junction. Oxidation stacking faults at this etch level were found both within and outside of the diode area [Fig. 10(b)]. The absence of OSF defects in the p -region in Fig. 10(a) shows that the presence of heavy boron acts as an effective getterer in the annihilation of electrically active stacking faults in silicon. It has been reported that stress introduced by the high concentration boron diffusion $> 10^{20}$ and solute lattice contraction results in some defect reduction (14). Observations of our leakage data also support these conclusions. In comparing decorated defect counts inside the individual diode areas after Wright etch (at the $1.8 \mu\text{m}$ etch level) with the leakage data associated with the particular diode no definitive correlation was found. This lack of sensitivity would support the conclusion that electrically active stacking faults were eliminated at least down to the junction

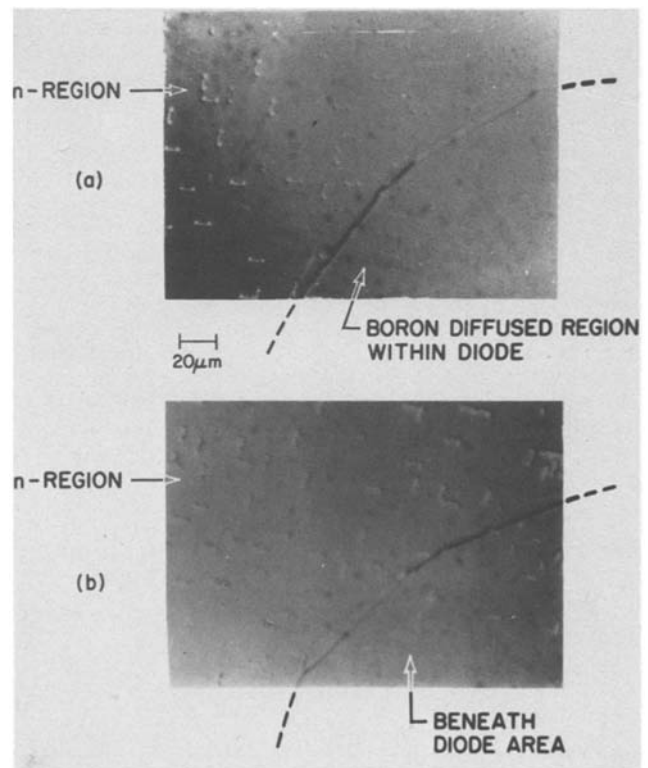


Fig. 10. Defect decoration in boron-diffused diodes: (a) within diodes, (b) beneath diode junction.

depth and probably gettered for some distance into the n-type regions surrounding the diode junction as well.

An experiment was also performed to investigate the influence of boron diffusion relative to the epitaxial-type stacking faults (SFepi). A similar boron diffusion at 1050°C was carried out for 2 hr to form 2 μm junction depth p-n diodes in a number of n-type epitaxial films. Following this a 1 min Wright etch was made on the structures removing 0.6 μm of silicon from the surfaces. Epitaxial stacking faults were exposed on the surface both inside and outside the boron-diffused diode areas. The SFepi densities inside the diode area were found to be a factor of 3-4 lower than those found in the nondiffused regions (Table III). In addition, the SFepi type artifacts found inside and outside the diode areas decorated differently with Wright etch, i.e., the SFepi within the diode area were found to be less sharply defined and difficult to see microscopically. Similar to the OSF type defect observation, there appears to be no correlation between the occurrence of the epitaxial stacking fault artifacts in the diode region and the diode leakage. The data in Table III show that a good part of SFepi were eliminated by boron diffusion, and the excellent diode characteristics would suggest that those which had not been eliminated were essentially "electrically deactivated."

Hillock-type Defects

There have been correlations made between the epitaxial hillock occurrence and the surface nucleated oxidation-induced stacking faults (OSF) (9, 10). A half minute Wright etch performed on an epitaxial wafer, in addition to revealing OSF and SFepi, usually also reveals small etch hillocks. The density of the hillocks vary from wafer to wafer and even from point to point on the same wafer. Densities in the range of from 10^2 to 10^7 cm^{-2} have been observed. High temperature steam oxidation causes some of these hillock-type defects to produce OSF's, however, it has been noted above that not all the etch hillocks decorate as oxidation stacking faults (Fig. 9). With anodic exposure, sometimes single hillocks on wafers not experiencing oxidation may develop etch pits. Such unpaired hillocks have been found to decorate less intensely with anodic etching as compared to that of the SFepi or the OSF type defects. They appear as circular structures with a central pit associated with them. In Fig. 11 a scanning electron microscope photo of such a pit is shown. A cleavage was made through the anodically etched pit to reveal its saucerlike shape. The scale shown is for 50 μm . Only about 10-20% of the hillock defects were observed to be electrically active anodically in these studies compared to 90% decoration for the epitaxial stacking fault types. It is believed that the impurity precipitation which is the critical factor in the nucleation of OSF (10, 15) must also play a decisive role in whether a hillock-type defect is or is not electrically active. It is believed that those hillocks which develop anodic etch pits on non-oxidized substrates by anodic exposure would probably nucleate to form OSF if they had been subjected to oxidation processing.

Summary and Conclusions

For the pre-epitaxial and postepitaxial gettering of epitaxial films the following observations were made: the pre-epitaxial gettering, when back-side gettering

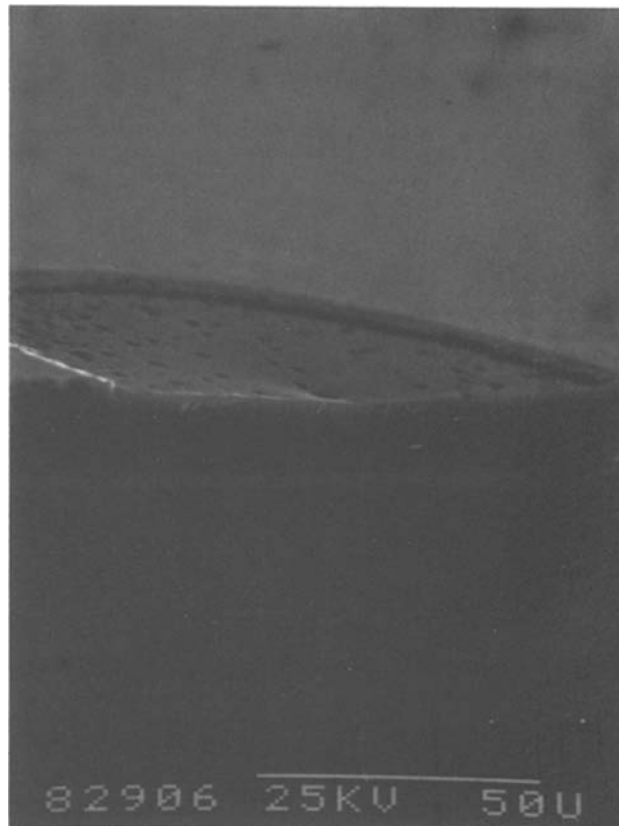


Fig. 11. Decorated unpaired hillock using anodic etch

alone was used, caused little reduction in SFepi. If the back-side gettering was used along with As I/I front-side treatment SFepi defects were significantly reduced.

The pre-epitaxial gettering on back sides of wafers reduce OSF counts to ≤ 10 cm^{-2} . When used in conjunction with As I/I on the front-side gettering of OSF defects in the epitaxial films is nearly 100% effective.

For the postepitaxial gettering case, of the two techniques tested (POCl_3 and Ar I/I), the Ar I/I method gave moderate OSF reduction in the films.

Both front-side gettering procedures were effective in significantly reducing OSF and SFepi-type defect counts.

Acknowledgments

The epi films and processing used in these experiments was carried out in the Si Processing Facility at IBM Yorktown as well as the IBM E. Fishkill location. The authors wish to thank B. M. Kemlage and H. B. Pogge at E. Fishkill for their cooperation. The authors are most grateful for many helpful suggestions and cooperation at Yorktown from the following: B. Ginsberg, assistance with epi films; L. Ephrath, H. Lazzari, and E. Petrillo for the Al-RIE wafer mapping; V. Maniscalco for I/I; K. E. Petrillo and M. Smyth for photolithography; H. Pinckney and G. Helmeyer for oxidation-diffusion processing; S. Tharas for CVD depositions; C. Altman for boron diffusions; E. Bassous for optical microscopy. In addition, we acknowledge the support and suggestions of J. Blum and C. M. Osburn in these studies.

Manuscript submitted April 9, 1980; revised manuscript received Aug. 7, 1980. This was Paper 566 presented at the Los Angeles, California, Meeting of the Society, Oct. 14-19, 1979.

Any discussion of this paper will appear in a Discussion Section to be published in the December 1981 JOURNAL. All discussions for the December 1981 Discussion Section should be submitted by Aug. 1, 1981.

Table III. Density of visible SFepi artifact (cm^{-2})

| Inside diode area | Outside diode area |
|-------------------|--------------------|
| 14 | 46 |
| 11 | 49 |
| 21 | 86 |

Publication costs of this article were assisted by IBM Corporation.

REFERENCES

1. K. V. Ravi, C. J. Varker, and C. E. Volk, *This Journal*, **120**, 533 (1973).
2. D. K. Seto, F. Barson, and B. F. Duncan, in "Semiconductor Silicon 1973," H. R. Huff and R. R. Burgess, Editors, pp. 651-657, The Electrochemical Society Softbound Proceedings Series, Princeton, N.J. (1973).
3. F. Barson, *IEEE J. Solid State Circuit*, **sc-11**, 505 (1976).
4. F. Barson, M. S. Hess, and M. M. Roy, *This Journal*, **116**, 304 (1969).
5. G. H. Plantinga, *IEEE Trans. Electron Devices*, **ed-16**, 394 (1969).
6. D. Pomerantz, *J. Appl. Phys.*, **38**, 5020 (1967).
7. G. A. Rozgonyi, R. P. Deysher, and C. W. Pearce, *This Journal*, **123**, 1910 (1976).
8. R. B. Marcus, M. Robinson, T. T. Sheng, S. E. Haszko, S. P. Murarka, and L. E. Katz, *J. Vac. Sci. Technol.*, **14**, 48 (1977).
9. M. Conti, G. Corda, R. Matteucci, and C. Ghezzi, *J. Mater. Sci.*, **10**, 705 (1975).
10. C. M. Hsieh and D. M. Maher, *J. Appl. Phys.*, **44**, 1302 (1973).
11. C. W. Pearce and R. G. McMahan, *J. Vac. Sci. Technol.*, **14**, 40 (1977).
12. G. A. Rozgonyi, P. M. Petroff, and M. H. Read, *This Journal*, **122**, 1925 (1975).
13. J. L. Deines, J. W. Philbrick, M. R. Poponiak, and D. B. Dove, *Appl. Phys. Lett.*, **34**, 746 (1979).
14. H. Hashimoto, H. Shibayama, H. Masaki, and H. Ishikawa, *This Journal*, **123**, 1899 (1976).
15. G. A. Rozgonyi, S. Mahajan, M. H. Read, and D. Brasen, *Appl. Phys. Lett.*, **29**, 531 (1976).
16. M. W. Jenkins, *This Journal*, **124**, 757 (1977).

Microdefect Elimination in Reduced Pressure Epitaxy on Silicon Wafer by Back Damage-Si₃N₄ Film Technique

Kohetsu Tanno, Fumio Shimura, and Tsutomu Kawamura

Central Research Laboratories, Nippon Electric Company, Limited,
4-1-1 Miyazaki, Takatsu-ku, Kawasaki, Japan

ABSTRACT

A gettering technique which prevents microdefect formation during oxidation processes after the growth of reduced pressure Si epitaxial layer for bipolar devices is described. A gettering process which consists of protection of the back damage layer with Si₃N₄ film is proposed. A microdefect density in epi-layers of $\sim 10^2$ cm⁻² is obtained by back damage with the Si₃N₄ film coating technique, on the contrary, the microdefect density reaches $\sim 10^6$ cm⁻² without the Si₃N₄ film. The critical thickness of Si₃N₄ film to eliminate microdefects in epi-layers is obtained 2500 and 200Å for substrates without and with back damage, respectively. It is found that the gettering action is closely correlated with induced defects in the back surface (OSF, dislocation, damage line, etc.) by sandblast-damaging and/or Si₃N₄ film.

Reduced pressure (RP) silicon epitaxy is an especially important technique for bipolar devices with buried layer containing high concentration of As or Sb. The advantage of RP epitaxy has attracted special interest for shallow junction devices. It has been reported that RP silicon epitaxy has more advantage in characteristics of layer [autodoping, pattern shift, and uniformity of epitaxial layer, etc. (1-5)], than those of atmospheric silicon epitaxy.

In general, a variety of defects such as stacking faults, slip dislocations (6,7), and microdefects correlated with impurities (8,9) is introduced in epi-layer during epi-processing. The stacking fault density can be obtained less than ~ 10 cm⁻² by gas etching prior to epitaxy and slip dislocations can be decreased to negligible extent by a radiant heating technique. However, the existence of microdefects in the epitaxial surface has become one of the most serious problems (e.g., collector-emitter leakage) for device characteristics.

In order to suppress nucleation sites for microdefects in epi-layer, a variety of gettering techniques has been proposed. These gettering techniques are based on mechanical damage (10,11), deposition of Si₃N₄ film on back surface (12), and intrinsic gettering (13-17), etc. (18-21). Although a number of workers have shown that stacking faults are produced in the atmospheric silicon epitaxial layer during thermal oxidation (22-26), none has reported the oxidation-induced

stacking faults and gettering of microdefects in RP epi-layers.

In RP epitaxy applying the microdefect gettering with a back-side damage technique, the gettering effect was found to be decreased by the reasons as follows (27): (i) the back damage layer is removed by HCl gas etching prior to epitaxial growth and by HCl gas produced from the SiH₂Cl₂ source during epitaxial growth; (ii) gas etching on the back surface is accelerated by a reduced pressure; and (iii) the back damage layer is annealed-out during a high temperature epitaxial process. Therefore, a protection of damage layer with Si₃N₄ films is proposed for a more effective gettering.

In the present paper, we describe the reduction of microdefects in RP epitaxial layer by sandblast-Si₃N₄ gettering technique and discuss the gettering mechanism on the basis of preferential etching and x-ray diffraction topography (XRT) data. In addition, we refer to the bow of substrates with Si₃N₄ film on the back surface.

Experimental Procedures

The p-type Si substrates used in this study were taken from a CZ-grown crystal with the resistivity of 10 ~ 20 Ω-cm. The wafers were 75 mm diam and 0.4 mm thick with the surface oriented approximately 3° from the (111) plane along the <110> direction. The front surfaces were mechanically-chemically polished and the back with and without sandblast-damage.

Key words: gettering, tensile stress, bow of wafer, oxidation-induced stacking fault.

The Si_3N_4 films were deposited on the back surface of silicon wafers prior to epitaxial growth by chemical vapor deposition using the system $\text{SiH}_4\text{-NH}_3\text{-N}_2$ at 770°C .

The silicon epi-layer was deposited in a commercial "AMC-7800-RP" cylindrical epi-reactor. The epi-layer was grown to the thickness of $2 \sim 3 \mu\text{m}$ at a rate of $0.3 \mu\text{m}/\text{min}$ at 1080°C in a reduced pressure of 80 Torr.

Finally, epitaxial substrates were annealed at 1140°C for 1 hr in wet O_2 for the evaluation of microdefects in epi-layers. Microdefects in an epi-layer were revealed using the Sirtl etchant for 15 ~ 30 sec and the XRT Lang method was also used to characterize the defects in an epi-layer and back surface.

The Si_3N_4 film thickness and bow were measured by an ellipsometer and a microsensors.

Results and Discussions

The sandblast gettering technique is commonly applied to reduce the microdefects in a substrate surface or epi-surface for MOS and bipolar devices. In the case of RP epitaxy, an annihilation of damage layer was confirmed by the decrease of oxidation-induced stacking fault (OSF) density in the back surface after gas etching and/or heat-treatment the same as the epi-process.

In general, a wafer surface is vulnerable to adsorbed oxygen or other impurities from the carbon susceptor. Metallic contamination is apt to take place as a result of the reaction between an SUS component and HCl gas or Cl gas dissociated from SiH_2Cl_2 source. Therefore, gettering processes are important for the suppression of microdefects caused by heavy metal contamination in the RP epitaxial layer. The damage layer can be protected by the deposited Si_3N_4 film which is an acid- and heat-stable material.

Gettering effect by Si_3N_4 film without back damage.
—Figure 1 shows the correlation between the micro-

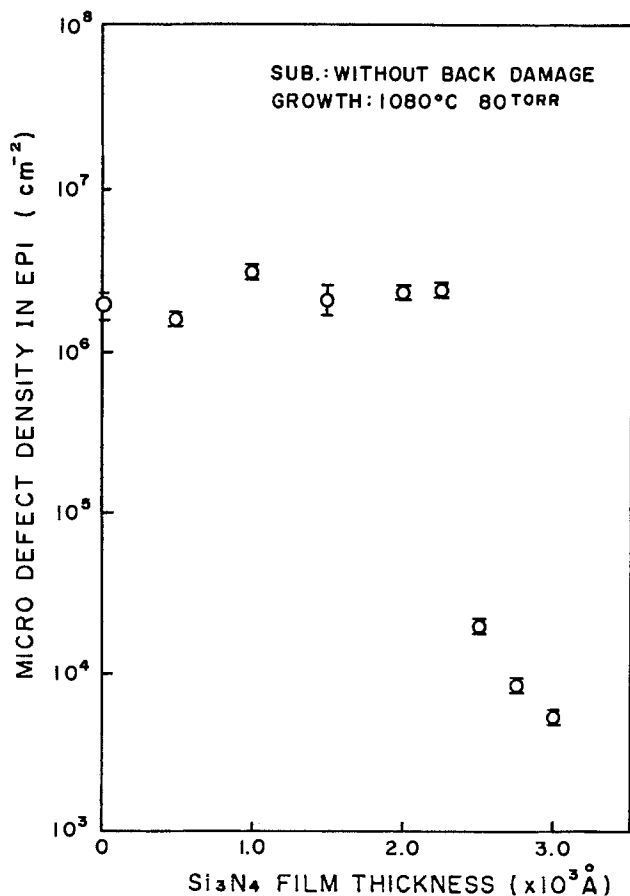


Fig. 1. Correlation between Si_3N_4 film thickness and microdefect density in epi-layer.

defect density in epi-layers and the Si_3N_4 film thickness.

In the Si_3N_4 gettering process, Petroff *et al.* (12) reported the elimination of nucleation centers and impurities which occur during oxide growth involved in the formation of SF by the preoxidation process prior to epitaxial growth. In the paper mentioned above, the Si_3N_4 film was deposited to 4000 \AA thick to eliminate microdefects in the substrate surface. In the deposition of a 4000 \AA thick Si_3N_4 film, we speculate that the bow of the substrate increases and many slip dislocations are introduced in the wafers.

As shown in Fig. 1, the microdefect density in an epi-layer drastically decreases from $\sim 10^6 \text{ cm}^{-2}$ to $\sim 10^3 \text{ cm}^{-2}$ when the 2500 \AA - Si_3N_4 film was deposited. Epitaxial defects were evaluated by Sirtl etching after a heat-treatment at 1140°C for 1 hr in wet O_2 . Sirtl-etched figures of epi-layers and back surfaces after removing Si_3N_4 films by hot H_3PO_4 solution are shown in Fig. 2(a) and (b), respectively.

Typical epitaxial microdefects, triangular shaped etch pits in the ungettered region observed by an optical microscope are shown in Fig. 3.

Damage line and dislocation pits, as shown in the bottom of Fig. 2(b), are observable in the back surface of gettered epi-wafer with an Si_3N_4 film of more than 2000 \AA thickness. These damage lines and dislocations are considered to be due to the stresses by an Si_3N_4 film.

Figure 4 shows that the microdefects in epi-layers are gettered when the Si_3N_4 film more than 2250 \AA thick is deposited. The Sirtl-etched epi-layer and back surface with an Si_3N_4 film are shown in Fig. 4(a) and (b), respectively. These damage lines have the tendency to run toward a definite direction as shown in Fig. 4(b). The remarkable correlation between the gettered region in epi-layer and the damage lines in back surface was observed in Fig. 4.

Figure 5 represents XRT of slip dislocations and damage lines in the substrate with a 3000 \AA -thick Si_3N_4 film. It is apparent from the topography that disloca-

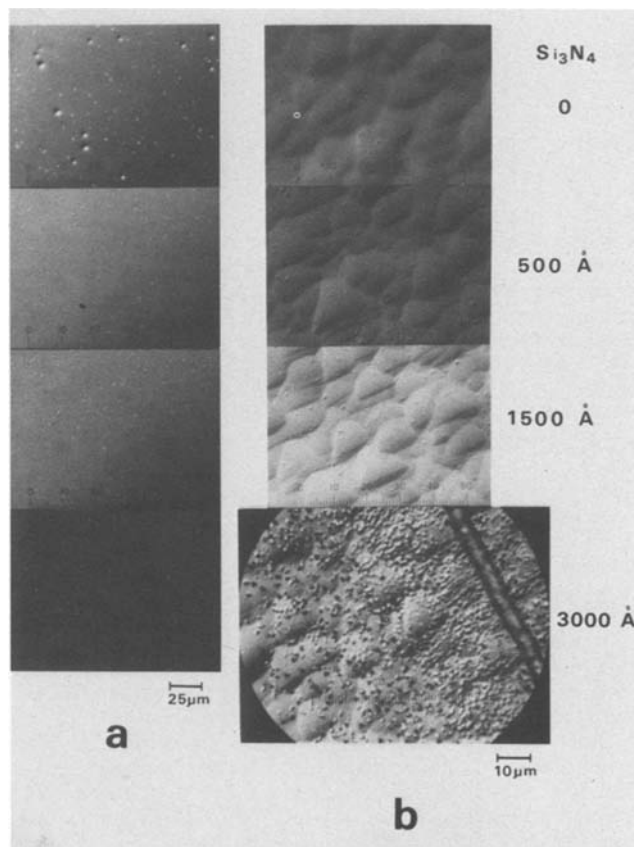


Fig. 2. Optical micrographs of defects in (a) epi-layer and (b) back surface removed Si_3N_4 film.

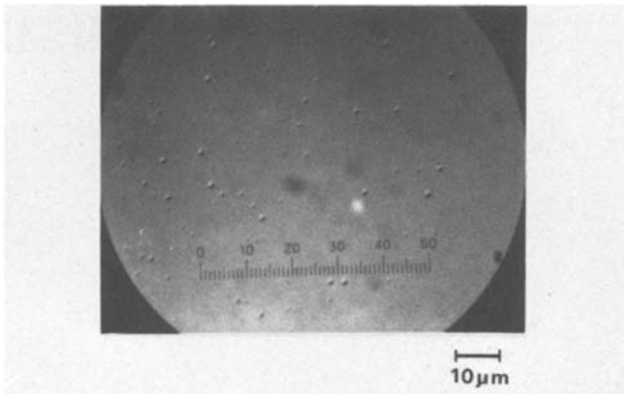


Fig. 3. Microdefects in RP epitaxial layer revealed by Sirtl etching.

tions are introduced around the damage lines, in accord with Fig. 2(b) (bottom).

The thick Si_3N_4 film is necessary to getter microdefects in an epi-layer with an Si_3N_4 film. That is, microdefects in epi-layer were reduced with Si_3N_4 films of 2500Å, 3000Å-thick without back damage, however the bow of the wafer becomes large in proportion to the Si_3N_4 film thickness as shown later and slip dislocations were introduced into the active layer as shown in Fig. 5. Consequently, the Si_3N_4 gettering technique without back damage has a problem which cannot be ignored for device processing.

Gettering effect by back damage with Si_3N_4 film.—In Fig. 6, the microdefect density in epi-layer is plotted as a function of the OSF density due to back damage by a sandblast technique prior to the deposition of a 1000Å-thick Si_3N_4 film. The microdefect density in an epi-layer is closely related to the density of OSF with back damage. It became evident that more than $5 \times 10^5 \text{ cm}^{-2}$ OSF's of density in the back-side damage is necessary to reduce epi-microdefects less than 10^3 cm^{-2} as shown in Fig. 6. Gettering experiments were

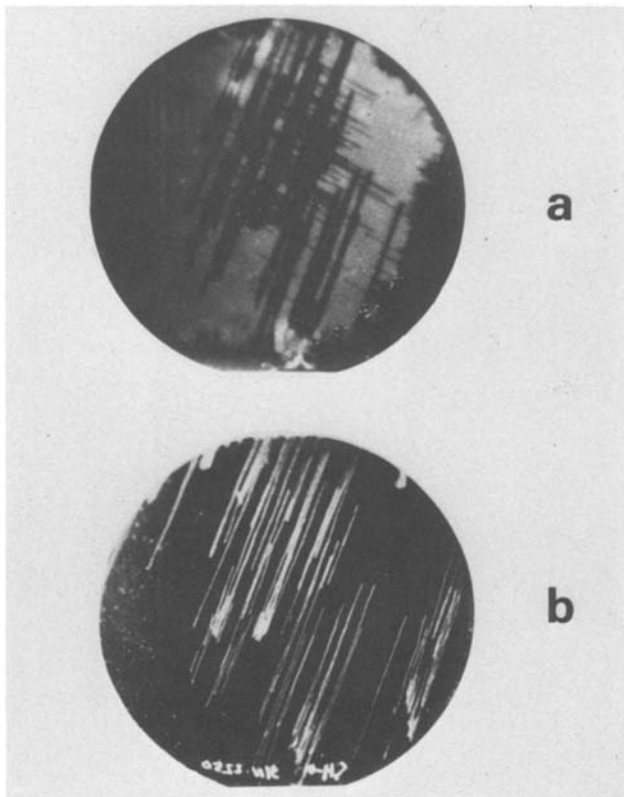


Fig. 4. (a) Sirtl-etched epi-surface and (b) its substrate back surface with 2250Å-thick Si_3N_4 film.

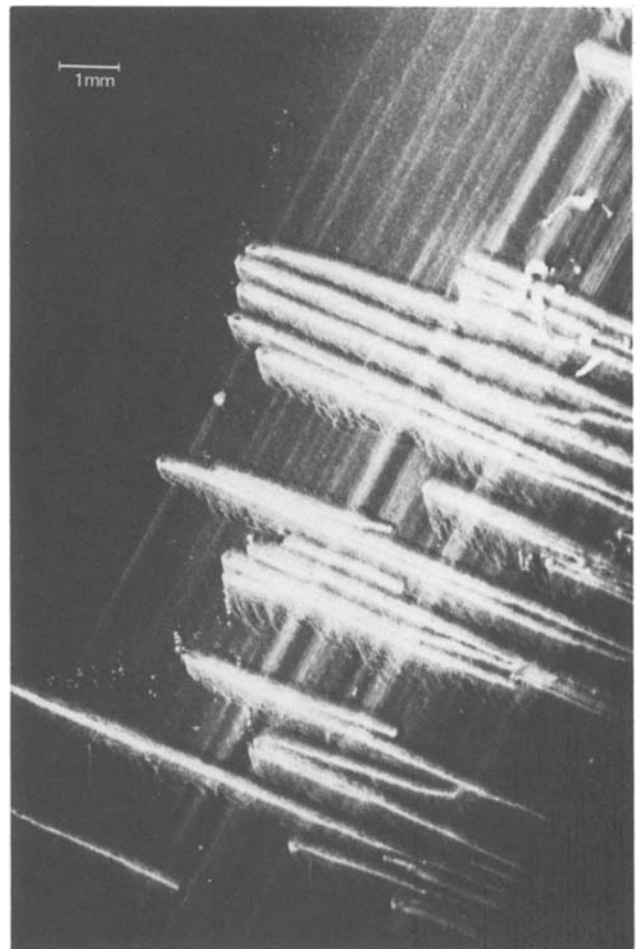


Fig. 5. X-ray diffraction topograph of epi-wafer with 3000Å-thick Si_3N_4 film. $g = [220]$.

carried out using back-damaged wafers with OSF's more than $5 \times 10^5 \text{ cm}^{-2}$ in the same wafer lots.

Figure 7 shows the dependence of epi-microdefect density on the Si_3N_4 film thickness. The epi-microdefect density decreased remarkably from 10^6 cm^{-2} to 10^3 cm^{-2} with the 200Å-thick film. When the Si_3N_4 film of 1000Å thickness was deposited, the microdefects in the epi-layer were reduced to the density of $5 \times 10^2 \text{ cm}^{-2}$.

Figure 8 shows etched figures of the epi-layer and back surfaces with sandblast damage. The Si_3N_4 film was removed by hot H_3PO_4 solution before Sirtl etching. The defects in the back surface (Fig. 8b) remarkably differ from those on the back surface shown in Fig. 2(b). OSF's due to sandblasting are observed in the back surface with Si_3N_4 films of more than 200Å thick as shown in Fig. 8(b). That is, the defect density in a back surface was kept with more than 10^5 cm^{-2} even after epitaxial growth. This shows that the extent of back damage with sandblasting remained at the same level before epitaxy, even though wafers were annealed in epitaxy and oxidation processes. It is suggested that the gettering action by back damage occurred effectively by covering with a thin Si_3N_4 film.

Bow of substrate with Si_3N_4 film.—A tensile stress of $10^{10} \text{ dynes cm}^{-2}$ has been reported for chemically vapor deposited (CVD) Si_3N_4 films on an Si wafer (28, 29). It is well known that Si substrates bend (30) with the stress of the Si_3N_4 film being vulnerable to cracks (31) with increasing Si_3N_4 film thickness and the process temperature. As a result of cracking due to Si_3N_4 film, dislocations are introduced into the wafers.

Figure 9 shows the bow dependence on the Si_3N_4 film thickness after the oxidation of the epi-layer at

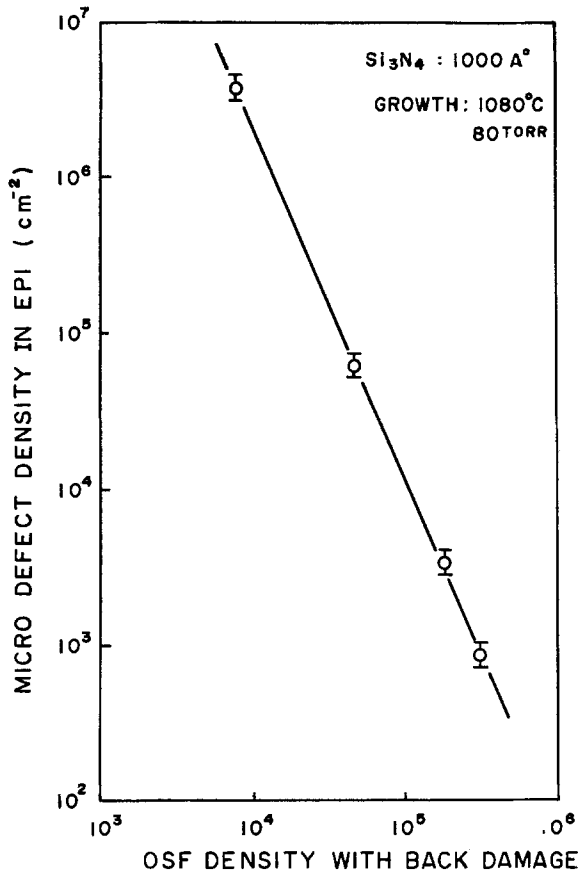


Fig. 6. Correlation between microdefect density in epi-layer and OSF density by back damage.

1140°C for 1 hr wet O₂. The cracks in Si₃N₄ films are observed after epitaxial growth and they accelerate, introducing dislocations into a substrate after an oxidation process. The minimum bow was found with the Si₃N₄ film of the thickness between 500 and 1000Å as shown in Fig. 9. In addition, the bow of wafers shows a tendency to approach a constant value with the Si₃N₄ film thickness above 2000Å which is the thickness of introducing cracks into a wafer. In the Si₃N₄ gettering without back damage, the constant bow region corresponds to the Si₃N₄ film thickness region with effective gettering in an epi-layer.

Since the bow of wafers becomes a serious problem in a photolithographic process after epitaxial growth, we may conclude that the effective thickness of an Si₃N₄ film with back damage is 500-1000Å for minimizing the bow of wafer and eliminating microdefects in an epi-layer.

Summary and Conclusion

The effective gettering of microdefects in an RP epitaxial layer has been shown in sandblast-wafers covering the back surface with a thin Si₃N₄ film. In both the gettering cases of applying Si₃N₄ film with and without back damage, it becomes clear that the elimination of the microdefects in an epi-layer is closely related to the induced defects in the back surface with sandblast-damage and Si₃N₄ film.

The conclusions reached are as follows.

1. The gettering of microdefects in an epi-layer occurs at the critical Si₃N₄ film thickness of 2500Å without back damage; however the bow of the wafer becomes large and many dislocations are introduced in the epi-layer.

2. The microdefect density in epi-layers shows a reciprocal correlation with the density of OSF in the back surface and good linearity in log-log plotting.

3. The gettering of the microdefects in an epi-layer occurs with more than 200Å-thick Si₃N₄ film with back

damage. The minimum microdefect density in an epi-layer obtained was $5 \times 10^2 \text{ cm}^{-2}$ with the 1000Å-thick Si₃N₄ film.

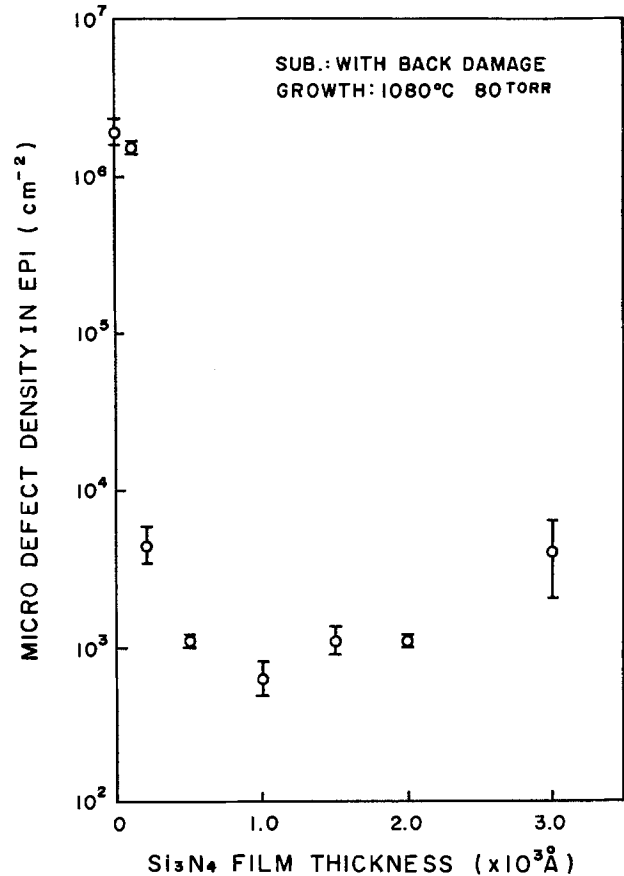


Fig. 7. Correlation between microdefect density in epi-layer and Si₃N₄ film thickness.

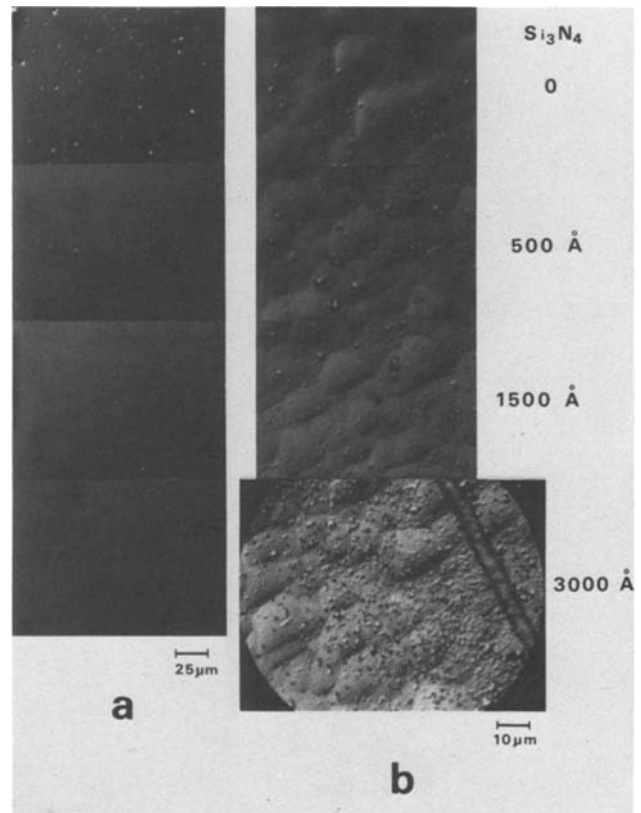


Fig. 8. Optical micrographs of defects in (a) epi-layer and (b) back surface removed Si₃N₄ film.

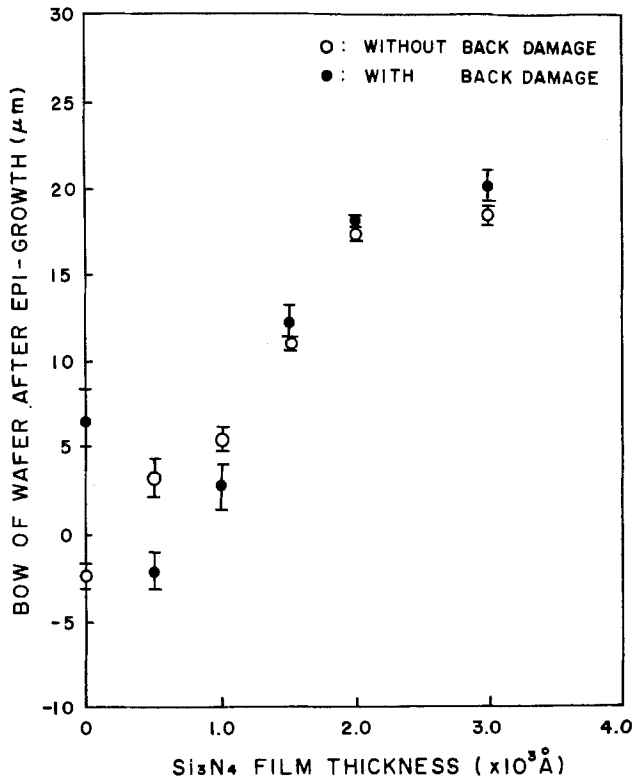


Fig. 9. Correlation between bow of wafer after epitaxial growth and Si₃N₄ film thickness.

4. The minimum bow of an epi-wafer with Si₃N₄-sandblast treatment after an epi-oxidation was found in the range of 500-1000Å in Si₃N₄ film thickness. The bow was saturated at the Si₃N₄ film thickness more than 2000Å. This coincides with the Si₃N₄ film thickness which introduces cracks for effective gettering.

Acknowledgments

The authors wish to acknowledge Dr. S. Asanabe and Dr. T. Okada for their continued interest and encouragement in the course of this study. They also wish to express their thanks to T. Takekawa for deposition of silicon nitride and T. Niyama for his technical assistance. This work was performed at Research Laboratories, NEC-TOSHIBA Information Systems, Incorporated.

Manuscript submitted May 12, 1980; revised manuscript received ca. Sept. 9, 1980.

Any discussion of this paper will appear in a Discussion Section to be published in the December 1981

JOURNAL. All discussions for the December 1981 Discussion Section should be submitted by Aug. 1, 1981.

Publication costs of this article were assisted by Nippon Electric Company, Limited.

REFERENCES

1. R. B. Herring, *Solid State Technol.*, **22**, 75 (Nov. 1979).
2. M. L. Hammond, *ibid.*, **22**, 61 (Dec. 1979).
3. M. Ogirima, H. Saida, M. Suzuki, and M. Maki, *This Journal*, **124**, 903 (1977).
4. M. Ogirima, H. Saida, M. Suzuki, and M. Maki, *ibid.*, **125**, 1879 (1978).
5. J. L. Deines and A. Spiro, Paper 62 presented at The Electrochemical Society Meeting, San Francisco, California, May 12-17, 1974.
6. L. D. Dyer, H. R. Huff, and W. W. Boyd, *J. Appl. Phys.*, **42**, 5680 (1971).
7. J. Bloem and A. H. Goemans, *ibid.*, **43**, 1281 (1972).
8. C. W. Pearce and R. G. McMahon, *J. Vac. Sci. Technol.*, **14**, 40 (1977).
9. G. B. Larrabee and J. A. Keenan, *This Journal*, **118**, 1351 (1971).
10. D. I. Pomerantz, *J. Appl. Phys.*, **38**, 5020 (1967).
11. E. J. Mets, *This Journal*, **112**, 420 (1965).
12. P. M. Petroff, G. A. Rozgonyi, and T. T. Sheng, *ibid.*, **123**, 565 (1976).
13. T. Y. Tan, E. E. Gardner, and W. K. Tice, *Appl. Phys. Lett.*, **30**, 175 (1977).
14. G. A. Rozgonyi and C. W. Pearce, *ibid.*, **32**, 747 (1978).
15. L. E. Katz and D. W. Hill, *This Journal*, **125**, 1151 (1978).
16. K. H. Yang, H. F. Kappert, and G. H. Schwuttke, *Phys. Status Solidi A*, **50**, 221 (1978).
17. H. Tsuya, K. Tanno, and F. Shimura, *Appl. Phys. Lett.*, **36**, 658 (1980).
18. G. A. Rozgonyi, R. P. Deysher, and C. W. Pearce, *This Journal*, **123**, 1910 (1976).
19. M. R. Poponiok, T. Nagasaki, and T. H. Yeh, *ibid.*, **124**, 1802 (1977).
20. C. W. Pearce and V. J. Zaleckas, *ibid.*, **126**, 1436 (1979).
21. G. H. Schwuttke, K. Yang, and H. Kappert, *Phys. Status Solidi A*, **42**, 553 (1977).
22. D. I. Pomerantz, *This Journal*, **119**, 255 (1972).
23. C. M. Drum and W. Van Gelder, *J. Appl. Phys.*, **43**, 4465 (1972).
24. M. Conti, G. Corda, and R. Matteucci, *J. Mater. Sci.*, **10**, 705 (1975).
25. C. M. Hsieh and D. M. Maher, *J. Appl. Phys.*, **44**, 1302 (1973).
26. K. V. Ravi, C. J. Varker, and C. E. Volk, *This Journal*, **120**, 553 (1973).
27. K. Tanno, Unpublished work.
28. M. Tamura and H. Sunami, *Jpn. J. Appl. Phys.*, **11**, 1097 (1972).
29. E. A. Irene, *J. Electron. Mater.*, **5**, 287 (1976).
30. S. Isomae, M. Nanba, Y. Tamaki, and M. Maki, *Appl. Phys. Lett.*, **30**, 564 (1977).
31. V. Y. Doo, D. R. Nichols, and G. A. Silvey, *This Journal*, **113**, 1279 (1966).

The Use of Si and Be Impurities for Novel Periodic Doping Structures in GaAs Grown by Molecular Beam Epitaxy

K. Ploog, A. Fischer, and H. Künzel

Max-Planck-Institut für Festkörperforschung, D-7000 Stuttgart 80, Germany

ABSTRACT

A new type of superlattice in GaAs consisting of a periodic sequence of ultrathin p- and n-doped GaAs layers (also called "nipi" crystal) has been achieved by molecular beam epitaxy (MBE). The individual p- and n-type GaAs layers of which the structure is composed were doped with beryllium as acceptor and silicon as donor impurities, respectively. Low temperature photoluminescence studies and transport measurements were performed first to attest a superior quality of the intentionally p- and n-doped constituent GaAs layers and of the characteristics of the individual p-n junctions prepared by MBE. The existence of a novel superlattice effect in the periodic p-n doping multilayer structures in GaAs was then established by studying the optical absorption tails which extend far into the gap of the unmodulated semiconductor ($\hbar\omega < E_g^{\text{GaAs}}$) depending on the constituent doping levels and on the artificially introduced periodicity of the crystal.

Doping structures in epitaxial GaAs thin films exhibiting abrupt variations of carrier concentration and/or carrier type in the submicron range have recently attracted great attention with respect to the optimization of standard-device performance as well as considering the exploration of novel device structures. Improved device operation of a number of GaAs microwave devices including mixer diodes (1), IMPATT diodes (2), and hyperabrupt varactor diodes (3) requires exactly tailored profiles of donor concentrations. In the field of improving the spatial resolution of GaAs doping profiles of only one carrier type (4) rapid progress has been made in recent years by applying the new growth technique of molecular beam epitaxy (MBE) (5). The superior characteristics of MBE are the ability to achieve reproducible ultrathin layers of extreme smoothness and tailoring doping profiles and/or composition on an atomic scale normal to the growth surface exactly to the desired function (6).

According to extensive theoretical calculations (7, 8), a novel type of a doping multilayer structure consisting of a periodic sequence of thin ($200\text{\AA} \leq D \leq 1500\text{\AA}$) p- and n-doped GaAs layers, possibly with intrinsic (i-) layers in between, (also called "nipi" crystals) should exhibit intriguing peculiarities because the bandgap and carrier concentration can be tuned within wide limits in these crystals. Although the first GaAs films with a periodic variation of carrier type (p- to n-type) produced by MBE have been reported in 1971 (9), only very limited progress has been made since. Also recent attempts to grow periodic p-n multilayer structures in GaAs by using a single dopant source containing the amphoteric element Ge and changing the As to Ga ratio on the growth surface have been successful only to some extent, because of the growth instabilities during Ga-stabilized (4×2) surface reconstruction (8, 10).

In the present paper we report now for the first time the preparation of a novel man-made superlattice in GaAs by MBE consisting of alternating p- and n-type layers with uniform dopant concentration within each individual layer and controlled thickness with constant periodicity by using Be as acceptor and Si as donor impurities. For an optimum performance of this new GaAs superlattice [e.g., electroluminescence application (7)],

a high quality with respect to majority as well as minority carrier properties has primarily to be assured to the constituent p- and n-doped layers and p-n junctions. First we present, therefore, experimental results indicating excellent uniformity of doping concentration, high carrier mobilities, and superior photoluminescence response of the individual Be- and Si-doped GaAs layers composing the periodic p-n multilayer structure. In some cases comparison is made with Sn- and Ge-doped layers grown in our laboratory in a previous study. We examine, furthermore, profiles of one carrier type in GaAs:Si and GaAs:Be layers and we discuss the abruptness of p-n junctions using (Be, Si)-doped GaAs layers. Finally, we provide convincing experimental evidence for the existence of a novel superlattice effect in the p-n multilayer structure from optical transmission measurements.

Experimental

At the present time the most important requirements for any significant advances in the quality of MBE grown III-V compound semiconductor structures and devices are (i) a careful selection of materials used for building the effusion cells as well as for the cell charges, (ii) the addition of a sample exchange load-lock system to the MBE growth chamber in order to eliminate the atmospheric contamination of the molecular beam sources during substrate introduction and removal, and (iii) a highly reproducible procedure for substrate preparation prior to epitaxial growth in order to avoid any effect of the substrate-active layer interface on the film properties.

MBE growth of the GaAs layer structures for this study was performed in a bakeable UHV system schematically shown in Fig. 1. The MBE system is of the vertical evaporation type, and it was designed for a growth process providing abrupt variation of dopants (p- to n-type) and/or of composition (GaAs to AlAs) without interruption of growth. Five effusion cells are installed in the growth chamber containing elemental arsenic, gallium, aluminum (not used in the present investigation), and the two dopant elements Be for p-type and Si for n-type doping. For cell materials, pyrolytic boron nitride (PBN) has been used for the high temperature evaporants (Ga, Al, and Si) and reactor-grade graphite for the As_4 and Be effusion cells. Each cell has its own mechanical shutter operated by a rotary feedthrough. The capacity of the

Key words: semiconductor thin films, molecular beam epitaxy (MBE), gallium arsenide, impurity incorporation, photoluminescence.

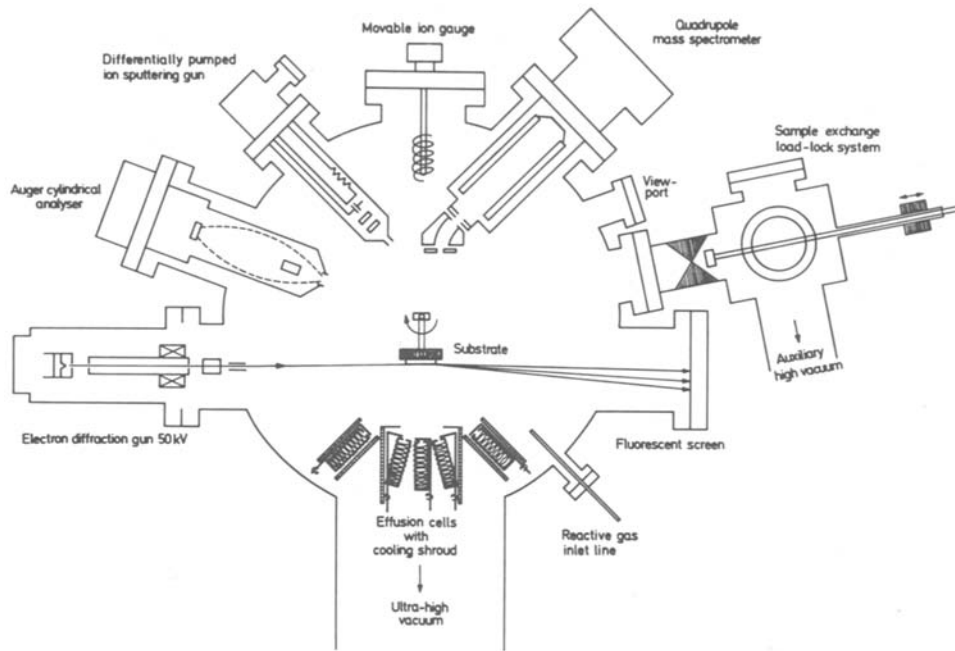


Fig. 1. Schematic cross section of the UHV system designed for molecular beam epitaxy of doped GaAs and $\text{Al}_x\text{Ga}_{1-x}\text{As}$ films (vertical evaporation type).

crucible containing As_4 is sufficient for deposition of an equivalent of more than $100 \mu\text{m}$ thick GaAs films before refilling is required. The complete multiple effusion cell assembly is surrounded by liquid-nitrogen cooled shrouds for cryopumping of condensable species in order to minimize outgassing into the reaction chamber. A more extended use of cryopanel completely surrounding the substrate was not used for this study.

The temperatures of the individual effusion cells and of the substrate heater block were measured with tungsten-rhenium (3% Re vs. 25% Re) thermocouples, and they were monitored by a computer-controlled temperature regulation system (11). In addition to the components used directly for the epitaxial growth process, the growth chamber shown in Fig. 1 contains several components of surface analytical techniques, the application of which during MBE growth has been described earlier (12).

The (100) oriented GaAs substrates were either Cr-doped (semi-insulating) for Hall effect and low temperature photoluminescence (PL) measurements or Si-doped ($n > 1 \times 10^{18} \text{ cm}^{-3}$)¹ for Schottky barrier or p-n junction current-voltage and capacitance-voltage characteristics of the grown films. Typically, a wafer was first polished with diamond paste to remove the initial saw-cut damage and etch-polished on an abrasive-free lens paper soaked with sodium hypochlorite solution leaving a mirrorlike finish. The slice was then successively rinsed in trichloroethylene, methanol, and double distilled water. After boiling in hydrochloric acid twice, the substrate was free-etched in a stagnant solution of $\text{H}_2\text{SO}_4:\text{H}_2\text{O}_2:\text{H}_2\text{O} = 3:1:1$ at 48°C for 1 min. Finally, the wafer was flooded with double distilled water to stop the etchant, rinsed in water, and blown dry with filtered nitrogen gas just before soldering it with liquid indium to a molybdenum plate under dust-free conditions.

Immediately after, the Mo mounting plate with the freshly prepared substrate was remotely exchanged with a plate holding the processed substrate from the previous growth run using an advanced sample exchange load-lock system² indicated in Fig. 1. The system was operated by a magnetically coupled transfer mechanism, and an all-metal isolation valve is utilized to separate the main growth chamber from the introduction chamber during epitaxy. The Mo mounting plate holding the substrate was fixed by a bayonet

joint to the internally heated Mo block which remains always inside the growth chamber. During sample exchange the cryopanel in the growth chamber were held at liquid-nitrogen temperature, and the effusion cells were kept at temperatures not far below their usual operation temperatures. The entire sample exchange procedure was completed in 10 min and a new growth run could be started rapidly without any distortion of the growth conditions.

Prior to epitaxy the substrate was outgassed by heating to a temperature of $50^\circ\text{--}80^\circ\text{C}$ higher than the final operating temperature in a beam of As_4 ranging from 10^{14} to 10^{15} molecules/ cm^2 sec for several minutes. This procedure produced a flat As-stabilized surface with a weak (2×4) reconstruction. Differently doped substrates required different time of heat-treatment.

During deposition the substrate temperature was maintained at 530°C for most of the Be- and Si-doped GaAs films yielding excellent majority carrier mobilities and PL efficiencies. The temperature was measured by a W-Re thermocouple and adjusted by the well-known oxygen desorption behavior of chemically etched (100) GaAs surfaces in a similar manner as described in Ref. (6). The temperatures of the Ga and As_4 effusion cells were kept constant throughout all growth runs resulting in a constant growth rate of $0.9 \mu\text{m}/\text{hr}$ and a constant As_4/Ga flux ratio of two. The temperatures of the Be and Si effusion cells were varied over wide ranges (cf. Fig. 2) according to the required dopant fluxes.

Most of the Be- and Si-doped GaAs films and of the doping structures used for this study were deposited without any buffer layer directly onto the appropriately doped substrate, and they had an overall thickness of not more than $2 \mu\text{m}$.

An important aspect in the growth of highly refined GaAs layers doped with Be was the selection of the Be source material. Most of the commercially available Be metal which is at best 99.9% contains considerable amounts of Fe, Al, Cr, Cu, and Ni. These impurity elements can also be incorporated into the growing GaAs during evaporation of Be. We have found that the best source for Be is a tiny block of material carefully cleaved from a highly refined Be single crystal (99.999%) which has been purified by several cycles of zone refining.³

¹ GaAs substrate material was supplied by Laser Diode Laboratories, Incorporated, New Brunswick, New Jersey 08901.

² ISA-Riber Model SPC 150.

³ Zone-refined Be material was supplied by the Pulvermetallurgisches Laboratorium, Max-Planck-Institut für Metallforschung, D-7000 Stuttgart 80, Germany.

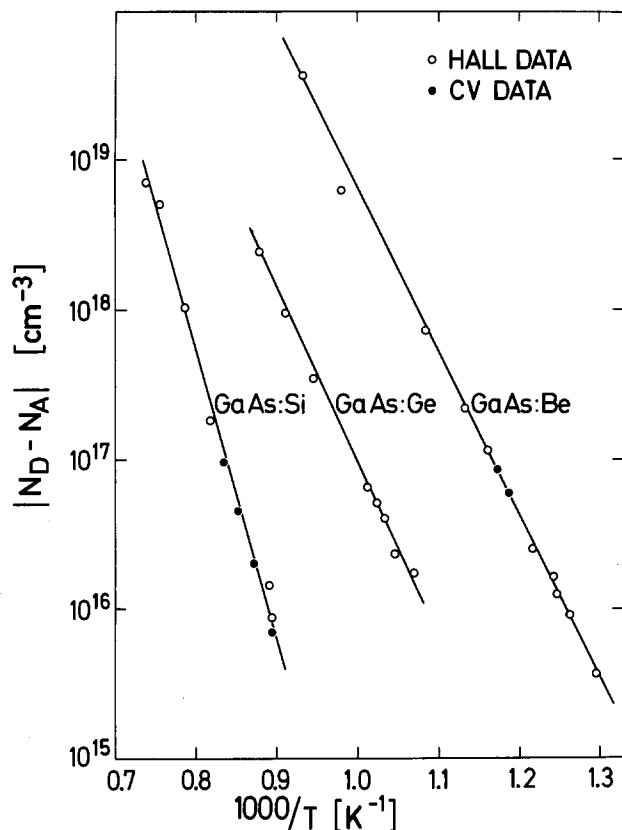


Fig. 2. Clausius-Clapeyron type plots of 300 K free-carrier concentrations of intentionally doped GaAs films as function of reciprocal dopant effusion cell temperatures for constant film growth rate, substrate temperature, and As_4 to Ga flux ratio.

The Ge-doped GaAs films which are in some cases cited for comparison with the Be- and Si-doped layers were grown in a separate growth system described earlier (13, 14), in order to prevent any Ge contamination of the system used for Be and Si doping.

Free-carrier concentrations and Hall mobilities of the $2 \mu\text{m}$ thick uniformly doped layers were measured in the temperature range of 77–300 K using the standard van der Pauw technique with contacts consisting of alloyed Sn (n-type samples) or Sn/Zn balls (p-type samples). Low current levels and a magnetic field of 5 kG were applied throughout these measurements. The ionized acceptor and donor concentrations were determined and separated by comparing the experimental 77 K data with the empirical curve of $\mu_{77\text{K}}$ vs. $[(N_D + N_A) \times (\text{Brooks-Herring screening factor})]$ derived by Stillman and Wolfe (15). No corrections were made for carrier depletion that occurs in epitaxial GaAs layers at their free surface and their interface with the semi-insulating substrate (16).

Free carrier profiles as a function of depth were derived from capacitance-voltage (CV) measurements of reverse-biased Schottky barriers or abrupt p-n junctions using the differential capacitance technique. The Schottky barriers on n-type films were formed by evaporating $0.2 \mu\text{m}$ Au through an Mo mask containing 0.5 mm diam holes in a separate vacuum system at 10^{-6} Torr and generally at room temperature. With p-n junctions the required contacts were obtained by successively depositing $0.02 \mu\text{m}$ Cr and $0.2 \mu\text{m}$ Au. Just prior to metallization, the surface of the GaAs film was carefully cleaned with hydrochloric acid for oxygen removal and rinsed in methanol for surface passivation. The ohmic contact on the back side of the heavily doped substrate wafer was formed by covering with liquid In/Ga = 4:1 alloy. Mesa diodes were obtained by removing the material between the metal dots to a depth of $\sim 10 \mu\text{m}$ with a standard mesa etch

($\text{CH}_3\text{OH}/\text{H}_3\text{PO}_4/\text{H}_2\text{O}_2 = 3:1:1$). Further efforts to avoid any leakage currents such as diffusing a guard ring were not made.

Acceptor impurities incorporated in the MBE GaAs films intentionally doped with either Be, Si, or Ge were identified by high resolution photoluminescence (PL) measurements which were performed with the sample immersed in liquid helium pumped to temperatures below 2 K. The samples were excited by the 6471 Å line of a Kr laser focused to a spot of area $\sim 10^{-3} \text{ cm}^2$. The laser excitation power was varied between 10^2 and 10^{-2} mW using neutral density filters. The luminescence light was analyzed by a grating monochromator with a resolution better than 1 Å and detected by a photon counting system attached to a cooled GaAs photocathode photomultiplier.

Optical transmission measurements on periodic p-n multilayer structures in GaAs at 1.6 K were made normal to the surface of the sample using a focused halogen lamp as light source and the same detection system as described before. Direct transmission was assured by placing the sample between two apertures with 4 mm diam holes. The transmitted light was focused onto the entrance slit of the monochromator.

Results and Discussion

Evaluation of Uniformly Doped GaAs:Si and GaAs:Be Layers

Electrical properties.—The elements Si and Be as well as Ge which have been used as dopants in the present study have unity sticking coefficients on (100) GaAs over a wide range of growth conditions, i.e., substrate temperature up to 630°C , impurity flux 10^9 – 10^{14} atoms/ cm^2 sec, As_4 to Ga flux ratio varied widely. This behavior is indicated by the Clausius-Clapeyron type plots of Fig. 2 which show the 300 K free-carrier concentration of a large number of intentionally doped GaAs films as a function of reciprocal temperature of the corresponding dopant effusion cells. The measured data fit well to an exponential $|N_D - N_A|$ vs. $1/T$ relation.

Ilegems (17), Wood *et al.* (18), and Shimano *et al.* (19) have pointed out that these $\log |N_D - N_A|$ vs. $1/T$ plots have exactly the same slope as the vapor pressure curves of Si, Ge, and Be also plotted vs. $1/T$. This means that one incident dopant atom produces one ionized impurity species in the GaAs films, and the observed doping level is simply proportional to the dopant arrival rate. In addition we have found that the free-carrier concentration profiles of either Si-, Ge-, or Be-doped GaAs films of varying thickness are completely flat over that part of the film depth measurable by the CV profiling technique.

The important aspect of doping MBE GaAs with Ge is that it is strongly amphoteric and it can thus be incorporated on Ga as well as on As sites depending on growth conditions (10, 14, 18). The result that the slope of the vapor pressure curve agrees well with the $1/T$ dependence of the free-electron concentration (Fig. 2) is significant. This suggests that for n-type films grown at a constant substrate temperature and with a constant As_4 to Ga flux ratio the degree of autocompensation of Ge in GaAs does apparently not depend on the doping level.

In the present study we have achieved lower and upper limits of 300 K free-carrier concentrations of $(N_D - N_A) = 4.1 \times 10^{15}$ to $6.1 \times 10^{18} \text{ cm}^{-3}$ for GaAs:Si, $(N_D - N_A) = 1.7 \times 10^{16}$ to $3.5 \times 10^{18} \text{ cm}^{-3}$ for GaAs:Ge and $(N_A - N_D) = 3.7 \times 10^{15}$ to $3.7 \times 10^{19} \text{ cm}^{-3}$ for GaAs:Be. For the group IV dopants Si and Ge the upper limit of $(N_D - N_A)$ is given by the autocompensation at high impurity concentrations. The lower limit of the Si- and Be-doped films depends on the total background doping level due to carbon species ($\sim 5 \times 10^{15} \text{ cm}^{-3}$ without cryopanel), whereas the relatively "high" lower level of Ge-doped films

is caused by the strong memory effect of as yet undefined Ge species during MBE.

In Fig. 3(a) and (b) Hall mobilities measured at 300 and 77 K are plotted as functions of free-electron concentration for various n-type GaAs films doped with either Si or Ge. For comparison, the results obtained from Sn-doped GaAs films of a previous study (20) and the theoretical curves calculated by Rode and Knight (21) for different levels of compensation ($N_A + N_D$)/ n are also included in Fig. 3(a).

For all three dopants, the deviation of experimental 300 K mobilities from the theoretical curve for zero compensation is significant at rather low [$(N_D - N_A) < 3 \times 10^{16} \text{ cm}^{-3}$] and at high [$(N_D - N_A) > 1 \times 10^{18} \text{ cm}^{-3}$] carrier concentrations thus indicating an increasing compensation ratio. When $(N_D - N_A)$ is below $3 \times 10^{16} \text{ cm}^{-3}$, the nearly constant acceptor concentration of between 5×10^{15} and $1 \times 10^{16} \text{ cm}^{-3}$ imposes a rather high degree of compensation and therefore has a significant influence on the majority carrier mobility. In the limit of large free-electron concentrations [$(N_D - N_A) \geq 1 \times 10^{18} \text{ cm}^{-3}$], on the other hand, the semiconductor becomes degenerate and the Born approximation used by Rode and Knight (21) probably becomes inadequate. In addition, the observed larger decrease of μ for Ge and Si doped films compared to the Sn-doped films must be attributed to the increasing autocompensation effect of these dopants in this region. In the range $5 \times 10^{16} \leq (N_D - N_A) \leq 1 \times 10^{18} \text{ cm}^{-3}$, the slightly lower mobility values of n-GaAs:Ge are due to a persistent amount of Ge acceptors on As sites even at growth temperatures below 530°C in addition to the residual C acceptors (14). This effect is less pronounced for the obviously less amphoteric Si in n-GaAs:Si.

The 77 K Hall mobilities of n-GaAs:Si and n-GaAs:Ge layers plotted in Fig. 3(b) fit well to an empirical "universal-value" curve introduced by Poth *et al.* (22). The authors compiled a large number of mobility data obtained from n-type GaAs films grown by LPE, MBE, and VPE with different dopants in various laboratories. All those experimental 77 K data were found to lie below the values predicted by Rode and Knight (21) for uncompensated material [dotted line in Fig. 3(b)]. The strongly amphoteric Ge in MBE-grown n-GaAs again causes a more pronounced deviation of $\mu_{77 \text{ K}}$ from the empirical curve.

Using deep level transient capacitance spectroscopy (DLTS) (23), we have detected not more than three deep electron traps in Si-doped GaAs films grown at 530°C, corresponding to the activation energies 0.297

eV (M2), 0.583 eV (M5), and 0.620 eV (M6) according to the notation of Lang *et al.* (24). Typical trap concentrations N_T in an n-GaAs:Si sample with $(N_D - N_A) = 1.7 \times 10^{16} \text{ cm}^{-3}$ were found to be $7.8 \times 10^{12} \text{ cm}^{-3}$ at $E_T = 0.620 \text{ eV}$, $9.4 \times 10^{12} \text{ cm}^{-3}$ at $E_T = 0.583 \text{ eV}$ and $1.14 \times 10^{13} \text{ cm}^{-3}$ at $E_T = 0.297 \text{ eV}$, respectively (25). This result confirms overall trap concentrations as low as 10^{-3} of the doping level.

Figures 4(a) and (b) show the dependence of 300 and 77 K Hall mobilities on the hole concentration for several p-type MBE GaAs films doped with Be or Ge. Also included are the data of a few nominally "undoped" as-grown p-type GaAs films containing a considerable amount of residual C acceptors. The solid line depicted in Fig. 4(a) simply follows the general trend of experimental data obtained from the best p-type GaAs samples prepared by LPE and VPE (26). The 300 K mobilities extracted from Be- and C-doped GaAs films grown by MBE are in excellent agreement with this empirical curve. The strong amphoteric character of Ge is again indicated by the lower mobilities of p-GaAs: Ge films.

With respect to Fig. 4(b) it is obvious that the 77 K mobilities of a number of Be-doped GaAs films prepared by MBE are higher in the range $(N_A - N_D) \geq 6 \times 10^{15} \text{ cm}^{-3}$ than the empirical curve derived by Wiley (26) does depict. This result demonstrates the superior quality of the MBE grown material prepared in the present study. The 77 K data of the Ge-doped p-type material, however, scatter considerably in the amount of carrier freeze out as well as in Hall mobility. The results obtained from C-doped p-type samples agree reasonably well with the empirical values.

Photoluminescence properties.—The results obtained from PL studies of the MBE-grown GaAs layers intentionally doped with either Si, Ge, or Be are displayed in Fig. 5 and 6. We restrict ourselves to the discussion of the high energy region of the PL spectra where recombination via shallow acceptors ($E_B \leq 100 \text{ meV}$) occurs which is significant to identify the dominant acceptor impurities in the material.

In PL spectra taken from Si-doped samples deposited at 530°C under standard As-stabilized growth conditions using an As_4 source, *i.e.*, As_4 to Ga ratio $\geq 2:1$, only three broad emission lines can be clearly resolved [full line in Fig. 5(a)]. The peak labeled BE is assigned to the bound exciton recombination. This line is smeared out because of the relatively high level of ionized impurities present which lead to a broadening of the individual excitonic lines. For the same reason, the band-acceptor recombination line labeled C is also

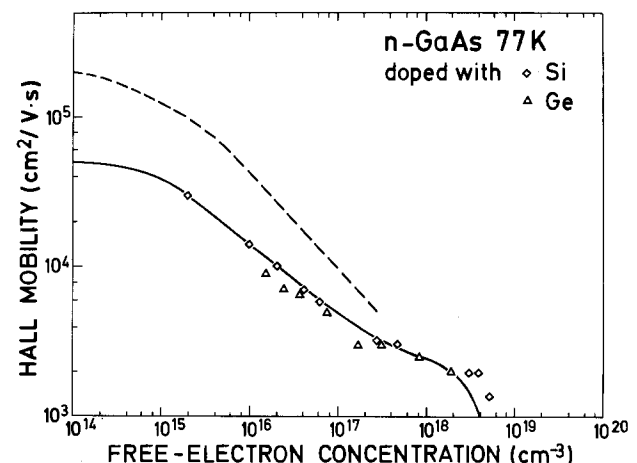
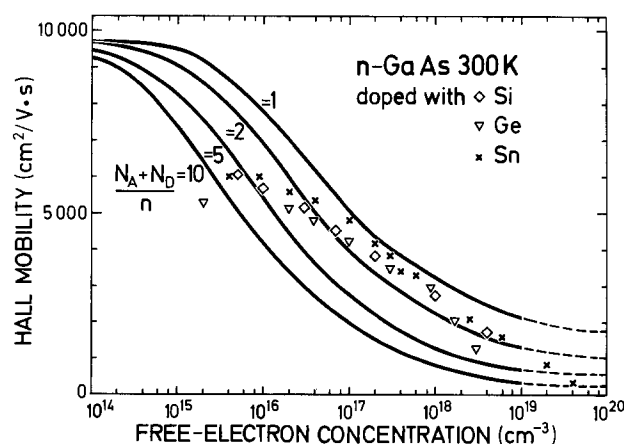


Fig. 3. Hall mobilities at (a, left) 300 K and (b, right) 77 K as a function of free-electron concentrations in MBE-grown 2 μm thick n-type GaAs films doped with either Si, Ge, or Sn. The solid lines in (a) and the dotted line in (b) follow the theoretical calculations of Rode and Knight (21) for different compensation ratios. The solid curve in (b) represents the empirical curve proposed by Poth *et al.* (22).

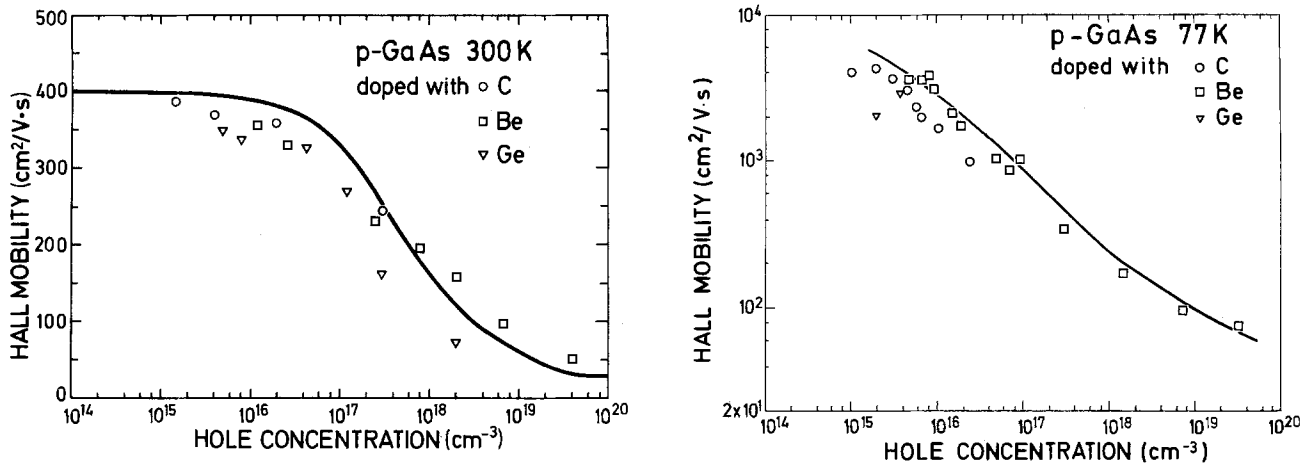


Fig. 4. Hall mobilities at (a, left) 300 K and (b, right) 77 K as a function of net-hole concentrations in MBE-grown 2 μm thick p-type GaAs films doped with either Be, C, or Ge. The solid lines represent the general trend of experimental data obtained from the best p-type GaAs samples prepared by LPE and VPE (26).

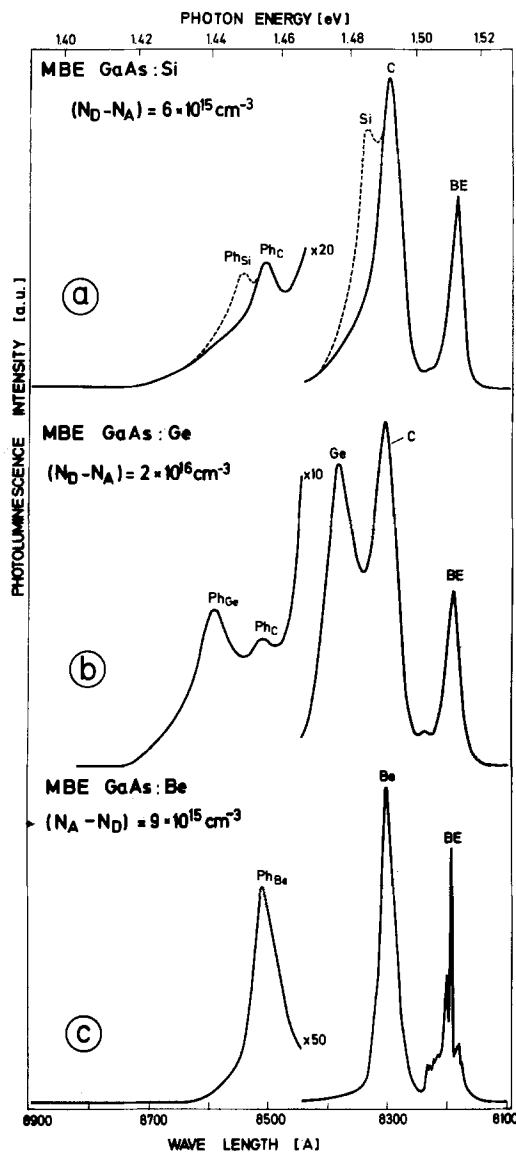


Fig. 5. Low temperature photoluminescence spectra taken at 1.6 K from intentionally doped GaAs films grown by MBE. (a) Si-doped, $(N_D - N_A) = 6.1 \times 10^{15} \text{ cm}^{-3}$; (b) Ge-doped, $(N_D - N_A) = 2.0 \times 10^{16} \text{ cm}^{-3}$; (c) Be-doped, $(N_A - N_D) = 8.9 \times 10^{15} \text{ cm}^{-3}$. Only the high energy regions of the spectra are shown. The various emission lines are labeled along their mechanisms (see text).

broadened and no evidence for the corresponding donor-acceptor transition is found. Ashen *et al.* (27) have shown in a fundamental study that this peak C may be attributed to carbon incorporated on arsenic sites. It is now generally accepted that carbon is the principal residual acceptor impurity associated with MBE growth of GaAs (28). We have hardly found any evidence for the BA recombination involving Si acceptors in MBE GaAs:Si layers of various doping levels when grown from an As₄ source with standard As-stabilized conditions. However, the peak at 1.485 eV corresponding to the BA emission due to Si incorporated on As sites does occur in samples grown (i) from an As₄ source and close to Ga-stabilized conditions, i.e., substrate temperature $>600^\circ\text{C}$ or As₄ to Ga ratio <1 , or (ii) from

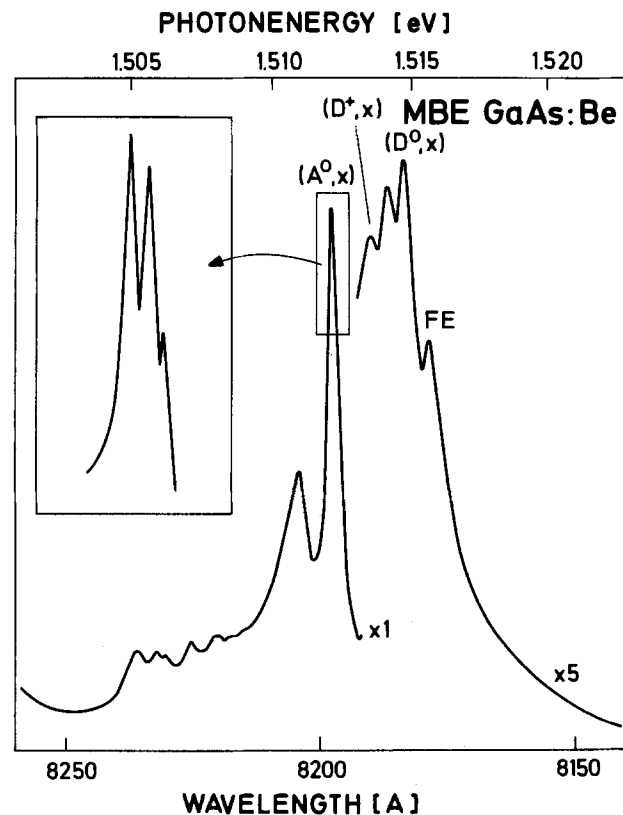


Fig. 6. 1.6 K photoluminescence spectrum of a Be-doped p-type GaAs layer of 2 μm thickness grown by MBE [$(N_A - N_D) = 8.9 \times 10^{15} \text{ cm}^{-3}$]. Only the excitonic region of the spectrum is shown. The various luminescence lines are labeled according to their recombination mechanisms (see text).

a GaAs source producing As_2 species. This additional peak is indicated by dotted lines in Fig. 5(a). The lines labeled Ph_{C, Si, Ge, Be} are the phonon replicas of the corresponding BA transition ($\hbar\omega_{LO} = 36$ meV).

The typical PL spectra obtained from Ge-doped n-type GaAs films [Fig. 5(b)] are very similar to those taken from Si-doped samples with the important features that (i) the BA transition due to Ge (1.479 eV) is much easier to separate from the BA transition assigned to C, and (ii) the intensity of this peak is generally much higher and it is detected even in the best n-type GaAs:Ge samples ($N_D/N_A = 4$) grown at 500°C. This must be attributed to the relatively large amount of Ge being incorporated on As sites even under strongly As-stabilized growth conditions (14).

Finally, the PL spectra of Be-doped GaAs layers [Fig. 5(c)] are to some extent similar to those of Si-doped layers. Two BA transition lines due to C and Be acceptors which are definitely present in these samples would be expected. However, we were not able to resolve both BA transitions in any of the measured PL spectra because the values of the binding energies of the C acceptor (26.0 meV) and of the Be acceptor (28.0 meV) (27) lie too close together. We assume that the peak labeled Be in Fig. 5(c) reflects the Be acceptor, since this peak is slightly shifted towards lower energies compared to the C_{As} related BA transition found in GaAs:Si.

Considering the PL spectra of Be-doped GaAs layers, an excellent resolution with excitonic fine structure was obtained for free-carrier concentrations up to 1×10^{16} cm^{-3} . For the first time, all sharp features as yet only seen in the best quality intentionally doped p-type VPE or LPE samples were observed in these layers grown by MBE in our laboratory (Fig. 6). Referring to the fundamental study of Heim and Hiesinger (29), the several spectral features were identified as a well-separated free-exciton (FE) recombination line at 1.5156 eV, a sharp line at 1.5140 eV due to excitons bound to neutral donors (D^0, x) as well as a peak due to the corresponding excited states at 1.5144 eV (not labeled), and a line at 1.5134 eV due to the recombination of ionized donors-bound excitons (D^+, x). The entire PL spectrum of this p-type GaAs:Be layer is dominated by the neutral acceptor-bound exciton (A^0, x) recombination line. The insert in Fig. 6 shows that this line is further split into a triplet at 1.5123, 1.5122, and 1.5120 eV. This splitting is caused by j-j coupling of the two holes and one electron resulting in $J = 1/2, 3/2, 5/2$ states (29).

Several additional lines in the energy range 1.511-1.504 eV (Fig. 6) are only found in GaAs layers grown by MBE using As_4 molecular beams. An interpretation of these new spectral features specific to MBE material is referred to a subsequent paper (30). As a result, the PL measurements on intentionally doped GaAs layers presented here attest an excellent quality of the MBE

grown material thus well suited as a component of highly refined III-V structures.

Dopant and Carrier Concentration Profiles

The incorporation behavior of the dopant elements Si, Ge, and Be in MBE GaAs was further studied by producing a number of structures consisting of stepwise changes in dopant beam intensity. For the case of doping with Si and Ge, the actual carrier profiles measured by the differential capacitance technique were compared with the corresponding dopant beam intensity vs. time profiles in Fig. 7. In these structures a 0.9 μm thick n^+ (2×10^{18} cm^{-3}) buffer layer was grown on the heavily Si-doped ($n = 2 \times 10^{18}$ cm^{-3}) substrate first. Then the 1 μm thick "active" n-GaAs layer was deposited which consisted of three narrow pulses of Si or Ge atoms, respectively, superimposed on a uniform doping background. Each pulse had a duration of time equivalent to the growth of 400Å GaAs. The width of the individual pulses was accurately controlled by opening and closing the mechanical shutters in front of the corresponding effusion cells.

The square traces in Fig. 7 reflect ideal profiles calculated from the dopant beam intensity which was modulated by the setting of the shutter. The ideal doping levels were extracted from the effusion cell temperatures related to the data of Fig. 2. The rectangular curves of Fig. 7 were calculated assuming a unity sticking coefficient of the dopants and neglecting surface segregation, bulk diffusion, and majority carrier diffusion.

The measured free-carrier profiles of the Si- and Ge-doped structures indicated by crosses in Fig. 7 differ significantly from one another. Using Si as dopant in GaAs, extremely abrupt profiles and a peak to background free-carrier ratio of nearly two orders of magnitude can easily be achieved, whereas in the case of the dopant Ge the actual carrier concentration decreases more slowly after the dopant beam has been cut off. Therefore, only less steep carrier profiles can be obtained with Ge doping. Note that in addition the background carrier concentration is one order of magnitude higher for Ge than for Si doping. The behavior of Ge must be attributed to its memory effect which gives rise to rather a high amount of Ge containing species remaining in the MBE growth chamber even after shuttering the Ge effusion cell and/or rapidly lowering the cell temperature.

The results obtained with Si doping have been used to verify doping profiles which are specifically designed for achieving Schottky barrier diodes with low diode noise temperature at cryogenic temperatures. Such diodes are required for cryogenically cooled millimeter wave mixers (1). The GaAs wafer consists of a heavily Si-doped substrate ($n = 2 \times 10^{18}$ cm^{-3}), a 1 μm thick n^+ buffer layer ($n = 2 \times 10^{18}$ cm^{-3}), and a 0.1-0.2 μm thick active layer having a carrier concen-

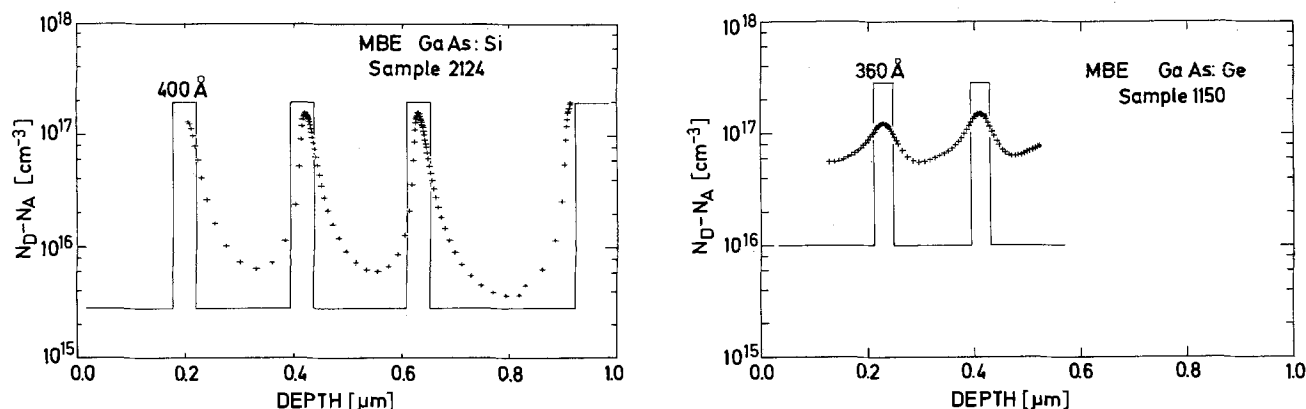


Fig. 7. Comparison of measured periodic doping profiles (indicated by crosses) of MBE-grown n-type GaAs layers doped with a pulsed beam of (a, left) Si and (b, right) Ge, respectively. The square traces are ideal profiles calculated from the dopant beam intensities.

tration of $n \approx 1 \times 10^{16} \text{ cm}^{-3}$. The donor concentration profile of the n^+ - to active layer interface must be as abrupt as possible. In order to determine the actual profile as a function of depth from the surface by the CV technique, thicker active n -type layers were grown in separate runs to account for the zero bias depletion layer. The resulting doping profile measured on a representative sample is shown in Fig. 9 (indicated by crosses), demonstrating an extremely abrupt transition from high to low carrier concentration. It should be noted that the actual profile is even more abrupt than the trace shown, because of the limited resolution of the profiling technique (cf. below).

In the doping profiles shown in Fig. 7 and 8 the actual free-carrier concentrations differ by several Debye-lengths [$\lambda_{\text{Debye}} \sim 450 \text{ \AA}$ for $(N_D - N_A) = 1 \times 10^{16} \text{ cm}^{-3}$ (31)] from the dopant concentrations due to majority-carrier diffusion. For this reason, the ultimate step sharpness of free-carrier profiles measured by the CV technique is limited. Moreover, Johnson and Panousis (32) have pointed out that there exist even small differences between the theoretical free-carrier profile (31) corresponding to the given dopant profile and the measured free-carrier profile, because the metal contacts necessary for CV measurements are not infinitely far away from one another. Using computer simulations for a stepwise change in doping concentration by, for instance, two orders of magnitude, these authors demonstrated that different carrier profiles are measured depending on the rectifying contact being placed on the high- or low-doped side. Slightly asymmetric free-carrier profiles as shown in Fig. 7 and 8 are, therefore, expected to be measured for rectangular dopant pulses.

For similar profiling measurements of Be-doped p -type GaAs layers, a number of n^+ (substrate)- n^+ - p - p^+ (contact) diode structures were produced. The n^+ -side of the p - n^+ junction was doped with Si ($n = 2 \times 10^{18} \text{ cm}^{-3}$). The p -layer consisted of three sharp Be doping pulses in time duration equivalent to the growth of 335 Å GaAs. A typical free-carrier profile obtained from measurements of mesa diodes fabricated on these structures is shown in Fig. 8. The solid line represents the rectangular profile calculated for the arriving dopant species. Note that also with Be extremely abrupt profiles in MBE GaAs with a peak-to-background free-carrier ratio of nearly two orders of magnitude have been obtained in this study. This outcome is an improvement of the actual carrier profile by one order of magnitude compared to the results of Ilegems (17). This improvement is simply a consequence of the superior quality of the Be doping material used in the present study.

p-n Junction Behavior

The results obtained from n -GaAs:Si [Fig. 7(a)] and p -GaAs:Be (Fig. 8) periodic doping structures can be combined in order to simulate the expected free-carrier profile of a step p - n junction in GaAs taking into account the two dopant cells Be and Si. The profile of the junction extracted in this way is shown in Fig. 10. The Si dopant cell is closed by the mechanical shutter during growth of the Be-doped GaAs layer and opened just when the Be dopant cell is mechanically shuttered (indicated by the dotted line). The expected free-carrier profile (solid line) can then be computed by a point by point subtraction of the two individual carrier profiles actually measured and shown in Fig. 7(a) and 8. With a final free-carrier concentration of $1.45 \times 10^{17} \text{ cm}^{-3}$ on both sides of the p - n junction, the width necessary to change the free-carrier concentration from n -type $1 \times 10^{17} \text{ cm}^{-3}$ to the same level p -type is found to be less than 200 Å. In this simulation procedure attention has been paid to all problems arising from CV profiling measurements discussed before. Therefore, the value of 200 Å demonstrates that hyperabrupt p - n junctions in GaAs with excellent char-

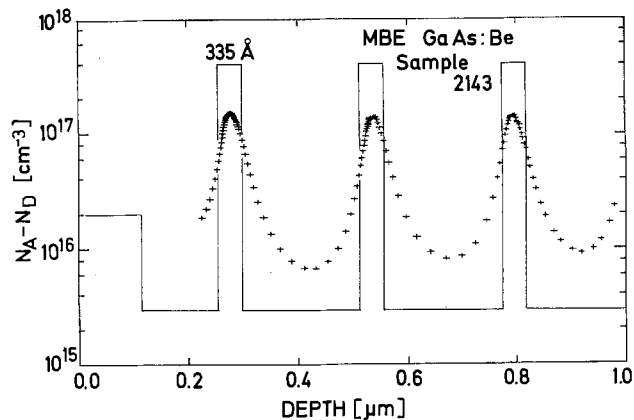


Fig. 8. Measured periodic doping profile (indicated by crosses) in a reverse-biased n^+ - p junction with pulsed Be dopant beam modulation in the p -region. The calculated ideal dopant profile is indicated by the solid line.

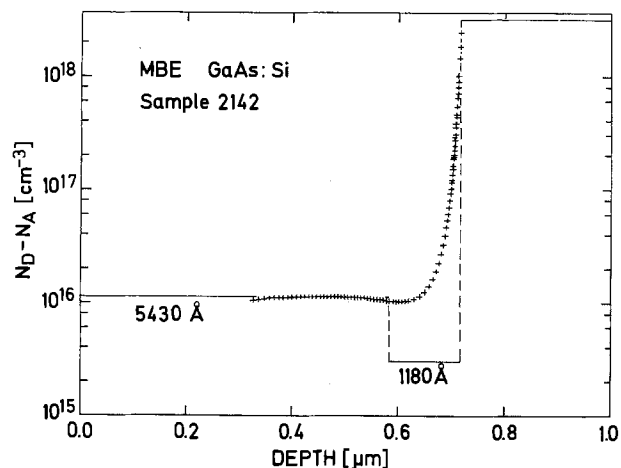


Fig. 9. Typical doping profile of a GaAs Schottky barrier diode designed for low diode noise temperature at cryogenic temperatures. In the actual mixer diodes the thickness of the active n -type layer is only 0.1-0.2 μm . The solid lines represent the ideal dopant beam intensity calculated from the cell temperature and shutter setting.

acteristics can be grown by MBE using Be and Si as p - and n -type dopants, respectively.

Based on the before-mentioned considerations one-sided abrupt p - n^+ junctions in GaAs were prepared using growth parameters established for periodic carrier profile growth. The diode structures consisted of an initial 1 μm thick Si-doped n^+ -layer ($n = 2 \times 10^{18} \text{ cm}^{-3}$) on the heavily Si-doped ($n = 2 \times 10^{18} \text{ cm}^{-3}$) substrate followed by a 1 μm thick Be-doped p -layer [$1.7 \times 10^{16} \leq (N_A - N_D) \leq 2.4 \times 10^{17} \text{ cm}^{-3}$] and a final 0.5 μm thick highly Be-doped p^+ -layer ($p = 2 \times 10^{18} \text{ cm}^{-3}$) for low resistance ohmic contacts. The constant free-hole level in the p -layer was systematically varied from sample to sample. The dopant type was selected by actuating the mechanical shutters in front of the Si and Be dopant cells. The abrupt increase of hole concentration at the p/p^+ transition was achieved by a step change of the Be cell temperature.

The properties of the (Be, Si)-doped GaAs p - n junctions were derived from IV and CV measurements on isolated mesa diodes. The results obtained for different doping levels of the p -region are summarized in Table I and in Fig. 11. In all diodes studied neither the forward nor the reverse characteristic showed evidence of leakage current. The current flow in the forward direction increases exponentially as $I = I_0 \exp(qV/nkT)$. The diode- n -value extracted from the slope of the linear fit to the measured $\ln I$ vs. V curve for $V \geq 3kT/q$ was found to be 1.8 ± 0.2 for all diodes.

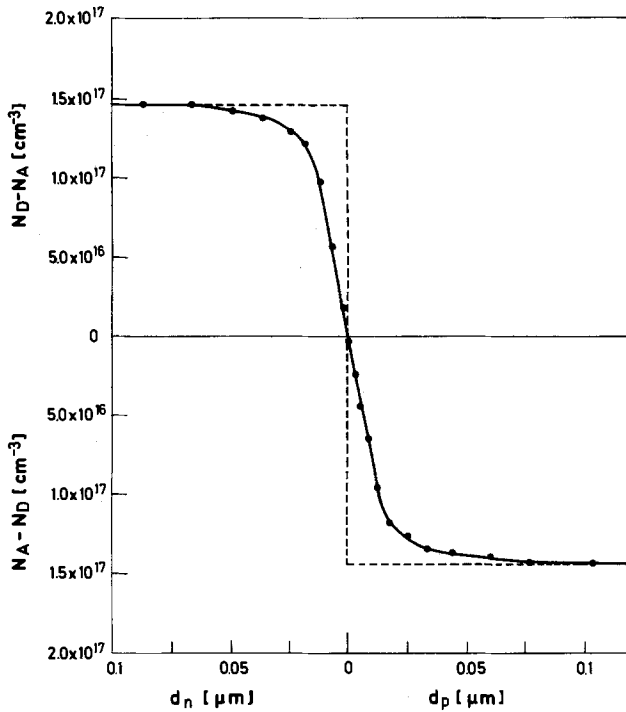


Fig. 10. Expected free-carrier profile (solid line) of a step p-n junction in (Be,Si)-doped GaAs grown by MBE computed by a point by point subtraction of the two individual measured carrier profiles shown in Fig. 7(a) and 8. The dotted line indicates the ideal profile extracted from the dopant beam intensities of Be and Si, respectively.

This value indicates that the current flow across these p-n junctions is dominated by recombination-generation processes ($n_{rec} = 2.0$) as opposed to diffusion mechanisms (33) ($n_{dif} = 1.0$). Minor deviations from the linear $\ln I$ vs. V behavior which may sometimes occur at higher current levels are caused by series resistance effects.

The current flow in the reverse direction is characterized by the junction breakdown voltage V_{Br} which increases exponentially with decreasing carrier concentration. The measured values for V_{Br} (associated with that voltage at which the current in the reverse direction reaches 10^{-4} A) are compiled in Table I and Fig. 11. The data points are in excellent agreement with the theoretical curve derived by Sze and Gibbons (34) for one-sided abrupt junctions assuming that avalanche multiplication dominates the breakdown characteristics. Small differences between observed and calculated V_{Br} values can be attributed to the nonguarded diode structure as well as to minor imperfections of the crystal (35) both of which reduce the actual breakdown voltage. This effect was not further studied throughout the present work.

Only the results obtained from sample 2162 (cf. Table I) seem to indicate severe discrepancies. The

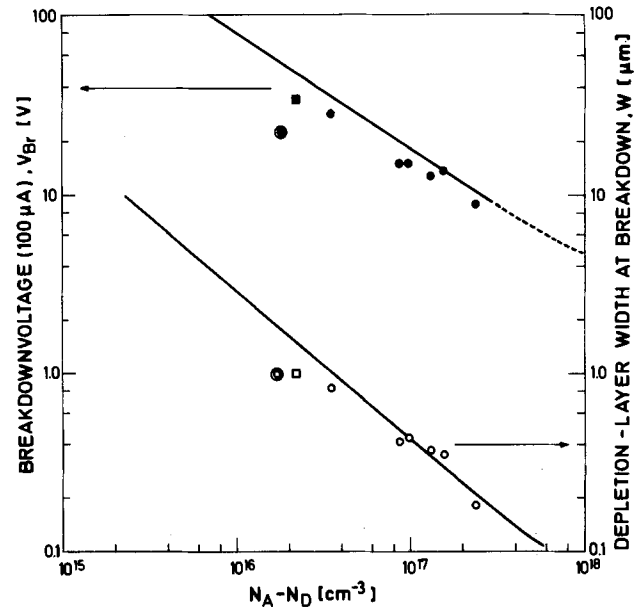


Fig. 11. Characteristics of one-sided abrupt p-n⁺ junctions in (Be,Si)-doped GaAs layers having different doping levels in the p-region as derived from IV and CV measurements (indicated by circles). The solid lines represent the theoretical values of breakdown voltage and depletion layer width, resp., as a function of carrier concentration in the p-region calculated by Sze and Gibbons (34). In the sample labeled by double circles, the 1 μ m thick p-type side of the junction is already totally depleted at 16V. The squares denote the results obtained from a p-n⁺ junction in GaAs doped with the amphoteric Ge only (10).

p-layer of this sample, however, having also a thickness of only 1 μ m, is almost totally depleted at 16V, thus yielding the limited value of V_{Br} . For comparison, the results extracted from a p-n⁺ junction in GaAs doped with the amphoteric Ge only are also included in Table I and in Fig. 11. This sample exhibited excellent characteristics, although the Ge-doped p-n junctions are certainly not quite as steep as are the (Be, Si)-doped ones (10, 14).

Additional detailed insight in the p-n⁺ junction behavior was deduced from CV profiling measurements. Outside the depletion region at $V = 0$, the measured doping profiles of the p-region as a function of depth were extremely flat, and the observed doping levels were in excellent agreement with the concentrations estimated from the Clausius-Clapeyron type plots of Fig. 2. The depletion layer width at breakdown voltage was derived and also compared with the theoretical width given for one-sided abrupt junctions in Ref. (34). As indicated in Fig. 11, there is a strict coincidence between measured and calculated depletion layer width for different doping levels. Finally, an extrapolation of the $1/C^2$ vs. V curve to $1/C^2 \rightarrow 0$ yields the built-in voltage V_{Bi} across the junction which was found to be 1.35 ± 0.15 V for the samples studied here.

Table I. Characteristics of one-sided abrupt p-n⁺ junctions in MBE grown GaAs layers having different doping levels in the p-region as derived from current-voltage and capacitance-voltage measurements

| Sample | Dopants | Carrier concentration in the p-region (cm ⁻³) | Breakdown voltage (V) | Diode-n-value | Depletion layer width (μ m) | Built-in voltage (V) |
|--------|---------|---|-----------------------|---------------|----------------------------------|----------------------|
| 2164 | Be, Si | 2.35×10^{17} | 8.8 | 1.89 | 0.18 | 1.31 |
| 2184 | Be, Si | 1.55×10^{17} | 13.6 | 1.69 | 0.35 | 1.49 |
| 2163 | Be, Si | 1.30×10^{17} | 12.7 | 1.70 | 0.37 | 1.23 |
| 2106 | Be, Si | 9.80×10^{16} | 15.0 | 1.94 | 0.43 | — |
| 2114 | Be, Si | 8.60×10^{16} | 15.0 | — | 0.41 | 1.48 |
| 2183 | Be, Si | 3.50×10^{16} | 28.4 | 1.82 | 0.82 | 1.30 |
| 2162 | Be, Si | 1.70×10^{16} | 16.0* | 1.86 | >1.0 | 1.21 |
| 1098 | Ge, Ge | 2.20×10^{16} | 34.0 | 1.6 | 0.98 | 1.21 |

* 1 μ m thick p-layer totally depleted at 16V.

Periodic p-n Multilayer Structures

Based on the foregoing experience, we have finally combined several p-n junctions in (Be, Si)-doped GaAs to build up a novel periodic multilayer structure in GaAs which is schematically depicted in Fig. 12. The structure is composed of a periodic sequence of thin p- and n-type GaAs layers with intrinsic (i-) layers in between. It is also called "nipi" structure (7, 8). The intrinsic layer denotes that region of the crystal in which the acceptor as well as the donor concentrations are as low as possible, i.e., both the Si and the Be shutter are closed for a controlled duration of time. This region may have a thickness close to zero without substantially modifying the electronic properties of a nipi crystal [cf. Fig. 12(b)].

Figure 13 displays a scanning electron micrograph of the (110) cleavage plane of one of these periodic p-n multilayer structures in GaAs which has recently been grown by MBE when actuating the shutters in front of the dopant cells in the appropriate manner. A total of 20 individual alternating p- and n-doped GaAs layers corresponding to 10 periods are clearly resolved. The structure was deposited on a $1 \mu\text{m}$ thick n^+ buffer layer ($2 \times 10^{18} \text{ cm}^{-3}$) which was first grown on a heavily Si-doped GaAs substrate ($n = 2 \times 10^{18} \text{ cm}^{-3}$) in order to facilitate light transmission measurements. Each doping layer has a thickness of $0.10 \mu\text{m}$ and was doped to a level of $(N_D - N_A) = 7.5 \times 10^{17} \text{ cm}^{-3}$ and $(N_A - N_D) = 2 \times 10^{18} \text{ cm}^{-3}$, respectively. The thickness of the intrinsic layer in the example shown was chosen to be close to zero by opening the Si shutter immediately after the Be shutter has been closed and vice versa. Using Be as acceptor and Si as donor impurities a uniform dopant concentration within each individual GaAs layer and a controlled thickness with constant periodicity has been successfully achieved. The interfaces between the individual GaAs layers remain extremely smooth down to atomic steps also for a large number of layers in sequence. We have varied the layer thicknesses d_n , d_p , and d_i ($0 \leq d_i \leq 0.1 \mu\text{m}$) and thereby the periodicity d as well as the individual doping levels over wide ranges according to the theoretical considerations of Döhler *et al.* (7, 8).

The 10 periods indicated in Fig. 13 are sufficient to bring about novel superlattice effects in these doping multilayer structures. The conduction and valence bandedges of a nipi multilayer structure in GaAs are

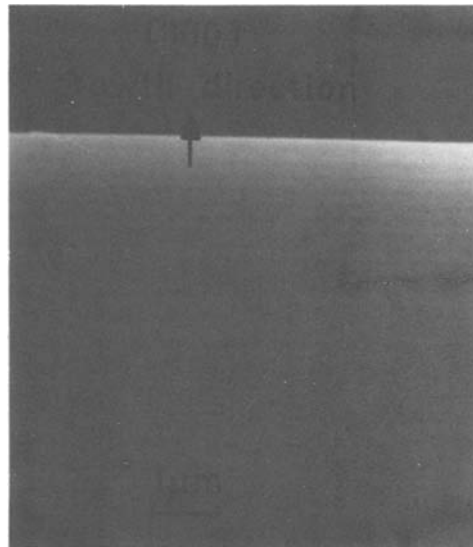


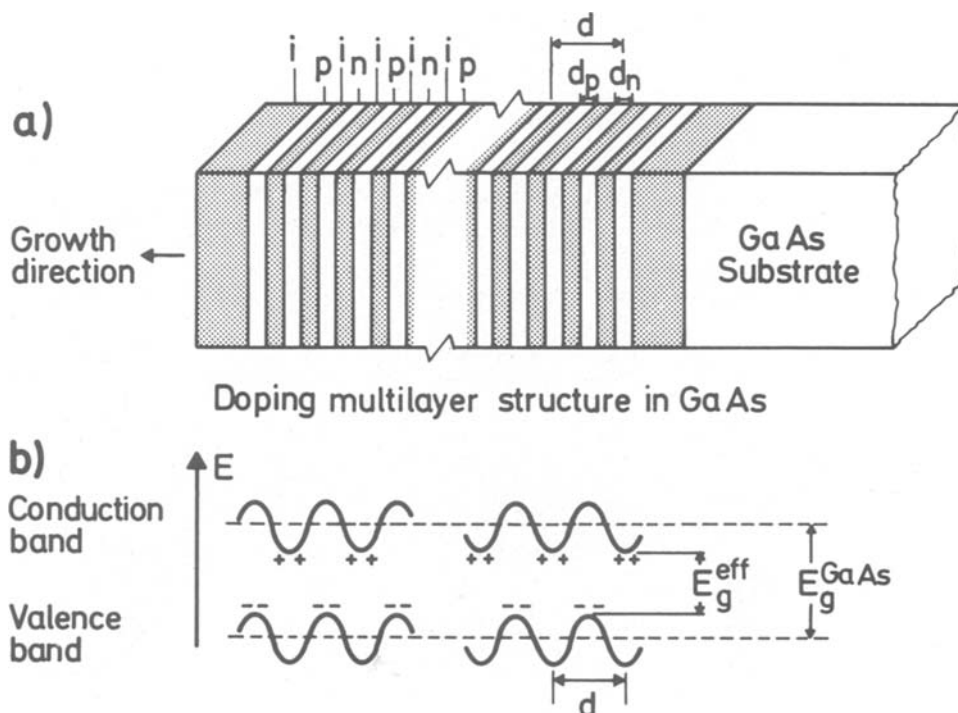
Fig. 13. Scanning electron micrograph of the (110) cleavage plane of a periodic p-n doping multilayer structure in GaAs consisting of 10 periods with a periodicity $d = 0.2 \mu\text{m}$. Each $0.1 \mu\text{m}$ thick individual layer was doped to a level of $(N_D - N_A) = 7.5 \times 10^{17} \text{ cm}^{-3}$ and $(N_A - N_D) = 2 \times 10^{18} \text{ cm}^{-3}$, respectively.

periodically modulated by the space charge field of the ionized impurity atoms per individual layer as depicted in Fig. 12(b). The important parameters which characterize the electronic structure of a nipi crystal are the period d and the concentrations of donors and acceptors per doping layer, i.e., $n_D \cdot d_n$ and $n_A \cdot d_p$, respectively. If the doping concentrations n_D and n_A are the same in the respectively doped layers and if, in addition, the number of dopants in the n- and p-type layers is equal, the amplitude of the space charge potential V_0 may be calculated as follows

$$V_0 \cong |\rho| \frac{d_n}{8 \cdot \epsilon \cdot \epsilon_0} \quad [1]$$

with ϵ = static dielectric constant [$\epsilon = 13.1$ for GaAs (36)], ϵ_0 = permittivity of free space, and ρ = charge

Fig. 12. Schematic illustration of a periodic doping multilayer structure, also called "nipi" structure, in GaAs of periodicity d . Also shown is the periodic modulation of the conduction and valence bandedges in this structure.



density per layer ($\rho \leq \text{Min}(|e|n_D d_n, |e|n_A d_p)$). The effective bandgap E_g^{eff} of a nipi crystal defined as the energy difference between the lowest conduction subband and the uppermost valence subband is

$$E_g^{\text{eff}} = E_g^{\text{GaAs}} - 2V_0 \quad [2]$$

As a result of the reduction of the effective energy gap in GaAs nipi crystals, the absorption of photons of energy

$$\hbar\omega > E_g^{\text{eff}} = E_g^{\text{GaAs}} - 2V_0 \quad [3]$$

is energetically allowed. Döhler (7) has proposed that the absorption coefficient $\alpha(\omega)$ should become large for photon energies well below the gap E_g^{GaAs} of the unmodulated semiconductor due to the overlap between conduction and valence subband wavefunctions. This absorption tail for $\hbar\omega < E_g^{\text{GaAs}}$ may be understood in some respect as a Franz-Keldysh effect due to the internal space charge fields in nipi crystals.

The effect of these internal fields on the absorption or transmission behavior, respectively, of GaAs nipi crystals with varying doping periods d is shown for two different samples in Fig. 14. In both samples the individual p- and n-doped GaAs layers composing the structure are doped to a rather high free-carrier concentration of $1 \times 10^{18} \text{ cm}^{-3}$, whereas the thickness of the individual layers is varied from 0.02 μm in sample 2227 ($d = 0.04 \mu\text{m}$) to 0.04 μm in sample 2228 ($d = 0.08 \mu\text{m}$). No intrinsic layers were interspersed between the alternating intentionally doped layers. These parameters yield a space charge potential V_0 of about 0.069 eV for sample 2227 and 0.276 eV for sample 2228.

In Fig. 14 the two transmission spectra of the periodic doping structures are compared with two spectra of a heavily Si-doped substrate wafer used for MBE growth and of a slightly Si-doped epitaxial layer deposited on n^+ -substrate. The strong shift of the absorption edge observed in the four layers is mainly due to the shift of the Fermi level at high carrier concentrations into the conduction band. In addition, the important feature in the optical transmission behavior of the p-n multilayer structures is the strong absorption tail observed particularly below the energy gap of the unmodulated material (indicated by an arrow in Fig. 14). These absorption tails are the result of the internal electrical field arising from the modulation of the bandedges [cf. Fig. 12(b)]. The differences between the two transmission spectra obtained from the p-n multilayer structures 2227 and 2228 are caused by the quantitative variation of the bandedge modulation. The values of

the maximum internal field strength as well as the layer thickness, in which a pronounced field strength exists, differ strongly and explain the remarkably lower transmission of sample 2228 compared to sample 2227.

As a result, the absorption tails observed for these periodic p-n doping multilayer structures extending far into the gap of the pure material can clearly be interpreted as internal Franz-Keldysh effect. The optical absorption at energies well below the gap of the unmodulated semiconductor is only one of the striking properties of this novel superlattice in GaAs first proposed by Döhler (7). A more extensive study of the effect of reduced effective bandgap and of the strongly anisotropic transport properties in these periodic p-n doping multilayer structures in GaAs is underway in this laboratory and detailed results are referred to in a subsequent paper (37).

Conclusion

The high degree of growth control during molecular beam epitaxy normal to the surface on an atomic scale, which was first established for MBE growth of GaAs/ $\text{Al}_x\text{Ga}_{1-x}\text{As}$ superlattices (38), has now been extended to the growth of a novel man-made superlattice in GaAs, also called "nipi" structure, consisting of a periodic sequence of ultrathin p- and n-type GaAs layers, possibly with intrinsic (i -) layers in between. The most stringent requirements for a successful growth of these periodic p-n multilayer structures are the superior electrical and optical quality of the individual p- and n-type GaAs layers composing the structures.

Using Be as acceptor and Si as donor impurities, respectively, for MBE grown GaAs, an excellent uniformity of doping concentration and high majority-carrier mobilities have been obtained. Low temperature photoluminescence measurements on GaAs:Be and GaAs:Si layers yielded highly resolved PL response with excitonic fine structure, thus attesting superior minority-carrier properties of these intentionally Be-doped MBE GaAs films never reported before. The measured periodic doping profiles normal to the surface in p-type GaAs:Be and in n-type GaAs:Si presented here exhibited peak to background free-carrier ratios which were a factor of two higher than those reported earlier. These results made feasible the MBE growth of extremely abrupt carrier profiles for p-n junctions in (Be, Si)-doped GaAs with a width of only 200 Å necessary to change the carrier concentration from p-type $1 \times 10^{17} \text{ cm}^{-3}$ to the same level n-type on the other side of the junction.

Based on this encouraging outcome, the MBE technique has then been further exploited to the successful growth of highly sophisticated periodic p-n doping multilayer structures in GaAs. The doping levels of the individual layers and the periodicity of these nipi structures have been varied over wide ranges according to the theoretical calculations of Döhler *et al.* (7, 8), in order to modify the resulting effective bandgap of the crystals.

Finally, the key features of this novel superlattice in GaAs, which are also evident for device applications, may be summarized as follows: (i) the effective bandgap E_g^{eff} in nipi crystals can have any value between the energy gap E_g^{GaAs} of the unmodulated bulk and zero, depending on the choice of layer thickness and doping concentration; (ii) nipi crystals are extremely anisotropic with respect to their transport properties; (iii) electrons and holes are spatially separated from each other which prevents direct electron hole recombination. As a consequence the carrier concentration and the effective bandgap of nipi crystals may be modulated within wide limits by external bias or absorption of light (7, 8).

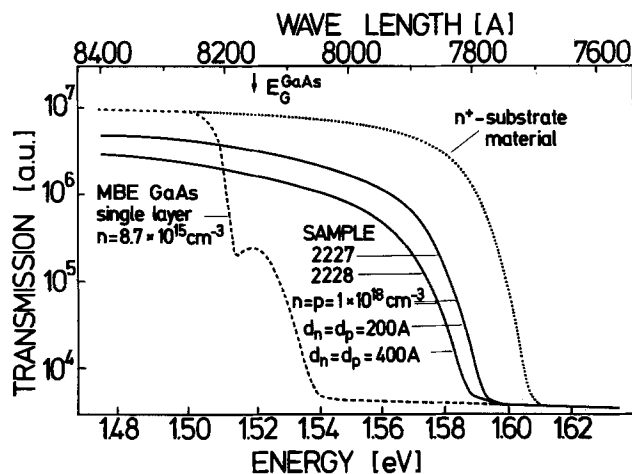


Fig. 14. 1.6 K optical transmission spectra of two representative periodic p-n doping multilayer structures in GaAs indicating the considerable absorption tails for $\hbar\omega < E_g^{\text{GaAs}}$ extending far into the gap of the unmodulated semiconductor (marked by an arrow). For comparison, also the optical transmission of the n^+ -substrate used and of a slightly n-doped GaAs layer are shown.

Acknowledgments

The authors are indebted to E. Jönsson for providing the highly refined Be source material, to W. Heinz, Mrs. G. Siegle, and Miss H. Willerscheid for excellent technical assistance, and to A. Rabenau for stimulating discussions and continuing interest. We are also grateful to G. H. Döhler and H. J. Queisser for many valuable discussions and for critically reviewing the manuscript. The work was sponsored by the Bundesministerium für Forschung und Technologie of the Federal Republic of Germany.

Manuscript submitted April 1, 1980; revised manuscript received Sept. 10, 1980.

Any discussion of this paper will appear in a Discussion Section to be published in the December 1981 JOURNAL. All discussions for the December 1981 Discussion Section should be submitted by Aug. 1, 1981.

Publication costs of this article were assisted by the Max-Planck-Institut für Festkörperforschung.

REFERENCES

- M. V. Schneider, R. A. Linke, and A. Y. Cho, *Appl. Phys. Lett.*, **31**, 219 (1977).
- A. Y. Cho, C. N. Dunn, R. L. Kuvvas, and W. E. Schroeder, *ibid.*, **25**, 224 (1974).
- D. W. Covington and W. H. Hicklin, *Electron. Lett.*, **14**, 753 (1978).
- A. Y. Cho, *J. Appl. Phys.*, **46**, 1733 (1975).
- A. Y. Cho and J. R. Arthur, *Prog. Solid-State Chem.*, **10**, 157 (1975).
- K. Ploog, in "Crystals, Growth, Properties, and Application," Vol. III, Springer, Heidelberg (1980).
- G. H. Döhler, *Phys. Status Solidi B*, **52**, 79 and 533 (1972).
- G. H. Döhler and K. Ploog, *Prog. Cryst. Growth Charact.*, **2**, 145 (1979).
- A. Y. Cho, *Appl. Phys. Lett.*, **11**, 467 (1971).
- K. Ploog, A. Fischer, and H. Künzel, *Appl. Phys.*, **18**, 353 (1979).
- A. Fischer, K. Graf, M. Hafendörfer, and K. Ploog, Submitted to *Rev. Sci. Instrum.*
- K. Ploog, *J. Vac. Sci. Technol.*, **16**, 838 (1979).
- K. Ploog and A. Fischer, *Appl. Phys.*, **13**, 111 (1977).
- H. Künzel, A. Fischer, and K. Ploog, *ibid.*, **22**, 23 (1980).
- G. E. Stillman and C. M. Wolfe, *Thin Solid Films*, **31**, 69 (1976).
- A. Chandra, C. E. C. Wood, D. W. Woodard, and L. F. Eastman, *Solid-State Electron.*, **22**, 645 (1979).
- M. Ilegems, *J. Appl. Phys.*, **48**, 1278 (1977).
- C. E. C. Wood, J. Woodcock, and J. J. Harris, *Inst. Phys. Conf. Ser.*, **45**, 28 (1979).
- T. Shimano, T. Muratoni, M. Nakatani, M. Otsubo, and S. Mitsui, *Surf. Sci.*, **86**, 126 (1979).
- K. Ploog and A. Fischer, *J. Vac. Sci. Technol.*, **15**, 255 (1978).
- D. L. Rode and S. Knight, *Phys. Rev. B*, **3**, 2534 (1971).
- H. Poth, H. Bruch, M. Heyen, and P. Balk, *J. Appl. Phys.*, **49**, 285 (1978).
- D. V. Lang, *ibid.*, **45**, 3023 (1974).
- D. V. Lang, A. Y. Cho, A. C. Gossard, M. Ilegems, and W. Wiegman, *ibid.*, **47**, 2558 (1976).
- H. Künzel, K. Wünstel, and E. Wagner, Unpublished results.
- J. D. Wiley, in "Semiconductors and Semimetals," Vol. 10, R. A. Willardson and A. C. Beer, Editors, p. 91, Academic, New York (1975).
- D. J. Ashen, P. J. Dean, D. T. J. Hurle, J. B. Mullin, and A. M. White, *J. Phys. Chem. Solids*, **36**, 1041 (1975).
- R. Dingle, C. Weisbuch, H. L. Störmer, H. Morkoc, and A. Y. Cho, *Appl. Phys. Lett.*, To be published.
- U. Heim and P. Hiesinger, *Phys. Status Solidi B*, **66**, 461 (1974).
- H. Künzel and K. Ploog, *Appl. Phys. Lett.*, **37**, 416 (1980).
- D. P. Kennedy, P. C. Murley, and W. Kleinfelder, *IBM J. Res. Dev.*, **12**, 399 (1968).
- W. C. Johnson and P. T. Panousis, *IEEE Trans. Electron Devices*, **ed-18**, 965 (1971).
- S. M. Sze, "Physics of Semiconductor Devices," Wiley, New York (1969).
- S. M. Sze and G. Gibbons, *Appl. Phys. Lett.*, **8**, 111 (1966).
- H. Kressel, *RCA Rev.*, **28**, 175 (1967).
- I. Strzalkowski, S. Joshi, and C. R. Crowell, *Appl. Phys. Lett.*, **28**, 350 (1976).
- H. Künzel, G. H. Döhler, A. Fischer, and K. Ploog, To be published in *Appl. Phys. Lett.*
- L. L. Chang, L. Esaki, W. E. Howard, and R. Ludeke, *J. Vac. Sci. Technol.*, **10**, 11 (1973).

Interfacial Arsenic Growth in Anodic Oxide/GaAs Structures

G. P. Schwartz,* G. J. Gualtieri, J. E. Griffiths, and B. Schwartz*

Bell Laboratories, Murray Hill, New Jersey 07974

ABSTRACT

Raman scattering has been employed to monitor both the structure and growth of elemental arsenic deposits thermally generated during the interfacial reaction which occurs between GaAs and the As_2O_3 component of its electrochemically anodized oxide. The band shape of the Raman scattering intensity is consistent with the formation of amorphous arsenic during the initial stages of reaction within the temperature interval 300°-366°C. The time and temperature dependence of a-arsenic growth can be approximated by

$$N(t,T) = 10^{28} \cdot t \cdot \exp(-2.3 \times 10^4/T) \text{ atoms/cm}^2$$

in the region where the Raman signal is linearly increasing with time and 300°C $\leq T \leq$ 366°C. Intensity variations due to multilayer interference were not observed during growth and have been neglected. The data suggest that more than one structural form of a-arsenic may evolve during the course of reaction.

Recent device-related applications utilizing native oxides on GaAs generated via thermal (1), anodic (2),

or plasma (3) techniques suggest that progress is being made in circumventing some of the obstacles previously encountered with such films. Nevertheless, the electrical and chemical properties of these films still present

* Electrochemical Society Active Member.

Key words: Raman scattering, oxides, anodization.

a major obstacle to applications in device technology. Recent studies of the equilibrium Ga-As-O phase diagram (4) have disclosed that the stable interfacial phase should consist of Ga_2O_3 and elemental As. As a result, native oxides containing As_2O_3 are subject to an interfacial reaction given by $\text{As}_2\text{O}_3 + 2\text{GaAs} \rightarrow \text{Ga}_2\text{O}_3 + 4\text{As}$ at sufficiently high temperatures where the diffusion and reaction barriers can be overcome. Experimental confirmation of this reaction has already been obtained in electrochemically anodized (5) plasma (rf and d.c.) oxidized (6), and thermally oxidized (7, 8) films.

Although the role interfacial arsenic deposits play in affecting the electrical properties at the oxide/substrate interface remains open to question, it seems reasonably certain from a device viewpoint that such compositional variations are an undesirable complication. Since crystalline arsenic is a semi-metal and the amorphous form is a small bandgap (1.1 eV) semiconductor, it was important to know more about its structure in the interfacial region. Therefore, the present study was undertaken to monitor both the growth rate and the structural form of elemental arsenic produced during the initial stages of interfacial reaction.

Experimental

Sample preparation and heating cell.—Bromine-methanol-polished Sn-doped ($n \sim 1-2 \times 10^{18} \text{ cm}^{-3}$) GaAs wafers of (100) orientation were electrochemically anodized at constant current (1 mA/cm²) up to 50V in a saturated aqueous solution of As_2O_3 buffered to pH 4.0 with dibasic ammonium phosphate. The resulting oxide films were approximately 1000Å thick and consisted of nearly equimolar mixtures of As_2O_3 and Ga_2O_3 .

The heating cell (Fig. 1) consisted of a ceramic insulation sleeve surrounding a beveled copper block into which a 400W cartridge heater was press fitted. Incident light entered the cell through a small hole and Raman scattered radiation passed through the quartz window to the collection optics. The cell was purged with argon in order to eliminate Raman scattering from the rotational bands of O_2 and N_2 .

Anodized samples were mounted onto the beveled face of the copper block and secured with two Be-Cu spring clips. A Chromel-Alumel thermocouple was also screwed down onto the beveled surface. Separate oil bath/thermometer calibrations of this thermocouple

were found to agree within $\pm 3^\circ\text{C}$ with tabulated (9) emf values over the range $20^\circ\text{-}300^\circ\text{C}$.

Raman spectra.—Spectra were collected on an Instruments S.A. Raman spectrometer (Model HG-2S) which was coupled to standard pulse counting electronics with analog recorder readout. Laser excitation at 5145Å was polarized in the plane of incidence and struck the sample surfaces at Brewster's angle. The polarization of the Raman scattered light was not analyzed. The spectra slit width, count rate meter time constant, laser power, and monochromator scan rate were held constant at values of 8 cm⁻¹, 10 sec, 700 mW, and 10 cm⁻¹/min, respectively. Analog spectra were subsequently digitized at 2 cm⁻¹ intervals. Spectral intensities for the as-anodized (prior to thermal reaction) wafers were normalized to the peak intensity of the GaAs LO phonon at 291 cm⁻¹.

Methodology.—An "interrupted reaction" scheme was employed which involved sequential steps of sample heating, cooling to room temperature, and data acquisition. The samples were never physically moved during repetitive sequences of these steps in order to avoid realignment errors. In addition, the laser excitation was kept off the sample during the heating and cooling parts of the cycle since arsenic growth and its crystallization could potentially be affected by the local heating associated with absorption of laser light during continuous monitoring of the reaction. At room temperature, the reaction rates were sufficiently slow that the local heating created during data acquisition was not observed to effect any changes. Further obstacles to making measurements at elevated temperatures during the reaction stemmed from background cell fluorescence and strongly enhanced plasma line scattering from the cell walls.

The adoption of an "interrupted reaction" sequence involves cumulative errors in defining the reaction time. With the small heat capacity of the copper block however, we were able to obtain the desired reaction temperature within 3-4 min. After a specified reaction time, the cartridge heater power was abruptly discontinued. The total cooldown times depended on the initial cell temperature, but in all cases the copper block had dropped to 300°C or less within the first 3 min following power discontinuation. Compared to a typical reaction time scale of hours, the error introduced by the response time of the heating block was considered to be acceptably small.

Results and Discussion

Spectral data and structural aspects.—All data were initially acquired in analog form under fixed instrumental conditions (see "Experimental" for details). A typical analog spectrum for as-anodized (100) GaAs wafer is shown in Fig. 2. In addition to the prominent first-order longitudinal and transverse optic mode (LO, TO) scattering from GaAs, weaker two-phonon

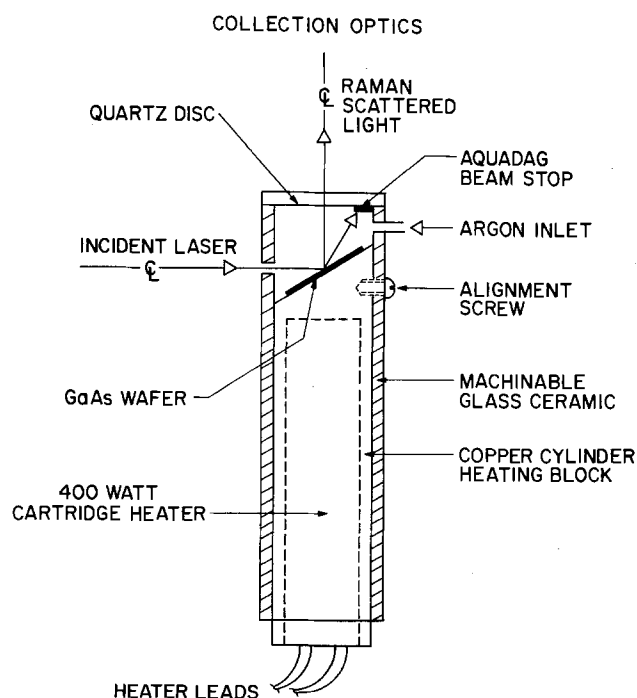


Fig. 1. Top view of the heating cell

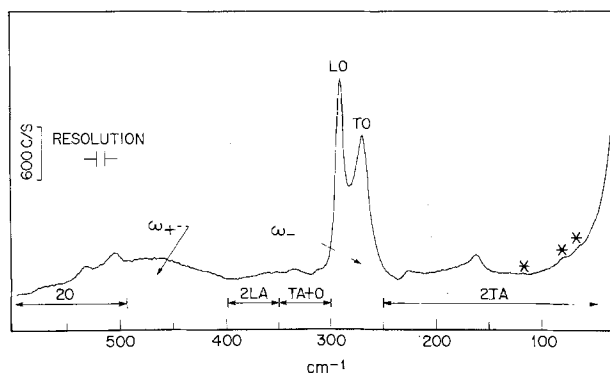


Fig. 2. Analog Raman spectrum of an as-anodized GaAs (100) wafer prior to thermal treatment. Data taken with 8 cm⁻¹ slits at a scan rate of 10 cm⁻¹/min with a 10 sec time constant. Power at the sample was approximately 400 mW; asterisks denote laser plasma lines.

features associated with the substrate are also observed. The two-phonon bands (10) are designated as overtone (2O), longitudinal and transverse acoustic (LA, TA), and combination (TA + O) modes where (O) refers to the optic modes. Coupled LO-plasmon (11, 12) modes are denoted by ω_+ and ω_- . Asterisks identify laser plasma lines. No bands explicitly associated with the amorphous oxide (13) film ($\sim 1000\text{\AA}$) are readily apparent. The Raman spectrum of amorphous arsenic (14, 15) is dominated by a relatively featureless broad band which extends from 180 to 280 cm^{-1} . Rhombohedral arsenic shows Raman peaks (16, 17) at 195 and 257 cm^{-1} , whereas orthorhombic arsenic (18) has its most intense modes located at ~ 222 and 254 cm^{-1} .

In order to separate the arsenic signal from the GaAs substrate background, the following analysis procedure was employed. The analog spectra were digitized at 2 cm^{-1} intervals and the Rayleigh wing and background components were fitted to a damped Lorentzian function plus a constant term. The low frequency plasma lines were removed in the initial digitization in order to avoid distorting the fit to the Rayleigh wing. The digitized version of the analog spectrum seen in Fig. 2 is shown in Fig. 3 along with the Rayleigh wing and background (solid line). Subtraction of the latter yields the digital data of Fig. 4. The substrate LO, TO, and ω_- modes were then fitted

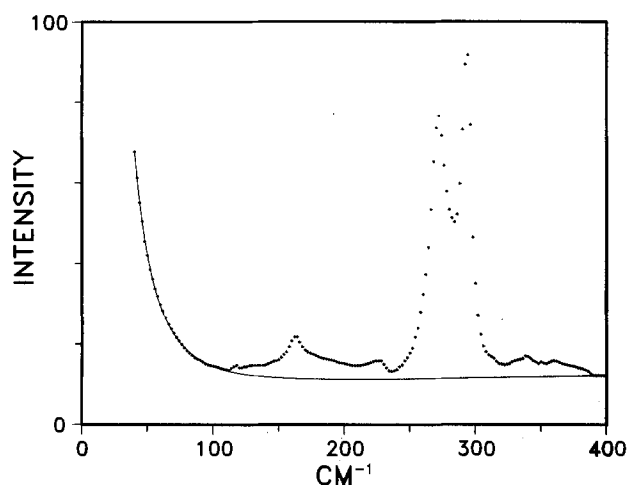


Fig. 3. Digitized (2 cm^{-1} intervals) version of Fig. 2 after removal of the 66 and 77 cm^{-1} plasma lines. The solid curve represents the nonlinear least-squares fit used to remove the Rayleigh wing and background between 30 and 400 cm^{-1} .

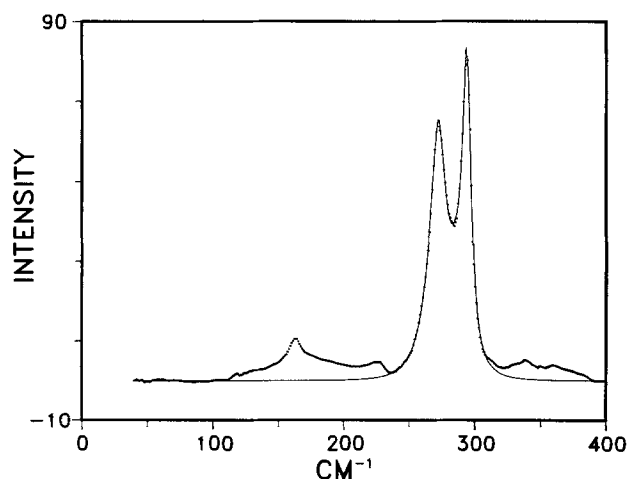


Fig. 4. Digital spectrum with the Rayleigh wing and background removed. The number of data points have been doubled using linear interpolation. The solid curve is the fit to the substrate LO and TO mode structure.

by an analytical function consisting of three damped Lorentzian using a nonlinear least squares routine. Prior to the fit, a linear interpolation routine was exercised in order to double the number of data points. This aided the fit to the wing which extends into the phonon combination (TA + O) mode region beyond $\sim 300 \text{ cm}^{-1}$. Removal of the Rayleigh wing, constant background, and LO, TO, and ω_- structures yielded the shape of the substrate two-phonon spectrum for the as-anodized wafer. This is shown in Fig. 5. The small oscillations observed between 240-280 cm^{-1} originate from curve-fitting errors and were subsequently smoothed. The resulting spectrum represents an intrinsic structured background due to the substrate (Fig. 6A). Figure 6(B-D) shows the resulting spectra in the 100-280 cm^{-1} region of an anodized GaAs sample after heating at 330°C for (B) 7.5, (C) 20, and (D) 29 hr respectively. These spectra represent the two phonon background of 6(A) plus the Raman scattering from any amorphous arsenic formed during heating.

Spectra for the arsenic generated during the reactions were obtained after subtraction of the as-anodized substrate two-phonon structure. Representative data for reaction at 330°C are presented in Fig. 7. A spectrum for bulk amorphous arsenic grown by thermally decomposing GaAs and condensing the evolved arsenic onto a 77 K coldfinger is also included (bottom) for comparison.

The systematic occurrence of a relatively sharp peak imposed on all the a-arsenic spectra (Fig. 7, A, B, C) is noted at $\sim 233 \text{ cm}^{-1}$. The intensity of this feature is essentially independent of either the reaction time or temperature. Its origin is believed to be associated with a slight broadening and shift of the substrate two-phonon background which accompanies the heating process and is not properly accounted for by using the as-anodized (unheated) spectra for base line subtraction.

A second peak at $\sim 200 \text{ cm}^{-1}$ is also obvious on the a-arsenic band shape after 29 hr of reaction at 330°C (Fig. 7C). The development of this feature in the reacted sample data was observed to be time and temperature dependent and was not observed in the 300 and 315°C data sets. Raman scattering data on a-arsenic by Lannin (14) and Nemanich *et al.* (15) clearly evidence a peak in this region in their samples which were prepared by prolytic decomposition of arsine. Lannin's (14) data for sputter deposited films do not show it, nor do ours for deposits prepared via thermal decomposition of GaAs (see Fig. 8A).

An unambiguous explanation of the evolution of the 200 cm^{-1} feature observed in Fig. 7C is complicated by at least two distinct types of structural considerations. The first of these deals with the implicit short-range order present in amorphous arsenic. Breiting (19) has

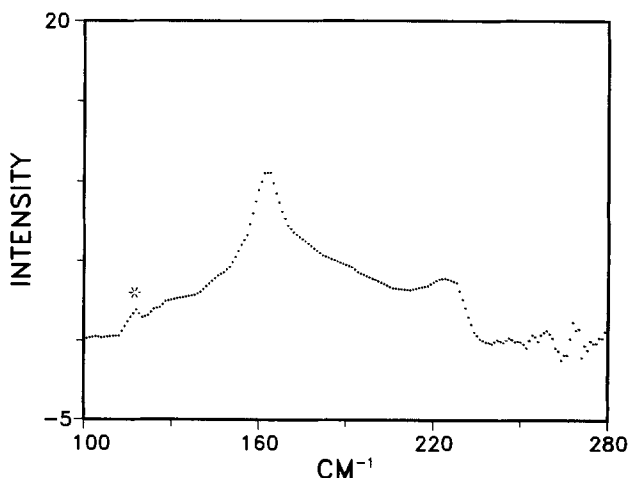


Fig. 5. Structure of the substrate two-phonon background in the region between 100 to 280 cm^{-1} . The asterisk denotes a laser plasma line.

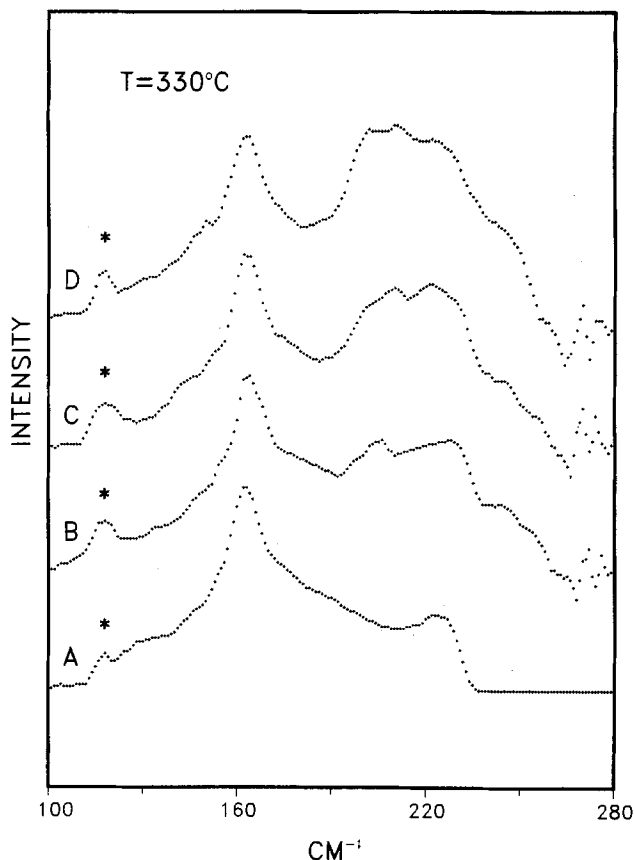


Fig. 6. Raman scattering intensity in the $100\text{--}280\text{ cm}^{-1}$ region for interfacial reaction at 330°C . Reaction times in hours are (A) 0, (B) 7.5, (C) 20.0, and (D) 29.0. Oscillations in (A) between 235 and 280 cm^{-1} have been smoothed. Asterisks denote laser plasma lines.

observed that the radial distribution functions obtained from evaporated and precipitated films of α -arsenic evidence distinctly different values for the shortest interlayer separations of 3.66 and 4.05 \AA , respectively. The growth of the 200 cm^{-1} peak could be indicative of a transformation from one distinct interlayer separation to the other. Alternatively, crystallization may be occurring to yield microcrystallites whose dimensions are small compared to the wavelength of the phonon modes. This process is expected to lead to a breakdown of the momentum selection rules in Raman scattering (20) and modify the bulk crystalline band shapes. Documentation on such phenomena on well-defined samples is quite limited. The work of Keramidas and White (21) on ZrO_2 suggests that crystallites of very small dimensions ($\sim 30\text{ \AA}$) can be detected by Raman scattering in the form of bands significantly broader than those expected for macroscopic crystals. As crystallization progresses, the bands sharpen and their peak intensities increase (21). More recently, Nemanich *et al.* (22, 23) reported Raman scattering from thin films ($50\text{--}60\text{ \AA}$) of polycrystalline Te and Ti. Broadening of the E_g mode of hexagonal Ti was observed. In the Te films, both the A_1 and E-type bands were slightly broadened compared with those observed for bulk material. Thus, crystallites of Ti and Te in which at least one dimension is not greater than 60 \AA give rise to Raman spectra characteristic of macroscopic crystals. For each situation described above, the particles are not isolated and strong intermolecular interactions may produce results that differ significantly from those expected for systems of small structurally and chemically separated scatterers. Ruppin (24) has reported that, for such systems, well-defined surface modes may be detectable and in fact the intensity of such modes are particle size dependent.

Returning to the case of arsenic, the growth of a broad band near 200 cm^{-1} during annealing without

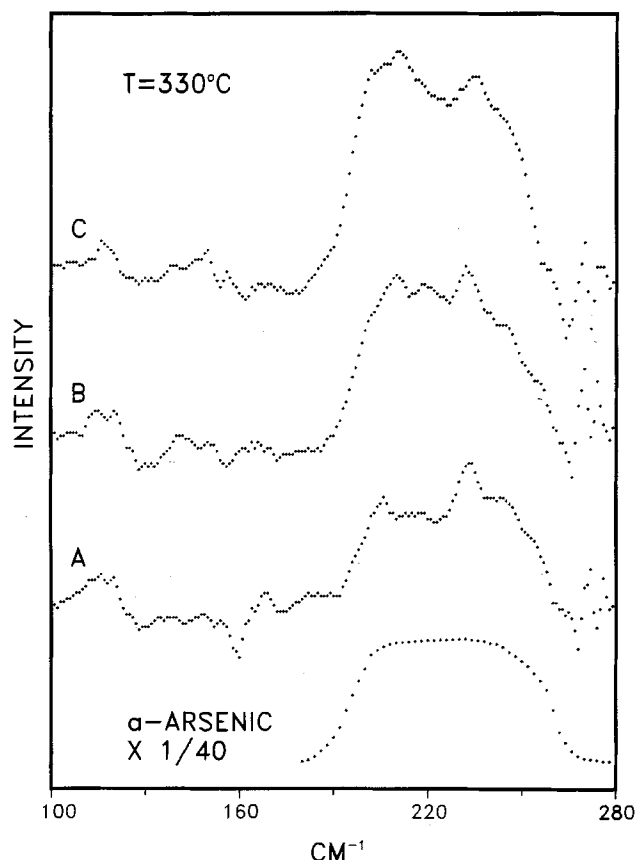


Fig. 7. The net Raman spectra for 330°C reaction after times of (A) 7.5, (B) 20.0, and (C) 29.0 hr following removal of the substrate two-phonon structure. The bottom panel shows the band contour obtained from a bulk sample of α -arsenic using a simple linear background subtraction as shown in Fig. 8.

observing the parallel growth of an A_1 -type band of crystalline arsenic suggests that the changes occurring do not involve a crystallization process. Instead, a change in the interlayer separation is favored. To test this interpretation, bulk films of amorphous arsenic were examined. The as-deposited film (Fig. 8A) was essentially featureless except for the laser plasma line artifact at 266 cm^{-1} . Annealing this sample at a copper block temperature of 220°C for 30 and 60 min yielded the spectra shown in Fig. 8B and 8C, respectively. One notes the growth of the 200 cm^{-1} spectral feature with essentially no evidence for the development of a corresponding band near 257 cm^{-1} . On the contrary, there appears to be a systematic decrease in intensity in the higher frequency region of the band envelope with increasing annealing time. Although our conclusions at the present time are quite speculative, we feel that the bulk of the evidence favors a structural interlayer separation change rather than crystalline size effects.

Reaction rates for interfacial arsenic formation.—To obtain an estimate of the interfacial arsenic growth rate, graphical integration of the α -arsenic intensity was performed for each sample and plotted *vs.* reaction time. The results are seen in Fig. 9. In extracting the integrated intensities the following two constraints were employed: (i) the α -arsenic band shape was assumed to be featureless, and (ii) the integration limits were taken at 180 and 270 cm^{-1} . The error introduced by neglecting the presence of the 200 cm^{-1} feature was approximately 10–15% in the worst case.

The heterogeneous nature of the interfacial reaction is further complicated by the presence of both diffusion and reaction barriers. In the following description of the interfacial α -arsenic growth we will assume that the time and temperature dependence are separable and of the empirical form

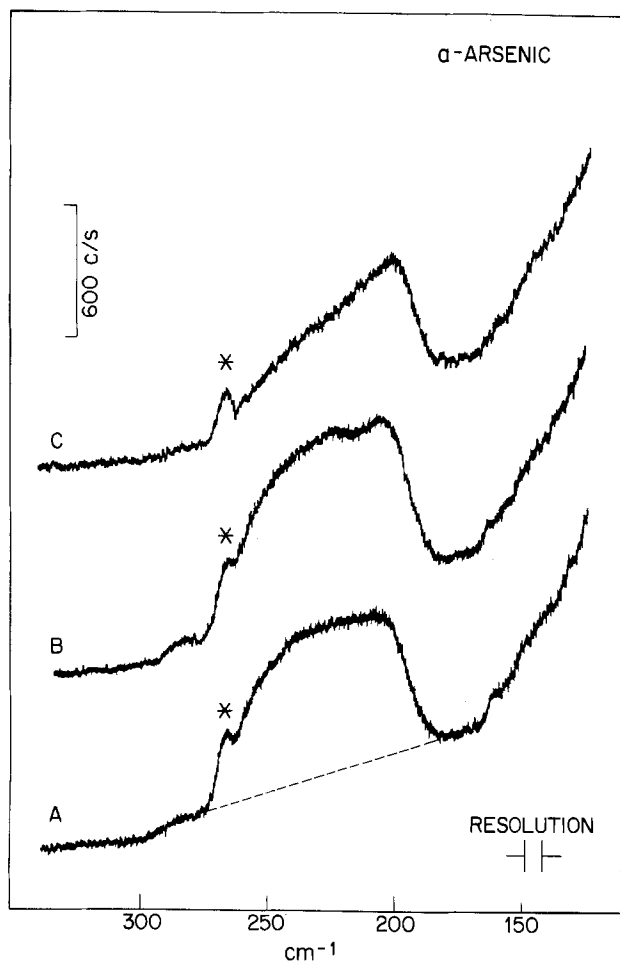


Fig. 8. Spectral lineshape changes observed in bulk α -arsenic after thermal annealing at 220°C. (A) as-deposited, (B) 30 min annealing, and (C) 60 min annealing.

$$N_{AS}(t, T) = N_0 \cdot f(t) \cdot \exp(-E/kT) \quad [1]$$

An attempt was made to obtain a nonlinear least-squares fit to the functional form $N_0 \cdot t^m \cdot \exp(-E/kT)$, but the fits obtained via this procedure always displayed a high degree of correlation between the parameters N_0 , m , and E . Consequently we have chosen to utilize only the initial regions of the growth curves in which $f(t)$ is well described as a linear function of time. Assuming the separability of the time and tem-

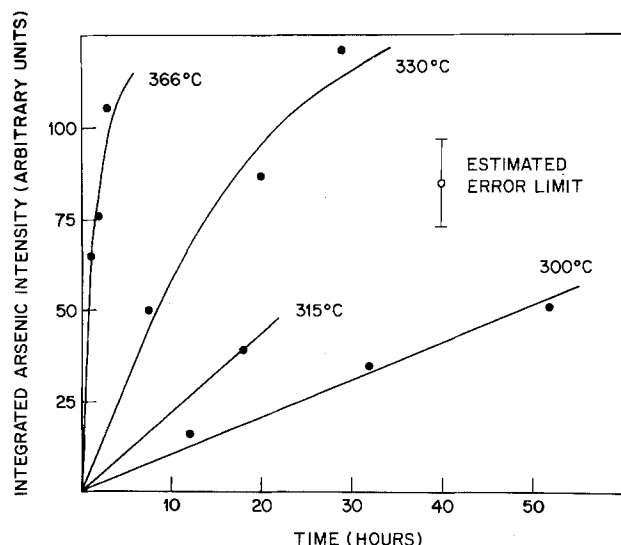


Fig. 9. Plot of the integrated α -arsenic intensity as a function of temperature and time.

perature variables appropriate to Eq. [1], one obtains the effective barrier energy E from the slope of a plot of $\log_e(\text{rate})$ vs. $1/T$, where the rate is the time derivative of the growth curves presented in Fig. 9. This plot is shown in Fig. 10 along with error bars constructed from estimated errors in the integrated intensities and reaction temperatures. The maximum possible deviations in slope constrained by the requirement that the lines intersect the error bars of all data points were also constructed in order to obtain upper and lower limits to the barrier energy E . In the limited temperature interval between 300°-366°C, we obtain a barrier energy $E = 46 \pm 9/14$ kcal per mole of arsenic atoms. Extension of the interfacial reaction data to higher temperatures is complicated by the onset of rapid crystallization and concomitant change in arsenic lineshapes. At lower temperatures the interfacial reaction is prohibitively slow.

In order to complete the description of interfacial arsenic growth via Eq. [1], it is necessary to convert the integrated intensities into some measure of equivalent thickness of amorphous arsenic. An estimate of this thickness is provided by monitoring the progressive attenuation of the GaAs LO intensity by an absorbing layer of thickness t and absorption coefficient α . Two implicit assumptions limit the accuracy of this technique. First of all, the α -arsenic layer is assumed to be continuous and of uniform thickness with an absorption coefficient α equal to that found in bulk (25) amorphous films. Secondly, reflectivity losses incurred at the oxide/ α -arsenic interface are difficult to assess and have been neglected. With the constraints of these assumptions, analysis of the data suggests that a uniform 8Å layer is equivalent to ~ 25 intensity units in Fig. 9. The uncertainty in this conversion is high however; we conservatively estimate that the absolute value of the 8Å figure may be in error by 100%.

Assuming a density of 4.7 g/cm³ for α -arsenic, an 8Å \times 1 cm² volume would contain $\sim 3 \times 10^{15}$ arsenic atoms. Since the laser beam spot size is not accurately known, we have chosen to express $N_{AS}(t, T)$ in units of atoms/cm² implying a finite depth of accrued arsenic. Within the temperature range 300°-366°C and for times sufficiently short that only α -arsenic is observed, we obtain an interfacial growth function given by

$$N_{AS}(t, T) = 10^{28} \cdot t \cdot \exp(-2.3 \times 10^4/T) \text{ atoms/cm}^2 \quad [2]$$

It should also be noted that this growth function is

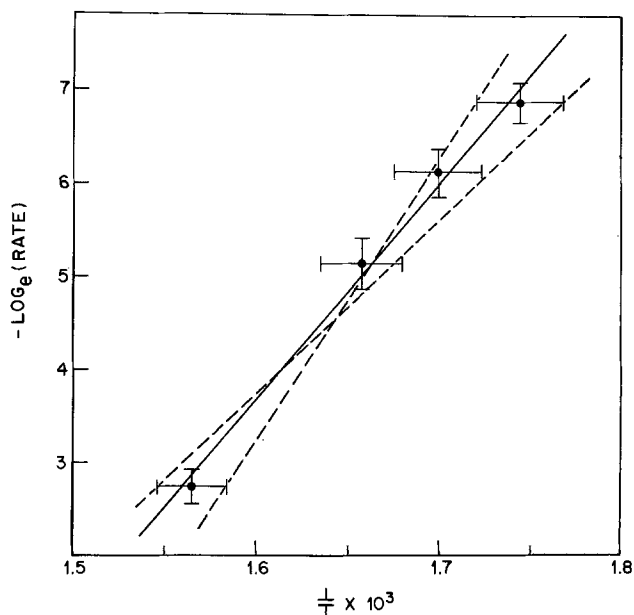


Fig. 10. Plot of the log of growth rate vs. inverse temperature. The solid line was fit by linear regression, the dashed lines represent upper and lower slope limits under the constraint that the error bars must be intersected.

probably specific to anodic oxide/GaAs interfaces and may be different for films produced by rf or d-c plasma anodization.

Summary

Structural and growth rate aspects of interfacial arsenic accumulation have been studied in thermally treated anodic films on GaAs. The initial stages of the interfacial reaction between As_2O_3 and the substrate yield deposits of amorphous arsenic in the reaction temperature range 300°-366°C. There is some evidence that more than one amorphous structure is observed. The growth of this amorphous arsenic is characterized by the equation

$$N_{AS}(t, T) = 10^{23} \cdot t \cdot \exp(-2.3 \times 10^4/T) \text{ atoms/cm}^2$$

where t is in seconds and T in degrees Kelvin.

Manuscript submitted June 11, 1980; revised manuscript received Sept. 5, 1980.

Any discussion of this paper will appear in a Discussion Section to be published in the December 1981 JOURNAL. All discussions for the December 1981 Discussion Section should be submitted by Aug. 1, 1981.

Publication costs of this article were assisted by Bell Laboratories.

REFERENCES

- H. Takagi, G. Kano, and I. Teramoto, *IEEE Trans. Electron Devices*, **ed-25**, 551 (1978).
- H. Tokuda, Y. Adachi, and T. Ikoma, *Electron. Lett.*, **13**, 761 (1977).
- F. Koshiga and T. Sugano, *Thin Solid Films*, **56**, 39 (1979).
- C. D. Thurmond, G. P. Schwartz, G. W. Kammlott, and B. Schwartz, *This Journal*, **127**, 1366 (1980).
- G. P. Schwartz, B. Schwartz, D. DiStefano, G. J. Gualtieri, and J. E. Griffiths, *Appl. Phys. Lett.*, **34**, 205 (1979).
- G. P. Schwartz, B. Schwartz, J. E. Griffiths, and T. Sugano, *This Journal*, **127**, 2269 (1980).
- J. A. Cape, W. E. Tennant, and L. G. Hale, *J. Vac. Sci. Technol.*, **14**, 921 (1977).
- R. L. Farrow, R. K. Chang, S. Mroczkowski, and F. H. Pollack, *Appl. Phys. Lett.*, **21**, 768 (1977).
- "Handbook of Chemistry and Physics," 43rd ed., p. 2654, Chemical Rubber Pub. Co., Cleveland (1961).
- T. Sekine, K. Uchinokura, and E. Matsuura, *J. Phys. Chem. Solids*, **38**, 1091 (1977).
- A. Pinczuk, G. Abstreiter, R. Trommer, and M. Cardona, *Solid State Commun.*, **21**, 959 (1977).
- G. Abstreiter, R. Trommer, M. Cardona, and A. Pinczuk, *ibid.*, **30**, 703 (1979).
- G. P. Schwartz, G. J. Gualtieri, J. E. Griffiths, C. D. Thurmond, and B. Schwartz, *This Journal*, **127**, 2488 (1980).
- J. S. Lannin, *Phys. Rev. B*, **15**, 3863 (1977).
- R. J. Nemanich, G. Lucovsky, W. Pollard, and J. D. Joannopoulos, *Solid State Commun.*, **26**, 137 (1978).
- R. N. Zitter, in "The Physics of Semi-Metals and Narrow Gap Semiconductors," D. L. Carter and R. T. Bate, Editors, p. 285, Pergamon Press, New York (1971).
- J. S. Lannin, J. M. Calleja, and M. Cardona, *Phys. Rev. B*, **12**, 585 (1975).
- J. S. Lannin and B. V. Shanabrook, 14th Intern. Conf. Phys. Semiconductors, Edinburgh, Scotland (1978).
- G. Breitling, *J. Non-Cryst., Solids*, **8-10**, 395 (1972).
- R. Shuker and R. W. Gammon, *Phys. Rev. Lett.*, **25**, 222 (1970).
- V. G. Keramidis and W. B. White, *J. Am. Ceram. Soc.*, **57**, 22 (1974).
- G. A. N. Connell, R. J. Nemanich, and C. C. Tsai, *Appl. Phys. Lett.*, **36**, 31 (1980).
- R. Ruppini, *J. Phys. C.: Solid State*, **8**, 1969 (1975).
- G. N. Greaves, E. A. Davis, and J. Bordas, *Philos. Mag.*, **34**, 265 (1976).

An AES/XPS Study of the Chemistry of Palladium on Hydrogenated Amorphous Silicon Schottky Barrier Solar Cells

J. H. Thomas III* and D. E. Carlson

RCA Laboratories, David Sarnoff Research Center, Princeton, New Jersey 08540

ABSTRACT

Thin layers of palladium (~100Å thick) on hydrogenated amorphous silicon have been used as diodes and photovoltaic devices (solar cells). Auger electron spectroscopy (AES) and x-ray photoelectron spectroscopy (XPS) in conjunction with ion-milling were used to characterize the interface region. At the interface, a thin oxide layer is observed along with possible palladium silicides. Palladium and palladium silicides extend well into the silicon substrate. Palladium silicide is due in part to ion-mixing. Heating device structures in D_2O caused considerable electrical degradation. Data indicate that the degradation is due to oxide formation at the Pd/a-Si:H interface.

Both Pt and Pd contacts have been used to form Schottky barriers on hydrogenated amorphous silicon (a-Si:H) (1). A recent study has shown that Pt/a-Si:H Schottky barriers exhibit degradation when exposed to water vapor (2). In the present investigation Auger electron and x-ray photoelectron spectroscopy were used to study Pd/a-Si:H junctions as formed and also after heat-treatments at 80°C for three weeks either in vacuum or in D_2O vapor. The junctions stored at 80°C in D_2O vapor exhibited significant

degradation compared to unaged junctions or those heat-treated in vacuum (1, 3). The goal of this study was to determine the junction chemistry and to see if any measurable difference is observed for samples treated in different ambients.

Experimental

Three samples of palladium (~100Å thick) evaporated on glow-discharge-deposited a-Si:H were fabricated. The a-Si:H was deposited in a d-c proximity glow discharge in SiH_4 at a substrate temperature of ~300°C. The discharge pressure was ~0.7 Torr and the

* Electrochemical Society Active Member.
Key words: ESCA, Auger, Schottky diodes, interfaces.

flow rate was ~ 90 sccm. The hydrogen concentration in the a-SiH was ~ 20 atomic percent (a/o) (3). One device was aged at 80°C in a rough vacuum of ~ 10 milliTorr. A second device was stored at 80°C in saturated D_2O vapor at approximately atmospheric pressure. The third device was an unaged control sample. The samples were subsequently electrically tested and subjected to surface analysis.

Elemental/chemical analysis was performed in a Physical Electronics Industries ESCA/Auger system. Auger electron spectra were excited with an electron beam energy of 3 keV at $10 \mu\text{A}$. A 3V peak-to-peak modulation was applied to the double pass cylindrical mirror analyzer (DPCMA) operating in a nonretarding mode. The narrow slit was used in obtaining the Auger spectra. X-ray photoelectron (or ESCA) spectra were excited with an achromatic magnesium $\text{K}\alpha$ x-ray source operated at 10 keV and 30 mA (300W). The DPCMA was operated in a retarding potential mode with the large slit. Survey and high resolution spectra were obtained at pass energies of 200 and 25 eV, respectively. Photoelectron pulse currents from the electron multiplier were detected and amplified with a Princeton Applied Research Model 1120 amplifier/discriminator. Data acquisition, display, and replotting were accomplished through the use of a computer-controlled data-acquisition system based on a Hewlett-Packard Model 1000 minicomputer and appropriate software.¹ Binding energies were internally referenced to the silicon 2p core photoelectron line due to elemental silicon at 99.40 eV (4). Curve deconvolution was accomplished with a gaussian curve-fitting program. Depth profiling for AES and XPS measurements was done with a Physical Electronics Industries ion gun (Model 20-045) operated at 1 keV at 20 mA, defocused slightly, in 5×10^{-5} Torr of xenon. The sputter rate for SiO_2 was $\sim 2 \text{ \AA}/\text{min}$. Xenon was used because of its small penetration depth (range) at 1 keV ($\sim 7 \text{ \AA}$) (5).

AES Results

The three samples were depth profiled. Auger spectra were measured in sputter time increments of ~ 2 min. The palladium MNN, carbon KLL, oxygen KLL, and silicon LVV Auger lines were tracked through the palladium film and well into the amorphous silicon substrate. Electrons emitted in the energy range below 500 eV, which includes all the transitions measured, have escape depths of less than 10 \AA (6). Elemental concentrations were obtained from the peak-to-peak derivative signal amplitudes using the sensitivity factors from Davis *et al.* (7). The concentrations at each point were normalized to 100%. The elemental depth profile for the unaged sample was identical to the profile of the 80°C vacuum-aged sample and is not shown for brevity.

Figure 1A and B show the depth profiles for the vacuum- and D_2O -aged Pd/a-Si:H samples. A significant amount of carbon is observed in the evaporated palladium layers of the vacuum-aged sample. Carbon on the immediate surface is contamination, probably from the ambient of the vacuum oven. Oxygen is observed at the Pd-Si interface of both samples. This is partly a native oxide that grew on the a-Si:H surface prior to metallization. The peak oxygen concentration in the vacuum-aged sample (~ 2 a/o) is less than in the D_2O -aged sample (~ 10 a/o). Palladium is observed in a-Si:H to a depth of greater than 50 \AA in both samples. The concentration is estimated as 4 a/o at this depth, in agreement with SIMS studies of similar films (2). The interface region is diffused in the three samples which may be in part due to ion mixing effects and crater formation during sputtering. An accurate measure of the interface width cannot be obtained from these data since the sputter rate of palladium is $\sim 5\times$ that of silicon. Qualitatively, the interface region of the three samples is similar.

¹ The basic data acquisition system was designed by J. R. Woolston and S. H. McFarlane.

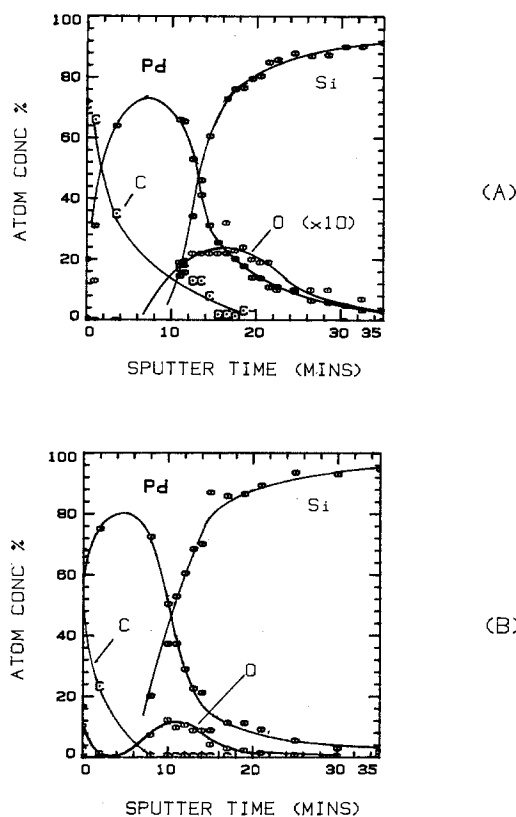


Fig. 1. (A) AES depth profile for the vacuum-aged Pd/a-Si:H device ($80^\circ\text{C}/3$ weeks). (B) AES depth profile for the D_2O -aged Pd/a-Si:H device ($80^\circ\text{C}/3$ weeks). The sputter rate of Si $\cong 2 \text{ \AA}/\text{min}$ and Pd $\cong 10 \text{ \AA}/\text{min}$. Surface O on (A) is $\sim 10\%$ (not shown).

XPS Results

Survey spectra (Fig. 2) were measured at most of the sputter times for which the Auger depth profile was measured. Elemental concentrations as a function of sputter time (depth) were calculated from the core photoelectron peak amplitudes and theoretical photoionization cross sections for Mg $\text{K}\alpha$ radiation (1253.6 eV) (8, 9). The general features of the AES depth profile are also observed in the XPS depth profiles for palladium, carbon, and silicon. The elemental concentration in each sample is quantitatively close to the concentration computed in the Auger depth profile and will be used later in computing bond concentrations.

High resolution spectra of the palladium $3d_{3/2,5/2}$ and silicon 2p photoelectron lines were obtained at a few points near the surface and in the interfacial region. Figure 2 shows a typical survey spectrum with insets of the Pd $3d_{3/2,5/2}$ and Si 2p lines. The high resolution spectra were obtained in an MCS (multichannel scaling) mode: 1 second/channel, and 30 scans. The secondary electron background was subtracted from the Si 2p and Pd 3d spectra, using Shirley's iterative method (10).

Structure, as indicated by the arrows, is observed on the high binding energy side of the Pd 3d and Si 2p lines (shown in the insets). The O 1s line is obscured by the palladium $3p_{3/2}$ line. An approximation of the oxygen line amplitude can be obtained by subtracting the estimated $3p_{3/2}$ amplitude from the total measured amplitude at 530 eV since the ratio of the Pd $3p_{1/2}$ to $3p_{3/2}$ intensity is constant. Separation of the Pd $3p_{3/2}$ and O $1s_{1/2}$ using the gaussian curve-fitting procedure was not attempted.

The Pd 3d and Si 2p lines were fitted with gaussian curves at sputter times of 3, 10, 13, 21, 25, and 30 min. The silicon 2p spectrum was fitted with a minimum of three peaks to adequately fit the spectra. Elemental silicon referenced to the Au $4f_{7/2}$ line occurs at 99.4 eV with an FWHM of 1.45 eV in this XPS system. Therefore, the binding energy scale has been shifted slightly

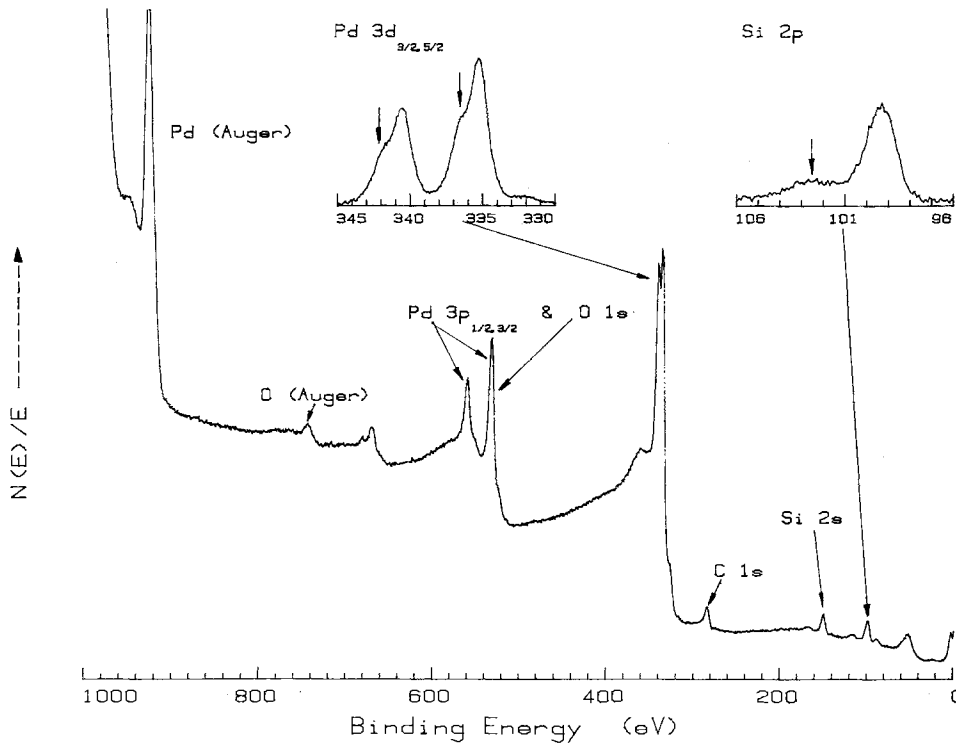


Fig. 2. Survey spectrum for vacuum-aged Pd/a-Si:H sputtered 11 min.

(± 0.1 eV) to account for minor instrumental changes. The other two gaussian peaks are centered at 103.0 ± 0.1 eV and 100.6 ± 0.2 eV and have FWHM's of 1.8 and 2.2 eV, respectively. A typical gaussian fitted spectrum is shown in Fig. 3A for silicon.

The gaussian fit to the Pd 3d lines was poor due to line asymmetry (11). This asymmetry which is about 10% of the 3d line area requires an additional gaussian

peak on the high energy side of the $3d_{3/2,5/2}$ lines which can be subsequently "subtracted" from the spectrum. The Pd $3d_{5/2}$ line consists of two gaussian components at 335.4 ± 0.1 eV and 336.8 ± 0.1 eV which vary in amplitude with sputter time. Their full widths at half maximum (FWHM) are 1.35 and 1.5 ± 0.05 eV, respectively. A typical gaussian fitted spectrum is shown in Fig. 3B.

The vacuum-aged sample is not significantly different from the D_2O -aged sample. However, the contribution of the 100.6 and 103.0 eV peaks relative to the 99.4 eV peak are somewhat greater in the D_2O -aged sample. Figures 4A and 4B show the Pd $3d_{3/2,5/2}$ and Si 2p spectra for the vacuum-aged samples as a function of sputter time (or depth). As the sputter time is increased, the contribution of the 103.0 eV peak decreases while elemental silicon increases. The contribution of the Pd 336.8 eV peak, relative to the 335.4 eV peak, increases with depth into the silicon substrate. Only a few of the Si and Pd spectra were plotted to demonstrate the trends observed. All the spectra plotted are shown with the secondary electron background removed. The vertical scale ($N(E)/E$) of the silicon spectra is 1/4 that of the palladium.

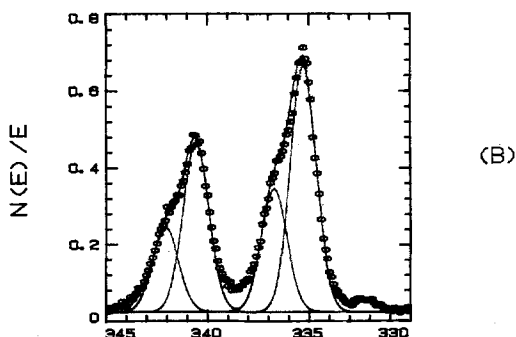
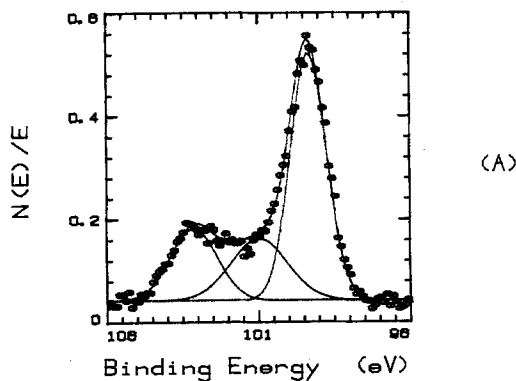


Fig. 3. (A) High resolution spectrum of the Si 2p region for the D_2O -aged sample sputtered 11 min. The gaussian fitted components are shown. (B) The same as Fig. 3(A) for the Pd $3d_{3/2,5/2}$ region.

Interpretation of XPS Peak Positions

The palladium $3d_{5/2}$ consists of two component gaussian peaks, 335.4 and 336.8 eV. A similar set of peaks are observed at the 3/2 spin doublet but will not be discussed. The peak at 335.4 eV is due to elemental palladium (Pd^E) and is in good agreement with Barr's results (12). The peak at 336.8 eV is close to 336.9 eV for Pd in PdO (12). However, from the AES results, <10 a/o of oxygen is present in the interface region. At the interface, (~ 10 min sputter time) both samples consist of about 50 a/o Pd of which equal amounts are at 335.4 and 336.8 eV. Therefore, the 336.8 eV peak cannot be attributed only to PdO. Some valence effects are observed in UPS studies of PdH_x (13). However, it is unlikely that the 3d state of Pd would be shifted by 1.4 eV due to the presence of hydrogen bonding. Therefore, we can conclude that the 336.8 eV peak is due to Pd in silicide form (Pd^B) and PdO.

The silicon 2p spectrum is resolved into three component gaussian peaks at 99.4, 100.6, and 103.0 eV. The 99.4 eV peak has been attributed to elemental silicon (Si^E) (4, 14). The 100.6 eV peak and a portion of the 103.0 eV peak appear to be associated with silicon in

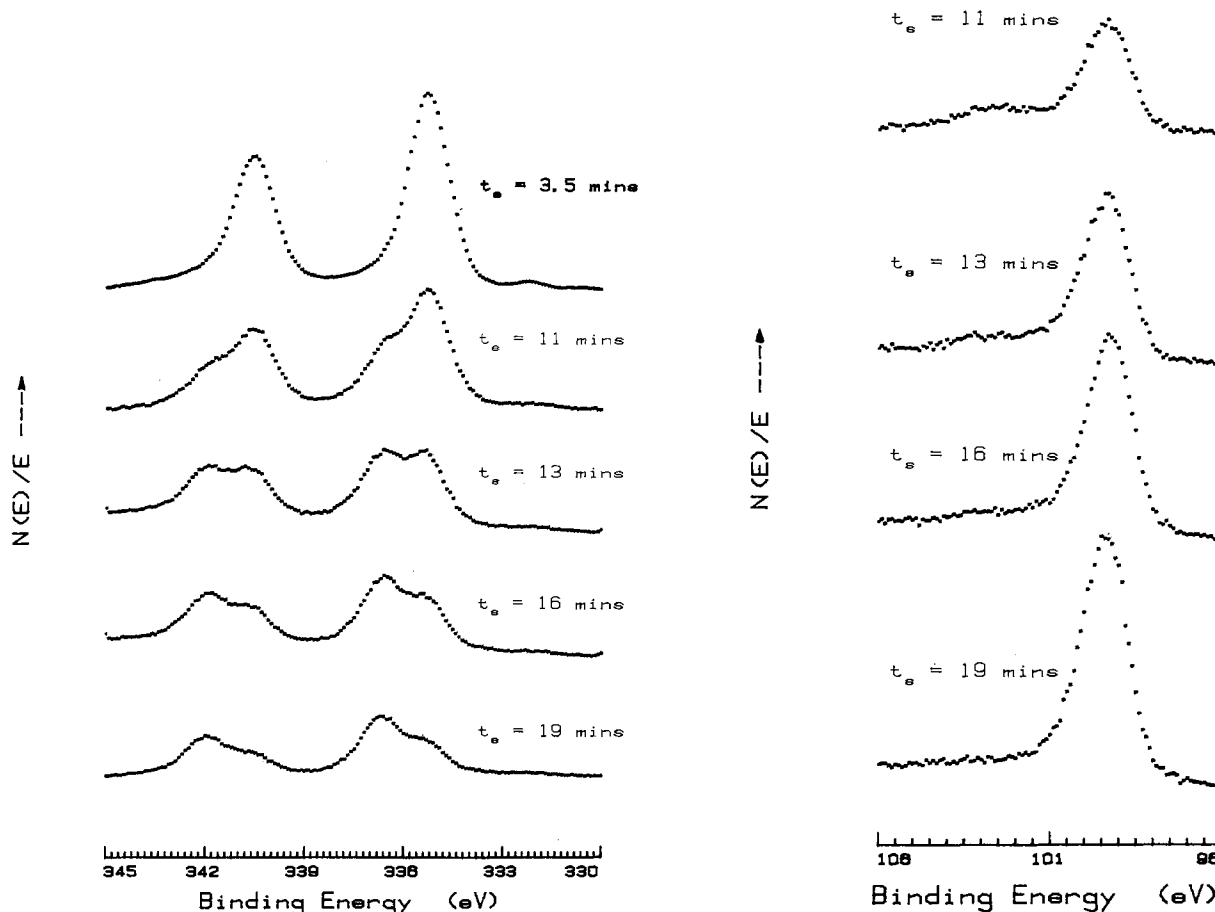


Fig. 4. (A, left) Palladium 3d_{5/2} spectrum as a function of sputter time for the vacuum-aged sample. (B, right) Silicon 2p spectrum as a function of sputter time for the vacuum-aged sample. The sputter rate is 2 Å/min Si and 10 Å/min Pd.

silicide form (15). Since oxygen is observed at the interface, these peaks are also related to nonstoichiometric silicon oxides which correspond to Si₂O₃ and Si₂O, respectively, in Raider and Flitsch's analysis (16). The broadened Si 2p line (FWHM = 1.45 eV) may indicate the presence of substantial hydrogen bonding in the material. For simplicity, it is assumed that the 103 eV Si 2p peak is Si^B and the 336.8 eV Pd 3d_{5/2} peak is Pd^B. The remaining Si 2p peak at 100.6 eV is termed intermediate (Si^I).

Integrating the gaussian components of the palladium and silicon spectra, the relative percentages of palladium and silicon in elemental and bound states are determined. Applying these percentages to the actual total palladium and silicon atom concentration as a function of sputter time (or depth), depth profiles of the bond state concentration of Si and Pd are obtained. These data are plotted in Fig. 5 and 6 for both samples as a function of sputter time. It is interesting to note that the curves due to the Pd^B and Si^B appear to track with depth between 10 and 20 min sputter time. The Si^I concentration is observed well into the silicon substrate material as is the Pd^B. Pd^E is also observed well into the substrate (as also observed by SIMS). The Si^B peak at 103 eV is not observed at these depths. The ratio of Pd^E to Pd^B remains ~1:4 to a sputter time of 35 min. Obviously, a stoichiometric palladium silicide is not formed. The silicide stoichiometry appears to continuously change with depth through the interface into the hydrogenated amorphous silicon substrate. The oxygen concentration after a sputter time of 35 min is ~0.2 a/o and appears to be chemically associated with the silicon (the Pd^B at that depth is associated with a silicide).

It has been implicitly implied that silicide is formed during the device fabrication or thermal aging process. However, the depth profiles were obtained by ion sputtering using 1 keV Xe⁺. Ion mixing effects are severe for Pd on Si and silicides of palladium are

readily formed at low ion doses and energies (17, 18). Therefore, the observed palladium in silicide form (Pd^B) may have formed as a result of sputtering and

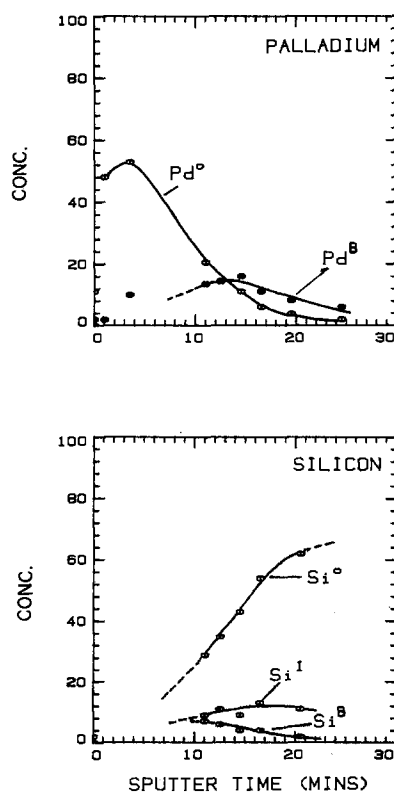


Fig. 5. Bond concentration profile of elemental and bound (A) Pd and (B) Si for the vacuum-aged sample.

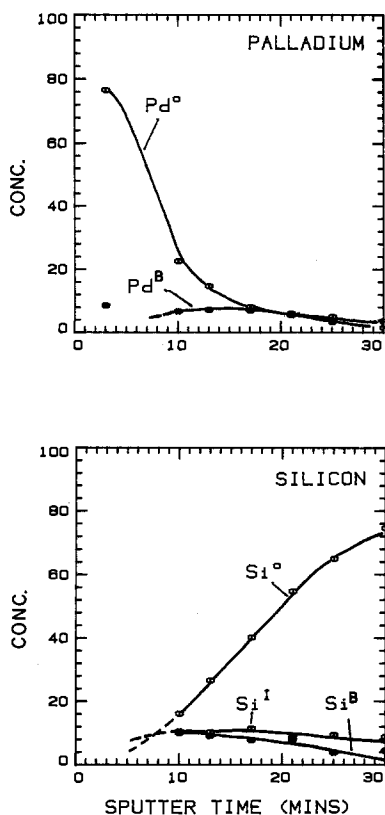


Fig. 6. Bond concentration profile of elemental and bound (A) Pd and (B) Si for the D_2O -aged sample.

subsequent ion-mixing. Using a simple model (see Appendix) which incorporates ion-mixing phenomena, a constant ratio, Pd^E/Pd^B , is predicted for long sputter times. SIMS data show a linear palladium gradient on log-linear coordinates (3, 19) that is, an exponential gradient. From the gradient of these data, the ratio, Pd^E/Pd^B , is found to be near 1:4. Therefore, the silicide observed away from the interface is created by ion-mixing and all the observed palladium is qualitatively elemental palladium.

Conclusions

This study has shown that palladium interdiffuses with hydrogenated silicon at relatively low temperatures to form a diffuse junction containing both oxides and possible silicides. Auger depth profiles show palladium and oxygen extending into the silicon substrate and are in good qualitative agreement with SIMS analysis of similar samples (3). Low temperature diffusion of palladium into single crystal silicon has been reported by Thomas and Terry (20), and the formation of Pd_2Si has been reported by Köster *et al.* (21) for Pd in contact with evaporated amorphous silicon at room temperature. The oxygen concentration is observed to broadly peak in the interface region between Pd and Si and is similar to the results of Pd on crystalline silicon (22). The shape of the peak oxygen distribution may be qualitatively explained by ion-mixing phenomena and a considerably larger oxygen peak content may be present (24). However, the tail into the silicon appears to be real and not an ion-mixing artifact. This is in agreement with SIMS results (3). Thermal aging of Pd/a-Si:H samples in D_2O vapor causes an increase in oxygen concentration ($\sim 5\times$) at the interface between the palladium and silicon relative to that observed in the vacuum-heated sample. Therefore, oxygen or D_2O diffuses through the palladium layer to the interface. SIMS (3) also indicates that deuterium (probably as D_2O) (2) diffuses through Pd.

XPS bond concentration profiles reveal that a transition region (interface), of about 30Å thick, exists. In this region, the palladium is observed to change from

a predominately elemental to the bound state. The bound palladium has tentatively been associated with oxide and ion-induced silicide. Also, in the transition region, silicon is observed in two bonding states believed to be associated in part with the existence of silicides (15). However, due to the small but measurable amount of oxygen extending well into the substrate, these states are also associated with suboxides of silicon (16).

Both the vacuum- and D_2O -aged Pd/a-Si:H samples have an interfacial layer of what appears to be in part a silicide intermixed with silicon suboxides, between 20 and 100Å in extent, depending upon the sputter rate used in the computation. Bound palladium and silicon are observed to peak in this region (Fig. 5 and 6). In comparing the vacuum-aged sample with the D_2O -aged sample, approximately $2\times$ more palladium is associated with silicide in the former. The bond concentration of the Si 103 eV peak is greater in the D_2O -aged sample due to the increased number of Si-O bonds and is in agreement with the Auger results of this study. The bond concentration of the Si 100.6 eV peak (intermediate) is about the same in each sample due to Si-O and Pd-Si bonding. The only significant difference as measured by XPS between the two samples is the Si-O bond concentration.

Diodes fabricated with palladium on a-Si:H exhibit good electrical characteristics (1) with an oxide layer at the interface. However, storing Pd/a-Si:H junctions at $80^\circ C$ in D_2O causes the photovoltaic conversion efficiency to fall by a factor of ~ 5 as compared to vacuum-aged devices (3). This degradation is probably caused by the presence of $\sim 5\times$ more oxygen at the interface of the D_2O -aged sample.

Manuscript submitted June 24, 1980; revised manuscript received Aug. 27, 1980.

Any discussion of this paper will appear in a Discussion Section to be published in the December 1981 JOURNAL. All discussions for the December 1981 Discussion Section should be submitted by Aug. 1, 1981.

Publication costs of this article were assisted by RCA Laboratories.

APPENDIX

Using SIMS depth profile data which indicates that palladium in a-Si:H varies exponentially with depth, x , into the a-Si:H layer and that ion-mixing creates a uniform concentration Pd_xSi region in the ion depth range, w , a simple expression for the XPS peak area ratio can be obtained. The usual expression for peak area which is given by (23)

$$dI_i = n_i \sigma_i K(E_k) \exp(-x/\lambda) dx$$

where I_i = intensity, n_i = atom density of i , σ_i = photoionization cross section, λ = electron escape depth, E_k = kinetic energy of electrons, and $K(E_k)$ = spectrometer transmission \times geometry \times detector efficiency.

To compute the intensity ratio of unbound to bound palladium over the sample depth range, it is assumed that $n_i \propto \exp(-x/x_0)$ at $x > w$ and $n_i = 0$ at $0 \leq x \leq w$. The amount of bound palladium is assumed constant at $0 \leq x \leq w$ and zero at $x > w$. x_0 is assumed as a parameter and will not be defined now. Two equations can be written for unbound and bound palladium, that is

$$I_{Pd^E} = \int_w^\infty n_{Pd^E} \sigma_{Pd} K \exp(-x/\lambda) \exp(-x/x_0) dx$$

and

$$I_{Pd^B} = \int_0^w x_0 N_{Pd^E} \sigma_{Pd} K \exp(-x/\lambda)$$

$$[1 - \exp(-w/x_0)] dx/w$$

where the average palladium concentration in $0 \leq x \leq w$ is given by $(1 - \exp(-w/x_0)) \times N_{Pd^E} x_0/w$. The above expressions are easily evaluated and the ratio $I_{Pd^E}/I_{Pd^B} = F$.

$$F^{-1} = \left\{ \exp \left[\frac{x_0 + \lambda}{x_0 \lambda} w \right] \right\} \{ [1 - \exp(-w/x_0)] [1 - \exp(-w/\lambda)] \} (x_0 + \lambda)/w$$

F was evaluated on an HP-1000 using a simple Fortran IV program as a function of w/λ for various values of x_0 and w . These data are not shown for brevity. However, if real numbers are substituted for λ , x_0 , and w (25, 500, and 15Å, respectively), F is found to be near 1/4. This calculation is very "model sensitive" and is intended to show, semi-quantitatively, how ion-mixing affects the measured XPS spectra. More detailed investigations are being performed in our laboratory.

REFERENCES

- C. R. Wronski, D. E. Carlson, and R. E. Daniel, *Appl. Phys. Lett.*, **29**, 602 (1976).
- D. E. Carlson and C. W. Magee, Photovoltaic Solar Energy Conference, Berlin, April 23-26, 1979.
- D. E. Carlson, *IEEE Trans. Electron. Devices*, ed. **24**, 449 (1977).
- J. H. Thomas, III and A. M. Goodman, *This Journal*, **126**, 1766 (1979).
- C. Wu, Private communication (1979).
- C. J. Powell, *Surf. Sci.*, **44**, 29 (1974).
- L. E. Davis *et al.*, "Handbook of Auger Electron Spectroscopy," Physical Electronics Industries, Eden Prairie, MN (1976).
- J. H. Scofield, *J. Electron. Spectrosc.*, **8**, 129 (1976).
- C. D. Wagner, W. M. Riggs, L. E. Davis, J. F. Moulder, and G. E. Muilenberg, "Handbook of X-Ray Photoelectron Spectroscopy," Perkin-Elmer Corp., Eden Prairie, MN (1979).
- D. A. Shirley, *Phys. Rev. B*, **5**, 4709 (1972).
- G. Wertheim and S. Hufner, *J. Inorg. Nucl. Chem.*, **38**, 1701 (1976).
- T. L. Barr, *J. Phys. Chem.*, **82**, 1801 (1978).
- D. E. Eastman, J. K. Cashion, and A. C. Switendick, *Phys. Rev. Lett.*, **27**, 35 (1971).
- F. J. Grunthaler and J. Maserjian, in "The Physics of SiO₂ and Its Interfaces," p. 389, Pergamon Press, New York (1978).
- J. H. Thomas III, Unpublished results on Pd, Pt, Mo silicides (1979).
- S. I. Raider and R. Flitsch, *IBM J. Res. Dev.*, **22**, 294 (1978).
- Z. L. Liao, B. Y. Tsaur, and J. W. Mayer, *J. Vac. Sci. Technol.*, **16**, 121 (1979).
- Z. L. Liao, J. W. Mayer, W. L. Brown, and J. M. Poate, *J. Appl. Phys.*, **49**, 5295 (1978).
- D. E. Carlson, C. W. Magee, and J. H. Thomas III, *Solar Cells*, **1**, 371 (1979/80).
- S. Thomas and L. E. Terry, *Appl. Phys. Lett.*, **26**, 294 (1978).
- U. Köster, D. R. Campbell, and K. N. Tu, *Thin Solid Films*, **53**, 129 (1978).
- L. L. Tongson, B. E. Knox, T. E. Sullivan, and S. J. Fonash, *J. Appl. Phys.*, **50**, 1535 (1979).
- C. J. Powell and P. E. Larson, *Appl. Surf. Sci.*, **1**, 186 (1978).
- P. Williams and J. E. Baker, *Appl. Phys. Lett.*, **36**, 842 (1980).

A New Technique for Antimony Diffusion into Silicon

M. Nanba

Hitachi Limited, Central Research Laboratory, Kokubunji, Tokyo 185, Japan

ABSTRACT

A new technique using auxiliary silicon wafers lapped with Al₂O₃ powder has been developed for Sb diffusion into silicon. Diffusion wafers are set face to face with those wafers in an open-tube system with Sb₂O₃ as the dopant source. This technique can easily attain a carrier concentration as high as the solid solubility of Sb in silicon without surface defects such as surface erosion. Carrier concentration is controlled by changing the distance between the diffusion and auxiliary wafers. In addition, it is confirmed that higher diffused areas on the diffusion wafers correspond to the lapped areas of the auxiliary wafers.

In bipolar IC fabrication technology, Sb buried layers are more effective than As buried layers for lowering the autodoping from the buried layer during epitaxial growth (1). However, two problems remain in conventional Sb diffusion with Sb₂O₃ source. One is surface defects such as surface erosion (2, 3), which hinders normal epitaxial growth. The other is the difficulty in obtaining high carrier concentrations at the surface of the diffused layer (4). Although SbCl₃ and Sb(C₂H₅O)₃ have been proposed as dopant sources to avoid the former problem, the latter problem has not been resolved (5, 6).

This work presents a new Sb diffusion technique which avoids both the problems described above. This new diffusion system consists of an open-tube furnace for use with Sb₂O₃ and auxiliary silicon wafers lapped with Al₂O₃ powder which are set face to face with the diffusion silicon wafers. The strong point of this technique is its utilization of auxiliary silicon wafers.

The diffusion silicon wafers employed in this study were CZ, (100) oriented, p-type, and 10-30 Ω-cm

wafers. The front surface of the diffusion wafer was damage-free mirror polished, and the back was chemically etched. Both surfaces of the auxiliary silicon wafers were polished with No. 1200-1500 grit Al₂O₃ powder. Before setting in a holder, these auxiliary wafers were thermally oxidized in wet oxygen atmosphere (O₂ bubbled through 90°C H₂O) to prevent the diffusion wafers from outdiffusion of Al₂O₃. Since the sheet resistance (ρ_s) of the diffusion wafer depended on the number of uses of the auxiliary wafer, the wafer was changed every experiment.

Figure 1 shows a schematic representation of the present diffusion system. Dry nitrogen was used as the carrier gas. In the first zone of the furnace shown in this figure, the Sb₂O₃ source was held in a platinum boat and heated to 750°C. In the second zone, the diffusion and auxiliary wafers were held on a fused silica holder at 1200°C. The front surface of the diffusion wafer (s) was set face to face with the auxiliary wafer. The distance between the diffusion and auxiliary wafers (d) was varied from 2 to 24 mm to investigate the influence of this distance on concentration profile. Concentration profiles of Sb were obtained by the

Key words: silicon, Sb diffusion, Sb₂O₃, auxiliary wafer, Al₂O₃.

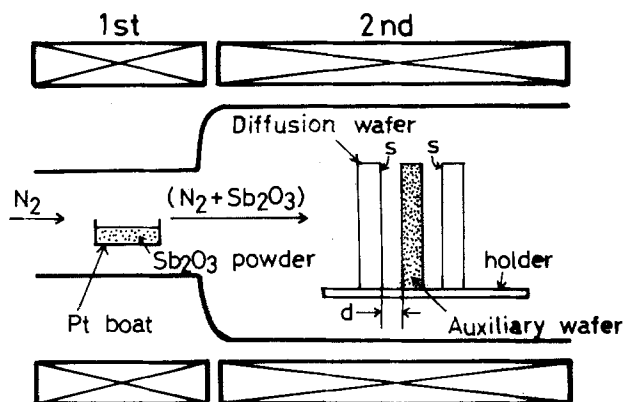


Fig. 1. Schematic design of the experimental apparatus. The marks s and d denote the front surface of the diffusion wafer and the distance between the diffusion and auxiliary wafers, respectively.

differential conductivity method (7) as well as Rutherford backscattering method. Surface erosion density was evaluated from optical microscopy. The sheet resistance (ρ_s) homogeneity map on a diffusion wafer was measured by a fully automated four-point probe.

The carrier concentration profiles obtained by the present and conventional techniques are shown in Fig. 2. Although the diffusion conditions of the present technique are quite similar to those of the conventional one, the concentration obtained by our technique is about 3 times as high as that by the conventional technique. Moreover, it should be noted that the surface concentration obtained by our technique is equal to the solid solubility ($6 \times 10^{19} \text{ cm}^{-3}$) (8), which is the highest concentration in the reported values at 1200°C (4, 9, 10).

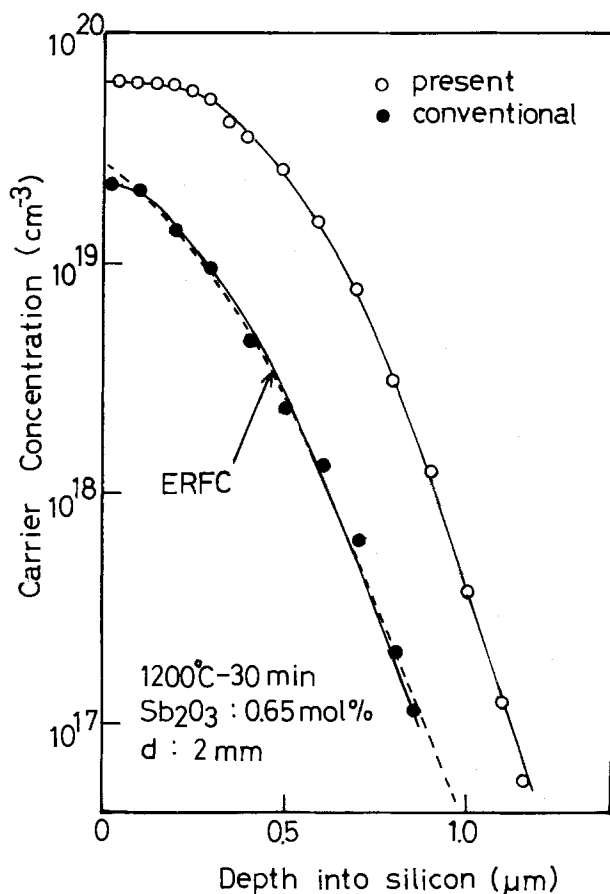


Fig. 2. Carrier concentration profiles obtained by the present (○) and conventional techniques (●).

In this figure, a plot of the error function complement (erfc) is also shown for comparison with the experimental data. Since the profile obtained by the conventional technique roughly fits the erfc, it is possible to estimate the effective diffusion coefficient ($2.6 \times 10^{-13} \text{ cm}^2/\text{sec}$), which agrees with that reported by Fuller *et al.* (9). On the other hand, the profile obtained by the present technique differs from the erfc. This suggests that the Sb diffusion coefficient depends on the surface concentration, as do phosphorus and boron (7, 11, 12).

When the ρ_s of the diffusion layer was $40 \Omega/\square$, the surface defect density in the wafer diffused by our technique was about 1 cm^{-2} , while that by the conventional one was about 10 cm^{-2} . Therefore, this technique is more useful than the conventional one in practical use.

Figure 3 shows the dependence of the carrier concentration on the distance (d). The surface concentrations are $6.0, 5.0, 4.0, 2.7,$ and $2.2 \times 10^{19} \text{ cm}^{-3}$ for d of 2, 4, 8, 16, and 24 mm, respectively. It is evident that the surface concentration can be controlled by changing the d . The effect of the auxiliary wafer becomes weak as the d increases. Then the carrier profile at the d of 24 mm is equal to that obtained by the conventional technique as known in Fig. 2. These results indicate that the auxiliary wafers play an important role on the Sb diffusion.

The reciprocal of the sheet resistance ($1/\rho_s$), *i.e.*, sheet conductance (σ_s), corresponds to the net carrier distribution in the diffusion wafer. The σ_s of the profiles shown in Fig. 3 are 42.5, 33.3, 24.2, 16.5, and 12.1 mV for d of 2, 4, 8, 16, and 24 mm, respectively.

Here we will define σ_s^p and σ_s^c as the sheet conductance obtained by the present and conventional techniques, respectively. Therefore, the value ($\sigma_s^p - \sigma_s^c$) can be considered to reveal the effect on the Sb diffusion obtained by the present technique. The ($\sigma_s^p - \sigma_s^c$) are 30.4, 21.2, 12.1 and 4.4 mV for d of 2, 4, 8, and 16 mm, respectively.

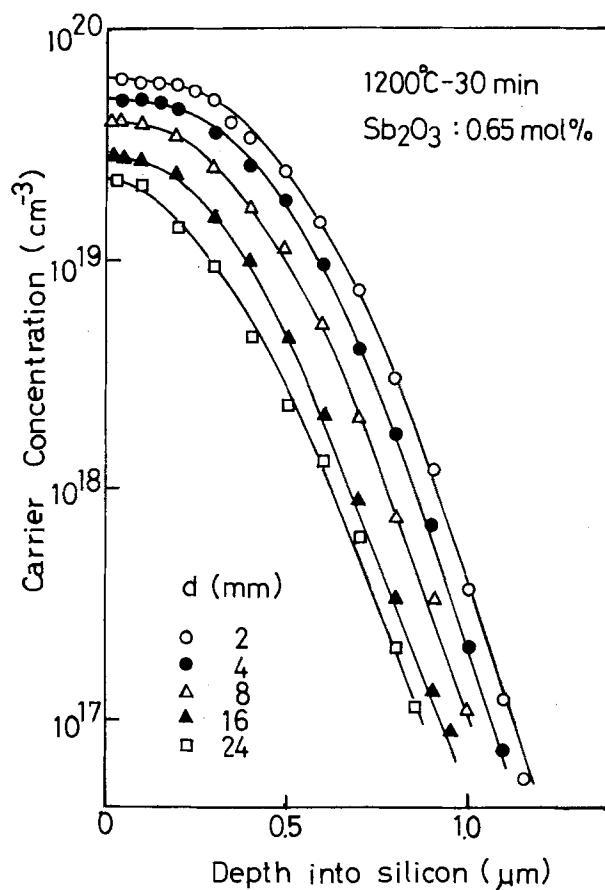


Fig. 3. Dependence of the carrier concentration on the distance between the diffusion and auxiliary wafers (d).

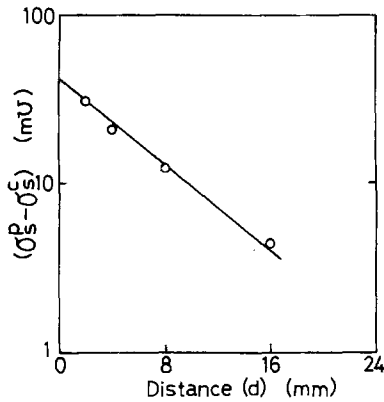


Fig. 4. The $(\sigma_s^p - \sigma_s^c)$ vs. the distance between the diffusion and auxiliary wafers (d). The σ_s^p and σ_s^c show the sheet conductance obtained by the present and conventional techniques.

Figure 4 shows the relation between the $(\sigma_s^p - \sigma_s^c)$ and the d . This relation is represented by

$$(\sigma_s^p - \sigma_s^c) = \sigma s o \exp\left(-\frac{d}{\lambda}\right) \quad [1]$$

where $\sigma s o$ is 43 mV and λ is 6.8 mm. From Eq. [1], it is easily seen that the smaller distance (d) is, the larger $(\sigma_s^p - \sigma_s^c)$ is.

Figures 5 (a)-(c) are surface photographs of the auxiliary wafers. Areas marked by M and L denote the mirror and lapped surfaces, respectively. Figures 5 (d)-(f) are the ρs homogeneity maps of the diffusion wafers obtained after Sb diffusion using the auxiliary wafers shown in Fig. 5 (a)-(c), respectively. This result shows that the areas of the lower ρs on the diffusion wafers agree with the lapped areas of the auxiliary wafers.

These results look as if some diffusant is emitted from the surface of the auxiliary wafers. The diffusant is estimated to be the dopant source (Sb_2O_3) or the abrasives (Al_2O_3). Therefore the Sb and Al contents in the Sb glass layer grown on the diffusion wafer should be analyzed. Further investigation is needed.

Figures 6(a) and (b) show 330 keV $^4\text{He}^+$ Rutherford backscattering spectra for the diffusion wafer with and without glass layer, respectively. The yield of Sb in a glass layer obtained by the present technique is about 10% that by the conventional one. On the other hand,

the yield of Sb in silicon obtained by the former technique is higher than that by the latter. This result is curious.

However, it should be noted that the spectrum in glass layer measured by Rutherford backscattering is mainly due to Sb_2O_3 , which is the main component in the layer (9). Since it is implausible that Sb_2O_3 diffuses into silicon (9), the contributory diffusant is not Sb_2O_3 , but elemental Sb. Thus, it is concluded that the Sb diffusion is not simply governed by the Sb_2O_3 concentration in the glass layer. If one allows the above interpretation, the results of Rutherford backscattering is not contrary to the carrier concentration profiles in Fig. 2 and 3.

From the point of view described above, it can be considered that the carrier concentration in silicon depends strongly on the diffusant concentration at the glass-silicon interface. In this case, it is reasonable to consider that the concentration of elemental Sb obtained with the present technique is higher than that obtained with the conventional one at the interface because the carrier concentration in silicon obtained with the former technique is higher than that with the latter one, as seen in Fig. 2 and 3.

Although this increase in the concentration of elemental Sb at the interface is clearly ascribable to the auxiliary wafer, it is not easy to explain this mechanism, nor the role of the auxiliary wafer, at present. Further investigation is necessary.

Acknowledgment

The author is indebted to Mr. M. Wada for his assistance in sample preparation; to Dr. K. Yagi for sheet

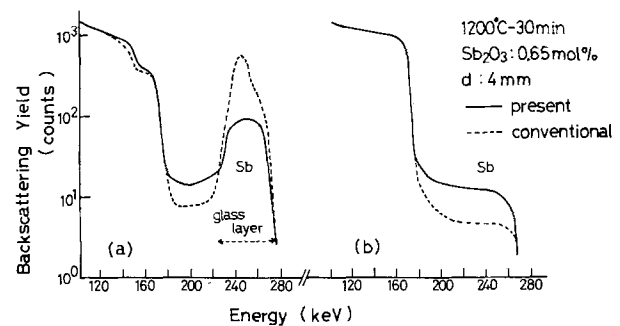
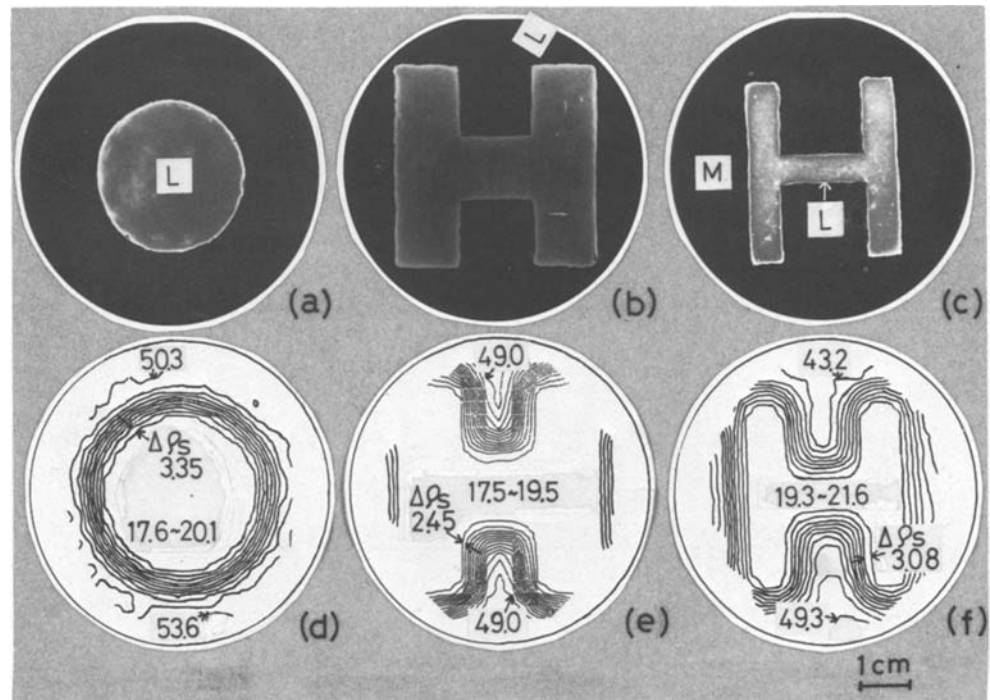


Fig. 6. Rutherford backscattering spectra (330 keV $^4\text{He}^+$) from the diffusion wafer with glass layer (a) and without glass layer (b).

Fig. 5. Relation between (a), (b), and (c) of the surface conditions in the auxiliary wafers and (d), (e), and (f) of the sheet resistance (ρs) homogeneity maps in the diffusion wafers. The marks M and L denote the mirror and lapped surfaces, respectively.



resistance homogeneity map measurement; and to Mr. N. Natsuaki for Rutherford backscattering measurement. The author is also indebted to Mr. H. Kozuka for his useful discussions and to Dr. A. Shintani and Mr. S. Isomae for a critical reading of the manuscript.

Manuscript submitted April 2, 1980; revised manuscript received Aug. 1, 1980.

Any discussion of this paper will appear in a Discussion Section to be published in the December 1981 JOURNAL. All discussions for the December 1981 Discussion Section should be submitted by Aug. 1, 1981.

Publication costs of this article were assisted by Hitachi, Limited.

REFERENCES

1. G. Mitsuhashi, *NEC Res. Dev.*, **36**, 68 (1975).
2. A. LaRocque, R. Yatsko, and A. Quade, *This Jour-*

3. A. Goetzberger, *Solid-State Electron.*, **5**, 61 (1962).
4. F. L. Gittler, and R. A. Porter, *This Journal*, **117**, 1551 (1970).
5. W. R. Runyan, "Silicon Semiconductor Technology," p. 146, McGraw-Hill Co., New York (1965).
6. F. L. Gittler, Paper 94 presented at The Electrochemical Society Meeting, Dallas, Texas, May 7-12, 1967.
7. E. Tannenbaum, *Solid-State Electron.*, **2**, 123 (1961).
8. F. A. Trumbore, *Bell System Tech. J.*, **39**, 205 (1960).
9. C. S. Fuller and J. A. Ditzenberger, *J. Appl. Phys.*, **27**, 544 (1956).
10. J. J. Rohan, N. E. Pickering, and J. Kennedy, *This Journal*, **106**, 705 (1959).
11. N. D. Thái, *J. Appl. Phys.*, **41**, 2859 (1970).
12. R. K. Jain and R. Van Overstraeten, *ibid.*, **44**, 2437 (1973).

Planarization of Phosphorus-Doped Silicon Dioxide

A. C. Adams* and C. D. Capiro

Bell Laboratories, Murray Hill, New Jersey 07974

ABSTRACT

A process has been developed for smoothing surfaces of phosphorus-doped silicon dioxide (P-glass). Samples are coated with a positive photoresist which flows during application to form a relatively smooth surface. The photoresist is etched in a CF_4 - O_2 plasma using conditions that etch the photoresist and the P-glass at nearly the same rates. Since the surface profile of the photoresist is preserved during etching, the P-glass is left with a relatively smooth surface. This process reduces step heights, usually by at least 50%, and decreases the angles at abrupt steps to 5° - 30° . In contrast to the flowed P-glass process, planarization does not require high temperatures and is independent of phosphorus concentration.

A primary cause of metallization failures in integrated circuit devices is incomplete metal coverage over oxide steps (1-3). Several techniques have been developed to improve the metal coverage by providing smaller or less abrupt steps. These techniques include: P-glass flow (3, 4), tapered etching (3, 5-9), and localized oxidation (3, 10-16). Recently another technique, surface leveling or planarization, which is shown schematically in Fig. 1, has been described (17, 18). In Fig. 1, an abrupt step in phosphorus-doped silicon dioxide (P-glass) is covered with a sacrificial organic coating. Since the organic material has a low viscosity, flow occurs during application or during a low temperature bake to give a relatively smooth surface with small, gentle steps. By etching the organic material using conditions that etch the sacrificial coating and the P-glass at nearly the same rates, the original profile of the coating material is maintained, leaving the P-glass surface with only small, gentle steps. This technique has been described for smoothing surfaces by sputter etching (17). The present paper describes a process for planarizing phosphorus-doped silicon dioxide films deposited over steps in polycrystalline silicon. The factors that affect the planarization are described, and the planarization technique is compared with the flowed glass process.

Experimental Procedure

The samples are etched in a parallel-plate, radial-flow reactor that has been described previously (19, 20). The etcher has an electrode spacing of 3.1 cm and an electrode area of 1250 cm². Ten 75 mm silicon wafers can be etched at one time. The phosphorus-doped sili-

con dioxide is deposited at 450°C using the reaction between silane, phosphine, and oxygen at atmospheric pressure. The phosphorus concentrations are determined by measuring sheet resistivities of the silicon substrates (on p-type monitor wafers) after a 20 min, 1100°C diffusion, and have been checked by infrared measurements and etch rate determinations (21). Unless stated otherwise, the phosphorus concentrations are approximately 6 weight percent (w/o).

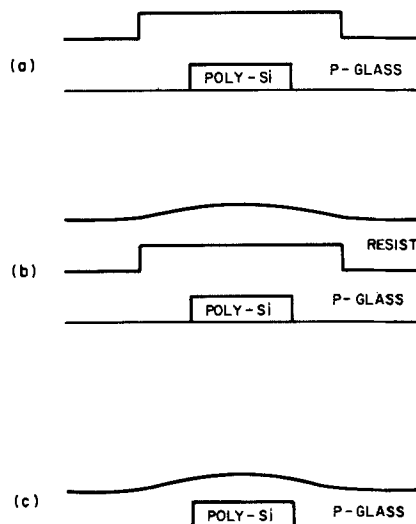


Fig. 1. Schematic representation of the planarization process: (a) poly-Si step covered with P-glass; (b) coated with resist; (c) after etching the resist leaving a relatively smooth P-glass surface.

* Electrochemical Society Active Member.

Key words: dielectrics, etching, integrated circuits.

Stylus measurements of the surface profiles are made with a Taylor-Hobson Talystep using a fine stylus, with a truncated pyramidal shape and a tip dimension of $0.1 \times 2.5 \mu\text{m}$. Most experiments use test structures containing $0.4 \mu\text{m}$ thick polycrystalline silicon, anisotropically etched in a $\text{Cl}_2\text{-C}_2\text{F}_6$ plasma to give vertical walls (20, 22), and covered with $1.0\text{-}1.5 \mu\text{m}$ of 6% P-glass. An alternate structure contains $1.2 \mu\text{m}$ of thermally grown silicon dioxide, etched to give a 45°C taper (7), and covered with $1.0 \mu\text{m}$ of 6% P-glass. The sacrificial coatings are all applied by standard photolithographic spinning techniques.

Planarization

Coatings.—Three organic resists have been examined as sacrificial coatings: HPR-204, a positive photoresist from Philip A. Hunt Chemical Corporation; AZ-111, a positive photoresist from Shipley Company, Incorporated; and PIQ, a polyimide resist from Hitachi Chemical Company. Surface profiles after P-glass deposition, after application of the organic coating, and after etching are given in Fig. 2. The profile of the P-glass after deposition shows cusps at the top of the step and crevices or thinning at the bottom. The maximum step height, from the top of the cusp to the bottom of the crevice, is $1.5 \mu\text{m}$. After coating, the profiles are smoother; the steps become much less abrupt and the maximum step height decreases to $0.6\text{-}0.8 \mu\text{m}$ because the coating materials tend to flow and fill-in at the bottom of the steps (curves marked A). The profile of the P-glass after etching the sacrificial layer tends to follow the original profile when the coating material is HPR-204 or PIQ (curves marked B). In both cases, the step heights increase by only $0.1 \mu\text{m}$ during etching to give final heights of $0.8\text{-}0.9 \mu\text{m}$ (compared to $1.5 \mu\text{m}$ in the original P-glass). The AZ-111 occasionally cracks during etching, possibly because of very strong adhesion between the resist and the P-glass, and leaves a crazed surface with little smoothing (as shown in Fig. 2). Of the three materials examined, the HPR-204 is preferred. It flows at a low temperature, produces a smooth surface, and etches at a rate similar to that of P-glass (discussed later).

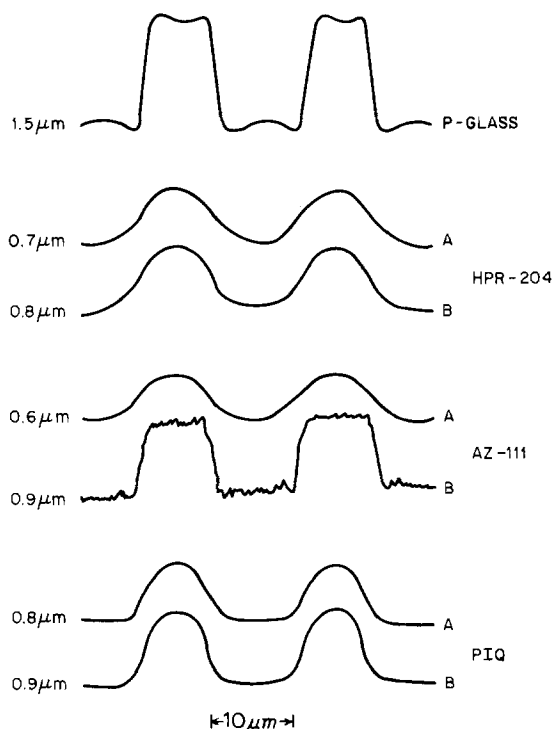


Fig. 2. Surface profiles with different coating materials: A, profiles of the resist surface after coating; B, profiles of the P-glass surface after planarization; step heights are given for each surface.

The amount of smoothing depends on the thickness of the coating material, as illustrated in Fig. 3 which shows the surface profiles obtained with different thicknesses of HPR-204 ($1.0, 1.4,$ and $1.8 \mu\text{m}$). After deposition, the P-glass has the characteristic cusps and crevices with a maximum step height of $0.61 \mu\text{m}$. Application of the HPR-204 provides a large reduction in step height and the formation of a very gentle topography. After etching, the step heights increase slightly but are still much less than the original height after deposition. The cusps and crevices are completely removed during planarization. In addition, the angles made by the P-glass going over the steps are reduced from about 90° after deposition to less than 20° after planarization. As the resist thickness increases, the surfaces become smoother. However, the thicker resists require longer etch times and cause a decrease in the reproducibility in the P-glass thickness after etching. Consequently, the $1.0 \mu\text{m}$ thickness is preferred.

The effect of baking the HPR-204 is shown in Fig. 4. At bake temperatures above about 150°C , the resist softens and flows providing a large decrease in step height (the solid circles) which is also observed in the P-glass surface after planarization (the open circles). The etch rate of the HPR-204 in a $\text{CF}_4\text{-O}_2$ plasma, measured in $\text{\AA}/\text{min}$ and shown by the squares, is independent of the bake temperature. The thickness of the HPR-204 is affected by the bake temperature, decreasing linearly from $1.10 \mu\text{m}$ after a 90°C bake to $0.82 \mu\text{m}$ after the 215°C treatment. Baking above 150°C is recommended because of the improved topography and because of decreased defects (discussed later).

The decrease in step height depends on the width of the line or space being covered. Relevant data using three thicknesses of HPR-204, all baked at 90°C , are given in Fig. 5. After P-glass deposition the maximum step height is about $0.60 \mu\text{m}$ and is independent of the feature size. After coating with the HPR-204, the step height is reduced to less than $0.25 \mu\text{m}$. As the

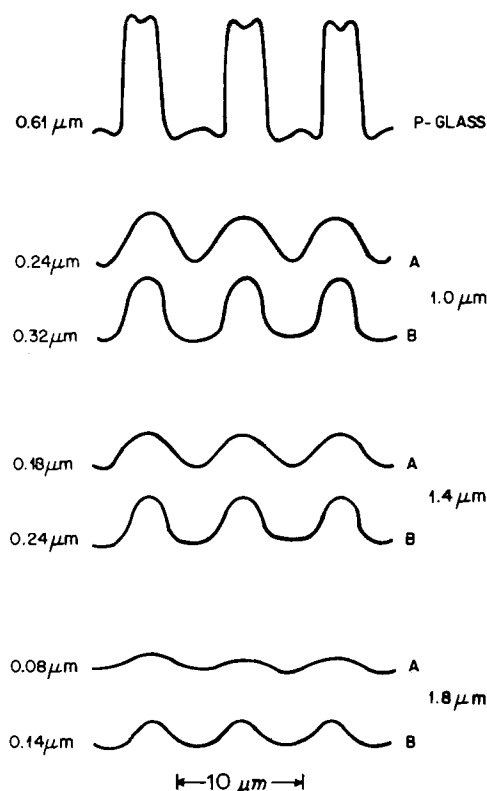


Fig. 3. Surface profiles obtained with different thicknesses of HPR-204; A, profiles of the resist surface after coating; B, profiles of the P-glass surface after planarization; step heights are given for each surface.

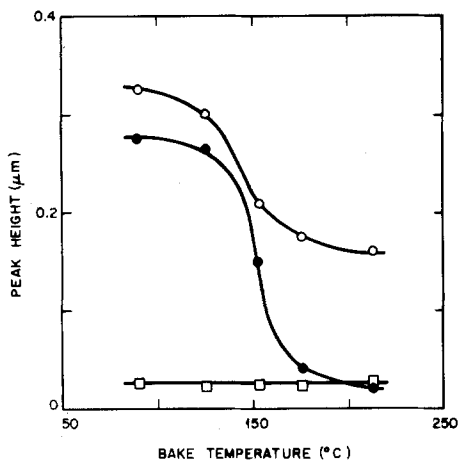


Fig. 4. Maximum peak height vs. bake temperature for HPR-204: solid circles, after coating; open circles, after planarization; squares, etch rate in Å/min of the HPR-204 in a CF₄-8% O₂ plasma.

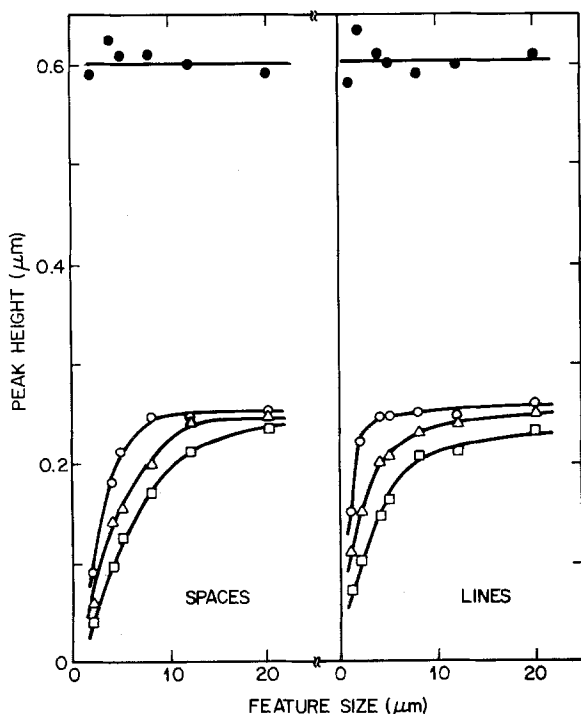


Fig. 5. Maximum peak height vs. feature size for three thicknesses of HPR-204 baked at 90°C: open circles, 1.0 μm ; triangles, 1.4 μm ; squares, 1.8 μm ; closed circles, P-glass after deposition.

feature size decreases the step height decreases further, and steps of less than 0.1 μm are observed for very narrow lines or spaces. The reduction in step height is greater for the thicker coatings, as previously shown. Flowing the resist at temperatures above 150°C gives step heights that are less than 0.1 μm and are nearly independent of feature size over the range measured. The P-glass surfaces after planarization show a similar behavior to Fig. 5 but with the step heights increased by about 0.1 μm . The angles made by the P-glass after planarization are about 13° and are nearly independent of the feature size and the resist thickness.

Etching.—The etch rates of HPR-204, PIQ, and P-glass in CF₄-O₂ plasmas are shown in Fig. 6-8. The etch rates increase in the order, P-glass < HPR-204 < PIQ for each of the variables investigated (gas composition, rf power, and sample temperature). Although the etch rates are affected by changes in these variables, the ratio of the HPR-204 etch rate to the P-glass etch rate remains nearly constant, and conditions giving equal etch rates have not been found. This

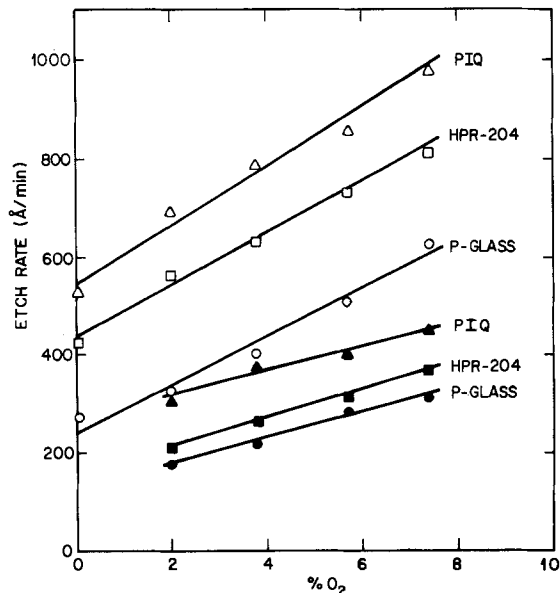


Fig. 6. Etch rate vs. gas composition for CF₄-O₂ mixtures at 0.4 Torr and 28°C: open points, 700W; closed points, 130W.

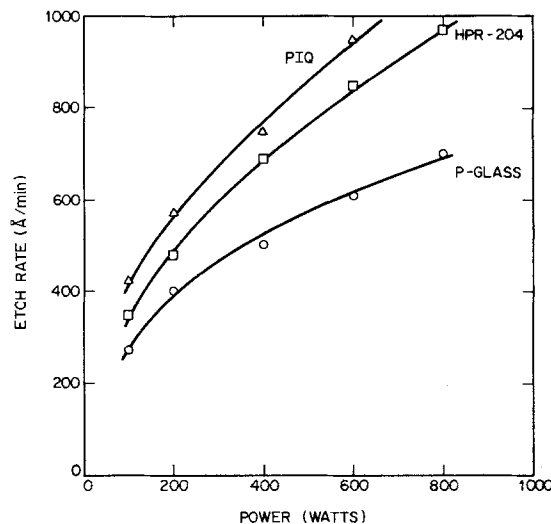


Fig. 7. Etch rate vs. power for CF₄-8% O₂ at 0.4 Torr and 28°C

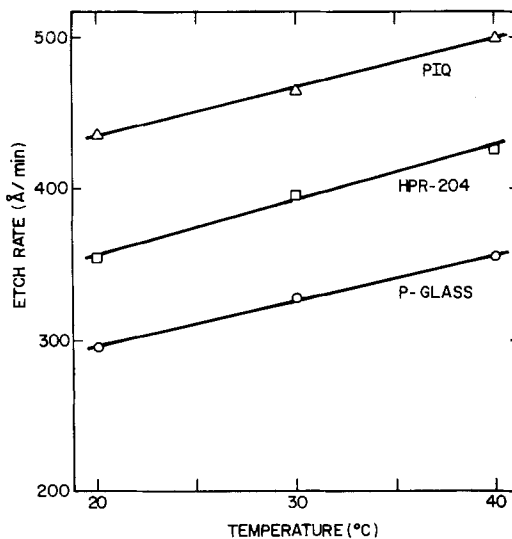


Fig. 8. Etch rate vs. sample temperature for CF₄-8% O₂ at 0.4 Torr and 130W.

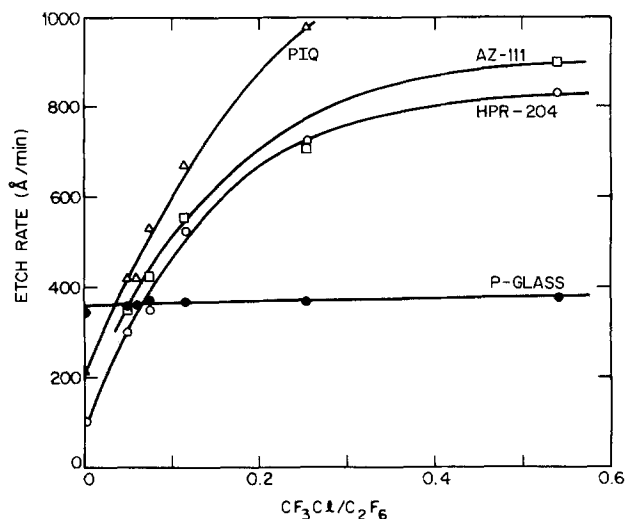


Fig. 9. Etch rate vs. gas composition for $\text{CF}_3\text{Cl}-\text{C}_2\text{F}_6$ mixtures at 0.4 Torr, 800W, and 28°C.

difference in etch rates causes the slight increase in step height as samples coated with HPR-204 are planarized (Fig. 2-4).

Etch rates in a $\text{CF}_3-\text{C}_2\text{F}_6$ plasma are shown in Fig. 9 as a function of the gas composition. The etch rates of the organic materials increase in the order: $\text{HPR-204} < \text{AZ-111} < \text{PIQ}$, and all increase as the $\text{CF}_3\text{Cl}/\text{C}_2\text{F}_6$ ratio increases. In contrast, the etch rate of the P-glass is nearly constant. Equal etch rates for the HPR-204 and the P-glass are obtained at a $\text{CF}_3\text{Cl}/\text{C}_2\text{F}_6$ ratio of about 0.07. Unfortunately, P-glass samples planarized with a $\text{CF}_3\text{Cl}-\text{C}_2\text{F}_6$ plasma are left with a very rough surface that consists of long nodules or fingers that increase in length as the etching time increases. This rough surface occurs with all three coating materials, and with $\text{CO}_2-\text{C}_2\text{F}_6$ plasmas and with C_2F_6 alone. The rough surface appears to be characteristic of P-glass planarization with C_2F_6 but has not been investigated further. The rough surface is not observed when samples are planarized with CF_4-O_2 .

The etch rate of silicon in a CF_4-O_2 plasma depends on the quantity of material being etched (the loading effect) (23). This effect also occurs when P-glass and resist are etched during planarization. The loading effect during planarization shown by the data in Fig. 10 is smaller than that observed for silicon (23). The small loading effect is a disadvantage of the CF_4-O_2 plasma etching, but it has not caused serious problems during the planarization of devices.

Planarization process.—The recommended processing sequence for planarization is as follows. The phos-

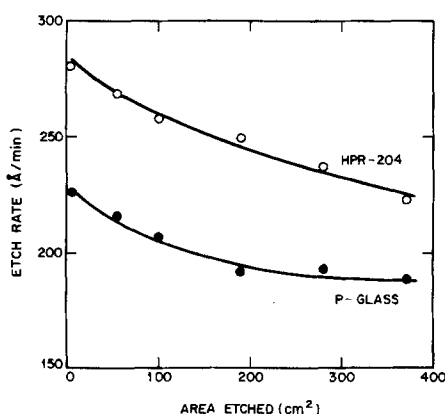


Fig. 10. The loading effect for HPR-204 and P-glass in $\text{CF}_4-8\% \text{O}_2$ at 0.4 Torr and 100W.

phorus-doped silicon dioxide (4-6 w/o P) is deposited to give a thickness of 1.5 μm . After deposition the samples are scrubbed to remove particles and then baked at 180°C for 45 min. The HPR-204 resist is applied (1.0 μm thick). The samples are given a final bake at 180°C for 20 min and then planarized using $\text{CF}_4-8\% \text{O}_2$ at 100W and 0.4 Torr. The thickness of P-glass after planarization is approximately 0.8 μm .

Surfaces and cross sections of samples after P-glass deposition and after planarization using the above process are shown in the SEM photographs in Fig. 11. It is evident that planarization completely removes the cusps and crevices and decreases the step height and the angle made by the P-glass. For most topographies, planarization reduces step heights by at least 50% and reduces the angles to less than 30°.

Defects.—Several types of defects associated with the planarization process have been observed. Pinholes or cracks in the P-glass lead to large holes in the silicon substrates since the etch rate of silicon in the CF_4-O_2 plasma, about 1000 Å/min, is much larger than the etch rate of P-glass. The holes in the silicon have been observed only on samples etched for very long times. Craters etched in the P-glass, usually 0.1-0.5 μm deep and about 10 μm in diameter, are occasionally observed. The craters are probably caused by moisture on the P-glass surface or solvent in the resist coating. The water or solvent vaporizes in the vacuum chamber to form a bubble in the HPR-204, thus allowing the P-glass to etch prematurely. These craters can be eliminated by baking the HPR-204 above 150°C. Mounds, approximately 10-20 μm in diameter and 0.5-1.0 μm high, have also been observed after planarization. These mounds, which are probably caused by particles on the original P-glass surface, are eliminated by scrubbing the P-glass after deposition. Striations are occasionally present in the HPR-204 and are transferred to the P-glass during planarization. The striations do not appear to cause serious problems since the thickness variations across the striations are only 0.05-0.10 μm .

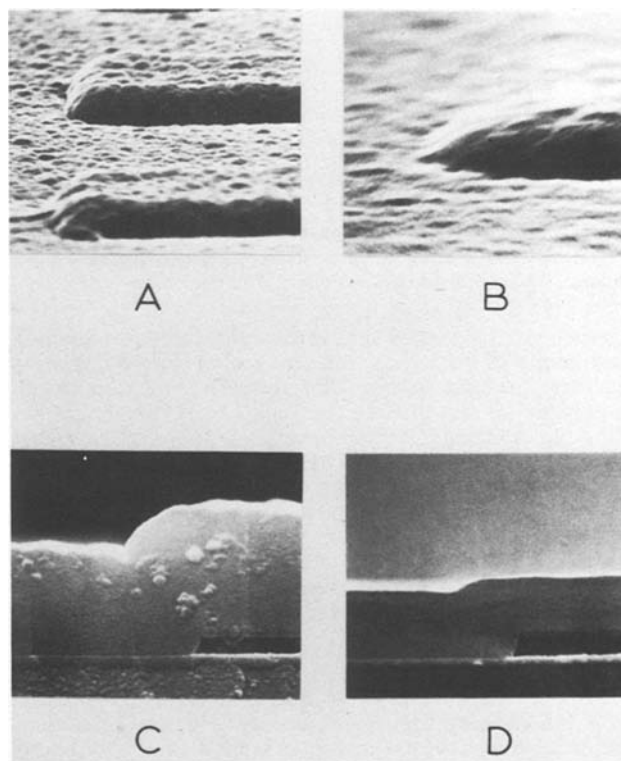


Fig. 11. SEM photographs of P-glass covering a polysilicon line: A, after deposition, 8 KX; B, after planarization, 26 KX; C, cross section after deposition, 15 KX; D, after planarization, 18 KX.

Comparison with P-glass Flow

Plasma planarization provides a smooth surface by altering the topography of the P-glass. Flowing the P-glass by heating to high temperatures also changes the P-glass topography. It is interesting to compare the two processes. The SEM photographs in Fig. 12 show a polycrystalline silicon line crossing an oxide step with the entire surface covered with P-glass (4.6 w/o P). The samples have been treated in steam at 1100°C for different times. Flow is indicated by the progressive loss of detail. As shown in Fig. 12, flow is normally a kinetic or rate phenomenon with the amount of flow strongly dependent on the time. Samples usually do not reach an equilibrium state during flow.

Flow is shown as a function of the phosphorus concentration in the SEM cross sections in Fig. 13. As deposited, the P-glass has a concave or retrograde angle with a cusp at the top of the step and a thin region at the bottom. As the phosphorus concentration increases, flow increases giving a decrease in the angle made by the P-glass going over the step.

Quantitative measurements of flow can be obtained from the SEM cross sections by measuring the angle made by the P-glass. The data in Fig. 14 show the angles for samples annealed in steam, nitrogen, or oxygen at 1100°C and in steam at 1050°C. Also shown are angles for planarized samples (the dashed line). The trends observed in Fig. 14 are in good agreement with those previously reported (14). Flow is similar in oxygen or nitrogen but increases significantly in steam. If flow occurs by the breaking and reforming of chemical bonds, then the increased flow in steam probably results from the rapid, reversible hydrolysis of the P-O bonds. The angle made by 6.5% P-glass after flowing at 1100°C for 20 min is 45°-65°. This is much greater than the angles observed on similar structures after planarization (28°, independent of the phosphorus concentration).

An additional comparison of planarization and P-glass flow is provided by the SEM photographs in Fig. 15. The cross sections show 1.5 μm of 7.2% P-glass covering 1.0 μm steps of polycrystalline silicon. Sam-

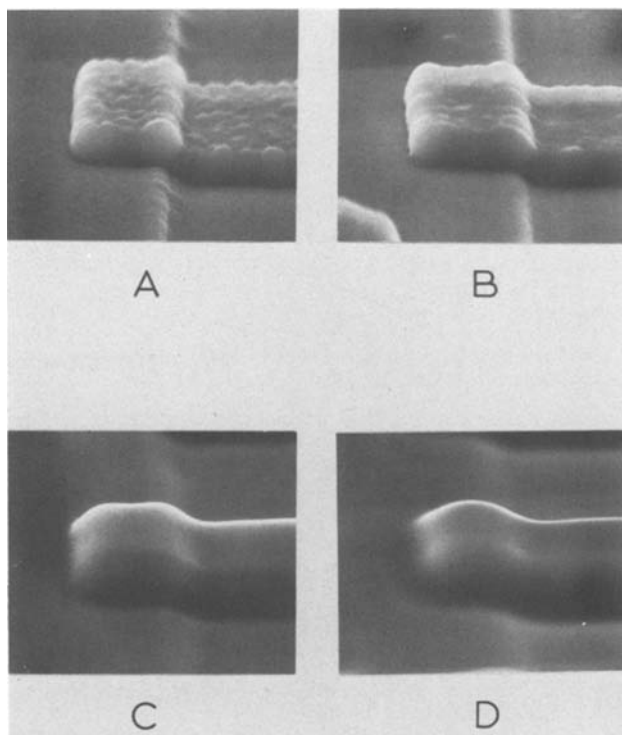


Fig. 12. SEM photographs at 3.2 KX showing surfaces of 4.6% P-glass annealed in steam at 1100°C: A, 0 min; B, 20 min; C, 40 min; D, 60 min.

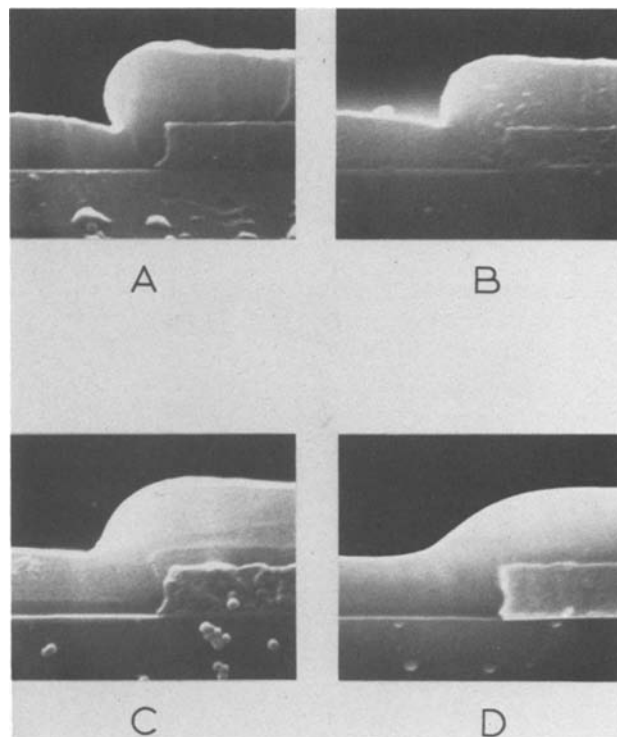


Fig. 13. SEM cross sections at 10 KX for samples annealed in steam at 1100°C for 20 min: A, 0.0% P; B, 2.2% P; C, 4.6% P; D, 7.2% P.

ples are shown after P-glass deposition, after flow in nitrogen at 1100°C for 20 min, and after planarization in a $\text{CF}_4\text{-O}_2$ plasma for 60 min. The sample showing the P-glass after deposition has been etched in dilute hydrofluoric acid to make the polycrystalline silicon easier to see. The step heights and angles for the three samples are: 1.60 μm and 122° after deposition; 1.32 μm and 42° after P-glass flow; and, 0.56 μm and 10° after planarization. It is obvious that planarization provides a greater reduction in step height and a much greater decrease in the angle made by the P-glass going over the step.

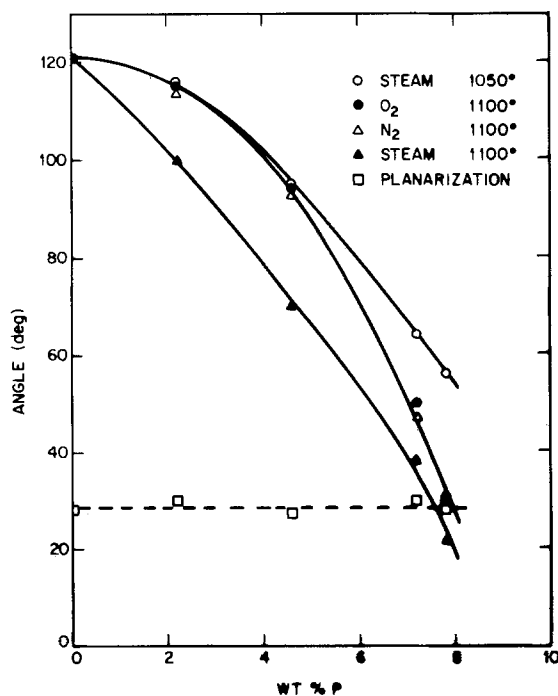


Fig. 14. Surface angles made by the P-glass vs. P-concentration for different annealing conditions.

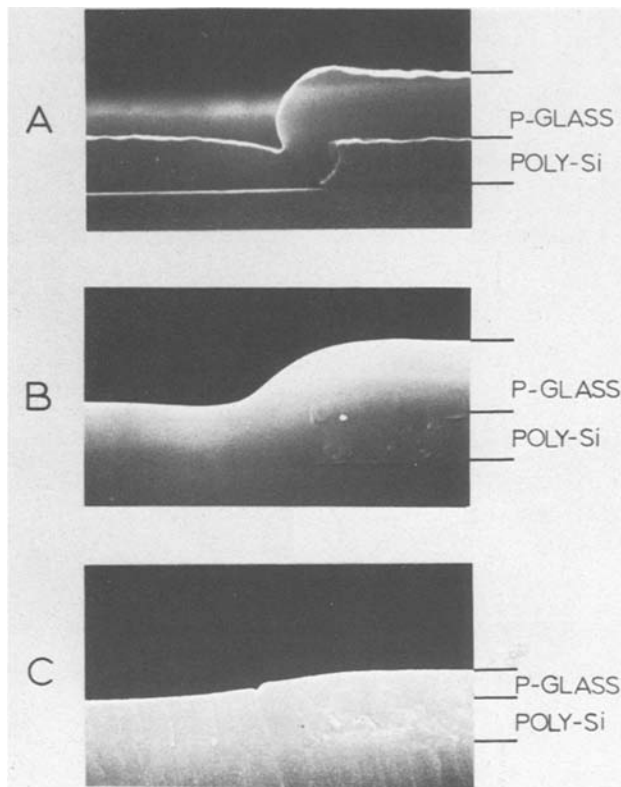


Fig. 15. SEM cross sections at 10 KX showing 7.2% P-glass: A, as deposited; B, after flow in N_2 at $1100^\circ C$ for 20 min; C, after planarization.

The viscosity of phosphorus-doped silicon dioxide can be calculated by assuming fourfold bonding and using known values for the viscosities and activation energies of SiO_2 and P_2O_5 (24). Calculated values are shown in Fig. 16 for three flow temperatures. Although the detailed relationship between viscosity and flow is not known, Fig. 16 can still provide useful information. Assuming that a sample containing 6.5% phosphorus has adequate flow at $1100^\circ C$, then decreasing the flow temperature to $1050^\circ C$ requires an increase

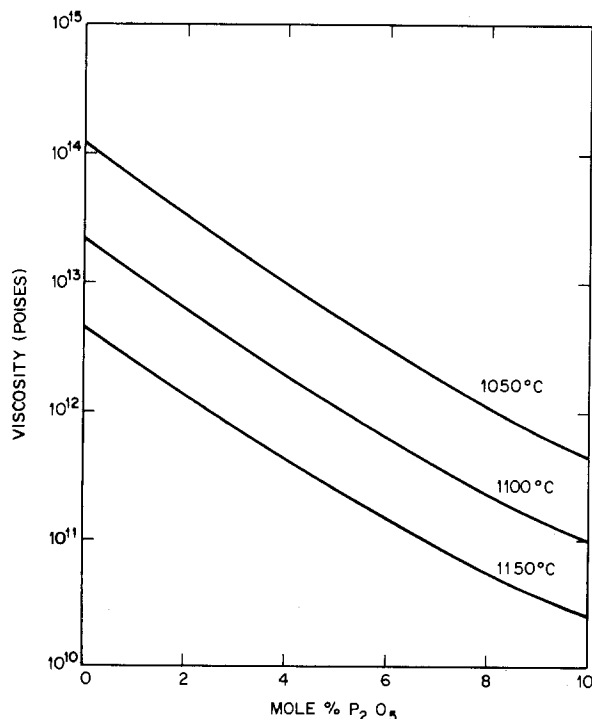


Fig. 16. Calculated viscosity of P-glass vs. composition

in phosphorus concentration to 9.5% (to obtain the same viscosity). Such a high phosphorus concentration is not compatible with aluminum metallization. Similarly, a decrease in phosphorus concentration to 3.5% P requires an increase in the flow temperature to $1150^\circ C$, which would have deleterious effects on diffused junctions in semiconductor devices. This illustrates the severe restrictions on the phosphorus concentration and on the flow temperature for the flowed glass process. These restrictions do not apply to the planarization process where the maximum temperature is less than $200^\circ C$ and where phosphorus concentrations of 0-8% P have been used with nearly equal results.

Summary and Conclusions

A process for smoothing or planarizing surfaces of phosphorus-doped silicon dioxide has been described. Planarization is achieved by coating the P-glass with a sacrificial coating and then plasma etching using conditions that etch the coating and the P-glass at nearly equal rates. The preferred material for the sacrificial layer is HPR-204. Other materials etch too rapidly or crack during etching. The preferred etching gas is CF_4 -8% O_2 . Gas mixtures containing C_2F_6 provide a better etch rate ratio, but leave a very rough surface. The planarization process typically reduces step heights by about 60% and reduces the angles made by the P-glass going over steps to less than 30° . However, the final surface depends strongly on the original topography and on the sacrificial layer. Surfaces become smoother for small feature sizes, and are made smoother by using thick resist and by flowing the resist before planarization.

Methods have been found for eliminating or minimizing the defects that are caused by planarization. These defects are: mounds, caused by particles on the P-glass; craters, caused by moisture on the surface or solvent in the resist; holes etched in the silicon substrate, caused by pinholes or cracks in the P-glass; and, striations in the P-glass caused by the striations in the resist.

The planarization process has been compared to the flowed glass process. Planarization reduces step heights and leaves angles of 5° - 30° . The flowed glass process gives very little reduction in step height and leaves surface angles of 45° - 65° . The flowed glass process requires temperatures of 1050° - $1100^\circ C$ and phosphorus concentrations of 6-7%. Planarization is a low temperature process, less than $200^\circ C$, and is nearly independent of the phosphorus concentration. These features make planarization a very attractive process for fabricating devices with small dimensions.

Acknowledgments

The authors would like to thank J. E. McNulty for much of the plasma etching; E. I. Povilonis for help in processing samples; and H. J. Levinstein and W. T. Lynch for many discussions.

Manuscript submitted May 7, 1980; revised manuscript received Aug. 12, 1980.

Any discussion of this paper will appear in a Discussion Section to be published in the December 1981 JOURNAL. All discussions for the December 1981 Discussion Section should be submitted by Aug. 1, 1981.

Publication costs of this article were assisted by Bell Laboratories.

REFERENCES

1. T. Yanagawa and I. Takekoshi, *IEEE Trans. Electron Devices*, **ed-17**, 964 (1970).
2. C. J. Santoro and D. L. Tolliver, *Proc. IEEE*, **59**, 1403 (1971).
3. J. L. Vossen, G. L. Schnable, and W. Kern, *J. Vac. Sci. Technol.*, **11**, 60 (1974).
4. W. E. Armstrong and D. L. Tolliver, *This Journal*, **121**, 307 (1974).
5. L. H. Hall and D. L. Crosthwait, *Thin Solid Films*, **9**, 447 (1972).

6. R. A. Moline, R. R. Buckley, S. E. Haszko, and A. U. MacRae, *IEEE Trans. Electron Devices*, ed-20, 840 (1973).
7. G. I. Parisi, S. E. Haszko, and G. A. Rozgonyi, *This Journal*, 124, 917 (1977).
8. J. C. North, T. E. McGahan, D. W. Rice, and A. C. Adams, *IEEE Trans. Electron Devices*, ed-25, 809 (1978).
9. H. Ono and H. Tango, *This Journal*, 126, 504 (1979).
10. J. A. Appels, H. Kalter, and E. Kooi, *Phil. Tech. Rev.*, 31, 225 (1970).
11. J. A. Appels, E. Kooi, M. M. Paffen, J. J. H. Schatorje, and W. H. C. G. Verkuylen, *Phil. Res. Rep.*, 25, 118 (1970).
12. J. A. Appels and M. M. Paffen, *ibid.*, 26, 157 (1971).
13. E. Kooi, J. G. van Lierop, W. H. C. G. Verkuiljen, and R. de Werdt, *ibid.*, 26, 166 (1971).
14. R. Edwards, R. S. Payne, C. F. Gibbon, M. L. Olmstead, R. A. Moline, D. L. Kushler, G. R. Weber, and R. T. Kraetsch, in "Semiconductor Silicon 1973," H. R. Huff and R. R. Burgess, Editors, p. 905, The Electrochemical Society Softbound Proceedings Series, Princeton, N.J. (1973).
15. E. Bassous, H. N. Yu, and V. Maniscalco, *This Journal*, 123, 1729 (1976).
16. H. Sakai, T. Yoshimi, and K. Sugawara, *ibid.*, 124, 318 (1977).
17. Y. Hom-ma, S. Harada, and T. Kaji, *ibid.*, 126, 1531 (1979).
18. E. F. Labuda, Private communication.
19. C. J. Mogab, A. C. Adams, and D. L. Flamm, *J. Appl. Phys.*, 49, 3796 (1978).
20. A. C. Adams and C. D. Capio, *This Journal*, 123, 366 (1981).
21. A. C. Adams and S. P. Murarka, *This Journal*, 126, 334 (1979).
22. C. J. Mogab and H. J. Levinstein, *J. Vac. Sci. Technol.*, 17, 721 (1980).
23. C. J. Mogab, *This Journal*, 124, 1262 (1977).
24. C. R. Hammond, *Phys. Chem. Glasses*, 19, 41 (1978).

Convective Interference and "Effective" Diffusion-Controlled Segregation during Directional Solidification under Stabilizing Vertical Thermal Gradients; Ge

Douglas E. Holmes¹ and Harry C. Gatos*

*Department of Materials Science and Engineering,
Massachusetts Institute of Technology, Cambridge, Massachusetts 02139*

ABSTRACT

Convection and segregation phenomena during vertical directional solidification of Ga-doped Ge under stabilizing vertical thermal gradients were investigated. Microscopic growth rates were determined by interface demarcation, compositional profiles by single point spreading resistance measurements, and thermal characterization of the melt by direct thermal probing. It was found that destabilizing horizontal temperature gradients, even in melts with a diameter as small as 3 mm, led to convection with pronounced effects on solidification. Turbulent convection resulted in microscopic growth rate-controlled dopant inhomogeneities similar to those observed for solidification under destabilizing vertical gradients. Under laminar convection dopant inhomogeneities were caused by perturbations in boundary layer thickness. Macro-segregation under both turbulent and laminar convection was controlled by the boundary layer thickness. A model based on diffusive and convective fluxes was developed describing laminar fluid flow and segregation; an experimental correlation between segregation and the Rayleigh number, consistent with the model, was obtained. Indirect evidence for diametrically antisymmetric fluid flow in the melt was obtained from lateral microsegregation across the interface. Theoretical and experimental results showed that complete elimination of convective interference is virtually impossible; however, "effective" diffusion-controlled segregation was achieved at relatively high growth rates and low Rayleigh numbers.

An understanding of the effects of convective heat and mass transport on the solidification process is of fundamental importance in assessing and/or defining the parameters which control the liquid-solid phase transformation. In addition, convective effects often preclude the extrapolation of macroscopic solidification parameters to segregation on a microscale, thereby preventing quantitative evaluation of cause-effect relationships between solidification parameters and materials properties.

Convection-related segregation effects have been recognized for many crystal growth configurations including the Czochralski (1), horizontal Bridgman (2),

and destabilizing vertical thermal gradient (3) geometries. Directional solidification under stabilizing vertical thermal gradients, on the other hand, has been employed for the purpose of minimizing convective interference (4). However, virtually no quantitative characterization of the effect of destabilizing horizontal temperature gradients in the melt, which are virtually unavoidable, has been carried out. Such gradients, although they may be reduced to very small values, invariably lead to convective flow. Recently, techniques have become available for the direct determination of solidification parameters on a macro- and microscale for dilute binary alloy semiconductor systems (3).

The present investigation was undertaken to study segregation in a vertical directional configuration with

* Electrochemical Society Active Member.

¹ Present address: Hughes Research Laboratories, Malibu, California 90265.

Key words: convection, solidification, interfaces.

stabilizing vertical thermal gradients employing recently developed techniques. Emphasis was placed on the correlation of convection and segregation processes, and on the identification of practical limitations associated with minimizing convective interference in high temperature systems in the light of horizontal thermal gradients.

Apparatus and Procedures

A diagram of the crystal growth apparatus employed in this investigation is shown in Fig. 1. A precast polycrystalline germanium charge doped with gallium to the desired level was brought into contact with a $\langle 100 \rangle$ germanium seed contained in a cylindrical ampul. The outer quartz tube positioned between two water-cooled brass-plates permitted control of the ambient atmosphere. Melting of the charge was carried out in two stages. First, with the outer heater the temperature of the system was raised to 800°C and was maintained constant throughout the experiment. Then, the inner heater was employed for melting the charge from top to bottom until the melt touched the seed. The system was then allowed to reach thermal equilibrium. Melting and equilibration were monitored visually through the gold-coated heat reflector and a window in the outer heater ceramic mandrel.

Solidification was initiated and allowed to proceed by controlled power reduction in the inner heater. Vertical temperature gradients in the melt during thermal equilibration ranged from 28° to 75°C/cm. Control of radial heat losses through the sample-ampul wall was achieved by adjusting the relative position of the inner and outer heaters and the ampul, and by independently controlling the power in each heater. The microscopic solidification rate would be varied up to 42 $\mu\text{m}/\text{sec}$.

Interface demarcation (5) was employed to determine the microscopic growth rates and interface morphology; pulses of 18 A/cm², of 50-80 msec duration, and at frequencies between 0.1-1 Hz were applied across the growth interface.

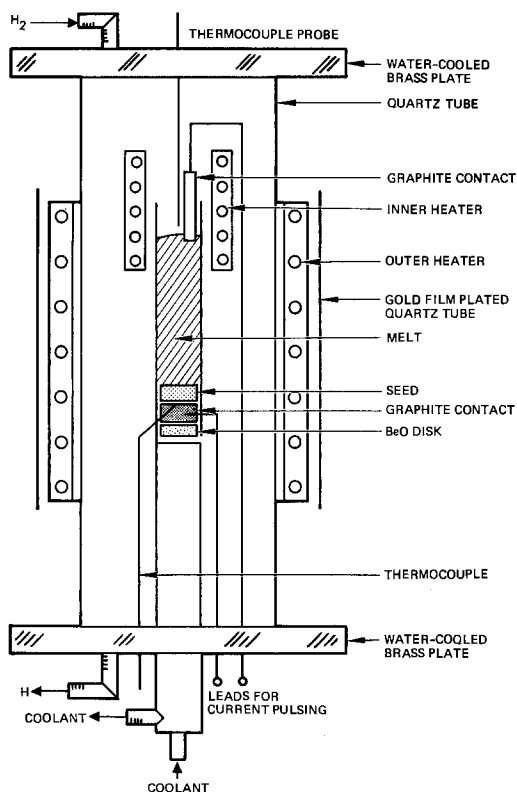


Fig. 1. Schematic arrangement of the apparatus used for the study of crystal growth under stabilizing vertical temperature gradients.

Growth and segregation analyses were performed on crystal segments cut along the growth axis, the segments were polished and etched (1 HF + 1 CH₃COOH + 1 H₂O₂) to reveal segregation effects and interface demarcation lines by interference contrast microscopy.

Carrier concentrations were determined with a single point spreading resistance probe (6) with a spacial resolution of about 5 μm . Spreading resistance data were converted directly to carrier concentration employing a calibration curve constructed from the average spreading resistance of 6 standard samples with carrier concentrations ranging from $9 \times 10^{16} \text{ cm}^{-3}$ to $1.2 \times 10^{20} \text{ cm}^{-3}$, as determined by Hall effect measurements.

Thermal characterization of the melt was carried out with a movable thermal probe (inserted through the top of the furnace) which could be positioned at any desired melt height. The most sensitive and durable probe was constructed of a 0.030 in. Omega Chromel-Alumel sheath thermocouple with a thin ceramic coating to prevent chemical attack and to provide electrical insulation. The time constant was 0.38 sec. A similarly constructed thermocouple was positioned just below the seed.

Temperature gradients in the liquid at the interface, during solidification, were determined by measuring the temperature at one position in the melt (typically 1.5 cm from the initial interface). The interface demarcation current pulses were inductively sensed by the thermal probe and were registered as instantaneous pen deflections on the temperature recorder. Thus, a direct time correspondence between the temperature at the probe tip and the interface demarcation lines (solidification behavior) could be made (3). Since the interface temperature is known, the gradient was calculated assuming a linear profile. The temperature gradient in the solid near the interface during solidification was obtained from the temperature registered by the thermocouple below the seed and the distance from the thermocouple to the advancing growth interface as determined from the interface demarcation lines in the crystal.

The temperature gradient in the liquid near the interface, G_L , was also determined by a second approach, i.e., it was calculated from the boundary condition for unidirectional heat flow at the solid-liquid interface, i.e.

$$G_L = \frac{k_s G_s - \rho H R}{k_L} \quad [1]$$

where k_s and k_L are the thermal conductivities of the solid and liquid, respectively, G_s is the temperature gradient in the solid, ρ is the density, H is the heat of fusion per gram, and R is the solidification rate. Agreement between the two types of determinations of G_L was generally within 20%.

A series of experiments were carried out in which the following geometrical, thermal, and growth parameters were studied: (i) the inside ampul diameter was varied from 3 to 9 mm, (ii) graphite and quartz ampuls were used which have relatively high and low thermal conductivity, respectively, (iii) the average vertical temperature gradient in the melt during solidification was varied from 15°C/cm to 60°C/cm, (iv) the average microscopic growth rate was varied from 8 to 21 $\mu\text{m}/\text{sec}$, (v) the amount and type of concentric thermal insulation was varied, and (vi) an ambient atmosphere of hydrogen and of argon were employed.

Results and Discussion

Thermal characterization of the melt.—In order to determine the temperature gradient as a function of melt height, continuous temperature recordings were obtained at various positions in the melt as the Ge charge was melted. Continuous recordings obtained from a 5.5 cm high melt in a 9 mm diam cylinder as

shown in Fig. 2, exhibited random temperature fluctuations throughout the melt with amplitudes of up to 7°C, indicating turbulent convective behavior.

The vertical temperature gradient in the central portion of this melt ($\partial T/\partial X$) was smaller than in the upper and lower regions ($\partial T'/\partial X$). This behavior is characterized by the Nusselt number, Nu, defined as the ratio of the total longitudinal heat flux in the melt and the conductive heat flux. In the present case, Nu can be expressed as

$$\text{Nu} = (\partial T'/\partial X)/(\partial T/\partial X) \quad [2]$$

and it was found to be > 1 .

It has been shown (8-10) that Nu exceeds 1 at the onset of turbulent convection. It is, thus, confirmed that turbulent convection prevailed in the above solidification configuration. Since the vertical gradient was stabilizing, the turbulent behavior resulted from unavoidable horizontal gradients. In all other experiments, in which the ampul diameter was 5 mm or less, the temperature fluctuations exhibited periods of 1.5 to 3.5 min and amplitudes between 0.1° and 0.7°C. Representative values of Nu measured in these melts equaled 1. These characteristics are indicative of laminar convection, although the presence of near-oscillatory convection (11) cannot be ruled out.

Microsegregation.—Microsegregation characteristics in the crystals grown were determined from high resolution etching in conjunction with phase contrast microscopy, compositional profiles, and microscopic growth rate measurements. Crystals grown in 9 mm diam ampuls generally exhibited pronounced dopant inhomogeneities over the 5 mm segment first to solidify, as shown in Fig. 3A. The inhomogeneities are identified as remelt striations which intersect each other at various angles and indicate a complex pattern of transient-backmelting occurring alternately on the right- and on the left-hand side of the crystals. The spacing of the striations corresponded to about 10 sec intervals. During this stage of solidification, the nature of the thermal field underwent a transition from static

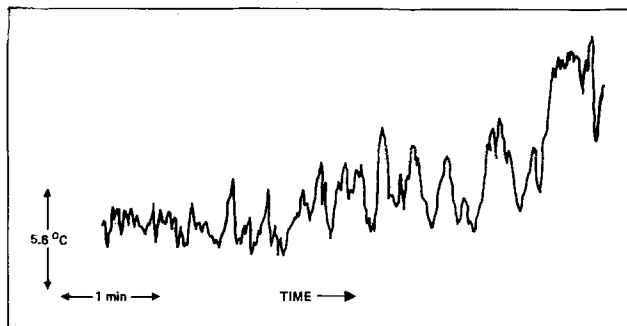


Fig. 2. Continuous temperature recording obtained during melt equilibration from a 9 mm diam, 55 mm high melt at a position 3 mm above the solid-liquid interface.

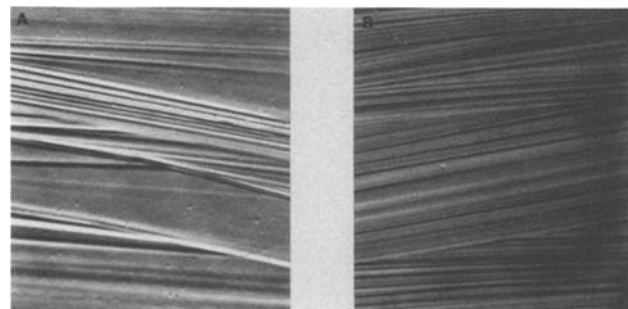


Fig. 3. Comparison of etched longitudinal segments of Ga-doped Ge crystals grown under turbulent convection resulting from destabilizing horizontal (A) and destabilizing vertical (B) thermal gradients. $\sim 200\times$.

(melt equilibration) to dynamic (programmed cooling) and the interface shape changed from convex (with respect to the solid) to wavy ("S"-shaped).

A one-to-one correlation between temperature fluctuations in the liquid adjacent to the solid-liquid interface during growth and remelt striations could not be made. However, the period of remelt striations was similar to the period of temperature fluctuations during melt equilibration (5-10 sec). Thus, it can be concluded that turbulent convection prevailed during the first stage of solidification. The virtual disappearance of the dopant inhomogeneities (as deduced from chemical etching) as growth proceeded, indicates a significant reduction in amplitude of the temperature fluctuations.

The segregation characteristics described above bear a striking similarity to those observed in an earlier study (Fig. 3B) on solidification under turbulent convection arising from destabilizing vertical gradients (3). In this earlier investigation an inverted Bridgman configuration was employed. With continued growth downward (decreasing melt height), the melt experienced successively turbulent, oscillatory, and laminar convection with correspondingly different growth and segregation behavior. Under conditions of turbulent convection, the frequency of remelt striations (shown in the figure) was found to correlate directly with the measured temperature fluctuations. By analysis of the measured microscopic growth rate and dopant concentration, the BPS relationship (12) was found to be applicable

$$C_s = \frac{k_0 C_L}{k_0 + (1 - k_0) \exp(-R\delta/D)} \quad [3]$$

where C_s is the dopant concentration in the solid, C_L is the dopant concentration in the bulk melt, k_0 is the equilibrium distribution coefficient, R is the microscopic growth rate, δ is the diffusion boundary layer thickness, and D is the diffusion coefficient of the dopant in the melt. It has been concluded that dopant inhomogeneities incorporated under turbulent convection were induced by changes in the microscopic growth rate and that boundary layer fluctuations were secondary.

A direct segregation analysis was not possible in the present investigation in view of the limited resolution of interface demarcation lines under pronounced backmelting. However, the similarity between segregation characteristics in the present and earlier studies and the correlation of remelt striations and temperature fluctuations in both cases can be taken as evidence that, in the present case also, microsegregation was controlled primarily by the microscopic growth rate under turbulent convection. This cause and effect relationship is apparently independent of the orientation of the destabilizing thermal gradient with respect to the gravitational field.

Pronounced dopant inhomogeneities were virtually eliminated under laminar convection. However, broadly spaced inhomogeneities were occasionally observed, as shown in Fig. 4A. These inhomogeneities were observed in regions grown under enhanced radial heat flow, as indicated by the pronounced concave shape of the demarcation lines.

The dopant concentration and microscopic growth rate along the spreading resistance impact traces visible in Fig. 4A are shown in Fig. 4B. It is seen that dopant concentration maxima do not coincide with growth rate maxima. Since the distribution coefficient of Ga in Ge is less than one, these results clearly indicate that in this case microsegregation is not controlled by the microscopic growth rate, but apparently by the boundary layer thickness.

Macrosegregation.—Longitudinal and radial macrosegregation profiles were obtained with spreading resistance by scanning at 50-250 μm intervals. The radial

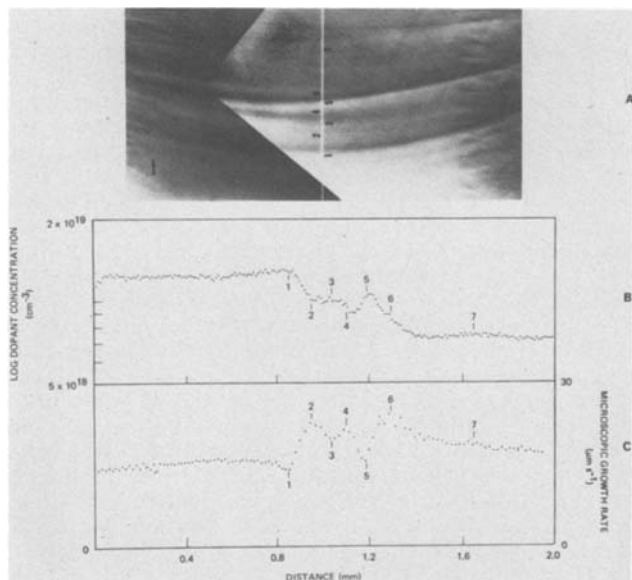


Fig. 4. Microsegregation analysis of Ge crystal grown under laminar convection: (A) micrograph of dopant inhomogeneities ("banding") across the crystal, (B) compositional analysis, (C) growth rate analysis. The increased concavity of the interface shape in this region suggests a transitory period of enhanced radial heat flow. Note that concentration maxima do not coincide with growth rate maxima.

scans were adjusted for interface curvature in order to represent the dopant concentration along the solid-liquid interface at a given time during growth.

The longitudinal macro-compositional profile of a 9 mm diam crystal is shown in Fig. 5 where the ratio of the dopant concentration at the growth interface (C_s) and the initial bulk liquid concentration (C_0) is plotted as a function of solidification distance (x). The experimental profile is shown together with the theoretical profile for diffusion-controlled segregation (13), given by

$$\frac{C_s}{C_0} = \{k_0 + (1 - k_0) [1 - \exp(-Rk_0x/D)]\} \quad [4]$$

and the normal freeze (complete stirring) profile (14) given by

$$\frac{C_s}{C_0} = k_0(1 - f_s)k_0^{-1} \quad [5]$$

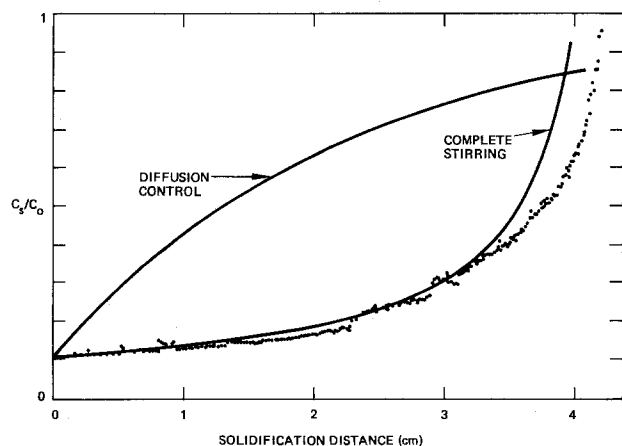


Fig. 5. Comparison of experimental longitudinal macrocompositional profile with theoretical curves for diffusion control and complete stirring (normal freeze). The experimentally determined average microscopic growth rate and bulk melt composition were $8 \mu\text{m sec}^{-1}$ and $1.1 \times 10^{19} \text{ cm}^{-3}$, respectively. For the calculations we took $D = 1.5 \times 10^{-4} \text{ cm}^2 \text{ sec}^{-1}$ and $k_0 = 0.087$.

where R is the average microscopic growth rate and f_s is the fraction solidified.

It is seen that the experimental profile is in good agreement with Eq. [5] indicating that high convective stirring reduces the diffusion boundary layer thickness to very small values. Thus, it is concluded that macrosegregation under turbulent convection is controlled by the boundary layer thickness. It is of interest to note that longitudinal compositional profiles of some 3 mm and 5 mm diam crystals grown under conditions of laminar convection indicated significant deviations from diffusion-controlled dopant segregation.

A characteristic value of the effective distribution coefficient (12), k_{eff} , defined as C_s/C_L in Eq. [3], was determined for each sample. For crystals grown under complete mixing conditions, $k_{\text{eff}} \rightarrow k_0$. For crystals in which the dopant concentration macro profiles were between the theoretical normal freeze and diffusion-controlled profiles, k_{eff} was determined iteratively by dividing the solid concentration by the bulk liquid concentration estimated for that fraction solidified consistent with the chosen value of k_{eff} . The measured values varied from k_0 to 0.8; the highest value was found in a 5 mm diam crystal. The results are presented and discussed below.

A series of radial concentration profiles of a 5 mm diam crystal together with the central longitudinal profile are shown in Fig. 6. The concentration maximum in the first scan was correlated experimentally with the lateral variation in microscopic growth rate as the initially concave growth front flattened out during the first 3 mm of solidification. However, subsequent changes in the asymmetry of the profiles were found to be unrelated to microscopic growth rate variations. Therefore, the concentration variation along an individual profile reflects a variation in the boundary layer thickness; variations between successive profiles indicate time variations in the boundary layer thickness. The implications with respect to the fluid flow pattern are discussed further below.

Model for segregation under laminar convection.—A model for laminar fluid flow and segregation was developed in order to analyze the experimental results on macrosegregation in terms of relevant growth parameters. The growth configuration is modeled in two dimensions. The fluid flow pattern ahead of the solid-liquid interface is assumed to be an axis-antisymmetric

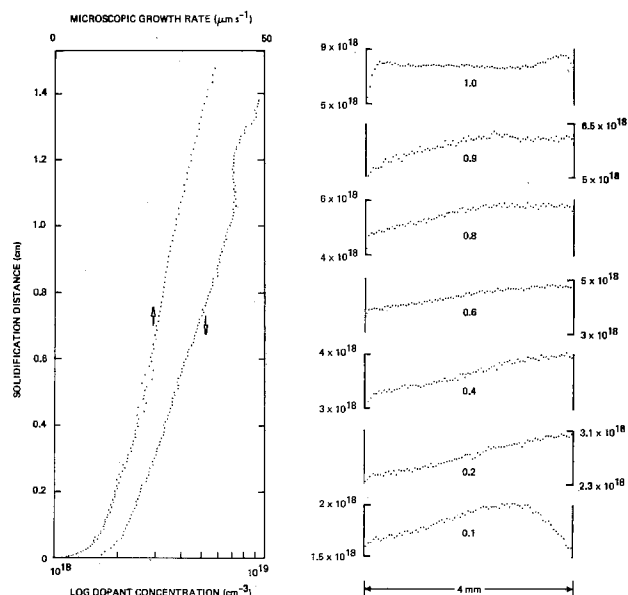


Fig. 6. Longitudinal (left) and lateral (right) concentration profiles of a 5 mm diam crystal. The lateral scans are plotted on a linear concentration scale. The number designating each lateral scan gives the respective solidification distance in centimeters.

cell with an aspect ratio of unity (circular flow pattern with fluid ascending and descending at opposite walls). Only the horizontal heat flow between the two vertical walls (held at different temperatures) is taken into account. Steady-state conditions are assumed.

Modeling of the segregation process was based on the establishment of a diffusion boundary layer thickness, δ_m , outside of which transport is convection-controlled. Here, δ_m was taken as the distance at which the diffusion flux equals 10% of the convection flux under steady-state conditions as suggested in a previous analysis of horizontal solidification (2). The diffusion flux was calculated from the dopant concentration gradient normal to the interface according to the approximation

$$\partial C/\partial x \approx C_0/\delta_m \left(\frac{k_{eff}}{k_0} - 1 \right) \quad [6]$$

The convective flux was calculated from the horizontal component of the laminar fluid flow velocity, v_y , across the solid-liquid interface, given by

$$v_y = \left(\frac{\kappa}{d} \right) \frac{\partial \psi}{\partial x} = \frac{-2}{3} \frac{\kappa}{d} y^2(1-y)^2 x(1-x)(1-2x) \quad [7]$$

where ψ is the dimensionless stream function for a fluid of unity aspect ratio confined between two vertical plates held at different temperatures (15), x and y are dimensionless lengths in units of the melt diameter and denote the vertical and horizontal directions, respectively, κ is the thermal diffusivity and d is the distance between the vertical plates; ψ is given by

$$\psi = \frac{1}{3} N_R x^2 (1-x)^2 y^2 (1-y)^2 \quad [8]$$

where N_R is the horizontal thermal Rayleigh number. N_R is given by

$$N_R = \frac{g\alpha}{\nu\kappa} d^3 \Delta T \quad [9]$$

where g is the acceleration due to gravity, α is the thermal expansion coefficient, ν is the kinematic viscosity, and ΔT is the temperature difference between the plates.

The values of v_y above the midpoint of the interface ($y = 0.5$) are shown in Fig. 7 as a function of distance from the interface for a 5 mm diam cylinder and various Rayleigh numbers. The magnitude of v_y increases from zero at the interface to a maximum value at about 1000 μm from the interface and decreases to zero at about 2500 μm since the flow pattern reverses direction at the upper portion of the convection cell.

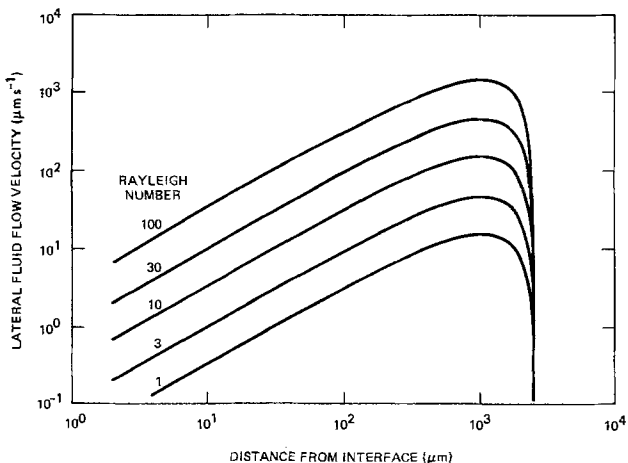


Fig. 7. Lateral fluid flow velocity in the center of a 5 mm diam cylinder as a function of distance from the center of a 5 mm diam cylinder over a range of Rayleigh numbers.

Equating the diffusion flux to 10% of the convective flux² and inserting the expression for v_y one obtains

$$\delta_m x (1-x)(1-2x) = \frac{15d}{\kappa N_R} \left[\frac{k_{eff}}{k_0} - 1 \right] / [y^2(1-y)^2] \quad [10]$$

In Fig. 8, δ_m is plotted as a function of N_R for a 5 mm diam cylinder and various values of k_{eff} . It is seen that δ_m increases with decreasing N_R (for constant d and k_{eff}) because the fluid velocity decreases with decreasing N_R and the boundary layer thickness can extend further into the melt before convection dominates.

The final parameter to be introduced into the model is the microscopic growth rate, R . The growth rate corresponding to the conditions specified in Fig. 8 was estimated from Eq. [10] employing the BPS relation [3]. Equation [3] gives a convenient theoretical expression for k_{eff} as a function of R and δ_m . Accordingly, the growth rate is plotted as a function of boundary layer thickness in Fig. 9 for various Rayleigh numbers and a cylinder diameter of 5 mm; δ_m increases with increasing R for constant N_R and decreases with increasing N_R for constant R .

As indicated in Fig. 9, as the growth rate increases, a point is reached where δ_m can no longer have a meaningful value because the diffusive flux is always greater than 10% of the convective flux. This condition is chosen as one criterion for diffusion-controlled

² The equation of fluxes normal and parallel to the interface seems justifiable when considering diffusive and convective flux distributions ahead of the interface. The present calculation does not apply away from the center of the cylinder where the component of fluid flow normal to the interface is not negligible.

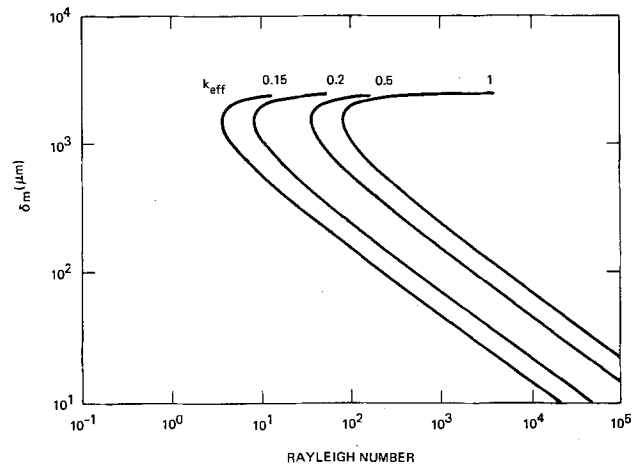


Fig. 8. Boundary layer thickness, δ_m , as a function of Rayleigh number in a 5 mm diam cylinder over a range of values of k_{eff} .

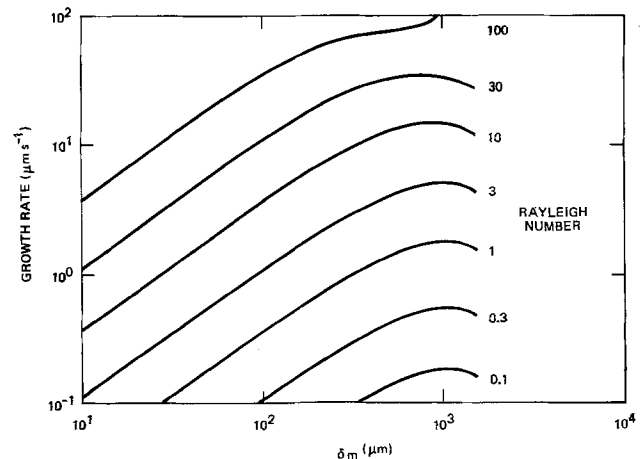


Fig. 9. Growth rate, R , as a function of boundary layer thickness, δ_m , in a 5 mm diam cylinder over a range of Rayleigh numbers.

segregation where the limit of k_{eff} becomes 1. A second criterion for diffusion control is

$$\delta_m > D/R \quad [11]$$

where D/R is the characteristic boundary layer thickness for diffusion-controlled segregation (13).

In order to present these calculations in a convenient graphical form representative of solidification under a wide range of conditions, Eq. [3], [10], and [11] were combined to determine k_{eff} as a function of growth rate for various hydrodynamic conditions. The results are shown in Fig. 10; they indicate a discontinuous rise in k_{eff} with increasing growth rate at constant Rayleigh number. The discontinuity results from the assumptions concerning the transition point from convection to diffusion control. The parameters used in the model can be readily modified to give a more realistic rise in k_{eff} as a function of growth rate. However, the essential features will remain the same: under a constant set of hydrodynamic conditions, diffusion-controlled segregation is predicted above a critical growth rate; the critical growth rate increases with increasing Rayleigh number. Thus, diffusion-controlled segregation is expected at sufficiently high growth rates and sufficiently low Rayleigh numbers.

Comparison of theory and experiment.—In order to analyze the experimental results on macrosegregation on the basis of the above, the magnitude of the destabilizing horizontal temperature gradients and the characteristic Rayleigh numbers during solidification were determined. The interface shape was revealed by demarcation lines and was found to be concave during the growth of all but the 9 mm diam crystals; thus, the horizontal gradients could be obtained from the vertical gradient and the experimental curvature parameters defined in Fig. 11 (taking the interface as isothermal). Both (near) symmetric and asymmetric interfaces were observed, as shown in the figure. The Rayleigh number for the symmetric (R_s) and asymmetric (R_a) interfaces are given by

$$R_s = \frac{1}{8} \frac{g\alpha}{\nu\kappa} G d^3 \Delta Z \quad [12]$$

$$R_a = \frac{g\alpha}{\nu\kappa} G \Delta Z \left\{ d \left(\frac{1}{2} + CP \right) \right\}^3 \quad [13]$$

$$R_a = \frac{g\alpha}{\nu\kappa} d^3 G \Delta A \text{ (the larger value)} \quad [14]$$

The geometric, hydrodynamic, and growth parameters obtained from seven crystals solidified under a wide range of growth conditions are shown in Table I. The analysis of the growth of the 9 mm crystals with

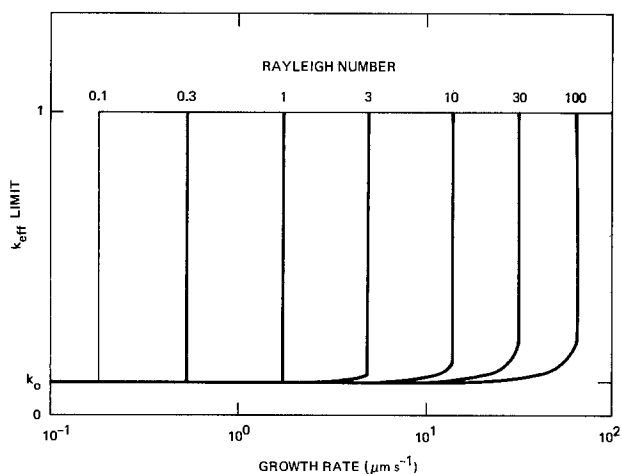


Fig. 10. The limit of k_{eff} as a function of growth rate in a 5 mm diam cylinder over a range of Rayleigh numbers.

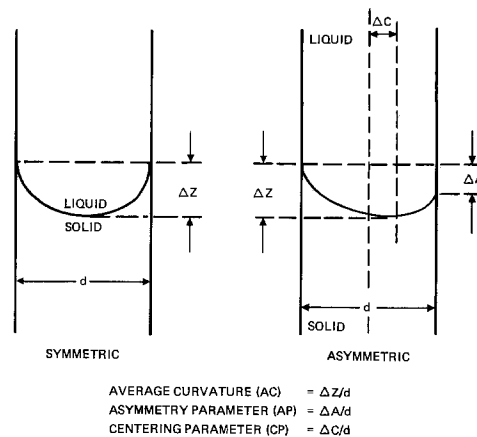


Fig. 11. Curvature parameters used to determine the Rayleigh number.

convex or "S"-shaped interfaces was also carried out on the same basis. By comparing experimental values of k_{eff} and growth rate, shown in the table, with the theoretical curves (such as those shown in Fig. 10) for 3, 4, 5, and 9 mm diam cylinders, it is found that theory and experiment are in good agreement.

In order to simplify the presentation of this analysis the theoretical curves for the 3-5 mm crystals were reduced to a plot of k_{eff} as a function of the ratio of Rayleigh number and growth rate at the transition of convection to diffusion control. Thus, a range of theoretical transition ratios is obtained and shown as a cross-hatched region in Fig. 12. This range was not extended to include 9 mm cylinders because macrosegregation was always convection controlled and the transition point was never approached. The experimental results are also shown in the figure. It is seen that the theoretical transition range is in good agreement with experimental data. Thus, diffusion-controlled segregation can be approached at sufficiently high growth rates and sufficiently low Rayleigh numbers. A representative Rayleigh number-to-growth rate ratio for the transition is 1 sec/ μm . However, approaching effective diffusion control, $k_{eff} > 0.9$, requires rigorous control of the radial heat losses and the shape of the solidification front.

The present model, which applies to macrosegregation behavior, cannot be successfully extended to transient microsegregation because steady-state laminar convection is assumed. However, the apparent suppression of turbulent convection and associated dopant inhomogeneities during growth in the small diameter

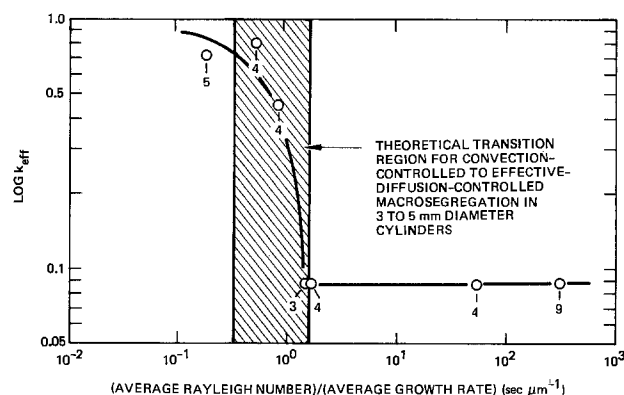


Fig. 12. Comparison of experimentally determined relationship between k_{eff} and the ratio of Rayleigh number and the theoretical transition region for convection-controlled macrosegregation in 3-5 mm diameter cylinders. The ampul diameter of each experiment is indicated in the figure in millimeters.

Table I. Geometric, growth, and hydrodynamic parameters of directional solidification experiments

| Sample No. | k_{eff} | Average microscopic growth rate ($\mu\text{m}/\text{sec}$) | Average Rayleigh No. | Ampul material | Ampul ID & OD (mm) | Concentric ampul insulation | Ambient |
|------------|-----------|--|----------------------|----------------|--------------------|-----------------------------|----------------|
| 1 | k_0 | 8 | 2250 | Quartz | 9; 11 | None | H ₂ |
| 2 | k_0 | 12 | 17.5 | Graphite | 3; 7 | None | H ₂ |
| 3 | k_0 | 7 | 35.5 | Graphite | 4; 9 | None | H ₂ |
| 4 | k_0 | 12 | 18 | Graphite | 4; 9 | Quartz | H ₂ |
| 5 | 0.45 | 16 | 13 | Graphite | 4; 5 | Quartz | H ₂ |
| 6 | 0.8 | 21 | 10.5 | Graphite | 4; 5 | Quartz | Ar |
| 7 | 0.7 | 17 | 3 | Quartz | 5; 8 | Lava | Ar |

ampuls (3-5 mm) as compared to growth in the larger diameter ampuls (9 mm) is consistent with established thermohydrodynamic criteria for the heating of a confined fluid from the side, on which the present model is based. It has been shown (15) that, in general, the transition from laminar to turbulent convection occurs at a critical Rayleigh number N_{R^C} . The value of N_{R^C} decreases with decreasing cylinder diameter for small aspect ratios (the ratio of the melt height and diameter), and is independent of diameter for large aspect ratios (keeping the melt height constant). Therefore, the critical aspect ratio for a 3 mm diam crystal growth ampul is actually smaller than for a 9 mm diam ampul. However, enhanced hydrodynamic stability was achieved in the present experiments by reducing the ampul diameter because the actual Rayleigh numbers could be controlled below the critical levels more effectively.

A theory applicable to the present solidification configuration which predicts the critical Rayleigh number as a function of aspect ratio for low Prandtl number fluids, such as Ge, heated from the side is not available. In order to consider the present experimental results in this light, the procedure outlined in Ref. (15) to determine the theoretical relationship between N_{R^C} and aspect ratio for air was used to obtain a similar curve for Ge. This was accomplished by substituting the appropriate materials constants for Ge, and by fitting the curve to an experimentally determined Rayleigh number of 2000 for the onset of turbulent convection in a 9 mm diam ampul. The result is shown in Fig. 13. It is seen that, as solidification progresses upward in a vertical direction solidification configuration, the critical Rayleigh number increases and the melt becomes progressively more stable. The experimental aspect ratios in this investigation ranged from zero (at the end of solidification) to a maximum value of 18 (at the beginning of solidification in the 3 mm diam ampul. The Rayleigh numbers measured for growth under laminar convection all lie below the curve at the corresponding aspect ratio, as shown in Fig. 13, indicating that the curve can serve as a guide-

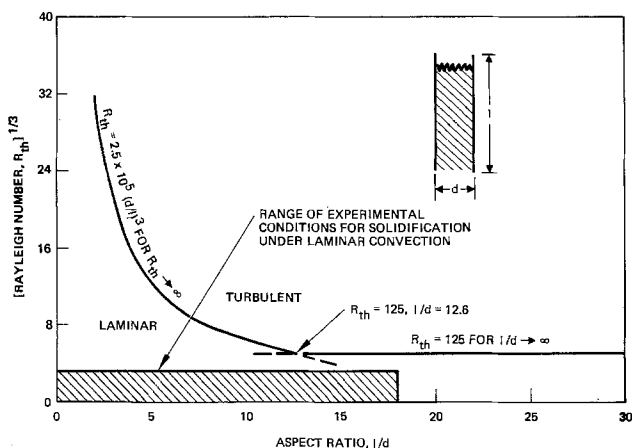


Fig. 13. Semi-empirical laminar-to-turbulent demarcation for directionally solidified Ge under stabilizing vertical thermal gradients.

line for laminar and turbulent convection regions for Ge growth in the present configuration. It is emphasized, however, that the curve is semi-empirical in nature and further theoretical work is needed.

The assumption in the present model of axis-antisymmetric flow is supported by the analysis of lateral segregation (Fig. 6) in which it was shown that the asymmetry of lateral compositional profiles reflects variations in boundary layer thickness. Thus, fluid descended on one side of the ampul, decreasing δ_m and k_{eff} , and ascended on the opposite side, increasing δ_m and k_{eff} . This conclusion is based on the consideration of the fluid flow velocity component normal to the growth interface as described in the BPS (12) analysis, which was not taken into account in the present model. However, if this indirect "sampling" of the fluid flow pattern is valid, then variations in the characteristics of successive lateral profiles indicate variations in the flow pattern. Thus, referring to the lateral scans in Fig. 6, the shift of the concentration maxima from the center of the crystal to the right, and then back toward the left, indicates an additional rotational component of the flow pattern about the axis along the direction of solidification; the flow pattern on one side of the ampul alternately shifts from ascending to descending with each half period of the rotational cycle. Therefore, a concentration minima becomes a maxima within the same time frame.

Three additional experimental observations support the presence of rotational displacement. First, analysis of broad dopant inhomogeneities which occurred under laminar convection (Fig. 4) revealed that the striations intersected successive demarcation lines continuously from one side of the crystal to the other. From the relative position of striations and demarcation lines, the apparent "lateral velocity" of the perturbation across the crystal could be measured; thus, for the striations shown in Fig. 4, it is about 1 mm/sec. (It should be pointed out that the actual three-dimensional nature of the striations was not determined, and it must certainly be much more complex.) It was observed that, while the first striation apparently travelled in one direction, successive striations travelled alternately in opposite directions. Although the precise mechanism of the formation of the striations has not been worked out, this result is consistent with the occurrence of rotational displacement in the melt during solidification.

The second observation, which is indicative of a rotational flow pattern, is the morphology of intersecting melt striations which occurred under turbulent convection (Fig. 3). Here, rotation of the hot fluid caused remelt on alternate sides of the crystal and the slope of the growth front shifted correspondingly from positive to negative with respect to a flat reference line.

Third, if alternate striations are formed as a result of flow reversal (due to rotation), then the spacing of successive striations must be related to the rotational period. Accordingly, the period of striations, ω , occurring under a wide range of hydrodynamic conditions was measured as a function of the local Rayleigh number with the aid of interface demarcation lines. The results, shown in Fig. 14, indicate that ω

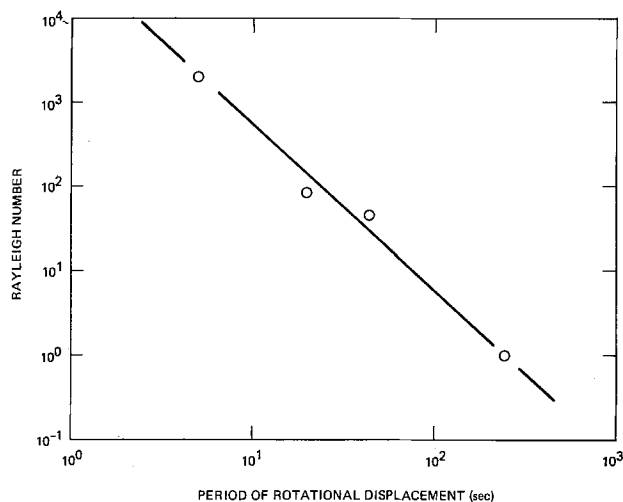


Fig. 14. Experimentally determined relationship between the Rayleigh number and period of fluid rotational displacement (deduced from the spacing of successive striations).

varies linearly with N_R . This trend agrees qualitatively with previous measurements of a confined fluid heated from the side (8, 11) and supports further the existence of fluid rotation.

Although the above segregation analysis represents a qualitative account of the fluid flow pattern adjacent to the solid-liquid interface, the three-dimensional flow behavior in the bulk of the melt cannot be ascertained. However, on the basis of the present results and existing theoretical analyses of similar configurations, such as a differentially heated inclined box (16) and a vertical tube with a square cross section heated from the side (17), it can be concluded that the flow pattern consisted of a single steady unicell under laminar convection and a series of cells, one above the other and with aspect ratios of 1, under turbulent convection. Further theoretical evaluation is necessary. Also, both the horizontal and vertical components of fluid flow must be taken into account to describe lateral segregation, although average longitudinal macrosegregation behavior predicted by the present model is in agreement with experiment.

To this point, only thermally driven convection has been considered. However, since the density of liquid Ge decreases with increasing Ga content, the contribution to the total vertical density gradient of the Ga concentration profile within the diffusion boundary layer is destabilizing. These conditions can lead to composition-driven, or solutal convection. The problem of fluid stability with simultaneous gradients of temperature and composition is complex and has received relatively little attention theoretically and experimentally; the potential influence of solutal convection in the present investigation can be evaluated semi-quantitatively at best. Calculated values of the total density gradient in the melt near the growth front were always positive (stabilizing); the density gradient due to the temperature was generally a factor of 5-10 times greater than that due to composition (18). Thus, the solutal effect would seem insignificant. On the other hand, theoretical calculations (19) predict that under certain conditions fluid instability can occur in spite of an overall stable density gradient when the thermal component is stabilizing and the compositional component is destabilizing. Although this theory is based on a thin film of infinite extent with stationary boundaries, and does not directly apply to the present experimental configuration, it indicates the possible significance of the solutal effect. The present experimental results, including thermal characterization, and macro- and microsegregation behavior, are consistent with convection driven by thermal density gradients.

Achievement of effective diffusion-controlled segregation.—It was one of the objectives of this study to determine the optimum vertical solidification configuration for minimal convective interference. As was shown above, the parameters leading to diffusion control are high growth rates, low vertical temperature gradients, small ampul diameter, and low interface curvature. The present apparatus allowed independent control of horizontal and vertical temperature gradients. However, the interface curvature and growth rate were found to be interdependent. As shown in Fig. 15, the curvature increased with increasing growth rate. In experiments carried out in quartz ampuls the curvature ($\Delta Z/d$) was found to be smaller and less sensitive to growth rate changes, $\left(\frac{\partial \Delta Z/d}{\partial R}\right)$, than

in those carried out in graphite ampuls. Thus, the curvature parameter, $\Delta Z/d$, represents the balance of longitudinal and radial heat flows, since radial heat losses decrease with decreasing ampul thermal conductivity and with increasing growth rate.

On the basis of these findings, three modifications of the growth configuration were made: (i) programmed cooling was introduced to the cooling shaft to enhance longitudinal heat flow and render the solid-liquid interface shape less concave; (ii) a 5 mm ID \times 8 mm OD quartz ampul was employed with concentric lava insulation to reduce heat losses; and (iii) the inner heater was positioned above the top of the melt to reduce radial heat flow in that region of the melt. With these modifications, it was found that the Rayleigh number was maintained below 0.9 and the curvature parameter at about 0.01.

A longitudinal macrocompositional profile of a crystal grown in this configuration is shown in Fig. 16. The microscopic growth rate was accelerated to 36 $\mu\text{m}/\text{sec}$ and the composition steadily increased to within 15% of the steady-state value as solidification progressed. Since no theories were available to analyze segregation under conditions of nonconstant growth rate, the data were compared with theoretical curves for diffusion control, expressed in (4), using the measured average microscopic growth rate of 18 $\mu\text{m}/\text{sec}$. In view of the uncertainty in the values of D and k_0 , a theoretical range was obtained by varying both parameters over the range of the published data, as shown in Fig. 16, bounded by curves calculated using values of D and k_0 of 2×10^{-4} cm^2/sec and 0.087, respectively, and of 1×10^{-4} cm^2/sec and 0.11. The experimental data lie within the theoretical range, indicating that within a margin of uncertainty, effective diffusion-controlled segregation prevailed. Furthermore, the ex-

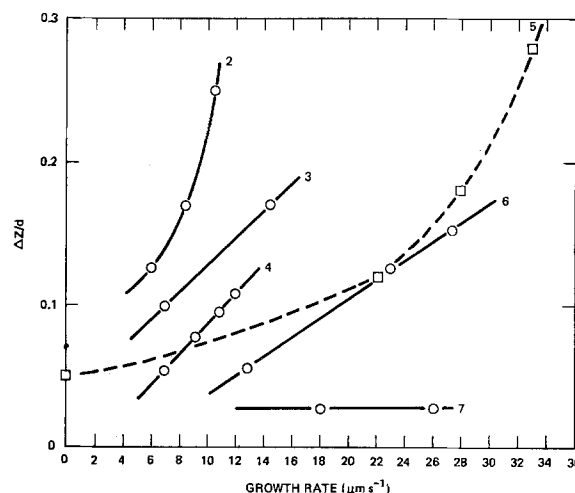


Fig. 15. Measured dependence of the curvature parameter, $\Delta Z/d$, on the growth rate, R , for the configurations given in Table I. The data for sample No. 1 are not given.

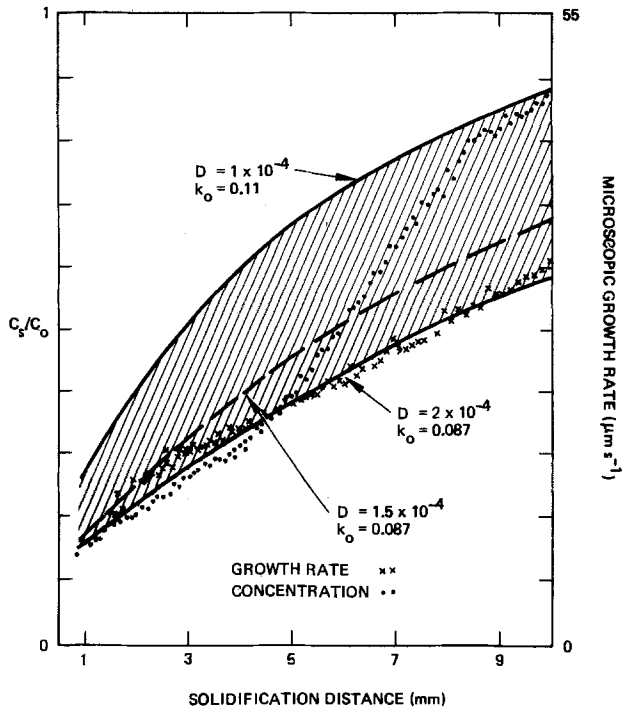


Fig. 16. Compositional and growth rate analysis of crystal grown under the highest achieved hydrodynamically stable conditions. The experimental concentration profile is compared with a range of theoretical curves for diffusion-controlled segregation (shaded area) corresponding to the uncertainty in the values of D and k_0 . The theoretical curve calculated with the commonly accepted values of D (1.5×10^{-4} cm²/sec) and k_0 (0.087) is also shown (dashed curve).

perimental curve first lags and then leads the theoretical curve calculated with the most commonly accepted value of D , 1.5×10^{-4} cm²/sec, and k_0 , 0.087. This behavior is expected for a diffusion-controlled growth under conditions of increasing growth rate and supports further that effective diffusion control was achieved.

Summary and Conclusion

Convection and convection-related segregation phenomena are dominant processes during directional solidification under stabilizing vertical thermal gradients due to the presence of unavoidable destabilizing horizontal thermal gradients. Under turbulent conditions the solidification rate is coupled to temperature fluctuations in the melt which leads to material with pronounced and random dopant inhomogeneities. This behavior is virtually eliminated under laminar convection. However dopant inhomogeneities broadly spaced are present due to perturbations in boundary layer thickness resulting from transient thermal con-

ditions in the melt. Macro-segregation in both convective regimes is controlled by the boundary layer thickness. Effective diffusion-controlled segregation is achieved at sufficiently high growth rates and sufficiently low Rayleigh numbers. Thus, the generally made assumption that diffusion control or minimal convective interference prevails during vertical directional solidification is not valid without experimental verification: direct thermal characterization of the melt, micro- and macrocompositional profiling, and the determination of horizontal temperature gradients and interface curvature are essential in the evaluation of convection and its effects on segregation.

Acknowledgment

The authors are grateful to the National Science Foundation for financial assistance.

Manuscript received June 26, 1980.

Any discussion of this paper will appear in a Discussion Section to be published in the December 1981 JOURNAL. All discussions for the December 1981 Discussion Section should be submitted by Aug. 1, 1981.

Publication costs of this article were assisted by the Massachusetts Institute of Technology.

REFERENCES

1. See, for example, K. Benson, *Electrochem. Tech.*, 11-12, 332 (1965); A. Murgai, H. C. Gatos, and A. F. Witt, *This Journal*, 123, 224 (1976).
2. J. Carruthers, *J. Cryst. Growth.*, 2, 1 (1968).
3. See, for example, K. M. Kim, A. F. Witt, and H. C. Gatos, *This Journal*, 119, 1218 (1972); K. M. Kim, A. F. Witt, M. Lichtensteiger, and H. C. Gatos, *ibid.*, 125, 475 (1978).
4. See, for example, L. Morris and W. Winegard, *J. Cryst. Growth*, 5, 361 (1969); R. Sharp and A. Hellowell, *ibid.*, 6, 253 (1970).
5. R. Singh, A. F. Witt, and H. C. Gatos, *This Journal*, 115, 112 (1968).
6. A. F. Witt, M. Lichtensteiger, and H. C. Gatos, *ibid.*, 120, 1119 (1973).
7. W. L. Lindberg and R. D. Haberstroh, *AIChE J.*, 18, 243 (1972).
8. M. Stewart and F. Weinberg, *J. Cryst. Growth*, 12, 217 (1972).
9. G. Cole, *Trans. AIME*, 239, 1287 (1967).
10. F. Chiesa and R. Guthrie, *Metall. Trans.*, 2, 2833 (1971).
11. D. T. J. Hurle, E. Jakeman, and C. P. Johnson, *J. Fluid Mech.*, 64, 565 (1974).
12. J. A. Burton, R. C. Prim, and W. P. Slichter, *J. Chem. Phys.*, 21, 1987 (1953).
13. W. A. Tiller, K. A. Jackson, J. R. Rutter, and B. Chalmers, *Acta Metall.*, 1, 248 (1953).
14. E. Scheil, *Z. Metallkd.*, 34, 70 (1942).
15. G. K. Batchelor, *Q. Appl. Math.*, 12, 209 (1954).
16. J. E. Hart, *Fluid Mech.*, 47, 547 (1971).
17. E. J. Martin, Private communication.
18. R. M. Sharp and A. Hellowell, *J. Cryst. Growth*, 12, 261 (1972).
19. J. O. Verhoeven, *Trans. AIME*, 242, 1937 (1968).

Partial Pressures over HgTe-CdTe Solid Solutions

I. Calibration Experiments and Results for 41.6 Mole Percent CdTe

J. P. Schwartz, Tse Tung, and R. F. Brebrick*

Metallurgy and Materials Science, Marquette University, Milwaukee, Wisconsin 53233

ABSTRACT

Calibration experiments are reported that enable the partial pressures of Hg, Te₂, and Cd to be calculated from measurements of the optical absorbance between 220 and 700 nm of the vapor phase. In particular, the self-broadening and Hg-broadening coefficients of the 228.7 and 325.7 Cd lines are established. The pressure ranges are between 10⁻² and 32 atm for Hg, 10⁻⁴ and 10⁻² atm for Te₂, and 10⁻⁷ and 10⁻⁵ atm for Cd. These calibrations are used in a study of the HgTe-CdTe solid solution containing 41.6 mole percent CdTe to determine all three partial pressures along the three-phase curve, the chemical potentials of HgTe and CdTe components, and the Gibbs free enthalpy of formation. Density and lattice parameter as a function of CdTe content are also reported.

HgTe and CdTe form a continuous range of solid solutions with the zinc blende structure in which the Hg and Cd atoms are distributed at random over the sites of one sublattice. The material is a semiconductor with a forbidden energy gap varying from about 2 eV for CdTe to a small negative value for the semi-metallic HgTe, and various HgTe-rich compositions are used as infrared detectors. Some values exist for the densities and lattice parameters of the solid solutions (1, 2). The pseudobinary phase diagram has been determined by thermal analysis (1, 3) and by chemical analysis of the first crystals to freeze from large volumes of melt (4). Total pressure measurements have been made by a reflux method for pseudobinary melts containing up to 60 mole percent (m/o) CdTe and these also furnish a few liquidus points (5). However, neither the partial pressures over the pseudobinary solid solutions have been reported nor has the Gibbs free enthalpy of formation for the various solid solutions.

It is observed that the concentration of electronic carriers in these materials for a given Hg to Cd ratio can be varied by equilibration at temperatures above 200°C under various mercury pressures (6-10). In accordance with the simple defect chemistry of solids, it is inferred that this implies a varying concentration of native atomic point defects, which can act as donors or acceptors, and consequently a small range of stability around an atomic fraction of one-half for Te. Statistical thermodynamic arguments show (11) that if the value of y in the formula (Hg_{1-x}Cd_x)_yTe_{1-y}(c) is restricted to values close to 1/2, then the sum of the chemical potentials of Hg and Te and that of Cd and Te are to a good approximation independent of y and functions of T and x (and weak functions of the total pressure, characteristic of condensed phases). Thus, for a given x and T , only one partial pressure need be fixed to fix all of the intensive variables, including the electronic carrier concentrations. For such purposes it is valuable to know the partial pressure of the predominant vapor species for both the metal-saturated and the tellurium-saturated solid solutions.

In the present paper we report measurements of the optical absorbance between 220 and 700 nm of the vapor coexisting with a solid solution of $x = 0.416$ between about 300° and 800°C. From these it is possible to obtain (i) the solidus temperature for this composition, (ii) the partial pressure of Hg along the three-phase curve, where the solid solution coexists

with the vapor and another condensed phase, (iii) all three partial pressures in certain ranges of T and y , and (iv) the Gibbs free enthalpy of formation. (Moreover, direct evidence of the narrow composition range of stability about $y = 1/2$ is obtained.) Extensive calibration experiments are required to convert the measured optical absorbances into partial pressures. This is particularly true in the case of Cd(g), which occurs at low partial pressures and shows an absorption line which varies from one that is narrower than our monochromator bandpass to one extensively broadened by mercury.

Measurements of the density and lattice parameter for various x -values were carried out to check the composition of the crystals and are also reported here.

Experimental

Materials.—The ternary solid solutions were furnished as large grain size samples by Mr. J. Schmit of Honeywell Corporate Research Laboratory in Bloomington, Minnesota. They were prepared by combining the weighed, spectroscopically-pure elements in sealed silica tubes with extra Hg to compensate for loss to a small volume of vapor phase, melting, cooling rapidly to below the solidus temperature, and annealing for long periods. The samples were slices cut from portions of the ingot where scanning electron microprobe analysis showed the Hg/Cd ratio typically to be the most uniform. The bottom one-third of each slice was discarded to further minimize any variation in Hg/Cd ratio following Mr. Schmit's experience. The remainder of each slice was then lightly lapped with 12 μ m grit alumina and rinsed with methyl alcohol. The density of roughly 5g samples was determined by weighing in air and in distilled water of measured temperature using an analytical balance with a sensitivity of 0.1 mg. The slices were then ground in an agate mortar and pestle and roughly 2g was further ground to pass a standard 44 μ m stainless steel sieve. Diffraction patterns were obtained with a Norelco diffractometer using CuK α radiation, a graphite monochromator in the diffracted beam, a 1/4° divergence slit, and a 4° scattering slit. Values of 2θ between 23° and 133° were scanned at 1/4°/min and a chart speed corresponding to 5.0 cm/° in 2θ . Thus angles could be read to 0.01°. The instrumental bandpass with this arrangement was 0.14°. The goniometer readings were corrected using ZnTe ($a_0 = 6.1027\text{\AA}$) as an external standard (12, 13).

In the instances in which it was necessary to add one or more of the elements to the slices, 6 nines pure elements from Cominco American, Spokane, Washington, were used.

* Electrochemical Society Active Member.

Key words: mercury-cadmium telluride, partial pressures, three-phase curve, free enthalpy, chemical potentials.

Optical cells.—The T-shaped optical cells were made of fused silica and consisted of a cylindrical cell-proper with roughly plane, parallel windows through which light passed and a 50 cm long sidearm attached at right angles to the cylindrical axis at its midpoint. The cells were ultimately sealed off under vacuum at the sidearm, leaving it 20 cm long. The extra length made it possible to attach the cell to a vacuum system and outgas the cell-proper and entire final 20 cm length of sidearm. The length of the cell-proper, exclusive of window thickness, ranged between 1 and 10 cm and was measured to the nearest 0.01 cm before attachment of the windows. For low pressure runs the cell-proper was 1.7 cm ID with a 0.15 cm wall and 0.2 cm thick windows. For runs in which the pressure exceeded 15 atm, the cell-proper was 0.8 cm ID with a 0.3 cm wall and 0.3 cm thick windows. Also for the high pressure cells, 15 cm of the sidearm length closest to the cell-proper was 0.16 cm ID capillary to minimize the vapor volume, only the 5 cm length furthest from the cell-proper being enlarged to 0.7 cm ID to hold the sample. High purity silica windows with a transmission exceeding 90% at 200 nm were used for all cells. The volume of the optical cell-proper and that of the sidearm as a function of length were determined by adding water from a burette with 0.05 ml divisions. That of the high pressure cells was determined by adding mercury and weighing. The cells were cleaned using a 15 sec rinse with 37 weight percent (w/o) HF, several distilled water rinses, and then drained dry. They were then outgassed for 16 hr at 1000°C and $3(10^{-7})$ Torr. Upon cooling the cells were ready for loading.

A weighed amount of solid solution passing a 125 μm sieve and being retained by a 44 μm sieve was loaded via a long funnel along with a weighed amount of Hg or Te into the optical cell-proper. The cell was then put on vacuum again and after 5-10 min sealed off with an $\text{H}_2\text{-O}_2$ torch to leave a 20 cm long sidearm. This was a sufficiently long period that the pressure was in the 10^{-7} Torr range for samples with added Te and about 10^{-6} Torr for those with added Hg. After seal-off the sample was shaken into the end of the sidearm. The small amount of fine material remaining in the cell-proper and upper portions of the sidearm was sublimed toward the bulk of the sample by imposing a temperature of 600°C over all the cell except the lower 6 cm of the sidearm, which was surrounded by a water-cooled copper cylinder. The sample was then homogenized by an isothermal anneal at about 500°C for 20 hr, the cell-proper and upper portions of the sidearm being held at higher temperature.

In order to determine the relation between optical absorbance and partial pressure a number of cells were prepared which contained pure Te, pure Hg, pure Cd, or weighed amounts of Hg and Cd.

Experimental arrangement.—Figure 1 is a schematic of the optical system which is a GCA McPherson RS10, 1m focal length, 12,000 grooves/cm grating monochromator arranged with reverse optics, and an open sample area large enough to accept a 30 cm long furnace. Light from a 75W high-pressure xenon lamp is sent through a chopper wheel and split into two beams. These are alternately sent into the entrance slit of a prism disperser (incorporated to eliminate higher orders and minimize stray light) by a flipper mirror that oscillates at 6.66 Hz between two stable positions, spending 50 msec in each. A small lamp and silicon diode mounted on opposite sides of the chopper wheel provide the synchronizing signal for a lock-in amplifier. Most of the measurements were taken with 200 μm settings for the entrance and exit slits of the monochromator giving a spectral bandpass of 0.17 nm. A recorder displayed the common logarithm of the ratio of reference beam to sample beam intensity, i.e., the optical absorbance. Measurements of the Cd line were also taken in transmission, with the flipper mirror stationary and sending the sample beam into the monochromator. Then the intensity of the transmitted sample beam was recorded and various slit widths between 20 and 100 μm were used. In operation a furnace containing an optical cell was placed in the sample beam so that the cylindrical axes of the cell-proper lay along the beam direction.

Figure 2 is a schematic of the split-T, 6-zone electrical resistance furnace with an optical cell in place. The furnace consists of two halves, each similar to that shown, that are hinged together along the upper edge of the upper leg of the T. Each zone is made of two heating elements connected in series, one in the lower half of the split-T, the other in the upper half, so that the two elements form a cylinder when the furnace is closed. The center zone of the upper leg of the T, Z2, is controlled electronically using a Platel II thermocouple located near the middle of the cell-proper and between the heating element and the steel liner. Slave controls furnish an adjustable percentage of the power sent to the center zone and to the adjacent end zones, Z1 and Z3. Power to the center sidearm zone, Z5, surrounding the sample, is also directly controlled and the end zone, Z6, is under slave control. The power to Z4 is controlled manually using an autotransformer and ammeter. The liners serve to position the optical cell, to hold some of the measuring thermocouples in position, to provide additional thermal mass to smooth out short-time temperature fluctuations, and, especially in the case of the silver liner, to minimize the temperature gradients in the cell-proper and around the sample. The eleven thermocouples used for temperature measurement were all $5(10^{-2})$ cm diam thermocouple grade Pt; Pt, 10% Rh wire from Englehard In-

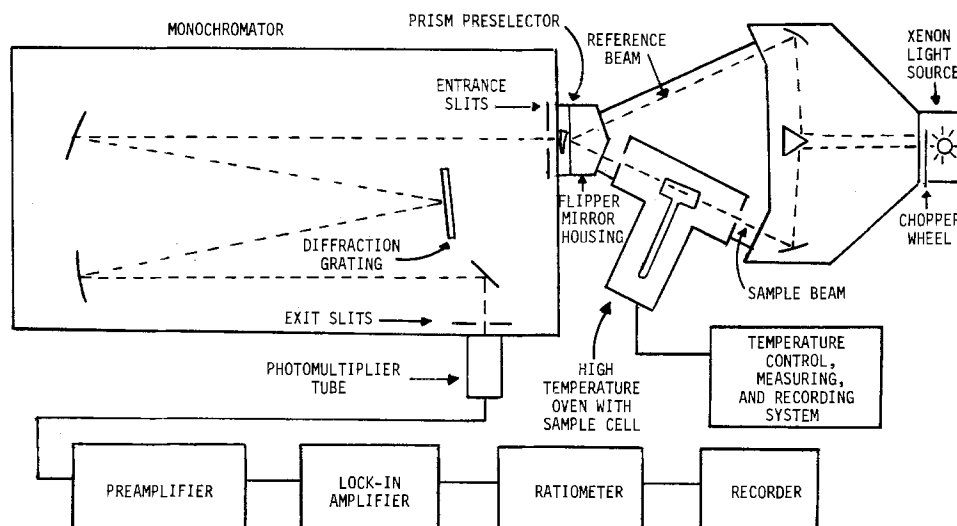


Fig. 1. Schematic of spectrophotometer with optical cell and furnace in place.

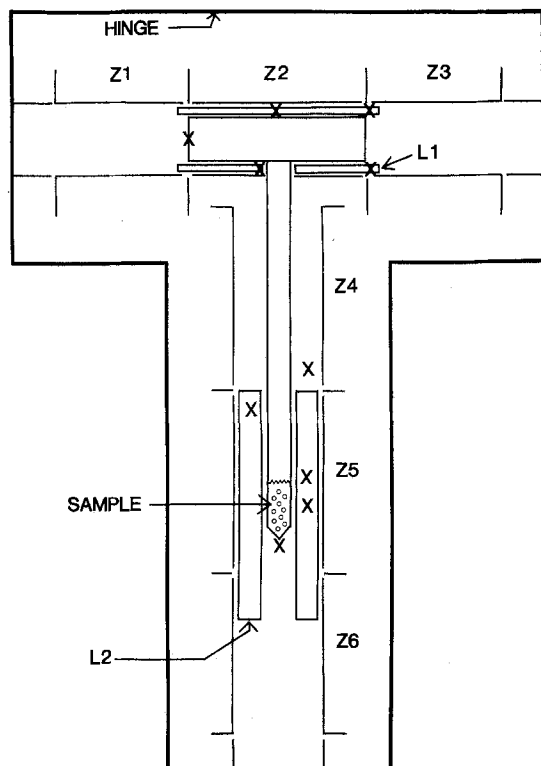


Fig. 2. Schematic cross section of hinged, split-T optical-cell furnace with cell in place. L1 is a 1.0 cm wall thickness, 10.2 cm long, split cylinder made of a high Ni-Cr steel (RA330; Rolled Alloy Products, Chicago, Ill.). L2 is a 0.89 cm wall, 12.5 cm long cylinder of silver. The walls of both liners contain thermocouple holes. Thermocouple positions are indicated by an X. There are two thermocouples at the end of the cell near the boundary of zones Z1 and Z2. One is at the bottom of the cell, the other near the top.

dustries, New Jersey. A certificate of calibration showed that thermocouples made from sample sections of this wire gave emf's matching the NBS tables to within -0.6° to -1.3°C between 400° and 1100°C . The temperatures of the six thermocouples distributed around the cell-proper were read to 0.75°C using a Multipoint Honeywell Potentiometric recorder. Those of four of the five thermocouples placed along the sidearm were read to the nearest 0.1°C using a Fluke, Model 2000, Digital Thermometer. The fifth thermocouple placed against the sidearm near the middle of the sample had a cold junction in an automatic ice bath and its emf was measured to the nearest $0.1\ \mu\text{V}$ using a Leeds and Northrup, Model 7564, differential potentiometer. Temperatures were obtained using the National Bureau of Standards Thermocouple Reference Tables. Consistency of the temperature readings from the three instruments was checked in separate experiments in which the thermocouple hot junctions were held as close together as possible in the middle of the silver liner. Readings from the digital thermometer and differential potentiometer agreed to within 1°C over the 400° - 800°C range while those of the Multipoint recorder agreed with these to within 5°C .

Experimental procedure.—In a set of measurements the temperature of the optical cell-proper was held fixed at 755°C with a variation of 3°C or less across the cell. For a few high sample temperature measurements with metal-saturated solid solutions, the optical cell temperature was held at 800°C . With the sample temperature near 200°C , and insufficient vapor present to give a measurable signal, the optical absorbance was measured between 200 and 700 nm. This measurement was repeated 2-5 times to furnish an average base line characterizing losses in the sample beam

$$D(\lambda) = \log_{10} \left(\frac{I_{RO}}{I_{SO}} \right) \quad [1]$$

where I_{RO} and I_{SO} are the initial intensities in the reference beam and sample beam, respectively. The sample temperature was then increased so absorption became measurable, measurements made, and the sample temperature increased again by 5° - 20°C . At a given sample temperature setting, the sample temperatures and the absorbance at some strongly adsorbing wavelength were recorded as a function of time. When both were steady the optical absorbance was measured as a function of wavelength. When Cd was present the transmission of the 228.7 and 325.7 nm lines was also recorded. Temperatures were recorded for the various positions along the cell-proper and sidearm. The net optical absorbance at a given wavelength was calculated by subtracting that of the base line from the total measured, $\log_{10} (I_R/I_{S,t})$, to give

$$D(\lambda, \text{net}) = \log (I_R/I_{S,t}) - \log (I_{RO}/I_{SO}) \quad [2]$$

where $I_{S,t}$ is the intensity of the light within the spectral bandpass at λ that is transmitted by the vapor-containing optical cell. Assuming (i) that no change occurs in the optical characteristics of the sample-beam path except that due to the changing vapor state and (ii) that any change in lamp output affects both beams equally so the $I_R = fI_{RO}$ and $I_{S,i} = fI_{SO}$, then the net optical density calculated from Eq. [2] can be written as

$$D(\lambda, \text{net}) = \log (I_{S,i}/I_{S,t}) \quad [3]$$

where $I_{S,i}$ is the intensity of the sample beam incident on the optical cell. The net optical absorbance is then a measure of the vapor absorbance alone. The assumed constancy of the base line with time was monitored at nonabsorbing wavelengths and occasionally was also checked after a run by cooling the sample to near 200°C and measuring the optical absorbance. The net optical densities at various wavelengths were plotted on a log scale against the reciprocal absolute sample temperature. Abrupt and significant base line shifts, which would appear as discontinuities, were not detected.

Accuracy of measurements.—The monochromator wavelength indicator was checked by locating the absorption maxima of Zn at 213.8 and 305.7 nm, of Cd at 228.7 nm, and Hg at 253.7 nm, with the vapors at a pressure of about 10^{-5} atm in each case. This showed the indicator was low by 0.4 nm at these wavelengths and so all wavelengths quoted here have been corrected by adding 0.4 nm to the reading. Wavelengths could be reproduced to within a few hundredths of a nanometer. Total optical absorbances were measured between 0.01 and 2.7. Reproducibility and noise were worse at 220 nm than at 300-700 nm. Typical noise amplitudes at 220 nm were ± 0.02 at optical absorbances between 0.01 and 1.0 and ± 0.1 at 2.0. One might then expect the partial pressures given in this paper to be accurate within 2% to 10%. In most cases, except for the partial pressure of Cd(g) and that of Hg(g) below 0.01 atm, several values for a partial pressure were obtained by using the optical absorbance at several different wavelengths and the average taken. These average values and the associated standard deviation are given in the tables that follow.

Photometric accuracy was checked by measuring the optical absorbance of Zn vapor in a 1000°C optical cell between 220 and 270 nm as a function of the temperature of the liquid Zn. Plots of the logarithm of the net optical absorbance vs. reciprocal absolute sample temperature could be well represented at all wavelengths as parallel straight lines with a slope twice that of the vapor pressure of zinc. Moreover the relative optical densities at different wavelengths agreed closely with those obtained elsewhere with a different monochromator and furnace (11, 14).

The response time for a full scale deflection from near zero absorbance to 3 was about 2.5 sec. Consequently when rapid changes in absorbance as a function of wavelength occurred the scanning rate was appropriately decreased, sometimes to zero.

The sample temperature was taken as the average of those recorded from the three thermocouples placed near either end of the sample and near the middle after adding a correction of + 1.0°C. The maximum temperature variation across the sample was about 3°C. We estimate our corrected average sample temperatures are accurate to $\pm 1.5^\circ\text{C}$. The temperature of the optical cell-proper is estimated to be correct to $\pm 3^\circ\text{--}5^\circ\text{C}$. For fixed partial pressures, the concentrations of the vapor species in the light path depend on the reciprocal absolute temperature of the optical cell. The uncertainty in the optical cell temperature therefore contributed an error of less than 1% to the measured optical absorbances.

Density and Lattice Parameter

Densities were determined at 20°C to within 0.1%. Lattice parameters were determined with a standard deviation of one part in 10^4 from a least squares fit to the corrected values of 2θ . Since the unit cell contains four formula units, $\text{Hg}_{1-x}\text{Cd}_x\text{Te}$, the value of x is given in terms of the density, d , in g/cm^3 and the lattice parameter, a_0 , in angstroms as

$$x = \frac{328.19 - (0.15056) da_0^3}{88.19} \quad [4]$$

The variation in lattice parameter from $x = 0$ to 1 is only 1/3% and if this is a linear variation, then Eq. [4] is a linear relation between x and d to an accuracy of 0.05% in d . In fact, the experimental values of x and d are well fit by a least squares straight line that goes through the densities of pure HgTe and CdTe

$$d = 8.077 - 2.225X \quad [5]$$

The experimental values obtained for x , d , and a_0 are given in Table I along with the standard deviation between measured and calculated values of 2θ . It is apparent the percentage variation of density with x is much larger than that in a_0 and so density measurements afford the more sensitive means of determining x . The use of Eq. [4] assumes the density samples are homogeneous and free of voids. The former was evidenced by the fact the half-width of the diffraction line was essentially equal to the instrumental bandpass of 0.14 even at the highest values of 2θ near 133° . Figure 3 shows a_0 as a function of x .

Our values and all but one of those from Blair and Newnham (1) fall close to straight line through the values for HgTe and CdTe. Those of Wooley and Ray (2) form a bow and are somewhat lower.

Calibration Measurements

Tellurium.—From a number of closely agreeing studies (15-18) the vapor pressure of Te above its melting point is given to within 2% by

$$\log P_{\text{Te}_2} (\text{atm}) = -5960.2/T + 4.7191 \quad [6]$$

Table I. Experimental values at 20°C for $\text{Hg}_{1-x}\text{Cd}_x\text{Te}$

| x | d (g/cm^3) | Lattice parameter, a_0 (Å) | Std. dev. of fit σ (2θ , deg) | Reference |
|-------|----------------------------|------------------------------|---|-----------|
| 0.00 | 8.077 | 6.4603 ± 0.001 | 0.0121 | This work |
| 0.00 | — | 6.4623 ± 0.0001 | — | (1) |
| 0.222 | 7.582 | 6.4658 ± 0.0005 | 0.0204 | This work |
| 0.277 | 7.462 | 6.4665 ± 0.0006 | 0.0231 | This work |
| 0.416 | 7.152 | 6.4689 ± 0.0005 | 0.0207 | This work |
| 1.00 | 5.852 | 6.4815 | — | (13) |

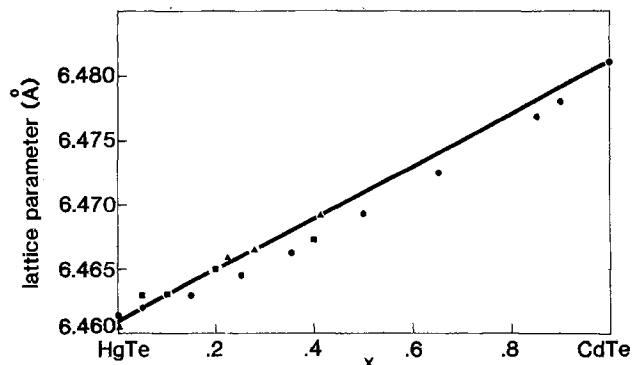


Fig. 3. Lattice parameter at 20°C as a function of the mole fraction of CdTe in HgTe-CdTe solid solutions. Triangles: this study. Circles: Wooley and Ray (2). Squares: Blair and Newnham (1).

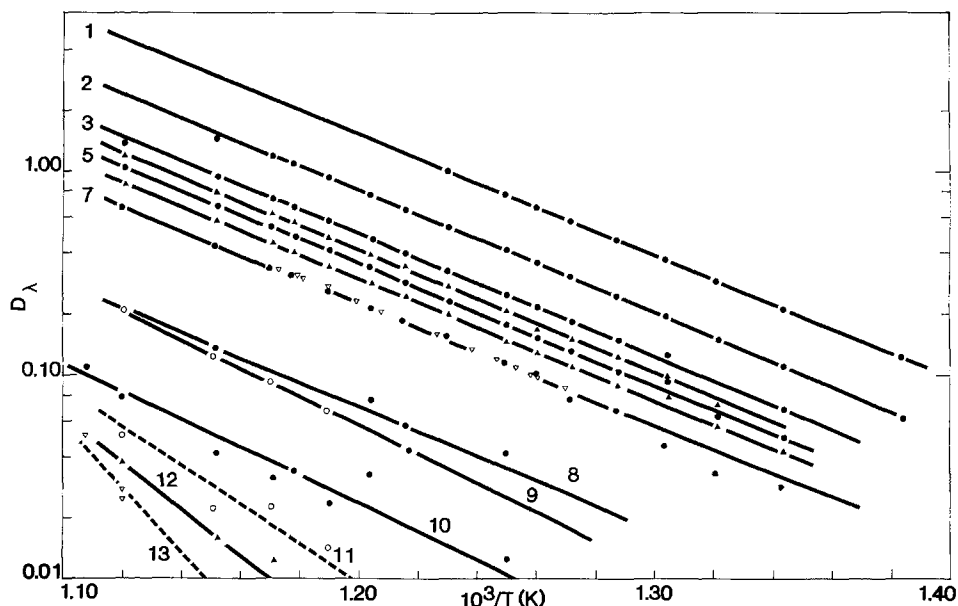
Selected values by Hultgren *et al.* (19), however, favor the data of Machol and Westrum (20), which show a decrease from values calculated from Eq. [6] that starts at about 620°C and amounts to about 20% at the 449.5°C melting point. The experimental points are relatively few in number between 450° and 500°C and the values are near the experimental limits of precision. In contrast, the optical absorbance of the strong Te_2 peaks in the 199.5-206.0 nm region indicate that Eq. [6] is followed down to the melting point (18). The present absorbance measurements in the visible also indicate that this is so to within $\pm 5\%$, the optical absorbance of a number of wavelengths being well represented by parallel straight lines with a slope of -5960 on a plot of $\log D$ vs. $10^3/T$ as shown in Fig. 4. We therefore choose Eq. [6] as the best representation for the vapor pressure of Te above its melting point. We should note that the tellurium calibration runs were made somewhat after the rest of those described here. The diameter of the sidearm section of the furnace was enlarged and a 20 cm long, 4.0 cm ID heat pipe inserted; one end being within 4.6 cm of the optical cell-proper and insulated from it except for a hole through which the optical cell sidearm passed. A 12.5 cm long sidearm cell was used. A close-fitting 12.5 cm long Ag liner was inserted inside the heat pipe and symmetrically around the part of the cell sidearm containing the $\text{Te}(1)$. Temperatures within the Ag liner and adjacent to the cell sidearm were constant to within 0.3°C over the 2 cm length of the sample and those measured by the digital voltmeter and differential potentiometer agreed to within $\pm 0.2^\circ\text{C}$. For an optical path at 755°C the net optical density for 200 μm slits is written as

$$P_{\text{Te}_2} (\text{atm}) \equiv P_2 = 9.78a_\lambda D_\lambda / L \quad [7]$$

where L is the optical path in centimeters and the values of a_λ are listed in Table II. The wavelengths listed include a number that were not tabulated in a previous study (21) using different instruments. For other wavelengths, the agreement with older values of a_λ is within 3%. The vibronic spectrum of $\text{Te}_2(\text{g})$ in the visible has been described previously (22). In particular, the vibronic peaks strongly overlap so that the difference in adjacent maxima and minima are only about 10% of the optical absorbance at the maximum. Moreover the latter values are independent of spectral bandpass between 0.08 and 0.17 nm (21). Finally, Lambert's law is followed and D varies linearly with path length.

Mercury.—It has been known for some time that the $5^1\text{S}_0\text{--}6^3\text{P}_1$ absorption line of Hg at 253.7 nm broadens extensively toward the visible for pressures greater than 1 atm. (The absorption lines of Zn(g) and Cd(g) associated with the ground states of these atoms behave similarly.) Consistent with the statistical theory

Fig. 4. Optical absorbance of $\text{Te}_2(\text{g})$ at various wavelengths plotted on a log scale vs. 1000 times the reciprocal absolute temperature of a liquid Te sample. Data taken with a 0.17 nm spectral bandpass and a 9.78 cm optical path at 755°C. The seven uppermost lines have the same slope as the vapor pressure of Te. The inverted triangles along the line for 500.4 nm are from Ref. (21). 1, 431.5 nm; 2, 464.0; 3, 481.8; 4, 485.6; 5, 490.2; 6, 496.8; 7, 500.4; 8, 340.4; 9, 255.4; 10, 330.4; 11, 280.4; 12, 320.4; 13, 310.4 and 300.4.



of broadening, the optical absorbance on the visible side of the line center depends on the square of the mercury concentration. The proportionality constants between optical absorbance and the square of the mercury pressure have already been determined (21) for a 755°C optical cell for wavelengths between 255 and 330 nm and for pressures between about 1 and 20 atm. The purpose of the present measurements was to redetermine these constants, to extend the measurements to 30 atm, to obtain a vapor pressure point in that vicinity, and to obtain a relation between absorbance and Hg pressures for pressures below 1 atm. These results are given below, but first it is necessary to discuss the vapor pressure of Hg(l) and the equation of state for Hg(g).

The vapor pressure of Hg(l) can be adequately represented between 0.1 and 38 atm by the equation

$$\log_{10} P_{\text{Hg}}^{\circ} (\text{atm}) = -3099/T + 4.920 \quad [8a]$$

Equation [8a] agrees with tabulated selected values (19) to 1% at 0.5 atm and to within 0.5% at 1 and 10 atm. Between 10 and 38.5 atm it agrees to within 1% with the measured values of Sugawara and Sato (23), who used a six term equation to fit their points to about 0.5%. These authors also developed an equation of state for Hg(g), based in part on their vapor pres-

sure measurements. For the saturated vapor, the difference between PV/RT and unity is -4.7% at 28.8 atm, -3.8% at 19.6 atm, -2.4% at 10 atm, and -0.44% at 1 atm. Another equation of state (24) based on vapor pressure data only up to 6 atm gives values for this difference that are in fair agreement and are, respectively, -4.0% , -3.1% , -2.1% , and -0.40% . Between 10^{-3} and 10^{-1} atm the selected values (19) of P_{Hg}° are given to within 1% by

$$\log P_{\text{Hg}}^{\circ} (\text{atm}) = -3157/T + 5.028 \quad [8b]$$

Figure 5 shows the optical absorbance at four wavelengths for a 755°C optical cell as a function of the Hg(l) sample temperature. The total Hg content of the cell was $0.2940 \pm 0.005\text{g}$. At 631°C ($10^3/T = 1.106$) and above the optical absorbance no longer increases with increasing temperature, indicating complete vaporization of the Hg(l). Knowing the volume of the cell and sidearm, assuming the temperature varied linearly along the sidearm between the values measured at four positions, and using Sugawara and Sato's equation of state, one calculates that $P_{\text{Hg}} = 31.4$ atm.

At 631°C Eq. [8a] gives 31.1 atm in good agreement. Below the complete vaporization temperature in Fig. 5, the data at each wavelength can be well represented by straight lines of $\log D$ vs. $1/T$ with a slope that is

Table II. Beers law constants, a_{λ} , from Eq. [7] for $\text{Te}_2(\text{g})$ obtained using a cell with a 9.78 cm optical path at 755°C

| | | | | | | | | |
|--------------------|--------|--------|---------|--------|--------|--------|--------|--------|
| λ | 363.4 | 383.2 | 404.2p* | 421.5p | 431.5p | 436.1p | 458.6p | 464.0p |
| $10^3 a_{\lambda}$ | 7.57 | 3.10 | 2.16 | 2.19 | 2.40 | 2.65 | 3.94 | 4.65 |
| λ | 472.5p | 481.8p | 485.6p | 490.2p | 496.8p | 499.4p | 500.4 | 550.4 |
| $10^3 a_{\lambda}$ | 5.89 | 7.60 | 9.10 | 10.54 | 12.65 | 15.00 | 16.37 | 22.76 |

* p after a wavelength indicates an absorption maximum.

Table III. Lineshape in long wavelength tail of 253.7 nm Hg(g) absorption line
 $P_{\text{Hg}} (\text{atm}) = b_{\lambda} D_{\lambda}^{1/2} = r_{\lambda} (D_{\lambda}/L)^{1/2}$ *

| | | | | | | | |
|---------------------------|--------|--------|--------|--------|-------|-------|-------|
| λ (nm) | 254.4 | 255.4 | 256.4 | 257.4 | 258.4 | 259.4 | 260.4 |
| b_{λ} | 0.3981 | 0.6456 | 0.9495 | 1.190 | 1.412 | 1.624 | 1.824 |
| r_{λ} | 1.248 | 2.024 | 2.977 | 3.731 | 4.427 | 5.09 | 5.72 |
| r_{λ} [Ref. (21)] | — | — | — | — | — | — | 5.38 |
| λ (nm) | 270.4 | 280.4 | 290.4 | 300.4 | 310.4 | 320.4 | 330.4 |
| b_{λ} | 3.511 | 5.282 | 7.725 | 10.666 | 14.79 | 22.75 | 36.14 |
| r_{λ} | 11.01 | 16.56 | 24.2 | 33.4 | 46.4 | 71.3 | 113.3 |
| r_{λ} [Ref. (21)] | 10.73 | 16.46 | 23.53 | 33.23 | 47.87 | 72.52 | 112.8 |
| λ (nm) | 340.4 | — | — | — | — | — | — |
| b_{λ} | 56.23 | — | — | — | — | — | — |
| r_{λ} | 176.3 | — | — | — | — | — | — |
| r_{λ} [Ref. (21)] | — | — | — | — | — | — | — |

* b_{λ} for a 9.83 cm optical path at 1028 K as obtained with a 0.17 nm spectral bandpass. L path length in cm. r_{λ} values from Ref. (21) are for wavelengths 0.4 nm shorter than listed and are increased by 1% to make them compatible with the Hg vapor pressure equation used here.

twice that in Eq. [8a]. Similar behavior is shown at lower pressures and shorter wavelengths and the results are in good agreement with those from a study (21) of HgTe(c) as can be seen in Table III. The range of pressures over which the constants in Table III were determined for each wavelength can be inferred from the path length and the fact that the measured net optical absorbances were in the 0.05-2.6 range. For wavelengths greater than 300 nm the measurements were made using a 2.92 cm path cell and the optical absorbances were normalized by multiplying by 9.83/2.92.

In contrast to the measurements of Te₂(g), those on Hg(g) discussed above were made with the monochromator wavelength scan-drive off. Thus the somewhat slow response time of the measuring electronics was not a factor when the optical absorbance changed rapidly with wavelength near 253.7 nm.

At low values of P_{Hg} the optical absorbance of the 253.7 nm line was scanned as a function of wavelength and the area of the line computed. The results are shown in Fig. 6. For values of $10^3/T$ less than about 2.4, where $P_{\text{Hg}} = 3.7(10^{-3})$ atm, the measured full line width at half-intensity is greater than the spectral bandpass of 0.017 nm and the absorbance area has a slope close to that of the vapor pressure on the log (area)- $10^3/T$ plot. Obtaining a least squares straight line to the high temperature portion of Fig. 6 and using Eq. [8b] to eliminate $10^3/T$ in favor of P_{Hg} , one obtains

$$\log P_{\text{Hg}} \text{ (atm)} = 0.9382 \log A - 1.763 \quad [9]$$

where the area of the absorbance curve, A , has the units of optical absorbance-angstroms. This equation is used here to establish P_{Hg} in the 0.001-0.20 atm range.

Cadmium.—The true area of an atomic absorption line on a plot of optical absorbance vs. λ is proportional to the number of atoms in the light beam that are in the initial state of the optical transition. In the experiments to be discussed, the partial pressure of Cd

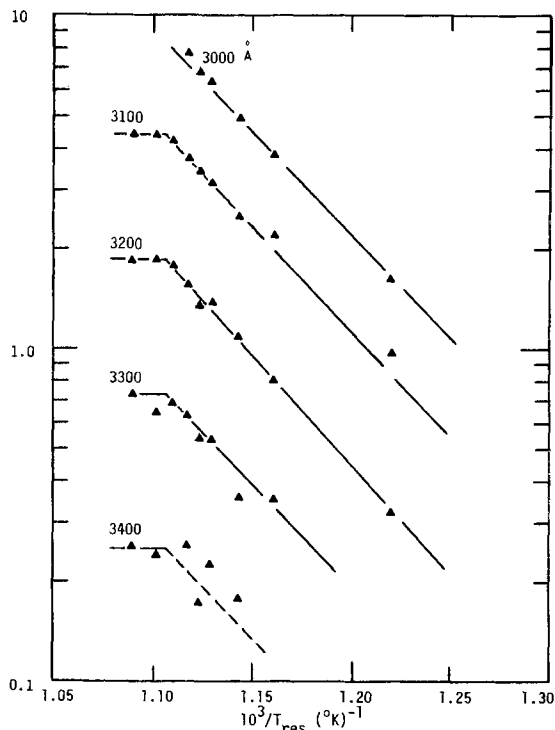


Fig. 5. Normalized optical absorbance on a long scale as a function of the reciprocal temperature of a liquid Hg sample. Absorbance is measured with a 0.17 nm spectral bandpass and a 2.92 cm optical path at 755°C. Measured values are normalized to a 9.83 cm path by multiplication by the factor 9.83/2.92. Labels give the wavelength in angstroms.

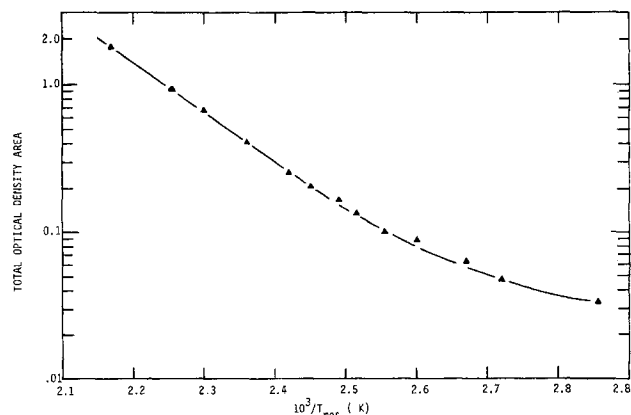


Fig. 6. Area of the 253.7 nm Hg line in units of optical absorbance-angstroms as a function of the reciprocal temperature of a liquid Hg sample. Data taken with a 0.017 nm spectral bandpass and a 9.83 cm optical path at 755°C.

varied over a range of low values while that of Hg was simultaneously in the 1-30 atm range. Correspondingly the true half-width of the Cd lines varied from values less than our smallest spectral bandpass of about 0.01 nm to values that were comparable or somewhat larger because of broadening by Hg. In such a case it is not possible to obtain reliable values of the partial pressure of Cd, P_{Cd} , from optical absorbance measurements unless extensive calibration measurements are made over a range of known P_{Cd} values for a set of known values of P_{Hg} . Moreover, the calibration results are unique to the slit settings and even to the particular monochromator used (25). We chose to shorten the labor somewhat, at the necessity of relying on the theory of lineshape, by making transmission measurements and obtaining the area in the transmission minima of the Cd lines. This is a common procedure when dealing with atomic lines and relies on the fact that although the transmission curve is distorted when the spectral bandpass is comparable to or larger than the true line half-width, the true area of the transmission curve is obtained to a first approximation. However, a knowledge of the absorption lineshape is necessary to extract the partial pressure of the absorber atom from the transmission area. The necessary results from lineshape theory are now summarized (26). If the intensities of the incident and transmitted beams at some frequency ν are I_0 and I_ν , respectively, then these are related by

$$I_\nu = I_0 \exp(-k_\nu L) \quad [10]$$

where L is the optical path length and k_ν is a frequency-dependent absorption coefficient. Comparison with Eq. [4] shows the net optical absorbance used here and k_ν are related by

$$D(\lambda, \text{net}) = k_\nu L / 2.303 \quad [11]$$

It is assumed that at sufficiently low P_{Cd} that the lineshape is the Voigt profile given by

$$k_\nu = \frac{k_0 a'}{\pi} \int_{-\infty}^{\infty} \frac{\exp(-z^2) dz}{(a')^2 + (\omega - z)^2} \quad [12]$$

where the reduced frequency ω is given in terms of the frequency of the line center, ν_0 , and the Doppler half-width $\Delta\nu_D$ by

$$\omega = 2(\nu - \nu_0) (\ln 2)^{1/2} / \Delta\nu_D \quad [13]$$

The parameter k_0 is proportional to the number of atoms, N , in the optical path that are in the initial state for the particular transition in question and to the oscillator strength of the transition, f , as given by

$$k_0 = 9.40 (10^{-2}) (\ln 2)^{1/2} N f / \pi \Delta\nu_D \quad [14]$$

The initial state for the optical transitions giving rise to the 228.7 and 325.7 nm lines observed here is the ground state of Cd(g). At the low temperatures and light intensities used, all of the Cd atoms are in the ground state and N is the concentration of Cd atoms. The Doppler half-width is given by

$$\Delta\nu_D = (2\nu_0/c) (2[\ln 2]RT/M)^{1/2} \quad [15]$$

where R is the gas constant, T is the optical cell temperature, and M is the gram-atomic weight of Cd. The width of the Voigt line is determined by the broadening parameter, a' , given by

$$a' = (\Delta\nu_N + \Delta\nu_S + \Delta\nu_F) (\ln 2)^{1/2} / \Delta\nu_D = a_N + a_S + a_F \quad [16]$$

where the natural half-width is determined by the lifetime of the excited state, τ

$$\Delta\nu_N = 1/(2\pi\tau) \quad [17]$$

and where the self-broadening contribution, a_S , is assumed to be proportional to the partial pressure of the absorber while the foreign gas contribution a_F is in general a sum of terms, one for each foreign gas that is proportional to the partial pressure of that foreign gas. It is necessary to experimentally determine a_S and a_F . The lifetimes τ , and equivalently, the oscillator strengths, of the 228.7 and 325.7 nm lines are known so that the natural half-width and the parameter k_0 in Eq. [14] can be calculated. Equation [12] predicts a lineshape that is symmetrical about ν_0 and the equation is valid sufficiently close to ν_0 and at low pressures. At frequencies sufficiently far from the line center and at high pressures the statistical theory of broadening holds and the Cd lines broaden extensively toward the visible. The proportionality between optical absorbance and the square of P_{Cd} has already been utilized (14) in determining the partial pressures along the three-phase curve for CdTe(c). In this study the Voigt lineshape was assumed to hold as long as the transmission curves were symmetrical. Finally, the total absorption as obtained in a transmission measurement is defined as

$$y' = \frac{(\ln 2)^{1/2}}{\Delta\nu_D} \int_0^\infty [1 - \exp(-k_\nu L)] d\nu \quad [18]$$

For a given value of a' , y' can be calculated as a function x' where

$$x' = 10.6k_0L = NfL (\ln 2)^{1/2} / \pi\Delta\nu_D \quad [19]$$

Curves of y' as a function of x' are known as curves of growth and are given for a few values of a' by Mitchell and Zemansky (26) and by Penner (27). The measured transmission areas correspond to the integral factor of Eq. [18] with $d\nu$ replaced by $d\lambda$ and the wavelength in angstroms. They are converted to the integral factor by multiplication by $\nu_0^2/3 (10^{18})$, where ν_0 is the frequency at the line center. Values of x' were calculated from Eq. [19] using published values of the oscillator strength and assuming that Cd(g) is an ideal gas whose pressure can be calculated from the Cd sample temperature and the vapor pressure equation given by

$$\begin{aligned} \log P_{Cd} \text{ (atm)} &= -5808/T + 5.956 & T < 594 \text{ K} \\ &= -5317/T + 5.119 & T > 594 \text{ K} \end{aligned} \quad [20]$$

Equations [20] match the tabulated values [19] to within 2% between 10^{-8} and 1 atm.

Figure 7 shows a few curves of growth along with the experimental points for the 228.7 Cd line. At low Cd pressures the experimental points follow closely the curve of growth for $a' = 0.023$, corresponding to natural and Doppler broadening. At higher pressures, the points cross the curves of growth indicating the onset of significant self-broadening. The 325.7 nm line shows a similar behavior except that at the lowest pres-

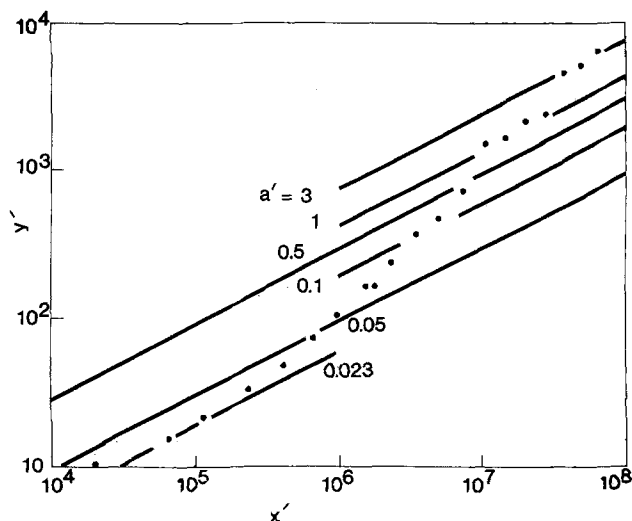


Fig. 7. Parameter y' of Eq. [18], which is proportional to the transmission area, plotted against x' of Eq. [19] for the 228.7 nm Cd line on a log-log scale. A few curves of growth are shown for labeled values of a' . Data taken with a 9.40 cm optical path at 755°C . $x' = 7.57(10^9) P_{Cd}(\text{atm})$.

sures the experimental points are somewhat above the theoretical curve for $a' = 2.69(10^{-5})$. If the self-broadening parameter, $a_S = a' - a_N$ is plotted against P_{Cd} , Fig. 8 results. The best straight lines of unit slope through the points are given by

$$a_S(228.7 \text{ nm}) = 108P_{Cd}(\text{atm}) \quad [21]$$

$$a_S(325.7 \text{ nm}) = 1.50P_{Cd}(\text{atm}) \quad [22]$$

In terms of the full frequency width at half-intensity, Eq. [21] and [22] correspond to

$$\Delta\nu_{\text{HW}}(228.7) = 2.75(10^{11})P_{Cd} \quad [23]$$

$$\Delta\nu_{\text{HW}}(325.7) = 2.74(10^9)P_{Cd} \quad [24]$$

Theoretical calculation (28, 29) of this half-width for resonance broadening is most accurate for lines with oscillator strengths near unity, such as the 228.7 line, and are of the form

$$\Delta\nu_{\text{HW}} = ke^2fN/8m\nu_0 \quad [25]$$

with k of the order of unity and equal to 1.45 for

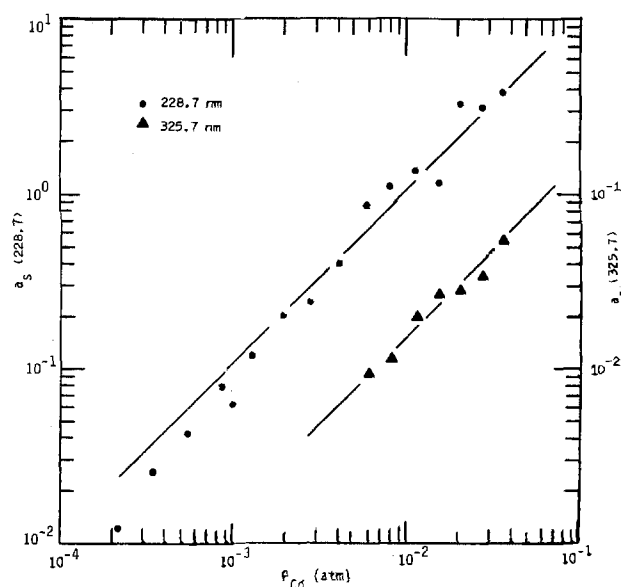


Fig. 8. Self-broadening parameters for the 228.7 and 325.7 nm Cd lines as a function of the pressure of Cd(g) in atmospheres.

$^1P_1-^1S_0$ and $^3P_1-^1S_0$ transitions. The proportionality constant between half-width and Cd pressure calculated from Eq. [25] is $2.77(10^{11}) \text{ sec}^{-1}$ for the 228.7 line and $6.3(10^8) \text{ sec}^{-1}$ for the 325.7 line. As can be seen the agreement with experiment is excellent in the former case and somewhat less so, as expected, in the latter case.

Mercury-cadmium.—The foreign gas broadening parameters representing the effect of Hg(g) on the Cd absorption lines were determined by measuring these lines in transmission for the vapor over Hg-Cd liquids for which P_{Hg} and P_{Cd} were known as a function of sample temperature. The area in the transmission minimum of a given line was converted to the van der Held parameter, y' , using Eq. [18] and the experimental points superimposed on a plot of the curves of growth. At each value of x' given by Eq. [19], the broadening parameter was determined. Subtracting the natural half-width contribution given by Eq. [16] and [17] and the self-broadening contribution given by Eq. [21] and [22] gave the Hg contribution, a_F , for each line.

Two slightly different techniques were used to obtain known values of P_{Hg} and P_{Cd} . In one, Hg-Cd solutions were prepared by weighing and successive dilution. Exposure of these solutions to the air was minimized by covering them with kerosene for the short time required for weighing and storing them in evacuated, sealed, silica tubes. For the experiments reported here the mercury surface remained clean and showed no sign of dark cadmium oxide even after heating in the optical cells. Sufficiently small, known weights of these solutions were sealed into optical cells so that the sample would completely vaporize at some sample temperature below the optical cell temperature of 755°C . An approximate temperature of complete vaporization was calculated assuming the Hg-Cd liquid was ideal. Measurements were then made for a few sample temperatures higher than this. Complete vaporization was confirmed by the fact that the transmission at the line center was only weakly dependent on sample temperature. The values of P_{Hg} and P_{Cd} were calculated from the known weight and atom fraction of the initial sample and the volume temperature profile in the cell and sidearm assuming the vapor was a mixture of ideal Cd(g) and imperfect Hg(g). The value of P_{Hg} could be independently obtained from the optical absorbance in the 255.0-340.0 nm interval using the results given in the section on Calibration Measurements, Mercury. The two values of P_{Hg} so obtained agreed to within a few percent. In the second technique, larger, known, sample weights were used so that dilution was not necessary, but the samples were never completely vaporized. For each sample temperature, P_{Hg} was obtained from the optical absorbance in the 255.0-340.0 nm interval and the composition of the liquid sample calculated assuming the vapor was essentially all Hg(g). A calculated value for P_{Cd} was then obtained for the known sample temperature and composition assuming the partial molar enthalpy and entropy for both Cd and Hg at 600 K are temperature independent. The equation used was

$$\ln P_{\text{Cd}} = \ln P_{\text{Cd}}^\circ + (\bar{h}_{\text{Cd}} - T\bar{s}_{\text{Cd}})/RT \quad [26]$$

where the vapor pressure P_{Cd}° is given by Eq. [20] and the relative partial molar enthalpy, \bar{h}_{Cd} , and entropy, \bar{s}_{Cd} , were interpolated between the values given by Hultgren *et al.* (30) at intervals of 0.1 in atom fraction.

The values of a_F are shown plotted vs. P_{Hg} in Fig. 9 and 10 along with the least squares straight lines obtained under the constraint of unit slope on the log-log plot. As indicated in the figure captions certain points corresponding to longer times at temperature were weighted more heavily in the fit. From these results and those given in the section on Calibration Measurements, Cadmium, the broadening parameters given in

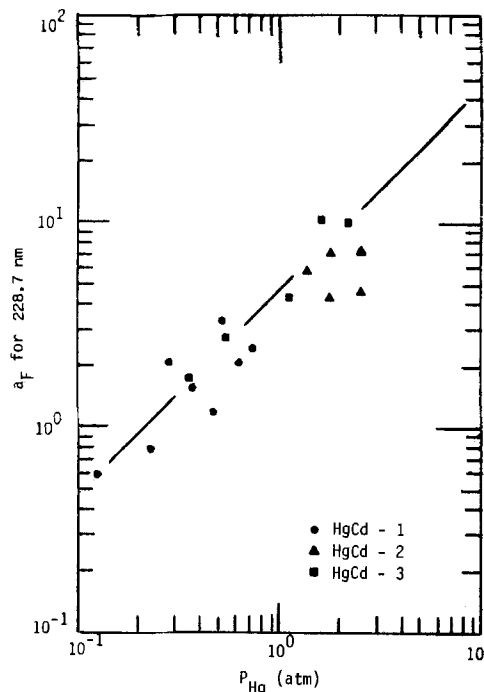


Fig. 9. Foreign gas broadening parameter for the 228.7 nm Cd line as a function of Hg(g) pressure. Data shown as squares represent 15-18 hr at sample temperature and are favored in determining the least squares line shown.

general by Eq. [16] can be written for a 755°C optical path as

$$a'(228.7) = 0.0236 + 108P_{\text{Cd}} + 4.60P_{\text{Hg}} \quad [27]$$

$$a'(235.7) = 2.69(10^{-5}) + 1.50P_{\text{Cd}} + 1.18P_{\text{Hg}} \quad [28]$$

where the pressures are in atmospheres.

The 228.7 line becomes slightly asymmetric and broadened toward the visible for P_{Hg} greater than about 0.5 atm. Table IV lists the literature values used and a few of the derived quantities used.

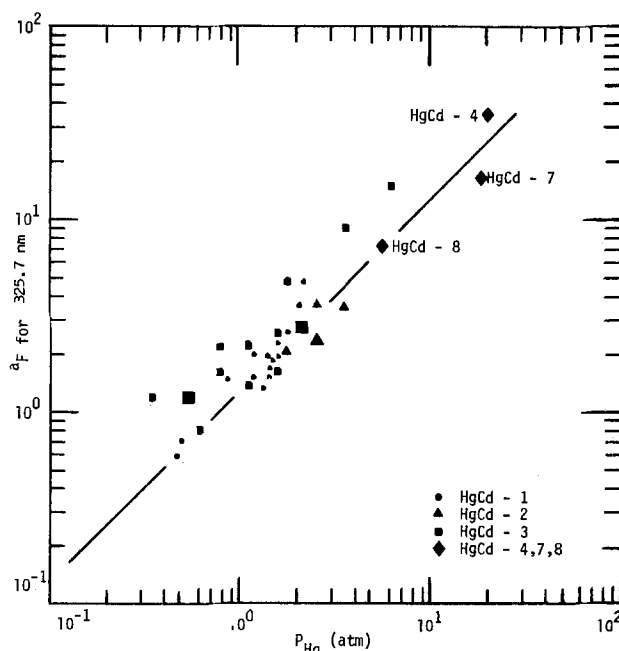


Fig. 10. Foreign gas broadening parameter for the 325.7 nm Cd line as a function of Hg pressure. Oversized squares, triangles, and diamonds represent 15-18 hr at sample temperature and are favored in determining the least squares line shown.

Table IV. Parameters for the Cd 228.7 and 325.7 absorption bands

| Parameter (units) | 228.7 | 325.7 | Reference |
|-------------------------------------|--------------------|-------------------|-----------|
| τ (s) | 1.99 (10^{-9}) | 2.5 (10^{-9}) | (26) |
| f (none) | 1.20 | 1.9 (10^{-3}) | (26) |
| $\Delta\nu_N$ (sec^{-1}) | 8.00 (10^7) | 6.4 (10^6) | — |
| $\Delta\nu_D$ (sec^{-1}) | 2.82 (10^9) | 1.98 (10^9) | — |

Calculation of Partial Pressures

Four optical cells containing $\text{Hg}_{1-x}\text{Cd}_x\text{Te}$ with $x = 0.416$ were prepared. One contained a known weight of Te in addition, three contained known weights of Hg. Of these last three, one was a high pressure cell described in the section Experimental, Optical cells. Except for this cell, whose optical path length was 2.92 cm, the cells had path lengths near 9.8 cm.

The partial pressure of $\text{Te}_2(\text{g})$ was calculated from the measured net optical absorbances between 363.4 and 550.4 nm where $\text{Hg}(\text{g})$ and $\text{Cd}(\text{g})$ do not absorb at the partial pressures encountered here. The partial pressure of $\text{Te}_2(\text{g})$ was calculated using Eq. [7]. Except at the lowest values of P_2 below 10^{-4} atm, at least three or four wavelengths gave values of D between 0.1 and 2.5 and corresponding values for P_2 . This procedure assumes no effect of the high mercury pressures on the $\text{Te}_2(\text{g})$ spectrum. The vibronic spectrum of Te_2 appeared qualitatively unchanged, although the maxima are broad and flat enough to obscure possible wavelength shifts of 0.1–0.4 nm. However, consistent with the above assumption, the relative optical densities in the visible remained the same as for pure $\text{Te}_2(\text{g})$ within experimental error, i.e., the values of P_2 calculated using Eq. [7] for the various wavelengths generally agreed within the expected accuracy (Experimental, Accuracy of measurements) of the optical absorbance values.

Except at values of 10^{-2} atm and below, the mercury pressure was also obtained as the average of generally closely agreeing values calculated from the absorbance at different wavelengths. First the $\text{Te}_2(\text{g})$ contribution to the net absorbance in the 255–340 nm region was calculated from the net absorbance due to $\text{Te}_2(\text{g})$ in the visible and the assumption that the relative values shown for D in Fig. 4 for pure $\text{Te}_2(\text{g})$ are unchanged in the presence of $\text{Hg}(\text{g})$. This, generally small, contribution was then subtracted from the net optical absorbance to give the contribution, $D(\lambda, \text{Hg})$, of Hg. The contribution of $\text{Hg}(\text{g})$ to absorption in the long wavelength tail of the 253.7 nm line is given by

$$D(\lambda, \text{Hg}) = LR^2C^2/t_\lambda^2 \quad [29]$$

where R is the gas constant, L is the optical path length, C is the concentration of $\text{Hg}(\text{g})$, and $1/t_\lambda^2$ is the product of the fraction of Hg atoms in the initial state of the transition (which is the ground state) and a transition probability. The linear dependence on L has been verified for the spectral band pass of 0.17 nm used here (21). Approximating $\text{Hg}(\text{g})$ as an ideal gas, Eq. [29] can be rewritten as

$$P_{\text{Hg}}(\text{atm}) = t_\lambda T_0 D_\lambda^{1/2} / L^{1/2} = b_\lambda D_\lambda^{1/2} \quad [30]$$

where T_0 is the temperature in the optical path and where b_λ is given in Table III for $L = 9.83$ cm and $T_0 = 755^\circ\text{C}$. Since the fraction of $\text{Hg}(\text{g})$ atoms in the ground state is essentially unity up to much higher temperatures than used here, t_λ is a constant for a given wavelength if the transition probability is independent of T_0 . Theoretical analysis of resonance broadening predicts such an independence (28). Moreover, runs on pure Hg with $T_0 = 860^\circ\text{C}$ give $b_\lambda(755)/b_\lambda(860)$ close to 0.90 for the same path length (31) and in close agreement with the value of $1028/1133 = 0.91$ expected from Eq. [30] and the assumed constancy of t_λ . [In Ref. (31) the theoretical dependence of b_λ on T_0 is stated incorrectly.] The necessary values of b_λ for

different path lengths and optical cell temperatures were calculated from those in Table III using the result of Eq. [30] i.e.

$$b_\lambda(L, T_0) = \left(\frac{T_0}{1028} \right) \left(\frac{9.83}{L} \right)^{1/2} b_\lambda(9.83, 755) \quad [31]$$

For values of P_{Hg} below about 0.2 atm, the partial pressures of Te_2 and Cd were below the detectable limits of, respectively, 10^{-4} and 10^{-7} atm. The contribution of foreign gas broadening to the 253.7 Hg line was therefore assumed negligible. The area obtained from a trace of optical absorbance vs. λ across the line was multiplied by $9.83/L$ to give a normalized area. Equation [9] was then used to calculate P_{Hg} .

Once P_{Hg} was known, the broadening parameters, a' , for the Cd lines were calculated using Eq. [27] and [28] with $a_s = 0$. A first approximation for P_{Cd} could then be calculated from the observed area in the transmission minima using the curves of growth. A computer program was written that numerically evaluated the van der Held parameter, y' , of Eq. [18] for given values of the broadening parameter, a' , and the parameter, x' , of Eq. [19]. A trial and error search was used to find the value of x' giving a value of y' in agreement with the value from experiment. This allowed an evaluation of the self-broadening parameter, a_s , according to Eq. [21] and [22] and a second approximation for a' for each wavelength. The values of P_{Hg} were so much larger than those of P_{Cd} that the first and second approximations for a' were close enough to lead to the same values of P_{Cd} within 1%. A small but clear asymmetry developed in the 228.7 line for P_{Hg} greater than about 0.5 atm, the long wavelength tail broadening. In this case the value of P_{Cd} was then calculated from the area of the 325.7 line in transmission.

The partial pressure of Hg was greater than that of either Cd or Te_2 in all of the measurements reported. Consequently the solid samples became progressively poorer in Hg with increasing sample temperature. From the partial pressures at a given sample temperature and the volume and temperature distribution along the optical cell and sidearm, the composition of the sample could be calculated assuming the vapor phase to consist of ideal $\text{Te}_2(\text{g})$ and $\text{Cd}(\text{g})$ and imperfect $\text{Hg}(\text{g})$. Writing the composition of the solid solution as $(\text{Hg}_{1-x}\text{Cd}_x)_y\text{Te}_{1-y}$, data for which $x = 0.416 \pm 0.01$ are grouped together here and taken as characteristic of the solid solution with $x = 0.416$.

Results for 41.6 m/o CdTe, HgTe-CdTe

The partial pressure of $\text{Te}_2(\text{g})$ over the Te-saturated solid solution is shown in Fig. 11 which also shows the vapor pressure of pure Te adopted here (see section on Calibration Measurements, Tellurium). Those partial pressures obtained with cell 38-TE1, to which excess Te was added, are given in Tables V and VI.

Figure 12 shows P_{Hg} for a cell to which Hg was added. At low temperatures the sample is metal saturated and P_{Hg} is very close to the vapor pressure of pure Hg. At 367°C ($10^3/T = 1.562$), $P_{\text{Hg}} = 1.2$ atm, the mercury pressure becomes nearly independent of temperature for a long interval. Complete vaporization of the added Hg would provide a vapor at 1.19 atm at 367°C , agreeing with the observed value within experimental error. Therefore we conclude that the solid solution sample used in this cell is essentially free of either Hg-rich or a Te-rich second phase. Upon heating above 367°C the small loss of Hg to the vapor phase causes the composition variable y in the formula $(\text{Hg}_{1-x}\text{Cd}_x)_y\text{Te}_{1-y}$ to move from its value at metal saturation to that at Te saturation, indicated by the sudden strong dependence of P_{Hg} on T . The point of Te saturation is $T = 624^\circ\text{C}$ ($10^3/T = 1.115$), $P_{\text{Hg}} = 1.29$ atm; $P_2 = 5.0 \times 10^{-3}$ and $P_{\text{Cd}} = 5.4 \times 10^{-7}$ atm. On log P vs. $10^3/T$ plots, P_2 and P_{Cd} show discontinui-

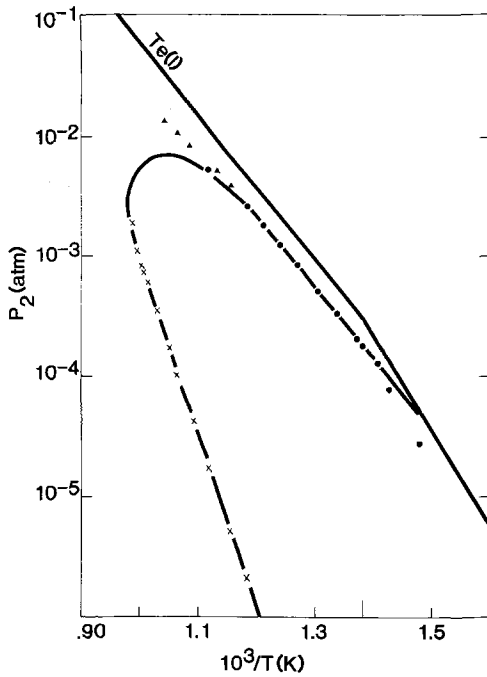


Fig. 11. Partial pressure of $Te_2(g)$ along the three-phase curve for 41.6 ± 1 m/o CdTe, HgTe-CdTe solid solution. Upper solid line is for the vapor pressure of Te. ● 38-TE1; ▲ 38-TE1, x value out of 0.416 ± 0.01 range; ▽ 40-HG3; × calculated from P_{Hg} in Table IX using Eq. [33] and first entry in Table X.

ties in slope at close to the same temperature as does P_{Hg} . Chronologically this cell was the first one used and it became apparent that, although P_{Hg} reached a steady-state value in a few hours, 15-18 hr were required for P_2 and P_{Cd} to do so with the particle size used here (see Experimental, Materials). Table VII summarizes the data for the runs of June 1977 for which the samples were 15-18 hr at temperature.

Table V. Partial pressures in atmospheres over a condensed phase of gross composition $(Hg_{1-x}Cd_x)_yTe_{1-y}$ obtained from cell 38-TE1 with a 9.40 cm optical path at 1028 K*

| T (K) | $10^2 \times P_{Hg}$ | $10^4 \times P_2$ | x | y |
|-------|----------------------|-------------------|-------|-------|
| 676.5 | 0.692 | 0.274 ± 0.001 | 0.416 | 0.492 |
| 700.6 | 1.81 | 0.784 ± 0.013 | | |
| 711.3 | 2.60 | 1.30 ± 0.06 | | |
| 724.7 | 2.53 | 1.71 ± 0.09 | | |
| 729.6 | 2.87 | 2.03 ± 0.14 | 0.417 | 0.491 |
| 748.5 | 4.29 | 3.32 ± 0.09 | 0.418 | 0.491 |
| 767.9 | 8.09 | 5.07 ± 0.06 | 0.419 | 0.490 |
| 787.5 | 15.8 | 8.53 ± 0.10 | 0.423 | 0.488 |
| 806.7 | 22.2 | 12.20 ± 0.02 | 0.426 | 0.487 |
| 826.2 | 29.0 | 17.66 ± 0.16 | 0.428 | 0.485 |
| 844.2 | 42.8 | 25.8 ± 0.1 | 0.434 | 0.482 |

* In general a partial pressure is obtained as the average of values calculated from the optical absorbance at several wavelengths. The uncertainties listed are the standard deviation of these values. For T up through 729.6 K, P_{Hg} is obtained using Eq. [9]. At higher T in this table and in Table VI, six values from D at λ between 255.0 and 270.0 nm are averaged. Two to six values from readings at λ between 421.5 and 500.4 nm are averaged to obtain P_2 , the partial pressure of $Te_2(g)$.

Table VI. Partial pressures in atmospheres from cell 38-TE1 at high temperatures. Cadmium pressures are obtained from 228.7 nm line except for the value at 959.5 K in brackets which is obtained from the 325.7 nm line.

| T (K) | P_{Hg} | $10^5 \times P_2$ | $10^5 \times P_{Cd}$ | x | y |
|-------|-------------------|-------------------|----------------------|-------|-------|
| 865.2 | 0.626 ± 0.019 | 3.87 ± 0.01 | 0.0146 | 0.444 | 0.476 |
| 883.2 | 0.830 ± 0.021 | 5.09 ± 0.06 | 0.494 | 0.450 | 0.473 |
| 920.9 | 1.436 ± 0.030 | 8.32 ± 0.21 | 1.91 | 0.48 | 0.457 |
| 939.9 | 1.869 ± 0.043 | 10.75 ± 0.02 | 3.69 | 0.504 | 0.445 |
| 959.5 | 2.276 ± 0.10 | 14.32 ± 0.08 | 5.03 | 0.533 | 0.431 |

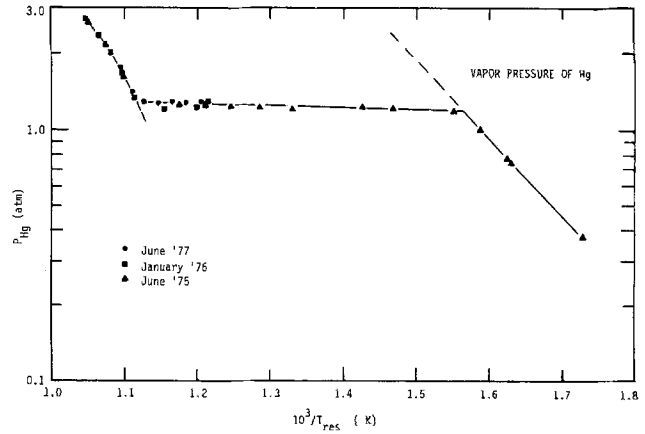


Fig. 12. Partial pressure of Hg on a log scale vs. reciprocal sample temperature for cell 38-HG1. The dashed line at upper right shows the vapor pressure of Hg. The data show the sample leaving the metal-saturated condition at low temperatures, crossing the homogeneity range, and attaining Te saturation.

The value of P_{Hg} along the three-phase curve for $x = 0.416$ is shown in Fig. 13. The lowest values are from the Te-saturated sample described earlier. One cell contained sufficient extra Hg to cross the stability field of the solid solution with P_{Hg} near 5 atm. This run furnished one metal-saturated point and one Te-saturated point in addition to a number of points within the stability field which can be used to calculate the chemical potentials of HgTe and CdTe and the standard Gibbs free enthalpy of formation from the elemental gases. The long-time points are given in Table VIII. From the data obtained with this cell the metal saturation point is at $10^3/T = 1.315$ and $P_{Hg} = 5.6$ atm. The Te-saturation point is at $10^3/T = 1.046$ and $P_{Hg} = 5.84$ atm. The highest mercury pressures were obtained using a high pressure cell. As shown in Fig. 13, P_{Hg}

Table VII. Partial pressures in atmospheres over a condensed phase of gross composition $(Hg_{1-x}Cd_x)_yTe_{1-y}$ as obtained from cell 38-HG1 with a 9.40 cm optical path at 1028 K. Uncertainties are standard deviations.

| T (K) | P_{Hg} * | $10^3 \times P_2$ ** | $10^7 \times P_{Cd}$ † | x | y |
|-------|-------------------|----------------------|------------------------|-------|-------|
| 830.0 | 1.276 ± 0.017 | 0.234 ± 0.004 | 1.11 | 0.416 | 0.500 |
| 845.0 | 1.275 ± 0.017 | 0.287 ± 0.010 | 1.79 | 0.416 | 0.500 |
| 859.1 | 1.279 ± 0.009 | 0.78 ± 0.02 | 4.65 | 0.416 | 0.500 |
| 873.0 | 1.272 ± 0.018 | 1.55 ± 0.02 | 4.82 | 0.415 | 0.501 |
| 888.1 | 1.277 ± 0.007 | 3.30 ± 0.05 | 5.39 | 0.415 | 0.501 |
| 901.1 | 1.401 ± 0.010 | 5.40 ± 0.09 | 8.58 | 0.420 | 0.498 |
| 914.7 | 1.754 ± 0.008 | 6.48 ± 0.08 | 21.9 | 0.434 | 0.490 |

* P_{Hg} is the average of seven values obtained from D between 256.4 and 280.4 nm.

** P_2 is the average of four to six values obtained from D between 363.4 and 458.6 nm.

† P_{Cd} is obtained from the 228.7 nm line.

Table VIII. Partial pressures in atmospheres obtained with cell 40-HG3, 9.81 cm optical path at 1028 K

| T (K) | P_{Hg} * | $10^5 \times P_2$ ** | $10^5 \times P_{Cd}$ † | x | y |
|-------|-----------------|----------------------|------------------------|-------|-------|
| 901.2 | 5.63 ± 0.05 | 0.369 ± 0.007 | 4.1 | 0.413 | 0.502 |
| 919.7 | 5.67 ± 0.06 | 0.68 ± 0.04 | 6.6 | 0.413 | 0.502 |
| 927.6 | 5.75 ± 0.05 | 1.22 ± 0.03 | 6.28 | 0.415 | 0.501 |
| 946.3 | 5.81 ± 0.05 | 3.04 | 7.62 | 0.415 | 0.501 |
| 955.5 | 5.84 ± 0.05 | 4.11 ± 0.46 | 8.73 | 0.416 | 0.501 |
| 970.2 | 6.08 ± 0.11 | 7.47 ± 0.49 | 10.8 | 0.420 | 0.498 |
| 919.6 | 5.67 ± 0.07 | 0.612 ± 0.011 | 6.63 | 0.413 | 0.502 |
| 937.8 | 5.76 ± 0.08 | 1.12 ± 0.02 | 9.11 | 0.415 | 0.501 |
| 909.0 | 5.62 ± 0.08 | 0.388 ± 0.03 | 5.56 | 0.413 | 0.502 |

* P_{Hg} is the average of four values calculated from D between 280.4 and 300.4 nm.

** P_2 is the average of three to four values calculated from D between 421.4 and 458.6 nm.

† P_{Cd} is from the 325.7 nm line.

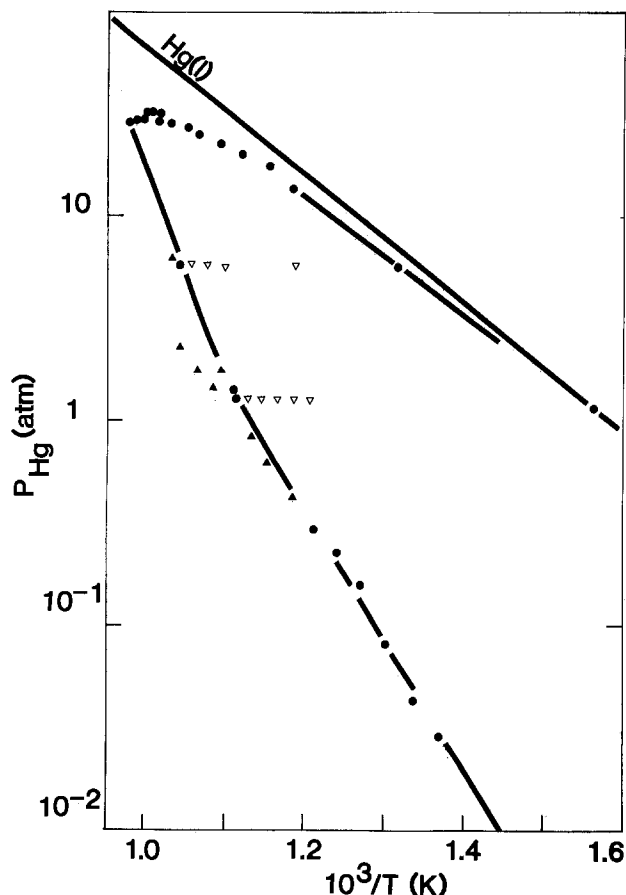


Fig. 13. Vapor pressure of Hg shown as uppermost line and partial pressure of Hg(g) along the three-phase curve for 41.6 ± 1 m/o CdTe, HgTe-CdTe solid solution. ● Saturation point or point on three-phase curve, ▽ inside field of stability, ▲ outside field of stability.

reaches at maximum of 32.0 atm near 723°C. The sample used to obtain these high pressures leaves the three-phase curve at $745 \pm 2^\circ\text{C}$, $P_{\text{Hg}} = 28.0$ atm, and the data undergo a reversal in slope. This is shown in more detail in Fig. 14 in which the optical absorbance is plotted. The temperature of $745 \pm 2^\circ\text{C}$ is interpreted as the solidus point for $\text{Hg}_{0.594}\text{Cd}_{0.416}\text{Te}(c)$. It agrees with the published data (4) within their scatter. The published data are from chemical analysis of the

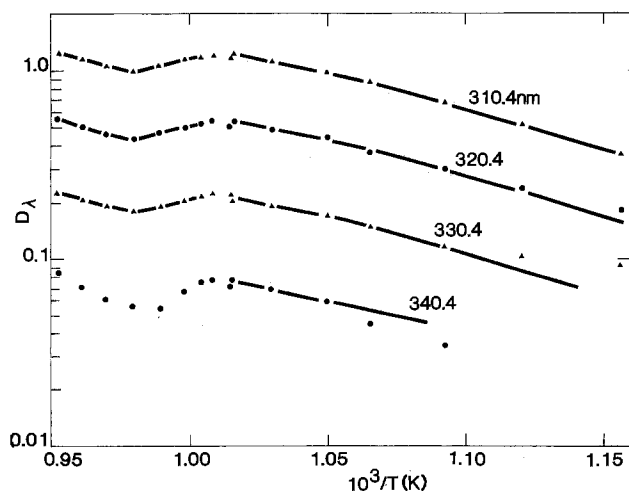


Fig. 14. Optical absorbance on a log scale and for different wavelengths as a function of reciprocal sample temperature for metal-saturated solid solution containing 41.6 ± 1 m/o CdTe. Data from cell 40-HG2 with a 2.92 cm optical path at 755° or 800°C . Pressures given in Table IX.

first crystals to freeze from a large volume of melt and furnish directly the compositions of coexisting liquid and solid solution phases. The corresponding temperature was taken from the smoothed liquidus line as determined by thermal analysis (1). The static technique used here to determine the solidus point is quite different and it is encouraging to obtain agreement. Steininger (5) has measured P_{Hg} over the pseudobinary melts by a reflux method. He found the unusual result that for several mole percents of CdTe between 0 and 60%, that the points all fell on the same straight line on a plot of $\log P_{\text{Hg}}$ vs. $10^3/T$. At 745°C he finds $P_{\text{Hg}} = 24$ atm in fair agreement with our value of 28 atm. The values of P_{Hg} from the measurements with the high pressure cell are summarized in Table IX. In order to minimize the time at high temperature and pressure the measurements necessary to obtain P_2 and P_{Cd} were omitted.

Discussion

For the experiments described here, in which the samples changed from a metal-saturated condition at low temperature to one of Te saturation at higher temperature, the calculated atomic percent of Te remained equal to 50% within an estimated experimental error of $\pm 0.2\%$. Hall measurements (6) on solid solution samples with $x = 0.40$ that were either metal saturated or Te saturated at high temperatures show an excess of holes over electrons for saturation temperatures above 350°C . At 600°C the excess of holes over electrons is about 10^{17} cm^{-3} for metal saturation and $2(10^{17}) \text{ cm}^{-3}$ for Te saturation. The data have been combined with the values of P_{Hg} reported here in a defect chemistry analysis (32). Assuming no significant concentration of native point defects that are inactive as donors or acceptors, $(\text{Hg}_{0.584}\text{Cd}_{0.416})_y\text{Te}_{1-y}(c)$ is always Te-rich, i.e., $y < 1/2$, above about 350°C and the range of y for a stable phase is restricted to values within $5(10^{-4})$ of $1/2$. Thus it is to be expected that the standard Gibbs free enthalpy of formation is independent of y to a good approximation. In fact, for such a narrow homogeneity range, statistical thermodynamic argument shows (11) that the chemical potentials of the thermodynamic components HgTe and CdTe are also independent of y to a good approximation. This theoretical prediction affords a check on the internal consistency of the measurements reported here which is discussed below. First, however, it should be noted that the independence of the chemical potentials of HgTe and CdTe from y implies a similar independence for the difference in the chemical potentials of Hg and Cd. Second, the discussion of HgTe and CdTe as thermodynamic components of the solid solution of course does not imply the existence of either HgTe or CdTe as structural units.

Table IX. Partial pressure of Hg in atmospheres from cell 40-HG2, 2.92 cm optical path at 1028 K or, starting with 985.1 K sample temperature, at 1073 K

| T (K) | P_{Hg}^* | x | y |
|--------|-------------------|-------|-------|
| 841.9 | 13.66 ± 0.23 | 0.399 | 0.511 |
| 865.4 | 17.43 ± 1.4 | 0.402 | 0.509 |
| 892.8 | 19.72 ± 0.26 | 0.404 | 0.508 |
| 915.5 | 22.06 ± 0.41 | 0.405 | 0.507 |
| 937.6 | 24.85 ± 0.33 | 0.407 | 0.505 |
| 952.1 | 26.68 ± 0.42 | 0.409 | 0.505 |
| 970.6 | 28.51 ± 0.40 | | |
| 984.8 | 29.82 ± 0.34 | 0.411 | 0.503 |
| 985.1 | 30.79 ± 0.41 | | |
| 995.8 | 32.09 ± 1.41 | 0.412 | 0.502 |
| 991.5 | 31.46 ± 0.43 | | |
| 1001.7 | 30.29 ± 0.19 | 0.410 | 0.503 |
| 1010.8 | 29.16 ± 0.19 | 0.410 | 0.504 |
| 1020.9 | 28.48 ± 0.19 | 0.409 | 0.504 |
| 1031.0 | 29.35 ± 0.20 | 0.410 | 0.504 |
| 1040.3 | 30.30 ± 0.04 | 0.410 | 0.503 |
| 1049.5 | 31.67 ± 0.54 | 0.411 | 0.503 |

* P_{Hg} is the average of three values calculated from D at 310.4, 320.4, and 330.4 nm.

Table X. Results of least squares fits to various thermodynamic functions for $\text{Hg}_{0.584}\text{Cd}_{0.416}\text{Te}(c)$

| Function | N^* | σ^{**} | σ_2^\dagger (cal) | $1/\langle 1/T \rangle^\ddagger$ (K) | Enthalpy§ (cal/mole) | Entropy§ (cal/K-mole) |
|---------------------|-------|---------------|--------------------------|--------------------------------------|----------------------|-----------------------|
| μ_{HgTe} | 20 | 0.124 | 232 | 878.2 | $-41,470 \pm 1201$ | -41.491 ± 1.383 |
| μ_{CdTe} | 17 | 0.114 | 220 | 924.7 | $-68,533 \pm 3053$ | -43.347 ± 1.566 |
| ΔG°_f | 13 | 0.0656 | 129 | 916.0 | $-50,995 \pm 2337$ | -40.318 ± 2.557 |

* N = number of data points.

** σ = standard deviation between measured and calculated values of μ/RT or $\Delta G^\circ_f/RT$.

† σ_2 = corresponding standard deviation for μ or ΔG°_f .

‡ $1/\langle 1/T \rangle$ = reciprocal of average $1/T$ value for experimental points.

§ The uncertainties in the enthalpies and entropies are at the 95% confidence level as calculated using the Student t -distribution with $N - 2$ degrees of freedom.

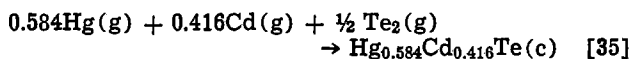
Assuming the vapor phase is ideal the chemical potentials relative to those of $\text{Hg}(g)$, $\text{Te}_2(g)$, and $\text{Cd}(g)$, each at 1 atm are

$$\bar{\mu}_{\text{HgTe}} = RT \ln P_{\text{Hg}} P_{\text{Te}_2}^{1/2} \quad [32]$$

$$\bar{\mu}_{\text{CdTe}} = RT \ln P_{\text{Cd}} P_{\text{Te}_2}^{1/2} \quad [33]$$

$$\bar{\mu}_{\text{Hg}} - \bar{\mu}_{\text{Cd}} = \bar{\mu}_{\text{HgTe}} - \bar{\mu}_{\text{CdTe}} = RT \ln P_{\text{Hg}}/P_{\text{Cd}} \quad [34]$$

The standard Gibbs free enthalpy of formation for the reaction



is given by

$$\Delta G^\circ_f = 0.584 \bar{\mu}_{\text{HgTe}} + 0.416 \bar{\mu}_{\text{CdTe}} \quad [36]$$

These quantities can be calculated from the entries in Tables V-VIII. Alternatively, the nonideal behavior of $\text{Hg}(g)$ could be taken into account using the equation of state of Sugawara and Sato (23) to calculate the fugacity. The largest corrections occur for the data given in Table VIII and amount to -10 to -15 cal for the chemical potential of Hg . Since these prove to be considerably less than the precision to which the chemical potential of HgTe can be fit, these corrections are neglected here. The negative of the chemical potential of HgTe is plotted as a function of T in Fig. 15. For completeness the figure includes some points outside the range $x = 0.416 \pm 0.01$. There are the three highest temperature points for 38-TE1 and the two highest temperature points for 38-HG1. These out of range points, as well as that at 830 K and the lowest point at 935.4 K are excluded from a least squares fit of μ_{HgTe}/RT to a straight line as a function

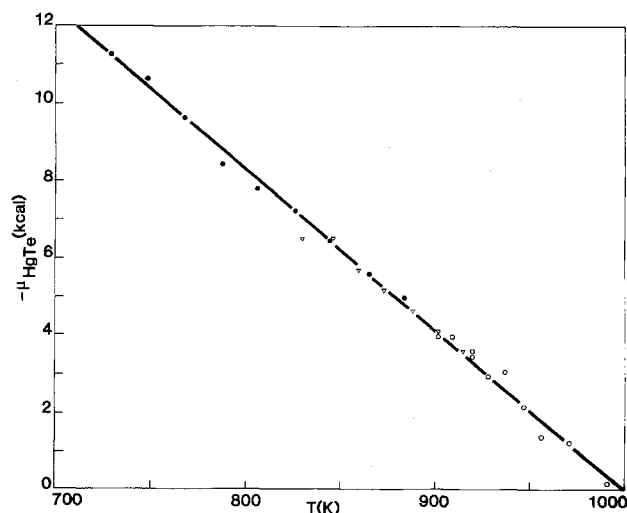


Fig. 15. The negative of the chemical potential of HgTe for a solid solution containing 41.6 ± 1 m/o CdTe as a function of absolute temperature. Solid line is from a least squares fit. ● 38-TE1, ▽ 38-HG1, ○ 40-HG3.

of $1/T$

$$\bar{\mu}_{\text{HgTe}}/RT = \bar{h}/RT - \bar{s}/R \quad [37]$$

where the partial molar quantities are assumed to be independent of T . The result is shown as the solid line in Fig. 15 and in the first entry of Table X. It should be noted that the partial enthalpy and entropy of HgTe are highly correlated. The most probable values fall essentially along a line segment in the \bar{h} - \bar{s} plane which passes through the best fit point, which has a slope of 871.8 K, and which is terminated with 95% confidence at values of \bar{h}_{Te} that are ± 1201 cal away from $-41,470$ cal (33). Mathematically, the most probable values are related by the equation

$$\bar{h} = -41,470 + 871.8 (\bar{s} + 41.491);$$

$$-44.05 \leq \bar{s} \leq -38.93 \text{ at 95\% confidence} \quad [38]$$

Analogous comments are valid for the fits to μ_{CdTe} and ΔG°_f . Figure 16 shows the chemical potential of CdTe and the least squares line. The two points for 38-TE1 are shown for completeness only. They correspond to x -values greater than 0.426 and were not included in the least squares analysis. A similar out of range point is the 914.7 K point for 38-HG1. The two lowest temperature points for 38-HG1 were excluded from the analysis because they were far from the least squares line obtained by including them. These same two points were also excluded from the analysis of ΔG°_f . A plot of the ΔG°_f - T points is shown in Fig. 17. Figure 18 shows a plot of the difference in the chemical potentials of Hg and Cd vs. T . Using Eq. [34] and

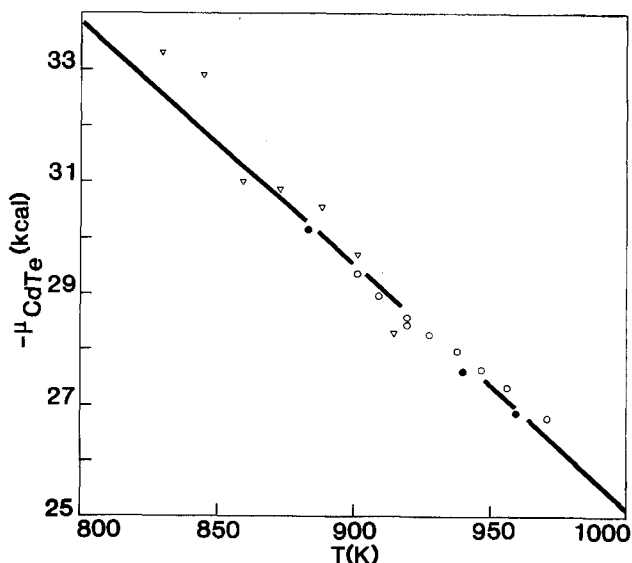


Fig. 16. Negative of the chemical potential of CdTe in a solid solution containing 41.6 ± 1 m/o CdTe as a function of absolute temperature. Symbols have the same meaning as in Fig. 15. Solid line is from a least squares fit.

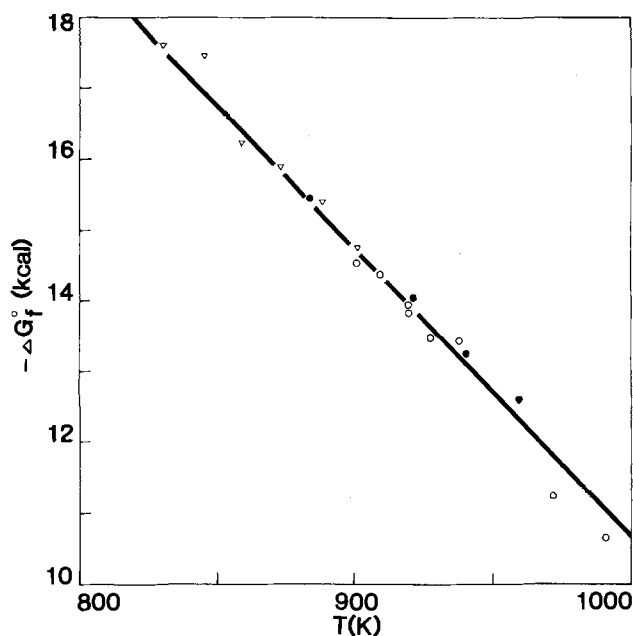


Fig. 17. Negative of the Gibbs free enthalpy of formation from $\text{Te}_2(\text{g})$, $\text{Hg}(\text{g})$, and $\text{Cd}(\text{g})$ of a solid solution containing 41.6 ± 1 m/o CdTe as a function of absolute temperature. Solid line is from a least squares fit. Symbols denote data from different cells as given for Fig. 15.

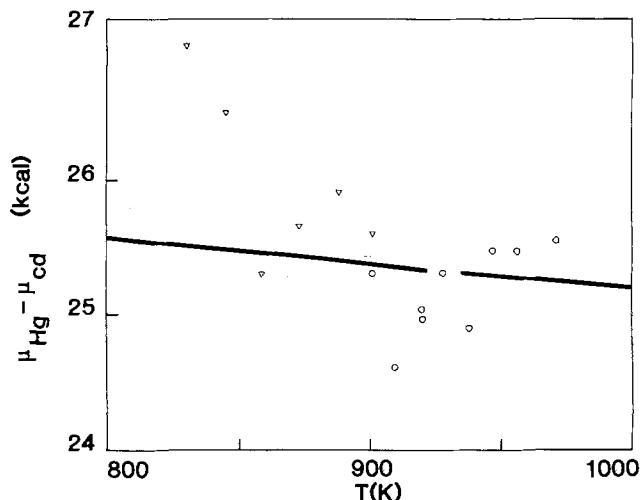


Fig. 18. Difference between the chemical potentials of Hg and Cd in a solid solution containing 41.6 ± 1 m/o CdTe as a function of absolute temperature. Solid line is from a least squares fit. Symbols retain same meaning as for Fig. 15.

Table X and not expressing the uncertainties, one obtains

$$\bar{\mu}_{\text{Hg}} - \bar{\mu}_{\text{Cd}} = 27,063. - 1.856T \quad [39]$$

Values for the partial pressures of $\text{Te}_2(\text{g})$ and $\text{Cd}(\text{g})$ along the three-phase curve can be calculated where they were not measured using the measured values of P_{Hg} , Eq. [32] and [33], and the entries in Table X. These are shown by the symbol, x, in Fig. 11 for P_2 and in Fig. 19 for P_{Cd} . The calculated points agree well with those measured directly. The utility of Eq. [32] and [33], which give two of the partial pressures if the third is known, is, of course, not limited to points along the three-phase curve. The equations are applicable for the entire composition stability field of $x = 0.416$.

The standard Gibbs free enthalpies of formation of $\text{HgTe}(\text{c})$ and $\text{CdTe}(\text{c})$ from $\text{Te}_2(\text{g})$ and the monoatomic metallic atoms have been determined from optical absorbance measurements at high temperatures

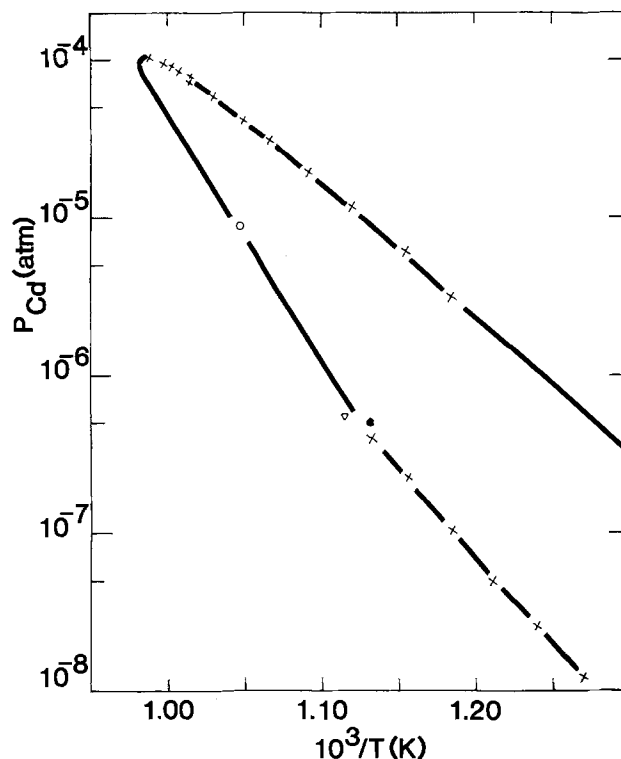


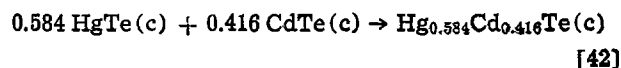
Fig. 19. Partial pressure of $\text{Cd}(\text{g})$ along the three-phase curve for a solid solution with 41.6 ± 1 m/o CdTe as a function of reciprocal absolute temperature. \bullet 38-TE1; ∇ 38-HG1; \circ 40-HG3; \times calculated from P_{Hg} in Table IX and Eq. [39] or, along bottom leg, from P_{Hg} in Table V and Eq. [39].

(21, 14) and are given, respectively, by

$$\Delta G^\circ_f(\text{cal/mole HgTe}) = -41,660. + 42.71T \quad [40]$$

$$\Delta G^\circ_f(\text{cal/mole CdTe}) = -68,640. + 44.94T \quad [41]$$

Combining these equations with the data in Table X, the ΔG°_f for the reaction



is

$$\Delta G^\circ_f = 1888. - 3.32T \quad [43]$$

If instead of starting with the last entry of Table X, one starts with the best fits to the chemical potentials of HgTe and CdTe individually and Eq. [36], one obtains for the reaction given by Eq. [42]

$$\Delta G^\circ_f = -155. - 1.37T \quad [44]$$

In either case, within the uncertainty limits inferred from Table X the enthalpy of formation from $\text{HgTe}(\text{c})$ and $\text{CdTe}(\text{c})$ is zero and the entropy of formation agrees with the value of 1.35 cal/K-formula weight for the random mixing of Cd and Hg on the metal sublattice.

Acknowledgment

This work was supported by the National Science Foundation under Grant DMR75-09332 and, in the latter stages and write-up, by the Air Force Office of Scientific Research, Air Force Systems Command, under Grant No. AFOSR-78-3611. Special thanks are due Mr. J. L. Schmit for kindly supplying the crystals used along with valuable suggestions, to Mr. D. Hovey, Reading, Massachusetts, for painstaking fabrication of the optical cells, and to Mr. Ozzie Werych, Lindberg Division of Sola Basic Industries, Watertown, Wisconsin, for assistance in furnace design. This paper was taken in part from a thesis submitted to the Graduate School of Marquette University in partial fulfillment of requirements for the Ph.D. degree in Materials Science (1977).

Manuscript submitted March 11, 1980; revised manuscript received Aug. 4, 1980. This was Paper 157 presented at the Seattle, Washington, Meeting, of the Society, May 21-26, 1978.

Any discussion of this paper will appear in a Discussion Section to be published in the December 1981 JOURNAL. All discussions for the December 1981 Discussion Section should be submitted by Aug. 1, 1981.

Publication costs of this article were assisted by Marquette University.

REFERENCES

1. J. Blair and R. Newnham, in "Metallurgy of Elemental and Compound Semiconductors," p. 393, Interscience Publications, New York (1961).
2. J. C. Wooley and B. Ray, *Phys. Chem. Solids*, **13**, 151 (1960).
3. J. L. Schmit and C. J. Speerschnieder, *Infrared Phys.*, **8**, 247 (1968).
4. T. C. Harman, in "Physics and Chemistry of II-VI Compounds," M. Aven and J. S. Prener, Editors, Chap. 15, North-Holland Publishing Co., Amsterdam (1967).
5. J. Steininger, *J. Electron. Mater.*, **5**, 299 (1976).
6. J. L. Schmit and E. L. Stelzer, *ibid.*, **7**, 65 (1978).
7. J. Nishizawka, K. Suto, M. Kitamura, M. Sato, Y. Takase, and A. Ito, *J. Phys. Chem. Solids*, **37**, 33 (1976).
8. A. J. Strauss and R. F. Brebrick, *ibid.*, **31**, 2293 (1970).
9. D. de Nobel, *Philips Res. Rept.*, **14**, 361 (1959).
10. F. T. J. Smith, *Metal. Trans.*, **1**, 617 (1970).
11. R. F. Brebrick, *J. Phys. Chem. Solids*, **40**, 177 (1979).
12. R. F. Brebrick, *This Journal*, **116**, 1274 (1969).
13. H. E. Swanson, M. C. Morris, E. H. Evans, and L. Ulmer, Standard X-ray Diffraction Powder Patterns, National Bureau of Standards Monograph 25, Section 3, p. 38 (July 1964).
14. R. F. Brebrick, *This Journal*, **118**, 2014 (1971).
15. L. S. Brooks, *J. Am. Chem. Soc.*, **74**, 227 (1952).
16. A. A. Kudryavtsev and G. P. Ustyugov, *Russian J. Inorg. Chem.*, **6**, 1227 (1961).
17. E. H. Baker, *J. Chem. Soc. (A)*, 1558 (1967).
18. R. F. Brebrick, *J. Phys. Chem.*, **72**, 1032 (1968).
19. R. Hultgren, P. Desai, D. Hawkins, M. Gleiser, and K. K. Kelley, "Selected Values of the Thermodynamic Properties of the Elements," American Society for Metals, Metals Park, Ohio (1973).
20. R. E. Machol and E. F. Westrum, *J. Am. Chem. Soc.*, **80**, 2950 (1958).
21. R. F. Brebrick and A. J. Strauss, *J. Phys. Chem. Solids*, **26**, 989 (1965).
22. R. F. Brebrick and A. J. Strauss, *J. Chem. Phys.*, **40**, 3230 (1964).
23. S. Sugawara and T. Sato, *Bull. Jpn. Soc. Mech. Eng.*, **5**, 711 (1962).
24. W. T. Hicks, *J. Chem. Phys.*, **38**, 1873 (1963).
25. S. Brodersen, *J. Opt. Soc. Am.*, **44**, 22 (1954).
26. A. C. G. Mitchell and M. W. Zemansky, "Resonance Radiation and Excited Atoms," Cambridge University Press (1961).
27. J. S. Penner, "Quantitative Molecular Spectroscopy and Gas Emissivities," p. 56, Addison-Wesley, Reading, Mass. (1959).
28. R. G. Breene, Jr., "The Shift and Shape of Spectral Lines," p. 231, Pergamon Press, New York (1961).
29. H. G. Kuhn and E. L. Lewis, in "Polarization, Matiere et Rayonnement," pp. 341-356, Presses Universitaires de France, Paris (1969).
30. R. Hultgren *et al.*, "Selected Values of the Thermodynamic Properties of Binary Alloys," American Society for Metals, Metals Park, Ohio (1973).
31. R. F. Brebrick, *J. Chem. Phys.*, **43**, 3846 (1965).
32. R. F. Brebrick and J. P. Schwartz, *J. Electron. Mater.*, To be published.
33. R. F. Brebrick, *High Temp. Sci.*, **8**, 11 (1976).

Partial Pressures over HgTe-CdTe Solid Solutions

II. Results for 10, 20, and 58 Mole Percent CdTe

Tse Tung, Leszek Golonka,¹ and R. F. Brebrick*

Metallurgy and Materials Science, Marquette University, Milwaukee, Wisconsin 53233

ABSTRACT

The partial pressures of Hg, Cd, and Te₂ are obtained along the three-phase curves for 10, 20, and 58 mole percent CdTe, HgTe-CdTe solid solutions by measuring the optical absorbance of the coexisting vapor between 220 and 700 nm. The pressure ranges covered are 10⁻²-32 atm for Hg, 10⁻³-10⁻⁵ atm for Cd, and 10⁻⁵-10⁻² atm for Te₂, and Hg is always the predominant vapor species. The data allow the calculation of the chemical potentials of HgTe and CdTe and the Gibbs free enthalpy of formation for the solid solutions. In addition, the solidus temperatures are obtained directly from the optical absorbance measurements.

In a previous paper (1), the calibration experiments required to obtain the partial pressures of Hg, Cd, and Te₂ and the results for an HgTe-CdTe solid solution containing 41.6 mole percent (m/o) CdTe were reported. Here we report similar experiments on 10, 20, and 58 m/o CdTe solid solutions. These experiments establish for each mole percent CdTe (i) the solidus temperature, (ii) all three partial pressures along the three-phase curve, (iii) the chemical potentials of HgTe and CdTe components in the solid solution, and (iv) the Gibbs free enthalpy of formation. To the best

of our knowledge, this is the first determination of items ii, iii, and iv. The predominant vapor species for both the metal-saturated and the Te-saturated solid solutions is Hg(g).

Experimental

The experimental details are the same as those described in Part I (1) with some important exceptions that are noted below. The mole percent of CdTe in the solid solution samples was determined as before from density measurements. The weight of solid solution and its particle size are noted in the table headings for each cell as well as the weight of any elements added. The experiments fell into two general classes. In the first, sufficient Hg was added along with the solid solution to provide a pressure of about 20 atm. In the sec-

* Electrochemical Society Active Member.

¹ Department of Electrical Engineering, Technical University of Wrocław, Wrocław, Poland.

Key words: mercury-cadmium-telluride, partial pressures, three-phase curve, free enthalpy, chemical potentials.

ond, the results of which are given in Tables IV, V, and VI, either excess Te or a small amount of Hg was added so that Te saturation was achieved at fairly low sample temperatures. For this second type of experiment, both sidearm portion of the furnace and the optical cells were modified. The modification of the furnace and the use of a heat pipe around the sample end of the sidearm are described in Calibration Measurements, Tellurium in Part I (1). Because of the heat pipe and its inner silver liner, the temperature variation over the roughly 5 cm length of the sidearm containing the sample was a few tenths of a degree centigrade or less. The sidearm of the cell consisted of two sections. The section attached to the cell-proper was 1.1 cm OD and 9 cm long. The section which was the end of the sidearm after seal-off was 2.0 cm OD and 3 cm long. Thus the overall sidearm length was about 12 cm, rather than 20, and approximately 5g samples could be spread out to provide a geometric surface area of about 3 cm². For the cells used in Part I (1), this area was about 0.5 cm². We believe this increased surface area was useful in minimizing equilibration times at high temperatures where the original particle size distribution tended to disappear because of sintering. It should be noted that, although there was sintering, there was no evidence of gross vapor transport along the sample section, attesting to the uniformity of temperature there.

As in Part I (1), the transmission over the Cd lines was measured rather than the optical absorbance. However, here the measurements were repeated at least three times and the integrated areas averaged.

Results

The optical absorbance measurements and the integrated area in the transmission valley for the Cd lines were converted to partial pressures as described in the section Calculation of Partial Pressures, in Part I (1).

As in Part I, it was found that the partial pressure of Hg, P_{Hg} , attained steady-state values within a few hours after a steady sample temperature was reached. In contrast the partial pressures of $Te_2(g)$, P_2 , and of Cd(g), P_{Cd} , required 4-15 hr or more depending on the temperature. A decrease in maximum particle size to 63 μm , see Table VI, seemed to reduce the time required for the attainment of a steady state.

Tables I through VI, with the exception of Table III, list the partial pressures measured. In all of these tables, the second column gives the number of hours the sample was at temperature before measurement. The measurement of optical absorbance and transmission (for the Cd lines) itself required an additional 40-60 min. The third column gives $10^3/T$, where T is the sample temperature in K. The last two columns titled x and y , respectively, are calculated values for the overall composition of the condensed phase or phases as expressed by the formula $(Hg_{1-x}Cd_x)_yTe_{1-y}$. These were obtained from the known weights of solid solution and added elements, the known volume of the cell and sidearm, the temperature distribution along the cell and sidearm, and the assumptions: (i) $y = 0.500$ for the solid solution added to the cell, (ii) Cd(g) and $Te_2(g)$ are ideal gases, and (iii) Hg(g) is a slightly imperfect gas with an equation of state given by Sugawara and Sato (see the section on Calibration Measurements, Mercury in Part I).

Tables I and II give P_{Hg} and P_2 for metal-saturated solid solution with x of, respectively, 0.108 and 0.198. These mercury pressures are also shown along the upper branches of the three-phase curves shown in Fig. 1. For comparison the data for HgTe (2) and for $x = 0.416$ from Part I (1) are also shown. The maximum values of P_{Hg} for $x = 0.108$ is 21 atm and occurs at 673°C. That for $x = 0.198$ is 24 atm and occurs at 683°C. Solidus temperatures were obtained from measurements with these cells and are given in Table III along with those for $x = 0$ and 0.416. The determination of the solidus temperature depends on the fact that the optical absorbance D , in the 254.0-340 nm re-

Table I. Partial pressures in atmospheres for metal-saturated, 10.8 ± 1 m/o CdTe, HgTe-CdTe.

Cell 137-1 2.495 cm optical path at 755° or 800°C. Cell loaded with 5.9812g of solid solution with $x = 0.108$ and with particle size between 44 and 250 μm plus 0.7465g Hg. Volume in cubic centimeters of cell-proper, upper part of sidearm, and sample end of sidearm minus sample volume are respectively, 4.27, 7.73, and 2.37. Five sidearm zones used in the calculation of the gross composition of the condensed phase or phases. This composition is written as $(Hg_{1-x}Cd_x)_yTe_{1-y}$.

| Run | Hr | $10^3/T$ | P_{Hg} | $10^4 \times P_2$ | x | y |
|------|-----|----------|----------|-------------------|--------|--------|
| 2203 | 0.8 | 1.1569 | 16.42 | 1.27 | 0.1047 | 0.5079 |
| 2204 | 0.5 | 1.1324 | 18.63 | 2.59 | 0.1068 | 0.5029 |
| 2205 | 1.2 | 1.1082 | 20.64 | 3.07 | 0.1087 | 0.4984 |
| 2206 | 0.8 | 1.0910 | 21.59 | 3.58 | 0.1096 | 0.4964 |
| 2307 | 4.0 | 1.0913 | 20.33 | 0.702 | 0.1082 | 0.4996 |
| 2308 | 0.6 | 1.0827 | 20.44 | 1.21 | 0.1082 | 0.4996 |
| 2309 | 0.7 | 1.0654 | 20.70 | 3.17 | 0.1082 | 0.4995 |
| 2310 | 0.5 | 1.0521 | 19.98 | 6.72 | 0.1073 | 0.5017 |
| 2311 | 0.7 | 1.0411 | 18.15 | 12.2 | 0.1053 | 0.5063 |
| 2312 | 0.9 | 1.0250 | 18.90 | 20.3 | 0.1059 | 0.5050 |
| 2313 | 0.8 | 1.0094 | 20.61 | 28.1 | 0.1074 | 0.5013 |
| 2314 | 0.7 | 1.0017 | 21.64 | 33.3 | 0.1084 | 0.4991 |
| 2315 | 0.7 | 0.9898 | 22.37 | 42.5 | 0.109 | 0.4978 |
| 2316 | 0.7 | 0.9800 | 23.90 | 49.7 | 0.1100 | 0.4955 |
| 2317 | 1.0 | 0.9701 | 25.26 | 60.8 | 0.1113 | 0.4926 |

Table II. Partial pressures in atmospheres for metal-saturated, 19.8 ± 1 m/o CdTe, HgTe-CdTe.

Cell H2, 2.910 cm optical path at 755° or 800°C. Cell loaded with 3.4373g of solid solution with $x = 0.198$ and with particle size between 44 and 250 μm plus 0.2021g Hg. Volume in cubic centimeters of cell-proper, upper part of sidearm, and sample end of sidearm minus sample volume are, respectively, 1.737, 0.653, and 0.920. Sidearm divided into seven zones in calculation of x and y .

| Run | Hr | $10^3/T$ | P_{Hg} | x | y |
|------|-----|----------|----------|--------|--------|
| 805 | 1.5 | 1.1448 | 17.5 | 0.1936 | 0.5057 |
| 806 | 0.5 | 1.1193 | 19.62 | | |
| 807 | 0.5 | 1.0950 | 21.26 | 0.1961 | 0.5024 |
| 808 | 0.5 | 1.0727 | 22.93 | | |
| 809 | 0.5 | 1.0518 | 23.67 | 0.1976 | 0.5005 |
| 810 | 1.5 | 1.0336 | 21.73 | | |
| 811 | 0.5 | 1.0282 | 20.69 | 0.1952 | 0.5035 |
| 812 | 0.5 | 1.0244 | 20.22 | | |
| 813 | 0.5 | 1.0197 | 20.10 | 0.1947 | 0.5042 |
| 814 | 0.5 | 1.0143 | 20.45 | 0.1949 | 0.5039 |
| 815 | 0.8 | 1.0049 | 21.68 | 0.1958 | 0.5028 |
| 1120 | 1.5 | 1.0034 | 22.18 | 0.1957 | 0.5029 |
| 1121 | 0.5 | 0.9937 | 23.35 | 0.1965 | 0.5019 |
| 1122 | 0.5 | 0.9785 | 25.52 | 0.1979 | 0.5001 |
| 1123 | 0.5 | 0.9644 | 27.64 | 0.1993 | 0.4984 |
| 1124 | 0.7 | 0.9519 | 29.72 | 0.2007 | 0.4966 |
| 1125 | 0.5 | 0.9435 | 31.40 | 0.2018 | 0.4952 |
| 1126 | 0.5 | 0.9626 | 27.92 | 0.1995 | 0.4981 |
| 1127 | 0.5 | 1.0086 | 21.49 | 0.1953 | 0.5034 |

gion where Hg(g) absorbs, increases with increasing temperature, attains a maximum value, decreases, and then increases linearly on a log D vs. $10^3/T$ plot. The behavior is similar to that shown in Fig. 14 of Part I (1). The high temperature, linear portion is characteristic of a liquid-solid solution equilibrium and its intersection with the decreasing segment of the log D vs. $10^3/T$ curve is taken as the solidus temperature. The evaluation of the solidus temperature for each x -value was made using D at a number of wavelengths and is independent of the accuracy with which P_{Hg} was established. Near the solidus temperature for $x = 0.108$ the optical absorbance for four wavelengths between 290.4 and 320.4 nm was in the reliable measurement range of 0.1-2.0 in D and all gave the same solidus temperature within $\pm 1^\circ C$. For $x = 0.198$ the solidus temperature was established to within $\pm 1^\circ C$ from the same type of reversal in the sign of the slope of a log D vs. $10^3/T$ plot for four wavelengths between 300.4 and 330.4 nm. The solidus temperatures given in Table III are obtained by an essentially static technique and so it is gratifying that they agree well with those obtained from chemical analysis of the first crystals to grow from large volumes of melt (3) combined with liquidus temperatures obtained by thermal analysis (4) (given only in the form of graph). The values of P_2 in Table I are the average of those calculated from the optical absorbance at 2-6 wavelengths between 400 and 500 nm.

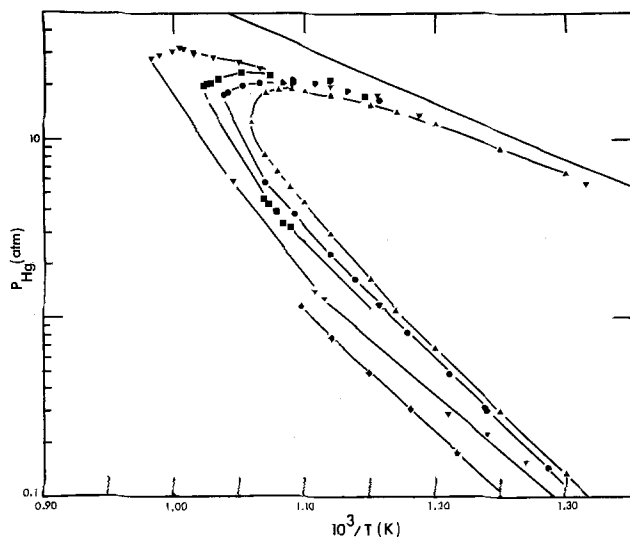


Fig. 1. Vapor pressure of Hg, shown as the uppermost line, and the partial pressure of Hg along the three-phase curves for various x -values of $\text{Hg}_{1-x}\text{Cd}_x\text{Te}(c)$ as a function of $10^3/T$. \blacktriangle , $x = 0.0$ [Ref. (2)]; \bullet , $x = 0.094, 0.108$; \blacksquare , $x = 0.196$; \blacktriangledown , $x = 0.416$; \blacklozenge , $x = 0.581$.

Table III also gives P_{Hg} at the solidus temperature as obtained here and as established by a reflux method (5). In the latter study, P_{Hg} falls along a common straight line on a $\log P_{\text{Hg}}-1/T$ plot for pseudobinary melts containing between 0 and 60 m/o CdTe. Therefore, the value of P_{Hg} at the solidus temperature for a given mole percent CdTe solid solution can be calculated knowing only the solidus temperature. As shown in Fig. 1 for $x = 0$, P_{Hg} along the three-phase curve has in principle an infinite slope at the solidus temperature, so that it can be difficult to establish its exact value. Data along the Te-rich leg and close to the solidus temperature, which we do not have, would serve to bracket this pressure. As it is, our values in Table III are upper limits and the agreement with Ref. (5) is satisfactory.

Table IV lists the partial pressures obtained for a Te-saturated solid solution with $x = 0.094 \pm 0.010$. For the last entry the loss of Hg in the vapor phase is large enough that the x -value differs by more than 0.01 from

Table III. Solidus temperatures in $^{\circ}\text{C}$ and P_{Hg} in atmospheres for $\text{Hg}_{1-x}\text{Cd}_x\text{Te}$ solid solutions

| x | 0 | 0.108 | 0.198 | 0.416 |
|----------------------------|------|---------------|---------------|-------------|
| T | 670 | 690.8 \pm 1 | 705.3 \pm 1 | 745 \pm 2 |
| P_{Hg} | 12.5 | 17.7 | 20.0 | 28.0 |
| P_{Hg} [Ref. (5)] | 13.8 | 16.3 | 18.2 | 24.1 |

Table IV. Partial pressures in atmospheres over Te-saturated, 9.4 m/o CdTe, HgTe-CdTe .

Cell 58C, 9.795 cm optical path at 755°C . Cell loaded with 5.3859g of solid solution with $x = 0.094$ and with particle size between 44 and 250 μm plus 0.01609g Te. Volume in cubic centimeters of cell-proper, upper part of sidearm, and sample end of sidearm minus sample volume are, respectively 17.0, 3.1, and 5.26.

| Run | Hr | $10^3/T$ | P_{Hg} | $10^3 \times P_2$ | $10^7 \times P_{\text{Cd}}$ | x | y |
|------|------|----------|-----------------|-------------------|-----------------------------|--------|--------|
| 1501 | 73 | 1.2862 | 0.146 | 0.700 | 0.0469 | 0.0943 | 0.4974 |
| 1602 | 18 | 1.2399 | 0.301 | 1.15 | 0.148* | 0.0945 | 0.4967 |
| 1703 | 43.5 | 1.2385 | 0.316 | 1.17 | 0.142 | 0.0946 | 0.4966 |
| 1804 | 20.5 | 1.2114 | 0.485 | 1.55 | 0.364 | 0.0949 | 0.4958 |
| 2105 | 4 | 1.1791 | 0.822 | 2.03 | 0.877 | 0.0955 | 0.4942 |
| 2206 | 16 | 1.1571 | 1.19 | 2.45 | 1.04* | 0.0962 | 0.4925 |
| 2207 | 4 | 1.1384 | 1.62 | 2.74 | 1.29* | 0.097 | 0.4904 |
| 2308 | 14 | 1.1200 | 2.26 | 3.04 | 6.23 | 0.0982 | 0.4874 |
| 2309 | 8 | 1.0326 | 3.80 | 3.30 | 17.7 | 0.1011 | 0.4799 |
| 2411 | 12.5 | 1.0705 | 5.72 | 3.61 | 25.8 | 0.1051 | 0.4702 |
| 2512 | 19 | 1.0494 | 7.98* | 3.74 | 57.4 | 0.1102 | 0.4585 |

* Entries marked with an asterisk in this table are omitted from the least squares fits to the chemical potentials of either HgTe or CdTe .

the nominal value. The values of P_{Hg} are shown in Fig. 1 along the lower leg of the three-phase curve for $x = 0.094$.

Table V gives the partial pressures for $x = 0.196$. The cell had only a small amount of added Hg and so left the metal-saturated condition and entered the solid solution single-phase field at 427°C with $P_{\text{Hg}} = 2.96$ atm. With increasing temperature the value of y increases by a small amount within the precision of our measurements, P_{Hg} remaining almost constant, and then finally attains Te saturation. Upon further increase in temperature, P_{Hg} starts to increase. From the discontinuities in the slopes of the optical absorbance at different wavelengths, Te saturation is attained at 646°C where $P_{\text{Hg}} = 3.2$ atm, $P_2 = 4.23 \times 10^{-3}$ atm, and $P_{\text{Cd}} = 1.92 \times 10^{-6}$ atm.

It is to be noted that the calculated values of x and y are constant to three significant figures up to $10^3/T = 1.0837$. Assuming the major errors are a 2% uncertainty in P_{Hg} and a 5% uncertainty in the volume of the optical cell implies approximate uncertainties of 0.5% in x and 0.25% in y . The maximum variation for the values in Table V are close to these estimates, being 0.4% in x and 0.1% in y .

Table VI lists the partial pressures for an x -value of 0.58. The partial pressures of $\text{Te}_2(g)$ along the three-phase curves for the various x -values are shown in Fig. 2 along with the vapor pressure of tellurium and a portion of the Te-rich leg for CdTe from Ref. (6). As can be seen there are not enough data points to define the maximum value of P_2 for $x = 0.416$.

A number of cells were prepared with added elemental Hg. As discussed above in connection with Table V, these left the metal-saturated condition with increasing T and entered the homogeneity range, where P_{Hg} was almost constant with increasing T . The values of $10^3/T$ and P_{Hg} at the metal-saturation points are given in Table VII since Fig. 1 does not extend to low enough T to include them all.

Discussion

For a narrow homogeneity range solid solution, $(\text{Hg}_{1-x}\text{Cd}_x)_y\text{Te}_{1-y}$, in which the solid is a stable phase only for a narrow range of y -values near 1/2, say less than 0.01 wide, certain chemical potentials are theoretically independent of y to a good approximation, i.e., they are stoichiometric invariants (7).

Assuming Cd and Te_2 behave ideally in the vapor phase and f_{Hg} is the fugacity of Hg(g), these are

$$\bar{\mu}_{\text{HgTe}} = RT \ln f_{\text{Hg}} P_2^{1/2} = \bar{h}_{\text{HgTe}} - T\bar{s}_{\text{HgTe}} \quad [1]$$

Table V. Partial pressures in atmospheres over 19.7 m/o CdTe, HgTe-CdTe

Cell I, 9.775 cm optical path at 755°C . Cell loaded with 4.8230g of solid solution of $x = 0.196$ and particle size between 44 and 125 μm plus 0.2060g Hg. Volume in cubic centimeters of cell-proper, upper part of sidearm, and sample end of sidearm minus sample volume are, respectively, 17.63, 2.8, and 6.97. Sidearm divided into six zones in calculation of x and y .

| Run | Hr | $10^3/T$ | P_{Hg} | $10^3 \times P_2$ | $10^9 \times P_{\text{Cd}}$ | x | y |
|------|------|----------|-----------------|-------------------|-----------------------------|--------|--------|
| 1815 | 5 | 1.1912 | 3.15 | 0.060 | 0.371* | 0.1969 | 0.4989 |
| 1816 | 6 | 1.1598 | 3.10 | 0.236 | 0.40* | 0.1966 | 0.4993 |
| 1917 | 3.5 | 1.1401 | 3.20 | 0.501 | 1.02* | 0.1969 | 0.4989 |
| 1512 | 15 | 1.1280 | 3.14 | 0.826 | 1.93* | 0.1966 | 0.4992 |
| 1918 | 3.5 | 1.1240 | 3.19 | 0.969 | 1.40* | 0.1968 | 0.4990 |
| 2019 | 17.5 | 1.1221 | 3.22 | 1.05 | 0.722* | 0.1969 | 0.4989 |
| 2732 | 96 | 1.1164 | 3.20 | 1.33 | 1.24 | 0.1968 | 0.4990 |
| 2020 | 4 | 1.1104 | 3.31 | 1.72 | 1.37 | 0.1973 | 0.4984 |
| 2733 | 6 | 1.1035 | 3.27 | 2.30 | 1.54 | 0.1971 | 0.4986 |
| 2123 | 13 | 1.0978 | 3.27 | 2.85 | 1.62 | 0.1970 | 0.4987 |
| 2834 | 8 | 1.0966 | 3.29 | 2.91 | 1.74 | 0.1971 | 0.4986 |
| 2835 | 6 | 1.0894 | 3.31 | 4.08 | 1.90 | 0.1972 | 0.4986 |
| 2125 | 3.5 | 1.0890 | 3.28 | 4.19 | 1.60* | 0.197 | 0.4987 |
| 2127 | 5 | 1.0837 | 3.46 | 4.44 | 1.93* | 0.1978 | 0.4978 |
| 2936 | 14 | 1.0780 | 3.99 | 4.73 | 2.42* | 0.2001 | 0.4949 |
| 2228 | 14 | 1.0733 | 4.37 | 4.90 | 2.53* | 0.2018 | 0.4928 |

* Entries marked with an asterisk are omitted from the least squares fits to the chemical potentials of CdTe.

Table VI. Partial pressures in atmospheres over Te-saturated, 58.1 m/o CdTe, HgTe-CdTe

Cell 64, 9.795 cm optical path at 755°C. Cell loaded with 4.116g of solid solution with maximum particle size of 63 μm and $x = 0.581$. Volume in cubic centimeters of cell-proper, upper part of sidearm, and sample end of sidearm minus sample volume are, respectively, 17.45, 6.9, and 2.74. Five sidearm zones used in calculation of x and y .

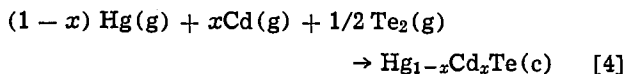
| Run | Hr | $10^3/T$ | P_{Hg} | $10^3 \times P_2$ | $10^3 \times P_{\text{Cd}}$ | x | y |
|------|------|----------|-----------------|-------------------|-----------------------------|--------|--------|
| 0826 | 1.3 | 1.4195 | 0.012* | 0.081 | | 0.5812 | 0.4999 |
| 0825 | 1.5 | 1.4014 | 0.013 | 0.114 | | 0.5812 | 0.4999 |
| 0824 | 32.0 | 1.3683 | 0.019 | 0.227 | | 0.5813 | 0.4999 |
| 0621 | 130 | 1.3391 | 0.029 | 0.343 | 0.00895* | 0.5814 | 0.4998 |
| 0622 | 4 | 1.3093 | 0.043 | 0.559 | 0.0161* | 0.5816 | 0.4997 |
| 0623 | 2.0 | 1.2894 | 0.060 | 0.763 | | 0.5818 | 0.4997 |
| 2409 | 3.5 | 1.2183 | 0.176 | 2.03 | 0.0538* | 0.5834 | 0.4990 |
| 2510 | 13.3 | 1.1817 | 0.310 | 3.15 | 0.103* | 0.5810 | 0.5000 |
| 2511 | 2 | 1.1505 | 0.491 | 4.52 | 0.213* | 0.5876 | 0.4972 |
| 2612 | 9 | 1.1232 | 0.772 | 6.06 | 0.989 | 0.5914 | 0.4957 |
| 3016 | 60 | 1.1064 | 1.00 | 7.27 | 1.93 | 0.5944 | 0.4944 |
| 2613 | 4 | 1.0976 | 1.17 | 8.12 | 2.73* | 0.5967 | 0.4934 |
| 3017 | 5 | 1.0848 | 1.37 | 9.45 | 3.24 | 0.5994 | 0.4923 |
| 2714 | 14 | 1.0720 | 1.72 | 10.6 | 5.07 | 0.6043 | 0.4903 |
| 2715 | 4.8 | 1.0618 | 1.95* | 12.0 | 5.76 | 0.6073 | 0.4891 |
| 3118 | 14 | 1.0453 | 2.44* | 14.0 | 10.1 | 0.6143 | 0.4862 |
| 0120 | 16 | 1.0218 | 3.36* | 17.6 | 19.3 | 0.6275 | 0.4810 |

* Entries marked with an asterisk are omitted from the least squares fits to the chemical potentials of either HgTe or CdTe.

$$\bar{\mu}_{\text{CdTe}} = RT \ln P_{\text{Cd}} P_2^{1/2} = \bar{h}_{\text{CdTe}} - T \bar{s}_{\text{CdTe}} \quad [2]$$

$$\bar{\mu}_{\text{Hg}} - \bar{\mu}_{\text{Cd}} = RT \ln f_{\text{Hg}}/P_{\text{Cd}} \quad [3]$$

Finally the standard Gibbs free enthalpy of formation of the solid solution according to the reaction



is given by

$$\Delta G^\circ_f = (1-x) \bar{\mu}_{\text{HgTe}} + x \bar{\mu}_{\text{CdTe}} = \Delta H^\circ_f - T \Delta S^\circ_f \quad [5]$$

The chemical potentials were calculated from the partial pressures given in the tables. Using the equation of state for Hg(g) given by Sugawara and Sato (8), one obtains

$$\begin{aligned} \bar{\mu}_{\text{Hg}} &= RT \ln f_{\text{Hg}} \\ &= RT \ln P_{\text{Hg}} + 4857.6 P_{\text{Hg}} (-1.793/T + 251/T^2 \\ &\quad + 0.001071) \quad [6] \end{aligned}$$

For the cases where both P_{Hg} and P_2 were measured, the correction term ranges from near zero to -70 cal/mole. Since the chemical potentials of HgTe and CdTe are independent of y , the solid solution can be described as effectively being a binary solution containing two thermodynamic components, HgTe and CdTe, for some purposes. In particular, the Gibbs-Duhem relation holds between $\bar{\mu}_{\text{HgTe}}$ and $\bar{\mu}_{\text{CdTe}}$. The experimental data obey the Gibbs-Duhem relation at least qualitatively in that $\bar{\mu}_{\text{HgTe}}$ increases at a given T with decreasing x while $\bar{\mu}_{\text{CdTe}}$ increases with increasing x .

Least squares straight lines were determined from the experimental values of $\bar{\mu}_{\text{HgTe}}/RT$ and $\bar{\mu}_{\text{CdTe}}/RT$, assuming that these quantities vary linearly with $1/T$. The temperature dependence of the corresponding en-

Table VII. Points on metal-saturated three-phase curves for various x -values. Vapor pressure of Hg, P_{Hg}° given for comparison. Cells 162, J1 used only to establish these points and not at high temperatures.

| Cell | x | $10^3/T$ (K) | P_{Hg} (atm) | P_{Hg}° (atm) |
|--------|-------|--------------|-----------------------|-----------------------------|
| 162 | 0.109 | 1.2037 | 12.5 | 15.48 |
| I | 0.197 | 1.428 | 2.96 | 3.12 |
| J1 | 0.199 | 1.2435 | 9.6 | 11.65 |
| 38-HG1 | 0.416 | 1.582 | 1.20 | 1.20 |
| 40-HG3 | 0.416 | 1.315 | 5.6 | 6.99 |

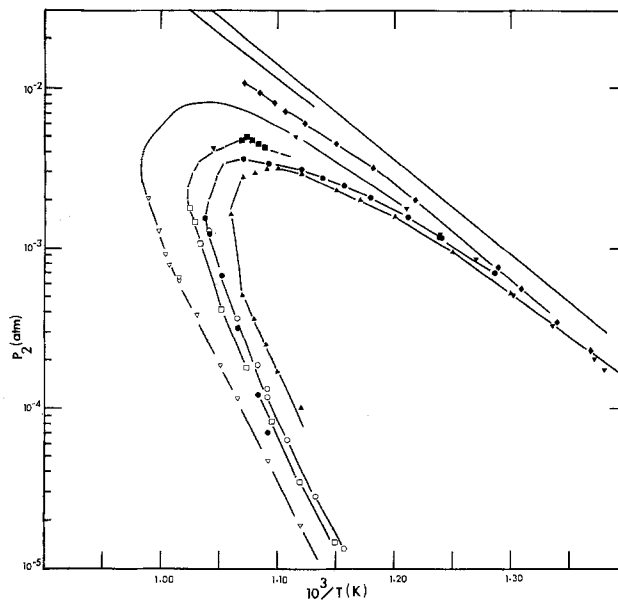


Fig. 2. Vapor pressure of Te, shown as the uppermost line, and the partial pressure of Te_2 along the three-phase curves for various x -values as a function of $10^3/T$. The short line segment just below the vapor pressure line, and without points, is a portion of the three-phase curve for CdTe from Ref. (6). Closed symbols have the same meaning as indicated in the caption for Fig. 1. Open symbols indicate values calculated as described in the Discussion section.

thalpies and entropies is thereby neglected and the values obtained are for a temperature near the midpoint of the temperature range. The results are summarized in Table VIII. Column 3 lists the standard deviation, σ^* , between measured and calculated values of $\bar{\mu}_{\text{HgTe}}$ etc., rather than of $\bar{\mu}_{\text{HgTe}}/RT$ etc., because the former seem to us to have a more immediately recognizable significance. Certain entries in Tables I, II, IV, V, and VI, indicated by an asterisk superscript, were excluded from these fits either because the value of x deviated by more than ± 0.01 from the nominal value or because the corresponding points fell too far from the least squares straight lines obtained by including them.

Table VIII. Results of least squares fits

Enthalpies, σ^* , and w in calories per formula unit, temperature in K. Uncertainties are at the 95% confidence limits as determined from the standard deviation between measured and calculated values, e.g., of $\bar{\mu}_{\text{HgTe}}/RT$, and the Student t -distribution. Entry for $x = 1.0$ from Ref. (2).

| N = No. pts | x | σ^* | $-\bar{h} \pm t\sigma$ | $-\bar{s} \pm t\sigma$ | $1/ <1/T>$ | w |
|--|---------------------|---------------------|------------------------|------------------------|------------|-----|
| A. Chemical potential of HgTe | | | | | | |
| 31 | 0.0 | 165 | 42169 ± 707 | 43.256 ± 0.399 | 870.18 | 60 |
| 10 | 0.094 | 31 | 41170 ± 405 | 41.969 ± 0.477 | 852.18 | 23 |
| 16 | 0.197 | 32 | 42317 ± 609 | 42.994 ± 0.677 | 898.67 | 17 |
| 16 | 0.416 | 126 | 41693 ± 739 | 41.721 ± 0.427 | 865.48 | 69 |
| 13 | 0.581 | 46 | 43187 ± 299 | 42.908 ± 0.363 | 825.77 | 28 |
| B. Chemical potential of CdTe | | | | | | |
| 8 | 0.094 | 230 | 67915 ± 2846 | 41.802 ± 3.30 | 865.0 | 197 |
| 6 | 0.197 | 28 | 70750 ± 4820 | 45.419 ± 5.31 | 907.1 | 37 |
| 17 | 0.416 | 220 | 68533 ± 3053 | 43.347 ± 3.30 | 924.7 | 114 |
| 7 | 0.581 | 117 | 67203 ± 4614 | 43.137 ± 4.95 | 931.4 | 138 |
| | 1.00 | | 68640 | 44.94 | Ref. (6) | |
| | 1.00 | | 67984 | 44.562 | Ref. (9) | |
| C. Gibbs free enthalpy of formation from the vapor | | | | | | |
| x | $-\Delta H^\circ_f$ | $-\Delta S^\circ_f$ | | | | |
| 0.094 | 43684 | 41.953 | | | | |
| 0.197 | 47890 | 43.469 | | | | |
| 0.416 | 52858 | 42.397 | | | | |
| 0.581 | 57140 | 43.041 | | | | |

The data for $x = 0.416$ reported in Part I (1) and the original data points for HgTe (2) were reanalyzed including the correction for the nonideality of Hg(g). For completeness these results are also listed in Table VIII, as well as the published (6, 9) standard enthalpy and entropy of formation of CdTe(s) from Cd(g) and $1/2 \text{Te}_2(\text{g})$. The chemical potential of HgTe can also be calculated for metal-saturated, $x = 0.108$, solid solution from the data in Table I. Except for the first four entries in Table I, and except for temperatures above the 691°C solidus, these fall very close to the least squares straight line determined from the data in Table IV for Te-saturated, $x = 0.094$, solid solution. The least squares line for μ_{CdTe} , $x = 0.196$, intersects that for $x = 0.094$ near 527°C . This of course cannot be correct. The error stems from the fact that the six data points cover only a 40°C range.

The enthalpy and entropy values shown in Table VIII are highly correlated in each case and their most probable values fall within an extremely elongated ellipse, which for practical purposes can be approximated by a thin rectangle in the enthalpy-entropy plane (10). The bisector of this rectangle is a line segment that goes through the best fit value for the enthalpy and entropy, has a slope given by the reciprocal of the mean value of $1/T$ listed in the next-to-last column of Table VIII, and is terminated at the 95% confidence limits by the uncertainty quoted for the enthalpy, or equivalently, that quoted for the entropy. Thus, for the first entry in Table VIII, the most probable values of \bar{h} and \bar{s} are related by

$$\bar{h} = -42,169 + 870.18(\bar{s} + 43.256) \pm w \quad [7]$$

$$-42.86 > \bar{s} > -43.66 \text{ for 95\% confidence limit}$$

where $2w$ is the width of the 95% probability ellipse at the best fit value of -43.256 for \bar{s} and is given in the last column of Table VIII for all of the fits. The value of w is the product of the uncertainty in \bar{h} and a factor $(1 - \rho^2)^{1/2}$. The correlation coefficient, ρ , in turn is given as the ratio of the average reciprocal temperature of the experimental points, $\langle 1/T \rangle$, to that of the square root of the average squared reciprocal temperature, $\langle (1/T)^2 \rangle^{1/2}$

$$\bar{\rho} = -\langle 1/T \rangle / \langle (1/T)^2 \rangle^{1/2} \quad [8]$$

It can be seen that the inclusion of the w term in Eq. [7] does not increase the uncertainty in \bar{h} significantly above the uncertainty associated with \bar{s} . Its presence is significant, however, in determining the uncertainty in the chemical potentials, which are much more precisely established than the corresponding individual values of \bar{h} and \bar{s} . Expressing the chemical potential in terms of its partial molar enthalpy and entropy, and using Eq. [7] to eliminate \bar{h} , for the first entry in Table VIII one obtains

$$\bar{\mu}_{\text{HgTe}} = -4528 + (870.2 - T)\bar{s} \pm w \quad [9]$$

Thus the uncertainty in the chemical potential depends on that in \bar{s} , but at 870.2 K reduces to a minimum value of $\pm w$ or $\pm 60 \text{ cal}$. At temperatures increasing removed from 870.2 K , the uncertainty in \bar{s} enters and increases that in the chemical potential above $\pm 60 \text{ cal}$.

The difference between the chemical potentials of Hg and Cd can be obtained as a function of T for a given value of x by using Eq. [1], [2], [3], and Table VIII.

Knowing the chemical potentials of HgTe and CdTe for the x -values listed, it is possible to calculate any two of the partial pressures, P_{Hg} , P_{Cd} , or P_2 , over the solid solution, given the third. The calculated points along the three-phase curves of Fig. 1 and 2 and the calculated values for P_{Cd} along the three-phase curves shown in Fig. 3 were obtained using the expressions for $\bar{\mu}_{\text{HgTe}}$ and $\bar{\mu}_{\text{CdTe}}$ established in Table VIII, Eq. [1], [2], [3], and the measured values of P_{Hg} given in Tables I

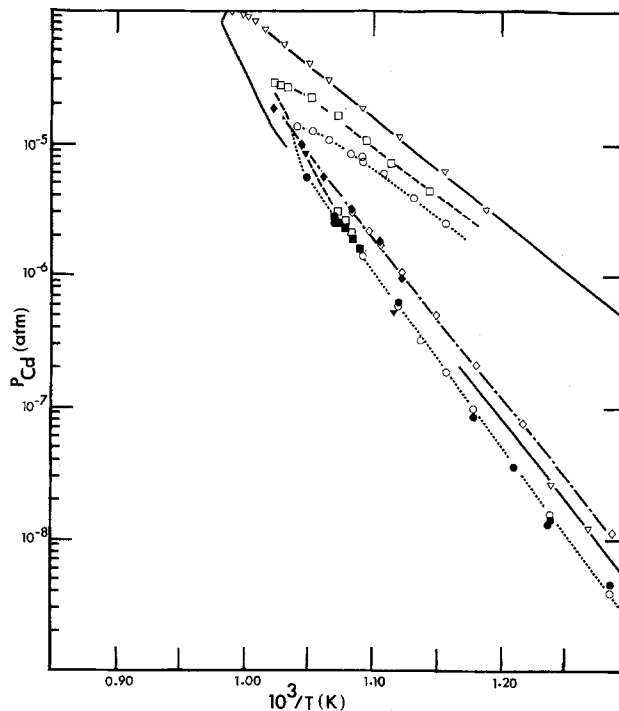
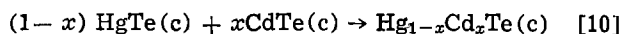


Fig. 3. The partial pressure of Cd along the three-phase curves for various x -values as a function of $10^3/T$. Closed symbols have the same meaning as indicated in the caption for Fig. 1. Open symbols are calculated values.

through VI. In contrast to the P_{Hg} and P_2 three-phase curves, those for P_{Cd} show that, at a given temperature, P_{Cd} is generally higher the larger x for both metal-saturated and Te-saturated solid solutions.

The standard enthalpies and entropies corresponding to the reaction given by Eq. [4] are given in the last section of Table VIII as calculated using the quantities for CdTe from Ref. (6). These were obtained using Eq. [5] and the individual fits to $\bar{\mu}_{\text{HgTe}}$ and $\bar{\mu}_{\text{CdTe}}$, rather than by a fit to the ΔG°_f points directly. Since the cadmium pressures were generally not measured over as wide a temperature range as the other two, the latter procedure would not include all the values of $\bar{\mu}_{\text{HgTe}}$ that were measured.

The standard enthalpy and entropy for the reaction



can be calculated using the data in Table VIII. The results are given in Table IX without the uncertainties attached.

Both ΔH°_f and ΔS°_f are small and at the 95% confidence limit are consistent with the interpretation that the solid solution is ideal with an entropy of mixing corresponding to the random mixing of Hg and Cd. Although the partial pressure measurements are fairly precise, as demonstrated by the fairly low values of w in Table VIII, the ΔG°_f values corresponding to Eq. [10] and Table IX are relatively small differences of large quantities. In spite of the above, one can attempt to gain further insight into the thermodynamics-of-mixing for the solid solution by considering the chemical potentials. Since the solid solution appears to be close to ideal, it seems reasonable to assume that it is a

Table IX. Standard enthalpy and entropy for the reaction, $(1-x) \text{HgTe}(c) + x \text{CdTe}(c) \rightarrow \text{Hg}_{1-x}\text{Cd}_x\text{Te}(c)$

| x | ΔH°_f (cal/ formula wt) | ΔS°_f (cal/ K-formula wt) |
|-------|---|---|
| 0.094 | -1492 | 1.46 |
| 0.197 | -533 | 0.12 |
| 0.416 | 323 | 1.56 |
| 0.581 | 409 | 1.19 |

simple solution, i.e.

$$\bar{\mu}_{\text{HgTe}} - \bar{\mu}^{\circ}_{\text{HgTe}} = \Omega x^2 + RT \ln(1-x) \quad [11]$$

$$\bar{\mu}_{\text{CdTe}} - \bar{\mu}^{\circ}_{\text{CdTe}} = \Omega(1-x)^2 + RT \ln(x) \quad [12]$$

where Ω is a function of T and $\bar{\mu}^{\circ}_{\text{HgTe}}$ and $\bar{\mu}^{\circ}_{\text{CdTe}}$ are the chemical potentials (or Gibbs free enthalpies of formation) of pure HgTe(c) and CdTe(c), respectively. Accordingly, the left-hand sides of Eq. [11] and [12] were calculated at 880 K, the average of the $1/\langle 1/T \rangle$ values in Table VII, and Ω evaluated for each x -value. Ideally, plots of Ωx^2 vs. x^2 and of $\Omega(1-x)^2$ vs. $(1-x)^2$ should yield two straight lines through the origin with the same slope, Ω . A superposition of the two plots should show points clustered around a common straight line. Actually, the chemical potentials of CdTe lead to points much higher than those derived from the chemical potentials of HgTe. If the former are all corrected by subtracting 720 cal, then Fig. 4 results. Two CdTe points are not shown. That for $x = 0.416$ occurs at $(1-x)^2 = 0.341$ and is at -481 cal. That for $x = 0.094$ occurs at 0.821 and is at 1378 cal. The presence of scatter in the points derived from $\bar{\mu}_{\text{HgTe}}$ is not surprising because the calculated values of Ωx^2 are not much larger than the 20-70 cal maximum precision with which the chemical potentials have been determined. Nevertheless they indicate a positive, nonzero value for Ω . In contrast, with the exception of $x = 0.416$, the values of $\Omega(1-x)^2$ derived from $\bar{\mu}_{\text{CdTe}}$ range from 800 to 2100 cal, large compared to the maximum precision of 100-200 cal in $\bar{\mu}_{\text{CdTe}}$ (see last column of Table VIII). We conclude that the value of $\bar{\mu}_{\text{CdTe}} - \bar{\mu}^{\circ}_{\text{CdTe}}$ for $x = 0.416$ is inconsistent with its values for

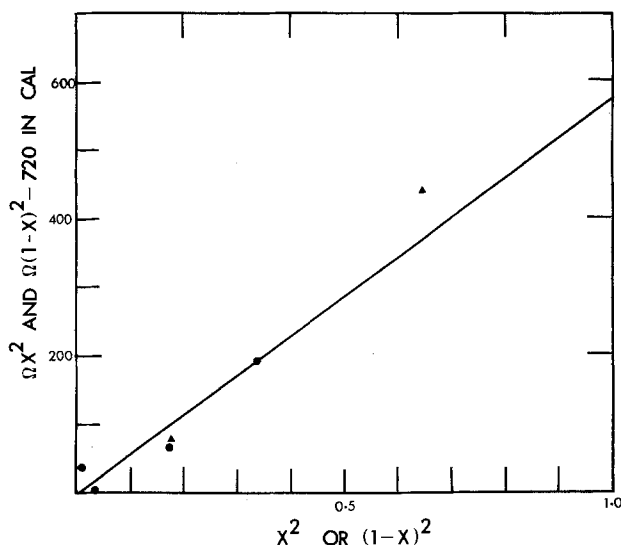


Fig. 4. The excess relative chemical potential of HgTe in $\text{Hg}_{1-x}\text{Cd}_x\text{Te(c)}$, Ωx^2 , plotted against x^2 and the analogous quantity for CdTe, $\Omega(1-x)^2$, plotted against $(1-x)^2$. ● Ωx^2 , ▲ $\Omega(1-x)^2$.

other x 's and should be ignored. Moreover, all the values for $\bar{\mu}_{\text{CdTe}} - \bar{\mu}^{\circ}_{\text{CdTe}}$ are most likely subject to a systematic error of about -720 cal/mole. A possible source for this error lies in the Gibbs free enthalpy of formation of CdTe(c) itself. The value of ΔG°_f for CdTe at 880 K calculated from Ref. (9) is 324 cal less negative than that from Ref. (6) and used here (see Table VIII). Another value (11), determined in the same high temperature range, is about 1 kcal less negative. The postulated error is therefore not unreasonable. This still leaves unexplained the high value of $\bar{\mu}_{\text{CdTe}} - \bar{\mu}^{\circ}_{\text{CdTe}}$ for $x = 0.094$. A true value of P_{Cd} only 0.6 of that measured would be required to reduce the corrected value of $\Omega(1-x)^2$ to 470 cal and put it on the line shown in Fig. 4. The above discussion of errors is speculative. However, we feel the values of Ωx^2 in Fig. 4, derived from the HgTe chemical potentials, do indicate a positive value for Ω that is roughly 600 cal at 880 K.

Acknowledgment

The authors wish to gratefully acknowledge support for this work from the Air Force Office of Scientific Research, Air Force Systems Command, under Grant No. AFOSR-78-3611. Special thanks are due Mr. J. L. Schmit, Honeywell Corporate Research Center, Bloomington, Minnesota, for supplying the crystals and for generous support and to Mr. D. Hovey, Reading, Massachusetts, for careful fabrication of the optical cells.

Manuscript submitted March 11, 1980; revised manuscript received Aug. 4, 1980.

Any discussion of this paper will appear in a Discussion Section to be published in the December 1981 JOURNAL. All discussions for the December 1981 Discussion Section should be submitted by Aug. 1, 1981.

Publication costs of this article were assisted by Marquette University.

REFERENCES

1. J. P. Schwartz, Tse Tung, and R. F. Brebrick, *This Journal*, **128**, 438 (1981).
2. R. F. Brebrick and A. J. Strauss, *J. Phys. Chem. Solids*, **26**, 989 (1965).
3. T. C. Harman, in "Physics and Chemistry of II-VI Compounds," M. Aven and J. S. Prener, Editors, Chap. 15, North-Holland Publishing Co., Amsterdam (1967).
4. J. Blair and R. Newnham, in "Metallurgy of Elemental and Compound Semiconductors," p. 393, Interscience Publications, New York (1961).
5. J. Steininger, *J. Electron. Mater.*, **5**, 299 (1976).
6. R. F. Brebrick, *This Journal*, **118**, 2014 (1971).
7. R. F. Brebrick, *J. Phys. Chem. Solids*, **40**, 177 (1979).
8. S. Sugawara and T. Sato, *Bull. Jpn. Soc. Mech. Eng.*, **5**, 711 (1962).
9. R. Hultgren *et al.*, "Selected Values of the Thermodynamic Properties of Binary Alloys," American Society for Metals, Metals Park, Ohio (1973).
10. R. F. Brebrick, *High Temp. Sci.*, **8**, 11 (1976).
11. M. R. Lorenz, *J. Phys. Chem. Solids*, **23**, 1449 (1962).

Estimated Thermodynamic Properties of the Solid Zirconium Iodides

Robert H. Lamoreaux and Daniel Cubicciotti*

SRI International, Menlo Park, California 94025

ABSTRACT

Literature values of ZrI_4 pressures in equilibrium with solids of the zirconium-iodine system have been used to calculate Zr and ZrI_4 activities as functions of composition at 700 K. These activities, along with estimated heat capacities and free energy functions, were used to derive values of the activity of iodine and of the enthalpies of formation of solid stoichiometric ZrI , ZrI_2 , and ZrI_3 . The estimated enthalpies of formation were: $\Delta H^\circ_{298}(ZrI,s) = -34.0 \pm 2.5$ kcal/mole; $\Delta H^\circ_{298}(ZrI_2,s) = -66.4 \pm 2.5$ kcal/mole; $\Delta H^\circ_{298}(ZrI_3,s) = -93.6 \pm 3.5$ kcal/mole.

The solid-state chemistry of the zirconium-iodine system, which must be known to understand the iodine-induced stress corrosion cracking of zirconium alloys, is complex and to a large extent undetermined. The earlier literature contains little thermodynamic information and is inconsistent about the compositions of solid phases. Recent torsion-effusion studies (1-3) of the pressure of ZrI_4 in equilibrium with solid zirconium iodides have established solid solution regions corresponding approximately to tetra-, tri-, di-, and mono-iodide.

Vaporization measurements on solid zirconium iodides determine the equilibrium pressure of ZrI_4 according to the generalized equation

$$\left(\frac{x+y}{y}\right) ZrI_{4-x}(s) = \left(\frac{x}{y}\right) ZrI_{4-x-y}(s) + ZrI_4(g) \quad [1]$$

Zirconium tetraiodide is the predominant gaseous metal iodide species in equilibrium with any condensed phase in the zirconium-iodine system below about 1000 K (2).

The equilibrium behavior of the condensed phases must conform to the phase rule. A two-component system with a gas phase is univariant when there are two condensed phases (i.e., two immiscible solids) and bivariant when there is only one condensed phase (i.e., one solid solution of variable composition). The number of condensed phases and their compositions can be deduced from the behavior of the pressure of ZrI_4 in the system as the composition of the solid changes during vaporization. As ZrI_4 is removed by vaporization from a solid by Eq. [1], the overall composition of the condensed phase becomes poorer in iodine. If the condensed phase consists of two solids, then the system is univariant and the equilibrium pressure of ZrI_4 depends only on the temperature of the system; in this case, removal of ZrI_4 by vaporization will not change the pressure, but will change only the amounts of the two solids present. If only one solid phase is present (a solid solution), then the system is bivariant and the pressure of ZrI_4 depends on the composition of the solid solution as well as on the temperature; in this case, removal of ZrI_4 will cause the composition of the solid solution to change and the equilibrium pressure to decrease at constant temperature.

The composition limits of zirconium iodide solid phases are listed in Table I (see also Fig. 1). These limits should vary somewhat with temperature, but the variation might be small, as found by Daake and Corbett (4) for the triiodide. The tetraiodide has been characterized, but there is no information about the range of composition over which it is stable. For this phase to be in equilibrium with triiodide, it must ex-

Table I. Composition limits of solid phases of the zirconium-iodine system

| Nominal phase | Composition range | Ref. |
|------------------|---|------|
| Zr | Zr-ZrI ₆ | — |
| ZrI | ZrI _{1.05} ± 0.1-ZrI _{1.30} ± 0.1 | (2) |
| ZrI ₂ | ZrI _{1.8} ± 0.1-ZrI _{2.1} ± 0.1 | (2) |
| ZrI ₃ | ZrI _{2.88} ± 0.05-ZrI _{3.48} ± 0.05 | (4) |
| ZrI ₄ | ZrI _{4-γ} -ZrI _{4+ε} | — |

tend to $ZrI_{4-\gamma}$, since stoichiometric $ZrI_4(s)$ vaporizes congruently (1). The ZrI solid solution composition limits were established by x-ray and chemical analysis of equilibrated samples (4), whereas those of the ZrI_2 and ZrI phases were established by observation of one- and two-solid-phase vaporization behavior (2, 3, 5). Two-solid-phase behavior was observed (3) between $ZrI_{1.05}$ and Zr. The two equilibrium solids in that region were determined from x-ray analysis of a sample of composition $ZrI_{0.1}$, which indicated that the only phases present were Zr and the monoiodide (3).

Heats of formation and free energy functions of solid zirconium monoiodide, diiodide, and triiodide are needed to assess their chemical reactivities with other materials. Since there are no measured values, we have estimated the free energy functions and utilized the limited amount of vaporization data to estimate the heats of formation. Thermodynamic functions used in

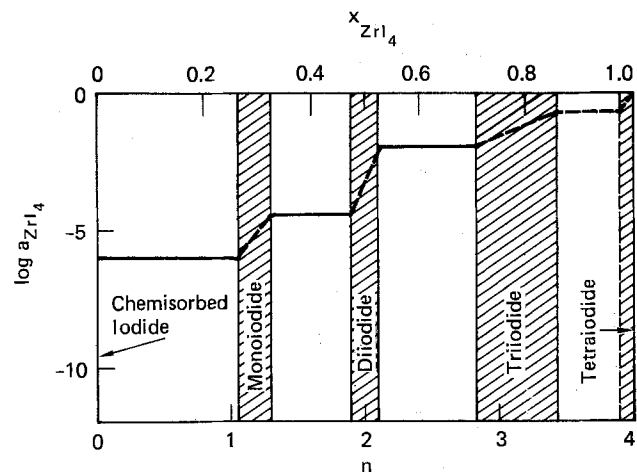


Fig. 1. Activity of ZrI_4 in solid phases of the Zr-I system at 700 K. The lower abscissa is the coefficient n in the formula ZrI_n . Dashed lines represent unknown values. Clear areas are 2 solid phase regions; diagonally ruled areas are 1 solid phase (solid solution) regions.

* Electrochemical Society Active Member.

Key words: enthalpies, sublimation, stoichiometry, free energy.

the calculations were taken from sources summarized in the Appendix.

Calculational Procedures and Results

Activities of Zr and ZrI₄.—Zirconium (component 1) and ZrI₄ (component 2) were taken to be the components of the Zr-I system. The pure solid at the temperature in question was used as the standard state for each component. The activity of ZrI₄ in a two-solid-phase region at a given temperature was calculated as $a_2 = p_2/p_2^\circ$, where p_2 was derived from the data of Table II, and p_2° was the pressure of ZrI₄ over pure, congruently vaporizing ZrI₄(s), calculated from the relationship given in Ref. (1)

$$\log p_2^\circ(\text{atm}) = -\frac{1}{4.575} [31880T^{-1} - 49.7 + 6.68 \times 10^{-3}T - 1.131 \times 10^{-6}T^2 + 8.06 \times 10^{-4}T^{-2}] \quad [2]$$

(450-670 K)

Existing ZrI₄ activity data for the Zr-I solid phase system are indicated in Fig. 1 by solid horizontal lines. The few pressure values reported in the literature for compositions in one-solid-phase regions of this system were considered unreliable because of the probable lack of equilibrium in effusion cells containing a solid phase whose composition changed as ZrI₄ was removed.

The procedure used was to (i) calculate the activities of ZrI₄ and Zr in the two-solid-phase regions, (ii) calculate these activities at compositions (ZrI₂, ZrI₃) within one-solid-phase (solid solution) regions, and (iii) use these activities and estimated free energy function to derive values of the enthalpy of formation for the solid iodides. The lack of experimental data for the triiodide-tetraiodide two-solid-phase region precludes exact calculation of activities within the ZrI₃ phase, but it will be shown that the enthalpy of formation of ZrI₃(s) may nevertheless be fixed within the stated uncertainties.

The activity of Zr was found by integrating the Gibbs-Duhem equation

$$d \ln a_1 = -\frac{x_2}{x_1} d \ln a_2 \quad [3]$$

Over a sufficiently narrow solid phase region it can be shown¹ that

$$\Delta \ln a_1 = -\left(\frac{x_2}{x_1}\right)_{\text{average}} \Delta \ln a_2 \quad [4]$$

or, in terms of n

$$\Delta \ln a_1 = -\left(\frac{n}{4-n}\right)_{\text{average}} \Delta \ln a_2 \quad [5]$$

This simple expression gave results for $\Delta \ln a_1$ in the mono- and di-iodide phases which were identical, at all values of n to results obtained by a more complex technique involving 3-term Margules expressions for the activity coefficients. The activities for stoichiometric ZrI₂ were thus obtained by interpolation. For ZrI, the activities were those of the Zr-ZrI_{1.05} two-solid-phase

¹The function $f(\ln a_2) = (x_2/x_1)$ expanded as a Taylor's series about $\ln a_2^\circ$ is truncated to $f(\ln a_2^\circ + h) = f(\ln a_2^\circ) + h f'(\ln a_2^\circ)$, then substituted on Eq. [3] for integration.

Table II. Pressures of ZrI₄ over two-solid phase regions of the zirconium-iodine system

| Two-solid-phase region | Log ₁₀ P (atm) = -AT ⁻¹ + B | | T range, K | Ref. |
|---|---|-------|------------|------|
| | A | B | | |
| Zr-ZrI _{1.05} | 13.217 | 12.83 | 735-780 | (3) |
| ZrI _{1.05} -ZrI _{1.0} | 9308 | 8.84 | 660-720 | (3) |
| ZrI _{2.1} -ZrI _{2.83} | 8700 | 10.45 | 586-641 | (5)† |

† Reference (5) assigned the data to the composition range ZrI_{1.0}-ZrI_{2.2}. The present assignment is from Ref. (2).

region; this procedure was justified by the uncertainty in the phase boundaries.

Because data are lacking for the ZrI_{3.43}-ZrI_{4-γ} region, activities for ZrI_{3.0} were calculated for the two limiting cases: (i) activities unchanged between ZrI_{2.83} and ZrI_{3.0}, and (ii) the activity of ZrI₄ reaches unity at ZrI_{3.0}. As shown below, both cases lead to closely agreeing values of the enthalpy of formation of ZrI₃(s).

The activities of Zr and ZrI₄ calculated at 700 K from the data of Tables I and II are shown in Table III. At this temperature, chosen to minimize extrapolation of ZrI₄ pressure relationships outside their experimental regions, $p_2^\circ = 0.937$ atm. The activity of Zr in the two-solid-phase region ZrI₃-ZrI_{1.05} was taken as unity because of the negligible solubility of iodine in metallic zirconium.

Thermodynamic functions for the solid zirconium iodides.—No experimental values of heat capacities, C_p , entropies, S° , or free energy functions, $\Phi_{298}^\circ = -(G^\circ - H^\circ_{298})/T$ were found for solid ZrI, ZrI₂, or ZrI₃. They were estimated by the method used by the authors of the JANAF Table (8) for ZrCl₂ and ZrCl₃ as follows. For the solid compound ZrI_n for which $n = 1, 2, \text{ or } 3$, or solid solution for which n is nonintegral, the quantity $Q(Q = C_p^\circ, S^\circ_T, \text{ or } \Phi_{298}^\circ)$ was estimated by subtracting (4- n) iodine-gram-atomic contributions from the molal quantity for ZrI₄(s) according to the relationship

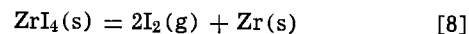
$$Q(\text{ZrI}_{n,s}) = Q(\text{ZrI}_{4,s}) - \frac{4-n}{4} [Q(\text{ZrI}_{4,s}) - Q(\text{Zr},s)] \quad [6]$$

We estimate the uncertainties introduced by this procedure are ± 1 cal/mole degree for C_p and ± 2 cal/mole degree for both S° and Φ_{298} . Table IV presents the thermal data used in Eq. [8] to evaluate the estimated quantities for the solids. Values for the nonstoichiometric solid solutions can be estimated by this procedure as well as for the stoichiometric compounds because the method assumes simply that the thermal quantities (Q) are arithmetic averages of the known values for the two components. The quantity of interest in the present work was the tempered Gibbs energy function, Φ_{298}° . That function for the zirconium iodide solid solutions can be represented in one equation as follows

$$\Phi_{298}^\circ(\text{ZrI}_{n,s}) = 7.53 + 0.0051T + n(10.91 + 0.00487T) \quad [7]$$

That equation is assumed to be applicable for n including nonintegral values, from 1 to 4 and over the temperature range 400-800 K.

Activity of I₂(g) and I(g).—In applications in which zirconium is exposed to attack by gaseous iodine, values of the activity of I(g) and I₂(g) over zirconium iodide solids are needed to understand the resulting chemical behavior. When ZrI₄ and Zr activities were known, the activity of I₂(g) with reference to the 1 atm perfect-gas standard state was calculated from the equilibrium



for which

$$\Delta G^\circ = -RT \ln K = -R \ln \frac{a_{\text{Zr}} a_{\text{I}_2}^2}{a_{\text{ZrI}_4}} \quad [9]$$

and

$$a_{\text{I}_2} = \left(\frac{K a_{\text{ZrI}_4}}{a_{\text{Zr}}}\right)^{1/2} \quad [10]$$

The standard Gibbs energy change for reaction [8] was calculated using tabulated values of Φ_{298}° and ΔH_{298}° (1, 8). At 700 K

$$K = 1.02 \times 10^{-30}$$

The activity of monatomic iodine was calculated from the equilibrium constant K_I for the reaction



Table III. Activities of ZrI_4 , Zr , I_2 , and I in equilibrium with condensed phases of composition ZrI_n at 700 K

| Standard States: $Zr(s)$, $ZrI_4(s)$, $I_2(g)$, $I(g)$ | | | | |
|---|--|---|---|--|
| n | a_{ZrI_4} | a_{Zr} | a_{I_2} | a_I |
| δ -1.05 \pm 0.1 | 9.5×10^{-7} | 1.00 | 9.8×10^{-19} | 1.0×10^{-19} |
| 1.30 ± 0.1 -1.9 \pm 0.1 | 3.7×10^{-5} | 0.22 | 1.3×10^{-17} | 3.8×10^{-18} |
| 2.00 | 8.5×10^{-4} | 1.1×10^{-2} | 2.8×10^{-16} | 1.8×10^{-11} |
| 2.1 ± 0.1 -2.83 \pm 0.5 | 1.2×10^{-2} | 6.9×10^{-4} | 4.2×10^{-15} | 6.9×10^{-11} |
| 3.00 | $\left\{ \begin{array}{l} 1.2 \times 10^{-2} \\ 1 \end{array} \right.$ | $\left\{ \begin{array}{l} 6.9 \times 10^{-4} \\ 4.9 \times 10^{-9} \end{array} \right.$ | $\left\{ \begin{array}{l} 4.2 \times 10^{-15} \\ 1.4 \times 10^{-11} \end{array} \right.$ | $\left\{ \begin{array}{l} 1.1 \times 10^{-11} \\ 4.0 \times 10^{-9} \end{array} \right.$ |

* Because ZrI_4 pressures are unknown in the $ZrI_{3.5}$ - $ZrI_{1.5}$ region, these activities are limiting values as discussed in the text.

Table IV. Parameters for use in Eq. [8] for thermal function of solid zirconium iodides^a

| T, K | Q(ZrI_4 , s) | | | Q(Zr , s) | | |
|------------------|-----------------|-------------|--------------------|--------------|-------------|--------------------|
| | C_p° | S_T° | Φ_{298}° | C_p° | S_T° | Φ_{298}° |
| 298 | 29.90 | 59.80 | 59.80 | 6.07 | 9.31 | 9.31 |
| 300 | 29.92 | 59.99 | 59.81 | 6.10 | 9.35 | 9.31 |
| 400 | 30.63 | 68.70 | 60.98 | 6.37 | 11.14 | 9.56 |
| 500 | 31.16 | 75.59 | 63.24 | 6.64 | 12.59 | 10.02 |
| 600 | 31.61 | 81.32 | 65.79 | 6.92 | 13.83 | 10.56 |
| 700 | 32.04 | 86.22 | 68.37 | 7.20 | 14.92 | 11.10 |
| 772 ^b | 32.34 | 89.37 | 70.18 | 7.40 | 15.63 | 11.49 |

^a Values are given in cal/mol deg, data is from sources cited in the Appendix.

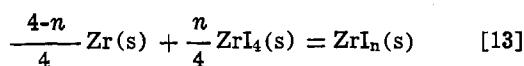
^b Melting point of ZrI_4 (s).

$$K_I = a_I^2/a_{I_2} \quad [12]$$

at 700 K, $K_I = 1.13 \times 10^{-6}$.

Activities of I_2 and I obtained in this way are given in Table III.

Enthalpies of formation of solid ZrI , ZrI_2 , and ZrI_3 .—The standard Gibbs energy changes, ΔG° , for formation of solid ZrI_n ($n = 1, 2, 3$, or 4) from solid Zr and ZrI_4 by the reactions of the type



were obtained from the activities of Zr and ZrI_4 at the composition ZrI_n (where $x_2 = n/4$); through the relationship

$$\Delta G^\circ = -RT \ln [a_{ZrI_n}/(a_{Zr})^{(4-n)/4} (a_{ZrI_4})^{n/4}] \quad [14]$$

or, since the ZrI_n activity of pure ZrI_n (s) is unity

$$\Delta G^\circ = RT \ln (a_{Zr})^{(4-n)/4} (a_{ZrI_4})^{n/4} \quad [15]$$

Since the method used (*i.e.*, Eq. [6]) for estimating heat capacities, entropies, and free energy functions of the solid zirconium iodides implies that ΔC_p° and ΔS° for Reaction [13] are zero at all temperatures, then $\Delta G^\circ_T = \Delta H^\circ_T = \Delta G^\circ_{298} = \Delta H^\circ_{298}$ for Reaction [13] so that

$$\Delta H_f(ZrI_n) = \Delta H_{13} + \frac{n}{4} \Delta H_f(ZrI_4) \quad [16]$$

and $\Delta H_{13} = \Delta G^\circ_{13}$ obtained in Eq. [15].

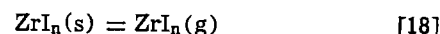
Activities of ZrI_4 and Zr at 700° from Table III were used to evaluate the enthalpies of formation. The values obtained for the stoichiometric compounds were $\Delta H^\circ_{298}(ZrI_4, s) = -34.0 \pm 2.5$ kcal/mole, $\Delta H^\circ_{298}(ZrI_2, s) = -66.4 \pm 2.5$ kcal/mole, and $\Delta H^\circ_{298}(ZrI_3, s) = -93.6 \pm 4.5$ kcal/mole. For purposes of comparison, for ZrI_4 (s), $\Delta H^\circ_{298} + -116.8 \pm 1.5$ kcal/mole (1). The uncertainties in ΔH°_{298} for ZrI (s) and ZrI_2 (s) are essentially due to uncertainties in Φ°_{298} . The difference in ΔG° between the two limiting activity cases for ZrI_3 was 0.5 kcal/mole, but the cumulative uncertainties in a_{Zr} increase the uncertainty in the value of ΔH°_{298} for ZrI_3 (s). The same procedure was used to obtain the enthalpies of formation of the nonstoichiometric solid

solutions. The results are presented graphically in Fig. 2. The lower curve gives the enthalpy of formation of the solid per gram atom of zirconium which is also the value per mole of solid ZrI_n . The upper curve gives the values per gram atom of iodide. The segments of that upper curve, which represent the approximate ranges of solid solution, fall on a straight line within experimental error. Thus, the enthalpies of formation of the solids per gram atom of iodide can be expressed by the rather simple equation

$$\Delta H_{298}(f, ZrI_n, s), \text{ kcal/g atom } I = -35.6 + 1.6 n \quad [17]$$

The enthalpy of formation per gram atom of iodine chemisorbed iodide was taken from Ref. (8) and represents a value obtained for a surface coverage of the order of a fraction of a monolayer. That value fits into Eq. [17] within experimental error. Therefore the range of values of n in Eq. [17] includes the value zero.

The enthalpies of formation of the gaseous iodide of zirconium can be combined with the enthalpies of formation of the solid stoichiometric iodides, given above, to derive enthalpies of sublimation for the four iodides. These values are given in Table V. These enthalpy changes correspond to the four reactions



It should be recognized that the equilibrium sublimations of all the iodides except the tetraiodide correspond to incongruent vaporization. That is, in general the major vapor species in gaseous ZrI_4 so that reaction [18] represents the equilibrium vaporization process. Nevertheless, reaction [2] can be considered *per se*. The values are in keeping with the relative pressures of species calculated for the equilibrium with zirconium at temperatures below about 1200 K in Ref. (7). That is, in the gas the monoiodide was the least important while the tetraiodide was the most important with the di- and

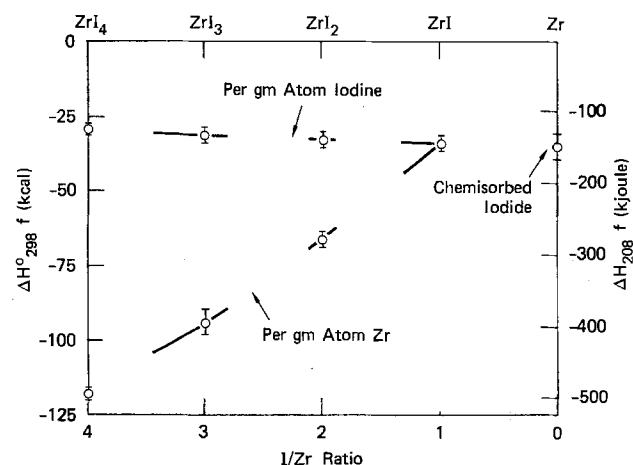


Fig. 2. Enthalpies of formation of the solid zirconium iodides. Values are presented per gram atom of zirconium (lower curve) or per gram atom of iodide in the solid (upper curve). The data points are the values for the stoichiometric solids. The curve segments represent values for the solid solution ranges.

Table V. Enthalpies of sublimation of zirconium iodides*

| | ΔH_{298}° (subl) kcal/mol |
|------------------|---|
| ZrI | 130 |
| ZrI ₂ | 99 |
| ZrI ₃ | 63 |
| ZrI ₄ | 31.9 |

* Values are hypothetical because all the iodides, except ZrI₄, vaporize incongruently to ZrI₄(g), see text.

tri-iodides intermediate, in keeping with the relative values of their sublimation enthalpies, which dominates the entropy at those lower temperatures.

Acknowledgment

This research was supported by the Division of Basic Energy, Sciences, Department of Energy, Dr. Robert P. Epple, Technical Monitor under Contract EY-76-S-03-1339.

Manuscript submitted April 16, 1980; revised manuscript received Aug. 18, 1980.

Any discussion of this paper will appear in a Discussion Section to be published in the December 1981 JOURNAL. All discussions for the December 1981 Discussion Section should be submitted by Aug. 1, 1981.

Publication costs of this article were assisted by SRI International.

APPENDIX

Sources of Thermocouple Information

ZrI₄(s).—The heat capacity and entropy values of Ref. (1) were used to derive the free energy function. The enthalpy of formation, $\Delta H_{298}^{\circ} = -116.8 \pm 1.5$ kcal/mole, was from the JANAF Tables (6).

ZnI₄(g).—The free energy function was taken from the JANAF Tables (6). The enthalpy of formation, $\Delta H_{298}^{\circ} = -84.9 \pm 1.6$ kcal/mole was from Ref. (1).

ZrI(g), ZrI₂(g), ZrI₃(g).—All data were taken from Ref. (7).

Zr(s,g).—Thermodynamic functions were taken from the JANAF Tables (6). The enthalpy of formation of Zr(g), $\Delta H_{298}^{\circ} = 143.4 \pm 1.2$ kcal/mole was from Ackermann and Rauh (9).

I₂(g), I(g).—Thermodynamic data were taken from the JANAF Tables (6).

REFERENCES

1. D. D. Cubicciotti, K. H. Lau, and M. J. Ferrante, *This Journal*, **125**, 972 (1978).
2. D. D. Cubicciotti and K. H. Lau, *ibid.*, **126**, 771 (1979).
3. D. D. Cubicciotti and K. H. Lau, To be published.
4. R. L. Daake and J. D. Corbett, *Inorg. Chem.*, **17**, 1197 (1978).
5. M. A. Bhatti, D. B. Copley, and R. A. J. Shelton, *J. Less-Common Metals*, **55**, 293 (1977).
6. JANAF Thermochemical Tables, NSRDS-NBS 37, U.S. Govt. Printing Office, Washington, D.C. (1971), and supplements.
7. P. D. Kleinschmidt, D. Cubicciotti, and D. L. Hildenbrand, *This Journal*, **125**, 1543 (1978).
8. G. N. Krishnan, B. J. Wood, and D. Cubicciotti, *ibid.*, **127**, 2738 (1980).
9. R. J. Ackermann and E. G. Rauh, *J. Chem. Thermodyn.*, **4**, 521 (1972).

Application of Wagner's Theory to the Parabolic Growth of Oxides Containing Different Kinds of Defects

I. Pure Oxides

F. Gesmundo and F. Viani

Centro Studi di Chimica e Chimica Fisica Applicata alle Caratteristiche d'Impiego dei Materiali del C.N.R., Genova, Fiera del Mare, Pad. D, Italy

ABSTRACT

A generalized treatment of the parabolic oxidation of pure metals forming electronically semiconducting oxides containing different kinds of defects is developed by extending the Kröger approach to Wagner's theory of oxidation based on the analysis of the diffusion of lattice defects. Only oxides with defects in the cation sublattice are considered for simplicity. It is shown how the generally used expressions for the dependence of the parabolic rate constant and the self-diffusion coefficient of the metal as functions of the oxygen activity through the scale are modified by the presence of more than one type of lattice defect. This treatment is then applied to the oxidation of cobalt in oxygen at 1000°C taking into account the actual defect structure of CoO, obtaining a reasonable agreement with the experimental results.

The oxidation of pure metals forming semiconducting oxides of p- or n-type is usually interpreted in terms of Wagner's theory of parabolic oxidation (1-4), assuming that only one kind of lattice defect predominates over the whole range of oxygen activities between the value of equilibrium metal/oxide and that prevailing in the gas phase. In some cases this assumption has led to a reasonably good agreement be-

Key words: parabolic oxidation, pure metals, theory.

tween the experimental values of the parabolic rate constant and those calculated by means of the diffusion coefficients of the migrating species obtained from independent measurements (5-14) and also in the reverse calculation (15-17). Frequently, however, the parameters giving the oxygen pressure dependence of the diffusion coefficient and the parabolic rate constant have not the exact integer values predicted by the theory for a single species of defects (1-4, 18). A pos-

sible reason for this discrepancy is the presence of interactions between defects, not accounted for by the theory, as pointed out recently by C. Wagner (19), but this may also depend on the simultaneous presence of different types of defects in the growing oxide. This situation has been recently discovered for oxides like CoO and NiO, since it has been found that at high temperatures their solid solutions contain a substantial concentration of metal interstitials in addition to the metal vacancies (20). It has also been found for CoO that the concentration of defects obtained from measurements of deviations from stoichiometry is smaller than the overall concentration, suggesting the presence of metal interstitials (Frenkel defects) (17, 21). In addition, the same type of lattice defect may present different electric charges, with the ratio between the concentrations of the differently charged defects depending on the actual value of the oxygen activity.

It seems therefore appropriate to examine the problem of the growth of pure and doped oxides on a metal in more detail than is usually done, considering the actual complexity of the defect structure of the oxides, even for those usually considered simple, like NiO and CoO, to see the effects that this may have on their oxidation behavior. An extension of Wagner's theory taking into account the participation of different kinds of defects to the mass transport during the metal oxidation has already been presented and applied to the oxidation of nickel and cobalt (12). This treatment is extended and generalized here to include the presence of any kind of defects in the cation sublattice.

Throughout the following analysis the Wagner theory of parabolic oxidation will be used as a basis, considering the diffusion of lattice and electronic defects according to the treatment developed by Kröger (22). Even if this approach to the metal oxidation is not exempt from criticism (23, 24), it represents a sufficiently approximate theory for the present purposes and at the same time has the advantage of being essentially simple. This procedure is also partly justified by the proof given by C. Wagner (25) that deviations from local equilibrium in a growing oxide are not likely to affect the final result appreciably. In addition, the many approximations involved in dealing with practical systems, as mentioned below, would prevent a completely rigorous treatment anyway.

Only electronically conducting oxides are considered here, and any kind of interaction between defects as well as defect aggregation will be neglected. This is undoubtedly a major approximation since defects, being generally electrically charged, will usually interact, so that the concept of free defects is a crude assumption when their concentration exceeds 10^{-3} - 10^{-4} in mole fraction (19, 26). Therefore, a correct treatment should make use of activities of defects instead of concentrations. The thermodynamic theory of lattice defects along these lines, however, is not yet completely developed (19, 26-27). In addition, the diffusion coefficients of the different defects are assumed to be equal and independent of their concentration, even if the theory does not require this limitation, since apparently there are no experimental results in this field. Furthermore it will be assumed that oxygen diffusion is negligible with respect to that of the metal.

In view of the many limitations mentioned above, the present treatment is considered only approximate, although it represents an improvement of the single-defect model generally used so far. Therefore, when applied to actual cases it is not expected to lead to a complete agreement with the experimental results. In fact, in addition to the improvements indicated above, this would also require a consideration of other frequently important factors such as the short-circuit diffusion, the presence of porosity and of mechanical stresses in the scale, the lack of scale adherence, and many others, many of which cannot be accounted for

quantitatively and whose consideration would make the theory extremely complex and not general.

This paper examines the oxidation behavior of pure metals; a following paper will discuss within the same framework the effect of the presence of a uniform concentration of aliovalent impurities on the growth of the scale on dilute alloys for oxides with simple or complex defect structure (28).

Theory

The most general model for the defect structure of a pure oxide should include all kinds of defects, also because under appropriate conditions even minority defects may play an important role. Therefore, we will consider the possibility of formation of both cation vacancies and metal interstitials, neglecting only for simplicity the presence of defects in the anion sublattice. This possibility may, however, be easily considered in this type of treatment. In addition, and in agreement with the above simplification, we assume that the contribution to the oxide growth by the oxygen diffusion is negligible.

The quasi-chemical equations for the formation of the different kinds of cation lattice defects in an oxide MO are



and for the electronic defects



where a simplified Kröger-Vink notation is used (22) since only metal vacancies are considered here. Each of the previous equations gives rise to a corresponding equilibrium constant K_i , where i represents the number of the equation in the scheme above. The concentrations of the different species so considered (expressed here as mole fractions) are therefore given by

$$[V^x] = K_1 P_{O_2}^{1/2} \quad [8]$$

$$[V'] = \frac{K_1 K_2}{p} P_{O_2}^{1/2} \quad [9]$$

$$[V''] = \frac{K_1 K_2 K_3}{p^2} P_{O_2}^{1/2} \quad [10]$$

$$[M_i^x] = \frac{K_4}{K_1 P_{O_2}^{1/2}} \quad [11]$$

$$[M_i'] = \frac{K_4 K_5}{n K_1 P_{O_2}^{1/2}} \quad [12]$$

$$[M_i''] = \frac{K_4 K_5 K_6}{n^2 K_1 P_{O_2}^{1/2}} \quad [13]$$

$$n = K_7/p \quad [14]$$

where n is the concentration of electrons and p that of the electron holes. By means of Eq. [14] the concentration of M_i' and M_i'' may also be given as a function of p . The previous equations show that the concentration of the lattice defects depends on the local oxygen activity.

A condition which must be fulfilled during the oxide growth is that of local electroneutrality, which in our case takes the form

$$p + [M_i'] + 2[M_i''] = n + [V'] + 2[V''] \quad [15]$$

Substituting in Eq. [15] the concentrations of the various defects as given by Eq. [8]-[14] and making

use of the oxygen activity defined as $a_o = P_{O_2}^{1/2}$ gives

$$2 \frac{K_4 K_5 K_6}{K_1 K_7 a_o} p^4 + \left(1 + \frac{K_4 K_5}{K_1 a_o} \right) p^3 - (K_7 + K_1 K_2 a_o) p - 2K_1 K_2 K_3 a_o = 0 \quad [16]$$

For any value of a_o , Eq. [16] gives the corresponding concentration of the electron holes and then Eq. [8]-[14] those of all the defects.

During the metal oxidation an oxygen activity gradient is built up between the inner and outer scale interfaces, producing therefore corresponding gradients in the concentrations of the different defects and thereby a flux of matter through the scale. For each kind of defect the diffusion flux is proportional to the corresponding gradient of the electrochemical potential (29) in the form

$$J_{def} = \frac{N_A d_{ox}}{M_{ox}} \left(-D_{def} \frac{d[def]}{dx} \pm v_{def} [def] \frac{d\phi}{dx} \right) \quad [17]$$

where x is the distance from the metal/scale interface, D_{def} the diffusion coefficient of the defect, v_{def} its mobility, and $-d\phi/dx$ the built-in electric field set up by the diffusion of charged species having a different mobility. The sign before the second term on the right-hand side of Eq. [17] is positive for a species with a negative effective charge and vice versa, while the factor $R = N_A d_{ox}/M_{ox}$ (where N_A is the Avogadro number, d_{ox} the oxide density, and M_{ox} its molar weight) is required to convert the concentrations of the defects from mole fractions to number of defects/cm³, which is also a common way of expressing the defect concentrations. The diffusion coefficient of each defect D_{def} is related to the mobility or to the transport number t_{def} of the same species by the relationships (29, 30)

$$D_{def} = v_{def} \frac{kT}{|z_i| q} \quad [18a]$$

and

$$D_{def} = t_{def} \frac{kT\sigma}{z_i^2 q^2 c_{def}} \quad [18b]$$

where c_{def} is the concentration of defects (number of defects/cm³), k the Boltzmann constant, q the electron charge, z_i the charge of the defect, T the absolute temperature, and σ the electrical conductivity.

During the growth of the oxide, the condition of local electroneutrality requires also that the various fluxes of defects are related by the restriction

$$J(h^\cdot) + J(M_i^\cdot) + 2J(M_i^{\cdot\cdot}) = J(e^-) + J(V^\cdot) + 2J(V^{\cdot\cdot}) \quad [19]$$

which is also called the "coupled current condition" (31). The previous equation may be used to obtain an expression for the diffusion electric field to substitute in Eq. [17]. This procedure may be simplified by considering only the motion of the electronic defects which are by far the most mobile species in the electronic conductors. It is easy to show that this is equivalent to putting equal to one the transport number of the electrons and the electron holes in the final expression for the overall flux of matter through the scale, as is usually done in the derivation of the expression of the parabolic rate constant according to Wagner's treatment (1-4, 22). A more thorough justification of this procedure has been given by Fromhold (32) with the introduction of the concept of "virtual current equilibrium" of the species giving the most important contribution to the electrical conductivity. For an oxide with prevailing electronic conduction the so-called "kinetic potential" or the actual electrostatic potential set up across the oxide by the diffusion of charged species may be deduced by setting

equal to zero the flux of the prevailing electronic defect or also by imposing the condition that the sum of the fluxes of electrons and electron holes is zero, taking into account the equilibrium for the intrinsic ionization of the oxide, as used here. Equating, therefore, the fluxes of electrons and electron holes as given by Eq. [17] yields then

$$E(x) = -\frac{d\phi}{dx} = \frac{kT}{q} \frac{d \ln p}{dx} \quad [20]$$

Upon introduction of Eq. [20] and [18a] and [18b] into Eq. [17], the fluxes of the lattice defects are obtained in the form

$$J(V^{\cdot\cdot}) = -D_{V^{\cdot\cdot}} \frac{d[V^{\cdot\cdot}]}{dx} R \quad [21]$$

$$J(V^\cdot) = -D_{V^\cdot} \left(\frac{d[V^\cdot]}{dx} + [V^\cdot] \frac{d \ln p}{dx} \right) R \quad [22]$$

$$J(V^{\cdot\cdot}) = -D_{V^{\cdot\cdot}} \left(\frac{d[V^{\cdot\cdot}]}{dx} + 2[V^{\cdot\cdot}] \frac{d \ln p}{dx} \right) R \quad [23]$$

$$J(M_i^{\cdot\cdot}) = -D_{M_i^{\cdot\cdot}} \frac{d[M_i^{\cdot\cdot}]}{dx} R \quad [24]$$

$$J(M_i^\cdot) = -D_{M_i^\cdot} \left(\frac{d[M_i^\cdot]}{dx} - [M_i^\cdot] \frac{d \ln p}{dx} \right) R \quad [25]$$

$$J(M_i^{\cdot\cdot}) = -D_{M_i^{\cdot\cdot}} \left(\frac{d[M_i^{\cdot\cdot}]}{dx} - 2[M_i^{\cdot\cdot}] \frac{d \ln p}{dx} \right) R \quad [26]$$

where D_i is the diffusion coefficient of the defect i . The overall flux of matter through the oxide is then given by

$$J_{ox} = -J(V^{\cdot\cdot}) - J(V^\cdot) - J(V^{\cdot\cdot}) + J(M_i^{\cdot\cdot}) + J(M_i^\cdot) + J(M_i^{\cdot\cdot}) \quad [27]$$

For simplicity sake the diffusion coefficients of the vacancies will be considered to be independent of their charge and have a common value D_v and in the same way a common value D_i is assumed for the interstitials: apparently there is no *a priori* theoretical reason for this, even though in some cases this condition has been found approximately true (12).

Introduction of Eq. [21]-[26] into Eq. [28] and use of the previous assumption gives then for the overall flux

$$J_{ov} = R \left[D_v \left(\frac{d[V^{\cdot\cdot}]}{dx} + \frac{d[V^\cdot]}{dx} + \frac{d[V^{\cdot\cdot}]}{dx} \right) + D_v ([V^\cdot] + 2[V^{\cdot\cdot}]) \frac{d \ln p}{dx} - D_i \left(\frac{d[M_i^{\cdot\cdot}]}{dx} + \frac{d[M_i^\cdot]}{dx} + \frac{d[M_i^{\cdot\cdot}]}{dx} \right) + D_i ([M_i^\cdot] + 2[M_i^{\cdot\cdot}]) \frac{d \ln p}{dx} \right] \quad [28]$$

Differentiation of Eq. [8]-[13] with respect to x and substitution into Eq. [28] gives finally

$$J_{ov} = \left[D_v ([V^{\cdot\cdot}] + [V^\cdot] + [V^{\cdot\cdot}]) \frac{d \ln a_o}{dx} + D_i ([M_i^{\cdot\cdot}] + [M_i^\cdot] + [M_i^{\cdot\cdot}]) \frac{d \ln a_o}{dx} \right] R = R F(a_o) \frac{d \ln a_o}{dx} \quad [29]$$

(where $F(a_o) = \Sigma D_{def} [def]$ is a function of a_o) for the overall flux which is now expressed as a function

of the concentrations of all the defects and the gradient of the oxygen activity through the scale.

For a fixed time and scale thickness, the overall flux of matter remains constant through the scale, neglecting the usually small changes in stoichiometry of the oxide. This assumption is essentially correct if the oxide has small deviations from the ideal composition: for large deviations it does not hold strictly, but it is still a reasonable approximation in view of the fact that in these cases other factors, such as interactions between defects, come into play. This point has been examined with particular care by Hirth (33) and Fromhold (34). Therefore, multiplication of both sides of Eq. [29] by dx and integration from $x = 0$ (corresponding to the metal/scale interface, with $a_0 = a_0'$) to $x = x_s$ (where x_s is the position of the scale/gas interface, with $a_0 = a_0''$) gives

$$J_{ov} x_s = k_t = R \int_{a_0'}^{a_0''} F(a_0) d \ln a_0 \quad [30a]$$

where k_t is the parabolic rate constant expressed in molecules of oxide formed per unit surface per unit time (35).

An alternative expression for the parabolic rate constant k_t may be obtained by defining a dimensionless distance parameter $y = x/x_s$, which upon differentiation gives $dx = x_s dy$. Introduction of this expression for dx into Eq. [29] and use of the definition of k_t as in Eq. [30] yields

$$J_{ov} x_s = k_t = R F(a_0) \frac{d \ln a_0}{dy} \quad [30b]$$

Integration of Eq. [29] between $x = 0$ and $x = x$ (with $x \leq x_s$) gives instead

$$J_{ov} x = R \int_{a_0'}^{a_0} F(a_0) d \ln a_0 \quad [31]$$

Division of Eq. [31] by Eq. [30a] yields then

$$x/x_s = y = \frac{R}{k_t} \int_{a_0'}^{a_0} F(a_0) d \ln a_0 \quad [32]$$

which defines the relationship between a_0 and the corresponding relative position within the scale y .

Using the rate constant k_x expressed as a function of the scale thickness by the relationship

$$x_s^2 = k_x t \quad [33]$$

and related to k_t by (35)

$$k_x = 2 \frac{M_{ox}}{N_A d_{ox}} k_t = 2k_t/R \quad [34]$$

Eq. [32] becomes

$$y = \frac{2}{k_x} \int_{a_0'}^{a_0} F(a_0) d \ln a_0 \quad [35]$$

For a fixed value of the oxygen activity in the gas phase a_0'' the rate constant k_x may be computed by means of Eq. [30a] and [34] and the profile of the oxygen activity through the scale by means of Eq. [35] once that the corresponding value of k_x has been obtained, using Eq. [8]-[13] and Eq. [16] to calculate the concentrations of all the defects as functions of a_0 . In addition, it is also possible to obtain the fractional flux of each kind of defects, i.e., the ratio between the flux of a defect and the overall flux, as a function of y , to detect the contribution of the different defects to the overall growth of the oxide at various positions in the scale. In fact, using the same procedure as before for the overall flux, the partial flux for any kind of defects is given by

$$J_{def} = R D_{def} [def] \frac{d \ln a_0}{dx} \quad [36]$$

and, dividing Eq. [36] by Eq. [29]

$$\frac{J_{def}}{J_{ov}} = \frac{D_{def} [def]}{F(a_0)} \quad [37]$$

where the ratio of the fluxes is a function of a_0 and/or y .

Equation [37] implies that the fractional flux of each defect changes with x even if J_{ov} remains constant, under a fixed x_s . In fact, in the simplest case where all the defects have the same diffusion coefficient, the fractional flux of each defect is simply proportional to its fractional concentration which is a function of the local value of the oxygen activity since the concentrations of the various defects have a different kind of dependence on a_0 , as shown by Eq. [8]-[13]. Therefore at any point in the scale the largest contributions to the matter transport come from the species having the largest concentrations. If the mobilities of the defects are different, then also this factor must be considered, as implied by Eq. [37].

A final subject to be considered is the expression of the electrical potential due to the migration of charged species in the oxide and of the electric field connected with it. The latter is given by Eq. [20] and is in general a function of x (or y) and x_s . For an oxide with several kinds of defects it can be computed by a numerical evaluation of $d \ln p/dx$. However, it is more convenient to compute the quantity $F(y) = x_s E(x)$ which is only a function of y and does not depend on x_s . This may be found by expressing dx as $x_s dy$ in Eq. [20] giving

$$x_s E(x) = F(y) = \frac{kT}{q} \frac{d \ln p}{dy} \quad [38]$$

In fact, since p is a function of a_0 and a_0 of y , $d \ln a_0/dy$ will depend only on y and not on x_s .

The expression of the electrostatic potential is obtained in a straightforward way by integration of Eq. [20] as

$$\begin{aligned} V(x) - V(0) &= -\frac{kT}{q} \int_0^x d \ln p \\ &= \frac{kT}{q} \ln \frac{p(0)}{p(x)} = V(x) \end{aligned} \quad [39]$$

(where $p(0)$ and $p(x)$ are the concentrations of electron holes at $x = 0$ and $x = x$, respectively), putting as usual the integration constant $V(0) = 0$. If the upper limit in the above integration is x_s , then we obtain

$$V(x_s) = \frac{kT}{q} \ln \frac{p(0)}{p(x_s)} \quad [40]$$

Equations [39] and [40] show that the electrostatic potential V is a function of the distance from the metal/scale interface x . However, since p is also a single-valued function of the relative position within the scale y through the local oxygen activity a_0 , the potential is also a function of y . Therefore, the potential at a point y in the scale is

$$V(y) = \frac{kT}{q} \ln \frac{p(a_0')}{p(a_0)} \quad [41]$$

where a_0' is the oxygen activity at $y = 0$ and a_0 that at $y = y$, while the potential across the scale is

$$V(1) = \frac{kT}{q} \ln \frac{p(a_0')}{p(a_0'')} \quad [42]$$

and does not depend on the actual value of the scale thickness x_s , but only on a_0' and a_0'' . Examples of calculation of $F(y)$ and $V(y)$ are given in the next section.

Oxides with a Simple Defect Structure

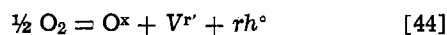
The previous equations for k_x as a function of a_0 and for a_0 as a function of y are reduced to the simple

expressions generally used if only one kind of defect is present in the oxide in the whole range of oxygen activities. In fact in this case the overall flux of matter through the scale is the same as that of the unique kind of defect to be considered and is given by

$$J_{ov} = \pm J_{def} = RD_{def} [\text{def}] \frac{d \ln a_o}{dx} \quad [43]$$

where the minus is for vacancies and the plus for interstitials. Using the same procedure described previously, one may easily obtain the expressions for k_x and a_o for these simple situations as shown below.

Oxides containing only one kind of metal vacancies.—If the oxide contains only vacancies with an effective charge r , the reaction for their formation becomes



with an equilibrium constant

$$K_V = \frac{[V^{r'}] p^r}{a_o} \quad [45]$$

and a neutrality condition (for $r \neq 0$) $p = r [V^{r'}]$. Substitution of this relationship into Eq. [45] gives the concentration of the vacancies in the form

$$[V^{r'}] = \left(\frac{K_V}{r^r} \right)^{1/m} a_o^{1/m} = [V^{r'}]^{\circ} a_o^{1/m} \quad [46]$$

where $m = r + 1$ and $[V^{r'}]^{\circ}$ is the concentration of vacancies when $a_o = 1$. Substitution of Eq. [46] into Eq. [43] yields

$$J_{ov} = -J_v = RD_v [V^{r'}]^{\circ} a_o^{1/m} \frac{d \ln a_o}{dx} \quad [47]$$

Integration of Eq. [47] between $x = 0$ and $x = x_s$ yields then

$$k_x = 2mD_v [V^{r'}]^{\circ} [(a_o'')^{1/m} - (a_o')^{1/m}] \quad [48]$$

or, using Eq. [46] and indicating with $[V^{r'}]'$ and $[V^{r'}]''$ the concentrations of the metal vacancies at $x = 0$ and $x = x_s$, respectively

$$k_x = 2mD_v \{ [V^{r'}]'' - [V^{r'}]' \} \simeq 2mD_v [V^{r'}]'' \quad [49]$$

since usually $[V^{r'}]'' \gg [V^{r'}]'$. The parabolic rate constant k_x can be put in a different form frequently used by means of the relationship (37)

$$D_M = D_v [V^{r'}] \quad [50]$$

where D_M is the self-diffusion coefficient of the metal in the oxide. When $a_o = 1$ Eq. [50] becomes

$$D_M^{\circ} = D_v [V^{r'}]^{\circ} \quad [51]$$

which, upon introduction into Eq. [48] gives finally

$$k_x = 2m [(a_o'')^{1/m} - (a_o')^{1/m}] D_M^{\circ} \quad [52]$$

where the dependence of k_x on the oxygen activity in the gas phase a_o'' is given more clearly.

Integrating again Eq. [47] between $x = 0$ and $x = x$, corresponding to an oxygen activity, a_o , dividing by Eq. [48] and regrouping gives finally, using Eq. [30b] and [34]

$$a_o^{1/m} = (a_o')^{1/m} + [(a_o'')^{1/m} - (a_o')^{1/m}] y \quad [53]$$

for the profile of a_o through the scale.

For these oxides, in view of the relationship between p and a_o as given by Eq. [46] and the appropriate electroneutrality condition, the electric field becomes

$$E(x) = \frac{kT}{qx_s} \frac{d \ln p}{dy} = \frac{kT}{qx_s} \frac{1}{m} \frac{d \ln a_o}{dy} \quad [54]$$

and, according to Eq. [53]

$$E(x) = \frac{kT}{qx_s} \frac{(a_o'')^{1/m} - (a_o')^{1/m}}{a_o^{1/m}} \quad [55]$$

showing that E is a function of y through a_o and of x_s as well: the product $x_s E$ however depends only on y .

Proceeding as for the general case, the electrostatic potential in the oxide will be

$$V(y) = \frac{kT}{q} \ln \left(\frac{p(0)}{p(y)} \right) = \frac{kT}{qm} \ln \left(\frac{a_o'}{a_o} \right) \quad [56]$$

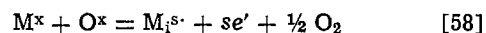
and the potential across the whole scale

$$V(1) = \frac{kT}{qm} \ln \left(\frac{a_o'}{a_o''} \right) \quad [57]$$

showing again the independence of $V(1)$ of the actual scale thickness x_s .

Equation [55] shows that the electric field within the oxide is not constant for a fixed x_s and therefore $V(x)$ is not a linear function of x . Actually, the condition of a constant electric field is not consistent with the condition of a constant flux of defects through the scale for a fixed oxide thickness. In fact, according to Eq. [54], a constant field requires a constant value of $d \ln p/dy$ and $d \ln a_o/dy$. However, since the flux of vacancies is given by Eq. [36], their concentration should be independent of y to produce a constant flux under a constant gradient of $\ln a_o$. This condition is, however, contradictory since the concentration of vacancies is related to the oxygen activity by Eq. [46] and must therefore change with a_o .

Oxides containing only one kind of metal interstitials.—The reaction for the formation of metal interstitials with an effective charge s is



with an equilibrium constant

$$K_I = [M_i^{s'}] n^s a_o \quad [59]$$

and a neutrality condition (for $s \neq 0$)

$$n = s [M_i^{s'}] \quad [60]$$

Upon introduction of Eq. [60] into Eq. [59] the concentration of interstitials becomes

$$[M_i^{s'}] = \left(\frac{K_I}{s^s} \right)^{1/t} a_o^{-1/t} = [M_i^{s'}]^{\circ} a_o^{-1/t} \quad [61]$$

where $t = s + 1$ and $[M_i^{s'}]^{\circ}$ is the concentration of $M_i^{s'}$ when $a_o = 1$. Substituting Eq. [61] into Eq. [43] gives then

$$J_{ov} = J_I = RD_I [M_i^{s'}]^{\circ} a_o^{-1/t} \frac{d \ln a_o}{dx} \quad [62]$$

Proceeding as before we get

$$k_x = 2tD_I [M_i^{s'}]^{\circ} [(a_o'')^{-1/t} - (a_o')^{-1/t}] \quad [63]$$

for k_x , or also, using Eq. [61] and indicating with $[M_i^{s'}]'$ and $[M_i^{s'}]''$ the concentrations of metal interstitials at $x = 0$ and $x = x_s$, respectively

$$k_x = 2tD_I ([M_i^{s'}]'' - [M_i^{s'}]') \simeq 2tD_I [M_i^{s'}]'' \quad [64]$$

since usually $[M_i^{s'}]'' \gg [M_i^{s'}]'$. The parabolic rate constant k_x may again be put in a different form by means of the self-diffusion coefficient of the metal D_M , which is related to the concentration of the interstitials by (37)

$$D_M = D_I [M_i^{s'}] \quad [65]$$

or, when $a_o = 1$, by

$$D_M^{\circ} = D_I [M_i^{s'}]^{\circ} \quad [66]$$

Introduction of Eq. [66] into Eq. [63] yields

$$k_x = 2tD_M^{\circ} [(a_o'')^{-1/t} - (a_o')^{-1/t}] \quad [67]$$

Proceeding as for the metal vacancies, the profile of a_o through the scale is obtained as

$$a_o^{-1/t} = (a_o')^{-1/t} - [(a_o'')^{-1/t} - (a_o')^{-1/t}] y \quad [68]$$

For these oxides, using the relationship between a_0 and p obtained by means of Eq. [14], [59], and [60], the electric field becomes

$$E = \frac{kT}{qx_s} \frac{d \ln p}{dy} = \frac{kT}{qx_s} \frac{1}{t} \frac{d \ln a_0}{dy} \quad [69]$$

and, using Eq. [68]

$$E = \frac{kT}{qx_s} \frac{(a_0')^{-1/t} - (a_0'')^{-1/t}}{a_0^{-1/t}} \quad [70]$$

so that E depends on y through $a_0^{-1/t}$ as given by Eq. [68]. The electrostatic potential across the scale is given by

$$V(y) = \frac{kT}{q} \ln \left(\frac{p(0)}{p(y)} \right) = \frac{kT}{qt} \ln \left(\frac{a_0'}{a_0} \right) \quad [71]$$

and the overall potential across the scale

$$V(1) = \frac{kT}{qt} \ln \left(\frac{a_0'}{a_0''} \right) \quad [72]$$

Equation [70] shows again that the electric field is a function of the position inside the scale, as discussed previously.

It is finally possible to show that the assumption of the existence of a single type of defect in an oxide leads necessarily to the consequence of the presence of a linear gradient of the concentration of the defect through the oxide as a result of the constancy of the flux of defects with respect to x for a constant x_s . In fact, if the oxide contains only metal vacancies with an effective charge r , their flux is given by Eq. [47] while their concentration is related to the local oxygen activity by Eq. [46]. Taking the logarithm of Eq. [46], differentiating with respect to x and substituting into Eq. [47] gives then

$$J_v = -RD_{vm} \frac{d[V^r]}{dx} \quad [73]$$

which, since J_v must be independent of x , requires a linear change of the concentration of the vacancies with x . In the same way, if the oxide contains only metal interstitials with an effective charge s , the flux of interstitials is given by Eq. [62], while their concentration depends on a_0 through Eq. [61]. Proceeding as before we get then

$$J_i = -RD_{it} \frac{d[M_i^s]}{dx} \quad [74]$$

showing again that the concentration of interstitials is a linear function of x . This situation is of course no longer true for oxides containing more than one kind of defect, since in this case the concentrations of defects are not related to the oxygen activity simply by equations of the form of Eq. [46] of Eq. [61].

The previous simplified expressions for k_x and a_0 are strictly valid only if a single kind of defect predominates over the whole range of oxygen activities from a_0' to a_0'' . In particular, Eq. [53] represents the equation derived by Pettit for the oxygen activity profile through the scale in case of p-type semiconducting oxides (38). This expression, however, is strictly correct only for special values of m , i.e., $m = 1, 2$, or 3 . Otherwise the complete expressions for J_{ov} , k_x , and a_0 should be used, dropping at most from them the terms corresponding to defects having only a negligible concentration everywhere.

Numerical Results

Since well-known analytical expressions are available for the different parameters examined above as functions of a_0 or y for oxides containing a single kind of defect, no particular discussion is required for these simple systems. On the contrary, we present here calculations for an oxide like CoO which has a more complex defect structure and for which approximate

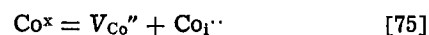
values of the different parameters required for the application of the theory are available. This oxide is selected as an example of the effect that the complex nature of the defects in the oxide may have on the oxidation behavior of the pure metal.

The high temperature oxidation of cobalt has been studied frequently so far (9-12, 39-46), like the defect structure (12, 16, 20, 21, 47-52) and the diffusion properties of CoO (9, 12, 16, 21, 50-60). There is a general agreement that Co oxidizes according to a parabolic rate law at high temperatures, the process being controlled by the diffusion of metal vacancies in the p-type semiconducting oxide (39-46). Neutral, singly, and doubly charged metal vacancies are present in CoO, their concentration being a function of the prevailing oxygen activity under a constant temperature. Around 1000°C and at high oxygen activities the vacancies are prevailing singly charged (12, 16, 21, 47-52), in agreement with the value of the oxygen pressure exponent in the dependence of the parabolic rate constant, the deviations from stoichiometry, and the self-diffusion coefficient of Co on $P(O_2)$ (16, 21, 39-60). Diffusion of oxygen is instead unimportant in this oxide (56).

In addition to metal vacancies, Co interstitials have been proposed as minority defects to explain the effect of Li doping on the electrical properties of CoO (61) and the difference between the concentration of defects deduced from the deviations from stoichiometry and that obtained from measurements of the oxidation rate of cobalt (21, 52). Metal interstitials have also been found by x-ray diffraction in solid solutions CoO-NiO (20) at high temperatures.

Recently, the presence of interstitials in CoO has been questioned on the basis of a comparison between the experimental dependence of the Co self-diffusion coefficient on a_0 and that predicted semi-quantitatively for different ratios between the diffusion coefficients of vacancies and interstitials (60). However, a more precise calculation of D_{Co} as a function of a_0 at 1000°C shows that the presence of a low concentration of Co interstitials is not inconsistent with the experimental findings, as shown below. Therefore, the following calculations are performed for both situations, i.e., for the presence of vacancies only (case 1) and of vacancies plus interstitials (case 2). In fact, even if for pure Co the presence of a low concentration of interstitials affects the oxidation behavior slightly, particularly under high oxygen activities, this may have a profound effect in case of doping, as shown elsewhere (28).

Experimental data.—To apply the calculations developed above to the cobalt oxidation we need the values of the equilibrium constants for the formation of the different defects. These have been measured by different authors in the high temperature range (12, 60, 61): we make use here of those calculated by Dieckmann (60) for the three kinds of metal vacancies, which at 1000°C take the values: $K_1 = 1.37 \times 10^{-3}$, $K_2 = 1.94 \times 10^{-2}$, and $K_3 = 1.89 \times 10^{-4}$, respectively. In the case of the presence of interstitials, three other constants would also be required: however, following Dieckmann (60), we adopt the simplification of considering only the presence of doubly charged interstitials according to the reaction



The corresponding equilibrium constant K_I is obtained assuming that at $a_0 = a_0'$ (Co/CoO equilibrium) the concentration of V_{Co}'' is equal to that of $Co_i^{\cdot\cdot}$, which represents an upper limit to the concentration of interstitials, since higher values would affect appreciably the self-diffusion coefficient of Co at low oxygen activities. In this way we get for K_I

$$K_I = 1.05 \times 10^{-10}$$

The equilibrium constant for the intrinsic ionization of

CoO is in the range 10^{-8} - 10^{-12} at 1000°C (61) and in the calculation we adopt the value $K_7 = 10^{-9}$.

The parabolic rate constant for the oxidation of cobalt at 1000°C and 1 atm O_2 ranges between 3.2×10^{-8} and $1.57 \times 10^{-8} \text{ g}^2 \text{ cm}^{-4} \text{ sec}^{-1}$ (9-12, 39-46), the lowest value being that measured by Mrowec *et al.* (46), which has been obtained by taking into account appropriate correction factors to the experimental value. Conversion of the latter value to the rate constant expressed in terms of scale thickness as used here yields at 1000°C

$$k_x = 1.07 \times 10^{-8} \text{ cm}^2 \text{ sec}^{-1}$$

Finally, the diffusion coefficient of vacancies in CoO has been measured many times with a sufficient agreement (12, 16, 54, 57, 60). For internal consistency, we make use of the value measured by Dieckmann (60), assuming that all the vacancies have the same diffusion coefficient which, at 1000°C , takes the value

$$D_V = 2.957 \times 10^{-7} \text{ cm}^2 \text{ sec}^{-1}$$

Using the previous values of the equilibrium constants for the formation of vacancies and of $\text{Co}_i^{\cdot\cdot}$ and the diffusion coefficient for vacancies reported above, the self-diffusion coefficient of Co in CoO at 1000°C is easily obtained as a function of a_0 by means of the relationship (60)

$$D_{\text{Co}} = D_V \Sigma [V_{\text{Co}}] + D_I [\text{Co}_i^{\cdot\cdot}] \quad [76]$$

putting $D_I = \alpha D_V$. The results are reported in Fig. 1 for case 1 (absence of interstitials) and case 2 (presence of interstitials) with different values of α . Comparison of these curves with the experimental results reported by Dieckmann (60) shows that the condition $[\text{Co}_i^{\cdot\cdot}] = [V_{\text{Co}}]$ at a_0' with $\alpha \leq 1$ is not contradictory with the data about D_{Co} . Therefore in the following the calculations for case 2 will be performed with the previous value of K_I and with $D_I = D_V$.

The oxygen pressure for the equilibrium Co/CoO at 1000°C is obtained from the standard free energy of formation of CoO as $P'(\text{O}_2) = 2.77 \times 10^{-12} \text{ atm}$, corresponding to $a_0' = 1.66 \times 10^{-6}$ (62).

Calculated properties.—The concentrations of the lattice and electronic defects in CoO at 1000°C calculated with the previous values of the different parameters are shown in Fig. 2 as functions of a_0' for cases 1 and 2, respectively. As expected, the difference between the two cases is rather small and limited to the region of low oxygen activities. Doubly charged vacan-

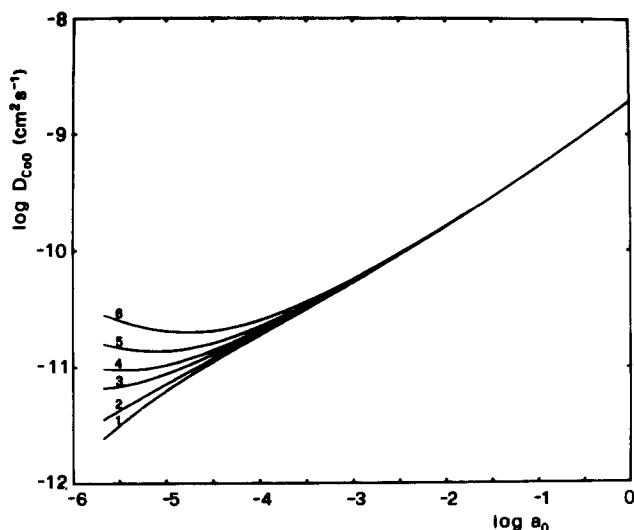


Fig. 1. Self-diffusion coefficient of cobalt in CoO at 1000°C as a function of the oxygen activity for several values of $\alpha = D_I/D_V$. Curve 1: case 1. Curves 2-6: case 2 for different values of α (curve 2, $\alpha = 0$; curve 3, $\alpha = 1$; curve 4, $\alpha = 2$; curve 5, $\alpha = 4$; curve 6, $\alpha = 8$).

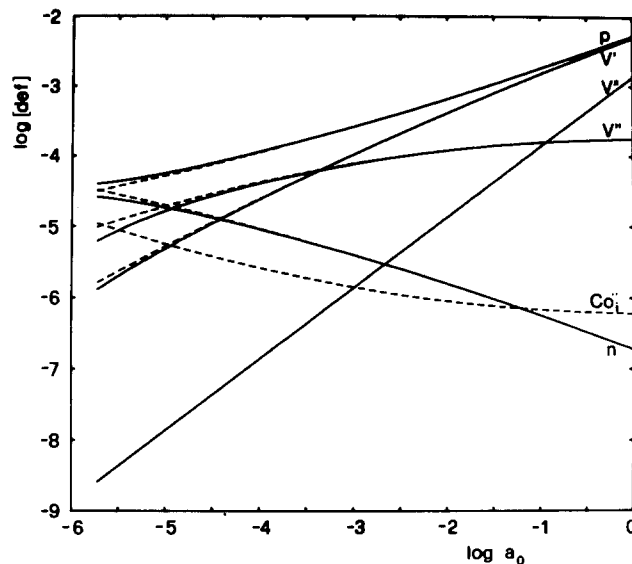


Fig. 2. Concentrations of the different defects in CoO at 1000°C as functions of the oxygen activity. Case 1, continuous lines; case 2, dotted lines.

cies are the prevailing defects from a_0' to about $a_0 = 4 \times 10^{-4}$, while above this value singly charged vacancies predominate. Neutral vacancies are instead minority defects everywhere, even if their concentration is larger than that of V'' above $a_0 = 0.12$. The presence of $\text{Co}_i^{\cdot\cdot}$ produces a decrease of p and a simultaneous increase of the concentration of the species with a negative effective charge, i.e., V' , V'' , and electrons, which is detectable however only close to a_0' , where the concentration of $\text{Co}_i^{\cdot\cdot}$ is larger. The oxide is of p-type everywhere, but close to a_0' it shows $p \approx n$, especially in presence of the interstitials. This is a consequence of the value selected for K_7 : a lower value would give a smaller concentration of electrons, but in lack of more precise information these plots are considered sufficiently accurate. Figure 3 shows the concentrations of the defects as functions of the normalized coordinate y for case 2 only, since those for case 1 are very similar. Comparison with Fig. 2 shows that the largest changes in the concentrations of all species occur for small values of y , i.e., close to the metal/scale interface.

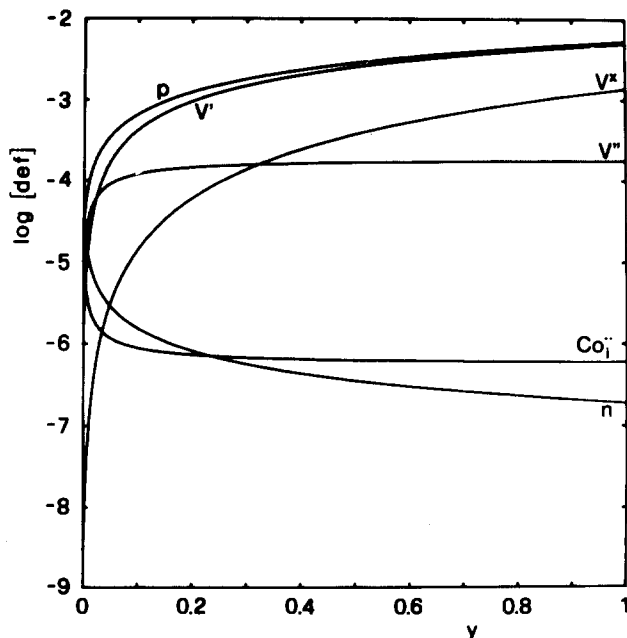


Fig. 3. Concentrations of the different defects in CoO at 1000°C as functions of the normalized distance $y = x/x_S$ for case 2.

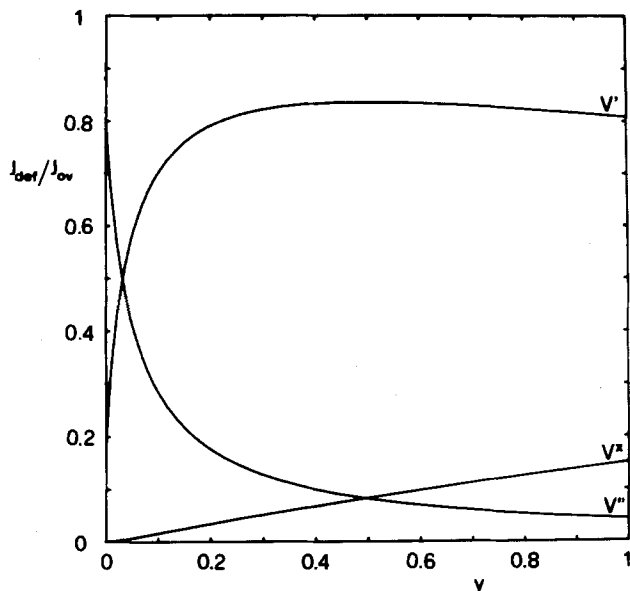


Fig. 4a. Fractional fluxes of the different defects in CoO at 1000°C as functions of the normalized distance $y = x/x_s$ for case 1.

The fractional fluxes of the different lattice defects as functions of y are reported in Fig. 4a and 4b for the two cases. Comparison of Fig. 4b with Fig. 3 shows that the transport through the scale is mainly by means of the doubly charged vacancies close to $y = 0$ where these vacancies prevail, while for the remainder of the scale thickness Co diffuses mainly by means of V' : the contribution of V^x is however significant particularly close to $y = 1$. Comparison of Fig. 4a with Fig. 4b shows instead that the presence of interstitials reduces the flux of V'' close to $y = 0$, so that this shows a sharp maximum at very small values of y . The contribution of the cobalt interstitials is significant only close to $y = 0$, in agreement with the rapid fall of their concentration with y .

The next parameter to be considered is the parabolic rate constant k_x : the plot of k_x as a function of a_0'' , calculated by means of Eq. [30a] and [34] is given in Fig. 5 for both cases. The consistent curvature of the plots at low oxygen activities is a consequence of the fact that in this range a_0'' is not negligible in com-

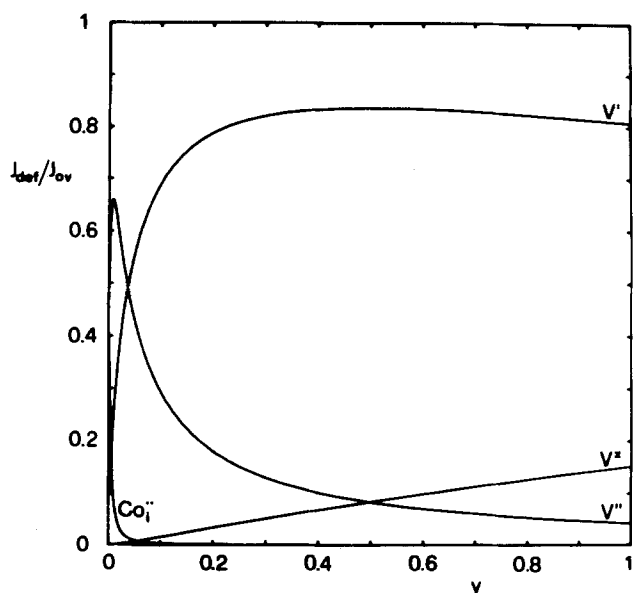


Fig. 4b. Fractional fluxes of the different defects in CoO at 1000°C as functions of the normalized distance $y = x/x_s$ for case 2.

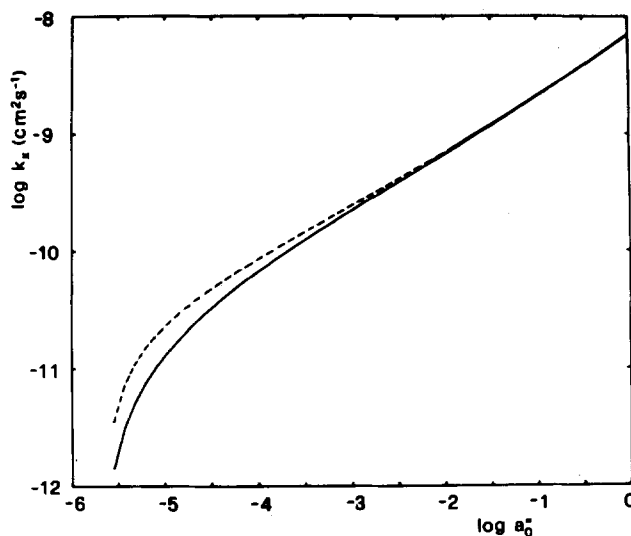


Fig. 5. Parabolic rate constant for the oxidation of pure Co at 1000°C as a function of the gas-phase oxygen activity a_0'' . Case 1 continuous line; case 2, dotted line.

parison with a_0' in the expression of k_x , so that the rate constant becomes a function of both a_0' and a_0'' and tends to zero as a_0'' approaches a_0' . The difference between the two curves is related, however, to the different defect structure assumed in the two cases and above $a_0 = 10^{-3}$ approximately is no longer affected by a_0' . In the region of high oxygen activities the two curves tend to coincide, so that it may be concluded that the presence of low concentrations of Co_i does not affect appreciably the oxidation kinetics of Co at 1000°C under sufficiently high oxygen activities in the gas phase. In presence of impurities, however, the presence of metal interstitials may play an important role, as will be shown elsewhere (28).

The numerical values obtained for k_x by the previous calculation with $a_0'' = 1$ amount to $7.015 \times 10^{-9} \text{ cm}^2 \text{ sec}^{-1}$ for case 1 and $7.045 \times 10^{-9} \text{ cm}^2 \text{ sec}^{-1}$ for case 2, very close together. These values are about 30% lower than the experimental value obtained by Mrowec (46), as reported above. The agreement is not good therefore, but is considered acceptable in view of the fact that the diffusion coefficient of the cobalt vacancies used here to obtain k_x (60) is smaller than the values reported by other authors (12, 57). No attempt is made here to improve the agreement between the calculated and experimental values of k_x by changing the diffusion coefficient of the metal vacancies also on account of the purpose of exemplification of the present calculations.

The dependence of the parabolic rate constant of oxidation of a metal and of the self-diffusion coefficient of the metal ions in its oxide D_M on a_0'' is usually expressed in the form

$$k_x \propto (a_0'')^{1/m} \text{ and } D_M \propto (a_0'')^{1/m'} \quad [77]$$

According to the previous discussion, the above relationships are not correct for oxides with a complex defect structure, but they may still be used to express in a simple way the dependence of these parameters on a_0'' . In these cases, however, m and m' will no longer be constant, but will change as functions of a_0'' . From Eq. [77] m and m' may be defined as

$$m = \frac{d \ln a_0''}{d \ln k_x} \text{ and } m' = \frac{d \ln a_0''}{d \ln D_M} \quad [78]$$

and may be calculated directly by a numerical differentiation procedure from the known dependence of k_x and D_M on a_0 . Plots of m and m' are reported in Fig. 6 for cases 1 and 2: they show that m and m' are indeed rather sensitive functions of a_0 and more-

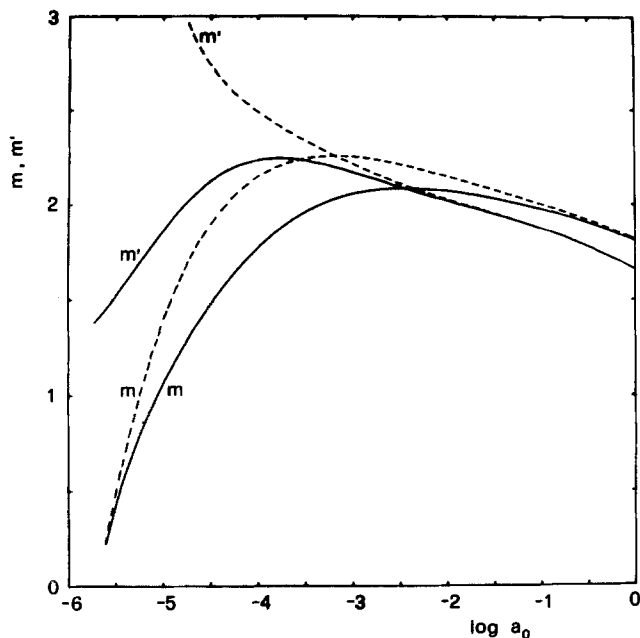


Fig. 6. Oxygen activity exponents of the parabolic rate constant for the Co oxidation (m) and the cobalt self-diffusion coefficient in CoO (m') at 1000°C as functions of the oxygen activity, a_0 . Case 1, continuous lines; case 2, dotted lines.

over that they are different even for the same model of defect structure of the oxide. While the anomalous values of m for low oxygen activities are a consequence of the fact that Eq. [77] does not hold for small values of a_0 , the change of m with a_0 at high a_0 values and that of m' in the whole range are an effect of the complex defect nature of the oxide. Both curves are affected by the presence of the interstitials in the region of low a_0 values, but this is particularly true for m' which shows a maximum in case 1, but is a continuously decreasing function of a_0 in case 2 with $D_I = D_V$. At $a_0 = 1$ we get for both cases $m = 1.812$ and $m' = 1.662$ to be compared with the experimental values $m = 1.725$ (46) and $m' = 1.7$ (45): the agreement seems rather satisfactory.

Finally, the product $x_s E = F(y)$ and $V(y)$ as defined by Eq. [38] and [41] are reported as functions of y in Fig. 7 for the two cases. The presence of interstitials affects the curves at some extent. In both cases, however, the potential is not a linear function of y , as has been found also for simple oxides, but shows a continuously changing gradient which is largest close to $y = 0$. It seems, therefore, that the conclusion that the presence of a potential which is a linear function of y is incompatible with a constant flux of matter through the scale applies also to oxides with a complex defect structure. Correspondingly the diffusion electric field is maximum close to the metal/scale interface and then decreases rather rapidly with y tending to a small value as y approaches 1.

In view of the many simplifications introduced into the present treatment and the uncertainty in the values of many parameters, the agreement between the calculated and experimental values of the various parameters examined here is considered satisfactory.

Conclusions

The previous calculations performed for the specific case of the oxidation of pure cobalt in oxygen at 1000°C show that the different parameters involved and relevant for the kinetics of oxidation of a pure metal are significantly affected by the actual structure of the defects of the oxide, and particularly even by minority defects. This applies even to oxides usually considered simple and seems to be a rather general rule since thermodynamics predict the presence of

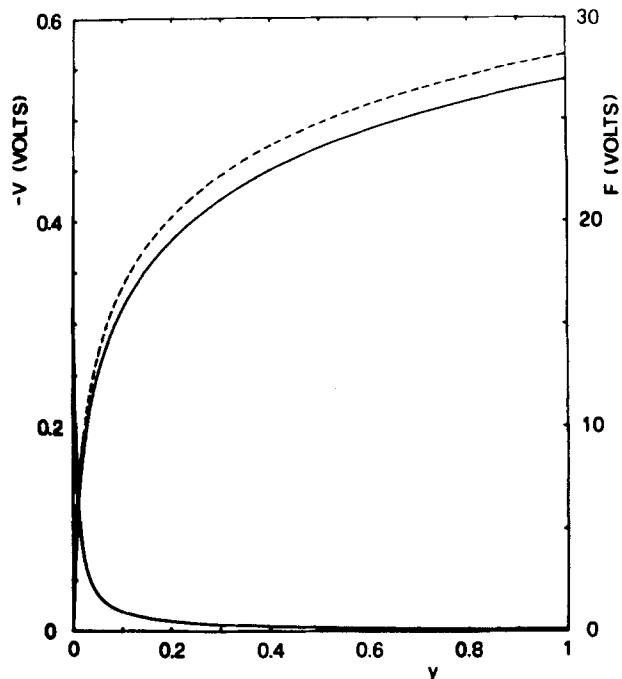


Fig. 7. Electrostatic potential V and product of the electric field by the scale thickness $F = x_s E$ as functions of the normalized distance $y = x/x_s$ for the oxidation of cobalt at 1000°C. Case 1, continuous lines; case 2, dotted lines. The plot of F for case 2 is practically coincident with that for case 1.

more than one kind of defect in any compound. Therefore a complete account of all the aspects connected with the oxidation of metals requires a careful consideration of the actual defect structure of their oxides. The theory presented here allows the calculation of all the quantities involved in the parabolic growth of a scale on a metal independently of the complexity of the oxide properties, overcoming even the difficulty connected in dealing with oxides showing a transition from n- to p-type semiconductivity with a change in the oxygen activity.

Unfortunately, the application of the present approach to the interpretation of the metal oxidation is generally prevented by the lack of sufficient knowledge of the relevant parameters involved. In addition, when the concentration of defects is rather large, interactions between defects become increasingly larger and should also be taken into account. It is hoped that in the future more fundamental research on the nature of defects and other basic properties of the oxides, mainly those of metals relevant for high temperature application, both pure and doped, will be developed, so that the interpretation of their oxidation behavior at high temperatures may be founded on a more solid basis and lead to a deeper understanding of the complex processes involved. In this connection we notice that the treatment developed here does not consider the effect of factors such as the contribution of short-circuit diffusion to the transport through the scale, which is of some importance at intermediate temperatures (13), or the presence of porosity and other possible complications. This represents obviously a limitation of the present approach which should be appreciated when it is applied to actual systems.

Manuscript submitted April 1, 1980; revised manuscript received Aug. 15, 1980.

Any discussion of this paper will appear in a Discussion Section to be published in the December 1981 JOURNAL. All discussions for the December 1981 Discussion Section should be submitted by Aug. 1, 1981.

Publication costs of this article were assisted by Centro Studi di Chimica e Chimica Fisica Applicata alle Caratteristiche d'Impiego dei Materiali del C.N.R.

REFERENCES

1. K. Hauffe, "Oxidation of Metals," Plenum Press, New York (1965).
2. P. Kofstad, "High-Temperature Oxidation of Metals," John Wiley & Sons, Inc., New York (1966).
3. S. Mrowec and T. Werber, "Gas Corrosion of Metals," Foreign Sci. Pub. Dept., Warsaw (1978).
4. J. Bénard, "Oxydation des Métaux," Gauthier-Villars, Paris (1964).
5. F. S. Pettit and J. B. Wagner, Jr., *Acta Metall.*, **12**, 35 (1964).
6. E. T. Turkdokan, W. M. McKewan, and L. Zwell, *J. Phys. Chem.*, **69**, 327 (1965).
7. G. Garnaud and R. A. Rapp, *Oxid. Met.*, **11**, 193 (1977).
8. F. Viani and F. Gesmundo, *Corros. Sci.*, **18**, 231 (1978); **19**, 437 (1979).
9. R. E. Carter and F. D. Richardson, *Trans. AIME*, **200**, 1244 (1954).
10. R. E. Carter and F. D. Richardson, *ibid.*, **203**, 336 (1955).
11. S. Mrowec, T. Walec, and T. Werber, *Corros. Sci.*, **6**, 287 (1966).
12. G. J. Koel and P. J. Gellings, *Oxid. Met.*, **5**, 185 (1972).
13. W. W. Smeltzer and D. J. Young, in "Progress in Solid State Chemistry," Vol. 10, J. O. McCaldin and G. Somorjai, Editors, p. 17, Pergamon Press, Oxford (1976).
14. C. Wagner and K. Grunewald, *Z. Phys. Chem. B*, **40**, 455 (1938).
15. K. Fueki and J. B. Wagner, Jr., *This Journal*, **112**, 970 (1965).
16. E. Fryt, S. Mrowec, and T. Waldec, *Oxid. Met.*, **7**, 117 (1973).
17. S. Mrowec and K. Przybylski, *ibid.*, **11**, 383 (1977).
18. P. Kofstad, "Nonstoichiometry, Diffusion and Electrical Conductivity in Binary Metal Oxides," Wiley-Interscience, New York (1972).
19. C. Wagner, in "Progress in Solid State Chemistry," Vol. 10, J. O. McCaldin and G. Somorjai, Editors, p. 3, Pergamon Press, Oxford (1976).
20. J. J. Stiglich, Jr., D. H. Whitmore, and J. B. Cohen, *J. Am. Ceram. Soc.*, **56**, 211 (1977).
21. E. Fryt, *Oxid. Met.*, **10**, 311 (1976).
22. F. Kröger, "The Chemistry of Imperfect Crystals," p. 832, North-Holland Publishing Co., Amsterdam (1964).
23. F. Morin, *Oxid. Met.*, **6**, 65 (1973).
24. A. T. Fromhold, Jr., "Theory of Metal Oxidation," p. 108, North-Holland Publishing Co., Amsterdam (1976).
25. C. Wagner, *Ber. Bunsenges. Phys. Chem.*, **78**, 611 (1974).
26. C. P. Flynn, "Point Defects and Diffusion," p. 46, Clarendon Press, Oxford (1972).
27. F. A. Kröger, *Ann. Rev. Mater. Sci.*, **7**, 449 (1977).
28. F. Gesmundo *et al.*, To be published.
29. F. Kröger, "The Chemistry of Imperfect Crystals," p. 834, North-Holland Publishing Co., Amsterdam (1964).
30. F. Kröger, *ibid.*, p. 829.
31. A. T. Fromhold, Jr., "Theory of Metal Oxidation," p. 104, North-Holland Publishing Co., Amsterdam (1976).
32. A. T. Fromhold, Jr., *ibid.*, p. 157.
33. J. P. Hirth and R. A. Rapp, *Oxid. Met.*, **11**, 57 (1977).
34. A. T. Fromhold, Jr., "Theory of Metal Oxidation," p. 69, North-Holland Publishing Co., Amsterdam (1976).
35. P. Kofstad, "High-Temperature Oxidation of Metals," p. 116, John Wiley & Sons, Inc., New York (1966).
36. P. Kofstad, *ibid.*, p. 121.
37. P. Kofstad, *ibid.*, p. 93.
38. F. S. Pettit, *This Journal*, **113**, 1249 (1966).
39. A. Preece and G. Lucas, *J. Inst. Metals*, **81**, 219 (1952).
40. S. F. Frederick and I. Cornet, *This Journal*, **102**, 285 (1955).
41. D. W. Bridges, J. P. Bauer, and W. M. Fassel, Jr., *ibid.*, **103**, 614 (1956).
42. F. S. Pettit and J. B. Wagner, Jr., *Acta Metall.*, **12**, 41 (1964).
43. F. R. Billman, *This Journal*, **119**, 1198 (1972).
44. G. N. Irving, J. Stringer, and D. P. Whittle, *Oxid. Met.*, **9**, 436 (1975).
45. M. E. El-Dahshan, D. P. Whittle, and J. Stringer, *Corros. Sci.*, **16**, 77 (1976).
46. S. Mrowec and K. Przybylski, *Oxid. Met.*, **11**, 365 (1977).
47. B. Fisher and D. S. Tannhauser, *J. Chem. Phys.*, **44**, 1663 (1966).
48. N. G. Eror and J. B. Wagner, Jr., *J. Phys. Chem. Solids*, **29**, 1957 (1968).
49. H. G. Sockel and H. Schmalzried, *Ber. Bunsenges. Phys. Chem.*, **72**, 745 (1968).
50. I. Bransky and J. M. Wimmer, *J. Phys. Chem. Solids*, **33**, 801 (1972).
51. M. Gvishi and D. S. Tannhauser, *ibid.*, **33**, 893 (1972).
52. S. Mrowec and K. Przybylski, in "Proceedings of 8th International Symposium on the Reactivity of Solids," J. Wood, O. Lindkvist, C. Helgesson, and G. Vannerberg, Editors, p. 177, Plenum Press, New York (1977).
53. W. K. Chen, N. L. Peterson, and W. T. Reeves, *Phys. Rev.*, **186**, 887 (1969).
54. J. B. Price and J. B. Wagner, Jr., *Z. Phys. Chem. N.F.*, **49**, 257 (1966).
55. J. B. Wagner, Jr., in "Mass Transport in Oxides," J. B. Wachtman, Jr. and A. D. Franklin, Editors, p. 65, National Bureau of Standards Spec. Pub. 296, Washington, D.C. (1968).
56. W. K. Chen and R. A. Jackson, *J. Phys. Chem. Solids*, **30**, 1309 (1969).
57. J. M. Wimmer, R. N. Blumental, and J. Bransky, *ibid.*, **36**, 269 (1975).
58. F. Morin, *Can. Met. Quart.*, **1**, 105 (1975).
59. S. R. Rahman and M. F. Berard, *J. Am. Ceram. Soc.*, **60**, 67 (1977).
60. R. Dieckmann, *Z. Phys. Chem.*, **107**, 189 (1977).
61. B. Fisher and J. B. Wagner, Jr., *J. Appl. Phys.*, **38**, 3838 (1967).
62. J. P. Coughlin, Bureau of Mines Bull. No. 542 (1954).

Application of Wagner's Theory to the Parabolic Growth of Oxides Containing Different Kinds of Defects

II. Doped Oxides

F. Gesmundo and F. Viani

Centro Studi di Chimica e Chimica Fisica Applicata alle Caratteristiche d'Impiego dei Materiali del C.N.R., Genova, Fiera del Mare, Pad. D, Italy

ABSTRACT

The theory of parabolic oxidation of metals forming oxides with a complex defect structure developed in a previous paper is applied here to the oxidation of dilute alloys with incorporation of aliovalent impurities in the scale. The treatment is limited, however, to the simple case of a uniform distribution of the dopant. First, the effect of the dopant on the oxidation rate is examined quantitatively for oxides containing a single kind of defect, obtaining simple analytical expressions for the relevant parameters for limiting situations. Then the growth of CoO on dilute cobalt alloys at 1000°C is analyzed by means of numerical calculations both in the case of the presence and of the absence of metal interstitials, allowing for the presence of metal vacancies of different electric charge. This case is examined as an example of the oxidation behavior of metals forming oxides with a complex defect structure in the presence of dopants. The treatment shows that in some cases even minority defects may change deeply the effect of impurities on the oxidation rate of the pure metal, even reversing the behavior predicted on the basis of a simpler defect model.

In a previous paper [Part I (1)] we have examined the oxidation behavior of pure metals forming electronically semiconducting oxides with a complex defect structure, extending Kröger's approach (2) to Wagner's theory of parabolic oxidation (3) and considering oxides in which only metal diffusion is important. We extend here the same analysis to the growth of doped oxides on dilute alloys, so that only the base oxide is formed in the process.

The rate constant for the parabolic oxidation of a metal is usually changed various extents by the addition of a second component forming a solid solution scale. Doping by foreign ions having the same valency as those of the matrix also affects the concentration of defects and the diffusion of matter through the scale (4-8), but this case will not be considered here. Doping by ions of different valency has, however, a stronger effect, since it produces a new kind of defect with an effective charge different from zero, the impurity itself. This is usually known as the Wagner-Hauffe effect (9-11) and is interpreted on the basis of the change of the concentration profiles of the lattice defects through the scale with respect to the pure oxide due to the incorporation of the aliovalent impurities. The change in the oxidation kinetics is usually analyzed assuming the presence of a single kind of defect even in the doped oxide. The thermodynamic theory of lattice defects shows, however, that the presence of impurities is able to change the concentrations of all the defects as well as their ratios, under a constant oxygen activity, since it affects the concentration of the electronic defects (12). In this way defects which may be neglected in the pure oxide may play an important role in the doped oxide. In some cases this may even lead to a change in the defect structure of the oxide, as found for example in Li-doped CoO (13). Therefore it is particularly important to take into account the actual defect structure of the base oxide when examining the effect of doping on the oxidation rate of a metal.

Key words: parabolic oxidation, dilute alloys, doping effects.

In this paper the effect of a dopant on the kinetics of oxidation of a metal is analyzed considering the particular but unlikely case of a uniform distribution of the dopant in the scale, such as has been considered in the derivation of the Wagner-Hauffe rules (9, 10). This simple treatment is, however, extended here to include the case of oxides having a complex defect structure, as has been done in a previous paper (1). The more complete problem of the growth of a doped oxide with a simple or complex defect structure and a nonuniform distribution of the dopant will be dealt with elsewhere (14).

Theory

The presence of aliovalent impurities in the oxide growing on a dilute alloy produces an unbalance of the electric charge, which must be compensated for by a change in the local concentration of the charged defects with respect to the pure oxide under the same oxygen activity. The concentrations of these species will then depend not only on the oxygen activity but also on the local dopant concentration. From the point of view of the parabolic growth of the scale this situation will affect in principle all the parameters involved, namely, the profile of the oxygen activity, the electric field within the scale, the partial and overall fluxes of the defects, and finally the parabolic rate constant itself.

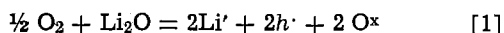
A primary factor for all these changes is clearly the profile of the concentration of the dopant in the scale, which in general will not be flat, but will show a preferential accumulation of the dopant either close to the metal/scale or to the scale/gas interface. The average concentration and the actual distribution of the dopant in the oxide will obviously depend on many factors, such as the bulk alloy composition, the difference between the affinity for oxygen of the two alloy components, the tendency of the impurity to oxidize internally if forming the most stable oxide, the solubility of the dopant in the matrix, and, above all, the relative diffusivities of the two kinds of cations in the scale. From this last point of view the ion moving

faster will clearly tend to accumulate close to the scale/gas interface.

The effect of all these factors on the overall scaling behavior of a binary alloy has already been thoroughly investigated in case of alloys producing a solid solution scale for any alloy composition (4-8) and will not be considered here. Even for aliovalent impurities a complete theory would involve the solution of the coupled equations for the diffusion of both the base metal and the impurity in the scale, as has been done by C. Wagner *et al.* for the oxidation of Ni-Cr alloys (15). However, this treatment introduces some parameters which are usually unknown, so that it may only be used as a qualitative criterion. The case of a uniform distribution is analyzed here with the purpose of obtaining indications of general character about the effects of doping, which require only a correct knowledge of the defect structure of the oxide. Actual cases of nonuniform distribution of the impurity in real systems must instead be solved individually taking specifically into account the different rates of diffusion of the two metal species and, while retaining their specific interest for the special system investigated, would lose any generality.

In the following it will be assumed that the dopant assumes only substitutional positions in the lattice of MO. Furthermore, only the case of monovalent and trivalent impurities will be considered: the extension to the case of impurities of higher valency is however obvious. In addition, the concentration of the impurity is considered sufficiently small so that the oxygen activity at the alloy/scale interface remains substantially unchanged with respect to the pure metal. It is finally assumed that the impurity is present in its normal charged state in the matrix: if this is not true, as has been found for Cr and Ti in CoO (16), the equilibrium between the states with a different electric charge of the impurity should also be considered. The same restrictions as used in Part I (1) are also assumed to apply here: in particular only defects in the cation sublattice are considered. The cases of presence of lower valent or higher valent impurities are examined in turn separately.

Lower valent impurities.—Since the oxide is assumed to have the composition MO, the lower valent impurity can only be monovalent. Li will be taken as an example of this class of dopants. In the presence of Li in substitutional positions in MO, in addition to the usual equations for the formation of the different lattice defects (1), the mechanism of incorporation of the impurity in a normal lattice site according to the reaction (17)



must also be considered. Equation [1] shows that the introduction of Li in MO produces an increase in the concentration of the electron holes: this in turn will lower the concentration of the charged metal vacancies or raise that of the charged metal interstitials in oxides containing only one kind of defect, but will affect simultaneously both concentrations in the case of oxides having both kinds of defects, according to Eq. [9]-[10] and [12]-[13] of Part I (1).

In the presence of Li as the impurity, the neutrality condition becomes

$$p + [\text{M}_i'] + 2[\text{M}_i''] = n + [\text{V}'] + 2[\text{V}'] + [\text{Li}'] \quad [2]$$

so that, expressing the concentrations of the charged defects by means of Eq. [9]-[14] of Part I (1) and rearranging, Eq. [2] becomes

$$2 \frac{K_4 K_5 K_6}{K_1 K_7 a_0} p^4 + \left(1 + \frac{K_4 K_5}{K_1 a_0} \right) p^3 - [\text{Li}'] p^2 - (K_7 + K_1 K_2 a_0) p - 2K_1 K_2 K_3 a_0 = 0 \quad [3]$$

as a final expression of p as a function of both a_0 and $[\text{Li}']$. For any given value of a_0 and $[\text{Li}']$ the previous equation may be solved for p and then the concentrations of all the defects may be calculated. Then the partial fluxes of the various kinds of defects, the overall flux, the parabolic rate constant, and the oxygen activity profile may be calculated as for the pure oxide (1), using only Eq. [3] rather than Eq. [15] of Part I (1) to compute p . For a nonuniform distribution of the dopant the solution of Eq. [3] requires a knowledge of $[\text{Li}']$ as a function of a_0 , which has to be obtained by some indirect procedure to be discussed elsewhere (14). The solution is instead much simpler if $[\text{Li}']$ is uniform since in this case p will be only a function of a_0 , but all the parameters must still be computed numerically for each specific case. Only in the case of the existence of a single kind of defect is it possible to obtain simplified expressions which, even though of limited use because based on excessively drastic approximations, may still be used to make a qualitative prediction of the effect of the dopant. These simplified expressions are given below for the different possible cases.

Neutral vacancies or neutral interstitials.—Since the presence of Li in substitutional positions with an effective charge -1 does not affect the concentration of the neutral lattice defects, J_{ov} and k_x are still given by Eq. [47] and [48] of Part I (1) with $r = 0$ for neutral vacancies, or by Eq. [62] and [63] of Part I (1) with $s = 0$ for neutral interstitials, so that no change of k_x or of the profile of a_0 is expected in this case. It is however to be noticed that this situation is very unlikely, particularly for high levels of doping, because in presence of high concentrations of electrons or electron holes the concentration of charged lattice defects may become important even in oxides in which they are usually insignificant. In fact, the assumption that a compound contains only neutral defects is only a simplifying approximation, since the equilibria between the differently charged states of the same kind of defect must always exist. In these cases, therefore, the complete treatment discussed above must be used.

Charged vacancies.—If a single kind of charged vacancy predominates in the doped oxide, then the electro-neutrality condition becomes (r being the effective charge of the vacancies)

$$p = n + r [\text{V}^r] + [\text{Li}'] \quad [4]$$

or, since $p \gg n$ for these oxides, particularly when Li doped

$$p \simeq r [\text{V}^r] + [\text{Li}'] \quad [5]$$

The previous equation may be used to compute p as a function of $[\text{Li}']$ and a_0 , expressing the concentration of the vacancies by means of the relationship (1)

$$K_v = \frac{[\text{V}^r] p^r}{a_0} \quad [6]$$

where K_v is the constant of the equilibrium for the formation of the vacancies.

A special situation arises when the concentration of the dopant is so high that $[\text{Li}'] \gg [\text{V}^r]$, so that Eq. [5] becomes

$$p \simeq [\text{Li}'] \quad [7]$$

and the concentration of the vacancies becomes, from Eq. [6]

$$[\text{V}^r] = \frac{K_v a_0}{[\text{Li}']^r} \quad [8]$$

The overall flux, which is given by J_v , becomes then (1)

$$J_{ov} = -J_v = RD_v [\text{V}^r] \frac{d \ln a_0}{dx} = RD_v \frac{K_v}{[\text{Li}']^r} \frac{da_0}{dx} \quad [9]$$

and, upon integration from $x = 0$ to $x = x_s$ (1)

$$k_x = 2D_V \frac{K_V}{[Li']^r} (a_0'' - a_0') \quad [10]$$

Alternatively, making use of the concentration of the metal vacancies in the pure oxide as obtained from Eq. [6] with the neutrality condition $p = r [V^r]$

$$k_x = 2D_V \frac{r^r}{[Li']^r} \{ ([V^r]_0'')^m - ([V^r]_0')^m \} \\ \approx 2D_V \frac{r^r}{[Li']^r} ([V^r]_0'')^m \quad [11]$$

where $[V^r]_0'$ and $[V^r]_0''$ are the concentrations of V^r in the pure oxide at the alloy scale interface and the scale/gas interface, respectively.

The ratio of the parabolic rate constant for the oxidation of the alloy k_x to that of the pure metal k_x° as given by Eq. [49] of Part I (1) becomes then

$$\frac{k_x}{k_x^\circ} = \frac{r^r}{m} \left\{ \frac{[V^r]_0''}{[Li']} \right\}^r \quad [12]$$

Equation [12] shows that under the conditions used to obtain it, k_x is smaller than k_x° , so that the introduction of Li slows down the oxidation rate with respect to the pure metal. In fact, apart from the numerical factor r^r/m which is close to one, one has $[Li'] \gg [V^r]_0''$ by hypothesis, so that $k_x \ll k_x^\circ$.

The profile of the oxygen activity is obtained as for the pure oxides by integration of Eq. [9] from $x = 0$ to $x = x$ and division by Eq. [10] in the form

$$a_0 = a_0' + (a_0'' - a_0') y \quad [13]$$

so that in this case a_0 is simply a linear function of y .

Charged interstitials.—The electroneutrality condition for these oxides which are essentially n-type semiconductors is, assuming that they contain only metal interstitials with an effective charge s

$$p + s [M_i^{s\cdot}] = n + [Li'] \quad [14]$$

where the concentration of $M_i^{s\cdot}$ depends on a_0 through the relationship (1)

$$K_I = [M_i^{s\cdot}] n^s a_0 \quad [15]$$

where K_I is the equilibrium constant for the formation of the interstitials. Equations [14] and [15] allow the calculation of p as a function of a_0 and $[Li']$.

A special situation is met also in this case in presence of high concentrations of Li, when $[Li'] \gg n$ and also $[M_i^{s\cdot}] \gg p$, so that Eq. [14] becomes

$$s [M_i^{s\cdot}] \approx [Li'] \quad [16]$$

leading to an approximately constant concentration of interstitials through the scale. The flux of interstitials will be then (1)

$$J_{ov} = J_I = RD_I [M_i^{s\cdot}] \frac{d \ln a_0}{dx} \\ = RD_I \frac{[Li']}{s} \frac{d \ln a_0}{dx} \quad [17]$$

from which, by integration from $x = 0$ to $x = x_s$ we obtain

$$k_x = 2D_I \frac{[Li']}{s} \ln \left(\frac{a_0''}{a_0'} \right) \quad [18]$$

The ratio of the rate constant k_x to that of the pure metal k_x° as given by Eq. [64] of Part I (1) will then be

$$\frac{k_x}{k_x^\circ} = \frac{1}{s(s+1)} \frac{[Li']}{[M_i^{s\cdot}]_0'} \ln \left(\frac{a_0''}{a_0'} \right) \quad [19]$$

where $[M_i^{s\cdot}]_0'$ is the concentration of $M_i^{s\cdot}$ in the pure oxide at $x = 0$, i.e., at $a_0 = a_0'$.

From Eq. [19] it follows that the introduction of Li produces an increase of the parabolic rate constant of oxidation in comparison with the pure metal under the same oxygen activity in the gas phase. In fact for the pure oxide $s [M_i^{s\cdot}]_0' = n_0'$, where n_0' is the concentration of electrons in the pure oxide at $a_0 = a_0'$, while for the doped oxide $s [M_i^{s\cdot}]' \approx [Li']$, but, because of reaction [1], one has also $[M_i^{s\cdot}]' \gg [M_i^{s\cdot}]_0'$; in addition, also the factor $\ln(a_0''/a_0')$ is greater than one, so that $k_x \gg k_x^\circ$.

The profile of a_0 through the scale is obtained by the usual procedure in the form

$$a_0 = a_0' \cdot (a_0''/a_0')^y \quad [20]$$

Higher valent impurities.—Chromium will be taken as an example of higher valent impurity in an oxide MO. The incorporation of chromium in substitutional positions occurs according to the reaction (17)



and produces, therefore, an increase in the concentration of electrons. As a consequence, the concentration of metal vacancies will increase and that of metal interstitials decrease according to the equilibria expressed by Eq. [9]–[10] and Eq. [12]–[13] of Part I (1). The condition for electroneutrality becomes in this case

$$p + [M_i \cdot] + 2[M_i \cdot \cdot] + [Cr \cdot] = n + [V'] + 2[V''] \quad [22]$$

and, expressing the concentrations of the different defects as functions of a_0 and p and regrouping, p is given by

$$2 \frac{K_4 K_5 K_6}{K_1 K_7 a_0} p^4 + \left(1 + \frac{K_4 K_5}{K_1 a_0} \right) p^3 + [Cr \cdot] p^2 \\ - (K_7 + K_1 K_2 a_0) p - 2K_1 K_2 K_3 a_0 = 0 \quad [23]$$

Equation [23] replaces Eq. [16] of Part I (1), which applies to the pure oxide, and allows the calculation of p when a_0 and $[Cr \cdot]$ are known. As in the case of monovalent impurities, the calculation of the parabolic rate constant, the fluxes of the different defects, and the profile of a_0 through the scale requires a complete solution of the relevant equations, obtaining p by solution of Eq. [23].

Simplified solutions may be obtained also in this case if it is assumed that essentially only one kind of defect is present in the whole range of stability of the oxide and that the impurity is uniformly distributed through the scale. As before, the different possibilities are examined in turn.

Neutral vacancies or neutral interstitials.—As for the case of the presence of monovalent impurities, no change in the rate constant or in the oxygen activity profile is expected in presence of these defects if it is assumed that the defect structure of the doped oxide remains the same as that of the pure oxide. However, as discussed above, this is only a crude approximation which is not expected to hold particularly for high doping levels.

Charged vacancies.—The electroneutrality condition in this case is

$$p + [Cr \cdot] = n + r [V^r] \quad [24]$$

or, since $p \gg n$ in these oxides

$$p + [Cr \cdot] \approx r [V^r] \quad [25]$$

which may be used to compute p as a function of $[Cr \cdot]$ and a_0 using Eq. [6] to express $[V^r]$ as a function of a_0 .

A special situation is met when the concentration of the dopant is much higher than p and independent of a_0 , since in this case Eq. [25] becomes simply

$$[Cr \cdot] = r [V^r] \quad [26]$$

The overall flux of matter through the scale is equivalent to J_V and becomes

$$J_{ov} = -J_V = RD_V [V^r] \frac{d \ln a_o}{dx} = RD_V \frac{[Cr \cdot]}{r} \frac{d \ln a_o}{dx} \quad [27]$$

Integration of Eq. [27] from $x = 0$ to $x = x_S$ yields

$$k_x = 2D_V \frac{[Cr \cdot]}{r} \ln \left(\frac{a_o''}{a_o'} \right) \quad [28]$$

In comparison with the oxidation of the pure metal we obtain, using Eq. [49] of Part I (1)

$$\frac{k_x}{k_x^\circ} = \frac{[Cr \cdot]}{mr [V^r]_o''} \ln \left(\frac{a_o''}{a_o'} \right) \quad [29]$$

or, expressing the concentration of charged vacancies V^r in the pure oxide as a function of a_o at $x = x_S$ by means of Eq. [46] of Part I (1)

$$\frac{k_x}{k_x^\circ} = \frac{[Cr \cdot]}{mr [V^r]_o^\circ} \frac{1}{(a_o'')^{1/m}} \ln \left(\frac{a_o''}{a_o'} \right) \quad [30]$$

where $[V^r]_o^\circ$ is the concentration of V^r at $a_o = 1$ in the pure oxide.

The previous equation shows that the presence of a higher valent impurity produces an increase in the parabolic rate constant for oxidation in comparison with the pure metals under the same oxygen activity in the gas phase. In fact for the pure oxide $p_o'' \approx r [V^r]_o''$, while for the doped oxide $r [V^r]'' \approx [Cr \cdot]$, but, as a consequence of reaction [21], $[V^r]'' \gg [V^r]_o''$, so that $[Cr \cdot]/[V^r]_o'' > 1$: in addition, also the factor $\ln(a_o''/a_o')$ is larger than one, so that $k_x \gg k_x^\circ$.

The profile of the oxygen activity is given in this case by the same equation as for the doping of MO by monovalent ions when the oxide contains only charged metal interstitials (Eq. [20]).

Charged interstitials.—The electroneutrality condition is now

$$p + s [M_i^{s \cdot}] + [Cr \cdot] = n \quad [31]$$

or, since $n \gg p$ in this case

$$s [M_i^{s \cdot}] + [Cr \cdot] \approx n \quad [32]$$

where the concentration of the interstitials depends on a_o by means of Eq. [15]. Equation [32] may be used in conjunction with Eq. [15] to compute p as a function of a_o if the concentration of chromium is known as a function of a_o too. The solution is obviously simpler if $[Cr \cdot]$ is independent of a_o .

If the concentration of the dopant is constant within the scale and much greater than the concentration of the metal interstitials, Eq. [32] becomes

$$[Cr \cdot] \approx n \quad [33]$$

and the concentration of metal interstitials is given by

$$[M_i^{s \cdot}] = \frac{K_I}{[Cr \cdot]^s a_o} \quad [34]$$

Under this situation the flux of metal interstitials, equivalent to J_{ov} , has the form (1)

$$J_I = J_{ov} = RD_I [M_i^{s \cdot}] \frac{d \ln a_o}{dx} = RD_I \frac{K_I}{[Cr \cdot]^s a_o} \frac{d \ln a_o}{dx} \quad [35]$$

From Eq. [35] the parabolic rate constant is obtained by the usual procedure in the form

$$k_x = 2D_I \frac{K_I}{[Cr \cdot]^s} \left(\frac{1}{a_o'} - \frac{1}{a_o''} \right) \quad [36]$$

or, using the concentration of interstitials in the pure oxide where the neutrality condition is $s[M_i^{s \cdot}] = n$, as given by (1)

$$[M_i^{s \cdot}] = [M_i^{s \cdot}]_o a_o^{-1/t} \quad [37]$$

even in the form

$$k_x = 2 \frac{D_I s^s}{[Cr \cdot]^s} \{ ([M_i^{s \cdot}]_o')^t - ([M_i^{s \cdot}]_o'')^t \} \approx 2 \frac{D_I s^s}{[Cr \cdot]^s} ([M_i^{s \cdot}]_o')^t \quad [38]$$

where $[M_i^{s \cdot}]_o'$ and $[M_i^{s \cdot}]_o''$ are the concentrations of $M_i^{s \cdot}$ in the pure oxide at $a_o = a_o'$ and $a_o = a_o''$, respectively.

In comparison with pure oxide we obtain, using Eq. [64] of Part I (1)

$$\frac{k_x}{k_x^\circ} = \frac{s^s}{t} \left\{ \frac{[M_i^{s \cdot}]_o'}{[Cr \cdot]} \right\}^s \quad [39]$$

Equation [39] shows that the introduction of chromium in an oxide containing metal interstitials produces a decrease of the parabolic rate constant for oxidation in comparison with the pure metal. In fact, a part from the numerical factor s^s/t , close to one, one has by assumption $[Cr \cdot] \gg [M_i^{s \cdot}]_o'$, so that $k_x \ll k_x^\circ$.

The profile of the oxygen activity is obtained as previously in the same form as holding for a pure oxide with prevailing neutral metal interstitials (Eq. [68] of Part I (1) with $t = 1$), or

$$a_o^{-1} = (a_o')^{-1} - ((a_o')^{-1} - (a_o'')^{-1})y \quad [40]$$

Numerical Results

This section is divided into two parts: first, the effect of the dopants on the parabolic rate constant of oxidation is evaluated as a function of the dopant concentration for a fixed oxygen activity in the gas phase or as a function of a_o' for fixed concentrations of the impurities for oxides having a single kind of defect. Then the effect of the presence of a constant concentration of impurities is evaluated for the growth of CoO on cobalt alloys at 1000°C both in the presence and in the absence of metal interstitials as an example of the behavior of oxides having a more complex defect structure.

Oxides containing a single kind of defect.—**Oxides with metal vacancies.**—As discussed above, the oxidation of metals forming oxides containing only neutral vacancies should not be affected by the addition of heterovalent impurities, but this case is not physically significant. We will therefore examine in detail the case of singly charged vacancies: oxides with doubly charged vacancies give similar results which are not reported here for brevity.

The numerical values of the various parameters required for the calculations are taken similar to those applying to the oxidation of cobalt at 1000°C. The diffusion coefficient of the metal vacancies is given the value $D_V = 10^{-7}$ cm² sec⁻¹; for the equilibrium constant K_V we take the value 10^{-4} , corresponding to a concentration of V' equal to 10^{-2} at $a_o = 1$. For the constant of the equilibrium for the intrinsic ionization K_I we use two values, namely $K_I = 10^{-9}$ and $K_I = 10^{-12}$, to show the effect that it may have on the concentrations of the various defects in the presence of impurities. Finally the oxygen activity corresponding to the metal/oxide equilibrium is taken equal to that prevailing for the Co/CoO equilibrium at 1000°C ($a_o' = 1.66 \times 10^{-6}$) (1).

Figure 1 shows the change of the parabolic rate constant k_x with the gas-phase oxygen activity a_o'' for the pure oxide and for some selected values of the concentration of the dopants, both monovalent and

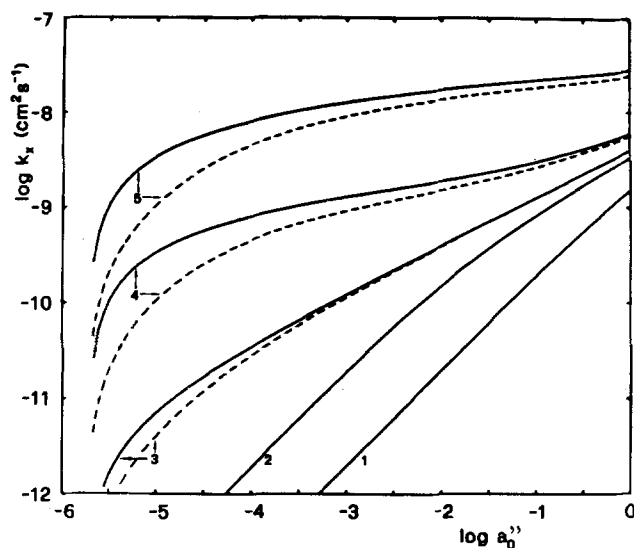


Fig. 1. Parabolic rate constant of oxidation of a metal as a function of the gas-phase oxygen activity a_0'' with formation of an oxide MO containing only metal vacancies V' . Continuous lines: $K_7 = 1 \times 10^{-12}$; dotted lines: $K_7 = 1 \times 10^{-9}$. Curves 1 and 2: oxide containing a monovalent impurity with a concentration 10^{-2} and 10^{-3} , respectively. Curves 3: pure oxide. Curves 4 and 5: oxide containing a trivalent impurity with a concentration 10^{-3} and 10^{-2} , respectively.

trivalent, and for the two values of K_7 . The effect of monovalent impurities is to produce a decrease of k_x and that of the trivalent impurities an increase, as expected. The curves tend to approach each other in the range of high oxygen activities while they diverge for low a_0 values. The curves corresponding to the same concentrations of monovalent impurities and the two values of K_7 are identical, while those for the trivalent impurities as well as for the pure oxide differ. This is an example of the importance of the value of the intrinsic ionization constant K_7 in establishing the concentrations of all the defects as functions of a_0 . For the pure oxide the expression of k_x as given by Eq. [49] of Part I (1)

$$k_x = 2mD_V [V']''_0 \quad [41]$$

holds only if the condition $p = [V'] = (K_V a_0)^{1/2}$ is fulfilled in the whole range of a_0 . Actually, however, the complete condition of neutrality is $p = n + [V']$, so that the equality between p and $[V']$ is only an approximation holding when $p \gg n$ or $[V'] \gg n$. Taking into account the two equilibria for the formation of vacancies, electrons and electron holes, the condition $p \approx [V']$ requires that $K_V a_0 \gg K_7$, a situation which is less likely to hold at small oxygen activities and in particular at $a_0 = a_0'$. In the present example, since $K_V = 10^{-4}$ and $a_0' = 1.66 \times 10^{-6}$, we obtain $K_7 \ll 1.66 \times 10^{-10}$ to have $p \approx [V']$. This condition is fulfilled if $K_7 = 10^{-12}$, but not if $K_7 = 10^{-9}$, leading in the latter case to a $[V']$ smaller than p at low oxygen activities. The consequence is that for $K_7 = 10^{-9}$ the parabolic rate constant is smaller than for $K_7 = 10^{-12}$ in the region of low a_0 , even if the effect tends to disappear at high a_0 . In the presence of monovalent impurities the concentration of the electron holes is increased and that of the electrons decreased with respect to the pure oxide, so that the value of k_x is no longer affected by the value of K_7 . On the contrary, the addition of trivalent impurities produces an increase in the concentration of the vacancies and electrons and a decrease in that of the electron holes so that, depending on the value of K_7 and the concentration of the impurity, the oxide may change from p- to n-type at least in the range of small oxygen activities. In addition, the concentration of electrons in the region of low a_0 may become

larger than that of V' , so that the condition $[V'] \approx [Cr']$ does no longer hold, but one has instead $[V'] < [Cr']$: for a fixed concentration of impurity these changes occur under an a_0 value which is smaller the larger is K_7 . This is shown in Fig. 2 where the concentrations of the different defects are plotted as functions of a_0 for the two values of K_7 and a concentration of the trivalent impurity equal to 10^{-2} . The consequence of this situation is that the k_x curves corresponding to $K_7 = 10^{-12}$ are higher than for the larger value of K_7 due to the higher concentration of vacancies in the former case in the region of low a_0 .

Figures 3a and 3b show the ratio between the parabolic rate constant for the formation of a doped oxide

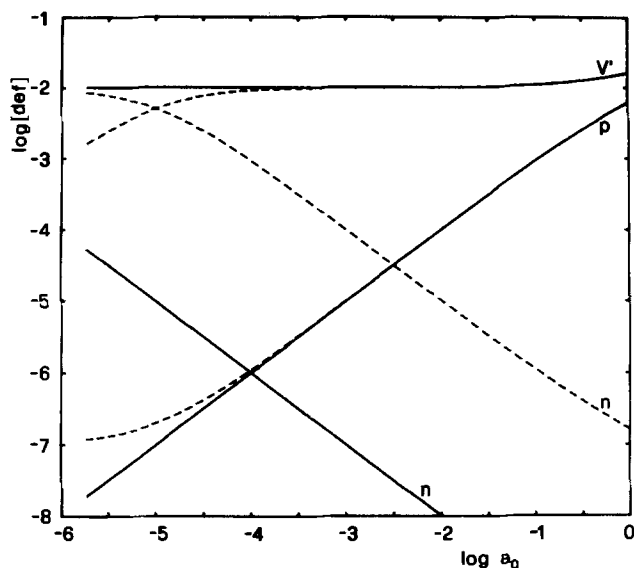


Fig. 2. Concentrations of the different defects as functions of the oxygen activity a_0 in an oxide MO containing only metal vacancies V' and a concentration of a trivalent impurity 10^{-2} . Continuous lines: $K_7 = 10^{-12}$; dotted lines: $K_7 = 10^{-9}$.

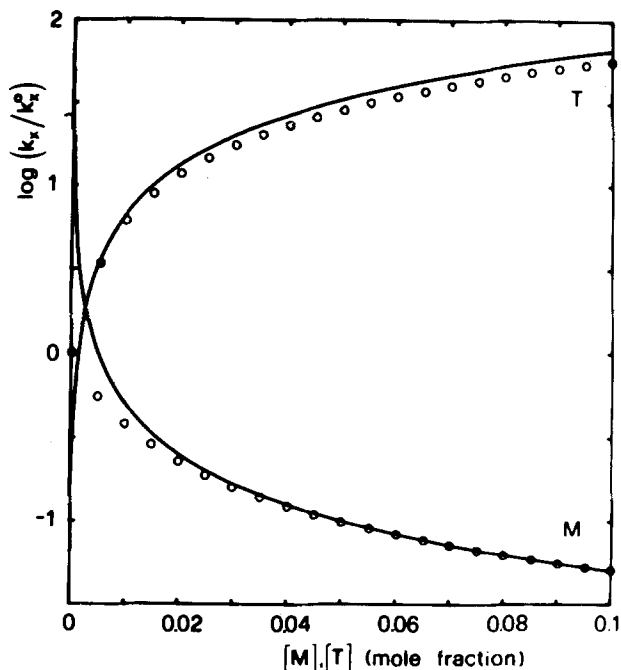


Fig. 3a. Ratio of the parabolic rate constant for the growth of a doped oxide k_x to that for the growth of the pure oxide k_x^0 under a gas-phase oxygen activity $a_0'' = 1$, as a function of the concentration of the dopant: M = monovalent impurity; T = trivalent impurity. Continuous lines obtained from Eq. [12] (M) and Eq. [29] (T), respectively. $K_7 = 10^{-9}$.

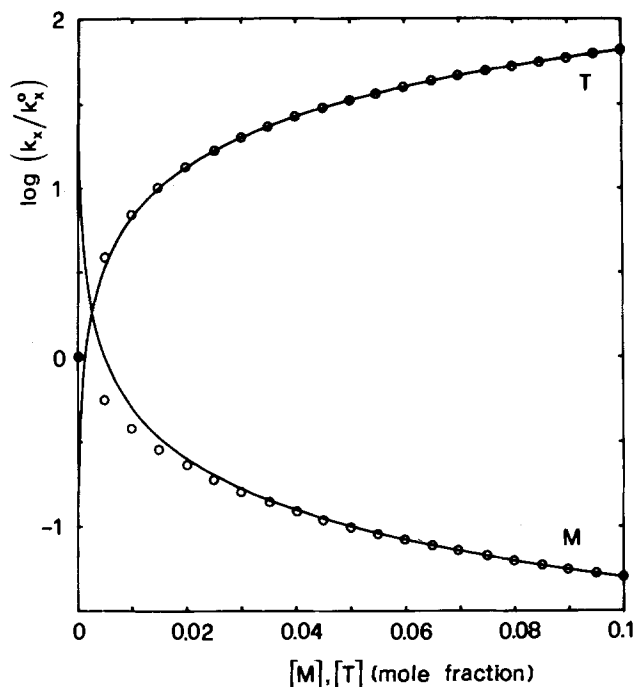


Fig. 3b. Ratio of the parabolic rate constant for the growth of a doped oxide k_x to that for the growth of the pure oxide k_x^0 under a gas-phase oxygen activity $a_0 = 1$, as a function of the concentration of the dopant: M = monovalent impurity; T = trivalent impurity. Continuous lines obtained from Eq. [12] (M) and Eq. [29] (T), respectively. $K_7 = 10^{-12}$.

k_x and that for the corresponding pure oxide k_x^0 , calculated for a fixed value of the gas-phase oxygen activity $a_0'' = 1$, as a function of the concentration of the dopants, both monovalent and trivalent, along with the curves corresponding to the limiting expressions as given by Eq. [12] for Li doping and Eq. [30] for Cr doping. The values of k_x/k_x^0 are calculated up to a high concentration of the dopants (10^{-1}) to show more clearly the effect of doping, but the results in this region are only indicative in view of the high concentrations of defects prevailing under this condition, requiring appropriate corrections to the simple expressions used here. The continuous curves corresponding to the limiting expressions are clearly wrong for low doping levels, since these equations do not extrapolate to this region where the approximations used to obtain them do not hold. At high dopant concentrations the curves are superimposed to the points calculated by the complete numerical procedure in the case of the presence of monovalent impurities for both values of K_7 , while this happens only for $K_7 = 10^{-12}$ in the case of trivalent impurities. In fact for the higher value $K_7 = 10^{-9}$ the calculated points lie below the simplified curve due to the reasons discussed above, i.e., to the fact that the condition $[V'] \approx [Cr]$ which has been used in the derivation of the analytical expression does not hold everywhere.

Regarding the effect of doping on the value of the parabolic rate constant for oxides containing only vacancies, substitution of $dx = x_S dy$ into Eq. [9] yields (1)

$$J_{ov}x_S = k_t = RD_V[V'] \frac{d \ln a_0}{dy} \quad [42]$$

where k_t is the parabolic rate constant expressed in molecules of oxide formed per unit surface area per unit time (18). Equation [42] shows that the value of k_t , and therefore also of k_x which is proportional to it (1), is related to two factors, namely, the concentration of defects and the gradient of $\ln(a_0)$ with respect to y . Using Eq. [42] to express k_t for the doped as well

as for the pure oxide, the ratio k_x/k_x^0 can be expressed in the form

$$\frac{k_x}{k_x^0} = \frac{[V^r]_{\text{doped}}}{[V^r]_{\text{pure}}} \frac{\left(\frac{d \ln a_0}{dy}\right)_{\text{doped}}}{\left(\frac{d \ln a_0}{dy}\right)_{\text{pure}}} = R_1 R_2 \quad [43]$$

with

$$R_1 = \frac{[V^r]_{\text{doped}}}{[V^r]_{\text{pure}}} \quad [44a]$$

and

$$R_2 = \frac{\left(\frac{d \ln a_0}{dy}\right)_{\text{doped}}}{\left(\frac{d \ln a_0}{dy}\right)_{\text{pure}}} \quad [44b]$$

Both factors R_1 and R_2 will in general contribute to fix the value of the ratio k_x/k_x^0 while for a fixed gas-phase oxygen activity a_0'' and a dopant concentration independent of x their product must remain constant through the scale, i.e., for any value of a_0 between a_0' and a_0'' . The individual values of R_1 and R_2 will, however, generally change with a_0 , so that it seems useful to examine the contributions of these factors to k_x/k_x^0 separately as functions of a_0 . This may be done easily by the usual numerical procedure by evaluating R_1 and R_2 as functions of a_0 : the result is shown in Fig. 4 for the same values of the parameters used above and $K_7 = 10^{-12}$ with a fixed concentration of impurities (10^{-2}). For a monovalent impurity the ratio k_x/k_x^0 under the conditions specified above becomes 0.379: the change of R_1 and R_2 reported in Fig. 4 shows that in this case R_1 always gives a contribution to the decrease of k_x with respect to k_x^0 , since it is smaller than one everywhere, while R_2 is larger than one below $a_0(1) = 0.211$ approximately and smaller than one above $a_0(1)$, so that the overall reduction of k_x with respect to k_x^0 has to be attributed to R_1 everywhere and to R_2 only above $a_0(1)$. In the region below $a_0(1)$ R_1 tends to produce a decrease of k_x while R_2 an increase, but the effect of R_1 is numerically prevailing. On the contrary for trivalent impurities, giving a

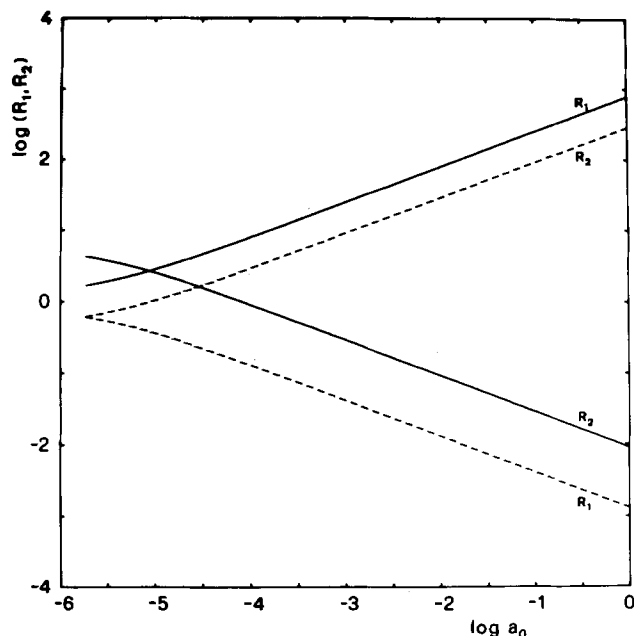


Fig. 4. R_1 and R_2 (defined in the text) as functions of the oxygen activity for the growth of an oxide MO containing only V' vacancies pure and doped with a concentration 10^{-2} of monovalent or trivalent impurities under a gas-phase oxygen activity $a_0'' = 1$. Continuous lines: monovalent impurity; dotted lines: trivalent impurity.

ratio $k_x/k_x^\circ = 6.919$, R_1 is always greater than one while R_2 is larger than one only above $a_0(1) = 2.24 \times 10^{-2}$ so that the increase of k_x with respect to k_x° is due mainly to R_1 . It may be concluded that for a uniform distribution of the dopant the change of k_x is related principally to the change in the concentration of the vacancies produced by the impurities, even though this is not the only factor to produce the observed effect.

Finally, different values of the equilibrium constant for the formation of the vacancies K_V yield results similar to those reported above: the effect of the dopants, however, increases for smaller values of K_V , since these correspond to smaller concentrations of vacancies in the pure oxide, in agreement with the theoretical predictions according to Eq. [12] and [29].

Oxides with metal interstitials.—Only oxides containing singly charged interstitials will be considered in detail. The diffusion coefficient of the interstitial metal atoms is taken again as $D_I = 10^{-7} \text{ cm}^2/\text{sec}^{-1}$ while for the constant of equilibrium for the formation of interstitials we take the value $K_I = 1.664 \times 10^{-10}$, corresponding to a concentration of interstitials 10^{-2} at the M/MO interface, using for a_0' the value $a_0' = 1.66 \times 10^{-6}$ as previously. Two different values are used for the intrinsic ionization equilibrium constant K_7 ($K_7 = 10^{-9}$ and $K_7 = 10^{-12}$) as for the vacancies to examine the effect of K_7 on the different parameters.

The change of k_x as a function of a_0'' for some selected values of the concentration of the dopant, both monovalent and trivalent, is reported in Fig. 5 for the two values of K_7 : the presence of monovalent impurities produces an increase and that of trivalent impurities a decrease of k_x with respect to the value for the pure metal k_x° , as expected. The curves show a fast increase of k_x at low oxygen activities and then tend to a constant value: this behavior is typical of oxides containing only metal interstitials. The curves corresponding to the presence of the same concentration of a trivalent impurity are coincident for the two K_7 values, while those for a monovalent impurity differ at high values of a_0 , those for $K_7 = 10^{-12}$ being higher than those calculated for $K_7 = 10^{-9}$. This is again a result of the relatively large value of K_7 in the

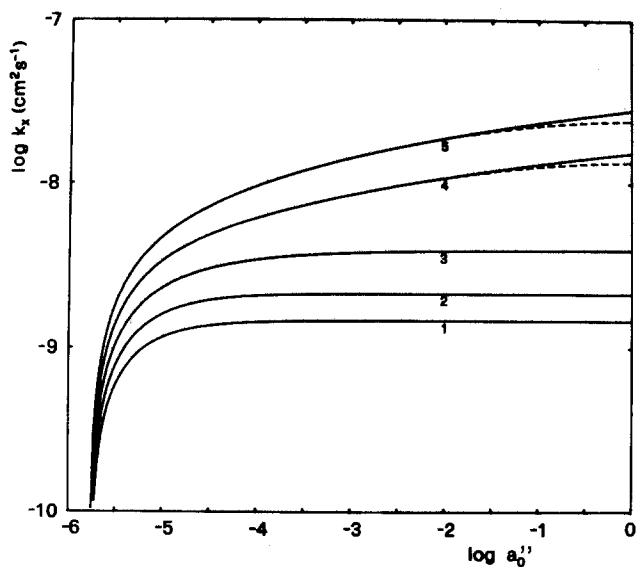


Fig. 5. Parabolic rate constant of oxidation of a metal as a function of the gas-phase oxygen activity a_0'' with formation of an oxide MO containing only metal interstitials M_i' . Continuous lines: $K_7 = 10^{-12}$; dotted lines: $K_7 = 10^{-9}$. Curves 1 and 2: oxide containing a trivalent impurity with a concentration 10^{-2} and 5×10^{-3} , respectively. Curve 3: pure oxide. Curves 4 and 5: oxide containing a monovalent impurity with a concentration 5×10^{-3} and 10^{-2} , respectively.

latter case. In fact, in the presence of monovalent impurities the concentration of interstitials and that of electron holes is increased with respect to the pure oxide and therefore that of electrons is decreased, so that the oxide tends to change from n- to p-type semiconductivity. Moreover, if K_7 is large and the concentration of the impurity great enough, the condition $[M_i'] < [Li']$ takes the place of the condition $[M_i'] \simeq [Li']$ holding for a lower K_7 value, as shown in Fig. 6 for a concentration of impurities equal to 10^{-2} and $K_7 = 10^{-9}$: this case yields, therefore, to a lower value of k_x .

The ratio k_x/k_x° as a function of the concentration of the dopant under $a_0'' = 1$ for monovalent and trivalent impurities is reported in Fig. 7a and 7b for the two values of K_7 along with the curves obtained from

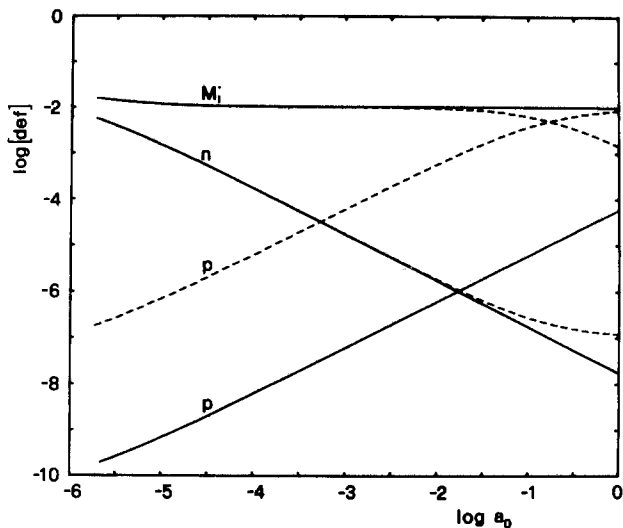


Fig. 6. Concentrations of the different defects as functions of the oxygen activity a_0 in an oxide MO containing only metal interstitials M_i' and a concentration of a monovalent impurity 10^{-2} . Continuous lines: $K_7 = 10^{-12}$; dotted lines: $K_7 = 10^{-9}$.

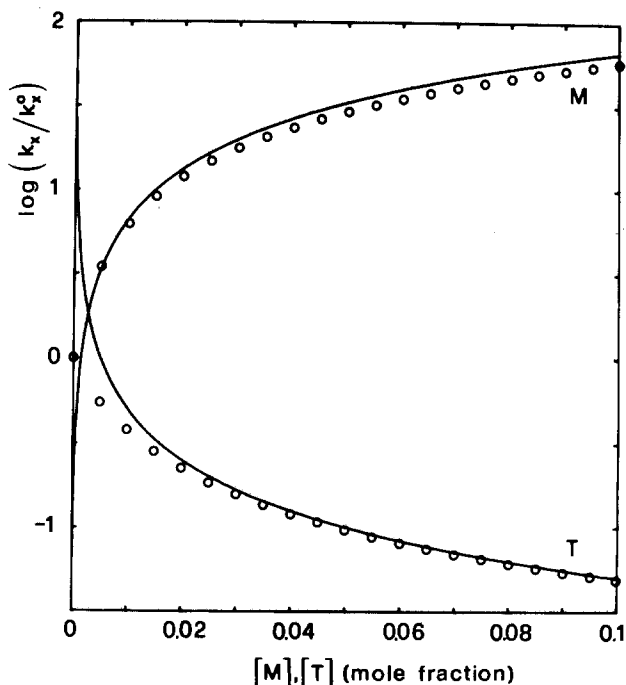


Fig. 7a. Ratio of the parabolic rate constant for the growth of a doped oxide k_x to that of the pure oxide k_x° under a gas-phase oxygen activity $a_0'' = 1$ as a function of the dopant concentration: M = monovalent impurity; T = trivalent impurity. Continuous lines obtained from Eq. [19] (M) and Eq. [39] (T), respectively. $K_7 = 10^{-9}$.

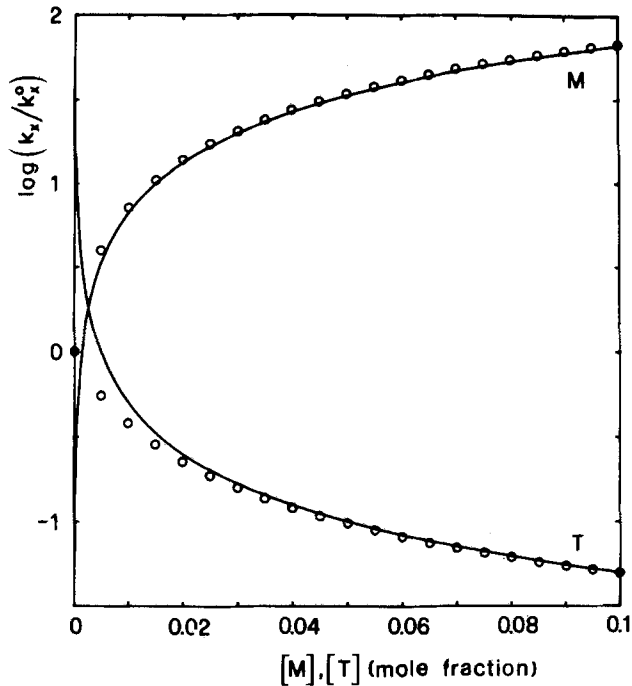


Fig. 7b. Ratio of the parabolic rate constant for the growth of a doped oxide k_x to that of the pure oxide k_x^0 under a gas-phase oxygen activity $a_{O''} = 1$ as a function of the dopant concentration: M = monovalent impurity; T = trivalent impurity. Continuous lines obtained from Eq. [19] (M) and Eq. [39] (T), respectively. $K_7 = 10^{-12}$.

the simplified limiting equations (Eq. [19] and [39]). For the lower K_7 value the points obtained by the complete calculation agree well with the simplified curves at sufficiently high doping levels. On the contrary, for $K_7 = 10^{-9}$ the agreement is obtained only for the trivalent, but not for the monovalent impurities, for which the complete calculation leads to results lower than those obtained from Eq. [19]. This behavior depends again on the high value of K_7 and on the effect it has on the concentration of metal interstitials, as discussed above.

Proceeding as for the vacancies, the ratio k_x/k_x^0 may be expressed in the form

$$\frac{k_x}{k_x^0} = R_1 R_2 \quad [45]$$

with

$$R_1 = \frac{[M_i']_{\text{doped}}}{[M_i']_{\text{pure}}} \quad [46a]$$

and

$$R_2 = \frac{\left(\frac{d \ln a_O}{dy}\right)_{\text{doped}}}{\left(\frac{d \ln a_O}{dy}\right)_{\text{pure}}} \quad [46b]$$

so that the ratio is affected by both factors R_1 and R_2 . These may be calculated separately as functions of a_O and are reported in Fig. 8 for $K_7 = 10^{-12}$ and a concentration of impurity equal to 10^{-2} either monovalent or trivalent. In the case of the addition of a uniform concentration of a monovalent impurity the ratio k_x/k_x^0 takes the value 7.0: R_1 is always greater than one while R_2 is greater than one only below $a_O(1) = 7.94 \times 10^{-5}$ approximately and smaller than one above $a_O(1)$. Therefore, below $a_O(1)$ both R_1 and R_2 act in the same direction to increase k_x , even if at a different extent; above $a_O(1)$ instead R_1 and R_2 act in the opposite way, but the effect of R_1 prevails over that of R_2 . For the same concentration of a trivalent impurity one obtains instead $k_x/k_x^0 = 0.367$

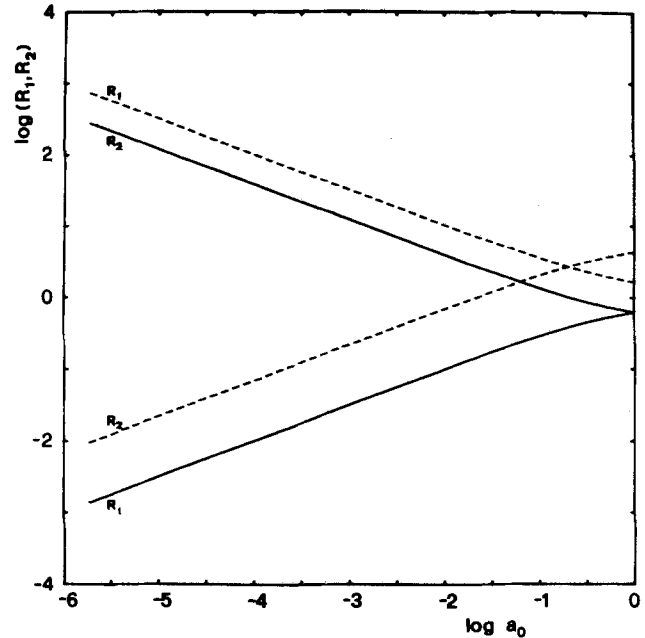


Fig. 8. R_1 and R_2 (defined in the text) as functions of the oxygen activity a_O for the growth of an oxide MO containing only metal interstitials M_i' pure and doped with a concentration 10^{-2} of monovalent or trivalent impurities under a gas-phase oxygen activity $a_O = 1$. Continuous lines: monovalent impurities; dotted lines: trivalent impurities.

and R_1 is always smaller than one while R_2 is smaller below $a_O(1) = 10^{-5}$ and greater above it. The general conclusion is therefore the same as for the charged vacancies, i.e., that the change of k_x is mainly due to the change in the concentration of the lattice defects produced by the incorporation of the impurity which is usually opposite and prevails over the change in the gradient of the logarithm of the oxygen activity through the scale.

Results similar to those reported here may be obtained for different values of the equilibrium constant K_1 or also for oxides containing doubly charged interstitials. In the former case a decrease of K_1 leads to a greater effect of the addition of the dopants on k_x , in agreement with the predictions based on Eq. [19] and [39].

Oxides with a complex defect structure: CoO.—The same values of the parameters as used for the calculation on pure CoO (1) are also used here. The calculation is performed for the case of the absence as well as for the presence of interstitial cobalt atoms, which are referred to as case 1 and case 2, respectively. In the latter case the concentration of interstitials is calculated assuming that at an oxygen activity corresponding to the Co/CoO equilibrium $[Co_i'] = [V'']$.

Figure 9a and 9b show the plots of k_x as functions of a_O'' for the oxide pure and doped with some selected concentrations of impurities either monovalent or trivalent for cases 1 and 2, respectively. In presence of trivalent impurities the curves corresponding to the two cases are exactly coincident. On the contrary, in the case of the presence of monovalent impurities the behavior of k_x is completely different in the two cases. In fact, while in absence of Co_i' the parabolic rate constant is decreased by the addition of Li with respect to pure Co, in the presence of Co interstitials it is increased even if these are minority defects in the pure oxide. This situation is related to the fact that the addition of a monovalent impurity carrying a negative effective charge produces a large increase in the concentration of the metal interstitials, particularly close to the metal/scale interface, as is shown in Fig. 10 for $[Li'] = 10^{-2}$, and this in turn produces an increase in the value of k_x with respect to k_x^0 particularly at

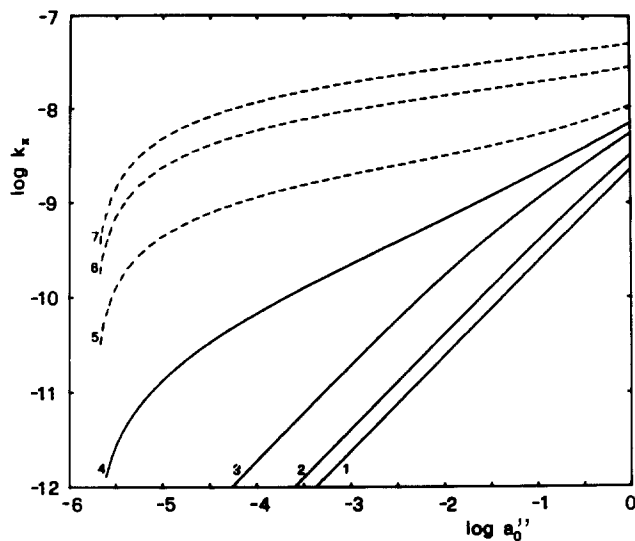


Fig. 9a. Parabolic rate constant for the growth of CoO at 1000°C pure or doped as a function of the gas-phase oxygen activity $a_0'' = 1$ for case 1 (absence of Co_i''). Continuous lines: pure oxide (curve 4) or oxide containing a monovalent impurity with a concentration 10^{-2} (curve 1), 5×10^{-3} (curve 2), and 10^{-3} (curve 3). Dotted lines: oxide containing a trivalent impurity with a concentration 10^{-3} (curve 5), 5×10^{-3} (curve 6), and 10^{-2} (curve 7).

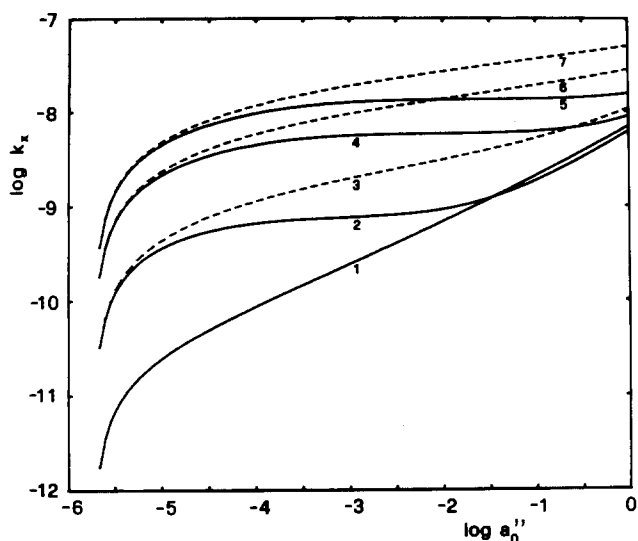


Fig. 9b. Parabolic rate constant for the growth of CoO at 1000°C pure or doped as a function of the gas-phase oxygen activity $a_0'' = 1$ for case 2 (presence of Co_i''). Continuous lines: pure oxide (curve 1) or oxide containing a monovalent impurity with a concentration 10^{-3} (curve 2), 5×10^{-3} (curve 4), and 10^{-2} (curve 5). Dotted lines: oxide containing a trivalent impurity with a concentration 10^{-3} (curve 3), 5×10^{-3} (curve 6), and 10^{-2} (curve 7).

low values of a_0'' . On the contrary, the addition of a trivalent impurity with a positive effective charge leads to a decrease of the concentration of the Co_i'' with respect to the pure CoO, where their role is already very limited, so that their presence has no effect in this situation.

The effect of the concentration of the impurity on the parabolic rate constant as measured by the ratio k_x/k_x° under a constant gas-phase oxygen activity $a_0'' = 1$ is presented in Fig. 11 for both cases 1 and 2. While the curve corresponding to the presence of trivalent impurities remains unaffected by the presence or the absence of Co_i'' , that corresponding to the addition of monovalent impurities is completely reversed, unless for very small values of $[\text{Li}']$, which lead to a

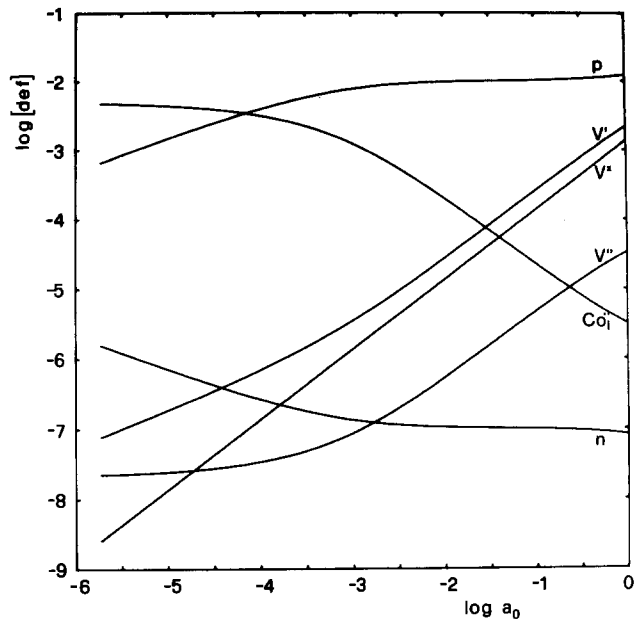


Fig. 10. Concentration of the different defects in CoO doped with a concentration 10^{-2} of a monovalent impurity as a function of the oxygen activity a_0 at 1000°C for case 2.

small decrease of k_x with respect to k_x° at low oxygen activities.

The previous conclusion about the effect of the addition of monovalent impurities on the oxidation rate of cobalt is supported by the results of the high temperature oxidation of a solid solution of copper in cobalt containing about 10 weight percent of Cu, which shows a small increase of the parabolic rate constant with respect to pure cobalt instead of a decrease as expected in the case of the absence of Co interstitials (19). This effect may be attributed to the presence of copper dissolved in CoO in the form of Cu^+ ions, at least in the region of low oxygen activities. A similar

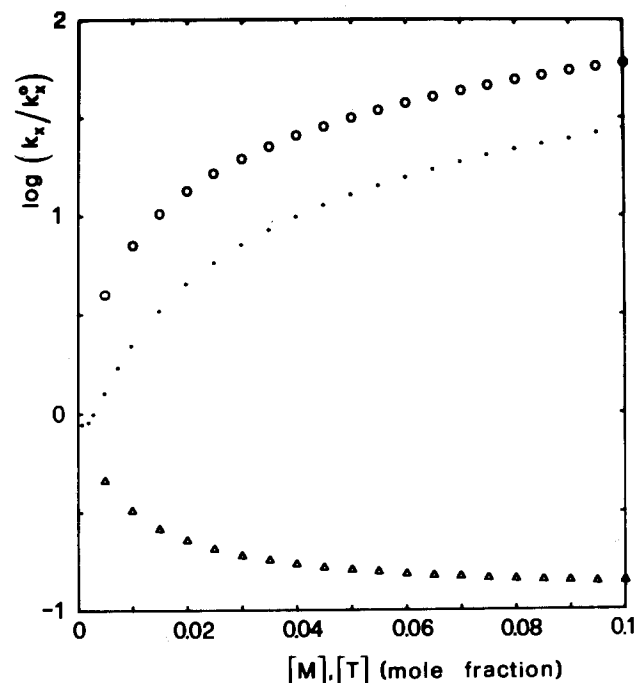


Fig. 11. Ratio of the parabolic rate constant for the growth of doped CoO to that of pure CoO at 1000°C and $a_0'' = 1$ as a function of the dopant concentration. Δ points calculated for a monovalent impurity for case 1; \circ calculated for a trivalent impurity for both cases 1 and 2.

effect has also been found in the oxidation of a copper-rich Cu-Ni alloy (20) and this could also have the same explanation.

The addition to cobalt or nickel of a second alloy component forming cations of valency higher than two has been found to produce an increase in the oxidation rate of the base metal, in agreement with the Wagner-Hauffe rules as given for a uniform concentration of the impurity (21-30). These impurities, however, show a tendency to accumulate preferentially close to the alloy/scale interface, thereby decreasing or even reversing the gradient of the concentration of the metal vacancies through the scale. In this situation the vacancies have to diffuse against their own concentration gradient in their motion inward from the scale/gas interface, a situation which at first sight seems physically unrealistic. The contradiction is, however, only apparent since the inward flux of charged vacancies is given by Eq. [22] or [23] of Part I (1) in the form

$$J_v = -RD_v \left(\frac{d[V^r]}{dx} + \tau [V^r] \frac{d \ln p}{dx} \right) \quad [47]$$

where the first term represents the flux due to the gradient of the concentration of the vacancies and the second that produced by the gradient of the electric potential due to the motion of the more mobile electronic species. It is therefore possible for the vacancies to move uphill with the help of an accelerating electric field which forces them to proceed inward.

It has been shown above that for oxides containing only one kind of metal vacancy and uniformly doped with a higher valent impurity the increase of k_x with respect to k_x^0 depends on two factors related respectively to the change of the concentration of the vacancies and of the gradient of the logarithm of the oxygen activity with respect to the normalized distance from the alloy/scale interface y . For that case the observed increase of k_x is due mainly to the first factor. However, if the distribution of the dopant is not uniform, it seems not possible to state *a priori* even if the addition of the impurity will enhance or depress the oxidation rate. In fact this may only be assessed by means of the appropriate calculations taking into account the actual distribution of the dopant in the scale, as will be attempted in a next paper (19). The experimental results point out, however, that the net effect of doping is to increase the oxidation rate, suggesting that the increase in the concentration of the vacancies produced by the impurities is still the dominating factor in modifying the oxidation rate for these systems.

Conclusions

The application of a theory for the parabolic oxidation of metals developed previously (1) to the growth of oxides doped with heterovalent impurities forming on dilute alloys confirms the conclusions already known as the Wagner-Hauffe rules for oxides containing a single kind of defects and a uniform distribution of the dopant, allowing however a more complete calculation of all the parameters involved. For oxides containing different kinds of defects it is shown that under suitable conditions defects which are unimportant in the pure oxide may play a substantial role leading to an effect of the dopant which may be very different or even reversed with respect to that predicted on the basis of a simpler defect model. These results point out again that a correct and complete interpretation of the oxidation behavior of dilute alloys as well as of pure metals can only be carried out if the actual defect structure of the oxide is known with sufficient accuracy. For the time being a complete understanding of the high temperature oxidation

behavior of pure metals and dilute alloys is generally prevented by the incomplete knowledge of this subject. Further progress should be possible, however, by a future development of the basic research in this field along with a consideration of all the other important factors also affecting the experimentally observed reaction rates.

Manuscript submitted April 1, 1980; revised manuscript received Aug. 15, 1980.

Any discussion of this paper will appear in a Discussion Section to be published in the December 1981 JOURNAL. All discussions for the December 1981 Discussion Section should be submitted by Aug. 1, 1981.

Publication costs of this article were assisted by Centro Studi di Chimica e Chimica Fisica Applicata alle Caratteristiche d'Impiego dei Materiali del C.N.R.

REFERENCES

1. F. Gesmundo and F. Viani, *This Journal*, **128**, 460 (1981).
2. F. A. Kröger, "The Chemistry of Imperfect Crystals," p. 832, North-Holland Publishing Co., Amsterdam (1964).
3. P. Kofstad, "High-Temperature Oxidation of Metals," p. 113, John Wiley & Sons, Inc., New York (1966).
4. C. Wagner, *Corros. Sci.*, **9**, 91 (1969).
5. A. D. Dalvi and D. E. Coates, *Oxid. Met.*, **3**, 203 (1971).
6. D. P. Whittle, B. D. Bastow, and G. C. Wood, *ibid.*, **9**, 215 (1975).
7. B. D. Bastow, D. P. Whittle, and G. C. Wood, *Corros. Sci.*, **16**, 57 (1976).
8. B. D. Bastow, D. P. Whittle, and G. C. Wood, *Proc. R. Soc. London, Ser. A*, **356**, 177 (1977).
9. K. Hauffe, "Oxidation of Metals," p. 176, Plenum Press, New York (1965).
10. P. Kofstad, "High-Temperature Oxidation of Metals," p. 265, John Wiley & Sons, Inc., New York (1966).
11. G. C. Wood, *Oxid. Met.*, **2**, 11 (1970).
12. P. Kofstad, "Nonstoichiometry, Diffusion and Electrical Conductivity in Binary Metal Oxides," p. 35, Wiley-Interscience, New York (1972).
13. B. Fisher and J. B. Wagner, Jr., *J. Appl. Phys.*, **38**, 3838 (1967).
14. F. Gesmundo *et al.*, To be published.
15. C. Wagner and K. E. Zimens, *Acta Chem. Scand.*, **1**, 547 (1947).
16. M. Gvishi and D. S. Tannhauser, *J. Phys. Chem. Solids*, **33**, 893 (1972).
17. K. Hauffe, "Oxidation of Metals," p. 20, Plenum Press, New York (1965).
18. P. Kofstad, "High-Temperature Oxidation of Metals," p. 116, John Wiley & Sons, Inc., New York (1966).
19. F. Gesmundo *et al.*, To be published.
20. D. P. Whittle and G. C. Wood, *Corros. Sci.*, **8**, 295 (1968).
21. G. C. Wood and T. Hodgkiess, *Nature*, **211**, 1358 (1966).
22. P. Kofstad and A. Z. Hed, *This Journal*, **116**, 224, 229 (1969).
23. G. C. Wood, I. G. Wright, T. Hodgkiess, and D. P. Whittle, *Werkst. Korros.*, **21**, 900 (1970).
24. G. C. Wood, *ibid.*, **22**, 491 (1971).
25. G. N. Irving, J. Stringer, and D. P. Whittle, *Oxid. Met.*, **9**, 427 (1975).
26. I. G. Wright and G. C. Wood, *ibid.*, **11**, 163 (1977).
27. F. H. Stott and G. C. Wood, *Corros. Sci.*, **17**, 647 (1977).
28. G. C. Wood, F. H. Stott, and J. E. Forrest, *Werkst. Korros.*, **28**, 395 (1977).
29. F. H. Stott, J. E. Forrest, and G. C. Wood, *Oxid. Met.*, **11**, 109 (1977).
30. F. H. Stott, I. G. Wright, T. Hodgkiess, and G. C. Wood, *ibid.*, **11**, 141 (1977).

Use of an Electron Beam to Separate Semiconductor Devices with Beam Leads

Irena Barycka, Bogusław Boratynski, Tomasz Ohly, Mirosław Szreter, and Helena Teterycz

Instytut Technologii Elektronowej, Politechniki Wrocławskiej, 50-372 Wrocław, Poland

and Olga Ikanowicz

Instytut Technologii Elektronowej NPCP CEMI 02-668 Warszawa, Poland

The division of silicon wafers covered with diodes, transistors, or integrated circuits into single structures presents a major difficulty in the manufacture of silicon devices with beam leads. The commonly used technique for division is laborious, since it involves many processes.

The wafer to be divided is first thinned down to a thickness of about 100 μm , then is coated (vacuum or CVD) with an SiO_2 film and photoresist and the areas to be etched are uncovered by photolithographic techniques. These uncovered areas are then etched in an alkaline solution. The procedure of matching the photomask with the patterns being on the opposite side of the wafer is very difficult, and the thinning of the wafer reduces its mechanical strength (1-3).

The fact that single crystal damaged regions have much higher etch rates than undamaged areas (4, 5) has been used by us as the basis for the separation of semiconductor devices with beam leads.

In this paper the results of an investigation using a technique utilizing an electron beam are presented. The electron beam was used to generate damage on selected areas of the silicon wafer (6). The damaged regions, which now have an increased etching rate, would enable the division of the wafer without reduc-

Key words: electron beam, semiconductor devices, silicon, beam leads, alkaline etching.

tion of thickness and without lithographic processing. Etching in alkaline solution is particularly sensitive to the crystallographic orientation of silicon (7, 8) and thus the course of the etching process will depend significantly on the orientation of the wafers used.

Experimental

The experiments have been conducted on typical polished single crystal silicon wafers 200 μm thick with (100) and (111) orientation. The resistivities of the samples were 10^{-3} - 10^{-1} Ωm , p- and n-type, and the dislocation density was up to 10^3 cm^{-2} .

A number of lines, parallel and perpendicular to the basic cutting directions, were ruled on the wafer surface with an electron beam. The pulsed beam was focused on the wafer surface. During exposure the wafer was shifted at a speed of 2 mm/sec.

After a preliminary investigation, it was found that a change in etch rate appeared only when the electron beam interaction resulted in melting of the silicon material.

In further experiments, electron accelerating voltages were chosen in the 100 to 120 kV range, pulse frequency 200 and 1000 Hz, and pulse duration 10 and 20 μsec . The electron beam current varied between 1 and 7 mA. The lines formed on the wafer surface due to exposure to the electron beam are shown in Fig. 1.

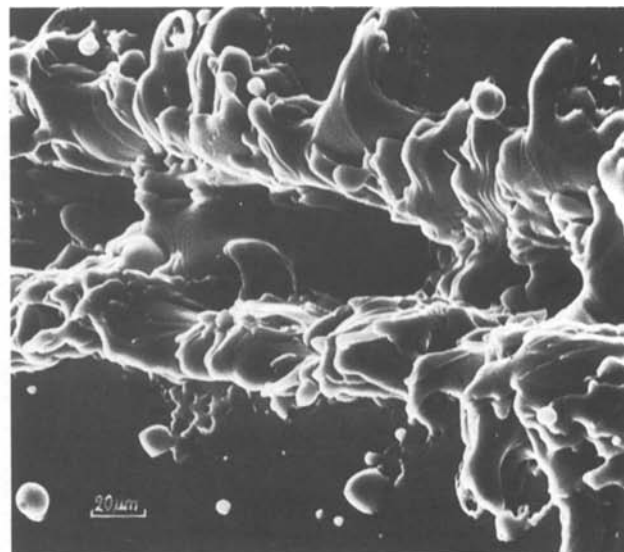
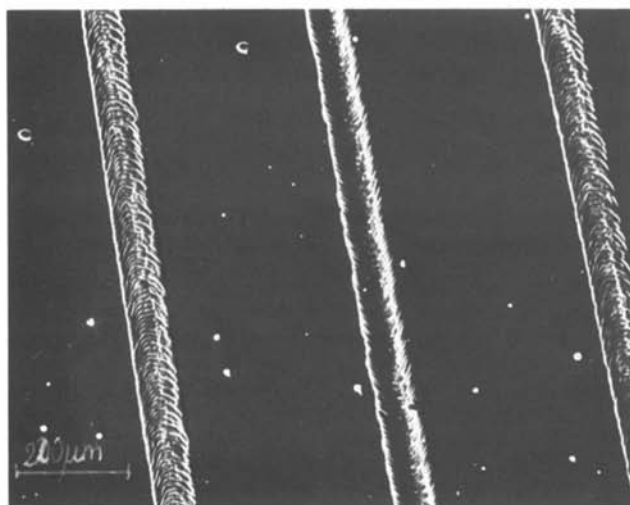


Fig. 1. Tracks formed on a (111) silicon wafer due to an electron beam, $U_p = 120$ kV, $f = 200$ Hz, $\tau = 10$ μsec (SEM). a. General view, $I = 4$ mA; b. selected fragment, $I = 7$ mA.

After exposure to the electron beam the wafers were placed on a rotating disk (250 rpm) and etched in 10M NaOH solution at 353 K.

Results

Exposure of the silicon wafer to the electron beam produces damaged regions (in the form of lines). To evaluate the range of damage produced in the material, the wafers were cut perpendicular to the electron beam trace and then etched in Sirtl etch solution, commonly used for defect detection in single crystal silicon. An example of such a cross section is shown in Fig. 2. The depth of the region damaged depends mainly on the intensity of the beam current and to a smaller degree on other beam parameters. The depth of the damaged region vs. current intensity is shown in Fig. 3. No dependence on crystallographic orientation



Fig. 2. Cross section through the irradiated (111) wafer. Beam parameters the same as in Fig. 1b (SEM).

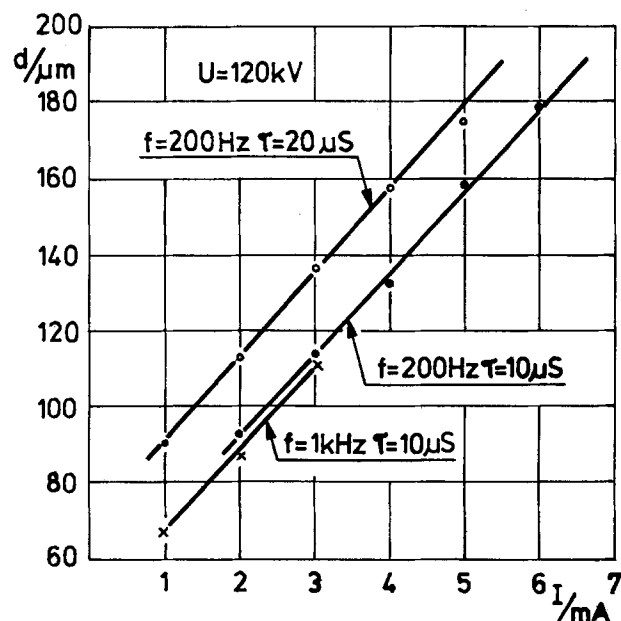


Fig. 3. The depth (d) of region damaged vs. beam parameters

of the specimen was observed in this portion of the investigation.

To evaluate the effects of etching, the wafers were placed in an NaOH solution and etching was carried out as described previously. Under the conditions used (10M NaOH, 353 K, 250 rpm) the etching rates were:

| orientation | (100) | (111) | damaged (100) and (111) |
|---------------------------------------|-------|-------|-------------------------|
| etching rate $\mu\text{m}/\text{min}$ | 1.16 | 0.168 | 2.3 |

The etch rates of the damaged regions were constant and were not dependent on the orientation. A series of grooves was formed as the result of the differences between the etch rates for damaged and undamaged silicon. The geometry of the grooves was examined by means of profilographs. Cross sections of the grooves were also made and their shape was observed using a scanning electron microscope (Fig. 4). The width and depth of the grooves obtained, as measured by both methods were in satisfactory agreement. There are some differences in groove formation between wafers oriented (111) and (100). Their dependence on the etching time and the exposure conditions as well as on the crystallographic orientation of the wafers is shown in Fig. 5 and 6.

After the damaged material had been removed from the (111) wafer, a flat bottom, terminated by the (111) plane was formed. This was then etched at the same rate as the undamaged wafer surface. Thus the depth of the groove remains constant during further etching, whereas its width increases rapidly. The inclination angle of the walls remains constant at 142°. This is shown schematically in Fig. 7a.

The deepening of grooves in the wafers with (100) orientation proceeds differently. After removal of the damaged material the etching proceeds perpendicularly to the (100) plane. The final shape of the groove is determined by the high etching rate of the lateral walls, as well as by the high etching rate of the (100) plane. That is why a flat bottom is formed on the



Fig. 4. Cross section of the groove after etching for 50 min, (111) wafer (SEM).

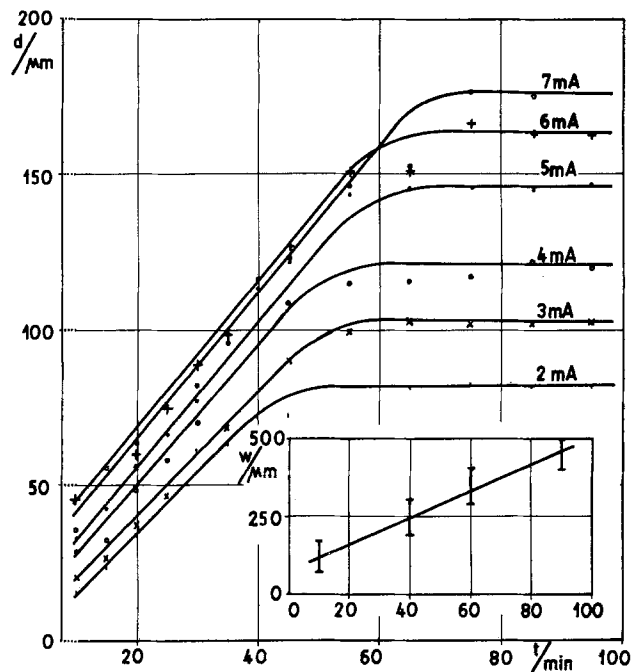


Fig. 5. Depth (d) and width (w) of groove vs. etching time (t) for silicon with (111) orientation, $U_p = 120$ kV, $f = 200$ Hz, $\tau = 10$ μ sec current I is given in the graph.

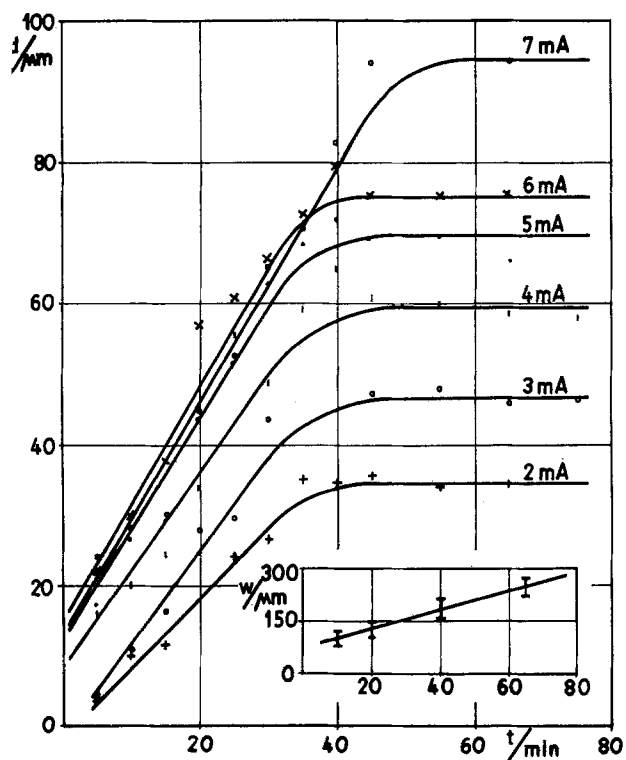


Fig. 6. Depth (d) and width (w) of the groove vs. etching time (t) for silicon with (100) orientation, $U_p = 120$ kV, $f = 200$ Hz, $\tau = 10$ μ sec, current I is given in the graph.

groove after a large quantity (approximately 100 μ m) of silicon is removed (Fig. 7b).

The structures on the wafer with (100) orientation can be separated without masking and without preliminary reduction of the wafer thickness. The exposure conditions should be chosen so that the damaged region reaches a specific depth, depending on the plate thickness and on the geometry of the beam leads. For

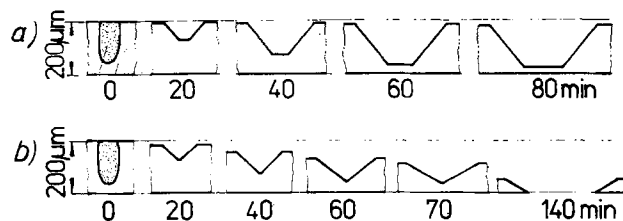


Fig. 7. Schematic representation of the etching process of electron beam exposed wafers. a, (111) and b, (100) orientation.

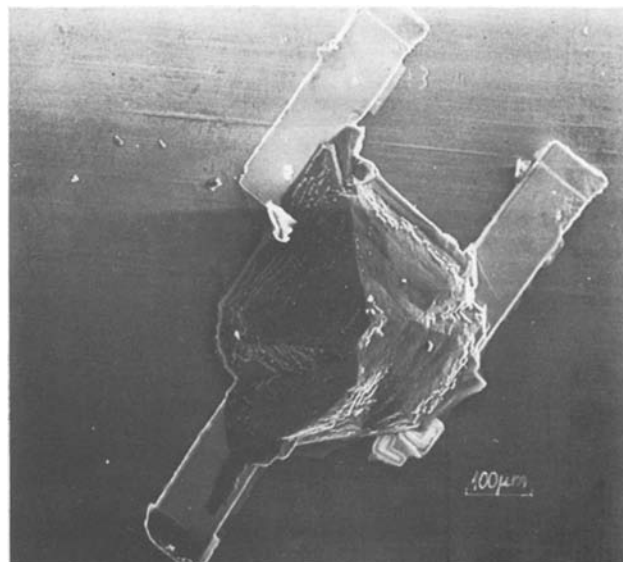


Fig. 8. Transistor with beam leads separated by means of an electron beam (SEM).

example, for a 200 μ m thick wafer and for a 100 μ m distance between the structures, the minimum required depth is 100 μ m. Under these conditions the structures separated by the etching technique yield pyramids or truncated pyramids about 50 μ m high. An example of a structure separated by this method is shown in Fig. 8.

It is also possible to separate the structures with beam leads made on a (111) wafer. Note that groove widening on the (111) plane proceeds at a high rate. Thus, this method requires a suitable arrangement of structures on the wafer: the beam leads must not be linked, and they must be separated by a distance of about 100 μ m. Here the exposure conditions should be chosen so that the defect region reaches the opposite side of the wafer. Etching should be continued until the defect region is completely removed and the beams are exposed along the length required. The structures obtained will have the shape of a truncated pyramid whose height is slightly less than that of the initial thickness of the wafer.

This method requires a certain decrease in packing density of the structures on the (111) surface. The effective packing density can be higher if the integration scale of each single chip is larger.

Manuscript submitted Aug. 3, 1979; revised manuscript received July 2, 1980.

Any discussion of this paper will appear in a Discussion Section to be published in the December 1981 JOURNAL. All discussions for the December 1981 Discussion Section should be submitted by Aug. 1, 1981.

REFERENCES

1. M. P. Lepselter, *Bell Syst. Tech. J.*, **XLV**, 233 (1966).
2. D. B. Lee, *J. Appl. Phys.*, **40**, 4569 (1969).

3. M. J. Declercq, *IEEE J. Solid State Circuits*, **sc-10**, 191 (1975).
4. D. G. Schimmel, *This Journal*, **123**, 734 (1976).
5. M. W. Jenkins, *ibid.*, **124**, 757 (1977).
6. G. W. Dudko *et al.*, *Electron. Obrab. Mater.*, **45**, No. 3 (1972).
7. J. W. Faust, Jr., in "The Surface Chemistry of Metals and Semiconductors," H. C. Gatos, Editor, New York (1960).
8. I. Barycka and H. Teterycz, Unpublished.

Mineralized Surfaces of the Dental Alloys

S. Yamaguchi*

2-72 Kotake-cho, Nerima-ku, Tokyo, 176, Japan

and T. Tsuchiya

2-15-4 Asakusa-bashi, Daito-ku, Tokyo, 111, Japan

It is of interest to study the dental gold/dental porcelain interface, as already reported by Sperner (1). In the present study, this problem has been treated in terms of RHEED (Reflection High Energy Electron Diffraction).

There are two types among the dental alloys of practical use. They are the solid solutions whose contents are given by Au(72)-Pt(13)-Pd(10)-Ag(3)-Rh(1)-Ir(0.5)-Sn(0.4)-Si(0.1) and by Au(72)-Pt(13)-Pd(10)-Ag(3.4)-Rh(1)-Ir(0.5)-Si(0.1), respectively. The former alloy contains Sn, whereas the latter is free from this element. These alloys are supposed to stick fast to the dental artificial porcelain that is composed of SiO_2 (43), Al_2O_3 (32), SnO_2 (10), K_2O (9), Na_2O (5), and a small amount of MgO , CaO , Li_2O .

In order to mate the alloys with the porcelain, one preheats the former in the air at about 1000°C . Figure 1 is the RHEED pattern from the surface of the 0.4% Sn alloy treated thermally for 30 min. All the reflections in this figure belong to the SnO_2 crystallites. The result of the analysis of Fig. 1 is given in Table I. This verifies that a selective oxidation (2) has taken place at the

* Electrochemical Society Active Member.
Key words: RHEED, adhesion, dental alloys.

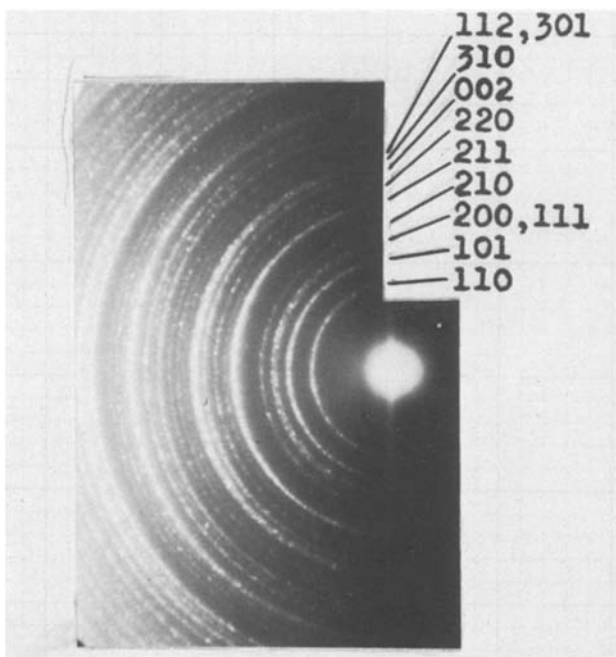


Fig. 1. RHEED pattern from the mineralized surface of the 0.4% Sn dental alloy. SnO_2 is formed as the result of selective oxidation. The Miller indexes corresponding to the space group $P4/mnm$ are attributed to the reflections. Wavelength of the electrons: 0.0347\AA . Distance between the object and the screen: 50 cm. Positive enlarged 2.3 times.

Table I. Result of the analysis of Fig. 1. $d(\text{\AA})$: interplanar spacings measured on Fig. 1; hkl : Miller indexes corresponding to the reflections; I : reflection intensities estimated in arbitrary units from Fig. 1. The lattice constants $a_0 = 4.74$ and $c_0 = 3.19\text{\AA}$ calculated coincide with those of SnO_2 crystal (space group: $P4/mnm$) (3).

| $d(\text{\AA})$ | hkl | I |
|-----------------|-------|-----|
| 3.35 | 110 | 7 |
| 2.64 | 101 | 8 |
| 2.37 | 200 | 5 |
| 2.31 | 111 | 5 |
| 2.12 | 210 | 2 |
| 1.76 | 211 | 10 |
| 1.67 | 220 | 2 |
| 1.59 | 002 | 3 |
| 1.50 | 310 | 3 |
| 1.44 | 112 | 6 |
| 1.41 | 301 | 6 |

specimen surface. This mineralized surface could stick fast to the dental porcelain containing SnO_2 .

The surface layer corresponding to Fig. 1 behaved in a chemically active manner. It began to deteriorate when exposed to the air at room temperature for several hours, succumbing to the attack of H_2O , CO_2 , and other gases in the air. In fact, the deteriorated specimen surface gave rise to an RHEED pattern different from Fig. 1. It was necessary to mate the alloy surface with the porcelain immediately after the former had been preheated in air. A strong adhesion was not obtained

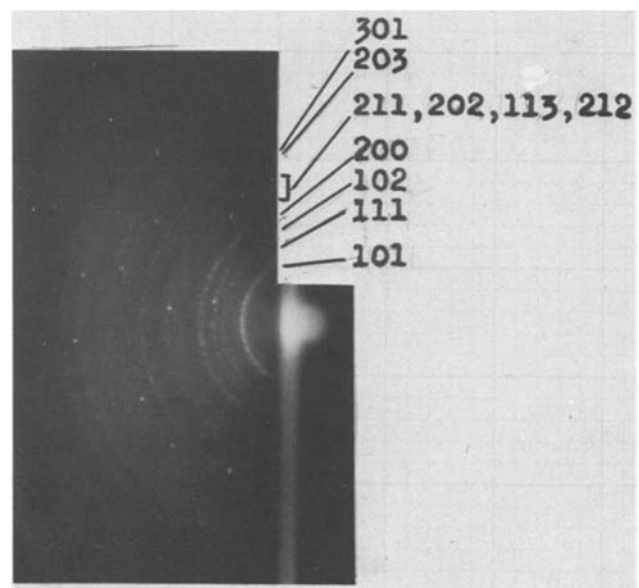


Fig. 2. RHEED pattern from the mineralized surface of the Sn-free 0.1% Si dental alloy. SiO_2 ($P4_12_12$) is formed as the result of selective oxidation. Wavelength of the electrons: 0.0329\AA .

between these two dental materials if one delayed this operation.

The RHEED pattern reproduced in Fig. 2 was observed from the surface of the Sn-free 0.1% Si alloy which was preheated at 1000°C in air. All the reflections found in Fig. 2 are characteristic of tetragonal SiO₂. The result of the analysis of Fig. 2 is given in Table II. This demonstrates that a selective oxidation has taken place at the specimen surface. The SiO₂

Table II. Result of the analysis of Fig. 2. $d(\text{Å})$: interplanar spacings measured on Fig. 2; hkl : Miller indexes corresponding to the reflections; I : reflection intensities estimated in arbitrary units from Fig. 2. The lattice constants calculated $a_0 = 4.94$ and $c_0 = 6.92\text{Å}$ coincide with those of SiO₂ crystal (P4₁2₁2) (4).

| $d(\text{Å})$ | hkl | I |
|---------------|-------|-----|
| 4.05 | 101 | 10 |
| 3.18 | 111 | 3 |
| 2.87 | 102 | 4 |
| 2.47 | 200 | 6 |
| 2.11 | 211 | 3 |
| 2.02 | 202 | 3 |
| 1.97 | 113 | 3 |
| 1.90 | 212 | 3 |
| 1.69 | 203 | 2 |
| 1.61 | 301 | 5 |

layer formed on the alloy could cement together with the porcelain rich in SiO₂.

It is empirically known that the 0.4% Sn alloy shows a stronger adhesion to the porcelain than the 0.1% Si. This is because the SnO₂ layer can adhere more firmly to the alloy substrate than the SiO₂.

Manuscript submitted Aug. 5, 1980; revised manuscript received ca. Aug. 17, 1980.

Any discussion of this paper will appear in a Discussion Section to be published in the December 1981 JOURNAL. All discussions for the December 1981 Discussion Section should be submitted by Aug. 1, 1981.

REFERENCES

1. F. Sperner, *Z. Metallk.*, **67**, 289 (1967); F. Sperner and N. Harmsen, *Mikrochim. Acta. Suppl.*, **7**, 415 (1977).
2. S. Miyake, *Scientific Papers of Inst. Phys. Chem. Research (Tokyo)*, **29**, 161 (1936); *Collected Papers of Prof. S. Miyake "Crystals and Waves,"* G. Honjo, Editor, p. 198, Tokyo (1972).
3. R. W. G. Wyckoff, "Crystal Structures," Vol. 1, 2nd ed., p. 251, Interscience Publishers, New York (1965).
4. ASTM X-Ray Diffraction Cards, Card Number 11-695.



A Mixed Rate Cathode for Lithium Batteries

M. Stanley Whittingham* and Allan J. Jacobson

Exxon Research and Engineering Company, Linden, New Jersey 07036

Many cathode materials for alkali metal anode batteries even though of high capacity are restricted in their application due to low rate characteristics, poor rechargeability and/or low electronic conductivity. Titanium disulfide, and some other dichalcogenides particularly those of vanadium, show high rate discharge and charge capabilities, essentially perfect reversibility and good electronic conductivity (1). The behavior of the former class of materials as shown in this paper can be improved by the addition of a minor amount of one of the dichalcogenides. The use of a good mixed, ionic and electronic, conductor such as TiS_2 should both assist in the transfer of ions between the active material particles, and minimize the need for the use of a non-electrochemically active conductive diluent such as carbon. In addition, the admixture of say TiS_2 with a higher energy density but lower rate cathode material should allow the retention of the latter's high capacity whilst permitting high current pulse discharging. This high rate capability will depend on the appropriate matching of the discharge voltage profiles of the two component materials.

In this paper this concept of a mixed rate cathode is tested using MoS_3 as the high energy component. This cathode as described previously (2) can react with up to 4 Li to give Li_4MoS_3 with a theoretical energy density of about 1.1 Whr/gm. However, at a continuous drain of

10 ma/cm² less than 30% of this capacity is attained (3). TiS_2 and VSe_2 were used as the high rate but lower capacity component; both exhibit almost 100% utilization at 10 ma/cm² (1) but have an energy density less than half that of MoS_3 . Both TiS_2 and VSe_2 have at least a part of their discharge voltage profile below that of MoS_3 so that under a high rate discharge pulse when the MoS_3 becomes polarized the dichalcogenide will react with the lithium. Then, when the pulse is off the MoS_3 will recharge the high rate component readying it for the next pulse. The sloping discharge of TiS_2 which crosses that of MoS_3 should also permit pulse charging.

The electrochemical cells were constructed as described earlier (1) using teflon bonded electrodes and a lithium perchlorate dioxolane electrolyte. The mixed cathodes were prepared by the thermal decomposition of the thiomolybdate, $(NH_4)_2MoS_4$ (2), mixed with 27 wt% of the dichalcogenide and 3 wt% teflon. The cells of area 2 cm² were then discharged at 20 ma, with the current on for 20 secs and then off for 20 secs. The same current cycle was used on charging but the rate was reduced to 4 ma. The first discharges of a mixed cathode and its components are shown in Fig. 1. The mixed cathode shows the highest capacity under these discharge conditions even though the pure MoS_3 cathode had a 20% greater theoretical capacity. This difference between the two cells increased continuously on subsequent cycling as shown in Fig. 2, and is even greater when the capacity is given in watt-hours rather than amp-hours due to a large polarization in the MoS_3 cell at 10 ma/cm². A cell constructed with VSe_2 in place of TiS_2 showed

*Electrochemical Society Active Member,

Present Exxon Address: P.O. Box 101, Florham Park, N.J. 07932

Key words: battery, cathode, titanium disulfide, vanadium diselenide

similar characteristics, indicating that the behavior is not unique to TiS_2 . By the 7th cycle both the mixed cathodes showed more than double the capacity of the single component cathode.

The data of Fig. 1 and Fig. 2 shows that the addition of a conductive high rate cathode material can enhance the discharge behavior of molybdenum trisulfide. The same enhancement is expected for many other cathodes such as MoO_3 , V_2S_5 , V_2O_5 and V_6O_{13} which have inherently high capacities for lithium but which have poor electronic conductivities and/or a low rate capability. In addition the replacement of the conductive diluent in some primary cells, such as the Li/FeS_2 and Li/MnO_2 cells, should also lead to an enhanced storage capacity. Preliminary studies (4) on FeS_2 cells in which the carbon diluent was replaced by titanium disulfide showed a 36% greater utilization of the FeS_2 itself and a 60% overall greater coulombic capacity, i.e. capacity of $\text{TiS}_2 + \text{FeS}_2$ over $\text{C} + \text{FeS}_2$.

REFERENCES

1. M.S. Whittingham, Progress in Solid State Chemistry, 12, 41 (1978).
2. A.J. Jacobson, R.R. Chianelli and M.S. Whittingham, Mater. Res. Bull., 14, 1437 (1979).
3. M.S. Whittingham, R.R. Chianelli, S.M. Rich and A.J. Jacobson, Proc. Nato Workshop on Batteries, Aussois, France, September 1979.
4. M.S. Whittingham and K. P. Glynn, to be published.

Manuscript submitted Sept. 29, 1980;
revised manuscript received Nov. 5, 1980.

Publication costs of this article were assisted by Exxon Research and Engineering Company.

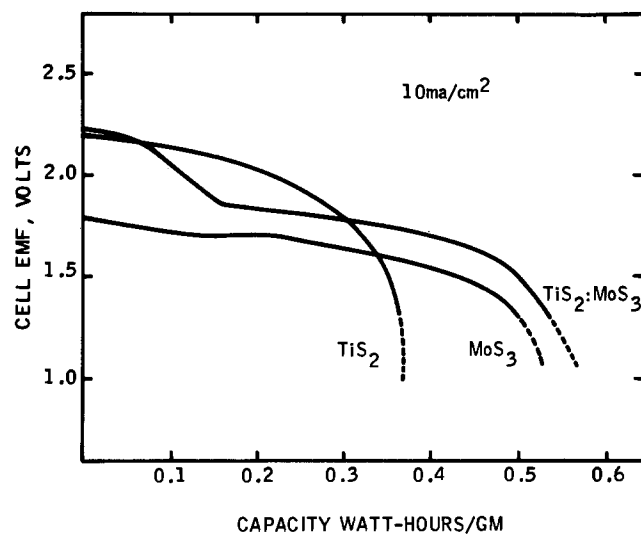


FIG 1 First discharge of TiS_2 , MoS_3 and $\text{TiS}_2:\text{MoS}_3$ mixture in lithium cells (theoretical capacity/gm electrode: $\text{TiS}_2 = 0.43$; $\text{MoS}_3 = 0.98$; mixture = 0.82 (0.67 MoS_3 , 0.15 TiS_2 ; wt $\text{MoS}_3/\text{TiS}_2 = 1.92$)).

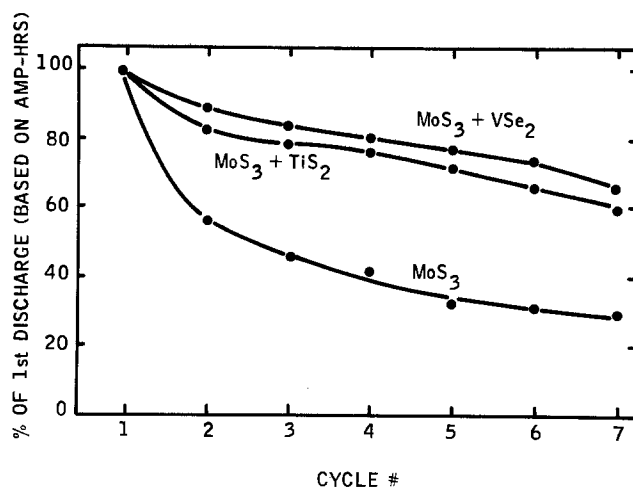


FIG 2 Change of discharge capacity with cycling

Some Observations on the Oxidation of an Fe-12% Cr Alloy in Gaseous Chlorine

Z. A. Foroulis*

Exxon Research and Engineering Company, Florham Park, New Jersey 07932

Only a few metallic oxides, sulfides and nitrides are ionic at room temperature and it is doubtful whether any of these compounds can be regarded as entirely ionic at elevated temperatures. Nevertheless, the oxidation mechanism of metals and alloys that form ionic conducting protective layers is a subject of considerable fundamental interest(1-5). Metal halides are more likely to be purely ionic than other metallic compounds. Silver bromide and silver chloride are such compounds which have been studied experimentally in the temperature range 200-400°C by Wagner(2). This brief communication presents experimental data which show that the oxidation of an Fe-12% Cr alloy in chlorine gas exhibits kinetics which can be interpreted by postulating kinetic control by electronic conductivity (along electron defects) through an outer $\text{CrCl}_3(\text{s})$ surface film formed during the chlorination reaction.

EXPERIMENTAL

The material used in this study was a commercial alloy with the following analysis (12% Cr, 0.6% Mn, 0.4% Si, 0.1% C and the balance iron). The oxidation kinetics were investigated by exposing alloy coupons in $\text{Cl}_2\text{-N}_2$ mixtures (chlorine partial pressure 0.5 to 3×10^{-2} atm.) and in the temperature range of 270-500°C. Rectangular coupons with a surface area of about 10 sq cm were placed in a horizontal quartz tubular reactor located inside a furnace capable of maintaining the reaction zone in the desired temperature. Mixtures of Cl_2 and N_2 were prepared by using conventional flow meters and a mixing coil. Steady-state reaction rates were determined by measuring the weight loss of test coupons before and after exposure. Coupons were polished with 6/0 emery paper and cleaned in acetone prior to weighing. After each experiment for weight loss deter-

mination, the reaction product surface films were removed by careful honing. Prior to each experiment, the test coupons were treated in situ at 497°C for at least one hour with pure hydrogen to reduce any surface oxide films. The kinetic data were supplemented with SEM, EDAX, X-ray diffraction and chemical analysis of the reaction product surface films.

RESULTS AND DISCUSSION

The reaction of the Fe-12% Cr alloy with low partial pressure chlorine gas was found to obey a parabolic kinetic law as shown schematically in Figure 1. This figure is a

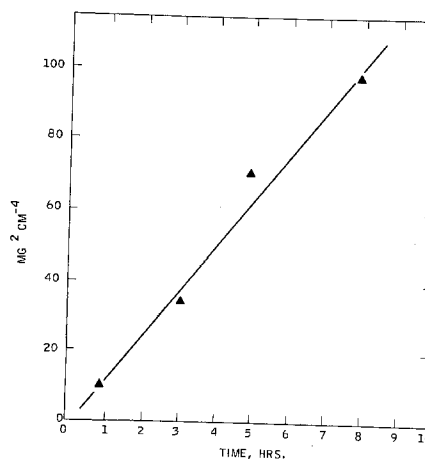


Figure 1. Variation of the Square of the Weight of the Alloy Converted to Reaction Products per Unit Surface Area Versus Exposure Time in a $\text{Cl}_2\text{-N}_2$ Mixture (0.01 Atm. Chlorine Partial Pressure) at 500°C.

plot of the square of the alloy weight converted to reaction products per unit surface area as a function of exposure time at 500°C in a $\text{Cl}_2\text{-N}_2$ mixture with a 0.01 atm. chlorine partial pressure. The kinetics of the alloy-chlorine gas reaction is influenced by the nature and composition of the reaction product surface film produced.

* Electrochemical Society Active Member.
Key Words: Oxidation, Chlorination,
Electronic Conductivity

The reaction product surface film formed with this alloy during the chlorination reaction is a well-adhering protective film consisting of two layers; an inner layer composed essentially of FeCl_2 and an outer layer consisting essentially of CrCl_3 . The FeCl_2 and CrCl_3 produced as a result of this reaction are solids with negligible vapor pressure(6) in the temperature studied. The temperature dependence of the parabolic rate constant for this reaction in the temperature range studied corresponds to an apparent activation energy of about 11 kcal/mole.

To gain a better understanding of the mechanism of this reaction, a series of experiments was also carried out at different chlorine partial pressures at 500°C. The chlorine partial pressure dependence of this reaction shown in Figure 2 indicates that the parabolic rate constant for this reaction varies with the 1/2 power of the chlorine partial pressure. In addition, gas velocity was found to have no effect on the reaction rate.

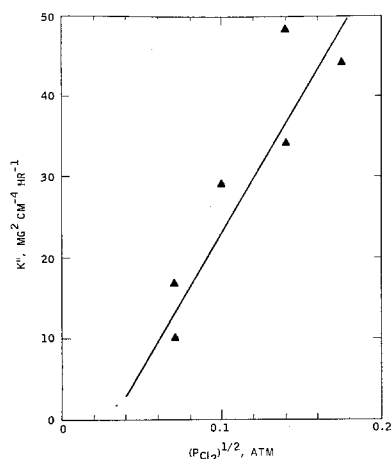
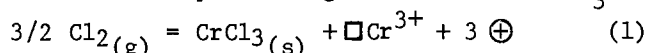


Figure 2. Dependence of the Parabolic Rate Constant for the Chlorination Reaction of a 12% Cr Alloy on the Chlorine Partial Pressure at 500°C.

The essential independence of this reaction on gas velocity and the parabolic law kinetics observed suggest that the reaction is limited by a solid-state migration process through the reaction product surface film. Diffusion through the inner FeCl_2 film is assumed not to be rate limiting, since for the iron-chlorine reaction (where the surface film consists only of FeCl_2) the overall kinetics have been shown to be controlled by migration of chlorine gas through the gas boundary layer or by the reaction of FeCl_2 with chlorine gas to form volatile FeCl_3 (7,8). Reaction of CrCl_3

with gaseous chlorine to form volatile CrCl_4 species via the reaction $\text{CrCl}_3 + 1/2 \text{Cl}_2 \rightarrow \text{CrCl}_4$ as a likely limiting reaction in the overall kinetics is not consistent with the observed parabolic kinetics and the insensitivity of the overall reaction on gas velocity. It is reasonable, therefore, to conclude that a migration process through the CrCl_3 surface film is the rate controlling process in the chlorination reaction of the Fe-12% Cr alloy.

The mechanism of the limiting solid-state migration process within the CrCl_3 outer surface film is not known. However, assuming that CrCl_3 , like several other metallic halides (e.g., AgCl , AgBr , etc.) exhibits ionic conductivity, it is reasonable to postulate that the rate-limiting process may be migration of electronic defects through the CrCl_3 film. In analogy with AgBr and AgCl , which were studied extensively by Wagner(2,9), the following reaction can be written as representing formation of CrCl_3 :



and the mass action equation:

$$[\oplus]^3 [\square \text{Cr}^{3+}] = k [\text{pCl}_2]^{3/2} \quad (2)$$

where $\square \text{Cr}^{3+}$ are ionic defects (cation vacancies), \oplus are positive holes, pCl_2 is the chlorine partial pressure, and k is the equilibrium constant.

In analogy with other metal halides which are predominantly ionic conductors, it is reasonable to assume that the normal concentration of $\square \text{Cr}^{3+}$ in CrCl_3 is likely to be relatively great so that it is not noticeably changed by the effect of chlorine. Hence, it follows from Eq. (2) that the concentration of positive holes ($[\oplus] \ll [\square \text{Cr}^{3+}]$) depends on chlorine partial pressure according to Eq. (3).

$$[\oplus] = \text{const.} [\text{pCl}_2]^{1/2} \quad (3)$$

where the quantity $\square \text{Cr}^{3+}$ is incorporated into the constant since it remains relatively unchanged. According to Eq. (3), the concentration of electronic defects and, therefore, the rate of chlorination reaction should be proportional to the square root of the chlorine partial pressure(10). This conclusion is consistent with the experimentally determined variation of the parabolic rate constant (Figure 2) according to the 1/2 power of the chlorine partial pressure. The postulated mechanism can, at present, be considered only as tentative. Additional work in this area is required, particularly

in the field of electronic properties of metal halides such as CrCl_3 , to confirm the postulated mechanism.

REFERENCES

- (1) K. Hauffe, *Metalloberfläche (A)*, 5, 1 (1951).
- (2) C. Wagner, *Z. Phys. Chem. (B)* 32, 447 (1936).
- (3) E. Koch and C. Wagner, *Z. Phys. Chem. (B)* 38, 295 (1937).
- (4) K. Hauffe and C. Gensch, *Z. Phys. Chem.* 195, 116 (1951).
- (5) A. B. Lidiard, "Ionic Conductivity" *Handbuch der Physik*, Volume XX, Springer-Verlag, Berlin (1957).
- (6) *The Chemistry and Metallurgy of Miscellaneous Materials* Ed. by L. L. Quill, McGraw-Hill Company, New York (1950).
- (7) R. F. Fruehan, *Met. Trans.* 3, 2585 (1972).
- (8) Z. A. Foroulis, "Metal-Slag-Gas Reactions and Processes" Edit. Z. A. Foroulis and W. W. Smeltzer, *The Electroch. Soc. Inc.*, Princeton, New Jersey, p. 571 (1975).
- (9) K. Hauffe in "Oxidation of Metals" *Plenum Press*, New York, New York, p. 151 (1965).
- (10) O. Kubaschewski and B. E. Hopkins, *Butterworths*, London, p. 116 (1962).

Manuscript received Nov. 12, 1980.

Publication costs of this article were assisted by Exxon Research and Engineering Company.



Electrosynthesis of Chlorate in the Nineteenth Century

H. Vogt

Fachbereich Verfahrenstechnik der Technischen Fachhochschule Berlin, D-1000 Berlin 65, West Germany

ABSTRACT

A critical review is given of the origins of the electrosynthesis of chlorate in 1802 to the beginning of industrial chlorate manufacture toward the end of the century. The contemporary efforts to establish the fundamentals of a theory of electrochemical chlorate formation are also discussed.

The Origin of Chlorate Electrosynthesis

The first chlorate produced by electrosynthesis dates back to 1802, earlier than currently written in historical reviews. This fact gives rise to the need for a critical review of the origins of the electrosynthesis of chlorate and on the development of technology and theory in the first 100 years, at the same time correcting a number of misconceptions.

Volta's famous letter to the Royal Society in London in 1800 prompted scientists all over Europe to study the effect of the electric current on chemical reactions. It was this interest in the new matter that induced Wilhelm von Hisinger together with Jöns Jakob Berzelius to run "experiments relating to the effect of the electrical pile on salts and their bases" (1). Neither men were professionals: Hisinger was a mine owner and Berzelius had become doctor of medicine and was at that time an unpaid assistant to a professor of medicine and pharmacy at the School of Surgery in Stockholm (2). The studies on the electrolytic decomposition of salts, dissolved in water, took several months in the autumn and winter of 1802 and were more than only cursory hobby activities. Runs with several solutions and various electrode materials showed an amazingly systematic manner.

In one of the series, sodium chloride solution was electrolyzed between silver wires, serving as electrodes in a U-type cell. After the anolyte had been evaporated and cooled down, sodium chloride precipitated. The remaining clear solution was found to contain sodium chloride and silver chloride and "perhaps, hyperoxygenized muriatic sodium and a formerly unknown silver salt" (1d).¹ The latter one was immediately identified by Gehlen (1a) with the "hyperoxygenized muriatic silver" which Chevenix had obtained through a chemical way (3). In fact, the salts were sodium chlorate and silver chlorate. A definite proof of the formation of chlorate through electrolysis of chloride solutions was given much later by Kolbe in 1847 (4).

A report on the joint studies of Hisinger and Berzelius was written in Swedish by Berzelius and published in German in February 1803 (1a). It was further published in French two years later (1b), in Swedish (1806) (1c), and once more in German (1807) (1d). "This treatise contains the fundamentals of those laws which the electrochemical theory later was based upon," Berzelius recapitulated with self-confidence many years later in his autobiography (5). However,

Key words: electrosynthesis, electrochemical chlorate formation.
¹ The passage cited is given after (1d); the first edition (1a) uses the expression "oxygennirt-salzsaurer Natron" instead of "überoxygennirt-salzsaurer Natron" (1d).

"the unknown names of the authors attracted no special attention." Indeed, in the chlorate literature of our century, the first preparation by electrosynthesis is erroneously dated throughout as of 1808 and attributed to Berzelius only.

Hisinger and Berzelius were not the first to prepare chlorate, which had already been prepared by Glauber in 1657 by chemical means (6,7) and rediscovered and identified by Berthollet (8) in 1786—nor were they the first who applied electrolysis to prepare it. It must be guessed that earlier electrolyses of chloride (9,10) would have led to chlorate, but they were the first who recognized having prepared chlorate.

Industrial Chlorate Production

Few years after Kolbe's observation, in 1851, a remarkable attempt at industrial application is reported. The chemist Charles Watt in Kensington, London, received a patent for the electrochemical decomposition of salt and other substances and separation into their components (11), Fig. 1. It is surprising that some features of modern chlorate process are anticipated in this first chlorate cell patent: the omission of a diaphragm, the relevance of high temperature to favor the chlorate formation, the separation of chlorate by crystallization, and the recycling of the mother liquor and its electrolysis after resaturation. Some of these characteristics were not realized with the first

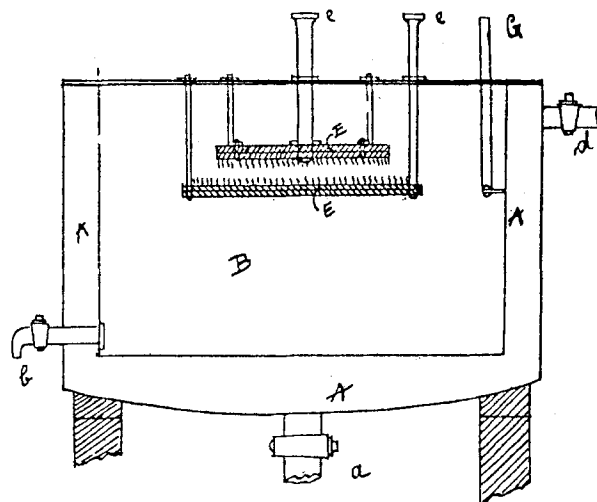


Fig. 1. Chlorate cell of the 1851 patent of C. Watt. The electrolyte vessel is surrounded by a steam-heated jacket.

industrial chlorate cells coming on stream and had to be rediscovered gradually.

A practical use of the patent is not reported and cannot be expected owing to the absence of powerful energy sources at that time. The only method of manufacture was the chemical process developed by Liebig. Chlorine was introduced into solutions of caustic potash or calcium carbonate to make chlorate (12).

After the dynamo machine was invented and improved for industrial use, the prerequisite for industrial electrosynthesis of chlorate was given. But even in 1888, the conviction was declared that electrochemical processes would have no future in the alkali industry (13). That happened two years after H. Gall and A. de Montlaur had started in 1886 the first plant in Villers-St. Sépulcre in Switzerland, where chlorate was electrochemically produced under industrial conditions.² The cell cases were reported to be made of wood and equipped with a diaphragm (14). The cells were operated at elevated temperatures. The concentration of chlorate in cell liquid was raised until crystals precipitated which were removed manually using enameled iron scoops. Cell voltage was 5V and a current was used of 1000A. Energy consumption per kg of potassium chlorate is reported to 24 hp (14) or 17.7 kW-hr/kg KClO₃, corresponding to a total current efficiency of 37%. The plant served as a prototype and was shut down in 1891, when the new bigger factory in Vallorbe (Switzerland) was ready to start (15). In 1896, the Société d'électrochimie started a second factory in St. Michel de Maurienne (France) (14).

The company was not the only electrochemical chlorate producer for long. In Sweden, the Superfosfat Fabriks AB started the manufacture in 1894 in Mansboe and in 1899 at Alby fall in Ljungan using the process of O. Carlson (16).

A big factory was started in Chedde (France) in 1896, which used the process of Corbin and Lederlin with bipolar electrodes. A description in detail was given by Kershaw (14).

At nearly the same time, electrochemical chlorate manufacture started in the U.S.A. (14). In 1896 and, 1897, the Chemical Construction Company operated a chlorate factory at Niagara Falls, New York, using the process of Blumenberg. The cell was equipped with a diaphragm and differs from contemporary types by the fact that chlorine gas was transported through a special pipe into the cathode compartment to mix with the catholyte remote from the cathode, but inside the cathode compartment. Owing to the cathodic reduction losses the process was not successful and production was finished in 1898 or 1899. As early as in 1905 the opinion was uttered (14) that Blumenberg would have had better results if he had carried out the reaction between chlorine and alkali in a vessel completely separated from the cell, an important process feature which was much later patented (17) and has come into industrial use since about 1970.

In 1894, Franchot and Gibbs started a test plant in Buckingham, Quebec. After the foundation of the National Electric Company an industrial plant was constructed in 1897 and started in 1898 at Niagara Falls. The cells had no diaphragm and were equipped with some kind of bipolar electrodes with pre-electrode and an electrode distance of only 1.5 to 3.0 mm (14).

In 1898, the North American Chemical Company, a subsidiary of the United Alkali Company of Liverpool was founded. Production started a little later in Bay City, Michigan, using a process of Brock with cells arranged in terraces (18).

In 1899, Oldbury Electro-Chemical Company started manufacturing potassium chlorate at Niagara Falls. The chlorate manufacture in the United States and Canada from that time on was reported in detail by Wallace (19).

²The year 1886 is sometimes erroneously reported in literature.

At the turn of the century, chlorate factories were operated in Switzerland (Vallorbe and Turgi), in France (St. Michel de Maurienne and Chedde), in the U.S.A. (Niagara Falls and Bay City), and in Sweden (Mansboe and Alby) (14, 19). Chlorate was not manufactured by electrosynthesis in Germany where the commercial electrochemical chlorate production started not before 1915, after first attempts at industrial scale, executed in 1887 in Leopoldshall, had failed. This situation is surprising since Germany, at that time, was the center of chlorate research.

The Controversy on the Theory of Electrosynthesis of Chlorate

With the beginning of the electrochemical chlorate production on an industrial scale, an interest in the knowledge of the processes of chlorate formation developed. At that time, it was the general belief that the electrosynthesis of chlorate took place in complete agreement with the chemical formation. Thus, chlorine and hydroxide "primarily" generated at anode and cathode were thought to react with each other to form "secondarily" hypochlorite and chlorate (20, 21)



Soon it became clear that these reactions did not completely describe the processes in the cell.

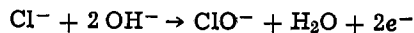
In 1889, Fogh (22) had subjected a neutral solution of alkali chloride to electrolysis without diaphragm and had found from a gas analysis that oxygen was also evolved at the anode. One of the reasons for the loss of current efficiency was found, irrespective of the question whether oxygen is generated by decomposition of water or by any other way.

Oettel, in 1894 (23), interpreted the finding as follows. "Primarily" chloride is anodically oxidized to chlorine. Secondarily, hypochlorite forms at both sides of the diaphragm. In the cathode compartment the hypochlorite is reduced at the cathode. In the anode compartment, part of the hypochlorite is "tertiarily" oxidized to chlorate, while the rest, together with some "tertiarily" formed chlorate is electrolytically decomposed



Additionally, an anodic discharge of hydroxyl is supposed. In any case, the formation of chlorate through anodic discharge of hypochlorite was unthinkable at that time. "The formation of oxygen compounds with chlorine is, therefore, attributed to purely chemical interaction between chlorine and potassium hydroxide," Oettel concluded (23).

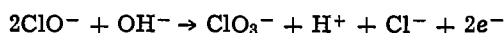
The reaction scheme established by Oettel was questioned a few years later in connection with studies on the electrolysis of hydrochloric acid. In 1898, Haber and Grinberg (24) concluded that simultaneously with the secondary (chemical) formation of hypochlorite and chlorate a primary (anodic) formation takes place



With this interpretation, the old theory of an exclusively chemical formation of chlorate was fundamentally shaken, stimulating extensive research at various places. The activities resulted in a complete revision of the chlorate theory, accompanied by sometimes violent discussions. The results of these fertile years shortly before and after the turn of the century form the basis of a theory which nowadays is essentially considered valid.

Oettel (25) compared the conclusions of Haber and Grinberg with older considerations and gathered that in neutral electrolytes chlorate is preferably formed from hypochlorite partly by "secondary" reactions in bulk of the solution, partly "primarily" by oxidation at the anode. In alkaline electrolytes he surmised a formation of chlorate predominantly by direct combination of chlorine and oxygen set free at the anode.

In 1898, Wohlwill (26), stimulated by his teacher Nernst, carried out experiments on the subject. In agreement with the Haber-Grinberg hypothesis he also stated that chlorate is not exclusively formed "secondarily" (i.e., by chemical reaction in bulk of the solution), but directly at the anode. From the observation that chlorate is never formed without the presence of hypochlorite he followed that chlorate is always generated from hypochlorite according to



while hypochlorite is formed "secondarily." From today's viewpoint the reaction cannot be considered valid since the concentration of OH^- in the bulk is usually small and its rate of diffusion toward the anode is negligible (27), but it is to Wohlwill's credit to have first given a formula for anodic discharge of hypochlorite to form chlorate and chloride.

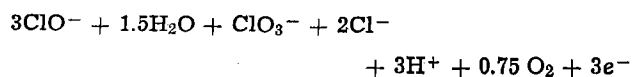
This construction, possibly kindled by the rude style of the paper and the direct attacks on Oettel and Haber, prompted the arousal of controversy on the central question of whether chlorate is formed "primarily" or "secondarily." In his famous Göttingen lecture in 1899, Foerster (28) reported on his essential finding that the electrolyte has to be slightly acidic to give way to the autoxidation of hypochlorite ($\text{ClO}^- + \text{HClO}$) to chlorate (29) which was a real novelty and stood in marked contrast to theory and practice of that time. But at the same meeting he strictly denied that chlorate formation took place at the anode. He had found that always, even in alkaline electrolytes, the electrolyte in the vicinity of the anode was acidic, and so he excluded the possibility of any anion discharge.

In an answer, Wohlwill (31) defended his construction against Foerster and uttered the opinion that in neutral or slightly acidic solutions chlorate is generated by primary as well as by secondary reactions. The aggressive mode of his comment on Foerster's theory provoked Foerster himself to a sneering answer (32) in which he insisted on his old conviction. The way this controversy was carried out obstructed the general acceptance of Wohlwill's theory, and probably was part of the phenomenon that Wohlwill's contribution to the chlorate theory is widely underesteemed.

One year later, Foerster published a study on the anodic processes (33) containing the untenable statement that oxygen is set free only to a very small extent and that chlorate is formed "anodically not in any appreciable extent." It was also in 1900 when Brochet (34) concluded from experiments that in alkaline solutions a primary chlorate formation does not occur.

The same year, Lorenz and Wehrin summarized the existing views and published their voluminous experimental results (35). The authors concluded that primarily hypochlorite is formed and that under certain conditions chlorate is formed at the anode, thus confirming Wohlwill.

Foerster continued to deny any anodic chlorate formation (36), but soon Foerster and Müller (37, 38) came to the definite conclusion that apart from autoxidation of hypochlorite requiring a slightly acidic region chlorate formation occurs by discharge of hypochlorite at the anode



They coined the expression of "anodic chlorate formation" which is still in use.

The Problem of Hypochlorite Reduction

The other relevant problem that occupied the science in the chlorate field was the question whether and how it was possible to prevent reduction of hypochlorite at the cathode. The formation of chlorate is favored by intensive mixing of anodic and cathodic products. But it was just this mixing that caused hypochlorite reduction to such an extent that current efficiency was held down and the economy of the whole process severely affected. To allow industrial operation, a diaphragm was generally used to separate anolyte and catholyte (20). "It is self-evident that the electrolysis of chlorides of potassium or sodium must be carried out with use of a membrane" (23).

When in 1894 Oettel (21) studied the conditions of electrochemical chlorate formation with the intention to check the assumed reaction equations, he concluded that the process should run best in the case where the diaphragm is omitted. In an extended test with a single compartment cell he was able to show that the current efficiency could be maintained at 80-82% without tendency of significant decrease (21). He soon obtained an efficiency of 87% when he operated such a cell with a strongly alkaline solution of calcium chloride (39). Oettel erroneously interpreted this current efficiency to be caused by the absence of hypochlorite during electrolysis. He was so enthusiastic that he called electrolysis without diaphragm "one of the most elegant processes that electrochemistry presents" (39), a statement which must be seen before the background of the enormous technical difficulties of making suitable diaphragms.

Independent of this realization, that same year the first industrial chlorate cell without diaphragm was started. As early as in 1890, Oscar Carlson had taken a Swedish patent (40) for a single-compartment cell. The process was used in the Mansboe factory. An advanced technology was used: "In a vessel alkali chloride is dissolved and the solution is then electrolyzed between an anode made of carbon or other convenient material and a cathode preferably made of iron under omission of a partition" (40). However, when discussing the question of priority of diaphragmless cells, Watt's patent of 1851 (11) has to be considered. Carlson was the first who used carbonates of alkaline earths as additive to the solution. The text of the patent (40) reveals that Carlson did not have a clear idea of the effect of this step. He was of the opinion that the hydroxides of alkaline earths react directly with the chlorine, thus playing an active role in the formation of chlorate. The disadvantageous side effect was that the layer of alkaline earth hydroxide attaching to the cathode continued to increase in thickness during electrolysis, causing a corresponding increase in voltage drop.

In 1898, Bischoff and Foerster (41) gave an interpretation of the way of action which also today is roughly valid: calcium hydroxide, being less soluble than alkali hydroxide, forms a diaphragm at the cathode surface thus obstructing the reduction of hypochlorite.

It was another Swede, J. Landin, who gave a definitely practicable solution of the problem (16, 42). In 1897, he proposed to use additives of compounds of those metals which occur in various valencies, particularly chromic acid. In 1898, Imhoff was granted a German and an American patent (43) (which was transferred to the United Alkali Company, Limited) for the addition of chromate.

Obviously without knowledge of Landin's and Imhoff's patents, Müller (44, 45) used potassium chromate additive with the intention of accelerating the conversion of hypochlorite to chlorate, but found that the additive was suitable to extensively suppress the cath-

odic reduction. "The electrolysis with chromate represents one of the most ideal diaphragm processes one can imagine" (46). Contemporary experiments showed that current efficiencies of 80-92% were attainable (33). A means thoroughly satisfying in industrial electrosynthesis of chlorate had been found. In 1905, world production of chlorate amounted to 15,000 tons per year, 65% of which were already made by electrosynthesis (14).

Manuscript received April 14, 1980.

Any discussion of this paper will appear in a Discussion Section to be published in the December 1981 JOURNAL. All discussions for the December 1981 Discussion Section should be submitted by Aug. 1, 1981.

REFERENCES

1. (a) W. Hisinger and J. J. Berzelius, *Neues Allg. J. Chem.*, **1**, 115; (1803) (b) W. Hisinger and J. J. Berzelius, *Ann. Chim.*, **51**, 167 (1805); (c) W. Hisinger and J. J. Berzelius, in "Avhandlingar Fysik Kemi och Mineralogi," Stockholm (1806); (d) W. Hisinger and J. J. Berzelius, *Ann. Phys.*, **27**, 269 (1807).
2. J. E. Jorpes, "Jac. Berzelius. His life and work." Berkeley, University of California Press (1970).
3. (a) R. Chevenix, *J. Phys. Chim. Hist. Nat.*, **55**, 85 (1802); (b) R. Chevenix, *Phil. Trans. Roy. Soc.*, **92**, 126 (1802); (c) R. Chevenix, *Ann. Phys.*, **12**, 416 (1803).
4. H. Kolbe, *Ann. Chem. Pharm.*, **49**, 393 (1847).
5. J. Berzelius, "Selbstbiographische Aufzeichnungen," H. G. Söderbaum, Editor, Leipzig: J. A. Barth (1903).
6. J. R. Glauber, "Des Teutschlandts Wohlfart, Amsterdam, J. Jansson 1656-1661."
7. H. Kopp, "Geschichte der Chemie," Vol. 3, Braunschweig (1845) (Reprint Hildesheim 1966).
8. C. Berthollet, *Mém. Acad. Roy. Sci.*, **3**, 385 (1786/1787), Turino 1788.
9. J. K. P. Grimm, *Ann. Phys.*, **7**, 348 (1801).
10. C. W. Böckmann, *ibid.*, **8**, 137 (1801).
11. C. Watt, *Brit. Pat.* 13,785 (1851).
12. B. Kerl, "Muspratt's . . . Chemie in Anwendung auf Künste und Gewerbe," 2nd ed., 3rd Vol., Braunschweig (1868).
13. F. Hurter, *J. Soc. Chem. Ind.*, **7**, 719 (1888).
14. J. B. C. Kershaw. "Die elektrolytische Chloratindustrie." Halle a. S.: Knapp (1905).
15. C. Häussermann, *Jahrb. Chem.*, **1**, 325 (1891).
16. J. Landin, *Z. Elektrochem.*, **6**, 480 (1900).
17. A. Schumann-Leclercq, French Pat. 772,326 (1933/34).
18. J. Brock, *Brit. Pat.* 9002 (1898).
19. W. Wallace, *This Journal*, **99**, 309C (1952).
20. C. Haeusermann and W. Naschold, *Chemiker-Ztg.*, **18**, 857 (1894).
21. F. Oettel, *Z. Elektrochem.*, **1**, 354 (1894).
22. J. Fogh, "Über die Vorgänge bei der Elektrolyse wässriger Chlorid-Lösungen," Diss. Jena (1889).
23. F. Oettel, *Chemiker-Ztg.*, **18**, 69 (1894).
24. F. Haber and S. Grinberg, *Z. Anorg. Chem.*, **16**, 329 (1898).
25. F. Oettel, *Z. Elektrochem.*, **5**, 1 (1898).
26. H. Wohlwill, *ibid.*, **5**, 52 (1898).
27. D. Landolt and N. Ibl, *J. Appl. Electrochem.*, **2**, 201 (1972).
28. F. Foerster, (E. Müller, F. Jorre), *Z. Elektrochem.*, **6**, 11 (1899).
29. F. Foerster and F. Jorre, *J. Prakt. Chem.*, **59**, 53 (1899).
30. F. Foerster, *Z. Anorg. Chem.*, **22**, 1 (1899).
31. H. Wohlwill, *Z. Elektrochem.*, **6**, 227 (1899).
32. F. Foerster, *ibid.*, **6**, 253 (1899).
33. F. Foerster and H. Sonneborn, *ibid.*, **6**, 597 (1900).
34. A. Brochet, *C.R. Acad. Sci. Paris*, **130**, 134, 718, 1624 (1900).
35. R. Lorenz and H. Wehrin, *Z. Elektrochem.*, **6**, 389, 408, 419, 437, 445, 461 (1900).
36. F. Foerster and E. Müller, *ibid.*, **8**, 8 (1902).
37. F. Foerster and E. Müller, *ibid.*, **8**, 633, 665 (1902).
38. F. Foerster and E. Müller, *ibid.*, **9**, 171 (1903).
39. F. Oettel, *ibid.*, **1**, 474 (1895).
40. O. Carlson, Swedish Pat. 3614 (1890).
41. H. Bischoff and F. Foerster, *Z. Elektrochem.*, **4**, 464 (1898).
42. J. Landin, Swedish Pat. 8820 (1897).
43. (a) P. Imhoff, Ger. Pat. 110,505 (1898); (b) P. Imhoff, U. S. Pat. 627,063 (1898).
44. E. Müller, *Z. Elektrochem.*, **5**, 469 (1899).
45. E. Müller, *Z. Anorg. Chem.*, **22**, 33 (1899).
46. E. Müller, *Z. Elektrochem.*, **7**, 398 (1901).



Mathematical Modeling of the Lithium-Aluminum, Iron Sulfide Battery

I. Galvanostatic Discharge Behavior

Richard Pollard*¹ and John Newman*

*Materials and Molecular Research Division, Lawrence Berkeley Laboratory
 and Department of Chemical Engineering, University of California, Berkeley, California 94720*

ABSTRACT

A mathematical model of the LiAl/LiCl, KCl/FeS high temperature battery is presented. The model considers a whole prismatic cell which consists of negative electrode, separator, electrolyte reservoir, and positive electrode. Physical phenomena described are ohmic potential drop and diffusion potential in the electrolyte, changes in porosity and electrolyte composition due to electrochemical reactions, local reaction rates, and diffusion, convection, and migration of electrolyte. In addition, the analysis includes finite matrix conductivities, variable physical properties, and the possibility of specific simultaneous reactions in the positive electrode. The theoretical results show many of the trends in behavior observed experimentally. The effects of state of charge, initial electrolyte composition, cell temperature, and current density are presented, and factors that can limit cell performance are identified.

The LiAl/LiCl, KCl/FeS₂ high temperature battery is a candidate for off-peak electrical energy storage and for electric vehicle propulsion. A mathematical model is needed to predict the operational characteristics of the system and to assess the influence of changes in design parameters on the cell performance.

Many models have been proposed to describe the behavior of flooded porous electrodes, and current and reaction distributions in a direction perpendicular to the separator have been considered in great detail (1). The electrode can be regarded as a homogeneous mixture of matrix and electrolyte (2) or as a single pore, provided that proper averages are taken over a cross section (3, 4).

The macrohomogeneous model has been applied to several specific battery electrodes. An analysis of the constant current discharge behavior of electrodes with sparingly soluble reactants, such as the Ag-AgCl and Cd-Cd(OH)₂ couples, has elucidated the relative importance of different failure modes in these systems (3). Transient and failure analyses have also been made of the zinc electrode (5) and the lead dioxide electrode (6, 7). An assessment of steady-state composition profiles in lithium/sulfur battery analogues has been made, but the results are restricted to nonporous systems (8).

Far less effort has been directed toward modeling complete cells and, up until now, only the lead acid cell has been considered in detail (9-12). In this paper, a one-dimensional model is presented for the LiAl/FeS system, which is currently being developed at the Argonne National Laboratory (13). A whole

prismatic cell is considered, consisting of negative electrode, separator, electrolyte reservoir, and positive electrode (see Fig. 1). The model can be used to identify system limitations and to help guide experimental research.

Model Development

The analysis is based on the macroscopic theory of porous electrodes in which the solution and matrix phases are treated as superposed continua without regard for the actual geometric details of the pores (2). With this approach, one can obtain a consistent framework for the description of isothermal transport processes in the molten salt electrolyte (14).

A material balance for species *i* is given by

$$\frac{\partial(\epsilon c_i)}{\partial t} = a_{j_{in}} - \nabla \cdot \mathbf{N}_i \quad [1]$$

where \mathbf{N}_i is the flux of species *i* in the pore solution averaged over the cross-sectional area of the electrode and where $a_{j_{in}}$ represents the transfer rate of species *i* from the solid phases to the pore solution per unit electrode volume. In addition, the superficial current density in the pore solution is due to the movement of the charged species

$$\mathbf{i}_2 = F \sum_i z_i \mathbf{N}_i \quad [2]$$

and, as a consequence of the condition of electrical neutrality, the divergence of the total current density is zero

$$\nabla \cdot \mathbf{i}_1 + \nabla \cdot \mathbf{i}_2 = 0 \quad [3]$$

For *j* simultaneous reactions of the form



* Electrochemical Society Active Member.

¹ Present address: Department of Chemical Engineering, University of Houston, Houston, Texas 77004.

Key words: porous electrodes, molten salt electrolyte, cell performance.



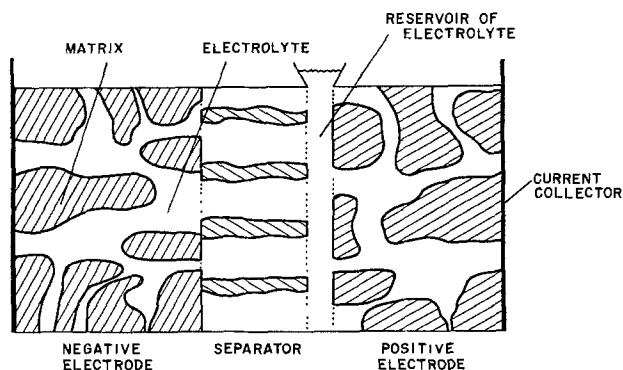


Fig. 1. Schematic diagram of LiAl/FeS cell

Faraday's law can be expressed as

$$aj_{in} = - \sum_j \frac{s_{ij}}{n_j F} a_{in_j} - \frac{1}{V_k} \frac{\partial \epsilon_{pk}}{\partial t} \quad [5]$$

provided that double layer charging can be ignored. The last term on the right side of Eq. [5] represents the removal of species i from the electrolyte as a result of precipitation of salt k . The transfer current per unit electrode volume $\nabla \cdot i_2$ is related to the individual average transfer current densities by

$$\nabla \cdot i_2 = \sum_j (a_{in_j})_j \quad [6]$$

A material balance on the solid phases indicates how the electrode porosity changes with the extent of reaction at each location within the electrode

$$\frac{\partial (\epsilon + \epsilon_p)}{\partial t} = \sum_j \sum_{\text{solid phases}} \frac{s_{ij} \tilde{V}_i}{n_j F} (a_{in_j})_j \quad [7]$$

where $\epsilon_p = \sum_k \epsilon_{pk}$.

The flux of mobile species in the electrolyte can be attributed to the combined effects of diffusion, migration, and convection. For the LiCl-KCl electrolyte, the fluxes of lithium and potassium ions are given by (14)

$$N_1 = - \frac{\epsilon D}{V} \nabla x_A + \frac{t^* i_2}{F} + x_A (c_A + c_B) v^* \quad [8]$$

$$N_2 = - \frac{\epsilon D}{V} \nabla x_B + \frac{t^* i_2}{F} + x_B (c_A + c_B) v^* \quad [9]$$

These relationships can be substituted into Eq. [1] to give, respectively

$$\frac{\partial (\epsilon x_A / \tilde{V})}{\partial t} + \nabla \cdot [x_A g + (x_B t^* i_1 - x_A t^* i_2) \frac{i_2}{F} - \frac{\epsilon D}{V} \nabla x_A] = aj_{1n} \quad [10]$$

$$\frac{\partial (\epsilon x_B / \tilde{V})}{\partial t} + \nabla \cdot [x_B g + (x_A t^* i_2 - x_B t^* i_1) \frac{i_2}{F} - \frac{\epsilon D}{V} \nabla x_B] = aj_{2n} \quad [11]$$

where

$$g = \frac{v^*}{V} + (t^* i_1 + t^* i_2) \frac{i_2}{F} \quad [12]$$

For the special case where $t^* i_1 = x_A/2$ and $t^* i_2 = x_B/2$, the direct dependence of Eq. [10] and [11] on current density is removed. The molar average velocity has been chosen as the reference frame because physical data for LiCl-KCl mixtures are often correlated with the mole fraction (see Appendix).

The movement of electrons in the matrix phase is governed by Ohm's law

$$i_1 = -\sigma \nabla \phi_1 \quad [13]$$

where σ is the effective conductivity of the matrix. In the electrolyte, the variation in solution potential is given by (14)

$$\frac{i_2}{\kappa} = -\nabla \phi_2 - \frac{1}{F} \left[\left(\frac{s_1}{n} + t^* i_1 \right) \frac{1}{x_B} - \frac{s_2 x_A}{n x_B} \right] \nabla \mu_A \quad [14]$$

where ϕ_2 is measured with a reference electrode that has stoichiometric coefficients s_i and number n of electrons transferred, and μ_A is the chemical potential of LiCl (see Appendix). Equations [13] and [14] may be combined to obtain variations in the overpotential $\eta = \phi_1 - \phi_2$ directly.

Polarization equations are needed to express the dependence of the local rate of each reaction on the various concentrations and on the potential difference driving force at the reaction interface. Electrode kinetics do not follow fundamental laws that can be expressed as reliably as Ohm's law or the law of conservation of matter. Consequently, the polarization relationships will be subject to further refinement, as one tries to account not only for the mechanism of the charge transfer process but also for the morphology of the electrode, the formation of covering layers, and the transport of species to and from the reaction site.

It is common to begin with a polarization equation of the form

$$i_{nj} = i_{oj} [e^{\alpha_{aj} F \eta_{sj} / RT} - e^{-\alpha_{cj} F \eta_{sj} / RT}] \quad [15]$$

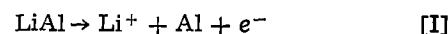
where η_{sj} is the local value of the surface overpotential, $\eta_{sj} = \eta - U_{j,o}$, and where the exchange current density can be written as

$$i_{oj} = i_{oj,ref} \prod_i \left(\frac{c_{j,o}}{c_{i,ref}} \right)^{\gamma_i} \prod_k a_k^{\gamma_k} \quad [16]$$

The theoretical open-circuit cell potential for reaction j is given by

$$U_{j,o} = U_j^\theta - U_{re}^\theta + \frac{RT}{n_{re} F} \sum_i s_{i,re} \ln a_{i,re} - \frac{RT}{n_j F} \sum_i s_{i,j} \ln a_{i,o} \quad [17]$$

The discharge reaction in the negative electrode is



In the fully charged state, it is assumed that the negative matrix consists of nonporous, spherical particles of β -LiAl. On discharge, the outermost region of a particle reacts first and a layer of α -Al is established which thickens gradually, at the expense of β -LiAl, as the reaction proceeds. The Butler-Volmer Eq. [15] should be modified to include the diffusional overpotential for mass transport of lithium across the α -phase to the solid-electrolyte interface.

The parameter

$$S = \frac{3.87(1-\epsilon)I}{nF\bar{c}_{Li}^\beta L a^2 D_\alpha} \quad [18]$$

can be used as a criterion to assess the importance of solid-state diffusion within an LiAl particle (16). Small values of S indicate that the time required for diffusion is much shorter than the time needed for complete utilization of the particle. Even though $S \sim 0(0.1)$ for this system, the influence of solid-state diffusion may be appreciable at high current densities or with low specific interfacial areas, particularly toward the end of discharge. However, for $S < 1$, it is reasonable to invoke the pseudo-steady state approximation to evaluate the composition profile within the α -phase. With this assumption, and with unit activity coefficients, the surface concentration of lithium can be written as (17)

$$\frac{(c_{Li^\alpha})_o}{(c_{Li^\alpha})_{sat}} = 1 - \frac{\nabla \cdot \mathbf{i}_2}{(\nabla \cdot \mathbf{i}_2)_{lim}} \quad [19]$$

The diffusion-limited transfer current is given by

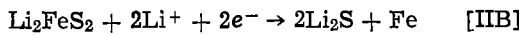
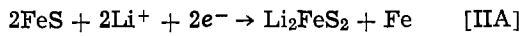
$$(\nabla \cdot \mathbf{i}_2)_{lim} = \frac{4\pi NFD_\alpha (c_{Li^\alpha})_{sat}}{(1 - \bar{x}_{Li^\alpha}) \left(\frac{1}{r_\beta} - \frac{1}{r_\alpha} \right)} \quad [20]$$

where r_α and r_β can be related to the state of charge (17). Combination of Eq. [6], [15], [19], and [20] gives

$$\nabla \cdot \mathbf{i}_2 = \frac{e^{\alpha_a F \eta / RT} - e^{-\alpha_c F \eta / RT}}{1} + \frac{e^{\alpha F a \eta / RT}}{4\pi N r_\alpha^2 i_{o,ref} \left(\frac{x_A}{x_{A,ref}} \right)^{\gamma_{Li^+}} + (\nabla \cdot \mathbf{i}_2)_{lim}} \quad [21]$$

where η is measured with a reference electrode of the same kind as the working electrode, but with a fixed lithium activity corresponding to saturated β -phase (see Table I). Implicit in Eq. [21] are the assumptions that there is no more reaction after the β -LiAl is completely transformed to α -Al and that there are no variations in electrolyte composition between the center of a pore and the adjacent solid surface.

The complicated discharge processes in the positive electrode are represented by two simultaneous reactions



Equation [15] is used to describe the rate of each reaction, and the reference electrode is taken to be the same kind as reaction [IIB] (see Table I). More sophisticated models for the positive electrode kinetics could include additional intermediate reactions, diffusion of reactants and products to and from reaction sites, and crystallization overpotentials for the formation of solid products. However, the detailed mechanism of the reactions and the juxtaposition of the different phases have not yet been formally established and are the subject of a separate study (18). At the high operating temperatures of the lithium/iron sulfide system, and with the relatively high concentration of lithium ions in the electrolyte, the rate of reaction is expected to be high and, therefore, the simplified kinetic analysis may be adequate.

The governing differential equations for the lithium-aluminum/iron sulfide system are subject to the following boundary conditions (see Fig. 1):

(i) at the current collectors

$$\begin{aligned} (a) \quad \mathbf{N}_i &= 0 \\ (b) \quad \mathbf{g} &= 0 \\ (c) \quad \mathbf{i}_2 &= 0 \end{aligned} \quad [22]$$

(ii) at the negative electrode/separator interface

Table I. Kinetic parameters used in model

| Negative electrode | | Positive electrode | |
|------------------------------|-----------------------|--------------------|--------------------------------|
| Parameter | Value | Value | Parameter |
| $\alpha_a = \alpha_c$ | 0.5 | 1.0 | $\alpha_{aj} = \alpha_{cj}$ |
| n | 1.0 | 2.0 | n_j |
| s_1 | -1.0 | -2.0 | $s_{1,j}$ |
| s_2 | 0.0 | 0.0 | $s_{2,j}$ |
| $(x_A)_{ref}$ | 0.58 | 1.0 | $(x_A)_{ref}$ |
| γ_{Li^+} | 0.5 | 1.0 | γ_{Li^+} |
| i_o (A/cm ²) | 2.8 | 2.0×10^8 | $(i_o)_j$ (A/cm ²) |
| D_a (cm ² /sec) | 4.0×10^{-10} | 0.0326 | $U_{IIA,o}$ (V) |
| \bar{x}_{Li^α} | 0.05 | 0.0 | $U_{IIB,o}$ (V) |

$$(a) \quad \mathbf{i}_2 = I$$

$$(b) \quad x_A, \mathbf{v}^\star \text{ continuous} \quad [23]$$

$$(c) \quad \left(\epsilon D \frac{\partial x_A}{\partial y} \right)_s = \left(\epsilon D \frac{\partial x_A}{\partial y} \right)_e$$

(iii) at the positive electrode/reservoir interface

$$(a) \quad \mathbf{i}_2 = I$$

$$(b) \quad x_A \text{ continuous} \quad [24]$$

$$(c) \quad \frac{V_R}{A} \frac{\partial x_{AR}}{\partial t} = \left(\epsilon D \frac{\partial x_A}{\partial y} \right)_e - \left(\epsilon D \frac{\partial x_A}{\partial y} \right)_s$$

where V_R/A can be estimated from

$$\frac{\partial (V_R/A)}{\partial t} = \mathbf{v}^\star_s - \mathbf{v}^\star_e + \frac{V_R}{A} \frac{d \ln \tilde{V}}{dx_A} \frac{\partial x_A}{\partial t} \quad [25]$$

The electrolyte composition is assumed to be uniform across the reservoir. It should also be noted that alternative formulations can be used for the boundary conditions at the front of the electrodes. These choose control volumes for the material balances that avoid the need for separate evaluation of the composition gradients at the interfaces (17). In the separator, the governing equations can be simplified in accordance with

$$(a) \quad \mathbf{i}_2 = I$$

$$(b) \quad \nabla \cdot \mathbf{i}_2 = 0 \quad [26]$$

$$(c) \quad \epsilon = \epsilon_s$$

The initial conditions are taken as

$$(i) \quad x_A = x_A^0$$

$$(ii) \quad \epsilon_e = \epsilon_e^0 \quad [27]$$

$$(iii) \quad \nabla \cdot (\tilde{V} \mathbf{g}) = \bar{V}_A a_{j1n} + \bar{V}_B a_{j2n} - \frac{\partial \epsilon}{\partial t}$$

$$+ \frac{\epsilon}{\tilde{V}} \frac{\partial \tilde{V}}{\partial T} \frac{\partial T}{\partial t} + \tilde{V} \nabla \cdot \left(\frac{\epsilon D}{\tilde{V}} \nabla x_A \right)$$

where Eq. [27(iii)] is derived from Eq. [10] and [11].

During discharge the temperature is assumed to be uniform throughout the cell sandwich, but it can change with time in response to reversible heat effects, Joule heating, overpotentials associated with electrode reactions, and precipitation or dissolution of electrolyte. The first law of thermodynamics gives

$$\frac{m \hat{C}_p}{2A} \frac{dT}{dt} = \left[U_o - V - T_o \frac{\partial \hat{U}_o}{\partial T} \right] I - h_o (T - T_A) + \sum_k \frac{L_k}{V_k} \int_0^{L_T} \frac{\partial \epsilon_{pk}}{\partial t} dy \quad [28]$$

where the heat transfer coefficient h_o is based on estimated heat losses for a battery module. The total cell potential V is obtained by integration of local matrix and electrolyte potential gradients in the electrodes and separator, in accordance with Eq. [13] and [14], respectively. Kirchhoff's voltage law requires inclusion of the surface overpotentials (with appropriate signs) at the front of each electrode as well as the difference in potential between the two types of reference electrode at one location. Resistances of the electrolyte reservoir and current-collector grid can also be included.

The LiAl/LiCl, KCl/FeS system can be described by the local variables x_A , ϵ , \mathbf{i}_2 , \mathbf{g} , and η , and by the governing Eq. [7], [10], [11], [14], and [15], subject to the specified boundary conditions. These relationships constitute a set of coupled, ordinary, nonlinear differential equations at each time step which are cast into finite

difference form accurate to $O(h^2)$, and solved simultaneously by a numerical technique (19). Each nonlinear equation is linearized properly to assure convergence, and each time-dependent equation is programmed symmetrically between the old time step and the present one, in order to attain stability.

Results and Discussion

Electrolyte composition.—Figure 2 shows composition profiles across the cell sandwich for several times during a constant current discharge of 41.6 mA/cm^2 . A lithium-rich electrolyte is used, and the dimensions and capacities of the fully charged electrodes correspond to those of the Argonne National Laboratory, Mark 1A cell (13). When the discharge is started, lithium ions are introduced into the electrolyte at the negative electrode and transported across the porous separator to the positive electrode, where they can react cathodically to form Fe and Li_2FeS_2 or Li_2S . Since the transference number of Li^+ is not unity, a concentration profile develops, and diffusion aids migration in the transport of lithium ions. An almost constant composition gradient is established across the separator that corresponds to the flux of lithium ions needed for the specified current density. The presence of the reservoir attenuates composition changes at the front of the positive but, within the electrode, the composition variations are accentuated by local porosity changes.

The details of the composition variations can be attributed to the combined effects of diffusion, migration, convection, and electrochemical reaction. The contribution of convection, which arises primarily from the influx or squeezing out of electrolyte as the porosity alters, is expected to be small for this system ($v^* \sim 0(10^{-5}) \text{ cm/sec}$). However, convection is included in the analysis to ensure that the accuracy of the electrolyte material balances is retained.

The importance of v^* was tested by repeating the simulation in Fig. 2, with the temperature dependence of the electrolyte molar volume included in a manner that caused oscillation in v^* , without adversely affecting the material balances. The results differed by less than 0.2%, except in the region with KCl precipitation, where the largest error in ϵ_p was 5%. The sensitivity of precipitation to temperature and composition indicates that a significant proportion of this error should

be associated with changes in \tilde{V} , rather than v^* .

If the cell temperature remains constant, the model predicts that the electrolyte composition in the negative electrode would cross the solubility limit for LiCl

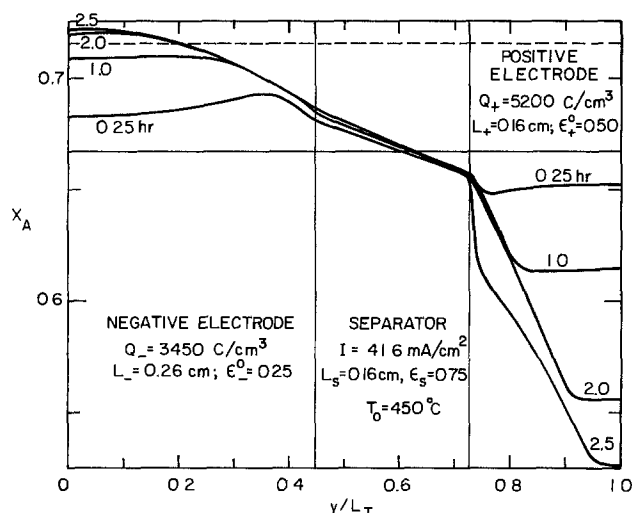


Fig. 2. Position dependence of mole fraction of LiCl at different discharge times. Dashed line represents saturation limit for LiCl at 450°C . Simulation parameters: $N = 1.1 \times 10^8 \text{ cm}^{-3}$; Tables I and III.

(indicated by the dashed line) after 1.5 hr. However, the average temperature rises by approximately 15°C during this period, and therefore precipitation of LiCl is avoided. Nevertheless, at about 54% depth of discharge, the composition has fallen markedly in the positive electrode and precipitation of KCl is predicted. This is illustrated in Fig. 3, which shows the variations in maximum and minimum electrolyte concentrations during the discharge, in comparison with the saturation compositions. The prediction of large variations in electrolyte composition during discharge emphasizes the need for inclusion of variable physical properties in the theoretical analysis.

The fraction of active material utilized within the negative electrode is shown in Fig. 4, at several discharge times. The large electrode surface area and the high operating temperature help to create fast reaction kinetics. As a result, a highly nonuniform reaction distribution, dominated by ohmic effects, is obtained. Initially, the sharp reaction front is restricted to the electrode/separator interface because an infinite matrix conductivity has been assumed for the simulation (2, 20). This reaction zone gradually moves through the electrode as active material is consumed and the potential required for the reaction becomes more positive. At the back of the electrode, the transfer current rises gradually in response to the composition-dependent term in the Ohm's law relationship for the electrolyte. This effect is more pronounced at high current densities and, as a result, the reaction front at a given state of charge is less sharp at higher discharge rates.

The complementary reaction distributions for the positive electrode are presented in Fig. 5. Reaction [IIA] starts first, and after 2 hr it has proceeded about two-thirds of the way through the electrode. The FeS is fully converted to Li_2FeS_2 behind this reaction front, which is itself relatively narrow. Subsequently, a front for reaction [IIB] begins to move through the electrode, and its influence on the composition can be seen in Fig. 2 at 2.5 hr.

The distance that the first reaction penetrates the electrode before onset of the second front is dependent on the operating conditions. Table II indicates that the

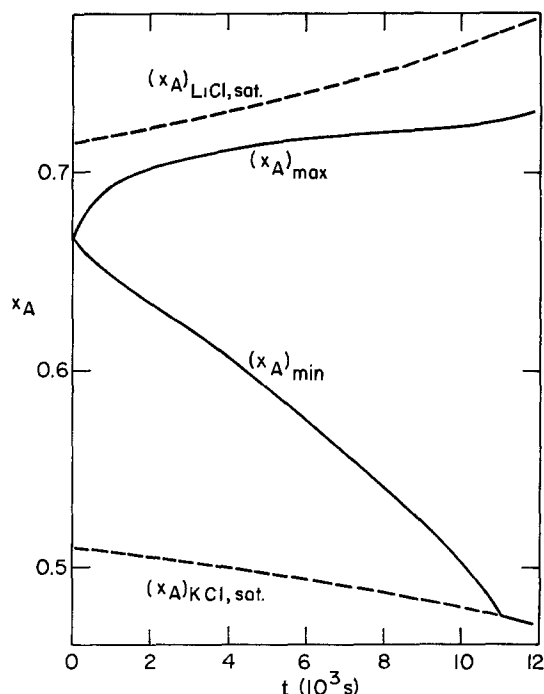


Fig. 3. Comparison of variations in saturation limits for LiCl and KCl and maximum and minimum electrolyte concentrations. Parameters as in Fig. 2.

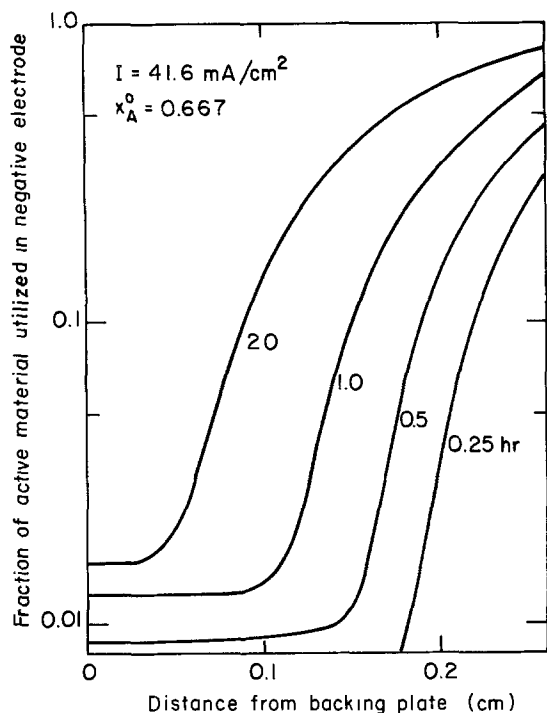


Fig. 4. Fraction of active material utilized in negative electrode at different discharge times. Parameters as in Fig. 2.

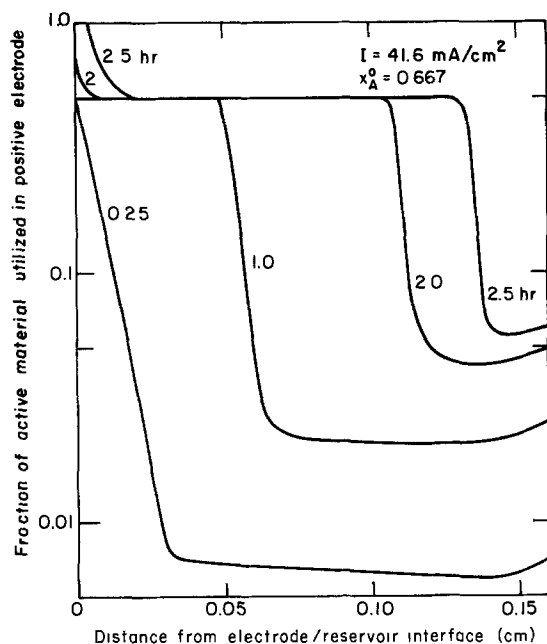


Fig. 5. Fraction of active material utilized in positive electrode at different discharge times. Parameters as in Fig. 2.

distance between the fronts is smaller, and hence the reactions are less distinct, with higher current densities or with lower initial electrolyte compositions.

The microstructure in the positive shortly after the second reaction has begun is shown in Fig. 6. In this example, the initial composition is that of the eutectic, 58 mole percent LiCl, and precipitation of KCl occurs at a relatively low depth of discharge. Precipitation is responsible for the extremely small value of the porosity ϵ at a distance of about 0.075 cm which effectively blocks off the back portion of the electrode. In this isolated region, self-discharge reactions can take place as a result of composition variations in the electrolyte and potential gradients in the matrix. The diagram shows that, in the depth of the electrode, reaction [IIA] has occurred to some extent, producing a certain vol-

Table II. Characteristics of reaction fronts in positive electrode

| | x_A^0 | | | |
|-----------------------------|---------|------|--------|------|
| | 0.58 | | 0.667 | |
| $I \text{ (A/cm}^2\text{)}$ | 0.0416 | 0.1 | 0.0416 | 0.1 |
| L_{gap}/L_+ | 0.40 | 0.18 | 0.63 | 0.30 |
| $100t_{12}/t_1$ | 22.7 | 12.2 | 33.6 | 17.7 |

Table III. Physical parameters used in analysis

| Parameter | Value |
|---|------------------------|
| $U_0 \text{ (V)}$ | 1.34 |
| $\partial U_0/\partial T \text{ (V/K)}$ | -1.55×10^{-4} |
| $C_p \text{ (kJ/kg} \cdot \text{K)}$ | 1.03 |
| $h_0 \text{ (W/m}^2 \cdot \text{K)}$ | 4.13×10^{-2} |
| $T_A \text{ (K)}$ | 298.15 |
| $\tilde{V}_{LiCl} \text{ (cm}^3\text{/mole)}$ | 20.50 |
| $\tilde{V}_{KCl} \text{ (cm}^3\text{/mole)}$ | 37.58 |
| $\tilde{V}_{FeS} \text{ (cm}^3\text{/mole)}$ | 18.55 |
| $\tilde{V}_{Fe} \text{ (cm}^3\text{/mole)}$ | 7.11 |
| $\tilde{V}_x \text{ (cm}^3\text{/mole)}$ | 46.23 |
| $\tilde{V}_{Li_2S} \text{ (cm}^3\text{/mole)}$ | 27.677 |
| $\sigma_{Fe} \text{ (}\Omega^{-1} \text{cm}^{-1}\text{)}$ | 8.23×10^4 |
| $\sigma_{FeS} \text{ (42) (}\Omega^{-1} \text{cm}^{-1}\text{)}$ | 1.90×10^9 |
| $\sigma_x \text{ (}\Omega^{-1} \text{cm}^{-1}\text{)}$ | 5.00×10^2 |
| $\rho_a \text{ (g/cm}^3\text{)}$ | 2.70 |
| $\rho_\beta \text{ (g/cm}^3\text{)}$ | 1.75 |
| $V_R/A \text{ (cm)}$ | 0.03 |

ume fraction ϵ_x of Li_2FeS_2 and slightly decreasing the porosity from its initial value of 0.5. Behind the central reaction front, there is a plateau for the values of ϵ_x , ϵ , and ϵ_{Fe} that corresponds to completion of reaction [IIA]. At distances less than 0.01 cm from the reservoir, the consequence of reaction [IIB] can be seen; Li_2FeS_2 is consumed, Li_2S is produced, and the porosity drops to a small value.

As the first reaction front moves back through the positive electrode, the precipitated region does so also, and it remains as a sharp spike located in the region of highest transfer current. The progression of the second reaction is accelerated by the isolation of the back of the electrode, and the region of precipitation can spread rapidly to affect a larger part of the electrode. The local reductions in porosity that result from the large molar volume of the Li_2S and the precipitation

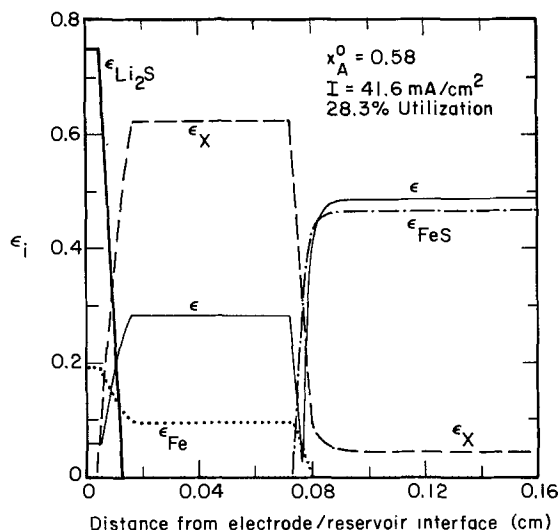


Fig. 6. Volume fractions of solid phases and electrolyte in positive electrode. Parameters as in Fig. 2, except as indicated.

of KCl lead to a reduction in local electrolyte conductivity in accordance with Eq. [A-2]. Consequently, a significant potential drop can develop across the low porosity region, and this may severely limit utilization of the electrode. The plugging of porous electrodes has been cited as a possible cause of failure in other electrodes (5, 21). In the zinc electrode, for example, a large volume fraction of ZnO can be produced at the front face early in a discharge, particularly if the reaction distribution is highly nonuniform.

Initial electrolyte composition.—An important consideration in the development of the LiAl/LiCl, KCl/FeS battery is the choice of initial electrolyte composition, x_A^0 . The dependence of composition changes on x_A^0 is illustrated in Fig. 7, at two different depths of discharge. The difference between the maximum and minimum electrolyte compositions is larger for smaller x_A^0 , and this effect becomes magnified as the discharge proceeds. The composition changes have a direct influence on the extent of precipitation and on the Nernst relationship for the cell potential.

With pure LiCl, there is no concentration polarization, but the minimum operating temperature would be 609°C. For molten salt mixtures with Li^+ as a common ion, the composition changes in the Li/FeS cell are expected to be small. The transport theory developed in Ref. (14) can be applied directly to binary electrolytes such as LiCl-LiF. It also applies to more complicated mixtures, such as LiCl-LiF-LiBr, provided that it is reasonable to assume that, from a mass transport standpoint, the anions can be lumped together to give only a single independent composition variable.

If the anions do not participate in the electrode reactions, the production term in the material balance equation is given by (14)

$$R_A = \tilde{V} a j_{3n} \left(\frac{c_2 t_1^r}{v_2^A v_3^A} - \frac{c_1 t_2^r}{v_1^A v_3^B} \right) \quad [29]$$

For electrolytes with unit stoichiometric coefficients, and for transference numbers that are directly proportional to concentration, Eq. [29] reduces to $R_A = 0$ and, therefore, the electrolyte composition is constant.

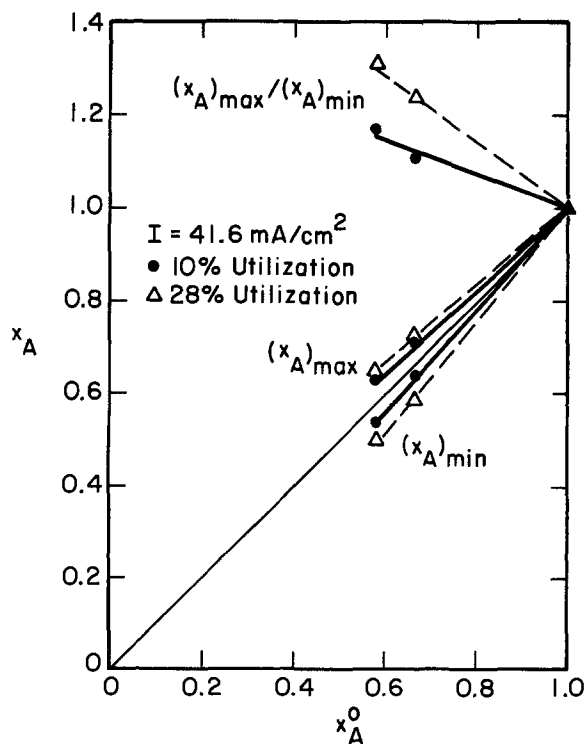


Fig. 7. Dependence of composition variables on initial electrolyte concentration. Parameters as in Fig. 2, except as indicated.

In practice, R_A is still expected to be small even with transference numbers not exactly proportional to concentration, and successful cell operation may be possible at temperatures much closer to the melting point than are permissible with the LiCl-KCl electrolyte.

Discharge curves.—An important capability of the model is to predict the dependence of total cell voltage on state of charge. Discharge curves for the Argonne Mark 1A cells are presented in Fig. 8 for several different operating conditions. The upper curves are for a current density of 41.6 mA/cm², and the highest of these is for a lithium-rich electrolyte, which has a larger bulk electrolyte conductivity than the eutectic mixture. Two curves are shown for the eutectic, which is the composition actually used in the Mark 1A cell design. Curve A takes account of precipitation of either component of the electrolyte, whereas curve B does not. For all three curves, the sharp reduction in cell voltage can be attributed to the localized porosity reductions in the fully reacted region of the positive electrode. Precipitation reduces the porosity still further, and the decline in voltage is correspondingly more acute. In practice, the porosity changes may not be quite so dramatic because it is possible for the electrodes to swell. Expansion may occur by compaction of the separator and displacement of the can walls during the formation cycles of the cell, or by motion of the electrodes relative to one another during a particular charge or discharge. The extent to which swelling can take place will depend on the stresses generated within the cell and the physical restraints on the container.

At the high current density, the initial cell voltage is considerably reduced as a result of the finite grid resistance (see Appendix). Also, the cell voltage declines more rapidly since there is less time available for diffusional processes to take place, and because the reaction distribution in the positive electrode is less uniform (see Table II).

The triangles in Fig. 8 indicate the onset of precipitation of KCl. They show that, at lower I or higher x_A^0 , precipitation is delayed. The exact time when precipitation begins is largely dependent on the details of the heat balance used to estimate the average cell temperature, Eq. [28]. Small changes in the rate of heat loss from the battery module, or slight differences in initial cell temperature, could have a significant impact on the extent of precipitation and, possibly, on the cell performance. In the examples shown, precipitation of LiCl is not predicted, even though the maximum composition is close to the solubility limit (see Fig. 3).

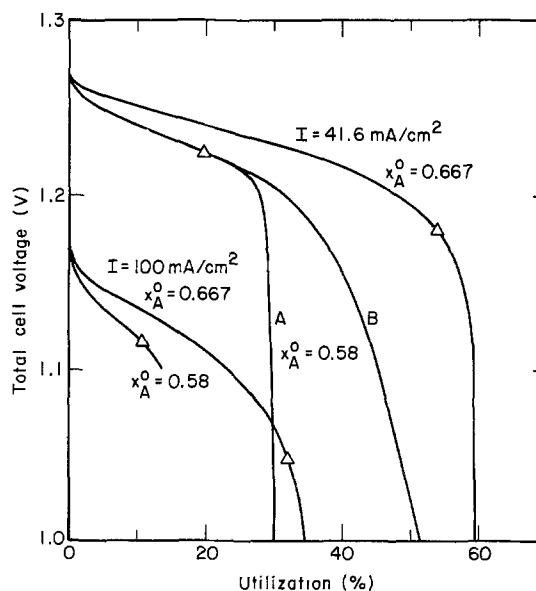


Fig. 8. Theoretical discharge curves for Argonne National Laboratory Mark 1A cells. Parameters as in Fig. 2, except as indicated.

Careful consideration of precipitation is needed for several additional reasons. The rate of mass transport from the electrolyte in the bulk of the pores to the matrix surface may influence the rate at which precipitation takes place. This has been included in previous studies of electrodes with sparingly soluble reactants (22-24), but the effects may not be so important in molten salt systems because the salt concentrations are generally much higher. The morphology of the precipitate may be important, particularly if it forms as a passivating layer over the active material. Furthermore, local thermal effects may influence the extent and nature of precipitation; heat generated as precipitate forms will tend to retard the precipitation process.

In Fig. 9, an experimental discharge curve is compared with theoretical predictions obtained at a similar current density. The experiment was done with a bicell (2 negative electrodes with a central positive plate) that was built with electrodes designed for the Mark 1A battery program (25). The computer simulation is based on the electrode capacities specified in Fig. 8, but it is assumed that the positive and negative electrodes have expanded 12.5% and 23%, respectively. It is also assumed that the heat transfer coefficient h_0 is twice as large as the value assumed for the Mark 1A battery model. The ambient temperature used in the model remains at 25°C, whereas it may be closer to 450°C in the experiments.

Theoretical curves A and B in Fig. 9 indicate the influence of initial cell temperature on the predicted system behavior. The cell temperatures rise by 18° and 26°C during the discharge, for low and high T_0 , respectively. Even with high operating temperatures and swollen electrodes, the maximum predicted utilization is still considerably below the experimental observations. Two possible reasons for this discrepancy are: (a) Larger local porosities in the positive electrode at a given stage of charge due to: (i) additional expansion, (ii) solid phase intermediates with relatively low molar volumes that are not included in the present model, and (iii) more uniform distribution of reactions. (b) Reduction in amount of KCl precipitation due to: (i) smaller composition variations as a result of larger porosities or free convection, (ii) high local temperatures, (iii) mass transport limitations, and (iv) modification of the equilibrium solubility limit by the presence of sparingly soluble species in the electrolyte or due to supersaturation.

Curve C in Fig. 9 represents the same simulation as curve B, except that precipitation of electrolyte is not

taken into account. The relatively good agreement with the experimental data, although possibly fortuitous, gives some support to the reduced precipitation concept and provides an incentive for a more detailed examination of the possible causes enumerated above. In particular, a force balance on the electrolyte in a direction parallel to the separator, together with Darcy's law, indicates that free convection is even less important than forced convection in vertical LiAl/FeS cells.

In addition, at the end of the simulation depicted by curve C in Fig. 9, $(x_A)_{\min} = 0.220$, whereas $(x_A)_{\text{sat}} = 0.437$. If local temperature effects dominated, the temperature in the positive electrode would need to be 155 K above the average cell temperature; temperature differentials of this magnitude are not expected to be observed in these cells because the electrodes are thin and the materials have relatively high thermal conductivities. Furthermore, large degrees of supersaturation would not be expected in the heterogeneous electrode medium. A separate study may be needed to monitor cell temperature and to investigate local variations in electrolyte composition, under closely controlled experimental conditions.

One can also speculate on the reasons for the differences between experiment and theory shown in Fig. 9, at low utilizations. The experimental curve rises more sharply than the model predictions at depths of discharge below approximately 25%. This can be attributed, at least in part, to the presence of about 15% Cu_2S in the positive electrode. Copper sulfide was added to the Mark 1A electrodes to minimize the formation of an intermediate sulfide, $\text{LiK}_6\text{Fe}_{24}\text{S}_{26}\text{Cl}$ (J-phase), which can adversely affect cell performance (26). There is now evidence to suggest that J-phase can also be suppressed by the use of lithium-rich electrolytes and increased operating temperatures (27). Elimination of Cu_2S from the positive would be advantageous because gross movement of Cu_2S to the separator, with subsequent cell shorting, can take place (28).

Small quantities of lithium are sometimes added to the negative to augment the electrode capacity. As with Cu_2S , addition of lithium tends to raise the total cell voltage. However, the lithium activity is increased, and this may cause operational difficulties, such as displacement of potassium from the electrolyte, reaction with the separator material, dendrite formation, shift of charge range in cycling, or failure to achieve full charge.

An alternative explanation for the differences at low utilizations resides in the higher potentials present during the preceding charge half-cycle, which persist for a while after discharge is begun. These would not be present in the computer simulation.

The small discrepancy between experiment and theory at approximately 30% utilization could result, among other reasons, from uncertainty in the estimation of the current collector and terminal resistance (see Appendix). The finite conductance of the grid will also lead to nonuniform current and potential distributions across the face of an electrode, which are not included explicitly in the one-dimensional cell model. A separate study has been made of ohmic drop in current collectors in order to help provide a rational basis for scale-up of cells (29).

An analysis of local variations in potential across the cell sandwich can provide additional insight into the behavior of the individual electrodes. Figure 10 shows potentials at different positions across the cell described in Fig. 9, relative to a saturated $\beta\text{-LiAl/LiCl}$, KCl reference electrode placed at the front face of the negative. The separator potential Φ_s is almost unchanged throughout the discharge, in keeping with the constancy of the composition profile across the separator (see Fig. 2). The open-circuit potential difference $(\Phi_s)_{=0}$, that would be measured by a reference electrode at the front face of the positive electrode, indicates the influence of concentration polarization, which

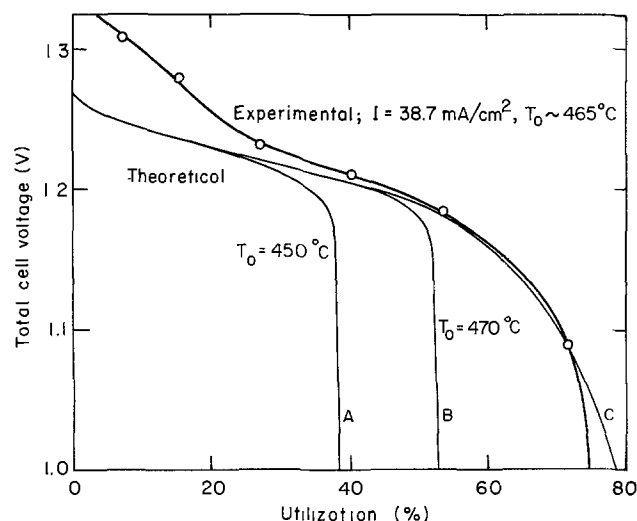


Fig. 9. Comparison of theoretical and experimental (25) discharge curves. Simulation parameters: $Q_- = 2800 \text{ C/cm}^3$, $Q_+ = 4630 \text{ C/cm}^3$, $L_- = 0.32 \text{ cm}$, $L_s = 0.16 \text{ cm}$, $L_+ = 0.18 \text{ cm}$, $\epsilon_- = 0.39$, $\epsilon_s = 0.75$, $\epsilon_+ = 0.555$, $x_A = 0.58$, $I = 41.6 \text{ mA/cm}^2$, $N = 5.5 \times 10^7 \text{ cm}^{-3}$, $h_0 = 8.25 \times 10^{-2} \text{ W/m}^2 \cdot \text{K}$.

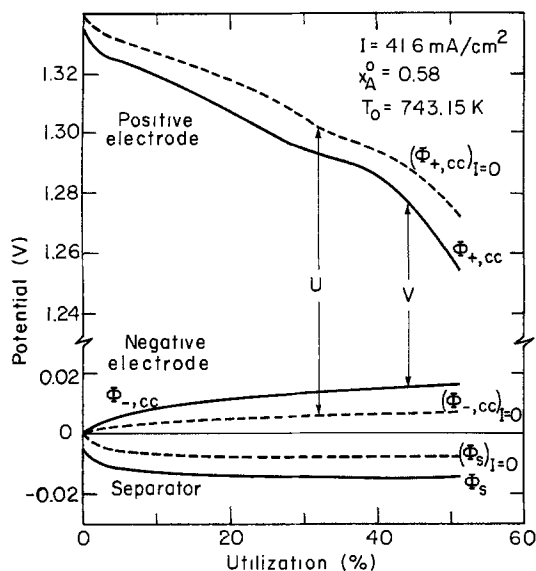


Fig. 10. Theoretical potential variations at different locations across the cell sandwich. Parameters as in Fig. 9. Dashed lines represent open-circuit potentials.

is characterized by the composition dependent term in Ohm's law, Eq. [14]. The curves marked $\Phi_{+,cc}$ and $\Phi_{-,cc}$ represent the potentials of the positive and negative current collectors, respectively. The difference between these potentials and their open-circuit counterparts can be regarded as the resistances of the individual electrodes. In the negative electrode, there is assumed to be no potential difference in the matrix phase, and, in the positive electrode, the matrix potential difference is too small to be discernable in Fig. 10 because the effective matrix conductivity calculated with Eq. [A-10] is large [$\sigma \sim 0(10^4) \Omega^{-1} \text{ cm}^{-1}$], throughout the discharge.

The components of the potential for the experimental cell depicted in Fig. 9 are presented in Fig. 11 (25). Both experimental and theoretical results indicate that changes in total cell voltage are largely dependent on the variations in apparent open-circuit cell potential U ,

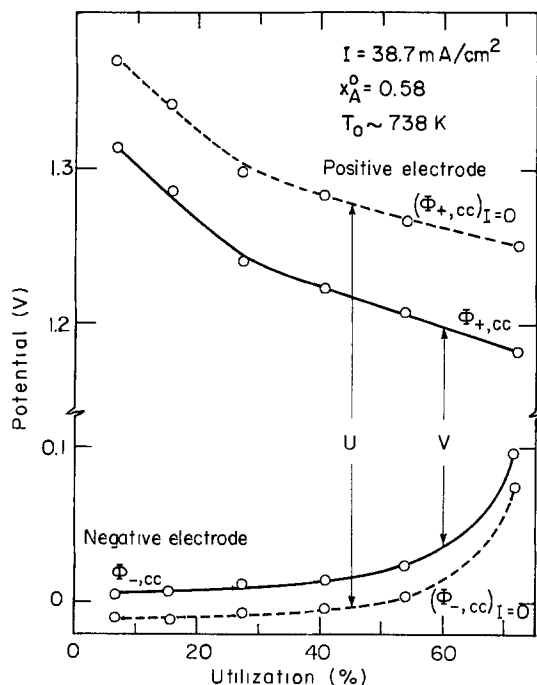


Fig. 11. Potentials at different locations across a cell sandwich measured with a reference electrode placed at the edge of the separator (25). Dashed lines represent open-circuit potentials, 15 sec after current interruption.

and that changes in electrode resistances are relatively small. The experimental results show that the positive is polarized more strongly than the negative electrode, but that the negative electrode potential rises more sharply toward the end of discharge. This could be interpreted as a negative electrode "limitation," although this term has not been carefully defined. In this context, it is not possible to distinguish between limitations caused by inherent electrochemical factors or by changes in the usable capacity of an electrode over a number of cycles. It might be expected that, with a sufficient increase in excess capacity in the negative electrode, the positive would limit cell performance on both charge and discharge.

For both electrodes, the model predicts resistances that are smaller than the observed values. This could be caused by overestimation of electrochemically active interfacial areas, exchange current densities, or matrix conductivities. Contact resistance or partial loss of electrical connectivity between electrode particles can lead to conductivities below those calculated from Eq. [A-10], which is based on the concept of parallel conduction paths. Separate experiments may be needed to establish the conductivity of each electrode matrix as a function of stage of charge. Contact resistances are not expected to be significant in the positive electrode during discharge because the large volume of solid products tends to increase the internal electrode pressure. Furthermore, the presence of Li_2S at the front of the positive electrode may not influence cell behavior markedly, since all the current will be carried in the electrolyte across the fully reacted region. However, the formation of a poorly conducting layer adjacent to the current collector could have a more profound effect on the predicted potential distribution.

Despite the underestimates for the electrode resistances, the model still gives voltages that lie below the experimental results in Fig. 9. This is directly associated with the estimated value of the current collector resistance R_g , which is included in the model only to improve the accuracy of the heat balance. The estimate of R_g could be refined with more precise experimental data for the polarization conductance Y of a cell element. This parameter (Y) could be obtained directly in a small, open test cell with current collectors large enough to ensure insignificant current and potential variations across the face of a plate and with voltage taps placed in direct contact with the current collectors.

Additional experiments may also be needed to elucidate the reasons for the observed rise in potential of the negative electrode toward the end of discharge (see Fig. 11). The theoretical calculations indicate that the increase in porosity as the discharge proceeds more than compensates for the additional distance the current must penetrate the electrode and that the current collector potential approaches a constant (see Fig. 10). The discrepancy between theory and experiment may result from: (a) reduction in negative electrode porosity caused by expansion of the positive, (b) gross morphology changes in the negative electrode, (c) reduction in the available electrode capacity and uncertainty in the state of charge caused by (i) segregation of active material from the bulk and (ii) cumulative coulombic losses, and (d) nonuniform initial distribution of reactants.

Agglomeration would reduce the electrochemically active interfacial area and increase the diffusional overpotential for transport of lithium atoms across the $\alpha\text{-Al}$. A computer simulation with the initial particle size r_0^0 increased by a factor of 4.5 shows an increased electrode resistance at a particular depth of discharge but, contrary to observations, the open-circuit potential $(\Phi_{-,cc})_{I=0}$ does not alter appreciably. The influence of the initial variation in state of charge across the negative electrode could be investigated by comparing potential distributions obtained

during two experiments; one where a considerable time interval was introduced between the discharge of interest and the previous charge, and the other where the discharge followed the charge immediately, but the overall initial state of charge matched the first experiment.

It should also be noted that a considerable quantity of lithium can be retained in the α -Al after the β -phase has been completely utilized. For the example B in Fig. 9, the characteristics of particles at the front of the electrode when the cutoff voltage is reached are: $r_\beta = 0.474 \times 10^{-3}$ cm, $r_\alpha = 1.115 \times 10^{-3}$ cm, and $(c_{Li^\alpha})_o / (c_{Li^\alpha})_{sat} = 0.78$. This indicates that the reaction is not limited by diffusion of lithium across the α -Al and that a minimum of approximately 7.8% of the total theoretical capacity could be stored in the α -Al when no β -LiAl remains. Consequently, the available capacity in the negative electrode may be significantly lower than the theoretical estimate, and this could contribute to the apparent limitation observed in this electrode.

Polarization characteristics.—In many applications it is important to know the effect of discharge rate and depth of discharge on the usable capacity of the cell. Figure 12 shows polarization curves that represent a voltage sweep of a cell that has been discharged at a specified constant current density for a given period of time. It should be emphasized that this is not simply a cross-plot of a number of constant current discharges. Before discharge begins, there is a single current-potential curve, but the polarization characteristics will change during the discharge in a manner that depends on the total applied current. In general, polarization is greater at larger depths of discharge and for higher current densities at a given depth of discharge.

An important feature of the curves in Fig. 12 is that they are substantially straight, and there is little error in approximating them by the equation

$$I = Y(U - \Phi_+ + \Phi_-) \quad [30]$$

where Y is the polarization conductance, given by the reciprocal of the slope of the lines, and U is the apparent open-circuit cell potential, given by the ordinate intercept. In this way, the polarization characteristics of the LiAl/FeS cell can be summarized by the dependence of U and Y on the operating conditions.

Figure 13 shows the dependence of electrochemical resistance on state of charge for several different current densities. Each curve shows that, in an overall sense, the resistance increases as more active material is consumed. However, for $I = 0.1$ A/cm², there is an almost discontinuous reduction in $1/Y$ at a time that corresponds to the onset of reaction [IIB] ($X + 2Li^+$

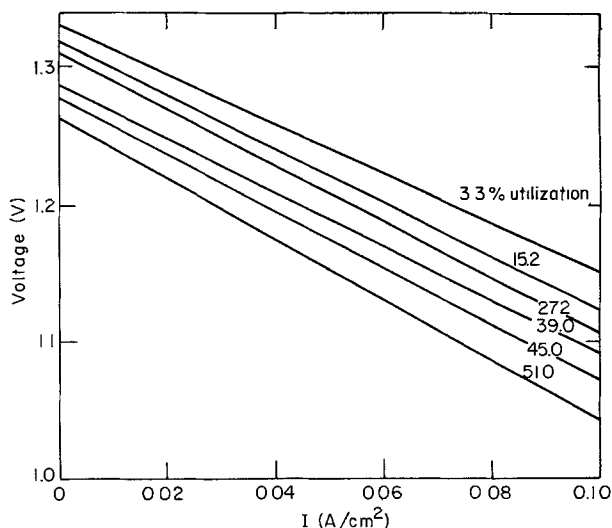


Fig. 12. Effect of state of charge on theoretical cell polarization behavior. Simulation parameters as in Fig. 9, $T_o = 470^\circ\text{C}$.

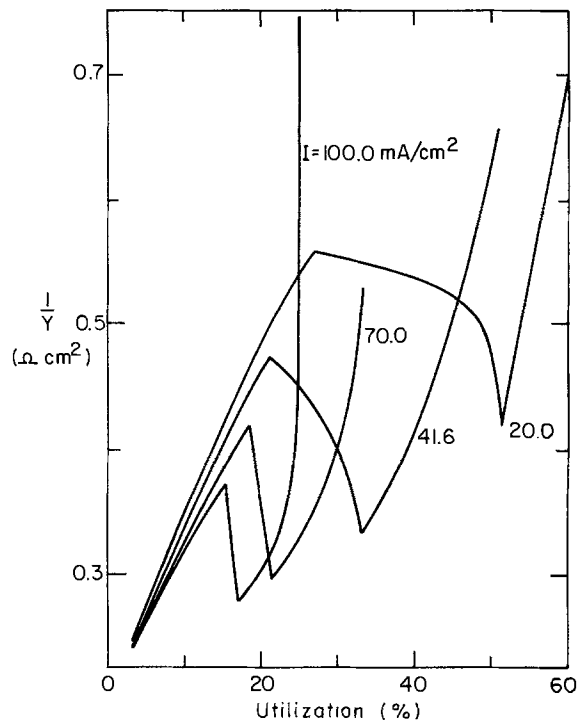


Fig. 13. Predicted dependence of polarization resistance on utilization at different discharge rates. Parameters as in Fig. 9, $T_o = 470^\circ\text{C}$.

$+ 2e^- \rightarrow 2Li_2S + Fe$) at the front of the positive electrode. At lower current densities the drop in resistance is neither as marked nor as abrupt, and it occurs later in the discharge (see Table II). At each current density, the resistance rises again as porosity variations in the positive electrode lower the effective electrolyte conductivity. In practice, there is much less distinction between the intermediate reaction steps in the positive electrode. Consequently, it is not expected that the sharp changes in resistance predicted with the model will be observed experimentally. It should also be emphasized that the model does not include the possibility for reaction of additives such as Cu_2S or CoS_2 , or for additional intermediates such as J-phase in the conversion of FeS to Li_2S and Fe.

The dependence of the apparent open-current cell potential on state of charge and discharge current density is presented in Fig. 14 and 15, for theory and experiment, respectively. In both cases, the value of U drops markedly during the discharge. The experimental results lie above the model predictions as a consequence of the presence of additives, such as Cu_2S , which raise the equilibrium open-circuit cell potential. For less than about 30% utilization, the experimental curves show no systematic dependence on current density. At greater depths of discharge, U changes more markedly at higher I , as predicted in Fig. 14.

The reduction in U during the discharge can be associated with concentration polarization caused by non-uniform utilization of active material. In the negative, lithium is preferentially removed from the front of the electrode first, as illustrated in Fig. 4, and a maximum in electrolyte composition can develop part of the way through the electrode. At open circuit, the region with highest electrolyte composition becomes cathodic with respect to the rest of the electrode, and local concentration cells are set up which act in a manner that tends to reduce the composition variations. These variations can be more substantial at higher discharge rates, for a given state of charge, and, consequently, the open-circuit resistance can be higher in the negative electrode, leading to smaller values for U .

In the positive electrode, the situation is complicated by the possibility of simultaneous reactions. Before re-

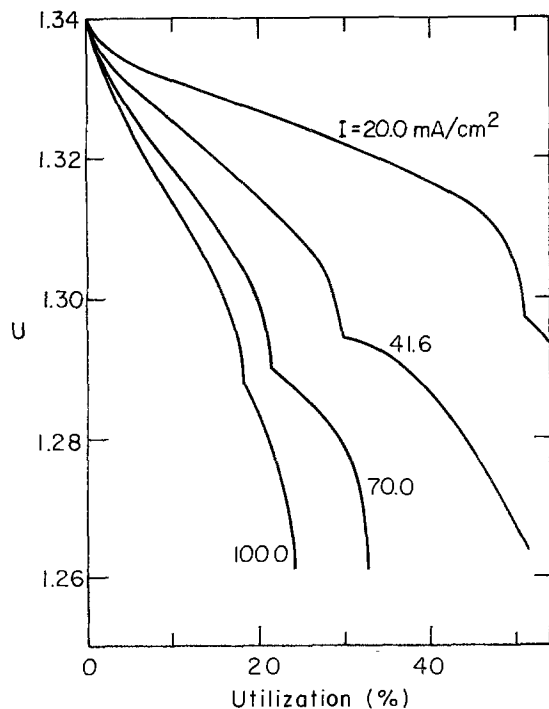


Fig. 14. Effect of discharge rate and state of charge on the theoretical apparent open-circuit cell potential. Parameters as in Fig. 9, $T_0 = 470^\circ\text{C}$.

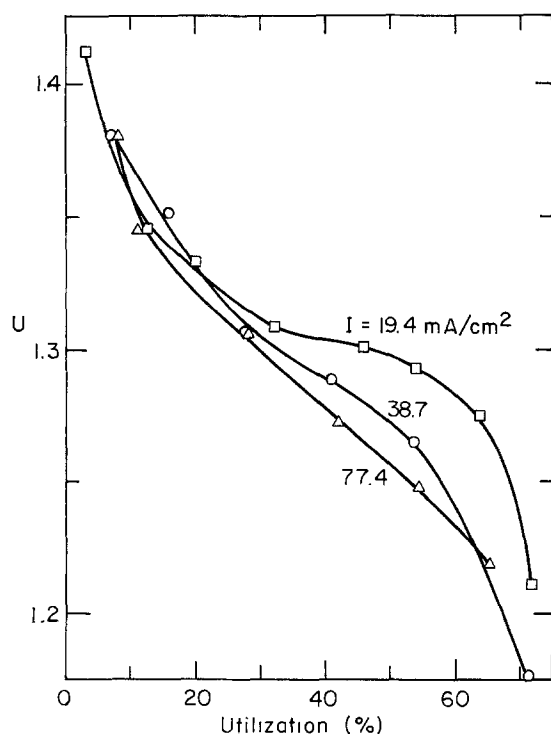


Fig. 15. Variation in experimental apparent open-circuit cell potential with discharge current density and utilization. Measurements taken 15 sec after current investigation (25).

action [IIB] begins, $(\Phi_{+,cc})_{I=0}$ is controlled by local concentration cells that result from electrolyte composition variations, in much the same way as described for the negative electrode. When reactions [IIA] and [IIB] both occur, a corrosion potential can be established on open circuit, which corresponds to cathodic formation of Li_2FeS_2 in the back of the electrode and anodic formation of Li_2FeS_2 toward the front. These reactions would be observed on current interruption, even in the absence of a composition gradient in the electrolyte. As the second reaction, [IIB], progresses,

the mixed corrosion potential shifts toward the equilibrium potential $U_{[\text{IIB}],0}$.

The positive electrode behavior is the major factor that leads to the predicted reduction in U . At higher current densities, reaction [IIB] begins earlier in the discharge and therefore U declines more rapidly. The less marked dependence of U on current density observed experimentally is further evidence to suggest that there is less distinction between the positive electrode reactions in practice.

Conclusions

A mathematical model has been developed that can describe the time-dependent and position-dependent behavior of a complete LiAl/LiCl,KCl/FeS cell. Composition and reaction distributions can be predicted, as well as variations in volume fractions of individual phases and electric potential within the electrodes. The results of the theoretical analysis show many of the general trends in discharge behavior that are observed experimentally. The model predicts that high internal resistance can develop in the positive electrode as a result of low local porosities which are, in turn, caused by large volume reaction products or precipitated KCl . This implies that, with the electrode capacities currently being considered for electric vehicle applications, swelling may be a prerequisite for successful operation and thermal management of battery modules may also be important. Furthermore, an investigation of the potential distribution across the cell sandwich indicates that, before porosity reductions become critical, variations in total cell voltage are controlled more by changes in apparent open-circuit cell potential than by changes in resistance across the individual electrodes.

Acknowledgment

The authors are extremely grateful to the members of the Chemical Engineering Division at the Argonne National Laboratory for many useful discussions and valuable suggestions. This work was supported by the Division of Solar, Geothermal, Electric and Storage Systems, Office of the Assistant Secretary of Energy Technology, U.S. Department of Energy under Contract No. W-7405-Eng-48.

Manuscript submitted Feb. 22, 1980; revised manuscript received ca Aug. 27, 1980.

Any discussion of this paper will appear in a Discussion Section to be published in the December 1981 JOURNAL. All discussions for the December 1981 Discussion Section should be submitted by Aug. 1, 1981.

Publication costs of this article were assisted by the University of California.

APPENDIX

Physical Properties of the LiAl/LiCl,KCl/FeS System

Electrolyte conductivity.—The dependence of bulk electrolyte conductivity on composition and temperature is described by

$$\kappa_{\infty} = (ax_A^2 + bx_A + c)e^{-E/T} \quad [\text{A-1}]$$

where: $a = 18.9803$; $b = -5.0170$; $c = 9.0903$; $E = 1425.76 \text{ K}$ (31, 32). The effective conductivity in the porous medium is estimated from

$$\kappa = \epsilon\kappa_{\infty}/\zeta^2 \quad [\text{A-2}]$$

where the tortuosity factor ζ is directly related to porosity by

$$\zeta = \epsilon^{(1-q)/2} \quad [\text{A-3}]$$

and the constant q is taken as 1.5.

Transference number.—Measurements of transference numbers in binary nitrate melts show that deviations from the relation $t_1^c = x_1$ are often relatively small (34). Experiments in LiCl-KCl melts (35) also tend to substantiate the use of this assumption which, for the molar average velocity reference frame, gives: $t_1^* = x_A/2$; $t_2^* = (1 - x_A)/2$.

Activity coefficient.—If dissociation of electrolyte is disregarded (36), the gradient of chemical potential of LiCl in the LiCl-KCl mixture can be written as

$$\nabla \mu_A = RT \left(1 + \frac{d \ln \gamma_A}{d \ln x_A} \right) \nabla \ln x_A \quad [\text{A-4}]$$

Information from the LiCl-KCl phase diagram can be used to obtain the composition and temperature dependence of the activity coefficient (37-39). A relationship of the form (40)

$$\ln \gamma_A = \frac{b}{T} \tanh \left(\frac{a(1 - x_A)^n}{bx_A} \right) \quad [\text{A-5}]$$

with $a = -1023.84$, $b = -1555.11$, and $n = 3$, has been chosen to represent the data.

Molar volume of electrolyte.—The molar volume of electrolyte is defined as $\tilde{V} = \sum_k M_k x_k / \rho$ where the density ρ is given by $\rho = 1.735 - 0.15x_A$.

Diffusion coefficient.—For the special case where the diffusion coefficients for binary interactions are all equal, it may be shown that

$$D_s = \frac{\kappa_s RT \tilde{V}}{2F^2} \left(1 + \frac{d \ln \gamma_A}{d \ln x_A} \right) \quad [\text{A-6}]$$

On this basis, it is assumed that

$$D_s = 2.442 \times 10^{-4} e^{-E/T} (x_A + 0.4) \quad [\text{A-7}]$$

over the composition and temperature range of interest. The molecular diffusion coefficient in the porous media can be characterized by

$$D = D_s / \xi^2 \quad [\text{A-8}]$$

together with Eq. [A-3].

LiCl-KCl phase diagram.—The equilibrium compositions that characterize the onset of precipitation of LiCl and KCl are approximated by (41)

$$(x_A)_{\text{LiCl,sat}} = 0.34080 - 4.773 \times 10^{-4}T + 1.376 \times 10^{-6}T^2 \quad [\text{A-9}]$$

$$(x_A)_{\text{KCl,sat}} = 0.14615 + 1.9117 \times 10^{-3}T - 1.948 \times 10^{-6}T^2$$

Matrix conductivity.—In general, the matrix conductivity can be influenced by the volume fraction of the conducting phases, the inherent conductivity of each solid phase, and the manner in which the particles of conducting phases are interconnected. As a first approximation, it has been assumed that parallel conduction pathways exist in the positive electrode so that

$$\sigma = \sum_i \sigma_i \epsilon_i^q \quad [\text{A-10}]$$

and q is taken to be 1.5. In the negative electrode, the conductivities of the active materials and the supporting grid are each very high ($\sigma_{\text{Li}} \cong 1.0 \times 10^5 \Omega^{-1} \text{cm}^{-1}$; $\sigma_{\text{Al}} \cong 2.2 \times 10^5 \Omega^{-1} \text{cm}^{-1}$; $\sigma_{\text{Fe}} \cong 2.34 \times 10^4 \Omega^{-1} \text{cm}^{-1}$, at $T = 450^\circ\text{C}$) and consequently the matrix conductivity is assumed to be infinite.

Current collector resistance.—The combined resistance R_g of the grid and terminal is obtained from a preliminary estimate of the polarization conductance, as defined by Eq. [30]. The resistance R_b of a bicell can be separated into electrochemical and current collector contributions, according to

$$R_b = \frac{1}{2A} \left(\frac{1}{Y} + R_g \right) \quad [\text{A-11}]$$

In the calculations, it is assumed that $R_b = 4 \text{ m}\Omega$, $Y = 1.013 \Omega^{-1} \text{cm}^{-2}$ (29), and $A = 316 \text{ cm}^2$. This yields $R_g = 1.55 \Omega \text{cm}^2$.

LIST OF SYMBOLS

a interfacial area per unit electrode volume (cm^{-1})
 a_k relative activity of species k
 A cross-sectional area of electrode (cm^2)
 c_i concentration of species i (mole/cm^3)

\hat{C}_p specific heat ($\text{J}/\text{g}\cdot\text{K}$)
 D diffusion coefficient (cm^2/sec)
 F Faraday's constant ($96,487 \text{ C}/\text{equiv.}$)
 g variable defined by Eq. [12]
 h mesh size (cm)
 h_o heat transfer coefficient ($\text{W}/\text{m}^2\cdot\text{K}$)
 i_o exchange current density (A/cm^2)
 i_1 superficial current density in matrix phase (A/cm^2)
 i_2 superficial current density in pore phase (A/cm^2)
 i_{nj} local current density due to reaction j (A/cm^2)
 I superficial current density to an electrode (A/cm^2)
 j = $\nabla \cdot i_2$, transfer current per unit electrode volume (A/cm^3)
 j_{in} pore wall flux of species i ($\text{mole}/\text{cm}^2\cdot\text{sec}$)
 L electrode thickness (cm)
 L_k latent heat of fusion of salt k
 L_T width of cell sandwich (cm)
 m mass of cell (kg)
 M_i symbol for the chemical formula of species i
 M_i molecular weight of species i (g/mole)
 n_i number of electrons transferred in electrode reaction j
 N number of LiAl particles per unit electrode volume (cm^{-3})
 N_i superficial flux of species i ($\text{mole}/\text{cm}^2\cdot\text{sec}$)
 r_i radius of β -LiAl in LiAl pellet (cm)
 r_o radius of LiAl pellet (cm)
 R universal gas constant ($8.3143 \text{ J}/\text{mole}\cdot\text{K}$)
 R_A parameter defined by Eq. [29]
 R_g grid resistance (Ωcm^2)
 s_{ij} stoichiometric coefficient of species i in electrode reaction j
 S parameter defined by Eq. [18]
 t time (sec)
 t_f final time (sec)
 t_{r2} time between start of discharge and onset of reaction [IIB] in positive electrode (sec)
 t_i^r transference number of species i with respect to reference frame, r
 T absolute temperature (K)
 T_A temperature of surroundings (K)
 T_o initial temperature (K)
 U apparent open-circuit cell potential (V)
 $U_{i,o}$ theoretical open-circuit potential for reaction j at the composition prevailing locally at the electrode surface, relative to a reference electrode of a given kind (V)
 U_j^0 standard electrode potential for reaction j (V)
 U_o open-circuit cell potential (V)
 v_3 velocity of common ion in molten salt mixture (cm/sec)
 v^* molar average velocity (cm/sec)
 \tilde{V} molar volume (cm^3/mole)
 \tilde{V}_k partial molar volume of salt k (cm^3/mole)
 V_R reservoir volume (cm^3)
 w reservoir width (cm)
 x_k mole fraction of salt k
 Y polarization conductance ($\Omega^{-1} \text{cm}^{-2}$)
 z_i valence or charge number of species i

Greek Letters

α_a transfer coefficient in anodic direction
 α_c transfer coefficient in cathodic direction
 γ mean molal activity coefficient
 γ_i exponent in Eq. [16]
 γ_k activity coefficient of salt k
 ϵ porosity or void volume fraction
 ϵ_i volume fraction of species i
 ϵ_p total volume fraction of precipitate
 ϵ_{pk} volume fraction of precipitate of salt k
 ξ tortuosity defined by Eq. [A-3]
 η $\Phi_1 - \Phi_2$
 κ effective solution conductivity (mho/cm)
 μ_k chemical potential of salt k (J/mole)
 ν_i^k number of ions of species i produced by dissociation of a mole of salt k
 ρ density (g/cm^3)
 σ effective matrix conductivity (mho/cm)
 Φ_1 electric potential in the matrix (V)
 Φ_2 electric potential in the solution (V)

Subscripts

A salt A, e.g., lithium chloride

| | |
|----------|----------------------------------|
| B | salt B, e.g., potassium chloride |
| cc | current collector |
| e | electrode |
| j | reaction j |
| k | salt A or B |
| lim | limiting value |
| o | at the electrode surface |
| ref | reference electrode |
| s | separator |
| sat | saturation value |
| α | α -Al |
| β | β -LiAl |
| + | positive electrode |
| - | negative electrode |
| ∞ | bulk solution property |

Superscripts

| | |
|----------|--|
| A | salt A, e.g., LiCl |
| B | salt B, e.g., KCl |
| o | initial value |
| α | α -Al |
| β | β -LiAl |
| * | relative to molar average reference velocity |

REFERENCES

- J. Newman and W. Tiedemann, *AICHE J.*, **21**, 25 (1975).
- J. Newman and C. W. Tobias, *This Journal*, **109**, 1183 (1962).
- J. S. Dunning, Dissertation, University of California, Los Angeles (1971).
- A. Winsel, *Z. Elektrochem.*, **66**, 287 (1962).
- W. G. Sunu, Dissertation, University of California, Los Angeles (1978).
- W. Stein, Ph.D. thesis, Rheinisch-Westfälischen Techn. Hochschule, Aachen (1959).
- K. Micka and I. Rousar, *Electrochim. Acta*, **18**, 629 (1973); *ibid.*, **19**, 499 (1974).
- C. E. Vallet and J. Braunstein, *This Journal*, **125**, 1193 (1978).
- K. Micka and I. Rousar, *Electrochim. Acta.*, **21**, 599 (1976).
- W. Tiedemann, J. Newman, and F. De Sua, *Power Sources*, **6**, 15 (1977).
- W. Tiedemann and J. Newman, in "Battery Design and Optimization," S. Gross, Editor, p. 23, The Electrochemical Society Softbound Proceedings Series, Princeton, N.J. (1979).
- W. Tiedemann and J. Newman, *ibid.*, p. 39.
- P. A. Nelson *et al.*, Progress Report for the period 11/78-3/79, ANL 79-39, Argonne National Laboratory (May 1979).
- R. Pollard and J. Newman, *This Journal*, **126**, 1713 (1979).
- R. White, Dissertation, University of California, Berkeley (1977).
- W. Tiedemann and J. Newman, *This Journal*, **122**, 1482 (1975).
- R. Pollard, Dissertation, University of California, Berkeley (1979).
- R. Pollard and J. Newman, Unpublished work.
- J. Newman, "Electrochemical Systems," Prentice-Hall, Englewood Cliffs, N.J. (1973).
- R. Pollard and J. Newman *Electrochim. Acta*, **25**, 315 (1980).
- D. Gidaspow and B. S. Baker, *This Journal*, **120**, 1005 (1973).
- J. S. Dunning, D. N. Bennion, and J. Newman, *ibid.*, **118**, 1251 (1971).
- J. S. Dunning, D. N. Bennion, and J. Newman, *ibid.*, **120**, 906 (1973).
- H. Gu, D. N. Bennion, and J. Newman, *ibid.*, **123**, 1364 (1976).
- L. Redey and D. R. Vissers, Personal communication.
- D. R. Vissers, K. E. Anderson, C. K. Ho, and H. Shimotake, in "Battery Design and Optimization," S. Gross, Editor, p. 416, The Electrochemical Society Softbound Proceedings Series, Princeton, N.J. (1979).
- M. L. Saboungi and A. E. Martin, Abstract 339, p. 919, The Electrochemical Society Extended Abstracts, Pittsburgh, Pennsylvania, Oct. 15-20, 1978.
- N. C. Otto and J. E. Battles, in Progress Report for the period 11/78-3/79, ANL 79-39, p. 50, Argonne National Laboratory (May 1979).
- J. Newman and R. Pollard, in Progress Report for the period 10/78-9/79, ANL 79-94, p. 109, Argonne National Laboratory (March 1980).
- C. A. Melendres, *This Journal*, **124**, 650 (1977).
- S. V. Karpachev, A. G. Stromberg, and V. N. Podchainova, *Zh. Obshchei Khim.*, **5**, 1517 (1935).
- E. R. van Artsdalen and I. S. Yaffe, *J. Phys. Chem.*, **59**, 118 (1955).
- J. Newman and W. Tiedemann, "Advances in Electrochemistry and Electrochemical Engineering," Vol. 11, H. Gerischer and C. W. Tobias, Editors, Wiley-Interscience (1977).
- J. Richter, U. Gasseling, and R. Conradt, *Electrochim. Acta*, **23**, 1165 (1978).
- C. T. Moynihan and R. W. Laity, *J. Phys. Chem.*, **68**, 3312 (1964).
- M. Blander, in "Molten Salt Chemistry," M. Blander, Editor, pp. 127-238, Interscience, New York (1964).
- E. Aukrust, B. Bjorge, H. Flood, and T. Forland, *Ann. N. Y. Acad. Sci.*, **79**, 830 (1960).
- B. Chu and J. J. Egan, *ibid.*, **79**, 908 (1960).
- J. Lumsden, "Thermodynamics of Molten Salt Mixtures," Academic Press, New York (1966).
- T. J. Edwards, J. Newman, and J. M. Prausnitz, *Ind. Eng. Chem. Fundam.*, **17**, 264 (1978).
- M. Hansen, "Constitution of Binary Alloys," Metallurgy and Metallurgical Engng. Series, 2nd ed., McGraw-Hill, New York (1958).
- J. P. Suchet, "Crystal Chemistry and Semiconduction in Transition Metal Binary Compounds," Academic Press, New York (1971).

Mathematical Modeling of the Lithium-Aluminum, Iron Sulfide Battery

II. The Influence of Relaxation Time on the Charging Characteristics

Richard Pollard*¹ and John Newman*

Materials and Molecular Research Division, Lawrence Berkeley Laboratory
and Department of Chemical Engineering, University of California, Berkeley, California 94720

ABSTRACT

A mathematical model of the LiAl/LiCl, KCl/FeS cell has been used to study the behavior of the system during relaxation and charging. The effects of state of charge, cell temperature, and current density are presented, and the influence of a period of relaxation on the subsequent charging operation is investigated. In addition, factors that can have a significant impact on the charging characteristics are identified.

The mathematical model of the LiAl/LiCl, KCl/FeS cell (1) can also be used to investigate the behavior of the system during relaxation and charging. The changes that take place under these conditions could influence the dependence of cell performance on the number of completed cycles.

In the laboratory, current interruption techniques can be used to assess the resistance within the electrodes, separator, and grids. Furthermore, in some experiments, such as post-mortem cell examinations, a period of relaxation may be needed before the temperature is low enough to begin the analyses. Current interruption may also be important in modules for electric vehicle propulsion, where it is anticipated that there will be significant periods when the battery is not in use. Cell behavior on charge can control the overall energy efficiency of the system and may also directly affect the nature of the subsequent cell discharge (2, 3). For these reasons, it is necessary to identify the factors that can limit the system during the relaxation and charging modes of operation.

The governing differential equations presented previously (1) can be used directly in the analysis, and it is only necessary to replace the initial conditions, $x_A = x_A^0$ and $\epsilon = \epsilon^0$, with the appropriate composition and porosity distributions and to modify the model for negative electrode kinetics. At any point in the electrode, it is assumed that an outer layer of β -LiAl forms as soon as charging begins and that the electrochemical reaction is restricted to the solid-electrolyte interface. The analysis of diffusion of lithium through the β -phase and the gradual reduction in thickness of the α -Al region parallels the model for discharge (1, 4), but the limiting transfer current becomes

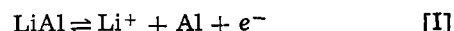
$$(\nabla \cdot \mathbf{i}_2)_{\text{lim}} = \frac{4\pi NFD_\beta (c_{\text{Li}^\beta})_{\text{sat}}}{(1 - x_{\text{Li}^\beta}) \left(\frac{1}{\tau_0} - \frac{1}{\tau_1} \right)} \quad [1]$$

and the reference concentration $(c_{\text{Li}^\alpha})_{\text{sat}}$ should be replaced by $(c_{\text{Li}^\beta})_{\text{sat}}$.

Results and Discussion

Relaxation.—Figure 1 shows composition profiles across the cell sandwich for several times after interruption of the current at the end of a discharge with $I = 41.6 \text{ mA/cm}^2$. The concentration variations diminish in both electrodes and, after 2 hr, the electrolyte composition is practically uniform. In the negative, the

region with highest x_A , at the back of the electrode, becomes cathodic with respect to the front portions. Local concentration cells, with the reaction



are established that reduce the initial composition variations. However, there is no driving force for equalization of the local state of charge within the α -Al, β -LiAl alloy, and the reactions that take place to give a uniform electrolyte composition accentuate the nonuniform utilization of reactants. The magnitude of this effect is dependent on the composition profile and the depth of discharge before current interruption.

In the positive electrode, the situation is complicated by the possibility of simultaneous reactions and by precipitation of electrolyte. Initially, the electrolyte concentration is almost uniform across the majority of the electrode due to precipitation of KCl as two spikes adjacent to the reaction fronts and self-discharge reactions in the isolated regions behind the spikes. Adjacent to the current collector, FeS reacts with lithium ions according to

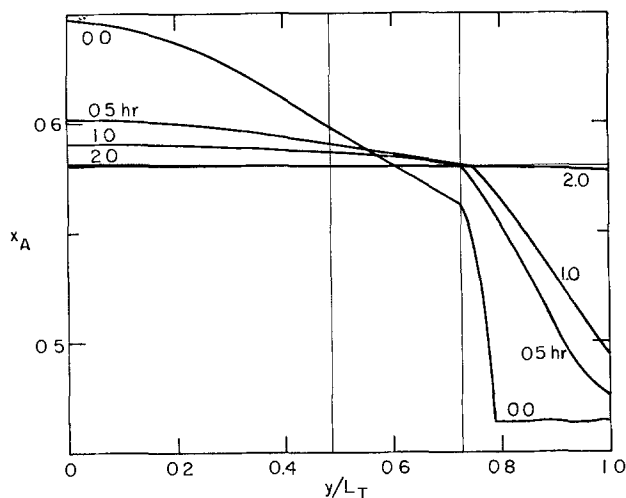
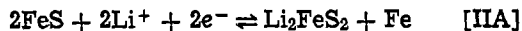


Fig. 1. Position dependence of mole fraction of LiCl at different times after current interruption. Simulation parameters: $Q_- = 2800 \text{ C/cm}^3$, $Q_+ = 4630 \text{ C/cm}^3$, $L_- = 0.32 \text{ cm}$, $L_s = 0.16 \text{ cm}$, $L_+ = 0.18 \text{ cm}$, $N = 5.5 \times 10^7 \text{ cm}^{-3}$, $h_0 = 8.25 \times 10^{-2} \text{ W/m}^2 \cdot \text{K}$, $R_g = 1.55 \Omega \text{ cm}^2$, $h = 0.004 \text{ cm}$, $w = 0$, $-c_{\text{Li}^\beta}/(c_{\text{Li}^\beta})_{\text{sat}} = 1.0$, $D_\beta = 4 \times 10^{-8} \text{ cm}^2/\text{sec}$. Parameters at start of previous discharge: $\epsilon_-^0 = 0.39$, $\epsilon_s = 0.75$, $\epsilon_+^0 = 0.555$, $T_0 = 470^\circ\text{C}$, $I = 41.6 \text{ mA/cm}^2$, $x_A^0 = 0.58$. Initial stage of charge, $\lambda(t=0) = 47.9\%$. Additional parameters specified in Tables I and III of Ref. (1).

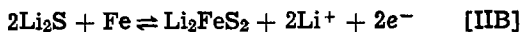
* Electrochemical Society Active Member.

¹ Present address: Department of Chemical Engineering, University of Houston, Houston, Texas 77004.

Key words: porous electrodes, molten salt electrolyte, cell performance.



whereas, near the front of the electrode, Li_2S reacts anodically with iron, thus



The transformation of Li_2S and FeS to the intermediate sulfide reduces the local variations in state of charge although, once all the FeS has been removed, it is not possible for the remainder of the Li_2S to react further. Consequently after approximately 1 hr, there are no more reactions in the positive, and the composition now relaxes under the influence of diffusion alone.

Characteristic times for other relaxation processes can also be identified from the composition profiles. In Fig. 1, the electrolyte concentration changes by less than 1% across the separator after 1.3 hr, whereas the 1% condition is achieved in the negative electrode after only 0.8 hr. This reflects, to some extent, the influence of the electrochemical reaction on the relaxation time (5). However, the 1% criterion is rather arbitrary and, even though the composition is fairly uniform at 0.8 hr, the concentration in the negative still needs to drop by another 2.5%, as diffusion takes place across the separator. In the positive, an additional characteristic time can be distinguished. Self-discharge reactions take place in the region where Li_2FeS_2 is only partially converted to Li_2S . Here, the portion closest to the front of the electrode becomes preferentially cathodic and, after approximately 4 min, a sharp reaction front for the second reaction has been formed.

Heat is not generated in the cell during relaxation, and the temperature falls in accordance with the specified rate of heat transfer to the surroundings. As a result, the saturation concentration for KCl can rise faster than the minimum electrolyte concentration and, under these circumstances, the total volume of precipitate becomes greater than the value at current interruption. However, the reduction in minimum composition soon dominates and, in this example, all the KCl has dissolved after 1500 sec.

Figure 2 shows the variations in total cell voltage that take place after the current is switched off, for simulations A and B described in Fig. 9 of Ref. (1). Curve A is for the example that had a temperature of 450°C at the start of discharge and that achieved 39.2% utilization before the cutoff voltage was reached. The second example had a higher initial temperature (470°C), and a greater utilization was attained before the termination of discharge. In both cases, there is an initial instantaneous rise in cell voltage. The magnitude of this step change can, in principle, be used as a basis for estimation of cell resistance. However, the numerical predictions cannot be used directly because the effects of double layer capacity are not included in the model, and because the final total cell voltage, prior to interruption, can be much lower than expected in practice, due to the acute nature of the predicted failure mechanism. Therefore, separate calculations are necessary to estimate the interrupter resistance.

At the instant of interruption, there is no change in the composition profile. The potential profile retains the same shape within the negative electrode, and the potential difference $\phi_1 - \phi_2$ in the positive is constrained to maintain the same value because of the double layer capacity. Consequently, at any point in the system, Ohm's law gives

$$\frac{i_1}{\sigma} - \frac{i_2}{\kappa} = -\nabla\eta = \frac{i_1^0}{\sigma} - \frac{i_2^0}{\kappa} \quad [2]$$

where the superscript refers to conditions just before interruption. Since $i_1 + i_2 = 0$ and $i_1^0 + i_2^0 = I$, one may write

$$i_1 - i_1^0 = -\frac{I\sigma}{\sigma + \kappa} \quad [3]$$

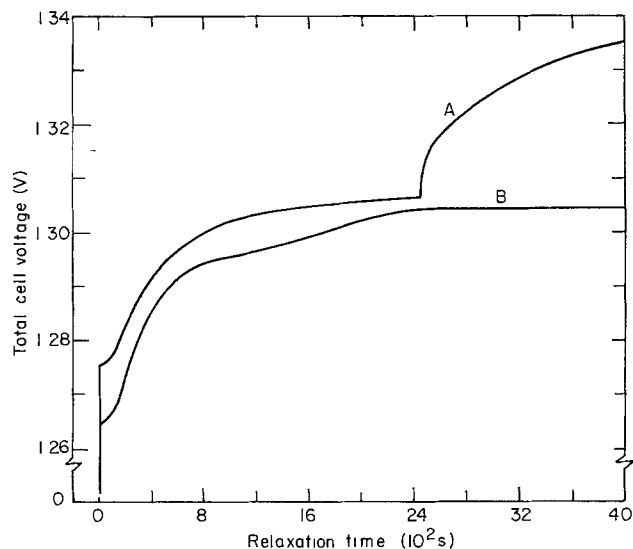


Fig. 2. Dependence of total cell voltage on relaxation time. Simulation parameters as in Fig. 1, except as indicated. Curve A: $\lambda(t=0) = 60.8\%$, $R_1 = 0.15 \Omega \text{ cm}^2$, $T(t=0) = 468.2^\circ\text{C}$, T_0 (at start of previous discharge) = 450.0°C . Curve B: $\lambda(t=0) = 47.9\%$, $R_1 = 0.14 \Omega \text{ cm}^2$, $T(t=0) = 496.2^\circ\text{C}$, T_0 (at start of previous discharge) = 470°C .

which indicates that the resistance of matrix and solution are effectively in parallel, even though each segment of the electrode is in series. Combination of Eq. [3] and Ohm's law for the matrix phase gives the change in cell voltage, $\Delta(V - V^0)$, as

$$\frac{\Delta(V - V^0)}{I} = \int_0^{L_T} \frac{dy}{\sigma + \kappa} \quad [4]$$

where the left side represents the interrupter resistance, R_1 . In the computer calculations, R_1 is dominated by the resistance across the separator because the matrix conductivity is assumed to be infinite in the negative and high in the positive electrode. The separator resistance changes only slightly during operation of the cell, in response to variations in electrolyte conductivity.

It should be emphasized that the theoretical models for the LiAl/FeS cell (6) do not include double layer effects since they are not generally regarded as being significant in the normal operation of a cell. Therefore, for the purpose of measuring the cell polarization characteristics, one may prefer the resistance to be measured after charging of the electric double layer has been completed. For this system, the double layer relaxation time, from point to point within an electrode, is estimated as approximately 50 msec (6), whereas relaxation of concentration profiles by diffusion and reaction is on the order of 3000 sec (see above).

After interruption, the voltage gradually approaches the equilibrium open-circuit cell potential. The shape of the curves is determined by the details of the reactions that occur in the individual electrodes. In particular, a corrosion potential is established in the positive by reactions [IIA] and [IIB]. In example A, all the Li_2S has been converted to Li_2FeS_2 after approximately 2450 sec, and the voltage rises sharply to the open-circuit value, $U_0 = 1.34\text{V}$. Curve B does not show this effect because some Li_2S still remains when reactions [IIA] and [IIB] are completed. In this case, the voltage slowly approaches the open-circuit potential, $U_0 - U_{[\text{IIA}],0} = 1.3074\text{V}$, as the electrolyte composition becomes more uniform. It should also be noted that the small initial rate of rise of cell voltage shown in the examples is atypical, and it results from potential drop across the sharp spike of precipitate that was responsible for the rapid decline in cell volt-

age before current interruption. Both theoretical and experimental results indicate that the initial voltage rise is more rapid when the current is interrupted before the cutoff voltage is reached (7).

Charging.—Figure 3 shows simulated composition profiles at different stages of a constant current charge. A relaxation time of 2 hr was included between the initial discharge and the start of the charging process. The parameter λ represents the overall state of charge; when the cutoff voltage of 1.65V is reached, 89.3% of the total theoretical capacity is available for the next discharge.

In contrast to discharge, lithium ions are now introduced into the electrolyte at the positive electrode and transported across the separator to the negative electrode, where they are incorporated into the LiAl alloy. The composition profiles represent the combined effects of diffusion, migration, and electrochemical reaction. An almost constant composition gradient is established across the separator, but the electrolyte concentration in the reservoir rises significantly during the charge. The model predicts that the electrolyte composition is almost uniform behind each reaction front.

The variations in electrolyte concentration in Fig. 3 can be compared with those in Fig. 4, for the same cell, but without relaxation between discharge and charge. At $\lambda = 77.6$, the profiles are very similar in the two cases, and there is little trace of the composition profile before the charge was started.

The average cell temperature in Fig. 3 falls from 753.5 to 740.0 K during the charge, as a result of reversible heat effects and heat transfer to the surroundings. Consequently, the saturation limit for KCl rises, and precipitation begins at the reaction front in the negative electrode when $\lambda = 85.9$. The temperature of the cell in Fig. 4 also falls, but over the range 769.4 to 751.6 K, and precipitation is delayed until $\lambda = 91.1$. For this reason, 93.7% of the theoretical capacity can be recovered before the resistance across the precipitated region becomes excessive and the cutoff voltage is reached.

The difference in charging behavior caused by the temperature drop during relaxation emphasizes the need for careful thermal management of battery modules. At lower charging current densities the temperature falls even more dramatically, but the maximum and minimum concentrations are smaller at a given state of charge, and precipitation of KCl no

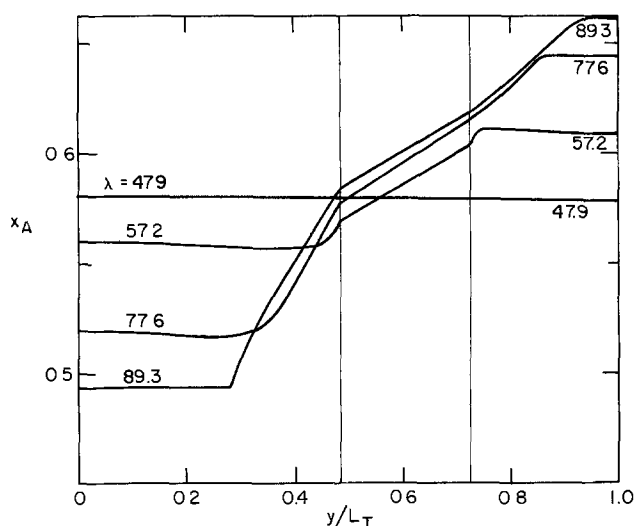


Fig. 3. Position dependence of mole fraction of LiCl at different states of charge for a constant current charge of -41.6 mA/cm^2 . A relaxation time of 2 hr is included between the end of the previous discharge and the beginning of the charging process. Simulation parameters: $T(t = 0) = 480.4^\circ\text{C}$, see also Fig. 1.

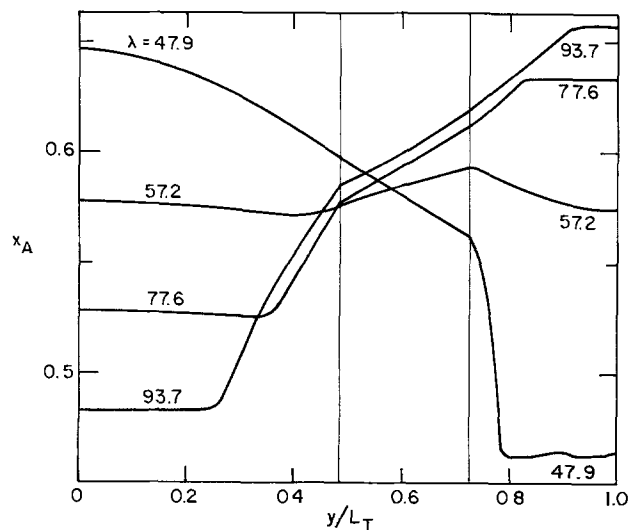


Fig. 4. Position dependence of mole fraction of LiCl at different states of charge for a constant current charge of -41.6 mA/cm^2 . No relaxation between the end of the previous discharge and the start of the charging process. Simulation parameters: $T(t = 0) = 496.2^\circ\text{C}$, see also Fig. 1.

longer controls the final value of λ . For the cell characteristics used in the simulations, a current density of -70 mA/cm^2 is needed to keep the average cell temperature reasonably constant.

Figures 5 and 6 show the fraction of active material utilized within the negative electrode, at several overall states of charge, for the examples in Fig. 3 and 4, respectively. A comparison of the curves at $\lambda = 47.9$ ($t = 0$) shows the increase in nonuniform utilization of reactants that results from relaxation of the electrolyte composition. The general charging mechanism is similar in two cases: the region closest to the electrode/separator interface is recharged first, and the reaction front moves back through the electrode as the alloy is completely reconverted to $\beta\text{-LiAl}$. Further reaction of the $\beta\text{-LiAl}$ is not included in the model because the necessary increase in overpotential of al-

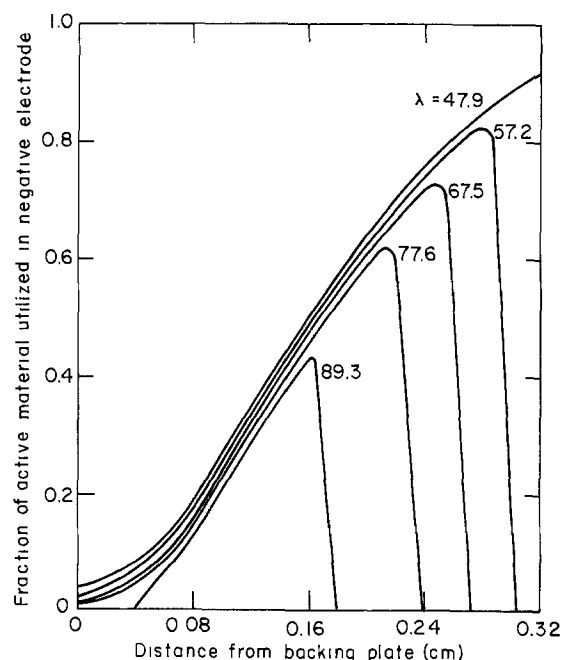


Fig. 5. Fraction of active material utilized in negative electrode at different overall states of charge during a constant current charge of -41.6 mA/cm^2 . A relaxation time of 2 hr is included between the end of the previous discharge and the beginning of the charging process. Simulation parameters are as in Fig. 1.

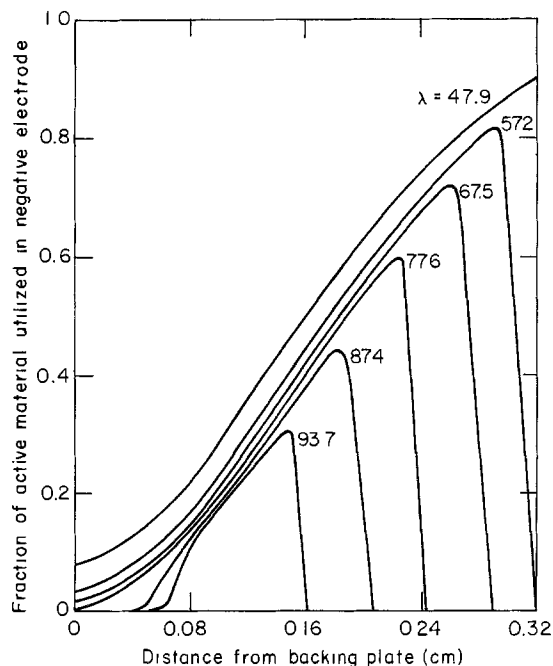


Fig. 6. Fraction of active material utilized in negative electrode at different overall states of charge during a constant current charge of -41.6 mA/cm^2 . No relaxation between the end of the previous discharge and the start of the charging process. Simulation parameters are as in Fig. 1.

most 0.3V (8) cannot be obtained with the specified cutoff voltage. However, recent evidence (9) suggests that the change in overpotential when a particle becomes completely converted to $\beta\text{-LiAl}$ may not be as dramatic as reported previously (8). Consequently, reaction may be possible at the surface of particles where no $\alpha\text{-Al}$ remains. In general, diffusion of lithium in the β -phase is considerably faster than in $\alpha\text{-Al}$ (10), and only very small concentration differences are predicted across the outer $\beta\text{-LiAl}$ layer.

The complementary reaction distributions for the positive electrode are presented in Fig. 7 and 8. The results at $\lambda = 47.9$ show explicitly the equalization in local state of charge that takes place during relaxation. Figure 7 shows that reaction [IIA] occurs preferentially at the front of the electrode, adjacent to the reservoir, and that a sharp reaction front moves through the electrode as Li_2FeS_2 is consumed. This mechanism also predominates in Fig. 8, although the final distribution of unreacted material is shifted from the back of the electrode. Figure 8 also indicates that, early in the charge and at a distance of approximately 0.14 cm, FeS reacts cathodically to form X-phase, in accordance with reaction [IIB]. This self-discharge process corresponds, in part, to the charge equalization predicted during relaxation. The effect is more pronounced at lower current densities.

The variations in total cell voltage for several constant current charges are presented in Fig. 9. In each case, there is a relatively sharp rise in electrode potential when reaction [IIB] is completed in the positive electrode because the corrosion potential can no longer be maintained. Also, precipitation of KCl in the negative electrode is predicted, and the local reduction in electrolyte conductivity that results causes a sharp increase in resistance at the higher current densities. At $I = -20 \text{ mA/cm}^2$, charging is completed before precipitation effects dominate. The time for onset of precipitation is sensitive to the cell temperature, and this is largely responsible for the lower final states of charge that are predicted when a period of relaxation is included in the operating cycle.

Experiments on the charging behavior of LiAl/FeS cells (7) show that the positive electrode current col-

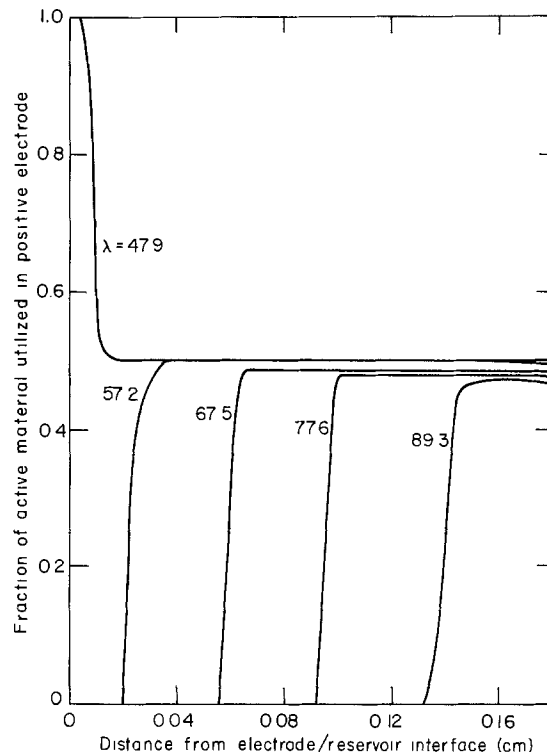


Fig. 7. Fraction of active material utilized in positive electrode at different overall states of charge during a constant current charge of -41.6 mA/cm^2 . A relaxation time of 2 hr is included between the end of the previous discharge and the beginning of the charging process. Simulation parameters as in Fig. 1.

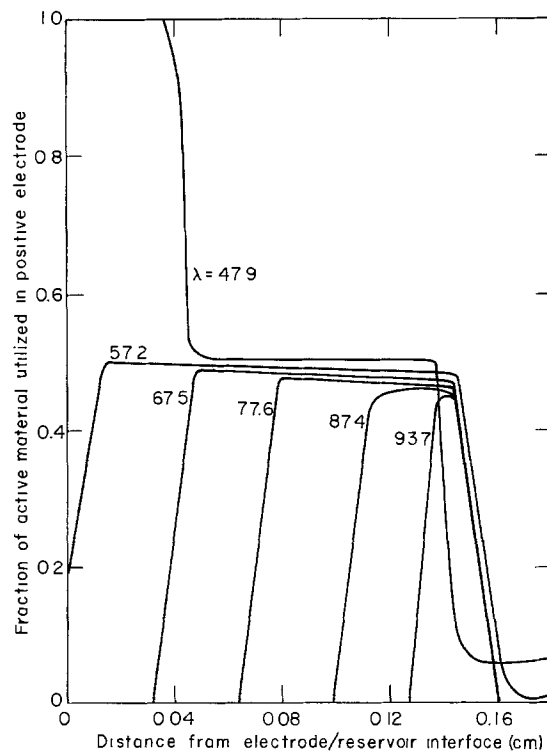


Fig. 8. Fraction of active material utilized in positive electrode at different overall states of charge during a constant current charge of -41.6 mA/cm^2 . No relaxation between the end of the previous discharge and the start of the charging process. Simulation parameters as in Fig. 1.

lector potential, measured relative to a reference electrode placed adjacent to the separator, can rise sharply toward the end of charge. The rate of change of this potential can be larger than that of the negative elec-

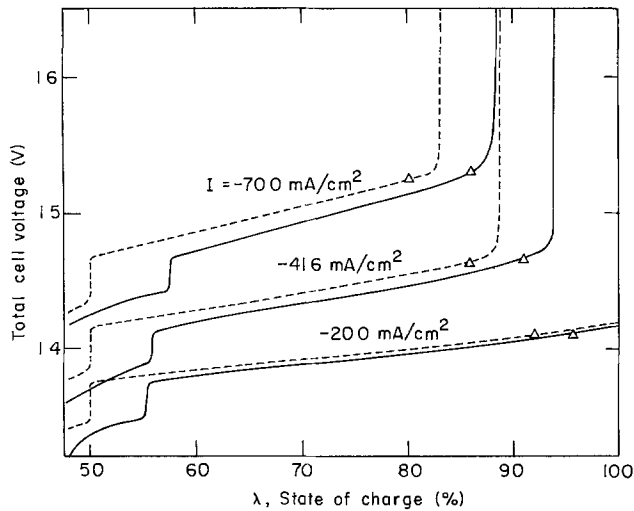


Fig. 9. Dependence of total cell voltage on state of charge during constant current charges. Simulation parameters as in Fig. 1 and $\lambda(t=0) = 47.9\%$. —: Charge begins immediately after discharge, $T(t=0) = 480.4^\circ\text{C}$; ---: 2 hr relaxation between discharge and charge, $T(t=0) = 496.2^\circ\text{C}$; Δ : onset of precipitation of KCl in negative electrode.

trode current collector, and this might be interpreted as a positive electrode limitation on charging. There are several possible reasons for this apparent discrepancy between experiment and theory: (i) reduction in positive electrode porosity caused by expansion of the negative, (ii) reduction in available electrode capacity and uncertainty in state of charge, and (iii) development of high matrix resistance in the positive electrode due to poor electrical connectivity of the phases or large contact resistances.

Additional experiments may be needed to obtain a clearer picture of the factors that limit the charging behavior and to assess the validity of the numerical predictions. The nature of overcharge reactions, and the potentials at which they become thermodynamically feasible, may also need to be investigated.

Conclusions

A mathematical model of the LiAl/FeS cell has been used to investigate the influence of relaxation on the charging characteristics of the system. The analysis indicates that composition variations become less pronounced during relaxation, but the local state of charge within the electrodes can become more non-uniform. The concentration changes induced on charging mask the effects of current interruption, and the effect of relaxation on cell temperature can be more important. The model shows that precipitation of KCl in the negative electrode can cause a rapid rise in applied potential toward the end of charge, but that the effect is not critical at low current densities. The results obtained are sensitive to the details of the heat balance used in the calculation, and this reflects a need for precise thermal management of LiAl/FeS battery modules.

Acknowledgment

The authors are extremely grateful to the members of the Chemical Engineering Division at the Argonne National Laboratory for many useful discussions and valuable suggestions. This work was supported by the Division of Solar, Geothermal, Electric and Storage Systems, Office of the Assistant Secretary of Energy Technology, U.S. Department of Energy, under Contract No. W-7405-Eng-48.

Manuscript submitted Feb. 22, 1980; revised manuscript received ca. Aug. 27, 1980.

Any discussion of this paper will appear in a Discussion Section to be published in the December 1981 JOURNAL. All discussions for the December 1981 Discussion Section should be submitted by Aug. 1, 1981.

Publication costs of this article were assisted by The University of California.

LIST OF SYMBOLS

| | |
|-----------|---|
| c_i | concentration of species i (mole/cm ³) |
| D | diffusion coefficient (cm ² /sec) |
| F | Faraday's constant (96,487 C/equiv.) |
| h | mesh size (cm) |
| h_o | heat transfer coefficient (W/m ² ·K) |
| i_1 | superficial current density in matrix phase (A/cm ²) |
| i_2 | superficial current density in pore phase (A/cm ²) |
| I | superficial current density to an electrode (A/cm ²) |
| L | thickness of electrode or separator (cm) |
| L_T | width of cell sandwich (cm) |
| N | number of LiAl particles per unit electrode volume (cm ⁻³) |
| r_1 | inner radius of outer region of β -LiAl in spherical pellet |
| r_o | radius of particle at solid/electrolyte interface |
| R_g | grid resistance (Ω cm ²) |
| R_I | interrupter resistance (Ω cm ²) |
| T_o | initial temperature (K) |
| $U_{j,o}$ | theoretical open-circuit potential for reaction j , relative to a reference electrode of a given kind (V) |
| V | cell voltage (V) |
| w | reservoir width (cm) |
| x_A | mole fraction of LiCl |

Greek letters

| | |
|------------|---|
| ϵ | porosity |
| η | $\Phi_1 - \Phi_2$ |
| κ | effective solution conductivity (mho/cm) |
| λ | state of charge (%) |
| σ | effective matrix conductivity (mho/cm) |
| Φ_1 | electric potential in the matrix (V) |
| Φ_2 | electric potential in the electrolyte (V) |

Subscripts

| | |
|---------|--------------------|
| lim | limiting value |
| s | separator |
| sat | saturation value |
| β | β -LiAl |
| + | positive electrode |
| - | negative electrode |

Superscripts

| | |
|---------|---------------|
| o | initial value |
| β | β -LiAl |
| - | average value |

REFERENCES

1. R. Pollard and J. Newman, *This Journal*, **128**, 491 (1981).
2. J. S. Dunning, D. N. Bennion, and J. Newman, *ibid.*, **120**, 1005 (1973).
3. H. Gu, D. N. Bennion, and J. Newman, *ibid.*, **123**, 1364 (1976).
4. R. Pollard, Dissertation, University of California, Berkeley (1979).
5. K. Nisancioglu and J. Newman, *This Journal*, **120**, 1339 (1973).
6. J. Newman and R. Pollard, in Progress Report for the Period 10/78-9/79, ANL 79-94, Argonne National Laboratory (March 1980).
7. L. Redey and D. R. Vissers, Personal communication.
8. J. R. Selman, D. K. DeNuccio, C. J. Sy, and R. K. Steuneberg, *This Journal*, **124**, 1160 (1977).
9. C. J. Wen, B. A. Boukamp, R. A. Huggins, and W. Weppner, *ibid.*, **126**, 2258 (1979).
10. C. A. Melendres, *ibid.*, **124**, 650 (1977).

Exothermic Reactions among Components of Lithium-Sulfur Dioxide and Lithium-Thionyl Chloride Cells

S. Dallek,* S. D. James,* and W. P. Kilroy*

Naval Surface Weapons Center, Electrochemistry Branch, White Oak Laboratory, Silver Spring, Maryland 20910

ABSTRACT

Differential scanning calorimetry measurements were made on various components of Li-SO₂ and Li-SOCl₂ cells to identify those combinations that react exothermically and might cause batteries to explode. The passivation of Li by SO₂ in acetonitrile (AN) was characterized over a wide range of SO₂ concentration (0.1-14M). In the absence of SO₂, trace additions of water greatly lower the exothermicity of the Li-AN reaction. The Li-SOCl₂-LiAlCl₄ mixture is inert over a wide range of temperature well above the melting point of Li. However, adding carbon black converts this inert mixture into one which is highly and consistently reactive. The addition of copper powder enhances carbon's catalytic effect on the reactivity of the Li-SOCl₂-LiAlCl₄ mixture while trace additions of water have the opposite effect.

Batteries based on the Li/SO₂ and Li/SOCl₂ electrochemical couples have shown great promise for use in military applications requiring high energy density power sources. However, hazards associated with these batteries may delay their use in future military devices. The incidents involving explosions of these cells under various conditions may be attributable to exothermic chemical reactions among initial cell constituents and/or discharge products.

A thermal analysis study was undertaken to determine the reactivity of various combinations of cell components which could cause thermal runaways resulting in cell explosions. Recent work in this area has been conducted on the Li/SO₂ (1-3) and on the Li/SOCl₂ (4, 5) systems. The present work involved the use of hermetically-sealed high pressure sample containers to extend our previous studies (1, 2) of Li/SO₂ cell components to include volatile substances. Another objective was to perform a similar study of the Li/SOCl₂ system using the high-pressure sample containers to obviate the problems associated with pressure bursts of sample containers encountered in other Li/SOCl₂ DTA studies (4, 5). Finally, the reactivity of the lithium-boron alloy was studied for comparison with that of lithium in combination with Li/SO₂ and Li/SOCl₂ cell components. This alloy has shown great promise for use as an anode material in molten salt batteries (6-8).

Experimental

Apparatus.—A du Pont Model 990 differential scanning calorimeter (DSC) was employed to measure the reaction initiation temperatures and the relative reactivity of various combinations of Li/SO₂ and Li/SOCl₂ cell constituents. In our DSC curves, since the ordinate corresponds to a rate of heat generation and the abscissa is proportional to time, a measure of the relative reactivity is accomplished by a comparison of peak areas and from the masses of the reactants. We sometimes mention the "temperature excursion" (not illustrated) noted for a particular reaction. This does not refer to a deflection of the DSC curves in the ordinate direction (which measures a rate of heat generation). This term refers to excursions of the actual reaction temperature above the programmed temperature. Most DSC curves were recorded at an ordinate sensitivity of 20 mcal/sec · in. (20×). A sensitivity of 5 mcal/sec · in. (5×) is four times as responsive to

enthalpy changes as is a setting of 20×. The sensitivity selection is included in the illustrations to allow comparison of the endothermic (endo) and exothermic (exo) areas. We deliberately used an insensitive recorder setting of 20× since we were mostly interested in comparing relatively vigorous reactions. Thus any reactions that involved relatively small amounts of heat change escaped our attention. The termination temperature on any DSC analysis is referred to in the test as the "cutoff" temperature.

All DSC measurements were made under a flowing atmosphere of dry argon at a programmed heating rate of 10°C/min. The DSC instrument was calibrated with pure metals melting over the temperature range studied (In, 156.6°C; Li, 180.5°C; Sn, 231.9°C; Zn, 419.4°C).

Thermal analysis of solids was performed in crimp-sealed du Pont-type Armco iron crucibles. Armco iron is inert to lithium and offers the advantage of excellent thermal response.

Mixtures containing volatile liquids were studied using high-pressure, corrosion-resistant Ni-Cr alloy (Nimonic) 500 μl crucibles purchased from Mettler Instrument Corporation, Princeton, New Jersey. Hermetic seals, capable of withstanding 100 atm of pressure, were achieved when an open-ended screw cap was tightened onto a gold diaphragm placed between the cap and the crucible. The hermeticity was confirmed by observing no loss of mass on reweighing the sample after the DSC run.

A comparison of the two types of sample cups is illustrated in Fig. 1. There is a large mass difference between the Armco cup (200 mg) and the Nimonic cup (2500 mg). The large size of the Nimonic cups necessitated modification of the DSC analytical procedure. Since the DSC chamber could not accommodate a second Nimonic cup for a reference, a stainless steel rod of similar mass was used as a reference and the instrument was then recalibrated. This disparity of sample cup and reference gives rise to a slightly sloping base line.

Sample preparation.—Lithium-boron alloy, containing 72 weight percent (w/o) lithium, was prepared as previously described (8). All solid mixtures containing either lithium-boron alloy or lithium (99.9% Foote Mineral) were prepared by sandwiching the other solid components into a single piece of the alloy or the lithium. The Li or Li-B fragment was pressed into a thin film and then the other solid powder was

* Electrochemical Society Active Member.
Key words: battery, carbon, discharge, catalysis.

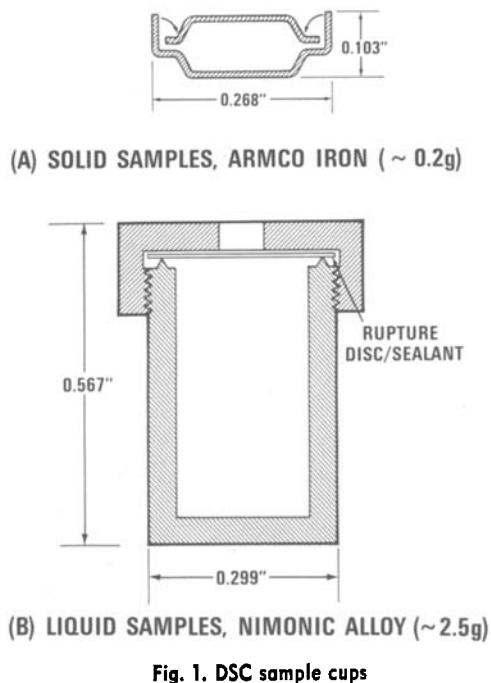


Fig. 1. DSC sample cups

pressed into this Li surface thus ensuring intimate contact. All samples were weighed, mixed, and sealed in a Dry Room maintained at 0.25% relative humidity. All salts, carbon, etc. were vacuum dried at appropriate temperatures. Lithium hexafluoroarsenate was obtained from U.S. Steel Corporation. The lithium tetrachloroaluminate was Matheson-Coleman-Bell "polar-quality" and was used as received. Lithium thiosulfate (Pfaltz and Bauer) was washed in carbon disulfide then in carbon tetrachloride. With the exception of the lithium bromide (Fisher) and the anhydrous lithium sulfide (Ventron), all the other salts used were anhydrous, Reagent-Grade chemicals. Methyl isocyanate (Aldrich) and thionyl bromide (Alfa) were used as received.

The "active" and "reserve" battery electrolytes (~14M in SO₂) were provided by Honeywell Power Sources Incorporated. The active battery electrolyte was approximately 70, 22, and 8 w/o in SO₂, CH₃CN, and LiBr, respectively. The reserve electrolyte was 72.6, 18.4, and 8.9 w/o in SO₂, CH₃CN, and LiAsF₆, respectively. The reserve electrolyte was developed for reserve, Li-SO₂ batteries where exceptional long-term stability of the electrolyte is needed.

Acetonitrile was doubly distilled, first over sodium hydride then over phosphorus pentoxide. Only the middle fractions were collected. Dilute solutions of SO₂ in acetonitrile were prepared by bubbling 99.9% SO₂ into the doubly distilled acetonitrile. The dilute solutions (0.1M) of SO₂ were analyzed by adding a known volume of the solution to an excess of standard iodine in acid buffer. The unreacted iodine was titrated with standard thiosulfate solution. The more concentrated solutions (1.7M) were analyzed by weighing the CH₃CN before and after absorption of the SO₂.

Thionyl chloride was refluxed with lithium for approximately 20 hr under an argon atmosphere followed by distillation under argon. Only the palest portion of the middle fraction was collected for use in the DSC studies. All other liquid chemicals were used as received.

A stock solution of 1.6M LiAlCl₄ was prepared in SOCl₂. A saturated solution of SO₂ in this electrolyte was prepared by bubbling the SO₂ into the LiAlCl₄-SOCl₂ solution cooled in powdered Dry Ice. This solution was allowed to equilibrate at room temperature and 1 atm pressure.

Discharge products were obtained by constant current discharge of a pressurized laboratory cell containing 30 ml of Li/SO₂ reserve battery electrolyte. Precaution was taken to insure that the carbon-Teflon current collector was very dry and that only clean-surfaced lithium was used. The cell was assembled under helium and discharged at approximately 2-3 mA/cm² current density at ambient temperature. The discharged cell was pumped dry overnight and disassembled in the Dry Room. The products were separated, washed with doubly distilled acetonitrile, and vacuum dried.

Results and Discussion

Sulfur Dioxide System

Table I summarizes the DSC data obtained in this system. The table is arranged in the order of increasing mixture complexity. Mixtures containing the Li-B alloy are segregated at the bottom. Figures 2B and 2C compare the thermal response of the relatively heavy, high-pressure Nimonic sample cups (2.5g) with that of the much lighter Armco iron containers (0.2g). For this purpose we chose the (Li + Li₂S₂O₃) reaction which is known to be very exothermic (2). The figure illustrates the generally greater sensitivity of the lighter Armco iron cups. The difference between Fig. 2B and 2C in exotherm initiation temperatures should not be attributed to the mass differences of the sample containers since heterogeneous sample mixtures can often generate irreproducible thermal data. In this connection we note that the curve of Fig. 2B differs slightly from that obtained previously (2). Most of the DSC runs reported herein were performed in duplicate, some in triplicate, to check for reproducibility. Generally, simple mixtures of solid components gave very reproducible results, whereas the initiation temperatures and enthalpic changes of more complicated mixtures, especially those containing liquids, were sometimes less reproducible.

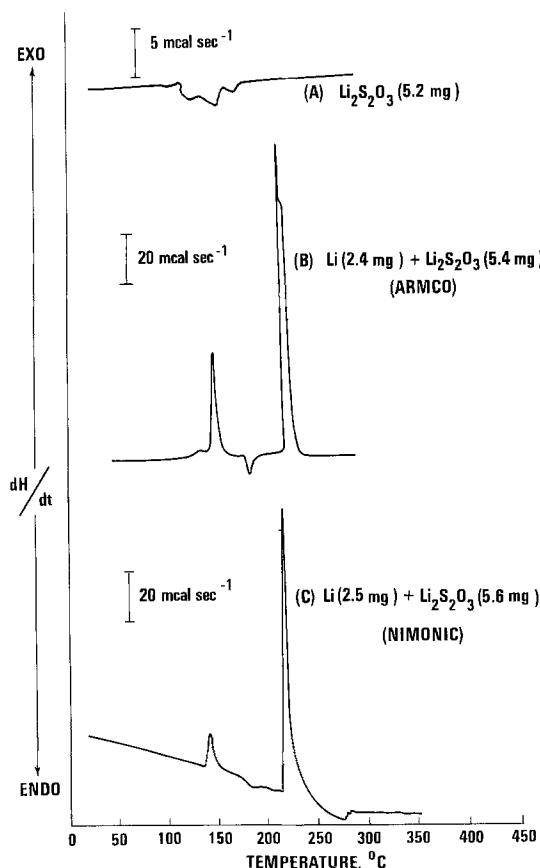


Fig. 2. Reactivity of lithium thiosulfate

Table I. Summary of DSC data for the Li/SO₂ system

| Reaction | Reactants | Cutoff temperature (°C)* | Transition temperatures (°C)** | |
|----------|--|--------------------------|--------------------------------|--------------------|
| | | | Endothermic | Exothermic |
| 1 | Li | — | 180 | — |
| 2 | S | — | 113, 118 | — |
| 3 | AN** | 284 | — | 241 |
| 4 | LiAsF ₆ | 300 | 258 | — |
| 5 | Na ₂ S ₂ O ₄ | 260 | — | 190 |
| 6 | Products of reaction 5 | 495 | 281, 365 | 440 |
| 7 | Li ₂ S ₂ O ₃ | 305 | 132 | — |
| 8 | Li + LiBr | 300 | 181 | 142 |
| 9 | Li + LiAsF ₆ | 400 | — | 187 (210) |
| 10 | Li + AN | 300 | 180 | 40 (5) |
| 11 | Li + S | 242 | 180 | 127 (100) |
| 12 | Li + Na ₂ S ₂ O ₄ | 353 | 180 | 190, 256 |
| 13 | Li + Li ₂ S ₂ O ₃ (ARMCO) | 290 | 181 | 147 (5), 222 (145) |
| 14 | Li + Li ₂ S ₂ O ₃ (NIMONIC) | 343 | 180 | 137 (5), 209 (20) |
| 15 | Li + Li ₃ N | 391 | 181 | — |
| 16 | Li + Li ₂ SO ₄ | 400 | 181 | — |
| 17 | Li + SOBr ₂ | 229 | 179 | — |
| 18 | Li + CH ₃ NCO | 408 | — | 152 |
| 19 | Active electrolyte† | 340 | 177 | — |
| 20 | Li + anode discharge product | 416 | 181 | — |
| 21 | Li + cathode discharge product | 452 | 181 | 251 (5) |
| 22 | Li + [AN-H ₂ O (0.2%)]‡ | 426 | 180 | 20 (minor) |
| 23 | Li + AN + LiBr | 295 | — | — |
| 24 | Li + [AN-LiBr (satd.)] | 400 | — | 35 (minor) |
| 25 | Li + AN + LiAsF ₆ | 300 | — | 50 (5), 181 |
| 26 | [AN-SO ₂ (0.1M)] + LiAsF ₆ | 268 | — | 266 (15) |
| 27 | Li + [AN-SO ₂ (0.1M)] | 305 | — | 142 (30) |
| 28 | Li + [AN-SO ₂ (1.7M)] | 400 | 186 | 122 |
| 29 | Li + S + S ₂ Cl ₂ | 265 | 180 | 261 |
| 30 | Li + active electrolyte | 343 | — | 156 (5), 180 |
| 31 | Li + reserve electrolyte§ | 387 | — | 180 (5) |
| 32 | Li + [AN-LiBr (satd.)] + C | 408 | 181 | — |
| 33 | Li + [AN-SO ₂ (0.1M) - LiBr (satd.)] | 429 | 179 | 86 (17) |
| 34 | Li + [AN-SO ₂ (1.7M)] + LiBr | 408 | 180 | 122, 181 |
| 35 | Li + [AN-SO ₂ (0.1M)] + LiAsF ₆ | 295 | — | 115 (10), 209 |
| 36 | Li + [AN-SO ₂ (1.7M)] + LiAsF ₆ | 400 | 181 | 142, 189, 217 |
| 37 | Li + [AN-SO ₂ (0.1M)-H ₂ O (0.07%)] + LiAsF ₆ | 276 | 180 | 98, 202 |
| 38 | Li + C + [AN-SO ₂ (1.7M) - LiBr (satd.)] | 266 | 180 | 35 |
| 39 | Li + C + reserve electrolyte | 324 | 181 | 142 |
| 40 | Li + PC** + active electrolyte | 348 | 172 | 174, 222 |
| 41 | Li-B alloy + AN | 372 | 180 | 50 (5) |
| 42 | Li-B alloy + S | 300 | 180 | 127 (80) |
| 43 | Li-B alloy + Li ₂ S ₂ O ₃ | 324 | 181 | 147 (5), 245 (10) |
| 44 | Li-B alloy + active electrolyte | 338 | — | 167 |
| 45 | Li-B alloy + cathode discharge product | 452 | 181 | 253 (5) |

* Temperature at which the DSC linearly programmed temperature scan was terminated.

** AN = acetonitrile; PC = propylene carbonate.

*** Figure in parenthesis represents the increase in the sample temperature above the linearly programmed temperature.

† Active electrolyte: 70, 22, 8% w/w in SO₂, AN, and LiBr (~14M SO₂).

‡ Ingredients within the square brackets are a homogeneous solution.

§ Reserve electrolyte: 72.6, 18.4, 8.9% w/w in SO₂, AN, and LiAsF₆ (~14M SO₂).

Lithium thiosulfate and sodium dithionite.—Figure 2A reveals that Li₂S₂O₃ begins to decompose endothermically at about 132°C. This indicates that the first exotherms in Fig. 2B and 2C are associated with the reaction of Li with these thiosulfate decomposition products. In agreement with the literature (9, 10), Fig. 3A shows rapid exothermic decomposition at 190°C for a sample of sodium dithionite (Na₂S₂O₄) containing 7.5% sodium sulfite and 2.5% sodium thiosulfate as impurities. This is as chemically similar as we could get to the commercially unavailable lithium dithionite which appears to be the primary product in discharged Li/SO₂ cells (18). Figure 3A agrees with previously published data (3). A repeated DSC run on the decomposed salt of Fig. 3A is shown in Fig. 3B. Contrary to a previous report (3) no evidence is seen for sulfur having been formed in Fig. 3A.

Cell discharge products.—Figure 4 shows thermal analysis of mixtures of Li with discharge products taken from an Li-SO₂ cell. This cell contained the "reserve" electrolyte (SO₂-AN-LiAsF₆) and was discharged at a constant current density of 2-3 mA · cm⁻² to a 0.2V cutoff voltage. A grayish-colored spongy product was scraped off the Li anode surface, mixed with Li, and analyzed as in Fig. 4A to a 400°C cutoff. In this range the trace is thermally featureless except for the 180°C endotherm for melting of Li. The discharged cathode was washed with pure acetonitrile to remove SO₂ and salt, dried by evacuation, and then a fragment of it was mixed with Li and thermally analyzed to give Fig. 4B. The sharp exotherm at 251°C appears to be due to the reaction of Li with decomposi-

tion products of Li₂S₂O₄. DSC curves of discharged cathodes in the absence of Li (not shown) reveal a minor exotherm due to decomposition of Li₂S₂O₄ with initiation temperatures from approximately 185° to 230°C. A small exotherm is also visible in Fig. 4B. The exotherm is minor because of the very small

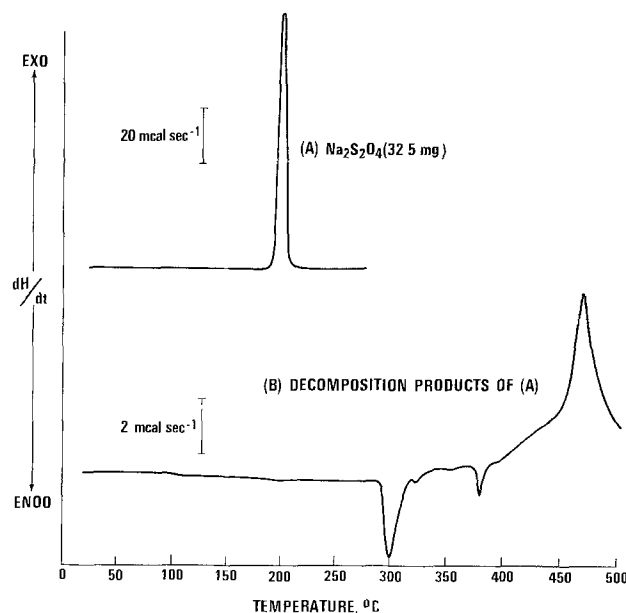


Fig. 3. Thermal decomposition of sodium dithionite

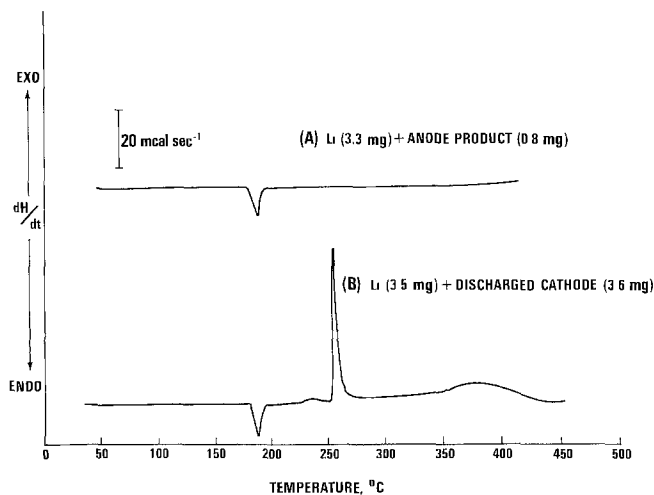


Fig. 4. Lithium reactivity with discharge products of Li-AN-SO₂-LiAsF₆ cell.

quantity of Li₂S₂O₄ (0.2-0.3 mg) imbedded in the (3.0-4.0 mg) of current collector. The variation in the initiation temperature is a function of the heterogeneous distribution of Li₂S₂O₄ in the carbon-Teflon collector. It is reasonable to speculate that under certain abusive conditions of battery discharge, Li₂S₂O₄ may undergo decomposition similar to the Na₂S₂O₄, thereby generating large temperature increases. The low broad exotherm at about 350°C is associated with the reaction between Li and Teflon binder from the cathode structure. This reaction was characterized thermally both previously (2) and in the present work.

Lithium-acetonitrile reaction.—Lithium and acetonitrile (AN) are unstable at ambient temperatures; a reaction starts slowly then accelerates and generates large amounts of heat. It is generally agreed that the heat and flammable gas generated in this reaction are a possible source of the explosions which have marred the generally good safety record of the Li-SO₂ battery. A typical DSC curve shown in Fig. 5A reveals a characteristic broad exotherm starting at about 40°C. Reaction rate is affected by purity both of Li and AN. Addition of 0.2% w/w of water to the AN greatly suppresses the exothermicity of the reaction (Fig. 5B). A similar suppression of Li-AN exothermicity is seen when the AN is saturated with LiBr (Fig. 5C). Lithium bromide additions were found to consistently mimic the effect of added water, whether or not excess solid LiBr was present. We presume this is indeed due to the presence of moisture in the very deliquescent LiBr. Even in a 0.2% relative humidity Dry Room, LiBr picks up water quite rapidly. DSC analysis of an (Li + LiBr) mixture gives an exotherm at 140°C despite starting with a vacuum-dried sample and working in a Dry Room (1, 3). This is apparently due to an Li-H₂O reaction. If an easily dried salt like LiAsF₆ is substituted for LiBr (Fig. 5D), the low temperature, Li-AN exotherm is again evident. The high temperature exotherm at the melting point of Li appears to involve the LiAsF₆, but is also in agreement with the previously recorded DSC curve (1) for Li plus the tetrasolvated salt, Li(AN)₄AsF₆ (11).

The effect of SO₂ concentration on the thermal behavior of the Li-AN system was studied in the presence of both the "active" (LiBr) and "reserve" (LiAsF₆) salts. Table II makes evident that the initiation temperature of the Li-AN reaction generally rises with increasing SO₂ concentrations. In the absence of SO₂ there is a slow, low temperature reaction as illustrated in Fig. 5A. At a level of 0.1M SO₂ (simulating that present in a discharged, SO₂-depleted Li-SO₂ cell) initiation temperature increases substantially. However, the delayed reaction is both more rapid and more exothermic (Fig. 6A, D, and E). At the 1.7M SO₂ level

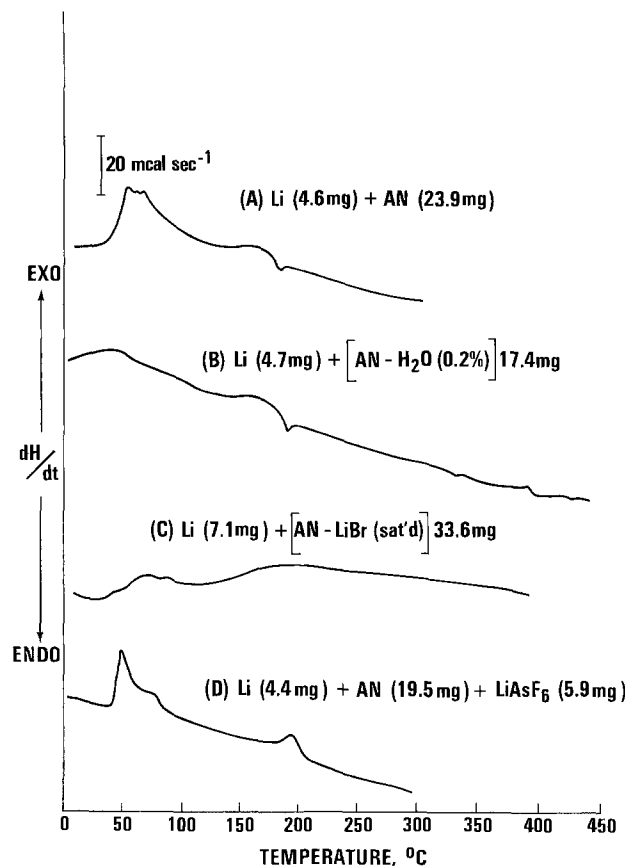


Fig. 5. Li-acetonitrile reactivity in absence of SO₂

(not illustrated) two exotherms were present corresponding to the Li-AN reaction and to one occurring at or near the melting point of Li. Finally, at concentrations of SO₂ found in the actual battery (about 14M), exothermic behavior occurs at higher temperatures (Fig. 6B and C). The heat liberated in the Li-AN reaction is similar to that noted in the absence of SO₂ and the dual peak behavior observed in 1.7M SO₂ is much less evident at these high SO₂ concentrations.

The quenching effect of water evident in Fig. 5 is no longer apparent in Fig. 6 when SO₂ is now present. Figure 6, curves D and E show big, sharp exotherms despite the addition of water. Perhaps the hydrolysis reaction between H₂O and SO₂ removes water from the system rendering it unable to quench the Li-AN reaction. The high temperature exotherm in Fig. 6D appears to result from the Li-LiAsF₆ reaction. This exotherm is regularly seen in the presence of LiAsF₆, but not in its absence (Fig. 6A).

Addition of propylene carbonate to a mixture of Li with the "active" battery electrolyte [AN-SO₂ (14M), LiBr] revealed that the Li-AN reaction is effectively quenched up to the vicinity of the melting point of Li (Table I, reaction 40).

Methyl isocyanate.—Rapid discharge caused by internal shorting has been reported to lead to the formation of methyl isocyanate (CH₃NCO) in the electrolyte

Table II. Effect of SO₂ concentration on initiation temperature for the Li-acetonitrile exotherm

| SO ₂ concentration (moles/liter) | Initiation temperature (°C) | | |
|---|-----------------------------|------|--------------------|
| | No salt | LiBr | LiAsF ₆ |
| 0 | 40 | 35 | 50 |
| 0.1 | 142 | 86 | 115 |
| ~1.7 | 122 | 122 | 142 |
| ~14* | — | 156 | 180 |

* Battery electrolyte.

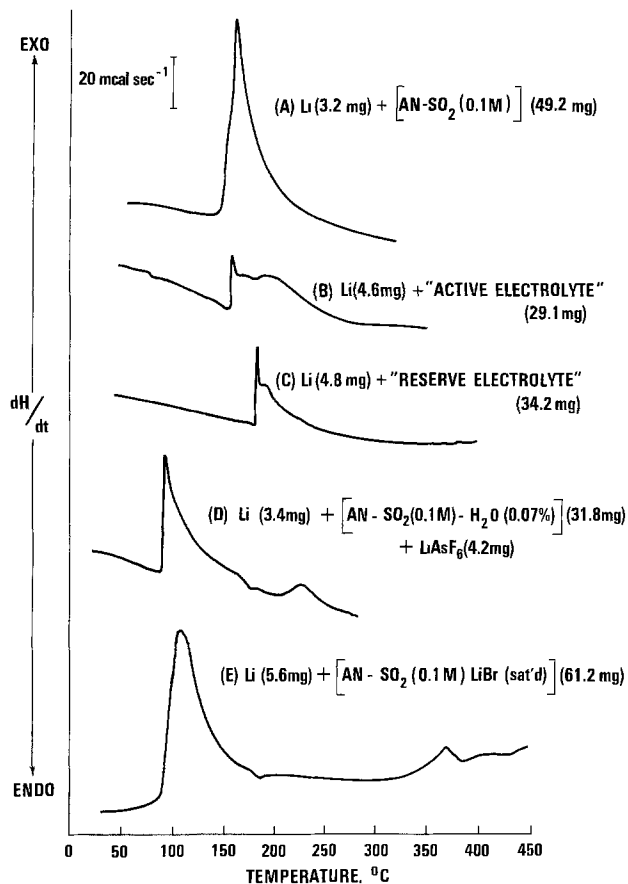


Fig. 6. Li-acetonitrile reactivity in presence of SO_2

of Li- SO_2 cells (12). The DSC curve for the reaction of Li with CH_3NCO is presented in Fig. 7. The reaction is slower than some of the explosive reactions reported here and elsewhere in this system (2). However it begins at 152° (below the melting point of Li) and generates substantial amounts of heat.

Thionyl Chloride System

Table III summarizes the data. The only previous thermal analysis work in this system is that of Dey *et al.* (5). Their work was limited to relatively low temperatures by the use of sealed glass ampuls as sample cups. In Li-containing mixtures, runs were usually terminated at little over 200°C by destructive reaction of molten Li with the glass container. Mixtures containing SOCl_2 developed high pressures which burst the cup at temperatures from 76° to 270°C . Cups used in

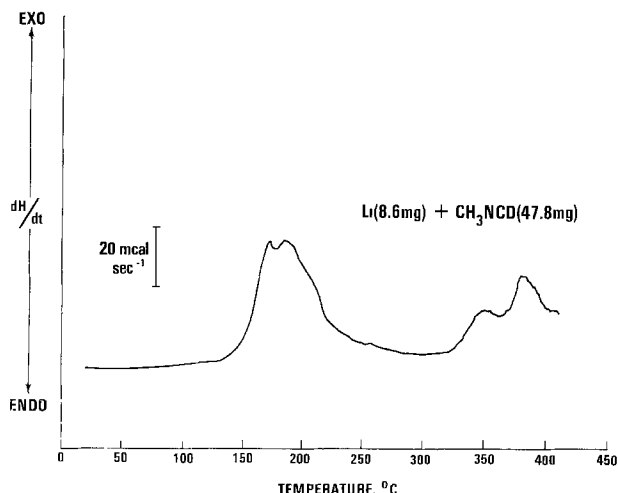


Fig. 7. Reactivity of lithium with methyl isocyanate

the present work were normally hermetic up to at least 500°C .

Initial components.—Figure 8E shows that the active materials of the Li- SOCl_2 battery display no reactivity together up to 335°C cutoff at which the DSC temperature scan was automatically terminated. The chloroaluminate by itself melts at about 143°C (Fig. 8A) in agreement with the literature. Mixed with Li in Fig. 8B, the salt rapidly and exothermically reacts near its melting point. Thionyl chloride alone (Fig. 8C) began breaking up (into $\text{SO}_2 + \text{S}_2\text{Cl}_2 + \text{Cl}_2$) at about 212°C , but the thermal effects are small. In Fig. 8D we see essentially the same thing with Li unreactive up to at least 345°C . Finally Fig. 8E brings together conductive salt and both active materials. This combination suppresses both the Li- LiAlCl_4 reaction of Fig. 8B and the SOCl_2 decomposition evident in Fig. 8C and D. Thus, the initially present components of an undischarged battery seem quite unreactive over a wide temperature range even after the lithium has melted.

Possible discharge products.—Under this heading we include products of the direct electrode reactions and also secondary products resulting from further reaction (e.g. direct product S further reacts giving secondary product Li_2S).

Sulfur.—Figure 9 shows DSC curves for combinations containing elemental sulfur. In combination with Li (Fig. 9A) the usual violent reaction at sulfur's melting point was observed. This Li-S reaction is noticeably absent from Fig. 9B where no exotherm appears at all until 400°C . In Fig. 9B's mixture, if all the S dissolved in the electrolyte, its concentration would be about 9M. The solubility of S in the electrolyte rises with temperature and is about 1.5M at 50°C (16). So in this run, above the melting point of S, both molten S and high concentrations of dissolved S should be present. Presumably the SOCl_2 protects Li from reacting with both molten and dissolved S by virtue of a passivating film of LiCl as in the battery. The 400°C exotherm may be a belated Li-S reaction occurring 300°C higher than usual. Thus we have confirmed a previous find of the beneficial effect of SOCl_2 (5) and extended it to 400°C . Figure 9C shows the in-

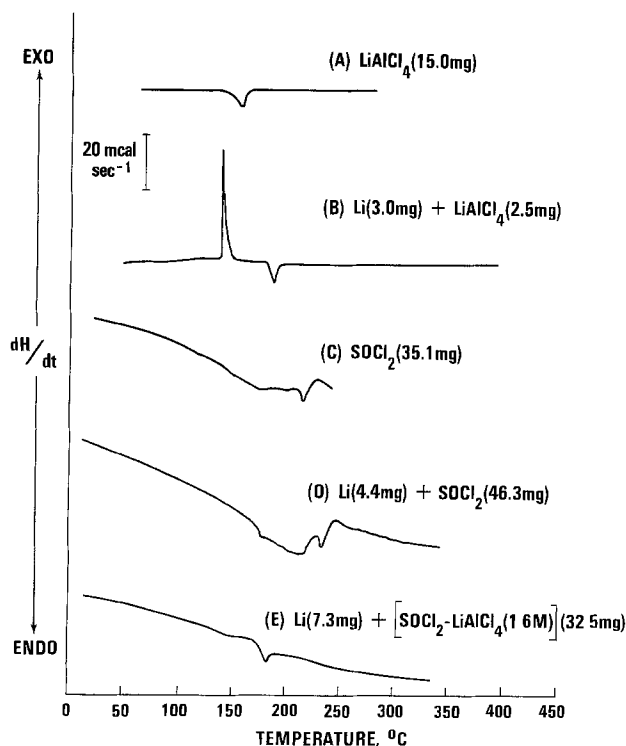


Fig. 8. Reactivity of the major initial components of the Li- SOCl_2 battery.

Table III. Summary of DSC results for Li/SOCl₂ system

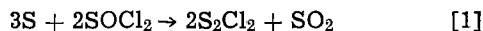
| Reaction | Reactants | Cutoff temperature (°C)† | Transition temperature (°C)‡ | |
|----------|--|--------------------------|------------------------------|-----------------|
| | | | Endothermic | Exothermic |
| 1 | SOCl ₂ | 241 | 212 | 214 |
| 2 | LiAlCl ₄ | 271 | 143 | — |
| 3 | Li + SOCl ₂ | 338 | 176 | 217, 231 |
| 4 | Li + LiAlCl ₄ | 410 | 181 | 137(5) |
| 5 | Li + Li ₂ SO ₄ | 400 | 181 | — |
| 6 | Li + S ₂ Cl ₂ | 343 | 172 | — |
| 7 | SOCl ₂ + Li ₃ N | 346 | — | 196(70) |
| 8 | SOCl ₂ + Li ₂ S | 276 | — | — |
| 9 | SOCl ₂ + C | 241 | — | — |
| 10 | Li + [SOCl ₂ -LiAlCl ₄]* | 329 | 177 | — |
| 11 | [SOCl ₂ -LiAlCl ₄] + S | 391 | 236 | — |
| 12 | [SOCl ₂ -LiAlCl ₄] + Li ₂ N | 367 | — | 132(150) |
| 13 | [SOCl ₂ -LiAlCl ₄] + Li ₂ S | 367 | — | — |
| 14 | Li + SOCl ₂ + C | 343 | 169 | — |
| 15 | Li + LiAlCl ₄ + C | 362 | 179 | 137(5) |
| 16 | Li + [SOCl ₂ -LiAlCl ₄] + C | 350 | — | 54, 326(25) |
| 17 | Li + [SOCl ₂ -LiAlCl ₄] + C | 302 | 167 | 169, 204 |
| 18 | Li + [SOCl ₂ -LiAlCl ₄] + C | 362 | 181 | 85 |
| 19 | Li + [SOCl ₂ -LiAlCl ₄] + Cu | 408 | 186 | — |
| 20 | Li + [SOCl ₂ -LiAlCl ₄] + S | 414 | 184 | 395(15) |
| 21 | [SOCl ₂ -LiAlCl ₄] + C + S | 384 | — | — |
| 22 | [SOCl ₂ -LiAlCl ₄] + C + Cu | 408 | — | — |
| 23 | Li + SOCl ₂ + LiCl + C | 362 | 187 | — |
| 24 | Li + SOCl ₂ + Li ₂ SO ₄ + C | 362 | 181 | — |
| 25 | Li + [SOCl ₂ -LiAlCl ₄ -1% H ₂ O + Cl] | 455 | 180 | 378 |
| 26 | Li + [SOCl ₂ -LiAlCl ₄ -SO ₂] (satd.) + S | 414 | 189 | — |
| 27 | Li + [SOCl ₂ -LiAlCl ₄] + C + Cu | 417 | 177 | 83(30), 348(25) |
| 28 | Li + [SOCl ₂ -LiAlCl ₄ -SO ₂ (satd.)] + C + S | 408 | 181 | 88, 181(75) |
| 29 | Li-B alloy + LiAlCl ₄ | 369 | 181 | 137 |
| 30 | Li-B alloy + SOCl ₂ | 343 | 192 | 231, 249 |
| 31 | Li-B alloy + [SOCl ₂ -LiAlCl ₄] | 343 | 172 | — |
| 32 | B + [SOCl ₂ -LiAlCl ₄] | 395 | — | — |
| 33 | Li-B alloy + [SOCl ₂ -LiAlCl ₄] + C | 391 | 172 | 59(20), 322(75) |

* Ingredients within the square brackets are a homogeneous solution.

† Temperature at which the DSC linearly programmed temperature scan was terminated.

‡ Figures in parenthesis are the increase in the sample temperature above the linearly programmed temperature.

ertness of S with the electrolyte. The addition of carbon black to the ingredients of Fig. 9C also gave an inert mixture (reaction 21, Table III). The DSC trace is not illustrated; it was thermally featureless in the range studied (up to 384°C). We have found carbon to catalyze the reaction of SOCl₂ with Li (see below) but evidently it has no effect on the (S + SOCl₂) reaction. The small endotherms in Fig. 9B and C at about 250°C may be associated with the reaction



Calculation indicates this to be an endothermic reaction (14). Furthermore we always observed a clear,

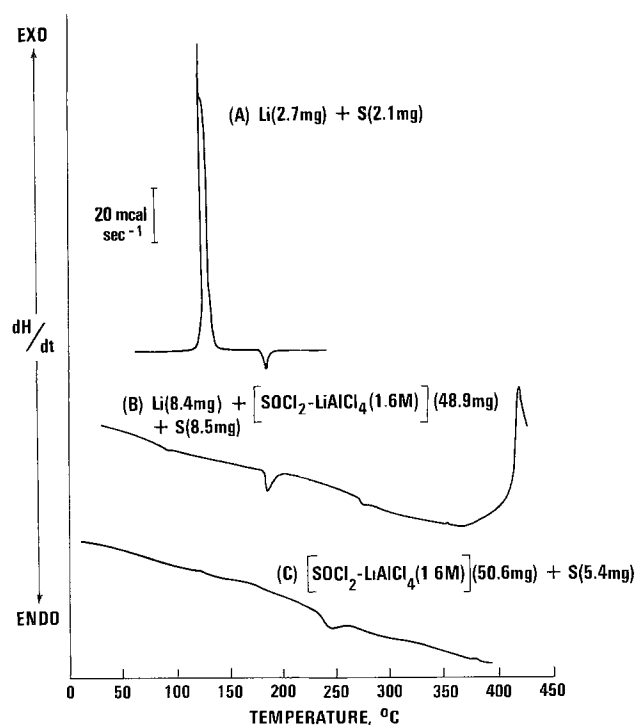


Fig. 9. Reactivity of mixtures containing elemental sulfur

boiling liquid (presumably SO₂ solution) when cups initially containing (S + SOCl₂) were unsealed at room temperature at the end of the run.

Lithium sulfide.—Some workers have reported (5, 13) that anhydrous Li₂S reacts violently with SOCl₂ generating considerable heat and gas while others (14) found this combination to be inert. The present work has shown that Li₂S is essentially unreactive with SOCl₂ up to a 276°C cutoff and with SOCl₂-1.6M LiAlCl₄ up to a 367°C cutoff. The DSC curves were basically featureless and they are not illustrated. (See Table III, reactions 8 and 13.)

Sulfur dioxide.—This is generally accepted as one of the main products of the battery discharge reaction. We showed above that SO₂ retards the Li-AN reaction. We now wished to determine if SO₂ could deactivate the most reactive mixtures in the SOCl₂ system. Accordingly, we saturated a portion of the 1.6M LiAlCl₄-SOCl₂ electrolyte with SO₂ at 1 atm and room temperature. The SO₂ concentration was 3-4M (16). A DSC curve recorded to 414°C for this solution with added Li and S (reaction 26, Table III) showed no significant change in reactivity *vs.* the SO₂-free solution illustrated in Fig. 9B. Furthermore, Fig. 10D shows that the catalytic effect of carbon on the Li-SOCl₂-LiAlCl₄ mixture (discussed below) proceeded unimpeded, by the presence of SO₂. Thus for these combinations, at least, SO₂ has no passivating effect in the SOCl₂ system.

Lithium sulfate, lithium chloride, sulfur monochloride.—Both sulfate and sulfite have been reported as low temperature discharge products of the thionyl chloride battery (14). Lithium sulfite has been previously studied (2, 5) with conflicting results, though the preponderance of evidence favors its nonreactivity. The present work has found lithium sulfate to be quite unreactive to Li up to a 400°C cutoff (reaction 5, Table III). It was also inert in combination with Li, C, and SOCl₂-LiAlCl₄. Sulfur monochloride, S₂Cl₂, is known to result from the thermal decomposition of SOCl₂ especially in the presence of trace catalysts like FeCl₃ (14) as described above. Thus we tested its reactivity with Li (reaction 6, Table III). It was quite inert over

the range studied, up to 346°C. Dey (5) had reported a strong exotherm at 302°C for $(\text{Li} + \text{S} + \text{SOCl}_2)$. Lithium chloride, one of the main discharge products formed in the cathode appears quite inert (to a 362°C cutoff) in combination with Li, C, and SOCl_2 (reaction 23, Table III). If LiAlCl_4 is substituted for LiCl, the mixture becomes extremely and consistently reactive; see discussion below of the effect of carbon in catalyzing reactions in this system (Fig. 10).

Catalysis of reactions by carbon black.—We invariably found that whenever an Li/C mixture was contacted with the 1.6M LiAlCl_4 - SOCl_2 electrolyte, a reactive mixture was produced. In these experiments the Shawinigan carbon black was pressed into both sides of a piece of flattened Li and the electrolyte dripped onto this sandwich. The mixture always warmed up the Nimonic cups to about 40°–50°C. Occasionally the reaction was so vigorous that the SOCl_2 boiled dry and more was added before the cup was sealed. Accordingly we began precooling cups in Dry Ice (–80°C) before adding electrolyte so as to postpone reaction and record it on the DSC trace. Figure 10 shows four DSC curves of mixtures involving Li-C- SOCl_2 - LiAlCl_4 . The addition of carbon black transformed the inert Li- SOCl_2 - LiAlCl_4 mixture into a consistently reactive one. However the data were unpredictable both as to peak height and even peak position. We include Fig. 10C, which actually contained Li-B alloy rather than Li, as the present work has shown the alloy behaves essentially the same as Li. The mixture of Fig. 10D contained S and SO_2 in addition to Li, C, SOCl_2 , and LiAlCl_4 . However, we believe that the reactivity of this mixture is due to the presence of carbon rather than to that of S and/or SO_2 . This is supported by the fact that the mixture $(\text{Li} + \text{SOCl}_2 + \text{LiAlCl}_4 + \text{S} + \text{SO}_2)$ was quite inert up to its 414°C cutoff (reaction 26, Table III). We should point out that the mixture referred to in Fig. 10D contains virtually all of the most reactive ingredients thought to be present in a partly-discharged thionyl chloride battery.

Of the four possible mixtures employing ternary combinations of the ingredients Li, C, SOCl_2 , and

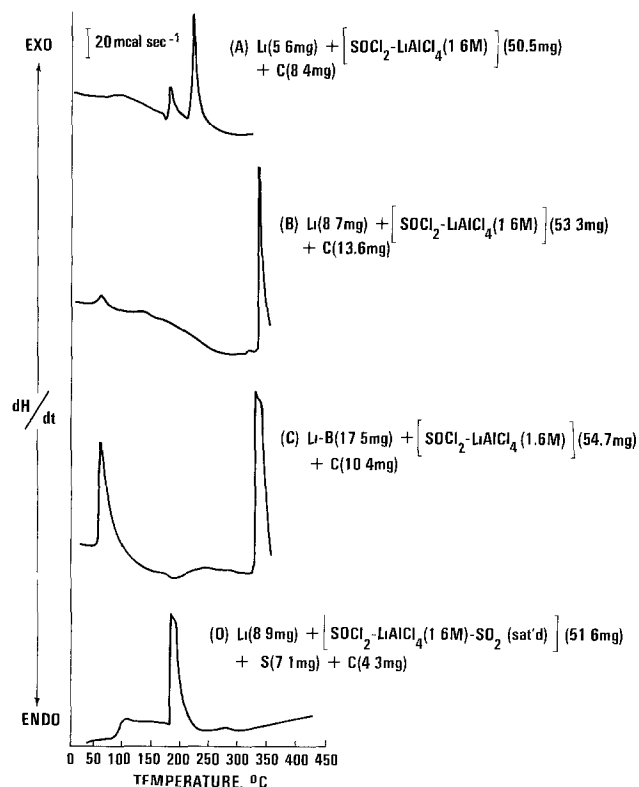


Fig. 10. Catalysis by carbon black of Li- SOCl_2 - LiAlCl_4 reactivity

LiAlCl_4 , none approached the reactivity of the quaternary mixture $(\text{Li} + \text{SOCl}_2 + \text{LiAlCl}_4)$ was inert, see Fig. 8E; $\text{Li} + \text{C} + \text{SOCl}_2$ was inert to a 343°C cutoff, see reaction 14; $\text{Li} + \text{C} + \text{LiAlCl}_4$ was no more reactive than $\text{Li} + \text{LiAlCl}_4$, see reaction 15; $\text{C} + \text{SOCl}_2 + \text{LiAlCl}_4$ was inert, even with added S to a 384°C cutoff, see reaction 21). Consistent strong reactivity was observed only when all four ingredients were together. This is understandable if we assume that a local cell is formed which activates the Li- SOCl_2 reaction. Carbon's function is to provide a catalytically active surface at which SOCl_2 can be cathodically reduced at high rates by electrons emanating from anodically dissolving lithium. Essentially we regard each carbon particle stuck in the Li surface as forming a tiny, short-circuited Li- SOCl_2 battery.

This is supported by the fact that the corrosion of a variety of metals in the LiAlCl_4 - SOCl_2 electrolyte is greatly accelerated if they are electrically contacted with carbon, probably due to the local cell effect (4). So the only function of LiAlCl_4 is to render the SOCl_2 highly conductive so as to complete the ionic part of the local cell circuit. Accordingly we tried to replace it with other conductive, nonreactive Li salts. We tried Li_2SO_4 and LiCl separately in mixtures with $(\text{Li} + \text{C} + \text{SOCl}_2)$. However DSC curves of these two mixtures showed them to be inert up to their 362°C cutoff (Table III, reactions 23 and 24). Apparently these salts did not impart the necessary ionic conductivity, probably due to a limited solubility in SOCl_2 .

The local cell idea is of course not new; it is very old and by now obvious to skilled electrochemists. However it is useful to point out the obvious if its important implications for battery safety have been previously overlooked. The above experiments are very suggestive in this connection. Cathode failure in one out of a chain of cells will cause Li to be plated out onto the carbon of the failed cathode. Indeed, complete reversal of cell voltage is not needed. Whenever cathode voltage falls below about 1V vs. Li, this potentially dangerous mixture may form by undervoltage deposition of Li into carbon (20). Recent work in our laboratories has shown that the situation may involve more than a simple Li-C mixture. ESCA (XPS) studies indicate that compound formation occurs in intimate mixtures of elemental Li and C.

Effect of copper.—In view of the use of powdered copper metal in the cathodes of some Li- SOCl_2 batteries (17) we studied the effect of added Cu on reactivity in this system. Figure 11 shows the effect of adding 99.9% pure Cu powder to the $(\text{Li} + \text{C} + \text{SOCl}_2$ - $\text{LiAlCl}_4)$ mixture. Reactivity seems to be enhanced vs. Fig. 10, not so much in terms of a more rapid reaction with high peak temperatures, but rather in terms of a larger total amount of heat liberated. The low temperature exotherm starting at about 80°C is much

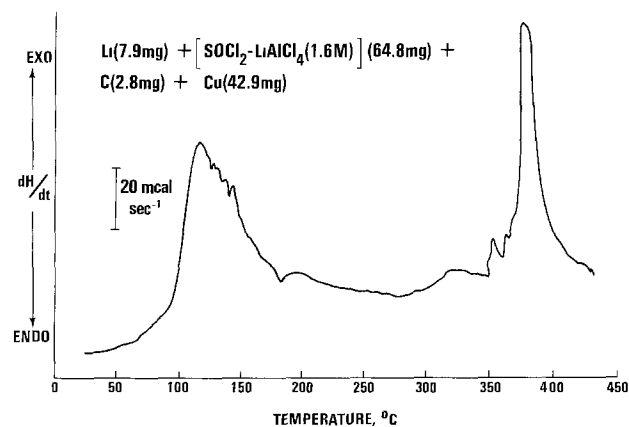


Fig. 11. Enhancement by copper of the carbon-catalysis of Li- SOCl_2 - LiAlCl_4 reactivity.

more pronounced than in the absence of Cu. Reactions 19 and 22 where first C then Li was omitted from the ingredients of Fig. 11 were quite inert up to 410°C. Thus both Li and C are necessary for reactivity. It appears that the basic reactivity of the system is accelerated by the highly conductive Cu.

Carbon catalysis in the SO₂-acetonitrile-electrolyte?—Preliminary work has produced evidence that carbon black is catalytically active also in this electrolyte. In an acetonitrile solution which was saturated with LiBr and 1.7M in SO₂, the Li-AN reaction initiation temperature was 122°C. However in the presence of carbon the reaction began at about 35°C (see reactions 34 and 38, Table I). On the other hand, in a solution that was identical except that it contained no SO₂, added carbon had no clear effect on the reactivity (reactions 24 and 32, Table I). More work is needed to better characterize carbon's effect in the SO₂ battery electrolyte.

Impurities.—Lithium nitride.—Li₃N is a very reactive material. When mixed with water it catches fire and burns violently with great heat. It was recently reported (14) to react violently with SOCl₂, but only if it was finely divided and if mixing were done in a normally humid atmosphere. In an argon atmosphere containing 1 ppm water, no reaction occurred. This applied both to the commercially obtained powder and to nodules of reaction product removed from air-reacted Li foil. The reaction with SOCl₂ could be hazardous if Li₃N forms on the Li anode during cell assembly or during the disassembly of discharged cells. In the present work no reaction was noted on mixing Li₃N with SOCl₂ in our Dry Room at 0.25% R.H. (81 ppm water). Figure 12A shows that Li and Li₃N commercial powder are quite inert together up to the 390°C cut-off, whereas 12B and 12C show that Li₃N undergoes violent exotherms with SOCl₂ and with SOCl₂-LiAlCl₄. At about 130°C, the exotherm shown in Fig. 12C was associated with the biggest temperature excursion

(150°C) observed in the present work (see reaction 12, Table III).

Water.—It is of interest to study the effect of added water on reactivities since this material is a ubiquitous contaminant which is very strongly absorbed by most battery active-materials. We added water only to the most consistently reactive combination, namely (Li + C + SOCl₂ + LiAlCl₄). Water added to the electrolyte to the extent of 1% by weight gave an immediate white precipitate. We homogenized the electrolyte before adding it to the Li/C sandwich so as to include some of this precipitate in the reaction mixture. This work is presently at an early stage, but it appears that this trace amount of water does exert some quenching effect on exothermicity in this system, at least in the lower half of the temperature range of Fig. 10. This contrasts with Dey's finding (5) that moisture enhances the reactivity of SOCl₂ with Li₂S, with Li₂O and with LiOH.

Relative Reactivities of Pure Lithium vs. Lithium-Boron Alloy

The Li-B alloy is a refractory Li-B solid compound permeated with fine pores filled with elemental Li. Because of its high temperature rigidity and the presence of the relatively inert boron, the alloy was considered as potentially safer than pure Li as a battery anode. In preparing reaction mixtures for DSC runs we used twice the mass of Li-B vs. that of pure Li. Since elemental Li forms 51% w/w of our alloy composition this provides for a just comparison of exothermicity. The results showed with two exceptions, no significant difference in reactivity between the alloy and pure lithium. Reaction initiation temperatures and temperature excursions shown in Tables I and III are quite similar for the two materials.

In only one case was Li-B clearly less reactive than Li. This occurred with Li₂S₂O₈, where temperature excursions for the major (~230°C) of the two exotherms were fifteen times greater for pure Li (150° vs. 10°, see reactions 13 and 43, Table I). The second difference with pure Li was in the C-SOCl₂-LiAlCl₄ system. Here the catalytic effect of carbon on this system's reactivity was somewhat greater with the alloy. This is illustrated in Fig. 10C.

Conclusions

1. For Li-SO₂-LiAsF₆ cell discharge products, the discharged cathode gave a significant exotherm with Li while films formed on the anode were inert to Li.
2. Trace additions of water greatly lower the exothermicity of the Li-acetonitrile (AN) reaction. Water entering the electrolyte via the extremely hygroscopic LiBr electrolyte-salt had the same effect.
3. The addition of SO₂ delays initiation of the Li-AN reaction to higher temperatures. An SO₂ concentration of 0.1M is sufficient to realize most of the rise in initiation temperature. The delayed, higher temperature reaction occurs more rapidly. The quenching effect of water on Li-AN reaction is no longer observed when SO₂ is present.
4. Addition of propylene carbonate to Li-AN-SO₂-LiBr delays the Li-AN reaction to the vicinity of the melting point of Li.
5. The Li-SOCl₂-LiAlCl₄ mixture is quite unreactive over a wide range of temperature, well above the melting point of Li.
6. The presence of carbon black converts the inert, Li-SOCl₂-LiAlCl₄ mixture into one which is highly and consistently reactive. This may affect battery safety because cathode failure in one out of a chain of cells will cause Li to be plated out onto the carbon of the failed cathode. Indeed complete reversal of cell voltage is not needed. Whenever the cathode voltage falls below about one volt vs. Li, this potentially dangerous mixture may form by undervoltage deposition of Li into carbon (20).

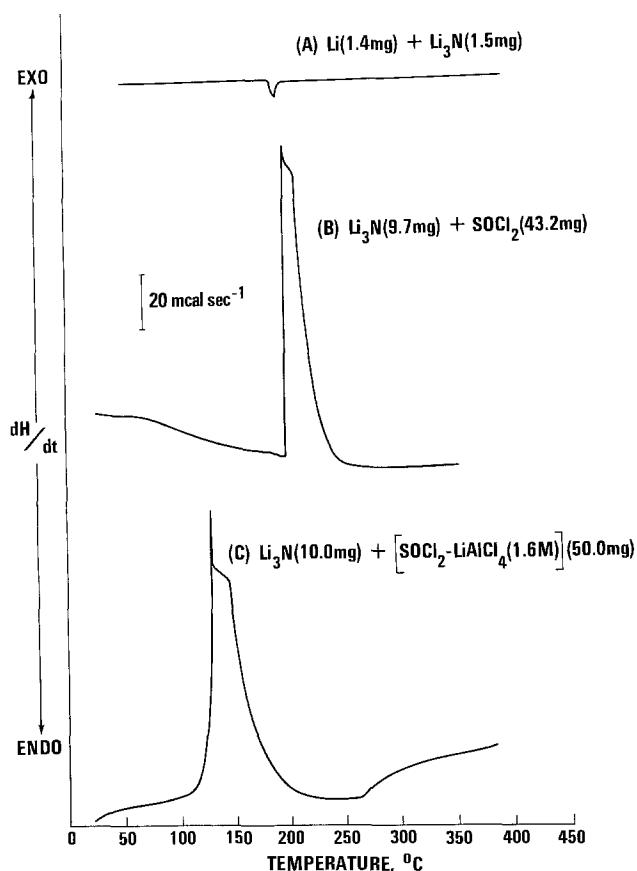


Fig. 12. Reactivity of lithium nitride

7. Some evidence was obtained for carbon catalysis also in the Li-SO₂ system.

8. The addition of copper powder enhanced carbon's catalytic effect on the reactivity of Li-SOCl₂-LiAlCl₄. Trace additions of water, on the other hand, had a counteracting effect on the carbon-catalyzed reactivity.

9. The presence of SOCl₂ delays the very exothermic Li-S reaction by at least 300°C.

10. We confirmed the nonreactivity of SOCl₂ with Li₂S.

11. Sulfur dioxide seems to have no retarding effect on reactions in the SOCl₂ system (in contrast to its suppression of the Li-AN reaction).

12. We confirmed the violent reactivity of Li₃N with SOCl₂.

13. We found no significant difference in chemical reactivity between lithium-boron alloy and pure lithium.

Acknowledgments

The authors thank the Independent Research Program of the Naval Surface Weapons Center and the Naval Sea Systems Command (PMS407) for financial support of this work.

Manuscript submitted June 3, 1980; revised manuscript received Oct. 20, 1980.

Any discussion of this paper will appear in a Discussion Section to be published in the December 1981 JOURNAL. All discussions for the December 1981 Discussion Section should be submitted by Aug. 1, 1981.

Publication costs of this article were assisted by the Naval Surface Weapons Center.

REFERENCES

1. W. P. Kilroy and S. Dallek, NSWC/WOL TR 78-156 (Nov. 13, 1978).

2. W. P. Kilroy and S. Dallek, *J. Power Sources*, **3**, 291 (1978).
3. A. N. Dey and R. W. Holmes, *This Journal*, **126**, 1637 (1979).
4. A. N. Dey, Final Report ERADCOM, DELET-TR-74-0109-F, P. R. Mallory and Co. Inc. (July 1978).
5. A. N. Dey, in Proceedings of the 28th Power Sources Symposium, Atlantic City, N.J., June 1978.
6. S. D. James and L. E. DeVries, *This Journal*, **123**, 321 (1976); **126**, 993 (1979).
7. B. F. Larrick, S. D. James, and R. Szwarc, in Proceedings of the 28th Power Sources Symposium, Atlantic City, N.J., June 1978.
8. S. Dallek, D. W. Ernst, and B. F. Larrick, *This Journal*, **126**, 866 (1979).
9. D. Lyons and G. Nickless, in "Inorganic Sulfur Chemistry," G. Nickless, Editor, p. 521, Elsevier Publishing Co., Netherlands (1968).
10. O. Dienes and G. Elstner, *Z. Anorg. Allg. Chem.*, **191**, 340 (1930).
11. W. P. Kilroy, *J. Solution Chem.*, **6**, 487 (1977).
12. G. Reinhard and A. R. Jones, Eastern Airlines Engineering Labs (MIAEL) Report, April 8, 1975, to Chromalloy Corp., Hollywood, Florida.
13. G. L. Holleck, M. J. Turchan, and D. R. Cogley, ECOM-74-0030-7 (January 1975).
14. C. R. Schlaikjer, F. Goebel, R. Staniewicz, and K. Kiinedinst, Final Report on Contract No. N00014-76-C-0524 (1-76 to 10-78) (January 1979).
15. C. R. Schlaikjer, F. Goebel, and N. Marincic, *This Journal*, **126**, 513 (1979).
16. K. A. Klinedinst and M. L. McLaughlin, *J. Chem. Eng. Data*, **24**, 203 (1979).
17. L. R. Giattino, U.S. Pat. 4,167,608 (1979).
18. W. P. Kilroy, Unpublished data.
19. P. M. Shah and W. J. Eppley, in Proceedings of the 28th Power Sources Symposium, Atlantic City, N.J., June 1978.
20. J. O. Besenhard and H. P. Fritz, *J. Electroanal. Chem. Interfacial Electrochem.*, **53**, 329 (1974).

Dynamic Microcalorimetry: Thermal Effects of Miniature Alkaline Cells under Load

Frank B. Tudron*

Union Carbide Corporation, Battery Products Division, Parma, Ohio 44130

ABSTRACT

A nonrigorous thermodynamic calculation is performed yielding an expression which relates the rate of heat evolution by a miniature battery under load to the current flowing through the cell. At small values of I , the expression predicts a linear plot of $-dQ/dt$ vs. I . To demonstrate this behavior, thermal effects of an Ag₂O-Zn cell are measured under various conditions of constant load. The heat evolution data vary linearly with I over the range 0.300 μ A, with a slope of 74.3 mV and an intercept of 2.1 μ W. The slope gives a value of -0.175 mV/K for $(\partial E/\partial T)_p$, corresponding to the formation of inactive ZnO as a discharge product at the anode. Additional data obtained for HgO-Zn and MnO₂-Zn cells with alkaline electrolytes are present. The heat release data do not vary linearly with current. Analysis of the discharge mechanism for the HgO system is possible. The discharge mechanism for the HgO cathode can be represented by a simple reduction to elemental mercury with formation of inactive ZnO as the discharge product at the anode.

Recently, the area of battery thermodynamics has shown significant activity (1-4). This activity is in part explained by the commercial availability of very sensitive differential calorimeters designed to accept miniature sized batteries. The utility of these so-called microcalorimeters has been demonstrated in a number of applications. One application is the evaluation of self-discharge processes in small batteries (1, 9). These

processes will, of course, determine the shelf-life of the cell and will also be important in determining the cell's operating life. Other processes, however, also contribute to the observed thermal effects. As they may not be related to capacity loss, a straightforward calculation of shelf-life from raw microcalorimeter data is often quite misleading. A second application is in the area of cell discharge mechanisms. Since the thermal effects measured are sensitive to the reaction path, mechanistic information can be obtained by comparing the results of the microcalorimeter experiment

* Electrochemical Society Active Member.

Key words: battery thermodynamics, silver oxide-zinc cells, mercuric oxide-zinc cells.

to predictions based on various models of the cell discharge (3, 4).

The purpose of the paper is twofold. The first goal is the derivation of an equation describing the dependence of the rate of heat release from a battery on the current flowing through the cell. The second goal is to present microcalorimeter data obtained for miniature alkaline cells of the types $\text{Ag}_2\text{O-Zn}$, HgO-Zn , and $\text{MnO}_2\text{-Zn}$ and to analyze these data by means of the equation presented, thereby relating the results to the discharge mechanism.

Theory

The dependence of the rate of heat release in a galvanic cell on current flowing in the cell has been previously derived in a rigorous fashion (5-8). This exercise will be performed here in a totally nonrigorous way merely to establish notation.

The first law of thermodynamics may be written $\Delta U = Q - W$, whereby the increase of the internal energy (ΔU) of the system (battery) is given by the heat flowing into the system less the work done by the system in the surroundings. What is measured by the microcalorimeter is the rate of heat flow out of the system (battery), i.e.

$$\frac{d}{dt}(-Q) = \frac{d}{dt}(-\Delta U - W)$$

Now $\Delta U = \Delta H - p\Delta V = \Delta H_f + \Delta H_{nf}$ where $p\Delta V$ term vanishes, the battery being a constant volume, sealed system.¹ Also, $\Delta H_f = \Delta G_f + T\Delta S_f$ and $\Delta H_{nf} = \sum_i \Delta H_{i\nu_i}$ where the sum is over all non-Faradaic processes. Thus

$$\begin{aligned} \frac{d}{dt}(-Q) &= \frac{d}{dt}[-\Delta G_f - T\Delta S_f - \sum_i \Delta H_{i\nu_i} - I^2 R t] \\ &= \frac{d}{dt} \left[nFE_o - TnF \left(\frac{\partial E}{\partial T} \right)_p - \sum_i \Delta H_{i\nu_i} - I^2 R_L t \right] \end{aligned}$$

where R_L is the load resistance. Faraday's law may be written $It = nF$. Consequently, for the Faradaic process $dn/dt = I/F$. For the non-Faradaic processes, $d\nu_i/dt = v_i$ where v_i is the rate of the i th process. The equation can now be written

$$\frac{d}{dt}(-Q) = IE_o - IT \left(\frac{\partial E}{\partial T} \right)_p - \sum_i \Delta H_{i\nu_i} - I^2 R$$

Now IR is the terminal potential and $E_o - IR$ is the polarization, η . Thus

$$\frac{d}{dt}(-Q) = \left[\eta - T \left(\frac{\partial E}{\partial T} \right)_p \right] I - \sum_i \Delta H_{i\nu_i} \quad [1]$$

which is the desired expression.

The shape of the curve obtained by plotting the calorimeter output vs. the current flowing through the battery will be determined by a number of factors. In the region of small polarization (i.e., for small I), the curve will be essentially linear. As the current increases, η becomes larger and a divergence from linearity is observed. This is magnified by the fact that the rates of certain parasitic processes, v_i , are dependent on the concentration of certain species in solution, and a current dependence arises due to the last term in the equation. What we have is a limiting expression: as I approaches zero, linear behavior is observed.

Experimental

The microcalorimeter used in the present study is the Tronac Model 351 RA battery calorimeter. This device has been described extensively in the literature (1). The batteries used in the study are "Eveready" miniature alkaline cells. Pertinent data concerning cell specifications are given in Table I.

¹The subscript "f" refers to Faradaic process, "nf" refers to non-Faradaic processes.

Table I. Specifications of batteries used in experiments

| Cell type | UCC designation | Diameter (in.) | Height (in.) | Rated capacity (mA-hr) | Voltage (V) |
|--------------------------|-----------------|----------------|--------------|------------------------|-------------|
| $\text{Ag}_2\text{O-Zn}$ | 386 | 0.455 | 0.165 | 120 | 1.60 |
| HgO-Zn | 354 | 0.455 | 0.165 | 150 | 1.35 |
| $\text{MnO}_2\text{-Zn}$ | 186 | 0.455 | 0.165 | 80 | 1.60* |
| HgO-Zn | E41 | 0.455 | 0.165 | 160 | 1.35 |

* Sloping discharge. Value reported is open-circuit voltage.

The value of the rate of heat release under open-circuit conditions was measured as follows. These cells were placed in an equilibration chamber immersed in the calorimeter water bath for 8-12 hr. The cells were then introduced into one of the microcalorimeter chambers designated as the sample chamber. The rate of heat release generally increased dramatically, but settled to a steady-state value within about 2 hr. This steady-state value minus the baseline value divided by the number of cells in the chamber is taken as the average rate of heat release.

Attempts to calculate shelf-life of a practical system from open-circuit microcalorimeter data are attended by many difficulties. As has been pointed out previously, many processes not associated with a decrease in capacity give rise to open-circuit heat production. As always, actual experimental determination of capacity following shelf storage is the most reliable indication of capacity maintenance.

To determine the rate of heat release under load, it was necessary to spot weld No. 25 AWG wires to both the cathode can and the anode cup of the cell. After equilibration, the cell was introduced into the sample chamber with the wires leading out to the surroundings. Here voltage measurements were obtained and resistors were attached. The wire was kept in good thermal contact with the aluminum calorimeter block to prevent spurious thermal effects.

To check the effectiveness of this technique, a 1 M Ω precision resistor was connected to two wires just as the cell was. Following equilibration, the resistor was placed in the sample chamber and the wires were connected to a Keithley Model 225 Current source. Figure 1 shows the result of successive applications of 1, 2, and 3 μA currents. The output power recorded agrees with that expected on the basis of heat dissipation due to $I^2 R$ loss. The wires exiting the chamber do not constitute a measurable heat leak.

All measurements were made at 25°C.

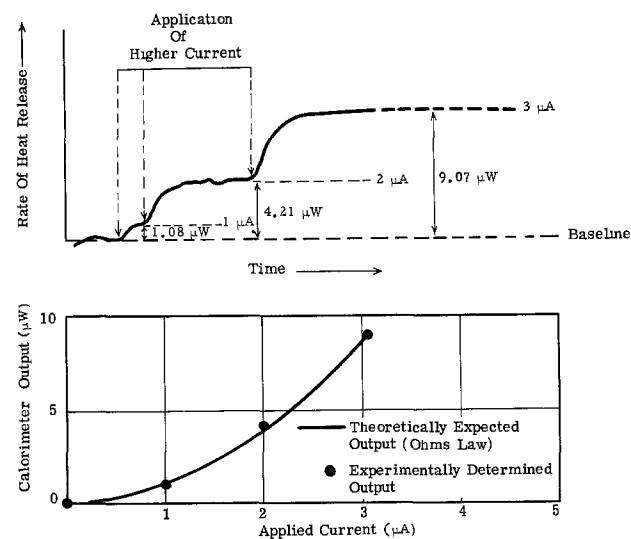
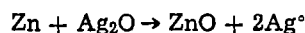


Fig. 1. Calibration of Tronac microcalorimeter by resistive technique.

Results and Discussion

The results of successive application of increasing loads to the cells, specified in Table I, are summarized along with polarization data and calculated values of current in Table II. The systems will be discussed individually.

Ag₂O-Zn.—Table II gives the values of the thermal effect along with the terminal voltage, load, polarization, and calculated current. As can be seen, the thermal output responds as would be expected: a smaller load results in a larger current and consequently, a larger thermal effect. The thermal effect is measured, as always, when the signal attains a steady-state value. Figure 2 is a plot of the rate of heat release (dQ/dt) vs. current (I). The discrete points are the experimental data. The data are linear over the region considered with intercept 2.1 μ W and slope 74.3 mV. The solid curves are calculated using Eq. [1] with values of $(\partial E/\partial T)_p$ corresponding to formation of the oxidized forms of Zn indicated. The lower curve, that corresponding to the reaction



fits the experimental values quite well. As is pointed out by Bode *et al.* (10), the thermal coefficient for the Ag₂O-Zn cell depends on the form in which the oxidized zinc deposits on the anode. Even if the electrolyte solution is not saturated with zincate, a thin film (oxide or hydroxide) is formed on the anode. It is this film that determines the anode thermodynamics, *i.e.*, the zinc electrode is an electrode of the second kind. If the film is inactive ZnO, the temperature coefficient for the cell is -0.177 mV/deg; if it is ϵ -Zn(OH)₂ the temperature coefficient is -0.337 mV/deg. Using Eq. [1] and the experimental slope (74.3 mV) yields an experimental value of $(\partial E/\partial T)_p$ of -0.175 mV/K. This analysis of the microcalorimeter data indicates that the discharge product is inactive ZnO.

HgO-Zn.—The No. 354 HgO-Zn cell attains steady-state values of heat release much as does the No. 386 Ag₂O-Zn. Table II summarizes the data. In an attempt to analyze the data using Eq. [1], the plots depicted in Fig. 3 were made. Two cell reactions were considered

Table II. Microcalorimetry data for miniature alkaline cells under load

| R_{Load} (k Ω) | V_{op} (V) | η (mV) | I (μ A) | $\frac{dQ}{dt}$ (μ W) |
|-----------------------------|-----------------|-------------|----------------|----------------------------|
| No. 386 Cell | | | | |
| 60 | 1.612 | 5 | 26.9 | 4.43 |
| 30 | 1.607 | 10 | 53.6 | 6.31 |
| 10 | 1.588 | 29 | 158.8 | 13.5 |
| 7 | 1.582 | 35 | 226.0 | 19.8 |
| 5 | 1.581 | 36 | 316.4 | 26.3 |
| O.C. | 1.617 | — | — | 2.03 |
| No. 354 Cell | | | | |
| 30 | 1.344 | 12 | 44.8 | 1.17 |
| 10 | 1.332 | 24 | 131.7 | 2.90 |
| 5 | 1.320 | 36 | 257.6 | 7.22 |
| 2 | 1.303 | 53 | 625.5 | 24.8 |
| O.C. | 1.356 | — | — | 0.93 |
| No. E41 Cell | | | | |
| 10 | 1.4655-1.4536 | 18.2-30.1 | 146-145 | 5.59-7.92 (2 hr) |
| 7 | 1.4417-1.4348 | 42.0-48.9 | 206-205 | 12.82-14.45 (1 hr) |
| 5 | 1.4215-1.4098 | 62.2-73.9 | 284-282 | Not measured |
| O.C. | 1.4837 | — | — | 3.26 |
| No. 186 Cell | | | | |
| 10 | 1.5685 | 6.9 | 156.9 | 6.06 |
| 7 | 1.5539 | 21.5 | 222.0 | 9.32 |
| 5 | 1.5423 | 33.1 | 308.5 | 13.51-14.91 (1 hr) |
| O.C. | 1.5754 | — | — | 2.33 |

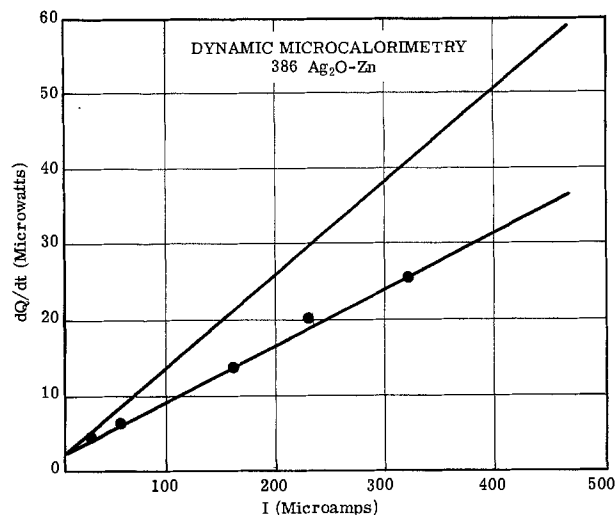


Fig. 2. Current dependence of the thermal effect for a No. 386 Ag₂O-Zn cell. The solid lines are calculated from theory based on Zn(OH)₂ (upper curve) and on ZnO (lower curve). The discrete points are experimental data.

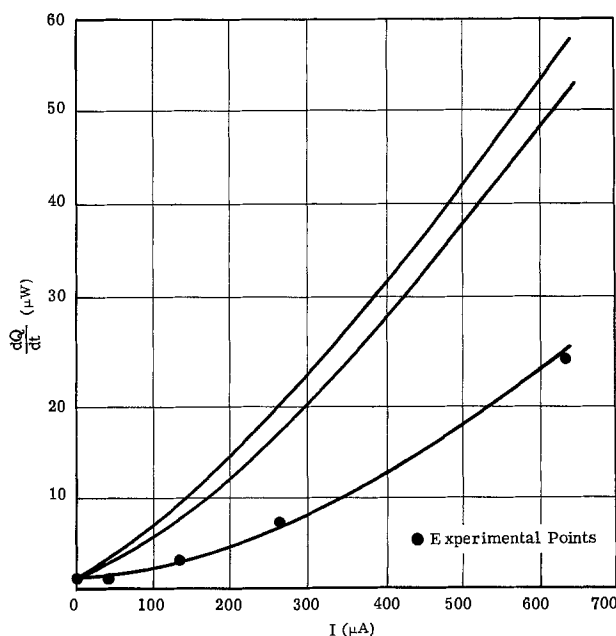
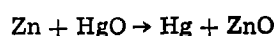
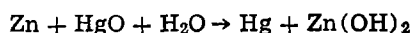


Fig. 3. Current dependence of the thermal effect for a No. 354 HgO-Zn cell. The solid lines are calculated from theory based on a two-electron reduction with Zn(OH)₂ formation (top curve), a two-electron reduction with ZnO formation (bottom curve), and a one-electron reduction with ZnO formation (middle curve).



$$\left(\frac{\partial E}{\partial T}\right)_p = 0.040 \text{ mV/K}$$

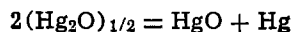
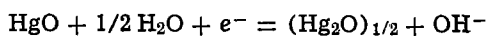


$$\left(\frac{\partial E}{\partial T}\right)_p = -0.123 \text{ mV/K}$$

As shown in the figure, the first reaction represents the experimental data well. Just as in the case of an Ag₂O-Zn cell, the discharge product at the anode is ZnO instead of Zn(OH)₂. That this is the case in these systems can be attributed to the small amount of water present in these limited electrolyte cells.

One other possibility which must be considered seriously is an alternate discharge mechanism proposed by Yosizawa *et al.* (11). According to this model, mercuric oxide is reduced to an intermediate product

which then disproportionates to elemental mercury and mercuric oxide



Using an estimated value of S° for Hg_2O (12) of 30 eu gives $(\partial E/\partial T)_p = -0.09$ mV/K. The resulting curve is also shown in Fig. 3. Clearly, it does not fit the data. Mercurous species are not part of the mechanism.

The behavior of the No. E41 cell is remarkably different from that of the No. 354 cell (see Fig. 4). The rate of heat release does not come to a steady-state value, but rather increases linearly with time. The difference between this cell and the No. 354 is the presence of MnO_2 in the cathode. The rate at which dQ/dt increases with time is a function of the current flowing through the cell, increasing with increasing current. Figure 4 shows the result of allowing the cell to remain on a 10 k Ω load. Increase of the thermal effect is observed for 17.5 hr. This corresponds to 91% of the MnO_2 contained in the cell, assuming a one-electron reduction. It should be noted that such an effect will not be seen in Ag_2O cells (e.g., No. 386) since the MnO_2 potential is lower than Ag_2O . The first material to discharge in an Ag_2O cell is Ag_2O .

The behavior of the cells is explained by recalling the sigmoid nature of the MnO_2 discharge curve. After a load is applied to the cell, the voltage, and consequently the current, continues to decrease for a rather long time. The basic microcalorimetry equation must be written

$$\frac{dQ}{dt} = \left[\eta(t) - T \left(\frac{\partial E}{\partial T} \right)_p \right] I(t) - \sum_{nf} \Delta H_{nf} \nu_{nf}$$

The variation of the voltage of a No. E41 cell is shown in Fig. 5. If this data is inserted into the above equation, the experimental data (represented by the symbol \odot) can be fit assuming a value of $(\partial E/\partial T)_p = -49$ $\mu\text{V}/\text{K}$ (see Fig. 6).

MnO_2 -Zn.—The fact that MnO_2 is responsible for the unique behavior of fresh E41 cells is corroborated by microcalorimetry experiments on the No. 186 MnO_2 -Zn cells. Figure 7 shows the data obtained by applying various loads to the cell. The same linear variation of thermal effect with time is observed indicating that MnO_2 is the material responsible for the unique behavior of the E41 cell. Reaction products cannot be determined by this method for systems with cathodes exhibiting such variations of operating potential with time.

Conclusions

It has been shown that microcalorimetry is an effective tool for the generation of mechanistic information for practical battery systems. An expression for the dependence of the rate of heat release on current has been derived. This expression has been used to analyze data obtained for an Ag_2O -Zn and for an HgO -Zn

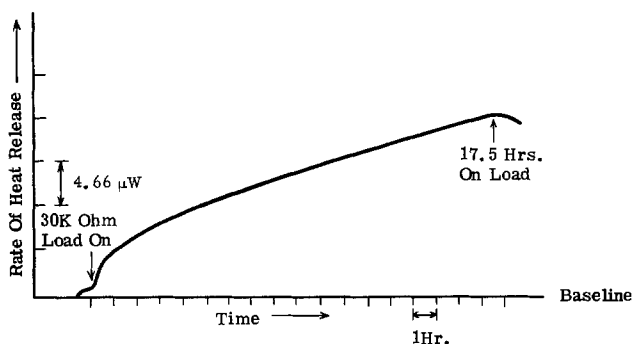


Fig. 4. Response of a No. E41 HgO-Zn cell to the application of a 30 k Ω resistive load.

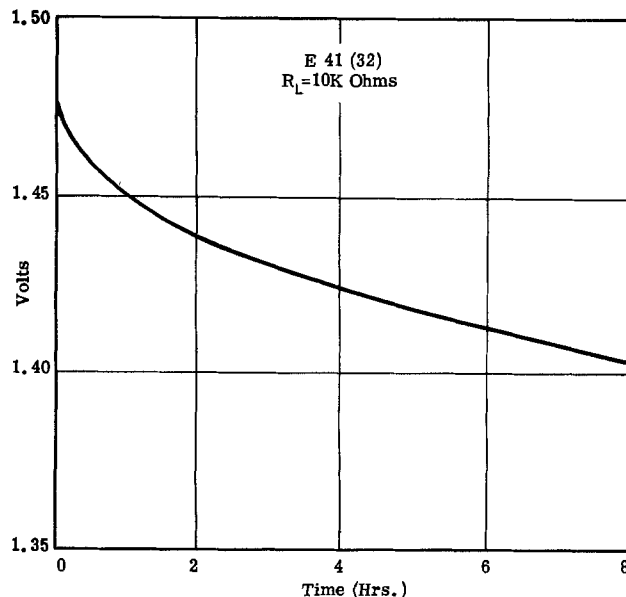


Fig. 5. Variation of the operating voltage of a No. E41 HgO-Zn cell under 10 k Ω resistive load.

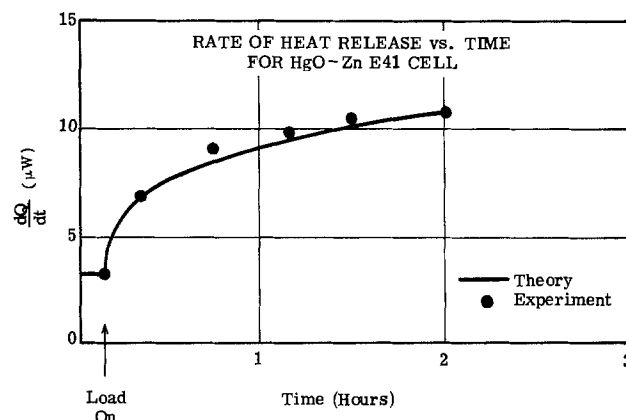


Fig. 6. Calculated response of a No. E41 HgO-Zn cell to a 10 k Ω resistive load. The procedure is described in the text.

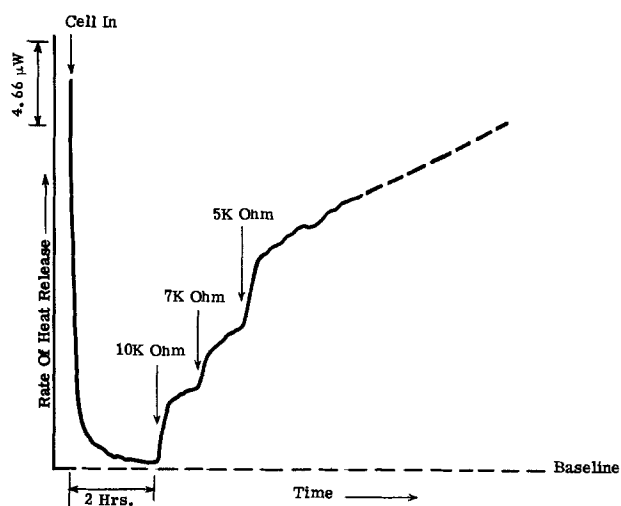


Fig. 7. Response of a No. 186 MnO_2 -Zn cell to the application of various resistive loads.

cell. In both cases it is found that ZnO is formed rather than $\text{Zn}(\text{OH})_2$ upon discharge. The effect of time variation of the cell polarization on the thermal effect has been observed in certain cells containing MnO_2 . This effect is attributed to the sigmoid nature of the MnO_2

discharge, and thus, ultimately, to the mechanism of MnO_2 reduction.

Acknowledgment

The authors would like to thank S. J. Cieszewski for her able assistance in performing the microcalorimeter experiments and in organizing the data.

Manuscript submitted Oct. 31, 1979; revised manuscript received Oct. 10, 1980. This was Paper 167 presented at the Los Angeles, California, Meeting of the Society, Oct. 14-19, 1979.

Any discussion of this paper will appear in a Discussion Section to be published in the December 1981 JOURNAL. All discussions for the December 1981 Discussion Section should be submitted by Aug. 1, 1981.

Publication costs of this article were assisted by Union Carbide Corporation.

REFERENCES

1. L. D. Hansen and R. M. Hart, *This Journal*, **125**, 842 (1978).
2. a. D. F. Untereker and B. B. Owens, Paper 13 presented at the 33rd Annual Calorimetry Conference, Utah State University, Logan, Utah, July 26-28, 1978; b. D. F. Untereker and B. B. Owens, Paper 24 presented at The Electrochemical Society Meeting, Atlanta, Georgia, Oct. 9-14, 1977.
3. P. Bro, *This Journal*, **125**, 674 (1978).
4. H. Frank Gibbard and C. C. Chen, Paper 12 presented at the 33rd Annual Calorimetry Conference, Utah State University, Logan, Utah, July 26-28, 1978.
5. J. M. Sherfey and A. Brenner, *This Journal*, **105**, 665 (1958).
6. S. Gross, *Energy Conversion*, **9**, 55 (1969).
7. T. Jacobsen and G. H. J. Broers, *This Journal*, **124**, 210 (1977).
8. H. F. Gibbard, *ibid.*, **125**, 353 (1978).
9. H. A. Cataldi, in Proceedings of the 27th Power Sources Symposium, Atlantic City, N.J., June 21-24, 1976.
10. H. H. Bode with V. A. Oliapuram, D. Berndt, and P. Ness, in "Zinc-Silver Oxide Batteries," A. Fleischer and J. J. Lander, Editors, John Wiley & Sons, Inc., New York (1971).
11. S. Yosizawa, Z. Takehara, and Y. Namba, *J. Electrochem. Soc., Jpn.*, **30**, 185 (1962) and references therein.
12. J. P. Coughlin, U.S. Bureau of Mines, Bulletin 542, p. 30.

Separation Between Deterministic Response and Random Fluctuations by Means of the Cross-Power Spectrum in the Study of Electrochemical Noise

Ugo Bertocci*

National Bureau of Standards, Chemical Stability and Corrosion Division, Washington, D.C. 20234

ABSTRACT

It is shown that by calculating the cross-power spectrum between the input (the electrode potential) and the output (the cell current) of an electrochemical system under potentiostatic conditions, it is possible to identify which part of the cell current is the response to the input voltage and which part is caused by random fluctuations of the parameters characterizing the electrode. The noise introduced by the amplifiers can be measured separately and then subtracted from the signal. As an example, the current noise of an aluminum electrode below and at the pitting potential is examined. Both electrode impedance and spectral power density of the random fluctuations are obtained. It is shown that below the pitting potential random fluctuations are below the minimum detectable value of $10^{-23} \text{ A}^2/\text{cm}^4 \text{ Hz}$.

In the analysis of electrochemical noise, an important problem is that of knowing which part of the output signal is caused by the input (*i.e.*, the deterministic response to the input) and which is caused by random fluctuations of the parameters characterizing the electrochemical system under study. Both parts can give important information, as long as they can be properly identified. The analysis is further complicated by the noise introduced by the amplifiers necessary to detect the generally small signals.

Digital signal processing equipment can be used, with the aid of the Fast Fourier Transform algorithm, to transform the signal received into the frequency domain, which simplifies the task of analyzing and manipulating the results. A two-channel spectrum analyzer can receive a signal which is the difference between reference electrode and working electrode as

well as a second signal proportional to the current flowing into a three-electrode, potentiostatted cell, and calculate the cross-power spectrum between the two signals. The purpose of this note is to show that the cross-power spectrum can be employed for separating the various components of the output signal.

Statement of the Problem and Mathematical Treatment

In electrochemical studies it is expedient in general to maintain the working electrode at constant potential by means of a potentiostat, and to observe and analyze the current output of the cell. Such a current output can be the deterministic response of the system to the input signal provided by the potentiostat or can be caused by internal fluctuations of the characteristics of the electrode, such as changes in surface area, crystal orientation of the surface, and film coverage, or processes such as passive film breakdown and repair, pitting, or other localized corrosion processes.

* Electrochemical Society Active Member.

Key words: aluminum, cross-power spectrum, electrochemical noise, electrode impedance, pitting.

The internally generated noise, therefore, can give information relative to the magnitude and relaxation times of the electrode processes (1). It has been used, for instance, for the detection of the onset of pitting (2), to monitor the effect of corrosion inhibitors (3), and to study electrocrystallization (4), and anodic dissolution (5).

The experimental problem consists in detecting the signal, that is, amplifying it to a level sufficient for processing, and distinguishing which part of the signal is deterministic, random, or caused by the instrumentation.

The circuit with its sources of signal can be schematized as shown in Fig. 1. The potentiostat delivers a control voltage, the input to the electrochemical cell, which consists of a constant (d-c) voltage and of broad-band noise caused by the instability of such a d-c level. To this a signal may be added, produced by a signal generator. This additional signal can be a constant amplitude sinusoid, a swept frequency signal ranging between two predetermined frequencies, or white noise. The symbol X represents here the a-c part of the input signal, expressed as a function of frequency, $X = X(\nu)$. Such a signal can be quite small, ranging in amplitude between 10^{-4} and 10^{-8} V. An amplifying stage is therefore necessary for its detection and processing, adding noise with spectrum $N_I(\nu)$ to the signal. The output of the first channel of the spectrum analyzer is therefore $A = X + N_I$.

The input signal generates a current in the cell. H represents the cell transfer function so that the output $Y(\nu)$ in the frequency domain is $Y = HX$. For an electrochemical cell H is the admittance, which is in general complex and frequency dependent. Random fluctuations of the electrode characteristics generate an additional noise current $N(\nu)$. The total current is transformed in an appropriate current-to-voltage converter (schematically indicated in Fig. 1) from which the signal emerges with noise $N_O(\nu)$ added at the output of the amplifying stage. The output of the second channel of the spectrum analyzer is therefore $B = Y + N + N_O$.

The auto- and cross-power spectra are, respectively

$$P_{AA} = (X + N_I)(X + N_I)^* = P_{XX} + P_{II} \quad [1]$$

$$P_{BB} = (HX + N + N_O)(HX + N + N_O)^* \\ = |H|^2 P_{XX} + P_{NN} + P_{OO} \quad [2]$$

$$P_{BA} = (HX + N + N_O)(X + N_I)^* = HP_{XX} \quad [3]$$

The terms marked with an asterisk are the complex conjugates of those without asterisk. In deriving [1], [2], and [3] it is assumed that all noise signals are uncorrelated with the input and with one another, so that the average values of the cross-products are zero

$$XN_I^* = N_I X^* = XN^* = NX^* = XN_O^* = N_O X^* = 0 \quad [4]$$

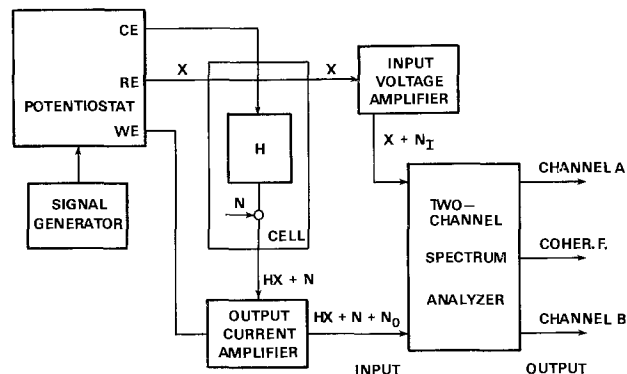


Fig. 1. Schematic representation of the measurement system with noise sources and spectrum analyzer outputs identified.

It should be remembered also that experimentally the spectrum analyzer averages out a large number of time records of the signals, so that, at least asymptotically, [4] is valid.

Taking [4] into account, Eq. [1], [2], and [3] contain five unknowns. It is therefore necessary to determine experimentally two of the unknowns in an independent way. This can be accomplished in the following manner: when the input of the amplifier of the voltage signal is short-circuited, X is effectively zero and therefore

$$(P_{AA})_{X=0} = P_{II} \quad [5]$$

the auto-power spectrum of the amplifier noise. This spectrum can be measured and stored in an appropriate memory. For the measurement of the current amplifier noise N_O it is sufficient to substitute the electrochemical cell with a resistor. Increasing the value of such a resistor decreases the current signal Y until the output of channel B becomes independent of the value of the resistance. In these conditions

$$(P_{BB})_{Y=0} = P_{OO} \quad [6]$$

Since a resistor has been substituted for the cell, no random fluctuations occur and therefore $N = 0$. The auto-power spectrum P_{OO} is also recorded and stored. Once P_{II} and P_{OO} are subtracted from P_{AA} and P_{BB} , it is easy to solve the system of equations so that H and N can be obtained.

Experimental Procedure

The measurements described here were taken with an experimental setup similar to that reported previously (6), which is a practical implementation of Fig. 1. The potentiostat employed, especially built for its low noise, has been described elsewhere (7). The analyzing instrument was a digital two-channel spectrum analyzer which provided the auto-power spectra of the two channels as well as the coherence function γ^2 , which is defined as

$$\gamma^2 \equiv \frac{|P_{BA}|^2}{P_{AA} P_{BB}} \quad [7]$$

and from which, therefore, the cross-power spectrum can be obtained. As it is well known, the coherence function γ^2 ranges from 1, when the output signal is entirely deterministic, to 0 when there is no casual relationship between P_{AA} and P_{BB} .

The electrochemical system investigated was aluminum in borate buffer (pH = 7.5), to which 0.01 mole/liter of NaCl was added. At potentials more positive than -650 mV vs. SCE this electrode undergoes pitting [8], whereupon the noise pattern of the current changes drastically (9). The measurements were carried out at -700 and at -650 mV vs. SCE. In some runs white noise of the order of a few $\mu\text{V}/\sqrt{\text{Hz}}$ were added to the control voltage of the potentiostat. The spectrum analyzer, which has a frequency resolution of $1/256$ of the range, was set for a 51.2 Hz range, so that the resolution was 0.2 Hz.

The results reported here were obtained manually; the spectra and the coherence function were recorded on an X-Y recorder and the calculations were done for only a few of the 256 points available. Such an experimental procedure is slow and tedious, but it was used to test the capability of the method. However, the spectrum analyzer can be interfaced to a computer so that acquisition, storage, and subtraction of the instrumental noise spectra P_{II} and P_{OO} , as well as all necessary calculations, can be carried out under software control with minimum time delay.

Experimental Results

The auto-power spectra of the noise N_I of the amplifier operating on the input signal (the electrode potential) and that of the noise N_O of the output amplifier operating on the cell current were measured over a

wide frequency range, and are shown in Fig. 2. Since P_{00} , the power spectrum of the current amplifier, is added to the current signal, it is given in current units, A^2/Hz . These spectra are averages over a number of repeat measurements, ranging from 512 at high frequency to 64 at low frequency, where the total acquisition times are of the order of 1 hr.

Results obtained on the Al electrode below (-700 mV vs. SCE) and at the pitting potential (-650 mV) in the absence of an external signal in the control voltage are shown in Fig. 3 and 4. The auto-power spectrum of the voltage is that of channel A and it is given in V^2/Hz . Channel B shows the current power spectrum in A^2/Hz . In order to facilitate comparisons the current spectra are not given in units of current density (P_{00} is independent of surface area), but they can be easily and quite precisely transformed into A^2/cm^4Hz by dividing by 10, since the electrode surface area in all experiments was 3.17 cm^2 . The figures show also the coherence function vs. frequency. Figure 5 shows power spectra and coherence function for an electrode at the pitting potential when white noise of $2 \mu V/\sqrt{Hz}$ was applied as an external signal.

From these data, according to the calculation method described earlier, the auto-power spectrum of the random fluctuations P_{NN} and the absolute value of the electrode impedance $|Z| = 1/|H|$ were obtained. They are shown in Fig. 6 and 7, respectively.

Discussion

The results presented here show a number of interesting features and illustrate the usefulness of quanti-

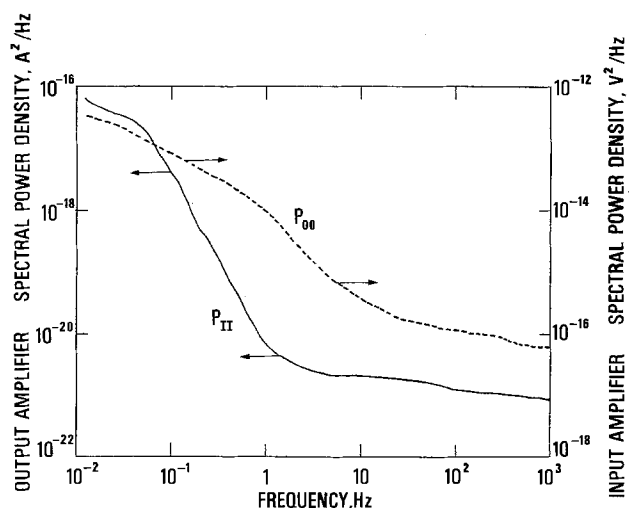


Fig. 2. Auto-power spectra of the instrumental noise of the input amplifier P_{II} (electrode potential) and output amplifier P_{00} (cell current).

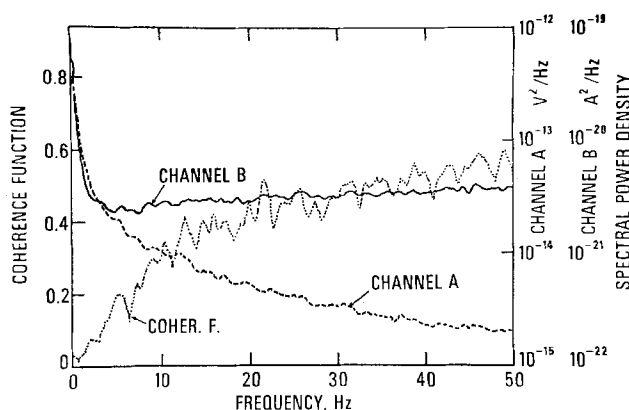


Fig. 3. Auto-power spectra and coherence function for Al in borate buffer + 0.01 mole/liter NaCl at -700 mV vs. SCE. Surface area = 3.17 cm^2 .

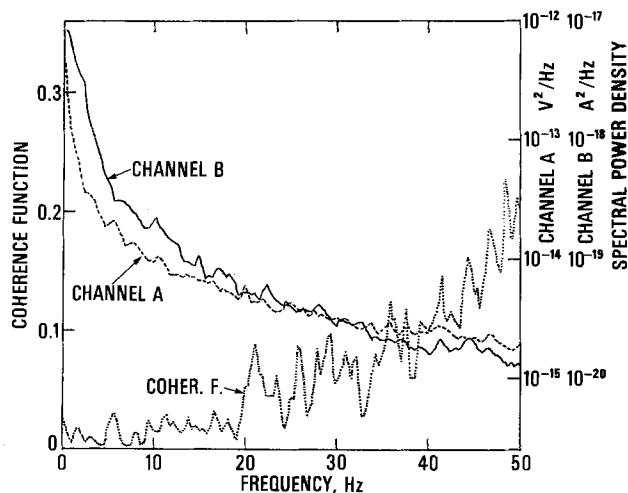


Fig. 4. Auto-power spectra and coherence function for Al in borate buffer + 0.01 mole/liter NaCl at -650 mV vs. SCE. Surface area = 3.17 cm^2 .

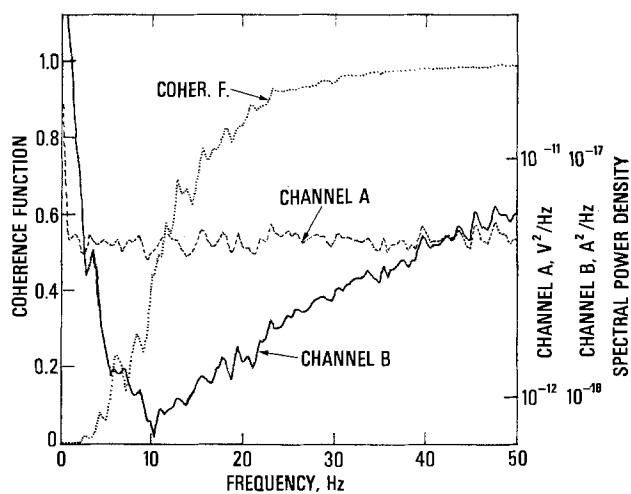


Fig. 5. Auto-power spectra and coherence function for Al in borate buffer + 0.01 mole/liter NaCl at -650 mV vs. SCE. Surface area = 3.17 cm^2 . White noise $2 \mu V/\sqrt{Hz}$ added to input signal.

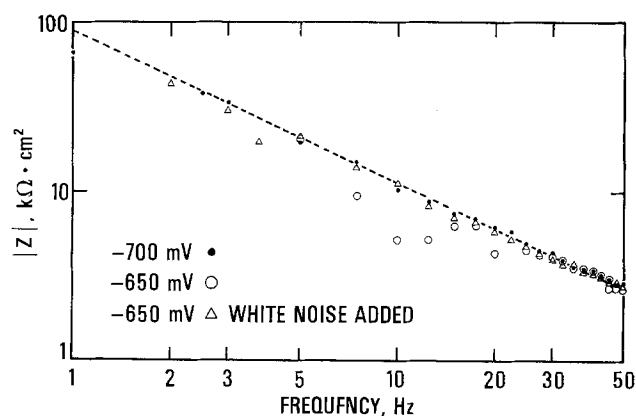


Fig. 6. Absolute value of the electrode impedance $|Z|$ per unit surface area derived from data of Fig. 3, 4, and 5. Squares: -700 mV. Circles: -650 mV. Triangles: -650 mV, white noise added to input.

tative criteria for identifying the sources of noise. For instance, although the voltage spectra in Fig. 3 and 4 are virtually identical, the current spectrum is much larger at -650 mV (Fig. 4), confirming that the noise level increases considerably when pitting begins (9). However, the coherence function in Fig. 3 indicates that a substantial part of the signal in channel B is not

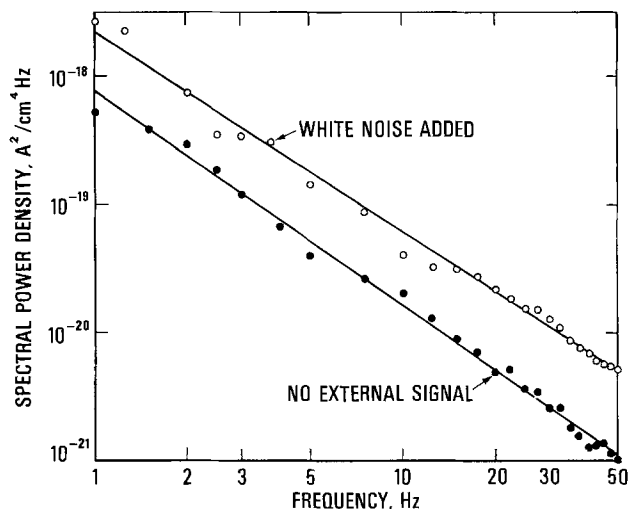


Fig. 7. Auto-power spectra P_{NN} of the random noise derived from data of Fig. 4 and 5 at -650 mV. Squares: no external input signal. Circles: white noise added to input.

causally related to the input, but such a noise may either be instrumental or may mark the beginning of the breakdown of the protective oxide film. However, when the separation of the noise sources is carried out, it is found that P_{NN} at -700 mV is practically zero over the whole frequency range studied. An upper value can be set for P_{NN} at about 10^{-22} A²/Hz (or 10^{-23} A²/cm²Hz), which is of the order of one-tenth of the instrumental noise as indicated by P_{00} . The difference between the value of the coherence function in Fig. 3 and unity can be accounted for entirely by the instrumental noise.

The impedance, shown in Fig. 6, corresponds essentially to the behavior of a capacitor of about $1.5 \mu\text{F}/\text{cm}^2$. The corrosion resistance cannot be determined with assurance because of the limited frequency range studied, but is larger than $60 \text{ k}\Omega \cdot \text{cm}^2$. Here the advantage of adding white noise to the input signal is shown by the data in Fig. 5, from which the deterministic response can be recovered in spite of the random fluctuations, while no reliable value of $|Z|$ can be calculated from Fig. 4 below 30 Hz because γ^2 is too close to zero.

In conclusion, with the aid of an instrument capable of processing voltage and current signals simultaneously and of calculating the cross-power spectrum, random noise can be separated from the deterministic response. Sensitivity is also enhanced, and noise about one-tenth of the instrumental noise can still be detected. However, it is evident that the noise level of the amplifier operating on the cell current is the main factor limiting the detectability of the random fluctuations of the electrode characteristics, and that its reduction would improve considerably the performance of the whole system.

As far as the pitting of Al is concerned, these rather limited results give nevertheless some interesting in-

formation. First of all, the impedance data of Fig. 6 show that, although pitting causes large current fluctuations, the deterministic behavior below and at the pitting potential is substantially the same. The random noise spectra of Fig. 7 show that reproducibility is only fair, as to be expected since number and size of the pits tend to vary from experiment to experiment. The major point seems to be that the amplitude of the fluctuations decays approximately as the reciprocal of the frequency, like the "flicker" noise observed in electronic devices (10). The decay with frequency also indicates that the capacitance of the electrode undergoes smaller fluctuations than the resistance during the pitting process (9).

Finally, the results have shown that the degree of random fluctuations below the pitting potential is so low that the picture of the protective film on aluminum as being in a state of dynamic equilibrium with continuous breakdown and repair does not seem to be supported by the experimental evidence.

Acknowledgment

The author wishes to thank Mr. S. Simms of the Hewlett-Packard Corporation for graciously lending part of the equipment used in this work.

Manuscript submitted May 5, 1980; revised manuscript received Oct. 15, 1980.

Any discussion of this paper will appear in a Discussion Section to be published in the December 1981 JOURNAL. All discussions for the December 1981 Discussion Section should be submitted by Aug. 1, 1981.

Publication costs of this article were assisted by the National Bureau of Standards.

REFERENCES

1. G. Blanc, I. Epelboin, C. Gabrielli, and M. Keddam, *J. Electroanal. Chem. Interfacial Electrochem.*, **62**, 59 (1975).
2. U. Bertocci, Seventh International Congress on Metallic Corrosion, p. 2010, Rio de Janeiro 1978, ABRACO (1979).
3. W. P. Iverson, *This Journal*, **115**, 617 (1968).
4. C. Gabrielli, M. Ksouri, and R. Wiart, *J. Electroanal. Chem. Interfacial Electrochem.*, **86**, 233 (1978).
5. G. Blanc, I. Epelboin, C. Gabrielli, and M. Keddam, *ibid.*, **75**, 97 (1977).
6. U. Bertocci, *This Journal*, **127**, 1931 (1980).
7. U. Bertocci and R. W. Shideler, *Nat. Bur. Stand. J. Res.*, **85**, 211 (1980).
8. J. R. Galvele and S. M. de DeMicheli, *Corros. Sci.*, **10**, 795 (1970); K. Nisancioglu and H. Holtan, *ibid.*, **18**, 835 (1978).
9. U. Bertocci and J. Kruger, "Proceedings of the International Conference on Non-Traditional Approaches to the Study of the Solid-Electrolyte Interface," Snowmass, CO (1979), in press.
10. D. K. C. MacDonald, "Noise and Fluctuations," p. 90, J. Wiley, New York (1962); A. van der Ziel, "Noise," p. 106, Prentice Hall, Englewood Cliffs, NJ (1970); A. H. W. Beck, "Statistical Mechanics, Fluctuations and Noise," p. 176, J. Wiley, New York (1976).

The Dissolution and Passivation of Zinc in Concentrated Aqueous Hydroxide

M. C. H. McKubre* and D. D. Macdonald*¹

SRI International, Materials Research Laboratory, Menlo Park, California 94025

ABSTRACT

The rotating ring-disk electrode has been applied in this study to the related phenomena of dissolution, current oscillation, and passivation of zinc in concentrated aqueous NaOH. The results of potentiostatic and potentiodynamic experiments are compared with those of previous workers, and a physical model is proposed to describe the anodic behavior of zinc in four successive potential regions: active dissolution, prepassivation, pseudopassivation, and true passivation.

The requirements for high specific energy, high specific power, and low cost make zinc an attractive negative electrode material for aqueous alkaline batteries in electric vehicular applications (1). However, a number of specific limitations await satisfactory resolution. Recent studies have been concerned with the limitations of cycle life associated with dendritic (2-5) and nonadherent (6-9) zinc deposition during charging, and with the problems of electrode shape change with cycling (1, 2, 10). The shelf life and cycle life of zinc battery electrodes is also limited by the corrosion of zinc in concentrated alkali (11-13).

In the present study we focus on the related processes of anodic dissolution and passivation. Rapid discharge of the zinc electrode is associated largely with the high solubility of Zn(II) as a zincate ion (14, 15) in alkaline solutions. At high currents, however, zinc discharge is often inhibited by the formation of a passivating zinc oxide or hydroxide layer by a dissolution-precipitation mechanism (16-28). Before the onset of passivation, the discharge of zinc is generally agreed (21) to proceed via the formation of complex hydroxyl zincate anion. The nature of this anion has been the subject of considerable thermodynamic (14, 29-31) and spectroscopic (15, 32-34) investigation, and is thought to have the form $Zn(OH)_4^{2-}$ in strongly alkaline solutions. However, the spectroscopic investigations of Jackovitz and Langer (32) suggest that "only a small fraction, about one-sixth of the anodically dissolved zinc, was converted to $Zn(OH)_4^{2-}$ "

Experimental Procedure

Experiments were performed using a rotating ring-disk electrode (RRDE). The importance of adequate hydrodynamic control in studies of zinc dissolution and passivation phenomena has been stressed by several authors (20, 26, 35, 36).

The RRDE was constructed using a vitreous carbon² ring with a 99.999% purity zinc disk, as shown in Fig. 1. Vitreous carbon constitutes a nearly ideal, nonporous, inert ring material for current collection at large cathodic potentials. The radius ratios r_3/r_2 and r_2/r_1 exceed those tabulated by Alberly *et al.* (37) and Pleskov (38), and the electrode collection efficiency was determined experimentally in 0.1M $K_3Fe(CN)_6$ with 1.0M NaOH supporting electrolyte. This calibration procedure has been described previously (39). At 20°C the measured collection efficiency was $70.9 \pm 0.2\%$. Details of the rotating ring-disk electrode construction are shown in Fig. 1.

* Electrochemical Society Active Member.

¹ Present address: The Fontana Corrosion Center, Department of Metallurgical Engineering, The Ohio State University, Columbus, Ohio 43210.

² Vitreous carbon was generously supplied by Dr. A. Norris, Fluorocarbon Corporation, Anaheim, California.

Experiments were conducted in an all Teflon cell shown in Fig. 2, situated in a water-ethylene glycol bath controlled to within ± 0.1 K. Potentiodynamic control of the disk and IR compensation were accomplished using a PAR Model 173 potentiostat and Model 175 potential programmer. The disk current and charge were recorded using a PAR model 179 digital coulometer. Potentiostatic control of the ring electrode was achieved using a purpose-built, high-speed potentiostat electrically isolated from the disk control circuit.

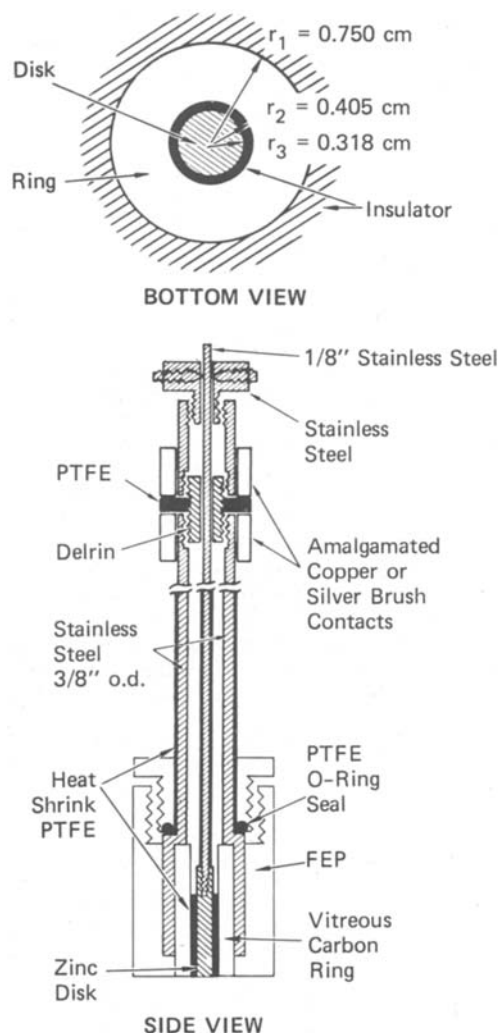


Fig. 1. Schematic diagram of RRDE construction and contact assembly.

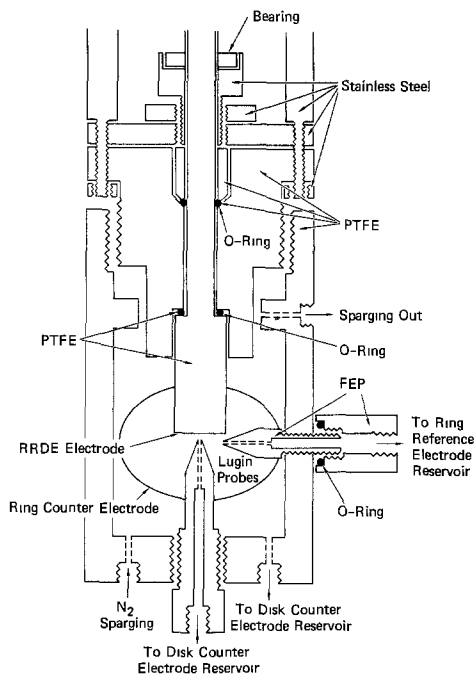


Fig. 2. RRDE cell construction

Details of the ring potentiostat, and six electrode cell geometry have been described previously (39, 40).

RRDE studies were performed in 9.78M [28 weight percent (w/o)] NaOH, prepared using analytical grade NaOH and water doubly distilled from deionized stock. The second distillation was under high purity nitrogen to exclude atmospheric CO₂, and the cell was continuously sparged with N₂ except during periods of measurement.

The RRDE electrode was polished with varying grades of carborundum paper, the final grade having 25 micron particle size. The electrode assembly was degreased with hot ethanol in an ultrasonic bath, then rinsed with distilled water immediately prior to use.

Results

Figure 3 shows schematically the general features observed during a slow anodic potentiodynamic sweep covering the zinc discharge region in initially zincate-free NaOH. The region "b" is characterized by an exponential dependence of the dissolution current on applied potential (31, 36, 41). The current increases in a nearly linear fashion with potential (25, 36) between "b" and "c" reaching a maximum at "d" and attaining a plateau value "e" before passivation. Two peaks in the region "cf" have been observed at very low potential sweep rates (< 1 mV sec⁻¹) by other workers (21, 26, 42). The peaks were interpreted by Powers and Breiter (21) in terms of growth of two surface

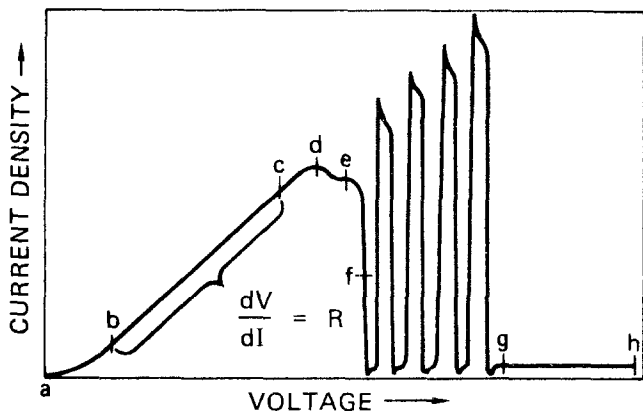


Fig. 3. Anodic potentiodynamic sweep of zinc in aqueous NaOH

oxide films. The features shown in Fig. 3 represent the limiting low rate potentiodynamic sweep behavior, and we have observed no evidence for a second peak under controlled hydrodynamic conditions.

Active dissolution.—We observed that the form of the repetitive sweep voltammogram depends critically on both electrode rotation speed and electrolyte temperature. Figure 4 shows the influence of rotation speed and Fig. 5 shows the influence of temperature on the zinc voltammogram. It is immediately apparent from Fig. 4 that the peak and plateau currents, as well as the slope in the linear *I-V* region, are strongly influenced by electrolyte convection at low sweep rates, suggesting that these are controlled not by factors at the zinc/electrolyte interface, but by processes within the diffusion layer.

The data in the region "bc" were analyzed as a function of temperature and rotation speed and the results are presented in Table I. The linearity of this portion of the current voltage curve is reflected in the near-unity values of the regression coefficients shown for an equation of the form

$$V = V_0 + IR$$

It is clear from the values in Table I that V_0 is effectively independent of ω , while R decreases monotonically with ω and T .

The linear dependence of the dissolution current on applied potential indicates that electrode discharge in

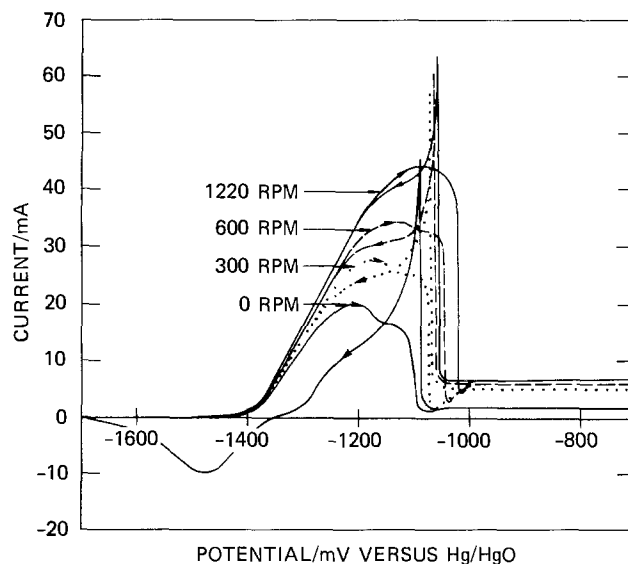
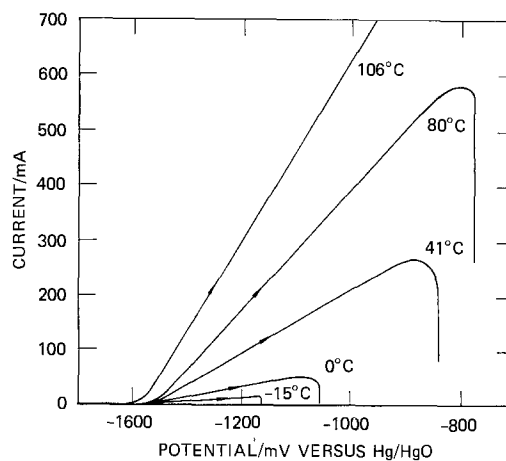
Fig. 4. The influence of electrode rotation speed on the zinc cycle voltammogram: 28 w/o NaOH, 0°C, sweep rate 5 mV sec⁻¹.Fig. 5. The influence of temperature on the potentiodynamic discharge of zinc: 28 w/o NaOH, 1200 rpm, sweep rate 5 mV sec⁻¹.

Table I. Linear regression of current vs. applied potential for the potentiodynamic discharge of Zn at 5 mV sec⁻¹

| T (°C) | ω (rpm) | V_0 /mV | R/ Ω | r^2 |
|--------|----------------|---------------------------|-------------|-------|
| -15 | 1160 | -1405 | 13.75 | 0.998 |
| -15 | 600 | -1406 | 15.00 | 0.999 |
| -15 | 300 | -1406 | 15.54 | 0.999 |
| -15 | 0 | -1403 | 15.88 | 1.000 |
| -15 | | $\bar{V}_0 = -1405 \pm 1$ | | |
| 0 | 1220 | -1387 | 5.44 | 0.999 |
| 0 | 600 | -1389 | 5.89 | 0.998 |
| 0 | 300 | -1389 | 6.23 | 1.000 |
| 0 | 0 | -1393 | 7.43 | 0.999 |
| 0 | | $\bar{V}_0 = -1390 \pm 3$ | | |
| 41 | 1200 | -1379 | 1.93 | 1.000 |
| 41 | 600 | -1381 | 2.18 | 1.000 |
| 41 | 300 | -1379 | 2.48 | 1.000 |
| 41 | 0 | -1379 | 2.48 | 1.000 |
| 41 | | $\bar{V}_0 = -1379 \pm 2$ | | |
| 80 | 1200 | -1360 | 0.925 | 0.999 |
| 80 | 600 | -1360 | 1.118 | 0.999 |
| 80 | 300 | -1358 | 1.501 | 0.995 |
| 80 | 0 | -1358 | 1.501 | 0.995 |
| 80 | | $\bar{V}_0 = -1359 \pm 1$ | | |
| 106 | 1200 | -1385 | 0.597 | 0.999 |
| 106 | 600 | -1384 | 0.656 | 0.996 |
| 106 | 300 | -1383 | 0.716 | 1.000 |
| 106 | 0 | -1378 | 1.077 | 0.995 |
| 106 | | $\bar{V}_0 = -1383 \pm 3$ | | |

Note: potentials are with respect to Hg/HgO. r^2 is the regression coefficient.

this region is not determined by ionic diffusion of OH⁻ to, or product from the interface. Sanghi and Fleischmann (42) discounted mass transport limitation by OH⁻ ions, observing that the maximum dissolution rate is only a fraction of the limiting diffusion current of hydroxyl ions at bulk concentration greater than 0.01M. However, resistive (migration) limitation, which is functionally dependent on the rate of electrolyte convection, suggests that the process that determines the Zn electrode discharge rate occurs either within the diffusion layer or within a surface film, the thickness of which is determined by ablation or dissolution to the bulk electrolyte.

As expected for a process occurring within the diffusion layer, the dissolution resistance values presented in Table I are approximately linear with the inverse square root of electrode rotation speed

$$T = -15^\circ\text{C}, R = 12.17 + 60.74 \omega^{-1/2}, r^2 = 0.992$$

$$T = 0^\circ\text{C}, R = 4.74 + 26.38 \omega^{-1/2}, r^2 = 0.968$$

$$T = 41^\circ\text{C}, R = 1.39 + 19.09 \omega^{-1/2}, r^2 = 0.997$$

$$T = 80^\circ\text{C}, R = 0.33 + 20.13 \omega^{-1/2}, r^2 = 0.992$$

$$T = 106^\circ\text{C}, R = 0.48 + 4.08 \omega^{-1/2}, r^2 = 0.991$$

Powers and Breiter (21) observed for Zn in KOH that, although faceting of the single crystal surfaces occurs in the linear- I - V region, there is no direct evidence of film formation until very near the potential at which the current density is a maximum, i.e., near "d." In a subsequent publication, Breiter (25) suggested that the linear region may result from the initial formation and spreading of a compact film across the surface. This proposal appears to conflict with their previous observation (21), and is clearly inconsistent with the rotation speed dependence of R observed in the present study. Armstrong *et al.* (36, 41) ascribe an observed I^{-1} vs. $\omega^{-1/2}$ linearity for the initial dissolution of Zn in NaOH to a $\text{Zn} \rightleftharpoons \text{Zn}(\text{OH})_4^{2-}$ equilibrium process in which current limitation is imposed by the diffusion of zincate to the bulk. This model has been extended (34) to predict an exponential dependence of I_∞ , the current extrapolated to the limit of

high rotation speed, on the applied overvoltage, $V - V_0$. Figure 6 shows plots of I_∞ and $\ln I_\infty$ vs. applied potential. Values of I_∞ were calculated by the linear regression of I^{-1} vs. $\omega^{-1/2}$ data, extrapolated to $\omega^{-1/2} = 0$, for varying temperatures and voltages in the region "bc," during a slow (5 mV sec⁻¹) anodic potentiodynamic sweep. While the data in Fig. 6(a) may be construed as straight lines in accordance with Armstrong's model (36, 41), a significantly better fit to the data is shown in Fig. 6(b). The vectors shown are regression lines for all data presented in Fig. 6(a).

To elucidate further the mechanisms of Zn dissolution, we determined the fraction of the dissolved zinc species that was reducible at the vitreous carbon ring. Three striking results immediately were apparent from the study.

1. Under all conditions, the fraction of dissolved zinc detected at the ring was less than that predicted by the calibrated collection efficiency.

2. The fraction at the dissolved zinc that was collected was a function at the electrode rotation speed.

3. When corrected for the increasing background current, the percentage of collected material increased with an increasing concentration of dissolved zinc in the bulk electrolyte.

Figure 7 shows the influence of rotation speed on disk and ring currents in initially zincate-free solution. The collection percentages shown at each rotation speed are determined from the current peaks for i_d and i_r , appropriately corrected for background currents, expressed as a percentage of the calibrated collection

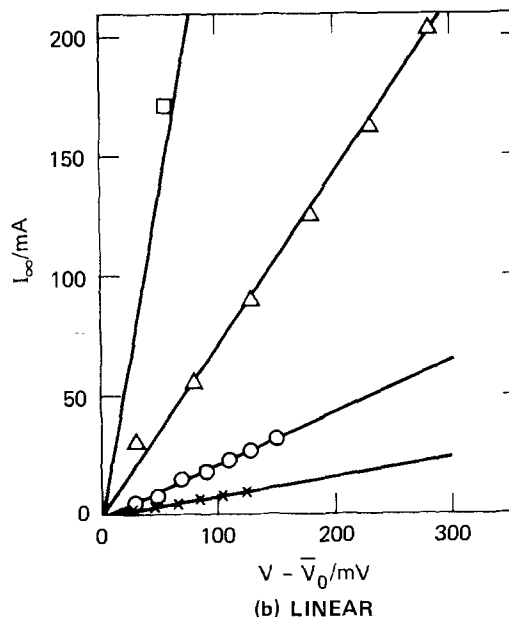
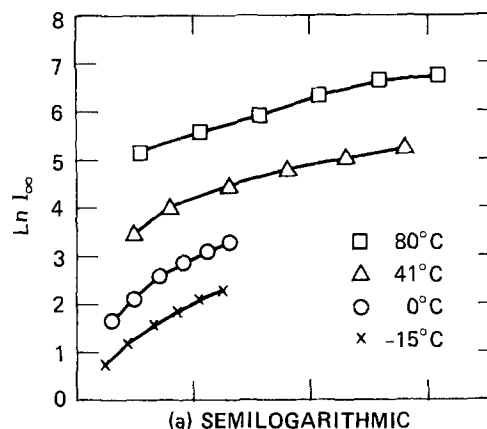


Fig. 6. The current extrapolated to infinite rotation speed vs. applied potential: 28 w/o NaOH, sweep rate 5 mV sec⁻¹.

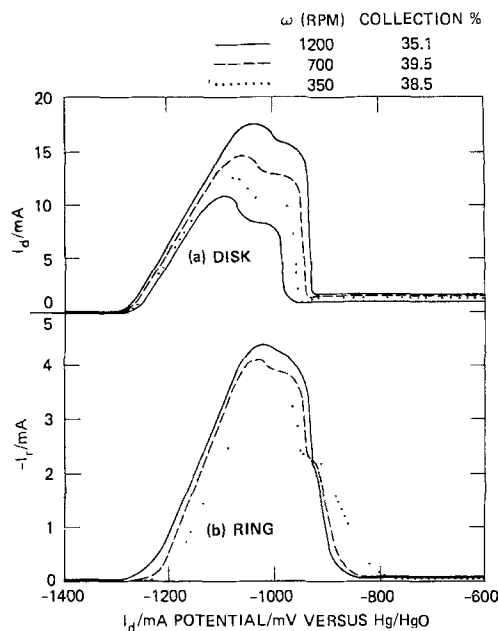


Fig. 7. RRDE study of zinc during anodic potentiodynamic sweep at 5 mV sec^{-1} : 28 w/o NaOH, 15°C .

efficiency. The concentration of dissolved zinc was then increased by controlled coulombic electrochemical dissolution of an auxiliary zinc electrode within the cell. Collection percentages determined at the peak are plotted vs. rotation speed in Fig. 8, together with data obtained at a single potential in initially zincate-free NaOH.

It is apparent from Fig. 8 that the percentage of dissolved zinc species that is reducible declines at high rotation speed, but increases with dissolved zinc concentration. The apparent small decreases in collection at very low rotation speeds seems to be an artifact of the ring disk system. A decrease in collection percentage at high rotation speed has been observed previously (17) and may be interpreted as follows. The

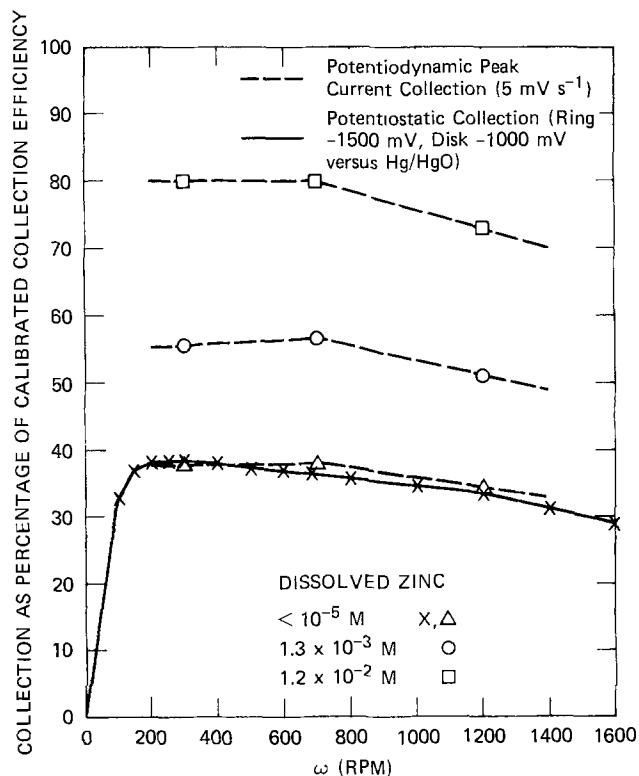
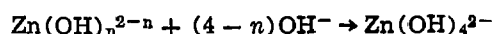
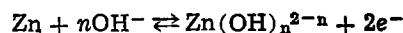


Fig. 8. Collection percentage vs. electrode rotation speed as a function of dissolved zinc concentration: 28 w/o NaOH, -15°C .

anodic charge transfer process produces an inactive intermediate, which transforms in time to the electrochemically active products by chemical dissolution. It is this final product that is reducible on the ring. Using laser Raman techniques, Kato and co-workers (17) suggested that this product is $\text{Zn}(\text{OH})_4^{2-}$. If we assume that the intermediate is a dissolved $\text{Zn}(\text{II})$ species, then the model for dissolution is consistent with that originally proposed by Gerischer (43) and provides a mechanism for subsequent passivation



where

$$0 \leq n \leq 3$$

This second reaction proceeds at a moderate rate. At high rotation speeds the intermediate species has insufficient time to transform to the reducible zincate ion, and the amount of species collected at the ring is less.

Passivation.—It is helpful to divide the passivation of Zn in concentrated aqueous hydroxide into three separate regions of applied potential: prepassive, pseudopassive or unstable, and true passive regions. The potentiokinetic current behavior within these regions is shown schematically in Fig. 3.

Prepassive region.—At potentials more positive than “d,” a white flocculent film is observed (21) to be deposited on the electrode. This has been associated (21, 24, 25) with the precipitation of $\text{Zn}(\text{OH})_2$ from a near-surface solution supersaturated with $\text{Zn}(\text{OH})_4^{2-}$. The dissolution current is reduced by the three-dimensional porous film, possibly as a consequence of the reduced effective surface area. A well-defined current plateau, “e” with current $\propto \omega^{1/2}$, is seen at low temperatures. It is apparent from the work of Breiter (21, 25) that passivation is not caused by the porous $\text{Zn}(\text{OH})_2$ film, but by a thin, compact, adherent film that forms directly on the zinc surface. We will adopt the nomenclature of Powers and Breiter (21), and refer to these films as types I and II, respectively. While the type I film is not passivating, we believe that its existence is required for the formation of a passivating type II film.

Unstable region.—The onset of passivation is rapid but not irreversible. Under potentiostatic or slow potentiodynamic sweep conditions, we have observed zinc electrodes to undergo an oscillatory activation/passivation process within a defined potential region “fg.” Current and potential oscillations have been observed previously (44-50) for a variety of systems including Zn in aqueous hydroxide (50, 51). Hampson *et al.* (18) observed that a passivated zinc electrode becomes depassivated after it is “rested for a few minutes,” and that depassivation becomes more rapid as the electrolyte temperature and concentration are increased. Breiter *et al.* ascribed fluctuations (21) and current oscillations (25) under potentiodynamic sweep conditions to buckling and tearing of the compact type II film. A close examination of this phenomenon provides a considerable insight into the mechanisms of passivation.

Figure 9 shows the broad potential region of current instability observable at elevated temperatures under single anodic potentiodynamic sweep conditions. The envelope of current peaks extends the region of current-voltage linearity discussed in the previous section. Thus, the current upon reactivation appears initially to be determined by the same diffusion layer resistance we believe is associated with active zinc dissolution.

Onset potentials for passivation are shown in Fig. 10, superimposed upon the reversible potential profiles calculated (52) for pertinent redox reactions in 9.7M NaOH. Under the conditions of our experiments, passivation occurs well into the potential regions of ZnO

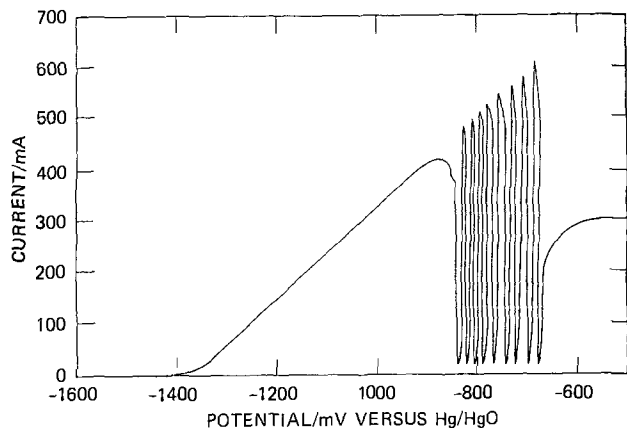


Fig. 9. Current oscillations of zinc during anodic potentiodynamic sweep at 5 mV sec^{-1} ; 28 w/o NaOH, 80°C , 600 rpm.

and $\text{Zn}(\text{OH})_2$ stability, and there is little correlation between initial passivation and the reversible potentials calculated for the formation of latently passivating oxide species. Under potentiodynamic conditions the passivation potential increases approximately linearly with temperature, with a slope that increases with increasing rotation speed.

Further information regarding current instability can be obtained by using the vitreous carbon ring to monitor the concentration of reducible Zn species adjacent to the electrode. Figure 11 shows the results of RRDE potentiostatic step experiments at 22.5°C and at 300 rpm. Under these conditions oscillation is confined to a $\pm 25 \text{ mV}$ region. On the time scale shown, passivation and reactivation occur virtually instantaneously. By using a Biomation Model 805 Wave Form Recorder in the pre-trigger mode, we ascertained that reactivation occurs in tens of milliseconds, and passivation somewhat less quickly. The nearly sinusoidal ring current perturbation reflects the concentration wave of

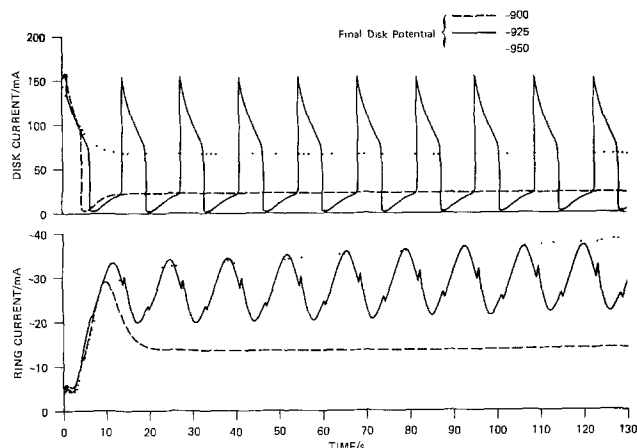


Fig. 11. RRDE potential step experiment for zinc in 28 w/o NaOH at 22.5°C . Ring potential and initial disk potential $-1500 \text{ mV vs. Hg/HgO}$.

reducible zinc ions that propagates through the electrolyte as a result of intermittent disk dissolution. The glitches appearing on the ring current sinusoid result from coupling of the ring and disk currents (40, 53) and are artifacts of the RRDE system.

Under controlled hydrodynamic conditions, oscillations appear to be sustainable indefinitely. However, both amplitude and period are markedly influenced by step potential, temperature, and rotation speed. Below room temperature, oscillation is observed at $\omega \leq 300 \text{ rpm}$. At 41°C , oscillation occurs for $\omega \leq 600 \text{ rpm}$, and above 80°C it may be sustained at all rotation speeds accessible to us (up to 1200 rpm). Figure 12 shows the limits of potential over which oscillation occurs in a quiescent system as a function of temperature.

Discussion

In the preceding sections we described the chronology of Zn anodization under controlled potential conditions, comparing our experimental results with the conclusions of previous authors, as a first step in the development of a self-consistent picture of the passivation of zinc. The sequence of important processes that require explanation may be summarized as follows.

1. Following an initial Tafel region, the zinc dissolution current increases linearly with applied potential, the resistance being proportional to the diffusion layer thickness.

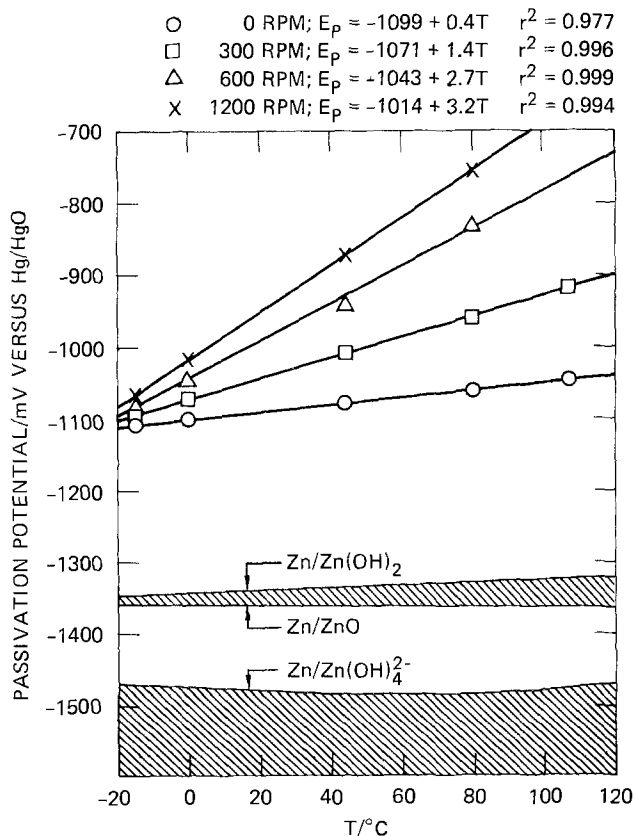


Fig. 10. Measured passivation onset potentials and calculated reversible potentials vs. temperature, for zinc in 28 w/o NaOH.

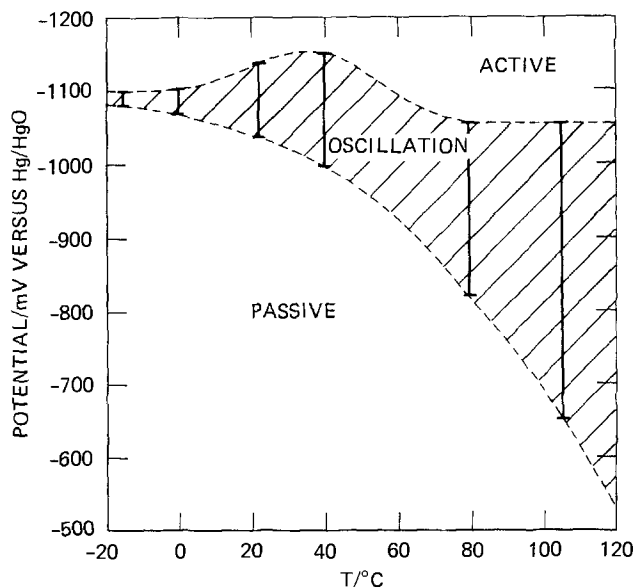


Fig. 12. Region of current instability for zinc in 28 w/o NaOH under quiescent conditions.

2. Zinc dissolves electrochemically via an intermediate species to a final product believed to be $\text{Zn}(\text{OH})_4^{2-}$.

3. $\text{Zn}(\text{OH})_2$ precipitates on the electrode in a pre-passive region, producing a loose flocculent film denoted as type I (21, 25).

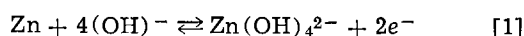
4. The temperature and convection dependence of passivation are consistent with a dissolution-precipitation mechanism, but the electrode is passivated by the formation of a compact, adherent (type II) film directly on the Zn electrode surfaces (21, 25).

5. Rapid reactivation may occur within a defined region of potential, the current initially attaining a value equivalent to the extrapolation of the linear I - V active dissolution region.

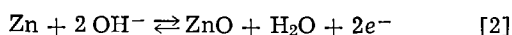
6. Current oscillations may effectively be sustained indefinitely and result in a near sinusoidal reducible Zn concentration wave in the electrolyte. The potential region of instability is strongly influenced by electrolyte temperature and convection, but is not correlated with known thermodynamic processes.

7. At sufficiently large anodic potentials, true passivation occurs, which results in a passive dissolution current independent of potential and time.

These observations are consistent with the following model. Initial dissolution proceeds according to the overall Eq. [1]

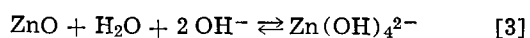


At a potential roughly corresponding to the onset of linear current-voltage behavior, the Zn/ZnO reversible potential is exceeded (51, 52) and the predominant electrode reaction becomes



Because hydroxide ions are the reactant in Eq. [2], there is no supporting electrolyte. Under these conditions an impedance term must be included to account for the migration resistance (54-58). We propose that at moderate current densities the resistance due to the migration of OH^- ions becomes rate limiting.

ZnO forms on the electrode and then dissolves by reaction with further hydroxide to form the zincate ion



When the electrolyte in the immediate vicinity of the electrode becomes supersaturated with zincate, $\text{Zn}(\text{OH})_2$ precipitates on the electrode forming a porous (type I) film. Dissolution proceeds according to reaction [3] until the pH within the porous film is reduced to the extent that ZnO is insoluble (24). At this stage the electrode passivates due to the surface formation of a thin compact ZnO (type II) layer. With the reduced dissolution current, the zincate concentration declines and the pH increases, redissolving the $\text{Zn}(\text{OH})_2$ (type I) and ZnO (type II) films. This mechanism is consistent with the observation (59) that Zn can be reactivated in a thin layer cell by the addition of very small amounts of fresh hydroxide. In the absence of the type I film, reactivation results initially in a current limited only by the hydroxide migration resistance. The next cycle is initiated with the precipitation of a new $\text{Zn}(\text{OH})_2$ film. The passivation onset potential and the period of oscillation are determined by the difference between the active dissolution current and rate of mass transport (diffusion plus convection) from the electrode surface.

To explain the true passive behavior of the Zn electrode, it is necessary to postulate that the pseudopassivating film undergoes a phase change to form a species that is relatively insoluble at high pH.

The model presented above can be used, at least qualitatively, to explain our experimental observations and those of other workers. However, it should not be regarded as definitive and requires substantive verification. A more detailed and quantitative study is currently under way in our laboratory.

Acknowledgment

Funding was provided by the Department of Energy under Contract EM-78-C-01-5159. The authors wish to thank Dr. S. Ruby and Dr. F. R. McLarnon of DOE for their continued interest in this study.

Manuscript submitted July 14, 1980; revised manuscript received Sept. 23, 1980.

Any discussion of this paper will appear in a Discussion Section to be published in the December 1981 JOURNAL. All discussions for the December 1981 Discussion Section should be submitted by Aug. 1, 1981.

Publication costs of this article were assisted by SRI International.

REFERENCES

1. E. J. Cairns, General Motors Research Publication GMR-2170 (1976).
2. J. McBreen, *This Journal*, **119**, 1620 (1972).
3. G. A. Dalin, in "Power Systems for Electric Vehicles," U.S. Department of Health, Education and Welfare, Cincinnati (1967).
4. P. Bauer, Batteries for Space Power Systems, NASA, Washington, D.C. (1968).
5. M. Eisenberg, in "Power Systems for Electric Vehicles," U.S. Department of Health, Education and Welfare, Cincinnati (1967).
6. I. Epelboin, M. Ksouri, and R. Wiart, *J. Electroanal. Chem. Interfacial Electrochem.*, **75**, 115 (1977).
7. H. G. Oswin and K. F. Blurton, in "Zinc-Silver Oxide Batteries," A. Fleischer, Editor, John Wiley, New York (1971).
8. H. K. Varmay and W. A. Smith, in "Batteries," D. H. Collins, Editor, Pergamon Press, New York (1963).
9. I. Epelboin, M. Ksouri, and R. Wiart, *This Journal*, **122**, 1206 (1975); *J. Less-Common Metals*, **43**, 235 (1975); I. Epelboin, M. Ksouri, E. Lejay, and R. Wiart, *Electrochim. Acta*, **20**, 603 (1975).
10. S. P. Poa and C. H. Wu, *J. Appl. Electrochem.*, **8**, 427 (1978).
11. P. Ruetschi, *This Journal*, **114**, 301 (1967).
12. L. Z. Vorkapic, D. M. Drazic, and A. R. Despic, *ibid.*, **121**, 1385 (1974).
13. V. S. Muralidharan and K. S. Rajagopalan, *J. Electroanal. Chem. Interfacial Electrochem.*, **94**, 21 (1978).
14. T. P. Dirkse, in "Zinc-Silver Oxide Batteries," A. Fleischer, Editor, John Wiley, New York (1971).
15. N. A. Hampson, in "Zinc-Silver Oxide Batteries," A. Fleischer, Editor, John Wiley, New York (1971).
16. R. D. Armstrong and G. M. Bulman, *J. Electroanal. Chem. Interfacial Electrochem.*, **25**, 121 (1970).
17. H. Kato, T. Yoshimura, and M. Yamashita, *Nippon Kagaku Kaishu*, **12**, 1811 (1977).
18. N. A. Hampson, M. J. Tarbox, and J. T. Lilley, *J. Electrochem. Technol.*, **2**, 309 (1964).
19. T. I. Popova, V. S. Bagotskii, and B. N. Kabanov, *Russ. J. Phys. Chem.*, **36**, 766 (1962).
20. M. A. V. Devanathan and S. Lakshamanan, *Electrochim. Acta*, **13**, 667 (1968).
21. R. W. Powers and M. W. Breiter, *This Journal*, **116**, 719 (1969).
22. J. O'M. Bockris, Z. Nagy, and A. Damjanovic, *ibid.*, **119**, 285 (1972).
23. T. P. Dirkse, in "Power Sources 3," D. H. Collins, Editor, Oriol Press, Newcastle-upon-Tyne (1971).
24. P. B. Mathur and K. R. Murti, *J. Ind. Chem. Soc.*, **44**, 407 (1967).
25. M. Breiter, *Electrochim. Acta*, **15**, 1297 (1970).
26. T. P. Dirkse and N. A. Hampson, *ibid.*, **17**, 387 (1972).
27. M. Yamashita, T. Yoshimura, Y. Imanaka, and H. Furuta, *Doshisha Daigaku Rikogaku Kenkyu Hokoku*, **18**, 204 (1977).
28. F. Jolas, *Electrochim. Acta*, **13**, 2207 (1968).
29. T. P. Dirkse, *This Journal*, **101**, 328 (1954).
30. H. H. Rode, V. A. Oliapuram, D. Berndt, and P. Ness, in "Zinc-Silver Oxide Batteries," A. Fleischer, Editor, John Wiley, New York (1971).
31. N. A. Hampson, G. A. Herdman, and R. Taylor, *J. Electroanal. Chem. Interfacial Electrochem.*, **25**, 9 (1970).

32. J. F. Jackovitz and A. Langer, in "Zinc-Silver Oxide Batteries," A. Fleischer, Editor, John Wiley, New York (1971).
33. J. S. Fordyce and R. L. Baum, *J. Chem. Phys.*, **43**, 843 (1965).
34. G. H. Newman and G. E. Blomgren, *ibid.*, **43**, 4393 (1965).
35. M. Eisenberg, H. F. Bauman, and D. M. Brettner, *This Journal*, **108**, 909 (1961).
36. R. D. Armstrong and G. M. Bulman, *J. Electroanal. Chem. Interfacial Electrochem.*, **25**, 121 (1970).
37. W. J. Albery and M. L. Hitchman, "Ring-Disc Electrodes," Clarendon Press, Oxford (1971).
38. Y. V. Pleskov and V. Y. Filinovskii, "The Rotating Disk Electrode," Consultants Bureau, New York (1971).
39. M. C. H. McKubre and D. D. Macdonald, "The Temperature Limitations of Primary and Secondary Battery Electrodes. Part I. Kinetics," SRI International, Final Report to the Department of Energy under Contract EM-78-C-01-5159 (1979).
40. M. C. H. McKubre and D. D. Macdonald, Submitted to *This Journal*.
41. R. D. Armstrong and M. F. Bell, *J. Electroanal. Chem. Interfacial Electrochem.*, **55**, 201 (1974).
42. I. Sanghi and M. Fleischmann, *Electrochim. Acta*, **1**, 161 (1959).
43. H. Gerischer, *Z. Phys. Chem.*, **202**, 302 (1953).
44. K. J. Vetter, "Electrochemical Kinetics," Academic Press, New York (1967).
45. J. Wojtowicz, in "Modern Aspects of Electrochemistry," Vol. 8, J. O'M. Bockris and B. E. Conway, Editors, p. 47, Butterworth, London (1973).
46. J. J. Podesta, R. C. V. Piatti, and A. J. Arvia, *This Journal*, **126**, 1363 (1979).
47. A. Y. Gokhshtein, *Dokl. Akad. Nauk. SSR*, **140**, 761 (1961).
48. A. Y. Gokhshtein and A. N. Frumkin, *ibid.*, **144**, 727 (1962).
49. C. Gabrielli, "Regulation et analyse des Systemes a Etats Stationnaires Multiples," Thesis, Paris (1973); I. Epelboin, C. Gabrielli, M. Keddam, J. Lestrade, and H. Takenouti, *This Journal*, **119**, 1632 (1972).
50. M. N. Hull, J. E. Ellison, and J. E. Toni, *This Journal*, **117**, 192 (1970).
51. U. F. Franck, *Z. Electrochem.*, **62**, 649 (1958).
52. D. D. Macdonald and M. C. H. McKubre, "The Temperature Limitations of Primary and Secondary Battery Electrodes. Part II. Thermodynamics," SRI International, Final Report to the Department of Energy under Contract EM-78-C-01-5159 (1979).
53. M. Shabrang and S. Bruckenstein, *This Journal*, **121**, 1439 (1974).
54. H. Chang and G. Jaffe, *J. Chem. Phys.*, **20**, 1071 (1952).
55. E. Levart and D. Schumann, *J. Electroanal. Chem. Interfacial Electrochem.*, **24**, 41 (1970).
56. E. Levart and D. Schuhmann, *ibid.*, **53**, 77 (1974).
57. J. R. Macdonald and D. R. Franceschetti, *ibid.*, **99**, 283 (1979).
58. D. R. Franceschetti and J. R. Macdonald, *ibid.*, **100**, 583 (1979).
59. T. Katan, J. R. Savory, and J. Perkins, *This Journal*, **126**, 1835 (1979).

Anodization of Metals Through Thin Solid Electrolyte Films of Calcia Stabilized Zirconia

J. Perriere and J. Siejka*

Groupe de Physique des Solides de l'Ecole Normale Supérieure,

Université Paris VII, 75221 Paris Cedex 05, France

and M. Croset*

Laboratoire Central de Recherches, Thomson-CSF, Corbeville 91401 Orsay, France

ABSTRACT

This paper shows that anodic oxidation of the metals Nb, Ta, and Al through thin solid electrolyte films of calcia stabilized zirconia (CSZ) is possible. The metal oxides grown are stoichiometric and the CSZ behaves like pure anodic oxide, since the electric field in CSZ in the 0.1-10 mA cm⁻² current density range is comparable with those in anodic oxides. Anodization of Nb|Ta|CSZ or Al|CSZ|Nb|Ta systems shows that only oxygen movements take place in CSZ during oxide growth (i.e., transport number of cations $t^+ = 0$), while both oxygen and cations take part in ionic current in the metal oxides underlying and overlying the CSZ layer (i.e., $t^+ \neq 0$). Thus the transport number of cations can be considered as an intrinsic property of an oxide layer, independent of the nature and of the position of the other layers. Possible microscopic transport mechanisms for oxygen and cations through superimposed oxide films are discussed.

Ionic transport under high electric field through oxide films is generally explained by the thermally activated motion, over discrete energy barriers, of charged point defects (1). It is generally assumed that these defects are injected in the oxide at one of the interfaces (2). For films sufficiently thick ($d > \approx 100\text{\AA}$) the anodization process is believed to be controlled by the migration in the bulk (1). The applied electric field E lowers the energy barrier W , leading

to an exponential type relationship between ionic current i and electric field E : $i \approx A \exp -(W - BE/Kt)$. This expression is obtained with the assumption of a sole migration specie, over a well-defined activation energy barrier. This is generally not the case for the anodization of valve metals, however in a first approach, this convenient theoretical expression has been generally used to describe anodic oxidation of valve metals [for example see Ref. (1-3) and references cited].

A number of works have been devoted to the study of cation or/and anion transport during anodic growth

* Electrochemical Society Active Member.

Key words: solid electrolyte, metals, oxidation, migration, nuclear reactions.

of oxide films. It has been clearly evidenced that the two species, oxygen and metal, may take part in the total ionic current during anodization (4-6), their motion obeying a neighbor-to-neighbor jump process (7, 8). It has been shown that the transport numbers of cations and of oxygen for several oxides (Al_2O_3 , Nb_2O_5 , and Ta_2O_5) have comparable values (5, 6, 9), although it seems unlikely that cation and oxygen defect species have similar activation energy of motion under a wide range of experimental conditions. Note however that during anodization of Zr only oxygen movements have been observed (10). Following Dignam (2) the microscopic mechanism of ionic movement during anodic oxidation of Ta or Al could be different from that of Zr: network defects (AlO^+ or AlO_2^- for example) in the first case, and oxygen point defects (vacancy or interstitialcy) in the second case.

The study of ionic movements during the anodization of superimposed metallic layers showed that it is possible to anodize a metal M_1 covered with a thin oxide film of a metal M_2 (11) even when their respective transport number for cations (t^+) are different; for example Nb can be anodized through thin Al_2O_3 films (12), or Zr through thin Ta_2O_5 films. In the last case the physical nature of moving defects in ZrO_2 and in Ta_2O_5 can also be different (2). Moreover a strong correlation has been evidenced between oxygen and cation jump probabilities during anodization of superimposed layers (13).

All these results did not allow one to construct an unambiguous model for the microscopic mechanism of ionic movements under high electric field. This is due to the fact that the nature of moving defects which are responsible for ion transport in Al_2O_3 , Ta_2O_5 as well as in ZrO_2 is unknown. A possible way to overcome this difficulty is to study ionic movements under high electric field through thin layers of solid electrolyte in which the thermally activated microscopic movements and the nature of moving defects are well known (14). This is the case for calcia stabilized zirconia (CSZ) which is a pure oxygen ion conductor via a vacancy-type mechanism (14). In fact, it has been recently shown (15) that dense and stoichiometric films of CaO doped zirconia of the fluorite-type structure can be obtained by rf sputtering. The conductivity and the activation energy of conduction (E_c) of these films were near to those found for oxygen conduction in bulk material of the same composition, i.e., $3 \times 10^{-7} (\Omega \cdot \text{cm})^{-1}$ at 300°C and $E_c = 1.2 \text{ eV}$ for $(\text{ZrO}_2)_{0.88}(\text{CaO})_{0.12}$. The study of Ni-NiO|CSZ|Pt-O₂ electrochemical cells (16, 17) allowed the authors to conclude that the oxygen transport number in rf sputtered thin CSZ films is near unity (0.99).

The aim of the present work was twofold: to study the ionic movements and the current field relationship in thin CSZ layers under high electric field, and to study cationic movements during anodic oxidation of various metallic substrates covered with superimposed thin CSZ and metallic films, i.e., anodization of metal|CSZ or metal|CSZ|metal systems.

The aim of our study of the current-field relationship in CSZ thin films during the anodization of metal/CSZ systems was to answer the following question: can the convenient theoretical expression

$$i = 2anvq \exp - \frac{W - qaE}{KT} \quad [1]$$

be used to describe the high field ionic transport in CSZ thin films? Let us notice that the CSZ represents the best case to apply this theoretical expression, since in CSZ a sole moving specie (oxygen vacancy) exists, the concentration of which is well known, while in the other classical cases, such as Ta, due to the presence of two migrating species, the theoretical expression has not been proven experimentally. Moreover all terms except the field are known in this expression for

$(\text{ZrO}_2)_{0.88}(\text{CaO})_{0.12}$ [i.e., $a = 1.27 \times 10^{-8} \text{ cm}$, $n = 3.14 \times 10^{21} \text{ cm}^{-3}$, $q = 2 \times 1.6 \times 10^{-19} \text{ C}$, $v = 10^{13} \text{ s}^{-1}$, $W = Ec = 1.2 \text{ eV}$ (17)], a theoretical electric field value can be calculated from the relationship [1], for each current density and so can be compared to the value experimentally determined. Thus, in principle, the concept of thermally activated point defects moving under the influence of electric field may be studied in the particular case of the high field ionic conduction in CSZ.

The study of cationic movements during the anodization of metallic substrates covered with thin films of CSZ was carried out in order to check the role played by interfaces in the injection of defects. Moreover in order to establish whether or not cation movements take place in the underlying oxides, anodization of Nb|Ta|CSZ or Nb|Al|CSZ systems were carried out since we have shown (11, 12) that the anodization of Nb|Ta and Nb|Al systems leads to a partial inversion of the order of cations due to cationic movements. In a similar way, we have studied the anodization of Al|CSZ|Nb|Ta systems in order to see if cationic movements exist in the metal oxides superimposed on the CSZ layer. All these experiments may permit us to elucidate the following problem: in the case of various superimposed oxide layers does a sole transport number of metal characteristic of the whole system exist? As the hypothesis of ionic movements in oxide films taking place by injection of point defects at one of the interfaces (metal-oxide or oxide-solution) implies the preservation of the cationic transport number (2), these experiments can give insights on the microscopic transport mechanism of cations.

This work is part of a general program devoted to the study of oxidation mechanisms of duplex layers and to their applications (18), and to thermal, anodic, and plasma treatments of solid surfaces covered with thin films of solid electrolytes acting as selective membranes (19).

Experimental

Sample preparation.—The metallic and CSZ thin films were deposited on silicon or aluminum substrates. The silicon samples were single crystal, [100] oriented with an n-type bulk resistivity of $10^{-2} \Omega \cdot \text{cm}$. Prior to deposition they were cleaned by successive dipping in HF, deionized water, and acetone. Niobium and tantalum films were deposited either by electron gun evaporation in high vacuum (less than 10^{-8} Torr during deposition) or by d-c triode sputtering in an argon plasma at a 0.13 Pa pressure. Ta and Nb sputtering targets were supplied by Kawecki Berylco Industries with a 99.98% purity for Ta and 99.9% for Nb. In the same way, Al films were obtained by d-c triode sputtering of an Al cathode in an argon plasma. CSZ films were made by rf sputtering of a sintered CSZ cathode supplied by LCC-France; the technique used is described in detail elsewhere (15).

Anodic oxidations were carried out at constant current density and temperature either in ammonium citrate solutions (0.5 or 2% by weight) or in ammonium borate solutions (0.5% by weight, pH kept at 9 by ammonium hydroxide additions). Exactly the same results were obtained whatever the solutions, thus in what follows, the electrolytes used will not be specified. Anodizations were performed using an anode assembly described elsewhere (20), in which a 1 cm^2 surface is delimited by a pressed Teflon O-ring. In the case of M_1 |CSZ and M_1 | M_2 |CSZ structures, an ohmic contact was made with a conducting Ag paste on the back side of the Al or Si substrate. When metallic layers were deposited on top of CSZ films ($\text{Si}|M_1$ |CSZ| M_2 structures), in order to anodize these metallic layers, we established outside the area in contact with the electrolyte an electrical contact (with Ag conducting paste) between the substrate and the metallic layers. Let us notice that it was not possible to anodize the metallic

layers on top of CSZ without the short circuit between these layers and the substrate. Hence we can exclude the presence of defects in CSZ layer which allowed the deposited metal layers to contact the substrate, so the CSZ takes part in the subsequent anodization. Due to possible roughness effects at the CSZ-M₂ interface, we cannot ascertain that all the deposited layer on top of CSZ was anodized without leaving unanodized metal islands. However, the same results were obtained for Si|M₁|CSZ|M₂ as well as for M₁|CSZ|M₂ structures, while the roughness effects must be more important in the last case. Thus we can reasonably assume that unanodized metal islands, if existing, are of very small dimensions (< 5 nm) and do not modify the anodization of the substrate.

Analysis of samples.—Nuclear microanalysis by the direct observation of nuclear reactions and of backscattering particles was used to study the samples before and after anodization. The experiments were carried out using the 2 MeV Van de Graaff accelerator of the Ecole Normale Supérieure.

The ¹⁶O content of the films was measured using the ¹⁶O(d,p)¹⁷O* nuclear reaction as described in detail by Amsel *et al.* (21). Absolute values were obtained by comparison with a reference target known to within ±3% (22).

Rutherford backscattering techniques were used to analyze the depth distribution of cations in the films and in their anodic oxides; lateral homogeneity was assumed for the interpretation of the spectra. The basic concepts and equations pertaining to Rutherford backscattering spectra interpretation can be found in Ref. (23) and will not be presented here; the application to the case of superimposed layers is described in detail in Ref. (11). In all analyses, ⁴He⁺ ion beams were used and the backscattered particles were detected at 165° angle by means of a surface barrier detector (21). The energy resolution being about 14 keV, it was possible to evaluate the depth distribution for Nb, Ta, Al, or Zr atoms in the oxide films with a depth resolution of about 20 nm.

Absolute amounts of Nb, Ta, Al, or Zr expressed in atoms/cm² were obtained (assuming the validity of the Rutherford law) by comparison with a Ta film taken as a standard (24). The film thicknesses will be given in nanometers, the equivalence atoms/cm² — nanometer being obtained by assuming, respectively, a density of 4.74 for Nb₂O₅ (25), 8.04 for Ta₂O₅ (25), 3.17 for Al₂O₃ (26), and 5.32 for CSZ [deduced from Ref. (17)].

Results and Interpretation

In order to describe our results on ionic movements under high electric field in terms of microscopic transport mechanisms, we use the concepts of oxygen and cationic transport events [see for details p. 1551, Ref. (11)]. By the term of cationic (or oxygen) transport events, one means the sequence of elementary jumps of one or more cations (or oxygen) which results in a transport of charges from their creation point to that of their recombination.

During the anodization of metals covered with a thin CSZ film some stresses can be developed at the metal oxide-CSZ interface, due to the increase of volume of the underlying metal oxide (Pilling-Bedworth ratio equal to 1.6 or 2.5 for Al or Ta for example). The ductility of anodic oxides is known to be very high (27); this should make easier the displacement of the CSZ layer located on the top of growing metal oxide. But this last phenomenon is not associated with an ionic migration and so will not be taken into consideration in what follows.

Relationships between oxidation potential *V* and time *t*: *V* = *f*(*t*).—Figure 1 shows some typical curves obtained by recording oxidation potential as a function of time during the anodization of Ta substrates covered

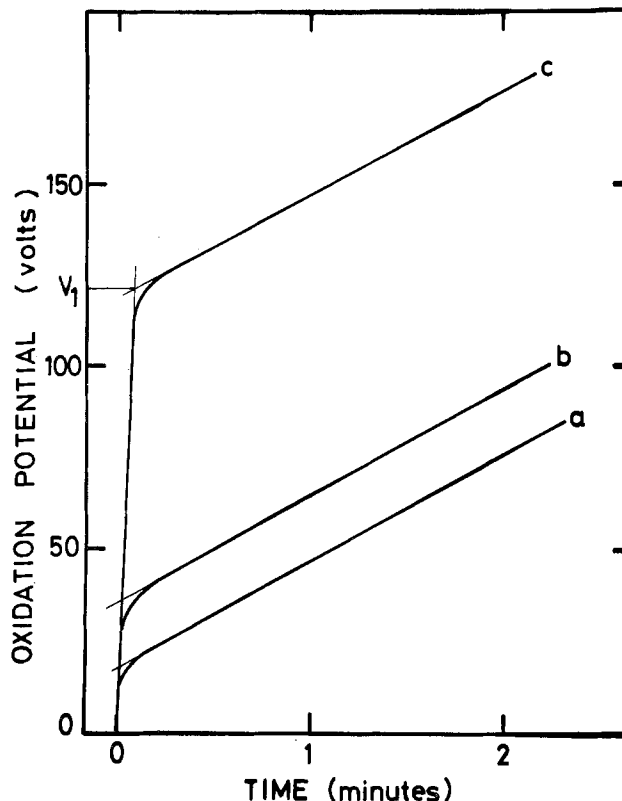


Fig. 1. Oxidation potential *V* as a function of time during anodization at ≈ 1.3 mA/cm² current density at a 23°C temperature for Ta substrates covered with thin CSZ films of various thicknesses: (a) 40 nm, (b) 80 nm, (c) 270 nm.

with CSZ thin films. The three curves of Fig. 1 were obtained for various thicknesses of the CSZ layer; these experiments were carried out at 23°C temperature with a current density of ~ 1.3 mA/cm².

Two linear regions can be distinguished on the three curves; the first region corresponds to a rapid potential increase, while the slope observed at high potential is the same as the one measured in the case of pure Ta₂O₅ growth. The nonabrupt transition between these two regions may be due to the roughness of the Ta-CSZ interface. As a slight thermal oxidation of the Ta substrate was observed (17) during CSZ film deposit, we cannot exclude some lateral inhomogeneity of the tantalum oxide thickness which could increase the roughness of the CSZ|Ta interface; let us notice that for Al|CSZ samples this transition region practically disappears.

The intercept of the two straight lines determines an oxidation potential *V*₁ which was taken as a measure of the potential drop in the CSZ layer. Since the thickness *d* of the CSZ films is determined by backscattering measurements (see experimental), we can evaluate the mean field *E*_{exp} in the CSZ layer by $E_{\text{exp}} = V_1/d$. The linear increase of the potential drop *V*₁ as a function of the thickness of the CSZ layer excludes any artifacts due to the possible presence of pores in the deposit.

The same values of *V*₁ were obtained during the anodization of Al or Nb substrates covered with thin CSZ layers of the same thicknesses. This shows that no appreciable influence of the substrate has been evidenced in these experiments.

In Table I, we present the values of the electric field *E*_{exp} in the CSZ layers at various current densities and for a temperature of 23°C. These values are mean values obtained by more than ten measurements performed either on Ta|CSZ or Al|CSZ systems. The values of the theoretical electric field *E*_{th} obtained from the expression

Table I. Values of the electric field E_{exp} in CSZ layers and in pure ZrO_2 as a function of current density; E_{th} calculated following Eq. [1]

| Current density | $E_{\text{exp}} \times 10^6$ V/cm in CSZ | $E_{\text{th}} \times 10^6$ V/cm | $E_{\text{exp}} \times 10^6$ V/cm in ZrO_2 |
|------------------------|---|-------------------------------------|--|
| 0.1 mA/cm ² | 3.5 ± 0.3 | 19.12 | 3.6 |
| 1 mA/cm ² | 4.3 ± 0.4 | 21.39 | 4 |
| 10 mA/cm ² | 5.5 ± 0.5 | 23.65 | 4.3 |

$$i = 2anvq \exp - \frac{W - qaE_{\text{th}}}{KT} \quad [1]$$

as described in the introduction are presented in Table I. The values of the electric field during anodization of zirconium, i.e., in pure anodic ZrO_2 , for the same experimental conditions, are also given for comparison (28).

Table I shows that E_{exp} in CSZ, which increases when i increases is always much lower than E_{th} . The difference between E_{exp} and E_{th} cannot be explained by our experimental uncertainties on E_{exp} which are of the order of 10%. These uncertainties preclude a precise determination of the $E_{\text{exp}} = f(\log i)$ relationship. However, it seems that E_{exp} in CSZ does not increase linearly with $\log i$. Such an effect is also observed in pure anodic ZrO_2 (28) for high current densities. The values of the electric field in CSZ and in ZrO_2 are similar for current densities of 0.1 and 1 mA/cm² and are different for 10 mA/cm². As most of the results presented in this work were obtained at current densities of about 1 mA/cm², in what follows we shall consider CSZ films like zirconia anodic oxides, i.e., with $t^+ \approx 0$ (10).

Note that this assumption (i.e., CSZ behaves like ZrO_2 anodic oxide) has been checked by experiments on oxygen movement which evidenced a partial inversion of the oxygen atom order in CSZ layers (29) during anodization of underlying metallic layers, like for pure zirconium anodization (28).

Anodization of Metal|CSZ systems.—Figures 2 and 3 represent, respectively, typical backscattering spectra for Ta|CSZ and Al|CSZ samples before and after anodization. In Fig. 2 the Zr spectrum is shaded, and the area of this spectrum does not change after anodization. This means that no dissolution from the CSZ layer occurs. In Fig. 3, the Zr, Hf, and Ca spectra which are clearly separated and isolated from Al background, are exactly the same before and after anodization. Thus it may be concluded that there is no dissolution of any cationic constituents of the CSZ layer.

Two plateaus are observed on the Ta spectrum after anodization (see Fig. 2); plateau 1 corresponds to Ta atoms in the Ta oxide layer while plateau 2 corresponds to unoxidized Ta atoms. As the ratio of plateau heights is the same as the one obtained in the case of pure Ta anodization, it can be assumed that pure Ta_2O_5 is formed during the anodization of Ta|CSZ systems. Similar conclusions for Al are obtained from the analysis of the Al spectrum in Fig. 3. Hence, the anodic oxidation of metal|CSZ systems leads to the formation of stoichiometric metal oxides.

The width of the front edge of the Ta (or Al) spectrum after anodization in Fig. 2 (or 3) is practically the same as the corresponding width before anodization. Note that the arrows in all figures indicate the position of elements at the surface of samples. This result demonstrates that metallic atoms did not enter the CSZ layer during anodization within our experimental resolution (about 20 nm). Let us notice, however, that we do not exclude a slight mixing between the metallic layers and CSZ during the deposit of the latter; the magnitude of such a mixing may be a function of the deposition conditions (17). The interpretation of these results, based on the necessary assump-

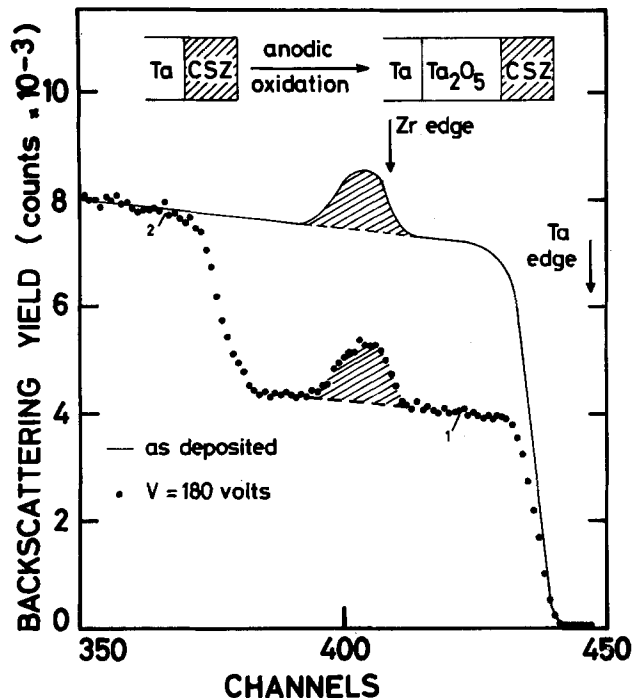


Fig. 2. Rutherford backscattering spectra of 1.6 MeV $^4\text{He}^+$ ions (3.2 keV/channel) for a CSZ film (48 nm) deposited on Ta substrate: before anodization (solid line) and after anodization (·) at $V = 180\text{V}$ and $i = 1\text{ mA/cm}^2$. The arrows indicate the position of elements at the surface of the sample.

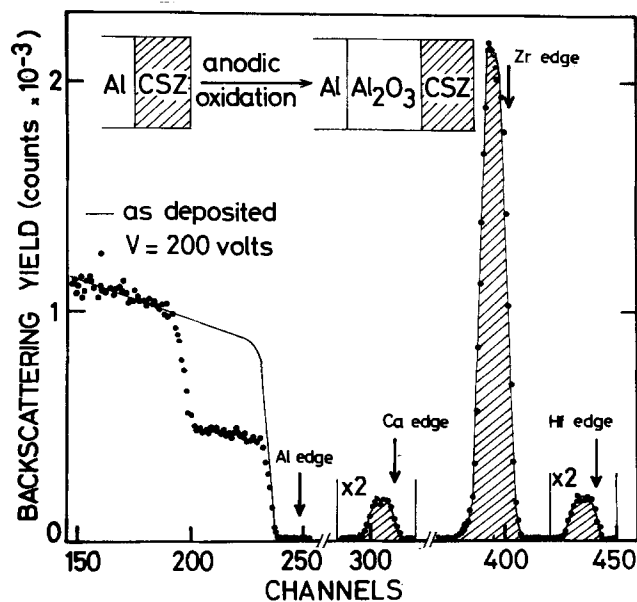


Fig. 3. Rutherford backscattering spectra of 1.8 MeV $^4\text{He}^+$ ions (3.3 keV/channel) for a CSZ film (53 nm) deposited on Al substrate: before anodization (solid line) and after anodization (·) at $V = 200\text{V}$ and $i = 1\text{ mA/cm}^2$. For arrows see Fig. 2.

tion of current continuity can be sought in the frame of one of the two following assumptions:

(1) The transport number of cations (t^+) is the same in each layer, i.e., in the CSZ layer and in the underlying metal oxide, the value of t^+ being determined by the mechanism of injection of transport events at the interfaces (oxide-solution or metal-oxide interface). This hypothesis means that the fluxes of anionic and cationic transport events are preserved through all the film (i.e., in the CSZ layer and in the metal oxide).

(2) The value of t^+ is different in the CSZ layer and in the underlying metal oxide. This hypothesis means that t^+ may be an intrinsic property of each layer, which does not depend on the other layers nor on the

position of the layer. In this case the t^+ values should be equal to 0.25 and 0.4 in Ta_2O_5 and in Al_2O_3 layers (6, 9), respectively, and to zero in CSZ layer.

The results presented on Fig. 2 and 3 can be explained by both assumptions. Let us now analyze the mechanisms of ionic movement involved in these two cases.

Two different mechanisms may be considered for the first hypothesis:

(a) The injection of point defects is determined by the nature of the oxide-solution interface. In the case of CSZ-solution interface, due to the properties of CSZ ($t^+ = 0$), it is logical to assume that only oxygen transport events are injected, i.e., the cationic current J_c is thus equal to zero in CSZ and in the underlying metal oxide (Fig. 4a). Following this mechanism (a) the anodization of Ta or Al substrates covered with a thin CSZ layer involves only oxygen movement.

(b) The injection of point defects is determined by the nature of the metal-oxide interface. In the case of Al| Al_2O_3 or Ta| Ta_2O_5 interfaces, both oxygen and cation transport events are observed ($t^+ \neq 0$) (6, 9) during the anodization of pure metals. According to this fact, in the frame of this mechanism (b) oxygen and cation movements must be preserved through the whole oxide, i.e., in the underlying metal oxide and in the CSZ layer (Fig. 4b). Thus cations move in the metal oxide and in the CSZ layer. As no broadening of the oxide-CSZ interface is observed, this cationic movement, if it takes place, must lead to the conservation of the order of cations. This is possible with some assumptions on the various jump probabilities of cations like those developed for Ta and Nb in a previous paper (11). In fact, to obtain the conservation or the order of cations, we must assume that the jump probability of Ta or Al cations (P_{Ta} or P_{Al}) are lower than that of Zr (P_{Zr}), Ca (P_{Ca}), and Hf (P_{Hf}). Moreover, since no relative movement of Zr, Ca, and Hf occurs (the cation distribution in CSZ film does not change after anodization, see Fig. 3), we must assume that $P_{Zr} = P_{Ca} = P_{Hf}$. Owing to the properties of CSZ previously defined, and to the fact that Zr cations do not seem to take part in the ionic current during Zr anodization (10), this mechanism (b) appears questionable.

The mechanism of ionic movement involved by hypothesis (2) is schematically presented on Fig. 5. In

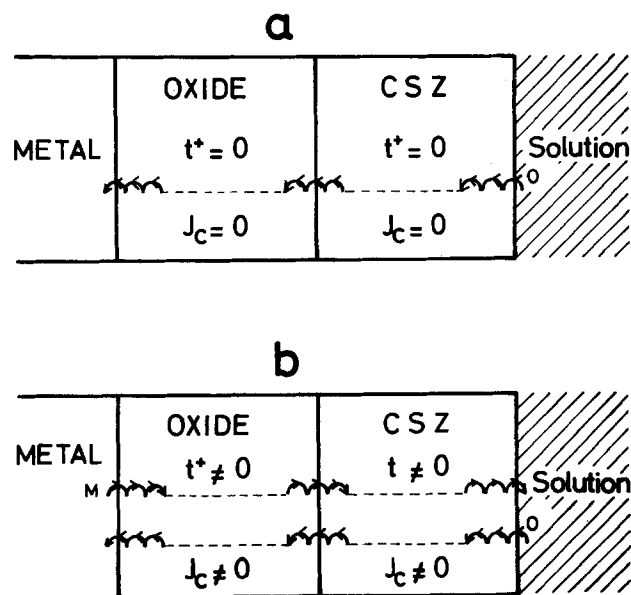


Fig. 4. Schematic representation of ionic movements during the anodization of Metal | CSZ systems with the same value of the transport number of cations t^+ in the whole oxide. (a) $t^+ = 0$, (b) $t^+ \neq 0$.

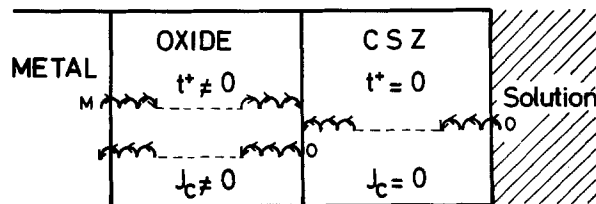


Fig. 5. Schematic representation of ionic movements during the anodization of Metal | CSZ systems with different values of t^+ in each layer.

this case, cationic and anionic movements exist in the underlying metal oxide ($J_c \neq 0$ and $t^+ \neq 0$) while there is only oxygen movement in the CSZ layer ($J_c = 0$ and $t^+ = 0$). With this hypothesis metallic atoms do not enter the CSZ layer and thus this means that metal oxide must be formed partially at the oxide-CSZ interface.

Anodization of $M_1|M_2$ |CSZ systems.—To establish whether cationic movements take place in the underlying metal oxide, anodization of Nb|Ta|CSZ systems was carried out. Figure 6 represents backscattering spectra obtained on such systems before and after anodization. As a result of the preceding experiments, these spectra were analyzed assuming that no dissolution of Zr occurs during oxide growth; therefore the

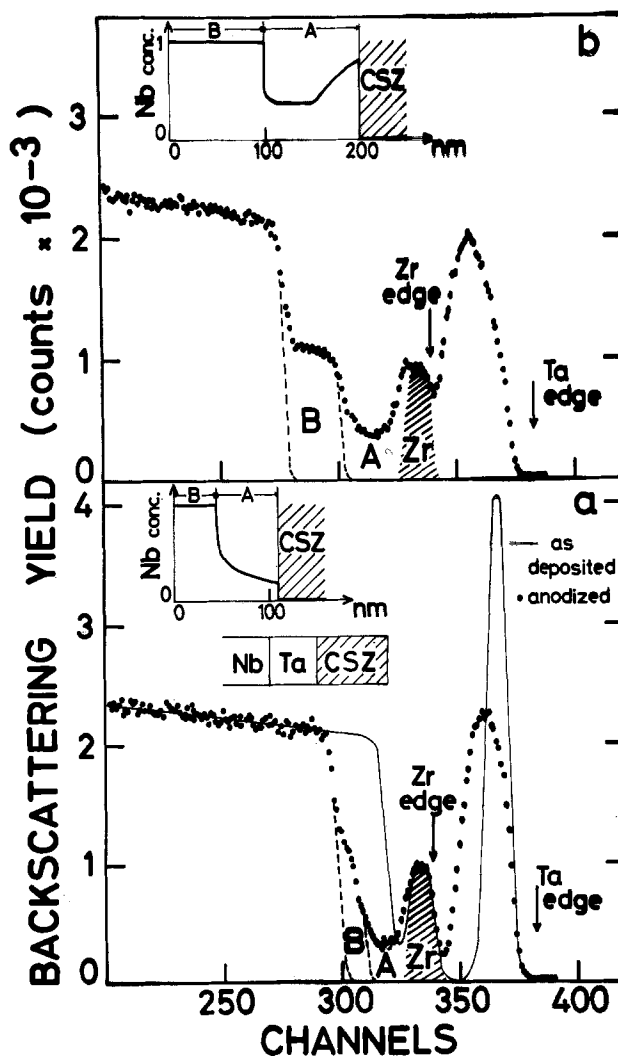


Fig. 6. Rutherford backscattering spectra of 1.8 MeV $^4He^+$ ions (3.2 keV/channel) for a CSZ layer (47 nm) superimposed on a Ta film (21 nm) deposited before and after anodization at two potentials: (a) $V = 80V$, (b) $V = 120V$, $i = 1 mA/cm^2$. The inserts represent the corresponding schematic Nb depth profiles in the oxide. For arrows, see Fig. 2.

Zr spectrum is shaded with a constant overall area on each figure. The front edge of the Ta peak before and after oxidation on Fig. 6a is located at the same energy, lower than for Ta atoms located at the surface of the sample (shown by the arrow Ta edge). This shift is due to the presence of the CSZ layer and means that Ta atoms did not enter the CSZ layer. On Fig. 6a two regions A and B can be defined in the Nb spectrum after anodization. Region A corresponds to Nb atoms which have entered the Ta oxide and thus have formed a Ta and Nb oxide mixture, while region B corresponds to the remaining oxidized Nb atoms [see Ref. (11) for details]. The corresponding Nb depth distribution in the oxide is schematically presented in the insert of the figure and it shows that Nb atoms have crossed the inner edge of the Ta atom distribution. This fact is evidence for cationic movements in the metal oxide underlying the CSZ layer. The behavior of Nb and Ta cations during oxidation of Nb|Ta|CSZ systems appears qualitatively similar to that observed during Nb|Ta anodization (11).

Figure 6b is obtained at a higher oxidation potential. The area of region A of the Nb spectrum increases when the potential increases. This means that more and more Nb cations penetrate into the Ta oxide layer as anodization is pursued. This is checked by the fact that the front edge of the Ta peak is broadened when the potential increases. It was already observed for Nb|Ta anodization (11). Moreover the Ta peak is not shifted toward high energies, this means that the Ta atoms do not enter the CSZ layer. Hence the broadening of the front edge of the Ta peak (Fig. 6b) is only due to the increase in Nb concentration at the metal oxide-CSZ interface. Penetration of Nb cations into the CSZ layer cannot be detected on the Zr or Nb spectrum, but the analysis of the Ta spectrum (shift of the peak to lower energies and broadening of the front edge) indicates that this Nb penetration, if it occurs, must be so weak that we cannot detect it within our experimental sensitivity. In what follows, we shall thus assume that Nb cations, like Ta or Al cations, do not enter into the CSZ layer during anodization.

The Nb depth distribution in the oxide is schematically represented in the insert on Fig. 6b. The various parts of the oxide film are hence: (i) a pure Nb₂O₅ layer at the metal-oxide interface (region B); and (ii) a region containing both Nb and Ta cations (region A). In this latter region the Nb concentration is maximum at the oxide-CSZ interface and then drops in the bulk down to a value which remains constant until region B is reached. These results demonstrate that cationic movements exist in the underlying metal oxide, and are consistent with the idea that Nb atoms do not cross the oxide-CSZ interface. Moreover, although no precise measurement of the fraction of the oxidized Nb atoms located in region A [i.e., F_t in Ref. (11)], was carried out, the results obtained on this system are similar to those observed on Nb|Ta samples.

These results allow us to eliminate the first mechanism of hypothesis (1) (only oxygen movement through all the film), since oxygen movement cannot lead to a cation mixing. Let us notice that they can be explained by the second mechanism of hypothesis (1), if we assume that the jump probabilities of Nb and Ta cations (P_{Nb} and P_{Ta}) are lower than that of Zr (P_{Zr}) so that Nb or Ta cations do not significantly penetrate in the CSZ layer. On the other hand the results are in good agreement with hypothesis (2), i.e., the transport number of cations is an intrinsic property of each layer.

Anodization of $M|CSZ|M_1|M_2$ systems.—In order to establish whether cationic movements take place in metal oxides located above a CSZ layer, i.e., at the oxide-solution interface, and in the underlying CSZ layer, the anodization of Al|CSZ|Nb|Ta systems was studied.

Figure 7 represents backscattering spectra after anodization at various potentials of an Al substrate covered with a CSZ layer (30 nm), itself covered with a 55 nm thick Nb layer on which a Ta film (22 nm) was deposited. On each figure, the Zr spectrum is shaded with a constant overall area. Figure 7a corresponds to an oxidation potential equal to 160V for which the Ta and Nb layers are fully oxidized, the potential drop in CSZ is established and the Al substrate just begins to be anodized. Due to the cationic movements during the anodization of Nb and Ta layers, Nb atoms have crossed the inner edge of the Ta atoms distribution, and thus have formed an Nb and Ta oxide mixture. These Nb atoms correspond to region A of the Nb spectrum, while region B corresponds to the remaining oxidized Nb atoms. The insert in the figure represents schematically the Nb depth profile in the near surface region of the film, as deduced from the spectrum.

On Figure 7b and c, the backscattering spectra correspond to the anodization of the Al substrate at higher

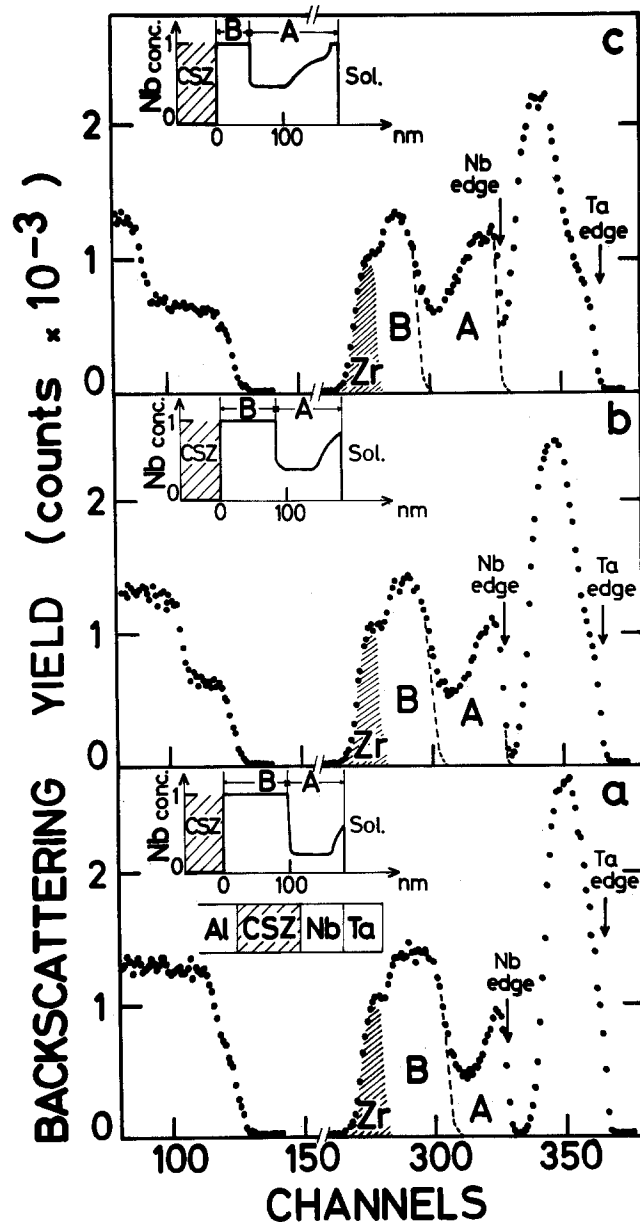


Fig. 7. Rutherford backscattering spectra of 1.8 MeV $^4\text{He}^+$ ions (3.5 keV/channel) for multi superimposed layers on Al substrate: Al | CSZ (30 nm) | Nb (55 nm) | Ta (22 nm) anodized at $i = 1$ mA/cm² and at various oxidation potentials: (a) $V = 160$ V, (b) $V = 210$ V, (c) $V = 270$ V. The inserts represent the corresponding schematic Nb depth profiles in the oxides. For arrows, see Fig. 2.

potentials. The comparison of these two figures with Fig. 7a shows that the area of region A of the Nb spectrum increases with oxidation potential. This demonstrates that Nb cations go on entering the Ta oxide layer whatever the potential. At the same time, the Al substrate is oxidized and Al_2O_3 is formed as the corresponding plateau can be observed in the Al spectrum. These results evidence cationic movements in the Nb and Ta oxide region, located above the CSZ layer, during the anodization of the Al substrate. It must be emphasized that cationic movements occur while the Nb and Ta oxide mixture is separated from the Al substrate by the CSZ layer.

The analysis of the spectra shown on Fig. 7 is consistent with the idea that Zr atoms (of the CSZ layer) have not entered the Nb oxide layer, and thus inserts in Fig. 7b and c represent schematically the Nb depth profile in the oxide with a sharp boundary at the interface with the CSZ layer.

The assumption of no penetration of Zr cations in the metal oxide was checked by experiments carried on Nb|CSZ|Ta samples. After anodization, the Ta_2O_5 layer at the oxide-solution interface and the Nb_2O_5 layer at the metal-oxide interface were separated by the CSZ layer without penetration of Zr cations into the Ta_2O_5 layer.

Another point to notice about Fig. 7 is that the front edge of the Al spectrum is wider than that observed on Fig. 3; however, as the oxidation potential increases, no further broadening occurs. This probably means that during the deposit of the CSZ layer some mixing with the Al substrate occurred, but during the anodization process no Al atoms entered the CSZ layer. On the three spectra the areas of the Nb and of the Ta components are constant; thus there is no appreciable dissolution of Nb or Ta during anodic oxidation.

These results allow us to eliminate mechanism (b). In fact in the frame of this mechanism, the cation movements evidenced in the Nb and Ta oxide mixture must be preserved in the whole oxide. In order to explain the preservation of the order of cations between the CSZ layer and the Nb and Ta oxide mixture, one must assume that P_{Ta} and P_{Nb} are higher than P_{Zr} . A contradiction appears, since in the frame of mechanism (b) the preceding results (anodization of Nb|Ta|CSZ systems) have been explained assuming P_{Ta} and $P_{\text{Nb}} < P_{\text{Zr}}$. As the mechanism (a) was eliminated previously, it appears that the hypothesis (1) [assuming the preservation of transport events through the whole oxide] is in contradiction with our experimental results and must be eliminated. It means that the cation constituents of CSZ layer (Zr, Ca, and Hf) do not move during anodization while cationic movements take place in the metal oxide layers located either on the top or under the CSZ layer. These results are in good agreement with hypothesis (2) which assumes that the transport number t^+ is an intrinsic property of each layer.

The results of this last experiment can be compared to those obtained during the anodization of Al|Nb|Ta systems (30) in which during the oxidation of the Al substrate, the Nb and Ta cation distribution, in the oxide mixture, goes on changing as the oxidation potential increases. These results were interpreted (31) assuming that cation transport events, coming from the underlying pure Al_2O_3 layer are preserved in the whole oxide, i.e., move through the mixed Ta and Nb oxide by a neighbor-to-neighbor type propagation process. Since the same results are obtained on Al|CSZ|Nb|Ta systems, we can conclude that the presence of the CSZ layer, in which only oxygen moves, does not eliminate cationic movements by a neighbor-to-neighbor jump in the Ta and Nb oxide mixture at the oxide solution interface.

Very similar results were obtained during the anodization of Al|CSZ|Nb|Al system, i.e., the cation distribution in the oxide in the near surface region of the

film undergoes strong changes whereas the Al substrate is oxidized as it is observed for the Al|Nb|Al system (29). In this case also, no penetration of Zr cations in the mixed oxide was evidenced.

Figure 8 represents schematically the main conclusion drawn from these experiments: the transport number of cations t^+ changes from one part of the film to another. t^+ is equal to zero in the CSZ layer, while there is cationic movement ($t^+ \neq 0$) in the metal oxide at the oxide-solution interface. Hence ionic current is transported by cation and oxygen in the outer part of the film while there is only oxygen movement in the CSZ layer.

Anodization of $M_1|M_2|CSZ|M'_1|M'_2$ systems.—All the preceding experimental results are in good agreement with hypothesis (2). In order to further confirm the validity of this hypothesis, we have studied the cation distribution in oxides formed by anodization of Nb|Al|CSZ|Nb|Ta systems. It was expected that cationic movements had to take place in metal oxides above and below the CSZ layer, while in the CSZ layer only oxygen movements have to take place.

Figure 9 represents backscattering spectra from Nb|Al (20 nm)|CSZ (85 nm)|Nb (36 nm)|Ta (14 nm) systems oxidized at two oxidation potentials. On the two figures, the Zr and Ta contributions are shaded while the two Nb parts corresponding to the Nb layer above the CSZ and to the Nb substrate are labelled Nb(1) and Nb(2). Figure 9a corresponds to an oxidation potential equal to 100V, for which the Ta and Nb layers are fully oxidized, part of the potential drop in the CSZ layer is established while the Al layer and the Nb substrate are not oxidized. As a result of cationic movements during the anodization of Ta and Nb layers, Nb atoms have crossed the inner edge of the Ta atom distribution and thus have formed the Ta and Nb oxide mixture at the oxide-solution interface. These Nb atoms correspond to region A of Nb(1), while region B of Nb(1) corresponds to the remaining oxidized Nb atoms. The insert in the figure shows schematically the Nb depth profile in the near surface region of the oxide.

Figure 9b corresponds to a potential equal to 200V for which the Al layer and the Nb substrate underlying the CSZ layer are oxidized. This figure shows that the area of part A of Nb(1) has increased; this indicates that Nb atoms have entered the Ta oxide layer during the anodic oxidation of metallic layers underlying the CSZ film. This result is identical to that obtained in the preceding experiments and can be interpreted by the fact that cationic movements take place in the oxide near the oxide-solution interface whereas the substrate is oxidized. Two regions (A' and B') can be distinguished on Nb(2) spectrum. Region B' represents Nb atoms in a pure Nb_2O_5 layer at the metal-oxide interface, while region A' corresponds to Nb atoms which have crossed the inner edge of the Al atoms distribution and thus have formed an Nb and Al oxide mixture. This result is similar to that obtained during the anodic oxidation of the Nb|Al system (12). The insert on the figure schematically represents the Nb depth profile in the film. The two Nb distributions (under and above the CSZ layer) are shown with sharp boundaries with the CSZ layer, i.e., assuming, as above, no penetration of Zr cations in the Nb and Ta oxide mixture superimposed on the CSZ layer, and

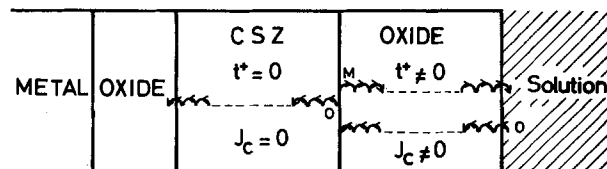


Fig. 8. Schematic representation of ionic movements during the anodization of Metal | CSZ | Metal systems with different values of t^+ in CSZ and in the metal oxide at the oxide solution interface.

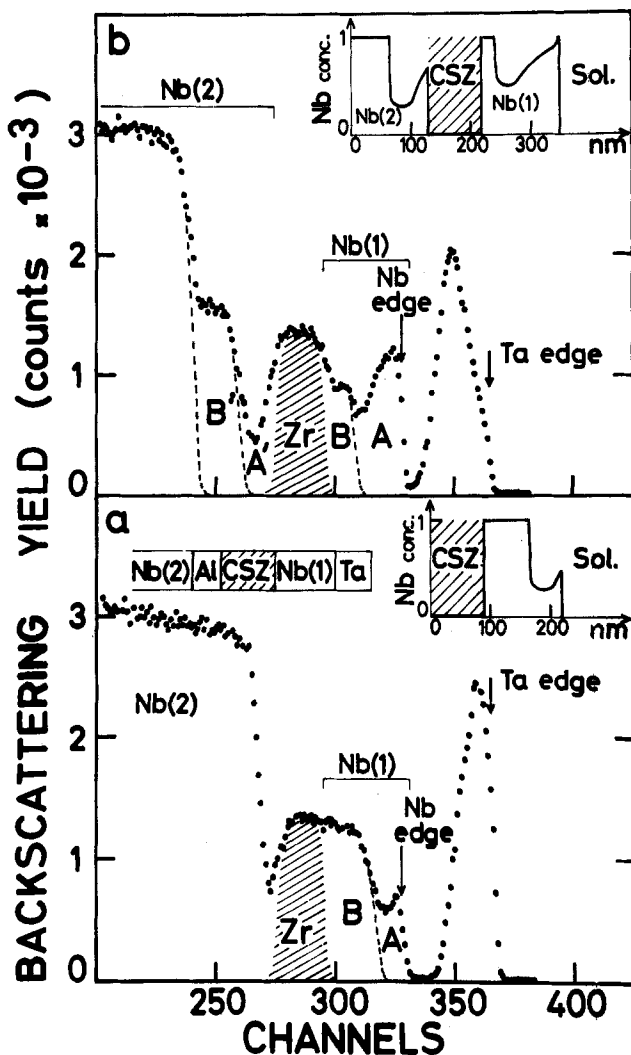


Fig. 9. Rutherford backscattering spectra of 1.8 MeV $^4\text{He}^+$ ions (3.5 keV/channel) for multi superimposed layers on Nb substrate: Nb | Al(20 nm) | CSZ(85 nm) | Nb(36 nm) | Ta(14 nm) anodized at $i = 1 \text{ mA/cm}^2$ at different potentials: (a) $V = 100\text{V}$, (b) $V = 200\text{V}$. The inserts represent the corresponding schematic Nb depth profiles in the oxides. For arrows, see Fig. 2.

without penetration of Nb coming from the underlying layer into the CSZ layer.

These results fully confirm the preceding results and are in agreement with hypothesis (2): cationic movements take place both under and above the CSZ layer during the anodization of the substrate. Figure 10 schematically represents this conclusion: the transport number of cations t^+ depends on the nature of each layer while cations move in the metal oxide located above and below the CSZ layer. Note that the confirmation of hypothesis (2) needs the knowledge of the values of t^+ in metal oxides overlying or underlying the CSZ layer. Our experimental conditions do not allow us to measure precise values of F_t , i.e., the transport number of cations in the Nb and Ta oxides located over and under the CSZ layer (11). Thus, at the present time, it is not possible to quantitatively compare these F_t values to that measured during pure Nb/Ta anodization. However, work is in progress to check hypothesis (2), since we have realized a computing calculation of backscattering spectra which allow us to precisely determine the cation distribution in the oxide films. Results of this study will be published in a later paper.

Discussion and Conclusions

In this work we have shown that it is possible to anodize metallic substrates (Nb, Ta, or Al) covered

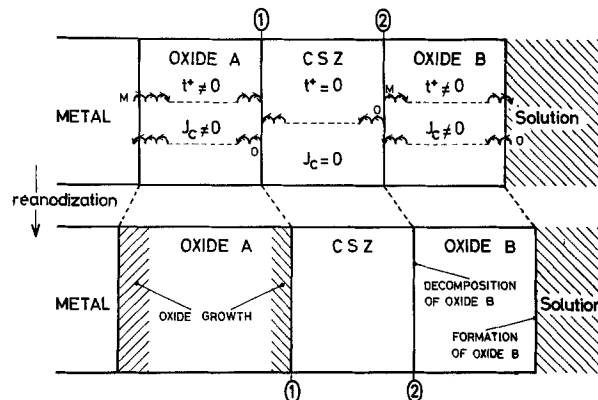


Fig. 10. Schematic representation of ionic movements during the anodization of Metal | CSZ | Metal systems with different values of t^+ in each layer, leading to oxide A growth while thicknesses of the CSZ layer and of oxide B are preserved.

with CSZ thin films. The growth rates of oxide on metallic substrates in metal|CSZ systems are similar to those observed for pure metals, and the current field relationship in CSZ appears similar to the one observed during pure Zr anodization. The anodization of $M_1|M_2$ |CSZ or $M_1|M_2$ |CSZ| M_1 | M_2 systems gives the experimental proof that cation movements take place in metal oxides located above and below the CSZ layer. Moreover, all these results are consistent with the idea that only oxygen atoms move through CSZ films, i.e., the cationic constituents of CSZ do not take part in ionic current. These results seem to indicate that the mechanism of high field conduction in CSZ film is similar to that of pure anodic ZrO_2 in which the transport number of oxygen is above 0.95 (10). This means that the introduction of 12 atomic percent of Ca to stabilize the fluorite structure of ZrO_2 does not notably affect the high field ionic conduction in zirconia oxide. Two possibilities appear in order to explain this last point: (i) anodization of Zr leads to the formation of a highly conducting phase, similar to the one obtained by inclusion of CaO in ZrO_2 . In this case, according to the presence in CSZ of a high oxygen vacancy concentration, oxygen ion movement takes place by a vacancy-type mechanism; (ii) oxygen ion movement does not take place by vacancy-type mechanism, neither in pure ZrO_2 film nor in CSZ film, in spite of the presence in CSZ of a high oxygen vacancy concentration with a low activation energy of movement (1.2 eV).

In hypothesis (i), one must explain the disagreement between E_{th} and E_{exp} (Table I). This disagreement seems to disappear if we use an effective field E_{eff} instead of the one of Maxwell, i.e., the experimental field ($E_{\text{Maxw}} = E_{\text{exp}}$), in the relationship [1]. In fact in ionic cubic crystals (32) (and the oxygen sublattice is of cubic symmetry), the following relationship is valid

$$E_{\text{eff}} \leq E_{\text{Maxw}} + \frac{\epsilon - 1}{3} E_{\text{Maxw}}$$

where ϵ is the static dielectric constant, i.e., $\epsilon = 25$ for CSZ thin films (17). This means that $E_{\text{eff}} \leq 9 E_{\text{Maxw}}$, i.e., $E_{\text{eff}} \leq 3.9 \times 10^7 \text{ V/cm}$ for $i = 1 \text{ mA/cm}^2$. A question arises whether E_{eff} or E_{Maxw} (i.e., E_{exp}) must be used in relationship [1]. Dignam has analyzed this question (2) and concludes that the Maxwell field must be used; however this problem has given rise recently to contradictory discussions (33) which indicate that Dignam's approach is not fully accepted.

The second possibility (ii) based on the fact that oxygen movement does not take place by a vacancy-type mechanism, implies that one must consider a new mechanism. Some essential features of such mechanism seem to be the following: injection of oxygen

charged species at the oxide-solution interface, which migrate by a neighbor-to-neighbor jump process, the activation energy of movement being lower than 1.2 eV. Works of Dignam (2), Fromhold (34), and Ortega (28) are attempts to provide at least partial informations on these migration mechanisms.

The second purpose of this work was devoted to study the mechanism of ionic movement through various superimposed layers having different values of cationic transport numbers. The essential results of this study are presented in Fig. 10. This figure shows schematically the presence of oxygen and cation transport events in metal oxides below and above the CSZ layer [respectively labelled (A) and (B)], and only of oxygen events in the CSZ film; at steady-state conditions the total ionic current (the electronic current can be neglected) must be preserved through the whole oxide, this means that $J_o(A) + J_c(A) = J_o(CSZ) = J_o(B) + J_c(B)$.

From the macroscopic standpoint, this figure indicates on the one hand the formation of oxide at the metal-oxide(A) and at the oxide(A)-CSZ interfaces, and on the other hand the decomposition of oxide(B) at the CSZ-oxide(B) interface, associated with the formation of the same quantity of oxide(B) at the oxide(B)-solution interface (see Fig. 10). In this way, the overall quantity of oxide(B) is preserved during anodization of the substrate as experimentally observed. It can be noticed that according to the fact that oxide(A) and (B) can have different values of cationic transport number, the quantity of oxide formed and eliminated at the interfaces of the CSZ layer are not necessarily equal. Thus, the role played by these interfaces appears to be very important. However it should be emphasized that the phenomena occurring at these interfaces (injection of charged species and oxide decomposition) are not the rate-determining steps of anodic growth since we have shown that the growth rates of oxide on metallic substrates (Ta or Al for example) covered with CSZ films are similar to those observed for pure metal anodization.

From the microscopic standpoint, the results summarized in Fig. 10 can be discussed by using the concept of oxygen and cationic transport events (see below).

Two extreme assumptions may be made to explain ionic movements in such superimposed layers. First, it could be assumed that oxygen and cation transport events are not distinct. There would be only one transport event implying the simultaneous movement of cations and anions. Thus, at a molecular scale, both cations and oxygen move in a ratio equal to the transport number which is a measure, at the macroscopic scale, of this movement and which appears as an intrinsic property of each oxide. In this frame, the results could be interpreted by assuming that each oxide layer preserves its own transport number. The microscopic jump process which can sustain this proposition could be searched in a similar way as that suggested by Fromhold (34), i.e., some sort of place exchange mechanism.

At the interface between the crystalline CSZ and the amorphous metal oxide, some rearrangement of the structure has to occur. This can be obtained by taking into consideration the property of plasticity (25) of anodic oxides related to their amorphous nature. It is, however, difficult to explain with such a mechanism the absence of noticeable mixing at the two interfaces of CSZ.

The other extreme assumption is that the oxygen and cation transport events are distinct (note that this does not mean that we consider these two charge transport events as independant since we have shown that a strong correlation exists (13) between oxygen and cation jump probability during anodic oxide growth. It appears, in this frame, that the role played by interface 2 is fundamental. In fact, at this CSZ-oxide(B) interface, the following processes must occur: injection of

oxygen charged species in the CSZ layer, and simultaneous generation of cationic transport events in the oxide(B). At the interface 1, the total current is due to oxygen injection in a way similar to the one taking place at an oxide-liquid electrolyte interface, CSZ acting thus as a solid electrolyte. Oxygen transport events have to exist in the whole oxide, but the associated charge q^- can be different in the CSZ layer and in metal oxide. For example at interface 2, oxygen transport events may be in the form of interstitialcy O^- in oxide(B) and in the form O^{2-} in CSZ layer. The current continuity, and the continuity of oxygen fluxes imply that a cationic charge M^+ has to be created at this interface. Here enough plasticity of anodic oxides must be assumed to explain the necessary rearrangement of the structure at the interface. In this assumption, the transport number in metal oxide(B) will be determined by the nature of the CSZ-metal oxide(B) interface. In the future work, we will try to answer this question.

Acknowledgments

The authors wish to express their thanks to G. Amsel, C. Ortega, and G. Velasco for helpful discussions. The technical assistance of MM. J. P. Enard, M. Guyery, and A. Laurent was much appreciated. This work was supported by the Centre National de la Recherche Scientifique (R.C.P. No. 157), by the D.G.R.S.T. and the D.R.E.T.

Manuscript submitted Feb. 20, 1980; revised manuscript received Sept. 12, 1980. This was Paper 189 presented at the Seattle, Washington, Meeting of the Society, May 21-26, 1978.

Any discussion of this paper will appear in a Discussion Section to be published in the December 1981 JOURNAL. All discussions for the December 1981 Discussion Section should be submitted by Aug. 1, 1981.

Publication costs of this article were assisted by the Laboratoire Central de Recherches Thomson—C.S.F.

REFERENCES

1. L. Young, "Anodic Oxide Films," Academic Press, New York (1961).
2. M. J. Dignam, in "Oxides and Oxide Films," Vol. 1, J. W. Diggle, Editor, Marcel Dekker, Inc., New York (1973).
3. C. J. Dell'Oca, D. L. Pulfrey, and L. Young, *Phys. Thin Films*, **6**, 1 (1971).
4. J. A. Davies, J. P. S. Pringle, R. L. Graham, and F. Brown, *This Journal*, **109**, 999 (1962).
5. J. A. Davies, B. Domeij, J. P. S. Pringle, and F. Brown, *ibid.*, **112**, 675 (1965).
6. J. P. S. Pringle, *ibid.*, **121**, 865 (1974).
7. G. Amsel and D. Samuel, *J. Phys. Chem. Solids*, **21**, 1707 (1962).
8. J. P. S. Pringle, *This Journal*, **120**, 1391 (1973).
9. F. Brown and W. D. Mackintosh, *ibid.*, **120**, 1096 (1973).
10. J. L. Whitton, *ibid.*, **115**, 58 (1968).
11. J. Perriere, S. Rigo, and J. Siejka, *ibid.*, **125**, 1549 (1978).
12. J. Perriere, S. Rigo, and J. Siejka, Abstract 194, p. 462, The Electrochemical Society Extended Abstracts, Seattle, Washington, May 21-26, 1978.
13. J. Perriere, S. Rigo, and J. Siejka, Abstract 196, p. 468, The Electrochemical Society Extended Abstracts, Seattle, Washington, May 21-26, 1978.
14. T. H. Etsell and S. N. Flengas, *Chem. Rev.*, **70**, 339 (1970).
15. M. Croset, J. P. Schnell, G. Velasco, and J. Siejka, *J. Appl. Phys.*, **48**, 775 (1977).
16. M. Croset, J. P. Schnell, G. Velasco, and J. Siejka, *J. Vac. Sci. Tech.*, **14**, 777 (1977).
17. J. P. Schnell, Thesis, Université Paris VI, Paris (1977).
18. S. Rigo and J. Siejka, French Pat. "Anvar No. 7193"
19. M. Croset and G. Velasco, French Pat. No. 77.27.470.
20. G. Amsel, J. P. Nadai, C. Ortega, and J. Siejka, *Nucl. Instr. Meth.*, **149**, 713 (1978).
21. G. Amsel, J. P. Nadai, E. D'Artemare, D. David, E. Girard, and J. Moulin, *ibid.*, **92**, 481 (1971).
22. G. Amsel, J. P. Nadai, C. Ortega, S. Rigo, and J.

- Siejka, *ibid.*, **149**, 705 (1978).
23. W. K. Chu, J. W. Mayer, A. Nicolet, T. M. Buck, G. Amsel, and F. Eisen, *Thin Solid Films*, **17**, 1 (1973).
 24. S. Rigo, C. Cohen, A. L'Hoir, and E. Backelandt, *Nucl. Instr. Meth.*, **149**, 721 (1978).
 25. A. J. Schrijner and A. Middlehoek, *This Journal*, **111**, 1167 (1964).
 26. W. J. Bernard and J. W. Cook, *ibid.*, **106**, 643 (1959).
 27. M. Propp and L. Young, Abstract 184, p. 438, The Electrochemical Society Extended Abstracts, Seattle, Washington, May 21-26, 1978.
 28. C. Ortega, Ph.D. Thesis, University Paris 7, Paris (1981).
 29. J. Perriere, J. Siejka, and M. Croset, Abstract 189, p. 448, The Electrochemical Society Extended Abstracts, Seattle, Washington, May 21-26, 1978.
 30. J. Perriere, S. Rigo, and J. Siejka, Abstract 129, p. 294, The Electrochemical Society Extended Abstracts, Toronto, Canada, May 11-16, 1975.
 31. J. Perriere, Thesis, Université Paris VII, Paris (1974).
 32. J. Tessman, A. Kahn, and W. Shockley, *Phys. Rev.*, **92**, 890 (1953).
 33. Panel discussion at The Electrochemical Society Meeting, Seattle, Washington, May 21-26, 1978.
 34. A. T. Fromhold, Jr., *This Journal*, **127**, 411 (1980).

On the Mechanism of Electrodeposition in the Dimercaptiothiadiazole/Copper Pyrophosphate System

Cameron Ogden* and Dennis Tench*

Rockwell International, Electronics Research Center, Thousand Oaks, California 91360

ABSTRACT

Cyclic voltammetric stripping results are presented which show that a dynamic equilibrium exists in the dimercaptiothiadiazole (DMTD)/copper pyrophosphate system involving a species which accelerates the copper deposition rate, a decelerating species, Cu^{+2} ions, and other bath constituents. The experimental data are well explained by assuming that the accelerator is the copper-complexed DMTD monomer species, whereas deceleration is produced by the DMTD dimer. A model is presented which explains the additive effects in terms of a critical balance between the nucleation of new growth centers by the accelerating additive species and copper ammine complexes, and the limitations on growth imposed by the decelerating additive species which functions by blocking growth sites. Based on this model, which is supported by a-c impedance data and morphological studies, the important deposit properties can be understood and predicted.

Copper pyrophosphate electroplating baths containing dimercaptiothiadiazole leveling additives (1,2) are widely used in applications for which throwing power, tensile strength, and ductility are important considerations, as in electroforming and the plating of through-hole interconnections in high reliability circuit boards. Our previous work (3) has shown that additives of this class function in a complex way, decelerating the copper deposition rate at higher concentrations while exerting an accelerating effect at lower levels. Such dual decelerating/accelerating behavior results in enhanced leveling power, but also underlies a strong dependence of the deposit uniformity (4) and tensile properties (5) on the additive concentration. Control of this system is rendered more difficult by the slow additive activation required to produce decelerated deposition (3). In the present paper, the additive species present in copper pyrophosphate baths and the mechanisms by which they affect copper deposition are discussed.

Experimental Details

System description.—Unless otherwise noted, all measurements were made in air-saturated copper pyrophosphate baths at 55°C containing 22.5 g/liter Cu^{+2} , 175 g/liter $\text{P}_2\text{O}_7^{4-}$, 2.25 g/liter NH_3 , and up to 50 $\mu\text{moles/liter}$ of the organic additive 2,5-dimercapto-1,3,4-thiadiazole (Aldrich Chemical Company). This pure compound was used as the additive since it is easier to control and has been shown (3-5) to yield results comparable to those for the proprietary formulation PY61-H (M & T Chemicals, Incorporated). Baths

were prepared from concentrates C10XB and C11XB (M & T Chemicals, Incorporated) and were operated at a pH of 8.3.

The cell was Pyrex glass with a Teflon top and had a volume of 150 ml. Temperature was maintained constant within $\pm 1^\circ\text{C}$ by water circulated through a cell jacket from a Haake FT circulator-controller. The Pt-40% Rh counterelectrode and commercial SCE reference were dipped directly in the bath.

Cyclic voltammetric stripping studies.—The cyclic voltammetric stripping (CVS) method (3) was used extensively in these studies to measure changes in the copper electrodeposition rate produced by additive species. In this method, the potential of an inert Pt electrode is cycled in copper pyrophosphate baths at 50 mV/sec between -0.700 and 1.000V vs. SCE so that a small amount of copper is alternately deposited on the Pt surface and stripped off by anodic dissolution. The charge required to oxidize the copper deposit is proportional to the average deposition rate for that cycle and is found to be related to the concentration of additive in the bath when adequate solution mass transport is provided. The latter is attained by mounting the Pt electrode in the standard disk configuration (6) and rotating it at 2500 rpm. The rotating Pt disk electrode used for the present studies and its pretreatment are described elsewhere (3).

The effects of other bath species which affect the electrodeposition rate are to some extent cancelled by using the internal standard provided by the static electrode in the same bath. When the electrode rotation is stopped, those additive species which are present in very small concentrations compared to other bath constituents become depleted at the electrode surface as they are destroyed by reduction and inclusion in the

* Electrochemical Society Active Member.

Key words: electroplating, copper pyrophosphate, additive effects, molecular dynamics.

deposit. Thus, the stripping peak area approaches that which would be obtained in the same bath without low-level additive species present. The ratio of the stripping peak area with rotation (A_r) to that for the static electrode in the same solution (A_s) yields a relative rate parameter which reflects only the effect of such additive species on the electrodeposition rate.

Measurements of A_r/A_s were made under complete computer control using a Hewlett-Packard Model 9825 minicomputer in conjunction with a PAR Model 173 Potentiostat/Galvanostat and a PAR Model 179 Digital Coulometer. A Hewlett-Packard Model 6940B Multi-programmer and a Model 98033A BCD were used as computer interfaces. Steady state for each measurement was assured by establishing a convergence limit of 4% for successive peak integrations.

A-C impedance analysis.—Measurements of the a-c impedance of the electrode during copper electrodeposition at constant potential were made from 0.1 Hz to 10 kHz using a Solartron Model 1174 Frequency Response Analyzer in conjunction with the PAR Models 173 and 179 instruments. Electrodes were rotated at 2500 rpm and comparable steady-state results were obtained with Pt (0.13 cm²) and Cu (0.30 cm²) substrates.

Results and Discussion

Additive activation studies.—A plot of A_r/A_s vs. the additive concentration for baths at operating temperature is shown in Fig. 1. Good sensitivity to the additive, which is the basis for use of this method as an analytical technique, is evident. It is also apparent that the additive accelerates the deposition rate at low concentrations ($A_r/A_s > 1$) but exerts a decelerating effect at higher levels ($A_r/A_s < 1$). The dependence of A_r/A_s on concentration is linear in the decelerating region and extrapolates to an A_r/A_s value of unity at zero concentration. This indicates that two additive species are involved, an accelerator and a decelerator, which act independently to affect the deposition rate. The presence of two species is also indicated by the observation that an activation period is required to produce deceleration on addition of the additive to the bath, whereas accelerated deposition is rapidly attained. The data in Fig. 1 were obtained after the baths were allowed to equilibrate for 16 hr at 55°C.

Plots of A_r/A_s as a function of time after addition of the additive to the bath at operating temperature

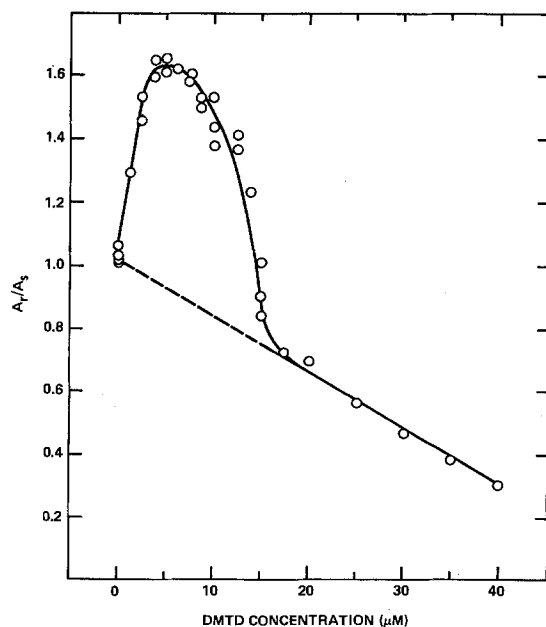


Fig. 1. Relative rate parameter (A_r/A_s) vs. additive concentration for copper pyrophosphate baths at 55°C (after 16 hr).

are shown in Fig. 2. It is evident that the accelerating species is formed almost immediately (A_r/A_s rapidly increases to a steady value), whereas the decelerator forms more gradually, at a rate which increases with initial concentration. The minima observed at the higher concentrations are discussed below.

Analog additive studies.— A_r/A_s ratios were measured at room temperature in baths containing molecular analogs of 2,5-dimercapto-1,3,4-thiadiazole for which amino ($-NH_2$) or methyl ($-CH_3$) groups were substituted for one or both of the mercapto ($-SH$) groups. To ensure equilibration, baths were heated at 55°C for 16 hr before measurements were made. Data are given in Fig. 3. Both acceleration and deceleration were produced by 2-amino-5-mercapto-1,3,4-thiadiazole, but this analog was less effective than the dimercapto compound. The 2-methyl-5-mercapto-1,3,4-thiadiazole and 2-mercaptothiazoline analogs produced only deceleration, whereas 2,5-dimethyl-1,3,4-thiadiazole had no effect on the deposition rate. These results indicate that acceleration requires two groups which can complex with Cu^{+2} (i.e., $-SH$ or $-NH_2$), whereas one such group can produce deceleration (after activation). It should be noted that other compounds that are not direct analogs of the dimercaptothiadiazoles but contain the $-S-C=N-$ group, like trithiocyanuric acid and sodium thiocyanate, also produce accelerated deposition. All of the accelerating species studied are capable of forming a ligand bridge between two copper ions which permits interaction via a conjugated framework.

Additive equilibria.—The simplest additive equilibrium scheme consistent with the available data is illustrated in Fig. 4. It should be borne in mind that the bath copper ions are highly complexed so that the concentration of free Cu^{+2} is extremely small (6) and may limit the rate of Cu^{+2} reactions. In aqueous solutions, the dimercaptothiadiazole (DMTD) additive (a) is expected (8-10) to exist predominately in the thiol-thione monoanion form (b) which readily complexes with Cu^{+2} ions. Since the analog additive studies showed that two donor groups capable of coordinating Cu^{+2} are required to produce acceleration, the accelerating species is presumably the copper-complexed monomer species (c and d). Since mercaptans also oxidatively dimerize (11), a DMTD dimer species (e) is also expected to form, although more slowly since the additive concentration is small and the oxidation reaction is bimolecular. That the DMTD dimer (e) and its complexed form (f) are the decelerating species is supported by the observation that increasing the Cu^{+2} concentration in the bath suppresses formation of the decelerator, presumably by tying up the DMTD monomer (b) required for dimerization. This is evident from the data in Table I which show that both the final A_r/A_s value and the time required for activation increase approximately linearly with Cu^{+2} concentration. As the additive level is decreased, the effect of increasing Cu^{+2} concentration saturates at progressively lower Cu^{+2} concentrations, as would be expected.

To corroborate the identity of the decelerator, the DMTD dimer (e) was synthesized (by oxidation of the monomer with iodine in acetonitrile/ethanol solution) and was found to be almost immediately active as a decelerator in copper pyrophosphate baths. Although the

Table I. Effect of Cu^{+2} concentration on the final A_r/A_s ratio and the time required for A_r/A_s to reach a plateau value for copper pyrophosphate baths containing 30 μ mole DMTD additive

| Cu^{+2} concentration (g/liter) | Final A_r/A_s | Time (hr) |
|-----------------------------------|-----------------|-----------|
| 20.0 | 0.36 | 0.3 |
| 22.5 | 0.65 | 1.2 |
| 24.8 | 0.80 | 2.2 |

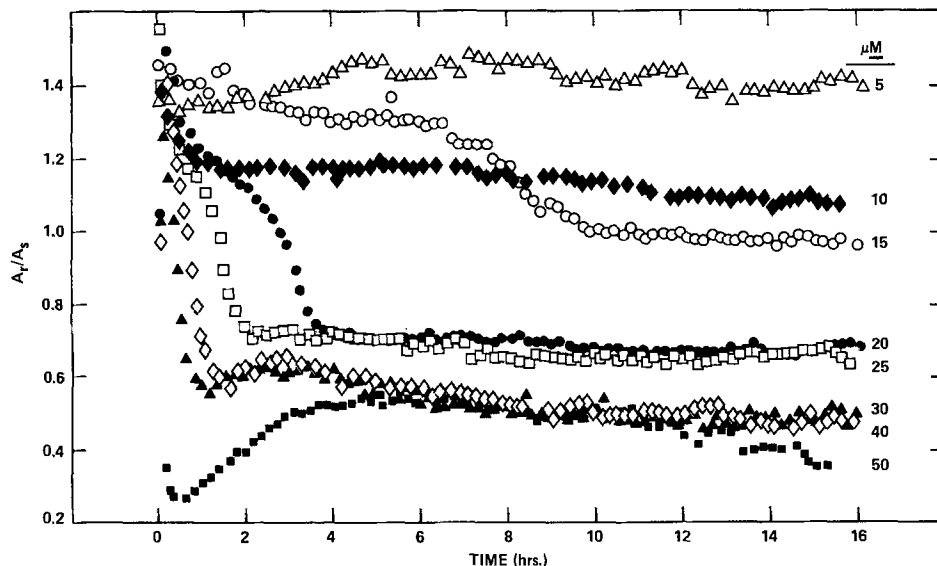


Fig. 2. Relative rate parameter (A_r/A_s) as a function of time after addition of various amounts of additive to copper pyrophosphate baths at 55°C.

dimer produces deceleration even at room temperature, its effectiveness increases with heating at bath operating temperature, which suggests that its copper complexes are more effective decelerators [(f) in Fig. 4 is the expected di-copper species]. Typical activation plots are shown in Fig. 5. At low dimer concentrations, there is a short induction period of several minutes, while low A_r/A_s values are obtained almost immediately at higher concentrations. This also suggests that the dimer must complex with Cu^{+2} in solution before it is active. A_r/A_s increases at longer times for low dimer concentrations (12.5 μmoles in Fig. 5) and accelerating baths are produced when low concentrations of dimer are allowed to equilibrate, indicating that a monomer/dimer equilibrium is established.

Additional strong support for a monomer/dimer equilibrium is found in the experimental verification that the initial monomer concentration must be double that of the dimer to produce approximately the same A_r/A_s value at equilibrium. Thus, a monomer concentration of 25 μmoles results in an A_r/A_s value of about 0.65 (Fig. 2) and the activation curve (Fig. 5) for 12.5 μmoles dimer approaches this value with time. An exact equivalence is difficult to obtain because of the difficulties involved in synthesizing and purifying the dimer and holding the bath composition (particularly

the ammonia level) constant for the long times required to reach equilibrium. Also, the dimerization/dissociation is a redox process which must involve other solution redox species (e.g., dissolved oxygen or Cu^+ species) that may be present in small concentrations.

The minimum in A_r/A_s observed early in the activation of higher concentrations of both the dimer and monomer and the peak observed at longer times (Fig. 2 and 5) presumably reflect the presence of appreciable amounts of intermediate species having varied activities. For example, the uncomplexed monomer species [(a) and (b) in Fig. 4] may be decelerating (unlike their Cu^{+2} complexes) so that the presence of significant amounts of these species in the early stages of the monomer and dimer activations could initially suppress A_r/A_s . A_r/A_s would then rise as most of the monomer was complexed with copper to form the accelerating species. The peak would be produced as A_r/A_s again decreased because of formation of di-copper dimer complex [(f) in Fig. 4] which is presumably much more effective as a decelerator than the mono-copper dimer species (not shown in Fig. 4).

It should be mentioned that, although this simple monomer/dimer scheme explains the data well, the situation is probably somewhat more complex. For

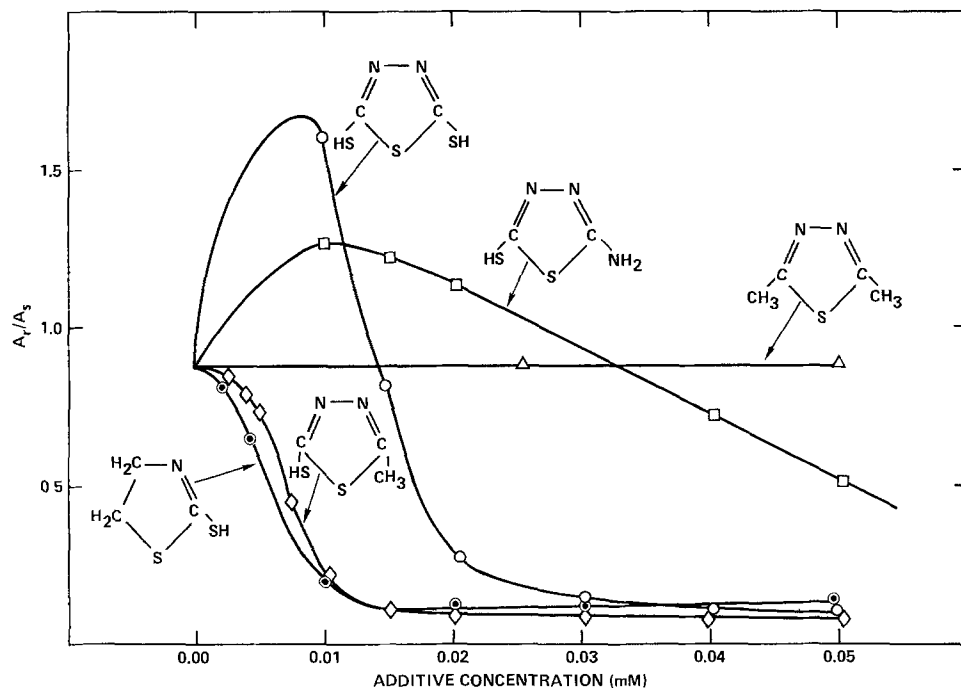


Fig. 3. Relative rate parameter (A_r/A_s) vs. the concentration of various additive analogs. Baths were heated at 55°C for 16 hr, then quenched to room temperature before the measurements.

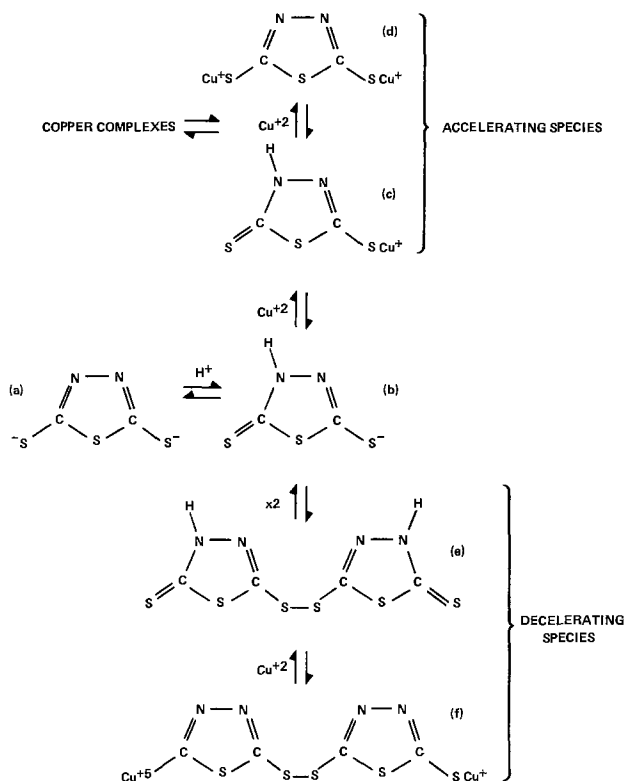


Fig. 4. Proposed equilibria involving the dimercaptotriadiazole additive in copper pyrophosphate baths.

example, in aqueous solutions, DMTD can exist as a monoanion or a dianion, and has several tautomeric forms which can coordinate with Cu^{+2} via mercapto groups, thione groups, an N-S chelate, or the diazo nitrogens of the ring system (9, 10). Large three-dimensional polymeric complexes with DMTD as the sole ligand have also been reported (8).

Considerable insight into the position of the accelerator/decelerator equilibrium and the relative effects of these two types of additive species on the deposition rate can be gained by plotting the A_r and A_s values from Fig. 1 separately vs. the overall additive concentration. Such a plot is shown in Fig. 6. These data indicate that the accelerator concentration is higher at equilibrium, but the decelerator produces the larger effect on the deposition rate (per molecule). Thus, A_s increases slowly with additive concentration

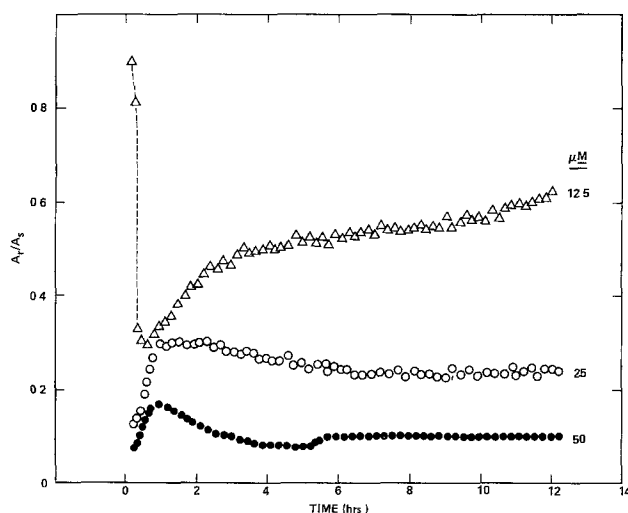


Fig. 5. Relative rate parameter (A_r/A_s) as a function of time after addition of various amounts of DMTD dimer to copper pyrophosphate baths at 55°C.

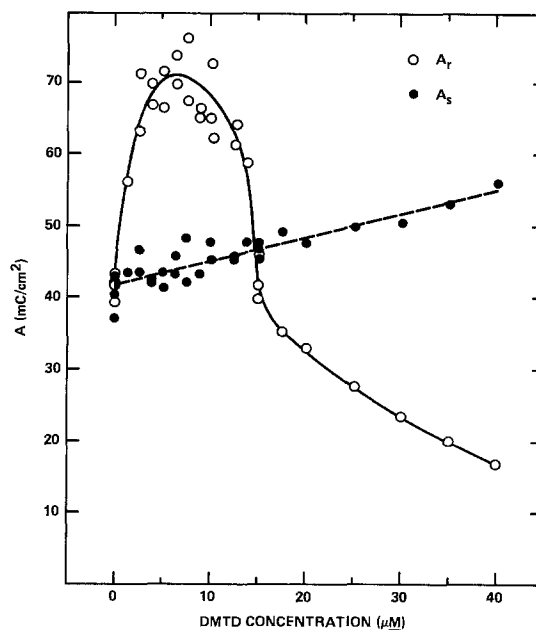


Fig. 6. Rate parameters (A_r and A_s) vs. additive concentration for copper pyrophosphate baths at 55°C (after 16 hr).

since in the absence of effective mass transport (electrode rotation), the decelerator concentration is exhaustively depleted at the electrode surface. With electrode rotation, the decelerator effect predominates at the higher concentrations for which sufficient decelerator is formed, so that A_r goes through a maximum then decreases sharply with additive concentration.

The analogous A_s plot is also expected to be linear. Consider the dimerization



for which the equilibrium constant is given by

$$K = C_D/C_M^2 \quad [2]$$

where C_D is the dimer concentration and C_M is the monomer concentration. When monomer is added to the bath, the initial concentration (C_0) is always given by

$$C_0 = C_M + 2C_D \quad [3]$$

so that

$$C_0 = C_M + 2KC_M^2 \quad [4]$$

Thus, if the effect of monomer on the deposition rate is directly proportional to its concentration, which will be shown to be a reasonable assumption, A_s should be linear in C_0 at equilibrium unless K is extremely large so that $2KC_M^2$ is not negligible.

It should be mentioned that ammonia in the bath also affects the copper deposition rate. This is not surprising since copper forms a series of ammine complexes, e.g., $[\text{Cu}(\text{NH}_3)_4]^{+2}$ and $[\text{Cu}(\text{NH}_3)_2]^+$, which have stability constants comparable to those of the copper pyrophosphate species (7), i.e., in the 10^{12} range. Mixed ammine/pyrophosphate copper complexes would also be expected. Since ammonia is an uncharged ligand, its copper complexes are less negatively charged than the pure pyrophosphate complexes so that copper discharge from the ammine complexes more readily occurs (12) and ammonia would thus be expected to accelerate deposition from copper pyrophosphate baths. As expected, the final A_r/A_s values after activation of copper pyrophosphate baths increase linearly with ammonia concentration. This is illustrated by the data in Table II. The time required for activation of the additive is not significantly affected by the presence of ammonia, indicating that ammonia does not play a major role in the activation process.

Mechanistic/a-c impedance studies.—In order to discuss the mechanism by which the additive species

Table II. Effect of NH_3 concentration on the final A_r/A_s value for copper pyrophosphate baths at 55°C

| NH ₃ concentration (g/liter) | Final A_r/A_s | |
|---|---------------------------|---------------------------|
| | 15 μmoles DMTD | 30 μmoles DMTD |
| 0 | 0.52 | 0.24 |
| 1.13 | 0.77 | 0.38 |
| 2.25 | 1.0 | 0.62 |

affect the copper electrodeposition rate, some additional data must be considered. First of all, we have observed by scanning electron microscopy that copper deposited from pyrophosphate baths in the absence of additives is large grained, whereas deposits from accelerating baths are nodular and those from decelerating baths are fine grained (4). Such dramatic differences in deposit morphology would be expected only if significant changes occurred in the deposition mechanism or rate-determining step. These additive-induced mechanistic changes can be investigated by determination of the charge transfer resistance and double layer capacitance from a-c impedance measurements. The double layer capacitance is particularly important since it reflects the surface concentration of copper adions, which are intermediates in the overall deposition process (13).

The principle of a-c impedance analysis is illustrated in Fig. 7. If we assume that the cathodic half-cell can be represented by the simple electrical network shown at the top of the figure, the electrode impedance can be calculated as a function of frequency (ω) in the complex plane as illustrated at the bottom of the figure (where R_s is the solution resistance, C_{DL} is the double layer capacitance, R_{CT} is the charge transfer resistance, and W is the Warburg impedance). The semicircle obtained is characteristic of a given combination of C_{DL} and R_{CT} , and the linear response at low frequencies is associated with the Warburg (diffusional) impedance.

Impedance diagrams determined during electrodeposition from copper pyrophosphate baths at -0.70 vs. SCE are shown in Fig. 8. Behavior is practically ideal for the additive-free and accelerated baths. The diagram for the decelerating bath approximates the ideal

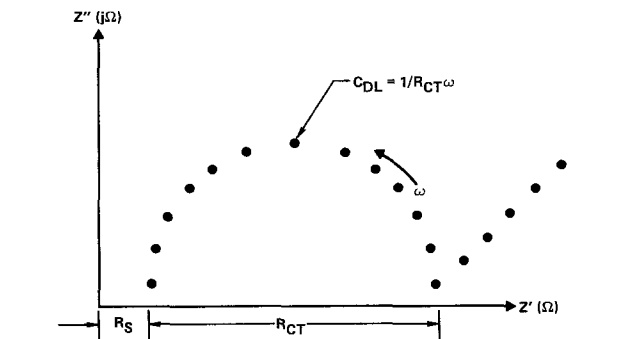
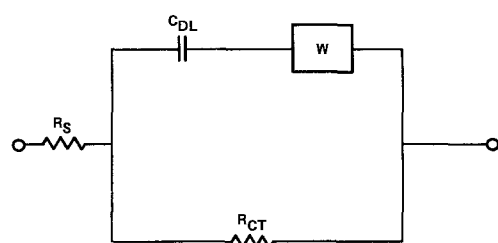


Fig. 7. Simple equivalent circuit for an electrode (top) and the expected a-c response in the complex plane (bottom).

semicircle and should provide semiquantitative information. Data derived from these impedance diagrams are given in Table III. As expected, R_{CT} is slightly smaller for the accelerating bath compared to the additive-free system, and considerably larger for the decelerating bath. The value of $11 \mu\text{F}/\text{cm}^2$ for C_{DL} is only slightly smaller in the accelerating system, but is a factor of 24 larger in the decelerating case. This may be interpreted as a significant increase in the copper adion concentration during additive-decelerated deposition since adions reside within the Helmholtz plane and thus reduce the overall extent of charge separation so that C_{DL} increases when the adion concentration increases.

Mechanism of additive effects.—These results provide the basis for understanding the mechanism by which the accelerating and decelerating additive species affect copper electrodeposition. First, consider the overall electrodeposition process in the absence of additives (13) which is illustrated in Fig. 9. Solvated/complexed Cu^{+2} ions in the electrolyte are discharged on surface planes to form partially solvated/complexed Cu^{+1} adions which surface diffuse over lattice planes and along steps to kink sites where they are discharged to Cu^0 and incorporated into the lattice. It is generally accepted that the rate-determining step at moderate current densities for acid copper sulfate baths is discharge of Cu^{+2} solution species to form adions (13) which has also been shown to apply to pyrophosphate copper deposition in the absence of additives (12). In this case, incorporation of adions into the lattice is fast and the adion surface concentration remains low; growth is orderly and deposits are large grained.

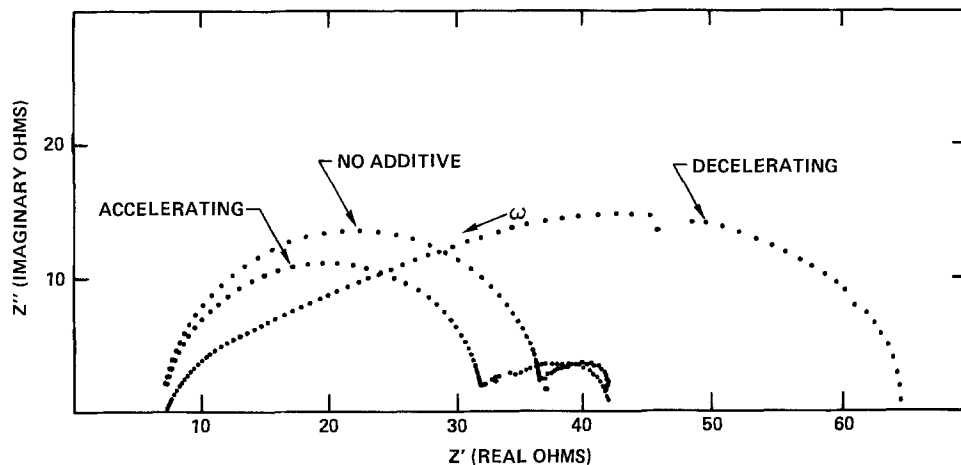
The situation for decelerated deposition is depicted in Fig. 10. In this case, the dimerized additive species adsorbed on the electrode surface interfere with surface diffusion of adions and block lattice growth at kink sites. This necessitates frequent renucleation to sustain a constant deposition rate which is reflected in the increased overvoltage, higher overall charge transfer resistance, and fine-grained deposit morphology. At sufficiently cathodic potentials, lattice incorporation, i.e., growth at kink sites, becomes the rate-determining step and the surface adion concentration increases sharply raising the measured C_{DL} . This change in rate-determining step from adion discharge to lattice incorporation is evident at an overpotential of 250 mV in the C_{DL} -overpotential plot shown in Fig. 11. It should be mentioned that the increased overvoltage may also affect the structure of the double layer electrostatically, especially since pyrophosphate anions are known to desorb at potentials more cathodic than -0.75V vs. SCE (14, 15). Such effects were probably minimal in our studies since the electrode potential was always held below this value.

The situation for accelerated deposition is illustrated in Fig. 12. The accelerating additive species apparently lowers the overpotential and overall charge transfer resistance by assisting in the nucleation of new growth centers on surface planes, which ultimately grow to form the almost spherical nodules observed by scanning electron microscopy. As also observed, C_{DL} would be expected to decrease slightly because of the reduction in adion concentration resulting from the shorter average surface diffusional path to the more numerous growth sites.

Table III. Charge transfer resistance (R_{CT}) and double layer capacitance (C_{DL}) during electrodeposition from copper pyrophosphate baths

| Additive concentration (μmoles) | A_r/A_s | R_{CT} (Ω) | C_{DL} ($\mu\text{F}/\text{cm}^2$) ² |
|--|-----------|-----------------------|---|
| 0 (additive-free) | 0.98 | 29 | 11 |
| 6 (accelerating) | 1.55 | 24 | 10 |
| 25 (decelerating) | 0.31 | 57 | 260 |

Fig. 8. Complex impedance data obtained during electro-deposition at $-0.70V$ vs. SCE from copper pyrophosphate baths at $55^{\circ}C$.



The way in which the accelerator might assist in nucleation of new growth centers on electrode surface planes can be visualized as follows. For the purposes of discussion, we will assume that the accelerator is the copper-complexed thiol-thione tautomer [(c) in Fig. 4], although the situation for the di-copper monomer species [Fig. 4 (d)] would be equivalent after the initial electron transfer. The accelerating species would be expected to adsorb on the electrode surface with the thiadiazole ring sulfur, which has a lone pair of electrons, serving as the attachment site. As the complexed Cu^{+2} is reduced to Cu^+ , and ultimately Cu^0 , to initiate the nucleation process, the charge would be redistributed via the ring structure to form the thiol-thione tautomer which is the mirror image of the original species. The thiol group thus generated would then be available to complex another Cu^{+2} from solution and the reduction process would be repeated. Thus, Cu^{+2} acquisition/ Cu^0 deposition would alternate between the thiol sites which would explain why two Cu^{+2} complexing groups are apparently required for accelerated deposition. If the thiadiazole sulfur-metal interaction is not too strong, the additive could move (via desorption/readsorption) along the surface of the growing nucleus, and the deposition of many Cu atoms could be facilitated before the additive was included in the deposit. The onset of spherical diffusion as the growing nuclei become three-dimensional would also

enhance the deposition rate and result in nodular deposits.

Quantitative treatment.—A more quantitative view of the effects of the accelerating species on the electro-deposition rate can be obtained by assuming that the accelerator and decelerator act more or less independently. As mentioned above, this appears to be a good assumption since the plot of the relative rate parameter (A_r/A_s) vs. additive concentration in Fig. 1 is linear at higher concentrations and extrapolates to unity for the additive-free system. Thus, we can subtract the decelerating effect of the dimer species according to the linear dashed line in Fig. 1 to obtain the plot shown in Fig. 13 of the accelerator effect on A_r/A_s . Based on the data in Fig. 6, we have assumed that the accelerator concentration is equivalent to the overall additive concentration in this concentration range.

Let us now assume that the monomer acceleration effect can be described in terms of birth and death of nodules so that the relative rate parameter after subtraction of the decelerator effect is given by

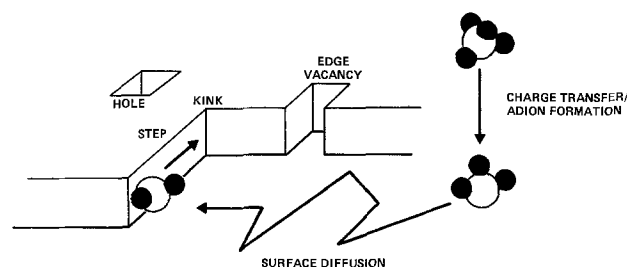


Fig. 9. Representation of copper electrodeposition in the absence of additives at moderate current densities.

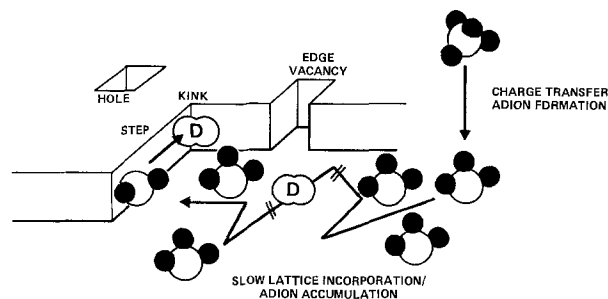


Fig. 10. Representation of additive-decelerated electrodeposition from copper pyrophosphate baths.

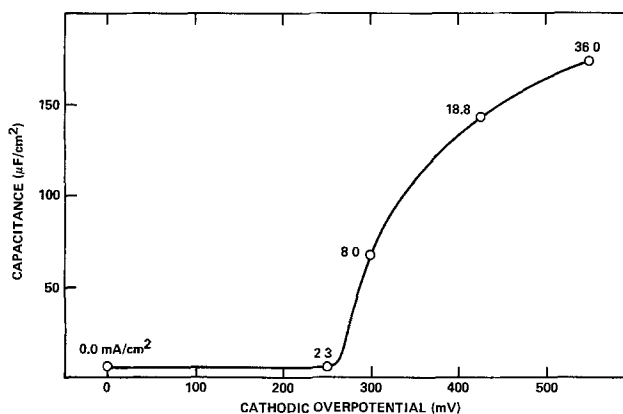


Fig. 11. Double layer capacitance vs. overpotential for additive-decelerated electrodeposition of copper from pyrophosphate baths at $55^{\circ}C$.

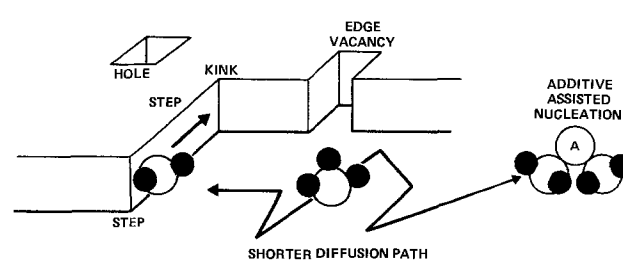


Fig. 12. Representation of additive-accelerated electrodeposition of copper from pyrophosphate baths.

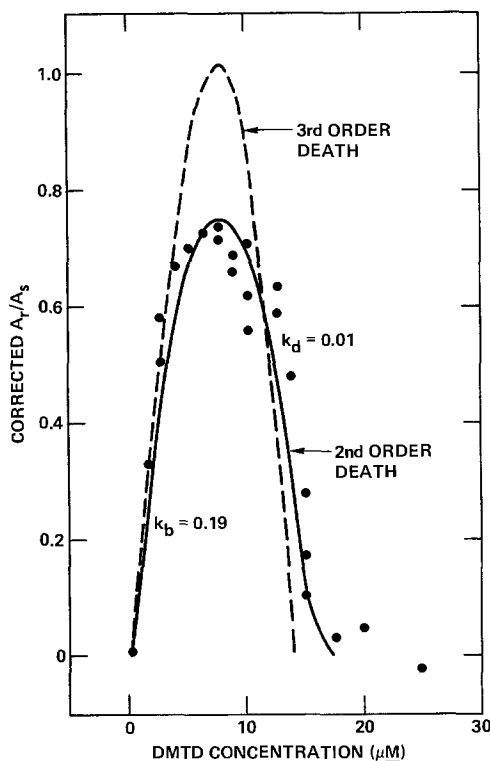


Fig. 13. Plot of A_T/A_S vs. additive concentration after subtraction of the decelerating effect of the dimer species.

$$A_T/A_S = 1 + k_b C_M - k_d C_M^x \quad [5]$$

where $(k_b C_M - k_d C_M^x)$ can only be positive. The assumptions concerning birth are that each nodule exerts an equivalent effect on the deposition rate and that the number of nodules formed is proportional to the monomer concentration. In this case, the accelerating effect on A_T/A_S is given by $k_b C_M$, where k_b is the proportionality constant. The death process which causes individual nodules to cease growing so that they no longer contribute to accelerated deposition is assumed to be collision with other nodules. Note that collision in this context means that the nodules interact at a small separation distance to stop growth. The collision frequency is assumed to increase with the number of nodules, which is in turn proportional to the monomer concentration so that the net decelerating effect of nodular death is $-k_d C_M^x$, where x is the number of collisions required to produce death and k_d is the death proportionality constant.

In order to test this model, we need to determine k_b and k_d . Assuming that death is unimportant when the density of nodules is low, k_b is obtained from the slope of the corrected A_T/A_S plot (Fig. 13) in the linear region at low additive concentrations. The value of k_d is determined by differentiating Eq. [5] and setting the differential equal to zero at the peak in the corrected A_T/A_S plot. For second-order death, $k_d = k_b/2C_M' = 0.01$, where C_M' is the additive concentration corresponding to the peak in the corrected A_T/A_S plot. The nodule death process seems to be second order as indicated by the excellent fit (solid line in Fig. 13) to the corrected A_T/A_S data. This implies that nodule death involves interruption of growth at specific sites, so that spherical diffusion of copper ions alone would not account for the accelerated deposition and nodular deposits. A plot for third-order death (dashed line) is included for comparison.

A unified model.—The results presented above show that there are two important additive species present in copper pyrophosphate baths. One of these suppresses (decelerates) deposition by blocking growth sites, whereas the other enhances (accelerates) depo-

sition by assisting in the nucleation of new growth centers. Ammonia also enhances deposition, presumably by forming complexes from which copper can be discharged at lower overpotentials to nucleate new growth centers. Nucleation via copper ammine complexes is supported by the observation of nodular deposits at high bath ammonia levels (12).

We propose here that the maintenance of the proper balance between the decelerating and accelerating bath species is critical to the attainment of acceptable pyrophosphate copper deposits. Consider deposition at a high overall additive concentration in the absence of ammonia in the bath. In this case, the limited number of growth sites are quickly blocked by the predominant decelerating dimer species and provisions for generating new sites are inadequate so that appreciable deposition can only occur at high cathodic overvoltages. Under these circumstances, nucleation occurs preferentially at surface microprotrusions where the electric field strength is highest and, once initiated, growth is extremely rapid and disorderly for the short time before it is blocked by adsorption of a new decelerating additive species. The resulting deposits are burnt and powdery with extremely poor crystallinity and mechanical properties.

To obtain acceptable deposits at reasonable current densities, provisions must be made for nucleation of a sufficient number of growth centers at low overvoltages where orderly deposition occurs and deposits are highly crystalline. This can be accomplished by lowering the additive concentration to attain a better balance between the accelerating and decelerating additive species, and by adding ammonia to the bath. On the other hand, sufficient decelerator must always be present to limit the extent to which individual nuclei are permitted to grow. Otherwise, as the nuclei expand in three dimensions, spherical diffusion enhances mass transport and consequently the growth rate, so that growth again becomes disorderly and nodular deposits are obtained. Within this model, it is readily apparent why ammonia is a critical constituent of copper pyrophosphate baths (1) and its concentration must be increased for plating at higher additive levels (16).

Practical implications.—In most applications for which copper pyrophosphate baths are used, the deposit tensile properties are of paramount importance. For example, to avoid cracking problems, plated through-hole deposits in multilayer circuit boards must be highly ductile to relieve stress generated by the excess thermal expansion of the laminant during soldering and must be sufficiently strong to resist fatigue failure upon thermal cycling (17). In addition, deposits must generally be uniform and adherent. Our previous work has shown that both the tensile properties and uniformity of pyrophosphate copper deposits depend strongly on the overall additive concentration and correlate well with cyclic voltammetric stripping data and morphological studies (3-5). Specifically, nodular deposits resulting from additive accelerated deposition were found to have poor tensile properties, and the nonuniform deposition within through-holes known as "foldback" was shown to be a consequence of the dual accelerating/decelerating nature of the additive.

The model presented here, which involves a critical balance between nucleation (initiated by the accelerating additive species and copper ammine complexes) and growth (limited by the decelerating additive species), provides a basis for improving control of copper pyrophosphate plating. First of all, since the three principal species (decelerator, accelerator, and ammonia) which affect the deposition rate (and consequently the deposit properties) vary in activity and concentration, it is clear that the bath additive and ammonia levels must be considered as interdependent variables. Control is therefore rendered considerably less difficult if the additive system is maintained near

equilibrium where the concentrations of additive species are fixed relative to one another. This also ensures that the concentration of monomer which must be balanced by dimer is minimal, so that the total amount of organic material included in the deposit is minimized. An excess of such included material can lead to deposit brittleness. Thus, the additive should be added in such a way as to ensure activation to the dimer form. This implies that, in some cases, making batch additions may be preferable to continuously feeding the additive. Of course, the optimum situation would involve approaching the equilibrium from the other direction by adding dimer directly, if this procedure can be shown to yield deposits with comparable mechanical properties.

Since the three species affecting the deposition rate vary in concentration and relative effectiveness, it might be expected that the effects of changes in bath agitation would be difficult to predict. Fortunately, the decelerator appears to be relatively low in concentration, but highly effective, so that changes in electrolyte mass transport primarily affect the magnitude of the decelerating effect. Thus, if the ammonia concentration is held constant and the additive system is close to equilibrium, variations in agitation can be countered by changes in the overall additive level. Nonetheless, caution should be exercised in making extrapolations for mass transport differences.

It should also be mentioned that the relative rate parameter (A_r/A_s) measured by cyclic voltammetric stripping (3) reflects primarily the concentration of the decelerating additive species in copper pyrophosphate baths. Thus, if the additive system is maintained near equilibrium and the bath ammonia level is held constant, this method provides excellent control of pyrophosphate copper plating.

Summary

The dimercaptothiadiazole/copper pyrophosphate system involves two additive species in dynamic equilibrium. One appears to be the copper complexed DMTD monomeric species which assists nucleation of new growth sites on crystal planes and can lead to nodular deposits. In this case, the electrodeposition rate is accelerated, presumably by some combination of additive-assisted growth randomly over the surface of the nodules, and the onset of spherical diffusion to the new isolated growth sites. The other additive species is apparently the DMTD dimer which decelerates the electrodeposition rate by blocking growth sites. Additive-accelerated deposition can be quantitatively described in terms of birth and death of nodules, where the birth rate is proportional to the accelerator concentration and death results from second-order collision of growing nodules.

Deposition in the dimercaptothiadiazole/copper pyrophosphate system can be understood by assuming that

a balance must be maintained between suppression of growth by the decelerating additive species and nucleation of new growth centers via the accelerating additive species and copper ammine complexes. This model could prove to be general for electrodeposition from highly complexed systems.

Acknowledgments

The authors gratefully acknowledge support of a portion of this work by the United States Air Force Materials Laboratory under contract No. F33615-79-C-5079. The authors are also indebted to Drs. D. O. Raleigh and L. F. Warren for many useful comments on the manuscript.

Manuscript submitted June 18, 1980; revised manuscript received ca. Sept. 22, 1980.

Any discussion of this paper will appear in a Discussion Section to be published in the December 1981 JOURNAL. All discussions for the December 1981 Discussion Section should be submitted by Aug. 1, 1981.

Publication costs of this article were assisted by Rockwell International.

REFERENCES

1. J. W. Dini, in "Modern Electroplating," 3rd Ed., F. A. Lowenheim, Editor, p. 205, Wiley-Interscience, New York (1974).
2. F. H. Wells and D. M. Lyde, Brit. Pat. 939,997 (1960).
3. D. Tench and C. Ogden, *This Journal*, **125**, 194 (1978); U.S. Pat. 4,132,605 (1979).
4. D. Tench and C. Ogden, *This Journal*, **125**, 1218 (1978).
5. C. Ogden and D. Tench, *Plating Surf. Finishing*, **66**, 30 (1979).
6. V. G. Levich, "Physicochemical Hydrodynamics," Prentice-Hall, Englewood Cliffs, N.J. (1962).
7. A. J. Bard, "Chemical Equilibria," p. 192, Harper and Row, London (1966).
8. M. R. Gajendragad and U. Agarwala, *Z. Anorg. Allg. Chem.*, **415**, 84 (1975).
9. S. Zaidi and D. Varshney, *J. Inorg. Nucl. Chem.*, **37**, 1804 (1975).
10. M. R. Gajendragad and U. Agarwala, *Indian J. Chem.*, **13**, 697 (1975).
11. D. Cram and G. Hammond, "Organic Chemistry," p. 440, McGraw-Hill, New York (1959).
12. O. Radovici, C. Vass, and I. Solacoln, *Electrodep. Surf. Treat.*, **2**, 263 (1973).
13. J. O'M. Bockris and A. K. N. Reddy, "Modern Electrochemistry," Vol. 2, Plenum Press, New York (1970).
14. H. Konno and M. Nagayama, *Electrochim. Acta*, **22**, 353 (1977).
15. H. Konno and M. Nagayama, *ibid.*, **23**, 1001 (1978).
16. D. E. Sherlin and L. K. Bjelland, *Circuit World*, **4**, 22 (1977).
17. J. K. Hagge, Proc. Printed Circuit World Expo '80, Pasadena, California, May 1980.

Energy Dependence of the Quantum Efficiency of CdSe Photoelectrochemical Cells

K. Colbow, D. J. Harrison, and B. L. Funt*

Departments of Physics and Chemistry, Simon Fraser University, Burnaby, Vancouver, B.C., V5A 1S6 Canada

ABSTRACT

Polycrystalline CdSe electroplated on nickel and titanium substrates was used as photoanode in electrochemical cells with S^{2-}/S_n^{2-} as a redox couple. When compared to a single crystal photoanode, the quantum efficiency is found to be larger for photon energies below the bandedge and smaller for those above the bandedge. The single crystal efficiency dependence on photon energy near the bandedge is well described by the Butler equation and dominated by variation of the absorption coefficient and the depletion layer width and less sensitive to the minority carrier diffusion length for the crystal under study. The electroplated samples may be assigned a bandgap of about 1.70 eV compared to 1.72 eV for the single crystal. Information about impurity content may be obtained from the photoresponse for energies below the bandedge.

The aim of this research was to understand the performance of electroplated and single crystal n-type CdSe as solar cells in terms of their fundamental semiconductor parameters, such as absorption coefficient (α), impurity concentration (N_D), depletion layer width (W), flatband potential V_{FB} , energy gap (E_g), hole diffusion length (L_p), and hole diffusion coefficient (D_p). To this end we studied the short-circuit photocurrent efficiency (η) as a function of wavelength in an aqueous electrolyte consisting of 1.0M NaOH, 1.0M Na₂S, and 1.0M S. Photoanodic dissolution does not occur under these conditions (1) and the electrode reactions are the oxidation of S_n^{2-} at the photoanode and the reduction of S_n^{2-} at the platinum dark electrode. We compared the data to the simple Butler equation (2)

$$\eta = \frac{I}{qA\phi_0} = 1 - \frac{e^{-\alpha W}}{1 + \alpha L_p} \quad [1]$$

where I is the short-circuit current, q the electronic charge, A the cell area, and ϕ the incident light flux. The depletion layer width is given by

$$W = \left\{ \frac{2\epsilon_0\kappa}{qN_D} (V - V_{FB}) \right\}^{1/2} \quad [2]$$

$\epsilon_0 = 8.85 \times 10^{-12} \text{C}^2 \text{N}^{-1} \text{m}^{-2}$ is the permittivity of free space, $q = 1.60 \times 10^{-19} \text{C}$ the electron charge, and V the measured or applied potential. The dielectric constant $\kappa = 10$ for CdSe (3).

For the flatband potential of CdSe with an S^{2-}/S_n^{2-} redox couple Gerischer and Gobrecht (4) obtained a value of -1.27V vs. NHE (normal hydrogen electrode) from capacitance measurements for CdSe single crystal whose surface had been converted to CdS. This corresponds to -1.51V vs. SCE (standard calomel electrode). Ellis *et al.* (1) obtained a flatband potential of -1.45V vs. SCE for single crystal CdSe from capacitance or open-circuit voltage at high light intensity and -1.40V from the less accurate onset of photocurrent at high light intensity. Noufi *et al.* (5) obtained -1.34V vs. SCE for pressed powder pellets and -1.30V for vacuum-deposited films of CdSe using the onset of photocurrent. We shall choose a value of -1.50V vs. SCE . Using a value of -0.72V for platinum in a polysulfide electrolyte *vs. SCE* (6, 7), we obtain $V_{FB} = -0.78 \text{V vs. platinum electrode in } S^{2-}/S_n^{2-}$, which was used in our experiments.

Experimental

Monochromatic excitation was obtained using a 1000W quartz iodine tungsten lamp and a Jarrel-Ash

* Electrochemical Society Active Member.

Key words: electroplating, photoanode, crystals.

grating monochromator with a 100Å bandpass. Infrared radiation was filtered out by passing the light through 2 in. of water, second-order grating effects were eliminated with a Corning 3.71 filter. The monochromatic beam was expanded by lenses to provide full sample illumination and a reasonably parallel beam.

Polycrystalline samples were prepared by an electrodeposition technique which evolved as an extension of a method reported previously (8, 9). Controlled electrodeposition was performed at -0.72V vs. SCE for 15 min on a titanium or nickel substrate, which had been etched, cleaned meticulously, and cathodized for 15 sec in an acidic oxidizing medium. The deposition bath consisted of 1M NH₄Cl, 0.5M CdSO₄, and 0.01M SeO₂. Electrodeposition at -0.76V and -0.64V vs. SCE was also performed in order to obtain electrodes lacking stoichiometry, being rich in Cd and Se, respectively. The plated photoelectrodes were about 1 μm thick and were subsequently heated under 100 Torr N₂ at 400°C for 15 min. The counterelectrode was platinum.

The single crystal CdSe was obtained from Cleveland Crystal Incorporated, its c-axis was perpendicular to the front surface. Electrical contact at the back side was made with a GaIn eutectic, and a copper wire was attached to this with Ag epoxy. This was then sealed with epoxy and mounted on a Teflon rod. The quartz cell had a flat window, allowing a 2-3 mm optical path length through the electrolyte. The cells were flushed with nitrogen gas prior to and after introduction of the electrolyte and then sealed from the atmosphere.

In order to test the polycrystalline electrodes under equilibrium conditions, the cells were left overnight in the electrolyte, and the open-circuit voltage V_{oc} was monitored to determine if a steady state had been reached. Steady open-circuit voltage always correlated with steady short-circuit current I_{sc} in the dark.

The "short-circuit" current was measured after the cells had equilibrated by determining the voltage drop across a 10Ω resistor in series with the photocell. The voltage in the dark and under illumination was measured and the difference was reported as the photocurrent.

Results and Discussion

Figure 1 shows the experimental points (□) for the quantum efficiency as a function of wavelength of the incident light. The data was obtained for a single crystal under low light intensity and corrected for light absorption by the solution. The curves represent Eq. [1] with the absorption coefficient α as function of wavelength taken from Parsons *et al.* (10) for light polarized perpendicular to the c-axis of the crystal.

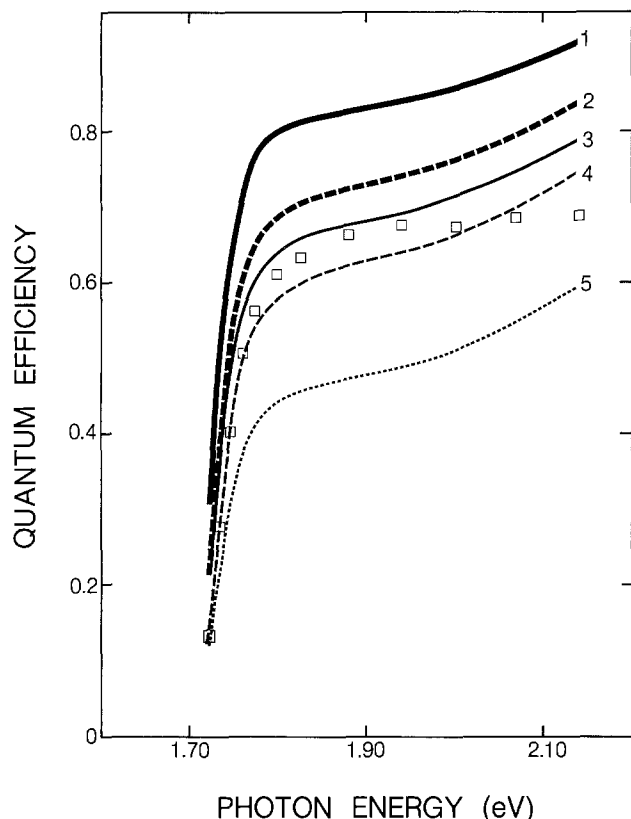


Fig. 1. Quantum efficiency vs. photon energy for a single crystal of CdSe (experiment: \square), and theoretical curves for W , L_p values of curve 1, 0.2, 0.1; curve 2, 0.2, 0; curve 3, 0.1, 0.1; curve 4, 0.15, 0, and curve 5, 0.1, 0 μm .

For W and L_p various values were chosen in order to demonstrate the sensitivity of the Butler equation to changes in these parameters. Curve 4 is a least squares fit to the experimental data. Using in Eq. [2] a dielectric constant $\kappa = 10$, and a flatband potential $V_{\text{FB}} = -0.78\text{V}$, a depletion layer width of $W = 0.15 \mu\text{m}$ corresponds to an impurity concentration of $N_D = 4 \times 10^{16} \text{cm}^{-3}$, which appears reasonable. The fact that Eq. [1] provides a reasonable fit to the data with negligible value of L_p merely suggests that $\alpha L_p < 1$ and thus most of the variation of efficiency comes through W .

To obtain a better fit between theory and experiment, one may consider that the most important neglect in the Butler equation is the assumption of no surface recombination. Analogous to Wilson's (11) treatment this may be rectified in the simplest way by multiplying the right-hand side of Eq. [1] by the ratio $S_t/(S_t + S_r)$, where S_t and S_r are the relative probabilities of surface transfer (S_t) and nonproductive surface recombination (S_r) of light-generated charge carriers at the semiconductor-electrolyte interface. This introduces one new parameter, namely the ratio of S_t/S_r . A more detailed theoretical treatment will be presented separately. Reiss' (12) more elaborate theory of photoelectrochemical cells also neglects surface recombination and gives a behavior similar to Butler's equation. A further complication to Eq. [1] arises for samples of thickness comparable to the inverse of the absorption coefficient ($\approx 1 \mu\text{m}$). This is a factor for our thin electroplated samples ($\approx 1 \mu\text{m}$ thickness), but not for the single crystal ($\approx 10^3 \mu\text{m}$ thickness) measurements.

Considering absorption coefficients such that $\alpha L_p \ll 1$ and $\alpha W \ll 1$, expansion of Eq. [1] yields

$$\eta \approx \alpha(W + L_p) \quad [3]$$

For $L_p \approx W \approx 0.1 \mu\text{m}$ this approximation is thus good for $\alpha \ll 10^5 \text{cm}^{-1}$.

The absorption coefficient α has different functional dependencies on photon energy $h\nu$, depending on the nature of the transition (13). For a direct gap material like CdSe near the absorption edge the absorption coefficient is described by

$$\alpha = \frac{A}{h\nu} (h\nu - E_g)^{1/2} \quad [4]$$

Combining Eq. [3] and [4], a plot of $(\eta h\nu)^2$ vs. $h\nu$ should give a straight line with intercept on the x-axis equal to the energy bandgap. This plot is shown in Fig. 2, curve 1, for the single crystal of CdSe.

For comparison we also show plots of $(\eta h\nu)^{1/2}$ vs. $h\nu$ (curve 2) and $(\eta h\nu)^{2/3}$ vs. $h\nu$ (curve 3), whose straight line sections extrapolate to the energy gap in the cases of an indirect semiconductor and a forbidden (phonon assisted) transition in a direct semiconductor, respectively (13). In curve 1 the full line extrapolates to an energy gap for CdSe of $E_g = 1.72 \text{eV}$. This compares with a quoted room temperature literature value of 1.74eV (14-16). Curves 2 and 3, which should not apply, extrapolate to energy gaps of 1.68 and 1.69eV , respectively. Figure 3 shows an expansion of the efficiency scale for photon energies below the bandedge for the single crystal of CdSe. The data indicates the typical Urbach exponential tail below the bandedge (above 1.60eV) and what we interpret as impurity absorption below 1.60eV . The peak at 1.50eV we believe is due to defect absorption. The peak is 0.240eV below the bandedge and in analogy to CdS may represent energy absorption by electrons bound to deep acceptors, possibly cadmium vacancies (17).

Figure 4 compares the wavelength dependence of the quantum efficiency for a single crystal of CdSe with electroplated samples of about $1 \mu\text{m}$ thickness. The latter were plated at -0.72V vs. SCE and subsequently heat-treated for improved response, as described earlier. Titanium substrates gave consistently higher efficiencies than nickel substrates, however, both had

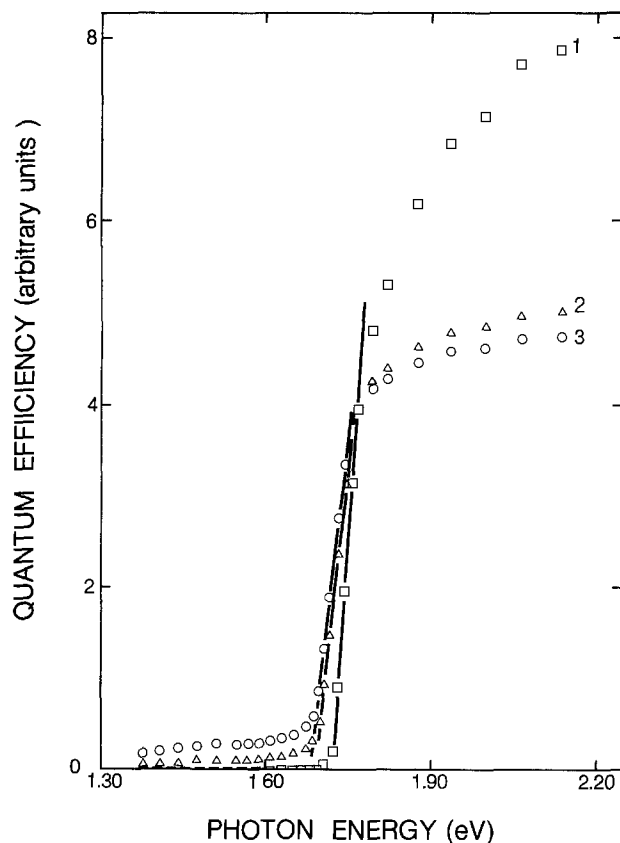


Fig. 2. Bandgap determination. Various fits of the single crystal quantum efficiency data for different functional forms of absorption coefficient vs. photon energy: 1, $(\eta h\nu)^2$, 2, $(\eta h\nu)^{1/2}$, 3, $(\eta h\nu)^{2/3}$.

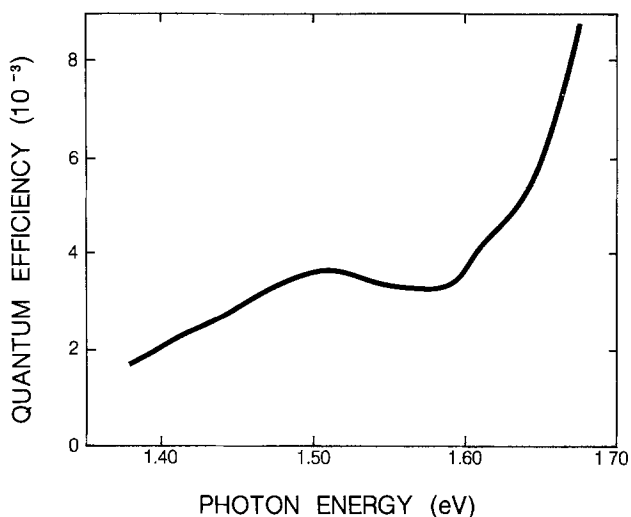


Fig. 3. Expansion of the experimental quantum efficiency (from Fig. 1) below the bandedge for single crystal CdSe.

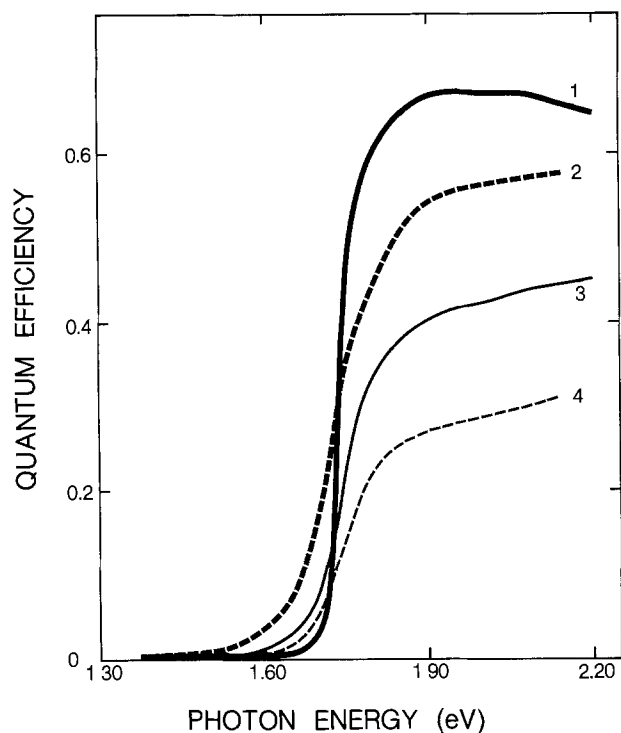


Fig. 4. Experimental quantum efficiency vs. photon energy of curve 1, CdSe single crystals; curve 2, electroplated samples on titanium substrate; curves 3 and 4, on nickel substrate.

a lower efficiency for photon energies above the band-edge and higher efficiencies for lower energy photons. Curves 3 and 4 show measurement on two different samples, which were prepared on different days under supposedly identical conditions to illustrate the reproducibility of sample preparation. Figure 5 shows a plot of $(\eta h\nu)^2$ vs. photon energy for two samples each, electroplated on nickel and titanium substrates. The straight line intercepts with the x-axis should give the energy bandgap of the CdSe (13). The samples on titanium substrate (curves 1 and 2) extrapolate to $E_g = 1.69$ eV and the samples on nickel substrate to 1.71 eV compared to our single crystal value of 1.72 eV.

Figure 6 compares electrodes plated at slightly lower (-0.76V) and higher potential (-0.64V) than the plating potential (-0.72V vs. SCE) that produces the most efficient electrodes (curve 1), corresponding to best stoichiometry. Plating at lower or higher potential probably produces electrodes rich in cadmium or selenium, respectively, which show a reduced efficiency

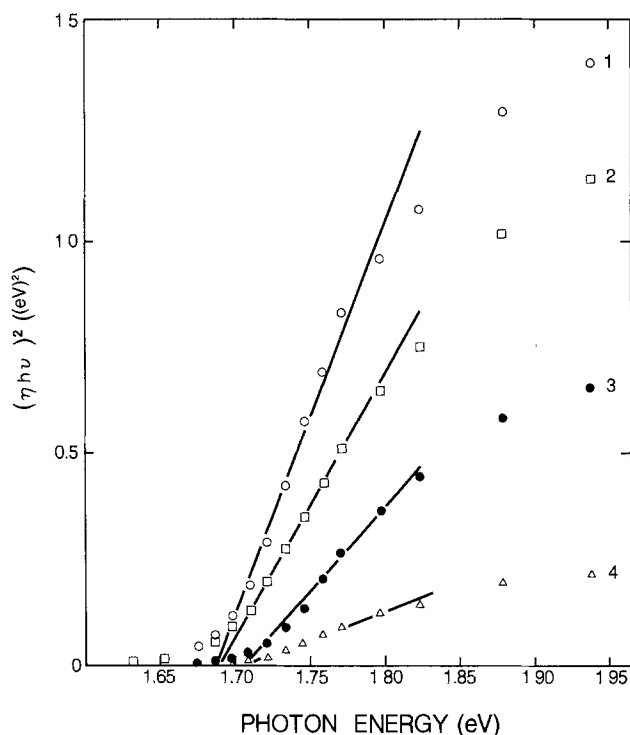


Fig. 5. Bandgap determination. $(\eta h\nu)^2$ vs. photon energy for electroplated CdSe on titanium (O, \square) and nickel (\bullet , \triangle) substrates.

at all wavelengths. In contrast to the samples in Fig. 4, those in Fig. 6 did not undergo heat-treatment after plating.

Figure 7 shows on an expanded efficiency scale the photoresponse of electroplated CdSe below the band-

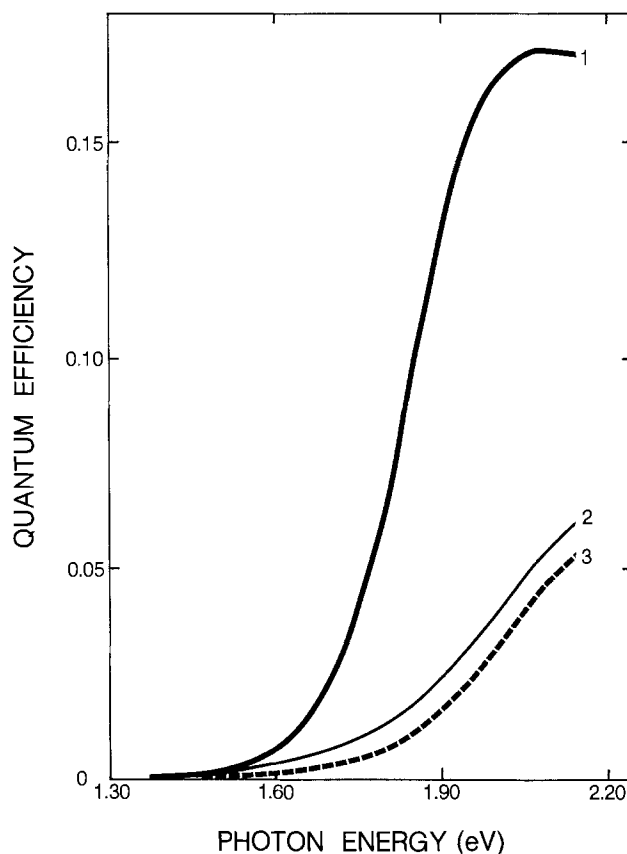


Fig. 6. Quantum efficiency vs. photon energy for CdSe electroplated on nickel substrates at plating potentials vs. SCE of curve 1, -0.72V, curve 2, -0.76V, and curve 3, -0.64V.

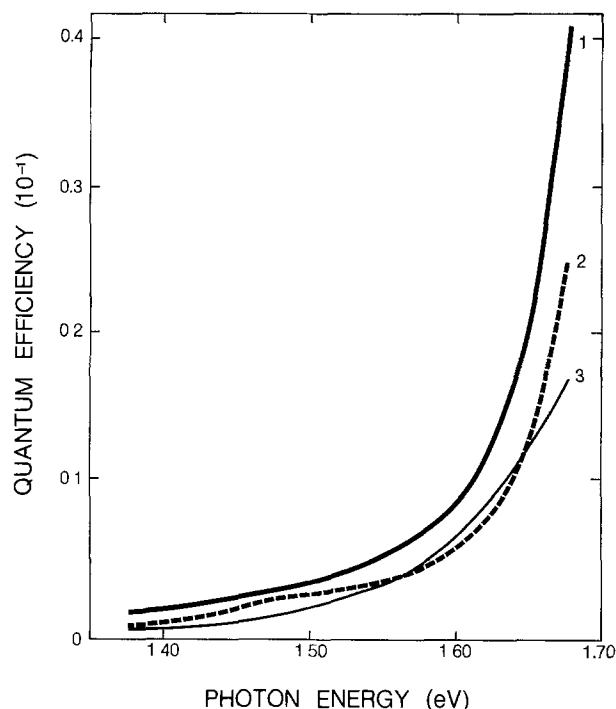


Fig. 7. Quantum efficiency vs. photon energy below the bandedge for CdSe electroplated on nickel substrate at $-0.72V$ vs. SCE. Samples for curves 1 and 2 were heat-treated but that for curve 3 was not heat-treated.

edge. While the response is large when compared to the single crystal data (Fig. 3), a 1.50 eV peak is not always as well defined, and no clear spectral differences due to heat-treatment were observable.

Conclusions

The Butler equation accounts reasonably well for the wavelength dependence of the quantum efficiency in single crystal CdSe for photons near the bandedge. The efficiency is controlled by the absorption coefficient and the depletion layer width, rather than the minority carrier diffusion length.

For photon energies below the bandedge a small photocurrent is observable in single crystal CdSe due to well-defined defect or impurity absorption.

In electroplated polycrystalline CdSe the efficiency above the bandedge is reduced by about a factor of two for 1 μm thick samples on nickel substrate and by half that for samples on titanium substrate, when com-

pared to thick single crystal of CdSe. The efficiency below the bandedge is increased in electroplated samples. The "impurity absorption" is much broader in the electroplated samples.

However, it appears that one still has a well-defined energy gap, which is only 20-30 meV smaller than our single crystal gap.

Preliminary experiments show that the electroplated CdSe efficiency can be enhanced with proper surface treatment.

Acknowledgments

This work was supported by a Strategic Grant from the National Science and Engineering Research Council of Canada.

Manuscript submitted July 17, 1980; revised manuscript received ca. Oct. 20, 1980.

Any discussion of this paper will appear in a Discussion Section to be published in the December 1981 JOURNAL. All discussions for the December 1981 Discussion Section should be submitted by Aug. 1, 1981.

Publication costs of this article were assisted by Simon Fraser University.

REFERENCES

1. A. B. Ellis, S. W. Kaiser, J. M. Bolt, and M. S. Wrighton, *J. Am. Chem. Soc.*, **99**, 2839 (1977).
2. M. A. Butler, *J. Appl. Phys.*, **48**, 1914 (1977).
3. S. M. Sze, "Physics of Semiconductor Devices," Wiley-Interscience, New York (1969).
4. H. Gerischer and J. Gobrecht, *Ber. Bunsenges. Phys. Chem.*, **80**, 327 (1976).
5. R. N. Noufi, P. A. Kohl, and A. J. Bard, *This Journal*, **125**, 375 (1978).
6. P. L. Allen and A. Hickling, *Trans. Faraday Soc.*, **53**, 1626 (1957).
7. W. M. Latimer, "The Oxidation States of the Elements and Their Potentials in Aqueous Solutions," Prentice Hall Inc., New York (1952).
8. J. Manassen, G. Hodes, and D. Cahen, *This Journal*, **124**, 931 (1977).
9. B. L. Funt, M. Leban, and A. Sherwood, *Am. Chem. Soc. Symp. Series No. 90*, 242 (1979).
10. R. B. Parsons, W. Wardzynski, and A. D. Yoffe, *Proc. Roy. Soc. A*, **262**, 120 (1961).
11. R. H. Wilson, *J. Appl. Phys.*, **48**, 4292 (1977).
12. H. Reiss, *This Journal*, **125**, 937 (1978).
13. R. H. Bube, "Photoconductivity of Solids," p. 211, John Wiley, New York (1960).
14. A. R. Hutson, "Semiconductors," N. B. Hannay, Editor, p. 541, Reinhold Publishing Corp., New York (1959).
15. R. H. Bube, *Proc. IRE*, **43**, 1836 (1955).
16. R. C. Weast, Editor, "Handbook of Chemistry and Physics," 59th ed., CRC Press (1978-79).
17. K. Colbow, *Phys. Rev.*, **141**, 742 (1966).

The Measurement of Fast Transients in the CdSe/S⁻, S^o Photoelectrochemical Cell

Z. Harzion

Department of Chemistry, University of Tel-Aviv, Ramat-Aviv, Israel

N. Croitoru

Department of Electronics, University of Tel-Aviv, Ramat-Aviv, Israel

and S. Gottesfeld*

Department of Chemistry, University of Tel-Aviv, Ramat-Aviv, Israel

ABSTRACT

Fast photocurrent transients were recorded in a CdSe/S⁻, S^o cell employing a spark-gap lamp as a source of illumination. From the measured dependence of the decay time on the value of the load resistor it is shown that photocurrent decay is controlled by an R-C time constant which is determined by the properties of the cell. The form of the decay is sensitive to the state of the photoelectrode surface, as shown by the pronounced effect of chemical etching which enhances the amplitude and reduces the decay time of the transients. The damaged surface layer produced by mechanical polishing increases the effective series resistance of the cell and decreases the photocharge obtained (per flash) through the external load.

The importance of kinetic parameters in the determination of the efficiency and stability of semiconductor (SC) photoelectrodes has been stressed by many authors (1). Transient techniques have served as an important tool for the evaluation of kinetic parameters in both electrochemical (2) and solid-state solar cells (3-10). The use of such techniques in photoelectrochemical cells has been introduced very recently (11-18). We present in this contribution results of fast transient measurements in the CdSe/S⁻, S^o photoelectrochemical system, and their analysis in terms of elements of an equivalent circuit.

Experimental

A block diagram of the experimental system for measuring fast transients in photoelectrochemical cells (PEC) is given in Fig. 1. A well-shielded spark-gap lamp served as a white light source, generating pulses of 10 nsec width and 50 Hz repetition rate. The peak power was 10³W and the spectrum was continuous, peaking around 330 nm. These light pulses were directed at the surface of a single crystal CdSe electrode immersed in a 4.5M NaOH, 0.2M S, 0.2M Na₂S solution.

The hexagonal n-type CdSe single crystals^{*} (Cleveland Crystals, Incorporated) were 1-2 mm thick, had a resistivity of 12.2 Ω cm, and a surface perpendicular to the C-axis. The ohmic contact to the crystal was prepared with an In/Ga eutectic, and the crystal was then attached to a copper foil with silver epoxy. The copper foil was coated by a layer of epoxy so that only a single surface of the CdSe crystal was in contact with the electrolyte. The exposed area varied from sample to sample in the range of 0.1-0.2 cm². Polishing was performed by 0.3 μm alumina and etching was carried out in 4:1 HCl:HNO₃. The duration of etching was 30 sec, followed by washing in alkaline polysulfide solution and rinsing in distilled water.

The PEC was completed by a load resistor and a reversible brass counterelectrode (19) of large area immersed in the same solution. The brass counterelectrode was wrapped by glass microfiber paper to avoid contamination of the solution by ZnS or CuS particles. The very short wires used to connect the electrodes to the load resistor, as well as the large areas of the

CdSe copper foil support and of the brass counterelectrode minimized the inductance of the total circuit. The PEC itself was well shielded electrically.

The high frequency photovoltaic signals were monitored using FET probes, (Type P6045 or plug-in unit 7A11, Tektronix). Photocurrents were measured under conditions close to external short circuit with a current-probe (P6022, Tektronix), and amplified when required by the current-probe amplifier (Type 134, Tektronix). To overcome problems due to lamp jitter and due to the initial delay of the boxcar unit, a compensated delay line was employed. The gate output of the scope (7904, Tektronix) was used to synchronize the scan delay generator (Brookdeal, 425A) while the amplified signal was applied through the delay-line to the linear-gate (Brookdeal, 415). The output signal from the boxcar was displayed on an X-Y recorder.

Results

Figure 2 demonstrates the pronounced effect of surface treatment on the amplitude and the decay time of the measured photocurrent transients: chemical etching of a mechanically polished CdSe electrode resulted in higher photocurrent peaks, in a larger charge per pulse, and in shorter decay times. The pronounced effect of surface treatment on the amplitude and decay time could be reproducibly repeated, while keeping the cell composition and electrode configuration con-

INSTRUMENTAL SYSTEM FOR FAST TRANSIENTS MEASUREMENTS IN PEC

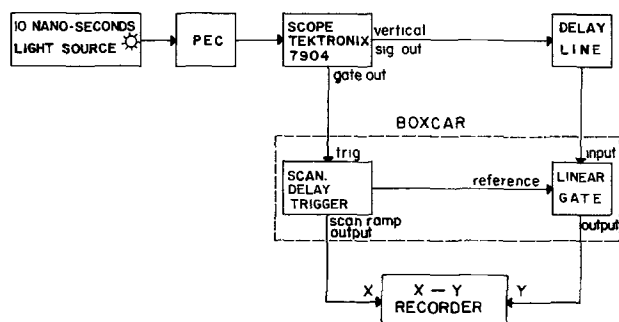


Fig. 1. The instrumental system for fast transient measurements in PEC.

* Electrochemical Society Active Member.
Key words: photocurrent, illumination, cell.

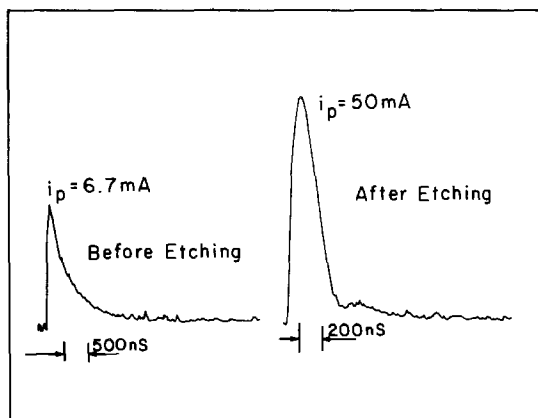


Fig. 2. Photocurrent transients for a mechanically polished (left) and for an etched (right) CdSe crystal, $R_L = 1\Omega$ in both cases. Semiconductor surface area = 0.2 cm^2 .

stant. This proved conclusively that interfacial effects were not masked in this mode of measurement by other possible contributions to the time constant of the complete circuit. Figure 3 shows the steady-state photocurrent-voltage curves obtained for the same mechanically polished CdSe electrode prior to and after etching. It is clear that large changes in the steady-state performance of the cell are brought about by the same surface treatment which causes the modification of the transients.

In an attempt to evaluate quantitatively the measured photocurrent decay curves, the dependence of the decay time τ on the value of the load resistor, R_L , was recorded under conditions of small potential perturbations, so as to keep the interfacial parameters practically constant. To ensure such conditions, the light intensity was attenuated by a neutral filter so that the total drop across the load would not exceed 25 mV. The quasipotentiostatic conditions and low intensities employed resulted in simple exponential decay with a single time-constant τ . Figure 4 demonstrates the difference in the shape of decay curves obtained under small and large perturbations. Such differences were pronounced especially for etched electrodes, for which saturation conditions due to bands flattening were reached at full lamp intensity. A τ vs. R_L plot recorded at small perturbations is presented in Fig. 5 (the same attenuating filter was employed for all values of R_L). It can be seen that for small values of R_L the curve is linear, but the slope becomes smaller at higher values of R_L . In the same measurement, τ was found to approach an almost constant level for load resistors higher than $5\text{ K}\Omega$. The effect of etching on the τ vs. R_L plot is demonstrated

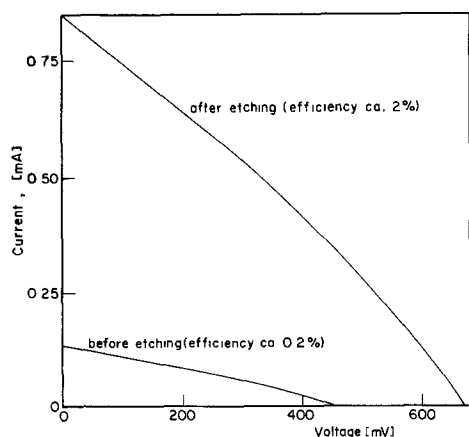


Fig. 3. Steady-state I vs. V curve for the polished and etched sample at which the transients of Fig. 2 were recorded.

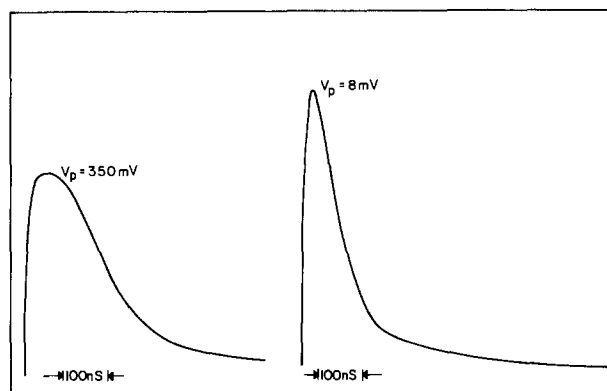


Fig. 4. Form of transients obtained for an etched electrode under saturation conditions at full light intensity (left), and with illumination attenuated by the use of neutral density filters (right). $R_L = 8.3\Omega$ in both cases. Semiconductor surface area = 0.1 cm^2 .

in Fig. 6. (Again, small perturbations were employed.) The insert in Fig. 6 is an enlargement of the linear sections (small R_L regions) of the plots obtained before and after etching. These linear sections were evaluated by a linear regression analysis for slope and intercept (correlation function better than 0.99 for both lines). It can be seen that the intercept of the plot has become lower as a result of etching, while the slope has become somewhat smaller.

Discussion

The decay of the photocurrent in solar cells following an illumination pulse may be controlled, in principle, by the following factors (3): (i) the diffusion time of minority carriers towards the junction; (ii) the transit time through the junction; (iii) the Maxwell relaxation time; (iv) the lifetime of minority nonequilibrium carriers; and (v) a combined cell-circuit R - C time constant. Since CdSe is a direct band-gap semiconductor (20), most of the light is absorbed in the space-charge region and factor (i) should be insignificant. Strong band bending, imposed by keeping the CdSe electrode close to the potential of the S^+/S° couple, makes factor (ii) unimportant. Factor (iii) is not expected to play an important role thanks to the low resistivity of both the SC and the electrolyte employed. The most important factors to be considered are thus (iv) and (v). *In situ* photoluminescence decay-time measurements, conducted for the same photoelectrode by employing a dye laser of 2 nsec

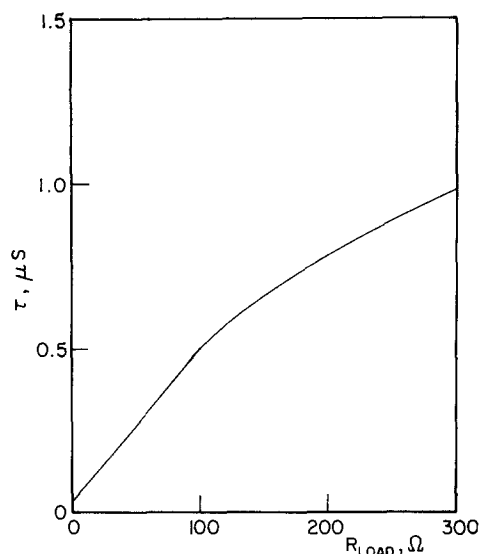


Fig. 5. τ vs. R_L recorded for an etched electrode under small photopotential perturbations. Surface area = 0.1 cm^2 .

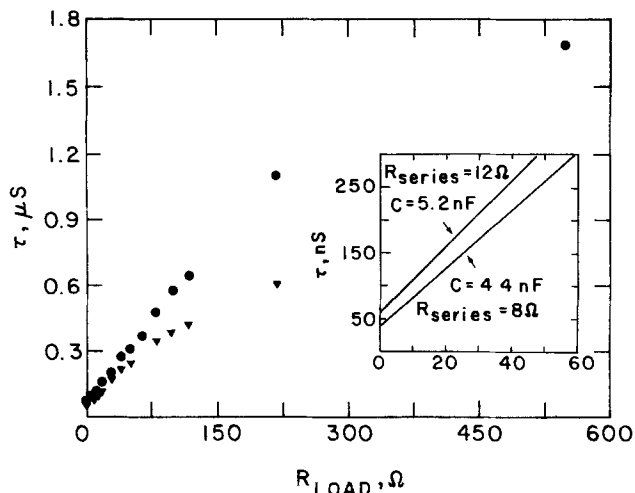


Fig. 6. τ vs. R_L plots taken before and after etching and recorded under small photopotential perturbations. Surface area = 0.1 cm² (same sample as in Fig. 4).

pulse width, revealed that the radiative band-to-band decay is completed in these CdSe samples (under small perturbation conditions) within 20 nsec. It thus seems from the above-mentioned arguments and results that in the time domain investigated ($t > 20$ nsec) photocurrent decay should be controlled by an R - C time constant.

The measured time dependence of τ on R_L (Fig. 5 and 6) verifies that τ is indeed controlled in our case by an R - C time constant which is determined by properties of the PEC and of the external circuit. The form of the measured variation of τ with R_L at small perturbations can be simulated by a very simple equivalent circuit, in which the semiconductor-electrolyte interfacial region is represented by a photocapacitor, C , with a shunt resistor, R_{in} , across it, while the rest of the cell and circuit is represented by a resistor R_{out} . R_{out} is given by

$$R_{out} = R_{series} + R_L$$

where R_{series} is a series combination of ohmic elements due to the PEC. To complete the equivalent circuit the photon flux is represented by a current source, according to the routine adopted in the analysis of solid-state solar cells (20), this leading to the circuit depicted in Fig. 7(a). The measured response of the real system to short light pulses can be simulated by the response of this simple R - C network to short current pulses. For a very short current pulse from the source (current delta function) the time variation of the current in the external circuit is calculated for circuit 7(a) [e.g., by Laplace transformation (21)] as

$$i_{out} = \frac{\Delta Q}{R_{out}C} \exp(-t/\tau) \quad [1]$$

where ΔQ is the charge injected by the source into the photocapacitor, and the decay time is given by $\tau = (R_{in} || R_{out})C$. For small values of R_L such that $R_{out} \ll R_{in}$, the decay time is given by $\tau = R_{out} \cdot C = (R_L + R_{series})C$. Under such conditions a plot of τ vs. R_L should be linear, with a slope of C and an intercept $R_{series} \cdot C$. On the other hand, at high values of R_L such that $R_{out} \gg R_{in}$, the decay time is given by $\tau = R_{in}C$ and is thus expected to be independent of R_L . This is indeed the general form of the experimental τ vs. R_L plots depicted in Fig. 5 and 6. It thus seems that for small values of R_L photocarrier decay occurs via the external circuit, while for large values of R_L the decay takes place via an internal leakage route, in the same way as the capacitor in circuit 7(a) discharges primarily via R_{out} or via R_{in} depending on their relative values.

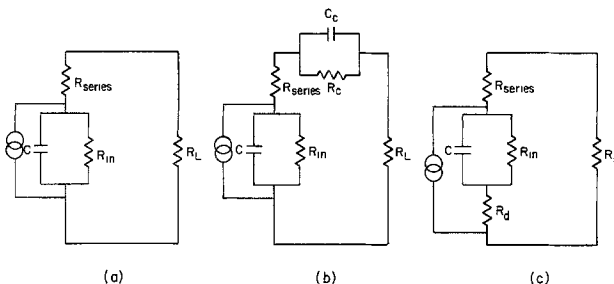


Fig. 7. Equivalent circuits used in the analysis of the photocurrent decay time (see text): C —photocapacitor; R_{series} —total series resistance of the PEC; R_L —load resistor; R_{in} —internal leakage resistor; R_c , C_c —the resistance and capacitance due to the counterelectrode interface; R_d —resistance due to the damaged surface layer.

Although the very simple equivalent circuit of Fig. 7(a) seems to explain the general form of the experimental τ vs. R_L plots, its validity should be examined considering the complete photoelectrochemical cell it is expected to represent. Thus, when additional elements representing the counterelectrode are added, the more complex circuit of Fig. 7(b) is obtained. Analysis of this circuit shows that the solution for the current in the external cell, following a delta source current perturbation, has the form

$$I_{out} = A_1 \exp(-t/\tau_1) + A_2 \exp(-t/\tau_2) \quad [2]$$

However, when $C_c \gg C$, the following relationships apply: $\tau_1 \sim (R_{out} || R_{in})C$, $\tau_2 \sim R_c C_c$ and $A_2 \ll A_1$. This means that circuit 7(b) will generate transients with, practically, a single decay time: $\tau = (R_{out} || R_{in})C$, provided $C_c \gg C$. This condition is fulfilled by the PEC employed, the counter being a metal electrode of large area. Any large capacitor in series with the small photocapacitor is expected, in fact, to act as a short during a fast transient measurement, and the simple circuit 7(a) is, thus, a high frequency form of 7(b) for $C_c \gg C$. This was further verified experimentally by replacing the brass counterelectrode by a gold wire, (while employing a 50 Ω resistor), resulting in no apparent effect on the measured transients, in accordance with the results reported in Ref. (16). Photocurrent transients with a single decay time may be, thus, expected for this cell when the decay is under pure R - C control, provided the potential perturbations are sufficiently small to ensure the constancy of C and R_{in} .

From the results of Fig. 6, it is seen that etching lowers the cell resistance, R_{series} , from 12 to 8 Ω . Assuming that mechanical polishing produces a damaged surface layer (or a surface film) which can be removed by chemical etching, then such a layer may behave as an additional ohmic element through which photocarriers have to be transported. The effect of such an additional ohmic element on the form of the transient can be examined with the aid of the equivalent circuit in Fig. 7(c), where the damaged layer is represented by the additional resistor R_d . The solution for a delta perturbation in this circuit is

$$I_{out} = \frac{\Delta Q \cdot R_{out}}{(R_d + R_{out})^2 C} \exp(-t/\tau) \quad [3]$$

where $\tau = C [R_{in} || (R_d + R_{out})]$. The resistor R_d thus explains the longer decay time and, to some extent, the lower amplitudes obtained in the presence of the surface film. Under short-circuit conditions, the amplitude is calculated to reduce by a factor of 2.5 due to the surface layer when $R_d = 4 \Omega$ and $R_{out} = 8 \Omega$. However, the description of the damaged layer in terms of the additional resistor, R_d , is not complete. From Fig. 3, it is clearly seen that this layer causes a substantial lowering of the open-circuit potential as well. This is not expected to occur due to the addition of R_d . It seems

that the damaged surface acts also as an active recombination region. If the recombinative process in this layer is very fast, it may not show up as a feature in the decay curve in the time window of our measurement ($t > 20$ nsec).¹ Its only apparent effect in terms of the equivalent circuit considered may be the lowering of the initial ΔQ on the photocapacitor, causing a reduction of the initial photopotential. The total amount of charge passing through the external load was indeed measured by us to increase 2-4 times after etching (Fig. 2). The role of the surface as a region of enhanced recombination has been described before by Nelson *et al.* (23) according to *ex situ* photoluminescence decay measurements. This may be the main kinetic significance of such a damaged layer under open-circuit conditions. However, the additional ohmic effect has to be considered when photocurrents are drawn from the cell.

The value of R_{series} evaluated from the photocurrent decay measurements after etching (8Ω in the case depicted in Fig. 6) is very close to the sum of bulk SC and electrolyte solution ohmic resistances calculated according to the specific resistivities, sizes, and geometries employed. The same value for the cell series was found also from the maximum photocurrent peak obtained for an etched electrode under saturation conditions (high pulse intensity): The maximum measured photocurrent peak was given by

$$(i_p)_{\text{max}} = \frac{\Delta\phi_{\text{max}}}{R_{\text{series}} + R_L}$$

where $\Delta\phi_{\text{max}} = 0.7V$ (complete band flattening) and $R_{\text{series}} = 8\Omega$. It is thus clear the value of R in the RC time constant found for photocurrent decay in this PEC is determined by the total series resistance of the cell. If R_{series} contains a contribution due to the finite rate of interfacial charge-transfer at the SC-electrolyte interface ("faradaic impedance") this contribution is apparently very small in this case. Further transient measurements with solutions containing less efficient hole acceptors should reveal if the faradaic impedance can be resolved when it is much larger than the ohmic elements due to the bulk SC and electrolyte.

Finally, the value of C evaluated from the τ vs. R_L plots is close to that found from a Schottky-Mott plot (80 nF cm^{-2}) for a similar CdSe electrode in an alkaline $S^=/S^\circ$ solution under the same applied potential (22). This simply means that the photocapacitor is located in the space-charge region of the semiconductor. Etching is expected to increase the value of C if its only effect were surface roughening. The slight lowering of C measured after etching (Fig. 6) probably means that some surface states contributing to the total C measured for a mechanically polished electrode are removed by etching, resulting in a lower capacity in spite of the increased surface area. It should be also noticed that the measured reduction in reflectance due to this mode of etching (24) is calculated to bring about not more than 20% enhancement of the photocurrent, i.e., this cannot be considered a major contribution to the measured effects.

¹Measurements conducted by us recently, using an Nd-YAG laser, showed that effects of the damaged surface layer on the effective lifetime of the photocarriers could be measured in the time window 10 psec-10 nsec.

Acknowledgment

One of us (S. G.) would like to thank Brookhaven National Laboratory for their assistance in the preparation of this manuscript for publication during his stay there as a Visiting Scientist (Summer 1980).

Manuscript received Aug. 6, 1980.

Any discussion of this paper will appear in a Discussion Section to be published in the December 1981 JOURNAL. All discussions for the December 1981 Discussion Section should be submitted by Aug. 1, 1981.

REFERENCES

1. "Semiconductor Liquid-Junction Solar Cells," A. Heller, Editor, The Electrochemical Society Softbound Proceedings Series, Princeton, N.J. (1977).
2. D. D. MacDonald, "Transient Techniques in Electrochemistry," Plenum Press, New York (1977).
3. S. M. Ryvkin, "Photoelectric Effects in Semiconductors," Consultants Bureau, New York (1969) and Ref. therein.
4. S. R. Dhariwal, L. S. Kothari, and S. C. Jain, *J. Phys. D: Appl. Phys.*, **9**, 631 (1976).
5. S. R. Dhariwal, L. S. Kothari, and S. C. Jain, *Solid State Electron.*, **20**, 297 (1977).
6. D. M. Bielle-Daspert and G. D. Gasset, *ibid.*, **21**, 1219 (1978).
7. H. Tade, *J. Appl. Phys.*, **37**, 4595 (1966).
8. J. L. Lindström, *Solid State Electron.*, **14**, 827 (1971).
9. J. E. Mahan, T. W. Ekstedt, R. I. Frank, and R. Kaplow, *IEEE Trans. Electron Devices*, **ed 26**, 733 (1979).
10. H. T. Weaver and R. D. Nasby, *Solid State Electron.*, **22**, 687 (1979).
11. V. A. Mayamlin and Y. V. Pleskov, "The Electrochemistry of Semiconductors," Plenum Press, New York (1967).
12. K. W. Frese and J. H. Kennedy, Paper 425 presented at The Electrochemical Society Meeting, Seattle, Washington, May 21-26, 1978.
13. G. A. Korsunovskii, *Russ. J. Phys. Chem.*, **53**, 123 (1979).
14. T. Sakata and T. Kawai, Paper 626 presented at The Electrochemical Society Meeting, Los Angeles, California, Oct. 14-19, 1979.
15. J. H. Richardson, S. B. Deutscher, J. E. Harrar, D. C. Johnson, S. P. Perone, and J. Zilmer, Paper 627 presented at The Electrochemical Society Meeting, Los Angeles, California, Oct. 14-19, 1979.
16. F. Kawai, H. Tributsch, and T. Sakata, *Chem. Phys. Lett.*, In press.
17. C. E. P. Krohn, Ph.D. Thesis, University of Texas at Austin (1978).
18. Z. Harzion, N. Croitoru, and S. Gottesfeld: (a) Bulletin of the Israel Physical Society, April 1980; (b) Extended Abstracts of the 3rd Intl. Conf. on Photochemical Conversion and Storage of Solar Energy, Boulder, Colorado, August 1980.
19. G. Hodes, J. Mannasen, and D. Cahen, Private communication.
20. A. Rothwarf and K. W. Böer, *Prog. Solid State Chem.*, **10**, 71 (1975).
21. See, for example, S. Goldman, "Laplace Transform Theory and Electrical Transients," Dover Publications, New York (1966).
22. D. Lando, Private communication.
23. R. J. Nelson, J. S. Williams, H. J. Leamy, B. Miller, H. C. Casey, Jr., B. A. Parkinson, and A. Heller, *Appl. Phys. Lett.*, **36**, 76 (1980).
24. R. Tenne, Private communication.



The Use of Rutherford Backscattering Spectroscopy for Characterization of Surface Films Produced by Aluminum/Water Reactions

R. C. McCune

Ford Motor Company, Engineering & Research Staff, Research, Dearborn, Michigan 48121

and C. J. Russo¹

General Ionex Corporation, Newburyport, Massachusetts 01950

Surface films formed during the reaction between aluminum metal and aqueous electrolytes at elevated temperatures are of considerable interest in situations where such films may afford some measure of resistance to the onset of pitting attack in the presence of aggressive anions (e.g., Cl^-). The reaction between aluminum or aluminum alloys and aqueous electrolytes may result in a variety of reaction products and surface film morphologies, and is reviewed in detail by Alwitt (1). For the specific case of aluminum alloy radiators in automotive cooling systems, the complexity of the electrolyte is accentuated by a variety of components including an antifreeze, various corrosion inhibitors, buffers, and antifoaming agents. Furthermore, the overall system may contain dissimilar metal components which can ultimately result in plating reactions on freshly exposed aluminum, in the absence of particular inhibitors for these reactions. Characterization of aluminum alloy surfaces used in an active cooling system involves not only an appraisal of aluminum/water reaction products on the surface, but also the degree of inhibitor uptake by the surface, the presence of any dissimilar metals, and the integrity of the surface film as a barrier to pitting attack.

The role of any films formed by surface reaction in the overall process of pitting attack is also of interest. While an initially dense oxide or oxyhydroxide (e.g., pseudoboehmite) film may be advantageous in limiting the rate of aggressive ion ingress, its ultimate role may be deleterious if the film serves to isolate a developing pit from the bulk of the electrolyte (2,3). In this latter case, the essentially unreactive film allows localized acidity conditions to develop within the pit so that metal dissolution proceeds without benefit of any diluent or buffering effects of the electrolyte external to the pit.

Electron and low energy (i.e., <10 keV) ion beam spectroscopies are often limited in their ability to rapidly assess such features as apparent thickness and overall elemental composition for water-grown films on aluminum. This is due primarily to experimental sampling depths (usually $\sim 100\text{\AA}$ or less) which can represent only a limited fraction of the thickest water-grown films [often approaching physical dimensions of $\sim 0.5\ \mu\text{m}$ (1)]. Since elemental depth profiles in these techniques are often achieved by concurrent sputter etching, the results may often require extensive times for data collection, and result in limited depth resolution

due to artifacts associated with the sputter process. In this work, the use of Rutherford Backscattering Spectroscopy (RBS) is described with particular application to reactions between a relatively clean aluminum surface and water containing a phosphate-based inhibitor. RBS has the distinct advantages in these applications of permitting the overall film characteristics to be assessed qualitatively, and in a relatively fast, (ca. 5 min spectrum acquisition time) though nondestructive manner.

The RBS technique has been employed by a number of investigators for analysis of surface oxides on aluminum and aluminum alloys (4-7). The experimental details are adequately described in the text by Chu, Mayer, and Nicolet (8). In general, a collimated source of monoenergetic high energy ions and associated scatter chamber and detector are used to acquire the energy distribution of ions scattered through a fixed angle from the target surface. For the simplest thin film, the mass of the surface atom is deduced from the kinetic energy of the backscattered ion, through application of simple binary scattering kinematics with the initial ion energy, its mass, and scattering angle as known quantities. Depth information may be obtained when energy losses in the target bulk are considered for the backscattered ions. For the case of $^4\text{He}^{2+}$ at primary energies of 2-3 MeV, the accessible depth is sufficient to permit penetration of the surface films, allowing extraction of compositional data for the free surface as well as the metal/oxide interface. Because of the relatively low atomic weights of aluminum and oxygen, the spectral peaks for heavier elements occur where there is minimal background contribution, and with somewhat larger sensitivities due to greater scattering cross sections (8).

In this work, the ion source consisted of a 3.0 MeV Tandemron accelerator manufactured by General Ionex Corporation. A scattering angle of approximately 160° was used, in conjunction with a barrier-type particle detector and counting electronics. The overall experimental resolution was estimated to be 25 keV.

Aluminum coupons of a commercial 1100 type material were prepared by mechanical and electrolytic polishing according to a procedure described elsewhere (9). Surface films were grown at 100°C by immersion of the coupons in either doubly distilled, deionized water or in similar water containing Na_2HPO_4 at 0.05M, which is a known inhibitor of the aluminum/water reaction (10). The surface treatments, as well as several experimental quantities are summarized in Table I.

¹ Present address: Varian Associates, Extrion Division, Gloucester, Massachusetts 01930.

Key words: backscattering, pseudoboehmite, aluminum, inhibitor.

Table I.

| Specimen | Film growth time (min.) | | ΔE_s Aluminum sub- strate energy shift (MeV) | O_{FWHM} (MeV) | Approximate film thick- ness (Å)* | Remarks |
|----------|-------------------------|---|---|------------------|---|------------------------------|
| | Water | 0.05M Na ₂ HPO ₄ | | | | |
| A | — | — | 0.0 | — | — | Electropolished surface only |
| B | 15 | 0 | 0.079 | 0.081 | 1450 | No iron peak observed |
| C | 0 | 15 | 0.044 | 0.050 | 850 | Distinct P and Fe |
| D | 15 | 15 | 0.117 | 0.122 | 2150 | Diffuse P and Fe |

* Calculated using density of 3.0 g/cm³ of AlOOH (boehmite) and tabulations outlined in Ref. (12) and (13).

The RBS spectra for the various surface treatments are shown in Fig. 1. The iron peak observed for the electropolished surface (spectrum A) is believed to be due to residual FeAl₃ particulates which remain on the surface following specimen preparation. Iron is the principal impurity in 1100 type alloys, present at levels typically less than 0.5% (wt). The role of the resultant FeAl₃ precipitates in corrosion of aluminum has been discussed elsewhere (11). In spectrum A scattering from the essentially clean aluminum substrate shows a spectral edge having the energy of the binary He-Al collision at roughly the half-height of the edge. The effect of growing a pseudoboehmite film in water (spectrum B) is evidenced by two new features of the spectrum: (i) the appearance of an oxygen peak due to growth of the oxyhydroxide film, and (ii) the displacement of the aluminum substrate scatter edge to a lower energy by the amount ΔE_s due to the associated loss of energy by the helium ions as the layer is traversed during the scatter process. As indicated in Table I, the aluminum substrate scatter edge is displaced by 0.079 MeV from the binary collision energy associated with the relatively clean surface in spectrum A. Because the surface pseudoboehmite film has a lower density of aluminum atoms per cm² than the aluminum metal substrate, the leading aluminum scatter edge occurs at an overall lower signal height. Thus, in principle, the film thickness is reflected in the breadth of the leading surface layer spectral edge (and corresponding ΔE_s for the substrate edge), while

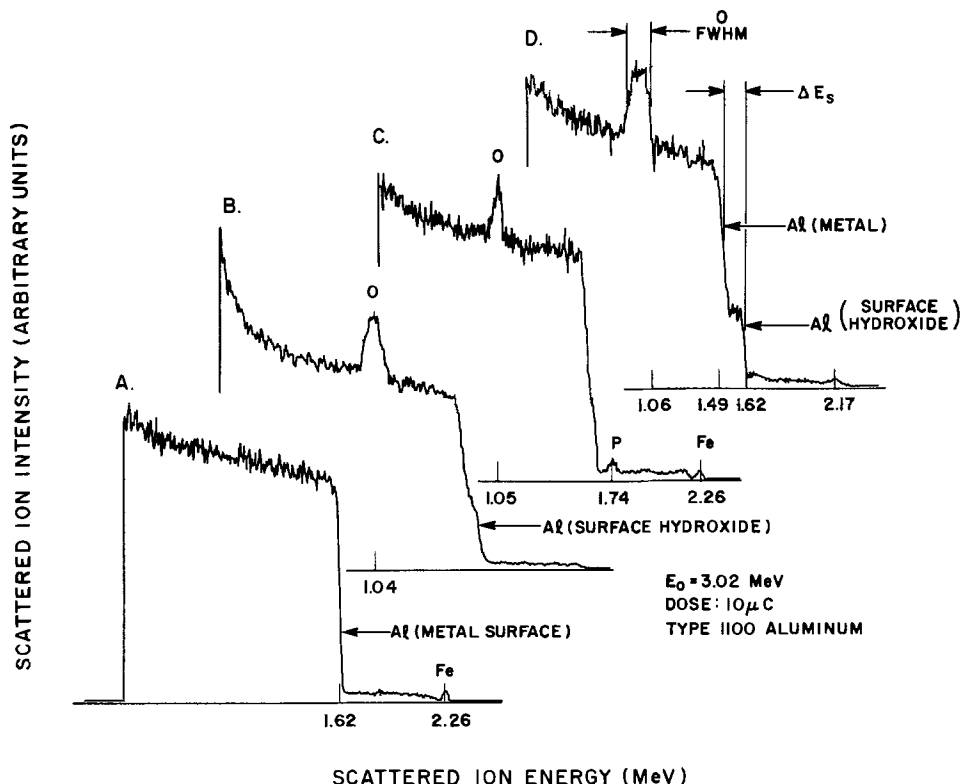
the height of this leading edge is a measure of the film density.

In spectrum C, the effect of the inhibitor is immediately apparent in that ΔE_s for the substrate, as well as the oxygen full width at half maximum (O_{FWHM}) are diminished from the values associated with the pure water grown film. The uptake of phosphorus in the surface layer is evidenced by the appearance of a distinct peak having the appropriate binary collision energy for He-P.

In spectrum D, the original 15 min pseudoboehmite film was exposed to an additional 15 min in the phosphate solution. The spectrum indicates continued film growth i.e., increased O_{FWHM} and ΔE_s , but with noticeably less phosphate uptake than that which occurred on the relatively fresh aluminum surface. The passivation of the surface by the original pseudoboehmite film is apparently responsible for retarding the fixation of the aluminophosphate complex as occurred in spectrum C. The original film produced by 15 min water exposure continues to develop with only slight uptake of phosphate.

It can be seen that RBS offers a unique insight into the mechanisms of film formation and growth. The inhibitive effect of phosphate at the fresh metal surface, as reported by Vermilyea and Vedder (10) is clearly observable, as well as the resulting phosphate uptake by the surface. The ability of RBS to observe cumulative elemental compositions in depth, may prove to extend the utility of the technique to a range which is unattainable with many other surface spectroscopies.

Fig. 1. Rutherford backscatter spectra for various surface treatments to type 1100 aluminum. A. Electropolished surface, B. 15 min pseudoboehmite film, C. 15 min film in phosphate inhibitor, D. combined 15 min pseudoboehmite, 15 min phosphate inhibitor.



Acknowledgments

The authors would like to thank P. J. Edwards for preparation of the specimens, and W. L. Winterbottom and R. R. Wiggle for review of the manuscript. The use of the General Ionex Facility and the cooperation of D. Mills and R. Suchanek for the work is appreciated.

Manuscript submitted July 22, 1980; revised manuscript received ca. Sept. 30, 1980.

Any discussion of this paper will appear in a Discussion Section to be published in the December 1981 JOURNAL. All discussions for the December 1981 Discussion Section should be submitted by Aug. 1, 1981.

Publication costs of this article were assisted by Ford Motor Company.

REFERENCES

1. R. S. Alwitt, "Oxides and Oxide Films," Vol. 4, J. W. Diggle and A. K. Vijh, Editors, p. 169, Marcel Dekker, Inc., New York (1976).
2. G. C. Wood, W. H. Sutton, J. A. Richardson, T. N. K. Riley, and A. G. Malakerbe, "Localized Corrosion," R. W. Staehle, B. F. Brown, J. Kruger, and A. Agrawal, Editors, p. 526. NACE, Houston (1974).
3. J. R. Galvele, "Passivity of Metals," R. P. Frankenthal and J. Kruger, Editors, p. 285, The Electrochemical Society, Princeton (1978).
4. M. Kamoshida, I. V. Mitchell, and J. W. Mayer, *J. Appl. Phys.*, **43**, 1717 (1972).
5. W. Bauer and R. G. Musket, *ibid.*, **44**, 2606 (1973).
6. F. Brown and W. D. Mackintosh, *This Journal*, **120**, 1096 (1973).
7. H. H. Strehblow, C. M. Melliar-Smith, and W. M. Augustyniak, *ibid.*, **125**, 915 (1978).
8. W. K. Chu, J. W. Mayer, and M. A. Nicolet, "Backscattering Spectrometry," Academic Press, New York (1978).
9. R. C. McCune, *J. Vac. Sci. Technol.*, **15**, 31 (1978).
10. D. A. Vermilyea and W. Vedder, *Trans. Faraday Soc.*, **66**, 2644 (1970).
11. J. Zahavi, A. Zavgvil, and M. Metzger, *This Journal*, **125**, 438 (1978).
12. J. F. Ziegler, "Helium Stopping Powers and Ranges in All Elemental Matter," Pergamon, New York (1977).
13. R. L. Shilts, Western Michigan University, Kalamazoo, MI (Private communication).

Erratum

In the paper "A Thermodynamic Theory of Dissolution Potential and Further Tests of the Theory" by R. P. Rastogi and S. A. Kahn, which appeared in the September 1980 issue of the JOURNAL, Vol. 127, No. 9, the following corrections should be noted: On page 1989, paragraph 3 should precede paragraph 2; on page 1990, in the third paragraph, it should read M = mass of phase; also on p. 1990, the right-hand side of Eq. [8] should read X_2 instead of J_c . On page 1991, the left-

hand side of Eq. [34] should read $(\Delta\phi)$ instead of $(\phi\Delta)$; on page 1991, Eq. [44] should read as $\frac{a_2^{(\text{sat'd})}}{a_2^\beta}$ instead of $\frac{a_1^{(\text{sat'd})}}{a_2^\beta}$. The title of Table II on p. 1993 should be "Dissolution potential of KCl in KCl-HCl aqueous mixtures." Also in Table II, the fourth line in the first column should read 0.025M HCl + 0.075M KCl.



Preparation and Properties of Zinc Oxide Films Grown by the Oxidation of Diethylzinc

James R. Shealy and B. Jayant Baliga*

General Electric Company, Corporate Research and Development Center, Schenectady, New York 12345

and R. Jett Field and Sorab K. Ghandhi*

Electrical and Systems Engineering Department, Rensselaer Polytechnic Institute, Troy, New York 12181

ABSTRACT

This paper describes the preparation and properties of zinc oxide films grown by the oxidation of diethylzinc. It is shown that growth above 250°C, with an oxygen to diethylzinc mole ratio in excess of 10, results in stable films of zinc oxide, free from carbon contamination or zinc-ethyl groups. Details are provided of these growth conditions and also of the resulting growth parameters in this paper. The physical properties of films grown by this technique are also described, with particular emphasis on their IR absorption characteristics, stoichiometry, refractive index, and crystallographic orientation, as a function of the growth conditions. Films are shown to have an oxygen deficiency which increases with growth temperature, as does their refractive index. Film orientation, along the c-axis, is also found to improve with increasing growth temperatures.

The properties of zinc oxide films have allowed the fabrication of devices such as heterojunction solar cells, surface acoustic wave devices, and optical waveguides. The highly aligned C-axis films which are obtained with the technique to be described display piezoelectric properties (1) and provide a medium for surface acoustic wave propagation (2). The bandgap of zinc oxide (3.3 eV) is sufficiently large to be transparent to most of the solar spectrum, and its conductivity may be controlled over a broad range. These facts together make zinc oxide useful in heterojunction solar cells application. For example, an n-ZnO/p-CdTe heterojunction solar cell has produced solar efficiencies of 4.6% and short-circuit current collection of 19 mA/cm² (3). The optical transmission spectrum for the zinc oxide films shows a strong absorption edge at wavelengths around 0.4 μm, with a transparent region in the range of 0.4–2.3 μm. This transparent window makes zinc oxide suitable for optical waveguide fabrication (4). In addition, the authors have used zinc oxide films as a source of zinc for open tube diffusions of zinc in gallium arsenide (5).

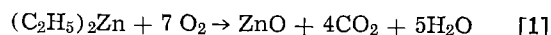
This paper describes the growth of zinc oxide utilizing a metal-organic chemical vapor phase deposition (CVD) process. These films are characterized using infrared transmission, resistivity measurements, x-ray diffraction, Auger analysis, and ellipsometry. The conditions for the deposition of stable, C-axis oriented, zinc oxide films grown by the oxidation of diethylzinc have been determined. It appears that zinc oxide films obtained with this process have desirable optical, electrical, and acoustical properties which are potentially suitable for the many applications mentioned above.

Apparatus

The apparatus used for the zinc oxide depositions was a resistance heated, cold wall system which is schematically illustrated in Fig. 1. The substrate heater was approximately 1½ in. in diameter. The reaction chamber geometry was vertical with gas flow normal to the substrate surface. The chamber was maintained at essentially atmospheric pressure with reactants entering at the top and exhausted out of the bottom of the chamber. The chamber was a 12 in. long, 3 in. diam quartz tube. Gases provided to this system were argon¹ and oxygen.¹ The diethylzinc² was contained in a stainless steel bubbler maintained at 25°C, and was transported into the reaction chamber by passing argon through the bubbler. An additional argon line was used for dilution purposes. Oxygen was introduced through a separate port at the top of the reaction chamber.

Film Deposition

In this study, the zinc oxide films were deposited by the reaction of diethylzinc with oxygen. Diethylzinc is a pyrophoric liquid which is known to react with air even at room temperature. The deposition of zinc oxide films using diethylzinc vapors was, therefore, studied over a wide range of temperatures ranging from room temperature (25°C) up to 500°C. The oxidation of diethylzinc may be expected to proceed by the following reaction



This equation indicates that it is necessary to perform the deposition under a high O₂/DEZ mole ratio to ensure complete oxidation of the diethylzinc.

* Electrochemical Society Active Member.

Key words: zinc oxide, chemical vapor deposition, organometallic CVD.

¹ UHP grade, Union Carbide Corporation.

² 5N Electronic grade, Ventron Corporation, Danvers, Massachusetts.

M.O. CVD SYSTEM SCHEMATIC FOR ZnO DEPOSITION

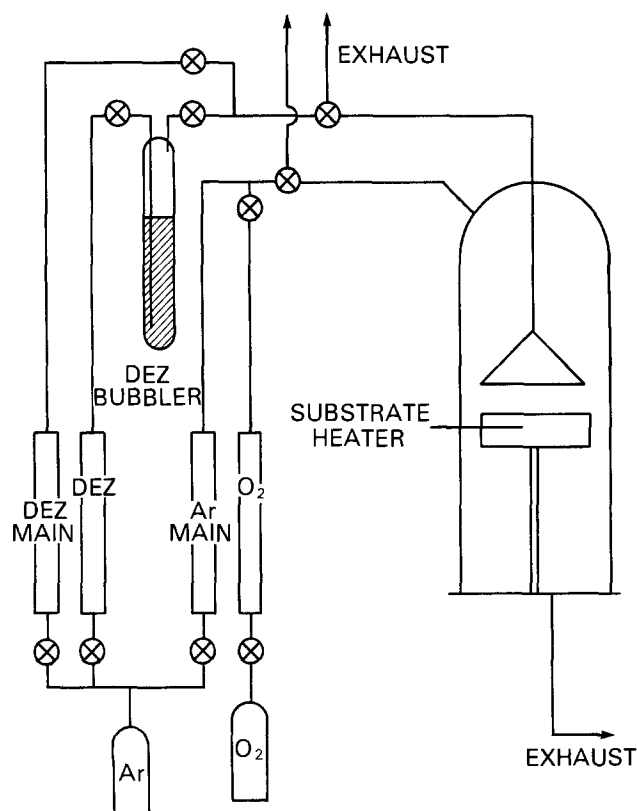


Fig. 1. Schematic diagram of zinc oxide deposition system

The deposition of the zinc oxide films was studied on (111) $\pm 0.5^\circ$ oriented, 30 Ω -cm, phosphorus-doped, silicon substrates under the following conditions:

(i) For a fixed partial pressure of diethylzinc and a fixed deposition temperature, the effect of the partial pressure of oxygen was observed by changing the oxygen flow.

(ii) Keeping the partial pressure of oxygen and the deposition temperature fixed, the effect of the partial pressure of diethylzinc was observed by changing the argon flow through the diethylzinc bubbler. Full saturation conditions were assumed for the argon passing through the bubbler.

(iii) Keeping the partial pressures of diethylzinc and oxygen fixed, the effect of the deposition temperature was observed. Prior to film deposition, the substrates were cleaned by degreasing, immersion in Caros solution, and a dip in HF prior to loading into the reactor. After deposition, the film thickness was determined by ellipsometry.

Oxygen flow.—In the absence of oxygen, diethylzinc will decompose at elevated temperatures into zinc-ethyl groups or even into elemental zinc if the temperature is sufficiently high. In this study, it was found that the films deposited with little or no oxygen present showed rapid changes in appearance upon exposure to air after deposition. The effect the introduction of oxygen had upon the growth rate of the films was examined at a deposition temperature of 350°C while maintaining all other gas flows constant. To obtain this data, the argon flow through the diethylzinc bubbler was maintained at 23 cm³/min and a total argon flow of 6.9 liters/min was used. The growth rate was found to be independent of oxygen flow when the oxygen to diethylzinc mole ratio exceeded 10. Films grown at oxygen to diethylzinc mole ratios of less than 10 showed changes in appearance on exposure to air. This

is in accordance with the high ratio of oxygen to diethylzinc indicated by Eq. [1] to ensure complete reaction. Consequently, care was taken in the experiments described below to maintain an oxygen to diethylzinc ratio of greater than 10 to ensure the deposition of stable zinc oxide films.

Diethylzinc flow.—The growth rate of the zinc oxide films could be varied over a broad range by controlling the argon flow through the DEZ bubbler while maintaining all other growth parameters constant. For a deposition temperature of 350°C, an oxygen flow of 12 cm³/min and a total argon flow of 6.9 liters/min, the growth rate was found to increase linearly with increasing argon flow through the DEZ bubbler as shown in Fig. 2. Similar results were obtained at other deposition temperatures. It should be noted that even at the highest DEZ concentrations used to obtain the growth rate data in Fig. 2, the oxygen to DEZ ratio was maintained at greater than 10 to ensure the formation of zinc oxide films.

Growth temperature.—The growth rate of the zinc oxide films was measured as a function of the deposition temperature over the range from room temperature (25°C) to 500°C, while maintaining all the gas flows constant. The gas flows chosen for these experiments were an argon flow through the DEZ bubbler of 23 cm³/min, an oxygen flow of 12 cm³/min, and a total argon flow of 6.9 liters/min. It was found that the films deposited at below 250°C changed their appearance on exposure to air. Consequently, the growth rate of films deposited at 250°-500°C is shown in Fig. 3. It can be seen that the deposition rate decreases when the growth temperature is increased. Reactant depletion at the substrate surface with increasing deposition temperature was found to be responsible for this decrease in the growth rate. This depletion in the reactant concentration at the substrate surface occurs due to a competing gas phase reaction between the diethylzinc and

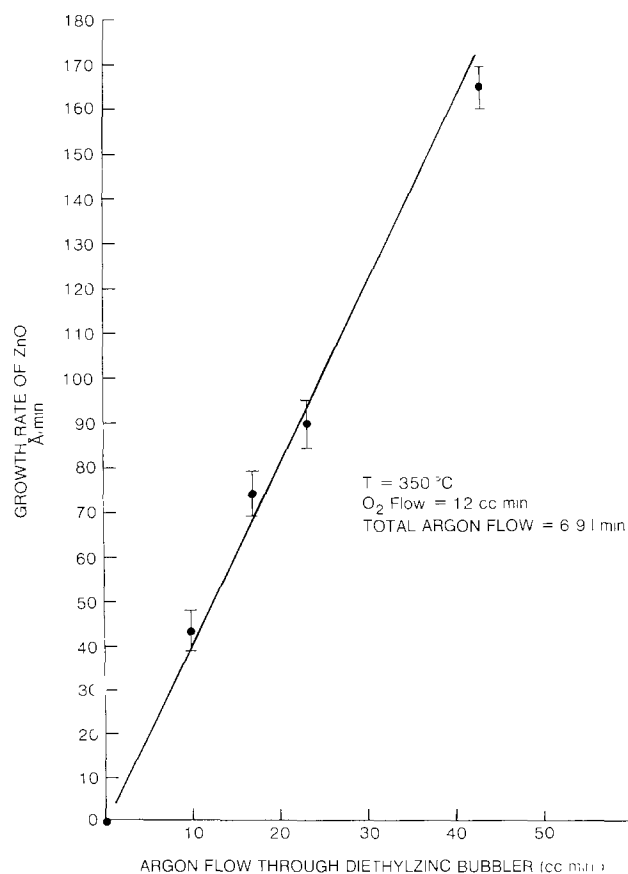


Fig. 2. Increase in the deposition rate of zinc oxide films with increase in argon flow through the diethylzinc bubbler.

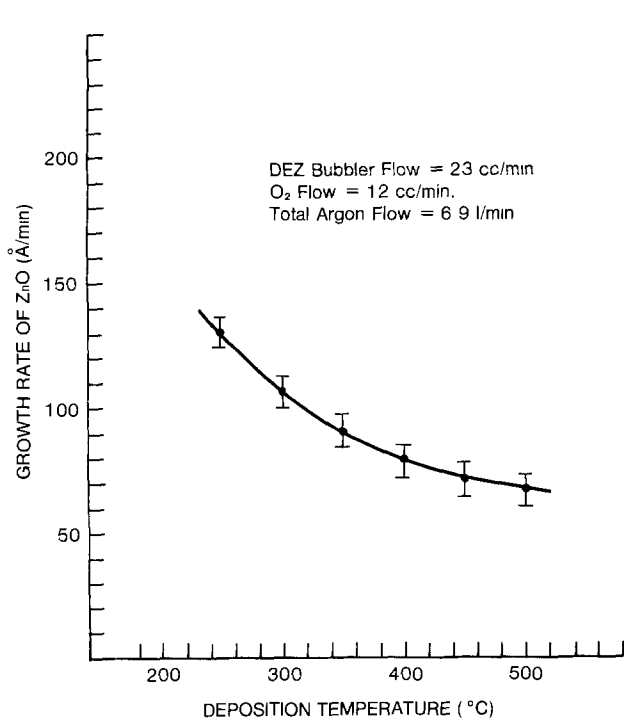


Fig. 3. Dependence of the growth rate of zinc oxide films upon the substrate temperature.

oxygen. Evidence supporting this was obtained by measuring the growth rate, at a fixed deposition temperature, while changing the spacing between the DEZ inlet to the reactor and the substrate surface. For a fixed partial pressure of DEZ in the reaction chamber, the growth rate showed a rapid increase with decreasing spacing between the DEZ inlet and the substrate surface. Although it may be concluded from these results that a small spacing between the DEZ inlet and the substrate surface is desirable for obtaining high growth rates, in practice the DEZ inlet position must be chosen so as to obtain the desired uniformity in the film thickness over the entire substrate area. As an example, for the above growth conditions, a spacing of 3 in. between the DEZ inlet and the substrate surface resulted in a variation in film thickness of less than $\pm 10\%$ over an area of 1.5 in. in diameter.

Film Properties

Chemical, physical, and electrical properties of the zinc oxide films deposited under various growth conditions are described below. This data can be used to evaluate the quality of these films for potential applications.

Infrared absorption.—Infrared absorption measurements over wavelengths ranging from 1 to 40 microns were taken on films deposited at temperatures ranging from room temperature (25°C) to 500°C. Films which were deposited at temperatures above 250°C showed the presence of an absorption band at a wavelength of 23 microns which was not observed in the case of films deposited at below 250°C. Typical absorption spectra for films deposited at 150° and 500°C are shown in Fig. 4 for comparison. Since this absorption band has been observed in bulk zinc oxide and is associated with the zinc-oxygen molecular bond, it can be concluded that zinc oxide films are deposited at substrate temperatures above 250°C, while films deposited below this temperature probably consist of unstable zinc ethyl groups.

Composition.—The stoichiometry of zinc oxide films deposited at temperatures ranging from 250° to 500°C was measured by Auger analysis using a polycrystalline zinc oxide sample as the standard. Films were found to contain an excess of zinc which increased with increas-

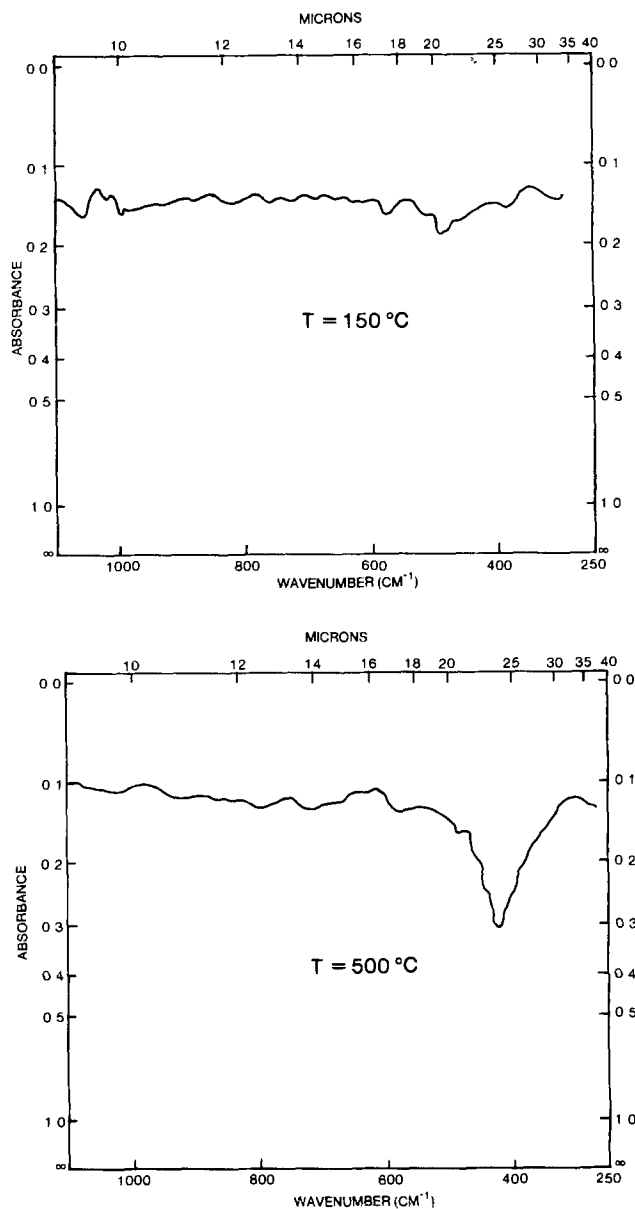


Fig. 4. Infrared absorption spectra of films deposited at substrate temperatures of 150° and 500°C.

ing deposition temperatures as shown in Fig. 5. A similar behavior has been observed in the case of the deposition of tin oxide films by the oxidation of tetramethyltin (6). The presence of excess zinc in the films, as detected by the Auger analysis, is important for understanding the variation in their refractive index and resistivity with growth temperature. It is also worth pointing out that the Auger analysis, taken on these films after ion milling approximately 50Å from the surface, showed that they were free of the carbon contamination that could arise from the use of the organometallic zinc source.

Refractive index.—The index of refraction was measured for films at a wavelength of 5461Å by ellipsometry. The conditions used to deposit these films on the silicon substrates were identical to those used to obtain the data shown in Fig. 3. The variation in the refractive index with deposition temperature is shown in Fig. 6. It can be seen that the index of refraction increases when the deposition temperature is increased. This increase in the refractive index with deposition temperature correlates with the observed increase in the excess zinc concentration as was shown in Fig. 5. While a refractive index of 2.03 has been reported for bulk ZnO (8), values similar to those given

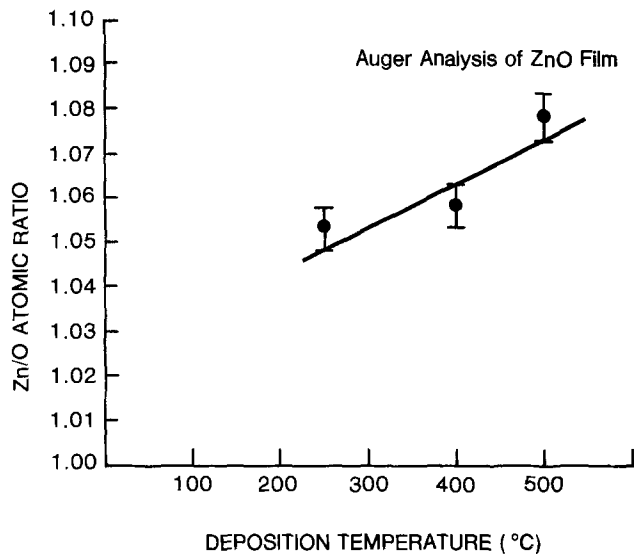


Fig. 5. Auger data of zinc oxide films revealing the increase of excess zinc in the films with increasing deposition temperatures.

in Fig. 3 have been observed for ZnO films deposited by other chemical vapor deposition techniques (9).

Crystal orientation.—X-ray diffraction measurements were made on films deposited on Corning Type 7059 glass at deposition temperatures ranging from 250° to 500°C. No diffraction peaks were observed for films grown at and below 300°C, indicating that these films were amorphous. However, films deposited at above 300°C showed x-ray diffraction peaks as illustrated in Fig. 7 for a film deposited at 400°C. This and other x-ray data taken on these films shows that the films have a high C-axis orientation which improves with increasing deposition temperature. This data as well as the results of deposition on other substrates has been discussed in greater detail elsewhere (7).

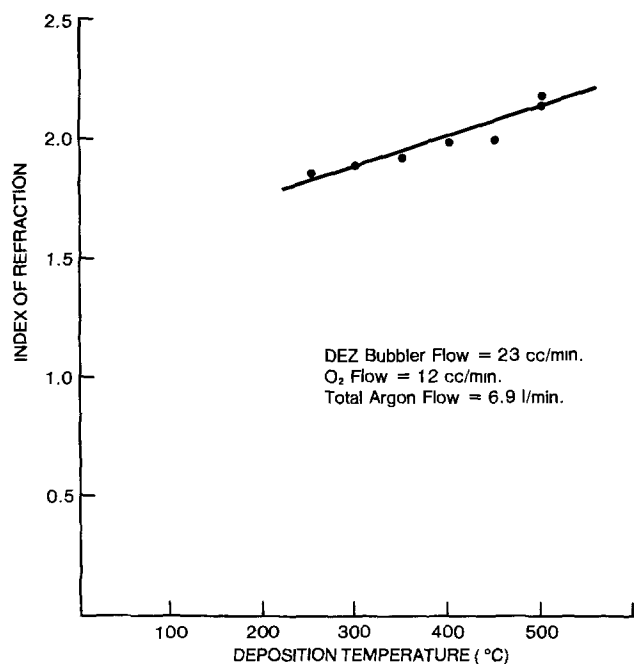


Fig. 6. Refractive index of zinc oxide films grown at deposition temperatures ranging from 250° to 500°C.

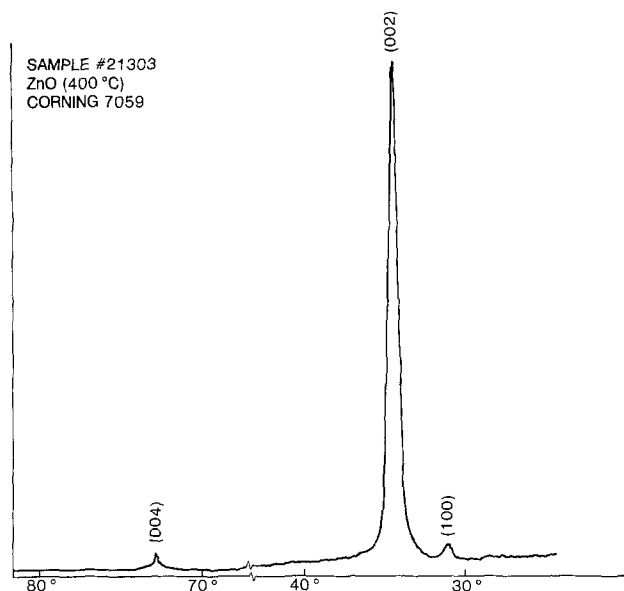


Fig. 7. X-ray diffraction data of a zinc oxide film grown at 400°C on Corning 7059 glass obtained using Copper K_α radiation.

Conclusions

A novel technique for the deposition of zinc oxide films at relatively low temperatures has been outlined. The physical properties of this material, which are of interest for a number of electronic applications, have also been described. It has been shown that films grown in this manner are highly oriented, and should find use in surface acoustic wave application. The use as a zinc source for open tube gallium arsenide diffusion has been outlined in an earlier paper. Further work needs to be done to explore other uses for zinc oxide thin films grown by this CVD technique.

Acknowledgment

The authors would like to thank R. Rafun for manuscript preparation. This work was partially supported (S.K.G. and R.J.F.) by Contract No. XI-9-8000-1 from the Solar Energy Research Institute, Golden, Colorado.

Manuscript submitted June 20, 1980; revised manuscript received Aug. 13, 1980.

Any discussion of this paper will appear in a Discussion Section to be published in the December 1981 JOURNAL. All discussions for the December 1981 Discussion Section should be submitted by Aug. 1, 1981.

Publication costs of this article were assisted by General Electric Company.

REFERENCES

1. A. R. Hutson, *Phys. Rev. Lett.*, **4**, 505 (1960).
2. T. Shiosaki, T. Yamamoto, A. Kawabata, R. S. Muller, and R. M. White, *IEDM Digest*, 151 (1979).
3. A. L. Fahrenbrach, J. Aranovich, F. Courregas, T. Chynoweth, and R. H. Bube, *IEEE Photovoltaic Spec. Conf.*, 13th, Washington, D.C., p. 281 (1978).
4. T. Shiosaki, S. Ohnishi, and A. Kawabata, *J. Appl. Phys.*, **50**, 3113 (1979).
5. J. R. Shealy, B. J. Baliga, and S. K. Ghandhi, *IEEE Electron Device Lett.* **ed1-1**, 119 (1980).
6. B. J. Baliga and S. K. Ghandhi, *This Journal*, **123**, 941 (1976).
7. S. K. Ghandhi, R. J. Field, and J. R. Shealy, *Appl. Phys. Lett.*, **37**, 449 (1980).
8. E. Mollwo, *Z. Agnew Phys.*, **6**, 257 (1954).
9. T. Shiosaki, S. Ohnishi, Y. Hirokawa, and A. Kawabata, *Appl. Phys. Lett.*, **33**, 406 (1978).

Comparison of the Properties of Molybdenum Silicide Films Deposited by D-C Magnetron and RF Diode Co-Deposition

Ronald S. Nowicki* and John F. Moulder

Perkin-Elmer, Physical Electronics Division, Mountain View, California 94043

ABSTRACT

We report a preliminary study in which the physical and electrical properties of d-c magnetron and co-deposited rf diode molybdenum silicide films of varying stoichiometry are compared. It is shown that the d-c magnetron films deposited from a composite target tend to be non-optimal in comparison to the rf diode co-deposited films of the same stoichiometry. Extensive degradation of the d-c magnetron films was frequently observed during heat-treatment at 1000°C in nitrogen or argon ambient. The rf diode films, however, appear to withstand heat-treatment without signs of degradation. There appear to be significant differences in film stress changes during heat-treatment, i.e., the d-c magnetron films exhibit a severe change in stress level resulting in a highly tensile state which causes film cracking and loss of adhesion, whereas the rf diode co-deposited film stress changes to minimal values during heat-treatment. Additional data on crystal morphology, resistivity change during heat-treatment, and general film properties are also discussed.

Refractory metal silicides have been proposed as alternatives to polycrystalline silicon ("polysilicon") for gate electrode or interconnection metallizations in field effect transistor devices of VLSI dimensions (1-4). This trend has evolved as a consequence of the prohibitive values of resistance encountered in conventional polysilicon gate technology as device geometries are reduced.

One significant problem with these newer materials appears to be the relatively high levels of contaminants (e.g., oxides, carbon, and alkalis) presently found in composite, hot-pressed sputtering sources (targets). These contaminants not only can alter device characteristics irreversibly, but also may result in the loss of film integrity during subsequent high temperature (1000°C) device processing steps.

Another potential problem with refractory silicide thin films may be the high levels of intrinsic film stress often found in these films. Additionally, many commercial sputter deposition systems do not provide a means of controlling this film stress through controlled d-c or rf substrate bias (5, 6). Films deposited with high levels of intrinsic stress can also fail in subsequent high temperature processing, where thermal expansion coefficient mismatch between film and substrate is exaggerated.

In this preliminary study, we describe a co-deposition technique in which rf sputtering is done from separate high purity targets of the refractory metal and silicon with and without substrate bias. Additionally, we compare the physical and electrical properties of molybdenum silicide films prepared by this technique with films deposited from a composite target by the d-c magnetron technique.

Experimental

D-C magnetron deposition of molybdenum silicide.—All d-c magnetron depositions were done in a Perkin-Elmer Model 4400 cryo-pumped sputtering system equipped with a hot-pressed source (target) of molybdenum disilicide of 99.9 purity (Metron). The target was solder-bonded to a standard water-cooled copper backing plate and magnet assembly. Depositions were done at ca. 7 W/cm² (averaged over entire target area of ca. 300 cm²) and 5 mTorr (0.67 Pa) of argon pres-

sure at system base pressure of ca. 5×10^{-7} Torr (7×10^{-5} Pa) and 10 rpm substrate table rotation. Deposition rates were typically ca. 35 nm/min. Films of ca. 250 nm nominal thickness, determined via profilometry of an etched step (HNO₃:HF-200:1), were deposited onto silicon wafers previously coated with ca. 100 nm of thermal silicon oxide, 100 nm of rf sputtered silicon nitride, and ca. 500 nm of LPCVD-deposited (640°C) polycrystalline silicon (polysilicon). Additional depositions with and without rf substrate bias were done onto 5 × 25 mm, 63 μm thick sapphire beams for evaluation of film stress and film integrity during subsequent heat-treatment.

Deposition of molybdenum silicide via the rf diode co-deposition technique.—These depositions were done in the same sputter system described above from separate targets of 99.99 purity molybdenum and silicon using the rf power-splitting feature of the system at 10 mTorr (1.33 Pa) argon pressure. For deposition of the silicon-rich (MoSi_{2.8}) films, typical target voltages and wattages were: Mo 850V, 300W; Si 2400V, 1500W. Substrate pallet rotation was 10 rpm in all cases. Under these conditions, ca. 0.1 nm of molybdenum and ca. 0.2 nm of silicon were deposited per one pallet revolution. The resultant deposition rate was ca. 2.7 nm/min. Deposition temperature was found to be ca. 120°C under these conditions (PTC Model 575 CM surface thermometer).

To study the influence of rf substrate bias on the film properties, additional depositions were done with varying degrees of bias. The effects of this parameter are elaborated upon later in the text (Results section).

Additional rf diode depositions were done from a composite target of 99.9 purity at 10 mTorr argon pressure and 5 W/cm² power density. The resultant deposition rate was ca. 4.7 nm/min.

Other experimental techniques.—Conventional four-point probe measurements were used for resistivity determinations.

All heat-treatments were carried out with a Lindberg "table top" (Model SB 54542) furnace and quartz diffusion tube using high-purity sources of nitrogen or argon at ca. 10 liters/min flow.

CV plotting was done with an MDC controller/plotter and Signatone probe with hot stage.

* Electrochemical Society Active Member.
Key words: films, gates, sputtering, analysis.

Auger and SIMS analyses were done with a Perkin Elmer Model 590 scanning Auger Microprobe.

The elemental sensitivity values reported by Davis *et al.* (7) were used to quantify the Auger electron spectra.

Helium ion backscatter analysis was done with the Cal Tech 3 MeV Van de Graaff accelerator using 4He^+ ions in the technique reported by Chu *et al.* (8).

Scanning electron microscopy (SEM) was done with a Hitachi S-450-1 system.

Determination of film stress was done on thin sapphire beams using the method reported (9) earlier.

X-ray diffractometry was done with a GE XRD diffractometer using $\text{CuK}\alpha$ radiation at 35 kV.

Results

Determination of molybdenum-silicon stoichiometry.

—Molybdenum/silicon ratios for both d-c magnetron and co-deposited rf diode films were determined initially in films deposited directly on silicon wafers. This was particularly essential for the co-deposited films, where no prior correlations existed between deposition parameters and stoichiometry. It was hoped that the d-c magnetron and rf diode films deposited from a single composite target of $\text{Mo}_{33}\text{Si}_{67}$ would serve as "standards" for the stoichiometric determinations. However, it can be seen (Fig. 1) that good stoichiometric correlation between the two deposition methods was not obtained, as shown by the Auger depth

profiles of the resultant films. It is apparent that molybdenum/silicon atomic ratio appears to be ca. 32:68 for the d-c magnetron films, whereas the ratio appears to be ca. 39:61 for the rf diode films.

In an attempt to resolve the question of film stoichiometry and to obtain a "standard" film, a sample of an rf diode co-deposited film having an apparent Mo/Si ratio of 32:68 by Auger analysis was analyzed via helium ion backscattering spectrometry (HIBS). The resultant Mo/Si ratio was found to be 26:74. Since the HIBS analyses are assumed to have an accuracy of approximately $\pm 5\%$, it is apparent that the Auger results are providing ratios that are Mo rich. It is possible that either differential sputtering effects or matrix effects on the shape of the Auger lines are contributing to this error (10). If the error is assumed to be constant (which may not be the case) a correction factor can be obtained by comparing the Auger and HIBS data. In this case the HIBS Mo/Si ratio was 0.35; the Auger Mo/Si ratio was 0.47. Therefore, a correction factor of 0.74 should be used as an attempt to correct the Auger data.

Figure 2 presents Auger depth profiles which depict the stoichiometry of two rf diode films, co-deposited with differing target voltages on the molybdenum and silicon. From Fig. 2(B), it is apparent that silicon enrichment may be present near the film surface. Appli-

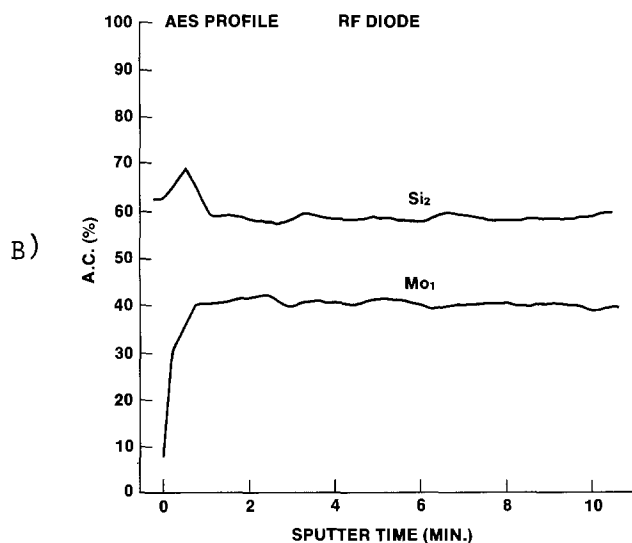
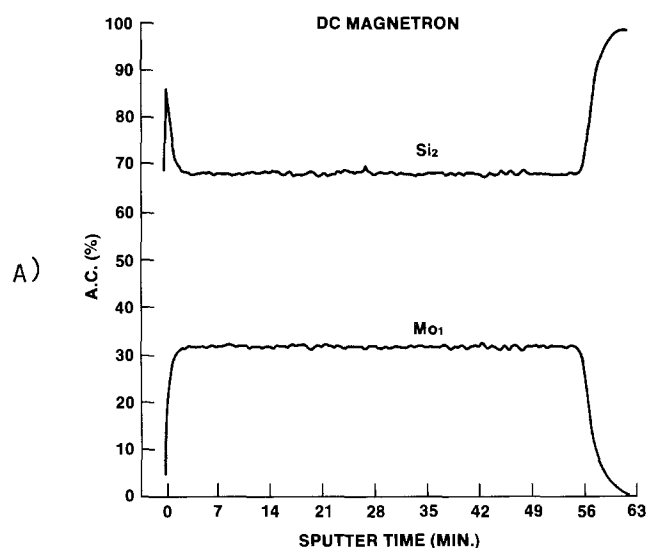


Fig. 1. Auger depth profiles of (A) d-c magnetron and (B) rf diode films sputtered from single composite targets of composition $\text{Mo}_{33}\text{Si}_{67}$.

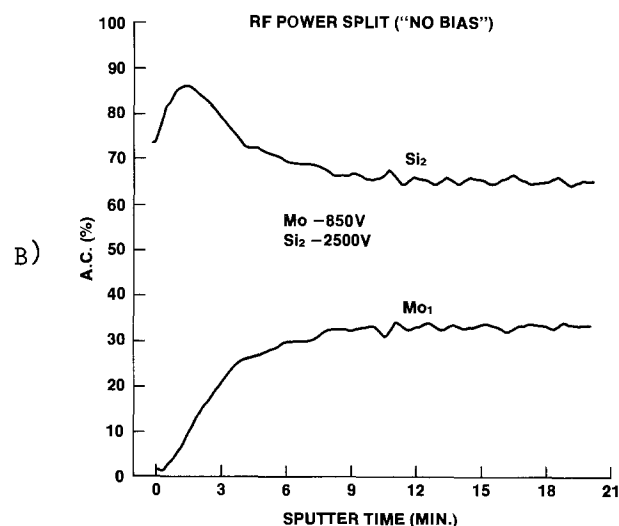
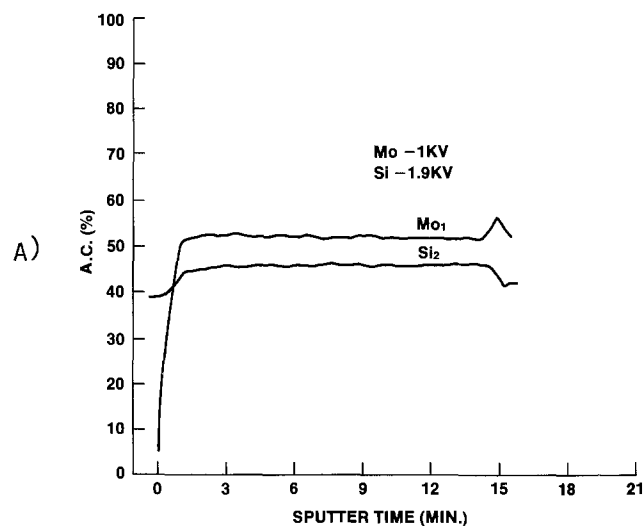


Fig. 2. Auger depth profiles of rf diode co-deposited molybdenum silicide films sputtered at different target voltages.

cation of the above correction factor to these spectra results in stoichiometric ratios of (a) $\text{Mo}_{46}\text{Si}_{54}$ and (b) $\text{Mo}_{26}\text{Si}_{74}$. For simplification, these films will be designated (a) "MoSi" and (b) "MoSi_{2.8}."

Comparison of morphology and integrity of as-deposited and heat-treated d-c magnetron and rf diode films.—The as-deposited films from all three types of depositions were metallic in appearance and exhibited no visible crystallinity or surface features at magnification up to 30 kX (SEM) on silicon oxide or nitride-coated silicon and sapphire. On polysilicon, all the as-deposited films tended to replicate the crystal morphology of the polysilicon. This observation is evident in Fig. 3(A), which shows the morphology of undoped polysilicon before (insert) and after deposition of the d-c magnetron molybdenum silicide without substrate bias. When this structure was subjected to 1000°C heat-treatment for 30 min in nitrogen or argon, severe cracking was observed in many instances, as shown in Fig. 3(B). Additionally, white fumes, presumably molybdenum oxide, were seen to evolve from the film during heat-treatment. The severity of this degradation precludes further processing. From Fig. 3, one may surmise that these cracks appear to be associated with a grain boundary or film stress phenomenon. The film stress-induced mode of degradation is

supported by the observation that the films tended to peel away from the substrate with concavity (Fig. 4A), indicative of tensile stress in the film. (See section on Film stress below for further comment.) This degradation is more severe in films deposited under high values of substrate bias (−120V).

For rf diode co-deposited films having Mo/Si ratios <0.5 on polysilicon, silicon oxide, or nitride, no observable film degradation was observed during and after heat-treatment, as shown by Fig. 4(B) and Fig. 5. From Fig. 4(B), it should be noted that the largest visible crystallites were <100 nm in width. Auger depth profile analysis of the films deposited under rf bias indicated that Mo-Si stoichiometry remained unchanged as a result of the heat-treatment [Fig. 6(A)] when the Mo/Si ratio was <0.5. However, one change which became apparent during heat-treatment was the appearance of a thin (ca. 5 nm) layer of silicon nitride on the surface of the silicide film. Figure 6(B) shows the Auger spectrum of the heat-treated film. No molybdenum was detected on the surface. The nitrogen peak, however, is readily apparent in the spectrum. For co-deposited films of molybdenum-rich stoichiometry (Mo/Si >0.5), extensive surface degradation was observed during heat-treatment. It should be noted that no detectable changes in thickness were observed for MoSi or MoSi_{2.8} films on silicon nitride or oxide as a result of heat-treatment.

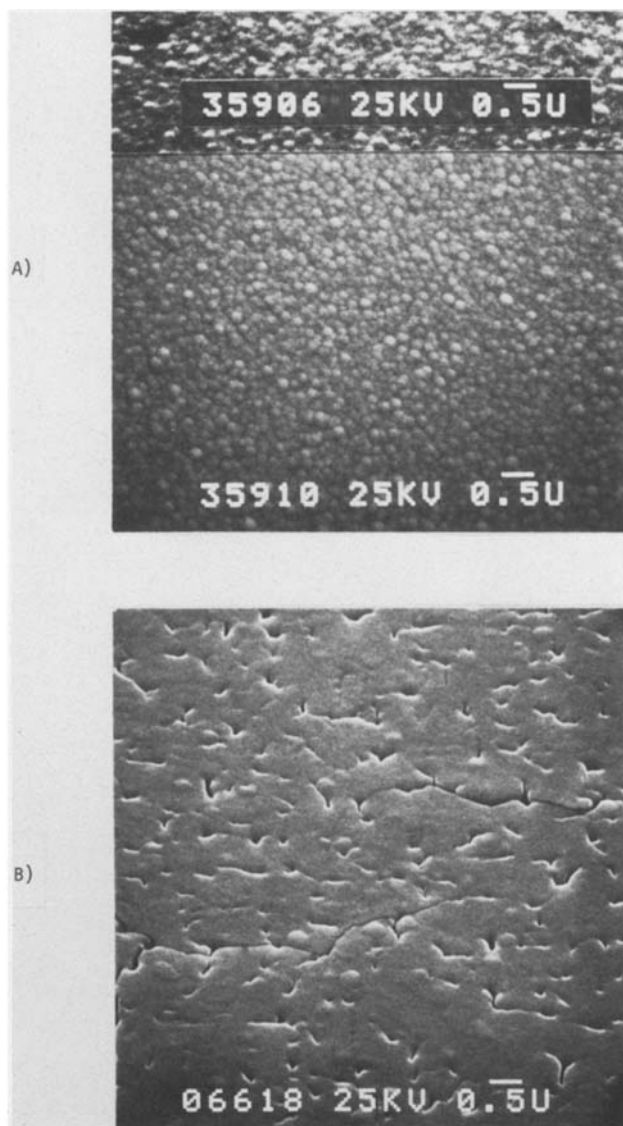


Fig. 3. SEM micrographies of d-c magnetron sputtered molybdenum silicide films on polysilicon, (A) as-deposited and (B) heat-treated in nitrogen at 1000°C for 30 min. Insert in (A) shows the uncoated polysilicon surface.

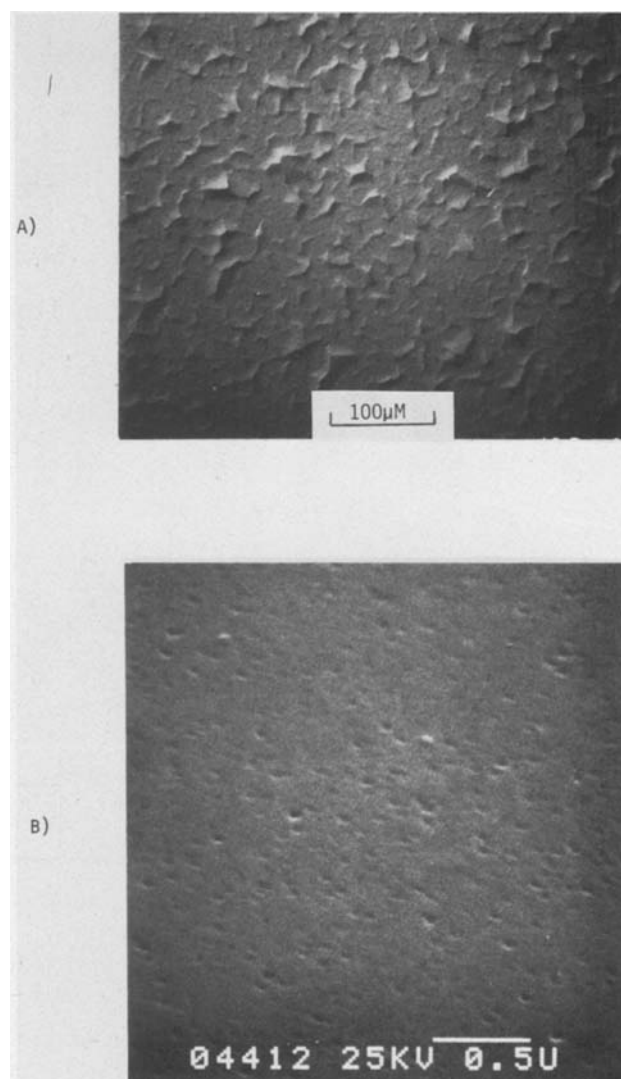


Fig. 4. Micrographs of (A) heat-treated d-c magnetron molybdenum silicide on polysilicon showing peeling morphology, and (B) heat-treated MoSi_{2.8} on oxide.

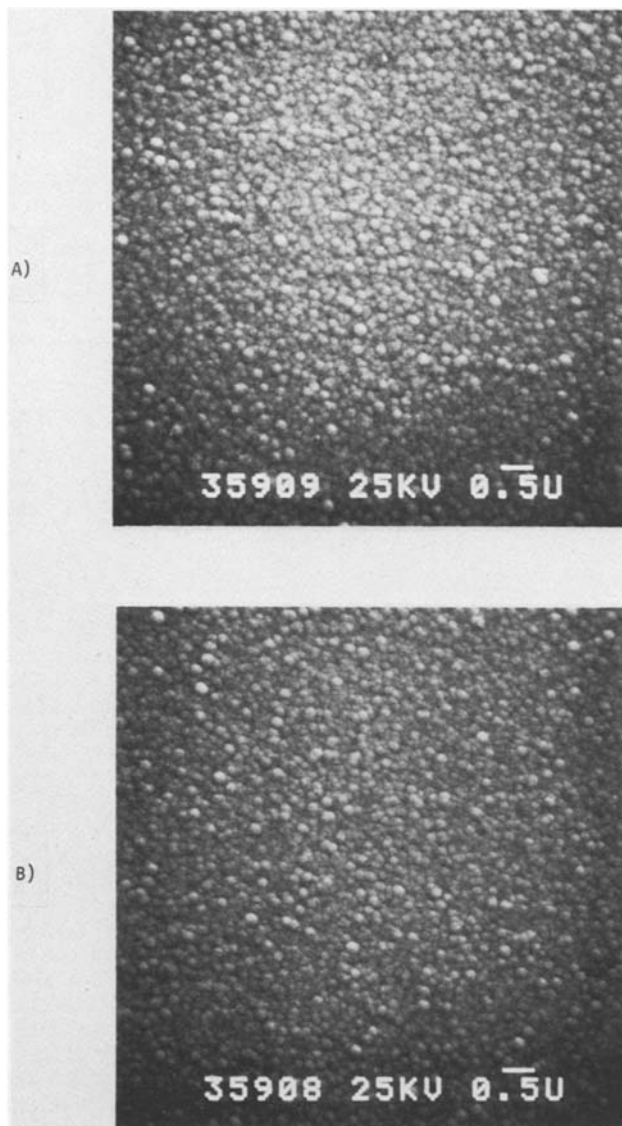


Fig. 5. SEM micrographs showing (A) as-deposited and (B) heat-treated $\text{MoSi}_{2.8}$ on polysilicon.

Comparison of the electrical properties of the d-c magnetron and co-deposited rf diode films.—The as-deposited d-c magnetron films had sheet resistance of ca. $20 \Omega/\text{sq}$ on silicon oxide or nitride. After heat-treatment at 1000°C in nitrogen or argon, the sheet resistance lowered to $4\text{--}5 \Omega/\text{sq}$ in cases when the film integrity was retained.

For the rf diode co-deposited films, the as-deposited sheet resistance values were dependent on molybdenum-silicon stoichiometry, as expected. Figure 7(A) shows the sheet resistance values plotted as a function of thickness for the composition $\text{MoSi}_{2.7}$. Figure 7(B) shows the resistivity plots as a function of Mo:Si ratio for as-deposited and heat-treated molybdenum silicide films of varying composition deposited under “no bias” (floating) conditions. With biased substrate depositions, (-25 to 50V), the heat-treated film resistivity appears to lower ca. 50% from the values shown. Thus, resistivity values of ca. $8 \times 10^{-5} \Omega\text{cm}$ can be obtained.

Capacitance-voltage plots of the d-c magnetron and rf diode co-deposited films were done before and after heat-treatment after using a metal mask to define $750 \mu\text{m}$ diam electrodes of the silicide on ca. 100nm of thermal oxide on n-type silicon wafers. Figure 8 shows the resultant plots for the as-deposited d-c magnetron film and the rf diode film after heat-treatment. The plot for the as-deposited rf diode film is not shown due to its severe distortion, presumably due to oxide “dam-

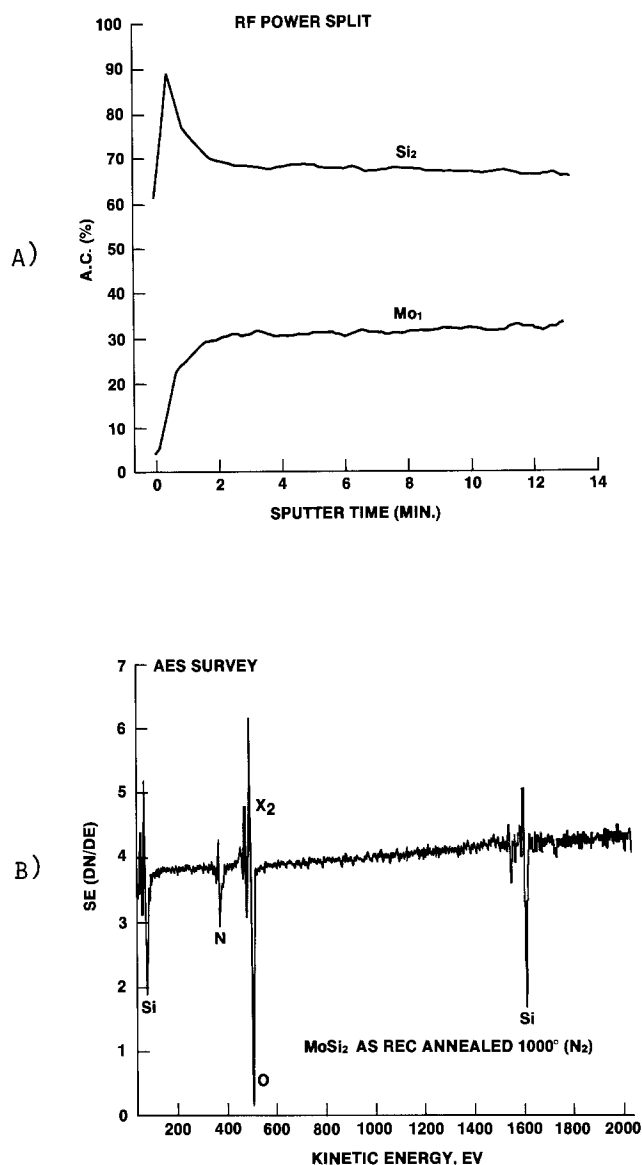


Fig. 6. Auger plots showing (A) depth profile of heat-treated rf diode co-deposited molybdenum silicide having as-deposited composition of $\text{Mo}_{32}\text{Si}_{68}$ (Auger), and (B) AES survey of film surface.

age” during deposition. From Fig. 8, it is apparent that alkali and hydrogen-induced flatband shifts (Q_m) (11) are excessively high (ca. 3×10^{12} charges/ cm^2) for the d-c magnetron films, whereas the heat-treated rf diode films have Q_m values of ca. $8 \times 10^{10}/\text{cm}^2$. The high Q_m values of the d-c magnetron films were considerably reduced to levels comparable to the rf diode films after heat-treatment at 1000°C in cases where film degradation did not occur. This reduction in Q_m with heat-treatment was reported by Learn (12).

X-ray diffractometry.—X-ray diffractometry was done on the as-deposited and heat-treated d-c magnetron and rf diode co-deposited films on silicon nitride coated wafers. The resultant spectra are shown in Fig. 9. Examination of these spectra show that both the as-deposited d-c magnetron and rf diode films [Fig. 9(a), their spectra were superimposable] exhibited minimal crystallinity. The silicon (211) cubic reflection in these spectra may be attributable to unreacted silicon in the as-deposited films; the intensity of this reflection is considerably diminished, or absent, after heat-treatment. Additionally, the heat-treated d-c magnetron film (b) shows strong tetragonal MoSi_2 reflections only. The rf diode co-deposited film designated “ MoSi ” (c) shows tetragonal and hexagonal MoSi_2 and cubic Mo_3Si reflections, whereas the film designated “ $\text{MoSi}_{2.8}$ ” (d)

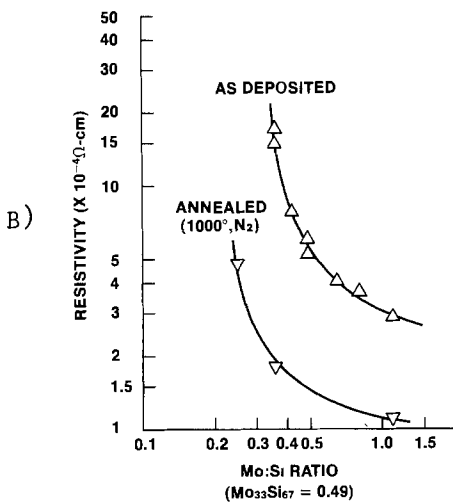
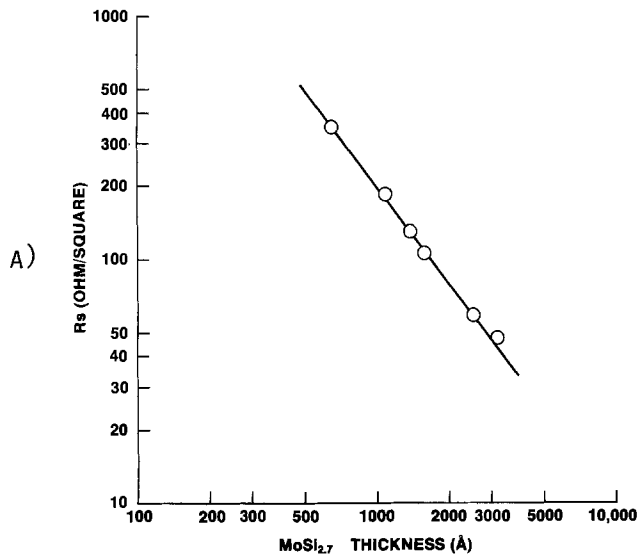


Fig. 7. Plots showing (A) sheet resistance vs. thickness for $\text{MoSi}_{2.7}$, and (B) as-deposited and heat-treated film resistivities for molybdenum silicide films of various stoichiometry.

shows only weak tetragonal MoSi_2 reflections consistent with the SEM micrograph shown earlier (Fig. 4B), indicative of very small crystallite size.

Film stress.—In the as-deposited d-c magnetron films on sapphire, film stress was compressive and was calculated to be $ca. 1 \times 10^{10}$ dyne/cm². During 1000°C heat-treatment, however, the intrinsic film stress

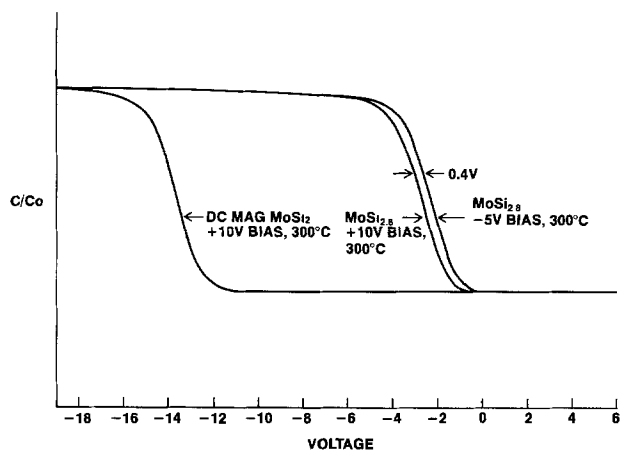


Fig. 8. Capacitance voltage plots of as-deposited d-c magnetron film and heat-treated rf diode co-deposited $\text{MoSi}_{2.8}$ film.

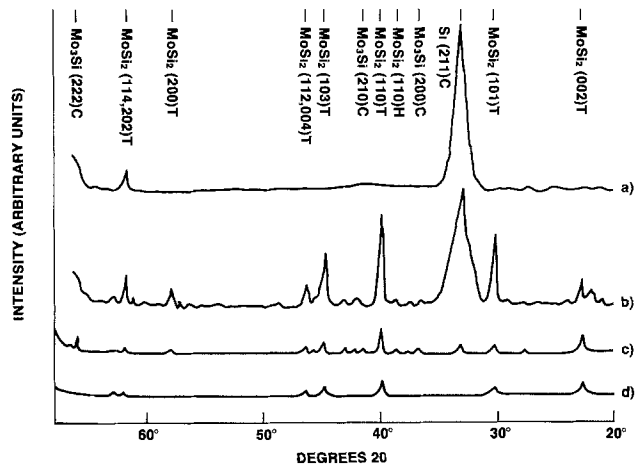


Fig. 9. X-ray spectra showing (a) as-deposited d-c magnetron and rf diode co-deposited $\text{MoSi}_{2.8}$ films, (b) d-c magnetron film after heat-treatment, (c) MoSi , and (d) $\text{MoSi}_{2.8}$ films after heat-treatment.

changed to high tensile stress values. This change could actually be observed during heat-up of the film; the substrate could be seen to curl rapidly from a convex to a concave condition, after which the film would tear away from the substrate producing fine particulates. In extreme cases, silicon wafers were seen to fracture during heat-treatment (13), especially when the deposition was done under high (-120V) substrate bias.

No such degradative changes in film stress were observed with the rf diode co-deposited films having Mo/Si ratios between 0.33 and 0.5. As-deposited, the film stress was minimally unmeasurable for films sputtered under "no bias" conditions or at -75V bias. Between -25 and -50V bias, film stress was $ca. 5 \times 10^{10}$ dyne/cm² (compressive). However, 1000°C heat-treatment of these films yielded a reduction of this stress to unmeasurable values. For films having Mo/Si ratios between 1.0 and 0.5, the film stress appeared to be in varying degrees of tension. Heat-treatment also appeared to reduce this stress to unmeasurable values. This stress behavior during heat-treatment differs from that reported (14) for co-sputtered titanium silicide.

Analysis of trace elements.—Analysis for trace elements and hydrogen was done on the as-deposited d-c magnetron and rf diode co-deposited films using the SIMS capability of the Physical Electronics 590 system. Additionally, film samples were also electron beam heated *in situ* and the resultant evolved gases were measured by mass spectrometry. The resultant spectra showed hydrogen and fluorine to be present in all the films. Quantification of the spectra could not be carried out easily using this technique.

Step coverage.—A 250 nm thick co-deposited film of composition $\text{MoSi}_{2.8}$ was sputtered onto an oxide-stepped silicon wafer at -50V substrate bias. The film was heat-treated at 1000°C, then photolithographically masked and etched in a parallel plate prototype reactor using Freon-14 as the etch gas. Figure 10 shows the SEM micrograph (in cross section) of the etched film over a one micron oxide step which is slightly "undercut." From Fig. 10, it is apparent that acceptable step coverage was obtained in the as-deposited film.

Oxidation rate.—RF diode co-deposited films of composition $\text{MoSi}_{2.8}$ and MoSi_2 were oxidized in dry oxygen at $ca. 6$ liters/min flow at 1000°C. The resultant oxidation rate (at $ca. 50$ nm oxide thickness) for the $\text{MoSi}_{2.8}$ was only $ca. 3$ Å/min, whereas the rate for the MoSi_2 was $ca. 400$ Å/min (resultant oxide thickness $ca. 300$ nm). Additional studies are underway in an attempt to gain more information on the oxidation of these films (15).

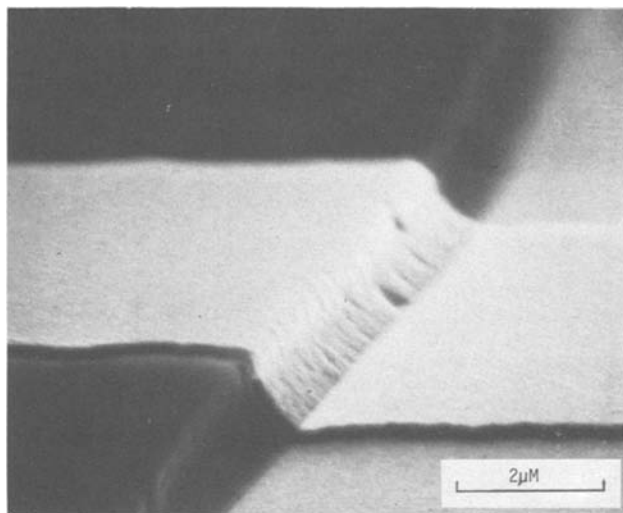


Fig. 10. SEM micrograph showing coverage of rf diode co-deposited film over oxide step.

Summary and Conclusions

This study has shown that molybdenum silicide films deposited by d-c magnetron sputtering from a composite target tend to be non-optimal during subsequent heat-treatment, *i.e.*, film degradation is often encountered for no easily apparent reason. The problem is more acute for films deposited under high values (-120V) of rf substrate bias.

RF diode films co-deposited from separate sources of molybdenum and silicon, however, do not exhibit this degradation when the Mo/Si ratio is ≤ 0.5 , providing that the films have not been subjected to acidic cleaning procedures (DI water cleans only are recommended) and annealing ambient is ensured to be inert. The reason for the difference in behavior between the d-c magnetron and rf diode co-deposited films is unclear at the present time. A possible model for the degradation is that trace impurities, *e.g.*, hydrogen, in the d-c magnetron films may result in severe changes in film stress during subsequent heat-treatment. This severe change in film stress level is indeed observed during heat-treatment of the d-c magnetron films and is not observed with the rf diode co-deposited films. However, film analysis by Auger and SIMS shows little differences, if any, in trace element content between the two types of films. Thus, it may be possible that the instrumental sensitivity to trace elements is insufficient to allow for correlations with film properties. However, the Auger analyses done

on the rf diode co-deposited films were shown to be essential for the establishment and monitoring of molybdenum-silicon stoichiometry in such a study.

In summary, it appears that the rf diode co-deposition technique is viable for the production of good quality molybdenum silicide films of low resistivity. Fully-operational gate arrays have been fabricated from these films, thus supporting the feasibility of the technique. Further details regarding these devices cannot be provided at this time due to proprietary considerations.

Manuscript submitted June 3, 1980; revised manuscript received Aug. 25, 1980. This was Paper 163 presented at the St. Louis, Missouri, Meeting of the Society, May 11-16, 1980.

Any discussion of this paper will appear in a Discussion Section to be published in the December 1981 JOURNAL. All discussions for the December 1981 Discussion Section should be submitted by Aug. 1, 1981.

Publication costs of this article were assisted by Perkin-Elmer.

REFERENCES

1. T. Mochizuki, K. Shibata, T. Inoue, K. Ohuchi, and M. Kashigawa, *Jpn. J. Appl. Phys.*, **17**, 37 (1978).
2. B. L. Crowder and S. Zirinsky, *IEEE J. Solid State Circuits*, **sc-14**, 291 (1979).
3. K. C. Saraswat, F. Mohammadi, and J. D. Meindl, Abstract 144, p. 388, The Electrochemical Society Extended Abstracts, Boston, Massachusetts, May 6-11, 1979.
4. S. Mantovani, G. Ottaviana, G. Magni, and F. Nava, Abstract 382, p. 967, The Electrochemical Society Extended Abstracts, Los Angeles, California, Oct. 14-19, 1979.
5. R. S. Nowicki, W. D. Buckley, W. D. MacKintosh, and I. V. Mitchell, *J. Vac. Sci. Technol.*, **11**, 675 (1974).
6. R. S. Nowicki, J. M. Harris, M.-A. Nicolet, and I. V. Mitchell, *Thin Solid Films*, **53**, 195 (1978).
7. L. E. Davis, N. C. MacDonald, P. W. Palmberg, G. E. Riach, and R. E. Weber, "Handbook of Auger Electron Spectroscopy," 2nd ed., Physical Electronics Industries, Inc., Eden Prairie, Minn. (1976).
8. W. K. Chu, J. W. Mayer, M.-A. Nicolet, T. M. Buck, G. Amsel, and F. Eisen, *Thin Solid Films*, **17**, 1 (1973).
9. R. S. Nowicki, *J. Vac. Sci. Technol.*, **14**, 127 (1977).
10. H. F. Winters and J. W. Coburn, *Appl. Phys. Lett.*, **28**, 176 (1976).
11. B. E. Deal, *This Journal*, **127**, 979 (1980).
12. A. J. Learn, *ibid.*, **122**, 1127 (1975).
13. F. Courreges, Private communication.
14. S. P. Murarka and D. B. Fraser, *J. Appl. Phys.*, **51**, 350 (1980).
15. K. C. Saraswat and R. S. Nowicki, Unpublished.

Fluorescent Screens for High-Resolution Real-Time X-Ray Topography

W. Hartmann

Max-Planck-Institut für Festkörperforschung, 7 Stuttgart 80, Germany

ABSTRACT

High-resolution real-time x-ray topography requires a fluorescent screen with high spatial resolution and good conversion efficiency of x-rays into visible light. We studied the spectral yield and the integral output with respect to screen thickness of common polycrystalline fluorescent materials. $Gd_2O_3:S:Tb$ has the best conversion efficiency and shows the highest spatial resolution with a grain size $\leq 1 \mu m$. The optimal screen thickness for our applications was $5 \mu m$. This choice results in a spatial resolution of about $10 \mu m$.

Real-time x-ray topography is a recent tool to study nondestructively the dynamics of defects, like dislocations, and strain fields in crystals under externally applied forces, for example temperature, strain, or magnetic and electric fields. A typical application is reported by Hagen, Miltat, and the present author (1). There are in principle two methods for real-time x-ray topography, the single-stage or direct *vs.* the multiple-stage or indirect method (2). In the single-stage arrangement the x-ray pattern is directly converted into an electronic charge pattern which is read out by an electron beam of a television tube. The resolution of such method is limited to typically $30 \mu m$ (3). In the multiple-stage method the x-ray pattern is first converted into an optical picture by a fluorescent screen and then imaged onto the target of a

Key words: fluorescent screen, real-time x-ray topography, spectral yield, spatial resolution.

TV camera by a lens system (4). The most important part in this arrangement is the fluorescent screen. It requires a high spatial resolution of a few micrometers and additionally a good conversion efficiency. Many studies have been made about resolution and yield of phosphors (5-12), but no information is available for this special x-ray topography purpose. This paper describes experiments about the spectral yield and the integrated intensity *vs.* screen thickness of various materials. We also investigated the spatial resolution.

Experimental

The experimental setup to study the spectral yield is shown in Fig. 1. A collimated x-ray beam enters an Si-crystal which is set in Bragg condition for the {220} reflection of MoK_{α} radiation. The diffracted beam is converted into an optical picture by a fluorescent screen. The resulting visible light is focused onto the entrance slit of a $\frac{1}{4}$ m-spectrometer which analyzes the emission spectra. The intensity is measured by a photomultiplier and amplified by an electrometer. The intensity *vs.* wavelength recording is made with an X-Y plotter. The fluorescent screens are prepared in the following way. A defined quantity of the material is weighed on a balance and then mixed with alcohol. The polycrystalline powder is deposited on a glass substrate by a centrifuge. The screen is characterized by density and thickness. The density is investigated

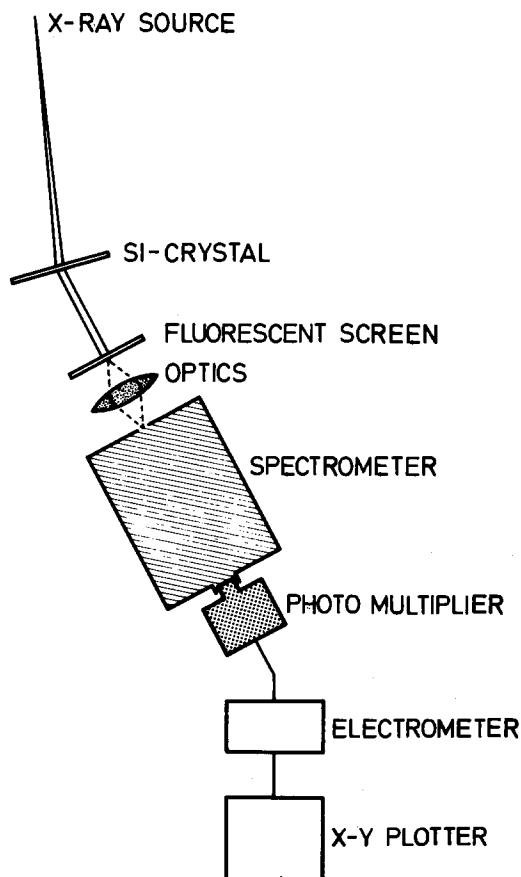


Fig. 1. Experimental setup to study the spectral yield of fluorescent screens for MoK_{α} radiation.

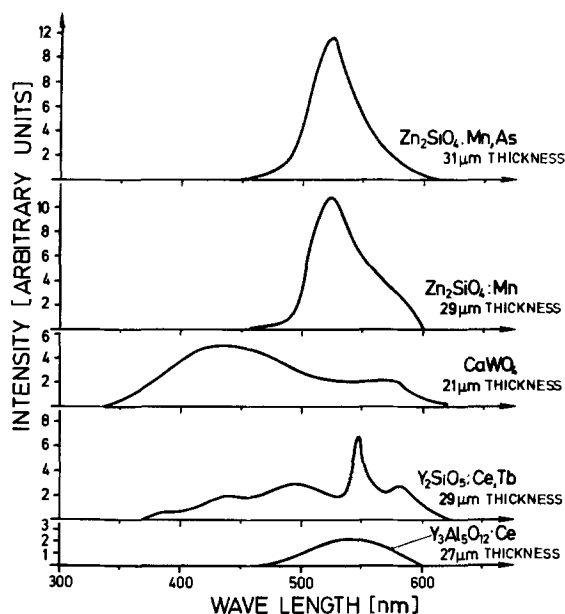


Fig. 2a. Emission spectra of $Zn_2SiO_4:Mn, As$ ($31 \mu m$ thick) $Zn_2SiO_4:Mn$ ($29 \mu m$ thick), $CaWO_4$ ($21 \mu m$ thick) $Y_2SiO_5:Ce,Tb$ ($29 \mu m$ thick), $Y_3Al_5O_{12}:Ce$ ($27 \mu m$ thick).

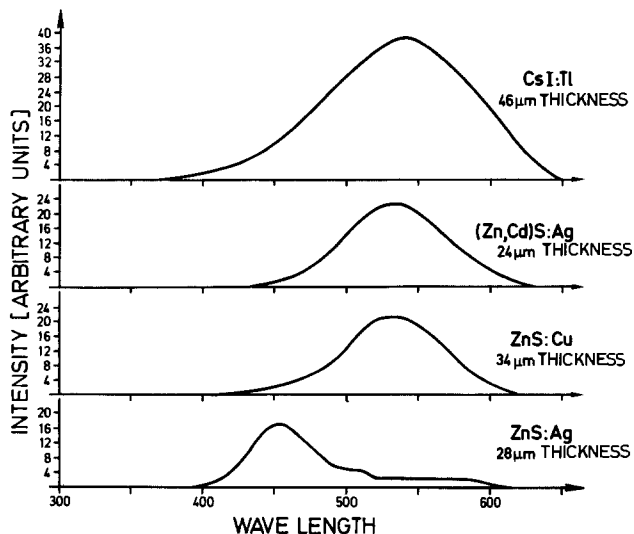


Fig. 2b. Emission spectra of CsI:Tl (46 μm thick), (Zn,Cd)S:Ag (24 μm thick), ZnS:Cu (34 μm thick), ZnS:Ag (28 μm thick).

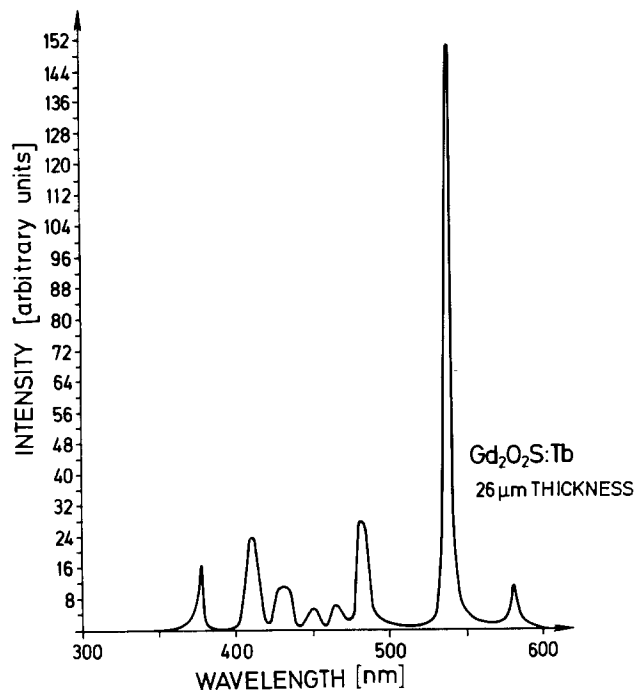


Fig. 2c. Emission spectra of Gd₂O₂S:Tb (26 μm thick)

by the weight of the screen minus the weight of the substrate divided by the screen area. The screen thickness is measured by an optical microscope.

Results and Discussion

Figures 2a-c show the spectral efficiency of the studied materials (Zn₂SiO₄:Mn,As; Zn₂SiO₄:Mn; CaWO₄; Y₂SiO₅:Ce,Tb; Y₃Al₅O₁₂:Ce; CsI:Tl, (Zn,Cd)S:Ag; ZnS:Cu; ZnS:Ag; and Gd₂O₂S:Tb) for one screen thickness.¹ Most of these materials emit light with a spectral intensity distribution over a broad wavelength region. Only Gd₂O₂S:Tb has eight sharp intensity peaks. This localized spectral recombination indicates that the ground and excited states of Tb, which are responsible for the emission spectra, have a small kinetic energy. That means the recombination centers are spatially localized in the material. This fact guarantees that the material is well suited for high spatial resolution.

¹ Some emission spectra differ slightly from the literature. The differences may be caused by contamination either from the producer of the fluorescent material and/or during screen preparation in our laboratory. However, these differences do not affect very much the results.

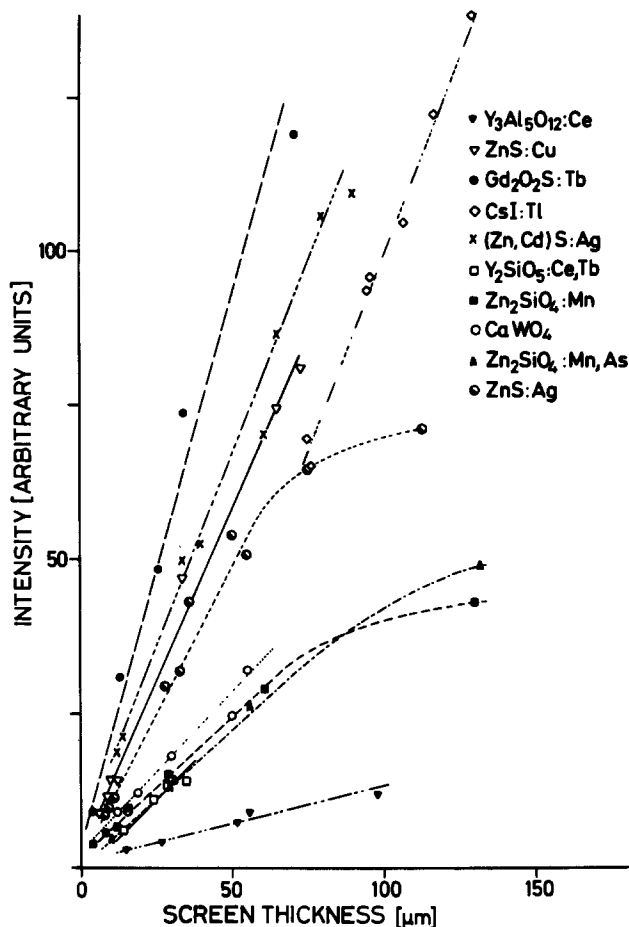


Fig. 3a. Integrated intensity vs. screen thickness of the studied materials. The intensity is calculated by digitizing the emission spectra and integrating the area below the curves.

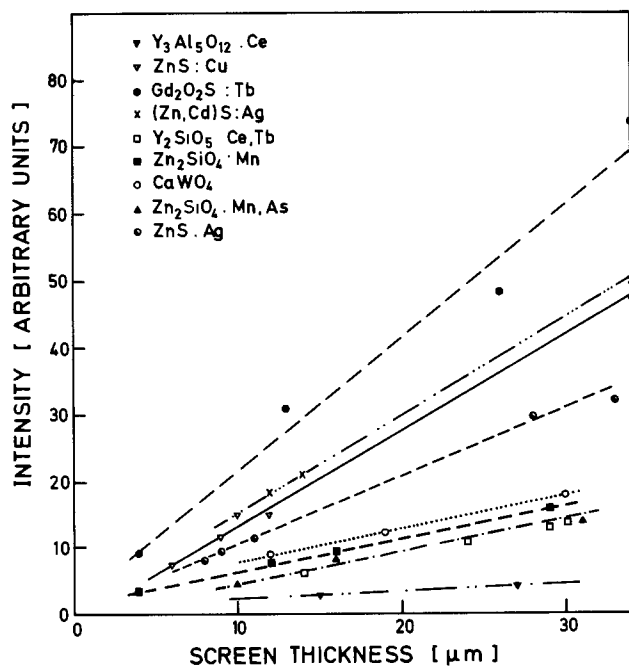


Fig. 3b. Blow-up of Fig. 3a in the thickness region up to about 30 μm. It shows more details at thinner screens which are important for real-time x-ray topography.

We have digitized the curves and integrated the area under each curve. Figure 3a shows the integrated intensity vs. the screen thickness. Gd₂O₂S:Tb has the best available efficiency. Figure 3b is a blow-up of Fig. 3a which shows more details of intensity differences in the thickness up to about 30 μm. One problem

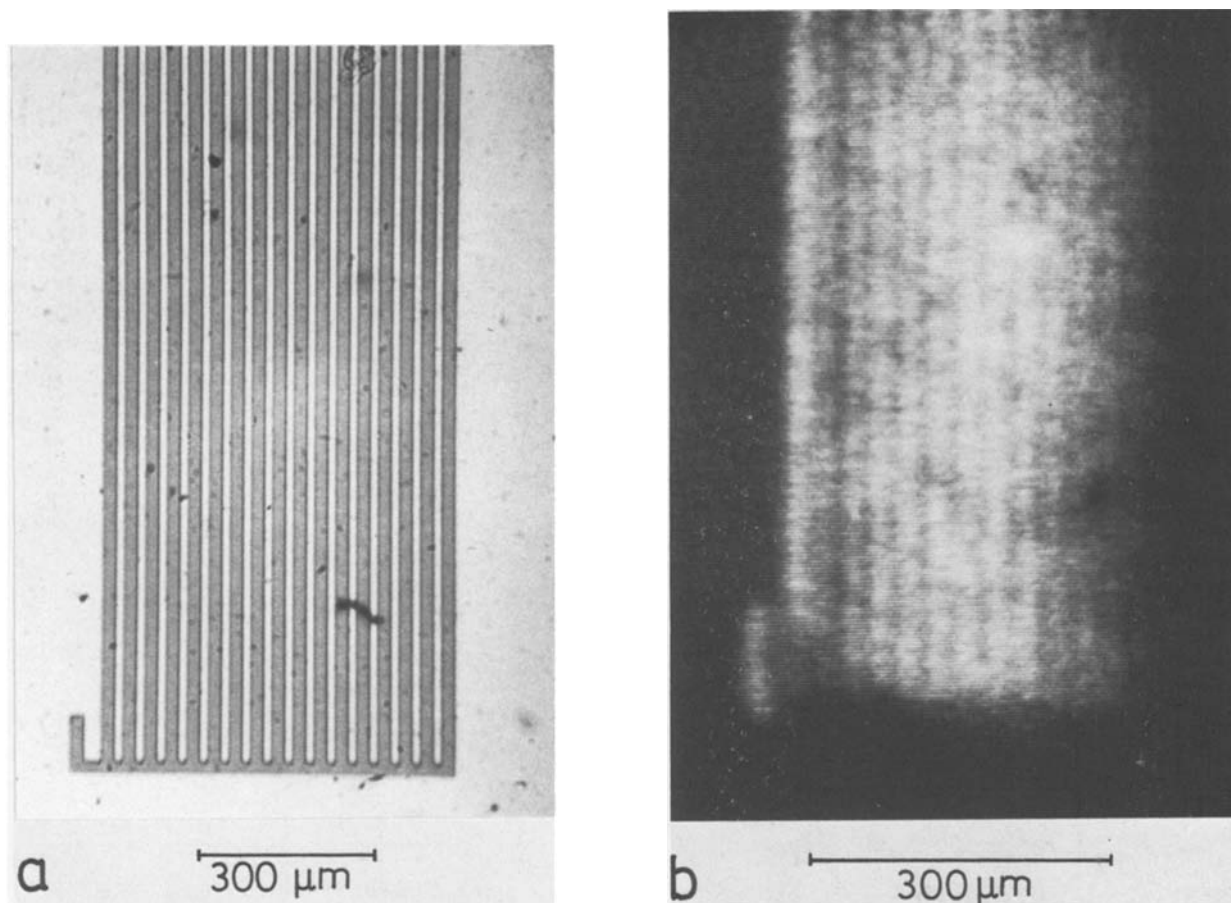


Fig. 4. (a) Optical micrograph of an excise stripe pattern on an Si-substrate with a periodicity of about $15 \mu\text{m}$. (b) Corresponding video topograph directly photographed off the TV monitor.

of polycrystalline fluorescent screens still remains. The density of $\text{Gd}_2\text{O}_2\text{S:Tb}$ is 7.4 g/cm^3 , but the density of a screen with $5 \mu\text{m}$ thickness is only about $2\text{-}3 \text{ g/cm}^3$. Thus, the achieved density is still well below the theoretical density and, therefore, we suffer a loss in the absorption of x-rays and in efficiency.

We need to achieve the highest possible spatial resolution in combination with sufficient yield. That means the grain size of the material used should be $\leq 1 \mu\text{m}$, with as little decrease as possible of internal conversion due to such a small grain size. The other parameter which limits the resolution is the screen thickness. The highest possible resolution is roughly twice the screen thickness. We achieved an optimal screen thickness of $5 \mu\text{m}$ and, therefore, a spatial resolution of $\sim 10 \mu\text{m}$. Figure 4a shows an optical micrograph of an oxide stripe pattern on an Si substrate and Fig. 4b is the corresponding video topograph directly photographed off the TV monitor. The contrast of the test pattern has a stripe periodicity of about $15 \mu\text{m}$ and shows the limitation of our present screens. The most difficult problem in fabricating the screens lies in achieving uniformity in thickness over the entire screen area. The screen preparation is rather difficult to handle. However, because of these difficulties it would be very helpful to have a single crystalline phosphor with a high spatial resolution. A single crystal with special features would combine the high material density and a good thickness uniformity. It would be possible to achieve thinner ($\sim 2\text{-}3 \mu\text{m}$) screens and, therefore, a better spatial resolution at the same conversion efficiency. Such experiments are currently under progress in our laboratory.

Acknowledgment

We gratefully acknowledge the support by the Bundesministerium für Forschung und Technologie.

We thank K. Düker for assistance in screen preparation and especially R. Kniep and W. Schmettow, who are members of the chemistry department in our institute, for discussions and collaboration in material preparation.

Manuscript submitted June 25, 1980; revised manuscript received Sept. 22, 1980.

Any discussion of this paper will appear in a Discussion Section to be published in the December 1981 JOURNAL. All discussions for the December 1981 Discussion Section should be submitted by Aug. 1, 1981.

Publication costs of this article were assisted by the Max-Planck-Institut für Festkörperforschung.

REFERENCES

1. W. Hartmann, W. Hagen, and J. Miltat, *Appl. Phys. Lett.*, **36**, 483 (1980).
2. W. Hartmann, in "Topics in Applied Physics," Vol. 22, H. J. Queisser, Editor, pp. 191-219, Springer-Verlag, Berlin, Heidelberg, New York (1977).
3. J. Chikawa, *J. Cryst. Growth*, **24/25**, 61 (1974).
4. W. Hartmann, in the Proceedings of the NATO Advances Study Institute, "Characterization of Crystal Growth Defects by X-Ray Methods," Durham, 1979 (To be published).
5. H. W. Leverenz and F. Seitz, *J. Appl. Phys.*, **10**, 479 (1939).
6. T. Yoshioka and O. J. Sovers, in "Proc. Rare Earth Res. Conf. 7th," pp. 575-583 (1968).
7. A. P. Wilska, in "Proc. Sept. Congrès Int. Microscopie Electr.," pp. 347-348, Grenoble (1970).
8. R. A. Buchanan, *IEEE Trans. Nucl. Sci.*, **19**, 81 (1972).
9. R. K. Swank, *J. Appl. Phys.*, **44**, 4199 (1973).
10. A. F. Shlensky, R. A. Buchanan, T. G. Maple, and H. N. Bailey, *This Journal*, **122**, 1089 (1975).
11. J. A. De Poorter and A. Bril, *ibid.*, **122**, 1086 (1975).
12. A. L. N. Stevels and A. D. M. Schrama-de Pauw, *ibid.*, **123**, 886 (1976).

Degradation of Bonding Strength (Al Wire-Au Film) by Kirkendall Voids

Katsuya Okumura

Toshiba Corporation, Toshiba Semiconductor Division, Kawasaki, Japan

ABSTRACT

Degradation in bonding strength of the Al wire-plated Au film system has been studied. When this bonding system is stored at elevated temperatures, the bonding strength degrades following one of the three degradation modes: (i) A-mode in which the bonding strength decreases with increasing thermal annealing period until reaching a certain value, (ii) B-mode in which the strength starts separating into two values after a certain period of annealing, and (iii) C-mode in which the strength rapidly drops down to zero. The physical mechanisms for the three degradation modes have been well explained by Kirkendall void formation at the gold-rich intermetallic phase of the aluminum-gold interface, where the growth rate of the gold-rich intermetallic phase plays a very important role on deciding the degradation modes. When gold film includes a large amount of Pb or Tl, this rate decreases and C-mode or B-mode will take place. Doping of Ag into the gold film sometime results in less degradation in the bonding strength.

The reliability of gold-aluminum bonding strength has a strong influence on the reliability of IC and LSI. Although there have been many reports about bonding of gold wire to evaporated aluminum film on silicon chip, only a few reports about bonding of aluminum wire to gold film have been published (1-4). It has already been discussed that the bonding of aluminum wire to gold film has a higher reliability than of gold wire to aluminum film as long as the ratio of the width of the aluminum wire bonding area to the thickness of the gold film is greater than four (1).

However, the physical mechanism as to why the value four appears to be a threshold value for the degradation in bonding strength has not been made clear.

The purpose of the present study is to obtain a better understanding of the nature of the gold film-aluminum wire metallurgical system and to reveal the degradation mechanism of the bonding strength.

Experimental Results

Sample preparation.—Substrates for bonding were prepared by plating nickel and gold sequentially on rectangular Kovar plates of $50 \times 7 \times 0.25$ mm. Typical layer thickness are $2 \mu\text{m}$ for nickel and $2\text{-}5 \mu\text{m}$ for gold. The plating solutions for nickel are a Watt bath and for gold a commercial cyanide solution.

Aluminum bonding wire of 2 mil in diameter, ultrasonic bonding grade including 1% silicon, is used, and 300 wires are bonded on each substrate. Here, bonding operations were made on the same ultrasonic wire bonder by the same technician in order to avoid poor reproducibility due to fluctuations coming from a different person and machine. Bonding strength was measured destructively on an automatic vertical pull tester, before and after annealing. Approximately 25 pull testings were carried out under each condition.

Thermal annealing was carried out in an air circulating oven controlled at $200^\circ \pm 5^\circ\text{C}$. After a certain period of annealing, 25 bonded wires were destructively pulled and the break strength was recorded for each test.

Pull strength as a function of annealing time.—The degradation modes of the pull strength at 200°C are phenomenologically classified into three kind of modes, as follows.

A-mode: The pull strength gradually decreases with annealing time and finally reaches a certain time-in-

dependent value as shown in Fig. 1. This value remained after 5000 hr at 200°C .

B-mode: The pull strength first decreases, and when annealing time exceeds a certain threshold, the degradation mode is divided distinctly into either A- or C-modes as shown in Fig. 2.

C-mode: The pull strength sharply drops down and becomes zero within a few hours as shown in Fig. 3.

Impurities in the plated gold film.—Impurities in the plated gold film are investigated by using ion mi-

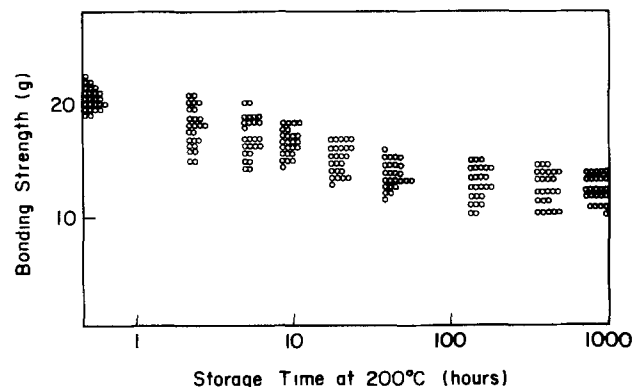


Fig. 1. The degradation appears to be A-mode. The bonding strength decreases with increasing heat-treatment until reaching a certain value.

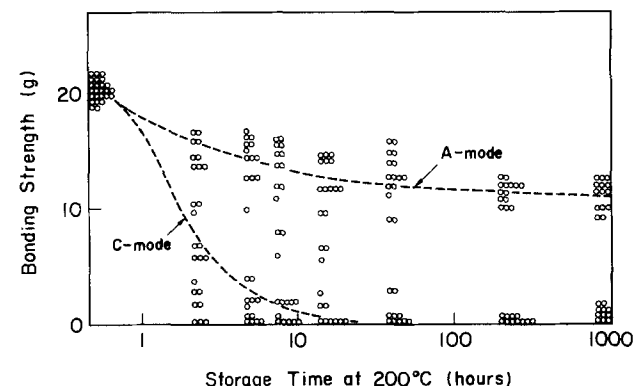


Fig. 2. The degradation appears to be B-mode. The bonding strength starts separating into two values after a certain period of the heat-treatment.

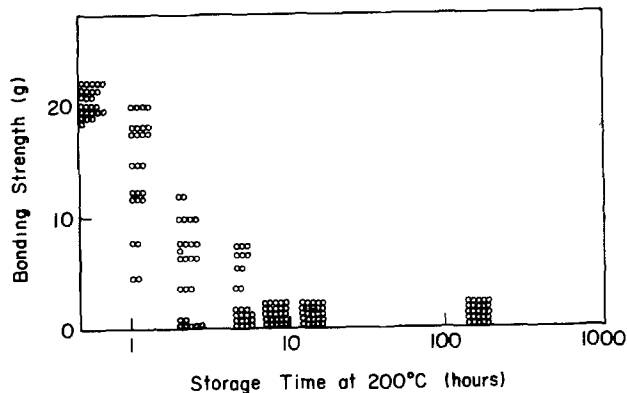


Fig. 3. The degradation appears to be C-mode. The bonding strength rapidly drops down and becomes zero within a few hours.

cromass analysis, IMA. The measuring conditions are as follows: Ar ions are used and accelerating voltage is 10 kV. Beam size is 760 μm in diameter, and the maximum measuring mass number is $M/e = 240$. The detected impurities are F, Na, K, Si, Al, Cl, Ca, Mg, Fe, Ni, Co, Ag, Tl, and Pb.

Results and Discussion

Correlations between impurities in Au film, thickness, and bonding strength.—Measured results of impurity concentration in gold, degradation mode, and gold film thickness are listed in Table I. Several characteristic features can be derived from Table I: (i) When a sample includes less Pb and Tl, the mode always becomes A-mode. (ii) When a sample has a large amount of Pb or Tl, the mode always becomes C-mode. (iii) When a sample has a few Ag even though it has a few Pb or Tl, the mode becomes A- or B-mode, but never C-mode. (iv) The thicker the gold film is, the more frequently B- and C-modes appear.

The effect of silver.—As pointed out above, even though there was a large amount of Pb or Tl in gold film, the influence of Pb or Tl was canceled by the presence of a small amount of silver. So, the following tests were carried out.

The substrate with a large amount of Tl and few Ag like in the sample No. 8 was prepared by depositing silver in a vacuum of $\sim 10^{-6}$ Torr. After being annealed, Al wire bondings were made on the preceding ultrasonic bonders. When about 400Å of Ag film is deposited, it is difficult to make bonds because of the

hardness of the silver-evaporated gold surface. On the other hand, it is easy to make bonds when about 50Å of silver film is deposited and annealing is carried out at 250°C for 30 min. The degradation mode of this sample has completely changed from C-mode to A-mode. In addition to this sample, other samples were also deposited with silver (50Å) by the same procedure. The results of these tests are summarized in Table II.

Mechanism of pull strength degradation.—Let us consider a mechanism that explains what happens when aluminum and gold films are coexisting and are stored at elevated temperatures, and why the pull strength significantly degrades in some cases, but not in other cases.

Many studies, (1, 5-7) have been reported that in the aluminum-gold binary system the growth rate of the gold-rich intermetallic phase is approximately 10 times as large as the growth rate of the aluminum-rich intermetallic phase, and the formation of Kirkendall voids is observed at the interface of the gold-rich intermetallic phase and gold.

At this point, let us set up two working hypotheses as follows: (i) The Kirkendall voids formed at the interface have a constant radius, r_0 , and the number of voids, n , is directly proportional to the square root of time. (ii) The Kirkendall voids are always at the interface. These voids pile up and condense to form an almost continuous line. This has a deleterious effect on the pull strength.

Kidson (8) has shown that if the mechanism of intermetallic phase formation is interdiffusion predominated by volume diffusion, growth rate of the intermetallic layer should follow a parabolic rate law as follows

$$d = k\sqrt{t} \quad [1]$$

where d is the intermetallic thickness, t is the storage time, and k is the growth rate of the phase.

In fact, the intermetallic phase layer thickness has been observed (3, 7), showing the square root of time dependence even though the storage temperature was as low as 200°C.

As illustrated in Fig. 4, aluminum wire comes in contact with gold film with bonding width W . The length along the gold-rich intermetallic phase-gold interface is given by

$$l = \pi d + W \quad [2]$$

By substituting Eq. [1] into Eq. [2]

$$l = \pi k\sqrt{t} + W \quad [3]$$

Table I. Correlations between impurities in gold film, thicknesses, and degradation modes

| | Sample number | | | | | | | | | | | | | | |
|-------------------------|---------------|-----|-----|-----|-----|-----|-----|-----|-----|-----|-----|-----|-----|-----|-----|
| | 1 | 2 | 3 | 4 | 5 | 6 | 7 | 8 | 9 | 10 | 11 | 12 | 13 | 14 | 15 |
| Peak height in IMA (mm) | | | | | | | | | | | | | | | |
| Ag | 2.1 | 180 | 20 | 75 | 6.2 | 150 | 6.1 | 8.4 | 6.2 | 4.1 | 4.2 | 1.1 | 1.2 | 17 | 5 |
| Pb | 0 | 0 | 1.9 | 1.2 | 1.4 | 1.0 | 1.2 | 0 | 1.1 | 0 | 0 | 2.2 | 30 | 26 | 0 |
| Tl | 8.4 | 84 | 2.3 | 3.8 | 3.0 | 4.2 | 1.5 | 8.1 | 1.1 | 30 | 10 | 0.1 | 0.1 | 0.1 | 40 |
| Au thickness | 4.0 | 3.6 | 4.8 | 2.5 | 3.2 | 2.0 | 4.0 | 2.0 | 3.8 | 2.2 | 2.2 | 2.5 | 2.7 | 1.5 | 3.8 |
| Degradation mode | C | B | B | A | A | A | A | C | A | C | B | A | C | A | C |

Table II. Changes in the degradation mode after silver doping

| Sample number | Initial degradation mode | Mode after silver doping | Au thickness (μm) | Peak height in IMA (mm) | | | | |
|---------------|--------------------------|--------------------------|--------------------------------|-------------------------|-----|---------|--------------|--|
| | | | | Tl | Pb | Ag | | |
| | | | | | | Initial | After doping | |
| 1 | C | B | 4.0 | 8.4 | 0 | 2.1 | 7 | |
| 8 | C | A | 2.0 | 8.1 | 0 | 8.4 | 18 | |
| 10 | C | B | 2.2 | 30 | 0 | 4.1 | 13 | |
| 13 | C | B | 2.7 | 0.1 | 30 | 1.2 | 9 | |
| 15 | C | C | 3.8 | 40 | 0 | 5.1 | 10 | |
| 2 | B | B | 3.6 | 84 | 0 | 180 | 185 | |
| 3 | B | A | 4.8 | 2.3 | 1.9 | 20 | 23 | |
| 11 | B | A | 2.2 | 10 | 0 | 4.2 | 13 | |

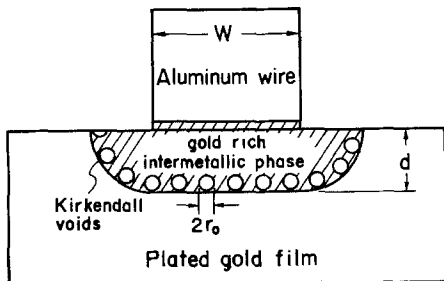


Fig. 4. Schematic representation of the degradation of bonding strength. Kirkendall voids are formed at the intermetallic phase-gold interface.

according to these working hypotheses, when the intermetallic phase grows up to the depth d , the number of Kirkendall voids, n , will be given by

$$n = \alpha\sqrt{t} \quad [4]$$

where α is the rate constant.

Total length of the voids projected to the intermetallic phase-gold interface is given by

$$v = 2r_0n \quad [5]$$

and thus

$$v = 2r_0\alpha\sqrt{t} \quad [6]$$

where r_0 is the radius of voids.

When Eq. [3] and [6] become equal, the Kirkendall voids form a continuous line and, consequently, the pull strength becomes catastrophically weak.

Equations [1], [3], and [6] are illustrated schematically in Fig. 5. When line 1 intersects line 2 at t_c , the voids form a continuous line at the intermetallic phase-gold interface and the pull strength degrades enormously. The depth of the intermetallic layer at t_c is defined as d_c .

The influence of gold film thickness.—Let us consider the influence of gold film thickness, D , the growth rate, k , and bonding width, W on the formation of Kirkendall voids. As shown in Fig. 6, the intermetallic phase-gold interface is divided into two parts; one is "P," the length of which grows as a function of πd and the other is "Q," the length of which stays constant at W .

When D is thicker than d_c , the voids will form a continuous line at both P and Q in the depth d_c and then the catastrophic weakness occurs, in other words, C-mode will appear.

Now, let us consider what can happen if D is thinner than d_c . When the intermetallic phase grows up and reaches the gold-nickel interface, the total projected length of the voids is represented as follows

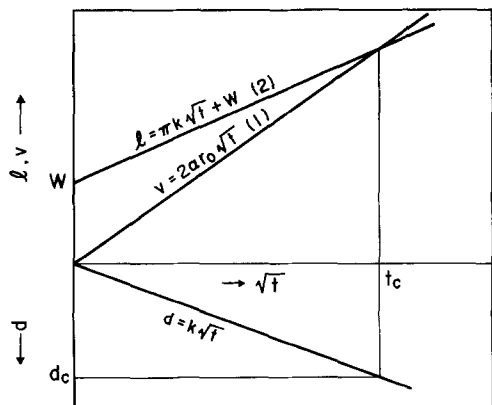


Fig. 5. Schematic representations for d , the intermetallic thickness; l , the length along the intermetallic phase-gold interface; and v , the total length of the voids projected to the interface as a function of t , the storage time.

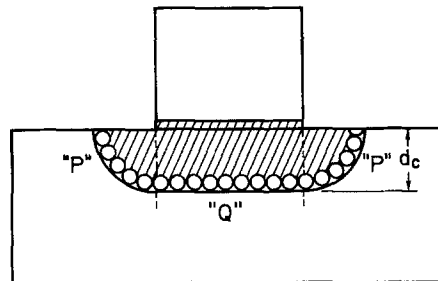


Fig. 6. Schematic representation. When gold film thickness is thicker than the critical depth, d_c , Kirkendall voids will form a continuous line along the intermetallic phase-gold interface.

$$v_0 = 2r_0\alpha\sqrt{t_0} \quad [7]$$

where t_0 is the time when the intermetallic phase reaches the gold-nickel interface.

After t_0 , there can be no increase in voids at Q, namely, the gold-nickel interface, on the other hand, the length of the interface along P, either $\overline{AB} + \overline{A'B'}$ or $\overline{CD} + \overline{C'D'}$ as shown in Fig. 7, is constant at πD but voids at P increase on and on until a continuous line is formed along $\overline{CD} + \overline{C'D'}$.

Let us find out the time t_1 , when the continuous line is formed eventually by the voids at the interface along P. To obtain t_1 , a graphical solution method is applied as shown in Fig. 8. The time when d grows up to D , namely, d_0 , is t_0 and at that time v and l are v_0 and l_0 , respectively. t_2 is imaginary time when v shall grow up to l_0 , that is, v_2 . The point X on $\overline{v_2t_2}$ divides v_2 into $W (= \overline{Xt_2})$ and $\pi k\sqrt{t_0} = \pi D (= \overline{v_2X})$. The point Y is defined as the cross point of $\overline{v_0t_0}$ and \overline{XO} .

At time t_0 , projected lengths of the voids on $\overline{AB} + \overline{A'B'}$ and $\overline{BB'}$, v_p , and v_q , are given by dividing $\overline{v_0t_0}$ by the ratio $\pi D:W$. On the other hand, the point Y

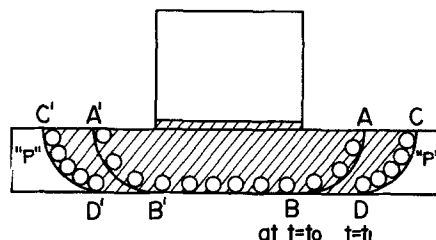


Fig. 7. Schematic representation. When gold film thickness is thinner than d_c , the intermetallic phase grows up and reaches the gold-nickel interface at the time t_0 , and then there is still increase in voids at "P" until the voids form continuous line at the time t_1 .

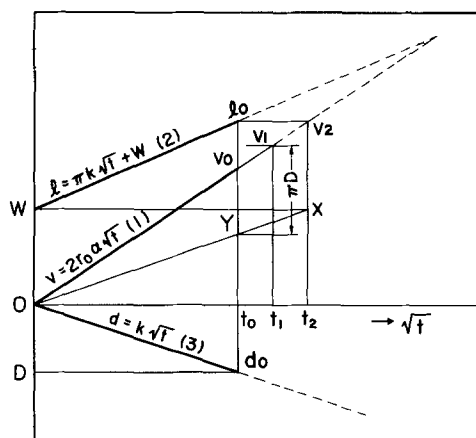


Fig. 8. Schematic representations of l , v , and d as a function of t when gold film thickness is thinner than d_c .

divides $\overline{v_0 t_0}$ by the ratio $\pi D:W$, then v_p and v_Q are equal to $\overline{v_0 Y}$ and $\overline{Y t_0}$, respectively.

After t_0 , the length of the interface along P is constant at πD as shown in Fig. 7, but v_p still grows up from $\overline{v_0 Y}$ to πD . t_1 is the time when v_p grows up to πD , that is, the voids along P form eventually a continuous line.

After t_1 , both the voids and the gold-rich intermetallic phase stop growing up, because the continuous line of voids shuts off the gold supply to the intermetallic phase and the gold-rich intermetallic phase will change into an aluminum-rich intermetallic phase by being supplied with a sufficient amount of aluminum from the aluminum wire. If the bonding strength at Q is sufficiently strong, the pull strength does not degrade, which results in A-mode.

Whether the gold film is thinner or thicker than d_c , Kirkendall voids ultimately form a continuous line along the interface between the gold and the gold-rich intermetallic phase. This phase will change into an aluminum-rich intermetallic phase after a sufficiently long period of time.

The influence of bonding width.—As shown in Fig. 9, when the bonding width becomes narrower, the critical depth d_c becomes shallower. That means C-mode will appear more easily. When the gold film thickness is slightly thinner than d_c , W plays a dominant role on the degradation, namely, a narrower W will lead to C-mode and a wider W will lead to A-mode.

The influence of the intermetallic phase growth rate.—Figure 9 shows that the critical depth d_c decreases with decreasing k . The influence of k is more prominent than W , because k can affect both Eq. [1] and [2].

The value of k , W , and d_c .—The samples were polished in the cross sections, and then the thickness of the gold-rich intermetallic phase was measured by using an optical microscope and SEM. Figure 10 shows one of the SEM photographs of the A-mode samples. Here, a crack is observed around the periphery of the bond. Figure 11 shows one of the SEM cross-section photographs of the C-mode samples. As noticed, a crack is observed not only in P but also in Q.

Bonding width, W ranges from 26 to 60 μm and its mean value is 40 μm . The thicknesses of the phase of A-mode samples after annealing for 1 hr are in the range of 2.4–3.2 μm and its mean value is 2.8 μm . By this measurement, k for A-mode is found to be 2.8 $\mu\text{m}/\sqrt{\text{hr}}$.

On the other hand, Kashiwabara and Hattori have reported (1) that $W/d_c \geq 4$ for the sample which is

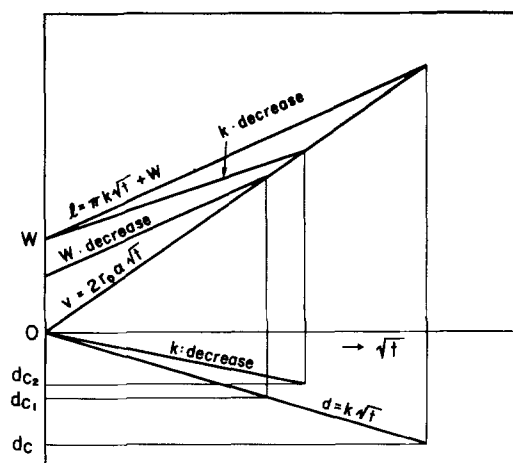


Fig. 9. Schematic representations of l , v , and d as a function of t taking bonding width W and intermetallic phase growth rate k as parameters.

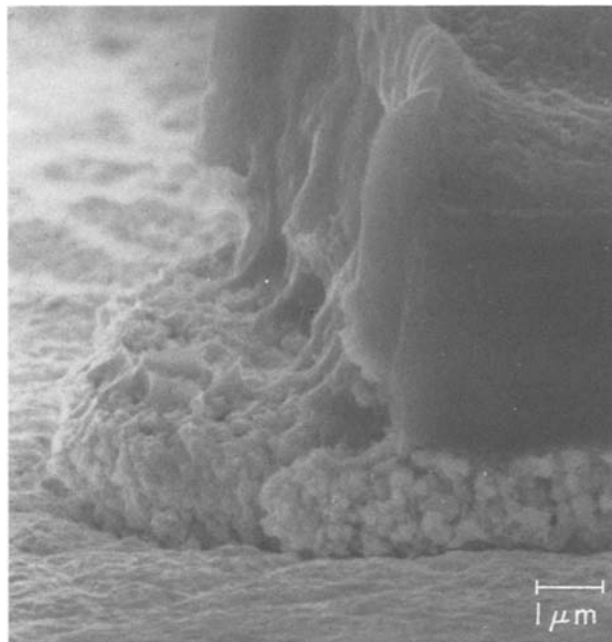


Fig. 10. An SEM photograph of Al-Au intermetallic compound formation (fluffy). A-mode sample stored at 200°C for 10 hr gives rise to the crack which is formed around the periphery of the bond.



Fig. 11. An SEM cross-section photograph of Al-Au intermetallic phase. C-mode sample stored at 200°C for 10 hr demonstrates the continuous line of Kirkendall voids along the interface of intermetallic phase-gold, in "P" and "Q."

equivalent to A-mode. These are summarized as follows, $W = 40 \mu\text{m}$, $k = 2.8 \mu\text{m}/\sqrt{\text{hr}}$ and $W/d_c = 4$. Substituting these values into Eq. [1], [3], and [6]

$$10 = 2.8\sqrt{t_c} \quad [8]$$

$$l' = 2.8\pi\sqrt{t_c} + 40 \quad [9]$$

$$l' = 2r_0\alpha\sqrt{t_c} \quad [10]$$

at $t = t_c$, l' is equal to v' , then

$$2.8\pi\sqrt{t_c} + 40 = 2r_0\alpha\sqrt{t_c} \quad [11]$$

From Eq. [8], $t_c = 12.7 \text{ hr}$, then $2r_0\alpha = 20 \mu\text{m}/\sqrt{\text{hr}}$. The critical time t_c is in good agreement with the time when B-mode starts separating into A- and C-modes in Fig. 2.

Table III. Growth rate of the gold-rich intermetallic phase, k

| Reference | k at 200°C ($\mu\text{m}/\sqrt{\text{hr}}$) | Purity of gold |
|-----------------|--|----------------------|
| Onishi (5) | 1.1 | Gold plate 99.99% |
| Kashiwabara (1) | 2.6 | Plated gold film |
| Philofsky (6) | 3.9-4.4 | 99.999% |
| Campisano (7) | 4.5-5.0 | Evaporated gold film |
| This work | 2.8 | Plated gold film |

Here, we compared the value of k with the previously published values which are summarized in Table III. As shown in Table III, Kashiwabara (1) obtained $k = 2.6 \mu\text{m}/\sqrt{\text{hr}}$ for gold-plating film and Onishi (5) found $k = 1.1 \mu\text{m}/\sqrt{\text{hr}}$ for gold plate where the purity of gold is 99.9%. Philofsky (6) and Campisano (7) found $k = 4-5 \mu\text{m}/\sqrt{\text{hr}}$ for evaporated gold film, which had a purity of more than 99.99%. These indicate that the lower the purity of gold, the more the value of k decreases.

At $t = t_c$, l is equal to v and $d_c = k\sqrt{t_c}$, then

$$\frac{1}{d_c} = \frac{2r_0\alpha}{W} \left(\frac{1}{k} - \frac{\pi}{2r_0\alpha} \right) \quad [12]$$

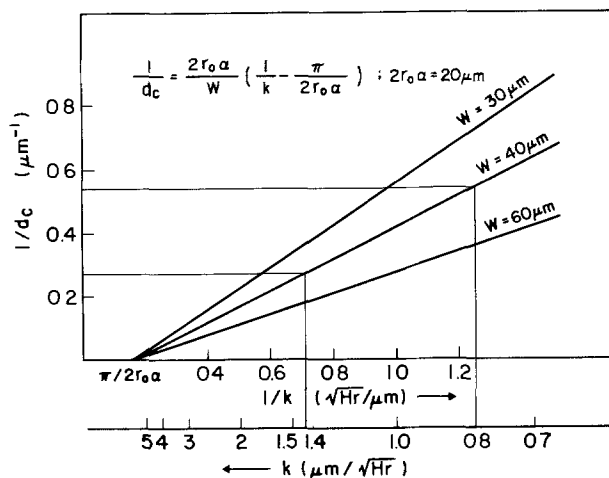
where

$$2r_0\alpha = 20$$

Figure 12 show the relationship between d_c and k for various values of W . When k decreases to be less than $1.4 \mu\text{m}/\sqrt{\text{hr}}$ and the thickness of the gold film is more than $3.6 \mu\text{m}$, C-mode will appear. Moreover, when k decreases to less than $0.8 \mu\text{m}/\sqrt{\text{hr}}$, even though the thickness of gold film was $1.8 \mu\text{m}$, C-mode should take place.

A large amount of Tl or Pb is found in the samples which provide B- or C-mode. Some of the samples have changed from C-mode to A- or B-mode by doping with a small amount of silver. This indicates that Tl or Pb may suppress the value of k drastically, but Ag has an ability to cancel this effect, although the mechanism for this is still uncertain.

Horsting (2) has experimentally shown that the presence of impurities in the gold caused the bondlift type of failure. However, he did not specify the kind of impurities responsible for the failure and the failure mechanism for the bondlift.

Fig. 12. Relationships between d_c and k for various values of W

On the contrary, in this study we have quantitatively made clear the mechanism of the degradation of bonding strength by introducing parameters such as k , n , W , and D . Our mechanism, described here, can also explain all of the facts which Horsting has found.

Conclusions

Degradation of bonding strength of the aluminum wire-gold film system has been investigated. The phenomena which take place at the aluminum-gold interface have been well explained by the Kirkendall void model.

1. When these bonding systems are heated at elevated temperatures, the degradation modes of the pull strength are classified into three modes: (i) A-mode in which the bonding strength decreases with increasing heat-treatment until reaching a certain value, (ii) B-mode in which the strength starts separating into two values after a certain period of heat-treatment, and (iii) C-mode in which the strength rapidly drops down to zero.

2. A large amount of Pb or Tl is found in the samples whose pull strength degrades rapidly and finally reaches zero.

3. Some of the samples including Pb or Tl are improved in the degradation mode by doping a small amount of silver into the gold film.

4. These phenomena can be well explained by the Kirkendall void model. According to this model, the growth rate of the gold-rich intermetallic phase plays a very important role on deciding the degradation modes. When this rate decreases, the pull strength frequently degrades very significantly.

5. The growth rate of the intermetallic phase, k , for A-mode, is found to be $2.8 \mu\text{m}/\sqrt{\text{hr}}$ at 200°C.

Acknowledgments

Thanks are due to A. Ogawa and Y. Naruse for their technical assistance in this work. Y. Yamaguchi, who performed the IMA analysis is acknowledged. The author wishes also to thank K. Takahashi and Dr. Y. Nishi for their helpful discussions and for critical review of the manuscript.

Manuscript submitted March 10, 1980; revised manuscript received Sept. 1, 1980.

Any discussion of this paper will appear in a Discussion Section to be published in the December 1981 JOURNAL. All discussions for the December 1981 Discussion Section should be submitted by Aug. 1, 1981.

Publication costs of this article were assisted by the Toshiba Corporation.

REFERENCES

1. M. Kashiwabara and S. Hattori, *Rev. Elect. Commun. Lab.*, **17**, 1001 (1969).
2. C. W. Horsting, in 10th Annual Proceedings IEEE Reliability Physics Symposium, p. 155 (1972).
3. E. Philofsky, in 9th Annual Proceedings IEEE Reliability Physics Symposium, p. 11 (1971).
4. G. Riga, in 11th Annual Proceedings IEEE Reliability Physics Symposium, p. 26 (1973).
5. M. Onishi and K. Fukumoto, *J. Jpn. Inst. Metals*, **38**, 148 (1974).
6. E. Philofsky, *Solid State Electron.*, **13**, 1391 (1971).
7. S. U. Campisano, G. Foti, and E. Rimini, *Philos. Mag.*, 903 (1975).
8. G. U. Kidson, *J. Nucl. Mater.*, **3**, 21 (1961).

Densification of SIPOS

H. R. Maxwell, Jr.* and W. R. Knolle*

Bell Laboratories, Reading, Pennsylvania 19604

ABSTRACT

Semi-insulating polycrystalline silicon (SIPOS) can be used as part of a passivation scheme on semiconductor devices. During processing the film experiences temperatures several hundred degrees higher than the SIPOS deposition temperature of 640°C. We have investigated the effect of high temperature anneals on the physical properties of SIPOS films containing 25 atomic percent oxygen. Heat-treatments of 900°C or greater in inert ambients densify the film resulting in a film thickness decrease (densification) on the order of 10% and decrease the etch rate of the film by a factor of 6 in a 6H₂O₂:1HF:10 NH₄F SIPOS etch solution. Also, the infrared transmission spectrum of the SIPOS film changes as a result of annealing. Similar infrared changes in SiO₂ films have been interpreted to be due to a relaxation of bond strain and a decrease in film porosity. Film stress has also been investigated before and after annealing and was found to change from tensile to compressive. This is consistent with the interpretation of the infrared data.

Semi-insulating polycrystalline silicon (SIPOS) films doped with oxygen (1) can be used as part of a passivation scheme on semiconductor devices. The film is deposited on the wafer by chemical vapor deposition (CVD) at a temperature of ~640°C. Typically, SIPOS is never used as the only passivation layer on a semiconductor device, but rather is followed by SiO₂ and Si₃N₄ layers deposited at 900°C or more. Therefore, it seemed natural to investigate more closely the behavior of SIPOS films after annealing in an inert ambient. In this paper we report the effects of high temperature anneals on the physical properties of SIPOS films containing 25 atomic percent (a/o) oxygen.

Experimental

SIPOS deposition.—An AMT low pressure (LPCVD) system was used to deposit the 25 a/o O SIPOS films by the reactive decomposition of silane (SiH₄) and nitrous oxide (N₂O) in N₂. For this work the deposition temperature was 637°C and the system pressure was 0.16 Torr. The reactant gas flow ratio, N₂O/SiH₄, was 0.22 with an N₂ carrier gas flow of 400 cm³/min for a deposition rate of 35 Å/min. The SIPOS film thickness was nominally 5000Å.

Two-inch diameter n-type (111) Si wafers were used throughout except for the stress measurements that were made on 3 in. diam n-type (100) Si wafers. Silicon nitride covered Si substrates were used for determination of the oxygen content of the SIPOS films by a gravimetric technique previously reported (2). In order to obtain a representative oxygen content the nitrided and bare Si wafers were alternately placed on a quartz boat with 0.375 in. spacing between them, loaded into the LPCVD furnace, and SIPOS deposited.

Etch rate and film thickness determination.—The SIPOS etch solution consisted of a mixture, by volume, of 6 parts H₂O₂-30%, 1 part HF-48%, and 10 parts of a 40% NH₄F (6:1:10) solution (1). The etch solution was allowed to equilibrate to 30°C for 5 min prior to etching.

The as-deposited etch rate was determined by half-waxing a wafer, cutting it into strips, and etching the strips for various times in the 6:1:10 SIPOS etch. After etching, the wax was removed and the step height measured on a Taylor Hobson Talystep. The effects of annealing in N₂ on etch rate after various times and temperatures were determined in a similar manner.

* Electrochemical Society Active Member.

Key words: semiconductor passivation technology, infrared spectroscopy, thin films.

The thickness change (densification) after annealing was determined by half-waxing the SIPOS deposited Si wafers and etching them in the 6:1:10 solution until bubbling on the wafer surface stopped, indicating that the SIPOS-Si interface was reached (etch rate of Si in 6:1:10 is ~260 Å/min). The height of the step was then measured on the Talystep. These Talystep wafers were then remeasured for the determination of the SIPOS thickness after annealing and were used for the infrared measurements.

Infrared spectra measurements.—The infrared transmission spectrum of the SIPOS sample was taken before and after each anneal or densification process. A clean Si substrate was placed in the reference beam of the Perkin-Elmer Model 621 Grating Infrared Spectrophotometer. The Si in the reference beam nulls out the absorption signal from the Si substrate in the sample beam. The absorbance, *A*, of an infrared peak was measured by the baseline technique (3) and the area of the absorption was approximated by *A*·*W* where *W* is the full width at half of the maximum absorbance.

Stress measurements.—The stress of the SIPOS film was measured with an optically levered laser technique (4). The difference between the radius of curvature of the Si wafer measured before and after deposition can be related to the stress in the deposited SIPOS film (SIPOS must be etched off the back of the wafer before the measurement is made). The measurements were made on 3 in. diam, 0.020 in. thick (100) Si wafers. The precision of the measurement is about ± 1 × 10⁹ dynes/cm².

Results

Etch rate.—The as-deposited SIPOS etch rate in the 6:1:10 SIPOS etch was determined and the data are plotted in Fig. 1 as the amount of SIPOS removed vs. etch time. The best fit for the data is shown and results in an average etch rate of ~1200 Å/min for the as-deposited 25 a/o O SIPOS film.

The effects of annealing temperature on etch rate are given in Fig. 2 where the SIPOS film etch rate in the 6:1:10 solution vs. annealing temperature is plotted. The anneals were done in N₂ for 1 hr. Initially, the etch rate decreases by a factor of 6 from the as-deposited value and then increases as the annealing temperature continues to increase. This increase in etch rate at the higher temperatures is attributed to the increase in the SiO₂ character of the film which will be discussed later. For reference, the etch rate of 1050°C steam-grown SiO₂ in 6:1:10 solution is shown.

The effect of annealing time on etch rate at the various temperatures is shown in Table I. The anneal

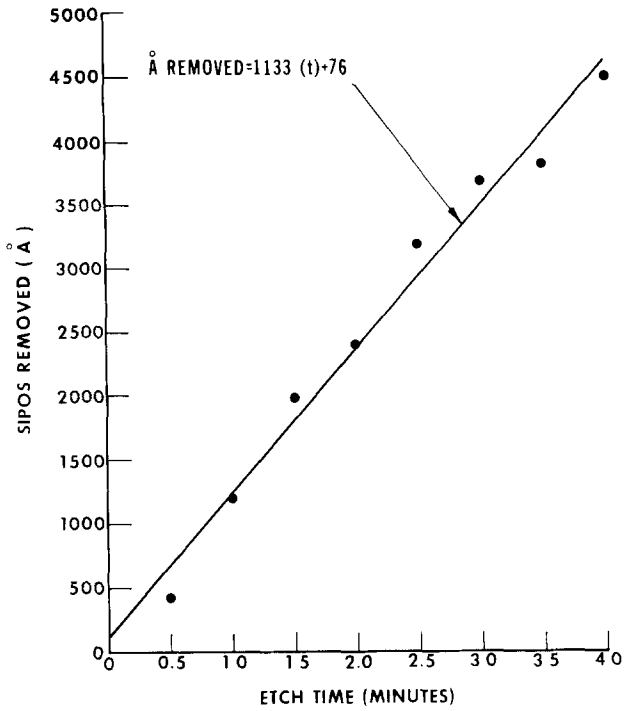


Fig. 1. Determination of the etch rate of 25 a/o O SIPOS in 6:1:10 SIPOS etch solution. The slope of the least squares line is the etch rate of the as-deposited SIPOS.

Table I. SIPOS etch rate after annealing in nitrogen. (6:1:10) (Error in etch rate is ~35 Å/min)

| Annealing temp (°C) | Annealing time (hr) | Etch rate (Å/min) |
|---------------------|---------------------|-------------------|
| 1100 | 2 | 240 |
| | 1 | 281 |
| | 0.5 | 250 |
| 900 | 2 | 150 |
| | 1 | 200 |
| | 0.5 | 225 |
| 800 | 2 | 350 |
| | 1 | 375 |
| | 0.5 | 500 |

plot it is apparent that after 30 min the SIPOS film has densified as much as it will at this temperature.

In Fig. 4 the percent densification of the SIPOS films after a 1 hr N₂ anneal has been plotted vs. the reciprocal of T from ~800°-1150°C so that an activation energy associated with the densification might be ob-

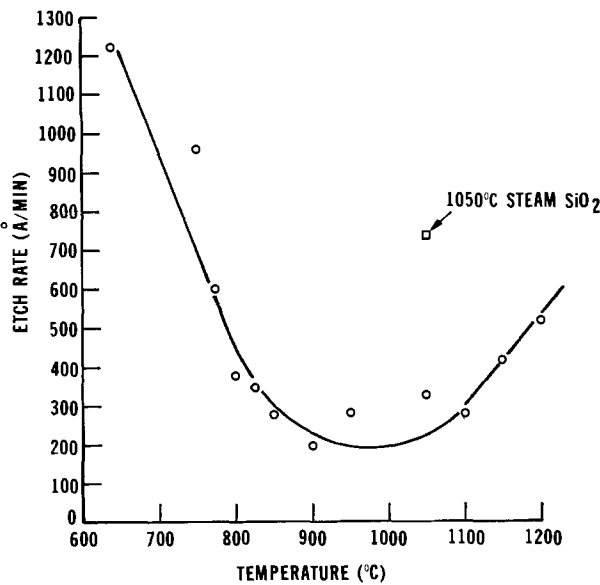


Fig. 2. Etch rate of 25 a/o O SIPOS in 6:1:10 SIPOS etch solution as a function of annealing temperature. Samples were annealed for 1 hr in N₂. The etch rate of a 1050°C steam-grown SiO₂ in 6:1:10 solution is represented by □.

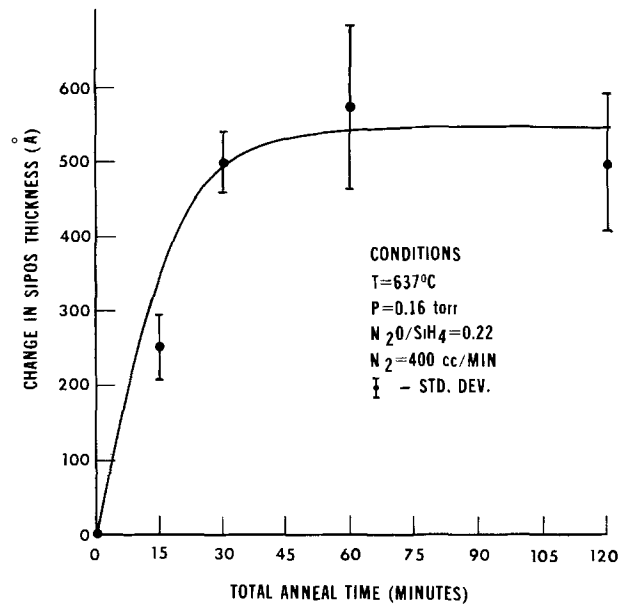


Fig. 3. Change in 25 a/o O SIPOS film thickness at 900°C in N₂ vs. annealing time. The change is a decrease in film thickness.

times of 1/2, 1, and 2 hr were used for the three annealing temperatures of 800°, 900°, and 1100°C. The 800° and 900°C temperatures are representative of typical SiO₂ and Si₃N₄ deposition temperatures. As shown, the 800°C anneals are not as effective at lowering the etch rate as the 900° and 1100°C anneals. Also, the etch rate decreases with increasing annealing time for the 800° and 900°C anneals, but does not continue to decrease for the 1100°C anneal. From the change in etch rate it is apparent that the SIPOS films have changed character due to the anneals.

SIPOS densification.—The anneals also cause the films to shrink or densify as shown in Fig. 3 where the change in the SIPOS film thickness (densification) vs. time is plotted for a 900°C N₂ anneal. From this

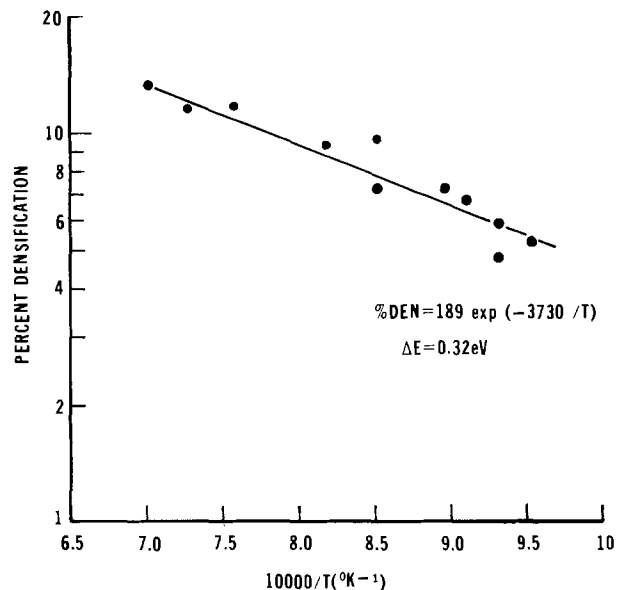


Fig. 4. Percent densification of 25 a/o O SIPOS vs. reciprocal temperature (K⁻¹). The SIPOS was annealed for 1 hr in N₂. Least squares analysis yields an activation energy of 0.32 eV.

$$\%DEN = 189 \exp(-3730/T)$$

$$\Delta E = 0.32 \text{ eV}$$

tained. The least squares analysis of the Arrhenius-type plot results in an activation energy of 0.32 eV.

Infrared measurements.—Thus far, it has been shown that the SIPOS etch rate decreases from its unannealed value and the film densifies with annealing. It will now be interesting to show how the film physically restructures. To do this, one can examine the infrared spectrum as shown in Fig. 5. This spectrum is for an as-deposited 25 a/o O SIPOS film and shows a strong absorption peak at 1030 cm^{-1} and a weak peak at 865 cm^{-1} . No peak is noted at $\sim 800\text{ cm}^{-1}$ which would be present in the infrared spectrum of SiO_2 (5).

The infrared spectra of SIPOS films after high temperature heat-treatments are shown in Fig. 6. This figure shows the effect of 1/2 hr N_2 anneals at 800° , 900° , and 1100°C on three different wafers. The major 1030 cm^{-1} absorption peak shifts to higher frequency with increasing annealing temperature. The strong absorption occurs at 1045 cm^{-1} for 800°C , 1080 cm^{-1} for 900°C , and 1095 cm^{-1} for the 1100°C anneal. Also the width of the major peak decreases from the initial value of 156 cm^{-1} to 125 cm^{-1} for 800°C , 121 cm^{-1} for 900°C , and 100 cm^{-1} for the 1100°C anneal. Moreover, the maximum absorbance increases in intensity as the temperature increases, yet the area of the strong absorption peak remains approximately the same for all temperatures and is an indication that the oxygen

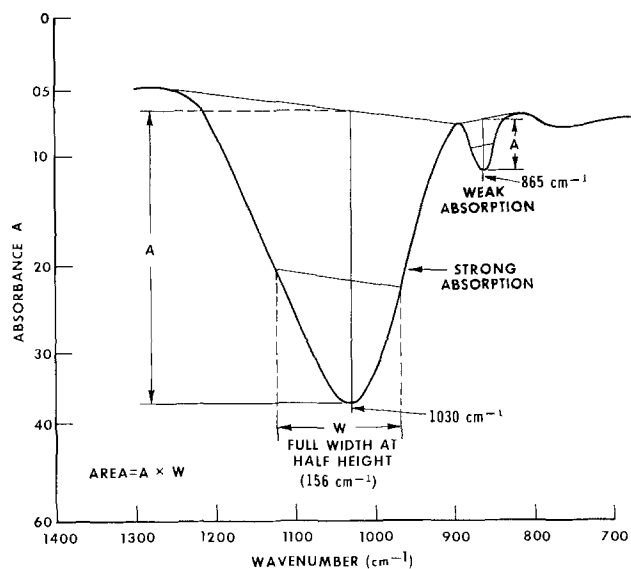


Fig. 5. Analysis of transmission infrared spectrum of 25 a/o O SIPOS film from 700 to 1400 cm^{-1} . The strong infrared absorption occurs at 1030 cm^{-1} while a weak absorption occurs at 865 cm^{-1} . Area of the 1030 cm^{-1} absorption is approximated by $A \cdot W$.

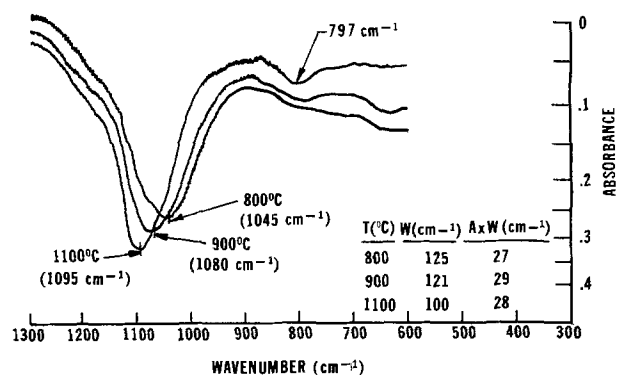


Fig. 6. Infrared spectra of SIPOS films after annealing. Note the shift in the position of the strong absorption to higher frequency with higher annealing temperature. The area of the strong absorption is constant, $28 \pm 1\text{ cm}^{-1}$, indicating no change in the oxygen content of the film.

Table II. SIPOS infrared peak and area ratios (2 hr nitrogen anneal)

| Annealing temp (°C) | SiO_2 (797 cm^{-1}) | |
|---------------------|---|------------|
| | Peak ratio | Area ratio |
| 1100 | 0.071 | 0.041 |
| 900 | 0.071 | 0.035 |
| 800 | 0.044 | 0.019 |

content is not changing. (This is confirmed by electron microprobe analysis of the same films.) Furthermore, the 865 cm^{-1} peak is eliminated and at 900° and 1100°C a weak peak at 797 cm^{-1} appears. This peak is usually associated with SiO_2 (5).

Obviously the heat-treatments restructure the SIPOS film. A relative measure of this restructuring is given in Table II. The ratio of the intensity of the 797 cm^{-1} peak to the strong absorption peak at $1045\text{--}1095\text{ cm}^{-1}$ may be an indication of how much restructuring has been done. In Table II these ratios for peak height and area are given. The 2 hr 900° and 1100°C anneals are roughly comparable and apparently caused more restructuring than the 800°C anneal. The peak ratios indicate less SiO_2 component (797 cm^{-1}) is formed at 800°C as compared to 900° and 1100°C . Likewise, the area ratio would indicate the higher temperature anneals are more effective in forming the 797 cm^{-1} peak.

A measure of the activation energy associated with the restructuring is given in Fig. 7 where the shift of the strong infrared absorption vs. the reciprocal of the annealing temperature is plotted. The least squares analysis for this Arrhenius plot results in an activation energy of 0.27 eV.

Additional infrared data resulting in an Arrhenius plot are presented in Fig. 8. The change or narrowing of the full width at half of the maximum absorbance for the strong infrared absorption vs. the reciprocal of annealing temperature is plotted and yields an activation energy of 0.27 eV. These activation energies are in reasonable agreement with the activation energy determined for the percent densification, 0.32 eV, (Fig. 4) and are all approximately one-sixth of the energy associated with forming the SIPOS film.¹

¹The energy for formation of the SIPOS film was determined from an Arrhenius plot of deposition rate vs. reciprocal of deposition temperature (6).

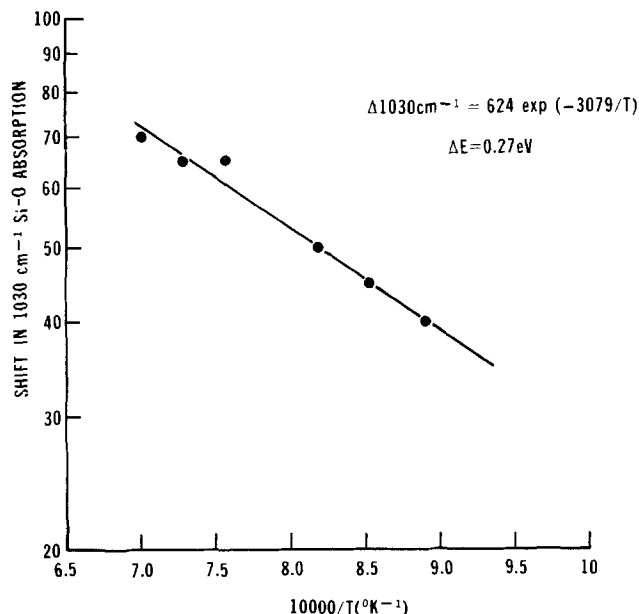


Fig. 7. Shift in the strong infrared absorption vs. reciprocal of the annealing temperature (K^{-1}). The SIPOS films were annealed for 1 hr in N_2 . The least squares analysis yields an activation energy of 0.27 eV.

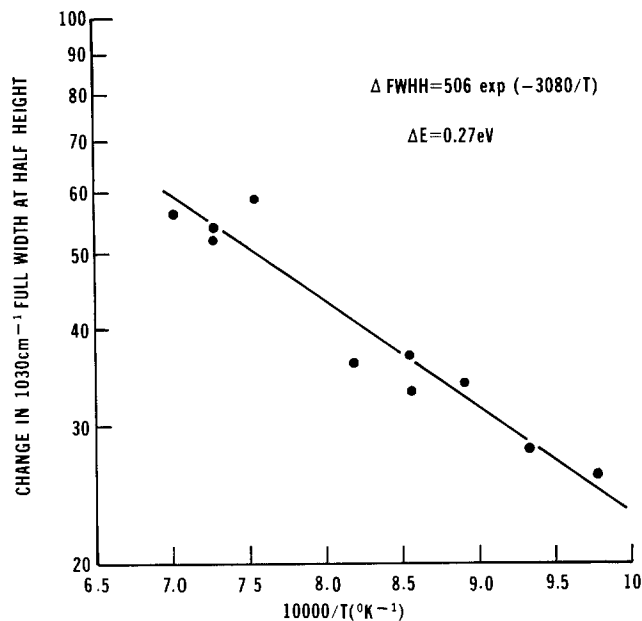


Fig. 8. Change in width of strong infrared absorption vs. reciprocal temperature (K^{-1}). The SIPOS films were annealed for 1 hr in N_2 . The least squares analysis yields an activation energy of 0.27 eV.

The results discussed, thus far, are from control wafers that were heat-treated. However, the same effects are observed in device processing during subsequent film depositions such as Si_3N_4 passivation (see Fig. 9). This figure shows the infrared spectra for a SIPOS film before and after Si_3N_4 deposition. The Si_3N_4 was etched off the sample before the infrared spectrum was taken. For this work, the Si_3N_4 was deposited in a LPCVD reactor at a temperature of approximately $892^\circ C$ by the reaction of SiH_2Cl_2 and NH_3 . As shown, the major infrared peak for SIPOS has shifted from 1030 cm^{-1} to 1070 cm^{-1} , the 865 cm^{-1} peak has disappeared, and a new peak at 797 cm^{-1} has appeared. This infrared spectrum is similar to the infrared spectrum of a SIPOS film that has been annealed at $900^\circ C$ (see Fig. 6).

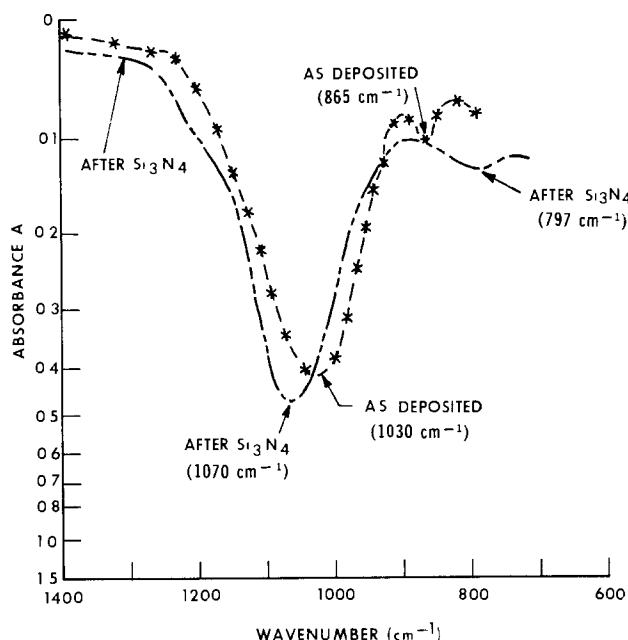


Fig. 9. Infrared spectra of SIPOS before and after deposition of Si_3N_4 at $892^\circ C$. —*— as-deposited SIPOS; — — — after Si_3N_4 deposition. Si_3N_4 was removed before infrared spectrum was recorded.

Stress measurements.—The restructuring caused by the high temperature anneals can be correlated with stress, as shown in Fig. 10, in which the measured stress is plotted for a 5000 \AA thick unannealed SIPOS film along with data after annealing at 900° and $1100^\circ C$ for 1 hr in N_2 . The stress for the as-deposited film is tensile and is $+1.2 \pm 0.9 \times 10^9$ dynes/cm 2 . After the $1100^\circ C$ anneal, the stress is compressive and is $-0.8 \pm 1.2 \times 10^9$ dynes/cm 2 .

The total stress (σ_t) of a film is given by

$$\sigma_t = \sigma_{th} + \sigma_i$$

where σ_i is the intrinsic stress and σ_{th} the thermal expansion coefficient mismatch stress. The latter is given by (7)

$$\sigma_{th} = (\alpha_f - \alpha_{Si}) \frac{E_f}{1 - \nu_f} \cdot \Delta T$$

where α_f and α_{Si} are the thermal expansion coefficients of the deposited film and the Si substrate, E_f and ν_f are Young's modulus and Poisson's ratio for the film, and ΔT is the difference in temperature between the film deposition temperature and the temperature at which the stress is measured. For these films, ΔT is about $620^\circ C$. For a 25 a/o O SIPOS film α , $E/(1 - \nu)$, and σ_i have been determined (8). These values are $\alpha = 2.18 \times 10^{-6}/^\circ C$, $E/(1 - \nu) = 1.31 \times 10^{12}$ dynes/cm 2 , and $\sigma_i = +1.5 \times 10^9$ dynes/cm 2 . Note that α lies between Si ($\alpha = 2.52 \times 10^{-6}/^\circ C$) and SiO_2 ($\alpha = 0.55 \times 10^{-6}/^\circ C$), as might be expected. Substituting the values for α and $E/(1 - \nu)$ into the expression for σ_{th} yields $\sigma_{th} = -2.8 \times 10^8$ dynes/cm 2 . If the high temperature annealing of SIPOS reduces the intrinsic stress, then SIPOS films should become more compressive according to the expression for σ_t and, in fact, this is what is observed, as shown in Fig. 10.

Discussion

The high temperature anneal of a 25 a/o O SIPOS film causes the film to shrink or densify about 10%. For deposited SiO_2 , densification on the order of 3% to 5% has been reported (5) after annealing. The etch rate of the annealed SIPOS in the 6:1:10 SIPOS etch solution has also decreased from the as-deposited value. This observation is consistent with the elimination of voids (reduction of porosity) at anneal temperatures above the deposition temperature. Amorphous thin films commonly have a void network (9). Moreover, the infrared spectrum of the densified SIPOS has changed as well. The strong absorption peak narrows and shifts to higher frequency. Similar

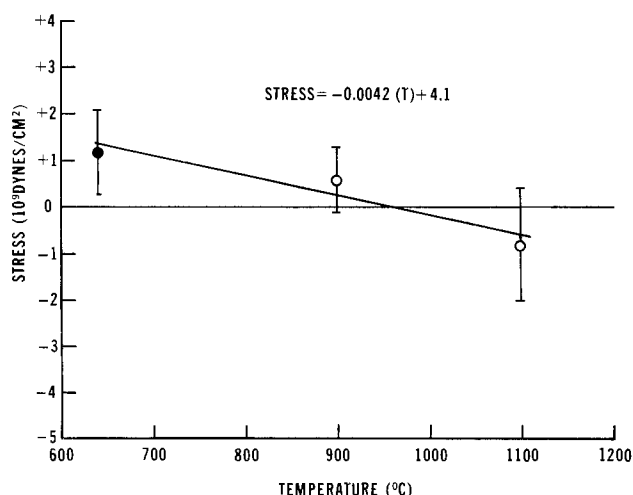


Fig. 10. SIPOS stress vs. annealing temperature. SIPOS was annealed for 1 hr in N_2 . The units of stress are 10^9 dynes/cm 2 . Tensile stress is positive and compressive stress is negative. The dark circle is the measured stress of the as-deposited SIPOS.

changes in the infrared spectrum of SiO₂ after annealing have been interpreted to be due to a relaxation of bond strain and a decrease in film porosity (5). In fact, if the temperature of the anneal is high enough, for example after an 1100°C anneal, the infrared spectrum of SIPOS resembles that of SiO₂. Even at 900°C, there is some SiO₂ character as evidenced by the presence of the weak 800 cm⁻¹ peak in the infrared spectra.

Other changes occur in the SIPOS film with annealing. For example, from previous work (10), it is known that the as-deposited 25 a/o O SIPOS film is amorphous and that after a 1050°C anneal an average grain size of 40Å is observed. Given the above, it is possible that the formation of polycrystalline Si grains in the SIPOS during the anneal could exclude oxygen from the polycrystalline Si regions (there may still be some oxygen interstitially dispersed). Therefore, more of the remaining Si, not in the polycrystalline region, should be bonded to more than one oxygen atom. Evidence for this is suggested by the infrared spectrum of annealed SIPOS films that show no oxygen is lost during annealing. Thus, it is reasonable that after high temperature annealing the infrared spectrum of a SIPOS film should resemble SiO₂.

The stress measurements of SIPOS before and after an anneal are also consistent with more SiO₂ character of the annealed SIPOS film, in that the SIPOS film stress tends to change from tensile to compressive after annealing (SiO₂ is a film in compression on Si).

We interpret the etch rate data in the 6:1:10 SIPOS etch to indicate that at higher temperatures, more of the SIPOS has been converted to SiO₂ and polycrystalline Si since the etch rate actually starts to increase with the very high temperature anneal.² Thus the densification of the SIPOS film after anneal and the change in the infrared spectrum reported here support the models of annealed SIPOS presented by Hamasaki *et al.* (12) and McGinn and Goodman (13).

Conclusions

We conclude that with high temperature annealing the SIPOS films densify. For the 25 a/o O SIPOS films evaluated, this densification is a strong function of temperature. Some time dependence has also been noted for the lower temperature anneals (800°C). The densification is the result of a restructuring of the amorphous as-deposited SIPOS film as evidenced by the change in the infrared spectrum. This same densification takes place during high temperature deposition

² The etch rate variation of SIPOS with anneal temperature may also be interpreted in terms of the stress in the SIPOS films. In Fig. 2 the lowest etch rate is at ~980°C. In Fig. 10, this temperature corresponds to about zero stress in the SIPOS film. At any other temperature the film is stressed and so the etch rate is higher than that at 980°C (11).

of Si₃N₄ or SiO₂ which are used as passivation layers on deposited SIPOS.

Evidence of grain growth at temperatures above the deposition temperature have been reported. Such grains exclude oxygen and result in the remaining Si atoms being bound to more than one oxygen atom (formations of SiO₂). The infrared changes and etch rate data are consistent with this interpretation. The change in the SIPOS stress due to the anneal is also consistent with more SiO₂ being formed. Finally, our results lend additional support to the models of annealed SIPOS presented by other workers.

Acknowledgment

We thank Dr. T. F. Retajczyk, Jr., at BTL-MH for the initial stress measurements.

Manuscript submitted March 19, 1980; revised manuscript received ca. Sept. 26, 1980. This was Paper 166 presented at the Boston, Massachusetts, Meeting of the Society, May 6-11, 1979.

Any discussion of this paper will appear in a Discussion Section to be published in the December 1981 JOURNAL. All discussions for the December 1981 Discussion Section should be submitted by Aug. 1, 1981.

Publication costs of this article were assisted by Bell Laboratories.

REFERENCES

1. H. Mochizuki, T. Aoki, H. Yamoto, M. Okayama, M. Abe, and T. Ando, *Suppl. Jpn. J. Appl. Phys.*, **15**, 41 (1976).
2. H. R. Maxwell, Jr. and W. R. Knolle, in "Semiconductor Characterization Techniques," P. H. Barnes and G. A. Rozgonyi, Editors, p. 180, The Electrochemical Society Softbound Proceedings Series, Princeton, N.J. (1978).
3. W. Bruegel, "An Introduction to Infrared Spectroscopy," p. 301, John Wiley & Sons, New York (1962).
4. A. K. Sinha, H. J. Levinstein, and T. E. Smith, *J. Appl. Phys.*, **49**, 2423 (1978).
5. W. A. Pliskin, *J. Vac. Sci. Technol.*, **14**, 1064 (1977).
6. H. R. Maxwell, Jr., Private communication.
7. A. K. Sinha, H. J. Levinstein, and T. E. Smith, *J. Appl. Phys.*, **49**, 2423 (1978).
8. T. F. Retajczyk, Jr., Private communication.
9. A. G. Dirks and H. J. Leamy, *Thin Solid Films*, **47**, 219 (1977).
10. H. R. Maxwell, Jr., A. R. Hartman, and T. T. Sheng, RNP 27 presented at The Electrochemical Society Meeting, Boston, Massachusetts, May 6-11, 1979; see *This Journal*, **125**, 257C (1978).
11. S. Schwarz, H. R. Maxwell, Jr., and W. R. Knolle, To be published.
12. M. Hamasaki, T. Adachi, S. Wayakama, and M. Kikuchi, *J. Appl. Phys.*, **49**, 3987 (1978).
13. J. T. McGinn and A. M. Goodman, *Appl. Phys. Lett.*, **34**, 601 (1979).

Transmission Electron Observations of the Early Stage of Epitaxial Growth of Silicon on Sapphire

S. Hamar-Thibault

L.T.P.C.M./E.N.S.E.E.G.—Institut National Polytechnique de Grenoble, B.P.44 38401 Saint Martin d'Herès, France

and J. Trilhe

Laboratoire M.E.A., LETI/C.E.N. de Grenoble—85 X 38041 Grenoble Cedex, France

ABSTRACT

A discontinuous silicon layer was produced on $(01\bar{1}2)$ oriented sapphire. The early growth of silicon was examined by transmission electron microscopy. During a very short time of deposition, it is shown that islands of $\{100\}$ orientation had nearly square or rectangular forms. We observed a very rapid decrease of $\{100\}$ crystallite density together with a nearly constant $\{110\}$ crystallite density. The lattice of epitaxial Si layers was measured to be distorted in the very early stage of the growth. The interfacial shear strain is calculated. The distortion of the silicon lattice decreases with growing time.

Devices fabricated from heteroepitaxial silicon films on sapphire sometimes presented backchannel leakage currents caused, at least in part, by the presence of defects and impurities in the silicon films. Several authors (1-4) using transmission electron microscopy have shown the presence of stacking faults and microtwins in silicon. Defect density in silicon is very high in the proximity of the sapphire interface, so it is very important to study the structure of the interface and the defects which are present.

In order to investigate the nature of the initially deposited silicon, we have studied, using transmission electron microscopy, the structure and the orientation of silicon islands at early stages of growth.

The presence of residual elastic stresses near the interface, which could affect electrical properties of integrated circuits, is proved by measuring lattice parameters by diffraction microscopy.

Experimental

The silicon was deposited from vapor phase at 980°C on $(01\bar{1}2)$ oriented CZ single crystal sapphire substrates by pyrolysis of diluted silane in H_2 . The sapphire substrates were polished wafers from Union Carbide.

Deposition was stopped at various times; with a growth rate of $0.67 \mu\text{m}\cdot\text{mn}^{-1}$, we obtained a series of samples with isolated islands of silicon. The samples examined were grown for 0.6, 1.2, 1.8, and 2.4 sec.

The samples were thinned by argon ion bombardment from the sapphire side only. Samples were observed by JEM 100 B electron microscope, operating at 100 keV.

Observations

We first present information contained in the diffraction patterns and electron microscopical images.

Diffraction pattern and electron micrographs.—The selected area diffraction pattern from a sample grown for 1.8 sec is shown in Fig. 1. The indexed pattern is given on the same figure with reference to the interpretation of Abrahams (1). It is seen in Fig. 1 that there are three orientations. The most important orientation of the silicon islands is $\{100\}$. For these $\{100\}$ domains, the plane $(2\bar{1}\bar{1}0)$ is parallel to the (001) plane of the silicon.

There are also two other orientations of silicon islands, that is to say two kinds of $\{110\}$ oriented domains. These three main orientations are always present with their twin configurations. Each two $\{110\}$

oriented domains have their twin pairs. They twinned about the $\langle 111 \rangle$ axis, which lies parallel to the $[011]$ and $[0\bar{1}1]$ directions of the (100) oriented domains. Only the two twin axes which are parallel to the substrate give well-developed twin crystals. All other spots may be due to multiple diffraction effects.

Bright and dark field electron micrographs of the sample grown for 2 sec are shown in Fig. 2. The micrograph 2a is the bright field image of a sample area. The micrograph 2b is a dark field image with an operative reciprocal lattice vector $\mathbf{g} = (004)$ of the same area. The $\{100\}$ oriented silicon islands appear light. In the micrograph 2c corresponding to the $\langle 111 \rangle$ reflection parallel to the $[0\bar{1}1]$ direction of the $\{110\}$ domains, the two $\{110\}$ domains appear light.

It is seen that the silicon films consisted of differently oriented domains smaller than 100 nm in diameter. The crystallites are often composed of one or two $\{110\}$ domains associated with $\{100\}$ domains.

We also observed that $\{110\}$ domains contain a very high density of twins and microtwins. Most of the twins are very thin, one or two atomic layers. The density of twins in $\{100\}$ domains is much smaller. The results given above concerned developed films before complete coverage. The observations are slightly different at earlier stages under the present growth conditions.

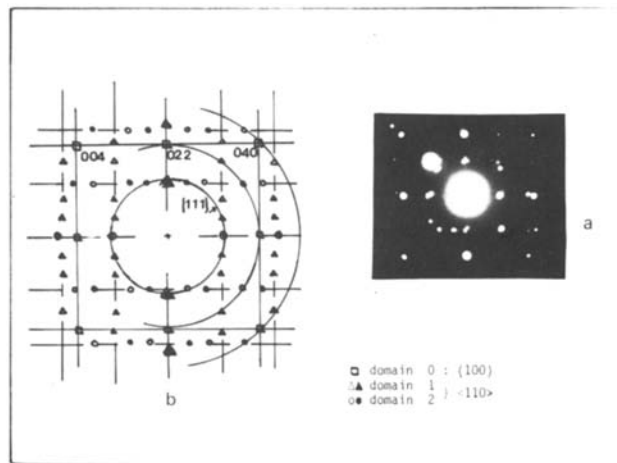


Fig. 1. Diffraction pattern of epitaxial silicon on sapphire. $(100)_{\text{Si}}/(01\bar{1}2)_{\text{Al}_2\text{O}_3}$. (a) Diffraction pattern, (b) indexed pattern of $\{100\}$ and $\{110\}$ domains.

Key words: dislocation, misfit, shear strain distortion.

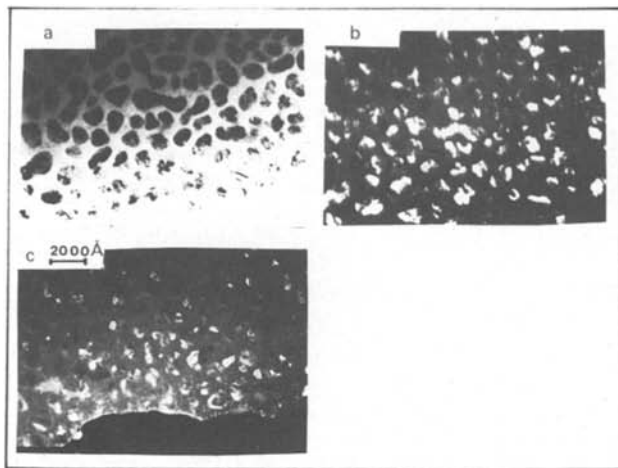


Fig. 2. Bright and dark fields electron micrographs: (a) bright field, (b) dark field $\{100\}$ domain $g = (022)$, (c) dark field $\{110\}$ domains $g = \langle 111 \rangle \parallel |0\bar{2}2|$.

The size of the $\{100\}$ domains is always larger than the corresponding $\{110\}$ domain.

Figure 3 presents for different growing times the silicon islands deposited on sapphire. As seen in Fig. 3, the mean diameter of silicon crystallites increases with growing time, as the density of $\{100\}$ domains decreases, as a result of island coalescence.

It is very interesting to note that for sample II ($t = 1.2$ sec, $v = 0.67 \mu\text{m}^{-1}$), rectangular or square particles are present. They are much less numerous than the particles of other forms. The sides of the square particles are parallel to the $[011]$ and $[0\bar{1}1]$ directions. These particles are always smaller than other particles. The mean diameter seems to be smaller than 200 or 300 Å. For longer growth time, the particles develop into larger conglomerates and the geometrical shape disappears.

Fine structure of electron diffraction patterns.—The fine structure in electron diffraction patterns for the sample with the smallest growth time shows: (i) elongation of spots (belonging to $[100]$ and $[110]$ domains) and (ii) distortion of the silicon lattice. Two distinct types of spot elongations are visible: circular elongation around the origin, and linear streaks. Figure 4 shows the diffraction pattern of $[100]$ zone of $\{100\}$ domains of silicon (sample II). Extreme variations in contrast made it difficult to obtain print that would

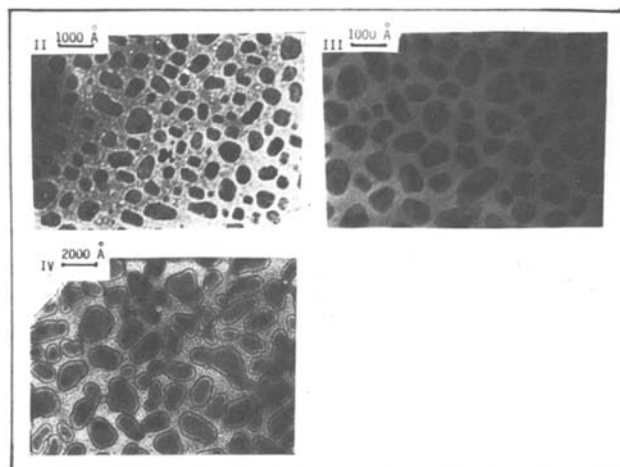


Fig. 3. Electron micrographs for different growing times. II = 1.2 sec; III = 1.8 sec; IV = 2.4 sec.

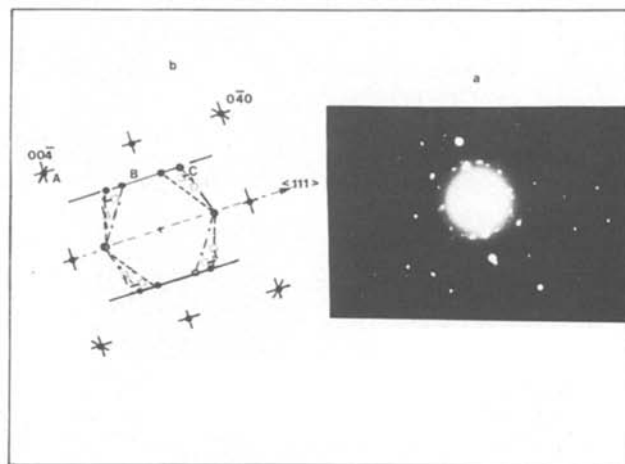


Fig. 4. Fine structure of a diffraction pattern

preserve the details of the relrods. These are shown in the accompanying tracing. The most readily identifiable type is circular elongations of the spots, which are due to small misorientations of the $\{100\}$ or $\{110\}$ domains.

This elongation is due to small misorientations. The mean angular spread of the spots from the $\{100\}$ domains is about 3° for the smallest growth time, and decreased to 1° for longer growth time. So experimentally, it is seen that silicon films on sapphire are like a mosaic of silicon islands, which becomes more perfect as the thickness of the films increases. This orientation spread of about 3° was interpreted by Abrahams (4) to nucleation of planes of the $\{100\}$ silicon islands parallel to sapphire planes; if some of the $(0\bar{2}2)$ planes of $\{100\}$ silicon nucleate parallel to the (2204) planes of sapphire, while some other of the $(0\bar{2}2)$ planes nucleate parallel to $(20\bar{2}4)$ planes of sapphire, the misorientation would be about 4° .

The second type of spot elongations in diffraction patterns appears as linear streaks in both $\{100\}$ and $\{110\}$ domains, arising from high density of stacking faults and microtwins (note B and C in Fig. 4). Diffraction patterns of the $\{110\}$ domains (B) are present at very early stages of growing time; high density of microtwins shows linear streaks in the $\langle 111 \rangle$ direction. Only elongations along the $\langle 111 \rangle$ twin axis parallel to $[011]$ and $[0\bar{1}1]$ directions of $\{100\}$ domains are well developed, as the twins. We obtain as the diffraction pattern, at very early stages of growth, a network with perpendicular streakings.

The $\{100\}$ domains are also twinned about the $\langle 111 \rangle$ twin axes; at the exact $[100]$ orientation, there are not spots due directly to the twins. But the spots noted C are extra spots due to double diffraction on those twins in $\{100\}$ crystals. These spots disappear when the growing time increases. Linear streaks are also seen near (004) , (022) spots and in the vicinity of the spots C, of the $\{100\}$ domains. The streaks are parallel to the $[010]$ and $[001]$ directions; they can indicate a high density of stacking faults.

Angular distortion, misfit, and misfit dislocations.—At early stages of growth, before complete coverage, observations of diffraction patterns show that the silicon lattice is distorted. The distortion decreased for increasing growth time deposition. There is an angular distortion, and together a contraction of the reciprocal lattice vector. As the substrate is not cubic, a shear stress exists, which can be established from the nonorthogonality of $(0\bar{4}0)$ and (004) reciprocal lattice vectors observed on the $[100]$ silicon films patterns.

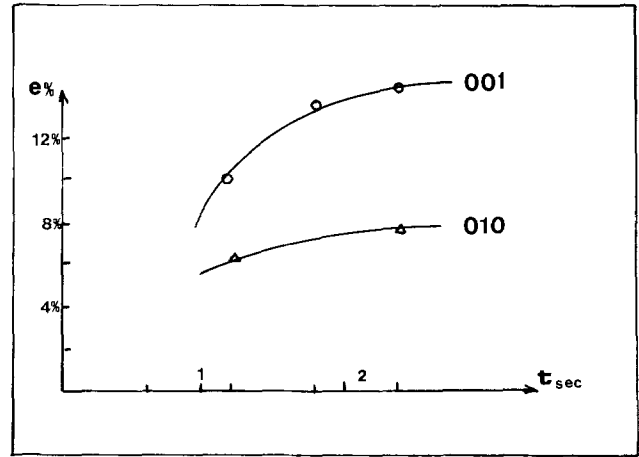
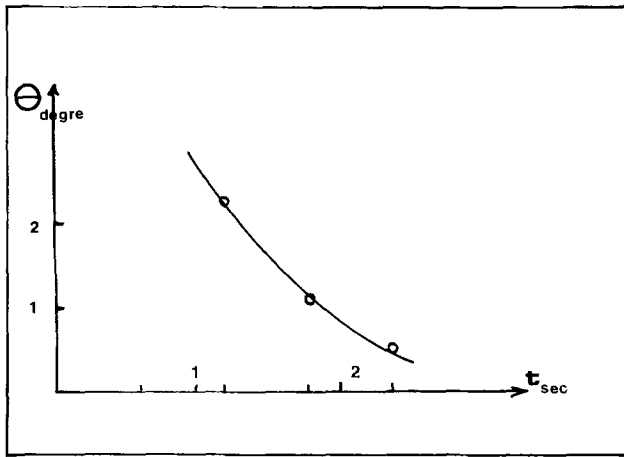


Fig. 5. Distortion of silicon lattice on sapphire at early stage of growth. (a) Deviation θ from theoretical angle between (004) and (040) reflections of epitaxial silicon, (b) misfit between distorted and nondistorted silicon lattice for the (004) and (040) reflection spots.

The angle between the (040) and (004) reciprocal lattice vectors was measured. This angle can be as large as 92°. The theoretical angle for the [100] orientation is 90°. 90° was subtracted from the measured angle to give the shift named θ . The variation of θ for different growth time is shown in Fig. 5(a). θ decreases with increasing growth time. The maximum observed value of θ is as large as 2° for 1 sec of growth time. θ reached zero after 3 sec of growth time.

In diffraction patterns, a misfit between the silicon and sapphire lattices can be observed. From the separation of g_{SI} and g_{SA} where g_{SI} and g_{SA} are, respectively, the reflection (004) of the silicon and (4220) of the sapphire, we deduce that there is a progressive increase in the misfit between silicon and sapphire lattices with increasing deposit time. If the misfit is defined as

$$e = \frac{a_{SA} - a_{SI}}{a_{SA}}$$

where a_{SA} and a_{SI} are the interatomic spacings in the interfacial plane in sapphire and silicon, then in terms of g_{SI} and g_{SA}

$$e = \frac{|g_{SA}| - |g_{SI}|}{|g_{SA}|}$$

assuming g_{SA}/g_{SI} .

Figure 5(b) shows that the misfit e increases from about 8% to 14% compared with a natural misfit e^0 of about 14%, for the (004) reciprocal lattice vector of silicon and the (4220) of sapphire. The misfits noted e_{004} and e_{040} are related to the (004) and (040) reflections spots for silicon.

The misfit is equal to the natural misfit after 2.4 sec of growth. For this sample, continuous networks of misfit dislocations are also seen in the silicon islands, as seen in Fig. 6. The fringes tend to lie parallel to the [011] and [011] directions. The Burgers vector of the dislocations is consistent with $a/2$ [110] which is the \mathbf{b} for dislocation in the diamond structure. Their spacing is equal to 38Å, which is in good agreement with the calculated value for pure edge type (37Å).

For this sample (2.4 sec of growing time) the linear density of misfit dislocations is $1/38\text{Å} = 2.6 \times 10^6$ dislocations·cm⁻¹. For the other samples with shorter growing time, we do not see any misfit dislocations. Misfit dislocations have also been observed by Abrahams (5).

It is very interesting to note the correlation between the lattice deformation of the silicon, which decreases with growing time, and the easy observation of misfit dislocations for longer growing time.

Results

Monoclinic distortion of the epitaxial layers.—If we assume the thickness of the epitaxial layer to be much

smaller than the dimensions of the substrate, we may neglect the strains in the substrate. Substrates that were not very thick became curved due to the stresses in the epitaxial layer.

The observations indicate that the silicon lattice at early stages of epitaxy is distorted. From measurements of several d spacings, it is concluded that there are compressional and shear strains in the silicon islands. The simplest distorted lattice is a monoclinic lattice.

Figure 7 gives a schematic drawing of a monoclinic distortion of a silicon layer on sapphire. The lattice



Fig. 6. Misfit dislocations of silicon on sapphire (growth time 2.4 sec).

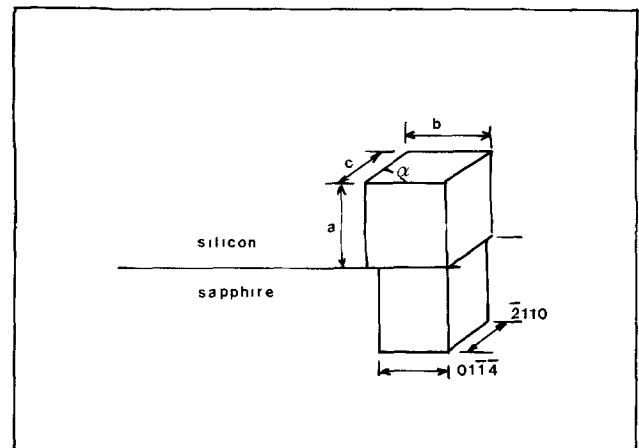


Fig. 7. Schematic representation of a monoclinic distorted silicon lattice on sapphire.

parameter of undistorted silicon is a_0 . If ϵ_{100} , ϵ_{010} , ϵ_{001} are the strains along the three axes, the parameters of a distorted lattice become a b c

$$a = a_0(1 + \epsilon_{100})$$

$$b = a_0(1 + \epsilon_{010})$$

$$c = a_0(1 + \epsilon_{001})$$

where α is the monoclinic angle between the [010] and [001] axis, as shown in Fig. 7. α is 90° if the silicon layer is not distorted.

Relations between observable quantities and strain components.—From [100] diffraction pattern, we obtain information about strains in the wafer plane along the [001] and [010] axis, that is to say, c , b , and α . From the angular deviation between (010) and (001) reflections, spots on [100] diffraction pattern, we obtained α , which is related to θ .

Strains ϵ_{001} and ϵ_{010} are approximately related to misfits by

$$\epsilon_{001} = \epsilon_{004^\circ} - \epsilon_{004}$$

$$\epsilon_{010} = \epsilon_{040^\circ} - \epsilon_{040}$$

Strain ϵ_{100} related to the [100] axis perpendicular to the epitaxial plane must be calculated from the [110] pattern of the {100} silicon domains. The parameter a is more difficult to calculate, these parameters can only be obtained from relations between c , b , α , d_{400} , and d_{220} , where d_{400} and d_{220} measured on the {110} diffraction pattern are interplanar spacings of (400) and (220) planes of silicon.

Figure 8 shows variations of lattice parameters ϵ and α of a distorted silicon layer on sapphire with deposition time. As seen in the figure, the lattice parameter normal to the wafer surface increases, while the two lattice parameters parallel to the wafer surface decrease. This result suggests that the first layers of silicon on sapphire are deformed to accommodate the sapphire lattice.

Stresses in epitaxial layer.—The elastic stresses in a cubic crystal are correlated to the strains by a tensor, whose elements are the elastic stiffness coefficients. The elastic stiffness coefficients are given by Hornstra (6). In thin epitaxial layers, forces of the substrate act only in the interface plane, and as the substrate is not cubic, shear strains are present, which are to be added to compressional strains (8).

We calculate stresses along the different axes using the variation of the lattice parameters; the result is for 1.2 sec of growing time (sample II)

$$\sigma_{100} \approx +1.2 \times 10^{10} \text{ dynes/cm}^2$$

$$\sigma_{010} \approx +2.9 \times 10^{10} \text{ dynes/cm}^2$$

$$\sigma_{001} \approx -5.9 \times 10^{10} \text{ dynes/cm}^2$$

The shear stress σ_S is calculated from the angular deviation θ by Abrahams (7)

$$\sigma_S = \text{tg } \theta \approx 2.7 \times 10^{10} \text{ dynes/cm}^2 \text{ for sample II}$$

The decay of the compressional and shear strains is very quick. For the sample III ($t = 1.8$ sec) these strains are about a factor of 10 less than the strains of the sample II ($t = 1.2$ sec). Along the [001] direction, we calculate the values

$$\sigma_{\text{II}} = -5.9 \times 10^{10} \text{ dynes/cm}^2$$

$$\sigma_{\text{III}} = -0.7 \times 10^{10} \text{ dynes/cm}^2$$

We also observed a very important difference between strains in [001] and [010] directions, which gives rise to a shear strain in the wafer plane.

The precision of our results are best appreciated along the [001] axis, where the compressional strain is the most important. The compressional strain of sample IV ($t = 2.4$ sec) is impossible to estimate with

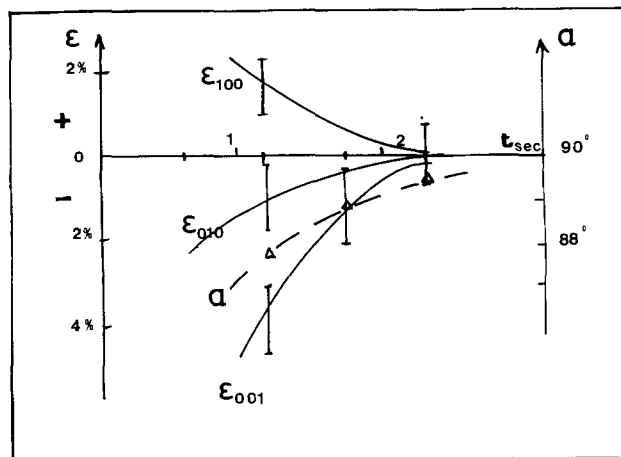


Fig. 8. Variation of lattice parameters of monoclinic silicon with deposit time.

our method; the precision of the diffraction patterns is too small. In opposition, the shear strain decreases slowly from $3 \cdot 10^{10}$ dynes/cm² for the sample II to 0.6×10^{10} dynes/cm² for sample IV, with increasing growth time.

Discussion

Two points are very important in our results, the geometrical form of the silicon islands and the stresses in the wafer plane before complete coverage. We compare first the morphology of the silicon islands with those of Abrahams (1); then some remarks are made concerning the magnitude of the calculated stresses and the asymmetric strains in the plane of the wafer.

The observations of the nucleation of silicon on sapphire are compared with the results of Abrahams. The growing conditions (temperature, growth rate) are approximately the same. They obtained near a rapid initial coverage rate, smooth forms of silicon islands. In opposition our silicon islands present geometric forms and the coverage of the substrate surface *vs.* time is represented by a sigmoid curve. Those islands present a partially coherent growth on the substrate. The morphology of the silicon islands differs only at a very early stage of growth. For longer growth time, our results are similar to those reported by Abrahams.

The important difference in the preparation of the substrate is hydrogen firing used by Abrahams. The surface of sapphire obtained by those authors seem to provide a high density of nucleation of silicon islands. As we do not use hydrogen firing, we obtain a lower density of silicon islands with a lower density of defects. Schmidt and Davey (13) have reported that after hydrogen firing, sapphire surfaces were ordered crystallographically but topologically poor.

Those silicon islands present, on the other hand, important compressional strains. Geometric or thermal considerations could explain the not equal compressional strains in the [001] and [010] directions, greater along the [001] axis. Stresses arise when the layers are cooled to room temperature. They are due to the difference between the thermal expansion coefficients of silicon and sapphire (8). The anisotropy of the thermal expansion coefficient of the sapphire (12) greater along c than perpendicularly gives rise to anisotropy of contraction of sapphire greater along the [010] than the [001] axis.

Crystallographical considerations could also induce stresses in the wafer plane. Nolder (11) compared the relative position of aluminum and oxygen atoms on a (01 $\bar{1}$ 2) plane in sapphire and the silicon atom on a (100) plane in the cubic lattice of the silicon.

It is seen that the aluminum sites form a face-centered array, which is similar to the arrangement of

silicon atoms in a (100) plane, with the [001] direction of silicon parallel to the $[2\bar{1}10]$ direction of the sapphire. The substitution of aluminum by silicon, leads to mismatches along the [001] and [010] directions of about 14 and 8% with reference to the $[2\bar{1}10]$ and $[0\bar{1}1\bar{4}]$ directions of sapphire. The observed strains are of the same order of magnitude and of the same direction as geometric strains.

In general, all the measurements of residual stresses in silicon films on sapphire lead to thermal stresses. Kamins and Meieran (9) calculated stresses of $7 \cdot 10^9$ dynes \cdot cm², Dumin (10) found residual stresses to be about $5 \cdot 10^9$ dynes \cdot cm⁻². Abrahams (7) gives shear stresses of $1.2 \cdot 10^{10}$ dynes \cdot cm⁻² near corners of silicon-sapphire interface. The magnitude of the calculated stresses ($5 \cdot 10^{10}$ dynes \cdot cm⁻² in the [001] direction) at an early stage of growth can exceed the thermal contribution by an order of magnitude. As the film grows, this contribution becomes very small rapidly. We think that there is a superposition of the two sorts of stresses. The crystallographical compressional strain, which is very important at early stage of growth, decreases very quickly with thickness. When the films are thicker, thermal compressional stresses remain the principal stresses.

Experimentally, we observed small islands at the first stage of the deposition of silicon on sapphire, which present the characteristics of partially coherent growth on the substrate surface. That is in opposition with the theory of Van Der Merve (14), which says that a totally coherent growth of a layer film (formed layer by layer) may be expected up until a certain thickness which is related with the misfit of the two lattices. This thickness is for the system Si/Al₂O₃ equal to 1Å, that is to say that the growth of silicon may be totally not coherent. In fact, the growth of islands of silicon instead of layers increases the possibility of coherent growing, by introducing a term of superficial energy of the island.

In conclusion, we observed at a very early stage of growth, a partial coherency of the silicon islands of sapphire. This partially coherent growth appears with

compressional strains in wafer plane and at the same time, the coverage of the substrate surface by silicon islands is represented by a sigmoid curve.

Acknowledgment

Thanks are due to Mr. G. Cullen and Mr. M. S. Abrahams for very useful discussions.

Manuscript submitted Feb. 28, 1980; revised manuscript received ca. Sept. 29, 1980. This was Paper 329 presented at the Los Angeles, California, Meeting of the Society, Oct. 14-19, 1979.

Any discussion of this paper will appear in a Discussion Section to be published in the December 1981 JOURNAL. All discussions for the December 1981 Discussion Section should be submitted by Aug. 1, 1981.

Publication costs of this article were assisted by the Institut National Polytechnique de Grenoble.

REFERENCES

1. M. S. Abrahams, C. J. Buiocchi, R. T. Smith, J. F. Corboy, Jr., J. Blanc, and G. W. Cullen, *J. Appl. Phys.*, **47**, 5139 (1976).
2. T. Hayashi and S. Kurosawa, *J. Cryst. Growth*, **45**, 426 (1978).
3. J. Trilhe, J. Borel, and J. P. Duchemin, *ibid.*, **45**, 439 (1978).
4. M. S. Abrahams and C. J. Buiocchi, *Appl. Phys. Lett.*, **27**, 324 (1975).
5. M. S. Abrahams, C. J. Buiocchi, J. F. Corboy, and G. W. Cullen, *ibid.*, **28**, 275 (1976).
6. J. Hornstra and W. J. Bartels, *J. Cryst. Growth*, **44**, 513 (1978).
7. M. S. Abrahams, J. Blanc, C. J. Buiocchi, and W. E. Hams, *J. Appl. Phys.*, **49**, 652 (1978).
8. D. M. Jefkins, *J. Phys. D. Appl. Phys.*, **3**, 770 (1970).
9. J. I. Kamins and E. S. Meieran, *J. Appl. Phys.*, **44**, 5064 (1973).
10. D. J. Dumin, *ibid.*, **36**, 2700 (1965).
11. R. Nolder and I. Cadoff, *Trans. Metal. Soc. AIME*, **233**, 549 (1965).
12. J. B. Wachtman, *J. Am. Ceram. Soc.*, **47**, 319 (1962).
13. W. A. Schmidt and J. E. Davey, *Nat. Bur. Stand. Spec. Publ.*, **348**, 259 (1972).
14. J. H. Van Der Merve, *J. Appl. Phys.*, **34**, 117 (1963).

Silicon Contamination of InP Synthesized under High Phosphorus Pressure

A. Yamamoto, S. Shinoyama, and C. Uemura

*Nippon Telegraph and Telephone Public Corporation,
Ibaraki Electrical Communication Laboratory, Tokai, Ibaraki 319-11, Japan*

ABSTRACT

An experimental study has been made of processes causing Si contamination of polycrystalline InP synthesized under high phosphorus pressure (~ 30 atm) via the horizontal Bridgman technique. Silicon content of the grown ingots was determined by measurement of carrier concentrations and by spark source mass spectrometry. The Si content increased by about two orders of magnitude when the maximum temperature in the indium melt was varied from 1050° to 1180°C. The Si content scarcely depended on phosphorus pressure in the range of 5-30 atm. Presence of indium oxides in the indium melt was found to lower the incorporated Si content. As a result of these investigations, high purity InP ($N_d - N_a = 3.2 \times 10^{15}$ cm⁻³, $\mu_{77K} = 37,000$ cm²/V \cdot sec) was reproducibly obtained by using a quartz boat at a growth rate of 3 mm/hr. The effective distribution coefficient for Si in InP was determined to be 0.53 by the analysis of intentionally Si-doped ingots.

Recent developments of InP-based devices such as InGaAsP-InP lasers or InP FET's require high quality

Key words: InP, Si contamination, effective distribution coefficient, synthesis of III-V compounds, horizontal Bridgman technique.

InP crystals as substrates. Single crystals of InP are currently grown by the liquid encapsulated Czochralski (LEC) method. The LEC method uses polycrystalline InP as the starting material. Reduction of residual donor impurities in the starting material is essential

to grow semi-insulating crystals or p-type crystals with low carrier concentrations.

Silicon is known to be a major residual donor impurity in InP and to be introduced from the silica envelope during synthesis or crystal growth (1, 2). Use of pyrolytic boron nitride (PBN) boats in the synthesis of InP is effective in reducing carrier concentrations in the grown ingots (3). Furthermore, the synthesis at lower temperatures ($\sim 950^\circ\text{C}$) and under lower phosphorus pressure (~ 2 atm) is successful in obtaining high purity InP with carrier concentrations lower than 10^{15} cm^{-3} (4). Although the reaction of SiO_2 and phosphorus vapor, which provides a source for Si contamination, has been proposed by Bachmann *et al.* (1), details of Si contamination process during synthesis or crystal growth have not been systematically studied.

Segregation behavior of Si in InP, on the other hand, has been unclear since the effective distribution coefficient for Si in InP, $k_e(\text{Si})$, has been scattered in the wide range of 10^{-3} in LEC (5) to 30 in LPE (6). This uncertainty for $k_e(\text{Si})$ is thought to be mainly caused by Si contamination during synthesis or crystal growth (2). Therefore, segregation behavior of Si must be evaluated with intentionally Si-doped materials in which an Si contamination level can be neglected as compared with the Si doping level.

In this work, we studied experimentally the Si contamination process of undoped InP synthesized under high phosphorus pressure via the horizontal Bridgman technique. By carrier concentration measurements and spark source mass spectrographic analyses, we found some factors in the synthesis which governed Si content incorporated into grown ingots. As a result of that, it was proved that bulk polycrystalline InP with carrier concentrations as low as those synthesized using PBN boats could be obtained by using quartz boats. We also obtained a reliable value of $k_e(\text{Si})$ from the analyses of intentionally Si-doped ingots.

Experimental

Not intentionally doped polycrystalline InP was synthesized from the elements via the horizontal Bridgman technique. Approximately 200g of indium (6-9's purity, Mitsubishi Metals or Yamanaka Semiconductors) were charged in a quartz boat. The quartz boat was placed in a quartz ampul (ID: 35 mm, length: 600 mm) together with approximately 100g of red phosphorus (6-9's purity, Mitsubishi Metals) charged in a separate quartz boat. Prior to the sealing of the ampul, the indium was prebaked in vacuum (pressure: 1×10^{-6} Torr) at a temperature in the range of 450°C – 950°C for 3 hr. After being evacuated and then sealed, the ampul was set in a three-zone horizontal Bridgman furnace. The furnace was in a water-cooled chamber that could be pressurized up to 35 atm with N_2 gas. The furnace was heated to the conditions shown in Fig. 1. The phosphorus pressure in the ampul was controlled by the temperature in the zone A, T_A , and estimated from the pressure-temperature relationship data reported by Bachmann *et al.* (7). T_A was varied from 400°C to 600°C , which corresponded to phosphorus pressure from 1.5 to 40 atm, respectively. To prevent breakage of the ampul due to such high phosphorus pressure, the N_2 gas pressure in the chamber was controlled to within ± 5 atm of the phosphorus pressure in the ampul. The indium was heated at the temperature in the zone B, T_B , and then traveled toward the zone A through the highest temperature zone C in which maximum temperature was T_{max} . T_B was fixed at 800°C through all experiments, and T_{max} was varied from 1050°C to 1200°C . The ampul was moved at a constant speed of 3 mm/hr when the desired temperature in each zone was reached.

Silicon-doped InP was also synthesized to study the segregation behavior of Si in InP. For Si doping, small pieces (2-5 mg) of an Si wafer (phosphorus-doped,

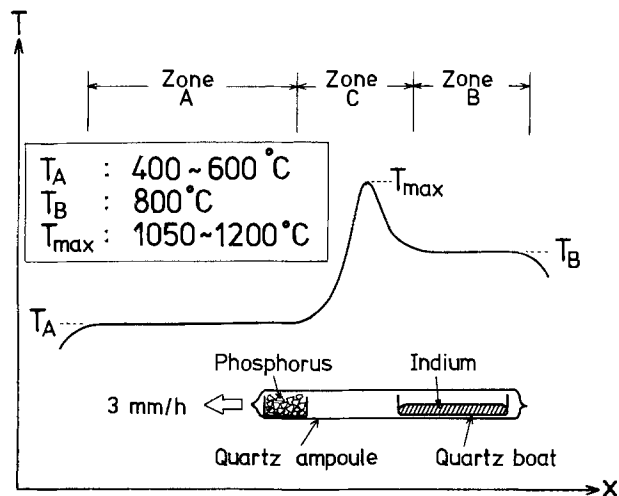


Fig. 1. Schematic of the horizontal Bridgman apparatus used for synthesis of InP.

50 $\Omega\text{-cm}$) were added to the indium before the prebaking of the indium.

The electrical properties of InP ingots synthesized were evaluated using Van der Pauw Hall measurements. The residual impurities in the ingots were determined using spark source mass spectrometry.

Results and Discussion

Silicon contamination of nominally undoped ingots.— We studied the dependence of carrier concentration or Si incorporated under various synthesis conditions such as maximum temperature in the zone C, T_{max} , phosphorus pressure in the ampul, P_P , and prebaking temperature of the charged indium, T_{pb} .

First, effects of T_{max} on carrier concentrations and Si contents in grown ingots will be described and discussed. Syntheses were performed under the following conditions: $T_{\text{pb}} = 500^\circ\text{C}$, $P_P = 7$ atm, and $T_{\text{max}} = 1050^\circ\text{C}$ – 1180°C . The InP ingots grown under these conditions were fully stoichiometric excepting the last-to-freeze end at which excess indium remained. Figure 2 shows a typical grown ingot weighing 250g. Samples for electrical measurements were sliced perpendicular to the growth direction from each position of the ingots. Figure 3 shows carrier concentration profiles along the growth direction in the ingots grown at different T_{max} . It can be seen that, with increasing T_{max} , the carrier concentration increases drastically and its distribution becomes flat. To confirm that the increase in carrier concentration with increasing T_{max} is due to an increase in Si content in the ingots, spark source mass spectrographic analyses for the ingots were performed. The analytical results for typical two samples as indicated by numbered squares in Fig. 3 are pre-

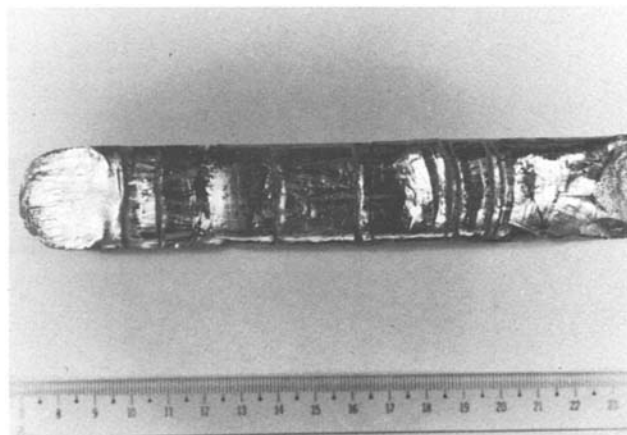


Fig. 2. A typical polycrystalline InP ingot grown, weighing 250g

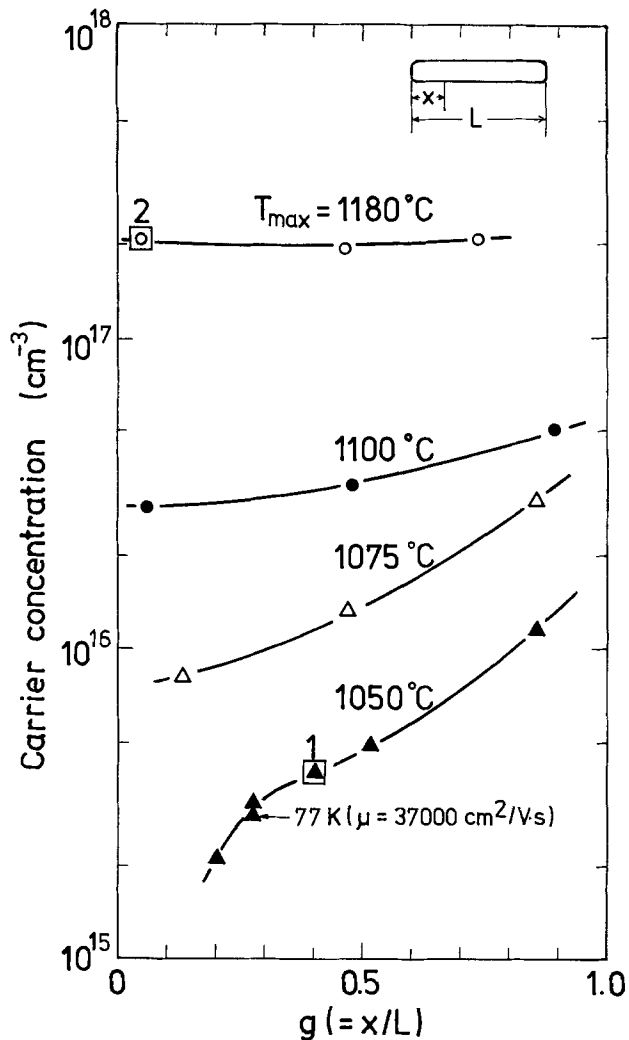


Fig. 3. Carrier concentration profiles along the growth direction for ingots grown at different maximum temperature in the indium melt (T_{\max}).

sented in Table I. A remarkable difference in Si concentrations between both samples are found, whereas no significant differences in concentrations of other impurities are found. Furthermore, no other donor impurities than Si are detected and the Si concentrations are in good agreement with the carrier concentrations. From these results, it is concluded that Si contents incorporated during synthesis dominate the carrier concentrations in the grown ingots and, also, that the increase in T_{\max} drastically enhances the reaction for Si contamination. Although high concentrations of C, N, and O were detected, they are thought to be incorporated during the sample preparation processes for the analysis.

The results shown in Fig. 3 also show that carrier concentrations as low as those in PBN-grown InP (3) can be obtained at a comparable growth rate (3-4 mm/hr) even if quartz boats are used. Hall data for

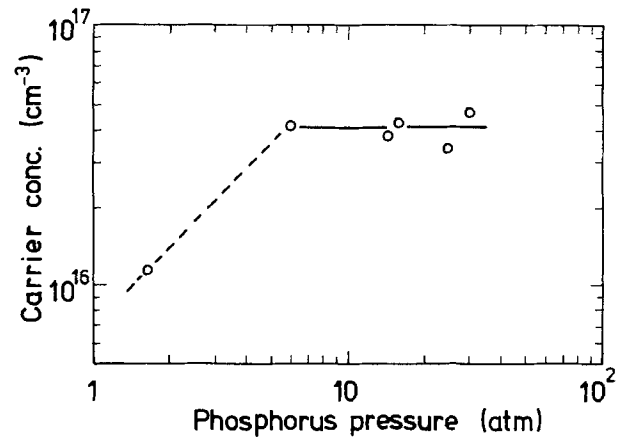


Fig. 4. Carrier concentrations at the first-to-freeze portion of grown ingots as a function of phosphorus pressure (P_P).

a typical ingot are $N_d - N_a = 3.2 \times 10^{15} \text{ cm}^{-3}$ and $\mu_{77\text{K}} = 37,000 \text{ cm}^2/\text{V}\cdot\text{sec}$.

It is obvious that curves in Fig. 3 do not represent the segregation behavior of Si because the distribution of Si is governed by the Si contamination process. The increase in "apparent" effective distribution coefficient with increasing Si content incorporated is a phenomenon commonly observed in this study. The segregation behavior will be discussed in the next section.

Next, a phosphorus pressure dependence of the carrier concentration in the grown ingot will be described. The ingots were grown under the following conditions: $T_{\text{pb}} = 800^\circ\text{C}$, $T_{\max} = 1100^\circ\text{C}$, and $P_P = 1.5\text{-}30 \text{ atm}$. When the synthesis was carried out using 200g of charged indium, inclusions of excess indium were contained in the ingots grown at P_P lower than about 5 atm. To avoid the In inclusions, it was necessary to reduce either the growth rate or the amount of charged indium. In this experiment, the amount of charged indium was reduced to 20g and, consequently, ingots free from inclusions were obtained at P_P in the range of 1.5-30 atm. Carrier concentrations at the first-to-freeze portions of grown ingots are plotted in Fig. 4 as a function of P_P . The effect of P_P on the carrier concentration is not as large as that of T_{\max} . The carrier concentration scarcely depended on P_P in the range of 5-30 atm. At lower P_P than about 5 atm, the carrier concentration seemed to depend on P_P . Similar P_P dependence of carrier concentration was found for InP crystals grown by the synthesis solute-diffusion method ($P_P = 0.6\text{-}1.2 \text{ atm}$) (8). Therefore, it is reasonable to assume that Si contamination level increases with increasing P_P , and becomes saturated at higher P_P ($\geq 5 \text{ atm}$).

We found that carrier concentrations in grown ingots were different depending on lot or supplier of the charged indium even if T_{\max} and P_P were fixed to certain values, as shown in Fig. 5. Differences in the carrier concentration profiles in Fig. 5 were found to be closely related to differences in degree of oxidation of the charged indium. The lowest profile was obtained for the ingot synthesized using the most heavily oxidized indium. The degree of oxidation of the charged

Table I. Spark source mass spectrographic analyses of nominally undoped InP ingots

| Sample (carrier conc.) | Impurity concentration (ppma) | | | | | | | | | |
|---|---|-----|------|-----|-----|-----|------|---|---|---|
| | Si | Sn | S | Te | Zn | Mg | Cu | C | N | O |
| No. 1 ($4 \times 10^{15} \text{ cm}^{-3}$) | 0.4 ($1.6 \times 10^{15} \text{ cm}^{-3}$) | ND* | ND** | ND* | 0.4 | 0.5 | 0.06 | 6 | 1 | 6 |
| No. 2 ($2 \times 10^{17} \text{ cm}^{-3}$) | 15 ($6 \times 10^{17} \text{ cm}^{-3}$) | ND* | ND** | ND* | 0.2 | 0.6 | 0.04 | 5 | 4 | 8 |

ND*: <0.1 ppma, ND**: <0.05 ppma.

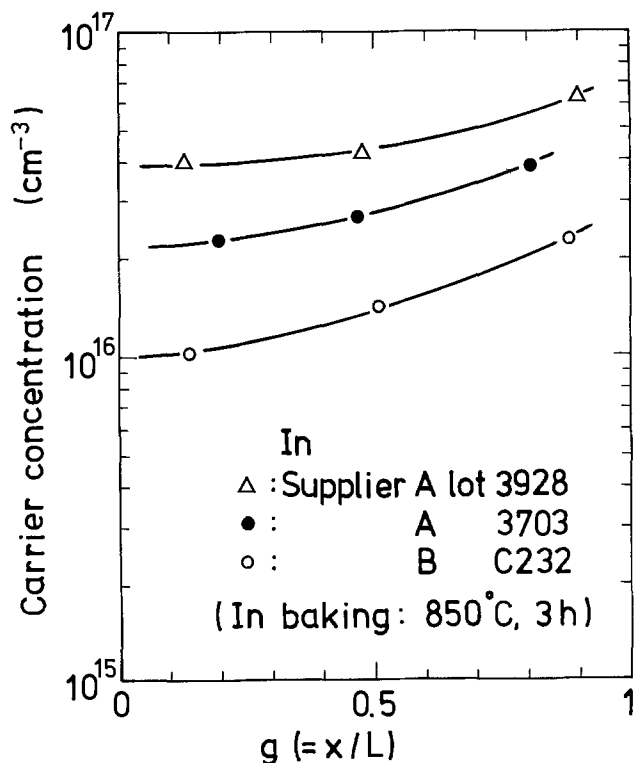
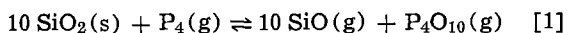


Fig. 5. Carrier concentration profiles for ingots grown by using charged indium of different lots or suppliers. Synthesis conditions are same for all samples.

indium was examined by an amount of a scum formed on a molten indium. This fact suggests that oxides of indium included in the charged indium have effects on the Si contamination process. Therefore, we tried to eliminate indium oxides contained in the charged indium, and examined effects of the elimination on the carrier concentration. The elimination was made by prebaking the charged indium in vacuum before synthesis. The prebaking temperature T_{pb} was varied from 450° to 950°C. All charged indium used here were from the same lot. The ingots were grown by using 200g of charged indium under the following conditions; $P_P = 8$ atm and $T_{max} = 1100^\circ\text{C}$. Figure 6 shows carrier concentration profiles for the ingots grown by using the charged indium baked at different T_{pb} . With increasing T_{pb} , the carrier concentration increases and its distribution becomes flat. Especially, a remarkable difference is observed in carrier concentrations between $T_{pb} = 700^\circ\text{C}$ and 800°C . This difference can be explained by the difference in removal rates of indium oxides at both temperatures, because indium oxides such as In_2O_3 , In_2O , or InO are sublimated or decomposed in vacuum at temperatures higher than about 800°C . From these results, it can be concluded that indium oxides in the charged indium suppress the reactions causing Si contamination. The effect of indium oxides on the reaction causing Si contamination can be understood qualitatively as follows. According to Bachmann *et al.* (1), an SiO vapor as a source for Si contamination is provided via the reaction



When indium oxides are present in the charged indium, they will be reduced by phosphorus vapor and a P_4O_{10} vapor will be produced prior to the reduction of SiO_2 . An increase in P_4O_{10} partial pressure in the ampul by the reduction of the indium oxides can force reaction [1] to proceed to the left-hand side, i.e., suppress the production of SiO vapor.

When the charged indium was prebaked in vacuum, most of the indium oxides were transported to a lower temperature region in the ampul. The presence of in-

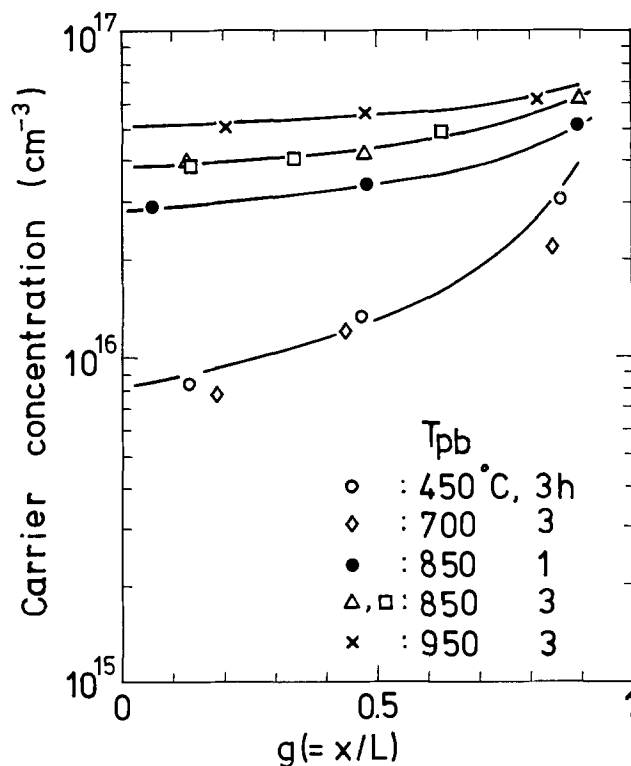


Fig. 6. Carrier concentration profiles for ingots grown by using charged indium prebaked at different temperature (T_{pb}).

dium oxides at a lower temperature region during synthesis had no effect on carrier concentrations in grown ingots. This fact means that the reduction of indium oxides, as well as the reduction of silica, by phosphorus vapor requires a high temperature ($\sim 1000^\circ\text{C}$).

Effective distribution coefficient for Si in InP, $k_e(\text{Si})$.—As described in the previous section, distributions of Si concentration in nominally undoped ingots are remarkably different depending on the Si contamination level. Therefore, it is meaningless to evaluate $k_e(\text{Si})$ for those ingots. We prepared Si-doped ingots with carrier concentrations higher than 10^{18}cm^{-3} to examine $k_e(\text{Si})$. The ingots were grown under the following conditions: $T_{pb} = 700^\circ\text{C}$, $T_{max} = 1050^\circ\text{C}$, and $P_P = 7$ atm. For successful Si doping, it was necessary to dissolve completely the Si pieces into the indium melt before the synthesis. When the Si pieces floated on the surface of the indium melt during the synthesis, they were attacked by phosphorus vapor and transferred to a low temperature region in the ampul and, consequently, Si doping was unsuccessful.

Typical carrier concentration profiles for Si-doped ingots along the growth direction are shown in Fig. 7. Doping efficiencies of Si for these ingots were about 50%. It is reasonable to assume that the profiles represent the segregation behavior of Si because the Si contamination levels in these ingots are estimated, from the growth conditions, to be lower than $2 \times 10^{16} \text{cm}^{-3}$. The profiles obey the normal freezing relationship and their slopes give $k_e(\text{Si}) = 0.53$. Figure 7 also shows carrier concentration profiles in LEC single crystals grown by using the nominally undoped ingots described in the previous section. We found that the average carrier concentrations in the LEC crystals were in good agreement with those in the starting materials (9). The profiles for the LEC crystals also obey the normal freezing relationship and have a same slope as that for the Si-doped ingots. These facts indicate that the carrier concentrations in the LEC crystals are dominated by Si contents involved in the starting materials.

Summary

We studied experimentally Si contamination of polycrystalline InP ingots synthesized using quartz boats

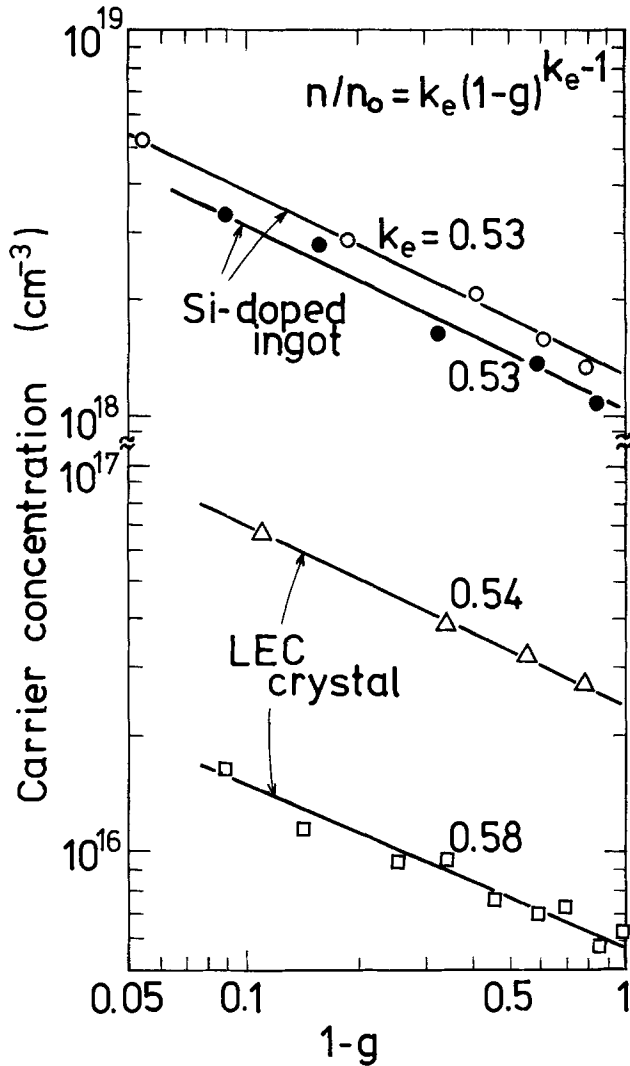


Fig. 7. Carrier concentration profiles for Si-doped ingots and for LEC crystals grown by using nominally undoped ingots. All curves obey the normal freezing relationship.

via the horizontal Bridgman technique. Silicon contamination levels were evaluated by measurements of carrier concentrations and by spark source mass spectrographic analyses. Good agreements between carrier concentrations and Si contents were obtained. Dependences of the Si contamination level on the synthesis conditions such as maximum temperature in the indium melt, phosphorus pressure in the ampul, and prebaking temperature of the charged indium were investigated. Among these conditions, maximum temperature in the indium melt was found to be the most dominant factor. Silicon contamination levels scarcely depended on phosphorus pressure in the range of 5-30 atm, while they decreased at lower phosphorus pressure than about 5 atm with decreasing phosphorus

pressure. With increasing prebaking temperature of the charged indium, Si contamination levels were increased. This result is explained by taking into account the fact that indium oxides in the charged indium, which suppress the reaction for Si contamination, are eliminated through the prebaking process.

As a result of the investigations described above, it has been enabled to prepare high purity InP ($N_d - N_a = 3.2 \times 10^{15} \text{ cm}^{-3}$, $\mu_{77K} = 37,000 \text{ cm}^2/\text{V} \cdot \text{sec}$) at a growth rate of 3 mm/hr even if quartz boats are used.

To examine the segregation behavior of Si in InP, we also prepared intentionally Si-doped ingots in which Si contamination levels were neglected as compared with Si doping levels. Carrier concentration profiles for these ingots along the growth direction obeyed the normal freezing relationship and, consequently, gave the effective distribution coefficient for Si in InP, $k_e(\text{Si}) = 0.53$. Carrier concentration profiles for LEC single crystals grown by using nominally undoped ingots contaminated by Si also obeyed the normal freezing relationship and had a same slope as that for the Si-doped ingots. This result indicates that carrier concentrations in the LEC crystals are dominated by Si contents involved in the starting materials.

Acknowledgment

The authors would like to thank Dr. N. Niizeki, Dr. H. Takata, and Dr. K. Kudo for their encouragement and support through this work, and Mr. C. Honma, Musashino Electrical Communication Laboratory, for spark source mass spectrographic analysis.

Manuscript submitted May 21, 1980; revised manuscript received Oct. 17, 1980.

Any discussion of this paper will appear in a Discussion Section to be published in the December 1981 JOURNAL. All discussions for the December 1981 Discussion Section should be submitted by Aug. 1, 1981.

Publication costs of this article were assisted by Nippon Telegraph and Telephone Public Corporation.

REFERENCES

1. K. J. Bachmann, E. Buehler, J. L. Shay, and D. L. Malm, "Gallium Arsenide and Related Compounds 1974," (Inst. Phys. Conf. Ser. No. 24) p. 21 (1975).
2. K. J. Bachmann, L. Clark, Jr., E. Buehler, D. L. Malm, and J. L. Shay, *J. Electron. Mater.*, **4**, 741 (1975).
3. R. L. Henry and E. M. Swiggard, *ibid.*, **7**, 647 (1978).
4. G. A. Antipas, "Gallium Arsenide and Related Compounds 1976," (Inst. Phys. Conf. Ser. No. 33b) p. 55 (1977).
5. J. B. Mulline, A. Royle, B. W. Straughan, P. J. Tuffton, and E. W. Williams, *J. Cryst. Growth*, **13/14**, 640 (1972).
6. G. G. Baumann, K. W. Benz, and M. H. Pilkun, *This Journal*, **123**, 1232 (1976).
7. K. J. Bachmann and E. Buehler, *ibid.*, **121**, 835 (1974).
8. A. Yamamoto and C. Uemura, *Jpn. J. Appl. Phys.*, **17**, 1869 (1978).
9. C. Uemura, S. Shinoyama, A. Yamamoto, and S. Tohno, Proceedings of ICCG-6, To be published.

Optical Properties of GaAs and Its Electrochemically Grown Anodic Oxide from 1.5 to 6.0 eV

D. E. Aspnes,* G. P. Schwartz,* G. J. Gualtieri, A. A. Studna, and B. Schwartz*

Bell Laboratories, Murray Hill, New Jersey 07974

ABSTRACT

Spectroscopic ellipsometry has been used to nondestructively study the optical and interface properties of the GaAs-electrochemically grown anodic oxide system over the energy range 1.5-6.0 eV. Values of the dielectric function of GaAs differ by up to 30% from previously published spectra due to improved sample preparation techniques. Values of the dielectric function of the oxide agree within several percent with previous measurements. Upper limits to the thickness of a layer modeled as amorphous arsenic (a-As) at the GaAs-oxide interface are 3 and 10Å for 60 and 75V oxides grown on $\langle 111 \rangle_B$ and $\langle 100 \rangle$ surfaces, respectively, at 0.1 mA cm⁻² constant current in a phosphoric acid/glycol based electrolyte. The major discrepancy between measurements and ideal three-phase model calculations arise from the interface region between oxide and ambient. This region shows a total distributed density deficit equivalent to 10Å lost material, probably due to leaching of As₂O₃. A complete description of the optical properties of the oxide requires a small absorptive component in the nominally transparent energy range below 4.5 eV. This absorptive component is equivalent to 0.2% and 0.9% by volume of a-As for the 60 and 75V oxides, respectively. The infrared refractive indexes for the two oxides, calculated from a Sellmeier dispersion relation with the absorptive component removed, are 1.777 and 1.717, respectively.

Intrinsic advantages of GaAs as a material for high-speed electronic devices have stimulated widespread research to develop a passivating oxide by thermal, plasma, and electrochemical anodization techniques. However, the composition, uniformity, and interface properties of native oxides on GaAs all depend rather strongly on the method by which the oxides are prepared. Thermally grown oxides consist almost entirely of Ga₂O₃ owing to the volatility of As and As₂O₃ at typical growth temperatures (1-4). Plasma-grown oxides are primarily mixtures of Ga₂O₃ and As₂O₃, but show accumulations of elemental As in both bulk and interface regions (3, 5-9). Although bulk uniformity and interface widths in electrochemically grown anodic oxides also depend on electrolyte and anodization conditions (10-12), recently reported Raman studies of thermal (13), plasma (14), and electrochemical (14) grown oxide films on GaAs indicate that the elemental arsenic content of the as-grown electrochemically formed oxides can be suppressed for low current density growth. A second feature associated with lowering the current density, and consistent with the Raman scattering results, appears to be a decrease in the width of the oxide-substrate interface region for electrochemically grown anodic oxides (12).

Preliminary reductions of complex reflectance ratio ($\tan\psi$, $\cos\Delta$) spectra that we measured for electrochemically grown anodic oxides supported the above conclusions, and indicated that nonuniformity and interface effects could be as much as an order of magnitude smaller than those observed in our previous work on films produced by rf-plasma (8, 9) and constant-voltage electrochemical (15) anodization methods. This suggested that more accurate values of the intrinsic dielectric response of anodic oxide films could be obtained. These data not only would be of interest in their own right, but also would serve as input data for determining more accurately from their dielectric response the composition, density, interface, and other microstructural parameters of other native oxides grown by different techniques. Moreover, since our previous investigations (15), methods using automatic spectroscopic ellipsometers have been developed (16,

17) for assessing the effectiveness of chemical stripping and cleaning procedures in real time, allowing dielectric function data that are more accurate than previously published spectra (18) to be obtained for the GaAs substrate material. Because these substrate data are used to determine interface and oxide parameters, more accurate analysis is made possible. Finally, we wished to establish new limits to the widths and possible compositions of the interface regions of the electrochemically grown oxides, taking advantage of the sensitivity of spectroscopic ellipsometry to these parameters (7-9, 19).

Since dielectric dispersion data are not available for both Ga₂O₃ and As₂O₃, we found it necessary to generalize the procedure that was previously developed for interface analysis with spectroscopic ellipsometry as it was applied to the thermally grown oxide on Si (20). This was done by using a Sellmeier representation to separate the slowly varying intrinsic dielectric response of the oxide from the more rapidly varying interface-related residual interference oscillations that appear in an approximate three-phase model solution. Thus both oxide and interface parameters could be obtained. This more general approach should also be useful for other oxide systems which can only be obtained in thin film form and for which bulk analytic dispersion expressions have not or cannot be determined.

Experimental

In this work, we analyze in detail two oxide films grown under 0.1 mA cm⁻² constant current conditions in a phosphoric acid/glycol-based [AGW (21)] electrolyte. The substrates used were n-type GaAs single crystals with carrier concentrations 2×10^{16} cm⁻³ and $\sim 1 \times 10^{18}$ cm⁻³. The surface orientation of the lightly doped sample was $\langle 111 \rangle_B$ and that of the heavily doped sample was $\langle 100 \rangle$. Surfaces were prepared by chemomechanical etch-polishing in bromine-methanol solutions. Surface quality was checked by measuring pseudo-(apparent) dielectric function spectra of chemically etched samples prior to anodization. Anodization was performed under white-light illumination to flood the space-charge region with carriers and eliminate any doping dependence of the anodization process. Final oxide thicknesses were ~ 1200 and

* Electrochemical Society Active Member.
Key words: ellipsometry, dielectrics, interface.

$\sim 1500\text{\AA}$ corresponding to limiting potentials of 60 and 75V for the lightly and heavily doped samples, respectively.

Optical data were obtained from 1.5 to 6.0 eV with an automatic spectroscopic ellipsometer described in detail elsewhere (22). The angle of incidence was 67.08° . The data were corrected for the optical activity of the quartz Rochon polarizers (23). Anodized samples were rinsed with methanol prior to measurement. Substrate spectra were obtained after chemically stripping the anodic films in a 1:1 mixture of HCl/methanol. This procedure yielded the highest ϵ_2 value [cleanest, least disordered, and/or microscopically smoothest surface (17)] at the 4.75 eV E_2 peak for these substrates. The peak ϵ_2 values after anodizing and stripping were ~ 0.5 higher than the corresponding values before anodizing, indicating that the anodizing/stripping sequence was improving surface quality (24). To minimize oxidation and contaminant adsorption effects, all chemical processing steps were performed with the samples already aligned in the ellipsometer and enclosed in a dry N_2 atmosphere in a windowless cell. $\tan\psi$, $\cos\Delta$, and pseudodielectric function spectra were obtained for the anodized and nominally bare stripped samples, respectively.

Optical Analysis

The basic procedure for determining interface properties from spectroscopic ellipsometric data was developed initially for application to the Si-SiO₂ system and is discussed in detail elsewhere (8, 20, 25). Briefly, in the previous work dielectric function data for crystalline Si, fused quartz, and various possible interface materials were used to calculate in an n-phase laminar model $\tan\psi$, $\cos\Delta$ spectra from 1.5 to 5.8 eV in terms of three frequency-independent free parameters, d_{ox} , f_v , and d_{int} . These free parameters represented the thickness and void fraction (density deficit) of the oxide and the thickness of the interface region, respectively. The calculated spectra were then compared to the measured spectra, with the best-fit values of the free parameters and the residual mean square deviation being determined systematically and objectively by linear regression analysis (LRA) (26). The LRA analysis also provided correlation coefficients and 90% confidence limits to show whether the data were in fact determining the parameters in addition to showing how well the models were fitting the data.

For the Si-SiO₂ system, the method was based on the existence of an accurate analytic Sellmeier expression for the dielectric response of fused quartz (27), which was used with the density deficit parameter f_v to represent the dielectric response of the SiO₂ overlayers. Although Sellmeier expressions have been given for GaAs oxide films (28, 29), the known sensitivity of oxide properties to preparation method suggests that a better approach in the absence of accurate bulk data would be to determine the Sellmeier coefficients themselves in the data reduction process. This is the procedure that we develop here.

Why should a Sellmeier representation be necessary? In principle, the dielectric response of the oxide can be obtained directly by solving the three-phase (substrate, oxide, ambient) laminar model given the $\tan\psi$, $\cos\Delta$ spectra and the dielectric functions of substrate and ambient. For example, the measured $\tan\psi$, $\cos\Delta$ spectra of the 60V AGW oxide on the $\langle 111 \rangle$ -B GaAs substrate shown in Fig. 1 and the approximate bulk dielectric response of this substrate shown in Fig. 2 can be used in the ideal three-phase model to calculate the approximate dielectric function of the oxide as shown in Fig. 3. Here, the thickness $d_{ox} = 1203\text{\AA}$ was chosen to make ϵ_2 "zero" in the transparency region below 4.5 eV. These results are calculated without regard to interface effects because the three-phase model supposes mathematically sharp boundaries.

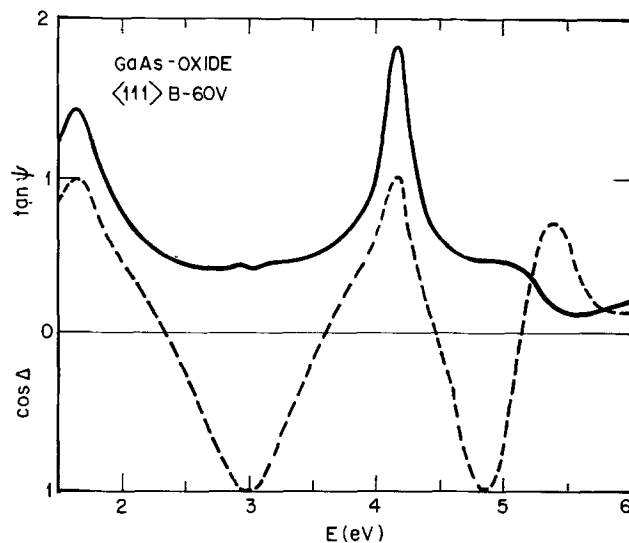


Fig. 1. $\tan\psi$, $\cos\Delta$ spectra for a $\langle 111 \rangle$ -B GaAs sample electrochemically anodized to 60V.

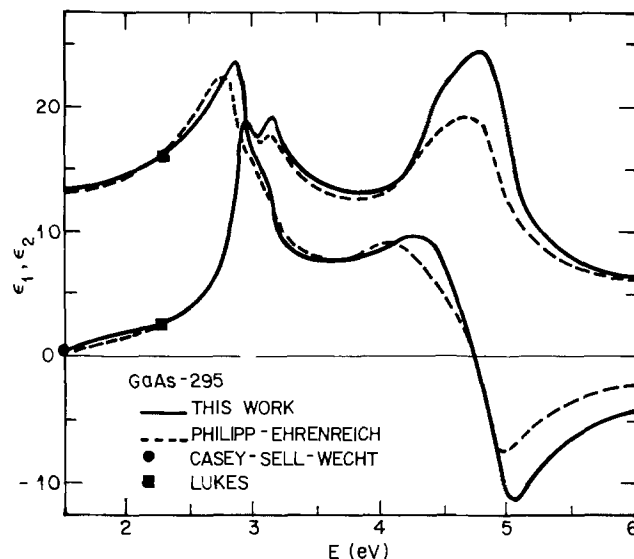


Fig. 2. Ellipsometrically determined dielectric response of the GaAs substrate for the sample of Fig. 1. Also shown for comparison are previous spectra [after Ref. (18)] and single-wavelength results [after Ref. (34) and (35)].

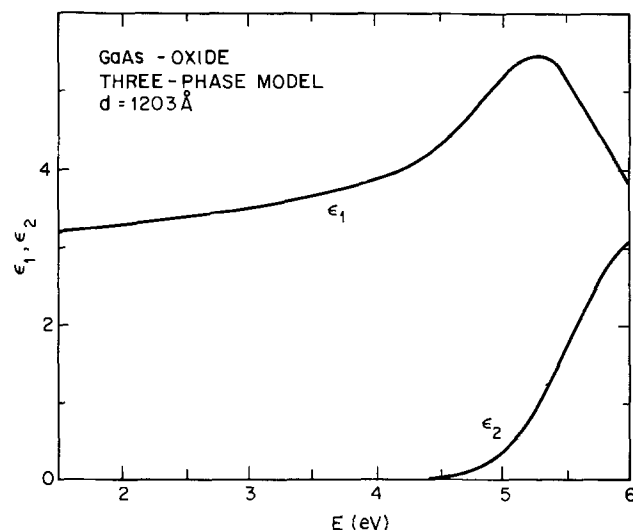


Fig. 3. Approximate dielectric response of a $\langle 111 \rangle$ -B-60V anodic oxide calculated in the three-phase model from the data of Fig. 1 and 2.

In fact, ϵ_2 is not zero but rather exhibits small oscillations about a slowly varying background. This can be seen clearly in Fig. 4, which shows the ϵ_2 results of Fig. 3 on an expanded scale. The period of the oscillations follows the thickness (compare 60V $\langle 111 \rangle$ B and 75V $\langle 100 \rangle$ oxide calculations), which shows that they are not part of the intrinsic response of the oxide. Rather, they appear because the three-phase model, with its mathematically sharp boundaries, does not fully describe this system. As previously discussed (8), these oscillations arise from the growth and collapse of s- and p-polarized standing waves within the oxide as the wavelength is scanned. The standing waves modify the field strengths at the film boundaries and consequently the sensitivity to the interface regions. They therefore carry the information desired about the interface regions. Qualitatively, Fig. 4 appears to show that the interface regions of the 60V $\langle 111 \rangle$ B AGW oxide are narrower than those of the 75V $\langle 100 \rangle$ oxide, but not so narrow as those of the Si-SiO₂ system (20) whose data are also shown for comparison. In fact, we shall show that the major source of the oscillations for the GaAs-oxide system is the oxide-ambient interface region, and that the GaAs-AGW oxide interface region is actually narrower than that between Si and its thermally grown oxide.

To analyze these data for the properties of the interface regions, it is clear that these oscillations must be separated from the slowly varying intrinsic dielectric response of the oxide. Because the oscillations are very small for the 60V oxide, of the order of 1% of $|\epsilon|$, the three-phase-model solution is already a fairly good approximation to the intrinsic response. Accordingly, for simplicity we first use LRA to fit a Sellmeier function to the three-phase solution for ϵ_1 in the region of transparency below 4.5 eV and therefore average out the oscillations that contain the interface information. ϵ_2 in the same region is simply set equal to zero. These analytic expressions are now used as the initial approximation to the oxide response.

A complete description of the oxide film (excluding interface regions) can now be accomplished over the region of transparency with the Sellmeier expression and three frequency-independent free parameters representing, respectively, the oxide thickness, d_{ox} , a volume void fraction or distributed density deficit, f_v , and a volume fraction of optically absorbing material, f_a . The total dielectric response of the oxide film can then be calculated by effective-medium theory (30) using these parameters, the Sellmeier expression for the approximate "intrinsic" response of the oxide, $\epsilon = 1 + i0$ for the voids, and a suitable representation for the dielectric response of the optically absorbing com-

ponent. Based on available data for this system, we choose the latter to be given by that of amorphous arsenic (a-As) (31), in which case $f_a = f_{a-As}$.

The reason for treating an optically absorbing component as an extrinsic feature can be understood by examining the absorptive tails in ϵ_2 in Fig. 4. These differ in all three cases, which shows that optical absorption is clearly not part of the intrinsic response of the oxide. The justification for f_v is less obvious. It concerns the boundary condition that d_{ox} shall be chosen so ϵ_2 is "zero" in the transparency region. This condition obviously cannot be satisfied over the entire transparency range because of the small interface oscillations. Model calculations quickly show that these oscillations may average about zero, or above zero, or below zero depending on interface compositions and widths. The requirement that ϵ_2 oscillate about zero is a fact completely arbitrary, and to make it imposes unintended constraints on the solution.

Now because the optical thickness $n_{ox}d_{ox} = \sqrt{\epsilon_{ox}}d_{ox}$ is the fundamental parameter describing interference effects in a thin transparent film, it is clear that changing d_{ox} to properly position ϵ_2 with respect to zero will also affect ϵ_1 since the energy at which interference structures occur is also fixed by the properties of the film. Thus ϵ_1 must be decoupled from d_{ox} . This is the purpose of f_v , which acts essentially as a simple scaling parameter, but one which also describes the amount of polarizable material per unit volume in the film. By incorporating f_v into the model we have generalized the boundary condition to the simple requirement that the interface oscillations shall vanish in the correct laminar model solution for the oxide properties. We re-emphasize that the use of an intermediate Sellmeier representation with corrections as outlined above is legitimate because the GaAs-AGW oxide system is already well approximated by the three-phase model, and that the interface corrections are very small.

Results

Dielectric function of GaAs.—The dielectric function that we consider to be most representative of the bulk dielectric response of the 2×10^{16} cm⁻³, $\langle 111 \rangle$ B-oriented n-type substrate used for the 60V anodization, and therefore that most appropriate for interface analysis, is shown in Fig. 2. This was obtained by *in situ* stripping of the AGW oxide with 1:1 HCl/methanol solution. The peak value observed for ϵ_2 was 23.89 at 4.75 eV. To obtain a better estimate of the intrinsic dielectric response of the substrate in the absence of etching-induced surface disorder, an additional 2Å of a-GaAs (32) was removed mathematically, bringing the ϵ_2 peak to 24.34. A direct experimental proof of the existence of such a disordered layer is not possible, but its presence can be inferred from similar measurements on Ge (33) and because the "bare substrate" dielectric function so obtained gave a somewhat lower residual in the interface analysis.

Whether the dielectric function obtained here accurately represents the intrinsic dielectric response of pure single crystal GaAs is a separate question and one more difficult to assess, but we believe that the ϵ spectra in Fig. 2 do so to within 5%. Bromine-methanol polished and anodized $\langle 111 \rangle$ B samples could be stripped with HCl/methanol, HCl/H₂O, or NH₄OH/H₂O solutions and consistently produced peak ϵ_2 values in the 23.0-23.9 range. By the "biggest-is-best" criterion (16, 17) the spectra corresponding to the largest peak value is the best approximation to the true response. Differences may represent surface roughness on a microscopic scale; the highest ϵ_2 values were generally observed by stripping once, with repeated treatments usually resulting in a gradual decline. This history-dependent sample behavior shows that in general the dielectric function spectrum actually used for analysis of very thin interfaces must be that measured on the

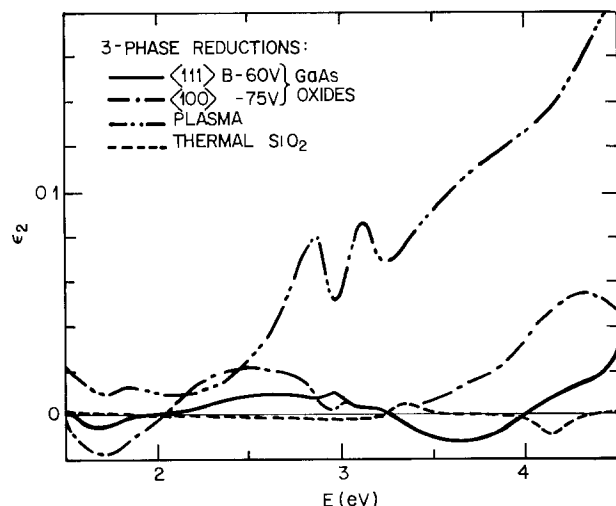


Fig. 4. Energy dependence of ϵ_2 on an expanded scale for selected oxide films in the region of transparency of oxides on GaAs.

stripped sample itself, and not taken from a different sample or from the literature.

Also shown for comparison in Fig. 2 are the previous best spectra for GaAs, obtained from a Kramers-Kronig transform of reflectance data measured over the range 1-27 eV (18). The differences in energy positions of the structures are probably due to the fact that the ellipsometric data were obtained with a 17 meV energy spacing, approximately one-third that of the reflectance data. Consequently, the ellipsometric data were able to follow the intrinsic GaAs structure more faithfully. The substantial discrepancy in absolute values is almost certainly due to the presence of natural oxide or contamination layers on the reflectance samples, which could not be stripped *in situ* as were the ellipsometric samples.

Other single-wavelength values also shown in Fig. 2 are those of Casey *et al.* (34) who found $\alpha = 1.6 \times 10^4 \text{ cm}^{-1}$ at 1.5 eV compared to our value of $1.5 \times 10^4 \text{ cm}^{-1}$, and Lukes (35), who obtained $\epsilon = (16.11 \pm 0.08) + i(2.41 \pm 0.40)$ at 5461Å (2.27 eV), compared to our value $16.13 + i2.80$. The agreement is satisfactory. We add that the ϵ_1 and ϵ_2 spectra obtained here were Kramers-Kronig consistent to better than 0.5%.

Approximate dielectric function of GaAs oxide.—The substrate dielectric function described above was used in the three-phase model to obtain the approximate dielectric response shown in Fig. 3. We now fit a four-term Sellmeier dispersion curve of standard form

$$\epsilon_1(E) = 1 + \sum_{i=1}^4 \frac{E_{gi}E_{oi}}{E_{gi}^2 - E^2} \quad [1]$$

to these data over the region of transparency. Two of the values E_{gi} are fixed by the known energies of the centroids of the lattice transitions at $E \approx 600 \text{ cm}^{-1} \approx 0.075 \text{ eV}$ (28, 36) and the ultraviolet bonding-antibonding transitions at $E \approx 16 \text{ eV}$ (37).

The value of E_{o1} that pertains to lattice absorption follows immediately from E_{g1} and the difference between the infrared dielectric constant [$\epsilon_\infty \sim 3.20$ (28)] and the 1 kHz dielectric constant ($\epsilon_0 \sim 8.2$) (38), that is, $E_{o1} \approx 0.35 \text{ eV}$. This presumes a contribution no greater than a few percent from water contained within the as-grown oxide, as seems reasonable from infrared absorption measurements on similar oxides (28), although the assumption is noncritical because this term has very little effect in the visible-near u.v. spectral range. Because the dispersion representation must describe near-edge absorption, Fig. 3 shows that 5.5 eV is a natural choice for E_{g2} . E_{g3} is essentially arbitrary, but a value of 7.5 eV will adequately describe midrange absorption.

The remaining three parameters are the amplitudes E_{o2} , E_{o3} , and E_{o4} . We determine them by fitting Eq. [1] by LRA to the real part of ϵ_1 in Fig. 3 from 1.5 to 4.8 eV, obtaining $1.62 \pm 0.27 \text{ eV}$, $5.5 \pm 1.9 \text{ eV}$, and $18.8 \pm 3.7 \text{ eV}$, respectively. The large uncertainties in E_{o3} and E_{o4} do not result from a poor fit, but rather originate because the third and fourth oscillators are highly correlated ($C_{34} = -0.994$). Since these values simply define a starting point for interface analysis, we shall

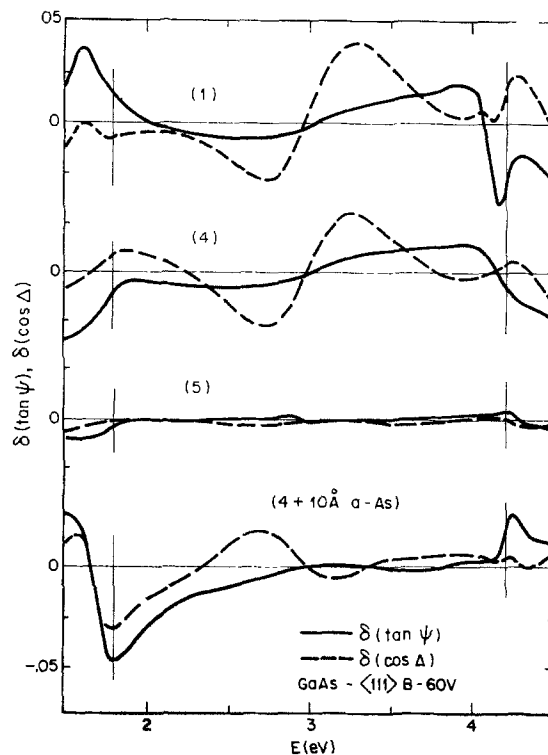


Fig. 5. Spectral dependences of discrepancies between experimental and theoretical spectra for various models for the $\langle 111 \rangle$ B-60V AGW oxide on GaAs: (top) 1-parameter model, using the Sellmeier oxide thickness as the single free parameter; (upper middle) 4-parameter model including an a-As interface, voids, and a-As in the oxide; (lower middle) as above, but including a density-deficient outer region; (lower) as above but with 10Å of a-As assumed at the GaAs-oxide interface.

defer a discussion about the fitted values until the section "Intrinsic oxide response."

Interface analysis.—Wavelength-dependent discrepancies between the $\tan \psi$, $\cos \Delta$ data of Fig. 1 and the predictions of selected models are shown for the electrochemically grown 60V anodic oxide in Fig. 5. Model parameters for this oxide are listed in Table I.

The simplest model assumes that the Sellmeier expression derived in the preceding section is directly applicable and that there are no interfaces. Then the only free parameter is the oxide thickness, d_{ox} . This is determined by LRA to be $1197.5 \pm 0.5 \text{ Å}$ with a residual 0.020 as summarized in Table I. The actual fitting was done over the range 1.8-4.2 eV to eliminate the effects of experimental artifacts at the low-intensity long-wavelength limit of the ellipsometer, and to eliminate intrinsic oxide absorption at higher energies which is not included in the Sellmeier model. The range is indicated by the vertical lines in Fig. 5. Neither $\tan \psi$ nor $\cos \Delta$ has its wavelength dependence predicted very accurately, but this is not surprising since interface effects are completely neglected. The result essentially establishes a point of reference from which to judge more elaborate models. It should be noted

Table I. Values of free parameters, 90% confidence limits, and residuals for models of an anodic oxide electrochemically grown to 60V on a $\langle 111 \rangle$ B GaAs substrate with $N_0 \sim 2 \times 10^{16} \text{ cm}^{-3}$

| Model | Inner interface | | | | Outer interface | | | Residual $10^3 \delta$ |
|-------|-----------------|-----------------|-----------------|---------------------|-------------------|-------------|-----------------|---------------------------|
| | Composition | d (Å) | $10^3 f_{a-As}$ | Oxide $10^3 f_v$ | d (Å) | Composition | d (Å) | |
| (1) | — | — | — | — | 1197.5 ± 0.5 | — | — | 20.0 |
| (2) | — | — | — | -2.9 ± 3.9 | 1195.3 ± 3.2 | — | — | 19.6 |
| (3) | — | — | 1.8 ± 0.6 | 20.5 ± 7.9 | 1212.16 ± 6.0 | — | — | 15.4 |
| (4) | a-As | -0.9 ± 1.9 | 1.4 ± 0.8 | 19.3 ± 8.1 | 1211.9 ± 6.1 | — | — | 15.3 |
| (5) | a-As | 0.31 ± 0.29 | 2.1 ± 0.1 | 14.9 ± 1.1 | 1151.8 ± 1.9 | 15% void | 67.6 ± 2.1 | 2.08 |
| (6) | — | — | 2.0 ± 0.1 | 14.6 ± 1.2 | 1151.8 ± 2.1 | 15% void | 67.6 ± 2.3 | 2.11 |
| (7) | a-As | 0.22 ± 0.30 | 1.8 ± 0.1 | 15.5 ± 1.3 | 1178.1 ± 1.5 | 25% void | 43.3 ± 1.6 | 2.37 |
| (8) | a-As | 0.18 ± 0.32 | 2.4 ± 0.4 | 15.1 ± 0.3 | 1121.2 ± 3.1 | 10% void | 96.9 ± 3.3 | 2.46 |
| (9) | a-As | 10Å (fixed) | 5.3 ± 1.0 | 13.8 ± 10.5 | 1136.4 ± 19.6 | 15% void | 77.6 ± 21.9 | 20.3 |

that the maximum excursion in $\delta(\tan\psi)$ is only 2% of the peak value in Fig. 1, re-emphasizing our earlier point that the three-phase model is already a very good approximation by the usual standards applied to ellipsometric data.

As the model is made more general by allowing a density change and an absorptive fraction in the oxide, very little improvement occurs as shown in Table I. Virtually no change occurs upon introducing the void fraction f_v , but that is expected because the initial solution from which the Sellmeier coefficients were determined had already set a zero-order density scale. A 25% reduction in the residual occurs when an absorptive component is allowed through a volume void fraction, f_{a-As} , of amorphous arsenic.

We now investigate the effect of interfaces. Since elemental arsenic is known or anticipated to be at the substrate-oxide interface from previous studies, we suppose an interface layer of a-As and determine its thickness by LRA. The results are shown in Table I and at the bottom of Fig. 5. The results show quite definitely that no a-As appears at the interface of this electrochemically grown anodic oxide. In fact, even with three additional free parameters with respect to the original three-phase model we have only succeeded in reducing the residual by 25%, with nearly all of that coming through the assumption of an absorbing fraction in the bulk oxide. Thus the main source of discrepancy between measurement and model must be due to yet another effect.

The small value of interface thickness makes it clear that the calculation has already been optimized with respect to the GaAs-oxide interface, and simply substituting other possible interface materials such as a-GaAs or mixtures of a-As with the oxide will not reduce the discrepancy between theory and experiment. We are thus led to look elsewhere for the cause of the remaining discrepancy.

Noting that radioactive tracer (10), photoemission (39, 40), and ISS (12) studies have all shown As_2O_3 depletion at the oxide-electrolyte interface for anodizations in glycol-based electrolytes, we are led to suppose a density-deficient outer layer at the oxide surface. We therefore generalize the model to include an exterior interface region by allowing an additional density deficit in the outer region of the oxide and using the thickness of this region as a fifth free parameter in an LRA analysis. The results assuming a 15% density-deficient outer layer are shown in Fig. 5 and Table I. The assumption of a density-deficient outer layer results in a sevenfold decrease in the residual and thus accomplishes what the preceding three free parameters could not, i.e., the virtual elimination of discrepancies between the experimental measurement and the $\tan\psi$, $\cos\Delta$ spectra. Furthermore, the discrepancies are essentially eliminated not only over the fitted region but also over the end regions as well. Thus the greatest single source of the discrepancy between the actual GaAs-oxide system and the ideal three-phase model does not occur at the GaAs-oxide interface, but rather at the oxide-ambient interface. The GaAs-oxide interface for electrochemically grown anodic oxides is in fact exceedingly sharp.

To emphasize that the sensitivity to the GaAs-oxide interface region is indeed real, we have calculated the

result of minimizing the remaining four parameters in LRA supposing that 10Å of a-As exists at the GaAs-oxide interface. As shown in Fig. 5 and Table I, this artificially imposed condition results in a residual that is larger than that calculated in the initial three-phase model solution, and the good agreement between measured and calculated $\tan\psi$, $\cos\Delta$ spectra is eliminated. We may conclude that 10Å of a-As or its equivalent, as for example an interface 40Å wide consisting of 25 volume percent (v/o) a-As, would be easily detected. Clearly, the statistically negligible thickness of the interface, $0.3 \pm 0.3\text{Å}$, makes meaningless the question of its composition. The point can be emphasized by noting that the residual increases only by 0.00003 if the GaAs-oxide interface region is eliminated from the model entirely.

We have also investigated the effect of changing the void fraction of the outer interface. As can be seen from Table I, the data do not discriminate among density deficits in the 10-25 v/o range. However, all solutions converge on an effective density deficit of 10Å. Our measurements cannot distinguish whether this represents a nonstoichiometry resulting from surface leaching or microscopic roughness. As mentioned above, however, this result is entirely consistent with previous observations of As_2O_3 depletion in the outer film surface of these systems (10, 12, 39, 40). Because the actual depletion depth is sensitive to details of the electrolyte pH, current density, and maximum applied voltage, a further detailed comparison with previous results is not warranted.

The results of a similar analysis for the 75V anodic oxide electrochemically grown on the $\langle 100 \rangle$ surface are given in Table II. From Fig. 4, it can be anticipated that a larger absorbing fraction will be necessary to describe this oxide. As expected, the fraction is about four times larger and nearly equivalent to 1 v/o of a-As. The absorbing component of the bulk oxide now represents the single most significant factor in reducing the residual.

Once again, a full five-parameter LRA shows "no" GaAs-oxide interface region to within statistical uncertainty, although the solution is sufficiently indeterminate to allow a few Å to be present. However, the presence of an oxide-ambient interface region very similar to that detected on the 60V oxide is unambiguous. It is interesting to note that the density of the $\langle 100 \rangle$ -75V oxide is significantly less than that of the $\langle 111 \rangle$ -B-60V oxide, indicating that oxide properties may be rather critically dependent on growth and substrate parameters.

Intrinsic oxide response.—The intermediate four-term Sellmeier oscillator representation of the oxides obtained in the three-phase model can now be replaced with expressions representing more accurately the intrinsic dielectric response of these oxides. We retain the characteristic oscillator energies, E_{gi} , and the amplitude, $E_{01} = 0.35$ eV, of the lowest oscillator and determine the remaining three amplitudes by an LRA fit to the dielectric function calculated in the effective-medium approximation from the intermediate representation and the void and a-As fractions calculated in the previous section. Values are given in Table III with and without the a-As contribution, although only

Table II. As Table I, but for an anodic oxide grown to 75V on a $\langle 100 \rangle$ GaAs substrate with $N_D \sim 10^{18} \text{ cm}^{-3}$

| Model | Inner interface | | $10^3 f_{a-As}$ | Oxide $10^3 f_v$ | d (Å) | Compositional | Outer interface d (Å) | Residual $10^3 \delta$ |
|-------|-----------------|---------------|-----------------|---------------------|-------------------|---------------|----------------------------|---------------------------|
| | Composition | d (Å) | | | | | | |
| (1) | — | — | — | — | 1439.6 ± 0.8 | — | — | 36.8 |
| (2) | — | — | — | -7.4 ± 5.7 | 1432.6 ± 5.5 | — | — | 34.5 |
| (3) | — | — | 8.2 ± 1.1 | 91 ± 14 | 1518.0 ± 12.7 | — | — | 17.1 |
| (4) | a-As | 4.3 ± 3.6 | 9.1 ± 1.3 | 91 ± 12 | 1515.9 ± 11.2 | — | — | 16.3 |
| (5) | a-As | 3.4 ± 3.3 | 9.3 ± 1.4 | 89 ± 11 | 1468.5 ± 12.4 | 15% void | 50.6 ± 15.9 | 14.8 |
| (6) | a-As | 3.4 ± 3.3 | 8.8 ± 1.5 | 87 ± 15 | 1492 ± 19.5 | 25% void | 26.7 ± 14.1 | 14.6 |
| (7) | a-As | 13.4 fixed | 11.0 ± 1.4 | 82 ± 17 | 1445.6 ± 38 | 15% void | 65 ± 34 | 18.2 |

Table III. Sellmeier oscillator energies for electrochemically grown anodic oxides on GaAs

| E_{si} | 60V | | 75V | |
|--------------|-----------|--------------|-----------|--------------|
| | with a-As | without a-As | with a-As | without a-As |
| E_{01} | 0.075 eV | 0.35 eV | 0.35 eV | 0.35 eV |
| E_{02} | 5.5 | 1.56 | 1.59 | 1.28 |
| E_{03} | 7.5 | 5.48 | 5.35 | 5.35 |
| E_{04} | 16.0 | 18.51 | 18.46 | 16.98 |
| n_{∞} | — | 1.781 | 1.777 | 1.734 |

the latter have meaning with respect to the intrinsic dielectric response of the oxide. Values of the infrared refractive index calculated from these results are also given.

Not surprisingly, a-As has its greatest effect on the lower-energy oscillators because its oscillator strength is greatest there. The reduction in amplitude of all oscillators, except that of the fixed term, E_{01} , is about 10% indicating a common dispersion characteristic (similar composition) for both, with basically a density difference responsible for the difference in dielectric response.

Discussion

The initial Sellmeier representation, together with the void and effective a-As volume fractions, define the wavelength-dependent dielectric response of these oxides over the region of transparency. The results for the 60 and 75V oxides of Tables I and II are shown in Fig. 6. The real and imaginary parts of the refractive index calculated from these spectra are shown in Fig. 7 along with selected results from the literature (28, 29, 36, 41-45) where with one exception (41) the effects of interfaces were neglected.

Figure 7 shows general agreement among refractive index values for as-grown oxides formed in glycol-based electrolytes. Specifically, our 60 and 75V spectra, those of Palik *et al.* (28), and the single-wavelength datum of Umeno (36) are reasonably close. Data from Dinges (41) represent AGW oxides heat-treated in hydrogen for 1 hr at 300°C and have a slightly higher index. Choosing $5461\text{\AA} = 2.27\text{ eV}$ as a common point, it is clear that the scatter is of the order of ± 0.03 units in n . This scatter may reflect differences in density as modeled here, but it could also represent small differences in the bulk film stoichiometry which arise from selective dissolution of one component in the electrolyte during growth. One should note that this latter feature is both current density and electrolyte

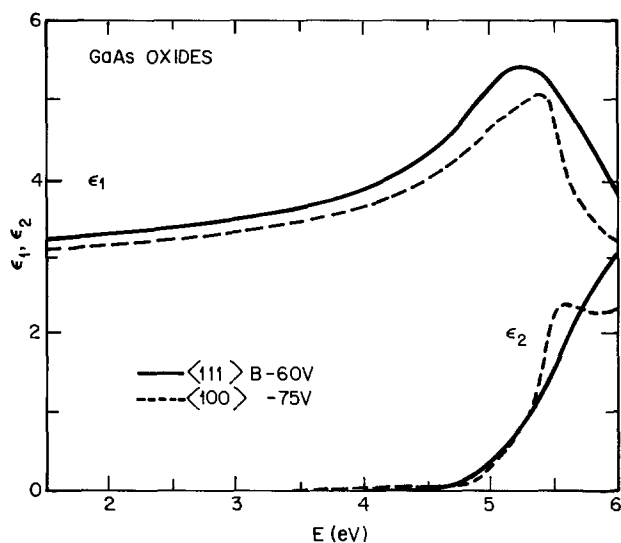


Fig. 6. Intrinsic dielectric functions for $\langle 111 \rangle$ -B-60V and $\langle 100 \rangle$ -75V electrochemically grown anodic oxides deduced from the analysis of the section "Optical Analysis."

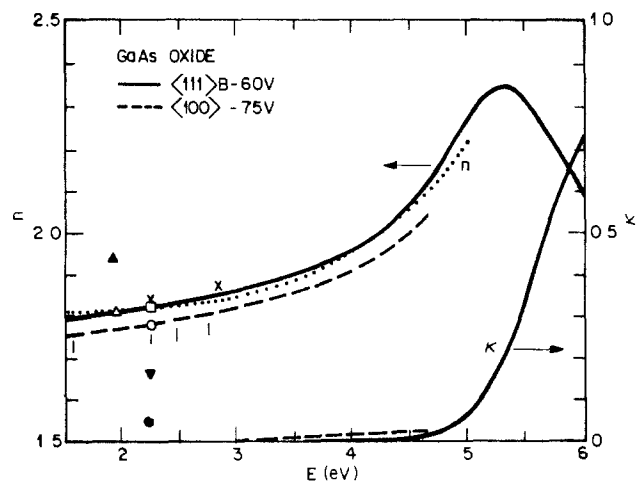


Fig. 7. As Fig. 6, but for refractive indexes. Selected data points and spectra are shown for comparison: AGW, as-grown: (...) Palik *et al.*, Ref. (28); (Δ) Umeno *et al.* Ref. (36). AGW, heat-treated: (||||) Barnes and Schinke, Ref. (29); (\blacktriangle) Umeno *et al.*, Ref. (36) (\times) Dinges, Ref. (41). Aqueous anodization: (\square) Dell'Oca *et al.*, Ref. (42). Oxygen plasma: (\circ) Weinreich, Ref. (43). Thermal: (\blacktriangledown) Lösche, *et al.*, Ref. (44); (\bullet) Navratil, Ref. (45).

dependent, making it difficult to compare these oxides directly. Oxides produced in nonglycol-based electrolytes show similar scatter; our previous results (15) on samples heat-treated 2 hr at 200°C are essentially identical to our 60V AGW data (and are not shown for that reason), while the Barnes-Schinke data (29) are systematically lower. The single datum of Dell'Oca *et al.* (42) coincides with our 60V AGW result, while the oxygen plasma-grown value of Weinreich (43) coincides with our 75V AGW result.

Similar scatter also appears in the infrared refractive index evaluated from the Sellmeier dispersion expressions. The values of Palik *et al.* (28) and of Barnes and Schinke (29), 1.79 and 1.707, respectively, can be compared with our values including a-As in Table III, which are 1.78 and 1.73 for the $\langle 111 \rangle$ -B-60V and $\langle 100 \rangle$ -75V oxides, respectively.

The measurement presented in Fig. 7 suggests that the index rises slightly by heat-treating in the 200°-300°C range, although it should be noted that Barnes and Schinke (29) reported a reduction in refractive index on five films heat-treated in N_2 at 250°C. We associate the general increase with heat-treating observed in most refractive index data with water removal and a slight densification. Ishii and Jepson (46) have studied the thermally induced desorption of products mass spectrometrically and observe that water is the primary species evolved below 300°C.

Heat-treatments above 300°C subject the film components to a variety of chemical reactions dependent on the nature of the ambient. In an inert atmosphere, the primary reactions involve the direct volatilization of As_2O_3 into the ambient and the reaction of As_2O_3 with the substrate according to the equation



The latter reaction has been verified experimentally using Raman scattering (47, 48) and explained thermodynamically based on a determination of the Ga-As-O phase diagram (49). Heat-treatments in reducing atmospheres (principally H_2) will reduce both oxides to their respective elemental forms starting at the oxide-ambient interface at sufficiently high temperatures; the interfacial reaction between As_2O_3 and GaAs will occur simultaneously at the substrate interface. The resulting oxide composition will be difficult to specify and will be dependent on the temperature and length of the heat-treatment. Heating at elevated temperatures in an oxidizing ambient (O_2 or air, typically)

produces similar changes as described for an inert ambient, but in addition the oxide-ambient surface region may contain some fraction of GaAsO₄ (50). The diversity of the oxide compositions resulting from the various heating procedures probably accounts for the contradictory nature of reported index of refraction data for films treated above 350°C.

An analysis of the separate Ga₂O₃ and As₂O₃ contents in these films is presently not feasible by spectroscopic ellipsometry due to lack of comprehensive dielectric response data on the structural forms of Ga₂O₃ and As₂O₃ likely to be found in these amorphous films. More definitive information on composition has generally been obtained from photoemission (11, 39, 50), RBS (46), ion-induced x-ray emission (51), ion scattering (12), radioactive tracer (10), and Auger profiling (3) studies. There is some variance in the literature concerning the As₂O₃/Ga₂O₃ ratio of the bulk films, but it should be kept in mind that selective dissolution into the electrolyte during growth coupled with the growth rate (current density) would need to be evaluated for each data set separately before a valid comparison could be made. In addition, ion profiling techniques are subject to selective sputtering during analysis and compensation for ion and electron beam reduction must also be induced. The generally observed trend for AGW oxides grown at current densities of ~1 mA/cm² yields a bulk oxide of ~1:1 ratio between As₂O₃ and Ga₂O₃.

In our opinion, the question of elemental arsenic content in these films is better addressed by the nondestructive optical techniques such as spectroscopic ellipsometry and Raman scattering than by either photoemission or Auger profiling. One does not have to contend with electron and ion beam reduction artifacts of As₂O₃ nor with background interferences close to the substrate which greatly complicate the separation of elemental arsenic and substrate signals. Comparison of our data with profiling data would also require, among other things, careful attention to the question of sample annealing, since it is now known (47-49) that As can be generated at the oxide-substrate interface even if it were not present in as-grown samples. The interface width obtained in spectroscopic ellipsometry is also not subject to sputtering rate, selective sputtering, and ion knock-on effects. The liability of spectroscopic ellipsometry is clearly that it requires either *a priori* knowledge of the disposition of oxide interfaces or considerable physical intuition before a viable model can be constructed.

Our data additionally allow us to draw some inferences about overall film homogeneity. Initial three-phase model analysis of the 60V AGW oxide yielded $|e_2| < 0.01$ (0.2% in $|e|$) in the region of film transparency. This represents roughly a factor of 5 improvement over previously analyzed oxides (15) grown in a dilute aqueous solution of orthophosphoric acid at high current densities. Moreover, the AGW oxides showed no ambiguities in the three-phase solutions above the oxide absorption edge. Such ambiguities result from a convergence of substrate and ambient branches of the mathematical solution as absorption in the film gradually closes off optical contact to the substrate. If the film is inhomogeneous so that the three-phase model solutions do not strictly apply, the result is a loss of continuity in the calculated spectra. This effect was observed previously (15) in anodic films and tends to be pronounced in d-c and rf plasma oxidized films [see, e.g., Fig. 5 and 6 in Ref. (8)]. The AGW oxides studied here display comparable bulk uniformity with thermally grown SiO₂ layers on Si. If the refractive indexes for Ga₂O₃ and As₂O₃ are taken to be of order 1.5 and 2.0, respectively, then these anodic films are homogeneous over the bulk (excluding boundary interfaces) to better than 2%.

The inner and outer interfaces deserve some final comment. The density-deficient oxide-air interface has

been mentioned previously; it is modeled here as a distributed density deficit equivalent to 10Å of material lost uniformly from a 60Å surface region. Available experimental results (10, 12, 39, 40) strongly suggest that the actual physical situation corresponds to non-uniform As₂O₃ depletion from a comparable region. With respect to the width and elemental arsenic content of the oxide-GaAs interface, our present measurements are at variance with numerous published Auger and photoemission profile studies. Once again we wish to stress the importance of accounting for the current density and any subsequent heat-treating steps before directly comparing data. The present measurements are in fact capable of much higher detection sensitivity than those of Raman scattering (48), another nondestructive analysis technique that failed to observe elemental As in as-grown films. The present results show essentially no ($0.3 \pm 0.3\text{Å}$) accumulated arsenic at the oxide-GaAs interface in the 60V oxide, although we feel that due to the possibility of systematic errors an absolute upper limit of 3Å is more reasonable. In addition to this elemental arsenic at the oxide-substrate interface, the bulk oxide would contain ~0.2% or another 2-3Å of absorbing material. The oxide-substrate interface width is essentially nil for AGW oxides produced under optimal (typically $I \leq 0.1$ mA/cm²) current density conditions. It is somewhat surprising to note that the present measurements indicate that oxide-GaAs interfaces can in fact be obtained with widths comparable to or less than those found in thermally oxidized Si-SiO₂ systems (20). This suggests that the high density of interface states typically observed in oxide-GaAs C-V studies may have its origin in parameters unrelated to or at least not dominated by interfacial sharpness.

Manuscript received Aug. 12, 1980.

Any discussion of this paper will appear in a Discussion Section to be published in the December 1981 JOURNAL. All discussions for the December 1981 Discussion Section should be submitted by Aug. 1, 1981.

Publication costs of this article were assisted by Bell Laboratories.

REFERENCES

1. I. Shiota, N. Miyamoto, and J. Nishizawa, *This Journal*, **124**, 1405 (1977).
2. D. N. Butcher and B. J. Sealy, *J. Phys. D*, **11**, 1451 (1978).
3. K. Watanabe, M. Hashiba, Y. Hirohata, M. Nishino, and T. Yamashina, *Thin Solid Films*, **56**, 63 (1979).
4. I. Sakai, M. Hirose, and Y. Osaka, *This Journal*, **127**, 713 (1980).
5. L. A. Chesler and G. Y. Robinson, *Appl. Phys. Lett.*, **32**, 60 (1978).
6. C. C. Chang, R. P. H. Chang, and S. P. Muraka, *This Journal*, **125**, 481 (1978).
7. J. B. Theeten, D. E. Aspnes, and R. P. H. Chang, *J. Appl. Phys.*, **49**, 6097 (1978).
8. D. E. Aspnes, J. B. Theeten, and R. P. H. Chang, *J. Vac. Sci. Technol.*, **16**, 1374 (1979).
9. J. B. Theeten, R. P. H. Chang, D. E. Aspnes, and T. E. Adams, *This Journal*, **127**, 378 (1980).
10. J. C. Verplanke and R. P. Tjiberg, *ibid.*, **124**, 802 (1977).
11. Y. Mizokawa, H. Iwasaki, R. Nishitani, and S. Nakamura, *J. Appl. Phys. Jpn.*, **17**, 327 (1978).
12. M. Croset, J. Diaz, D. Dieumegard and L. Mercandalli, *This Journal*, **126**, 1543 (1979).
13. R. L. Farrow, R. K. Chang, S. Mroczkowski, and F. H. Pollak *Appl. Phys. Lett.*, **31**, 768 (1977).
14. G. P. Schwartz, B. Schwartz, J. E. Griffiths, and T. Sugano, *This Journal*, **127**, 2269 (1980).
15. D. E. Aspnes, B. Schwartz, A. A. Studna, L. Derick, and L. A. Koszi, *J. Appl. Phys.*, **48**, 3510 (1977).
16. D. E. Aspnes, in *Surf. Sci.*, **101**, 84 (1980).
17. D. E. Aspnes, *J. Vac. Sci. Technol.*, **17**, 1057 (1980).
18. H. R. Philipp and H. Ehrenreich, *Phys. Rev.*, **129**, 1550 (1963).

19. J. B. Theeten and D. E. Aspnes, *Thin Solid Films*, **60**, 183 (1979).
20. D. E. Aspnes and J. B. Theeten, *Phys. Rev. Lett.*, **43**, 1046 (1979); *This Journal*, **127**, 1359 (1980).
21. H. Hasegawa, K. E. Forward, and H. L. Hartnagel, *Appl. Phys. Lett.*, **26**, 567 (1975); *This Journal*, **123**, 567 (1976); H. Hasegawa and H. L. Hartnagel, *ibid.*, **123**, 713 (1976).
22. D. E. Aspnes and A. A. Studna, *Appl. Opt.*, **14**, 220 (1975); *SPiE Proceedings*, **112**, 62 (1977); *Rev. Sci. Instrum.*, **49**, 291 (1978).
23. D. E. Aspnes, *J. Opt. Soc. Am.*, **64**, 812 (1974).
24. C. C. Chang, P. H. Citrin, and B. Schwartz, *J. Vac. Sci. Technol.*, **14**, 3602 (1978).
25. D. E. Aspnes, J. B. Theeten, and F. Hottier *Phys. Rev. B*, **20**, 3292 (1979).
26. E. S. Keeping, "Introduction to Statistical Interference," Chap. 12, Van Nostrand, Princeton, N.J. (1962).
27. I. H. Malitson, *J. Opt. Soc. Am.*, **55**, 1205 (1965).
28. E. D. Palik, N. Ginsburg, R. T. Holm, and J. W. Gibson, *J. Vac. Sci. Technol.*, **15**, 1488 (1978).
29. P. A. Barnes and D. P. Schinke, *Appl. Phys. Lett.*, **30**, 26 (1977).
30. D. A. G. Bruggeman, *Ann. Phys. (Leipzig)*, **24**, 636 (1935).
31. G. N. Greaves, E. A. Davis, and J. Bordes, *Philos. Mag.*, **34**, 265 (1976).
32. J. Stuke and G. Zimmerer, *Phys. Status Solidi B*, **49**, 513 (1972).
33. D. E. Aspnes and A. A. Studna, *Surf. Sci.*, **96**, 294 (1980).
34. H. Casey, Jr., D. D. Sell, and K. W. Wecht, *J. Appl. Phys.*, **46**, 250 (1975).
35. F. Lukes, *Optik*, **31**, 83 (1970).
36. M. Umeno, M. Yoshimoto, H. Shimizu, and Y. Amemiya, *Surf. Sci.*, **86**, 314 (1979).
37. R. N. Dexter, Private communication.
38. S. Varadarajan, I. Littlejohn, and J. R. Hauser, *Thin Solid Films*, **56**, 235 (1979).
39. P. A. Breeze, H. L. Hartnagel, and P. M. A. Sherwood, *This Journal*, **127**, 454 (1980).
40. G. P. Schwartz and G. J. Gualtieri, To be published.
41. H. W. Dinges, *Thin Solid Films*, **50**, L17 (1978).
42. C. J. Dell'Oca, G. Yan, and L. Young, *This Journal*, **124**, 1784 (1977).
43. O. A. Weinreich, *J. Appl. Phys.*, **37**, 2924 (1966).
44. K. Lösche, G. Kühn, H.-J. Bilz, and G. Leonhardt, *Thin Solid Films*, **19**, 81 (1973).
45. K. Navratil, *Czech. J. Phys. B*, **18**, 266 (1968).
46. T. Ishii and B. Jeppson, *This Journal*, **124**, 1784 (1977).
47. G. P. Schwartz, B. Schwartz, D. DiStefano, G. J. Gualtieri, and J. E. Griffiths, *Appl. Phys. Lett.*, **34**, 205 (1979).
48. G. P. Schwartz, J. E. Griffiths, and B. Schwartz, *J. Vac. Sci. Technol.*, **16**, 1383 (1979).
49. C. D. Thurmond, G. P. Schwartz, G. W. Kammlott, and B. Schwartz, *This Journal*, **127**, 1366 (1980).
50. G. P. Schwartz, G. J. Gualtieri, G. W. Kammlott, and B. Schwartz, *ibid.*, **126**, 1737 (1979).
51. L. C. Feldman, J. M. Poate, F. Ermanis, and B. Schwartz, *Thin Solid Films*, **19**, 81 (1973).

The Electromigration Directions of Liquid Au-Ag Alloy Droplets in Single Crystals of Si

T. R. Anthony

General Electric Research and Development Center, Schenectady, New York 12301

ABSTRACT

The electromigration directions and velocities of liquid Au-Ag alloy droplets in single crystals of Si were measured as a function of alloy composition at a temperature at which the electromigration velocities of Ag-Si and Au-Si liquid droplets are equal in magnitude, but opposite in direction. The electromigration null point composition of these ternary alloy droplets occurs at an alloy work function that roughly agrees with an electromigration-null-point work function previously determined with binary alloy droplets in Si.

Liquid metal droplets in a silicon single crystal through which a direct electric current is passing will migrate either towards the anode (+) or the cathode (-) (1-6). The motion of the liquid droplets is caused by a flux of dissolved silicon atoms across the inclusion, induced by the electric current passing through the liquid inclusion. To feed this flux of silicon atoms across the inclusion, silicon atoms dissolve into the inclusion at the forward face, while dissolved silicon atoms deposit on the rear face of the inclusion.

In the redeposited silicon trail left behind the electromigrating inclusion (Fig. 1), trace amounts of the metals comprising the droplet are left behind equal to the solid solubility limit of the metals in crystalline silicon. If one of the metals making up the inclusion is a donor or an acceptor element in silicon, then the redeposited silicon trail will be doped either n-type or p-type, respectively. By electromigration of an acceptor liquid metal droplet through n-type silicon or a donor liquid metal droplet through p-type silicon, p-n junctions can be formed in the silicon crystal. Because the electromigration velocities of liquid metal droplets

are orders of magnitude greater than solid-state diffusion coefficients of the same metals, liquid droplet electromigration provides a means of forming p-n junctions all the way through silicon wafers in a manner of minutes instead of days.

Not all liquid metal droplets electromigrate in the same direction in silicon. As shown in Table I, a liquid

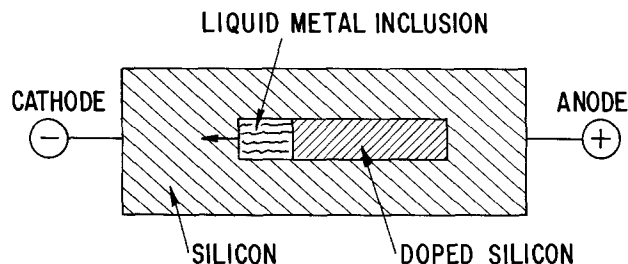


Fig. 1. A metal-rich liquid droplet electromigrating through a silicon single crystal toward the cathode. The redeposited silicon trail behind the electromigrating droplet contains the solid solubility limit in crystalline silicon of the metals comprising the inclusion.

Table I. The electromigration directions of nine liquid metal droplets in silicon and the work functions of these metals. The null-point work function for silicon is 4.55 eV. The work function of silicon is 4.85 eV. The electromigration directions are taken from Ref. (5) and the work functions from Ref. (8)

| Element | Electromigration direction | Work function (eV) |
|-----------|----------------------------|--------------------|
| Palladium | Anode (+) | 5.12 |
| Gold | Anode | 5.10 |
| Copper | Anode | 4.65 |
| Antimony | No electromigration | 4.55 |
| Tin | Cathode (-) | 4.42 |
| Aluminum | Cathode | 4.28 |
| Silver | Cathode | 4.26 |
| Gallium | Cathode | 4.20 |
| Indium | Cathode | 4.12 |

droplet of a metal with a work function greater than 4.55 eV electromigrates toward the anode, while a liquid droplet of a metal with a work function less than 4.55 eV electromigrates toward the cathode (5, 6) in silicon.

To manufacture a particular semiconductor device, it may be desirable to have a liquid droplet that electromigrates toward the anode and that dopes the silicon p-type. From Table I, it is seen that all of the acceptor droplets (Al, Ga, and In) electromigrate toward the cathode. Hence, to obtain an inclusion that will both electromigrate toward the anode and dope the silicon p-type, an alloy inclusion must be formed of, say, Al and Pd in the right proportions.

In order to be able to obtain the correct inclusion composition in this and other cases, some information is required on the electromigration directions of inclusions composed of more than one metal. *A priori*, one would expect that the correlation of the work function of the metal comprising the droplet with the electromigration direction of the droplet found for the pure metals might carry over to droplets made up of more than one metal.

To test this hypothesis, the electromigration directions of droplets of Au-Ag alloys of varying compositions were measured. Au and Ag were selected for several reasons. First, both of these noble metals are chemically similar and have almost identical atomic radii. In addition, they form continuous solid and liquid solutions so that extraneous factors such as eutectic points, intermetallics, or liquid immiscibility do not complicate the study. Of particular importance to the investigation is the fact that inclusions of these two noble metals electromigrate in opposite directions: Au-Si droplets move toward the anode, while Ag-Si droplets move toward the cathode (5). Also, a temperature (880°C) can be selected where the absolute magnitudes of the oppositely directed velocities of Au and Ag droplets are equal (5) (Fig. 2). Finally, the work functions of Au-Ag alloys of varying compositions are available in the literature (7) so that a comparison of the electromigration direction of a particular alloy composition with its work function is possible.

Experimental

Sample preparation.—Rectangular samples $4 \times 1 \times 1$ cm were cut from an n-type $10 \Omega\text{-cm}$ Si ingot. The long dimension of the rectangular specimen was parallel to the $\langle 111 \rangle$ direction. The top and side faces were perpendicular, respectively, to the $\langle 1\bar{1}0 \rangle$ and the $\langle 11\bar{2} \rangle$ directions. On the top ($1\bar{1}0$) face of the sample, thirteen holes were ultrasonically drilled halfway through the crystal (Fig. 3). One hole was 2 mm in diameter and served as the thermocouple cavity, while the other twelve holes were 0.75 mm in diameter and were used to hold Au-Ag alloy droplets of varying composition.

Eleven Au-Ag alloys of various compositions from 0 to 100% Au at 10% composition intervals (i.e., 0%,

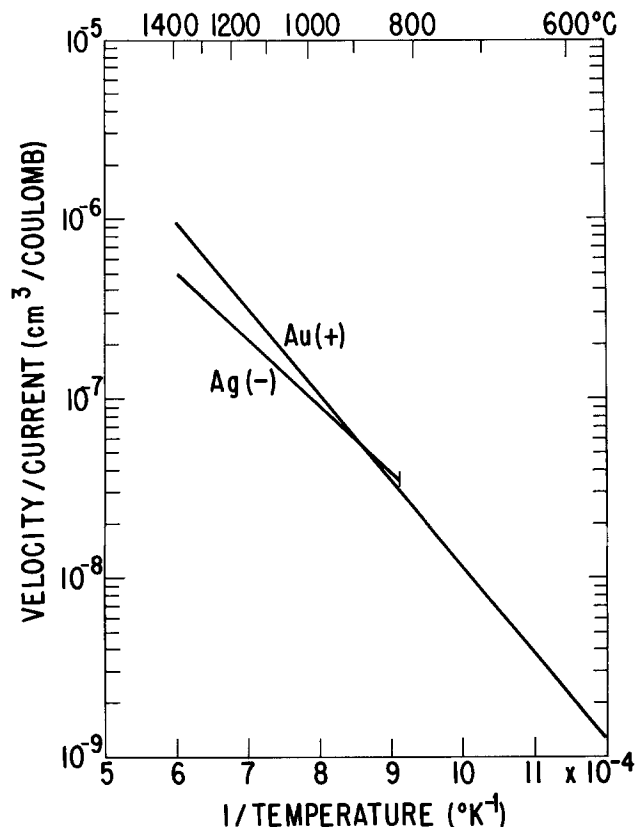


Fig. 2. The electromigration velocities of liquid droplets of Ag and Au in Si. In the temperature range of 880°-900°C, the electromigration velocities of Au and Ag-rich droplets are equal and opposite with Au migrating toward the anode (+) and Ag migrating toward the cathode (-).

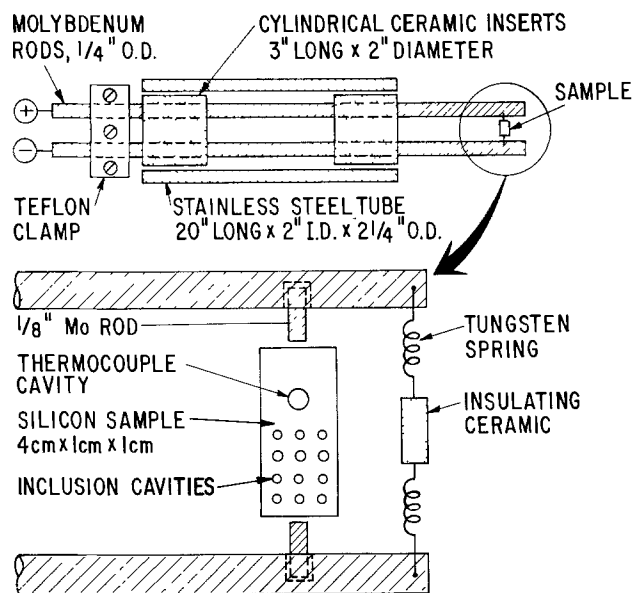


Fig. 3. The electrode jig used to pass current through the Si sample. The stainless steel tube is inserted part way into a diffusion furnace and current is passed through the Si sample in the furnace via the 1/4 in. molybdenum rods that extend outside of the furnace. The replaceable 1/8 in. molybdenum contact electrodes are pressed against the silicon sample throughout the electromigration experiment by the adjacent tungsten springs.

10%, 20%, etc.) were cut and weighed from 99.99% Au and Ag wires and melted under vacuum in sealed quartz tubes. During melting the sealed quartz ampuls were mechanically jostled to ensure complete homogeneous mixing of the Au and Ag. Following melting, the alloys were quenched in water. The cast alloys

were hammered into thin sheets from which were cut small pieces that were inserted into the sample cavities in the silicon crystal (Fig. 3).

The silicon specimen with the eleven different alloy compositions in eleven separate sample cavities was placed in an annealing furnace with flowing H_2 at $1100^\circ C$ for 3 hr to form the series of eleven Au-Ag liquid alloy droplets that would later be electromigrated. The silicon specimen was then cooled and removed from the annealing apparatus.

The electromigration apparatus.—The electromigration apparatus consisted of a diffusion furnace to attain the temperature of the electromigration run and an electrode jig, shown in Fig. 3, to apply current to the sample. One-eighth in. replaceable molybdenum electrodes were used as electrode contacts to the silicon sample. A tungsten spring provided contact pressure between the molybdenum electrodes and the Si sample during the high temperature electromigration experiments. A direct current of $15 A/cm^2$ at a temperature of $884^\circ C$ was used in the electromigration experiments. The temperature was selected so that the liquid inclusions of pure Ag and pure Au would have equal and opposite velocities (5). The current was produced by a Hewlett-Packard 6269B constant direct current power supply. A constant current supply was necessary, because the decrease in the resistivity of silicon with temperature would otherwise lead to an unstable situation. A voltage drop of 4.1V was required by the power supply to drive the $15 A/cm^2$ current in the silicon specimen. Most of this voltage drop occurred at contact points in the circuit rather than in the specimen itself.

Measurement of Au-Ag electromigration directions.—Infrared transmission micrographs were taken of the pre-annealed silicon sample with a Research Devices (Elizabeth, New Jersey) infrared microscope. The silicon sample had been previously polished to a $1 \mu m$ finish and fiduciary lines had been scribed on the top surface of the sample with a diamond marker. These fiduciary lines were used as reference points to measure the movement of the alloy liquid droplets through the silicon.

The specimen was then placed in the electrode jig shown in Fig. 3 and inserted in a diffusion furnace. After temperature equilibration at $884^\circ C$, a constant direct current of $15 A/cm^2$ was passed through the silicon sample for 24 hr. The temperature of the sample was continuously monitored during the experiment with a Chromel-Alumel thermocouple inserted in the thermocouple cavity (Fig. 3) of the specimen. A flow of a nonexplosive gas mixture of 95% $N_2 + 5\% H_2$ was used to prevent oxidation of the electrode jig.

Following the electromigration anneal, the electrode jig was withdrawn from the furnace tube and allowed to cool. The Si sample was removed from the jig and infrared transmission micrographs were taken again of the Si sample to determine the movement of the eleven liquid Au-Ag alloy droplets through the silicon. Measurements of the inclusion displacements were made on the photomicrographs with respect to the diamond-scribed fiduciary lines on the surface of the sample. Care was taken to center each droplet in the middle of its respective photomicrograph to avoid parallax errors arising from the difference in depths between the droplets in the middle of the sample and the fiduciary lines on the surface of the sample.

Experimental Results

Figure 4 shows the electromigration velocities of eleven Au-Ag alloys vs. composition. The velocities are averages of several experiments. Ag-rich alloys electromigrated toward the cathode, while Au-rich alloys electromigrated toward the anode. The null-point crossover composition is approximately 79 atomic percent (a/o) Au-21 a/o Ag. Between 30-60 a/o Ag, the

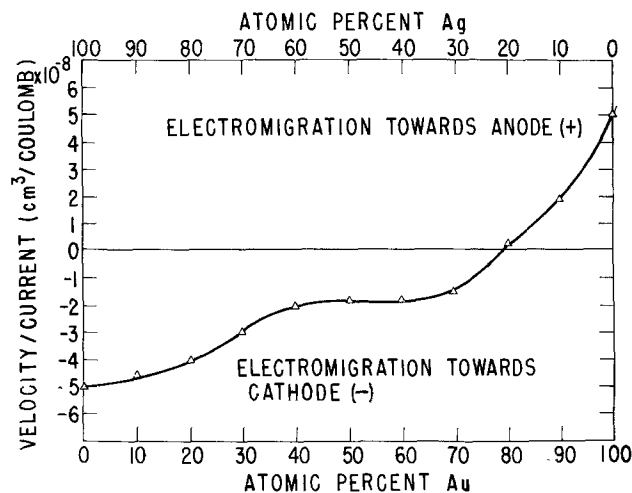


Fig. 4. The electromigration velocities and directions of a series of Au-Ag liquid droplets at $884^\circ C$ vs. composition of the droplet. Droplets with more than 21 a/o Ag electromigrate toward the cathode, while droplets of Au-Ag alloys of less than 21 a/o Ag electromigrate toward the anode.

droplet velocity is independent of composition with experimental error.

Discussion of the Electromigration Direction

In a previous paper, it was found that the electromigration directions of pure metals in silicon (5, 6) and germanium (11) show a strong correlation with the work functions (5) of the pure metals comprising the droplets. Table I shows that droplets of metals with work functions greater and less than 4.55 eV electromigrate, respectively, toward the anode and cathode in a silicon single crystal. In germanium crystals, liquid droplets of metals with work functions greater and less than 5.0 eV (the work function of Ge) electromigrate toward the anode and cathode, respectively, as shown in Table II.

A rationale for the relation between the work function of a metal and its electromigration direction as a liquid droplet in a host semiconductor crystal can be made qualitatively in terms of the electron-atom momentum exchange force that drives electromigration. [Electric field drift and Peltier-induced TGZM contribute less than a few percent of the observed electromigration velocities (2, 5, 6).] The work function of an element is a measure of the attraction between that element and an electron. That is, the larger is the work function, the greater will be the attraction. If two elements are mixed together, one would expect, as a first-order approximation, that some electron transfer would occur from the element with the small work function to the element with the large work function. Because the ion size of an element is a very sensitive function of

Table II. The work functions and electromigration directions of liquid metal droplets in germanium. The work function of germanium is 5.0 eV. The work functions are taken from Ref. (8) and the electromigration directions from Ref. (1)

| Element | Electromigration direction | Work function (eV) |
|-----------|----------------------------|--------------------|
| Platinum | Anode (+) | 5.65 |
| Nickel | Anode | 5.15 |
| Palladium | Anode | 5.12 |
| Gold | Anode | 5.10 |
| Tellurium | Cathode (-) | 4.95 |
| Copper | Cathode | 4.65 |
| Antimony | Cathode | 4.55 |
| Tin | Cathode | 4.42 |
| Aluminum | Cathode | 4.28 |
| Silver | Cathode | 4.26 |
| Lead | Cathode | 4.25 |
| Bismuth | Cathode | 4.22 |
| Gallium | Cathode | 4.20 |
| Magnesium | Cathode | 3.66 |

its valence state, the electron scattering cross section for an element losing electrons (the low work function element) would be expected to decrease, while the scattering cross section for the element gaining electrons would increase. These respective changes in electron scattering cross sections would be in the direction such that when the liquid alloy is subjected to a direct electric current, the electron wind would tend to preferentially blow the element with the larger work function toward the anode in accord with the experimental observations listed in Tables I and II.

A simple dilute solution theory using the difference in the work function of the metal comprising the droplet and an empirical null-point work function, as the driving force for electromigration, can be formulated as follows.

At the rear interface of the electromigrating droplet, conservation of mass requires that the flux J of silicon atoms impinging on the rear interface equal the velocity V of the inclusion times the difference in silicon concentrations per unit volume between the solid and the liquid

$$J = V(C_s - C_L) \quad [1]$$

where C_s and C_L are, respectively, the concentrations of silicon per unit volume in crystalline silicon and in the liquid droplet.

The flux J of silicon atoms in the liquid metal is given by

$$J = \text{Force} \times \text{Mobility} \times \text{Solubility} \quad [2]$$

The force f on the dissolved silicon atoms can be represented by

$$f = \alpha I \Delta W \quad [3]$$

where I is the electric current density, ΔW is the difference between the work function of the metal comprising the droplet and the empirical null-point work function, and α is an unknown numerical factor. This is a result of an empirical relationship found earlier (5).

The mobility M of dissolved silicon atoms in the inclusion is given by the Einstein Relation

$$M = \frac{D}{RT} \quad [4]$$

where D is the diffusion coefficient of dissolved silicon atoms in the liquid metal droplet, R is the gas constant, and T is the absolute temperature. The combination of Eq. [1]-[4] gives

$$\frac{V}{I} = \left[\alpha \left(\frac{C_L}{C_s - C_L} \right) \frac{D}{RT} \right] \Delta W \quad [5]$$

Unfortunately, no data are available for silicon in Au-Ag alloys that would allow one to evaluate the bracketed expression. However, the null-point composition at which the electromigration velocity passes through zero can be predicted by the Au-Ag composition where the work function deviation ΔW of the alloy equals zero.

Figure 5 shows the work function of Au-Ag alloys plotted vs. composition. The null-point work function for silicon of 4.55 eV corresponds to a predicted electromigration null-point composition of 60% Au-40% Ag. Since at the temperature of the electromigration experiments, the electromigration velocities of pure Au and pure Ag droplets are equal and opposite, a simple use of the law of mixtures would indicate that the null-point composition would be 50 a/o Au-50 a/o Ag. In the experiments, a shift of the null point to a gold-rich composition is found instead. This shift to a gold-rich composition is predicted by the nonlinear work function of Au-Ag alloys that shows a much steeper change on the gold-rich side of the work-function-composition diagram than on the silver side. Thus, there is qualitative agreement between the experimental null point and the null point predicted by the work functions of the alloys as far as the shift to the gold-rich side of the diagram. However, quantitatively, the predicted null-

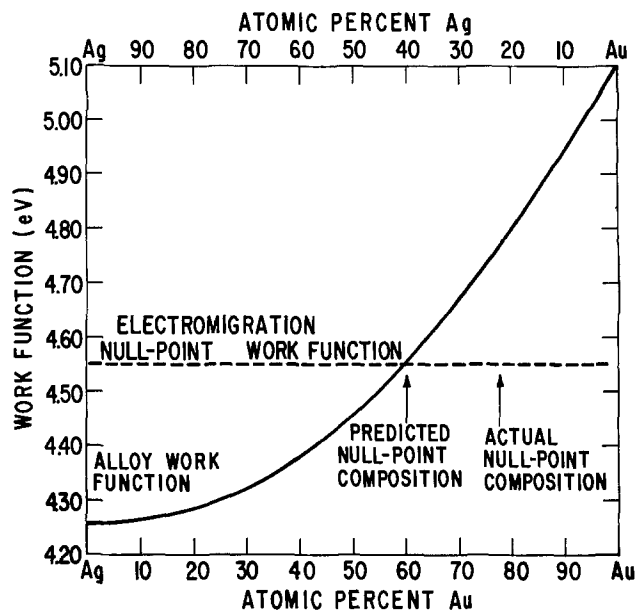


Fig. 5. The work function vs. composition of Au-Ag alloys taken from Ref. (7) and (8). The electromigration null-point work function for various metals is shown along with the predicted and experimental null-point alloy compositions.

point alloy composition of 60% Au-40% Ag does not agree with the experimentally observed null-point composition of 79% Au-21% Ag. This quantitative disagreement is not surprising, since the work function of a pure alloy crystal at room temperature, no doubt, does not equal the work function of the same alloy liquid containing dissolved silicon at 880°C. In view of this quantitative disagreement in the alloy case, the perfect correlation of electromigration directions with work functions found for the pure liquid metal droplets (5) is even more remarkable.

Summary

The electromigration directions of a series of liquid Au-Ag droplets were measured as a function of composition in Si. The electromigration experiments were carried out at a temperature where the electromigration velocities of Au-Si and Ag-Si liquid droplets are equal in magnitude but opposite in direction. Although the law of mixtures would predict an electromigration null-point composition of 50% Au-50% Ag, the actual null-point composition was shifted to a gold-rich composition of 79% Au-21% Ag. This gold-rich shift is predicted qualitatively by a model relating the driving force of electromigration to the deviation of the nonlinear work function of Au-Ag alloys from an electromigration-null-point work function determined previously with simple liquid metal inclusions in Si.

Manuscript submitted May 12, 1980; revised manuscript received Sept. 8, 1980.

Any discussion of this paper will appear in a Discussion Section to be published in the December 1981 JOURNAL. All discussions for the December 1981 Discussion Section should be submitted by Aug. 1, 1981.

Publication costs of this article were assisted by General Electric Company.

REFERENCES

1. W. G. Pfann, K. E. Benson, and J. H. Wernick, *J. Electron.*, **2**, 597 (1957).
2. D. T. J. Hurlle, J. B. Mullin, and E. R. Pike, *Philos. Mag.*, **9**, 423 (1964).
3. J. K. Howard, *J. Appl. Phys.*, **46**, 1910 (1975).
4. J. K. Howard, *ibid.*, **44**, 1977 (1973).
5. T. R. Anthony, *ibid.*, **51**, 6348 (1980).
6. T. R. Anthony, *ibid.*, **51**, 6356 (1980).
7. S. C. Fain, Jr. and J. M. McDavid, *Phys. Rev. B*, **9**, 5099 (1974).
8. H. B. Michaelson, *IBM J. Res. Dev.*, **22**, 72 (1978).

An Improved Model for Analyzing Hole Mobility and Resistivity in p-Type Silicon Doped with Boron, Gallium, and Indium

L. C. Linares¹ and S. S. Li*

Department of Electrical Engineering, University of Florida, Gainesville, Florida 32611

ABSTRACT

Using the relaxation time approximation, and a three-band model (i.e., nonparabolic light-hole band, parabolic heavy-hole, and split-off bands), theoretical calculations of hole mobility and resistivity were carried out for p-type silicon doped with boron, gallium, and indium for dopant densities from 10^{14} to 10^{18} cm^{-3} and temperatures between 100 and 400 K. The theoretical analysis did not consider the effects of compensation, but scattering contributions from acoustical and optical phonons, and ionized and neutral impurities were considered. In addition, interband scattering, the effect of hole-hole scattering, and the nonparabolic nature of the valence bands were also taken into account in the mobility formulations. To verify our theoretical calculations, resistivity measurements were performed on silicon samples (relatively free of compensating impurities) doped with boron, gallium, and indium with dopant densities ranging from 4.25×10^{15} to 9.05×10^{17} cm^{-3} , for $100 \leq T \leq 400$ K. Agreement between the calculated and measured resistivity values and the published mobilities (4) was within 10% over the range of temperature and dopant density studied.

For purposes of device design it is necessary to know the correct relationship between resistivity and dopant density at different temperatures. Evaluation of the characteristics of semiconductor devices and the study of transport phenomena in semiconductors requires an accurate knowledge of variations in ohmic mobility and carrier density with changes in temperature and dopant density. Because of this, numerous studies of mobility, resistivity, and carrier density in p-type silicon have been carried out (1-15). However, due to the complexity of the valence band of silicon and the various scattering mechanisms involved, these studies, for the most part, have either been conducted in temperature and dopant density ranges designed to explore only a particular type of scattering mechanism, or have not advanced the theory necessary to describe the experimental results. For example, Costato and Reggiani (1) calculated the mobility of holes for pure p-type silicon in which lattice scattering dominates; Braggins (2) considered the nonparabolicity of the valence band and all the relevant scattering mechanisms with the exception of hole-hole (h-h) scattering, but he limited his investigation to dopant densities below 5×10^{16} cm^{-3} and low temperatures; Morin and Maita (3) considered wide ranges of temperature and dopant concentration, but did not provide a theoretical examination of the data. Recently, Li (4) developed a theoretical model capable of describing the mobility and resistivity of p-type silicon over a wide range of temperatures and dopant densities. This improved model was applied to the case of boron-doped silicon with great success (4). The improvement in Li's theoretical treatment of mobility and resistivity consists mainly of the inclusion of h-h scattering effects, and consideration of the nonparabolic nature of the valence band.

With some exceptions (13-15), most of the research in p-type silicon has been conducted with boron as the doping impurity, since boron is the shallowest acceptor in silicon and this material is widely available. A limited amount of data is available on silicon doped with

deeper impurities such as gallium and indium. These dopants, especially indium, are of great interest to modern technology because of their application to photo-detector devices. Curves of resistivity and mobility as a function of dopant density (5-7) have been applied to characterizing boron-doped starting material and diffused boron layers in silicon, and have proven to be highly useful. Similar curves developed in this study may be expected to be equally useful for characterizing and integrating infrared detectors based on the deeper levels of indium and gallium with on-chip silicon electronics.

The purpose of this paper is to improve Li's (4) theoretical model by including consideration of interband transitions in the development of scattering relaxation time due to lattice phonons, and to apply this theory to the study of silicon doped with boron, gallium, and indium. The theoretical investigation is carried out over a temperature range from 100 to 400 K and a dopant density range from 10^{14} to 10^{18} cm^{-3} . Because of the complexities brought about by heavy doping effects and uncertainties in accounting for hole density and impurity density at high dopant densities, we have restricted the present analysis to densities below 10^{18} cm^{-3} in which the use of Boltzmann statistics is justified.

In the next section we describe the theoretical approach, presenting the formulation of effective mass in the nonparabolic valence band, and the relaxation time and mobility formulation. Resistivity and carrier density are also analyzed in this section. Next, the theoretical and experimental results are compared. The theory is further verified by comparison with other published data. The section "Summary and Conclusions" summarizes the main conclusions derived from this work.

Theoretical Approach

In this section we present the model used for the valence band of silicon, and the approach used to determine effective masses in the nonparabolic band. The mobility and resistivity in p-type silicon is obtained by considering contributions from lattice, ionized impurity, and neutral impurity scattering. The effects of h-h scattering and valence band nonpara-

* Electrochemical Society Active Member.

¹ Present address: U.S. Air Force Academy, Physics Department, Colorado Springs, Colorado 80840.

Key words: hole mobility, resistivity, dopant.

bolicity are also taken into account in the scattering relaxation time formulation. Interband transitions are considered only for lattice phonon scattering.

Valence band and hole effective masses.—The valence bands of silicon have an extremum at $\bar{k} = 0$ and are degenerate there. The constant energy surfaces for this case are warped spheres. Although warped, the bands are parabolic for small values of \bar{k} . However, for larger values of \bar{k} , the bands become nonparabolic, and along the $\langle 100 \rangle$ and $\langle 111 \rangle$ directions the heavy- and light-hole bands are parallel over most of the Brillouin zone. The derivation of an expression for a valence band effective mass which incorporates the nonparabolic nature of the individual bands begins with a simplified model of the warped structure based on the work of Kane (16) and Barber (17). In this model, the heavy-hole band is characterized by holes with an energy independent but direction dependent effective mass, and the light-hole band is characterized by holes with an energy and direction dependent effective mass. The split-off band is separated at $\bar{\kappa} = 0$ by an energy $\Delta = 0.044$ eV (18), and is characterized by an effective mass which is temperature dependent. Thus the heavy-hole band is treated as parabolic for the range of temperature considered in this work, while the light-hole band is parabolic only for very low values of \bar{k} . At higher values of $\bar{\kappa}$, the light-hole band has an energy dependent curvature which takes on the same characteristics as the heavy-hole band for energies greater than 0.02 eV.

Using the above band model, expressions were derived for density-of-states and conductivity effective masses, based on the following definitions (19): the density-of-states effective mass, m_D^* , enters in the normalization of the distribution function, and the conductivity effective mass, m_C^* , is the mass of a mobile charge carrier under the influence of an external electric field. Since the crystal structure of silicon has cubic symmetry, ohmic mobility will be isotropic. The warping and nonparabolic character of the bands enters the isotropic mobility via the effective mass formulation. The values of m_C^* and m_D^* calculated in (19) were obtained assuming the Fermi-Dirac distribution function, and unequal relaxation times in the individual bands (20). These values are valid in the temperature range considered in this study, where the warping nature of the heavy-hole band is not strong and this band can be assumed parabolic. The values of m_C^* and m_D^* calculated in Ref. (19) for $100 \leq T \leq 400$ K are listed in Table I.

Mobility and scattering relaxation time formulation.—The calculation of the mobility of holes in the valence band of silicon is accomplished by evaluating the mobility separately in the heavy-hole band, the light-hole band, and the split-off band considering all appropriate scattering mechanisms. The overall mobility is then evaluated as a weighted average of the single-band mobilities over the individual hole densities in each band.

The conductivity mobility in each of the three valence bands is calculated from

Table I. Density-of-states and conductivity effective masses of holes in p-type silicon for $N_A = 10^{14} \text{cm}^{-3}$ and $100 \leq T \leq 400$ K (19) (masses in units of electron rest mass)

| T (K) | 100 | 150 | 200 | 250 | 300 | 350 | 400 |
|------------|--------|--------|--------|--------|--------|--------|--------|
| m_{D1}^* | 0.5503 | 0.5547 | 0.5592 | 0.5638 | 0.5685 | 0.5733 | 0.5782 |
| m_{D2}^* | 0.2486 | 0.3092 | 0.3533 | 0.3865 | 0.4123 | 0.4337 | 0.4502 |
| m_{D3}^* | 0.0080 | 0.0249 | 0.0443 | 0.0627 | 0.0793 | 0.0940 | 0.1071 |
| m_D^* | 0.6567 | 0.6997 | 0.7340 | 0.7624 | 0.7865 | 0.8081 | 0.8265 |
| m_{C1}^* | 0.4271 | 0.4323 | 0.4375 | 0.4429 | 0.4484 | 0.4541 | 0.4599 |
| m_{C2}^* | 0.3285 | 0.4319 | 0.4839 | 0.5099 | 0.5222 | 0.5283 | 0.5286 |
| m_{C3}^* | 0.2410 | 0.2443 | 0.2474 | 0.2511 | 0.2532 | 0.2598 | 0.2596 |
| m_C^* | 0.3604 | 0.4143 | 0.4454 | 0.4633 | 0.4743 | 0.4820 | 0.4859 |

$$\mu_i = \frac{e \langle \tau_i \rangle}{m_{C1}^*} \quad [1]$$

where

$$\langle \tau_i \rangle = \frac{\int \epsilon^{3/2} \tau_i (\partial f_0 / \partial \epsilon) d\epsilon}{\int \epsilon^{3/2} (\partial f_0 / \partial \epsilon) d\epsilon} \quad [1]$$

for the case of Fermi-Dirac statistics, $\epsilon = E/k_0T$ is the reduced energy, and m_{C1}^* and τ_i are the conductivity effective mass (19), and the total scattering relaxation time in band i , respectively.

At temperatures above absolute zero, in any semiconductor, the charge carriers may be scattered by a number of different mechanisms. Because each scattering mechanism has its own dependence on scattering energy, a simple closed form expression for total scattering relaxation time as a function of temperature cannot be obtained. The use of numerical techniques is necessary to solve for the relaxation time. In the case of p-type silicon, the peculiarities of a degenerate, warped, and nonparabolic valence band must be taken into account (2). The possibility of interband as well as intraband transitions must also be taken into account in the analysis. With the inclusion of interband scattering as given by Bir *et al.* (21), the total relaxation time in the heavy- ($i = 1$) and light- ($i = 2$) hole bands is given by

$$\tau_i = \frac{1}{\delta} \left(1 + \frac{m_{D1}^*}{m_{Dj}^*} \frac{\tau_{ji}}{\tau_{ij}} \right) \tau_{ii} \quad i \neq j; \quad i = 1, 2; \quad j = 1, 2 \quad [3]$$

where

$$\delta = 1 - \frac{\tau_{11}\tau_{22}}{\tau_{12}\tau_{21}} \quad [4]$$

and τ_{ii} is obtained by adding reciprocally the contributions from scattering by acoustical phonons, optical phonons, ionized impurities, and neutral impurities with i as the band index. The total relaxation time in the split-off band ($i = 3$) is obtained in the same manner. Only transitions between the light- and heavy-hole bands are considered; the relaxation time τ_{ji} takes into account a transition from band i to band j .

The procedure for including the nonparabolicity of the band structure into calculations of relaxation time, consists of modifying the relaxation time for a given scattering process by replacing the temperature independent effective mass of the parabolic band by the temperature dependent effective mass of the nonparabolic band. This procedure has been successfully applied to the study of acoustic phonon scattering in nonparabolic bands by Radcliffe (22). Optical phonon and ionized impurity scattering in nonparabolic bands have been considered by Barrie (23) in the same manner. Braggins (2) has used the same method to include nonparabolicity in his study of p-type silicon. In this work, the relaxation times appropriate to degenerate, parabolic valence bands have been used and modified according to the prescription of Radcliffe (22), Barrie (23), and Braggins (2). The anisotropy of the energy spectrum is not considered in this model, because from the transport theory for parabolic bands it is known that this anisotropy has no influence on the temperature dependence of mobility, but only on its absolute value (24). Each of the four scattering mechanisms will now be discussed.

Acoustical phonon scattering.—The relaxation time for scattering by acoustical phonons includes both the possibility of interband as well as intraband scattering. The treatment of the acoustical phonons has been based on the theory of Bir, Normantas, and Pikus (21) where the relaxation times can be expressed in terms of a single constant, τ_0 , which controls the overall magnitude of the scattering. Both transverse and longitudinal phonons participate in the scattering so that

$$\tau_{ac1}^{-1} = \frac{m_{D1}^{*3/2}}{\tau_0} \left\{ L_{11}^{(2)} + \gamma^3 L_{11}^{(1)} + \frac{C_l^2}{C_t^2} \eta^2 \right. \\ \left. (T_{11}^{(2)} + \gamma^3 T_{11}^{(1)}) \right\} T^{3/2} \epsilon^{1/2} \quad [5]$$

and

$$\tau_{ac2}^{-1} = \frac{m_{D2}^{*3/2}}{\tau_0} \left\{ L_{22}^{(2)} + \gamma^3 L_{22}^{(1)} + \frac{C_l^2}{C_t^2} \eta^2 \right. \\ \left. (T_{22}^{(2)} + \gamma^3 T_{22}^{(1)}) \right\} T^{3/2} \epsilon^{1/2} \quad [6]$$

for intraband scattering, while

$$\tau_{ij}^{-1} \gamma^{-5} = \tau_{j1}^{-1} \\ = \frac{m_{D1}^{*3/2}}{\tau_0} \left\{ L_{ij}^{(2)} + \frac{C_l^2}{C_t^2} \eta^2 (T_{ij}^{(2)}) \right\} T^{3/2} \epsilon^{1/2} \quad [7]$$

for interband scattering. In the split-off band, the scattering relaxation time is given by

$$\tau_{ac3}^{-1} = \frac{m_{D3}^{*3/2}}{\tau_0} (\epsilon - \Delta/k_0 T)^{1/2} T^{3/2} \quad [8]$$

In these equations

$$\frac{1}{\tau_0} = \frac{k_0^{3/2} a^2 m_0^{3/2}}{\sqrt{2} \pi \hbar^4 \rho_s C_l^2}, \quad \gamma^2 = \frac{m_{D2}^*}{m_{D1}^*}, \quad n = b/a$$

a and b are valence band acoustic deformation potential constants in the Picus and Bir (25) notation, ρ_s is the density, C_l and C_t are the longitudinal and transverse sound velocities in silicon, and L_{ij} and T_{ij} are the functions of η and γ defined in (21).

Optical phonon scattering.—Optical phonon scattering, while negligible at very low temperatures, cannot be ignored at high temperatures. Ehrenreich and Overhouser (26) have calculated the mobility of holes in silicon and its dependence on temperature. The calculated mobility follows a $T^{-2.3}$ dependence for reasonable choices of the parameters which describe the mixing of optical and acoustical phonon scattering. This agrees with experimental results (3, 7). The relaxation time for scattering by nonpolar optical phonons is given by (27)

$$\tau_{oi}^{-1} = \frac{m_{Di}^{3/2}}{\tau_0} W \theta T^{1/2} \{ (n_0 + 1) (\epsilon - \theta/T)^{1/2} \\ + n_0 (\epsilon + \theta/T)^{1/2} \}, \quad i = 1, 2, 3 \quad [9]$$

where θ is the Debye temperature, $n_0 = (\exp(\theta/T) - 1)^{-1}$ is the phonon distribution function, and W is a constant which determines the relative coupling strength of the holes to the optical phonon mode compared to the acoustical phonon mode, $W = D_0^2 \hbar^2 C_l^2 / 2k_0^2 a^2 \theta^2$, where D_0^2 is the optical deformation potential constant. The first term in the brackets of Eq. [9] corresponds to optical phonon emission and is relevant only when this is energetically possible ($\epsilon > \theta/T$). The second term in the brackets corresponds to optical phonon absorption.

Ionized impurity scattering.—The Coulombic interaction between ionized impurities and charge carriers drifting through the crystal under the action of an applied electric field causes scattering of the charge carriers. Scattering by ionized impurities was first considered by Conwell and Weisskopf (28). The basic assumption is that the Coulomb field is cut off at half the distance between charged impurities. This is equivalent to assuming that a charge carrier sees only one charged impurity at a time, the effect of the other charged impurities being sufficiently screened as to be negligible. This approach was improved by Brooks (29) and Herring (30) who associated the cutoff of the Coulomb potential with a screening distance, the free

carriers being assumed to provide screening against the charge of the impurities. We have used the Brooks-Herring formula in our calculations.

Neutral impurity scattering.—Scattering by neutral impurities in semiconductors has been considered by Erginsoy (31) as a variation of the problem of the scattering of electrons by neutral hydrogen atoms. The result is a temperature independent relaxation time. Sclar (32, 33) has included the possibility of bound states in the evaluation of electron-hydrogen impurity scattering by using a three-dimensional square well to estimate the influence of a weakly bound state on the scattering. In this case the relaxation time is given by

$$\tau_{Ni}^{-1} = \frac{2^{3/2} \pi \hbar^2 N_N}{(k_0 T)^{1/2} m_{Di}^{*3/2}} \left\{ \epsilon^{1/2} + \frac{E_1}{k_0 T \epsilon^{1/2}} \right\}, \quad i = 1, 2, 3 \quad [10]$$

where

$$E_1 = 1.136 \times 10^{-19} \left(\frac{m_D^*}{m_0} \right) \left(\frac{\epsilon_0}{\epsilon_s} \right)^2$$

is the binding energy of neutral acceptors.

McGill and Baron (34) report a more accurate calculation of neutral impurity scattering which is not subject to any of the previous approximations to the scattering, and represents an accurate implementation of the neutral-hydrogen approximation. Using this calculation, Baron *et al.* (35) show that neutral impurity scattering is inversely proportional to the ionization energy of the impurity. McGill and Baron's calculations, while predicting significant deviations from the results of Erginsoy and Sclar at low temperatures, agree in general with the predictions of Eq. [10] at higher temperatures ($36 < T < 181$ K for In).

For silicon doped with shallow impurities, neutral impurity scattering is important at low temperatures where neutral impurities may outnumber ionized impurities. The more accurate calculations of McGill and Baron are appropriate in this case, especially for the deeper level impurities. In this study, however, because of the temperature range involved, we felt that Sclar's calculation could accurately represent neutral impurity scattering.

Effect of hole-hole scattering.—The expressions thus far presented for scattering relaxation time neglect the effect of hole-hole (h-h) scattering. Although h-h scattering does not affect the current density directly since it cannot alter the total momentum, it tends to randomize the way in which this total momentum is distributed among holes of different energies. When the scattering mechanism is such as to lead to a non-uniform distribution, h-h scattering gives rise to a net transfer of momentum from holes which dissipate momentum less efficiently to those which dissipate momentum more efficiently, resulting in an overall greater rate of momentum transfer, and lower mobility (36). Thus the size of the effect of h-h scattering on the scattering relaxation time is a function of the energy dependence of the relaxation time. The h-h factor, γ_{hh} , can be derived by means of a classical formulation introduced by Keyes (37). When hole-hole collisions are much more frequent than hole-acceptor collisions, the average relaxation time for a parabolic band in the Keyes (37) approximation approaches the limiting form

$$\langle \tau_{hh} \rangle = \frac{\int \epsilon^{3/2} (\partial f_0 / \partial \epsilon) d\epsilon}{\int \epsilon^{3/2} \tau^{-1} (\partial f_0 / \partial \epsilon) d\epsilon} \quad [11]$$

where f_0 is the Fermi-Dirac distribution function. On the other hand, if h-h collisions are neglected, the average relaxation time is given by Eq. [2].

Thus the h-h reduction factor (*i.e.*, the ratio of $\langle \tau_{hh} \rangle$ to $\langle \tau \rangle$) can be expressed as

$$\gamma_{hh} = \left\{ \frac{\int e^{3/2} \tau (\partial f_0 / \partial \epsilon) d\epsilon \int e^{3/2} \tau^{-1} (\partial f_0 / \partial \epsilon) d\epsilon}{[\int e^{3/2} (\partial f_0 / \partial \epsilon) d\epsilon]^2} \right\}^{-1} = \frac{1}{\langle \tau \rangle \langle \tau^{-1} \rangle} \quad [12]$$

For optical phonon scattering, and γ_{hh}^o , the h-h reduction factor is evaluated from Eq. [12].

For acoustical phonon scattering it is assumed that γ_{hh}^a decreases linearly with increasing dopant density from a value of one to a value of $\gamma_{hh}^a = 9\pi/32 \stackrel{\Delta}{=} 0.88$ (4) in a certain range of impurity concentration. The exact relationship ($\gamma_{hh}^a = 1.0004 - 4.013378 \times 10^{-19} N_A$, $10^{15} \leq N_A \leq 3 \times 10^{17}$) is determined empirically with a best fit of the experimental data.

Luong and Shaw (38) using a one-particle-like approximation from the Hartree-Fock theory, have shown that by inclusion of h-h scattering, the Brooks-Herring (29, 30) formula is reduced by a factor which can be expressed in closed form as

$$\gamma_{hh}^i = (N_A^- / p') [1 - \exp(p' / N_A^-)] \quad [13]$$

where N_A^- is the ionized acceptor density and p' is the screening hole density.

In the case of neutral impurity scattering, h-h scattering has no significance because τ_N is independent of hole energy. Thus the overall scattering relaxation time in each hole band is calculated by adding the contributions from the different scattering mechanisms, each properly corrected for the effects of h-h scattering. The conductivity mobility in each individual band is calculated from Eq. [1] and the combined conductivity mobility in the valence band is then evaluated as a weighted average of the single-band mobilities over the population of holes in each band.

Resistivity and hole density.—The resistivity for p-type silicon is given by

$$\rho = \frac{1}{e\mu_C p} \quad [14]$$

where μ_C is the hole conductivity mobility and p is the hole density

$$p = \frac{4}{\sqrt{\pi}} \left[\frac{2\pi k_0 T m_D^*}{h^2} \right]^{3/2} F_{1/2}(\eta) \quad [15]$$

for the general case of Fermi-Dirac statistics. Here, m_D^* , the density-of-states effective mass, contains information pertaining to the nonparabolic nature of the valence band (19). In the limit of low dopant densities, Eq. [15] reduces to $p = N_v \exp(-\eta)$ where $N_v = 2 (2\pi m_D^* k_0 T / h^2)^{3/2}$ is the effective density of valence band states. For the range of temperatures considered in this study, the hole density is determined by assuming that the density of carriers is determined by the impurities present in the silicon sample. The density of ionized acceptor impurities in p-type silicon is computed from the charge neutrality equation, which reduces to $p \simeq N_A^-$ for the case of uncompensated materials.

The density of ionized acceptors is (39)

$$N_A^- = \frac{N_A}{1 + g \exp\left(\frac{E_A - E_F}{k_0 T}\right)} \quad [16]$$

where E_A is the acceptor ionization energy, and g is the ground state degeneracy. Excited states have a very minor influence on the carrier concentration due to the large separation between the ground state and the excited states (2, 39). Letting

$$g = 4 + 2 \exp(-\Delta / k_0 T) \quad [17]$$

enables us to include contributions from the lowest energy state associated with the split-orbit band. Equa-

tion [17] assumes that this state is bound to the split-orbit band with the same energy as the ground state is bound to the light- and heavy-hole bands. Calculations of Zwerdling, *et al.* (18) and Baldereschi and Lipari (40) show that this assumption leads to underestimation of the percentage of impurity ionization. On the other hand, tacit acceptance of $g = 6$ (41), overestimates ionization density and introduces a larger error than the assumption of Eq. [17]. The density of ionized acceptors is computed by iterating E_F in Eq. [15] and [16] until $|p - N_A^-| < 0.001$.

Experimental evidence shows that the acceptor ionization energy E_A is not a constant, but decreases with increasing dopant density (9). Penin *et al.* (42) have determined in a study of heavily doped silicon from 4 to 300 K that for shallow impurities such as boron and phosphorus the ionization energy decreases and finally disappears altogether for impurity densities greater than $3 \times 10^{18} \text{ cm}^{-3}$. For impurities with deeper activation energies, it is also expected that at some impurity concentration, the impurity activation energy should become a function of the impurity concentration. However, in this case this should happen at higher impurity concentrations than for the shallower level impurities. This is due to the smaller geometrical dimensions of the wave functions applicable to the deeper levels, so that overlapping effects which promote the reduction in activation energy require higher impurity concentrations (13). For shallow impurities such as boron and phosphorus, empirical expressions (9, 42) relating the dependence of ionization energy to dopant density have been established. In the case of Ga, there are data (14) on activation energy *vs.* concentration, but not enough on which to base an accurate relationship. For this reason the value of $E_A = 0.065 \text{ eV}$ (43, 44) was used. For In, $E_A = 0.156 \text{ eV}$ (45) was used.

Theoretical and Experimental Results

Using the theoretical expressions derived in the previous section and the parameters listed in Table II, we have calculated the hole mobility as a function of hole density at 300 K for boron-doped silicon. The constant, τ_0 , was found by fitting the mobility to experimental points in the lattice-scattering-limited range. Our value of τ_0 is equivalent to an acoustic deformation potential constant of 8.099 eV. The optical phonon coupling constant, W , was then found by fitting the mobility to the high temperature experimental data. Our value of W is equivalent to an optical deformation potential constant of $6.024 \times 10^8 \text{ eV/cm}$. Curve 1 in Fig. 1 represents this theoretical calculation, and curve 2 was reproduced from Wagner (7). Our calculated values are within 6% of the values reported by Wagner for $N_A \leq 3 \times 10^{17} \text{ cm}^{-3}$. For higher values of hole density our calculated values are substantially higher than those of Wagner. As previously explained by Li (4), this discrepancy is due to Wagner's assumption of complete ionization of boron impurities. This assumption is valid only at low dopant densities or at high temperatures where full ionization

Table II. Values of physical parameters used in the calculations of hole mobility in p-type silicon

| Parameter | Value | Unit |
|--------------|------------------------|----------------------|
| Δ | 44.0 | meV |
| a | -6.4* | eV |
| b | -1.36* | eV |
| Cl/Ct | 2.09* | |
| θ | 735 | K |
| ρ_s | 2.329×10^3 | kg/m ³ |
| ϵ_s | 11.7 | ϵ_0 |
| τ_0 | 6.96×10^{-10} | sec K ^{2/3} |
| W | 2.44 | |

* J. C. Hensel and G. Feher, *Phys. Rev.*, **129**, 1041 (1963).

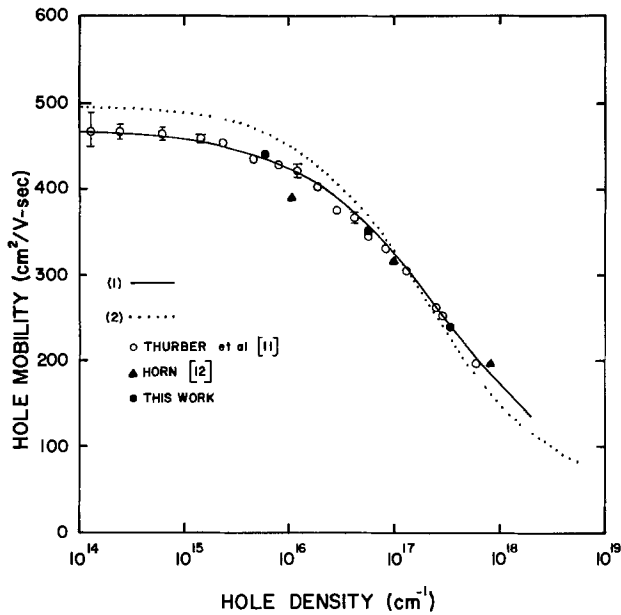


Fig. 1. Hole mobility vs. hole density for boron-doped silicon at 300 K. Curve 1 is the theoretical calculation and curve 2 is reproduced from Wagner (7). Shown also are the experimental results of this work, Horn (12), and Thurber *et al.* (11). All data points have been corrected for deionization effects.

of boron atoms prevails. The inclusion of interband scattering in the theoretical development results in a minor improvement in the quantitative agreement between theoretical and experimental results for boron-doped silicon. While Li's (4) model predicts a mobility of 475 cm²/V-sec for low-doped silicon at 300 K, the model presented in this paper predicts a mobility of 465 cm²/V-sec, and provides better agreement with the data of Thurber *et al.* (11). This value also agrees closely with direct measurements of drift mobility reported by Otaviani *et al.* (46). The theoretical calculation is in excellent agreement (within 3%) with experimental data reported by Thurber *et al.* (11). This gives support to the validity of ionization calculations based on Eq. [15] through [17]. Mobility values reported by Horn (12) are also in reasonable agreement with our theoretical results. The data points shown in Fig. 1 were corrected for deionization effects via Eq. [15] through [17].

The equations derived in the previous section were used to calculate the hole mobility for silicon doped with boron, gallium, and indium as a function of temperature with dopant density as a parameter, for 100 ≤ T ≤ 400 K. The results are displayed in Fig. 2 through 4. A major use for Ga- and In-doped silicon is as infrared detectors. In this use it is essential that any residual boron be overcompensated. In the calculations of mobility in silicon doped with gallium and indium, we assumed that very lightly compensated boron impurities were also present. The Ga- and In-doped samples used in this study were specifically prepared with minimum compensation. Values of net background boron density (10¹³ and 5 × 10¹³ cm⁻³ in the gallium- and indium-doped samples, respectively) were deduced from a best fit of the experimental data. For this reason, especially in the case of indium-doped silicon, the actual role of the impurities at low temperatures and/or low dopant densities is masked by the action of the always present boron impurities. As the dopant density and temperature increase, the assumed background density of boron impurities becomes insignificant compared to the density of ionized dopant atoms, and Fig. 2 through 4 accurately depict the influence of the particular type of impurity on the mobility of holes in p-type silicon. The figures also show that for the case of the shallower ionization energies,

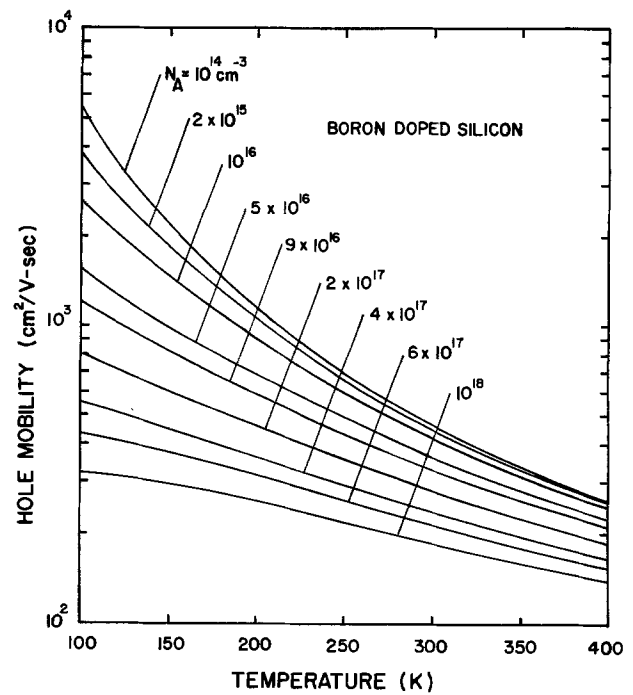


Fig. 2. The calculated hole mobility vs. temperature for boron-doped silicon with dopant density as a parameter.

mobility depends more strongly on temperature for the lightly doped case where lattice scattering is dominant, and becomes less temperature dependent as the dopant density increases.

In order to verify the adequacy of the theoretical model developed in this work, resistivity measurements were performed on silicon slices doped with boron, gallium, and indium for temperatures between 100 and 400 K. The data were obtained from NBS-4 test patterns fabricated on the silicon slices. Resistivity measurements were made on four-probe square array resistors and collector Hall effect resistors, while the net dopant density in the specimens was determined by the junction C-V method on a gated base-collector diode. These test structures are part of the test pattern NBS-4 (47), and are described in detail elsewhere

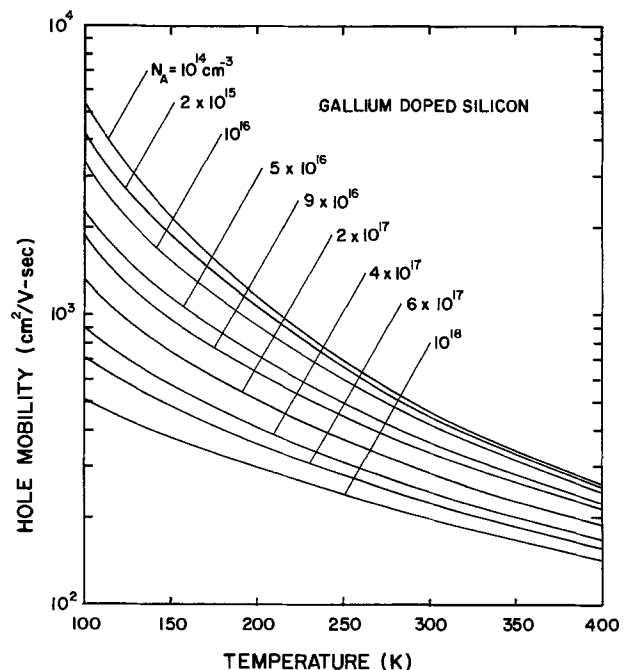


Fig. 3. The calculated hole mobility vs. temperature for gallium-doped silicon with dopant density as a parameter.

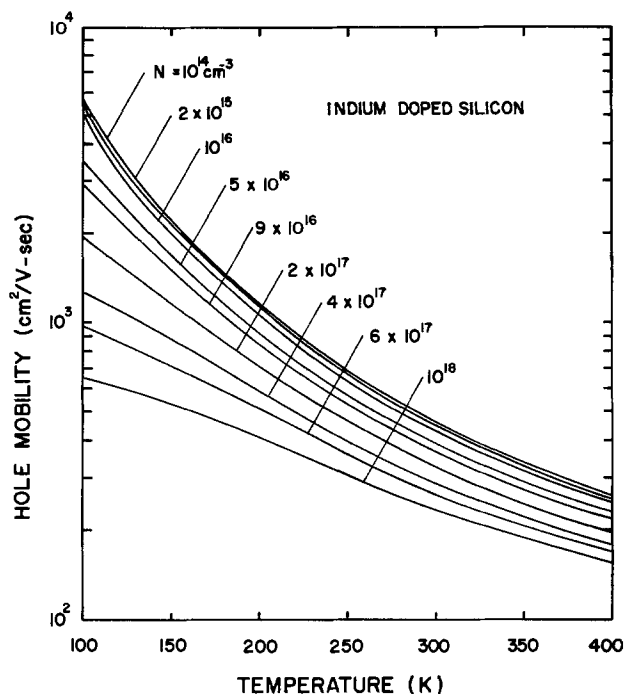


Fig. 4. The calculated hole mobility vs. temperature for indium-doped silicon with dopant density as a parameter.

(47, 48). Mean values of resistivity were determined by measuring 5-8 selected test cells with a standard deviation in resistivity values under 5%. Figure 5 shows the resistivity vs. dopant density relationship for boron-doped silicon at 300 K. The solid line represents theoretical calculations using Eq. [14], and the solid dots are our experimental data from boron-doped silicon. Resistivity values predicted by this model differ from those calculated by Li (4) by no more than 2% (at 300 K, for $N_A = 10^{14} \text{ cm}^{-3}$, our model predicts a resistivity of $134.1 \text{ } \Omega\text{-cm}$, while Li's model predicts a

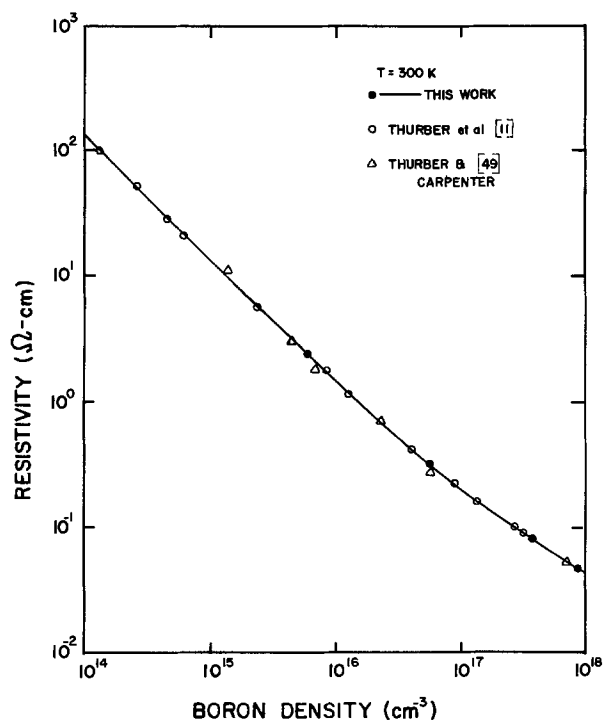


Fig. 5. Resistivity vs. dopant density for boron-doped silicon at 300 K. Shown are the theoretical calculations from Eq. [19] and the experimental results of this work, Thurber and Carpenter (49), and Thurber et al. (11).

value of $131.4 \text{ } \Omega\text{-cm}$). Wagner's (7) resistivity curve and the theoretical line coincide over most of the total boron density range. Our theoretical calculations agree with Wagner's resistivity data within 6% over the entire range of boron densities considered at $T = 300 \text{ K}$. Excellent agreement exists between our experimental data and the theoretical calculations at $T = 300 \text{ K}$. Figure 5 also shows excellent agreement between our theoretical calculations and the data of Thurber et al. (11). Good agreement was obtained with the data of Thurber and Carpenter where total boron density was obtained by the nuclear track technique (49).

Figure 6 shows the resistivity of gallium- and indium-doped silicon as a function of total dopant density for $T = 300 \text{ K}$. As expected, because of the deeper ionization energy of indium as compared to gallium, values of resistivity for gallium-doped silicon are lower than values of resistivity for indium-doped silicon at the same total dopant density. Figure 6 does not show this at low dopant densities because of the assumed values of background boron impurity densities. Excellent agreement was obtained between our experimental data and that obtained from Wolfstirn (14) for gallium-doped silicon, and our theoretical calculations at $T = 300 \text{ K}$. Wolfstirn's data quotes values for activation energy ranging from 0.052 to 0.070 eV as the dopant density changes from 1.62×10^{18} to $1.26 \times 10^{18} \text{ cm}^{-3}$. While Wolfstirn acknowledges that compensation plays a significant role in determining the degree of ionization of excess acceptors, she does not specify the degree of compensation of the samples used. Data obtained from the two indium-doped samples showed good agreement with the theoretical calculations, but the same was not true for the data of Schroder et al. (50), and Backenstoss (15). As seen in Fig. 6, for each value of measured resistivity, Schroder et al. (50) report two different values of measured indium density. The lower value of indium density was obtained by C-V and junction breakdown methods, while the higher value was obtained by Hall measurements and curve fitting. Because of uncertainties in the value of the Hall scattering factor, Schroder

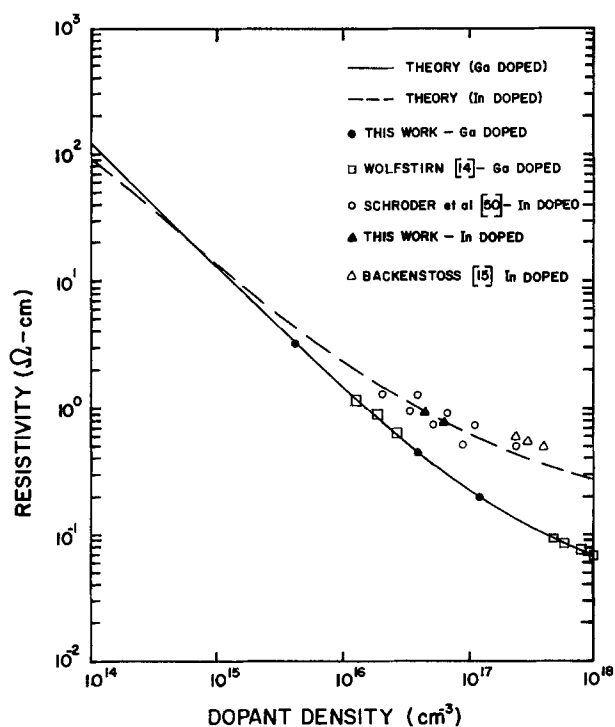


Fig. 6. Resistivity vs. dopant density for gallium- and indium-doped silicon at 300 K. Shown are theoretical calculations from Eq. [19] and the experimental results of this work, Wolfstirn (4), Schroder et al. (50), and Backenstoss (15).

et al. consider the lower value of density more reliable. Note that our theoretical calculation falls between the two values of dopant density reported by Schroder *et al.* (50). Values of resistivity of indium-doped silicon reported by Backenstoss (15) are about 25% higher than our calculated values. The work of Backenstoss (15), however, was done in the high doping region where dopant densities approach the limit of solid solubility. Backenstoss found that for dopant densities greater than $4 \times 10^{17} \text{ cm}^{-3}$ there was a considerable amount of indium precipitation. Thus it is possible that part of the discrepancy between our theoretical calculations and the data of Backenstoss is due to the low solid solubility limit of indium in silicon. Recent theoretical results of Sclar (13) for In-doped silicon also agree very closely with our theoretical calculations at 300 K. Neither Schroder *et al.* (50) nor Backenstoss (15) have indicated the degree of compensation of the samples used in their work.

To find out the adequacy of our theoretical model for temperatures other than 300 K, we compared the calculated and measured values of resistivity for silicon samples doped with boron, gallium, and indium for temperatures ranging from 100 to 400 K. Figure 7 shows the comparison between theoretical and measured resistivities for boron-doped silicon. Except for a couple of data points, agreement between the theoretical and measured values was within 8% over the entire range of temperatures. Figures 8 and 9 show the comparison between theoretical and measured resistivities for gallium- and indium-doped silicon, respectively. Agreement here was not as good as in the boron-doped case, but except for a couple of data points, agreement between theory and experiment was within 10%. For indium-doped samples, the largest discrepancies occurred at low temperatures. This is suggestive of some degree of compensation in the samples. Because the materials used were very carefully prepared to minimize compensation, an experimental estimate of percentage of compensation was not made for any of the silicon samples studied in this work.

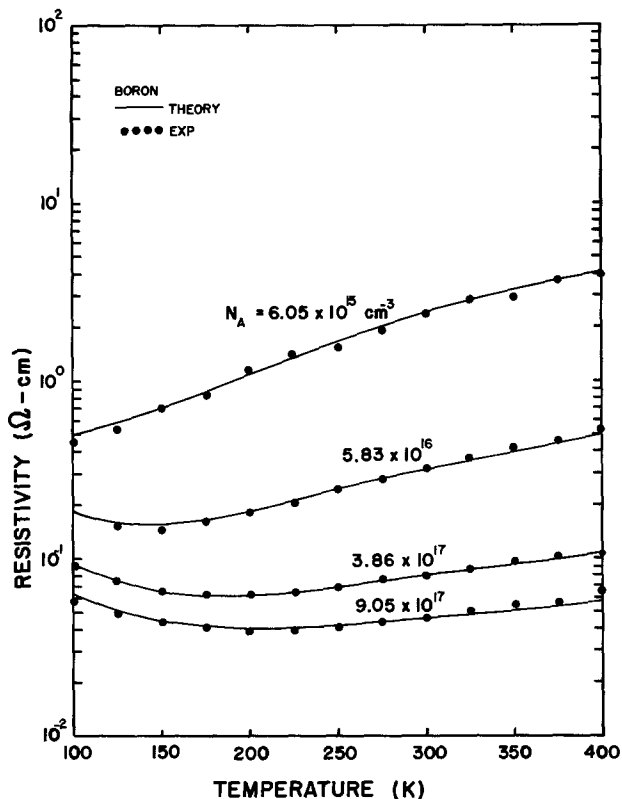


Fig. 7. Resistivity vs. temperature for the boron-doped silicon samples. Solid lines are the theoretical calculations and solid dots are the experimental data.

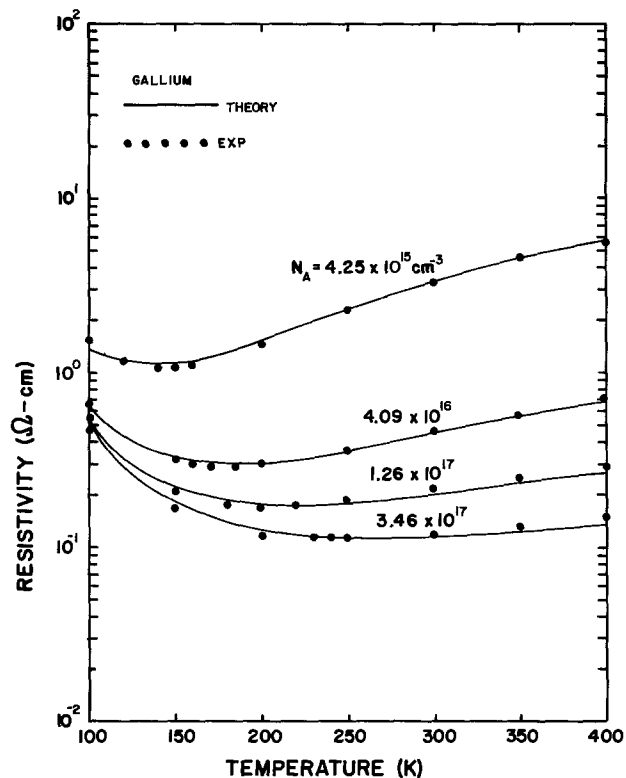


Fig. 8. Resistivity vs. temperature for the gallium-doped silicon samples. Solid lines are the theoretical calculations and solid dots are the experimental data.

Summary and Conclusions

Theoretical expressions have been derived to compute hole mobility and resistivity as functions of dopant density and temperature for silicon doped with boron, gallium, and indium. The valence band of silicon was represented by a three-band model which takes into account the nonparabolic nature of the bands. This attribute of the valence band is included in the

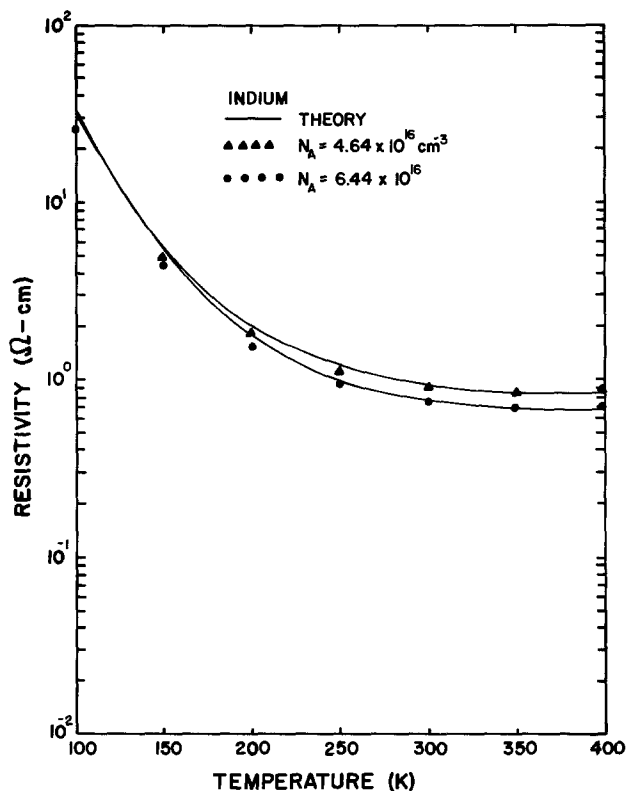


Fig. 9. Resistivity vs. temperature for the indium-doped silicon samples. Solid lines are the theoretical calculations.

effective mass calculations. Contributions from scattering by acoustical and optical phonons, ionized impurities, and neutral impurities were considered in the calculation of average relaxation time. In addition, our model also takes into account the effect of (h-h) scattering on both lattice and ionized impurity scattering relaxation times, and the effect of interband transitions on the acoustic phonon scattering relaxation time.

The resistivity analysis for the boron-, gallium-, and indium-doped silicon samples showed agreement between experimental and theoretical results within 10% over the entire range of temperature, $100 \leq T \leq 400$ K. Note that best agreement between theory and experiment was obtained for boron-doped samples, followed by gallium- and indium-doped samples. This may be due to the fact that we neglect the compensation effect and the possible dependence of ionization energy on dopant density in the theoretical calculations for gallium- and indium-doped samples. An experimental estimate of degree of compensation was not made for any of the silicon samples studied here. Data points representing a resistivity-dopant density pair are estimated to have a total error of around 6%.

A comparison between our calculated mobility values with those of Wagner's (7) data on boron-doped silicon at 300 K shows that agreement is within $\pm 6\%$ for $N_A \leq 3 \times 10^{17} \text{ cm}^{-3}$. Discrepancies at higher dopant densities can be eliminated if the effect of deionization of boron impurities were included in Wagner's calculations (7). Excellent agreement was found between our theoretical calculations of mobility in boron-doped silicon and the data of Thurber *et al.* (11) at 300 K. We have obtained excellent agreement between theoretical values of resistivity and our experimental data for boron-, gallium-, and indium-doped silicon at 300 K; our theoretical calculations also agreed with the resistivity data by Thurber *et al.* (11) for boron-doped silicon, and Wolfstirn (14) for gallium-doped silicon. From this study, we have found that the theoretical expressions derived in this work are adequate for mobility and resistivity calculations for p-type silicon valid for $10^{14} \leq N_A \leq 10^{18} \text{ cm}^{-3}$ and $100 \leq T \leq 400$ K. The work presented here may be considered as a further refinement and extension over that published recently by Li (4) for p-type silicon.

Acknowledgment

The financial support received from the National Bureau of Standards and the National Science Foundation is gratefully acknowledged. Thanks are due to Dr. W. M. Bullis and W. R. Thurber of the National Bureau of Standards for their critical review of the manuscript, and their continued interest in this work.

The authors are also indebted to M. R. Riley for preparation and measurement of the boron-doped test structures, and to D. Yuen for resistivity measurements on the gallium- and indium-doped samples. Assistance by H. Mehta in carrying out the numerical computations is also gratefully acknowledged. This research was jointly supported by the National Bureau of Standards Contract 7-35741 and the National Science Foundation Grant ENG 76-81828.

Manuscript submitted July 30, 1979; revised manuscript received Sept. 15, 1980. This was Paper 551 presented at the Los Angeles, California, Meeting of the Society, Oct. 14-19, 1979.

Any discussion of this paper will appear in a Discussion Section to be published in the December 1981 JOURNAL. All discussions for the December 1981 Discussion Section should be submitted by Aug. 1, 1981.

Publication costs of this article were assisted by the University of Florida.

REFERENCES

1. M. Costato and L. Reggiani, *Il Nuovo Cimento*, **68**, 64 (1970).
2. T. T. Braggins, Thesis, Syracuse University (1975).
3. F. J. Morin and J. P. Maita, *Phys. Rev.*, **96**, 28 (1954).
4. S. S. Li, *Solid State Electron.*, **21**, 1109 (1978).
5. J. C. Irvin, *Bell Syst. Tech. J.*, **16**, 387 (1962).
6. S. M. Sze and J. C. Irvin, *Solid State Electron.*, **11**, 599 (1968).
7. S. Wagner, *This Journal*, **119**, 1570 (1972).
8. G. W. Ludwig and R. L. Watters, *Phys. Rev.*, **101**, 1699 (1956).
9. G. L. Pearson and J. Bardeen, *ibid.*, **75**, 865 (1949).
10. M. Prince, *ibid.*, **93**, 1204 (1954).
11. W. R. Thurber, R. L. Mathis, and Y. M. Liu, *Nat. Bur. Stand. Spec. Publ.*, **400-36** (1978).
12. F. H. Horn, *Phys. Rev.*, **97**, 1521 (1955).
13. N. Sclar, *IEEE Trans. Electron Devices*, **ed-24**, 709 (1977).
14. K. B. Wolfstirn, *J. Phys. Chem. Solids*, **16**, 279 (1960).
15. G. Backenstoss, *Phys. Rev.*, **108**, 1416 (1957).
16. E. O. Kane, *J. Phys. Chem. Solids*, **1**, 82 (1956).
17. H. D. Barber, *Solid State Electron.*, **10**, 1039 (1967).
18. S. Zwerdling, K. J. Button, B. Lax, and L. M. Roth, *Phys. Rev. Lett.*, **4**, 173 (1960).
19. L. C. Linares and S. S. Li, *Phys. Status Solidi.*, To be published (1980).
20. M. Tiersten, *J. Phys. Chem. Solids*, **25**, 1151 (1964).
21. G. H. Bir, E. Normantas, and G. E. Pikus, *Soviet Phys. Solid State*, **4**, 867 (1962).
22. J. M. Radcliffe, *Proc. Phys. Soc. London Ser. A*, **68**, 675 (1955).
23. R. Barrie, *Proc. Phys. Soc. London Ser. B*, **69**, 553 (1956).
24. M. Ashe and J. vonBorzeszkowski, *Phys. Status Solidi*, **37**, 433 (1970).
25. G. E. Pikus and G. L. Bir, *Sov. Phys. Solid State*, **1**, 136, 1502 (1959).
26. H. Ehrenreich and A. W. Overhauser, *Phys. Rev.*, **104**, 649 (1956).
27. E. M. Conwell, *J. Phys. Chem. Solids*, **8**, 234 (1959).
28. E. M. Conwell and V. F. Weisskopf, *Phys. Rev.*, **77**, 388 (1950).
29. H. Brooks, in "Advances in Electronics and Electron Physics," Vol. 7, L. Marton, Editor, pp. 85-182, Academic Press, New York (1955).
30. C. Herring, *Bell Syst. Tech. J.*, **36**, 237 (1955).
31. C. Erginsoy, *Phys. Rev.*, **104**, 1559 (1956).
32. N. Sclar, *ibid.*, **104**, 1548 (1956).
33. N. Sclar, *ibid.*, **104**, 1559 (1956).
34. T. C. McGill and R. Baron, *Phys. Rev. B*, **11**, 5208 (1975).
35. R. Baron, M. H. Young, and T. C. McGill, in "Proc. of 13th Conf. on the Physics of Semiconductors," L. G. Fumi, Editor, p. 1158, Tipographia Marves, Rome (1977).
36. S. S. Li, *Nat. Bur. Stand. Spec. Publ.*, **400-33**, March (1977).
37. R. S. Keyes, *J. Phys. Chem. Solids*, **6**, 1 (1958).
38. M. Luong and A. W. Shaw, *Phys. Rev. B*, **4**, 2436 (1971).
39. J. S. Blakemore, "Semiconductor Statistics," Pergamon Press, New York (1962).
40. A. Baldereschi and N. O. Lipari, in "Proc. of 13th Int. Conf. on The Physics of Semiconductors," L. G. Fumi, Editor, p. 595, Tipographia Marves, Rome (1977).
41. H. J. Mason, Jr. and J. S. Blakemore, *J. Appl. Phys.*, **43**, 2810 (1972).
42. N. A. Penin, B. G. Zhurkin, and B. A. Volkov, *Sov. Phys.-Solid State*, **7**, 2580 (1966).
43. A. G. Milnes, "Deep Impurities In Semiconductors," John Wiley & Sons, New York (1973).
44. S. M. Sze, "Physics of Semiconductor Devices," John Wiley & Sons, New York (1969).
45. W. Scott, Paper presented at IRIS Specialty Group on IR Detectors, Colorado Springs, CO, March 21-23, 1977.
46. G. Ottaviana, L. Reggiani, C. Canali, F. Nava, and A. Alberigi-Quaranta, *Phys. Rev. B*, **12**, 3318 (1975).
47. W. R. Thurber and M. G. Buehler, *Nat. Bur. Stand. Spec. Publ.* **400-32**, April (1978).
48. M. Buehler and W. R. Thurber, *IEEE Trans. Electron Devices*, **ed-23**, 968 (1976).
49. W. R. Thurber and B. S. Carpenter, *This Journal*, **125**, 654 (1978).
50. D. K. Schroder, T. T. Braggins, and H. M. Hobgood, *J. Appl. Phys.*, **49**, 5256 (1978).

Measurement and Identification of Distortion, Alignment, and Mask Errors in IC Processing

K. H. Nicholas,* I. J. Stemp, and H. E. Brockman

Philips Research Laboratories, Redhill, Surrey, England

ABSTRACT

Measurement and identification of misregistration between patterns in integrated circuits is becoming increasingly important as finer geometry processes are being developed for VLSI. Various forms of the Stickman resistor pattern are described. These enable measurement of the alignment errors, mask errors, and distortions that occur when using any alignment apparatus. The properties of the different forms of Stickman resistors are compared and examples of applications to studying mask making errors, slice/mask distortions, projection distortions, and process induced slice distortions are described. It is shown that misregistrations of 0.1 micron or even less can be measured and identified. Direct measurements on simple apparatus are shown to be reproducible to ± 0.003 micron and accuracy is estimated at 5% of the misregistration with simple apparatus and 2% for a one micron misregistration if on chip measurement of sheet resistance is made.

Automatic measurement of the misregistration between patterns in integrated circuits and identification of the causes are necessary to the development of high packing density circuits. A resistor pattern for measuring misregistrations automatically has been described (1) that is more accurate and sensitive than other methods (2-5). In this paper three forms of the pattern (1), called the Stickman pattern from its shape, are described. They enable measurement of mask errors, alignment, and distortion in any alignment apparatus.

The basic pattern is first outlined and then the standard, small displacement, and protected edge forms are described and compared. Examples of measurements of mask faults and slice and image distortions are given to illustrate the flexibility and accuracy of the methods.

Throughout the paper misalignment is used to describe errors in aligning the new pattern with the slice as a whole and generally has only one value per slice. There can be several values with steppers. Misregistrations refer to errors at each measurement site including misalignment. Residual misregistrations are the values when apparent alignment errors have been removed. Distortions are the misregistrations when alignment and mask errors have been eliminated.

Stickman Types

Basic pattern.—The basic Stickman resistor pattern is shown in Fig. 1. It can be formed by a conducting layer on a mask or slice substrate or by doping in a silicon slice. The two resistors connected at one end are formed by two definition stages. One defines the outside edges shown with a solid line while the inside edges, shown by a dotted line, are defined at the other stage. Misregistration leads to differences in widths and hence to differences in resistances. It can be shown (1) that the misregistration, Δx , is given by

$$\Delta x = \frac{1}{2} \rho L (R_1^{-1} - R_2^{-1})$$

where ρ is the sheet resistance, L is the resistor length, and R_1 and R_2 are the resistances. The length of the resistor and sheet resistance are scaling factors. The sheet resistance can be measured on van de Pauw patterns adjacent to the Stickman patterns and the length is made large. The value for Δx is independent of resistor width and so is independent of systematic lithographic variations. Accuracy is better than 2% (0.02 micron for 1 micron misregistration) with typical measuring apparatus and linewidths.

Devices to measure misregistrations in X and Y directions are generally formed at each site. A pattern of resistors to do this is shown in Fig. 2. A constant current is passed from I to 0 and voltages across the resistors (1-2, 2-3, etc.) measured to evaluate their resistances.

The values can be analyzed in a computer to produce misregistrations and these are further analyzed in the computer in terms of position on the slices.

Standard.—The two patterns used to define resistors in the standard method are on two separate masks if conventional lithography is used. The patterns are indicated by different cross hatching in Fig. 3. Such patterns can be included on appropriate mask levels in production integrated circuit processes. The standard form is therefore ideal for monitoring total misregis-

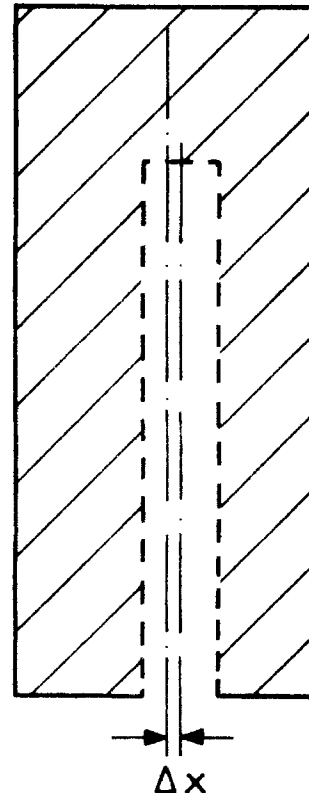


Fig. 1. Basic resistor pattern

* Electrochemical Society Active Member.

Key words: integrated circuits, resistivity, semiconductor.

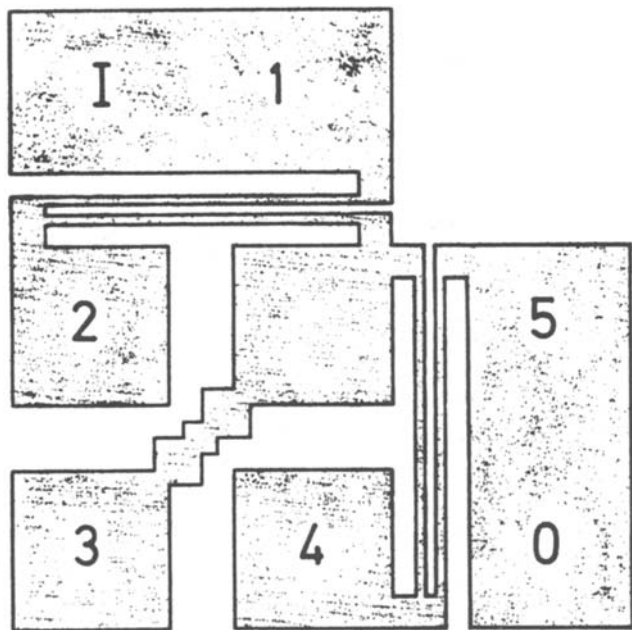


Fig. 2. Pattern with probe pads for misregistrations in both directions.

trations in integrated circuit process lines and can be used on any aligner.

Errors in alignment can generally be separated from other effects in the computer analysis program (6) but mask effects and distortions cannot necessarily be separated. In principle mask errors can be checked by using a "low distortion" process and finding errors that are reproduced on several slices. Some errors can be observed by this method or by studying the pattern of misregistrations but it is only generally possible if the errors are of the order of $0.1 \mu\text{m}$ or greater and a genuine "low distortion" process can be achieved. Subtracting the values of mask errors so obtained can allow distortion values to be derived but again the accuracy is limited.

The standard form can be used to assess mask makers directly. The two patterns are exposed successively on a bright chrome mask and the chrome layer defined. The thin film chrome resistors and the sheet resistance of the chrome can then be measured to give values for the misregistrations produced in the mask maker. This method can be extremely sensitive and accurate as will be shown in the Results section.

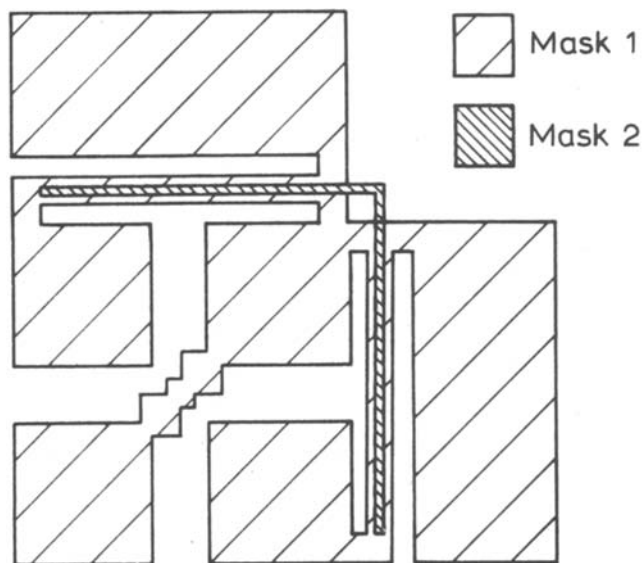


Fig. 3. Standard two mask level form

The mask stepping error can be greatly reduced by including both patterns on the same mask and displacing the second mask to superimpose it. Step and repeat errors of translation are virtually eliminated but any slight rotation of the chip leads to errors because the displacement has to be hundreds of microns to clear the pad areas. Also, it is not possible to misalign by hundreds of microns accurately in some aligners. The standard pattern is therefore unsuitable for accurate measurement of distortion.

Small displacement.—The small displacement pattern (7) was designed to eliminate mask stepping and some mask lithographic errors by using a single mask and reducing the displacement at the second alignment to a few microns. A single pattern has only to be misaligned by about ten microns. Chip rotation effects are negligible and the displacement only has to be accurate to about $2.5 \mu\text{m}$. The pattern is shown in Fig. 4. If, for example a conducting layer is being etched, the layer is first defined to leave the shaded area. At the second definition stage the mask is misaligned by a small amount so that the small square at the top right falls in the larger one and the layer is redefined. The resulting pattern is shown in Fig. 4b, with the resistors indicated by heavy shading.

Distortion values are the misregistrations with the misalignment values removed by the computer (6) as mask errors are virtually eliminated. The misalignment values are not generally meaningful because of the special alignment situation associated with the displacement. The small displacement pattern cannot be used with most automatic aligners because of the need for a larger displacement to accommodate the larger auto-align mask.

Protected edge.—A new form for measuring distortion on an automatic aligner and for measuring alignment accurately has been developed. It is called the protected edge form because there are two edge protection masks as well as one critical mask. The critical mask is shown in Fig. 5a. It is designed to be like a perfectly aligned final pattern.

If a conducting layer is defined with negative resist the procedure is most straightforward because the layer has to remain where either the critical mask or

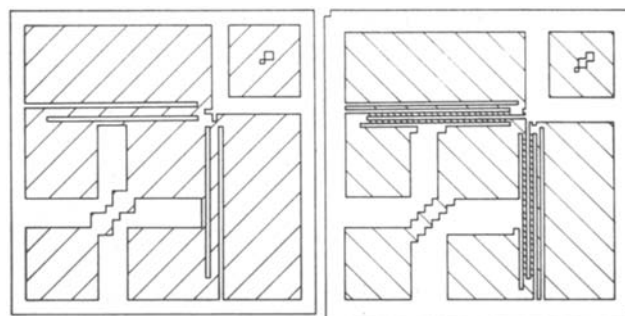


Fig. 4. Small displacement form

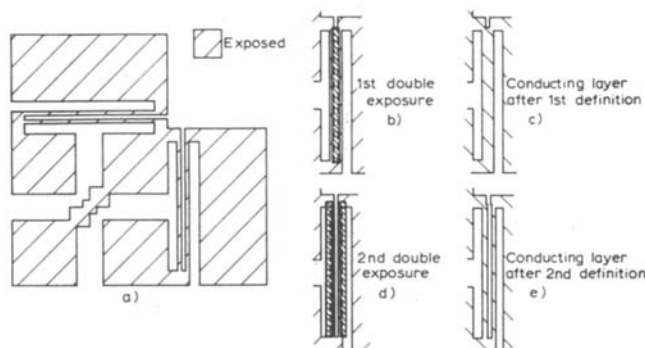


Fig. 5. Protected edge form

the edge protection mask is clear. The critical mask and the inner edge protection mask (dotted) are both exposed as shown for the X-direction in Fig. 5b. The layer is then etched leaving the layer shown in Fig. 5c with outside edges defined by the critical mask. At the second definition step the critical mask is again exposed but an outer edge protection mask is used for the second exposure as shown in Fig. 5d. This time the inside edges are defined by the critical mask and so after etching the final pattern shown in Fig. 5e is obtained.

The misregistration so measured is independent of step and repeat mask errors because resistor edges are defined by the same critical mask. The accuracy with which the resistors are matched on the critical mask will affect these results but this can be measured by a separate test in which only the critical mask is exposed and a measurement made. These measurements can then be removed from other results to give the true misregistration values. The matching on masks is often good enough to make the correction unnecessary.

The independence from step and repeat errors and smallness of other mask errors makes the protected edge form suitable for accurate measurement of distortion. It is ideal for measuring alignment as the same critical mask is used twice so that errors between alignment marks and patterns do not affect the results. The only disadvantages are the more complex processing and somewhat lower sensitivity. The lower sensitivity follows from the need for the protected edge masks to protect one edge of the resistors but not the other. This requires the resistors to be wider.

Comparison between different forms.—In this section the different forms of Stickman pattern are compared. The comparison is summarized in Table I. All forms can be used with any integrated circuit process though some modifications may be necessary.

Alignment apparatus can be assessed on both the standard and protected edge forms, but in the case of the standard form mask errors may be included particularly if alignment markers and measurement patterns are separately exposed. The small displacement pattern has special alignment requirements and so it is not generally suitable.

The standard form is ideal for overall misregistration measurements, particularly on work slices in production, and alignment errors can be separated even with the few process control sites normally present on such slices. The standard form is also the one to use for mask error studies. This can be done using a "low distortion" process, such as double exposure of a single resist layer to define resistors, and look-

ing for common pattern of errors on different slices. The accuracy is then limited by residual distortions including temperature effects. The assessment of mask makers is best done using bright chrome mask layers to form thin film resistors after double exposure.

Distortions can be measured accurately by the small displacement and protected edge forms. The former cannot be used with most automatic aligners but has the advantage of simpler processing and higher accuracy.

Typical device length is 200 microns and an average resistor width of three microns is used to measure errors up to two microns. The minimum lithographic dimension on the mask is six microns as the resistor edges are defined in separate exposures. The only case of a complete resistor appearing on a mask is in the protected edge critical mask when the width is greater anyway. The greater width reduces sensitivity from 6.7% resistor difference per 0.1 μm to 3.3% difference in resistance per 0.1 μm . As misregistrations are decreased finer geometries can be used and sensitivity is further increased. The only limitation is that the resistivity is linear with width and so in general widths should be much greater than conductive layer thicknesses. It is generally possible to measure resistor values to better than 1% on a normal automatic probe and measurement apparatus if four terminal measurements are used. The accuracy is therefore better than 0.01 μm for a 1 μm misregistration. In the Results section it is shown that small misregistrations can be measured with a reproducibility of an order of magnitude smaller than this.

The different forms are suitable for different applications but at least one is suitable for any particular measurement.

Results

Applications are described that illustrate the usefulness of the technique in measuring and identifying causes of misregistration. The different forms can be used to study misalignments, mask errors, and distortions. The measurement of misalignment is straightforward, as described earlier, and the applications outlined here are to the measurement of mask errors and distortions.

Mask errors.—Mask errors have been identified by repetition of errors on different slices (6) and by the pattern of errors (1) using the standard form. Distortion variations were minimized but they do limit the accuracy.

A better method for studying errors on mask machines is to double define bright chrome layers in the mask making machine, again using the standard patterns, and measuring the thin film chrome resistors so formed. The technique has been applied to optical and electron beam mask makers.

Rotational misalignment has little meaning on mask makers or on direct slice writers working from marker arrays. It is useful in these cases to dispense with computer processing of data and have direct read-out of misregistrations. A circuit for direct reading onto a chart recorder is shown in Fig. 6. The resistors r_1 and r_2 are chosen to have the same value but much lower than the Stickman resistors R_L and R_R . By applying the same circuit and voltage V to X and Y direction devices and the outputs to an X-Y recorder, misregistration vectors can be drawn. The technique is also applicable on slices to Y-misregistrations in columns and X-misregistrations in rows where displacements due to rotation are virtually constant. The technique is not applicable if sheet resistance of the conducting layer is variable or if contact resistance is large and variable.

The two standard patterns had to be exposed consecutively on a widely used commercial mask maker as there was no facility for aligning reticles accurately with masks. Even so some misregistrations were ob-

Table I. Main properties of different Stickman forms

| Device pattern | Standard (STD) | Small displacement (SD) | Protected edge (PE) |
|--------------------------------|----------------|-------------------------|---------------------|
| <i>Measured directly</i> | | | |
| Alignment | yes | | yes |
| Overall misregistration | yes | | |
| Mask errors | yes | | |
| Distortions | | yes | yes |
| <i>Fabrication</i> | | | |
| No. exposures | 2 | 2 | 4 |
| No. masks | 2 | 1 | 3 |
| On work slices | yes | | |
| <i>Typical geometries</i> | | | |
| Length μm | 200 | 200 | 200 |
| Average width μm | 3 | 3 | 6 |
| <i>Sensitivity</i> | | | |
| % difference/0.1 μm | 6.7 | 6.7 | 3.3 |
| <i>Lithography</i> | | | |
| Photo-contact | yes | yes | yes |
| Photo-projection (P-E) | yes | yes | yes |
| Automatic stepper | yes | | yes |
| Electron image proj. | yes | yes | yes |
| Direct slice writing | yes | | |
| X-ray | yes | | yes |

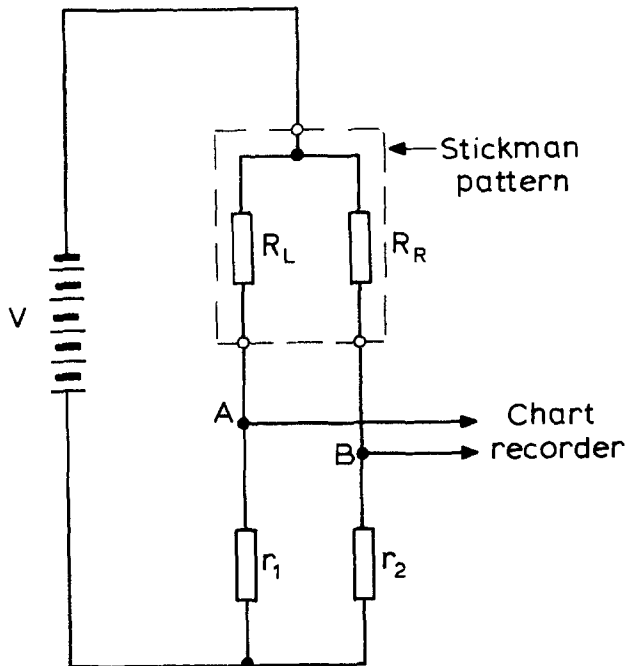


Fig. 6. Circuit for direct recording of misregistrations

served. The reticle contains an 8×8 array of devices. Misregistrations in the X-direction for two rows of devices (extending in the X-direction) are shown in Fig. 7(a) and (b). There is a repetitive pattern every 3.8 mm equal to the step and repeat distance. Errors within the pattern (up to $0.06 \mu\text{m}$) are due to errors or distortion in the reticle or rotational errors in its placement. It was made on widely used commercial equipment. Misregistration values for each position in a chip are compared to the equivalent position in the first chip to evaluate step and repeat errors. The average values and standard deviations for the 16 positions are plotted against chip number in Fig. 8. Reproducibility over the chip is generally about $\pm 0.003 \mu\text{m}$ (a few atomic layers) showing how sensitive the technique is. The absolute accuracy is limited by sheet resistance variations and accuracy of the voltage measuring apparatus to about 5% of the misregistration. Step and repeat errors are less than $0.04 \mu\text{m}$ except for the relatively large change by about $0.15 \mu\text{m}$ around chip 7. This represents two $\lambda/8$ counts on the laser interferometer ($\lambda = 633 \text{ nm}$). The reason for the counting error is being investigated.

It is possible to position patterns on masks with some more advanced mask makers enabling patterns to be written at well-separated times. This gives a more realistic measurement of alignment between different masks or different layers in direct slice writing. Results on an experimental electron beam pattern generator, with a six weeks gap between exposures and

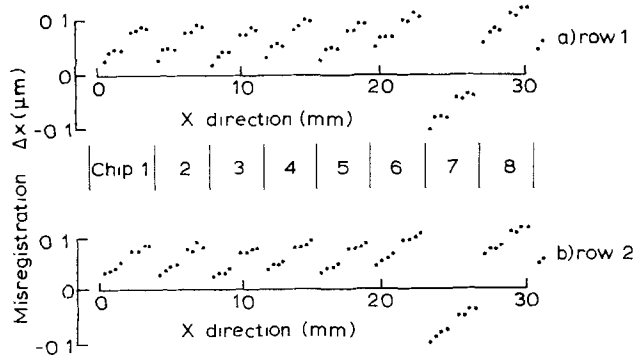


Fig. 7. Misregistrations in double written mask from optical mask maker.

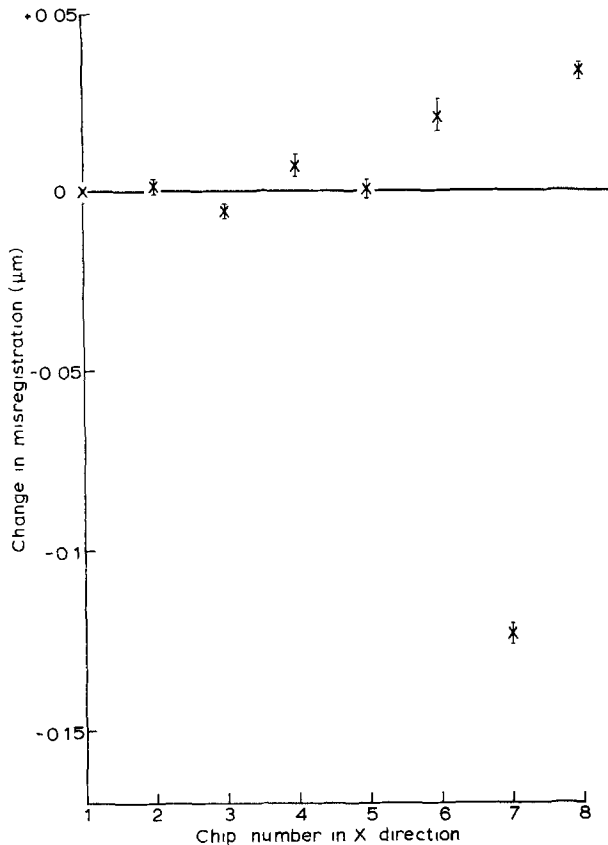


Fig. 8. Step and repeat errors in optical mask makers

incorrect adjustment the second time, are shown in Fig. 9. The outside rectangle represents the edge of the chip and the vectors give errors at 16 places in the chip. The scale for the vectors is given at the top. The sets of three vectors represent three different chips. There can be seen to be a general magnification error common to all chips which is due to a setting up error, but closer inspection shows an additional error in the X-direction. The corners of each chip are defined by markers. The markers in chip 3 (crosses) were read correctly but it appears that the bottom left-hand marker in chip 1 (diamonds) which determines the origin in the X-direction was differently read on the two occasions by about $0.08 \mu\text{m}$. This led to differences in the X-direction from chip 3 on the left-hand side of the chip but improving agreement on moving to the right. The same marker was misread in chip 2 (plus signs) but this time it was the right-hand marker and so there is a magnification error causing increasing errors to the right of the chip. This illustrates how the causes even

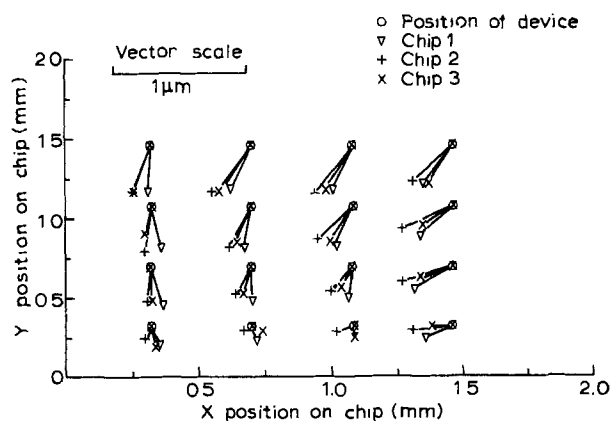


Fig. 9. Repetitive errors in different chips due to electron beam machine adjustment errors.

of small errors can be identified so that steps can be taken to reduce them. Errors were generally less than $0.1 \mu\text{m}$ when the machine was correctly adjusted (1).

Matching of pairs of resistor patterns is required for the critical mask in the protected edge form. If the critical mask alone is used to define resistors the matching can be investigated. Even with a mask made on an experimental pattern generator errors were only $+0.007 \mu\text{m}$ and correction for such errors is normally unnecessary.

Distortions.—Misregistrations caused by lateral distortions can be measured with the small displacement or protected edge forms. The three common causes are (i) mask/slice distortion in the alignment equipment, (ii) pattern distortion on projection, and (iii) process-induced slice distortion. Distortions only contribute to misregistrations if they change between the two alignment stages.

An example of mask/slice distortion difference is shown in Fig. 10. Vectors representing misregistrations with alignment effects removed are shown in their position on the slice. The misregistrations are due to thermal expansion as the temperature (6) at the two alignment stages differed and the mask had a much higher temperature coefficient of expansion than the silicon slice. The effect can be reduced in some advanced alignment apparatus but such expansion is still important.

One way of compensating for the effect in some aligners is by intentional pattern distortion (8). Such distortion is shown in Fig. 11 where a contraction has been produced intentionally on an electron image projector. Analysis shows the contraction to be linear. On this machine any expansion can be compensated for automatically using signals from markers on the slice.

Distortion of slices by processing have also been observed. Most distortions are roughly linear but if stresses are very large nonlinear effects can occur. An example is shown in Fig. 12 where large stress was intentionally produced by a $0.14 \mu\text{m}$ thick layer of silicon nitride with a very thin oxide layer below. Such nonlinear distortions have only been found in the presence of a large density of defects.

Conclusions

Three forms of the Stickman resistor pattern (i) the standard (ii) the small displacement, and (iii) the protected edge forms have been described and compared.

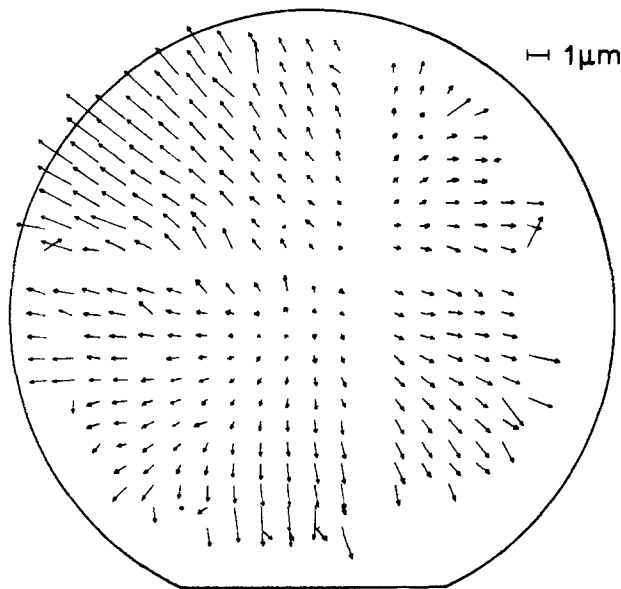


Fig. 10. Expansion due to temperature change

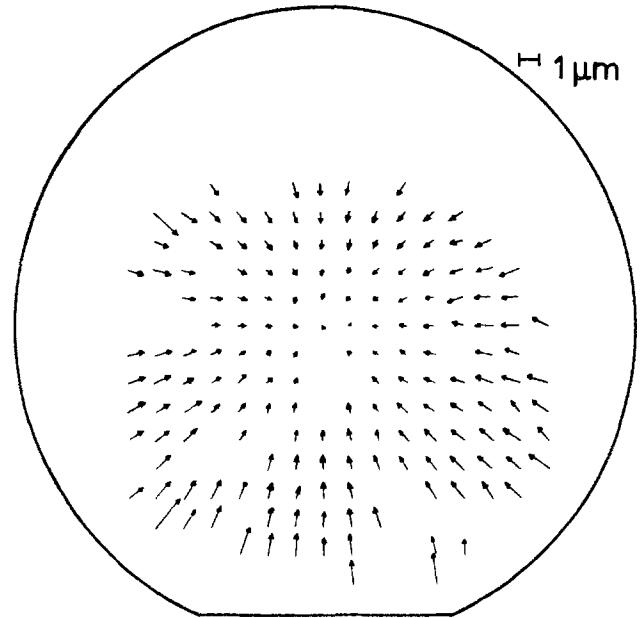


Fig. 11. Contraction of patterns in an electron image projector

It has been shown that alignment, mask errors, and distortions can be measured on any aligner using the appropriate form.

Identifications of errors in optical and electron beam mask makers have been described and observations of slice/mask distortion, projection distortion, and slice distortion outlined.

It has been shown that sensitivity and reproducibility are such that misregistration effects much less than $0.1 \mu\text{m}$ can be identified and measured to reproducibility of $\pm 0.003 \mu\text{m}$ using simple apparatus. Accuracy of measurement is limited to about 5% of the total misregistration if the simple apparatus is used but improved to 2% for $1 \mu\text{m}$ misregistration if sheet resistance is measured on each chip.

Acknowledgments

We would like to acknowledge the assistance of Mrs. C. Glaister in fabrication of devices and useful discussion with Dr. P. J. Daniel. We would also like to thank colleagues in Philips for providing masks and slices for measurement.

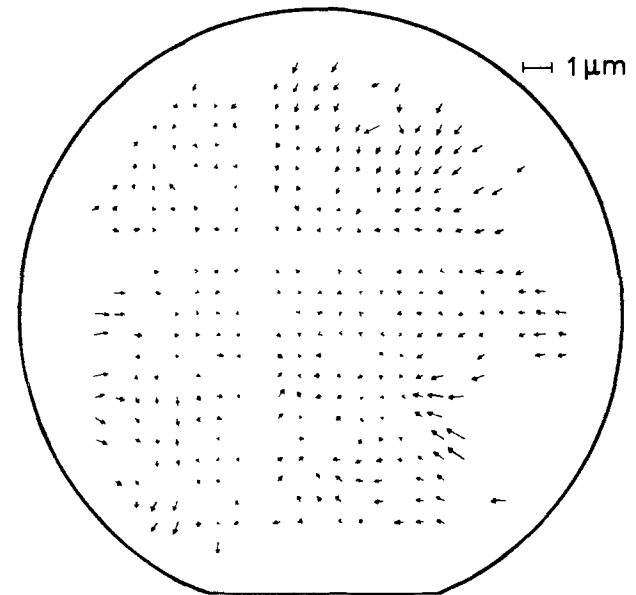


Fig. 12. Nonlinear distortions due to a silicon nitride layer

Manuscript submitted June 19, 1980; revised manuscript received ca. Sept. 16, 1980. This was Paper 184 presented at the Pittsburgh, Pennsylvania, Meeting of the Society, Oct. 15-20, 1978.

Any discussion of this paper will appear in a Discussion Section to be published in the December 1981 JOURNAL. All discussions for the December 1981 Discussion Section should be submitted by Aug. 1, 1981.

Publication costs of this article were assisted by Philips Research Laboratories.

LIST OF SYMBOLS

| | |
|----------------------|--|
| $\Delta x, \Delta y$ | misregistration in X and Y direction (μm) |
| ρ | sheet resistance Ω/\square |
| L | length of resistors (μm) |
| R_1, R_2 | Stickman resistor values (Ω) |
| R_L, R_R | left and right resistor values (Ω) |
| r_1, r_2 | measurement resistors (Ω) |
| V | applied voltage V (volts) |

REFERENCES

1. I. J. Stemp, K. H. Nicholas, and H. E. Brockman, Proc. Conf. Microcircuit Engineering '78, Cambridge, England, April 1978.
2. D. S. Ferloff, *IEEE J. Solid State Circuits*, **sc-13**, 436 (1978).
3. T. J. Russell, T.F. Leedy, and R. L. Mattis, *Tech. Dig. IEDM*, p. 7A (IEEE), Dec. 1977.
4. R. G. Gegenworth and R. P. Lamming, *S.P.I.E. V100 Semiconductor Microlithography II*, p. 66 (1977).
5. L. D. Yau, *Appl. Phys. Lett.*, **33**, 756 (1978).
6. I. J. Stemp, K. H. Nicholas, and H. E. Brockman, *IEEE Trans. Electron Devices*, **ed-26**, 729 (1979).
7. I. J. Stemp, K. H. Nicholas, and H. E. Brockman, Abstract 184, p. 491, The Electrochemical Society Extended Abstracts, Pittsburgh, Pennsylvania, Oct. 15-20, 1978.
8. R. Ward, To be published.

Surface Charges in a Zinc-Borosilicate Glass/Silicon System

Y. Misawa, H. Hachino, S. Hara, and T. Ogawa

Hitachi Limited, Hitachi Research Laboratory, Hitachi, Ibaraki, Japan

and H. Yagi

Hitachi Limited, Hitachi Works, Hitachi, Ibaraki, Japan

ABSTRACT

Surface charges in a zinc-borosilicate glass/silicon system were studied by measuring capacitance-voltage curves of metal-glass-silicon capacitors at various temperatures. The capacitance-voltage curves change remarkably with measurement frequency and temperature. The density of positive fixed charge decreases significantly with increasing glass firing temperature and also when nitrogen gas is added to the oxygen firing atmosphere. On the other hand, the density of the surface state is about $(2-6) \times 10^{12} \text{ cm}^{-2} \cdot \text{eV}^{-1}$ and insensitive to glass firing conditions. The surface charge is positive for n-type silicon and negative for p-type silicon when the Fermi level is near the intrinsic energy level. The surface charges are reversed, however, when the Fermi level is near the bandedge.

Surface passivation using glass powder is effective for achieving good reliability in high voltage silicon power devices since glass is electrically stable, easy to coat as a thick film, resistant to humidity, and has a low ion mobility. Therefore, many glass passivated silicon devices, such as thyristors, transistors, and diodes, have recently been developed.

Glasses as passivants for silicon devices are classified roughly into zinc-based glass and lead-based glass. Zinc-based glass is very stable at high temperature and high electric fields (1, 2), and therefore, is more suitable for achieving high reliability.

It is necessary to know better the surface charge configuration in a glass/silicon system in order to design glass passivated silicon devices accurately. However, not many investigations on this topic have been reported before. It is known that surface charge density changes with glass firing conditions, such as firing temperature and the content of the ambient (3). Many surface states exist at the glass/silicon interface (1, 2) and the flatband voltage is positive for n-type silicon and negative for p-type silicon (2).

However, the changes of surface charge configuration in a glass/silicon system with glass firing conditions have not been studied.

Key words: charge, films, glass.

In this paper, the variations of fixed charge density and surface state density with glass firing conditions and the conductivity-type of silicon substrates are discussed by measuring capacitance-voltage (C-V) curves at various temperatures.

Experimental

In this work, surface charge in a glass/silicon system was measured by metal-glass-silicon (MGS) capacitors at various temperatures. This method, as proposed by Gray and Brown (4), can separate the effects of the fixed charge in glass and surface states at glass/silicon interface, on the surface potential. Table I shows the properties of silicon substrates. The composition of the glass used is: ZnO, 65 weight percent (w/o); B₂O₃, 21 w/o; SiO₂, 8.5 w/o; PbO, 4 w/o; SnO, 1 w/o; and Sb₂O₃, 0.5 w/o. This glass has a

Table I. Properties of silicon substrates

| Conduction type | N | P |
|---------------------------------------|---------------|---------------|
| Dopant | Phosphorus | Boron |
| Resistivity, $\Omega \cdot \text{cm}$ | 9-15 | 8-12 |
| Crystal orientation | (111) | (111) |
| Method of production | CZ | CZ |
| Surface | Mirror polish | Mirror polish |

softening point of 645°C, crystallization point of 719°C, and thermal expansion coefficient of $4.0 \cdot 10^{-6}/^\circ\text{C}$. MGS capacitors were prepared by following procedure. The glass powder was deposited on the silicon substrate by the electrophoretical method. The colloidal suspension used consisted of isopropyl alcohol as a suspension medium with a small amount of additive electrolyte and glass powder whose size was controlled by decantation. The glass film thickness was controlled to about $10 \mu\text{m}$. The deposited glass powder was fired in an oxygen or a nitrogen-oxygen (4:1) mixture at various temperatures. The metal electrodes were formed on the glass film by evaporating aluminum. Capacitance of the MGS was measured in the evacuated chamber at various temperatures by a capacitance bridge. The measurement frequency was 1 MHz unless otherwise noted.

Results and Discussion

Effects of measurement frequency and temperature on the C-V curves.—Figure 1 shows the effect of measurement frequency on the C-V curves for samples made with the glass fired on n-type silicon at 710°C in a nitrogen-oxygen mixed atmosphere. The C-V curve shifts to the positive voltage direction with increasing frequency. It can be seen from this that many surface states with various time constants exist. Figure 2 illustrates the effect of measurement temperature on the C-V curves for the same sample. Here the C-V curve shifts significantly to the negative voltage direction with increasing measurement temperature.

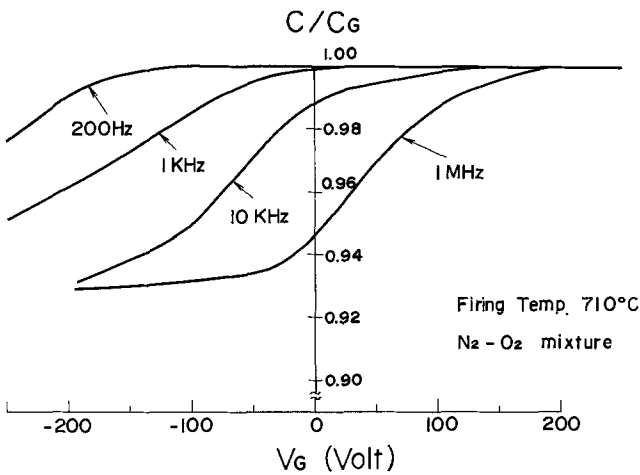


Fig. 1. The effect of measuring frequency on the capacitance-voltage curves of the sample made with the glass fired on n-type silicon at 710°C in a nitrogen-oxygen mixture.

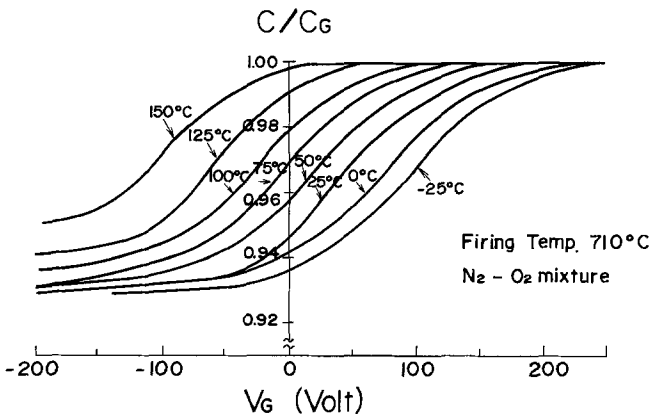


Fig. 2. The effect of measuring temperature on the capacitance-voltage curves of the sample made with the glass fired on n-type silicon at 710°C in a nitrogen-oxygen mixture.

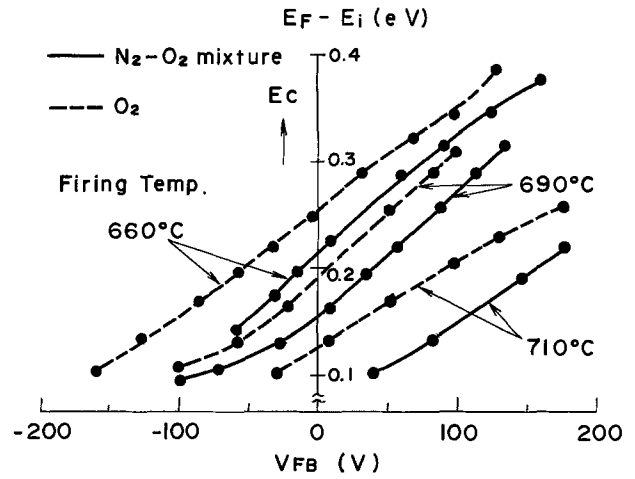


Fig. 3. Flatband voltage of the samples made with the glass fired on n-type silicon at various conditions vs. energy level.

This shows that the surface states are distributed over a wide range of energy levels.

Effect of glass firing condition on surface charge configuration.—Figure 3 shows flatband voltage (V_{FB}) of the samples made with the glass fired on n-type silicon at various temperatures in an oxygen or a nitrogen-oxygen mixed atmosphere vs. energy level $E_F - E_i$, where E_F is the Fermi level and E_i is the intrinsic level. The energy level decreases with increasing measurement temperature. The flatband voltage increases with increasing energy level and the curves shift in the positive voltage direction as the glass firing temperature increases. That is, the net surface charge density is more negative as the glass firing temperature increases. These curves are nearly linear and their slopes, nearly equal. That is, the surface state density is nearly equal over a wide range of energy levels. The surface state density for glass firing temperature of 660°C is shown in Fig. 4, as calculated

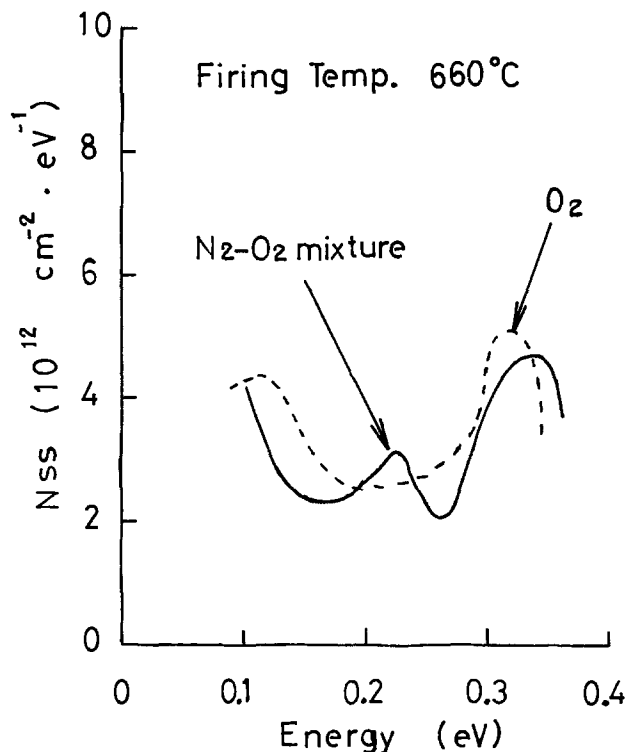


Fig. 4. Surface states density of the samples made with the glass fired on n-type silicon at 660°C in an oxygen or nitrogen-oxygen mixture vs. energy level.

from the experimental results given in Fig. 3. The surface state density is $(2-6) \times 10^{12} \text{ cm}^{-2} \cdot \text{eV}^{-1}$. Therefore, it is felt that the variation of the flatband voltage with the glass firing temperature is due to the fixed charge rather than surface states. So, the positive fixed charges decreases as the glass firing temperature increases. The flatband voltage for the firing atmosphere of a nitrogen-oxygen mixture is larger than that for an oxygen alone. The positive fixed charge decreases when nitrogen is added to the oxygen firing atmosphere.

Effect of the conductivity type of silicon substrate on surface charge configuration.—Figure 5 shows the flatband voltage of the samples made with the glass fired on n-type and p-type silicon vs. energy level. The flatband voltage of the glass fired on p-type silicon decreases as the Fermi level moves closer to the valence band. On the other hand, the flatband voltage of the glass fired on n-type silicon shifts to the positive voltage direction, as the energy level moves closer to the conduction band. That is, the flatband voltage of the glass fired on p-type silicon varies differently with measurement temperature as compared to that of the glass fired on n-type silicon. However, the change of flatband voltage with energy level for n-type and p-type silicon are qualitatively the same. The slopes of curve for n-type silicon is nearly equal to that for p-type silicon. Saying it differently, the surface states are distributed similarly in the energy level of the conduction band side and the valence band side as in Fig. 6 calculating from Fig. 5. Only the displacement of the curve along the flatband axis is different. Flatband voltage for p-type silicon at room temperature is negative and that for n-type silicon is positive. These results agree with the results of Goodwin (2). This difference is considered as the difference of the sign of fixed charge. That is, the fixed charge for n-type silicon is positive, that for p-type silicon is negative.

Conclusions

Surface charges in a zinc-borosilicate glass/silicon system were studied by measuring capacitance-voltage

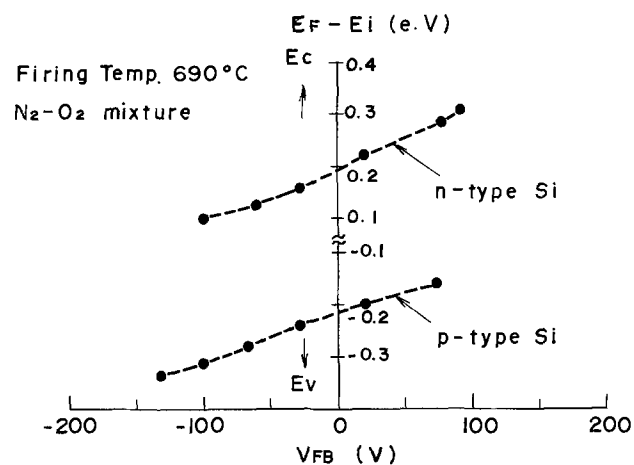


Fig. 5. Flatband voltage of the samples made with the glass fired on n-type or p-type silicon at 690°C in a nitrogen-oxygen mixture vs. energy level.

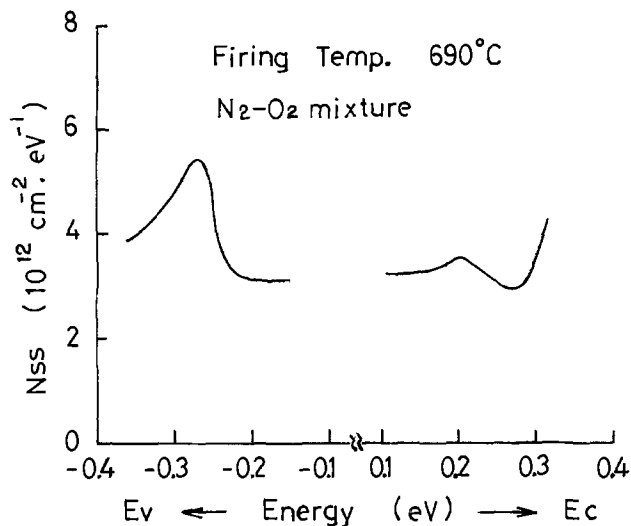


Fig. 6. Surface states density of the samples made with the glass fired on n-type or p-type silicon at 690°C in a nitrogen-oxygen mixture vs. energy level.

curves of metal-glass-silicon capacitors at various temperatures. Capacitance-voltage curves changed remarkably with measuring frequency and temperature due to the existence of many surface states. Net surface charge density varies with glass firing conditions as follows. The positive fixed charge density decreased remarkably with increasing glass firing temperature and also when nitrogen gas was added to the oxygen firing atmosphere. On the other hand, surface state density was about $(2-6) \times 10^{12} \text{ cm}^{-2} \cdot \text{eV}^{-1}$ and hardly changed with glass firing conditions. Moreover, the surface charge was positive for n-type silicon and negative for p-type when the Fermi level is near the intrinsic energy level. On the other hand, the surface charge was reversed when the Fermi level is near the bandedge.

Acknowledgments

The authors wish to thank Messrs. S. Kawai, K. Wajima, and K. Morita and Dr. Okamura for their helpful suggestions and encouragements during this study.

Manuscript submitted Dec. 17, 1979; revised manuscript received Sept. 8, 1980.

Any discussion of this paper will appear in a Discussion Section to be published in the December 1981 JOURNAL. All discussions for the December 1981 Discussion Section should be submitted by Aug. 1, 1981.

Publication costs of this article were assisted by Hitachi, Limited.

REFERENCES

1. K. Miwa, K. Ikeda, and K. Aoki, *NEC Res. Dev.*, **42**, 1 (1976).
2. C. A. Goodwin, Paper 353 presented at The Electrochemical Society Meeting, Las Vegas, Nevada, Oct. 17-22, 1976.
3. K. Miwa, Y. Moriguchi, M. Kanno, T. Kawamura, and T. Shibuya, *Denki Kagaku*, **40**, 478 (1972).
4. P. V. Gray and D. M. Brown, *Appl. Phys. Lett.*, **8**, 321 (1965).

Tapered Windows in SiO₂, Si₃N₄, and Polysilicon Layers by Ion Implantation

J. Götzlich and H. Ryssel

Fraunhofer-Institut für Festkörpertechnologie, 8000 München 60, Germany

ABSTRACT

In integrated circuit production, tapered windows are important for good step coverage of subsequent deposited layers. We show that by implantation of Ar and As ions into SiO₂, Si₃N₄, and polysilicon layers the slope angle of window walls can be reduced. The slope angle is determined by the ratio of the etch rates of the undamaged region to the damaged top region of the layer. Depending on ion species, ion dose, ion energy, and etching conditions we could achieve minimum angles of about 10° in these layers.

In semiconductor technology, the definition of structures in layers of SiO₂, Si₃N₄, or polycrystalline silicon is usually made by photolithography, which is followed by chemical or plasma etching of the film. If the etched structure is coated by another film, the step coverage of this second film at the windows is determined by the wall contour of the window. The step coverage is especially important with metal layers, since at a steep edge the metal is thinner and can cause severe problems with reliability (1). Many investigations have been performed to optimize step coverage by a proper design of the evaporation equipment. New evaporation techniques using magnetron sputtering have brought a significant improvement. The most reliable method is, however, the tapering of the slope of window walls.

Since all layers to be tapered are amorphous or polycrystalline, they are etched isotropically using wet chemical etches or standard plasma etching. If the adherence of the etching mask is good, the slope of the window wall will reach asymptotically 90° in case of overetching (2). Shallow slopes in homogeneous films can be produced by lifting-off the photoresist during the etching process. The slope angle is then determined by the ratio of lateral lift-off rate to the etching rate of the film. However, this technique is hard to control and therefore the results are not well reproducible.

A more reliable and very often used method is the reflow of phosphorus-silicon-glass (PSG). PSG is deposited at low temperatures from silane, oxygen, and phosphine in a nitrogen atmosphere and reflowed at about 900°C, resulting in very smooth window edges (9). Another reliable method for tapering windows is the application of a two-level structure, in which the top part of the layer etches faster than the lower part. The sine of the slope angle of the lower part of the layer is given by the ratio of the etching rates of the two components of the film. Even if the layer is overetched, this angle will have a constant value (3). This sandwich structure can be achieved in two different ways: First, by changing the chemical compounds during the deposition of the layer (*e.g.*, CVD layers) (4), and second, by bombardment of the layer with energetic ions which damage the surface and thus enhance the etching rate.

Moline *et al.* (5) reported on the tapering of SiO₂ using Ar ions. North *et al.* (3) also used Ar ions to taper PSG glass and Bell and Hoepfner (6) used Ar ions from an ion-etching machine for tapering SiO₂ layers.

In this paper we report on the tapering of window walls in SiO₂, Si₃N₄, and polysilicon layers by ion implantation using argon, arsenic, and boron ions with subsequent chemical or plasma etching.

Key words: ion implantation, tapered windows, damage enhanced etching.

Experimental Techniques

For all experiments, phosphorus-doped <111>-oriented silicon with a resistivity of 1-10 Ωcm was used. For the experiments with SiO₂, the silicon wafers were oxidized at 1000°C for 1 hr in a wet oxygen atmosphere, forming an SiO₂ layer of about 0.4 μm. The silicon nitride layers were deposited in an SiH₄-NH₃-N₂ atmosphere at 800°C. The film thickness was 0.4 μm. The deposition of the polysilicon layers was done in an SiH₄-N₂ atmosphere at 700°C. The 0.9 μm thick polysilicon was deposited on a thin SiO₂ layer, which acted as an etch stop.

The wafers were then implanted with Ar-, As-, and B-ions at energies between 50 and 200 keV and doses of 10¹²-10¹⁶ cm⁻². To obtain the different implantation doses, a variable beam stopper was used, which made it possible to implant up to six various doses on one wafer. Thus, all samples to be compared were processed in the same way during the photolithographic and etch processes.

Before applying the photoresist to define the etch windows in SiO₂ and polysilicon, the wafers were baked in a nitrogen atmosphere at 300°C for 30 min. Nevertheless, it was necessary to apply an adhesion promoter solution to obtain reliable results. The nitride layers were CVD coated with a 200 nm thick oxide layer in an SiH₄-O₂-N₂ atmosphere at 450°C. The SiO₂ was etched in buffered hydrofluoric acid. The Si₃N₄ was etched at 160°C in conc H₃PO₄, using the SiO₂ layer as a mask. The etching solution for the polysilicon consisted of 100 HNO₃:3HF:4H₂O. Besides these procedures, polysilicon layers were etched in a CF₄ plasma in order to compare plasma etching with wet chemical etching.

The etching times were 2-4 min for the SiO₂, 60-80 min for the Si₃N₄, and 0.5-1 min for the polysilicon layers. The relative amount of overetching after etching through the layer was about 10%. After etching, the samples were cleaned using organic solvents and then cleaved. The cross section of the window wall was determined using a scanning electron microscope (SEM). The uncertainty in the determination of the slope angle of the window walls was ± 2°. The reproducibility was also ± 2°.

Results and Discussion

In Fig. 1, SEM photographs are shown for typical etched structures in Si₃N₄ layers implanted with argon ions. For all doses shown, a reduction in the slope angle can be seen. The top layer of 1000Å shows a steeper slope. This can be attributed to the thickness of the damaged layer, which shows a nearly constant enhanced etching rate. Using lower implantation energies, this effect can be reduced.

The implantation of Si₃N₄ layers with As ions (80 keV) reduced the taper angle to 11° for a dose of

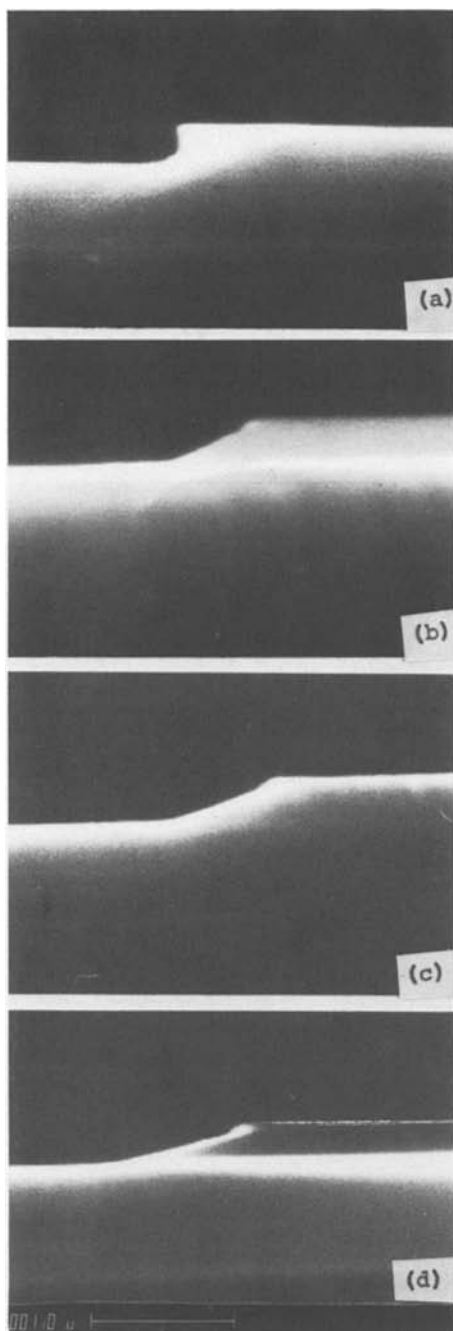


Fig. 1. Scanning electron micrographs of wall profiles in Si_3N_4 layers after Ar implantation with 50 keV and various doses: (a) no implantation; (b) $1 \cdot 10^{15} \text{ cm}^{-2}$; (c) $5 \cdot 10^{15} \text{ cm}^{-2}$; (d) $1 \cdot 10^{16} \text{ cm}^{-2}$.

10^{16} cm^{-2} (Fig. 2). There seems to be a saturation effect for the higher ion doses. This saturation does not occur until doses greater than 10^{15} cm^{-2} . The same dependence is observed for the implantation of 50 keV Ar ions; the slope angle decreases continuously to 14° for the 10^{16} cm^{-2} dose. In both cases (Ar and As ions), there was a step in the profile for doses greater than $5 \times 10^{14} \text{ cm}^{-2}$ (see Fig. 1). This step was not taken into consideration for the results in Fig. 2. The height of this step (about $0.1 \mu\text{m}$) should indicate the depth to which the enhanced etching occurs.

In Fig. 3, the slope angles of window walls in SiO_2 after implantation with Ar and As ions, respectively, with different ion doses are shown. Implanting Ar ions with 50 keV or As ions with 80 keV, the slope angle can be reduced to 11° or 12° , whereas by implantation of Ar ions with 200 keV the minimum angle is about 24° . In all cases there is a saturation effect which depends on ion dose, species, and energy. This saturation

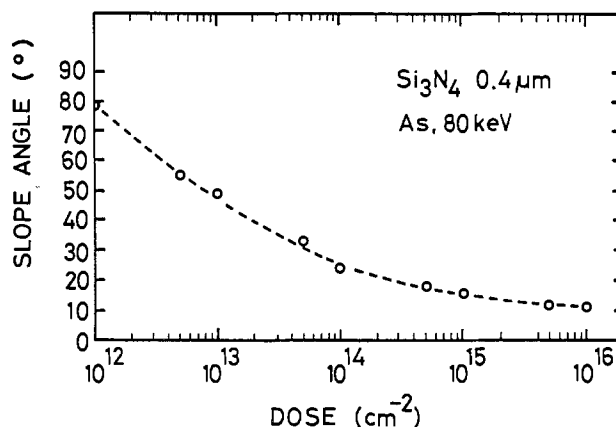


Fig. 2. Slope angles of window walls in Si_3N_4 vs. ion dose after implantation with 80 keV As.

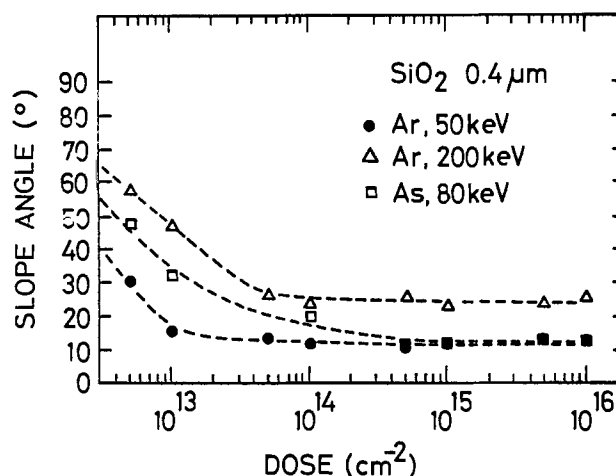


Fig. 3. Slope angles of window walls in SiO_2 vs. ion dose after implantation with 50 keV and 200 keV Ar and 80 keV As.

effect should be correlated with the saturation of defects produced by ion implantation. The As-implanted samples showed a step in the window profile for doses greater than $5 \times 10^{13} \text{ cm}^{-2}$. The height was the same as for the Si_3N_4 layers (see above). In the case of Ar implantation, no step could be observed.

The results of the experiments with polysilicon layers are shown in Fig. 4 and 5. These measurements showed no effect of the ion implantation on the etching rate for doses up to 10^{13} cm^{-2} , e.g., a steep slope of 80° - 90° was observed. For ion doses greater than

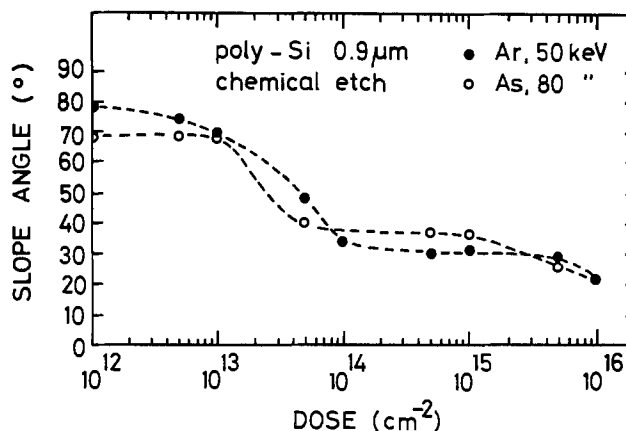


Fig. 4. Slope angles of window walls in polysilicon vs. ion dose after implantation with 50 keV Ar and 80 keV As and chemical etching.

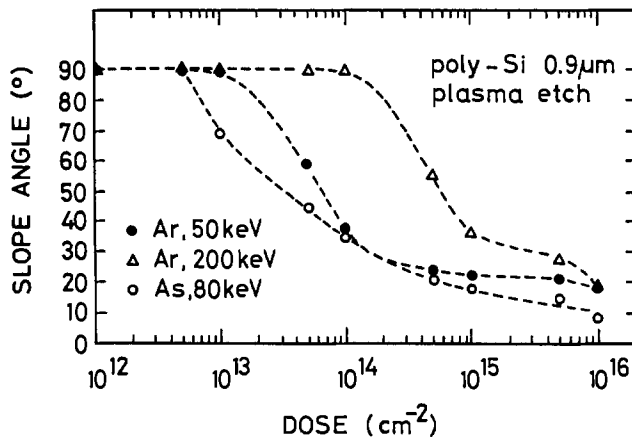


Fig. 5. Slope angles of window walls in polysilicon vs. ion dose after implantation with 50 keV and 200 keV Ar, 80 keV As and plasma etching.

10^{13} cm^{-2} there was a reduction of the slope angle in the case of the 50 keV Ar and the 80 keV As implantation for the chemically etched samples as well as for the plasma-etched layers. The minimum slope angle achieved with plasma-etched samples was 9° (1×10^{16} As/ cm^2 , 80 keV), whereas with the chemically etched samples the angle could only be decreased to 23° (1×10^{16} cm^{-2} , 80 keV As and 50 keV Ar). There is also a different behavior in respect to the formation of a step in the wall profile between the two sets of samples. The chemically etched samples showed no step, whereas for the plasma-etched samples, there was a step with a height of $0.1 \mu\text{m}$ (Ar, 50 keV) or $0.2 \mu\text{m}$ (As, 80 keV) for doses greater than 5×10^{14} cm^{-2} . The implantation of Ar with 200 keV in polysilicon layers only had an influence on the slope angle for ion doses greater than 1×10^{14} cm^{-2} . The slope angle of these 200 keV samples could only be measured in the case of plasma etching because of the steep overhanging step in the case of chemical etching. The height of this step was about $0.25 \mu\text{m}$. This step can be explained by a lower etch rate at the surface, since the damage is produced predominantly in a deeper region. The plasma-etched samples showed only a step for the 10^{16} cm^{-2} implantation; the height was as above.

The implantation of B ions with 60 keV in SiO_2 and polysilicon layers gave no reliable results. At the higher ion doses (10^{15} - 10^{16} cm^{-2}) a taper angle of about 40° could be observed but the reproducibility was only $\pm 10^\circ$. Most of the samples also showed a high step of about $0.3 \mu\text{m}$ in the wall profile, due to the large range of the ions.

All layers (SiO_2 , Si_3N_4 , poly-Si) showed the formation of a step profile for some implantation conditions such as high ion energy or high ion doses. The height of this steeper step on top of the layers was generally greater than the range of the implanted ions, and especially greater than the range of the damage created

during the ion bombardment. Usually, the height of this step is about 0.05 to $0.1 \mu\text{m}$ more than the projected range of the ions. A possible explanation is that there exists a transition region with the above thickness, in which the steep slope at the surface is passed into the reduced slope (which is determined by the ratio of the etching rates of the damaged to the undamaged region). This observation should be taken into account if one adjusts the ion energy for tapering window walls. Moreover, one should take into consideration that any annealing of the implantation damage could change the slope angle of the wall profile. Such an annealing can occur not only during technological processes at low temperatures, but also already during the implantation process due to substrate heating (7, 8).

Conclusion

We have shown that in SiO_2 , Si_3N_4 , and polysilicon layers, the slope angle of window walls can be tapered by ion implantation. The slope angle depends on ion species, ion dose, and ion energy. The minimum angles achieved here were about 10° , e.g., the etch rate of the damaged surface region showed a maximum enhancement of about 6 by ion implantation. The observed step in the profile can be reduced by reducing the ion energy. The reduction of the energy at lower ion doses gives the same slope angle as with the higher energy.

Acknowledgment

The authors wish to thank Mr. H. Kranz and Miss E. Traumüller for the implantations, Mrs. M. Ramin for the photolithography, and Miss D. Boehm for the SEM investigations.

Manuscript submitted July 15, 1980; revised manuscript received Sept. 12, 1980.

Any discussion of this paper will appear in a Discussion Section to be published in the December 1981 JOURNAL. All discussions for the December 1981 Discussion Section should be submitted by Aug. 1, 1981.

Publication costs of this article were assisted by the Institut für Festkörpertechnologie.

REFERENCES

1. J. L. Vossen, G. L. Schnable, and W. Kern, *J. Vac. Sci. Technol.*, **11**, 60 (1974).
2. R. G. Brandes and R. H. Dudley, *This Journal*, **120**, 140 (1973).
3. J. C. North, T. E. McGahan, D. W. Rice, and C. Adams, *IEEE Trans. Electron Devices*, **ed-25**, 809 (1978).
4. B. A. Boxall, *Solid-State Electron.*, **21**, 1173 (1978).
5. R. A. Moline, R. R. Buckley, S. E. Haszko, and A. U. MacRae, *IEEE Trans. Electron Devices*, **ed-20**, 840 (1973).
6. G. Bell and J. Hoepfner, in "Etching for Pattern Definition," H. G. Hughes and M. J. Rand, Editors, p. 47, The Electrochemical Society Softbound Proceedings Series, Princeton, N.J. (1976).
7. P. D. Parry, *J. Vac. Sci. Technol.*, **15**, 111 (1978).
8. P. D. Parry and S. P. Bristol, *ibid.*, **15**, 664 (1978).
9. W. Kern and R. S. Rosler, *ibid.*, **14**, 1082 (1977).

Neutron Activation Study of a Gettering Treatment for Czochralski Silicon Substrates

L. E. Katz and P. F. Schmidt*

Bell Laboratories, Incorporated, Allentown, Pennsylvania 18103

and C. W. Pearce*

Western Electric Company, Allentown, Pennsylvania 18103

ABSTRACT

A pre-process gettering treatment is described for Czochralski silicon substrates which removes essentially any transition group metal contaminants present in the wafer and continues to getter contaminants during subsequent device processing. Laser induced damage (LID) on the back surface of the wafer, a modified high temperature HCl treatment, and formation of oxygen precipitates in the bulk of the wafer only, are used as a three-step gettering process. Neutron activation analysis (NAA) was used to monitor the gettering behavior of each individual contaminant species and shows that the combined treatment is indeed nearly 100% effective in removing impurities, both from starting substrates and from processed wafers. Removal of impurities from the starting substrates is important in order to prevent the formation of oxidation induced stacking faults (OSF), which are nucleated by impurities and then become decorated with impurities making them much harder to getter (1). Holdtime performance of 4K and 16K dynamic RAM's fabricated on substrates treated in this manner served to evaluate the effectiveness of the treatment. Significant improvement can be achieved for bulk substrates. However, the performance of epitaxial silicon on low resistivity substrates cannot be matched since the low resistivity substrate in the EPI case additionally suppresses the minority carrier diffusion current from the bulk of the wafer. The individual steps of the treatment are: (i) produce laser induced damage on the back surface of the wafers by means of powerful, partially overlapping laser pulses; (ii) ramp from 950° to 1250°C in 0.5% O₂, 0.5% HCl, balance argon; (iii) oxidize at 1250°C for 8 hr in dry O₂ + 0.5% HCl, then ramp down to 950°C. Keeping the oxygen concentration to 0.5% during step (ii) is important to prevent formation of a thick oxide film during this step. The long oxidation at 1250°C both depletes interstitial oxygen at the Si surface, thus preventing formation of OSF, and causes formation of oxygen precipitates in the bulk if the initial O_i concentration is high enough. Oxygen precipitates in the bulk are a valuable means of gettering.

The detrimental effect of transition group metal impurities on device performance is well documented, both through the formation of microdefects in the silicon lattice during high temperature treatments and through their action as regeneration-recombination centers. The microdefects are in fact decorated by impurity precipitates. Impurities located at the surface are implicated in the formation of oxidation-induced stacking faults. Careful cleaning, prior to oxidation is a necessary but often insufficient condition for avoiding the OSF. The device sensitivity to transition group metal contamination depends on the required performance of the device and on the process technology used.

Metal impurities can be "gettered" from the bulk of the silicon by a variety of means, such as volatilization as chlorides during heat-treatment in Cl-containing ambients, diffusion into regions of enhanced metal solubility (N+ or P+ regions), or precipitation at deliberately introduced crystal defects. A number of techniques have been used for the controlled introduction of such crystal defects, such as ion implantation damage, stress-inducing surface films, surface abrasion, and oxygen precipitates, to which now is being added lattice damage from laser pulses of sufficient power to cause local melting of the silicon. The wavelength employed determines the distance over which the energy is absorbed by the silicon, and hence the depth of damage introduced. All of the lattice-damage-type gettering procedures require that the damaged region be located remote from the device areas; usually the

back side of the wafer is used for this purpose (except in certain ion implantation applications) (2). The metal impurities are then made to diffuse into the deliberately damaged regions during a high temperature treatment, where they are held quite tenaciously and are not then involved in space charge leakage currents, provided the lattice damage survives the subsequent heat-treatments.

Gettering by oxygen precipitates poses certain problems of its own. Oxygen is a regular unintentional dopant in Czochralski grown silicon, though the level of oxygen concentration depends on several factors, such as rotational speed during crystal growth (3), ingot diameter, distance from the seed end, etc. If the oxygen concentration is high enough for precipitation of oxygen to occur during heat-treatments, then precipitates can form in the device areas, giving rise to microdefects and deterioration of device performance. On the other hand, oxygen precipitates are a valuable means of gettering. Their presence is thus desirable, but only in the bulk of the silicon, not in the device areas near the front surface of the wafer. The means of achieving this oxygen distribution was previously (4) described; it requires a prolonged heat-treatment in oxygen at 1250°C.

Gettering treatments are usually applied fairly well into the processing sequence, often as one of the last high temperature treatments. At this stage, however, the original crystal perfection of the surface-near layers of the wafer may already have been degraded, and impurities are precipitated at lattice defects where they are difficult to getter. In a way, the gettering treatment is being applied too late. Table I shows how

* Electrochemical Society Active Member.

Key words: gettering, HCl, laser damage, silicon defects.

inefficient N⁺ diffusion gettering from the back surface can sometimes be at this stage. In this example, a 4K dynamic RAM wafer pulled from the processing sequence, the gold contamination was reduced significantly, but the copper contamination remained high; the inverse occurs just as frequently, sometimes even both Au and Cu remain high.

Gettering studies in the past have mostly utilized device performance after the gettering step as the main diagnostic criterion. However, no detailed information about the concentrations of the different contaminant species present in the device regions of silicon wafers before and after the gettering step can be obtained in this way. In view of the exceedingly small amounts of contaminants already sufficient to degrade device performance, only neutron activation analysis has the necessary sensitivity to produce such information. NAA has therefore been applied throughout this study and has given firm quantitative results. Device performance after gettering confirmed the predictions based on NAA and expected from general principles. Systematic NAA is also a valuable and versatile method of process control.

Table II illustrates the correlation between level of contamination and generation lifetime or device holdtime. Concentrations of more than a few times 10¹² atoms of Cu or Au per 3 in. silicon wafers are definitely to be avoided. While Cu and Au are among the most deleterious contaminants, other transition group metals also give rise to deep lying recombination-generation levels in silicon and can be equally detrimental. The concentration at which a given impurity species begins to cause trouble is a complex function of its capture cross sections for electrons and holes, its solubility and diffusivity, etc. However, one may expect that these concentrations will be higher than for Cu or Au.

The ideal gettering treatment for transition group metals in silicon should accomplish the following objectives:

1. It should remove detrimental impurities from the surface-near layers of the silicon wafer prior to the first high temperature oxidation step while maintaining the perfection of the silicon lattice near the surface where devices will be located.
2. It should continue to exert a gettering action throughout the device fabrication process, *i.e.*, the gettering mechanism must be able to survive prolonged high temperature treatments.
3. In particular, it must prevent impurities introduced into the silicon during later steps of device fabrication from becoming lodged at crystal defects near

Table I. Gettering of impurities by N⁺ diffusion on back surface of processed bulk silicon wafers. (A 4K dynamic RAM wafer pulled from processing sequence.)

| | Cu (atoms cm ⁻²) | Au (atoms cm ⁻²) |
|--|---------------------------------|---------------------------------|
| After phosphorus diffusion | 3.8E12 | 6.2E12 |
| After removal of N ⁺ region and P-glass by etching | 2.6E12 | 1.8E11 |

Table II. Correlation between copper and gold contamination and generation lifetime or device holdtime

| Impurity concentration per 3 in. diam wafer | | | |
|---|---------------|--------|---------------|
| MOS wafers | | | |
| Mos generation lifetime | 100 μ sec | | 2.0 μ sec |
| Copper | — | | 5.0E14 |
| Gold | 2.5E11 | | 3.1E12 |
| 4K dynamic RAM's on bulk silicon | | | |
| Holdtime at room temperature | 100 sec | 3 sec | 0.8 sec |
| Copper | 1.0E12 | 6.8E13 | 2.5E14 |
| Gold | 1.7E12 | 8.2E12 | 7.3E13 |

the sensitive front surface, in other words, it must prevent formation of oxidation-induced stacking faults throughout the device fabrication process.

These objectives can be achieved by a 3-step gettering process which consists of the following steps:

1. Applying laser induced damage (LID) to the back surface of the silicon wafers. The resulting damage is so severe that it survives essentially any annealing steps without losing its gettering ability, as demonstrated in separate experiments (5).

2. A high temperature HCl treatment in the presence of only a trace of oxygen. Some oxygen is necessary to prevent attack on the silicon, but higher concentrations of oxygen would cause growth of a thick ($\geq 1000\text{\AA}$) oxide film; this impedes the outdiffusion of many transition group elements which therefore cannot react with and be transported away by the chlorine. Gold and the platinum group metals cannot be gettering by the HCl treatment because of the thermodynamic instability of their chlorides at high temperatures. For the gettering of these elements, a solid-state sink (LID layer, oxygen precipitates, or N⁺ diffused layers) is thus indispensable.

3. Depletion of interstitial oxygen (O_i) in the surface-near layers of the silicon wafers to a depth of about 120 microns by means of a high temperature anneal in oxygen (4). Formation of a thick oxide film eventually starves the Si/SiO₂ interface of oxygen from the gas phase (parabolic rate law), so that apparently the interstitial oxygen near the silicon/SiO₂ interface is consumed by this reaction. This depletion of oxygen in the surface-near layers has been proved both by charged particle activation analysis (¹⁶O(³He, xp)F¹⁸; work performed for Bell Labs at the Texas A&M University, Center for Trace Characterization), and by microscopic examination in conjunction with cleavage and Secco-etch studies.

We have chosen 450 min at 1250°C in dry O₂ + 0.5% HCl for this step. In silicon wafers with an initial (O_i) content of more than about 30 ppm,¹ this treatment also results in the simultaneous precipitation of oxygen-silicon complexes in the bulk, but not in the surface-near layers of the wafers. These precipitates then become sinks for impurities introduced via the front surface during device processing. On silicon wafers with less than about 30 ppm (O_i) such precipitates cannot form and here the LID layer on the back surface continues to exert its gettering action. This is an important point because the interstitial oxygen concentration on some ingots can be less than 30 ppm and can also be nonuniform, so that even an average oxygen content above 30 ppm does not really guarantee formation of oxygen precipitates forming a continuous sheet in the bulk of any given wafer. This is particularly true of the butt end of an ingot. The thick oxide film grown during the 1250°C anneal can also be used as the initial oxide for device fabrication.

Experimental

Materials preparation.—All of the silicon wafers were cut from Czochralski boron-doped (100) oriented ingots of 3 in. diam and a fairly high oxygen content (~35 ppm). The resistivity ranged from 5.5–9.3 Ω -cm, and nominal thickness of the finished substrates was 20 mils. They were chem-etched on both sides and polished on one. Their back surfaces were subjected to laser damage as detailed in Table III. Prior to use they were again cleaned in hot ammonium hydroxide-hydrogen peroxide solution.

In many experiments previously oxidized and then neutron activated wafers were used for investigation of the three separate gettering mechanisms (HCl, LID, layer, oxygen precipitates). The activity of these samples had decayed to essentially zero over periods of

¹ The infrared oxygen concentration determination is based on ASTM F-121-79 "Interstitial atomic oxygen content of silicon by infrared absorption."

Table III. Details of laser treatment used

| | |
|---|--|
| Laser type | ND:YAG, 8W-Cw, TEM ₀₀ |
| Dislocation density produced | 300/mm (counted along a cleavage face) |
| Propagation distance after a 1100°C, 1 hr oxidation | 50 microns |
| Laser repetition rate | 20 kHz |
| Machined spot diameter | 45 microns |
| Spot overlap | 30% |

many months of storage, but their impurity contents were accurately known from the previous NAA results. These wafers, of course, contain initially very severe lattice damage from the previous neutron activation step. Some but not all of this damage can be annealed out. [During our neutron irradiation, fast neutrons with energies above 1 MeV were present as well, at a concentration of about 10% of the thermal neutrons. While fast neutrons do not contribute to the activity of isotopes formed by (n,γ) reactions, they cause most of the lattice damage; this severe damage, in conjunction with appreciable contamination, makes complete annealing of lattice defects very difficult.] These wafers are therefore especially difficult to getter, and results obtained on them represent "worst possible cases."

High temperature treatments.—Table IV summarizes the separate steps of the cleaning-gettering-oxidizing treatment. Step 2 details the HCl cleaning and gettering during ramp-up from 950° to 1250°C, step 3 the 1250°C anneal in dry O₂ + 0.5% HCl. Neither the oxygen nor the HCl concentration is very critical; in fact, it is quite difficult to maintain a flow rate of exactly 0.5%. However, the oxygen concentration, on the one hand, should be kept to the level necessary to prevent pitting of the silicon surface, but, on the other, should be low enough that not more than 100–200 Å of oxide will grow during step 2. The HCl concentration, on the one hand, should be kept high enough to remove contaminants from the silicon as chlorides and to prevent indiffusion of additional impurities during the 8 hr 1250°C anneal in dry O₂, but, on the other hand, must be low enough to avoid any trouble due to phase segregation at the Si/SiO₂ interface (6). Throughout this work we have not observed troubles neither due to phase segregation, nor due to penetration of dislocations from the LID layer to the front surface, however, these are potential difficulties one has to watch for.

Neutron activation and analysis.—Many of the transition group metals, especially those of the stainless steel family, produce only very long-lived radioisotopes under neutron bombardment. In order to have sufficient sensitivity for these elements at the concentration levels at which they can be detrimental in silicon, long irradiation and long spectrum acquisition times are required (the saturation factor of the activity reached during neutron irradiation is given by $S = 1 - e^{-\ln 2 \cdot T_{irr}/T_{1/2}}$, where T_{irr} is the time in the reactor, and $T_{1/2}$ the half-life of any given isotope, both measured in the same time units. It is obvious that S will remain very small if $T_{irr}/T_{1/2}$ is a small quantity). Samples were therefore routinely irradiated for 120 hr at core face of the Union Carbide Research Reactor at Tuxedo, New York 10987; the flux at this position is approximately 7E12 thermal neutrons cm⁻² sec⁻¹ (averaged over the diameter of a 3 in. wafer), with an epithermal component of about 3%. Further details are given in the preceding paper by Schmidt and Pearce. (7).

Table IV. Details of gettering procedure

1. Subject back surface to laser-induced damage (LID).
2. Ramp up from 950° to 1250°C over a period of about 20 min in a mixture of 0.5–1% O₂, 0.5–1% HCl, balance argon.
3. At 1250°C, substitute dry O₂ for the argon, but keep HCl flowing; keep at 1250°C for about 8 hr. Ramp down to 950°C in the same ambient.

After cleaning, wafers were measured for 18 hr in close proximity to the end cap of a 46 cm³, closed-one-end coaxial lithium-drifted detector, connected via a spectroscopy amplifier and ADC to a computerized 4096 channel analyzer. The measuring system and the concentration evaluation have been described in Ref. (8). It should perhaps be pointed out that the volume of data generated by this study as well as by continual production control was so large that it could not have been handled readily by conventional neutron activation analysis in which a standard for each element to be determined is co-irradiated with the unknown samples. The Absolute Counting method of analysis does not require such standards and is consequently much faster. It is also described in Ref. (8).

Distribution of impurities between the silicon wafer and the LID layer were determined by measuring the same wafer before and after etch-off of the LID layer in 5 parts nitric, 3 parts hydrofluoric, 3 parts acetic acid mixture. The acid etch was always followed by a double clean in hot HCl-H₂O₂ solution to remove chemisorbed impurities from the silicon surface; without this precaution, especially gold determination can give completely misleading results.

Device fabrication.—4K and 16K dynamic memory devices were fabricated on substrates of the description given under "Materials preparation." Half of the wafers received the laser treatment only, the other half received LID plus the "full treatment"² (see Table IV) prior to being fed into the normal device fabrication process. Split lots of the normal production served as controls. In the case of 4K dynamic RAM's, comparison was made between the performance of devices on untreated bulk substrates and on bulk substrates having undergone the procedures of Table IV described before. In the case of 16K dynamic RAM's, a comparison was also made between the performance of devices on gettered bulk substrates and on epitaxial silicon on highly doped but nongettered substrates.

Results

Table V shows impurity concentrations on two starting substrates of good crystal quality before and after removal by etching of the LID layer. Only a few impurities show up, and their concentration, with the exception of gold, is very low. This is a consequence either of the purity of the starting material or of the gettering by the HCl treatment. Removal of the LID layer then eliminates the remaining impurities.³

The situation changes drastically if previously oxidized and then neutron activated substrates are used for the experiment as shown in Table VI. As shown in a companion paper (7), oxidation in steam or in dry oxygen without HCl leads to a strong contamination of the silicon. These impurities are tightly held at crystal defects produced by the oxidation and by the neutron irradiation and mostly refuse to be gettered into the LID layer. Note, in particular, the very high

² By "full treatment" we mean LID + 0.5% HCl-0.5% O₂ ramp-up in argon + 8 hr heat-treatment at 1250°C in dry oxygen.

³ The high temperature treatments were performed in a furnace located in a laboratory otherwise engaged in gold metallurgy on silicon. As a consequence, contamination with small amounts of gold was very difficult to avoid.

Table V. Effectiveness of "full LID treatment" on starting substrates of good lattice perfection. Wafers activated after LID treatment.

| | Cu | Cr | Fe | Co | Ni | Au |
|-----------------------------|----|----|----|--------|--------|--------|
| Before removal of LID layer | * | * | * | 1.8E11 | 6.9E13 | 6.2E11 |
| After removal of LID layer | * | * | * | — | — | 3.6E11 |
| Before removal of LID layer | * | * | * | * | 8.4E13 | 1.3E11 |
| After removal of LID layer | * | * | * | * | — | 1.3E10 |

* These impurities already gettered by the HCl step of the "full treatment."

Table VI. Relative inefficiency of LID gettering if the HCl treatment is omitted on silicon wafers with strong lattice damage from previous neutron activation

| | Cu | Cr | Fe | Co | Ni | Au | Ta |
|---------------------------|--------|--------|--------|--------|--------|--------|--------|
| Before removing LID layer | 3.9E14 | 7.3E14 | 6.9E15 | 2.7E13 | 5.6E14 | 1.1E12 | 2.7E12 |
| After removing LID layer | 1.0E14 | 6.1E12 | — | 8.9E12 | 2.7E14 | 3.1E10 | 1.0E12 |
| Before removing LID layer | 2.8E14 | 3.6E13 | 1.2E15 | 1.1E13 | 2.3E14 | 9.0E11 | 1.1E12 |
| After removing LID layer | 2.5E14 | — | 3.0E14 | 6.6E12 | 1.2E14 | 9.0E11 | 8.0E11 |

remaining copper concentration, a consequence of the omission of the HCl gettering step in this experiment.

Table VII shows that the combination of gettering by HCl and LID layer is capable of extracting the impurities even from a severely damaged silicon lattice. Only the gold concentration remained unchanged. As pointed out in footnote 3, we cannot be sure in the case of gold that we are not looking at an accidental recontamination after the high temperature treatment. Combining the information of Table VI and VII leads to an interesting conclusion. If depleting impurities at the silicon/ambient interface were the only function of the HCl at high temperature, *i.e.*, providing a concentration gradient, then one would expect that the concentration gradient provided by the LID layer should also suffice to attract impurities into the LID layer (case of Table V); this, however, essentially does not happen in the absence of HCl.

In the presence of HCl, however, impurities do diffuse into the LID layer and remain there, at least in part, in spite of the presence of the HCl. It appears that the impurities in the silicon are mobilized in the presence of HCl in a high temperature ambient.

It is generally considered that chlorine (the active species resulting from the interaction of HCl with oxygen) does not penetrate into the silicon. Neutron activation studies on silicon wafers oxidized in dry oxygen + 1% HCl at 1150°C have indeed shown that essentially all of the chlorine present on the sample is contained in the oxide film near the SiO₂/Si interface, and disappears from the sample upon etching in HF.⁴ This result, however, was obtained on wafers cooled down to room temperature after the oxidation in dry O₂ + 1%

* P. F. Schmidt, unpublished work.

Table VII. Effectiveness of "full LID treatment" including HCl step on previously neutron activated wafers containing strong lattice damage

| | Cu | Cr | Fe | Co | Ni | Au |
|---------------------------|--------|--------|----|--------|--------|--------|
| Before removing LID layer | 2.0E13 | 5.3E12 | * | 8.0E11 | 2.0E14 | 1.0E12 |
| After removing LID layer | — | — | — | — | — | 1.0E12 |

* Iron completely removed, concentration of other impurities decreased by the ramp-up 950°-1250°C in 0.5% HCl-0.5% O₂.

Table VIII. High temperature HCl gettering of impurities from oxidized silicon wafers containing strong lattice damage from previous neutron activation step. 20 min in 0.5% HCl at 950°-1250°C.

| | | Cu | Cr | Fe | Co | Ni |
|--|----------------------|--------|--------|--------|--------|--------|
| Other thickness | | | | | | |
| 10,800Å | Before HCl treatment | 5.7E14 | 2.2E14 | 9.7E14 | 8.1E12 | 6.7E14 |
| | After HCl treatment | — | 2.0E13 | + | 8.1E12 | 6.0E14 |
| 8500Å | Before HCl treatment | 6.5E14 | 8.8E13 | 3.9E14 | 5.0E12 | 4.6E14 |
| | After HCl treatment | — | 1.0E13 | — | 5.0E12 | 4.1E14 |
| Oxide thickness | | | | | | |
| 1000Å | Before HCl treatment | 2.4E16 | 1.6E13 | 3.9E14 | + | 9.1E13 |
| | After HCl treatment | — | 1.3E13 | — | — | 5.0E12 |
| Initially bare 200Å grown during HCl treatment | Before HCl treatment | 1.4E13 | 1.4E14 | 9.6E14 | 2.8E12 | 1.1E14 |
| | After HCl treatment | — | — | — | 1.8E12 | 5.7E13 |

HCl and does not give information about the presence of chlorine in the silicon at the high temperature.

All observed facts would find a logical explanation if chlorine is indeed to some extent soluble in silicon at high temperature, but is expelled from the crystal during cool-down due to a strong retrograde solubility as a function of temperature.

The effect of oxide films on suppressing the out-diffusion of certain impurities during the 950°-1250°C ramp-up in 0.5% HCl (no LID gettering) is shown in Table VIII. Only copper is always gettering under these circumstances. The getterability of Fe and of Cr depends on their location: if contained in the oxide film itself (probably even in the outer layers of the oxide film) they are quantitatively removed. But if contained in the silicon substrate, they are not. This effect is discussed in a companion paper (7). Co and Ni are very difficult to getter from a damaged Si lattice in the presence of an oxide film. Data on gold have been omitted in this table since gold cannot be gettering by high temperature HCl treatment due to the thermodynamic instability of its chloride. The conventional "dry oxygen + 1% HCl" treatment at 1000°-1100°C is thus not really a gettering treatment. It keeps additional impurities from getting into the silicon, but the concentration of impurities already in the silicon, with the exception only of copper, will not be strongly decreased by this treatment.

Oxygen precipitates forming in the bulk of the silicon wafer will eventually compete with the LID layer for the available impurities. Thus removing a LID layer from the wafer which has seen the 1250°C anneal in oxygen +0.5% HCl will result in a wafer which appears to be slightly more contaminated than a wafer which was merely subjected to the ramp-up-and-down in 0.5% each of O₂ and HCl, balance argon, with the LID layer in place. However, the impurities remaining on the wafer are tied down in oxygen precipitates and are not located near the surface of the wafer.

A comparison between device performance on gettered *vs.* nongettered bulk substrates, and also between gettered bulk substrates *vs.* epi on low resistivity p-type substrates, is given in Table IX in terms of the ratio of the percentage of devices failing the 4.4 msec Holdtime test. The gettered bulk substrates outperform the nongettered bulk substrates significantly, but the devices made on epitaxial silicon also outperform the devices on gettered bulk substrates by a similar margin.

Table IX. Improvement of hold time by pre-gettering of substrates

| Dynamic RAM's on bulk Czochralski silicon | |
|---|--------------------------------------|
| Ratio % of device failing 4.4 millisecond test (at 90°C) | |
| 4K Dynamic RAM, lot 819 | Non-gettered |
| | Gettered = 3.28 |
| 4K Dynamic RAM, lot 7228 | Non-gettered |
| | Gettered = 1.91 |
| 16K Dynamic RAM, lot 1044 | Non-gettered |
| | Gettered = 1.57 |
| 16K Dynamic RAM's, lot 1044 and devices made on epi on low resistivity substrates | Gettered bulk substrates |
| | Epi on low resistivity p-type = 2.52 |

This is a consequence of the suppression of the minority carrier diffusion current from the bulk of the wafer by the low resistivity epi substrates. This component of the leakage current is especially significant at elevated temperatures (9). Suppression of the diffusion component of the leakage current on bulk silicon can also be achieved by buried isolation diffusions.

Conclusions

The treatment described removes essentially any transition group metals from the front surface-near layers of the silicon, thus preventing formation of OSF, and resulting in improved holdtime performance of devices prepared on bulk Czochralski substrates gettered in this manner. However, the performance of devices fabricated on epitaxial silicon on low resistivity substrates cannot be matched since the low resistivity substrates suppress the minority carrier diffusion current from the bulk of the wafer.

To our knowledge this is the first deliberate gettering approach in which the gettering action continues

throughout the device fabrication process and is not eliminated by high temperature treatments.

High temperature HCl gettering in the presence of only a very thin oxide film has been shown to be a much more effective means of removing transition group metals than is the conventional "dry oxygen + 1% HCl" treatment.

Manuscript submitted April 14, 1980; revised manuscript received July 31, 1980.

Any discussion of this paper will appear in a Discussion Section to be published in the December 1981 JOURNAL. All discussions for the December 1981 Discussion Section should be submitted by Aug. 1, 1981.

Publication costs of this article were assisted by Bell Laboratories.

REFERENCES

1. G. A. Rozgonyi, S. Mahajan, and D. Brasen, *Appl. Phys. Lett.*, **29**, 531 (1976).
2. G. A. Rozgonyi, R. P. Deysher, and C. W. Pearce, *This Journal*, **123**, 1910 (1976).
3. L. E. Katz and D. W. Hill, *ibid.*, **125**, 1151 (1978).
4. C. W. Pearce and G. A. Rozgonyi, in "Semiconductor Silicon, 1977," H. Huff and E. Sirtl, Editors, pp. 606 ff, The Electrochemical Society Softbound Proceedings Series, Princeton, N.J. (1977).
5. V. J. Zaleckas and C. W. Pearce, Unpublished work.
6. J. Monkowski, R. E. Tressler, and J. Stach, *This Journal*, **125**, 1867 (1978); D. H. Hess and R. C. McDonald, *Thin Solid Films*, **42**, 127 (1977).
7. P. F. Schmidt and C. W. Pearce, *This Journal*, **128**, 630 (1981).
8. P. F. Schmidt and D. J. McMillan, *Anal. Chem.*, **48**, 1962 (1977); P. F. Schmidt, J. E. Riley, and D. J. McMillan, *ibid.*, **51**, 189 (1979).
9. R. Sun and J. T. Clemens, Abstract 499, p. 1266, The Electrochemical Society Extended Abstracts, Los Angeles, California, Oct. 14-19, 1979. See also U.S. Pat. 4,216,489 (August 1980).

AES Investigation of the Chemical Structure of Plasma-Deposited Silicon Nitride

H. H. Madden

Sandia Laboratories, Albuquerque, New Mexico 87185

ABSTRACT

Auger electron spectroscopy (AES) measurements have been made on a 500Å thick, plasma-deposited silicon nitride film. The refractive index of the film was 2.06, and it was deposited at 300°C. The silicon- $L_{2,3}VV$ uncorrected derivative signal had a sharp, high energy feature whose energy location and shape were suggestive of those from elemental silicon. Based on the supposition that the Si- $L_{2,3}VV$ signal from the plasma nitride is a superposition of signals, the background-corrected, loss-deconvoluted integral signal could be resolved into three signals: one which represented elementally bound silicon (and which was modeled by the signal from the silicon substrate); a second which was representative of silicon-hydrogen bonding; and a third which was found to have the shape of a signal from pyrolytically deposited silicon nitride. Because hydrogen is not directly detectable by AES measurement, and its effects on the shape of the Si- $L_{2,3}VV$ signal are small and more subtle than those of either oxygen or nitrogen, the effects of hydrogen on the Si- $L_{2,3}VV$ signal decomposition could only be assessed by making use of auxiliary data from a separate study of the silicon-hydrogen system. The uncorrected peak-to-peak, first derivative signals from oxygen and silicon in the plasma nitride indicated an oxygen content of less than 0.5 atomic percent (a/o). This was consistent with the lack of any indication of oxygen influence on the shape of the plasma-nitride Si- $L_{2,3}VV$ signal. These results for plasma-nitride are compared with the results of a similar study of silicon-oxynitride samples.

Silicon nitride is a dielectric material that has been found useful for a number of applications in the semiconductor-device industry. It is mostly used in the form of amorphous films, and although a number of other film growth techniques have been studied, chemical vapor deposition (CVD) and reactive plasma deposition are the most common thin film fabrication processes used. Films deposited by these methods may have electrical and structural properties which are strongly influenced by the presence of excess silicon or of contaminants in the films. The most important contaminants are thought to be oxygen, which results for oxidants present during the deposition reactions, and hydrogen derived from the hydrogen-bearing gases, silane and ammonia, used in both the CVD and plasma processes. The effects of nonstoichiometry and of oxygen and hydrogen impurities in silicon-nitride films are subjects of continuing interest. The persisting uncertainties in these subjects are consistent with the complex nature of silicon-nitrogen chemistry (1).

Of the many physical properties used in defining the characteristics of silicon nitride films, the index of refraction is the most widely used in practice. It has been found that excess silicon in a film causes an increase in the refractive index above the value of ~ 2 which is thought to be indicative of stoichiometric Si_3N_4 . An oxygen contamination causes a decrease in the refractive index toward a value of 1.44 characteristic of SiO_2 . The effect of hydrogen on the refractive index has not been clearly delineated.

Direct Si, N, and O signals appear in the AES spectrum and they have been employed for compositional analysis (2). There have been some disagreements in the interpretations of the lineshape of the silicon signals, however. Some authors (3,4) have described the shape of the uncorrected derivative silicon $L_{2,3}VV$ -AES signal from stoichiometric Si_3N_4 as being composed of a strong negative peak on its high energy side, with a broader shoulder at its low energy end. The energy location of the high energy peak is close to that

of the corresponding signal from elemental silicon. This has led other workers (2, 5) to interpret this peak as being due to elemental or "free" silicon and thus the shape of the Si- $L_{2,3}VV$ signal as being due to the superposition of a low energy signal from silicon in silicon nitride and a high energy signal due to free silicon.

In contrast to these interpretations, recent results from our laboratories (6) have indicated that the $L_{2,3}VV$ lineshapes from oxygen-contaminated CVD silicon-nitride films may also have the high energy peak/low energy shoulder structure but that the high energy peak is due to the presence of oxygen in the films. These results are in agreement with the AES and x-ray photoelectron spectroscopy (XPS) results of Wittberg, Hoenigman, Moddeman, Cothorn, and Gullett (7), also on oxygen-contaminated CVD nitride films, which showed that the "free" silicon in such CVD films was less than 3 a/o. In our study the CVD nitride film with the least oxygen contamination exhibited only a single peak in the location (~ 84 eV) of the shoulder of the two-feature signals. This single peak line was judged to be the "true" AES lineshape for silicon bonded to nitrogen.

The apparent contradiction in interpretation of the high energy peak in the more complex AES lineshape, together with an expectation that the signal from a silicon-rich nitride film should be the simple superposition of a nitride-related signal and a signal from "free" silicon, prompted the measurements reported below. The plasma-nitride films used in this new investigation had an Si/N ratio closer to 1.05 than to the stoichiometric value of 0.75; and although oxygen was detectable, its level was very low. After corrections for instrumental and electron-energy-loss distortions, the integral $[N(E)]$ silicon- $L_{2,3}VV$ signal from our plasma-nitride samples could indeed be resolved into a "free"-silicon signal superimposed on a silicon-nitride-like (6) signal, but with a third component representing silicon-hydrogen bonding in the film.

Other measurements (8) on nitride films deposited under nearly identical conditions to those in this AES

Key words: silicon nitride, hydrogen, chemical bonding.

study indicate that the films contain some 20-25 a/o hydrogen. A large portion of this hydrogen is bonded to the excess silicon and the question naturally arises as to the role that hydrogen plays in determining the shape of the $L_{2,3}VV$ silicon line. Although direct AES signals from hydrogen do not exist, the effects of hydrogen could be reflected in silicon lineshape changes. This possibility has been ignored in the interpretations cited above (2-6). While separate studies (9) on the chemisorption of hydrogen onto a clean silicon surface have shown that the changes in the silicon AES lineshape due to hydrogen-silicon bonding are less dramatic than the changes that accompany nitrogen- or oxygen-bonding to a silicon surface, the changes are discernable and the results of our plasma-nitride silicon lineshape decomposition are consistent with the idea that the high energy component is due to some hydrogen-bonded silicon and not solely to excess "free" silicon.

Experimental

The plasma-nitride films were deposited to a thickness of $\sim 500\text{\AA}$ in an AMT Plasma I reactor. This is a production scale system incorporating a rotating horizontal platen, capacitive-coupling to drive the glow discharge in a radially flowing gas mixture, and a stationary resistance-heater block positioned below the rotating platen to control its temperature. The temperature of the $3\ \Omega\text{-cm}$, n-type (111) Si wafers onto which the films were deposited was 300°C ; and the gas-discharge mixture consisted of an N_2 carrier gas fed at a rate of $670\ \text{std cm}^3/\text{min}$ with ammonia and silane fed at a flow ratio of 2.67:1 ($\text{NH}_3\text{-}360\ \text{cm}^3/\text{min}$; $\text{SiH}_4\text{-}135\ \text{cm}^3/\text{min}$). The refractive index of our film was 2.06. Other predeposition processing and deposition conditions were identical to those described in the report by Stein, Wells, and Hampy (8), where the results of a series of optical, structural, and electrical measurements made on these films are discussed. The major difference between the films used for our AES investigations and those studied by Stein *et al.* was the thickness. Their films were some 8-10 times thicker. Anderson (10) has discussed the effects on radiation hardness in the use of these plasma-nitride films for passivation of CMOS integrated circuits.

The AES data are taken with a single-pass cylindrical-mirror analyzer (CMA) using a 5 keV, $5\ \mu\text{A}$ primary electron beam from an electron gun coaxial with the CMA. The modulation voltage was 2V p-p and the data was recorded using signal-averaging techniques in the first-derivative mode. Before processing to arrive at a loss-corrected integral $[N(E)]$ signal the data were first corrected for the linear dependence of the CMA response on energy. The "true" Auger signal must be extracted from the raw data by corrections for electron-energy-loss features. These include simple subtraction of a secondary-electron-background function (11) and a subsequent iterative deconvolution procedure (12) to remove a low energy tail from the background-corrected $N(E)$ signal. This tail results from Auger electrons which have suffered energy losses before leaving the solid. The deconvolution technique makes use of a near-elastic spectrum of back-scattered electrons as an approximation to the total system (spectrometer resolution and Auger-electron loss features) response function. It was the loss-corrected $N(E)$ signal that was analyzed in terms of a superposition of signals from silicon atoms in different chemical environments.

During the transfer of the samples from the deposition system to the AES unit, the nitride films developed an oxide layer (13). This layer was removed by sputtering with 1 keV argon ions prior to analysis. A representative sputter profile recorded during our investigations of oxynitride films (6) is shown in Fig. 1 with the $L_{2,3}VV$ -silicon AES signals taken at various sputter depths given in the insert to this figure. The silicon lineshape taken before sputtering, A, is "SiO₂-

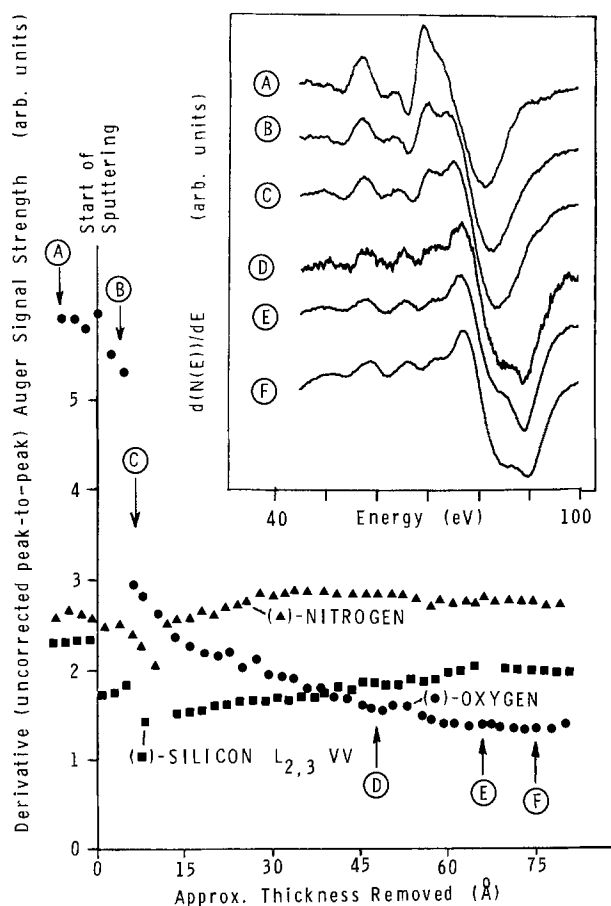


Fig. 1. AES sputter profile for a silicon-oxynitride film with ~ 10 a/o bulk oxygen [this film denoted as "74 ppm" in Ref. (6)]. Insert gives silicon- $L_{2,3}VV$ spectra taken at various points indicated on the sputter profile. The differences in signal-to-noise for curves D through F in the insert are the result of differing numbers of scans used in data averaging. For general survey work one set of scans (e.g., curve D) was taken while, for data that were to be used in deconvolution (curve E or F) a larger number of scans was taken so that the buildup of noise expected in the deconvolution process [Ref. (12)] could be mitigated.

like," but without the electron-beam-reduction peak (6, 14) at ~ 90 eV. Signals B and C are typical of a superposition of an SiO_2 and an oxynitride line. Only when a "plateau" was reached, e.g., curves D-F in Fig. 1, did the silicon lineshape become "nitride-like." Similar changes in the $\text{Si-L}_{2,3}VV$ lineshape with sputter depth were observed for the plasma-nitride film. All of the AES data presented below were taken in the sputter-plateau region, i.e., after the surface oxide layer had been removed.

The AES data were taken with the ion-bombardment beam off and only after the argon pressure in the experimental chamber had fallen below 7×10^{-7} Pa (the base pressure was $\sim 3 \times 10^{-8}$ Pa). In earlier work (14) it was found that AES data taken during ion bombardment were subtly distorted. These distortions were found to be related to the presence of argon gas at ion-bombardment pressures ($\sim 5 \times 10^{-8}$ Pa) in the experimental system during AES measurements. The samples in the present work were not annealed and hence contained embedded argon. Studies (15) of argon-ion bombarded, single crystal silicon samples, however, indicated that the presence of embedded argon and the associated damage does not have a very significant effect on the silicon AES lineshape. Carbon was a persistent contamination but for the data discussed below the carbon level was always low enough that it did not have an effect on the silicon lineshape (15).

Results and Discussion

Si-N, Si-Si, and Si-H contributions to the Auger lineshape.—Figure 2 shows both the uncorrected derivative $L_{2,3}VV$ signal (left-hand column) and the corresponding, loss-corrected $N(E)$ signal (right-hand column) from a plasma-nitride sample. For comparison, signals from elemental silicon, from our lowest-oxygen-content CVD nitride sample (6), our 74 ppm CVD oxynitride sample (6), and from an SiO_2 sample (16) are also plotted in this figure. The elemental silicon signals were obtained from the silicon substrate after sputtering through the plasma-nitride film. The energy location and shape of the high energy feature in the derivative spectra from our plasma-nitride and oxynitride samples are indeed suggestive of elemental Si. The SiO_2 data shown in Fig. 2 were recorded (16) in the presence of an oxygen atmosphere in order to minimize the electron beam reduction effects which give rise to a sharp peak commonly seen in the derivative spectrum from silicon dioxide at ~ 90 eV, which is also interpreted as due to elemental Si. Of the other $N(E)$ signals of Fig. 2 (right-hand column) the plasma-nitride signal most closely resembles the CVD nitride and oxynitride signals on their low energy sides in shape and energy location.

In order to test the supposition that the high energy feature in the uncorrected, derivative spectrum from the plasma nitride is due to elemental or "free" silicon, an elemental-silicon signal in the loss-corrected $N(E)$ form (Fig. 2) was subtracted from the $N(E)$ plasma-nitride signal (Fig. 2) to get a difference signal whose shape could be checked against the CVD-nitride signal (Fig. 2). The elemental-silicon signal was scaled in the resolution such that it had the maximum amplitude without resulting in a difference signal exhibiting negative $N(E)$ portions. This is a condition that one would expect for a simple superposition of signals. For the results presented here the curves involved in the resolution were not shifted in energy relative to one another. Allowing relative energy shifts would have introduced an additional (undesirable) adjustable parameter into the curve resolution. Some shifts might

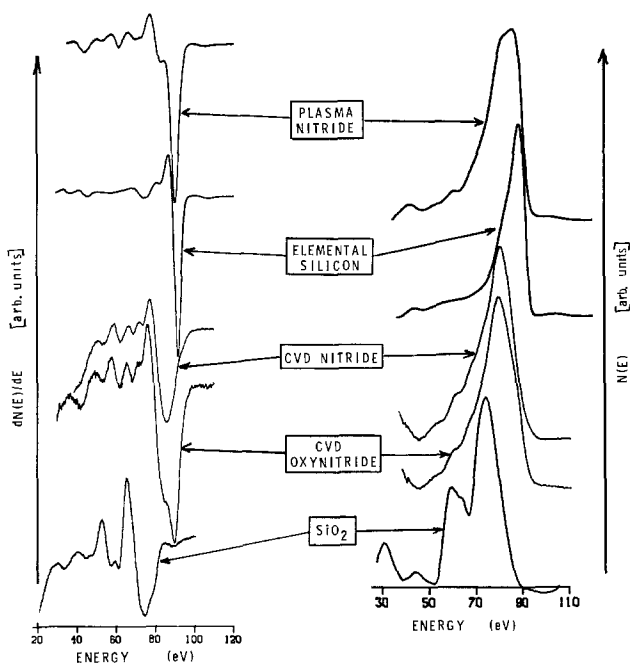


Fig. 2. Silicon- $L_{2,3}VV$ signals from plasma-nitride; elemental-silicon; CVD-nitride [Ref. (6)]; CVD-oxynitride [74 ppm, Ref. (6)]; and SiO_2 [Ref. (16)] samples. The left-hand side of this figure gives uncorrected, first-derivative signals while corresponding background-corrected, loss-deconvoluted integral signals are shown as the right-hand side. Zero levels for the integral signals are given by the right-hand side of each $N(E)$ curve.

indeed be appropriate due to core-level shifts or to differences in work functions for the surfaces involved. Such differences, although not measured, were assumed to be negligible however, and the only adjustable parameter in the curve resolution was the scaling factor, as was also true for the our oxynitride studies published earlier (6).

The difference signal from our plasma-nitride curve resolution, using the elemental silicon signal as one of only two components, is shown as the solid curve in Fig. 3a. It is seen to closely resemble (6, 14) a signal from an oxynitride sample with appreciable oxygen content. This might be interpreted to suggest that there is a third, oxygen-related component in the difference signal for plasma nitride, but the low oxygen concentration in the film determined by AES peak-height analysis runs counter to this suggestion. What was needed to obtain a more nitride-like difference curve was a different component signal which was more-or-less elemental-Si-like in shape but which occurred ~ 1 eV lower in energy than the elemental-Si signal used in Fig. 3a. Such a signal was found (9) in the $L_{2,3}VV$ signal from a hydrogen-covered silicon surface. A component curve that reflects Si-H bonding might indeed have been expected because infrared measurements indicated appreciable Si-H bonding in these plasma-nitride films (8).

Although a direct AES signal from hydrogen does not exist, hydrogen may be detected indirectly by its effects on an AES line of its host material. Such an effect of hydrogen on the Si- $L_{2,3}VV$ line is shown in Fig. 4, the results of a study of the chemisorption of hydrogen onto a clean (100) silicon surface (9). The amount of hydrogen on the hydrogen-covered surface for the signal shown in Fig. 4 was enough to have two

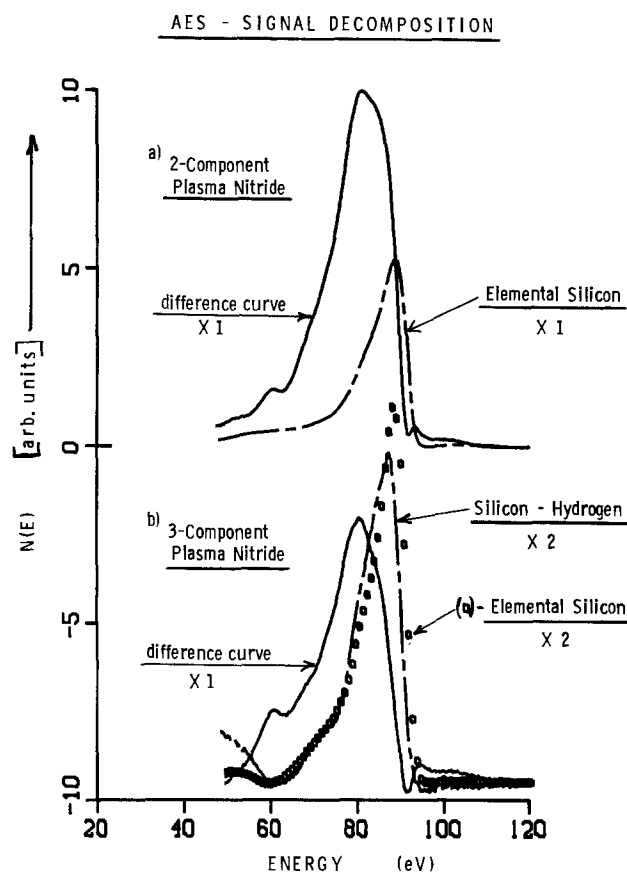


Fig. 3. $L_{2,3}VV$ -silicon component signals for a plasma-nitride sample. a) 2-component decomposition using only an elemental-Si signal as the high energy component; b) 3-component decomposition using both the elemental-Si and the Si-H signals from Fig. 4 as the high energy components. The solid curves are the difference curves in both cases.

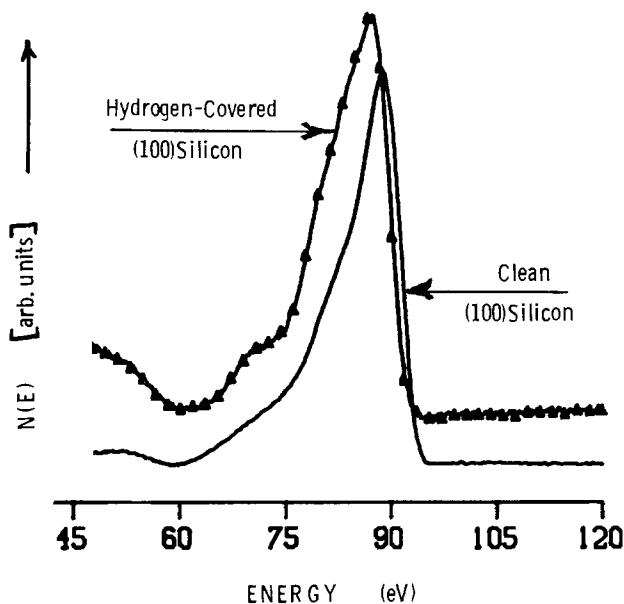


Fig. 4. Loss-corrected $N(E)$, $L_{2,3}VV$ signals from a clean, and a hydrogen-covered (100) silicon surface. Zero levels for the signals are given by the right-hand side of each curve. Triangles mark the curve for the hydrogen-covered surface.

hydrogen atoms bonded to each surface silicon atom (17). Thus each surface silicon atom is bonded to two hydrogen atoms and to two substrate silicon atoms. The hydrogen chemisorption caused the reconstructed (2×1) surface characteristic of the clean (100) surface to form a (1×1) structure characteristic of the dihydride layer on this substrate (17). The $L_{2,3}VV$ signal from the hydrogen-covered surface (Fig. 4) is a superposition of a hydrogen-influenced signal from the surface region and an elemental-Si signal from the substrate. This signal by itself was thus thought to be a better approximation to the high energy component curve in the plasma-nitride-film case than is the elemental-Si signal.

Subtracting this hydrogen-covered-surface signal from the plasma-nitride signal did produce a difference curve that was a better fit to the CVD nitride signal in the region near the peak but the lower part of the high-energy side of the difference curve was still too broad. The best-shaped difference curve was obtained by using both the hydrogen-covered-surface signal and the elemental-Si signal from Fig. 4. This difference curve is shown as the solid curve in Fig. 3b and once again in Fig. 5a. For comparison the CVD-nitride signal is also plotted in Fig. 5a. The good agreement in shape between these two curves indicates that the $L_{2,3}VV$ signal from our plasma-nitride sample can indeed be regarded as the superposition of three components: the silicon-nitride signal, the elemental-Si signal, and a signal due to Si-H bonding in the film.

Comparison of spectra from plasma-nitride and CVD-oxynitride.—These results for the plasma-nitride film are in sharp contrast to our earlier results (6) for CVD-oxynitride films. There the uncorrected derivative Si- $L_{2,3}VV$ signal also had a high energy feature that had earlier been interpreted as being due to free silicon but which our curve-resolution results found to be more indicative of silicon-oxygen bonding than to free silicon. The difference curve for the CVD oxynitride had a double-peak structure that resembled the SiO_2 signal more closely than it did the elemental-Si signal. Despite the similarities in shape of the oxynitride-difference and SiO_2 curves, there are significant differences that should be discussed. The prominent peak of the difference signal occurs some 13 eV higher than the corresponding peak in the SiO_2 signal. The peak separation in the difference signal is also some-

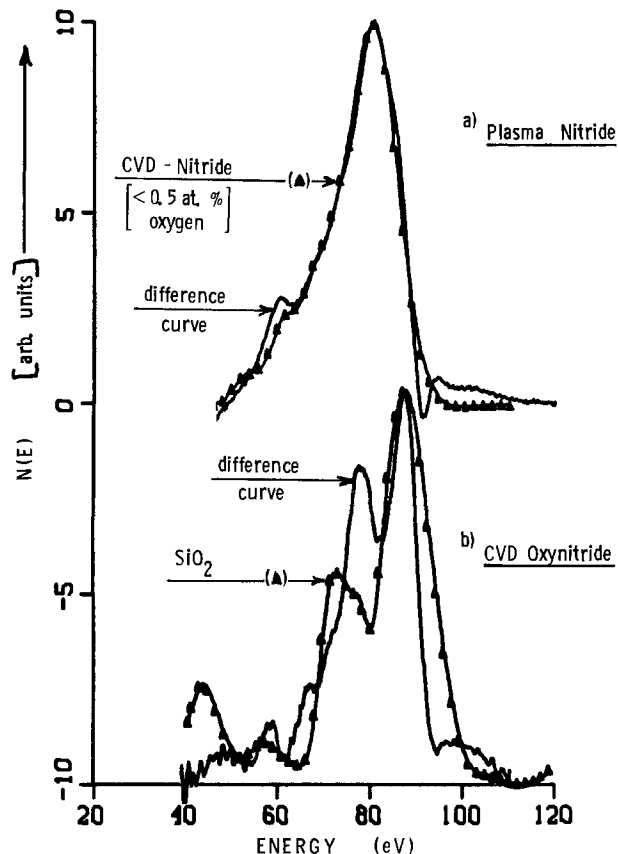


Fig. 5. Comparisons of a) curve-resolved difference curve from 3-component plasma-nitride decomposition results of Fig. 3b with our CVD-nitride signal [Ref. (6) and Fig. 2] and b) curve-resolved difference curve from our CVD-oxynitride results [Fig. 2 of Ref. (6)] with an SiO_2 signal [Ref. (16)]. The SiO_2 signal has been shifted higher in energy by 13 eV, but the CVD-nitride signal is in its original energy location. Both the CVD-nitride and SiO_2 signals are marked with triangles.

what less than in the SiO_2 curve. This is seen in Fig. 5b where the SiO_2 curve has been shifted up in energy so that the prominent peaks of the two curves are aligned.

The differences in shape between the two curves in Fig. 5b suggest that the difference curve is not simply an SiO_2 -like curve shifted up in energy relative, perhaps, to formation of a suboxide in the films. The prominent peak of the SiO_2 curve occurs fairly close to (~ 3 eV below) the secondary peak of the difference curve. Thus the high energy peak of the difference curve could alternatively be interpreted as a spectrum feature peculiar to the incorporation of oxygen in the amorphous silicon nitride matrix. It should be remembered that AES is a local probe of a material's electronic configuration. The prominent peak in the oxynitride difference curve could signal a local configurational change in the nitride. If the oxygen enters the nitride substitutionally, as suggested in our earlier report (6), the divalent oxygen will leave one unsaturated bond which could lead to so-called dangling-bond states at the local sites of the replaced trivalent nitrogen.

Alternatively, the incorporation of oxygen into the nitride could be accompanied by a local restructuring of the nitride matrix and the formation of new and different Si-Si and Si-H bonds. Such local "disordering of the nitride skeleton by oxygen" has already been suggested by the results (18) of a study of short-range order in silicon-oxynitride films using the method of radial distribution functions determined from electron diffraction measurements. AES is a probe of the local electronic structure of a material and should hence be sensitive to such local disorder. In any case the AES

data indicate that, below an oxygen level of ~ 50 a/o, the incorporation of oxygen into the nitride does not lead to a simple mixture of SiO_2 and silicon nitride but to a more unique substance. On the other hand, the fact that signals indicating Si-Si and Si-H bonding can be reasonably shown to be components of the $\text{Si-L}_{2,3}\text{VV}$ lineshape for plasma nitride suggests that excess silicon and silicon bonded to hydrogen may exist as independent entities in a two (or three) phase amorphous mixture with silicon nitride in plasma-nitride films.

Comments and Conclusions

The high energy peak in the uncorrected, derivative $\text{Si-L}_{2,3}\text{VV}$ signal from a plasma-nitride film is due to Si-Si bonds in the film. In our sample this peak is also identifiable with some Si-H bonding. The overall $\text{L}_{2,3}\text{VV}$ lineshape for our plasma-nitride sample is thus consistent with the presence of excess silicon, of silicon bonded to hydrogen, and of silicon bonded to nitrogen in the film. The AES signal decomposition indicates that the Si-Si and Si-H bonding in the plasma nitride can be detected as separate signals from the Si-N signal. This suggests that plasma-nitride films prepared with excess silicon may be simple mixtures of silicon (with incorporated hydrogen) and silicon nitride.

These decomposition results are in contrast to our earlier results (6) for CVD silicon-oxynitride films where the $\text{Si-L}_{2,3}\text{VV}$ signal, which in its uncorrected derivative form also has a high energy peak that has been interpreted as being due to free silicon, was found to be composed only of a component indicating silicon-nitrogen bonding and a second component indicating silicon-oxygen bonding. No clear-cut elemental (or "free") silicon component was found. This contrast indicates that the assignment of compositional information based primarily on the energy locations of AES lines in uncorrected, derivative spectra can be misleading and that more careful attention should be given to the shape of the AES lines in interpreting AES results.

The analysis of our $N(E)$ data might perhaps be considered speculative. It is based on the supposition that the background-corrected, loss-deconvoluted AES signal is a simple superposition of component signals. This is certainly not unreasonable; and the decomposition (or curve-resolving) that was done was performed with the restriction that no adjustments of relative energy positions of the as-measured component signals was allowable. This meant that whereas the high energy portion of the plasma-nitride signal could actually have been modeled by two elemental-Si signals shifted relative to one another, the physical and chemical significance of such a pair of elemental-Si signals must be considered unclear, at the least. The Si-H signal used in the curve-resolving presented above, while not differing greatly in shape from the elemental-Si signal, does give the energy shift needed with a chemically identifiable reason for the shift. In this regard, it should be noted that the 13-eV shift made to the SiO_2 signal in Fig. 5b was not involved in the curve-resolving procedure (6), but was made merely to make the shape comparison with the silicon-oxynitride difference curve easier.

These results illustrate the utility of AES as a probe of the chemical, as opposed to merely elemental, com-

position of solid surfaces. Energy (chemical) shifts of Auger lines can be larger than corresponding shifts of XPS lines; and, with care, these shifts can provide useful information about the chemistry of materials. Auger lineshape changes have been shown to aid in such interpretations.

Acknowledgments

The preparation of the plasma nitride films by J. J. Clement and the assistance of W. O. Wallace in making the Auger measurements are gratefully acknowledged. Very useful information concerning other measurements on these films was supplied by H. J. Stein prior to publication. This work was supported by the U.S. Department of Energy under Contract DE-AC04-76-DP00789.

Manuscript submitted Jan. 24, 1980; revised manuscript received Aug. 6, 1980.

Any discussion of this paper will appear in a Discussion Section to be published in the December 1981 JOURNAL. All discussions for the December 1981 Discussion Section should be submitted by Aug. 1, 1981.

Publication costs of this article were assisted by Sandia Laboratories.

REFERENCES

- U. Wannagat, in "Advances in Inorganic Chemistry and Radiochemistry," H. J. Emeleus and A. G. Sharpe, Editors, pp. 225-277, Academic Press, New York (1964).
- S. Thomas and R. J. Mattox, *This Journal*, **124**, 1942 (1977).
- W. A. Lanford and M. J. Rand, *J. Appl. Phys.*, **49**, 2473 (1978).
- P. H. Holloway, *Surf. Sci.*, **54**, 506 (1976).
- Y. E. Strausser and J. S. Johannessen, NBS Special Publ. 400-23, ARPA/NBS Workshop IV, "Surface Analysis for Silicon Devices," A. G. Lieberman, Editor, p. 119 (March 1976); J. S. Johannessen, W. E. Spicer, and Y. E. Strausser, *Phys. Scr.*, **19**, 355 (1979).
- H. H. Madden and P. H. Holloway, *J. Vac. Sci. Technol.*, **16**, 618 (1979).
- T. N. Wittberg, J. R. Hoenigman, W. E. Moddeman, C. R. Cothorn, and M. R. Gullett, *ibid.*, **15**, 348 (1978).
- H. J. Stein, V. A. Wells, and R. E. Hampy, *This Journal*, **126**, 1750 (1979).
- H. H. Madden, 39th Annual Conference on Physical Electronics, Univ. of Maryland, June 20, 1979; and to be published.
- R. E. Anderson, *IEEE Trans. Nucl. Sci.*, **ns-26**, 5180 (1979).
- E. N. Sickafus, *Rev. Sci. Instrum.*, **42**, 933 (1971).
- H. H. Madden and J. E. Houston, *J. Appl. Phys.*, **47**, 3071 (1976); *Adv. X-Ray Anal.*, **19**, 657 (1976).
- S. I. Raider, R. Flitsch, J. A. Aboaf, and W. A. Pliskin, *This Journal*, **123**, 560 (1976).
- H. H. Madden, G. Moore, and P. H. Holloway, "An Auger-Electron Line-Shape Study of CVD Silicon Nitride Films," Report No. SAND77-0584, Sandia Labs., Albuquerque, NM (1977), Unpublished work.
- J. E. Houston, G. Moore, and M. G. Lagally, *Solid State Commun.*, **21**, 879 (1977).
- J. E. Houston and M. G. Lagally, *J. Vac. Sci. Technol.*, **13**, 361 (1976); and unpublished results.
- T. Sakurai and H. D. Hagstrum, *Phys. Rev. B*, **14**, 1593 (1976).
- F. L. Edelman, B. N. Zaitzen, V. Z. Latula, and A. A. Khoromenko, *Phys. Status Solidi A*, **51**, 49 (1979).

A Neutron Activation Analysis Study of the Sources of Transition Group Metal Contamination in the Silicon Device Manufacturing Process

P. F. Schmidt*

Bell Laboratories, Allentown, Pennsylvania 18103

and C. W. Pearce*

Western Electric Company, Allentown, Pennsylvania 18103

ABSTRACT

A survey is given of the sources, species, and quantities of transition group metals residing on starting silicon substrates and introduced during the device manufacturing process. The survey begins with the polysilicon feed for silicon ingot fabrication and extends through all customary device fabrication steps, such as wafering, polishing, oxidations, epitaxy, ion implantation, etc. High temperature furnace operations in the absence of HCl, such as steam oxidations, are presently the major source of contamination if all other steps of the fabrication process are under full control. However, contaminated polishing slurries, contaminated handling tools or carriers, impure SiC boats or susceptors, or choice of unsuitable materials for beam catcher plates, etc. in ion implantation, can also lead to trouble. Several options are available to avoid the contamination introduced during high temperature treatments, and these are reviewed.

Minority carrier lifetime is an important parameter in silicon (integrated) device technology. However, the amounts of contaminants which suffice to degrade lifetime are so small that they cannot be detected and quantified by conventional chemical analysis. Only neutron activation analysis (NAA) has this capability among techniques applicable to measuring the total impurity concentration.¹ A systematic application of NAA to the silicon device manufacturing process does not seem to have been carried out before.

We report here on NAA starting with the polysilicon used for crystal growth and extending through the fabrication process. Some of the results are what one would expect to find, others came as surprises.

Some Background Information

Gamma-ray spectrometry of reactor neutron activated samples has a very high sensitivity for most elements of the periodic system beyond neon. Notable exceptions are the light elements B, P, and S, and the heavy elements Tl, Pb, and Bi, which do not become gamma-ray emitters but only beta emitters.² Since the electrons emitted in beta decay have a continuous spectrum, beta spectroscopy is not an attractive tool to identify individual elements among a multitude of beta emitters. However, determination of the half-life and maximum beta energy can sometimes be used to measure some beta emitters, especially phosphorus. We shall limit ourselves here to gamma-ray emitters.

Among the gamma-ray emitters, there exist also a few elements (V, Al, Cl, and F being the most important) whose half-lives are so short that their determination must be carried out immediately after end of reactor irradiation, and these elements are therefore not seen at all if analysis is carried out a

day or so after end of irradiation. Manganese, too, has a relatively short half-life (2.58 hr) and will be detectable a day after end of irradiation only if the total number of manganese atoms in the sample approaches about $1E15$.

Si-31, the only radioisotope formed during reactor irradiation of silicon, has a short half-life of 2.62 hr. This fact is of great help in the instrumental analysis of silicon samples: about 27 hr after even a long irradiation, the emission intensity from the silicon matrix has decayed to the extent that the samples can be analyzed nondestructively, without any need for chemical separations. The high purity of semiconductor silicon also guarantees that there are no self-shielding effects for any of the impurities contained in the silicon, and the thermal cross sections and infinite dilution resonance integrals given in the literature for the various isotopes can be used without correction factors for concentration determinations. This fact makes absolute counting of silicon samples especially attractive. In this method, one does not need standards for each element to be determined, one must merely measure accurately the thermal and epithermal flux in the reactor at the time and location of irradiation. A method of measuring the thermal and epithermal flux in a very convenient manner has been described before (1). Since silicon is a light element, there is also very little self-absorption of the emitted gamma rays, and again one does not have to worry about correction factors when applying instrumental analysis.

Two of the common dopants in silicon, boron, and phosphorus do not become gamma-ray emitters after irradiation. Phosphorus, however, becomes a 14-day half-life emitter of high energy betas, which in turn give rise to copious generation of Bremsstrahlung x-rays, raising instrumental deadtime and background at lower energies to unacceptable levels. Thus highly phosphorus-doped silicon samples are not very suitable for nondestructive analysis. Boron, on the other hand, is an ideal dopant for NAA purposes. The fission reaction of B-10 with thermal neutrons, resulting in the emission of Li-7 or of alpha particles, generates no radioactivity, and the beta activity resulting from the B-11 (n,gamma) B-12 reaction has a half-life of much

* Electrochemical Society Active Member.

Key words: carrier lifetime, diffusion, silicon dioxide, IC processing, contaminants.

¹ Ion microprobes have similar sensitivities as NAA in terms of total number of atoms needed for detection, but in the microprobe case these atoms are confined to the very small volume being sputtered, i.e., representing relatively high concentrations. NAA is a global technique, does not give information about impurity distributions in very small volumes, and is most useful for determination of impurities present in extreme dilution. The two techniques are thus complementary.

² Except boron.

less than 1 sec. Thus boron-doped silicon is ideally suited for investigating at which process steps contaminants are being introduced. Most of the work described in this paper was performed with 3" ϕ boron-doped Czochralski silicon.

There are certain practical constraints on the maximum or minimum number of samples one usually activates together during a reactor irradiation. Since the irradiations are fairly expensive, one clearly wants to co-irradiate as many samples as possible. On the other hand, one should be able to measure all samples before the short-lived species on the last samples to be measured have decayed to too low levels of activity. One thus needs a high throughput capability of the measuring equipment and computer evaluation of the gamma-ray spectra becomes a practical necessity.

There are many computer programs described in the literature which take spectrum evaluation to the point where identification of the isotopes present as well as determination of the intensities of the various photopeaks has been accomplished. Converting these intensities to concentrations, however, is usually done by comparison to the intensities of standards for each element co-irradiated with the unknown samples. A hybrid technique in which standards for each element are irradiated in a very well-known flux, and comparison to the spectra obtained in another reactor or a different flux is made possible through the co-irradiation of so-called comparators, has also been described (2). These techniques, however, involve a considerable amount of computation and [in the hybrid technique (2)] some degree of control over the irradiation facility.

The method of absolute counting (1), by contrast, requires the co-irradiation of only two flux monitors and the use of a minicomputer and is applicable to irradiations in any reactor. It is therefore much faster and only slightly less accurate than the relative method. Altogether, in survey work of this type precision is more important than accuracy, and the precision of absolute counting is excellent. The large volume of data generated in this study could not readily have been handled by a relative method.

Experimental

Whenever feasible, boron-doped silicon wafers were used, mostly in the resistivity range 4-9 Ω -cm, and of (100) or (111) orientations. Samples were cleaned in hot H_2O_2 - NH_4OH and H_2O_2 - HCl solutions prior to insertion into the process steps to be tested, prior to measurement after neutron irradiation, and, of course, also prior to neutron irradiation if the purpose of the test was to determine the impurities worked into the silicon surface rather than deposited on the surface (slicing, lapping, and polishing of wafers).

Samples were irradiated for 120 hr with rotation at core face of the Union Carbide reactor³ at Tuxedo, New York, and were measured nondestructively the next day. All samples were measured first for 2000 sec only for determination of short-lived species and were then measured again for 13.2 hr for determination of the long-lived species. Coarse profiling of impurity distributions was done by removal of oxide films in HF followed by cleaning in HCl - H_2O_2 , by etching in 5:3:3 nitric:hydrofluoric:acetic acid mix (sometimes with one surface masked against attack) followed by cleaning in H_2O_2 - HCl , and also by removing the peripheral portions of the wafer by scribing and breaking in order to learn about the lateral distribution of the impurities. Autoradiography served the same purpose on wafers with only one predominant emitter.⁴

³ Typical flux of 1.5×10^{13} thermal neutrons $cm^{-2} sec^{-1}$, with 3-5% epithermal neutron.

⁴ One should bear in mind that the sensitivity of the photographic plate is much higher for betas than for gammas and that presence of pure beta emitters could completely falsify an autoradiograph. Presence or absence of beta emitters can usually be inferred from the low energy x-ray background (below 100 keV) generated by a given sample.

Both the measuring equipment and the method of absolute counting used, as well as the method of flux determination by means of Fe-Ru flux monitors, has been discussed before (1).

In irradiating high purity materials it is necessary to use high purity materials as irradiation containers. Impurities contained in the irradiation container can be transferred and implanted into the unknown sample by knock-on events of fast neutrons and cannot always be removed by nondestructive cleaning. One also needs a container material which does not become very radioactive even after long irradiations, so that samples can be handled readily after irradiation, and the containers reused after some cool-down periods to let induced activities decay. These considerations limit the practical choice of irradiation containers to silicon, quartz, graphite, or vanadium, all of the highest purity. The half-lives of V-51 and of Si-31 are 3.76 min and 2.62 hr, respectively, thus containers made from quartz, silicon, or vanadium can be handled after conveniently short waiting periods. On the other hand, the neutron capture cross section of C-13 is so low (0.9 millibarns, at an abundance of 1.11%) and the half-life of C-14 so long (5730 years) that the activity generated in the matrix is very low even after long irradiations⁵ and in any case stems only from a very low energy beta emitter. We have chosen 7 nines pure graphite for irradiation containers, both because of its ready availability and its ease of machinability.

While the graphite matrix is extremely pure, surfaces of graphite workpieces can be significantly contaminated from contact with metal or carbide tools during fabrication. We have especially noted significant molybdenum contamination on some batches. Fortunately, these surface contaminants can be removed by the manufacturer by means of a high temperature cleaning treatment at little extra cost. Their elimination is necessary because of the knock-on and implant events during irradiation already mentioned. Especially molybdenum seems to diffuse quite deeply into silicon during reactor irradiation. Contamination of graphite containers inevitably will also occur from contact with the (contaminated) silicon wafers placed into the containers. It is, however, possible to repurify the graphite (at a somewhat lower temperature than the original heat-treatment) after the activities of these surface contaminants have decayed. Long-lived impurities located deeper in the graphite will have little tendency to be released since they were not removed by the original heat-treatment at the higher temperature.

Our graphite containers consisted of 1.5 in. high cylindrical boxes with screw-on lids, and 1 mm thick graphite spacers to be inserted between the 10 silicon wafers (full load) for avoidance of cross contamination between wafers.

Results

Starting materials and fabrication of starting substrates.—Crystal growth.—The polysilicon used for crystal growth is extremely pure, with only weak traces of impurities detectable.⁶ The crystals grown from this polysilicon also proved to be exceedingly pure, with only traces of Cr, Co, Ta, W, Sb, and Na being present. The polysilicon residue in the quartz crucible, however, turned out to be severely contaminated as shown in Table I. The residue constitutes

⁵ The activity generated as a function of irradiation time is given by the saturation factor $S = 1 - \lambda/t_{irr}$, with $\lambda = \ln 2/T_{1/2}$; $T_{1/2}$ is the half-life of the radioactive species formed.

⁶ By weak traces we mean photopeaks which are still clearly discernible as to their position in energy, but too weak for meaningful quantitative evaluation because of the statistical uncertainty involved. Detection limits for the more important transition group metals, using our detectors, irradiation, and counting conditions, as stated above, and decay times of about 2 weeks, would be approximately (for 3" ϕ silicon wafers): Fe, 1E14 atoms; Ni, 5E13; Zr, 7E13; Cr, 1.5E12; Mo, 1E11; Co, 5E10; Au, 1E9. Detection limits depend, of course, on the background, i.e. are higher in the presence of longer lived species having photopeaks at higher energies.

Table I.

| Silicon residue in crucible I | | Silicon residue in crucible II | |
|-------------------------------|--|--------------------------------|--------------------------|
| Cu | 2.6×10^{-1} ppm = $(3.7E15 \text{ cm}^{-3})^*$ | Cu | 1.5×10^{-1} ppm |
| Au | 5.3×10^{-5} ppm | Au | 5.0×10^{-5} ppm |
| Cr | $4.2 \times 10^{+0}$ ppm | Cr | 7.2×10^{-1} ppm |
| Mn | 2.9×10^{-1} ppm | Mn | 4.5×10^{-2} ppm |
| Fe | 2.3×10^{-1} ppm | Fe | $4.2 \times 10^{+0}$ ppm |
| Co | 6.8×10^{-2} ppm | Co | 1.7×10^{-2} ppm |
| Ni | $4.1 \times 10^{+0}$ ppm | Ni | $1.1 \times 10^{+0}$ ppm |
| Mo | 2.0×10^{-1} ppm | Mo | 7.1×10^{-2} ppm |
| Ag | 4.7×10^{-2} ppm | Ag | n.d. |
| Hf | Positive | Hf | 7.2×10^{-3} ppm |
| Ta | 3.6×10^{-6} ppm = $(2.8E11 \text{ cm}^{-3})^*$ | Ta | 4.4×10^{-3} ppm |
| W | 8.2×10^{-3} ppm | W | 2.2×10^{-3} ppm |
| As | 1.9×10^{-3} ppm | As | 2.9×10^{-3} ppm |
| Sb | 2.5×10^{-3} ppm | Sb | 1.8×10^{-3} ppm |

* Conversion from ppm to atoms/cm³ involves the atomic weight of the impurity species. For readers more familiar with the atoms/cm³ notation, the concentrations have been expressed in this manner for a typical light (Cu) and a typical heavy (Ta) metal.

about 10% of the original charge, its level of contamination subsequent to crystal growth thus cannot be due simply to the reduced volume. Since the hot silicon melt dissolves a substantial amount of the crucible during a run, it was initially thought that impurities in the crucible were responsible for the buildup of contamination in the melt, and the quartz from several suppliers was analyzed (see Table II). While the amount of impurities in the quartz is not negligible, it is not sufficient to explain the massive contamination of the melt; the contamination had to originate somewhere else in the crystal grower. Next we suspected the quality of the graphite susceptor, but it, too, proved to be quite clean (Table III). However, when the upper edge of the susceptor was examined, it was found to be severely contaminated with molybdenum and with the various components of stainless steel (Table IV). The source of contamination turned out to be seed shafts made from molybdenum or stainless steel and attached to the graphite chuck carrying the silicon seed crystal. These were positioned close enough to the hot portions of the crystal grower to reach obviously excessive temperatures. Since not only the silicon melt became contaminated, but the edge of the surrounding graphite susceptor as well, a major portion of the contamination must have occurred through the vapor phase.

Table II. Impurities detected in various crucible quartz. Concentrations given in ppm.

| Quartz from crucible I | Quartz from crucible II | Quartz from supplier* | | | |
|------------------------|-------------------------|-----------------------|-----------|-----------|-----------|
| | | 1 | 2 | 3 | 4 |
| Cr | $2.0E-1$ | n.d. | $1.3E-1$ | n.d. | n.d. |
| Mn | n.d. | $1.7E-1$ | $7.5E-1$ | $7.2E-3$ | $9.0E-3$ |
| Fe | $5.9E-0$ | n.d. | $1.3E-0$ | $1.6E-0$ | $3.3E-1$ |
| Co | $1.0E-2$ | n.d. | $7.6E-3$ | $3.8E-3$ | n.d. |
| Ni | $9.0E-1$ | n.d. | Not meas. | Not meas. | Not meas. |
| Cu | $2.3E-1$ | $1.6E-1$ | n.d. | $3.4E-1$ | $9.3E-2$ |
| Zn | $1.1E+1$ | n.d. | $1.5E-2$ | $5.5E-2$ | n.d. |
| Zr | $1.1E+1$ | $8.6E-0$ | Not meas. | Not meas. | Not meas. |
| Mo | $5.1E-0$ | $4.1E-0$ | $7.0E-1$ | n.d. | n.d. |
| Hf | $2.7E-1$ | $5.8E-1$ | $1.6E-1$ | $2.1E-1$ | n.d. |
| Ta | $3.9E-3$ | $2.4E-0$ | $2.1E-3$ | $9.0E-3$ | $2.8E-3$ |
| W | $4.8E-2$ | $7.1E-2$ | $2.5E-1$ | $2.8E-1$ | n.d. |
| Ag | $4.9E-2$ | n.d. | n.d. | n.d. | n.d. |
| Au | n.d. | $1.4E-5$ | n.d. | n.d. | n.d. |
| Pt | n.d. | n.d. | $7.5E-0$ | $9.7E-1$ | n.d. |
| Ir | n.d. | n.d. | $2.0E-4$ | $2.0E-4$ | n.d. |
| Na | $3.7E-0$ | $1.2E-0$ | $7.0E-1$ | $2.2E-0$ | $2.0E-1$ |
| K | n.d. | n.d. | $6.6E-1$ | $3.3E-0$ | n.d. |
| As | $5.1E-3$ | $1.4E-3$ | n.d. | n.d. | $2.0E-2$ |
| Sb | $2.6E-3$ | $2.3E-3$ | $3.5E-2$ | $2.7E-2$ | $4.2E-2$ |
| Sn | $9.8E-0$ | n.d. | Not meas. | Not meas. | Not meas. |
| U | n.d. | n.d. | $2.6E-1$ | $1.3E-1$ | n.d. |
| Ce | $1.1E-0$ | n.d. | $3.1E-2$ | $4.6E-2$ | n.d. |

* Note: The data for these 4 quartz samples by J. E. Riley, M. T. Kelley and G. Gleason, Talk presented at the American Nuclear Society Conference, Mayaguez, 1978.

Table III. Graphite from center of susceptor. All concentrations in ppm.

| | |
|----|-----------|
| V | $5.6E-1$ |
| Cr | $1.5E-1$ |
| Mn | $1.0E-1$ |
| Fe | n.d. |
| Co | n.d. |
| Ni | $4.0E-1$ |
| Mo | $1.1E-01$ |
| Zr | $3.2E+0$ |
| Hf | $1.9E-2$ |
| Au | $3.7E-4$ |
| Ca | $1.0E+2$ |
| Sr | $1.2E+0$ |
| Sc | $2.3E-1$ |
| Sn | $2.3E+0$ |
| Sb | $7.4E-3$ |
| Se | + |
| La | $2.1E+0$ |
| Ce | $2.8E+0$ |

Rare earths in the 10^{-2} - 10^0 range

Table IV. Graphite from edge of susceptor. All concentrations in ppm.

| | |
|----|----------|
| V | $5.0E-1$ |
| Cr | $1.6E+0$ |
| Mn | $4.6E-1$ |
| Fe | $3.7E+2$ |
| Co | $6.6E-1$ |
| Ni | $3.1E+1$ |
| Mo | $6.3E+1$ |
| Zr | $3.6E+0$ |
| Hf | n.d. |
| Au | $2.4E-4$ |
| Ca | $9.1E+1$ |
| Sr | $1.2E+0$ |
| Sc | $1.2E-1$ |
| Sn | $1.8E+0$ |
| Sb | $5.9E-3$ |
| Se | $4.1E+0$ |
| La | $1.5E+0$ |
| Ce | $1.6E+0$ |

Rare earths in the 10^{-2} - 10^0 range

The high purity of the silicon crystals pulled from the contaminated melt is thus due to the large segregation coefficient for transition group metals. A rough calculation based on the observed concentrations of the various impurities in the crucible residue showed that the impurity traces in the silicon ingot just correspond to the segregation factors. Since the quality of the ingot material is adequate, the observed contamination of the melt is not serious as long as the polycrystalline residue in the crucible is indeed discarded and is not added to further silicon charge. Somewhat surprising is the purity of the silicon ingot in spite of its contact with the vapors of the contaminants.

Slicing, mechanical and chemical lapping, and polishing.—Slicing and mechanical lapping are very dirty operations, carried out on industrial equipment not designed for maintaining cleanliness. Wafers at this stage are therefore badly contaminated with a variety of impurities, not always removable by simple cleaning. The level and species introduced during slicing and mechanical lapping depend on the kind of slicing saw, the lapping compound, and the composition and corrosion resistance of other metal parts involved in the process. Fortunately, almost all of this contamination is again removed in the chem-etching step, thus there is little purpose in listing specific contaminants observed in the slicing or mechanical lapping process. Some comments, however, are in order concerning the edge beveling and the chem-etching steps.

Until recently, edge beveling wheels had their diamonds embedded in a solder consisting of a mixture of Cu, Ni, Mn, and Sn. This type of wheel deposited large amounts of impurities at the wafer periphery, which, strangely enough, could not be efficiently removed by chem-etching, even when the duration of the chem-etching step was extended by a factor of 4. The only reasonable explanation for this kind of behavior appears to be the assumption that the high density of vacancies generated at the silicon surface during beveling, in conjunction with local high tempera-

Table V.

Impurities in a silica based polishing slurry as determined by neutron activation

| Impurity species Conc in ppm | V | Mn | Cr | Fe | Co | Ni | Cu | Zn | Zr | In | Hf | Ta |
|---------------------------------|-----|-----|------|------|--------|------|-----|-----|-----|------|-----|--------|
| | 7.5 | 3.3 | 0.45 | 96.8 | 5.7E-2 | 2.52 | 2.6 | 3.8 | 145 | 0.45 | 3.3 | 8.8E-3 |

Impurities in ppm in polishing compounds from different manufacturers. Determination by means of atomic absorption spectrometry.

| | V | Cr | Fe | Cu |
|------------|------|------|-----|------|
| Supplier 1 | <0.5 | 0.30 | 47 | 0.20 |
| Supplier 2 | <0.5 | 0.45 | 43 | 1.0 |
| Supplier 3 | <0.5 | 0.35 | 40 | 0.28 |
| Supplier 4 | <0.5 | 0.28 | 124 | 0.20 |
| Supplier 5 | <0.5 | 0.50 | 84 | 3.8 |
| Supplier 6 | <0.5 | 3.20 | 228 | 1.9 |

tures, caused impurity diffusion into the silicon and that these impurities retreated before the advancing solution/silicon interface during chem-etching in the manner described by Wagner for copper in aluminum during electrolytic polishing (3).

More recently, beveling wheels have become available in which the diamonds are embedded in nickel only, with an increased ratio of diamonds/nickel binder. These wheels seem to deposit next to no contamination, not even nickel, at least when new.

In view of the heavy contamination of sliced or mechanically lapped wafers with transition group metals, it is necessary to change the etching solution frequently enough to prevent impurity buildup in the solution. Otherwise the electrochemical potential of the impurities can rise to the point where the solution ceases to be an effective cleaning agent. This phenomenon is quite analogous to the deposition of heavy metals on silicon from contaminated nitric acid-hydrofluoric acid solutions reported by Politycki and Rädlein (4).

Polishing slurries usually appear to be clean enough not to deposit large amounts of impurities on the polished silicon surfaces (Table V), but again it is necessary to limit the length of time the same solution may be reused by recycling. Table VI shows the disastrous results of using a polishing slurry for too long.⁷

The analysis of an alumina-based lapping compound is given in Table VII. These are only examples and may not be typical of other lapping compounds or slurries. An interesting aspect of contamination during polishing is the difference in susceptibility to contamination of differently doped and differently oriented silicon surfaces. (100) and (111) oriented silicon wafers, boron (p-type) and phosphorus (n-type) doped in the 10^{14} cm⁻³ range, were polished using an alkaline, SiO₂-based slurry deliberately contaminated with very dilute copper sulfate. The (100) oriented surface of the p-type wafers became plated with a continuous copper film, the (111) oriented large surface of the n-type wafers remained visually free of any copper, but showed some copper deposition on the edge; the amount of copper on the other two combinations, (111) oriented p-type and (100) oriented n-type silicon, was intermediate. This behavior is in accord with the known electrochemical behavior of silicon crystals, but should be kept in mind: (100)-oriented p-type silicon is most prone to contamination during polishing.

Device fabrication.—Wafer handling.—Prior to entering the device fabrication process, polished substrates are cleaned in different ways, all of which seem to do an adequate job of removing impurities adhering to the surfaces. The wafers are then subjected to a variety of processing steps, which require handling of the wafers for inspection, insertion in furnaces,

⁷ Impurities on silicon wafers are usually concentrated in surface near layers, but their exact distribution is not known. We prefer to give impurities detected on silicon wafers in terms of atoms/wafer. Conversion of atoms/wafer to ppm requires knowledge of the wafer thickness at a given diameter. A 20 mil thick, 3 in. diam silicon wafer contains about $1.15E23$ atoms silicon, and weighs about 5.39g.

Table VI. Impurities on a wafer polished with an alkaline SiO₂ based polishing slurry which became contaminated during excessive use of the same solution

| | Concentrations in atoms/3" ϕ wafer |
|----|--|
| Cr | 5.9E15 |
| Fe | 8.5E15 |
| Co | 4.0E15 |
| Ni | 3.4E15 |
| Cu | 1.4E15 |
| Zn | + |
| Mo | 3.6E15 |
| Ta | 1.6E12 |
| W | 1.4E14 |

Table VII.

Impurities in a fresh alumina lapping compound. Concentration in ppm.

| | |
|----|-----------|
| Cr | 7.2 |
| Fe | 1100 |
| Zn | 34.2 |
| Cu | Not meas. |
| Ni | 28.7 |
| Mo | 4.1 |
| Hf | 2.1 |
| W | 3.9 |
| Au | 0.023 |
| Na | 4600 |

Other elements detected: As, Ga, Sc, La, Ce, Nd, Eu, Tb, Yb

Impurities in alkaline solution (density 1.18 g/ml) of colloidal silica.* Concentration in ppm of liquid.

| | |
|----|-------|
| Cr | 0.14 |
| Fe | 31.0 |
| Zn | 0.43 |
| Cu | 0.085 |
| Ni | 0.084 |
| Mo | 0.025 |
| Mn | 0.125 |
| V | 0.250 |

* Atomic Absorption Data courtesy of T. Y. Kometani, Bell Labs, Murray Hill, N.J.

application of photoresist, etc. Until fairly recently, metal tweezers were in widespread use for this purpose. Table VIII shows that this is not the best way of handling wafers, especially bare silicon wafers which are hard enough to abrade the tweezer material; an oxidized wafer is much "softer" in this respect. More recently, plastic tweezers have been substituted, and the "roll-over" technique from one (plastic) container

Table VIII. Contamination of bare silicon wafers handled with metal tweezers

| | Control (atoms/3" ϕ wafer) | Wafer lifted 20 times with metal tweezer (atoms/ 3" ϕ wafer) | Tweezer composition concentration (%) |
|----|---------------------------------------|--|--|
| Fe | — | 4.2E13 | 73.15 |
| Cr | 5.0E11 | 1.3E13 | 14.30 |
| Ni | 1.4E13 | 5.6E13 | 10.90 |
| Cu | — | — | 0.059 |
| Au | 1.1E11 | 1.5E11 | Contaminated |

to another has eliminated much of the handling of individual wafers, resulting in a considerable reduction in the degree of contamination with stainless steel components. There persist two rather insidious modes of contamination: use of the same containers or of the same tweezers for handling metallized and virgin wafers. Containers or tools used for handling metallized wafers should not be used at earlier fabrication steps.

Once oxidized, the silicon surface becomes much less vulnerable to contact contamination, including contact with liquids. Etching with HF, however, generates a highly active silicon surface on which noble metals, if present, will readily plate out by contact potential. If a contamination problem seems to exist on the line, an HF etching step exposing bare Si should always be followed by a cleaning in hot H_2O_2 -HCl, which both cleans and oxidizes the silicon surface.

Deposition of epitaxial silicon.—In the MOS technology epitaxial silicon is usually deposited on low resistivity substrates, which has a high solubility for transition group metals. This is a fortunate feature in that the substrate effectively blocks the transfer of impurities, emanating from impure graphite or SiC susceptors, into the epitaxial layer by solid-state diffusion. Because of the lower metal solubilities at lower temperatures, there is, of course, a practical limit to the degree of blockage even a low resistivity substrate can exert (5), and cleanliness of the susceptors, especially absence of particulate impurities, is still very important. Diffusion of impurities from the susceptors through the vapor phase into the growing epitaxial layer is essentially prevented by the presence of chlorine or chlorine-containing species during the epitaxial deposition process. In addition, the low oxygen content and the purity of the higher resistivity epitaxial silicon offers few sites for precipitation of contaminants.

The effect of particulate (*i.e.*, highly concentrated) contamination in the susceptor was demonstrated by Pearce and McMahon (6). Dragging a stainless steel tweezer over the surface of an SiC susceptor resulted in the appearance of the same pattern in the epitaxial layer of a wafer placed over the contaminated area for epitaxy. The pattern in the epilayer consisted of stacking faults and saucer pits (after Secco etching). Contamination of graphite susceptors with nickel and copper-containing particulate matter was revealed also by laser-induced emission spectroscopy (7) and by autoradiography of wafers neutron-activated after epitaxial deposition: the radioactive spots were confined to the back surface of the wafer. These particulate sources of contamination probably stem from the machining process and could perhaps be removed by the manufacturer by a cleaning treatment subsequent to the shaping operation.

Oxidation.—High temperature oxidations, in the absence of HCl, especially steam oxidations for production of the "initial oxide" are probably the process step normally introducing the largest quantities of detrimental impurities. Yet this need not be so.

Table IX shows the typical contamination resulting from a high temperature steam oxidation as well as from an oxidation in dry oxygen (no HCl) at about the same temperature and for the same length of time. There is not much difference between the level of contamination, thus it is not necessary to speculate on

Table IX. Typical level of contamination observed after oxidation in steam or in dry O_2 without HCl. Concentrations in atoms/ $3'' \theta$ wafer.

| | Cu | Cr | Fe | Co | Ni |
|------------------------------|--------|--------|--------|--------|--------|
| Steam at 1170°C for 1 hr | 1.3E15 | 4.8E14 | 2.1E15 | 1.2E14 | 5.4E14 |
| Dry O_2 at 1150°C for 1 hr | 1.5E15 | 1.3E15 | 6.6E16 | 2.7E14 | 3.8E15 |

transportation of volatile impurity species by the steam: the impurities must be diffusing out of the quartz tube. Table X gives the analysis of a piece of an unused quartz tube. While the level of contamination is not insignificant, it is obvious that the total amount of impurities present could not possibly act as the reservoir for the observed contamination of the silicon wafers over an extended period of time. In steady state, impurities must be diffusing from the outside through the walls of the quartz tube.

Quartz tubes are conventionally operated inside mullite or SiC liners; both of these materials are, however, very impure and can serve as a virtually inexhaustible reservoir of impurities. Table XI gives impurity concentrations in mullite and in SiC from furnace liners.

Diffusion of transition group metals through quartz furnace tubes possesses an extremely steep temperature dependence. In one set of experiments the existing temperature gradient in a furnace was utilized, with silicon wafers positioned at locations of accurately measured temperatures. The concentrations of Fe, Co, Ni, and Cr were all found to increase by a factor of 200 over a temperature range of only 30°C (1140°-1170°C), whereas copper and tantalum increased only by a factor of 3. The ambient, dry oxygen or steam, did not appear to be a factor. We believe, however, that these results do not reflect a true activation energy for diffusion, but rather a different degree of devitrification of the quartz tube kept at the different temperatures for a long period of time, and thus providing more or

Table X. Impurities in an unused quartz furnace tube. Concentrations in ppm.

| | |
|----|-----------|
| Cr | 3.3E-2 |
| Mn | Not meas. |
| Fe | 3.4 |
| Co | 8.6E-3 |
| Ni | 2.4E-1 |
| Zn | 2.4E-1 |
| Cu | 0.28 |
| Mo | 0.26 |
| Zr | 5.3 |
| Hf | 0.17 |
| Ta | 5.6E-3 |
| Se | 0.57 |
| Te | 0.08 |
| Th | 0.15 |
| U | 0.55 |
| Na | 1.8 |
| Cd | 0.72 |

Other elements detected: Ca, Ba, La, Sc, rare earth (in part fission products from the reactions on U and Th).

Table XI.

Impurities in a SiC furnace liner. Concentrations in ppm.**

| | |
|----|--------|
| Fe | 19,300 |
| Co | 51.1 |
| Ni | 195 |
| Zr | 9,300 |
| Hf | 3.5 |
| Mn | 10.3 |
| Cr | 75.1 |
| Ir | 0.23 |
| W | 0.42 |
| Na | 19,900 |
| K | 1,860 |

La, Sc, Sm, Eu—all in the 0.X ppm range

Impurities in a mullite furnace liner. Concentrations in ppm.**

| | | | |
|----|-------|----|-------|
| Fe | 8,180 | Ga | 75.0 |
| Co | 5.7 | Na | 980 |
| Ni | 9.4 | K | 7,570 |
| Cr | 62.9 | Ca | 2,200 |
| W | 8.2 | Cs | 12.7* |
| Ta | 3.6 | Ba | 152* |
| Th | 2.2 | Sc | 15.6 |
| U | 0.12 | Zr | 210* |
| Hf | 6.2 | Yb | 35.8 |
| Sb | 0.77 | La | 6.26 |
| Au | 0.12 | | |

* There may be some contribution from the fission of U-235.
** Cu could not be determined nondestructively on this sample but was present.

easier diffusion paths. Fe, Co, Ni, and Cr thus appear to diffuse preferentially along (incipient) grain boundaries, the lower "activation energy" of copper may be indicative of a bulk diffusion process.

Table XII shows impurity concentrations on silicon wafers oxidized at the same temperature, but for different periods of time in steam. It can be seen that there exists probably a sublinear time dependence. Combining these two results suggests that from the contamination point of view it would be advantageous to carry out steam oxidations at the lowest feasible temperature.

Table XIII gives the impurities on a wafer oxidized in dry oxygen + 1% HCl at 1000°C for 1 hr. The presence of the HCl prevents contamination of the silicon; unfortunately, no such protection occurs during steam oxidation in HCl, not to mention the exceedingly corrosive nature of the steam-HCl mixture.

A particularly insidious, but easily avoidable, source of contamination during high temperature furnace treatments are impure SiC boats or paddles (or impure graphite coated with a thin layer of SiC). Table XIV shows the enormous contamination that can result from the use of such boats. This particular oxidation was carried out in dry O₂ + 1% HCl, otherwise the contamination would have been even worse. Autoradiography also showed that the contamination was heaviest where the wafer had been in contact with the boat. Contamination can also result from the use of impure diffusion sources. Table XV shows the impurity content of a BN diffusion disk. This BN disk, as well as others, were found to be very nonuniform, and segments from one and the same disk gave strongly different results. The isotopes Cu and Mn could not be determined on this sample, the 511 keV peak of the positron annihilation radiation due to Cu-64 being interfered by pair-production from other high energy

gamma emitters, and the Mn-56 emission having decayed due to the short half-life of Mn-56 (2.58 hr). From the absence of the weak 1345.6 keV gamma line of Cu-64 it can be inferred that the Cu concentration must have been less than about 10¹⁴ atoms cm⁻³.

By analyzing the impurities not in the BN disk but on silicon wafers diffused from BN disks it has been shown that Cu and Mn are in fact impurities transferred from the BN disks to the silicon during diffusion treatment. Which impurities are significantly volatile will depend on the activity coefficient of the impurity in the BN matrix, a topic on which essentially nothing is known. In calculating the impurity concentrations in boron or BN from the gamma-ray spectra of neutron-activated samples one must take into consideration the reduction in thermal neutron flux inside the sample, due to the extremely large cross section of B-10 for thermal neutrons (8).

Ways to avoid contamination during steam oxidation.—

1. A guaranteed way to eliminate contamination would be the use of a double-walled quartz tube with an HCl-containing gas being passed between the inner and outer walls of the tubes (and discharged into a separate outlet from the steam). This would increase the outer diameter of the tube, but would eliminate the need for a furnace liner.

2. High purity alumina liners are available, an analysis of this material is shown in Table XVI. The high purity alumina is orders of magnitude cleaner than the customary mullite liners (and therefore also more expensive). There should be very little transition group metal diffusion into quartz tubes heated inside high purity alumina liners, as long as the alumina liner does not become saturated with impurities diffusing from the heating elements of the furnace, etc. We do not have at this time experimental data to clarify this question.

3. Another attractive approach is the use of low temperature-high pressure steam oxidation. Table XVII shows results obtained on wafers oxidized in a system built at Bell Labs, Allentown (9). In this particular system the steam comes in direct contact with a highly corrosion resistant cobalt alloy, a condition avoided in commercially available systems. The contamination with cobalt, nevertheless, is moderate. The wafers after oxidation are rather clean, except for an unaccounted for contamination with some copper. Es-

Table XII. Impurity buildup as a function of oxidation time in steam at 950°C. Concentrations in atoms/3" θ wafer.

| | Cu | Fe | Co | Ni | Cr | W |
|---------|--------|--------|--------|--------|--------|--------|
| 60 min | 2.8E14 | 3.2E15 | 1.7E13 | 5.9E14 | 7.5E14 | 4.1E11 |
| 122 min | 5.1E14 | 3.9E15 | 2.0E13 | 1.5E15 | 1.0E15 | 3.1E12 |

Table XIII. Typical level of contamination observed on a very clean substrate after oxidation for 1 hr at 1000°C in dry oxygen + 1% HCl. Atoms/3" θ wafer

| | |
|----|--------|
| Cu | — |
| Cr | — |
| Fe | — |
| Co | 3.8E11 |
| Ni | + |
| Ta | 1.5E11 |

Table XIV. Impurities on originally clean substrate oxidized in dry O₂ + 1% HCl for 1 hr at 1000°C in SiC boat. Atoms/3" θ wafer.

| | |
|----|--------|
| Cu | 2.8E16 |
| Co | 6.6E12 |
| Ni | 3.5E14 |
| Ta | 8.4E11 |

Table XV. Impurities on a BN diffusion disk. Concentrations in ppm.

| | |
|----|---------|
| Fe | 97.0E-0 |
| Co | 1.0E-2 |
| Ni | 1.3E-3 |
| Mo | 5.0E-4 |
| Zr | 4.6E-1 |
| Pt | 1.1E-1 |
| Hf | 3.0E-0 |
| Ta | 3.0E-1 |
| Au | 3.0E-4 |
| W | 6.4E-1 |
| U | 7.0E-1 |
| Th | 8.1E-1 |

Many rare earths, in part from the fission reaction of U-235

Table XVI. Impurities on a piece of high purity alumina furnace liner. Concentrations in ppm.

| | |
|----|--------------------------------------|
| Cu | Not measured because of interference |
| Cr | 7.1 |
| Fe | 512 |
| Co | 0.37 |
| Ni | 9.4 |
| Zr | 1,000 |
| Mo | 0.30 |
| Hf | 1.72 |
| W | 1.61 |
| Na | 350 |
| K | 143 |
| Ca | 217 |

Other elements detected: Ba, Ce, La, Ga, Sc, Nd, Eu, Tb, Yb

Table XVII. Contamination during low temperature (750°C)-high pressure (20 atm) oxidation for 70 min in steam. Steam in direct contact with pressure vessel alloy. Atoms/3" θ wafer.

| | Before oxidation | After oxidation |
|----|------------------|-----------------|
| Cu | 5.8E13 | 1.9E14 |
| Cr | 6.1E13 | 6.1E13 |
| Co | — | 2.3E12 |
| Ni | Very weak | 2.1E13 |
| Fe | Very weak | Very weak |
| W | — | 1.3E11 |
| Na | 1.5E14 | 1.1E14 |
| As | 8.7E11 | 7.3E11 |
| Sb | 9.9E10 | 7.6E10 |

essentially all contamination should be avoidable, at 750°C!, in a system which prevents the steam from coming in contact with any metal parts.

Ion implantation.—Our experiments were carried out on two different types of implanters. One is a high voltage, low current commercial machine in which only one wafer at a time is being implanted. The other is a low voltage, high current machine designed and built internally. In this latter machine up to 30 wafers may be implanted simultaneously, a large target holder moving in front of the stationary beam. The commercial high voltage-low current machine has excellent focusing and mass resolution, and no contamination with transition group metals attributable to the implantation step was detectable. In the low voltage, high current machine, on the other hand, the ion beam is permitted to strike the walls of the waveguide, the beam stop, and the beam catcher plate. Impurities can and are being sputtered off these metal parts, and attention must therefore be paid to the material from which they are made. Table XVIII shows an example of the contamination resulting from the use of a stainless steel beam catcher plate. The contamination was not confined to the back surface of the wafer, about 1/3 was found on the front surface. Impurities from the material of the hot cathodes were also shown to find their way to the silicon wafers, but this does not appear to constitute a major problem.

Plasma etchers.—Plasma etching is beginning to replace wet chemical etching steps due to the better resolution and avoidance of undercutting. The plasma, however, constitutes a very effective means of redistributing impurities deposited outside the target area in previous runs. Thus, for instance, plasma etchers which have been used to pattern gold metallurgy should not be used for other work without very thorough cleaning if the sample to be etched will undergo still some high temperature treatments after the plasma etch. Exposed copper parts also have been shown to be a source of contamination, as is the copper contained in aluminum-copper alloys used as the base plate in some etchers; in the latter case, however, the aluminum plate becomes oxide covered if the working gas in the etcher contains oxygen, and the contamination decreases with time.

Packaging.—At this stage, wafers are no longer exposed to high temperatures, thus contaminants other than those that give rise to electrolytic conduction, such as NaCl, are no longer of importance. A special case, however, is the packaging of static memories in alumina ceramics. Information in static memories is not periodically refreshed, but must be maintained indefinitely. Alumina ceramics, however, often contain small amounts of uranium and thorium and other members of the uranium decay chain, all of them alpha emitters. Due to the large energy of alpha particles, and the very small charge stored on an individual capacitor in such memory arrays, direct hits by alpha particles can result in loss of information. This fact requires that static memories be shielded against direct alpha hits, a relatively easy task in view of the very short range of alpha particles in matter. Most of the alpha emission, incidentally, does not stem from the very long-lived U-238, but from shorter lived members of the decay chain. However, the (n,gamma) reaction on U-238 is the most convenient method for de-

Table XVIII. Impurities on a silicon wafer boron implanted at a dose of $6.7E16$ /wafer at a beam current of 0.5 mA with a low voltage-high current implanter built internally. Tungsten hot filament, stainless steel beam catcher plate. Atoms/ $3'' \theta$ wafer.

| Cu | Fe | Co | Ni | Cr | W | Mo |
|--------|--------|--------|--------|--------|--------|--------|
| 1.9E14 | 5.4E15 | 1.6E13 | 6.0E14 | 1.6E15 | 7.4E11 | 1.7E15 |

Table XIX. Impurities from the ceramic of an integrated circuit package. Concentration in ppm or in %.

| | |
|----|----------|
| Na | 0.48% |
| Ca | 5.1% |
| Cr | 0.51% |
| Zr | 0.35% |
| Hf | 130 ppm |
| W | 21 ppm |
| Ta | 7 ppm |
| U | 0.79 ppm |
| La | 0.34 ppm |
| Sc | 0.42 ppm |
| Sm | 0.25 ppm |
| Yb | 1.70 ppm |

termining the uranium content, and hence establishing the presence or absence of the problem (Table XIX).

Summary

A survey has been given of the sources of contamination in silicon device processing. The polysilicon used for growing ingots is very pure, but very strong contamination of the silicon melt can occur from the exposure of metal parts (Inconel and/or molybdenum in our case) in the crystal growers to high temperatures. Transfer of the contamination appears to occur preponderantly through the vapor phase. The large segregation coefficients of the transition group metals protect the silicon ingot against significant contamination provided the polysilicon residue in the crucible is not recycled.

Lapping and polishing can be sources of very undesirable contamination of the starting substrate surface if the lapping and polishing compounds are dirty to start with or are being reused for too long. Edge beveling wheels of a new design were found to introduce very little if any contamination as compared to older types of wheels. High temperature oxidations in the absence of HCl were shown to be preponderant sources of contamination. The impurity diffusion through the walls of the quartz tubes and into the silicon approximately follows an exponential behavior with temperature. Presence of HCl suppresses this contamination. Possible alternatives for preventing contamination during high temperature furnace treatments are described. The special role of HCl (or other chlorine-containing compounds) in removing contaminants as chlorides during high temperature gettering is examined in a companion paper.

Acknowledgment

The authors are indebted to T. Y. Kometani, Bell Labs, Murray Hill, New Jersey, for atomic absorption spectrometric determinations of impurities in polishing compounds.

Manuscript submitted April 14, 1980; revised manuscript received July 31, 1980.

Any discussion of this paper will appear in a Discussion Section to be published in the December 1981 JOURNAL. All discussions for the December 1981 Discussion Section should be submitted by Aug. 1, 1981.

Publication costs of this article were assisted by Bell Laboratories.

REFERENCES

1. P. F. Schmidt and D. J. McMillan, *Anal. Chem.*, **48**, 1962 (1976); P. F. Schmidt, J. E. Riley, Jr., and D. J. McMillan, *ibid.*, **51**, 189 (1979).
2. R. Van der Linden, F. De Corte, and J. Hoste, *Anal. Chim. Acta*, **71**, 267 (1974); L. Moens, F. De Corte, J. Haste, and A. Simonits, *J. Radioanal. Chem.*, **45**, 221 (1978).
3. H. W. Pickering and C. Wagner, *This Journal*, **114**, 698 (1967); see also H. H. Strehblow, C. M. Melliar-Smith, and W. M. Augustyniak, *ibid.*, **125**, 915 (1978).
4. A. Politycki and G. Rädlein, *Z. Naturforsch., Teil A*, **19**, 1216 (1964).

5. R. N. Hall, *J. Phys. Chem. Solids*, **3**, 63 (1957); R. N. Hall and J. H. Racette, *J. Appl. Phys.*, **35**, 378 (1964).
6. C. W. Pearce and R. G. McMahon, *J. Vac. Sci. Technol.*, **14**, 40 (Jan/Feb. 1977).
7. T. H. Briggs, Personal communication.
8. Y. U. Yakovlev and N. N. Dogadkin, *Uspekhi Anal. Khim.*, **124** (1974).
9. L. E. Katz and B. F. Howells, *This Journal*, **126**, 1822 (1979).

Metal Silicon Reactions Induced by CW Scanned Laser and Electron Beams

T. Shibata,¹ T. W. Sigmon,* J. L. Regolini,² and J. F. Gibbons*

Stanford Electronics Laboratories, Stanford, California 94305

ABSTRACT

Scanned CW-laser and electron beams have been utilized to react thin metal films of Pd, Pt, Mo, W, and Nb deposited by electron beam evaporation onto single crystal silicon substrates to form silicides. Formation of large area uniform layers of Pd₂Si or PdSi is controlled by selection of the power level of the scanning laser or electron beam. Single phase MoSi₂, WSi₂, and NbSi₂ are also found after CW-beam reaction. For the Pt/Si system mixed phase silicides are found after CW-laser reaction with a superconducting ($T_c \cong 4$ K) metastable compound, Pt₂Si₃, observed as the dominant phase. In contrast, single-phase PtSi is found after electron-beam reaction. Comparison is also made with electron beam evaporated films and argon sputter-deposited films.

The reaction of thin metal films with both single and polycrystalline silicon to form silicide compounds is an area which has received wide attention in the past few years. Future integrated circuit technology will require increased device packing density along with decreased dimensions resulting in a need for low resistance interconnects. Desirable properties of these interconnects will include high temperature process compatibility and controlled metal-silicon-interface reactions for both Schottky and ohmic contact reliability (1-3). The bulk of the research to date has been carried out in thermal equilibrium furnace reactions and an excellent review is given in Ref. (4). There both the film deposition and furnace annealing processes are discussed in detail along with useful measurement techniques for determining reacted film composition and quality.

Certain limitations have been found in the furnace thermal equilibrium processing, however. As a result of these limitations, within the last year, the use of energetic beams to react metal silicon films has been investigated by a number of research groups. Both laser (5-7) and electron beam (8) reaction and ion beam mixing (9) have been used in this work. Each of these techniques has led to several unique results, differing in many cases from that found for standard furnace processing.

The main features offered by the laser or electron beam processing of these films include shorter reaction times, localized heat-treatment, and rapid heating and cooling rates. Similar to the case of energetic beam annealing of semiconductors, a natural division of the physical mechanisms and results can be made for pulsed vs. scanned CW energetic beam-induced reactions. In this paper we will discuss results we have obtained using scanned CW-laser and electron beams to react various metal/silicon systems. In contrast to the results found for the pulsed case, uniform, essentially single-phase silicide films are obtained with the scanned CW beams. However, under certain conditions, metastable mixed-phase systems are also obtained.

Both MeV Rutherford backscattering and glancing angle x-ray diffraction analysis have been utilized for characterizing the structure of the layers. Four-probe resistivity measurements have been utilized to obtain bulk resistivity using the film thickness data obtained from the backscattering.

Experimental

In Table I we list the various metal/silicon systems reacted in this work. Also listed are the pertinent properties characterizing each system, such as thickness and whether or not a silicon overcoating is used. All metal films were deposited by electron beam evaporation onto p-type <100> silicon substrates in a high vacuum oil-free system, unless otherwise noted. Thin amorphous silicon layers were deposited on the metal layers to be reacted by the laser to provide an anti-reflection coating for the metal surface. Without the silicon overcoating, a high laser power is required to compensate for the power reflected from the metal surface. However, the smaller reflectance of the silicide compound results in an increased power absorption in the film during the reaction, leading to difficulty of control of the reaction. This problem can be avoided by the use of this thin silicon overcoating. Naturally, since the reflectance does not change for the electron beam this overcoating layer is not required for the scanned electron beam experiments.

The laser used in this work was a CW argon laser operating in the multiline mode. The laser output was focused by a 135 mm lens onto the sample and scanned by the apparatus described in Ref. (10). Typical pa-

Table I. Summary of samples used in the experiments

| Beam process | Si-over-coating | Metal layer | Substrate |
|-----------------------|-----------------|---|-----------------|
| Scanned-laser beam | Si (200Å) | Pd (1300Å) Pt (1000Å) Mo (530Å) W (440Å) Nb (1100Å) | p-type <100> Si |
| Scanned-electron beam | None | Pd (1400Å) Pt (1100Å) Nb (1250Å) | |

* Electrochemical Society Active Member.

¹ On leave from Integrated Circuits Laboratory, Toshiba R and D Center, Toshiba Corporation, Kawasaki, Japan.

² Present address: CNEA Bariloche, Argentina.

Key words: silicides, laser anneal, e-beam anneal, contacts.

rameters used in these experiments were, approximately 50 μm spot size and 12 cm/sec beam scan speed. The substrate was held at fixed temperatures during the laser irradiation. The substrate temperatures used for the various reactions are listed in Table II. Electron beam irradiation was performed in a Hamilton Standard electron beam welder, Model EBW7.5 at a working vacuum of 10^{-4} Torr. The samples were mounted on a copper heat sink with Dow Corning 340 heat sink compound and maintained near room temperature during the reaction. Typical electron beam parameters used for the reactions were, substrate temperature approximately 50°C, electron beam energy 31 keV, current 0.1-0.3 mA, beam spot size (as measured by the reacted path) approximately 100 μm , scan rate of 13 cm/sec, and a step size of less than 100 μm . All reacted layers were studied by MeV ^4He ion backscattering, glancing angle x-ray diffraction analysis in a Read camera, Nomarsky optical microscopy, and four-probe resistivity measurements.

Results and Discussion

Pd/Si.—In Fig. 1 we show an optical micrograph of a sample consisting of Si (200Å)/Pd (1300Å)/Si <100> laser beam scanned as a function of laser power levels. It can be seen from Fig. 1 that the reaction of the Pd/Si is initiated at about 4W of laser power. The laser-induced reaction is easily detected by the unaided eye through a surface color change. For this particular sample the reaction began at a power level of 4W where the surface color changed from blue (unreacted film) to yellow (reacted film, low power phase). This low power phase was found to be stable to a threshold power of about 7.0W, above which a different high power phase appears in the center of the beam scan line. At this power level, the surface color changes to a gray color characteristic of the high power phase. In order to obtain uniformly annealed areas, overlapped scans were performed in such a way that each adjacent scan line overlapped by at least 40%.

For the remainder of this paper we will normalize the output power level of the laser (P) to the power at which the surface of a virgin silicon wafer just begins to melt (P_0). This normalized power ($p \equiv P/P_0$) is experimentally reproducible, thereby minimizing the dependence on the laser system and/or other conditions. For our experimental configuration, typical values of P_0 are 9.0 and 5.0W for 50° and 350°C substrate temperatures, respectively. This normalized laser power is also related to the important parameter of the CW-beam process, i.e., the ratio of beam power to the spot radius (P/w). This relation is given by P/w ($W/\mu\text{m}$) = $0.337p$ or $0.191p$ for $T_{\text{sub}} = 50^\circ$ or 350°C , respectively, using the formulation of Ref. (11). Here the beam radius, w , is defined by the $1/e$ point of the beam intensity assuming a Gaussian distribution. Since

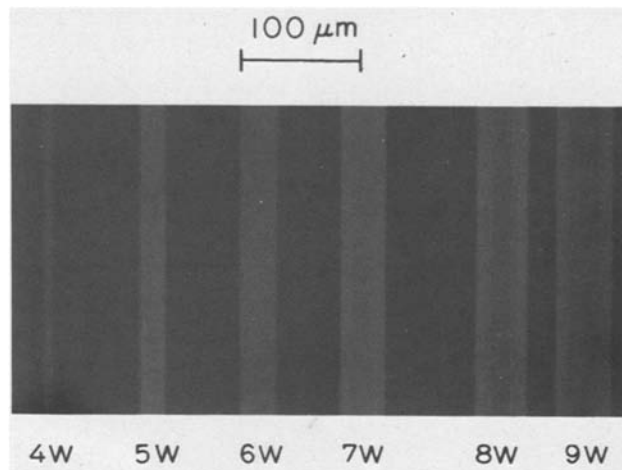


Fig. 1. Optical micrograph of a sample consisting of Si (200Å)/Pd (1300Å)/Si <100> after single laser scans at various laser power levels. The low power phase is formed between 4 and 7W and the high power phase at and above 8W.

the actual power absorbed by the sample is reduced by the reflection, the essential power parameter is $(1 - R)P/w$, where R denotes the reflectance of the sample. This parameter is listed in Table II and has been calculated by using experimentally determined values for R . Since reflectance is not important for the electron beam experiments the actual P/w values are listed in Table II. For the electron beam data the beam diameter used was determined by measuring the width of the reacted material for a single scan. This technique gives a slightly different value for w as compared to the laser case, where w is determined from the melting power (P_0).

Backscattering spectra for the Pd/Si samples which were laser annealed at $p = 0.71$ (low power phase) or $p = 1.1$ (high power phase) are shown in Fig. 2(a). The spectrum for the unreacted sample is shown by the solid line. Since this is a sample prepared for laser annealing, the peak in the solid line near 1.2 MeV on the energy scale is the signal from the 200Å of silicon antireflection overcoating previously discussed. The peak at higher energy is the signal from the Pd, and the step in the backscattered yield at about 1.1 MeV represents the signal from the underlying silicon substrate. It is clearly seen in Fig. 2(a) that the entire metal layer has been reacted with the substrate and surface silicon after laser irradiation. From the areas underlying the backscattering spectra for the different atomic species, one can determine the average composition of the reacted materials. This was determined to be Pd_2Si for the low power phase and PdSi for the

Table II. Summary of beam process parameters and resultant reactions

| | Metal film | Reacted phase | Reacted thickness* (Å) | p (normalized laser power) | Power parameter** ($W/\mu\text{m}$) | T_{sub} (°C) | Resistivity ($\mu\Omega \cdot \text{cm}$) |
|-----------------------|------------|--------------------------------|------------------------|------------------------------|---------------------------------------|-----------------------|---|
| Laser beam reacted | Pd | Pd_2Si | 1930 | 0.71 | 0.154 | 50 (± 0.5) | 37 |
| | Pd | PdSi | 2600 | 0.9 ~ 1.4 | 0.2 ~ 0.3 | 50 (± 0.5) | 31 |
| | Pt | $\text{Pt}_2\text{Si}^\dagger$ | — | 0.69 | — | 50 (± 0.5) | — |
| | Pt | PtSi_2^\ddagger | — | 0.86 | 0.185 | 50 (± 0.5) | — |
| | Mo | MoSi_2 | 1450 | 0.88 | 0.093 | 350 (± 1.0) | 190 |
| | W | WSi_2 | 1200 | 0.85 | 0.087 | 350 (± 1.0) | 110 |
| | Nb | NbSi_2 | 1350 | (10 scans) 0.9 | 0.089 | 350 (± 1.0) | — |
| | (21 scans) | | | | | | |
| Electron beam reacted | Pd | Pd_2Si | 2280 | | 0.112 | ~50 | 39 |
| | Pd | PdSi | 2730 | | 0.136 | ~50 | 20 |
| | Pt | PtSi | 1670 | | 0.093 | ~50 | 28 |
| | Nb | NbSi_2 | 1200† | | 0.173 | ~50 | — |
| | | | | | | | |

* Calculated from backscattering spectra using the near-surface approximation for the energy loss.

** Calculated values of absorbed power/beam radius: $(1 - R)P/w$.

† A mixed phase compound including metastable Pt_2Si_3 .

‡ Thickness of a partially reacted film.

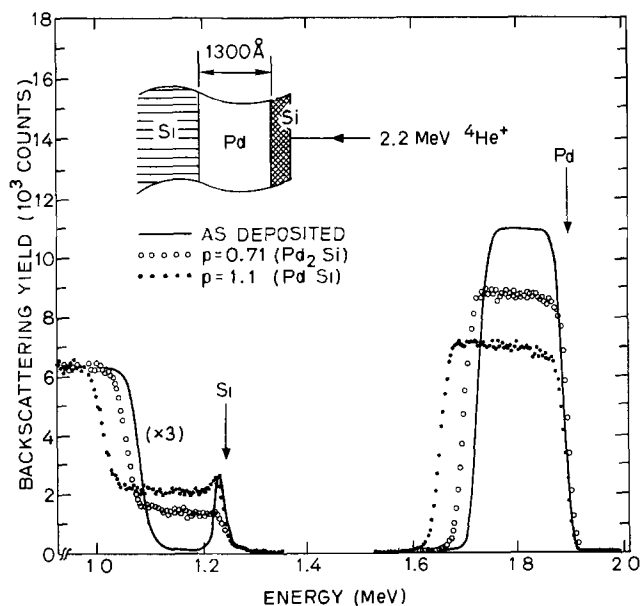


Fig. 2. (a). Backscattering spectra for Si/Pd/Si laser annealed samples for various normalized laser power levels. The solid line (—) represents data taken on unreacted samples, the circles (○ ○ ○) on samples reacted at low powers, and the closed circles (● ● ●) samples reacted at high power levels.

high power phase. It should be noted that the spectrum of the high power phase (PdSi) did not change significantly with laser powers ranging from $p = 0.9$ to 1.4 . This result is quite different from those obtained using a pulsed laser beam, where the average composition of the silicide layers are observed to change continuously with increasing laser power (5, 12). In Fig. 2(b) we show the x-ray diffraction pattern obtained from the sample reacted at high power ($p = 1.1$) using a Read x-ray camera. The lines from the PdSi phase are indicated by the solid circles and the most intense lines from the Pd₂Si phase by the open circles. It can be seen from this diffraction pattern that the compound is essentially single-phase PdSi containing a trace amount of Pd₂Si, thereby verifying the backscattering results. Similar results were obtained for the sample reacted at low power where the compound was found to be mainly Pd₂Si, with a trace amount of PdSi observed. Identical results were also found for the electron beam reacted Pd/Si samples. These results are also in contrast with those obtained using a pulsed laser beam, where the reacted layer was found to con-

sist of PdSi, Pd₂Si, Pd₄Si, Pd₅Si, and Si precipitations (12, 13).

It should be noted that the formation of uniform PdSi layers is difficult by conventional furnace techniques unless ion beam mixing (14) is used, usually leading to a PdSi island microstructure containing Si between or inside the islands (15). In Table II various properties of the PdSi and Pd₂Si films formed by both the laser and electron beams are presented.

The surface morphology of the Pd₂Si layers can be best described as a rather patchy surface appearance similar to that obtained in the furnace reacted case (15). The effective temperature calculated for the laser-scanning conditions used to form the Pd₂Si is about 778°C for $p = 0.71$, with an effective annealing time of $T_{eff} = 12.1$ msec. This results in a calculated Pd₂Si thickness of about 1530 Å assuming that the furnace annealing data (16) holds for the laser process. [The formulas in Ref. (11) have been used for the calculation.] These calculations are in good agreement with the experimentally observed result (1930 Å) determined by backscattering (Table I). These results indicate that the formation of Pd₂Si by the CW laser occurs by a process quite similar to that of the furnace reaction. Using recently obtained furnace annealing data for the activation energy of the Pd₂Si formation (17), we have concluded that the formation of this phase proceeds via a solid-state interdiffusion mechanism (18).

The PdSi films exhibit a laminar-like surface morphology indicative of a spontaneous nucleation process. A Nomarsky interference micrograph of the surface is shown in Fig. 3. Although the mechanism responsible for the PdSi formation is not completely understood, we have evidence indicating that a nucleation-induced process is responsible (7).

Pt/Si.—Scanned laser reaction of the Si (200 Å)/Pt (1000 Å)/Si <100> samples resulted in surface color changes similar to those found for the Pd/Si samples. The reaction was found to begin at $p = 0.5$ with the transition from a low power to a high power phase occurring at a value $p = 0.74$. The backscattering and x-ray diffraction results were found to be quite different from those obtained for the Pd/Si films. In Fig. 4(a) we show backscattering data for the laser-reacted Pt/Si films, and in Fig. 5 similar data is shown for the electron-beam reacted layers.

The average composition calculated from the backscattering spectrum in Fig. 4 for the low power laser-reacted sample is close to Pt₂Si; however, it was found from x-ray analysis that the layer consisted mainly of Pt₃Si and PtSi with trace amounts of Pt₁₂Si₅ and Pt₂Si.

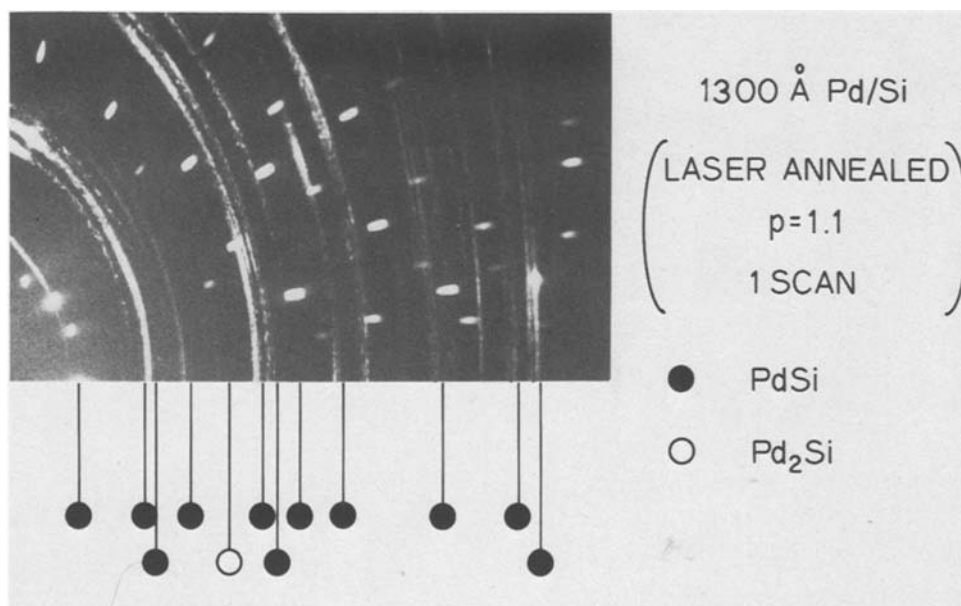


Fig. 2. (b) Glancing angle x-ray diffraction pattern from a Read camera on the sample reacted at high power as shown in Fig. 2(a). The line indicated by ○ is the most intense diffraction line from Pd₂Si.

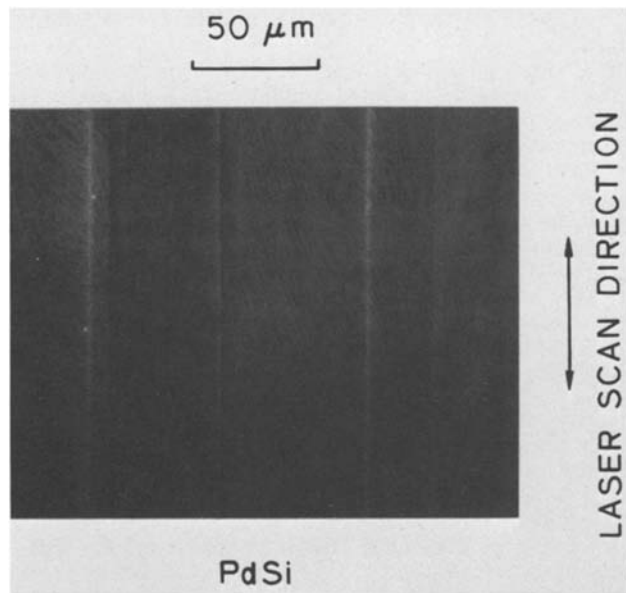


Fig. 3. Nomarsky interference micrograph of a PdSi layer formed by scanned laser reaction.

The average composition determined from Fig. 4 for the high power phase was approximately PtSi_2 . This compound does not exist in the equilibrium phase diagram (19). The x-ray diffraction pattern obtained from the high power phase (PtSi_2) is shown in Fig. 4(b). The intense lines appearing in this diffraction pattern cannot be fit by any equilibrium Pt/Si compounds. However, they are found to fit very well the diffraction pattern of metastable Pt_2Si_3 (20). Small amounts of Pt_2Si_3 were also found in the samples reacted at low power. To further verify the existence of this phase for these samples we performed superconductivity measurements. The observed transition temperature (T_c) was found to be approximately 4 K corresponding well to that observed in Ref. (20).

In Fig. 5 backscattering data obtained for the Pt/Si films reacted by scanned electron beams are shown. Using the near-surface approximation for the energy loss and cross section, this data indicates the entire film has been reacted to form PtSi. That this is a uniform reaction is indicated by the uniformity of the platinum and silicon signals corresponding to the PtSi layer.

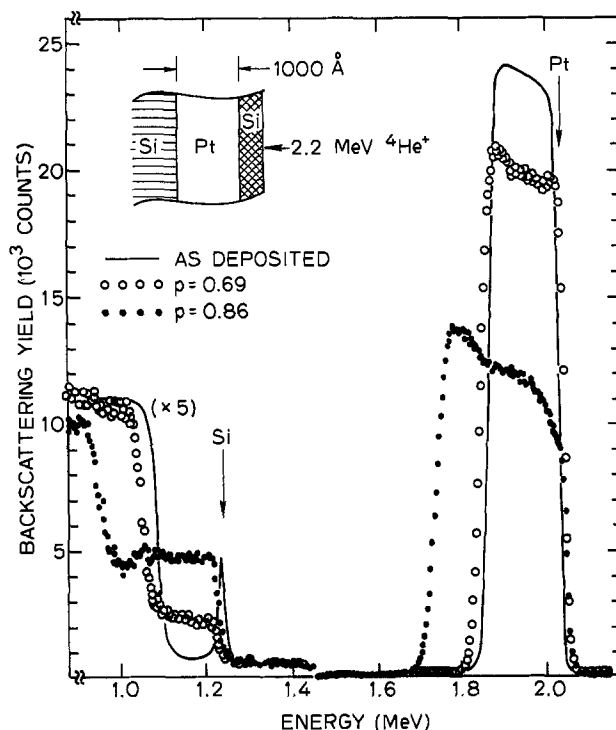
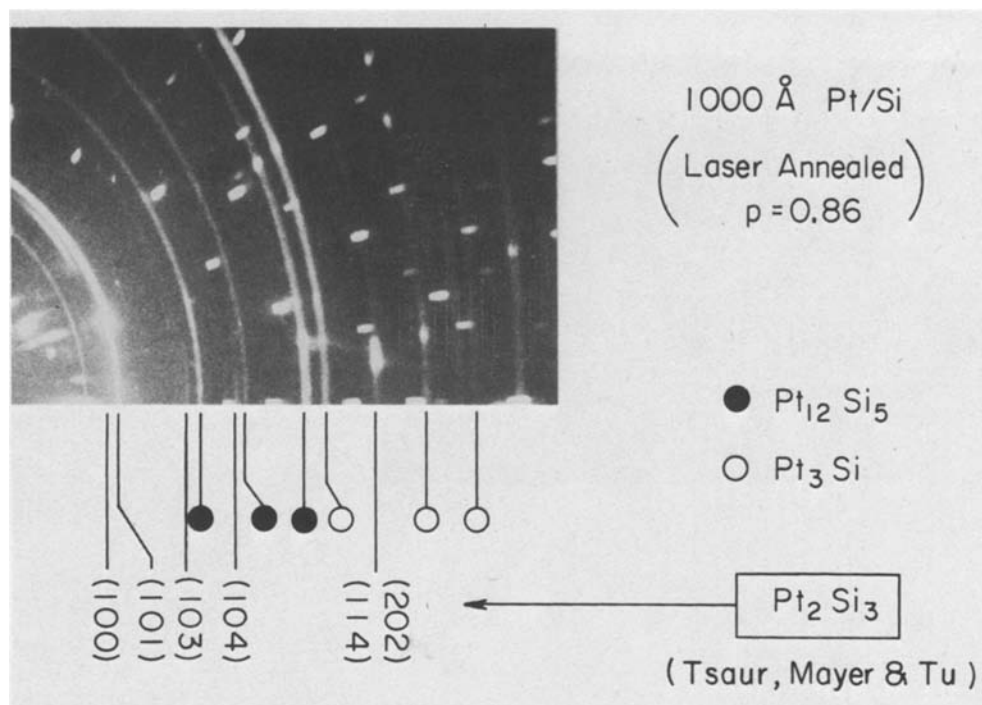


Fig. 4. (a) Backscattering spectra for as-deposited (—) Si/Pt/Si structures and laser annealed [(○○○) $p = 0.69$ and (●●●) $p = 0.89$] Si/Pt/Si structures.

This is in contrast to that observed in Fig. 4(a), for the Pt/Si layers reacted by the laser. Glancing angle x-ray diffraction analysis of the electron-beam reacted layers confirm the results of the backscattering that we do indeed have single-phase PtSi. Further parameters measured for these films are listed in Table II.

The observed difference between the laser and electron beam ability to form PtSi can be caused by two phenomena. The basic physical differences between the laser and electron beam experiments are sample structure and beam energy deposition profile. Although we cannot rule out the possibility of interfacial effects (such as bond breaking) created by penetration of the electron beam into the Pt/Si interface, we speculate

Fig. 4. (b) Glancing angle x-ray diffraction pattern for the Pt/Si structure laser annealed at $p = 0.86$ as shown in Fig. 4(a). Formation of superconducting Pt_2Si_3 phase is evident.



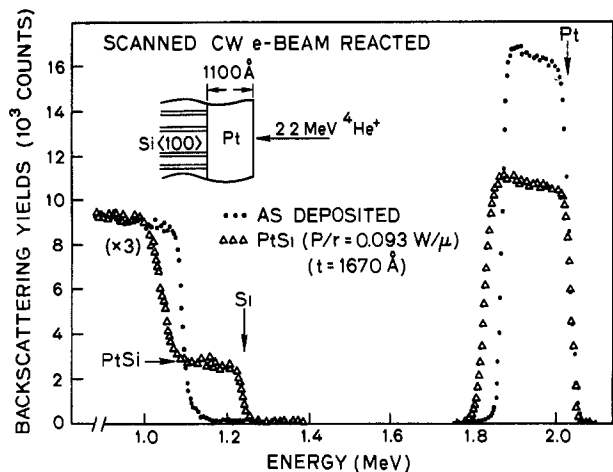


Fig. 5. Backscattering spectrum shown for Pt/Si film reacted by a scanning electron beam. The closed circles (●●●) represent the spectrum from the as-deposited film while the triangles (△△△) are for the e-beam reacted.

that the observed difference is due to the presence of the thin overcoating of silicon on the laser-reacted samples.

Refractory metals (Mo, W, Nb)/silicon.—We have successfully used the scanned CW laser and/or electron beam to react thin films of Mo, W, and Nb with Si. For films to be reacted by the laser a thin overcoating of silicon was again used to control reflectivity. In Fig. 6(a) we show backscattering spectra for both before and after CW laser irradiation of Si(200Å)/Mo(530Å)/Si <100> samples. It can be seen from this data that the deposited film of Mo was completely reacted with the Si after laser irradiation at a normalized power of $p = 0.88$. The average composition of resulting layer can be calculated from the spectrum and was found to be MoSi₂. The x-ray diffraction pattern, shown in Fig. 6(b), also verifies that the reacted layer is single-phase MoSi₂ free from unreacted Mo or Si precipitates.

For both the W/Si and Nb/Si samples multiple laser scans were required to fully react the metal with the underlying silicon. For example, for the Si(200Å)/W(440Å)/Si <100> and Si(200Å)/Nb(1100Å)/Si <100>, laser irradiation at a normalized power of $p = 0.85$ and 0.90 , respectively, resulted in only a limited amount of reaction observed at the interface between the metal and silicon. The results of backscattering analysis for both the W/Si and Nb/Si samples are shown in Fig. 7(a) and 8, respectively. In Fig. 7(a) it can be seen that the 440Å tungsten layer was completely reacted

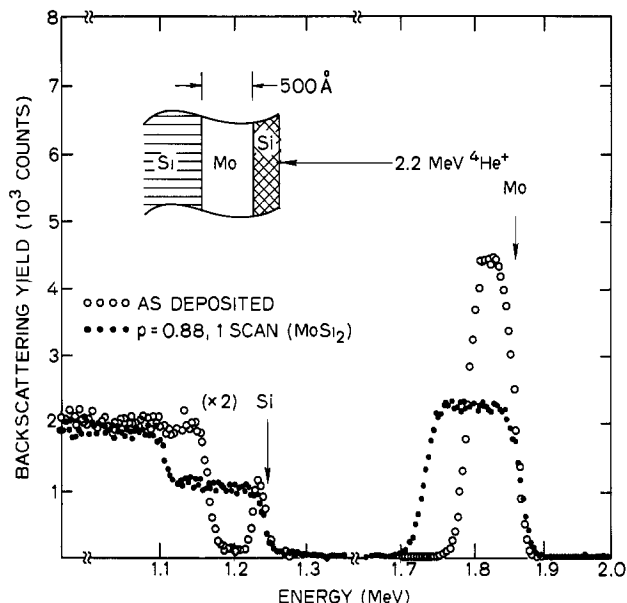


Fig. 6. (a) Backscattering spectra for Si(200Å)/Mo(530Å)/Si <100> structures before (○○○) and after (●●●) laser reaction. A layer of MoSi₂ of about 1450Å thickness was obtained after 1 laser scan at $p = 0.88$.

forming a WSi₂ layer of about 1200Å in thickness. It should also be noted that ten passes with the laser were required to complete this reaction. The backscattering data show that the film is quite uniform with a well-defined interface at the silicide/silicon crystal interface. In Fig. 7(b) the x-ray diffraction pattern obtained for this sample is shown. The major lines of WSi₂ are seen without presence of W and/or Si precipitate lines.

In Fig. 8 the backscattering spectra for the Nb/Si samples are shown. Here we see the advancement of the interface between the silicon and niobium occurring for constant laser power as a function of the number of laser scans. It can be seen that the thickness of the silicide film (NbSi₂) increases with the number of scans. The average composition of this reacted layer is found to be NbSi₂, determined from the backscattering spectra and verified by x-ray diffraction analysis. Using the near-surface S factor, $[S_0]_{Nb}^{NbSi_2} = 83.7$ eV/Å, the film thickness *vs.* the number of scans are plotted in Fig. 9. One can clearly see that a parabolic growth behavior exists for the NbSi₂ film since the number of scans is proportional to an effective annealing time. This result is in agreement with the general behavior of the refractory metals which form disilicides

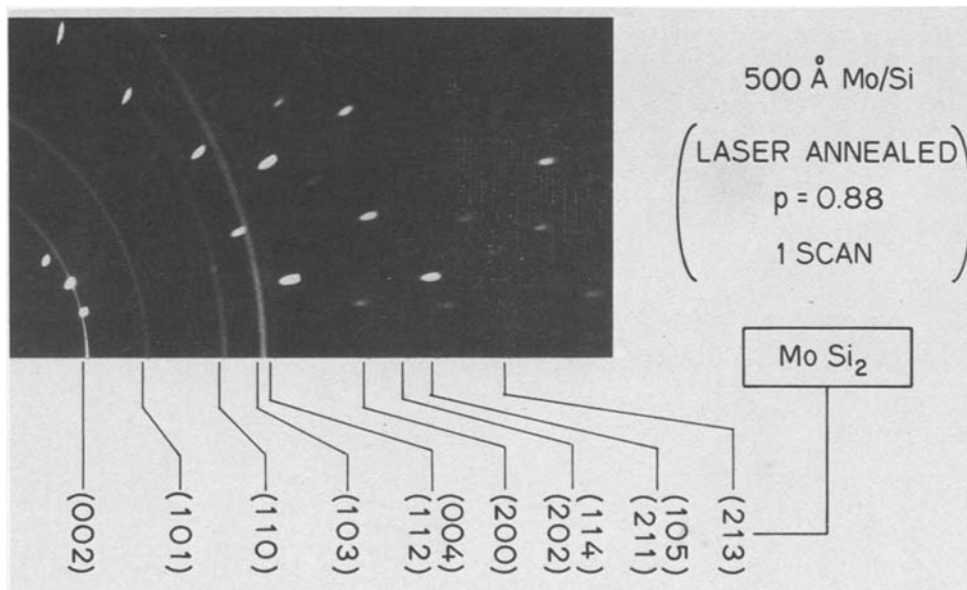


Fig. 6. (b) X-ray diffraction pattern obtained from the Mo/Si sample laser annealed at $p = 0.88$.

by furnace annealing (4). The facts suggest that the laser-induced reaction for NbSi_2 formation occurs essentially by a solid-phase diffusion mechanism.

In Fig. 10 we show backscattering data taken on unreacted Nb/Si and e-beam reacted NbSi_2 for two different values of P/w (0.155, 0.173 W/μ). The growth front of the NbSi_2 layer into the Nb/Si couple can be seen directly from this data. Verification of the NbSi_2 phase has been done again using x-ray diffraction. The calculated thicknesses of the two layers are 780 and 1200 Å for the 0.155 and 0.173 W/μ power levels, respectively.

Sputtered films (Pd, W)/Si.—The thin film samples used in the experiments discussed so far were all prepared by e-beam evaporation of the metal and silicon layers in an oil-free vacuum system. Similar experiments have been performed on samples prepared by argon sputtering of the layers. However, significant differences have been found in the resulting reacted films from those prepared by evaporation.

The Si(200Å)/Pd(1000Å)/Si <100> samples prepared by argon sputtering were laser irradiated at power levels of $p = 0.5$ –1.4. For the lower power

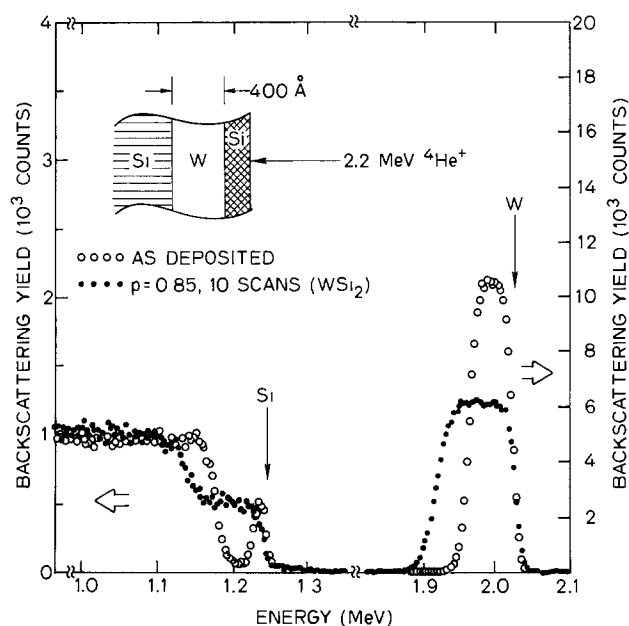


Fig. 7. (a) Backscattering spectra for Si (200Å)/W (440Å)/Si <100> structures. About 400 Å of W (○ ○ ○) is completely reacted to form a WSi_2 film (● ● ●) of about 1200 Å thickness after 10 laser scans at $p = 0.85$.

Fig. 7. (b) X-ray diffraction pattern obtained from the Si/W/Si structure laser annealed at $p = 0.85$ for 10 scans.

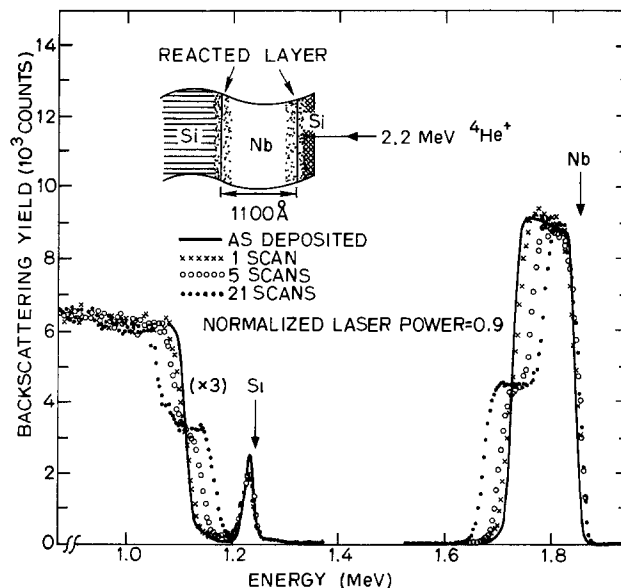
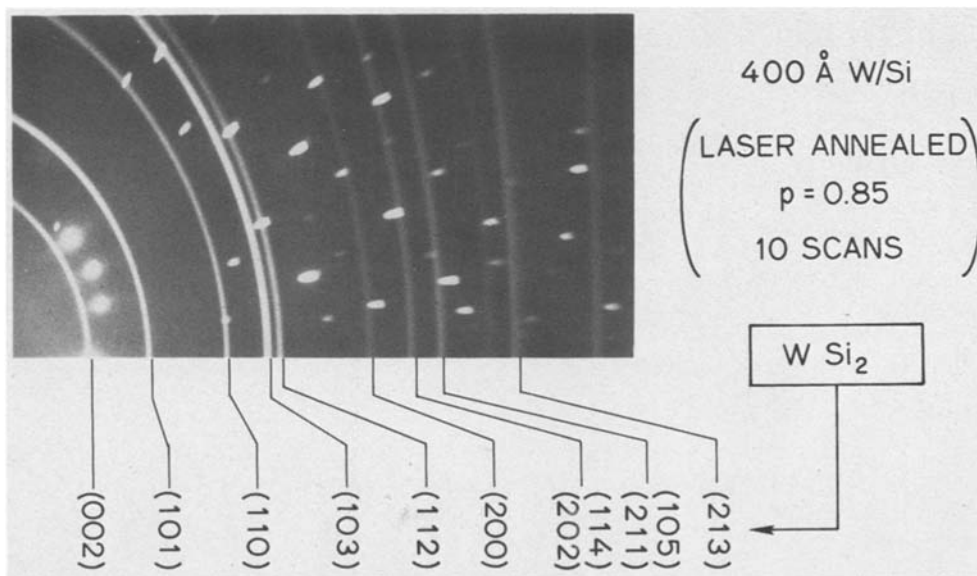


Fig. 8. Backscattering spectra for Si (200Å)/Nb (1100Å)/Si <100> samples with multiple laser scans. The thickness of the silicide (NbSi_2) increases with the number of scans.

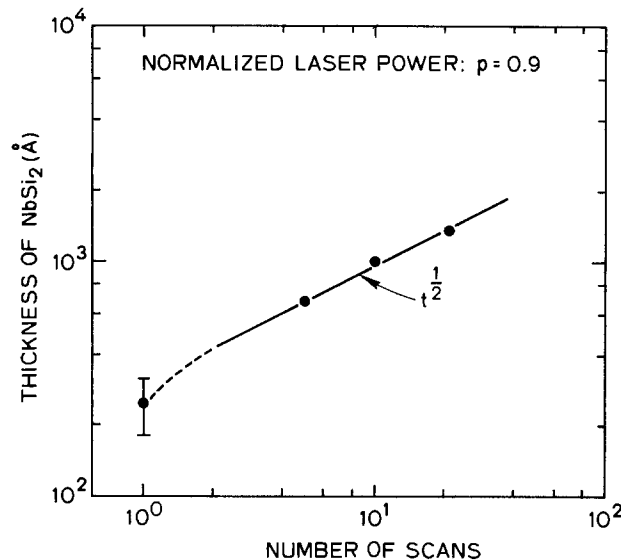


Fig. 9. Thickness of NbSi_2 as a function of the number of laser scans. The data show the parabolic growth for NbSi_2 formation since the number of scans is proportional to the annealing time.

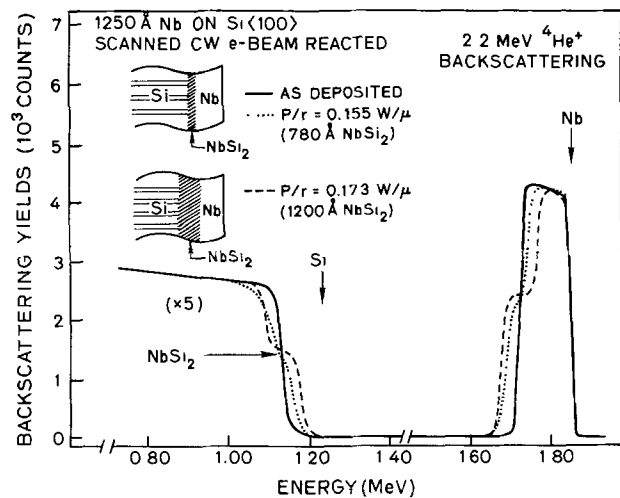


Fig. 10. Backscattering spectra for Nb (1250Å)/Si <100> samples electron beam scanned at various power levels. The thickness of the silicide is seen to increase with increasing power.

levels (0.5-1.0), the surface color changes observed optically were similar to those observed for the e-beam evaporated films, i.e., the surface color changed from blue (unreacted film) to yellow (low power reaction). However, at the higher power levels ($p \geq 1.0$), a damaged surface was observed optically in contrast to the high power phase appearing for the e-beam, evaporated samples.

In Fig. 11(a) we show an optical micrograph of a sputtered Pd/Si sample laser irradiated at a power level of $p = 1.2$. A severely damaged surface can be seen to result. This micrograph should be compared to that shown in Fig. 3 for the e-beam evaporated Pd/Si sample laser irradiated under similar conditions. The backscattering spectrum of a sputtered sample which was laser irradiated at a power of $p = 0.98$, slightly below the power causing surface damage, is shown by the solid line in Fig. 11(b). The spectrum for an unreacted sample is also shown by the solid circles in this figure for comparison. Only a limited amount of reaction is observed from this data at the Pd/Si interfaces (to be compared with Fig. 1). Also a small peak can be seen at an energy of 1.48 MeV in the spectrum of the as-deposited sample, corresponding to argon in the near-surface region. Although it is not observed in the backscattering spectrum, considerable amounts of Ar can exist in the Pd films. The argon atoms and/or other possible impurities (such as carbon, oxygen, etc.) can be incorporated during the sputtering process. These impurities can have a crucial effect on the silicide-forming reactions (21). Similar results were obtained for the W/Si samples prepared by argon sputtering.

Conclusions

Silicide-forming reactions induced by scanned CW laser and electron beams have been described. The characteristic features of the scanned CW-beam process found differentiating it from those using pulsed beam systems are: scanned CW beams can be used to form large area, uniform, essentially single-phase silicides; different phases within a particular system (such as Pd₂Si or PdSi) can be formed by adjusting the beam power level; and the reactions proceed basically by a solid-phase mechanism.

We have also succeeded in forming both the PdSi silicide and metastable Pt₂Si₃ silicide phases. These phases are difficult or impossible to form by conventional furnace annealing techniques. Both laser and electron beams have exhibited similar reaction effects for most of the metal/Si systems examined here, an exception occurring for the Pt/Si system. We speculate that the effects from the thin overcoating of silicon on

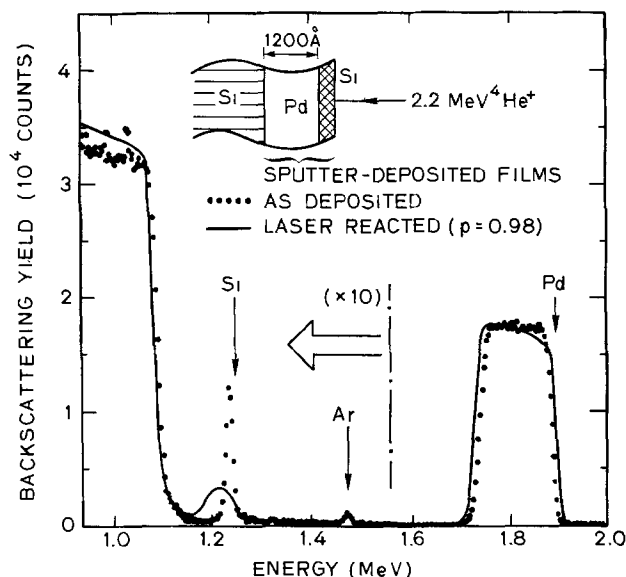
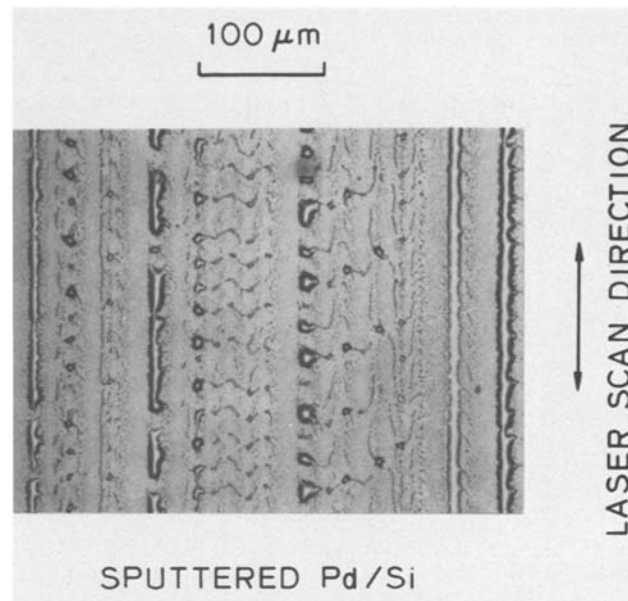


Fig. 11. (a) Optical micrograph of a sputtered Si/Pd/Si sample laser irradiated at a power level of $p = 1.2$. (b) Backscattering spectra of as-deposited (●●●) and laser reacted (—) Si/Pd/Si sputter deposited films. A small peak corresponding to Ar in the surface Si layer is seen.

the laser-reacted samples could be responsible for this difference. At this writing further experiments are underway to verify this hypothesis. Finally, it is pointed out that for the case of sputter-deposited metal films impurities incorporated into the films during sputter deposition have a deleterious effect on silicide formation.

Acknowledgments

We would like to thank Dr. S. S. Lau, Cal Tech for providing the e-beam evaporations and D. Keith, CMR Stanford for providing the sputter-deposited films. We also would like to acknowledge Dr. R. Reynolds for continued encouragement and support of this work through DARPA contracts MDA903-78-C-0290 and MDA903-78-C-0128 and one of us (T. Shibata) would like to acknowledge partial support of Toshiba Corporation during the course of this work.

Manuscript received May 27, 1980.

Any discussion of this paper will appear in a Discussion Section to be published in the December 1981 JOURNAL. All discussions for the December 1981 Discussion Section should be submitted by Aug. 1, 1981.

Publication costs of this article were assisted by Stanford University.

REFERENCES

1. B. L. Crowder and S. Zirinsky, *IEEE Trans. Electron Devices*, **ed-26**, 369 (1979).
2. P. L. Shah, *ibid.*, **ed-26**, 631 (1979).
3. H. N. Yu, A. Reisman, C. M. Osburn, and D. L. Critchlow, *ibid.*, **ed-26**, 318 (1979).
4. "Thin Films Interdiffusion and Reactions," J. M. Poate, K. N. Tu, and J. W. Mayer, Editors, Wiley-Interscience, New York (1978).
5. J. M. Poate, H. J. Leamy, T. T. Sheng, and G. K. Celler, *Appl. Phys. Lett.*, **33**, 918 (1978).
6. Z. L. Liau, B. Y. Tsaur, and J. W. Mayer, *ibid.*, **34**, 221 (1979).
7. T. Shibata, J. F. Gibbons, and T. W. Sigmon, *ibid.*, **36**, 569 (1980).
8. T. W. Sigmon, J. L. Regolini, J. F. Gibbons, S. S. Lau, and J. W. Mayer, Abstract 388, p. 981, The Electrochemical Society Extended Abstracts, Los Angeles, California, Oct. 14-19, 1979.
9. B. Y. Tsaur, Z. L. Liau, and J. W. Mayer, *Appl. Phys. Lett.*, **34**, 168 (1979).
10. A. Gat and J. F. Gibbons, *ibid.*, **32**, 142 (1978).
11. R. B. Gold and J. F. Gibbons, *J. Appl. Phys.*, **51**, 1256 (1980).
12. M. von Allmen and M. Wittmer, *Appl. Phys. Lett.*, **34**, 68 (1979).
13. M. Wittmer and M. von Allmen, *J. Appl. Phys.*, **50**, 4786 (1979).
14. B. Y. Tsaur, S. S. Lau, and J. W. Mayer, *Appl. Phys. Lett.*, **35**, 225 (1979).
15. G. A. Hutchins and A. Shepela, *Thin Solid Films*, **18**, 343 (1979).
16. R. W. Bower, D. Sigurd, and R. E. Scott, *Solid State Electron.*, **16**, 1461 (1973).
17. N. Cheung, S. S. Lau, M.-A. Nicolet, and J. W. Mayer, in "Thin Film Interfaces and Interactions," J. E. E. Baglin and J. M. Ponte, Editors, p. 494, The Electrochemical Society Softbound Proceedings Series, Princeton, N.J. (1980).
18. T. Shibata, T. W. Sigmon, and J. F. Gibbons, Proceedings of Laser and Electron Beam Processing of Materials Symposium of Materials Research Society, Boston (1979), To be published.
19. M. Hansen, "Constitution of Binary Alloys," McGraw-Hill Book Co., New York (1958).
20. B. Y. Tsaur, J. W. Mayer, and K. N. Tu, in "Thin Film Interfaces and Interactions," J. E. E. Baglin and J. M. Ponte, Editors, p. 264, The Electrochemical Society Softbound Proceedings Series, Princeton, N.J. (1980).
21. Ref. (4), p. 103.

Evaluation of Dislocation Generation at Si_3N_4 Film Edges on Silicon Substrates by Selective Oxidation

Y. Tamaki, S. Isomae, S. Mizuo, and H. Higuchi*

Hitachi Limited, Central Research Laboratory, Kokubunji, Tokyo 185, Japan

ABSTRACT

The density of dislocations generated at Si_3N_4 film edges on silicon substrate by selective oxidation is measured and the relation between the selective oxidation conditions and dislocation generation at the film edges is investigated. Dislocations are observed using Secco etching. The results show that the density of dislocations does not continuously increase with oxidation temperature, but decreases markedly at temperatures above 1000°C . A further experiment with recessed oxide structure reveals that the generation of dislocations depends strongly on the cross-sectional structure of the sample. These results are interpreted in terms of viscous flow of SiO_2 film. Another experiment suggests that high pressure oxidation is not effective for suppressing dislocation generation, although it is useful for reducing oxidation time. Finally, collector-emitter shorts of transistors in bipolar integrated circuits are examined quantitatively using a simple statistical method in relation to the dislocations generated at Si_3N_4 film edges.

In silicon device technology, chemical vapor deposited (CVD) Si_3N_4 films on silicon substrates have been widely used as selective oxidation masks or passivating films. These Si_3N_4 films on silicon substrates have a large intrinsic stress of about 10^9 N/m^2 that often leads to the generation of dislocations in silicon substrates during thermal treatment (1-3). Since these dislocations are detrimental to the characteristics of transistors, insertion of SiO_2 film between Si_3N_4 film and silicon substrate has been used in order to avoid generation of dislocations. However, in selective oxidation the SiO_2 film causes the formation of a long bird's beak at the perimeter of the silicon islands (4, 5). This bird's beak constitutes an insuperable barrier to reducing the dimensions of oxide-isolated devices. Therefore, selective oxidation conditions that can pre-

vent the generation of dislocations on silicon substrate without inserting an SiO_2 film have been sought. Although several papers dealing with the generation of dislocations in selective oxidation have been reported (5-8), no reports which quantitatively examine the oxidation condition have been published.

In this paper, first the relation between the heat-treatment conditions (Si_3N_4 film thickness, temperature, time, atmosphere, etc.) and dislocation generation at the film edges is described quantitatively using the dislocation density per unit length of Si_3N_4 film edge. From this experiment the difference in the temperature dependence of dislocation generation between N_2 annealing and selective oxidation becomes clear. Then the cause of this phenomenon is discussed, taking the behavior of SiO_2 films grown during oxidation into account. The effects of Si etching and high pressure oxidation on dislocation generation are also examined. The influence of sample structure on dislocation gen-

* Electrochemical Society Active Member.

Key words: defect density, mechanical property, viscosity of SiO_2 , bipolar transistor.

eration and the suitability of high pressure oxidation are also discussed. Next, in order to examine the effect of dislocations on collector-emitter shorts of transistors, defect density obtained from transistor yield was compared to the dislocation density after selective oxidation.

Experimental Procedures

Sample preparation.—The samples were (001) oriented p-type, 0.2–0.3 Ω -cm, dislocation-free, 350 μm thick Czochralski-grown silicon wafers with $10 \times 10 \mu\text{m}$ square masks consisting of only an Si_3N_4 film. The Si_3N_4 film was deposited by reacting SiH_4 and NH_3 in N_2 at 950°C. The deposition rate was 25 nm/min and the NH_3/SiH_4 flow rate ratio was 150. The films were 100–200 nm thick. The pattern of the film was formed by conventional H_3PO_4 etching technique using phosphorus-doped SiO_2 film as a mask.

The force acting on the Si_3N_4 film edge is proportional to the film thickness, with a constant of proportionality of about 9.2×10^{-1} N/m per nanometer of film thickness (9). For some samples the exposed silicon substrate was anisotropically etched 0.9 μm using KOH solution containing isopropyl alcohol in order to make a recessed oxide structure.

Thermal treatment and oxidation.—In order to investigate dislocation generation at the film edges, the samples were divided into three groups. The samples in the first group were annealed at 950°–1150°C for 2 hr in N_2 atmosphere. The samples in the second group were oxidized at 900°–1150°C for 2 or 16 hr in wet O_2 atmosphere. Some of the samples were silicon-etched before oxidation for comparison. The samples in the third group were silicon-etched and oxidized to grow 1.8 μm thick SiO_2 at 900°–1125°C in wet O_2 under atmospheric pressure (1 atm) or high pressure (7 atm) to form recessed oxide structures. The conditions for the third sample group correspond to those for isolation oxidation of bipolar integrated circuits. Cross sections of the samples were observed by scanning electron microscope (SEM) to evaluate the bird's beak and bird's head.

Dislocation observation.—In order to detect dislocations generated at the film edges, surface films were removed from the samples using diluted hydrofluoric acid after heat-treatment. Photographs of dislocations revealed by Secco etching (10) are shown in Fig. 1. In this figure, dislocation pits appear near the film edges. Since the force acting on the Si_3N_4 film edge is very large, it is expected that the density of dislocations depends on the perimeter length of the film edges. If the occurrence of dislocations can be represented by a Poisson distribution, the yield of patterns (the probability that a pattern has no dislocations) is given by

$$Y = e^{-\lambda l}$$

where λ is the dislocation density per unit length of the film edge and l is the perimeter length of the pattern. Consequently the dislocation density can be obtained by measuring the yield of $10 \times 10 \mu\text{m}$ square patterns.

Transistor fabrication.—In order to apply the above results to the fabrication of integrated circuits and investigate the relations between dislocations generated by selective oxidation and collector-emitter shorts of bipolar transistors, npn array-transistors were fabricated by a conventional planar process. A 150 nm thick Si_3N_4 film was deposited directly on the silicon substrate and selective oxidation was performed at 1100°C in wet O_2 under high pressure (7 atm) to reduce oxidation time. The time required to grow 1.8 μm thick SiO_2 film was only 50 min. The base and emitter were formed by boron ion-implantation and arsenic diffusion in an ampul tube, respectively.

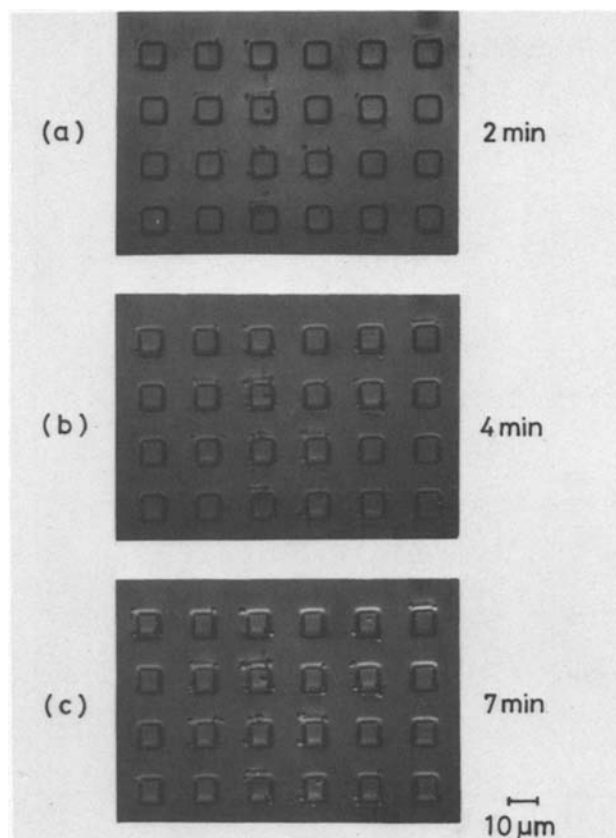


Fig. 1. Photographs of dislocation pits revealed by Secco etching for various etching time. Dislocation pits become more clear as the etching time increases. The square patterns were the regions covered by 150 nm thick Si_3N_4 film during oxidation.

Results and Discussion

Dislocation generation in N_2 annealing.—The samples in the first group were annealed for 2 hr in N_2 at 950°–1150°C. Dislocation densities of these samples are shown in Fig. 2, where “x,” “ Δ ,” and “o” represent the results for 200, 150, and 100 nm thick Si_3N_4 films, respectively. It is easily seen that the dislocation density increases with annealing temperature. This is because the critical stress for dislocation generation in Si becomes smaller as temperature increases. Since the force acting on the Si_3N_4 film edges is proportional to the film thickness, dislocation density increases with Si_3N_4 film thickness. Figure 3 shows the annealing time dependence of the dislocation densities at 1000°C. This figure indicates that the dislocation density becomes larger with annealing time.

From these results it is clear that the dislocation generation depends on the force acting on the Si_3N_4 film edges, annealing temperature, and annealing time. The data of a creep experiment (11) indicate that the time required to generate dislocations becomes shorter with increasing temperature.

Dislocation generation in oxidation.—The samples in the second group were oxidized for 2 or 16 hr in wet O_2 at 900°–1150°C. Dislocation densities of the samples oxidized for 2 and 16 hr are shown in Fig. 4 and 5, respectively. A distinguishing feature of both figures is that the dislocation density decreases with increasing temperature above 1000°C. It should be noted that the present results are entirely different from the results obtained in N_2 , which are shown in Fig. 2. This suggests that SiO_2 film grown during oxidation plays an important role in dislocation generation.

Two factors that reduce the stress effect during oxidation are considered. One is reduction in Si_3N_4 film thickness. During oxidation the surface of Si_3N_4 film is gradually converted to SiO_2 film (12). The reduc-

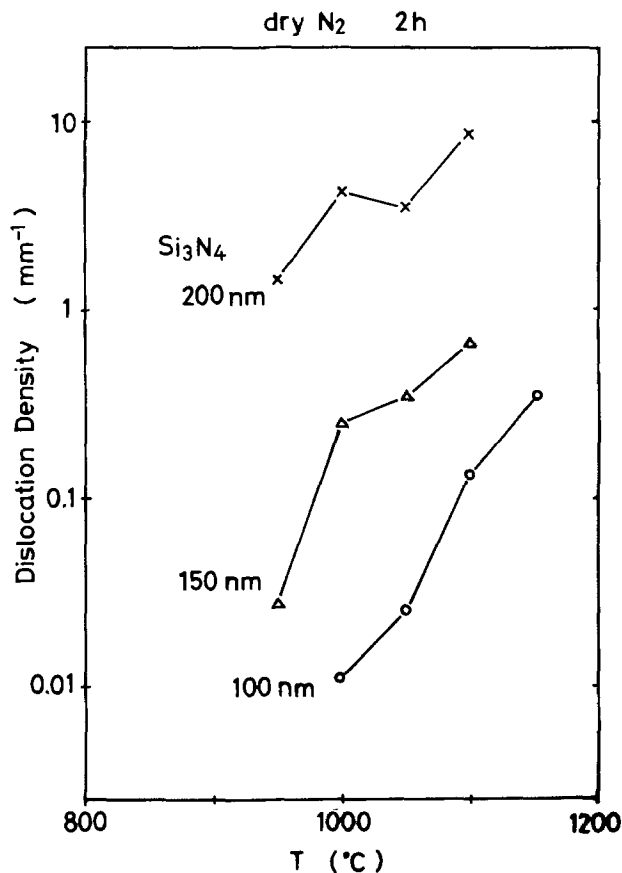


Fig. 2. Temperature dependence of dislocation densities of the samples annealed for 2 hr in N_2 . The marks "x", " Δ ", and " \circ " show that the thickness of Si_3N_4 films were 200, 150, and 100 nm, respectively.

tion in Si_3N_4 film thickness by oxidation are shown in Table I. The other is relaxation due to the viscous flow of SiO_2 film grown under the Si_3N_4 film edges. The dislocation density of the sample with 150 nm Si_3N_4 film oxidized in wet O_2 at $1100^\circ C$ is smaller than that of the sample with 100 nm Si_3N_4 film annealed in N_2 at

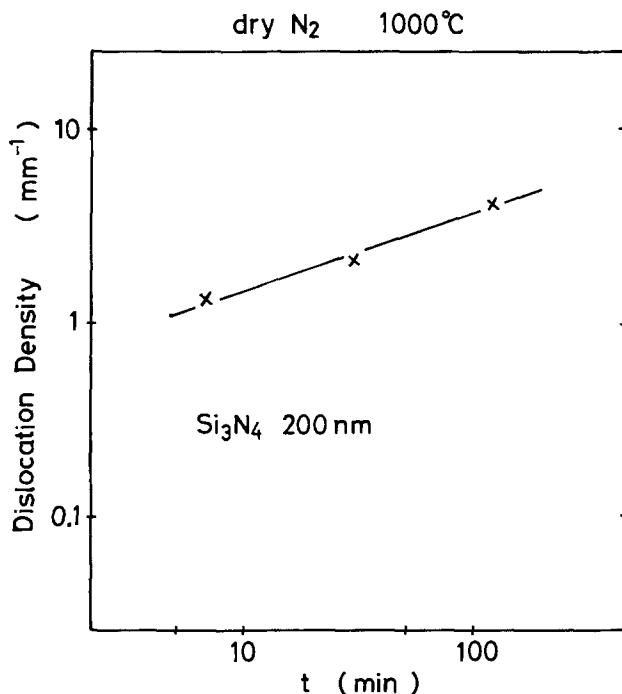


Fig. 3. Annealing time dependence of dislocation densities at $1000^\circ C$.

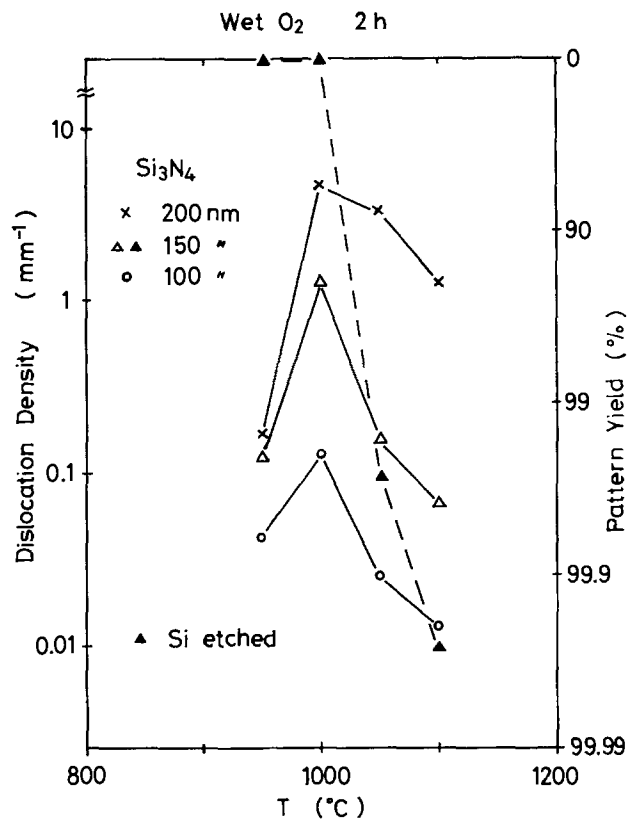


Fig. 4. Temperature dependence of dislocation densities of the samples oxidized for 2 hr in wet O_2 . Pattern yield means the probability that a $10 \times 10 \mu m$ square pattern has no dislocations. Dashed line shows the results for samples with $0.9 \mu m$ Si etching before oxidation.

$1100^\circ C$, as seen from Fig. 2 and 4. This suggests that the effect of the latter factor is much larger than that of the former. It is known that the viscosity of SiO_2 decreases rapidly with increasing temperature and that viscous flow of SiO_2 occurs at temperatures around $950^\circ C$ (13-15). Consequently, it is expected that the dislocation density tends to decrease with temperature, as shown in Fig. 5. Since relaxation of the stress

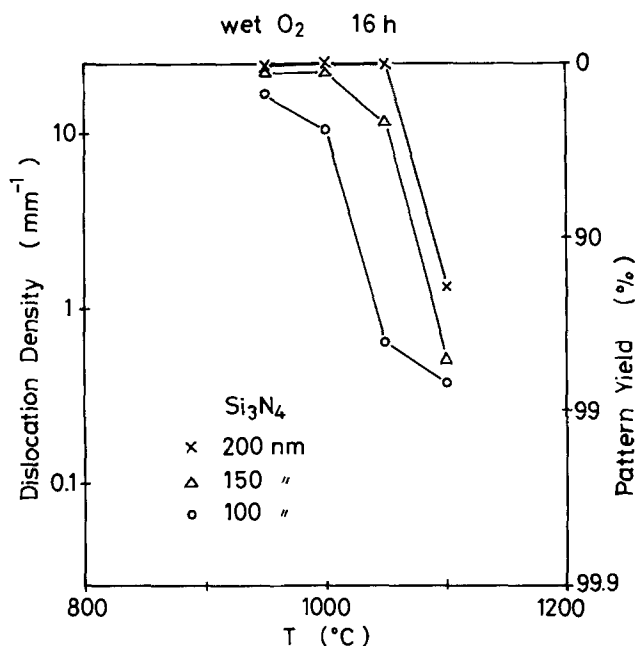


Fig. 5. Temperature dependence of dislocation densities of the samples oxidized for 16 hr in wet O_2 .

Table I. Reduction in Si_3N_4 film thickness by oxidation (in wet O_2 at 1 atm)

| | Oxidation Temperature | Oxidation time | |
|--|-----------------------|----------------|-------|
| | | 2 hr | 16 hr |
| | 1000°C | 6 nm | 30 nm |
| | 1100°C | 22 nm | 98 nm |

is caused by the SiO_2 film grown under the Si_3N_4 film, the degree of the relaxation depends on the stress fields in the silicon substrate under the Si_3N_4 film edges and the extent of lateral oxidation (in this case this is nearly half of the SiO_2 film thickness). Therefore, when the SiO_2 film is thin, relaxation will not occur. Although the stress fields near the film edges are different from the theory of elasticity (9, 16), the extent of lateral oxidation that the generation of dislocations can be suppressed is estimated to be 0.4-0.5 μm from the thickness of the SiO_2 film (0.8 μm) grown at 1050°C in wet O_2 for 2 hr. Because the temperature that the dislocation density in Fig. 4 becomes smaller than that in Fig. 2 is about 1050°C. As the results of oxidation for 2 hr at temperatures under 950°C are similar to those of N_2 annealing, stress relaxation due to oxide does not occur in these conditions. Thicknesses of SiO_2 films were about 0.4 μm at 950°C and 0.3 μm at 900°C. For these reasons, the maximum of dislocation density is found at about 1000°C in Fig. 4 (solid line).

In order to examine the effect of Si etching on dislocation generation, Si substrate is etched and oxidized for 2 hr. As the stress due to the expansion of SiO_2 grown by oxidation concentrates, the effect of viscous flow of SiO_2 film becomes dominant. Therefore, the dislocation densities of these samples are large at temperatures below 1000°C and decrease rapidly with temperature at temperatures above 1000°C, as shown in Fig. 4 (dashed line).

From these results it is concluded that the dislocation generation at Si_3N_4 film edges by selective oxidation depends on the strength of Si crystal, the thickness of Si_3N_4 film, the viscosity of SiO_2 , and the topological structure of the Si substrate. Although the latter two factors are not so important in N_2 annealing, they play an important role in selective oxidation.

Dislocation generation in recessed oxide structure.—The samples in the third group were silicon-etched and oxidized to grow 1.8 μm thick SiO_2 at 900°-1125°C in wet O_2 under atmospheric pressure or high pressure. This coplanar structure is used for high speed bipolar integrated circuits. As the oxidation time is inversely proportional to the pressure, high pressure oxidation is useful to reduce the oxidation time drastically (17). Dislocation densities and oxidation times of the samples with this structure are shown in Fig. 6 and Table II, respectively. It is seen that the dislocation density decreases rapidly with temperature. The results are ascribed to the effect of viscous flow of SiO_2 film. The effect may be understood by observing the cross section of the sample. Photographs of the samples observed by SEM are shown in Fig. 7. The shape of SiO_2 film grown by selective oxidation changes with oxidation temperature. Inspecting the shape near the edge of SiO_2 , Si is lifted up and a number of etch patterns

Table II. Oxidation times of the samples in Fig. 6

| Oxidation Temperature | Oxidation pressure | |
|-----------------------|--------------------|---------|
| | 1 atm | 7 atm |
| 900°C | 32 hr | 200 min |
| 1000°C | 16 hr | 100 min |
| 1050°C | 10 hr | 68 min |
| 1100°C | 7 hr | 50 min |

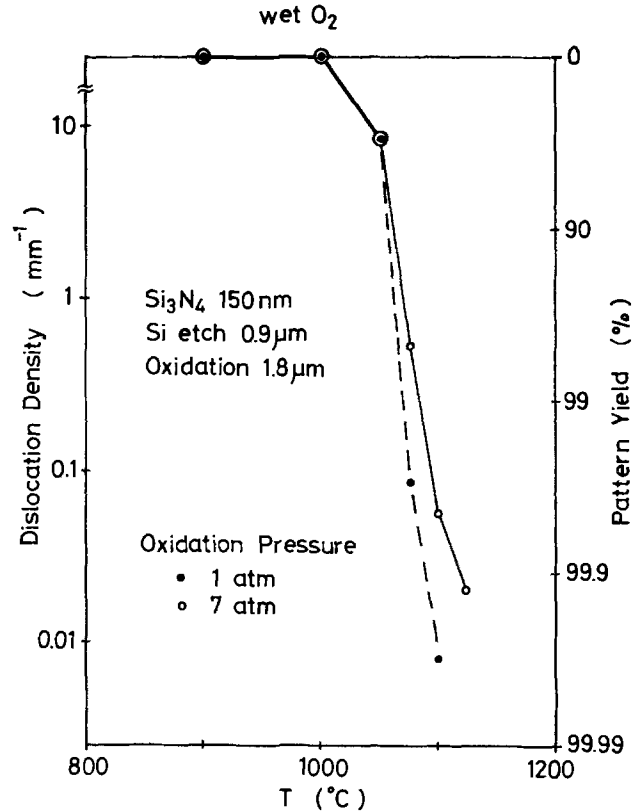


Fig. 6. Temperature dependence of dislocation densities of the samples with recessed oxide structure. After Si substrate was etched 0.9 μm , 1.8 μm thick SiO_2 was grown under atmospheric pressure (solid line) or high pressure (dashed line).

produced by large strain in Si are seen at temperatures of 1000° and 1050°C. The amounts of the lift-up were 0.15, 0.09, and 0 μm at 1000°, 1050°, and 1100°C, respectively. The higher the oxidation temperature is, the smaller the deformation of Si becomes. The lift-up and etch patterns correspond to the generation of dislocations in Si substrate. This temperature dependence of dislocation generation coincides with that in Fig. 6. Since the viscosity of SiO_2 becomes very small at 1100°C, the stress produced by the growth of SiO_2 is almost relaxed by the viscous flow of SiO_2 . The stress acting on Si substrate is reduced to a great extent, and thus dislocation generation is prevented. Although the generation of dislocations can be suppressed by oxidizing at 1100°C, the bird's beak lengthens to about 0.3 μm . The bird's beak is defined as the distance between the Si_3N_4 mask edge and the top of the beak. From Fig. 7 the beaks were 0.60, 0.61, and 0.92 μm at 1000°, 1050°, and 1100°C, respectively. It is expected that the bird's beak reduces the stress acting on the silicon substrate. In order to evaluate the increment in bird's beak, the oxidation mechanism of Si, and the mechanical strength of Si, SiO_2 and Si_3N_4 at high temperatures must be considered. Further investigation will be necessary.

Next, the effect of pressure during oxidation is discussed. It is seen that the dislocation density at 7 atm is larger than that at 1 atm. As the growth rate of SiO_2 is proportional to the oxidation pressure, the time required to grow SiO_2 of a given thickness becomes shorter with increasing pressure. If the generation of dislocations depended only on oxidation time, the dislocation density at 7 atm might be smaller than that at 1 atm. Therefore it is concluded that the generation of dislocations depends not only on oxidation time but on oxidation rate. This behavior is considered to be related to the relaxation time τ of viscous flow of SiO_2 . Here, τ is defined by $\tau = \eta/E$, where η and E are, respectively, the viscosity and the shear modulus of the

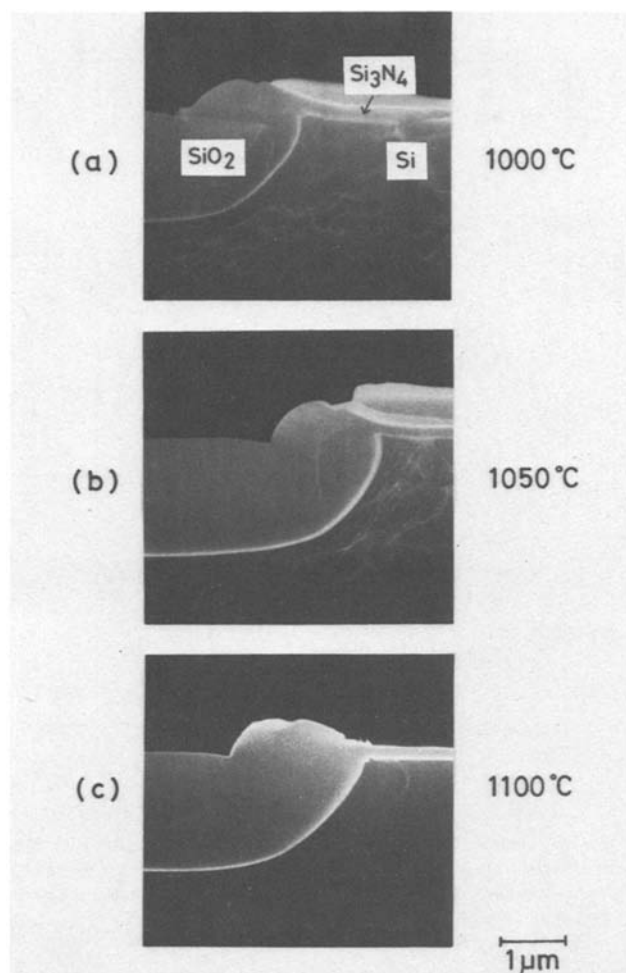


Fig. 7. Cross sections of recessed oxide structure for various oxidation temperatures. The samples were lightly etched by HF-HNO₃ before SEM observation.

SiO₂ film. Using the values of η and E for vitreous silica (18, 19), τ is estimated to be around 1 min at 1100°C. This is different from EerNisse's estimated time, which is only a few seconds (14). Although it is not certain which time is correct, it is clear that the effect of viscosity appears at the beginning of the oxidation. As the initial oxidation rate is very large, the effect is reduced in high pressure oxidation.

Transistor characteristics.—It is known that process-induced dislocations cause collector-emitter shorts of bipolar transistors (20). However, the relation between the collector-emitter shorts and the dislocation density after selective oxidation has seldom been investigated. In this study, in order to treat the shorts quantitatively, collector-emitter breakdown voltages (BV_{CEO}) of fabricated transistors were measured and the transistors with $BV_{CEO} > 5V$ at $I_{CE} = 10 \mu A$ were defined as good. If the occurrence of defects can be represented by a Poisson distribution, the yield of good transistors is given by (21)

$$Y = e^{-(\lambda_A A + \lambda_L L)}$$

where λ_A is the defect density per unit emitter area, λ_L is the defect density per unit length of the emitter perimeter, and A and L are the emitter area and perimeter length per transistor, respectively. From the yield of transistors with emitter size of $3 \times 5 \mu m^2$ and $70 \times 110 \mu m^2$, $\lambda_A = 0.24 \text{ mm}^{-2}$ and $\lambda_L = 0.048 \text{ mm}^{-1}$ were obtained. Comparison of λ_L with λ at 1100°C in Fig. 6 shows that they are in good agreement. Since the size of the emitter is about 1/3 that of the pattern with selective oxidation, it is expected that about 1/3 of the transistors with dislocations generated by selective oxidation fail by collector-emitter shorts. In order

to examine the close relation between the dislocations and the collector-emitter shorts, further investigation of multiplication and movement of dislocations are needed.

Conclusions

From the results obtained in this study, several conclusions can be made.

1. The density of dislocations generated at Si₃N₄ film edges by selective oxidation decreases with increasing oxidation temperature. This phenomenon is explained by the effect of the viscous flow of SiO₂ film.

2. When Si is etched and oxidized to form a recessed oxide structure, the effect of the viscosity of SiO₂, i.e., oxidation temperature dependence of dislocation generation, becomes significant. This effect is confirmed by observation of cross sections of samples. Furthermore, the Si substrate is deformed by selective oxidation with Si₃N₄ mask at temperatures below 1050°C.

3. The dislocation generation at Si₃N₄ film edges by selective oxidation depends on Si₃N₄ film thickness, oxidation temperature, oxidation time, and oxidation rate.

4. The dislocations generated by selective oxidation cause collector-emitter shorts of bipolar transistors. The probability of the occurrence of collector-emitter shorts caused by dislocations depends on the heat-treatment conditions and the pattern geometry. This is considered to be related to the multiplication and movement of dislocations.

Acknowledgments

The authors wish to thank Drs. K. Sugawara, M. Maki, and M. Ogirima for useful discussions.

Manuscript submitted May 28, 1980; revised manuscript received Aug. 15, 1980.

Any discussion of this paper will appear in a Discussion Section to be published in the December 1981 JOURNAL. All discussions for the December 1981 Discussion Section should be submitted by Aug. 1, 1981.

Publication costs of this article were assisted by Hitachi Limited.

REFERENCES

- W. A. Westdorp and G. H. Schwuttke, in "Thin Film Dielectrics," F. Vratny, Editor, p. 546, The Electrochemical Society Softbound Proceedings Series, Princeton, N.J. (1969).
- M. Tamura and H. Sunami, *Jpn. J. Appl. Phys.*, **11**, 1097 (1972).
- E. A. Irene, *J. Electron. Mater.*, **5**, 287 (1976).
- J. A. Appels and M. M. Paffen, *Phil. Res. Rep.*, **26**, 157 (1971).
- E. Bassous, H. N. Yu, and V. Maniscalco, *This Journal*, **123**, 1729 (1976).
- B. O. Kolbesen and H. Strunk, "Proc. 5th Int. Conf. on High Voltage Electron Microscopy," p. 637, Kyoto (1977).
- A. Bohg and A. K. Gaiand, *Appl. Phys. Lett.*, **33**, 895 (1978).
- K. Shinada, S. Shinozaki, K. Kurosawa, and K. Taniguchi, "Int. Electron Devices Meet. Dig. Tech. Papers," p. 344, IEEE (1979).
- S. Isomae, Y. Tamaki, A. Yajima, M. Nanba, and M. Maki, *This Journal*, **126**, 1014 (1979).
- F. S. d'Aragona, *ibid.*, **119**, 948 (1972).
- S. Isomae, M. Nanba, Y. Tamaki, and M. Maki, *Appl. Phys. Lett.*, **30**, 564 (1977).
- I. Franz and W. Langheinrich, *Solid State Electron.*, **14**, 499 (1971).
- J. R. Patel and N. Kato, *J. Appl. Phys.*, **44**, 965 (1973).
- E. P. EerNisse, *Appl. Phys. Lett.*, **30**, 290 (1977).
- E. P. EerNisse, *ibid.*, **35**, 8 (1979).
- S. M. Hu, *ibid.*, **32**, 5 (1978).
- J. R. Ligenza, *This Journal*, **109**, 73 (1962).
- R. Brückner, *J. Non-Cryst. Solids*, **5**, 123 (1970).
- R. Brückner, *ibid.*, **5**, 177 (1971).
- F. Barson, *IEEE J. Solid-State Circuits*, **sc-11**, 505 (1976).
- S. M. Hu, S. P. Klepner, R. O. Schwenker, and D. K. Seto, *J. Appl. Phys.*, **47**, 4098 (1976).

Interdiffusion of Titanium and Gold: A Comparison of Thin Films Deposited in Technical Vacuum and Ultrahigh Vacuum

G. W. B. Ashwell and R. Heckingbottom

British Telecom Research Laboratories, Martlesham Heath, Ipswich IP5 7RE, England

ABSTRACT

Thin films of 0.5 μm Ti and 0.5 μm Au have been deposited on Si and SiO_2 substrates in technical vacuum (HV, $\leq 10^{-6}$ Torr) and ultrahigh vacuum (UHV, 10^{-9} Torr). After deposition and subsequent annealing in N_2 containing $\leq 1\%$ O_2 at 300°-350°C, the films were analyzed, principally using Auger sputter ion profiling, but also using electrical resistivity, x-ray, Rutherford backscattering, and SEM/microprobe measurements. While the UHV films were clean to the techniques used, several percent of C and O were present in the HV deposited Ti films. On SiO_2 substrates the reaction proceeded via formation of Au_4Ti and oxidation of Ti to TiO_2 as it came in contact with the air interface. The rate of alloy formation was almost an order of magnitude faster in the UHV deposited films and the oxidation rate was also enhanced. The importance of these usually unmonitored impurities in determining the reactivity of films deposited in technical vacuum is stressed.

Gold is widely accepted as the preferred metallic conductor for interconnection patterns on semiconductors, particularly where high current densities are encountered. Its advantages include high electrical conductivity, corrosion resistance, and full compatibility with gold wire thermocompression bonding. Its two main drawbacks, poor metallurgical bonding to the semiconductor and catastrophic reduction of carrier lifetime in the semiconductor, can both be solved by the use of an intermediate layer of titanium between the gold and the semiconductor. While more complex three-layer metallizations incorporating a third layer of Pd or Pt to reduce the Au-Ti interaction are widely used, extremely reliable transistors can be fabricated using Au-Ti metallization only (1).

The interaction of Au-Ti thin film couples under thermal stressing and varying humidity has been studied previously (2-4), reflecting its importance both individually and as part of the three-layer metallization schemes. All these studies used films prepared in technical vacuum comparable with that used in device fabrication. As part of a wider program aimed at optimization of the Ti-Au system we have also studied films prepared in ultrahigh vacuum. This paper describes the significant differences between films formed in the two different ways. Resistivity/anneal time plots have been used to identify distinct stages in the interaction and compositional analysis, principally by Auger electron spectroscopy with sputter ion profiling, was carried out at these points. The importance of low levels of impurities such as oxygen and carbon in determining the stability of the layers used in device fabrication is clearly illustrated.

Experimental

Sample preparation.—The main series of Au-Ti layers were deposited on a thermally grown SiO_2 layer (3500Å thick) on Si(111) slices to allow simple resistivity determinations. Other series of Au-Ti layers, deposited directly on Si(111) substrates, were also subjected to compositional analysis to check for any effects due to the introduction of the SiO_2 layer. A standard deposition sequence involved (i) deposition of 0.5 μm Ti with a substrate temperature of 75°C, (ii) increase of the substrate temperature to 250°C followed by deposition of a further 250Å of Ti, and (iii) deposition of 0.5 μm Au with the substrate at 250°C. Matched dep-

osition sequences were carried out in technical vacuum (HV) and in ultrahigh vacuum (UHV). In both cases beam pressures were $\approx 5 \cdot 10^{-6}$ Torr with background pressures of $\approx 10^{-6}$ and $\approx 10^{-9}$ Torr, respectively. There was a detectable drop in the former background pressure during Ti evaporations. Additional samples with only 0.1 μm Au layers were prepared for Rutherford backscattering analysis (RBS).

Analysis techniques.—Auger analysis was performed with a conventional CMA analyzer at 3 keV primary beam energy. The sputter ion profiling used argon ions at 500 eV from a broad focused gun. RBS spectra were generated using 1.5 MeV He^+ ions and were provided by Dr. P. L. F. Hemment of the University of Surrey, England. A separate examination for nitrogen was carried out using x-ray photoelectron spectroscopy (XPS) because of a partial overlap between N and Ti peaks in the Auger spectrum. The XPS analysis was provided by Dr. R. M. Waghorne at Fulmer Research Institute, England. The x-ray data was produced using a cylindrical texture camera (5). In this technique the sample is rotated normal to its surface which is at a glancing angle to the incident x-ray beam. The resulting pattern of arcs of diffracted x-ray reveals the extent of any orientation effects in the thin surface layers in addition to the lattice spacings. Scanning electron microscopy (SEM) with energy dispersive microprobe facilities was also used to check for any spatial heterogeneity in the samples.

Results

Electrical resistivity.—Standard 0.5 μm Ti-0.5 μm Au layers on SiO_2 were annealed in N_2 containing $\leq 1\%$ O_2 for varying times at 350°C. The changes in sheet resistance with anneal time are shown in Fig. 1 for layers formed in HV and UHV systems. Several distinct stages in the plots are present for both samples, with the time taken to reach a given stage being almost an order of magnitude shorter for the UHV plot. The actual values of resistance at each stage are also significantly lower for the UHV samples for reasons considered in the discussion. These differences show through in Fig. 1, even though R_T/R_0 is plotted, as R_0 values were similar in the two cases: $3\text{-}4 \cdot 10^{-6} \Omega \text{ cm}$ for HV films and $3.5\text{-}4.0 \cdot 10^{-6} \Omega \text{ cm}$ for UHV films, cf. $2.06\text{-}2.44 \cdot 10^{-6} \Omega \text{ cm}$ for bulk Au. For convenience in the following descriptions we may distinguish the following regions in the plots. First a slow initial in-

Key words: reaction rate, impurities, Auger profiling.

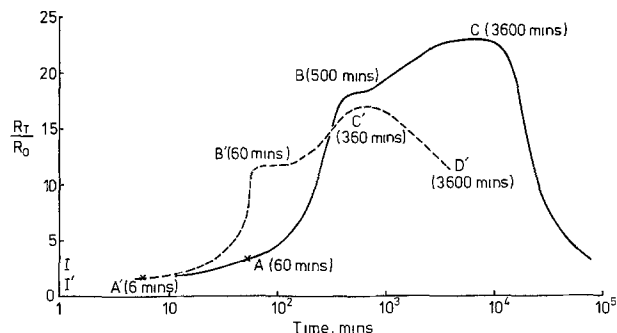


Fig. 1. Resistivity vs. anneal time plots for Au-Ti films deposited on SiO_2 in technical vacuum — and ultrahigh vacuum ---, and annealed in air at 350°C . Points A, A' etc. are described in the text.

crease with time (stage A), second a rapid climb to a plateau (stage B), third a further steady climb to a peak (stage C), and finally a fall off (stage D). The UHV plot stages will be further distinguished by a prime e.g., A'.

Auger sputter ion profiles.—Auger profiles were recorded at each of the key stages identified in the resistivity plots. First, however, the as-deposited films were examined. In Fig. 2a a standard film on SiO_2 , deposited in technical vacuum is shown. Several important features are immediately apparent. The gold film is clean by Auger criteria, with a small amount of carbon contamination on the surface. The titanium film, on the other hand, has up to $\approx 10\%$ of oxygen and carbon impurity, levels which increase as the deposition continues, i.e., they are quite different from an

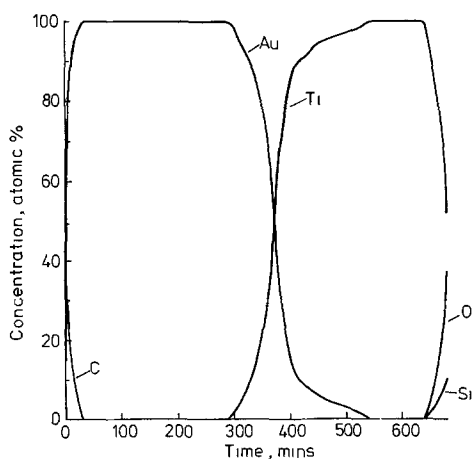
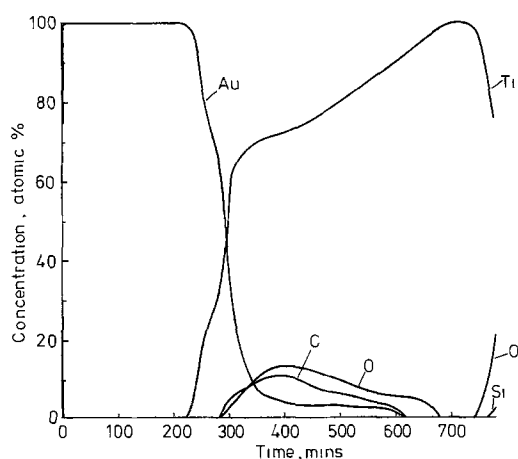


Fig. 2. Compositional depth profiles of as-deposited films determined by Auger electron spectroscopy with sputter ion profiling, (a, top) deposited in technical vacuum and (b, bottom) deposited in ultrahigh vacuum.

initial surface contamination broadened by the sputtering process. In contrast, the SiO_2 surface was free from carbon contamination. By comparison, both the metal films deposited in UHV (Fig. 2b) were free from impurities. In both cases there was a detectable amount of apparent interdiffusion at the Au/Ti interface with a significant Au tail extending into the Ti. In neither case had the Ti penetrated to the Au surface.

The initial stage of interaction on annealing is shown in Fig. 3. The profile was taken after annealing a UHV deposited film for 6 min (stage A'). The major change is that Ti has penetrated to the Au surface and has accumulated with oxygen. Though there has been measurable broadening of the Au/Ti interface, the Ti level within the gold film has remained undetectable. An example of slightly increased reaction (still in stage A) is shown in Fig. 4. In the HV deposited film annealed for 60 min, some Ti is detectable throughout the Au film, but there is a marked concentration gradient approximately half-way through the Au film. An increased amount of Ti and O have accumulated on the Au surface.

Stage B is illustrated in Fig. 5 where the profile was obtained from a sample deposited in technical vacuum and annealed for 500 min. The new feature is the alloying of all the Au layer. The titanium oxide buildup on the surface has increased toward 2000\AA and the Au tail has extended to the SiO_2 substrate. Traces of Fe and Ni are detectable on the outer surface in this sample. Oxygen is present throughout the film with Ti. All the same major features were present at stage B' for the UHV deposited sample (not shown). As this stage was

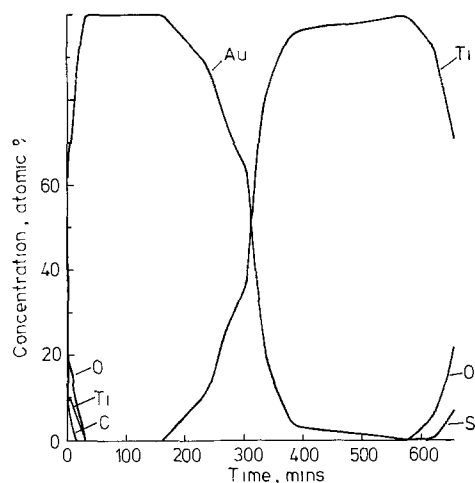


Fig. 3. Composition/depth profile of an Au-Ti film deposited in UHV on an SiO_2 substrate and annealed for 6 min at 350°C .

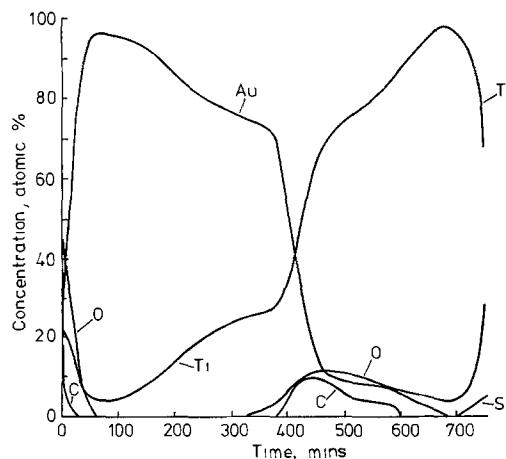


Fig. 4. Composition/depth profile of an Au-Ti film deposited in HV on an SiO_2 substrate and annealed for 60 min at 350°C .

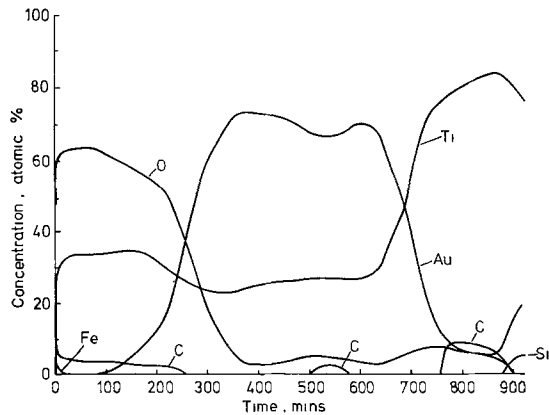


Fig. 5. Composition/depth profile of an Au-Ti film deposited in HV on an SiO_2 substrate and annealed for 500 min at 350°C .

reached after only a 60 min anneal the oxide buildup on the surface amounted to only a few hundred angstroms. A more substantial level of Fe impurity persisted throughout the film in this sample.

The final distinctive stage in the reaction is shown in Fig. 6. This profile corresponds to stage C' on a UHV deposited sample annealed for 360 min. Here the key feature is that the oxidation of the Ti is so extensive that all elemental Ti has reacted either with O or Au. As in the earlier samples, several percent of C are present in the oxide film. Again Fe persists as an impurity throughout the films on this sample. A comparison of the fourth stage, D', with C' shown in Fig. 6 revealed no major differences. There was, however, a measurable enhancement of the Au level vs. Ti both near the peak of the Au signal and at the interface with the SiO_2 . Stage C was only reached after annealing for 4000 min and, although the outlines of the profiles were similar to those shown in Fig. 6, there had clearly been much more intermixing in C between the Au/Ti alloy and the titanium oxide layers.

The similar series of samples prepared on Si substrates proved unsuitable for Auger profiling after annealing at 350°C . Although after a 6 min anneal of the UHV deposited sample the reaction had started in a similar manner to that shown in Fig. 3 a separate heterogeneous interaction (described later) rapidly began to dominate.

Further series of samples with $0.1 \mu\text{m}$ Au on $0.5 \mu\text{m}$ Ti on both Si and SiO_2 substrates were prepared and annealed at 300°C . These samples were more suitable for RBS analysis. Anneal times of 960 and 1380 min were used and no differences due to the two kinds of substrates were observed in the Auger profiles under these conditions. Both anneal periods were sufficient for the whole of these thinner layers of Au to have reacted with the Ti. The longer anneal periods differed

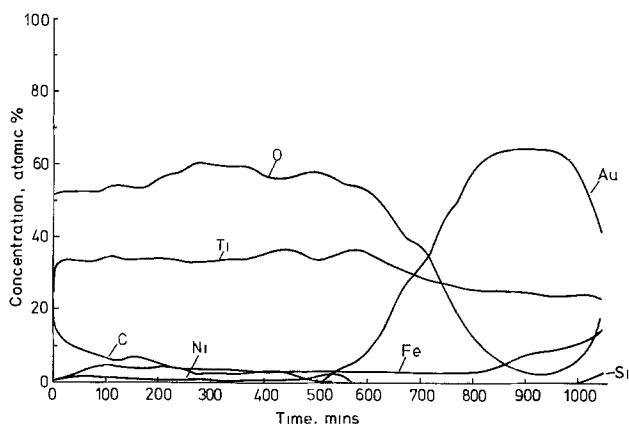


Fig. 6. Composition/depth profile of an Au-Ti film deposited in UHV on an SiO_2 substrate and annealed for 360 min at 350°C .

only in that a thicker layer of titanium oxide formed above the Au/Ti layer. The extent of oxidation was also greater on the UHV prepared samples. That is a thicker oxide layer had formed after 960 min on the UHV sample than had formed after 1380 min on an HV sample. On the other hand, the surface oxygen did not penetrate beyond the Au/Ti layer in the UHV deposited sample, whereas in the HV deposited sample oxygen from the surface merged with that already in the Ti as shown in Fig. 5.

X-ray, RBS, XPS, and SEM/electron microprobe.—The x-ray diffraction data were dominated by the contributions from the layers containing gold. In addition to Au itself, the only phase detected was Au_4Ti , as identified in earlier work (3). This phase was present in all the films where Auger indicated significant interaction between Au and Ti. Both identifiable layers showed marked texturing.

As can be seen from Fig. 7 the RBS analysis supported the overall results from Auger and x-ray measurements. The slight interdiffusion during deposition was confirmed, particularly by the high energy edge of the Ti signal. Following the anneal, the appearance of Ti on the surface and throughout the gold layer is clearly evident. It is also clear, however, (particularly from the rounding of the gold peak in the annealed sample spectrum) that there is some continuous variation of composition with depth. The composition of the Au/Ti is not quite as straightforward as might be inferred from the x-ray data. While the identification of the main phase as Au_4Ti is supported, the Au/Ti ratio corresponding to the Au peak in the annealed sample RBS spectrum is ≈ 4.7 .

No nitrogen could be detected in the films, using XPS combined with argon ion sputtering.

SEM/electron microprobe analysis on the majority of the samples confirmed that the layers remained intact, so that the averaging implicit in the broad area technique described above retained validity. Two conditions occurred where this situation broke down, however. First, after very long anneal times at 350°C for layers on SiO_2 substrates (stage C) where the Auger profiles for different elements showed much overlapping, this was shown to be due to a physical mixing of different matrices. SEM/microprobe analysis following a light etch in 40% HF solution showed that the Au_4Ti remaining had been honeycombed with titanium oxide.

A second, more serious exception, invalidated the profiling approach for layers on Si substrates annealed at 350°C . After about 10 min anneal a reaction involving film break-up began to spread from local

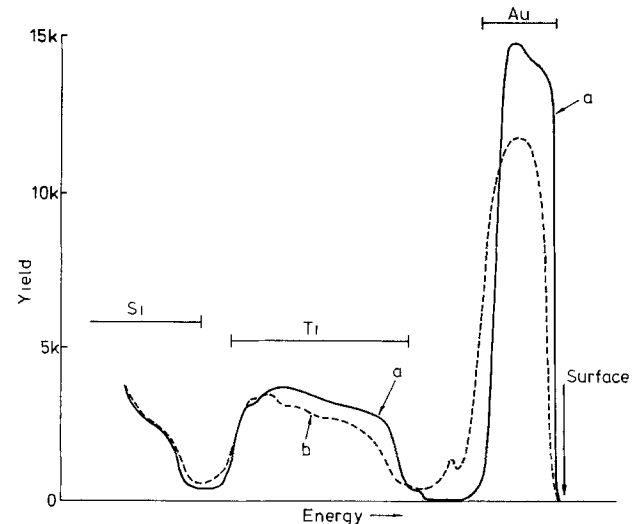


Fig. 7. Rutherford backscattering spectra of $0.1 \mu\text{m}$ Au/ $0.5 \mu\text{m}$ Ti films deposited in HV on SiO_2 substrates, (a) as deposited — and (b) after annealing for 23 hr at 300°C - - -.

areas often at the sample edge. By 30 min the reaction had occurred over the entire surface. High magnification pictures of the reaction at different stages are shown in Fig. 8. The Ti_5Si_3 crystallites were identified by electron microprobe analysis and x-ray diffraction following removal of the surrounding Au in I_2 solution. This etching also revealed that the formation of pinholes in the Ti film preceded the crystallite formation (Fig. 8c). Subsequent removal of the crystallites in 40% HF solution revealed small amounts of Au be-

tween them and the Si substrate, which had been protected from the earlier iodine etch.

Discussion

The detailed Auger profiles in Fig. 2-6 allow considerable progress to be made in understanding the basic resistivity data of Fig. 1 and the underlying interaction between Au and Ti. The basic difference between the HV and UHV deposited layers is the significant concentration of C and O in the Ti layers of the former. These impurities are the most likely cause of the slower interdiffusion rates (by almost an order of magnitude) in the HV samples. The higher resistivity at stage B compared with B' is also likely to be dominated by these impurities, though in the comparison of C with C' the honeycombing of the intermetallic layer by oxide will also be important. It should be stressed that these contaminant levels are to be expected for all evaporations of active metals in vacuum systems with background pressures of $\approx 10^{-6}$ Torr. Most films studied previously (2-4) and in general use will be of the contaminated kind. The "pumping" of the background gases during the evaporation is exactly the same phenomenon that makes titanium sublimation pumps an effective aid to obtaining UHV. As a first approximation the contaminant content will reflect the ratio of the bombardment rate of the background gas molecules on the sample ($\approx 10^{15} \text{ cm}^{-2} \text{ sec}^{-1}$ at 10^{-6} Torr) and the evaporant flux (which may be calculated from the amount of film deposited in a given time).

The main interaction sequence appears to be similar in the UHV and HV deposited films. It simply occurs faster in the former. Thus from Fig. 3 it seems most likely that the Ti has reached the surface by grain boundary diffusion through the gold. This mechanism is thus identified as the fastest process, as first recognized by Tisone and Drobek (2). However, as pointed out by Hall and Morabito (6) in their studies of the Au/Pd system, diffusion within the grains is also required to explain any substantial compositional change in the Au layer. Simple application of the formula $x = (Dt)^{1/2}$ to the position of the diffusion front in Fig. 4 allows an estimate of this bulk diffusion constant D . Taking x as 3000Å for $t = 3600$ sec gives $D \approx 2.5 \cdot 10^{-13} \text{ cm}^2 \text{ sec}^{-1}$. As noted previously for Pd-Au (6), values of this kind are five or six orders of magnitude higher than would be expected by extrapolation of data obtained for bulk diffusion couples at higher temperatures (2). In general this result would be expected in samples cooled from high temperatures; at some point the activation energy obtained in high temperature measurements (which includes both formation and mobility of defects) would cease to apply and a lower value (which represents only the mobility term) would replace it. What is interesting is that it seems to be the norm that films formed directly at lower temperatures also have extremely high values of defects in them. Any growth methods that reduced these nonequilibrium concentrations of defects could lead to much improved metallization systems.

Figure 4 also shows that these enhanced diffusion rates within the grains are becoming comparable to the grain boundary diffusion rate. Thus the original Ti/Au interface is a more effective source of Ti than the grain boundaries, at least when the latter are also acting as a source for the oxidation. Otherwise one would not see a concentration gradient in Ti but a steady rise with time of a flat Ti level through the Au layer as discussed by Poate *et al.* (3) in their analysis of RBS profiles of the Pd-Au system.

Although the experiments were primarily designed to study the intermetallic layers, it is also possible to learn something from them about the accompanying oxidation of titanium which reaches the surface. First, it is clear that the UHV deposited layers also oxidized much faster than the HV deposited layers. Thus in Fig. 6 there is approximately three times as much oxide as

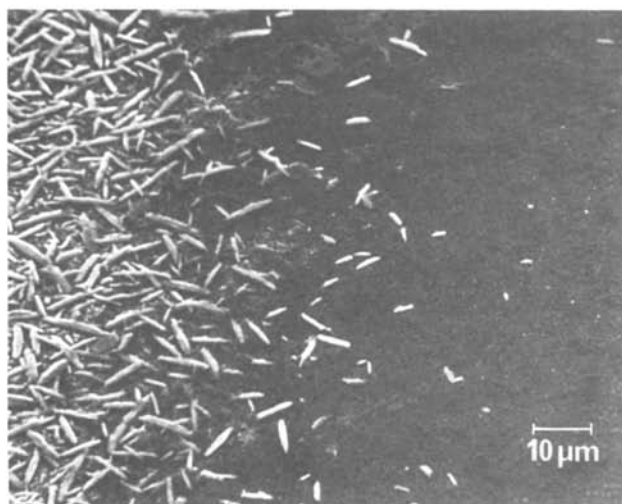
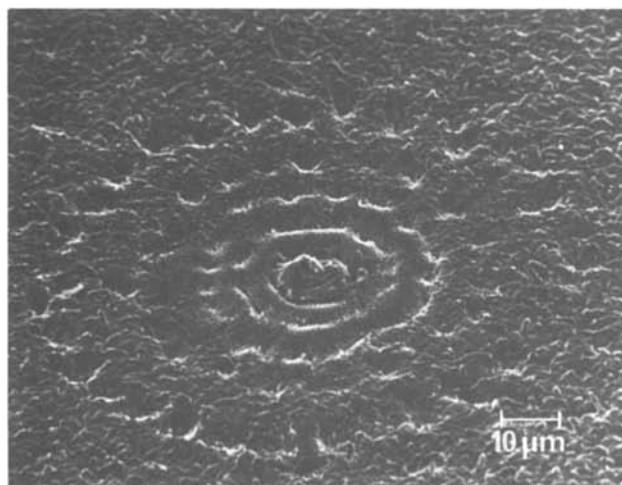
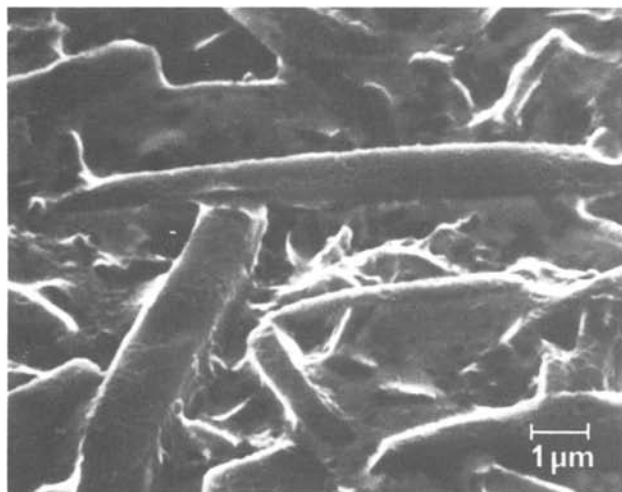


Fig. 8. Scanning electron micrographs of stages in the Au-Ti-Si interaction at 350°C : (a, top) the reaction product of elongated Ti_5Si_3 crystallites in an Au matrix, (b, center) the center of a reacted zone, and (c, bottom) the edge of a reaction zone (after removing the gold).

in Fig. 5 even though the anneal time in the former is shorter. A similar conclusion is provided by the data from the 300°C anneals. Second, all the oxidation rates are much greater than expected from extrapolation of literature values obtained at high temperatures. Close comparison is difficult because of the variety of rate laws reported for low temperature oxidation of titanium (7). However, the size of the effect can be gauged from the following estimate. At 600°C a parabolic oxidation law is followed (8) with $kp = 0.16 \exp(-45,000/RT) \text{ g}^2 \text{ cm}^{-4} \text{ sec}^{-1}$. Extrapolation to 350°C gives $kp \approx 2.8 \cdot 10^{-17} \text{ g}^2 \text{ cm}^{-4} \text{ sec}^{-1}$, whereas from Fig. 5 with 3000Å of oxide formed in $3 \cdot 10^4 \text{ sec}$ $kp = 5.3 \cdot 10^{-13} \text{ g}^2 \text{ cm}^{-4} \text{ sec}^{-1}$ which is some four orders of magnitude higher. Even without assuming the parabolic rate law at 350°C there is the simple comparison that a slightly thicker oxide layer has grown at 350°C than in the earlier experiments with titanium (8) at 600°C. More recent work on titanium (9,10) also shows no evidence of the faster oxidation rates reported here. However Poate *et al.* (3) did find a comparable amount of oxidation, suggesting that the faster rate is characteristic of the gold-rich Au/Ti alloys. In both these studies of the Au/Ti alloys the presence of excess nitrogen in the gas phase had no detectable effect.

The above discussion of diffusion has not depended on accurate quantitative elemental concentrations from the Auger profiles. However, it is clear from Fig. 2-6 that the Auger data is providing a good quantitative guide at many points. The values shown were obtained using Chang's basic formula (11) together with our

own elemental and compound standards. The thicker layers of oxide are very close to TiO_2 . The apparent excess of Ti is due to the presence of TiC also, as it is clear from the shape of the C_{272} peak that the carbon is present as carbide not in a graphitic form. In the Au/Ti alloy, on the other hand, the composition indicated by the Auger profile is too rich in Ti; in Fig. 5 the Au/Ti ratio is only ≈ 2.7 not 4. Errors in alloy composition are to be expected when elemental standards are used (12). For instance the Ti signal in the alloy should be enhanced due to the greater backscattering coefficient from the Au in the alloy. Also, as reported earlier for Ti and TiO samples (13), the Ti Auger spectrum undergoes strong changes in the relative intensities of the two peaks at 387 and 418 eV with matrix. Although this makes detailed quantitative work difficult it can be turned to advantage and used as a guide to the chemical state of the titanium. In Fig. 9 this region of the Ti spectrum is illustrated for the four distinct matrices occurring in the present work. The Ti_5Si_3 spectrum was recorded after an iodine etch removal of the Au, similar to that described in the SEM results section, but on a completely reacted sample. These peak intensity differences may often be amplified for ease of detection during profiling by choice of appropriate modulation voltage (14).

Following the chemical analysis, the main features of the resistivity plots shown in Fig. 1 can be interpreted as follows. The initial slow rise in resistivity is due to "removal" of free Au by alloying with Ti, as the Au layer is expected to carry $\approx 95\%$ of the current initially (15). By stage B no free Au remains and

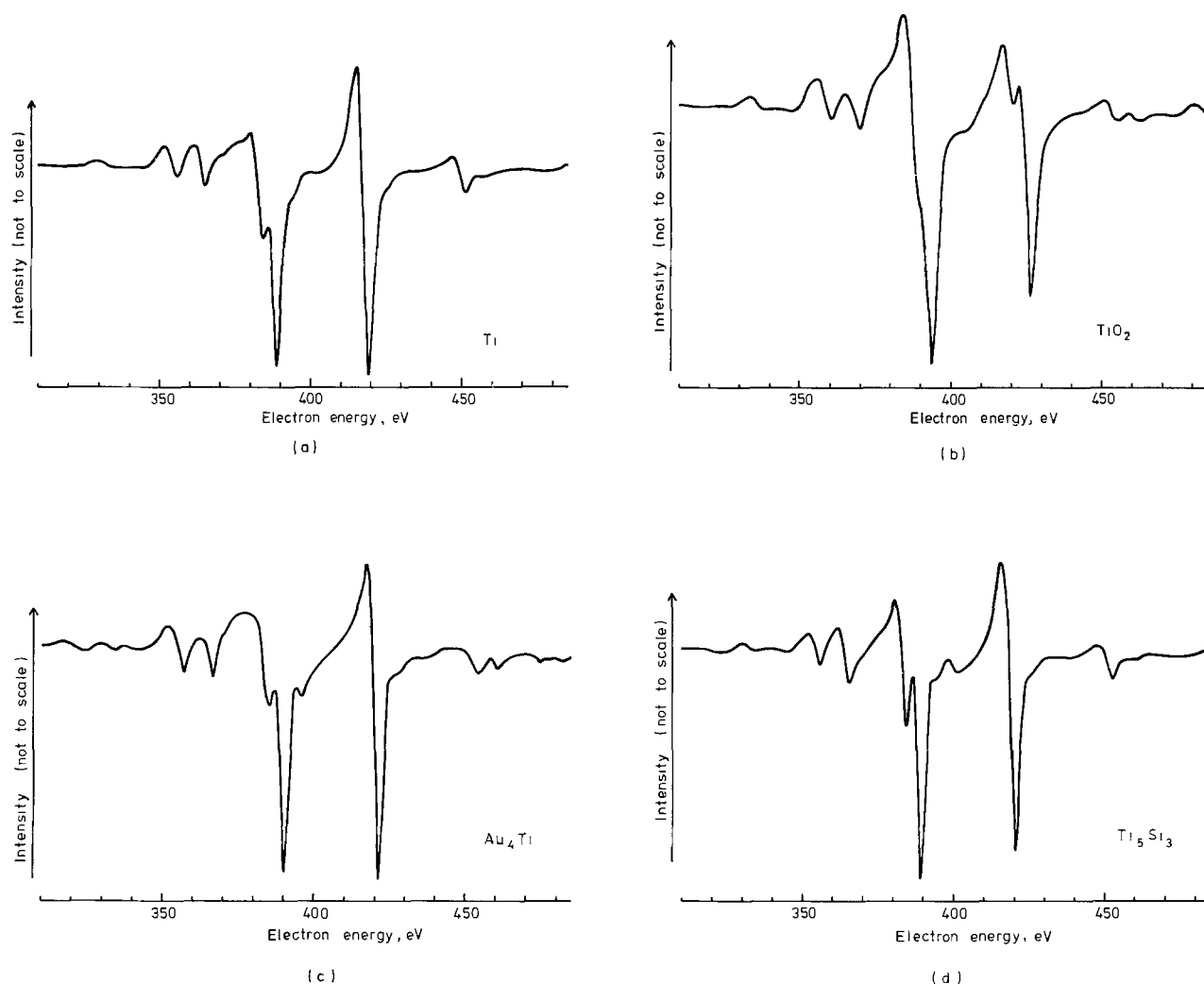


Fig. 9. Auger spectra from titanium in the 350-450 eV energy range taken with an energy resolution of 0.6% and showing the effect of different chemical matrices on the relative peak intensities: (a) metallic Ti, (b) TiO_2 , (c) Au_4Ti , and (d) Ti_5Si_3 .

the current is carried by both Au₄Ti and Ti layers. At stage C all the Ti has been oxidized and only the Au₄Ti layer remains conducting. A comparison between stages C and B suggests the conductivity of the Au₄Ti is comparable with that of Ti, perhaps $\approx 30\%$ higher. Finally, as oxidation proceeds further, some free Au is regenerated and the resistance falls again quite markedly.

Sylwestrowicz *et al.* (4) have rightly stressed that some of the mechanisms of interaction studied at high temperature may not be relevant to metallizations used on devices operated nearer room temperature. On SiO₂ substrates we have three mechanisms at least, grain boundary diffusion, bulk diffusion of Ti-Au, and oxidation of Ti, all influencing the reaction. In principle these reactions could all show quite different dependences on temperature. In practice, however, they are all likely to be quite similar. The temperature dependence of the defect mobility term in the bulk diffusion coefficient has been found to be 0.80-0.85 eV for several metals in Au (16, 17). Similarly the equivalent defect mobility term in TiO₂ has been estimated at ≈ 1.0 eV (7). There appears to be no direct measurement of the activation energy for grain boundary diffusion of Ti in Au but an estimate of 0.87-0.9 eV has been calculated for Pd in Au (3, 6) and initial penetration of Ti through Au occurs at similar temperatures to Pd in Au (3). Thus in the system studied here the high temperature results reported should provide a worthwhile guide to the expected behavior of metallizations used in long-lived devices.

The results from high temperature anneals (350°C) of Au-Ti on Si substrates clearly illustrate Sylwestrowicz's point, and it is likely that they were quite unrepresentative of room temperature behavior. The detailed mechanism is not established, but it appears that a Ti-Au-Si eutectic which is molten at 350°C must form. Starting at discrete flaws in the film, the reaction then spreads rapidly. A similar phenomenon was reported by Sinha in the Si/SiO₂/W/Au system (18). Both the appearance of the reaction zone in Fig. 8b and the complete envelopment of the Ti₅Si₃ crystallites in the Au matrix strongly support the idea of melting during reaction. Figure 8c suggests that the spread of the molten zone, like many other reactions, proceeds first at grain boundaries. Independent of the precise details of the reaction mechanism, it is evident that the reaction product Ti₅Si₃ is more stable than the possible Au-containing alloys, a point that it might be possible to exploit in future metallization schemes.

Conclusions

Auger sputter ion profiling has shown that deposition of Ti films in technical vacuum results in the incorporation of C and O impurities at the 1-10% level. Comparison with films deposited in UHV, and so free from

the above impurities, shows that the C and O play a crucial role in determining the interdiffusion rates and hence effective lifetimes of Ti-Au thin film couples. The results suggest that monitoring and control (even controlled introduction) of such impurities, normally ignored in device production, might lead to significant improvements in current metallization schemes.

Acknowledgments

The authors would like to thank C. H. Ling, P. Walmsley, and S. J. Wright for film preparation, C. H. Ling for resistivity measurements, P. J. Carter for x-ray measurements, and A. P. Skeats for SEM/microprobe determinations. Acknowledgment is also made to the Director of the British Telecom Research Laboratories for permission to publish this paper.

Manuscript submitted June 18, 1980; revised manuscript received Sept. 18, 1980.

Any discussion of this paper will appear in a Discussion Section to be published in the December 1981 JOURNAL. All discussions for the December 1981 Discussion Section should be submitted by Aug. 1, 1981.

Publication costs of this article were assisted by British Telecom Research Laboratories.

REFERENCES

1. D. Baker, P.O. Res. D. Report No. 641 (1977).
2. T. C. Tisone and J. Drobek, *J. Vac. Sci. Technol.*, **9**, 271 (1971).
3. J. M. Poate, P. A. Turner, W. J. De Bonte, and J. Yahalom, *J. Appl. Phys.*, **46**, 4275 (1975).
4. W. D. Sylwestrowicz, H. A. Elkholy, and G. W. Kammlott, *J. Mater. Sci.*, **14**, 873 (1979).
5. C. A. Wallace and R. C. Ward, *J. Appl. Crystallogr.*, **8**, 255 (1975).
6. P. M. Hall, J. M. Morabito, and J. M. Poate, *Thin Solid Films*, **33**, 107 (1976).
7. O. Kubaschewski and B. E. Hopkins, "Oxidation of Metals and Alloys," p. 214, Butterworths, London (1962).
8. A. E. Jenkins, *J. Inst. Met.*, **84**, 1 (1955).
9. W. D. Sylwestrowicz, *This Journal*, **122**, 1504 (1975).
10. T. Smith, *Surf. Sci.*, **38**, 292 (1973).
11. C. C. Chang, *ibid.*, **48**, 9 (1975).
12. P. M. Hall and J. M. Morabito, *ibid.*, **83**, 391 (1979).
13. J. T. Grant, T. W. Haas, and J. E. Houston, *J. Vac. Sci. Technol.*, **11**, 227 (1974).
14. J. T. Grant, T. W. Haas, and J. E. Houston, *Surf. Sci.*, **42**, 1 (1974).
15. "Handbook of Chemistry and Physics," R. C. Weast, Editor, p. f145, Chemical Rubber Co., Cleveland, Ohio (1973).
16. W. Jost, "Diffusion in Solids, Liquids and Gases," p. 234, Academic Press Inc., New York (1952).
17. P. G. Shewmon, "Diffusion in Solids," p. 74, McGraw-Hill, New York (1963).
18. A. K. Sinha, *Thin Solid Films*, **20**, 115 (1974).

Liquid Phase Epitaxial Growth of $(\text{Hg}_{1-x}\text{Cd}_x)\text{Te}$ from Tellurium-Rich Solutions Using a Closed Tube Tipping Technique

J. A. Mroczkowski* and H. R. Vydyanath*

Honeywell Electro-Optics Center, Lexington, Massachusetts 02173

ABSTRACT

The liquidus temperatures for $(\text{Hg}_{1-x}\text{Cd}_x)_{1-y}\text{Te}_y$ have been determined for $x = 0.067$, $x = 0.10$, and $0.7 \leq y < 1.0$ compositions by differential thermal analyses. $(\text{Hg}_{1-x}\text{Cd}_x)\text{Te}$ films with compositions of $x = 0.35$, 0.31 , and 0.24 have been grown by liquid phase epitaxy on CdTe (111)A oriented substrates. The Cd segregation coefficient has been determined to be $k = 3.5 \pm 0.1$. Films grown at around 550°C from 3 mm thick melts at slow cooling rates showed thicknesses close to those expected for equilibrium growth. The residual impurity in the LPE films was usually n-type and was less than 10^{15} cm^{-3} in the better films. Photovoltaic diodes fabricated in the films have shown performance comparable to those fabricated in bulk grown crystals.

The II-VI compounds of CdTe and HgTe form a continuous series of solid solutions with cubic zincblende structure. $(\text{Hg}_{1-x}\text{Cd}_x)\text{Te}$ consists of a mixture of the wide gap semiconductor CdTe ($E_g = 1.6\text{ eV}$) with the semimetallic compound HgTe which can be considered as a semiconductor having a negative energy gap. The gap in the alloys varies nearly linearly with x between the two end-point values. Alloys of $\text{Hg}_{1-x}\text{Cd}_x\text{Te}$ with x -values in the range 0.2-0.4 corresponding to bandgap energies in the range 0.1-0.5 eV are of particular interest for the detection of infrared radiation in the 2-20 micron range.

Initial LPE $(\text{Hg}_{1-x}\text{Cd}_x)\text{Te}$ film growth was pursued from pseudobinary melts due to the absence of phase diagram information in the Hg-rich and Te-rich corners. Since the pseudobinary film growth involved temperatures around 700°C and Hg pressures on the order of 10 atm a closed tube tipping technique was adopted. The work reported here concerns the subsequent determination of liquidus temperatures and LPE $(\text{Hg}_{1-x}\text{Cd}_x)\text{Te}$ film growth development from Te-rich solutions.

LPE $(\text{Hg}_{1-x}\text{Cd}_x)\text{Te}$ film growth from Te-rich solutions has only recently been reported in "open" systems (1-3), but no liquidus data covering a range of x, y values has been documented. Our initial use of a closed tube system for film growth at temperatures around 550°C , where the Hg pressure is about 1/3 atm, has permitted the study of film growth under near equilibrium conditions without concern over melt composition changes from Hg loss due to evaporation.

With phase diagram information limited to binary and pseudobinary compositions initial work was concentrated on determining the liquidus temperatures for Te-rich $(\text{Hg}_{1-x}\text{Cd}_x)_{1-y}\text{Te}_y$ solutions suitable for $x = 0.20$ to $x = 0.40$ film growth. Subsequently, stoichiometric $(\text{Hg}_{1-x}\text{Cd}_x)\text{Te}$ films were grown from slightly undersaturated 3 mm thick LPE melts. Measured film thicknesses and composition gradings obtained from slow growth conditions were then compared with calculated values based on measured liquidus temperatures and the Cd segregation coefficient.

Liquidus Temperatures

Thermal analyses were conducted by the slow cooling of homogenized $(\text{Hg}_{1-x}\text{Cd}_x)_{1-y}\text{Te}_y$ liquid samples. Charges with weights close to 15g were placed in 12 mm ID, 1 mm thick wall quartz ampuls with a thin

2 cm re-entrant thermocouple well. The free space inside the ampuls was about 5 cm^3 . The change in composition due to evaporation was calculated to result in an error in the liquidus temperature interpolation of much less than 1°C . A similar ampul containing silicon was used as a reference. After sealing, the ampuls were placed very close together in two symmetrical cavities drilled in a nickel cylinder fitted with a nickel lid. A Chromel-Alumel thermocouple was inserted in each ampul, and the two were connected for simultaneous recording of the sample temperature and the temperature difference between the sample and reference as a function of time. To obtain high sensitivity sample and differential temperature readings, the sample signal was largely balanced out with a potentiometer, and the differential signal was amplified ten times. The two signals were then fed into an XYY' recorder.

Temperature data for each composition were taken after at least 6 hr of solution homogenization at temperatures at least 15°C above the anticipated liquidus temperatures. Cooling rates were typically $2^\circ\text{C}/\text{min}$, an order of magnitude larger than used in the subsequent LPE film growths. Supercooling was observed in all the thermal analysis runs, and from later liquidus temperature interpolations supercooling at the cooling rates used was found to range mostly between 5° and 15°C .

The actual liquidus temperatures were estimated by extrapolation from a plot of the degree of supercooling vs. temperature at which supercooling stopped. The amplitude of the differential temperature overshoot was used as a measure of the degree of supercooling.

Heating runs for the eutectic temperatures gave a range of values lying between 410° and 420°C . Since the eutectic compositions cannot be specifically defined under nonequilibrium cooling conditions the eutectic temperatures are not displayed.

The thermal analysis data taken for $x = 0.067$ and $x = 0.10$ compositions together with $x = 0$ data for Hg_2Te^4 are summarized in Table I and displayed in Fig. 1. The data for the liquidus slopes at varying composition^s x, y defined as $m_x = \partial T / \partial x)_y$, $^\circ\text{C}/\text{mole}$ and $m_y = \partial T / \partial y)_x$, $^\circ\text{C}/\text{mole}$ were obtained from the best slope fitting of the data shown in Fig. 1.

LPE Film Growth Procedures and Results

LPE film growth using the tipping technique was accomplished in a POCO DFP 3-2 grade graphite boat shown in Fig. 2. The outer radius of the base of the graphite boat was designed to fit the inside radius of an evacuated sealed quartz ampul. The component

* Electrochemical Society Active Member.

Key words: LPE, II-VI ternary semiconductor, phase diagram, equilibrium growth theory.

Table I. Liquidus temperature and slope data for low x-value Te-rich $(\text{Hg}_{1-x}\text{Cd}_x)_{1-y}\text{Te}_y$ solutions

| y | Liquidus temperatures ($^{\circ}\text{C}$) | | Liquidus surface | |
|-------|--|-------------|--|--|
| | $x = 0.067$ | $x = 0.10$ | $\frac{\partial T}{\partial y}_x$ $^{\circ}\text{C}/\text{mole}$ | $\frac{\partial T}{\partial x}_y$ $^{\circ}\text{C}/\text{mole}$ |
| | | | $0.067 < x < 0.10$ | $0 < x < 0.10$ |
| 0.70 | 585 ± 4 | 607 ± 8 | -672 | 500 |
| 0.725 | — | 590 ± 3 | -707 | 530 |
| 0.75 | 551 ± 4 | 568 ± 3 | -770 | 600 |
| 0.775 | — | 545 ± 3 | -862 | 630 |
| 0.80 | 506 ± 3 | 530 ± 3 | -960 | 645 |
| 0.825 | — | 499 ± 5 | -1170 | 650 |
| 0.85 | 445 ± 10 | — | — | — |
| 0.90 | 430 ± 10 | — | — | — |

preparation and the film growth processes are described in the following.

The LPE melt was usually obtained from a section of a rapidly quenched $(\text{Hg}_{1-x}\text{Cd}_x)_{1-y}\text{Te}_y$ ingot. Six nines purity quadruply zone refined Cominco Cd and Te were used for the compounding. *In situ* preparation of the melt from HgTe, CdTe, and Te in the graphite boat just before growth was also used. In both of the preparation methods the elements were homogenized in closed ampuls in the LPE tipping furnace used in

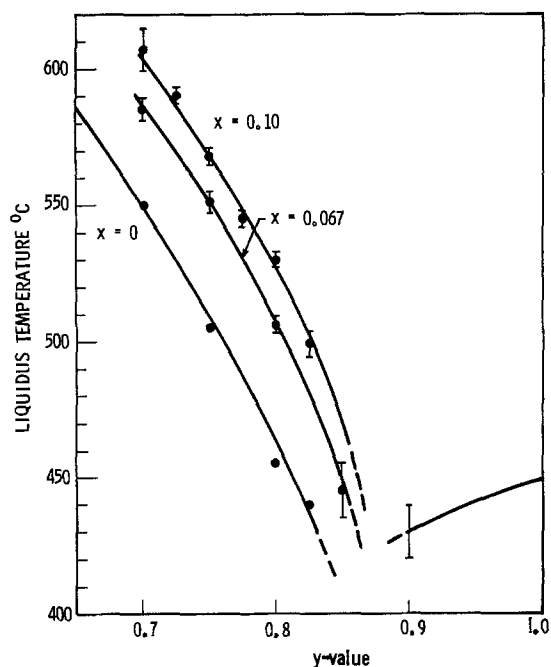


Fig. 1. Liquidus temperature data on $x = 0.067$ and $x = 0.10$ $(\text{Hg}_{1-x}\text{Cd}_x)_{1-y}\text{Te}_y$ solutions. $x = 0$ data is from Ref. (4).

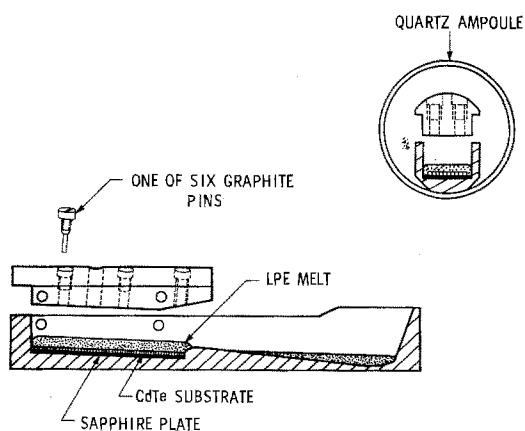


Fig. 2. Exploded view of LPE graphite boat shown in the growth position with the Te-rich solution tipped over the substrate.

a rocking mode. In the case of the *in situ* preparation method, the rocking angles were chosen such as to prevent the melt contacting the CdTe substrates before the actual growth process was initiated.

The dimensions of the CdTe substrates used were typically 10×37 mm; the substrates, purchased from II-VI Incorporated, were also prepared from 6 nines pure Cd and Te obtained from Cominco. Almost all the substrates used were (111)A oriented. The initial polishing of the substrates to mirror flatness involved a method using diamond milling with a single diamond edge along a select direction (5). Subsequent surface preparation involved light chemical-mechanical and chemical etching in a bromine methanol solution with the final chemical etch being performed immediately before the loading of the growth ampul.

To ensure a minimum of process contamination, the $(\text{Hg}_{1-x}\text{Cd}_x)_{1-y}\text{Te}_y$ compounding and the pre-LPE growth component assembly procedures were all performed in a VAC argon glove box which included a Mettler Electronic balance. Quartz ampuls used for compounding or film growth were baked out at 800°C under ion pump vacuum. LPE graphite boats were rf baked before each film growth run for 3 hr at 1600°C under a diffusion pump vacuum of 2×10^{-7} mm pressure. Component transfer between the glove box and vacuum stations either under vacuum or with the glove box atmosphere was performed with the use of closed bellows valves which isolated the inside of the ampuls from the ambient.

For each LPE film growth run, $10 \pm \frac{1}{2}$ g of $(\text{Hg}_{1-x}\text{Cd}_x)_{1-y}\text{Te}_y$ were used. The CdTe substrate and $(\text{Hg}_{1-x}\text{Cd}_x)_{1-y}\text{Te}_y$ were placed at opposite ends of the graphite boat. To prevent substrate to graphite sticking a 0.010 in. thick sapphire plate was placed in between.

After loading the graphite boat and components into a quartz ampul and subsequent evacuation and sealing, the quartz ampul with the contents was placed in the growth furnace near the center of a 12 in. sodium heat pipe. The steady-state temperature profile was $\pm \frac{1}{4}^{\circ}\text{C}$ over the 6 in. length of the ampul. The thermal history of each growth run was recorded using the analog output of an Omega 2176A thermometer with simultaneous digital display reading to 0.2°C . The temperature and the times involved in a typical growth run are shown in Fig. 3. The recording thermocouple was checked against the melting point of Te; the melting point of Te was recorded at 452.6°C .

In most growth runs slight undersaturation was used. The CdTe substrate was then allowed to equilibrate with the solution at constant temperature for about 15 min before a slow linear cool was initiated for typically a $5^{\circ}\text{--}7^{\circ}\text{C}$ temperature drop. Figure 4 illustrates the small changes in liquidus composition after the 15 min equilibration time, and at the end of near equilibrium film growth. At the end of the cooling cycle, the solution was decanted off the film and the ampul was removed from the furnace.

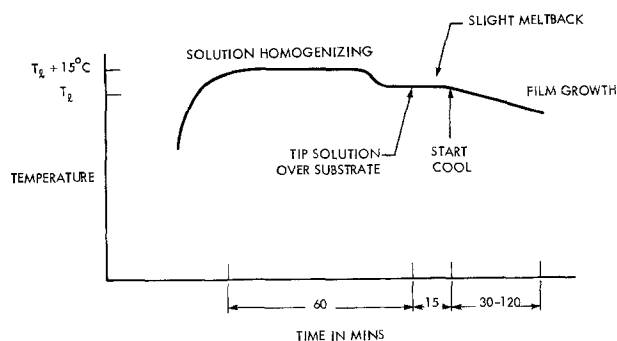


Fig. 3. Typical thermal history of an LPE film growth run; the liquidus temperature is denoted by T_1 .

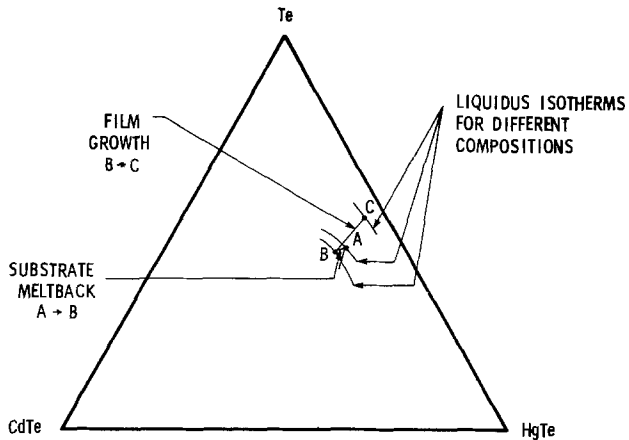


Fig. 4. Schematic of changes in the LPE solution composition (A→B→C) following the growth conditions shown in Fig. 3.

Some problems that develop in the LPE film surface morphology during growth can be traced to local changes in the melt depletion region composition. Several triggering situations are possible, including initial surface unevenness and/or substrate contamination affecting the initial nucleation and melt trace impurities. Any of these situations can result in an increasingly irregular interface, as melt diffusion in the affected areas takes on a nonuniform three-dimensional aspect. Depressed growth areas can then become increasingly covered by slightly lower liquidus temperature compositions resulting in further slow down of the growth rate in those areas and the problem can escalate, particularly under severely diffusion-limited growth conditions. Since, in the initial portion of this work, fast film growth rates appeared to be detrimental to film surface morphology, most of the film growth concentrated on slow growth rates controlled by slow cooling rates.

Film thickness *vs.* temperature drop data for films grown from solution compositions initially compounded as $(\text{Hg}_{0.90}\text{Cd}_{0.10})_{0.225}\text{Te}_{0.775}$ and $(\text{Hg}_{0.933}\text{Cd}_{0.067})_{0.25}\text{Te}_{0.75}$ are shown in Fig. 5. All of the solutions used for growing these films were undersaturated by 0 to 3°C at the time of the initial contact with the substrate. Under these conditions, after 15 min of equilibration, the new very slightly different solution compositions were considered to be very close to their liquidus temperatures.

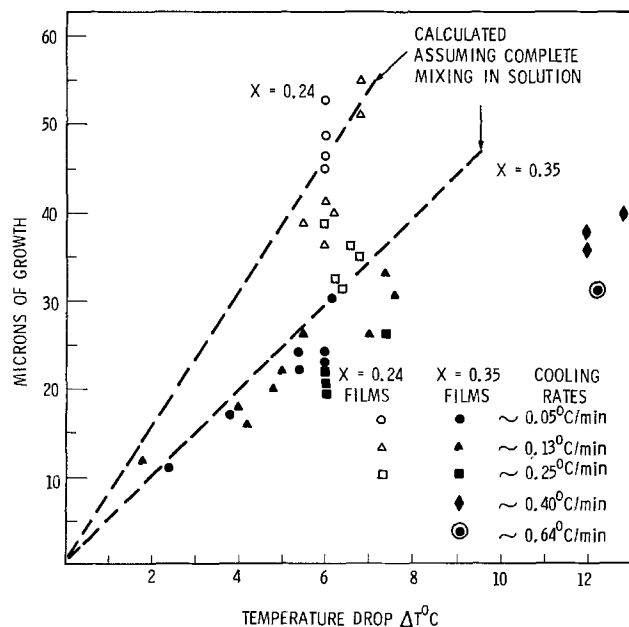


Fig. 5. Film growth thicknesses *vs.* temperature drop for $(\text{Hg}_{0.90}\text{Cd}_{0.10})_{0.225}\text{Te}_{0.775}$ and $(\text{Hg}_{0.933}\text{Cd}_{0.067})_{0.25}\text{Te}_{0.75}$ solutions.

The film thickness measurements were made optically from cleaved $(1\bar{1}0)$ planes perpendicular to the $(111)A$ film surface. The film thickness was readily identified from a distinctly different visible reflectivity of $(\text{Hg}_{1-x}\text{Cd}_x)\text{Te}$ compared to that of the CdTe substrate. The film growth thickness was taken as the total thickness less 4 microns of interdiffusion into the substrate side of the interface.

Measured film growth thicknesses *vs.* temperature drop data given in Fig. 5 show that for cooling rates on the order of 0.05°C/min the film thicknesses were close to those expected for equilibrium film growth from 3 mm thick solutions.

X-ray microprobe analyses were performed across $(1\bar{1}0)$ cleaved surfaces of the films perpendicular to the $(111)A$ surface. HgTe and CdTe were used as standards and the composition of films was determined using a KEVEX Magic 5 program with a ZAF correction. Composition profiles shown in Fig. 6 were made on lightly etched film surfaces and also on as-grown surfaces.

The microprobe measurements on the as-grown films and films which were lightly etched indicated that the Cd concentration increases near the as-grown surface. Evidence of an increase in the Cd concentration near the film surface was also provided by visible color differences of the film surfaces before and after etching which were the same as those seen in cleaved film sections between the CdTe substrate and the $(\text{Hg}_{1-x}\text{Cd}_x)\text{Te}$ film. Auger and ellipsometer analyses on the as-grown and etched surface areas confirmed that the composition increased by about $\Delta x = 0.5$ within about a tenth of a micron of the surface.

The increase in surface *x*-value after the LPE solution is decanted off, and the closed ampul cools to ambient temperatures in about 5 min. The probable explanation for this is that during cooldown the ratios of the activities of Hg and Cd over the melt and film change in a manner that favor the formation of a CdTe-rich surface layer on the film.

Infrared transmission scans were used to determine the composition of films with *x*-values around $x = 0.35$. For a linearly graded film composition the fraction of energy transmitted relative to the peak transmission can be expressed as (6)

$$I_{tr} = I_{pk} \exp - (2K/3\beta m) (E - E_s)^{3/2} \quad [1]$$

where E_s denotes the surface bandgap energy, E the

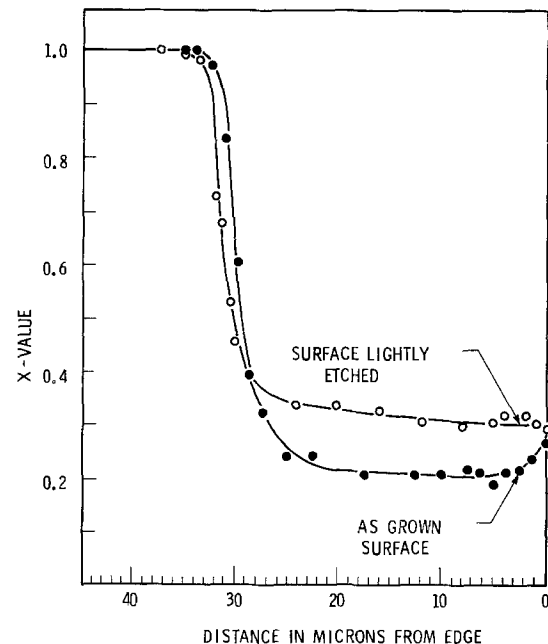


Fig. 6. X-ray microprobe data on films grown from $(\text{Hg}_{0.90}\text{Cd}_{0.10})_{0.225}\text{Te}_{0.775}$ and $(\text{Hg}_{0.933}\text{Cd}_{0.067})_{0.25}\text{Te}_{0.75}$ solutions.

photon energy satisfies $E_s + \beta md \geq E \geq E_s$, m is the composition grading/unit distance, β is the incremental change in energy gap/Cd mole, d is the depth from the film surface in which absorption can take place, and the parameter K is related to the bandgap energy E_g through the standard expression $\alpha = K(E - E_g)^{1/2}$ where α is the absorption coefficient at the photon energy E . Transmission curve fitting to Eq. [1] and the use of calibrated data for the absorption coefficient at $\alpha(E) = 500 \text{ cm}^{-1}$ vs. x -value (7) enabled an accurate assessment of the film surface composition to be made.

Films grown from $(\text{Hg}_{0.90}\text{Cd}_{0.10})_{0.225}\text{Te}_{0.775}$ solutions around 550°C with thicknesses around 25 microns beyond the interdiffused region showed surface x -values close to $x = 0.345$. Films which were grown from $(\text{Hg}_{0.91}\text{Cd}_{0.09})_{0.232}\text{Te}_{0.768}$ solutions at the same temperatures showed surface compositions of around $x = 0.31$ close to those expected for a 10% reduction in solution x -value. A few films which were grown from $(\text{Hg}_{0.90}\text{Cd}_{0.10})_{0.175}\text{Te}_{0.825}$ solutions at around 500°C indicated essentially no discernible change in the segregation coefficient with increase in y -value.

The segregation coefficient of Cd, k , obtained from the more extensively investigated $x = 0.10$ and $x = 0.09$ LPE solutions at growth temperatures around 550°C was taken to be $k = 3.5 \pm 0.1$. The more accurate composition determinations of films grown from $x = 0.067$ solutions at around 550°C were made using infrared spectral response measurements at 77 K; the composition of these films was $x = 0.235$, which agreed with the value kx expected from the definition of k .

Most of the film growths were carried out on (111)A CdTe substrate surfaces rather than on the (111)B and (100) surfaces. Evaluation of over 100 films grown from Te-rich solutions has shown that the best films were grown using only about 1°C of undersaturation resulting in a slight meltback of the substrate surface which could not be detected in optical examination of the film cross sections.

For 3°C of undersaturation, substrate meltback was uneven and film morphologies were very uneven, particularly when relatively fast cooling rates were used. In addition, the LPE solution was trapped in the more heavily depressed film regions after the melt decanting operation. When growth conditions used solutions estimated to be supersaturated by 2°C the quality of the film surface was generally poorer and homogeneously precipitated $(\text{Hg}_{1-x}\text{Cd}_x)\text{Te}$ crystals deposited on the film surface. It appeared that without some undersaturation, initial nucleation on the substrate may have been inhibited by traces of oxides on the substrate in the closed tube growth. The cross section of a typical LPE film is shown in Fig. 7.

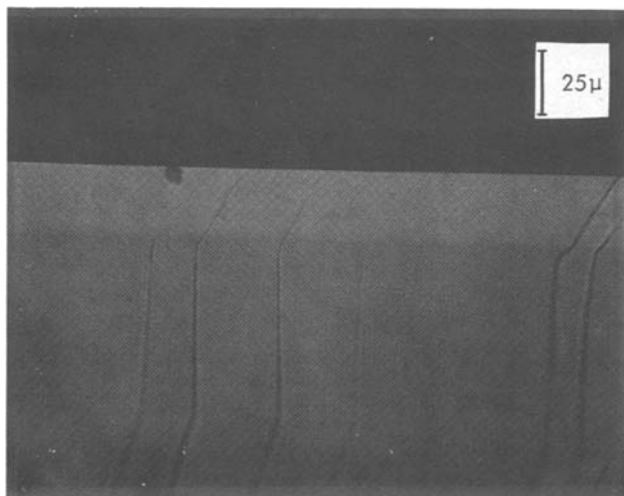


Fig. 7. Section of an $(\text{Hg}_{0.65}\text{Cd}_{0.35})\text{Te}$ film at $400\times$

A feature observed to some degree on most film surfaces was the presence of isolated, very flat plateau areas surrounded by depressed areas as seen in the micrograph of Fig. 8. The completely flat areas were exact (111)A planes with dimensions up to 1 mm across. The changes in film thickness between these areas were fairly gradual and generally within 3 microns for film thicknesses typically averaging 30 microns. However, in a few cases, thicknesses varied by more than a factor of two over distances on the order of 1 mm. These features appeared most prominently in films grown at slow cooling rates, when initial undersaturation was relatively high and when (111)A substrates oriented to within 5 min were used. Figure 8 shows the plateau areas adjacent to the more depressed areas. These morphological features are believed to be caused by convection currents in the melt since the lower, more depleted melt regions are less dense. Estimates of the solution stability using a Reynolds number criterion such as reported by Crossley and Small (8) support the possibility of solution convection during LPE film growth from Te-rich solutions, particularly when slow cooling rates are used.

Electrical characteristics.—Electrical characterization of the LPE films was used to determine the residual impurity concentration, the carrier mobilities, and the carrier concentrations. Since the CdTe substrates used for the growth of the LPE films were almost insulating it was assumed that the LPE films were electrically isolated from the CdTe substrates and therefore the electrical measurements were made on the films without etching away the substrate. Hall effect and resistivity measurements were made using the Van der Pauw method (9).

The residual impurity as measured from the Hall effect measurement at 77 K (subsequent to an Hg-rich anneal at a temperature of 250°C or less) was usually of the donor type (possibly indium) and varied between 3×10^{14} to $1 \times 10^{15} \text{ cm}^{-3}$ in the better films.

The electron mobility at 77 K in the better films exceeded $10^5 \text{ cm}^2/\text{V sec}$ for $x = 0.2$ and $2 \times 10^4 \text{ cm}^2/\text{V sec}$ for $x = 0.3$ compositions. These values compare well with those reported for the bulk grown crystals (10) and, hence, indicate the crystallinity of the films to be sound.

Diode characteristics.—Some n^+p diodes were fabricated in the LPE films. Figure 9 shows the characteristics of these diodes at 130 K in terms of R_0A (product of the zero bias resistance and p-n junction area) vs. the material cutoff wavelength $\lambda_{1/2}$. Data for some of the better diodes fabricated in bulk grown material are included in Fig. 9 for comparison purposes. Details of

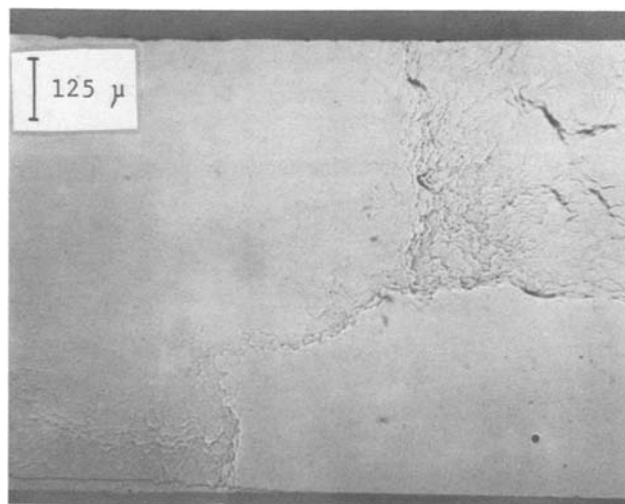


Fig. 8. Micrograph of film showing slightly elevated flat plateau areas surrounded by terraced areas.

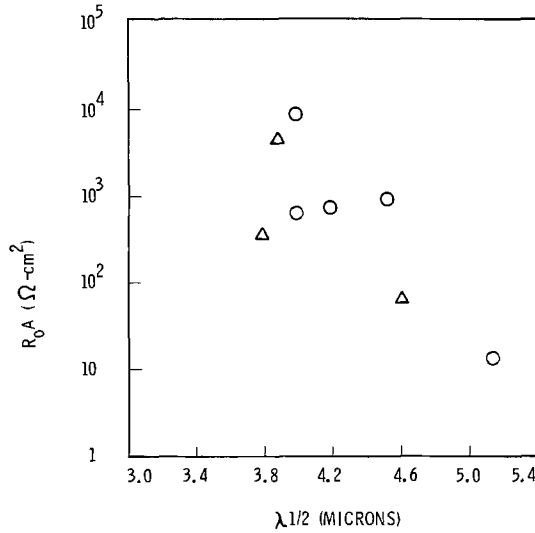


Fig. 9. R_0A data measured at 130 K vs. $\lambda/2$. Circles represent diodes fabricated in bulk grown material while triangles refer to diodes fabricated in the LPE material.

the LPE diode characteristics will be presented elsewhere.

Discussion

Calculations of the film thicknesses and composition gradings due to Cd and Hg depletion in the solution, based on equilibrium growth conditions, have been made. These calculations provided an additional method for estimating solution liquidus temperatures based on the depth of meltback from excessively undersaturated solutions. Solution undersaturation was then optimized to provide the best film surface morphology.

A slight change in the LPE solution composition occurs during the heat up of the growth system and subsequent homogenization of the solution. This composition change is due to the interaction of the CdTe substrate with the vapor species in the growth ampul before the melt contacts the substrate. In order to assess the extent of this interaction, a CdTe substrate that was exposed only to the vapor interaction was microprobed as shown in Fig. 10. If one assumes that all the Cd loss from the CdTe substrate in exchange for Hg is uniformly dissolved in the $(\text{Hg}_{1-x}\text{Cd}_x)_{1-y}\text{Te}_y$

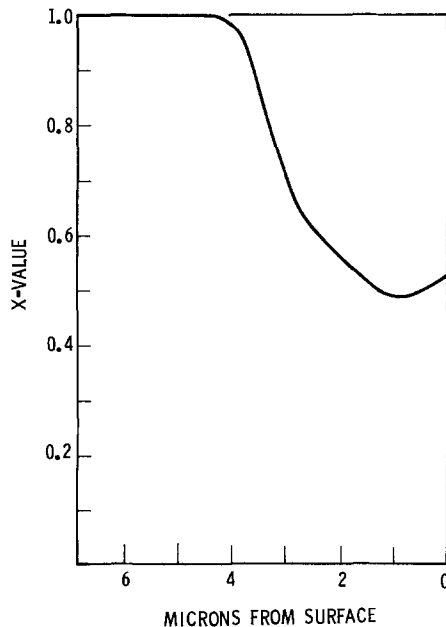


Fig. 10. X-ray microprobe analysis of a CdTe substrate exposed to the vapor (Hg, Cd, and Te_2 species) of a $(\text{Hg}_{1-x}\text{Cd}_x)_{1-y}\text{Te}_y$ growth solution during heat up and homogenization of an LPE growth run.

solution, the increase in x -value of the solution can be estimated to be about $\Delta x = 0.003$ resulting in an increase of the liquidus temperature of 2°C . These changes were expected to be reproducible in film growth runs using comparable homogenization times and temperatures.

Consider N mole fractions of $(\text{Hg}_{1-x}\text{Cd}_x)_{1-y}\text{Te}_y$ very slowly precipitating ΔN moles of stoichiometric solid $(\text{Hg}_{1-kx}\text{Cd}_{kx})_{0.5}\text{Te}_{0.5}$ following a temperature drop $\Delta T^\circ\text{C}$ below the liquidus temperature. Cd precipitation satisfies the following equation

$$\Delta[Nx(1-y)] = \Delta Nx(1-y) + \Delta xN(1-y) - Nx\Delta y = 0.5kx\Delta N \quad [2]$$

Similarly, Te precipitation gives

$$\Delta[Ny] = N\Delta y + y\Delta N = 0.5\Delta N \quad [3]$$

An additional constraint on the final solution composition is given by

$$\Delta T = \left(\frac{\partial T}{\partial x} \right)_y \Delta x + \left(\frac{\partial T}{\partial y} \right)_x \Delta y \quad [4]$$

where $\partial T/\partial x)_y = m_x$ and $\partial T/\partial y)_x = m_y$ are the liquidus slopes for $(\text{Hg}_{1-x}\text{Cd}_x)_{1-y}\text{Te}_y$. From Eq. [2] to [4]

$$\Delta x = \left[\frac{x(k-1)}{m_x x(k-1) - m_y(2y-1)(1-y)} \right] \Delta T \quad [5]$$

$$\Delta y = \left[\frac{-(2y-1)(1-y)}{m_x x(k-1) - m_y(2y-1)(1-y)} \right] \Delta T \quad [6]$$

$$\frac{\Delta N}{N} = 2 \left[\frac{(1-y)}{m_x x(k-1) - m_y(2y-1)(1-y)} \right] \Delta T \quad [7]$$

The change in the Cd concentration C in the solution for a given change in x and y is given by

$$\Delta C = (1-y)\Delta x - x\Delta y$$

Using Eq. [5] and [6], the liquidus slope for equilibrium growth defined in terms of the Cd concentration is given by

$$m = \frac{\partial T}{\partial C} = \frac{m_x x(k-1) - m_y(2y-1)(1-y)}{(1-y)(k+2y-2)x} \quad [8]$$

For film thickness determination the densities of the LPE melt and precipitated solid $(\text{Hg}_{1-x}\text{Cd}_x)\text{Te}$ are taken as $\rho_m(x,y)$ and $\rho_f(kx,0.5)$, respectively. The LPE film thickness l_f for equilibrium growth can then be obtained with the use of Eq. [7] and [8], while noting that the ΔN for the film is opposite in sign to that for the solution. Denoting the molecular weights of the film and melt by M_f and M_m we obtain

$$l_f = - \frac{\rho_m(x,y)M_f}{\rho_f(kx,0.5)M_m} \left[\frac{2l_m\Delta T}{m_x(k+2y-2)} \right]$$

Estimates of $\rho_m(x,y)$ were obtained from the sum of the proportionately weighted stoichiometric solid and pure Te densities $\rho(x,0.5)$ and ρ_{Te} , respectively, i.e.

$$\rho_m(x,y) = 2(1-y)\rho(x,0.5) + (2y-1)\rho_{\text{Te}}$$

The density of solid $(\text{Hg}_{1-x}\text{Cd}_x)\text{Te}$ at room temperature (11) was taken as

$$\rho(x,0.5) = 2.226(3.628 - x)$$

and the density of pure Te at 550°C (12) was taken as 5.75 g/cm^3 .

Table II lists some of the growth parameters used to obtain films with compositions of $x = 0.35$ and $x = 0.24$, and also the calculated equilibrium values of film growth thickness/ $^\circ\text{C}$ of temperature drop and the composition grading/micron of growth from 3 mm thick solutions.

Under equilibrium growth conditions the change in the solution x -value due to the depletion of Cd and Hg

Table II. Summary of film growth parameters and calculated substrate meltback depths and film composition changes due to initial solution undersaturation, and film thickness and composition gradings in subsequent film growth

| Parameters | | Film compositions | |
|---|---|---|---|
| | | Hg _{0.66} Cd _{0.34} Te | Hg _{0.768} Cd _{0.232} Te |
| Melt thickness | l_m mm | 3 | 3 |
| Melt composition | (Hg _{1-x} Cd _x) _{1-y} Te _y | (Hg _{0.60} Cd _{0.40}) _{0.225} Te _{0.775} | (Hg _{0.633} Cd _{0.367}) _{0.25} Te _{0.75} |
| Liquidus slopes | m_x °C/mole m_y °C/mole | 630 -862 | 600 -770 |
| Densities: melt | m °C/Cd mole | 3850 | 3915 |
| film | $\rho_m(x,y)$ g/cm ³ | 6.7 | 6.8 |
| Segregation coefficient | $\rho_f(kx, 0.5)$ g/cm ³ k (Cd ratio) | 7.3 3.5 | 7.5 3.5 |
| Film growth | | | |
| Thickness | l_t microns/°C $d(kx)$ | 4.9 | 7.35 |
| Film grading | $\frac{d}{dl_t}$ Cd moles/micron | -0.0007 | -0.0004 |
| Meltback Hg _{0.5} Cd _{0.5} Te surface | | | |
| Effective segregation coefficient | k' Cd ratio | 5.0 | 7.46 |
| Liquidus slope | m' °C/mole | 3504 | 3053 |
| Film x -value increase | $k\Delta x$ Cd moles/°C | 0.0039 | 0.0043 |
| Meltback depth | l_d microns/°C | -3.6 | -4.0 |
| Meltback CdTe surface | | | |
| Effective segregation coefficient | k' Cd ratio | 10.0 | 14.9 |
| Liquidus slope | m' °C/mole | 3135 | 2716 |
| Film x -value increase | $k\Delta x$ Cd mole/°C | 0.0047 | 0.0050 |
| Meltback depth | l_d microns/°C | -1.9 | -2.2 |

during growth results in proportional changes in the precipitated solid composition x -values. From Eq. [5] and [8], $\Delta x/x$ in solution can be expressed as

$$\frac{\Delta x}{x} = \frac{(k-1)\Delta T}{(k+2y-2)(1-y)m}$$

The change in the x -value of the film is then

$$k\Delta x = \frac{k(k-1)\Delta T}{(k+2y-2)(1-y)m} \quad [9]$$

Using Eq. [9], the change in x -value as a function of film thickness can be obtained

$$\frac{d(kx)}{dl_t} = -\frac{\rho_f(kx, 0.5)M_m}{\rho_m(x, y)M_f} \left[\frac{(k-1)kx}{2(1-y)l_m} \right] \quad [10]$$

To estimate substrate meltback depths and the increase in the film composition profile resulting from a Cd and Hg increase in the solution the same formalism as used for growth can be used for meltback, provided that k and m are appropriately redefined by their effective values in meltback, that is k' and m' . On the basis of the microprobe data shown in Fig. 10 two values of k' have been considered for the meltback process. First, for the case of light meltback of no more than about 2 microns of the substrate surface with x -value around $x = 0.5$, k' was taken as $0.5/x$ where x is the solution x -value. Second, for the case of significant meltback involving essentially pure CdTe k' was taken as $1/x$. The increase in the whole film x -value profile for ΔT '°C of undersaturation could then be obtained from

$$k \left[\frac{(k'-1)\Delta T'}{(k'+2y-2)(1-y)m'} \right] \quad [11]$$

With most undersaturated solution contact temperatures controlled to within $\pm 1/2$ °C of each other the measured film x -value variations between films of comparable thickness, grown from the same solution compositions, were observed to be within $\Delta x = \pm 0.002$. These results are consistent with the composition variations expected on the basis of Eq. [11] and listed in Table II.

Average meltback depths l_d into Hg_{0.5}Cd_{0.5}Te and separately into CdTe substrate surface compositions were determined from

$$l_d = -\frac{\rho_m(x, y)M_s}{\rho_s(k'x, 0.5)M_m} \left[\frac{2l_m\Delta T'}{m'x(k'+2y-2)} \right]$$

where M_s and ρ_s denote the molecular weight and density of the surface with composition $k'x$. The calculated values of l_d in Table II show that the meltback depth per °C of undersaturation is significantly less on CdTe than on Hg_{0.5}Cd_{0.5}Te. In films grown from supersaturated solutions the Cd/Hg interdiffusion depth on the CdTe substrate was typically 4 microns. Based on this information, the meltback depth data in Table II and observation on over a hundred films showing that excessive undersaturation led to uneven meltback reaching into the CdTe, we have associated an undersaturation of about 2°C as the temperature at which meltback could just be seen. Using meltback observations as a reference point for estimating solution undersaturation, it was estimated that the optimum degree of solution undersaturation for the best film morphology appeared to be about $1 \pm 1/2$ °C.

Two liquidus temperatures estimated from thermal analyses and meltback considerations are given in Table III. The liquidus temperature data obtained from thermal analysis appear to be about 3°C higher than those interpreted from LPE film growth. This temperature difference is believed to be largely due to the interaction between the substrate and solution via the vapor phase before solution tipping over the substrate. Allowing also for the solution depletion during growth, the Cd segregation coefficient for solutions with $y \geq 0.75$ and low x -values is estimated to be $k = 3.5 \pm 0.1$.

Summary

Thermal analyses have been made of Te-rich (Hg_{1-x}Cd_x)_{1-y}Te_y solutions with compositions suitable for growing (Hg_{1-x}Cd_x)Te films with compositions

Table III. Liquidus temperatures obtained by DTA and from LPE films

| Solution composition | | Film surface kx | Liquidus temperatures determined from | |
|----------------------|-------|-------------------|---------------------------------------|---------------|
| x | y | | DTA | LPE |
| 0.10 | 0.775 | 0.35 | 545 \pm 3°C | 549 \pm 1°C |
| 0.067 | 0.75 | 0.24 | 551 \pm 4°C | 554 \pm 1°C |

$x = 0.2-0.4$. The liquidus temperatures obtained in this way are consistent with estimates inferred from substrate meltback prior to the film growth process.

LPE $(\text{Hg}_{1-x}\text{Cd}_x)\text{Te}$ films grown at slow cooling rates under almost nondiffusion limited conditions showed thicknesses and composition gradings close to those calculated for equilibrium growth. In the absence of Hg loss in the closed system used, an accurate assessment of the Cd segregation coefficient was possible for low x -value $(\text{Hg}_{1-x}\text{Cd}_x)_{1-y}\text{Te}_y$ solutions with $y \cong 0.75$; the value obtained was $k = 3.5 \pm 0.1$.

Using slight undersaturation, smooth films up to 40 microns thick were grown. Electrical characterization of the LPE films showed electron mobility and residual impurity concentration characteristics comparable to bulk grown material. In addition, the performance of photodiodes made in the LPE films was similar to those made in the bulk grown material.

Acknowledgments

The authors wish to express their thanks to Mr. P. Guzelf for growing films and P. Crickard for electrical evaluation. This work was supported, in part, by the Air Force Materials Laboratory, Air Force Systems Command, United States Air Force, Wright Patterson AFB, Ohio 45433, under Contract No. F33615-78-C-5156.

Manuscript submitted April 28, 1980; revised manuscript received Sept. 12, 1980.

Any discussion of this paper will appear in a Discussion Section to be published in the December 1981 JOURNAL. All discussions for the December 1981 Discussion Section should be submitted by Aug. 1, 1981.

Publication costs of this article were assisted by Honeywell Electro-Optics Center.

REFERENCES

1. T. C. Harman, in Abstracts of the 1979 Electronic Materials Conference, June 28, 1979.
2. J. L. Schmit and J. E. Bowers, *Appl. Phys. Lett.*, **35**, (6) (1979).
3. C. C. Wang, S. H. Shin, M. Chu, M. Lanir, and A. H. B. Vanderwyck, *This Journal*, **127**, 175 (1980).
4. R. Brebrick and A. Strauss, Private communication.
5. J. A. Mroczkowski, To be published.
6. J. Mroczkowski, P. Lovecchio, D. Polla, and H. R. Vidyantath, "($\text{Hg}_{1-x}\text{Cd}_x$)Te Technology Development for MSP Support," Interim annual report to Air Force Materials Laboratory under Contract No. F33615-73-C-5156 (1979).
7. M. W. Scott, *J. Appl. Phys.*, **40**, 4077 (1969).
8. M. B. Crossley and I. Small, *J. Cryst. Growth*, **27**, 35 (1974).
9. L. J. Van der Pauw, *Philips Tech. Rev.*, **20**, 220 (1959).
10. W. Scott, *J. Appl. Phys.*, **43**, 1055 (1972).
11. J. Blair and R. Newman, in "Metallurgy of Elemental and Compound Semiconductors," Vol. 12, p. 393, Wiley-Interscience, New York (1961).
12. CRC Handbook, 55 ed., p. B-237 (1974-1975).

Stress-Induced Dark Line Defect Formation in GaAlAs:Si LED's

A. K. Chin,* W. C. King, T. J. Leonard, R. J. Roedel, C. L. Zipfel, V. G. Keramidis,*
and F. Ermanis

Bell Laboratories, Murray Hill, New Jersey 07974

ABSTRACT

Homojunction, graded bandgap GaAlAs:Si LED's have been demonstrated to be highly reliable. During accelerated aging (30 mA forward bias, 250°C), these LED's generally degrade slowly without the formation of dark lines or dark spots. It has recently been found, however, that some LED's show a rapid reduction of light output even when aged without current bias at 200°C. $\langle 110 \rangle$ oriented dark lines appeared in the electroluminescence image of heavily degraded devices. To determine the source of the DLD's, the material quality of degraded LED's and unaged LED's from the same wafer was assessed using etch pitting and transmission cathodoluminescence. Examination of the devices revealed the presence of small pyramids, composed mainly of silicon, on the p-surface of some of the LED's; no unusual features were found on the remaining LED's. A dislocation network surrounding each pyramid was found to be initially present. Due to bonding and thermal stresses applied to the pyramids, these networks enlarged with aging along the $\{111\}$ planes and appeared as $\langle 110 \rangle$ DLD's in the electroluminescence image upon reaching the p-n junction. In degraded LED's from pyramid-free regions of the wafer with pyramids, $\langle 110 \rangle$ DLD's initiate at dicing damage and regions of the p-surface subject to high bonding stress, i.e. edges and corners. The growth of these DLD's is identical to those initiating at pyramids. A similar study of LED's from a wafer that is totally free of pyramids shows that DLD's are not formed in devices that degrade slowly.

Graded-bandgap, homojunction GaAlAs:Si LED's are presently used as high efficiency light sources for opto-isolators (1, 2). Bias tests of these devices, accelerated by applying a thermal stress, demonstrated high reliability; with 30 mA forward current bias, a mean-time-to-failure (MTTF) of $\sim 10^5$ hr at 250°C

(1) and $\sim 10^8$ hr at 25°C (3) was determined. The electroluminescence of degraded diodes appears to differ from unaged devices only in relative brightness. Both degraded and unaged LED's exhibit uniform light emission; no dark lines or spots are observed. Recently, however, aging studies (4) have shown that some LED's degrade rapidly when aged at 200°C even without current bias; degradation to 10% of initial efficiency occurred within 400 hr. Examination of the

* Electrochemical Society Active Member.

Key words: cathodoluminescence, electron microscopy, reliability.

electroluminescence image of many of the most heavily degraded devices showed the presence of $\langle 110 \rangle$ oriented dark line defects (DLD's). The drop in LED efficiency is thus attributed to nonradiative recombination at the DLD's. Since dark line formation has not been previously observed in graded bandgap GaAlAs:Si LED's, this paper reports on their origin and growth behavior.

Formation of dark spots and dark lines oriented in the $\langle 100 \rangle$ and $\langle 110 \rangle$ directions is a degradation mode for LED's fabricated from many semiconductors, e.g., GaP (5), GaAs/GaAlAs (6-13), and GaAsP (14, 15). $\langle 110 \rangle$ DLD's grow by glide motion of dislocations on the $\{111\}$ slip planes (6, 7, 9, 10) whereas the growth of $\langle 100 \rangle$ DLD's is consistent with climb of dislocations (11-13). Studies have shown that formation of $\langle 100 \rangle$ DLD's require minority carrier injection whereas $\langle 110 \rangle$ DLD formation can be induced with either minority carrier injection or stress (7). Since the GaAlAs:Si LED's under discussion developed $\langle 110 \rangle$ DLD's without current bias, a source of stress was searched for.

Studies of stress-induced DLD's in GaAs/GaAlAs double heterostructure crystals provide a useful background for the present study. These studies showed that a threshold stress is required to form $\langle 110 \rangle$ DLD's (6, 7, 9, 10). This threshold level decreases for increasing minority carrier injection (6, 7, 10). For no injection, the threshold stress is $\sim 8 \times 10^9$ dynes/cm² (7). This value rapidly decreases to $\sim 2 \times 10^9$ dynes/cm² under the low excitation level of 3 W/cm² from a 6471A Kr-ion laser beam, equivalent to a current density of $J \sim 1$ A/cm² (7). A lower stress level of $\sim 6 \times 10^8$ dynes/cm² is found for $J = 58$ A/cm² (10). These stress values are comparable with values from typical sources of stress. Stresses from dielectric coatings can be as high as 10^{10} dynes/cm² (15), stresses due to dicing damage are $2-7 \times 10^7$ dynes/cm² (14), and the thermal stress on a mounted LED, assuming a 100°C temperature difference between header and LED, can be $\sim 10^9$ dynes/cm² (8).

In a reliability study by King (4), LED's from the same wafer as those that showed poor reliability were examined visually. Pyramidal protrusions of various sizes were found on the p-surface of some of the LED's (4). These pyramids occasionally occur in this device material and their exact cause is presently under in-

vestigation. LED's from the same wafer were separated into groups with and without pyramids. Bonded LED's with pyramids were found to degrade at a faster rate than those without pyramids, but both groups degraded faster than previous devices (1, 3, 4). A mean-time-to-failure (MTTF) of $\sim 10^5$ hr (250°C, 30 mA forward current) has been found for the latter whereas the LED's with pyramids show a MTTF of $\sim 4 \times 10^2$ hr even under reduced stress conditions (200°C, 0 mA forward current). Dark regions and lines in the electroluminescence image were observed only in the devices degraded to less than $\sim 10\%$ of their initial efficiency.

In the present study, the material quality of unaged and aged devices from a wafer exhibiting pyramids on the p-surface was determined by KOH etch pitting (17) and transmission cathodoluminescence (TCL) (18). A dislocation network was found to surround each pyramid initially. During aging, $\langle 110 \rangle$ DLD's develop from these networks. In the pyramid-free LED's, $\langle 110 \rangle$ DLD's initiate at processing damage and at high stress points (e.g., edges and corners) on the p-surface. To determine whether bonding stress or internal stress is responsible for the growth of the DLD's, a defect study was made of similar unbonded LED's aged at 200°C without current bias. Finally, a high dislocation density ($\sim 10^5$ cm⁻²) and stacking faults were found in the degraded devices. This result suggests that the susceptibility of the pyramid-free LED's to stress-induced DLD's may be simply due to a high dislocation density or to the presence of stacking faults. Low and high defect density GaAlAs:Si LED's fabricated from a wafer without pyramids on the p-surface were then tested. High reliability was found for the LED's irrespective of the defect density. The degradation of these LED's did not involve the formation of DLD's. These experiments and results are summarized in Table I. The remainder of this paper comprise the details of this study.

Experimental

Device characteristics.—The GaAlAs:Si LED's were grown by a single-step liquid phase epitaxy (LPE) technique as described by Dawson (1). A schematic of the LED structure is presented in Fig. 1. An epitaxial layer of ~ 200 μ m thickness is grown on a $\langle 100 \rangle$ oriented GaAs substrate. The aluminum content of this

Table I.

| Experiment | Analysis technique | Results |
|--|--|--|
| 1. Material evaluation | Nomarski interference microscopy Secondary electron imaging in SEM TCL KOH etch pitting X-ray microanalysis on SEM | Pyramids on p-surface Dicing damage Etch used to remove dicing damage removes more of the n-layer 10^5 dislocation/cm ² Stacking faults Dislocation network surrounding pyramids Pyramids consist mainly of silicon |
| 2. Reliability of bonded LED's with pyramids | Aging at 200°C, 0 mA Electroluminescence imaging TCL of p-surface TCL of LED side | MTTF ≤ 400 hr DLD's observed for $\eta/\eta_0 \leq 0.1$ DLD's initiate from dislocation networks surrounding pyramids DLD's propagate on $\{111\}$ planes and terminate at p-n junction |
| 3. Reliability of unbonded LED's with pyramids | Aging at 200°C, 0 mA Electroluminescence imaging TCL | Aging time = 10^8 hr No DLD's No change in dislocation networks surrounding pyramids |
| 4. Reliability of pyramid-free bonded LED's from wafer with pyramids | Aging at 200°C, 0 mA Electroluminescence imaging TCL of p-surface TCL of LED side | MTTF $\leq 10^8$ hr DLD's observed for $\eta/\eta_0 < 0.1$ DLD's initiate from dicing damage and high stress points on p-surface DLD's propagate on $\{111\}$ planes and terminate at p-n junction |
| 5. Reliability of bonded LED's from pyramid-free wafer | Aging at 250°C, 30 mA, 5-15 dislocations/LED Aging at 250°C, 30 mA, 20-40 dislocations/LED and stacking faults TCL of p-surface | MTTF $\sim 10^5$ hr MTTF $\sim 10^5$ hr LED's do not degrade by DLD formation Dislocations and stacking faults not sources of DLD's |

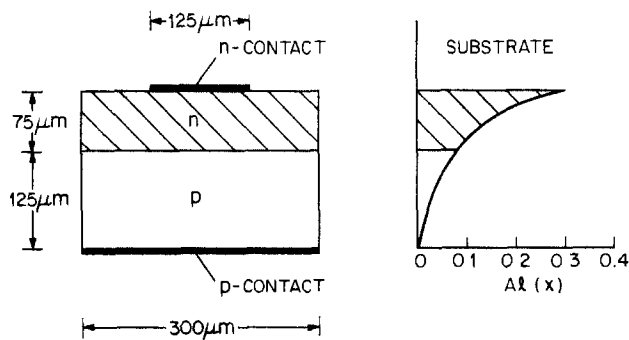


Fig. 1. Schematic of GaAlAs:Si LED

layer varies from an initial value of $x \sim 0.30$ to a final value of $x \sim 0.0$. The p-n junction is formed by Si amphoteric doping; the aluminum concentration is $x \sim 0.08$ at this junction which is located $\sim 75 \mu\text{m}$ from the substrate-epilayer interface. After epi-growth, the GaAs substrate is chemically removed from the LPE layer, contacts are evaporated, and the wafer is diced into $300 \times 300 \mu\text{m}$ square diodes. The p-surface receives a full surface metallization of 1% BeAu alloy whereas the n-contact consists of a $125 \mu\text{m}$ diam dot of SnAu. To minimize dicing damage, the saw cuts are aligned along the $\langle 100 \rangle$ directions (45° from the $\langle 110 \rangle$ cleavage directions) and then etched to remove the sawing damage. The etch consists of 30% H_2O_2 whose pH is adjusted to 8.4 by the addition of NH_4OH (1). The devices are bonded with epoxy with the p-surface toward the header so that the higher aluminum content, i.e., higher bandgap, n-layer forms a window for the light emitted at the p-n junction. The typical operating condition is 10 mA forward current, corresponding to a current density of $J \sim 10 \text{ A/cm}^2$.

Material evaluation technique.—As noted above the material quality of degraded and undegraded devices was assessed using KOH etch pitting (17) and transmission cathodoluminescence (TCL) (18). Dislocations appear as dark spots in the TCL image due to nonradiative recombination. An exact one-to-one correspondence between dislocation pits produced by the KOH etch and dark spots in TCL images of the $\{100\}$ surface of GaAlAs:Si has been previously established (18). For most of the study the TCL technique was used since etch pitting of small devices is difficult.

Both etching and TCL require removal of the LED from the header used for aging and testing. Other techniques for detecting material defects, e.g., cathodoluminescence (CL) and electron beam induced current (EBIC), that do not require demounting of the LED, were tried unsuccessfully. Although mechanical damage appears as a dark region in TCL, CL, and EBIC images, grown-in dislocations and DLD's are apparent only in the TCL images (19, 20).

For TCL measurements, the devices were carefully demounted from the TO-18 headers by softening the bonding epoxy with heat ($T \sim 300^\circ\text{C}$) applied to the header. The residual epoxy was removed using an oxygen plasma. The contact metallization was chemically stripped with a solution of 450g KI, 150g I_2 , and 400 ml H_2O . Since the contact is alloyed into the semiconductor and since the metallization etch mildly attacks GaAlAs, the etched surfaces are rougher than the as-grown surface. This surface is, however, sufficient for TCL imaging.

Material quality and degradation.—Figure 2 shows an electroluminescence image of a typical, rapidly degraded LED. The dark circle in the center is the n-contact. Several $\langle 110 \rangle$ oriented DLD's are observed. These dark lines are located at the p-n junction where the light is emitted. To determine the source of the DLD's, the degraded LED's were first visually in-

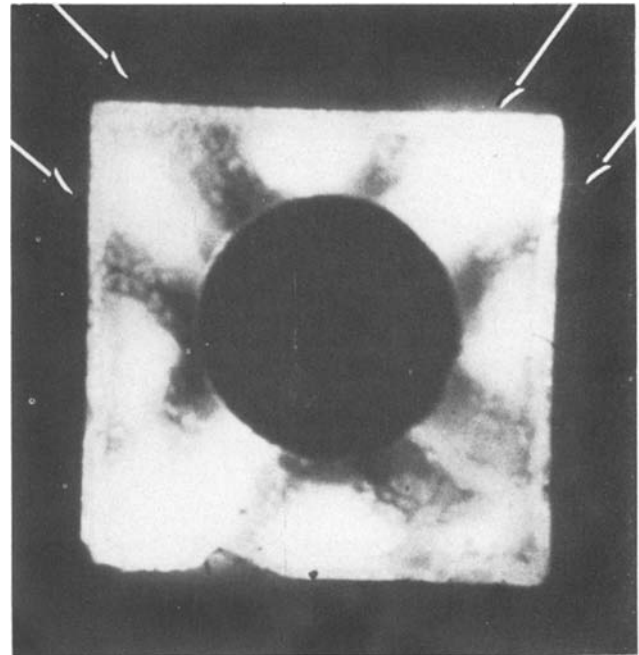


Fig. 2. Electroluminescence image of the n-surface of a degraded LED. The black dot in the center is the n-contact. The arrows indicate the $\langle 110 \rangle$ DLD's.

spected on the headers using the SEM and Nomarski interference microscopy. Some damage was found, but it was not considered unusual or excessive. After demounting the LED's, small pyramids of various sizes were found on the p-surface of some of the LED's. Figure 3a is a secondary electron (SE) image of an unaged LED with several pyramids. X-ray microanalysis on an SEM showed that these pyramids are composed mainly of silicon (21).

Figure 3b is the TCL image of the region shown in Fig. 3a. The pyramids appear dark due to the low luminescence efficiency of these regions. In addition to dark regions, dark lines extending from the pyramids along the $\langle 110 \rangle$ directions are observed. These dark regions and lines are part of a dislocation network and have no corresponding features in the SE image of Fig. 3a. These dislocation networks are probably a result of lattice mismatch between the GaAlAs epilayer and the Si pyramid. Using the KOH defect etchant (17), these dislocation networks are also revealed. The surface of a wafer, examined with Nomarski interference microscopy before and after etching, is shown in Fig. 4a and 4b. A comparison of the two figures shows that the pyramids have been etched away by the KOH. The dislocation network surrounding the pyramids appears as a rectangular region containing a high density of etch pits. The $\langle 110 \rangle$ dark lines appear as a series of pits after KOH etching.

Figures 5a and 5b are, respectively, the SE and TCL images of the p-surface of typical degraded, bonded LED's. Although Fig. 3 and 5 correspond to two different LED's, comparison of these figures shows clearly that with aging the dislocation networks originating at the pyramids enlarge along the $\langle 110 \rangle$ directions and form $\langle 110 \rangle$ DLD's. A similar study of unbonded LED's was performed to determine whether bonding stress or internal strain was responsible for the growth of the DLD's. The TCL images of the aged, unbonded LED's were similar to Fig. 3b. No noticeable growth of the dislocation networks was found. It is thus concluded that bonding stresses applied to the pyramids is one source of DLD's. These stresses include those that result from the differences in the thermal expansion coefficient of the LED, header, and bonding material.

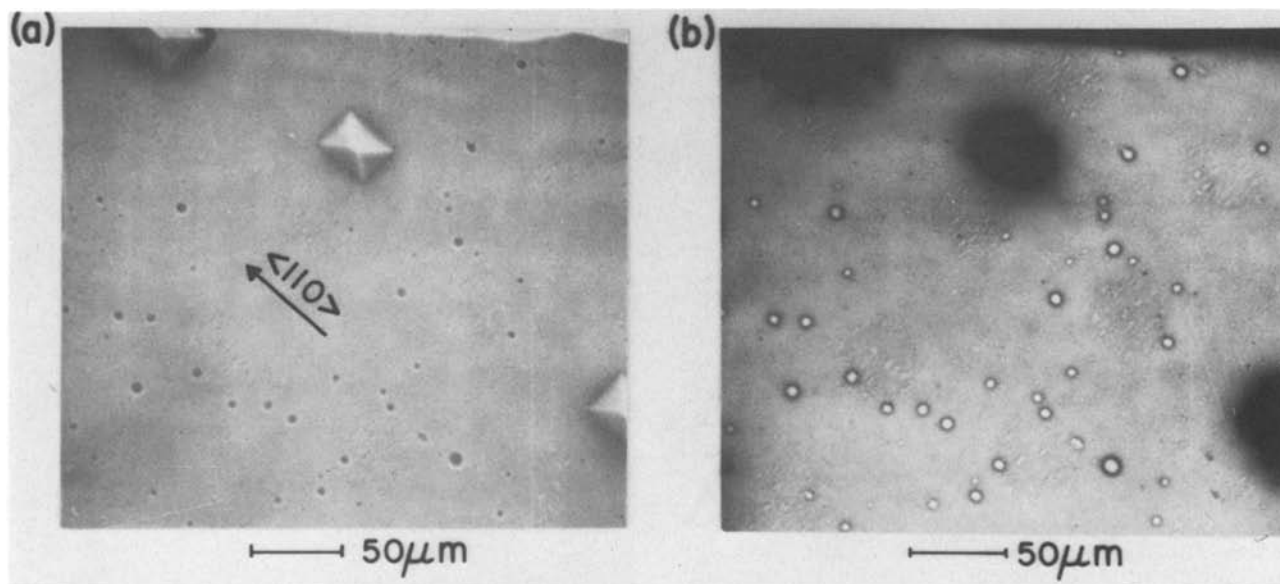


Fig. 3. a. Secondary electron image of the p-surface of an unaged LED with pyramids. The sides of the pyramids are parallel to the $\langle 110 \rangle$ directions. b. TCL image of the region in Fig. 3a. The dark area surrounding each pyramid is a dislocation network. The short dark lines are dislocations extending along the $\langle 110 \rangle$ directions.

Bonded devices without pyramids selected from the same wafer as the LED's in Fig. 3 and 5 were also found to degrade although at a slower rate (4). After 10^3 hr at 200°C without current bias, the efficiency is generally reduced to $\lesssim 0.1$ of its initial efficiency. As in diodes with pyramids, $\langle 110 \rangle$ DLD's were observed in the electroluminescence image only after the efficiency had fallen below $\lesssim 0.1$ of its initial efficiency.

TCL examination shows $\langle 110 \rangle$ DLD's initiating at dicing damage and high stress points, e.g., edges and corners, on the p-surface. Typical DLD's are shown in Fig. 6. Dicing damage is visible in the SE image of Fig. 6a; DLD's extending from the dicing damage are visible in the TCL image of Fig. 6b. These DLD's are found in the TCL image of all aged LED's examined, even those that do not show DLD's in the electroluminescence image. Although similar damage was found

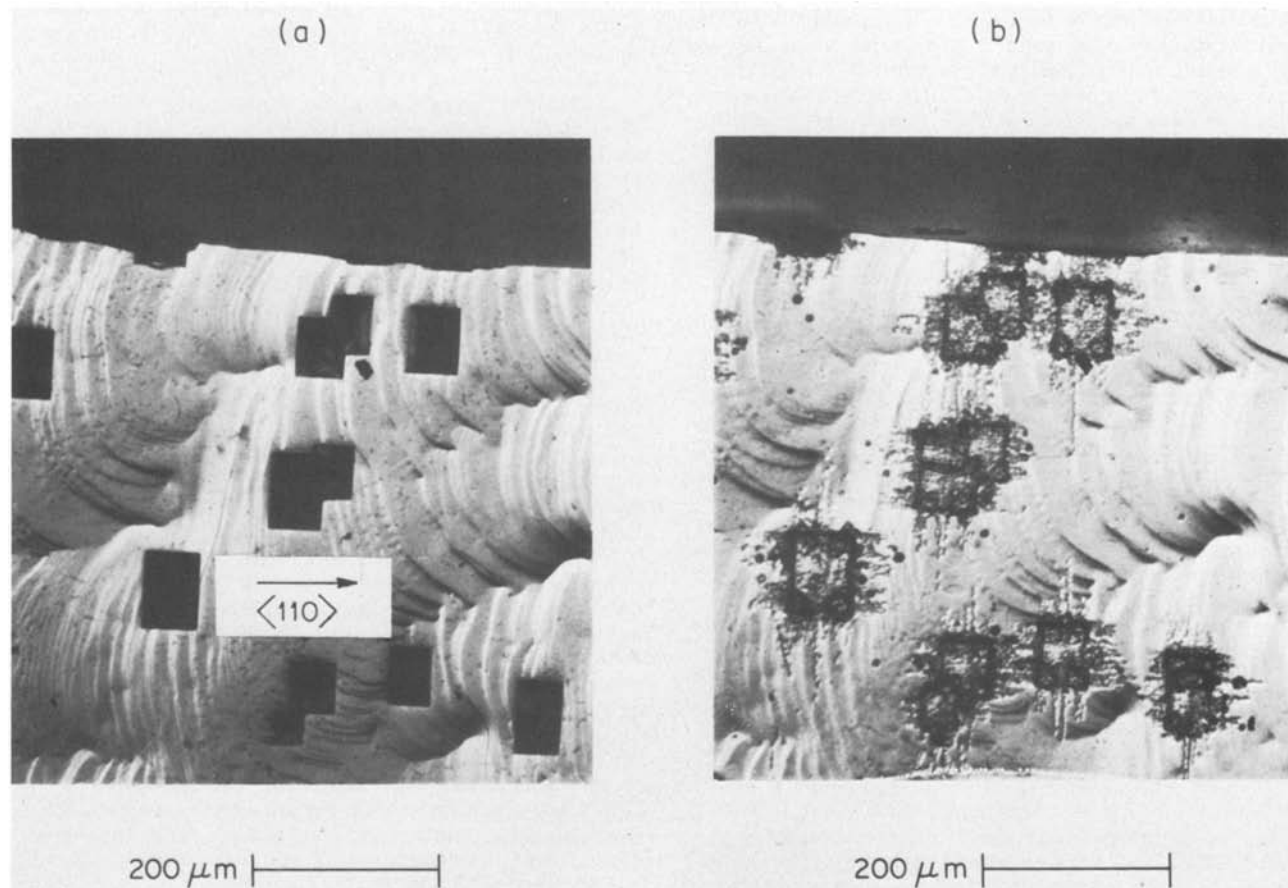


Fig. 4. a. Region of p-surface containing pyramids. b. Region of p-surface after etching in KOH. The pyramids have been removed by the etch and a high density of etch pits is observed beneath the pyramid (rectangular regions of pits). Linear arrays of pits extend along the $\langle 110 \rangle$ directions.

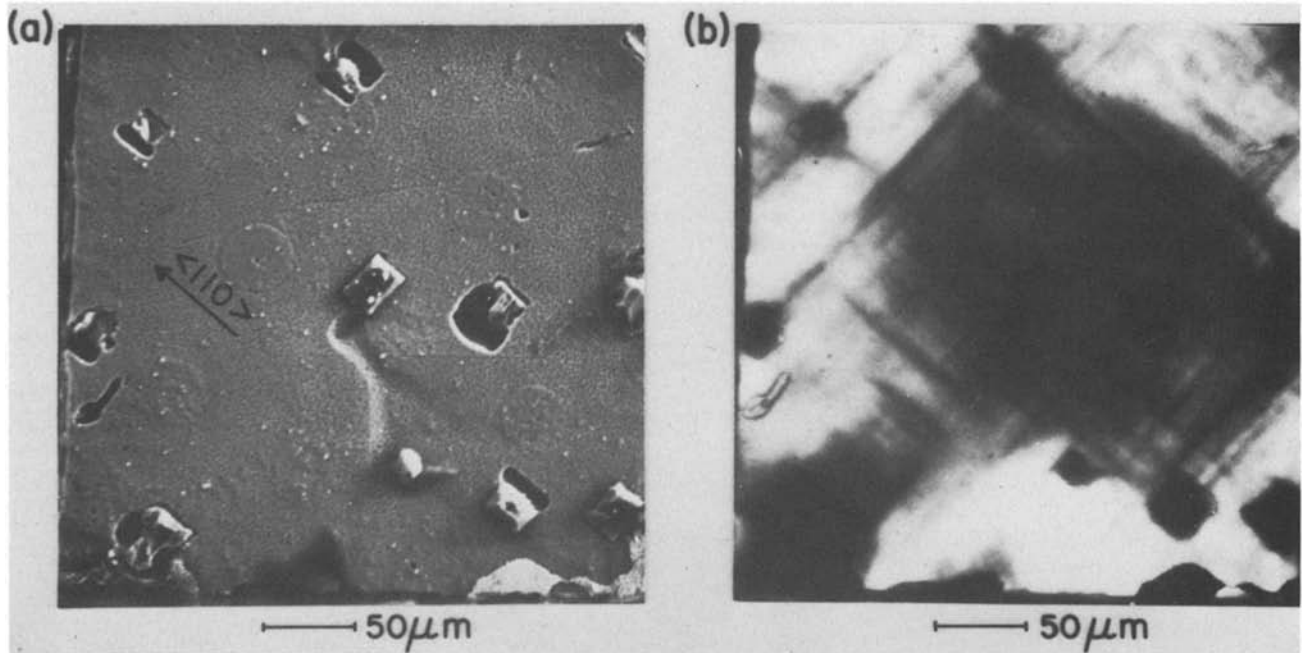


Fig. 5. a. SE image of the p-surface of a degraded LED with pyramids. b. TCL image of region in Fig. 5a. $\langle 110 \rangle$ DLD's initiate at the pyramids.

in unaged devices, only dark regions and not dark lines were associated with them. It will be shown below that the susceptibility to DLD formation is peculiar to the device wafers with silicon pyramids.

DLD growth behavior.—The study in the above section concentrated on the p-surface due to the presence of pyramids there. To determine whether the DLD's originate only on the p-surface, the top n-surface and

(100) sides of the LED's need to be examined. In unaged devices, the usual dislocations, stacking faults, and processing damage were found on these surfaces. In degraded devices, TCL images of the n-surface were similar to those of unaged LED's, but $\langle 110 \rangle$ DLD's were found on the sides. By examining the sides of partially and highly degraded LED's, the DLD's were found to initiate at the p-surface and propagate

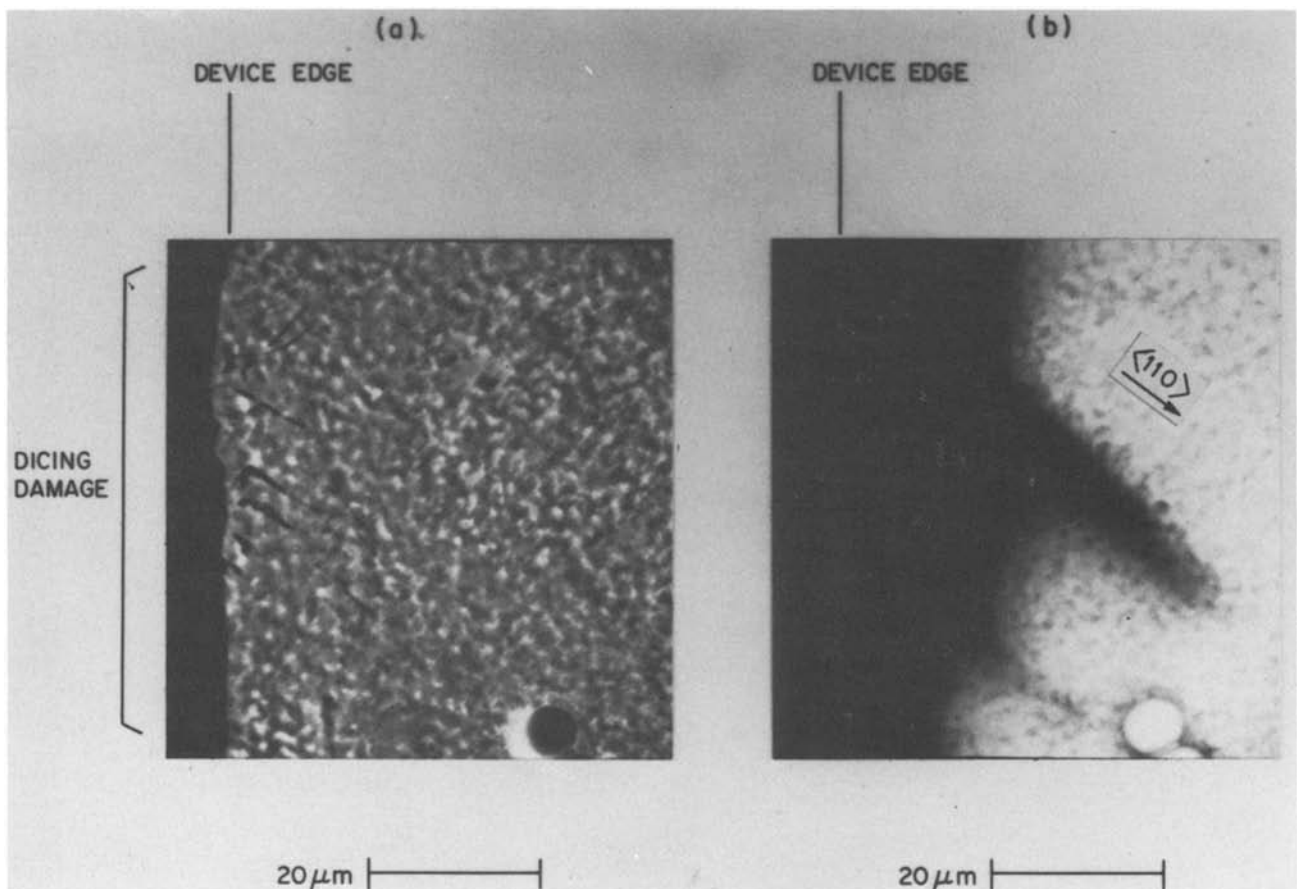


Fig. 6. a. SE image of the p-surface of an LED showing dicing damage along an edge. b. TCL image of the region in Fig. 6a. $\langle 110 \rangle$ DLD's initiate at the damage.

toward the p-n junction; the DLD's did not extend beyond the p-n junction into the n-region even in the most heavily degraded LED's ($\eta/\eta_0 < 0.01$).

SE and TCL images of the {100} side of a partially degraded LED are shown in Fig. 7. The SE image shows that the etch used to remove dicing damage removes more of the n-layer. The p-n junction appears as a dark line in the TCL image since the built-in electric field separates the electron-hole pairs generated by the electron beam and prevents recombination (22). The n-layer is brighter than the p-layer due to higher intrinsic luminescence efficiency rather than a result of degradation. DLD's were not observed in the electroluminescence image although the luminescence efficiency was 0.62 of its initial efficiency. However, DLD's were found by TCL imaging of the p-surface and the sides. The DLD's initiate at dicing damage on the p-surface and extend up the side as shown in Fig. 7b. The DLD's intersect the {100} p-surface at an angle of 45° , suggesting that the DLD's lie on the {111} slip planes.

Figures 8a and 8b are the SE and the TCL image of the {100} sides of heavily degraded LED. After aging, this {100} side was ground with $3\ \mu\text{m}$ alumina grit and etched in Br/methanol to observe the p-n junction clearly. The efficiency was $\lesssim 0.01$ of the initial value; DLD's were observed in the electroluminescence image. As shown in Fig. 8b, the DLD's propagate up to the p-n junction, but do not penetrate into the n-layer.

Similar examination of LED's with various degrees of degradation shows that the DLD's always initiate at the p-surface and propagate toward the p-n junction.

The DLD's stop their growth upon reaching the p-n junction probably due to lower stress in the n-layer. Since the etch used to remove the saw damage removes more of the n-layer than the p-layer, the n-layer may have a lower surface damage induced stress. A high internal electric field at the p-n junction is unlikely to hinder the propagation of the DLD's. Similar stress-induced $\langle 110 \rangle$ DLD's in GaAs/GaAlAs wafers have been shown to propagate through the p-n junction (23). Further study, e.g., an examination of degraded LED's using transmission electron microscopy or a reliability study of LED's that have been etched more uniformly, is required to determine the exact cause of this effect. Such studies are beyond the scope of this work.

Degradation of high and low defect density LED's.— During evaluation of device wafers with pyramids, a high dislocation density (up to $\sim 10^5\ \text{cm}^{-2}$, ~ 100 dislocations/LED) and stacking faults were found. Additionally, the dislocation networks beneath the pyramids were resolved as individual dislocations or parts of dislocation loops even after 50–100 μm of material have been chemically etched from the p-layer. The susceptibility of the pyramid-free LED's to DLD formation was thus possibly a result of a high defect density. To investigate the influence of such defects, a separate set of LED's from a wafer completely free of

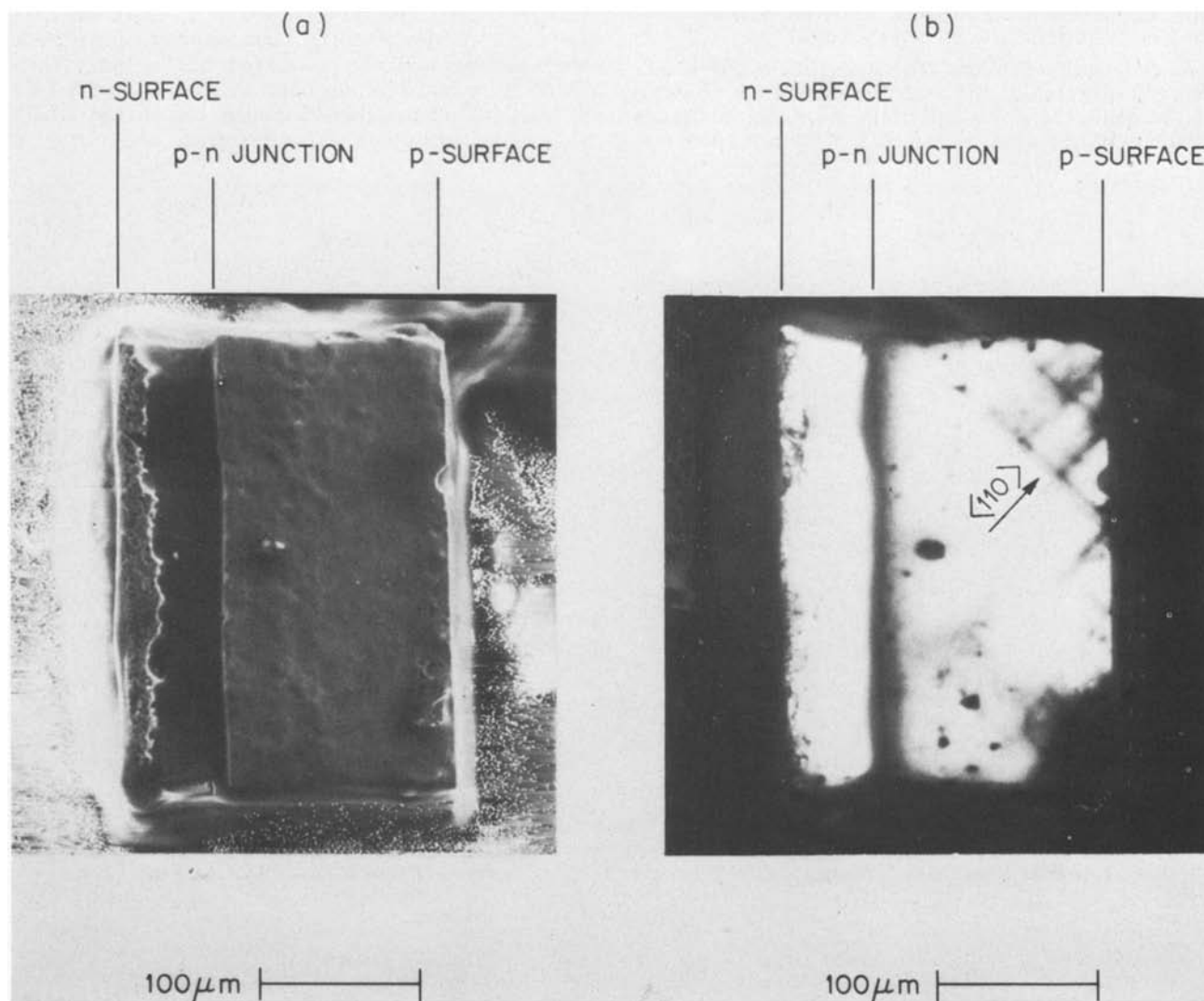


Fig. 7. a. SE image of {100} side of a partially degraded ($\eta/\eta_0 = 0.62$) LED. b. TCL image of the region in Fig. 7a. $\langle 110 \rangle$ DLD's initiate at the p-surface and propagate along the {111} planes toward the p-n junction.

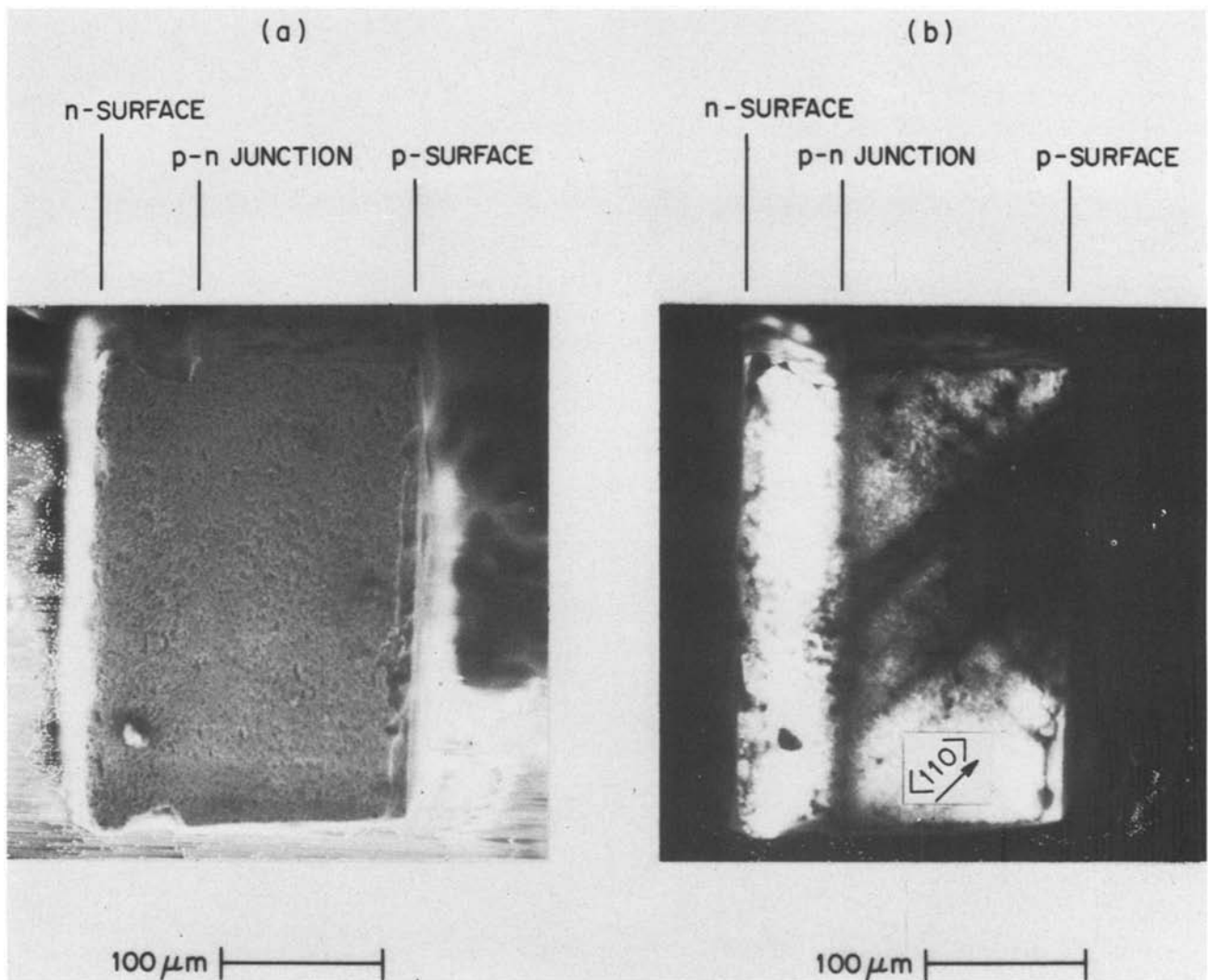


Fig. 8. a. SE image of the $\{100\}$ side of a heavily degraded ($\eta/\eta_0 = 0.01$) LED. The surface has been ground and etched. b. TCL image of the region in Fig. 8a. $\langle 110 \rangle$ DLD's initiate at the p-surface, propagate along the $\{111\}$ planes toward the p-n junction, and terminate at the p-n junction.

pyramids was separated into a group containing a high defect density (stacking faults and 20-40 dislocations/LED) and a group containing a low defect density (5-15 dislocations/LED). The two groups were then tested in the usual fashion (250°C, 30 mA forward bias).

The defect density of each diode was determined in the following manner. The surface of the device wafer was Br/methanol polished to provide a smooth surface; $\sim 25 \mu\text{m}$ of material was removed. Saw cuts, $25 \mu\text{m}$ deep, were made into the wafer to define the locations of the LED's. The p-surface of each LED was imaged using TCL to determine the defect content. After processing, the wafer was diced along the original saw marks. The LED's were demounted from the cutting block and individually etched to preserve their identity.

The results of the reliability study on these LED's are plotted in Fig. 9. The average efficiency of each group is plotted vs. the square root of time in hours; each group contains 10 LED's. Essentially, the results show that the defect density of the devices from a wafer free of pyramids has little or no effect on the reliability. From the data in Fig. 9, an MTTF of $\geq 10^5$ hr at 250°C with 30 mA forward current is estimated for both high and low defect density LED's. These values of MTTF are similar to those found by Dawson (1). No catastrophic degradation was observed in any of the devices, and no DLD's were observed in the

electroluminescence image after the ~ 4000 hr of operation.

Ten of the LED's were demounted and examined using TCL. In general, some additional dark spots developed during aging, but short ($\leq 25 \mu\text{m}$), dark lines were found only in one of the devices. These dark lines were present at the edge of the LED on the p-surface as shown in Fig. 10. Figures 10a and 10b are the SE and TCL images, respectively. Two $\langle 110 \rangle$ DLD's and

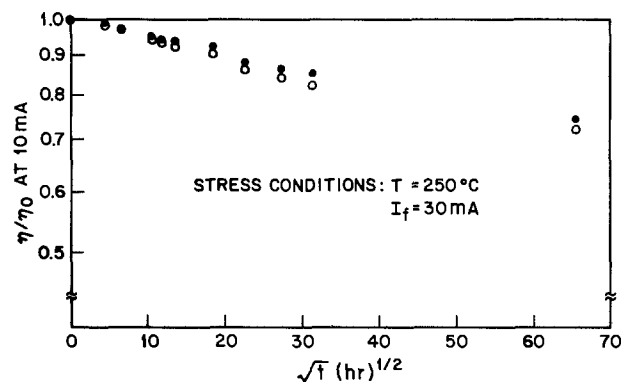


Fig. 9. Normalized efficiency vs. \sqrt{t} for two sets of LED's. LED's in set 1 (dots) contain stacking faults and 20-40 dislocations. LED's in set 2 (open circles) contain 5-15 dislocations.

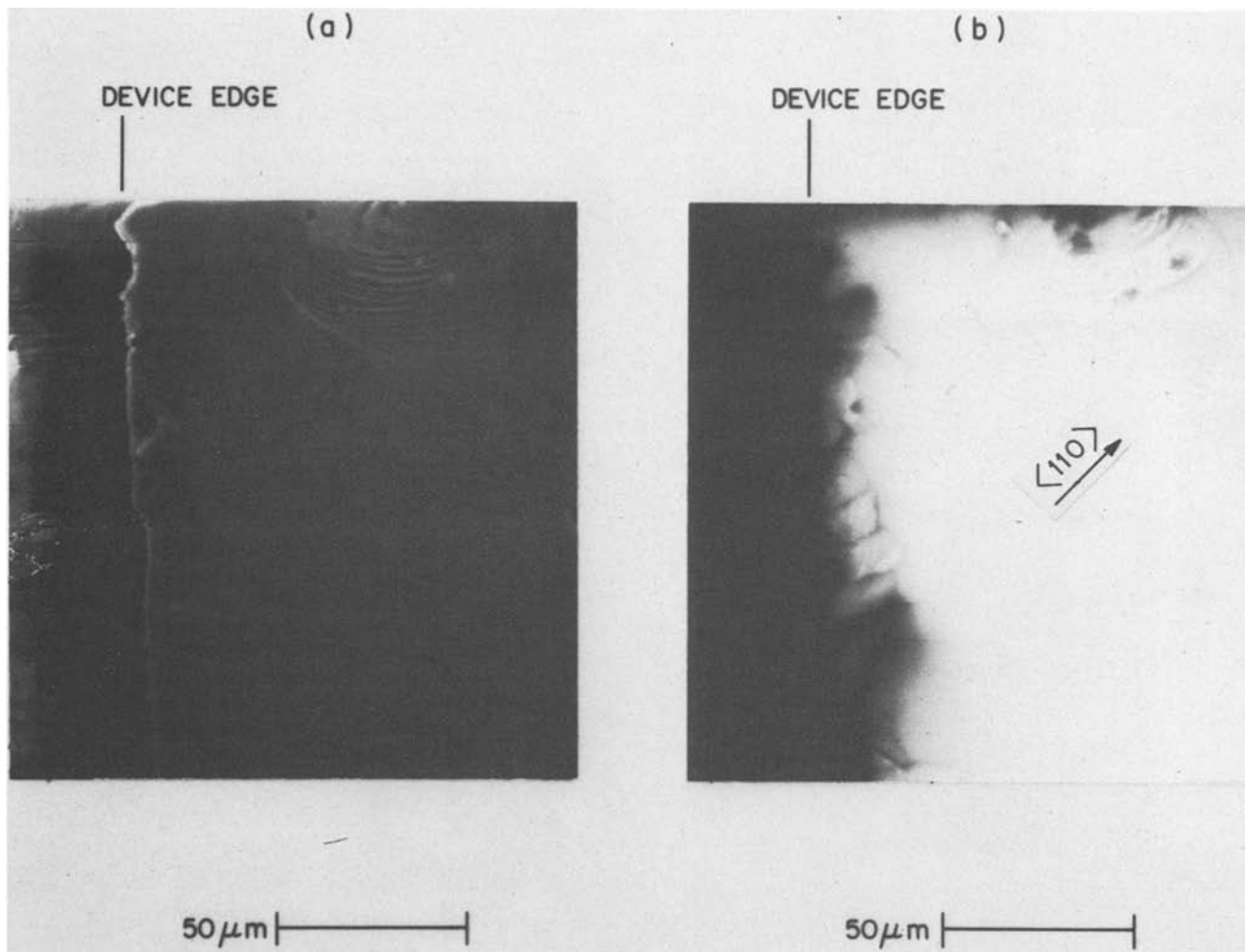


Fig. 10. a. SE image of the p-surface of an LED aged for 4000 hr at 250°C and $I_f = 30$ mA. b. TCL image of region in Fig. 10a. Two $\langle 110 \rangle$ DLD's and one $\langle 100 \rangle$ DLD are apparent at the device edge.

one $\langle 100 \rangle$ DLD are observed in Fig. 10b. The presence of this $\langle 100 \rangle$ DLD is unusual and suggests that these DLD's are not stress induced (11-13).

Summary and Conclusions

The present results show that GaAlAs:Si LED's fabricated from wafers with Si pyramids on the p-surface are prone to stress-induced $\langle 110 \rangle$ DLD formation. The origin of the silicon pyramids is not presently known and requires further study. Two sources of DLD's were found. First, a dislocation network was shown to initially surround the pyramids. These networks with the addition of bonding and thermal stresses extended on $\{111\}$ planes toward the p-n junction. When they reached the p-n junction they were observed in the electroluminescence image. No DLD's were found in the n-layer. The etch used to remove dicing damage removes more of the n-layer and thus reduces the associated stress.

An internal stress of $2-7 \times 10^7$ dynes/cm² due to dicing damage was found by Hirahara *et al.* (16) in GaP LED's; this stress was sufficient to enhance the degradation rate of such devices. A similar stress is probably present in the GaAlAs:Si LED's. At room temperature, it is known that a threshold stress level of 8×10^9 dynes/cm² produces $\langle 110 \rangle$ DLD's in GaAlAs/GaAs double heterostructure crystals (7). This threshold level is probably greatly reduced for the GaAlAs:Si LED's at 200°C and the presence or absence of internal stress may cause the total strain to either exceed or be below the threshold required for stress-induced DLD's. Additionally, DLD's on devices selected from pyramid-free regions of the wafer with pyramids were found to initiate at mechanical

damage or high stress points of the p-surface. The DLD growth proceeded as in devices with pyramids, but at a slower rate. Since LED's from pyramid-free wafers do not degrade by DLD formation, the presence of pyramids indicates a material problem. A high density of precipitates, unresolved either by KOH etching or TCL, may be present in wafers with pyramids.

The susceptibility of the LED's from wafers with pyramids to stress-induced DLD's was shown not to be a result of a high dislocation density or the presence of stacking faults. The tests used to determine the influence of such defects showed that the reliability of normal GaAlAs:Si LED's seems to be relatively independent of the diode defect density. Examination of normal LED's operated at 250°C, and 30 mA forward bias for 4000 hr shows that the degradation mechanism is not DLD formation.

Acknowledgments

We wish to thank H. Temkin for aging the LED's and for helpful discussions, E. Lassiter for mounting and demounting the LED's, D. D. Roccasecca for some device processing, K. B. Bauer for electroluminescence imaging, S. Jabbar for supplying some of the LED's, and O. G. Lorimor and R. H. Saul for helpful discussions.

Manuscript submitted Aug. 22, 1980; revised manuscript received Oct. 21, 1980. This was Paper 515 presented at the Hollywood, Florida, Meeting of the Society, Oct. 5-10, 1980.

Any discussion of this paper will appear in a Discussion Section to be published in the December 1981 JOURNAL. All discussions for the December 1981 Discussion Section should be submitted by Aug. 1, 1981.

Publication costs of this article were assisted by Bell Laboratories.

REFERENCES

1. L. R. Dawson, *J. Appl. Phys.*, **48**, 2485 (1977).
2. J. S. Jayson and S. Knight, *Appl. Solid State Sci.*, **6**, 119 (1976).
3. C. L. Zipfel, Unpublished.
4. W. C. King, Unpublished.
5. M. Iwamoto and A. Kasami, *Appl. Phys. Lett.*, **28**, 591 (1976).
6. S. Kishino, N. Chinone, H. Nakashima, and R. Ito, *ibid.*, **29**, 488 (1976).
7. H. Nakashima, S. Kishino, N. Chinone, and R. Ito, *J. Appl. Phys.*, **48**, 2771 (1977).
8. G. Zaeschmar and R. S. Speer, *ibid.*, **50**, 5686 (1979).
9. K. Ishida, T. Kamejima, and J. Matsui, *Appl. Phys. Lett.*, **31**, 397 (1977).
10. T. Kamejima, K. Ishida, and J. Matsui, *Jpn. J. Appl. Phys.*, **16**, 233 (1977).
11. P. W. Hutchinson and P. S. Dobson, *Philos. Mag.*, **32**, 745 (1975).
12. P. Petroff and R. L. Hartman, *Appl. Phys. Lett.*, **23**, 469 (1973).
13. P. Petroff and R. L. Hartman, *J. Appl. Phys.*, **45**, 3899 (1974).
14. N. Shimano, *Jpn. J. Appl. Phys.*, **17**, 1323 (1978).
15. N. Shimano, Y. Kawai, and M. Sakuta, *J. Appl. Phys.*, **51**, 1227 (1980).
16. K. Hirahara, Y. Iizuka, T. Beppu, and A. Kasami, 3rd IEEE Specialist Conference on the Technology of Electroluminescent Diodes, Session B1 (1978).
17. J. G. Grabmaier and C. B. Watson, *Phys. Status Solidi.*, **32**, K13 (1969).
18. A. K. Chin, H. Temkin, and R. J. Roedel, *Appl. Phys. Lett.*, **34**, 476 (1979).
19. R. J. Roedel, A. R. Von Neida, R. Caruso, and L. R. Dawson, *This Journal*, **126**, 637 (1979).
20. A. K. Chin, V. G. Keramidias, W. D. Johnston, Jr., S. Mahajan, and D. D. Roccasecca, *J. Appl. Phys.*, **51**, 978 (1980).
21. F. Ermanis, Unpublished.
22. D. B. Wittry and D. F. Kyser, *J. Appl. Phys.*, **36**, 1387 (1965).
23. K. Ikeda, T. Tanaka, M. Ishii, and A. Ito, *GaAs Relat. Comps.*, **24**, 174 (1974).

The Properties of Iron in Silicon

K. Graff and H. Pieper

AEG-Telefunken, Serienprodukte AG, Semiconductor Division, D-7100 Heilbronn, West Germany

ABSTRACT

The properties of iron in n-type and p-type silicon were studied by means of DLTS, carrier lifetime measurements, and infrared absorption spectroscopy. Only one donor level was observed, situated at $E_v + 0.43$ eV and correlated to iron on an interstitial site. In p-Si:B iron-boron pairs were formed at room temperature. Their activation energy was determined to be $E_v + 0.10$ eV. The reaction proceeded in two phases. In the second phase a thermal equilibrium between iron and iron-boron pairs was found which could be shifted by annealing and illuminating the specimen, respectively. In aluminum-doped silicon crystals two levels were observed after iron diffusion correlated to iron-aluminum pairs. Their activation energies were determined to be $E_v + 0.21$ and 0.13 eV. It is assumed that iron-boron pairs form also two levels, a donor and an acceptor. The acceptor must be situated in the upper half of the silicon bandgap. Reaction mechanisms are discussed.

Iron is one of the main heavy metal impurities in silicon devices. Because of its considerable high solubility and fast diffusion at high temperature iron is easily introduced into silicon crystals during heat-treatments. Hence it has been detected even after presumably clean annealing and quenching processes (1-3).

First investigations on the behavior of iron in silicon were carried out in the fifties and early sixties applying radiotracer techniques, resistivity measurements, and ESR spectroscopy (4-7). The fundamental knowledge about the properties of iron in silicon are based on these results: after quenching iron-doped specimens from high temperature iron forms a deep donor level at $E_v + 0.4$ eV which is paramagnetic in neutral state and detectable by ESR as iron on an interstitial site. This interstitial iron reacts with shallow acceptors such as B, Al, Ga, and In even at room temperature forming pairs which are oriented in $\langle 111 \rangle$ -direction with the exception of FeIn showing $\langle 100 \rangle$ -symmetry. These pairs dissociate during annealing at moderate temperatures and finally iron precipitates at somewhat higher temperature (100°-200°C).

Recently an increasing number of papers concerning the properties of iron in silicon was published showing a growing interest in this subject. This may

be due to further increasing requirements to device performance accompanied by the development of improved measurement techniques including Deep-Level-Tansient-Spectroscopy (DLTS) (8), Mössbauer-spectroscopy, and neutron activation analysis of higher sensitivity (9). On the other hand, investigations on thermally induced donors resulted in a correlation of these defects to electrically active iron impurities (2, 10-12). Most of the publications show, however, a wide spread in results as shown in Fig. 1. Various experimentally determined activation energies of iron in silicon are scaled in the bandgap of silicon (2, 5, 7, 11, 13-23). The histogram deduced from these values at the right side of the figure shows a peak at $E_v + 0.42$ eV and a second broader one at $E_c - 0.60$ eV. The spread of values can be caused by (i) additional undesired impurities introduced especially during extended treatments of the specimens at high temperatures, (ii) iron reactions with dopant atoms or other impurities, and (iii) precision of differing method for the determination of the activation energy (resistivity, photoconductivity, Hall-measurements, and DLTS).

In order to avoid systematic errors, more sophisticated experiments were carried out in the present study, regarding specifications of the silicon crystals and utmost cleanliness of specimen preparation and heat-treatment. The undesired introduction of additional impurities was checked and the concentrations

Key words: iron-boron pairs, iron-aluminum pairs, room temperature impurity reactions, haze.

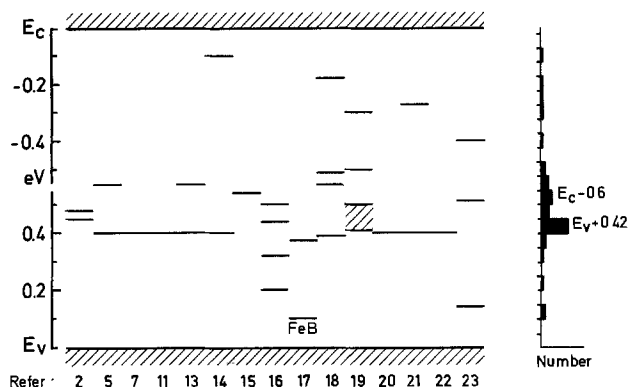


Fig. 1. Activation energies of iron in silicon as published in the literature and histogram deduced from these results.

of defect levels were monitored. The reaction mechanism of iron in p-type silicon was studied by observing variations of the levels as a function of time elapsed after quenching the specimen. This paper shall contribute to clarify the properties of iron in silicon taking into account results obtained by the following measurement techniques: four-point probe, DLTS, carrier lifetime measurements, infrared absorption, and Sirtl-etch technique.

Experimental Procedure

Specimen preparation.—Iron doping experiments were performed on p-type and n-type silicon wafers with resistivities in the range 1–100 Ωcm . The crystals were grown dislocation-free by Czochralski and floating-zone techniques, respectively. Most of the crystals were free of swirl-defects.

Iron contamination was performed either by evaporation of iron onto the polished clean surface of the wafer or by scraping with a piece of iron wire on the rougher back side. Before scraping the iron wire was etched. This procedure, so far, seems to be the cleanest method to obtain intentional impurity contamination.

Diffusion of iron was carried out in an oven with silica tube and specimen holder. The silicon wafer was mounted on top of two oxidized silicon specimens preventing a direct contact of the wafer to the silica substrate holder. The atmosphere in the furnace tube consisted of oxygen or nitrogen. Some diffusions were performed in argon and hydrogen, respectively. High cooling rates were achieved by quenching the specimen in Diffilen, ethylene glycol, or liquid nitrogen. In order to achieve low cooling rates the power of the furnace was switched off.

After diffusion 50–100 μm were removed from both surfaces by etching the specimen in a mixture of nitric acid, hydrofluoric acid, and acetic acid. For applying DLTS, Schottky contacts 1 mm in diameter were evaporated using Pd for n-type and Ti or Mg for p-type silicon. Silicon specimens $2.5 \times 5 \times 25 \text{ mm}^3$ in size were used for the determination of the carrier lifetime. Ohmic contacts were prepared onto the two small opposite sites of these specimens by rubbing gallium onto the silicon surfaces.

Measurement techniques.—Several measurement techniques were applied in order to gain more information about the properties of iron in silicon. Usual Sirtl-etch technique revealed the distribution of iron after diffusing wafers containing iron scratches on the surface. Four-point probe measurements exhibited the degree of free-carrier compensation after diffusion of iron in p-type silicon. Measurements of the recombination lifetime of minority carriers were carried out by applying an improved photoconductive decay (PCD) technique as reported previously (24).

The reactions of iron with shallow acceptors boron and aluminum were studied by means of infrared ab-

sorption spectroscopy which enabled us to determine the concentration of boron and aluminum at low measurement temperatures. For this purpose a Perkin-Elmer 621 double-beam grating infrared spectrometer was used. Specimens $2 \times 2 \text{ cm}^2$ in size were cut from the wafers and cooled to about 25 K with the aid of a CTI Cryogenics refrigerator, which was mounted in the measurement beam. The boron concentration [B] was calculated from the absorption coefficient α of the main absorption band at 320 cm^{-1} applying the following calibration factor (25)

$$[B] = 3.5 \times 10^{13} \alpha \text{ cm}^{-3}$$

No absolute values were determined for the concentration of aluminum.

For deep-level analysis the improved double-correlation equipment (DDLTS) of Lefèvre and Schulz (26) was applied. Spectra were recorded during the cooling cycle of the refrigerator mentioned above. The specimen temperature was determined by means of a calibrated silicon diode. The Schottky diodes were usually supplied with a reverse bias of 5V. The first pulse of 5V resulted in a final reverse bias of zero volts. The second pulse was adjusted to 1V. Pulse durations of 70 μsec were used. An emission time of 1.42 msec was achieved by adjusting the correlator-windows at 1 and 2 msec, respectively. Most of the spectra were recorded between 310 and 50 K.

In order to determine the activation energy of an unknown defect level the temporal signal decay was studied for several fixed temperatures in the region of maximum DDLTS-signal. The decay curves were stored in 100 storage channels of a Waveform Eductor and the corresponding lifetime was determined with the aid of a digital voltmeter and a calculator. The activation energy finally resulted from the best fit of an Arrhenius plot.

Experimental Results

Intentionally iron-doped silicon.—Intentionally iron-doped n- and p-type silicon specimens exhibited no deep-level impurities in DLTS if slow cooling rates were applied after iron diffusion. Quenching n-type silicon specimens after iron diffusion resulted in two levels of minor concentrations in the upper half of the bandgap which, however, were not correlated to iron. They appear after any etching procedure showing a steeply decreasing concentration towards the bulk of the wafer.

Quenching p-type silicon specimens after diffusion of iron resulted in one strongly marked deep-level impurity with an activation energy of $E_v + 0.43 \text{ eV}$. This level was also observed in n-type silicon when light pulses were applied for discharging the defects. The same level was found in iron-doped p-type silicon specimens which were slowly cooled from 900°C for the first time, shortly annealed at 900°C for a second time, and finally quenched to room temperature. The concentration of this level depended on the diffusion temperature applied and to a minor extent on the atmosphere during annealing. A reducing atmosphere yielded somewhat higher final impurity content in the silicon crystal than an inert gas atmosphere or oxygen. The impurity concentration as a function of annealing temperature was found to be in good agreement with the solubility of interstitial iron as published by Weber and Riotte (ESR results) (1). After iron diffusion in p-type silicon the resistivity of the specimens increased more or less depending on its initial value and the respective iron concentration. At the same time the minority carrier lifetime was considerably reduced.

Room temperature reactions in boron-doped silicon.—In iron-doped p-type silicon crystals containing higher boron concentrations a second shallower impurity level was observed. Its activation energy was

determined to be $E_v + 0.10$ eV. This level was also obtained in high resistivity crystals after a certain period of time elapsed after quenching the specimen. The appearance of this shallower level was accompanied by the disappearance of the deeper level, the sum of both concentrations remaining constant. The time required for this transmutation of impurity levels was found to depend on the initial boron concentration of the starting material, being short for high concentrations and longer for low boron content. After an appropriate time the deep level disappeared completely in all specimens studied so far. Investigations were performed, however, in specimens where the boron concentration always exceeded the iron content in order to enable quantitative measurements by means of DLTS.

During this level transmutation no changes were observed neither in resistivity nor in carrier lifetime, both of which were compatible with the respective change in impurity concentration. Soon after quenching the iron-doped specimens the concentration of the boron acceptor was strongly reduced, as determined by means of infrared absorption spectroscopy. A further storage of this specimen at room temperature for several days resulted only in an additional minor reduction in boron concentration although the level transmutation in similar material took place within this period of time.

Reaction in aluminum-doped silicon.—Experiments performed on a p-type silicon crystal doped with boron and aluminum resulted in the formation of two further levels after a certain period of time elapsed after quenching the iron-doped specimen. The activation energies of these levels were determined to be $E_v + 0.13$ and $E_v + 0.21$ eV, respectively. Besides the disappearance of the boron acceptor, infrared absorption spectra showed a considerable reduction in the absorption bands correlated to the aluminum acceptor. These results are shown in Fig. 2. The concentration of the aluminum acceptor still decreased with the storage time of the specimen at room temperature. The two additional DLTS signals $E_v + 0.13$ and $E_v + 0.21$ eV correlated to aluminum increased in the same way with the elapsed time as the boron-correlated signal ($E_v + 0.10$ eV), whereas the deep level ($E_v + 0.43$ eV) decreased simultaneously as shown in Fig. 3.

Reactions during illumination of boron-doped silicon.—When the level transmutation in boron-doped p-type silicon was terminated, resulting in only one impurity level at $E_v + 0.10$ eV, the reaction could be

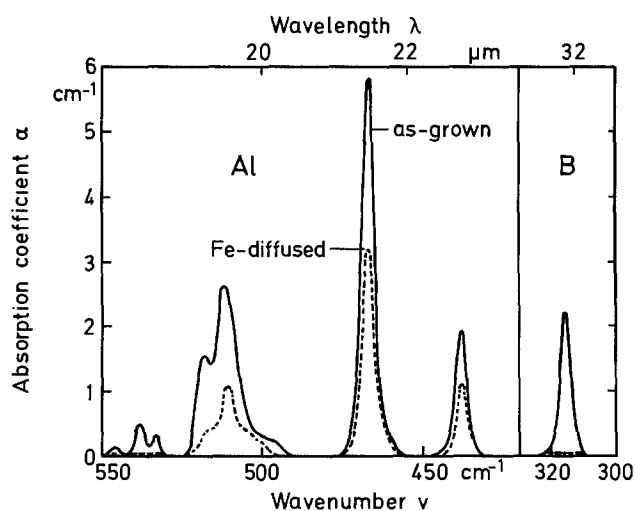


Fig. 2. Reduction of aluminum and boron infrared absorption bands due to complexing with iron observed at 25 K in a p-type silicon wafer doped with boron and aluminum before (solid curve) and after (dashed curve) iron diffusion.

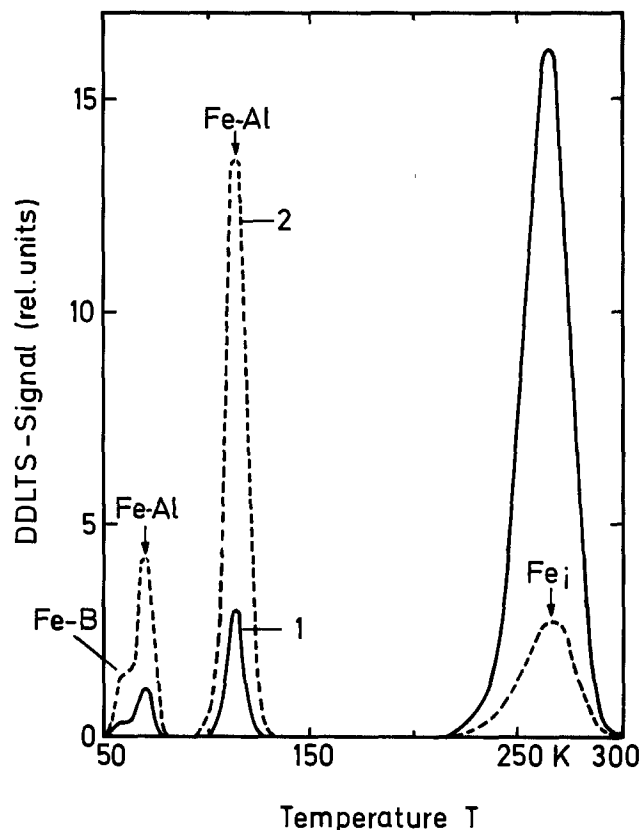


Fig. 3. Deep-level spectra after iron diffusion in a p-type silicon crystal doped with boron and aluminum at two different elapsed times (1: solid curve = initial, 2: dashed curve = final) after quenching of the specimen.

reversed in a rather short time by illuminating the specimen with intense white light. This was carried out by focusing the light of a 50W halogen lamp on the surface of the silicon specimen. The illuminated area amounted to about 0.5 cm in diameter. During illumination the specimen was kept at room temperature by mounting it on a heat sink which was cooled by the aid of compressed air. After illuminating the specimen for 1 hr Schottky contacts were evaporated again and deep levels were monitored. As in the initial state soon after quenching the specimen the impurity was concentrated in the 0.43 eV level. This is shown in Fig. 4. Similar results were obtained repeatedly in crystals of various specifications. Infrared absorption spectra showed an increase in boron concentration with the duration of the illumination. For the application of infrared absorption the illuminated area was considerably extended and the intensity of the light correspondingly reduced. After illumination was terminated the level transmutation from the deeper to the shallower one preceded as observed soon after quenching the specimen.

Annealing properties of boron-doped silicon.—During transmutation of the 0.43 eV level into the 0.10 eV level a storage of the iron-doped specimen at elevated temperature (100°C) was obviously of no influence. This is shown in Fig. 5 phase 1, where the ratio of the concentration of 0.10 eV level to the total concentration is plotted as function of storage time at 100°C . When, however, the transmutation was terminated (after about 10 days room temperature storage, phase 2) the ratio of the concentration of the shallow level to the total iron content proved to be dependent on the temperature resulting in a thermal equilibrium. This is shown in Fig. 5 and 6 as function of annealing duration at 100° and 130°C and temperature, respectively. At higher temperatures this equilibrium shifted to increasing deep level and vanishing shallow level.

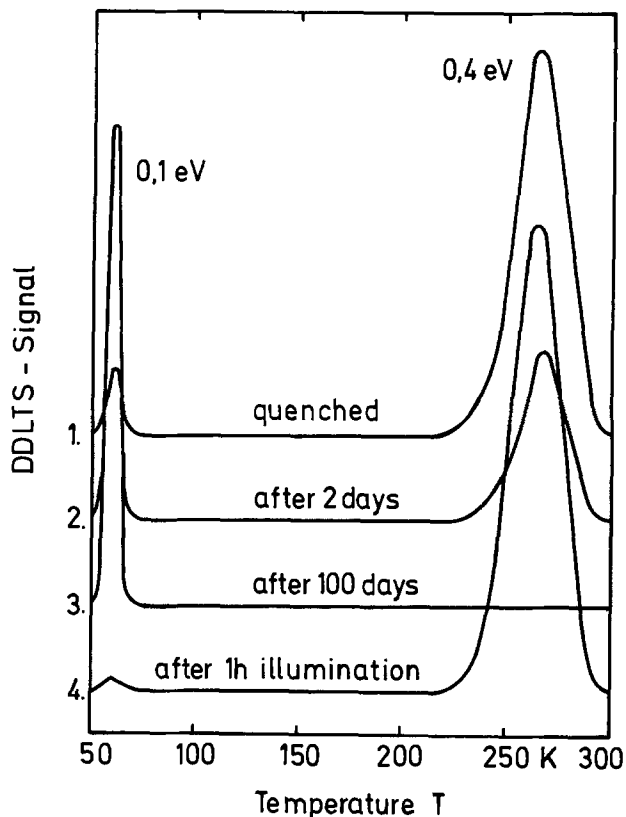


Fig. 4. Deep-level spectra after iron diffusion in boron-doped p-type silicon at three different elapsed times after quenching of the specimen and finally after illumination of the specimen.

Beyond about 150°C the total concentration of both levels decreased after extended annealing durations. This latter reaction was accelerated at higher temperatures. At the same time the boron (and aluminum) acceptor increased finally up to the initial value of the starting material as deduced from infrared absorption spectra and shown in Fig. 7. Simultaneously the resistivity of the specimen was restored. The electrical activity of the iron impurity could not be restored before a second treatment at high temperatures and quenching was performed.

Diffusion properties of iron.—Even during quenching iron-doped silicon wafers from high temperatures iron tends to diffuse to the surfaces of the specimen. This resulted in lower iron contents for shallow penetration depths. In order to obtain bulk values the sur-

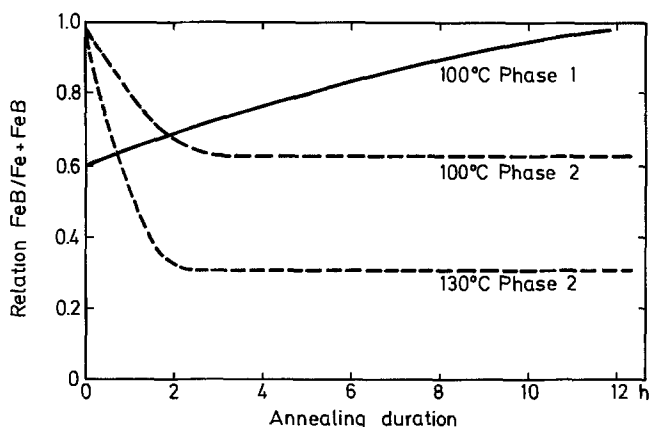


Fig. 5. Ratio of the concentration of the 0.10 eV level and the total iron content as function of storage time at elevated temperatures (100° and 130°C). Phase 1 (solid curve): soon after quenching the specimen, phase 2 (dashed curve): after completing complex formation about 10 days later.

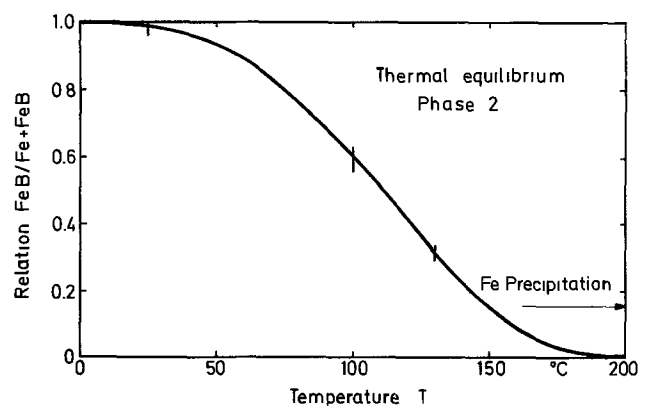


Fig. 6. Ratio of the concentration of the 0.10 eV level and the total iron content as function of storage temperature in phase 2.

faces were removed after heat-treatment. Moderately fast cooling rates after iron diffusion (within 5 min from 1050°C to room temperature) already resulted in the formation of precipitates which were detected by x-ray topography. Whereas the Lang-topography exhibited the area of distorted silicon lattice the section topography showed an accumulation of precipitates within the middle of the wafer. Towards both surfaces the density of precipitates was strongly reduced. The distribution of iron after diffusion was also detected by usual Sirtl-etching of the wafer showing an accumulation of shallow etch pits in the same area as marked by the Lang-topography. The distribution of these etch pits is frequently called "haze." One example is shown in Fig. 8. The symbol "Fe" was scratched on the back side of a Czochralski-grown p-type silicon wafer with the aid of a piece of iron wire. The wafer was then annealed at 1150°C for 10 min, moderately cooled to room temperature within 5 min, and treated by Sirtl-etch. For taking the photograph the wafer was illuminated by means of a spot light. Whereas the Sirtl-etch technique works for Czochralski-grown and floating-zone silicon, x-ray topography resolved precipitates and strain only in the case of Czochralski-grown silicon. This is probably caused by the larger size of precipitates in pulled crystals due to initially formed oxygen agglomerates.

Iron content in as-grown silicon crystals.—After having investigated intentionally iron-doped silicon crystals the undesired iron content of some commercially available crystals of various specifications was determined. Measurements were carried out in as-received state and after a short heat-treatment at 1000°C and quenching. Utmost clean conditions were observed for handling and heat-treating the specimens. The iron content of as-received silicon crystals

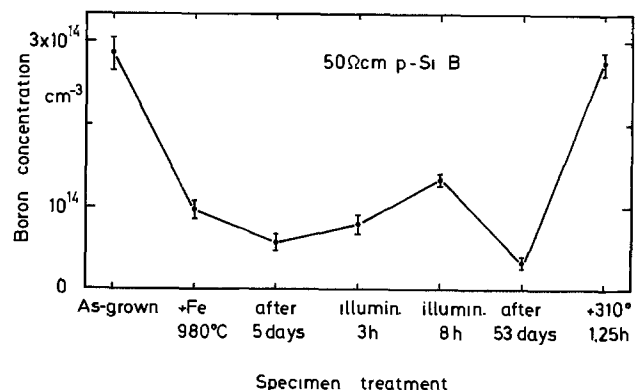


Fig. 7. Boron concentration calculated from infrared absorption of a boron-doped p-type silicon wafer before and after iron diffusion, illumination, and annealing of the specimen.

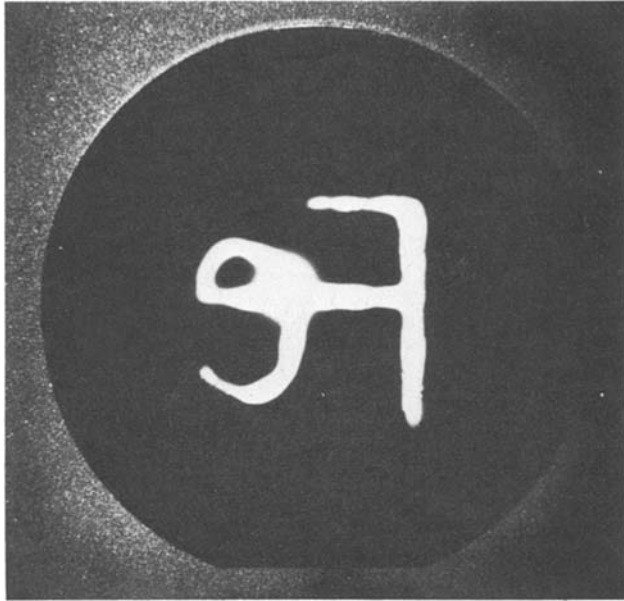


Fig. 8. Czochralski-grown silicon wafer with "Fe" scratched on the back side with the aid of a piece of iron wire, annealed at 1150°C for 10 min and treated in Sirtl-etch.

investigated so far did not exceed the detection limit (about 10^{-4} of the carrier concentration). After quenching these specimens, rather low iron concentrations were observed not exceeding $5 \times 10^{11} \text{ cm}^{-3}$ in floating-zone and $5 \times 10^{12} \text{ cm}^{-3}$ in Czochralski-grown crystals. These results are in contrast to previous publications (1, 12).

Discussion

From the experimental results the following properties of iron in silicon were deduced: only one impurity level is formed by electrically active iron in n- and p-type silicon situated at $E_v + 0.43 \pm 0.04 \text{ eV}$. This level is obviously correlated to iron on an interstitial site as detectable by means of ESR spectroscopy. This level has the properties of a donor. The best fit to our experimental results for the solubility of iron in silicon as function of the temperature $[\text{Fe}]$ is represented by the Arrhenius equation published by Weber and Rottke (1)

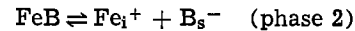
$$[\text{Fe}] = 5 \times 10^{22} \exp(7.3 - 2.87 \text{ eV}/kT) \text{ cm}^{-3}$$

Because of the high diffusion coefficient of iron in silicon even at rather low temperatures, iron tends to precipitate during a cooling cycle if the specimen is not quenched rapidly. The precipitates can be dissolved once more by a second heat-treatment of the specimen up to a concentration corresponding to the respective solubility.

So far no infrared absorption bands correlated to iron in silicon were observed. As a deep level impurity iron reduced the carrier lifetime in n- and p-type silicon. The capture cross section for holes in n-type silicon $\sigma_p^0 = 3 \times 10^{-16} \text{ cm}^2$ (27) seemed to be in reasonable agreement with most of our experimental lifetime results. The electron capture cross section in p-type silicon $\sigma_n^+ = 15 \times 10^{-16} \text{ cm}^2$ (27), however, is still doubtful, since the iron donor is not stable in p-type silicon but reacts with all common shallow acceptors even at room temperature.

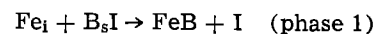
The iron-boron pairs formed in p-type silicon after quenching the specimen were detected by means of DLTS and a level at $E_v + 0.10 \text{ eV}$ was found. This value is identical with recent results of Feichtinger (17). So far no infrared absorption bands could be correlated to this complex. If the boron concentration exceeded the iron content in the crystal all interstitial iron reacted with boron in an appropriate time which

depended on the boron concentration. In the first stage after quenching the specimen this reaction took place quantitatively, independent of the storage temperature within the range 20°-150°C. In a second phase, after termination of the level transmutation, a thermal equilibrium between interstitial iron and iron-boron pairs was observed, following the mechanism



This equilibrium could be shifted to the right side by increasing the temperature and by illuminating the specimen, respectively. At higher temperatures exceeding about 150°C most of the complexes were dissociated. Since the thermal mobility of iron is rather high, the iron then precipitated irreversibly after an appropriate time.

In order to explain the reaction mechanism in phase 1 two facts were illuminating: the thermal equilibrium was not observed soon after quenching the specimen and at the same time the concentration of the boron acceptor was strongly reduced although almost no pairs were detected. To explain these observations it was assumed, that the boron acceptor reacted with an intrinsic defect during quenching the specimen. Then the following reaction may take place



I symbolizes an intrinsic defect being a vacancy or self-interstitial, which is formed at high temperatures in the silicon lattice and which is highly mobile even at room temperature. In the present case a self-interstitial seems more likely to react in the same way as iron on an interstitial site. After the formation of the iron-boron pairs the isolated intrinsic defect can react with a second boron atom or finally diffuse to the surface of the specimen. This reaction proceeds only in one direction because one participant disappears. When all the intrinsic defects have disappeared then the phase 2 reaction takes place.

During the reaction of iron with boron no strongly marked change in carrier lifetime was observed as would be expected during the change of a deep-level impurity into a shallow one. This could be explained by assuming the existence of a second level for the pair which must be situated in the upper half of the silicon bandgap and which must be a deep level. Usually a level in the upper half of the bandgap cannot be observed by DLTS in p-type material by applying Schottky contacts. On the other hand the iron-boron pair is not formed in n-type silicon, so the second level of this pair is not detectable by this method. In some specimens which were highly compensated because of high iron concentrations, however, an additional level was observed after the formation of the complexes was completed. The activation energy of this level was determined to $E_v + 0.6 \text{ eV}$, so it must be situated in the upper half of the bandgap. This result agrees well with the value $E_c - 0.55 \text{ eV}$ published repeatedly in the literature as an additional impurity level of iron in silicon (Fig. 1). Furthermore in aluminum-doped silicon two levels were detected which were correlated to iron-aluminum pairs.

If an ionic binding in the iron-boron pairs predominates, the charge carriers may be bound to one atom. Only the following three charge states are possible: (Fe^0B^-) , (Fe^+B^-) , and (Fe^+B^0) . (Fe^0B^0) is not existent, since Fe^0 and B^0 are always situated on opposite sites of any Fermi level as shown in Fig. 9. The sum of the charge states of iron and boron determines the charge of the complex. From the figure it is deduced that the $E_v + 0.10 \text{ eV}$ level then forms a donor (change from positive to neutral charge) whereas the $E_c - 0.55 \text{ eV}$ level forms an acceptor (change from neutral to negative charge). This assumption would explain all experimental findings and can be extended in the same way to explain the two levels of the iron-

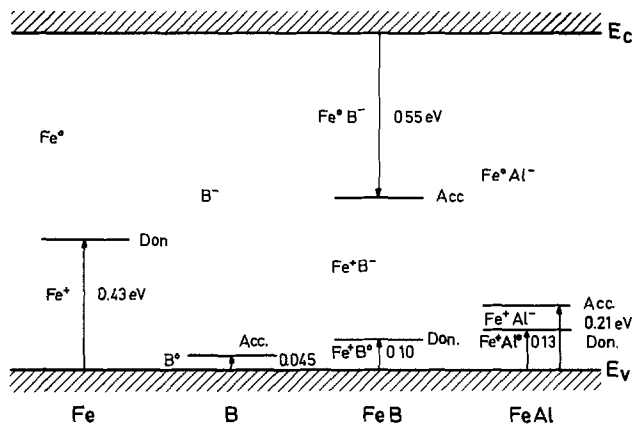


Fig. 9. Activation energies of iron, boron, iron-boron, and iron-aluminum pairs in silicon.

aluminum pairs. In this pair the ionic character of the binding may be reduced so the two levels approach one another. The formation and detection of the iron-boron acceptor level and its correlation to the iron-boron pair should be proved, however, by another measurement technique.

Conclusion

The knowledge of the impurity level of iron in silicon and those of the most frequent iron-acceptor pairs is quite useful for the examination of the impurity content in silicon crystals especially after technological processes for device production. Usually iron is precipitated at least partly. Therefore a certain preparation technique is needed to transform it into a detectable electrically active impurity. The experimental finding, that iron-boron pairs dissociate during illumination of the specimen facilitates the detection of the total iron content of a specimen. The iron analysis is then limited to usual measurement temperatures (270 K). The DLTS-signal of the FeB, however, is not observed at temperatures exceeding 60 K applying an emission time constant of 1.42 msec.

The present investigations were limited to impurity reactions of iron with boron, aluminum, and phosphorus. In order to complete the knowledge about possible reaction mechanisms further impurities should be added intentionally and the resulting deep-level spectra studied.

Acknowledgment

The authors want to thank J. Hilgarth for performing x-ray topographies. They are grateful to Dr. Goldbach for his interest and for stimulating discussions. This work was supported by the Bundesministerium für Forschung und Technologie of the FRG.

Manuscript submitted June 19, 1980; revised manuscript received ca. Aug. 29, 1980.

Any discussion of this paper will appear in a Discussion Section to be published in the December 1981 JOURNAL. All discussions for the December 1981 Discussion Section should be submitted by Aug. 1, 1981.

Publication costs of this article were assisted by AEG-Telefunken.

REFERENCES

1. E. Weber and H. G. Riote, *J. Appl. Phys.*, **51**, 1484 (1980).
2. J. D. Gerson, L. J. Cheng, and J. W. Corbett, *ibid.*, **48**, 4821 (1977).
3. H. Feichtinger, A. Gschwandtner, and J. Waltl, *Phys. Status Solidi A*, **53**, K71 (1979).
4. J. D. Struthers, *J. Appl. Phys.*, **27**, 1560 (1956).
5. C. B. Collins and R. O. Carlson, *Phys. Rev.*, **108**, 1409 (1957).
6. H. H. Woodbury and G. W. Ludwig, *ibid.*, **117**, 102 (1960).
7. W. H. Sheperd and J. A. Turner, *J. Phys. Chem. Solids*, **23**, 1967 (1962).
8. D. V. Lang, *J. Appl. Phys.*, **45**, 3023 (1974).
9. U. Herpers, H. G. Riote, and E. Weber, To be published.
10. Y. H. Lee, R. L. Kleinhenz, and J. W. Corbett, *Inst. Phys. Conf. Series*, **46**, 521 (1979).
11. H. J. Rijks, J. Bloem, and L. J. Giling, *J. Appl. Phys.*, **50**, 1370 (1979).
12. E. Weber and H. G. Riote, *Appl. Phys. Lett.*, **33**, 433 (1978).
13. N. T. Bendik, V. S. Garnyk, and L. S. Milloskii, *Sov. Phys. Solid State*, **12**, 1340 (1970).
14. B. J. Boltaks, M. K. Baknadyrkanov, and G. S. Kulikov, *ibid.*, **13**, 2240 (1972).
15. L. K. Ermakov, *Sov. Phys. Sem.*, **12**, 732 (1978).
16. A. O. Evwaraye and P. L. Andersson, in "Semiconductor Characterization Techniques," P. A. Barnes and G. A. Rozgonyi, Editors, p. 61, The Electrochemical Society Softbound Proceedings Series, Princeton, N.J. (1978).
17. H. Feichtinger, *Inst. Phys. Conf. Series*, **46**, 528 (1979); The Institute of Physics, Bristol, London (1979).
18. M. Okuyama, N. Matsunaga, J. W. Chen, and A. G. Milnes, *J. Electron. Mater.*, **8**, 501 (1979).
19. M. A. Abdugafurova, L. M. Kapitanova, L. S. Kostina, A. A. Lebedev, and S. L. Makhkamov, *Sov. Phys. Sem.*, **9**, 450 (1975).
20. M. A. Abdugafurova, A. A. Lebedev, A. T. Mamadalimov, and Sh. Makhkamov, *ibid.*, **8**, 1409 (1975).
21. J. W. Chen and A. G. Milnes, in "Proc. Nat. Workshop on Low-Cost Polycryst. Silicon Solar Cells," T. L. Chu and S. S. Chu, Editors, Dallas (1976).
22. K. D. Glinchuk and N. M. Litovchenko, *Sov. Phys. Solid State*, **6**, 2963 (1965).
23. W. Fahrner and A. Goetzberger, *Appl. Phys. Lett.*, **21**, 329 (1972).
24. K. Graff and H. Fischer, "Carrier Lifetime in Silicon and Its Impact on Solar Cell Characteristics, Topics in Appl. Phys.," Vol. 31, B. O. Seraphin, Editor, p. 173, Springer Verlag, Berlin (1979).
25. B. O. Kolbesen, *Appl. Phys. Lett.*, **27**, 353 (1975).
26. H. Lefèvre and M. Schulz, *IEEE Trans. Electron. Devices*, **ed-24**, 973 (1977).
27. E. Schibli and A. G. Milnes, *Mater. Sci. Eng.*, **2**, 229 (1967/68).

Effects of Multiple Slice Epitaxy and Front End Processing on Generation Threshold Current in Bubble Memory Devices

R. L. Guldi, R. E. Fontana, Jr., and D. C. Bullock

Texas Instruments, Incorporated, Dallas, Texas 75265

ABSTRACT

The factors affecting generate threshold current, I_g , (the minimum current required to reliably nucleate a bubble under a hairpin generator) are reviewed. I_g data are presented for bubble memory devices fabricated using YSL-CaGe garnet (1) epitaxial films with nominal bubble sizes of 5.3 and 3.8 microns. Where multiple slice epitaxy employing large vertical stacks (up to 16 singly spaced slices/stack) is used, it is found that I_g measured on an aluminum generator without overlying Permalloy elements or passivation is shown to depend on position in the epitaxy stack, decreasing by as much as 4 mA (1%) per slice position with increasing depth of slices in the melt. In contrast, slices ion milled to remove a 0.4 micron thick surface layer show no dependence of I_g on stack position. Removal of the surface layer has the additional effect of significantly decreasing the variation of I_g across a slice by up to 67%. These observations are interpreted in terms of the existence of a low anisotropy surface layer approximately 0.2-0.5 microns thick grown as slices are slowly withdrawn from the epi melt without rotation. The properties of this layer are discussed. In particular, the layer is shown to have a lower anisotropy than the bulk film, and it is estimated that the growth rate appropriate to the surface layer is approximately 20% of the value for normal film growth (0.4-1.0 microns/min). Finally the dependence of I_g on subsequent front end processing is presented, and it is shown that the I_g value measured on an aluminum generator without overlying oxide and Permalloy is reduced by approximately 30% after subsequent oxide and Permalloy processing steps.

Generate threshold current (I_g), or the minimum current required to reliably nucleate a bubble under a hairpin generator, is a parameter that must be understood and controlled in order to produce reliable, interchangeable, and easily used bubble memory devices. Some of the factors contributing to I_g variations in devices have been discussed previously by Wolfe and Johnson (2) who have related I_g variation to stress effects in the epitaxial garnet layer due to the silicon oxide and the aluminum metallization and to changes in the stress because of the presence of the overlying layers, and through annealing effects arising during oxide and Permalloy deposition.

This paper describes another major source of I_g variation that can be found in slices grown using multiple slice epitaxy employing large vertical stacks of slices, namely a contribution from an anomalous surface layer on the top of the epitaxial garnet film.

Experimental

Figure 1 shows an artist's concept of the particular type of multiple slice holder used in this study. This holder has capacity for 16 singly spaced, 2 in. diam slices. The circular ring that ties the legs of the holder together for extra strength in the center of the holder separates the top eight slices from the bottom eight and increases the distance between the eighth and ninth slices in the stack, producing an effect on the stack dependence of I_g that will be discussed later.

The generator geometry for this investigation is shown in Fig. 2. The generator element is a conventional hairpin generator, made of evaporated aluminum containing approximately 2 weight percent (w/o) copper, separated from the epitaxial film by a plasma-deposited silicon oxide layer, and patterned by ion milling at an angle of 45 degrees. Silicon oxide and aluminum thicknesses are 4000 and 5000Å, respectively,

Key words: magnetic garnet epitaxy, liquid phase epitaxy, generate threshold current, multiple slice epitaxy, bubble memory devices.

for five micron bubble circuits and 4000 and 4000Å for three micron bubble circuits. The dimensions given in Fig. 2 apply to a three micron bubble circuit which is a scaled-down version of a five micron circuit as far as considerations dealing with the generator are concerned. All data reported were taken on neon-implanted slices (2.5 E14 at 100 keV for 5 micron films and 2.0 E14 at 100 keV for 3 micron films).

Generate threshold data as reported in this paper are taken on the structure shown in Fig. 2 without overlying oxide and Permalloy layers in order to avoid effects due to stress or problems with the alignment of aluminum and Permalloy elements. I_g measurements are made by contacting the generator lead structure with fine-tipped probes, pulsing the generator with a 500 nsec current pulse with a rep rate of 500 Hz to minimize heating, and increasing the pulse amplitude until the first bubble is observed optically. It is estimated that the I_g values obtained are reproducible

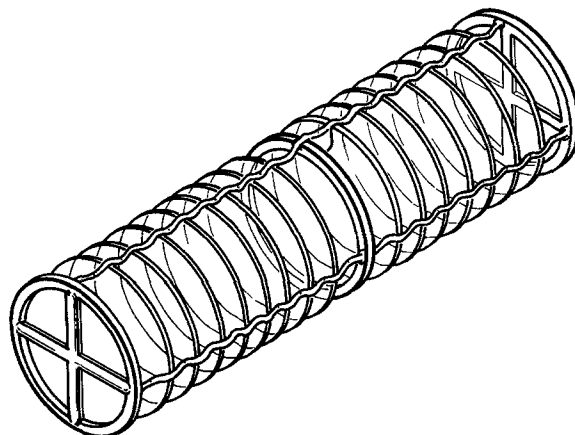


Fig. 1. Slice holder for LPE of 16 singly spaced wafers

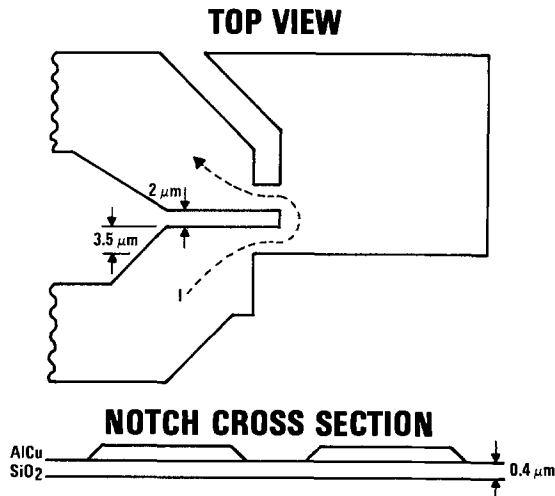


Fig. 2. Generator design for 3 micron bubble circuits

to about ± 5 mA. All data presented were taken at room temperature. For consistency the threshold is measured with the bias field 10 Oe below free bubble collapse. It will be noticed that the I_g values discussed throughout the paper are approximately 30% higher than those found in actual packaged devices. This discrepancy arises because I_g decreases with annealing during the high temperature processing used in depositing subsequent oxide and Permalloy layers, as will be described later.

Results

The dependence of I_g on position in the epitaxy holder for a typical epitaxial run is shown in Fig. 3 for three micron bubble films. The X-axis is drawn using a linear distance scale as measured from the top slice holder ring, with numbers labeling the position of each slice in the stack, starting with the No. 1 slice at the top of the stack. The larger than average separation between the eighth and ninth slices results from the presence of the middle support ring on the slice holder (see Fig. 1). The top eight slices in the stack show practically no dependence of I_g upon stack position, but slices in the lower eight positions show a decrease in I_g with stack position of up to 7 mA/slice position.

This type of dependence of I_g on stack position is typical of both 5 and 3 micron bubble films. Run-to-run variations in the degree of stack dependence in the range of approximately 2-7 mA/stack position exist and these are correlated with a variation in epitaxial film anisotropy throughout the stack which is associated with small vertical temperature gradients in the epi-melt. Runs for which the measured film anisotropy is higher for slices from the top of the stack than for

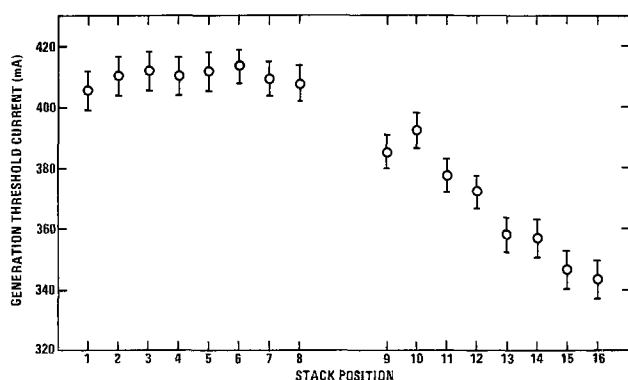


Fig. 3. Average generation threshold current, I_g , on aluminum generators without overlying oxide and Permalloy elements vs. position in the epitaxy slice holder for 3 micron bubble films. Stack position No. 1 is located toward the top of melt.

slices from the bottom show an increased I_g stack variation compared to runs for which the measured film anisotropy gradient is reversed, but in all cases I_g decreases with increasing stack position. Another common trend is for the I_g value for slices in position 1 and 9 to be slightly less than the average for adjacent slices in the stack, and it is interesting that these films are grown with the device side faced down whereas all other films are grown with the device side faced up. However, the universal trend is that slices from the bottom of the stack exhibit reduced I_g . It should be noted that there is a minimal dependence of I_g on spacer oxide thickness, aluminum thickness, and generator linewidth provided these parameters are controlled within $\pm 5\%$.

As an explanation for the dependence of I_g upon stack position, it was proposed that a low anisotropy surface layer grown on the epitaxial film during withdrawal from the melt is responsible for controlling I_g . In order to investigate this hypothesis, 5 micron films from alternating stack positions were ion-milled to remove a 5000Å thick surface layer before ion implanting and beginning generator processing. The results of this experiment are shown in Fig. 4. The unmilled slices exhibit a strong dependence of I_g on stack position, but the milled slices do not. Hence the existence of a surface epi layer which controls I_g was verified.

To investigate this effect further, four slices, one each from positions 2, 6, 10, and 16 of a sixteen slice 5 micron bubble stack, were quartered and each quarter was ion-milled to remove either 0, 2000, 4000, or 6000Å of material before generator processing (see Fig. 5), and generators were fabricated on these quartered slices. The measured I_g values were independent of milled thickness for slices 2 and 6, which are from the top of the stack, but increased dramatically with increasing thickness milled for slice 16, which was grown at the bottom of the stack.

Slices No. 10 and 11 were processed as whole slices. Slice No. 10, which was not milled, showed an I_g value approximately 20 mA less than the slice grown in the adjacent stack position No. 11, which had 6000Å of material removed by milling before generator processing.

Again the quarters of all four slices which received no milling show the same type of dependence of I_g on stack position presented in Fig. 3 and 4, while practically no stack dependence is found on the quarters of the slices which had a sufficiently large thickness removed, namely 6000Å. Hence, one could estimate the maximum thickness of the surface layer for the 16th slice in the stack as approximately 6000Å.

In a related experiment, the variation of I_g over a single slice was investigated. Figure 6 shows the distribution of I_g measured for slices number 2 and num-

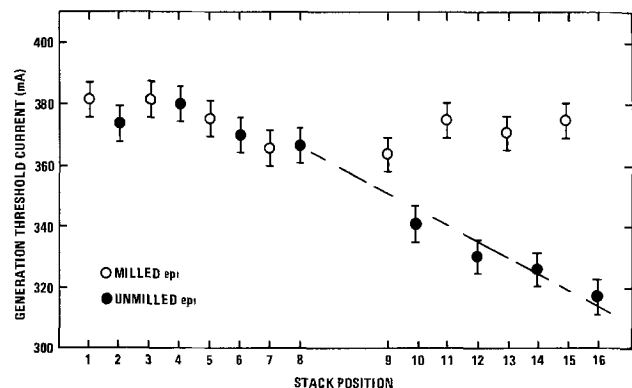


Fig. 4. Average generation threshold current, I_g , on aluminum generators without overlying oxide and Permalloy elements vs. position in the epitaxy slice holder for 5 micron bubble films. Alternate slices were ion milled to remove a 5000Å thick surface layer before beginning generator processing.

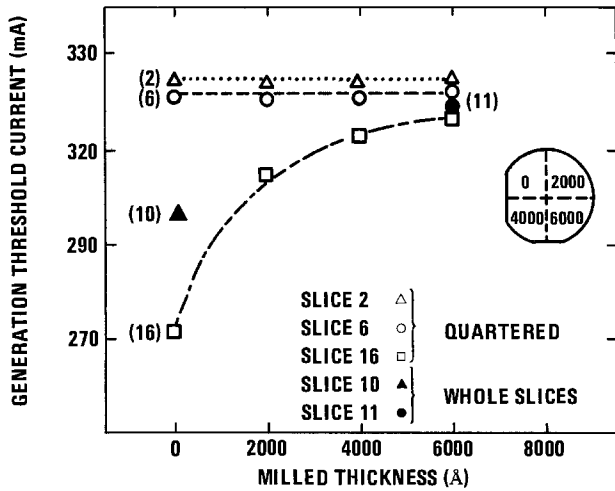


Fig. 5. Average generation threshold current, I_g , on aluminum generators vs. thickness of material removed by ion milling before beginning generator processing as a function of stack position. Slices No. 2, 6, and 16 were quartered, and each quarter had a different amount of material removed before processing. Slices No. 10 and 11 were processed as whole slices.

ber 15 in a sixteen slice stack of three micron bubble films. A tighter distribution of I_g about the mean value is found for the slice from the top of the stack ($\sigma = 3.8$ mA for slice No. 2 vs. $\sigma = 6.7$ mA for slice No. 15). Consistent with previous data, slice No. 15 also shows a lower value of I_g .

The I_g distribution for all chip positions in all 16 slices from the same three micron epitaxial run was also investigated. Alternating slices were either unmilled or milled to remove a 5000Å layer before generator fabrication. The I_g distributions measured after aluminum patterning and also after Permalloy patterning are shown in Fig. 7. For this lot after aluminum patterning, a fairly narrow distribution was observed for milled slices, while a broader distribution was observed for unmilled slices. After the NiFe was patterned, both distributions broadened somewhat with the unmilled distribution still broader than the milled. In this example, the I_g broadening arising from epi-related effects is approximately 3 times more significant than broadening related to aluminum or Permalloy processing.

In order to confirm the existence of a surface layer of composition different from the bulk, SIMS or ion probe profiles of composition vs. depth were obtained for epitaxial films. Figure 8 shows one such profile for a three micron bubble film. For simplicity the Y, Ca, and Fe profiles which were relatively constant are not shown. Similar results have been obtained for both

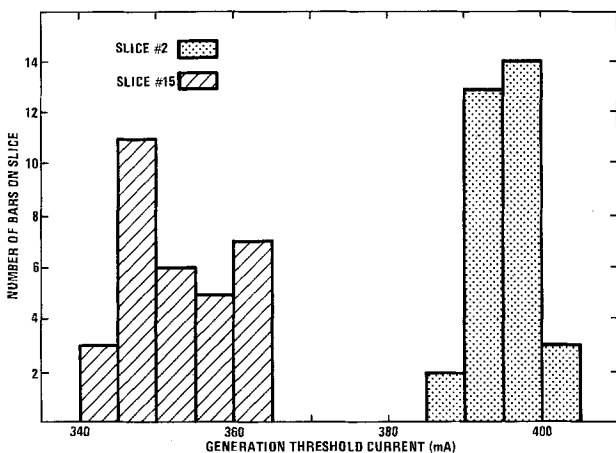


Fig. 6. Distribution I_g for slices No. 2 and 15 in a 16 slice stack of 3 micron films.

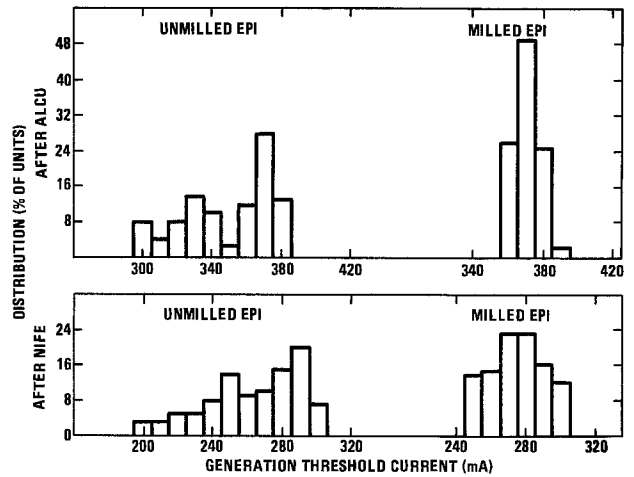


Fig. 7. I_g distribution for all chip positions in a lot of 16 slices from the same 3 micron epitaxial run. Alternating slices were either unmilled or ion milled to remove a 5000Å layer before generator fabrication. Distributions are shown for measurements after AlCu patterning without overlying oxide and Permalloy elements and for measurements after NiFe patterning.

three and five micron films. In general there exists on all films a surface region with a composition significantly different from the bulk of the film, although the exact nature of the profiles in the surface region varies considerably from epi run to epi run. For the slice at the bottom of the stack, the thickness of the surface region is approximately 5000Å. Usually the surface region is lower in components that contribute to anisotropy such as samarium and lutetium, or it is lower in germanium content than the bulk, a condition that would tend to increase $4\pi M_s$ and decrease anisotropy.

The existence of an anomalous surface layer on epitaxial films is consistent with the basic understanding of the epitaxial growth process. During the growth of the primary film, extensive melt mixing occurs because of the stirring action of the rotating slices. Indeed mixing is required in order to maintain the proper concentrations of the various components sufficiently near the surface of the growing film to incorporate the correct amount of each component into the film as required to achieve desired film properties (3-5). It has also been shown that the rotation conditions used during immersion of slices into an epi melt can significantly affect film coercivity and lattice parameter because of compositional variations near the film-substrate interface (6). After primary film growth terminates, the stack of slices is slowly withdrawn from

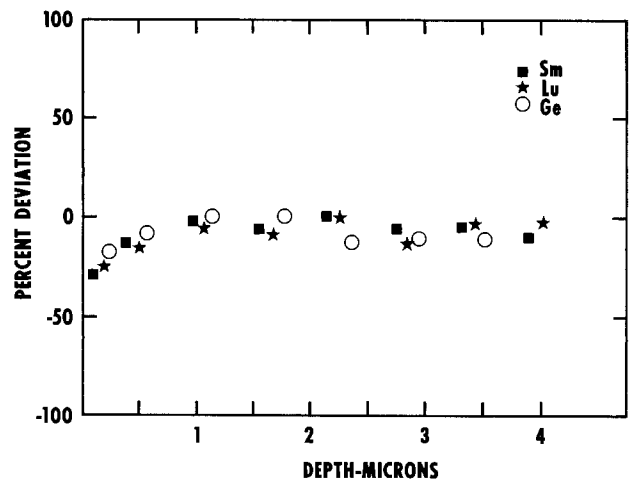


Fig. 8. Composition profiles of garnet wafer determined by ion probe (SIMS). The Y, Ca, and Fe contents were relatively constant.

the melt without rotation in order to minimize the occurrence of flux droplets which cause defects on the slice. The lack of rotation during withdrawal from the melt significantly reduces melt mixing so that growth then occurs under drastically different conditions such as with a reduced growth rate, a wider diffusion boundary at the film-melt interface, and changed values of the segregation coefficients of the constituents. Reduced surface anisotropy at reduced growth rate is consistent with reduced segregation coefficients of high anisotropy components such as samarium and lutetium and with a reduced effective segregation coefficient for germanium, all of which have segregation coefficients less than unity. The reduced samarium and lutetium concentrations directly decrease the anisotropy of the surface layer, while the reduced incorporation of germanium leads to a tendency toward higher $4\pi M_s$ and lower l , conditions which are also associated with reduced anisotropy.

One can estimate the reduction in growth rate that occurs during withdrawal of slices from an epitaxial melt without rotation in the following manner. The milling experiments suggest that the surface layer thickness, t , for a bottom slice in a 16 slice stack is approximately 0.5 microns. For the withdrawal rate of slices from the melt used in this work, 7.5 cm/min, and for conditions in which the bottom slice is grown at a depth of 18 cm below the melt surface, the withdrawal time, T , for the bottom slice is calculated to be 2.4 min. The average growth rate, R' appropriate for growth of the surface layer is then calculated as t/T or 0.21 microns/min. Since R , the growth rate which applies during the growth of the primary portion of the epitaxial film while slice rotation and melt mixing are present, is of the order of 1 micron/min, one can calculate a value for the growth rate reduction factor during withdrawal as $R'/R = 0.21$. Hence during withdrawal, the growth rate drops to approximately 1/5 its normal value.

In order to relate measurements of I_g on aluminum generators without overlying Permalloy elements to measurements on finished devices, we have measured I_g after specific stages of front end processing. Figure 9 shows the reduction that occurred in the average I_g for a slice as it progressed through normal processing and was measured after plasma resist stripping at 75°C,

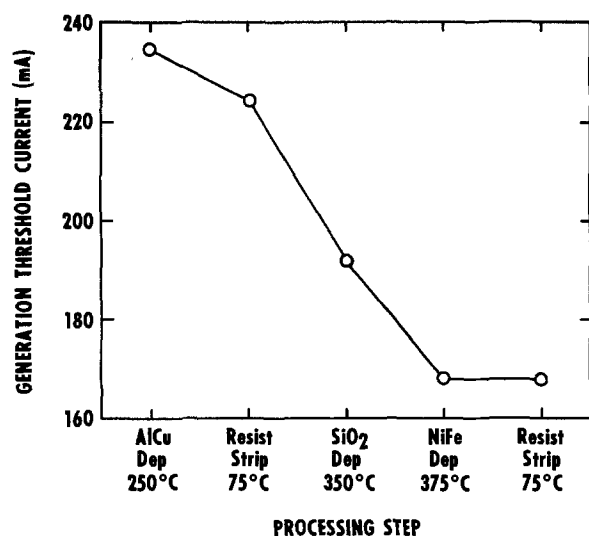


Fig. 9. Generation threshold current after various front end processing steps.

plasma oxide deposition at 350°C, NiFe sputtering at 375°C followed by ion milling and plasma resist stripping. All temperatures cited are nominal. When I_g was measured on slices after generator patterning and then remeasured after annealing the slices through the NiFe time-temperature schedule, a 14% decrease in I_g was found, compared with a 30% decrease when oxide and NiFe layers were actually deposited and patterned. These results are similar to data presented by Wolfe and Johnson (2) who attributed the I_g reduction to a localized decrease in film anisotropy caused by stresses from overlying oxide and metallization layers and to annealing effects which modify the stresses of the conductor metallization on the garnet film.

Conclusions

An anomalous surface layer with composition and anisotropy different from the bulk exists on slices grown in large vertical stacks in LPE melts and withdrawn slowly from the melt. Although the composition and anisotropy of this layer depend upon melt temperature and on melt temperature gradient, the primary dependence of surface layer thickness is on stack position, with a maximum surface layer thickness approximately 0.5 micron being found for a slice in the lowest position of a sixteen slice stack. For the withdrawal speeds used, the growth rate during withdrawal from the melt (without mixing) is estimated as 0.2 micron/min for melts in which the nominal film growth rate is 1.0 micron/min.

The variation in generation threshold current due to the anomalous surface layer presents a problem that may become increasingly more severe as film thickness is reduced to produce smaller bubble films required for advanced devices. Although I_g is the only device parameter presently identified as being sensitive to the presence of the surface layer, it is reasonable to expect other device parameters to be influenced by this layer. The control of I_g and other such parameters may involve techniques to reduce the surface layer thickness such as increasing the withdrawal rate or reducing stack height, or it may involve techniques to remove the layer such as milling or etching. Alternatively, new device designs which are less sensitive to epi surface film layers would be attractive.

Acknowledgment

The authors wish to thank Dr. C. Castro and Dr. S. Parker for illuminating discussions leading to the identification of the anomalous surface layer.

Manuscript submitted June 9, 1980; revised manuscript received Sept. 10, 1980.

Any discussion of this paper will appear in a Discussion Section to be published in the December 1981 JOURNAL. All discussions for the December 1981 Discussion Section should be submitted by Aug. 1, 1981.

Publication costs of this article were assisted by Texas Instruments, Incorporated.

REFERENCES

1. S. L. Blank, J. W. Nielsen, and W. A. Biolsi, *This Journal*, **123**, 856 (1976).
2. R. Wolfe and W. A. Johnson, *IEEE Trans. Mag.*, **mag-13**, 1595 (1977).
3. S. L. Blank, B. S. Hewitt, L. K. Shick, and J. W. Nielson, *A.I.P. Proc.*, **10**, 256 (1972).
4. J. E. Davies, G. Galli, and J. C. Suits, *J. Appl. Phys.*, **49**, 1859 (1978).
5. S. J. Lewis, *IBM J. Res. Dev.*, **22**, 422 (1978).
6. S. G. Parker, *Solid State Commun.*, **31**, 403 (1979).

Chemical Reaction of Sulfur Dioxide at High Humidity and Temperature: Implications for Accelerated Testing

Daniel L. Flamm, D. D. Bacon, E. Kinsbron, and Alan T. English

Bell Laboratories, Murray Hill, New Jersey 07974

ABSTRACT

The interaction of SO₂ with humid air was studied in a Teflon chamber (SEAT facility) as a function of flow rate (50-180 std. liters/min), humidity (7-87%), temperature (23°-85°C), and SO₂ concentration (2-9 ppm). Both SO₂ and the reaction products were monitored using wet chemical and pulsed fluorescence techniques. Sulfur dioxide is oxidized to SO₃/H₂SO₄ in dark reactions at elevated temperature and humidity. The experimental data were represented by the rate equation

$$\frac{dp_{\text{SO}_2}}{dt} = -k(T) p_{\text{SO}_2} p_w$$

where p_{SO_2} is the partial pressure of SO₂ in the chamber, p_w the partial pressure of water vapor, and $k(T)$ the rate constant. The reaction has a low activation energy (~ 5 kcal/mole) and appears to occur in the gas phase rather than on the chamber walls. The significance of secondary corrosive products in the design and use of accelerated tests is covered in detail. When field failure of a device occurs via the attack of SO₂ and water vapor alone, the quantity of product acid in accelerated test chambers should be carefully limited. It is shown how this requirement can be quantitatively specified in the form of an operating diagram derived from the rate expression. Other simulation regimes and the significance of catalytic oxidation processes are also discussed.

Introduction

Accelerated test environments.—Assurance of long-term reliability is an important consideration for most mechanical and electronic equipment in the telecommunications industry. The development of a sound basis for prediction and specification of reliability is thus a vital research and engineering objective. Typically, components are expected to function continuously and without interruption for a number of years. To provide timely information, reliability tests must be short; therefore, they must somehow be "accelerated" with respect to normal conditions of use in order to produce failures within a reasonable period of time.

Usually, elevated temperature and/or high humidity have been used to realize this acceleration: tests at 85°C and 85% relative humidity (RH) have been extensively employed for Bell System studies. Accelerated reliability tests have been used to make qualitative comparisons which are useful for device selection or for identification of the predominant modes of failure (1, 3b, 4). In a few cases there has been a post hoc attempt to determine scaling factors which relate failure times under field conditions to those observed in the laboratory test (2). More often, the extrapolation from laboratory to use conditions is based on some assumptions concerning the mechanism of failure and the dependence of the kinetics of that process on accelerated test parameters.

The concern with chemical pollutants in our environment has extended to reliability studies (3). A number of workers (3b, 4, 6) have introduced various pollutants into the test environment in an attempt to mimic the effects of atmospheric contaminants on chemical or "corrosion" sensitive failure. A crucial problem in this work is the unavailability of scientific or empirical guidelines which can be used to specify a suitable polluted atmosphere for use in accelerated tests, or a method to calculate or even to estimate the resulting acceleration factors.

Key words: atmosphere, oxidation, kinetics, corrosion.

Recently, Schwartz and Bacon (5) proposed theoretical guidelines for "Simulated Environment Accelerated Tests" (SEAT). It was assumed that the effect of atmospheric contaminants on failure could be attributed to the solution of these compounds in a thin adsorbed layer of water and by the sequential reaction of dissolved species with devices. With the exception of those involving NO and NO₂, the rate of chemical degradation processes leading to failure were assumed to be of the form

$$r_p = A_p \prod_i C_{i,s}^{n_i} C_{\text{H}_2\text{O},s} e^{-\Delta E/kT} \quad [1]$$

where A_p is a numerical coefficient, $C_{\text{H}_2\text{O},s}$ is the surface concentration of adsorbed water, $C_{i,s}$ are the average concentrations of contaminants on the surface, n_i is the reaction order (exponent) of the i^{th} component, ΔE is the activation energy, and kT , the Boltzmann constant and temperature. It was further assumed that the surface concentrations, $C_{i,s}$, could be obtained by Henry's law equilibria and that $C_{\text{H}_2\text{O},s}$ would be nearly a function of relative humidity alone. In general it was presumed that the various atmospheric contaminants underwent no synergistic reactions (outside of the failure interaction, Eq. [1]) as long as the temperature in the accelerated environment was restricted to 85°C.¹

According to the procedure stipulated by Schwartz and Bacon, accelerated failure would be accomplished by a manipulation of the variables in the rate expression, Eq. [1]. In particular, it was proposed that the rate could be increased by an increase in temperature, thereby relating failure rate in the field to failure rate under accelerated conditions by an Arrhenius law

$$\frac{r_p^{\text{accel}}}{r_p^{\text{field}}} = e^{-\frac{\Delta E}{k} \left(\frac{1}{T_{\text{accel}}} - \frac{1}{T_{\text{field}}} \right)} \quad [2]$$

where ΔE is the activation energy for the failure re-

¹ Several exceptions to this scheme were explicitly given.

action. Relative humidity (RH) was to be held constant—it was argued that the surface concentration of water, $C_{H_2O,s}$, would be nearly unchanged under these conditions. Finally, the concentration of each species in aqueous solution was to be maintained near the upper end of the range of values encountered in field use (3a). It was stated that this would occur if the gas phase partial pressure of each component was adjusted at each temperature in proportion to the corresponding value of its Henry's law constant in a pure solution

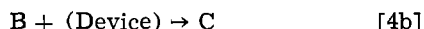
$$\frac{p_i^{\text{accel}}}{p_i^{\text{field}}} = \frac{H(T_{\text{accel}})}{H(T_{\text{field}})} \quad [3]$$

There was no experimental confirmation of these propositions.

Schwartz and Bacon (5) constructed a heated Teflon chamber (SEAT facility) in order to apply these principles to actual failure tests in the presence of SO_2 , NO_2 , and ozone. In initial experiments, employing humid air and SO_2 analysis of the chamber ambient was attempted using a pulsed fluorescence analyzer to monitor the concentration of SO_2 ; there was an apparent discrepancy between the quantity of SO_2 entering the chamber and that detected in the humid air emerging downstream. This effect was again confirmed in subsequent reliability studies involving the electroplated leads of light emitting diodes (LED's) (6). Furthermore, when SO_2 , NO_2 , and O_3 were introduced in various combinations, there was a large interaction between contaminants as the loss of each was dependent on the concentrations of the other components.

These results are highly significant since other workers have carried out accelerated tests under the assumption that gases introduced into a test chamber maintain their chemical integrity (7). Kemmerer and Hartwig (7a), for example, assumed that 0.5 ppm SO_2 introduced into a stream of air at 85°C and 80% RH provides an atmosphere containing 0.5 ppm SO_2 for the exposure of metallizations in a test chamber; however the SEAT studies (5, 6) demonstrate that large SO_2 losses occur and, as will be shown, SO_3 and sulfuric acid are the main corrosive agents under those test conditions.

Restrictions on the simple model.—Clearly there are a number of additional assumptions implicit in the simple model, Eq. [1]. As noted by the authors (5), it is assumed that the relative humidity is a proper scaling factor. Consecutive chemical processes of all kinds are neglected. For instance, if pollutant A forms a product B and B is the corrosive agent, then the corrosion process



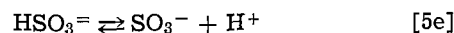
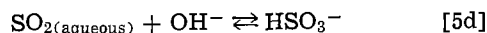
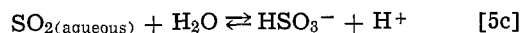
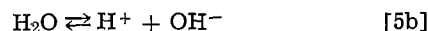
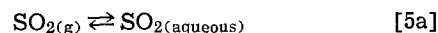
cannot, in general, be characterized by a single reaction and activation energy. Thus the attack of metallizations by sulfuric acid, alluded to above, falls outside of the scope of this model. Of course far more complex multiple reaction schemes are conceivable and the actual failure process (as opposed to precursor formation, as illustrated above) may involve several consecutive reactions and even alternate pathways.

The elementary model also neglects mass transfer limitations. A pollutant must be transferred to the interface solution and, ultimately, to the liquid-device interface. In addition, the actual corrosive agent may be formed through intermediate reactions at the gas-liquid or solid-liquid phase boundaries. A simple universal rate of the form given in Eq. [1] can only apply when consumption or transport of reactant in one of these processes is always slow (and therefore dominant) compared with the others. If these requirements are not met, then the rate law and detailed chemistry of failure will be a function of the specific concentrations, temperature, humidity, and gas flow parameters in the test.

Previous studies of SO_2 oxidation.—The oxidation of SO_2 in the atmosphere is an important process in the chemical evolution of air pollutants and as such has received a great deal of attention (8). While there seems to be many parallels with the present study, including synergistic effects on the reaction from NO_2 and water vapor (9), the atmospheric process is photochemical and therefore differs fundamentally from the dark reaction occurring in the present study. In the polluted atmosphere, hydroxyl radicals are formed from photochemical reactions involving other species (e.g., NO, hydrocarbons) and the oxidation process can be quite complex (10). In the laboratory, the formation of SO_3 and subsequent nucleation of sulfate has been studied through photochemical oxidation involving excited states of SO_2 and the ground state of oxygen. In any case the homogeneous photo-oxidation of SO_2 in the atmosphere is very slow ($\sim 2\%/hr$ in sunlight at solar zenith) (11). In the presence of water, laboratory photolysis rates (12) are greatly increased (about 200 times), presumably due in part to hydration of SO_2 molecules which promotes H_2SO_4 formation. Negligible oxidation occurs at ambient temperature in the absence of irradiation (12).

The homogeneous dark oxidation of SO_2 has, by comparison, been little studied. Tokunaga *et al.* (13) found that in dry mixtures of SO_2 and high purity synthetic air, no oxidation could be observed, even at 100°C and after irradiation by 10 Mrad of 1-2 MeV electrons. In the presence of water, irradiation produces substantial oxidation. However these workers did not report the rate, if any, of oxidation of the wet mixtures without irradiation. Urone *et al.* (14) found no homogeneous reaction in an SO_2 /air mixture (~ 10 -20 ppm) at 25°C and 50% RH. Evidently there are no other published data for the homogeneous oxidation of SO_2 in air at elevated temperature.

A number of workers have investigated the oxidation of SO_2 by molecular oxygen in aqueous solution (15). At 25°C, the oxidation proceeds via the mechanism² (15a)



where the oxidation of SO_3^- to SO_4^- occurs by a first-order reaction as indicated and no oxidation of HSO_3^- occurs directly. To a good approximation, the rate of oxidation is given by (15a)

$$\frac{d[SO_4^-]}{dt} = 1.58 \times 10^{11} [H]^{-2.16} p_{SO_2} \frac{\text{moles } SO_4^-}{\text{liter-s-atm.}} \quad [6]$$

where p_{SO_2} is the partial pressure of SO_2 in equilibrium with water; the overall reaction appears to be rate controlled by the oxidation of sulfite (Eq. [5f]), even in a static chamber, and the rate was verified for pH between 2 and 6 and temperatures of 3° and 25°C. The reaction rate was zero order with respect to O_2 over a wide range of concentrations.

Finally, it is well known that certain metal oxides catalyze the air oxidation of SO_2 to SO_3 (14) and a number of transition metal ions catalyze the oxidation of sulfite to sulfate in solution (17). The action of some catalysts is clearly very temperature sensitive since, for instance, vanadium and chromium oxides produce very slow oxidation at room temperature (14, 18), whereas vanadium pentoxide is a catalyst for sulfuric acid

² It should be noted that some workers studying the oxidation of other sulfur species in aqueous solution were apparently unaware of this previous work and utilized erroneous assumptions for the oxidation of sulfite (16).

production at $\sim 400^\circ\text{C}$ (18). Metallic catalysts also can enhance the photochemical oxidation of SO₂ (14).

In this connection it should also be noted that higher alcohols and phenols inhibit the aqueous oxidation of sulfite (18, 19). The wet chemical analysis, described below, utilized isopropanol as an inhibitor in order to separately collect sulfate.

Scope of the investigation.—SO₂ is one of the most pervasive pollutants and it is known to accelerate failure and corrosion in a variety of situations. Compared to the complex chemistry which occurs in many gas mixtures, or even with other elementary pollutants such as NO₂, SO₂ represents a simple contaminant system. Nevertheless, as mentioned above, several investigators have been unable to obtain a mass balance on humid, SO₂-contaminated air streams entering an empty Teflon chamber; one objective of the present study was to characterize any chemical processes which occur and could account for the loss of SO₂. A second objective was to identify those conditions for which the loss of SO₂ and the formation of secondary corrosive agents would be negligible—only under these circumstances would there be some hope of establishing an analytical relationship between SO₂-induced failure processes in the field and those observed in an accelerated laboratory test environment.

Low concentrations (1-5 ppm) of SO₂ were added to the humid air and the effluent composition was measured as a function of temperature (23°-85°C), humidity (7-87% RH), and flow rate (50-185 std. liters per minute [slpm]) in an empty Teflon (SEAT) chamber. Wet chemical and instrumental analyses were in good agreement and revealed that substantial amounts of SO₂ in the feed gas were converted to SO₃ and sulfuric acid. The kinetics of this reaction were determined and it was found that the loss of SO₂ in an accelerated environment can be minimized by the judicious selection of residence time, temperature, and humidity.

Apparatus and Technique

SEAT flow system.—The SEAT test facility, which has been described previously (5), was modified and used to conduct the present investigation. Its construction and current mode of operation will be discussed briefly.

A schematic of the entire apparatus is shown in Fig. 1. Dry nitrogen and oxygen were metered in a 1:4 ratio through a Tylan mass flowmeter gas blending unit. This stream passed through a packed column containing activated charcoal and molecular sieves to insure the absence of reactive trace impurities. This "synthetic air" then flowed over a humidification tray in the oven that housed the Teflon SEAT chamber and into a mixing plenum leading to the chamber proper (Fig. 2). A precalibrated SO₂ mixture (5% SO₂ in N₂) was metered through a separate mass flowmeter and injected into the mixing plenum (Fig. 2) of the 16 × 17 × 15 in. chamber.

The chamber temperature was measured using a sheathed thermocouple inserted via the exhaust port, and humidity was measured with a Humitemp Model PCRC-55HPT humidity/temperature sensor, a wet/dry bulb system built into the oven, and water collected by condensation of the chamber effluent (water collection

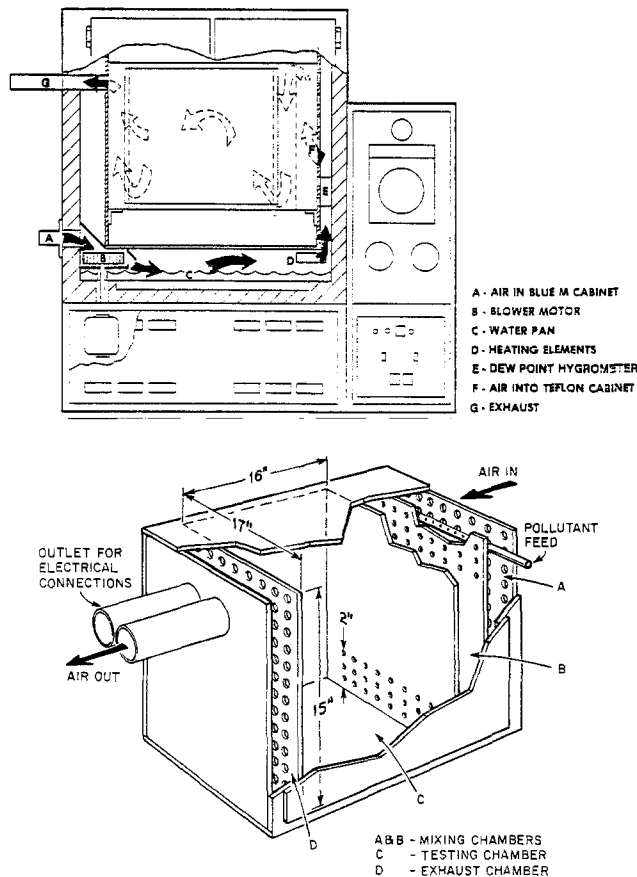


Fig. 2. SEAT Chamber. (a, top) humidity oven and airflow, (b, bottom) chamber detail.

occurred as part of the chemical analysis—see below). SO₂ concentrations in the effluent were determined by pulsed fluorescence while an independent chemical technique was used to analyze SO₂ and the combined quantity of SO₃ and H₂SO₄.

The SO₂ flowmeter was periodically calibrated against a Brooks mercury-sealed piston displacement calibrator and the N₂ and O₂ flow rates were calibrated against a wet test meter. The wick of the wet/dry bulb sensor deteriorated with use and this measurement was not consistently made through all the experiments. In order to insure against chemical degradation of the Humitemp sensor, the remote element was regularly replaced with a new, calibrated unit. The precision of water collection was best at high temperatures and moderate to high humidity; under favorable conditions the humidity determined in this way was in good agreement with the humitemp measurements ($\pm 3^\circ\text{C}$ dewpoint).

Sampling and analyses.—SO₂ concentrations reported in previous investigations with the SEAT facility (5, 6a) were determined using the sampling system in Fig. 1 and a Thermolectron Model 43 pulsed Fluorescence SO₂ Analyzer. While this method of analysis was continued throughout the present investigation, *a priori* its accuracy was uncertain due to possible losses in the sampling process and the failure of previous investigators to obtain an SO₂ mass balance (5, 6a). However, parallel wet chemical determinations made during the present study were in good agreement with the analyzer and thus verified its accuracy (Fig. 3).

The fluorescent analyzer is essentially a transfer standard and must be carefully calibrated to make absolute measurements. Periodically, the analyzer was zeroed and spanned against a dry, standard 1 ppm (nominal) SO₂/N₂ mixture and a dynamic SO₂ permeation tube system. Independently, the 5% SO₂/N₂ supply tank was standardized using the wet chemical procedure (see below) and diluted with "synthetic air" to

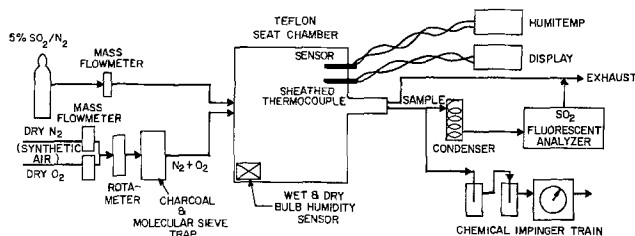


Fig. 1. Schematic of apparatus

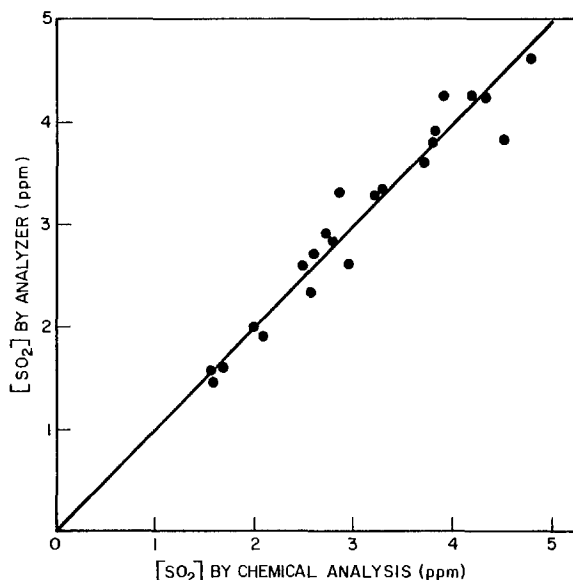


Fig. 3. SO_2 analyzed chemically vs. SO_2 measured by pulsed fluorescence ($46^\circ\text{--}85^\circ\text{C}$, 7-90% RH).

verify the analyzer calibration. These procedures were also used to standardize new tanks of SO_2/N_2 mixture.

The atmosphere emerging from the Teflon SEAT chamber is generally hot and humid. Since the analyzer will not function under such conditions, a glass water-cooled condenser was used to cool and dehumidify the gas (Fig. 1). Evidently, negligible SO_2 is absorbed during this process because (i) the condensate is acidic due to dissolved sulfuric acid and SO_2 is relatively insoluble in neutral and acid solution and (ii) the contact time is short.

A possible cause for the earlier mass balance discrepancies was the oxidation of SO_2 in the chamber. In order to quantify the significance of this process and to account for all products in the effluent, we added a wet chemical sampling train (Fig. 4) and titrimetrically analyzed SO_2 and its oxidation products. The method used was a modification of the hydrogen peroxide "stack sampling" technique (20, 17, 19b). Approximately 100 liters of the chamber effluent was sampled at 0.25-0.5 liter/min into two Smith-Greenberg impingers (Fig. 4). A small auxiliary vacuum pump was used to draw the sample and total gas volume was measured with an in-line wet test meter. Typical collection times were ~2-4 hr. Both impingers were immersed in an ice bath to condense water vapor and the short sample line sloped downward in order to drain any condensate into the first impinger.

Impinger 1 was charged with 150 ml of a fresh solution containing 80% isopropanol in distilled water. The

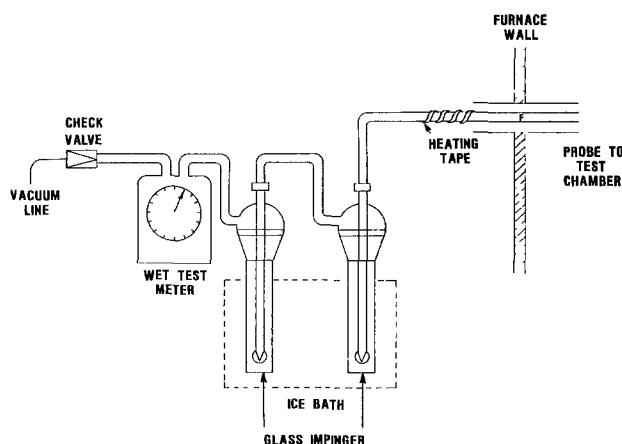


Fig. 4. Impinger train for sample collection

second impinger contained 150 ml of 3% hydrogen peroxide solution. SO_3 , H_2SO_4 aerosol, and water vapor in the sampled stream are collected in the first impinger, while SO_2 is captured in impinger 2. After the sample has been collected, dry air is passed through the train for several minutes to sweep any traces of SO_2 in the first impinger out and into the second impinger. SO_2 is relatively insoluble in the aqueous, acidic isopropanol solution in impinger 1 and the isopropanol inhibits the slow oxidation of SO_2 to sulfate in solution (17, 19). The hydrogen peroxide in impinger 2, on the other hand, rapidly absorbs SO_2 and oxidizes it to sulfate (17). The quantity of water vapor collected in impinger 1 was measured by the volume or weight change and provided an independent measure of relative humidity. Negligible water accumulated in impinger 2 under these conditions.

The efficacy of this collection process was verified in several distinct ways. Blank runs using SO_2 alone confirmed that negligible SO_2 was collected in the first impinger. A third impinger with peroxide absorbent was temporarily inserted into the train after impinger 2; this also failed to collect SO_2 and thus proved that impinger 2 had a high absorption efficiency. The combination of SO_2 and $\text{SO}_3/\text{H}_2\text{SO}_4$ determined by this analysis consistently agreed with the total quantity of SO_2 fed to the chamber. Finally, as already mentioned, these SO_2 analyses were in good agreement with pulsed fluorescence.

The absorbent solutions were analyzed as follows. 80 ml of isopropanol was added to 20 ml aliquots of the impinger samples. These were then titrated with 0.005M BaClO_4 using 6 drops of 0.013% methylene blue solution and 6 drops of 0.2% thiorin as an indicator (17). At the endpoint of the reaction



the greenish color changes to pink.

Results and Discussion

Reaction and rate.—The chemical analysis revealed that SO_2 is converted to SO_3 and H_2SO_4 in the SEAT chamber. Under steady-state operation, the total sulfur determined by chemical analysis of the product gas was ordinarily within 5% of that based on the feed gas flow rates and there was no accumulation of water or acid in the chamber; therefore any H_2SO_4 so formed must emerge as an aerosol or fine mist. Reaction data for 100 slpm air feed rate and various temperatures are shown in Fig. 5. At high temperature and humidity more than 70% of the SO_2 was converted to products. No significant reaction was observed at 23°C . Experiments performed at constant temperature, humidity, and air flow rate, but with varying concentrations of SO_2 in the feed (2-9 ppm), revealed that the extent of reaction is independent of SO_2 concentration. Thus at least in this 0-10 ppm SO_2 range, the curves in Fig. 5 apply for any concentration of pure SO_2 introduced into the SEAT chamber.

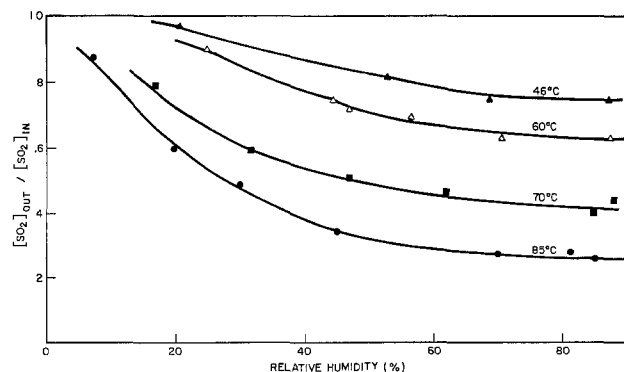


Fig. 5. Unreacted fraction of SO_2 vs. relative humidity at 100 slpm and various temperatures. SO_2 concentrations were 5-7 ppm.

If the kinetics of this reaction process were of the form given by Eq. [1], where relative humidity determines $C_{H_2O,surf}$, then the logarithm of SO₂ conversion plotted against RH would be a straight line at each temperature; however the data do not support this hypothesis. In fact the data are consistent with the first-order rate equation

$$\frac{dp_{SO_2}}{dt} = -k(T)p_{SO_2}p_w \quad [8]$$

This may be seen as follows. Equation [8] is integrated to give

$$\ln \frac{p_{SO_2,out}}{p_{SO_2,in}} = -k(T)p_w\tau \quad [9]$$

where τ is the mean residence time. If the chamber gas is well mixed

$$\tau = \tau_0 \equiv V/F \quad [10]$$

where V is the volume of the chamber, approximately 66.86 liters, and F is the total combined volumetric flow rate of air and water vapor entering the chamber (the volume of SO₂ is neglected). On the other hand, even if mixing were incomplete, τ and τ_0 would only differ by a constant factor as long as the degree of mixing were insensitive to changes in the flow rate. Equation [9] may then be rewritten in the form

$$\log_{10} \frac{p_{SO_2,out}}{p_{SO_2,in}} = -k'(T)p_w\tau_0 \quad [11]$$

where

$$k'(T) = k(T) \frac{\tau}{\tau_0} \log_{10} e \quad [12]$$

If the data obey this relation, a plot of $\log(p_{SO_2,out}/p_{SO_2,in})$ against p_w will form a distinct straight line at each temperature. Figures 6 and 7 show the experimental data plotted in this fashion. If the 85°, 50 slpm data (upper line) in Fig. 7 are temporarily disregarded, it may be concluded that the results are indeed in satisfactory agreement with Eq. [11].

As noted, the 85°C, 50 slpm data form a distinct group. While superficially, this appears to be contrary

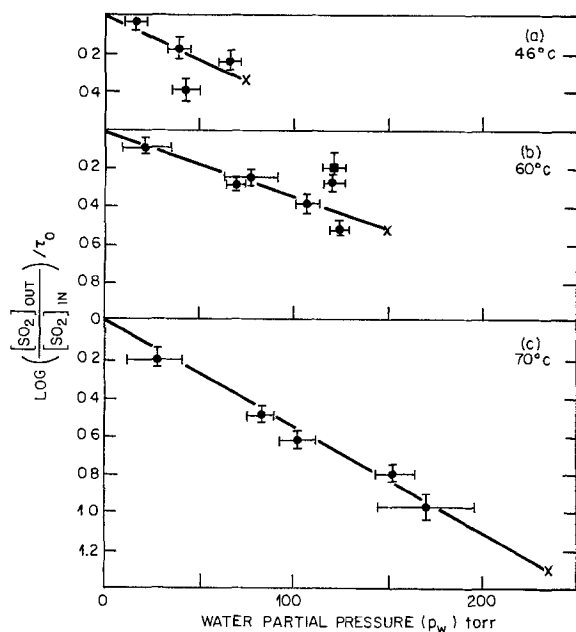


Fig. 6. $-\log \frac{[SO_2]_{out}}{[SO_2]_{in}} / \tau_0$ vs. p_w at (a) 46°C, (b) 60°C, and (c) 70°C. The dry air flow rate was 100 slpm except (■) 50 slpm. Inlet SO₂ concentrations ranged from 5 to 13 ppm. The lines terminate at saturation (100% RH denoted by x's).

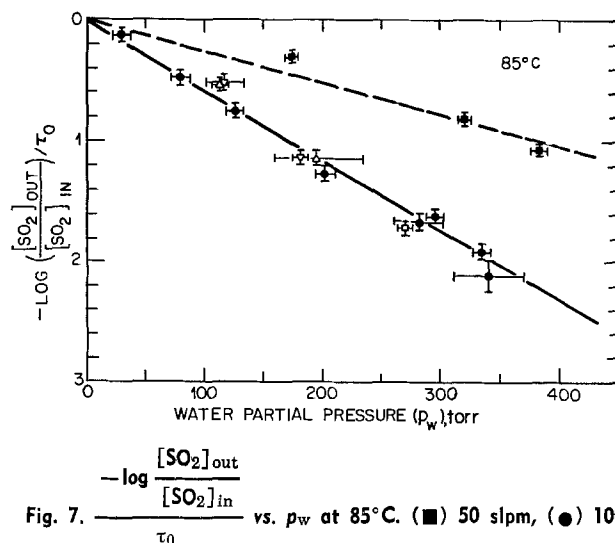


Fig. 7. $-\log \frac{[SO_2]_{out}}{[SO_2]_{in}} / \tau_0$ vs. p_w at 85°C. (■) 50 slpm, (●) 100 slpm, (▽) 120 slpm, (□) 150 slpm, (△) 180 slpm dry air flow rates. SO₂ concentrations ranged from 5 to 11 ppm. The lines terminate at 100% RH [$p_w(85^\circ C) = 433.6$ Torr].

to Eq. [11], it is possible to rationalize these data within the above framework. Feed gas entering the bottom of the chamber wall (Fig. 2) creates a complex flow pattern due to entrainment of the surrounding fluid, the effect of nearby surfaces, and, possibly, flow separation. Temperature gradients may also influence the flow. Since the Peclet number (based on the lengths subtended by the feed jet array) is large (~ 350) and the Reynolds number is moderate ($N_{Re} \approx 500$), the mixing within the chamber is primarily brought about by flow circulation rather than diffusion or turbulence. By analogy to other hydrodynamic phenomena, it is reasonable to assume that this circulation pattern will exhibit drastic changes at particular values of the Reynolds number. Thus without direct experimental evidence, it might be assumed that there is less circulation at the lowest flow (50 slpm, 85°C); this will lower τ . A decrease in τ results in a smaller $k'(T)$, (Eq. [12]) which is in accordance with the data.

The available precision and range of the present data foreclose the possibility of detecting a similar mixing effect at the lower temperatures (60° and 46°C). At low p_w and temperature, little SO₂ reacted and the variability in conversion was comparable to its magnitude. A large p_w cannot be used under these conditions since p_w is limited by the vapor pressure at saturation and this decreases rapidly with temperature (Fig. 6 and 7).

The slopes of the (high flow) 85°C and 60°C lines (Fig. 7 and 8) correspond to rate constants [$k'(T)$] of 0.0058 and 0.0035 Torr⁻¹ min⁻¹, respectively. The derived activation energy is $\sim 5 \pm 2$ kcal/mole, but this is a very crude estimate because of the scatter and the possibility that part of it can be attributed to systematic changes in τ/τ_0 .

Mechanism of reaction.—There is insufficient information to infer detailed mechanisms for the oxidation of SO₂ in the SEAT chamber. However, some rather general observations suggest that the reaction does not take place on the chamber walls. A combination of homogeneous reaction, and reaction at the surface of sulfuric acid aerosol nuclei is consistent with recent photochemical oxidation studies and the present data.

Since water vapor is required for the reaction to proceed at a measurable rate, the direct oxidation of SO₂ to SO₃ on the Teflon walls may be excluded. Furthermore, in the presence of water, sulfuric acid should be the principal oxidation product. Sulfuric acid has a negligible vapor pressure and thus any acid produced on wall sites would accumulate in the chamber and absorb additional water vapor from the humid

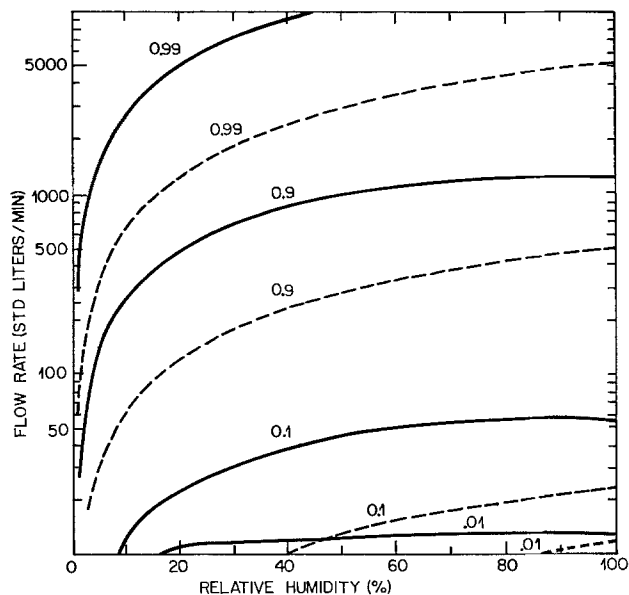


Fig. 8. Theoretical air flow/relative humidity operating curves for a constant fraction of unreacted SO_2 in the SEAT chamber (based on Eq. [13]). Fraction noted on curves. Solid lines (—) at 85°C ; dashed lines (---) at 60°C .

gas. Since (i) liquid did not normally accumulate in the chamber and (ii) essentially all sulfur was accounted for in the emerging product gas, this type of process can be excluded.

It has been proposed (21) that SO_2 may cluster with water molecules in the gas phase at high humidity. Such hydration would facilitate its oxidation and nucleation to form an H_2SO_4 aerosol. The surface of aerosol droplets could, in turn, provide sites for subsequent heterogeneous oxidation within the gas phase. Substantial homogeneous reaction within the liquid phase of aerosol droplets is unlikely, since the total volume of liquid would be small and the rate of this oxidation process (Eq. [5]–[6]) is retarded by low pH.

Significances of reliability tests.—These experiments show that secondary products can be highly significant in contaminative humid atmospheres at elevated temperature. Since the temperature, humidity, residence time, and flow profile will greatly influence the chemical environment, the chamber composition should be monitored and these variables manipulated to attain the desired test composition.

Ideally, a test should not be sensitive to small fluctuations in the operating parameters. Thus the temperature, flow rate, and humidity should be chosen so that only a small extent of reaction is possible or, alternatively, so that gaseous reactions proceed to near-completion. These requirements may be expressed as a series of "operating curves" as shown in Fig. 8. In Fig. 8, SEAT isothermal $[\text{SO}_2]_{\text{out}}/[\text{SO}_2]_{\text{in}}$ isopleths are shown on the RH-air flow plane. The curves are computed from Eq. [11] using $k'(T)$ values determined from Fig. 6 and 7 (see above). Thus more than 90% of SO_2 in the inlet gas will be unreacted for values of flow and RH which lie above and to the left of the $[\text{SO}_2]_{\text{out}}/[\text{SO}_2]_{\text{in}} = 0.9$ isopleths. Likewise, for example, the extent of reaction will be more than 90% for flow and RH values which lie below and to the right of the $[\text{SO}_2]_{\text{out}}/[\text{SO}_2]_{\text{in}} = 0.1$ isopleths. In fact, the curves in Fig. 8 may overstate conversion somewhat since they do not include possible effects of flow rate on τ (see Reaction and Rate, above).

Another consideration is the relation of chamber data to field conditions. If field failure of a device occurs via the attack of SO_2 and water vapor alone, exposure to SO_3 and H_2SO_4 may lead to unrepresentative failure modes. In this case the test should be conducted in the

low conversion regime of Fig. 8. In other instances, field failure may be induced by sulfuric acid from the dark or photo-oxidation of SO_2 on oxide or metallic surfaces. In that event, a test environment containing SO_2 and its oxidation products may be quite appropriate.

This point has been overlooked in previous studies. Feinstein and Sbar (7b), for example, report that both nickel sulfite and nickel sulfate were formed on the metallizations in their accelerated tests using 0.5 ppm SO_2 at 85°C and 85% RH. While those workers and others (7) attribute the sulfate corrosion to SO_2 attack, this premise should be carefully scrutinized in light of the present findings.

Even when SO_3 and H_2SO_4 are normal ingredients in SO_2 induced field failure processes, more sophisticated analyses will be required to carry out scalable accelerated tests. Consider a case in which SO_2 is catalytically oxidized on the surface of a component under test. The product acid may be responsible for failure in both field and accelerated test environments; however surface reactions will be rate limiting in the field, whereas the supply of $\text{SO}_3/\text{H}_2\text{SO}_4$ in a chamber can be governed by volume production.

Conclusions

Sulfur dioxide is oxidized during accelerated life test at elevated temperature and humidity. The products are sulfuric acid, and possibly, SO_3 . The reaction is first order in SO_2 and water concentrations and appears to occur in the gas phase, either homogeneously or on aerosol nuclei, rather than on the walls of a Teflon test chamber. A rate equation has been formulated to represent the experimental data, but at present its numerical values should only be applied to the SEAT test facility.

In order to conduct meaningful tests which mimic the effects of atmospheric contaminants, it is necessary to consider the oxidation and interaction of pollutants since secondary corrosive agents are formed under accelerated conditions. The acceleration guidelines proposed by Schwartz and Bacon (5) require stringent assumptions which do not appear to be met in practice.

The formation of product acid from SO_2 can be controlled by a judicious selection of operating parameters. The manifolds of constant product formation are two dimensional; it is therefore possible to select various combinations of temperature and humidity which accelerate failure, and simultaneously to control product formation by adjusting the gas flow rate.

Manuscript received July 21, 1980.

Any discussion of this paper will appear in a Discussion Section to be published in the December 1981 JOURNAL. All discussions for the December 1981 Discussion Section should be submitted by Aug. 1, 1981.

Publication costs of this article were assisted by Bell Laboratories.

REFERENCES

1. F. G. Peters and N. Schwartz, TM 77-1528-31; G. T. Kohman, H. W. Hermance, and G. H. Poanes, *Bell Syst. Tech. J.*, **34**, 1115 (1955).
2. J. C. Harrison, *Microelectron. Reliab.*, **16**, 233 (1977).
3. (a) T. E. Graedel and N. Schwartz, *Materials Performance*, **16**, 17 (1977); (b) K. L. Schiff and N. Harmsen, *Z. Elektrotech (ETZ-B)*, **28**, 896 (1976).
4. N. Harmsen, *ibid.*, **28**, 902 (1976).
5. N. Schwartz and D. D. Bacon, *This Journal*, **125**, 1487 (1978).
6. (a) N. N. Schwartz, G. L. Link, D. D. Bacon, and D. R. Falcone, Unpublished results (1977); (b) E. Kinsbron, D. D. Bacon, and A. T. English, Unpublished results (1978).
7. (a) C. T. Kemmerer and C. T. Hartwig, Unpublished results (1979); (b) L. G. Feinstein and N. L. Sbar, *IEEE Trans. Comp. Hybrids Manuf. Tech.*, **chmt-2**, 159 (1979); (c) L. G. Feinstein

- and N. L. Sbar, Unpublished results (1975).
8. R. B. Husar, J. P. Lodge, Jr., and D. J. Moore, Editors, "Sulfur in the Atmosphere," Proceedings of the International Symposium on Sulfur in the Atmosphere, Dobrovnik, Yugoslavia, September, 1977 (Pergamon Press, 1978).
 9. K. Iwamoto, N. Presser, and J. Ross, *J. Chem. Phys.*, **68**, 663 (1978).
 10. T. E. Graedel, *Rev. Geophys. Space Phys.*, **15**, 421 (1977); T. E. Graedel, "Atmospheric Photochemistry," in *Hand. Env. Chem.*, O. Hutzinger, Editor, In press, Springer (Berlin) 1980; J. T. Herron, R. E. Huie, J. A. Hodgeson, Editors, "Chemical Kinetic Data Needs for Modeling the Lower Troposphere," NBS Special Publ. 57, U.S. Dept. Commerce, Wash. D.C. (1979); R. D. Cadle and E. R. Allen, *Science*, **167**, 243 (1970).
 11. H. W. Sidebottom, C. C. Badcock, G. E. Jackson, J. G. Calvert, G. W. Reinhardt, and E. K. Damon, *Env. Sci. Tech.*, **6**, 72 (1972).
 12. J. P. Smith and P. Urone, *ibid.*, **8**, 742 (1974).
 13. O. Tokunaga, K. Nishimura, and M. Washino, *Int. J. Appl. Rad. Iso.*, **29**, 87 (1978).
 14. P. Urone, H. Lutsep, C. M. Noyes, and J. F. Parcher, *Env. Sci. Tech.*, **2**, 611 (1968).
 15. (a) S. Beilke, D. Lamb, and J. Müller, *Atmos. Environ.*, **9**, 1083 (1975); (b) W. D. Scott and P. V. Hobbs, *J. Atmos. Sci.*, **24**, 54 (1967); (c) J. M. Miller and R. G. de Pena, *J. Geophys. Res.*, **77**, 5905 (1972); (d) H. A. C. McKay, *Atmos. Environ.*, **5**, 7 (1971).
 16. D. J. O'Brien and F. B. Birkner, *Env. Sci. Tech.*, **11**, 1114 (1977).
 17. J. N. Driscoll and A. W. Berger, "Improved Chemical Methods For Sampling and Analysis of Gaseous Pollutants from the Combustion of Fossil Fuels, Vol. I Sulfur Oxides," National Tech. Inform. Service PB 209 267/APTD 1106 (1971).
 18. D. Bienstock, L. W. Brunn, E. M. Murphy, and H. E. Benson, "Sulfur Dioxide—Its Chemistry and Removal From Industrial Waste Gases," U.S. Bureau of Mines, Circular 7836 (1958).
 19. (a) H. N. Alvea and H. L. J. Bäckström, *J. Am. Chem. Soc.*, **51**, 90 (1929); (b) D. Flint, *JSCI*, **67**, 2 (1948).
 20. Texas Department of Health, Air Pollution Central Services "Compliance Sampling Manual," II41-II-50, Austin, Texas (1972).
 21. (a) D. C. Marvin and H. Reiss, *J. Chem. Phys.*, **69**, 1897 (1978); (b) P. Mirabel and J. L. Clavelin, *ibid.*, **68**, 5025 (1978); (c) R. H. Heist and H. Reiss, *ibid.*, **61**, 573 (1974).

Preparation of Tin Oxide Films from Ultrafine Particles

Hisahito Ogawa, Atsushi Abe, Masahiro Nishikawa, and Shigeru Hayakawa

Matsushita Electric Industrial Company, Limited, 1006 Kadoma, Osaka, 571 Japan

ABSTRACT

A highly reproducible procedure for preparing films from ultrafine particles of metal oxides has been developed. The ultrafine particles of several tens of angstroms in size are grown by the evaporation of the metal in low oxygen gas pressure, and subsequently, the film is constructed from the ultrafine particles aligned in a specific direction on the substrate. The particles' size and film structure were studied under various deposition conditions, i.e., oxygen gas pressure, rf activation power, evaporation temperature, and others. The ultrafine particle films prepared with this procedure may serve as a highly sensitive gas sensor.

Increasing attention is being paid to studies on tin oxide materials, especially on the method of preparation of sintered materials and thin films of tin dioxide and evaluation of their electrical properties for gas sensors. It is important to pay special attention to the surface quality of the tin oxide materials, because the change in conductance of gas sensors takes place at the boundary between the gaseous and solid states.

The specific surface area of crystals, i.e., the surface area of the crystals per unit weight (cm²/g), increases as the particle size decreases. Hence, if one studies the physical properties associated with the crystal surface, such as gas adsorption and light dispersion, the properties are strongly dependent on the particle size (1-3), and may be enhanced with ultrafine particles. In order to supply samples for studying the physical properties of ultrafine particles, we have studied the preparation of ultrafine particles in the size range of several tens of angstroms and films of these particles deposited on a glass substrate.

The preparation methods for fine particles which are usually considered are the following: (i) mechanically grinding large particles to a smaller desired size, and (ii) nucleation and growth of particles by chemical reaction of the constituent elements under controlled

conditions. The latter method, combined with a gas-evaporation technique, which can easily produce low surface distortion, high purity, and small size particles, is preferable to the grinding one. Many studies on the growth and morphology of metallic particles (4-8) have been carried out by the gas-evaporation technique. A few reports have been made on metal oxides (9, 10). None of these studies, however, supplies enough information on the formation of films made with ultrafine particles of metal oxides which is the subject of this report.

We found a new procedure for growing the appropriate ultrafine particles of certain metal oxides in oxygen atmosphere, and subsequently, a method for producing films consisting of the ultrafine particles aligned in a specific direction on the substrate. The details of the preparation and the optimized conditions will be described below.

Deposition of Metal Oxides

The vacuum deposition chamber used in this study is illustrated in Fig. 1. The specific features arranged in the chamber were (a) a quartz cylinder guiding the ultrafine particles from an evaporator boat to a substrate, and (b) an rf coil electrode consisting of several turns of stainless steel tubing. The rf coil was operated with a 13.56 MHz oscillator through a matching box.

Key words: ultrafine particle films, tin oxide, gas-evaporation technique, oxygen gas plasma, gas sensor.

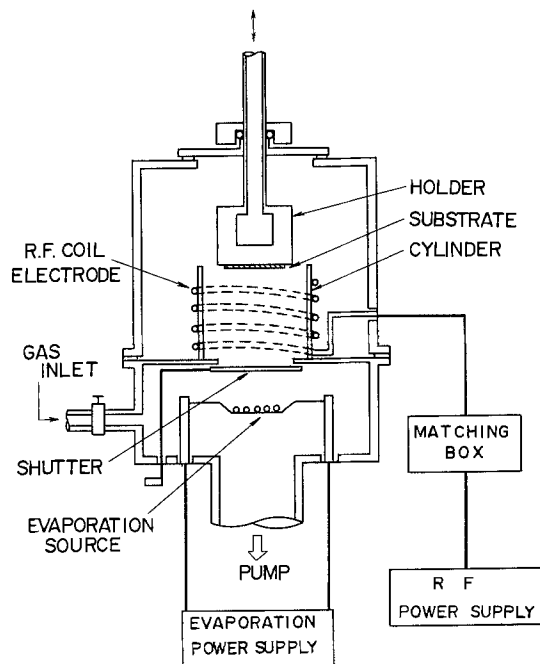


Fig. 1. The apparatus arrangement in this experiment

The glow discharge of the oxygen in the vacuum chamber was produced in the region adjacent the rf coil by applying the high oscillating field between the coil and chamber.

The samples were prepared using the following procedures. A glass substrate was supported by a sample holder. A high purity metal (greater than 99.99%) such as Sn, Mn, Zn, or Cu was placed in the evaporator boat. The chamber was pumped down to approximately 2×10^{-6} Torr and then oxygen gas was introduced into the chamber. A glow discharge in the oxygen gas (white color) was produced by applying the rf power. Then power was supplied to the boat to evaporate the metal. The growth of the ultrafine metal oxide particles in the glow discharge of oxygen gas was easily detected with the observation of the discharge color turning to purple (in the case of tin oxide) from white.

When the boat temperature was stabilized, a shutter was opened to deposit the ultrafine metal oxide particles on the substrate. The deposition was continued for several minutes, depending on the desired thickness of the final ultrafine particle film.

The metal oxides deposited on the substrate were significantly dependent, both physically and chemically, upon the oxygen gas pressure in the vacuum chamber. Most of our studies were with Sn as the metallic reactant and are thus the principal subject of this report. Evaporation of Sn metal yields a film consisting of a mixture of SnO_2 and SnO for oxygen gas pressures between 0.1 and 10 Torr. It can be seen that no peaks from tin metal ultrafine particles exist in the x-ray diffraction spectrum, indicating extensive chemical reaction between evaporating tin atoms and oxygen molecules in the chamber. The percentage (Γ) of SnO_2 content in the final products was estimated from the ratio of the intensities of the given x-ray diffraction lines of SnO_2 (at $2\theta = 26.6^\circ$) and SnO (at $2\theta = 29.9^\circ$), with the aid of a calibration curve made from a physical mixture of SnO_2 and SnO powders. As described later, the value of Γ was a sensitive function of the oxygen gas pressure, evaporation temperature, and activation power in the plasma.

The appearance of the metal oxide ultrafine particle films deposited on the substrate is also affected by the oxygen gas pressure. Figure 2 shows photomicrographs, taken by a scanning electron microscope, of tin oxide ultrafine particle films deposited at oxygen gas pressures of 0.05, 0.5, and 5.0 Torr, respectively. It may be

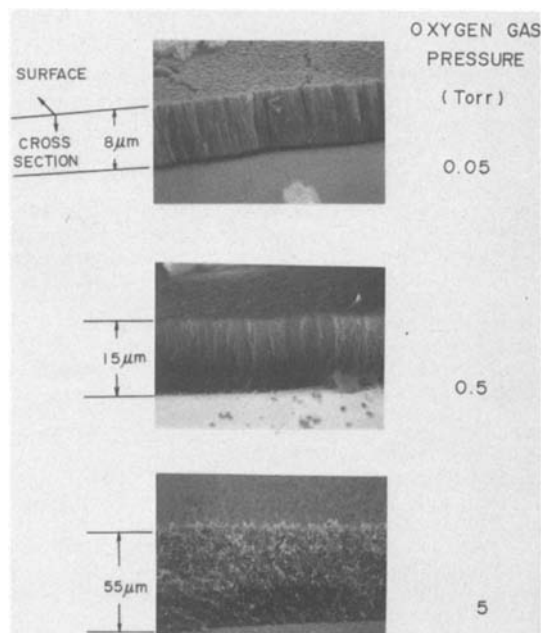


Fig. 2. Scanning electron micrographs showing the structure of tin oxide ultrafine particle films deposited at three different oxygen gas pressures.

seen that the structure and thickness of the ultrafine particle films are markedly dependent upon the oxygen gas pressure and vary from oriented columnar to spongy structures. When the oxygen gas pressure is less than 0.05 Torr, the ultrafine particle film has a smooth, flat surface with an inferior columnar structure perpendicular to the surface of the substrate. For oxygen gas pressures greater than 0.2 Torr, derangement occurs in the columnar structure and the thickness of the ultrafine particle film is increased. The growth of the ultrafine particle film is accelerated with the oxygen gas pressure at 5 Torr, resulting in a spongy appearing film with a rough surface.

Determination of Particle Size

An ultrafine particle film, even a single column in the film, consists of an agglomeration of many ultrafine particles, of the order of tens of angstroms in size. The particle sizes and crystallization of the ultrafine particles were determined first from observation with an electron microscope.

Figure 3 shows an electron micrograph and an electron diffraction pattern of ultrafine tin oxide particles.

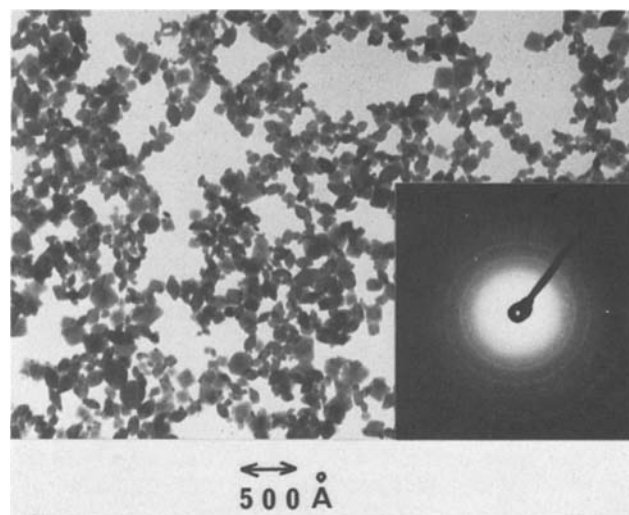


Fig. 3. Transmission electron micrograph and electron diffraction pattern of ultrafine tin oxide particles.

One may see the spotty diffraction rings, indicating that the ultrafine particles are crystallized well. This is consistent with the observation of flat crystal faces in the micrograph. Microcrystallites consisting of octahedra and truncated octahedra are clearly evident (9). The distribution of sizes of the ultrafine particles is log-normal. The sizes of 185 particles on the micrograph were measured by a ruler, and the result is shown in Fig. 4 in a size distribution histogram. The calculated curve of the log-normal distribution is also shown with a solid line. The median particle size (\bar{x}) is calculated from the data to be 152Å.

The determination of particle size distribution by the electron microscope may be accurate and precise, but is very tedious. It is found that the mean particle size D of the ultrafine particles can also be estimated from the broadening of the lines in the x-ray diffraction spectrum, by applying Hall's equation (11)

$$\frac{\beta \cos \theta}{\lambda} = \frac{1}{D} + 2\epsilon \frac{\sin \theta}{\lambda} \quad [1]$$

where λ is the wavelength of x-ray used (in this case, $\lambda = 1.5404\text{Å}$), β is the width of the line at the half-maximum intensity, and ϵ is the degree of crystal distortion. The estimated values of D and ϵ (for the same sample observed in the electron microscope) were $D = 160\text{Å}$ and $\epsilon = 3 \times 10^{-3}$, respectively. This means particle size D is in good agreement with the value of the median particle size D measured using the electron microscope. Thus, we can determine the size of the ultrafine particles by means of the x-ray diffraction lines, instead of the tedious method by the electron microscope. We used the x-ray diffraction method for further size measurements of ultrafine particles in deposited films.

Particle Size Dependence on the Oxygen Gas Pressure

Figure 5 shows the curves of the D values for ultrafine tin oxide particles determined from the x-ray diffraction spectrum as a function of oxygen gas pressure under the evaporation conditions of the evaporation temperature $T = 1100^\circ\text{C}$, the rf power $RF = 0$ watt (i.e., no plasma), and the distance between the evaporation source and substrate $L = 7$ cm. Similar results were also obtained with different T and L . The results shown in Fig. 5 indicate that the growth

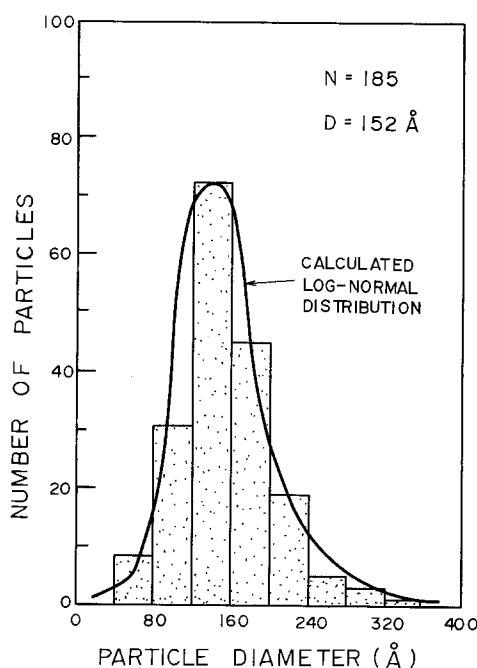


Fig. 4. A histogram of the particle size of tin oxide (shaded). The solid curve represents a log-normal distribution calculated for $\bar{x} = 152$, $\sigma = 1.4$.

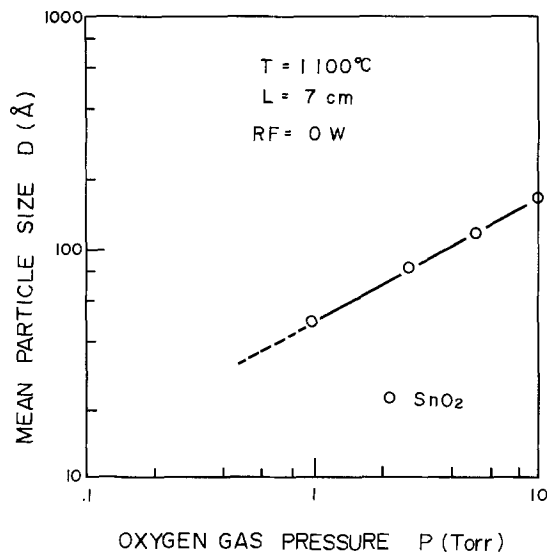


Fig. 5. The mean particle size D of SnO_2 particles as a function of oxygen gas pressure.

rate dependence of ultrafine particle films of SnO_2 on oxygen gas pressure (P) can be expressed by

$$D = kP^{1/2} \quad [2]$$

where k is a constant determined by T and L .

The growth mechanism of ultrafine metal oxide particles on the substrate is not yet well understood, even though a mutual collision-coalescence of particles and a complicated chemical reaction of the oxidation between metal atoms and oxygen molecules have obviously occurred during the deposition. Therefore, we cannot propose a model to explain the sublinear dependence of the particle size on the oxygen gas pressure.

Evaporation Conditions for Tin Oxide Films

As already mentioned, the composition of the film of the ultrafine tin oxide particles (i.e., SnO_2 and SnO), as revealed by the x-ray diffraction analysis, is markedly dependent on the evaporation conditions. Figure 6 shows the values of D and Γ as a function of the distance L between the evaporation source and substrate, for two evaporation temperatures of 1100° and 1350°C . For evaporation temperatures below 1100°C , the values of D and Γ are essentially independent of both T and L , ($D_{\text{SnO}_2} = 40\text{Å}$ and $\Gamma = 16\%$). For $T > 1100^\circ\text{C}$, the values of D and Γ are increased with increasing T and L , showing an increase in the content of large SnO_2 particles in the film with T and L . The measured temperature of the oxygen atmosphere for different values of L are also plotted in Fig. 6. These temperature profiles show that in the case of $T = 1350^\circ\text{C}$, the oxygen gas at $L < 7$ cm is heated enough for the conversion of SnO to SnO_2 (the conversion easily occurs above 170°C , as described later). Thus, the increase in the values of both D and Γ is caused by the reaction in the oxygen gas. If $\text{SnO} \rightarrow \text{SnO}_2$ is the sequence of the reaction of the evaporating metal particles with the active oxygen gas, this reaction would be favored by the particles travelling longer distances, i.e., large D and Γ would result for large L . The heated oxygen gas may be active at the evaporation temperature of 1350°C . When an rf field is applied, the oxygen plasma gas should be very active for oxidation even at a lower temperature. This has been examined for $T = 1100^\circ\text{C}$.

The rf power (RF) was varied from 0 to 500W. Figure 7 shows the dependence of D and Γ on the rf power. The mean particle size D_{SnO_2} of SnO_2 particles in the film increased from 40 to 52Å as the rf power was increased to 150W, and the percentage of SnO_2 progressively increased from 16 to 66%. The values of

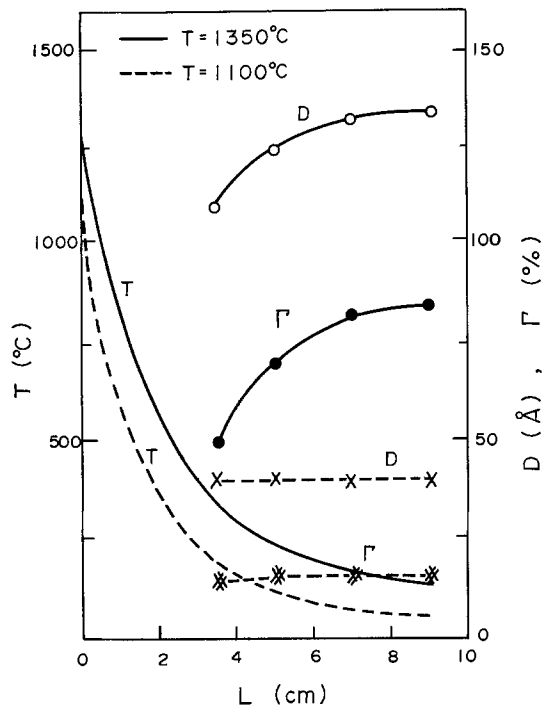


Fig. 6. The mean particle size D of tin oxide particles and the percentage Γ of SnO_2 content in films as a function of the distance L between the substrate and source. The tin oxide particles were prepared at temperatures $T = 1350^\circ\text{C}$ and 1100°C .

D and Γ increased linearly with rf power up to 100W and, for rf power greater than 150W, the values of D and Γ were almost constant ($D \sim 50\text{\AA}$ and $\Gamma \sim 70\%$). The temperature of the oxygen gas slightly increased during the operation of the rf discharge, less than 150°C even with an rf power of 500W, therefore, the growth of SnO_2 ultrafine particles could not be attributed solely to the temperature rise of the oxygen gas. Thus, the oxidation of SnO ultrafine particle is promoted in the active oxygen gas plasma even though the oxidation is not completed; the value of Γ is saturated at 67%. To obtain a pure SnO_2 film with $D = 52\text{\AA}$, another treatment was necessary.

In order to understand the conversion of SnO to SnO_2 , we have studied the thermogravimetry (TG)

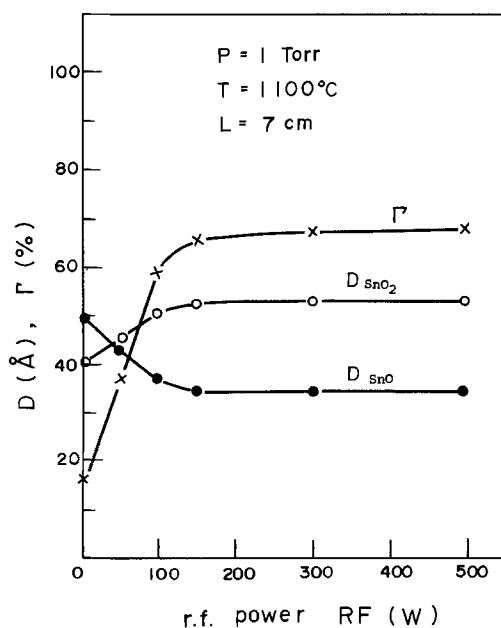


Fig. 7. The mean particle sizes D_{SnO_2} and D_{SnO} and the percentage Γ of SnO_2 content in films as a function of rf power (RF).

and differential temperature analysis (DTA) of the film in air. Two samples prepared under the following conditions were tested.

Sample No. 1 $P = 1$ Torr, $T = 1100^\circ\text{C}$, $RF = 150\text{W}$,
 $\Gamma = 66\%$

Sample No. 2 $P = 1$ Torr, $T = 1100^\circ\text{C}$, $RF = 0\text{W}$,
 $\Gamma = 16\%$

Figure 8 shows the TG and DTA curves obtained with the temperature rising at a rate $10^\circ\text{C}/\text{min}$. The results show the complete oxidation of SnO to SnO_2 at 300°C . This is confirmed by the x-ray diffraction analysis. The SnO is stable below 150°C . As the temperature is raised, the DTA curve shows an exothermic band, between 170° and 300°C with the peak at 220°C , showing that the oxidation of SnO to SnO_2 occurs in this temperature region. The TG curve shows an increase in weight, in the same temperature range, also indicating the oxidation of SnO to SnO_2 . On the basis of these observations, we could say that the conversion of SnO to SnO_2 by means of the heat-treatment is dependent on the initial value of Γ . To confirm the oxidation of SnO to SnO_2 , the ultrafine particle films prepared were annealed at various temperatures up to 250°C . Each sample was held for 30 min in air at the given temperature. The results obtained are shown in Fig. 9.

For the ultrafine particle film prepared under no plasma ($RF = 0\text{W}$) (Sample No. 2), the values of D and Γ increased progressively with annealing temperature, to a maximum of $D = 70\text{\AA}$ and $\Gamma = 84\%$ which did not fit our requirements. Because, in detecting combustible gases, the tin oxide film comprising 100% SnO_2 ultrafine particles (i.e., $\Gamma = 100\%$) has high sensitivity as compared with the film comprising mixed SnO-SnO_2 ultrafine particles. It is also found that there is an optimum particle size for the gas sensing film.

On the other hand, the samples deposited under $RF = 150\text{W}$ (Sample No. 1) convert completely to pure SnO_2 with only a small increase in size (from 52 to 56\AA at 250°C). Observation of the annealed ultrafine particle film with the scanning electron microscope re-

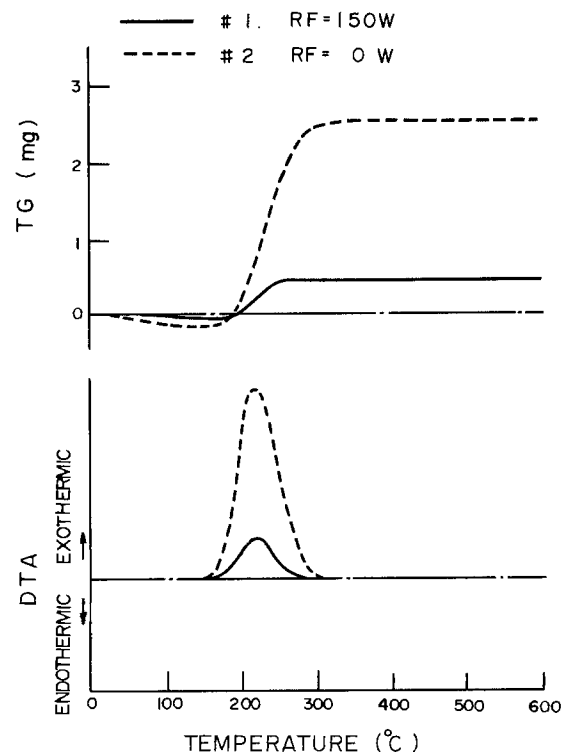


Fig. 8. Thermogravimetry and differential temperature analysis curves of tin oxide particles prepared with two different rf powers, $RF = 150\text{W}$ and 0W .

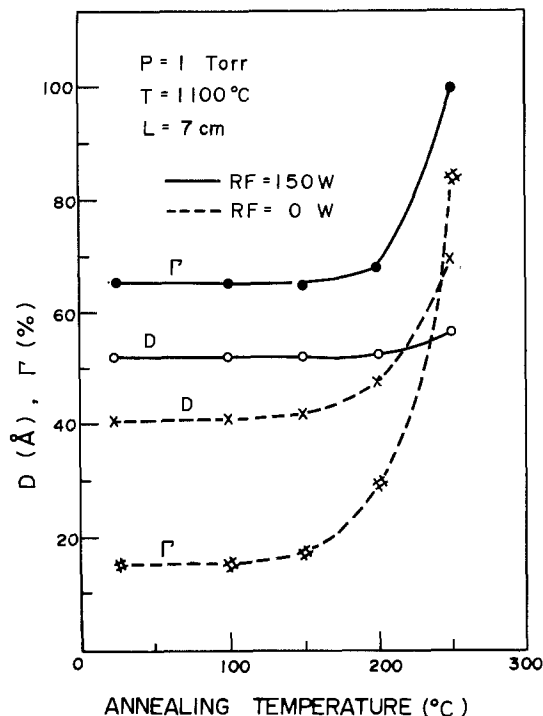


Fig. 9. The mean particle size D of SnO_2 particles and the percentage Γ of SnO_2 content in films of Fig. 7 as a function of annealing temperature.

vealed the columnar structure. Thus, the film structure is not altered by the annealing. Because the D -values of SnO_2 and SnO ultrafine particles grown at 1100°C in $RF = 150\text{W}$ are less sensitive to deposition conditions, good reproducibility was obtained for the film.

Summary and Conclusions

We have developed a procedure for preparing a columnar structure film of SnO_2 . A film comprising 100% SnO_2 particles about 50\AA in size was realized with a high reproducibility by the following procedure.

An initial deposit of mixed SnO-SnO_2 ultrafine particles was prepared in an oxygen gas plasma with an rf power input of 150W , subsequent heating of this deposit at 250°C in air for 30 min fully converted the film to SnO_2 without significant particle growth. This film may serve as a highly sensitive gas sensor.

Acknowledgments

The authors would like to express our hearty thanks to Dr. T. Nemoto, Dr. S. Sekido, and Dr. M. Mikoda for their deep interest throughout the progress of the work, and Professor R. Kiriyama and Dr. L. Ozawa for many useful discussions, and Messrs. T. Murakami and M. Fujii for the electron micrograph analysis. This work was supported by MITI subsidy for important technological research and development.

Manuscript submitted July 28, 1980; revised manuscript received Oct. 20, 1980.

Any discussion of this paper will appear in a Discussion Section to be published in the December 1981 JOURNAL. All discussions for the December 1981 Discussion Section should be submitted by Aug. 1, 1981.

Publication costs of this article were assisted by Matsushita Electric Industrial Company, Limited.

REFERENCES

1. D. B. Tanner, A. J. Sievers, and R. A. Buhrman, *Phys. Rev. B*, **11**, 1330 (1975).
2. J. R. Anderson, R. F. Macdonald, and Y. Shimoyama, *J. Catal.*, **28**, 147 (1970).
3. J. C. Slater and K. H. Johnson, *Phys. Today*, Oct., 34 (1974).
4. C. G. Graugvist and R. A. Buhrman, *J. Appl. Phys.*, **47**, 2200 (1976).
5. K. Kimoto, Y. Kamaya, M. Nonoyama, and R. Uyeda, *Jpn. J. Appl. Phys.*, **2**, 702 (1963).
6. Y. Saito, S. Yatsuya, K. Mihama, and R. Uyeda, *ibid.*, **17**, 291 (1978).
7. G. H. Comsa F. Hensel, and F. Ringelmann, *Le Vide*, **30**, 113 (1975).
8. M. Rappaz and F. Feas, *J. Appl. Phys.*, **46**, 3273 (1975).
9. C. Kaito, K. Fujita, H. Shibahara, and M. Shiojiri, *Jpn. J. Appl. Phys.*, **16**, 697 (1977).
10. M. Kato, *ibid.*, **15**, 757 (1976).
11. W. H. Hall, *Proc. Phys. Soc., A*, **62**, 741 (1949).

On the Kinetics of the Thermal Oxidation of Silicon

III. Coupling with Other Key Phenomena

William A. Tiller

Department of Materials Science and Engineering, Stanford University, Stanford, California 94305

ABSTRACT

A new model of transformation is proposed which leads to a much reduced excess free energy storage. Silicon is transformed to α -cristobalite plus interstitial Si ions. Subsequent oxidation of these interstitials produces rapid distortion of the lattice and speedy transformation of the structure to vitreous silica. The model allows a satisfactory qualitative explanation of both the orientation and temperature dependence of oxidation-enhanced diffusion (OED), oxidation-induced stacking faults (OISF), interface states (N_{it}), fixed oxide charge (Q_f), oxidation velocity (V), oxide density interface stoichiometry (SiO_x), and silicon interstitial partition coefficient (k_I).

In Part I (1) of this series a general overview was given of the partitioning of the total driving force for the oxidation process into the key parallel subprocesses. Attention was focused on the free volume sup-

Key words: semiconductor processing, thermodynamics, point defects, silicon dioxide, interstitials.

ply condition needed to sustain such a transformation and on the specific mechanism available for free volume generation. In Part II (2), the transport subprocess was predicted to be electric field and orientation dependent and to involve charged as well as neutral species. The excess free energy subprocess due to the

large molecular volume difference between Si and SiO₂ was shown to dominate the Si/SiO₂ oxidation and to lead to a possible interface structure wherein a cross-grid of extra half-planes terminated at the Si side of the Si/SiO₂ interface. Propagation of the interface to the Si phase required continuous removal of these extra atoms via one of several mechanisms.

Associated with the oxidation process in Si, there are a number of other phenomena that beckon for understanding. There is the oxidation-enhanced diffusion (OED) phenomenon (3-6), the oxidation-induced stacking fault (OISF) formation phenomenon (5, 7), plus the interface charge (N_{it}) and fixed oxide charge (Q_f) phenomena which all need to be understood in relationship to the oxidation process. One would also wish to understand their orientation and temperature dependences.

The primary purpose of this paper is to present a new way of looking at the oxidation process that allows one to qualitatively explain all of the foregoing phenomena with their associated orientation and temperature dependences as well as the orientation and temperature dependence of the oxidation velocity, V , the interface oxide density, and the interface stoichiometry SiO_x. Some quantitative assessment of these phenomena is given as well.

Analysis

Structural model of phase change.—Let us first consider what crystalline phase of SiO₂ would be the best match to continuously transform Si in the $\langle 100 \rangle$ direction. We shall assume that the system selects that phase which lowers the excess free energy contribution, ΔG_E (1, 2), the most, and then we shall look at the consequences of this choice and this approach.

The SiO₂ molecular volume increases from β -quartz (38.8Å³) to α -cristobalite (43.6Å³), β -cristobalite (45.3Å³), and then to tridymite (52.0Å³) compared to the atomic volume of Si (20.0Å³) and vitreous silica (44.5Å³). Transformation of the Si phase to these SiO₂ phases requires massive reconstruction except for the cristobalites and the vitreous phase. Direct intrusion of O atoms between each Si-Si bond in the Si lattice creates the β -cristobalite lattice under a compressive strain of 31%. Similar direct formation of vitreous SiO₂ from the Si lattice results in an amorphous film under a 30% compressive strain. However, the direct formation of α -cristobalite seems to offer a potentially much lower value of ΔG_E .

Consider the (100) face of the Si unit cell and the (100) face of the tetragonal α -cristobalite unit cell whose projections are shown in Fig. 1. In the Si unit cell we have 8 atoms. By completely removing the 4-Si atoms at the $\frac{1}{4}$ and $\frac{3}{4}$ positions and slightly displacing the other 4-Si atoms followed by oxidation of these 4

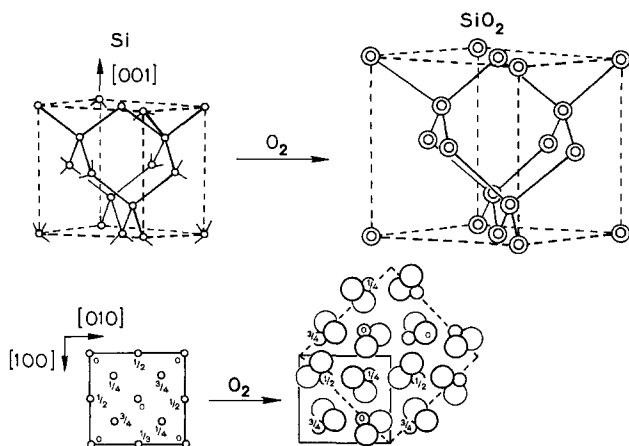


Fig. 1. Projection of the Si and the α -cristobalite unit cells onto their (100) planes. The dashed square represents the pseudo-diamond cubic unit cell of α -cristobalite.

remaining Si atoms, we obtain the α -cristobalite unit cell. This produces a biaxial tension in the film parallel to the interface of $\sim 9\%$ and no strain in the perpendicular direction because the unit cell can expand freely in this direction. This would yield a strain energy $< 9\%$ of that generated by forming the β -cristobalite directly. However, we still have the 4 removed Si atoms per unit cell to place back into the system in interstitial positions and this will move the system toward compressive strain and will increase the excess free energy. Placing these interstitials into the Si and the SiO₂ at the interface will stretch the respective unit cells to varying degrees depending on the degree of partitioning of these 4 extra Si atoms between the two phases. Thus, if the majority of these extra Si atoms enter the SiO₂, we can expect relaxation to occur at the interface such that some extra half-planes on the Si side will terminate at the interface (see Fig. 2). The number of these planes per unit area of interface will depend on the partitioning ratio of the Si interstitials between the two phases. Since the dangling bonds at the interface ends of these half-planes constitute interface electronic states, this is probably the source of N_{it} (8). We thus see that the magnitude of N_{it} depends critically on the interstitial partitioning ratio at the interface. In addition, we note in Fig. 1 that, at 45° to the α -cristobalite unit cell, the structure is pseudo diamond-cubic with a lattice spacing slightly smaller than that of β -cristobalite. Thus, the proposed transformation leads to a relatively well-matched diamond-cubic phase that is then stressed in compression by the interstitials placed therein. This leads to an increased density of the interfacial silicate and to an interface silicate stoichiometry of SiO_x where $x \approx 1$. If the β -cristobalite phase or the vitreous phase had formed directly from the Si, it would not have been possible to obtain this interface stoichiometry or excess interfacial density.

The key point of this concept is that the SiO₂ forms a suitable structure with extra atoms being placed in interstitial positions rather than forms a structure without interstitials. We shall see later that the former choice is the energetically favorable one. The second point concerning this concept relates to the actual structure that the interface SiO₂ takes. There is only a slight preference for α -cristobalite over β -cristobalite since both produce extra half-planes of Si at the interface that must end up in interstitial positions. There is less reason to choose vitreous SiO₂ because this requires some additional disordering mechanism and there is no rationale for choosing which Si atoms are destined to become interstitial species. We shall see later that a mechanism exists for the rapid transition of the crystalline SiO₂ phase to the vitreous SiO₂ phase within a few molecular distances of the interface. The crystalline SiO₂ phase thus exists only as a buffer layer between the Si and the vitreous SiO₂, but it plays a crucial role in the overall transformation process.

Point defect thermodynamics.—Neglecting any electric field or strain field effects, Appendix A gives the

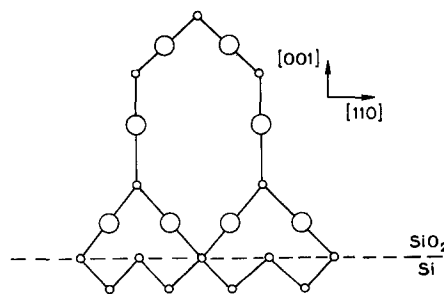


Fig. 2. Projection of Si/SiO₂ interface cross section illustrating the extra half-planes of Si that terminate at the interface with α -cristobalite.

chemical potential of defect species i , $i = \text{vacancy (V)}$ or interstitial (I), in each phase $j = \text{Si or SiO}_2$ to be (9)

$$\mu_{ij} = kT \ln \left[\frac{n_{ij}(n_{sj} - n_{ij}^*)}{n_{ij}^*(n_{sj} - n_{ij})} \right] \quad \begin{array}{l} i = \text{V, I} \\ j = \text{Si, SiO}_2 \end{array} \quad [1]$$

Here, n_i is the average number of i -defects per unit cell, n_{sj} is the number of possible i -defect sites per unit cell, and n_i^* is the average equilibrium number of i -defects given by

$$\frac{n_i^*}{n_{sj} - n_i^*} = e^{\Delta S_i^V/k} e^{-\Delta H_i/kT} \quad [2]$$

where ΔS_i^V is the vibrational entropy contribution and ΔH_i is the enthalpy of formation of the i -defect. In general, we expect $n_i^* \ll n_s$ for each phase. For Si, $n_{sV} = 8$, $n_{sI} = 5$ (10), $\Delta H_V = 2.4$ eV while $\Delta H_I \sim 8$ eV (11). For α -cristobalite, $n_{sV} = 4$ for Si, O, or SiO₂ vacancies, while $n_{sI} \sim 15$ (one I-defect adjacent to each O site in a ring), and no information is available on the ΔH values; however, it is well known that many different kinds of interstitial ions enter the interstitial spaces in natural β -cristobalite so it is expected that ΔH_I will be small for this defect in SiO₂ (10). Certainly, it is expected that $\Delta H_{I\text{SiO}_2} \ll \Delta H_{I\text{Si}}$ (11, 12). For the vacancy species as well as the interstitial species in SiO₂, one must consider Si, O, O₂, SiO, SiO₂, SiO₃, SiO₄, and (O-Si-O)_n chains as candidates. For each of these defect species, the free energy change for the phase, ΔG_{ij} , has the form given by Fig. 3 where the minimum gives the location of the equilibrium i -defect content, n_i^* ($\mu_i^* = 0$). For our interest here, we will generally be interested in i -defect contents far removed from n_i^* where ΔG_{ij} is no longer negative, but may have a large positive value.

Since so little is known about point defects in SiO₂, let us consider the consequences of adding large numbers of I-defects to the Si phase. Since the I-defects are so much more energetic than the V-defects, the free energy of the system will be lowered by recombination events between I- and V-defects. If there were no vacancy sources in the system, the V-concentration would be greatly reduced until its chemical potential, μ_V , had been sufficiently reduced that

$$\frac{\partial G}{\partial n_I} + \frac{\partial G}{\partial n_V} = 0 \quad [3a]$$

or

$$\frac{n_V n_I}{n_V^* n_I^*} \left[\frac{(n_s - n_I^*)}{(n_s - n_I)} \right] \approx 1 \quad [3b]$$

Thus, since μ_I will be large and positive, μ_V will be large and negative. At this point, the recombination

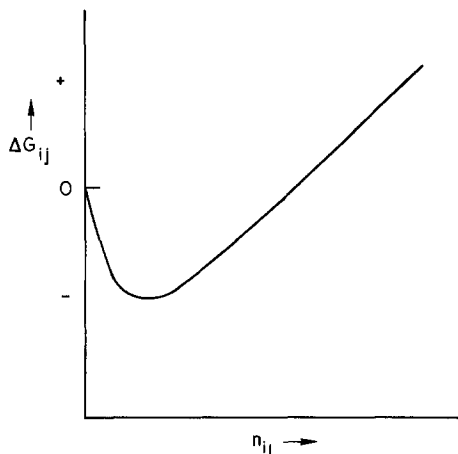


Fig. 3. Excess free energy of formation, ΔG_{ij} , of i -type defects in phase j as a function of number of defects per unit cell, n_{ij} .

process no longer lowers the free energy of the system and it will stop. This leaves us with $n_I \gg n_I^*$ and $n_V \ll n_V^*$. In general, we can expect two or three types of vacancy sources in the system. The first is the small voids in the Si created by vacancy supersaturation due to initial cooling of the crystal from the melting temperature. This should give a total potential vacancy supply of $\sim 10^{15}/\text{cm}^3$ (i.e., all those formed at the melting point). The second is dislocation lines which can climb in a direction so as to generate vacancies (total potential supply $< 10^{14}/\text{cm}^3$, i.e., $\sim 10^3$ lines/ $\text{cm}^3 \times \sim 4 \times 10^7$ sites/line $\times \lesssim 2500$ climb steps/site). The third is the Si/SiO₂ interface where vacancies in the SiO₂ lattice may transfer to the Si phase. Depending on the kinetics of supply of vacancies from these sources, the vacancy concentration of bulk Si may or may not be reduced to levels such that Eq. [3] is satisfied.

The probability of interstitial annihilation, P_A , is given by the product of P_{VN} = probability that a vacancy is in a neighboring site and P_J = probability of a net jump into the vacant site. Thus, since there are 6 possible lattice sites in the ring surrounding each interstitial site, we have

$$P_A = 6X_V \frac{\nu}{6} e^{-Q_A^*/kT} (1 - e^{-(\mu_I - \mu_V)/kT}) = P_A' n_V \quad [4]$$

where X_V is the fraction of vacancies, $P_A' = P_A/8$, ν is the vibrational frequency, and Q_A^* is the activation barrier between the ring center and a lattice site on the ring. The differential equation governing the interstitial content is

$$D_I \nabla^2 n_I - P_A' n_V n_I = \frac{\partial n_I}{\partial t} \quad [5]$$

While that governing the vacancy content is

$$D_V \nabla^2 n_V - P_A' n_I n_V + \dot{Q}_V^S = \frac{\partial n_V}{\partial t} \quad [6a]$$

where \dot{Q}_V^S is the volume source supply rate per unit cell of Si. The strength of this vacancy source is given by (13)

$$\dot{Q}_V^S = \frac{A_V^S \nu}{\Omega^{2/3} 6} e^{-Q_S^*/kT} [f_V^S - X_V e^{(\mu_V - \delta E)/kT}] \quad [6b]$$

where Ω is the atomic volume of Si, A_V^S is the active area of the vacancy source, f_V^S is the fraction of surface sites from which a vacancy can be introduced into the Si with activation energy Q_S^* , and δE is the energy change of the source due to the loss of one vacancy, i.e.

$$\delta E = \left(\frac{dE_V^S}{dr} \right) \Delta r = \frac{2\Omega\gamma}{r} \quad [6c]$$

for a spherical source of radius r and surface energy γ . In Eq. [6b], μ_V is negative.

Interstitial partition coefficient.—The equilibrium partition coefficient, k_1^* , between the concentration of interstitial species in SiO₂ at the interface to the concentration in Si at the interface will be determined by the equality of the electrochemical potential, η_i , of this defect species, Si_i, in each phase at the interface

$$\eta_{I\text{Si}} = \eta_{I\text{SiO}_2} \quad \text{at Si/SiO}_2 \quad [7]$$

Neglecting any electric field or strain field effects, Eq. [1] is inserted in Eq. [7] with $\eta_I = \mu_I$. It should be noted in Eq. [1] that the value of n_{ij}^* is dependent on the actual conditions applying at the interface; i.e., on thermal expansion stresses, disregistry stresses due to interfacial orientation constraints when one alters the Si orientation, and on the presence of electric or macroscopic stress fields. Thus, in general, $\eta_I \neq \mu_I$. These refinements will be considered as second-order effects for this paper; however, it should be recognized that

there will undoubtedly be some circumstances when they may become first-order effects.

We are actually interested in the nonequilibrium partition coefficient, k_I , for the I-defect at the interface. The initial I-defects can be thought of as being created in the α -cristobalite lattice by the breaking of Si-Si bonds (thermally activated process) so that the corner Si atoms are free to become SiO₂ while the 4 inner Si atoms become I-defects. The entrance of the I-defects into the Si side of the interface then involves an activation step because the enthalpy of formation of the I-defect in Si is expected to be much higher than in SiO₂ (11, 12). This is conceptually illustrated in Fig. 4. Actually, instead of the two-step process proposed above, the process of I-defect partitioning is a single-step process which is outlined mathematically in Appendix B. However, because the two-step process is more tractable mathematically at this stage in our understanding, we shall utilize it.

For the two-step process, a chemical potential difference, $\Delta\mu_I(V, \theta)$, develops between the I-defects on the SiO₂ side of the interface compared to the I-defects on the Si side of the interface in order to supply I-defects to the Si at a rate determined by the oxidation rate, V . This can be thought of in analogy with water trickling through a leaky dam; the higher the water level, the greater the leak rate. As indicated in Appendix B, this leak rate is expected to be a function of orientation, θ , because the activation barrier existing right at the interface in Fig. 4 is expected to be a function of orientation. It is also expected to be a function of interface velocity, V , since the flux, J_{I1} , of I-defects into the Si depends on V . Using classical reaction rate theory for the two-step process (see Appendix B), we expect to find

$$J_{I1} \approx Ae^{-Q(\theta)/kT} e^{\Delta\mu/kT} \quad [8a]$$

where A is a constant with a slight orientation dependence for a given number of I-defects in the SiO₂ and

$$Q(\theta) = \Delta H_I^{Si} + Q^*(\theta) - \Delta H_I^{SiO_2} \quad [8b]$$

(see Fig. 4). Thus, instead of Eq. [7], for the zero interface field case we must use

$$\Delta\mu(V, \theta) + \mu_I^{Si} = \mu_I^{SiO_2} \quad [9]$$

to determine the nonequilibrium interface partition coefficient, $k_I(V, \theta)$.

Utilizing Eq. [9], [7], and [1], k_I is given by

$$k_I(V, \theta) = \frac{n_{I2}(O)}{n_{I1}(O)} = \frac{\beta}{\left[1 + \frac{n_{I1}(O)}{n_{s2}} \left(\beta - \frac{n_{s2}}{n_{s1}} \right) \right]} \quad [10a]$$

where the subscripts 1 \equiv Si and 2 \equiv SiO₂ and where

$$\beta = \left[\frac{1 - n_{I1}^*/n_{s1}}{1 - n_{I2}^*/n_{s2}} \right] \frac{n_{I2}^*}{n_{I1}^*} \exp[\Delta\mu(V, \theta)/kT] \quad [10b]$$

In our case, $n_{I1}^*/n_{s1} \ll 1$ and probably $n_{I2}^*/n_{s2} \ll 1$ as well so that the first term on the right of Eq. [10b] is ~ 1 . From Eq. [8a], we also note that $\beta \propto J_{I1}$. Although we do not have any information on $\Delta\mu(V, \theta)$ or on n_{I2}^*/n_{I1}^* , we can evaluate k_I in terms of β . In Fig. 5, plots of k_I and $n_{I2}(O)$ are given as a function of $n_{I1}(O)/n_{s2}$ for a range of β -values. We note that k_I decreases from its saturation value of $\sim \beta$ at very small values of $n_{I1}(O)$ to an inverse dependence on $n_{I1}(O)$ at large values of $n_{I1}(O)$. We note from the previous discussion that $n_{I2}(O) = k_I n_{I1}(O)$ increases toward its ultimate value of 4 per unit cell of Si transformed as $n_{I1}(O)$ increases and at a rate less than linear.

If we make the approximation that $n_{I2}(O) \approx 4$ in the derivation leading to Eq. [10a], then we are led to the result that

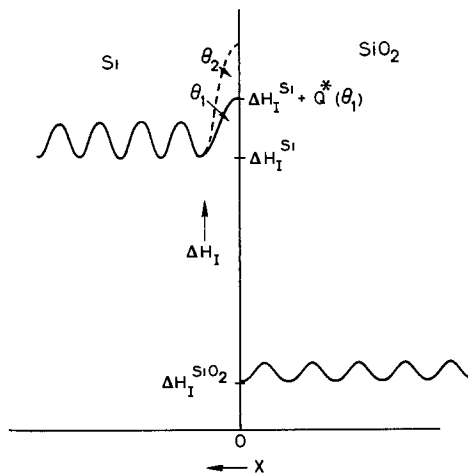


Fig. 4. Schematic illustration of the enthalpy of formation, ΔH_I , for I-defects as a function of distance from the interface. Also included is the interface barrier for two different Si wafer orientations θ_1 and θ_2 .

$$k_I \approx \beta \left(1 - \frac{4}{n_{s2}} \right) + \frac{4}{n_{s1}} \quad [11]$$

since $k_I \approx 4/n_{I1}(O)$. Thus, in this limit, from Eq. [8a] and [10a], we see that $k_I \propto J_{I1}$. For this same approximation, we shall find the excess free energy stored in I-defects, ΔG_E , to be given by (see Appendix A)

$$\Delta G_E = mkT \left\{ 4 \ln \left[\frac{4(n_{s2} - n_{I2}^*)}{n_{s2} n_{I2}^*} \right] + (n_{s2} - 4) \ln \left(\frac{n_{s2} - 4}{n_{s2}} \right) \right\} \quad [12a]$$

$$\approx mkT \{ 4 \ln(4/n_{I2}^*) + 11 \ln(11/15) \} \quad [12b]$$

assuming that $n_{s2} = 15$ for α -cristobalite. For $n_{I2}^* = 10^{-2}$ and 10^{-4} , this amounts to values of $\Delta G_E \approx 6.5$ and 12.4 kcal/mole, respectively, at $\sim 1100^\circ\text{C}$. Thus by the type of structural transition involving interstitials proposed here rather than a direct transition with no interstitials, the value of ΔG_E is reduced from ~ 150 kcal/mole to ~ 20 kcal/mole for this step in the process.

Interstitial conservation condition.—There are 4 Si atoms per unit cell of Si transformed that become

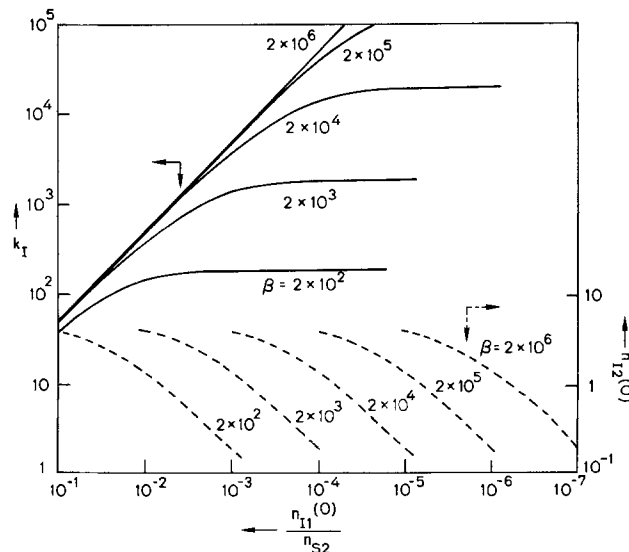


Fig. 5. Plot of k_I and $n_{I2}(O) = k_I n_{I1}(O)$ as a function of $n_{I1}(O)/n_{s2}$ for several values of the parameter β .

I-species. Thus, the interface conservation condition is given, on an Si unit cell basis, as

$$\frac{4V}{\lambda_0^3} = J_{I1} - J_{I2} \quad [13a]$$

where λ_0 is the unit cell size of the Si. Neglecting any interface field effects, this becomes

$$\frac{4V}{\lambda_0^3} = -\frac{D_{I1}\nabla n_{I1}}{\lambda_0^3} - \frac{Vn_{I1}}{\lambda_0^3} + \frac{D_{I2}\nabla n_{I2}}{\lambda_0^3} + \frac{Vn_{I2}}{\lambda_0^3} \quad [13b]$$

Here, D_{Ij} is the interstitial diffusion coefficient in the j -phase. From Eq. [13b]

$$[4 - (k_1 - 1)n_{I1}(O)]V \approx \frac{D_{I1}[n_{I1}(O) - n_{I1}(x_1^*)]}{x_1^*} + \frac{D_{I2}[n_{I2}(O) - n_{I2}(x_2^*)]}{x_2^*} \quad [13c]$$

where x_j^* is the characteristic diffusion length in the j -phase. In Eq. [13b] and [13c], drift of the interstitial species in either an electric or a stress field at the interface has been neglected. In phase 2, subsequent oxidation of the I-defects tends to fill the interstitial spaces with SiO complexes. This increases the formation energy and decreases the diffusion coefficient of the I-defect with increasing distance from the interface. Thus, an interface field effect must really be introduced to model J_{I2} . Diffusion in this phase extends only a short distance ($x_2^* \sim 15\text{\AA} - 25\text{\AA}$) before it is almost completely stopped and D_{I2} has dropped to very small values. This leakage into the region $|x| > |x_2^*|$ is the limiting value of $J_{I2} - (Vn_{I2}/\lambda_0^3)$. The value of $x_1^* \approx \sqrt{\pi D_{I1}t}$ should be used for semi-infinite Si and $x_1^* \approx l$ for an Si slab of thickness $2l$ at times $t \gtrsim l^2/\pi D_{I1}$.

From the earlier discussion, it is clear that $n_{I1}(O)$ and k_1 are functions of time, especially since J_{I1} and V are functions of time in the oxidation process. In the limit where almost all of the I-defects remain in the SiO₂, $k_1 \propto J_{I1}$ from Eq. [11] and $n_{I1}(O) = b/J_{I1}$ where b is an orientation-dependent constant. With this approximation, the flow of interstitials into the Si can be uncoupled from the flow into the SiO₂ and we can treat each phase in turn. For the SiO₂ phase, we choose $J_{I1} \ll -J_{I2}$ in Eq. [13a] and let $n_{I2}(O) \approx 4$. For the Si phase, we choose $n_{I2}(O) \approx 4$ and let k_1 have the value given by Eq. [11]. Following this procedure, we can consider time-dependent events in each phase.

Consequences for the Si-phase.—The I-defects partitioned into the Si slab of thickness $2l$ will diffuse into the bulk Si and some will recombine with vacancies to deplete the population. At short times, Eq. [5] will govern the diffusion of the I-defects subject to the conditions (i) $n_I = 0$ at $t = 0$ for all x , (ii) $\partial n_I/\partial x = 0$ at $x = 0$ for all t , and (iii) $J = J_{I1}$ from Eq. [8a] at $x = \pm l$ for all t . Initially, let us assume that $P_A' = 0$ (no interstitial sinks) and look for a solution in the time domain $t \gtrsim 10^3$ sec. In this time domain, diffusion in a slab $l \sim 10^{-1}$ cm with $D_I \sim 10^{-5}$ cm²/sec is almost complete. If we assume that diffusion is complete, then we have the average slab I-defect concentration, \bar{n}_{I1}

$$\bar{n}_{I1} \approx n_{I1}(O) = \frac{1}{l} \int_0^t J_{I1} dt' \quad [14]$$

which leads to

$$\frac{dn_{I1}(O)}{dt} = \frac{J_{I1}}{l} \quad [15]$$

Combining Eq. [1] and [9] with [8a], we find that

$$J_{I1} = Ae^{-q(\theta)/kT} \left[\frac{(n_{I2}/n_{I1})(n_{s2}/n_{s1})n_{s1}}{(n_{I2}^*/n_{I1}^*)(n_{s2} - n_{I2})} \right] \quad [16a]$$

which yields

$$n_{I1}(O) \approx \frac{4}{J_{I1}} Ae^{-q(\theta)/kT} \left[\frac{n_{s2}(n_{I1}^*/n_{I2}^*)}{(n_{s2} - 4)} \right] \quad [16b]$$

Inserting Eq. [16a] into Eq. [15] leads to

$$n_{I1}^2(O) \approx \frac{8Ae^{-q(\theta)/kT}}{l} \left[\frac{n_{s2}(n_{I1}^*/n_{I2}^*)}{(n_{s2} - 4)} \right] t \quad [17]$$

Thus, in the time domain $t \gtrsim t_0 \sim 0$, $n_{I1}(O)$ increases as $t^{1/2}$ provided we neglect recombination events with vacancies or other sinks. Incorporating the effects of such events will decrease the time exponent in this relationship.

To incorporate the effect of vacancy recombination events, let us assume that $P_A'n_V$ in Eq. [5] is independent of x and is a slowly varying function of t . Then, following Carslaw and Jaeger (14), we find our new I-defect content in the Si, n_{I1}^\dagger , to be given by

$$n_{I1}^\dagger = n_{I1}e^{-P_A'n_V(t-t_0)} + P_A'n_V \int_0^{t-t_0} n_{I1}(t')e^{-P_A'n_V t'} dt' \quad [18]$$

where $n_{I1}(t)$ is given from Eq. [17].

Because n_V has been so strongly decreased in the Si close to the oxidizing interface, vacancies flow in from the bulk Si to reduce n_V close to the interface. This diffusion of V-defects along substitutional sites produces a type of "vacancy wind" which moves substitutional solutes deeper into the Si. The movement of I-defects deeper into the Si also produces an "interstitial wind" of strength proportional to J_{I1} . The analogue for this wind effect comes from electromigration experiments where the momentum exchange between electrodes and lattice ions often causes movement in the opposite direction from that expected based on ionic charge. In terms of the thermodynamics of multicomponent systems, the flux, J_a , of species a is given in terms of the mobilities, M_{ia} , and the electrochemical potential gradients, $\nabla\eta_i$, of the various species i by (15)

$$\bar{J}_a = - \sum_{i=1}^n M_{ia} \nabla\eta_i \quad [19]$$

Thus, depending on the sign of M_{ia} and the $\nabla\eta_i$ ($i \neq a$), the diffusion of a may be greatly enhanced. Here, for $i = I$, $\nabla\eta_I \propto J_{I1}$. This enhanced drift of the substitutional species has been labeled oxidation enhanced diffusion (OED). We see that it arises from the interstitial flux generated at the Si/SiO₂ interface as a natural consequence of the oxidation model described here.

From Eq. [18] we expect n_{I1}^\dagger to build up in the Si slab in a manner proportional to t^p where $p < 1/2$. At some time, t_1 , the supersaturation of I-defects will be sufficient that stacking faults will nucleate and begin to grow and Eq. [5] must then be replaced by

$$D_I \nabla^2 n_I - P_A' n_V n_I - \dot{Q}_{SF} = \frac{\partial n_I}{\partial t} \quad [20a]$$

where

$$\dot{Q}_{SF} = \frac{2\pi b N_{SF}}{\Omega_I} \bar{r} \frac{d\bar{r}}{dt} \quad [20b]$$

with N_{SF} and \bar{r} as the number and average radius, respectively, of the stacking faults as a functions of time, b is the thickness of the fault, and Ω_I is the atomic volume of the condensed I-defect in Si. This interstitial sink should deplete the supply in the bulk Si. However, it is noted that significantly changing N_{SF} has a negligible effect on $d\bar{r}/dt$ (16), which suggests that the interface source strength is so strong, I-defect diffusion in Si is so fast, and the barrier to attachment at the stacking fault edge so large that $n_{I1}(O)$ remains relatively unaltered by the increased sink strength. Eventually, of course, the total line length of stacking fault increases to the point that the drain of interstitials

exceeds the supply and $d\bar{r}/dt$ must shrink to zero. The retrograde portion of the stacking fault growth curve can then come about either by continued vacancy supply from bulk sources plus from the Si/SiO₂ interface or by a change in diffusive flux of I-defects into the bulk SiO₂ from the interface so that N_{12} decreases. If the latter occurs, N_{11} begins to decrease and I-defects begin to flow from the Si to the SiO₂ so that the stacking faults then become the I-defect sources.

Consequences to the SiO₂.—Let us now look in the opposite direction, i.e., to the interstitials flowing into the SiO₂. It is most probable that these will be partially charged, but they will not be nearly as mobile as those in the Si. In fact, they may be fairly immobile because of the incoming oxygen species. These interstitials, almost 4 per unit cell, will swell the unit cell in the direction lateral to the interface making the interface SiO_x more dense than the bulk SiO₂ (17, 18). As oxygen diffuses through the SiO₂ and reaches the interface region, it will oxidize these interstitial Si ions partially blocking the outward diffusion paths of other Si ions. This immobilized group reacts further to form O-Si-O polymer chains. These chains may be thought to interconnect the interstitial spaces in the diamond cubic structure until flow produces enough volume that the more stable SiO₄ tetrahedra may form. It is well known that SiO₄ tetrahedra link together by sharing two of the four corners to form a continuous chain of composition (SiO₃)_n (12) constituting the pyroxene group of chain silicates. In the amphibole group, the SiO₄ tetrahedra are linked to form chains having double the pyroxene chain width and having a composition (Si₄O₁₁)_n. The mica group of silicates form sheet structures with hexagonal nets which lead to a composition of Si₄O₁₀ (12).

Several features are important to note about the proposed interstitial chains. First, they may be considered to have a range of enthalpies of formation and some particular distribution of chain lengths will minimize the free energy of SiO₂ (short chain lengths probably). Second, the strain energy will increase with the degree of advancement of the oxidation process and very quickly exceed a few kcal/mole so that the α -cristobalite lattice will quickly distort to the vitreous-type structure. Third, the incompletely oxidized Si (chain ends) are expected to contain unsatisfied bonds which will be positively charged. Since the positive ions occupy less space, the reduced strain energy favors the ionization. This is proposed as the origin of Q_f . Fourth, since these chains place the unit cell under swelling stresses, there will be a slow yielding of the SiO_x as free volume flows into the interface region from the bulk SiO₂ via viscoelastic processes (19). As the system yields, complete oxidation of these interstitial I-defects become possible and they may make the transition to stable SiO₄ tetrahedra which completely transforms the SiO_x to vitreous SiO₂. Thus, an interface layer of enhanced density and thickness, ΔZ , exists wherein the stoichiometry is of the form SiO_x with $1 \lesssim x < 2$. This layer becomes a steady-state condition moving with the interface wherein new bare Si or SiO interstitials enter at one side and completely oxidized interstitial chains or interstitial tetrahedra exit at the other side. The point here is not to make a case for chains vs. partial tetrahedra, but to allow both possibilities at this qualitative stage. Important thermodynamic calculations need to be made concerning these various interstitial defect species and such subsequent calculations will allow discrimination between these two possibilities. A residual interstitial density, such as to produce a swelling stress equal to the SiO₂ flow stress at the oxidation temperature, is predicted in accordance with the findings of Taft (20). For high pressure oxidation, this residual density effect will be higher because of the decreased SiO₂ viscosity at the higher pressure.

An important point to be underlined here is that the oxidation of Si occurs via two streams. In the first stream, 4 Si atoms per unit cell of Si oxidize directly to SiO₂ and form the lattice of α -cristobalite. In the second stream, almost 4 I-defects per unit cell of transformed Si oxidize in steps as SiO_x with an increased activation energy and decreased free energy release being associated with oxidation as x increases from 1 to 2. The larger x is for this stream, the slower the oxidation process because of the associated strain energy. From qualitative theoretical reasoning, one expects x to increase from ~ 1 to ~ 2 in about 4 unit cell distances. This internal swelling and flow process cannot help but produce a highly densified and integral oxide.

Temperature dependence.—As the temperature is increased, the yield stress of the α -cristobalite is reduced and the system flows more easily. Thus, the stored strain energy due to the I-defects in SiO₂ will be reduced, which will reduce $\Delta\mu$ for the same value of N_{12} . This will cause a decrease in $J_{11}(O)$ and an increased fraction of the I-defects are partitioned to the SiO₂. Since there are fewer I-defects flowing into the Si as T increases, the driving force for both the OED and the OISF phenomena must decrease beyond a certain temperature as T increases. From the work of Eernisse (19), we see that the critical temperature range for strong changes in the vitreous SiO₂ flow properties is $\sim 950^\circ$ - 1000° C. Thus, changes in OED and OISF should begin to be seen at $T \gtrsim 1000^\circ$ C.

With respect to expected Q_f and n_{it} changes with T , since $J_{11}(O)$ decreases and k_f increases as T increases, one might expect that the total positive charge at chain ends would increase and that Q_f should increase also. However, n_{12} increases only very slightly as T increases but, because the system flows more easily at the higher temperatures, the oxidation should be more complete, the number of oxy-silicon chain ends should decrease, and Q_f should decrease in accord with the results of Deal (8). At the higher T , the reaction between the Si atoms at the ends of the extra half-planes and oxygen will be more rapid and, thus, more complete so that N_{it} should also decrease as T increases. Of course, the reactivity of minor constituents like H or C should also be altered, which will, in turn, alter the observable N_{it} (21).

Orientation dependence.—We assume the same epitaxial match, (100)Si/(100)SiO₂, but now we focus attention on the (111) plane of Si as the interfacial plane and notice that it is lined up with the (120) plane of the pseudo-diamond cubic cell of α -cristobalite (see Fig. 1). As Herman *et al.* (22) have noted, the interface model of (100)Si parallel to (100) β -cristobalite, with this latter rotated by 45° , is the simplest interface model constructable between these two phases. In our case, the (100)Si/(100) α -cristobalite with parallel $\langle 100 \rangle$ directions gives almost exactly the result of Herman *et al.* (22). If we look into the α -cristobalite pseudo cube along the $\langle 120 \rangle$ or into the β -cristobalite along this direction, we note easy access to the $\langle 110 \rangle$ tunnels through the diamond cubic structure.

Thus, for this direction, the second term of Eq. [13c] may be larger than for Si orientations where the interface normal is not lined up with the tunnel direction. If this is so, then $n_{11}(O)$ will be reduced and so will the OED and the OISF. We are not yet in a position to evaluate the magnitude of this effect. The dominant orientation effect, however, is expected to arise as a consequence of its influence on the magnitude of β . As V increases at fixed $n_{12}(O)$, J_{11} is fixed; however, for fixed oxide thickness, \bar{n}_{11} is reduced because it takes less time to form this layer and thus t , in Eq. [14], is smaller. For constant diffusive transport rate in the oxide, $n_{12}(O)$ should increase as V increases (less transported away per unit film thickness). Thus, \bar{n}_{11} should decrease as V increases, but a little less than

linearly with V . Since V increases as p_{O_2} increases, a similar change in $n_{II}(O)$ should develop for increasing p_{O_2} . In changing the Si wafer orientation from (100) to (111), the change in $n_{II}(O)$ arises from the fact that $V_{(111)} > V_{(100)}$. Thus, this effect is expected to lower $n_{II}(O)$ for the (111)Si wafers compared to the (100)Si wafers for fixed oxide thickness, in accord with observations.

Because of the increase of k_I for the (111)Si compared to the (100), Q_f will increase, OED will decrease, and OISF will decrease. Since larger k_I means more I-defects in the SiO_2 , this means greater lateral swelling stresses as the interstitial Si becomes oxidized. The increased lateral swelling stresses are expected to cause the SiO_2 at the interface to relax to a larger average spacing and leave more Si half-planes per unit interface area on the Si side terminating at the interface. Thus, we also expect N_{it} to increase for the (111) over that for the (100).

Oxidation velocity.—Because the number of I-defects in Si is greater for the (100) orientation than for the (111) orientation, the reverse situation holds for the SiO_2 phase. The greater Q_f for the (111) orientation means an enhanced electric field in the oxide for this orientation. Since the Q_f is associated with positive charge, the interface region will be more positive for the (111) orientation than for the (100). This means that the diffusion rate of $O=$ ions through the oxide will be enhanced for the (111) oxidation compared to the (100) so the oxidation velocity for (111) oxidation will be greater than for the (100) oxidation. As shown in Part II (2), the field effects enter both the linear and parabolic rate coefficients so both the short-time and the long-time oxidation rates should be affected by this mechanism. Of course, as the temperature is increased, the enhanced flow process allows almost all of the I-defects to enter the SiO_2 phase and differences in the field-driven diffusion for the two orientations disappear. Thus, the oxidation velocities for the (111) and the (100) become almost equal at high temperatures.

Discussion

The most important concept of this paper is the formation of a transitory crystalline SiO_2 layer containing interstitial species. The utilization of this concept allows one to see how a host of ancillary phenomena can occur and be associated with the oxidation process. Consideration of a direct transition to vitreous SiO_2 without interstitial species leaves one with no ready pathway to simply account for these other phenomena. Certainly there is no apparent way to see their interconnectedness. Since the free energy difference between any one SiO_2 phase and another is only ~ 2 kcal/mole, which is $\sim 1\%$ - 2% of the total free energy available for the reaction, the choice of specific interface SiO_2 structure is of second order to the overall process. In this paper, the slight favorite has been α -cristobalite.

The paper has, for reasons of simplicity, considered that the Si atoms at the ends of the extra half-planes remain unoxidized until after they jump into SiO_2 interstitial positions. In actual fact, many of these atoms will have formed a single Si-O bond and some may have formed O-Si-O bonds. Thus, not only will we have Si interstitials being generated from this interface source but SiO interstitials and some O-Si-O interstitials as well. Of course, this will increase the interface density and the value of x somewhat in the overall interface stoichiometry, SiO_x . We would expect that, in the interface reaction control regime at low temperatures or high O_2 pressures, the oxygen supersaturation at the interface would be greatest, so more of the terminating Si atoms would be partially oxidized, more SiO interstitials would enter the SiO_2 , and x would be larger for SiO_x at the interface. At the other extreme, for thick oxides where diffusion control is dominant, the interface oxygen supersaturation

will be small and most of the terminating Si atoms will be bare and will enter the SiO_2 interstitial positions as bare Si. Of course, during cooling to room temperature, the excess oxygen in the SiO_2 will move to the interface and partially oxidize these terminating Si species.

For the bare Si atoms in terminal positions at the interface, one might picture them with dangling bonds; however, it is more likely that bond reconstruction will occur and only a few dangling bonds will exist. The density of these dangling bonds is likely to be much lower at room temperature than at oxidation temperatures and to depend on both the quenching rate from high temperature and the quenching environment. This should be governed by the natural bond reconstruction rate which is expected to be a function of the orientation of the extra half-planes terminating at the interface; i.e., it should be a function of interface orientation. We should always expect some bare dangling bonds, even in the equilibrium reconstructed state, for entropic reasons. Given the difference in bond energy, ΔE^* , between the dangling and reconstructed states, the fraction of dangling bond sites, x_{db} , in the equilibrium reconstructed state is simply

$$x_{db} \sim e^{-\Delta E^*/kT} \quad [21a]$$

When some of these terminal atoms are partially oxidized, we must mix the three unique species (dangling bonds, reconstructed bonds, and oxygenated bonds) among these available terminating atoms. For a fixed fraction x_o of oxygenated terminal Si species, Eq. [21a] becomes

$$x_{db} = (1 - x_o) e^{-\Delta E^*/kT} \quad [21b]$$

As x_o approaches unity, it can no longer be held fixed in the calculation and we return to a result like Eq. [21a], but with ΔE^* replaced by $\Delta E^* + \Delta E_B$ where ΔE_B is the decrease in bond energy in going from a bare reconstructed bond to a singly oxidized bond.

The conceptual features of this overall model are expected to be fairly representative of the experimental reality for the thermal oxidation of Si. However, much fine tuning of the model is still needed to produce the desired quantitative match with experiment. Many significant theoretical hurdles still stand in the way of this goal.

Conclusions

A qualitative model has been proposed based on the initial transformation of silicon to α -cristobalite plus almost 4 interstitial Si ions per unit cell of Si transformed, with the remainder interstitial Si ions rejected into the bulk silicon phase. Subsequent oxidation of the interstitial Si ions in the SiO_2 matrix produces rapid distortion and transformation of the structure to the vitreous form. The following are the qualitative predictions of the model:

1. OED, OISF, N_{it} , and Q_f can be accounted for.
2. The orientation dependence gives, in accordance with experiment

$$\begin{aligned} k_{I(100)} &< k_{I(111)} \\ OED_{(100)} &> OED_{(111)} \\ OISF_{(100)} &> OISF_{(111)} \\ Q_{f(100)} &< Q_{f(111)} \\ N_{It(100)} &< N_{It(111)} \\ V_{(111)} &> V_{(100)} \end{aligned}$$

3. The temperature dependence gives k_I increasing as T increases above $\sim 950^\circ C$ so that all the orientation dependences tend to decrease.

4. At the lower growth temperatures, a layer of increased density SiO_2 will exist at the Si interface which will yield an increased index of refraction for the layer in accordance with experiment (17). The chemical stoichiometry of the layer will range from almost SiO

(slightly Si deficient) at the interface with Si to almost SiO₂ (slightly O deficient) at the transition with bulk density vitreous SiO₂ which occurs within ~3-5 unit cell distances of the interface.

In addition, a quantitative expression for k_I has been derived and the I-defect content in the Si is predicted to increase for short times as t^p , where $p < 0.5$.

Acknowledgments

This work was partially supported by the Defense Advanced Research Projects Agency under Contracts No. DAAB07-77-C-2684 and MDA 903-79-C-0484. The author wishes to thank Dr. A. Lin for many informative discussions.

Manuscript submitted Feb. 22, 1980; revised manuscript received June 26, 1980.

Any discussion of this paper will appear in a Discussion Section to be published in the December 1981 JOURNAL. All discussions for the December 1981 Discussion Section should be submitted by Aug. 1, 1981.

Publication costs of this article were assisted by Stanford University.

APPENDIX A

Neutral Interstitial Partition Coefficient at the Si/SiO₂ Interface

Let the neutral interstitial enthalpy of formation in Si and in SiO₂ be given by ΔH_{I1} and ΔH_{I2} , respectively. In each phase, the entropy of the I-species, S_D , permuted amongst the mn_s available interstitial sites for m unit cells, is given by

$$S_D = k \ln [(mn_s)! / (mn_I)! (mn_s - mn_I)!] \quad [\text{A-1}]$$

Here, $n_s = 5$ for diamond cubic with one atom or ion per site. However, in SiO₂ it may be possible to have more than one I-species per interstitial site because the sites are so large. Thus, $n_s^{\text{SiO}_2}$ is not fully specifiable at this time.

The equilibrium number of interstitials per unit cell, n_I^* , in each phase is given by

$$\frac{n_{Ij}^*}{n_{sj} - n_{Ij}^*} = e^{\Delta S_j^v/k} e^{-\Delta H_{Ij}/kT} \quad j = 1, 2 \quad [\text{A-2}]$$

where ΔS_j^v is the vibrational entropy contribution of the I-defects. Both n_{I1}^* and n_{I2}^* are expected to be small relative to n_{s1} and n_{s2} and $n_{I1}^* \ll n_{I2}^*$ is also expected. In our area of interest, large values of n_I are being generated at the Si/SiO₂ interface and the excess free energy of each phase for $n_{Ij} \gg n_{Ij}^*$ is given by (9)

$$\Delta G_{\text{ex } j} = mkT \left\{ n_{Ij} \ln \left[\frac{n_{Ij} (n_{sj} - n_{Ij}^*)}{n_{Ij}^* n_{sj}} \right] + (n_{sj} - n_{Ij}) \ln \left[\frac{n_{sj} - n_{Ij}}{n_{sj}} \right] \right\} \quad j = 1, 2 \quad [\text{A-3}]$$

for the m unit cells ($m = N/8$ for a mole of Si or α -cristobalite where $N = \text{Avogadro's number}$). The chemical potentials of the interstitials at these excess concentrations are, in turn, given by

$$\mu_{Ij} = \frac{\partial G_{\text{ex } j}}{\partial n_{Ij}} = kT \ln \left[\frac{n_{Ij} (n_{sj} - n_{Ij}^*)}{n_{Ij}^* (n_{sj} - n_{Ij})} \right] \quad j = 1, 2 \quad [\text{A-4}]$$

APPENDIX B

Interstitial Partitioning of Si

One-step process.—Consider unit area of interface where the environment for Si I-defects is like that in Fig. 4. The concentration of the I-defects in SiO₂ is such that a chemical potential difference, $\Delta\mu_0$, exists between SiO₂ and Si for this species. The number of Si atoms jumping out of the interface layer per unit time into interstitial sites in Si $\equiv 1$ and SiO₂ $\equiv 2$ is given by

$$R_{\text{out}} = \frac{N_s(\theta)}{2} \frac{v}{6} (e^{-Q_2^*/kT} + e^{-Q_1^*/kT}) \quad [\text{B-1}]$$

where $N_s(\theta)$ is the average number of atoms per unit

area of the interface and v is the vibrational frequency. The number jumping back into the interface layer per unit time from these phases is

$$R_{\text{in}} = N_{I2} \frac{v'}{6} e^{-[Q_1^* - (\Delta H_{I2} + \Delta\mu)]/kT} + N_{I1} \frac{v''}{6} e^{-[Q_1^* - \Delta H_{I1}]/kT} \quad [\text{B-2}]$$

The net result arising as a result of interface motion is

$$R_{\text{out}} - R_{\text{in}} = \frac{4V(\theta)}{\lambda_0^3} \quad [\text{B-3}]$$

where λ_0 is the Si unit cell size and V is the interface velocity. Placing Eq. [B-1] and [B-2] into [B-3] leads to

$$\frac{4V(\theta)}{\lambda_0^3} = \left[\frac{N_s(\theta)v}{12} - \frac{N_{I2}v'}{6} e^{(\Delta H_{I2} + \Delta\mu)/kT} \right] e^{-Q_2^*/kT} + \left[\frac{N_s(\theta)v}{12} - \frac{N_{I1}v''}{6} e^{\Delta H_{I1}/kT} \right] e^{-Q_1^*/kT} \quad [\text{B-4}]$$

At $V = 0$, $\Delta\mu = 0$ and $N_{I2} = k_I^* N_{I1}$, so a relationship between some of the parameters is possible; however, it is essentially too complex to be readily useful.

Two-step process.—Let all of the I-defects first be liberated into the SiO₂ (with an activation energy that requires Si-Si bond breaking). Then, some of the I-defects are partitioned into the Si interstitial spaces. For this second step, we have

$$R_L = N_{I2} \frac{v}{6} e^{(Q^* - \Delta\mu)/kT} \quad [\text{B-5}]$$

and

$$R_R = N_{I1} \frac{v}{6} e^{-Q^*/kT} \quad [\text{B-6}]$$

where R_L means from the SiO₂ to the Si, while R_R is from the Si to the SiO₂. Therefore, the number of I-defects entering the Si per unit time, J_1 , is given by

$$J_1 = R_L - R_R = N_{I2} \frac{v}{6} e^{-Q^*/kT} \left(e^{\Delta\mu/kT} - \frac{1}{k_I} \right) \quad [\text{B-7a}]$$

$$\approx \frac{N_{I2}v}{6} e^{-Q^*/kT} e^{\Delta\mu/kT} \quad [\text{B-7b}]$$

since k_I^{-1} is very small and $\Delta\mu/kT \gg 1$ generally. It should also be noted that J_1 is somewhat proportional to V since the interface conservation condition is

$$\frac{4V}{\lambda_0^3} = J_1 - J_2 \quad [\text{B-8}]$$

and the minus sign is used because J_2 is in the opposite direction to J_1 .

REFERENCES

- W. A. Tiller, *This Journal*, **127**, 619 (1980).
- W. A. Tiller, *ibid.*, **127**, 625 (1980).
- P. S. Dobson, *Philos. Mag.*, **24**, 567 (1971).
- P. S. Dobson, *ibid.*, **26**, 1301 (1972).
- S. M. Hu, *J. Appl. Phys.*, **45**, 1567 (1974).
- D. A. Antoniadis, A. M. Lin, and R. W. Dutton, *Appl. Phys. Lett.*, **33**, 1030 (1978).
- S. P. Murarka, *Phys. Rev. B*, **16**, 2849 (1977).
- B. E. Deal, *This Journal*, **121**, 198C (1974).
- R. A. Swalin, "Thermodynamics of Solids," p. 218, John Wiley & Sons, Inc., New York (1962).
- R. G. Rhodes, "Imperfections and Active Centers in Semiconductors," p. 12, MacMillan, Pergamon Press, New York (1964).
- J. S. Van Vechten, *Phys. Rev.* **5**, **17**, 3197 (1978).
- W. A. Deer, R. A. Howie, and J. Zussman, "An Introduction to the Rock-Forming Minerals," John Wiley & Sons, Inc., New York (1966).
- K. A. Jackson, *Philos. Mag.*, **5**, 43 (1960).
- H. S. Carslaw and T. C. Jaeger, "Conductor of Heat

- in Solids," p. 63, Clarendon Press, Oxford (1959).
15. P. G. Shewmon, "Diffusion in Solids," p. 122, McGraw-Hill Book Co., New York (1963).
 16. A. Lin, Private communication.
 17. E. Taft and L. Cordes, *This Journal*, **126**, 131 (1979).
 18. H. Z. Massoud and J. A. Plummer, Private communication.
 19. E. P. Eernisse, *Appl. Phys. Lett.*, **30**, 290 (1977).
 20. E. A. Taft, *This Journal*, **125**, 968 (1978).
 21. C. M. Svensson, in "The Physics of SiO₂ and Its Interfaces," S. T. Pantelides, Editor, p. 328, Pergamon Press, New York (1979).
 22. F. Herman, I. P. Batra, and R. V. Kasowski, in "The Physics of SiO₂ and Its Interfaces," S. T. Pantelides, Editor, p. 333, Pergamon Press, New York (1979).

Technical Notes



Formation of Recombination Centers in Epitaxial GaAs due to Rapid Changes of the Growth Velocity

L. Jastrzebski

RCA Laboratories, Princeton, New Jersey 08540

and J. Lagowski and H. C. Gatos*

Department of Materials Science and Engineering,
Massachusetts Institute of Technology, Cambridge, Massachusetts 02139

It was established that recombination centers in epitaxial GaAs are formed upon abrupt acceleration of the growth. The corresponding effect of abrupt deceleration of the growth is only minor. In the case of backmelting, recombination centers are also introduced, however, not due to backmelting itself, but rather due to the subsequent acceleration of the growth. The abrupt changes in growth velocity were achieved by corresponding changes in the current density during electroepitaxial growth.

It has been recently demonstrated experimentally and theoretically that liquid phase electroepitaxy provides a unique means for achieving essentially independent control of the interface temperature and the growth velocity (1, 2). In the present study we have utilized this feature of electroepitaxy in the growth of GaAs with intentionally imposed controlled changes of the growth velocity in order to study the role of growth dynamics in the formation of recombination centers.

In electroepitaxy growth is initiated and sustained by passing an electric current through the solution-substrate interface. An electric field, $E = \rho J$, (ρ is the resistivity and J is the current density) in the solution (GaAs in the present case) causes electromigration of solute species (As in the present case) to the interface providing an effective means for the mass transport required for epitaxial growth (1). In addition, electric current flow leads to a change, ΔT_p , of the interface temperature due to the Peltier effect; $\Delta T_p \sim \pi J d$ where π is the Peltier coefficient with a sign depending on the conductivity type of the substrate (n or p) and d is the thickness of the substrate. It is apparent that by using thin substrates, current-induced change of the interface temperature can be minimized (down to a fraction of 1°C) and thus growth can be controlled by electromigration. The velocity (1, 2), $v_E = C_0 \alpha E J / (C_s - C_0)$, (where C_0 and C_s are the equilibrium solute concentration in the solution and in the solid, respectively, and μ is the mobility of solute species) can be programmed by programming the current density as a

function of time. The electromigration flux adjusts instantaneously to changes in electric current density and thus the time-lag between rapid changes of J and of the growth velocity, v_E , is negligible. For thick substrates, ΔT_p becomes of significance (of the order of a few degrees C). However, the thermal relaxation time of the interface temperature is typically of the order of 0.1 sec, which is much longer than the relaxation time of the growth velocity associated with solute electromigration changes.

In the present study controlled growth velocity changes were introduced during electroepitaxial growth of Sn-doped ($n \approx 6 \times 10^{16} \text{cm}^{-3}$) GaAs from Ga-rich solution at 950°C with an apparatus described elsewhere (3). The minority carrier lifetime microprofiling in the grown layers was performed utilizing SEM-electron beam-induced current (EBIC).

A current collecting Schottky barrier was formed by evaporating gold on the surface of the epitaxial layer cleaved parallel to growth direction. As shown in Fig. 1, the collection efficiency of the electron beam-induced current was measured while scanning the beam across the regions subjected to changes of growth velocity. The position of these regions (and thus the corresponding values of growth velocity) was determined with differential etching (AB etchant).

EBIC measurements were carried out under plasma generation conditions so that the observed changes of collection efficiency reflect primarily the changes of minority carrier lifetime and thus the concentration of recombination centers (a decrease in collection efficiency corresponds to an increase in the concentration of recombination centers). The experimental results showing the effect of growth velocity changes on the formation of recombination centers are shown in Fig. 2 and 3.

It is evident from Fig. 2a that an abrupt increase of growth velocity¹ from 2 to 4 $\mu\text{m}/\text{min}$ produces a pronounced minimum in collection efficiency in the corre-

¹ The change of the current level was brought about in 1 msec; it is believed that the corresponding change of growth velocity took place in approximately the same period of time.

* Electrochemical Society Active Member.
Key words: growth, electroepitaxy, current.

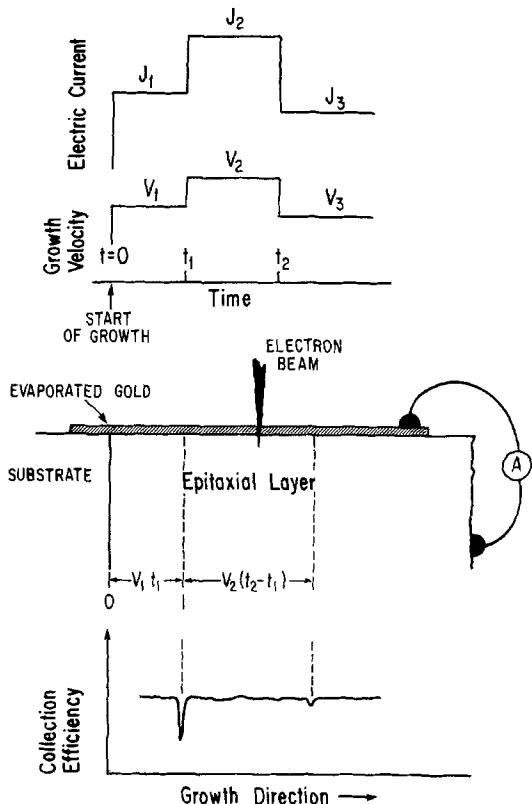


Fig. 1. Schematic representation of current-controlled changes of the growth velocity (upper portion) and corresponding configuration employed in SEM-electron beam-induced current (EBIC) measurements.

sponding transition region. Higher growth velocity changes (from 2 to 14 $\mu\text{m}/\text{min}$; or from 8 to 20 $\mu\text{m}/\text{min}$) reduce the collection efficiency by as much as 30%. It should be pointed out that the recovery of the

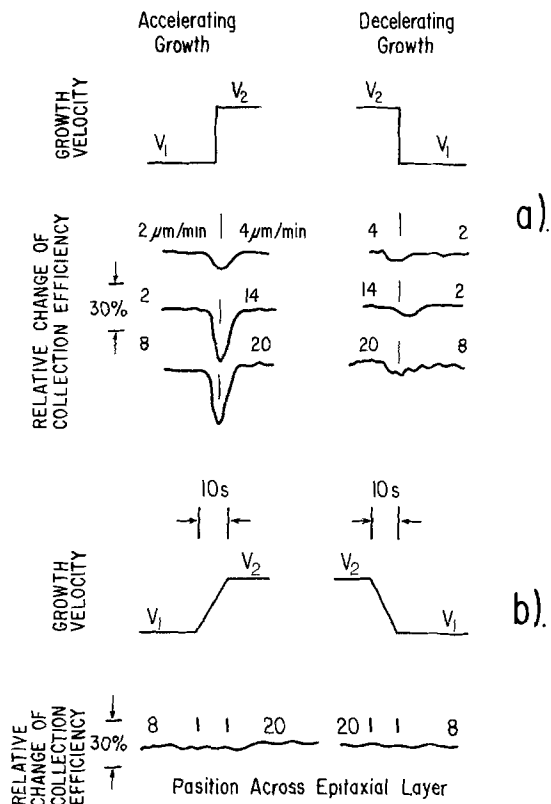


Fig. 2. EBIC microprofiles reflecting formation of recombination centers upon abrupt changes of growth velocity (a) and upon similar changes spread over a period of 10 sec (b).

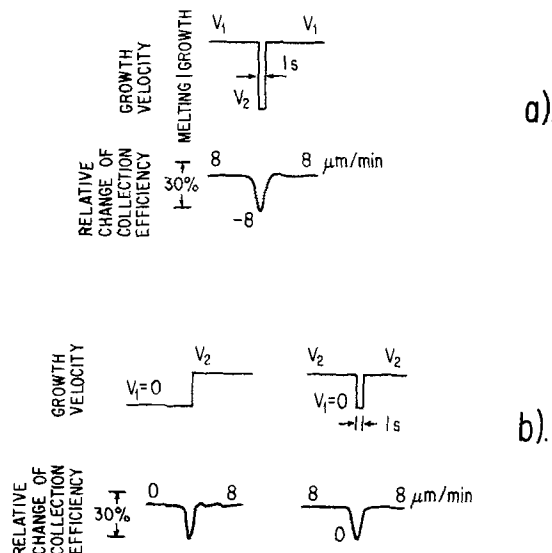


Fig. 3. EBIC microprofiles corresponding to backmelting (a) and to abrupt changes of growth velocity without backmelting (b). (See text.)

collection efficiency (concentration of recombination centers) following the step-like change in growth velocity indicates that the acceleration of the growth (dV/dt) rather than the absolute value of growth velocity (V) is responsible for the formation of recombination centers. This conclusion is confirmed by the results of Fig. 2b, whereby the growth velocity was changed from 8 to 20 $\mu\text{m}/\text{min}$, however, not instantaneously but during a period of 10 sec. In this case no noticeable amount of recombination centers was introduced.

The results shown on the right-hand side of Fig. 2(a, b) indicate that the effect of deceleration of the growth on recombination centers is about one order of magnitude smaller than that of acceleration of the growth.

Experiments, as discussed above, were also carried out with substrates of different thickness, and thus under different current-induced changes of the interface temperature. No significant differences were observed from the results of Fig. 2 obtained with thin substrates. Apparently, changes in interface temperature are of secondary importance compared to changes in growth velocity.

Typical results regarding the effect of backmelting on the formation of recombination centers are shown in Fig. 3. In the upper portion of Fig. 3 backmelting is introduced with 1 sec electric current pulse of polarity opposite than required for growth. It is seen that a minimum in collection efficiency is introduced by this pulse.

In order to verify whether the observed increase in concentration of recombination centers is caused by phenomena taking place during backmelting of the grown crystal or by the subsequent increase of the growth velocity to the original value of 8 $\mu\text{m}/\text{min}$, the following experiments were carried out. Growth was arrested for an extended period and then it was abruptly increased to 8 $\mu\text{m}/\text{min}$. In addition, the growth was interrupted for 1 sec and then restored abruptly to its original value of 8 $\mu\text{m}/\text{min}$. As seen in the lower part of Fig. 3, the results are the same as those obtained for backmelting (upper part of Fig. 3). Thus, it is concluded that the recombination centers introduced into the epitaxial layer during backmelting are formed primarily by the acceleration of the growth following backmelting.

In summary, we have demonstrated the importance of growth dynamics, and in particular, the importance of the acceleration of growth in the formation of re-

combination centers during liquid phase epitaxy. It is likely that these recombination centers originate from point defects generated at the growth interface in response to abrupt increases in growth velocity (abrupt deviations from steady-state growth conditions). It is apparent that surface nucleation effects commonly considered of no significance in the LPE process with slowly varying growth velocity can in fact be of primary importance in the case of abrupt increases in growth velocity. The limited framework of existing theoretical treatments of point defect formation on growth interfaces (4-7) does not provide an adequate basis for further, even qualitative explanation of the present findings.

Acknowledgments

The authors are grateful to the National Aeronautics and Space Administration and to the National Science Foundation for financial support.

Manuscript received Sept. 12, 1980.

Any discussion of this paper will appear in a Discussion Section to be published in the December 1981 JOURNAL. All discussions for the December 1981 Discussion Section should be submitted by Aug. 1, 1981.

Publication costs of this article were assisted by the Massachusetts Institute of Technology.

REFERENCES

1. L. Jastrzebski, J. Lagowski, H. C. Gatos, and A. F. Witt, *J. Appl. Phys.*, **49**, 5909 (1978).
2. T. Bryskiewicz, J. Lagowski, and H. C. Gatos, *ibid.*, **51**, 988 (1980).
3. L. Jastrzebski, Y. Imamura, and H. C. Gatos, *This Journal*, **125**, 1140 (1978).
4. W. W. Webb, *J. Appl. Phys.*, **33**, 1961 (1962).
5. J. A. Van Vechten, *Appl. Phys. Lett.*, **26**, 593 (1975).
6. A. J. R. de Koch, P. J. Roksner, and P. G. T. Boonen, *J. Cryst. Growth*, **22**, 311 (1974).
7. J. Chikawa and S. Shirai, *Jpn. J. Appl. Phys.*, **18**, Supplement 18-1, 153 (1979).

The Archival Stability of Tellurium Films for Optical Information Storage

David Y. Lou

Philips Laboratories, Briarcliff Manor, New York 10510

Optical storage of information by means of laser micromachining of thin metal films is currently the subject of a great deal of interest (1-3). One of the major potential applications of this technology is the high density, low cost archival storage of information. Thus, the archival properties of the recording medium are examined. We report in this paper data obtained for tellurium films deposited on polymethyl methacrylate (PMMA) substrates, where the recording medium is fabricated into a protective air sandwich structure (2, 3).

Experimental Procedure

Several options exist in the choice of parameters to monitor the degradation of optical disks. One possibility is to monitor the degradation in the recording characteristics of the disk, such as the sensitivity to laser machining and the recovered bit error rate. This would yield information about the shelf life of the optical disk (4). Another important parameter concerns the degradation in the characteristics of a recorded disk, which gives us the archival life of stored information. Obviously, a complete map of errors over the entire disk gives the most information. Such data are, however, also most expensive to come by. Measurements of the fundamental optical properties of the film material, such as reflection, transmission, or subjective appearance, undoubtedly give information directly related to film degradation, and are much easier to perform (5). However, the translation of these properties into degradation characteristics of digital information is problematic, especially when the degradation is nonuniform over the disk surface. The most representative description of the degradation of recorded digital information is the bit error rate, averaged over a meaningful portion of the recordable disk surface area. This is the parameter we have chosen to measure.

Figure 1 shows the electronic instrumentation that was used to measure the bit error rate. The clock for

the pattern generator section of the HP 3780A was derived from a Syntest frequency synthesizer for a data rate of 1.85 Mbits/sec. Two bit patterns were used for testing, a 16 bit word, 1010 1010 1010 1010 (1010//4) and a pseudorandom bit sequence $2^{15}-1$ bits long (PRBS-15). The Miller modulated version of these bit sequences were used to drive the acousto-optic modulator in the recorder.

The experiments were carried out on air sandwiches (2) assembled from two tellurium-coated disks. The recorder used in this series of experiments was of fairly standard design. Laser radiation of 633 nm was obtained from an He-Ne laser and modulated by an

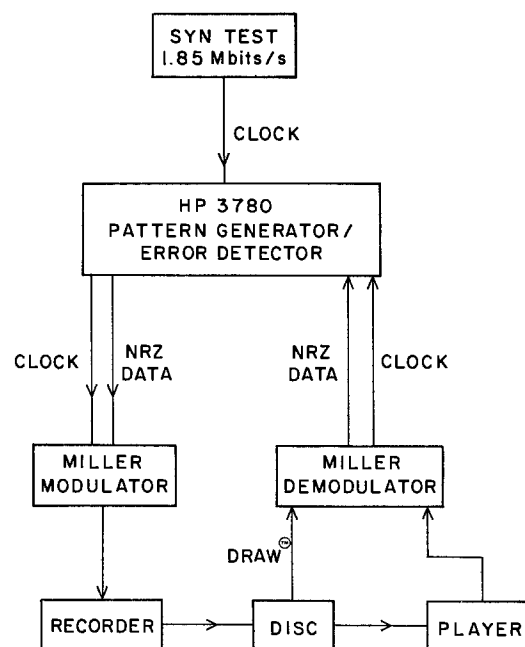


Fig. 1. Electronic system

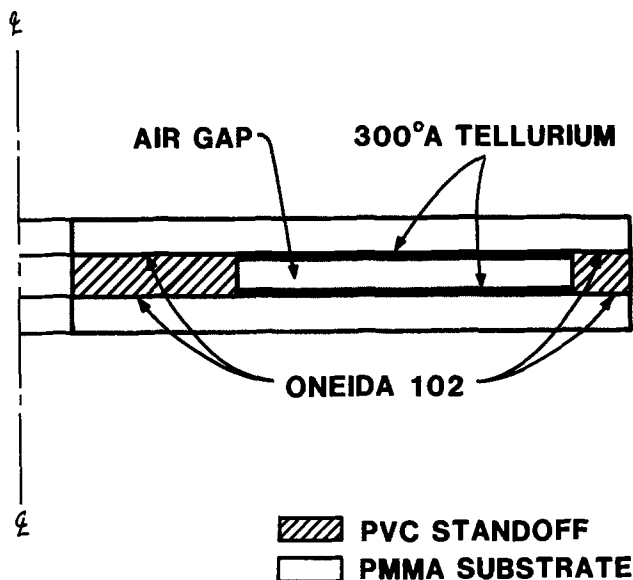


Fig. 2. The air sandwich™ structure

acousto-optic modulator. The sandwiches were mounted on an air-bearing spindle driven by a pancake motor. The focusing lens was a 0.45 N.A. Zeiss objective designed for the Philips Videodisc player. The calculated spot size of the recording beam is $0.7 \mu\text{m}$ FWHM. Active focusing was obtained by sensing the error signal with an infrared side beam system, and driving the objective with a standard Videodisc type voice coil. The entire focusing optics assembly was mounted on a rectangular Dover air-bearing sled and driven by a linear motor. The readout signal was obtained by splitting off a portion of the laser beam before modulation and aligning it to trail the main recording beam by a few microns on the recorded track.

Typically, each disk has four recorded bands of information, each approximately 2 mm wide, 120 sec long. Recordings of the 1010//4 pattern were made at the inner (75 mm), middle, and outer (95 mm) radii of the disk, together with a PRB5-15 pattern somewhere in between. For each recorded band, the recording parameters were adjusted to minimize the bit error rate of the readout signal.

After recording, the disks were stress aged in a temperature humidity oven at 45°C 95% relative humidity. Periodically, the disks were taken out, and the bit error rates were measured. Playback was on a modified version of the standard Philips Videodisc player. The Miller output from the player preamplifier was

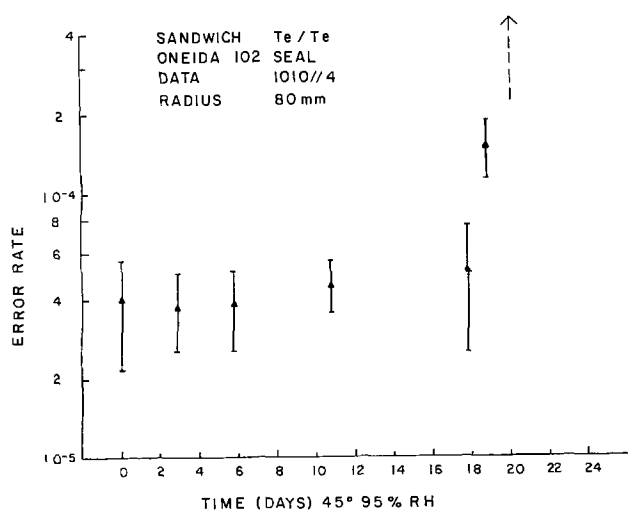


Fig. 3. Error rate degradation for double-sided tellurium air sandwich™, inner radius.

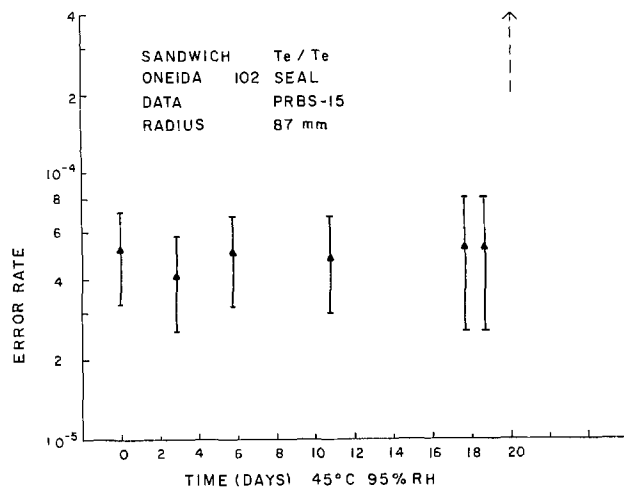


Fig. 4. Error rate degradation for double-sided tellurium air sandwich™, middle radius.

demodulated. The bit error rate of the recorded data was measured in the error detector section of the HP 3780A over data segments 10^6 bits in length. With a gating time of 1 sec on the HP 3780A, each recorded band contains approximately 100 readings. The average and standard deviation of these bit error rate readings are taken as the descriptor for the condition of the disk.

Results

Figures 3-5 show the data obtained for a double-sided sandwich, which has 300Å Te coated on both recordable surfaces. Standard Glasflex PMMA disks were cleaned by an acetone/alcohol rinse, immersion in an ultrasonic detergent bath, and deionized water rinse. The sandwich was bonded together with a polyvinyl chloride standoff using Oneida 102 cyanoacrylate as a seal (Fig. 2). Figure 3 gives the behavior for a 1010//4 pattern recorded at a radius of 80 mm. The recorded data show an initial error rate in the mid 10^{-5} range and are stable at 45°C 95% relative humidity for up to 18 days, after which it rapidly deteriorates. Figure 4 shows the behavior of PRB5-15 data at 87 mm, and Fig. 5 shows the behavior of 1010//4 data at 95 mm, on the same disk. The degradation in the fundamental signal characteristics, as measured by the carrier to noise ratio and carrier to second harmonic ratio, is given in Fig. 6. Figure 7 gives the data for a 1010//4 pattern on a double-sided sandwich which has extensive recordings made on the opposite recordable

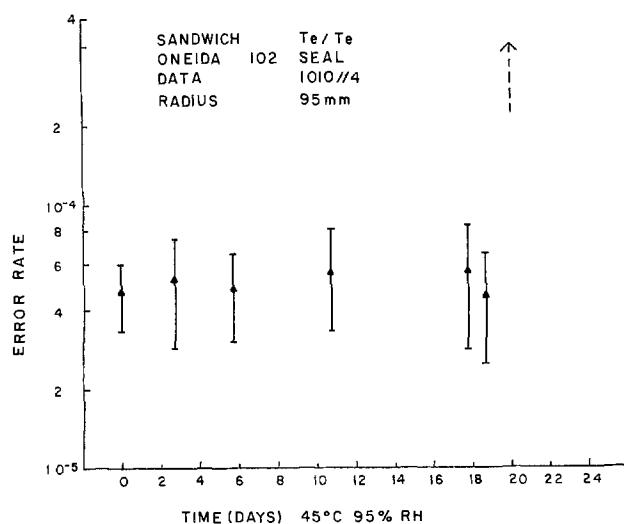


Fig. 5. Error rate degradation for double-sided tellurium air sandwich™, outer radius.

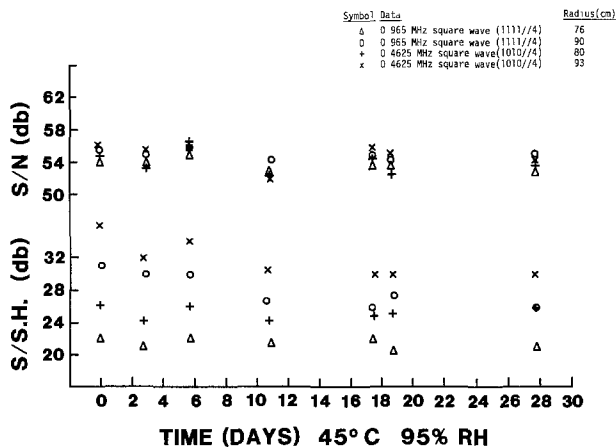


Fig. 6. Signal-to-noise and signal-to-second-harmonic degradation for double-sided tellurium air sandwich™.

surface. The results are typical of the behavior of tellurium air sandwiches.

Conclusions

Recorded data on these tellurium sandwich disks will remain stable in a 45°C and 95% relative humidity environment for at least 15 days. Stability is independent of recording radius, recorded data patterns, and whether recordings have been made on the opposite side. At present, extrapolation of these data to room ambient is uncertain. If one were to adopt the model proposed by Milch and Tasaico (4), developed

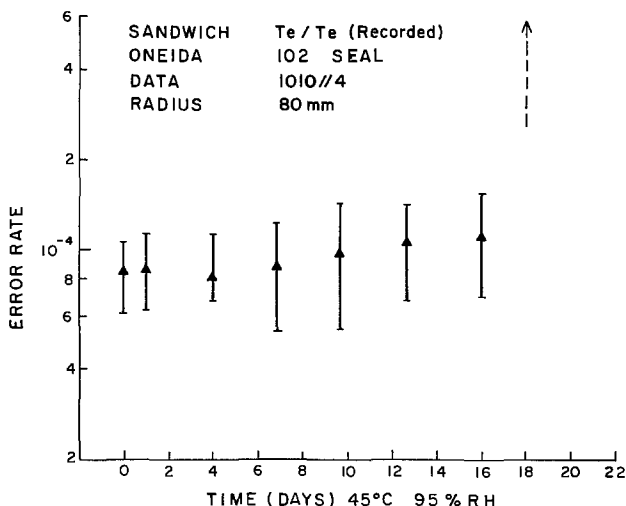


Fig. 7. Error rate degradation for double-sided tellurium air sandwich™ with recordings on opposite side.

for the extrapolation of shelf-life data, these results imply an archival life of at least 10 years for tellurium sandwiches at room ambient (25°C, 50% relative humidity). Failure of the air sandwich consists of a dramatic increase (several orders of magnitude) in the error rate, developing over a comparatively short time (a day or so). The direct cause of failure is apparently the development of localized defects on the disk. The catastrophic failure was not observed in the macroscopic signal characteristics, the film properties, or the integrity of the air sandwich structure. Lifetime data based on macroscopic optical measurements of transmission and reflection may well give overly optimistic results. Analogue information storage based on these macroscopic signal characteristics will probably have substantially longer lifetimes than 14 days at high humidity.

Several possible pathways exist for improving the archival life of the tellurium sandwich. The degradation is primarily associated with humidity. Hermetic sealing of the sandwich (6), or storage at elevated temperatures (4), have been used successfully. Substantially improved stability has also been observed by introducing appropriate impurities in the tellurium film. These results will be reported in a subsequent paper.

Acknowledgments

We would like to thank A. Chan and J. Nadan for the electronics instrumentation used in these experiments, and F. Zernike for the recorder. Sandwiches were fabricated by A. Weeks and M. Jaso, and S. Tan carried out the data analysis. We would also like to acknowledge G. Blom and G. Kenney for reviewing the manuscript.

Manuscript submitted June 24, 1980; revised manuscript received Sept. 15, 1980.

Any discussion of this paper will appear in a Discussion Section to be published in the December 1981 JOURNAL. All discussions for the December 1981 Discussion Section should be submitted by Aug. 1, 1981.

Publication costs of this article were assisted by Philips Laboratories.

REFERENCES

1. R. Bartolini, H. Weakleim, and B. Williams, *Opt. Eng.*, **15**, 99 (1976).
2. G. Kenney, D. Lou, R. McFarlane, A. Chan, J. Nadan, T. Kohler, J. Wagner, and F. Zernike, *IEEE Spectrum*, **16**, No. 2, 33 (1979).
3. K. Bulthuis, M. G. Carasso, J. P. J. Heemskerk, P. J. Kivits, W. J. Kleuters, and P. Zalm, *ibid.*, **16**, No. 8, 26 (1979).
4. A. Milch and P. Tasaico *This Journal*, **127**, 884 (1980).
5. S. Yonezawa, T. Maeda, T. Sugiyama, and H. Takahashi, *Tech. Dig., CLEOS* (1980).
6. M. deHaan, *ibid.*, CLEOS (1980).

Tarnishing of Silver by Sulfur Vapor: Film Characteristics and Humidity Effects

B. T. Reagor* and J. D. Sinclair*

Bell Laboratories, Holmdel, New Jersey 07733

In laboratory and field studies over the past several years, we have noted that in some environments the average tarnishing rate of silver seemed to be less

* Electrochemical Society Active Member.
Key words: sulfadation, dendrite, SEM, growth.

dependent on relative humidity (RH) than the dramatic dependence that has commonly been observed in the laboratory with hydrogen sulfide (1-15). We have also noted that the tarnish film thickness was often nonuniform. These effects were especially evident

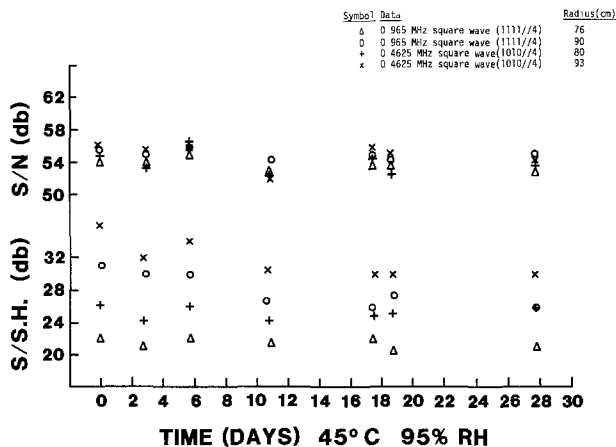


Fig. 6. Signal-to-noise and signal-to-second-harmonic degradation for double-sided tellurium air sandwich™.

surface. The results are typical of the behavior of tellurium air sandwiches.

Conclusions

Recorded data on these tellurium sandwich disks will remain stable in a 45°C and 95% relative humidity environment for at least 15 days. Stability is independent of recording radius, recorded data patterns, and whether recordings have been made on the opposite side. At present, extrapolation of these data to room ambient is uncertain. If one were to adopt the model proposed by Milch and Tasaico (4), developed

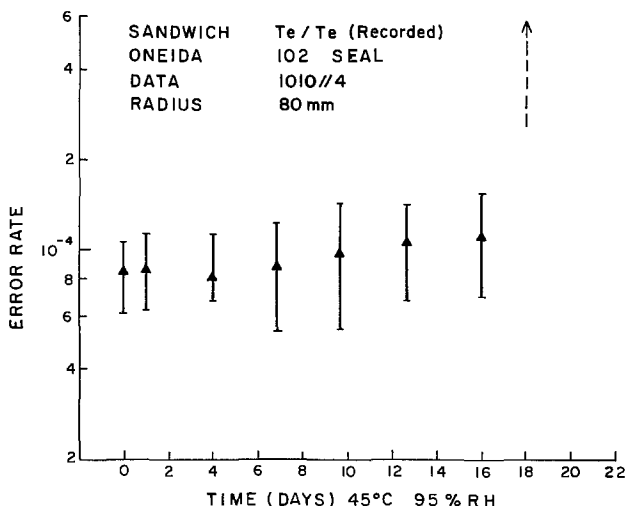


Fig. 7. Error rate degradation for double-sided tellurium air sandwich™ with recordings on opposite side.

for the extrapolation of shelf-life data, these results imply an archival life of at least 10 years for tellurium sandwiches at room ambient (25°C, 50% relative humidity). Failure of the air sandwich consists of a dramatic increase (several orders of magnitude) in the error rate, developing over a comparatively short time (a day or so). The direct cause of failure is apparently the development of localized defects on the disk. The catastrophic failure was not observed in the macroscopic signal characteristics, the film properties, or the integrity of the air sandwich structure. Lifetime data based on macroscopic optical measurements of transmission and reflection may well give overly optimistic results. Analogue information storage based on these macroscopic signal characteristics will probably have substantially longer lifetimes than 14 days at high humidity.

Several possible pathways exist for improving the archival life of the tellurium sandwich. The degradation is primarily associated with humidity. Hermetic sealing of the sandwich (6), or storage at elevated temperatures (4), have been used successfully. Substantially improved stability has also been observed by introducing appropriate impurities in the tellurium film. These results will be reported in a subsequent paper.

Acknowledgments

We would like to thank A. Chan and J. Nadan for the electronics instrumentation used in these experiments, and F. Zernike for the recorder. Sandwiches were fabricated by A. Weeks and M. Jaso, and S. Tan carried out the data analysis. We would also like to acknowledge G. Blom and G. Kenney for reviewing the manuscript.

Manuscript submitted June 24, 1980; revised manuscript received Sept. 15, 1980.

Any discussion of this paper will appear in a Discussion Section to be published in the December 1981 JOURNAL. All discussions for the December 1981 Discussion Section should be submitted by Aug. 1, 1981.

Publication costs of this article were assisted by Philips Laboratories.

REFERENCES

1. R. Bartolini, H. Weakleim, and B. Williams, *Opt. Eng.*, **15**, 99 (1976).
2. G. Kenney, D. Lou, R. McFarlane, A. Chan, J. Nadan, T. Kohler, J. Wagner, and F. Zernike, *IEEE Spectrum*, **16**, No. 2, 33 (1979).
3. K. Bulthuis, M. G. Carasso, J. P. J. Heemskerk, P. J. Kivits, W. J. Kleuters, and P. Zalm, *ibid.*, **16**, No. 8, 26 (1979).
4. A. Milch and P. Tasaico *This Journal*, **127**, 884 (1980).
5. S. Yonezawa, T. Maeda, T. Sugiyama, and H. Takahashi, *Tech. Dig., CLEOS* (1980).
6. M. deHaan, *ibid.*, CLEOS (1980).

Tarnishing of Silver by Sulfur Vapor: Film Characteristics and Humidity Effects

B. T. Reagor* and J. D. Sinclair*

Bell Laboratories, Holmdel, New Jersey 07733

In laboratory and field studies over the past several years, we have noted that in some environments the average tarnishing rate of silver seemed to be less

* Electrochemical Society Active Member.
Key words: sulfidation, dendrite, SEM, growth.

dependent on relative humidity (RH) than the dramatic dependence that has commonly been observed in the laboratory with hydrogen sulfide (1-15). We have also noted that the tarnish film thickness was often nonuniform. These effects were especially evident

in laboratory studies in which sulfur vapor was the tarnishing agent and in field studies at Artesia, New Mexico.

While sulfur vapor is a significant atmospheric tarnishing agent in only a few field environments (16), mercaptans and organic sulfides and disulfides can be more widely found as a result of natural processes and anthropogenic activity. Crossland *et al.* (11) have reported that mercaptans do not tarnish silver, but work in this laboratory indicates that atmospheres generated from organic sulfides and disulfides rapidly tarnish silver, especially in the presence of light (17). Very recently carbonyl sulfide, a major atmospheric sulfur-containing constituent was found to tarnish silver at elevated RH (18). The effect of RH on tarnishing by any of these carbon containing agents is unknown.

In a paper on precious metal alloys, Abbott (19) briefly reported on the tarnishing of silver by sulfur at 30°C in a flowing atmosphere. His data were summarized in a single linear plot that represented all N₂-O₂-SO₂-sulfur-H₂O environments studied. Chiarenzelli (5) claimed tarnishing would not occur in the absence of moisture. We report here the results of a study on sulfide film uniformity and humidity effects, using sulfur vapor as the tarnishing agent for silver coupons exposed in a closed environment at room temperature and 50°C.

Experimental

Tarnish film morphology was studied with an AMR-1000 Scanning Electron Microscope (SEM) in the secondary electron mode using an accelerating voltage of 30 kV. Average sulfide film thickness was measured by cathodic reduction (20). Nonuniformity in film thickness was estimated from sulfur (K α) to silver (L α) x-ray intensity ratios using a calibration plot based on cathodic reduction measurements. The x-ray intensities were measured with a Princeton Gamma-Tech x-ray detector and Tracor Northern 880 multichannel analyzer in conjunction with the SEM.

Square silver coupons (½ in. on a side) were cut from 0.005 in. thick Sargent-Welch silver foil. The coupons were cleaned and etched by two sets of successive immersions in concentrated nitric acid and then ammonia, the first set involving 10 min immersions and the second set 5 min immersions. Each immersion was followed by multiple rinses in pure water. The coupons were air dried for several hours prior to initiation of the experiments. This procedure produced a uniform and reproducible white matte surface on the coupons.

Sulfide films were grown on coupons suspended individually by glass hooks in bell jars that were approximately 8 cm high with a diameter of 6.5 cm. Sulfur vapors were evolved from a large excess of aged flowers of sulfur spread across a crystallization dish that was placed at the bottom of the bell jar. The vapor pressure of sulfur at room temperature is approximately 0.2 mPa (21), while that at 50°C is approximately 10 mPa (21). The molecular composition of sulfur vapor in equilibrium with the solid is approximately 96% S₈ and 4% S₆ at 50°C (22). A saturated salt solution, pure water, or Drierite, each contained in a 10 ml beaker, was placed at the bottom of the bell jar in the center of the crystallization dish for RH control. The salts used were lithium chloride, calcium nitrate, and ammonium sulfate. A survey of literature data on the vapor pressures of saturated salt solutions (23-32) indicated that the RH over the calcium nitrate solution used at room temperature was approximately 51%, while the RH's over the lithium chloride, ammonium sulfate, and calcium nitrate solutions used at 50°C were 11, 79, and 35-45%, respectively.

Coupon exposures at room temperature (23° ± 2°C) were accomplished on laboratory benches under ordinary fluorescent lighting. Studies at elevated tempera-

tures were carried out in a GCA/Precision Scientific oven that was modified to include a Leeds and Northrup temperature controller. The temperature of the oven was 50° ± 2°C.

Results and Discussion

The sulfide tarnish film thickness on freshly cleaned and etched silver coupons that were exposed for up to 50 and 18 days at room temperature and at 50°C, respectively, is shown in Fig. 1 and 2 as a function of exposure time. The error bars indicate 95% confidence limits. The data confirm that in a closed environment relative humidity does not have an appreciable effect on the average rate of silver sulfide formation in the presence of sulfur vapor either at room temperature or at 50°C. The independence of the rate on relative humidity is further evidence that the probable function of moisture in tarnishing by hydrogen sulfide is to provide a medium for the oxidation of hydrogen sulfide to free sulfur (2, 10).

The average rate of silver sulfide film formation (at all humidities) was 0.5 Å/hr at room temperature and 13.3 Å/hr at 50°C. Similar to previous work, the observed linearity of the sulfiding rate at the conditions of this study indicates that the process is controlled by the arrival of sulfur at the silver surface (12, 19, 33, 34). An approximation for the rate of arrival of S₈ vapor to the coupon surface was calculated with the equation

$$S/t = DqCe/l$$

from the cylindrical model of Jost (35), where S is the quantity of S₈ arriving in time t , D is the diffusivity of S₈ in air, l is the distance from the sulfur source to the center of the coupon (5 cm), q is the cross-sectional

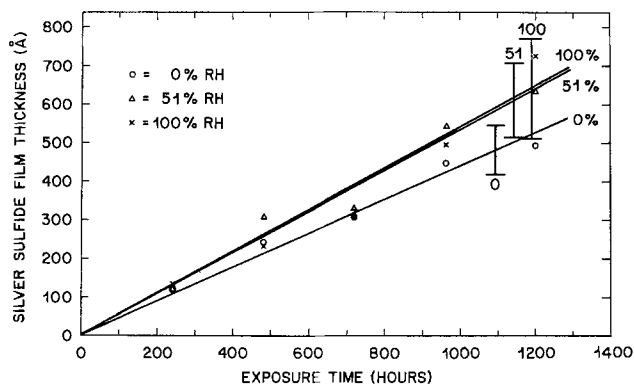


Fig. 1. Sulfide tarnish film formation on silver by sulfur vapor at room temperature.

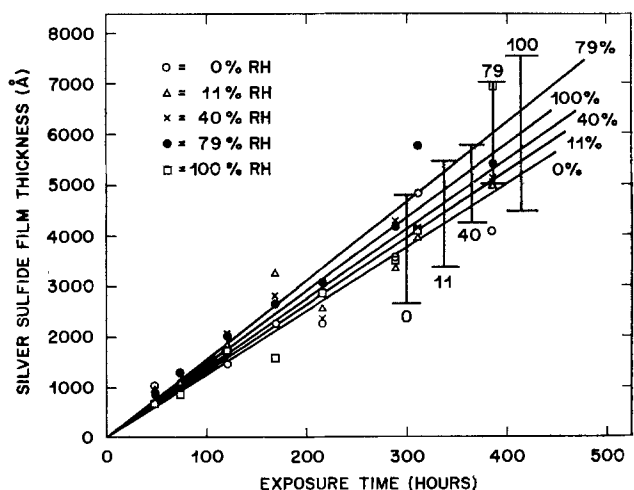


Fig. 2. Sulfide tarnish film formation on silver by sulfur vapor at 50°C.

area of the bell jar, and C_e is the equilibrium concentration of S_8 obtained from the vapor pressure above the solid. The model assumes an S_8 concentration of zero at the silver surface, i.e., all S_8 striking the coupon surface is consumed by silver. The diffusivity of S_8 at room temperature was estimated from the diffusivity of air and the relationship

$$\frac{D_{\text{sulfur}}}{D_{\text{air}}} = \sqrt{\frac{MW_{\text{air}}}{MW_{\text{sulfur}}}}$$

to be 0.036 cm²/sec. With this model the calculated rate of silver sulfide formation at room temperature was 0.7 Å/hr in reasonable agreement with the experimental rate. Unfortunately the diffusivity of silver in silver sulfide is not well known below 90°C, which prohibits calculating a silver diffusion limited tarnishing rate. Parabolic kinetics have been observed at considerably higher tarnishing agent concentrations (> 1 ppm hydrogen sulfide) (6). For initial film formation rates in excess of approximately 10 Å/hr at room temperature, the diffusivity of silver in silver sulfide appears to be rate controlling.

The morphology of the tarnish films formed at 50°C under the conditions of this study was not appreciably affected by the relative humidity, as the micrographs in Fig. 3 and 4 indicate. The high magnification micrographs in Fig. 3 of approximately 5000Å sulfide films exhibit the crystallinity in the surface film that was observed on the tarnished coupons. The apparent greater crystallinity seen in micrograph d relative to that in micrographs b and c is a result of random variations across the coupon surfaces.

In all cases examined, the tarnish film thickness at the coupon edges was greater than the thickness at the center. The micrographs in Fig. 4 show the extensive dendritic growths observed at the coupon edges and a rapid drop in dendrite density immediately interior to the edges. The tarnish film thickness variations on these coupons, as determined by the SEM/x-ray method, are summarized in Table I. The tarnish film thickness at the coupon centers is from 1240 to 2940Å less than the average thickness at the corners. The trend toward increasing thickness away from the center can be attributed to the statistical distribution of the sulfur diffusion paths as affected by convection

Table I. Silver sulfide tarnish film thicknesses by S/Ag x-ray intensity ratio (18 day exposure at 50°C)

| Percent RH of test atmosphere | Thickness (Å) | | |
|-------------------------------|------------------------|------------------------|---------------|
| | Four corners of coupon | Average of the corners | Coupon center |
| 0 | 5770, 5770, 6500, 5710 | 5940 | 3900 |
| 51 | 5120, 5250, 5180, 5370 | 5230 | 3990 |
| 100 | 5180, 5960, 5820, 5770 | 5680 | 4020 |

currents from the sulfur source to the coupon surface. Most of the film thickness measurements for the four corners are within 200Å of the average of the corners and can be considered essentially identical. However, the corners of the coupons exposed at 0 and 100% RH that exhibited thicknesses of 6500 and 5180Å, respectively, are significantly different from the average.

These nonuniformities indicate that the wide scatter in tarnish rate data found for films analyzed by cathodic reduction in this study and in others could be at least partially caused by random fluctuations in the surface condition prior to tarnishing that may be experimentally caused but that would be most difficult if not impossible to avoid. They could also relate, in part, to convective effects on the sulfur arrival rates. Mechanistic interpretations utilizing film thickness data based on cathodic reduction or other averaging techniques may not always be as straightforward as is often thought. In some cases, for example the mixed oxide, sulfide films that usually form on copper, regional fluctuations in the rates of competing reactions may occur across the surface of test coupons. For silver, the variations in sulfide thickness could result in or be caused by localized mechanistic differences or nonuniform surface energetics but do not appear to influence the average rate of the sulfur limited reaction.

Some of the previous studies of sulfidation of silver have documented the growth of dendrites, whiskers, or platelets. Drott (3), using 2% hydrogen sulfide in water saturated air at room temperature, noted that the appearance of whiskers occurred simultaneously with a sudden increase of the reaction rate. The whisker growth was uniformly distributed and oc-

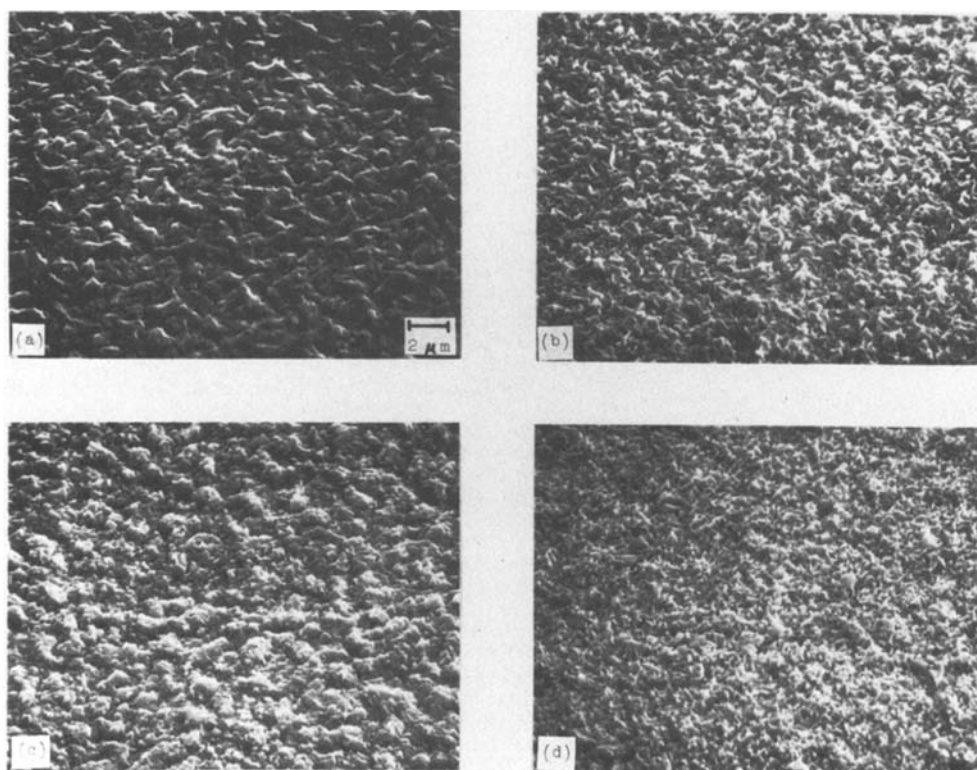


Fig. 3. Morphology of the interior surfaces of silver coupons: (a) untarnished coupon; (b-d) coupons tarnished to a sulfide film thickness of approximately 5000Å at 0, 51, and 100% RH, respectively.

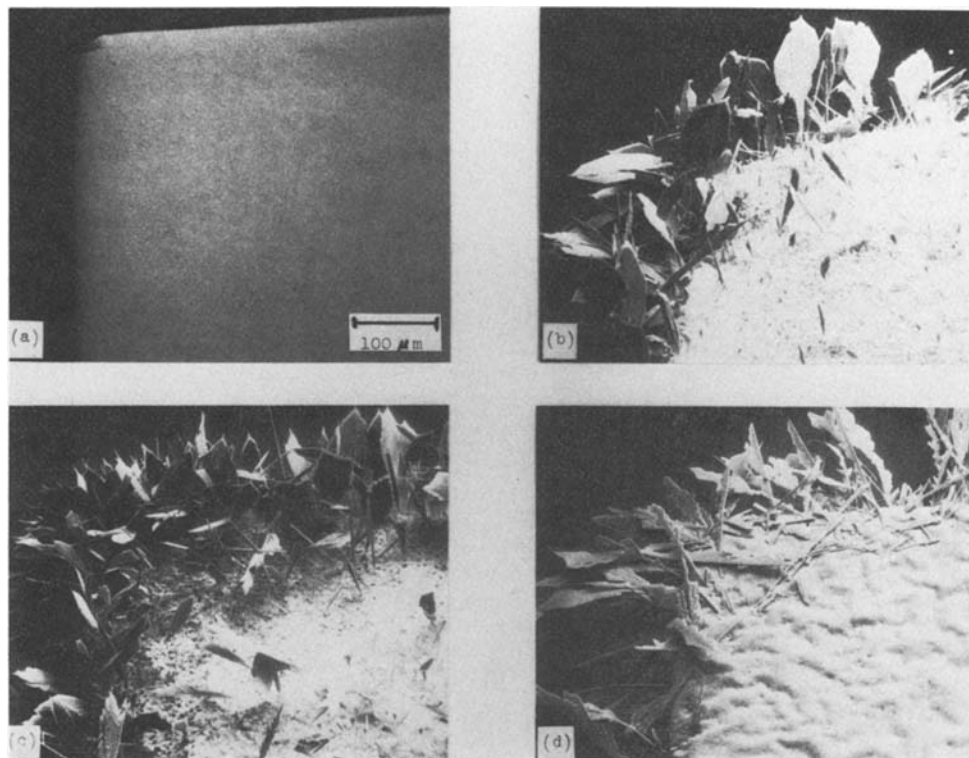


Fig. 4. Dendritic growths at the corners of silver coupons: (a) untarnished coupon; (b-d) coupons tarnished to a sulfide film thickness of approximately 5000 Å at 0, 51, and 100% RH, respectively.

curred after the formation of discrete mounds whose distribution was unrelated to the grain structure of the metal. It was suggested that whiskers sprouted when critical mound conditions existed that were brought about by mechanical tension due to rapid growth. Backlund *et al.* (4) and Bennett *et al.* (9) reported similar findings.

At the very high tarnishing agent concentrations of Drott the increase in tarnishing rate coincident with whisker growth can be attributed to the sudden availability of silver in a silver-limited environment. In the sulfur limited environment of this study an increased growth rate coincident with whisker growth would not occur. The preferential growth of dendrites at the edges indicates that the rate of arrival of sulfur there was sufficiently large to create a mechanically stressed surface. The surplus silver available at the outer ends of the easy diffusion paths apparently allows whisker growth to start. After initiation, the sulfur arrival process and the surface diffusion paths available on the dendrites would probably be expected to produce preferential growth on the whiskers. The average growth rate would remain linear.

Manuscript submitted June 12, 1980; revised manuscript received *ca.* Sept. 24, 1980.

Any discussion of this paper will appear in a Discussion Section to be published in the December 1981 JOURNAL. All discussions for the December 1981 Discussion Section should be submitted by Aug. 1, 1981.

Publication costs of this article were assisted by Bell Laboratories.

REFERENCES

- W. H. J. Vernon, *Trans. Faraday Soc.*, **31**, 1668 (1935).
- S. Liienfeld and C. E. White, *J. Am. Chem. Soc.*, **52**, 885 (1930).
- J. Drott, *Arkiv För Kemi*, **15**, 181 (1960).
- P. Backlund, B. Fjellström, S. Hammerbäck, and B. Majgren, *ibid.*, **26**, 267 (1966).
- R. V. Chiarenzelli, *IEEE Trans. Parts, Mater., Packag.*, **pmp-3**, 89 (1967).
- D. Pope, H. R. Gibbens, and R. L. Moss, *Corros. Sci.*, **8**, 883 (1968).
- W. H. Abbott, "Proceedings of the Holm Seminar on Electrical Contact Phenomena," p. 53, Chicago, Ill. (1968).
- W. E. Campbell and U. B. Thomas, *ibid.*, p. 233 (1968).
- H. E. Bennett, R. L. Peck, D. K. Burge, and J. M. Bennett, *J. Appl. Phys.*, **40**, 3351 (1969).
- J. A. Lorenzen, "Proceedings of the Institute of Environmental Sciences," p. 110, Mt. Prospect, Ill. (1971).
- W. A. Crossland, E. Knight, and C. R. Wright, "Proceedings of the Holm Seminar on Electrical Contact Phenomena," p. 265, Chicago, Ill. (1973).
- W. H. Abbott, *IEEE Trans. Parts, Hybrids, Packag.*, **php-10**, 24 (1974).
- H. Schmidt-Brücken and W. Betz, *Metalloberfläche Angew. Elektrochem.*, **28**, 373 (1974).
- K. L. Schiff and H. Becker, *Electr. Contacts*, **24**, 295 (1978).
- D. Simon, J. Bardolle, and M. Bujor, "Proceedings of the Holm Seminar on Electrical Contact Phenomena," p. 55, Chicago, Ill. (1979).
- B. T. Reagor, Publication in preparation, unpublished work.
- J. D. Sinclair, Publication in preparation.
- T. E. Graedel, G. W. Kammlott, and J. P. Franey, Publication in preparation.
- W. H. Abbott, *IEEE Trans. Parts, Mater., Packag.*, **pmp-5**, 156 (1969).
- W. E. Campbell and U. B. Thomas, *Trans. Electrochem. Soc.*, **76**, 303 (1939).
- A. N. Nesmeyanor, "Vapor Pressure of the Chemical Elements," translated from 1961 Russian ed., pp. 314-320, Elsevier, New York (1963).
- "The Sulphur Data Book," W. N. Tuller, Editor, pp. 26-28, McGraw-Hill Book Co., New York (1954).
- F. E. M. O'Brien, *J. Sci. Instr.*, **25**, 73 (1948).
- C. P. Hedlin and F. N. Trofimenkoff, "Humidity and Moisture," Vol. 3, A. Wexler and W. A. Wildhack, Editors, 1963 International Symposium on Humidity and Moisture, Washington, D.C.
- A. Wexler and S. Hasegawa, *J. Res. Nat. Bur. Stand.*, **53**(1), 19 (1954).
- R. H. Stokes and R. A. Robinson, *Ind. Eng. Chem.*, **41**, 2013 (1949); R. A. Robinson and R. H. Stokes, "Electrolytic Solutions," 2nd ed., Butterworths, London (1959).
- W. A. Wink and G. R. Sears, *TAPPI*, **33**, 96 (1950); *Chem. Abstr.*, **44**, 10416 (1950).
- F. H. Huttig and F. Reyscher, *Z. Anorg. Chem.*, **137**, 155 (1924).
- G. Edgar and W. O. Swan, *J. Am. Chem. Soc.*, **44**, 570 (1922).
- J. R. Adams and A. R. Merz, *Ind. Eng. Chem.*, **21**, 305 (1929).

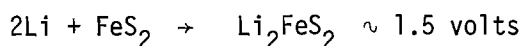
31. J. Obermiller and M. Goertz, *Z. Phys. Chem.*, **109**, 145 (1924).
32. A. Lannung, *ibid.*, **A170**, 134 (1934).
33. H. Rickert, *Werkst. Korros.*, **19**, 869 (1968).
34. H. Rickert and K. H. Tostmann, *ibid.*, **21**, 965 (1970).
35. W. Jost, "Diffusion in Solids, Liquids, Gases," p. 9, Academic Press Inc., New York (1970).

Niobium Triselenide in a Lithium Dioxolane Cell

M. Stanley Whittingham*¹ and Gerald H. Newman*

Exxon Research and Engineering Company, Linden, New Jersey 07036

For many applications there is a need for a secondary battery with a high volumetric energy density. Although the lithium titanium disulfide cell has very good rechargeability and gravimetric energy density, it has a rather low volumetric energy density compared with some primary cathodes such as MnO_2 and FeS_2 . The oxide has a higher potential and the sulfide reacts with about two lithium:



In contrast to the disulfide, titanium trisulfide will react with three lithium to give the compound Li_3TiS_3 . However, this compound shows very poor reversibility, less than one lithium being discharged on the 2nd cycle, because of structural changes (1). Niobium triselenide is much more reversible (2), but even here the best reported cycling showed a 60% loss in capacity in going from the first to the third cycle (3). The capacity then fell in the range 26-30% of the first cycle capacity for the next sixty cycles.

The reversibility of the Li/TiS_2 cell was maximized when dioxolane was used as the electrolyte solvent (4). We therefore conducted experiments on the trichalcogenides using dioxolane as the solvent. The cells were constructed as described earlier (5), using as electrolyte a 2.5 molar solution of lithium perchlorate in dioxolane. They were then cycled (6) continuously at 2 ma/cm^2 between voltage limits of 2.65 and 1.45 volts. On the first discharge 2.33 lithium were incorporated into the niobium triselenide lattice, 78% of the theoretical value. This decayed slowly on cycling as shown in Fig. 1.

This figure also compares the data in the dioxolane solvent with that obtained (3) in a LiClO_4 /propylene carbonate cell to which 3 wt.% of an ether additive, tetraglyme, has been added. The latter in turn was much improved over a pure propylene carbonate solvent (3). Just as for titanium disulfide, dioxolane gives the best cycling performance for niobium triselenide. The reason for this is not clear but is related to a number of factors, probably including its lithium plating capability which minimizes formation of lithium "sludge", its greater resistance than propylene carbonate to react at the cathodic lithium potentials and better wetting of the cathode and separators.

The experiments were extended to two other trichalcogenides, NbS_3 and TiS_3 , to see whether their cycling could also be improved. The NbS_3 was discharged at 2 ma/cm^2 for the first two cycles and then at 1 ma/cm^2 thereafter; charging throughout was at 1 ma/cm^2 . The TiS_3 cathode was discharged at 2 ma/cm^2 but due to the very low capacities the charge rate was only 0.5 ma/cm^2 ; this was further reduced to 0.25 ma/cm^2 after the 27th discharge. The cycling behavior of these two cathodes are compared with despite the less demanding cycling regime. Thus on the 20th cycle, the capacities are 66%, 30% and 2.6% for NbSe_3 , NbS_3 and TiS_3 respectively. This behavior is probably a result of an inherent irreversibility of at least part of the lithium in the two sulfides, rather than a function of the electrolyte, as described elsewhere (1,5,7-9). When TiS_2 cells are cycled under similar conditions the loss of capacity over 60 cycles is about 20%. This was reduced to about 0.1%/cycle by applying pressure to the cells (10), and it is anticipated that the capacity of NbSe_3 cells would be similarly improved as Jacobson (11) has shown in very slow cycling tests that NbSe_3 is inherently totally reversible. In addition, a low capacity, 4 mAhr , NbSe_3 cell has recently been cycled to over 80% of 3 Li/Nb sixty times (12).

*Electrochemical Society Active Members
1. Present Exxon Address: P. O. Box 101,
Florham Park, N. J. 07932

REFERENCES

1. M. S. Whittingham, J. Electrochem. Soc. 123, 315 (1976).
2. J. Broadhead and F. A. Trumbore, Abstract 178 p. 445, The Electrochemical Society Extended Abstracts, Chicago, Illinois, May 13-18, 1973 and U.S. Pat. 3,864,167.
3. J. Broadhead, T. M. Putvinski & F. A. Trumbore, U.S. Patent 3,928,067.
4. L. H. Gaines & G. H. Newman, Can. Pat. 1,066,766.
5. M. S. Whittingham, Progress in Solid State Chem., 12, 41 (1978).
6. M. S. Whittingham & G. H. Newman, U.S. Patent 4,086,403.
7. R. R. Chianelli & M. B. Dines, Inorg. Chem., 14, 2417 (1975).
8. D. W. Murphy & F. A. Trumbore, J. Electrochem. Soc., 123, 960 (1976).
9. G. L. Holleck, F. S. Shuker & S. B. Brummer, Proc. 10th IECEC Mtg., Delaware, 10, 444 (1975).
10. M. S. Whittingham & J. A. Panella, Mat. Res. Bull., 16, 1 (1981).
11. A. J. Jacobson, to be published.
12. J. Broadhead, 5th Australian Electrochemistry Conference, to be published.

Manuscript submitted Sept. 29, 1980;
revised manuscript received Dec. 17, 1980.

Publication costs of this article were
assisted by Exxon Research and Engineering
Company.

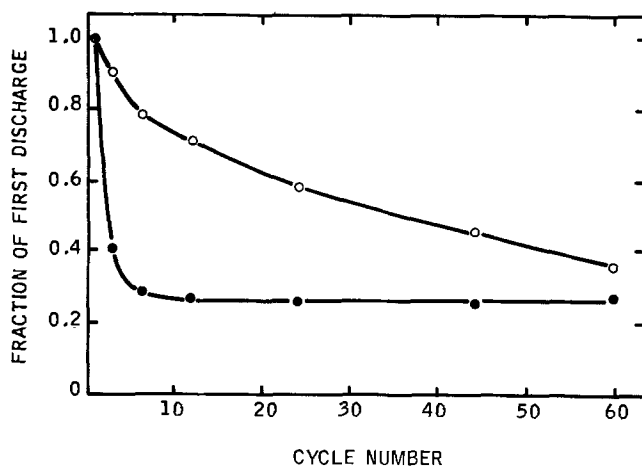


FIG 1 Discharge capacity of NbSe_3 in lithium cells containing as electrolyte solvent (o) dioxolane and (●) propylene carbonate/3% tetraglyme

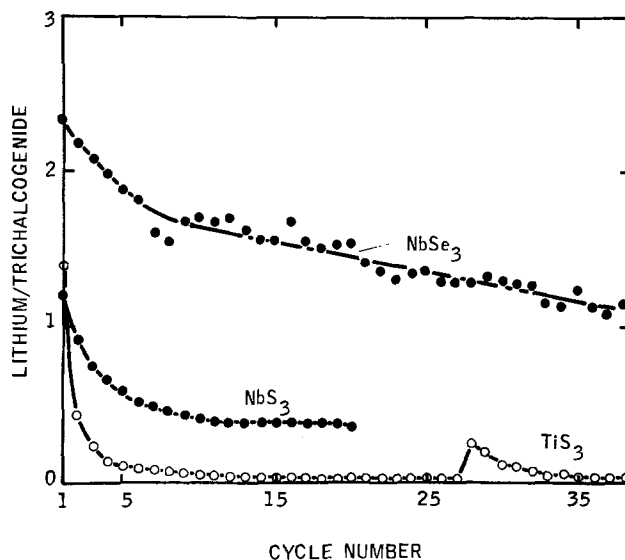


FIG 2 Discharge capacity of NbSe_3 , NbS_3 and TiS_3 in lithium cells using a lithium perchlorate/dioxolane electrolyte and no conductive diluent in the cathode

Low Pressure Deposition of Silicon Nitride by SiCl_4 and NH_3 Reaction

I. Szendro and E. Marton

TUNGSRAM, H-1340, Budapest, Hungary

Low pressure deposition processes utilizing SiH_4 - NH_3 and SiH_2Cl_2 - NH_3 have been reported. The former reaction is extremely sensitive to wafer spacings and system configurations [1.,2./]. The SiH_2Cl_2 - NH_3 [1.,3./] reaction yields excellent film uniformities and reproducibilities. However, to achieve this, care should be taken of the control of temperature and pressure, and at 900°C it requires a rather high capacity vacuum system [1./].

In our study we have applied the SiCl_4 - NH_3 reaction [which is well known at atmospheric, cold wall conditions/ to a low pressure hot wall system as this nitride forming process was expected to be less sensitive to process variations.

Experiments. -- The LPCVD system consisted of a normal resistance heated furnace and a quartz tube /80/74 mm/ without any special tube inserts. The 2 inch diameter wafers were held in four basket type quartz carrier with wafer plane perpendicular to the tube axis. One wafer carrier consisted 25 slots with 3,2 mm spacings. The vacuum exhaust system was based on a LN_2 trap followed by a mechanical vacuum pump of 585 l/min capacity. The pressure could be independently controlled by introducing N_2 gas directly into to vacuum inlet line of the pump. Pressure was measured at the front of the tube by a Baratron 221 type capacitance manometer, temperatures reported here were measured in the subatmospheric reaction zone.

Gases were controlled by taper

Key words: LPCVD, silicon nitride

tube flowmeters [Matheson Gas Prod./, the SiCl_4 /Merck, zur Synthese/ was held in a stainless steel reservoir, and its vapour was introduced into the reactor zone by N_2 carrier gas. In some experiments undiluted, pure SiCl_4 vapour was introduced into the reactor with the help of a mass flow controller, connected between the outlet of the reservoir and the inlet of the reactor quartz tube. In those cases, the N_2 gas inlet of the SiCl_4 reservoir was closed and only the SiCl_4 vapour / ~ 260 mbar at 20°C / feeded the MFC inlet. This set up is useful if one needs a high SiCl_4 partial pressure in the reactor, because no N_2 carrier is needed. The E.G. ammonia and diclorosilane [for comparative nitride depositions/ was supplied by Matheson Gas Prod., the N_2 was obtained from liquid nitrogen source and after purification its oxygen and water concentration was less than 2 ppm. All thickness and refractive index measurements were made with a laser ellipsometer.

Results. -- The deposition rate was studied as a function of temperature and the results are plotted in Fig. 1. The Arrhenius curves show that the SiCl_4 - NH_3 - N_2 process is about half as sensitive to temperature change / $\sim 0,9\% / ^\circ\text{C}$ / as the SiH_2Cl_2 - NH_3 process / $\sim 1,7\% / ^\circ\text{C}$ /. On Fig.2. the SiCl_4 and SiH_2Cl_2 partial pressure effect on the nitride growth rate is shown and the advantages of SiCl_4 over SiH_2Cl_2 are significant as to deposition rate change versus pressure change. Deposition rate versus wafer spacing was determined for several system pressures and there was no difference between the two nitride forming process.

Film uniformity within a wafer and

within wafer to wafer in a 100 wafers load was studied as a function of pressure and temperature slope. In order to get a better uniformity within a wafer than $\pm 2,5\%$ and a better than $\pm 4\%$ within wafer to wafer the pressure must be below 1,1 mbar, wafer spacings 3,2 mm, and as high as $1,5^\circ\text{C}/\text{cm}$ temperature slope should be achieved in the reactor zone declining towards the gas inlet.

The physical and chemical properties of the silicon nitride layers produced by the $\text{SiCl}_4\text{-NH}_3$ LPCVD process was found to be similar to those deposited by the $\text{SiCl}_4\text{-NH}_3$ reaction at atmospheric conditions [4.] or by the $\text{SiH}_2\text{Cl}_2\text{-NH}_3$ LPCVD process [1.]. The refractive index is $1,98 \pm 0,01$, the etch rate in 40% HF at 25°C is 11 nm/min, the i.r. absorption maximum is at 830 cm^{-1} .

It is known that at atmospheric deposition conditions trace amounts of oxygen and water can cause off stoichiometric silicon nitride layers [5.]. We have carried out some experiments to see how the gas phase O_2 and H_2O contamination affects the LPCVD silicon nitride film properties. The preliminary results are surprising and further experiments have to be made. It is found that up to 50 ppm O_2 concentration in the $\text{SiH}_2\text{Cl}_2\text{-NH}_3$ process and 50 ppm H_2O in the $\text{SiCl}_4\text{-NH}_3$ process has no effect on such nitride properties as refractive index, etch rate, i.r. absorption. The possible explanation is that in the hot wall reactors the O_2 and H_2O can not reach the wafers surface because they react in the hot gas phase much faster with SiH_2Cl_2 and SiCl_4 than NH_3 does, and the oxide forming reaction is finished already in the colder inlet side of the reactor.

Acknowledgment. -- Authors are grateful to Gy. Motal for his encouragement during this work and to F. Nagel for his help in building the LPCVD equipment.

Manuscript submitted March 26, 1980;
revised manuscript received Dec. 9, 1980.

REFERENCES

1. R.S. Rosler, Solid State Technology, vol. 20, pp. 63-70. Apr. 1977
2. E.Tanikawa, O. Takayama and K.Maeda, Proc. 4th Int. Conf. on C.V.D., 1973. pp 261-274
3. W-A. Brown, T.I. Kamins, Solid State Technology, pp 51-57. July 1979.
4. M.J. Grieco, F.L. Worthing and B. Schwartz, J. Electrochem. Soc. vol. 115, no.5. pp 525-531 May 1968.
5. V.A. Wells and M.V. Hanson, Proc. 7th. Int. Conf. on C.V.D., 1979 pp 190-197.

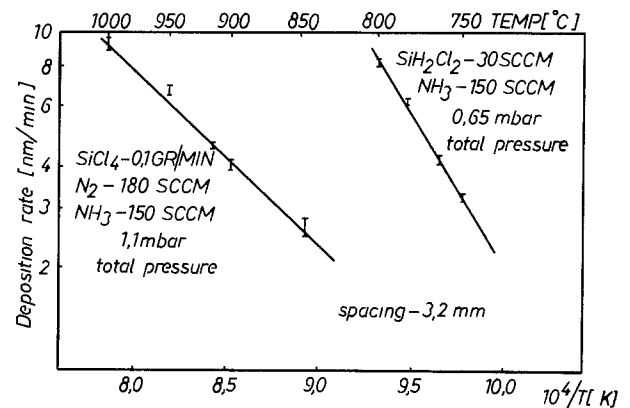


Fig.1. Silicon nitride deposition rate versus $1/T$.

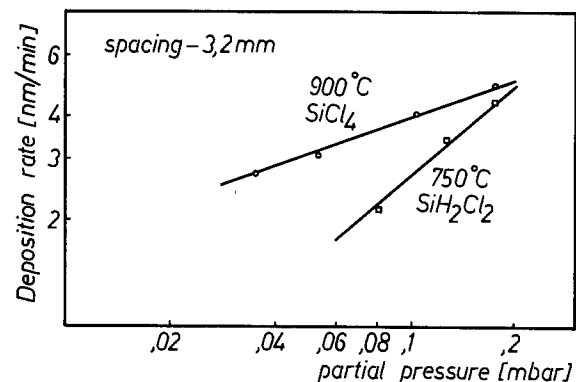


Fig.2. Silicon nitride deposition rate versus SiCl_4 and SiH_2Cl_2 partial pressure

Al/FeS₂ Secondary Cells Using Organic Electrolytes

Setsuko Takahashi and Nobuyuki Koura*

*Department of Industrial Chemistry, Faculty of Science and Technology,
Tokyo University of Science, 2641 Yamazaki, Noda Chiba 278, Japan*

Aluminum is a common and inexpensive metal with a high theoretical capacity and a negative potential, but for use as the negative electrode of cells, it has some drawbacks, oxide film formation, self corrosion, and dendritic deposit. Therefore, there are few practical cells with an Al electrode (1).

It is considered that if the above drawbacks can be overcome, aluminum is highly promising as the active material for the negative electrode of advanced secondary cells. We have investigated Al/AlCl₃-NaCl-MCl_x/FeS₂ cells for load-leveling applications and in electric vehicles (2), and there are many other investigations (1) showing that a smooth, dense aluminum deposit forms in organic electrolytes. For this reason, Al/AlCl₃-organic solvent/FeS₂ cells have been developed. It was expected that these cells will offer a long service life and high terminal voltage at around room temperature.

The Al electrodes were spiraled rods (ϕ 5 mm, 99.99% purity) with areas five to seven times the areas of the FeS₂ electrodes. Details of the FeS₂ electrode are given elsewhere (2). The FeS₂ electrode (7 mm thick, ϕ 25 mm) was degassed and immersed in the organic bath in vacuo to wet both the FeS₂ powder and the current collector completely with the electrolyte.

AlCl₃ and lauryl pyridinium chloride (LPC) were dried at 80°C for 10 h in vacuo. In tetrahydrofuran (THF) system, LiAlH₄ was added to the THF, the solution was refluxed at 70°C for 6 h, and the AlCl₃ was put in a THF-benzene or a THF solution to which was added the THF-LiAlH₄ solution. Electrolyte preparation was done under a dry N₂ atmosphere. The cell comprises an upper Al electrode and a lower FeS₂ electrode

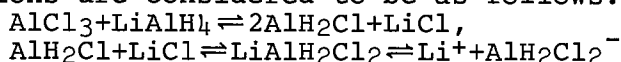
(distance: 5 ~ 10 mm). Cell performance was observed during about 30 repetitions (1 ~ 2 months) of the discharge (cutoff: 0.5 V) - charge (cutoff: 2.1 ~ 3.0 V) cycle under the N₂ atmosphere. The ohmic drop (IR drop) was checked once every 30 minutes with a relay. Potential-current curves were given potentiostatically.

After several cycles the cell performance was steady, therefore, the data (IR-free) of each 10th cycle are presented. Although charge curves are not shown, the coulombic efficiencies were from 80 to 100%. Discharge curves for the LPC systems are shown in Fig. 1. In the case of a 63.0 mol% AlCl₃ - 37.0 mol% LPC bath, in which the current density at the FeS₂ electrode was 3 mA/cm² and bath temperature was 125 °C, although the discharge capacity was only 0.03 Ah and the IR drop was large (0.5 V), the open circuit voltage (OCV) was 1.50 V. When toluene was added to the bath to lower its temperature, discharge capacity fell to 0.02 Ah at 100°C. For an FeS₂ electrode with a 38% graphite additive, however, discharge capacity for the above bath rose to 0.07 Ah at 60°C and 0.1 Ah at 100°C. The additive had no pronounced effect either on OCV or IR drop. Since THF baths are very favorable to Al deposition, and can be operated at relatively low temperatures, it was decided to test this system (Fig. 2). The discharge capacity rose no higher than 0.32 Ah (ca. 20% of the theoretical capacity). However at room temperature and 5 mA/cm², the discharge curve showed a high voltage plateau of about 2.3 V and a low voltage plateau of about 1.0 V. Moreover, in the case of a vitreous carbon current collector, the high voltage plateau capacity increased significantly. These facts indicate that THF systems are very promising.

Potential-current curves for Al

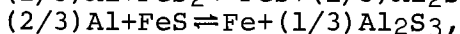
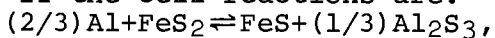
*Electrochemical Society Active Member
Key words: aluminum, FeS₂, secondary cell, organic electrolyte

anode in LPC and THF systems showed the limiting current of 0.7 mA/cm² for the LPC systems and 7 mA/cm² for the THF systems. In THF systems the reactions are considered to be as follows:



It is also known that the lower the concentration of LiAlH₄, the smaller is the conductivity of the electrolyte (3). In the case of the bath B in Fig. 2, the conductivity was 5.47x10⁻³ Ω⁻¹/cm. We suggest that ionic species (AlH₂Cl₂⁻, etc.) may be present in insufficient quantities in the electrolyte, and that this is the reason why this cell has a big IR drop and a small discharge capacity. Thus the immediate need is to improve the electrolyte. The fact that the addition of graphite greatly raised the discharge capacity but had little effect on IR drop further corroborate the above reasoning. In a molten-salt cell (Li-Al/LiCl-KCl/FeS₂), it is known that the problem of FeS₂ electrode conductivity is not so severe, due to the existence of certain phases (4), while in the organic solvent cells studied, such phases were not detected by X-ray analysis. Therefore, it is considered that a conductive material should be added to the FeS₂ electrode of organic cells in order to raise the discharge capacity. Since the graphite did not affect the OCV, it would seem that there can have been no effect from a 'carbon-metal complex' (5).

If the cell reactions are:



two plateaus should appear in the discharge curve as seen in Fig. 2. FeS and Al₂S₃ were detected by X-ray analysis of a discharged FeS₂ electrode. But the e.m.f. values calculated from free energy values for the above reactions do not correspond to those observed. It should be considered that some complex compounds may be formed in the FeS₂ electrode by the interaction of Al₂S₃ with iron-sulfur compounds such as in the Li-Al/FeS₂ cell (4).

It is suggested that through improvement of the electrolyte and investigation of suitable additives for the FeS₂ electrode, the promise of this cell can be realized in the development of an advanced, high-capacity secondary cell.

REFERENCES

1. N.Koura and S.Takahashi, *Alutopia*, **10**, 49 (1980) and references cited.
2. N.Koura, *This Journal*, **127**, 1529 (1980).
3. M.Yoshio and N.Ishibashi, *J. Appl. Electrochem.*, **3**, 321 (1973).
4. F.C.Mrazek and J.E.Battles, *This Journal*, **124**, 1556 (1973).
5. E.S.Buzzelli, U. S. Patent, 3650834 (1972).

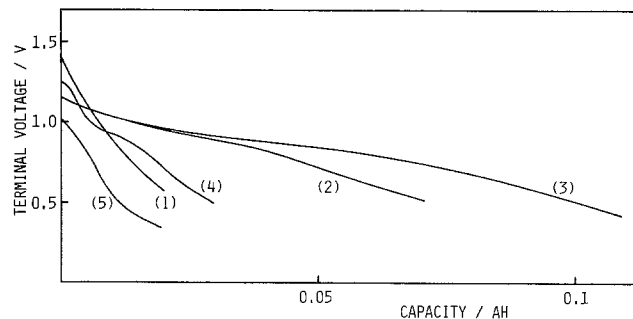


Fig. 1 Discharge curves for (A) 63mol% AlCl₃+37mol% LPC bath or (B) (A)+sat. toluene bath. (1) bath B, 50°C, FeS₂ 4g+C 3g; (2) bath B, 60°C, FeS₂ 4g+C 3g; (3) bath B, 100°C, FeS₂ 4g+C 3g; (4) bath A, 125°C, FeS₂ 8g; (5) bath B, 100°C, FeS₂ 8g. C.D.: 3 mA/cm².

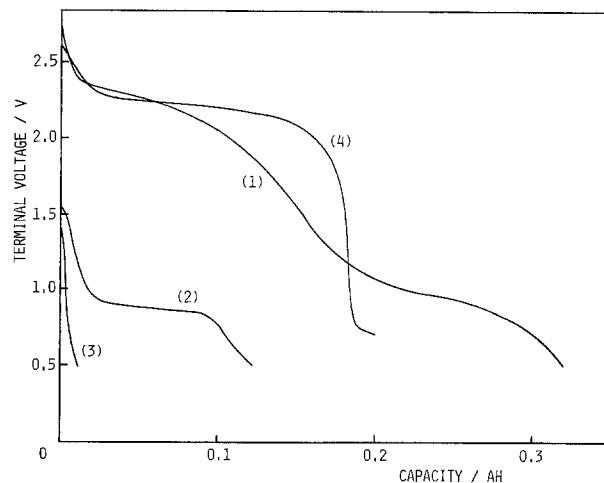


Fig. 2 Discharge curves for (A) 1.5M AlCl₃+0.3M LiAlH₄+80vol% THF+20vol% benzene bath and (B) 0.5M AlCl₃+0.5M LiAlH₄+THF bath. (1) bath B, room temperature, 5 mA/cm², FeS₂ 4g+C 3g; (2) bath A, 50°C, 3 mA/cm², FeS₂ 4g+C 3g; (3) bath A, 50°C, 3 mA/cm², FeS₂ 8g; (4) bath B, room temperature, 5 mA/cm², FeS₂ 4g, vitreous carbon c. c.

Manuscript received Sept. 11, 1980.

Publication costs of this article were assisted by Tokyo University of Science.

Surface Treatment Induced Sub-Band Gap Photoresponse of GaP Photoelectrodes

M. A. Butler* and D. S. Ginley*

Sandia National Laboratories, Albuquerque, New Mexico 87185

The efficiency and behavior of most photoelectrodes depend strongly on the nature of the surface and near surface region of the semiconductor. Thus it is to be expected that the electrodes are sensitive to surface treatment.⁽¹⁾ The predominant mechanism is thought to be the introduction or removal of localized states near the surfaces which can act as recombination centers or can modify the kinetics of the redox reaction. Such localized states, which may be in the band gap of the semiconductor, can provide a mechanism for a photoresponse at energies below the band gap.⁽²⁾ In this paper we demonstrate that such a sub-band gap photoresponse can be generated in GaP photoelectrodes either by mechanically damaging the surface or by cathodic aging of the electrode.

The p-GaP samples were single crystal wafers cut perpendicular to the [111] axis and Zn doped to a density of $5 \times 10^{17} \text{ cm}^{-3}$. The contacts were made by sputtering In:Zn alloy and then annealing in vacuum. A conventional 3-electrode electrochemical cell was used with a PAR 173 potentiostat and a saturated calomel reference electrode. The illumination was by a quartz iodine lamp with a Schoeffel grating monochromator. Unless specified otherwise all experiments were run in 0.1M HClO₄ electrolyte. Typical sub-band gap spectra for various surface treatments are shown in Figure 1.

Figure 1a shows that etching of the photoelectrodes $\sim 4 \mu\text{m}$ with a specific GaP etchant⁽³⁾ removes any sub-band photoresponse that may have existed.

*Electrochemical Society Active Member.

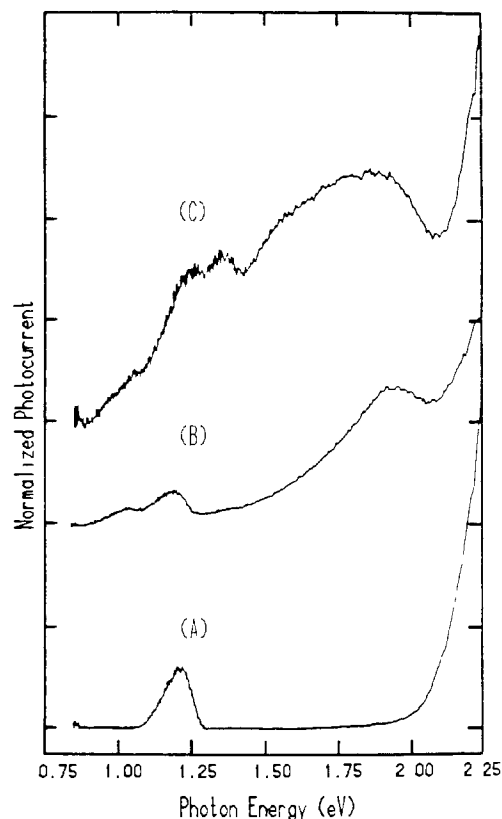


Figure 1. The sub-band-gap photoresponse of p-GaP with various surface treatments. The spectra are normalized to light intensity and the zero level is offset for (b) and (c) by an amount indicated by the left side of the spectra. All measurements were made at -2.0 V(SCE) in 0.1M HClO₄ using a filter to cut off the optical response above $\sim 2.5 \text{ eV}$. (a) Polished surface etched $4 \mu\text{m}$. (b) Surface mechanically polished using $1/4 \mu$ diamond paste. (c) Cathodic aging under constant current conditions 5 mA for 1 hr. The peak at 1.2 eV is due to the second order reflection of the grating.

Polishing the surface either wet or dry using various materials including diamond paste, aluminum oxide and SiC produces a sub-band gap response such as shown in Figure 1b. Similar behavior but with somewhat broader spectral features is produced by cathodic aging of the sample as shown in Figure 1c.

A sub-band gap response has also been observed in an n-GaP photoanode which was doped with sulfur to a density of $2 \times 10^{18} \text{ cm}^{-3}$. The general features were the same as observed in p-GaP although a complete set of experiments on this sample have not been performed.

Etching for fixed time periods to profile the surface treatment effects shows that both polishing and cathodic aging produce damage extending $\sim 1500 \text{ \AA}$ into the surface. These results are confirmed by the potential behavior of the photocurrent shown in Figure 2. For a small optical absorption coefficient α it has been shown⁽⁴⁾ that the photocurrent is:

$$J = \phi \alpha \left(\frac{2\epsilon q}{N_D} \right)^{1/2} (V - V_{fb})^{1/2} \quad [1]$$

where ϕ is the photon flux, ϵ the dielectric constant, q the electronic charge, N_D the dopant density and V the applied potential. Since the width of the depletion layer is given by:

$$W = \left(\frac{2\epsilon}{qN_D} \right)^{1/2} (V - V_{fb})^{1/2} \quad [2]$$

the linear relationship between J^2 and V shown in Figure 2 means that $J \propto W$. The observed photoresponse is a bulk effect arising throughout the depletion layer region. The maximum applied potential, $-4V(\text{SCE})$, corresponds to a depletion layer thickness of $\sim 0.09 \mu\text{m}$. Thus, the linear region in Figure 2 indicates that the surface treatment effects are uniform between $\sim 0.06 \mu\text{m}$ and $\sim 0.09 \mu\text{m}$. The deviation from linearity between 0 and $-1V$ has been shown to arise from recombination in the near-surface region⁽⁵⁾.

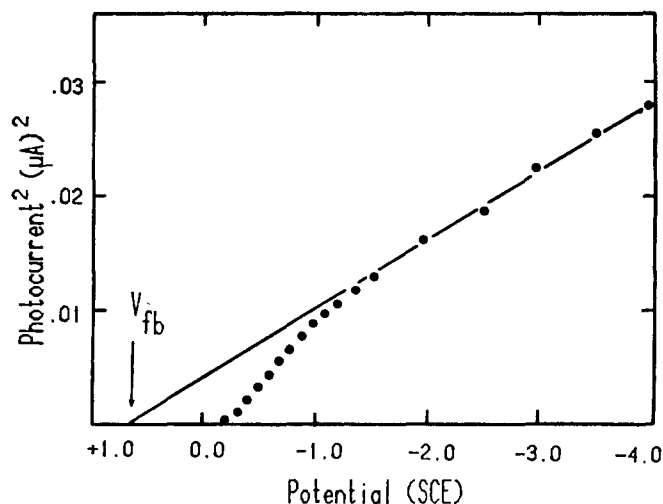


Figure 2. Potential behavior of the photoresponse at 1.75 eV of a polished sample taken in 0.1M HClO_4 . Note the difference between photocurrent onset and flatband potential (V_{fb}) as determined by capacitance measurements.

In addition to etching, which removes the damaged near surface region, the sub-band gap photoresponse can be removed by anodic aging or by heat treating the sample. Treatment at 800°C for 1 hr. in vacuum totally removes the effect. Since at this temperature the partial pressure of P is higher than the partial pressure of Ga,⁽⁶⁾ the heat treatment should change the stoichiometry of the near surface region by lowering the P/Ga ratio. Thus the sub-band gap response may arise from Ga vacancy related defects.

This idea is consistent with the production of a sub-band gap response by cathodic aging and its removal by anodic aging. These two bias conditions represent reductive and oxidative surface conditions which tend to remove Ga and P respectively from the surface.⁽⁵⁾ The exact nature of the defects responsible for the states in the gap is not known.

While the sub-band gap photoresponse induced by mechanical damage or cathodic aging can be removed by similar means, there are differences in such treated electrodes other than the obvious spectral differences

which can be observed. Simultaneously with the sub-band gap photoresponse measurements the capacitance of the interface and the photoresponse above the band gap were measured. Both of these measurements provide further information concerning the nature of the induced electronic states.

For a freshly etched surface in a 0.1M HClO₄ electrolyte a Mott-Schottky plot gives a straight line with an intercept of $\sim +0.7$ V(SCE) and a slope indicative of a donor density of $\sim 7 \times 10^{17} \text{cm}^{-3}$. The flat band potential is in good agreement with previously reported values⁽⁵⁾ and the donor density is in agreement with the known bulk value of $5 \times 10^{17} \text{cm}^{-3}$. Anodic or cathodic aging of the sample does not significantly change either slope or intercept of the Mott-Schottky plot even though the cathodic aging induces a sub-band gap photoresponse. The photoresponse in 0.1M HClO₄ at 500nm (2.48eV) of a freshly etched surface has an onset at ~ 0.0 V(SCE) again consistent with previously reported results. The discrepancy between the photocurrent onset and the flatband potential arises from recombination at bulk states in the band gap.⁽⁵⁾ This behavior is also observed for anodically and cathodically aged samples.

For the mechanically damaged (polished) samples considerable changes are observed. The capacitance is drastically reduced although the intercept remains the same. The slope of the linear part of the Mott-Schottky plot suggests a reduction of the doping density by an order of magnitude with some variation from sample to sample. This interpretation is supported by the photoresponse at 500nm (2.48eV) which shows that the photocurrent increases by approximately a factor of three as would be expected for a lower doping levels and consequently increased depletion layer widths.

Thus it seems that the two processes which produce a sub-band gap photoresponse induce states of considerably different character. Cathodic aging produces states which do not change the overall doping

level while polishing results in states which seem to compensate the p-type GaP samples. Both of these processes produce sub-band gap responses which are similar in spectral dependence.

REFERENCES

1. R. H. Wilson, L. A. Harris and M. E. Gerstner, J. Electrochem. Soc. 127, 884 (1979).
2. M. A. Butler, M. Abramovich, F. Decker and J. F. Julia, J. Electrochem. Soc. (in press).
3. Manufactured by the TRANSENE Company Rt. 1, Rowley, Mass. 01969.
4. M. A. Butler, J. Appl. Phys. 48, 1914 (1977).
5. M. A. Butler and D. S. Ginley, J. Electrochem. Soc. 127, 1273, (1980).
6. M. Ilegums, M. B. Panish and J. R. Arthur, J. Chem Thermodynamics 6, 157 (1974).

ACKNOWLEDGMENT

This work was supported by the Materials Sciences Division, Office of Basic Energy Sciences, U.S. Department of Energy, under Contract DE-AC04-76-DP00789.

Manuscript received July 22, 1980.

Publication costs of this article were assisted by Sandia National Laboratories.

Transference Number Measurements for the Polymer Electrolyte Poly(ethylene oxide) NaSCN

R. Dupon, D. H. Whitmore,* and D. F. Shriver

*Departments of Chemistry and Materials Sciences, and Materials Research Center,
Northwestern University, Evanston, Illinois 60201*

Current interest in the development of high energy density batteries has focused considerable attention on solid electrolytes. The leading solid electrolytes in developmental batteries are hard ceramic materials, which usually are employed at elevated temperatures with liquid electrodes. A more compliant solid electrolyte, such as a polymer electrolyte, should enable contact to be maintained at the electrode-electrolyte interfaces in an all solid state battery and lower operating temperatures might be facilitated. Potential application of ion-containing polymers as battery electrolytes, and electrical measurements on salt complexes with poly(ethylene oxide) and with poly(propylene oxide) have been presented by Armand (1,2), and structural studies of poly(ethylene oxide) salt complexes have been reported from our laboratory (3). The original synthesis and characterization of these materials was reported by Wright (4,5) and extended by James (6).

A fundamental parameter in the characterization of any solid electrolyte is the fraction of the total current which is carried by the mobile ion, i.e. the transference number. Prior to the present work, a rigorous determination of the transference number for poly(ethylene oxide) based electrolytes was not available. The present study is based on the measurement of emf between ion reversible amalgam electrodes which are separated by the solid electrolyte in a concentration cell (7,8).

Experimental Procedure. -- Poly(ethylene oxide) with an average molecular weight 600,000 was obtained from Aldrich. The polymer was purified by ion-exchange of an aqueous solution and the solvent was subsequently removed under high vacuum. Reagent

grade NaSCN (B & A) was recrystallized from methanol and dried under high vacuum. Reagent grade methanol (MCB) was dried by distillation from iodine-activated magnesium under a nitrogen atmosphere.

A PEO·NaSCN complex, 4.5:1 mole ratio of polymer repeat unit to salt, was prepared from stoichiometric quantities of the polymer and salt in anhydrous methanol. Following complete dissolution of the two solids, the methanol was removed under vacuum. All manipulations were carried out using standard inert atmosphere techniques (9). The identity of the PEO·NaSCN complex was confirmed by infrared spectroscopy and differential scanning calorimetry, and in previous research the material prepared by this same procedure has been characterized by optical microscopy and x-ray diffraction, which demonstrate the absence of free NaSCN.

Amalgams were prepared with triple distilled mercury and reagent grade sodium (MCB). Molten sodium was filtered through fritted glass to remove sodium oxide. The concentration of the stock amalgam, solution No. 1, Table I, was determined gravimetrically and checked by the gasometric method based on the amount of hydrogen evolved from the reaction of the sodium amalgam with hydrochloric acid. Concentrations of the remaining solutions were determined gravimetrically by successive dilution of the stock amalgam.

The sample and amalgams were placed in a cell which permitted exclusion of the atmosphere, Fig. 1. A pressed pellet of the PEO·NaSCN complex, 4.5:1, was fitted into an o-ring which was then clamped between the side arms. All loading of the polymer complex was carried out in a nitrogen filled dry box. One side arm was filled with the stock amalgam solution while the other was successively filled with the dilutions of the stock. Introduction of amalgam solutions was done with a gas-tight syringe under a flush of dry nitrogen.

Key words: Solid electrolyte, polymer electrolyte, transference number, poly(ethylene oxide).

*Electrochemical Society Active Member.

The potentials of the cell were measured using a Keithley 177 multimeter together with an electrometer containing an RCA CA3140 E MOS/FET operational amplifier designed to increase the input impedance of the measuring device to 10^{12} ohms. All measurements were made at room temperature, 23.5 ± 0.2 °C, which was monitored using an iron-constantan thermocouple and millivolt meter. The cell and connecting leads were placed in an aluminum box designed to shield the system from extraneous radiation. Reversing the cell polarity produced insignificant changes in the magnitude of the observed potentials. The emf was read after the potential had maintained a stable (± 0.3 mV) value over a period of one hour. Typical stabilization times were of the order of one to two hours. The measured results are given in Table I. As a check on these measurements, emf values were determined on a different batch of the polymer electrolyte using different amalgam preparations. Agreement between the data sets was good.

A value of the cell impedance was obtained by loading standard resistors in parallel with the cell and observing the change in emf. The observed room temperature cell impedance of $3.9 \times 10^6 \Omega$ was well within the capability of the measuring device and yielded a D.C. conductivity of $6.3 \times 10^{-8} (\Omega \text{ cm})^{-1}$, which is in general agreement with the A.C. value shown by Armand (2).

The emf of the concentration cell $\text{Hg-Na}(x_1) | \text{PEO} \cdot \text{NaSCN} | \text{Hg-Na}(x_2)$ is expressed by (8):

$$E_{\text{obs}} = (1 - t_e)E_{\text{id}} = (1 - t_e) \frac{RT}{nF} \ln \frac{a_1}{a_2} =$$

$$(1 - t_e) \frac{RT}{nF} \ln \frac{\gamma_1 x_1}{\gamma_2 x_2}$$

The activity coefficients for dilute amalgams (present case) may be calculated from the relationship (10):

$$\log \gamma = Qx$$

where

$$Q = 18.720 - 8.00 \times 10^{-3} T$$

From this, E_{id} may be calculated:

$$E_{\text{id}} = \frac{RT}{F} 2.303 \log \frac{x_1}{x_2} + \frac{RT}{F} 2.303 Q(x_1 - x_2)$$

A plot of E_{obs} vs. E_{id} for each x_2 (x_1 being

fixed as the stock amalgam, solution No. 1) yields a straight line (Fig. 2) of slope $(1 - t_e)$.

Results and Discussion. -- For a purely ionic conductor the value of $(1 - t_e)$ should be unity. Least squares treatment of E_{obs} vs. E_{id} produced slope 1.005 ± 0.005 , Fig. 2. This result establishes that the electronic contribution to the total electrical conductivity of $\text{PEO} \cdot \text{NaSCN}$ is negligible and that the ionic component is responsible for the conduction. Since sodium-reversible electrodes were employed and since the conductivity is close to the published A.C. data, the sodium ion is implicated as the major charge carrier in the $\text{PEO} \cdot \text{NaSCN}$ complex.

Table I. Ideal and observed emf's of concentration cell at room temperature.

| Solution No. | x_{Na} | E_{id} (mV) | E_{obs} (mV) |
|--------------|-----------------|----------------------|-----------------------|
| 1 | 0.04103 | - | - |
| 2 | 0.03426 | 11.13 | 10.98 |
| 3 | 0.02944 | 19.64 | 19.47 |
| 4 | 0.02406 | 29.99 | 29.11 |
| 5 | 0.01928 | 40.25 | 40.89 |
| 6 | 0.01440 | 52.36 | 52.10 |
| 7 | 0.009477 | 67.84 | 68.34 |

E_{obs} = the measured emf

t_e = electronic transference number

E_{id} = ideal emf, value of E_{obs} when $t_e = 0$

R = universal gas constant

T = absolute temperature

n = number of electrons transferred

F = Faraday constant

a_1, a_2 = activities of sodium in the amalgams

γ_1, γ_2 = activity coefficients of sodium in the amalgams

x_1, x_2 = mole fractions of sodium in the amalgams

Acknowledgment. -- We wish to thank Mr. J. R. Anderson for discussions and help with the instrumentation. This research was supported in part by the Office of Naval Research.

REFERENCES

1. M. Armand, J. M. Chabagno, and M. J. Duclot, Abstract 6.5, Extended Abstracts, Second International Conference on Solid Electrolytes, St. Andrews, Scotland, Sept. 20-22, 1978.
2. M. Armand, J. M. Chabagno, and M. J. Duclot, in "Fast Ion Transport in Solids," P. Vashishta, J. N. Mundy, and G. K. Shenoy, Editors, p. 131, North-Holland, Amsterdam (1979).
3. B. L. Papke, M. A. Ratner, and D. F. Shriver, *J. Phys. Chem. Solids*, in press.
4. D. E. Fenton, J. M. Parker, and P. V. Wright, *Polymer*, **14**, 589 (1973).
5. P. V. Wright, *Br. Polym. J.*, **7**, 319 (1975).
6. D. B. James, R. S. Stein, and W. J. Macknight, *Bull. Am. Phys. Soc.*, **24**, 479 (1979).
7. L. Hsueh and D. N. Bennion, *This Journal*, **118**, 1128 (1971).
8. R. Galli, F. A. Tropeano, P. Bazzarin, and U. Mirarchi, in "Fast Ion Transport in Solids," W. van Gool, Editor, p. 573, North-Holland, Amsterdam (1973).
9. D. F. Shriver, "The Manipulation of Air-Sensitive Compounds," McGraw-Hill, New York (1969).
10. T. Mussini, A. Maina, and A. Pagella, *J. Chem. Thermodyn.* **3**, 281 (1971).

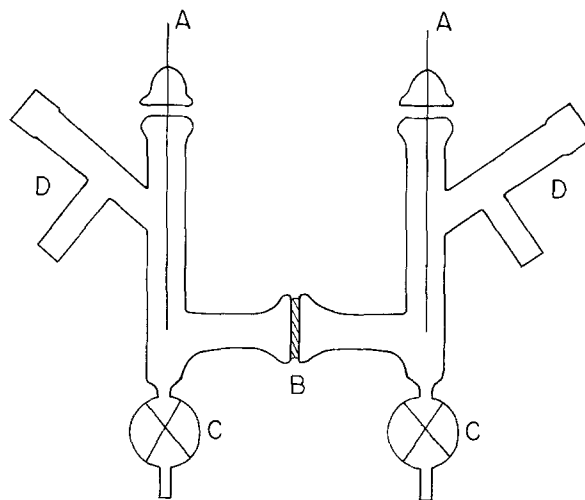


Fig. 1. Cell for transference number measurements. A, nickel electrode; B, polymer electrolyte; C, stopcock; D, Teflon in glass valves for N_2 inlet.

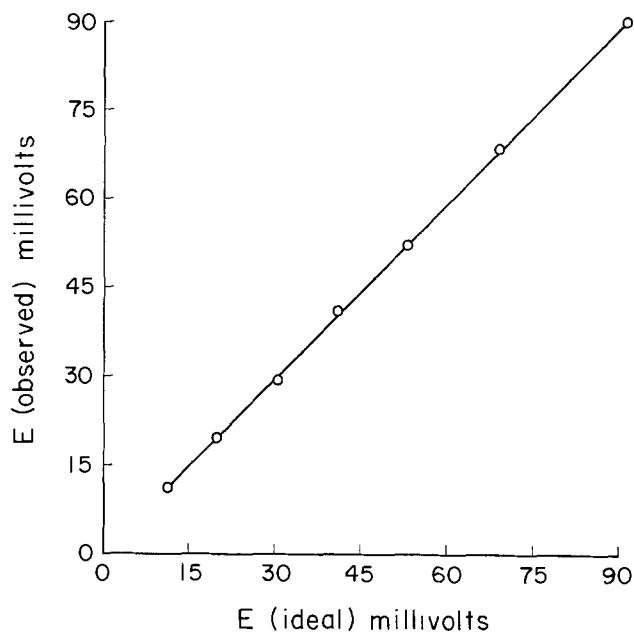


Fig. 2. Observed vs. ideal emf values for a Na/Hg concentration cell with NaSCN·PEO polymer electrolyte.

Manuscript received Nov. 17, 1980.

Publication costs of this article were assisted by Northwestern University.



Formation of Tetrabasic Lead Sulfate at Room Temperature

T. G. Chang* and M. M. Wright*

Cominco Limited, Product Research Centre, Sheridan Park, Mississauga, Ontario, Canada L5K 1B4

ABSTRACT

A study was made of the formation of tetrabasic lead sulfate, $4\text{PbO} \cdot \text{PbSO}_4$, in oxide-sulfate mixtures between room temperature and 80°C for reaction times of up to 4 weeks. Under certain conditions it is a reaction product at room temperature, a finding contrary to the generally held view that this compound can form only above 70°C .

Tetrabasic lead sulfate, $4\text{PbO} \cdot \text{PbSO}_4$, is, in some cases, a major component in the cured paste of a lead-acid battery plate. In our experience its presence enhances the mechanical strength of the paste, perhaps due to the interlocking of its rodlike crystals. This would not only better preserve the integrity of the plate during the manufacturing process, but it might contribute to a longer cycle life in battery service. Thus, according to Burbank (1), the transformation of $4\text{PbO} \cdot \text{PbSO}_4$ to PbO_2 during electrochemical formation is largely metasomatic after the original crystals, and Bell Telephone Laboratories (2-6), who have been engaged for years in research on the direct use of $4\text{PbO} \cdot \text{PbSO}_4$ in battery pastes, have reported that such batteries have a longer cycle life. Although the formation of this compound has been much investigated, there is still uncertainty as to the necessary conditions. It is generally accepted that an elevated temperature ($>70^\circ\text{C}$) is required (2, 7, 8-13). On the other hand, Mrgudich (14), and Bode and Voss (7) have reported that $4\text{PbO} \cdot \text{PbSO}_4$ was found in pastes cured at room temperature. There is also disagreement in the literature as to whether or not the tetragonal form of PbO

can react with sulfates to produce $4\text{PbO} \cdot \text{PbSO}_4$ (2, 8, 12-14).

The present investigation was carried out to elucidate the effects of temperatures and lead monoxide morphology on the formation of $4\text{PbO} \cdot \text{PbSO}_4$ in lead-acid battery pastes.

Experimental

Lead monoxide.—Several commercially available lead monoxides were used in this investigation. They are listed in Table I together with data on specific surface area, particle size distribution, and composition. The surface area data were obtained by a 4-point BET method on a Micromeritics Model 2100 surface area instrument and the particle size distribution data by the x-ray sedimentation method on a Micromeritics Sedigraph 500 using Sedisperse as dispersing medium. The proportions of orthorhombic and tetragonal lead monoxide, $\text{PbO}(o)$ and $\text{PbO}(t)$, were determined by x-ray diffractometry and the metallic lead content by chemical analysis (15). Tetragonal lead monoxide, $\text{PbO}(t)$, was prepared by conversion from the orthorhombic form by suspension in boiling water for 1 hr. Reference will be made to these oxides by name of supplier and number, as given in Table I.

* Electrochemical Society Active Member.

Key words: lead-acid battery, paste curing, thermodynamics.

Table I. Surface area, particle size, and composition of lead monoxides

| Oxide No. | Manufacturer* | Cat. No. | Lot No. | Surface area (m^2/g) | Particle size (μm) | | | Composition (% wt) | | |
|-----------|---------------|----------|-----------|--|---------------------------------|----------------|----------------|--------------------|-----------------|-------------|
| | | | | | Median | Upper quartile | Lower quartile | $\text{PbO}(o)$ | $\text{PbO}(t)$ | Metallic Pb |
| 1a | JTB | 2238 | 41125 | 1.97 | | | | 100 | 0 | 0 |
| 1b | | | 44313 | 1.97 | | | | 100 | 0 | 0 |
| 1c | | | 45199 | 2.28 | 1.1 | 1.5 | 0.82 | 100 | 0 | 0 |
| 2a | ACP | AC-5398 | 070921 | 0.66 | 3.8 | 5.7 | 2.4 | 82 | 18 | 0 |
| 2b | | | 960602 | 0.58 | 3.8 | 5.5 | 2.6 | 90 | 10 | 0 |
| 2c | | | 860313 | 0.79 | 3.4 | 5.2 | 2.2 | 90 | 10 | 0 |
| 2d | | | 271023 | 0.57 | 4.1 | 6.0 | 2.6 | 88 | 12 | 0 |
| 2e | | | 670114 | 0.57 | 4.3 | 6.1 | 2.6 | 94 | 6 | 0 |
| 3 | FS | L-71 | 732611 | 0.45 | 5.5 | 8.0 | 3.3 | 90 | 10 | 0 |
| 4a | BDH | 10146 | 1243-3291 | 0.16 | 11.2 | 17.0 | 7.9 | 98 | 2 | 0 |
| 4b | | | 80285 | 2.05 | | | | 100 | 0 | 0 |
| 5 | | | | 1.18 | | | | 0 | 100 | 0 |
| 6 | | | | 1.17 | | | | 0 | 100 | 0 |

* JTB = Baker Analyzed Reagent, J. T. Baker Chemical Company.

ACP = Chemical Reagent, Anachemia Chemical Products, Limited.

FS = Fisher Certified Reagent, Fisher Scientific Company Limited.

BDH = "AnalaR," BDH Chemicals.

† Prepared in this laboratory (see text).

Sulfate reagent.—In addition to sulfuric acid the following lead sulfates were used as sources of sulfate ion: normal lead sulfate, PbSO_4 (of reagent grade, from Anachemia Chemical Products Limited), monobasic lead sulfate, $\text{PbO}\cdot\text{PbSO}_4$, and tribasic lead sulfate, $3\text{PbO}\cdot\text{PbSO}_4\cdot\text{H}_2\text{O}$. The latter two compounds were synthesized in this laboratory using the slurry method (1).

The reaction of lead monoxide with a sulfate was studied under three different conditions, as described below. In each case the mole ratio, PbO/SO_3 , was 10/1.

Slurries.—Lead monoxide (10g) and the sulfate were reacted as a stirred suspension in 200 ml of water.

Pastes.—For reaction with sulfuric acid, lead monoxide was first mixed with water and then the acid (1.325 sp gr) added, with mixing, over a period of 5-10 min. Mixing was then continued for an additional 5 min. When using the normal and basic lead sulfates, the solids were first mixed together by grinding, packed into a plastic Petri dish, and then water added dropwise without further mixing. In a few cases (which will be indicated) there was further mixing during the addition of water. In all cases the water content was such as to give a wet paste density of 4.0 g/cm³. All pastes were cured at room temperature in air at 100% relative humidity.

Sediments.—This refers to the reaction in the settled solids of a slurry following a stirring period of a few seconds for its preparation. When sulfuric acid was used, lead monoxide (30g) was first mixed with 50 ml of water and then acid (4.2M, 3.2 ml) added. When a lead sulfate was used, the solids were first ground together and then the water (50 ml) added. After settling, the volume was adjusted to 80 ml by adding water slowly without disturbing the sediments. After a given reaction time, during which the sediments remained undisturbed, the samples were taken out and dried *in vacuo* at room temperature.

X-ray diffraction patterns were recorded on a Philips diffractometer which was equipped with a graphite monochromator (PW 1152) and a pulse height analyzer (PHA, PW 4620). A PW 2113/00 diffraction tube (1.2 kW) with a copper target was employed. The samples were packed in a flat rotating specimen holder (PW 1064/100).

The morphology of the starting materials and products was also studied on a scanning electron microscope, the Etec Autoscan.

Results

Morphology of lead monoxides.—Figure 1 gives the scanning electron micrographs of four commercial lead monoxides: Baker (No. 1a), Anachemia (No. 2a), Fisher, and BDH (No. 4a). Baker oxide No. 1a is very

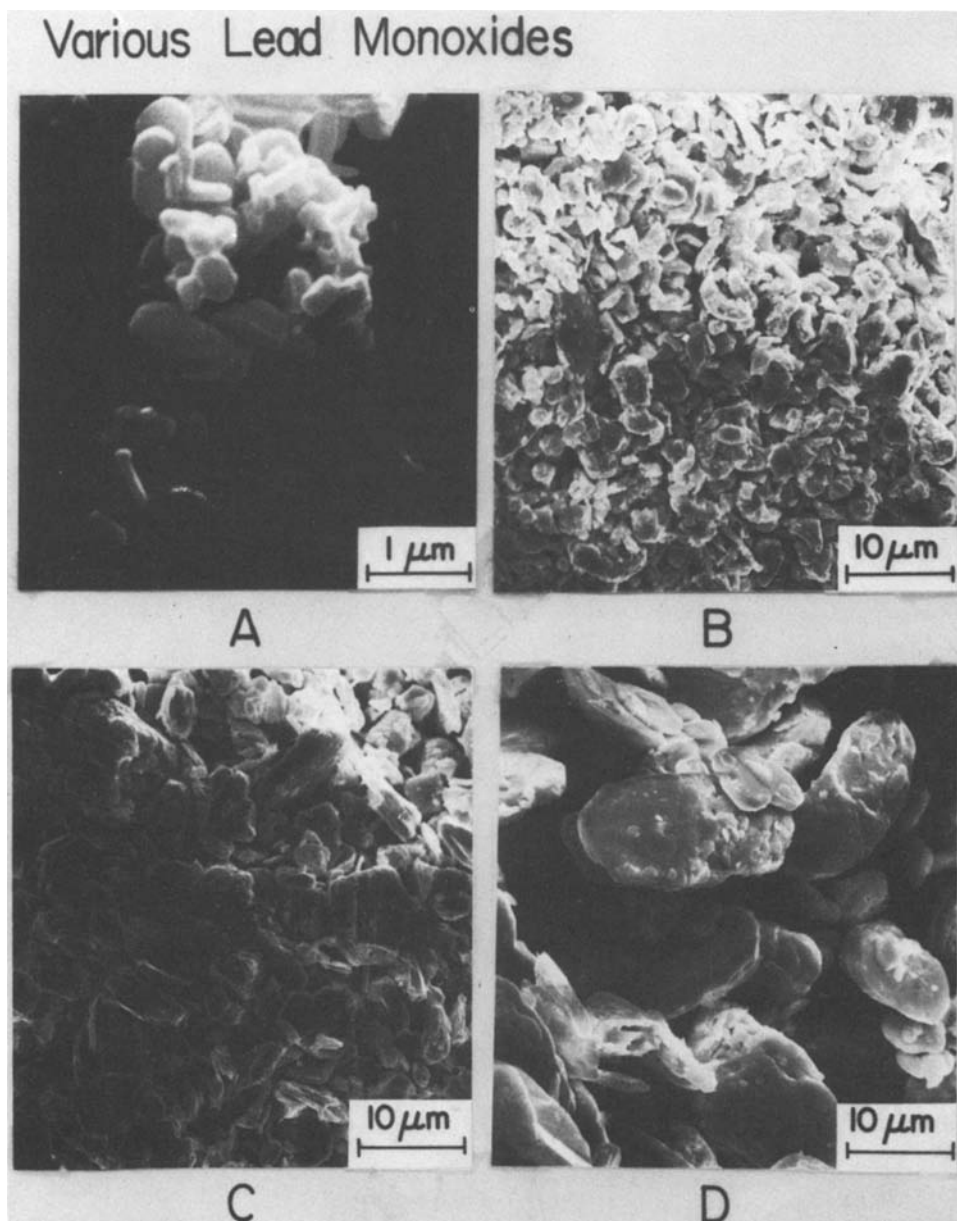


Fig. 1. Electron micrographs of commercial lead monoxides (see also Table I): A. Baker (No. 1a); B. Anachemia (No. 2a); C. Fisher (No. 3); and D. BDH (No. 4a).

fine and well crystallized. X-ray diffractometry showed it to be a pure $\text{PbO}(o)$ of high crystallinity. Baker oxides No. 1b and No. 1c of Table I, though of different lot numbers, have the same morphology as No. 1a. Anachemia PbO has particles of nondescript irregular form. Each particle appears to be an agglomerate of numerous small particles. Fisher and BDH No. 4a are similar to the Anachemia oxide, but larger in particle size, especially the latter. However, BDH No. 4b (see Table I; not shown in Fig. 1) is quite different; it is identical in particle size and appearance to the Baker oxides. These latter oxides are believed to be fume oxides (16), prepared by burning a stream of finely divided molten lead. The other oxides are thought to have been made by further processing of a Barton Pot oxide.

X-ray diffractometry showed that Anachemia (No. 2a-e), Fisher, and BDH No. 4a are oxides of low crystallinity, especially Anachemia No. 2a, and the latter two.

Scanning electron micrographs of tetragonal lead monoxide, No. 5 and No. 6, prepared from Baker No. 1a and Anachemia No. 2a (see Table I), are shown in Fig. 2. The particles are small and tabular in form. Many of the crystals of oxide No. 5 appear as regular octahedral platelets.

Production of $4\text{PbO}\cdot\text{PbSO}_4$.—Slurries.—At room temperature no $4\text{PbO}\cdot\text{PbSO}_4$ was produced in an agitated slurry within up to 28 days. The result was the same no matter which polymorph of PbO or which form of sulfate (H_2SO_4 , PbSO_4 , $\text{PbO}\cdot\text{PbSO}_4$, or $3\text{PbO}\cdot\text{PbSO}_4\cdot\text{H}_2\text{O}$) was used in the reaction. The products were found to be, invariably, a mixture of $3\text{PbO}\cdot\text{PbSO}_4\cdot\text{H}_2\text{O}$ and unreacted PbO . When the temperature was raised to 85°C , $\text{PbO}(o)$ reacted quickly with each of the sulfates to form $4\text{PbO}\cdot\text{PbSO}_4$. However, no $4\text{PbO}\cdot\text{PbSO}_4$ was produced from $\text{PbO}(t)$ even at 85°C .

Pastes.—The finely divided and well-crystallized oxides, Baker No. 1a and BDH No. 4b, as shown in Table II, produced no $4\text{PbO}\cdot\text{PbSO}_4$ at room temperature, even after 28 days. However, the coarser and less well-crystallized Anachemia No. 2a produced some

$4\text{PbO}\cdot\text{PbSO}_4$ after as little as 7 days. The x-ray diffraction patterns of Fig. 3 and 4 show the progress of this reaction. Thus, Fig. 3A shows that in the reaction with H_2SO_4 the only product after 2 weeks is $3\text{PbO}\cdot\text{PbSO}_4$, as indicated by the peak at $27.3^\circ 2\theta$. However, after 4 weeks the presence of $4\text{PbO}\cdot\text{PbSO}_4$ is clearly indicated by the peak at $27.7^\circ 2\theta$. Figure 3B shows that in the reaction with PbSO_4 the peak at $27.7^\circ 2\theta$ is detectable after 2 weeks, and very prominent after 4 weeks. Figure 4 shows that the reaction is faster still between this oxide and $\text{PbO}\cdot\text{PbSO}_4$; the peak at $27.7^\circ 2\theta$ is observable after only 1 week. The growth of the $4\text{PbO}\cdot\text{PbSO}_4$ peak at $10.8^\circ 2\theta$ is also shown in Fig. 4. Of the five lots of Anachemia PbO (No. 2a-e), No. 2a was the most reactive; three lots produced no detectable $4\text{PbO}\cdot\text{PbSO}_4$ even after 4 weeks. The still coarser and less well-crystallized BDH No. 4a was more active yet in the formation of $4\text{PbO}\cdot\text{PbSO}_4$. Its reaction with PbSO_4 is shown in Fig. 5, and the scanning electron micrographs of the products after 2 and 4 weeks are shown in Fig. 6.

The two samples of $\text{PbO}(t)$, oxides 5 and 6, produced no $4\text{PbO}\cdot\text{PbSO}_4$ at room temperature.

When the temperature was raised to 40°C , Baker No. 1a and Anachemia No. 2d, both inactive at room temperature, now gave substantial yields of $4\text{PbO}\cdot\text{PbSO}_4$, in some cases, in as little as 3 days, as shown in Table II. When the temperature was increased further to 60°C , the only measurable product for these oxides was $4\text{PbO}\cdot\text{PbSO}_4$. On the other hand, $\text{PbO}(t)$ (oxides 5 and 6) was inactive at 40°C ; it became active at 60°C , but gave a much lower yield than did lead oxide in the orthorhombic form.

Table II also shows that when $3\text{PbO}\cdot\text{PbSO}_4\cdot\text{H}_2\text{O}$ was used as the sulfate reactant there was no yield of $4\text{PbO}\cdot\text{PbSO}_4$ at room temperature in any case. Some $4\text{PbO}\cdot\text{PbSO}_4$ was produced when the temperature was raised to 40°C , but the yield was much lower than when other sulfate compounds were used.

Sediments.—The formation of $4\text{PbO}\cdot\text{PbSO}_4$ by reaction in sediments over a 28-day period at room temperature is reported in Table III, and x-ray patterns for selected cases are shown in Fig. 7. The results are similar to those for reaction in pastes. The oxides of very

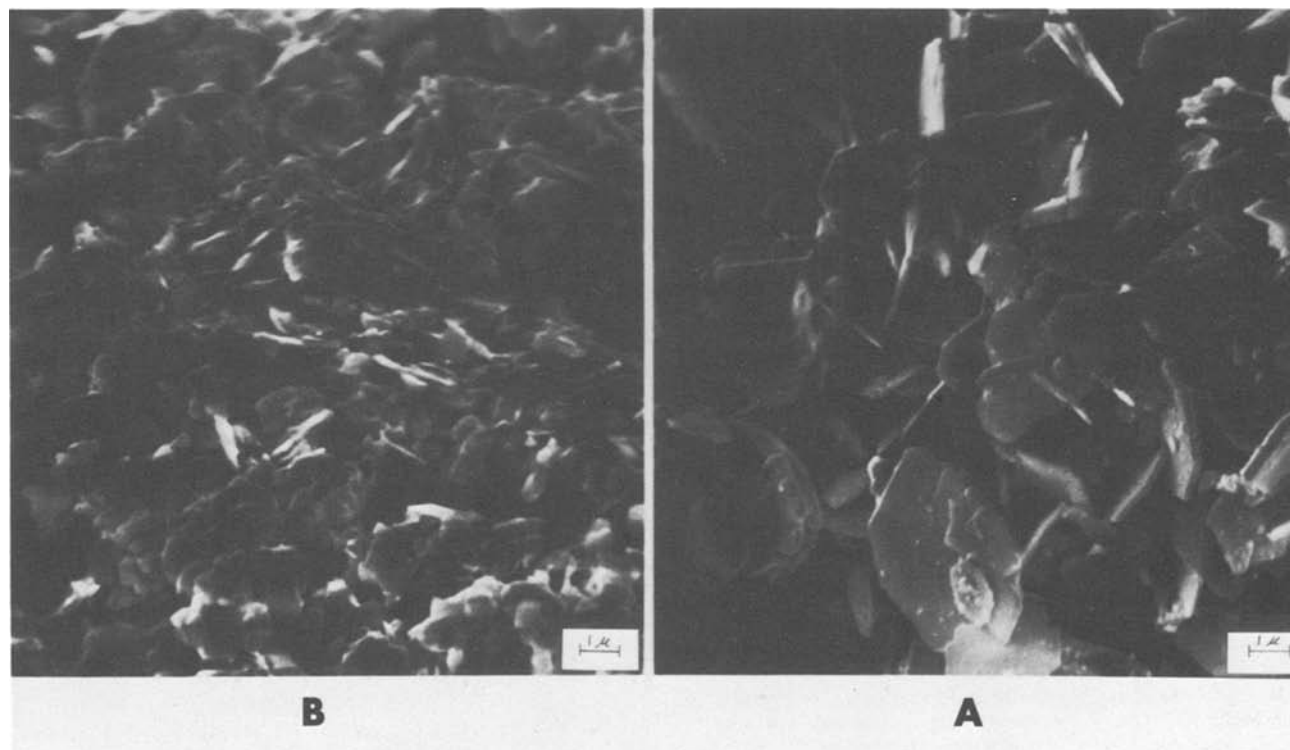


Fig. 2. Electron micrographs of two tetragonal lead monoxides: A. No. 5 and B. No. 6 (see Table I)

Table II. Formation of $4\text{PbO}\cdot\text{PbSO}_4$ in pastes

| No.* | Lead oxide PbO(o)/ PbO(t) | Source of sulfate** | Temper- ature (°C)*** | $W_{\text{tet}}/W_{\text{tri}}\dagger$ Curing time (days) | | | | |
|------|---------------------------------|------------------------|-----------------------------|--|------|------|------|------|
| | | | | 3 | 7 | 14 | 21 | 28 |
| 1a | 100/0 | A, B, C, D | RT | 0.0 | 0.0 | 0.0 | 0.0 | 0.0 |
| 1a | 100/0 | A | 40 | 0.06 | 0.97 | 6.6 | — | H |
| 1a† | 100/0 | B | 40 | 0.17 | 8.2 | H | — | H |
| 1a† | 100/0 | C | 40 | 0.0 | 1.6 | H | — | H |
| 1a† | 100/0 | D | 40 | 0.0 | 0.0 | 0.48 | — | H |
| 1a† | 100/0 | B, C, D | 60 | H | H | H | H | H |
| 2a | 82/18 | A | RT | — | 0.0 | 0.0 | 0.0 | 0.08 |
| 2a | 82/18 | B | RT | — | 0.0 | 0.0 | 0.15 | 0.4 |
| 2a | 82/18 | C | RT | — | 0.01 | 0.05 | — | 0.2 |
| 2a | 82/18 | D | RT | — | 0.0 | 0.0 | — | 0.0 |
| 2b | 90/10 | A, B | RT | — | — | — | — | 0.05 |
| 2c | 90/10 | A, B | RT | 0.0 | 0.0 | 0.0 | — | 0.0 |
| 2d | 88/12 | A, B | RT | 0.0 | 0.0 | 0.0 | — | 0.0 |
| 2e | 94/6 | B | RT | — | 0.0 | 0.0 | 0.0 | 0.0 |
| 2d | 88/12 | A | 40 | 0.0 | 60 | H | — | H |
| 2d† | 88/12 | B | 40 | 0.3 | H | H | — | H |
| 2d† | 88/12 | C | 40 | 0.6 | H | H | — | H |
| 2d† | 88/12 | D | 40 | 0.0 | 0.25 | H | — | H |
| 2d† | 88/12 | B, C, D | 60 | H | H | H | — | H |
| 3 | 90/10 | A | RT | 0.0 | 0.0 | 0.0 | — | 0.1 |
| 3 | 90/10 | B | RT | — | 0.05 | 0.12 | 0.2 | 0.5 |
| 4a† | 98/2 | B | RT | — | 0.0 | 0.07 | 0.25 | 1.73 |
| 4b | 100/0 | B | RT | — | 0.0 | 0.0 | 0.0 | 0.0 |
| 5 | 0/100 | A, C, D | RT | — | 0.0 | 0.0 | — | 0.0 |
| 5 | 0/100 | A | 80 | — | 0.0 | 0.03 | — | 1.4 |
| 6 | 0/100 | A, B | RT | 0.0 | 0.0 | 0.0 | — | 0.0 |
| 6 | 0/100 | A, B, C, D | 40 | 0.0 | 0.0 | 0.0 | — | 0.0 |
| 6 | 0/100 | A, B | 60 | 0.0 | 0.0 | 0.0 | — | 0.05 |
| 6 | 0/100 | C | 60 | 0.0 | 0.3 | 0.05 | — | 0.10 |
| 6 | 0/100 | D | 60 | 0.0 | 0.0 | 0.0 | — | 0.0 |
| 6 | 0/100 | B, D | 80 | — | H | H | — | H |

* See Table I.
 ** A = H_2SO_4 ; B = PbSO_4 ; C = $\text{PbO}\cdot\text{PbSO}_4$; D = $3\text{PbO}\cdot\text{PbSO}_4\cdot\text{H}_2\text{O}$.
 *** RT = room temperature, $23^\circ \pm 2^\circ\text{C}$.
 † Weight ratio of tetrabasic to tribasic sulfate. H = $W_{\text{tet}}/W_{\text{tri}} > 50$.
 ‡ The paste was mixed for 5 min after the addition of water.

small particle size (ca. $1\ \mu\text{m}$) and high crystallinity (i.e., Baker oxides and BDH No. 4b) produced only $3\text{PbO}\cdot\text{PbSO}_4\cdot\text{H}_2\text{O}$, while the coarsest oxide, BDH No.

4a, gave only $4\text{PbO}\cdot\text{PbSO}_4$. In general, the yield of $4\text{PbO}\cdot\text{PbSO}_4$ increased with increase in oxide particle size and decrease in oxide crystallinity.

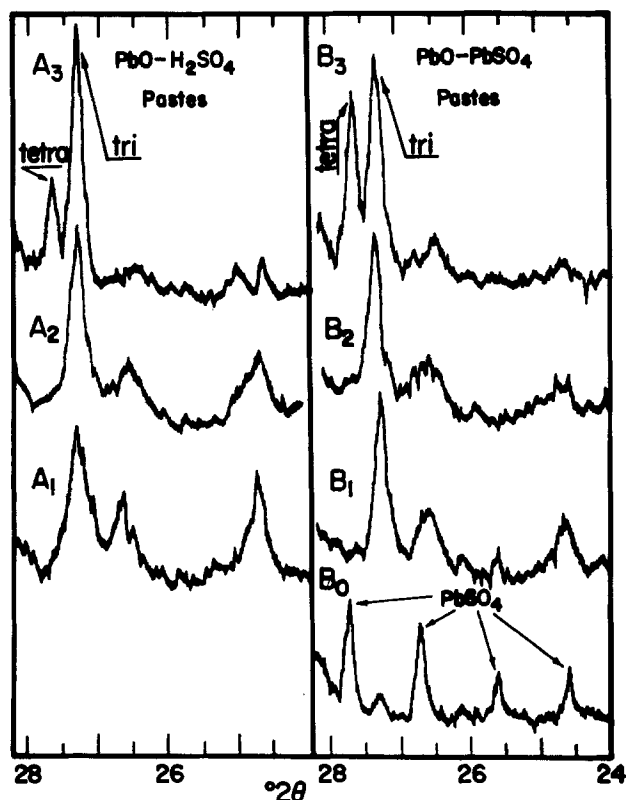


Fig. 3. X-ray diffraction patterns for the reaction products of Anachemia PbO (No. 2a) in pastes with: A, sulfuric acid; and B, PbSO_4 , each cured at room temperature for 1 week (A_1 and B_1), 2 weeks (A_2 and B_2), and four weeks (A_3 and B_3). B_0 is mixture B before the addition of water.

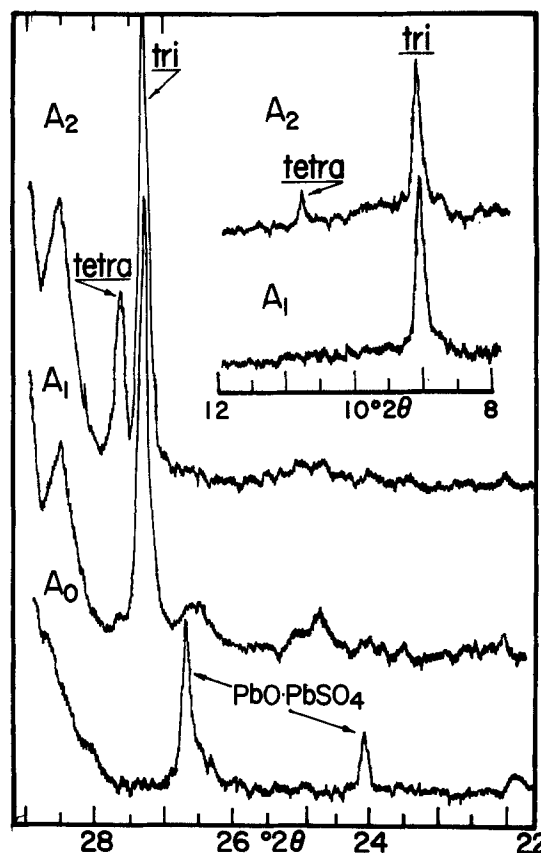


Fig. 4. X-ray diffraction patterns for the reaction of Anachemia PbO (No. 2a) in a paste with $\text{PbO}\cdot\text{PbSO}_4$, cured at room temperature for 1 week (A_1) and four weeks (A_2). A_0 is the mixture before the addition of water.

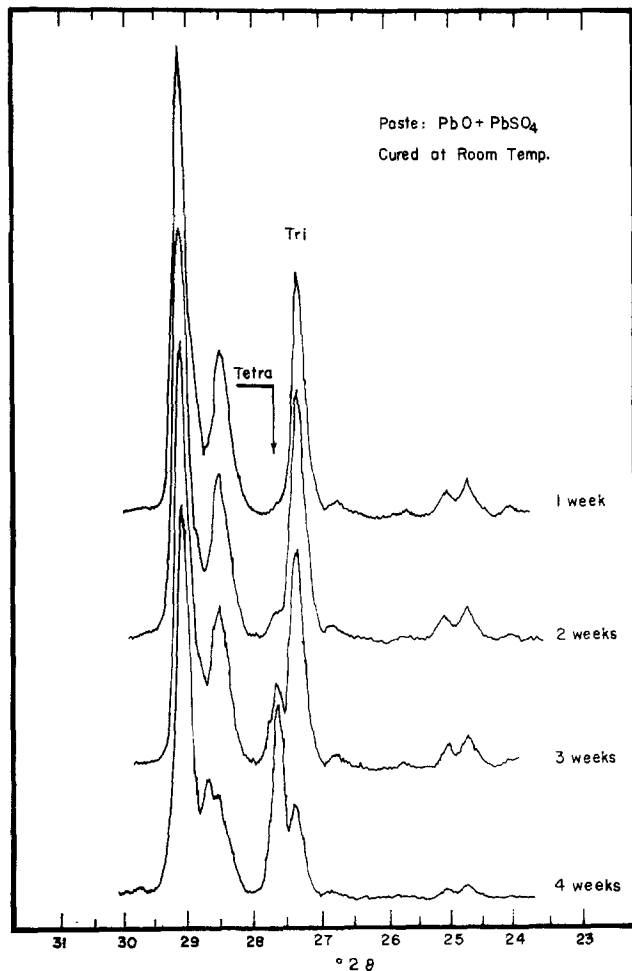


Fig. 5. X-ray diffraction patterns for the reaction products of BDH PbO (No. 4a) in a paste with PbSO₄.

Stability of 4PbO·PbSO₄.—When a cured paste is ground and suspended in water, further phase changes usually occur over time. Two examples, A and B (replicates), are shown in Fig. 8. Both pastes were prepared from Anachemia No. 2a and PbSO₄ and cured for 4 weeks at room temperature. They were then ground and suspended in water. Figure 8 shows that the ratio of tetrabasic to tribasic sulfate increased with time from 0.6 and 0.3 to 0.9 and 2.4, for pastes A and B, respectively, after 10 days. The amount of tribasic increased after 1 day, thereafter remaining approximately constant for paste A, and decreasing for paste B. In case B the increase in tetrabasic content was obviously at the expense of tribasic.

Discussion

These experiments show that 4PbO·PbSO₄ can form at room temperature, although the formation rate is low. Given the necessary conditions and sufficient time, 4PbO·PbSO₄ can be the only sulfate in the product. The necessary conditions are evidently that PbO be in the orthorhombic form and of large particle size and low crystallinity and that the reaction mixture be quiescent. Also associated with the reaction is a long induction period. Thus, Table II and Fig. 3-5 all show that the rate increases markedly beyond the initial 2 weeks. This may be a nucleation period for 4PbO·PbSO₄.

Some information on the way in which 4PbO·PbSO₄ forms is revealed by scanning electron microscopy. Thus, in the 2-week paste of Fig. 6, small crystals of 3PbO·PbSO₄·H₂O, about 2-4 μm long and 0.5 μm wide, can be seen to lie lengthwise on the surface of large PbO particles, irregular platelike forms about 10 μm in diameter (see Fig. 1D), and completely cover them

Table III. Formation of 4PbO·PbSO₄ in sediments

| Lead monoxide | | | | |
|---------------|-------------------|--|-----------------------|--|
| No. | PbO(o)/ PbO(t) | Surface area (m ² /g) | Source of sulfate* | W _{tet} /W _{tri} ** after 28 days |
| 1a | 100/0 | 1.97 | A, B, C | 0.0 |
| 1b | 100/0 | 1.97 | A, B, C | 0.0 |
| 1c | 100/0 | 2.28 | A, B, C | 0.0 |
| 2a | 82/18 | 0.66 | A | 0.25 |
| 2a | | | B | 0.57 |
| 2a | | | C | 0.28 |
| 2b | 90/10 | 0.58 | B | 0.06 |
| 2c | 90/10 | 0.79 | B | 0.12 |
| 2c | | | C | 0.07 |
| 2d | 88/12 | 0.57 | B | 0.0 |
| 2e | 94/6 | 0.57 | B | 0.0 |
| 3 | 90/10 | 0.45 | B | 5.3 |
| 4a | 98/2 | 0.16 | B | H |
| 4b | 100/0 | 2.05 | B | 0.0 |

* Source of sulfate: A = H₂SO₄, B = PbSO₄, and C = PbO·PbSO₄.

** W_{tet}/W_{tri} = weight ratio of tetrabasic to tribasic lead sulfate. H = W_{tet}/W_{tri} > 50.

so that only their outlines show. The few large elongated crystals, 20 μm long and 2 μm wide, are 4PbO·PbSO₄. It can be seen that one end of these large crystals is almost always attached to a PbO particle. The 4-week paste is different. There is, now, a large number of 4PbO·PbSO₄ crystals, again, most of them attached to a PbO particle. Some appear to have their ends submerged in a PbO particle, and some to be just emerging from one. It appears, therefore, that the growth of a 4PbO·PbSO₄ crystal originates at the surface of a PbO particle and that this point of attachment is retained.

Based on these observations the formation of 4PbO·PbSO₄ may be described as follows. Sulfate ions, SO₄²⁻, derived from the sulfate reagent, diffuse to the surface of a PbO particle and assimilate into the oxide lattice without precipitation of any known stoichiometric compound (14). (We have found, in agreement with this concept, that with the uptake of sulfate in a paste there is less than the equivalent increase in crystalline sulfate compounds.) An imperfection in the oxide crystal structure may facilitate this process. When the reaction mixture is not stirred the sole means of mass transport is diffusion, which is slow. Therefore, the pH at the surface of the PbO particle can approach its maximum value. A greater solubility and, hence, a higher pH may also be expected if the crystallinity of the PbO particle is low. Moreover, because large particles of PbO are agglomerates of smaller particles, which, in most cases, appear to be fused together, the resultant tiny crevices and holes would also contribute to regions of high pH. Therefore, nuclei of 4PbO·PbSO₄ may now form on PbO particles, due to the presence of sulfate ion in regions of high pH. This is the induction period. Once the nuclei are formed their growth rate appears to be quite high. If, however, the reaction mixture is stirred the rate of mass transport is greater; the local pH is therefore not as high and conditions for nucleation are less favorable.

PbO(t) has a much lower activity for 4PbO·PbSO₄ formation than has PbO(o); thus, none is formed below 40°C and, with agitation, none below 85°C. This may be due to its lower solubility (16) and, hence, lower pH, or to a higher energy barrier in the initial absorption or assimilation of sulfate ion. Iliev and Pavlov (13) reported that when the initial reaction mixture contained 30%-60% PbO(t), the rate of formation of 4PbO·PbSO₄ was highest. They also reported (12, 13) that the polymorphic transformation of PbO(o) to PbO(t), or vice versa, took place during the paste reaction at 35° and 80°C. We have found, however, that the extent of the polymorphic transformation in either direction is negligible. Even when the orthorhombic form, PbO(o), which is unstable under 390°C (16), was used as the starting material, no ap-

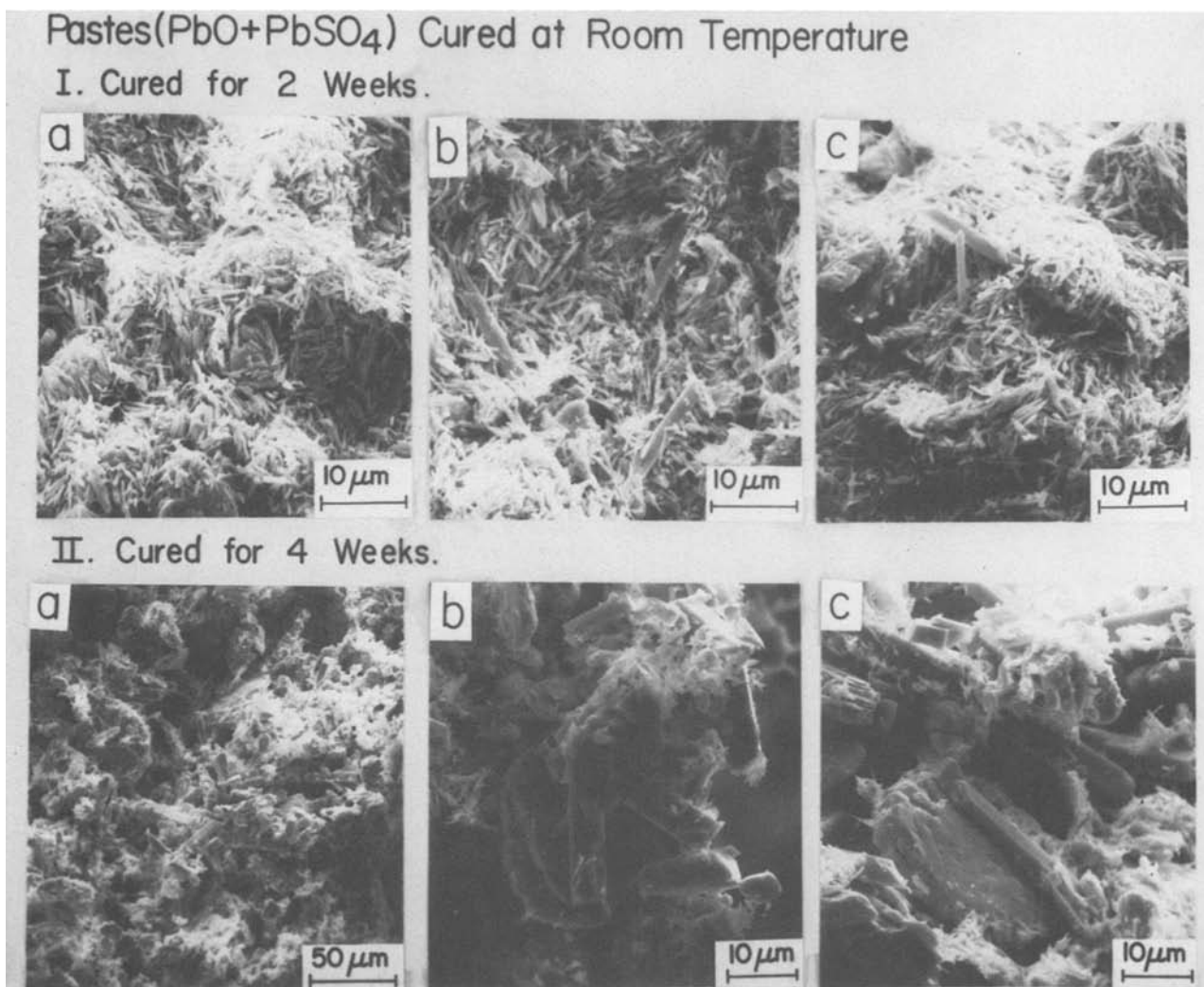


Fig. 6. Electron micrographs of pastes made from BDH (No. 4a) and PbSO_4 after being cured at room temperature for 1, 2 weeks and II, 4 weeks. (a, b, and c show different fields in the same sample).

preciable amount of $\text{PbO}(t)$ was found in reactions at temperatures up to 85°C , with or without agitation. It appears that the presence of sulfates in the mixture inhibits the transformation.

When crystalline $3\text{PbO}\cdot\text{PbSO}_4\cdot\text{H}_2\text{O}$ is the source of sulfate ion the formation of $4\text{PbO}\cdot\text{PbSO}_4$ is not observed at room temperature. However, the reaction does occur after the induction period, as shown in Fig.

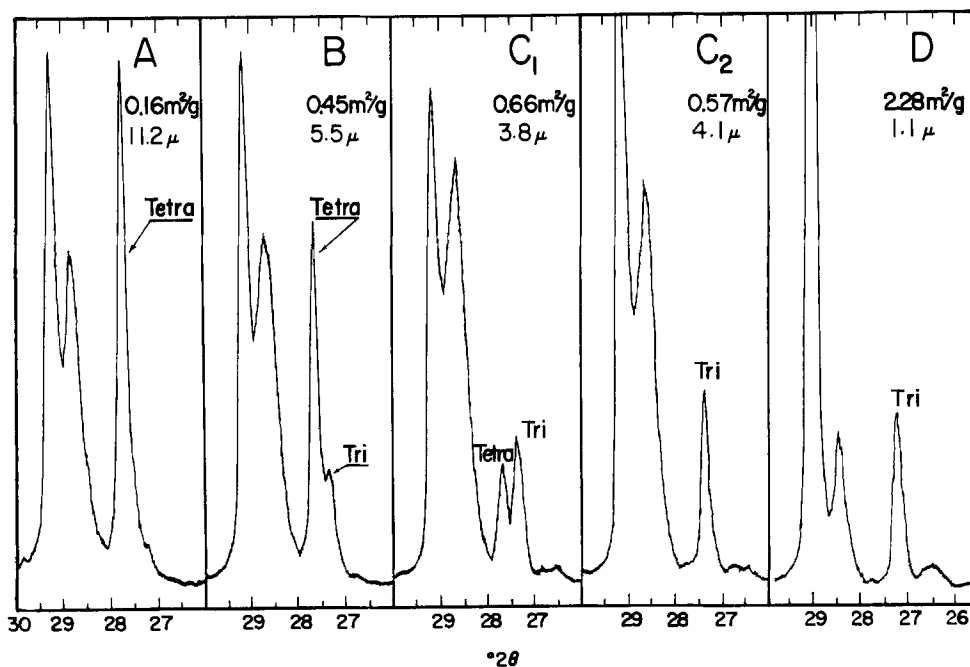


Fig. 7. X-ray diffraction patterns of products in the sediments from the reaction of PbSO_4 with oxides: A, BDH (No. 4a); B, Fisher (No. 3); C₁, Anachemia (No. 2a); C₂, Anachemia (No. 2d); D, Baker (No. 1a). The values in the upper right corner of each section are the specific surface area and median particle size of the oxide.

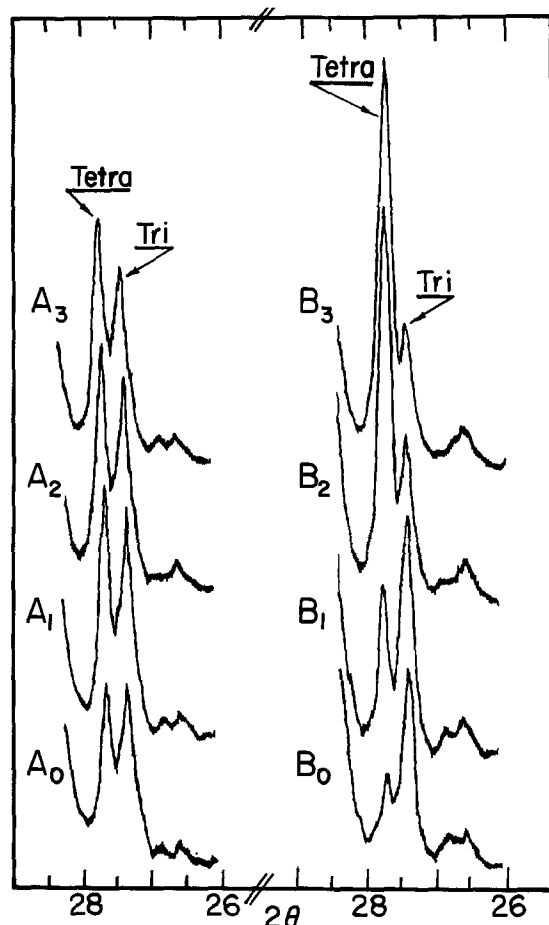


Fig. 8. X-ray diffraction patterns of two examples (A_0 and B_0) of pastes prepared from Anachemia PbO (No. 2a) and $PbSO_4$, and cured at room temperature for 4 weeks. They were then ground and suspended in water at room temperature for 1 day (A_1 and B_1), 4 days (A_2 and B_2), and 10 days (A_3 and B_3).

5 and 8. The nucleation process is evidently much slower for the reaction with crystalline $3PbO \cdot PbSO_4 \cdot H_2O$. This suggests that the nucleation site is the ternary interface between the aqueous phase, a growing structure energetically close to tribasic sulfate and the PbO surface, one that, in a quiescent state, would be well established and have a high pH. With tribasic

sulfate as the added reactant, and in a well-crystallized form, such an interface may not readily be formed.

All the evidence seems to suggest that, in the presence of excess PbO , $4PbO \cdot PbSO_4$ is the stable sulfate at room temperature. If so, further studies on the $PbO-SO_3-H_2O$ system, its thermodynamic aspects and potential-pH diagram, are warranted.

Acknowledgment

This work was supported, in part, by the Industrial Research Assistance Program of the National Research Council of Canada. Most of the experimental work was done by N. A. Haneke and R. J. Lloyd.

Manuscript received Aug. 12, 1980. This was Paper 13 presented at the Las Vegas, Nevada, Meeting of the Society, Oct. 17-22, 1976.

Any discussion of this paper will appear in a Discussion Section to be published in the December 1981 JOURNAL. All discussions for the December 1981 Discussion Section should be submitted by Aug. 1, 1981.

Publication costs of this article were assisted by Cominco Limited.

REFERENCES

1. J. Burbank, *This Journal*, **113**, 10 (1966).
2. R. V. Biagetti and M. C. Weeks, *Bell Syst. Tech. J.*, **49**, 1305 (1970).
3. C. F. Yarnell, U.S. Pat. 3,788,898 (1974).
4. R. V. Biagetti, U.S. Pat. 3,765,943 (1973).
5. C. F. Yarnell, *This Journal*, **125**, 1934 (1978).
6. C. F. Yarnell and M. C. Weeks, *ibid.*, **126**, 8 (1979).
7. H. Bode and E. Voss, *Electrochim. Acta*, **1**, 318 (1959).
8. S. Ikari, S. Yoshizawa, and S. Okada, *J. Electrochem. Soc. Jpn.*, **27**, E-167 (1959).
9. S. C. Barnes and R. T. Mathieson, in "Batteries 2," D. H. Collins, Editor, p. 41, Pergamon Press, Oxford (1965).
10. A. C. Simon and E. L. Jones, *This Journal*, **109**, 760 (1962).
11. K. R. Bullock, *ibid.*, **127**, 662 (1980).
12. D. Pavlov and G. Papazov, *J. Appl. Electrochem.*, **6**, 339 (1976).
13. V. Iliev and D. Pavlov, *ibid.*, **9**, 555 (1979).
14. J. N. Mrgudich, *Trans. Electrochem. Soc.*, **81**, 165 (1942).
15. M. Denby, in "Batteries," D. H. Collins, Editor, p. 439, The MacMillan Company, New York (1963).
16. N. E. Hehner and E. J. Ritchie, "Lead Oxides, Chemistry-Technology-Battery Manufacturing Uses—History," Independent Battery Manufacturers Assoc., Inc., (1974).

All-Solid Lithium Electrodes with Mixed-Conductor Matrix

B. A. Boukamp,* G. C. Lesh, and R. A. Huggins*

Department of Materials Science and Engineering, Stanford University, Stanford California 94305

ABSTRACT

The concept of a novel all-solid composite electrode is presented. One example of such a composite contains a finely dispersed reactant, Li_9Si , in a solid mixed-conducting matrix, $Li_{2.6}Sn$. Repeated charging and discharging of such electrodes without appreciable loss of capacity has been demonstrated. The polarization is found to be comparable to values typical of highly porous electrode systems in molten salt electrolytes.

The use of elemental lithium electrodes in high temperature lithium/metal sulfide battery systems presents serious problems, as it is highly corrosive, dif-

ficult to contain, and dissolves in the molten salt electrolyte causing severe self-discharge. These problems can be reduced by using solid lithium-metal alloys which have a lower lithium activity. In order to provide high current densities, these electrodes are typically made as a highly porous salt-filled sponge [Li-Al

* Electrochemical Society Active Member.
Key words: composite, battery electrodes, chemical diffusion, lithium-silicon, lithium-tin.

system (1, 2)], or as a powder contained in a mesh cage [Li-Si system (3, 4)]. Such lithium-metal alloys are often found to lose capacity with cycling.

A different approach, an all-solid composite electrode, which has the potential of being an attractive alternative is presented here. This composite has a microstructure in which a reactant, (e.g., Li_yAl or Li_ySi) is finely dispersed in a solid mixed-conducting matrix, so that there is a large (internal) reactant surface area. The compound that is used as the matrix phase should be a good electronic conductor, should have a high diffusion constant for the electroactive species (e.g., Li), and except for the transfer of the electroactive species, should not react with the reactant phase. It must also be stable over the range of potential at which the reactant is operated. The matrix phase determines and maintains the microstructural morphology of the dispersed reactant, is the current collector, and is also a fast transport medium for the electroactive species, while the reactant acts as the storage system.

While some preliminary experiments have been performed with different combinations of reactants and matrix compositions, the data presented here, showing the feasibility of this concept, deal with experiments done on the $\text{Li}_y\text{Si}/\text{Li}_{2.6}\text{Sn}$ system. The important electrochemical and structural parameters are given in the next two paragraphs.

A number of phases exist in the Li-Sn system (5-11). They all exhibit rather high chemical diffusion for Li (12). The $\text{Li}_{2.6}\text{Sn}$ (or $\text{Li}_{13}\text{Sn}_5$) phase has the highest

chemical diffusion constant, with $\tilde{D}_{\text{Li}} = 5 \times 10^{-5}$ increasing to 7.6×10^{-4} cm^2/sec with increasing lithium activity at 415°C , which is even greater than typical molten salt values of $1-5 \times 10^{-5}$ cm^2/sec . The stability range of this phase is between 0.390 and 0.286V with respect to lithium at 415°C (5) (for increasing α_{Li}). The position of all Li-Sn phases and two-phase voltage plateaus is given in Fig. 1, together with those for the reactant, Li_ySi . The variation in stoichiometry, δ , for $\text{Li}_{13+\delta}\text{Sn}_5$, is small, ranging from -0.04 to $+0.025$ with increasing α_{Li} (12). The volume per Sn atom varies with increasing Li content, in some cases causing appreciable volume changes upon the conversion of one Li-Sn phase into the next. The important parameters pertaining to this are given in Table I.

Much doubt has existed about the true compositions of the Li-Si phases. Recent electrochemical measurements in our laboratory (13, 14) and careful x-ray analysis elsewhere (11, 15-18) have shown that the phases in the Li-Si system are $\text{Li}_{1.71}\text{Si}$ (or $\text{Li}_{12}\text{Si}_7$)

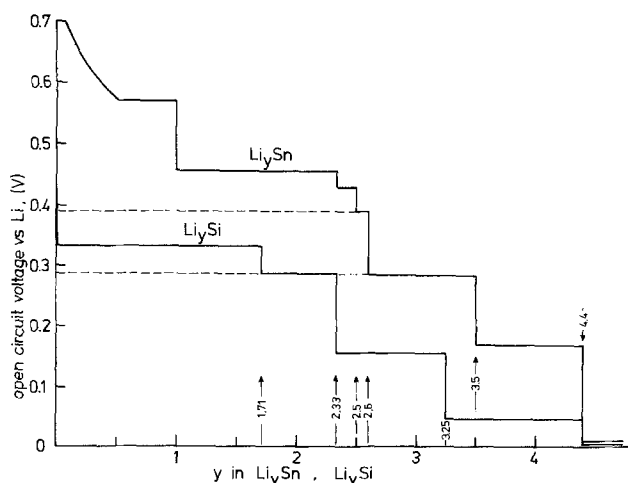


Fig. 1. Coulometric titration curve showing two-phase plateaus and ranges of stability of single phases for the Li-Sn (5) and Li-Si (13, 19-21) systems.

Table I. Crystal structure, unit cell volume, number of formula units per unit cell, crystal volume per Sn atom, and theoretical density for the Li-Sn system

| Compound and crystal structure | Unit cell volume (\AA^3) | Formula units per unit cell | Volume per Sn-atom (\AA^3) | Theoretical density (g/cm^3) | Ref. |
|--|-------------------------------------|-----------------------------|---------------------------------------|--|--------|
| LiSn | | | | | |
| Monoclinic | 132.2 | 3 | 41.1 | 5.07 | (6, 7) |
| Li_7Sn_3 , ($\text{Li}_{2.33}\text{Sn}$) | | | | | |
| Monoclinic | 367.1 | 2 | 61.2 | 3.66 | (8) |
| Li_5Sn_2 , ($\text{Li}_{2.5}\text{Sn}$) | | | | | |
| Rhombohedral | 385.8 | 3 | 64.3 | 3.51 | (9) |
| $\text{Li}_{13}\text{Sn}_5$, ($\text{Li}_{2.6}\text{Sn}$) | | | | | |
| Hexagonal | 327.5 | 1 | 65.5 | 3.47 | (10) |
| Li_7Sn_2 , ($\text{Li}_{3.5}\text{Sn}$) | | | | | |
| Orthorhombic | 642.4 | 4 | 80.3 | 2.96 | (7) |
| $\text{Li}_{25}\text{Sn}_8$, ($\text{Li}_{3.125}\text{Sn}$) | | | | | |
| Cubic | 773.9 | 16 | 96.7 | 2.56 | (11) |

(15), $\text{Li}_{2.33}\text{Si}$ (or $\text{Li}_{14}\text{Si}_6$) (16), $\text{Li}_{3.25}\text{Si}$ (or $\text{Li}_{13}\text{Si}_4$) (17), and $\text{Li}_{4.4}\text{Si}$, (or $\text{Li}_{22}\text{Si}_5$). The stability ranges of these phases with respect to the lithium activity, and the two-phase voltage plateaus according to Ref. (13) and (19-21) are given in Fig. 1. From this figure it is clearly seen that the Si- $\text{Li}_{1.71}\text{Si}$ two-phase plateau voltage is positioned in the middle of the stability range of the matrix phase $\text{Li}_{2.6}\text{Sn}$.

For the Li-Si system the volume per Si atom also varies appreciably among the phases encountered upon increasing the Li content. The volume per Si and the theoretical densities for all Li-Si phases are given in Table II.

Experimental Procedures

The matrix, Li_ySn , was prepared by the careful addition of lithium (99.9%, Alfa) to molten tin (99.9%, Baker) in a molybdenum crucible at $\sim 400^\circ\text{C}$ followed by heating to 600°C for 20-30 min. The crucible was closed, but not tightly sealed, with a molybdenum lid. After rapid cooling by removal of the crucible from the furnace, the metallic gray product was broken in a mortar and milled to a fine powder in a ball mill. All handling was done in a helium atmosphere glove box, or in a protective, leak-tight enclosure. No chemical analysis was necessary, as the composition could be readily determined by electrochemical titration.

The matrix material was then mixed and ground with Si powder (99.95%, Alfa) in a mortar, the Si/Sn ratio being 0.617. The particle size of 90% of the powder mixture was smaller than 45 micron. Pellets were pressed from this mixture in either 3/8 in. (0.93 cm) or 5/16 in. (0.794 cm) diameter evacuated steel dies at a pressure of 2700 kg/cm^2 . This resulted in an overall density over 80% of the theoretical value. This is considerably greater than that typically found in finely divided porous electrodes. The pellets were then placed in a molybdenum holder which was tightened around the cylindrical edge of the sample, exposing the flat planparallel surfaces to the molten electrolyte.

Reference and counterelectrodes were prepared in the same manner using an Al/LiAl mixture of nominal

Table II. Crystal structure, unit cell volume, formula units per unit cell, crystal volume per Si atom, and theoretical density for the Li-Si system

| Compound and crystal structure | Unit cell volume (\AA^3) | Formula units per unit cell | Volume per Si-atom (\AA^3) | Theoretical density (g/cm^3) | Ref. |
|---|-------------------------------------|-----------------------------|---------------------------------------|--|----------|
| Si | | | | | |
| Cubic | 160.2 | 8 | 20.0 | 2.33 | |
| $\text{Li}_{12}\text{Si}_7$, ($\text{Li}_{1.71}\text{Si}$) | | | | | |
| Orthorhombic | 2436 | 6 | 58.0 | 1.15 | (15) |
| $\text{Li}_{14}\text{Si}_6$, ($\text{Li}_{2.33}\text{Si}$) | | | | | |
| Rhombohedral | 308.9 | 1 | 51.5 | 1.43 | (16) |
| $\text{Li}_{13}\text{Si}_4$, ($\text{Li}_{3.25}\text{Si}$) | | | | | |
| Orthorhombic | 538.4 | 2 | 67.3 | 1.38 | (17) |
| $\text{Li}_{22}\text{Si}_5$, ($\text{Li}_{4.4}\text{Si}$) | | | | | |
| Cubic | 6592 | 16 | 82.4 | 1.18 | (11, 18) |

overall composition $\text{Li}_{0.82}\text{Al}$. The three electrode system (LiAl/Al counter and reference; Li-Sn-Si working electrode) was then placed in the molten LiCl-KCl electrolyte (Lithcoa), contained in an Al_2O_3 crucible in a furnace, the temperature being maintained at $\sim 410^\circ\text{C}$. The electrochemical experiments also were carried out in a helium atmosphere glove box.

Experiments were performed using an Aardvark Model V potentiostat/galvanostat, an Aardvark Model BA-1 buffer amplifier, and a Model 379 PAR digital coulometer. Voltages were measured using a Keithley digital multimeter and a stripchart recorder. Experiments were either performed potentiostatically or galvanostatically.

Experiments and Results

Experiments were performed on electrode systems in which the starting composition of the matrix was $\text{Li}_{1.56}\text{Sn}$, (or $\text{LiSn} + 0.74 \text{Li}_{2.33}\text{Sn}$). Lithium was added electrochemically to the sample until its potential reached 0.350V with respect to lithium. At this point virtually no lithium has been incorporated in the single-phase Si reactant, as the solubility of Li in silicon has been estimated to be less than 0.36 atomic percent (a/o) at 415°C (13). The matrix then goes through two phases, $\text{Li}_{2.33}\text{Sn}$ and $\text{Li}_{2.5}\text{Sn}$, before arriving at the equilibrium composition $\text{Li}_{2.6}\text{Sn}$. The influence of this recrystallization process upon the mechanical strength of the sample is still under investigation.

The first few charging (adding lithium to the reactant) and discharging (removing lithium from the reactant) cycles were performed potentiostatically, the charging potential being set at 0.300V vs. Li and the discharging potential at 0.375 vs. Li. The current was integrated by a coulometer and recorded on a strip-chart recorder. In this way the capacity of the reactant could be measured. The coulombic capacity was found to be within the experimental error of the calculated value for the $\text{Si-Li}_{1.71}\text{Si}$ plateau. During the course of the experiment potentiostatic cycles were run in order to monitor the coulombic capacity. It was found that it remained virtually constant over the duration of the experiments (16-20 cycles, one charge and discharge counted as one cycle) indicating negligible capacity loss on cycling.

During this potentiostatic cycling possible slow second phase nucleation was observed for the reactant. At the onset of the charge or discharge cycle the current had an initial high value, which decreased rapidly due to the small change in stoichiometry of the matrix phase which is associated with the instantaneous change in lithium activity. The current then went through a minimum which is probably associated with the slow nucleation of the second phase ($\text{Li}_{1.71}\text{Si}$ for the charge and Li-saturated Si for the discharge cycle) as under this potentiostatic cycling the reactant is driven into its single-phase regime.

A number of cycles were performed galvanostatically in order to establish the polarization characteristics of the mixed-conducting matrix electrodes. No special precaution was taken with respect to the placement of the electrodes; a simple triangular arrangement was used. In order to start from the same composition, or lithium activity, the electrodes were equilibrated potentiostatically at 0.375V vs. Li before charge, and 0.300V before discharge. Thus, as each cycle started with a single-phase reactant, what appeared to be slow second-phase nucleation again was observed as a voltage dip in the polarization at the onset of the charge cycle, and a voltage peak at the onset of the discharge cycle, as shown in Fig. 2.

When the galvanostatic charge and discharge cycles were terminated before reaching the ends of the two-phase plateau, this slow second-phase nucleation was not observed, as both phases were then always present in the reactant (see Fig. 3).

The overpotential as a function of the current density (taking both sides of the sample into account) is

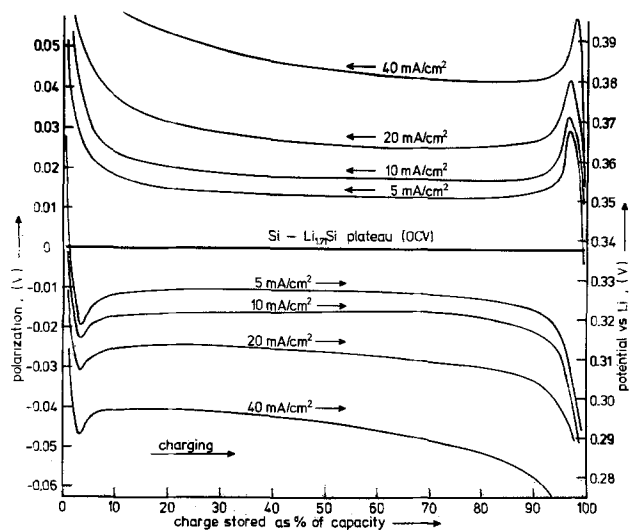


Fig. 2. Electrode polarization as function of the state of charge for several current densities.

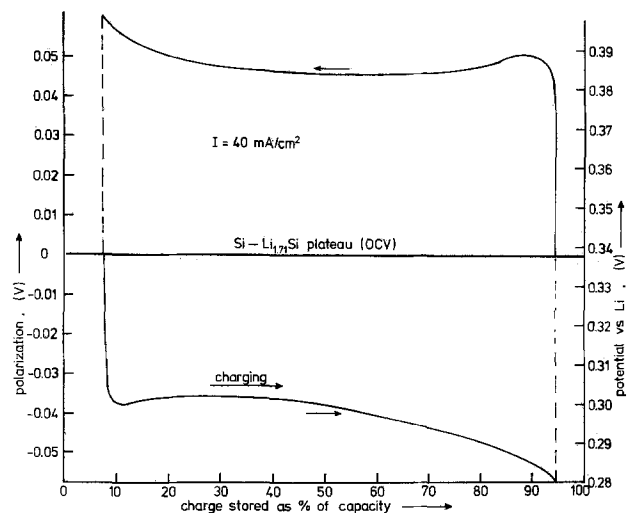


Fig. 3. Electrode polarization as function of the state of charge demonstrating the disappearance of the nucleation related dips and peaks when not cycled to the ends of the plateau.

shown for a 50% state of charge in Fig. 4. The overpotential was found to be small, of the order of 1 mV per mA per cm^2 of macroscopic surface area, being slightly larger near the end of the charge or discharge cycle.

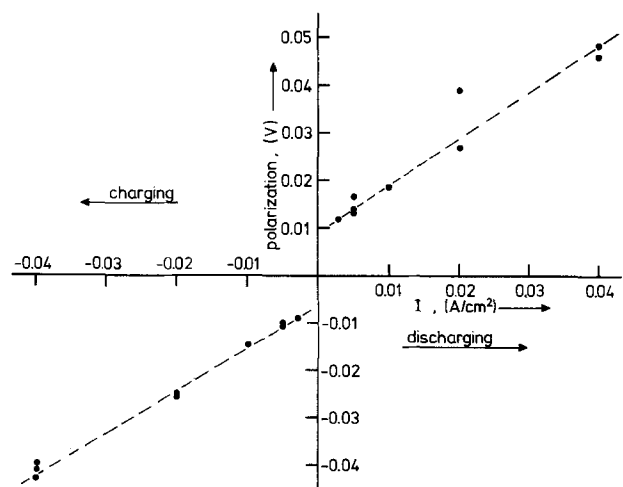


Fig. 4. Electrode polarization as function of the current density for a state of 50% charge stored.

If the matrix electrode is charged with more lithium the potential falls to that of the next two-phase plateau where $\text{Li}_{2.33}\text{Si}$ begins to form. The matrix could also enter a two-phase region with the formation of $\text{Li}_{3.5}\text{Sn}$ at about the same potential [0.282V vs. Li for $\text{Li}_{1.71}\text{Si}/\text{Li}_{2.33}\text{Si}$ (19-21) and 0.286V vs. Li for $\text{Li}_{2.6}\text{Sn}/\text{Li}_{3.5}\text{Sn}$ (5)].

Figure 5 shows a complete galvanostatic cycle, measured at a current density of 5 mA/cm^2 in which the two additional plateaus can be observed. From the length of these plateaus it follows that the first additional plateau is the $\text{Li}_{1.71}\text{Si}/\text{Li}_{2.33}\text{Si}$ two-phase region, as its length is ~ 0.3 times the length of the first, i.e., $\text{Si-Li}_{1.71}\text{Si}$, plateau. The OCV was measured to be 0.288V at 410°C , the same as found by Ref. (13), but slightly higher than reported by Ref. (19-21). The second additional plateau is associated with the $\text{Li}_{2.6}\text{Sn}/\text{Li}_{3.5}\text{Sn}$ two-phase region. Its length was equivalent to about 0.9 times the amount of Sn in the sample. The OCV for this plateau was measured to be 0.276V vs. Li, (at 410°C) which is 10 mV lower than reported by (5).

These extended charging and subsequent discharging did not seem to affect the integrity of the sample, or the overall kinetic behavior of the electrode. The coulombic capacity of the first plateau remained virtually unchanged.

Discussion

In the preceding section the feasibility of this mixed conducting matrix electrode concept has been clearly demonstrated. It is, however, important to discuss its merits with regard to the conventional porous, salt-filled electrodes. The solid matrix phase is obviously heavier than the chloride molten salt which typically exists in the pores of electrode structures prepared by the consolidation, or mechanical containment, of powders (the density of $\text{Li}_{2.6}\text{Sn}$ is 3.47 g/cm^3 , whereas the density of the eutectic composition of the LiCl-KCl salt is 1.66 g/cm^3). The matrix phase acts, on the other hand, simultaneously as the current collector, so no additional material needs to be included for that purpose. Nor is a metallic (e.g., nickel, which has a density of 8.90 g/cm^3) sponge necessary to hold the reactant powder in place.

While this may lead to a slight loss of weight efficiency in this approach, there could be kinetic advantages, as the chemical diffusion coefficient is greater in this metallic matrix than the typical value of about $10^{-5} \text{ cm}^2/\text{sec}$ for molten salts. In this way the possibility of electrolyte freezing inside the pores of the

salt-filled electrodes, due to a local depletion or enrichment of Li in the eutectic electrolyte (22) is avoided.

The theoretical coulombic capacity of such an electrode with an Si/Sn atom ratio of 0.62, operated only within the first Li-Si two-phase region is 0.46 A-hr/cm^3 . In comparison, the "contained powder" Li-Si electrode of Seefurth and Sharma (3, 4) contained 0.68 A-hr/cm^3 when charged to the same Li/Si atom ratio. If the composite electrode were utilized to higher Li contents, i.e., to $\text{Li}_{3.5}\text{Sn}$ and $\text{Li}_{2.33}\text{Si}$, which involved reaction with both the silicon and the tin, the capacity increases to 0.93 A-hr/cm^3 . Under these conditions, the pure Li-Si electrode of Seefurth and Sharma also has 0.93 A-hr/cm^3 . The measured overvoltages were somewhat larger than those measured by Seefurth and Sharma (3, 4) although no corrections for electrolyte resistance were applied.

Although there have not been very many experiments to date, present indications are that there is negligible loss of capacity upon cycling electrodes with this type of composite structure. This is what would be expected if the microstructure returned to its original state after the completion of each full cycle.

This approach avoids the typical problems of densification and particle growth which often play a role in decreasing the useful capacity in conventional liquid-permeated electrode structures.

Further work is being undertaken to investigate the microstructural features of the operation of such composite electrodes as well as their range of applicability.

Acknowledgment

This work was supported by the U.S. Department of Energy under LBL Subcontract No. 4503110.

Manuscript submitted July 1, 1980; revised manuscript received Nov. 10, 1980.

Any discussion of this paper will appear in a Discussion Section to be published in the December 1981 JOURNAL. All discussions for the December 1981 Discussion Section should be submitted by Aug. 1, 1981.

Publication costs of this article were assisted by Stanford University.

REFERENCES

1. N. P. Yao, L. A. Heredy, and R. C. Saunders, *This Journal*, **118**, 1039 (1971).
2. E. C. Gay, D. R. Vissers, F. J. Martino, and K. E. Anderson, *ibid.*, **123**, 1591 (1976).
3. R. N. Seefurth and R. A. Sharma, *ibid.*, **124**, 1207 (1977).
4. R. N. Seefurth and R. A. Sharma, *ibid.*, **127**, 1101 (1980).
5. C. J. Wen and R. A. Huggins, *ibid.*, To be published.
6. W. Muller and H. Schafer, *Z. Naturforsch.*, **28b**, 246 (1973).
7. U. Frank, W. Muller, and H. Schafer, *ibid.*, **30b**, 6 (1975).
8. W. Muller, *ibid.*, **29b**, 304 (1974).
9. U. Frank, W. Muller, and H. Schafer, *ibid.*, **30b**, 1 (1975).
10. U. Frank and W. Muller, *ibid.*, **30b**, 316 (1975).
11. E. I. Gladyshevskii, G. I. Oleksov, and P. I. Kripyakevich, *Sov. Phys.-Cryst.*, **9**, 269 (1964).
12. C. J. Wen and R. A. Huggins, *J. Solid State Chem.*, To be published.
13. C. J. Wen, Ph.D. Dissertation, Stanford University (1980).
14. C. J. Wen and R. A. Huggins, *J. Solid State Chem.*, To be published.
15. H. G. von Schnering, R. Nesper, K.-F. Tebbe, and J. Curda, Unpublished results (1980).
16. H. G. von Schnering, R. Nesper, K.-F. Tebbe, and J. Curda, *Z. Metallk.*, **71**, 357 (1980).
17. U. Frank, W. Muller, and H. Schafer, *Z. Naturforsch.*, **30b**, 10 (1975).
18. H. Axel, H. Schafer, and A. Weiss, *ibid.*, **21b**, 115 (1966).
19. R. A. Sharma and R. N. Seefurth, *This Journal*, **123**,

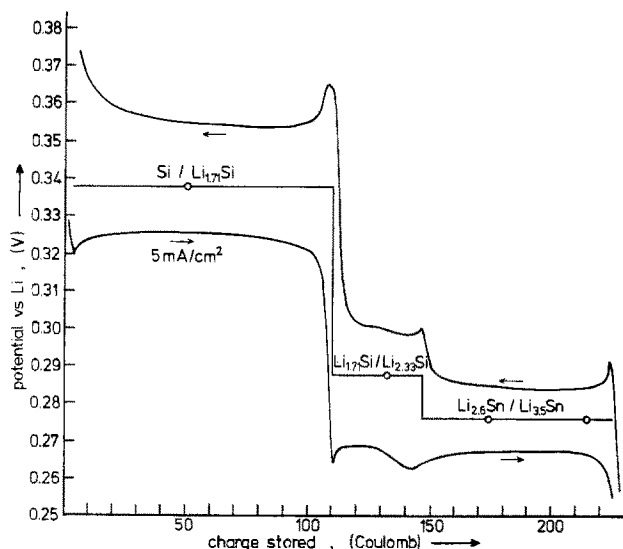


Fig. 5. Electrode polarization at 5 mA/cm^2 as function of the charge stored during a complete charge-discharge cycle to lower voltages. The circles represent measured open-circuit voltages.

1763 (1976).

20. L. R. McCoy and S.-C. Lai, in "Proceedings of the Symposium and Workshop on Advanced Battery Research and Design," U.S. ERDA Report No.

ANL-76-8, p. B-167, March, 1976.

21. S.-C. Lai, *This Journal*, **123**, 1196 (1976).

22. J. Braunstein and C. E. Vallet, *ibid.*, **126**, 960 (1979).

Influence of the Growth Conditions of Al_2O_3 Passivating Layers on the Corrosion of Aluminum Films in Water

J. Grimblot¹ and J. M. Eldridge

IBM Research Laboratory, San Jose, California 95193

ABSTRACT

The effects of water vapor on the oxidation kinetics of UHV-deposited Al films have been investigated using *in situ* ellipsometric measurements. For a given exposure time, the presence of $\sim 33\%$ H_2O increases the Al_2O_3 thickness by $\sim 50\%$ and roughly doubles the extinction coefficient of the oxide. We attribute the nonzero extinction coefficients (with a range in values from 0.05 to 0.18) as being due to the presence of excess Al in the oxide. The "wet"-grown Al_2O_3 layers oxidize at least twice as fast as "dry"-grown layers on storing of samples in a normal laboratory environment. Furthermore, the relative effectiveness of the passivation provided to the underlying Al is greater for the "dry"- than the "wet"-grown Al_2O_3 layers. Gravimetric and electrical resistance data from samples exposed to an aqueous corrosion test are given to support this.

The lifetimes of Al conductor lines in integrated circuits is highly dependent on the quality of the thin ($\sim 20\text{\AA}$) air-formed Al_2O_3 layer. In an effort to better understand processing effects on Al_2O_3 quality as a passivant, *in situ* ellipsometry studies have been used to evaluate the growth and optical properties of oxide layers grown in dry O_2 on UHV-deposited Al films (1). The sensitivity afforded by this approach has clearly shown that the reaction rate is not significantly pressure sensitive and only moderately temperature dependent.

In this paper we report on the effects of water vapor on the oxide growth and properties, as determined by *in situ* ellipsometric measurements. Electrical resistance and weight change determinations were carried out *ex situ* to compare the passivating characteristics of "dry" and "wet" grown Al_2O_3 .

Al films (2000 \AA thick) were deposited under UHV conditions as described elsewhere (1), and exhibited a very strong (111) preferred orientation. The effects of moisture [up to 33 volume percent (v/o)] on Al oxidation at 274°C is shown in Fig. 1. The data are presented according to a direct logarithmic growth law, although our earlier analysis (1) suggests the well-known Mott-Cabrera inverse log law is probably more correct. Note that the presence of 33% water increases the oxide thickness by roughly 50%.

As reported for the Al-dry O_2 reaction (2), the oxide layer is slightly light-absorbing at $\lambda = 5461\text{\AA}$. For dry O_2 , the optical extinction coefficient (k) of thin Al_2O_3 layers varies from 0.07 to 0.05 as the oxide grows from roughly 20 to 30 \AA . For "wet" grown oxides, k varies from ~ 0.18 to 0.10 for the same thickness range. We attribute the small light absorption as being due to the presence of a very small ($\sim 10^{19}/\text{cm}^3$) concentration of Al atoms in excess of the stoichiometric ratio. Similar effects have been seen in the In_2O_3 -In system (2).

We have attempted to use *ex situ* ellipsometric measurements in an effort to compare the relative passivi-

ties provided by the "dry" and "wet" Al_2O_3 layers. However, the results were quite difficult to interpret, perhaps owing to the formation of quite discontinuous islands of hydroxide, pits, blisters, etc. Indeed, it may only be possible to study the very initial reaction of materials in corrosive solutions via ellipsometry (3). Accordingly, we used ellipsometry here to measure thickness increases of the above oxides due to prolonged exposure to laboratory air (*i.e.*, $\sim 25^\circ\text{C}$, 40-50% RH, and some unknown levels of corrosive pollutants). For periods up to roughly 40 days, we found the "wet" Al_2O_3 layers continued to grow in ambient air at $\sim 1\text{\AA}/\text{day}$, whereas "dry" Al_2O_3 grew at $\sim 0.4\text{\AA}/\text{day}$.

In an effort to better differentiate between the reactivity of these oxides, more extensive tests were conducted using various aqueous reactive ambients. We regard the aqueous test results as significant because: DI-water rinses are integral to all IC processing (4);

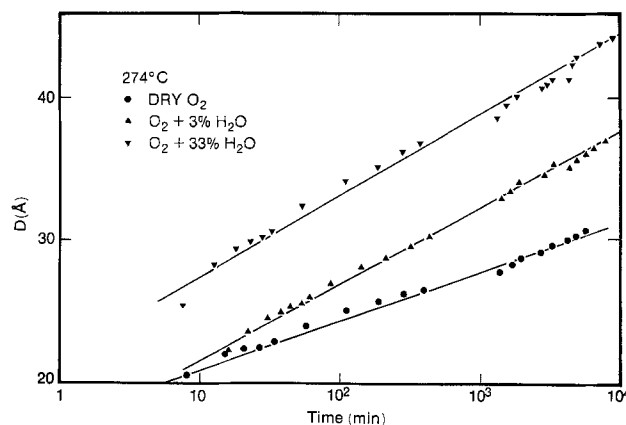


Fig. 1. Plot of the thickness as a function of log time (min). ● Dry O_2 (50 Torr) at 274°C ; ▲ $\text{O}_2 + 3\% \text{H}_2\text{O}$ (50 Torr total pressure) at 274°C ; ▼ $\text{O}_2 + 33\% \text{H}_2\text{O}$ (100 Torr total pressure) at 274°C .

¹Permanent address: Université des Sciences et Techniques, Lille, France.

Key words: accelerated corrosion, thin films, semiconductor reliability.

and, adsorbed water layers lead to Al corrosion in electronic circuits of all types (5). For this purpose, weight change and resistance increase measurements were used to monitor the effects of exposure of films to various aqueous solutions. In each case, three nominally identical samples were used to minimize effects of specimen inhomogeneities. Experiments were conducted using samples with roughly the same Al_2O_3 thickness: 30Å for "dry" oxide (formed in 4200 min at 274°C); and, 35Å for "wet" oxide (grown in 200 min at 274°C with 33% H_2O in O_2).

Figure 2 shows weight losses of various samples due to immersion in different solutions at room temperature. The NaF solution is too corrosive, removing entire 2000Å thick Al films (i.e., ~230 μg) in 3-20 hr depending on concentration. The KCl solutions are less corrosive but still sufficiently large as to mask significant differences amongst the oxide layers.

For our comparisons, we finally decided to use a DI H_2O solution containing Al^{3+} ions (obtained by boiling the water with an excess of ultrapure Al slugs). In this way, we hoped to minimize effects due to dissolution-precipitation processes, even though the solubility product of $\text{Al}(\text{OH})_3$ in water is very low (6) at room temperature. The weight change vs. time curves in Fig. 2 for this solution are quite complex and beyond our total understanding at this time. This is not unexpected in view of the well-known complexities of the Al- H_2O interactions (7-8). However, two well-defined regions emerge here. In the first, an incubation period (IP) appears with no noticeable weight loss. We attribute the IP to the time needed to hydroxylate the Al_2O_3 since this period is smaller for the "wet" oxide. The IP characteristics of Table I show this value decreases with storage of "dry" grown Al_2O_3 samples, becoming essentially identical to freshly prepared "wet" oxide after roughly 25 days. Since hydroxylated Al_2O_3 layers have a more open structure wherein corrosive species diffuse more readily, the above observations may have an important practical aspect. Namely, so-called "dry" processing and subsequent storage in inert ambients should enhance the passivity of Al conductor lines. Such effects are likely to become more important as VLSI technologies are developed where all reasonable precautions should be taken to prevent metal corrosion with attendant yield loss, etc.

The second stage of the result in Fig. 2 is characterized either by weight loss and/or small hole formation

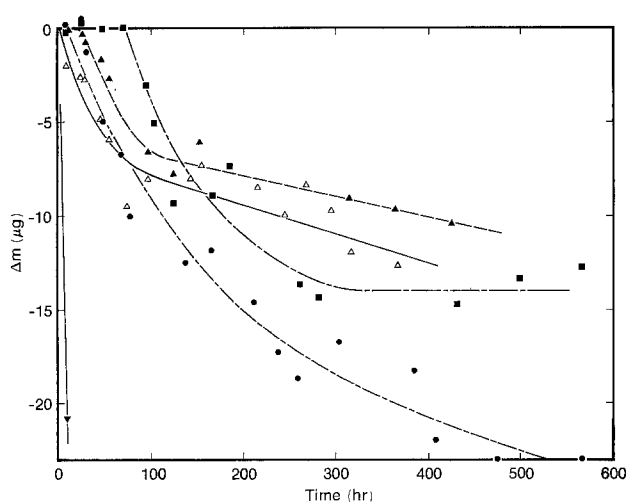


Fig. 2. Plot of weight change in μg (averaged over 3 identical samples) as a function of time (hr). ∇ "Dry" oxide in NaF (0.01M); \bullet "dry" oxide in KCl (0.1M)—5 days between preparation and corrosion test; \blacksquare "dry" oxide in water—4 days between preparation and corrosion test; \blacktriangle "dry" oxide in water—25 days between preparation and corrosion test; \triangle "wet" oxide in water—21 days between preparation and corrosion test.

Table I. Characteristics of the incubation period

| Sample | Time between preparation and corrosion test (days) | Solution | Incubation period (hr) | Symbol used in Fig. 2 |
|--------|--|-----------------------------|------------------------|-----------------------|
| Dry | 5 | KCl (0.1M) | 20 | ● |
| Dry | 4 | Water (+ Al^{3+}) | 75 | ■ |
| | 12 | Water (+ Al^{3+}) | 60 | ▲ |
| | 25 | Water (+ Al^{3+}) | 15 | ▲ |
| Wet | 1 | Water (+ Al^{3+}) | 25 | ▲ |
| Wet | 21 | Water (+ Al^{3+}) | 0 | △ |

through the films. We then expect that adhesion of some corrosive products is poor to the glass substrate. It is probably one of the reasons why our findings disagree with previous results (7) indicating weight gain by immersion of bulk Al sheets in water (from 20° to 80°C). Since hole formation seems to occur randomly, it is difficult to compare absolute weight losses from different samples.

Probably similar effects have to be invoked to explain the resistance variations of typical "dry" and "wet" samples when immersed in the test solution (Fig. 3). Hole formations in the aluminum film and insulator produce growth that can give acceptable explanations of the observed resistance increases, but the presence of a sharp maximum after ~40 hr of immersion is still unclear. Note also that the "wet" oxide samples exhibit a larger resistance increase with time, similar to the weight change results of Fig. 2. In addition, the "wet" oxides exhibit much smaller IP values, as expected.

In conclusion, this paper clearly shows that introduction of water vapor in O_2 modifies unambiguously the kinetics of aluminum film oxidation. Moreover, the "wet"-formed oxide is less stoichiometric because its extinction coefficient is relatively higher. Secondly, the "wet" Al_2O_3 layers are less effective as passivants on storing Al films in a normal laboratory environment. Thirdly, immersion of the samples in DI water yields an incubation period which can be observed gravimetrically and electrically. Both techniques show that IP is higher for the "dry" compared to the "wet" oxide. Since significant corrosion only starts after the completion of this IP, we conclude that the fresh "dry" oxide is more protective than the "wet" oxide.

Acknowledgment

The authors are indebted to J. M. Brown for his helpful experimental assistance.

Manuscript submitted Sept. 16, 1980; revised manuscript received Nov. 21, 1980.

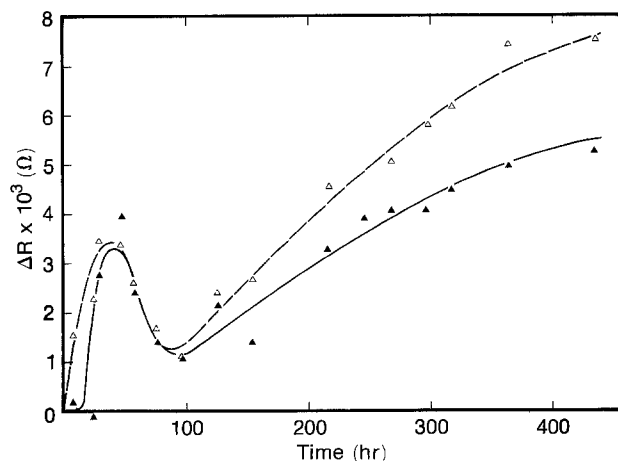


Fig. 3. Plot of resistance change (Ω) as a function of time (hr). \blacktriangle , \triangle same symbol as in Fig. 2.

Any discussion of this paper will appear in a Discussion Section to be published in the December 1981 JOURNAL. All discussions for the December 1981 Discussion Section should be submitted by Aug. 1, 1981.

Publication costs of this article were assisted by IBM Corporation.

REFERENCES

1. J. Grimblot and J. M. Eldridge, Submitted to *Surf. Sci.*
2. J. M. Eldridge, Y. J. Van Der Meulen, and D. W. Dong, *Thin Solid Films*, **12**, 447 (1972).
3. K. A. Pha Tak, S. S. Tamhankar, and K. Sathianandan, *ibid.*, **41**, 137 (1977).
4. C. C. Chang, D. B. Fraser, M. J. Grieco, T. T. Sheng, S. E. Haszko, R. E. Kerwin, R. B. Marcus, and A. K. Sinha, *This Journal*, **125**, 787 (1978).
5. G. F. Cerofolini and C. Rovere, *Thin Solid Films*, **47**, 83 (1977).
6. L. Meites, Editor, "Handbook of Analytical Chemistry," McGraw-Hill, New York (1963).
7. R. K. Hart, *Trans. Faraday Soc.*, **53**, 1020 (1957).
8. W. Vedder and D. A. Vermilyea, *ibid.*, **65**, 561 (1969).

High Rate Electrodeposition of Niobium from Molten Fluorides Using Periodic Reversal Steps and the Effects on Grain Size

Uri Cohen¹

Department of Materials Science and Engineering, Stanford University, Stanford, California 94305

ABSTRACT

Application of periodic reversal (PR) technique, in which a cathodic (depositing) step is followed by an anodic (polishing) step, was found very beneficial to the increase of electroplating rate of coherent niobium. With no mechanical agitation, the application of the PR technique facilitated an electroplating rate increase by a factor of about 10 over the direct current method. The morphology of the deposits was found to be of the columnar structure. The columns became more oriented along the [100] direction, and of smaller diameters as the rate of electrodeposition increased. Unexpectedly, beyond a certain rate and under certain conditions, the columnar grains became large once again. Under such conditions a pronounced heteroepitaxial effect of the substrate (Cu) grains on the deposit grain size and orientation was observed.

Niobium (1, 2), as well as other refractory metals (2-7), were first demonstrated by Senderoff and Mellors to be capable of electroplating in coherent and dense coatings from molten alkali fluoride solvents. In addition, Senderoff and Mellors also investigated the electrode reactions of niobium (8) and the other refractory metals (3, 5) by chronopotentiometry. They reported three steps in the reduction of Nb(V) (which is used as the solute source):

$$\text{Nb(V)} \xrightarrow{e^-} \text{Nb(IV)} \xrightarrow{3e^-} \text{Nb(I)} \xrightarrow{e^-} \text{Nb}$$

They also investigated its anodic oxidation to the hexavalent state on inert anodes (9). The decomposition potentials of the solute salt K_2NbF_7 in the molten alkali fluoride solvent, as well as those of several other metal salts, were measured by Cohen (10, 11). In addition, Cohen also studied the behavior of niobium electrode by slow cyclic voltammetry and by a newly developed technique, reversal current step voltammetry (RCSV) (10). The latter technique provides steady-state polarization curves while greatly eliminating the deleterious effects (13-15) associated with prolonged electrodeposition at high rates onto solid electrodes. These studies showed that niobium is capable of both electrodeposition and electropolishing in the same molten fluoride electrolyte.

Molten alkali fluorides, due to their high decomposition potentials (>3V) (10, 11), provide inert media from which many metals and alloys can be readily deposited. Some of these metals and alloys cannot be deposited from other solvents with smaller decomposi-

tion ranges (such as water) due to the latter decomposition. This advantage, as well as several other attractive features of the alkali fluoride solvents (such as the fluxing effect of metal surface oxides, the complex ion stability, the high ionic conductivity, and the low melting point eutectics) have been discussed previously (10, 12).

Electrodeposition with the periodic reversal (PR) current was first developed by Jernstedt (16, 17). The technique was originally applied to the plating of Cu, Ag, and brass from their aqueous cyanide baths. It was further investigated by other workers (18-25). Several review papers are now available (26-28). The technique was shown to be particularly useful for coating properties such as coherency, density, smoothness, brightness, uniformity, and the reduction of internal stresses. Very low frequencies, typically in the range of few cycles per minute, have been found most beneficial. The anodic current magnitude has not, in general, exceeded the cathodic current magnitude. The average PR plating rate has been, in general, about the same or somewhat higher than the conventional direct current (d-c) plating. The PR method was reported to be very beneficial to copper plating from its cyanide bath (27, 29), but to have no such effects when applied to the acid copper sulfate bath (30). Despic and Popov (31) related the positive PR effects to systems operating under diffusional control of the deposition process, but to have no such effects with systems operating under activation-controlled deposition process.

In the present work, much larger anodic than cathodic current magnitudes were employed, and the anodic periods were shorter than the cathodic periods.

¹ Present address: Department of Materials Engineering, Technion, Haifa, Israel.
Key words: fused salts, electrode, current density, electrodeposition.

The larger anodic current magnitude ensured polishing rather than etching. The large current magnitudes were facilitated by the large decomposition potential range of the alkali fluoride solvent.

Recently, Jackson and Miller (32) described a new method of thermal cycles for remelting and regrowth. Utilizing *in situ* microscopic observations of the growing crystals, they reported significant improvements in the crystal perfection and grain size increase. Several mechanisms which they suggested for the cyclic thermal growth seem to be also valid for some observations made in the present study.

The basic principles of the PR steps technique, utilized in this study, are schematically illustrated in Fig. 1. Figure 1(a) defines the operating parameters of a PR-current signal. Similar parameters are likewise defined for PR-potential signal. Figure 1(b) shows the effect of a PR cycle. The original flatness of the solid-liquid interface prior to the cycle ($t = 0$) is restored at the end of the cycle ($t = t_c + t_a$). Thus, although the cathodic pulse may drive into the diffusion-controlled regime, giving rise to interface protrusions forming after some initiation period (31, 33, 34), the latter may then be taken off during the following anodic polishing pulse. The next cathodic deposition step will start again with a fresh smooth and flat interface.

Experimental

The experimental setup has been described in detail elsewhere (10). An inert atmosphere of purified helium was maintained in the vacuum-tight chamber (with a slow flow rate). Three electrodes insulated from each other and from the chamber, could be replaced through special "rescue chambers" without having to open the main chamber. The latter consisted of an Inconel can fitted with an O-ring seal and a water cooled top flange. The Inconel can was inserted into an electrically heated tube furnace. The crucible was typically

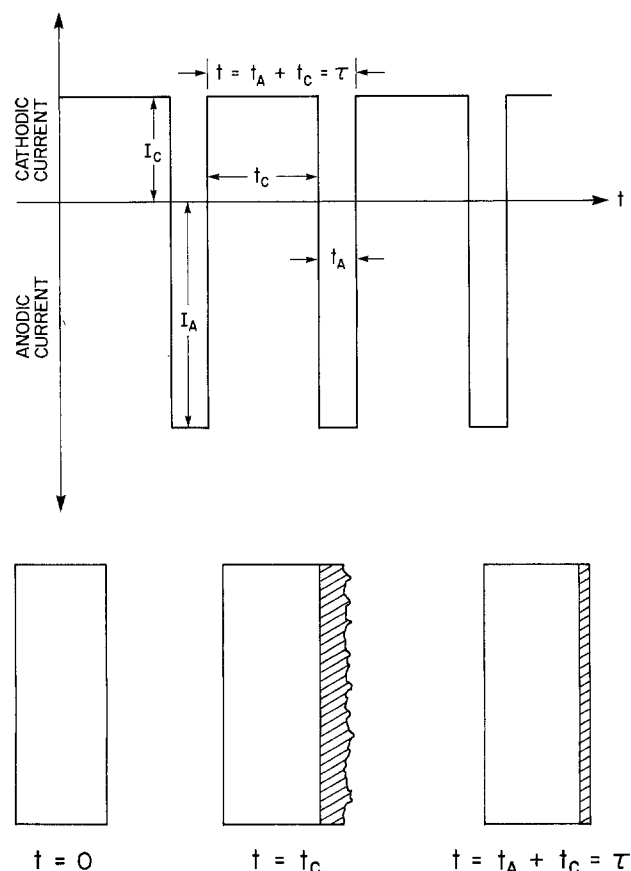


Fig. 1. (a, top) PR-current (PRC) signal and its parameters, (b, bottom) schematic profile cross section of the cathode and its coating during a PR cycle.

made of Ni or Mo metals, and was protected from contamination originating on the Inconel walls by an Mo liner.

A convenient salt mixture containing 6 mole percent (m/o) K_2NbF_7 , 10 m/o KHF_2 , and balance $LiF:KF$ (47:37 m/o), was first melted in a manner which was described elsewhere (10, 35). A niobium anode piece was then immersed in the melt in order to equilibrate the niobium valences (1)



A pre-electrolysis run was then performed with a copper strip cathode. This pre-electrolysis substantially reduced the more noble metal impurities. Thus, an initial contamination of the niobium deposit with 0.2 weight percent (w/o) Fe, dropped to below 0.05 w/o Fe after an overnight electrolysis at 10 mA (total bath of 3 moles).

A practical quasi-reference electrode² was the redox couple electrode Cu/Nb(V), Nb(IV). The reaction [1] was shown (1) to reach equilibrium at a mean valence of 4.5. The ratio of $[Nb(V)]/[Nb(IV)] \approx 1$ suggests a stable redox potential since concentration fluctuations will only slightly affect the redox potential. The anode was always a dissolving niobium sheet, and both copper and molybdenum strips were used as substrates.

The electrical signals for both electrodeposition and voltammetric studies were produced by the combination of a potentiostat and a signal programmer PAR 173/PAR 175.

The samples were analyzed by x-ray diffraction (XRD) for preferred orientation. Scanning electron microscopy (SEM), and sample sectioning and metallography were used to study the morphology. The sectioned samples were mounted in a plastic mold and ground and polished. They were then etched in a solution which contained H_2O (50 ml), HF (20 ml), HNO_3 (10 ml), and H_2SO_4 (15 ml). Superconducting transition temperature measurements were performed by Professor Geballe's Cryogenic Group at Stanford University.

Results

Electrodeposition at constant current.—Constant current electrodeposition experiments were done at $750^\circ \pm 5^\circ C$, from a solution of 6 m/o K_2NbF_7 . No mechanical agitation was used. Figure 2 shows a sample which was prepared during the pre-electrolysis purification stage. A constant current density of 3.3 mA/cm² was applied. The deposit was dense and coherent. Its cross section reveals a columnar microstructure, and XRD analysis of the as-deposited sample indicated strong preferred orientation along the [100] direction. The deposit had a light gray matte color, and was of dull appearance due to its surface roughness. The unusual pyramidal morphology is believed to be due to the adsorption of impurities. Following the purification stages, the application of a constant current density of 5 mA/cm² to the pure solution yielded the sample shown in Fig. 3. This deposit was of high quality but had also a dull appearance. Application of a constant current density of 25 mA/cm² resulted in a deposit revealing the onset of deterioration beyond a thickness of about 100 μm . The deposit is shown in Fig. 4. An upper limit of about 25 mA/cm² on the useful range of constant current was thus established.

Electrodeposition with periodic reversal (PR) pulses.—Experiments with PR were also performed with a solution of 6 m/o K_2NbF_7 , and at $750^\circ \pm 5^\circ C$. Cu and Mo strips of 1 cm width were used as cathodes, and

²The potential of immersed metal Cu in this melt is not well defined. The slightly soluble (8) species Nb(I) may greatly affect it. However, the potential of this electrode reaches a steady-state value after a few minutes of immersion. That potential is stable (within about ± 1 mV) over periods of several days. As this quasi-reference electrode was only used to monitor variations in the working electrode potential over short durations, its actual potential was considered of secondary importance.

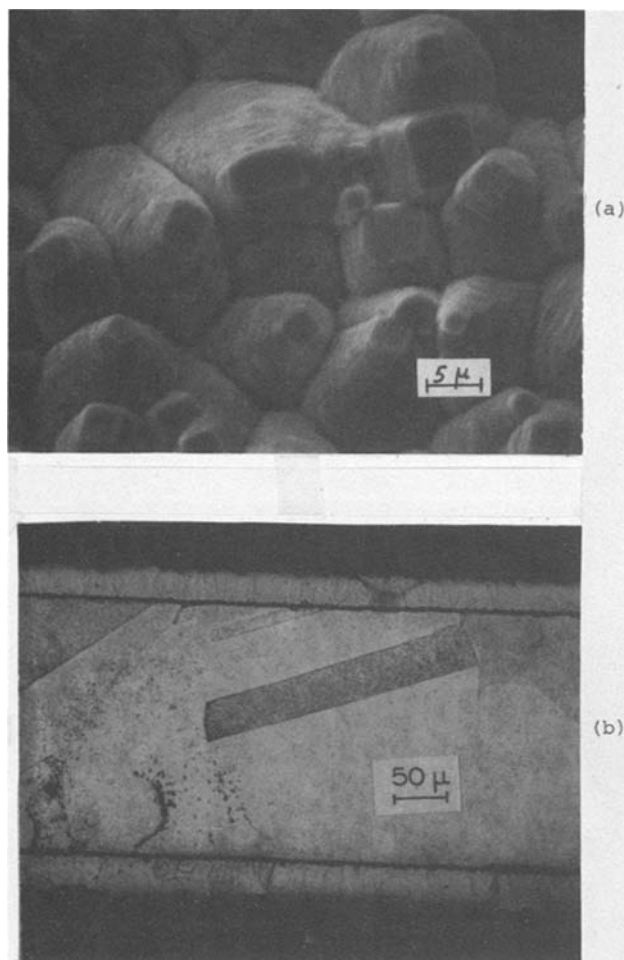


Fig. 2. Nb deposit obtained by constant current (d-c) pre-electrolysis at $i_c = 3.3 \text{ mA/cm}^2$. (a) SEM photograph of the coating surface, (b) optical micrograph of a vertical cross section.

a niobium sheet was used as a dissolving anode. Cu/Nb(IV), Nb(V) was used as a quasi-reference electrode. No mechanical agitation was used. Both methods of PR-potential (PRP) and PR-current (PRC) were examined. Figure 5 shows the traces of a PRP controlling signal and the current response with time. Figure 6 shows the traces of a PRC controlling signal and the potential response with time. The deposit shown in Fig. 7 was obtained from the application of the PRP signal of Fig. 5. The deposit was of high quality with a very smooth, polished, and shiny appearance, but had etch pits on the surface. The average cathodic current density on this sample was about 90 mA/cm^2 . The average anodic dissolution current density was about 110 mA/cm^2 . The Q -ratio for this sample was about 4.1, where Q is defined by

$$Q = |Q_C/Q_A| = |t_{cic}/t_{aia}| \quad [2]$$

The signal parameters are defined in Fig. 1.

Figure 8 shows another sample which was grown by PRP. For this sample, however, the average deposition current density was 300 mA/cm^2 , and the Q -ratio was about 8.0. The bad morphology of this deposit is seen in the poor filling and coherency. The more the deposit grows, the worse its quality becomes.

PRC offers a better control of the Q -ratio as the currents do not drift during the deposition run. Figures 9 and 10 show the effect of reducing the Q -ratio when PRC steps were applied. The sample shown in Fig. 9 was grown by the PRC signal of Fig. 6 with $Q = 4.0$. The sample shown in Fig. 10 had $Q = 2.0$. Both samples were grown with identical cathodic current density, $i_c = 300 \text{ mA/cm}^2$.

Increasing the frequency showed a slight improvement of the deposit brightness, but decreased uniformity. A sample which was prepared under similar conditions to those of Fig. 10, but at a ten times higher frequency, yielded a somewhat brighter deposit on the flat surface. However, large dendrites were found on the strip edges, due to the higher local current density there.

Concentration effects.—A mixture containing 0.8 mole K_2NbF_7 , 0.1 mole KHF_2 , and 0.1 mole LiF (total of 1 mole) was heated and melted according to a procedure previously described (10, 35) (on cooling, the first freezing was observed at $705^\circ \pm 5^\circ\text{C}$). The niobium valences were then equilibrated with niobium metal according to (1). A dissolving Nb anode was used and the cathodes were either Cu or Mo strips.

Using a PRC signal to deposit Nb from the 80 m/o K_2NbF_7 solution was less favorable than from the 6 m/o solution. Figure 11 shows samples which were grown with $i_c = 50 \text{ mA/cm}^2$ and $Q = 2.0$ from the 80 m/o solution. The deposit was shiny and of high quality and coherence. However, at higher PRC cathodic current densities, large dendrites began to appear on the substrate edges, and an "umbrella" of deposit rapidly grew at the liquid surface perpendicular to the substrate surface. Thus the maximum deposition rate obtainable from the highly concentrated solution is significantly lower than from the 6 m/o solution. The Nb dissolving anode, after operation in the 80 m/o solution, is shown in Fig. 12. Notice the highly polished appearance of this anode.

Superconductivity tests.—Superconducting transition temperature, T_c , was measured by magnetic suscepti-

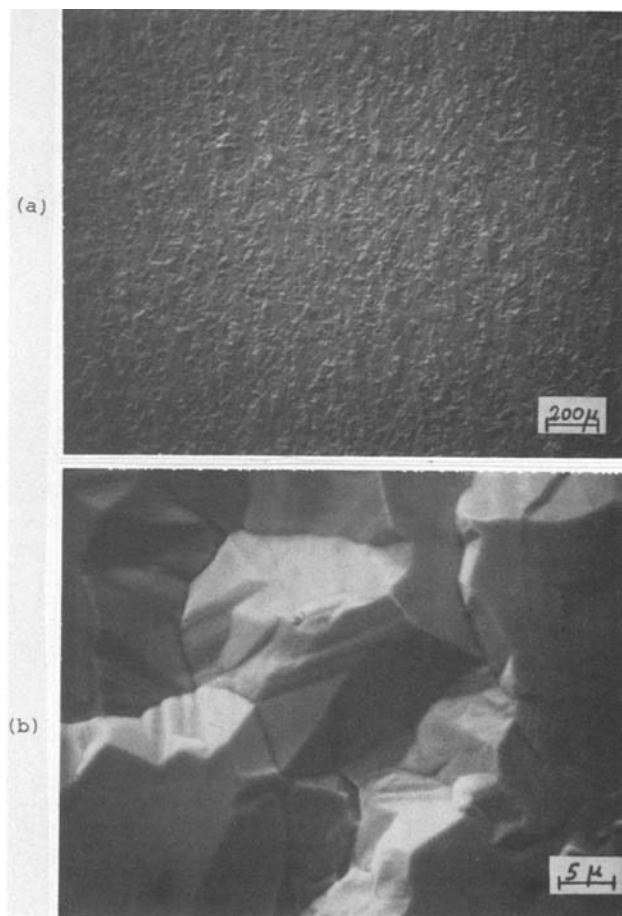


Fig. 3. SEM photographs of Nb deposit obtained with constant current density of 5 mA/cm^2 . Mo substrate; pure solution.

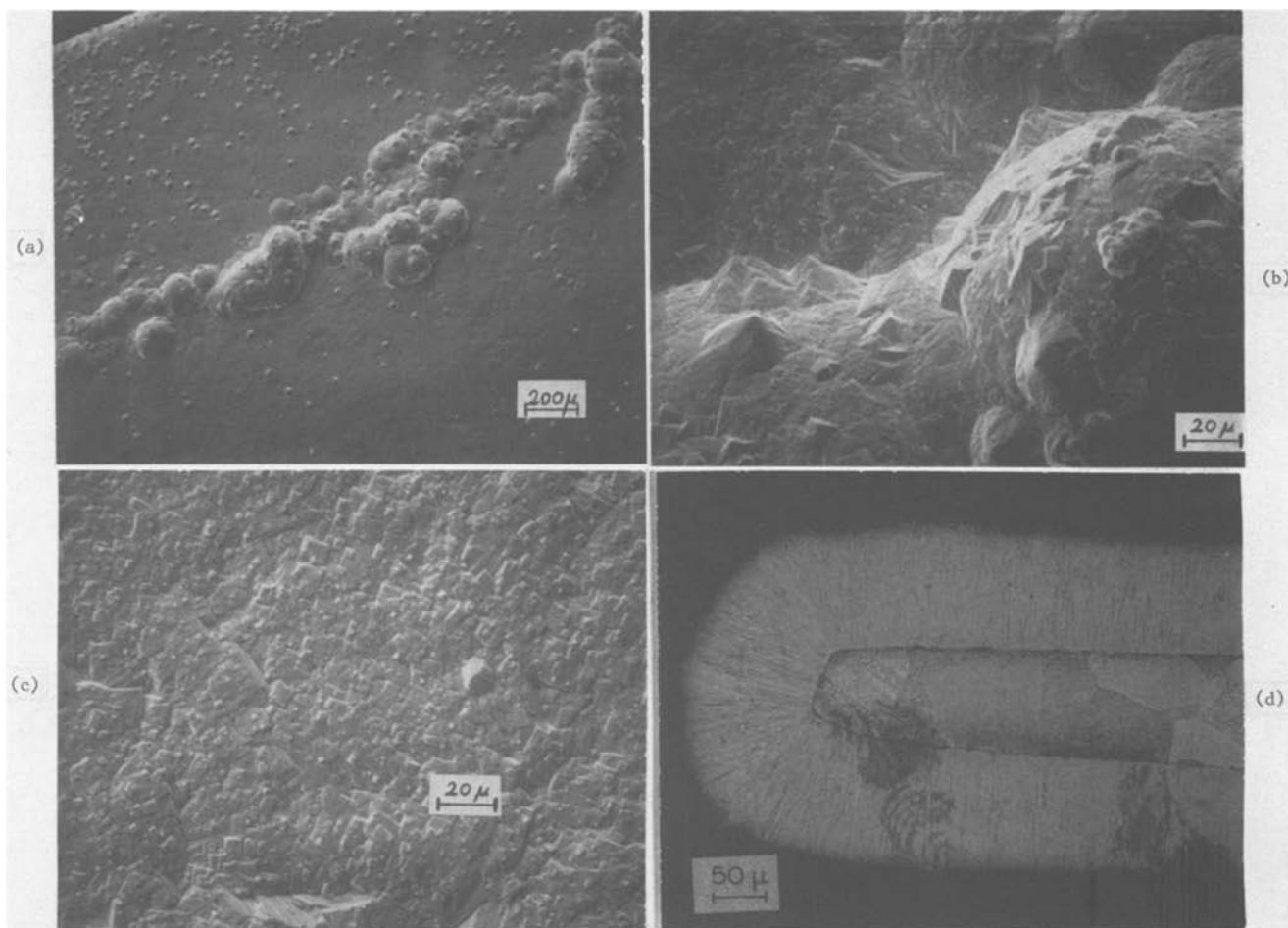


Fig. 4. Nb deposit obtained with constant current density, $i_c = 25 \text{ mA/cm}^2$. (a) and (b) SEM of deteriorating surface, (c) SEM of smooth area, (d) vertical cross section.

bility. Both frequency shift and oscillation amplitude methods were utilized (36).

Strongly oriented deposits along the [100] direction with fine columnar grain structure, such as seen in Fig. 7, revealed wide transition temperature interval, $\Delta T_c = 5.2\text{--}9.1 \text{ K}$. The interval decreased as the grains became larger, less oriented, and less coherent. Thus, the deposit shown in Fig. 10 had $\Delta T_c = 8.3\text{--}9.1 \text{ K}$, and the one shown in Fig. 4 had $\Delta T_c = 8.8\text{--}9.15 \text{ K}$. The high transition limits indicate that the deposits were very pure. For a comparison, the impure Nb deposit which was obtained during the pre-electrolysis stage (shown in Fig. 2), had only $\Delta T_c = 7.9\text{--}8.4 \text{ K}$. The latter contained between 0.2–0.05 w/o of Fe, as revealed by electron microprobe analyses before and after the deposition, respectively. Analysis by electron microprobe of Nb deposits with high T_c failed to reveal any impurities (detection limit of about 0.01 w/o).

The superconducting transition temperature ranges, along with other relevant properties and preparative parameters of representative samples, are summarized in Table I.

Discussion

Anodic dissolution of niobium.—Anodic and cathodic polarization curves of niobium electrode in molten fluorides were described elsewhere (10). The anodic curve was nearly linear for current densities below about 5 A/cm^2 . The etch pits observed in Fig. 7(b) are believed to be due to an insufficient anodic current density pulse (110 mA/cm^2). This sample was prepared from a 6 m/o K_2NbF_7 solution in which the rate of the anodic dissolution was probably insufficient to reach a level of saturation and passivity. The dissolution was therefore of a discriminative etching nature. Such

pitting was not observed when higher anodic current densities were used. The samples shown in Fig. 9–10 were prepared with anodic current pulses of 375 mA/cm^2 . It is of interest to note in this context that the niobium anode of Fig. 12, which was used in the 80 m/o solution of K_2NbF_7 , was very smooth and shiny. Relatively low anodic current pulses were applied to this anode (75 mA/cm^2). However, grain boundaries and other features (dislocations?) related to preferred dissolution are clearly observed. The very concentrated solution is expected to enhance passivity due to saturation of anodic products. An insoluble salt film covered this anode when it was removed from the molten bath. When immersed in a dilute HCl solution, the film dissolved with a vigorous hydrogen liberation. It is believed that a lower niobium valence salt such as NbF (8) constituted the film. Hydrogen evolution was then a result of the reaction $\text{Nb(I)} + 4\text{H}^- = \text{Nb(V)} + 2\text{H}_2$. Anodic current densities in excess of 100 mA/cm^2 are believed to be essential for successful electro-polishing.

Effects of PR plating on the deposition rate.—The definition of the plating limiting current density (not to be confused with the diffusion-limited current) is not unambiguous. It is based on the surface roughening which is also a function of the deposit thickness. Thus, for a very thin deposit, very high current densities might be used without appreciable surface deterioration. On the other hand, for very thick coatings, much lower current densities may cause severe surface roughening. Ideally, the limiting current density should be determined only for well-defined surface roughness and thickness of the deposit. Many other parameters, such as substrate surface preparation and composition,

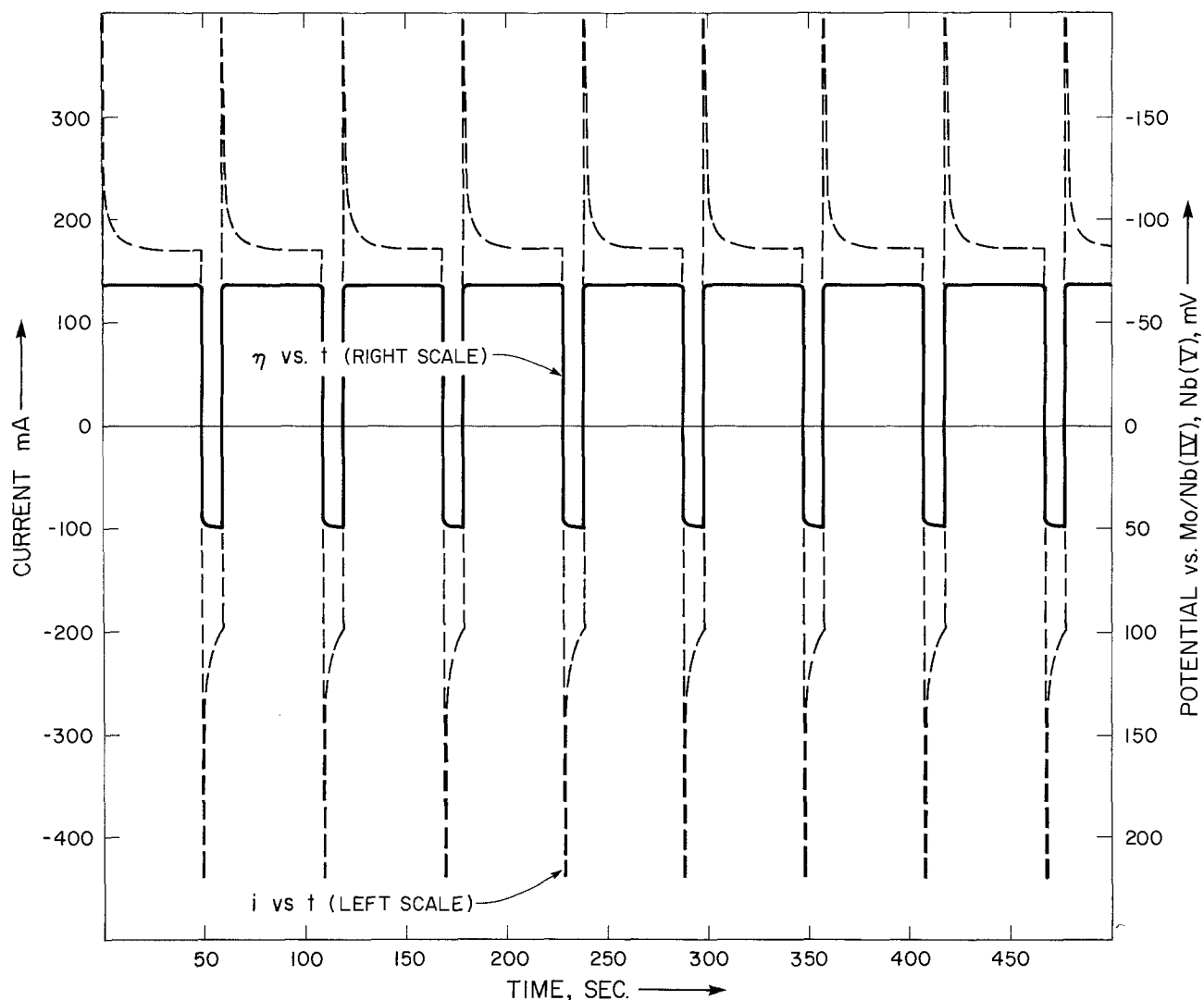


Fig. 5. PR-potential (PRP) for the deposition of Nb from 6 m/o K_2NbF_7 . $\eta_C = -70$ mV; $t_C = 50$ sec; $\eta_A = 50$ mV; $t_A = 10$ sec; $Q \cong 4.1$.

temperature, bath concentration and purity, and mechanical agitation may appreciably affect the deposit character and vary this definition, accordingly.

Senderoff and Mellors (1) reported a constant current density range of 5-125 mA/cm² for the electro-deposition of coherent niobium. However, they did not report some important parameters such as the mechanical agitation. In this work, under the stated operating variables, the limiting constant current density was found to be between 5-25 mA/cm². This definition is specified as follows: no mechanical agitation, copper strip substrate which was chemically polished in HNO₃/HF mixture (7:3), 750°C, and 6 m/o K_2NbF_7 in the KF-LiF solvent. A deposit thickness of at least 100 μ m, and the appearance of local macrodeterioration were used as criteria. Thus, Fig. 3 shows a stable growth at 5 mA/cm², whereas the onset of surface deterioration is observed in Fig. 4 of a sample which was grown at 25 mA/cm².

The effects of the PR variables were not comprehensively investigated. Several trends, however, were clearly observed. It was found that the most important parameter was the Q -ratio (defined by [2]). The closer was Q to unity, the better were the coherency and smoothness of the deposits. The PR-potential (PRP) method was found hard to control since the currents varied in time and, as a result, the Q -ratio varied too. It was found desirable to use anodic pulse amplitudes as high as possible to ensure electropolishing rather than electroetching. Anodic current densities of $i_A > 100$ mA/cm² were found essential for successful elec-

tropolishing. The pulse periods, t_C and t_A , were found to have influence on the Q -ratio mostly through their ratio t_C/t_A . Very long periods, $t_C \geq 1$ min, were found to be deleterious due to the formation of large protrusions which could not be completely removed by electropolishing. Frequencies from about 1 cycle per minute to about 1 cycle per second were investigated. The increase of the frequency showed some improvement in the brightness and coherency, but fast deterioration

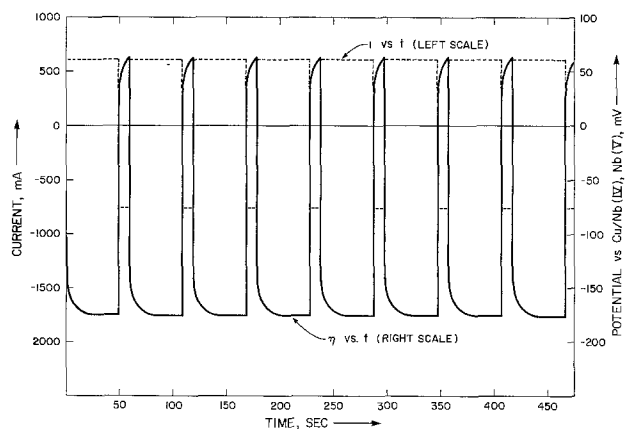


Fig. 6. PRC for the deposition of Nb from 6 m/o K_2NbF_7 . $i_C = 600$ mA (300 mA/cm²); $t_C = 50$ sec; $i_A = 750$ mA (375 mA/cm²); $t_A = 10$ sec; $Q = 4.0$.

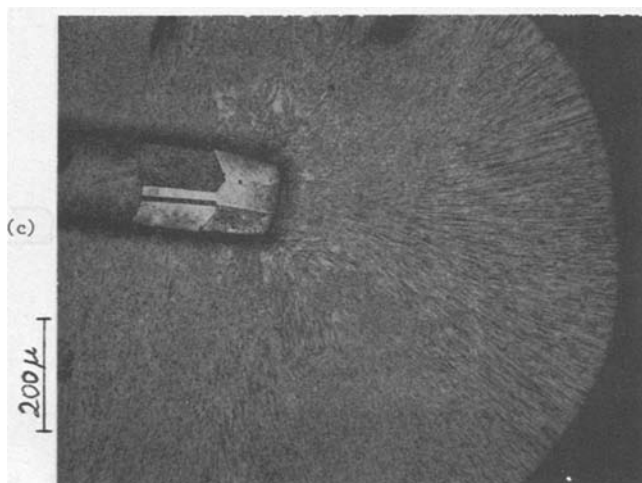
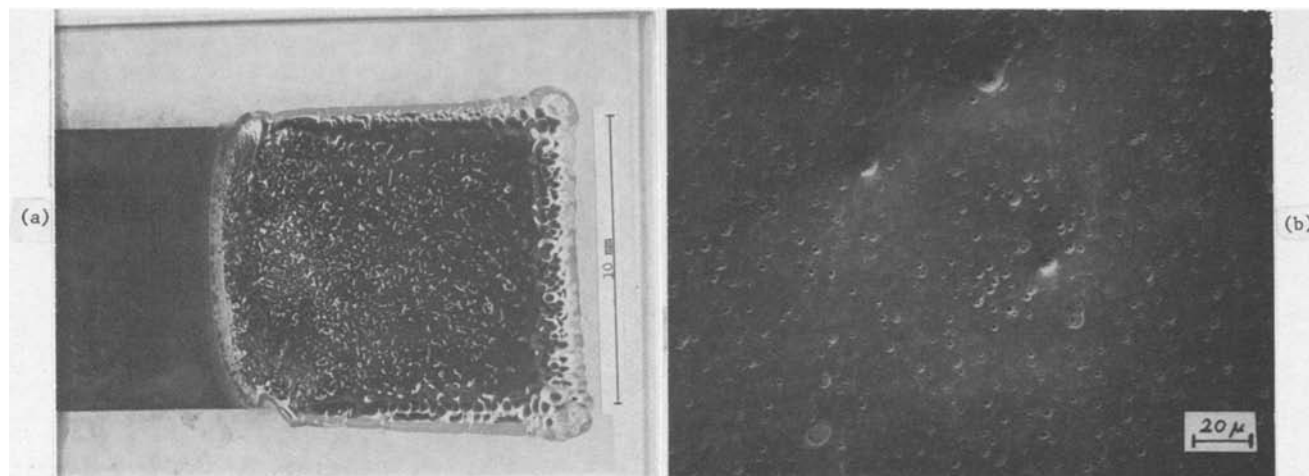


Fig. 7. Nb coating obtained with PRP steps. $\eta_C = -70$ mV; $t_C = 50$ sec; $\eta_A = 50$ mV; $t_A = 10$ sec; $Q \cong 4.1$; $i_C \sim 90$ mA/cm²; $i_A \sim 110$ mA/cm². (a) Full view, (b) SEM of surface, (c) vertical cross section.

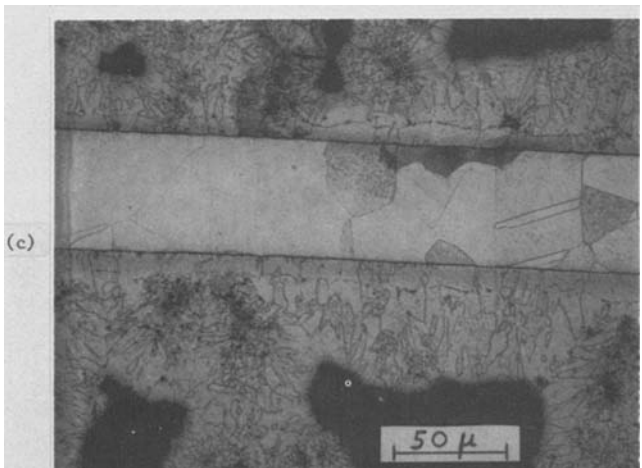
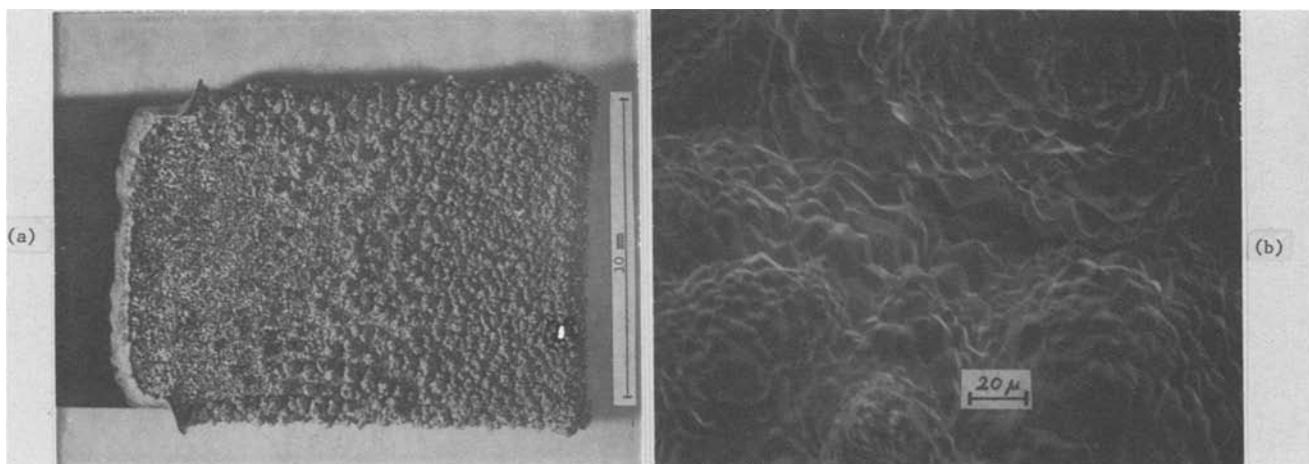


Fig. 8. Nb deposit obtained with PRP steps. $\eta_C = -155$ mV; $t_C = 50$ sec; $\eta_A = 5$ mV; $t_A = 10$ sec; $i_C \sim 280$ mA/cm²; $i_A \sim 180$ mA/cm²; $Q \cong 8.0$. (a) Full view, (b) SEM of surface, (c) vertical cross section.

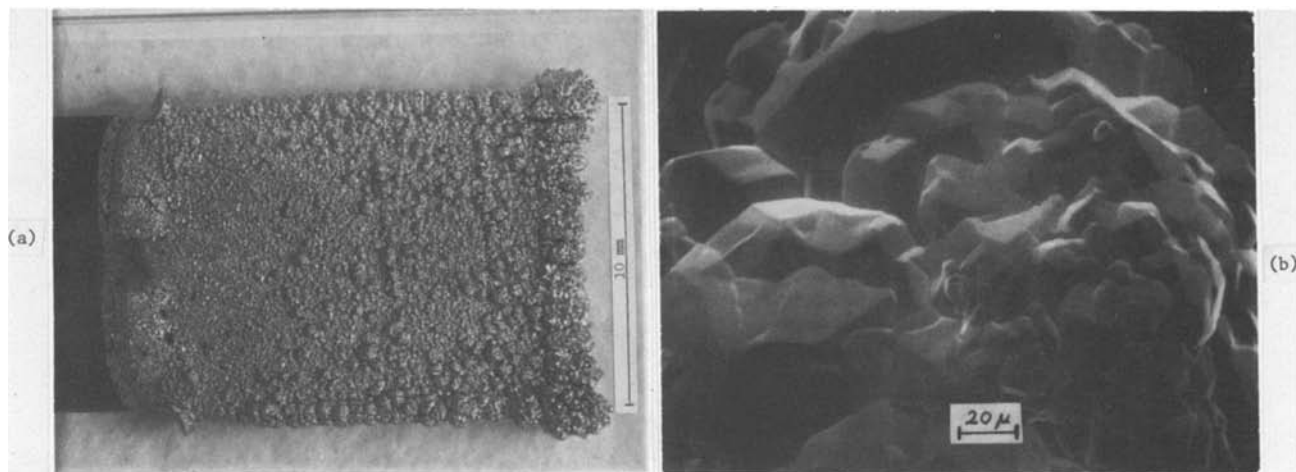


Fig. 9. Nb deposit obtained with PRC steps. $i_C = 300 \text{ mA/cm}^2$; $t_C = 50 \text{ sec}$; $i_A = 375 \text{ mA/cm}^2$; $t_A = 10 \text{ sec}$; $Q = 4.0$. (a) Full view, (b) SEM of surface, (c) vertical cross section.

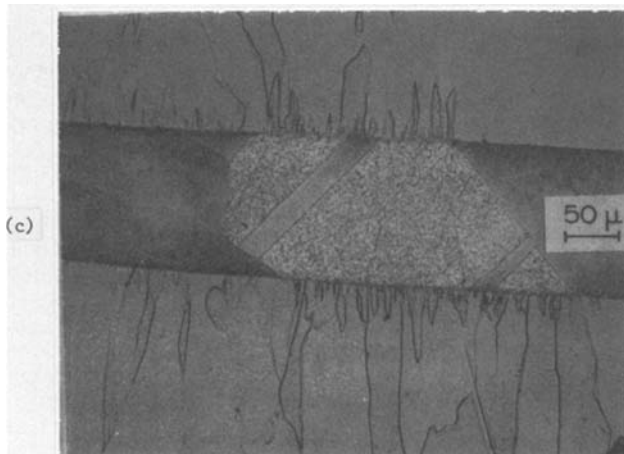
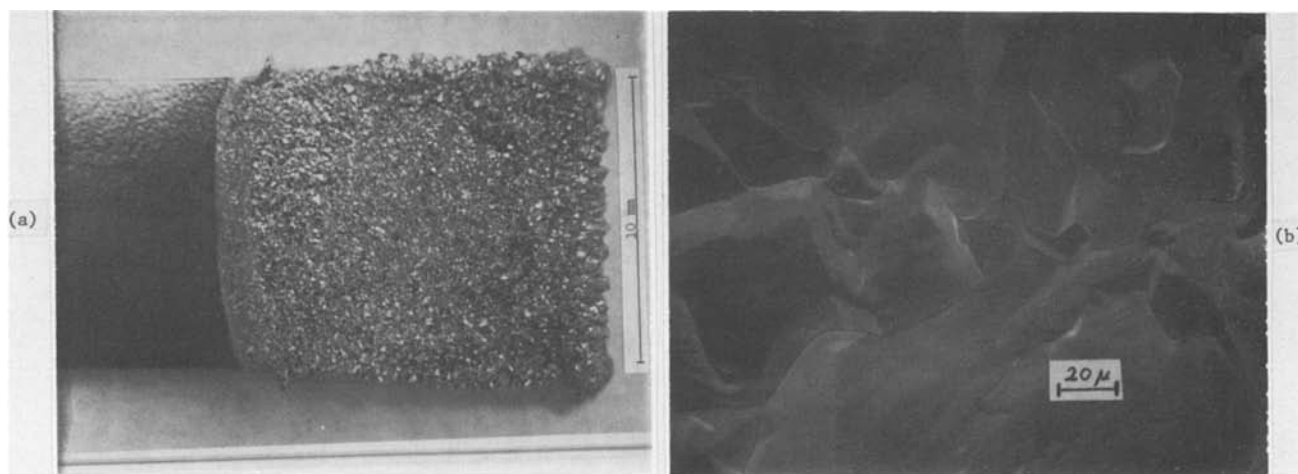


Fig. 10. Nb coating obtained with PRC steps. $i_C = 300 \text{ mA/cm}^2$; $t_C = 25 \text{ sec}$; $i_A = 375 \text{ mA/cm}^2$; $t_A = 10 \text{ sec}$; $Q = 2.0$. (a) Full view, (b) SEM of surface, (c) vertical cross section. Note the hetero-epitaxial relationship of the deposit to the substrate (Cu) grains.

Table I. Summary of Nb plating experiments

| K ₂ NbF ₇ conc. m/o | Subst. | Temp. (°C) | Electrical parameters | Coating thickness (μm) | Cathodic current efficiency (%) | *Preferred orientation XRD | T _c (K) | Comments |
|---|--------|------------|---|------------------------|---------------------------------|---|--------------------|---|
| 6 | Cu | 770 | d-c <i>i</i> _C = 3.3 mA/cm ² | ~40 | 60 | (110) — 76 (200) — 100 (211) — 18 | 7.9-8.4 | Pre-electrolysis run. See Fig. 2. |
| 6 | Mo | 751 | d-c <i>i</i> _C = 5.0 mA/cm ² | ~50 | 53 | (110) — 14 (200) — 100 (211) — 25 | — | Sample is shown in Fig. 3. |
| 6 | Cu | 755 | d-c <i>i</i> _C = 25 mA/cm ² | ~100 | 95 | (110) — 0 (200) — 100 (211) — 0.4 | 8.8-9.15 | Deteriorating interface growth. See Fig. 4. |
| 6 | Cu | 755 | PRP; <i>Q</i> ≅ 4.1 <i>η</i> _C = -70 mV; <i>t</i> _C = 50 sec <i>η</i> _A = +50 mV; <i>t</i> _A = 10 sec | ~500 | ~70 | (110) — 0 (200) — 100 (211) — 0 | 5.2-9.1 | See Fig. 7. Long superconducting transition tail. |
| 6 | Cu | 765 | PRP; <i>Q</i> ≅ 8.0 <i>η</i> _C = -159 mV; <i>t</i> _C = 50 sec <i>η</i> _A = +11 mV; <i>t</i> _A = 10 sec | ~675 | ~82 | (110) — 61 (200) — 17 (211) — 100 | — | Unstable growth. See Fig. 8. |
| 6 | Cu | 760 | PRC; <i>Q</i> = 4.0 <i>i</i> _C = 300 mA/cm ² ; <i>t</i> _C = 50 sec <i>i</i> _A = 375 mA/cm ² ; <i>t</i> _A = 10 sec | ~685 | 95 | (110) — 31 (200) — 5 (211) — 100 | — | Coating somewhat porous. See Fig. 9. |
| 6 | Cu | 760 | PRC; <i>Q</i> = 2.0 <i>i</i> _C = 300 mA/cm ² ; <i>t</i> _C = 25 sec <i>i</i> _A = 375 mA/cm ² ; <i>t</i> _A = 10 sec | ~660 | 91 | (110) — 63 (200) — 100 (211) — 19 | 8.3-9.1 | Excellent coating with large grain size. See Fig. 10. |
| 6 | Cu | 760 | PRC; <i>Q</i> = 2.0 <i>i</i> _C = 300 mA/cm ² ; <i>t</i> _C = 2.5 sec <i>i</i> _A = 375 mA/cm ² ; <i>t</i> _A = 1.0 sec | ~690 | 96 | (110) — 1 (200) — 100 (211) — 8 | — | Sample is not shown. |
| 80 | Cu | 740 | PRC; <i>Q</i> = 2.0 <i>i</i> _C = 50 mA/cm ² ; <i>t</i> _C = 10 sec <i>i</i> _A = 250 mA/cm ² ; <i>t</i> _A = 1 sec | ~60 | 19 | (110) — 95 (200) — 37 (211) — 100 | — | Sample is shown in Fig. 11 (a). |
| 80 | Mo | 745 | PRC; <i>Q</i> = 2.0 <i>i</i> _C = 50 mA/cm ² ; <i>t</i> _C = 10 sec <i>i</i> _A = 250 mA/cm ² ; <i>t</i> _A = 1 sec | ~104 | 25 | (110) — 66 (200) — 28 (211) — 100 | — | Sample is shown in Fig. 11 (b). |

* For a random Nb powder, the normalized diffraction intensities are $I_{(110)} = 100$; $I_{(200)} = 20$; $I_{(211)} = 30$.

at the edges (with higher local current density) was also observed. The diminution of the beneficial effects

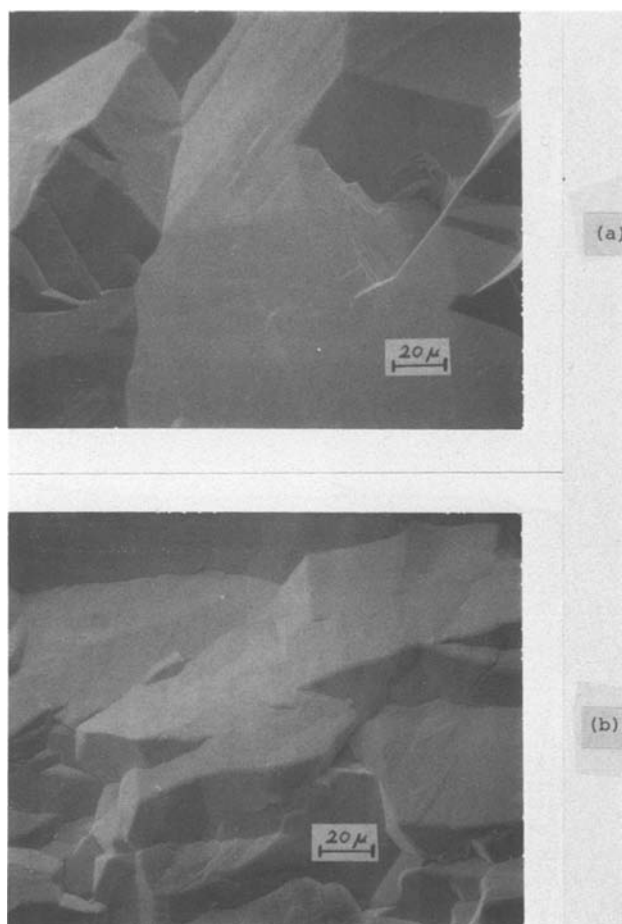


Fig. 11. SEM of Nb deposit surface. 80 m/o K₂NbF₇ solution; *i*_C = 50 mA/cm²; *t*_C = 10 sec; *i*_A = 250 mA/cm²; *t*_A = 1 sec; *Q* = 2.0. (a) Cu substrate, (b) Mo substrate.

of the PR technique with the increase of the frequency is believed to be due to the growing share of the non-faradaic currents (e.g., double layer charging) with the frequency increase. The current spikes of Fig. 5 are probably due to such currents. The net result is the lessening of the available current to remove the interface protrusions during the anodic pulses. It may be noted that the high values of these current spikes do not appear to adversely affect the deposit morphology. It is possible, however, that they facilitate nucleation and thus finer grain size. The best results were obtained with cycles of periods in the range of 3-50 sec.

With PRC plating, cathodic current densities of 300 mA/cm² (corresponding to an instantaneous growth rate of about 5 μm/min) were successfully achieved. The average current density is, of course, lower. For *i*_C = 300 mA/cm² and *Q* = 4.0, the average current density is 187.5 mA/cm². The latter is only 107.1 mA/cm² for *Q* = 2.0. The present study, which is only preliminary, already demonstrates that the application of the PR technique can facilitate increase of the useful plating rate by about an order of magnitude over the constant (d-c) current technique, under otherwise identical conditions.

Effects of concentration.—Low concentrations usually reduce the limiting current density. On the other hand, the increase of solute concentration (in the present system) raises the liquidus temperature so that higher operating temperatures are necessary. The higher temperatures cause coherence deterioration, probably due to the dissociation of the complex ionic species present (1), and higher volatility of the solute and rapid bath depletion. For the eutectic LiF-NaF-KF (Flinak) solvent, a limit of about 7.5 m/o K₂NbF₇ was cited (1). The system KF-K₂NbF₇ was found (37) to have low eutectics at 20 m/o K₂NbF₇ (723°C), and at 80 m/o (706°C). In this work, a solution of 80 m/o K₂NbF₇ in the "solvent" KF (10 m/o)-LiF (10 m/o) was found to freeze at 705° ± 5°C; the effect of substituting LiF for part of KF being very small. The very concentrated solution was found to offer no advantage for the electrodeposition of niobium. A lower electrodeposition rate, by at least a factor of 3 compared with the 6 m/o solution, was found. This is believed to



Fig. 12. Nb dissolving anode which was used in the 80 m/o K_2NbF_7 solution. $i_C = 375 \text{ mA/cm}^2$; $t_C = 1 \text{ sec}$; $i_A = 75 \text{ mA/cm}^2$; $t_A = 10 \text{ sec}$; $Q = 0.5$.

be due to a higher viscosity which lowers the ionic conductivity and diffusion rates. In addition, the highly concentrated solution had high vapor pressure of NbF_5 over the melt, resulting in excessive volatilization and bath depletion. The concentrated solution, however, may prove to be more useful for electropolishing of niobium.

Grain size control.—The columnar grains of the niobium deposits become more oriented and of smaller columnar diameter as the rate of plating is increased. Unexpectedly, it was found that, beyond a certain PR plating rate and appropriate Q -ratio, the columns become very large. This is demonstrated in the series of experiments shown in Fig. 2(b), 4(d), 7(c), and 10(c). These figures show vertical cross sections of samples which were grown at various cathodic currents and modes. A gradual decrease in the columnar diameter is seen through Fig. 2(b) (d-c plating at 3.3 mA/cm^2), 4(d) (d-c plating at 25 mA/cm^2), and 7(c) (PRP plating at 90 mA/cm^2). Figure 10(c) (PRC plating at 300 mA/cm^2), however, shows large columnar grains with an apparent heteroepitaxial correlation with the copper substrate grains. Such a correlation is not observed at the lower current densities.

It is believed that the anodic pulses, in addition to removing the solid interface protrusions, may also act to remove precursors defective solid material. Thus, adsorption of foreign species may gradually hinder the normal crystallization process, eventually leading to nucleation and growth of new grains. The periodic regression of the solid interface removes the blocking species at the interface along with the solid material. It thus yields fresh, adsorption-free, crystalline interface for the next growth cycle. Such mechanism may avoid secondary nucleation, and result in much larger grains. Other defects may similarly be avoided. Jackson and Miller (32), utilizing thermal cycles for remelting and regrowth, observed significant increase of grain size and improvement of crystal perfection. They forwarded a mechanism by which the slow-growing crystals (or grains) with low index plane parallel to the interface, are preferentially selected, yielding large grains with flat interface. They also reported the removal of inclusions and gas bubbles by the process. In addition to the above mechanisms, it is conceivable that the large amplitude current pulses applied in the PR technique, may cause additional convection mode in the liquid interface. This may significantly reduce the effective diffusion layer thickness, thereby eliminating much of the deleterious effects caused by concentration polarization. The simple method of controlling the columnar grain size may be of considerable practical significance. Mechanical properties as well as superconducting properties depend on the grain size.

A smaller grain size generally results in harder materials and, for superconductors, this means stronger magnetic flux pinning, and therefore larger critical current densities. The superconducting transition temperature, T_c , with no magnetic field applied, is not expected to be affected by the grain size (38). The latter was verified by the T_c measurements, as described above. Applications of niobium superconductors requiring high pinning capability along a certain direction may find the PR plating technique, with its easy grain control, very attractive.

Conclusions

The results of the present preliminary study indicate that electroplating with the PR technique is very beneficial to the increase of plating rate of coherent niobium. With no mechanical agitation, the rate could be increased by about an order of magnitude over d-c plating.

Beyond a certain rate, and under certain conditions of PR plating, the columnar grains of the Nb deposit become very large, revealing a clear heteroepitaxial correlation with the substrate grains.

The simplicity of the PR technique, and the already achieved high rate of deposition of Nb, combined with the high purity and quality of the coatings, may very likely find ready future applications in the production of superconducting and refractory metal coatings. The PR technique is also likely to be beneficial in the electrodeposition of other refractory metals such as Ta, Mo, W, V, Cr, and perhaps Zr from molten fluoride electrolytes.

Acknowledgments

The author wishes to express his gratitude to Professor W. A. Tiller for his comments, suggestions, and discussions. He is also indebted to Dr. K. A. Jackson for reviewing the manuscript and his many helpful comments. The technical assistance of R. Koch, L. J. Anderson, and Professor Geballe's Cryogenic Group, from Stanford-CMR, is gratefully acknowledged. This paper is based on the author's Ph.D. thesis [Ref. (10)]. The research was supported, in part, by the Center for Materials Research at Stanford University under the NSF-MRL Program.

Manuscript submitted June 25, 1979; revised manuscript received Sept. 2, 1980. This was Paper 147 presented at the Dallas, Texas, Meeting of the Society, Oct. 5-9, 1975.

Any discussion of this paper will appear in a Discussion Section to be published in the December 1981 JOURNAL. All discussions for the December 1981 Discussion Section should be submitted by Aug. 1, 1981.

REFERENCES

- G. W. Mellors and S. Senderoff, *This Journal*, **112**, 266 (1965).
- G. W. Mellors and S. Senderoff, *Can. Pat.* 688,546 (1964).
- S. Senderoff, G. W. Mellors, and W. J. Reinhart, *This Journal*, **112**, 840 (1965).
- G. W. Mellors and S. Senderoff, *ibid.*, **113**, 60 (1966).
- G. W. Mellors and S. Senderoff, *ibid.*, **114**, 586 (1967).
- G. W. Mellors and S. Senderoff, *Plating*, **51**, 972 (1964).
- S. Senderoff, *Met. Rev.*, **11**, 97 (1966).
- G. W. Mellors and S. Senderoff, *This Journal*, **113**, 66 (1966).
- G. W. Mellors and S. Senderoff, *ibid.*, **112**, 642 (1965).
- U. Cohen, Ph.D. Dissertation, Stanford University (1977).
- U. Cohen, Paper 346 presented at The Electrochemical Society Meeting, Pittsburgh, Pennsylvania, Oct. 15-20, 1978.
- N. C. Cook, J. D. Evans, and B. A. Fosnocht, in "Proc. Int. Conf. on Protection Against Corrosion by Metal Finishing," Basel (1966).
- Iu. Delimarskii and B. F. Markov, "The Electrochemistry of Fused Salts," Sigma Press, Wash-

- ington, D.C. (1961).
14. H. A. Laitinen, C. H. Liu, and W. S. Ferguson, *Anal. Chem.*, **30**, 1266 (1958).
 15. G. Torsi and G. Mamantov, *J. Electroanal. Chem. Interfacial Electrochem.*, **30**, 193 (1971).
 16. G. W. Jernstedt, *Proc. Am. Electroplating Soc.*, **36**, 63 (1949), and **37**, 151 (1950).
 17. G. W. Jernstedt *et al.*, U.S. Pat. 2,451,340 (1948); 2,451,341 (1948); 2,470,775 (1949); 2,524,912 (1950); 2,575,712 (1951); 2,636,850 (1953); 2,678,909 (1954).
 18. J. Teres, M.S. Thesis, Ohio State University (1950).
 19. N. W. Hovey, J. L. Griffin, and A. Krohn, *This Journal*, **102**, 470 (1955).
 20. G. T. Bakhvalov, *Izv. Vyssh. Uchebn. Zaved. Tsvetn. Metall.*, **3**, 136 (1958).
 21. P. M. Walker, N. E. Bentley, and L. E. Hall, *Trans. Inst. Metal. Finish.*, **32**, 349 (1955).
 22. N. A. Marchenko, I. N. Lekhovitskiy, and A. N. Buyanova, *Zhur. Priklad. Khim.*, **31**, 1511 (1958).
 23. A. M. Yampolsky, *Electroplating Metal Finishing*, **16** (3), 76 (1963).
 24. A. Hickling and H. P. Rothbaum, *Trans. Inst. Metal Finish.*, **34**, 53 (1957), and **34**, 119 (1957).
 25. G. A. Conn, *Plating*, **56** (9), 1038 (1969).
 26. G. W. Dini, *Metal Finish.*, **61** (7), 52 (1963).
 27. G. T. Bakhvalov, "New Technology of Electrodeposition of Metals," *Izd. Met.*, (in Russian) (1966).
 28. M. Ceresa, in "Electroplating Engineering Handbook," 3rd ed., A. K. Graham, Editor (1971).
 29. D. Rossi, *Galvanotechnics*, 793 (1953).
 30. V. I. Cherenko *et al.*, *Elektrokhimiya*, **4**, 519 (1968).
 31. A. R. Despic and K. I. Popov, in "Modern Aspects of Electrochemistry," Vol. 7, B. E. Conway and J. O'M. Bockris, Editors, Plenum Press (1972).
 32. K. A. Jackson and C. E. Miller, *J. Cryst. Growth*, **42**, 364 (1977).
 33. N. Ibl and K. Schadegg, *This Journal*, **114**, 54 (1967).
 34. A. R. Despic, J. W. Diggle, and J. O'M. Bockris, *ibid.*, **115**, 507 (1968), and **116**, 1503 (1969).
 35. U. Cohen, U.S. Pat. 3,983,012 (1976) and 4,142,947 (1979).
 36. S. F. Meyer *et al.*, "A Susceptibility Apparatus for Materials Research," To be published.
 37. A. Mukhtar and R. Winand, *Compt. Rendn.*, **260**, 3675 (1965).
 38. T. H. Geballe and M. R. Beasley, in "Energy and Materials," G. C. Libowitz and M. S. Wittingham, Editors, Academic Press (1976).

Electrodes for Alkaline Water Electrolysis

D. E. Hall*

Inco Research & Development Center, Incorporated, Sterling Forest, Suffern, New York 10901

ABSTRACT

Electrodes for alkaline water electrolysis have been made by applying high specific surface area coatings of nickel or nickel-iron alloy to steel or nickel substrates. The coatings are applied as polysilicate-based paints containing particles of the desired metals. The coating is sintered into a porous structure which is bonded firmly to the substrate. The present electrode preparation method has been used to coat a variety of substrate forms, such as flat plates or wire screens, and is compatible with commercial alkaline electrolysis equipment. The resulting electrodes were found to be particularly effective as anodes for oxygen evolution. The efficiency of the electrodes was greatly influenced by coating microstructure. This microstructure, in turn, could be controlled by adjusting the sintering conditions. Electrochemical operating characteristics of the electrodes in 30 w/o KOH at 80°C were determined. Comparable oxygen evolution efficiencies were obtained with coatings made from nickel powders, nickel flake, and nickel-iron alloy powder.

Hydrogen has been produced commercially by alkaline water electrolysis for many years. Recent indications are that significant improvements can be made in the electrolysis efficiency of practical cells (1). Thus, despite advances in other electrochemical hydrogen production methods (2), much research continues to be done in alkaline water electrolysis to improve efficiency and develop more durable cell materials (3).

There are several approaches to improving the efficiency of alkaline water electrolysis. Raising the electrolysis temperature, for example, lowers the voltage required to maintain a given cell current density (4). Improvements in cell design, separator structures, and materials, etc., will also contribute to better cell performance. Whatever advances are made, it will remain necessary to develop electrodes, compatible with the system design and operating conditions, which will give the lowest possible overpotentials. This can be achieved by two methods, which can sometimes be combined for maximum benefit. In the first, catalytically active materials such as NiCo_2O_4 (5) are applied to the electrode surface. The second method involves greatly increasing the electrode surface area (*i.e.*, its "roughness factor,"

defined as the ratio of its real surface area to its apparent, or geometric, area), thereby lowering the real current density and the associated activation overpotential.

Efficiency gains, as a rule, must be balanced against the additional capital cost incurred (6). For this reason, work continues to be done to minimize oxygen and hydrogen overpotentials on inexpensive electrode materials such as nickel (7) and nickel alloys (8, 9), which are the least expensive electrode materials currently known that can be used as both anodes and cathodes. These materials function most efficiently when fabricated as high surface area electrode forms.

Because the electrode structures used in commercial alkaline electrolyzers vary, it is desirable to have a method of increasing the surface area without regard to whether the electrode is a corrugated or flat plate, wire cloth, or a combination of these or other structures. This paper reports the development of such electrodes, in which a high surface area coating is applied to metal substrates, using a paint containing particulate nickel or nickel-iron alloys. Although nickel, nickel-iron alloy, and steel substrates have all been used to prepare electrodes, the present paper is concerned mainly with coatings on steel sheets and nickel screen.

* Electrochemical Society Active Member.

Key words: alkaline water electrolysis, electrodes.

The coated steel sheets are intended for use primarily in low temperature ($T \leq 80^\circ\text{C}$) electrolysis characteristic of today's commercial practice.

Experimental

Electrode coatings were prepared using polysilicate-based paints, in which the metal particles described below were suspended. The parent nickel powders, known commercially as Inco Type 123 and Inco Type 287, are high purity powders prepared by the thermal decomposition of nickel tetracarbonyl (10). These powders are referred to in this paper as "Ni 123" and "Ni 287," respectively. Their surfaces are highly spiky and angular. The specific surface area of Ni 123 is $\sim 0.4 \text{ m}^2/\text{g}$ and that of Ni 287 is $\sim 0.6 \text{ m}^2/\text{g}$. Using these values, a typical Ni 123 coating 50% dense and $100 \mu\text{m}$ thick would provide a maximum surface roughness factor of about 180 to a coated electrode. A nickel-iron alloy powder (37% Ni), similar in structure to Ni 123, and a nickel flake produced by ballmilling Ni 123 powder were also used.

The coatings were applied to flat panels of AISI 1008 steel which had been sandblasted to improve coating adhesion. The metal-containing paints were spread over the steel surfaces with drawbars; coating thickness was varied by using drawbars with different gauge wire wrappings. Coatings were also applied to nickel wire screen, an electrode form found in some commercial electrolysis units. The nickel screen was 20 mesh, with a wire diameter of 0.38 millimeters. Screens were immersed in the polysilicate paint and then shaken to remove any excess paint which filled the spaces between adjacent wires. Roller- and spray-coating of screens were also used.

The coatings were dried and then sintered in a cracked ammonia atmosphere at selected temperatures between 760° and 980°C for 5–60 min. Exact sintering conditions for particular electrodes are given in the text. Coating thicknesses were determined from photomicrographs of polished electrode cross sections. Coatings less than $\sim 125 \mu\text{m}$ thick were uniform; thicker coatings on the flat steel panels showed broad, shallow striations caused by the wire wrappings on the drawbars. The average thickness was used for analysis of the experimental results.

Electrodes were made from the coated steel panels and nickel screens by cutting them to appropriate size and tack-welding a nickel wire to each. The wire was insulated with epoxy resin. The back and edges of each coated steel panel were also coated, with epoxy lapped over the front (coated) side of the panel to prevent direct contact of the uncoated steel with the electrolyte solution during electrochemical experiments. The geometric areas of finished electrodes were typically $3\text{--}7 \text{ cm}^2$.

The structures of the electrode coatings were examined using photomicrographs of polished electrode cross sections. In addition, the coating surface structure and the morphologies of individual coating particles were characterized by scanning electron microscopy.

Electrochemical measurements.—The electrochemical cell used for current *vs.* potential measurements was a straight-walled cylindrical polypropylene beaker with a Teflon cover machined to fit. The cell, containing 30 weight percent (w/o) KOH electrolyte, was immersed in a water bath which maintained the cell temperature at $80^\circ \pm 0.5^\circ\text{C}$. A large planar nickel counterelectrode was positioned facing the working electrode, at a distance of about 3 cm from it. A saturated calomel electrode (SCE) was used as the reference electrode. The SCE was inserted into a Luggin probe, the tip of which was positioned at the center of the working electrode. Overpotentials were determined from current *vs.* potential data using the reversible hydrogen electrode potential *vs.* SCE in 30 w/o KOH at 80°C (9) and the theoretical water electrolysis voltage at 80°C (11).

The experimental current density *vs.* overpotential data were then corrected for the effects of ohmic resistance using a computer method developed by LeRoy *et al.* (12). The Tafel slopes and exchange current densities reported below are based on the resistance-corrected data. The overpotential corrections produced by the program were typically 10–20 mV at current densities of 200 mA cm^{-2} .

Current density *vs.* electrode potential measurements were made galvanostatically. A constant current density of 200 mA cm^{-2} was imposed on each electrode for ~ 6 hr. At roughly 1 hr intervals, electrode potentials were measured at several current densities from 600 to 0.5 mA cm^{-2} in descending order. The last set of measurements from each electrode was used for the data analysis given in this paper. Potentiostatic measurements of $\log i$ *vs.* E were also made for several 2.0 cm^2 electrodes, in slow potential-sweep experiments. Because of the similarities of results from the galvanostatic and potentiostatic experiments, only the former are discussed here.

Results

Nickel and Nickel-Iron Alloy Anode Coatings

Coating structure.—The coatings prepared from Ni 123, Ni 287, and nickel-iron alloy powders consist of porous networks with unit particle diameters characteristic of the powders used to make them. Figure 1a shows the surface structure of a typical coating on a mild steel sheet. The cross section of this coating, shown in Fig. 1b, indicates that the structure is quite uniform from the base of the coating to its surface. Porosity pockets with diameters several times larger than the particles themselves are spread evenly through the coatings.

Nickel flake coatings, applied to mild steel panels, have a laminar structure in which the flakes and the porous channels between them are preferentially oriented parallel to the steel base. This structure is shown in Fig. 1c.

Electrochemical characteristics.—Overpotentials for oxygen evolution (η_{O_2}) at the high surface area nickel anode coatings on steel sheets are less than or equal to those at nickel anode forms such as nickel-plated steel (13), nickel cloth, and nickel sinter (7). Typical current density *vs.* overpotential data for the oxygen evolution reaction (OER) at two types of nickel powder-coated steel electrodes are plotted in Fig. 2. Tafel slopes of η_{O_2} *vs.* $\log i$ plots were generally 30–40 mV/decade for the electrodes studied in this work; slopes greater than 40 mV/decade were, however, obtained at some electrode coatings sintered at the higher end of the $760^\circ\text{--}980^\circ\text{C}$ temperature range used. The average slope of ~ 35 mV/decade is considerably lower than Lu and Srinivasan's value of 62 mV/decade at smooth nickel electrodes tested under identical conditions (14).

The efficiency of nickel screen anodes was also improved significantly by the nickel powder coatings. For example, a coating $\sim 40 \mu\text{m}$ thick was sintered onto nickel screen at 760°C for 30 min. The oxygen evolution overpotentials at current densities of 100 and 200 mA cm^{-2} were about 80 mV lower than on uncoated nickel screen anodes.

Nickel flake coatings, sintered at 760°C for 60 min onto mild steel sheets had a laminar structure, as described above and shown in Fig. 1c. Despite this preferred orientation of pore channels perpendicular to the direction of electrolyte penetration and gas evolution, the nickel flake anode coating performed well. The Tafel slope was 33 mV/decade and overpotentials were comparable to those obtained at Ni 123 (Table I) and Ni 287 powder coatings.

Nickel-iron alloy anode coatings on mild steel sheets, sintered at 760°C for 60 min, had current density *vs.* overpotential characteristics which were nearly equal

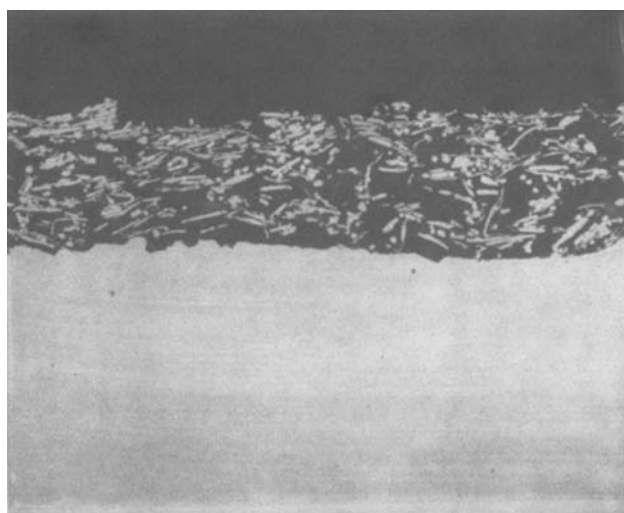
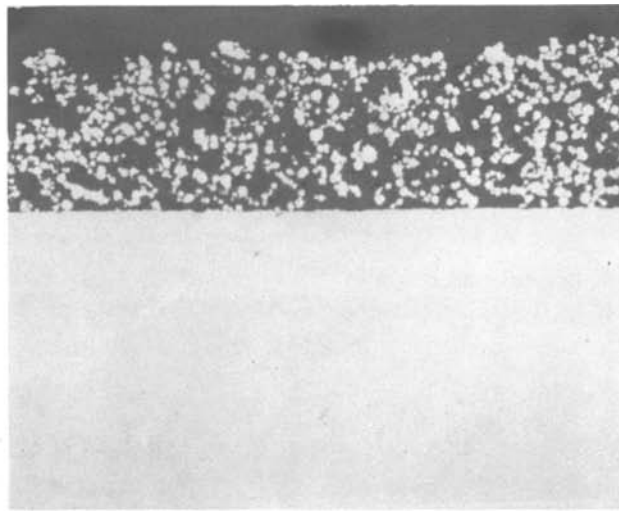
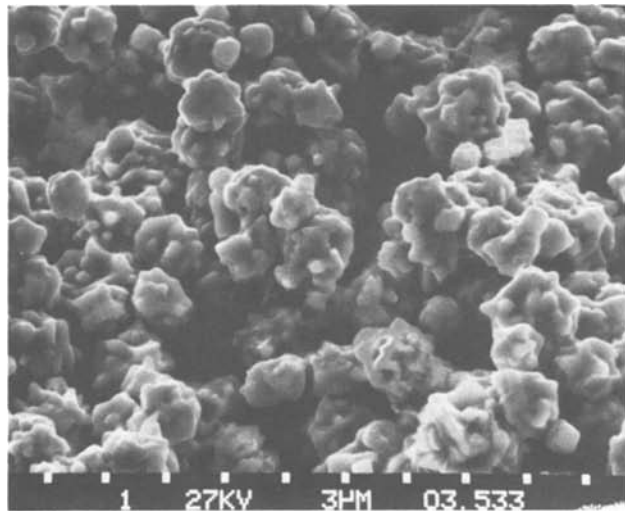


Fig. 1. (a, top left) Ni 123 coating on mild steel, sintered at 760°C for 60 min (Fischer subsieve of Ni 123 powder = 3-7 μm) 3000 \times ; (b, top right) cross section of same coating, 300 \times ; (c, bottom left) cross section of Ni flake coating, 300 \times .

to those obtained with similar Ni 123 coatings, as shown in Table I.

Effect of sintering conditions on coating microstructure and anode efficiency.—The sintering conditions of the electrode coatings, as expected, were found to have a significant effect on their oxygen evolution efficiencies and microstructures. The overall structure of the porous network, shown in Fig. 1a and 1b, is not greatly changed over a broad range of sintering times and temperatures. However, the coating microstructure, i.e., the morphology of the individual particles which

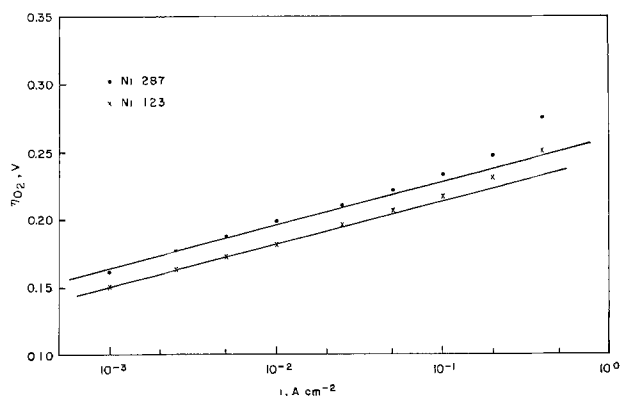


Fig. 2. Current density vs. overpotential for oxygen evolution in 30 w/o KOH at 80°C. Ni 123 anode coating: 85 μm thick, sintered at 870°C for 10 min. Ni 287 anode coating: 85 μm thick, sintered at 760°C for 60 min.

make up the coating network, is sensitive to sintering conditions. At low sintering temperatures, much of the particle morphology is preserved; however, as one would expect, as the sintering temperature is raised or the sintering time is increased, the particle surfaces tend to spheroidize and the contact areas between adjacent particles increase. The result is a reduction in electrode surface area. This can be seen by comparing the coating structures in Fig. 3.

To determine the effects of coating microstructure on the efficiency of oxygen evolution, nine Ni 123 electrode coatings on mild steel panels were prepared as described in Table II. Coatings were all applied using the same drawbar; the average thickness was $\sim 60 \mu\text{m}$. After sintering and prior to electrode fabrication, a portion of each coating was tested for adhesion with a simple tape test, in which cellophane tape was applied firmly to the coating and then pulled away. Coatings 5-9 successfully resisted the test, but succes-

Table I. Fe-37Ni alloy, Ni flake, and Ni 123 anode coatings. Comparison of current density vs. potential characteristics. All coatings sintered at 760°C for 60 min

| Electrode composition | Coating thickness, μm | η_{O_2} (V) at (mA cm $^{-2}$) | | | | |
|-----------------------|----------------------------------|---|------|------|------|------|
| | | 1 | 10 | 100 | 200 | 400 |
| Fe-37Ni | 38 | 0.17 | 0.20 | 0.24 | 0.25 | 0.26 |
| Fe-37Ni | 58 | 0.16 | 0.20 | 0.23 | 0.24 | 0.25 |
| Fe-37Ni | 107 | 0.16 | 0.19 | 0.23 | 0.24 | 0.25 |
| Ni 123 | 36 | 0.16 | 0.19 | 0.22 | 0.23 | 0.24 |
| Ni 123 | 64 | 0.16 | 0.19 | 0.23 | 0.24 | 0.25 |
| Ni 123 | 112 | 0.14 | 0.18 | 0.21 | 0.22 | 0.23 |
| Ni flake | 84 | 0.16 | 0.19 | 0.22 | 0.23 | 0.24 |

Table II. Sintering conditions of Ni 123 electrode coatings on mild steel sheets used to determine the effect of coating microstructure on electrocatalytic efficiency

| Electrode | Temp, °C | Time, min | Microstructure (by SEM) |
|-----------|----------|-----------|--|
| 1 | 760 | 5 | Most of Ni 123 structure preserved. Some rounding of surface spikes. |
| 2 | 760 | 10 | |
| 3 | 760 | 30 | Substantial rounding of spikes. |
| 4 | 870 | 5 | Spikes lost, but particles are still angular. |
| 5 | 870 | 10 | |
| 6 | 870 | 30 | Ni 123 structure lost. Particles are rounded, indistinct; interparticle contact areas are large. |
| 7 | 980 | 5 | |
| 8 | 980 | 10 | |
| 9 | 980 | 30 | |

sively increasing amounts of nickel powder were removed from coatings 4 (minimal) through 1 (substantial). Because the relationship of this test to the mechanical stability requirements for practical electrolyzer anodes was not known, all coatings were used as anodes. A clear relationship between coating microstructure and overpotential at a constant current density was obtained (Fig. 4). Increasing the temperature and/or time of the sintering operation, *i.e.*, reducing the effective anode surface area, caused a greater than 70 mV overpotential increase at 200 mA cm⁻² and an associated increase in Tafel slope between coatings 2 and 9. Anode 1 was an exception; it was mechanically unstable under conditions of vigorous oxygen evolution. Thus some coating material was lost, causing a reduction in surface area and a consequent increase in overpotential.

Effect of coating thickness on anode efficiency.—The porous, open structure of the nickel coatings suggests the likelihood that the interior surfaces of the anode coatings catalyze the oxygen evolution reaction to some extent. This was investigated using Ni 123 and Ni 287 coatings covering a wide range of thicknesses. The coatings were prepared on mild steel panels using identical sintering conditions (760°C, 60 min). Despite some fluctuations in the data, Fig. 5A shows that an increase in Ni 123 coating thickness from 23 to 150 μm causes some reduction in η_{O₂} at a given current density. For Ni 287 coatings (Fig. 5B), the change in η_{O₂} with thickness is somewhat smaller.

An increase in coating thickness also causes an increase in the exchange current density. At the Ni 123 coated anodes described in Fig. 5A, for example, *i*₀ ranged from 2.8 × 10⁻⁸ A cm⁻² at the 23 μm thick coating to 1.9 × 10⁻⁷ A cm⁻² at the 150 μm thick coating. The data from these experiments were compared to the behavior expected assuming that the entire coating thickness had equal electrocatalytic activity, which was determined as follows.

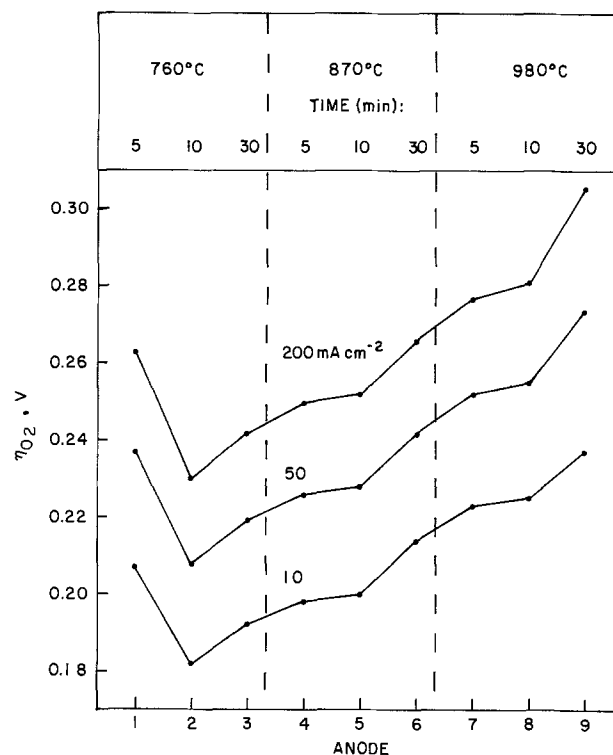
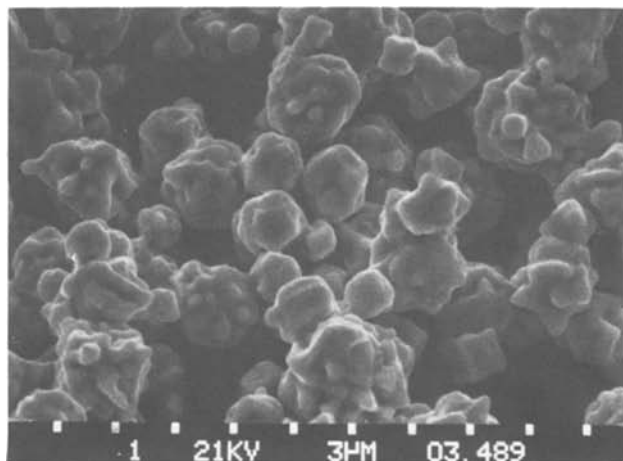


Fig. 4. η_{O₂} at selected current densities, for Ni 123 coatings on mild steel (from Table II). Effect of coating microstructure changes caused by variation of sintering conditions.

If the entire microstructural surface of the coating catalyzes the OER with equal effectiveness, the effective surface area of the electrode, *A*_{eff}, is proportional to the coating thickness. The exchange current density per unit effective surface area is a constant, characteristic of the electrode material and the reaction which takes place. Thus, the experimentally measured exchange current will be proportional to coating thickness (*x*)

$$i_0 = Mx + B \quad [1]$$

M is the slope of a plot of exchange current density *vs.* coating thickness. The *B* term includes exchange current on accessible portions of the substrate surface (if any) and on the extra microstructural area available in the top layer of sintered particles; at large *x* (compared to the surface roughness of the substrate and the coating unit particle diameter), *B* should be much less than *Mx*.

Under conditions of net current flow, the Tafel relationship $\eta = a + b \log i$ obtains. Strictly, the current density in this equation is based on effective surface area, and thus $\eta \propto \log (I/A_{\text{eff}})$, where *I* is the total

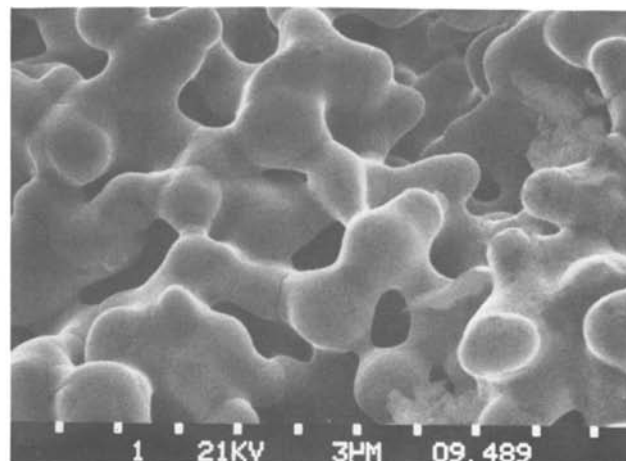


Fig. 3. Ni 123 coatings on mild steel, sintered for 30 min at (a, left) 760°C and (b, right) 980°C. 3000×

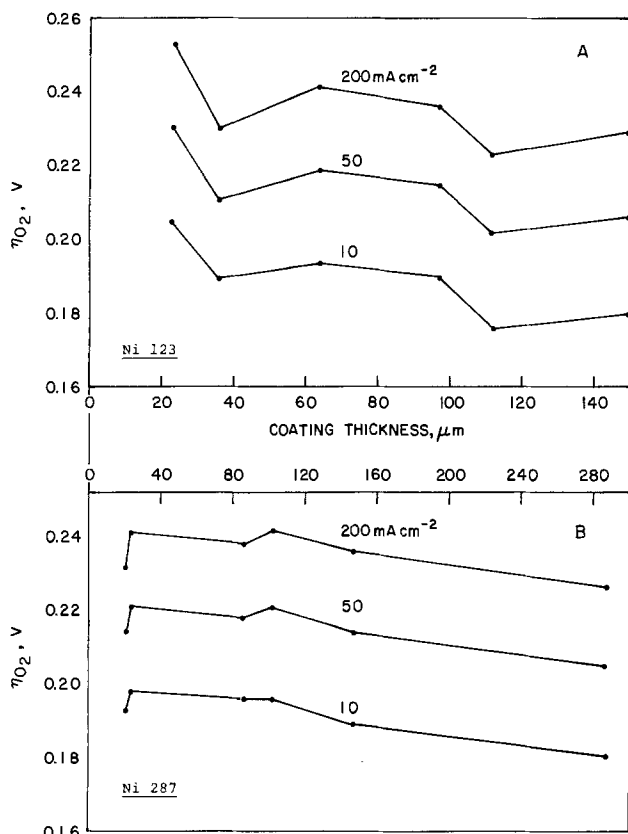


Fig. 5. η_{O_2} at selected current densities: effect of coating thickness. All coatings sintered at 760°C for 60 min. (A) Ni 123 coatings on mild steel sheets, (B) Ni 287 coatings on mild steel sheets.

current. A_{eff} is proportional to coating thickness, and thus

$$\eta_{O_2} = C - D \log x \quad [2]$$

where D is the slope of a plot of η_{O_2} vs. $-\log x$, and C is a constant. This equation, like Eq. [1], will be valid for coating thicknesses greater than several unit particle diameters.

Regression fits of experimental data from the anodes of Fig. 5 to Eq. [1] and [2] were used to determine how effectively the coating interiors were utilized. For Eq. [1], the "goodness-of-fit" (F value) indicated that the regressions were significant at the 99% level for both Ni 123- and Ni 287-coated anodes. At Ni 123-coated anodes, an increase of $10 \mu\text{m}$ in the coating thickness produced an average $1.4 \times 10^{-8} \text{ A cm}^{-2}$ increase in i_0 (Fig. 6); for Ni 287 anode coatings, the corresponding i_0 increase was smaller, about $3.5 \times 10^{-9} \text{ A cm}^{-2}$.

It is interesting to compare the above results with data from Appleby *et al.*, who found [Fig. 7 of Ref. (7)] that i_0 at 90°C was ~ 55 times higher on a $150 \mu\text{m}$ thick sintered nickel plaque than on a smooth nickel surface. Using the i_0 value at smooth nickel obtained by those authors ($\sim 7 \times 10^{-10} \text{ A cm}^{-2}$), this increase is then about $3.8 \times 10^{-8} \text{ A cm}^{-2}$, or roughly $2.6 \times 10^{-9} \text{ A cm}^{-2}$ for each $10 \mu\text{m}$ of sintered nickel thickness. This value is comparable to that reported above for Ni 287 coatings.

The nickel sinter used by Appleby *et al.* had an available electrode surface area, according to BET measurements, of 140 cm^2 per square centimeter of the sintered plaque. If all of this area were electrochemically active, one would expect the exchange current density measured on the plaque to be 140 times higher than on the smooth nickel electrode. It is noteworthy that this is nearly three times higher than the ~ 55 -fold increase in i_0 actually obtained, indicating that the BET surface area may substantially overestimate the

effective surface area of a particular electrode with a high roughness factor. This would, of course, be expected under conditions of copious gas evolution, resulting in areas where electrode-electrolyte contact is lost. However, it is apparently also true when gas blockage is not a major consideration, i.e., when the current density is low: the linear region of the Tafel plot extrapolated to obtain the i_0 value at the sintered nickel plaque anode extended from $10^{-2} \text{ A cm}^{-2}$ down to almost $10^{-6} \text{ A cm}^{-2}$ [Fig. 6 of Ref. (7)].

Overpotentials at 200 mA cm^{-2} were used in Eq. [2], to assess coating interior participation in the oxygen evolution reaction during copious gas formation. Goodness-of-fit was less satisfactory than with Eq. [1]; correlation of Ni 287 coating data with Eq. [2] was poor. For Ni 123 coatings, the regression was significant at about the 90% level; the coefficient D was 24 mV/decade . If the entire coating microstructure participated equally in the oxygen evolution reaction, the expected decrease in η_{O_2} would be equal to the Tafel slope at Ni 123 anode coatings, or $\sim 35 \text{ mV/decade}$. Thus, there is probably some pore blockage by evolved gas, which increases the observed overpotential by reducing the active anode surface area and increasing the resistance loss within the coating pores. This problem is apparently more severe with the Ni 287 coatings examined, and may be due to the chainlike structure of Ni 287 powder, although this was not evident from SEM photomicrographs of the coatings.

Nickel Powder Cathode Coatings

The electrochemical behavior of nickel cathode coatings on mild steel sheets was interpreted using criteria similar to those applied to anodes in the preceding sections. At normal operating current densities (200 mA cm^{-2}), cathode overpotentials were $0.1\text{--}0.2\text{V}$ higher than corresponding anode overpotentials for the same coatings. Tafel slopes on Ni 123 cathode coatings were $130\text{--}175 \text{ mV/decade}$, while i_0 varied from 1.6×10^{-4} to $3.4 \times 10^{-4} \text{ A cm}^{-2}$. On Ni 287 coatings, Tafel slopes ranged from 134 to 167 mV/decade , with most between $134\text{--}144 \text{ mV/decade}$. The exchange current density varied from 8.8×10^{-5} to $4.2 \times 10^{-4} \text{ A cm}^{-2}$. The higher exchange current densities are com-

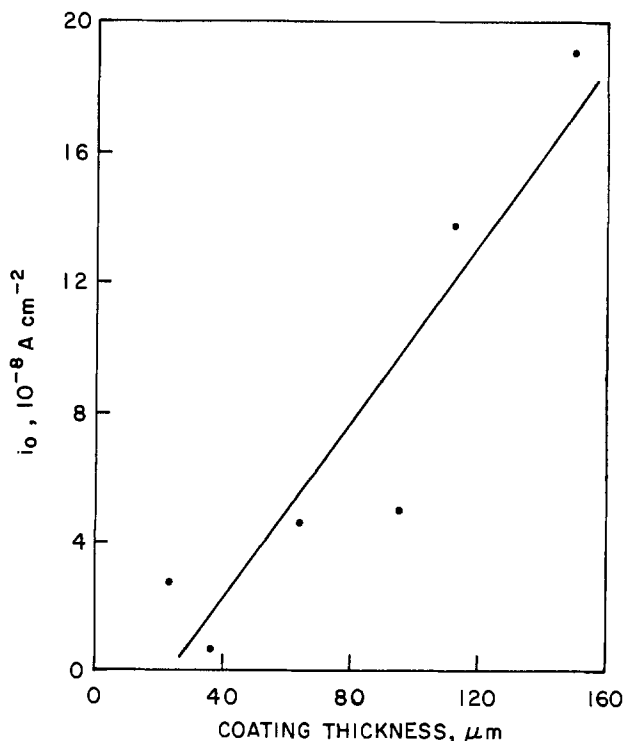


Fig. 6. Exchange current densities vs. thickness of Ni 123 coatings on mild steel. Points: experimental. Line: best fit of Eq. [1].

parable to those observed by Appleby *et al.* (7) on screen-reinforced sintered nickel under similar conditions. However, the hydrogen evolution overpotentials at higher current densities reported by those authors are significantly lower (by >70 mV at 10 mA cm^{-2}) than observed on high surface nickel coatings in the present work. The explanation for this behavior may lie in the fact that gas may exit only from the front face of the coatings on steel sheets rather than from both faces in the case of porous sintered nickel. This should be relatively more important in H_2 evolution than in O_2 evolution, due to the twofold difference in gas volume produced at equal current densities. However, when Ni 123 coatings were applied to Ni cathode screens, no significant overpotential reduction was obtained.

There is a trend toward higher overpotentials at coatings with reduced microstructural surface area, caused by more severe sintering conditions, as shown in Fig. 7. However, this trend did not include the most highly sintered cathode (No. 9), which showed an unexpected decrease in η_{H_2} . No explanation for this behavior was evident from photomicrographs of the coatings. It is possible that this increase in efficiency at the nickel coating with the smoothest surface morphology is a result of easier gas release from coating pores; the fact that similar behavior was not observed for O_2 evolution may be due to the smaller size of evolving H_2 gas bubbles. It is also noteworthy that coating No. 1 failed in anodic operation but not as a cathode. This indicates that cavitation forces which may rupture the sintered coating structure may be more dependent on gas bubble size (larger for O_2) than on total gas volume (larger for H_2).

Appleby and co-workers (7) suggested that the interior of screen-reinforced sintered nickel was largely accessible for the hydrogen evolution reaction, as a

consequence of the small bubble size of evolved H_2 . Using the technique applied above to anode coatings, the electrochemical activity of the inner surfaces of Ni 287 cathode coatings was investigated as part of the present work. A regression analysis of the hydrogen evolution data for Ni 287 coatings from ~ 20 to 290 μm thick showed that each 10 μm increase in coating thickness produced a 1.1×10^{-5} A cm^{-2} increase in i_0 . For one decade of increase in coating thickness, η_{H_2} at 200 mA cm^{-2} was reduced by 55 mV. This is less than half of the overpotential reduction expected if the entire surface of the coating were catalyzing the reaction equally. Similarly, Appleby *et al.* (7) point out that the apparent exchange current density for the hydrogen evolution reaction at their sintered nickel electrode was only 30 times higher than at smooth nickel. This is substantially below its roughness factor of 140, as measured by the BET technique.

Discussion

The electrodes described in the present paper are prepared by applying particulate metal coatings to metal substrates. The use of a paint-like suspension of the metal particles makes it possible to achieve uniform coatings of controlled thickness using a variety of coating techniques. This electrode fabrication method, which appears to be well suited for preparing anodes for alkaline water electrolysis, has two main advantages: (i) the coating technique can be used to add considerable surface roughness to existing electrode structures of many kinds; (ii) the materials and procedures used to prepare the electrodes are relatively inexpensive. Both of these factors are in keeping with the capital cost restraints on commercial alkaline electrolysis equipment.

The efficiencies of the coated electrodes and their microstructures, can be varied significantly by changing the coating preparation conditions. The interior surfaces of both anode and cathode coatings participate in the electrode reactions to some extent; thus, overpotentials can be reduced by increasing the electrode coating thickness. However, the use of thick anode coatings to improve electrolysis efficiency is of doubtful value on economic grounds, since the overpotential reduction obtained is small. This would be true even under ideal conditions, in which the overpotential reduction for a tenfold increase in coating thickness is given by the Tafel slope, which is only ~ 35 mV, as shown earlier.

Although the electrode structure developed in the present work is less suitable for hydrogen evolution than for oxygen evolution, the cathode overpotential reduction with increased coating thickness is larger. This is not due to the more effective utilization of the electrode coating interior for hydrogen evolution than for oxygen evolution, but is rather a consequence of the difference in Tafel slopes for the two processes.

The optimum electrode coating microstructure, for any given cell and set of operating conditions, is that which gives adequate strength and stability while maintaining the highest possible surface roughness factor. The present work indicates that different coating strengths are necessary, depending on whether the coated electrodes are used as anodes or cathodes. The efficiency improvements which can result from choosing proper sintering conditions are large enough to be significant. In addition, sintering no more than necessary for adequate mechanical integrity of the coating minimizes sintering costs.

The use of steel substrates with porous coatings as anodes in alkaline electrolysis raises questions regarding their durability, since unprotected mild steel corrodes rapidly under anodic service. None of the electrodes used in this work showed evidence of corrosive failure in six-hour electrolyses. A report of the operating characteristics and corrosion resistance of nickel

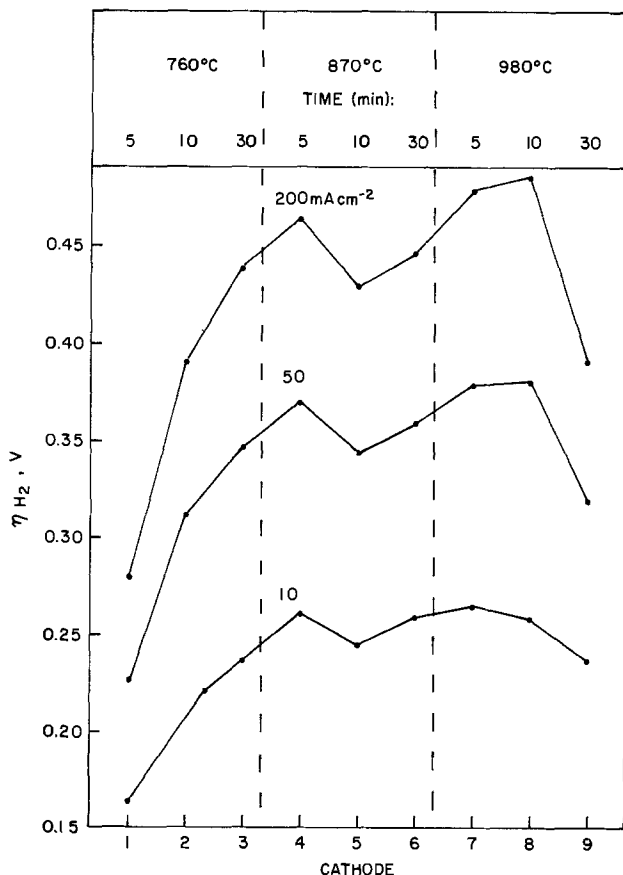


Fig. 7. η_{H_2} at selected current densities, for Ni 123 coatings on mild steel (from Table II). Effect of coating microstructure changes caused by variation of sintering conditions.

powder-coated mild steel-based anodes in 1200 hr tests will be made in a future publication.

Acknowledgments

Electrode coatings were prepared by W. A. Petersen and J. A. Travis. Their cooperation in this work is gratefully acknowledged. Electrode polarization data were obtained with the skillful assistance of A. M. Rapun. Permission to publish this work was granted by MPD Technology, Incorporated of Wyckoff, New Jersey, holders of commercial rights to the electrodes described in this paper.

Manuscript submitted July 14, 1980; revised manuscript received ca. Nov. 20, 1980.

Any discussion of this paper will appear in a Discussion Section to be published in the December 1981 JOURNAL. All discussions for the December 1981 Discussion Section should be submitted by Aug. 1, 1981.

Publication costs of this article were assisted by Inco Research & Development Center, Incorporated.

REFERENCES

1. A. J. Appleby and G. Crépy, in "Electrode Materials and Processes for Energy Conversion and Storage," J. D. E. McIntyre, S. Srinivasan, and F. G. Will, Editors, p. 382, The Electrochemical Society Softbound Proceedings Series, Princeton, N.J. (1977).
2. J. H. Russell, in "Industrial Water Electrolysis," S. Srinivasan, F. J. Salzano, and A. R. Landgrebe, Editors, p. 77, The Electrochemical Society Softbound Proceedings Series, Princeton, N.J. (1978).
3. A. J. Smith and J. D. Hatfield, *ibid.*, p. 143.
4. M. H. Miles, G. Kissel, P. W. T. Lu, and S. Srinivasan, *This Journal*, **123**, 332 (1976).
5. A. C. C. Tseung and S. Jasem, *Electrochim. Acta*, **22**, 31 (1977).
6. D. P. Gregory, K. F. Blurton, and N. P. Biederman, in "Industrial Water Electrolysis," S. Srinivasan, F. J. Salzano, and A. R. Landgrebe, Editors, p. 54, The Electrochemical Society Softbound Proceedings Series, Princeton, N.J. (1978).
7. A. J. Appleby, G. Crépy, and J. Jacquelin, *Int. J. Hydrogen Energy*, **3**, 21 (1978).
8. J. M. Gras and M. Pernot, in "Electrode Materials and Processes for Energy Conversion and Storage," J. D. E. McIntyre, S. Srinivasan, and F. G. Will, Editors, p. 425, The Electrochemical Society Softbound Proceedings Series, Princeton, N.J. (1977).
9. M. H. Miles, *Electroanal. Chem. Interfacial Electrochem.*, **60**, 89 (1975).
10. "Inco Nickel Powders: Properties and Uses," The International Nickel Company, Inc. (1975).
11. F. J. Salzano, Editor, "Hydrogen Storage and Production in Utility Systems," 3rd Quarter Progress Report, Brookhaven National Laboratory, (BNL 19520), October 1974.
12. R. L. LeRoy, M. B. I. Janjua, R. Renaud, and U. Leuenberger, *This Journal*, **126**, 1674 (1979).
13. R. L. LeRoy, M. B. I. Janjua, R. Renaud, and U. Leuenberger, in "Industrial Water Electrolysis," S. Srinivasan, F. J. Salzano, and A. R. Landgrebe, Editors, p. 63, The Electrochemical Society Softbound Proceedings Series, Princeton, N.J. (1978).
14. P. W. T. Lu and S. Srinivasan, *This Journal*, **125**, 265 (1978).

An SEM Study of the Nature of the Electrochemical Deposit in Reversible Electrodeposition Displays

H. J. Stocker, L. G. VanUitert, T. C. Loomis, and F. B. Koch*

Bell Laboratories, Murray Hill, New Jersey 07974

ABSTRACT

SEM-x-ray spectroscopic studies of display cells based on reversible electrodeposition (RED's) conclusively show that the deposit is composed of elemental silver, regardless of its color (gold, gray, black, red-brown, etc.) A gold deposit is shown to consist of finely dispersed (colloidal) silver particles, while the black deposit consists of a spongy type of deposit of elemental silver. This fact means that the mechanism of operation of these dispersive displays is due to collective electromagnetic scattering effects of colloidal silver. Confirming evidence that TiO₂ particles form in-depth contacts is also presented.

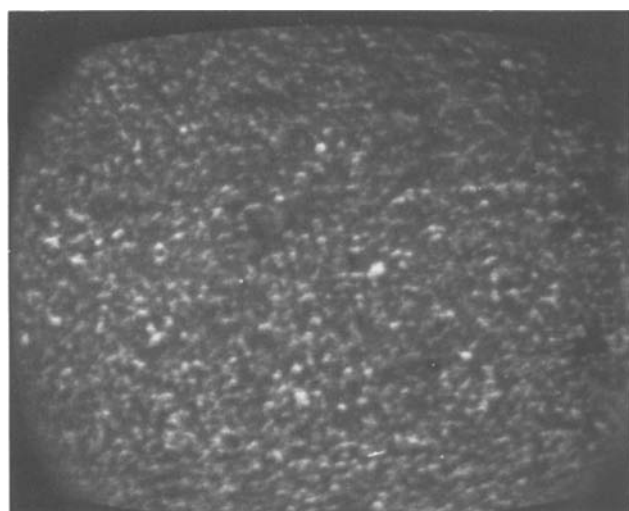
Display cells based on reversible electrodeposition (RED's) are under active study (1, 2).

Experimental cells are constructed of two parallel plates of indium-tin oxide (ITO) coated glass. The intervening space is filled with a paste electrolyte consisting of silver iodide (AgI), tetralkylammonium iodide (RN₄I), and a solvent (dimethylformamide or DMF). The use of the tetralkylammonium iodide permits the use of high silver concentrations in organic solvent based electrolytes (2). Sometimes a mixture of TiO₂ powder and fine ZEOLITE particles (molecular SIEVE) is added to the mixture. The function of the TiO₂ is twofold: one, it serves as an opacifier (white background) and second it extends the electrical contact into the interior of the cell, thus enlarging the volume in which the electrochemical reactions take place. The molecular sieve is added in an empirically

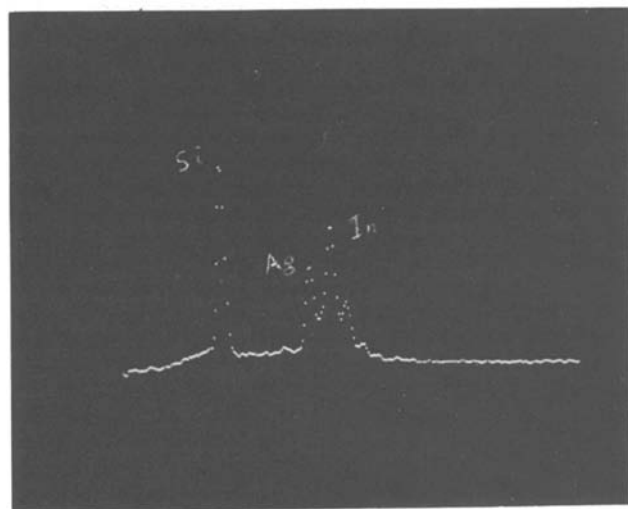
determined proportion to adjust the conductivity of the mixture for maximum contrast. The functions of these components are more fully described in Ref. (2). Upon application of voltage pulses of 1-2V magnitude and several hundred millisecond durations, coloration is observed at the cathode. A variety of colors, including gray, black, gold, green-gold, red, red-brown, light-blue, and navy blue reproducibly result from plating in these experimental display cells. Several colors may be observed in the same display cell, depending on driving conditions. For instance, a brief high amplitude pulse (duration 0.1 sec) in a DMF/AgI/TBAI/TiO₂-SIEVE cell (TBAI is tetrabutyl ammonium iodide) produces a bright red color, while a low amplitude pulse of 1 sec duration produces a dark gray color. Similarly, in cells without the TiO₂/SIEVE filler, a golden color can often be observed with a low driving current, while a gray to black deposit develops if the cell is driven harder.

* Electrochemical Society Active Member.

Key words: spectroscopy, electrodeposition, deposits.



— 1 μm (a) 5000 X



(b)

Fig. 1. (a) A 5000 \times picture of the gold-colored deposit showing clearly the finely dispersed particles. (b) X-ray energy spectrum belonging to Fig. 1a. Si and In are due the substrate. Ag is clearly present but there is no I peak, supporting the conclusion that the deposit consists of colloidal silver.

These puzzling coloration effects cannot be understood as a straightforward electroplating of silver, which had been the basis of earlier work in aqueous solutions by Zaromb (3, 4).

We will consider two fundamentally different hypotheses, namely, (i) that the different colors correspond to the different electrochemical reaction products (e.g., Ag, $\text{Ag}_0(\text{AgI})_x$, etc.) or (ii) that only Ag is deposited and the different colors result from collective electromagnetic scattering effect of a collection of colloidal silver particles. The latter effects, first studied by Carey-Lea in 1889 (5) in silver electrolytes cause many fascinating colors, including most of the colors seen in display cells. The particular colors observed correlate with the size of the colloidal silver particles. A summary of such phenomena is given in Gmelin's handbook (6). It is this key question of the physical and chemical nature of the deposit to which our SEM-x-ray spectroscopic study was addressed in experiments A and B, described below.

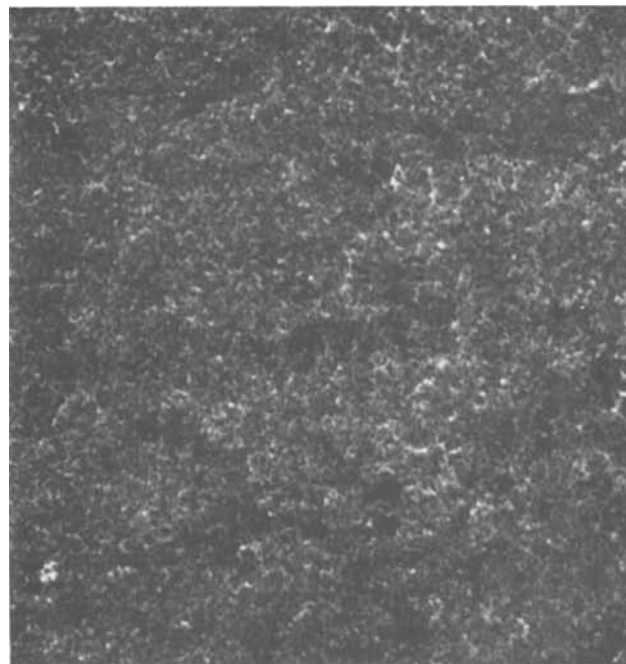
Experiment C clarifies the role of the TiO_2 particles sometimes used in the pastes. The working hypothesis

that the TiO_2 , by virtue of its conductivity, allows plating to occur throughout the volume of the paste rather than just on the planar electrode is confirmed by this experiment.

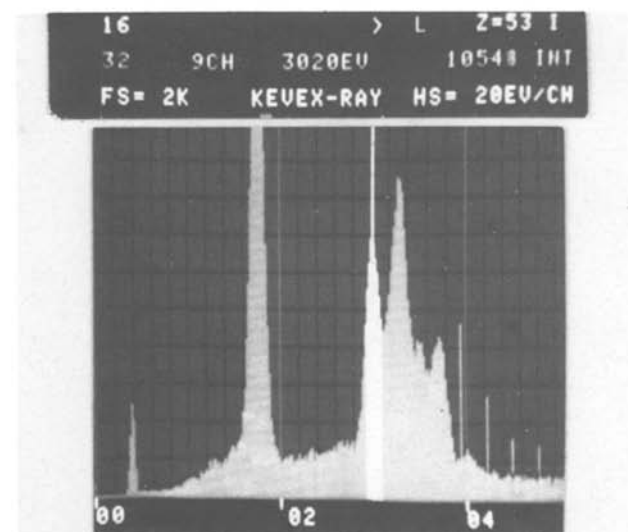
Results

In experiment A, a cell containing an $\text{NR}_4\text{I}/\text{AgI}/\text{DMF}$ solution but no filler was cycled with 1 Hz square waves of 2.5V amplitude so that a gold color developed. With the gold color remaining on the first electrode, the cell was opened and the deposit washed with acetone and then subjected to SEM analysis.

The SEM examination revealed both a submicron structure of finely dispersed particles and a large number of Maltese-cross and bar-shaped crystals. There is strong evidence that these crystals are an experimental



(a) 5000 X



(b)

Fig. 2. (a) SEM picture at 5000 \times of a black deposit, showing a dense spongy structure. (b) X-ray energy spectrum showing the presence of Si, Ag, and In but no I.

artifact in the form of AgI precipitated from a supersaturated solution when the cell was opened and the solvent evaporated. The elemental ratios, found using energy dispersive x-ray analysis correspond to the ratios obtained from an AgI standard. Also, the growth of similar crystals could be observed directly with an optical microscope as the solvent evaporated. The gold color seen in an unopened cell thus must be attributed to light scattering from the submicron structure rather than the AgI-salt crystals.

Figure 1(a) shows a detail of the gold-colored deposit in an area free of AgI crystals at a magnification of 5000 \times , where the morphology of the finely dispersed particles can clearly be resolved. Their size is approximately 50 nm. The corresponding x-ray energy spectrum in Fig. 1(b) shows only the presence of Ag from the particles, In from the transparent conductive coating, and Si from the substrate. We therefore conclude that silver is present in colloidal form in this area.

In experiment B, a cell containing ASI/TBAI/DMF (ASI is ammonium silver iodide) was colored with several 1 sec, 2V d-c pulses until a dark gray to blackish deposit had formed. The cell was then opened and the deposit carefully washed with acetone and distilled water. The deposit has a spongy form as indicated in Fig. 2(a) (5000 \times). The composition is again entirely elemental silver, with no iodine present [Fig. 2(b)]. This experiment thus conclusively shows that the deposit, when driven hard enough to produce black color, is entirely elemental silver, and furthermore is of a spongy, loose structure. The only difference between the black deposits [Fig. 2(a)] and the golden deposit formed at lower driving currents [Fig. 1(a)] is that the silver particles which were isolated in the golden deposit have been agglomerated into a deep spongy form in the black deposit.

In experiment C, an ASI/TBAI/DMF/TiO₂/SIEVE cell was colored to a red-brown color with a d-c pulse of 300 msec duration and 2V amplitude. The cell was then taken apart carefully and the paste near the electrode examined under the SEM. Figure 3 is a 5000 \times



Fig. 3. SEM picture and elemental distribution maps of the TiO₂/SIEVE paste mixture, after cell had been colored red-brown. The preferential occurrence of Ag on the TiO₂-particles confirms their role as an in-depth contact.

SEM picture of the paste together with elemental distribution maps for Al, Ti, and Ag. The Al map indicates the position of the zeolite (NaAlSi₂O₆) particles, the Ti map the position of the TiO₂ particles. A careful comparison of the elemental maps lead to the conclusion that the Ag is indeed distributed predominantly on the TiO₂ particles. This confirms the hypothesis that the TiO₂ acts as an in-depth-contact, so that dispersed silver is formed within much of the volume of the paste.

A cell which appears red-brown when viewed normally (*i.e.*, perpendicular to the electrode plane) may appear greenish when viewed at a $\sim 75^\circ$ angle. We have not studied these complicated effects in detail but we believe they are consistent with the hypothesis of formation of a silver colloid, in fact provide further evidence for it. Theoretically (7), one expects different colors to be seen at different angles in a colloid of silver particles, because the light scattering efficiency, as calculated for uniform particle size in Mie's theory, predicts dependence on both the angle ϕ and the wavelength λ . The resulting array of colors is known as higher order Tyndall spectra (7).

Conclusions

The major conclusion of this study is that the chemical composition of the deposit in dispersive RED display cells is elemental silver for both the dispersive colors and the more conventional electroplated deposit at the cathode. This conclusion is consistent with studies of the cyclic voltammograms of such cells which show a smooth behavior consistent with the electrochemical reaction $\text{Ag}^+ + e \leftrightarrow \text{Ag}$ but no structure which would indicate the electrodeposition of other reaction products.

As larger amounts of currents are passed through the cell, the colloidal particles (gold color) apparently agglomerate to larger structures whose optical properties make them look black.

A second result of our study is confirmation that the TiO₂ particles indeed do form in-depth contacts and therefore act as a dispersing agent. This effect is believed to enhance the electromagnetic scattering effects attributable to a colloid vis-a-vis the more conventional electroplating effects at the electrode.

Manuscript submitted Nov. 9, 1979; revised manuscript received March 17, 1980.

Any discussion of this paper will appear in a Discussion Section to be published in the December 1981 JOURNAL. All discussions for the December 1981 Discussion Section should be submitted by Aug. 1, 1981.

Publication costs of this article were assisted by Bell Laboratories.

REFERENCES

1. I. Camlibel, S. Singh, H. J. Stocker, L. G. VanUitert, and G. J. Zydzik, *Appl. Phys. Lett.*, **33**, 793 (1978).
2. L. G. VanUitert, I. Camlibel, R. M. DeLaRue, T. R. Kyle, R. Pawelek, S. Singh, H. J. Stocker, and G. J. Zydzik, *ibid.*, **34**, 232 (1979).
3. S. Zaromb, *This Journal*, **109**, 903 (1962).
4. I. Mantell and S. Zaromb, *ibid.*, **109**, 992 (1962).
5. M. Carey Lea, *Am. J. Sci.*, **37**, 476 (1889).
6. Gmelin-Handbuch, Vol. 61 Ag[A3], p. 209-212.
7. M. Kerker, "The Scattering of Light," Academic Press, New York (1969).

Electroluminescence during the Anodic Growth of Tantalum Pentoxide

V. Kadary¹ and N. Klein

Department of Electrical Engineering, Technion, Israel Institute of Technology, Haifa, Israel

ABSTRACT

Light emission during the anodic growth of tantalum pentoxide was found to grow quasi-exponentially with electric field and oxide thickness. Data on the spectrum were obtained with six narrow bandpass filters. Largest light output was found for 4.8 eV photons. This light component was strongly absorbed in the oxide, since its bandgap is 4.6 eV. The light emission was interpreted as an electroluminescent (EL) effect due to electron avalanching and to recombination of hot electrons with trapped holes for most of the light components. The nonabsorbed light components could in part be due also to first-order kinetics EL processes. Relations derived for the EL output fitted experimental results well, giving $\alpha = 1.12 \times 10^5/\text{cm}$ for the coefficient of impact ionization at a field of 6.26 MV/cm. Earlier breakdown investigations resulted in $\alpha = 1.4 \times 10^5 \pm 10\%/ \text{cm}$. The difference in α values can be due to approximations made in deriving relations for the two phenomena. Since both breakdown and EL theories were developed with the same avalanche model, independent evidence was obtained on impact ionization in tantalum pentoxide from two phenomena.

It has been known since the end of the last century that a steady light emission accompanies the anodic growth of oxides. The effect was termed galvanoluminescence (1) and surveyed in an excellent review article by Ikonopisov (2). The survey shows that this luminescence is not well understood and that there are many contradictions in observations and insufficiencies in interpretations.

Light output during the growth of aluminum oxide was found to increase quasi-exponentially with the electric field in the oxide and also with thickness (3). This thickness dependence could not be explained by chemiluminescence due to electrochemical reactions at the electrolyte interface (4), or at flaws (5). Many investigators assume that the light emission is an electroluminescent (EL) effect (2).

A mechanism for the EL in aluminum oxide was proposed by van Geel *et al.* (3), assuming that impact ionization by electrons and avalanching take place during anodization at a field of nearly 9 MV/cm in the oxide. EL was ascribed to excitation of impurities by hot electrons and subsequent radiative de-excitation. The thickness dependence of EL was explained with the exponential increase of hot electrons with thickness by avalanching. The luminescent impurity centers were thought to be metallic (6), or organic ions (5), and addition of manganese to aluminum was found to enhance the EL manifold (7). Anderson suggested radiative hole-electron recombination as an alternative EL mechanism (8).

Most of the EL investigations were confined to aluminum oxide (2). Publications on light emission during the anodic growth of tantalum pentoxide were fewer and less detailed (4, 7-10). Investigating electrical breakdown processes during the anodic growth of oxides on tantalum (11) and aluminum (12), we found that breakdown events could be well explained by the succession of avalanches breakdown model (13). The question arose whether the light emission is also connected with avalanching processes in tantalum pentoxide and whether light emission observations could provide independent data on avalanching. We therefore investigated light emission in parallel with electrical breakdown during anodic growth.

We describe below results of light emission observations in tantalum pentoxide. It is shown that most of the light emission is an EL process, explained by the effects of avalanching and by radiative hole-electron recombinations. The magnitude of the coefficient of impact ionization, α , is derived from EL data and found to be in reasonable agreement with α obtained from breakdown experiments.

Samples and Experimental System

The sample and experimental system were described in the publication on breakdown in tantalum pentoxide (11) and we recapitulate here the main features. Figure 1 illustrates the sample. The anodizations were carried out on 500 nm thick, sputtered, lightly nitrogen-doped, β tantalum films. The sample was placed horizontally in the electrolytic bath. This was an aqueous solution of citric acid with a range of concentrations from 2.5×10^{-3} to 1.8 weight percent (w/o), the corresponding electrolyte resistivities varying from 21,000 to 260 $\Omega\text{-cm}$ at 1 kHz. Anodizations were carried out at constant current densities of 0.5, 1.0, 5.0, or 10.0 mA/cm². The corresponding mean electric fields in the oxide were 6.14, 6.26, 6.56, and 6.7 MV/cm, respectively

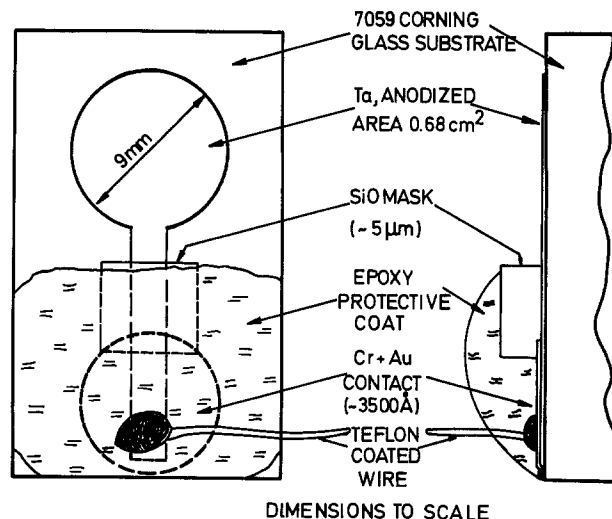


Fig. 1. Tantalum sample for anodization

¹ Present address: Israel Aircraft Industries, Yahud, Israel.
Key words: electroluminescence, insulator, anodization, breakdown.

(11). Magnetic stirring of the bath reduced temperature rises to less than 1°C in the sample for a current density of 1 mA/cm^2 and oxide thickness of about 500 nm .

Light emitted from the sample was collected with a vertical 100 mm long, 10 mm diam quartz light guide. The collecting face of the light guide was concentric with and 10 mm above the sample in all experiments. The light guide was coupled to an RCA Type 1P28 photomultiplier, sensitive over the spectral range of $220\text{--}620\text{ nm}$, with a maximum sensitivity close to 330 nm . The photomultiplier had potted leads and was cooled with solid CO_2 . Electrolytic bath, light guide, and photomultiplier were enclosed in an aluminum box, impervious to external light.

Measurements recorded light emission and voltage across the oxide *vs.* time of anodization. The output of the photomultiplier was amplified and the light emission was plotted on a Hewlett Packard strip chart recorder. Voltage was measured across a capacitor connected in parallel with the electrolytic bath. The voltage across the oxide layer was obtained by subtracting voltage drops in the electrolyte and in a series resistor. Light emission observations extended from the smallest to close to the breakdown voltages. Breakdown sparks foiled observations in the breakdown range of voltages.

Experimental Results

Results were presented in plots of light emission during anodic growth *vs.* voltage across the oxide, or *vs.* the oxide thickness, w . The oxide thickness was calculated from the voltage and the oxide field data given above.

The field dependence of the light emission *vs.* thickness is presented in Fig. 2, with mean field in the oxide as parameter. The solid line results were obtained with continuous anodic growth experiments and the broken line results at fields lower than applied for anodizations. The latter results were obtained from sequences of light emission measurements indicated by arrows in Fig. 3. The anodic growth was interrupted in this ex-

periment near $100, 150,$ and 200 V and light emission was measured rapidly at decreasing and again at increasing voltages, followed by resumption of anodic growth. We estimated that the growth in the thickness of the oxide film was insignificant during a voltage decrease period, owing to the rapidity of voltage decrease and due to the quick decrease in ionic current density with field reduction. We obtained thus approximate field-dependent data on light emission below fields for anodic growth.

The data of Fig. 2 were replotted and showed that (i) the light emission grows in a superlinear manner with current density of anodization and (ii) the light emission grows exponentially with oxide field at a given oxide thickness. A semilogarithmic plot of emission consists of two ranges, one with a relatively low slope at lower fields and one with a relatively large slope at fields of anodic growth.

The effect of the electrolyte resistivity, ρ_e , on the light emission is illustrated by Fig. 4. An increase of ρ_e from 285 to $21,000\ \Omega\text{-cm}$ produced no significant change in the light emission; observations of this nature were made earlier also with aluminum oxide (7, 10). The effect of temperature on light emission was found to be small in the range of $3^{\circ}\text{--}50^{\circ}\text{C}$ as is indicated by the curves in Fig. 5. In contrast, the light emission of aluminum oxide was found to change and increase with temperature in an inorganic electrolyte, but decrease with temperature in an organic electrolyte (5).

Data on the spectrum of the light emission were obtained by a series of anodizations performed under identical conditions at a current density of 1 mA/cm^2 . The light emission was measured through a different narrow bandpass interference filter on each of the anodization runs. Balzer filters of a half-bandwidth of about 10 nm were used, of wavelengths $259, 313, 366, 408, 434,$ and 545 nm at their maximum transmittance. The peak transmittance of the filters varied between 20% and 30% .

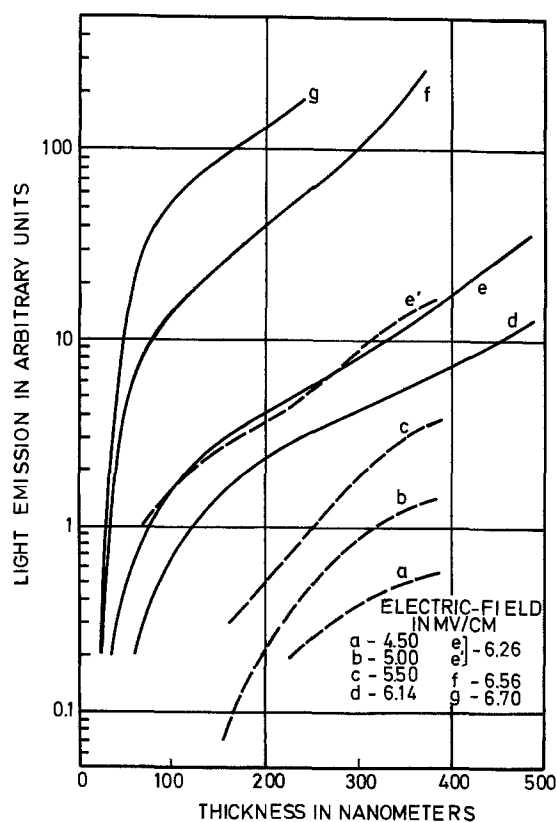


Fig. 2. Light emission *vs.* thickness with field as parameter. Electrolyte resistivity $7000\ \Omega\text{-cm}$.

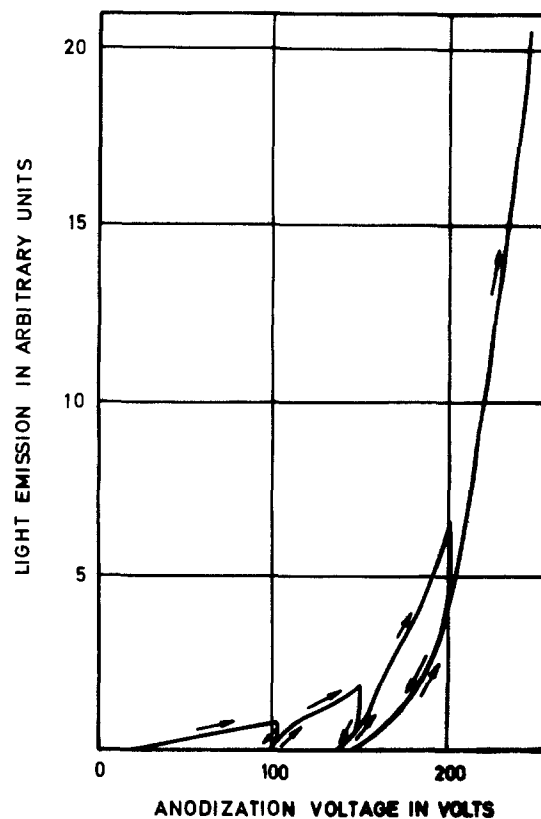


Fig. 3. Light emission *vs.* voltage with interruptions of anodic growth near $100, 150,$ and 200 V . Current density 0.5 mA/cm^2 , electrolyte resistivity $7000\ \Omega\text{-cm}$.

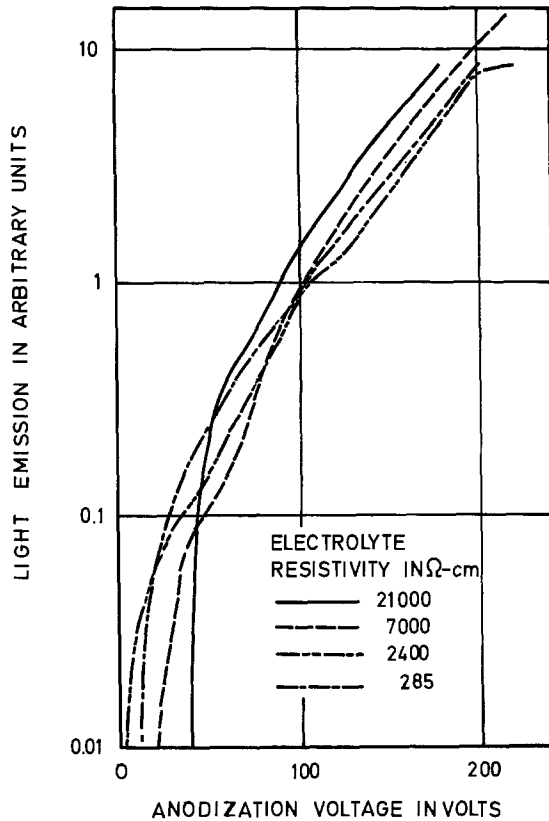


Fig. 4. Light emission vs. voltage with electrolyte resistivity as parameter. Current density 1 mA/cm².

For the evaluation of the light measurements, the transmission of the filters and the quartz light guide was determined with a Cary 14 type spectrometer and the photomultiplier spectral response was calibrated using a Jarrel-Ash monochromator Model 83-410 and

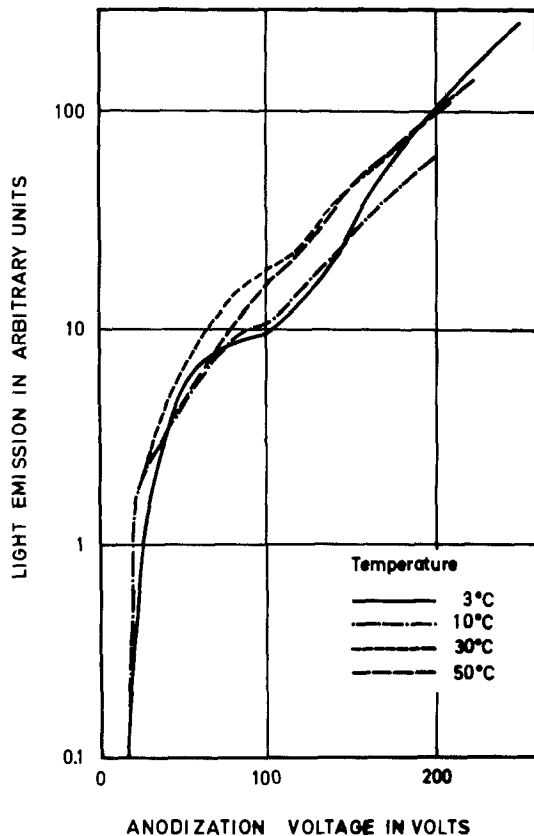


Fig. 5. Light emission vs. voltage with temperature as parameter. Current density 1 mA/cm², electrolyte resistivity 7000 Ω-cm.

an Eppley thermopile. Light readings were corrected for transmission losses in the system and for differences in the photomultiplier spectral response.

Results are shown in Fig. 6, where the narrow-band light emission, *L*, is plotted in relative units vs. anodization voltage with wavelength as parameter. The light emission component at 259 nm is of special interest with photon energies centered at 4.8 eV. The band-gap of anodically grown tantalum pentoxide was found to be smaller by photoconduction, 4.6 eV (14). Thus the 259 nm light emission was expected to be affected by light absorption in the oxide. Spectrophotometrical measurements showed that the coefficient of absorption *K* has a value between 1.8 and 2.0 × 10⁵/cm at 259 nm in good agreement with earlier results of Bray *et al.* (15). A slight absorption was found at 313 nm wavelength with *K* < 5 × 10³/cm.

Mechanisms of Electroluminescence

Avalanching.—The near-exponential increase of light emission with thickness in Fig. 2, 4-6 suggests that the light emission is connected with avalanching, as found by van Geel *et al.* (3) for aluminum oxide. Since electrical breakdown investigations confirmed that impact ionization and avalanching accompany the anodic growth of tantalum pentoxide (11), we proceed examining avalanche models for the interpretation of light emission. The properties of impact ionization and avalanching are recapitulated first.

Fitting experimental data to breakdown theory it was found that the coefficient of impact ionization, α , is related to the field by $\alpha = 4.4 \times 10^6 \exp(-21.5/F)/\text{cm}$ in the range of fields, *F*, 6.1-6.7 MV/cm with *F* given in MV/cm. The current density, *j*, of most anodizations was 1 mA/cm² at a field of 6.26 MV/cm and the corresponding value of α was 1.4 × 10⁵/cm with an estimated uncertainty of ±10%.

Electrons injected into the oxide produce avalanches by impact ionization. Electrons are little affected by trapping and traverse the oxide in the order of picoseconds. In contrast, holes produced on impact are deeply trapped, drift slowly toward the electrolyte,

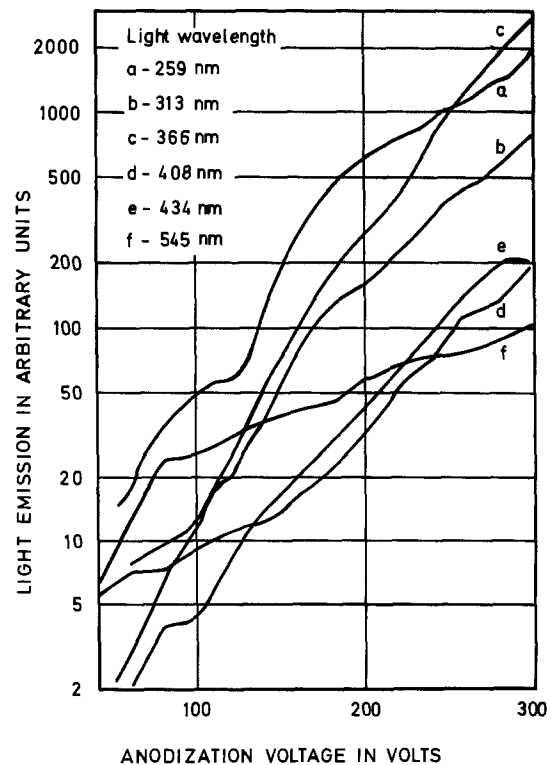


Fig. 6. Light emission through narrow bandpass filters vs. voltage. Parameter wavelength at maximum transmittance of filters. Current density 1 mA/cm², electrolyte resistivity 7000 Ω-cm.

and traverse the oxide in the order of micro- to milli-seconds. Figure 7a shows a schematic oxide cross section with avalanche cones of holes at various stages of drift through the oxide. Most positive charge clusters drift out of the insulator. There is, however, some probability that a drifting cluster is hit by an electron injected from the electrolyte. Such an electron produces a second avalanche and a succession of avalanches at one spot produces breakdown (11).

The average number N , of electrons in an avalanche, as a function of distance x from the electrolyte interface is (11)

$$N = \exp \left(\int_0^x \alpha dx' \right) \quad [1]$$

There is an upper limit to the avalanche size, since positive charges produced and left behind keep decreasing the field at the propagating front of the avalanche until impact ionization stops (16, 13). The limiting avalanche size N_1 was found to produce about 2000 carriers of each sign in tantalum pentoxide (11). Since the avalanche size is an exponential function of x , the effect of positive charges becomes significant only in the last few ionizing steps of an N_1 size avalanche. The avalanche sizes were limited by oxide thickness in the light emission experiments, so that usually $N \ll N_1$ and N could be approximated by

$$N \approx \exp(\alpha x) \quad [1a]$$

The number of holes produced in an avalanche $P = N - 1$. Figure 7b presents a second illustration of hole clusters drifting toward the electrolyte. The hole cones are not limited in this sketch by spatial extension in the electrode direction, but by curves approximating the hole density as function of x .

First-order kinetic processes.—The light emission can be examined by processes of first- and of second-order kinetics and we start with first-order processes. These produce light in proportion to the electron current. Photon emissions are due to events such as de-excitation of impurities, radiative trapping, geminate recombination, or de-excitation of excitons.

We assume that the rate of light emission by these processes dL from the wavelength band $\Delta\lambda$ and from the space between x and $x + dx$ is proportional to $\exp(\alpha x)$, and to the rate of electrons injected, I_e/q , and

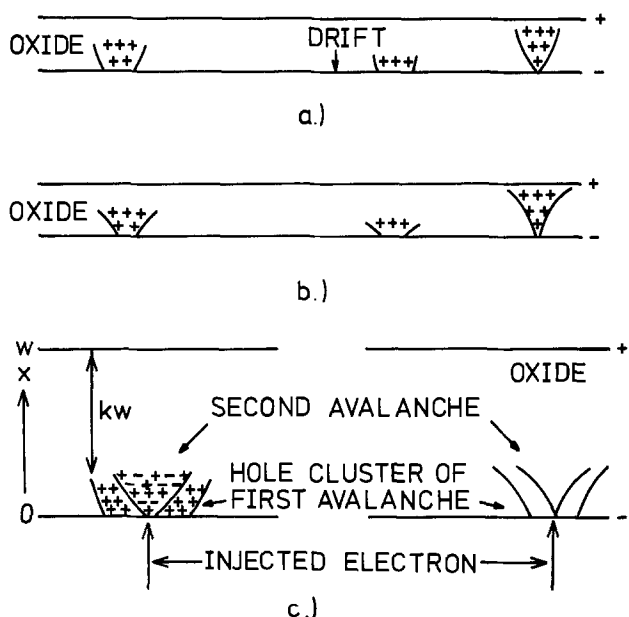


Fig. 7. Sketches showing (a) space occupied by avalanche hole clusters drifting through oxide; (b) hole density of drifting clusters as function of x ; (c) EL event, left, spatial extensions and, right, hole density of overlapping avalanche clusters.

$$dL = A_\lambda I_e \exp(\alpha x) dx/q$$

I_e is the electron current, q the electronic charge, and A_λ is a constant dependent on the wavelength λ . Integrating between the limits 0 and w , the oxide thickness, the relation for light emission L is obtained in the absence of light absorption, $K = 0$, and

$$L = \frac{A_\lambda I_e}{\alpha q} [\exp(\alpha w) - 1] \quad [2]$$

This relation was derived by van Geel *et al.* (3). When account has to be taken of light absorption

$$dL = A_\lambda I_e \exp(\alpha x) \exp(-Kx) dx/q$$

and integration over the oxide thickness gives

$$L = \frac{A_\lambda I_e}{q(\alpha - K)} [\exp(\alpha - K)x - 1] \quad \text{for } \alpha > K \quad [3a]$$

and

$$L = \frac{A_\lambda I_e}{q(K - \alpha)} \{1 - \exp[-(K - \alpha)x]\} \quad \text{for } K > \alpha \quad [3b]$$

It is important to differentiate between the two cases: L grows quasi-exponentially with w , when $\alpha > K$. L saturates with w when $K > \alpha$, because light is detected only from a roughly $1/(K - \alpha)$ thick layer adjacent to the electrolyte.

The spectral data of Fig. 6 were examined with Eq. [2] first. Some difficulties were experienced in fitting results to Eq. [2] owing to a wavy structure superposed on the curves, which may perhaps be due to interference effects. We fitted by the least squares method and derived values for the coefficient of impact ionization α . These were tabulated for four wavelengths in Table I.

The results for the wavelengths 313 and 366 nm are remarkable, since they coincide closely with $\alpha = 1.4 \times 10^5/\text{cm}$ obtained from breakdown observations (11). The agreement is less good for the 408 and 434 nm minor light components. Another minor component at 545 nm does not fit Eq. [2] and increases roughly in a linear manner with thickness.

The light emission at 259 nm is subject to light absorption. It could be fitted to Eq. [3a] resulting in $\alpha - K = 1.1 \times 10^5/\text{cm}$. Since the coefficient of absorption $K \approx 2.0 \times 10^5/\text{cm}$, $\alpha = 3.1 \times 10^5/\text{cm}$ results. This contradicts the values obtained at longer wavelengths and on breakdown (11). Alternatively we can use $\alpha = 1.4 \times 10^5/\text{cm}$ and $K = 2.0 \times 10^5/\text{cm}$ to describe the dependence $L(w)$ with Eq. [3b]. This equation predicts saturation in L which is not found with the exponentially rising 259 nm curve in Fig. 6. Thus first-order kinetics cannot explain the light emission at 259 nm.

Second-order kinetics processes.—We continue examining a second-order kinetics model for radiative hole-electron recombinations. These can take place on the chance event of an injected electron hitting an avalanche cluster of holes. A second avalanche is produced and recombination of holes of the first and electrons of the second avalanche can result in light emission. The probability of such an event, s , is $j_e(F_c) A_v t_t / q$ (13), $j_e(F_c)$ is the electron current density and F_c the cathode field at a hole cluster, A_v is the cross section of an average avalanche at the tantalum electrode, t_t the hole cluster transit time, and q the electronic charge. When electron injection takes place by tunneling, $j_e(F_c) \propto \exp(-B/F_c)$. The cathode field $F_c = \beta F$,

Table I. The coefficient of impact ionization, α from first-order kinetics processes

| Wavelength, nm | 259 | 313 | 366 | 408 | 434 | 545 |
|-----------------------------|-----|------|------|------|------|-----|
| Photon energy, eV | 4.8 | 4.0 | 3.4 | 3.0 | 2.85 | 2.3 |
| α , $10^5/\text{cm}$ | | 1.38 | 1.36 | 1.04 | 1.15 | |

where $\beta > 1$ is the field enhancement factor at a hole cluster.

The cathode field F_c keeps increasing during the drift of an avalanche cluster toward the cathode because most holes were produced near the anode. Increase of F_c increases $j_e(F_c)$ and s exponentially with $1/F_c$. The probability s will thus be largest in the vicinity of the cathode.

Figure 7c illustrates with two sketches the EL event resulting from hole-electron recombinations. The left-hand sketch shows the spatial extensions of the drifting hole cluster and of the new avalanche produced by a centrally hitting electron. The right-hand sketch indicates hole and electron densities of the first and second avalanche in the manner of Fig. 7b.

A relation for the EL emission can be readily derived with the help of a simplified model. We assume that injection of an electron into a hole cluster and light emission take place when the hole cluster has drifted a fraction kw of the insulator thickness toward the cathode (see Fig. 7c). The recombination light, dL_a , emitted by one avalanche in the wavelength band $\Delta\lambda$ and between x and $x + dx$ is $dL_a = r_\lambda N (\partial P/\partial x) dx$. Here r_λ is a constant, a function of the wavelength λ . $N = \exp(\alpha x)$ is the approximate size of the second electron avalanche crossing the space between x and $x + dx$ and $(\partial P/\partial x) dx$ are the holes produced in the space between x and $x + dx$ by the first avalanche.

Since on impact ionization $\partial N/\partial x = \partial P/\partial x$, we find with Eq. [1a] that $(\partial P/\partial x) dx = \alpha \exp(\alpha x) dx$ at the time of avalanche production. When the hole cluster drifts the distance kw toward the cathode, $(\partial P/\partial x) dx = \alpha \exp \alpha[(x + kw)] dx$ and

$$dL_a = \alpha r_\lambda \exp(\alpha x) \exp[\alpha(x + kw)] dx$$

To account for absorption of light, dL_a is replaced by an expression dL_{aa}

$$dL_{aa} = \exp(-Kx) dL_a = \alpha r_\lambda \exp(\alpha kw) \exp[(2\alpha - K)x] dx$$

The EL light emission is obtained by integrating dL_{aa} across the hole cluster from $x = 0$ to $(1 - k)w$ and by multiplying by the rate of light emitting clusters, sI_e/q . The resulting relation for L is

$$L = \frac{sI_e r_\lambda \alpha}{q(2\alpha - K)} \exp(\alpha kw) \{ \exp[(2\alpha - K)(1 - k)w] - 1 \} \quad [4]$$

When absorption is absent

$$L = \frac{sI_e r_\lambda}{2q} \exp(2kw) \{ \exp[2\alpha(1 - k)w] - 1 \} \quad [5]$$

Examination of the expression for dL_a , or of Fig. 7c, quickly reveals that most of the light is produced in a thin layer, a distance $x = (1 - k)w$ from the electrolyte interface.

The simplifications in the derivation of Eq. [4] and [5] are connected with the use of continuum instead of single electron calculations and with the omission of the effect of fluctuations in k and the place of electron injection with respect to the hole cluster. Owing to fluctuations in k and due to hole diffusion, the light emitting layer is expected to be broader than found with Eq. [4] and [5]. A further simplification is the assumption for the expression dL_a that the size of the second avalanche N is $\exp(\alpha x)$. Due to a dead space for ionization at the cathode and due to recombinations, N grows slower with x than $\exp(\alpha x)$, but faster owing to the increased rate of impact ionization by the enhanced field at the hole cluster.

The applicability of the recombination EL model was examined assuming that the major light components of Fig. 6 at 259, 313, and 366 nm are all due to radiative hole-electron recombinations. Equation [4] was fitted

for this purpose to the experimental data at 259 nm and Eq. [5] to the data at 313 and 366 nm, using the same values of k and α . The small absorption at 313 nm was neglected.

The results are presented for better legibility separately, in Fig. 8, where full lines plot experimental data and the dotted line curves fitted with $\alpha = 1.12 \times 10^5/\text{cm}$, $k = 0.78$, and $K = 2 \times 10^5/\text{cm}$. A slightly better fitting results for nonabsorbing components, when only a pair of components is fitted. Thus if fitting is restricted to the 259 and 313 nm components, $\alpha = 1.105 \times 10^5/\text{cm}$ and $k = 0.795$ is obtained. The pair of components of 259 and 366 nm gives $\alpha = 1.135 \times 10^5/\text{cm}$ and $k = 0.765$. Thus the fitting procedure results in fairly precise values for α and k . The influence of the coefficient of absorption is not strong and a decrease of K to $1.8 \times 10^5/\text{cm}$ has but a small effect on the fitting of the 259 nm curve to experimental data.

The breakdown investigations resulted in $\alpha = 1.4 \times 10^5 \pm 10\%$ at a field of 6.26 MV/cm (11). The difference from the α value found here is not unexpected owing to approximations in the models of the phenomena. A further difficulty is added by the lack of assessment of the influence of the wavy superstructure on the emission curves of Fig. 6. It was not thought warranted for this reason to derive EL relations more accurate than Eq. [4] and [5].

The total light production at 259 nm was determined too. Comparison of Eq. [4] and [5] shows that the total light is obtained by multiplying the measured light emission by

$$\frac{2\alpha}{2\alpha - K} \frac{\exp[(2\alpha - K)(1 - k)w] - 1}{\exp[2\alpha(1 - k)w] - 1} \quad [6]$$

The resulting total light production is plotted as a broken line curve in Fig. 8. The calculated total light emission curves of Fig. 8 show that the ratio of the light emissions L at 259, 313, and 366 nm wavelengths is 1:0.14:0.3.

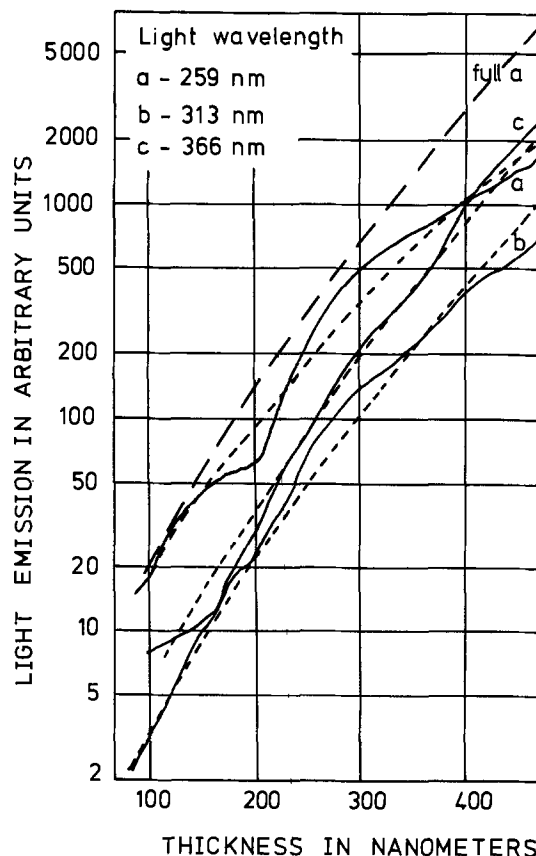


Fig. 8. Solid lines replot light emission curves of Fig. 6 for the wavelength 259, 313, and 366 nm. Dotted lines represent calculated results and the broken line is the full light production at 259 nm.

Discussion of the Luminescence

We first turn our attention to an assessment of the energy levels of the recombining conduction band electrons and trapped holes. Considering that the band-gap is 4.6 eV and using the photon energy data of Table I, we find that the hole traps are at least $q\phi_t = 1.2$ eV above the valence bandedge, if light emission is ascribed to the components 259, 313, and 366 nm only. If the components at 408 and 434 nm are also produced by recombination $q\phi_t = 1.85$ eV at least.

Further indication about the magnitude of $q\phi_t$ can be obtained from results of the breakdown investigations (11). These show that holes must be deeply trapped, since shallow traps would be empty at the fields of anodization larger than 6 MV/cm. There is also an upper limit for $q\phi_t$, since the mobility of trapped holes, μ_t , was estimated to be larger than 10^{-8} cm²/Vsec.

While these data are insufficient to calculate $q\phi_t$ we will attempt assessments of $q\phi_t$ with the help of assumptions. We start with the ratio of the hole density p in the valence band and the trapped hole density p_t . We equate p/p_t with the ratio of hole mobilities μ_t/μ_v , where μ_v is the hole mobility in the valence band. When the oxide thickness and the avalanches are small we assume that $p \ll p_t \ll P_t$, where P_t is the hole trap density. Boltzmann statistics apply in this case (17) and

$$\frac{\mu_t}{\mu_v} = \frac{p}{P_t} = \frac{N_v}{P_t} \exp \left\{ -\frac{q}{k_T T} \left[\phi_t - \left(\frac{qF}{\pi \epsilon_0 \epsilon} \right)^{1/2} \right] \right\} \quad [7]$$

Equation [7] permits one to calculate $q\phi_t$. N_v is the equivalent density of states in the valence band, k_T the Boltzmann constant, T the temperature, ϵ_0 the permittivity of empty space, and ϵ the relative permittivity of the oxide. We assume that $\mu_t = 10^{-8}$ cm²/Vsec, $\mu_v = 10$ cm²/Vsec, $N_v/P_t = 10^5$, $T = 300$ K, and $F = 6.26$ MV/cm. The magnitude of ϵ lies for Eq. [7] between the static value 25 and the optical value 4.5. We assumed first $\epsilon = 5$ and calculation with Eq. [7] resulted in $q\phi_t = 1.6$ eV. The calculation with $\epsilon = 15$ resulted in $q\phi_t = 1.24$ eV.

Avalanches grow to large sizes when the oxide thickness is large; p_t may reach values of 10^{18} /cm³ (11) and may be close to the magnitude of P_t then. We assessed $q\phi_t$ in these cases too, obtaining values slightly larger than when p_t is small. Examination of these results indicates that the hole trap level, or possibly levels, are situated approximately 1.5 eV above the valence bandedge. Addition of the photon energies of Table I to the hole energy level gives the energy level of the recombining electrons; for the 259, 313, and 366 nm light components these are 1.7, 0.9, and 0.3 eV above the conduction bandedge, respectively. These energy levels and recombination processes are illustrated with the schematic energy band diagram of Fig. 9.

The minor light components at 408 and 434 nm could also be ascribed to hole-electron recombination processes. Equation [5] would then apply to the light components 408 and 434 nm with the same constants α and k as to the components 313 and 366 nm. Figure 6 shows that this is not the case, since the slopes of the light emission curves at 408 and 434 nm wavelengths are smaller than at 313 and 366 nm. This discrepancy is expressed also in the difference of the corresponding α values in Table I. The reason for this difference may be indicated by the minor light emission at 545 nm (Fig. 6), which rises with thickness in a linear manner only. This emission cannot be ascribed to an EL process by avalanching and its origin is not known. It is feasible that the light emission at 408 and 434 nm is only in part due to recombination EL but in part due to processes which produce the 545 nm light component.

The discussion shows that radiative hole-electron recombinations can explain most of the spectrum observed. First-order kinetics processes can also interpret

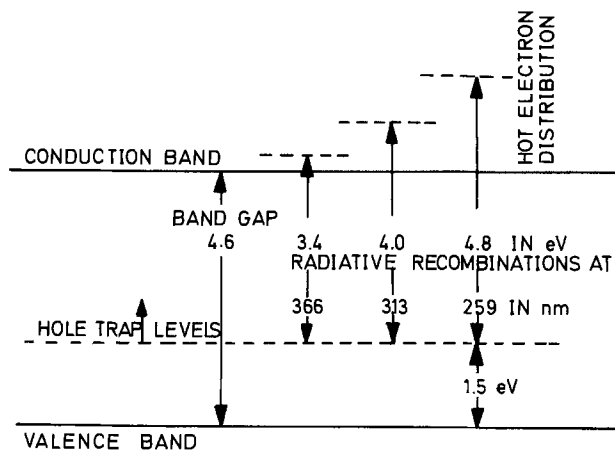


Fig. 9. Schematic band diagram for the illustration of the hole-electron EL recombination mechanism.

the light components not absorbed by the oxide, but not the largest component at 259 nm, partly absorbed by the oxide. Whatever the order of the process, a continuous spectrum is expected, as was observed on the anodic growth of aluminum oxide (18). It appears also that the total light output measured during the anodization of tantalum represents the sum of light emissions by different processes, of which recombination EL is preponderant. Total light output data are presented in Fig. 2, 4, and 5. Owing to differences in EL light processes, the data of Fig. 2, 4, and 5 will be discussed in a qualitative manner only.

We consider first the influence of the electrolyte (Fig. 4), which can affect the EL through the magnitude of the injected electron current, I_e . The light emission is proportional to I_e in first-order processes and to $sI_e \propto I_e^2$ in second-order processes (see Eq. [2]-[5]). Since the results of Fig. 3 show that L is not influenced by changes in the electrolyte, we find that I_e is unaffected by changes ranging from 2.5×10^{-3} to 1.8 w/o in the concentration of the aqueous citric acid electrolyte.

The rapid increase of EL emission with field shown by Fig. 2 is expected with Eq. [2]-[5] owing to exponential field dependences of I_e and α in these equations. The electron current I_e can be proportional to $\exp(-B/F)$ and the coefficient of impact ionization is related to F by $\alpha = \alpha_0 \exp(-H/F)$, with α_0 and H constants (11).

Figure 5 illustrates the temperature dependence of light emission observed on anodizations at a current density of 1 mA/cm². Calculating fields of anodization (19), $F = 6.5$ MV/cm is found for the 3°C experiment and 5.8 MV/cm for the 50°C experiment. This decrease in F with increasing temperature implies large decreases in I_e and α , hence also in L according to any of the Eq. [2]-[5]. Figure 5 shows but little change in L between 3° and 50°C indicating the effect of compensating processes, contained perhaps in the temperature variation of the coefficient τ_λ in Eq. [4] and [5].

Conclusion

The quasi-exponential increase of light emission with thickness during the anodic growth of Ta₂O₅ suggests that the process is an EL effect connected with avalanching. The light can originate from a number of de-excitation processes. An indication of their nature was found in observations on the largest light component at 259 nm. The light emission of this component increases quasi-exponentially with thickness, in spite of the fact that the component is strongly absorbed by the oxide. This could be well explained by radiative hole-electron recombinations, but not with first-order kinetics processes. Approximate relations derived for the thickness dependence of hole-electron recombination

light could be quite well fitted not only to experimental results of absorbed, but also of nonabsorbed, light components. Thus most of the light can be ascribed to recombination light, although it is feasible that nonabsorbed light components are in part due to first order kinetics EL mechanisms. A minor light component at 545 nm wavelength increased roughly linearly with thickness. This component cannot be explained with an EL mechanism connected with avalanching.

Fitting of experimental data on the major light components to theory resulted in fairly precise value for the coefficient of impact ionization, $\alpha = 1.12 \times 10^5/\text{cm}$ at a field of 6.26 MV/cm. Comparison of electrical breakdown observations with theory gave $\alpha = 1.4 \times 10^5 \pm 10\%/\text{cm}$ at this field. The difference in the α values was not unexpected, owing to the approximations made in deriving relations for the two phenomena. A further difficulty in the determination of α by EL was due to a wavy superstructure on the EL observations. The influence of this structure on the emission curves could not be assessed.

We used the same avalanche model in the development of theory for light emission and electrical breakdown. Theories could be well fitted to experimental observations and the magnitudes of the coefficient of impact ionization derived from EL and breakdown data were in fair agreement. Thus independent evidence was obtained on avalanching processes in tantalum pentoxide from two phenomena.

Acknowledgment

We gratefully acknowledge the help of Dr. M. Basches of the Bell Laboratories, who supplied the tantalum-coated substrates. Thanks are due to Professor M. Auwärter, Balzers for the loan of optical filters and to Dr. E. Finkman for the measurements of optical constants. This work was submitted by V. K. in partial fulfillment of requirements for the D.Sc. degree to Technion.

Manuscript submitted Oct. 7, 1980; revised manuscript received Nov. 20, 1980.

Any discussion of this paper will appear in a Discussion Section to be published in the December 1981 JOURNAL. All discussions for the December 1981 Discussion Section should be submitted by Aug. 1, 1981.

REFERENCES

1. H. F. Ivey, "Electroluminescence and Related Effects," pp. 161-166, 255-256, Academic Press, Inc., New York (1963).
2. S. Ikonopisov, *Electrochim. Acta*, **20**, 783 (1975).
3. W. Ch. van Geel, C. A. Pistorius, and B. C. Bouma, *Philips Res. Rep.*, **12**, 465 (1957).
4. Yu. E. Gardin, L. L. Odyneets, and B. C. Tumakov, *Elektrokhimiya*, **6**, 1562 (1970); Yu. E. Gardin, V. M. Kulabukhov, and V. A. Legostaev, *Elektron. Techn. (Ser. 5)*, **27**, 83 (1972).
5. S. Tajima, K. Shimizu, N. Baba, and S. Matsuzawa, *Electrochim. Acta*, **22**, 845 (1977); K. Shimizu, S. Tajima, N. Baba, and S. Matsuzawa, *Thin Solid Films*, **41**, L35 (1977).
6. W. P. Ganley, *Thin Solid Films*, **11**, 91 (1972).
7. A. Güntherschulze and H. Betz, "Die Elektrolytkondensatoren," M. Krayn, Berlin (1937).
8. S. Anderson, *J. Appl. Phys.*, **14**, 601 (1943).
9. R. Audubert and van Doormal, *E. R. Acad. Sci., Paris* **196**, 1883 (1933); R. Audubert and O. Viktorin, *J. Chim. Phys. (France)*, **34**, 18 (1937).
10. R. T. Dufford, *J. Opt. Soc. Am.*, **18**, 17 (1929).
11. V. Kadary and N. Klein, *This Journal*, **127**, 139 (1980).
12. N. Klein, V. Moskovici, and V. Kadary, *ibid.*, **127**, 152 (1980).
13. N. Klein, *Adv. Phys.*, **21**, 605 (1972).
14. L. Apker and E. A. Taft, *Phys. Rev.*, **88**, 58 (1952).
15. A. R. Bray, P. W. M. Jacobs, and L. Young, *J. Nucl. Mater.*, **4**, 356 (1959).
16. J. J. O'Dwyer, *J. Phys. Chem. Solids*, **28**, 1137 (1967).
17. P. C. Arnett, *J. Appl. Phys.*, **46**, 5236 (1975).
18. K. Guminski, *Bull. Acad. Pol. Sci., (Ser. A)*, No. 3-4A, 145 and No. 8-9A, 457 (1936).
19. L. Young, *Proc. R. Soc. London, Ser. A*, **258**, 496 (1960).

Electrochemical and *In Situ* Laser Raman Spectroscopy Studies on Carbon-Supported Iron Phthalocyanine Electrodes

C. A. Melendres* and F. A. Cafasso

Argonne National Laboratory, Chemical Engineering Division, Argonne, Illinois 60439

ABSTRACT

Cyclic voltammetry has been used to characterize the electrochemical behavior of iron phthalocyanine (FePc) films on glassy carbon electrodes in 0.05M H₂SO₄ solution. The films were found to catalyze oxygen reduction but deactivate on continuous cyclic scans. Films prepared by evaporation of a solution containing FePc and organic solvents, as well as by immersion in such a solution, showed significantly higher activity than those prepared by vapor deposition. This difference was attributed to the difference in the polymorphic forms of the FePc films. *In situ* laser Raman spectroscopy studies of this film indicated coordination of the FePc with water molecules in solution. The vibrational spectra, however, appear to be independent of potential in the region of 0.4 to -0.9V vs. Hg/Hg₂SO₄.

Considerable interest exists in the use of transition-metal macrocyclic compounds as a catalyst for the electrochemical reduction of oxygen (1). Iron phthalocyanine (FePc) and its derivatives, supported on carbon, appear to be among the most promising such catalysts. A number of electrochemical studies of this material both as an adsorbed layer or thick films on carbon have been reported in the literature (2-6). Spectroscopic studies have also been undertaken to

* Electrochemical Society Active Member.

Key words: electrocatalysis, iron phthalocyanine, Raman spectroscopy.

characterize the physicochemical properties of FePc (6-9). Despite these investigations, our understanding of the mechanism of O_2 electrocatalysis by FePc is far from complete. For example, little information exists concerning the molecular electronic structure of FePc on the electrode surface during electrolysis. The electrochemical behavior toward oxygen reduction of FePc films prepared by solution precipitation (2) and those prepared by vapor deposition (3) is apparently different; the reason for this is yet unexplained. Furthermore, the nature of the interaction of FePc with O_2 during electrocatalysis and the structure of a possible FePc- O_2 complex (8) have not been determined. In a program of basic research at Argonne National Laboratory, we are seeking correlations between the structure and intermolecular interactions of transition-metal macrocyclic compounds and their electrocatalytic properties. In this communication, we report some results on the interfacial behavior of carbon-supported FePc films in 0.05M H_2SO_4 , as determined by cyclic voltammetry and laser Raman spectroscopy studies.

Experimental

Glassy carbon rods ($\frac{1}{4}$ in. diam, from Fluorocarbon Corporation, Anaheim, California) were cut at an angle of 45° - 60° then ground and polished to a mirror finish. These rods were then sheathed in heat shrinkable Teflon, leaving exposed only the elliptical-shaped, polished surface. FePc was obtained from Eastman Kodak Company (Rochester, New York) and used without further purification. Sample purity was established by infrared, Mössbauer, and atomic emission spectroscopy together with elemental (carbon, hydrogen, nitrogen) analysis. The FePc material was supported on the glassy carbon surface in a number of ways: (i) the carbon electrode was dipped in a solution of 0.25 weight percent (w/o) FePc in pyridine or 0.1 w/o FePc in dimethyl formamide (DMF) for 30 min to 4 hr, (ii) a portion of the same solution was evaporated on the surface, and (iii) FePc was vapor deposited onto the surface under vacuum. In all cases, the resulting electrode was washed thoroughly with distilled water before use. The average thickness of the FePc layer was determined from the amount of solution taken for evaporation or vaporization and/or by the use of a Varian A-scope Interferometer Model 980-4000. A Princeton Applied Research Model 173 Potentiostat and 179 Universal Programmer were used for cyclic voltammetry. Electrode potentials were measured against an Hg/Hg_2SO_4 reference. The 0.05m H_2SO_4 solution was prepared from triply distilled water and deaerated by bubbling through it ultrahigh purity He (which had less than 2 ppm O_2 initially, then passed through molecular sieves at liquid nitrogen temperature). A special H-type, three-compartment cell fitted with a quartz optical window at an angle of 60° from horizontal was constructed for *in situ* measurements using laser Raman spectroscopy. A Spex Model 1401 double monochromator with a photomultiplier tube detector was used for these Raman measurements. Slit widths of 150-250 μm were employed with spectral resolution of 2-4 cm^{-1} . The signal was recorded following the usual d-c amplification. The cell and a diagram of the Raman setup are shown in Fig. 1. Sample excitation was by Ar^+ and/or Kr^+ lasers (Coherent Radiation Model 52G).

Results and Discussion

Electrochemical measurements.—Figure 2 shows typical cyclic voltammograms obtained from the pure glassy carbon electrode (no FePc) in 0.05M H_2SO_4 solution. Figure 3 shows a typical cyclic voltammogram in solution saturated with helium obtained for glassy carbon electrodes with FePc films prepared by methods (i) and (ii) given in the experimental section. Three cathodic (Ic, IIc, and IIIc) and three anodic waves (Ia, IIa, and IIIa) were observed in the voltage range

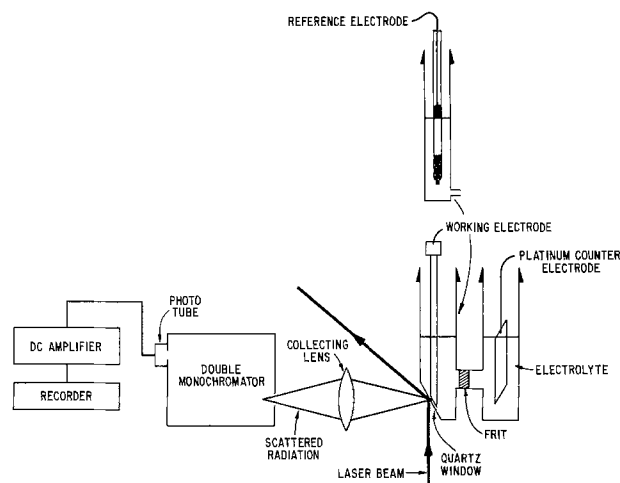


Fig. 1. Experimental setup

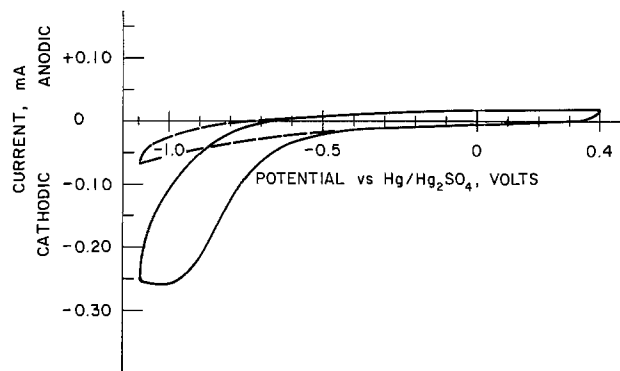


Fig. 2. Cyclic voltammograms of GC electrode: (1) — O_2 saturated, (2) - - - He saturated.

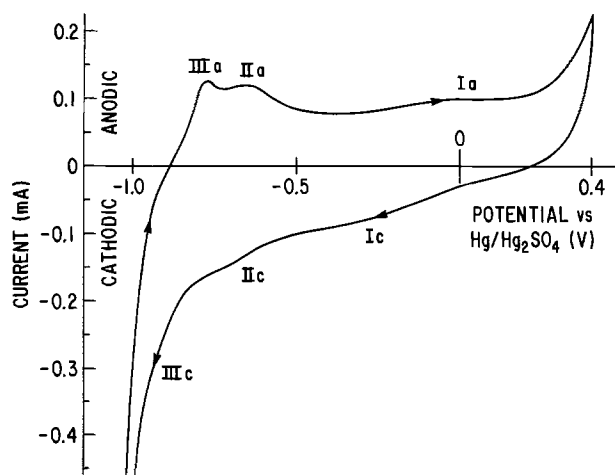


Fig. 3. Cyclic voltammogram of GC with FePc film prepared by solution evaporation: He saturated, avg. film thickness = 11000Å, apparent area = 0.57 cm^2 , scan rate = 100 mV/sec.

of 0.4 to $-1.0V$ vs. Hg/Hg_2SO_4 . Figure 4 shows a number of scans made on the FePc-C electrode in oxygen-saturated solution. In contrast to Fig. 3, waves IIa and IIIa are not evident, while waves Ic and IIIc increase and become the dominant waves. Voltametric peak IIIc appears to coincide with the position of the cathodic peak produced in the reduction of O_2 on pure glassy carbon electrodes (Fig. 2). This suggests that this wave represents the reduction of oxygen on bare carbon surface in the FePc-coated electrode. Optical and electron microscopic examinations of the electrodes showed the existence of bare spots and a rather non-uniform coating distribution for films prepared by evaporation of FePc solutions. Wave Ic appears to be

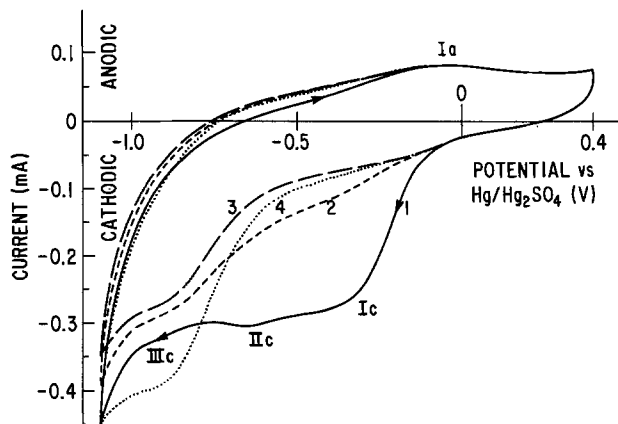


Fig. 4. Cyclic voltammograms of GC with FePc film: O_2 saturated, avg. film thickness $\sim 11000\text{\AA}$, apparent area = 0.57 cm^2 , scan rate = 100 mV/sec . (1) — first scan, (2) - - - second scan, (3) — — fifth scan, (4) on stirring and bubbling O_2 ; sixth scan.

associated with the reduction of oxygen on the FePc film. The variation of peak current with the square root of scan rate for this wave is linear (Fig. 5), indicating that the process is diffusion controlled. Furthermore, the peak potential of I_c shifts to more cathodic values as the scan rate increases, implying a slow electron transfer process. This wave persists even after bubbling He through the solution for 2-3 hr, and we have been unable to eliminate it completely. Presumably, some residual oxygen remains in the solution or is adsorbed on the FePc surface.

It is interesting to note here that the well-defined voltammetric wave, I_c , was obtained only on the first scan and its intensity is diminished considerably on continuous scanning (see Fig. 4). By waiting for about 1 hr at open circuit until the initial open-circuit potential of about $0.15\text{V vs. Hg/Hg}_2\text{SO}_4$ is reestablished, we are able to retrace the original wave (solid line in Fig. 4). The time to reestablish this open-circuit potential appeared to be independent of whether or not O_2 was present in the solution. This apparent "deactivation" of the electrode for the reduction of oxygen

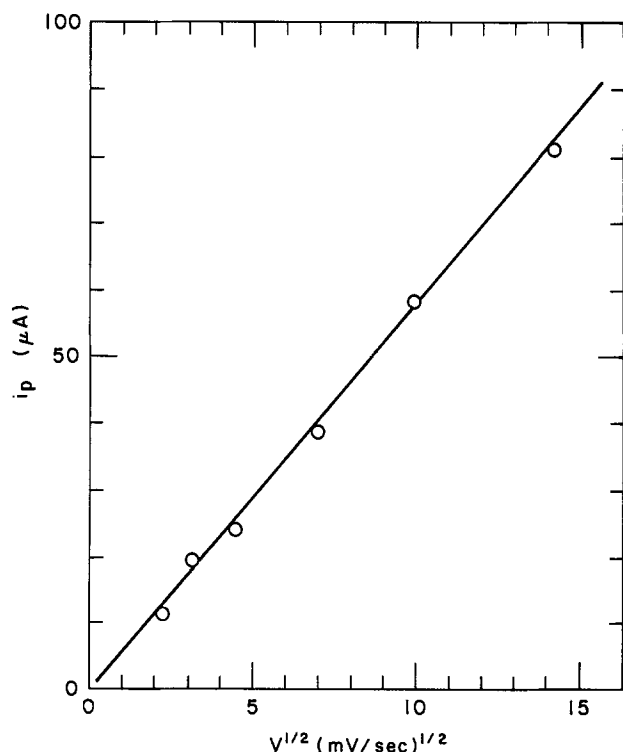


Fig. 5. Scan rate dependence of peak current for I_c

with repeated scanning was first noted by Kozawa *et al.* (2), who thought that it was due to high cathodic potentials (-0.8V vs. SCE in acid solutions). Although some loss in activity occurred in our electrodes when cycled to about $-1.1\text{V vs. Hg/Hg}_2\text{SO}_4$, this loss appears to be primarily due to desorption of the catalyst and/or breakdown of the film, which was brought about by the onset of gas evolution. Even under this condition, wave I_c reappeared when the cell was retained on open circuit for $\sim 1\text{ hr}$. Our electrodes deactivated even when switching potentials of -0.8V were used. Stirring the solution or bubbling O_2 through it during subsequent scans did not increase the cathodic current for I_c , although it increased that for III_c . We are conducting further investigations to establish the origin of this deactivation phenomenon. Some possible causes are: (i) deactivation by peroxide electrogenerated on the bare electrode surface, (ii) blockage of active surface sites on the electrodes, or (iii) some limitation in the transport of charge carriers within the electrode. The third possible cause might be expected if, in line with Faulkner's hypotheses (5), FePc is considered a p-type semiconductor. Depletion of electrons or limitation in their transport can lead to saturation-type currents, which have been observed with semiconductor electrodes (10).

Electrochemical behavior similar to that of electrodes prepared by method (ii) was observed for our electrodes prepared by soaking the glassy carbon in solutions of FePc in pyridine or DMF (method i). For such electrodes, the peak current of wave III_c is, however, often higher, indicating that a larger area of the carbon surface had been exposed. The intensities of the waves vary considerably from electrode to electrode, the efficiency of the dipping process for FePc attachment being facilitated by slightly roughening the glassy carbon surface.

Some difference was observed in the electrochemical behavior of the vapor-deposited FePc films (method iii). Figure 6 shows the cyclic voltammogram for an electrode with 3000\AA thick FePc film vapor deposited on glassy carbon ($0.05\text{M H}_2\text{SO}_4$ electrolyte solution). The absence of wave III_c is notable in this voltammogram. Coverage by the vapor-deposited film on the electrode appeared uniform and no bare spots were visible microscopically. The absence of III_c is thus explained. For the case of O_2 -saturated solution, waves III_a and II_a also disappear, while an increase in background current in the region of II_c causes this wave to increase. Only a small peak for I_c is observed. The increase in residual current at -0.35V in the presence of oxygen is slight. This appears to support Tachikawa and Faulkner's (5) claim that O_2 is not significantly reduced on their vapor-deposited film electrodes.

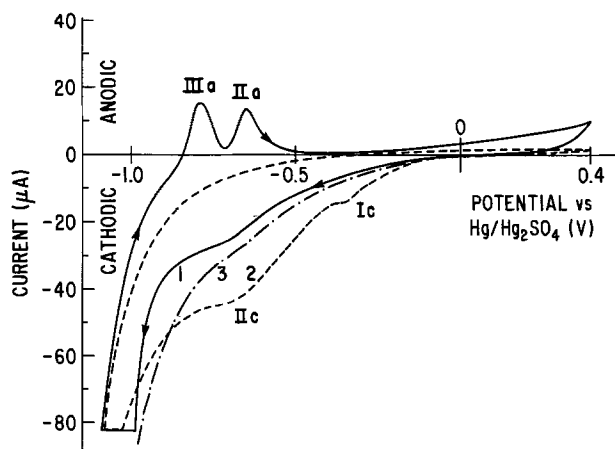


Fig. 6. Cyclic voltammograms of vapor-deposited FePc film on GC electrode: scan rate = 100 mV/sec , apparent area = 0.42 cm^2 . (1) — He saturated; (2) - - - O_2 saturated, first scan; (3) — — O_2 saturated, second scan.

Table I. Oxygen reduction on FePc-glassy carbon electrodes

| Method of electrode preparation* | Avg. film thickness (Å) | Cathodic current** ($\mu\text{A}/\text{cm}^2$) |
|--|-------------------------|--|
| 1) Vapor deposited | 3000 | 17 |
| 2) Vapor deposited | 1500 | 23 |
| 3) Vapor deposited | 500 | 21 |
| 4) Evaporation of 0.1 w/o FePc/DMF solution | 2000 | 145 |
| 5) Evaporation of 0.1 w/o FePc/DMF solution | 6000 | 192 |
| 6) Same as (4) and (5) but on rough carbon substrate | 11,000 | 354 |
| 7) Soaking in 0.25 w/o FePc/pyridine solution (roughened slightly) | — | 95 |
| 8) Soaking in 0.1 w/o FePc/DMF solution (roughened slightly) | — | 296 |

* Highly polished carbon substrate unless otherwise specified.
 ** At -0.35V ; scan rate = $100\text{ mV}/\text{sec}$.

In Table I, we present the oxygen reduction currents at about -0.35V for FePc films on carbon prepared by the three methods. It is evident that, while all the films catalyze O_2 reduction, the activity of vapor-deposited FePc films is significantly lower than that of films prepared from pyridine or DMF. It also appears that the activity of the latter film does not depend on the solvent used since the same cathodic current has been observed by Kozawa on films prepared by precipitation of FePc from concentrated H_2SO_4 solutions (2). The difference in electrocatalytic activity of the films is probably attributable to their different structures. Films prepared by vapor deposition (or sublimation) are known to crystallize in the β -polymorphic form of FePc while those precipitated from solution take the α -form (11). The former is more stable, but the latter has higher electrical conductivity and is more active towards the uptake of oxygen. In the β -polymorph, the nitrogen atoms of the neighboring molecules are situated axially above and below the central metal atoms at about 3.38\AA . In the α -form, the nitrogen atoms of the nearest molecules are not in axial positions, thereby, allowing access of electronegative ligands (e.g., O_2) to the iron site (6). Our Raman spectroscopy results, described in the next section, provide concrete evidence for the difference in structure of the two types of film.

We feel confident about the assignment of waves Ic and IIIc for films prepared by all 3 methods. Waves IIc, IIIa, and IIa appear to be characteristic of the FePc itself. From their symmetrical shapes, they appear to be surface processes (12). The integrated charges under each wave indicate that the bulk of the FePc film is not involved. Wave Ia has been difficult to characterize owing to the presence of a coincident wave on the pure carbon electrode. This wave may be partially attributable to a surface process on the FePc, with a component also due to the anodic oxidation of the carbon surface. A similar deactivation phenomenon is observed with IIc as with Ic. The possibility that IIc has a component which is a consecutive reaction to Ic cannot be ruled out at this time. The possibility that the voltammetric waves observed here were due to impurities has also been considered. We feel this is unlikely. Analyses of our FePc showed insignificant organic contaminants and only a faint trace ($< 10\text{ ppm}$) of a number of metals. Impurities tend to give rise to a high background residual current rather than well-defined waves. Moreover, the same general voltammetric behavior is observed with different sample preparation procedures which should lead to varying impurity levels in the electrode and solution. Further electrochemical investigations of the redox processes associated with the above voltammetric waves are needed. To help elucidate these phenomena, spectroscopic measurements were undertaken. Some initial results are presented in the following section.

In situ laser Raman spectroscopy studies.—Raman spectroscopic measurements for the FePc films on glassy carbon electrodes in $0.05\text{M H}_2\text{SO}_4$ were conducted *ex situ* and *in situ* as a function of applied potential. Laser excitation with a Kr^+ laser at 647.1 nm was principally employed to take advantage of resonance enhancement of the Raman effect. (FePc has an electronic absorption band in the $600\text{--}800\text{ nm}$ region.) Typical spectroscopic results are shown in Fig. 7. Essentially the same spectra are obtained *ex situ* for FePc films on glassy carbon prepared by method (ii), solution evaporation, and method (i), immersion in solution. Some difference was observed when the film was prepared by method (iii), vapor deposition. Bands at 1330 and 1600 cm^{-1} due to the carbon substrate appear for all the electrode specimens; their intensities relative to the FePc bands vary inversely with film thickness. The *in situ* spectra for films prepared from organic solutions appear to be the same as the *ex situ* spectra with the following exceptions: a new band appeared at 1513 cm^{-1} and the 1526 cm^{-1} band increased in intensity following immersion of the electrode in the solution (Fig 8). To ascertain the origin of the 1513 cm^{-1} band, *in situ* spectra were taken in pure water both in the presence and absence of oxygen. The 1513 cm^{-1} band was observed in both cases, indicating that this band is associated with an interaction of the FePc film with water. This band appears to increase with time following immersion of the electrode in water, while the adjacent band at 1500 cm^{-1} decreases proportionately with time. Removal of the electrode from water results in reappearance of the 1500 cm^{-1} band and a proportional decrease in intensity of the 1513 cm^{-1} band. Based mainly on infrared spectral studies on metalloporphyrins (13, 14) and metal phthalocyanines (15-17) together with a normal coordinate analysis of the vibrational spectra of metalloporphyrins (19), we have assigned the 1500 cm^{-1} band to the C-N stretching mode. A shift in the frequency of this band to 1515 cm^{-1} is consistent with coordination of water to the bridge nitrogen site in FePc. This assignment is supported by the x-ray and u.v. photoelectron spectroscopy studies of Kawai *et al.* (20) on the adsorption of water on metal phthalocyanines. This last study as well as that of Sidorov (18) indicate adsorption of a hydrogen in the water molecule onto the bridge nitrogen site. Furthermore, from the intensity of the 1530 cm^{-1} band, it can be deduced that the water is incorporated into the bulk of the phthalocyanine film rather than just on the surface layer.

We are as yet unable to assign a mode for the 1526 cm^{-1} band; its intensity change follows closely that of the 1513 cm^{-1} band and can, to a large extent, be accounted for by its partial overlap with this band.

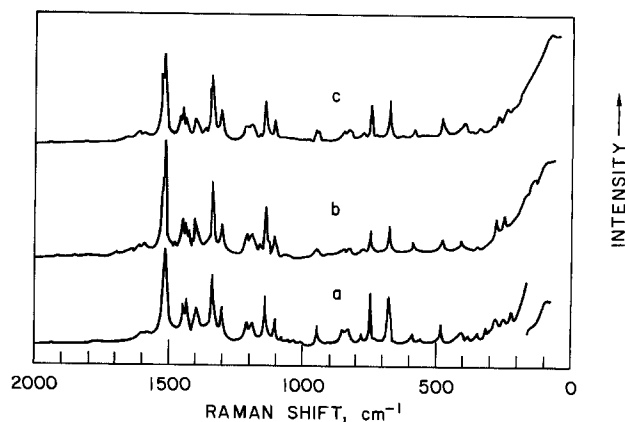


Fig. 7. Raman spectra of FePc film on glassy carbon electrode: (a) *ex situ* spectra, (b) *in situ* at $E = 0.4\text{V}$, (c) *in situ* at $E = -0.8\text{V}$. Avg. film thickness $\approx 500\text{\AA}$, Kr^+ Laser, $\lambda = 647.1\text{ nm}$, $P = 140\text{ mW}$.

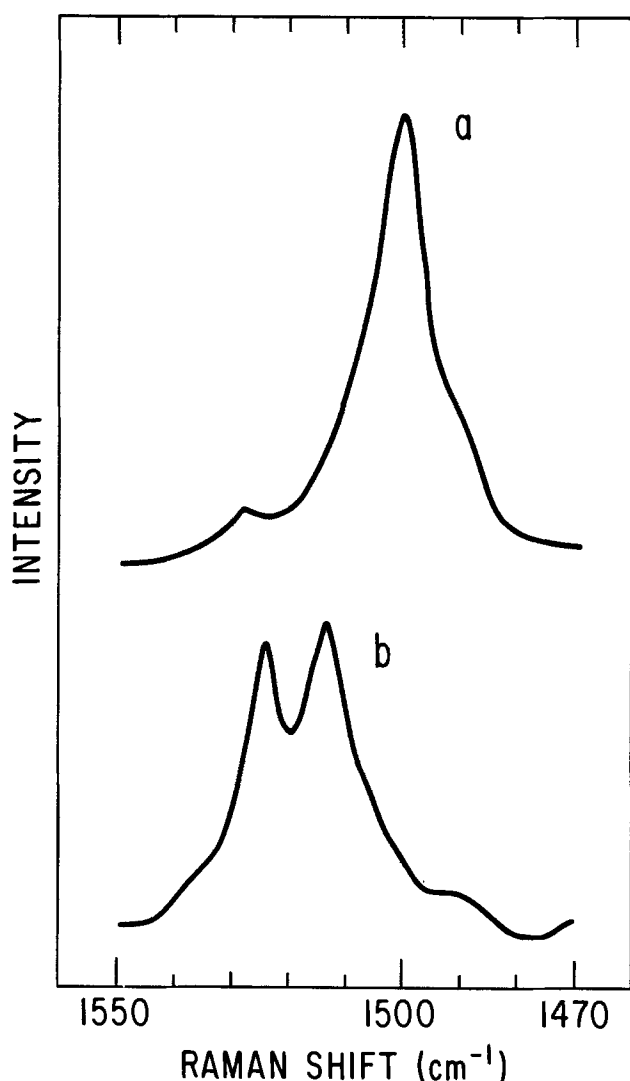


Fig. 8. Raman spectra of FePc-on-glassy carbon electrode (partial). Film prepared by evaporation of DMF solution (α -form). (a) *Ex situ* spectra, (b) *in situ* after 15 min following immersion of electrode in solution. Avg. film thickness $\sim 3500\text{\AA}$, Kr^+ Laser, $\lambda = 647.1\text{ nm}$, $P = 95\text{ mW}$.

The difference in *ex situ* spectra of vapor-deposited FePc film and films prepared by methods (i) or (ii) can be seen by comparison of Fig. 9 and Fig. 8a. In Fig. 9, strong bands at ~ 1513 and $\sim 1526\text{ cm}^{-1}$ are observed in addition to the 1500 cm^{-1} band. These two bands again increase in intensity on immersion of the electrode in water or $0.05\text{M H}_2\text{SO}_4$ solution, while the 1500 cm^{-1} band decreases. The appearance of the 1513 cm^{-1} band in the vapor-deposited films, even in the absence of water, can be rationalized in terms of the structure of the β -form of FePc. As previously stated, in this form, the iron is coordinated above and below the bridge nitrogen site, hence the spectrum is similar to that taken *in situ* for the α -form coordinated with water molecules. As a result of this coordination, the C-N stretching frequency shifts. We also find a weak band at $\sim 278\text{ cm}^{-1}$ which is specific to the vapor-deposited FePc; this is in addition to all other bands observed for films prepared from solution. This weak band probably involves an iron-ligand vibrational mode, which is expected to occur in the region of $100\text{--}300\text{ cm}^{-1}$.

We have also studied the dependence of the vibrational spectrum of FePc on the applied potential. Starting at an open-circuit potential of about $0.15\text{V vs. Hg/Hg}_2\text{SO}_4$, the potential was changed to the desired value and the spectrometer was scanned from 100 to 2000 cm^{-1} . Spectra were obtained at constant poten-

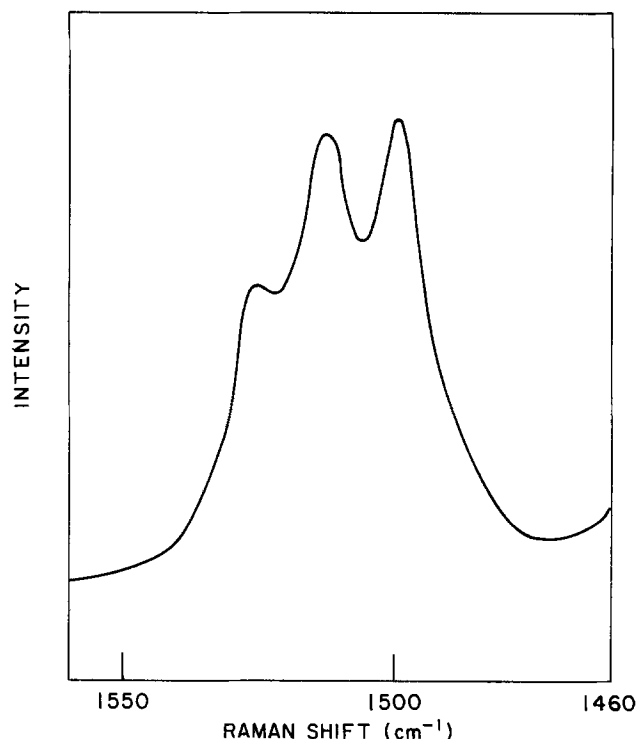


Fig. 9. Raman spectra of vapor-deposited FePc film on GC (β -form). Average thickness = 3000\AA .

tials from $+0.4$ to -1.0V . Apart from a marked decrease in intensity of the bands with the passage of current, the spectra were essentially the same as the one obtained at open circuit (Fig. 7a and 7b); no significant shift in frequency of the bands occurred and no new bands appeared. The 1513 and 1526 cm^{-1} bands appear unaffected by the applied potential and cycling. A continuous deterioration of the spectra (poor signal-to-noise ratio), however, occurs with time of cathodization and at the more negative potentials. The latter is probably associated with the formation of gas bubbles, which were observed on the electrode surface.

The independence of the vibrational spectra of FePc on applied potential implies either the structure of the FePc film is unaffected by potential or the laser Raman spectroscopic technique is insensitive to any structural changes that are occurring, or both. It is likely that no structural change occurs in the bulk of the FePc film as a function of potential. If the bulk of the film were ionized, frequency shifts of the bands and the appearance of new ones would be expected (22). The laser Raman technique is sensitive to bulk structural changes. Whether it is able to monitor electronic structural changes of the surface layer in the present system was of interest to us. The passage of current certainly indicates the occurrence of electrochemical reactions at the electrode surface. To see if we can follow the structural changes associated with these reactions, *in situ* spectra of FePc on glassy carbon prepared by dipping the electrode in a solution of FePc in pyridine, to obtain monolayer coverage, were obtained. The spectra were not significantly different from those of the thick film as far as can be established. The signal-to-noise ratio, however, was rather poor; in many instances, only the most intense band at about 1500 cm^{-1} was observed. Again, no potential dependence was observed for this band. Initial attempts to obtain spectra *in situ* for FePc adsorbed on high-surface-area carbon electrodes have not been successful.

To recapitulate, we have reported in this publication some results on the interfacial behavior of carbon-supported FePc films in $0.05\text{M H}_2\text{SO}_4$. Our cyclic voltammetry measurements showed similar electrochemical

behavior of FePc films prepared by solution evaporation or dipping and by vapor deposition. The FePc films catalyze the electrochemical reduction of oxygen to varying degrees but deactivate on continued scanning. The mechanism for this deactivation process is not known; it is likely to be associated with the slow transport of charge carriers within the semiconductor film electrode. "In situ" laser Raman spectroscopy investigations indicate coordination of the FePc with water molecules in solution. This finding should be considered in any attempt to correlate electrocatalytic activity of FePc films with structural features. The "in situ" laser Raman technique can monitor structural changes in the bulk of the FePc film; the α and β forms of FePc can be distinguished. The vibrational modes of the bulk film, however, appear independent of applied potential.

Acknowledgment

The authors are grateful to Dr. J. Unik and Dr. J. Ferraro of the Chemistry Division, ANL, for allowing us the use of their Raman spectrometer, to Al Smirvickas for assistance in its operation, and to Dr. R. Varma for initial introduction to the technique.

This work was carried out under the auspices of the Materials Science Office of the Department of Energy's Division of Basic Energy Sciences.

Manuscript submitted June 9, 1980; revised manuscript received Nov. 3, 1980.

Any discussion of this paper will appear in a Discussion Section to be published in the December 1981 JOURNAL. All discussions for the December 1981 Discussion Section should be submitted by Aug. 1, 1981.

Publication costs of this article were assisted by Argonne National Laboratory.

REFERENCES

1. H. Jahnke, M. Schönborn, and G. Zimmerman *Top. Curr. Chem.*, **61**, 133 (1976).
2. A. Kozawa, V. E. Zillinois, and R. J. Brodd, *This Journal*, **117**, 1470 (1970).
3. H. Alt, H. Binder, and G. Sandstede, *J. Catal.*, **28**, 8 (1973).
4. J. Zagal, R. K. Sen, and E. Yeager, *J. Electroanal. Chem. Interfacial Electrochem.*, **83**, 207 (1977).
5. H. Tachikawa and L. R. Faulkner, *J. Am. Chem. Soc.*, **100**, 4379 (1978).
6. A. J. Appleby, J. Fleisch, and M. Savy, *J. Catal.*, **44**, 281 (1976).
7. H. Meier, U. Tschirwitz, *et al.*, *J. Phys. Chem.*, **81**, 712 (1977).
8. B. Z. Nikolic, R. R. Adzic, and E. B. Yeager, *J. Electroanal. Chem. Interfacial Electrochem.*, **103**, 281 (1979).
9. C. A. Melendres, *J. Phys. Chem.*, **84**, 1936 (1980).
10. J. B. Flynn, *This Journal*, **105**, 715 (1958).
11. T. R. Srivastava, J. L. Przyblinski, and A. Nath, *Inorg. Chem.*, **13**, 1562 (1974).
12. E. Laviron, *Bull. Soc. Chim. Fr.*, 3717 (1967).
13. L. J. Boucher and J. J. Katz, *J. Am. Chem. Soc.*, **89**, 1340 (1967).
14. H. Ogoshi, N. Masai, *et al.*, *Bull. Chem. Soc. Jpn.*, **44**, 49 (1971).
15. H. Ogoshi, E. Watanabe, Z. Yoshida, *et al.*, *J. Am. Chem. Soc.*, **95**, 2845 (1973).
16. T. Kobayashi, *Spectrochim. Acta*, **26A**, 1313 (1970).
17. T. Kobayashi, F. Kurokawa, *et al.*, *ibid.*, **26A**, 1305 (1970).
18. A. N. Sidorov and I. P. Kotlyar, *Opt. Spectrosc.*, **11**, 92 (1961).
19. H. Ogoshi, Y. Saito, and K. Nakamoto, *J. Chem. Phys.*, **57**, 4194 (1972).
20. T. Kawai, M. Soma, and Y. Matsumoto, *et al.*, *Chem. Phys. Lett.*, **37**, 378 (1976).
21. A. N. Sidorov, *Opt. Spectrosc.*, **11**, 379 (1961).
22. I. V. Aleksandrov, Y. S. Bobovich, V. G. Maslov, and A. N. Sidorov, *Opt. Spectrosc.*, **37**, 265 (1974).

Reactions of FeS Electrodes in LiCl-KCl Electrolyte

Z. Tomczuk,* S. K. Preto,* and M. F. Roche*

Argonne National Laboratory, Chemical Engineering Division, Argonne, Illinois 60439

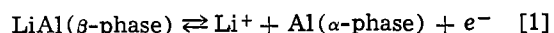
ABSTRACT

The reactions of FeS electrodes in LiCl-KCl electrolytes of various compositions were determined by a combination of phase studies, cyclic voltammetry, and emf measurements. The effect of temperature, charge-cutoff voltage, and electrolyte composition on the phases present in the sulfide electrode were determined. Six electrochemical and four chemical reactions can occur. The emf's of three of the six electrochemical reactions were measured over a temperature range of 380°-530°C and were computed for the other three electrochemical reactions. The free energy changes for the chemical reactions were also calculated.

Since the early 1970's Argonne National Laboratory has been developing high-performance batteries for use as power sources for vehicle propulsion and as energy storage devices for electric utilities. In the ongoing development work, the battery cells are operated at 400°-500°C and consist of molten LiCl-KCl electrolyte, Li-Al alloy negative electrodes, and FeS or FeS₂ positive electrodes. The LiAl/FeS cell has received the greatest attention, primarily because an inexpensive current collector (iron) can be used in the FeS electrode and because the capacity retention of this cell is superior to that of the LiAl/FeS₂ cell (1, 2).

The electrochemical properties of the Li-Al alloy have been reported in considerable detail (3-8). The

potential of this electrode in LiCl-KCl electrolyte at 400°C is approximately 300 mV less anodic than that of liquid lithium, and the electrode reaction is simply



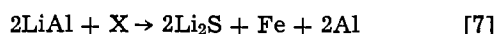
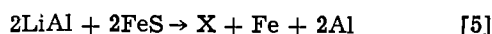
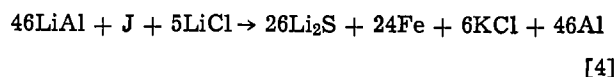
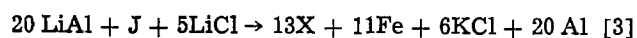
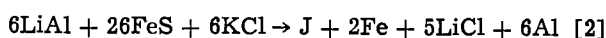
Some properties of the FeS electrode, which has a voltage of about 1.34V vs. Li-Al, have also been reported (9-17). Five phases have been identified: FeS, LiK₆Fe₂₄S₂₆Cl (≡J-phase), Li₂FeS₂ (≡X-phase), Li₂S, and Fe. The FeS phase corresponds to a fully charged electrode, the J- and X-phases are present at intermediate states of discharge or charge, and the Fe and Li₂S phases correspond to the fully discharged electrode. Additional phases are formed when cells are overcharged (12). These higher voltage phases were usually avoided in the present study.

* Electrochemical Society Active Member.

Key words: fused salts, free energy, voltammetry, emf.

The objectives of this study were: (i) to determine the sequence of phase transitions that occurs in the FeS electrode during discharge and charge, (ii) to obtain information on the effects of electrolyte composition and cell temperature on the electrode reactions, and (iii) to determine the thermodynamic properties of the reactions.

Thermodynamic preliminaries.—Because so many phases are involved in the FeS electrode reactions, some thermodynamic preliminaries are useful to outline the relationships among them. The condensed phases in the positive electrode consist of the liquid electrolyte, iron, and the sulfide phases. All of these phases can be prepared from five components: LiCl, KCl, FeS, Li₂S, and Fe. The Gibb's phase rule for condensed systems, in which pressure and the gas phase are ignored, states that six conditions (coexisting phases and defined intensive variables) must be met to define a five-component condensed system at equilibrium (18). Four such conditions for the electrochemical reactions of FeS are: (i) iron is present, (ii) liquid electrolyte is present, (iii) the cell has a known temperature, and (iv) the electrolyte has a known ratio of LiCl to KCl. If any two of the sulfide phases are then present, an electrode of fixed potential is defined. Six such combinations of the four known sulfides are possible as shown in Fig. 1. The LiAl/FeS cell discharge reactions that correspond to the arrows in Fig. 1 are as follows



The arrows in Fig. 1 are labeled with the free energy change of the electrochemical reaction

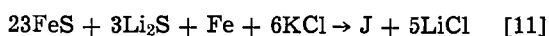
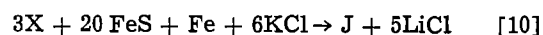
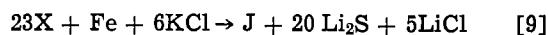
$$\Delta G_i = -n_i F E_i \quad [8]$$

where n_i is the Li-Al coefficient in reaction [i], F is the Faraday, and E_i is the emf of reaction [i]. For instance, the free energy change for reaction [2] is given by $\Delta G_2 = -6FE_2$.

Certain combinations of three E_i define the thermodynamic properties: any three E_i not forming a triangle in Fig. 1 may be selected independently. For instance, the discharge path consisting of reactions [2], [3], and [7] has the net effect of reducing FeS to Fe plus Li₂S and gives one set of three independent volt-

ages from which the other three voltages can be calculated.

It will occasionally be necessary to consider mixtures of three sulfide phases with iron. Such mixtures can be at equilibrium in a given electrolyte at only one temperature. At other temperatures in the same electrolyte, the three sulfide phases are not in equilibrium, and a chemical reaction tends to consume one of them. These chemical reactions are derived by eliminating Li-Al (and Al) between any two of the electrochemical reactions [2]-[7]. Four chemical reactions, two of which are independent, are derived in this way. These are



The free energy changes of these chemical reactions (ΔG_9 to ΔG_{12} , respectively) are related to the emf's of the electrochemical reactions as follows

$$\Delta G_9 = -46F(E_7 - E_4) = -20F(E_7 - E_3) \quad [13]$$

$$\Delta G_{10} = -20F(E_5 - E_3) = -6F(E_2 - E_5) \quad [14]$$

$$\Delta G_{11} = -46F(E_6 - E_4) = -6F(E_2 - E_6) \quad [15]$$

$$\Delta G_{12} = -2F(E_5 - E_6) = -F(E_5 - E_7) \quad [16]$$

Measurement of two of these ΔG_i vs. T and one of the E_i vs. T is sufficient to describe the system's thermodynamic properties. For example, Saboungi, Marr, and Blander (15) have obtained the ΔG_i at several temperatures through determination of the sulfide-ion activity required to convert FeS to J-phase or J-phase to X-phase in LiCl-KCl eutectic electrolyte. These ΔG 's may be combined with E_i data to define the system. In other experiments, Saboungi and Martin (16) have conducted metallographic studies to determine several combinations of temperatures and LiCl-to-KCl ratios that correspond to either $\Delta G_9 = 0$ or $\Delta G_{10} = 0$. Under these $\Delta G = 0$ conditions, three sulfide phases coexist with iron, and, according to Eq. [13] and [14], three of the E_i coincide. These data may also be combined with E_i data to derive the system's thermodynamic properties. Thus, a variety of techniques may be employed to determine the thermodynamic properties of the LiAl/FeS cell.

In this study, we began by establishing the FeS electrode phases under various cycling conditions through metallographic and x-ray examinations. Cyclic voltammetry experiments were then conducted to aid in determining the dominant reaction paths in electrolytes of various compositions and temperatures. Finally emf measurements were combined with other available data to obtain the thermodynamic properties of the electrode.

Experimental

The LiCl-KCl eutectic (mp 352°C) was obtained from Anderson Physics Laboratory and was polarographic grade. It was analyzed to confirm its composition [58 mole percent (m/o) LiCl]. Polarographic grade LiCl was also obtained from the Anderson Physics Laboratory. The KCl was reagent grade (Baker) and had been dried at 100°C under vacuum for about 1 hr. The iron sulfide was stoichiometric FeS, obtained from Great Western Inorganic, that was ground and sieved (either -80, +170 mesh, or -325 mesh). Chemical analysis indicated that the purity was >99% and x-ray diffraction analysis showed that the material was single phase. The iron and lithium sulfide powders were obtained from Cerac/Pure, Incorporated and Foote Minerals, respectively. The stated purity of the iron was 99.9%, and the stated purity of the lithium sulfide was >97%. The purity of both materials was verified by chemical analysis. The Li-Al alloy powder

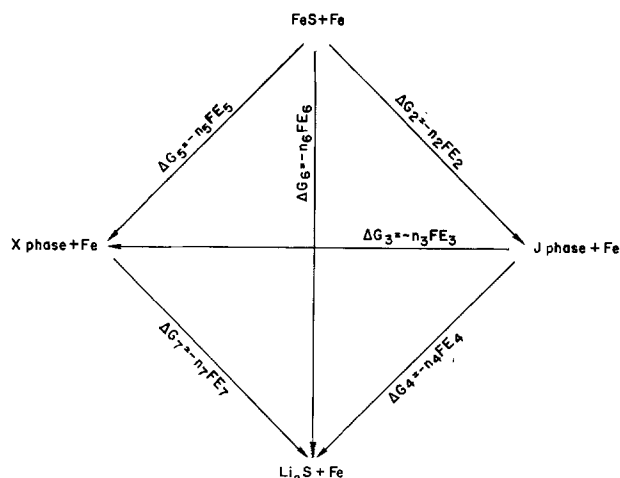


Fig. 1. Electrochemical reactions of the FeS electrode

was obtained from KBI, Incorporated and contained 48 atom percent (a/o) lithium. The aluminum powder was obtained from Alcoa Aluminum Company and was >99% pure.

The cell design is shown in Fig. 2. The cells contained an iron sulfide working electrode and lithium-aluminum counter and reference electrodes. These were immersed in about 80 ml of electrolyte contained in a 250 ml alumina crucible. The Li-Al reference electrode was required only for cyclic voltammetry experiments; the Li-Al counterelectrode served as a reference electrode in the phase studies and emf measurements. In some phase studies, a liquid lithium counterelectrode (9) was used instead of Li-Al. We have converted any voltage data from these cells to the equivalent voltage vs. Li-Al. Thus, all cell voltages are given vs. an Li-Al reference electrode.

The FeS working electrodes were prepared by loading the FeS (or an equivalent amount of Fe and Li₂S) into the cavity (5 cm² × 0.6 cm) of an ATJ¹ graphite cup. A disk of porous graphite (PG-60¹) was then graphite-cemented to the face of the cup to serve as a particle retainer. Other designs of working electrode were employed in a few experiments. For example, an iron or molybdenum cup (1 cm² × 0.5 cm), covered with fine screens and containing FeS with a five-fold excess of iron powder, was used in some of the voltammetry work. Molybdenum cups (2.5 cm diam × 0.6 cm deep) were also substituted for the graphite cups in a few cell tests. The theoretical capacity of the working electrodes was 0.5-1 A-hr (0.8-1.6g FeS) in the phase studies and emf measurements, but was much smaller in the cyclic voltammetry experiments (20-80 mA-hr).

The Li-Al counterelectrodes (42 a/o Li) were prepared by vibrating a mixture of 6g Li-Al powder (~5 A-hr Li) and 1.5g Al powder into a porous iron Retimet² disk (2.5 cm diam × 1.2 cm thick) which was contained in an iron or nickel cup. Fine stainless steel screens were welded to the face of the cup to retain the powders. The Li-Al reference electrodes (42 a/o Li) were similar in construction to the counterelectrodes, but were smaller (1 cm diam) and contained 1.6g Li-Al and 0.4g Al. These reference electrodes were wrapped in BN fabric so they could be placed close to the working electrodes (within 0.5 cm) without shorting.

Procedures.—The cells were operated at temperatures ranging from 370° to 520°C in a furnace well (7.5 cm ID) which was attached to a helium-atmosphere glove box. The helium was continuously purified

¹ A product of Union Carbide Corporation.

² A product of Dunlop Limited, Coventry, England.

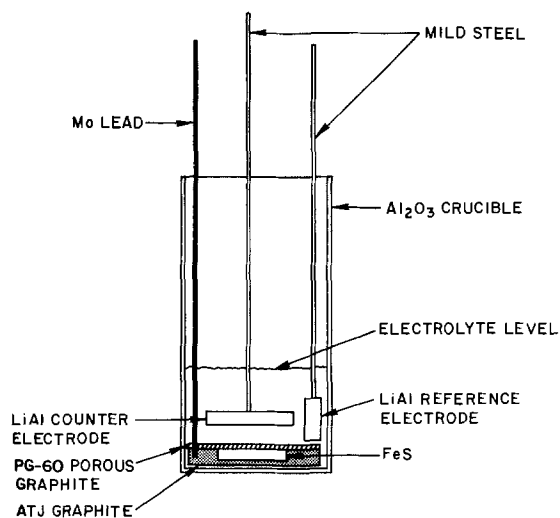


Fig. 2. Design of the LiAl/FeS cell

(<3 ppm O₂ and H₂O) by a combination of molecular sieves and cold traps. The furnace controller maintained the cell temperature within 1°C of the pre-selected value during cell operation. A sheathed Chromel-Alumel thermocouple that had been calibrated against an NBS standardized thermocouple was used to monitor the temperature of the cell vs. an ice point reference.³ Since the thermocouple was wired to the cell exterior, a correction was required for the temperature drop through the alumina crucible. Interior vs. exterior temperature measurements on one cell gave a linear temperature correction ranging from 8° to 13°C for interior temperatures of 370°-520°C. In another cell (operated in a different furnace well), the correction was 2°C over the same temperature range. The reported cell temperatures include this type of temperature correction and are believed to be within 0.5°C of the actual cell temperature.

The cells used for phase studies were cycled at constant charge and discharge current densities of 10-50 mA/cm². The cell temperature employed during this cycling ranged from 400° to 490°C. The cycler consisted of a Hewlett-Packard Model 620B constant-current power supply equipped with a voltmeter-controlled relay system that reversed the direction of cell current at charge and discharge cutoff voltages of about 1.6 and 1.0V, respectively.

For the phase studies, some of cell tests were stopped during their initial charge or discharge, and others were stopped after subjecting them to five or more full cycles (generally, the coulombic efficiency was greater than 90% and the utilization of the FeS electrode capacity was greater than 80% in each of these cycles). In most of these tests, the electrodes were removed immediately after interrupting the current, and the electrodes were cooled to ambient temperature in the glove box. However, in some cases, the cells were allowed to approach equilibrium (either on open circuit or at some constant voltage) for several days prior to removal of the electrodes.

The positive-electrode phases were then examined by metallography and x-ray diffraction. The polishing equipment and microscopes for the metallographic work were located in a helium-atmosphere glove box to prevent reactions between the electrode samples and air. The glass capillaries for x-ray diffraction work were filled with electrode samples and were temporarily sealed with Apiezon grease prior to removal from the glove box. Upon removal, a section of the capillary between the sample and grease was fused to form a permanent seal.

For the cyclic voltammetry studies, the three-electrode cells were controlled by a Wenking Model 70HC3 potentiostat and a Wenking Model VG72 voltage scan generator, and the data were recorded on a Hewlett-Packard Model 7045A X-Y recorder. The procedure consisted of repeated cathodic and anodic sweeps to obtain steady-state voltammograms at each electrolyte composition and temperature. The tests were conducted using LiCl-KCl electrolyte (52-75 m/o LiCl) at temperatures of 389°-481°C. To resolve the various electrode-reaction peaks, low scan rates (about 0.02 mV/sec) were usually employed; a typical voltammetry cycle (1200 mV) required ~17 hr. These cycling rates are comparable to the rates at which the LiAl/FeS cells were cycled, and thus the phase data from cells could be related to the voltammetry data. The small capacity and large volume of the cyclic voltammetry electrodes precluded direct phase determinations on them.

For the emf measurements, cells of high coulombic efficiency were selected. These cells were first conditioned by cycling them for at least five full cycles at a current density of 15 mA/cm² and a temperature of 420°C. In these cycles, the coulombic efficiencies exceeded 99%, and the utilization of the FeS electrode

³ A product of J. Kaye Company, Cambridge, Massachusetts.

capacity was greater than 80%. After being cycled, the cells were either discharged or charged to a selected fraction of their capacity and were placed on open circuit. The emf was then measured at the operating temperature of the cell as well as higher and lower temperatures with a Dana Model 5330 digital voltmeter ($10^{10}\Omega$). An emf was recorded only after the open-circuit voltage at each temperature was stable within 0.1 mV for at least 4 hr. Most of the data includes a 16-20 hr check of stability, although the voltage had usually stabilized within 1-2 hr. In some special cases, however, very long relaxation times (in excess of 100 hr) were employed to test for the possible effects of slow chemical reactions.

The cells for the emf measurements employed electrolyte of eutectic composition. However, it was recognized that the J-phase reactions would shift the composition. The maximum shift in composition was computed from the known weights of cell electrolyte and FeS and the stoichiometries of reactions [2], [3], and [4]. It never exceeded 0.3 m/o, and thus could be ignored.

A thermal emf, which resulted from the use of dissimilar metal leads (molybdenum on the positive elec-

trode and iron on the negative electrode), was subtracted from the cell emf data. The thermal emf was measured by shorting the fully discharged electrodes to each other within the cell and reading the residual voltage at various temperatures. The thermal emf varied linearly from 3.3 mV at 370°C to 4.4 mV at 520°C.

Results and Discussion

Electrode phases.—In the first discharge of relatively large FeS particles ($\sim 160\ \mu\text{m}$ diam), different surface reactions and core reactions were evident, as shown in Fig. 3. With an equivalent amount of more finely divided FeS particles ($< 45\ \mu\text{m}$ diam) in the electrode, the surface reactions tended to go to completion, and the cores were then absent in all but a few larger particles. This difference between equivalent amounts of larger and smaller particles indicates that the layering effect in larger particles is caused by limited diffusion within the surface layer. Since the FeS particles in well-cycled electrodes become very fine ($< 20\ \mu\text{m}$ diam), their discharge reactions are much simpler than those shown in Fig. 3. Nevertheless, an examination of the first discharge of large particles is of interest because the limitations of some of the

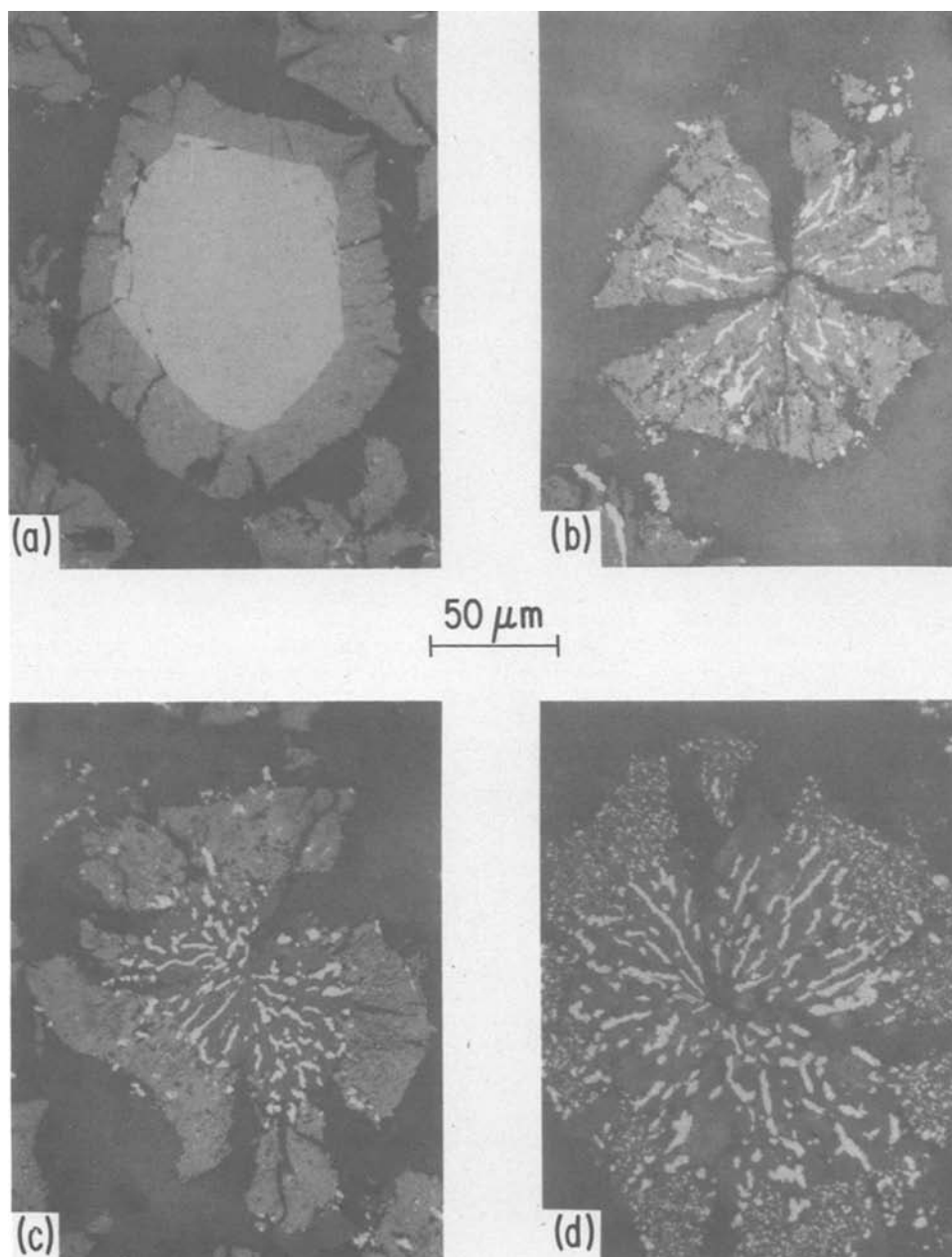


Fig. 3. Phases formed during the first discharge of large FeS particles (matrix phase is electrolyte): (a) core is FeS and surface layer is J-phase plus fine iron particles, (b) core is X-phase (gray) plus iron (white) and surface layer is J-phase plus fine iron particles, (c) core is Li_2S (gray) plus iron (white) and surface layer is J-phase plus fine iron particles, and (d) core and surface are Li_2S and iron.

reactions are readily observed. The first discharge of Cu_2S -modified FeS electrodes (20 m/o Cu_2S) has been reported (14). In that system the first reaction was like that shown in Fig. 3(a), but subsequent reactions also involved the Cu_2S and the distinct surfaces and cores were not as evident.

The particles shown in Fig. 3 came from various electrodes that were 20-100% discharged in eutectic electrolyte at 409°-430°C and were then cooled immediately to room temperature. The state of discharge of each particle can be crudely estimated from the relative areas of the phases and the stoichiometry of discharge reactions [2], [4], [5], and [7]; the particles in Fig. 3 are discharged approximately (a) 8%, (b) 25%, (c) 40%, and (d) 100%. Any one electrode usually contained a variety of such particle types. For instance, an electrode stopped at 20% discharge contained a mixture of unreacted FeS, particles like (a) and (b), and four-phase particles that combined features of (a) and (b). These four-phase particles each had a core of FeS, an intermediate layer of X-phase and Fe, and a surface layer of J-phase and Fe. These mixtures of particle types clearly were not in equilibrium, but the overall reaction sequence could still be deduced by examining the individual particles.

This examination showed that the first discharge of large FeS particles proceeded in four successive stages: I, FeS on the surface discharged to J-phase and iron; II, FeS in the core discharged to X-phase and iron; III, X-phase in the core discharged to Li_2S and iron; and IV, J-phase on the surface discharged to Li_2S and iron. The core reactions (stages II and III) only required Li^+ ions (and electrons) for their completion, while the surface reaction (stage I) also required K^+ and Cl^- to satisfy the stoichiometry of J-phase. Preferential diffusion of Li^+ through the J-phase surface layer was evident from the occurrence of the core reactions. It was also evident that the discharge of J-phase (stage IV) had a relatively low voltage; stages II and III were completed before stage IV occurred. Since the formation of J-phase was diffusion limited and the discharge of J-phase was a lower voltage reaction, suppressing these reactions (and accentuating the X-phase reactions) seemed desirable for high electrode performance.

One possible method of suppressing the J-phase is to employ an electrolyte with a high LiCl -to- KCl ratio, which tends to drive chemical reactions [9]-[11] to the left (15, 16). A first discharge of FeS in LiCl -saturated (68 m/o LiCl) electrolyte at 425°C provided an initial test of this possibility. The J-phase surface layers generated under these conditions were only one-fifth as thick as the surface layers shown in Fig. 3. Subsequent cell tests (19) established the beneficial effects of LiCl -rich electrolytes on cell performance, and such electrolytes are now routinely used in high-performance Li-Al/FeS cells (20).

The phases in well-cycled FeS electrodes and their relationship to cell voltage curves will now be described. Voltage curves for a well-cycled FeS cell are shown in Fig. 4; two voltage regions, A and B, are apparent. A charge cutoff voltage of 1.78V, which is somewhat higher than the normal 1.65V, was used to reveal region A, which corresponds to the $\text{J} \rightarrow \text{FeS}$ reaction on charge and the $\text{FeS} \rightarrow \text{J}$ reaction on discharge. A reference electrode showed that the higher voltage of region A was caused by shifts in the potential of the FeS electrode. The phase progression in regions A and B during discharge is simpler than that during charge and will be described first.

As noted previously, well-cycled FeS electrodes contain very fine particles ($<20\mu\text{m}$ diam) which undergo mainly the surface discharge reactions of larger particles (i.e., stages I and IV). Thus, at least in terms of observed phases, the cell discharge presents a simple, two-stage sequence that can be represented as $\text{FeS} \rightarrow \text{J} \rightarrow \text{Li}_2\text{S}$. Early in the discharge (region A of Fig. 4),

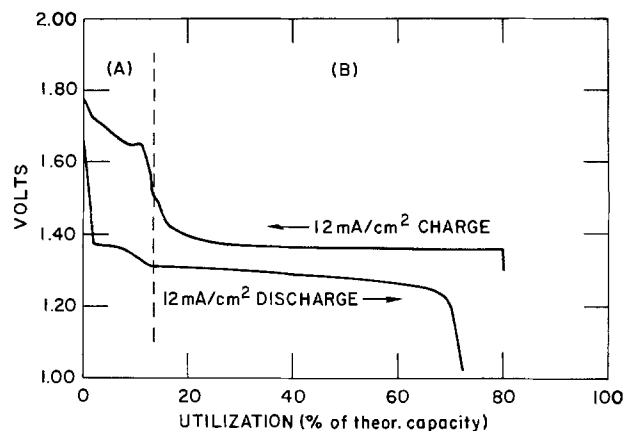


Fig. 4. Voltage curves for an Li-Al/FeS (0.45 A-hr) cell operated at 443°C using electrolyte of eutectic composition.

the phases are FeS, J, and Fe, and, for the remainder of the discharge (region B of Fig. 4), the phases are J, Li_2S , and Fe. Very little X-phase can be found in well-cycled electrodes that are stopped during discharge at normal cell temperatures (450°C or less). These results may be compared with metallographic studies (16) of chemical reactions [9] and [10]. These showed that mixtures of FeS, J-phase, and Fe were more stable than mixtures of FeS, X-phase, and Fe at temperatures up to 623°C in eutectic electrolyte. Similarly, mixtures of J-phase, Li_2S , and Fe were more stable than mixtures of X-phase, Li_2S , and Fe at temperatures up to 455°C in eutectic electrolyte. Thus the phase mixtures found in cycled cells that are discharged at normal temperatures are the equilibrium phase mixtures.

The phase mixtures found in well-cycled FeS electrodes that were stopped on charge were more complex than those on discharge. For example, X-phase was always found in cells stopped during charge anywhere in voltage region B of Fig. 4. In the first charge (5% theoretical) of fine Li_2S and Fe powders (~ 200 mesh) at 430°C, we found coexisting mixtures of X-phase, J-phase, Li_2S , and Fe. In fact, whenever X-phase was present, J-phase, Li_2S , and Fe were also found in the electrode, with the ratio of X-phase to J-phase being dependent on temperature and state of charge. In cells with eutectic electrolyte, the X-phase was more evident at higher temperatures and lower states of charge.

In spite of the complicated, nonequilibrium phase mixtures, the successive stages of the charge reaction could be outlined by examining contiguous regions of electrodes that were at increasing states of charge. Photomicrographs that illustrate various phase mixtures present in small regions of the electrodes, and that also represent successively higher states of charge, are shown in Fig. 5. From such examinations, we believe that the major stages during charge are as follows: I, Li_2S and Fe charge mainly to X-phase and Fe (with concurrent formation of J-phase tending to obscure this reaction); II, X-phase and Fe charge to J-phase and Fe; and III, J-phase and Fe charge to FeS. These charge stages were not as well defined as the discharge stages because of the involvement of X-phase, which is a nonequilibrium phase at normal cell temperatures.

Stages I and II occurred in region B of the charge curve in Fig. 4, while stage III occurred in region A. The voltage of the charge curve in region A was highly temperature sensitive, ranging from $\sim 1.7\text{V}$ at 390°C to $\sim 1.45\text{V}$ at 480°C; the other portions of the voltage curves varied only slightly with temperature. The difference between the charge and the discharge voltages in region A suggests poorer reversibility at low temperatures (large difference) and better reversibility at high temperatures. To confirm the indications that a

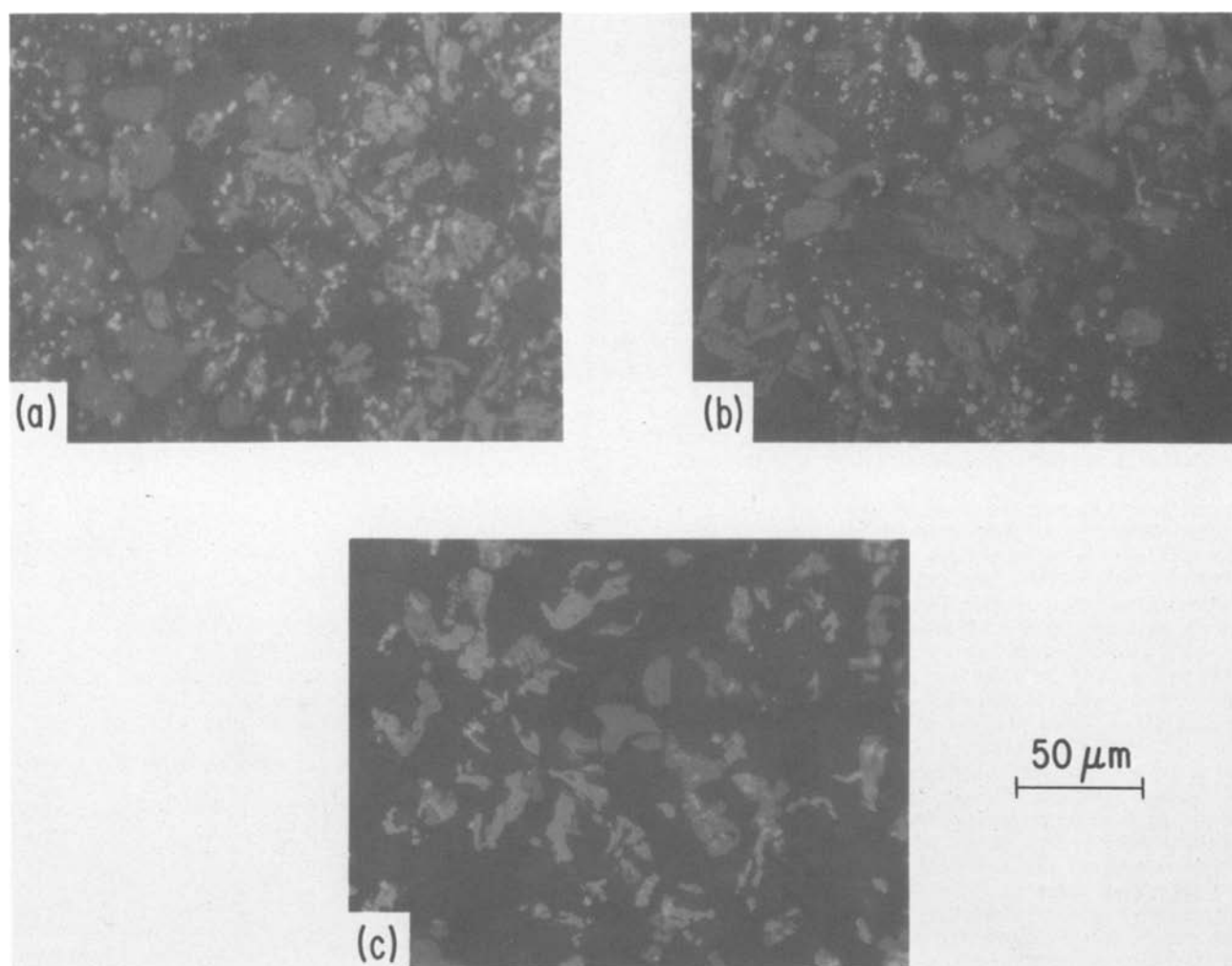


Fig. 5. Phases formed in well-cycled FeS electrodes during charge (matrix phase is electrolyte): (a) conversion of Li_2S and Fe (gray and white particles, respectively, on the left) to X-phase and Fe (gray and white particles, respectively, on the right), (b) conversion of X-phase and Fe (gray and white particles, respectively, on the left) to J-phase and Fe (gray and white particles, respectively, on the right), and (c) conversion of J-phase (darker gray) and Fe to FeS (lighter gray).

high cell voltage is required to drive the stage III reaction, we potentiostated two well-cycled cells at 1.50V for about 100 hr at a cell temperature of 400°C. The positive electrodes taken from these cells contained only J-phase and Fe; no FeS was generated.

From these phase studies, it was evident that well-cycled FeS electrodes had a different phase sequence on charge ($\text{Li}_2\text{S} \rightarrow \text{X} \rightarrow \text{J} \rightarrow \text{FeS}$) than on discharge ($\text{FeS} \rightarrow \text{J} \rightarrow \text{Li}_2\text{S}$) when eutectic electrolyte and cell temperatures less than 450°C were employed. However, one other feature of low-temperature cell operation needs to be considered. In addition to the usual solid phases, KCl or LiCl crystals may also be formed by current-induced shifts in salt composition (21, 22). We have occasionally seen evidence that such crystals were formed in cells operated at high current densities ($\sim 50 \text{ mA/cm}^2$) and low cell temperatures ($\sim 430^\circ\text{C}$). In qualitative agreement with expectations, excess KCl was found near full discharge and excess LiCl near full charge. Such shifts in electrolyte composition, although not ordinarily detected, are in a direction that would tend to stabilize J-phase relative to X-phase on discharge and, conversely, stabilize X-phase relative to J-phase on charge. Thus, electrolyte composition shifts may partly account for the X-phase being more evident on charge than discharge at lower cell temperatures. However, the electrochemical and chemical reaction sequences are also a factor in accentuating X-phase on charge and suppressing it on discharge, as will be seen in the analysis of cyclic voltammetry data.

A few cells with eutectic electrolyte were tested at temperatures of 480°-500°C during the course of the phase studies. The results of these tests tend to support the chemical-reaction studies (16) which showed X-phase becomes an equilibrium phase at high temperatures in eutectic electrolyte. For example, we found that X-phase was apparently in equilibrium with J-phase and Fe at a temperature of 500°C in a 20% discharged cell that had been placed on open circuit for 50 hr prior to removal of the electrodes. In another cell, operated at $\sim 490^\circ\text{C}$ and stopped at 43% charge, X-phase and iron were dominant; only traces of J-phase were found. In a cell operated at $\sim 490^\circ\text{C}$ and stopped near full charge, FeS, J-phase, and Fe were still the dominant phases. Although these studies of phases present at high temperatures are less extensive than the studies of phases present at low temperatures, the phase sequence seems reasonably certain. Higher temperatures lead to similar sequences of sulfide phases during charge and discharge; namely, $\text{Li}_2\text{S} \leftrightarrow \text{X} \leftrightarrow \text{J} \leftrightarrow \text{FeS}$. However, the cyclic voltammetry studies indicate that the electrode reactions are not quite as reversible as this simple sequence implies.

It should be noted that no significant variations in either the x-ray diffraction patterns or metallographic characteristics of the electrode phases were detected in the above studies. Furthermore, there were always at least two coexisting sulfides (e.g., FeS and J-phase) during an electrode reaction. Thus each of the reactions is expected to have a fixed emf.

Although we have sometimes used a shorthand notation (e.g., $\text{Li}_2\text{S} \rightarrow \text{X}$) for reactions, we have purposely delayed the assignment of specific reactions (from the list of ten in the first part of the paper) to the observed phase sequences. The problem in making such assignments is that a variety of plausible combinations of electrochemical and chemical steps can lead to the same mixtures of phases. More detailed reaction assignments are given in the discussion below.

Cyclic voltammetry.—Cyclic voltammograms at high scan rates (5–50 mV/sec) for iron immersed in Li_2S -saturated LiCl-KCl eutectic electrolyte have been presented (11, 17). Their interpretation is difficult because the peaks may reflect transient intermediates rather than known electrode phases. In the present study, we concentrated on very low scan rates (0.01–0.02 mV/sec) that were comparable to the cell-cycling rates used in the phase studies. This type of voltammetry is similar to coulometry since the area of a current peak (in coulombs) is approximately the theoretical peak capacity and each peak can be reasonably associated with known electrode phases.

The effects of increasing scan rates are shown in Fig. 6 in which cyclic voltammograms at scan rates of 0.015, 0.1, and 0.2 mV/sec are given. In this case, the electrode consisted of 20 mA-hr of FeS (and a five-fold excess of iron) in a molybdenum housing ($1 \text{ cm}^2 \times 0.5 \text{ cm}$). These voltammograms indicate that the dominant peaks (one on discharge and two on charge) are under ohmic control since the peak currents and peak potentials are both proportional to the square root of the scan rate. This type of ohmic behavior has been noted previously for the discharge peaks (11). Each of the peaks in Fig. 6 seems to exhibit more structure as the scan rate increases. Consequently, we believe that our reaction assignments, which will be based on the lower rates, will not define all the possible reactions at higher rates.

Figures 7 and 8 illustrate some of the effects of changes in cell temperature and electrolyte composition on voltammograms taken at scan rates of 0.01–0.02 mV/sec. The voltammograms in Fig. 7 are for eutectic electrolyte (58 m/o LiCl) at (a) 400°C and (b) 455°C , while those in Fig. 8 are for LiCl -rich electrolyte (67 m/o LiCl) at (a) 453°C and (b) 481°C . Since the mole ratio of electrolyte to FeS was very high (100:1) within the electrode cavity and a very large excess of electrolyte was present in the cell, the effects shown in these figures are not due to shifts in electrolyte composition.

Two general features of these voltammograms are of interest. First, the voltammograms indicate that the dis-

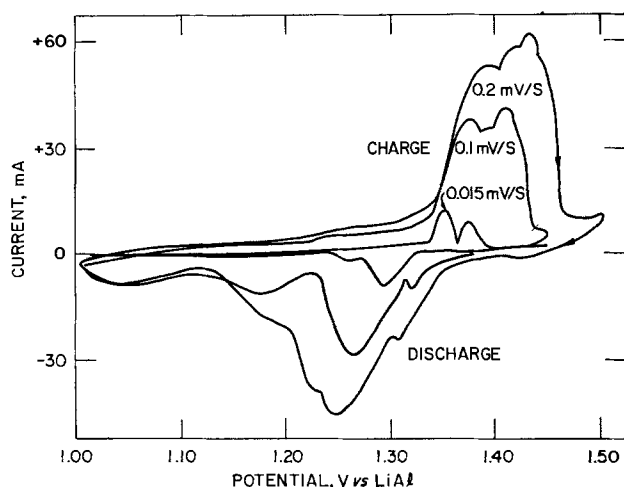


Fig. 6. Effects of increasing scan rates on cyclic voltammetry peaks of FeS electrode (20 mA-hr capacity) operated in eutectic electrolyte at 430°C .

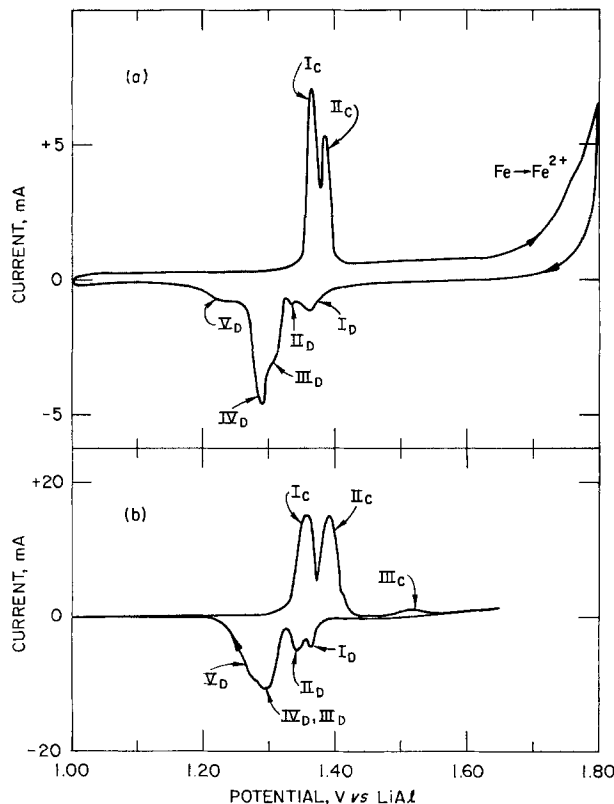


Fig. 7. Voltammograms for FeS electrodes operated in eutectic electrolyte (a) 400°C , 0.015 mV/sec, 18 mA-hr FeS and 90 mg Fe in molybdenum housing, and (b) 455°C , 0.01 mV/sec, 80 mA-hr FeS in graphite housing.

charge electrochemistry is more complex than the charge electrochemistry. The phase studies showed an opposite effect, the phase sequences being more complex during charge. To explain these contrasting effects, a combination of chemical and electrochemical reactions is required. Second, the voltammograms indicate that many of the reactions do not have the sort of ideal reversibility that is desirable for emf measurements; the discharge peaks have different areas than the charge peaks and seem to be located at different potentials.

The major reaction paths were derived by combining the data from cyclic voltammetry and the phase studies. An electrochemical reaction (from the list of six in the beginning of the paper) was assigned to each voltammetry peak on the basis of its size, location, and response to changes in electrolyte composition, cell temperature, and charge-cutoff voltage. These assignments were compared with the emf of each reaction (given in the next section) to ensure that the discharge peak was below the emf and the charge peak was above the emf. The chemical reactions were then considered as required to reconcile any differences between the electrochemical assignments and the observed electrode phases. These chemical reaction assignments were also compared with the emf data, using Eq. [13]–[16], to ensure that the reactions were capable of proceeding in the desired direction.

The electrochemical reactions assigned to charge peaks I_c and II_c in Fig. 7 and 8 are, respectively, $\text{Li}_2\text{S} \rightarrow \text{X}$ (E_7) and $\text{X} \rightarrow \text{FeS}$ (E_5). These assignments are based primarily on the observation that the areas of the two peaks remain nearly equal over a wide range of conditions (see Fig. 7 and 8). However, the assignments are also supported by an analysis of the response of the peak voltages to changes in electrolyte composition and temperature. This analysis is based on the voltage at the leading edge of each peak, which approximates the emf of each reaction. The voltage,

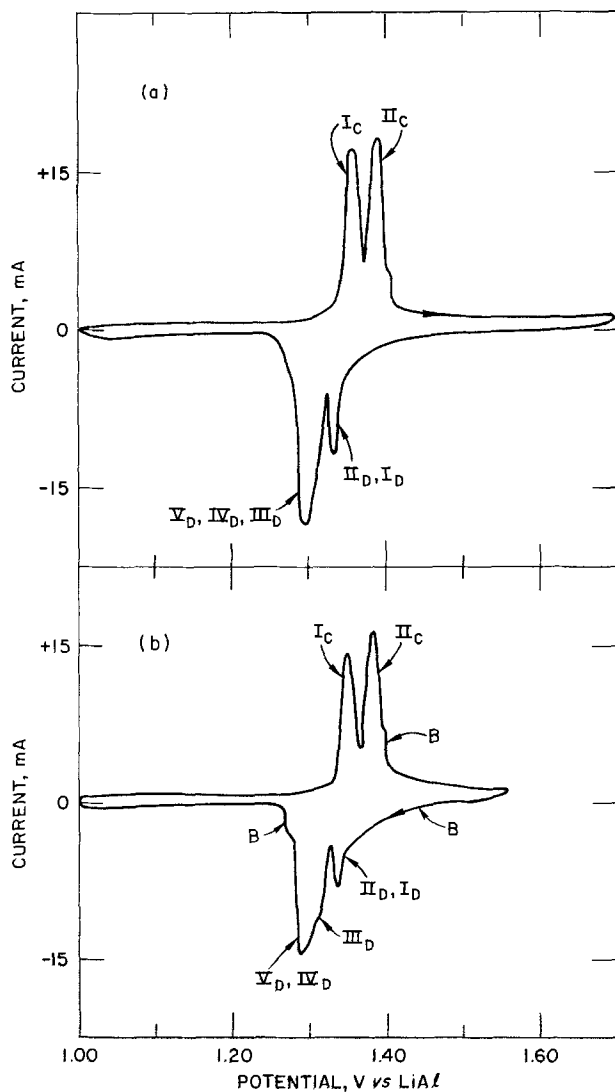


Fig. 8. Voltammograms (0.02 mV/sec) for FeS electrode (40 mA-hr in graphite housing) operated in LiCl-rich electrolyte (67 m/o LiCl) at (a) 453°C and (b) 481°C.

$V(I_C)$, was obtained by linear extrapolation of the left side of peak I_C to zero current, and the voltage, $V(II_C)$, was obtained by adding the peak separation to $V(I_C)$. The voltages obtained in this way for a variety of electrolyte compositions and cell temperatures are presented in Table I and Fig. 9. The voltages in Table I are independent of electrolyte composition, which is in accord with the assigned reactions and excludes J-phase reactions. Furthermore, the voltages have the same temperature dependence as the emf's of the assigned reactions, which are derived in the next section and are also presented in Fig. 9. The slight difference (10-15 mV) in Fig. 9 between the voltages obtained from the voltammograms and the actual emf's

Table I. Voltages of major charge reactions

| Temperature (°C) | Electrolyte composition (m/o LiCl) | $V(I_C)$ (V) | $V(II_C)$ (V) |
|------------------|------------------------------------|--------------|---------------|
| 400 | 58 (eutectic) | 1.345 | 1.366 |
| 425 | 58 | 1.339 | 1.364 |
| 433 | 64 | 1.337 | 1.362 |
| 433 | 67 | 1.335 | 1.360 |
| 433 | 67 | 1.336 | 1.363 |
| 440 | 67 | 1.336 | 1.366 |
| 451 | 67 | 1.335 | 1.366 |
| 451 | 67 | 1.334 | 1.365 |
| 455 | 58 | 1.332 | 1.363 |
| 455 | 52 | 1.332 | 1.363 |
| 481 | 67 | 1.330 | 1.362 |
| 481 | 75 | 1.326 | 1.359 |

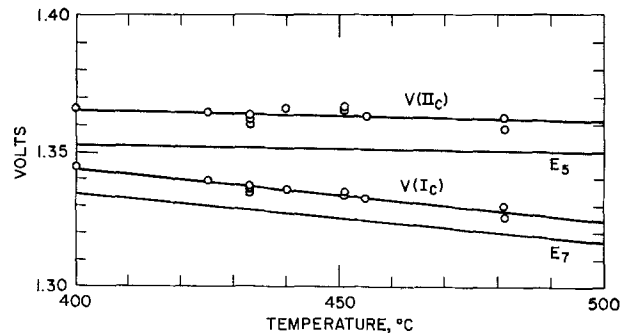


Fig. 9. Comparison of the voltages of the major charge reactions, I_C and II_C , with the emf of the assigned reactions $E_7(X \leftrightarrow Li_2S)$ and $E_5(FeS \leftrightarrow X)$, respectively.

is reasonable; the voltages obtained from the voltammograms may include overpotentials that are not removed by linear extrapolation techniques. Thus, the peak areas and the response of the peaks to changes in electrolyte composition and temperature all tend to support the reaction assignments.

Peaks I_C and II_C are equivalent to charge region B of Fig. 4. According to the phase studies for this region, J-phase is formed to some extent during reaction $I_C(Li_2S \rightarrow X)$ and it is the final product of reaction $II_C(X \rightarrow FeS)$. Thus, chemical reactions [9] ($X \rightarrow J + Li_2S$) and [10] ($X + FeS \rightarrow J$) are required to reconcile the differences between the electrochemical assignments and phase studies. These reactions form J-phase at temperatures as high as 455° and 623°C, respectively, in eutectic electrolyte, according to Saboungi and Martin (16). Certain rate conditions are implicit in these assignments (namely, [9] is slow and [10] is fast), but the rates have not been measured.

The J-phase that is formed in the above reactions is equivalent to approximately 90% charge. The remaining 10% of the charge reaction ($J \rightarrow FeS$) occurred in cell tests on a poorly defined plateau (see Fig. 4) that was temperature sensitive ($\sim 1.7V$ at 390°C; $\sim 1.45V$ at 480°C). In the cyclic voltammetry, we had great difficulty in locating a corresponding current peak. At low temperatures (400°C), the peak may have been masked by the $Fe \rightarrow Fe^{2+}$ charge reaction, which is shown in Fig. 7(a). When this reaction was avoided by reversing the charge scan at 1.7V instead of 1.8V, the leading discharge peak, I_D , was only 50% as large. This indirect evidence suggests that the conversion of J-phase to FeS occurred in the neighborhood of 1.7V. At a higher temperature of 455°C a small peak (III_C) was barely discernible above the background current in Fig. 7(b). This peak shifted from ~ 1.5 to $\sim 1.6V$ when KCl was added to the electrolyte (decreasing the LiCl concentration from 58 to 52 m/o). Such a shift is in the expected direction according to emf calculations which are discussed later. Therefore, we have tentatively assigned the reaction $J \rightarrow FeS(E_2)$ to peak III_C .

In the scans employing LiCl-rich electrolytes (Fig. 8), no high-voltage charge peak for the $J \rightarrow FeS$ reaction could be detected above the background current, but indirect evidence again suggested that a relatively high voltage was required to complete the reaction. For instance, the discharge peak I_D , II_D shown in Fig. 8(a) was only half as large when the charge scan was reversed at 1.56V instead of 1.7V. A peak representing 10%-12% of the charge capacity in Fig. 7 and 8 would have been readily detected if the reaction occurred over a narrow voltage range like peaks I_C and II_C ; we believe therefore, that the III_C peak was usually too broad to detect.

In Fig. 8(b), two poorly resolved peaks and much of the high-voltage region are labeled as background B. These features became noticeable only after high-temperature ($\sim 450^\circ C$) cycles. We concluded that the B-reactions were not associated with the normal FeS re-

actions because they did not decline with cycling as sulfide was lost from the electrode (probably through dissolution of Li_2S in the large volume of cell electrolyte). Over a period of ten cycles of the type shown in Fig. 8(b), the FeS reaction peaks all declined by a factor of three while the background features remained constant. The background peaks and much of the 1-3 mA background current at high voltages may have resulted from intercalation of electrode material in the graphite housing; graphite will intercalate iron chloride and iron sulfides at high temperatures (23). The background problem is also present in the scan shown in Fig. 8(a) (the same electrode, but an earlier cycle), and one of the background peaks seems to be present in Fig. 7(b) to the right of peak II_c (this electrode also employed the graphite housing). With a molybdenum housing, the peaks were absent, but high-voltage background currents were still a problem.

The discharge electrochemistry was very complicated. For example, five discharge peaks are noted in Fig. 7(a), yet only two phase mixtures (FeS, J and Fe or J, Li_2S and Fe) are found on discharge at such low cell temperatures (400°C). Thus, at low temperatures, there are too many electrochemical steps and not enough phase mixtures to account for them. Since X-phase is present in the charge reactions and in the higher temperature discharges, we shall assume that it is also an intermediate in the lower temperature discharges. This situation is basically no different than that with charge peak II_c , where the electrochemical evidence warranted choosing FeS as a charge intermediate even though J-phase was the final product. However, the problem in choosing the intermediate is more obvious on discharge since X-phase will be required for three of the five low-temperature peaks.

The discharge peaks in Fig. 7 and 8 can be divided into two groups using the emf of the $\text{J} \rightarrow \text{Li}_2\text{S}$ reaction ($\sim 1.32\text{V}$ from the emf measurements). From the known phase mixtures above and below this emf, the two higher voltage reactions convert FeS to J-phase and the three lower voltage reactions convert J-phase to Li_2S . As the temperature and LiCl concentration were increased the separate peaks in each region tended to merge; the multiple labels on a peak thus reflect the probable occurrence of more than one reaction.

The electrochemical reactions assigned to peaks I_D and II_D are $\text{FeS} \rightarrow \text{J}$ (E_2) and $\text{FeS} \rightarrow \text{X}$ (E_5), respectively. As with the charge peak II_c ($\text{X} \rightarrow \text{FeS}$), we shall require chemical reaction [10] ($\text{X} + \text{FeS} \rightarrow \text{J}$) to occur with the discharge peak II_D ($\text{FeS} \rightarrow \text{X}$). Thus the final product of I_D and II_D is J-phase. The combined areas of these two peaks are consistent with the conversion of FeS to J-phase ($\sim 10\%$ of the discharge capacity). At high temperatures and LiCl concentrations, these peaks tended to merge at the location of the II_D peak which is in accord with the assignments since the stability of the X-phase relative to J-phase increases under these conditions.

The electrochemical reactions assigned to peaks III_D , IV_D , and V_D are $\text{J} \rightarrow \text{X}$ (E_3), $\text{X} \rightarrow \text{Li}_2\text{S}$ (E_7), and $\text{J} \rightarrow \text{Li}_2\text{S}$ (E_4), respectively. These peaks merge in a complex manner as the LiCl concentration and temperature of the cell are raised (compare Fig. 7 and 8). The last of the peaks, V_D , is assigned the $\text{J} \rightarrow \text{Li}_2\text{S}$ reaction because it is present under conditions of lowest X-phase stability relative to J-phase (lower temperatures and lower LiCl concentrations). The other two peaks, which are poorly resolved, are assigned the $\text{J} \rightarrow \text{X}$ (III_D) and $\text{X} \rightarrow \text{Li}_2\text{S}$ (IV_D) reactions merely because the $\text{J} \rightarrow \text{X}$ transition has to precede the $\text{X} \rightarrow \text{Li}_2\text{S}$ transition. The poor resolution implies that the reactions tend to occur simultaneously. Consequently, X-phase, if it is indeed the intermediate in this doublet, need not appear as a major phase during the $\text{J} \rightarrow \text{X} \rightarrow \text{Li}_2\text{S}$ sequence. The III_D - IV_D reaction assignments are thus in accord with the phase studies.

With a stoichiometric FeS electrode at a temperature of 400°C , peak V_D was much more prominent than shown in Fig. 7(a). Its area was equivalent to $\sim 50\%$ of the discharge capacity, and it was a more definite, but very broad peak that was centered at $\sim 1.19\text{V}$ and extended from $\sim 1\text{V}$ into the trailing edge of the III_D - IV_D peaks. With a large excess of Fe in the electrode [Fig. 7(a)], this broad V_D peak was partially suppressed and the III_D - IV_D peaks were accentuated. A more efficient method of suppressing V_D is to reverse the direction of chemical reaction [9] ($\text{X} \rightarrow \text{J} + \text{Li}_2\text{S}$) through the use of higher temperatures and higher LiCl concentrations. These conditions tend to promote the $\text{J} \rightarrow \text{X} \rightarrow \text{Li}_2\text{S}$ reaction sequence (peaks III_D and IV_D) and diminish the contribution from the direct $\text{J} \rightarrow \text{Li}_2\text{S}$ reaction (peak V_D). However, from the way in which the peaks merge as the cell temperature and LiCl concentration are increased, we believe all three reactions occur simultaneously and have labeled the voltammograms in Fig. 8 accordingly. The X-phase will tend to appear during these simultaneous reactions since it is an equilibrium phase at higher temperatures and LiCl concentrations.

In the above assignments we have not employed the $\text{FeS} \rightarrow \text{Li}_2\text{S}$ (E_6) reaction. Although this reaction will no doubt be required to explain high-scan-rate data, it does not represent an equilibrium mixture of cell phases under any of our test conditions.

The reaction assignments are summarized in Fig. 10 for two general cases, (a) lower LiCl concentrations and temperatures, and (b) higher LiCl concentrations and temperatures. The connecting lines are labeled with the assigned peaks (rather than the E_i used in Fig. 1), and the broad arrows show the effects of the chemical reactions [9] and [10]. Note that the $\text{X} \rightarrow$

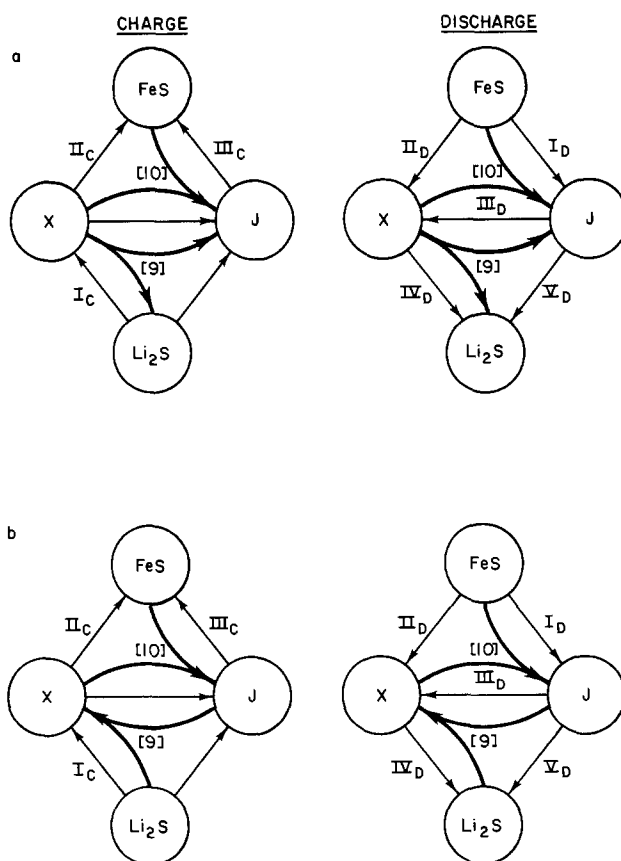


Fig. 10. Summary of reaction assignments for two general cases (a) lower LiCl concentrations and temperatures and (b) higher LiCl concentrations and temperatures. Peak assignments from cyclic voltammetry (roman numerals) and the directions of chemical reactions [9] ($\text{X} \leftrightarrow \text{J} + \text{Li}_2\text{S}$) and [10] ($\text{X} + \text{FeS} \leftrightarrow \text{J}$) are shown.

$J(E_3)$ and $Li_2S \rightarrow J(E_4)$ lines have no peak assignments on charge. The results of emf measurements show that E_3 and E_4 are reversible under some conditions. Consequently, these reactions must occur, but may be masked by the other reactions. The only notable difference between cases (a) and (b) in Fig. 10 is that reaction [9] tends to form J-phase in (a) and X-phase in (b). This accentuation of X-phase at higher LiCl concentrations and temperatures leads to greatly improved cell performance (19, 20), without completely eliminating J-phase from the reaction scheme.

Emf measurements and thermodynamic properties.— Voltage vs. temperature data are given in Fig. 11 and 12. The data in Fig. 11 are from one cell on which measurements were made at 15%-30% discharge (squares) and at 20% charge (circles). The data in Fig. 12 are from a second cell on which measurements were made at 80% charge. The lines E_3 , E_4 , and E_7 in these figures are linear regression curves through selected data (the selection process is based on reversibility tests, and is described below). The dashed curves labeled α , β , and γ in the figures pass through data that represent measurements on various nonequilibrium mixtures of electrode phases (see below); the potentials of such mixtures are often called "mixed" potentials.

Other types of voltage vs. temperature patterns can be obtained depending on the cell operating temperature, the percent of discharge or charge, and the direction of

temperature change during the voltage measurements. For example, a cell was discharged about 52% at a temperature of 400°C, and the open-circuit voltages were recorded as the temperature was first increased to 500°C and was subsequently decreased to 400°C. What is expected here is a pattern similar to the 15%-30% discharge data shown in Fig. 11, but the high temperature data should lie on the $X \leftrightarrow Li_2S$ line instead of the $J \leftrightarrow X$ line because, beyond 50% discharge, the high temperature equilibrium phases are X, Li_2S , and Fe. The results when increasing the temperature were in accord with expectations; the data at temperatures below 470°C were near the $J \leftrightarrow Li_2S$ line, and, above 470°C the data were near the $X \leftrightarrow Li_2S$ line. However, when the temperature was then decreased in several stages from 500° to 400°C, in an attempt to retrace the $X \leftrightarrow Li_2S$ and $J \leftrightarrow Li_2S$ lines, the data were near the $X \leftrightarrow Li_2S$ and α -lines. Thus, the voltage patterns can be extremely complex.

An emf may be extracted from such data only when certain reversibility criteria are satisfied. For instance, the $J \leftrightarrow X(E_3)$ data are obtained at both 20% discharge (Fig. 11) and 80% charge (Fig. 12) which are equivalent states of charge approached from different directions. This is an indication of reversibility. In addition, we found the J, X, and Fe phases in apparent equilibrium at this emf by phase determinations on a cell that had been equilibrated for 50 hr at 20% discharge and 500°C. Thus, we consider the $J \leftrightarrow X(E_3)$ line to be well established and have calculated E_3 by a linear-regression analysis of the 480°-525°C data near E_3 in Fig. 11 and 12. This emf⁴ is given by

$$E_3(J \leftrightarrow X) = 1238.6 + 0.1753T \quad [17]$$

The $J \leftrightarrow Li_2S(E_4)$ data in Fig. 11 were collected in several experiments: (i) The cell was discharged ~15% at 486°C, and measurements were made on the $J \leftrightarrow X(E_3)$ line prior to lowering the temperature to measure the $J \leftrightarrow Li_2S(E_4)$ line. (ii) The cell was discharged ~20% at 400°C, and measurements were made on the $J \leftrightarrow Li_2S(E_4)$ line prior to increasing the temperature to measure the $J \leftrightarrow X(E_3)$ line. The data from (i) and (ii) coincided, indicating reversibility. (iii) The cell was discharged ~30% at 443°C and the procedure described in (ii) was repeated, giving the same results. In this case, however, the temperature was lowered again in an attempt to retrace the $J \leftrightarrow Li_2S(E_4)$ line; the data appeared instead on the α -line (the two square symbols on this line in Fig. 11).

From such measurements, we have found that the $J \leftrightarrow Li_2S(E_4)$ line can be observed when the cell is discharged at low temperatures to avoid large amounts of the X-phase. No data for this line were obtained during charge, where the X-phase interferes. Because of the difficulty in establishing reversible behavior, we consider this line to be less well defined than the $J \leftrightarrow X(E_3)$ line. A linear regression analysis of the 400°-450°C data along E_4 in Fig. 11 gives

$$E_4(J \leftrightarrow Li_2S) = 1346.0 - 0.0525T \quad [18]$$

The $X \leftrightarrow Li_2S(E_7)$ data shown in Fig. 11 are for 20% charge; data near the E_7 line have also been obtained at >50% discharge, indicating reversibility. The persistence of X-phase at low temperatures leads to various nonequilibrium extensions of the E_7 line into the J-phase field. These extensions, which are labeled α , β , and γ in Fig. 11 and 12, would lie on the E_4 line if X-phase were absent. Consider the α -line data in Fig. 11. The data, most of which were obtained at 20% charge, are as much as 10 mV above the $J \leftrightarrow Li_2S$ data, which were obtained near 20% discharge. However, 20% discharge is actually the higher state of charge, being equivalent to 80% charge. Thus, the α -data are definitely for a nonequilibrium state; the emf at 20%

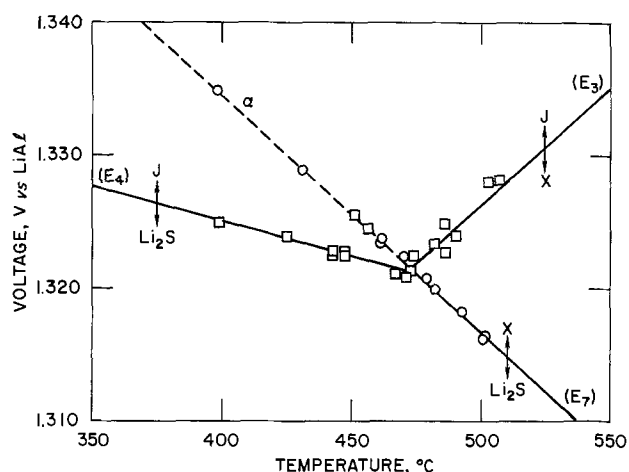


Fig. 11. Voltage measurements on LiAl/FeS cells at 15%-30% discharge (squares) and 20% charge (circles). Emf assignments and a nonequilibrium curve, α , are also shown. Electrolyte is LiCl-KCl eutectic.

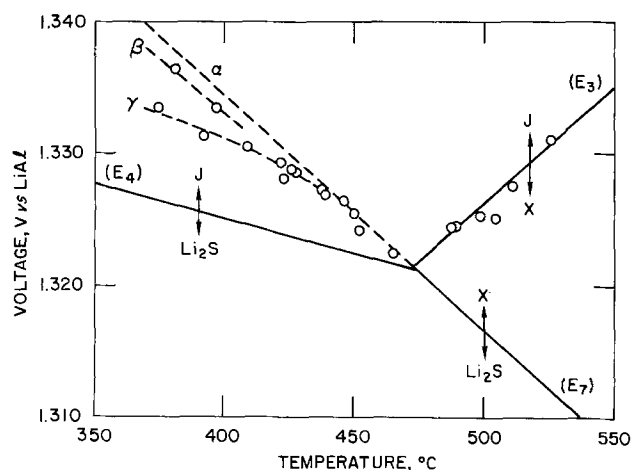


Fig. 12. Voltage measurements on LiAl/FeS cell at 80% charge. Emf assignments and three nonequilibrium curves (α , β , γ) are also shown. Electrolyte is LiCl-KCl eutectic.

⁴ All emf equations are given with the temperature in degrees centigrade and the emf in millivolts.

charge cannot exceed the emf at 20% discharge. Despite the lack of equilibrium, the α -line data represent quite stable voltages; the data at 398° and 431°C showed less than 0.1 mV drift in 100 hr open-circuit measurements. The colinear data along the α -line and E_7 line in Fig. 11 give the following equation for E_7

$$E_7(X \leftrightarrow \text{Li}_2\text{S}) = 1405.8 - 0.1781T \quad [19]$$

The data along the γ -line in Fig. 12 were obtained during an attempt to eliminate the X-phase by extended open-circuit relaxations at a high state of charge. (At a high state of charge the ratio of J-phase to X-phase is high.) Eight measurements were made along the γ -line over a 300 hr period as the temperature was lowered. It can be seen that data lying between the lines E_4 and α were obtained, suggesting that traces of X-phase were still affecting the results. The cell was then heated at $\sim 500^\circ\text{C}$ to generate additional X-phase, and two voltage measurements were made over a 90 hr period at low temperatures. The data were on the β -line in Fig. 12, indicating a somewhat higher level of X-phase in these shorter time measurements. It was evident from the above tests that many hundreds of hours would be required to completely eliminate the X-phase at low temperatures.

The $J \leftrightarrow \text{Li}_2\text{S}$, $J \leftrightarrow X$, and $X \leftrightarrow \text{Li}_2\text{S}$ lines in Fig. 11 and 12 intersect at $473^\circ \pm 2^\circ\text{C}$ and 1321.4 ± 0.2 mV. This is a point of four-phase equilibrium (J, X, Li_2S , Fe) at which $\Delta G_9 = 0$ in Eq. [13]. Metallographic studies have indicated temperatures of $455^\circ \pm 4^\circ\text{C}$ (16) and $465^\circ \pm 7^\circ\text{C}$ (24) for this intersection. Considering the difference in techniques, we believe the measurements are in fair agreement.

One test of the emf equations given for E_3 , E_4 , and E_7 is provided by Eq. [13] which can be written as follows

$$(E_7 - E_3) = 2.30 (E_7 - E_4) \quad [20]$$

This equation can be used to calculate E_4^* from the measurements of E_3 (Eq. [17]) and E_7 (Eq. [19])

$$E_4^*(J \leftrightarrow \text{Li}_2\text{S}) = 1333.0 - 0.0245T \quad [21]$$

The difference between E_4 (Eq. [18]) and E_4^* is only 1.7 mV at 400°C . In view of the difficulties in establishing the E_4 line, we consider the agreement between E_4 and E_4^* to be acceptable. In fact, we prefer to use E_4^* in our subsequent calculations since E_4 is slightly above E_4^* , which may reflect the presence of some residual X-phase during the E_4 measurements.

Note that only two of the emf equations presented so far are independent; one additional emf is needed to determine the thermodynamic properties of the FeS electrode. We attempted to measure the emf of the $\text{FeS} \leftrightarrow J(E_2)$ transition, but could not obtain stable readings. For example, when a cell was charged at 446°C to $\sim 95\%$ of its theoretical capacity, where the $\text{FeS} \leftrightarrow J$ transition is known to occur, the open-circuit voltage steadily declined from 1.49V at 1 hr to 1.42V at 24 hr. When the same cell was taken to full charge and then discharged $\sim 5\%$, the open-circuit voltage rose to 1.43V at 1 hr, but then declined to 1.355V at 24 hr. We will be able to compute the emf of the $\text{FeS} \leftrightarrow J(E_2)$ reaction (assuming it has a fixed emf), but we consider the calculated value to be uncertain since direct measurement was not possible.

To obtain the additional emf equation that was required for a complete description of the electrode, we calculated the emf of the $\text{FeS} \leftrightarrow \text{Li}_2\text{S}(E_6)$ reaction from available thermodynamic data (3, 25-27). This emf, which is probably uncertain by ± 25 mV, is

$$E_6^*(\text{FeS} \leftrightarrow \text{Li}_2\text{S}) = 1383 - 0.10T \quad [22]$$

The $J \leftrightarrow X$, $X \leftrightarrow \text{Li}_2\text{S}$, and $\text{FeS} \leftrightarrow \text{Li}_2\text{S}$ equations were then combined with Eq. [13]-[16] to calculate the emf of the $\text{FeS} \leftrightarrow X$ reaction and $\text{FeS} \leftrightarrow J$ reaction. These

* An asterisk on an emf indicates that it has been calculated from other data.

calculated emf equations are given by

$$E_5^*(\text{FeS} \leftrightarrow X) = 1361 - 0.022T \quad [23]$$

$$E_2^*(\text{FeS} \leftrightarrow J) = 1769 - 0.68T \quad [24]$$

Five emf equations are plotted in Fig. 13 to show the regions of stability of the various electrode phases in eutectic electrolyte. The equation for E_6^* , which is simply the average of E_5^* and E_7 , is omitted. Note the location of an intersection between E_2^* , E_5^* , and E_3 at a temperature of 621°C . This temperature is in excellent agreement with metallographic studies, which have located the intersection at $623^\circ \pm 7^\circ\text{C}$ (16) and $624^\circ \pm 4^\circ\text{C}$ (24); the four solid phases in equilibrium here are FeS, J, X, and Fe. Because of the excellent agreement with metallographic studies, we believe the E_5^* line is accurate to within a few millivolts. It follows that the E_6^* equation must have a similar accuracy, although the thermodynamic data from which E_6^* was calculated were not that precise.

It will be noted that the $\text{FeS} \leftrightarrow X(E_5^*)$, $J \leftrightarrow X(E_3)$, and $X \leftrightarrow \text{Li}_2\text{S}(E_7)$ lines have been extended in Fig. 13 to low temperatures. These extensions were required to treat both the phase data and the cyclic-voltammetry peaks at lower cell temperatures.

The $\text{FeS} \leftrightarrow J(E_2^*)$ line in Fig. 13 is located at a relatively high voltage ($\sim 1.5\text{V}$ at 400°C ; $\sim 1.46\text{V}$ at 450°C). The cyclic voltammetry studies gave lower voltages than E_2^* on discharge (1.4V at 400°C , 1.38V at 450°C), but higher voltages on charge ($\sim 1.7\text{V}$ at 400°C , $\sim 1.5\text{V}$ at 455°C). In cells potentiostated at 1.50V for 100 hr at 400°C , no FeS was formed from J-phase. Thus, the proposed emf for the $J \leftrightarrow \text{FeS}$ transition is in accord with the experimental data.

The emf's of reactions [2], [3], and [4] depend on the electrolyte composition. The changes in E_2^* , E_3 , and E_4^* can be calculated from the reaction stoichiometry and the changes in the activity of LiCl and KCl with electrolyte composition (28). The calculated emf equations for an LiCl-rich electrolyte containing 67 m/o LiCl are as follows

$$E_2^{*'} = 1738 - 0.71T \quad [25]$$

$$E_3' = 1247.8 + 0.1843T \quad [26]$$

$$E_4^{*'} = 1.337.1 - 0.0205T \quad [27]$$

These equations (and E_5^* and E_7) are plotted in Fig. 14 to show the effects of the LiCl-rich electrolyte on the regions of stability of the various electrode phases. The emf-intersection temperatures decrease from 473° and 621°C in eutectic electrolyte (Fig. 13) to 436° and 549°C , respectively, in the LiCl-rich electrolyte (Fig. 14). These shifts cause the field of J-phase stability to

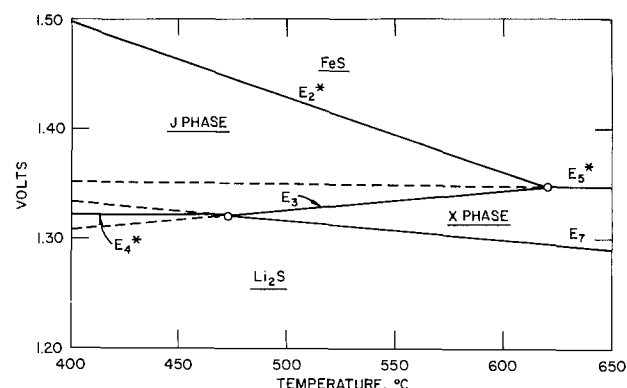


Fig. 13. Regions of stability of FeS, J-phase, X-phase, and Li_2S in LiCl-KCl electrolyte of eutectic composition. Extensions of the $\text{FeS} \leftrightarrow X(E_5^*)$, $J \leftrightarrow X(E_3)$, and $X \leftrightarrow \text{Li}_2\text{S}(E_7)$ reactions into the low temperature region are indicated by dashed lines. An asterisk indicates a calculated emf.

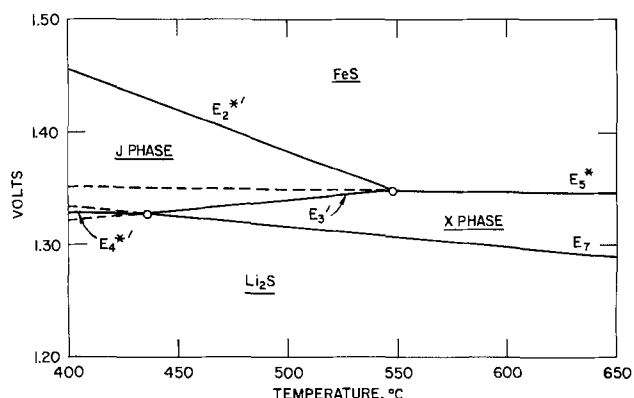


Fig. 14. Regions of stability of FeS, J-phase, X-phase, and Li₂S in LiCl-rich electrolyte (67 m/o LiCl). Extensions of the FeS ↔ X(E₃*), J ↔ X(E₃'), and X ↔ Li₂S(E₇) reactions into the low temperature region are indicated by dashed lines. An asterisk indicates a calculated emf. Note that E₂*', E₃*', and E₄*' are shifted from their corresponding values in eutectic electrolyte (E₂*, E₃, E₄*), and the field of J-phase stability is therefore much smaller.

become much smaller. A cell temperature of 460°C and an electrolyte containing ~67 m/o LiCl are known to be sufficient to suppress the harmful effects of the J-phase on electrode performance (19). According to Fig. 14, the reaction sequence under these conditions is FeS ↔ J ↔ X ↔ Li₂S.

Another calculation that can be made from the emf equations and the activities of LiCl and KCl is the emf-intersection temperatures in LiCl-saturated electrolyte. For example, the intersection of E₂*', E₅*', and E₃, which occurs at 621°C in eutectic electrolyte, is calculated to occur at 481°C in electrolyte saturated with LiCl [75.2 m/o LiCl (29)]. This temperature is in excellent agreement with the metallographically determined temperature of 481 ± 5°C (16). Similar calculations for the intersection of E₃, E₄*', and E₇ (which occurs at 473°C in eutectic electrolyte) give a value of 429°C in LiCl-saturated electrolyte [68.4 m/o LiCl (29)], which is in reasonable agreement with the 419 ± 2°C temperature determined in the metallographic studies (16). The above temperature calculations rely on the reaction stoichiometries and certain emf differences, while the metallographic studies only require the presence or absence of phases. The good agreement between these independent methods tends to confirm the emf equations and the reaction stoichiometries. Therefore, the free energy changes of the chemical reactions can be calculated with a reasonable degree of confidence.

The free energy changes of the chemical reactions [9]-[12] were calculated from the emf equations and Eq. [13]-[16]. For the calculations we selected the eutectic electrolyte as the standard state and used the following relationships

$$\Delta G^{\circ}_9 = -20 F(E_7 - E_3) = -322.6 + 0.682T \quad [28]$$

$$\Delta G^{\circ}_{10} = -20 F(E_5^* - E_3) = -236 + 0.380T \quad [29]$$

$$\Delta G^{\circ}_{11} = -6F(E_2^* - E_6^*) = -223 + 0.336T \quad [30]$$

$$\Delta G^{\circ}_{12} = -F(E_5^* - E_7) = 4.32 - 0.015T \quad [31]$$

where the temperatures are in °C and the free energy changes are in kJ. Calculated values are given in Table II for temperatures ranging from 400° to 600°C. This table shows the decreasing stability of J-phase (first three reactions) and increasing stability of X-phase (last reaction) with increasing temperature.

The ΔG[°]₁₂ values in Table II are in good agreement with an earlier study (15), which gave values of -1.38 ± 0.84 kJ at 450°C and -3.01 ± 0.84 kJ at 500°C. The ΔG[°]₁₁ values in Table II are more negative than those obtained in the earlier study, which gave values of

Table II. Standard free energy changes for the four chemical reactions

| ΔG [°] ₁ (reaction) | Standard free energy change (kJ) | | | | |
|---|----------------------------------|-------|-------|-------|-------|
| | 400°C | 450°C | 500°C | 550°C | 600°C |
| ΔG [°] ₉ (X → J + Li ₂ S) | -50 | -16 | 18 | 52 | 87 |
| ΔG [°] ₁₀ (X + FeS → J) | -84 | -65 | -46 | -27 | -8 |
| ΔG [°] ₁₁ (Li ₂ S + FeS → J) | -89 | -72 | -55 | -38 | -21 |
| ΔG [°] ₁₂ (Li ₂ S + FeS → X) | -1.7 | -2.4 | -3.2 | -3.9 | -4.7 |

-25.9 ± 7.5 kJ at 400°C, -25.5 ± 1.2 kJ at 450°C, and -28.9 ± 2.5 kJ at 500°C. These values were obtained by determining the sulfide-ion activity required to cause J-phase formation from FeS in eutectic electrolyte. The method used was equivalent to a cell discharge, and the location of the FeS ↔ J(E₂) discharge peak in the cyclic voltammograms (Fig. 7) is indeed in accord with the earlier measurements. However, we prefer the higher voltage calculated from Eq. [24] for the FeS ↔ J(E₂) reaction since it seems to be more representative of the combined data for discharge and charge.

One measure of the uncertainty in the ΔG[°]₁₁ values given in Table II is provided by an alternative calculation. Note that Eq. [15] gives two methods of calculating ΔG[°]₁₁, one based on E₂ (which was used for Table II) and another based on E₄, which was both measured (Eq. [18]) and calculated (Eq. [21]). Of course, the value of ΔG[°]₁₁ that would be obtained from the calculated E₄(E₄*) would agree with the results given in Table II. However, the equation that results from the measured E₄ is

$$\Delta G^{\circ}_{11} = -164 + 0.211T \quad [32]$$

This equation differs significantly from Eq. [30] and gives values ranging from -80 kJ at 400°C (vs. -89 kJ in Table II) to -38 kJ at 600°C (vs. -21 kJ in Table II). Clearly, alternative methods of measuring this free energy change are needed. The problem is to find reversible conditions under which the emf of the FeS ↔ J(E₂) reaction can be measured; the use of LiCl-rich electrolytes for this particular emf measurement may be appropriate.

Conclusions

A reasonably complete description of the electrochemistry and chemistry of the FeS electrode in LiCl-KCl electrolytes at low cycling rates was obtained by combining phase studies, cyclic voltammetry data, and emf measurements. In many cases, the measurements are in excellent agreement with other studies, but in one particular area, the thermodynamics of the J-phase (LiK₆Fe₂₄S₂₆Cl), more study is needed. The problem with the J-phase is the poor reversibility of its electrochemical reactions, which leads to large uncertainties in the thermodynamic properties.

In agreement with other studies, high LiCl concentrations in the LiCl-KCl electrolyte tend to improve the cell performance by suppressing the adverse effects of the J-phase. The required mole ratio of LiCl to KCl is approximately 2:1. This electrolyte accentuates the reactions of X-phase (Li₂FeS₂), which are more reversible than the J-phase reactions.

To date, emf measurements have been conducted only in the eutectic electrolyte. Measurements will also be needed in LiCl-rich electrolytes and in electrolytes containing only lithium salts (e.g., LiCl-LiBr-LiF) to more firmly establish the thermodynamics of the six electrochemical and four chemical reactions that are required to describe the FeS electrode. Methods of establishing the identity of transient intermediates in the electrode reactions are also desirable; at present, the reactions are understood only at low cycling rates.

The very complex chemistry and electrochemistry of the FeS electrode has not prevented its use in high-performance (>100 W-hr/kg), long-lived (>300

cycles) Li-Al/FeS cells. The performance and cycle life of this cell may be even higher than they are at present once the FeS electrode reactions are fully understood.

Acknowledgments

The authors would like to express their thanks to A. E. Martin and N. C. Otto for their metallographic analyses and to B. S. Tani for his x-ray diffraction studies. The active support and encouragement of D. R. Vissers, R. K. Steunenberg, D. L. Barney, P. A. Nelson, and L. Burris during the course of this study are also appreciated. Discussions with M. Blander and M. L. Saboungi were particularly helpful and are gratefully acknowledged. Special thanks are due to J. Harmon for editorial assistance. This work was conducted under the auspices of the U.S. Department of Energy.

Manuscript submitted June 9, 1980; revised manuscript received Nov. 14, 1980.

Any discussion of this paper will appear in a Discussion Section to be published in the December 1981 JOURNAL. All discussions for the December 1981 Discussion Section should be submitted by Aug. 1, 1981.

Publication costs of this article were assisted by Argonne National Laboratory.

REFERENCES

1. E. C. Gay, W. E. Miller, R. F. Malecha, and R. C. Elliott, Proceedings of 13th IECEC, Society of Automotive Engineers, Inc., Warrendale, PA, pp. 690-696 (1978).
2. F. J. Martino, T. D. Kaun, H. Shimotake, and E. C. Gay, *ibid.*, pp. 709-716.
3. N. P. Yao, L. A. Heredy, and R. C. Saunders, *This Journal*, **118**, 1039 (1971).
4. E. C. Gay, D. R. Vissers, F. J. Martino, and K. E. Anderson *ibid.*, **123**, 1591 (1976).
5. R. K. Steunenberg and M. F. Roche, in "Electrode Materials and Processes for Energy Conversion and Storage," J. D. E. McIntyre, S. Srinivasan, and F. G. Will, Editors, p. 869, The Electrochemical Society Softbound Proceedings Series, Princeton, NJ (1977).
6. C. J. Wen, B. A. Boukamp, and R. A. Huggins, *This Journal*, **126**, 2258 (1979).
7. C. A. Melendres, *ibid.*, **125**, 727 (1978).
8. K. M. Myles *et al.*, in Proceedings of Symposium and Workshop on Advanced Battery Research and Design, Argonne National Laboratory Report ANL-76-8, pp. B67-B70 (1976).
9. D. R. Vissers, Z. Tomczuk, and R. K. Steunenberg, *This Journal*, **121**, 665 (1974).
10. R. A. Sharma, *ibid.*, **123**, 448 (1976).
11. C. A. Melendres, C. C. Sy, and B. Tani, *ibid.*, **124**, 1060 (1977).
12. Z. Tomczuk, A. E. Martin, and R. K. Steunenberg, Abs. 47, p. 131, The Electrochemical Society Extended Abstracts, Las Vegas, Nevada, Oct. 17-22, 1976.
13. B. Tani, *Am. Mineral.*, **62**, 819 (1977).
14. F. C. Mrazek and J. E. Battles, *This Journal*, **124**, 1556 (1977).
15. M. L. Saboungi, J. J. Marr, and M. Blander, *ibid.*, **125**, 1567 (1978).
16. M. L. Saboungi and A. E. Martin, Abs. 339, p. 919, The Electrochemical Society Extended Abstracts, Pittsburgh, PA, Oct. 15-20, 1978.
17. J. Phillips and H. F. Gibbard, Abs. 335, p. 909, The Electrochemical Society Extended Abstracts, Pittsburgh, PA, Oct. 15-20, 1978.
18. E. Levin, C. Robbins, and H. McMurdie, in "Phase Diagrams for Ceramists," M. Reser, Editor, pp. 8-28, The American Ceramic Society, Columbus, Ohio (1969).
19. D. R. Vissers, Z. Tomczuk, K. E. Anderson, and M. F. Roche, U.S. Pat. 4,156,758 (1979).
20. D. Barney *et al.*, Argonne National Laboratory Report No. ANL-79-94 (1980).
21. C. E. Vallet and J. Braunstein, *This Journal*, **125**, 1193 (1978).
22. R. Pollard and J. Newman, *ibid.*, **126**, 1713 (1979).
23. A. K. Holliday, G. Hughes, and S. M. Walker, in "Comprehensive Inorganic Chemistry," J. C. Bailar, H. J. Emeleus, R. Nyholm, and A. F. Trotman-Dickenson, Editors, p. 1292, Pergamon Press Ltd., Oxford (1973).
24. A. E. Martin, Argonne National Laboratory Report ANL-78-94, pp. 178-179 (1978).
25. K. C. Mills, "Thermodynamic Data for Inorganic Sulfides, Selenides, and Tellurides," Butterworth, and Co., London (1974).
26. D. R. Stull and H. Prophet, JANAF Thermochemical Tables, NSRDS-NBS 37 (1970).
27. R. Hultgren, P. D. Desai, D. T. Hawkins, M. Gleiser, and K. K. Kelley, "Selected Values of the Thermodynamic Properties of the Elements," American Society of Metals, Metals Park, Ohio (1973).
28. J. Lumsden, "Thermodynamics of Molten Salt Mixtures," Academic Press, New York (1966).
29. B. Chu and J. Egan, *Ann. NY Acad. Sci.*, **79**, 908 (1960).

Properties of LiAlCl₄-SOCl₂ Solutions for Li/SOCl₂ Battery

H. V. Venkatesetty* and D. J. Saathoff

Honeywell Corporate Material Sciences Center, Bloomington, Minnesota 55420

ABSTRACT

Conductance and viscosity of LiAlCl₄-SOCl₂ solutions covering a wide range of concentration (10⁻⁴-2.0M) have been measured at 25°C and for concentrated solutions these measurements have been made at several temperatures. Parameters characteristic of ion-ion and ion-solvent interactions and the energy of activation for conductance and for viscous flow have been obtained. Cyclic voltammograms of LiAlCl₄-SOCl₂ solutions at several concentrations have been obtained and the effect of the additives, such as S₂Cl₂, SCl₂, SO₂, and SO₂Cl₂ on the reduction behavior of SOCl₂ has been studied as some of these are reduction products of SOCl₂. The implications of these studies on the performance and safety of the lithium-thionyl chloride battery are discussed.

The lithium-thionyl chloride battery system has become technologically important as a high-energy density and high-power density battery with potentially long shelf-life (1-4). In a lithium-thionyl chloride (Li/SOCl₂) battery, thionyl chloride serves both as a solvent for the solute and a depolarizer for the cell. The common solute used for primary active cells is lithium aluminum chloride (LiAlCl₄) in SOCl₂ at fairly high concentration (1.5-1.8M). It is well known that the transport properties and the structure of these solutions play an important role in the performance of the battery. The charge transfer rate is very much influenced by the nature of the electrical double layer at the phase boundary, and the double layer structure is dependent on the properties of the electrolyte solution. Recently the electrical conductance, viscosity, density of LiAlCl₄-SOCl₂ solutions, and diffusion coefficient of electroactive species, namely, SOCl₂, have been reported (5).

A better understanding of the overall reaction mechanism and the reaction products during the discharge of lithium-thionyl chloride battery is necessary to improve the performance and safety of the battery. There is no complete agreement on the lithium thionyl chloride cell reaction and several cell reactions have been proposed (1, 2, 6). It has been reported that the products of electrolysis of SOCl₂ above 0°C are SO₂, S₂Cl₂, and Cl₂ (7). This paper reports the results obtained on conductance, viscosity, and density of LiAlCl₄-SOCl₂ solutions covering a wide range of concentration (10⁻⁴-2.0M) and temperature. Parameters characteristic of ion-ion and ion-solvent interactions and the energy of activation for conductance and for viscous flow have been obtained. Cyclic voltammetric studies on LiAlCl₄-SOCl₂ solutions at several concentrations have been obtained and the effect of additives such as S₂Cl₂, SCl₂, SO₂, and SO₂Cl₂ on the reduction behavior of LiAlCl₄-SOCl₂ solutions have been examined. The implications of these studies on the performance and safety of lithium-thionyl chloride battery are discussed.

Experimental

Thionyl chloride (MC/B) was mixed with triphenylphosphite (16% by volume) and distilled under a positive pressure of dry nitrogen. The distillate from the first distillation was redistilled with a cut-off point at 80°C, and the middle fraction of the second distillation was used for this study. Anhydrous LiAlCl₄ prepared in this laboratory was used. All chemicals were

weighed to 0.1 mg inside the dry box which was purged with dry argon. All solutions were prepared in the glove bag under a positive pressure of dry nitrogen. Electrochemical measurements were carried out using different batches of LiAlCl₄-SOCl₂ solutions and the experimental data were reproducible. Conductance measurements were made using a Jones bridge with accessories and Jones and Bollinger type conductance cells with bright platinum disk electrodes. A constant temperature oil bath with a control of $\pm 0.05^\circ\text{C}$ at 15° and 25°C and $\pm 0.5^\circ\text{C}$ at 40° and 60°C was used. Viscosity was measured using calibrated Cannon-Fenske type viscometer with guard tube attachment to minimize moisture contamination. Densities were measured using a calibrated density bottle. Cyclic voltammetric studies were carried out using Princeton Applied Research Corporation Model 173 potentiostat/galvanostat with a Model 175 universal programmer. A three-electrode cell with compartments separated by a medium porosity fritted disk was used. A glassy carbon electrode was the working electrode, with platinum spiral counterelectrode, and Li/Li⁺ with a solution of LiAlCl₄ of the same concentration as in the working electrode compartment in SOCl₂ in a tube with fritted disk was used as a reference electrode. The glassy carbon electrode was polished to a mirror finish with alumina powder, washed with 0.05M H₂SO₄ and with distilled water. The cyclic voltammograms were run at different scan rates after cleaning the electrode and the voltammograms were reproducible.

Results and Discussion

The basic conductance, viscosity, and density data for LiAlCl₄ in SOCl₂ solutions covering a wide range of concentrations are given in Tables I and II. The specific conductances of LiAlCl₄-SOCl₂ solutions measured over a range of concentration (3 × 10⁻⁴-2.0M) show that the conductance increases with concentration and reaches a maximum at about 1.8M. A plot of equivalent conductance (Δ) vs. C^{1/2} shows that the value of Δ is high at low concentration, decreases rapidly with increase of concentration, reaches a maximum around 0.8M, and decreases again (Fig. 1). This behavior is characteristic of weak electrolytes in solvents of low dielectric constant (8, 9). The data for dilute solutions (< 0.00544M) were treated theoretically using an equation of a form similar to that of Fuoss-Shedlovsky (10) except for the function S(Z). The equation is

$$\frac{1}{\Delta} = \frac{1}{\Delta_0} + \frac{CA}{Kd(\Delta_0)^2}$$

* Electrochemical Society Active Member.

Key words: lithium battery, thionyl chloride, conductance, viscosity, cyclic voltammetry.

Table I. Conductance, viscosity, and density of LiAlCl₄-SOCl₂ solutions

| Concentration (mole/liter) | Equivalent conductance (cm ² Ω ⁻¹ equiv. ⁻¹) |
|----------------------------|--|
| 0.000313 | 13.51 |
| 0.00052 | 13.40 |
| 0.00104 | 11.94 |
| 0.00313 | 8.089 |
| 0.005216 | 7.025 |
| 0.007824 | 6.264 |
| 0.01043 | 5.228 |
| 0.04 | 6.228 |
| 0.09 | 7.134 |
| 0.1448 | 8.758 |
| 0.25 | 10.662 |
| 0.4999 | 13.717 |
| 0.7498 | 14.489 |
| 0.9998 | 14.114 |
| 1.25 | 13.69 |
| 1.50 | 12.659 |
| 1.75 | 11.487 |
| 2.00 | 10.255 |

Table II. Conductance, viscosity, and density of LiAlCl₄-SOCl₂ solutions

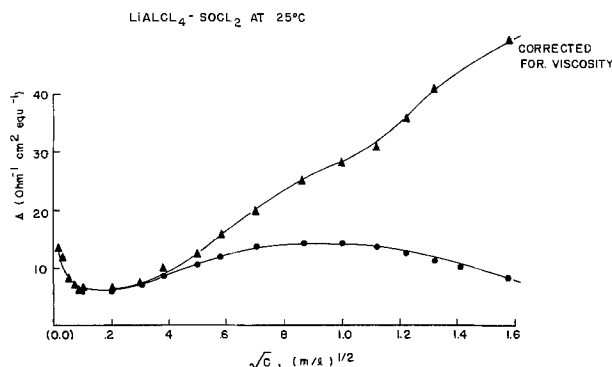
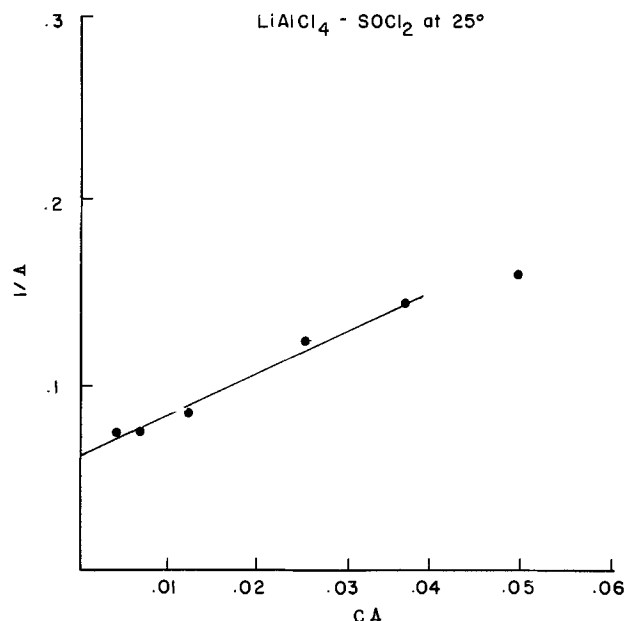
| Concentration (mole/liter) | Viscosity (cp) | Density (g/cm ³) |
|----------------------------|----------------|------------------------------|
| 0.00249 | 0.63684 | 1.6438 |
| 0.00997 | 0.64506 | 1.6443 |
| 0.03046 | 0.6522 | 1.6451 |
| 0.04985 | 0.65563 | 1.64599 |
| 0.0997 | 0.70841 | 1.64820 |
| 0.200 | 0.7357 | 1.6525 |
| 0.35 | 0.76133 | 1.65903 |
| 0.50 | 0.78731 | 1.66555 |
| 0.65 | 0.88218 | 1.67206 |
| 0.75 | 0.95589 | 1.6764 |
| 0.90 | 1.11729 | 1.68293 |
| 1.00 | 1.25061 | 1.68727 |
| 1.50 | 1.7746 | 1.7090 |

where Λ_0 is the limiting equivalent conductance and Kd is the dissociation constant for the ion-pairs. A plot of $1/\Lambda$ vs. $C\Lambda$ is linear (Fig. 2), the intercept gives $\Lambda_0 = 16.51$, and the slope gives $Kd = 1.605 \times 10^{-3}$. The data for solutions in the concentration range of 0.005M to about 0.5M were treated by Fuoss and Kraus method (8, 9). The equation is given by

$$\Lambda = \sqrt{\frac{Kd}{C}} \Lambda_0 + \frac{\sqrt{Kd}C}{k} \Lambda_{03}$$

where k is the dissociation constant for triple ions and Λ_{03} is the limiting equivalent conductance for triple ions. A plot of $\Lambda C^{1/2}$ vs. concentration gives a linear relationship from which the value of $k/\Lambda_{03} = 1.21 \times 10^{-3}$ is obtained.

The low value for Λ_0 and high value for Kd indicate appreciable amounts of ion-solvent and ion-ion interactions in these solutions. For concentrated solutions, the viscosity plays an important role which is evident from the plot of conductance corrected for

Fig. 1. Equivalent conductance vs. the square root of concentration of LiAlCl₄ in SOCl₂ at 25°C.Fig. 2. $1/\Lambda$ vs. $C\Lambda$ for LiAlCl₄ in SOCl₂ at 25°C

viscosity (Fig. 1). The viscosity measurements have been carried out over the entire concentration range (Table II) and the data have been treated using Jones-Dole equation (11), $\eta/\eta_0 = 1 + AC^{1/2} + BC$ for low concentrations and for high concentrations, an extended form of this equation (12, 13), $\eta/\eta_0 = 1 + AC^{1/2} + BC + DC^2$ has been used. Here η is the viscosity of the solution, η_0 is the viscosity of the solvent, C is the concentration in moles/liter, and the constants A and B are characteristic of ion-ion and ion-solvent interactions. The data for dilute solutions can be represented by the equation $\eta/\eta_0 = 1 + 0.1326C^{1/2} - 0.632C$ and for concentrated solutions, the data can be represented by the equation $\eta/\eta_0 = 1 + 0.1326C^{1/2} - 0.2759C + 1.0887C^2$. For concentrated solutions, both conductance and viscosity were measured at 25°, 40°, and 60°C. The plots of $\log \Lambda$ vs. $1/T$ and $\log \eta$ vs. $1/T$ were linear from which energies of activation for conductance and for viscous flow were obtained (Table III). The large increase in the energy of activation for conductance and for viscous flow with increase of concentration can be explained in terms of strong ion-ion and ion-solvent interactions giving rise to complex aggregates, particularly at high concentrations. The cyclic voltammetric studies have been carried out on 2.0, 1.8, 1.5, 1.0, and 0.6M solutions of LiAlCl₄-SOCl₂ solutions. The voltammogram of the 1.5 LiAlCl₄-SOCl₂ solution shows a large reduction peak around 2.7V and two very small peaks around 1.8 and 1.4V vs. Li/Li⁺ (Fig. 3). In the anodic direction, a very small, but broad peak appears around +2.65V vs. Li/Li⁺. Similar cyclic voltammo-

Table III. Energy of activation for conductance

| Concentration | |
|--|-------------|
| (moles/liter) | (kcal/mole) |
| LiAlCl ₄ -SOCl ₂ solutions | |
| 0.5 | 0.144 |
| 0.75 | 0.422 |
| 1.0 | 0.568 |
| 1.25 | 0.816 |
| 1.50 | 0.949 |
| 1.75 | 1.214 |
| 2.0 | 1.383 |
| Energy of activation for viscous flow | |
| 0.5 | 1.942 |
| 1.0 | 2.041 |
| 1.5 | 2.426 |
| 2.0 | 3.270 |

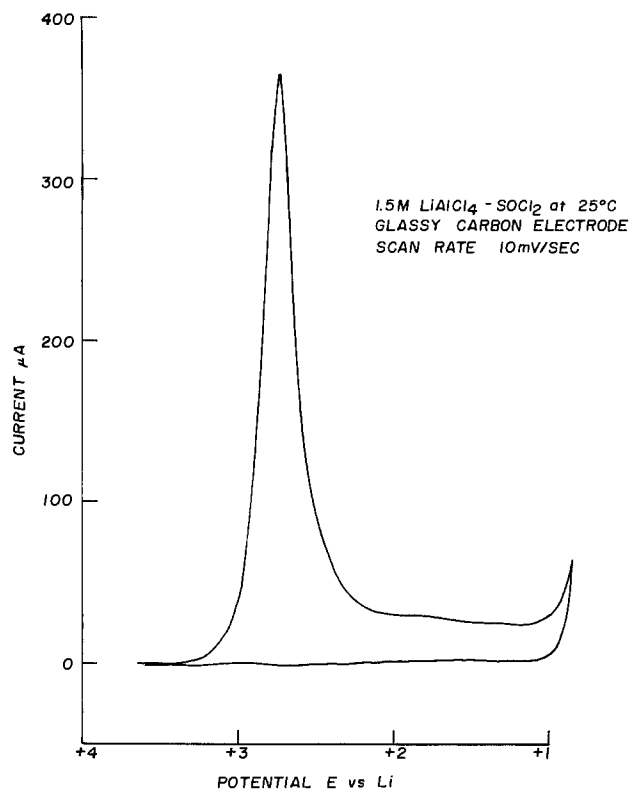


Fig. 3. Cyclic voltammetry of $\text{LiAlCl}_4\text{-SOCl}_2$ solution at 25°C

grams were observed for 2.0, 1.8, 1.0, and 0.6M $\text{LiAlCl}_4\text{-SOCl}_2$ solutions. The peak currents for the large reduction peak around 2.7V increased with increasing scan rate and the peak potentials shifted to more negative potentials indicating that the reduction involves an irreversible charge transfer process (14). The large reduction peak occurring around 2.7V vs. Li/Li^+ can be attributed to the electrochemical reduction of thionyl chloride represented by one of the following reduction reactions in lithium-thionyl chloride cell (1, 2, 6)



It has been shown that during the reduction of thionyl chloride in lithium-thionyl chloride cell, products such as sulfur monochloride (2, 4, 6) and sulfur dichloride (15) are formed. Therefore, the cyclic voltammograms of 1.8M $\text{LiAlCl}_4\text{-SOCl}_2$ solution containing small amounts of sulfur monochloride (S_2Cl_2) were studied. The cells have a slight increase in open-circuit potential. The main peak of SOCl_2 appearing around 2.7V vs. Li/Li^+ shows an increase in amplitude (Fig. 4) and the remaining peaks are the same as in $\text{LiAlCl}_4\text{-SOCl}_2$ solutions. The cyclic voltammogram of 1.8M $\text{LiAlCl}_4\text{-SOCl}_2$ solution containing 2% (by volume) of sulfur dichloride (S_2Cl_2) shows an increased open-circuit potential (3.9V) and three reduction peaks at about 3.65, 3.5, and 2.7V vs. Li/Li^+ (Fig. 5). Since S_2Cl_2 is known to undergo dissociation to S_2Cl_2 and Cl_2 (16) according to



the peaks observed at 3.65 and 3.5V can be attributed to the reduction of chlorine. When a solution of 1.5M $\text{LiAlCl}_4\text{-SOCl}_2$ is maintained for 5 min at 4.5V vs. Li/Li^+ using glassy carbon and platinum electrodes and the cyclic voltammogram is run in the cathodic mode, two reduction peaks are observed at about 3.65 and 3.5V vs. Li/Li^+ (Fig. 6). On bubbling dry nitrogen

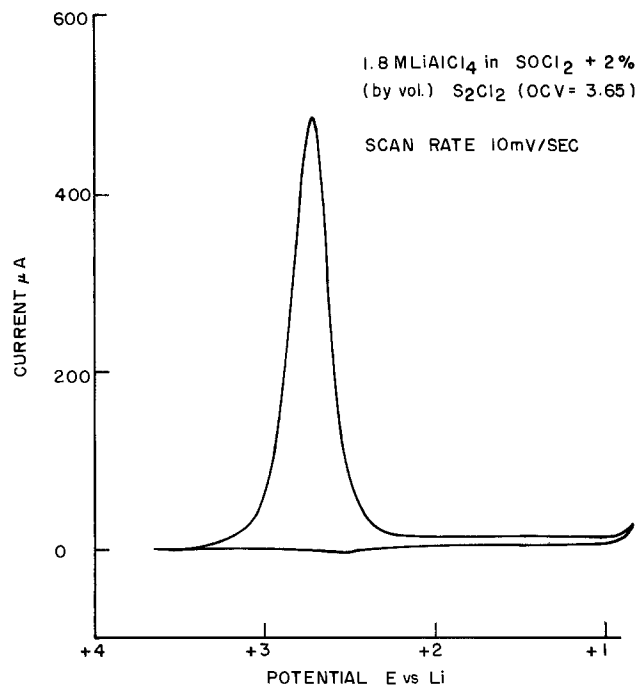


Fig. 4. Cyclic voltammetry of $\text{LiAlCl}_4\text{-SOCl}_2$ solution with 2% (by volume) of S_2Cl_2 .

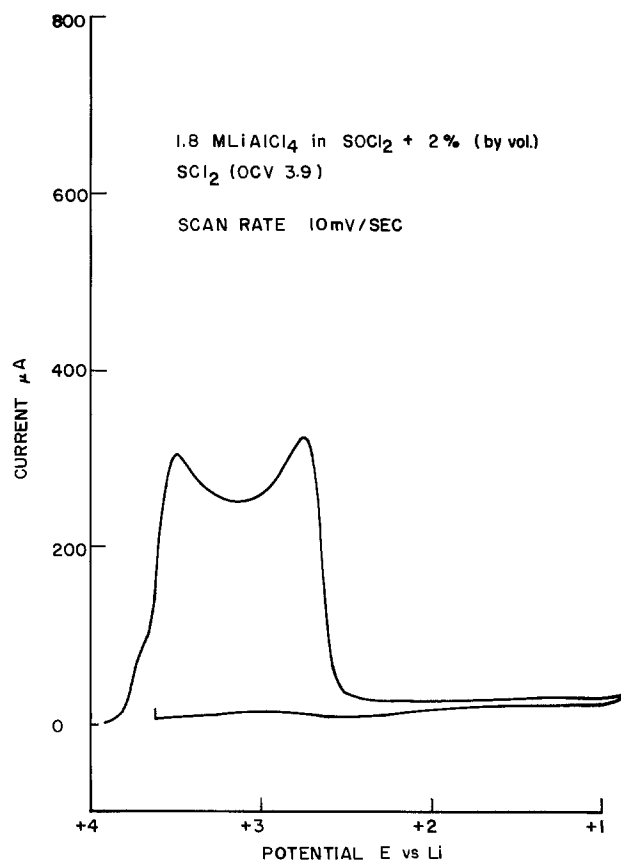


Fig. 5. Cyclic voltammetry of $\text{LiAlCl}_4\text{-SOCl}_2$ solution with 2% (by volume) of SCl_2 .

through this solution and then running cyclic voltammetry, only one peak around 3.5V vs. Li/Li^+ is observed. It is possible that when chlorine is generated anodically at the glassy carbon electrode, there is free chlorine and chlorine combined with SOCl_2 . On bubbling dry nitrogen, the free chlorine is removed and the chlorine in combination with the solvent SOCl_2 remains in solution and undergoes reduction at about 3.5V. This interpretation is verified by bubbling chlo-

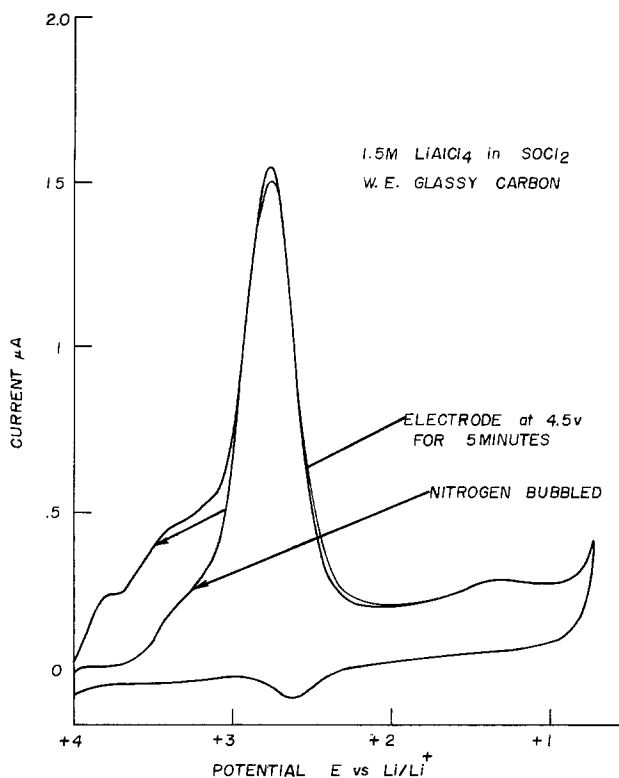


Fig. 6. Cyclic voltammetry of LiAlCl₄-SOCl₂ solution

rine gas through a solution of 1.5M LiAlCl₄-SOCl₂ and running cyclic voltammetry. There are two small peaks at 3.65 and 3.4V vs. Li/Li⁺ and a large peak at 2.75V vs. Li/Li⁺ (Fig. 7).

The cyclic voltammogram of 1.8M LiAlCl₄-SOCl₂ solution saturated with sulfur dioxide (OCV = 3.6V) at 25°C shows a large reduction peak around 2.7V followed by two very small peaks at about 1.8 and 1.4V vs. Li/Li⁺ (Fig. 8). When the voltammogram for this solution was run at 0°C, the amplitude of the main peak appearing around 2.7V decreases, whereas the small peaks at about 1.8 and 1.4V take a fairly well-defined shape and a small and broad oxidation peak appears around 2.8V. The cyclic voltammograms of

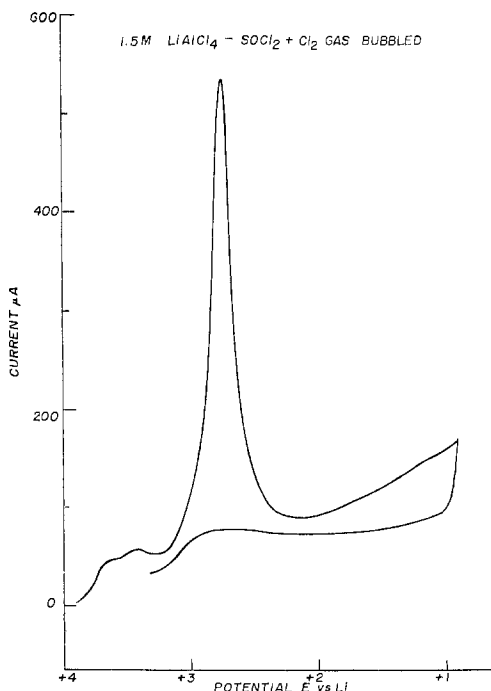


Fig. 7. Cyclic voltammetry of LiAlCl₄-SOCl₂ solution + Cl₂ gas bubbled.

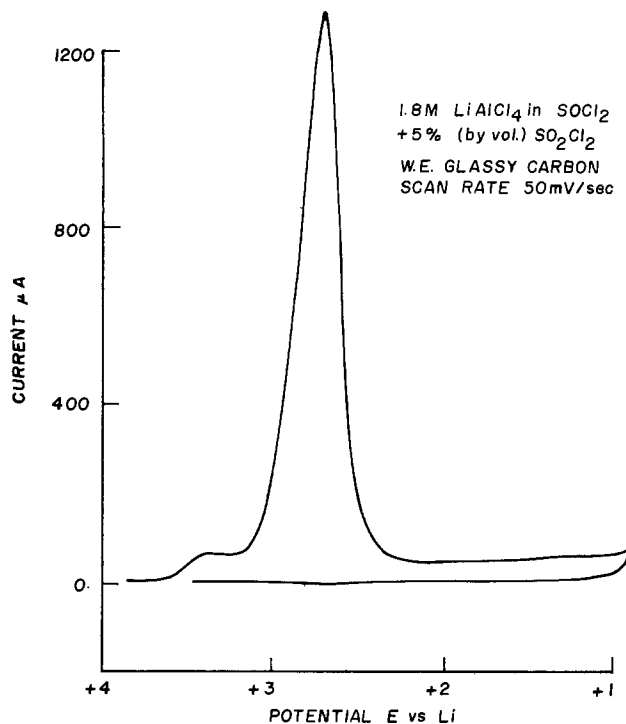


Fig. 8. Cyclic voltammetry of LiAlCl₄-SOCl₂ solution saturated with SO₂.

1.8M LiAlCl₄-SOCl₂ solutions containing 5% and 13% (by volume) of sulfuryl chloride (SO₂Cl₂) (OCV = 3.9) show a reduction peak around 3.45V followed by the major reduction peak for SOCl₂ at about 2.7V vs. Li/Li⁺ and small reduction peaks at about 1.8 and 1.4V vs. Li/Li⁺ (Fig. 9). The peak around 3.45V can be attributed to the reduction of chlorine produced by the decomposition of SO₂Cl₂ (17), according to the equation

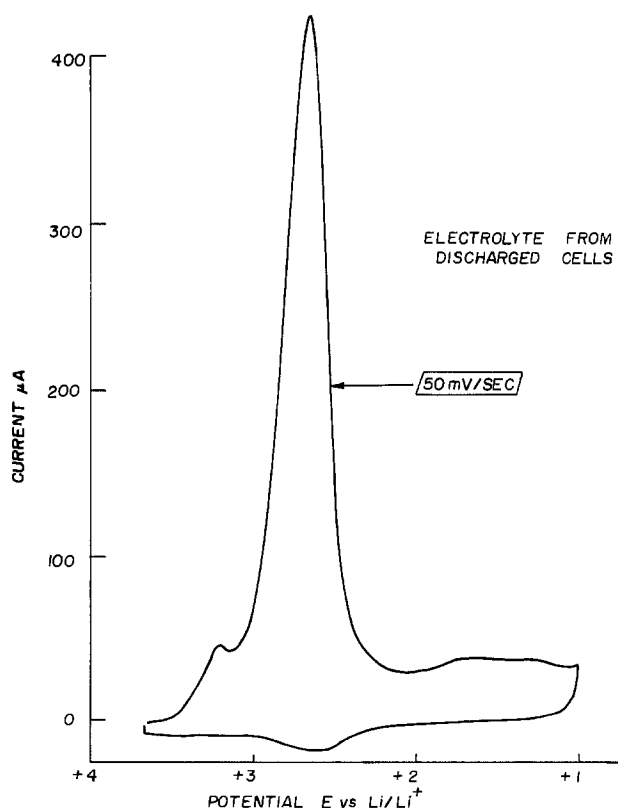
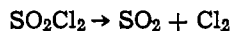


Fig. 9. Cyclic voltammetry of LiAlCl₄-SOCl₂ solution with 5% (by volume) of SO₂Cl₂.



The cyclic voltammogram of $\text{LiAlCl}_4\text{-SOCl}_2$ solution from a battery discharged to 0.0V shows a peak around 3.35V, a large peak around 2.7V, and two small peaks around 1.8 and 1.4V vs. Li/Li^+ (Fig. 10). These results seem to suggest that the electrolyte solution from a discharged cell contains chlorine and sulfur dioxide. Chlorine can possibly result due to the dissociation of SOCl_2 to S_2Cl_2 and Cl_2 .

Sulfur monochloride, being a good solvent for sulfur, may minimize lithium sulfur reaction which is highly exothermic (4). Chlorine evolved may interact with the oxidant giving rise to oxides of chlorine which are explosive in the presence of reducing agents (16, 18).

Conclusion

The conductance and viscosity data indicate that the electrolyte LiAlCl_4 is highly associated in SOCl_2 . The associated electrolyte can affect the mass transport and the charge transfer process during Li/SOCl_2 cell dis-

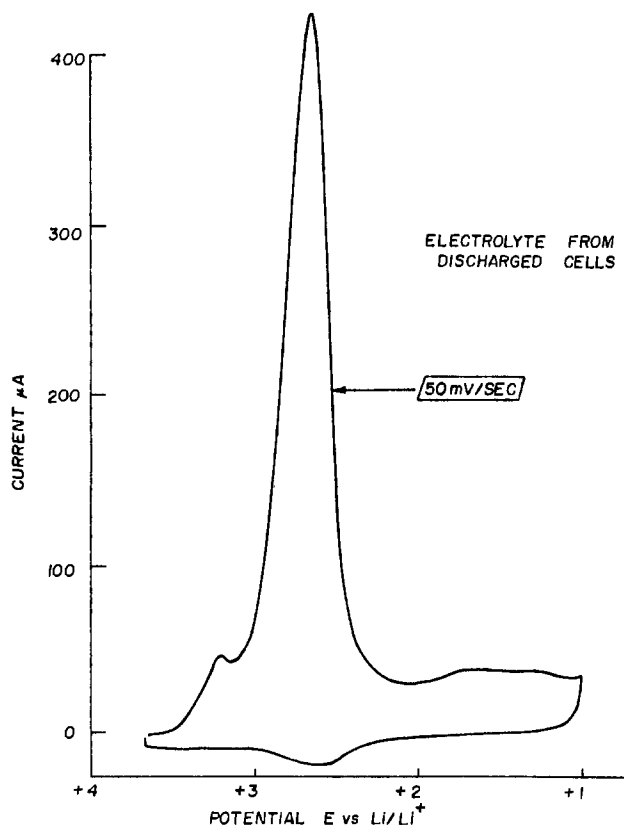


Fig. 10. Cyclic voltammetry of $\text{LiAlCl}_4\text{-SOCl}_2$ solution from cell discharged to 0.0V.

charge, particularly at low temperatures. The cyclic voltammetric studies show that chlorides of sulfur and chlorine are likely to be generated during the cell discharge.

Acknowledgment

The authors thank B. K. Patel for his technical assistance.

Manuscript submitted Aug. 18, 1980; revised manuscript received Nov. 3, 1980.

Any discussion of this paper will appear in a Discussion Section to be published in the December 1981 JOURNAL. All discussions for the December 1981 Discussion Section should be submitted by Aug. 1, 1981.

Publication costs of this article were assisted by Honeywell Corporate Material Sciences Center.

REFERENCES

1. J. J. Auborn, K. W. French, S. I. Lieberman, V. K. Shah, and A. Heller, *This Journal*, **120**, 1613 (1973).
2. W. K. Behl, J. A. Christopoulos, M. Ramirez, and S. Gilman, *ibid.*, **120**, 1619 (1973).
3. J. F. McCartney, W. H. Shipman, and C. R. Gunderson, in Proceedings of 11th IECEC, p. 457 (1976).
4. D. L. Chua, S. L. Deshpande, and H. V. Venkatesetty, in "Battery Design and Optimization," S. Gross, Editor, p. 365, The Electrochemical Society Softbound Proceedings Series, Princeton, N.J. (1979).
5. H. V. Venkatesetty and W. B. Ebner, Paper presented at the 29th Power Sources Conference, Atlantic City, N. J., June 1980.
6. A. N. Dey and C. R. Schlaikjer, in Proceedings of 26th Power Sources Symposium, Atlantic City, N. J. (1974).
7. V. H. Spandu, A. Beyer, and F. Preugschat, *Z. Anorg. Allg. Chem.*, **306**, 13 (1960).
8. R. M. Fuoss and C. A. Kraus, *J. Am. Chem. Soc.*, **55**, 2387 (1933).
9. C. A. Kraus and R. M. Fuoss, *ibid.*, **57**, 1 (1935).
10. R. M. Fuoss and T. Shedlovsky, *ibid.*, **71**, 1496 (1949).
11. G. Jones and M. Dole, *ibid.*, **51**, 2950 (1929).
12. M. Kaminsky, *Discussions Faraday Soc.*, **24**, 171 (1957).
13. J. E. Desnoyers and G. Perron, *J. Solution Chem.*, **1**, 199 (1972).
14. R. S. Nicholson and I. Shain, *Anal. Chem.*, **36**, 706 (1964).
15. G. L. Blomgren, V. Z. Leger, T. Kalnoki-Kis, M. L. Kronenberg, and R. J. Brodd, in Proceedings of International Power Sources Symposium, Brighton, England, p. 583 (1978).
16. F. A. Cotton and G. Wilkinson, "Basic Inorganic Chemistry," John Wiley & Sons, Inc., New York (1976).
17. "Encyclopedia of Chemical Technology," Vol. 14, K. Othmen, Editor, p. 398 (1969).
18. T. Moeller, "Inorganic Chemistry," pp. 431-432, John Wiley & Sons, Inc., New York (1952).

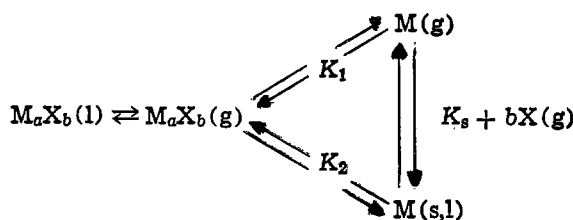
Chemical Reactivity in Halide Discharges: Effects of Condensed Phases and Common Components

D. M. Speros, R. K. Datta, and D. A. Lynch

General Electric Company, Lighting Research and Technical Services Operation, Nela Park, Cleveland, Ohio 44112

ABSTRACT

Theoretical analysis of the cyclic equilibria



defines the conditions leading to (i) condensation of metal M and (ii) suppression of dissociation of halide M_aX_b by halogen X(g). The analysis is extended to include cases in which X is a common component of several coexisting halides. The theoretical conclusions are applied to the system $\text{M}_a\text{X}_b\text{-SiO}_2\text{-W}$ where M is reactive toward SiO_2 . It is shown that chemical reactivity in this system is determined by the thermodynamic activity of M in the gas phase. This result is applied to a common type of halide discharge lamp and leads directly to the proposal of a mechanism of reaction between the halides, the vitreous silica envelope, and the tungsten electrodes. Experimental investigations employing both established and new techniques confirm each step of the reaction sequence and the reaction sequence as a whole. It is concluded that outlines are provided for: (i) a thermodynamic basis for electrode-atmosphere cycles, (ii) an overall mechanism for wall-atmosphere interactions, (iii) experimental methods for the study of chemical reactivity in discharges, and (iv) an interpretive basis for experimental results.

Introduction and Basic Concepts

In a previous publication on molecular arcs (1), the origin, consequences, and applications of a condensed phase of Sn in discharge envelopes containing tin halides were described. Likewise, the role of Sn vapor as a "common component" between SnI_x and SnCl_y vapors in the discharge atmosphere was elucidated. It was shown that a condensed phase of "excess" Sn is necessary in order to obtain a chemically stable discharge system.

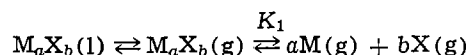
This paper reports investigations of the occurrence and effects of condensed phases when the condensing metal, unlike Sn, is reactive toward the walls and electrodes of the discharge, and the common component is not a metal but a halogen. Specifically, the factors determining chemical reactivity in the system $\text{M}_a\text{X}_b\text{-SiO}_2\text{-W}$ were explored. M_aX_b is the halide of metal M which is reactive toward SiO_2 . Examples of such metals include Al, lanthanides such as Dy, actinides such as Th, and the alkali metals, Zr, Sc, Ti, Si, etc. Of these, the iodides of Na, Sc, and Th were chosen for study. The reason for this choice is that combinations of these iodides find applications in discharge lamps of widespread use especially in outdoor lighting (2, 3). Thus, the experimental part of this investigation included actual lamps of various configurations as, for example, that of Fig. 3 in Ref. (1) which is of sub-centimeter dimensions.

The common component effect is completely analogous to the well-known "common ion effect" in solution chemistry: the dissociation of halide M_aX_b in the discharge atmosphere will be suppressed by the presence of another halide which has a common component, halogen X or metal M, with M_aX_b .

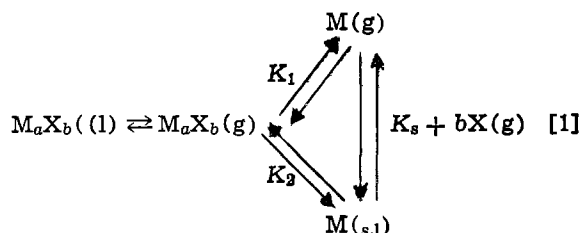
Key words: lamps (halide), high temperature chemistry, transport of silicon and silica, tungsten silicides, electrodes.

Of special importance is the fact that the dissociation will be suppressed also if excess M or X is introduced in the discharge either deliberately, as was the case with the Sn system, or because of reaction between the metal M of M_aX_b and the walls of the discharge device thereby liberating unassociated or "excess" halogen X. The latter is the case of interest here.

Condensed phases can occur because of supersaturation when the partial pressure of M, P_M , from the dissociation of M_aX_b is higher than the saturation or equilibrium pressure of M, $P_M(\text{satd.})$, over condensed M. Therefore, it is not sufficient to consider only the dissociation



because it is necessary to consider also the possibility of condensation. This is expressed here by the cyclic equilibria



from which it is readily shown that

$$P_M = \frac{K_1}{K_2} \leq K_s = P(\text{satd.}) \quad [2]$$

The unequal sign refers to conditions under which P_M is not sufficiently large to attain $P(\text{satd.})$, and

therefore condensation does not occur. As can be seen from these relations, examples of such conditions include: (i) $K_s \gg K_1$ as is the case with NaI, (ii) limited amount of M_aX_b in the discharge envelope, and (iii) excess of X which suppresses dissociation of M_aX_b due to common component effect.

The last case is of particular importance because it shows the interrelation between the effects of common components and condensed phases.

Finally, according to Eq. [1], the gaseous and condensed phases of all species are in equilibrium at each locale. Therefore, the tendency for reaction of each species is thermodynamically indistinguishable from that of another species. For example, reduction of P_M because of reaction of $M(g)$ with the wall will cause some $M(s, l)$ to evaporate, and depletion of $M(s, l)$ because of reaction with the wall will cause some $M(g)$ to condense, all phases being replenished by further evaporation of $M_aX_b(l)$ and dissociation of $M_aX_b(g)$. In summary, what counts is the thermodynamic activity of M in the gas phase.

These concepts would be implicitly included in comprehensive free energy minimization computations; however, their explicit application to the systems of Th and Sc halides in the following section leads directly to the proposal in the section on Reaction Mechanism and Experimental Results of a set of reaction mechanisms between the halides, the vitreous silica envelope, and tungsten electrodes and to experimental investigations confirming each step of the reaction sequence as a whole.

Theoretical Results and Confirming Experimental Evidence

It is possible to obtain a semiquantitative description of the effects of common components and condensed phases by making the following approximations:

1. Local thermodynamic equilibrium is assumed.
2. The vapor pressure of the halides is determined by the temperature of the coldest region in the discharge envelope. At this region exists a liquid phase reservoir of the halides.
3. Almost certainly the liquid phase cannot be considered an ideal solution since, for example, molecular complexes of NaI-ScI₃ are known to exist (4); however, since disagreements in reported vapor pressure data seem difficult to reconcile (4), it may be preferable at present to employ ideal solution relations.
4. Lower iodides such as ThI₂ are neglected not only because of paucity in thermodynamic data but also because (i) the complete dissociation of the iodides represents the limiting case of interest here and (ii) the procedure of involving the lower iodides is the same except for added mathematical complexity.

Because of these approximations, it is emphasized that this analysis forms only a base line on which to "factor" the effects of other possible variables, particularly molecular complexing. Conversely, analysis of the effects of other variables must take into account the results given here.

Established procedures (1, 3) are adapted to this set of constraints, see Appendix, to obtain the partial pressures of the species as a function of temperature. These are plotted in Fig. 1 for the ScI₃-NaI system and in Fig. 2 for the ThI₄-NaI system; in both cases the mole fraction, N , of NaI has been taken as equal to 0.9 for the sake of correspondence to actual systems. The liquid phase reservoir temperature has been taken as equal to 1100 K.

Common component effect.—In Fig. 1, the dashed lines show the partial pressures of Na, curve B, and Sc, curve C, calculated without taking into account the common component effect of iodine. When this effect is taken into account, the partial pressure of Sc is severely suppressed as shown by the thin solid line, curve D. The partial pressure of Na (not plotted) is suppressed to a lesser extent. Likewise, the suppression

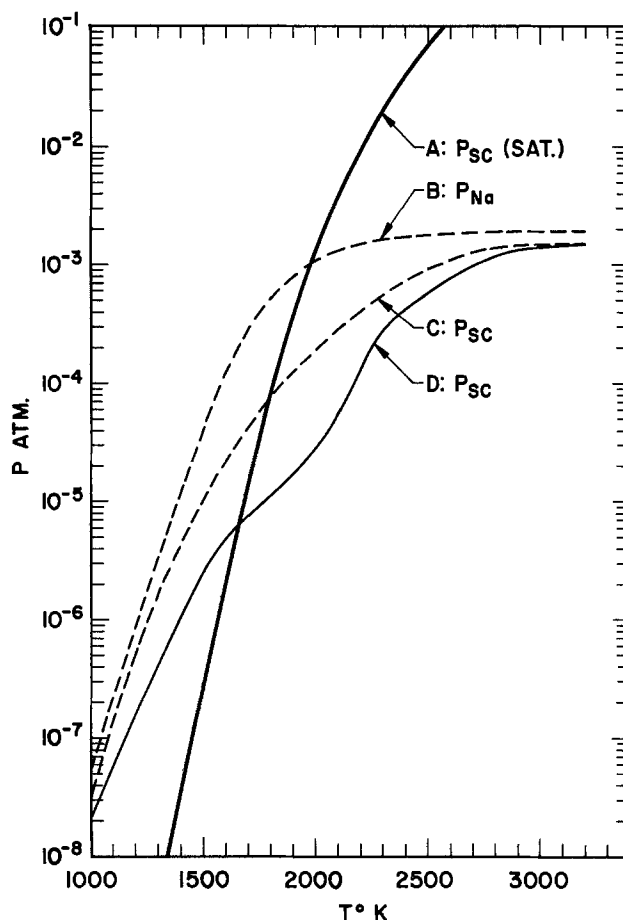


Fig. 1. Partial pressures of Na and Sc over liquid phase reservoir at 1100 K containing mole fractions $N_{NaI} = 0.9$ and $N_{ScI} = 0.1$. A: equilibrium pressure of Sc(g) over condensed Sc(c). B and C: partial pressures of Na and Sc, respectively, calculated without taking into account the common component effect. D: calculated partial pressure of Sc taking into account the common component effect.

of the partial pressures of Na and Th are shown in Fig. 2 and are discussed below.

These results show that the effect of the iodine common component is to suppress the vapor pressures of the metallic vapors; consequently, the intensity of metal atom spectral lines should decrease.

Experimental confirmation of this is seen in the spectra of Fig. 3A and 3B.¹ Figure 3A shows the spectrum of a discharge of NaI and ScI₃ of mole fractions $N_{NaI} = 0.9$ and $N_{ScI_3} = 0.1$ and containing in addition Hg and A. Figure 3B shows the spectrum of the same discharge, but to which a small amount of ThI₄ ($N_{ThI_4} = 0.01$) has been added. It is seen that the lines of Na and Sc are suppressed as predicted. The intensity of the Hg lines is essentially unaffected, Hg being completely vaporized in either case.

It is concluded that changes such as these in discharge spectra affecting severely lamp color and efficacy (lumens/watt) can be accounted for, at least in part, by the effect of common components.

Condensed phase effects.—In Fig. 1, it is seen that the partial pressure of Sc, P_{Sc} , curve D, from the dissociation of ScI₃ is higher than the equilibrium vapor pressure of Sc, $P_{Sc}(\text{satd.})$ over condensed Sc, curve A, up to approximately 1650 K. Therefore, up to this temperature Sc should tend to condense.

In Fig. 2 is seen that P_{Th} , curve E, is higher than $P_{Th}(\text{satd.})$, curve A, for all temperatures in the range of the figure and, therefore, condensation of Th should likewise be expected.

¹ Obtained by G. Kazek.

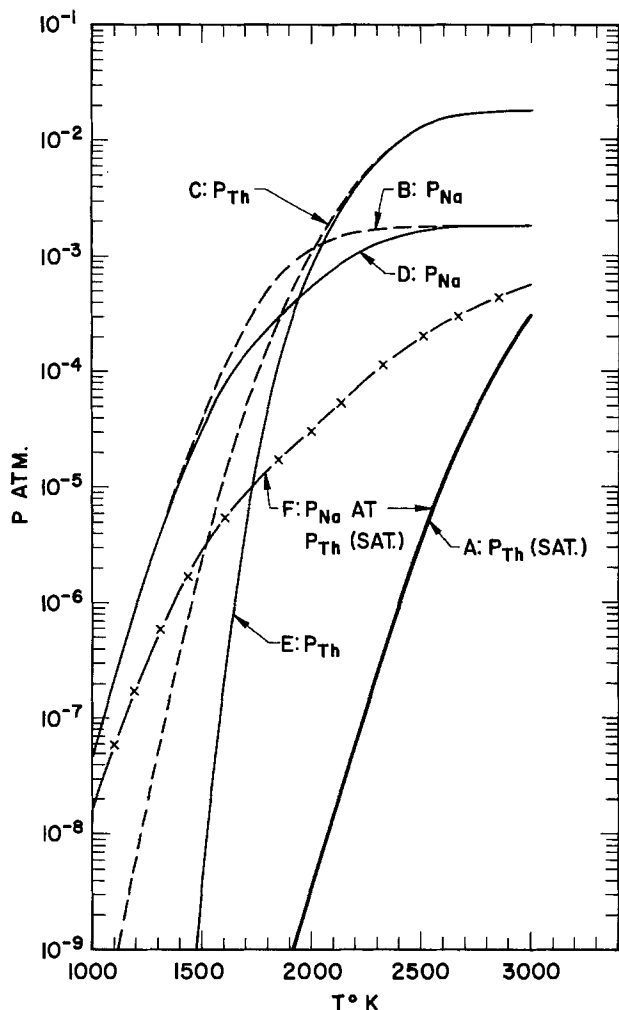


Fig. 2. Partial pressures of Na and Th over liquid phase reservoir at 1100 K containing mole fractions $N_{\text{NaI}} = 0.9$ and $N_{\text{ThI}_4} = 0.1$. A: equilibrium pressure of Th(g) over condensed Th(c). B and C: partial pressures of Na and Sc, respectively, calculated without taking into account the common component effect. D and E: calculated partial pressures of Na and Th, respectively, taking into account the common component effect. F: partial pressure of Na when there is sufficient excess iodine to prevent condensation of Th.

$P_{\text{Na}}(\text{satd.})$ is of the order of 10^{-1} atm already at 1000 K, i.e., higher than P_{Na} and, therefore, no condensation of Na should be expected.

Elemental Sc and Th can be expected to come in contact with the SiO_2 walls and the electrodes. In particular, Th can be expected to condense even on the hottest parts of the electrodes, i.e., at temperatures often exceeding 2500 K. The earliest published evidence for this is photograph 9.9, p. 248 of Ref. (2), which shows a hemispherical deposit of Th on the W electrode of a lamp containing ThI_4 . Electron emission measurements from cathodes under discharge conditions using the methods developed in this laboratory (5) confirm that electron emission is enhanced under conditions conducive to Th deposition because Th reduces the work function from the 4.5 eV of bare W to the 3.5 eV of Th.

According to Fig. 1 and 2, condensation could take place in the gaseous phase provided nucleation conditions exist. Our observations confirm the statement in Ref. (2), p. 285 that occasionally a fog of metal droplets is seen within the gaseous phase of the discharge.

Finally, Fig. 1 and 2 indicate that condensation could take place on the walls of the discharge envelope where reactions between Th and Sc species and SiO_2 can be expected. This is the subject of the remainder of the paper; however, since excess iodine will be formed as

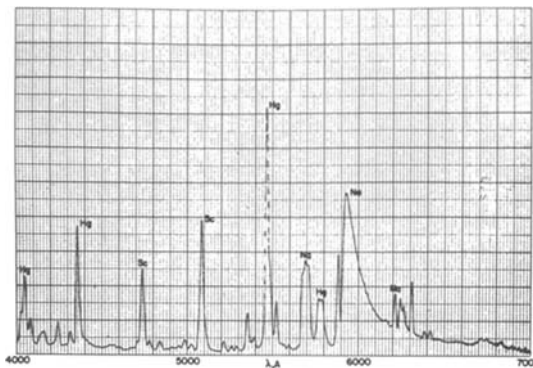


Fig. 3A. Spectrum of discharge of NaI and ScI_3 of mole fraction $N_{\text{NaI}} = 0.9$ and $N_{\text{ScI}} = 0.1$ (also involving Hg and A).

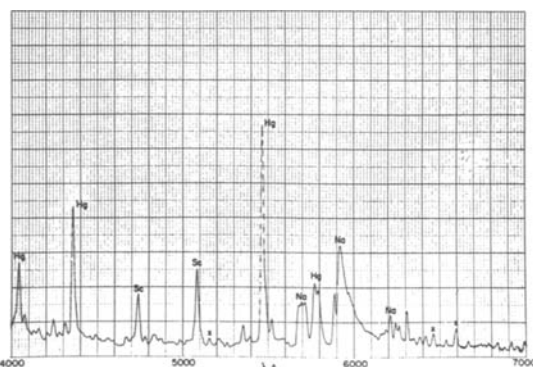


Fig. 3B. Spectrum of same discharge as in Fig. 3A but also containing a small amount of ThI_4 ($N_{\text{ThI}} = 0.01$).

a result of these reactions, an important effect of this excess iodine is treated immediately below.

Suppression of condensation by excess iodine.—The amount of excess iodine, P_I , is calculated (Appendix) which will be sufficient to suppress the dissociation of the iodides, due to common component effect, until P_{Th} and P_{Sc} are equal to their respective $P(\text{satd.})$. In other terms, the values of P_I are calculated which will cause in Fig. 1 curve D to coincide with curve A up to 1650 K; and in Fig. 2 curve E to coincide with curve A at all temperatures shown. These then will be the partial pressures of iodine which will just suffice to prevent condensation of Th and Sc.

The results are shown in Fig. 4: curve A gives the partial pressures of excess iodine as a function of temperature that will prevent condensation of Th. Curve B is the equivalent curve for the Sc case. This is compared to curve C which shows the iodine pressure from the normal dissociation of the ScI_3 and NaI, i.e., the iodine pressure in the absence of excess iodine. It is seen that above 1650 K this is sufficient to prevent condensation of Sc as already deduced from Fig. 1.

In addition to suppressing the dissociation of Th and Sc iodides, excess iodine will also suppress the dissociation of NaI. In Fig. 2, curve F shows the partial pressure of Na when there is sufficient iodine to cause P_{Th} , curve E, to coincide with $P_{\text{Th}}(\text{satd.})$, curve A. It is seen that P_{Na} is severely suppressed and consequently the spectral lines of Na of discharges containing excess iodine should be severely suppressed. This is an additional reason for the suppression of Na and Sc lines in the spectrum of Fig. 3B as confirmed by the fact that an amount of red HgI_2 , formed by the reaction between excess iodine and Hg, was visible on the walls of this lamp at room temperature. In new lamps where wall reactions have not progressed sufficiently for excess iodine to form to the extent that HgI_2 is visible, the suppression of Na lines is less but nevertheless occurs, demonstrating the common component effect due only to iodide dissociation.

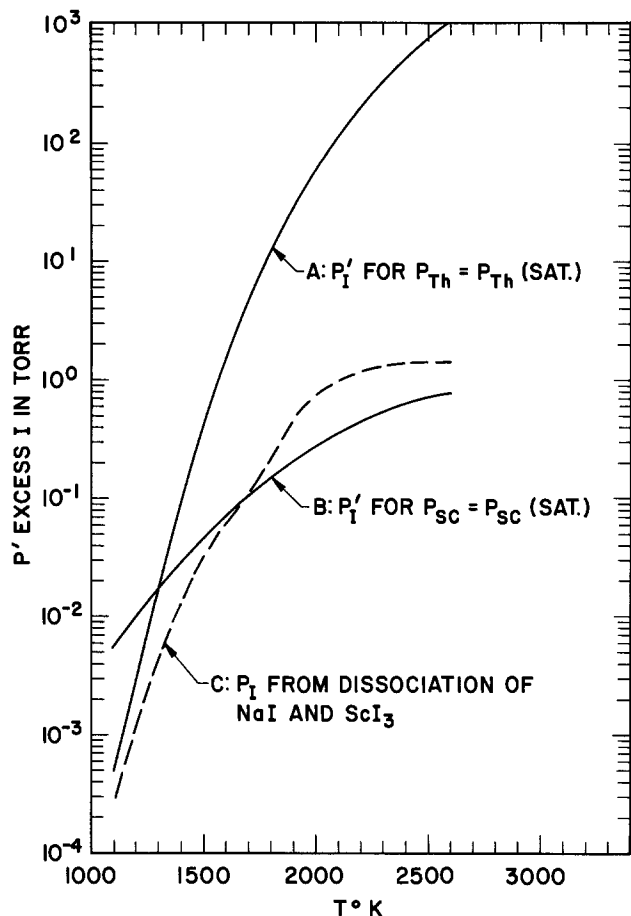


Fig. 4. Partial pressure, P_I , of excess iodine necessary to prevent condensation of Th and Sc. A: P_I to prevent condensation of Th. B: P_I to prevent condensation of Sc. C: iodine pressure from normal dissociation of ScI_3 and NaI , mole fractions $N_{\text{ScI}} = 0.1$ and $N_{\text{NaI}} = 0.9$. Liquid phase reservoir temperature in all cases is 1100 K.

Reaction Mechanism and Experimental Results

The considerations in the previous sections indicate the conditions under which reactivity should be expected between discharge components. These are applied here to the example of a vitreous silica envelope containing a halide reservoir with a ThI_4 or ScI_3 component and tungsten electrodes.

Table I gives a summary of the understanding that seems to be emerging of the overall mechanism of reaction between discharge atmosphere electrodes and walls for the case of ThI_4 . ScI_3 gives completely analogous behavior.

On the left-hand side of the table are given the steps of the reaction sequence. On the right-hand side is given the kind of experimental evidence obtained in support of each step.

The effects of the reactivities in Table I are intricately interrelated and cover the range from subtle to obvious. Therefore, it proved necessary to employ not only established experimental procedures but also to devise new ones. In this paper only the bare essentials of these techniques are given pending their full description elsewhere, particularly of the "closed system" high temperature x-ray diffraction, and near-infrared spectroscopic detection of reaction products in high intensity gas discharge lamps. At the other extreme, in some cases confirming experimental results or observations already existed such as the appearance of red HgI_2 on the walls, and the distortion of electrodes of lamps containing Th and Sc iodides.

Step 1: According to Eq. [1], the gaseous and condensed phases of M_aX_b , M and I_x are at equilibrium at each locale. This is expressed by the equation of Step

1 in the table.

Step A: According to the theoretical and experimental evidence, Th condenses on the electrodes enhancing electron emission.

Step 2: This step postulates attack of the SiO_2 wall by Th to produce condensed products such as interoxides, " Th_xO_y -excess SiO_2 ," (and possibly oxyiodides), and volatile $\text{SiO}(\text{g})$. Formation of $\text{SiO}(\text{g})$ is postulated because, as will be explained in detail below, transport of SiO_2 is observed within the envelope.

(a) Detection of wall attack: Microscopic and scanning electron microscope (SEM) examination of SiO_2 envelopes of discharges involving Th and/or Sc iodides revealed that these were etched possibly because of evolution of SiO . Figure 5 is an SEM photograph² of such an attacked region.

(b) Detection of condensed products: Energy dispersive mode SEM revealed Th and Sc in these regions.

(c) Detection of volatile Si product(s) from the Th- SiO_2 interaction by means of ion scattering spectroscopy.³

In order to determine whether any volatile products such as SiO could result from this interaction, a mixture of Th and vitreous SiO_2 powders, the latter in great excess, was placed in the vitreous silica sample container of an Ainsworth thermobalance, Fig. 6. Above the furnace region of the thermobalance tube was placed a platinum cylinder which had been cleaned with 25% HF solution. The system was evacuated to 10^{-6} Torr and the sample was heated between 900 and 1000 K for 1 hr. A slight decrease in weight was indicated and a light brown deposit was obtained on the platinum cylinder. Examination of a small piece of the Pt cylinder by means of ion scattering spectroscopy revealed that the brown deposit contained Si in a thin ($\sim 100\text{\AA}$) layer.

X-ray diffraction of the reacted mixture in the container gave the peaks corresponding to ThO_2 and a pattern of broad bands. These matched the bands obtained from a commercial (Union Carbide) preparation of " SiO ."

It is concluded that these experimental results are consistent with the second step of the proposed mechanism.

Step 3: This step postulates transport of SiO_2 . Examination of the same discharge envelopes that show etching also revealed deposits in other regions as seen in Fig. 7. These spheroidal deposits proved to be pure SiO_2 as determined by electron microprobe, ion scattering spectroscopic, and energy dispersive SEM

² Obtained by S. K. Gupta.

³ In collaboration with S. K. Gupta.

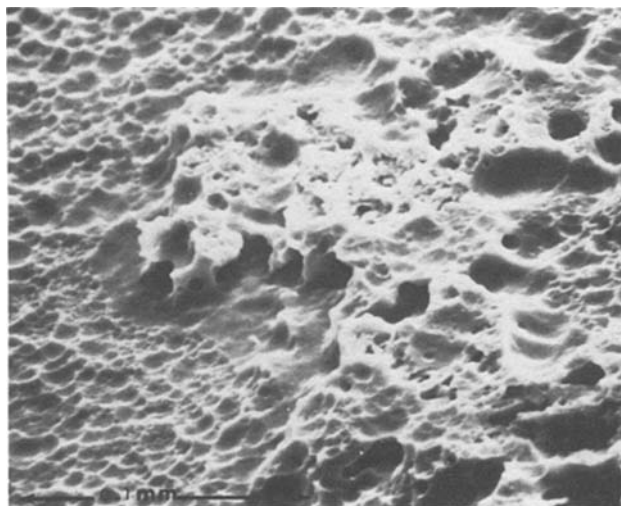


Fig. 5. Scanning electron microscope photograph showing wall attack.

Table I. Proposed reaction mechanism

| Step | Reaction* | Experimental evidence |
|------|---|---|
| A. | $M + xsW \rightarrow M \cdot xsW$ ↑ electrode | Electrode activation |
| 1. | $M_aX_b(g) \rightleftharpoons aM(g,c) + bX(g)$ | Sections on Theoretical Results and Confirming Experimental Evidence and on Reaction Mechanisms and Experimental Results |
| 2. | $M(g,c) + xsSiO_2 \xrightarrow{\text{wall}} M_xO_y \cdot xsSiO_2(c) + SiO(g)$ | |
| 3. | $2SiO(g) \rightarrow SiO_2(s) + Si(s)$ | Observed etching of wall I.S.S. identification of Si in brown deposit (T.G.A. experiments) X-ray diffraction identification of ThO_2 |
| 4. | $Si(s) + X(g) \rightarrow Si_xX_y(g)$ | Observed transport of SiO_2 in envelope (identification by electron microprobe, etc.) |
| 5. | $Si_xX_y(g) \xrightarrow{W \text{ electrode}} WSi_x(s,l) + yX(g)$ | Spectroscopic identification in atmosphere |
| 6. | $yX(g)$ | Observed electrode distortion Identification of WSi_x product by closed-system high T x-ray diffraction Electron microprobe x-ray backscattering identification of Si on electrodes Formation of red HgI_2 and changes in lamp characteristics |

* $xs = \text{excess}$, x, y : stoichiometric parameters.

analyses which were corroborated by high temperature mass spectroscopic studies.⁴

This evidence is consistent with Step 3 of the proposed mechanism since SiO is known (6) to disproportionate into SiO_2 and Si . The absence of elemental Si in the regions of the deposit is related to the next process, Step 4, of the mechanism indicating reaction between this Si and excess iodine to form volatile SiI_4 .

Step 4: This reaction relies on the existence of excess iodine: the initiation of the chain of Steps 1-6 depends on iodine from the dissociation of the iodides in Step 1 which is left unassociated by the interaction of Th with SiO_2 in Step 2. Chain propagation then is possible by

⁴ In collaboration with S. K. Gupta.

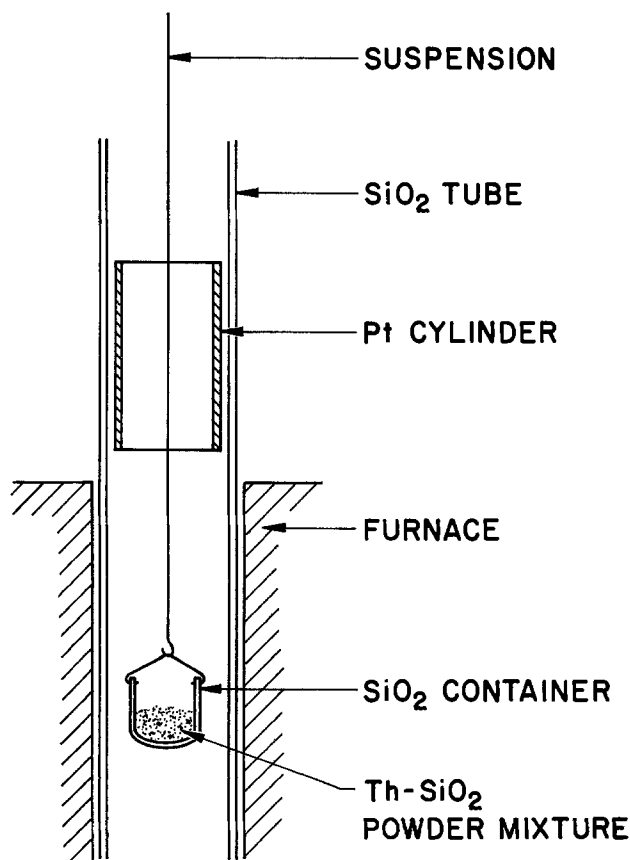


Fig. 6. Experimental arrangement for the detection of volatile Si compounds from the interaction between Th and SiO_2 .

excess iodine increasing with each reaction cycle, Steps 1-6.

Commonly used halide lamps contain large amounts of Hg which is completely vaporized. Calculations (3) indicate that the resulting P_{Hg} can vary from 4 atm to in excess of 10 atm depending on lamp type. A consideration of the $Si-I-Hg$ system shows that, since K_{SiI} and K_{HgI} are within one or two orders of magnitude of each other

$$P_{SiI_4} \cong 10^{-3} P_{HgI_2}^2$$

for P_{Hg} of the order of 10 atm. Even for $P_I \cong 100$ Torr (see Fig. 4) $P_{HgI} \cong 10^{-4}$ atm and, therefore, $P_{SiI_4} \cong 10^{-11}$ atm. Consequently, the excess iodine will be manifested in the discharge as $Hg-I$ species much more than as $Si-I$ species.

This was demonstrated by means of near-infrared spectroscopy using a Hitachi 340 Recording Spectrophotometer modified slightly in order to obtain emission spectra of high intensity lamps situated externally to the instrument.

Figure 8 is the spectrum of a discharge lamp containing a small amount of SiI_4 and sufficient Hg to result in P_{Hg} of several atmospheres, in addition to approximately 100 Torr of A (cold pressure). Except for minor differences, this spectrum is the same as that obtained when the SiI_4 is replaced by HgI_2 . These spectra show the reported Hg lines (7) and additional lines marked U in the figure. Between 800 and 1400 nm a broad band is prominent.

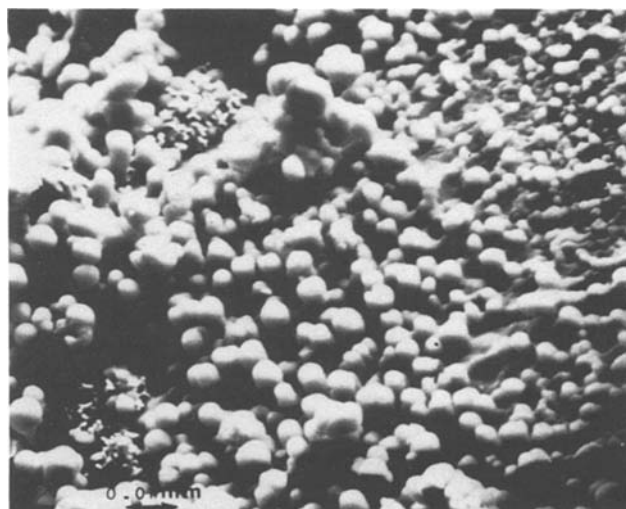


Fig. 7. Spheroidal deposits of pure SiO_2 on the discharge envelope

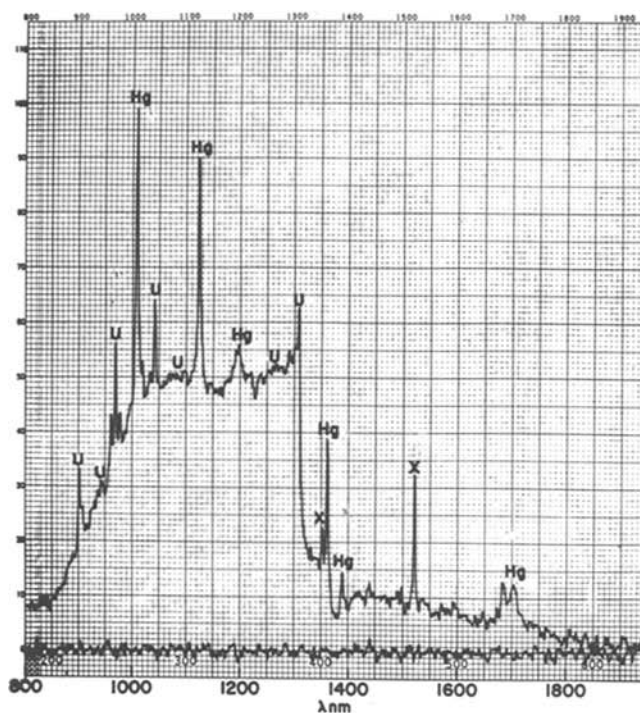


Fig. 8. Near-infrared spectrum of discharge lamp containing a small amount of SiI_4 in addition to Hg vapor at several atmospheres and 100 Torr A (cold pressure).

The U lines and the band are seen in lamps containing Th and/or Sc iodides, Fig. 9. They do not occur in lamps containing only NaI, Fig. 10.

These results are consistent with Step 4 with respect to formation of excess iodine, but proof of the coexistence of SiI_4 is based on the evidence given for Step 5.

Step 5: This step postulates attack of W electrodes by SiI_4 to form silicides whose melting point is considerably lower than that of W. In addition, silicon solution-precipitation effects can be expected along the electrode

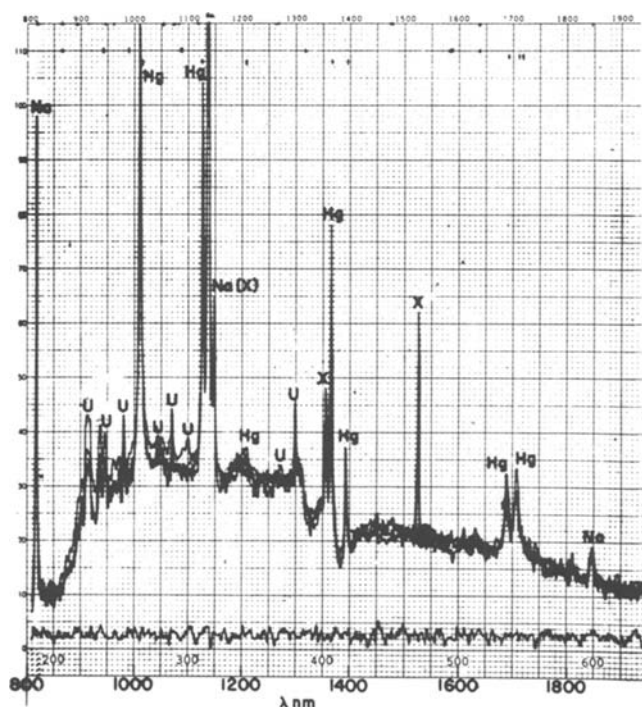


Fig. 9. Near-infrared spectrum of discharge lamps containing Th and/or Sc iodides and the same amounts of Hg and A as in Fig. 8.

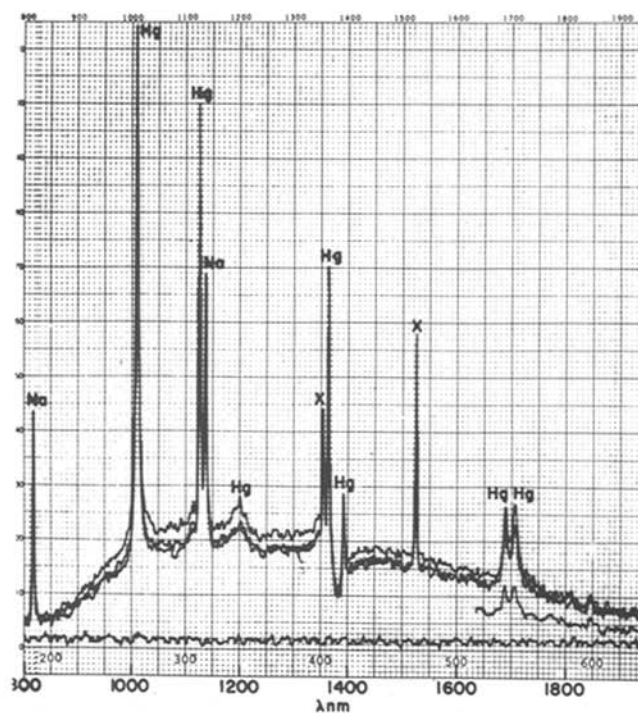


Fig. 10. Near-infrared spectrum of discharge lamps containing only NaI and the same amounts of Hg and A as in Fig. 8 and 9.

temperature gradient (8). The net effect will be distortion of the electrode structure. Figure 11 is a photograph of an electrode, originally ending in a well-defined tip, after operation for a few hours in a discharge lamp containing ScI_3 . This type of distortion also occurs in lamps containing ThI_4 .

A key check of the postulated mechanism is to confirm that this distortion involves SiI_4 .

(a) Direct evidence: Although the spectra of lamps containing HgI_2 and SiI_4 are essentially the same, the electrodes of the lamps containing HgI_2 remained intact but the electrodes of lamps containing SiI_4 were distorted during the short (minutes) time of spectroscopic examination. The distorted appearance is very similar to that observed in lamps containing Th and/or Sc iodides, Fig. 11.

(b) Electron microprobe identification of Si: Electrodes such as that of Fig. 11 were subjected to electron microprobe x-ray backscattering examination.



Fig. 11. Photograph of electrode originally ending in a well-defined tip after operation in discharge containing ScI_3 . This distortion also occurs in discharges containing ThI_4 .

Figure 12 shows that large amounts of Si are associated with the distorted area (end-on view).

(c) Scanning electron microscopy: SEM micrographs of distorted regions reveal peculiar growths, Fig. 13. These do not appear to be only the result of a simple melting process but also of a complex interaction to be discussed in the next section.

(d) Identification of WSi_2 formation by means of "closed system" high temperature x-ray diffraction: The interaction between $\text{SiI}_4(\text{g})$ and $\text{W}(\text{s})$ to form Si-W condensed phases was proven by means of the experimental arrangement shown in Fig. 14.⁵

The first column of Table II gives the d values of the W peaks (9) before and after heating the system. The second column gives the d values of new peaks appearing after heating the silica envelope to approximately 100°C (~ 5 Torr of $\text{SiI}_4(\text{g})$) for 30 min while

⁵This method was developed in collaboration with J. R. Cooper of this laboratory. It is pointed out that result reproducibility is dependent on precise positioning of the sample in the x-ray beam (i.e., use of a micro-manipulator), secure coupling of reaction tube to support, and the geometry of the target. The optional lower electrode can be used for reactivity studies under discharge conditions and/or measurement (5) of changes of the work function of the target (upper electrode) as a result of its interaction with the atmosphere. The attenuation of the x-ray beam by the walls of the reaction vessel did not prove to be a serious problem. Absorption measurements were in agreement with calculated values using the Victoreen procedure (11); thus, for two 1 mm wall thicknesses of vitreous silica, the attenuation proved to be $\sim 50\%$.

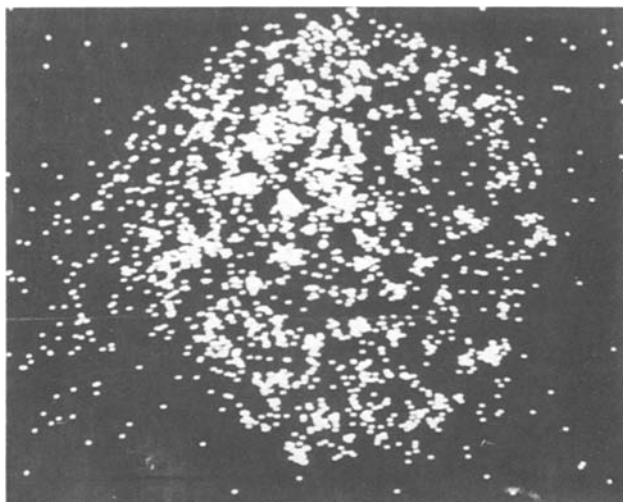


Fig. 12. Detection of Si associated with the distorted area of the electrode of Fig. 11 by means of electron microprobe x-ray back-scattering.

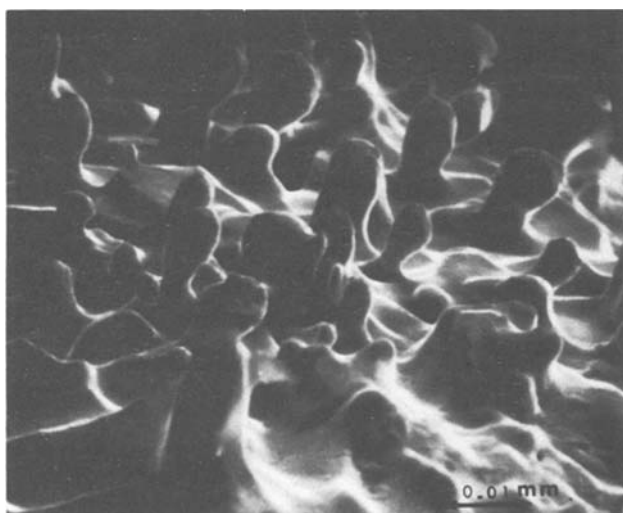


Fig. 13. Scanning electron photomicrograph of distorted region of the electrode of Fig. 11.

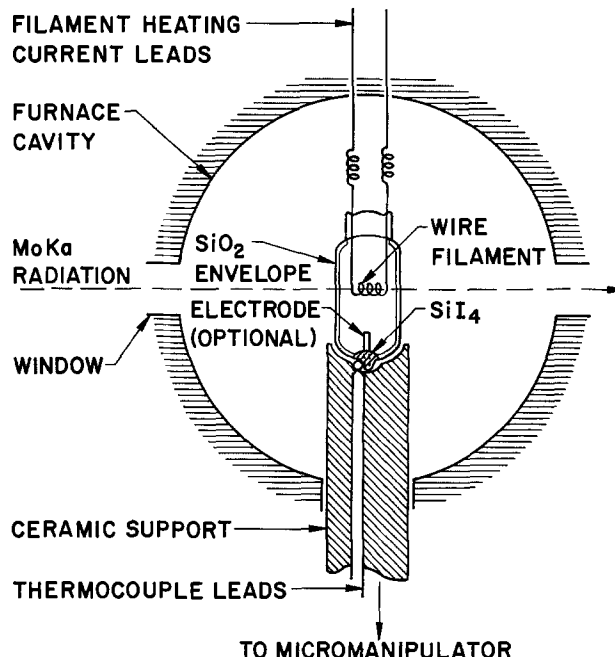


Fig. 14. Experimental arrangement of "closed system" high temperature x-ray diffraction for the study of gas-solid interactions involving condensable, corrosive, or toxic gases.

holding the W filament to an estimated temperature of 1400°C . The d values of the new peaks correspond (10) to those of WSi_2 .

These results are consistent with Step 5 of the mechanism; it is concluded that electrode distortion involves SiI_4 .

Step 6: Self-regulation of reaction mechanism: At low temperatures, the excess iodine combines with Hg to form HgI_2 which is observed as a red deposit on the discharge envelope. At higher temperatures ($>100^\circ\text{C}$ – 200°C), HgI_2 dissociates to Hg and gaseous iodine. The quantity of excess iodine increases with each reaction cycle, Steps 1-6. Eventually this provides the degree of self-regulation of the reaction mechanism described in the previous sections of this paper.

One of the effects will be the suppression of condensation of Th on the electrodes (Step A) and discharge characteristics will begin to change also because of reduction in electron emission from the electrodes. Such changes have been observed (5).

Discussion and Conclusions

Equations [1] and [2] and those in the Appendix outline a thermodynamic basis for electrode-atmosphere interactions. The exact predictions of this interaction, Fig. 1 and 2, will require more exact thermodynamic data. For example, nonideality of solution between ThI_4 and the other species in the reservoir, or formation of oxyiodides could reduce P_{Th} , i.e., lower curve E in Fig. 2, by several orders of magnitude. Reduction by three orders of magnitude would result in curve E intersecting curve A, i.e., the Th saturated pressure, at approximately 2500 K. Consequently, Th would not condense at the electrode tip. Reduction by four orders of magnitude would result in curve E intersecting

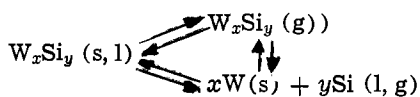
Table II. X-ray diffraction data

| 2 θ and d values for W before and after heating | | 2 θ and d values for WSi_2 after heating | |
|--|-------|--|-------|
| 2 θ | d | 2 θ | d |
| 25.90 | 1.582 | 19.74 | 2.97 |
| 31.80 | 1.29 | 20.80 | 1.96 |
| 45.70 | 0.915 | 25.50 | 1.61 |
| 49.46 | 0.849 | 28.0 | 1.47 |
| 63.60 | 0.674 | 29.0 | 1.412 |
| 69.60 | 0.622 | 38.1 | 1.09 |

curve A at two points, one at approximately 2300 K and another at a lower temperature. Then the deposition of Th would occur only at a zone of the electrode between these two temperatures.

Finally excess iodine, Fig. 4, would prevent Th deposition altogether.

The experimental evidence supports the proposed mechanism for envelope-atmosphere interactions in Table I. However, the mechanism does not consider "sub-mechanisms" *i.e.*, ultimate reactions and species. For example, it does not attack the problem of the mechanism of formation of the spheroidal deposits of SiO₂ in Fig. 7, or of the peculiar growths in Fig. 13 from the interaction of Si species with W. The W_xSi_y phases formed may be involved in the cyclic process



causing not only the growths of Fig. 13 by fractional distillation of Si but also wall blackening.

From both the fundamental and practical viewpoints, it is important to establish the kinetic rates of the steps of the mechanism and especially of the rate-determining step. This is difficult not only because of the intricacy of the mechanism but also because of the overlapping influence of cataphoretic and other effects.

The experimental methods described here could be useful in such kinetic studies. With the exception of the near-infrared spectra for Hg lamps given by Elenbaas (8c), we are not aware of previous studies of gas discharge lamps involving halides by means of near-infrared spectroscopy. The closed system high temperature x-ray diffraction technique illustrated in Fig. 14 is recommended for the study of gas-solid interactions involving condensable, corrosive, or toxic gases.

It is concluded that this work provides outlines for: (i) a thermodynamic basis for electrode-atmosphere cycles, (ii) an overall mechanism of wall-atmosphere interactions, (iii) experimental methods for the detection, monitoring, and study of chemical reactivity in discharges, and (iv) an interpretive basis for experimental and test results.

These results supplement those of previous investigations of the effects of oxygen containing impurities (1, 3) and photoelectron-induced electrolysis (2, 3) in halide discharges.

Acknowledgments

It is a pleasure to acknowledge consultations with Professors K. D. Carlson, D. E. Rosner, and F. E. Williams, collaboration with J. R. Cooper in the x-ray studies, with M. E. Blech and J. W. Moyer in the preparation of experimental systems, with W. M. Collins in all aspects of this work, and discussions with numerous colleagues but especially with R. M. Potter. This work has drawn heavily on exploratory studies by S. K. Gupta and G. J. Kazek.

Manuscript received Sept. 3, 1980.

Any discussion of this paper will appear in a Discussion Section to be published in the December 1981 JOURNAL. All discussions for the December 1981 Discussion Section should be submitted by Aug. 1, 1981.

Publication costs of this article were assisted by General Electric Company.

APPENDIX

A complete set of equations describing the atmosphere composition in discharge lamps is given in Ref. (1). For the set of constraints given in the section on Theoretical Results and Confirming Experimental Evidence, these are simplified as follows

$$\begin{aligned} P_{\text{W}_x\text{Si}_y} &= N_{\text{W}_x\text{Si}_y} \cdot P_{\text{M}_x\text{X}_b} \\ P_{\text{W}_x\text{Si}_y} &= P_{\text{M}_x\text{X}_b} + aP_{\text{M}} + bP_{\text{X}} \end{aligned}$$

where P^{W} is the pressure of M_xX_b over the liquid phase reservoir, P the partial pressure of the species indicated by the subscripts anywhere in the envelope, N_{MX} the mole fraction of the halide in the liquid reservoir and P_{MX}^* the vapor pressure of the pure halide.

Introducing these equations into the expressions for the equilibrium constants of the binary system of ScI₃ and NaI results in

$$\begin{aligned} K_{\text{NaI}} &= \frac{P_{\text{Na}} [P_{\text{Na}+3} P_{\text{Sc}}]}{P_{\text{WNaI}} - 2P_{\text{Na}}} \\ K_{\text{ScI}_3} &= \frac{P_{\text{Sc}} [P_{\text{Na}+3} P_{\text{Sc}}]^3}{P_{\text{WScI}_3} - 4P_{\text{Sc}}} \end{aligned}$$

and equivalent expressions are obtained for the NaI-ThI₄ system.

These equations are solved by iteration to obtain P_{Na} , P_{Sc} , P_{Th} , and the partial pressures of the undissociated halides as a function of temperature.

The amount of excess iodine, P_{I} , which will be sufficient to suppress P_{Th} until it is equal to $P_{\text{Th}}(\text{satd.})$, *i.e.*, to suppress the tendency of Th to condense, is calculated by setting

$$P_{\text{I}} = MP_{\text{Th}}$$

$$P_{\text{Th}} = P_{\text{Th}}(\text{satd.}) = K_{\text{s}}$$

Then

$$K_{\text{ThI}_4} = \frac{K_{\text{s}} [P_{\text{Na}} + K_{\text{s}}(4 + M)]^4}{P_{\text{WThI}_4} - 5K_{\text{s}}}$$

$$K_{\text{NaI}} = \frac{P_{\text{Na}} [P_{\text{Na}} + K_{\text{s}}(4 + M)]}{P_{\text{WNaI}} - 2P_{\text{Na}}}$$

and analogous expressions are obtained for the ScI₃-NaI system. These equations are also solved by iteration as a function of temperature.

The Gibbs free energy, ΔG_{T} , adopted for the dissociation of ThI₄(s) to form Th(s) and 2I₂(g) in the range 298-839 K is that reported by Fuger and Brown (12). This was combined with fusion and vaporization data for ThI₄ (13) and Th (14) and with dissociation data for I₂ (15) to arrive at the approximate relation

$$\Delta G_{\text{T}}(\text{ThI}_4) = 370,000 - 132T$$

for ΔG_{T} of dissociation above 839 K.

The equivalent expression for the dissociation of ScI₃ was also taken to be a linear function of temperature and after review of the literature (13, 15-20) was estimated to be approximately

$$\Delta G_{\text{T}}(\text{ScI}_3) = 144,000 - 21T$$

ΔG_{T} data for the dissociation of NaI was taken from the JANAF compilation (15) and Ref. (13) and (19).

REFERENCES

- D. M. Speros, R. M. Caldwell, and W. E. Smyser, *High Temp. Sci.*, **4**, 99 (1972).
- J. F. Waymouth, "Electric Discharge Lamps," p. 285, M.I.T. Press, Cambridge, MA (1971).
- R. E. Hanneman, W. E. Smyser, and D. M. Speros, Unpublished report (1968).
- For example, C. Hirayama, P. M. Castle, C. S. Liu, and R. J. Zollweg, *J. Illum. Eng. Soc.*, **209** (July 1977).
- D. M. Speros and P. R. Buccilli, *J. Appl. Phys.*, **41**, 1512 (1970) and previous references given therein.
- For example, W. Hertl and W. W. Pultz, *J. Am. Ceram. Soc.*, **50**, 378 (1967).
- For near infrared spectra of pertinent interest, see (a) S. Baskin and J. O. Stoner, Jr., "Atomic Energy and Grotrian Diagrams," Vol. 1, North Holland/American Elsevier. (b) A. C. G. Mitchell and M. W. Zemansky, "Resonance Radiation and Excited Atoms," Cambridge University Press (1961). (c) W. E. Elenbaas, "The High Pressure Mercury Vapour Discharge," p. 127, North Holland/Interscience (1951).
- J. F. Waymouth, "Electric Discharge Lamps," pp. 247-249, M.I.T. Press, Cambridge, MA (1971).
- ASTM Card No. JCPDS 4-806.
- ASTM Card No. JCPDS 11-195.
- J. A. Victoreen, *J. Appl. Phys.*, **20**, 1141 (1949).
- J. Fuger and D. Brown, *J. Chem. Soc. Dalton*

Trans., Part I, 428 (1973).

13. O. Kubaschewski, E. LL. Evans, and C. B. Alcock, "Metallurgical Thermochemistry," 4th ed., Pergamon Press, New York (1967).
14. Derived from vapor pressure data by E. Honig and D. A. Kramer, R.C.A. Laboratories, Princeton, NJ (1968).
15. JANAF 1970 and later supplements.
16. L. Brewer, in "Chemistry and Metallurgy of Miscellaneous Materials," L. L. Quill, Editor, McGraw-Hill, New York (1950).
17. R. F. Rolsten, "Iodide Metals and Metal Iodides," John Wiley & Sons, Inc., New York (1961).
18. C. E. Wicks and F. E. Block, Bureau of Mines Bulletin 605, U.S. Printing Office, Washington, DC (1963).
19. T. B. Reed, "Free Energy of Formation of Binary Compounds," M.I.T. Press, Cambridge, MA (1971).
20. D. A. Lynch, Unpublished report (1973).

Comparison of Computer Curve-Fitting and Graphical Data Evaluations of the Galvanostatic Double Pulse Relaxation Technique for the Measurement of Kinetics of Electrode Reactions

Z. Nagy*

Argonne National Laboratory, Chemical Engineering Division, Argonne, Illinois 60439

ABSTRACT

The fields of applicability of the graphical and computer curve-fitting methods of data analysis for the double pulse galvanostatic relaxation technique are evaluated and compared using numerical computer simulation. The field of applicability is evaluated in terms of τ_c , the time constant of the double layer capacitance-reaction resistance system, and τ_d , the time constant of the diffusion impedance-reaction resistance system, and is graphically represented on a $\log \kappa$ vs. $\log \tau_c$ diagram, where κ , the rate constant parameter, is equal to $(\pi/4\tau_d)^{1/2}$. Within the field of applicability, the technique can be used to obtain the exchange current density with an error of less than $\pm 20\%$. It is shown that a modified graphical method of data evaluation can extend the field of applicability of the technique over that of the graphical evaluation method generally used in the past. The modified technique overcomes the experimental difficulty of measuring the overpotential immediately after the prepulse and also produces a mathematically more accurate description of the overpotential-time curve. As a result, the field of applicability is extended to reactions that are about 0.5 to 2 orders of magnitude faster than measurable with the unmodified technique. The computer curve-fitting data-evaluation method further extends the field of applicability, beyond that of the modified technique, because it uses an exact overpotential-time equation in the numerical evaluation; the improvement is about one order of magnitude in the measurable rates of reactions. Furthermore, the computer curve-fitting method generally results in smaller errors for the determination of the exchange current density than the graphical methods, and, in most cases, the values of the diffusion parameter and the double layer capacitance can also be obtained from the same measurement. A comparison of the fields of applicability of the single pulse and double pulse galvanostatic techniques reveals the general superiority of the latter with the improvement being about one order of magnitude in the measurable rates of reactions.

Computer curve-fitting data-evaluation methods have been shown to be superior to graphical methods for the coulostatic (1, 2) and galvanostatic (3) relaxation techniques. The possible advantages of curve-fitting data evaluation has not been previously examined for the galvanostatic double pulse technique.

The galvanostatic double pulse technique was developed by Gerischer and Krause (4) and Matsuda, Oka, and Delahay (5) as an improved galvanostatic relaxation technique. A high-current, short-duration prepulse is applied, before the measuring pulse, to charge the double layer of the electrode. As a consequence, the technique can be used to make kinetic measurements at times short enough to avoid the disturbing diffusional effects before they become overwhelming. The theory of the original technique required that the prepulse be adjusted to produce a

minimum in the overpotential-time curve exactly at the end of the prepulse. A modified theory of the technique has recently been developed (6) which takes into account the experimental fact that exact potential values cannot be measured during a short time immediately after the prepulse. The theory of the technique was extended to the case in which the minimum in the overpotential curve appears at some time after the prepulse, in a time region where exact potential measurements are possible. Two specific cases were investigated: $t_m = t_1 + \Delta t$ and $t_m = qt_1$ where Δt and q are kept constant within a series of measurements. It has also been shown that, for experimental reasons, the ideal case of $t_m = t_1$ can never be achieved and that all previous applications of the technique have probably (albeit tacitly) used the case in which $t_m = t_1 + \Delta t$. This case will henceforth be called the unmodified technique, whereas the case of $t_m = qt_1$ will be called the modified technique. In this communication, the

* Electrochemical Society Active Member.

Key words: computer, chronopotentiometry, kinetics, transients.

graphical data evaluation for these two cases will be compared to a computer curve-fitting data evaluation.

Procedures

Theory.—The theory of the galvanostatic double pulse technique has been described before and will not be repeated here. The full overpotential-time equation has been described for the case of an ideal galvanostat, having zero risetime (5, 6), and also for the more realistic case of linearly rising current pulses (7). It is assumed that all restrictions and assumptions leading to these equations are fulfilled, including the assumption that the current density-overpotential relation can be linearized if the total overpotential (activation + concentration) is less than 5 mV. There is some controversy in the literature about this point. Kooijman *et al.* (8) showed that linearization may be valid only for much smaller overpotentials, but numerical calculations on the coulstatic (9) and galvanostatic (10) relaxation techniques indicated that they are applicable to overpotentials as large as 20-25 mV, even though a linear current density-overpotential relation is assumed.

The three quantities that are potentially determinable with this technique are (i) the ratio of the exchange current density to the stoichiometric number (i_0/ν), (ii) the diffusion parameter ($1/D_0^{1/2}C_0 + 1/D_R^{1/2}C_R$), and (iii) the capacitance of the double layer. The first one of these is usually the main objective of the measurement, and its determination will be emphasized in this communication. It is to be noted that, since the technique is limited to the linear current density-overpotential range, the value of the exchange current density cannot be directly determined from a simple measurement. The determinable quantity is the ratio of the exchange current density to the stoichiometric number. For the sake of simplicity, the term "exchange current density" will refer to the i_0/ν ratio in the following, unless it is specifically stated to be i_0 .

The full overpotential-time equations are too complicated to be used in a simple graphical data evaluation, and, for this purpose, the zero risetime equation is simplified by some series expansion which is valid only for small or for large arguments (5, 6). A graphical evaluation method is not available for the case of linearly rising pulses. Because of the inadequacies of the above-mentioned simplifications, the graphical analysis introduces an error into the determination of the exchange current density that can limit the applicability of the method, as will be shown below. It is the purpose of the computer curve-fitting data evaluation to eliminate this error by using the full overpotential-time equation, either in the form that assumes ideal pulses or in the extended form that assumes a linear rise for the pulses.

Computational techniques.—In the computer curve-fitting data evaluation, a numerical calculation was carried out to determine the values of the exchange current density, diffusion parameter, and double layer capacitance that give the best fit between the measured and calculated overpotential-time curves, using a multidimensional, nonlinear least squares technique. The curve-fitting subroutine used in this work was LMDER from the MINPACK-1 package developed by the Applied Mathematics Division of Argonne National Laboratory (11). A modified version of the driver program LMDER1 was used to access LMDER. The modifications were made to avoid large initial changes of the estimate of the solution vector by the program, in its search for the minimum in the sum of squares. These modifications were needed, in this particular case, because, in addition to the absolute minimum to be determined, there seemed to exist several local minima which would have trapped the program had the solution vector come too close to any of them. The changes in LMDER1, as compared to the published version (11),

were as follows. The statement LMR11310 was replaced by

DATA FACTOR, ZERO/1.D-01, 0.0D0

and the statement LMR11450 was replaced by the following statements

MODE = 2

DO 99 I = 1, N

99 WA(I) = 1.D0/DABS(X(I))

The value of TOL was always set to 10^{-8} , as recommended in the documentation for LMDER1. The graphical evaluation was also carried out with the computer, using a linear least squares extrapolation of the overpotential to $t_1 = 0$.

During the computer calculations, the function $g(z) = \exp(z^2) \operatorname{erfc}(z)$ has to be evaluated repeatedly, often for complex values of z . Several algorithms were evaluated for this purpose, and their claimed precision and relative computing times are summarized in Table I. The algorithms were compared for a large number of values of the argument, and were found to agree among each other to at least their claimed precision and often to a precision that was many orders of magnitude better. They were compared also by use in the curve-fitting program. The first three algorithms in Table I gave very similar results, whereas Tacher's algorithm resulted in a somewhat larger range of applicability for the determination of the exchange current density. The Tacher algorithm was used for all final calculations. These results indicate that the curve-fitting is influenced by the accuracy of the evaluation of the function $g(z)$ and that an algorithm is needed that approaches machine precision as closely as possible. (The machine precision was sixteen significant digits in this work.) The basic algorithms calculate the function $w(z) = \exp(-z^2) \operatorname{erfc}(iz)$ in the first quadrant only. But $g(z) = w(iz)$, and the following symmetry relations can be utilized to obtain the function in all four quadrants: $w(-z) = 2 \exp(-z^2) - w(z)$, and $w(\operatorname{conj}g(z)) = \operatorname{conj}g(w(-z))$. The algorithm is correct for all values of the argument but, because of computer limitations, it could not be used when the real part of the argument was less than -13.1 . It should be noted that, while there is no physical meaning attached to negative values of any of the three parameters to be determined, the curve-fitting program will occasionally assign negative values during its search for a minimum.

Error analysis.—The errors of the determination of the exchange current density can be conveniently divided into systematic and random errors. The systematic errors include those resulting from the inadequacies of the mathematical approximations used in the theory of the techniques and from the neglect of the finite risetime of the pulse generator. The random errors are caused by the uncertainties of the measurements of the current density, the electrode potential, and the time. In this discussion, the errors of the potential and time will be combined; that is, it will be assumed that all the errors of a potential-time data pair are concentrated in the error of the potential measurement. This error also includes the error of the correction or compensation for the IR drop between the working and reference electrodes.

Table I. Comparison of precision and relative computing times of algorithms for the calculation of the complex exponential error function

| Author | Claimed precision | Relative computing time requirements | Ref. No. |
|----------|-------------------|--------------------------------------|------------|
| Nagy | 16^{-6} | 3 | (3) |
| Gautschi | 10^{-10} | 1 | (12), (13) |
| Gautschi | 10^{-10} | 1 | (12) |
| Tacher | 10^{-16} | 1.5 | (14) |

The following procedure was used to calculate the error of the exchange current density using the different data-evaluation methods. Synthetic data were generated using the full overpotential-time equation. These data were then treated as experimental data and the exchange current density was calculated with the appropriate method. The known and calculated exchange current densities were then compared to arrive at the relative error of the method. Both the data generation and evaluation were carried out with a computer.

The following general conditions were used in the calculations. It was assumed that the ringing occurring after the prepulse will subside in such a short time that the minimum in the overpotential-time curve will be observable in the time range of 50-100 nsec after the prepulse. The minimum prepulse length was set to 100 nsec. The shallowness of the minimum in the overpotential-time curve was also considered. The shallowest minimum was required to have a potential change twice that of the uncertainty of the potential measurement in a time duration not longer than ten times the prepulse length. The prepulse length and the position of the minimum were then systematically varied, during the data generation, to find a data set with an observable minimum. To minimize the effect of diffusion, the minimum was set close to the end of the prepulse; usually Δt was equal to the shortest t_1 of the series and q was equal to 1.5. For the graphical data evaluation, a series of four data sets were used with t_1 varying in proportion to 1, 2, 3, 4. For the curve-fitting, the data set with the shortest t_1 was used with $q = 1.5$. The error of the exchange current density determination was calculated for a large number of conditions, systematically varying τ_c and τ_d (see below).

To determine the effect of the accuracy of the overpotential measurements on the error of the determination of the exchange current density, the synthetic data values were rounded off either to the nearest tenth of a millivolt or to the nearest hundredth of a millivolt, creating data sets with ± 50 and $\pm 5 \mu\text{V}$ random errors. A $50 \mu\text{V}$ accuracy can be achieved by the best analog oscilloscopes and the $5 \mu\text{V}$ accuracy is available with some digital oscilloscopes (transient recorders). The effect of the error of the current density was determined by offsetting the values of the current densities used in the data generation and those used in the data evaluation.

The effect of the risetime of the galvanostat was also investigated. For this purpose the synthetic data were generated with a full equation which takes into consideration the risetime (7). This equation assumes a linear rise of the current (constant slew rate) to the desired value.

The applicability diagram.—Although it has been customary (15, 16) to express the limitation of a technique as the largest measurable first-order heterogeneous rate constant, an inspection of the theory of the technique will immediately reveal that the determination of the exchange current density is influenced not only by the magnitude of k_0 but also by many other parameters. Kooijman and Sluyters (17) have suggested the use of certain dimensionless parameters for the error analysis of the galvanostatic and coulometric techniques. While this is a useful approach, it seems more appropriate, from the standpoint of obtaining a clear physical picture, to express the errors as a function of certain characteristic times of the electrode system and the length of the measuring pulse. This approach was found useful for previous error analyses of transient techniques employing galvanostatic double pulse (6), potential and voltage step (18), and galvanostatic single pulse (3).

A simple electrochemical reaction can be described by an electrical analog of series-coupled reaction resistance and diffusion impedance, both being shunted by the double layer capacitance. Neglecting one component at a time, one can obtain three simple time

constants. Only two of these are, of course, independent and it is convenient to select

$$\tau_c = \frac{\nu RTc}{nF i_0} \quad [1]$$

and

$$\tau_d = \frac{\pi \nu^2 n^2 F^2}{4 i_0^2 \left(\frac{1}{D_0^{1/2} C_0} + \frac{1}{D_R^{1/2} C_R} \right)^2} \quad [2]$$

Here, τ_c is the well-known τ_c time constant of the double layer-reaction resistance system (neglecting the diffusion impedance) and is defined by

$$\eta = \frac{\nu RT i}{nF i_0} \left[1 - \exp \left(-\frac{t}{\tau_c} \right) \right] \quad [3]$$

And, τ_d is the time constant of the reaction resistance-diffusion impedance system (neglecting the double layer capacitance) and is defined by (19)

$$\eta = \frac{\nu RT i}{nF i_0} \left[1 + \left(\frac{t}{\tau_d} \right)^{1/2} \right] \quad [4]$$

As indicated by Eq. [4], at $t = \tau_d$, the activation and diffusion parts of the total overpotential are equal. To define the limitations of a technique and to allow meaningful comparison with other relaxation techniques, the errors of the measurement should be evaluated as a function of these time constants and the length of the measuring pulse.

The experimenter has full control over the pulse length although the values of τ_c and τ_d can also be varied somewhat through the control of concentrations and temperature. It is therefore practical to describe the limits of a technique as a function of τ_c and τ_d while using reasonable values for the length of the measuring pulse. It was found convenient to use the parameter κ , called the rate constant parameter, in place of τ_d . They are simply related

$$\kappa = (\pi/4\tau_d)^{1/2} = \frac{i_0}{\nu n F} \left(\frac{1}{D_0^{1/2} C_0} + \frac{1}{D_R^{1/2} C_R} \right) \quad [5]$$

The advantage of the rate constant parameter is that it can be directly related, under simplified conditions, to the first-order standard heterogeneous rate constant. If one assumes that $D_0 = D_R = D$, $C_0 = C_R$, and $\nu = 1$, then $\kappa = 2k_0/\sqrt{D}$; and for $D = 10^{-5} \text{ cm}^2 \text{ sec}^{-1}$, $\kappa = 632k_0$.

Using the results of an error analysis, a diagram of κ vs. τ_c can be constructed on a log-log scale, and a field of applicability of the technique is defined in such a way that if an electrode reaction system falls within the limits of this field, its exchange current density is determinable with less than a given error. The error limit was set to $\pm 20\%$ in this work. For example, a diagram of $\log \kappa$ vs. $\log \tau_c$ is shown in Fig. 1. A description of some general features of this type of representation is needed. The main scales ($\log \kappa$ and $\log \tau_c$) are exact and valid for any combinations of the parameters they contain; under general conditions, only these scales can be used to define the position of an electrode system on the diagram. There are also three approximate, auxiliary scales shown (i_0 , k_0 , and C). These are convenient because they define a system with familiar parameters, but they are exact only under restricted conditions. The i_0 scale assumes that $c = 20 \mu\text{F cm}^{-2}$, $T = 298 \text{ K}$, and $n = \nu = 1$. The concentration scale further assumes the $D_0 = D_R = 10^{-5} \text{ cm}^2 \text{ sec}^{-1}$ and $C_0 = C_R = C$. All these restrictions apply to the k_0 scale.

Results

Graphical data evaluation.—Error analyses of the method, considering the systematic errors only, have already been published (6, 7). To construct the applicability diagrams, a systematic investigation of the random errors was also conducted.

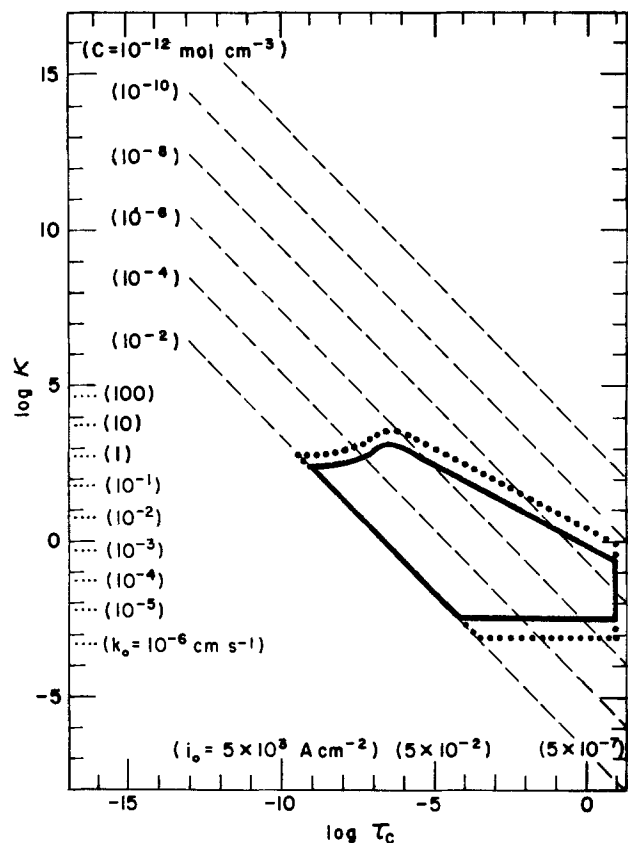


Fig. 1. Applicability diagram of the unmodified galvanostatic double pulse technique with graphical data evaluation ($t_m = t_1 + \Delta t$). The solid line marks the field of applicability for measuring the exchange current density with a maximum error of $\pm 20\%$, with an accuracy of overpotential measurement of $\pm 50 \mu\text{V}$. The dotted line extends the field for the $\pm 5 \mu\text{V}$ accuracy case.

The applicability diagram constructed for the unmodified method ($t_m = t_1 + \Delta t$) is shown in Fig. 1. The solid line demarcates the area within which the exchange current density can be measured with an error of less than $\pm 20\%$ if the overpotential is measured with an accuracy of $\pm 50 \mu\text{V}$. The dotted line extends the field to the case of $\pm 5 \mu\text{V}$ accuracy. The effects limiting the applicability of the method are different on each section of the diagram. They will be discussed proceeding clockwise from the upper left-hand corner. At first, the applicability is limited by the mathematical approximations that are needed to produce the simplified equations used in the graphical data evaluation. Proceeding clockwise, the measurable κ increases as the system approaches the validity range of the small-argument approximation. This is because the error caused by the inadequacy of the mathematical approximations is larger for the large-argument expansion than for the small-argument expansion of the unmodified method (6). The following decline of the measurable κ arises from a combination of two experimental limitations. As the value of τ_c increases, one needs larger t_m values to produce an observable minimum in the overpotential-time curve. Consequently, the kinetic content of the overpotential (ratio of the activation overpotential to the total overpotential) decreases and this causes an increase in the error of the determination of the exchange current density. All the above limitations can be counteracted by more precise measurements of the overpotential, as indicated in Fig. 1. The maximum allowed τ_c was set to 10 sec; at larger values, the measuring current density becomes small (less than nA cm^{-2}) and difficult to measure because of the small signal to noise ratio. If this limitation is removed, the range of applicability can be enlarged by linearly extending the upper and lower limits. The lower limit is also set by experimental effects. Below

this limit, the pulse lengths required to produce an observable minimum are so long that natural convection of the solution will interfere with the diffusional mass transport. The onset of the convection was taken to be about 1 min (20). Finally, the highest usable concentration was set at 10^{-2} mole cm^{-3} , which, considering solubility limitations and the requirement of a large excess of supporting electrolyte, is probably as high as one will ever use. The approximate nature of the concentration scale should, however, be kept in mind.

Figure 2 shows the applicability diagram of the modified technique ($t_m = qt_1$). The main improvement, compared to the unmodified method, occurs at small τ_c values at the upper left-hand corner of the applicability field. As has been shown before (6), the large- and small-argument approximations give equally good results for the modified method and, therefore, the limitation at small τ_c values is due to the kinetic content of the overpotential, rather than the breakdown of the large-argument approximation. Proceeding clockwise, the maximum measurable κ goes through a minimum, being limited by the mathematical approximations of the simplified equations, since in this intermediate range neither the large- nor the small-argument expansions are good approximations. The rest of the limitations are the same as those for the unmodified technique (Fig. 1). It is to be noted, however, that the measurable κ levels are somewhat larger for the modified method at all values of τ_c . The reason for this is the generally smaller errors of the small-argument approximation for the modified method (6).

Another experimental restriction which may, in principle, limit the field of applicability is the largest practically achievable current density. This has been shown (3) to be outside the fields of applicability defined by Fig. 1 and 2.

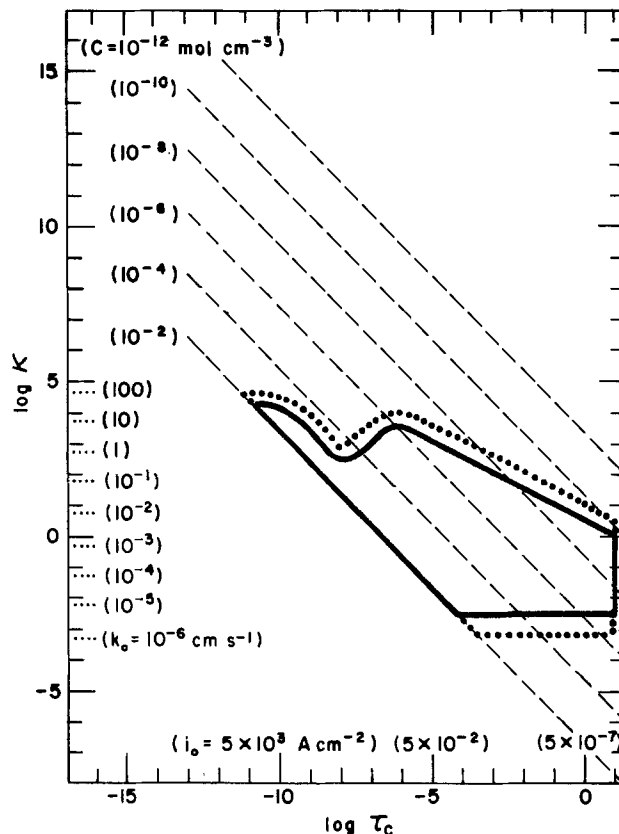


Fig. 2. Applicability diagram of the modified galvanostatic double pulse technique with graphical data evaluation ($t_m = qt_1$). The solid line marks the field of applicability for measuring the exchange current density with a maximum error of $\pm 20\%$, with an accuracy of overpotential measurement of $\pm 50 \mu\text{V}$. The dotted line extends the field for the $\pm 5 \mu\text{V}$ accuracy case.

The effect of the error of the measuring current density is not large. An error of the measuring current density will introduce a very nearly equal error in the exchange current density which will be approximately additive to the other errors. Figures 1 and 2 were calculated for a $\pm 1\%$ error of measuring current density. An increase of the error to $\pm 5\%$ will decrease the field of applicability only slightly.

The risetime of the galvanostat was found to have only a small effect, as has been shown previously (7). Figures 1 and 2 were calculated for a risetime of 15 nsec, but increasing the risetime to 50 nsec (and even to 0.5 μsec , for prepulses of 1 μsec or longer) will leave the fields of applicability practically unchanged.

Computer curve-fitting data evaluation.—The curve-fitting method is expected to be superior to the graphical data evaluation method because it uses the full overpotential-time equation and therefore the error introduced by the inadequacy of the simplified equations is eliminated. Indeed, as indicated by Fig. 3, the range of applicability is improved in the area where the graphical method is limited by the simplified equations. No other improvements were produced because the limiting conditions (kinetic content of data, shallowness of minima, etc.) are equally applicable to both data-evaluation methods. Therefore, the limiting effects of Fig. 3 are the same as those of Fig. 2, with the exception of the limitation resulting from the use of simplified equations for the graphical data evaluation. On the other hand, a further benefit of the curve-fitting evaluation method is the generally higher accuracy of the exchange current density determination. The error of the exchange current density is equal to or less than that resulting from the graphical method everywhere within the field of applicability. The error of the curve-fitting method can be as much as one order of magnitude less than that of the graphical method. The field

of applicability shown on Fig. 3 is, however, subject to the following caveats.

In the computer curve-fitting method, there is no need for a fixed relation between t_1 and t_m , since only one measurement is used rather than the series of measurements needed for the graphical case. Therefore, one cannot distinguish between the cases of $t_m = t_1 + \Delta t$ and $t_m = qt_1$. However, to assure that the double layer is precharged, the technique still requires that $t_1 < t_m$ and that the minimum in the overpotential-time curve be observable.

The method was found to be very sensitive to the risetime of the galvanostat when using the equation assuming ideal pulses; this effect can be diminished, however, by using an extended equation assuming linearly rising pulses (7). To achieve the field of applicability shown on Fig. 3, the extended equation was used; in this case, risetimes up to 50 nsec were examined and were found to have no effect on the results. In these evaluations, the rise and fall of the prepulse were assumed to be linear (7), which is a good approximation of the pulses produced by modern pulse generators. Any deviation from this assumed linearity will introduce some error in the determination of the exchange current density; this error was not evaluated, but is expected to be considerably less than the error caused by the complete neglect of the risetime. This latter case is illustrated in Fig. 4. For this graph, the synthetic data were generated with the equation that takes into consideration the finite rise of the pulses (7), whereas the data evaluation was carried out with the equation assuming zero risetime (6). A comparison with Fig. 3 reveals that a risetime even as short as 5 nsec has a deleterious effect on the accuracy of the determination of the exchange current density and decreases the field of applicability. Of course, if zero risetime data had been used in conjunction with the zero risetime equation in the curve-fitting program,

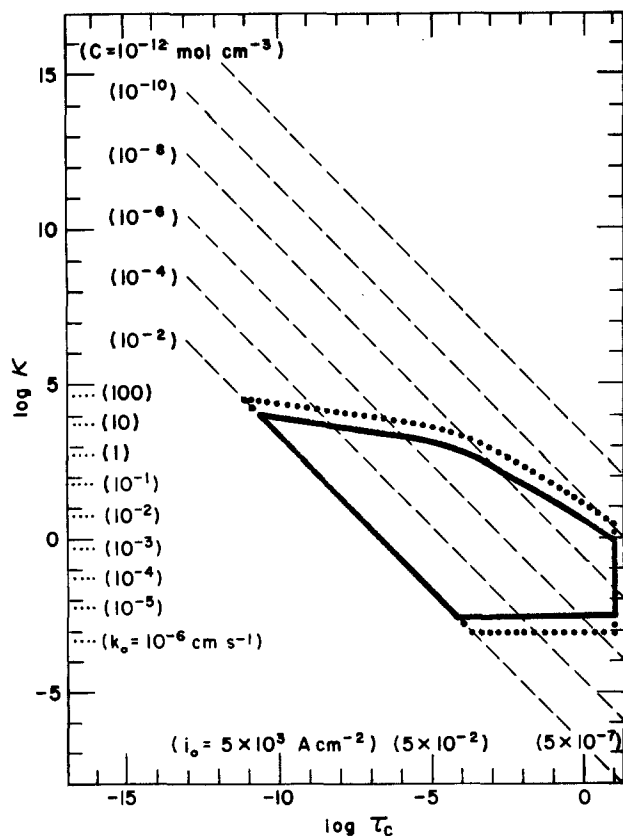


Fig. 3. Applicability diagram of the galvanostatic double pulse technique with computer curve-fitting data evaluation. The solid line marks the field of applicability for measuring the exchange current density with a maximum error of $\pm 20\%$, with an accuracy of overpotential measurement of $\pm 50 \mu\text{V}$. The dotted line extends the field for the $\pm 5 \mu\text{V}$ accuracy case.

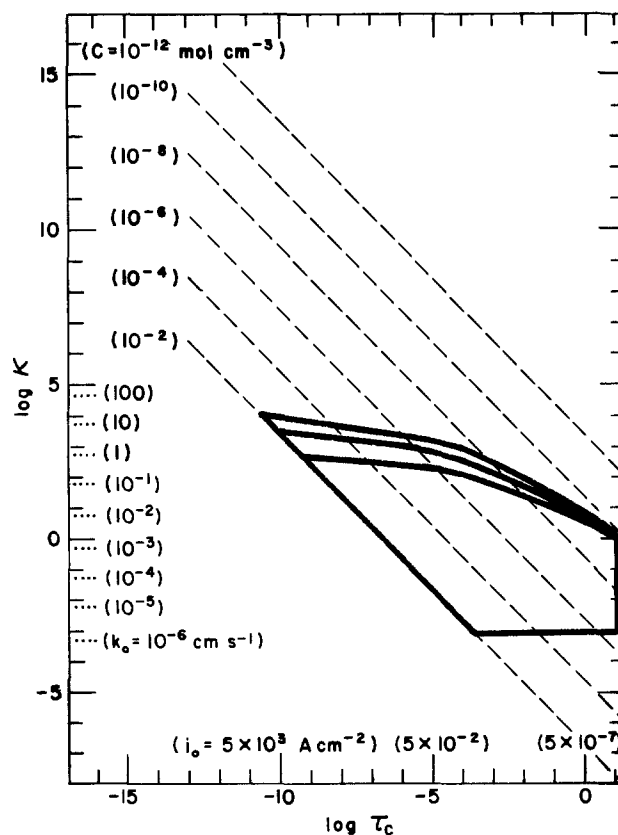


Fig. 4. Effect of the risetime of the galvanostat on the field of applicability of the curve-fitting method, with $5 \mu\text{V}$ overpotential accuracy. The upper limits represent, in decreasing order, a risetime of 5, 15, and 50 nsec.

the field of applicability in Fig. 3 would have been duplicated.

The method was also found to be sensitive to errors of the measurement of the overpotential and current density. Similar accuracies were assumed for the two measurements; for the case of the 50 μV potential error, the maximum current density error was set to $\pm 1\%$; and for the 5 μV case, the current error was limited to $\pm 0.1\%$. The combined effect of these errors is shown in Fig. 3.

In the calculations leading to Fig. 3 and 4, the number of data points was always 50, with the points being uniformly spaced during the measuring pulse. The first point was always taken at 0.1 μsec after the end of the prepulse to assure that all initial distortions of the potential, due to induction effects and ringing, are avoided in the data. Fifty is probably the maximum number of points obtainable with an analog oscilloscope, while thousands could be obtained with a digital oscilloscope or transient recorder. Increasing the number of data points can decrease the error of the determination of the exchange current density, at the price of longer computation times, but will not significantly change the field of applicability. The use of as many as 2000 data points can decrease the error by one order of magnitude. The computation time for 50 data points averages around 30 sec, and it increases approximately in proportion to the number of points.

To start the calculation, the curve-fitting program requires a set of initial guesses for the three parameters to be determined, (i_0/ν , the diffusion parameter, and the double layer capacitance). It is desirable to start with guesses that are close to the actual values. Figures 3 and 4 are valid for guesses that do not deviate by more than a factor of three from the actual values. A factor of two will produce very similar results. The field of applicability will start to shrink considerably when the factor is four or larger. This is not a serious limiting effect since the initial guess for the exchange current density can be obtained within the desired limits by the graphical data evaluation method of the double pulse technique. The required values of the diffusion parameter and the double layer capacitance can be obtained within the desired limits from the long-time and short-time slopes of galvanostatic transients.

The computer curve-fitting data-evaluation method permits one to calculate the diffusion parameter ($1/D_O^{1/2}C_O + 1/D_R^{1/2}C_R$), and the capacity of the double layer, in addition to the exchange current density. The fields of applicability, of course, are not necessarily the same for these parameters as for the exchange current density, and these limits were not examined in this work. However, the following observations are relevant. The field of applicability of the diffusion parameter is larger than that of the exchange current density, and its field of applicability completely overlaps that of the latter. Within the field of applicability shown on Fig. 3, the diffusion parameter can be determined with an error that is much less than that of the exchange current density. The fields of applicability for the determination of the capacity of the double layer and the exchange current density overlap only partially. The capacity can be determined with an error less than $\pm 20\%$ on the right-hand side of the field shown in Fig. 3; but on the left-hand side, the field is limited approximately by the $\tau_c = 10^{-8}$ line. This is probably due to the fact that at small values of τ_c the usual prepulse length is much longer than τ_c .

Conclusions

A comparison of the unmodified and modified techniques, coupled with graphical evaluation, reveals the general superiority of the modified technique. This is caused by the fact that the simplified equation needed for the graphical evaluation is a better approximation for the modified case. In general, the field of applicability is enlarged by about one-half order of magni-

tude of κ , and for very fast reactions it is enlarged by about two orders of magnitude.

The computer curve-fitting data-analysis method further extends the field of applicability of the technique because this method uses the full overpotential-time equation as the basis of the data evaluation and the approximation errors of the simplified equations are eliminated. This extends the field of applicability by about one order of magnitude of κ at τ_c values around 10^{-8} . At smaller and larger τ_c values, the curve-fitting method is approximately equivalent to the modified graphical method because they are both limited by the same experimental factors. Further advantages of the computer curve-fitting method are that the error of the determination of the exchange current density will generally be smaller, and that, in most cases, the values of the diffusion parameter and the double layer capacitance can also be obtained from the same measurement.

A comparison of the field of applicability of the galvanostatic single pulse technique (3) with that of the double pulse technique shows that at large κ values (fast reactions) the exchange current density can be measured with smaller error using the double pulse technique, but for slower reactions only the single pulse technique is applicable. Comparing the graphical evaluation methods of both techniques, one can conclude that the modified double pulse technique can be used to measure the exchange current density of reactions that are up to one and a half order of magnitude faster than those measurable with the single pulse technique. The unmodified double pulse technique is applicable to reactions about one order of magnitude faster than the single pulse technique at τ_c values larger than 10^{-6} , but it is worse at smaller τ_c values. Furthermore, using the criterion of maximum measurable κ at any τ_c , the unmodified double pulse technique is indeed inferior to the single pulse technique, as has been predicted by Sluyters and co-workers (21-23). The application of computer curve-fitting data evaluation increases the field of applicability of both the single pulse and the double pulse techniques but the double pulse technique remains equal to or better than the single pulse technique, with the improvement being up to one order of magnitude in measurable κ .

Acknowledgments

The author is indebted to Dr. W. J. Cody for his help and advice with the algorithms for the evaluation of the complex exponential error function. This work was performed under the auspices of the Division of Materials Sciences, Office of Basic Energy Sciences, U.S. Department of Energy.

Manuscript submitted Aug. 11, 1980; revised manuscript received ca. Nov. 18, 1980.

Any discussion of this paper will appear in a Discussion Section to be published in the December 1981 JOURNAL. All discussions for the December 1981 Discussion Section should be submitted by Aug. 1, 1981.

Publication costs of this article were assisted by Argonne National Laboratory.

LIST OF SYMBOLS

| | |
|-------|--|
| c | capacity of the double layer (F cm^{-2}) |
| C_j | concentration of species j in the bulk solution (mole cm^{-3}) |
| D_j | diffusion coefficient of species j ($\text{cm}^2 \text{sec}^{-1}$) |
| F | Faraday constant |
| i | current density (A cm^{-2}) |
| i_0 | apparent exchange current density (A cm^{-2}) |
| k_0 | apparent standard heterogeneous rate constant (cm sec^{-1}), $k_0 = i_0/nFC_O^{\alpha_a/n}C_R^{\alpha_c/n}$ where α_a and α_c are the anodic and cathodic transfer coefficients |
| n | total number of electrons transferred in the overall reaction |
| O | (index) oxidant |
| R | (index) reductant |
| R | universal gas constant ($\text{J K}^{-1} \text{mole}^{-1}$) |

q constant ratio between t_1 and t_m in the modified technique (sec)
 t time (sec)
 t_1 end of the prepulse (sec)
 t_m time of occurrence of minimum in the overpotential-time curve (sec)
 Δt constant difference between t_1 and t_m in the unmodified technique (sec)
 T temperature (K)
 η overpotential (V)
 κ rate constant parameter, defined by Eq. [5]
 ν stoichiometric number of the reaction mechanism
 τ_c time constant of the double layer capacitance-reaction resistance system (sec)
 τ_d time constant of the diffusion impedance-reaction resistance system (sec)

REFERENCES

- R. F. Martin and D. G. Davis, in "Computers in Chemistry and Instrumentation," Vol. 2, Chap. 4, J. S. Mattson, H. B. Mark, and H. C. MacDonald, Editors, Marcel Dekker, Inc., New York (1972).
- J. M. Kudirka, P. H. Daum, and C. G. Enke, *Anal. Chem.*, **44**, 309 (1972).
- Z. Nagy, *Electrochim. Acta*, In press.
- H. Gerischer and M. Krause, *Z. Phys. Chem. (Frankfurt)*, **10**, 264 (1957).
- H. Matsuda, S. Oka, and P. Delahay, *J. Am. Chem. Soc.*, **81**, 5077 (1959).
- Z. Nagy, *This Journal*, **126**, 1148 (1979).
- Z. Nagy, *ibid.*, **125**, 1809 (1978).
- D. J. Kooijman, M. Sluyters-Rehbach, and J. H. Sluyters, *Electrochim. Acta*, **11**, 1197 (1966).
- J. M. Kudirka and C. G. Enke, *Anal. Chem.*, **44**, 614 (1972).
- F. H. Beyerlein and R. S. Nicholson, *ibid.*, **44**, 1917 (1972).
- J. J. More, B. S. Garbow, and K. E. Hillstrom, Argonne National Laboratory Report, ANL-80-74 (1980).
- W. Gautschi, *SIAM J. Numer. Anal.*, **7**, 187 (1970).
- W. Gautschi, *Comm. ACM*, **12**, 635 (1969).
- H. J. Tacher, Jr., in "Blanche Anniversary Volume," B. Mond, Editor, p. 315, Aerospace Research Laboratory, Wright-Patterson AFB, Ohio (1967) (Avail. NTIS. AD-657323).
- P. Delahay, in "Advances in Electrochemistry and Electrochemical Engineering," Vol. 1, Chap. 5, P. Delahay and C. W. Tobias, Editors, Interscience Publishers, Inc., New York (1961).
- J. Kuta and E. Yeager, in "Techniques of Electrochemistry," Vol. 1, Chap. 3, E. Yeager and A. J. Salkind, Editors, Wiley-Interscience, New York (1972).
- D. J. Kooijman and J. H. Sluyters, *Electrochim. Acta*, **12**, 1579 (1967).
- Z. Nagy, *ibid.*, **25**, 575 (1980).
- T. Berzins and P. Delahay, *J. Chem. Phys.*, **23**, 972 (1955).
- P. Delahay, "New Instrumental Methods in Electrochemistry," p. 46, Interscience, New York (1954).
- D. J. Kooijman and J. H. Sluyters, *J. Electroanal. Chem. Interfacial Electrochem.*, **13**, 152 (1967).
- H. P. van Leeuwen and J. H. Sluyters, *ibid.*, **42**, 313 (1973).
- M. Sluyters-Rehbach and J. H. Sluyters, in "Topics in Pure and Applied Electrochemistry," p. 15, S. K. Rangarajan, Editor, SAEST, Karaikudi (1975).

Mass Transfer in a Porous Trielectrode Reactor under Steady-State and Recirculating Conditions

Patrick K. Ng*

GM Research Laboratories, Electrochemistry Department, Warren, Michigan 48090

ABSTRACT

A porous electrode sandwiched between two counterelectrodes was investigated for the recovery of silver from dilute silver cyanide solution. Both single-pass steady-state and recirculating experiments were conducted with this trielectrode reactor, and the results were compared with those of a traditional bielelectrode reactor containing only one counterelectrode. A more uniform potential distribution was observed in the cathode of the trielectrode reactor, and a higher volumetric reaction rate is thus possible. A model was developed to derive an overall mass transfer coefficient (K_m) from the results of recirculating experiments. The correlation is in good agreement with the one calculated from steady-state experiments and is best represented by $K_m = 4.1 \times 10^{-4} \text{ Re}^{0.48}$.

Flow-through porous electrodes in which the flows of current and solution are parallel to each other have been studied to a great extent both experimentally and theoretically. The merits of such electrodes lie in the fact that they can provide a substantial amount of surface area and a high mass transfer rate. An extensive literature survey of porous electrodes can be found in review papers by Newman and Tiedemann (1, 2). Data furnished by Houghton and Kuhn (3, 4) indicated that porous flow-through electrodes have the highest volumetric reaction rate among electrodes, including planar, rotating cylinder, and fluidized bed. This high volumetric reaction rate makes porous electrodes a suitable candidate, under the present stringent environmental regulations, for treating dilute effluents from electroplating rinsing waste waters.

The performance of a porous electrode is considered at its optimum if the whole electrode is operated under diffusion control, or is limited by the transfer rate of reactants to the electrode surface. This condition can be sustained only with a reasonably uniform potential distribution in the electrode. The low conductivity associated with dilute electrolytes makes this condition difficult to maintain and, as a result, the electrode is not performing up to its full capacity. A great deal of work has been done on predicting and measuring the potential distribution (5-11), and the mass transfer characteristics of the electrode (12, 25, 26). In general, an optimum design involves an electrode that is thin in the direction of current flow to maintain the necessary diffusion-limiting condition in the electrode. This design has a very short contact time for the solution and is not practical for application. One of the proposed remedies for the problem has been to flow the electro-

* Electrochemical Society Active Member.

Key words: cathode, current efficiency, mass transfer, transient.

lyte perpendicular to the current field (13-16), and this is best represented by the "Swiss-roll" cell (14, 17). With this variation, the electrode can be constructed such that it is thin in the direction of current flow and is long in the direction of solution flow. A separator, however, is necessary and the fabrication of such an electrode can be cumbersome.

To maintain a high recovery efficiency in once-through systems, the electrolyte has to be pumped very slowly through the electrode. Sioda (18) gave an equation for the calculation of this critical velocity. Too low a flow rate, however, is also not practical when thousands of gallons of effluents have to be treated. A recirculating operation is thus more applicable and its behavior has been investigated theoretically (19-21) by considering the porous electrode as the analog of a chemical reactor. Experimental work has also been carried out for treating dilute solutions of copper (22, 23, 25) and antimony (24).

The purpose of this work was to develop an improved reactor design that is easy to fabricate and, at the same time, ensures diffusion-control condition over the whole electrode. This design consists of a porous working electrode (cathode) sandwiched between two porous counterelectrodes (anodes), and is referred to as the trielectrode reactor. With the current penetrating from both sides of the working electrode, the potential distribution is more uniform, and a higher volumetric reaction rate is possible. This reactor is useful when products from the counterelectrodes would not interfere with reactions on the working electrode. The behavior of the trielectrode reactor was examined and its performance was compared with that of a traditional bi-electrode reactor. Mass transfer correlations were obtained and compared under both steady-state and recirculating conditions. Recovery of silver from a dilute alkaline silver cyanide solution was chosen for study because of the environmental toxicity and the escalating value of silver.

Experimental

Apparatus.—The reactor was fabricated from acrylic tubing (5.7 cm ID) and is shown schematically in Fig. 1. The cathode working electrode was constructed by pressing together silver-plated brass spheres (0.45 cm diam) to a height of 5 cm between two silver screens on which silver wire was welded for electrical contact. Its porosity and specific surface area (a) were calculated to be 0.39 and 8.05 (cm)⁻¹, respectively. Each anode was made of stainless steel balls (0.3175 cm diam), also packed between two stainless steel screens to a height of 5 cm. A stainless steel rod (0.635 cm diam) was inserted into each anode for electrical contact. The cathode was insulated from each anode by a plastic screen. Glass beads (0.23 cm diam) were packed at both the entrance and exit regions to ensure uniform flow. Only the bottom anode was connected when experiments for the bi-electrode reactor were conducted. The electrolyte was prepared by diluting the silver plating bath solution to a concentration approximately 40 g/liter in KCN and 4 g/liter in KOH. Two initial silver concentrations, 150 and 250 ppm, were used during the experiments. Table I illustrates the physical properties of the solution. Three mercuric oxide reference electrodes were used for measuring the overpotential of the cathode via a capillary at three different positions, i.e., the inlet, the middle, and the outlet.

Flow rates were controlled by a tubing pump and were calibrated with electrolytes by precision rotameters. The potential between the working cathode and the inlet reference electrode was kept constant by a po-

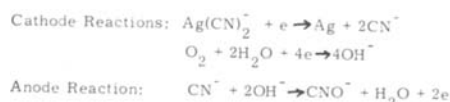
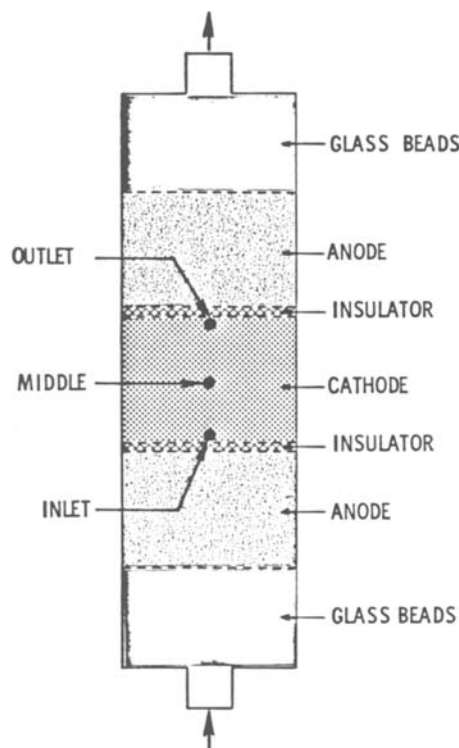


Fig. 1. Schematic diagram of the reactor

tentiostat. Current flowing through each anode was obtained by measuring the potential across a shunt (0.1Ω) connected in series with anode. A 4-pen recorder was employed for continuous tracing of the currents, and a data logger was used for recording measurements on the cell voltage, the cathode overpotentials, and the anode overpotentials.

Procedures.—For single-pass (steady-state) experiments, the electrolyte was pumped from a 113.5 liter reservoir upward through the reactor. The electrolyte was deaerated for at least 4 hr before each experiment with N₂ gas at a flow rate of 1500 cm³/min. After a constant electrolyte flow rate was maintained, the electrical circuit was then switched on. Steady state was usually attained in four to five residence times, and an outlet sample was collected for Ag analysis by an atomic absorption spectrophotometer. The applied potential was then increased and the procedures repeated. Caution was taken not to increase the applied potential to a level where the undesired hydrogen gas starts evolving. Another flow rate was then chosen and the entire process repeated.

For the recirculating experiments, the deaerated electrolyte was pumped from a solution volume of 1.5 liter. Samples from the reservoir were taken at predetermined time intervals. In order to minimize the effect of changing volume, only a small amount (2 or 3 ml) of solution was sampled, keeping the overall volume change at less than 2% for all experiments. The applied potential between cathode and inlet reference electrode was kept at 1.2V, under which limiting current condition prevailed over the whole cathode of the trielectrode reactor.

Results and Discussion

Single-pass (steady-state) systems.—Polarization curves obtained from single-pass experiments are shown in Fig. 2 for both the trielectrode and bi-electrode reactors. Typical outlet silver concentrations in ppm are also shown in the parentheses. The trielectrode

Table I. Physical properties of silver cyanide electrolyte

| | |
|---------------------------|-----------------------------------|
| Viscosity (μ) | 1.036×10^{-2} g/(cm-sec) |
| Density (ρ) | 1.033 g/cm ³ |
| Conductivity (κ) | 0.07 (Ω-cm) ⁻¹ |

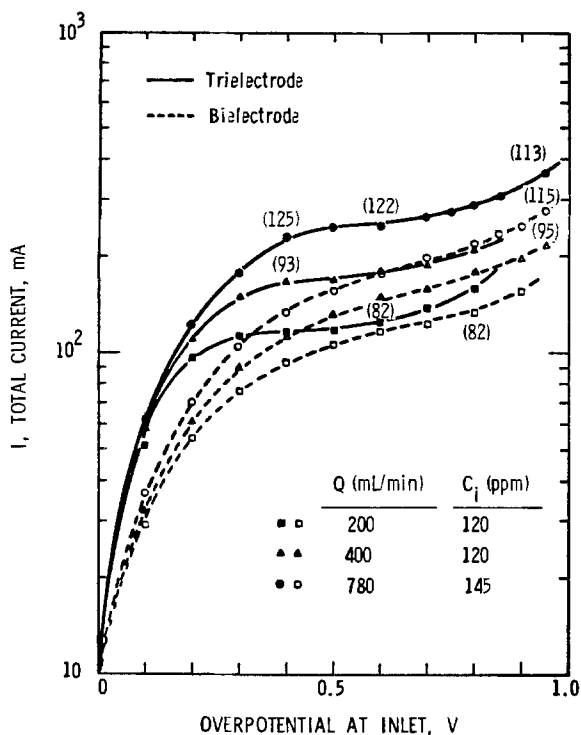


Fig. 2. Polarization curves at steady state.

reactor shows a definite limiting current plateau for all flow rates, indicating a mass transfer limiting condition over the whole cathode. This plateau falls in the potential range of 0.3 to 0.6V and shrinks with increasing flow rate. Hydrogen bubbles have been observed at overpotentials higher than 0.6V. The bielectrode reactor, on the other hand, indicates no plateau even at slow flow rates. Limiting current condition is not maintained and the reacting zone is confined near the inlet due to a highly nonuniform potential distribution. Current efficiencies for both reactors remained high (95-100%) until hydrogen gas started evolving. In general, the trielectrode reactor has a higher volumetric reaction rate than the bielectrode reactor, based on the outlet silver concentrations. Figure 3 shows typical potential distributions within the cathode when the overpotential between the cathode and the inlet reference electrode was maintained at 0.5V. It must be pointed

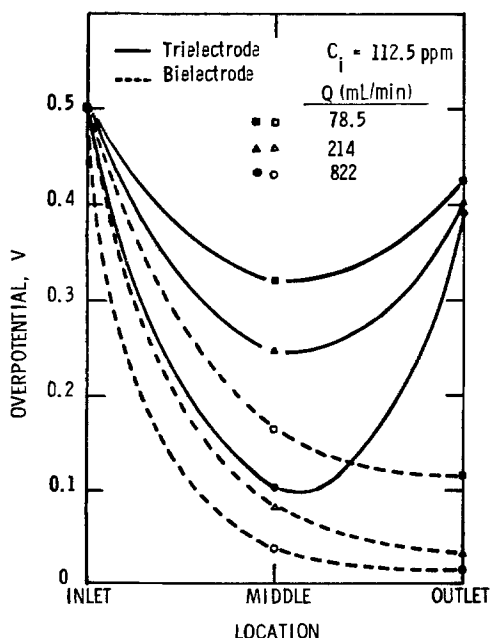


Fig. 3. Steady-state potential distribution in the cathode

out that each curve is only an approximation of the actual potential distribution. The overpotential in a bielectrode reactor is highest near the inlet and decreases rapidly, whereas the overpotential is relatively more uniform in the trielectrode reactor, particularly at low flow rates. With the additional anode, the potential near the outlet reaches about the same value as the inlet, and a minimum in potential exists near the middle of the cathode. The gain in overpotential or volumetric reaction rate, by the trielectrode reactor is obvious. At high flow rates, even the trielectrode reactor cannot maintain a sufficiently high overpotential near the middle portion of the cathode.

Since the electrode is limited by mass transfer, the measured current is related to the mass transfer coefficient by the following equation

$$I = nFav_T K_m C_i / 10^3 \quad [1]$$

Equation [1] assumes a flat velocity profile in the electrode and a velocity such that $v \gg aK_m L$, where L is the electrode length. A correlation between the calculated K_m and the Reynolds number (Re) is generally in the form of

$$K_m = B Re^m \quad [2a]$$

where B is a constant containing system parameters. Figure 4 shows the plot of K_m vs. Re for both reactors. A least square fit to the trielectrode reactor gives the following correlation

$$K_m = 4.1 \times 10^{-4} Re^{0.48} \quad [2b]$$

in which the exponent is in reasonable agreement with values obtained by other workers (10, 26). The bielectrode reactor follows closely the same correlation but deviates significantly at large Reynolds numbers where limiting current condition cannot be maintained.

The above polarization curve measurements established the proper control potential for the recirculating experiments. A value of 1.2V was subsequently chosen between the porous cathode and the inlet reference electrode, and is equivalent to a cathodic overpotential of about 0.45V.

Recirculating systems.—Previous work (22-25) on recirculating experiments has indicated that the reservoir concentration varied exponentially with time. This work also suggested this simple relationship and typical results are shown in Fig. 5 and 6 for both reactors. Referring to the flow circuit in Fig. 7, the reservoir silver concentration can be represented by

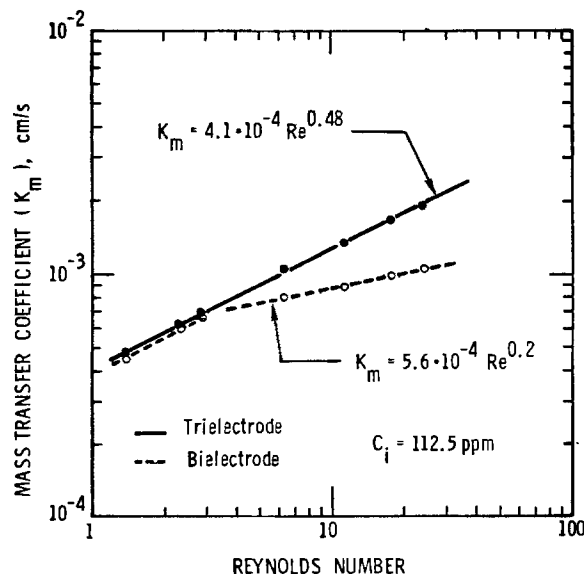


Fig. 4. Mass transfer correlation under once-through conditions

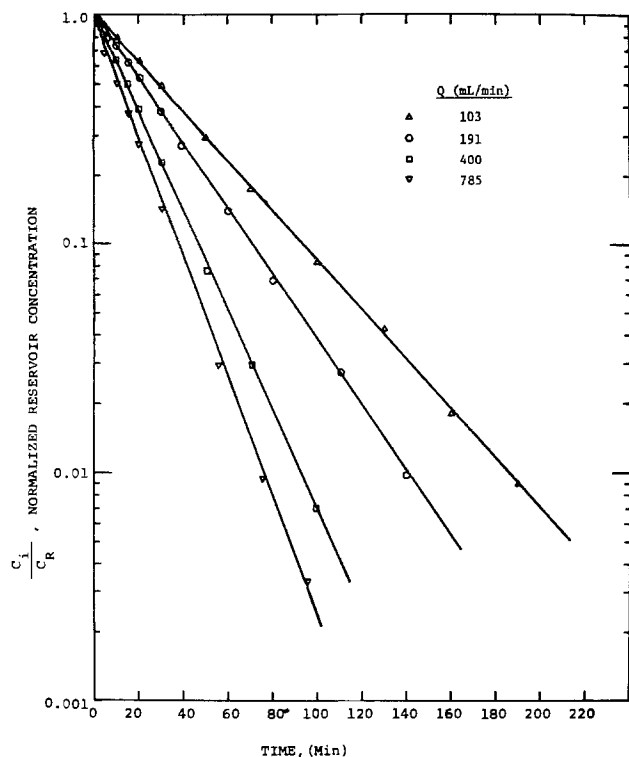


Fig. 5. Concentration transients for trielectrode reactor, $V_R = 1.5$ liters, $C_R = 150$ ppm.

$$C_i = C_R e^{-Ht} \quad [3]$$

where H is the slope of the straight lines in Fig. 5 and 6. The reservoir can thus be considered as a reactor with a first-order reaction, and H is the rate constant. For initial concentrations (150 and 250 ppm) studied in this work, the trielectrode reactor gives only one slope, whereas the bielectrode reactor has two. This is consistent with the fact that the trielectrode reactor has a more uniform potential distribution. Figure 8 illustrates a transient variation of overpotential at differ-

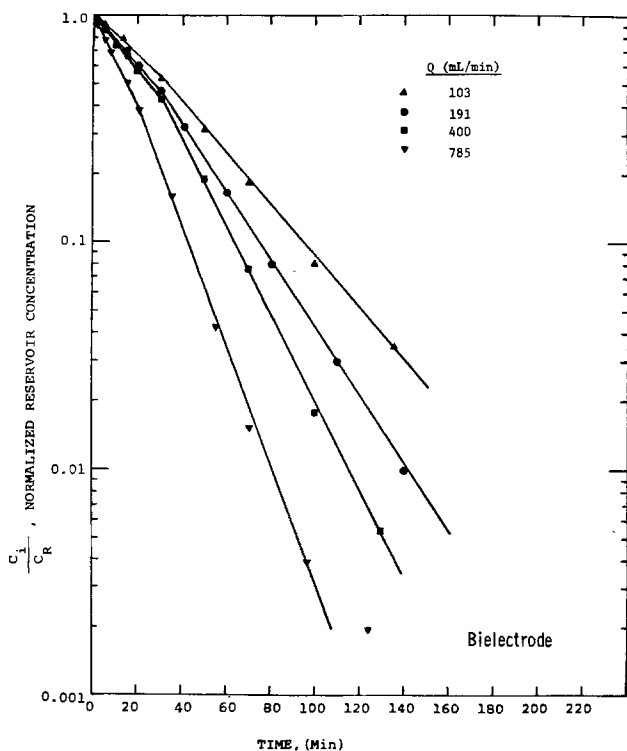


Fig. 6. Concentration transients for bielectrode reactor, $V_R = 1.5$ liters, $C_R = 150$ ppm.

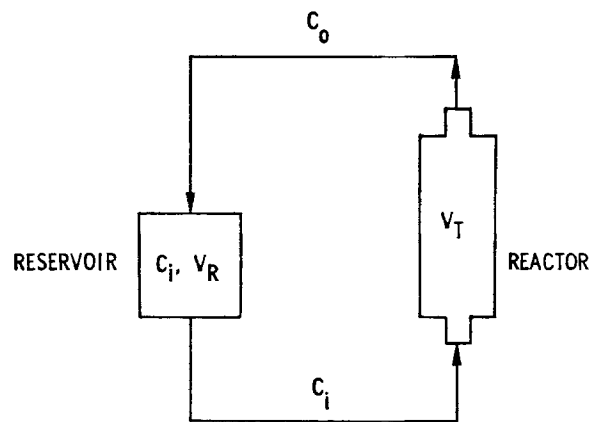


Fig. 7. Flow circuit for recirculating experiments

ent locations of the cathode. For the trielectrode reactor, the middle position reaches the limiting current condition (above 200 mV) in a very short time (about 10 min), and the whole cathode is recovering silver effectively. On the other hand, the cathode of the bielectrode reactor has only the inlet region reacting for as long as 40 min before the middle and the outlet positions reach the same limiting condition. The reservoir rate constant is thus a measure of the performance of the reactor, and a close scrutiny of the rate constant would lead to the characterization of mass transport in the porous cathode under recirculating condition.

Figures 5 and 6 can be used to obtain two volumetric reaction rates, namely, an instantaneous (J_t) and an overall (J_T). Instantaneous volumetric reaction rate is the rate at a particular inlet concentration (C_i) and is best calculated by the following equation

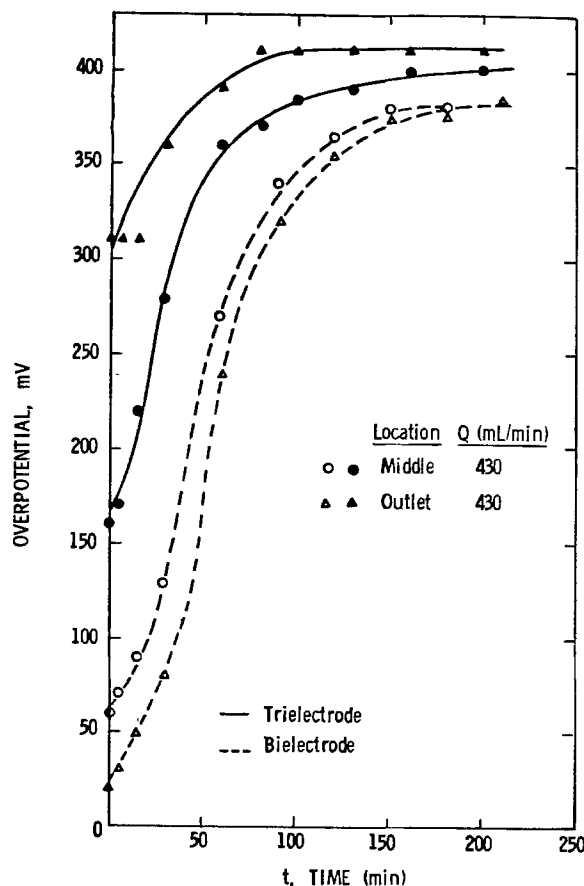


Fig. 8. Overpotential transients at different locations, $V_R = 1.5$ liters, $C_R = 150$ ppm.

$$J_t = -\frac{V_R}{V_T} 10^3 \frac{dC_i}{dt} = 10^3 C_i H \frac{V_R}{V_T} \quad [4]$$

At the beginning of experiments, the trielectrode reactor definitely has a much higher J_t because of a higher rate constant (H). The bielectrode reactor has the same rate constant after about 40 min and starts having a higher J_t due to a higher C_i in the reservoir. However, the overall volumetric reaction rate (J_T), which is the overall rate calculated over any time interval starting from $t = 0$, remains high for the trielectrode reactor, as illustrated in Fig. 9. The trielectrode reactor can also reduce the problem of plugging by extending the reacting zone over the whole cathode.

Two current efficiencies can be defined: instantaneous (η_t) and overall (η_T). Instantaneous current efficiency is the efficiency at a particular inlet concentration (C_i) and can be estimated from experimental data. This was done by calculating the current efficiency between two sampling points and assigning it as the η_t at the midpoint. One of these results is shown in Fig. 10 in terms of concentration. The error of calculation is greatest at the beginning of the experiment where η_t has to jump from 0 to almost 100%, causing the scattering of data. In general, η_t is high at the beginning when silver ions [in the form of $\text{Ag}(\text{CN})_2^-$] are plentiful. As the silver concentration drops with time, η_t decreases

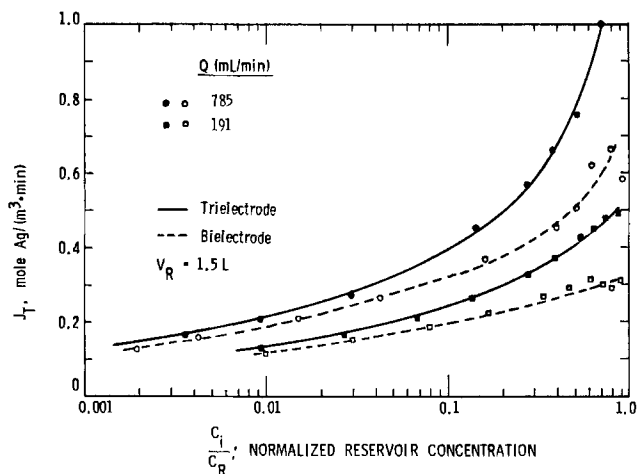


Fig. 9. Dependence of J_T on silver concentration

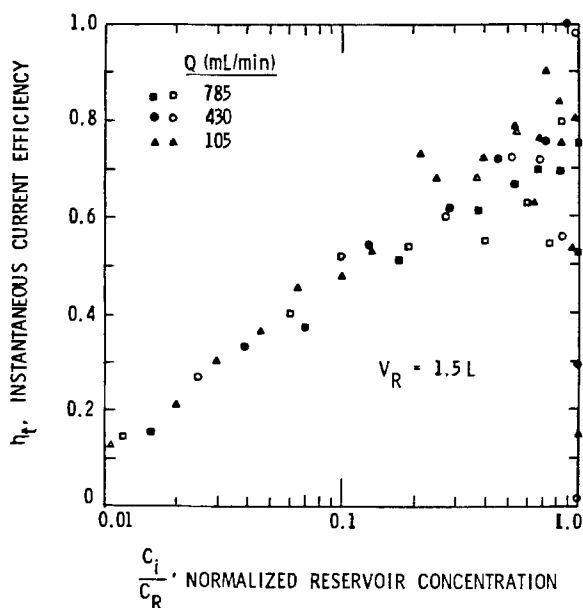


Fig. 10. Dependence of η_t on concentration for trielectrode reactor (closed symbols) and bielectrode reactor (open symbols).

drastically, and oxygen reduction becomes the major reaction. For example, η_t is only 50% when 90% of the silver is deposited. The overall current efficiency (η_T), which is the current efficiency over the period of each experiment, remains at about 60% due to a high η_t at the beginning.

An overall mass transfer coefficient (K_m) of the trielectrode reactor under recirculating condition can also be obtained by mass balance equations of the cathode and the reservoir. The porous electrode is assumed to be pseudo-homogeneous with a uniform velocity profile (plug flow). In the recirculating experiments, the inlet silver concentration varied with time, and during each passage of electrolyte through the electrode, the silver concentration changed only slightly. It is assumed that, at any particular time, the bulk silver concentration in the electrode is uniform and equal to the outlet concentration (C_o). The experimental current is then related to C_o by an equation similar to Eq. [1], or

$$\eta_t I = n F a V_T K_m C_o / 10^3 \quad [5]$$

where η_t is the instantaneous current efficiency. The value of C_o can be calculated by considering an overall mass balance of the cathode, that is

$$Q(C_i - C_o) = 60 K_m a V_T C_o \quad [6]$$

Thus

$$C_o = C_i \frac{Q}{Q + 60 K_m a V_T} \quad [7]$$

Substituting Eq. [7] into Eq. [5], one has

$$\eta_t I = \frac{a n F V_T K_m C_i}{10^3} \frac{Q}{Q + 60 K_m a V_T} \quad [8]$$

A plot of $\eta_t I$ vs. C_i yields a slope in which K_m can be calculated. The effect of the reservoir, or the rate constant H , is included in C_i which varied according to Eq. [3]. The correlation between K_m and Reynolds number is given in Fig. 11 and can be represented by

$$K_m = 4.0 \times 10^{-4} \text{Re}^{0.45} \quad [9]$$

Equation [9] compares remarkably well with Eq. [2], considering the complexity and uncertainty in calculating η_t . This not only justifies the assumptions of the model, but also confirms the belief that K_m obtained from steady-state condition can be confidently used in recirculating condition. Equation [2] is probably the better representation of the mass transfer in the cathode.

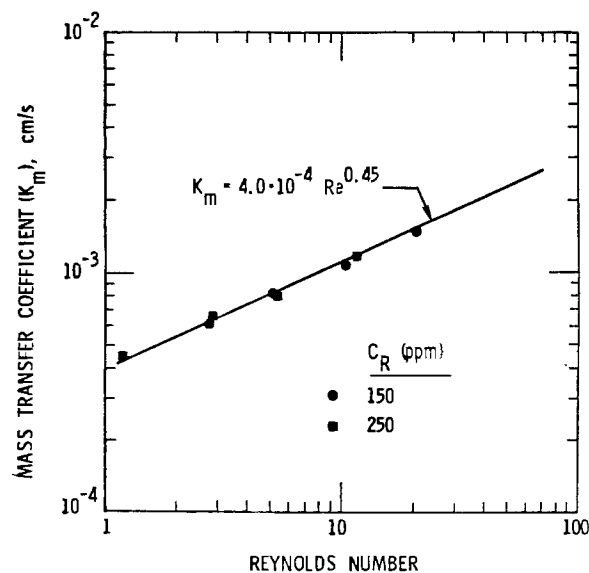


Fig. 11. Mass transfer correlation for trielectrode reactor under recirculating conditions.

Conclusions

Porous electrodes, although they can provide high volumetric reaction rate, are vulnerable to potential variation due to high solution resistivity. An optimum design includes a very thin electrode and a very slow solution flow rate, neither of which is practical. A tri-electrode reactor can attenuate these drawbacks by placing the porous working electrode between two counterelectrodes. The additional counterelectrode greatly improves the uniformity of potential and expands the diffusion-control regime over the whole working electrode. As a result, a substantial increase in volumetric reaction rate can be expected, and experimental results substantiate this advantage of the tri-electrode reactor. Furthermore, a more uniform reaction rate can extend the operating lifetime of the reactor, reducing maintenance requirements. This is particularly true when using the more practical continuously recirculating system for treating a large amount of solution.

Correlations for the overall mass transfer coefficient were obtained for the trielectrode reactor under recirculating and steady-state conditions. The results indicate that both conditions provide the same correlation. Literature correlations from steady-state experiments can thus be confidently applied to recirculating processes.

Manuscript submitted July 16, 1980; revised manuscript received Nov. 25, 1980. This was Paper 404 presented at the St. Louis, Missouri, Meeting of the Society, May 11-16, 1980.

Any discussion of this paper will appear in a Discussion Section to be published in the December 1981 JOURNAL. All discussions for the December 1981 Discussion Section should be submitted by Aug. 1, 1981.

Publication costs of this article were assisted by General Motors Research Laboratories.

LIST OF SYMBOLS

English characters

| | |
|-------|--|
| a | specific surface area, cm^2/cm^3 electrode volume |
| C_i | reactor inlet concentration, mole Ag/liter |
| C_o | reactor outlet concentration, mole Ag/liter |
| C_R | initial reservoir concentration, mole Ag/liter |
| d_p | cathode particle diameter, cm |
| F | Faraday's constant, C/g-equiv. |
| H | reservoir rate constant, 1/min |
| I | current, A |
| J_t | instantaneous volumetric reaction rate, mole Ag/ $(\text{m}^3 \cdot \text{min})$ |
| J_T | overall volumetric reaction rate, mole Ag/ $(\text{m}^3 \cdot \text{min})$ |
| K_m | overall mass transfer coefficient, cm/sec |
| L | electrode length, cm |
| n | number of electrons |
| Q | volumetric flow rate, ml/min |

| | |
|-------|---|
| Re | Reynolds number, (vd_p/ν) , dimensionless |
| t | time, min |
| v | superficial solution velocity, cm/sec |
| V_R | reservoir volume, liter |
| V_T | geometrical cathode volume, liter |

Greek characters

| | |
|----------|---|
| η_t | instantaneous current efficiency |
| η_T | overall current efficiency |
| ν | kinematic viscosity, cm^2/sec |
| μ | viscosity, $\text{g}/(\text{cm} \cdot \text{sec})$ |
| ρ | solution density, g/cm^3 |
| κ | solution conductivity, $1/(\Omega \cdot \text{cm})$ |

REFERENCES

1. J. Newman and W. Tiedemann, *AIChE J.*, **21**, 25 (1975).
2. J. Newman and W. Tiedemann, in "Advances in Electrochemistry and Electrochemical Engineering," Vol. 11, H. Gerischer and C. W. Tobias, Editors, Wiley-Interscience, New York (1978).
3. R. W. Houghton and A. T. Kuhn, *J. Appl. Electrochem.*, **4**, 173 (1974).
4. A. T. Kuhn and R. W. Houghton, *Electrochim. Acta*, **19**, 733 (1974).
5. M. Paulin, D. Hutin, and F. Coeuret, *This Journal*, **124**, 180 (1977).
6. R. E. Sioda, *Electrochim. Acta*, **16**, 1569 (1971).
7. A. Gaunand, D. Hutin, and F. Coeuret, *ibid.*, **22**, 93 (1977).
8. R. Alkire and B. Gracon, *This Journal*, **122**, 1594 (1975).
9. J. A. Trainham and J. Newman, *ibid.*, **124**, 1528 (1977).
10. D. N. Bennion and J. Newman, *J. Appl. Electrochem.*, **2**, 113 (1972).
11. J. A. Trainham and J. Newman, *This Journal*, **125**, 58 (1978).
12. P. W. Appel and J. Newman, *AIChE J.*, **22**, 979 (1976).
13. R. Alkire and P. K. Ng, *This Journal*, **124**, 1220 (1977).
14. A. Storck, P. M. Robertson, and N. Ibl, *Electrochim. Acta*, **24**, 373 (1979).
15. D. T. Chin, *AIChE J.*, **23**, 434 (1977).
16. J. M. Williams and K. B. Keating, *Du Pont Innovation*, **6**, 6 (1975).
17. P. M. Robertson, F. Schwager, and N. Ibl, *J. Electroanal. Chem. Interfacial Electrochem.*, **65**, 883 (1975).
18. R. E. Sioda, *J. Appl. Electrochem.*, **8**, 297 (1978).
19. D. J. Pickett, *Electrochim. Acta*, **18**, 835 (1973).
20. D. J. Pickett, *ibid.*, **20**, 803 (1975).
21. A. T. S. Walker and A. A. Wragg, *ibid.*, **22**, 1129 (1977).
22. A. K. P. Chu, M. Fleischmann, and G. J. Hills, *J. Appl. Electrochem.*, **4**, 323 (1974).
23. A. K. P. Chu and G. J. Hills, *ibid.*, **4**, 331 (1974).
24. A. T. Kuhn and R. W. Houghton, *ibid.*, **4**, 69 (1974).
25. A. Tentorio and U. Casolo-Ginelli, *ibid.*, **8**, 195 (1978).
26. R. Alkire, B. Gracon, T. Grueter, J. Marek, and P. Blackburn, *This Journal*, **127**, 1085 (1980).

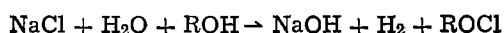
The Electrochemical Production of Organic Hypochlorite Compounds

Ronald L. Dotson* and Richard W. Lynch

Olin Corporation, Charleston Technology Center, Charleston, Tennessee 37310

ABSTRACT

The electrochemical synthesis of organic hypochlorite compounds is important as a process for direct production of reactive halofunctionalization agents (1, 2). These materials are useful as intermediates which contain a halogen in the plus one valence state, and applicable to the manufacture of industrial chemicals such as propylene oxide (2) and calcium hypochlorite (3-5). This electroorganic synthesis requires a raw material feed of aqueous brine, organic alcohol, and organic solvent in an undivided cell without separator, and no solvent in a second multi-chambered cell having a membrane. For example, tertiary butyl hypochlorite can be prepared by the electrolysis of aqueous sodium chloride brine and tertiary butyl alcohol. High product yield, current density, and current efficiency is achieved by the proper choice of anode-cathode or anode-membrane gap, proper control of the pH, and cell temperature control. The addition of an organic solvent such as carbon tetrachloride can be used in the "gap-cell" to extract the organic hypochlorite formed within the aqueous brine phase during or after the electrolysis step, according to the following overall reaction



The objectives of this research were: (i) to evaluate the use of electrochemical gap and membrane type cells for the manufacture of tertiary butyl hypochlorite from tertiary butyl alcohol and sodium chloride, and (ii) to optimize cell performance with respect to the operating conditions. This product is useful as a source of pure hypochlorous acid and can be used for the preparation of propylene oxide and calcium hypochlorite (6-8).

Experimental

Tertiary butyl hypochlorite was produced electrochemically in bench scale gap and membrane electrochemical cells.

Gap cell studies.—The test system used is shown in Fig. 1. All tests were run batchwise in a 2000 ml glass reaction flask produced by Tudor Scientific Glass Company. To this cell were added 1500 ml of saturated sodium chloride solution, 50 ml of *t*-butyl alcohol, and 350 ml of carbon tetrachloride. The cell contained an anode made up as a length of 5/16 in. diam titanium rod coated with ruthenium oxide at the standard firing temperatures. These anodes were prepared by sequentially painting on seven thin coatings from an aqueous solution of RuCl_3 dissolved in acidified *o*-butyl titanate and butanol, then fired in a muffle furnace for 1 hr at 520°C after each coating. This 5/16 in. diam titanium rod was masked down to an exposed length of 3 in. in each case. The cathode of this cell was formed of 1/32 in. thick 316 stainless steel plate rounded in a semi-circular shape with an exposed length of 3 in., as seen in Fig. 1.

All of the studies in the gap cell were made at a constant current of 3.4A, with a current density of 1.6 kA/m^2 , based on the entire exposed anode area. The d-c power was supplied from two Heath SP-2730 Power Supplies. The cell voltage was measured with a digital Weston Voltmeter.

The experimental sequence is illustrated by the following example. The cell had a 1/8 in. anode-cathode gap and subtended angle cathode concentric about the anode rod. To the cell was added a volume of 1500 ml of saturated brine at a pH of 7.5. The brine was electrolyzed and stirred for 1 hr at ambient temperature.

A 10 ml sample of the electrolyzed brine was then analyzed for the available chlorine using 7.6 ml of 0.1N sodium thiosulfate in an iodometric titration. To the remaining 1490 ml of electrolyzing brine was added 50 ml of *t*-butyl alcohol and 350 ml of carbon tetrachloride, and then electrolysis with mechanical stirring resumed at room temperature. The solution pH was constantly regulated to a pH of 7.5 by adding HCl at regular intervals. A nitrogen purge of the top section of the cell prevented the buildup of an explosive mix-

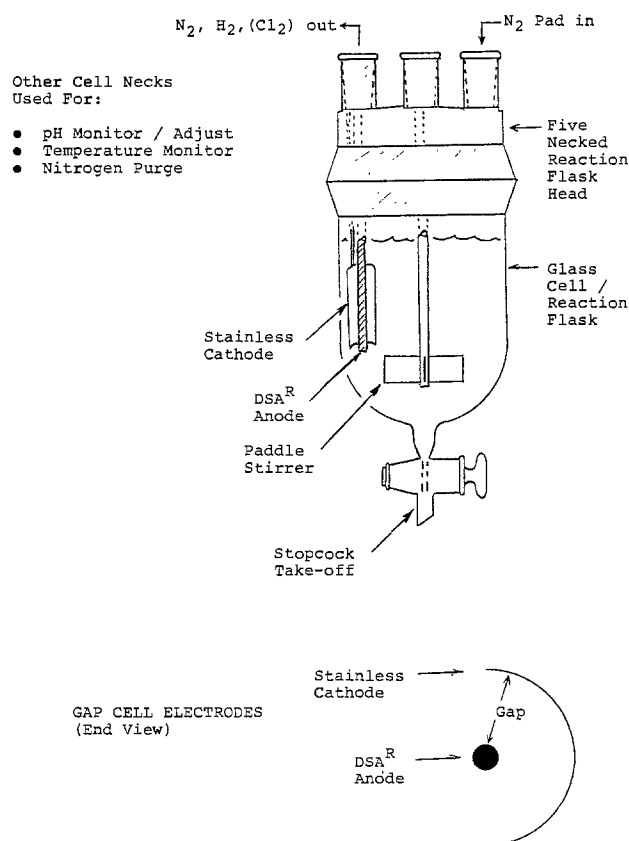


Fig. 1. Batch gap cell (empty)

* Electrochemical Society Active Member.
Key words: organic, industrial chemicals, electrolysis.

ture of hydrogen, chlorine, and oxygen. After line-out at a constant load, the cell voltage was observed to be about 3.2V in all cases. The electrolyte mixture in the cell became progressively more yellow in color as time passed until electrolysis was terminated after the passage of 6.8 A-hr of electricity. After mechanical stirring was stopped, the electrolyte was allowed to stand and to phase separate into a dense yellow organic layer and a clear aqueous layer. A 20 ml sample of the total 370 ml organic layer required 160.6 ml of 0.1N sodium thiosulfate for the total available chlorine titration. A 10 ml sample from the corresponding 1500 ml aqueous layer required 2.2 ml of 0.1N sodium thiosulfate for the available chlorine titration. This typical result of 92% anode current efficiency was determined after considering the available chlorine control of the initial electrolyzed brine layer and the final aqueous layer. The yellow-green product formed in the organic layer was *t*-butyl hypochlorite, C_4H_9OCl (9).

Membrane cell studies.—A block diagram for the membrane test cell is shown in Fig. 2. All runs were made batch-wise using a flow-through membrane cell constructed from du Pont Teflon®. The glass anolyte vessel was a 2000 ml reaction flask. The anolyte volume was 2000 ml and contained 1700 ml of brine along with 300 ml of alcohol. The anode of this cell was made from a 2.75×5.75 in. sheet of expanded titanium mesh coated with ruthenium dioxide; and the cathode was of the same dimensions but made of stainless steel. The membranes used were composed of the 427 and 295 du Pont Nafion® fluorocarbon cation exchange materials. The cell was designed to provide adjustable electrode-membrane gaps. The cell voltage varied with electrode-membrane gaps, and also both anolyte and catholyte solutions were circulated with inert pumps.

The membrane cell was normally operated at constant current of 20.5A, or 2 kA/m² current density. The cell voltage varied with electrolyte gap between membrane and electrode, and current density.

The experimental sequence is illustrated in the following example. This example uses an anode-membrane gap of $\frac{1}{2}$ in., a cathode-membrane gap of $\frac{1}{8}$ in., a Nafion® 427 membrane, a volume of 1700 ml of saturated brine at a pH of 7.5, and 300 ml of *t*-butanol added to the anolyte storage vessel. The electrolyte was circulated through the anode chamber of the cell and back into the anolyte storage vessel by an anolyte pump at a rate of 200 ml/min. A 500 ml volume of NaOH solution of 207 g/liter concentration was added to the catholyte storage vessel, and circulated through the cathode chamber of the cell and back again to the catholyte storage vessel. It was started circulating through the cathode chamber of the cell and back to the catholyte storage vessel by the circulating pump at a flow rate of 50 ml/min. Electrolysis was started and

the cell voltage determined to be 5.2V throughout the run. The anolyte pH was held at 7.5 by addition of 50% caustic at regular intervals, and the anolyte became progressively more yellow with time of run. After 2 hr, 41 A-hr of charge passed, and then the electrolysis was stopped and both anolyte and catholyte solutions collected in separate vessels. A volume of 750 ml of carbon tetrachloride was added to the anolyte in order to ease separation of the concentrated *t*-butyl hypochlorite product after each run. The inclusion of this step is thought to be safer, but not essential (10, 11).¹ The anolyte was separated into a 750 ml yellow organic phase and 1670 ml clear aqueous phase. A 10 ml sample of the organic phase used 178 ml of 0.1N thiosulfate for the available chlorine titration, while a 20 ml sample of the aqueous phase required 0.8 ml of 0.1N thiosulfate, and thus showed little hypochlorite remaining. A total volume of 570 ml of NaOH coproduct was collected, and analyzed as 257 g/liter or 21% caustic.

A current efficiency of 85% was determined for the anode portion of the cell, taking into account the small amount of available chlorine present in the final aqueous phase. The current efficiency for the cathode part of the cell was determined to be 68%. A minor amount of *t*-butanol was found in the catholyte solution, about 0.1% plus a small amount of NaCl, of 0.1%.

Results and Discussion

These studies in this work are unique and present viable commercial approaches to direct electro-synthesis of hypochlorite compounds from alcohols in one step in an electrochemical cell (12, 13).

Gap Cell Studies

Organic solvent.—The kinetics at the anode are thought to be the same for the membrane and gap cell studies. The major difference becomes apparent in the case of the gap cell where carbon tetrachloride is added before electrolysis. The current efficiency of the gap cell experiment was improved from 27 to 95% by solvent addition. This large difference results from the extraction of the very organic-soluble *t*-butyl hypochlorite moiety into the organic liquid phase where it can become insulated from the cathode surface thereby preventing its electrochemical reduction.

Electrode gap.—A series of identical experiments were run varying only cathode to anode gap distance. These runs showed the cell current efficiency reached a maximum of 93% at $\frac{1}{8}$ in. electrode gap. Note in Fig. 3, where at a gap of inches/16 vs. cell voltage, the voltage coefficient, V/kA/m², and the current efficiency are described and calculated

$$\% \text{ Current Efficiency} = [m/EW/Q/F] \times 100$$

where *m* is the mass of the product in grams, *EW* is the equivalent weight in grams per equivalent, *Q* is the quantity of electricity consumed, and *F* is the Faraday constant.

Electrolyte pH.—The pH of the electrolyte of the gap cell is important in determining the cell current efficiency and the resulting yield of *t*-butyl hypochlorite obtained. The theoretical optimum point of pH is 7.49, which is the *pK_a* for hypochlorous acid. Figure 4 provides the data from a series of experiments run at different pH's and electrode gaps at 27°C in a gap cell. The optimum pH is 7.5 and optimum at an electrode gap of $\frac{1}{8}$ in. for a 93% current efficiency, in the pH range of 5.8-9.2 and electrode gaps of 1/16 to 1/2 in. Acidic conditions cause decomposition of the *t*-butyl hypochlorite with liberation of chlorine in the pres-

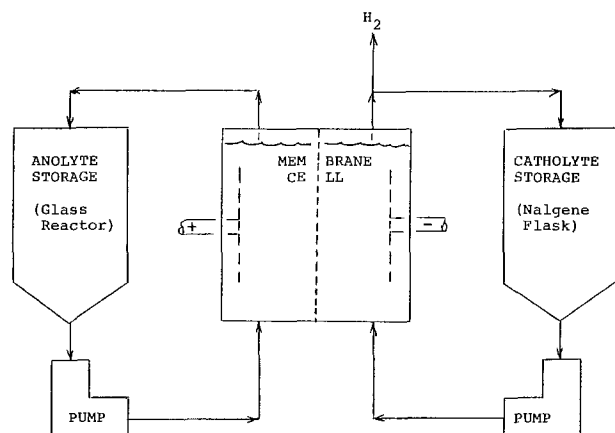
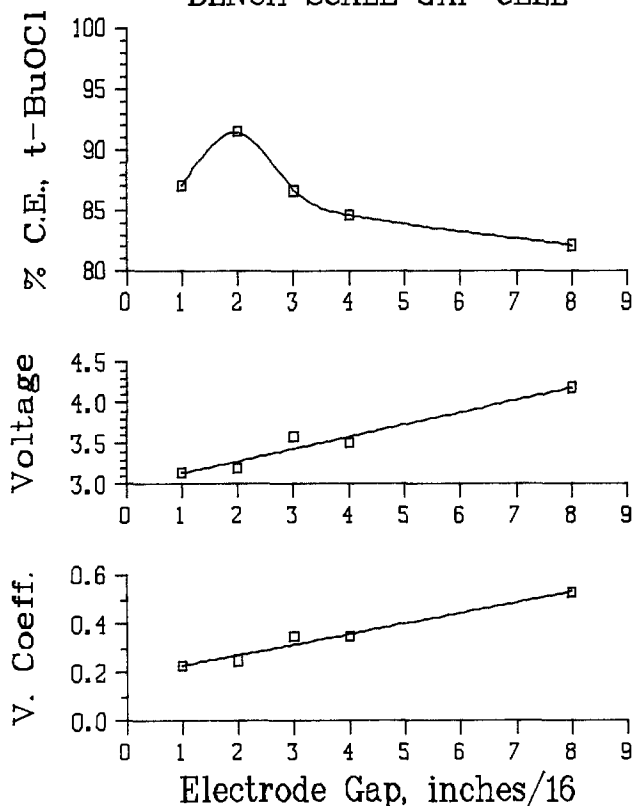


Fig. 2. Membrane cell system block diagram

¹ Bradshaw and Nechvatal (11) reported that during the preparation of *t*-butyl hypochlorite an explosion occurred during the chlorination step of *t*-butyl alcohol due to lack of temperature control. They recommend that the temperature of the reaction never exceed 20°C; however, our runs were made at over 27°C with no problems in the electrochemical cells.

ELECTROCHEMICAL FORMATION OF t-BUTYL HYPOCHLORITE IN BENCH SCALE GAP CELL



Plots of Current Eff., Cell Voltage, and Voltage Coeff. vs. Electrode Gap

Fig. 3. Plots of current eff., cell voltage, and voltage coeff. vs. electrode gap: 27°C, pH 7.5, CCl_4 in organic phase. 6.5 A-hr/run norm.

ence of chloride, while basic conditions cause the hydrolysis of the t-butyl hypochlorite to inorganic hypo-

ELECTROCHEMICAL FORMATION OF t-BUTYL HYPOCHLORITE IN BENCH SCALE GAP CELL

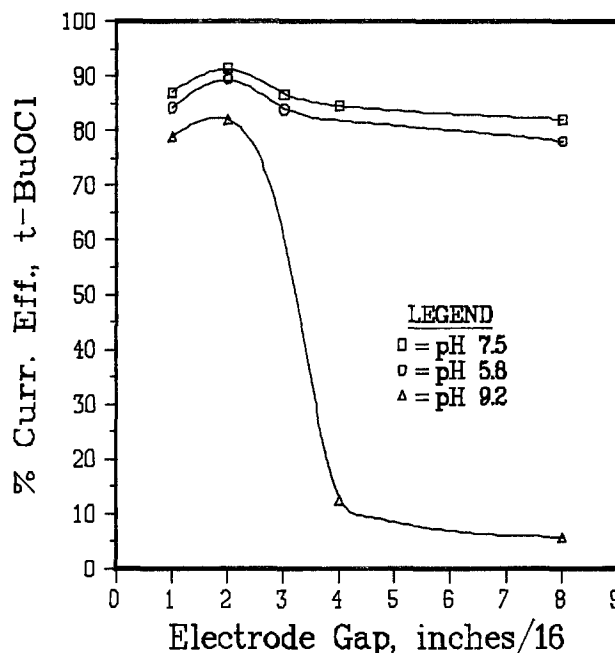


Fig. 4. Plot of curr. eff. vs. electrode gap: 27°C, CCl_4 solvent in organic phase. 6.5 A-hr/run norm.

chlorite. Both routes lead to undesirable by-products, such as chlorates and chlorinated organics.

Membrane Cell Studies

Anode-membrane gap.—The best anode current efficiency obtained with the membrane cell was found to be 85% for t-butyl hypochlorite formation. During the membrane cell operation, the anode current efficiency depends on the anode-membrane gap, since efficiency increases with increasing gap and then levels as seen in Fig. 5. There appears to be an optimum gap at $\frac{1}{2}$ in. giving maximum efficiency, and Fig. 6 shows the cell potential to rise more rapidly above $\frac{1}{4}$ in.

ELECTROCHEMICAL FORMATION OF t-BUTYL HYPOCHLORITE IN BENCH SCALE MEMBRANE CELL

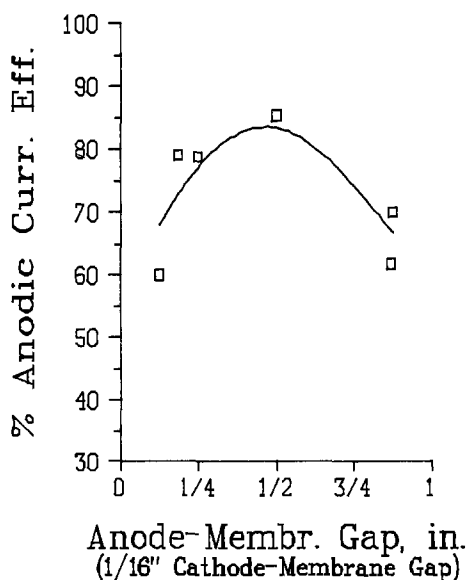
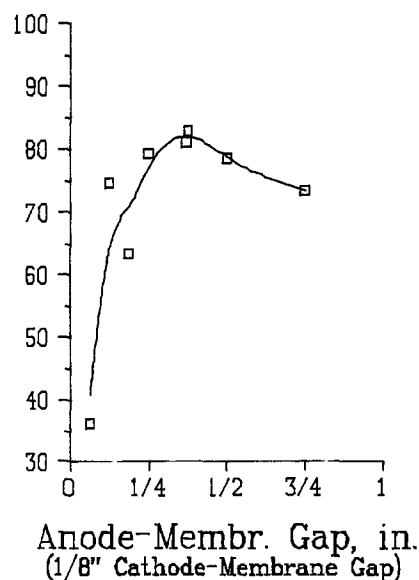


Fig. 5. 25°C, Nafion[®] 427 membrane, anolyte pH = 7.5, 2 kA/m^2 , DSA[®] anode, stainless steel cathode. 43 A-hr/run norm.



ELECTROCHEMICAL FORMATION OF t-BUTYL HYPOCHLORITE IN BENCH SCALE MEMBRANE CELL

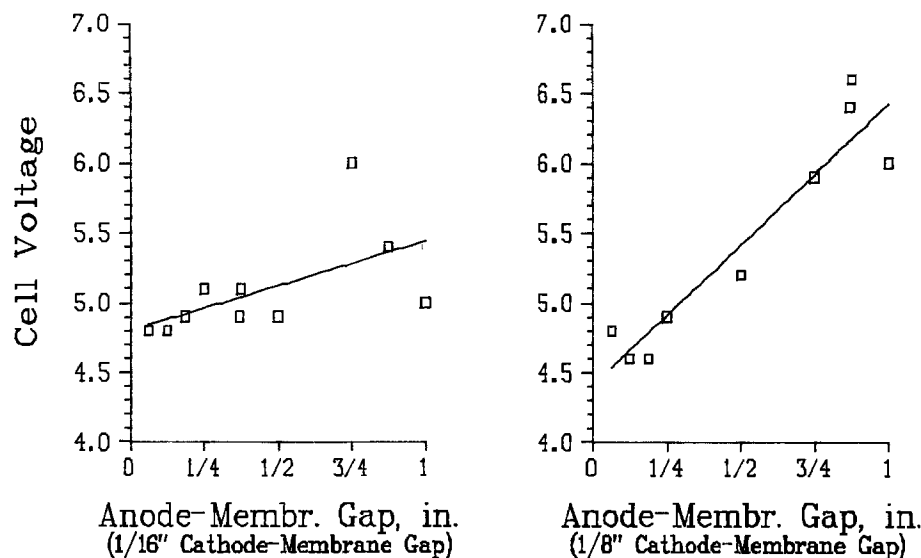


Fig. 6. 25°C, Nafion[®] 427 membrane, anolyte pH = 7.5, 2 kA/m², DSA[®] anode, stainless steel cathode.

Cathode-membrane gap.—The cathode-membrane gaps have little effect on the anode current efficiency, and the plots are shown in Fig. 5 nearly the same for 1/16 and 1/8 in. cathode-membrane gaps. Cathode current efficiencies do not have any clear-cut relationship to anode-membrane gaps or the cathode-membrane gaps, as seen from the large scatter of points in these cases. During the entire series of tests run producing t-butyl hypochlorite, cathode current efficiencies averaged 65-70% for the Nafion[®] 427 membranes.

Membrane type.—An alternate membrane, Nafion[®] 427, was used in some of these experiments and compared to the Nafion[®] 295 membrane. The anode current efficiency for this membrane was dependent on gap as was the 295; however, the cathode current efficiency increased dramatically to 85-90% for the 295.

The Nafion[®] 295 membrane appears to be the best membrane for this application.

Conclusions

In this study bench scale gap and membrane cells were operated to produce organic hypochlorites safely, economically, and pollution-free in highly pure form. The gap cell synthesis of t-butyl hypochlorite requires an inert organic liquid to dissolve the product as it is formed, but the membrane cell does not require any solvent.

The membrane cell production of t-butyl hypochlorite is safer than the gap cell production and in addition gives pure product. However, the explosive mixtures of hydrogen, chlorine, and oxygen must be purged from the gap cell system.

Acknowledgments

The authors are grateful to the Olin Corporation for its support of this work, and to Garland Hilliard of Olin for his superior efforts exerted to achieve these results.

Manuscript submitted Aug. 12, 1980; revised manuscript received Nov. 18, 1980.

Any discussion of this paper will appear in a Discussion Section to be published in the December 1981 JOURNAL. All discussions for the December 1981 Discussion Section should be submitted by Aug. 1, 1981.

Publication costs of this article were assisted by the Olin Corporation.

REFERENCES

1. J. Ghoroghchian, R. E. W. Jansson, and D. Jones, *J. Appl. Electrochem.*, 309 (1977).
2. J. A. M. Leduc, U.S. Pat. 3,288,692; Fr. Pat. 1,375,973 (1963).
3. R. W. Lynch and R. L. Dotson, U.S. Pat. 4,183,907 (1980).
4. M. C. Taylor, C. A. Gammal, and R. E. Gegenheimer, U.S. Pat. 1,481,039 (1924).
5. R. B. MacMullin, U.S. Pat. 1,632,483 (1925); 1,632,484 (1925); 1,632,485 (1925).
6. L. Ebersson, K. Nyberg, and H. Sternerup, *Chem. Scr.*, 3, 12 (1973).
7. R. L. Dotson and R. W. Lynch, U.S. Pat. 4,177,115 (1979).
8. K. H. Simmrock, *Chem. Ing. Tech.*, 48, 1085 (1976).
9. R. W. Lynch and R. L. Dotson, U.S. Pat. 4,182,661 (1980).
10. H. M. Teeter and E. W. Bell, *Org. Synthesis*, 32, 125 (1952).
11. C. P. C. Bradshaw and A. Nechvatal, *Proc. Chem. Soc.*, 213 (1963).
12. A. P. Tomilov, S. G. Mairanovskii, M. Ya. Fioshin, and V. A. Smirnov, "Electrochemistry of Organic Compounds," John Wiley & Sons, Inc., New York (1972).
13. S. Swann, Jr. and R. Alkire, "Bibliography of Electro-Organic Syntheses," pp. 312-317, Port City Press, Inc., Baltimore, MD (1980).

Electroreduction of 1-Methyl-2-, 3-, and 4-Carbomethoxypyridinium Ions

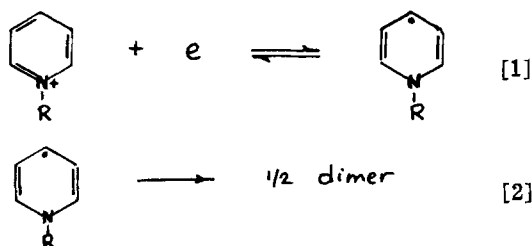
S. Kashti-Kaplan, J. Hermolin, and E. Kirowa-Eisner

Department of Chemistry, Tel-Aviv University, Ramat Aviv, Israel

ABSTRACT

The character of both polarographic waves of the three isomers 1-methyl-2-, 3-, and 4-carbomethoxypyridinium ions (2^+ , 3^+ , and 4^+ , respectively) has been studied in acetonitrile and in methanol. The first wave is due to a one-electron reduction under DC and normal pulse polarographic (NPP) conditions. Whereas a stable free radical $4\cdot$ is reversibly formed in the reduction of 4^+ and a dimer is irreversibly formed in the reduction of 3^+ , the 2^+ reversibly forms radical $2\cdot$ at low concentration and short pulse width and a dimer under DC conditions. The equilibrium constant and the rate constants for the dimerization reaction $2\cdot \rightleftharpoons \frac{1}{2}$ dimer have been determined by the reverse-pulse polarographic method (RPP). The radicals $2\cdot$ and $4\cdot$ have been identified by RPP, and the formal potentials of the couples $2^+/2\cdot$ and $4^+/4\cdot$ are reported. The second reduction wave of the three compounds is diffusion controlled in protic media (methanol) and yields dihydropyridine as a product. In acetonitrile, the pyridinium salts (n^+) exhibit quite complicated behavior, which is dependent on the nature of the pyridinium ion (position of the carbomethoxy group on the ring) and its concentration, the nature of the cations present in the solution, and the time scale in which the electrochemical method is applied. The 3^+ isomer does not undergo a second reduction step in this solvent. The anions 2^- and 4^- react with the cations to form nH (dihydropyridines), nLi , nNa , or the corresponding dimers $n-n$ (reaction with the starting material n^+). The latter reaction causes a decrease in the amplitude of the second wave and is the most favored reaction in the presence of the indifferent bulky tetrabutylammonium cation, under which conditions the anions (2^- and 4^-) are most stable and are easily detected. The formal potential of the couples $2\cdot/2^-$ and $4\cdot/4^-$ are reported.

The observation that NAD^+ and $NADH$ participate in biological oxidation/reduction reactions was made quite long ago (1), but the debate about the exact mechanism of this reaction, namely, hydride transfer (2) *vs.* stepwise electron-proton transfer (3), still continues (4, 5). The implication that radicals may be involved in this important reaction and also the search for the mechanism by which paraquat, a common and important herbicide, acts on the plants (6) have given rise to considerable research on the properties of pyridinyl radicals. Electrochemical techniques have been used in the systematic investigation of chemical phenomena involving NAD^+ and model molecules (7-9). Most pyridinyl radicals formed by electroreduction follow the reaction scheme (8-10)

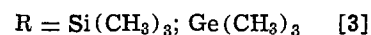
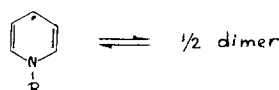


However, Kosower and collaborators (11) were able to show that withdrawing substituent groups on the γ -position of the pyridinium ring may limit the above mechanism to the formation of the stable free radicals in equilibrium with the pyridinium ion (Eq. [1]), with no subsequent chemical reaction (Eq. [2]). Reversible dimerization processes are common features in radical chemistry (12) and are usually accompanied by marked changes in color. Reversible π -merization¹ of Wurster's blue cation radical, which is usually revealed by the appearance of spectacular colors, was

Key words: polarography, dimerization, carbonethoxypyridinium salts.

¹ Denotes a π -type charge transfer complex formation between two radicals. The products, π -mers, exhibit spectacular colors (6).

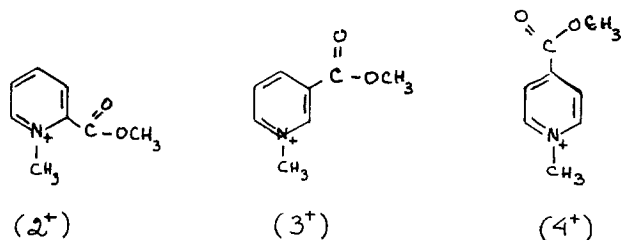
detected by Hausser and Murrell (13) and later for pyridinyl radicals by other investigators (14, 15). Reversible dimerization of 1-trimethylsilyl and 1-trimethylgermyl-pyridinyl radicals (Eq. [3]), which gave rise to a covalent bond between the reacted species has been reported by Neumann and collaborators (16-18)



Earlier reports (19) on reversible dimerization of pyridinyl radicals based on color changes proved later to be incorrect (20).

Recently Kosower and collaborators (21-23) were able to show that 1-alkylpyridinyl radical, suitably substituted, can also undergo reversible dimerization to form covalent dimers. The behavior of 1-methyl-2-carbomethoxypyridinyl radical, $2\cdot$, in acetonitrile and in 2-methyltetrahydrofuran indicated beyond any doubt that reversible dimerization to yield covalent dimers takes place in solution over a considerable temperature range (21). π -mers of $2\cdot$ were obtained only under special conditions, which were described in detail (22).

In this article we would like to report on the detailed electrochemical behavior of 1-methyl-2-carbomethoxypyridinium salt (2^+) in comparison to its two isomers, 1-methyl-3- and 4-carbomethoxypyridinium salts (3^+ and 4^+ , respectively), and also in comparison to results obtained previously (6-11, 21-24). Employing DC, normal-pulse (NP), and reverse-pulse (RP) polarography it was possible to detect intermediate stability radical species and to determine some of their thermodynamic and kinetic constants



Experimental

A modified PAR 174 polarographic analyzer (25) with pulse width 0.8–90 msec, sampling time 0.6 msec, and memory time constant of 0.04 msec was used for DC, NP, and RP polarography. The current-potential curves were recorded on a Yokogawa XY Recorder, Model 3077. A 3.5 digit voltmeter was used for setting the initial potential. All experiments were performed at 22°C. Potentials were corrected for iR drop according to the spherical symmetry calculations for a three-electrode system (26), where $V_{iR} = i\rho/4\pi r_0$ (ρ , the specific resistivity of the solution; r_0 , the radius of the mercury drop; and i , the current at a given part of the polarogram). This correction is necessary for polarograms for which limiting currents are larger than 10 μA ($\rho \sim 50 \Omega\text{cm}$). The flow rate of the dropping mercury electrode was 1.08 mg/sec.

An Ag/Ag^+ (0.01M), LiClO_4 (0.25M), CH_3CN reference electrode (27) was used both in acetonitrile and in methanol. The reference electrode compartment was a glass tube on the end of which a "thirsty glass" plug (Corning Type 7930 glass) was sealed with epoxy glue. The solution in this compartment was renewed every day. The liquid junction stability of this electrode in methanol was very good (drifts smaller than 1 mV/day were observed).

Mercury and nitrogen were purified by standard techniques. The nitrogen was bubbled through acetonitrile or methanol before entering the cell.

Acetonitrile (Merck, Uvasol) and methanol (Merck, proanalysis) were used. Freshly purified² acetonitrile was used for comparison with the commercial grade; no difference in the electrochemical behavior was observed. LiClO_4 (anhydrous, Fluka-purum) and tetrabutylammonium perchlorate (G. Frederick Smith Chemical Company) were used as electrolytes. 1-Methyl 2-, 3-, and 4-carbomethoxy-pyridinium perchlorates (mp = 112°–113°C, 88°–89°C, 110°–111°C, respectively) were prepared from the corresponding iodides by treatment with AgClO_4 [in methanol, followed by crystallization from methanol-ether (4)]. 1-t-Butyl-4-carbomethoxy-pyridinium perchlorate was prepared according to Ref. (28).

For large scale electrolytic preparation of the dimer, a mercury pool cathode ($A \sim 7 \text{ cm}^2$) was used. Its potential was controlled against an Ag/Ag^+ reference electrode. The platinum counterelectrode was separated by a Quickfit rotaflow stopcock. During the electrolysis the solution was stirred with a magnetic stirrer and deaerated with nitrogen. The electrochemical behavior of the dimer was tested with a DME inserted in the electrolysis cell itself.

Results and Discussion

We have investigated the electrochemical reductions of 1-methylpyridinium salts substituted with a carbomethoxy group at position 2, 3, or 4. The substituent is an electron-withdrawing group which stabilizes the radical species in the order $4 > 2 > 3$, thus giving rise to fundamental differences in their chemical and electrochemical behavior. In both acetonitrile and methanol, all isomers yield two polarographic waves except

² The acetonitrile was dried over a molecular sieve (4A) 24 hr and then stored over Mg turnings and 1,1'-trimethylene-bis-(4-carbomethoxy-pyridinium)iodide, effectively removing oxygen and other reactive impurities. Samples of distilled solvent were collected under high vacuum ($\sim 10^{-5}$ mm Hg) and used immediately.

the 3-carbomethoxy-pyridinium ion in acetonitrile which displays only wave (Fig. 1a–3a, 5a).

The electrochemical studies were carried out by conventional electrochemical methods, such as DC and normal-pulse polarography (NPP) and the recently introduced reverse-pulse polarographic (RPP) technique (29, 30). RPP is a pulse-polarographic technique that has the quantitative merits of the double-potential-step method and the diagnostic strength of cyclic voltametry. RPP has advantages over cyclic voltametry, since the capacitance currents are much smaller and thus faster reactions can be studied; mathematical treatment is easier and there are no complications due to simultaneous accumulation of products from different potential regions.

The principle of RPP is that during almost the entire life of the mercury drop, $\tau - t_p$, (seconds) a constant potential is applied at which the reaction of interest takes place. Products and intermediates are accumulated in the diffusion layer and their electroactivity is displayed during the application of a short anodic or cathodic potential pulse (milliseconds) during which the resulting current is measured. Examples of RPP in electrode kinetics have been given elsewhere (29, 30).

First Wave

1-Methyl-3- and 4-carbomethoxy-pyridinium (3⁺ and 4⁺) ions.—The electrochemical behavior of the two isomers 3⁺ and 4⁺ at the first wave is well understood (9, 11). We only briefly describe our results to facilitate the comparison of their electrochemical behavior with that of 1-methyl-2-carbomethoxy-pyridinium (2⁺) ion.

Reduction of 4⁺ under polarographic conditions yields a one-electron reversible wave with the formation of the corresponding radical



in acetonitrile (Fig. 1a) or in methanol as solvents and LiClO_4 or TBAP as supporting electrolytes. The radical is directly observed by its oxidation wave in the RP mode (Fig. 1c wave with $E_{1/2} = -1081 \text{ mV}$). The reversibility of the charge transfer was proved by the Nernstian behavior of the DC, NP, and RP waves. The half-wave potentials are a good estimate for the formal potential E° of the redox couple $4^{\cdot}/4^+$.

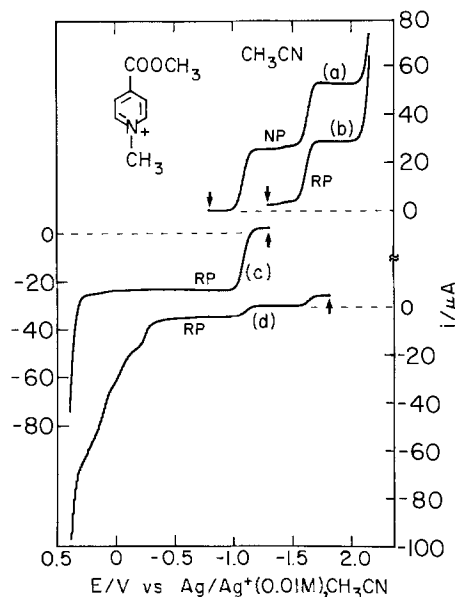
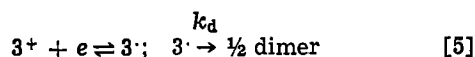


Fig. 1. NPP and RPP (constant E_{in} mode) of 0.65 mM 4^+ ClO_4^- in 0.25M $\text{LiClO}_4\text{-CH}_3\text{CN}$. $\tau = 1.1 \text{ sec}$, $t_p = 3.1 \text{ msec}$. Arrows indicate E_{in} . E_p is plotted on the X-axis.

RP measurements reveal that the radical is the only product at short pulse duration as well as in DC measurements (up to 8 sec) in both methanol and acetonitrile (11). Because of the short times involved, the slow reaction of 4^{\cdot} with methanol (6) does not interfere.

The reduction of 3^+ results in a one-electron wave, the limiting current of which is diffusion-controlled under DC and NP conditions. The shape of the wave and the dependence of $E_{1/2}$ on time and concentration (Table I) corresponds to a reversible one-electron step followed by irreversible dimerization (Eq. [5])



Semilogarithmic analysis (31) (Eq. [6]), corresponding to reaction scheme [5]

$$E = E_{1/2} + \frac{RT}{F} \ln \frac{2^{1/3}(i_{NP} - i)}{i^{2/3} \cdot i_{NP}^{1/3}};$$

$$E_{1/2} = E^{\circ'} + \frac{RT}{3F} \ln(4.2k_d t C_2) \quad [6]$$

was carried out with data from DC polarograms (drop time 1-5 sec) in the presence of Triton X-100 (required for the suppression at the maximum) and yielded the expected slope (Table I). The dimer formed during the electroreduction of 3^+ was directly observed by the RP technique. RP carried out with an initial potential in the plateau region of the first wave displays a well-defined two-electron wave of the dimer oxidation in both acetonitrile (Fig. 2c, $E_{1/2} = -400$ mV) and methanol (Fig. 3c, $E_{1/2} = -330$ mV).

The characteristic experimental parameters are reported in Tables I, II, and Fig. 1-4.

1-Methyl-2-carbomethoxy pyridinium (2^+) ion.—The behavior of 2^+ is more complex than that reported previously (24) and offers a special case in which both the pure charge transfer process

Table I. Characterization of first polarographic wave of 4^+ , 2^+ , and 3^+ in acetonitrile and in methanol, 0.25M LiClO₄*

| | | |
|-------|-----|---|
| 4^+ | DC | $0.5 \text{ sec} < \tau < 8 \text{ sec}; 10^{-5} \text{M} < C_4^+ < 5 \times 10^{-3} \text{M}$ |
| | | $\frac{\partial E_{1/2}}{\partial \log \frac{i_{DC} - i}{i - i_{RP}}} = 59.0 \pm 0.6; \frac{\partial E_{1/2}}{\partial \log C_4^+} = 0; \frac{\partial E_{1/2}}{\partial \log \tau} = 0;$ |
| | | $\frac{\partial \log i_{DC}}{\partial \log \tau} = 0.20 \pm 0.02$ |
| | NPP | $1 \text{ msec} < t_p < 90 \text{ msec}; 10^{-5} \text{M} < C_4^+ < 5 \times 10^{-3} \text{M}$ |
| 3^+ | DC | $\tau > 0.5 \text{ sec}; C_3^+ > 0.3 \text{ mM}, 2 \times 10^{-3} \% \text{ Triton X-100}$ |
| | | $\frac{\partial E_{1/2}}{\partial \log \frac{i_{DC} - i}{i - i_{RP}}} = 60 \pm 1; \frac{\partial E_{1/2}}{\partial \log C_3^+} = 20 \pm 2; \frac{\partial E_{1/2}}{\partial \log \tau} = 20 \pm 2; \frac{\partial \log i_{DC}}{\partial \log \tau} = 0.20 \pm 0.02$ |
| | NPP | $t_p < 1.8 \text{ msec}; C_3^+ < 17 \mu\text{M}; \frac{\partial E_{1/2}}{\partial \log t_p} = 0; \frac{\partial E_{1/2}}{\partial \log C_3^+} = 0$ |
| | RPP | $10 \text{ msec} < t_p < 90 \text{ msec}; C_3^+ > 1 \text{ mM}$ |
| 2^+ | DC | $4 \text{ sec} < \tau < 8 \text{ sec}; 0.2 \text{ mM} < C_2^+ < 3 \text{ mM}$ |
| | | $\frac{\partial E_{1/2}}{\partial \log \frac{(i_{DC} - i)^2}{i - i_{RP}}} = 29.6 \pm 1; \frac{\partial E_{1/2}}{\partial \log C_2^+} = 29 \pm 1;$ |
| | | $\frac{\partial E_{1/2}}{\partial \log \tau} \approx 0; \frac{\partial \log i_{DC}}{\partial \log \tau} = 0.20 \pm 0.01$ |
| | NPP | $t_p < 1.8 \text{ msec}; C_2^+ < 17 \mu\text{M}; \frac{\partial E_{1/2}}{\partial \log t_p} = 0; \frac{\partial E_{1/2}}{\partial \log C_2^+} = 0$ |
| 2^+ | DC | $4 \text{ sec} < \tau < 8 \text{ sec}; 0.2 \text{ mM} < C_2^+ < 3 \text{ mM}$ |
| | | $\frac{\partial E_{1/2}}{\partial \log \frac{(i_{DC} - i)^2}{i - i_{RP}}} = 29.6 \pm 1; \frac{\partial E_{1/2}}{\partial \log C_2^+} = 29 \pm 1;$ |
| | | $\frac{\partial E_{1/2}}{\partial \log \tau} \approx 0; \frac{\partial \log i_{DC}}{\partial \log \tau} = 0.20 \pm 0.01$ |
| | NPP | $10 \text{ msec} < t_p < 90 \text{ msec}; C_2^+ > 1 \text{ mM}$ |
| 2^+ | DC | $4 \text{ sec} < \tau < 8 \text{ sec}; 0.2 \text{ mM} < C_2^+ < 3 \text{ mM}$ |
| | | $\frac{\partial E_{1/2}}{\partial \log \frac{(i_{DC} - i)^2}{i - i_{RP}}} = 29.6 \pm 1; \frac{\partial E_{1/2}}{\partial \log C_2^+} = 29 \pm 1;$ |
| | | $\frac{\partial E_{1/2}}{\partial \log \tau} \approx 0; \frac{\partial \log i_{DC}}{\partial \log \tau} = 0.20 \pm 0.01$ |
| | NPP | $10 \text{ msec} < t_p < 90 \text{ msec}; C_2^+ > 1 \text{ mM}$ |

* Semilogarithmic slopes are given in millivolts.

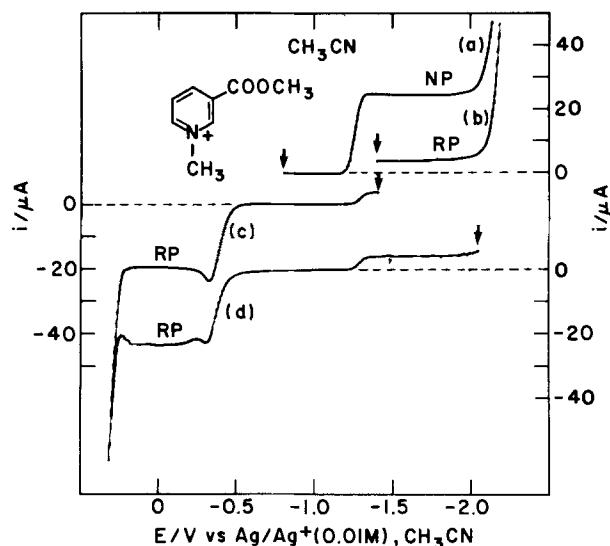


Fig. 2. NPP and RPP (constant E_{in} mode) of $1.3 \text{ mM } 3^+ \text{ ClO}_4^-$ in $0.25 \text{ M LiClO}_4\text{-CH}_3\text{CN}$. $\tau = 0.55 \text{ sec}$, $t_p = 5.1 \text{ msec}$. Arrows indicate E_{in} . E_p is plotted on the X-axis.

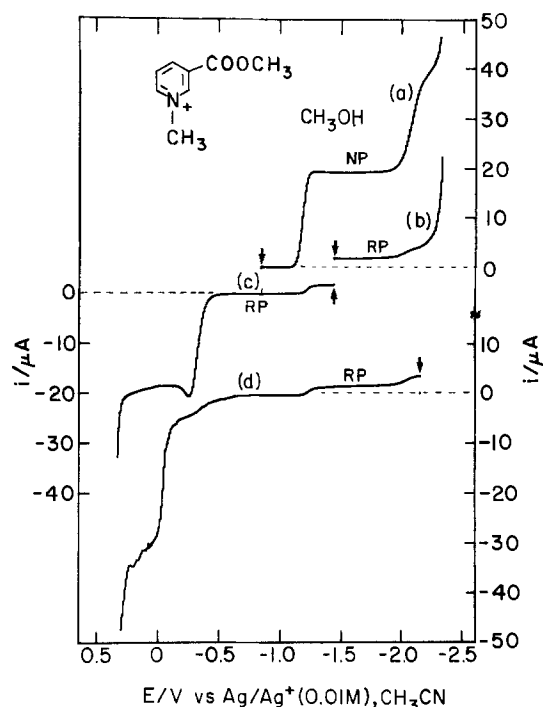
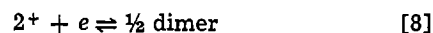


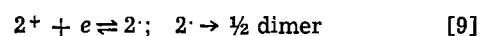
Fig. 3. NPP and RPP (constant E_{in} mode) of $0.54 \text{ mM } 3^+ \text{ ClO}_4^-$ in $0.25 \text{ M LiClO}_4\text{-CH}_3\text{OH}$. $\tau = 1.1 \text{ sec}$, $t_p = 3.1 \text{ msec}$. Arrows indicate E_{in} . E_p is plotted on the X-axis.



and the dimer formation



can be observed separately by merely choosing the proper time scale. In the millisecond range, only the reversible formation of the 2^{\cdot} radical (Eq. [7]) is observed, while at much longer times (seconds) the reversible dimer formation (Eq. [8]) takes place. In an intermediate time range the dimerization process of 2^{\cdot} radical following the charge transfer step (Eq. [9]) is irreversible



The experimental data concerning the behavior described above are summarized in Table I.

Table II. Electrode reactions: first wave

| Compound | Conditions | Electrode reaction | Acetonitrile* | Methanol* | Remarks |
|----------|--|--|---|---|--|
| 4+ | NP and DC | $4^+ + e \rightleftharpoons 4\cdot$ | $E_{0.4^+/4\cdot} = -1.081V^{**}$ $E_{0.4^+/4\cdot} = -1.095V^\dagger$ | $E_{0.4^+/4\cdot} = -1.019V^{**}$ | w; rev. at NP and DC; diff. contr. limiting current; $D(\text{AN}) = 1.7 \times 10^{-5}$; $D(\text{MeOH}) = 1.4 \times 10^{-5}$ cm ² sec ⁻¹ |
| 2+ | NP ($t_p \leq 2$ msec; $C_{2^+} \leq 2 \times 10^{-5}M$) NP (10 msec $\leq t \leq$ 90 msec; $C_{2^+} \cong 2$ $\times 10^{-3}M$) DC ($\tau \cong 4$ sec; C_{2^+} $\cong 2 \times 10^{-4}M$) | $2^+ + e \rightleftharpoons 2\cdot$ $2\cdot \rightarrow \frac{1}{2}$ dimer $2^+ + e \rightleftharpoons 2\cdot$ $2\cdot \rightleftharpoons \frac{1}{2}$ dimer $3^+ + e \rightleftharpoons 3\cdot$ | $E_{0.2^+/2\cdot} = -1.166V^{**}$ $E_{0.2^+/2\cdot} = -1.159V^\dagger$ $k_d = 1.3 \times 10^4 M^{-1} \text{sec}^{-1**,\dagger}$ $E_{0.2^+/dimer} = -1.038V^{**}$ $k_d = 6.3 \times 10^4 M^{-1**,\dagger}$ | $E_{0.2^+/2\cdot} = -1.111V^{**}$ $k_d = 2.5 \times 10^4 M^{-1} \text{sec}^{-1**}$ $E_{0.2^+/dimer} = -0.976V^{**}$ $k_d = 6.9 \times 10^4 M^{-1**}$ | w; rev. at NP ($t \leq 2$ msec); rev. at DC ($\tau > 4$ sec); diff. contr. limiting current; 2 \cdot detected; $D(\text{AN}) = 1.7 \times 10^{-5}$; $D(\text{MeOH}) = 1.4 \times 10^{-5}$ cm ² sec ⁻¹ |
| 3+ | NP and DC | $3^+ \rightarrow \frac{1}{2}$ dimer | $E_{1/2} = -1.155V^\ddagger$ | $E_{1/2} = -1.101V^\ddagger$ | w; irr. at DC and NP; polarogr. maximum at DC; diff. contr. limiting current; $D(\text{AN}) = 1.7 \times 10^{-5}$; $D(\text{MeOH}) = 1.4 \times 10^{-5}$ cm ² sec ⁻¹ |

* Reference electrode: Ag/Ag⁺(0.01M), 0.25M LiClO₄ in CH₃CN.

** Supporting electrolyte: 0.25M LiClO₄.

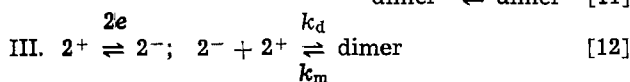
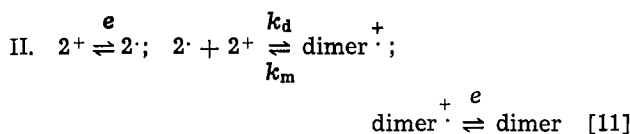
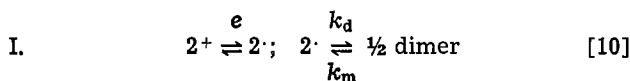
† Supporting electrolyte: 0.25M TBAP.

‡ Calculated from NPP.

§ Calculated for $\tau = 1$ sec and $C_{2^+} = 1M$ by extrapolation from short times and low concentrations.

Pathway of Dimerization

Dimerization can proceed in different pathways. Those proposed by Bard *et al.* (32) will be discussed



At short time/low concentration measurements, the contribution of the dimerization reaction is negligible ($tC_{2^+} < k_d^{-1}$). One electron reduction wave was observed (cf. Table I) excluding II as a possible mechanism.

Distinguishing between mechanism I and II was based on measurements of the ratio of RP current of radical to RP current of dimer at varying initial potentials along the DC polarographic wave of 2⁺. This ratio decreases with increasing DC for mechanism I

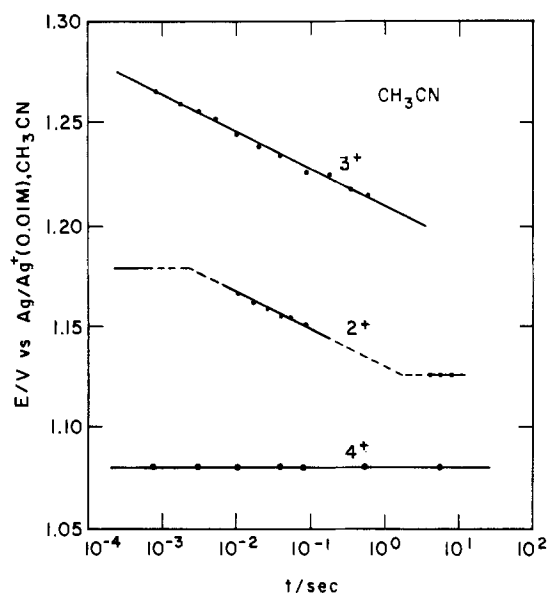


Fig. 4. Half-wave potential/time dependence for the first reduction wave of 2.5 mM 2⁺, 3⁺, and 4⁺ in 0.25M LiClO₄-CH₃CN. Data derived from NP, RP, and DC polarography.

and increases for mechanism II. The experimentally measured ratios indicate unequivocally that mechanism I is operative in the reduction at the first wave.

It will be shown later in this work that mechanism III is operative at the second-reduction wave and may become dominant under proper conditions.

The Reverse Pulse Method for Characterization of the Redox Couple 2⁺/2[·]

NPP in a limitingly low concentration range of 2⁺ (8-17 μM) and short times (0.8-1.8 msec), corresponds to a one-electron reversible wave (without dimerization) as manifested by constancy of $E_{1/2}$ (Table I). The reversibility under these conditions could not be supported by a semilogarithmic analysis of the NPP wave (because of charging-current distortion), but was unambiguously proved by analyzing the RPP waves as will be shown later.

By applying RPP (potentiostating the DME at the plateau of the first wave for $\tau \cong 1$ sec, and sampling the current at $t_p \leq 3$ msec and $C_{2^+} \leq 2$ mM), the following observations were made: (i) the mixed cathodic-anodic wave ($E_{1/2} = -1.166V$, Fig. 5c) has Nernstian behavior for a simple one-electron charge transfer process; (ii) $E_{1/2}$ is independent of pulse

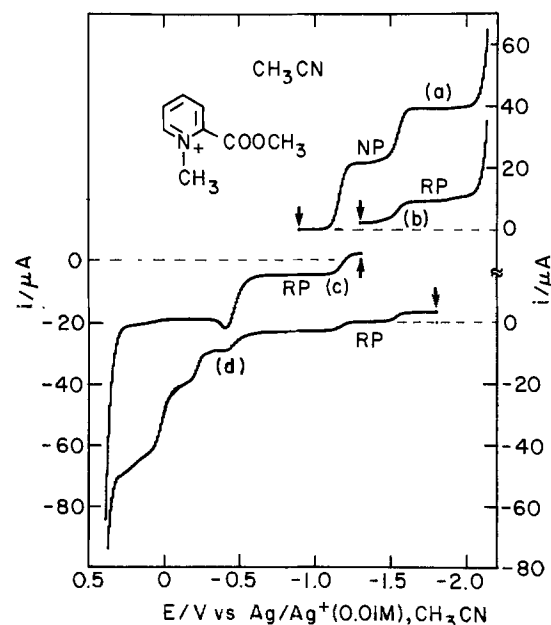


Fig. 5. NPP and RPP (constant E_{in} mode) of 0.57 mM 2⁺ ClO₄⁻ in 0.25M LiClO₄-CH₃CN. $\tau = 1.1$ sec, $t_p = 3.1$ msec. Arrows indicate E_{in} . E_p is plotted on the X-axis.

width and concentration; and (iii) $i_{RP,D}/i_{RP,R}^2$ is independent of pulse width.

We thus conclude that the chemical reactions (monomerization and dimerization) are frozen and the simple charge transfer [7] is observed.

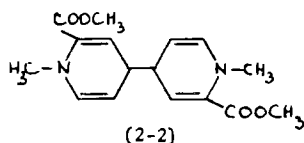
The main difference between the NP and RP modes stems from the fact that under RPP, the radicals have been allowed to dimerize over a long enough time ($\tau \cong 1$ sec), thus diminishing substantially the contribution of the dimerization process during the pulse.

The observation that at the same pulse width, monomerization is frozen at RPP, while dimerization is not frozen at NPP, indicates that $k_m < k_d C_{2^+}$ ($0.1 \text{ mM} \leq C_{2^+} \leq 2 \text{ mM}$).

The RP mixed cathodic-anodic wave is a good estimate for the formal potential of the couple $2^+/2^+$: $E^{\circ}_{2^+/2^+}(\text{AN}) = -1166 \text{ mV}$ and $E^{\circ}_{2^+/2^+}(\text{MeOH}) = -1111 \text{ mV}$.

Products of the Dimerization Process

RPP proved to be a useful tool to analyze the reduction products of 2^+ at the electrode. The RPP of 2^+ (Fig. 5c) includes two waves, one with cathodic and anodic components ($E_{1/2} = -1.166 \text{ V}$, represents the reduction-oxidation process [7]) and the other, the anodic wave at -0.48 V . The following facts indicate that the anodic wave represents the oxidation of only one product

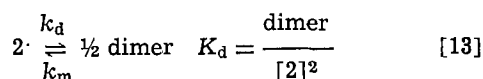


1,1'-dimethyl-2,2'-dicarbomethoxy-4,4'-tetrahydrobipyridine: $\lambda_{\text{max}}(\epsilon) = 332 \text{ nm}(2000); 245 \text{ nm}(10000)$ sh

(i) The reduction products of 2^+ in $\text{CH}_3\text{CN}-\text{LiClO}_4$ [obtained by Na-Hg reduction or by macroscale reduction on Pt or Hg electrodes (21)] exhibit the same oxidation wave at -0.48 V . RPP of this solution indicates that the 2^+ is the product of the electrochemical process taking place at -0.48 V . (ii) Introduction of oxygen into the system causes a decrease in the oxidation wave at -0.48 V and a subsequent increase in the reduction wave of the starting material, (2^+). The formation of 2^+ is also revealed by the appearance of the absorption band at 270 nm and the disappearance of the absorption spectrum of the dimer, (2-2) [cf. (21)]. (iii) The photodissociation spectrum of the electroreduction products of 2^+ , measured by RPP technique (33), corresponds very well to the absorption spectrum of the dimer (2-2) in this solution (21). A detailed discussion on the assignment of the structure of (2-2) is given elsewhere (21).

Determination of K_d , k_d , and k_m

The progress of the reaction



can be followed by RPP. Under conditions at which the dimerization and monomerization processes are frozen, the RP limiting anodic currents for the radical ($i_{RP,R}$) at -1.166 V and of the dimer ($i_{RP,D}$) at -0.48 V are proportional to the concentration of these species in the diffusion layer at time τ , prior to the application of the pulse. The ratio $i_{RP,D}/i_{RP,R}^2$ reflects the progress of reaction [13] during the time τ at which E_m is applied. Therefore we define a kinetic parameter K_d'

$$K_d' = \frac{\bar{C}_D}{\bar{C}_R^2} = \frac{1}{2} \frac{i_{RP,D}}{i_{RP,R}^2} \cdot \frac{i_{NP,1}}{C_{2^+}} \quad [14]$$

where \bar{C}_R and \bar{C}_D are the average concentrations of the radical and the dimer, respectively, in the diffusion layer at the time of pulse application.

A typical set of results obtained for $1.0 \text{ mM } 2^+$ in $0.25 \text{ M LiClO}_4\text{-TBAP}$, $5 \times 10^{-3}\%$ Triton X-100, exemplifies the dependence of K_d' on τ :

| | | | | | | |
|--------------|------|------|------|------|------|------|
| $\log K_d'$ | 3.42 | 3.57 | 3.78 | 3.99 | 4.12 | 4.16 |
| τ (sec) | 0.36 | 0.57 | 1.12 | 2.24 | 3.35 | 5.47 |

Since $\log K_d'$ approaches constancy at large τ , the value 4.2 is a first approximation for the equilibrium constant. A simulation technique, treating a second order following reactions with diffusion taken into account, has been elaborated (30) and applied on the 2^+ reduction process, yielding values for K_d , k_d , and k_m .

The equilibrium and rate constants in acetonitrile were determined in two different supporting electrolytes, LiClO_4 and TBAP, in order to examine the effect of the cations on the dimerization reaction. [The effect of cations on the stability of various pyridinyl radicals has been discussed recently (34).] No effect was observed in the concentration range of supporting electrolytes used (25-250 mM).

To exclude the possibility of adsorption of the dimer at the electrode surface with subsequent dissociation into radicals (33), measurements were carried out also in the presence of 0.01% Triton X-100, but only a small increase (0.1 log units) in K_d was observed. In acetonitrile (with LiClO_4 or TBAP): $\log K_d = 4.8 \pm 0.1$; $\log k_d = 4.1 \pm 0.1$; $\log k_m = -0.7 \pm 0.05$. In methanol-0.25M LiClO_4 : $\log K_d = 4.8 \pm 0.1$; $\log k_d = 4.4 \pm 0.1$; $\log k_m = 0.4 \pm 0.05$.

A value of $\log K_d \cong 5$ in acetonitrile, obtained by a titration method, is reported elsewhere (21).

k_d was also estimated from NPP carried out at intermediate pulse widths, $10 \text{ msec} < t_p < 90 \text{ msec}$. As shown above, reversible electroreduction is observed at shorter pulse durations, while reversible electroreduction is approached at $\tau \cong 4 \text{ sec}$. At pulse widths ranging from 10-90 msec and $C_{2^+} > 1 \text{ mM}$, the current-potential relationship according to Eq. [6] is followed up to $i \sim \frac{1}{2} i_d$.⁴ $E_{1/2}$ is shifted in this time range by 20 mV per decade of time (Fig. 4). Based on the value of E° obtained earlier, k_d was calculated: $\log k_d(\text{AN}) = 4.2 \pm 0.1$; $\log k_d(\text{MeOH}) = 4.4 \pm 0.1$; these values are in good agreement with those obtained by the simulation method (30).

Second Wave

The second wave of 2^+ , 3^+ , and 4^+ is strongly dependent on the type of solvent (protic or aprotic), the type of supporting electrolyte (size of cation), the concentration of depolarizer, and the timing of the experimental measurement (τ , t_p).

In methanol, independent of the type of electrolyte, the amplitude of the second wave of the isomers equals that of the first wave, and its limiting current is diffusion controlled (with the exception of a small deviation in the case of 3^+).

In acetonitrile, with LiClO_4 as supporting electrolyte, the amplitude of the second wave of 4^+ is equal to that of the first wave, while with TBAP, the amplitude of the DC, but not the NP wave, is smaller in comparison of the first wave. The 2^+ isomer exhibits a slightly decreased amplitude in the second wave (in both DC and NP modes) in LiClO_4 with a more pronounced decrease in TBAP. No second wave for the 3^+ isomer was detected up to -2.5 V .

Reacting Species of the Second Wave

RPP has been used to identify the reacting species of the second wave. The principle is similar to that of exhaustive electrolysis at the plateau of the first wave, where the electroactivity of the products is tested

³ At very short τ , K_d' will be determined mainly by k_d ; at very long τ , at which equilibrium conditions are approached, it will be determined by k_d/k_m .

⁴ Simulated NPP curves using K_d and k_d values obtained above agreed with the measured curves (35).

in the potential region of the second wave. The difference between the exhaustive electrolysis method and the RPP method is that in RPP the products of the first wave are prepared in the diffusion layer only (1-5 sec electrolysis) so that no separation is needed between anode and cathode. The electroactivity of the products is displayed by applying short potential pulse (milliseconds) in the potential region of the second wave. The advantages of the RP method are due to the short time scale electrolysis in which even unstable products of the first wave can be detected as plausible reactants of the electrode process at the second wave; at long-term electrolysis the products may undergo chemical changes and thus are not necessarily identical to those of DC or NP polarography.

The diagnostics of the RPP display are based on the following: (i) If the product formed at the first wave is the reactant at the second wave, the limiting RP current is identical to the limiting current of the starting material under NP conditions (in both cases the total amount of species in the diffusion layer able to react is identical)

$$i_{RP,2} = i_{NP,2} \quad [15]$$

$i_{RP,2}$ depends inversely on the square root of pulse width. (ii) If the product formed at the first wave is not the reactant of the second wave the RP current $i_{RP,2}$ will result only from the relatively small amount of starting material diffusing toward the electrode from the bulk of the solution. The rate of diffusion is equivalent to the DC limiting current at second wave. Thus

$$i_{RP,2} = i_{DC,2} \quad [16]$$

where $i_{RP,2}$ is independent of pulse width.

Such a test has been carried out on the compounds of interest 4^+ , 3^+ , and 2^+ with LiClO_4 as supporting electrolyte (Fig. 1b, 3b, 5b). 4^+ behaves according to Eq. [15] in both acetonitrile and methanol in the pulse width range 1-90 msec. The conclusion is that the product of the first wave (4^\cdot) is further reduced along the second wave and does not undergo any chemical changes preceding the second charge transfer.

3^+ yields a second DC and NP wave in methanol, but not in acetonitrile. The RP limiting current $i_{RP,2}$ in methanol behaves according to Eq. [16] in the time range 1-90 msec. This indicates that the dimer, which is the product of the first wave of 3^+ , is not further reduced at the potential range of the second wave. The appearance of the second wave under DC and NP conditions, at potentials where the dimer is stable to reduction, indicates that the second electron transfer is very rapid compared to the dimerization reaction of radicals formed at the first wave. It must then be the radical 3^\cdot which is reduced along the second wave. The same conclusion has been reached for the reduction of NAD^+ and related compounds (8, 9) on the basis of exhaustive electrolysis.

The RPP of 2^+ is somewhat more complicated than those of 4^+ and 3^+ (Fig. 5b). The value of the RP limiting current is somewhere between i_{NP} and i_{DC} of the second wave in both acetonitrile and methanol. We have already shown that in the case of 2^+ substantial fractions of both 2^\cdot and the dimer exist as final products of the first wave on the time scale of the experiment. If, as with the two other compounds, the radical is the reacting species, the limiting RP current of 2^+ should be higher than that of 3^+ and lower than 4^+ . The RP current $i_{RP,2}$ for such a case will be the sum of (i) the reduction of 2^\cdot present in the diffusion layer, which is expressed by the absolute value of the RP anodic current, $i_{RP(R)}$ and (ii) the reduction of 2^+ diffusing toward the electrode at the time of the pulse, which is expressed by $i_{DC,2}$

$$i_{RP,2} = i_{DC,2} + |i_{RP,R}| \quad [17]$$

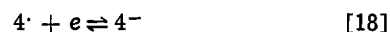
The RP polarograms at different pulse widths gave

currents in agreement with the calculated values from Eq. [17]. Thus the reacting species of the second wave is the radical.

In conclusion, the reacting species of the three carbomethoxypyridinium compounds at the second wave is the corresponding pyridinyl radical.

Intermediate Species and Products at the Second Wave

$\text{CH}_3\text{CN-TBAP}$.—In CH_3CN containing TBAP the NPP and RPP waves of 4^+ have Nernstian slopes according to Eq. [5] and [6] and the $E_{1/2}$ is independent of pulse width in the time range of 1-40 msec (Fig. 6). Thus, under such conditions, simple charge transfer is observed



with a formal potential $E^{\circ'}_{4^+/4^\cdot} = -1.910\text{V}$. The $E_{1/2}$ of the DC wave is shifted to more anodic potentials with the increasing τ , and the ratio of the limiting currents $i_{DC,2}/i_{DC,1}$ is smaller than unity (while under NP conditions it is equal to unity). An explanation of this phenomena is given below in the discussion of dimerization processes at the second wave.

An attempt was made to determine the formal potential of the $2^-/2^\cdot$ couple at low concentrations of 2^+ (necessary to avoid dimerization, Eq. [23]). However, the relatively low concentration of 2^+ and the large background currents did not allow an accurate semi-logarithmic analysis of the wave. Thus, a rough estimate of the formal potential yields a lower limit of $E^{\circ'}_{2^-/2^\cdot} \sim -1.83\text{V}$.

$\text{CH}_3\text{CN-TBAP-Li}^+$.—Addition of Li^+ to $\text{CH}_3\text{CN-TBAP}$ solutions containing 2^+ or 4^+ has the following effects on the second wave: (i) At molar ratios $[\text{Li}^+]/[4^+] = 0-1$ the wave splits; a new wave at more anodic potentials is formed at the expense of the original wave, reaching full height at a molar ratio of unity (Fig. 7). Further addition of Li^+ (molar ratios 10-100) shifts the $E_{1/2}$ by 30 mV per decade of $[\text{Li}^+]$, and by 30 mV per decade of time (in the time range of 1-100 msec).⁵ (ii) The addition of Li^+ restores the amplitude of the second wave to its full diffusion controlled height. (iii) The amplitude of the RP wave (E_{in} set on the plateau of the second wave) in the presence of Li^+ is considerably smaller than that measured with TBAP alone (Fig. 6). (iv) The reduction wave of Li^+ at $E_{1/2} = -2.3\text{V}$ makes its appearance only at molar ratios larger than unity. Plots of the amplitude of the Li^+ wave as function of $[\text{Li}^+]$ have the shape of an

⁵ For a EC scheme of reversible charge transfer followed by irreversible chemical reaction, $E_{1/2} = E^{\circ'} + \frac{RT}{F} \ln 0.89 \left(\frac{D_0}{D_R} C_{Mkt} \right)^{1/2}$, where C_M is the concentration of the metal ion (31).

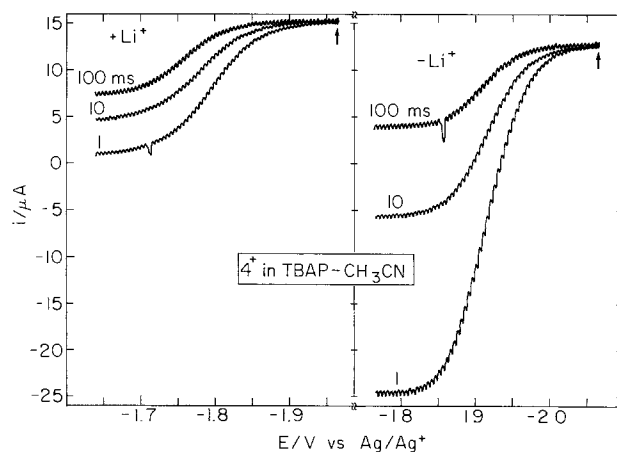


Fig. 6. RPP (constant E_{in} mode) of 2.3 mM 4^+ClO_4^- in 0.25M TBAP- CH_3CN at different pulse widths. Right: no Li^+ added; left: $+4.08 \text{ mM LiClO}_4$. $\tau = 0.5 \text{ sec}$. Arrows indicate E_{in} . E_p is plotted on the X-axis.

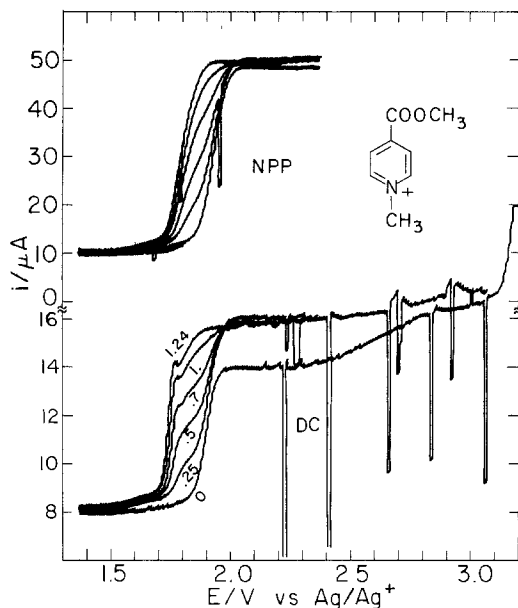


Fig. 7. Polarograms of 2.3 mM 4^+ ClO_4^- in 0.25M TBAP- CH_3CN with additions of LiClO_4 . The values of the molar ratio $[\text{Li}^+]/[4^+]$ are marked on bottom curves. $\tau = 0.5$ sec, $t_p = 10$ msec.

amperometric titration with an increase of current starting at the equivalent point (molar ratio unity). (v) The electrochemical behavior of the system is independent of the presence of TBAP, which acts as an indifferent electrolyte. The effect of tetrabutylammonium ion was tested in acetonitrile, which contained no other electrolyte, under conditions in which the current ratio $i_{\text{DC},2}/i_{\text{DC},1}$ is considerably smaller than unity (4 mM 4^+). A gradual increase of TBAP concentration did not change the ratio and had the expected effect of decreasing the iR drop and the migration current. (vi) In solutions containing LiClO_4 alone, the anions 2^- and 4^- were also detected, although to a much smaller extent than in TBAP.

$\text{CH}_3\text{CN-TBAP-Na}^+$.—Addition of Na^+ to $\text{CH}_3\text{CN-TBAP}$ solutions shifts the reduction wave to more positive potentials and restores the amplitude of the second wave to its full diffusion-controlled height. The shift of the wave is less pronounced than in the case of Li^+ at the same molar ratios, and the reduction wave of Na^+ ($E_{1/2} = -2.2\text{V}$) appears at molar ratios smaller than unity, depending on time (t_p or τ).

$\text{CH}_3\text{CN-TBAP-proton donor}$.—Addition of methanol as proton donor has an effect similar to that of Li^+ , with, however, molar ratios much larger than unity ($\sim 5 \times 10^3$ in the case of 4^+) being required for full development of the new wave.

In the case of 1-methyl-4-cyanopyridinium ion, the behavior of which is similar to that of 4^+ , acetic acid was used as proton donor. Only a 1:1 molar ratio of $[\text{HAc}]/[4^+]$ was required for the new wave to reach full height.

CH_3OH .—The electrochemical behavior in methanol is similar to that of acetonitrile solutions containing at least 20% (V) of methanol. The type of electrolyte does not affect the amplitude of the second wave or its location (differences of few millivolts are related to liquid junction potential).

The above experimental facts undoubtedly prove that the anions 2^- , 3^- , and 4^- are involved in a fast irreversible reaction with cations (Li^+ , Na^+ , H^+) present in solution.

Dimerization Processes at the Plateau of the Second Wave

The observation of a decrease of the current ratio ($i_{\text{DC},2}/i_{\text{DC},1}$ or $i_{\text{NP},2}/i_{\text{NP},1}$) is concurrent with the appearance of a dimer oxidation wave in the RPP mode

(E_{in} set on the plateau of the second wave). In $\text{CH}_3\text{CN-TBAP}$ solutions, the decrease is most pronounced with 2^+ ($i_{\text{DC},2}/i_{\text{DC},1} \rightarrow 0$ for 2^+ , 3 mM; $i_{\text{NP},2}/i_{\text{NP},1} < 1$ and depends on t_p). With 4^+ only the DC ratio is decreased (i.e., $i_{\text{DC},2}/i_{\text{DC},1} \sim 1/2$ at 3 mM). In $\text{CH}_3\text{CN-LiClO}_4$ solutions only the 2^+ exhibits this behavior (Fig. 5d), but a lesser degree than in $\text{CH}_3\text{CN-TBAP}$.

The identification of the dimer of the 2^+ isomer, formed at the plateau of the second wave, was made by comparing $E_{1/2}$ of its oxidation wave (Fig. 5d) with that of the dimer produced at the first wave (wave with $E_{1/2} = -0.48\text{V}$ in Fig. 5c). Such comparison could not be carried out for the 4^+ isomer, since no dimer formation takes place at the first wave. In all cases in which the current ratios were smaller than unity the following behavior was observed: (i) The current ratio increases with decreasing depolarizer concentration, reaching unity at low concentrations. For example, the DC and NPP ratio for 2^+ in 0.25M $\text{LiClO}_4\text{-CH}_3\text{CN}$ is:

| $[2^+]$, mM | 2.60 | 1.15 | 0.61 | 0.06 |
|---------------|------|------|------|------|
| Current ratio | 0.72 | 0.87 | 0.98 | 1.00 |

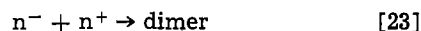
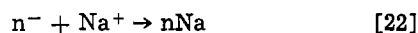
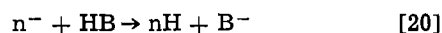
(ii) For a given isomer, the current ratio in acetonitrile is lowest with TBAP as electrolyte and increases with additions of equimolar amounts of small cations (H^+ , Li^+ , Na^+ , Mg^{++}) or larger amounts of a proton donor such as CH_3OH . (iii) The second wave of 4^+ recorded in a pulse mode with E_{in} set on the plateau of the first wave has a considerably larger amplitude than with E_{in} set at a potential region in which no reduction takes place (NPP). (iv) In methanolic solutions (LiClO_4 or TBAP as electrolytes), only 3^+ yields a small amount of dimer with the potential set on the plateau of the second wave (Fig. 3d) (this accounts for the small decrease in the amplitude of the second wave).

Summary of the Electrode Processes at the Second Wave

From the results described above we conclude that the anions n^- (2^- , 3^- , or 4^-) formed in a reversible charge transfer reaction [19] (at the potential region of the second wave)



react irreversibly with cations or abstract protons from the solvent as follows



The general idea that pyridinium cations may react with anions has been extensively discussed in the literature [i.e., Ref. (36, 37)]. Dimerization of tropylium cation with its anion, formed by electrochemical reduction, (reaction similar to [23]) was observed by Breslow and Drury (38).

Reaction [20] dominates in protic solvents. The product, dihydropyridine, nH , is revealed by the RPP oxidation waves at about 0V (i.e., see Fig. 3d for 3^+).

In acetonitrile solutions, n^- reacts with the cations of the electrolyte (reactions [21], [22]) or with the corresponding pyridinium cation, n^+ (reaction [23]).

The rate of the reaction with Li^+ is higher than that with Na^+ .

No reaction between n^- and the bulky tetrabutylammonium cation takes place on the polarographic time scale. Thus, $\text{CH}_3\text{CN-TBAP}$ solutions offer the most favorable conditions for the observation of anions, n^- , and dimers, $n\text{-n}$, formed according to reaction [23]. Whenever the dimerization process takes place, the amplitude of the second wave is decreased (as described above), since the net number of electrons involved in this wave is less than one.

The dimer formed on the plateau of the second wave results from a reaction between n^- and n^+ (reaction [23]), while along the wave, its formation from radicals also takes place

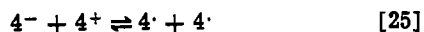


To exemplify this point, the formation of the dimer (2-2) at the second wave is followed by measuring the RP current at a potential set on the plateau of the oxidation wave of the dimer (-0.36V), with the initial potential making excursions into the range of interest (Fig. 8c). The contribution of the oxidation currents of 2^- and 2^+ are evaluated by recording a reverse pulse polarogram as above, but the potential of the pulse is set at the plateau of the oxidation of the radical ($\sim -0.80\text{V}$) at which 2^- and 2^+ , but not the dimer are oxidized (Fig. 8b). Subtraction of curve 8c from 8b yields the oxidation current of the dimer, which is proportional to its amount generated at different initial potentials.

The formation of (4-4) dimers at the second wave (Eq. [23]), is most interesting, since no (4-4) dimers are formed under the conditions of the polarographic first wave (Eq. [24]). Dimerization of 4^- radicals has only been observed in thin films (22b) or in the case of 1,1'-dimethylene or trimethylene-bis (4-carbomethoxy-pyridinyl) radicals (34, 39). The (4-4) dimers are very unstable in solutions and dissociate immediately into the 4^- radicals. On the polarographic time scale, dimers are formed only according to reaction [23], but not according to reaction [24], leading us to the conclusion that the respective dimerization rate constants are substantially different.

Experiments performed with 1-t-butyl-4-carbomethoxy-pyridinium ion gave rise to greater amount of the respective anion and smaller amount of the dimer compared to 4^+ under similar conditions. Considering steric effect, we assume that the dimerization takes place at the 2-position of the ring, at least, for one of the participants of reaction [23].

From the thermodynamic point of view, it is of interest to calculate the equilibrium constant of reaction [25]



$\log K = (E^{\circ'}_{4^-/4} - E^{\circ'}_{4^+/4}) / (2.3 RT/F) = 13.8$, was calculated with values of $E^{\circ'}$ determined in CH_3CN -TBAP (Tables II and III). Reaction [25] has been discussed by Mohammad *et al.* (40).

The processes along the second wave are summarized in Table III.

Acknowledgments

The authors would like to thank Professors E. Gileadi and E. M. Kosower for their interest in this

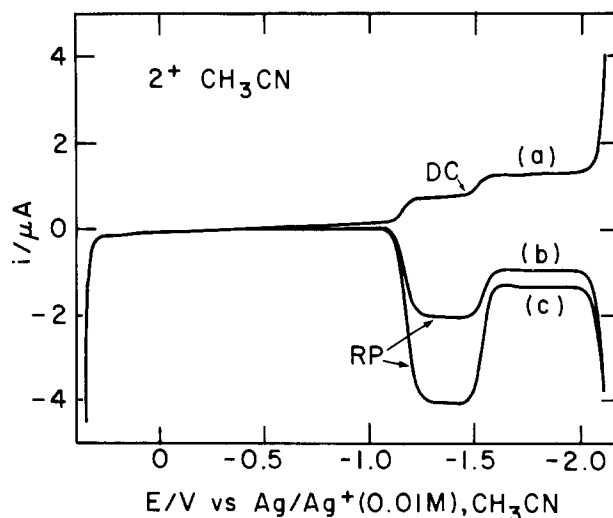


Fig. 8. DC and RPP (constant E_p mode) of $0.28 \text{ mM } 2^+ \text{ClO}_4^-$ in $0.25\text{M LiClO}_4\text{-CH}_3\text{CN}$. $\tau = 0.55 \text{ sec}$, $t_p = 5.1 \text{ msec}$. The value of E_{in} is plotted on the X-axis. (a) DC polarogram; (b) RPP with E_p set at the plateau of the oxidation waves of 2^- ($E_p = -0.80\text{V}$); (c) RPP with E_p set at the plateau of the oxidation wave of the dimer ($E_p = -0.36\text{V}$).

work. The contribution made by D. Talmor with the simulation calculations is appreciated.

Manuscript submitted May 12, 1980; revised manuscript received Nov. 12, 1980.

Any discussion of this paper will appear in a Discussion Section to be published in the December 1981 JOURNAL. All discussions for the December 1981 Discussion Section should be submitted by Aug. 1, 1981.

LIST OF SYMBOLS

| | |
|------------------------------|---|
| C_{2^+} (C_D) | bulk concentration of 2^+ (dimer) |
| C_D (\bar{C}_R) | average concentration of dimer (radical) in the diffusion layer ($\delta = (\pi D t_p)^{1/2}$) at the time of pulse application |
| D_{2^+}, D_D, D_O, D_R | diffusion coefficients of 2^+ , dimer, oxidized and reduced form |
| E° ($E^{\circ'}$) | standard (formal) potential |
| E_{in} | potential applied from the beginning of the drop growth up to time $\tau - t_p$. In the RPP mode, products and intermediates are generated at this potential |
| E_p | potential of pulse |
| i_{DC} (i_{NP}) | DC (NP) limiting current |
| $i_{DC,1}$ ($i_{NP,1}$) | DC (NP) limiting current for the first wave |

Table III. Electrode reactions: second wave

| Compound | Conditions | Electrode reactions | Acetonitrile* | Methanol* | Remarks |
|----------|---------------------------------|---|--|--|--|
| 4+ | NP ($t_p < 40 \text{ msec}$)† | $4^+ + e \rightleftharpoons 4^-$ | $E^{\circ'}_{4^+/4^-} = -1.910\text{V}^\dagger$ | | w; diff. contr. limiting current; $i_{DC,2}/i_{DC,1} < 1$; 4^- detected |
| | NP, DC** | $4^+ + e = 4^-$ $4^+ + M^+ \rightarrow 4M$ $M^+ = H^+, Li^+, Na^+$ $4^+ + 4^+ \rightarrow \text{dimer}^\ddagger$ | $E_{1/2} = -1.564\text{V}^{**,\dagger}$ | $E_{1/2} = -1.412\text{V}^{**,\ddagger}$ | |
| 2+ | NP ($t_p < 2 \text{ msec}$)† | $2^+ + e = 2^-$ | $E^{\circ'}_{2^+/2^-} \sim 1.83\text{V}^\dagger$ | | w; $i_{NP,2}/i_{NP,1} < 1$; 2^- detected |
| | NP, DC** | $2^+ + e = 2^-$ $2^+ + M^+ \rightarrow 2M$ $M^+ = H^+, Li^+, Na^+$ $2^+ + 2^+ \rightarrow \text{dimer}^{**,\dagger,\ddagger}$ $2^+ + 2^- \rightleftharpoons \text{dimer}^{**,\dagger,\ddagger}$ | $E_{1/2} = -1.505\text{V}^{**,\ddagger}$ | $E_{1/2} = -1.371\text{V}^{**,\ddagger}$ | $i_{DC,2}/i_{DC,1} < 1$; 2^- detected |
| 3+ | NP, DC | No wave in AN | — | | |
| | | $3^+ + e = 3^-$ $3^+ + BH \rightarrow 3H + B^-$ $3^+ + 3^+ \rightarrow \text{dimer}^{**,\dagger}$ | | $E_{1/2} = -2.06\text{V}^{**,\ddagger}$ | w; 3^- detected |

* Reference electrode: $\text{Ag/Ag}^+(0.01\text{M})$, 0.25M LiClO_4 in CH_3CN .

** Supporting electrolyte: 0.25M LiClO_4 .

† Supporting electrolyte: 0.25M TBAP .

‡ DC measurements at $\tau = 1 \text{ sec}$.

§ Reaction taking place along the wave and at the limiting current region (in acetonitrile solutions).

§§ Reaction taking place along the wave, but not at the limiting current region.

| | |
|------------------------------|---|
| $i_{DC,2}$ ($i_{NP,2}$) | DC (NP) limiting current for the second wave |
| $i_{RP,D}$ ($i_{RP,R}$) | reverse pulse limiting current of oxidation of dimer (radical) generated at an initial potential on the plateau of the first wave |
| $i_{RP,2}$ | reverse pulse limiting current measured at the potential of the second wave (postsubscript) with an initial potential on the plateau of the first wave (presubscript) |
| K_d | equilibrium constant of dimerization |
| K_d' | kinetic parameter, defined by Eq. [14] |
| k_d (k_m) | rate constant of dimerization (monomerization) |
| n^+ , n^- , n^- | pyridinium cation, pyridinyl radical and anion of the 2, 3, and 4 carbomethoxy isomers, respectively |
| RPP (constant E_{in} mode) | reverse pulse polarography with constant value of E_{in} and variable E_p |
| t_p ; τ | pulse duration; drop time |

REFERENCES

- P. Karrer and O. Warburg, *Biochem. Z.*, **285**, 297 (1936).
- F. H. Westheimer, *Adv. Enzymol.*, **24**, 241 (1962).
- L. Michaelis, *Ann. N.Y. Acad. Sci.*, **40**, 39 (1949).
- E. M. Kosower, A. Teuerstein, H. A. Burrows, and A. Y. Swallow, *J. Am. Chem. Soc.*, **100**, 5185 (1978).
- A. Ohno, M. Ikeguchi, T. Kimura, and S. Oka, *ibid.*, **101**, 7036 (1979).
- E. M. Kosower, in "Free Radicals in Biology," Vol. II, W. A. Pryor, Editor, Chap. 1, Academic Press, New York (1976).
- R. W. Burnett and A. L. Underwood, *Biochem.*, **7**, 3328 (1968).
- A. L. Underwood and R. W. Burnett, in "Electroanalytical Chemistry," (A Series of Advances), Vol. 6, A. J. Bard, Editor, p. 1, Marcel Dekker, New York (1973).
- P. Y. Elving, C. O. Schmakel, and K. S. V. Santhanam, *CRC-Crit. Rev. in Anal. Chem.*, **6**, 1 (1976).
- S. G. Mairanovski, "Catalytic and Kinetic Waves in Polarography," p. 231, Plenum Press, New York (1968).
- W. M. Schwarz, E. M. Kosower, and I. Shain, *J. Am. Chem. Soc.*, **83**, 3164 (1961).
- A. R. Forrester, J. M. Hay, and R. H. Thomson, "Organic Chemistry of Stable Free Radicals," Academic Press, New York (1968).
- K. H. Hasuser and J. N. Murrell, *J. Chem. Phys.*, **27**, 500 (1957).
- E. M. Kosower and J. L. Cotter, *J. Am. Chem. Soc.*, **86**, 5524 (1964).
- M. Itok and S. Nagakura, *ibid.*, **89**, 3959 (1967).
- B. Schroeder, W. P. Neumann, J. Hollaender, and H. P. Becker, *Angew. Chem. Int. Ed.*, **12**, 850 (1972).
- W. P. Neumann and K. Reuter, *Chem. Ber.*, **112**, 936 (1979).
- W. P. Neumann and K. Reuter, *ibid.*, **112**, 950 (1979).
- O. Mumm and H. Ludwig, *Ber.*, **59**, 1605 (1926).
- A. T. Nielson, D. W. Moore, G. M. Muka, and K. H. Berry, *J. Org. Chem.*, **29**, 2175 (1964).
- J. Hermolin, M. Levin, Y. Ikegami, M. Sawayanagi, and E. M. Kosower, Submitted to *J. Am. Chem. Soc.*
- J. Hermolin, M. Levin, and E. M. Kosower, Submitted to *J. Am. Chem. Soc.* (a) Thin film optical spectroscopy of 1-alkyl-2-carbomethoxy and -2-acetylpyridinyl radical monomers and dimers, (b) 1-alkyl-4-carboalkoxy- and -carbamidopyridinyl radicals in solution and in thin films.
- E. M. Kosower, Am. Chem. Soc. National Meeting (1979).
- R. E. Mackay, J. R. Landolph, and E. J. Poziomek, *J. Am. Chem. Soc.*, **93**, 5026 (1971).
- R. H. Abel, J. H. Christie, L. L. Jackson, J. Osteryoung, and R. A. Osteryoung, *Chem. Instr.*, **7**, 123 (1976).
- E. Gileadi, E. Kirowa-Eisner, and J. Penciner, "Interfacial Electrochemistry," p. 206, Addison-Wesley Publishing Co., Reading, Mass. (1975).
- C. K. Mann and K. K. Barnes, "Electrochemical Reactions in Nonaqueous Systems," p. 20, Marcel Dekker, New York (1970).
- E. M. Kosower, H. P. Waits, A. Teuerstein, and L. C. Butler, *J. Org. Chem.*, **43**, 800 (1978).
- J. Osteryoung and E. Kirowa-Eisner, *Anal. Chem.*, **52**, 62 (1980).
- J. Osteryoung, D. Talmor, J. Hermolin, and E. Kirowa-Eisner, Submitted to *J. Phys. Chem.*
- J. Heyrovsky and J. Kuta, "Principles of Polarography," Academic Press, New York (1956).
- W. V. Childs, J. T. Maloy, C. P. Keszthelyi, and A. J. Bard, *This Journal*, **118**, 874 (1971).
- J. Hermolin, E. Kirowa-Eisner, and E. M. Kosower, Submitted to *J. Am. Chem. Soc.*
- J. Hermolin and E. M. Kosower, Submitted to *J. Am. Chem. Soc.*
- D. Talmor, Ph.D. Progress Report, Tel-Aviv University (January 1980).
- K. Walienfels and H. Schuly, *Ber.*, **621**, 86 (1959).
- U. Eisner and J. Kutan, *Chem. Rev.*, **72**, 1 (1972).
- R. Breslow and R. F. Drury, *J. Am. Chem. Soc.*, **96**, 4702 (1974).
- J. Hermolin, S. Kashti-Kaplan, and E. Kirowa-Eisner, Submitted to *J. Electroanal. Chem.*
- M. Mohammad, A. Y. Khan, M. Igbal, R. Igbal, and M. Razzaq, *J. Am. Chem. Soc.*, **100**, 7658 (1978).

Evidence for Metallic Ag at the Surface of Ag/Ag₂S Electrodes

J. Gulens*

Atomic Energy of Canada Limited, General Chemistry Branch, Chalk River, Ontario, Canada, K0J 1J0

and D. W. Shoesmith*

Atomic Energy of Canada Limited, Research Chemistry Branch, Pinawa, Manitoba, Canada, R0E 1L0

ABSTRACT

Varying amounts of metallic Ag are detected by x-ray diffractometry at the surface of Ag/Ag₂S electrodes that have been exposed to alkaline-ascorbic acid solutions. These electrodes give a voltammetric response to redox couples in solution and this response is interpreted as providing further proof of the presence of Ag metal at the electrode surface. The metallic Ag accumulates at the electrode surface primarily as a result of redox reactions between the Ag₂S and the ascorbic acid present in the solution in which the electrode is used.

Solid-state Ag₂S membrane electrodes that have an internal silver metal contact (Ag/Ag₂S) may give rise to negative deviations from Nernstian response (super-Nernstian response) at sulfide concentrations less than 10⁻⁶ mole/liter in an alkaline-ascorbic acid solution (1). A deposit or film that had appeared on the surface of one such electrode was previously studied in a scanning electron microscope (SEM), and deposits that were rich in silver but depleted in sulfur were observed; it was concluded that these could be deposits of metallic silver, thereby giving rise to the super-Nernstian response because of the measurement of mixed potentials (1). The internal silver metal contact was proposed to be the primary source of the metallic silver (1). This paper presents results from x-ray diffractometry (XRD) studies that show varying amounts of metallic Ag to be present at the outer Ag₂S surface of other Ag/Ag₂S electrodes that had been exposed for varying periods of time to alkaline-ascorbic acid solutions.

However, the presence of metallic silver at the electrode surface should not in itself cause interference with the Nernstian response of the electrode to low levels of sulfide ion in solution; the solid-state Ag₂S membrane electrode can be regarded as an electrode of the second kind (2), and the potential of the latter electrode is not affected by the extent of coverage of the silver wire by the silver salt (2, 3). The potential of an electrode of the second kind may be sensitive to the presence of redox couples in solution since bare silver metal may be exposed to the solution either directly or through the pores in the relatively thin layer of salt deposited on its surface (2, 3); the potential of the solid-state Ag₂S membrane electrode, however, is claimed to be insensitive to the presence of redox couples (4-6), since the metallic silver is isolated from the solution by a thick nonporous polycrystalline pressed pellet membrane. Metallic silver present at the outer surface of the solid-state membrane electrode may interfere with the Nernstian response of this electrode if the silver can alter sufficiently the electronic conductivity of the membrane electrode such that the latter can respond to the presence of redox couples in solution, *i.e.*, measure mixed potentials (1).

At room temperature, Ag₂S is both an ionic and electronic conductor. The ionic conductivity is high, $\sigma_i = 0.36 \times 10^{-3} \Omega^{-1} \text{cm}^{-1}$, both in cell I, Ag/Ag⁺(aq)/Ag₂S/Ag⁺(aq)/Ag and cell II, Ag/Ag₂S/Ag⁺(aq)/Ag, and is attributed to the presence of Frenkel defects, silver vacancies, and silver interstitials (4). The elec-

tronic conductivity σ_e , however, varies strongly with the nature of the contact to the Ag₂S membrane; for a liquid contact as in cell I, $\sigma_e = 0.004 \times 10^{-3} \Omega^{-1} \text{cm}^{-1}$ while for a silver metal contact, cell II, $\sigma_e = 2.5 \times 10^{-3} \Omega^{-1} \text{cm}^{-1}$ (4). The high electronic conductivity of an Ag₂S electrode in contact with metallic Ag, Ag/Ag₂S, is attributed to the presence of excess silver in the crystal which acts as an electron donor (4); despite this, it has been claimed that the presence of redox couples in solution has little or no effect on the measured potential at an Ag/Ag₂S electrode because of the high resistance at the Ag₂S/solution interface to the transfer of electrons to redox species in solution (4, 5). However, the results presented in this paper show that our used Ag/Ag₂S electrodes give a well-defined voltammetric response to redox couples in solution, similar to the response observed at an Ag wire electrode; these voltammetric results provide further indirect evidence that metallic Ag is present at the outer surface of these used Ag₂S electrodes. It is proposed that the metallic Ag alters the electronic conductivity of the Ag₂S membrane to the extent that the electrode can measure mixed potentials.

From the results of the voltammetric and surface studies, it is concluded that the metallic silver accumulates at the electrode surface primarily as a result of the redox reaction between the Ag₂S and the ascorbic acid present in the solution in which the electrode is used.

Experimental

All Ag₂S membrane electrodes were obtained from Orion Research Incorporated; metal-contacted (Ag/Ag₂S) electrodes were purchased (Orion 94-16A) while the graphite-contacted (C/Ag₂S) electrodes were kindly provided by Orion. The Ag/Ag₂S electrodes were labeled alphabetically to identify them during use.

The surfaces of the Ag/Ag₂S electrodes were examined by x-ray diffractometry and scanning electron microscopy, using equipment described previously (7). X-ray reference data were obtained from Joint Committee for Powder Diffraction Standards (Swarthmore, Pennsylvania) file cards 4-0783 (Ag), 14-72 (Ag₂S), and 12-793 (Ag₂O).

The voltammetric studies were done at room temperature in solutions prepared from reagent grade chemicals using deionized-distilled water and deaerated with N₂. Stock (0.1 mole/liter) iron solutions were prepared by dissolving (NH₄)₂Fe₂(SO₄)₃ in 0.1 mole/liter HClO₄, and FeCl₃ in distilled water; microliter portions of these stock solutions were added to the deaerated electrolytes as required. A Princeton Applied Research

* Electrochemical Society Active Member.

Key words: membrane, electrode, x-ray, voltammetry.

(PAR) Model 174 Polarographic Analyzer was used, together with a conventional single-compartment cell (PAR Model K60). A Pt wire was used for the counter-electrode, while a saturated calomel electrode, separated from the test solution by a 0.1 mole/liter KNO_3 solution, was used as the reference electrode. A Moseley Model 2D-2 X-Y recorder and an HP Moseley 7100B X-t recorder were used to record the voltammetric and chronoamperometric results, respectively.

Results

Surface analyses.—Initially, electrodes J and M were examined by XRD. Electrode M had failed to give Nernstian response after continuous use for approximately one month in an H_2S -in-water monitor (8); on removing it from the monitor, a coarse crystalline deposit was present on its surface. Electrode J had been used extensively in the laboratory to study response to sulfide ions in alkaline-ascorbic acid solutions; it would rapidly acquire a surface film during use. After J had been stored for 3 weeks in an alkaline-ascorbic acid solution, a coarse granular deposit was present on its surface. X-ray diffractometry showed that Ag metal was the major component of the surface deposits on both electrodes. After the deposit was scraped from the surface of M, the Ag_2S counts were enhanced three-fold while the Ag counts were reduced by $\sim 60\%$; x-ray powder diffraction photographs showed that the scraped material contained both Ag and Ag_2S . After electrode J was scraped, the Ag counts from the surface were reduced by $\sim 20\%$ and the Ag_2S counts increased by $\sim 50\%$; the scraped material in this case was essentially Ag with no detectable Ag_2S . Silver oxide, Ag_2O , was not detected at either electrode.

Further XRD and SEM analyses of other Ag/ Ag_2S electrodes are summarized in Table I. Electrode H, used and treated similarly to electrode J, also had acquired a thick coarse layer on its surface during its 4 week storage in an alkaline-ascorbic acid solution. This layer was pitted and consisted almost entirely of Ag. The Ag layer was removed by polishing the electrode on 600 grit paper; the resultant exposed surface contained only Ag_2S and was porous and pitted. Another layer of Ag was subsequently grown on the surface of electrode H on re-exposure to alkaline-ascorbic acid, and this again could be removed by polishing. Electrode D had also been used extensively in the laboratory but had been stored dry, in air. The surface of D contained numerous large visible pits and consisted primarily of Ag_2S with some Ag, but Ag was not detected at electrode Z.

It had been previously presumed that the Ag diffused to the electrode surface from the internal silver metal contact (1); attempts to observe this diffusion process by heating an Ag/ Ag_2S electrode in air were unsuccessful. Electrode T was a new electrode that gave Nernstian response to 3×10^{-7} mole/liter sulfide; metallic Ag was not detected by XRD at its surface neither before nor after heating for 102 hr at 371 K, nor after a

further 380 hr at 398 K, despite a two-fold decrease in electrode thickness caused by polishing of the electrode during periodic examination while being heated.

Silver oxide was again not detected at any of the electrode surfaces.

Electrochemical Studies

Ag/ Ag_2S electrode.—Numerous Ag/ Ag_2S electrodes that had undergone "normal use" gave a voltammetric response to electroactive species in solutions. These electrodes had been used to measure sulfide in alkaline-ascorbic acid solutions, but were stored in air between use and were polished occasionally. There were no visible deposits or films on their surface. In an oxalate electrolyte (pH 4) containing Fe(II), a well-defined oxidation peak was observed at -50 mV as the electrode was scanned from negative to more positive potentials, Fig. 1A; a corresponding reduction peak for Fe(III) was not observed on the reverse scan even in the presence of added Fe(III), prior to the reduction of the Ag_2S at potentials more negative than -500 mV. The anodic peak current increased linearly with Fe(II) concentration over the range $0.1\text{--}4 \times 10^{-3}$ mole/liter, Fig. 2, and also with the square root of the scan rate (ν),

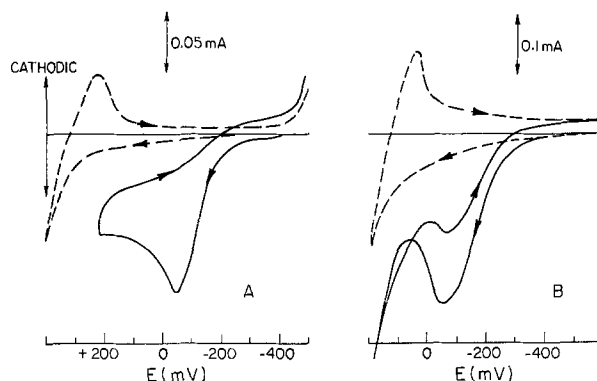


Fig. 1. Voltammetric response of Ag/ Ag_2S electrode at 50 mV/sec to solutions of: (A) 2×10^{-3} mole/liter Fe(II) in 0.2 mole/liter $\text{Na}_2\text{C}_2\text{O}_4$ (pH ~ 4); (B) 2×10^{-3} mole/liter ascorbic acid in 1 mole/liter NaOH; - - - electrolyte only, — electrolyte plus electroactive species.

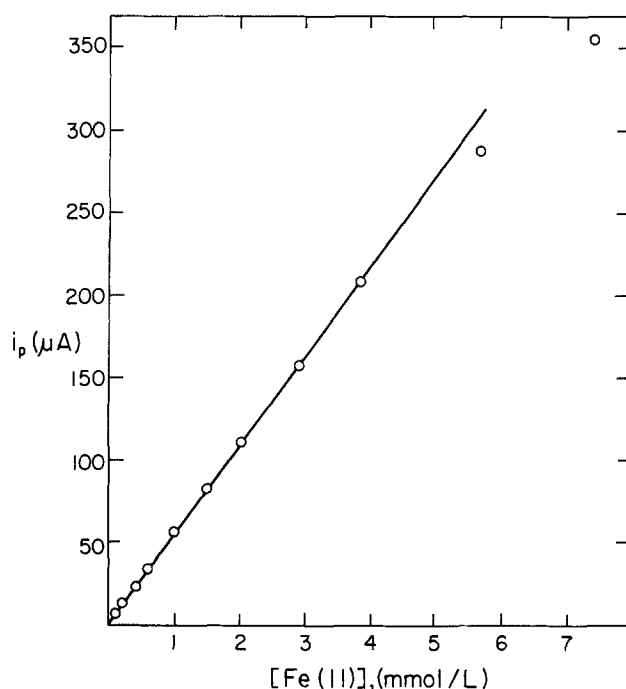


Fig. 2. Variation of peak current at Ag/ Ag_2S electrode with Fe(II) concentration at 50 mV/sec in a 0.2 mole/liter $\text{Na}_2\text{C}_2\text{O}_4$ (pH 4) solution.

Table I. XRD, SEM study of Ag/ Ag_2S electrodes

| Electrode | XRD* | SEM | Comments |
|--------------|---|-------------------------------------|---|
| C | — | Ag, Ag_2S pitted | Used in H_2S monitor |
| M | <u>Ag</u> , Ag_2S | — | Used in H_2S monitor |
| J | <u>Ag</u> , Ag_2S | — | Lab use Stored in alkaline-ascorbic acid |
| H | <u>Ag</u> , Ag_2S | Pitted | Lab use Stored in alkaline-ascorbic acid |
| H (polished) | Ag_2S | Porous | — |
| T | Ag_2S | — | No Ag after heating |
| Z | Ag_2S | Pitted | Lab use |
| D | Ag, <u>Ag_2S</u> | Pitted | Air storage Lab use Air storage |

* Major surface component underlined.

Fig. 3; deviations from linear response were observed at Fe(II) concentrations $>4 \times 10^{-3}$ mole/liter and at scan rates >50 mV/sec. At a given scan rate, the peak potential for the oxidation of Fe(II) varied by 100-200 mV from one electrode to another, and with the condition of the electrode surface. The anodic peak potential also shifted to more positive values with increasing scan rate; some electrodes appeared to follow an $E_p - \nu^{1/2}$ relationship while others appeared to follow an $E_p - \ln \nu$ relationship ($1 \leq \nu \leq 200$ mV/sec). Both in the absence and in the presence of Fe(II), large anodic currents were observed at potentials more positive than +300 mV on the forward scan, and a corresponding reduction peak was observed on the reverse scan at +200 mV, Fig. 1A.

Similar results were observed in alkaline solutions containing ascorbic acid: an oxidation peak was observed at -100 mV on both the forward and reverse scans, Fig. 1B. The anodic peak current on the forward scan increased linearly with ascorbic acid concentration over the range $0.1-1 \times 10^{-3}$ mole/liter; the peak current $-\nu^{1/2}$ dependence in the ascorbic acid system was nonlinear, Fig. 3.

If the Ag/Ag₂S electrode was scanned to potentials more negative than -800 mV in the alkaline solution, the cathodic current increased markedly, Fig. 4; a well-defined anodic peak was observed on the reverse scan and the anodic peak current increased either as the switching potential became more negative or as sulfide ions were added to the solution. When the electrode was scanned to positive potentials, large oxidation currents that increased linearly with time (voltage) were observed. The well-defined reduction peak observed at +100 mV on the reverse scan increased in height as the switching potential for the forward scan was made more positive.

Potential-step chronoamperometry provided further information on the nature of the processes occurring at the positive potentials in the alkaline solutions. The oxidation current at +300 mV remained constant or

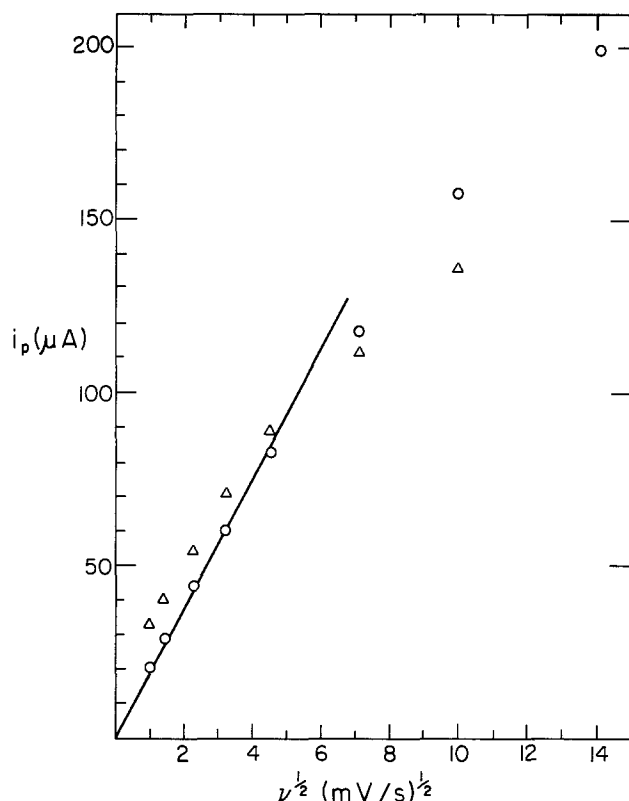


Fig. 3. Variation of peak current at Ag/Ag₂S electrode with square root of scan rate; \circ , 2×10^{-3} mole/liter Fe(II) in 0.2 mole/liter Na₂C₂O₄ (pH \sim 4); Δ , 2×10^{-3} mole/liter ascorbic acid in 1 mole/liter NaOH.

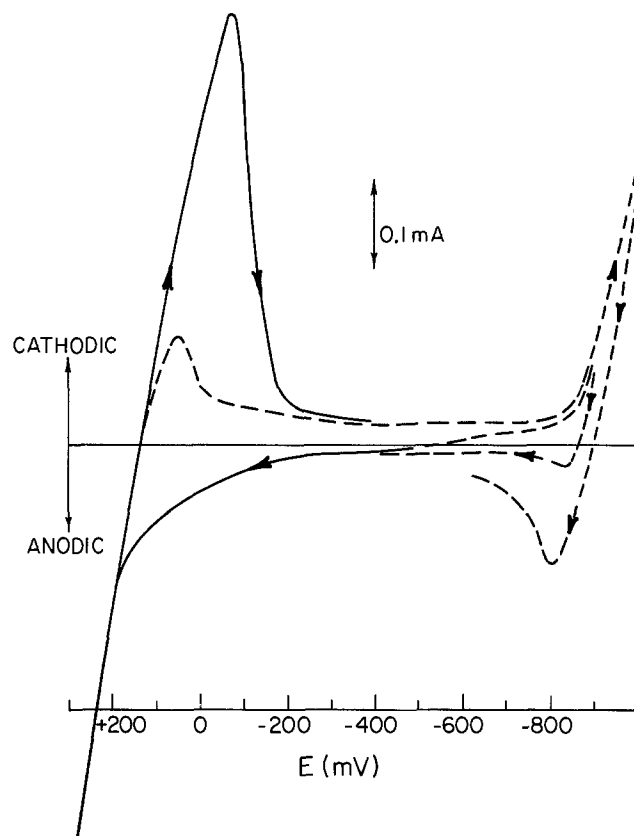


Fig. 4. Voltammetric response of Ag/Ag₂S electrode at 50 mV/sec in 1 mole/liter NaOH. Electrode was scanned: — from -500 to +300 to -400 mV; - - - from -500 to -900 to +300 to -1000 to -600 mV.

decreased only gradually, Fig. 5; a dark deposit formed on some electrodes during this oxidation step. When the potential was stepped to -300 mV, the reduction current first increased with time, then decreased gradually, and finally decreased very rapidly; the black deposit was removed from the electrode surface during the reduction step. Equal amounts of charge were consumed by the anodic and cathodic processes.

The voltammetric responses of numerous Ag/Ag₂S electrodes to the oxalate-Fe(II) solution and to the alkaline-ascorbic acid solution were qualitatively similar, regardless of whether the electrodes gave good or poor Nernstian response to low levels of sulfide.

C/Ag₂S electrode.—Voltammograms obtained with the C/Ag₂S electrode, Fig. 6, were considerably different from those obtained with the Ag/Ag₂S electrode. Much lower background currents were observed and the oxidation processes, when Fe(II) was present,

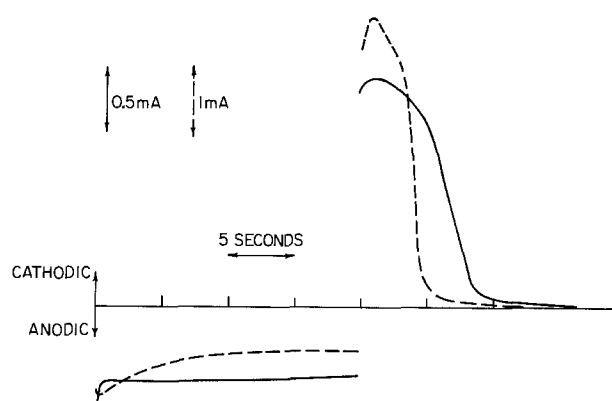


Fig. 5. Chronoamperometry at different Ag/Ag₂S electrodes in 1 mole/liter NaOH; anodic step at +300 mV, cathodic step at -300 mV.

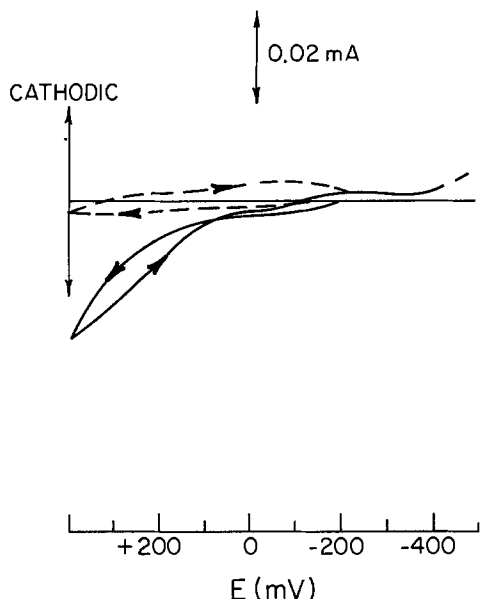


Fig. 6. Voltammetric response of C/Ag₂S electrode at 50 mV/sec; - - - - 0.2 mole/liter Na₂C₂O₄ (pH ~ 4), ——— 2 × 10⁻³ mole/liter Fe(II) added.

occurred at considerably more positive potentials (+300 mV) and appeared to be ill-defined (hysteresis).

Ag electrode.—The voltammetric response of an Ag electrode to the redox species studied was qualitatively similar to the response of the Ag/Ag₂S electrode. A well-defined anodic peak for the oxidation of Fe(II) in the oxalate electrolyte was observed at -200 mV on the forward scan, and a corresponding reduction peak for the Fe(III) formed at the electrode surface was observed on the reverse scan, Fig. 7A. An anodic peak for the oxidation of ascorbic acid in an alkaline solution was observed at -300 mV, Fig. 7B.

Discussion

Surface studies.—The XRD results show that metallic silver had accumulated at some Ag/Ag₂S electrode surfaces. The layer of metallic silver present on the surface of electrodes H, J, and M could be removed by polishing or scraping, thereby renewing the surface. In the case of the scraped electrodes, surface roughening may also partially account for the variation in the x-ray counts. A small amount of metallic silver is de-

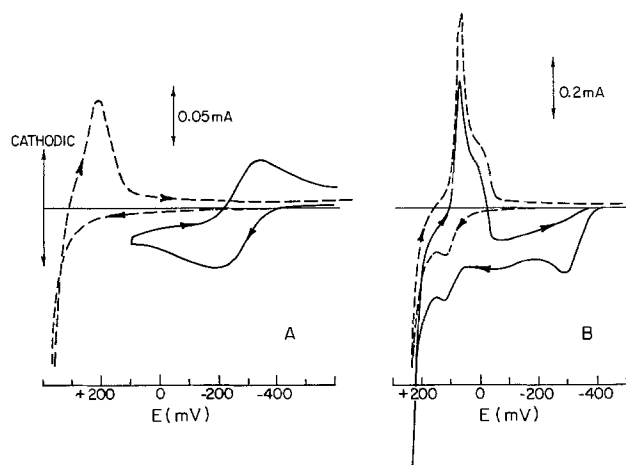
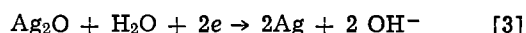
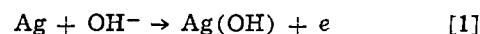


Fig. 7. Voltammetric response of Ag electrode at 50 mV/sec to solutions of: (A) 2 × 10⁻³ mole/liter Fe(II) in 0.2 mole/liter Na₂C₂O₄ (pH ~ 4); (B) 2 × 10⁻³ mole/liter ascorbic acid in 1 mole/liter NaOH; - - - - electrolyte only, ——— electrolyte plus electroactive species.

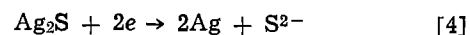
tected at the surface of electrode D, presumably in the readily visible pits; metallic Ag is not detected by XRD at the surface of electrodes Z and T, despite the fact that the latter has undergone prolonged heating. Because the detection limit for XRD is ~5%, small but significant amounts of metallic silver may nonetheless be present at these electrode surfaces. These XRD results confirm our previous proposal, which was based on SEM results (1), that metallic silver accumulates at the Ag₂S/solution interface.

Electrochemical studies.—Further evidence that Ag metal is present at the surface of the Ag/Ag₂S electrodes is provided by the fact that the voltammetric response of the Ag/Ag₂S electrodes is qualitatively similar to the response of an Ag wire electrode, both in the presence and absence of electroactive species. In the absence of electroactive species, both electrodes undergo oxidation at the same positive potentials and give rise to the same well-defined reduction peak on the reverse scan, Fig. 1 and 7. For the Ag electrode in alkaline solutions, the anodic processes occurring at potentials more positive than +100 mV have been ascribed to the formation and reduction of Ag₂O (9, 10); the reactions can be represented as



These reactions can also be applied to explain the response of the Ag/Ag₂S electrodes in alkaline solutions, Fig. 4 and 5. The oxidation of metallic silver, Eq. [1], gives rise to the large anodic currents observed at potentials more positive than +100 mV, while the cathodic peak present on the reverse scan is due to the reduction of Ag₂O to Ag, Eq. [3]. During the chronoamperometric measurements at +300 mV, the oxidation of metallic Ag to Ag₂O, Eq. [1] and [2], gives rise to the black deposit of Ag₂O on the electrode surface; during the subsequent reduction step at -300 mV, the black deposit is removed as the Ag₂O is reduced to Ag, Eq. [3]. The electrodeposition of metallic Ag is controlled by the rate of nucleation and growth of overlapping two-dimensional centers of silver metal on the electrode surface (11); this electrodeposition process is characterized by current-time curves (11) that are very similar to the ones observed in the chronoamperometric reduction process at -300 mV, Fig. 5.

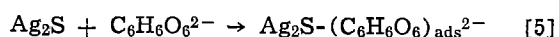
Reduction of the Ag₂S to metallic Ag occurs at potentials more negative than -900 mV in alkaline solutions, Fig. 4

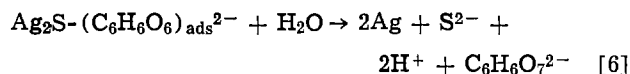


The sulfide ion released at the electrode surface is consumed during the oxidation of Ag metal to Ag₂S in the reverse scan, giving rise to the anodic peak at -800 mV. The same reaction occurs at -400 mV in the pH 4 oxalate solution.

Species such as Fe(II) or ascorbic acid are oxidized at both the Ag and Ag/Ag₂S electrodes; the oxidations occur at slightly more positive potentials (by 250 mV) at the latter electrode, Fig. 1 and 7. At the Ag/Ag₂S electrode, these oxidations are diffusion controlled over a limited range of concentrations, Fig. 2, and scan rates, Fig. 3. The variation in the peak potential with scan rate indicates that factors such as charge-transfer kinetics (12) and/or electrode membrane resistance (13) are also limiting the current at this electrode.

The voltammetric behavior of ascorbic acid on Ag₂S appears similar to that observed at Pt (14). The non-linear $i_p \nu^{-1/2}$ behavior, Fig. 3, suggests adsorption of ascorbic acid while the increased anodic currents observed on the reverse scan, Fig. 1, suggest that the oxidized product, dehydroascorbic acid is being desorbed. The following overall mechanism appears plausible (15)



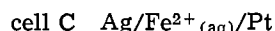
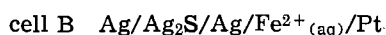


Ascorbic acid is adsorbed at a silver ion site on the surface and electron transfer is assumed to occur via the adsorbed complex; the desorption of the dehydroascorbic acid allows the nucleation and growth of the Ag centers on the electrode surface.

Other workers have previously concluded that Ag/Ag₂S electrodes do not respond to the presence of redox couples in solution (4-6), in direct contrast to our results. The presence of Ag metal on our electrode surfaces as a result of their exposure to alkaline-ascorbic acid solutions may explain this discrepancy. Koebel *et al.* (4) measured the resistance to charge transfer in the cells Ag/Ag₂S/Fe²⁺-Fe³⁺/Pt and Pt/Fe²⁺-Fe³⁺/Ag₂S/Fe²⁺-Fe³⁺/Pt to be $4 \times 10^3 \Omega$ and $1 \times 10^6 \Omega$, respectively, by using a 10^{-2} mole/liter Fe(II)- 5×10^{-3} mole/liter Fe(III)-0.5 mole/liter H₂SO₄ solution and by applying a square wave current. They concluded that this large resistance to electron transfer was located at the Ag₂S/solution interface and attributed it to the semiconductor properties of Ag₂S (4); a specific redox reaction usually requires a larger overpotential at a semiconductor electrode than at a metal electrode [(4, 16) and references therein]. Although the difference between the formal potentials of the redox couples used in our and Koebel's work may have some influence on the electron transfer kinetics at the semiconductor surface (16), we conclude that the facile electron transfer observed at our electrodes is primarily due to the Ag metal on our electrode surface, *i.e.*, the surface is heterogeneous. The Ag/Ag₂S electrodes used by others (4, 5) presumably had not been exposed to a reducing environment and thus did not have Ag at their surface.

Further support for this conclusion of a heterogeneous surface is provided by a comparison of our voltammetric results with those of Van de Leest. Van de Leest observed (17) the anodic dissolution of an Ag/Ag₂S electrode in a nitrate electrolyte only at potentials more positive than +800 mV, while on the addition of bromide ions a new anodic peak was observed at +650 mV and ascribed to AgBr formation. These potentials are considerably more positive than the standard potentials for Ag metal and are also more positive than the potentials we observe at our Ag/Ag₂S electrodes in a nitrate electrolyte (anodic dissolution occurs at +400 mV as in the oxalate solution, Fig. 1A).

Redox reactions at a heterogeneous surface.—If the electrode surface is in fact heterogeneous, the current attributed to the redox couples can flow via different cells



Cell B is considered to have isolated patches of Ag metal at the electrode surface, while in cell C it is considered that there are continuous "threads" of metallic silver extending from the silver metal contact at the back of the electrode through the Ag₂S crystal to its outer surface, *i.e.*, a pure Ag electrode exposed to the solution. The current flowing through each cell is governed primarily by the total interfacial area (A_j) of each cell and the exchange current density at each surface, i_j ; the net observed current is the sum of the individual cell currents. On the basis of the XRD results of "normal" electrodes, *i.e.*, those that have not been stored or used for prolonged periods in an alkaline-ascorbic acid solution, it can be assumed that $A_A \gg A_B \simeq A_C$. Despite the larger surface area of cell A, the exchange current density at a semiconductor/solution interface is usually several orders of magnitude smaller than at a metal electrode (16, 18, 19); we thus conclude that the current in cell A will be con-

siderably smaller than cell B or cell C. The heterogeneous rate constant for the oxidation of Fe(II) ions in an oxalate electrolyte at an Ag electrode is 1×10^{-3} cm/sec (20), and thus the exchange current density at the Ag/Fe²⁺(aq) interface for both cell B and cell C should be large.

Cell B, however, is expected to have a higher resistance than cell C; the electrical conductivity of Ag/Ag₂S at room temperature, $\sigma_e = 2.5 \times 10^{-3} \Omega^{-1} \text{cm}^{-1}$ is orders of magnitude smaller than that of Ag metal, $\sigma_e = 6.25 \times 10^5 \Omega^{-1} \text{cm}^{-1}$ (21). In addition, cell B contains two separate solid/solid contacts and it has been concluded that the Ag/Ag₂S interface not only has a small exchange current density but also becomes strongly polarized under conditions of current flow (5). Koebel *et al.* (4) also noted that the nature of the Ag/Ag₂S contact was very important, as certain contacts were highly polarizable and irreproducible, giving high resistances; Buck has recently observed similar effects (22). The "patches" of metallic silver in cell B can arise because of redox interactions between the Ag₂S membrane and reducing agents in solution (*vide infra*); it is very probable that these "patches" have a large contact resistance, as it has been shown that silver films, produced by the interaction of various reducing agents with silver ions or complexes in solution, can have variable resistivities and compositions (23). We thus conclude that the observed redox currents are measured primarily via cell C, *i.e.*, the continuous "threads" of metallic Ag through the Ag₂S membrane.

Ag accumulation at electrode surface.—We had previously proposed that the primary means of metallic Ag accumulation at the outer Ag₂S surface resulted from the diffusion of Ag from the silver metal contact at the inner membrane surface (1). Attempts to observe this diffusion process by heating an Ag/Ag₂S electrode and examining the Ag₂S surface for the appearance of Ag by XRD were unsuccessful, perhaps because of the detection limit of XRD or because the conditions of our experiment were not optimal. However, it is well documented that Ag has a high interdiffusion coefficient in the system Ag/Ag₂S (2, 5, 24, 25) and diffusion of metallic silver through the membrane to the outer surface should occur.

We had also proposed previously that Ag could be formed at the electrode surface as a consequence of redox interactions between the Ag₂S membrane and reducing agents in solution (1). This mechanism now appears to be of primary importance; the XRD results show that those electrodes that had been either stored or used for a prolonged period in an alkaline-ascorbic acid solution had a surface deposit whose major component was metallic silver, and that the silver layer could be removed by polishing. The voltammetric results support this conclusion and provide a mechanism for this redox interaction; the voltammetric results indicate that ascorbic acid is adsorbed onto the Ag₂S surface prior to the electron-transfer step, Eq. [5], and that after the electron transfer the dehydroascorbic acid is desorbed from the surface, Eq. [6], to permit the nucleation and growth of the Ag centers. The silver deposited in this manner would also tend to diffuse inward into the Ag₂S membrane and could thus meet the silver diffusing outward from the back of the membrane to give rise to the continuous "threads" of metallic silver proposed in cell C.

Potentiometric vs. voltammetric response.—We are puzzled by the fact that there is no apparent correlation between the potentiometric and voltammetric response of these electrodes; all Ag/Ag₂S electrodes gave qualitatively the same voltammetric response, regardless of whether they gave good or poor Nernstian response to low levels of sulfide. A possible explanation may be the fact that the potentiometric response is much more sensitive to electrode surface effects (changes in composition and conductivity of the surface) than the voltammetric response where changes in

the electrode itself may have occurred, or are continuously occurring, because of the measurement process. Although the C/Ag₂S electrodes do not appear to give a well-defined voltammetric response to Fe²⁺, we have observed (26) that on some occasions these electrodes give a Nernstian potentiometric response to varying concentration ratios of Fe³⁺/Fe²⁺ in the oxalate electrolyte. The reproducibility of this potentiometric response for the C/Ag₂S electrodes is poor, however, as on other occasions they give no response; the reproducibility of the potentiometric response to varying ratios of Fe²⁺/Fe³⁺ for the Ag/Ag₂S electrodes is generally better, but also varies from one electrode to another, and from time to time. Further work is required to understand this response.

Minimizing interference to Nernstian response.—On the basis of the foregoing results and discussion, it is evident that metallic Ag is present at the electrode surface and that the heterogeneous surface responds to, or senses, redox species in solution; the resulting mixed potentials interfere with the Nernstian response. Interference from mixed potentials could be minimized by the following:

1. Use of C/Ag₂S electrodes. These electrodes do not appear to be as sensitive to redox couples as the Ag/Ag₂S electrodes because of their lower electronic conductivity (4, 25). However, the electronic conductivity (4) and the standard potential of these electrodes (25) varies with the stoichiometry of the Ag₂S. Use of these electrodes in an alkaline-reducing environment would result in the deposition of metallic silver on the electrode surface, leading to gradual changes in the stoichiometry and hence conductivity and standard potential of the electrode.

2. Elimination of reducing agents. Since the reducing agents in solution not only give rise to the metallic silver deposit on the electrode surface but also are sensed by the silver on the electrode, it may be advantageous to eliminate them. Problems in the measurement of low concentrations of sulfide in alkaline solutions would result, because the reducing agents are required to maintain anaerobic conditions to prevent the rapid oxidation of sulfide in the alkaline solution by traces of dissolved oxygen; bubbling an inert gas through the solution is not sufficient to overcome this problem (27).

3. Working in acidic media. The rate of oxidation of H₂S by dissolved oxygen is much smaller in acidic than in highly alkaline solutions (28); by using acidic conditions to measure the dissolved sulfide, the reducing agents could be eliminated thus minimizing interference. Due to the high volatility and toxicity of H₂S, problems in sample handling and storage may be encountered under acidic conditions; these problems, however, are not major. A new continuous H₂S-in-water monitor is now commercially available wherein the H₂S is measured in an acidic (pH 5) solution by a sulfide electrode/glass electrode system (29). This monitor has been evaluated and tested in a laboratory and is currently being tested in the field, where its performance over the past 12 months has been excellent; electrode failure has not been observed.

Summary

On the basis of the XRD and voltammetric results, we conclude that Ag metal is present at the outer surface of Ag/Ag₂S electrodes. The Ag metal accumulates at this outer surface as a result of redox reactions between the Ag₂S membrane and the ascorbic acid present in solution, and perhaps also by diffusion from the Ag metal contact at the inner membrane surface. The Ag metal interferes with the Nernstian response of these electrodes to low sulfide concentrations in alkaline-ascorbic acid solutions, by responding to the

redox couples present in solution and generating mixed potentials. This interference can be minimized by working in acidic solutions in the absence of reducing agents.

Acknowledgments

We thank Dr. P. Taylor and A. M. Duclos for the x-ray analysis results; J. Gulens thanks Dr. J. W. Ross of Orion Research Incorporated, for the gift of the C/Ag₂S electrodes and valuable discussions.

Manuscript submitted March 25, 1980; revised manuscript received Oct. 16, 1980. This was Paper 670 presented at the Los Angeles, California, Meeting of the Society, Oct. 14-19, 1979.

Any discussion of this paper will appear in a Discussion Section to be published in the December 1981 JOURNAL. All discussions for the December 1981 Discussion Section should be submitted by Aug. 1, 1981.

Publication costs of this article were assisted by Atomic Energy of Canada Limited.

REFERENCES

1. J. Gulens and B. Ikeda, *Anal. Chem.*, **50**, 782 (1978).
2. R. P. Buck and V. R. Shepard, *ibid.*, **46**, 2097 (1974).
3. R. P. Buck, *ibid.*, **40**, 1432 (1968).
4. M. Koebel, N. Ibl, and A. M. Frei, *Electrochim. Acta*, **19**, 287 (1974).
5. K. Camman and G. A. Rechnitz, *Anal. Chem.*, **48**, 856 (1976).
6. J. W. Ross, in "Ion Selective Electrodes," R. A. Durst, Editor, Natl. Bur. Stand. (U.S.), Spec. Publ. 314, p. 82 (1969).
7. D. W. Shoesmith, P. Taylor, M. G. Bailey, and B. Ikeda, *Electrochim. Acta*, **23**, 903 (1978).
8. J. Gulens, K. Jessome, and C. K. MacNeill, *Anal. Chim. Acta*, **96**, 23 (1978).
9. J. Ambrose and R. G. Barradas, *Electrochim. Acta*, **19**, 781 (1974).
10. J. M. M. Droog, P. T. Alderliesten, and G. A. Bootsma, *J. Electroanal. Chem.*, **99**, 173 (1979).
11. J. A. Harrison and H. R. Thirsk, in "Electroanalytical Chemistry, Vol. 5," A. J. Bard, Editor, p. 67, Marcel Dekker, New York (1971).
12. R. S. Nicholson and I. Shain, *Anal. Chem.*, **36**, 706 (1964).
13. A. J. Calandra, N. R. deTacconi, R. Pereiro, and A. J. Arvia, *Electrochim. Acta*, **19**, 901 (1974).
14. M. Brezina, J. Koryta, T. Loucka, D. Marsikova, and J. Pradac, *J. Electroanal. Chem.*, **40**, 13 (1972).
15. J. J. Ruiz, A. Aldaz, and M. Dominguez, *Can. J. Chem.*, **56**, 1533 (1978).
16. R. Memming, in "Electroanalytical Chemistry, Vol. 11," A. J. Bard, Editor, p. 1, Marcel Dekker, New York (1979).
17. R. E. Van de Leest, *Analyst*, **101**, 433 (1976).
18. S. Y. Ahmed and H. Gerischer, *Electrochim. Acta*, **24**, 705 (1979).
19. H. Gerischer, in "Physical Chemistry," Vol. 9A, M. Eyring, D. Henderson, and W. Jost, Editors, p. 463, Academic Press, New York (1970).
20. B. E. Conway, "Electrochemical Data," p. 356, Greenwood Press, Westport, Conn. (1969).
21. C. Kittel, "Introduction to Solid State Physics," 5th ed., John Wiley & Sons, Inc., New York (1976).
22. R. K. Rhodes and R. P. Buck, *Anal. Chim. Acta*, **110**, 185 (1979).
23. W. R. Momyer and D. J. Levy, *This Journal*, **121**, 484 (1974).
24. C. Wagner, *J. Chem. Phys.*, **21**, 1819 (1953).
25. M. Koebel, *Anal. Chem.*, **46**, 1559 (1974).
26. J. Gulens, Unpublished results.
27. D. J. Crombie, G. J. Moody, and J. D. R. Thomas, *Anal. Chim. Acta*, **80**, 1 (1975).
28. K. Y. Chen and J. C. Morris, *Environ. Sci. Technol.*, **6**, 529 (1972).
29. Orion Model 1516 Sulfide Monitor, Orion Research Inc., Cambridge, Mass.

A Rotating Ring-Disk Electrode Study of Soluble Lead (IV) Species in Sulfuric Acid Solution

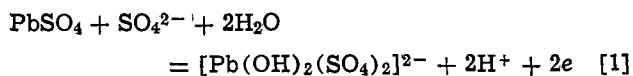
Maria Skyllas Kazacos*

Bell Laboratories, Murray Hill, New Jersey 07974

ABSTRACT

The rotating ring-disk electrode technique was used to detect the presence of soluble Pb(IV) species generated during the anodic charging of the lead dioxide electrode in H₂SO₄. By potentiostatting a gold ring at 0.2V vs. Hg/Hg₂SO₄ while scanning the lead disk between 0.8 and 1.7V, it was possible to observe a small cathodic ring current corresponding to the anodic current waves on the PbO₂ disk, and attributable to the reduction of Pb(IV) to Pb(II). This paper presents evidence for the generation of soluble Pb(IV) as an unstable intermediate during the charging of the PbSO₄/PbO₂ electrode. The effect of addition of small amounts of H₃PO₄ to the H₂SO₄ electrolyte is also illustrated.

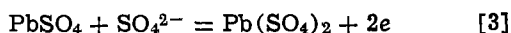
The possible existence of soluble Pb(IV) species in sulfuric acid solution is important in the lead-acid battery, particularly with regard to their effect on the performance of the positive lead dioxide electrode. Although considerable research has been carried out in this area, there still remains a number of unsolved problems concerning the behavior of this electrode. An early hypothesis of Feitknecht and Gaumann (1) assumed the formation of intermediate lead (IV) compounds during the charging process which are not stable in the acid, but decompose spontaneously or are hydrolyzed



followed by



or



followed by



Another proposed mechanism assumes that at a certain overpotential applied to the Pb/PbSO₄ electrode, the pH of the solution in the pore volume will reach the value where the reaction



becomes possible. The Pb(OH)₂ formed is immediately oxidized further by solid-state reaction to PbO₂ (2).

β-PbO₂ has been reported to dissolve to the extent of approximately 0.2 mM in 33 weight percent (w/o) H₂SO₄; however, it is generally believed that soluble Pb(IV) species are not detected in sulfuric acid solution (3). The existence of two relatively stable tetra-valent lead phosphate species, 2PbO₂ · P₂O₅ · nH₂O and PbO₂ · P₂O₅ · nH₂O, has been reported in phosphoric acid-containing sulfuric acid solutions (4-7). Polarographic measurements by Amlie and Berger (8) have confirmed the presence of soluble lead(IV) phosphate species produced both chemically and electrochemically in sulfuric/phosphoric acid solutions. They also developed an amperometric titration technique to determine quantitatively the Pb(IV) species concentration in these solutions. They could not, however, generate either chemically or electrochemically, any detectable soluble Pb(IV) species in pure 35% sulfuric acid solutions.

* Electrochemical Society Active Member.
Key words: metals, potential, voltammetry.

If soluble Pb(IV) species are formed during the charging process in the sulfuric acid battery, they would be unstable and decompose spontaneously (3). Since a rotating ring-disk electrode (RRDE) (9, 10) can be used for the detection at the ring of soluble species discharged by the disk, such an experiment was set up to study the generation of any soluble lead species at the lead dioxide electrode.

This technique is particularly useful in the study of unstable intermediates of the disk processes since it provides a virtually instantaneous quantitative analysis of the disk product (11).

Experimental

The RRDE construction and electronics employed here have previously been described by Miller (12). Ring disk measurements were made on a rotating Au ring-Pb disk electrode (disk area = 0.18 cm²) which used lead of 99.999% purity. A two-compartment Pyrex electrolytic cell was used in all experiments and the counterelectrode consisted of lead rod, 99.999% pure.

The electrolyte consisted of 29 w/o H₂SO₄ which was prepared from analytical-grade sulfuric acid and deionized water. Before use, the solution was preelectrolyzed (2 liters) using two Pb electrodes with a current of 100 mA for 48 hr. All potentials were measured vs. an Hg/Hg₂SO₄ reference electrode containing the same electrolyte as used in the electrolysis cell. A thin Luggin capillary was mounted approximately 2-4 mm below the center of the disk electrode.

Unless otherwise specified, all measurements were carried out at a rotation speed of 2500 rpm and a potential scan rate of 10 mV sec⁻¹. Nitrogen gas was passed through the solution prior to electrolysis, as well as during the experiments to remove any O₂ generated at the PbO₂ electrode. All experiments were conducted at room temperature.

Results and Discussion

The curves of Fig. 1(a) show the typical behavior of a Pb disk electrode in H₂SO₄, when the potential is scanned between 0.8 and 1.7V vs. an Hg/Hg₂SO₄ reference electrode. The increase in faradaic current observed in the first scan [curve 1 of Fig. 1(a)] at potentials greater than 1.5V, corresponds to the coformation of O₂ and PbO₂. Although no current arrest corresponding to PbO₂ formation is observed on the initial scan, a definite black deposit corresponding to a PbO₂ film can be observed on the electrode surface. As sufficient PbO₂ forms on subsequent cycles to stabilize the PbSO₄/PbO₂ reversible electrode, a definite peak

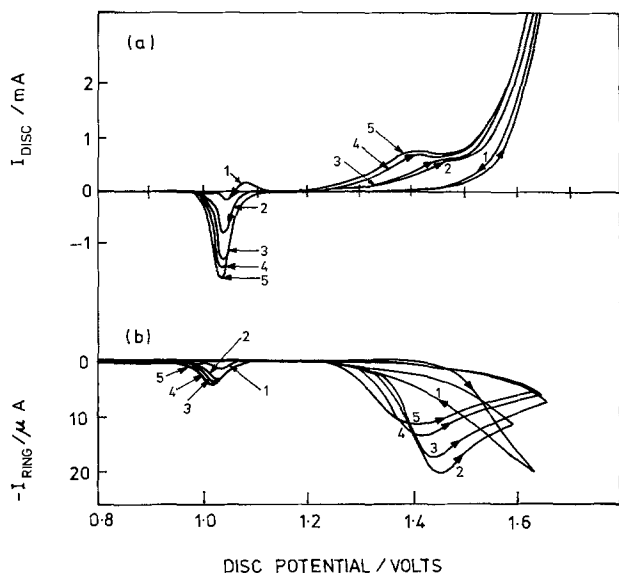


Fig. 1. (a) Consecutive controlled potential sweep cycles at a 0.18 cm^2 lead disk electrode in 29 w/o H_2SO_4 . Potential range = 0.8 to 1.7V vs. $\text{Hg}/\text{Hg}_2\text{SO}_4$; sweep rate, $\nu = 10 \text{ mV sec}^{-1}$; rotation speed, $\omega = 2500 \text{ rpm}$. Numbers on curves refer to the cycle number. (b) Ring current traces for lead disk scans of Fig. 1(a). $E_R = 0.2\text{V}$.

corresponding to PbO_2 formation can be distinguished, as seen in curves 2-5 of Fig. 1(a). Reversal of the potential scan gives rise to the cathodic peak corresponding to the reduction of PbO_2 to PbSO_4 .

If soluble Pb(IV) ions were being formed at the PbO_2 disk during charge or discharge, by potentiostating the gold ring at the appropriate potential, it should be possible to observe a current at the ring for the reduction of Pb(IV) to Pb(II) or to Pb , depending on the potential of the ring electrode. Thus, if the ring is held at a potential less than approximately 1.0V but more positive than that required for Pb deposition a current corresponding to the reaction $\text{Pb(IV)} + 2e \rightarrow \text{Pb(II)}$ would be expected. It is also necessary to select a potential at which reduction of O_2 evolved at the disk will not interfere with, or mask, the reduction of interest at the ring. The ring was therefore potentiostatted at 0.2V vs. $\text{Hg}/\text{Hg}_2\text{SO}_4$ while the disk was scanned between 0.8 and 1.7V. The curves of Fig. 1(b) show the ring currents corresponding to the disk currents of Fig. 1(a). A reduction peak is indeed observed at the ring electrode during PbO_2 formation. In fact the ring peak closely follows the position of the PbO_2 peak as it moves to less positive potentials on successive cycles. The ring current decreases with each cycle, due to the increasing coverage of the ring with the insulating PbSO_4 layers. Furthermore, this ring peak is not present at a gold ring-gold disk electrode in the same solution, indicating that the species detected is peculiar to the reactions taking place at the lead electrode, and not to the reduction of oxygen evolved at the disk.

Reversal of the disk potential gives rise to a second smaller cathodic ring peak at potentials corresponding to PbSO_4 formation. Since the ring potential is too positive to detect Pb^{2+} in solution, the cathodic peaks observed at the ring electrode must be due to the reduction of soluble Pb(IV) species formed at the $\text{PbSO}_4/\text{PbO}_2$ electrode during charge and discharge.

If Pb(IV) ions are indeed reduced at the ring electrode at +0.2V, it should be possible to detect the presence of PbSO_4 on the surface of the ring. Previous workers (12) have shown, however, that during reduction of PbO_2 , Pb^{2+} can also be detected at a gold ring. This is evidenced also by the considerable increase in the ring current during PbSO_4 formation, when the ring is potentiostatted at -1.1V (Fig. 2). The Pb(IV)

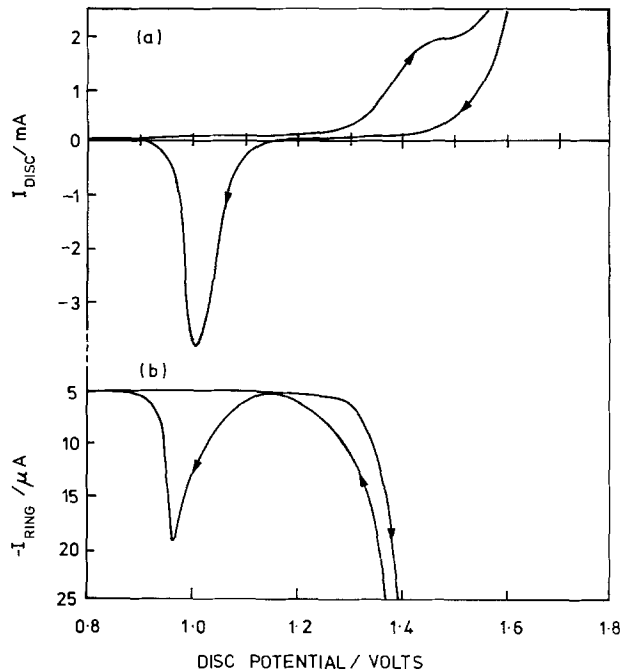


Fig. 2 (a) Controlled potential sweep cycle at a precycled lead disk electrode. Conditions as for Fig. 1. (b) Ring current traces at constant ring potential for the lead disk scan of Fig. 2(a). $E_R = -1.1\text{V}$.

ring peak at disk potentials corresponding to PbO_2 formation, however, can no longer be detected, due to O_2 interference. Since Pb^{2+} is generated during the reaction $\text{PbO}_2 \rightarrow \text{PbSO}_4$, it would be expected that Pb^{2+} be precipitated by SO_4^{2-} and deposit on the ring. It is therefore important to ensure that any PbSO_4 on the ring is due to the reduction of Pb(IV) ions and not to precipitation of Pb^{2+} ions generated during the discharge reaction.

The electrode was repolished using 3 micron aluminum oxide paper to remove any PbSO_4 which may have been present from previous experiments. After immersing in the H_2SO_4 , the ring was scanned negative from +0.2V to the potential for H_2 evolution and then reversed to the initial potential. Figure 3(a) shows the voltammogram obtained. No wave corresponding to PbSO_4 reduction or Pb reoxidation can be detected on the gold.

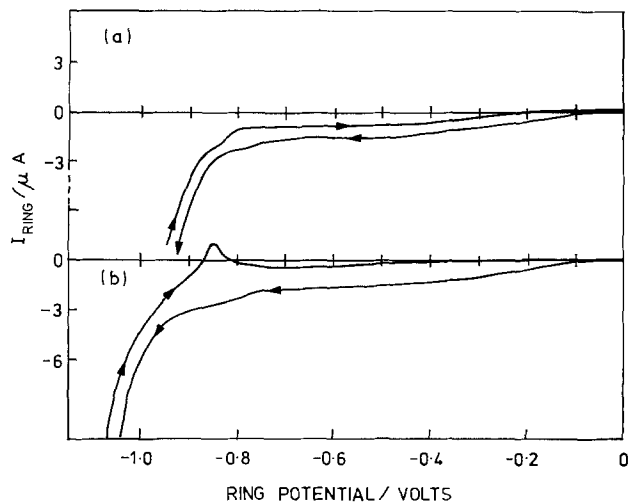


Fig. 3. (a) Potential sweep cycle of gold ring between 0.2 and -1.1V. Lead disk not previously cycled. (b) Potential sweep cycle of gold ring which had been previously potentiostatted at 0.2V, while lead disk scanned between 0.8 and 1.7V in H_2SO_4 .

The ring was then open-circuited while the disk was scanned from 0.8 to 1.7V and then back to 1.2V. Holding the disk at 1.2V and being careful not to allow PbO_2 reduction, the ring was then cycled negative from zero volts. A voltammogram, similar to Fig. 3(a) was again obtained showing that no PbSO_4 was present on the ring. Thus, scanning the disk from 0.8 to 1.7V does not lead to deposition of PbSO_4 on the ring from precipitation of Pb^{2+} .

The ring was then potentiostatted at +0.2V while the disk was scanned as above. When the ring was subsequently scanned negative from 0.2V and reversed after H_2 evolution, the voltammogram of Fig. 3(b) was obtained. Although no wave corresponding to the reduction of PbSO_4 can be distinguished due to the coevolution of H_2 on the gold, reversal of the potential gives rise to an anodic peak at a potential corresponding to the reaction $\text{Pb} \rightarrow \text{PbSO}_4$. Thus, as the ring potential was initially scanned beyond -1.2V, the PbSO_4 on the ring was reduced to Pb and on reversal a distinct peak for the reoxidation of Pb was obtained. This may be compared to Fig. 4 which shows the characteristic behavior of a lead electrode in sulfuric acid. This experiment thus verifies the presence of PbSO_4 on the ring electrode, the presence of which could only be due to the reduction of a Pb(IV) species generated at the disk during PbO_2 formation.

Previous workers (4-8) have demonstrated that the presence of H_3PO_4 increases the solubility of Pb(IV) in H_2SO_4 due to the formation of relatively stable Pb(IV) phosphate complexes. Addition of 0.5 w/o H_3PO_4 to the sulfuric acid effects the performance of the $\text{PbSO}_4/\text{PbO}_2$ electrode, as previously reported (13), and as seen from Fig. 5(a). Thus, the addition of small amounts of phosphoric acid results in the reduction peak shifting in the positive direction with a simultaneous decrease in height, as well as the appearance of a second more negative peak. The anodic peak is also seen to shift to a more positive potential in the presence of H_3PO_4 , in agreement with other investigators (13, 14). The beneficial effect of phosphoric acid has been reported in the patent literature (15-19). However, higher concentrations can be detrimental to battery performance, as seen by excessive mossing at higher phosphate concentrations (16), probably related to the increased solubility of lead (IV) under these conditions. The ring current [Fig. 5(b)], corresponding to the disk scan of Fig. 5(a) shows a marked increase in the soluble Pb(IV) species on addition of H_3PO_4 , as expected, again supporting the presence of Pb(IV) ions in solution during PbO_2 formation. This observation also rules out the possibility that the ring current may be due to colloidal PbO_2 particles which

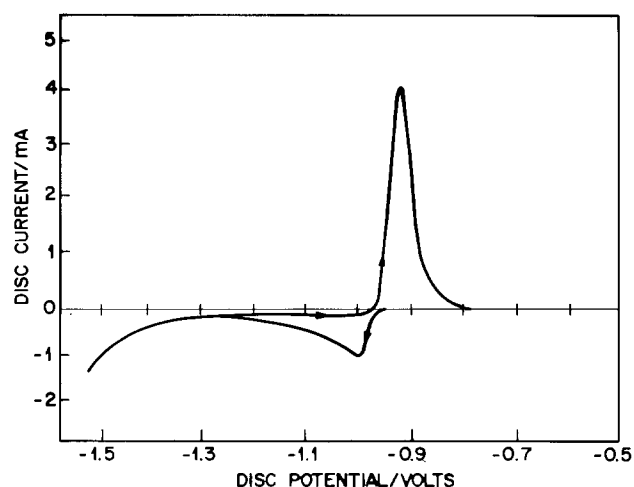


Fig. 4. Controlled potential sweep cycle at a 0.18 cm^2 lead disk electrode in 29 w/o H_2SO_4 . Potential range -0.7 to -1.5V vs. $\text{Hg}/\text{Hg}_2\text{SO}_4$; $\nu = 10 \text{ mV sec}^{-1}$; $\omega = 2500 \text{ rpm}$.

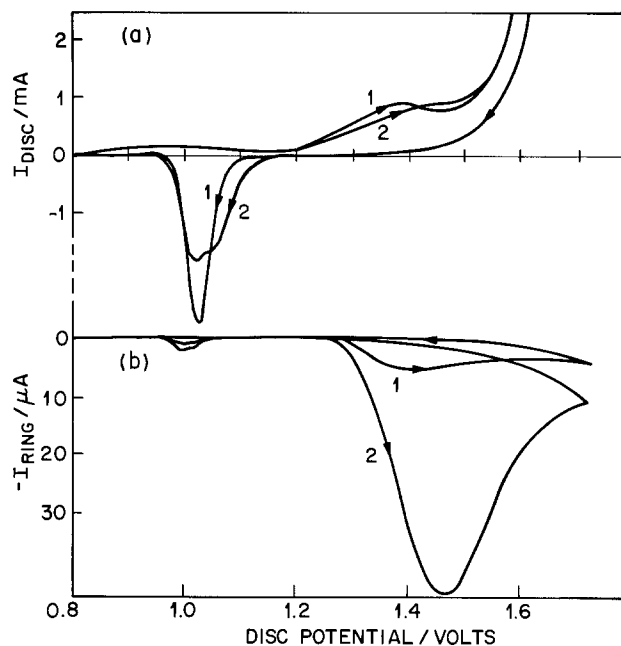


Fig. 5. (a) Curve 1: Potential sweep cycle at lead disk in H_2SO_4 . Condition as for Fig. 1(a). Curve 2: Effect of addition of 0.5 w/o H_3PO_4 to H_2SO_4 solution. (b) Ring current traces corresponding to lead disk voltammograms of Fig. 5(a).

become detached from the electrode surface and are reduced at the ring, since such a phenomenon should not be affected by the presence of H_3PO_4 in the electrolyte.

Further support for the existence of the soluble Pb(IV) species may also be obtained by comparing the magnitude of the ring currents at ring potentials of 0.2 and -1.1V. At the first potential, the Pb(IV) would be reduced to Pb(II), while at the more negative potential, Pb would be produced, resulting in an increase in the ring current by a factor of 2.

Before performing such an experiment however, two problems had to be overcome. Firstly, and as previously mentioned, at a ring potential of -1.1V, the Pb(IV) peak would be hidden by the oxygen reduction wave. To minimize this effect, the disk was precycled several times so as to stabilize the $\text{PbSO}_4/\text{PbO}_2$ electrode and increase the oxygen overpotential. The scans were also performed at lower sweep rates (2 mV/sec) to further separate PbO_2 formation from O_2 evolution.

The second difficulty arises from the low H_2 overpotential at a gold electrode which means that at a potential of -1.1V, the high H_2 evolution would prevent detection of a distinct wave corresponding to the reduction of Pb(IV) to Pb. This was overcome by first plating the gold ring electrode *in situ* with lead which has a much higher H_2 overpotential. The lead plating was accomplished by potentiostating the ring at -1.1V while sweeping the disk between -0.8 and -1.4V. During this cycle, the disk electrode is charged, ($\text{PbSO}_4 \rightarrow \text{Pb}$) and discharged ($\text{Pb} \rightarrow \text{PbSO}_4$). During the discharge reaction, Pb^{2+} ions are generated at the disk (20) and swept across to the ring where they are reduced to Pb, thus plating the gold ring. As more and more Pb is deposited at the ring with continuous cycling of the lead electrode, the ring current decreased due to the increase in H_2 overpotential.

Using the lead-plated ring electrode which was potentiostatted at 0.2V, the disk was again scanned between 0.8 and 1.7V, with a sweep rate of 2 mV sec^{-1} [Fig. 6(a)]. Since this experiment required the use of a very slow sweep rate, a much lower current would be expected at the ring. In order to improve the sensitivity, therefore, 0.5 w/o H_3PO_4 was added to the sulfuric acid so as to increase the amount of Pb(IV) generated during the charge reaction. Figure 6(b),

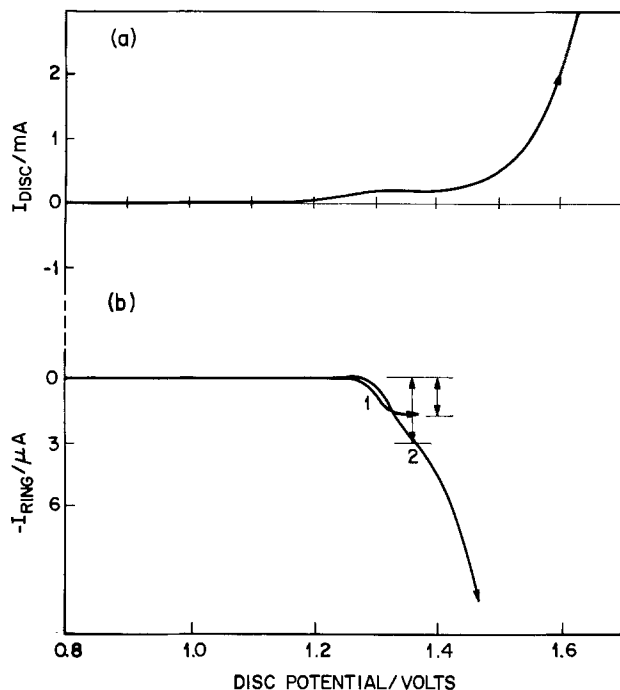


Fig. 6. (a) Voltammogram of lead disk in H_2SO_4 for $\nu = 2 \text{ mV sec}^{-1}$. Other conditions as for Fig. 5(a). (b) Ring current traces at constant ring potential for lead disk scans of Fig. 6(a). Curve 1: $E_R = 0.2\text{V}$; curve 2: $E_R = -1.1\text{V}$.

curve 1 shows the characteristic Pb(IV) wave obtained at the ring at $E_R = 0.2\text{V}$. Setting the ring potential at -1.1V and sweeping the disk as above, gave rise to the wave seen in Fig. 6(b), curve 2. A comparison of the ring currents at the two potentials does indicate that the ratio of the electrons transferred at -1.1 and 0.2V is approximately 2:1 as would be expected if the ring currents were due to the reduction of Pb(IV).

Conclusion

In this study, evidence has been presented for the generation and detection of soluble Pb(IV) ions in sulfuric acid solution during charge and discharge of the PbO_2 electrode. This was accomplished with the use of a rotating ring-disk electrode which is a particularly useful technique for the study of unstable intermediates of the disk reaction, as would be expected with Pb(IV) ions. This phenomenon could help to elucidate the mechanism of the reactions occurring

at the positive electrode of the lead-acid battery which still presents a great deal of uncertainty and disagreement.

Acknowledgments

The author wishes to thank the Australian Commonwealth Scientific and Industrial Research Organization for its support for this work. She is also indebted to Barry Miller for many helpful discussions as well as to David Feder, John Broadhead, and Richard Biagetti for their suggestions and encouragement.

Manuscript submitted Aug. 1, 1979; revised manuscript received Feb. 3, 1980.

Any discussion of this paper will appear in a Discussion Section to be published in the December 1981 JOURNAL. All discussions for the December 1981 Discussion Section should be submitted by Aug. 1, 1981.

Publication costs of this article were assisted by Bell Laboratories.

REFERENCES

1. W. Feitknecht and A. Gaumann, *J. Chim. Phys.*, **49**, 135 (1952).
2. H. R. Thirsk and W. F. K. Wynne-Jones, *ibid.*, **49**, 131 (1952).
3. L. N. Vanyukova, M. M. Isaeva, and B. N. Kabanov, *Dokl. Akad. Nauk. SSSR*, **143**, 32 (English translation) (1962).
4. P. Ness, *Electrochim. Acta*, **12**, 161 (1967).
5. E. Voss, "Proceedings of the Second International Symposium on Batteries," Bournemouth, England Paper No. 16 (1960).
6. H. Bode and E. Voss, *Electrochim. Acta*, **6**, 11 (1962).
7. F. Huber and M. S. A. El-Meligy, *Z. Anorg. Allg. Chem.*, **367**, 154 (1969).
8. R. F. Amlie and T. A. Berger, *J. Electroanal. Chem. Interfacial Electrochem.*, **36**, 427 (1972).
9. A. N. Frumkin, L. N. Nekrasov, N. Levich, and Ju. Ivanov, *J. Electroanal. Chem.*, **1**, 84 (1959).
10. A. N. Frumkin and L. N. Nekrasov, *Dokl. Akad. Nauk. SSSR*, **126**, 115 (1959).
11. Yu. N. Pleskov and V. Yu. Filinovskii, "The Rotating Disc Electrode," Chap. 8, H. S. Wroblowa and B. E. Conway, Editors, Consultants Bureau, N.Y. (1976).
12. B. Miller, *This Journal*, **116**, 1675 (1969).
13. K. R. Bullock and D. H. McClelland, *ibid.*, **124**, 1478 (1977).
14. W. Visscher, *J. Power Sources*, **1**, 257 (1977).
15. M. Krugel, German Pat. 480,149 (1926).
16. D. Evers, U.S. Pat. 3,011,077 (1961).
17. E. A. Willihnganz, French Pat. 1,517,629 (1968).
18. S. Tudor, A. Weisstuch, and S. H. Davang, U.S. Pat. 3,447,969 (1969).
19. K. Yonetsu *et al.*, Japanese Pat. 48-5175 (1973).
20. B. Miller and M. Bellavance, Unpublished data (1972).

The Electrochemical Reduction of Molten Perchlorate and Chlorate Salts

M. H. Miles* and A. N. Fletcher*

Naval Weapons Center, Chemistry Division, China Lake, California 93555

ABSTRACT

The electrochemical reduction of molten LiClO_4 occurs much more readily on nickel electrodes than on platinum electrodes. This is likely related to the catalytic effect of the nickel oxide that forms on the electrode surface in oxidizing electrolytes. Both the thermal decomposition and the electrochemical reduction of molten chlorates and perchlorates require the rupture of Cl—O bonds. Such bond breaking processes appear to be catalyzed by the positive field of nearby cations and by p-type oxides. Cyclic voltammetric studies show that LiClO_4 is more readily reduced than NaClO_3 and that both form insoluble oxides as products. Potential *vs.* temperature measurements at a constant current density show nearly linear behavior between about 260°–380°C for the electrochemical reduction of LiClO_4 on nickel. Kinetic parameters calculated from these measurements yield 0.2 for the transfer coefficient, 15 kcal/mole for the activation energy, and 5×10^{-4} A/cm² for the exchange current density at 350°C. The transfer of the first electron accompanied by breakage of the Cl—O bond is postulated to be the slow step in the reduction reaction.

The melting points of LiClO_3 (129°C), NaClO_3 (263°C), KClO_3 (357°C), and LiClO_4 (247°C) are well separated from their thermal decompositions by temperature ranges of 100°–200°C (1). These molten oxychloride salts, therefore, may find use as oxidizing electrolytes in battery systems somewhat analogous to the use of thionyl chloride, SOCl_2 (2, 3). Electrochemical studies of fused LiClO_4 and LiClO_3 have been reported by other workers (4, 5), and electrochemical cells utilizing fused lithium chlorate with lithium anodes have been described (6). Mixtures of perchlorate salts with nitrate salts are also of interest due to their low melting temperatures and wide ranges of thermal stabilities. For example, an equimolar mixture of LiClO_4 – LiNO_3 melts at about 160°C and appears to resist thermal decomposition up to about 450°C.

Previous studies of the electrode reduction of molten nitrates show that cations exert a major catalytic effect on the reaction (7, 8). Overvoltages for nitrate reduction increase with increasing size of the metal cation present, and the oxide ions produced by the reaction become more prone to oxidation to form peroxides or superoxides (8). Our interest in molten nitrate and oxyhalide systems is related to their possible use as oxidizing electrolytes in thermal battery cells (9).

Experimental

The electrochemical cell used in the cyclic voltammetric studies was constructed from Pyrex glass tubing with dimensions similar to the cell used previously (10). Uncompensated solution resistance was minimized by using a small working electrode ($A \sim 0.01$ cm²) positioned close to a Luggin capillary tip. The platinum and nickel working electrodes were constructed from wires sealed in glass with one end polished smooth. All potentials were measured against an Ag/AgNO₃ (0.1M) reference electrode as described previously (10). The counterelectrode generally consisted of a platinum wire spiral contained in fritted glass tubing that prevented any gaseous products from contacting the working electrode. The electrochemical cell was also equipped with a glass tube used for bubbling helium gas through the melt to remove residual water. The helium was passed through tubes of anhydrous calcium sulfate (indicating Drierite) and P₂O₅ prior to entering the cell. Despite using anhy-

drous LiClO_4 (J. T. Baker or G. F. Smith Reagent) that was dried in a vacuum oven at 130°C for several days, considerable water still remained in the salt. The water-wave on platinum in molten LiClO_4 , similar to that observed in molten LiNO_3 (8), showed that the bubbling of dried helium gas through molten LiClO_4 at 300°–350°C for several hours was required to remove the final traces of water. The problem of water retention by NaClO_3 , in contrast, was very minor. Temperature control was maintained within $\pm 5^\circ\text{C}$ by the use of a fluidized sand bath (Tecam).

Potential *vs.* temperature measurements of the cathodic reaction at a selected constant current density were made on nickel electrodes ($A = 0.32$ cm²) using the electrode arrangement in an open pan as described previously (7). The only difference was that a platinum pan was used in place of nickel to minimize both the catalytic decomposition of molten LiClO_4 and the corrosion of the pan. A fiberglass filter served as a separator and contained most of the molten salt in these thin cells that used calcium as the anode to approximate conditions in thermal battery cells. Galvanostatic studies of the cathodic reaction at a fixed temperature were also made in these same cells.

Constant current measurements were obtained using a PAR Model 173 potentiostat/galvanostat and results were plotted using a strip chart recorder (HP 7100B). For cyclic voltammetric measurements, a PAR Model 175 programmer was also used and results were displayed with an X-Y recorder (HP 7047A).

Results

The electrochemical reduction of molten LiClO_4 occurs much more readily on nickel electrodes than on platinum electrodes. This is in sharp contrast to the electrochemical reduction of molten nitrates that occurs at about the same potential on both electrodes (7, 8). Figure 1 shows a cyclic voltammetric trace for the reduction of molten LiClO_4 at 300°C on nickel. The cathodic reaction begins at about -0.5V on nickel and at about -1.1V on platinum (Fig. 2). Although a reduction peak was observed on both metals, the peak was usually rather irregular on nickel and is not shown in Fig. 1. At a potential sweep rate of 100 mV/sec, typical peak potentials were about -0.8V on nickel and -1.5V on platinum. By varying the cathodic sweep limit, the following anodic peak was found to be directly related to the reduction reaction. Comparisons with previous results in molten LiNO_3 indi-

* Electrochemical Society Active Member.

Key words: catalysis, cathode, fused salts, voltammetry.

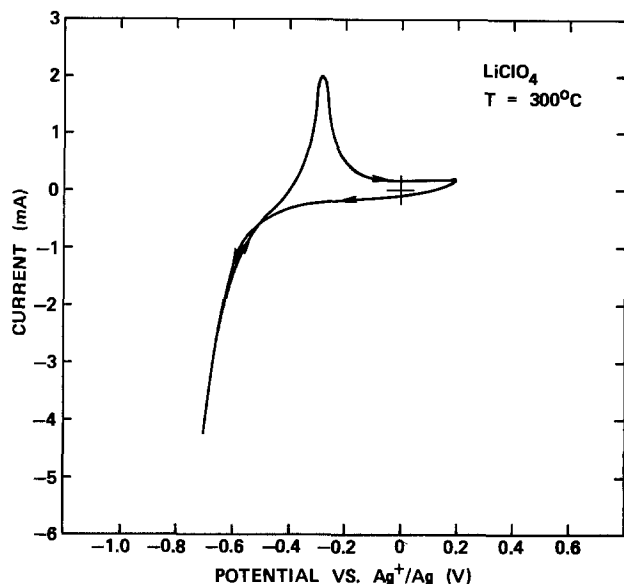


Fig. 1. Cyclic voltammogram study on nickel at 100 mV/sec. Results are for molten LiClO_4 at 300°C . Potential sweep was begun at 0.0V and swept first cathodically, then anodically, and finally cathodically to the starting potential.

icates that the anodic peak is due to the oxidation of insoluble Li_2O to form Li_2O_2 (8). Slight gas evolution observed immediately following the anodic peak suggests the decomposition of the unstable peroxide formed. Similar gassing was also observed following the anodic peak on molten NaClO_3 (Fig. 2).

Cyclic voltammogram studies of molten LiClO_4 at 300°C on platinum are shown in Fig. 2 at four potential sweep rates. For comparisons, a similar cyclic voltammogram trace at 100 mV/sec on platinum in molten NaClO_3 is also shown. Although molten LiClO_4 reduction begins at quite different potentials on nickel and platinum electrodes, the Li_2O oxidation peak remains at about the same potential. The water-wave on platinum in molten LiClO_4 occurs prior to the LiClO_4 reduction peak (4) and, as found in molten LiNO_3 (8), is not detected on nickel electrodes.

Figure 2 indicates that molten NaClO_3 is much more difficult to reduce than molten LiClO_4 and that insoluble Na_2O is produced by the electrode reaction. Oxidation of the Na_2O to the peroxide apparently occurs on the anodic sweep similar to previous studies

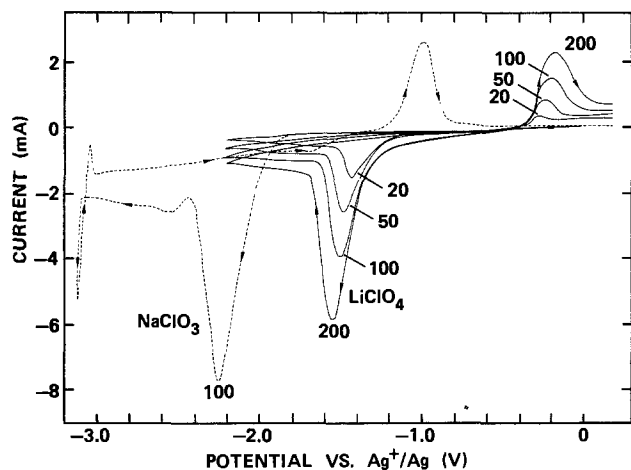


Fig. 2. Cyclic voltammogram studies on platinum in molten LiClO_4 and NaClO_3 at 300°C . The studies in LiClO_4 (solid lines) were made at potential sweep rates of 20, 50, 100, and 200 mV/sec. All potential sweeps began at 0.0V and were swept first cathodically and then anodically.

in molten NaNO_3 (8). The different areas of the reduction and oxidation peaks in Fig. 2 likely reflect the partial dissolution of the oxide product. The extended cathodic sweep in molten NaClO_3 shows the reduction of sodium ions to metallic sodium at about $-3.1\text{V vs. Ag}^+/\text{Ag}$. This metallic sodium likely reacts quickly with molten NaClO_3 to form sodium oxide. The solubilities of both Li_2O and Na_2O at 300°C , as determined from acidimetric titrations, were 0.2 mole percent (m/o) in molten NaClO_3 and 0.8 m/o in molten LiClO_4 .

Studies of the LiClO_4 reduction peak were often complicated by rather irregular traces caused by gas bubbles forming at the working electrode. This effect was much greater with nickel electrodes than with platinum electrodes and persisted even at open circuit, suggesting the catalytic decomposition of LiClO_4 . Although smooth cyclic voltammogram traces were often difficult to obtain, the potential sweep studies of LiClO_4 reduction on both platinum and nickel electrodes generally showed that the peak current was proportional to the square root of the sweep rate while the peak potential becomes more negative with increasing rate of potential change. It should be noted, however, that the peak currents are likely due to blockage of the electrode surface by insoluble oxides rather than by diffusion limitations of the reactants. Similar reduction peaks due to oxide blockage are obtained in molten LiNO_3 and NaNO_3 (8, 11, 12).

Figure 3 presents a cyclic voltammogram study of an equimolar mixture of LiClO_4 - LiNO_3 . On platinum, reduction of the LiNO_3 occurs more readily than the reduction of LiClO_4 and gives a peak potential of about -0.95V . The reduction of molten LiClO_4 beginning at about -1.1V (see Fig. 2) gives an unsymmetric shape to the reduction peak. Insoluble Li_2O is produced by the reduction of both LiNO_3 and LiClO_4 , hence a single oxidation peak is observed on the following anodic sweep. Preliminary studies of equimolar mixtures of KClO_3 - LiNO_3 and NaClO_4 - LiNO_3 at 350°C indicated less satisfactory performance than the LiClO_4 - LiNO_3 mixtures. In particular, gassing was a serious problem. Differential scanning calorimetry studies of the KClO_3 - LiNO_3 mixture gave thermal decomposition characteristics that related more closely to molten LiClO_3 than to KClO_3 . Thermogravimetric experiments indicate that LiClO_3 decomposes more readily than LiClO_4 (1). These results suggest that the use of molten LiClO_3 as the oxidizing electrolyte might be less satisfactory than the use of LiClO_4 in the temperature range of $250^\circ\text{--}400^\circ\text{C}$.

The analyses of potential vs. temperature measurements at constant current densities can yield various

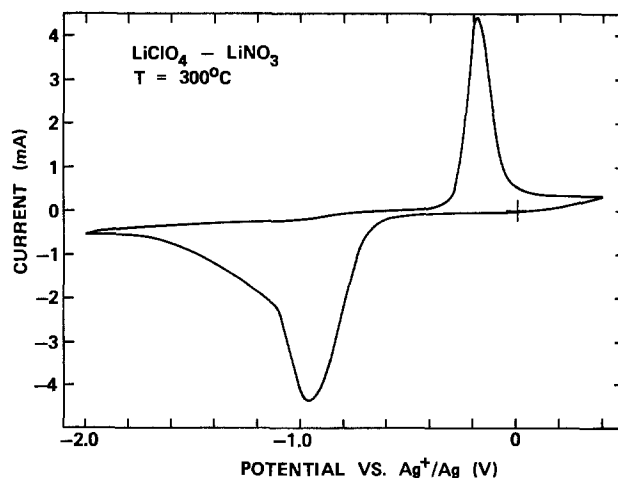


Fig. 3. Cyclic voltammogram study on platinum in equimolar LiClO_4 - LiNO_3 at 300°C . Potential sweep rate was 100 mV/sec.

kinetic parameters since the constants in the empirical equation

$$E_c = a + (b_1 + b_2 \ln i)T \quad [1]$$

can be theoretically related to these parameters (7). Typical results for such experimental measurements on nickel electrodes in molten LiClO_4 and LiNO_3 are presented in Fig. 4. Both studies show an approximately linear potential change with temperature as predicted theoretically (7); however, for molten LiClO_4 , the linear range is limited to about 280°–380°C. The upper limit is likely related to the thermal decomposition of molten LiClO_4 that begins at about this temperature (1). Table I presents the average values for the empirical constants obtained from nine separate studies in molten LiClO_4 as well as the kinetic parameters calculated from these constants. For comparisons, average results from similar studies of molten LiNO_3 reduction are also shown. For molten LiClO_4 reduction, the transfer coefficient (α_c) is calculated to be 0.20, the free energy of activation (ΔG^{\ddagger}) is about 15 kcal/mole, and the exchange current density (i_0) is 5×10^{-4} A/cm². The calculations of the ΔG^{\ddagger} and i_0 values involved the assumption that the equilibrium potential at 350°C is 0.2V for LiClO_4 reduction and 0.0V *vs.* Ag^+/Ag for LiNO_3 reduction (7). These values are supported by both thermochemical calculations and experimental observations. The i_0 values presented are based upon the apparent electrode area that may vary from the real surface area depending upon the relative effects of electrode blockage by insoluble Li_2O and the roughness of the electrode surface. Similar studies on platinum electrodes gave poor results; this could likely be due to interference from the water-wave that occurs on platinum but is not detected on nickel (8).

Table II presents average Tafel and kinetic parameters obtained galvanostatically at 350°C from potential *vs.* current density measurements. Linear Tafel regions were generally observed between about 1–10 mA/cm². The α_c and i_0 values show reasonable agreement with those obtained from the potential *vs.* temperature measurements under galvanostatic conditions (Table I). The parameters for molten LiNO_3 reduction obtained in these thin cells containing a calcium anode and exposed to the atmosphere also agree favorably with previous results obtained potentiostatically in stirred solutions under a helium atmosphere (8).

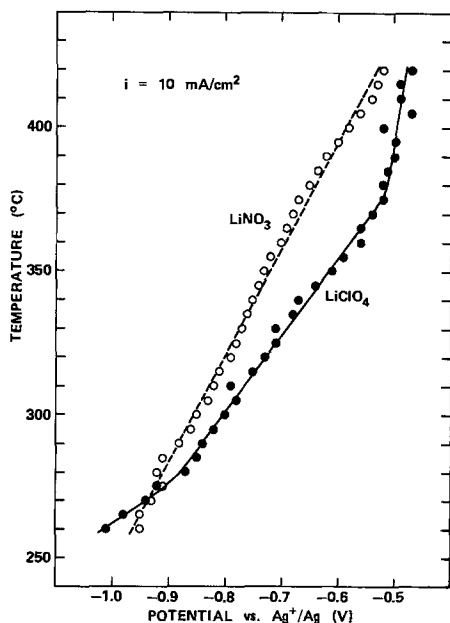


Fig. 4. Potential *vs.* temperature measurements for the electrochemical reduction of molten LiClO_4 and LiNO_3 salts on nickel electrodes at a constant current density of 10 mA/cm².

Table I. Average empirical constants and kinetic parameters for the electrochemical reduction of molten LiClO_4 and LiNO_3 salts on nickel electrodes. These values were obtained from potential *vs.* temperature measurements at constant current densities in thin cells that used calcium as the anode

| Salt | a (V) | b_1 (V/K) | b_2 (V/K) | α_c | ΔG^{\ddagger} (kcal/mole) | i_0^* (A/cm ²) |
|------------------|---------|-----------------------|------------------------|------------|-----------------------------------|------------------------------|
| LiClO_4 | -2.84 | 1.57×10^{-3} | -0.43×10^{-3} | 0.20 | 15 | 5×10^{-4} |
| LiNO_3 | -2.78 | 1.99×10^{-3} | -0.22×10^{-3} | 0.39 | 25 | 3×10^{-5} |

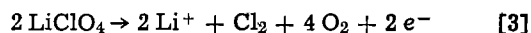
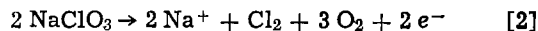
* At $T = 350^\circ\text{C}$.

Table II. Average Tafel and kinetic parameters for the electrochemical reduction of molten LiClO_4 and LiNO_3 salts on nickel electrodes. These values were obtained from steady-state galvanostatic measurements at 350°C in thin cells that used calcium as the anode

| Salt | b (V) | α_c | i_0 (A/cm ²) |
|------------------|---------|------------|----------------------------|
| LiClO_4 | 0.45 | 0.27 | 3×10^{-4} |
| LiNO_3 | 0.28 | 0.44 | 4×10^{-5} |

Figure 4 and Tables I and II show that on nickel electrodes, the reduction of molten LiClO_4 occurs more readily than the reduction of molten LiNO_3 . This is reversed from the observations on platinum electrodes.

The stability limit with respect to electrochemical oxidation was investigated for molten NaClO_3 and LiClO_4 at 300°C on platinum electrodes, and the cyclic voltammograms (Fig. 5) show that NaClO_3 oxidizes more readily than LiClO_4 . The major anodic wave begins at about 0.8V in NaClO_3 and at about 1.7V in LiClO_4 . On nickel electrodes, the major anodic wave begins at about 0.7V in molten NaClO_3 and at about 1.5V in molten LiClO_4 at 300°C. The oxidation reactions



likely involve the loss of an electron by the oxychloride anion followed by decomposition of the resulting radical (13). Mass spectrometric analysis of the gases produced at the anode during electrolysis of pure LiClO_4 showed no fragments containing Cl—O bonds (4). The slowly rising anodic current in the molten LiClO_4 study suggests the presence of small amounts of the more readily oxidized chlorate compound.

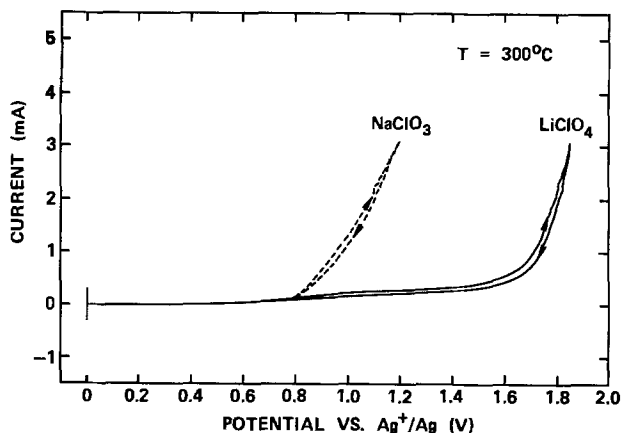
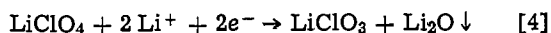


Fig. 5. Cyclic voltammetric studies of the electrochemical oxidation of molten NaClO_3 and LiClO_4 at 300°C. Potential sweeps began at 0.0V and were swept first anodically and then cathodically. Potential sweep rate was 100 mV/sec.

Discussion

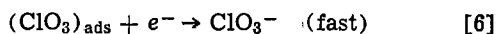
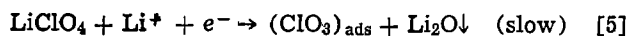
Anders and Plambeck (4) have presented evidence that the reduction peak observed in molten LiClO_4 is due to the net reaction



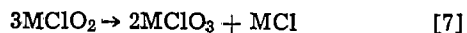
The expected electron:oxide ratio was obtained but not the expected electron:chlorate ratio. This is not surprising considering the various decomposition and disproportionation reactions that may occur in molten chlorates and perchlorates (1). The Li_2O produced in the electrode reduction reaction can have a large catalytic effect on the decomposition reaction (1, 4). For example, we observed that 20g of molten LiClO_4 at 350°C in a quartz container was quite stable until 0.1g of Li_2O was added that produced immediate gassing and complete decomposition of the melt to a white solid (LiCl) within 30 min. The presence of LiClO_3 as an intermediate in the decomposition reaction or the reaction of chlorate with the oxygen produced, $\text{LiClO}_3 + \frac{1}{2}\text{O}_2 \rightleftharpoons \text{LiClO}_4$, could account for variable electron:chlorate ratios. Constant current exhaustive electrolysis experiments involving small amounts of LiClO_4 and LiNO_3 added to LiCl-KCl melts at 390°C indicated that both LiClO_3 and LiNO_2 reduction products react readily with oxygen to regenerate the reactants.

The chemistry of alkali metal nitrates depends greatly upon the nature of the metal cation that is present (7, 8). Increase of the electric field strength (polarizing power) of the cation results in a decrease in overvoltage for the electrochemical reduction. Although the rather high melting points of some of the alkali metal chlorates and perchlorates prevented a systematic investigation of cation effects in these molten oxyhalides, cation effects similar to those observed for molten nitrate reduction are to be expected. For example, the observation that fused NaClO_3 is more difficult to reduce than LiClO_4 (Fig. 2) may be largely due to the weaker electric field of the sodium ion since the electrochemical reduction of molten LiClO_3 apparently occurs readily even at 140°C (5, 6).

For alkali metal chlorates and perchlorates, it is generally observed that the greater the electric field strength of the cation, the lower the temperature at which the compounds begin to decompose (1). Both the thermal decomposition and the electrochemical reduction of molten chlorates and perchlorates require the rupture of Cl-O bonds; thus the positive electric field of a nearby cation apparently weakens such bonds via strong electron withdrawing effects. The equations



represent a mechanism for LiClO_4 reduction that is consistent with the kinetic parameters obtained (Tables I and II) and similar to the mechanism proposed for the reduction of molten LiNO_3 (7). A possible mechanism for chlorate reduction similar to that for perchlorate would involve formation of $(\text{ClO}_2)_{\text{ads}}$ in the slow step followed by reduction to chlorite. Since any chlorite formed in the reduction process would tend to disproportionate with chloride being the final product (1)



the reduction of LiClO_4 could conceivably yield a total of eight electrons per molecule. A six electron reaction has been proposed for the reduction of LiClO_3 (5).

Various metal oxides in addition to Li_2O are capable of increasing the rates of decomposition of chlorates and perchlorates to a considerable extent, and the p-type oxides (MnO_2 , CuO , and NiO) tend to be among the most effective catalysts (1, 14, 15). It has been proposed that the mechanism for the catalytic

decomposition of oxyhalides on p-type oxides involves the transfer of an electron from the adsorbed oxyhalide anion to a positive hole in the oxide (1). After rupture of the Cl-O bonds to form oxygen, the electron is transformed back to the chlorine atom to form Cl^- . Nickel undergoes spontaneous passivation in nitrate melts due to formation of a nickel oxide film (16). Since nickel electrodes also form a dark oxide film in the molten oxyhalide salts (4), the observed gas bubbles formed at the nickel electrode even at open circuit suggests the catalytic decomposition of molten LiClO_4 and NaClO_3 by nickel oxide. On platinum electrodes, the irregular cyclic voltammetric traces produced by gas bubbles seemed to be related to the presence of insoluble Li_2O since the removal of Li_2O from the electrode surface resulted in less gassing and smoother traces.

The effectiveness of nickel electrodes in the electrochemical reduction of molten LiClO_4 is likely related to the catalytic properties of nickel oxide. Both the positive hole of the nickel oxide and the positive electric field of the Li^+ ion could contribute to the weakening of the Cl-O bond of the adsorbed perchlorate. The observation that platinum electrodes are much less effective than nickel electrodes in catalyzing the reduction of molten LiClO_4 is likely related to the noble behavior of platinum with respect to oxide film formation in fused LiClO_4 (4). Studies in condensed phosphates indicate a strong cation effect in the form of $-\text{P}-\text{O}-\text{P}-$ bond weakening by induction (17, 18). The strong polarizing power of the lithium ion probably plays an important role in the oxidation of nitrite ions in molten LiClO_4 (19).

Explosive reactions may occur following the deposition of lithium metal at the cathode in molten LiClO_4 (4, 20). In our studies, the deposition of lithium metal at a nickel electrode in molten LiClO_4 at 350°C resulted in a sharp explosion shortly after switching the cell to open circuit. However, no explosive reactions were observed in the use of calcium anodes in molten LiClO_4 over a variety of conditions. A passive oxide film offers protection to the solid calcium (mp = 838°C) and isolates it from the molten LiClO_4 , however, stable film formation is not possible with the liquid lithium (mp = 181°C) metal and its contact with the molten perchlorate gives a very unstable condition. Explosion hazards in the handling of sodium chlorate should also be noted (21).

Manuscript submitted Aug. 27, 1980; revised manuscript received Nov. 19, 1980. This was Paper 523 presented at the St. Louis, Missouri, Meeting of the Society, May 11-16, 1980.

Any discussion of this paper will appear in a Discussion Section to be published in the December 1981 JOURNAL. All discussions for the December 1981 Discussion Section should be submitted by Aug. 1, 1981.

Publication costs of this article were assisted by the Naval Weapons Center.

REFERENCES

1. F. Solymosi, "Structure and Stability of Salts of Halogen Oxyacids in the Solid Phase," pp. 16-20, 33-37, 44-54, 126-144, John Wiley and Sons, New York (1977).
2. A. N. Fletcher and D. A. Fine, in "28th Power Sources Symposium," pp. 92-94, Atlantic City, N.J. (1978).
3. R. Gangadharan, P. N. N. Namboodiri, K. V. Prasad, and R. Viswanathan, *J. Power Sources*, **4**, 1 (1979).
4. U. Anders and J. A. Plambeck, *This Journal*, **115**, 598 (1968).
5. S. S. Wang and D. N. Bennion, Paper 132 presented at The Electrochemical Society Meeting, Los Angeles, California, October 14-19, 1979.
6. S. Wang and D. N. Bennion, Paper 556 presented at The Electrochemical Society Meeting, Seattle,

- Washington, May 21-26, 1978.
7. A. N. Fletcher, M. H. Miles, and M. L. Chan, *This Journal*, **126**, 1496 (1979).
 8. M. H. Miles and A. N. Fletcher, *ibid.*, **127**, 1761 (1980).
 9. M. H. Miles and A. N. Fletcher, *J. Appl. Electrochem.*, **10**, 251 (1980).
 10. M. H. Miles, D. A. Fine, and A. N. Fletcher, *This Journal*, **125**, 1209 (1978).
 11. S. Shibata and M. P. Sumino, *Electrochim. Acta*, **20**, 871 (1975).
 12. H. S. Swofford, Jr. and H. A. Laitinen *This Journal*, **110**, 814 (1963).
 13. O. de Nora, P. Gallone, C. Traini, and G. Meneghini, *ibid.*, **116**, 146 (1969).
 14. M. Shimokawabe, R. Furuichi, and T. Ishii, *Thermochim. Acta*, **24**, 69 (1978).
 15. L. W. Collins, *Inorg. Chim. Acta*, **39**, 53 (1980).
 16. A. J. Arvia and N. R. De Tacconi, *Thin Solid Films*, **43**, 173 (1977).
 17. J. L. Copeland and L. Gutierrez, *J. Phys. Chem.*, **77**, 20 (1973).
 18. J. L. Copeland, A. S. Metcalf, and B. R. Hubble, *ibid.*, **80**, 236 (1976).
 19. D. W. James, *ibid.*, **72**, 876 (1968).
 20. K. F. Denning and K. E. Johnson, *Electrochim. Acta*, **12**, 1391 (1967).
 21. J. A. Lamb, *Chem. Br.*, **15**, 125 (1979).

Solid Electrolyte Interphase (SEI) Electrode

II. The Formation and Properties of the SEI on Magnesium in $\text{SOCl}_2\text{-Mg}(\text{AlCl})_2$ Solutions

A. Meitav and E. Peled*

Institute of Chemistry, Tel-Aviv University, Ramat Aviv, Tel Aviv, Israel

ABSTRACT

Magnesium metal immersed in thionyl chloride solutions becomes covered by a passivating layer which has properties of solid electrolyte. The buildup and the electrochemical properties of this layer were studied. Tafel slopes measured on freshly immersed Mg electrodes depend linearly on the apparent thickness of the SEI. The reaction resistance and the differential capacitance, on Mg and W electrodes, were measured by several methods. Values of the electrochemical parameters depend on the bias potential. The metal/solution interfacial capacitance of W electrode is higher by an order of magnitude than that of Mg electrode. This higher capacitance decreases markedly, under cathodic polarization.

The alkali and alkaline-earth metals show no significant corrosion in many strong oxidizing solvents (1). This apparent stability is explained by the existence of a passivating layer (PL), which is formed instantly by the contact of the metal with the solution. This layer consists of some insoluble products of the reaction of the metal with the solution (2-13). It acts as an interphase between the metal and the solution and has the properties of solid electrolyte, through which electrons are not allowed to pass. Therefore, it is called "solid electrolyte interphase (SEI)" (8). The electrochemical behavior of SEI electrodes are primarily governed by the properties of the SEI (8-13). Therefore an understanding of the SEI buildup and the conduction mechanism through it, is of practical and theoretical importance.

It was found that the PL of lithium immersed in thionyl-chloride (TC) solutions consists of lithium chloride crystals (7). The electrochemical properties of lithium in TC were recently investigated (10-11). The resistivity of this layer was found to be ca. 10^8 Ωcm and the apparent resistance was proportional to the SEI thickness. In aged electrodes the linear portion of the polarization (I/V) curves expanded up to 0.5V, indicating Tafel slope greater than 3V. On the basis of these and other results, it was concluded that the rate-determining step (rds) for the deposition-dissolution process of lithium in TC solutions is the migration of lithium cations through the SEI.

The behavior of pure magnesium and magnesium alloys has been reported in Ref. (6, 9, 12, 13). The in-

vestigations deal with TC solutions employing two electrolytes: $\text{AlCl}_3\text{-MgCl}_2$ and $\text{FeCl}_3\text{-MgCl}_2$. It was found that magnesium rapidly corrodes in $\text{AlCl}_3\text{-TC}$ solution, being completely dissolved. However, in solutions saturated with MgCl_2 it practically does not corrode. Magnesium was electrodeposited on a nickel wire in $\text{Mg}(\text{FeCl}_4)_2$ solution (12). However, the electrolysis does not occur according to a simple electrodeposition mechanism. The magnesium deposits only after the nickel cathode has been coated by a PL. This layer is formed during the first period of the electrolysis by electroreduction of TC. The reduction products of TC precipitate on the cathode surface and inhibit the farther electron transfer through the interface. In experiments employing magnesium alloys it was found that the alloying elements affect the growth rate of the SEI, but not the resistivity of the SEI (13).

All these electrochemical measurements employing magnesium and magnesium alloys were taken near the OCP only. The primary goal of this work was to investigate in more details the formation and properties of the PL on magnesium, at OCP and during anodic and cathodic polarization; as well, to study the influence of the surface pretreatment on the electrochemical behavior of the magnesium metal in TC solutions. The second goal was to investigate the metal-solution interfacial properties. As the PL on alkali and alkaline-earth metals in TC forms spontaneously and immediately; the double layer (DL) capacitance of the metal-solution interface cannot be obtained. Therefore an inert tungsten electrode was used and its electrochemical behavior, at OCP and under cathodic polarization, was studied.

* Electrochemical Society Active Member.

Key words: thionyl chloride, magnesium anode, solid electrolyte formation.

Experimental

All solutions were prepared and cells were assembled inside an argon-filled glove box. The Merck zur synthesis TC was twice distilled under vacuum. Fluka puriss AlCl_3 was vacuum sublimed at $120^\circ\text{--}140^\circ\text{C}$ and dissolved in distilled TC. Roc/Ric MgCl_2 (98%) was vacuum dried at $80^\circ\text{--}120^\circ\text{C}$ for 24 hr and dissolved (in 5% excess) in the AlCl_3 -TC solution. Then the TC was pumped out of the solution and another volume of twice-distilled TC was added to the residual electrolyte, to form 0.6M $\text{Mg}(\text{AlCl}_4)_2$ solution. The experimental cell was constructed of three magnesium electrodes or of a tungsten working electrode and magnesium reference and counterelectrodes. A detailed construction of the cell is described in Ref. (12). The standard pretreatment of the magnesium consists of etching the metal (for about 10 sec at room temperature) in 5% HNO_3 (A.R.) and rinsing in distilled water. Then the electrode is fitted into the electrochemical cell, which is evacuated and transferred to the glove box. There, the cell is filled with the solution and the desired experiments are performed. All experiments, with saturated solutions, were carried out in 0.6M $\text{Mg}(\text{AlCl}_4)_2\text{SOCl}_2$.

The reaction resistance was calculated from galvanostatic micropolarization curves at steady state and from a-c measurements. The galvanostatic measurements were performed by a homemade pulse galvanostat with a rise time of about 1 μsec . The a-c measurements were performed with the use of a lock-in analyzer (PAR Model 5204), attached to a PAR Model 173 potentiostat. An IR correction was made in all experiments. All experiments were carried out at room temperature.

The differential capacitance of the magnesium-solution interphase was determined by an a-c method and from the initial slope of the η vs. t transients, using the equation

$$C = \frac{i}{(dv/dt)t \rightarrow 0} \quad [1]$$

The minimum apparent thickness of the SEI (d) was calculated according to the measured differential capacity with the use of the equation for a parallel-plate capacitor and under the assumption that the dielectric constant is 5 (12). The dielectric constant of many calcium and magnesium compounds is about 5-10. The dielectric constant (ϵ) of MgCl_2 was not found in the literature. Moreover, these values of solid-state dielectrics are probably correct for single crystals. The true ϵ value of the polycrystalline MgCl_2 in the SEI may differ from that for a single crystal and should depend on many other parameters. As we have no ways to precisely determine ϵ , it was assumed, as a first approximation, that its value is constant in all experimental conditions. Therefore this calculation gives the minimum apparent thickness of the SEI.

Results

Electrochemical Properties of Magnesium Electrode

Unsaturated solution.—The reaction resistance (R_r) and the calculated thickness of the SEI (d) of a magnesium electrode immersed in a solution unsaturated with MgCl_2 are presented in Fig. 1. The composition of the solution was 1.2M $\text{AlCl}_3 + 0.3\text{M}$ MgCl_2 . A comparison of the calculated resistivity (R_r/d) of a magnesium electrode in a saturated and unsaturated solution vs. the immersion time is shown in Fig. 2. The magnesium electrode in the unsaturated solution disintegrated almost completely after about 70 hr of immersion in the electrolyte.

Surface pretreatment.—Under the described experimental conditions, the magnesium electrode introduced into the cell is covered by a thin oxide film. In order to investigate the possible dependence of the electrochemical properties of the magnesium on the primary

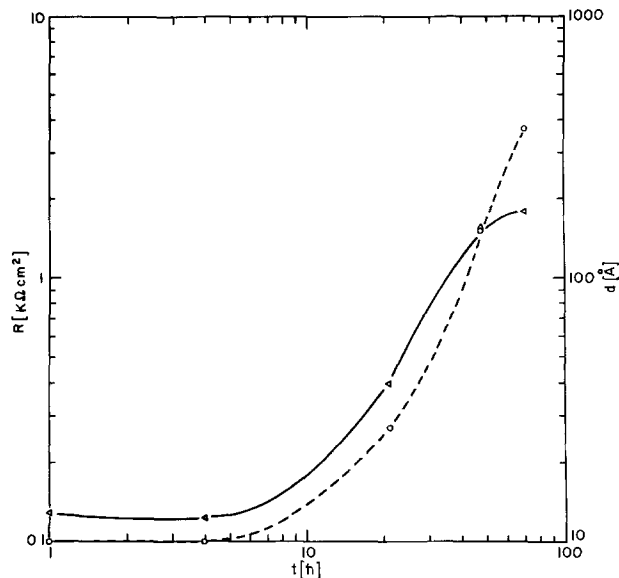


Fig. 1. Reaction resistance and calculated thickness of the SEI of magnesium electrode in acidic solution (1.2M AlCl_3 -0.3M MgCl_2 - SOCl_2) vs. the immersion time. Δ , Thickness; \circ , resistance.

layer which coats it prior to its immersion in the TC solution, three sets of differently pretreated magnesium electrodes were examined: (i) standard pretreated electrodes, (ii) electrodes pretreated as in (i), followed by 50 hr of immersion in distilled water, (iii) electrodes degreased only. Scanning electron micrographs of the three magnesium electrodes after these pretreatment procedures are shown in Fig. 3-5. The white zones seen in Fig. 4 are the areas from which the hydrogen bubbles were evolved during immersion in water. The SEI resistivity-time plot of these electrodes, immersed in 0.6M $\text{Mg}(\text{AlCl}_4)_2$ solution, are presented in Fig. 6.

A-C measurements.—The differential capacity of magnesium electrode was measured as a function of time by an a-c technique, while constant anodic or cathodic overvoltages were applied. The a-c frequency was 100 Hz and rms amplitude was 30 mV. The d-c

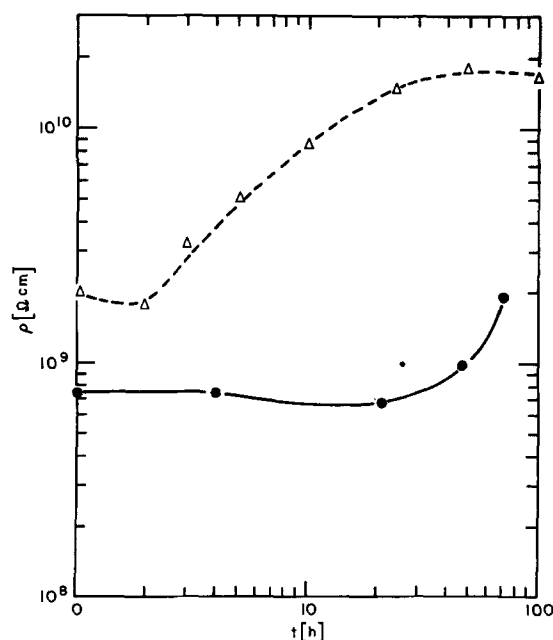


Fig. 2. The resistivity of the SEI of magnesium in saturated and unsaturated (acidic) solutions vs. the immersion time. Δ , Saturated solution, 0.6M $\text{Mg}(\text{AlCl}_4)_2$ TC; \circ , unsaturated solution, 1.2M AlCl_3 -0.3M MgCl_2 - SOCl_2 .



Fig. 3. SE micrograph of a magnesium electrode pretreated by standard procedure. Magnification 500X. The line drawn on the picture presents length of 20 microns.

current and the differential capacitance during anodic polarizations of 50, 100, 200, and 300 mV are presented in Fig. 7 and 8. Figure 9 shows a-c differential capacity and d-c currents for cathodic overvoltages of 100, 200, 300, 800 mV. Passage of high cathodic currents is possible only if the cathodic polarization follows a previously applied anodic macropolarization. Under these experimental conditions the cathodic currents are much higher and a rapid gas evolution and a yellow precipitate on the cathode are observed. A marked increase in resistance and decrease in capacity are observed after such a polarization.

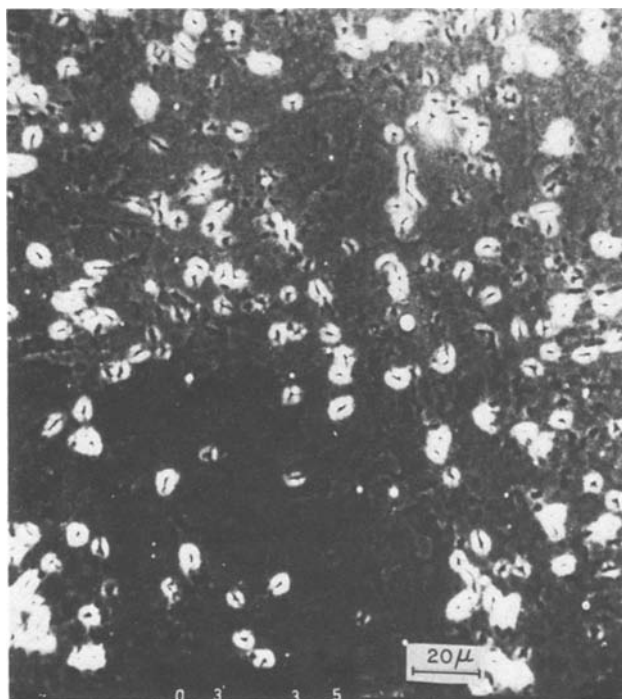


Fig. 4. SE micrograph of a magnesium electrode held for 50 hr in distilled water, after the standard pretreatment. Magnification 500X. The line drawn on the picture presents length of 20 microns.

Tafel plots.—With short current pulses it was possible to obtain Tafel plots for electrodes which were im-

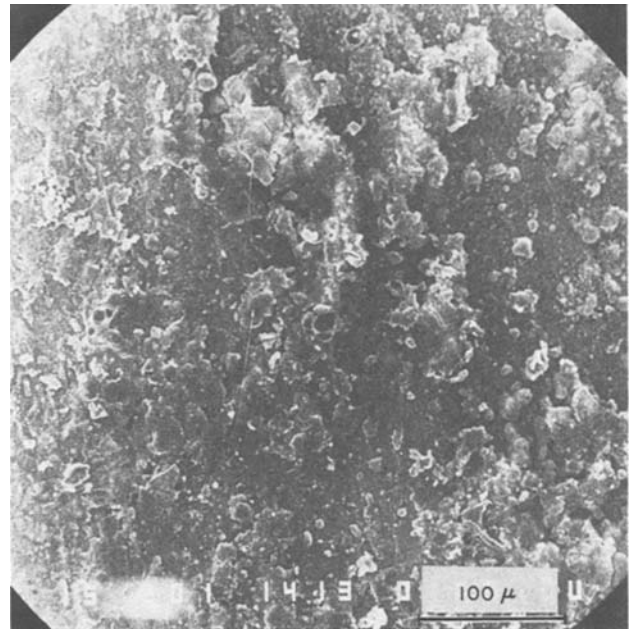


Fig. 5. SE micrograph of a magnesium electrode degreased only. Magnification 300X. The line drawn on the picture presents length of 100 microns.

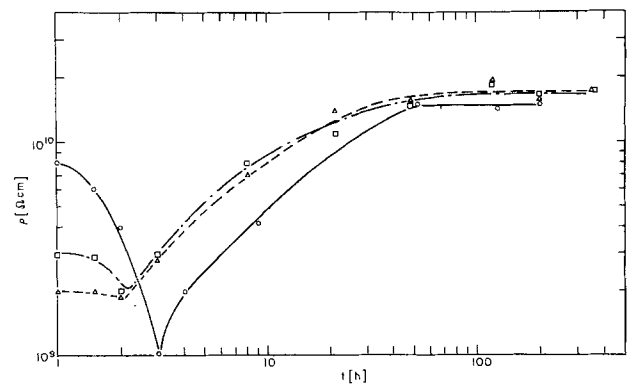


Fig. 6. Resistivity of three different pretreated magnesium electrodes vs. immersion time in 0.6m $Mg(AICl_4)_2$ TC solution. Δ , Standard pretreated electrode; \square , electrode immersed in distilled water for 50 hr, after standard pretreatment; \circ , electrode degreased only.

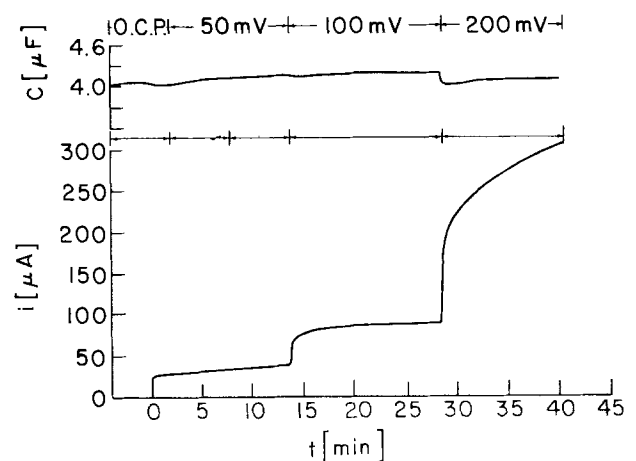


Fig. 7. D-C current and differential capacitance during application of anodic overvoltages of 50, 100, and 200 mV on magnesium electrode. The electrode area is 2.2 cm².

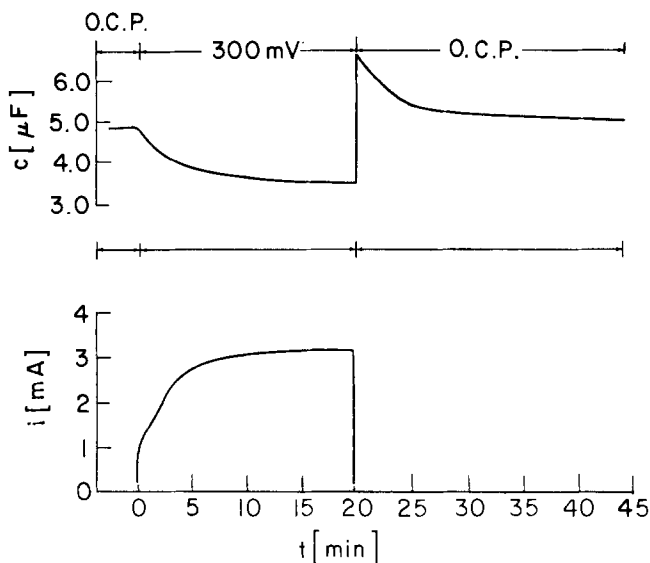


Fig. 8. D-C current and differential capacitance during application of anodic overvoltage of 300 mV on a magnesium electrode. The electrode area is 2.2 cm².

mersed in 0.6M Mg(AlCl₄)₂ solution, for up to 40 hr. The plots are shown in Fig. 10. The plots were obtained after different times of immersion: 1, 20, and 40 hr. The Tafel slopes are 280, 350, and 430 mV, respectively. On polarizing magnesium electrodes immersed for longer periods of time, the Tafel plots deviate from linearity (on a semilogarithmic scale). The linear portion of the η vs. i curves measured for electrodes immersed for longer periods of time reaches up to 300 \pm 100 mV.

Electrochemical Properties of Tungsten Electrode

The OCP of tungsten in 0.6M Mg(AlCl₄)₂ TC solutions is about 1.9V vs. Mg reference electrode (RE). The differential capacitance and the reaction resistance of the tungsten electrode were measured by an a-c technique, in the frequency range of 40-1500 Hz. In this frequency range the differential capacitance did not depend significantly on the frequency, its value at OCP being about 30 μ F/cm². Figure 11 shows two successive cyclic voltammograms at 500 mV/sec sweep rate. It should be noted that the cathodic current maximum of the first sweep disappears on the succeeding one. However, a current maximum does appear on the succeeding sweep when the sweep rate is decreased (smaller than 0.3 V/sec).

The current maximum observed on the first potential sweep rises as the sweep rate is increased. However, when the sweep rate is reduced a new cathodic

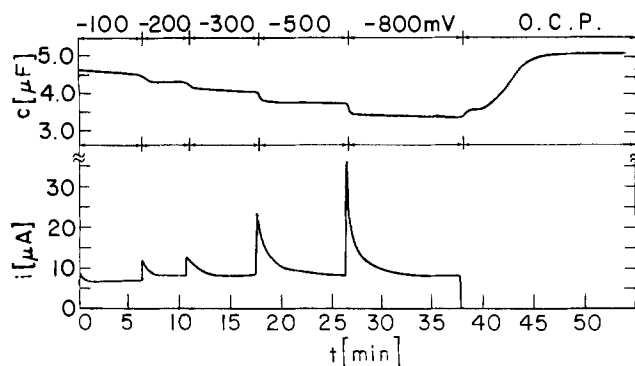


Fig. 9. D-C current and differential capacitance during application of cathodic overvoltages of 100, 200, 300, and 800 mV on a magnesium electrode. Electrode area 2.2 cm².

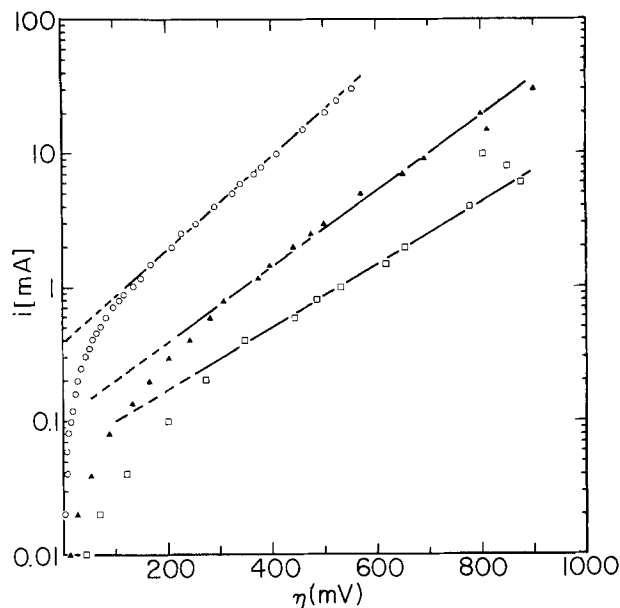


Fig. 10. Tafel plots of magnesium electrode immersed for 1, 20, and 40 hr in 0.6M Mg(AlCl₄)₂ TC solution. \circ , 1 hr; Δ , 20 hr; \square , 40 hr. The electrode area is 2.2 cm².

current peak is detected on the backward potential scan (i.e., going from 0 to 1.8V vs. MgRE). This is peak B in Fig. 12. Figure 12 shows cathodic d-c current (dashed line) and the interfacial capacitance as a function of an applied potential scanned at a rate of 2 mV/sec. It should be noted in Fig. 12 that the decrease of the cathodic current (after passing the peak) is associated with a sharp decrease of the electrode capacitance.

Supplementary to the a-c technique, the differential capacitance, at the tungsten-TC interface, was calculated from the I-V plots which were obtained at high sweep rates, in the potential range 2.0-1.8V vs. Mg RE. In this range the currents are mainly capacitive, Fig. 13.

The capacity values obtained at different sweep rates are presented in Table I.

Discussion

Formation and properties of the SEI.—It should be emphasized that the system investigated is thermodynamically unstable and the apparent stability is due to the kinetic properties of the system. These properties are directly dependent on the SEI features which are determined by: (i) thickness, porosity, and adhesion; (ii) electronic and ionic transference numbers (t_{e^-} , $t_{cath.}$, t_{anodic}); and (iii) ionic mobility. The main factors determining the ionic conductivity are the type of the structural defects (Frenkel, Schottky) and their concentration.

According to this work it seems that it is possible to define two different states of the magnesium SEI

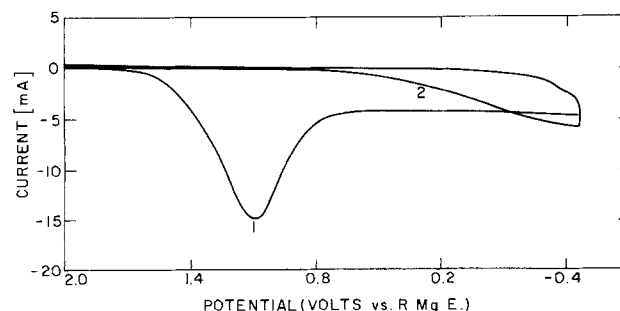


Fig. 11. Two successive voltammograms on tungsten electrode. Sweep rate 500 mV/sec. Electrode area 1.7 cm².

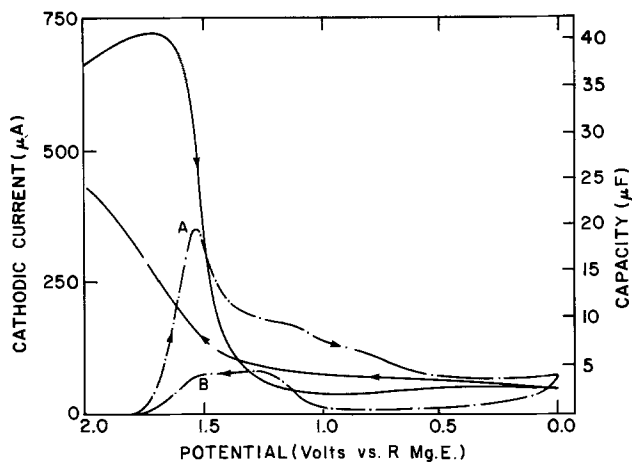


Fig. 12. Current and a-c capacitance vs. potential applied on tungsten electrode. Potential sweep rate 2 mV/sec. Electrode area, 1.7 cm². — current, — — — a-c differential capacitance.

electrode: (i) Electrodes that are held under OCP condition for sufficiently long durations (50 hr or more). Under these "steady-state" conditions, the SEI would have the relatively highest integrity and compactness. Consequently, the ionic and electronic conductivities will have the minimum intrinsic value. (ii) Electrodes handled under nonsteady-state conditions, such as: (a) acidic solutions, (b) freshly immersed electrodes, and (c) continuous heavy anodic polarization.

In all these circumstances the SEI is relatively thinner and may have a highly disordered structure, which leads to high ionic and electronic conduction.

In acidic solutions (excess of AlCl₃), the corrosion rate of magnesium is much higher than in neutral solutions (saturated with MgCl₂). Accordingly, the apparent electrode resistance and the calculated resistivity (Fig. 2) are smaller by an order of magnitude than their values in neutral solutions. This may result from the continuous process of redissolving of the precipitated corrosion product (MgCl₂).

The behavior of magnesium in saturated solution during the first hours of immersion is very similar to its behavior in the unsaturated solution. The resistivity, during the first 3 hr, does not differ much from the values in the unsaturated solution. It seems that in both cases the same process of dissolution of the PL establishes these relatively low values. It is possible that these lower values are accompanied by a high rate of corrosion. During this process there is a rearrangement of the surface layer on the immersed electrode. The oxide layer dissolves and a new (most likely MgCl₂) layer is built up. The formation of the MgCl₂ is thermodynamically preferred over MgO by 35 kcal/mole (MgO + SOCl₂ → MgCl₂ + SO₂ - 35 kcal/mole).

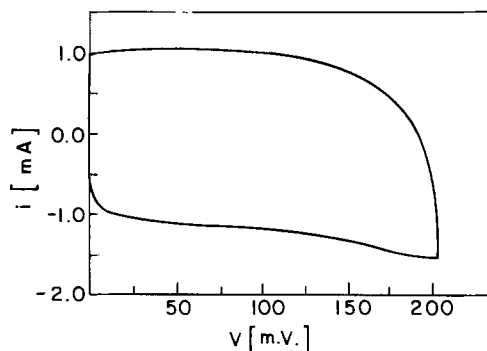


Fig. 13. *I*-*V* curve on tungsten electrode, obtained at sweep rate 20 V/sec in the potential range 2-1.8V vs. MgRE (Recorded on oscilloscope.)

Table I. The differential capacitance calculated from double layer charging currents, at different potential-sweep rates

| Sweep rate (V/sec) | 0.2 | 20 | 100 | 200 | 500 | Average |
|--------------------------------|-----|----|-----|-----|-----|---------|
| Capacity (μF/cm ²) | 24 | 29 | 26 | 24 | 24 | 25 ± 1 |

This exchange process causes a very defective interphase, which has a highly disordered structure. However, with the growth of the MgCl₂ layer, the corrosion ceases, the layer becomes more compact and ordered, and the resistivity reaches its steady-state value. This proposed mechanism of film exchange, on freshly immersed electrodes, is also supported by several other experimental results:

1. The original state and composition of the magnesium surface film has no influence on the SEI properties after 30-50 hr of immersion.

2. The resistivity of magnesium electrodes which are covered by a thick oxide layer (Fig. 4) falls by almost an order of magnitude during the first 2-5 hr of immersion. Then it passes through a minimum and increases slowly for 40-60 hr, until it reaches an almost steady-state value of $(1.8 \pm 0.2) \times 10^{10} \Omega \text{cm}$.

3. The OCP of magnesium vs. tungsten increases by about 0.2V, within the first few days. The lower OCP during this time may be caused by the high corrosion rate.

Deposition-dissolution mechanism of the SEI magnesium electrode.—From the significantly different electrochemical behavior of the magnesium electrode during cathodic and anodic macropolarization, it appears that the anodic and cathodic processes are essentially different. In the anodic process, the dissolution of the metal beneath the PL causes a process of breakdown and repair of the SEI. This process becomes faster as the dissolution current is increased. As a result, a very disordered SEI is formed which has a high ionic (and probably electronic) conductivity. However the SEI cannot be completely removed by anodic dissolution. It was found that a current density of 5 mA/cm² passed for 1 hr (which removed about 13 microns of magnesium) did not have significant influence on the differential capacity. It does not exceed 2 μF/cm² during the anodic-dissolution and does not exceed 4 μF/cm² immediately after turning off the current. The calculated thickness of the SEI during this polarization was ca. 25Å. These capacitance values are much lower in comparison with 25-30 μF/cm², the tungsten-solution interfacial capacitance.

As opposed to anodic-dissolution experiments, under cathodic polarization, the d-c current and the electrode capacitance remain almost unchanged as the cathodic overvoltage is increased up to -800 mV vs. Mg RE. On stepping the potential more cathodically there are some transient phenomena which are not observed on anodic polarization (Fig. 9). These indicate that under prolonged cathodic polarization there is some kind of blocking mechanism. The relatively low cathodic currents measured prove that the SEI remains quite a good electronic insulator even under such high electric fields (10⁶ V/cm). Only a previously applied anodic macropolarization enables passage of relatively high cathodic currents, which are accompanied by a rapid gas evolution and a yellow precipitate (probably SO₂ and S) on the electrode. A possible explanation for these phenomena is as follows: the pre-applied anodic macropolarization decreases markedly the thickness of the SEI and enhances its electronic and ionic conductivity. Under these conditions, in a subsequent high cathodic polarization, a direct reduction of the TC solvent can take place. Supplementary to this, under high electric field, the magnesium cations may be reduced within the SEI, without reaching the metal-solid electrolyte interface. The precipitated metallic magnesium may cause a short-circuit through the SEI thus markedly enhancing the direct reduction of TC.

Tafel slopes.—High Tafel slopes are a well-known phenomena in literature dealing with oxide films (14, 15). The explanation for these phenomena involves the basic assumption that a major fraction of the applied metal-solution overpotential falls across the PL. The same may be expressed differently by saying that the rds of the redox reaction is the migration of the ions through the SEI. Accordingly the current-voltage relation should obey the law of migration of ions in a solid electrolyte, while the Tafel slope (b) depends on thickness (d) of the SEI according to Eq. [2]

$$b = \frac{2.3RT}{azF} \cdot d \quad [2]$$

where $2a$ is the jump distance of the mobile ion and z is the valence of the mobile ion.

In this work it was found that for aged magnesium electrodes there is a linear relationship between the overpotential and the current, up to 300-400 mV. This indicates that the Tafel slope is higher than 2V. However to reach the Tafel region it was possible only for freshly immersed electrodes. In these cases Tafel slopes depend on immersion time. These results support a previous conclusion that the rds is the migration of Mg^{2+} ions in the solid electrolyte. The SEI thickness calculated from the Tafel slopes correlated well with the thickness calculated from the differential capacity (Table II). However, good correlation was observed only on freshly immersed electrodes. Tafel curves obtained on electrodes immersed for longer times deviate from linearity. This occurs as a result of the necessity to pass higher currents in order to reach the Tafel region. These currents partially destroy the SEI structure.

Tungsten Electrode

The interpretation of the electrochemical measurements performed on active metal electrodes coated by a passivating layer, which is a poor electronic conductor, is based on the following assumptions: (i) the rds of charge transfer is the ion migration through the SEI and (ii) the double layer capacities of the two interfaces, metal-SE and SE-solution, are much higher than the SEI capacity. Only under these conditions would the apparent resistance and capacity represent the properties of the SEI.

The spontaneous formation of PL on alkaline-earth metals prevents the possibility of carrying out any electrochemical measurements at the metal-solution interface. Employing the "inert" tungsten electrode permitted the determination of the DL capacitance of the metal-TC interface. With the use of an a-c technique the differential capacity of the metal-solution interface at OCP was found to be about $30 \mu F/cm^2$. The values of the DL capacity calculated from DL charging currents are in perfect agreement with the values obtained in the a-c measurements. The small increment of the capacity in the first 200 mV of the cathodic overvoltage (Fig. 12) may result from specific adsorption, since in this potential range the faradaic current is negligible. Comparison of these values with the differential capacity measured for magnesium ($2-0.1 \mu F/cm^2$) clearly indicates the existence of the PL on magnesium and underlines the basic difference between the "bare" tungsten electrode and the "covered" magnesium. In $Mg(AlCl_4)_2$ solution saturated with $MgCl_2$, the chloride produced by the reduction of TC

($2SOCl_2 + 4e \rightarrow SO_2 + 4Cl^- + S$) may precipitate as $MgCl_2$ on the tungsten electrode and form a PL. This PL has a low electronic conductivity and so it slows further reduction of the solvent. The significant decrease of the capacitance [to $1.6 \mu F/cm^2$ (Fig. 12)] and the appearance of a current maximum are due to the above-mentioned process. When potential returns to the OCP, the capacitance rises to about its initially high value (Fig. 12). It would appear that a slow chemical dissolution of the PL occurs in parallel with the reduction of the solvent. These two opposing processes (formation and dissolution) determine the dependence of the reduction current on the sweep rate. If two consecutive voltammograms are performed at high sweep rates, the PL formed is not dissolved at the end of the first sweep. Consequently, it completely inhibits a further solvent reduction on the second sweep (Fig. 11). However, on slow scanning of the potential the PL has enough time to dissolve, thus enabling further solvent reduction in the second sweep, or even in the reverse direction of the first one. The small cathodic current peak on the reverse branch (Fig. 12) is due to this process.

The apparent resistivity of the PL on tungsten is $(0.5-1) \times 10^{10} \Omega cm$ (assuming the same ϵ as for magnesium electrode). These values correlate quite well with the steady-state resistivity of the SEI on magnesium $(1-2) \times 10^{10} \Omega cm$.

The thickness of the PL on tungsten was calculated by two independent methods: (i) from the reduction charge, passed during the cathodic sweep and (ii) from the differential capacitance.

Because of the chemical dissolution of the PL, the "efficiency" of the PL formation depends on the sweep rate. Figure 14 shows the thionyl chloride reduction charge vs. the sweep rate. The two curves show the charge passed up to the peak of the reduction current and up to the plateau (0.5 vs. Mg RE). It can be seen that the charge reaches a constant value at high sweep rates. It was found that the solvent reduction is inhibited by the formation of a PL of 30-40Å thickness ($1.5-2$ mcoulomb/cm²). This value corresponds quite well with the electron-tunneling path in insulators (16), the thickness of passivating oxides (at Vp) in aqueous solutions (17), and with the minimum thickness of the SEI on magnesium. The reduction ceases almost completely as the thickness reaches 80-90Å ($4-4.5$ mcoulomb/cm²).

The thickness of the PL on tungsten electrode, which is calculated according to the interfacial capacitance assuming $\epsilon = 5$, do not differ significantly from that calculated according to the cathodic charge (Fig. 14).

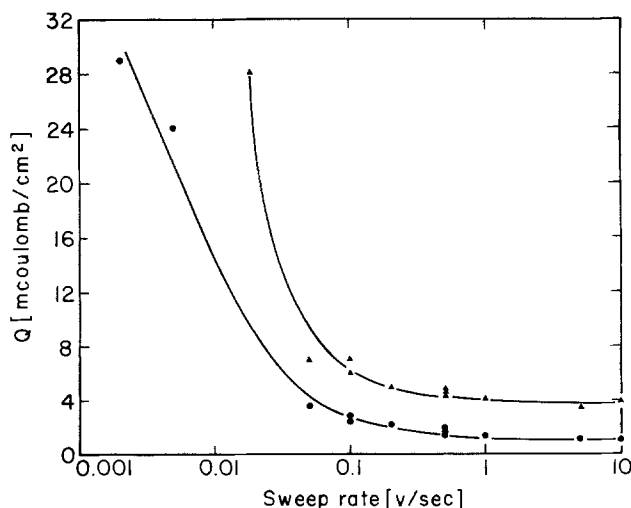


Fig. 14. Reduction charge passed during cathodic potential sweep vs. the sweep rate. ● Charge passed up to the peak of the reduction current. ▲ Charge passed up to the plateau.

Table II. The SEI thickness calculated from Tafel and capacity data

| Immersion time (hr) | 1 | 20 | 40 |
|--|-----|-----|-----|
| Tafel slope (mV) | 280 | 350 | 430 |
| Thickness [Å]* based on Tafel data | 19 | 23 | 29 |
| Thickness [Å]** based on capacity data | 17 | 24 | 30 |

* The thickness was calculated according to Eq. [2], where it was assumed that $a = 2\text{Å}$ and $z = 2$.

** The dielectric constant was assumed to be 5.

The corresponding values are 30 and 80-90Å, respectively. The discrepancy of these values is attributed to the two different experimental methods. SEM studies pointed out that the surface of the PL on magnesium is very rough. The PL formed on tungsten may be rough too. The interfacial capacitance is mainly contributed by the thinner parts of the layer. Consequently, the calculated thickness, according to the interfacial capacitance, is smaller than the geometric average value [for details see Ref. (11)], which is calculated from the passivating charge. So, the above-mentioned experimental discrepancy seems quite reasonable. Moreover, in addition to the results of Tafel experiments, it points out that the assumed value of the dielectric constant is quite suitable for these systems.

Acknowledgments

We wish to express our appreciation to the French Friends of Tel-Aviv University (AFAUTA) who partially supported this work.

Manuscript submitted May 29, 1980; revised manuscript received Nov. 13, 1980.

Any discussion of this paper will appear in a Discussion Section to be published in the December 1981 JOURNAL. All discussions for the December 1981 Discussion Section should be submitted by Aug. 1, 1981.

REFERENCES

1. R. Jasinski and S. Carroll, *This Journal*, **117**, 218 (1970).
2. R. Jasinski, *Coll. Czech. Chem. Commun.*, **36**, 1079 (1977).
3. A. N. Dey, Paper 62 presented at The Electrochemical Society Meeting, Atlantic City, New Jersey, Oct. 4-8, 1970.
4. A. K. Vijh, *Surf. Technol.*, **4**, 401 (1976).
5. G. W. Jackson and G. E. Blomgren, *This Journal*, **116**, 1483 (1969).
6. E. Peled and H. Straze, Abstract 127, 27th I.S.E. Meeting, Zurich, Switzerland (September 1976).
7. A. N. Day and C. R. Schlaikjes, 26th Power Sources Symposium (1974).
8. E. Peled, *This Journal*, **126**, 2047 (1979).
9. A. Meitav and E. Peled, 30th I.S.E. Meeting, Trondheim (Aug. 27-31, 1979).
10. E. Peled and H. Yamin, Proceedings of the 28th Power Sources Symposium (1978).
11. E. Peled and H. Yamin, *Israel J. Chem.*, **18**, 131 (1979).
12. E. Peled and H. Straze, *This Journal*, **124**, 1030 (1977).
13. E. Peled and A. Meitav, Paper 554 presented at The Electrochemical Society Meeting, Seattle, Washington, May 21-26, 1978.
14. A. K. Vijh, in "Electrochemistry of Metals and Semiconductors," Chap. 6, Marcel Dekker, Inc., New York (1973).
15. L. Young, in "Anodic Oxide Films," Academic Press, New York (1961).
16. Y. Coutts, "Electrical Conduction in Thin Metal Films," Chap. 2, Elsevier Scientific Publishing Co., London (1974).
17. J. W. Diggle, in "Oxide and Oxide Films," Vol. 1, p. 42, Marcel Dekker, Inc., New York (1972).

Ohmic Potential Drop in Flow-Through and Flow-By Porous Electrodes

Peter S. Fedkiw*

Department of Chemical Engineering, North Carolina State University, Raleigh, North Carolina 27650

ABSTRACT

The limiting current analysis has been applied to the flow-through and planar flow-by porous electrodes using a recently developed low flow rate mass transfer coefficient correlation. At the limiting current, the maximum ohmic drop in the solution is developed. The flow-through electrode analysis is identical to that first given by Bennion and Newman. In the flow-by electrode, the two-dimensional structure of the potential field is taken into account. It is shown that given a maximum solution ohmic potential drop and reactant conversion, a flow-by electrode with an aspect ratio $L/d > 5$ is superior to a flow-through electrode in that the maximum processing rate will always be higher for the range of parameters presented in this work. If the aspect ratio L/d (length-to-width) of the flow-by electrode is large, it is reasonable to assume that the potential field is governed by a one-dimensional Laplace equation. This simplifying assumption has been examined and shown to overestimate the maximum ohmic potential drop. Given the two constraints mentioned above, a flow-by electrode will have an optimum aspect ratio L/d which is determined by an economic balance between greater current-volume of the bed as L/d increases vs. greater pumping and separator (if required) costs which also increase with L/d .

Packed bed electrodes (three-dimensional) have the major advantage of large surface area available for reaction per unit volume of the reactor in comparison to the more conventional flat (two-dimensional) electrode configuration. The reaction distribution in packed beds can vary significantly, however, because of ohmic, geometric, and mass transfer effects; this can become an undesirable problem. The spatial variation in reaction rates is accompanied with a consequential variation in the potential difference between the electrode

and adjacent electrolyte. The reaction selectivity and and reactant conversion may become significantly affected in a multiple step (parallel or series) reaction network (1-5).

An upper bound can be determined on the solution phase potential variation by analyzing the current distribution in a bed with a single reaction taking place under mass transfer controlled conditions. An upper bound is established because the rate of any reaction cannot exceed the rate of its reactant supply.

The purpose of this paper is to examine the solution phase potential variation in a packed bed electrode

* Electrochemical Society Active Member.

Key words: current, flow-by electrode, potential.

operating with a single reactant under mass transfer controlled conditions. Two configurations of the packing of the electrode are considered and compared (Fig. 1): (i) the flow-through electrode where the current and fluid flow are parallel (fluid flows through the current collector) and (ii) the flow-by electrode configuration where the current and fluid flow are approximately perpendicular (fluid flows by the current collector). Focus is fixed on a single packed bed electrode in the cell, that is, it is assumed that the counter-electrode effects can be ignored.

The limiting current analysis as outlined here cannot, of course, determine absolute electrochemical driving potentials at any position in the bed. Other information such as the specific kinetics of the reaction (or reaction sequence) must be known. To incorporate such effects into an analysis of the electrode adds complexity to the resulting model equations. (A short review of previous detailed analysis is presented in the following paragraph.) The limiting current analysis is useful because of its simplicity, and it enables a first-order engineering design of the reactor to determine maximum permissible flow rate and packing depth (parallel and/or perpendicular to current flow) as was shown by Newman and Tiedemann (6) for the flow-through electrode.

Bennion and Newman (7) first analyzed the flow-through configuration using the limiting current deposition of Cu^{++} as a test reaction. They derived an analytical expression (assuming convective transport of reactant only) which related the solution phase ohmic potential drop to the physical and operational parameters. [Other workers have rederived this result as reviewed in Ref. (6). In this same reference, Newman and Tiedemann expanded the earlier work to account for axial dispersion.] Alkire and Ng (8,9) have studied extensively the flow-by electrode configuration. These publications were mostly concerned with calculating the spatial reaction distribution and reactant conversion with a single electrode reaction. Some attention was directed at evaluating the maximum potential variation under limiting current conditions (9). However, it was assumed that the potential varied strongly in the direction perpendicular to the fluid flow only.

A recently developed correlation (10) for low Reynolds number mass transfer coefficients will be applied in the governing equations in this work in order to calculate the solution phase potential drop. The results

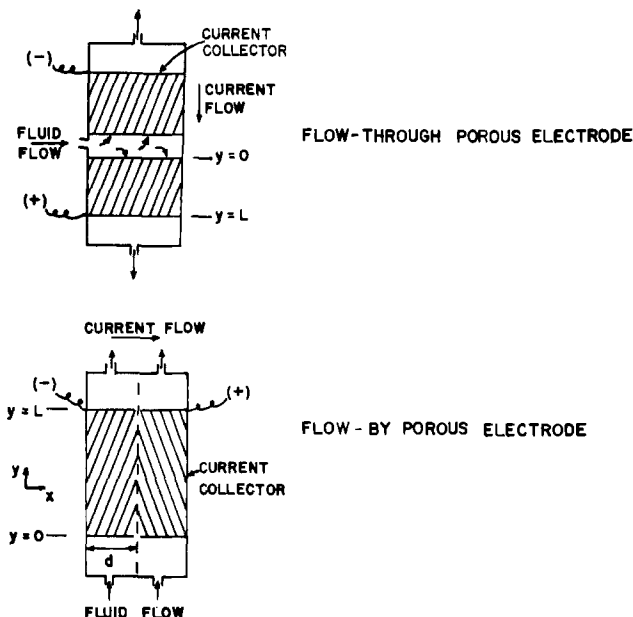


Fig. 1. Flow-through and planar flow-by electrode configurations with both packed bed working and counterelectrodes.

are expressed in terms of the relevant dimensionless parameters of the system. In addition, the two-dimensional Laplace equation is solved to describe the potential variation in the flow-by electrode. The conditions under which the one-dimensional approximation used by Alkire and Ng is valid is also examined. It is shown that neglect of the two-dimensional structure will overestimate the solution phase potential drop.

Model Formulation

It is assumed that the packed bed can be modeled as a superposition of two continuum. The reaction rate term then appears as a pseudo sink or source term in the species and charge conservation equations (11). It is also assumed that a single reaction takes place in a well-supported electrolyte at the limiting current under steady-state conditions. This reaction is written in a general form as



The reactive species of molar concentration C is transported through the electrode by convective means only. The dispersive flux is assumed negligible. Under the above conditions the equations which govern the concentration and potential are

$$v \frac{dc}{dy} = -ak_m C \quad [2]$$

$$-\kappa \nabla^2 \phi_2 = \frac{nF}{s_R} ak_m C \quad [3]$$

Both equations apply to the flow-through and flow-by electrodes. The conductivity κ has been corrected from its free stream value κ_0 and is assumed to be much less than the matrix conductivity, thus the matrix is isopotential. The mass-transfer coefficient k_m depends on the velocity v , the diffusivity of the reactive species, and the packing geometry. For both electrode geometries, we shall examine the solution to each of these equations under appropriate boundary conditions.

Flow-Through Electrode

The solutions to Eq. [2] and [3] for this geometry have been given by Bennion and Newman. They assumed that the potential varies only in the streamwise direction and hence, only second-order derivatives of the potential with respect to the streamwise coordinate appear on the left-hand side of Eq. [3]. The boundary conditions on the potential depend on the placement of the counterelectrode which can be placed upstream or downstream of the fluid inlet to the bed. Assume an upstream counterelectrode with the reference potential set at the solution phase entrance to the bed; the boundary conditions become

$$y = 0 \text{ (fluid inlet) } C = C_F, \phi_2 = V \quad [4a]$$

$$y = L \text{ (fluid exit) } \frac{\partial \phi_2}{\partial y} = 0 \quad [4b]$$

In dimensionless form the solution to Eq. [2], [3], and [4] for the concentration and potential can be written

$$\frac{C}{C_F} = \exp \left(-\frac{aL}{\epsilon} \frac{\text{Sh}_B}{\text{Pe}_B} \frac{y}{L} \right) \quad [5]$$

$$\Delta \phi_2 \equiv \frac{\phi_2 - V}{-\epsilon n F D_0 C_F} = \left\{ \frac{\text{Pe}_B^2}{\text{Sh}_B} + \frac{aL}{\epsilon} \text{Pe}_B \frac{y}{L} \right. \\ \left. \exp \left[-\frac{aL}{\epsilon} \frac{\text{Sh}_B}{\text{Pe}_B} (1 - y/L) \right] \right\} \\ \exp \left[-\frac{aL}{\epsilon} \frac{\text{Sh}_B}{\text{Pe}_B} \frac{y}{L} \right] - \frac{\text{Pe}_B^2}{\text{Sh}_B} \quad [6]$$

In order to calculate accurate conversions and potential drops, it is necessary to have accurate values for the dimensionless mass transfer coefficient Sh_B (bed Sherwood number).

Equation [6] is a special case of the more general relationship derived by Newman and Tiedemann (6) who did not neglect the axial dispersive term for the reactant in Eq. [2]. However for most cases of practical importance, inclusion of dispersion only adds a minor correction.

The concentration profile (Eq. [5]) is independent of the counterelectrode placement at the limiting current. However, the solution phase potential drop is highly sensitive to the counterelectrode placement. When the counterelectrode is placed downstream of the fluid exit at the limiting current, it can be shown that the potential drop across the solution from the front to the back of the electrode asymptotically increases linearly with the packing depth (6). [Trainham and Newman (12) have recently analyzed the effect of counterelectrode placement on reaction rate distribution below the limiting current.] Since the potential drop continually increases with an increase of bed length, we shall concentrate on the flow-through electrode with an upstream counterelectrode placement.

Flow-By Electrode

Because the fluid and current flow are not parallel in this electrode configuration, the analysis of the potential field is more complex than that in the flow-through electrode. We shall assume that $L/d \geq 1$ and furthermore that the bed shown in Fig. 1 is of infinite extent in the direction which is mutually perpendicular to the current and fluid flow. The potential will vary only in the x and y coordinates. The concentration profile within the reactor will be a function only of the streamwise coordinate, a direct consequence of the limiting current assumption. (Below the limiting current the concentration will vary in the x direction.) If the dispersive flux of reactant is neglected, the concentration profile is still given by Eq. [5]. The potential will satisfy

$$\frac{\partial^2 \phi_2}{\partial x^2} + \frac{\partial^2 \phi_2}{\partial y^2} = - \frac{nFak_m C_F}{s_R \kappa} e^{-\frac{ak_m}{v} y} \quad [7]$$

subject to the assumed boundary conditions

$$y = 0, \frac{\partial \phi_2}{\partial y} = 0 \quad [8a]$$

$$y = L, \frac{\partial \phi_2}{\partial y} = 0 \quad [8b]$$

$$x = 0, \frac{\partial \phi_2}{\partial x} = 0 \quad [8c]$$

$$x = d, \phi_2 = V \quad [8d]$$

Any packing material must be physically supported at the bottom of the bed ($y = 0$). A compression-type support at the top of the bed ($y = L$) is usually used to restrain the bed from expanding under the stress of the flowing fluid and to ensure good interparticle contact. Both of these supports must be porous for the fluid to pass through. It is assumed that the effective conductivity of the fluid in these porous supports is much less than the effective conductivity of the fluid in the bed. Under these circumstances, little current can flow through these supports which accounts for boundary conditions [8a] and [8b]. No current leaks out the back side (farthest away from the counterelectrode) which gives Eq. [8c]. The final boundary condition [8d] assumes that either the conductivity of the counterelectrode compartment is much larger than that of the working electrode, or that the counterelectrode is very near the separator. Under these conditions

the potential on the counterelectrode side of the electrode will be uniform. The Appendix examines this assumption in more detail. For a bed of large aspect ratio L/d , it is shown that the potential at $x = d$ is not constant in the streamwise direction. Since more current flows to the region of the bed near $y = 0$, the potential along $x = d$ must be less than V due to the ohmic drop. However, the solution potential drop across the working electrode is seen to be independent of the counterelectrode separation.

Equations [7] and [8] have been solved by superposition of a particular solution and three Fourier-series type homogeneous solutions. In a dimensionless form the potential can be written

$$\begin{aligned} \frac{\phi_2 - V}{Sh_B \left(\frac{aL}{\epsilon R}\right)^2} &\equiv \frac{\phi_2 - V}{\frac{-\epsilon n F D_o C_F}{s_R \kappa} Sh_B \left(\frac{aL}{\epsilon R}\right)^2} \\ &= \frac{R^2 e^{-\gamma R y/L}}{(\gamma R)^2} + \phi_2^a + \phi_2^b + \phi_2^c \quad [9] \end{aligned}$$

where

$$\phi_2^a = \sum_{n=1}^{\infty} \left[\frac{(-1)^n 2R}{\gamma R \lambda_n^2 \sinh \lambda_n R} \right] \cosh \lambda_n (Y - R) \cos \lambda_n X$$

$$\phi_2^b = \sum_{n=1}^{\infty} \left[\frac{(-1)^{n+1} 2R e^{-\gamma R}}{\gamma R \lambda_n^2 \sinh \lambda_n R} \right] \cosh \lambda_n Y \cos \lambda_n X$$

$$\begin{aligned} \phi_2^c &= \sum_{n=0}^{\infty} \left[\frac{2R^2 / (\gamma R)}{(1 + \delta_{n,0}) \cosh \lambda_n} \right] \\ &\quad \cdot \frac{(-1)^n e^{-\gamma R} - 1}{(\gamma R)^2 + (n\pi)^2} \cosh \lambda_n X \cos \lambda_n Y \end{aligned}$$

where

$$\gamma R = \frac{Sh_B}{Pe_B} \frac{aL}{\epsilon}, \quad \lambda_n = \left(n - \frac{1}{2} \right) \pi$$

$$\hat{\lambda}_n = \frac{n\pi}{R}$$

$$X = x/d$$

$$Y = y/d$$

Alkire and Ng solved Eq. [7] in the limit of $R \rightarrow \infty$ where it is anticipated that all derivatives of potential with respect to the streamwise direction will be zero. Equation [7] with the y derivatives neglected can be solved subject to [8c] and [8d] to yield

$$\begin{aligned} \phi_2 - V &\equiv \frac{\phi_2 - V}{\frac{-\epsilon n F D_o C_F}{s_R \kappa}} \\ &= Sh_B \left(\frac{aL}{\epsilon R}\right)^2 \left(\frac{X^2}{2} - \frac{1}{2}\right) e^{-\gamma R y/L} \quad [10] \end{aligned}$$

Maximum Potential Drop

Equations [6] evaluated at $y = L$ indicates the maximum potential drop for the flow-through electrode. In the flow-by electrode the maximum potential drop will occur at the fluid inlet to the bed where the largest current is flowing. Equation [9] evaluated at $X = 0$, $Y = 0$ gives the maximum potential drop. One may be suspicious of the appropriateness of applying Eq. [10] near the bed inlet due to the validity of its assumptions. Near $y = 0$ we anticipate the existence of a region wherein the streamwise derivatives cannot be neglected, but this is exactly the region in which we are interested in calculating the potential drop. Equation [10] was derived by neglect of all y derivatives. It can be shown by a singular perturbation solution to

Eq. [7] and [8] that the maximum dimensionless potential drop is given as

$$\left[-\frac{1}{2} + 0 \left(\frac{1}{R} \right) \right] \text{Sh}_B \left(\frac{aL}{\epsilon R} \right)^2$$

in the limit of $R \rightarrow \infty$ which conforms to Eq. [10]. Three regions were delineated in the singular perturbation analysis: two inner regions, one near the fluid inlet and the other near the fluid exit of the bed; and a common outer region which encompasses the remainder of the bed.

Mass-Transfer Coefficient

The maximum potential drop will depend on the mass-transfer coefficient. It is important to have an adequate estimate of this quantity in order to calculate both the total reactant consumption and the potential drop.

Packed bed electrodes are usually operated at low fluid velocities. This is particularly true for the flow-through configuration. A recent extensive review (10) of the chemical engineering literature for low velocity, liquid phase mass transfer coefficients showed a sparsity of data and a large variation in the few reported results. Sometimes even conflicting asymptotic trends of the data were reported. An experimental and theoretical program was undertaken to develop a mass transfer coefficient correlation which would be useful for the low Reynolds number regime. Figure 2 is a plot of the resulting correlation in comparison to experimental data. The correlation related Sh_B at creeping flow to the Péclet number and the dimensionless streamwise depth (aL) of the bed. The correlating equation and further details may be found in Ref. (10). This Sherwood number correlation was used in Eq. [6], [9], and [10] to generate the results given in this paper.

Results and Discussion

When comparing the performance of a flow-by electrode to a flow-through electrode, a common basis for the evaluation must be established. Consider the two-electrode configurations with a given equal cross-sectional flow area and volume. Under these two constraints, at a set flow rate, the consumption rate (conversion) of reactant is identical in both reactors. It might seem that the current must traverse a longer path in the flow-through electrode than in the flow-by electrode (recall $L/d \cong 1$), hence a larger ohmic drop must occur in the flow-through configuration. The results of this work demonstrate quantitatively, however, that this is not true for all L/d values. There is a lower limit to this ratio below which it becomes more

advantageous to use the flow-through configuration. Table I lists a comparison between the calculated solution phase ohmic potential drop in the flow-through and flow-by reactors at three values of conversion each at two Péclet numbers. It is seen from this table that a lower limit for L/d exists below which the ohmic potential drop in the flow-through electrode is less than that in the flow-by electrode. It is also seen that this lower limit decreases as the conversion decreases at a given Péclet number. However, for all L/d greater than five in the range of parameters varied in this study, the flow-by electrode was always the preferred choice over the flow-through electrode. This conclusion is expanded on below.

Figure 3 is a plot of the maximum dimensionless ohmic drop in a flow-through electrode as a function of the conversion and Péclet number. Figures 4a, 4b, and 4c are similar to Fig. 3, but are for the flow-by elec-

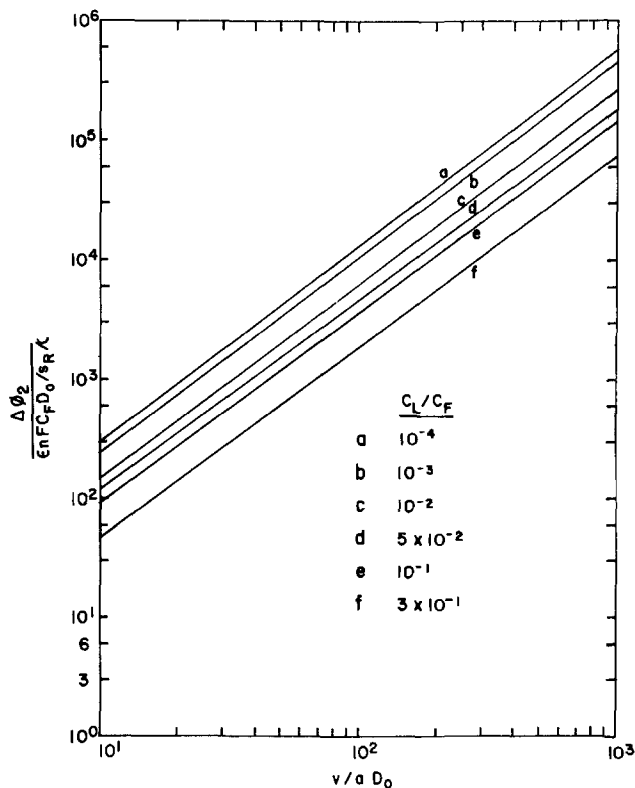


Fig. 3. Maximum solution phase ohmic drop in a flow-through electrode at the limiting current.

Fig. 2. Low Reynolds number mass transfer coefficient correlation. Taken from Ref. (10).

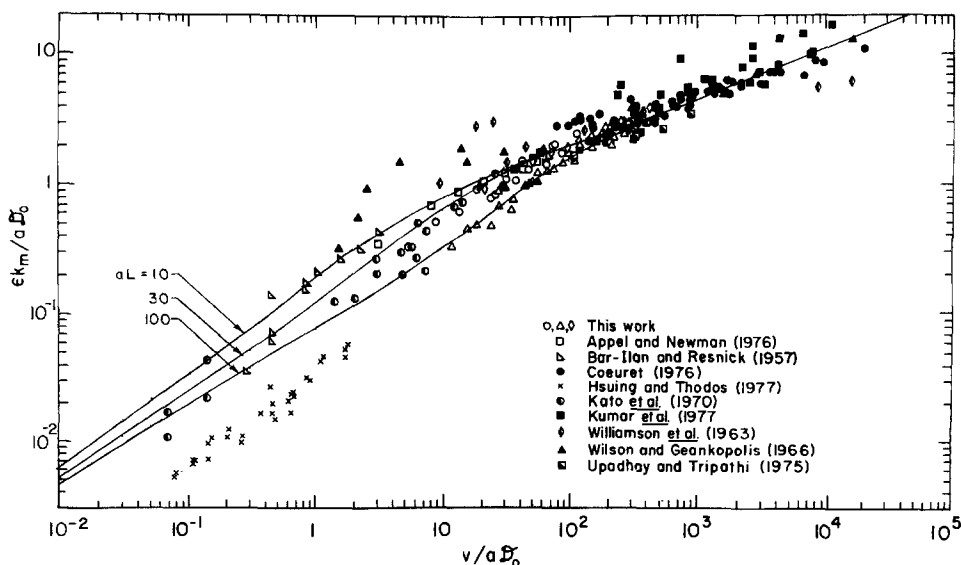


Table 1. Comparison of maximum ohmic potential drop in a flow-through porous electrode to that in a flow-by porous electrode at various aspect ratios

| | | Flow-through | $-\Delta\Phi_2$ | | | | |
|------------------|---------------|--------------|-----------------|--------|--------|-------|-------|
| | | | $L/d = 1$ | 2 | 3 | 4 | 5 |
| $\theta = 0.001$ | $v/aD_0 = 10$ | 245 | 1,170 | 445 | 256 | 170 | 122 |
| | $= 100$ | 10,200 | 49,000 | 18,700 | 10,800 | 7,130 | 5,100 |
| $\theta = 0.01$ | $v/aD_0 = 10$ | 157 | 478 | 170 | 94.1 | 60.6 | 42.4 |
| | $= 100$ | 6,130 | 19,100 | 6,810 | 3,760 | 2,420 | 1,690 |
| $\theta = 0.1$ | $v/aD_0 = 10$ | 95.9 | 161 | 50.6 | 26.0 | 15.9 | 10.7 |
| | $= 100$ | 3,360 | 6,290 | 1,980 | 1,020 | 622 | 421 |

trode of L/d ratio 5, 10, and 40, respectively. Also indicated by the dotted lines on Fig. 4 is the ohmic drop predicted by Eq. [10]. The lower limit of 10 for the Péclet number was chosen so that axial dispersion does not become important in any of the calculations. A comparison between Fig. 3 and 4 shows that at a given conversion and maximum permissible voltage drop, the flow-by electrode will permit a larger Péclet num-

ber (processing rate) than the flow-through electrode. The flow-by electrode is inherently the better of the two arrangements from ohmic considerations for $L/d \geq 5$. We shall focus our attention in the remainder of this paper on the more promising flow-by electrode.

The dimensionless streamwise depth of the packing will vary along each curve of Fig. 3 and 4. The specification of the conversion and Péclet number permits

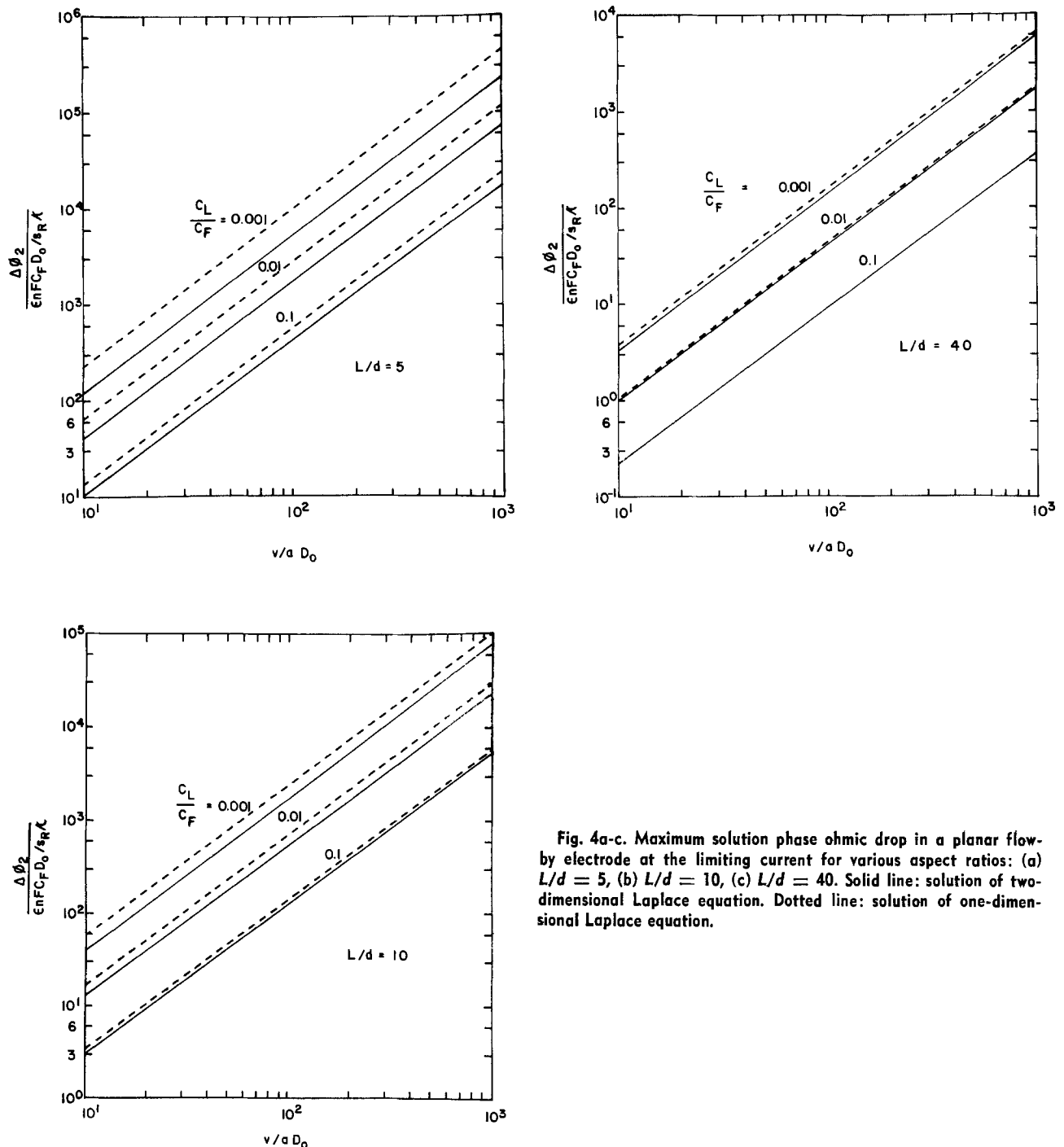


Fig. 4a-c. Maximum solution phase ohmic drop in a planar flow-by electrode at the limiting current for various aspect ratios: (a) $L/d = 5$, (b) $L/d = 10$, (c) $L/d = 40$. Solid line: solution of two-dimensional Laplace equation. Dotted line: solution of one-dimensional Laplace equation.

the use of Eq. [5] (evaluated at $y = L$) along with the Sherwood number correlation to calculate the resulting value of aL . Table II lists these packing depths for selected values of conversion and Péclet number.

Figure 4 is a log-log plot and consequently it is difficult to appreciate the difference between the potential drop predicted by Eq. [9] and that by Eq. [10]. Figure 5 illustrates more clearly the error associated with assuming that a one-dimensional approximation for the limiting current potential field is valid. This is a plot of Eq. [9] and the ordinate which is proportional to the maximum solution potential drop has been normalized such that it is one when the one-dimensional approximation is valid. The curves are for three different Péclet numbers (conversions). As $L/d \rightarrow \infty$ all lines converge to the common ordinate value of one. We note, however, that at a given Péclet number and identical ordinate, a larger value of L/d is required for the deeper bed ($aL = 100$, Fig. 5b) than for the shallower bed ($aL = 30$, Fig. 5a). Also note that the larger the Péclet number (or equivalently, C_L/C_F), a smaller L/d ratio is required to ensure that the one-dimensional approximation is valid. These results are also reflected in Fig. 4 and they can be interpreted physically. As the C_L/C_F ratio increases, the more uniform will be the reaction distribution in the streamwise direction; the scaled potential field will consequently vary weakly in the y direction and more dominantly in the x direction which is the basis for the one-dimensional approximation. Also, as aL increases for a given Péclet number (or equivalently, as C_L/C_F decreases), the reaction distribution becomes highly nonuniform with most of the reactant consumed near the entrance of the bed. However, it is precisely this region which is ignored in the one-dimensional approximation. Therefore, the one-dimensional simplification is not a good approximation in this circumstance.

In all situations it is seen that Eq. [10] overestimates the maximum potential drop. A designer who utilizes Eq. [10] will construct a conservative design for a packed bed electrode. In the proper set of circumstances this conservative design will not permit the full utilization of the bed. Consider as an example a flow-by electrode which is to have an L/d ratio of 10 (Fig. 4b) and C_L/C_F equal to 0.001. A typical value for the ordinate of Fig. 4 is 10^3 . Equation [10] (dotted line) predicts that the maximum permissible Péclet number is 55. However, the full solution to the Laplace equation (solid line) predicts a maximum Péclet number of 72. For the conditions of this particular bed, a maximum production rate 31% larger is predicted when no approximations are made in solving Laplace's equation.

In order that Eq. [9] be a better approximation than Eq. [10] to the actual solution phase potential distribution in a flow-by electrode, the no-current boundary conditions (Eq. [8a], [8b]) imposed at the bottom and top of the bed must be a good approximation to reality. If the bed support at $y = 0$ does permit an appreciable current to enter through its bottom face from the counterelectrode compartment (and likewise for the support at the top), Eq. [8a] and [8b] must be replaced with a more complex boundary condition that

Table II. Dimensionless packing depth (aL) required to obtain the specified conversion at various Péclet numbers in a flow-by or flow-through porous electrode at the limiting current

| v/aD_0 | C_L/C_F | | |
|----------|-----------|------|------|
| | 0.001 | 0.01 | 0.1 |
| 10 | 62.7 | 29.5 | 12.2 |
| 25 | 118 | 50.4 | 20.6 |
| 50 | 182 | 76.9 | 31.2 |
| 100 | 282 | 118 | 47.6 |
| 250 | 510 | 212 | 84.5 |
| 500 | 800 | 331 | 132 |
| 1000 | 1260 | 519 | 206 |

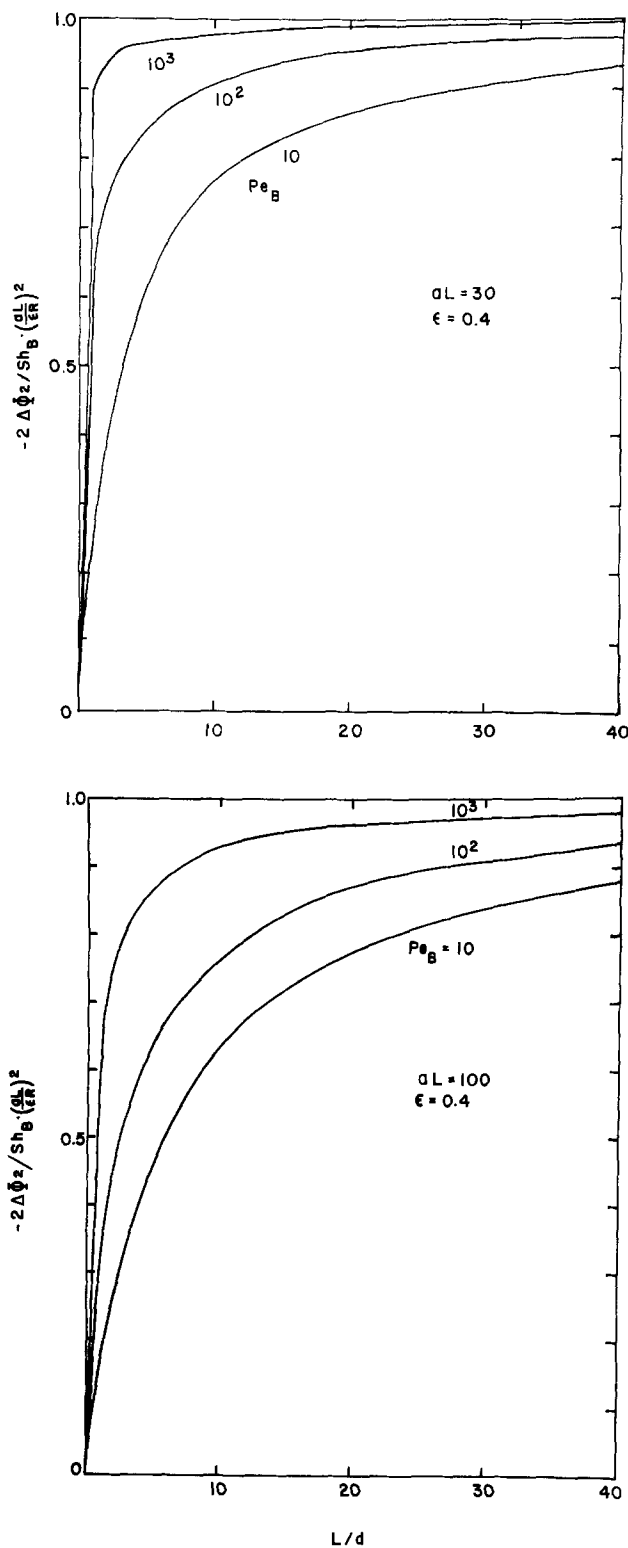


Fig. 5a-b. Normalized maximum solution phase ohmic potential drop in a flow-by electrode at the limiting current for (a) $aL = 30$ and (b) $aL = 100$.

cannot be stated independent of considering the counterelectrode placement and total cell geometry. Truly, this is a more complex problem and is not considered quantitatively here. However, qualitatively we can extrapolate from the results obtained here and state that the maximum solution phase ohmic drop with a given flow-rate will be less with a "leaky" support than with an insulator. Hence a higher maximum processing rate is possible for a specified $\Delta\phi_2$.

The example of two previous paragraphs arbitrarily chose a value for the L/d ratio. As part of the cell design, however, this number must be determined from

a total system economic analysis. From ohmic considerations it would be beneficial to make L/d as large as possible. Figure 4 indicates that the maximum Péclet number will increase as L/d increases. However, in order to meet the design criteria, other variables must also change. In the following discussion a simple qualitative analysis of the factors to be considered in determining an L/d ratio is presented. As a specific example suppose that the conversion has been set at 99% and the maximum ohmic drop corresponds to an ordinate value on Fig. 4 of 10^3 . Let us also assume that the packing material has been chosen which specifies a and that a bed of unit width is under consideration. An optimal value of L/d can be found with a corresponding maximum production rate as shown below.

Table III presents for selected L/d ratios the Péclet number and corresponding aL value calculated from Eq. [5] and [9] which satisfies the given conversion and ohmic constraints. The bed height must increase with L/d to obtain a given conversion (line 2), but the maximum processing rate will also increase (line 1). The bed height can become so great that a purely mechanical constraint may determine the maximum packing depth. Entry 3 of this table is proportional to the volume of the bed which increases proportionally with L/d . The total current through the electrode is proportional to the entry of line 4. It also increases with L/d but at a greater rate than the volume such that the current/volume (line 5) of the bed also increases with L/d . Since the current/volume is directly proportional to the amount of product produced per capital cost of the reactor, this ratio should be as large as possible for an operating reactor. As L/d increases the pumping cost will increase because of both the higher flow rate and narrower flow area and eventually overtake the positive benefit of a greater current/volume of the reactor. If a separator is required, its cost will also increase with L/d and must also be considered. The optimum L/d is thus seen to be determined by minimizing the total cost of running the electrochemical reactor which is a sum of the depreciated capital equipment costs which decrease with L/d and the operating costs which increase with L/d .¹

Summary

The limiting current analysis has been applied to a flow-through and flow-by porous electrode. The two-dimensional nature of the potential distribution within the flow-by electrode was taken into consideration. It is shown that the maximum processing rate obtainable in a flow-by electrode ($L/d \geq 5$) is always greater than that in a flow-through electrode given a conversion and maximum solution phase potential drop. The one-dimensional approximation to the solution of Laplace's equation in a flow-by electrode was compared to the two-dimensional solution and was found to give conservative estimates for the maximum reactant processing rates. A procedure for choosing an

¹ In the review process of this manuscript, it was pointed out to the author that an M.S. thesis exists (13) which utilizes a similar optimization procedure as outlined here.

Table III. Various computed results from a limiting current analysis of a flow-by electrode with $C_L/C_F = 0.01$, $-\Delta\Phi_2 = 10^3$

| | | L/d | | |
|----|-------------------------------|-------|------|------|
| | | 5 | 10 | 40 |
| 1. | v/aD_0 | 70 | 150 | 740 |
| 2. | aL | 93 | 150 | 420 |
| 3. | $\frac{(aL)^2}{R}$ | 1700 | 2300 | 4400 |
| 4. | $\frac{v}{aD_0} \frac{aL}{R}$ | 1300 | 2300 | 7800 |
| 5. | $\frac{v/aD_0}{aL}$ | 0.75 | 1 | 1.8 |

optimum L/d ratio in a flow-by electrode was qualitatively outlined.

Acknowledgment

My association with Professor John Newman was beneficial in establishing the quantitative "tools" used in the analysis.

This work was partially supported by NSF grant CPE80-06703.

Manuscript submitted Feb. 21, 1980; revised manuscript received ca. Oct. 15, 1980.

Any discussion of this paper will appear in a Discussion Section to be published in the December 1981 JOURNAL. All discussions for the December 1981 Discussion Section should be submitted by Aug. 1, 1981.

APPENDIX

Comments on the Potential Boundary Condition for a Flow-By Electrode

Let us consider the correct boundary condition for the electrical potential along the face $x = d$ in a flow-by electrode as shown in Fig. 1.

Suppose that the counterelectrode (anode for sake of argument) is a planar electrode and is separated a distance d_A from the back face of the cathode. At the limiting current, the potential in the anode and cathode compartments obey, respectively

$$\nabla^2 \phi_2^A = 0 \quad [\text{A-1}]$$

$$\nabla^2 \phi_2^C = - \frac{nFak_m C}{s_R \kappa} \quad [\text{A-2}]$$

subject to the boundary conditions

$$\phi_2^A = V \quad \text{at } x = d_A$$

$$\frac{\partial \phi^C}{\partial x} = 0 \quad \text{at } x = 0 \quad [\text{A-3}]$$

$$\frac{\partial \phi_2^{A(\text{or } C)}}{\partial y} = 0 \quad \text{at } y = 0, L$$

Here V is the applied cell voltage.

If the length to width ratio L/d is $\gg 1$ Eq. [A-1] and [A-2] reduce to

$$\frac{\partial^2 \phi_2^C}{\partial x^2} = \frac{-nFak_m C_F}{s_R K} \cdot e^{-\gamma y} \quad [\text{A-4}]$$

$$\frac{\partial^2 \phi_2^A}{\partial x^2} = 0 \quad [\text{A-5}]$$

Equation [A-4] and [A-5] can be solved subject to [A-3] and requiring the continuity of potential and current between the anode and cathode compartment at $x = d$.

In a nondimensional form the two solutions may be written

$$\frac{\Phi_2^C - \gamma}{\left(\frac{aL}{eR}\right)^2 \text{Sh}_B} = \left(\frac{X^2 - 1}{2} + \frac{1 - X_A}{r} \right) e^{-\gamma R y / L} \quad [\text{A-6}]$$

$$\frac{\Phi_2^A - \gamma}{\left(\frac{aL}{eR}\right)^2 \text{Sh}_B} = (X - X_A) \frac{e^{-\gamma R y / L}}{r} \quad [\text{A-7}]$$

where r is the ratio of the anode compartment conductivity κ_A to that of the cathode κ and X_A is d_A/d . For convenience sake, it has been assumed that the separator is of negligible thickness and resistance. Equation [A-6] demonstrates that the potential along $X = 1$ is not uniform unless X_A is near one or r is large. However $\Delta\Phi_2^C$ is unaffected by these parameters.

LIST OF SYMBOLS

| | |
|-------|---|
| a | specific interfacial area of bed, cm^2/cm^3 |
| C | concentration, mole/ cm^3 |
| d | bed depth perpendicular to fluid flow direction, cm |
| D_0 | free stream diffusion coefficient, cm^2/sec |
| F | Faradays constant, coulomb/equiv. |

| | |
|---------------|---|
| k_m | mass transfer coefficient, cm/sec |
| L | bed depth in streamwise direction, cm |
| n | number of electrons transferred in reaction |
| Pe_B | Péclet number, v/aD_0 |
| R | aspect ratio, L/d |
| Sh_B | Sherwood number, $\epsilon k_m/aD_0$ |
| s_R | stoichiometric coefficient of reactant |
| v | superficial fluid velocity, cm/sec |
| x, y | coordinates, cm |
| X, Y | dimensionless coordinates $x/d, y/d$ |
| ψ | dimensionless applied potential |
| γ | $(aL \cdot Sh_B)/(\epsilon \cdot R \cdot Pe_B)$ |
| δ_{ij} | Kronecker delta function |
| ϵ | bed porosity |
| κ | conductivity, $(\Omega \text{ cm})^{-1}$ |
| ϕ_2 | solution potential, V |
| Φ_2 | dimensionless solution potential, $\phi_2(-enFD_0C_F/s_R\kappa)$ |

Subscripts

| | |
|---|----------------|
| F | feed condition |
| L | exit condition |

REFERENCES

1. R. Alkire and R. Gould, *This Journal*, **123**, 1842 (1976).
2. R. Gould and R. Alkire, *ibid.*, **126**, 2125 (1979).
3. J. Trainham and J. Newman, *ibid.*, **124**, 1528 (1977).
4. G. Sakellaropoulos, *AIChE J.*, **25**, 781 (1979).
5. G. Sakellaropoulos and G. Frances, *This Journal*, **126**, 1928 (1979).
6. J. Newman and W. Tiedemann, *Adv. Electrochem. Electrochem. Eng.*, **11**, Wiley-Interscience, New York (1978).
7. D. Bennion and J. Newman, *J. Appl. Electrochem.*, **2**, 113 (1972).
8. R. Alkire and P. Ng, *This Journal*, **121**, 95 (1974).
9. R. Alkire and P. Ng, *ibid.*, **124**, 1220 (1977).
10. P. Fedkiw, Ph.D. Dissertation, University of California, Berkeley (December 1978).
11. J. Newman and W. Tiedemann, *AIChE J.*, **21**, 25 (1975).
12. J. Trainham and J. Newman, *This Journal*, **125**, 58 (1978).
13. S. Ghosh, M.S. Thesis, UCLA (1979).

Technical Notes



The Hydrogen Evolution Reaction on Electrodeposited Gold, Nickel, and Zinc Rotating Disk Electrodes

P. C. Andricacos* and H. Y. Cheh*

Department of Chemical Engineering and Applied Chemistry, Columbia University, New York 10027

Consider a first-order irreversible cathodic reaction occurring on a rotating disk electrode (RDE) to which a step potential has been applied. The relation between the steady-state current density under mixed diffusion-kinetic control, i , and the rotation speed, ω , of the RDE is given by the following equation (1)

$$i^{-1} = i_k^{-1} + (0.620 n F c^b D^{2/3} \nu^{-1/6})^{-1} \omega^{-1/2} \\ = i_k^{-1} + i_l^{-1} \quad [1]$$

where i_k is the purely kinetic current density, i_l is the diffusion-limiting current density, D is the diffusion coefficient of the reacting ion, ν is the kinematic viscosity of the electrolyte, and c^b is the bulk concentration of the reacting ion. Equation [1] predicts that i^{-1} is a linear function of $\omega^{-1/2}$ for a fixed potential; the slope is proportional to $D^{2/3}$, $(c^b)^{-1}$, and $\nu^{-1/6}$, and the intercept is the reciprocal of i_k . If the i^{-1} vs. $\omega^{-1/2}$ line is plotted for various values of the potential, parallel lines should result. The value of the Tafel slope can then be extracted from the intercepts of these lines. Equation [1] was used by Frumkin and Tedoradze (2, 3) for the study of Cl_2 reduction and by Zurilla *et al.* (4) for O_2 reduction. It was augmented by Jahn and Vielstich (5) to include the reverse (anodic) reaction. The augmented form was experimentally verified by these authors and later by Viswanathan and Cheh (6).

In the present note, Eq. [1] is applied to interpret data obtained for the hydrogen evolution reaction (HER) on electrodeposited Au, Ni, and Zn RDE's. It offers the advantage that data obtained at high overpotentials and/or electrolytes with low H^+ concentrations can be treated despite diffusion limitations. Such

experimental conditions are necessary if the HER occurs on substrates which corrode in the electrolyte. Its disadvantage in the particular case of the HER is that it applies only to those mechanisms which have a first-order dependence on the surface concentration of H^+ . Furthermore, the surface coverage with adsorbed hydrogen must be constant over the entire potential and current density regions studied. Such mechanisms are those involving a charge transfer or electrochemical desorption steps as rate determining, the former proceeding at low coverage and the latter at high coverage (7).

Experiments were conducted on electrodeposited Au, Ni, and Zn RDE's. Table I summarizes plating condi-

Table I. Plating conditions

| Metal | Bath | g/liter | $T, ^\circ C$ | ω , rpm | Current waveform |
|-----------|--|---------|---------------|----------------|--|
| Au (8, 9) | KAu(CN) ₂ KCitrate KH ₂ PO ₄ | 20 | 55 | 2500 | Single step pulse $i_p^{(1)} = 2.5, 5.5, 5.2, 5$ mA/cm ² $\theta_1^{(2)} = \theta_2^{(3)} = 1$ msec |
| | | 150 | | | |
| | | 40 | | | |
| Ni (10) | NiSO ₄ ·6H ₂ O NiCl ₂ ·6H ₂ O H ₃ BO ₃ | 330 | 60 | 2500 | Two step pulse $i_1^{(4)} = 3, 14, 14, 14$ mA/cm ² $\mu^{(5)} = 0.1$ $\theta_1 = \theta_2 = 1$ msec |
| | | 45 | | | |
| | | 38 | | | |
| Zn (10) | ZnO NaCN NaOH Na ₂ CO ₃ | 25 | 25 | 1600 | Single step pulse $i_p = 10, 10, 10, 10$ mA/cm ² $\theta_1 = \theta_2 = 1$ msec |
| | | 50 | | | |
| | | 80 | | | |
| | | 60 | | | |

(¹) Peak current density; (²) duration of the pulse ON period; (³) duration of the pulse OFF period; (⁴) current density during the first step; (⁵) ratio of the second to first step current densities.

* Electrochemical Society Active Member.

Key words: electrodeposition, electrolyte, diffusion.

tions for each metal. Single or two step galvanostatic pulses were used throughout. A two step pulse was employed in the deposition of Ni to cathodically protect the deposit during the relaxation period (11). Typically 4-5 layers of deposit were necessary to produce a satisfactory surface as judged by the metal under investigation. This was established by separate cyclic voltammetric tests. The duration of plating each layer was approximately 1 hr, followed by mechanical polishing to produce a mirror-like surface. Current densities used are shown in Table I. The deposit thickness cannot be calculated because of the polishing procedure.

Measurements were conducted in a conventional three compartment cell. The counterelectrode was a Pt spiral and the reference electrode was an SCE. A glass electrode was also immersed for pH control together with the SCE. The electrolyte was a 0.25M Na_2SO_4 solution acidified to a pH of 3.2 by the addition of 9.1 ml of a 1% (by volume) solution of H_2SO_4 . It was prepared from triply distilled H_2O and analytical grade reagents without further purification, and was continuously saturated with H_2 .

The i^{-1} vs. $\omega^{-1/2}$ plots for the three metals are shown in Fig. 1-3. Figure 4 is a Tafel plot, where i_k are the reciprocals of the intercepts in Fig. 1-3. The Tafel slopes in Fig. 4 and the exchange current densities calculated by extrapolation to zero overpotential are reported in Table II. The equilibrium potential was calculated from the measured pH value. The fourth column is the reciprocal of the slope of the i^{-1} vs. $\omega^{-1/2}$ plots, which is equal to the slope of a Levich plot, i.e., i_l vs. $\omega^{1/2}$. Its value depends on ν , D , and c^b . If the latter is not known exactly, one can still check for consistency by measuring limiting current densities directly, constructing a Levich plot, and then comparing its slope with the reciprocal of the i^{-1} vs. $\omega^{-1/2}$ slope. Such experiments were performed for the limiting current densities of the HER on a commercial (Pine Instruments, DT6) Pt RDE of a different geometrical area in the same solution. The slope of the Levich plot was 3.78×10^{-4} A/cm² sec^{1/2}, which is within 11% of the values reported in Table II. The discrepancy might be attributed to surface area variations caused by the polishing procedure.

The values of the Tafel slope and the first-order dependence on the surface concentration of H^+ for both Au and Ni are consistent with a mechanism in which the electrochemical desorption step is rate determining and proceeds at high coverages. Since the H^+ concentration is not known exactly, one cannot compute the

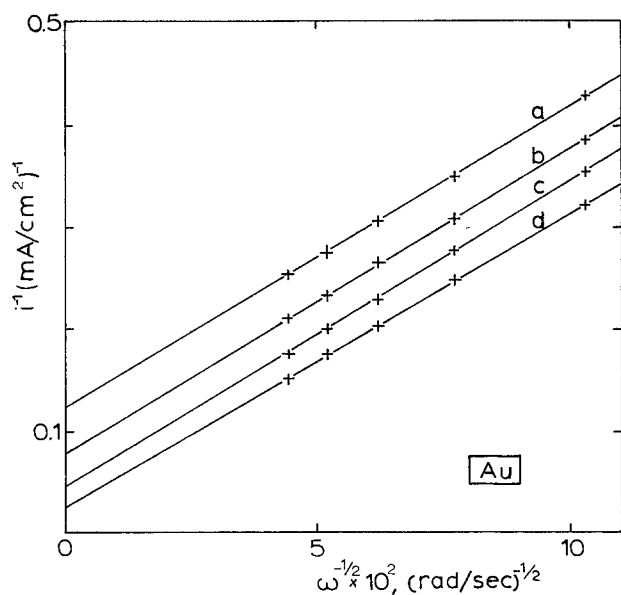


Fig. 1. i^{-1} vs. $\omega^{-1/2}$ plots for the HER on an Au-plated RDE. Curve a: -1.060V vs. SCE; curve b: -1.085 ; curve c: -1.110 ; curve d: -1.140 .

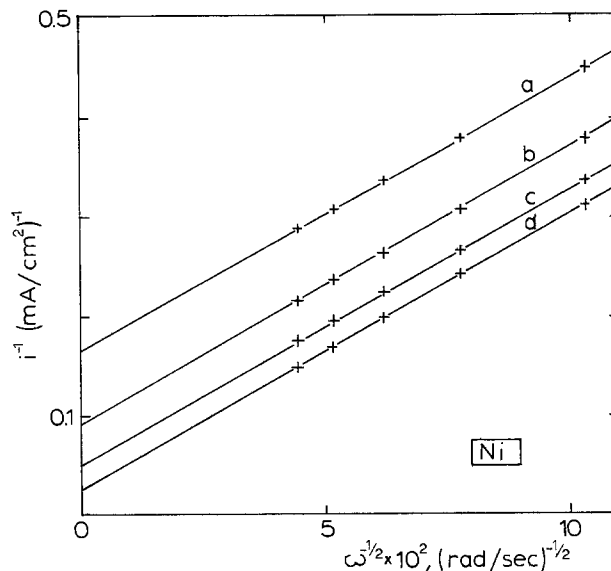


Fig. 2. i^{-1} vs. $\omega^{-1/2}$ plots for the HER on a Ni-plated RDE. Curve a: -1.060V vs. SCE; curve b: -1.090 ; curve c: -1.120 ; curve d: -1.160 .

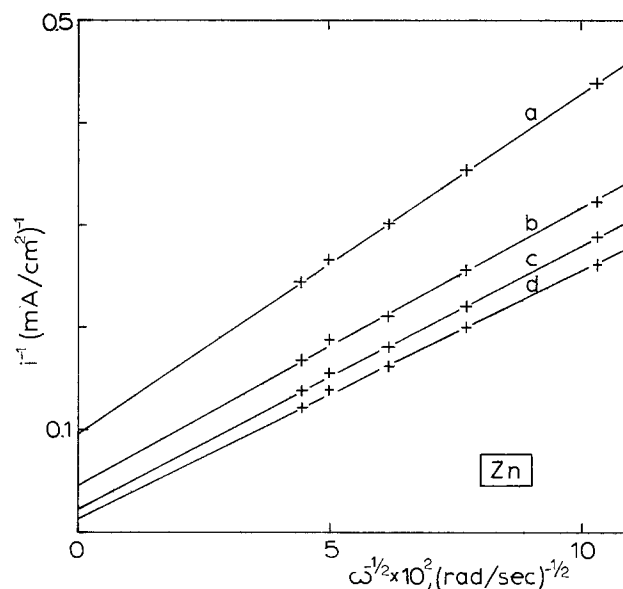


Fig. 3. i^{-1} vs. $\omega^{-1/2}$ plots for the HER on a Zn-plated RDE. Curve a: -1.270V vs. SCE; curve b: -1.320 ; curve c: -1.370 ; curve d: -1.420 .

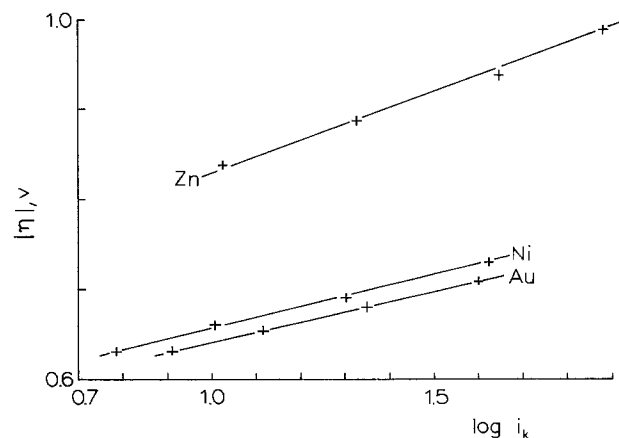


Fig. 4. Tafel plots for the HER on plated Au, Ni, and Zn RDE's (i_k is in mA/cm²).

Table II. Data extracted from Fig. 1-4

| Metal | Tafel slope, V | Exchange C.D. $\times 10^6$, A/cm ² | (Slope) ⁻¹ $\times 10^4$, A/cm ² sec ^{1/2} |
|-------|----------------|---|--|
| Au | 0.113 | 2.2 | 3.38 \pm 0.08 |
| Ni | 0.120 | 3.6 | 3.56 \pm 0.02 |
| Zn | 0.172 | 14.2 | — |

exchange current density that the present measurements would predict for acid strengths typically reported in the literature. However, assuming complete dissociation of H₂SO₄, the predicted value for 1M acid is about 10 μ A/cm², which is in agreement with the literature values (12, 13).

Results in Fig. 3 and 4 indicate that the Tafel slope of the HER on Zn is considerably higher than the one predicted for a charge transfer rate-determining step (14) and consequently, the value of the exchange current density is also abnormally high. Zn data were difficult to reproduce; however, the increase of the i^{-1} vs. $\omega^{-1/2}$ slope with decreasing cathodic potentials was a common feature in all runs. If one assumes a simultaneous anodic dissolution with a first-order overall dependence on the concentration of Zn²⁺, such discrepancies are expected (5). However, they cannot be taken into account quantitatively, since both Zn²⁺ concentration and anodic overpotential are unknown. The possibility of substrate dissolution was also evidenced by an increase in the net cathodic current from the initial to the steady-state value, as opposed to Au and Ni for which the initial HER current was higher than the steady-state value. Initially, there is an infinite tendency for Zn corrosion, since no Zn²⁺ ions exist in the electrolyte. As the Zn²⁺ concentration increases, the corrosion current decreases, and the net current increases.

To summarize, our results indicate that hydrogen evolution on Au and Ni in the electrolytes studied

proceeds at high coverages of H⁺ with electrochemical desorption as the rate-determining step, whereas hydrogen evolution and Zn dissolution occur simultaneously.

Manuscript submitted July 9, 1980; revised manuscript received Nov. 17, 1980.

Any discussion of this paper will appear in a Discussion Section to be published in the December 1981 JOURNAL. All discussions for the December 1981 Discussion Section should be submitted by Aug. 1, 1981.

REFERENCES

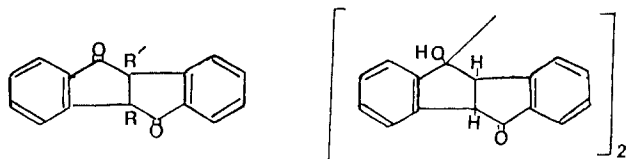
- V. G. Levich, "Physicochemical Hydrodynamics," p. 72, Prentice-Hall, Englewood Cliffs, N.J. (1962).
- A. N. Frumkin and G. A. Tedoradze, *Dokl. Akad. Nauk SSSR*, **118**, 530 (1958).
- A. N. Frumkin and G. A. Tedoradze, *Z. Elektrochem.*, **62**, 251 (1958).
- R. W. Zurilla, R. K. Sen, and E. Yeager, *This Journal*, **125**, 1103 (1978).
- D. Jahn and W. Vielstich, *ibid.*, **109**, 849 (1962).
- K. Viswanathan and H. Y. Cheh, *ibid.*, **125**, 1616 (1978).
- J. O'M. Bockris and A. K. N. Reddy, "Modern Electrochemistry," Vol. 2, p. 1231, Plenum Press, New York (1970).
- H. Y. Cheh, P. C. Andricacos, and H. B. Linford, *Plating Surf. Finish.*, **64** (7), 42 (1977).
- P. C. Andricacos, H. Y. Cheh, and H. B. Linford, *ibid.*, **64** (9), 44 (1977).
- "Modern Electroplating," 3rd ed., F. A. Lowenheim, Editor, pp. 314 and 420, John Wiley, New York (1974).
- P. C. Andricacos and H. Y. Cheh, *J. Electroanal. Chem. Interfacial Electrochem.*, in press.
- A. T. Kuhn and M. Bryne, *Electrochim. Acta*, **16**, 391 (1971).
- J. O'M. Bockris and E. C. Potter, *J. Chem. Phys.*, **20**, 614 (1952).
- A. L. Rotinyan, N. P. Fedotieff, and L. Yu. Sok, *Zh. Fiz. Khim.*, **31**, 1295 (1957).

Electrochemical Reduction of 4b,9b-Dihydroindeno[2,1-a]indene-5,10-diones

Stanley Wawzonek*

Department of Chemistry, The University of Iowa, Iowa City, Iowa 52242

The electrochemical reduction of 4b,9b-dihydroindeno[2,1-a]indene-5, 10-dione (1a) in dimethylformamide was investigated as a possible method for simplifying the preparation of 3,4,7,8-dibenzocycloocta-1,5-dione which originally was prepared (1) from this diketone 1a by a lengthy three step synthesis in a 30% overall yield. This research was predicated on



1a R=R'=H

b R=CH₃; R'=H

c R=R'=CH₃

the report that the electrochemical reduction of cyclohexan-1,4-dione gave a 1,4-diradical which cleaved to

hexane-2,5-dione. The yield of the latter was only 6% but 63% of the starting material was recovered (2).

In the present work it was hoped that a 1,4-diradical would be formed by generating anion radical moieties at each of the carbonyls in 1a and that cleavage would then occur between the 4b and 9b carbons and form 3,4,7,8-dibenzocycloocta-1,5-dione.

The formation of such a 1,4-diradical was prevented by an unexpected reaction which is described in the present paper.

Experimental

Melting points are uncorrected. Infrared spectra were recorded on a Perkin-Elmer Infracord Model 137B spectrophotometer. NMR spectra were obtained with a Bruker HX-90 Fourier transform NMR spectrometer.

Electrochemical reduction of 4b,9b-dihydroindeno[2,1-a]-indene-5,10-dione (1a) (5).—A solution of the diketone 1a (5) (4.68g, 0.02 mole) in dimethylformamide (320 ml) containing tetrabutylammonium bromide (20.6g) was degassed for 1 hr with nitrogen and then reduced at a mercury cathode (area: 63 cm²) under nitrogen. The anode compartment was a porcelain cylinder (5 cm in diameter and 2 cm high) and

* Electrochemical Society Active Member.

Key words: pinacols, self-protonation, dimethylformamide.

contained 0.2M tetrabutylammonium bromide in dimethylformamide and a platinum gauze anode. The reference electrode was mercury in a dimethylformamide solution containing 0.2M tetrabutylammonium bromide and was separated from the cathode compartment with a porous glass disk. The electrolysis was carried out at a potential of $-1.2V$ using a PAR Model 371 Potentiostat. Polarographically **1a** shows two one-electron waves at -1.03 and $-1.38V$ (*vs.* Hg pool). The large scale reduction results were similar to those obtained at $-1.2V$ if an applied potential between -1.4 and $-1.7V$ was used in the electrolysis. The initial current of 0.05A decreased to 0.01A after 11 hr. The resulting solution which contained a red solid was treated with excess methyl iodide and stirred until the red color disappeared. Removal of the dimethylformamide under reduced pressure was followed by the addition of water. The resulting solid was dissolved in methylene chloride and the solution was dried and the solvent was removed. Addition of ethyl acetate resulted in the precipitation of the tetrabutylammonium iodide formed in the reaction. The filtrate gave an oil which was taken up in benzene and chromatographed on alumina using benzene as an eluant. The first fraction after fractional crystallization using petroleum ether (bp 60° - 68°) gave *cis*-4b-methyl-4b,9b-dihydroindeno[2,1-a]indene-5,10-dione (**1b**) (1.74g) and the starting material (**1a**) (0.08g). *cis*-4b-Methyl-4b,9b-dihydroindeno[2,1-a]indeno-5,10-dione (**1b**) melted at 93° - 95° after two crystallizations from petroleum ether (bp 60° - 68°). This compound (**1b**) has been prepared by the methylation of **1a** in ethanolic potassium hydroxide and is reported to be a viscous oil (3). Repetition of this method gave the same crystalline solid. Its spectral properties were identical to those reported for the oil (3). *Anal.* Calcd. for $C_{17}H_{12}O_2$: C, 82.26; H, 4.84. Found: C, 82.30; H, 4.96.

Further elution of the alumina with benzene and with chloroform gave a mixture of pinacols (**2**) (1.14g) which could be separated by fractional crystallization from benzene and from ethanol. One isomer after crystallization from benzene melted at 180° with gas evolution; IR(Nujol) 2.91(OH), 5.88 μ (CO); NMR($DCCl_3$) δ 3.00(s, 2H, OH), 3.92(d, 2H, 11-H ($J = 6.65$ Hz)), 4.14(s, 2H, 10-H ($J = 6.65$ Hz)), 7.11-7.88 (m, 16H, aromatic Hs). *Anal.* Calcd. for $C_{32}H_{22}O_4$: C, 81.70; H, 4.68. Found: C, 82.11; H, 4.99.

The second isomer after crystallization from benzene melted at 240° - 255° with decomposition; IR(Nujol) 2.87(OH), 5.83 μ (CO); NMR($DCCl_3$) δ 2.83(s, 2H, 20 Hs), 3.99(d, 2H, 11-Hs ($J = 6.59$ Hz)), 7.13-7.66(m, 16H, aromatic Hs). *Anal.* Calcd. for $C_{32}H_{22}O_4$: C, 81.70; H, 4.68. Found: C, 82.33; H, 5.07.

Further elution using ethyl acetate gave a solid (0.4g) melting at 285° - $290^{\circ}C$ with decomposition and resembling the high melting product obtained from the diketone **1a** with alkali (5).

cis-4b,9b-Dimethyl-4b,9b-dihydroindeno[2,1-a]indene-9,10-dione (**1c**).—*cis*-4b-Methyl-4b,9b-dihydroindeno[2,1-a]indene-9,10-dione (**1b**) 2.54g) was dissolved in dimethylformamide (50 ml) and treated successively with 0.1M tetrabutylammonium hydroxide (23 ml) in methanol and methyl iodide (2 ml) until no more red color was produced by the base. The resulting pale yellow solution was treated with water and the solvent was removed under reduced pressure. The resulting solid was taken up in ethyl acetate and the precipitated tetrabutylammonium iodide was filtered. The filtrate was evaporated to dryness and the resulting solid was dissolved in benzene and the resulting solution was passed through an alumina column. Removal of the benzene gave **1c** (1.78g) melting at 128° - $30^{\circ}C$. One crystallization from petroleum ether (bp 60° - $68^{\circ}C$) gave white crystals melting at 130° - $132^{\circ}C$ [lit. 3] 126° - $128^{\circ}C$). The infrared and NMR spectra were identical to those reported (3).

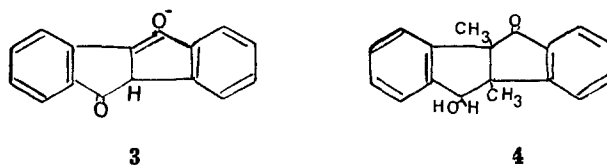
Electrochemical reduction of cis-4b-9b-dimethyl-4b,9b-dihydroindeno[2,1-a]indene-5,10-dione (**1c**).—A solution of **1c** (1.57g) in dimethylformamide (100 ml) containing 0.2M tetrabutylammonium bromide was electrolyzed under nitrogen at a mercury cathode at a constant potential of $-1.8V$. The anode was a platinum gauze electrode and the reference electrode was mercury in a dimethylformamide solution of 0.2M tetrabutylammonium bromide. Polarographically **1c** shows two one-electron waves at -1.09 and $-1.65V$ (*vs.* Hg anode) in a dimethylformamide solution of 0.2M tetrabutylammonium bromide. The current observed was 0.2A which slowly dropped to 0.1A in the course of 2 hr. The solution during the electrolysis turned a dark green. Acidification with dilute acetic acid gave a pale yellow solution. Removal of the solvent gave a solid which was dissolved in benzene and chromatographed on silica. Using benzene as an eluant gave as the first fraction the starting diketone (**1c**) (0.51g). The second fraction (0.28g) gave **4** melting at 175° - 180° . Recrystallization from benzene gave a sample melting at 179° - 180° . IR(Nujol) 2.79(OH), 5.89 μ (CO), NMR($DCCl_3$) δ 1.48(J, 3H, 10- CH_3), 1.57(s, 3H, 11- CH_3), 1.85(broad s, 1H, OH), 5.21 (broad s, 1H, 9-H), 7.23-7.82(m, 8H, aromatic H). Addition of D_2O sharpened the singlet at δ 5.21 and eliminated the singlet at δ 1.85. *Anal.* Calcd. for $C_{18}H_{16}O_2$: C, 81.82; H, 6.06. Found: C, 81.63; H, 6.03.

Results

The electrochemical reduction of **1a** did not proceed as planned but gave results which were considered to be important enough to report.

Reduction of **1a** (under nitrogen) in dimethylformamide containing 0.2M tetrabutylammonium bromide proceeded with the formation of a deep red colored compound. Acidification of the solution caused decolorization and gave a mixture of pinacols **2** and the starting material (**1a**). Repetition of the electrolysis followed by treatment with methyl iodide instead of acid gave the same mixture of pinacols and *cis*-4b-methyl-4b,9b-dihydroindeno[2,1-a]indene-5,10-dione (**1b**) (3) in place of **1a**.

These results indicate that the anion radical formed from **1a** is protonated by another molecule of **1a** and dimerizes to the pinacols **2**. The red colored compound formed is therefore the mono-tetrabutylammonium salt of the enolate (3). The di-tetrabutylammonium salt was eliminated as a possible structure since



none of the *cis*-4b,9b-dimethyl-4b,9b-dihydroindeno[2,1-a]indene-5,10-dione (**1c**) was isolated. This salt would be expected to react stepwise with methyl iodide and form first the enolate of **1b** and then the dimethyl derivative **1c**. The plausibility of the second step was demonstrated chemically; treatment of **1b** in dimethylformamide with tetrabutylammonium hydroxide and methyl iodide gave **1c**.

The possibility of an anion-radical structure for **3** was eliminated by the reaction of the diketone **1a** with tetrabutylammonium hydroxide in dimethylformamide; a similar colored species was formed.

The unusual proton donor capability of **1a** in dimethylformamide was verified by its effect on the polarographic reduction of azobenzene in dimethylformamide containing 0.2M tetrabutylammonium bromide. In this medium azobenzene gave two reduction waves at -0.6 and $-1.28V$ (*vs.* Hg pool), with a ratio of wave heights of 1:0.96. Addition of 1.11 mmoles of **1a** to 0.66 mmoles of azobenzene changed the ratio of the two waves to 1:0.196. The decrease in height of the sec-

ond wave indicated that 80% of the initial anion radical formed from azobenzene is diprotonated by a CEC mechanism and that 1.06 mmoles of protons are involved. Since 1.11 mmoles of **1a** were added originally, its (**1a**) utilization as a proton source is 95% efficient.

The benzyl ketone moiety present must be responsible for the proton capability of **1a** since dibenzylketone had the same effect upon the polarographic behavior of azobenzene in dimethylformamide. Acetophenone and cyclohexanone which do not have this grouping, had no effect on the polarographic behavior of either azobenzene or benzophenone in dimethylformamide.

To circumvent the possibility of enolization *cis*-4b-9b-dimethyl-4b,9b-dihydroindeno[2,1-a]indene-5,10-dione (**1c**) was electrolyzed in dimethylformamide containing tetrabutylammonium bromide at a mercury cathode at a potential of -1.80V . The resulting deep green anion radical (**3**) produced gave upon acidification a mixture of the alcohol **4** and the starting material (**1c**). No products corresponding to the eight-membered ring diketone or its reduction products were isolated.

The alcohol **4** could be formed in two ways. The anion radical from **1c**, which is a mixed valence anion radical (**3**), is an intermediate in the 2-electron reduc-

tion and could be formed under the large scale reduction conditions used. Treatment with dilute acid would convert this species into the alcohol **4** and the diketone **1c** in a similar fashion to that reported for the ketyl of benzophenone (**4**). The second possibility is the reduction of the anion radical to an unsymmetrical dianion which on protonation forms **4**.

Manuscript submitted Aug. 20, 1980; revised manuscript received Nov. 17, 1980. This was Paper 424 presented at the St. Louis, Missouri, Meeting of the Society, May 11-16, 1980.

Any discussion of this paper will appear in a Discussion Section to be published in the December 1981 JOURNAL. All discussions for the December 1981 Discussion Section should be submitted by Aug. 1, 1981.

REFERENCES

1. S. Wawzonek, *J. Am. Chem. Soc.*, **62**, 745 (1940).
2. E. Kariy and B. J. Cohen, *J. Chem. Soc. Perkin II*, **1972**, 509 (1972).
3. A. H. Schroeder and S. Mazur, *J. Am. Chem. Soc.*, **100**, 7339 (1978).
4. W. E. Bachmann, *ibid.*, **55**, 355 (1933).
5. W. Roser, *Justus Liebig Ann. Chem.*, **247**, 152 (1888).



The Role of Defects in the Fracture of Oxide Films on Metals

D. R. Arnott,¹ W. J. Baxter, and S. R. Rouze

General Motors Research Laboratories, Physics Department, Warren, Michigan 48090

ABSTRACT

The extent of fracture of anodic oxide films during tensile deformation of aluminum is shown to be controlled by the density of defects in the oxide. The density of defects was monitored by the "leakage" resistance of the film, while the extent of fracture of the oxide was obtained from measurements of re-anodization current transients. Other experiments in a photoelectron microscope showed that these oxides are ruptured at emerging slip steps. This provided the basis of a simple model for oxide fracture, which requires the presence of a defect in the oxide at the site of an emerging slip step. A relationship between the leakage resistance and fracture susceptibility of the oxide was derived and confirmed by experiment, showing that both properties are controlled by the same type of defect. The density of these defects may be controlled by the surface preparation prior to anodization. If the density of defects is greatly reduced, even a thin (28 nm) oxide becomes strong enough to suppress slip step formation during tensile deformation.

Various properties of oxide films on metals are often ascribed to the presence of imperfections or flaws. For example, defects in the oxide are held responsible for: (i) the finite conductivity (leakage currents) of these oxide films (1,2); (ii) the occurrence of pitting in a corrosive environment (3); and (iii) the initiation of mechanical failure of the film during deformation (4, 5).

The precise nature of the defects is usually indeterminate, particularly for thin oxide films. However, the development of pores in aluminum oxide has been well documented by electron microscopy and demonstrated to be responsible for an increase of leakage current (1, 2, 6). On the other hand, defects are often attributed to surface contamination of the metal or the presence of inclusions in the metal. For example, it has been reported that impurities decrease the ductility of anodic oxide films formed on the surface of tantalum (4).

In this study of thin barrier layer anodic oxide films on aluminum, it is shown that there is a systematic relationship between the conductivity and the strength of thin (<30 nm) anodic films, indicating that, in this case at least, the same defect controls both properties. These oxides are shown to rupture at emerging slip steps provided that defects are present in the oxide. If the density of defects in the oxide is reduced sufficiently, even a very thin oxide (28 nm) becomes strong enough to suppress slip step formation during tensile deformation of aluminum.

Experimental

The present series of experiments was centered upon the influence of chromic acid cleaning treatment on

the properties of anodic films formed on 1100-0 aluminum.

Specimens of 1100 aluminum were degreased with acetone and cleaned further by immersion for 10 min or less in chromic acid solution² at 70°C. After rinsing with water and alcohol, the oxide film was then grown by anodization in a solution of 3% tartaric acid, adjusted to pH = 5 with NH₄OH. To obtain oxides of well-controlled thickness, the current density during anodization was limited to ~1 mA/cm² until the required voltage (V) was attained, and then allowed to decay for a period of 10 min. The specimens were then removed from the electrolyte, rinsed with water and alcohol, and blown dry. Auger sputter profiling of a few samples confirmed that the oxide thickness was essentially constant and independent of the precleaning treatment.

The leakage currents through the anodized film were measured by reimmersing the anodized specimen in the tartaric acid solution, then applying a potential ½V. This procedure ensured that the measured current was primarily due to leakage processes and not a continued growth in oxide thickness.

The mechanical properties of the anodic films were examined with the following techniques.

1. The extent of fracture of the oxide produced by known amounts of tensile deformation was measured quantitatively by the reanodization current transient method described previously by Baxter and Gifford (7). Briefly, after tensile deformation the microcracks produced in the 28 nm oxide (formed at 20V) were reanodized at a lower voltage (10V), and the current transient recorded on a digital oscilloscope. The decay time (τ) of this current transient is directly proportional to the area of metal being reanodized, i.e., the total area of the microcracks produced in the 28 nm

¹ Present address: Capricornia Institute of Advanced Education, Rockhampton, Queensland, Australia.

Key words: defects, films, oxide fracture.

² 7g Cr₂O₃, 20 ml H₂SO₄, 200 ml H₂O.

oxide over the deformed gauge section of the sample. The results are expressed as τ/A , where A is the surface area of the entire specimen gauge section.

2. The mode of fracture of the oxide was observed directly and continuously during tensile deformation of small samples in the photoelectron microscope (PEM) (8). These samples were all mechanically polished, prior to the chromic acid and anodization procedure, to improve the resolution of the image obtained in the microscope. In these experiments, any microcracks produced in the oxide appear as regions of much stronger photoelectron emission, often referred to as photostimulated exoelectron emission (9, 10). Such observations provide both a measure of the strain required to fracture the oxide as well as defining the mode of fracture. These specimens were also examined subsequently by conventional optical and scanning electron microscopy.

Leakage Current

The leakage current through the oxide, at $\frac{1}{2}V$ after anodizing at V , decreases dramatically with increase of precleaning time in chromic acid. As shown in Fig. 1 for a 14 nm oxide, a period of 5 min was sufficient to reduce the leakage current by two orders of magnitude. Thus it may be concluded that the precleaning of the aluminum substrate in chromic acid greatly reduces the concentration of flaws in the subsequently formed oxide film. This simple result provided an opportunity to compare the mechanical properties of aluminum oxide films of the same thickness, but with widely different concentrations of defects.

Reanodization Current Transients

Two sets of measurements are shown in Fig. 2. One series of specimens were deformed to a tensile strain of 6×10^{-2} . The decay time of the current transient for these specimens decreases rapidly with increasing duration of the chromic acid treatment. In fact, the form of this curve provides an interesting comparison with that in Fig. 1, the reduction of both leakage current and reanodization time constant being essentially

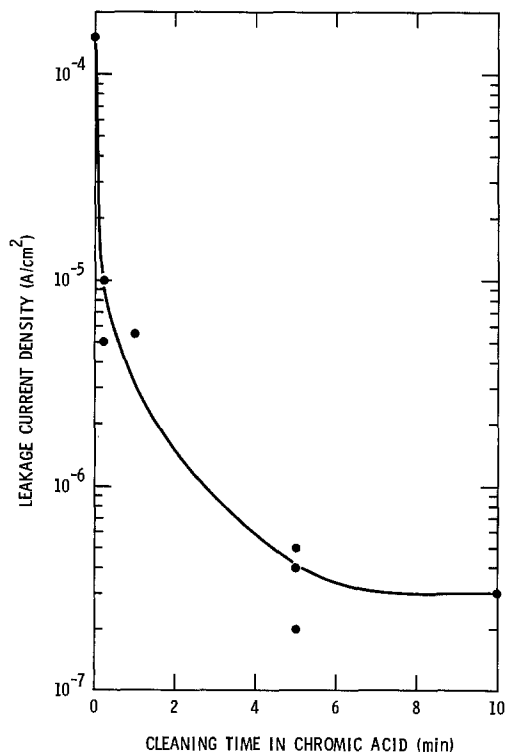


Fig. 1. Effect of duration of precleaning of aluminum in chromic acid on the leakage current density of a subsequently deposited 14 nm anodic oxide film. Leakage current measured at 5V with specimen immersed in anodizing electrolyte.

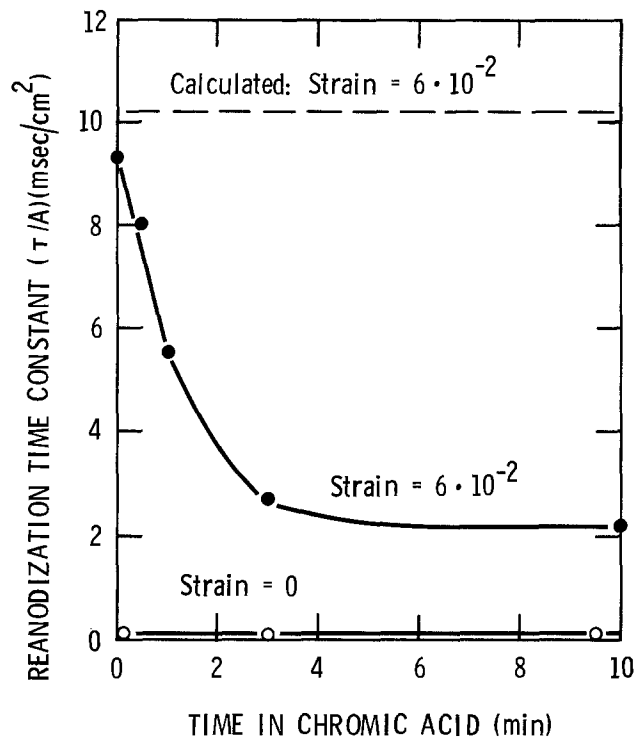


Fig. 2. Effect of duration of precleaning of aluminum in chromic acid on the time constant for reanodization after tensile deformation. Samples coated initially with 28 nm oxide (at 20V), and reanodized at 10V. Tensile strain as indicated in figure.

completed by a 5 min treatment. By contrast the decay time for undeformed specimens is very small and independent of the chromic acid treatment. This transient is simply that required to charge up the oxide film and the time constant is controlled by the oxide thickness, which has a constant value for all specimens.

The calculated curve shown in Fig. 2 is for a perfectly brittle oxide film. This value of τ/A was calculated on the following basis.

1. A series of calibration measurements on small samples of known area showed that

$$\tau = K\delta A \quad [1]$$

where δA is the area of metal being anodized, and K , for our experimental arrangement, had a value of 300 msec/cm².

2. For a perfectly brittle oxide, the area of fresh metal revealed by the microcracks is equal to the geometrical increase of surface area of the specimen (δA). The value of δA may be calculated for a given tensile strain (ϵ_1) on the basis of constant specimen volume, i.e.

$$\epsilon_1 + \epsilon_2 + \epsilon_3 = 0 \quad [2]$$

where ϵ_1 , ϵ_2 , and ϵ_3 are the strains in the three principal directions. Also it is known empirically that the changes in width and thickness of the sample are simply related by

$$\epsilon_2 = R\epsilon_3 \quad [3]$$

where $R \approx 0.7$ for this material (11). From these relationships it is easily shown that for our specimen geometry

$$\frac{\delta A}{A} = 0.57 \epsilon_1 \quad [4]$$

Combining Eq. [1] and [4], the value of $\tau/A = 170 \epsilon_1$ msec/cm². Thus for a tensile strain of 6×10^{-2} , $\tau/A = 10.2$ msec/cm². This value is only slightly greater than that observed experimentally for the oxide film formed without any prior chromic acid treatment. The small difference can be accounted for simply by assuming that the oxide behaves elastically

until attaining a strain of 6×10^{-3} , whereupon fracture is initiated. This value of the fracture strain is in fact in the range of values reported by other investigators (5, 10, 12-14).

The difference between the calculated and the experimental curves for a tensile strain of 6×10^{-2} , may be regarded as a measure of the effective ductility of the oxide film. The precleaning in the chromic acid can apparently reduce the concentration of flaws in the oxide sufficiently to produce a fivefold reduction in the extent of rupturing of the oxide. For example, the saturation level of $\tau/A = 2.2$ msec/cm² could be interpreted in terms of most of the strain (4.7×10^{-2}) being accommodated elastically by the oxide. This dramatic difference in the fracture resistance of these oxide films merited further investigation on a more microscopic level as outlined below.

Photoelectron Microscopy

Two types of specimens were examined; one was precleaned with chromic acid for 20 min while the other received no chromic acid treatment. Both were anodized to form a 28 nm oxide. The tensile strain required to initiate the fracture of these oxides, as determined by the onset of exoelectron emission, was essentially the same irrespective of the chromic acid treatment. The onset of oxide rupture always occurred at strain levels of 5×10^{-3} to 1×10^{-2} . By contrast, however, the total extent of cracking of these oxides differed markedly. This is illustrated by the photoelectron micrographs in Fig. 3 which show the sources of exoelectron emission produced after a tensile strain of 4×10^{-2} . The sample which was not precleaned with

chromic acid has developed many sources of exoelectron emission, i.e., microcracks in the oxide (Fig. 3a), while there are only a few in the oxide on the sample which had been treated with chromic acid (Fig. 3b). The mode of fracture appears to be the same in the two cases, namely the microcracks are in grain confined arrays and are associated with slip step emergence.

Thus the major effect of precleaning with chromic acid is that the subsequently formed anodic oxide film is considerably more difficult to rupture. A number of explanations could be proposed to account for this effect. For example, it could be argued that the chromic acid treatment actually etched away the work hardened layer near the surface, so that during subsequent deformation the slip steps would develop on a much finer scale and not be large enough to rupture the oxide. However an explanation along these lines is refuted by similar experiments in the PEM, where only the very thin natural oxide had been allowed to form after the initial cleaning of the specimens. As shown by the photoelectron micrographs in Fig. 4, the natural oxide develops numerous arrays of microcracks irrespective of the chromic acid treatment.

Another possible explanation could be formulated in terms of the chromic acid treatment leaving a contaminating film, perhaps only a monolayer, so that the anodic oxide film is not as well bonded to the metal substrate. If this were the case, the oxide film might tend to peel rather than rupture, as outlined analytically by Grosskreutz and McNeil (15) several years ago. Peeling of thicker oxides during tensile deformation has in fact been reported by several authors (4, 16,

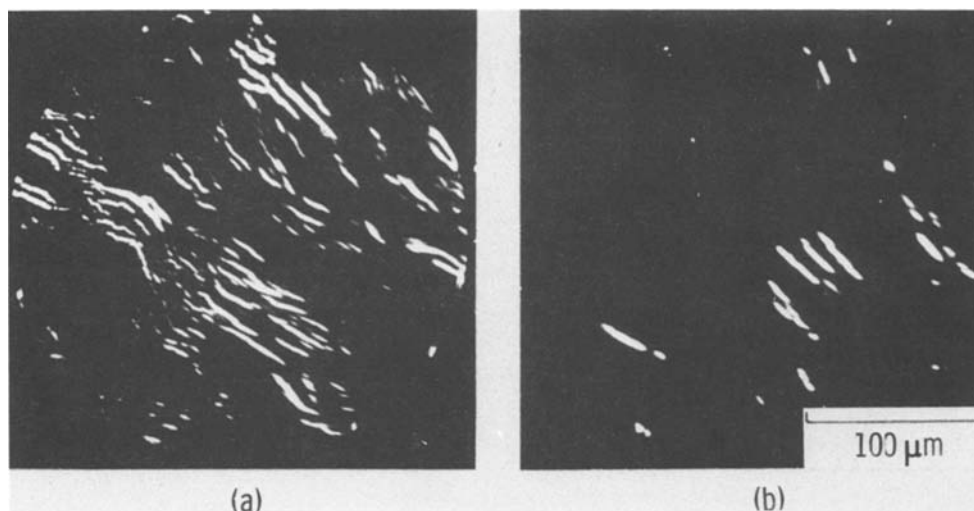


Fig. 3. Photoelectron micrographs of 1100 aluminum coated with 28 nm anodic oxide, showing sources of exoelectron emission after a tensile strain of 4×10^{-2} . (a) Precleaned with acetone, (b) precleaned with chromic acid for 20 min, prior to anodization.

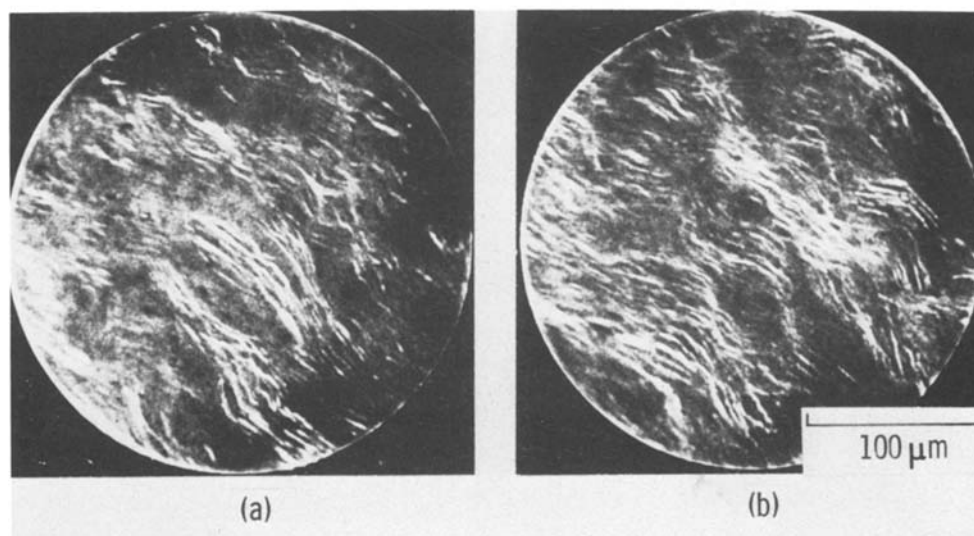


Fig. 4. Photoelectron micrographs of 1100 aluminum coated with thin natural oxide, showing sources of exoelectron emission after a tensile strain of 4×10^{-2} . (a) Precleaned with acetone, (b) precleaned with chromic acid.

17), but in our experiments we have not detected any evidence of peeling even for oxides as thick as 200 nm.

The 28 nm oxide formed after chromic acid treatment behaves quite differently from the oxides formed under the other three conditions considered above. Subsequent examination of these specimens with an optical microscope showed that in the case of the three oxides exhibiting a similar and high degree of susceptibility to fracture, the specimens had developed the usual multitudinous arrays of slip lines. On the other hand hardly any slip lines were visible on specimens which had been coated with the more fracture resistant 28 nm oxide. Closer examination of the latter, at higher magnification in a scanning electron microscope, did reveal a few isolated arrays of what appear to be microcracks in the surface oxide (Fig. 5a). But these are quite different in character from the strongly defined slip steps which always develop on specimens with the other less fracture resistant oxides (e.g., Fig. 5b).

Thus of the four surface oxides under consideration here, the 28 nm oxide with low leakage current is unique in that it is apparently strong enough to suppress slip step development during tensile deformation. The other three oxides are much weaker, are apparently of similar strength, and are much more easily ruptured by the relatively freely emerging slip steps.

Flaw Controlled Fracture of Oxide Films

The above experiments show that the extent of fracture of surface oxides during tensile deformation of the metal substrate is closely related to the concentration of flaws initially present in the oxide film. This conclusion is consistent with the observations of oxide fracture by photoelectron microscopy, as well as the quantitative measurements of the extent of fracture by the reanodization current transient technique. On the other hand, the experiments in the PEM also showed that the tensile strain required to initiate oxide fracture was approximately independent of the concentration of flaws in the oxide (as measured by the leakage current). Thus we conclude that the fracture process is a highly localized phenomenon and requires only the presence of a flaw at the site of an emerging slip step.

Thus the following picture of the process emerges. During the early stages of tensile deformation slip steps are initiated over the entire surface of the sample, producing highly localized stress concentrations in the strongly bonded oxide film. In the model of Grosskreutz and McNeil (15) the oxide film is regarded as having two choices, either fracture or peel, depending upon the strength of the film and the strength of the bond to the substrate. In the metal-oxide system studied here we have never observed peeling of the oxide. Instead the two alternatives are that either the oxide fractures or the slip step is suppressed, i.e., the oxide acts as a barrier to slip step development. This was clearly

demonstrated for the 28 nm oxide (Fig. 3 and 4), but was not observed for the much thinner natural oxide. The latter may simply not be strong enough to withstand the stresses produced by an emerging slip step, so always fractures. On the other hand, the 28 nm oxide may either fracture or suppress the slip. The degree to which these two alternatives occur is dependent upon the strength of the oxide in the immediate vicinity of the emerging slip steps, i.e., on the probability of the presence of a debilitating flaw in the oxide.

Let us consider in more detail the implications of this model for the more interesting case of the 28 nm oxide. The nature of the flaws controlling the leakage current and the fracture strength of this oxide is not clear. Let us simply assume that they are point defects when viewed perpendicular to the surface, such as for example the pores which have been reported to form in similar anodic films even during the first 10 min of anodization (6). The leakage current density of such an oxide film will be

$$I_1 = \alpha N \quad [1]$$

where N is the concentration of defects and α is a constant.

If these defects are randomly distributed with an average spacing d , then

$$Nd^2 = 1 \quad [2]$$

The occurrence of oxide fracture is determined by the probability (P) of an emerging slip line of length D (and negligible but finite width) encountering a defect. There are three regimes to consider.

I. If $D \gg d$, $P \sim 1$. This is the case of a high density of defects so all slip steps will rupture the oxide with ease. The reanodization time constant (τ/A) for a given value of tensile strain will be independent of I_1

$$\text{i.e., } \tau/A = \text{constant} \quad [3]$$

II. $D \sim d$. In this regime of intermediate flaw density

$$P \sim \frac{D}{d} \sim DN^{1/2} \quad [4]$$

Thus the reanodization time constant (τ/A) for a given tensile strain will depend upon $N^{1/2}$, or

$$\tau/A \sim I_1^{1/2} \quad [5]$$

III. If $D \ll d$, $P \sim N$. Thus for a low density of flaws

$$\tau/A \sim I_1 \quad [6]$$

The experimental relationship between I_1 and τ/A can be obtained from the results in Fig. 1 and 2. Values of I_1 and τ/A , for equal periods of cleaning time in chromic acid, were taken from the curves drawn through this original data. The relationship between these values of I_1 and τ/A are shown in Fig. 6. The regimes of high defect density (I), and intermediate defect density (II) are clearly apparent and in good

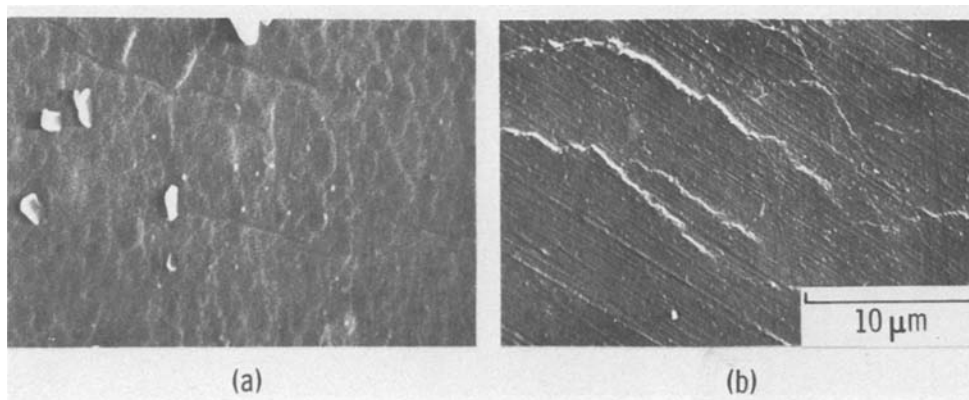


Fig. 5. Scanning electron micrographs of two samples of 1100 aluminum coated with 28 nm anodic oxide. Tensile strain 4×10^{-2} . (a) Pre-cleaned with chromic acid, (b) pre-cleaned with acetone, prior to anodization.

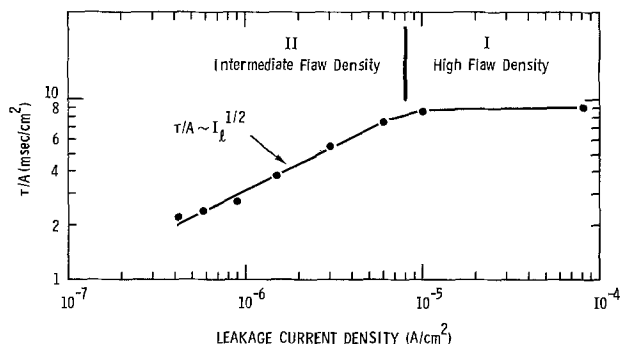


Fig. 6. Relationship between leakage current density and re-anodization time constant after tensile strain of 6×10^{-2} . Data obtained from Fig. 1 and 2 (see text).

agreement with Eq. [3] and [5]. The third regime of low defect density was apparently not achieved in these experiments.

This analysis, particularly the confirmation of Eq. [5], provides further support for our contention that the same defects control both the leakage current and the fracture strength of the oxide film. These defects were present in a high concentration since the analysis of Fig. 6 shows that $d \leq D$. The length of a slip line D approximates the average grain diameter, so the defects apparently reside in regions corresponding to the interior of the grains of the substrate metal. Presumably they form around pre-existing defects in either the very thin initial natural oxide film and/or in the surface layers of the substrate metal.

Summary

During tensile deformation of aluminum, the extent of fracture of anodic oxide films on the surface is controlled by the density of defects initially present in the oxide. For oxide thicknesses ≤ 30 nm, the fracture occurs at slip steps emerging from the underlying metal, provided that the oxide contains debilitating defects in the immediate vicinity of the step. In these experiments the same defects controlled both the susceptibility to fracture as well as the leakage current, or effective resistivity, of the oxide film. In fact these two properties can be related in terms of a simple model involving only the probability of a defect in the oxide being located in the path of an emerging slip step.

The density of defects in these thin barrier layer type of anodic oxides is determined by the condition of the aluminum surface prior to anodization. Thus the defects originate either from flaws in the initial natural oxide upon which the anodic film grows, or from impurities or inclusions in the substrate metal. The density of defects can be greatly reduced by cleaning the surface with chromic acid prior to anodization. This increases the strength of the oxide film, so that even a thin (28 nm) oxide suppresses slip step formation during tensile deformation.

Manuscript received Sept. 10, 1980.

Any discussion of this paper will appear in a Discussion Section to be published in the December 1981 JOURNAL. All discussions for the December 1981 Discussion Section should be submitted by Aug. 1, 1981.

Publication costs of this article were assisted by General Motors Corporation.

REFERENCES

1. P. G. Anderson and O. F. Devereux, *This Journal*, **122**, 267 (1975).
2. Y. H. Choo and O. F. Devereux, *ibid.*, **122**, 1645 (1975).
3. G. C. Wood, W. H. Sutton, J. A. Richardson, T. N. K. Riley, and A. G. Malherbe, "Localized Corrosion," 526 NACE-3 (1971).
4. S. F. Bubar and D. A. Vermilyea, *This Journal*, **113**, 892 (1966).
5. J. C. Grosskreutz, *ibid.*, **116**, 1232 (1969).
6. T. P. Hoar and J. Yahalom, *ibid.*, **110**, 614 (1963).
7. W. J. Baxter and F. E. Gifford, "Reanodization Current Transients After Plastic Deformation of Aluminum," General Motors Research Laboratories, Warren, MI, Research Publication GMR-2960, April 6, 1979.
8. W. J. Baxter and S. R. Rouze, *Rev. Sci. Instrum.*, **44**, 1628 (1973).
9. W. J. Baxter and S. R. Rouze, *J. Appl. Phys.*, **44**, 4400 (1973).
10. W. J. Baxter and S. R. Rouze, *ibid.*, **49**, 4233 (1978).
11. S. S. Hecker, *Met. Eng. Quart.*, **14**, 30 (1974).
12. D. H. Bradhurst and J. S. L. Leach, *Trans. Br. Ceram. Soc.*, **62**, 793 (1963).
13. J. C. Grosskreutz, *Surf. Sci.*, **8**, 173 (1967).
14. O. F. Devereux, T. A. Libsch, Y. H. Choo, and A. K. Bambri, *Corros. Sci.*, **15**, 361 (1975).
15. J. C. Grosskreutz and M. B. McNeil, *J. Appl. Phys.*, **40**, 355 (1969).
16. N. J. Cochrane and R. J. Block, *This Journal*, **117**, 225 (1970).
17. R. J. Block, *ibid.*, **117**, 788 (1970).

LPE Growth of Silicon from Poly Si/Si Structure Using CW Argon Laser

S. Minagawa,* K. F. Lee, and J. F. Gibbons*

Stanford Electronics Laboratories, Stanford University, Stanford, California 94305

and T. J. Magee and R. Ormond

Advanced Research and Applications Corporation, Sunnyvale, California 94086

ABSTRACT

Epitaxial layers were grown by melting the surface of a polysilicon/silicon structure with a scanning cw argon laser beam. Topographical features and crystalline perfection associated with the laser-induced recrystallization were investigated by transmission electron microscopy (TEM) and optical microscopy. The regrown layers obtained were relatively free of defects, as revealed by TEM analysis. Large concentrations of dislocation lines and twinning zones were not detected in these studies; however, dense dislocation networks were observed in the substrate beneath the epitaxial layer.

Laser annealing, particularly by cw laser scanning, has been used in a variety of experiments to grow thin layers of silicon crystal. Recrystallization of an ion-implanted amorphized layer (1-4), grain growth of both poly and single crystal silicon on an insulating layer (5, 6), and graphoepitaxy (7, 8) are the major achievements obtained to date.

However, epitaxial growth from the polysilicon/single crystal silicon structure, utilizing cw laser scan techniques has not been reported, although epitaxial growth (9-12) and bridging epitaxial growth (13) are known to occur by melting the surface with a high energy density ($10^7 \sim 10^8$ W/cm²) laser pulse.

This paper describes the grain growth obtained when a poly-Si/Si structure is scanned by a separated single beam of a cw Ar laser, with an energy density high enough to melt the surface. Under appropriate conditions, epitaxial growth of silicon is obtained.

* Electrochemical Society Active Member.
Key words: semiconductor, epitaxy.

Experimental

The scanning laser setup has been described elsewhere (14). It consists of a 25W cw Ar laser operated in a multiline mode, an X-, Y-beam deflection system implemented with galvanomirrors, a heated vacuum-chuck sample holder, and control electronics.

The samples were prepared by depositing 2000Å polysilicon layers on (100) Si wafers using the hydrogen reduction of silane at 630°C at 0.8 Torr (LPCVD). The grain size was on the order of 500Å or less as measured by transmission electron microscopy (TEM).

The scanning speed of the laser beam was 12 cm/sec. In area scan experiments, the separation between the two successive scanning lines was set to about 11 μm so that the melted zones were well overlapped to assure the occurrence of uniform growth over the total area scanned. This assures overlap of more than 50%

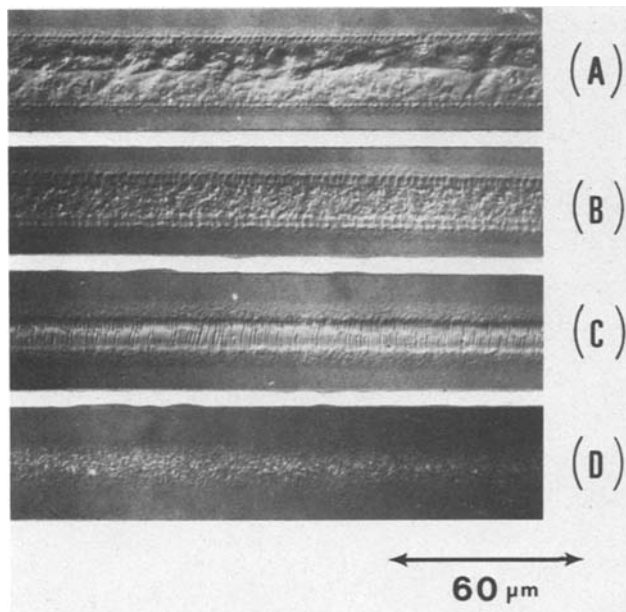


Fig. 1. Optical micrographs showing the surface topography induced after single line scans: (A) 10W, (B) 9W, (C) 8W, (D) 7W.

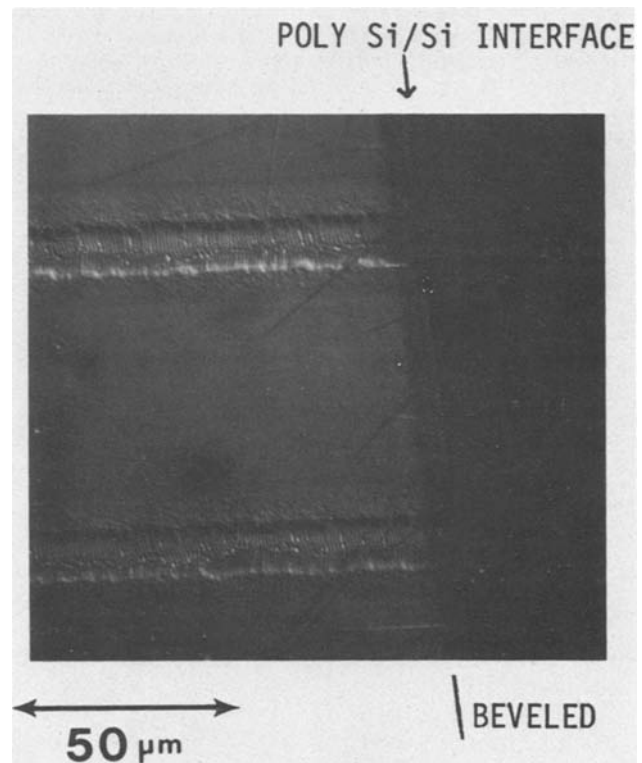


Fig. 2. Laser traces on a beveled and etched sample

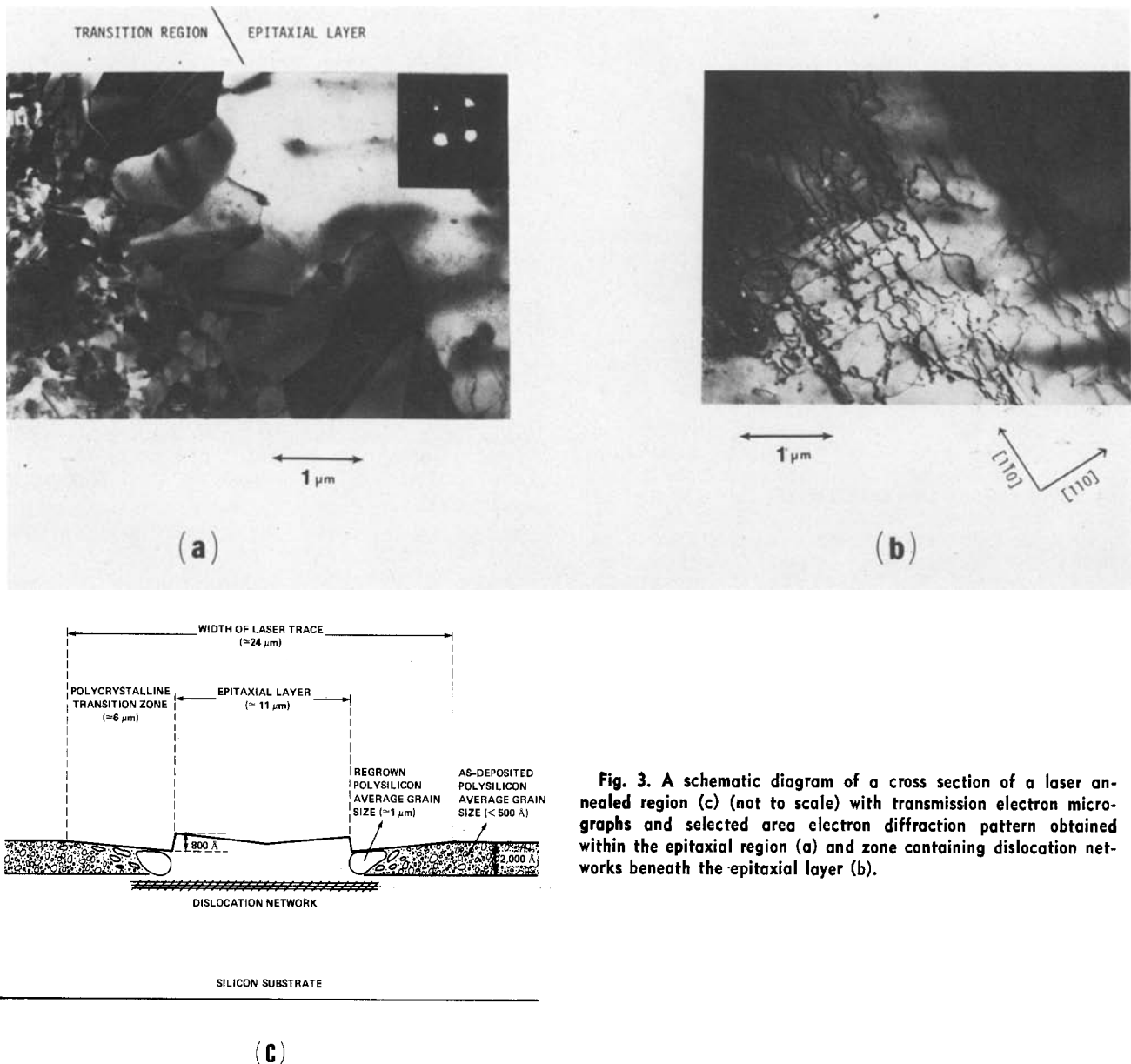


Fig. 3. A schematic diagram of a cross section of a laser annealed region (c) (not to scale) with transmission electron micrographs and selected area electron diffraction pattern obtained within the epitaxial region (a) and zone containing dislocation networks beneath the epitaxial layer (b).

of the laser traces. The substrate temperature was 350°C in all anneal experiments. Bevel polishing was done at an angle of $1^{\circ}9'$ on a Plexiglas plate with Metadi grits. The etchant used to delineate the polysilicon/silicon substrate boundary was a diluted Sirtl etch with the composition $\text{CrO}_3:\text{H}_2\text{O}:\text{HF} = 5\text{g}:10\text{ml}:1\text{ml}$.

Results

The samples were annealed under various output powers in the single line scan mode. The development of surface topographic features with the output power of the cw laser is shown in Fig. 1. At low power, the trace of a laser beam shows a dotted surface structure [Fig. 1(D)], which was found to be a result of the grain growth of polycrystalline silicon when examined by TEM. Increasing the laser power to a threshold value turned the center portion of the beam trace band into a ripple pattern [Fig. 1(C)]. Further increase in laser power smeared out the ripples into a rather coarse and irregular pattern [Fig. 1(A) and (B)]. Although the dotted and ripple structures have already been reported in pulse experiments (12), the latter irregular feature was not known. It did not disappear even at an output power level as high as 15W which is the maximum output of the cw laser used in this experiment. This can be associated with the longer melt duration in the cw laser irradiation than that in the short pulse case.

The bevel polish and etching show the existence of the polysilicon/single silicon substrate boundary in samples annealed at low laser powers. However, the boundary disappeared under the ripple pattern indicating that melting occurred into the substrate and suggesting the epitaxial regrowth of the polysilicon layer (Fig. 2). The beveling also shows the minute variation of the cross-sectional height of the beam trace as illustrated in Fig. 3(c). TEM examination of these single line scanned samples was employed to study the possible occurrence of epitaxial growth.

The change in the crystal structure brought about by cw laser anneal is shown in Fig. 3(a) for an 8W annealed sample with the ripple structure. The grain size of polycrystals increases from the edge toward the center of the laser beam trace and turns into single crystal epitaxial layer at the onset front of the ripple structure. The quality of the epitaxial layer is good as judged by the (100) transmission electron diffraction pattern, and by the absence of twin boundaries or dislocation lines. However, the electron micrograph of the epitaxial layer shows a periodic contrast associated with surface undulations, thereby duplicating the characteristic ripples observed on the surface of the regrown layer. This periodic ripple (thickness) contrast can probably be ascribed to the periodic change of stress accompanying crystal regrowth. The regularly defined (thickness) contrast variations disap-

peared in the sample annealed at 10W. The layer grown at 10W was also shown to be single crystal by diffraction, with no structural irregularity observed by TEM.

Another feature revealed by the TEM observation is the dislocation network which appeared in the substrate crystal below the epitaxial layer [Fig. 3(b)]. From micrographs obtained on a large number of samples, we observed that the dislocation lines extend from the epitaxial layer to the transition region where polycrystals develop, depending on the laser energy they receive. Since no periodic variation in contrast is observed for long dislocation lines, with the foil oriented at the exact Bragg condition ($S_g \approx 0$), these lines are believed to lie on (100) planes extending in $\langle 110 \rangle$ directions. All these results are summarized in Fig. 3(c), which schematically shows the crystallographic changes when a surface of a polysilicon/silicon structure is swept by a laser beam.

Area scanning was used in an attempt to obtain large epitaxial layers. Scan conditions were chosen as stated in the Experimental section, using the results obtained for single line scan experiments. The surfaces of the area scanned sample are seen to reflect the topographical features of single line scans. One example is shown in Fig. 4, which retains the ripple structure observed in a single line sample. Electron diffraction demonstrates that the polysilicon layer was re-grown as an epitaxial layer by area laser beam scanning.

Discussion

A lower bound on the propagation velocity of the recrystallization front along the direction of scan can be estimated, postulating that the ripples are generated by standing waves from interference of laser beam on crystal surface (12, 16, 17).

This propagation velocity should be an order of magnitude faster than the scan speed, because the crystal growth pattern (the ripples) caused by the variation of laser power distribution by interference

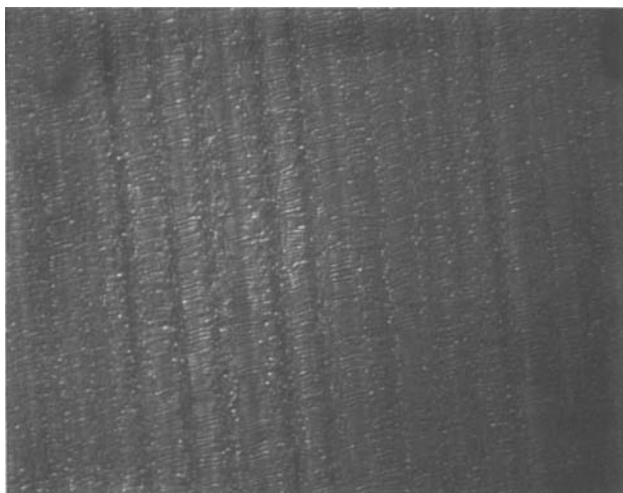


Fig. 4. An optical micrograph showing the surface topography of an epitaxial layer grown by overlapping laser scans (8W).

is not smeared out by scanning. Therefore, the lower limit of this velocity is estimated to be around 1 m/sec in the ripple growth condition. This value is well within a reasonable range for the laser-induced liquid phase epitaxial growth, from the discussion on the crystal growth velocity in a previously published paper (15).

Conclusion

Liquid phase epitaxial growth from polysilicon/single crystal structures utilizing a cw Ar laser was demonstrated. The epitaxial layer was of relatively good crystal perfection in that the layer included few dislocations and twins. However periodic pile up of stress at some power levels, surface roughness, and high density dislocations under the epitaxial layer indicate the need for further study.

Acknowledgment

One of the authors (S.M.) would like to thank Dr. T. Doi, Dr. T. Tokuyama, and Dr. M. Tamura of Central Research Laboratory, Hitachi, Limited, and to Dr. Y. Yamada of HISL, Incorporated for their support in various ways.

Manuscript submitted Sept. 3, 1980; revised manuscript received Dec. 1, 1980.

Any discussion of this paper will appear in a Discussion Section to be published in the December 1981 JOURNAL. All discussions for the December 1981 Discussion Section should be submitted by Aug. 1, 1981.

Publication costs of this article were assisted by Stanford University.

REFERENCES

1. A. Gat, J. F. Gibbons, T. J. Magee, J. Peng, V. R. Deline, P. Williams, and C. A. Evans, *Appl. Phys. Lett.*, **32**, 276 (1978).
2. A. Gat, J. F. Gibbons, T. J. Magee, J. Peng, P. Williams, and C. A. Evans, Jr., *ibid.*, **33**, 389 (1978).
3. D. H. Auston, J. A. Golovchenko, P. R. Smith, C. M. Surko, and T. N. C. Venkatesan, *ibid.*, **33**, 539 (1978).
4. J. S. Williams, W. L. Brown, H. J. Leamy, J. M. Poate, J. W. Rogers, D. Rouseau, G. A. Rozgonyi, J. A. Shelnut, and T. T. Sheng, *ibid.*, **33**, 542 (1978).
5. A. Gat, L. Gerzberg, J. F. Gibbons, T. J. Magee, J. Peng, and J. D. Hong, *ibid.*, **33**, 775 (1978).
6. J. F. Gibbons, K. F. Lee, T. J. Magee, J. Peng, and R. Ormond, *ibid.*, **34**, 831 (1979).
7. M. W. Geis, D. C. Flanders, and H. I. Smith, *ibid.*, **35**, 71 (1979).
8. M. W. Geis, D. C. Flanders, H. I. Smith, and D. A. Antoniadis, *J. Vac. Sci. Technol.*, **16**, 1640 (1979).
9. G. K. Celler, J. M. Poate, and L. C. Kimerling, *Appl. Phys. Lett.*, **32**, 464 (1978).
10. S. S. Lau, W. F. Tseng, M.-A. Nicolet, J. W. Mayer, R. C. Eckerd, and R. J. Waner, *ibid.*, **33**, 130 (1978).
11. J. C. Bean, H. J. Leamy, J. M. Poate, G. A. Rozgonyi, T. T. Sheng, J. S. Williams, and G. K. Celler, *ibid.*, **33**, 227 (1978).
12. H. J. Leamy, G. A. Rozgonyi, and T. T. Sheng, *ibid.*, **32**, 535 (1978).
13. M. Tamura, H. Tamura, and T. Tokuyama, *Jpn. J. Appl. Phys.*, **19**, L23 (1980).
14. A. Gat and J. F. Gibbons, *Appl. Phys. Lett.*, **32**, 142 (1978).
15. G. Foti and E. Rimini, *Appl. Phys.*, **15**, 365 (1978).
16. C. T. Walters, *Appl. Phys. Lett.*, **25**, 696 (1974).
17. G. N. Maracus, G. L. Harris, C. A. Lee, and A. McFarlane, *ibid.*, **33**(5) 453 (1979).

Comparison of Aluminum Etch Rates in Carbon Tetrachloride and Boron Trichloride Plasmas

K. Tokunaga,* F. C. Redeker,* D. A. Danner, and D. W. Hess*

Department of Chemical Engineering, University of California, Berkeley, California 94720

ABSTRACT

Etch rates of aluminum and "native aluminum oxide" films were studied as a function of substrate temperature in a parallel plate plasma etcher using CCl_4 and BCl_3 plasmas. Differences in the inhibition period for CCl_4 vs. BCl_3 etching were attributed to the relative abilities of these etchants to scavenge oxygen and water vapor and to etch native aluminum oxide. The temperature dependence of the etch rates suggested basic differences in the rate-controlling steps for CCl_4 vs. BCl_3 plasma etching. The surface chemistry of the electrode materials played an important role in the etch rates observed with CCl_4 and BCl_3 .

Plasma or reactive ion etching of aluminum and aluminum alloys is vitally important to the VLSI effort. A number of papers have appeared recently describing the etching of aluminum films in carbon tetrachloride or boron trichloride plasmas using parallel plate plasma etch systems (1-10). However, these publications have not directly compared etch rate results for carbon tetrachloride and boron trichloride in the same etch system. In this paper we investigate the etch rates of aluminum films in carbon tetrachloride and boron trichloride as functions of substrate temperature in a parallel plate plasma etcher.

Experimental Procedure

The detailed operation of the parallel plate plasma etcher used in this study has been described previously (10), so only a brief description will be given here. Filament-evaporated or S-gun sputtered aluminum films on either Pyrex cover slips or on oxidized 2 in. diam silicon wafers were placed on the grounded lower electrode, which was temperature controlled. Power from a 13.56 MHz rf generator was supplied to the upper electrode, which was separated from the lower electrode by a distance of 2.5 cm. Etch gases entered the system through holes in the hollow upper electrode, and were exhausted through the lower electrode support column.

The etch runs described below were carried out at 100W rf power (0.3 W/cm^2) and 13 Pa (0.1 Torr) pressure. Since etching proceeded from the substrate edge to the center, the etch time was taken as the time required to completely remove the aluminum film.

Results

Many investigators have noted that the native aluminum oxide film present on aluminum surfaces etches slowly (compared to aluminum) in chlorine-containing etch gases (2-6, 10, 11). By utilizing both a thin (30-40 nm) and a thick (>500 nm) aluminum film during each etch run, an estimate of the etch rates of aluminum and of native aluminum oxide has been made as shown in Fig. 1 (10). Of course, this etch rate analysis assumes that the native aluminum oxide coating is the sole cause of the slow initiation step in aluminum etching. As indicated previously (10), this assumption is not entirely correct, since water vapor or oxygen in the etching chamber also inhibit aluminum etching (8, 9, 12). Nevertheless, such an analysis allows comparisons to be made between the ability of different etch gases to minimize or control oxygen or water vapor effects, and to etch native aluminum oxide.

* Electrochemical Society Active Member.

Key words: aluminum plasma etching, boron trichloride plasma, carbon tetrachloride plasma, oxygen scavenging, water vapor scavenging.

CCl_4 etching.—Using anodized aluminum electrodes (10), controllable aluminum etching was achieved in pure CCl_4 plasmas as shown in Fig. 1. However, Fig. 1 indicates that a large discrepancy (approximately a factor of 100) is observed between the etch rate of the "oxide" (which is composed of oxygen and water vapor scavenging, and native aluminum oxide etching) and the etch rate of the aluminum.

In an attempt to determine an order-of-magnitude estimate of the etch rate of native aluminum oxide, aluminum oxide was sputtered onto silicon wafers using a Model 304 Randex rf sputtering system. The sputtering atmosphere was 20% O_2 /80% Ar, at a pressure of 0.01 Torr, which resulted in an aluminum oxide film with a refractive index of 1.60. At 100°C substrate temperature, the sputtered aluminum oxide etch rate was $\sim 0.1 \text{ nm/sec}$, which is approximately a factor of two higher than that indicated in Fig. 1 for "oxide." This difference is no doubt related to the fact that native aluminum oxide has a different composition than

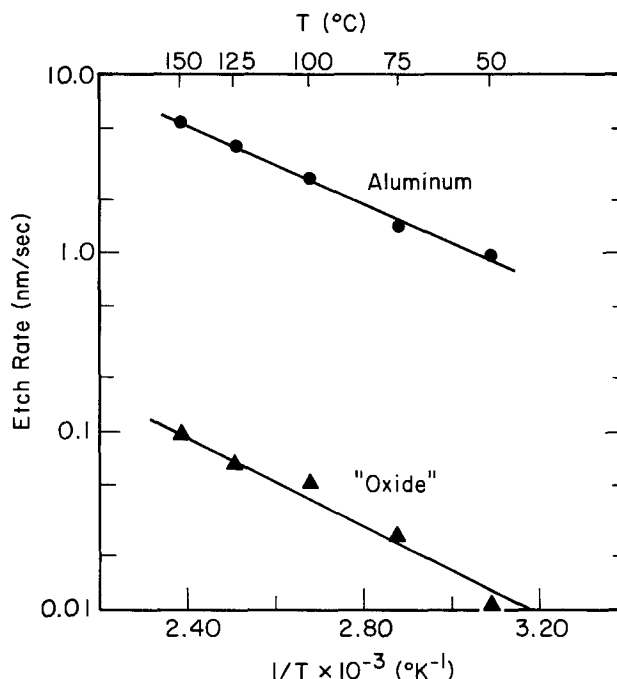


Fig. 1. Etch rate of aluminum and "oxide" (composed of oxygen and water vapor scavenging plus native aluminum oxide etching) films in CCl_4 as a function of electrode temperature on anodized aluminum electrodes.

sputtered aluminum oxide, since scavenging effects should be similar in both cases.

The etch rate data of Fig. 1 also indicate that the activation energies for aluminum and "oxide" etching are nearly equal (~ 0.2 eV/mole). The meaning of the equality of the activation energies is not clear, since the "oxide" etch rate is composed of oxygen and water vapor scavenging, along with native aluminum oxide etching. All that can be said at present, is that under the conditions used in this study, the overall inhibition period displays an activation energy of ~ 0.2 eV/mole.

A few comments can be made in regard to the portion of the inhibition period due to native aluminum oxide etching. Atomic chlorine appears to be the etchant for aluminum, while a chlorocarbon species is believed to be the primary etchant for aluminum oxide (2, 6). Indeed, this is in agreement with results in our system as well as others (2), that demonstrate the inability of Cl_2 plasmas to effectively and uniformly etch aluminum. However, if substrate bombardment is enhanced, as in the case of RIE, aluminum oxide can be etched successfully in Ar/Cl_2 atmospheres (6, 13).

BCl_3 etching.—An Arrhenius plot of the etch rate of aluminum and "oxide" films in BCl_3 using anodized aluminum electrodes, is shown in Fig. 2. Unlike the results obtained with CCl_4 , BCl_3 displays little temperature dependence of the etch rates—activation energy ~ 0.02 eV/mole for aluminum, and ~ 0.03 eV/mole for "oxide." These observations suggest basic differences in the rate-controlling steps for BCl_3 vs. CCl_4 plasma etching of aluminum.

BCl_3 was also used to etch sputtered aluminum oxide. At a substrate temperature of 100°C , the etch rate was ~ 0.01 nm/sec, which is a factor of two lower than that determined via our analysis on "oxide" films.

Discussion

One of the primary differences between CCl_4 and BCl_3 etching of aluminum involves the ability of CCl_4 to form unsaturated chlorocarbons, and thus polymer films in a glow discharge. With CCl_4 , and an active surface as stainless steel (SS), chlorine atom recombination, chlorocarbon recombination, and reaction of chlorine with the electrode material are all likely

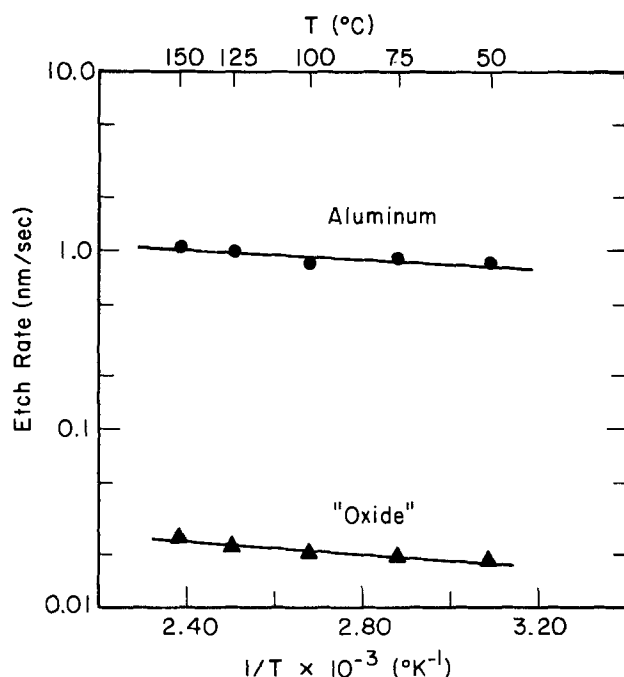


Fig. 2. Etch rate of aluminum and "oxide" (composed of oxygen and water vapor scavenging plus native aluminum oxide etching) films in BCl_3 as a function of electrode temperature on anodized aluminum electrodes.

processes, and contribute to the concentration of unsaturated chlorocarbons and thus to polymerization (10). Under the high pressure and low power conditions utilized in our previous study (10), polymerization of CCl_4 on SS electrodes was difficult to avoid, although at lower pressures, where ion and electron energies are higher, polymerization can be minimized, and etching can proceed, even with low power densities. For instance, at 0.1 Torr, both BCl_3 and CCl_4 exhibit aluminum etch rates approximately a factor of two lower with SS than with anodized aluminum electrodes.

Since boron does not form the same type of polymer structures as does carbon, no polymer is observed on the samples or on the electrodes with BCl_3 using SS or anodized aluminum electrodes. Boron compounds (possibly a combination of BCl_3 and boron oxychlorides) do condense or adsorb on the bell jar walls with anodized aluminum or SS electrodes, because when the etch chamber is vented to the atmosphere, a white deposit ($\text{B}(\text{OH})_3$) forms immediately. Such deposits are never observed with CCl_4 .

Aluminum oxide etching and oxygen scavenging.—Under the present plasma conditions, the etch rate of sputtered aluminum oxide is an order of magnitude higher with CCl_4 than with BCl_3 as discussed previously. Thus, if native aluminum oxide etching is the primary cause of the inhibition period for aluminum etching, the inhibition period should be shorter for CCl_4 than for BCl_3 , at least to the extent that the etch rate of native aluminum oxide can be equated to that of sputtered aluminum oxide. Indeed, the inhibition period is slightly shorter for CCl_4 etching than for BCl_3 etching, at higher temperatures (100°C), but the difference is less than expected on the basis of sputtered aluminum oxide etch rates. However, the inhibition period is always more variable with CCl_4 than with BCl_3 .

In order to compare the abilities of CCl_4 and BCl_3 to scavenge oxygen and water vapor from the chamber atmosphere, and thereby to estimate the relative importance of scavenging in the inhibition period, the effluent gases from 1% mixtures of oxygen in CCl_4 and in BCl_3 were monitored with a UTI Model 100 C quadrupole mass spectrometer. Figure 3a demonstrates that when a plasma is ignited in the O_2/CCl_4 mixture, the intensity of the O_2^+ peak decreases as expected, due to the reaction of carbon-chlorine fragments with O_2 , but O_2 is still present in the plasma effluent. However, when an O_2/BCl_3 plasma is struck, the intensity of the O_2^+ peak goes to zero, and remains there until the plasma is extinguished (Fig. 3b). Further, with BCl_3 , the O_2^+ peak intensity is zero with an O_2 content in the inlet of approximately 5 volume percent.

In addition, the H_2O^+ peak intensity decreases when a plasma is ignited in either a BCl_3 or a CCl_4 plasma, but does not go to zero in either case. Nevertheless, the inhibition time is more reproducible in a BCl_3 than in a CCl_4 plasma. These results indicate that BCl_3 is a more efficient oxygen and possibly water-vapor scavenger than is CCl_4 . As a result, etch reproducibility should be improved with BCl_3 compared to CCl_4 , since etching should not be as critically dependent upon residual oxygen and water vapor in the etch chamber. Indeed, such conclusions have been demonstrated in our system, and these studies are consistent with the effects of oxygen and water vapor on CCl_4 etching (8, 9, 12).

Additional evidence for the scavenging differences between BCl_3 and CCl_4 arises from consideration of the reflected power observed in CCl_4 and BCl_3 plasmas. The reflected power for a CCl_4 plasma is shown as a function of time in Fig. 4. Approximately 1 min is required from plasma ignition until the reflected power reaches a minimum value. However, only 15 sec is required when BCl_3 is used (Fig. 4). The exact time

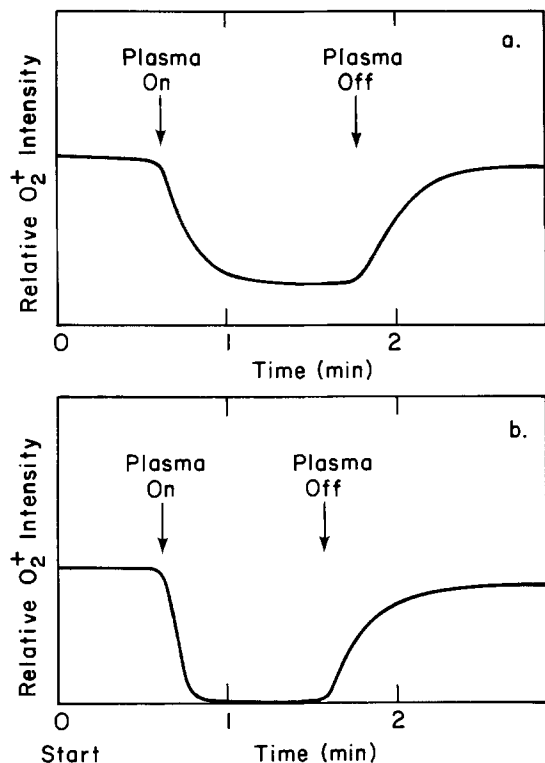


Fig. 3. (a) Relative O₂⁺ peak intensity in a 1% O₂/99% CCl₄ plasma as a function of discharge time. (b) Relative O₂⁺ peak intensity in a 1% O₂/99% BCl₃ plasma as a function of discharge time.

required to reach a minimum varies slightly (apparently due to water concentration); however, the trend is always the same. Further, the minimum reflected power is less with BCl₃ than with CCl₄, and this observation apparently depends upon water concentration also. These results are consistent with the mass spectrometer studies shown in Fig. 3, in that oxygen is still present in the plasma effluent when a plasma is ignited in a 1% O₂/CCl₄ mixture, but is absent with a 1% O₂/BCl₃ mixture. Also, Fig. 3 and 4 demonstrate a more rapid change in O₂⁺ peak intensity and reflected power, respectively, for BCl₃ as compared to CCl₄. Thus the reflected power may indicate the portion of the inhibition period due to oxygen and water vapor scavenging. In fact, in aluminum etch runs, the alu-

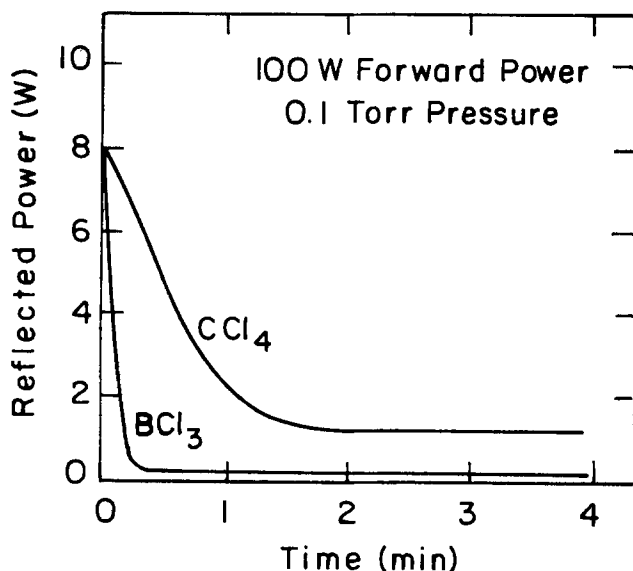


Fig. 4. Reflected power in BCl₃ and CCl₄ plasmas as a function of discharge time.

minum has not begun to etch at the point in time where the reflected power reaches a minimum. Rather, it begins to etch after approximately one additional minute of plasma exposure.

The above results are consistent with discharge impedance monitoring of CCl₄ plasmas during aluminum etching using RIE (14). In that study, a gradual decrease (over ~1 min) of electrode voltage was observed after ignition of the CCl₄ plasma. Thus, it is quite likely that oxygen or water vapor scavenging was in part responsible for the impedance changes observed at the start of the etch process.

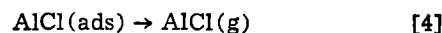
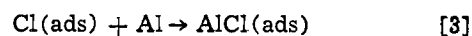
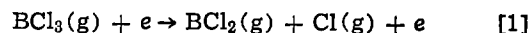
Since BCl₃ is a reasonably efficient scavenger of oxygen and water vapor, one can assume that the inhibition period for BCl₃ etching is primarily due to native aluminum oxide etching. However, the etch rate estimate from aluminum samples is ~2 times higher than that observed for sputtered aluminum oxide. This discrepancy is no doubt related to the heavily hydrated nature of native aluminum oxide surfaces (15). Since BCl₃ reacts readily with water, the native oxide is probably more reactive toward BCl₃ than is sputtered aluminum oxide.

CCl₄, on the other hand, displays an "oxide" etch rate that is ~2 times lower than that of sputtered aluminum oxide. Again, this is probably due to the high moisture content of the native oxide surface, since CCl₄ plasmas are not efficient oxygen and water vapor scavengers, and, in fact, these species tend to inhibit aluminum etching. Currently, it is not clear why CCl₄ plasmas can etch sputtered aluminum oxide more rapidly than BCl₃ plasmas. However, such results may be related to differences in the plasma and electrode potentials between CCl₄ and BCl₃, or to different concentrations of etchant species generated by the two etch gases.

Chemistry of BCl₃ and CCl₄ etching.—Etch rate studies with BCl₃ and CCl₄ have indicated that the aluminum etch rate is higher on anodized aluminum than on SS electrodes. This difference may be partly due to higher recombination and/or reaction rate of chlorine free radicals, which have been proposed to be the etchant species for aluminum, on SS surfaces. Such conclusions are consistent with studies of fluorine atom recombination on steel vs. alumina surfaces (16). These latter studies have shown that steel is a better recombination surface for fluorine atoms than is alumina.

Another consideration with regard to electrodes involves the effect of oxygen from the electrode material (10, 23). Oxygen could promote the removal of boron from the aluminum surface if boron oxychlorides are formed, and in addition can generate additional chlorine atoms by reaction with boron-chlorine fragments. Thus, enhanced aluminum etch rates may be expected.

Comparison of Fig. 1 and 2 suggests that under the plasma conditions investigated in this study, basic differences exist in the rate-limiting steps for BCl₃ vs. CCl₄ etching of aluminum. A possible reaction sequence for the etching of aluminum in BCl₃ plasmas can be written as follows

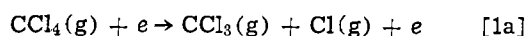


The dissociation of BCl₃ via electron collisions into BCl₂ has been indicated previously, since rf glow discharge dissociation of BCl₃ represents a high yield pathway for the formation of B₂Cl₄ (17). Also, the adsorption of chlorine gas and/or chlorine atoms onto clean aluminum surfaces has been reported (18). Clearly, gas phase species other than Cl₂ or Cl might

adsorb onto aluminum surfaces (for instance, CCl_2 or BCl_2), but for the purpose of the following discussion, these possibilities need not be considered. AlCl has been observed by emission spectroscopy of CCl_4 plasmas (19). Of course, AlCl (ads) can further react on the aluminum surface, the electrode surface, or in the gas phase, to form AlCl_2 and/or AlCl_3 as the final reaction product. The above mechanism (Eq. [1]-[4]) is in principle similar to that proposed for the etching of silicon in CF_4 plasmas (20). The present mechanism, however, considers the adsorption of Cl atoms on the aluminum surface, as well as the possibility of desorption of various aluminum-chlorine fragments in addition to AlCl_3 . Indeed, fragment desorption has been demonstrated for the etching of silicon with fluorine-containing gases (21).

Since reactions [2]-[4] are surface reactions, a temperature dependence is expected for these steps. On the other hand, reaction [1] represents a gas phase generation of chlorine free radicals, which is independent of substrate temperature. Thus, the rate-determining step for BCl_3 etching of aluminum on anodized aluminum or stainless steel electrodes is probably the gas phase generation of etchant species. Such conclusions are consistent with previous aluminum etch studies using BCl_3 on stainless steel electrodes (2).

A similar reaction sequence for CCl_4 etching can be written by replacing reaction [1] with [1a]



Indeed, mass spectrometric studies have shown that CCl_3 is prevalent in CCl_4 discharges (22). Since a substrate temperature dependence is observed for CCl_4 , one (or more) surface reactions of the type [2]-[4] control the etch rate.

Reactions similar to [1]-[4] can be written for the etching of native aluminum oxide. However, the composition of this layer is uncertain, and so no specific reactions are proposed. Nevertheless, if it is assumed that oxygen assists the removal of boron or carbon species, the chlorine is left to react with aluminum. Indeed, carbon oxides and oxychlorides are well known, and gas-phase oxychlorides of boron have been reported (24). These considerations are consistent with the improved etching characteristic of CCl_4 and BCl_3 on anodized aluminum electrodes compared to stainless steel electrodes. On stainless steel, an efficient means of removing carbon and boron is not available after the native aluminum oxide coating has been removed. However, with anodized aluminum electrodes, small concentrations of oxygen are present to assist removal of carbon (23) or boron species but the concentrations are sufficiently low to prevent inhibition of aluminum etching by aluminum oxide formation.

The scavenging studies discussed above indicate that the relative reactivity of oxygen with aluminum *vs.* CCl_x or BCl_x is an important aspect of aluminum plasma etching. Apparently, in the competition for oxygen between BCl_x and Al, BCl_x is the preferred reactant, whereas with CCl_x , aluminum may be the better scavenger. Certainly, the etch rate of aluminum samples decreased when oxygen was added to CCl_4 (10), and our analysis indicated that both the "oxide" and the aluminum etch rates decreased. However, small additions (~1%) of oxygen to BCl_3 resulted in a decrease in the "oxide" etch rate, but an increase in the aluminum etch rate, such that the overall etch rate increased. Higher oxygen concentrations result in boron oxide deposition. These results are consistent with previous studies which report an increase in overall aluminum etch rate with oxygen addition to BCl_3 plasmas (7).

In CCl_4 etching, oxygen reacts with aluminum or carbon species, while with BCl_3 , oxygen reacts preferentially with boron to form oxides or oxychlorides, thus generating additional chlorine atoms, which en-

hance the aluminum etch rate. This latter reaction is analogous to that observed when oxygen is added to CF_4 during silicon etching (25).

If CCl_4 is a better etchant for aluminum films than is BCl_3 , and if BCl_3 is a better scavenger for oxygen and water vapor than is CCl_4 , then an improved etchant for aluminum may be some mixture of the two. Indeed, preliminary studies in our laboratory indicate that such mixtures display higher etch rates and better reproducibility than either CCl_4 or BCl_3 individually. However, boron residues may preclude their usefulness.

Summary

The etch rates of aluminum and "native aluminum oxide" (composed of native aluminum oxide etching and oxygen and water vapor scavenging) in CCl_4 and BCl_3 plasmas were investigated as functions of substrate temperature in a parallel plate plasma etcher. Oxygen and water vapor scavenging appeared to be the most important process in initiating aluminum etching in CCl_4 plasmas, while aluminum oxide etching was the primary factor in the inhibition period with BCl_3 plasmas. These results suggest a chemical competition for oxygen or water vapor between aluminum and either boron-chlorine or carbon-chlorine fragments, with boron compounds being the better scavengers.

The etch rates of aluminum in CCl_4 plasmas on anodized aluminum electrodes were critically dependent upon temperature, indicating that surface reactions were rate controlling. However, BCl_3 etching on anodized aluminum or on SS electrodes showed little or no temperature dependence, suggesting that the rate-controlling step(s) involved gas phase generation of etching species.

The etch rate of aluminum using BCl_3 was dependent upon the electrode material, with the etch rate being greater by a factor of 2 with anodized aluminum than with SS electrodes. The differences observed are believed to be due to increased chlorine atom recombination on SS electrodes and/or to the ease of surface boron removal and additional chlorine atom generation when oxygen is available from the electrode material.

Acknowledgments

The authors would like to thank Mr. G. Au at Amdahl Corporation for supplying the sputtered aluminum films used in this study. This material is based upon work supported by the National Science Foundation under Grant ENG-7812236.

Manuscript submitted Sept. 8, 1980; revised manuscript received Nov. 17, 1980.

Any discussion of this paper will appear in a Discussion Section to be published in the December 1981 JOURNAL. All discussions for the December 1981 Discussion Section should be submitted by Aug. 1, 1981.

Publication costs of this article were assisted by the University of California.

REFERENCES

1. A. R. Reinberg, in "Etching for Pattern Definition," H. G. Hughes and M. J. Rand, Editors, p. 91, The Electrochemical Society Softbound Proceedings Series, Princeton, N.J. (1976).
2. R. G. Poulsen, H. Nentwich, and S. Ingrey, in "Proceedings of the International Electron Devices Meeting," p. 205, Washington, D.C. (1976).
3. T. O. Herndon and R. L. Burke, Interface '77 Kodak Microelectronics Symposium, Monterey, California, 1977.
4. R. Reichelderfer, D. Vogel, and R. L. Bersin, Abstract 151, p. 414, The Electrochemical Society Extended Abstracts, Atlanta, Georgia, Oct. 9-14, 1977.
5. A. Yasuoka, H. Nagata, H. Harada, and T. Enomoto, IPC Technical Report, 1977.

6. P. M. Schaible, W. C. Metzger, and J. P. Anderson, *J. Vac. Sci. Technol.*, **15**, 334 (1978).
7. M. Nakamura, M. Itoga, and Y. Ban, Abstract 114, p. 298, The Electrochemical Society Extended Abstracts, St. Louis, Missouri, May 11-16, 1980.
8. T. Y. Fok, Abstract 115, p. 301, The Electrochemical Society Extended Abstracts, St. Louis, Missouri, May 11-16, 1980.
9. D. K. Ranadive and D. L. Losee, Abstract 116, p. 304, The Electrochemical Society Extended Abstracts, St. Louis, Missouri, May 11-16, 1980.
10. K. Tokunaga and D. W. Hess, *This Journal*, **127**, 928 (1980).
11. R. L. Bersin, *Solid State Technol.*, p. 117, (April, 1978).
12. R. Le Claire, *ibid.*, p. 139, (April, 1979).
13. N. Heiman, V. Minkiewicz, and B. Chapman, *J. Vac. Sci. Technol.*, **17**, 731 (1980).
14. K. Ukai and K. Hanazawa, *ibid.*, **16**, 385 (1979).
15. M. S. Hunter and P. Fowle, *This Journal*, **103**, 482 (1956).
16. P. C. Nordine and J. D. Le Grange, *AIAA Journal*, **14**, 644 (1976).
17. T. Wortik, R. Moore, and H. J. Schlesinger, *J. Am. Chem. Soc.*, **71**, 3265 (1949).
18. T. Smith, *Surf. Sci.*, **32**, 527 (1972).
19. B. J. Curtis and H. J. Brunner, *This Journal*, **125**, 829 (1978).
20. H. F. Winters, *J. Appl. Phys.*, **49**, 5165 (1978).
21. V. M. Donnelly and D. L. Flamm, Abstract 123, p. 323, The Electrochemical Society Extended Abstracts, St. Louis, Missouri, May 11-16, 1980.
22. C. M. Melliari-Smith and C. J. Mogab, in "Thin Film Processes," J. L. Vossen and W. Kern, Editors, p. 497, Academic Press, New York (1978).
23. J. W. Coburn, H. F. Winters, and T. J. Chuang, *J. Appl. Phys.*, **48**, 3532 (1977).
24. J. Blauer and M. Farber, *J. Chem. Phys.*, **39**, 158 (1963).
25. C. M. Melliari-Smith and C. J. Mogab, in "Thin Film Processes," J. L. Vossen and W. Kern, Editors, p. 505, Academic Press, New York (1978).

Reduction of Grain Boundary Effects in Indium Phosphide Films by Nitridation

T. L. Chu* and Shirley S. Chu*

Southern Methodist University, Dallas, Texas 75275

C. L. Lin* and Y. C. Tzeng*

Poly Solar Incorporated, Garland, Texas 75041

and L. L. Kazmerski and P. J. Ireland

Solar Energy Research Institute, Golden, Colorado 80401

ABSTRACT

Indium phosphide, a direct gap semiconductor with a room temperature energy gap of 1.35 eV, is a promising photovoltaic material for thin film devices. Thin films of indium phosphide have been deposited on tungsten-coated graphite substrates by the reaction of indium, hydrogen chloride, and phosphine in a gas flow system. Without intentional doping, the deposited films are n-type with a carrier concentration of about 10^{17} cm^{-3} . Schottky barriers prepared from these films have been found to exhibit low rectification ratios, high dark currents, and poor photovoltaic response due to the shunting effects of grain boundaries. The grain boundary effects can be partially reduced by heat-treatment in an ammonia atmosphere, converting the surface of grains into indium nitride. The formation of indium nitride has been verified by Auger electron spectroscopy and x-ray photoelectron spectroscopy.

Direct gap semiconductors with bandgap energy of 1.3-1.8 eV are most promising materials for thin film photovoltaic devices. Because of their sharp optical absorption edges and large absorption coefficients, solar radiation with energy in excess of the bandgap energy are essentially all absorbed within 2-3 μm of the surface. Thus, the grain size and minority carrier diffusion length requirements are less stringent than those required of indirect-gap materials. Among III-V compounds, gallium arsenide with a room temperature energy gap of 1.43 eV and indium phosphide with a bandgap energy of 1.35 eV are considered as most promising. For example, gallium arsenide films deposited on graphite or tungsten-coated graphite substrates by the halide process have an average grain size of about 10 μm , and large area (10 cm^2) MOS solar cells have been fabricated from this type of polycrystalline films (1, 2). The AM1 efficiency of thin film gallium arsenide solar cells is higher than 8%; while

their short-circuit current density is about 80% of that of single crystalline gallium arsenide solar cells, their open-circuit voltage is considerably lower. Indium phosphide films have also been deposited on foreign substrates such as carbon and molybdenum, and small area (3 mm^2) thin film solar cells of the configuration n-CdS/p-InP/p⁺-GaAs/carbon fabricated. Although the photocurrent from thin film cells is similar to that from single crystalline CdS/InP cells, thin film cells have considerably lower open-circuit voltage and fill factor, resulting in a conversion efficiency of about 5.7%.

The considerably lower open-circuit voltage in thin film cells is due presumably to the high saturation current which arises from the poor grain structure or grain boundary effects. In this work, indium phosphide films have been deposited on tungsten-coated graphite substrates by the halide process. Schottky barrier devices prepared from these films exhibit excessive dark currents due to the shunting effects of grain boundaries. The grain boundary effects can be reduced sub-

* Electrochemical Society Active Member.

Key words: semiconductor, photovoltaic, thin films.

stantially by the heat-treatment of indium phosphide films in an ammonia atmosphere, due to the formation of indium nitride at the grain surface. The experimental procedures and results are discussed in this paper.

Deposition of Indium Phosphide Films

Graphite is an economical substrate for large area solar cells. Several types of low-cost graphite, such as grade PLC graphite manufactured by POCO Graphite Incorporated, have a linear thermal expansion coefficient very similar to that of indium phosphide ($4.5 \times 10^{-6} \text{ }^\circ\text{C}^{-1}$). Graphite is chemically inert under the conditions used for the deposition of indium phosphide. Also, graphite has high thermal and electrical conductivities and may be used as an ohmic contact to the solar cell. However, the density of low-cost graphite is 1.65-1.75 g/cm^3 (theoretical density of graphite: 2.2 g/cm^3), corresponding to a porosity of 20-25%. Consequently, the surface of graphite has a high concentration of pits, and uniform nucleation of indium phosphide cannot be expected. To provide a homogeneous surface, a thin layer (2-3 μm) of tungsten, an impervious material, was deposited on graphite substrates by the reduction of tungsten hexafluoride with hydrogen at 500°C.

The deposition of indium phosphide films on tungsten/graphite substrates was carried out by the reaction between indium, hydrogen chloride, and phosphine using the apparatus shown schematically in Fig. 1. A typical temperature profile with the positions of indium and substrate are also shown. The reaction tube was made of fused silica and was of 55 mm ID; the use of a relatively large diameter reaction tube facilitates the preparation of large area indium phosphide films of uniform properties. The reaction tube is held in a four-zone furnace with each zone separately heated and controlled. The temperature profile and the composition and flow rate of the reactant mixture are important factors affecting the deposition rate of indium phosphide.

To carry out the deposition of indium phosphide, an indium container and the substrate are placed in the appropriate temperature zones. A hydrogen-hydrogen chloride mixture is introduced into the reaction tube over the indium container, where indium is converted into volatile indium monochloride. At the same time, phosphine is introduced into the reaction zone near the substrate surface. The reaction between indium monochloride and phosphine on the substrate surface deposits indium phosphide. In the deposition experiments, the temperature of indium was maintained at 745°-755°C, and the flow rate of hydrogen was 0.5-1.5 liters/min. The substrate temperature was varied in the range of 500°-650°C, and the flow rates of hydrogen chloride and phosphine were 10-45 ml/min and 30-135 ml/min, respectively (a PH_3/HCl molar ratio

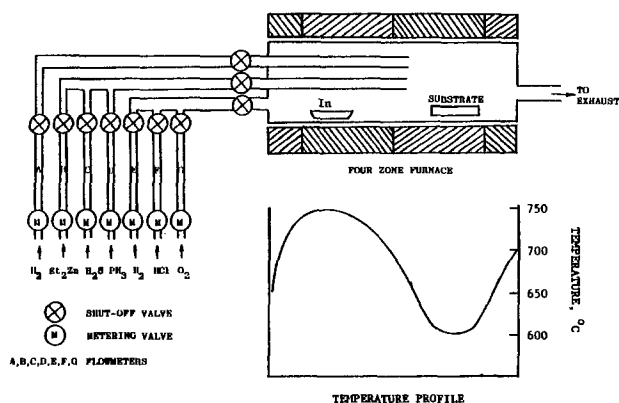


Fig. 1. Schematic diagram of the apparatus for the deposition of indium phosphide films and a typical temperature profile used in the deposition process.

of 3 or higher was always used to minimize any phosphorus deficiency in the deposit). The results of a number of deposition experiments indicate that the deposition parameters can only be varied over a limited range in order to obtain continuous films. During the initial stage of deposition, a high flux of reactant mixture, by using a relatively high flow rate of hydrogen through indium, for example, must be maintained at the substrate surface. Once a continuous film is formed, the deposition rate of indium phosphide may be reduced by reducing the flow rate of hydrogen chloride.

The microstructure of indium phosphide films on tungsten/graphite substrates were examined using optical microscope and scanning electron microscope on the as-deposited and fractured cross-section surfaces. One example is shown in Fig. 2 where the scanning electron micrographs of the as-grown and fractured cross-section surfaces of an indium phosphide film deposited on a tungsten/graphite substrate at 600°C using a hydrogen chloride flow rate of 45 ml/min are reproduced. The crystallites in these films are of random shape and size; x-ray diffraction examinations indicate that the films are essentially polycrystalline with no appreciable preferred orientations.

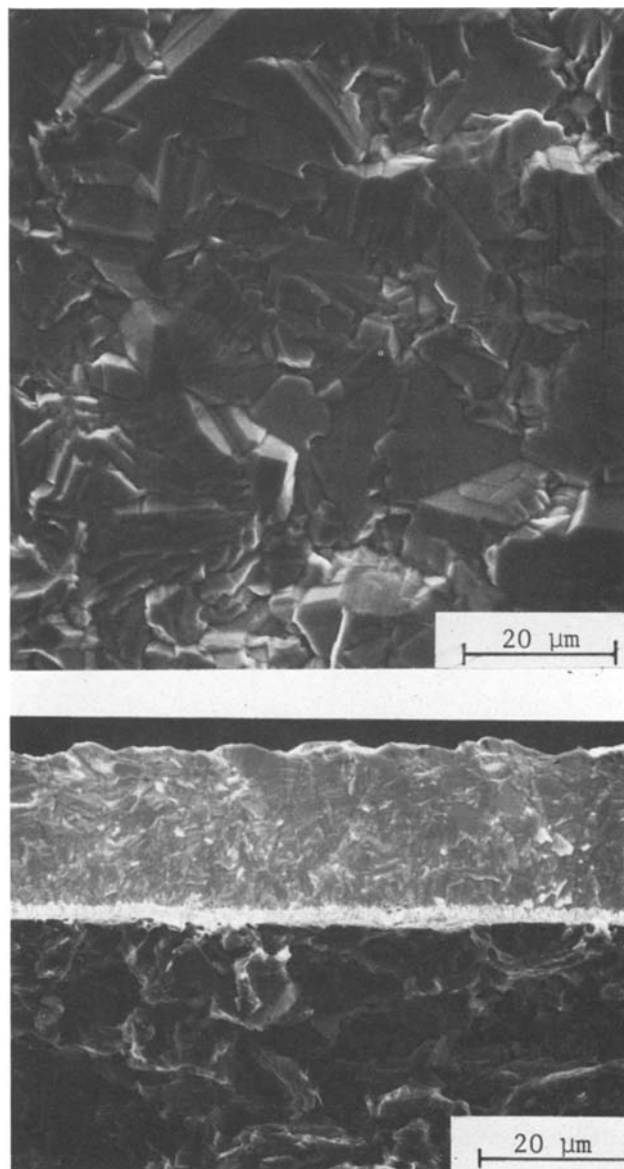


Fig. 2. Scanning electron micrographs of the as-grown and fractured cross-section surfaces of an indium phosphide film deposited on a tungsten/graphite substrate.

Electrical Properties of Indium Phosphide Films

Without intentional doping, indium phosphide films deposited on tungsten/graphite substrates are always n-type. The carrier concentration in indium phosphide films determined by differential capacitance method is in the range of $(0.5-3) \times 10^{17} \text{ cm}^{-3}$; lower carrier concentrations were obtained when the indium source was saturated with phosphine prior to the deposition process. The n-InP/W interface is ohmic with an interface resistance of less than $10^{-3} \Omega\text{-cm}^2$ at a current density of 10 mA/cm^2 .

The electrical properties of indium phosphide films on tungsten/graphite substrates were evaluated by measuring the dark current-voltage characteristics of Schottky barriers prepared from these films. Schottky barriers were prepared by the evaporation of silver dots of $1-2 \text{ mm}^2$ area onto the specimen surface through a metal mask under a pressure of less than 10^{-6} Torr, and their dark current-voltage characteristics measured at room temperature. To evaluate the photovoltaic properties of indium phosphide films, Schottky barrier solar cells of 1 cm^2 area were prepared by the evaporation of a thin silver film (60-80 Å thickness) and the grid contacts (10 lines per cm) onto the specimen surface, and their illuminated current-voltage characteristics measured under AM1 conditions. All Ag/n-InP/W/graphite devices were found to show excessive dark currents and poor rectification ratios. As an example, Fig. 3 shows the characteristics of an Ag/n-InP/W/graphite structure of about 1 mm^2 area, where the forward current density exceeds 1 A/cm^2 at 0.3 V , the diode quality factor "n" is about 5, and the rectification ratio is less than 10. However, when a semispherical gold pressure contact is used instead of the evaporated contact, the current-voltage characteristic is often improved significantly. Figure 4 shows such a characteristic, where the diode quality factor is less than 2 and the rectification ratio at 0.3 V exceeds 1000. This difference in characteristics between evaporated and pressure contacts is due presumably to the fact that the grains in indium phosphide films are not tightly packed and metals penetrate through grain boundaries during contact formation, causing shunting effects. Auger and SIMS studies on fractured cross sections have shown that the segregation of impurities,

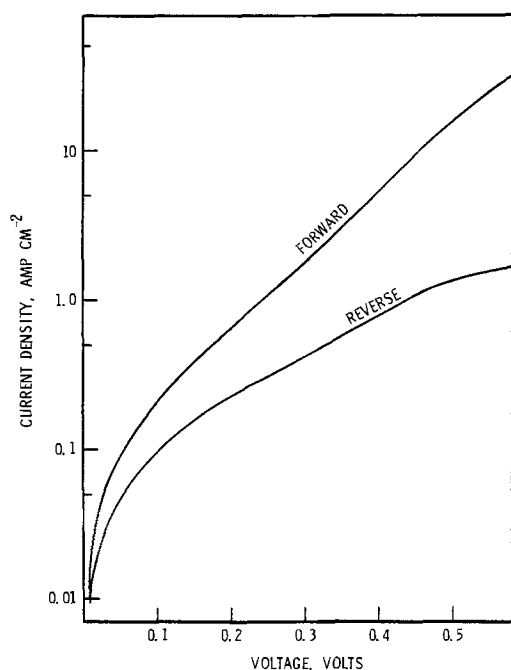


Fig. 3. Dark current-voltage characteristics of a silver Schottky barrier of about 1 mm^2 area prepared from an n-type indium phosphide film on a tungsten/graphite substrate.

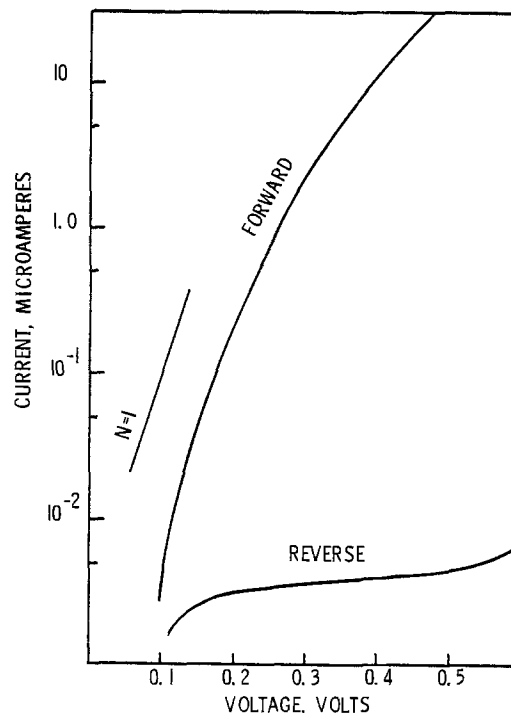


Fig. 4. Dark current-voltage characteristics of a semispherical gold pressure contact on an n-type indium phosphide film on a tungsten/graphite substrate.

such as sulfur, at grain boundaries is also a major factor contributing to the shunting effects.

Because of the high dark current, Schottky barrier solar cells of 1 cm^2 area exhibit poor photovoltaic characteristics. Under AM1 conditions, the open-circuit voltage and short-circuit current density are usually in the range of $5-10 \text{ mV}$ and $1-3 \text{ mA/cm}^2$, respectively. Schottky barrier solar cells were also prepared from n-type indium phosphide films deposited on aluminum-coated graphite substrates; their characteristics were inferior to those on tungsten-coated graphite substrates. Auger and SIMS studies on fractured and cross sections have shown that aluminum from the substrate diffused into the indium phosphide film preferentially along the grain boundaries. The diffusion of aluminum into indium phosphide generates phosphorus vacancies, thereby increasing the donor concentration in, and electrical conductivity of, grain boundaries. Thus, impurity segregation at grain boundaries is a major factor contributing to the shunting effects.

Reduction of Grain Boundary Effects by Nitridation

The high dark current in Schottky barriers from indium phosphide films is contributed by the shunting effects of grain boundaries in the films. The electrical conductivity of grain boundaries dominates over that of the grains due to at least two factors: dopant segregation at grain boundaries and the presence of minute voids between grains in indium phosphide films. The shunting effects of grain boundaries associated with impurity segregation may be reduced by using a higher bandgap material at the grain surface. Indium nitride with a bandgap energy of about 3 eV appears to be a promising candidate; this material has been prepared by the reaction of indium (III)oxide with ammonia and is stable in air at temperatures up to 300°C (4).

Because of the greater stability of indium nitride, the surface of indium phosphide can be converted into indium nitride by treatment with ammonia at high temperatures. A number of indium phosphide films were heated in an ammonia flow at $500^\circ-650^\circ\text{C}$ for a period of 15 min to 2 hr. Subsequently, silver contacts

were evaporated onto the ammonia-treated surface, and the dark current-voltage characteristics of the resulting MNS structures were used to determine the effects of temperature and duration of the ammonia treatment. At temperatures of 550°C and below, the conversion of indium phosphide into indium nitride is negligible, and the decomposition of indium phosphide becomes apparent at 650°C. Ammonia treatment at 600°C for 20 min appears to be optimum for reducing dark currents without introducing a large series resistance. The *in situ* ammonia treatment of indium phosphide films immediately after the deposition process has produced the same results.

To determine the composition and chemistry of ammonia-treated indium phosphide films, high resolution scanning Auger electron spectroscopy (AES) and x-ray photoelectron spectroscopy (XPS) using a Physical Electronics Industries Model 590 SAM/SIMS and a Model 550 XPS/SAM were carried out. For AES, pulse counting with 10 nA currents and 5 kV beam voltages were used. For the XPS studies, the argon ion source was operated at 10 kV with a magnesium anode; the pass energy was 10 eV providing a 0.3 eV instrument resolution. Figure 5 shows an Auger depth-compositional profile for an ammonia-treated indium phosphide film. The surface layer of indium phosphide, about 50Å thickness, has been converted into a nitride, and an orderly transition from the nitride to the phosphide is observed. To determine the chemical composition of the ammonia-treated indium phosphide films, XPS data were obtained at two points, α and β shown in Fig. 5, during the depth profile. The positions of the indium $3d_{3/2}$ and $3d_{5/2}$ peaks in the XPS spectra are shown in Fig. 6. These peaks were compared to the $3d_{3/2}$ (451.2 eV) and $3d_{5/2}$ (443.6 eV) peaks from an in-

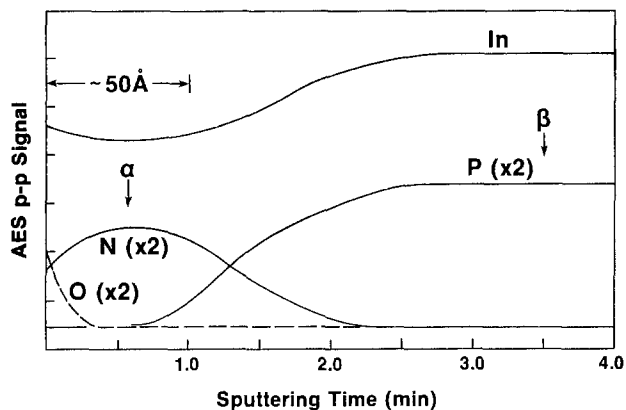


Fig. 5. AES depth-compositional profile from an ammonia-treated indium phosphide film on a tungsten/graphite substrate showing the indium nitride layer at the surface.

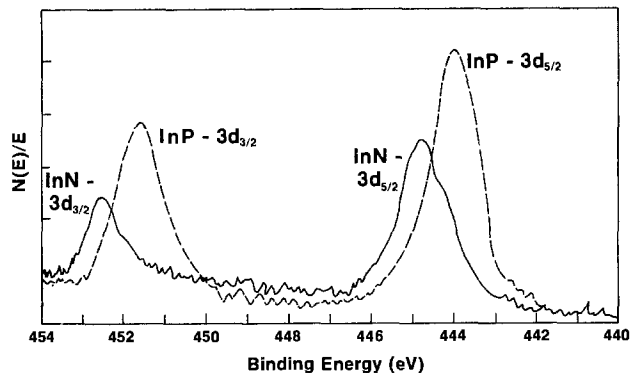


Fig. 6. XPS spectra taken at two points of the depth-compositional profile shown in Fig. 1: Dashed line—indium phosphide spectrum taken at point β in Fig. 1; Solid line—indium nitride spectrum taken at point α in Fig. 1. (Mg anode, 10 keV source; instrument resolution: 0.3 eV).

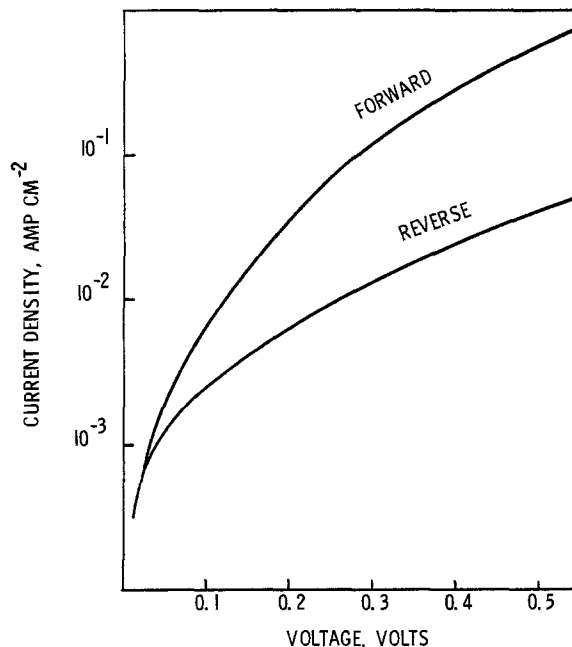


Fig. 7. Dark current-voltage characteristics of a Schottky barrier solar cell of 1 cm² area prepared from an ammonia-treated n-type indium phosphide film on a tungsten/graphite substrate.

dium standard. The spectrum taken at point β shows $3d_{3/2}$ and $3d_{5/2}$ peaks at 451.6 and 444.0 eV, respectively, which correspond to indium phosphide. The spectrum taken at point α shows $3d_{3/2}$ and $3d_{5/2}$ peaks at 452.6 and 445.0 eV, respectively, which correspond to indium nitride. No other signals over this binding energy range were observed.

Schottky barriers prepared from ammonia-treated indium phosphide films show considerably improved characteristics. Figure 7 shows the dark current-voltage characteristics of a solar cell of 1 cm² area with the configuration Ag/InN/n-InP/W/graphite. The dark current is reduced considerably as compared with the Schottky barrier structure (Fig. 3), and the rectification ratio is also improved. However, the dark current is still too high for efficient solar cells. Under AM1 conditions, the open-circuit voltage and short-circuit current density are 125 mV and 6.5 mA/cm², respectively.

Summary and Conclusion

Indium phosphide films have been deposited on tungsten-coated graphite substrates by the reaction of indium, hydrogen chloride, and phosphine. The electrical properties of these films are determined predominantly by the shunting effects of grain boundaries due to at least two factors: (i) the segregation of dopants at grain boundaries, and (ii) the loose packing of grains in the films. The shunting effects may be reduced to some extent by converting the surface of indium phosphide into indium nitride; however, more efficient passivation techniques are necessary in order to produce efficient solar cells.

Acknowledgment

This research was supported by the Electric Power Research Institute under Contract No. 1193-2.

Manuscript received Sept. 19, 1980.

Any discussion of this paper will appear in a Discussion Section to be published in the December 1981 JOURNAL. All discussions for the December 1981 Discussion Section should be submitted by Aug. 1, 1981.

Publication costs of this article were assisted by Southern Methodist University.

REFERENCES

1. S. S. Chu, T. L. Chu, and M. S. Lan, *J. Appl. Phys.*, **50**, 5805 (1979).
2. S. S. Chu, T. L. Chu, and Y. T. Lee, *IEEE Trans. Electron Devices*, **ed-27**, 640 (1980).
3. J. L. Shay, S. Wagner, M. Bettini, K. J. Bachman, and E. Buehler, *ibid.*, **ed-24**, 483 (1977).
4. G. V. Samsonov and M. D. Lyutaya, *Chem. Abstr.*, **59**, 14864 (1960).

In Situ Semiconductor Heterostructure Arrays: Ge-GaAs

D. E. Holmes¹

Hughes Research Laboratories, Malibu, California 90265

ABSTRACT

The experimentally determined microstructure of the directionally solidified Ge-GaAs eutectic, studied for the first time, was characterized as an aligned array of GaAs rods in a Ge matrix. Alignment occurred within faceted grains on the order of 100 μm wide. Possible causes of the grain structure are discussed. Based on these findings, the growth characteristics and properties of several new *in situ* semiconductor heterostructure materials (directionally solidified composites) containing group IV, III-V, and II-VI compounds were evaluated.

The potential for producing semiconductor heterostructures in a one-step process has been virtually overlooked. Heterostructures are conventionally grown layer by layer. Yet, aligned *in situ* composites of metals and oxides have been produced by techniques such as directional solidification of eutectics (1-4), eutectoid decomposition (5), and directional decomposition of noncrystalline solid single phase materials (6). Although a limited number of directionally solidified composites containing semiconductors have been grown (7-11), semiconductor-semiconductor composites containing group IV, III-V, and II-VI compounds have not been studied systematically.

This investigation concerned new *in situ* semiconductor composites with emphasis on the structure and properties of the internal phase boundaries. Attention was focused on the directional solidification of eutectics (12). The Ge-GaAs system was chosen for experimental study because (i) the pseudobinary phase diagram has been shown to contain a eutectic (13-15) and (ii) the difference between the lattice parameters of Ge and GaAs is very small ($\sim 0.004\text{\AA}$), providing an excellent lattice match at the phase boundaries.

Apparatus and Procedures

Mixtures of GaAs and Ge of the approximate eutectic composition (75 atomic percent Ge) were melted in 1-cm-diam graphite crucibles contained in evacuated quartz ampuls. The melt height was about 2 cm. The solution was solidified directionally in a vertical Bridgman apparatus by lowering the ampul through a heater at a rate of about 2 mm hr^{-1} . Although the measured vertical temperature gradient in the furnace was about 25°C cm^{-1} , the actual gradient in the melt during solidification could have been much lower because of the heat-leveling effect of the ampul. The ingots were cut parallel and perpendicular to the solidification direction and polished using Linde A and B.

The electrical properties of bulk samples were determined by Hall effect measurements. Compositional analyses and compositional microprofiles were obtained by energy dispersive x-ray analysis (EDAX Model 5-150), electron spectroscopy for chemical analysis (Perkin-Elmer ESCA-SAM Model 550), and scanning Auger microscopy (Perkin-Elmer SAM Model 590). Microstructures were determined by examination with

the optical microscope and the SEM (Cambridge Stereoscan Model 150).

Results and Discussion

A characteristic feature of the microstructure of the material is faceted grains, as shown in Fig. 1. The grains were delineated by plasma (LFE-PDE 100 $\text{CF}_4\text{-O}_2$) and chemical [AB etch, Ref. (16)] etching. The grain size ranged from about 10 to 300 μm , and the larger grains were distributed toward the end of the ingot that was last to solidify.

A regular intragranular structure characterized by continuous bands of two alternating phases was revealed in several grains in unetched samples, as shown in Fig. 2. The phase of lower volume fraction occurred in 0.1-0.4 μm wide bands with an average separation of about 1.3 μm . The delineation of the structure apparently resulted from preferential polishing. The average concentration of Ga, Ge, and As in the regions depicted in Fig. 2, as determined by EDAX measurements, corresponded to the original composition of the melt. ESCA studies confirmed the presence of Ga and As in compound form and of elemental Ge (see Table I). The

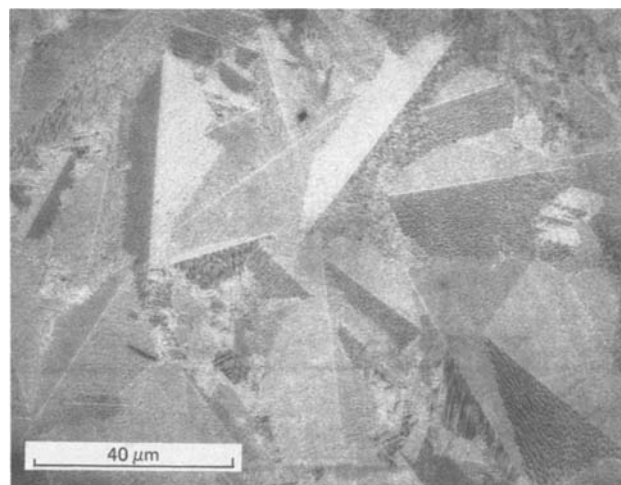


Fig. 1. SEM photomicrograph of chemically etched sample showing faceted grain structure.

¹ Present address: Rockwell International, Thousand Oaks, CA 91360.

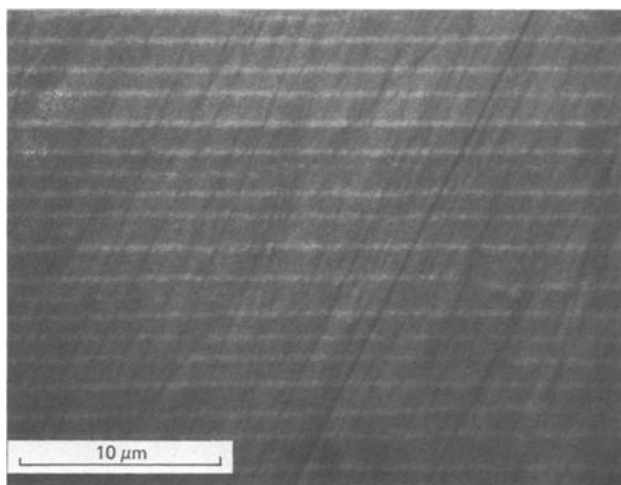


Fig. 2. SEM photomicrograph of polished sample showing alternating light and dark bands of GaAs and Ge, respectively.

spatial relationship between the structures revealed by the SEM (Fig. 2) and the actual distribution of the compounds was studied by making SAM compositional profiles across the aligned structures. The results (Fig. 3) showed that the Ge and GaAs phases did indeed alternate along the surface of the sample. Examination of regions depicted in Fig. 2 before and after chemical etching for 1 sec revealed that the regular structure extended continuously only within one grain; the relative orientation of the regular structure from grain to grain appeared to be random.

The intragranular structure of most of the grains in the plasma-etched samples was characteristic of a rod-matrix structure, where bundles of aligned rods in the different grains intersected the surface of the sample at random angles. The rods appeared to be aligned close to perpendicular to the sample's surface in several grains, as shown in Fig. 4. The projections corresponded in diameter and spacing to the GaAs phase depicted in Fig. 2.

The results above show that the Ge-GaAs eutectic can be grown with a regular structure over regions on the order of 100 μm wide. However, the question arises as to the cause of the faceted grains. This issue is discussed below in the light of prevailing theoretical models (18-25).

Hunt and Jackson (22) have treated the general problem of the microstructure of two-phase materials by extending Jackson's (26) original work describing single-phase materials in which he correlated the growth kinetics and morphology of the solid-liquid interface with the α -factor.¹ They found the following three guidelines to be generally consistent with experiment: (i) eutectics in which neither phase forms a facet ($\alpha < 2$ for both phases) have regular rod-matrix or lamellar structures; (ii) eutectics in which both phases form facets ($\alpha > 2$ for both phases) have irreg-

¹ $\alpha = \epsilon \Delta S / R$ where $\Delta S / R$ is the dimensionless entropy of melting and ϵ is the ratio of nearest neighbor coordination in the plane of the growth front to that in the bulk.

Table I. Summary of ESCA analysis of Ge-GaAs composite

| | BINDING ENERGY, eV | | |
|---------------------------|--------------------|-------|-------|
| | Ga 3d | As 3d | Ge 3d |
| COMPOSITE | 18.8 | 40.8 | 28.9 |
| GaAs STANDARD | 18.7 | 40.7 | |
| Ge STANDARD ¹⁷ | | | 28.9 |

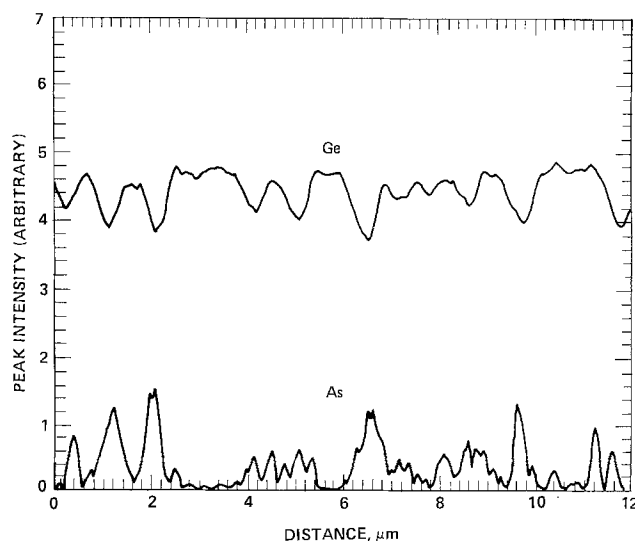


Fig. 3. Scanning Auger compositional microprofile taken across aligned structures depicted in Fig. 2. The experimental resolution was about 2000 Å. As a result, the electron beam was always incident on some region of the Ge matrix.

ular structures; (iii) eutectics in which one forms a facet ($\alpha > 2$) and the other does not ($\alpha < 2$) have complex-regular structures (regular structures extending over small distances).

The Ge-GaAs eutectic is a borderline case according to the criteria above (see Table II). This is because Ge and GaAs crystallize in the zincblende structure, which has possible values of ϵ ranging from 0.5 to 0.75. The precise value depends on the crystallography of the phase boundaries, which is unknown. As a result, the α -factor for compounds with entropies of melting between 2.7 and 4 are close to the critical value of 2.²

The faceted nature of the grains, taken with the regular structure within each grain, indicates complex-regular behavior overall. However, this assignment is not definitive for three reasons. First, although a crystallographic relationship is often observed between grains in a complex-regular structure (22), the orientation of sets of rods from grain to grain in Ge-GaAs appears to be random. Second, the experimentally determined average rod spacing is an order of magnitude smaller than expected. Atoms rejected into the

² More detailed calculations of the single-phase α -factors taking into account the effects of compound formation and solid-solid miscibility (25, 26) could not be made because the phase diagram is not known in sufficient detail to obtain the necessary thermodynamic parameters.

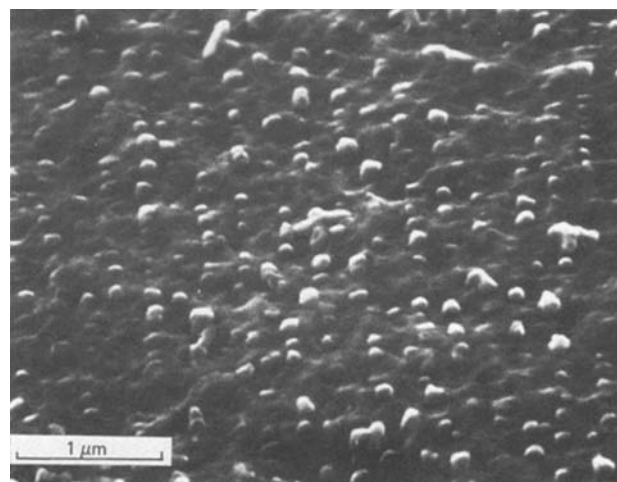


Fig. 4. SEM photomicrograph of plasma-etched sample indicative of a rod-matrix structure. 60° tilt.

Table II. Survey of *in situ* semiconductor heterostructure materials

| COMPOSITE MATERIALS | | ENTROPY OF MELTING (CAL/g-ATOM ⁻¹ K ⁻¹) | | MICROSTRUCTURE BASED ON α -FACTOR ^a | MICROSTRUCTURE BASED ON VOLUME FRICTION ^b | DIFFERENCE IN BANDGAP $ E_1-E_2 $ (eV) ^c | DIFFERENCE IN REFRACTIVE INDEX $ n_1-n_2 $ | RESISTIVITY RATIO | REFERENCES |
|---------------------|---------------------|---|---------|---|--|---|--|----------------------|----------------|
| PHASE 1 | PHASE 2 | PHASE 1 | PHASE 2 | | | | | | |
| Ge | GaAs | 3.3 | 3.5 | R, C, B, I | R(2) | 0.78 (ID) | 0.7 | | 13-15, 34, 35 |
| Si | GaAs | 3.5 | 3.5 | " | L | 0.32 (ID) | 0.1 | | 15, 34, 36-39 |
| Si | GaP | 3.5 | | " | L | 1.15 (II) | 0.2 | | 36 |
| Si | GaAlAs ^d | 3.5 | | " | | | | | 39 |
| Ge | GaAlAs ^d | 3.3 | | " | | | | | 35 |
| Ge | InSb ^e | 3.3 | 3.6 | " | R(1) | 0.47 (ID) | 0.2 | | 35, 40-47 |
| GaAs | CrAs ^f | 3.5 | | " | R(2) | | | > 10 ⁶ | 34 |
| InP | CrP ^f | | | " | R(2) | | | > 10 ³ | 34 |
| Ge | ZnGeP ₂ | 3.3 | | " | R(2) | 1.69 (II) | | | 35, 53 |
| CdTe | InAs | 2.0 | 3.3 | <u>R, C, B</u> | L | 1.14 (DD) | 0.7 | | 42, 43, 54, 55 |
| CdTe | GaAs | 2.0 | 3.7 | " | R(1) | 0.80 (DD) | 1.0 | | 43-46, 55, 56 |
| ZnTe | GaSb | 2.2 | 3.7 | " | R(1) | 1.50 (DD) | 0.7 | | 43-46, 56, 57 |

a. R-REGULAR, C-COMPLEX REGULAR, B-BROKEN REGULAR, I-IRREGULAR. THE SYMBOL OF MOST LIKELY MICROSTRUCTURE(S) IS UNDERLINED.

b. L-LAMELLAR, R-RDD/MATRIX, ROD PHASE INDICATED BY NUMBER.

c. I AND D INDICATE INDIRECT OR DIRECT BANDGAP OF PHASES 1 AND 2, RESPECTIVELY.

d. EXPECTED TO FORM OVER SOME RANGE OF LIQUID COMPOSITIONS BUT PHASE DIAGRAM INFORMATION IS NOT AVAILABLE.

e. MAY NOT BE A TRUE QUASI-BINARY.

f. ALTHOUGH CrAs AND CrP DO NOT FALL IN THE GENERAL SEMICONDUCTOR GROUPS CONSIDERED IN THIS PAPER, THESE COMPOSITES ARE OF INTEREST.

melt at the growth interface ahead of one phase diffuse laterally and incorporate with the adjoining phase. The size and spacing of the microstructural features therefore decrease as the growth rate increases and the diffusion coefficients decrease. For comparison, the lamellar spacing of Pb-Sn (1) solidified at a rate corresponding to the present experiments was about 7 μm . Because the diffusion coefficients of Ga, Ge, and As are higher than Pb and Sn under the respective growth conditions (29, 30), rod spacings of at least 10 μm were anticipated for the Ge-GaAs system. Third, the gradation of the grain size along the ingots is inconsistent with a constant solidification rate.

One explanation consistent with these observations is that, in the present experiments, solidification occurred rapidly and uncontrollably from an undercooled melt. This situation was possible because the melts were not seeded. Solidification under these conditions could account for the faceted grain structure.

Further evaluation of the microstructure showed that, from a consideration of the surface energy of the phase boundaries (23), a rod-matrix structure is favored over a lamellar structure when the volume fraction of one phase is less than $1/\pi$. On this basis, the directionally solidified Ge-GaAs eutectic would be predicted to have a microstructure of GaAs rods in a Ge matrix (see Table II), which is in agreement with the present experimental results. A lamellar structure should be possible by adjusting the melt composition off the eutectic (1).

Hall measurements indicated that the Ge-GaAs composite is p-type with a free carrier concentration greater than $8 \times 10^{19} \text{ cm}^{-3}$. The degenerate doping behavior probably results from mutual doping: Ge is an acceptor in GaAs; Ga, an acceptor in Ge with a distribution coefficient of about 0.1, is incorporated at a higher concentration than As, a donor with a distribution coefficient of 0.02.

Because our analysis of the directionally solidified Ge-GaAs eutectic showed that a regular structure was possible, a survey was conducted to find other potential

in situ semiconductor heterostructure materials. Several pseudobinary phase diagrams of group IV, III-V, and II-VI materials have a eutectic, as shown in Table II. The microstructures predicted on the basis of volume fraction and single phase α -factor criteria are indicated. The properties of the composites were evaluated by comparing the relative properties of each phase: The application of heterostructures generally depends on the property variations across the hetero-interface. The refractive index, optical bandgap, and electrical resistivity were compared for illustration (see Table II). The properties of the individual phases were used for comparison, and the effects of mutual doping could not be assessed quantitatively in the absence of detailed phase diagrams. The property difference, or property ratio, varied widely from composite to composite. Further, in the case of the GaAs-CrAs and InP-CrP composites, a high resistance ratio is anticipated because Cr, as a deep acceptor, would cause semi-insulating behavior in these compounds (32, 33).

Summary and Conclusions

This investigation shows that a two-phase, aligned array of Ge and GaAs can be produced by directional solidification. Alignment was observed to extend in grains over distances of up to 300 μm . We concluded that the small size of the microstructural features within the grains and the formation of the grains themselves could have resulted from rapid and uncontrolled solidification from a supersaturated melt. Future work with Ge-GaAs will include seeded growth experiments to prevent supersaturation and to determine whether or not rod alignment can be promoted over greater distances. An evaluation of potential *in situ* heterostructure materials containing group IV, III-V, and II-VI compounds indicates that regular structures could be achieved in many cases because the α -factors are similar to that of Ge and GaAs. Mutual doping was identified as a fundamental limitation to the control of the electrical and optical properties of some of these materials.

Acknowledgments

The author wishes to acknowledge the patient and skillful assistance of Merry Nell Colborn with the SEM analysis. The contribution of Dr. Marion Clark in making the plasma etching studies is deeply appreciated. Dr. John Moulder of Perkin-Elmer (Surface Science Division, San Jose, California) is gratefully acknowledged for conducting the ESCA and SAM analyses.

Manuscript received Oct. 3, 1980.

Any discussion of this paper will appear in a Discussion Section to be published in the December 1981 JOURNAL. All discussions for the December 1981 Discussion Section should be submitted by Aug. 1, 1981.

Publication costs of this article were assisted by Hughes Research Laboratories.

REFERENCES

1. F. R. Mollard and M. C. Flemings, *Trans. AIME*, **239**, 1526, 1534 (1967).
2. E. R. Thompson and F. D. Lemkey, *Met. Trans.*, **1**, 2799 (1970).
3. J. L. Fihey, M. Neff, R. Roberge, M. C. Flemings, S. Foner, and B. B. Schwartz, *Appl. Phys. Lett.*, **35**, 715 (1979).
4. J. Van Der Boomgard, D. R. Terrell, R. A. J. Born, and H. F. J. I. Giller, *J. Mater. Sci.*, **9**, 1705 (1974).
5. C. Zener, *Trans. AIME*, **167**, 550 (1946).
6. F. M. A. Carpay and W. A. Cense, *Scripta Met.*, **8**, 11 (1974).
7. B. Paul, H. Weiss, and M. Wilhelm, *Solid-State Electron.*, **7**, 835 (1964).
8. A. Muller and M. Wilhelm, *J. Phys. Chem. Solids*, **26**, 2021 (1965).
9. W. K. Liebmann and E. A. Miller, *J. Appl. Phys.*, **34**, 2653 (1963).
10. S. E. R. Hiscocks, *J. Mater. Sci.*, **4**, 773 (1969).
11. M. D. Khyilstovskaya, G. N. Zotova, L. G. Elanskaya, and E. P. Rashevskaya, *Izv. Akad. Nauk SSSR Neorg. Mat.*, **11**, 413 (1975).
12. M. C. Flemings, "Solidification Processing," McGraw-Hill, New York (1974).
13. M. B. Panish, *J. Less-Common Metals*, **10**, 416 (1966).
14. Y. Takeda, T. Hirai, and M. Hirao, *This Journal*, **112**, 363 (1965).
15. O. V. Pelevin, *Izv. Akad. Nauk SSSR Neorg. Mat.*, **11**, 51 (1975).
16. M. S. Abrahams and C. J. Buiocchi, *J. Appl. Phys.*, **36**, 2855 (1965).
17. "Handbook of X-Ray Photoelectron Spectroscopy," Perkin-Elmer (1979).
18. D. T. J. Hurle and E. Jakeman, *J. Cryst. Growth*, **3-4**, 574 (1968).
19. K. A. Jackson, *Trans. AIME*, **242**, 1275 (1968).
20. H. E. Cline, *ibid.*, **242**, 1613 (1968).
21. J. D. Hunt, D. T. J. Hurle, K. A. Jackson, and E. Jakeman, *Met. Trans.*, **1**, 318 (1970).
22. J. D. Hunt and K. A. Jackson, *Trans. AIME*, **236**, 843 (1966).
23. K. A. Jackson and J. D. Hunt, *ibid.*, **236**, 1129 (1966).
24. J. D. Hunt and D. T. J. Hurle, *ibid.*, **242**, 1043 (1968).
25. M. N. Croker, D. Baragar, and R. W. Smith, *J. Cryst. Growth*, **30**, 198 (1975).
26. K. A. Jackson, "Liquid Metals and Solidification," p. 174, ASM, Cleveland, Ohio (1958).
27. M. R. Taylor, R. S. Fidler, and R. W. Smith, *Met. Trans.*, **2**, 1793 (1971).
28. R. S. Fidler, M. N. Croker, and R. W. Smith, *J. Cryst. Growth*, **13-14**, 739 (1972).
29. D. L. Rode, *ibid.*, **20**, 13 (1973).
30. K. M. Kim, A. F. Witt, and H. C. Gatos, *This Journal*, **125**, 475 (1978).
31. J. A. Burton, E. D. Kolb, W. P. Slichter, and J. D. Struthers, *J. Chem. Phys.*, **21**, 1991 (1953).
32. G. R. Cronin and R. W. Haisty, *This Journal*, **111**, 874 (1964).
33. G. A. Antypas, *J. Cryst. Growth*, **33**, 174 (1976).
34. D. Richman and E. Hockings, *This Journal*, **112**, 461 (1965).
35. E. Greiner, *J. Metals*, **4**, 1044 (1952).
36. A. S. Jordan and M. E. Weiner, *This Journal*, **121**, 1634 (1974).
37. M. B. Panish, *ibid.*, **113**, 1226 (1966).
38. L. A. Borisova and N. A. Valisheva, *Izv. Akad. Nauk SSSR Neorg. Mat.*, **10**, 1263 (1974).
39. D. R. Stull and H. Prophet, "JANAF Thermochemical Tables," 2nd ed. (1971).
40. J. C. Wooley and D. G. Lees, *J. Less-Common Metals*, **1**, 192 (1959).
41. K. Lehovec and A. Slobodskoy, *This Journal*, **111**, 65 (1964).
42. R. K. Cox and N. J. Poole, *J. Chem. Eng. Data*, **12**, 247 (1967).
43. R. K. Willardson and H. L. Goering, "Compound Semiconductors—Preparation of III-V Compounds," Reinhold, New York (1962).
44. B. D. Lichter and P. Sommelet, *Trans. AIME*, **245**, 99 (1969).
45. R. Blachnik, *Met. Trans.*, **1**, 1087 (1970).
46. W. F. Schottky and M. B. Bever, *Acta Met.*, **6**, 320 (1957).
47. J. Terpilowski and W. Trzebiatowski, *Bull. Acad. Pol. Sci. Ser. Sci. Chim.*, **8**, 95 (1960).
48. B. W. Straughan and D. T. J. Hurle, *J. Cryst. Growth*, **21**, 117 (1974).
49. V. M. Glazov, A. N. Kretovnikov, and V. A. Nagiev, *Izv. Akad. Nauk SSSR Neorg. Mat.*, **10**, 585 (1974).
50. M. Schafer and K. Weiser, *Z. Phys. Chem.*, **61**, 1424 (1957).
51. J. G. Greenfield and R. Z. Smith, *Trans. AIME*, **203**, 351 (1955).
52. R. Holl, *This Journal*, **110**, 385 (1963).
53. E. Buehler, J. H. Wernick, and J. D. Wiley, *J. Electron. Mater.*, **2**, 445 (1973).
54. G. I. Bazhenova, E. A. Balagurova, A. A. Ryantsev, and E. N. Khabarov, *Izv. Akad. Nauk SSSR Neorg. Mat.*, **10**, 1770 (1972).
55. D. R. Mason and B. M. Kulwicki, "Phase Diagram for the Binary System Cd-Te," University of Michigan, Ann Arbor, Michigan, 1960, AD-235, 831.
56. V. M. Glazov, L. M. Pavlova, and N. L. Gryazeva, *Izv. Akad. Nauk SSSR Neorg. Mat.*, **11**, 418 (1975).
57. V. N. Vigdorovich, O. V. Pelevin, and E. V. Ufimtseva, *ibid.*, **8**, 753 (1972).

Ohmic Contacts to Lightly Doped n-AlGaAsSb

R. A. Milano, Raymond Chin, and Y. Z. Liu

Rockwell International Electronics Research Center, Thousand Oaks, California 91360

ABSTRACT

Two different metallization schemes, AuGe/Pt/Au and Sn/Ag/Ni have been used to fabricate ohmic contacts to lightly doped n-type $\text{Al}_x\text{Ga}_{1-x}\text{As}_y\text{Sb}_{1-y}$ ($x \sim 0.3$, $y \sim 0.01$). The electrical characteristics of each have been studied and the metallurgy has been examined using Auger electron spectroscopy (AES) sputter analysis. The results show that the AuGe/Pt/Au system is undesirable owing to the rapid diffusion of Au and Ge into the AlGaAsSb, even at very low temperatures (275°-300°C). The Sn/Ag/Ni system, however, forms a satisfactory ohmic contact and all of the constituents remain in a very shallow region near the semiconductor surface. The lowest specific contact resistance for this system is $1.3 \times 10^{-3} \Omega\text{-cm}^2$ obtained at an alloy temperature of $\sim 425^\circ\text{C}$.

The quaternary alloy AlGaAsSb is an important material for the fabrication of optoelectronic devices. To date, lasers (1), detectors (2), and solar cells (3) have been fabricated using AlGaAsSb. More recently, the observation of charge transfer (4) in this material has stimulated work on the fabrication of a heterojunction CCD imager to respond in the 1-2 μm spectral region. Ohmic contacts are an important component of all of the above listed devices. In order to optimize the device performance, it is necessary to fabricate contacts with the lowest possible contact resistance. The formation of ohmic contacts to a CCD channel layer is particularly difficult because of the doping and layer thickness requirements necessary for optimum performance. Typically $N_D - N_A \sim 1-3 \times 10^{16} \text{ cm}^{-3}$ and $d \leq 1.0 \mu\text{m}$. The constituents of the contact must form a shallow, heavily doped region. The use of a rapidly diffusing element may result in the formation of ohmic contacts; however, the I - V characteristics of the underlying p-n heterojunction will be degraded.

Ohmic contacts to p- and n-type AlGaAsSb are usually formed with Ag-Mn (1, 3) and Au (3), respectively. The contacts are made to relatively thick ($> 2 \mu\text{m}$, typically) layers of heavily doped material. The fabrication of an ohmic contact to a thin, lightly doped n-type layer using Au has been attempted without success. Two new metallizations, AuGe/Pt/Au and Sn/Ag/Ni, have been used to form ohmic contacts to AlGaAsSb. The diffusion of the various elements into the epilayer after alloying has been measured using AES and the electrical characteristics have been examined.

Experimental Procedure and Results

$\text{Al}_x\text{Ga}_{1-x}\text{As}_y\text{Sb}_{1-y}$ ($x \sim 0.3$, $y \sim 0.01$) layers were grown on n^+ and p^+ GaSb substrates by LPE using a slider boat apparatus (5). The initial growth temperature was 500°C and the cooling rate was $1.5^\circ\text{C}/\text{min}$. Te was used as the dopant. Differential C - V analysis was used to determine the doping and layer thickness. For all samples used in these experiments, $N_D - N_A \approx 2-5 \times 10^{16} \text{ cm}^{-3}$ and $d \approx 0.5-1.0 \mu\text{m}$. Standard photolithographic techniques were used to define an array of dots on each wafer. The contact metals were deposited by E-beam evaporation at a pressure of $1-2 \times 10^{-6}$ Torr. Prior to deposition, the regions to be contacted were cleaned with solvents and etched with 10:1 DI:HF for 30 sec. After deposition the samples were alloyed in palladium-purified flowing H_2 .

AuGe/Pt/Au Contacts

The AuGe/Pt/Au metallization consists of 2000Å AuGe (88%:12%), 150Å Pt, and 1000Å Au evaporated sequentially. Previous attempts to fabricate ohmic con-

tacts to AlGaAsSb/GaSb n/p⁺ heterojunctions using this system have indicated that for alloy temperatures greater than 330°C the underlying heterojunction was no longer rectifying (6). The sample was, therefore, alloyed at 275°C for 2 min. The I - V characteristics between contact dots were measured using a curve tracer and found to be extremely nonlinear, as shown in Fig. 1. A subsequent heat-treatment at 300°C for 2 min resulted in no significant improvement. The nonlinearity of the I - V characteristics prevented a meaningful determination of the contact resistance.

In order to understand the nonlinear effects observed, the metallized regions were analyzed using AES sputter profiling to determine the depth of penetration of the contact constituents into the epitaxial layer. The sputtering rate used was $\sim 1 \text{ A}/\text{sec}$. The results of the analysis are shown in Fig. 2 where the Auger signal amplitude is plotted as a function of sputtering time. The Al peak defines the location of the epitaxial layer. A relatively high concentration of Ga is found at the surface. This behavior is characteristic of Au-based ohmic contacts on GaAs (7). The low concentration of Sb at the surface and its movement from the epilayer toward the surface indicates that a significant amount of Sb evolves from the surface during alloying. A similar effect is observed during Zn diffusion into GaSb (8). Both Au and Ge are present throughout the epitaxial layer and Au is found in the substrate as well. The Pt was contained in a region

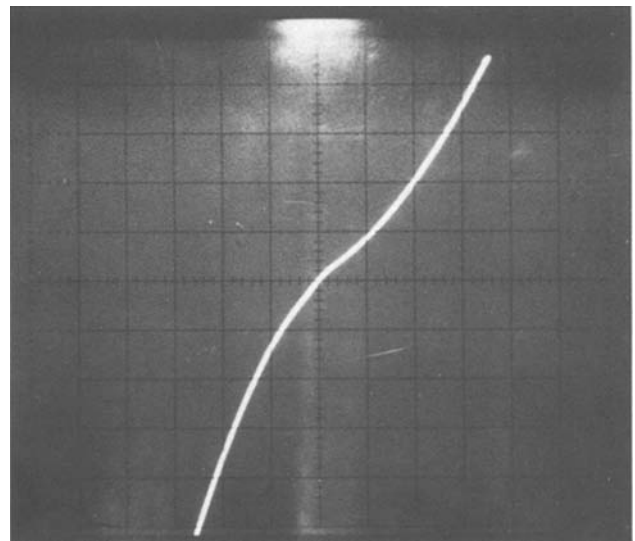


Fig. 1. I - V characteristics of AuGe/Pt/Au metallization after 275°C alloy. Vert. scale: 1 mA/div., horiz. scale: 0.5 V/div.

Key words: metallization, AES, semiconductor.

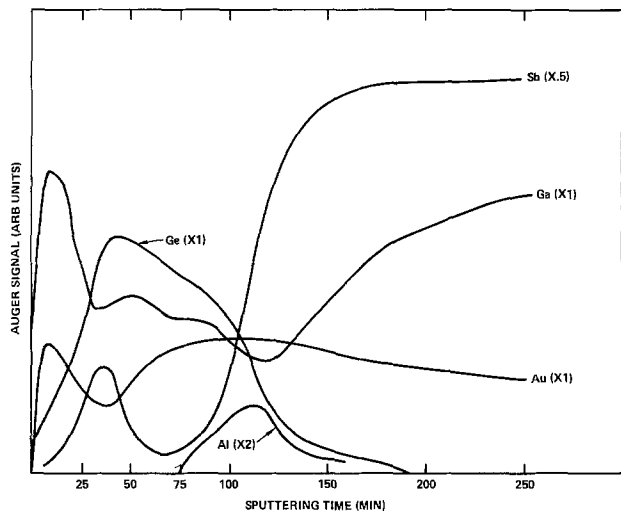


Fig. 2. Depth composition profile for AuGe/Pt/Au metallization determined by AES.

between 0 and 4000 sec and has been omitted from Fig. 2 to preserve clarity.

The large Au and Ge signals located in the range of 3000-5000 sec, where a minimum in the Sb signal is located, provide a possible explanation for the observed behavior. At alloy temperatures below the AuGe eutectic temperature ($T_{eut} = 356^\circ\text{C}$), significant movement of the constituents is not expected (7). However, if a large concentration of vacancies exist, generated by the movement of Sb towards the surface, then interstitial-substitutional diffusion due to the atom size of Au and Ge is possible. The I - V data shown in Fig. 1 are characteristic of field emission tunneling (9), indicating that the incorporation of Ge into the material has produced a heavily doped region to which the Au/Ga surface layer makes contact.

Sn/Ag/Ni Contacts

Ohmic contacts were formed by sequentially evaporating 100Å Sn/200Å Ag/500Å Ni. The sample was cleaved into nine pieces and each piece was alloyed for 5 min. An alloy temperature range of 275°-475°C was investigated in 25°C increments. The I - V characteristics between dots with varying center-to-center spacings were examined on a curve tracer. Samples that were alloyed at $\leq 350^\circ\text{C}$ had nonlinear I - V characteristics and the resistance uniformity was very poor. For alloy temperatures $\geq 375^\circ\text{C}$, the uniformity and linearity improved significantly with the best results in the 400°-425°C range. A typical I - V characteristic of Sn/Ag/Ni contacts alloyed at 425°C is shown in Fig. 3. The total resistance measured between the contacts is independent of contact separation indicating that the resistance of the contact dominates the measurement. Specific contact resistance was calculated using the expression $R_c = (R_T/2)A$, where R_T is the total measured resistance between the contacts and A is the contact area (10). The minimum R_c was obtained for an alloy temperature of 425°C. At this temperature, $R_c \leq 1.3 \times 10^{-3} \Omega\text{-cm}^2$.

The results of the AES analysis of the contacts alloyed at 375° and 475°C are shown in Fig. 4(a) and (b), respectively. It is important to note that the sputtering times are 10× less than in Fig. 2. At 375°C, Ag remains localized in a region very near the surface of the semiconductor. Only a small amount of Sn has penetrated into the material. The relative positions of the Ag and Sn peaks indicate that at this temperature Sn is moving into the Ni cap layer. Alloying at 475°C produces a somewhat broader interface region; however, relative locations of Ag and Sn and the depth of penetration of each into the semiconductor is essentially unchanged. An Ni cap was originally chosen

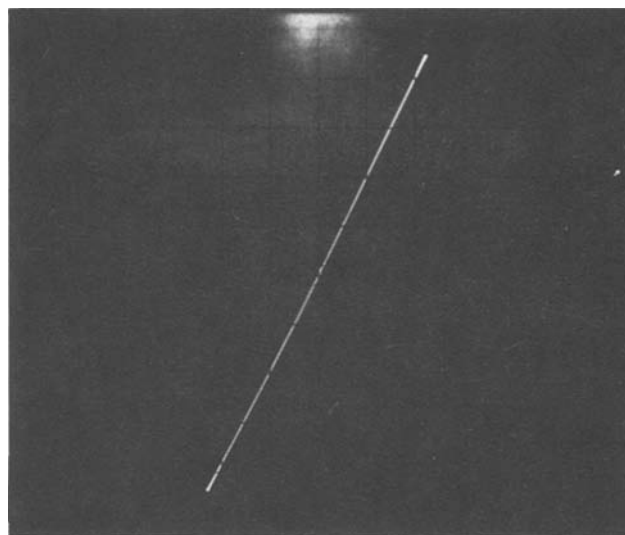


Fig. 3. I - V characteristics of Sn/Ag/Ni metallization after 425°C alloy. Vert. scale: 20 mA/div., horiz. scale: 0.5 V/div.

to prevent the contact metals from balling up for $T > 229^\circ\text{C}$ (eutectic temperature of Ag-Sn). As shown in Fig. 4(a) and (b), it effectively stops the outdiffusion of Ga and Sb from the semiconductor. Very few vacancy sites are therefore available for the dopant atoms to occupy; consequently the contact resistance of this system is relatively high.

Discussion

As described by Rideout, a heavily doped region of semiconductor next to the deposited metal is necessary to form low resistance ohmic contacts (9). The heavy doping in the semiconductor allows tunneling to occur through the thin potential barrier which exists at the metal-semiconductor interface. Formation of a low resistance contact to lightly doped material then presents a problem. One possible solution is to deposit a eutectic metal(s) which has a dopant as one of its constituents. During the subsequent alloying process, the constituent which acts as the dopant diffuses into the semiconductor, thus allowing a selective ohmic contact to be formed while preserving the lightly doped material elsewhere.

Application of this technique to the quaternary AlGaAsSb requires special considerations. Owing to the low growth temperature (400°-600°C) of AlGaAsSb and hence lower bond strength, it is necessary to use alloys with low eutectic temperatures. Both AuGe and AgSn form low temperature eutectics; however, Ge is known to be a p-type dopant in solution grown AlGaSb (11) and AlGaAsSb (12), while Sn can be used to grow either p- or n-type GaSb (13).

In order to form an n-type contact, outdiffusion of Sb from the semiconductor must be prevented. This is not the case for the AuGe/Pt/Au contact, where the outdiffusion of Sb through the Pt barrier and the indiffusion of Au and Ge result in a p-type region. In the case of the Sn/Ag/Ni contact, severe Sb outdiffusion is prevented. The net effect is to create an n⁺-type region at the metal-semiconductor interface. Since Sn is an amphoteric dopant (13) and a large Ga vacancy concentration is not readily available, a very heavily doped region cannot be formed. Therefore, the contact resistance is rather large.

Conclusions

In conclusion, it has been shown that Sn/Ag/Ni ohmic contacts can be formed to lightly doped ($N_D - N_A \sim 10^{16} \text{ cm}^{-3}$) n-type $\text{Al}_x\text{Ga}_{1-x}\text{As}_y\text{Sb}_{1-y}$ ($x \sim 0.3$, $y \sim 0.01$) epitaxial layers. Control of the column III and V vacancies must be maintained in order to allow

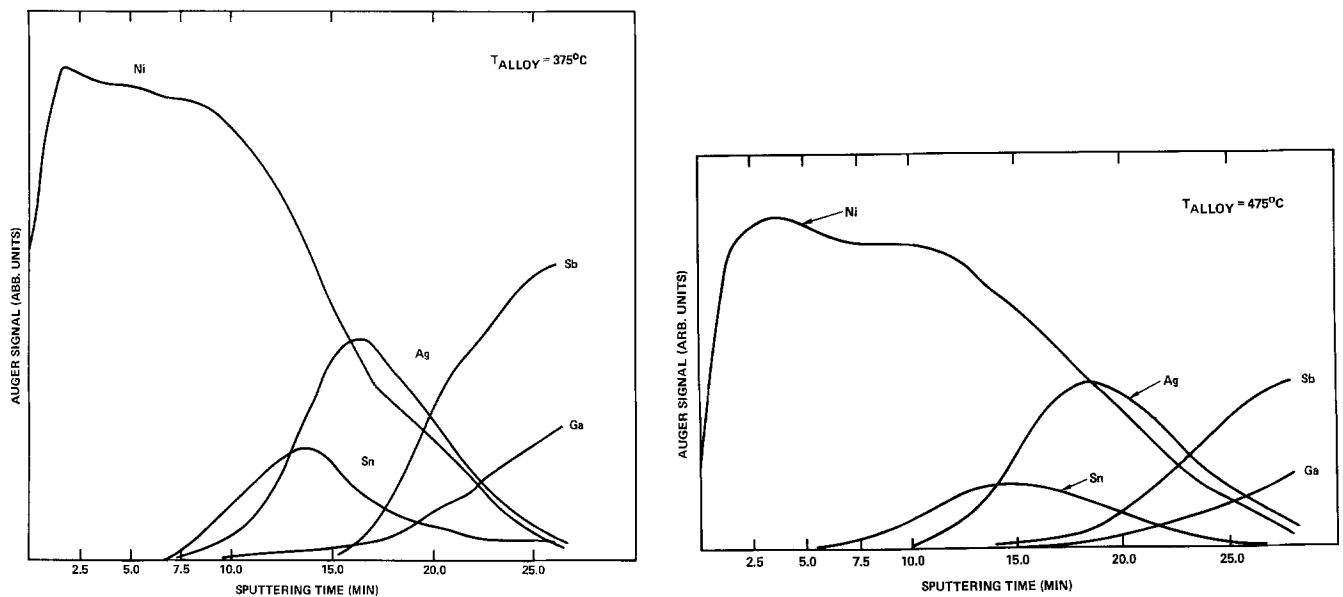


Fig. 4. Depth composition profile for Sn/Ag/Ni metallization determined by AES. The data for all elements is $\times 1$. All data has been deleted for clarity. (a, left) 375°C alloy for 5 min; (b, right) 475°C alloy for 5 min.

the desired substitution of the amphoteric doping such as Sn to occur in the proper vacancy. This can be achieved with the proper eutectic metals and alloying conditions, allowing either p- or n-type contacts to be made to AlGaAsSb.

Acknowledgments

The authors would like to acknowledge the technical assistance of W. E. Burke and the many helpful discussions with H. D. Law, J. S. Harris, Jr., and J. R. Waldrop.

Manuscript received Oct. 12, 1980.

Any discussion of this paper will appear in a Discussion Section to be published in the December 1981 JOURNAL. All discussions for the December 1981 Discussion Section should be submitted by Aug. 1, 1981.

Publication costs of this article were assisted by Rockwell International.

REFERENCES

1. H. D. Law, J. S. Harris, K. C. Wong, and L. R. Tomasetta, *Proc. 7th Int. Symp. on GaAs, Inst. Phys. Conf. Ser.*, No. 45, 420 (1979).
2. H. D. Law, L. R. Tomasetta, K. Nakano, and J. S. Harris, *Appl. Phys. Lett.*, **33**, 416 (1978).
3. Y. Z. Liu, H. T. Yang, and J. S. Harris, Jr., "Proc. 14th IEEE Photovoltaic Specialists Conference," January, 1980.
4. Y. Z. Liu, I. Deyhimi, J. S. Harris, R. J. Anderson, J. Appelbaum, and J. R. Pollard, *Appl. Phys. Lett.*, **36**, 458 (1980).
5. R. Chin, H. D. Law, K. Nakano, and R. A. Milano, *ibid.*, **37**, (Accepted for publication).
6. R. J. Anderson, Private communication.
7. G. Y. Robinson, *Solid State Electron.*, **18**, 331 (1975).
8. R. Chin, Private communication.
9. V. L. Rideout, *Solid State Electron.*, **18**, 541 (1975).
10. M. Itoh, S. Suzuki, T. Itoh, Y. Yamamoto, and K. G. Stephens, *ibid.*, **23**, 447 (1980).
11. S. J. Anderson, F. Scholl, and J. S. Harris, *Proc. 6th Intl. Conf. on GaAs, Inst. Phys. Conf. Ser.*, **33b**, 346 (1977).
12. H. D. Law, Private communication.
13. A. I. Lebedev and I. A. Strel'nikova, *Sov. Phys. Semicond.*, **13**, 10 (1979).

Reduction of Defects in Ion Implanted Bipolar Transistors by Argon Back Side Damage

James A. Topich*

Tektronix, Incorporated, Beaverton, Oregon 97077

ABSTRACT

The effectiveness of argon backside implants on the reduction of defects in an implanted bipolar process has been investigated. Insertion of an argon backside implant at two places in the processing sequence has been found to be beneficial. A backside implant before initial oxidation of the wafers will minimize the density of epitaxial defects for both arsenic diffused or implanted buried layers. For diffused buried layers, the backside damage offers only minimum improvement in yield because of the gettering action of the diffused arsenic itself. For implanted buried layers, the backside damage allows for higher arsenic doses and shorter HCl etch-back prior to epi growth, resulting in lower sheet resistance while still maintaining acceptably low defect levels. Correlation of electrical parameters and crystal defects showed that small defects in the emitter, probably dislocations generated by the implanted emitter process are responsible for "piped" transistors, leaky base emitter junctions, and poor low current beta. An argon backside implant just prior to emitter processing will reduce the density of these small defects and improve device yield.

The reduction of emitter-collector shorts in bipolar integrated circuit processing is of critical importance as chip densities and circuit complexity increase. The shorts or "pipes" are caused by a number of processing-induced defects, among them epitaxial defects, oxidation induced stacking faults, slip lines, and dislocations (1). It is a well-established fact that backside damage due to ion implantation will getter metallics (2, 3) and that both MOS and bipolar circuit yield (4, 5) is improved by the inclusion of such a step in the processing sequence. The work reported here focuses on (i) the effect of argon backside implants on the reduction of epi defects for both arsenic diffused and arsenic implanted buried layers and (ii) the use of a pre-emitter argon backside implant for improving device yield.

Experimental

The test vehicle was a current production process for high frequency bipolar integrated circuits. The starting material was commercially obtained 2 in. silicon wafers, Czochralski grown, 10-50 Ω -cm resistivity, boron doped, with (111) surface orientation. The oxygen content of the wafers was not specified and the back surface was chem-mechanical polished. The nominal epi layer thickness which was grown over either the diffused or implanted buried layers was 3 microns. The active base and emitter were implanted using boron and arsenic, respectively. Resulting junction depths are approximately 0.2 microns for the base-emitter junction and 0.3 microns for the base-collector junction. Maximum f_T for the devices is in the range of 6-7 GHz.

In order to study the effects of the backside argon implants, the wafers were pulled from the normal processing sequence at various steps, stripped of all oxide and Wright etched (6) to delineate crystal defects. Some of the wafers were electrically probed after the contact openings were cut, and mapped for "piped" devices, leaky base-emitters, and poor low current beta. These wafers were subsequently Wright etched and observed defects correlated with electrical measurements.

No attempt was made to optimize or improve the overall yield by varying any of the processing parameters other than the insertion of the backside argon

implant at various stages in the fabrication sequence. The only exceptions to this were the implant dose and energy for the implanted buried layer, and the HCl etch-back in the subsequent epitaxial growth step. These changes, however, were made in order to see how far the implanted buried layer process could be pushed to reduce the resulting sheet resistance while maintaining an acceptably low defect density.

Results and Discussion

Buried layer and EPI gettering.—For the diffused buried layer process, a significant reduction in overall defect density after epi growth resulted from a backside argon implant when the implant was done before initial oxidation. Figure 1 shows a comparison of two wafers processed identically except that wafer (b) was implanted on the backside with argon at a dose of 1×10^{16} cm^{-2} and an energy of 190 keV. Defect reduction for wafer (b) however, is primarily in the field region and not over the buried layer regions where the active devices will be subsequently fabricated. The lack of defects in the buried layer regions for both wafers (a) and (b) can be attributed to the gettering effect of high arsenic concentration diffusion which annihilates the small stacking faults formed during the initial silicon oxidation (7). These stacking faults, which show up as small saucer or S-pits when preferentially etched, act as nucleation sites for defects in the epitaxial layer. With the backside argon implant, epi defects are also eliminated in the field region due to dislocation networks generated in the backside by the implantation process. These dislocations getter metallics (8) which can precipitate and form the previously mentioned S-pits. The TEM photo in Fig. 2 shows the interference fringes of one of these small stacking faults and resulting strain contrast due to the precipitates.

During the initial gettering studies, rather high doses and energies were used for the backside implant. Further tests showed that these parameters could be reduced substantially while not only maintaining but improving gettering efficiency. The stacking fault density after epi growth as a function of argon dose implanted at 100 keV is shown in Fig. 3. The transition around a dose of 2×10^{14} cm^{-2} coincides quite closely with the argon dose needed to produce an amorphous layer in silicon. The decrease in gettering efficiency at the higher doses is believed to be due to precipitation of the implanted species around the dislocations, thus

* Electrochemical Society Active Member.

Key words: gettering, defects, semiconductor, epitaxy.

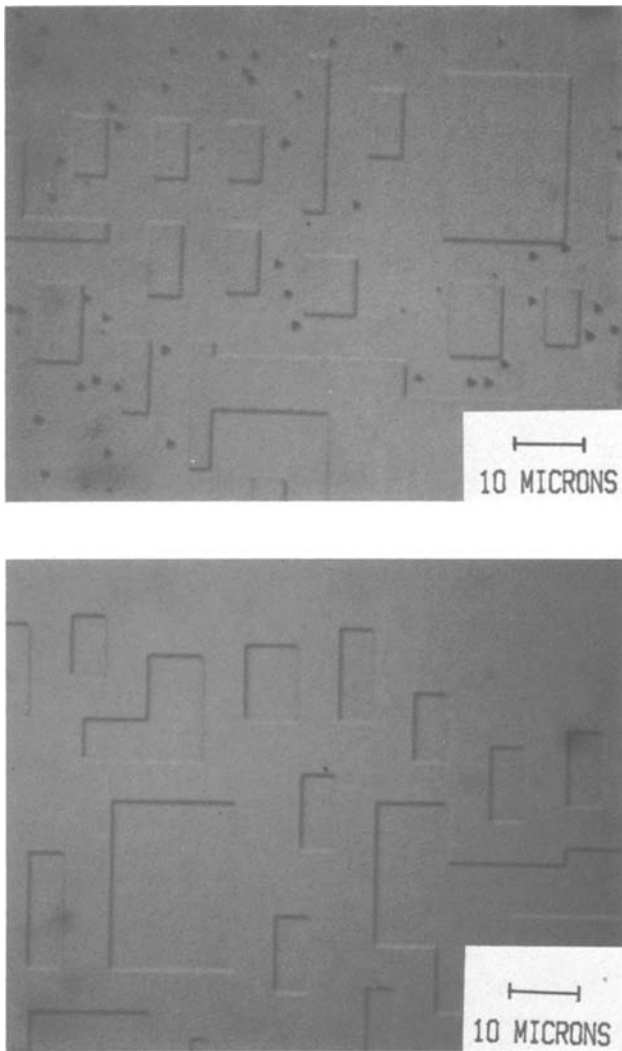


Fig. 1. Defect reduction for diffused buried layers (a, top) without backside damage, (b, bottom) with backside damage.

reducing their effectiveness in gettering metallics (8). A dose of 5×10^{14} cm $^{-2}$ at 100 keV is sufficient for producing the desired gettering effect. Since most of the experimental runs were started before the minimum argon dose and energy were determined, the results presented here are for higher doses and energies.



Fig. 2. TEM photo of small stacking fault formed during initial oxidation.

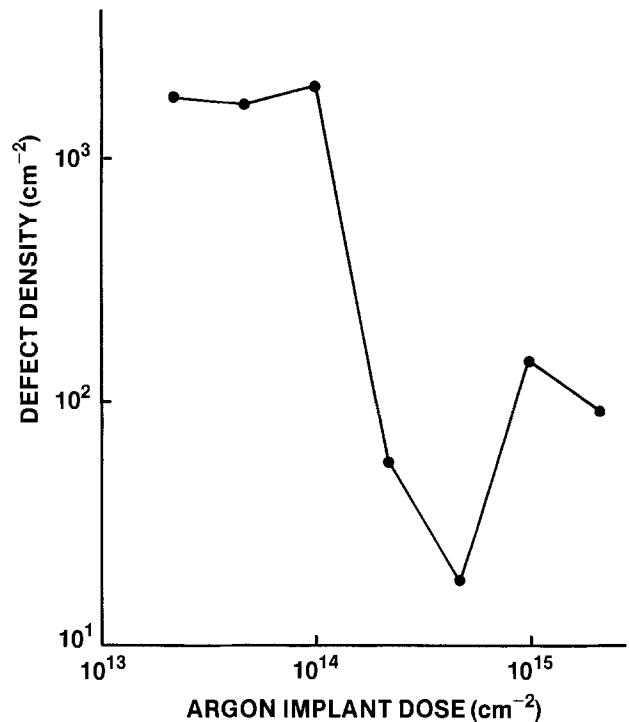


Fig. 3. Stacking fault density after epi growth as a function of argon backside dose.

For arsenic implanted buried layers the defect problem is of a different nature than that of diffused buried layers. If drive cycles after a buried layer implant and HCl etch-back prior to epi growth are not optimized, a large number of defects can be generated over the buried layer regions. These defects, directly in the active device areas, are extremely detrimental to device performance and circuit yield.

Appropriate drive cycles for the implanted buried layer and epi growth conditions have been reported previously (9) and are only briefly outlined below. After a buried layer implant of 5.5×10^{15} arsenic ions per cm 2 at 50 keV, a two-step anneal is used. The first is a 600°C soak in dry oxygen for 1 hr. This is above the recrystallization temperature for silicon (550°C) and allows for the solid-state epitaxial regrowth of the amorphous layer. The second is a 30 min ramp from 1100° to 1250°C, a 1 hr soak at 1250°C, and slow ramp back to 1100°C. This process serves to fully activate and drive in the implanted arsenic ions as well as removing residual defects remaining after the low temperature anneal. This annealing cycle is also done in a dry oxygen ambient. A recent paper (10) reported that a low defect density could not be obtained for arsenic implanted buried layers if the drive-in is done in an ambient containing more than 10% oxygen. The anneals used in this work were conducted in 100% oxygen and essentially defect-free buried layers were obtained.

The depth of silicon removed by the HCl etch-back prior to epi growth was also found to be critical for obtaining low defect densities. It was determined experimentally that approximately 0.4 microns of silicon had to be etched away in order to achieve an acceptable low defect density in the epi layer.

The above-mentioned processing can be used to obtain epi layers with low defect densities even without the use of an argon backside implant. With the implant however, some processing constraints can be relaxed resulting in lower sheet resistance for the buried layer while still maintaining at low defect density. Figure 4 shows photomicrographs of two wafers, one with a backside implant and one without. The buried layer implant and epi parameters were not optimized for these samples in order to demonstrate defect reduction achieved with a backside argon implant. A significant

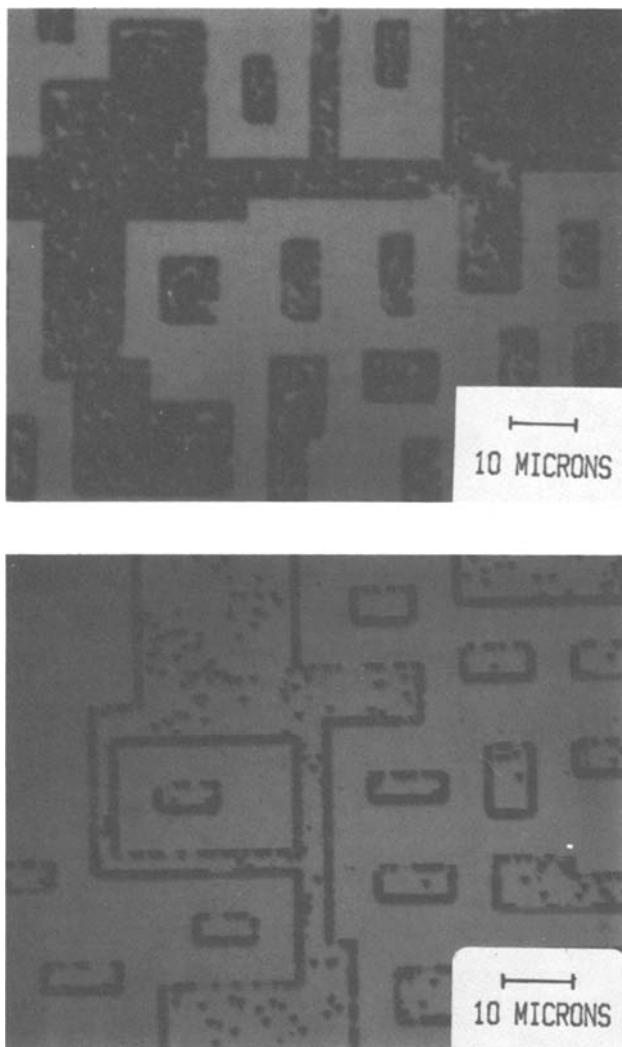


Fig. 4. Defect reduction for implanted buried layers (a, top) without backside damage (b, bottom) with backside damage.

improvement is evident with the backside implant, but it does not completely eliminate defects. Figure 5 shows defect densities observed after epi growth for various arsenic buried layer dose-energy products using optimized anneal and epi processing parameters and an argon backside implant of 1×10^{16} at 190 keV before initial oxidation. A reasonable correlation is shown between the buried layer dose-energy prod-

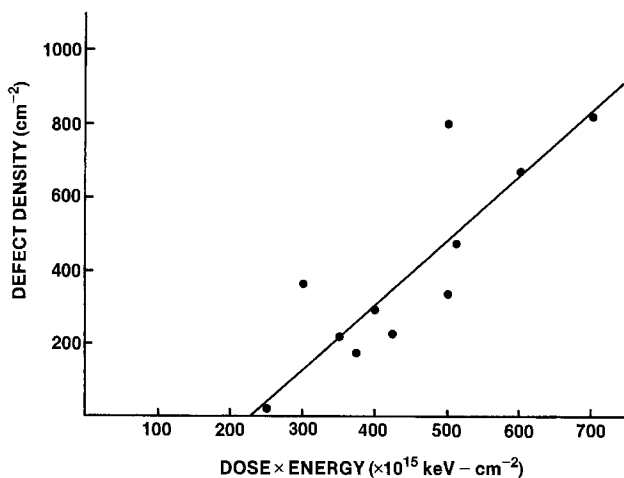


Fig. 5. Defect density as a function of buried layer dose-energy product.

uct and the defect density. For comparison, a buried layer implant with a dose energy product of 400×10^{15} keV-cm⁻² ($50 \text{ keV} \times 8 \times 10^{15} \text{ cm}^{-2}$) and without the backside implant had a defect of over 1600 cm⁻² which is well off the figure. The implant parameters used in the production process mentioned previously give a dose-energy product of 275×10^{15} keV-cm⁻², resulting in a defect density on the order of 100 per cm².

The use of a backside argon implant also permits a decrease in HCl etch-back prior to epi growth while still maintaining an acceptably low defect density. Figure 6 shows data from a number of tests where parameters such as HCl flow rate, etch-back time, and buried layer implant dose were varied. The two lines were fitted to data points from samples which received a backside argon implant, but were subjected to different HCl etch-back conditions. The 0.1 micron/min etch rate is used in our lab for arsenic diffused buried layers while the 0.4 micron/min etch rate is used for arsenic implanted buried layers. A 1 min etch time is typically used, but in these tests times of 20, 40, and 60 sec were used. For a given implant dose there were only small variations in defect densities for the three different etch times at each etch rate. These variations did not always correlate with the etch time, thus for the sake of clarity only the two solid lines corresponding to the data are shown without the data points. It can be said however, that an HCl etch-back which removes approximately 0.13 microns of silicon is sufficient for implant doses up to 7×10^{15} cm⁻² on wafers which have previously had a backside argon implant, a similar set of HCl etch-back tests were conducted using the same buried layer implant doses but without the backside implant. Results from these tests are shown as the data points in Fig. 6. Again, there was no correlation between the etch time used and the observed defect densities, but the data spread was almost three orders of magnitude. It is obvious that without the argon backside implant the defect density is quite unpredictable. Some samples may have a very low defect density while others which underwent similar processing have unacceptably high defect densities.

The curves in Fig. 7 show the interrelationship between the arsenic implant dose, HCl etch-back time (at an etch rate of 0.4 microns per minute), and resulting buried layer sheet resistance prior to epi growth. Final sheet resistance is smaller than the pre-epi value due to increases in carrier mobility as the arsenic concentration per unit volume decreases due to diffusion. For the implanted buried layer process as originally developed, a dose of 5.5×10^{15} cm⁻² and an HCl etch-back of 60 sec were used. This gives a sheet resistance of approximately 18 Ω /square. With the

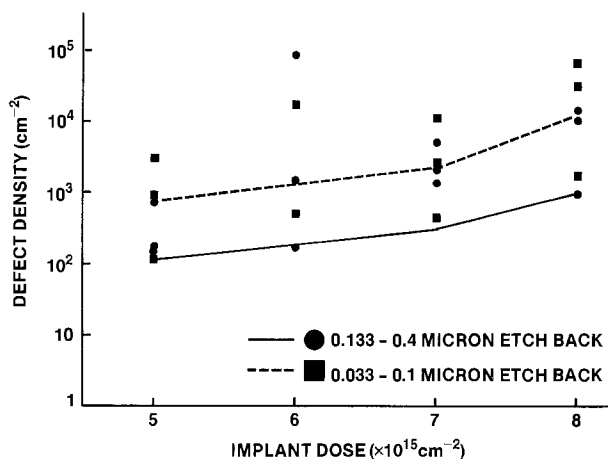


Fig. 6. Effects of HCl etch-back and implanted buried layer dose on epitaxial defects.

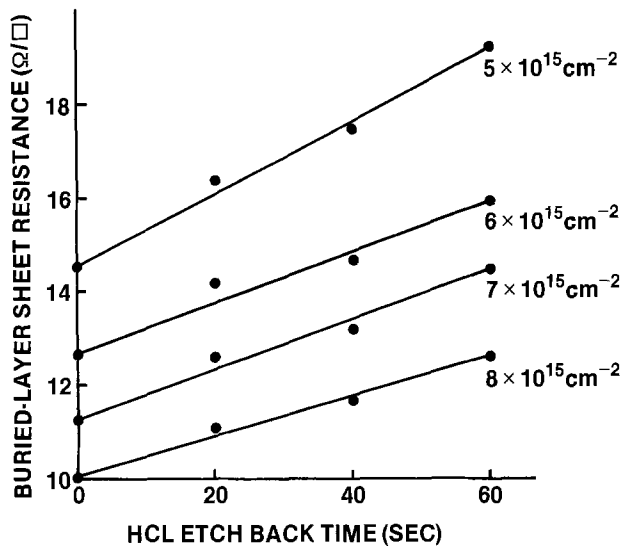


Fig. 7. Buried layer sheet resistance as a function of arsenic dose and HCl etch-back time at an etch rate of 0.4 microns per min.

argon backside implant, the buried layer dose could be increased to $7 \times 10^{15} \text{ cm}^{-2}$ and the HCl etch-back time decreased to 20 sec, with a subsequent drop in the buried layer sheet resistance to 12 Ω per square. Lower sheet resistance can be used to improve the high frequency performance of the resulting transistors.

When an argon backside implant was incorporated into the complete bipolar processing sequence using either diffused or implanted buried layers, no significant yield improvement or change in yield distribution was observed and the percentage of test transistors with emitter-collector shorts remained essentially the same. Such results were not unexpected since the diffused buried layer acts as a getterer itself, almost completely eliminating epi defects in the active regions. The argon backside implant serves only to reduce the defect density in the field regions away from the active devices as was shown in Fig. 1. The implanted buried layer process conditions (anneal, drive-in, and epi) had already been optimized for low defect levels (9), thus the argon backside implant was not expected to offer significant improvement.

Base and emitter gettering.—Poponiak, Nagasaki, and Yen (5) showed that an argon backside implant before emitted processing significantly reduced the number of "piped" devices. Because of that work a number of gettering techniques were incorporated into the bipolar process previously mentioned, and the resulting defects were studied at various stages of the processing sequence. The gettering techniques employed were backside argon implants (i) before initial oxidation, (ii) before base processing, or (iii) before emitter processing and phosphorus backside diffusion. Also included for comparison were wafers where no intentional gettering was used. (Phosphorus backside diffusion was done during deep collector processing early in the fabrication sequence and is not as effective as that done during a phosphorus emitter diffusion because of the many high temperature processes still to be performed in which defects can be generated and impurities introduced.)

When samples were stripped of all oxide and Wright etched after emitter processing was completed, two types of defects were observed. One was large epi stacking faults which occurred primarily in the field region of those wafers which did not receive a backside implant before initial oxidation. The other was a small defect that occurred primarily in the P^+ base contact and the emitter regions; these were called "shallow pits" because of their appearance. From our observations, these defects are not formed until base

P^+ contacts or emitters are implanted. They are most likely dislocations generated by the implant process and decorated with metallics.

Figure 8 shows defect densities for both epi stacking faults and shallow pits as observed after emitter processing, for each of the gettering techniques incorporated into the diffused buried layer process. The argon backside implant before initial oxidation is shown to be most effective in reducing epi stacking fault density; this is as expected considering the formation mechanism. The largest reduction in shallow pit density occurred for an argon backside implant just prior to emitter processing. This is most probably due to metallic contaminants being pulled to the backside, having been introduced and/or redistributed during various high temperature processing steps. No other gettering technique studied came close to the backside implant before emitter processing in reducing shallow pit defect density.

In order to correlate poor device performance with crystal defects in the silicon, a mask set was used which contained a $2000 \mu\text{m}^2$ emitter test transistor on each chip. This large device area permitted electrical measurements to be made without the need of metallization. Thus it was possible to map the wafers for "piped" transistors, leaky base-emitter junctions, and poor low current beta and then remap for defects after Wright etching. In this way a direct correlation between electrical performance and crystal defects could be made. Many of the devices had both emitter-collector shorts and leaky base-emitter junctions but were put only in the "piped" transistor category for the statistical analysis.

For the processing runs from which the data in Table I was collected, only one epi stacking fault was found in any of the emitters after Wright etching. Shallow pits, however, were found in many of the emitter regions. Those wafers which received an argon backside implant before emitter processing had a much lower incidence of pits. The use of an argon backside implant before initial oxidation either alone or in conjunction with the pre-emitter backside implant did not of itself affect the shallow pit density.

Table I lists the results of the correlation between poor electrical performance and the presence of shallow pits in the emitter regions. It should be pointed out that when the term "gettered" is used in Table I it refers only to pre-emitter argon backside implant gettering. The results show that (i) pre-emitter argon backside implant reduces the incidence of shallow pits, (ii) piped transistors, leaky base-emitter junctions, and poor low current beta can be strongly correlated to the

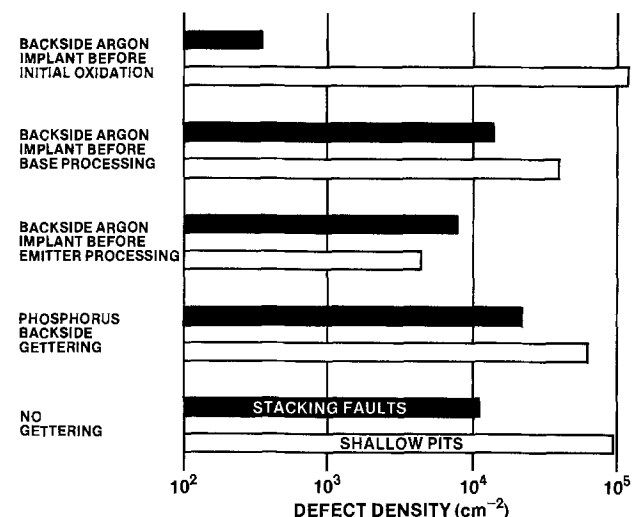


Fig. 8. Defect densities for both epi stacking faults and "shallow pits" for various gettering techniques observed after emitter processing.

Table I. Results of correlation between electrical parameters and "shallow pits" in the emitter

| | Gettered | Ungettered |
|---|----------|------------|
| Number of devices tested | 418 | 380 |
| Number of devices with "shallow pits" | 45 | 214 |
| Number of "piped" devices | 9 | 38 |
| Number of "piped" devices with "shallow pits" | 4 | 36 |
| Number of leaky base-emitter junctions | 0 | 52 |
| Number of leaky base-emitter junctions with "shallow pits" | 0 | 52 |
| Number of devices with poor low current beta | 0 | 8 |
| Number of devices with poor low current beta and "shallow pits" | 0 | 7 |

presence of these shallow pits, (iii) a shallow pit in the emitter is not always detrimental to performance as the 62% good devices with shallow pits indicates. Approximately 1% of the devices tested had poor electrical performance, but no defects were observed in the emitters. This may have resulted from the Wright etch washing out a very small pit since the etch consumed a quantity of silicon greater than the original active device depth, or there may in fact not have been a defect in those devices.

Some wafers which did not receive a pre-emitter argon backside implant were probed and mapped for electrical performance. There were appreciable numbers of piped devices, leaky base-emitter junctions, and devices with poor low current beta. The wafers then received a post-emitter argon backside implant and a 30 min anneal at 900°C in argon. The thermal cycle would not have a detrimental effect on the impurity profiles. When the wafers were reprobed after the gettering step only one spiked device remained. All others had normal transistor characteristics. When the wafers were Wright etched only 5% of the devices had shallow pits in the emitter. The "piped" device that remained had an epi defect in the emitter which was not affected by the post-emitter gettering. These results are contrary to the results of Barson, Klepner, and Seto (11) who found that the "pipes" in their relatively deep structures were not cured by a post-emitter gettering step even though the gettering did reduce the number of soft diodes. This apparent inconsistency can be reconciled by considering that the devices of this study were fabricated with very shallow junctions, and defects associated with shallow pits can be in many instances sufficiently long so as to traverse the entire base width. For the deep devices used in Ref. (11) it is quite possible that two different defects were responsible for "piped" devices and soft junctions, and only one was affected by the post-emitter annealing. The fact that the "piped" devices in this study could be cured by a post-emitter argon backside implant gettering step indicates that collector-emitter leakage is not due to enhanced diffusion of the arsenic from the emitter along the defect, but most likely it is due to metallic precipitates.

Conclusions

Use of an argon backside implant in silicon wafer processing can result in a reduction of crystal defects.

The type of defect minimized and the ultimate effect on circuit performance depends on when the backside implant is incorporated into the fabrication sequence. A backside implant prior to initial oxidation can reduce epitaxial defects for both diffused and implanted arsenic buried layers. This will not necessarily improve circuit yield since both processes can be implemented so as to minimize epitaxial defects in the active device regions without a backside implant. For the implanted buried layer process however, use of an argon backside implant allows for an increase in the arsenic implant dose and/or a decrease in the HCl etch-back prior to epi growth. Both of these changes provide lower buried layer sheet resistance while still maintaining low defect levels.

The defect found to be primarily responsible for the majority or "piped" transistors, leaky base-emitter junctions, and poor low current beta for the process described appears as "shallow pits" when Wright etched. These defects can be greatly minimized by an argon backside implant immediately prior to the arsenic emitter implant. Resulting reduction in "shallow pit" density correlates with the reduction in the percentage of "piped" transistors, leaky base-emitter junctions, and poor low current beta. These defects, associated with the implanted emitter, can be cured by a post-emitter gettering step using a backside argon implant, but the most logical procedure is to incorporate the backside implant prior to emitter processing and utilize the emitter drive cycle to activate the gettering action.

Manuscript submitted April 14, 1980; revised manuscript received Nov. 14, 1980.

Any discussion of this paper will appear in a Discussion Section to be published in the December 1981 JOURNAL. All discussions for the December 1981 Discussion Section should be submitted by Aug. 1, 1981.

REFERENCES

1. F. Barson, *IEEE J. Solid State Circ.*, **sc-11**, 505 (1976).
2. T. E. Seidel, R. L. Meek, and A. G. Cullis, *J. Appl. Phys.*, **46**, 600 (1975).
3. T. W. Sigmon, L. Csepregi, and J. W. Mayer, *This Journal*, **123**, 1116 (1976).
4. W. K. Tice and H. J. Geipel, Paper 496 presented at The Electrochemical Society Meeting, Los Angeles, California Oct. 14-19, 1979.
5. M. R. Poponiak, T. Nagaskai, and Y. H. Yen, *This Journal*, **124**, 1802 (1977).
6. M. W. Jenkins, *This Journal*, **124**, 757 (1977).
7. G. A. Rosgonyi, R. P. Deysher, and C. W. Pearce, *ibid.*, **123**, 1910 (1976).
8. H. J. Geipel and W. K. Tice, *Appl. Phys. Lett.*, **30**, 325 (1977).
9. V. C. Kannan and G. Roper, Paper 116 presented at The Electrochemical Society Meeting, Seattle, Washington, May 7-14, 1978.
10. L. C. Parrillo, R. S. Payne, T. E. Siedel, McD. Robinson, G. W. Reutlinger, D. E. Post, and R. L. Fields, Paper 14.7 IEDM Technical Digest (1979).
11. F. Barson, S. P. Klepner, and D. K. Seto, Paper 144 presented at The Electrochemical Society Meeting, Toronto, Canada, May 11-16, 1975.

Conductivity Profiling of GaAs/(AlGa)As Multilayer Structures

J. L. Zilko and P. J. Anthony

Bell Laboratories, Murray Hill, New Jersey 07974

ABSTRACT

A simple method for profiling the conductivity of GaAs/(AlGa)As multilayer structures is presented. The technique consists of step etching the sample using a chemical etch while measuring sample resistance after each etch step. An annulus geometry is used for the electrical measurement with the contact metallization also serving as an etch mask. Sample preparation is simple so that the technique can be used as a routine process monitor. The results from profiling single and multilayer heterostructure (AlGa)As laser materials grown by liquid phase epitaxy (LPE) are presented. Of particular interest is the ability of this technique to measure the resistivity of underlying layers.

The electrical conductivity of the various layers of multilayer GaAs/(AlGa)As structures, such as those that make up heterostructure lasers, can strongly affect the performance of the devices. For example, a high resistance P-(AlGa)As confinement layer in heterostructure lasers can significantly increase the lasing threshold current and its temperature dependence (1-3). However, several investigators (4, 5) have noted that the measured conductivity of a liquid phase epitaxial (LPE) Ge-doped $\text{Al}_{0.4}\text{Ga}_{0.6}\text{As}$ layer in a multilayer structure can be substantially different from that of a similar single layer grown on a semi-insulating substrate. Thus, the ability to measure the conductivity of the actual multilayer structures including underlying epitaxial layers is of primary importance for the evaluation of crystal growth processes and device material. While the conductivity of single layers can be determined from capacitance (6) or Hall effect (7) techniques which are relatively straightforward and easily interpretable, this is not the case for layers buried within multilayer structures. The conductivity of moderately or highly doped layers is particularly difficult to profile due to the decrease in depletion layer width with doping level.

In this paper, we present a simple technique for measuring the conductance of multilayer structures as a function of depth using chemical etching of the layers. Several examples of the resulting conductance profiles are given for both single layer and multilayer structures and the sources of error in this measurement technique are discussed.

Experimental

Crystal growth was accomplished by conventional LPE techniques (8) using the source-seed method (9). The substrates were Si-doped n^+ -GaAs which were degreased and etched immediately prior to insertion into the LPE reactor. Single layer (AlGa)As, 6-layer experimental structures, and 4-layer laser structures were grown. The laser structures consist of N- $\text{Al}_{0.4}\text{Ga}_{0.6}\text{As}$, p' - $\text{Al}_{0.08}\text{Ga}_{0.92}\text{As}$, P- $\text{Al}_{0.4}\text{Ga}_{0.6}\text{As}$, and p^+ -GaAs layers grown sequentially on the n^+ -GaAs substrate. The layer thicknesses ranged from 1.50 μm for the N layer, 0.1 to 0.2 μm for the p' layer, 0.8 to 1.8 μm for the P layer, and 0.4 to 0.8 μm for the p^+ layer.

The conductance profiling was carried out by incrementally chemically etching the sample, followed each time by a measurement of the sample resistance. The sample geometry consisted of an annulus as shown schematically in Fig. 1 with electrical contact made at the center and outer contact pads. This geometry was chosen in order to eliminate edge effects and minimize

the effects of misalignment of the contacts on the measurement (10). Junction isolation confined the current to the p-type layers close to the surface. The inner diameter of the annulus was 0.15 cm, the outer diameter 0.30 cm, and typical sample dimensions were 0.4 by 0.4 cm. For a laterally homogeneous single layer with annular contacts, the measured resistance is

$$R_s = \frac{\ln r_2/r_1}{2\pi} \frac{1}{\int_0^t dx/\rho(x)} \quad [1]$$

where $\rho(x)$ is the depth dependent resistivity and r_2/r_1 is the ratio between the outer and inner radii of the annulus. In this expression we assume that the effective resistance of the layers under the contacts is negligible compared to the resistance between contacts. Equation [1] can be rewritten in a more useful form as

$$\frac{d(1/R_s)}{dx} = \frac{2\pi/\rho(x)}{\ln r_2/r_1} \quad [2]$$

The multilayer structures in general consist of a series of layers each with a constant value of resistivity so that, for example, as profiling is carried out through the p^+ -GaAs layer, Eq. [1] becomes

$$\frac{d(1/R_{p^+})}{dx} = \frac{2\pi/\rho_{p^+}}{\ln r_2/r_1} \quad [3]$$

Similar expressions can be written as etching proceeds through subsequent layers. In addition, for controlled etching conditions, the distance etched into the sample

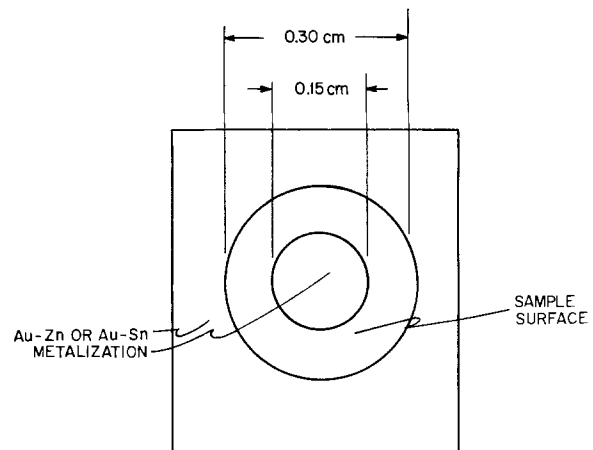


Fig. 1. Sample geometry for conductance profile measurements

is proportional to time. Thus, a plot of $1/R_s$ vs. etch time for the entire sample should give a series of straight lines with slopes inversely proportional to the resistivities of each p-type layer.

Ohmic contacts were made to the P or p^+ surface by evaporating an Au-Zn alloy through a contact mask. These contacts also served as the etch mask. Simple press contacts were made to the metallization. The voltage applied between contacts was kept constant at 0.1V in order to maintain junction isolation of the p-type layers from the n-type layers, and the current flowing through the sample was monitored at each step.

The samples were etched with voltage applied to the sample contacts using a solution consisting of H_2SO_4 , H_2O_2 , and H_2O in volume ratios of 40:1:1 or 10:1:1 at room temperature. The 10:1:1 etch is faster than the 40:1:1 and proved useful in profiling samples with thick layers.

A controlled amount of the etch was applied to the sample surface for a time of 5 ± 0.5 sec after which the etch was washed away by $\sim 10^6$ Ω -cm deionized water. No evidence was found to suggest electrochemical etching. It was noted that careful degreasing of the samples prior to metallization prevented separation of the metallization from the semiconductor surface during etching.

The layer thickness and etch rate of each sample was measured after resistance profiling using scanning electron microscopy (SEM) of cleaved and stained sample edges. The etch rate of GaAs and (AlGa)As was generally found to vary spatially by less than 10%. In addition, the etch rate of each layer appeared to be time independent. Both the small lateral dimensions of the sample and the short time of each etching increment improve the controllability of the etch. Figure 2 is an SEM micrograph of the cleaved cross section of a profiled laser structure showing the edge of the etched region. In order to improve contrast, the sample was etched for 30 sec in a solution consisting of H_2O_2 and NH_4OH at a pH of 7.5 which preferentially attacks binary material (11). The four epitaxial layers as well as the metallization can be seen in this figure. Etching was carried out in this case through the p^+ , P, and p' layers to the N-(AlGa)As layer.

Results

Figure 3 is a plot of sample conductance, $G \equiv 1/R_s$, as a function of etching time for a p-type Ge-doped $Al_{0.4}Ga_{0.6}As$ single layer grown on an n^+ -GaAs substrate. The layer thickness was $4.0 \mu m$. G varies approximately linearly with etching time indicating a constant value of ρ . The value of ρ obtained from the

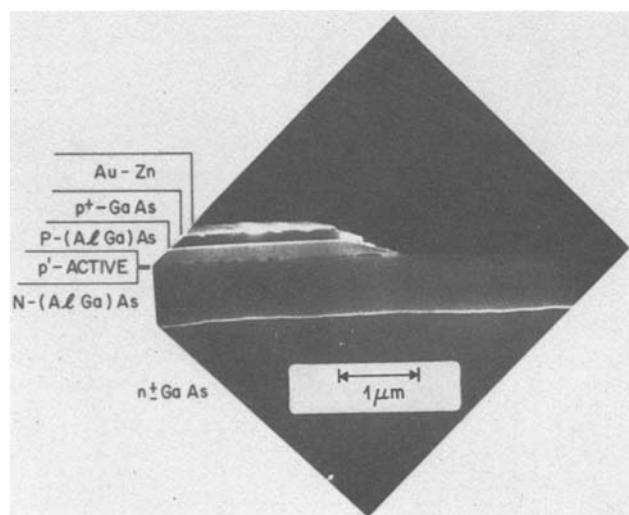


Fig. 2. SEM micrograph of the cleaved cross section of profiled heterostructure laser material.

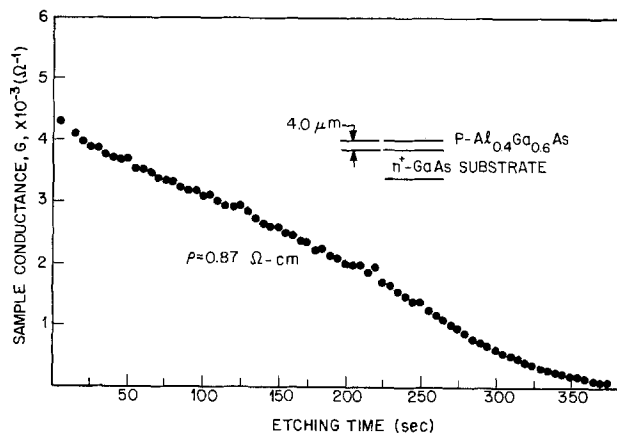


Fig. 3. Sample conductance as a function of etching time for a p-type $Al_{0.4}Ga_{0.6}As$ single layer grown on an n^+ -GaAs substrate.

slope of the G vs. etch time curve in Fig. 3 and the layer thickness was 0.87Ω -cm. We have generally found the value of ρ measured by the profiling technique to be within 20% of the value of ρ obtained from Hall effect measurements.

Figure 4 is a conductance profile of a typical laser structure obtained using the 40:1:1 etch. Only the p^+ -GaAs and P-(AlGa)As layers can be distinguished. The thin ($\sim 1000 \text{ \AA}$) p' layer buried beneath the p^+ and P layers is partially inaccessible within the junction depletion width and is not identifiable in the measurements. Because most of the current is initially shunted through the high conductivity p^+ -GaAs, the conductance decreases rapidly as etching proceeds through that layer. The lower conductivity of the P-(AlGa)As layer results in a less rapid decrease in G with etch time. The measured resistivity of the p^+ layer is $1.5 \times 10^{-2} \Omega$ -cm compared to 0.24Ω -cm for the P layer. The measured value of ρ_{p^+} is thus a factor of 17 less than that of ρ_P for this sample. The conductance profile of a second similar standard laser structure is shown in Fig. 5. The profile in Fig. 5 has the same general appearance as the profile in Fig. 4 but with values of ρ_{p^+} and ρ_P of $1.6 \times 10^{-2} \Omega$ -cm and 0.55Ω -cm, respectively. Conductivity profiling of a large number of wafers has indicated that the conductivity of the P layer can be perturbed by over a factor

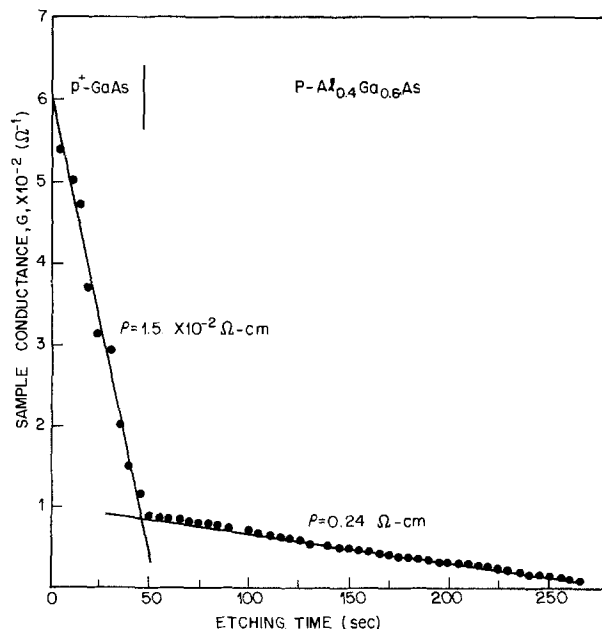


Fig. 4. Sample conductance as a function of etching time for heterostructure laser material.

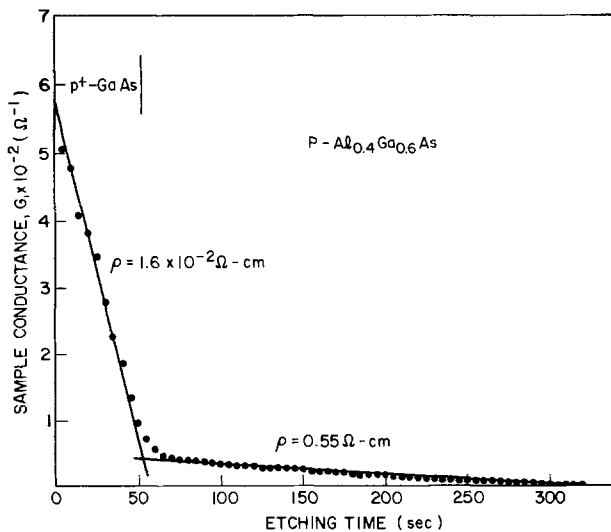


Fig. 5. Sample conductance as a function of etching time for heterostructure laser material from a second wafer.

of 5 by changes in LPE process variables and the profiling technique has been used as a primary analytical tool for this study. The results of this study will be discussed in detail in a future publication.

In order to demonstrate the depth resolution that can be achieved using this technique, a 6-layer structure consisting of N- $\text{Al}_{0.4}\text{Ga}_{0.6}\text{As}$ ($2.5 \mu\text{m}$), p^- - $\text{Al}_{0.08}\text{Ga}_{0.92}\text{As}$ ($0.1 \mu\text{m}$), P_1 - $\text{Al}_{0.4}\text{Ga}_{0.6}\text{As}$ ($1.1 \mu\text{m}$), p'' - $\text{Al}_{0.12}\text{Ga}_{0.88}\text{As}$ ($0.15 \mu\text{m}$), P_2 - $\text{Al}_{0.4}\text{Ga}_{0.6}\text{As}$ ($0.6 \mu\text{m}$), and p^+ -GaAs ($0.5 \mu\text{m}$) layers was grown sequentially on an n^+ substrate. The doping levels for the P_1 , P_2 , and p'' layers were chosen such that $\rho_{\text{P}_2} > \rho_{\text{P}_1} > \rho_{\text{p}''}$. The conductivity profile was obtained using 10:1:1 etch and is shown in Fig. 6. The p^+ layer has been eliminated for clarity. The profile indicates that $\rho_{\text{P}_2} > \rho_{\text{P}_1} < \rho_{\text{p}''}$ as predicted from the doping levels. More importantly, the $0.15 \mu\text{m}$ thick p'' layer is observable in the profiles even at a depth of over $1 \mu\text{m}$ beneath the surface and even using the relatively fast 10:1:1 etch. This indicates that etching proceeds uniformly through the layers using the step etching technique and that thin layers beneath the surface can be adequately profiled.

Discussion

Using a simple step etching technique, the conductivity of a variety of single and multilayer structures can be measured. Of particular interest is the ability to measure the conductivity of buried layers that are difficult to measure using other techniques. A conduc-

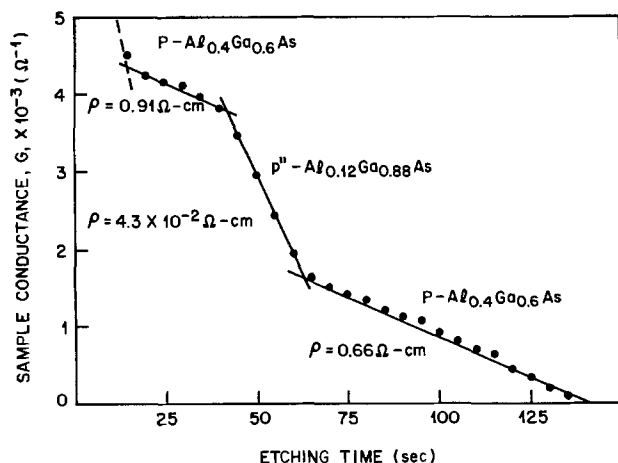


Fig. 6. Sample conductance as a function of etching time for a 6-layer structure. A $0.15 \mu\text{m}$ $\text{Al}_{0.12}\text{Ga}_{0.88}\text{As}$ layer was grown between the two $\text{P-Al}_{0.4}\text{Ga}_{0.6}\text{As}$ layers $1.1 \mu\text{m}$ beneath the surface.

tivity profile of a laser structure can typically be done in 30-40 min after contact formation so that this technique can be used as a routine process monitor for device material.

The principal errors of this measurement are: (i) spatial variations in layer thicknesses, (ii) spatial variations in the etch rate, (iii) errors in the time of each etch step, (iv) variations of the sample temperature during measurement, and (v) lateral inhomogeneities in the resistivity. It was found that spatial inhomogeneities in layer thickness were typically $\sim 20\%$ and that etch rate variations across a sample were typically less than 10% . The primary effect of these errors is to make the measured interface between the p^+ and P layers more diffuse. Errors in the length of each etch increment are estimated to be generally $\pm 10\%$ although the error can be greater than that for isolated data points. The effect of this source of error is diminished by the use of a large number of data points. Sample temperatures during the conductance measurements can have a large effect on the measured value of R_s but can be minimized by taking care to provide a constant temperature environment during the measurement. Lateral inhomogeneities in resistivity caused, for example, by metallic inclusions in the semiconductor layers affect both the accuracy of the resistivity measurement and the lateral uniformity of the etch rate.

In some extreme cases, for example in highly resistive layers, the resistance from the metal contacts to the edges of the etched region may be neither negligible nor constant. The measured resistivity of such a layer would then overestimate the actual layer resistivity. We have thus far studied no wafers of this type.

The primary advantages of this technique are: simplicity of experimental technique, the speed with which routine profiles can be taken, and the ability to measure the conductivity of buried layers. The primary disadvantages are that no information about carrier concentration or mobility separately can be obtained and such experimental errors as spatial inhomogeneity of etch rate can introduce errors in the profile that are difficult to subtract out.

In conclusion, we have demonstrated that useful information concerning the resistivity of buried layers in multilayer structures can be obtained by chemically etching the structure in short (5 sec) increments. The technique has proved to be useful in the evaluation of heterostructure laser structures grown by LPE. The major errors in measurement are nonuniform layer thicknesses and etching and errors in the etch increment. The technique is simple, the results easily interpretable, and the information can be obtained only with considerable difficulty using other techniques.

Acknowledgment

The authors would like to thank N. E. Schumaker for proposing this project, S. M. Woelfer, J. W. Lee, and K. R. Stiles for technical assistance, and W. B. Joyce for helpful discussions.

Manuscript submitted Aug. 18, 1980; revised manuscript received Oct. 27, 1980.

Any discussion of this paper will appear in a Discussion Section to be published in the December 1981 JOURNAL. All discussions for the December 1981 Discussion Section should be submitted by Aug 1, 1981.

Publication costs of this article were assisted by Bell Laboratories.

REFERENCES

1. P. J. Anthony and N. E. Schumaker, *Electron. Device Lett.*, **ed1-1**, 58 (1980).
2. P. J. Anthony and N. E. Schumaker, *J. Appl. Phys.*, **51**, 5038 (1980).
3. N. K. Dutta, *ibid.*, To be published.
4. B. Wakefield, J. L. Stevenson, R. M. Redstall, and T. Ambridge, *Appl. Phys. Lett.*, **35**, 347 (1979).
5. P. J. Anthony, J. L. Zilko, V. Swaminathan, N. E.

- Schumaker, and W. R. Wagner, Unpublished.
6. See, for example, G. P. Donzelli, G. Guarini, and V. Svelto, *IEEE Trans. Electron. Devices*, **ed-26**, 811 (1979).
 7. G. E. Stillman and C. M. Wolfe, *Thin Solid Films*, **31**, 69 (1976).
 8. H. C. Casey, Jr. and M. B. Panish, "Heterostructure

- Lasers Part B: Materials and Operation Characteristics," Academic Press, New York (1978).
9. D. L. Rode, *J. Cryst. Growth*, **20**, 13 (1973).
 10. W. B. Joyce and S. H. Wemple, *J. Appl. Phys.*, **41**, 3818 (1970).
 11. R. A. Logan and F. K. Reinhart, *ibid.*, **44**, 4172 (1973).

Localized GaAs Etching with Acidic Hydrogen Peroxide Solutions

Don W. Shaw*

Texas Instruments Incorporated, Dallas, Texas 75265

ABSTRACT

Control of the morphologies or profiles produced by localized etching of GaAs structures has assumed increasing importance with the current emphasis being placed on microdefinition and surface relief optimization for GaAs monolithic circuits. To obtain a better understanding of the complex anisotropic etching behavior observed in GaAs, the morphologies produced by various acidic hydrogen peroxide solutions were evaluated. The degree and nature of the anisotropy is shown to vary extensively and systematically with the etchant composition. Both highly anisotropic and essentially isotropic etching may be obtained by selection of the appropriate etchant composition.

Gallium arsenide semiconductor technology is progressing toward increasing levels of integration. Analog, monolithic integrated circuits for microwave applications and digital circuits for high speed logic are under development. However, integrated circuit development places new requirements on GaAs processing technology, particularly with respect to chemical etching. Unlike the elemental semiconductors, GaAs has a noncentrosymmetric crystal structure, which results in unusual etching characteristics. For example, in defining a step on the usual {100} GaAs wafer, chemical etching generally produces step profiles that are grossly nonequivalent for steps running in orthogonal <011> directions. An etched mesa with a rectangular shape and aligned with the cleavage directions will have two sides with gradually sloping walls, while the other two sides will have obtuse-angled walls that are unsuitable for metallization steps or crossovers. This phenomenon greatly complicates circuit design and layout, if chemical etching steps are required in subsequent processing.

As GaAs technology develops it becomes increasingly important to understand, control, and exploit these unique etching characteristics. For some device and circuit applications, highly anisotropic etchants are desirable, e.g., formation of crystallographically defined "vee grooves." In other cases, isotropic etchants are required to obtain symmetrical structures in spite of the noncentrosymmetric nature of the GaAs crystal structure. This report describes one stage of a systematic evaluation of GaAs etchants. Included in the evaluation is an assessment of the profiles produced in etching, the degree of undercutting in the presence of an inert mask, the relative anisotropy, and the kinetics for room temperature etching. The results should provide guidance for efficient selection of requisite GaAs etchants and etching processes.

Etchants are generally composed of an oxidant and a solvent or solubilizing agent. The most common oxidants for GaAs are hydrogen peroxide and halogens, such as bromine. However, other agents such as $K_3Fe(CN)_6$, $Ce(SO_4)_2$, and $KMnO_4$ are also effective oxidants. The oxides produced in GaAs oxidation are

amphoteric in nature and may be dissolved in either acidic or basic aqueous solutions or, in some cases, in organic solvents such as methanol. As will become evident, the different etchant compositions, although similar in principle, produce widely varying etching characteristics.

In the limiting cases the rate of etching may be determined by one of two basic events: the chemical processes that occur at or upon the semiconductor surface or the mass transport processes that occur within the liquid to supply fresh etchant species to the etching surface or to remove the reaction products. Etchants whose rates are limited primarily by mass transport are particularly useful for polishing. Surface protrusions have more favorable access to the incoming etchant species and tend to be etched more rapidly so that the surface becomes smoother. Mass-transport-limited etchants also tend to be more isotropic with respect to crystallographic orientation. Conversely, kinetically or surface-limited etchants tend to preserve the original configuration of an initially planar surface; and, since the etch rate is determined principally by the surface reaction rate, their etch rates are relatively insensitive to the nature and degree of agitation. Kinetically limited etchants are often highly anisotropic. e.g., the orientation-dependent etchants that are highly coveted for producing precisely defined shapes or cross sections in semiconductor crystals. As will be subsequently shown, both types of behavior can be observed when etching gallium arsenide with acidic hydrogen peroxide solutions.

Experimental Approach

For each etchant composition included in the present study, the following parameters were evaluated: etch rate, cross-sectional morphology, undercutting, and relative anisotropy (as defined in a later section). Particular emphasis was placed on identification of the principal morphology-determining crystallographic orientations, since procedures are described in a related publication (1) for using this data to predict the shapes expected as a function of the wafer surface orientation and mask geometry.

All studies were performed on {100} GaAs slices, which were not intentionally doped. The measured carrier density was $1.5 \times 10^{16} \text{ cm}^{-3}$ (n-type). After being

* Electrochemical Society Active Member.

Key words: etching, dissolution, semiconductor, topography, kinetics.

chemically polished on both sides, the slices were coated with a plasma-deposited silicon nitride film, which served as an etch mask. The nitride film was patterned using photolithography to expose GaAs in the stripe and circle configuration shown in Fig. 1. The stripes, which were visually aligned with respect to the $\langle 110 \rangle$ cleavage planes of the slice, were used to evaluate the etch rate and cross-sectional anisotropy. The circular regions or rings allowed evaluation of the azimuthal anisotropy, particularly with respect to undercutting. In practice, a patterned slice would be incrementally etched for sufficient total time in a given etchant composition to produce a channel depth within the stripes of $\sim 10 \mu\text{m}$. Typically the time increments would be chosen to remove 2-3 μm in each stage; and, prior to beginning the next etch stage or increment, small pieces would be cleaved in each of the two fundamental $\langle 110 \rangle$ directions (two orthogonal directions). The depths were measured on each of the cross sections; and by plotting the depth as a function of time, the etch rates were obtained. Any variation in etch rate as a function of time could also be detected.

In each experiment the etching was performed with the slice in a rotating (135 rpm) beaker, which was inclined by 30° from an upright position. The rotation direction was reversed midway during each time increment. Unless otherwise specified, all etchant compositions were freshly prepared from reagent-grade or semiconductor-grade starting materials, and all etching experiments were performed at room temperature. When necessary, the etchant solutions were allowed to cool or warm to room temperature prior to etching. This took no more than 2 hr after solution preparation in any case.

The extent of undercutting was assessed by the ratio, w/d , where w is the lateral etch distance just below the nitride film measured parallel to the cleavage direction in question, and d is the channel depth. Angular measurements were made on micrographs of the cleaved cross sections or by use of an optical microgoniometer.

Results and Discussion

The characteristics observed for the thirteen etchant compositions selected for investigation are summarized in Table I. The compositions are expressed as volume ratios (of the concentrated reagents) and molar concentrations. Included in the tabulated experimental data are the undercut ratio as previously defined, the etch rate perpendicular to the $\{100\}$ surface, and the relative anisotropy. The latter parameter is chosen to provide some measure of the degree of anisotropy of the etch rate with respect to crystallographic orientation. The relative anisotropy is estimated from the observed azimuthal variation in undercutting of the circular masked region on a $\{100\}$ slice. It is arbitrarily

defined as the difference between the maximum and minimum extents of undercutting (U_{max} and U_{min} , respectively) normalized by the average of these two values, i.e.

$$\text{relative anisotropy} = \frac{U_{\text{max}} - U_{\text{min.}}}{\frac{1}{2}(U_{\text{max}} + U_{\text{min.}})}$$

Also shown in Table I are cross-sectional profiles for the two orthogonal cleavage sections. These profiles are drawn to scale from optical micrographs of the cross sections. The angles and relative dimensions (including the degree of undercutting) are correct as shown. To aid in comparison of the cross sections for various etchant compositions the sections have been drawn to the same etch depth (normalized with respect to depth).

Sulfuric acid based compositions.—Sulfuric acid is the most widely employed reagent for acidification of hydrogen peroxide based GaAs etchants. The nine $\text{H}_2\text{SO}_4\text{-H}_2\text{O}_2$ etchant compositions listed in Table I were chosen to represent systematic compositional variations such as dilution at fixed $\text{H}_2\text{O}_2/\text{H}_2\text{SO}_4$ concentration ratio, variations in H_2SO_4 concentration at constant H_2O_2 concentration, etc.

Consider first the effects of diluting a basic 1:8:1 etchant as represented by the first five compositions in Table I. As expected, the etch rate decreases as both the acid and H_2O_2 concentrations are diminished, with a nearly linear decrease in rate with dilution for the less concentrated solutions. However, the most interesting effect of dilution occurs with the cross-sectional profiles. Although the profiles produced by these etchants are given in Table I, it is instructive, at least with the first series, to refer to the actual micrographs of the orthogonal cross sections given in Fig. 2.

Two cross-sectional micrographs, representing portions of cleaves through both of the different, orthogonal cleavage directions ($[011]$ and $[0\bar{1}\bar{1}]$) lying in the $\{100\}$ plane, are shown for each composition. The $(0\bar{1}\bar{1})$ sections¹ (right-hand side of Fig. 2) reveal flat bottoms in the etched channels between the stripes. Connecting the channel bottoms with the upper surface are acute-angled walls, which, in the sections etched with the more dilute compositions, are sharply defined planar walls corresponding to $\{111\}$ surfaces (55°). However, it is evident on closer inspection that the sidewalls of the two most concentrated compositions (1:8:40 and 1:8:1) are not planar but curved. Indeed the walls from the 1:8:1 etched section appear to be

¹ Assignment of polarities to the two orthogonal sections is made by assuming that the acute-angled walls, which make an angle of $\sim 55^\circ$ with the $\{100\}$ surface, are the $\{111\}_A$ or $\{111\}_B$ orientation. These directions are generally known to be the slowest etching directions in GaAs.

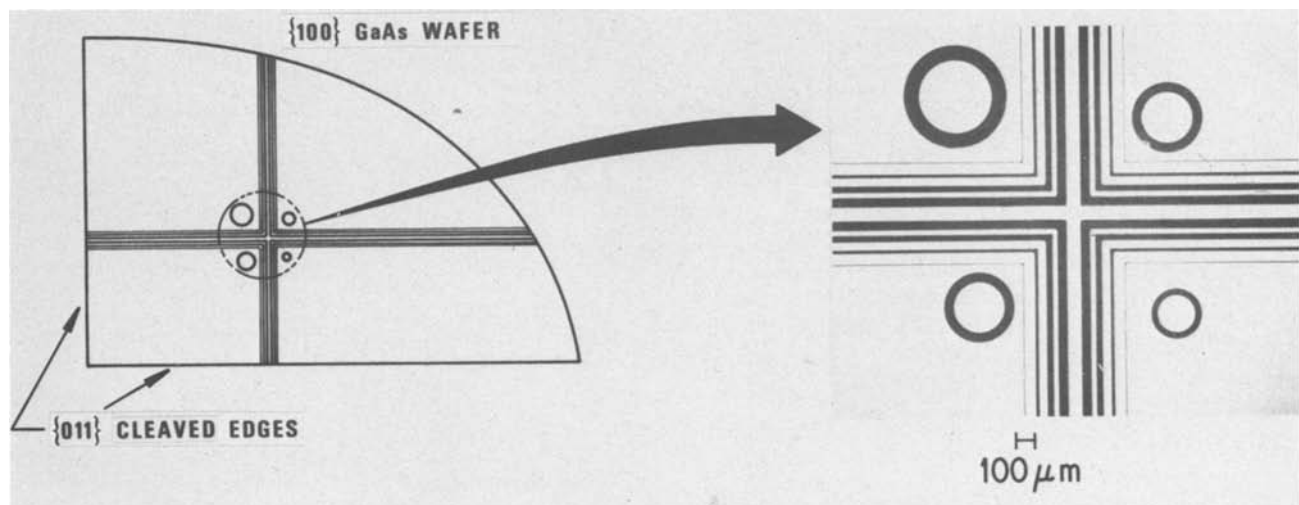


Fig. 1. Etch mask design and alignment configuration

Table I. Characteristics of acidic hydrogen peroxide etchants for GaAs

| ACID | VOLUME RATIOS * | CONCENTRATION (mol/l) | | RATIO OF UNDERCUT TD ETCHED DEPTH | | | RELATIVE ANISOTROPY | ETCH RATE (100) ($\mu\text{m min}^{-1}$) | CROSS-SECTIONAL PROFILES | |
|--------------------------------|-----------------|-----------------------|-------------------------------|-----------------------------------|-------|-------|---------------------|--|--------------------------|---------------|
| | | ACID | H ₂ O ₂ | <011> | <011> | <100> | | | (011) SECTION | (011) SECTION |
| H ₂ SO ₄ | 1:8:1 | 1.8 | 8.0 | 0.30 | 0.30 | 0.90 | 1.0 | 14.6 | | |
| H ₂ SO ₄ | 1:8:40 | 0.36 | 1.6 | 0.89 | 0.68 | 1.2 | 0.55 | 1.2 | | |
| H ₂ SO ₄ | 1:8:80 | 0.20 | 0.90 | 0.62 | 0.62 | 0.86 | 0.32 | 0.54 | | |
| H ₂ SO ₄ | 1:8:160 | 0.10 | 0.47 | 0.71 | 0.71 | 0.93 | 0.27 | 0.26 | | |
| H ₂ SO ₄ | 1:8:1000 | 0.018 | 0.079 | 0.82 | 0.76 | 0.95 | 0.22 | 0.038 | | |
| H ₂ SO ₄ | 1:1:8 | 1.8 | 1.0 | 0.77 | 0.53 | 1.0 | 0.61 | 1.3 | | |
| H ₂ SO ₄ | 4:1:5 | 7.1 | 1.0 | 0.49 | 0.29 | 0.70 | 0.83 | 5.0 | | |
| H ₂ SO ₄ | 8:1:1 | 14.0 | 1.0 | 0.52 | 0.43 | 0.61 | 0.35 | 1.2 | | |
| H ₂ SO ₄ | 3:1:1 | 11.0 | 2.0 | 0.44 | 0.44 | 0.53 | 0.19 | 5.9 | | |
| HCl | 1:4:40 | 0.27 | 0.87 | 0.51 | 0.28 | 0.97 | 1.1 | 0.22 | | |
| HCl | 1:1:9 | 1.1 | 0.89 | 0.22 | 0.18 | 0.37 | 0.69 | 0.20 | | |
| HCl | 40:4:1 | 10.6 | 0.87 | 0.54 | 0.54 | 0.54 | ~ 0 | >5.0 | | |
| HCl | 80:4:1 | 11.2 | 0.46 | 0.7 | 0.7 | 0.7 | ~ 0 | 1.1 | | |

* ACID (CONCENTRATED): H₂O₂(30%): H₂O

composed of two basic surface orientations, making angles of 55° ($\{111\}$) for the portion of the wall nearest the upper surface, and $\sim 40^\circ$ for that nearest the channel bottom.

The effects of etchant composition are even more pronounced with the profiles obtained with the (011) sections (left side of Fig. 2). The most concentrated etchant composition (1:8:1) yields a section with obtuse-angled walls. These walls are inclined with respect to the upper surface by an angle of ($90^\circ + 65^\circ = 155^\circ$). Note that this does not correspond to a $\{111\}$ surface (145°) even though this is the configuration where the $\{111\}$ orientation would be expected based on the results of the (011) sections. Later, this point will be discussed in detail, but at present, note that at the extreme lower portion of the walls of the 1:8:1 (011) section a small acute-angled surface exists. The relative portion of the walls made up of this acute-angled surface in comparison with the obtuse one increases progressively as the etchant composition is successively diluted. The lower, acute-angled surface yields projected angle of $\sim 55^\circ$ on the micrographs. This then represents a $\{\bar{1}\bar{1}\bar{1}\}$ As or $\{111\}$ B which is of opposite polarity to the acute-angled $\{111\}$ surfaces on the (011) sections to the right. Evidently, as the etchant becomes more dilute the $\{\bar{1}\bar{1}\bar{1}\}$ etch rate decreases relative to the rate for the orientation that forms the obtuse-angled surface.

As previously mentioned the noncentrosymmetric nature of GaAs crystals complicates fabrication of semiconductor devices. In etching mesas on the usual $\{100\}$ GaAs wafers, if the mesa mask pattern is rectangular with the sides aligned parallel to the cleavage directions in the customary manner, then the mesa will

have two opposing acute-angled sides with the other two sides being obtuse angled. The obtuse-angled sides are unsuitable for metallization and the device design is constrained. Silicon, on the other hand, yields equivalent mesas, with all four sides having the desirable acute-angled walls. Since, the extent of the lower, acute-angle wall increases with increasing dilution in the first four etchants in Table I (Fig. 2), it was hoped that even greater dilutions would result in symmetrical mesas with acute-angled walls similar to those obtained with silicon. With the 1:8:1000 solution this situation was approached, with only a small obtuse-angled wall at the top of the (011) section; however, at this dilution the etch rate had dropped to a very low value ($0.038 \mu\text{m min}^{-1}$). Thus, a completely symmetrical acute-angled mesa etch solution was not obtained with etch rates comparable to those commonly employed.

The angles of the various planar regions comprising the walls of these locally etched crystals may be analyzed using a graphical procedure (1). In this way the relative etch rates of the orientations yielding the various etched facets or portions of the etched walls may be ascertained and compared. The procedure yields the minimum permissible rates as a function of crystallographic orientation that are consistent with an observed cross-sectional morphology. Application to the cross sections shown in Fig. 2 yields the polar diagrams shown in Fig. 3 for each of the four etchants under discussion. These diagrams are not to be considered the actual rate vs. orientation diagrams, but rather the minimum rates as a function of orientation. Thus, minima present on these diagrams may result in etched facets; however, the intermediate orientations (angles on the diagram) between minima are merely

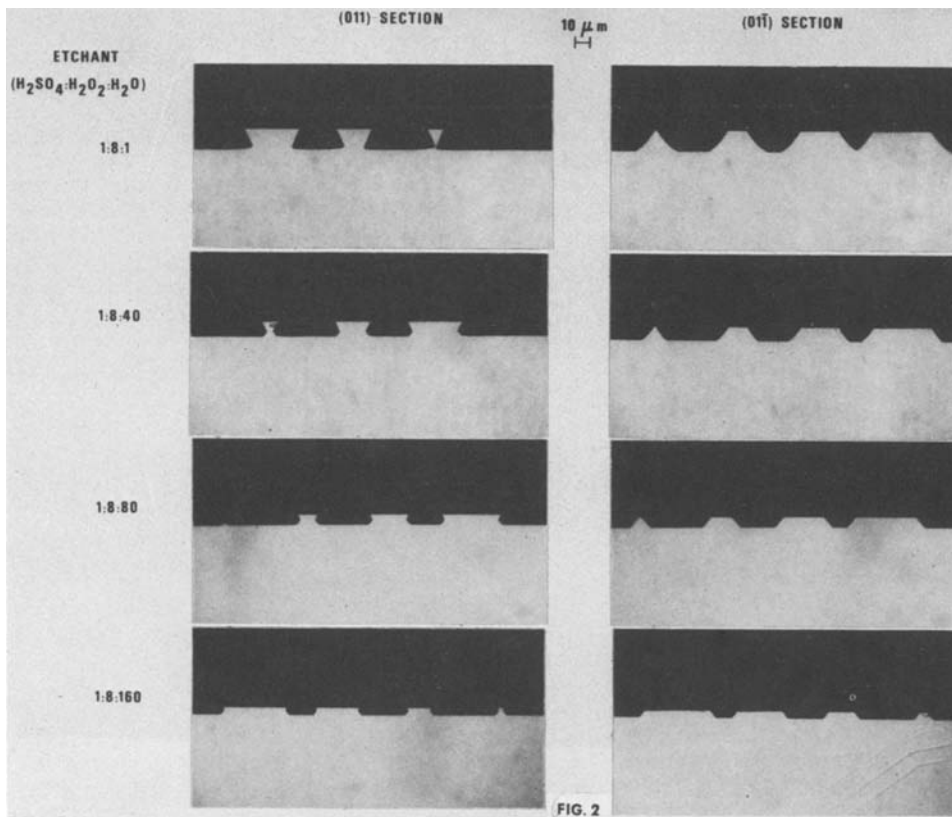


Fig. 2. Micrographs of orthogonal cross sections cleaved from slices etched in $H_2SO_4:H_2O_2:H_2O$ solutions.

the minimum rates consistent with the observed cross sections, and the actual rates for intermediate angles will generally exceed these values. On the other hand, the etched morphologies are principally determined by

the minima. The diagrams were constructed on the basis of measurements of the extent of undercutting just beneath the etch mask, the measured intersection angles between the planar regions (or their geometrical

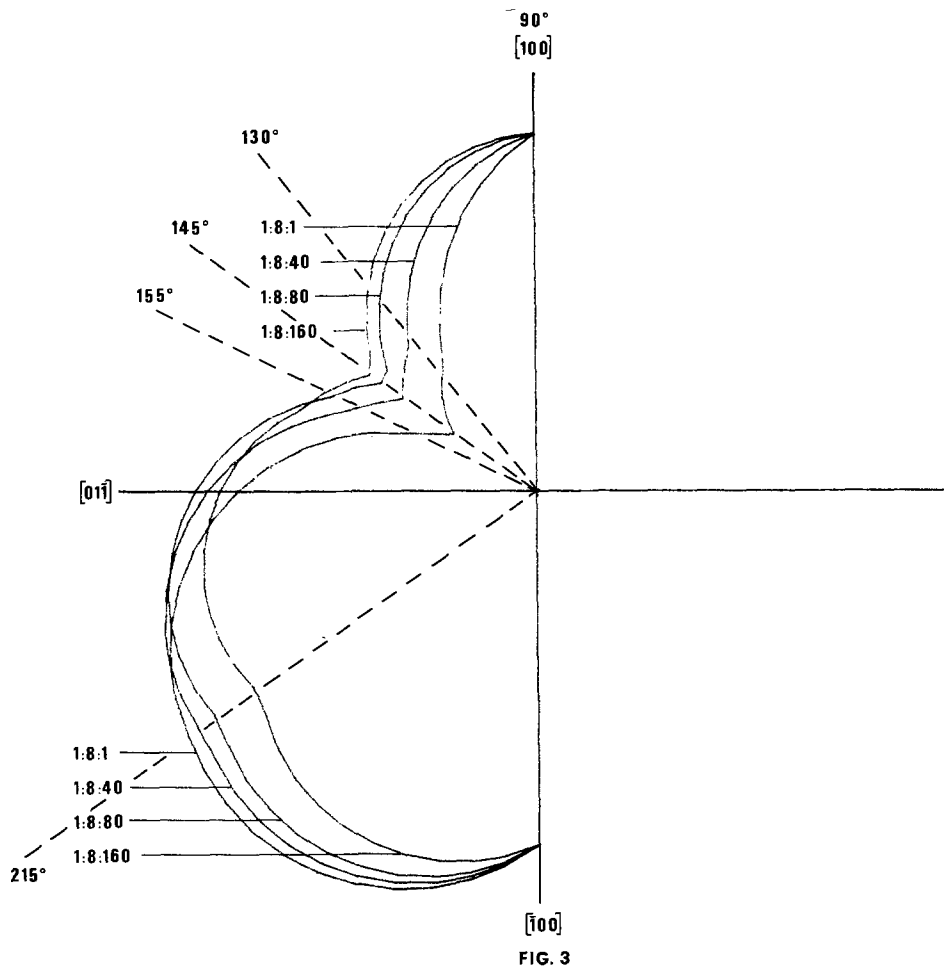


Fig. 3. Minimum-rate polar diagrams for GaAs etching with $H_2SO_4:H_2O_2:H_2O$ solutions of the designated compositions (by volume of concentrated reagents).

extensions) and the upper surface, and the etch rate or depth perpendicular to the surface in regions significantly distant from the mask edge that a planar etch front parallel to the original surface is evident.

The derived polar diagrams may be verified by comparison of the experimental cross sections in Fig. 2 with predicted cross sections geometrically constructed from the diagrams. This construction, which is discussed in detail in Ref. (1), consists of locating the origin of the polar diagram at a position representing the edge of the etch mask with the correct orientation normal to the slice surface. Radius vectors are then extended from the origin to their intersection with the polar diagram. Normals are drawn to the ends of these radius vectors, and the predicted cross-sectional profile is defined by an envelope-of-normals, which consists of all normals or portions of normals that may be

reached from the origin without intersecting any others. The machine-drawn, predicted cross-sectional profiles for the four 1:8:X etchants under consideration are shown in Fig. 4 and 5. For purposes of comparison they are all normalized to a uniform etch depth.² Comparison of the predicted profiles with the actual micrographs in Fig. 2 supports the validity of the minimum-rate polar diagrams.

Consider the diagrams of Fig. 3. All four etchants have minimum etch rates at $\sim 145^\circ$, which corresponds to the $\{111\}$ orientation. As previously mentioned, this

² It should be noted that if the relative etch rates do not vary with time, the polar diagrams and hence the basic cross-sectional profiles will be independent of the extent of etching. This was confirmed experimentally with each etchant by observing that the cross-sectional shapes did not change with incremental etching. In other words with increased etching time the etched grooves or channels enlarged, but the basic cross-sectional profiles were invariant.

Fig. 4. Predicted (011) cross-sectional morphologies based on the polar diagrams in Fig. 3 for $\text{H}_2\text{SO}_4:\text{H}_2\text{O}_2:\text{H}_2\text{O}$ solutions.

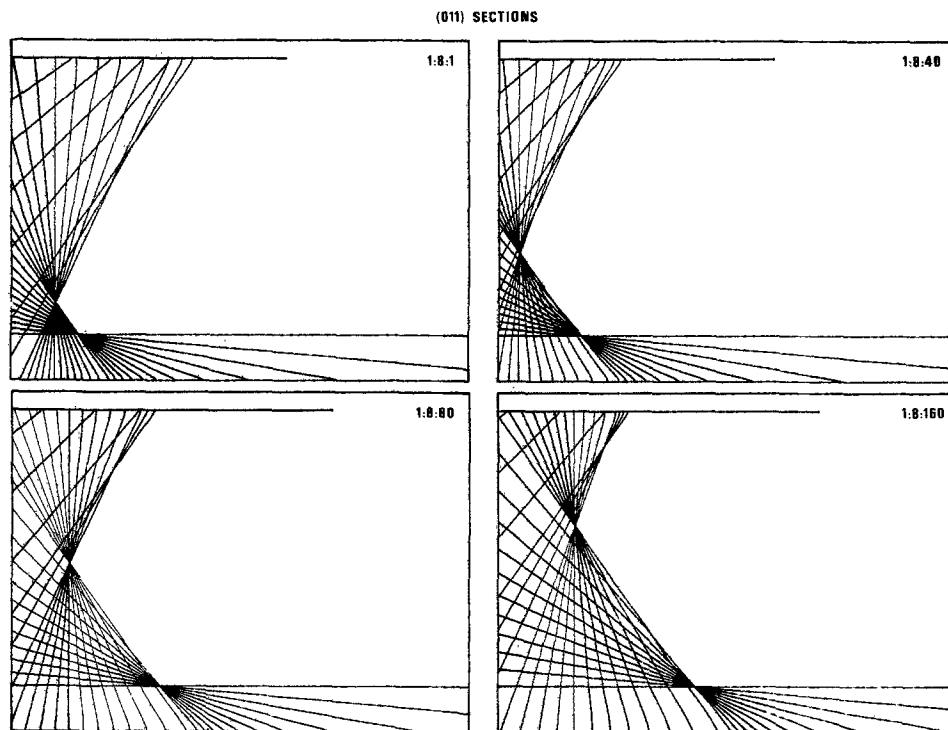
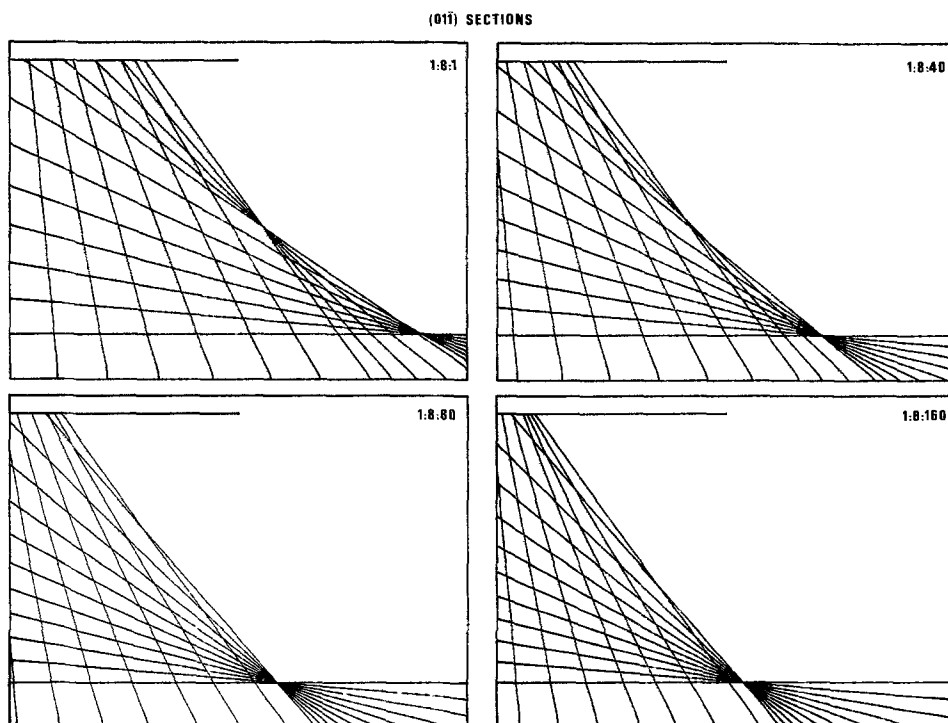


Fig. 5. Predicted (01 $\bar{1}$) cross-sectional morphologies based on the polar diagrams in Fig. 3 for $\text{H}_2\text{SO}_4:\text{H}_2\text{O}_2:\text{H}_2\text{O}$ solutions.



is assumed to be the {111}A, since the electron deficient, Ga-rich {111}A surface is resistant to chemical oxidation and generally is the slowest etching orientation for GaAs crystals. The {111}A etch rate is responsible for the acute-sloped facets near the upper surface of the (01 $\bar{1}$) sections. Three other minima directions also contribute to the resulting shapes. First among these is the orientation occurring at 215° which corresponds to a {111}B or {111}As. Obviously the chemical properties of the surface atoms are not the sole factor determining etch rate, because the electron-rich character of the {111}B surface should make it one of the most rapidly etching orientations. Most likely the minimum at {111}B is due to the great packing density of the close-packed {111}B surface relative to the adjacent orientations. The most important criterion for faceting is not the absolute rate of a given orientation, but rather its rate relative to the adjacent orientations. Thus, the {111}B produces faceting even though it has a relatively high etch rate. The relatively minor perturbation to the polar diagrams at 215° results in the lower, acute-angled facets that appears on the (011) cross sections (Fig. 2 and 4).

The orientations corresponding to the other two minima (130° and 155°) are somewhat unexpected because no low index orientations lie at these angles. The angle, 155°, corresponds to the {332} orientation; however, this relatively high index orientation has been previously (2) associated with facet formation with a Br₂:CH₃OH etchant composition. The 130° minimum appears to be even more complex. Only a very high index surface would appear at 130° in the [0 $\bar{1}\bar{1}$] direction where the facet appears to be located on the (01 $\bar{1}$) sections (lower acute facet notable in the sections for the 1:8:1 and 1:8:40 compositions in Fig. 2). However, lying close to the [0 $\bar{1}\bar{1}$] zone axis (within 12°) are two {332} orientations whose apparent facet angles if projected into the (01 $\bar{1}$) viewing surface would be 130.3°. These {332} are the only likely orientations responsible for the clearly defined lower facets observed on some (01 $\bar{1}$) cross sections.

From Fig. 3 it is evident that relatively minor local minima or perturbations, such as those at 130° and 155°, can be associated with pronounced effects on the morphology, primarily because of the angles where they occur. An interesting question concerns why local rate minima are found at {332}, but not at other high index planes lying in the zone, e.g., {221}, {331}, {211}, etc. The other orientations in the immediate vicinity of {332} do not contribute significantly to the morphology or otherwise the sharply defined obtuse facet near the mask surface on the (011) sections would be more rounded than the very planar regions observed. Thus we are faced with the conclusion that {332} possesses unique characteristics that tend to resist etching by the etchants with higher H₂O₂ concentrations. Koszi and Rode (2) observed precisely defined {332} etched facets with a Br₂:CH₃OH etchant. Presumably the etch rate inhibition is due to either the chemical properties and/or the geometrical atomic arrangement of the {332} surfaces, surface steps, or kinks.

Since the polar etch rate diagrams in Fig. 3 are all normalized to the same [100] etch rate, the effect of etchant composition on the etch rate anisotropy is readily apparent. As the basic 1:8:1 etchant is successively diluted the etch rate becomes more isotropic with respect to orientation. This is evident from Table II where the relative rates (rate ratios) of the two polar {111} rates are displayed. It should be noted, however, that the decrease rate ratios in Table II result from a simultaneous increase in the {111}A etch rate and a decrease in the {111}B etch rate (relative to {100}) with dilution. Of course, a truly isotropic etchant would exhibit an unperturbed, circular polar diagram. The decrease in anisotropy with dilution is also apparent in the "relative anisotropy" column in Table

Table II. Influence of etchant composition on etch rate anisotropy for polar {111} orientations

| Etchant composition (conc. H ₂ SO ₄ :H ₂ O ₂ (30%):H ₂ O (by volume)) | Etch rate ratio |
|--|---|
| | $\frac{R(\bar{1}\bar{1}\bar{1})B}{R(111)A}$ |
| 1:8:1 | 4.2 |
| 1:8:40 | 2.6 |
| 1:8:80 | 2.1 |
| 1:8:160 | 1.5 |

I. Note, however, that even on dilution to 1:8:1000 the anisotropy is still significant, having a value of 0.22 as compared with zero for an isotropic etchant.

Examination of the degree of undercutting (ratio of undercutting to etched depth) in Table I shows that the greatest undercutting occurs in the <100> azimuthal direction. Although only three directions are tabulated in Table I, examination of the patterned rings on the etched slices confirmed that the <100> direction is, indeed, the most susceptible to undercutting. This is due to the absence of slow-etching planes with {111} character in the <100> zone. Other trends are also evident from Table I. Consider the H₂SO₄-based series, 1:8:80, 1:1:8, 4:1:5, and 8:1:1, where the H₂SO₄ concentration is increased at nearly constant H₂O₂ concentration (~1.0 mole/liter). At low concentrations the etch rate increases as the H₂SO₄ concentration is raised, in a manner similar to that observed by Iida and Ito (3). Accompanying the increase in H₂SO₄ concentration is an increase in solution viscosity, which becomes particularly apparent with H₂SO₄ concentrations above ~4 mole/liter (4). Thus, whereas the H₂SO₄ may initially increase the surface dissolution kinetics, the high viscosities at elevated H₂SO₄ levels decrease the mass transport rates in the liquid to the degree that the overall etch rate decreases. This hypothesis is consistent with previous observations (3) that at high H₂SO₄ concentrations the etch rate becomes sensitive to stirring effects and the apparent activation energy decreases, effects generally associated with mass transfer control of the etch rate.

If the etch rate becomes mass transport limited, the etch rate anisotropy should decrease. This is evident from Table I where the relative anisotropy first increases and then decreases with increasing H₂SO₄ concentration in the same manner as the etch rate for the series 1:8:80, 1:1:8, 4:1:5, and 8:1:1. Note also the rounded profiles obtained with the (011) cross sections for the two highest H₂SO₄ compositions, 8:1:1 and 3:1:1. Of course, these etchants are not completely isotropic because some angular or faceted behavior is apparent near the mask surface on the (011) sections, and the (01 $\bar{1}$) sections are clearly faceted.

The 8:1:1 and 3:1:1 compositions also provide a comparison of the effects of increasing H₂O₂ concentrations at high H₂SO₄ levels. The etch rate increases strongly as the H₂O₂ concentration is doubled from 1.0 to 2.0 moles/liter. However, the relative anisotropy actually decreases, indicating that there is no simple relationship between the (100) etch rate and the relative anisotropy.

Hydrochloric acid based compositions.—All of the H₂SO₄-based etchants exhibited to a greater or lesser extent an obtused-angled facet on the (011) sections. Even etchants with apparent mass transfer limitations such as 8:1:1 and 3:1:1, [where the (011) section showed rounded, less-angular walls] still retained the small obtuse facet near the mask surface. Obtuse-angled walls are undesirable for many electronic device configurations. Fortunately, some HCl-based etchants yield significantly different profiles.

The etching characteristics of four HCl-based compositions are presented at the bottom of Table I. At high dilutions and/or low HCl concentrations, etchants

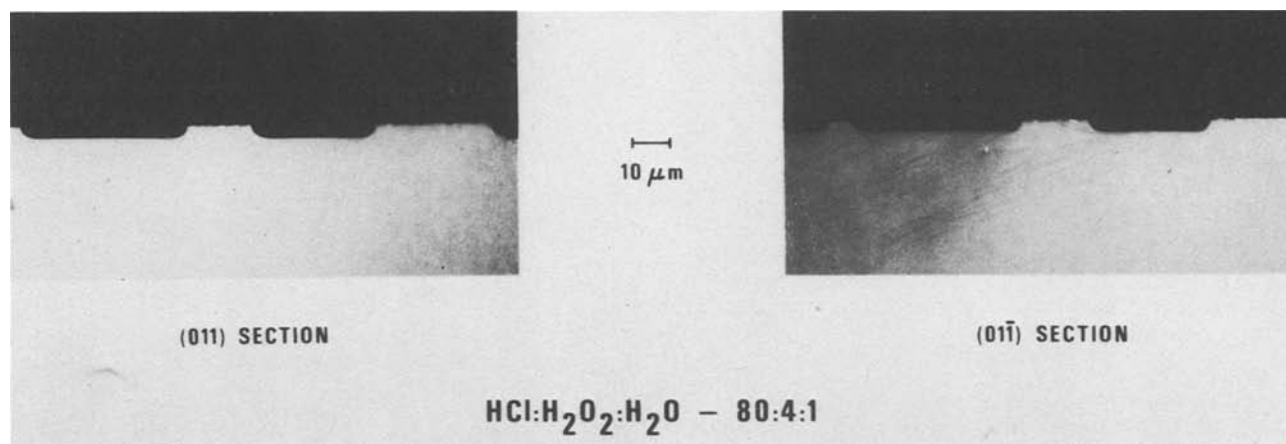


Fig. 6. Micrographs of orthogonal cross sections cleaved from GaAs slice etched in HCl:H₂O₂:H₂O-80:4:1 solution

exhibit orientation-dependent rate characteristics similar to the H₂SO₄-based solutions, although the lower acute-angled facet previously observed on the (011) sections is not evident with the 1:1:9 HCl:H₂O₂:H₂O solution. If, however, the HCl concentration is increased to the neighborhood of 10 moles/liter, an unexpected effect is observed. The etchants become essentially isotropic. This is apparent from comparison of the (011) and (011 $\bar{1}$) cross-sectional profiles for the last two compositions (40:4:1 and 80:4:1) given in Table I. Here the cross-sectional profiles are smoothly rounded, and essentially identical profiles are obtained for both orthogonal cross sections. The actual cross-sectional micrographs obtained from wafers etched in the 80:4:1 solution are shown in the lower part of Fig. 6. Unlike previous GaAs etchant compositions, the 80:4:1 HCl:H₂O₂:H₂O solution produces virtually identical (011) and (011 $\bar{1}$) cross-sectional profiles. Furthermore, the degree of undercutting was azimuthally uniform, both on the inside and outside perimeters of the ring pattern, as expected for an isotropic etchant.

More quantitative assessment of the isotropic character of some HCl-based etchants may be obtained from the relative anisotropy column of Table I. For low HCl concentrations the etchants are quite anisotropic. Indeed, the 1:4:40 composition yielded the highest anisotropy of all etchants tabulated in Table I. However, as the HCl concentration is increased, the relative anisotropy falls and becomes essentially zero for the last two compositions with HCl concentrations in excess of 10 moles/liter.

The isotropic, HCl-based compositions should be useful for any application where uniform orientation-independent etching is required. However, their isotropic rate characteristics are accompanied by a mass transfer controlled behavior, and the etch rates become particularly sensitive to the degree and nature of agitation employed during etching. The etch rates given in Table I for the 40:4:1 and 80:4:1 correspond to the particular agitation conditions employed, and significant deviations should be expected for other conditions. Likewise, it is necessary to provide very uniform agitation to obtain uniform morphologies.

Another interesting feature is the low degree of mask undercutting produced by the 1:1:9 composition. The ratio of undercut to etched depth for each azimuthal direction is lower for the 1:1:9 etchant than for any other composition in Table I.

Summary and Conclusions

The GaAs etch rates and morphologies produced by a wide range of acidic hydrogen peroxide etchants have been examined. Through analyses of the cross-sectional morphologies obtained from locally etched samples, the etch rate anisotropy with respect to crystallographic orientation can be assessed. The principal slow-etching and morphology-determining orientations are {111}Ga, {111}As, {332}Ga, and {100}. Sulfuric acid based etchants are generally anisotropic with respect to orientation; but, the degree of anisotropy decreases with high-H₂SO₄-concentration etchants, where mass transport rate limitations are encountered. Hydrochloric acid based etchants are also anisotropic if the HCl concentration is low. However, at higher HCl concentrations (*e.g.*, greater than 10 moles/liter), the etchants are essentially isotropic. Thus, HCl:H₂O₂:H₂O compositions are identified, which, during localized etching, produce uniformly rounded etched profiles independent of the azimuthal crystallographic direction.

Acknowledgments

Appreciation is expressed to Mr. D. E. Todd for his experimental assistance. In addition, the author wishes to thank Drs. D. J. Coleman, Jr. and W. R. Frensley for carefully reviewing the manuscript. This research was supported by the Air Force Office of Scientific Research (AFSC) under Contract No. F44620-75C-0036.

Manuscript submitted June 18, 1980; revised manuscript received Oct. 21, 1980.

Any discussion of this paper will appear in a Discussion Section to be published in the December 1981 JOURNAL. All discussions for the December 1981 Discussion Section should be submitted by Aug. 1, 1981.

Publication costs of this article were assisted by Texas Instruments Incorporated.

REFERENCES

1. D. W. Shaw, *J. Cryst. Growth*, **47**, 509 (1979).
2. L. A. Kozi and D. L. Rode, *This Journal*, **122**, 1676 (1975).
3. S. Iida and K. Ito, *ibid.*, **118**, 768 (1971).
4. E. W. Washburn, Editor, *International Critical Tables*, Vol. V, p. 12, McGraw-Hill, New York (1929).

Delineation of Shallow Junctions in Silicon by Transmission Electron Microscopy

T. T. Sheng and R. B. Marcus

Bell Laboratories, Murray Hill, New Jersey 07974

ABSTRACT

A method has been developed for delineating arsenic implanted n+p junctions in silicon by selective etching in 0.5% HF in HNO₃ and examination by transmission electron microscopy. This method is particularly applicable to shallow junction ($\lesssim 0.1 \mu\text{m}$) devices where conventional methods are no longer applicable. The n⁺ region is selectively etched, and delineation occurs at a depth corresponding to a concentration of $1 \times 10^{19} \text{ As/cm}^3$.

The trend in silicon VLSI MOS technology is toward smaller geometries with shallower junction depths and shorter gate lengths. As these dimensions approach $1 \mu\text{m}$ and below, traditional methods for measuring these distances are no longer useful. Angle lap-stain methods as normally applied are limited by the spacing of interference lines, which is $0.275 \mu\text{m}$ for Xe light. Samples cleaved through a junction, selectively etched and examined in the SEM offer an improvement in resolution as well as information on the lateral extent of the junction (1), but quantitative information is limited by the resolution of the SEM and uncertainty about the spatial relationship between the chemical delineation and the junction. Spreading resistance probing of a shallow angle-lapped surface (2) is limited in resolution due to the probe tip size. Auger electron spectroscopy (3) and Rutherford backscattering (4) methods are useful for depth measurements for shallow junctions, but give no information on the lateral extent of the junction.

In this paper a method is described for accurately and reproducibly determining junction profiles using transmission electron microscopy (TEM) on cross-section samples. This method has been demonstrated to provide a precision of $\pm 45 \text{ \AA}$ on a 1180 \AA junction depth sample and gives sharp delineation in both vertical and lateral directions.

Experimental

P-type, (100) oriented 6-8 $\Omega\text{-cm}$ 75 mm diam silicon wafers were used as starting material for these experiments. Two types of samples were processed as described in Table I. The test pattern samples were fabricated from a two-level mask set that produced a repetitive array of 1.0, 2.0, and 4.0 μm gates bounded by 2.0 μm source/drain regions; adjacent "IGFET's" were separated by 2.0 μm field oxide regions. In the orthogonal direction these features ran the length of the wafer. A very large number of cross-section preparations for TEM study could be made from each wafer. These preparations were primarily used to evaluate different chemical etchants to determine reproducibility and accuracy and to determine the doping level which corresponded with the delineation; most of the studies were performed on these test pattern samples. Unpatterned samples were also used to evaluate accuracy and to determine the location of the delineation.

The method for preparing cross-section samples has been described elsewhere (5). Each preparation for TEM study contained four to six specimens, all from the same wafer. In a typical case (for the test pattern samples) 5-10 gates could be examined in one sample, so 20-60 gates in one preparation could be examined by TEM.

Key words: junction delineation, pn junction, VLSI technology, electron microscopy.

Chemical etchants were examined in terms of their ability to produce reproducible and accurate junction delineations. Reproducibility was determined by using the following procedure:

1. Prepare TEM sample.
2. 5-60 sec buffered HF [34.6 weight percent (w/o) NH₄F, 6.8 w/o HF], rinse and dry, and treat in etchant.
3. Deposit calibrated latex balls (6) over TEM preparation for internal magnification standard.
4. TEM study and evaluation.
5. Ion mill (6.5 kV, 100 μA Ar⁺ ions/gun) 5 min-2 hr and repeat steps 2-4.

The latex balls, nominally 0.312 μm diam, were calibrated against a replica of a diffraction grating with a known period of 0.715 μm .

The accuracy of the method was found by determining the doping level which corresponded to the etched delineation. This was done by comparing measurements with junction depths calculated from variation 3 of the SUPREM II diffusion model (7) (with clustering; $M = 4$), which in turn was calibrated against junction depths measured by Auger electron spectroscopy (3) and Rutherford backscattering (4).

The chemical etchants examined were a combination of HF and HNO₃ (8), and a copper plating solution (9), all at room temperature. A variety of etch times and concentrations (for the HF-HNO₃ system) were studied, including an evaluation of the effect of illumination. Vapor etching was also studied. In all cases the etching was preceded by 5-60 sec treatment in buffered HF (BHF) followed by a 1 sec rinse and quick dry by blotting. The HF-poor etchants produced very little thinning of SiO₂, and in order to produce a more uniform contrast in micrographs the SiO₂ was pre-thinned, in these cases, by exposure to 60 sec of BHF.

Table I. Description of samples

| | |
|--------------------------------|--|
| A. Test pattern samples | |
| Source/drain doping: | Arsenic implant, 30 keV, $7 \times 10^{15} \text{ ions/cm}^2$, 900°C, 35 min |
| | O ₂ drive-in |
| Gate: | 3500 Å undoped polysilicon on 250 Å SiO ₂ . Gate length = 1.0, 2.0, 4.0 μm |
| Field oxide: | 3500 Å SiO ₂ . Oxide length = 2.0 μm |
| B. Unpatterned samples | |
| n ⁺ doping: | Arsenic implant, 30 keV, $7 \times 10^{15} \text{ ions/cm}^2$, 900°C 35 min. |
| | O ₂ drive-in |
| Additional thermal treatments: | 15 min 950°C Ar |
| | 30 min 950°C Ar |
| | 60 min 950°C Ar |
| | 120 min 950°C Ar |

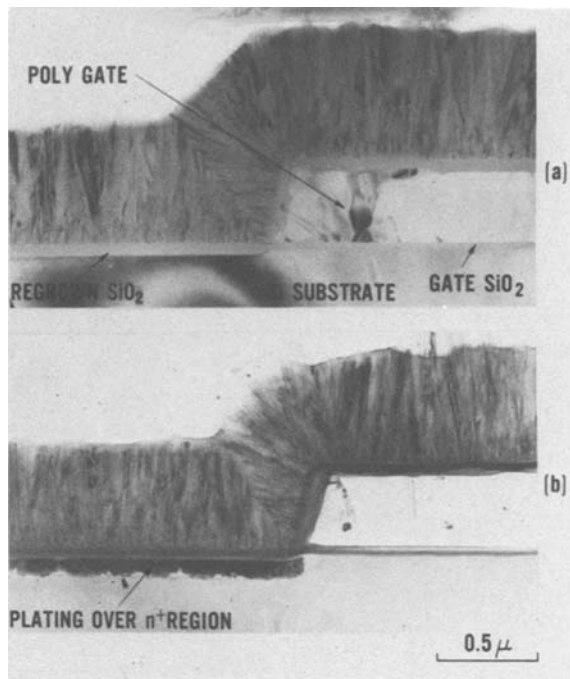


Fig. 1. TEM photograph of a vertical section through test pattern structure containing n^+p junction before (a) and after (b) copper plating. The copper grains plate preferentially on the n^+ region.

Results

A copper plating treatment has been reported to give clear pn junction delineation when examined by optical microscopy (9). Baths were prepared using 8

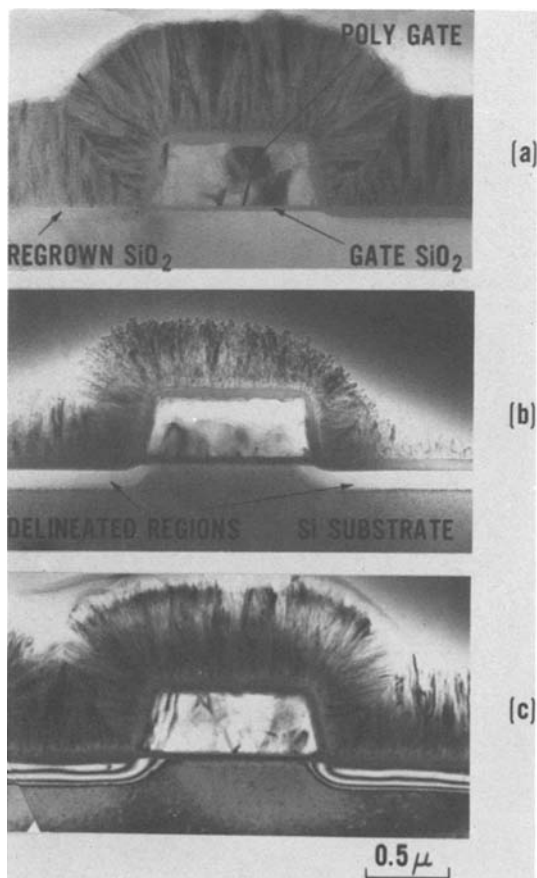


Fig. 2. TEM photographs of a vertical section through test pattern structure containing gate, source, and drain regions before etch (a) and after 9 sec etch in 0.5% HF-HNO₃ solution (b). Tilting the sample revealed thickness contours in the n^+ region (c).

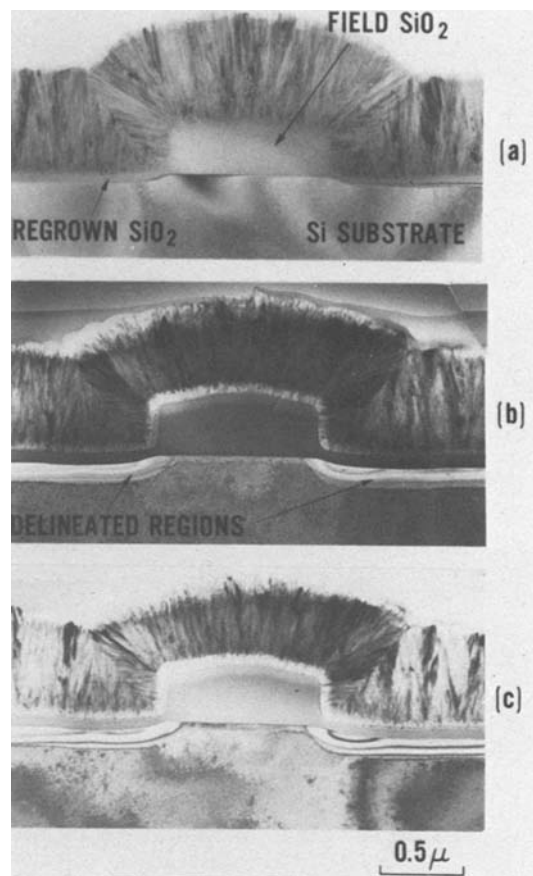


Fig. 3. TEM photographs of a vertical section through test pattern structure containing field oxide, source, and drain regions before etch (a) and after 9 sec 0.5% HF-HNO₃ etch (b). Tilting the sample revealed thickness contours in the n^+ region (c).

g/liter of CuSO₄·5H₂O and 10 ml/liter of concentrated HF. TEM test pattern preparations were etched using plating times of 5 sec. In one case strong illumination was used during plating and in another case plating was performed in the dark. In all experiments it was found that n^+ material was preferentially etched, but the plating overlay on the n region contained grains too large ($\sim 0.1 \mu\text{m}$) to permit clear delineation. A micrograph of such a sample is shown in Fig. 1.

Various mixtures of HNO₃-HF were examined. Although HF-rich solutions tend to remove oxide at a fast rate thus destroying part of the structure of a sample under study, these solutions were examined since they are typically used for routine angle lap-strain procedures. Solutions of 0.25, 0.5, 1.0, 1.5, 2.0, and 4.0% HNO₃ in HF were used on TEM test pattern preparations for times of 1-8 sec, both with and without strong illumination. Results were variable, ranging from 1000 to 2400 Å, with no clear correlation of measured delineation depth with any of the above variables.

Attempts have been made to delineate junctions by holding the TEM preparation in the vapor from a 33% HNO₃ in HF solution heated to boiling. Although junctions have been delineated by this method (5), reproducibility is poor.

The most successful results were obtained with dilute solutions of HF in HNO₃. Although 1% solutions gave delineations whose depths increased with increasing etching time, 0.5% solutions gave reproducible depth independent of etch time as shown in Table II. TEM preparations 1, 2, and 3 (Table II) were etched for 5, 9, and 7 sec, respectively, and each preparation contained 4-6 specimens. The average delineation depth measured from the test pattern samples (10 measurements on two preparations) was 995 Å with a standard

Table II. Junction delineation using 0.5% HF in HNO₃

| Sample | TEM preparation | Etch time (sec) | Delineation depth (Å) | Calculated junction depth (Å) | (Calculated depth)-(delineated depth) (Å) | {As} at delineated depth (atom/cm ³) |
|------------------|-----------------|-----------------|--|-------------------------------|---|--|
| Test pattern | 1 | 5 | 923 | 1180 | 185 | 1.0×10^{19} |
| | | 5 | 933 | | | |
| | | 9 | 1035 | | | |
| | | 9 | 1040 | | | |
| | | 9 | 988 | | | |
| | | 9 | 957 | | | |
| | | 9 | 1055 | | | |
| | | 9 | 966 | | | |
| | | 9 | 1040 | | | |
| | | 9 | 1010 | | | |
| | | | Average = 995Å, $\sigma = 45\text{Å}$ | | | |
| Unpatterned 15m | 3 | 7 | 1470 | 1780 | 310 | 2.0×10^{19} |
| Unpatterned 30m | 3 | 7 | 1932 | 2140 | 208 | 5.0×10^{18} |
| Unpatterned 60m | 3 | 7 | 2435 | 2700 | 265 | 4.0×10^{18} |
| Unpatterned 120m | 3 | 7 | 3044 | 3510 | 466 | 1.3×10^{18} |

deviation of 45Å. Figures 2 and 3 show micrographs of TEM test pattern structures before (a) and after (b and c) etch in 0.5% HF in HNO₃. The micrographs in Fig. 2 and 3 are from polygate and field oxide regions, respectively. Delineations are sharp, and the magnitude of lateral junction penetration under a gate can be easily measured. The ratio of lateral to vertical delineation (*c/a* in Fig. 4, measured from the positions of the polysurface before reoxidation and the silicon surface after reoxidation) was found to range from 0.75 to 0.95 μm.

Discussion

The use of 0.5% HF in HNO₃ as a junction delineation etchant was found to give reproducible results, both for measurements on a number of samples within a preparation, and for measurements on different preparations. The determination of accuracy is not quite as easy to evaluate. At present we assume variation 3 of SUPREM II computation (with clustering; *M* = 4) to be correct, and Auger electron spectroscopy (3) and Rutherford backscattering (4) measurements confirm

that the model is correct to within ~ 300Å for shallow junctions.

The doping concentrations which correspond to the delineated depths measured from the TEM photographs are calculated from the SUPREM II model and are shown in the last column of Table II. A profile calculated for the test pattern samples is shown in Fig. 5. These data indicate that the delineation occurs at a concentration of ~ 1×10^{19} /cm³. A plot of the measured delineation from the micrographs vs. the calculated depth which corresponds to 1.0×10^{19} As/cm³ for the unpatterned samples is shown in Fig. 6. The curve passes through the origin and lends support to the argument that delineation corresponds to a concentration level of ~ 1×10^{19} As/cm³.

The steepness of the profile for concentrations < 10^{19} /cm³ for the test pattern samples (see Fig. 5) places the true junction only a short distance deeper than the delineations. With increasing junction depth the steepness of the concentration profile diminishes slightly, and for the 120 min unpatterned sample with a junction depth of 3510Å, the junction would be ~ 470Å deeper than the delineation; this trend can be seen in the fifth column of Table II. Although the precise location of the junction is subject to errors in the SUPREM II model, these errors are likely to have

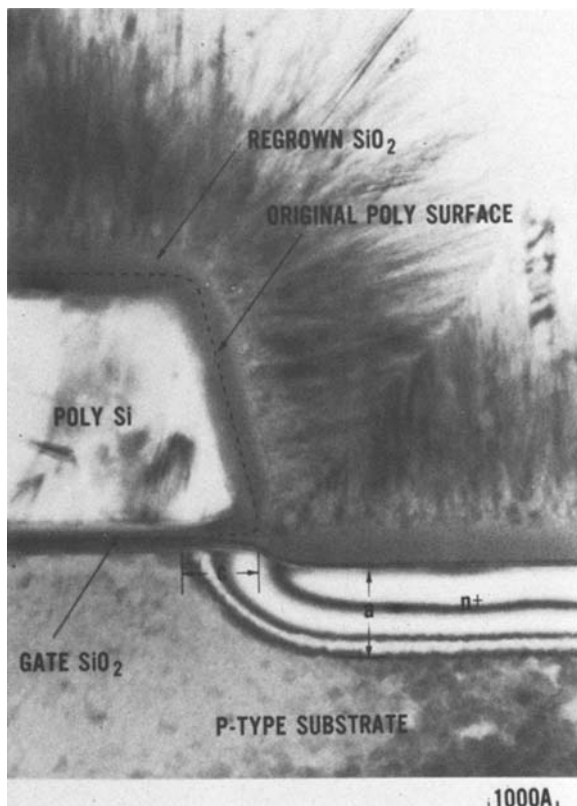


Fig. 4. TEM photograph of vertical section through test pattern structure at edge of gate after 9 sec. etch in 0.5% HF-HNO₃. The parameters *a* and *c* are, respectively, the junction depth and the lateral penetration of the junction from the position of the original edge of the implant (before reoxidation).

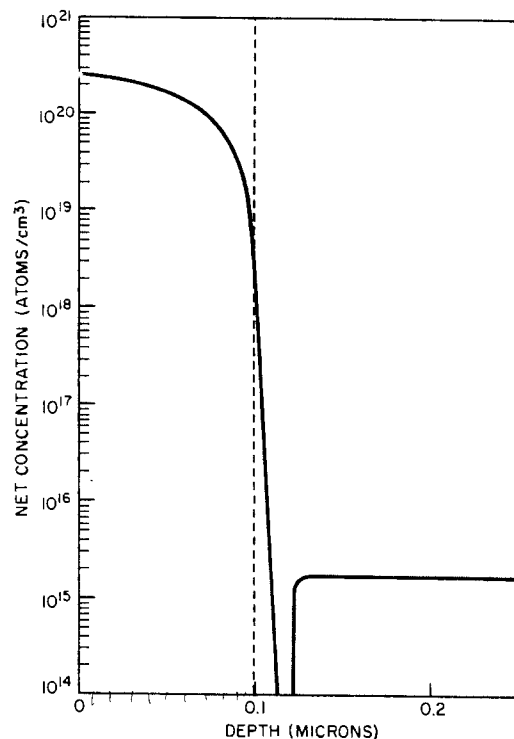


Fig. 5. Arsenic profile calculated for the test pattern samples using variation 3 of SUPREM II with clustering. The dotted line indicates the average depth measured from the TEM samples.

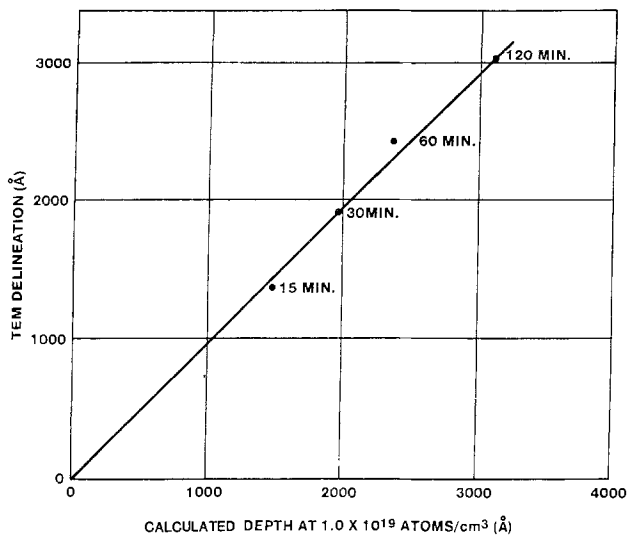


Fig. 6. Plot of delineation depth vs. calculated depth corresponding to $\{As\} = 1 \times 10^{19}$. Data obtained from the unpatterned samples using variation 3 of SUPREM II.

no effect on the profile for the higher arsenic levels where Auger and Rutherford scattering measurements show little difference between the two variations of the SUPREM model.

It may be incidentally noted that oxide thickness on the sidewalls of the poly is 30-50% thinner than oxide on the poly surface. This is thought to be due to the higher As doping of the poly surface (due to the normal direction of incidence of the implantation) and the known faster oxidation of implanted poly. The extreme thinning of oxide sometimes seen at polycorners is a different phenomenon that is discussed elsewhere (10).

Conclusion

A method has been found for delineating arsenic implanted n+p junctions in silicon with a reproducibility and resolution that has not been previously realized. The delineation method uses 0.5% HF in HNO₃ to selectively remove silicon with an arsenic concentration greater than $1 \times 10^{19}/\text{cm}^3$; the delineation is ob-

served in the transmission electron microscope. Measurements were made on arsenic implanted and annealed samples with and without gate structures, and delineation data were correlated with junction profiles calculated from SUPREM II modeling with clustering. This method is particularly applicable to shallow junction arsenic implanted source/drain structures where the doping profile falls off sharply for concentrations below $1 \times 10^{19}/\text{cm}^3$. Ten measurements on samples which represent etch time of 5 and 9 sec gave an average delineation depth of 995Å with a standard deviation of 45Å.

Acknowledgments

The help of T. Smith in computer profiling and C. C. Chang and E. Kinsbron in discussions is gratefully acknowledged.

Manuscript submitted June 9, 1980; revised manuscript received Sept. 2, 1980.

Any discussion of this paper will appear in a Discussion Section to be published in the December 1981 JOURNAL. All discussions for the December 1981 Discussion Section should be submitted by Aug. 1, 1981.

Publication costs of this article were assisted by Bell Laboratories.

REFERENCES

1. E. S. Meieran and T. I. Kamins, *Solid State Electron.*, **16**, 545 (1973).
2. N. Goldsmith, R. V. D'Aiello, and R. A. Sunshine, in *Proceedings of Spreading Resistance Symposium*, Gaithersburg, MD, June 13-14, 1974, Nat. Bur. Stds. Special Publication, 406-10, p. 223.
3. C. C. Chang, Unpublished.
4. E. Kinsbron, Unpublished.
5. T. T. Sheng and R. B. Marcus, *This Journal*, **127**, 737 (1980).
6. Latex balls obtained from E. F. Fullam, Inc., Schenectady, N.Y.
7. D. A. Autoniadis, S. E. Hansen, and R. W. Dutton, U.S. Army Technical Report No. 5019-2, June 1978.
8. W. R. Runyan, "Semiconductor Measurements and Instrumentation," p. 980, McGraw-Hill, New York (1975).
9. C. P. Wu, E. C. Douglas, C. W. Mueller, and R. Williams, *This Journal*, **126**, 1982 (1979).
10. R. B. Marcus, Unpublished.

Cosmetic Defects in CCD Imagers

L. Jastrzebski, P. A. Levine, W. A. Fisher,* and A. D. Cope

RCA Laboratories, Princeton, New Jersey 08540

and E. D. Savoye and W. N. Henry

RCA Optoelectronics Division, Lancaster, Pennsylvania 17604

ABSTRACT

The requirement to fabricate CCD imagers free of defects brings about the need to identify the origin of the defects in an effort to improve the imager technology. The following defects in the video display were commonly observed: vertical and horizontal lines, localized spots, and striations. Their origin was analyzed using a combination of optical microscopy, chemical etching, and EBIC. It was established that they are related to defects present in the oxide and polysilicon, defects introduced into the bulk silicon by processing, and defects present in the starting material. A detailed discussion of their relation to the starting material, device processing steps, and their appearance in the displayed output as a function of the device operating conditions is given.

One of the more challenging problems of VLSI technology is the fabrication of large area devices free of localized defects. This is particularly important for photosensitive mosaics such as CCD imagers intended for use as the image sensor of a television camera. The history of camera tubes, which spans some fifty years, has been dominated by the efforts to improve the image quality of each successive generation of devices. Silicon technology is the latest to be applied to this application, first in the diode array of the silicon vidicon and now in CCD's.

As has been previously reported (1-5), there are ample opportunities for defects to be present since a sensor area of 1.5 cm^2 contains between 1 and 3×10^5 picture elements (pixels). Any defect producing a video signal anomaly in the order of 1%-2% of the peak signal, which corresponds to a current change in the order of 10^{-9} A , is observable in the video display of the sensor output.

A successful program to eliminate image blemishes must first identify the origin of each type of electrically active defect and then establish a correlation between a particular type and a specific part of the fabrication process. With this information the efforts to upgrade the device processing can proceed in a purposeful manner.

This paper reports the results of our investigation into the origin of electrically active defects found in the SID 52501 CCD imager (6) manufactured by the Electro-Optics Department of the RCA Solid State Division. We believe that the results presented here are typical of any frame transfer imager.

The majority of point and some line defects observed in the television display of the output signal from these devices have involved the malfunction of one or more pixels, failures which can be eliminated by improved control over processes such as mask fabrication, photolithography, etching, and ion implantation that are used in fabricating the CCD structure. Other defects arise from inhomogeneities and defects in the single crystal substrate which can originate during processing, but most frequently are present in the virgin wafer. Our analysis shows that defect densities can be minimized and increased yields of cosmetically pleasing CCD imagers are within the capability of present integrated circuit technology. Cost reductions resulting from improved yields will follow from further improvement in the state-of-the-art.

* Electrochemical Society Active Member.
Key words: CCD imagers, process and crystallographic defects, device performance.

Experimental Approach

The SID 52501 CCD imager (Fig. 1) whose die size is $1.25 \times 1.95 \text{ cm}$ is fabricated on a $10 \Omega \text{ cm}$ float zone p-type silicon wafer. It uses a three-phase single level polysilicon gate structure and contains a parallel array of 320 surface channel linear CCD's each having 512 stages of $30 \times 30 \mu \text{m}$ area. The array is subdivided into two identical areas of 320×256 stages, one part serving as the image sensing register, the other as a storage register. In the normal TV camera system the device is operated in the frame transfer mode. An optical image is focused on the image register where the photogenerated charges are integrated for $1/60 \text{ sec}$. The entire charge image is then transferred into the storage register during the 1.3 msec blanking interval in order that the next image integration cycle can be started. Simultaneously, the first charge image is transferred one line at a time out of the storage register and into a 320 stage buried channel CCD output register. Each successive line of charge is transferred through the output register and read serially by a floating gate output transistor amplifier. This readout is continued until a complete field has been removed from the storage register at which time the entire cycle is repeated.

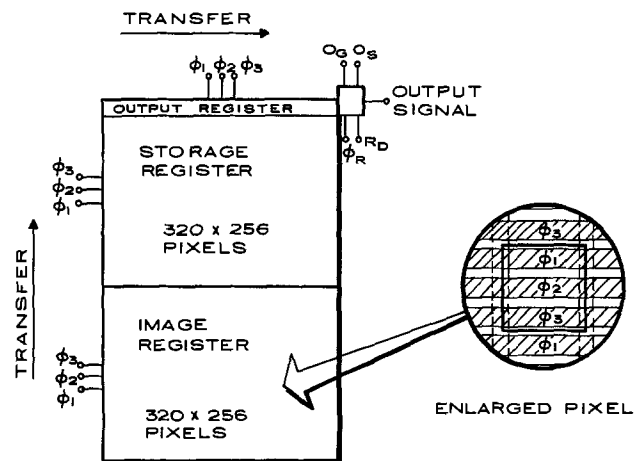


Fig. 1. Schematic diagram of a three-phase frame transfer CCD imager showing the image, storage, and output registers. In the diagram of the enlarged pixel the horizontal polysilicon gates are shown by the solid lines and the vertical channel stops by the dashed lines.

By forming the integrating wells under the $\phi 1$ gates for the odd numbered fields and under $\phi 2$ for the even, a display of two interlaced fields on the TV monitor produces a 512 line image (7). In a fully operational device, defective pixels in any of the 320 parallel CCD channels can introduce blemishes in the transduced image producing either a high signal (white) defect by the injection of spurious charge, or a low signal (black) defect because charge is lost before it reaches the output stage. Such a signal loss originates either from a localized region having low photosensitivity or a defective channel blocking the complete transfer of charge.

Because the camera system used for this study has the capability to vary the number of clock cycles used during transfer of the charge image from the image to the storage register, a simple means is available for distinguishing between defects in these two sections of the device. If the apparent location of the defect as observed in the displayed output changes as the number of cycles of the transfer clocks is altered, then the defect is within the area of the imaging register. Defects whose position is not altered are in the storage register area.

After having determined that a blemish seen in the displayed output was located in a particular register and could be classified by its electrical and optical characteristics, the next step was to determine its origin. The exact position was established by observing in the video display of the output from the operating device the coincidence of its signal with that generated by a stationary $5\ \mu\text{m}$ diam light probe as the device was moved about on a microscope stage. A $500\times$ microscope with a long focal length objective was used to examine the area surrounding the defect and also to guide the operator in scribing a square around the defective pixel using a micromanipulator probe as a stylus. As shown in Fig. 2 the CCD structure consists of a number of lamina formed on the silicon substrate. A defect can originate in any part of the superstructure or in the substrate itself and can rarely be found by optical examination of the top surface. Using either KOH or HF etching to strip each successive layer, the newly exposed lamina was examined by Nomarski microscopy to determine its mechanical integrity in the region of the defect. When the entire superstruc-

ture had been removed, the substrate was given a Dash etch followed by microscopic examination to determine if microdefects such as edge dislocations, saucer pits, and mounds were present. In addition, EBIC (electron beam induced current) scans (8) were made in the defect region to determine whether crystallographic defects were electrically active.

By repeating these analytical procedures for each type of blemish on many samples, a classification was made of the various electrically active defects and common origins for each class were established. Following each step of the fabrication process the presence or absence of the established origin for a particular defect was used to assess the need for a process change and as the means by which to compare the results from modified procedures. In this manner controls could be established over an improved processing schedule which either eliminates or reduces the number of electrically active defects of a particular class.

Classification of Defects and Their Origin

In the video display of the output signal from a CCD imager the contrast of a blemish can vary between the extremes of the full well charge storage capacity (white signal) to a zero signal charge (black). Typical examples of the various CCD image defects are shown in Fig. 3. Blemishes have been observed whose contrast with respect to the surrounding background varies with operating voltage, rate of charge transfers, illumination intensity, and illumination wavelength. Some exhibit voltage or illumination thresholds. Table I lists a variety of spurious signal defects along with their location and identifying characteristics. These are discussed more fully in the following paragraphs.

Striations.—The ring-type bands of varying contrast observed in the background of the displayed image produced by the SID imager are striations. Their contrast increases with both increasing wavelength of the incident illumination and with a change of the barrier gate bias from depletion (positive voltage) to accumulation (negative voltage). Although the contrast variations in the image associated with the striations ordinarily do not exceed 4% and are usually less than 1%, their coherent nature makes them cosmetically unacceptable (Fig. 3c).

It was established by an extensive study (9) that striations are caused by a combination of inhomogeneities in the distribution of recombination centers and localized resistivity variations in the as-grown wafers. These nonuniformities modulate the collection efficiency of photogenerated charges which must diffuse through a field-free region before reaching a charge storage well. Since material inhomogeneities form concentric rings in the wafer, the appearance of the stria-

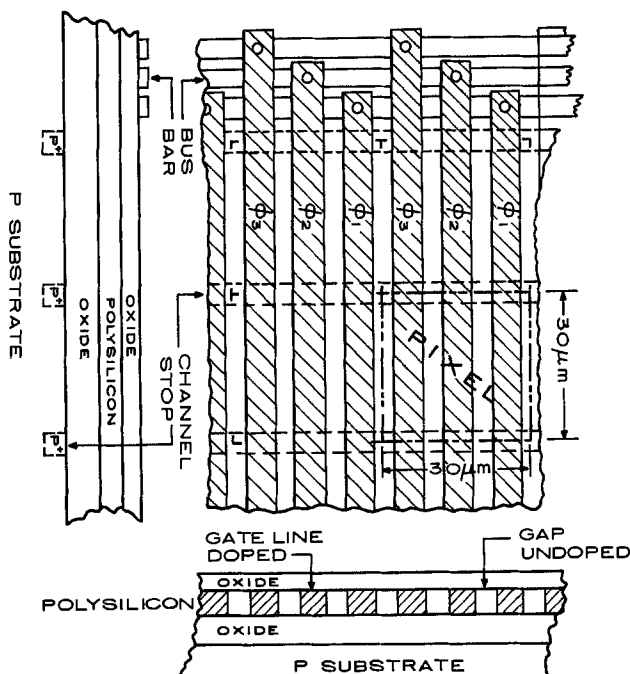


Fig. 2. Plan and cross-sectioned views of the CCD structure which was used for this study.

Table I.

| | Image register | Storage register | Contrast constant | Contrast voltage variable | Contrast illumination variable |
|------------------------|----------------|------------------|-------------------|---------------------------|----------------------------------|
| Striations | X | | | X | X (wavelength) |
| Slip | X | | | X | |
| Black vertical lines | X | X | | | X (intensity) X (intensity) |
| Black horizontal lines | X | | | X | X (intensity) X (intensity) |
| White spots | X | | X | X | X (wavelength) |
| White vertical lines | | X | X | X | X (wavelength) X (wavelength) |
| Black spots | X | | X | X | X (wavelength) |
| | | X | X | X | |

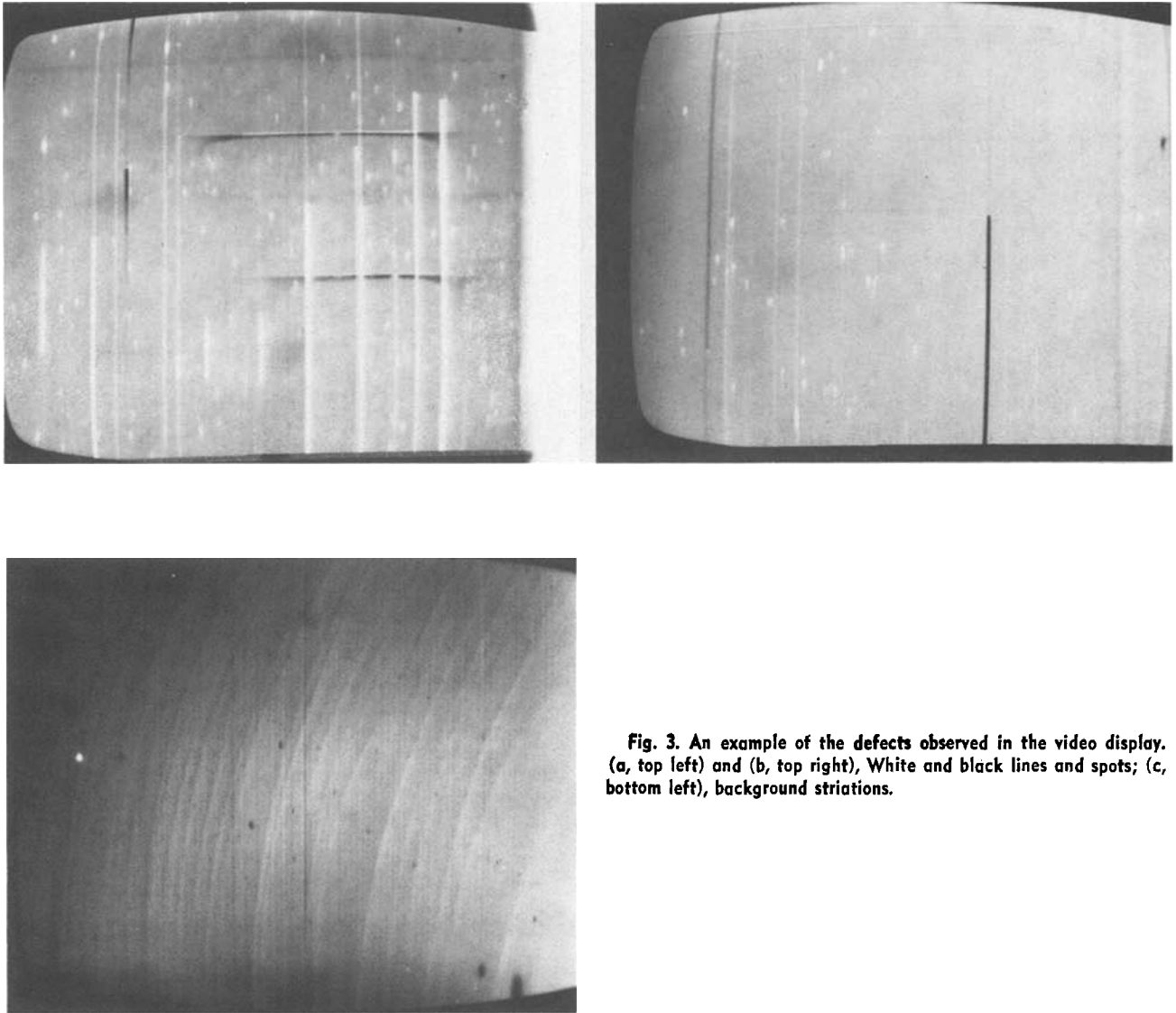


Fig. 3. An example of the defects observed in the video display. (a, top left) and (b, top right), White and black lines and spots; (c, bottom left), background striations.

tion pattern in the displayed image will depend on the location of a particular device on the wafer.

Slip.—The clusters of short horizontal and vertical line segments in the displayed CCD image of Fig. 4a are caused by crystallographic slip in that area of the substrate occupied by the image and/or storage registers of the SID device. The contrast of these bright lines is enhanced by increasing the voltage applied to the storage gates in the image register during the integration period. Figure 4 is an example of a device having slip lines in the displayed output image (Fig. 4a) which exhibit a one-to-one correlation with the crystallographic slip present (Fig. 4b) in the bulk silicon in the same part of the register. These substrate features were revealed by a Dash etch. In the present work it has been found that in order for the slip lines to be observed in the displayed image, the crystallographic slip has to be electrically active. The crystallographic slip observed after chemical etching, but not revealed by EBIC, did not give the slip lines in the displayed image. Although the means by which the crystallographic slip becomes decorated to make it electrically active is not clearly understood, it is known that the propagation of slip from the edge of the wafer into the central area occupied by the devices occurs during processing. The slip is introduced at the wafer edge (10) and is spread by the combined effects of the strain generated by fast heating and cooling cycles (11) and by the stresses produced by the formation of the silicon dioxide and polysilicon layers (12) of the

device superstructure. Control over the heating and cooling rates during device processing and adjustment of the conditions under which the various lamina are formed so that stress is minimal has been shown to reduce crystallographic slip in the device areas by a significant amount.

Black vertical lines.—Black vertical lines in the displayed image from a frame transfer CCD imager (Fig. 3) can originate in either the image or storage registers and are the result of a defect which inhibits the transfer of charge along a channel. It has been determined that the defects were formed by an unintentional diffusion of p^+ dopants into the region between the channel stops (Fig. 5). If a complete bridge is formed between a pair of channel stops, no charge will be transferred beyond the defective pixel. If a partial blockage occurs then only a portion of the charge will be transferred, particularly during the high speed transfer of the charge image from the image to the storage register. A few examples have been observed where there is a combined blockage of a channel and a break in an adjoining channel stop. In such a case charge packets whose transfer is blocked in one channel can shift to the adjacent column and in the displayed image a black line is paired with a bright line beyond the defect site.

Unintentional p^+ diffusions are the result either of a poor quality masking oxide or problems encountered during photolithographic definition of the channel stop lines.



(a)



(b)

Fig. 4. Comparison between (a) slip (cross-hatched pattern) observed in the displayed image and (b) crystallographic slip in silicon substrate revealed by Dash etch. Lower left corner in Fig. 4a corresponds to lower left corner in Fig. 4b.

Black horizontal lines.—Black horizontal lines such as seen in the Fig. 3 image display result from a discontinuity in a transfer gate or a shorted pair of gates located in either the image or storage register. A gate in this part of the device consists of a $6\ \mu\text{m}$ wide doped line in the polysilicon layer which extends across the full width of the device and is connected to a metal

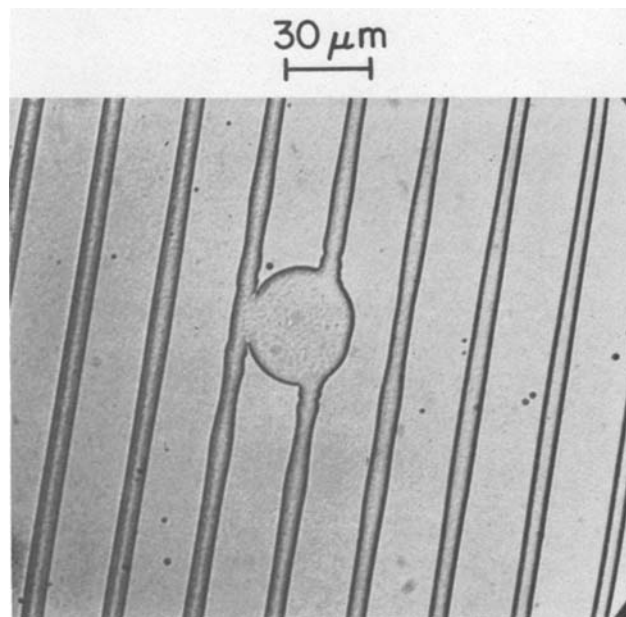


Fig. 5. An example of a defective channel stop diffusion which blocks the CCD channel. (Nomarski micrograph of a Dash etched crystalline substrate.)

bus at each end. Figure 6 is a micrograph of a typical discontinuity or break in a gate line.

Pixels located along the defective line are driven by clock pulses from one end of the line whereas the pixels in nondefective lines are driven from both ends so that the high frequency clock pulse encounters different attenuation along the open line than along nondefective lines. This leads to the distortion of the clock pulse shape and phase applied to those pixels situated under the defective line, which results in an incomplete transfer of charge. It has been established that the effect is the strongest for the breaks located in the vicinity of metal buses and that for breaks located in the center of the gate where no pulse distortion should take place the defect in the image is of minimum contrast. It has been observed that the contrast of the defects is enhanced by the increase of transfer speed and high signal level (peak illumination intensity). Similar incomplete charge transfer is also caused by shorts between the gates.

Shorts or breaks in the gate lines of the polysilicon layer are caused by defects in the patterned oxide mask which defines the regions to be doped by diffusion from a phosphorous glass overlayer and are the result of problems related to the photolithographic definition of the oxide pattern.

White spots and lines.—A single pixel size white spot or one column wide white vertical line is caused by a charge injecting defect at a given pixel site (Fig. 3). The amount of spurious charge added to any packet of photogenerated charge will depend on the amount of time it occupies a defective pixel site. In the image register during the integration period this amounts to 15.5 msec and the result is a single high signal charge packet which appears as a discrete spot in the displayed image. By comparison, other charge packets transferred through this defective pixel during the transfer from the image to the storage register will generally pick up an insignificant amount of spurious charge during the $\approx 1\ \mu\text{sec}$ occupancy.

Defect sites in the image register having exceptionally high injection rates are capable of generating a low contrast vertical line in the displayed image because sufficient spurious charge is added to each packet during the image-to-storage register transfer to produce a visible image. In the display the bright

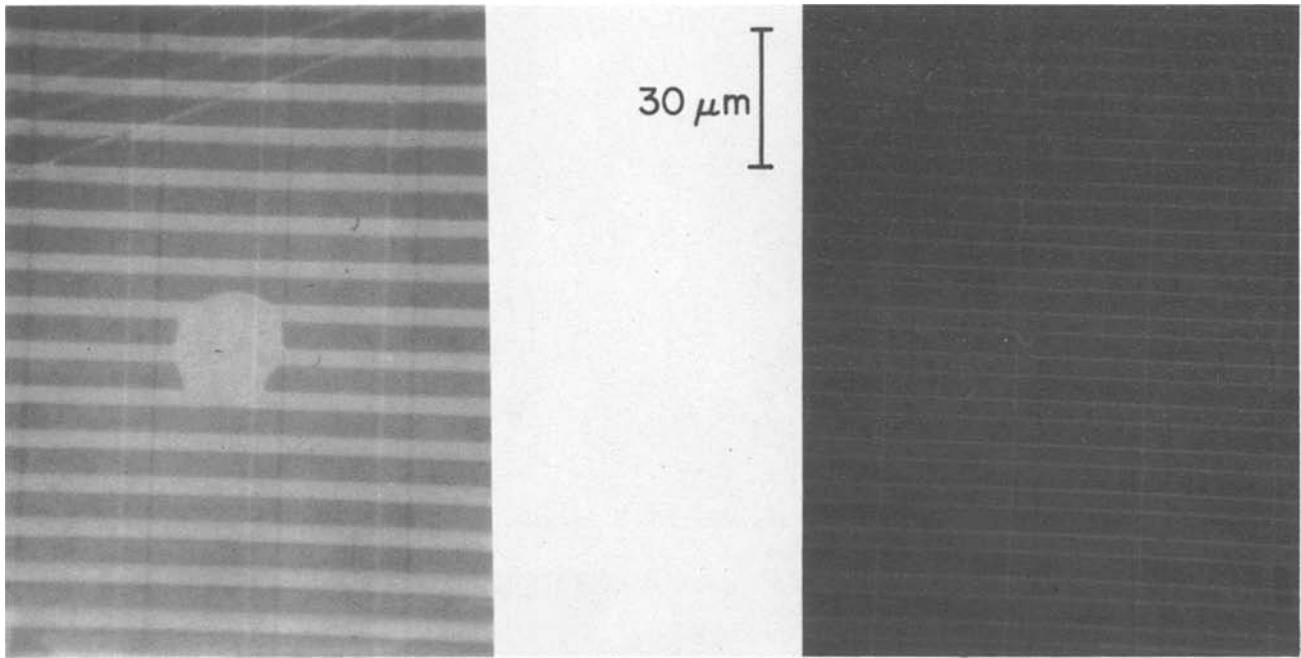


Fig. 6. Typical defects observed in the polysilicon gate structure. Highly doped regions are the darker lines

point image, which will have become enlarged by blooming, is trailed by a low contrast smear.

In the storage register each charge packet spends one line time ($64 \mu\text{sec}$) in each pixel site as it moves along a column on its way to the output register so there is ample time for a sufficient amount of spurious charge to be added to each packet transferred through a defective pixel to produce a high current vertical line in the displayed image which extends from the defect to the bottom edge of the display. The rate at which charge is injected in the storage register well of a defective pixel determines the contrast of the vertical line seen in the displayed image.

As shown in Table II six types of charge injecting defects have been identified which differ in their characteristic behavior as the result of changes in storage gate potential and illumination wavelength.

An electrical short between the polysilicon gate layer and the substrate through a pinhole in the channel oxide will produce a defective pixel whose injected charge amplitude is strongly dependent on both the maximum voltage applied to the gate and the rate of transfer. Such shorts form junctions between the n-doped polysilicon and the p-doped substrate which exhibit a reverse bias breakdown threshold. In the image register the peak gate voltage is applied during the rapid transfer of the charge image from the image to the storage register. Because the p-type substrate is patterned with p^+ channel stops and the intrinsic polysilicon layer is patterned with n^+ doped gate lines, the makeup of a substrate short can vary de-

pending on its location, ($p\text{-}i\text{-}n^+$ or $p^+\text{-}n^+$) and each variant will have a somewhat different threshold and gate voltage dependence.

Another source of point defects are unintentional phosphorus diffusions through pinholes in the masking oxide used to define the source/drain sites. These can form small $n^+\text{-}p^+$ junctions at the edge of a channel stop. Such defects exhibit a breakdown above a critical gate bias voltage (usually about 8V) which produces a high signal point defect in the displayed image. An n^+ diffusion which does not contact a p^+ region will not act as an injection spot because the breakdown voltage of an $n^+\text{-}p$ junction is much higher than those used in the CCD operation.

Damage to the wafer surface which can either be present in the virgin wafers or be introduced during processing will produce high current generation sites whose injection rate is usually independent of operating conditions. It should be noted that the residual surface damage responsible for this type of defect usually cannot be seen by optical examination of the original wafer prior to processing. The damage sites are revealed on the surface of a wafer only after etching or with EBIC scanning. However, the damage becomes visible when the wafer is oxidized because the oxide usually grows at a different rate in the damaged area.

The last three categories listed in Table II are crystallographic defects in the substrate which may be present in the as-grown crystals or be introduced during device processing. Dislocation networks introduced by diffusion of the dopant for the channel stops have been observed previously (13) and are caused by the strain resulting from the lattice mismatch between the doped and undoped regions of the crystal. The blemishes in the displayed image which are the result of this type of injecting defect do vary in contrast as the integrating voltages are altered. These dislocation networks can be eliminated by decreasing the dopant concentration in the channel stop region below a critical value.

Other crystallographic defects are the edge dislocations which are responsible for low contrast white spots in the displayed image whose intensity is critically dependent on the device operating conditions. A micrograph of the etch pits formed at one of these dislocation sites is shown in Fig. 7. The data on Table III indicate that when such defects are located in the

Table II. Charge injecting defects

| Type of defect | Contrast varied by changes in | | | |
|-------------------------------------|-------------------------------|---------------------|----------------------|------------------|
| | Illumination wavelength | Integrating voltage | Barrier gate voltage | Transfer voltage |
| 1. Pinhole | No | Yes, no | No | Yes, threshold |
| 2. n^+ diffusion | No | Yes, threshold | No | No |
| 3. Surface damage | No | No | No | No |
| 4. Channel stop dislocation network | No | Yes | No | No |
| 5. Edge dislocation | Yes | Yes | Yes | No |
| 6. Microprecipitates | Yes, no | Yes, no | Yes, no | No |

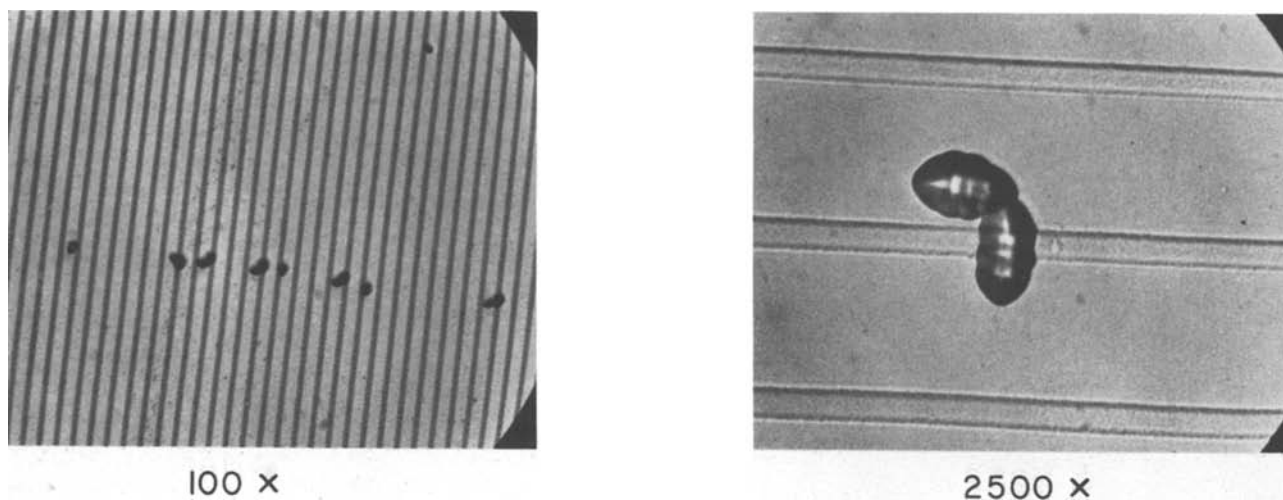


Fig. 7. Nomarski micrograph of the etch pits (Dash etch) which are related to edge dislocations

image register the contrast of the spots they produce in the displayed image can be changed by varying either or both the storage gate potential and the wavelength of the incident illumination. The mechanism of the edge dislocations formation during processing has been reviewed in Ref. (10).

The last category of defect listed in Table II is related to defects present in as-grown crystals and called here, for convenience, microprecipitates. They appear as hillocks [similar to those observed in CZ silicon (14)] when observed by Nomarski microscope examination of the surface of an etched sample. They can also be seen without etching on the surface of an oxidized wafer as shown in Fig. 8. Some of the white spots in the displayed image resulting from charge injection by these microprecipitates were observed to be independent of device operating conditions, while others exhibited the same dependence as those spots arising from edge dislocations. Usually the contrast of the spots related to microprecipitates is greater than that associated with edge dislocations.

Not all of the crystallographic defects in these last two categories are electrically active. Figure 9(a) shows an example of electrically active defects observed by EBIC scanning while Fig. 9(b) shows the edge dislocations present in the same area as revealed by a Dash etch. Only two of the four defects giving etch pits are electrically active. Similar data was obtained for microprecipitates.

It must be pointed out that the fraction of crystallographic defects which are electrically active increases during processing. For example, in a virgin wafer about 10% of the microprecipitate sites are electrically active. After initial oxidation about 30% have become active and after complete processing of the device the active fraction has increased to about 50%. During wafer processing the probability for a crystallographic defect to be electrically active has been found to increase just as the average concentration of recombination centers increases. Table IV shows the relationship between the average value of diffusion length, as measured by surface photovoltage (15), and those white spots in the



Fig. 8. Nomarski micrograph of hillock observed on the surface of a nonetched oxidized wafer. These hillocks are caused by microprecipitates present in the as-grown wafer.

image originating from edge dislocations. No correlation was claimed if there were no white spots in the displayed image which could be associated with the edge dislocation sites located in the image register as revealed by Dash etching of the substrate. It was ob-

Table III. Dependence of edge dislocation related spots on the integrating gate voltage and illumination wavelength

| Integrating gate voltage | Blue light | Green light | Red light | Infrared light |
|--------------------------|---------------------|---------------------|-------------|----------------|
| 3V | High contrast white | White | Not visible | Black |
| 9V | High contrast white | High contrast white | White | Not visible |

Table IV. Relationship between diffusion length and white spots caused by edge dislocations

| Sample | Diffusion length | Correlation? |
|--------|------------------|--------------|
| 1 | 70 | Yes |
| 2 | 40 | Yes |
| 3 | 65 | Yes |
| 4 | 160 | No |
| 5 | 180 | No |

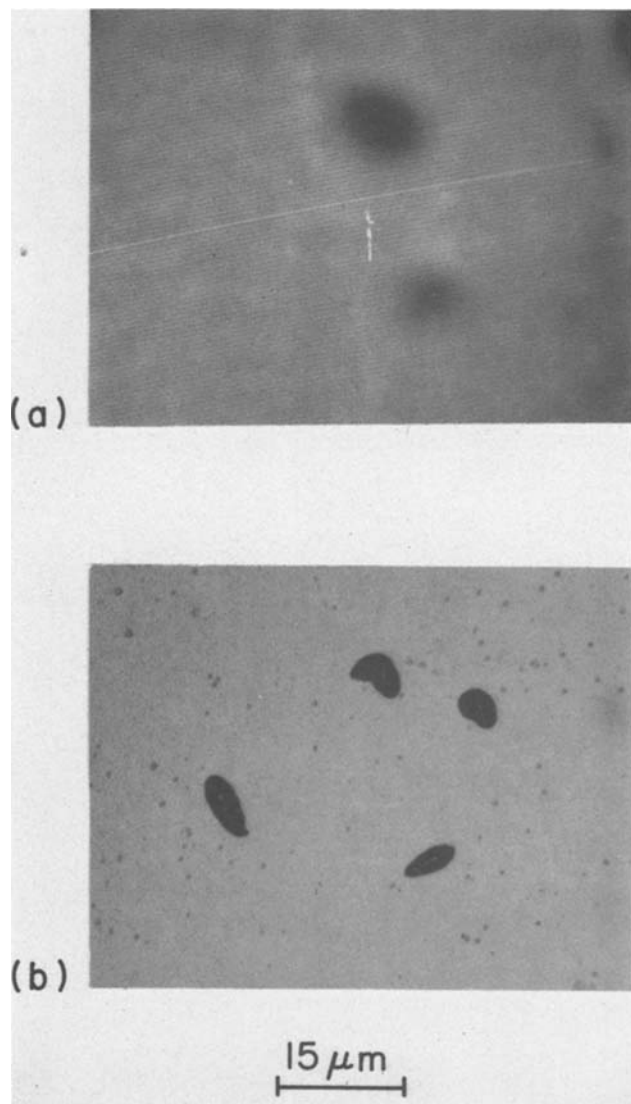


Fig. 9. Comparison between (a) electrically active edge dislocations as observed by EBIC and (b) dislocations in the same area revealed by a Dash etch.

served that only in those wafers with the shorter diffusion length (higher concentration of recombination centers) could a correlation be established between edge dislocations and white spots in the displayed image. These data indicate that changes in the density of recombination centers as small as a factor of four can lead to substantial differences in the percentage of electrically active crystallographic defects.

Black spots.—Black spots in the displayed image fall into two categories, one being defects which cover several pixels, the other one pixel size blemishes of low contrast. The large spots were found to be associated with anomalies in the polysilicon layer. Defects such as hillocks or voids can affect either the light transmission through the polysilicon or the charge transfer through a given pixel (in much the same manner as an open gate line). The small spots are caused by a low photosensitivity region in the substrate. These result from the presence of a crystallographic defect under one pixel which produces a region with a higher than average concentration of recombination centers. The contrast of this type spot depends strongly on both the storage gate potential and the illumination wavelength.

As shown in Table III the same defect which appears in the displayed image as a black spot when the defective pixel is illuminated with infrared light can also appear as a white spot under short wavelength

illumination. This is interpreted as indicating the presence of an electrically active crystallographic defect which acts as a generation center when it is located inside the depletion region and a recombination center when it is located outside the depletion region. Most of the charge generated by short wavelength light originates within the depletion region and a defective pixel collects both the photogenerated and the injected carriers. Alternatively, most of the photogenerated charge resulting from long wavelength light originates outside the depletion region where it is subject to recombination losses. The number of carriers which recombine before reaching the depletion region can be greater than the injected carriers with the result that the defective pixel will show a lower signal contrast than its neighbors. The depletion region contracts as the potential applied to the storage gate of a pixel is reduced, therefore, one can account for the observed decrease in the number of white spots and the increase in the number of black spots which occurs as the barrier gate voltage is switched from shallow depletion to accumulation (the anti-blooming mode of operation) (16).

Summary and Conclusions

The origin of cosmetic defects in CCD imagers and dependence of their contrast on operating conditions has been analyzed. It was established that all defects observed in the displayed image could be correlated with defects present in the superstructure (e.g., pin holes in the oxide layer, defects in polysilicon) or with defects present in the substrate. The substrate defects could be divided into three categories: obvious defects introduced by processing such as unintentional n^+ or p^+ diffusions, process-induced crystallographic defects such as dislocations networks, slip, or edge dislocations, and defects present in virgin wafers such as striations or microprecipitates. The process-dependent defects visible either in the superstructure or in the substrate are easily recognized and can be eliminated by attention to the techniques of LSI fabrication. Less well understood and more difficult to control are crystallographic defects, whether present in the virgin wafers or introduced by processing. Although processing steps responsible for the formation of crystallographic defects have been identified, an important unresolved issue still remaining is how nucleation and propagation of crystallographic defects, especially edge dislocations, can be prevented. At the completion of processing only a fraction of the crystallographic defects have become electrically active, the requirement for their producing cosmetic defects in the displayed image. Therefore, the mechanisms by which crystallographic defects become decorated should be investigated. The important issue to be solved is related to the sources of contamination; are they introduced from outside during processing or rather they are caused by redistribution and change of state of those defects which are already present in the original wafers (17, 18)? Only detailed understanding of these problems will provide the basis for process changes which will result in significant improvement of CCD imagers quality.

Manuscript submitted July 28, 1980; revised manuscript received Nov. 21, 1980.

Any discussion of this paper will appear in a Discussion Section to be published in the December 1981 JOURNAL. All discussions for the December 1981 Discussion Section should be submitted by Aug. 1, 1981.

Publication costs of this article were assisted by RCA Laboratories.

REFERENCES

1. For review, see R. Melen and D. Buss, "Charge Couple Devices: Technology and Applications," IEEE Press, New York (1977).
2. Y. Hokari and H. Shiraki, *Jpn. J. Appl. Phys.*, **16**, 585 (1977).

3. Y. Hayafuji, T. Shimada, and S. Kawado, in "Semiconductor Silicon 1977," H. R. Duff and E. Sirtl, Editors, p. 750, The Electrochemical Society Soft-bound Proceedings Series, Princeton, NJ (1977).
4. H. Shiraki, in *ibid.*, p. 546.
5. H. E. Murphy, Proceeding of the SPIE, Vol. 203, pp. 80-87, San Diego, CA (1979).
6. R. L. Rodgers III, p. 196 of Ref. 1.
7. C. H. Sequin, *IEEE Trans. Electron Devices*, ed-20, 535 (1973).
8. For tutorial introduction, see H. J. Leamy, L. C. Kimerling, and S. D. Ferris, "Scanning Electron Microscopy," Vol. 1, p. 717, SEM Inc., AMF O'Hare, IL (1978).
9. L. Jastrzebski, P. A. Levine, A. D. Cope, W. F. Kosnocky, W. N. Henry, and D. F. Battson, *IEEE Trans. Electron. Devices*, ed. 27, 1694 (1980).
10. For review, see S. M. Hu, *J. Vac. Sci. Technol.*, 14, 17 (1977).
11. A. W. Fisher and G. L. Schnable, *This Journal*, 123, 434 (1976).
12. T. Suzuki, A. Mimura, and T. Ogawa, *ibid.*, 124, 1776 (1977).
13. H. F. Schaake, C. G. Roberts, and A. J. Louis, Advance Research Project Agency Report, Contract No. M00-173-76-C-0280 (1979).
14. G. A. Rozgonyi, *Appl. Phys. Lett.*, 29, 531 (1976).
15. For measurements of diffusion length done by surface photovoltage, see e.g., Annual Book of ASTM Standards, p. 752, ASTM, Philadelphia (1974).
16. W. F. Kosnocky, J. C. Carnes, M. G. Kovec, P. Levine, F. V. Shallcross, and R. L. Rodgers, *RCA Rev.*, 35, 2 (1974).
17. L. Jastrzebski and J. Lagowski, Paper 152 presented at The Electrochemical Society Meeting, St. Louis, Missouri, May 11-16, 1980.
18. L. Jastrzebski and P. Zanzucchi, To be published in "Semiconductor Silicon 1981," Minneapolis, MN (May 1981).

Bulk Impurity Charge Trapping in Buried Channel Charge Coupled Devices

M. J. McNutt* and W. E. Meyer

Rockwell International, Anaheim, California 92803

ABSTRACT

Buried channel charge coupled devices are particularly sensitive to the effects of bulk state impurities on such device characteristics as thermal leakage current, charge transfer efficiency, and noise. This paper reviews the statistics relevant to these effects and describes an improved application of the double pulse experiment for probing bulk impurities. This experiment found that the dominant impurity in our devices had an energy level 0.404 eV from one of the bandedges and determined a lower limit of 10^{13} cm^{-3} for the concentration. A close match with previously reported results suggests that this energy level is referenced to the valence band and represents iron. By eliminating the corrosive HCl gas used to getter sodium in the thermal oxides, the source of iron was removed and the affected device characteristics improved about two orders of magnitude.

Bulk impurities, especially in buried channel devices, give rise to several undesirable charge coupled device (CCD) characteristics. Among these are enhanced thermal leakage current, bulk state trapping, and bulk state trapping noise. Thermal leakage current generates charge internally and limits the time during which an empty charge packet can be stored. Bulk state trapping and subsequent emission smears charge into trailing charge packets, thus degrading the signal, and also gives rise to a partition-type bulk state trapping noise. The trapping noise can also dominate as a generation-recombination noise in the output circuit due to the proportionality of this noise power to the square of the bias current.

Mohsen and Tompsett (1) discussed the effects of bulk traps on the performance of buried channel CCD's and described the double pulse technique they used to determine the trap emission time constant. Our purpose in this paper is to review the trapping statistics that include the effects of both energy bands and to describe an efficient implementation of the double pulse measurement technique. We are also interested in identifying the appropriate impurities, and, in our example, we will find a large iron distribution and discuss its source and eventual elimination.

Bulk Impurity Statistics

Figure 1 is a band diagram describing the four possible Shockley-Read-Hall (2) trapping transitions assumed to dominate in the device. (a) and (b) are electron capture and emission rates, and (c) and (d) are hole capture and emission rates at a trap with energy, E_T . E_C and E_V are the conduction and valence band energies. The relevant statistics can be described by three rate equations

$$dn/dt = (b) - (a) = e_n n_T - c_n n p_T \quad [1]$$

$$dp/dt = (d) - (c) = e_p p_T - c_p p n_T \quad [2]$$

$$dn_T/dt = (a) - (b) - (c) + (d)$$

$$= c_n n p_T - e_n n_T - c_p p n_T + e_p p_T \quad [3]$$

n and p are the electron and hole concentrations, and n_T and p_T are the filled and empty electron bulk state concentrations. c_n and c_p are the electron and hole capture coefficients, and e_n and e_p are the electron and hole emission coefficients.

At equilibrium

$$dn/dt = 0$$

$$n = n_o = N_C \exp [(E_F - E_C)/kT]$$

$$dp/dt = 0$$

$$p = p_o = N_V \exp [(E_V - E_F)/kT] \quad [4]$$

* Electrochemical Society Active Member.

Key words: iron, bulk impurities, charge coupled devices.

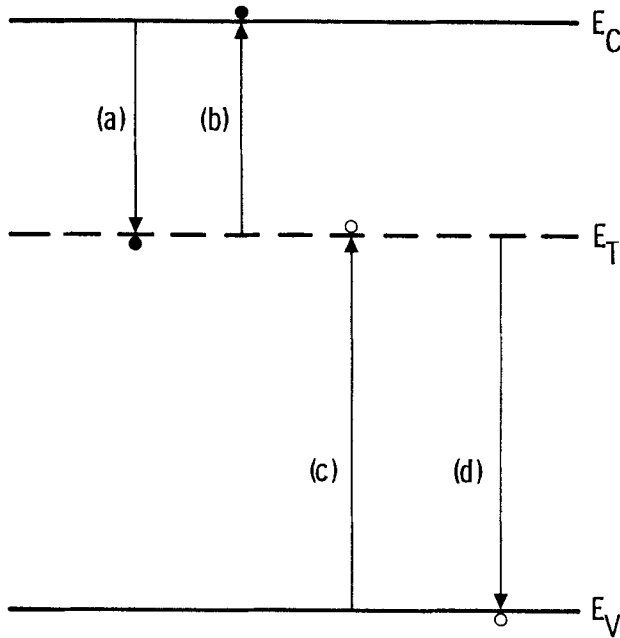


Fig. 1. Energy band diagram indicating bulk state trapping processes.

where N_C and N_V are the effective density of states at the two bandedges and E_F is the Fermi energy. Substituting Eq. [4] into [1] and [2] gives

$$\begin{aligned} e_n &= c_n N_C \exp[(E_T - E_C)/kT] \\ e_p &= c_p N_V \exp[(E_V - E_T)/kT] \end{aligned} \quad [5]$$

To obtain this result we used the Fermi occupation factor in n_T and p_T such that

$$\begin{aligned} n_T &= N_{TT}/(1 + \exp[(E_T - E_F)/kT]) \\ p_T &= N_{TT} \exp[(E_T - E_F)/kT]/ \\ &\quad (1 + \exp[(E_T - E_F)/kT]) \end{aligned} \quad [6]$$

where $N_{TT} = n_T + p_T$ is the total bulk state concentration. Also in equilibrium

$$\begin{aligned} dn_T/dt &= 0 \\ n_T &= N_{TT} (c_n n_0 + e_p) / (c_n n_0 + e_n + c_p p_0 + e_p) \end{aligned} \quad [7]$$

where Eq. [3] was substituted along with $p_T = N_{TT} - n_T$.

As noted by Sah (3), Eq. [5] are strictly valid only at thermal equilibrium where they are derived. However, for small deviations from equilibrium we can assume that the electric fields are not large enough to make the capture and emission coefficients field dependent. Also, we will be primarily interested in the temperature dependence of the emission coefficient rather than its absolute value, thus minimizing the effects of nonequilibrium on the measurement accuracy.

In depletion, we have $p = n = 0$, so the emission transitions, (b) and (d), dominate the capture events, (a) and (c), in Eq. [3] giving

$$\begin{aligned} dn_T/dt &\simeq -e_n n_T + e_p p_T \\ &= -(e_n + e_p) n_T + e_p N_{TT} \end{aligned} \quad [8]$$

The solution to Eq. [8] is

$$n_T = \Delta n_T \exp(-t/\tau) + (\tau/\tau_p) N_{TT} \quad [9]$$

where $\tau^{-1} = e_n + e_p$ and $\tau_p^{-1} = e_p$. Let $t = 0$ be the time when the device is switched from equilibrium to depletion so that $n_T(0)$ is given by Eq. [7]. Then from [7] and [9] at $t = 0$ we get

$$\Delta n_T = N_{TT} [e_n c_n n_0 - e_p c_p p_0] / [(e_n + e_p)(c_n n_0 + e_n + c_p p_0 + e_p)] \quad [10]$$

In some cases, [10] can be greatly simplified. For example, in N-type material $n_0 \gg p_0$, and, if the impurity level is near the middle of the bandgap, $c_n n_0 \gg e_n$, e_p so that $\Delta n_T \simeq N_{TT} e_n / (e_n + e_p)$. Furthermore, if the energy level is in the upper half of the bandgap, we should have $e_n \gg e_p$ and $\Delta n_T \simeq N_{TT}$.

Depending on the location of the impurity energy level, either e_n or e_p normally dominates in τ . For example, if E_T is closer to E_C than E_V , we expect $e_n \gg e_p$ from Eq. [5] and so

$$\tau \simeq e_n^{-1} = \{c_n N_C \exp[(E_T - E_C)/kT]\}^{-1} \quad [11]$$

The capture coefficient, c_n , is proportional to $T^{1/2}$ since it contains the thermal velocity factor, and the effective density of states, N_C , is proportional to $T^{3/2}$ (4). Thus, there is a T^2 factor built into the $c_n N_C$ product. This factor can be eliminated by multiplying Eq. [11] by T^2 . Then when we take the natural logarithm we get

$$\ln(\tau T^2) = \ln(T^2/c_n N_C) + (E_C - E_T)/kT \quad [12]$$

Now if $\ln(\tau T^2)$ is plotted against $(kT)^{-1}$, the slope of the straight line is $E_C - E_T$ which identifies the impurity energy level. In the other case, if $e_p \gg e_n$ (e.g., E_T closer to E_V), then

$$\ln(\tau T^2) = \ln(T^2/c_p N_V) + (E_T - E_V)/kT \quad [13]$$

and the data slope gives $E_T - E_V$.

Trapping occurs when a charge packet in the CCD is transported into a cell that has previously been empty or in depletion. This means that the exponential term in Eq. [9] has at least partially decayed. When the charge packet arrives, electrons fill these empty impurity states almost instantaneously due to the high capture rate caused by the large carrier concentration. However, when the charge packet is transported to the next cell, these electrons stay trapped in the impurity states. We are back to a depletion condition and these electrons are only emitted from the traps according to the exponential time term in Eq. [9]. As the electrons are emitted from the traps they are picked up by trailing charge packets. This total process tends to smear out the CCD signal in time.

The trapping process also gives rise to partition noise in the CCD charge signal due to the constant reapportionment of charge among adjacent cells. Also, there is substantial generation-recombination noise in any currents flowing in the device, particularly in the output circuit where the currents can be substantial. This noise is derived from the constant emission and capture of the current carriers even in a nearly equilibrium condition where the total concentration is constant.

Experimental Procedure

In order to obtain some direct quantitative information on these bulk states, we performed a double pulse charge transfer experiment similar to that of Mohsen and Tompsett (1). This experiment is illustrated in Fig. 2. The device is encased in a controlled temperature environment, and the analog signal charge transfer is driven by a four-phase clock driver. The driver also triggers a double pulse generator at a predetermined interval based on an integral number of clock periods. The double pulse generator puts out two pulses, one immediately following the trigger signal and a second pulse that is delayed from the trigger signal. The delay is manually adjustable, and the width of the two pulses is also adjustable, but the width is normally at least two clock periods. The double pulse output signal from the pulse generator is applied to the shift register input, which samples the signal every clock period and converts voltage to proportional charge. The sampled signal charge is transferred through the shift register where it loses charge to empty bulk state energy levels. Eventually, the diminished signal charge reaches the output where

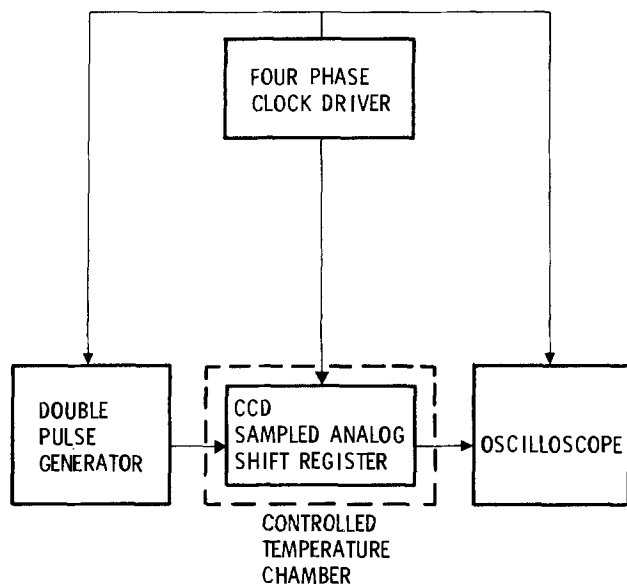


Fig. 2. Block diagram of CCD variable delay double pulse trapping experiment.

it is proportionally converted back to voltage and displayed on the oscilloscope. The oscilloscope uses the same trigger as the pulse generator. Figure 3 contains typical examples of the input and output signals, where, in this case, the output signal has been time shifted to eliminate the shift register delay that would normally occur. As shown in the figure, the pulses applied to the CCD input extend over two clock periods. For each input signal pulse, the resulting output then gives two sample pulses corresponding to the two charge packets that each input signal pulse forms. A more negative output corresponds to a larger charge packet of electrons.

As seen in the output circuit signal, the first charge packet or cell is greatly reduced during transfer down the CCD channel. This is due to trapping of charge by the bulk states. Since most of the traps are filled by the first charge packet, the second charge packet transfers through the CCD with very little loss. There is some loss, however, since the first charge packet is not exposed to all the traps in the channel because of decreases in the charge packet volume due to charge loss.

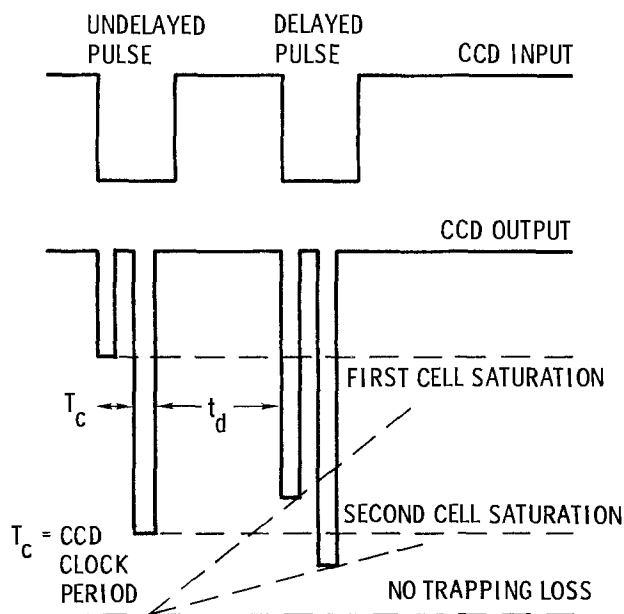


Fig. 3. Variable delay double pulse trapping experiment input and output signals.

These remaining traps are nearly all filled (in this example) by the second charge packet or the second sample of the first input signal pulse.

In the extreme case of a very large impurity concentration, more than two charge packets may be required to fill the trapping levels. This does not substantially affect the measurement technique as long as a sufficient number of charge packets is provided. This is accomplished by extending the signal pulse width over additional clock periods.

There is a delay, t_d , between the second charge packet from the first input pulse and the first charge packet from the second input pulse as shown in the figure. During this time electrons are emitted from the traps according to the depletion statistics of Eq. [9]. Then when the next charge packet comes along, it fills the recently emptied traps such that its trapping loss is equal to the emission that occurred in the t_d interval. If the emission of trapped charge is large, some of these traps may be missed by the reduced first delayed charge packet. These are then filled by the second delayed charge packet or any additional charge packets that may be required.

If $t_d = 0$, no significant emission from the traps occurs between the charge packet pairs so that no trapping loss occurs in the second pair. At the other extreme, if $t_d \gg \tau$, where τ is the trap emission time constant, all the traps empty during t_d and the second charge packet pair experiences the same trapping loss as the first pair. For values of t_d in between these extremes, the second pair trapping loss follows the form

$$Q(t_d) = Q(\infty) + [Q(0) - Q(\infty)] \exp(-t_d/\tau) \quad [14]$$

$$[Q(t_d)/Q(0)] \exp(-t_d/\tau) \quad [14]$$

In Eq. [14], $Q(t_d)$ is the remaining charge at the CCD output in a charge packet delayed by t_d , while $Q(0)$ and $Q(\infty)$ are the remaining charge for charge packets with zero and infinite delays. The quantity $Q(0) - Q(\infty)$ is the charge potentially subject to trapping, and the exponential factor is that of the trap emission rate. As the charge packet moves along the CCD channel losing charge to trapping centers, its volume is reduced and it is exposed to a smaller volume of trapping centers. In a uniform buried channel, this is represented by the factor $Q(t_d)/Q(0)$ where the charge packet volume is assumed proportional to the amount of charge. Finally, we can isolate $Q(t_d)$ in [14] to get

$$Q(t_d) = Q(\infty) / \{1 - [1 - Q(\infty)/Q(0)] \exp(-t_d/\tau)\} \quad [15]$$

Of course the CCD output voltage is proportional to $Q(t_d)$. Thus, by varying t_d and observing the corresponding change in the output voltage, τ can be deduced.

Frequently if the trapping effect is not too large, we have $[1 - Q(\infty)/Q(0)] \ll 1$, and Eq. [15] can be approximated by

$$Q(t_d) \approx Q(\infty) \{1 + [1 - Q(\infty)/Q(0)] \exp(-t_d/\tau)\} \quad [16]$$

This approximation becomes more accurate as the exponential factor decays. Since we now have a purely exponential time term in Eq. [16], the time constant, τ , can be determined without regard to the absolute values of $Q(\infty)$ and $Q(0)$. Sometimes the first sample of the delayed signal pulse experiences very large trapping losses such that $Q(\infty) \approx 0$ and [16] cannot be used. In that case, a second or third sample will have less trapping loss and thus qualify for using Eq. [16]. Since we have to take as many samples of each signal pulse (i.e., stretch the signal pulse over more clock periods) as necessary to get at least one undiminished sample, we can always apply Eq. [16] to one of the sample pulses.

Although the time delayed trapping data can be taken in the usual point-by-point manner, a more efficient technique gives a much faster result with an increase in accuracy. This technique uses the fact that the sampling nature of the CCD provides the same size charge packets at the same sample times even as the signal pulse is delayed up to one full clock period. However, when the signal pulse edge passes through the sample aperture time, the charge packet abruptly changes. Thus, when the time delay between pulses is continuously varied, the CCD output photographed by a time exposure clearly indicates the corresponding charge loss variation in the delayed charge packets. Each of the time delayed outputs is displayed for the time it takes to adjust the delay through one CCD clock period. If this time is long enough to expose the film and the delay is varied in a roughly uniform fashion, a good photograph will result. In practice, this typically requires opening the camera shutter for about 5 sec while turning the delay knob on a double pulse generator.

In performing the experiment, it is important to choose a CCD clock period that is much less than τ in order to get many samples of the exponential decay to match with Eq. [15]. Also, the time between the end of the delayed signal pulse and the start of the next signal pulse pair must be long enough to allow all the trapped carriers to be emitted. In other words, the signal pulse pair repetition period must be many τ time constants longer than the longest delay between the two pulses. The first signal pulse then provides the $Q(\infty)$ reference values.

The accuracy of the single photograph method can be better than the technique of recording each time delayed sample separately, even though the individual sample resolution may be less. This is because there is much less opportunity for calibration or temperature drift between t_d readings. Therefore, the relative accuracy between data points is excellent, which is most important in obtaining the time constant, τ , by matching experimental results with Eq. [15]. It should also be noted that this technique of probing bulk impurities by using CCD's is potentially more sensitive than normal capacitance transient methods (5) because the charge packet flows through a number of cells losing trapped charge in each one. In more traditional measurements, only the equivalent of one cell is used. Thus, sensitivity is multiplied by the number of CCD cells. However, to take advantage of this enhanced sensitivity, CCD noise sources such as transfer efficiency noise and output FET noise must be minimized.

Although the double pulse experiment does not by itself give the impurity concentration, N_{TT} , except in the special cases where $N_{TT} \approx \Delta n_T$, it can give the impurity energy level by finding the slope of Eq. [12] or [13]. This can identify the impurity involved. Since the technique directly measures the adverse CCD characteristic, namely charge transfer trapping loss, it always identifies the impurity that is most injurious to the device, and the measurement can be made near the normal operating temperature.

Experimental Result

An example of the determination of the time constant, τ , at a single temperature is shown in the oscilloscope photo of Fig. 4. This photo is a long time exposure showing the first charge packet pair and a sequence of second charge packet pairs at various delays. The delay time was adjusted continuously from 0 to the edge of the oscilloscope scale while the camera shutter was open. The result is the two exponential decays vividly displayed for the first and second delayed charge packets. The two undelayed charge packet signals are also shown, somewhat bloomed due to the long exposure time. They indicate the long delay values of the delayed charge packets so that the time constant can be determined. They also define the ref-

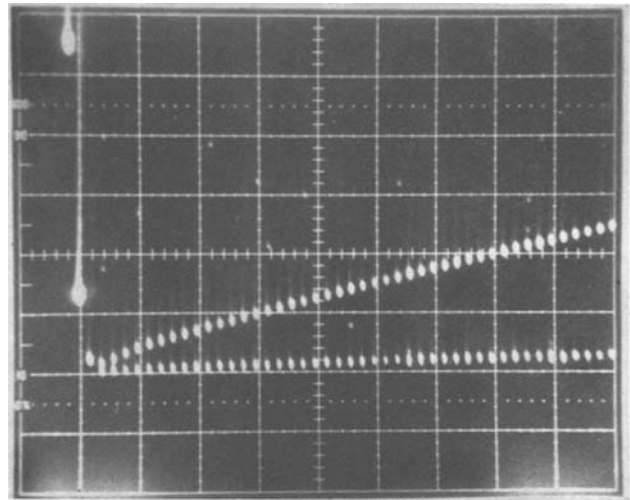


Fig. 4. Long exposure photo of CCD output during variable delay double pulse trapping experiment. Device 30338-1-4-37B; CCD Clock Rate = 50 KHz; Horizontal scale = 100 $\mu\text{sec}/\text{div.}$; Vertical scale = 0.1 V/div.; temperature = 55°F.

erence time. Since the trapping loss is about 25% of the total first charge packet (the zero charge level is well above the top of the scope display), Eq. [16] approximates [15], and a simple exponential decay can be assumed.

For example, let 0V be the top of the vertical scale as an arbitrary reference. The undelayed first charge packet signal is at -0.05V . The delayed first charge packet when the delay is zero (*i.e.*, no charge loss) is at -0.60V , giving a maximum charge loss equivalent to 0.55V. We see a charge loss equivalent to 0.20V at a delay of 700 μsec , so that

$$\begin{aligned} 0.55 - 0.20 &= 0.55 \exp(-700 \times 10^{-6}/\tau) \\ \tau &= 700 \times 10^{-6} / \ln(0.55/0.35) \\ &= 1550 \mu\text{sec at } T = 55^\circ\text{F} \end{aligned}$$

Naturally, curve-fitting techniques could be used with Eq. [15] to get more precise values of τ if required. By repeating the experiment at several temperatures, we can plot $\ln(\tau T^2)$ vs. $(kT)^{-1}$, and from Eq. [12] and [13], we expect a straight line of slope $E_C - E_T$ or $E_T - E_V$. The experimental results are plotted for a single CCD device in Fig. 5 and they do in fact fall on a least squares fit straight line of slope 0.404 eV = $E_C - E_T$ or $E_T - E_V$. This is an energy level that lies near the midgap of silicon, where we know it can give rise to the most thermal leakage current. The reported energy level closest to this number in silicon is $E_T - E_V = 0.40$ eV for iron (6-8). Iron is known to have one of the highest diffusion coefficients of any impurity in silicon, and its solid solubility is larger than 10^{15} cm^{-3} at our lowest furnace temperatures. An obvious source of iron is the stainless steel plumbing for the gas flow systems and the gas storage tanks. The potentially corrosive HCl gas system used to getter mobile sodium ions from the gate oxides was particularly suspect. By eliminating the HCl gas flow and relying on clean processing and gettering of sodium by our phosphorus-doped polysilicon gates, we obtained an immediate reduction of about two orders of magnitude in thermal leakage and charge trapping in finished devices.

The concentration of trap states from which carriers are emitted after a certain time is given by the first term in Eq. [9], and the concentration of emptied traps after steady state is achieved is represented by the factor Δn_T . As seen in Eq. [10], Δn_T is only a fraction of the total impurity concentration, N_{TT} , with the fraction determined by the values of the emission and

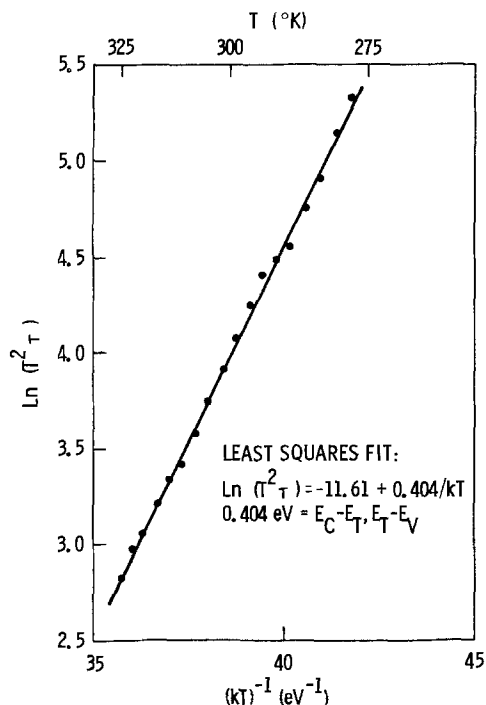


Fig. 5. Experimental data plot yielding bulk state energy level

capture coefficients and the equilibrium doping concentrations.

In our buried N-channel device we have $c_n n_0 \gg c_p p_0$, and, since the impurity level is near the midgap energy, $c_n n_0 \gg e_n e_p$ by comparing Eq. [4] and [5]. Finally, we have assumed that the impurity level emits holes to the valence band so that $e_p \gg e_n$. Combining these approximations in Eq. [10], we get $\Delta n_T \approx (e_n/e_p) N_{TT}$. We have determined $e_p = \tau^{-1}$, but e_n can only be found by another measurement technique. However, we have determined that the concentration of trapped and reemitted carriers, Δn_T , is much less than the impurity concentration or $N_{TT} \approx (e_p/e_n) \Delta n_T \gg \Delta n_T$.

Referring to Fig. 4, after the traps have emptied in a full depletion mode so that the first term in Eq. [9] is zero, a full charge packet loses charge represented by a 0.55 drop in output voltage. A second charge packet experiences a 0.13 voltage drop and succeeding full charge packets lose nothing because the traps have reached the equilibrium condition of Eq. [7]. The output circuit has a sensitivity of about 10^{12} V/C, so the 0.55V and 0.13V represent 0.55×10^{-12} C and 0.13×10^{-12} C or a combined total of 4.3×10^6 electrons. These electrons are trapped in a CCD channel that is $250 \mu\text{m}$ wide \times $1540 \mu\text{m}$ long \times $1 \mu\text{m}$ deep for a total volume of 3.8×10^{-7} cm³. Therefore, the concen-

tration of trapped electrons that can be reemitted is $\Delta n_T = 4.3 \times 10^6 / 3.8 \times 10^{-7} = 1.1 \times 10^{13}$ cm⁻³. This represents a lower limit on N_{TT} .

Conclusions

By employing the temperature dependent transfer inefficiency of a CCD, we have been able to identify the impurity causing that inefficiency as iron with an energy level 0.40 eV above the silicon valence band. We have also been able to place a lower limit on the iron concentration of 1.1×10^{13} cm⁻³. A simplified single photograph variation of the double pulse method greatly facilitated determination of the required emission time constants.

This impurity identification immediately threw suspicion on the furnace plumbing for the HCl gas used to getter the threshold shifting sodium ions in isolation oxides. This plumbing contains iron in the stainless steel tubing and the HCl tanks. By eliminating the HCl gas system, an immediate reduction of about two orders of magnitude in thermal leakage current and in charge trapping was observed in finished devices.

Acknowledgments

We would like to thank R. A. Bredthauer, S. Chung, R. L. Maddox, W. P. Waters, and E. F. Wojtkowski for helpful discussions on the source of iron contamination and its elimination.

Manuscript submitted June 24, 1980; revised manuscript received Nov. 17, 1980.

Any discussion of this paper will appear in a Discussion Section to be published in the December 1981 JOURNAL. All discussions for the December 1981 Discussion Section should be submitted by Aug. 1, 1981.

Publication costs of this article were assisted by Rockwell International.

REFERENCES

1. A. M. Mohsen and M. F. Tompsett, *IEEE Trans. Electron Devices*, **ed-21**, 701 (1974).
2. R. N. Hall, *Phys. Rev.*, **83**, 228 (1951); *ibid.*, **87**, 387 (1952); W. Shockley and W. T. Read, Jr., *ibid.*, **87**, 835 (1952).
3. C. T. Sah, *Proc. IEEE*, **55**, 654 (1967).
4. S. M. Sze, "Physics of Semiconductor Devices," pp. 26-27, John Wiley & Sons, New York (1969).
5. C. T. Sah, L. Forbes, L. L. Rosier, and A. F. Tasch, Jr., *Solid State Electron.*, **13**, 759 (1970).
6. S. M. Sze, "Physics of Semiconductor Devices," pp. 30-32, John Wiley & Sons, New York (1969).
7. A. O. Eywaraye and P. L. Anderson, in "Semiconductor Characterization Techniques," P. A. Barnes and G. A. Rozgonyi, Editors, pp. 61-70, The Electrochemical Society Softbound Proceedings Series, Princeton, N.J. (1978).
8. M. Okuyama, N. Matsunaga, J. W. Chen, and A. G. Milnes, *J. Electron. Mater.*, **8**, 501 (1979).

High Temperature Oxidation Mechanism of CoO to Co₃O₄

K. Przybylski¹ and W. W. Smeltzer*

Department of Metallurgy and Materials Science, McMaster University, Hamilton, Ontario, Canada, L8S 4M1

ABSTRACT

Growth of Co₃O₄ layers on the (100) surface of single crystal CoO was investigated in air at 700° and 800°C. These layers were of duplex structure due to simultaneous inside and outside growth. Measurements on the position of inert gold markers demonstrated that cobalt migration outward in Co₃O₄ was the dominant diffusion mechanism. The oxidation kinetics were parabolic; the parabolic rate constant at 800°C was used to obtain an estimate of $D_{Co} = 3.0 \times 10^{-12}$ cm²/sec for the self-diffusion coefficient of cobalt in Co₃O₄.

The kinetics and mechanism of the growth of Co₃O₄ on CoO have been studied only by a few investigators (1-6). This reaction was found to follow parabolic kinetics at temperatures between 600° and 714°C for exposures extending from 1 to 30 hr in oxygen at 1 atm pressure (1). Growth of Co₃O₄ layers on CoO in air between 700° and 910°C followed cubic or parabolic relationships (2). The initial oxidation rates during 0.05-1 sec between 500° and 1000°C in oxygen at 1-5 atm are much slower than those rates for extensive oxidation and they are strongly influenced by oxygen pressure (3). Oxidation of sintered CoO samples in air at 600°-900°C for periods up to 12 hr have been reported to be determined by Co₃O₄ nucleation processes (4). Attempts using inert gold marker measurements to interpret the reaction mechanism have been inconclusive since inward oxygen (5) and outward cobalt (6) migration have been advanced to account for Co₃O₄ layer growth.

A review of the published literature illustrates that there are many discrepancies among the investigations and that the oxidation kinetics and mechanisms for Co₃O₄ growth on CoO are not understood. It appears that the most important undefined source of errors is associated with the low density of the polycrystalline CoO specimens resulting from cracks and pores. To explain the discrepancies in kinetics and proposed mechanisms, we decided to investigate the growth of Co₃O₄ layers on the (100) surface of CoO single crystals.

Experimental

A crystal of CoO (99.92 weight percent pure) grown by the Verneuil process was homogenized in air at 1200°C for 24 hr. It was oriented by means of Laue x-ray back reflection and a typical diffraction pattern of a (100) face is shown in Fig. 1. Rectangular sheets, 10 × 5 × 0.5 mm, were prepared from this crystal with the large lateral surface at (100) orientation. A suspension hole, 0.5 mm diam, was drilled ultrasonically in each specimen after its surface was abraded by 800 grit SiC. The crystal surfaces then were metallographically polished with kerosene as lubricant to a 1 μm diamond paste finish and they were cleaned ultrasonically using acetone as solvent.

These CoO specimens were subsequently thermally homogenized and subjected to oxidation in air at atmospheric pressure at 700° and 800°C. In the oxidation runs, several specimens were simultaneously exposed from quartz rods using Pt wire in a mullite reaction tube placed horizontally in an electric furnace controlled to ±2°C.

The schedules of the homogenization and oxidation experiments can be explained with reference to the

thermodynamics of the CoO-Co₃O₄ system. A wide range of thermodynamic data has been published, which has been discussed by Ingraham (7) who proposes that the equilibrium oxygen pressure for CoO-Co₃O₄ coexistence is given by

$$\log P_{O_2} \text{ (atm)} = 12.809 - 1.580 \times 10^4/T \text{ (1086-1219 K)}$$

where P_{O_2} is the oxygen pressure and T is the temperature. Part of the diagram for the compositions of cobalt oxides as a function of temperature and oxygen pressure given by Holappa (6) based on results of two investigations (8,9) is shown in Fig. 2. Accordingly, the CoO crystal homogenized at 1200°C in air ($P_{O_2} = 0.21$ atm) and quenched to room temperature would be expected to exhibit Co₃O₄ precipitates. The degree of this precipitation is illustrated in the micrograph of Fig. 3. The CoO matrix is probably near stoichiometry, because Carter and Richardson (10) have shown that its lattice parameter remains constant independent of thermal pretreatment and quenching method. Specimens of this investigation were subjected to the following thermal pretreatments to minimize Co₃O₄ precipitation. They were heated to 1200°C in a flowing Ar-O₂ atmosphere set at $P_{O_2} = 1.2 \times 10^{-2}$ atm (point A of Fig. 2), slowly cooled to 800°C, and held in this atmosphere (point B of Fig. 2) for 2 weeks before quenching to room temperature. Those specimens to be

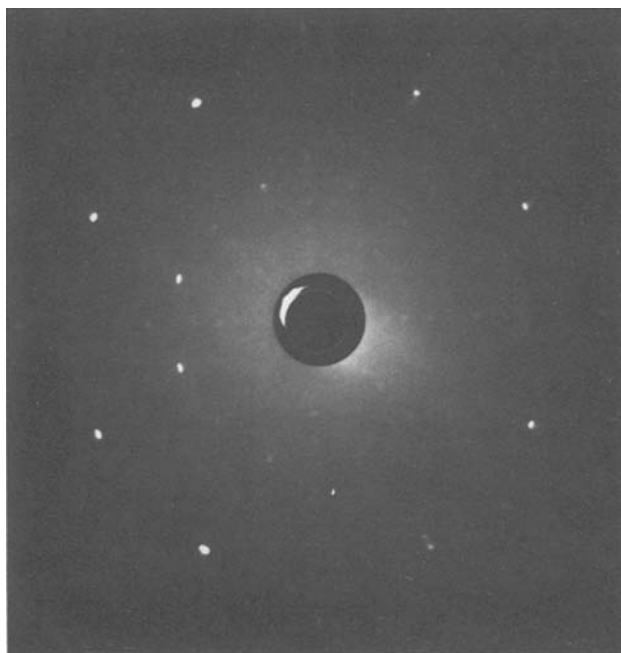


Fig. 1. Laue back reflection x-ray diffraction pattern with incident beam perpendicular to the (100) CoO face.

* Electrochemical Society Active Member.

¹ Present address: Institute of Materials Science, Academy of Mining and Metallurgy, Krakow, Poland.

Key words: semiconductor, kinetics, mass transport, diffusion.

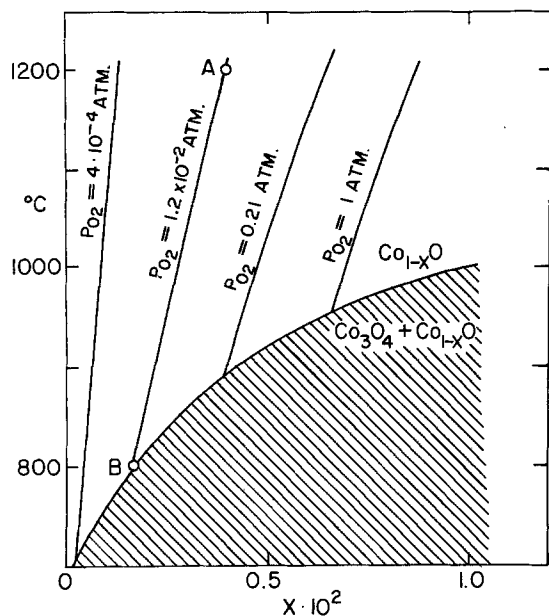


Fig. 2. Composition diagram of Co_{1-x}O between 700° and 1200°C showing its nonstoichiometry at several oxygen pressures.

oxidized at 700°C were sealed in an evacuated quartz tube containing a $\text{CoO} + \text{Co}_3\text{O}_4$ mixture and equilibrated at this temperature ($P_{\text{O}_2} = 3.7 \times 10^{-4}$ atm) for 2 weeks before quenching to room temperature.

It was confirmed by x-ray and reflection electron diffraction that Co_3O_4 was the only product upon oxidizing CoO . Co_3O_4 layer thicknesses and distances within these layers were obtained from scanning electron microscopy (SEM) images of specimen cross sections prepared by metallographic polishing and by fracture. Experiments using inert markers were carried out to determine the predominant diffusion species in Co_3O_4 during its growth. Gold markers, ~ 0.5 – $1 \mu\text{m}$ thick, were deposited by evaporation on several CoO specimens through masks made up of two microscope copper grids ($20 \times 200 \mu\text{m}$) tilted to obtain triangles $\sim 100 \mu\text{m}$ long and 7 – $10 \mu\text{m}$ wide at the base. The lateral size of these markers was reduced to 1 – $3 \mu\text{m}$ by careful mechanical removal of gold from the specimen mounted on the stage of an optical microscope. The gold markers and their positions in the Co_3O_4 layer of a metallographically prepared oxidized CoO specimen cross section could be definitively identified

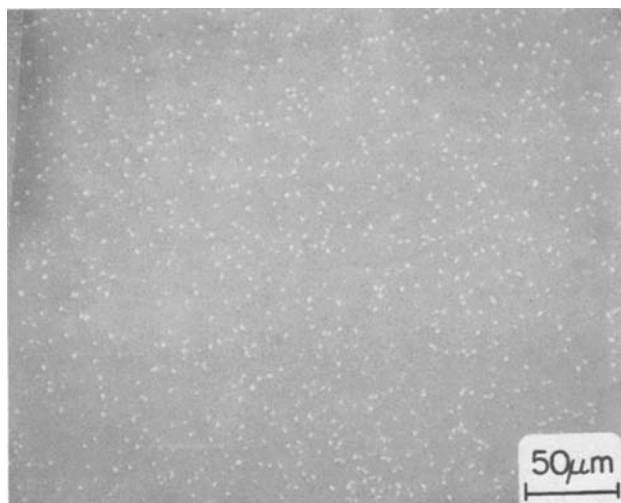


Fig. 3. The (100) CoO surface exhibiting Co_3O_4 precipitates after the specimen was annealed at 1200°C in air for 24 hr and subsequently quenched in air.

by energy dispersive x-ray analysis (EDAX) and the (SEM) images, respectively.

Results

The microstructures of the Co_3O_4 layers formed at 800°C during exposures extending from a few minutes to 672 hr are illustrated in the micrographs of Fig. 4–7. A complete layer developed within 4 min (Fig. 4a) and an examination of its exterior surface showed that the uppermost region of this layer was composed of small grains (Fig. 4b). Although the CoO crystal was at (100) orientation (Fig. 4c), the thin Co_3O_4 layer was polycrystalline (Fig. 4d). This layer during long exposure developed a distinct duplex structure composed of an inner layer of large columnar grains and an outer layer of smaller more equiaxed grains (Fig. 5, 6). Distinct voids occurred at the boundary between the inner and outer layers which lay parallel to the direction of the

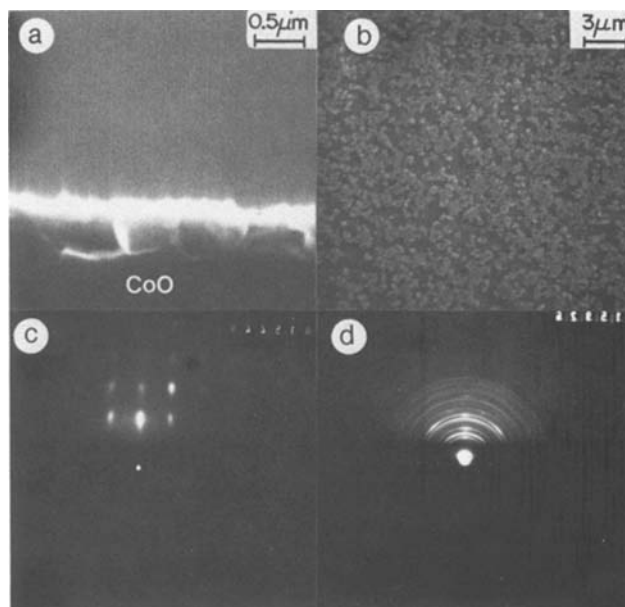


Fig. 4. Co_3O_4 formed on (100) CoO oxidized at 800°C in air for 4 min: (a) SEM image of fracture cross section, (b) SEM image of Co_3O_4 external surface, (c) reflection electron diffraction pattern from (100) CoO surface before oxidation, (d) reflection electron diffraction pattern from Co_3O_4 surface.

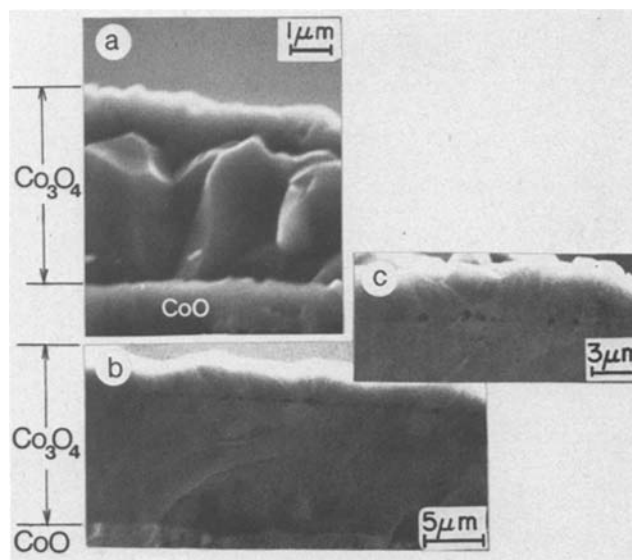


Fig. 5. SEM images of fracture cross sections of Co_3O_4 formed on (100) CoO at 800°C in air after (a) 1 hr, (b) 24 hr, and (c) 24 hr. The image in (c) shows details of the boundary between the inner and outer layers of the duplex Co_3O_4 layer.

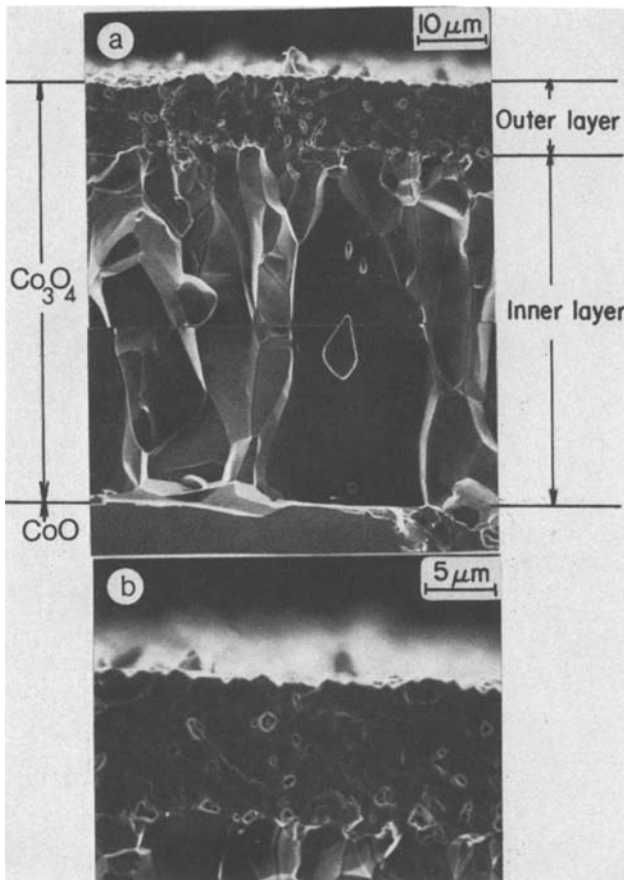


Fig. 6. SEM images of fracture cross sections of Co₃O₄ formed on (100) CoO at 800°C in air after (a) 672 hr and (b) the outer layer of the duplex layer shown in (a).

CoO surface after 24 hr (Fig. 5b). The number and size of these voids increased with time and at exposures extending longer than 200 hr voids of approximately the same size were observable at grain boundaries in the outer layer (Fig. 6, 7). The Co₃O₄ layer retained intimate bonding to the CoO surface; voids were not observed at this essentially planar interface as depicted in the specimen cross sections shown in Fig. 7.

Thicknesses of the total, inner, and outer Co₃O₄ layers were evaluated from metallographic and fracture cross sections of CoO specimens oxidized at 800°C. Eight to ten layer thickness measurements were made on each specimen and these results are recorded in Table I. It was found that growth of these layers follow a parabolic rate equation

$$X^2 = 2k_p t + C \quad [1]$$

where X represents a layer thickness after time t , k_p is a parabolic rate constant, and C is a constant. The re-

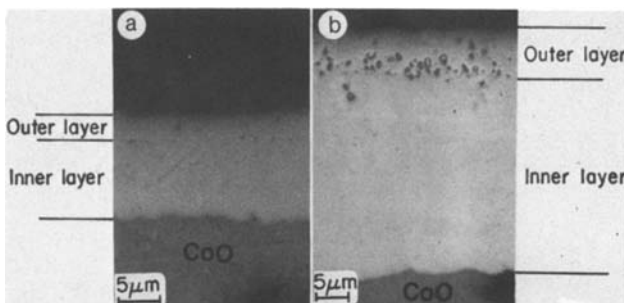


Fig. 7. Optical images of metallographic cross sections of Co₃O₄ layers formed on (100) CoO at 800°C in air after (a) 15 hr and (b) 218 hr.

Table I. Summary of results for Co₃O₄ growth on CoO in air at 800°C

| Time (hr) | Total oxide thickness (μm) | Inner layer thickness (μm) | Outer layer thickness (μm) | Thickness ratio: outer layer/total layer (%) | Ratio of marker depth to total thickness (%) |
|-----------|----------------------------|----------------------------|----------------------------|--|--|
| 15 | 12.5 | 9.4 | 3.1 | 24.8 | |
| 24 | 15.2 | 11.5 | 3.7 | 24.3 | |
| 24 | 16.1 | 12.2 | 3.9 | 24.2 | |
| 24 | 14.5 | 11.1 | 3.4 | 23.4 | |
| 40 | 17.1 | 13 | 4.1 | 24 | 24.1 |
| 40 | 18.2 | 13.9 | 4.3 | 23.6 | |
| 48 | 19.2 | 14.7 | 4.5 | 23.4 | |
| 72 | 22.2 | 16.9 | 5.3 | 23.9 | |
| 72 | 21.6 | 16.6 | 5.0 | 23.1 | |
| 96 | 25.3 | 19.4 | 5.9 | 23.3 | |
| 96 | 24.4 | 18.8 | 5.6 | 23 | 23.4 |
| 120 | 26.7 | 20.3 | 6.4 | 24 | |
| 140 | 29.2 | 22.4 | 6.8 | 23.3 | |
| 140 | 28.8 | 22.2 | 6.6 | 22.9 | |
| 160 | 31.2 | 24.1 | 7.1 | 22.8 | 22.6 |
| 160 | 31.6 | 24.3 | 7.3 | 23.1 | |
| 181 | 32.6 | 25 | 7.6 | 23.3 | |
| 181 | 33.1 | 25.3 | 7.8 | 23.6 | |
| 200 | 34.8 | 26.9 | 7.9 | 22.7 | |
| 218 | 36.2 | 28.6 | 7.6 | 21 | |
| 242 | 37.5 | 29.3 | 8.2 | 21.9 | 21.6 |
| 242 | 38.1 | 30.1 | 8 | 21 | |
| 260 | 39.4 | 30.7 | 8.7 | 22.1 | |
| 260 | 38.9 | 30 | 8.9 | 22.9 | |
| 282 | 40.6 | 32.1 | 8.5 | 20.9 | |
| 305 | 41.8 | 32.9 | 8.9 | 21.3 | |
| 384 | 47.7 | 37.2 | 10.5 | 22 | 22.8 |
| | | | | 23 ± 2 | 22.9 ± 1.5 |

sults from Table I are plotted in Fig. 8 according to this relationship. The values for the parabolic rate constants are

$$k_p \text{ (total Co}_3\text{O}_4 \text{ layer)} = (7.65 \pm 0.1) \times 10^{-12} \text{ cm}^2/\text{sec}$$

$$k_p \text{ (inner Co}_3\text{O}_4 \text{ layer)} = (4.69 \pm 0.08) \times 10^{-12} \text{ cm}^2/\text{sec}$$

$$k_p \text{ (outer Co}_3\text{O}_4 \text{ layer)} = (3.6 \pm 0.2) \times 10^{-13} \text{ cm}^2/\text{sec}$$

An example of results obtained using the inert gold markers to determine the predominant diffusion species during growth of Co₃O₄ at 800°C is presented in Fig. 9. The markers were found at the boundary between the inner and outer layers which corresponds to the initial location of the CoO surface. In this specific example, 23% of the layer thickness is outside the marker. Average values obtained by measuring the positions of four to five markers on each CoO specimen subjected to a different exposure period are recorded in Table I. The ratio of the outer to total Co₃O₄ layer thickness ob-

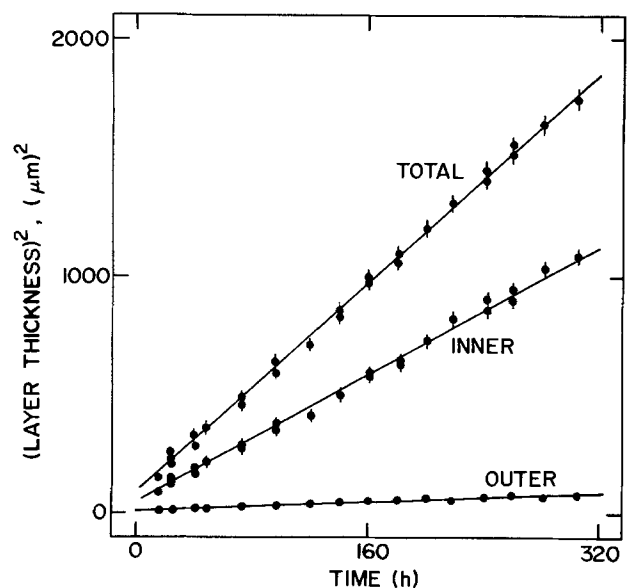
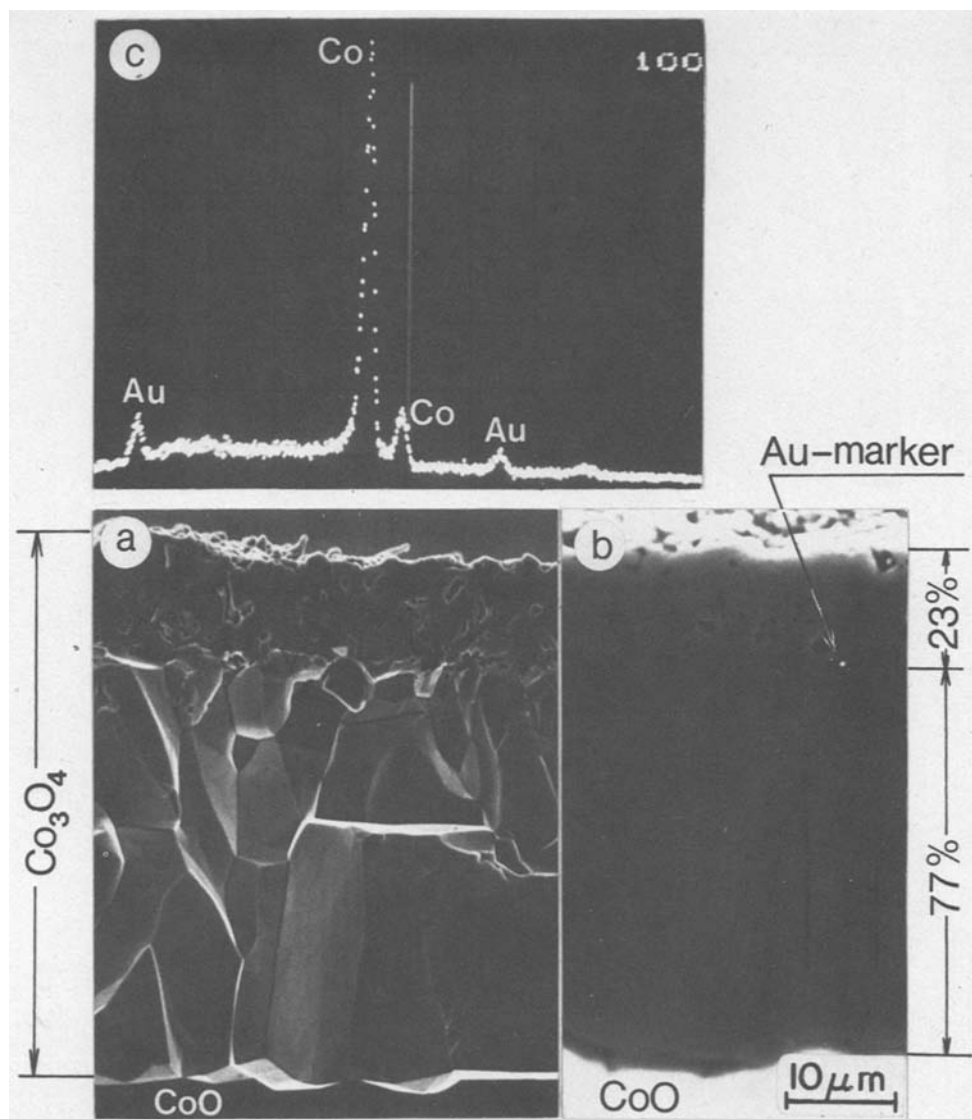


Fig. 8. Co₃O₄ layer growth on (100) CoO at 800°C in air according to a parabolic rate relationship: (layer thickness)² vs. time. Plots are given for growth of outer, inner, and total Co₃O₄ layers.

Fig. 9. Co_3O_4 layer formed on (100) CoO at 800°C in air after 384 hr: (a) SEM image of fracture cross section, (b) SEM image of metallographic cross section showing Au marker in Co_3O_4 layer, and (c) EDAX spectra for Au.

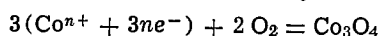


tained from direct measurements of layer thicknesses and of marker positions are in agreement.

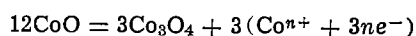
These general features of Co_3O_4 layer growth at 800°C were also found for the growth of the layers over long time intervals at 700°C . Five exposure tests extending from 24 to 480 hr were completed. Growth of the individual and total Co_3O_4 layers followed parabolic kinetics. The microstructural features were identical and the position of the gold markers was at the boundary between the inner and outer layers as shown in Fig. 10.

Discussion

The parabolic kinetics for growth of the Co_3O_4 layer, the position of the inert metal marker within this layer, and its morphological development to a duplex structure by simultaneous inside and outside growth can be explained by outward cobalt diffusion. A model illustrating growth of the near stoichiometric Co_3O_4 layer is shown in Fig. 11. Outward ambipolar diffusion of Co ions and electrons probably via positive holes (6) across this layer leads to formation of 1 mole of oxide at the $\text{Co}_3\text{O}_4/\text{O}_2$ interface I by the reaction

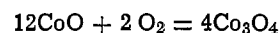


upon formation simultaneously of the cobalt reactant by the following displacement reaction at the $\text{CoO}/\text{Co}_3\text{O}_4$ interface III



In these reactions, $n^+ = 2.67$ is the effective charge for the diffusing Co^{2+} and Co^{3+} ions. The mass balance

for these two reactions is



where 1 and 3 moles of Co_3O_4 are formed at the $\text{Co}_3\text{O}_4/\text{O}_2$ and $\text{CoO}/\text{Co}_3\text{O}_4$ interfaces, respectively. An inert metal marker placed initially on the CoO surface, interface II, is therefore positioned at a fractional depth of 25% into the Co_3O_4 layer when distances are measured from its external to interior surface.

Ambipolar diffusion of cobalt through the Co_3O_4 layer leads to parabolic growth kinetics described by the Wagner theory (11). The parabolic rational rate constant k_r can be expressed as

$$k_r \text{ (equiv./cm sec)} = C_{\text{equiv.}} \int_{a_o'}^{a_o''} \frac{Z_{\text{Co}}}{|Z_o|} D_{\text{Co}} d \ln a_o \quad [2]$$

where $C_{\text{equiv.}}$ is the cobalt concentration in equivalents/cm³, the valencies $Z_{\text{Co}} = 2.67$ and $|Z_o| = 2$, D_{Co} is the cobalt self-diffusion coefficient and a_o is the oxygen activities having values a_o'' and a_o' at the $\text{Co}_3\text{O}_4/\text{O}_2$ and $\text{CoO}/\text{Co}_3\text{O}_4$ interfaces, respectively. Upon expressing this rate constant in terms of k_p from Eq. [1], one obtains

$$k_p \text{ (cm}^2\text{/sec)} = \frac{4}{3} C_{\text{equiv.}} \tilde{V} \int_{a_o'}^{a_o''} \frac{Z_{\text{Co}}}{|Z_o|} D_{\text{Co}} d \ln a_o \quad [3]$$

In this latter equation, \tilde{V} is the equivalent volume of Co_3O_4 and the factor equal to $4/3$ occurs because only $1/3$ mole of Co_3O_4 is formed by 1 mole of cobalt diffusing across the layer to react with oxygen for

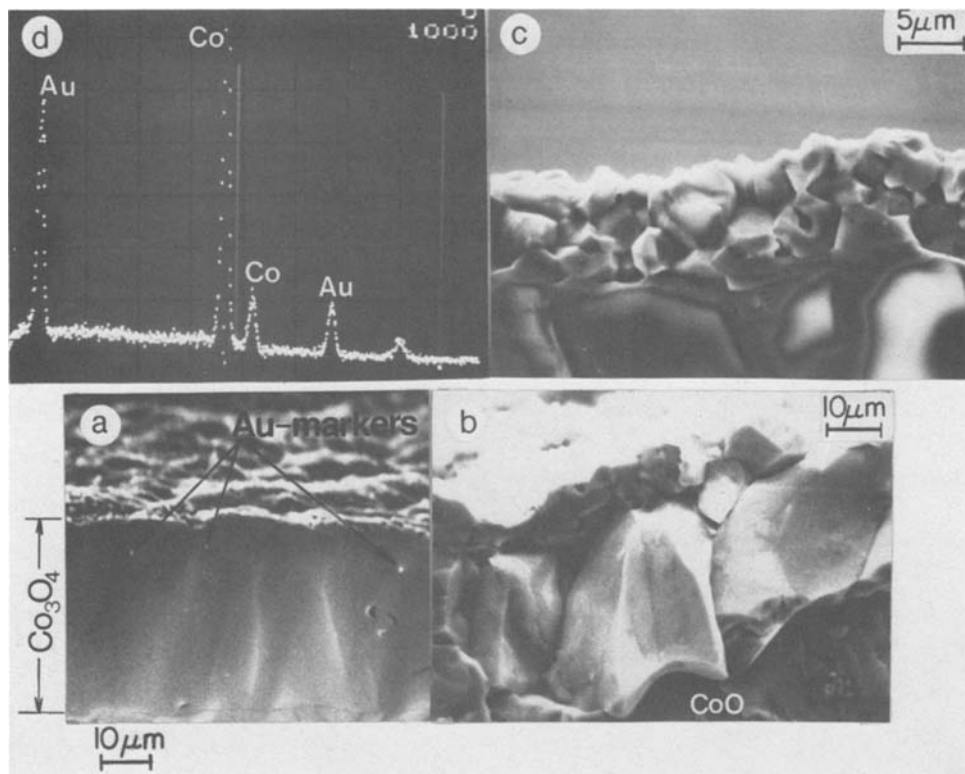


Fig. 10. Co_3O_4 layer formed on (100) CoO at 700°C in air after 480 hr: (a) SEM image of metallographic cross section showing Au markers in this layer, (b) SEM image of fracture cross section, (c) fracture cross section of outer layer region, and (d) EDAX spectra for Au.

each mole of Co_3O_4 simultaneously formed at the $\text{CoO}/\text{Co}_3\text{O}_4$ interface.

Examination of the results in Table I and Fig. 9 and 10 shows that the position of the gold marker in the Co_3O_4 layers is in close agreement with the prediction from the growth model based on cobalt diffusion and a simultaneous displacement reaction at the $\text{CoO}/\text{Co}_3\text{O}_4$ interface. This position at a fractional depth beneath the external surface of $22.9\% \pm 1.5\%$ from the extensive measurements at 800°C and 23% from the measurement at 700°C compares favorably with the predicted value of 25% . Holappa (6) also found that gold markers were $\sim 20\%$ within the Co_3O_4 layer upon oxidizing polycrystalline CoO at 860°C in air for 366 hr. Alcock and Hocking (5) have suggested, however, that Co_3O_4 grows by inward oxygen diffusion since gold markers were positioned at the $\text{Co}_3\text{O}_4/\text{O}_2$ interface

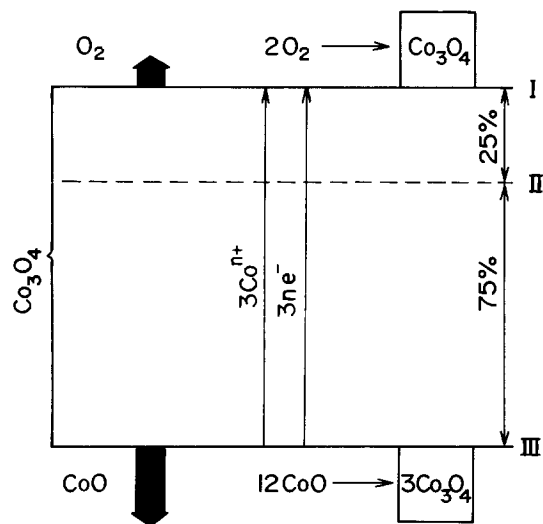


Fig. 11. Schematic model for growth of the Co_3O_4 layer on CoO by oxidation. One mole of Co_3O_4 grows at the $\text{Co}_3\text{O}_4/\text{O}_2$ interface by outward diffusion of cobalt to react with oxygen and 3 moles of Co_3O_4 are formed at the $\text{CoO}/\text{Co}_3\text{O}_4$ interface from the reaction of 12 moles of CoO. Designations are I, $\text{Co}_3\text{O}_4/\text{O}_2$ interface; II, initial position of CoO surface; and III, $\text{CoO}/\text{Co}_3\text{O}_4$ interface.

upon oxidizing polycrystalline CoO for 168 and 72 hr at 688° and 850°C , respectively. The oxidation experiments of this investigation carried out for exposures up to 384 hr on CoO single crystals utilizing minute gold markers have demonstrated, notwithstanding, that growth of a Co_3O_4 layer proceeds by cobalt diffusion. This type of mechanism for Co_3O_4 layer growth is identical to the mechanism advanced by Davies *et al.* (12) for the growth of Fe_3O_4 layers on FeO by iron diffusion.

Co_3O_4 is a member of the M_3O_4 transition metal oxides of spinel structure which exhibit cation vacancies in octahedral and tetrahedral positions and positive holes as point defects (13, 14). Its defect properties have not been investigated, but it has been shown that the value of the electrical conductivity at 900°C remains unchanged over the oxygen pressure range from 0.21 to 1 atm (15). Moreover, Co_3O_4 transforms at 800°C to CoO at oxygen pressures not far removed from 1 atm as shown in Fig. 2. We have obtained, therefore, an estimate of the self-diffusion coefficient of cobalt for Co_3O_4 at 800°C by integrating the right-hand side of Eq. [3] with the assumption that this diffusivity is not dependent on oxygen pressure over the very small pressure range from 0.21 to 1.2×10^{-2} atm which corresponds to the oxygen pressures at the $\text{Co}_3\text{O}_4/\text{O}_2$ and $\text{CoO}/\text{Co}_3\text{O}_4$ interfaces, respectively. A value of $D_{\text{Co}} = 3.0 \times 10^{-12}$ cm²/sec is obtained using the experimental value of $k_p = 7.65 \times 10^{-12}$

cm²/sec and $\bar{V} = 5.0$ cm³/equiv. The assumption that cobalt is the predominant diffusion species is reasonable because the self-diffusion coefficient of oxygen in this polycrystalline oxide is $D_{\text{O}} = 3.3 \times 10^{-14}$ cm²/sec (16) yielding $D_{\text{Co}}/D_{\text{O}} \approx 10^2$.

The gold markers were positioned at the boundary between the columnar and equiaxed layers of a duplex Co_3O_4 layer. Apparently outward growth of Co_3O_4 by cobalt diffusion led to development of a relatively large number of equiaxed grains, while inward penetration of Co_3O_4 into CoO, resulting from the simultaneous displacement reaction, led to development of a relatively smaller number of large, columnar grains. These growth features and the voids observed at this boundary between the different structural layers possibly

arose from imperfections and impurities, since the boundary is situated at the position of the initial metallographically prepared CoO surface. These voids and those observed at grain boundaries within the outer layer would enlarge by acting as sinks for cobalt vacancies migrating across the Co_3O_4 layer during its growth. Thus, any small decrease of the cobalt flux across the outer layer, due to the migration of vacancies to voids and the lateral areal barrier of these voids to cobalt diffusion, can account for the variation to slightly smaller values of the fractional depth of the internal boundary and marker position with increasing exposure time. These fractional depths, as shown in Table I, corresponded to the predicted value of 25% during early periods up to 24 hr, but they decreased slightly to final values of $\sim 22\%$ as voids became distinctly observable at and within the outer layer of the duplex Co_3O_4 layers during long exposures.

Conclusions

Oxidation of (100) CoO single crystals produced adherent, uniformly thick Co_3O_4 layers of duplex structure. During oxidation, voids developed at the boundary between the inner and outer layers and within the outer layer. Marker measurements and texture analysis showed that Co_3O_4 grew as a duplex layer due to simultaneous inside and outside growth. It was found that the oxidation kinetics of CoO to Co_3O_4 obeyed a parabolic relationship resulting from the dominating mechanism of cobalt ambipolar diffusion outward through the Co_3O_4 layer. An estimate of $D_{\text{Co}} = 3.0 \times 10^{-12}$ cm²/sec was obtained at 800°C for the value of the cobalt self-diffusion coefficient of Co_3O_4 .

Acknowledgments

K. Przybylski expresses his appreciation for the opportunity of a one-year (1979) study period at McMaster University under the Canada-Poland Academic Exchange Program. The authors gratefully acknowledge financial support for this research from

the National Science and Engineering Research Council of Canada.

Manuscript received Oct. 15, 1980.

Any discussion of this paper will appear in a Discussion Section to be published in the December 1981 JOURNAL. All discussions for the December 1981 Discussion Section should be submitted by Aug. 1, 1981.

Publication costs of this article were assisted by McMaster University.

REFERENCES

1. G. Chauvenet, *Compt. Rend.*, **209**, 886 (1939).
2. M. G. Vallee and J. Paidassi, *J. Metaux*, **42**, 360 (1967).
3. A. R. Reti, P. L. T. Brian, and L. C. Hoagland, *Ind. Eng. Chem.*, **5**, 171 (1966).
4. W. R. Ott and D. T. Rankin, *J. Am. Ceram. Soc.*, **62**, 203 (1979).
5. C. B. Alcock and M. G. Hocking, *Trans. Inst. Min. Metall.*, **75C**, 27 (1966).
6. L. E. K. Holappa, *Acta Polytech. Scand. Chem. Metall. Ser.*, **92**, 40 (1970).
7. T. R. Ingraham, *Can. Met. Quart.*, **3**, 221 (1964).
8. B. Fisher and D. S. Tannhauser, *J. Chem. Phys.*, **44**, 1663 (1966).
9. R. J. Makonnen, Tech. Lic. Thesis, Technical University Helsinki (1965).
10. R. E. Carter and F. D. Richardson, *Trans. AIME*, **203**, 336 (1955).
11. C. Wagner, "Atom Movements," p. 153, ASM, Cleveland (1951).
12. M. H. Davies, M. T. Simnad, and C. E. Birchenall, *Trans. AIME*, **197**, 1250 (1953).
13. W. L. Roth, *J. Phys. Chem. Solids*, **25**, 1 (1964).
14. R. Dieckmann and H. Schmalzried, *Z. Phys. Chem., N. F.*, **96**, 331 (1975).
15. C. Wagner and E. Koch, *Z. Phys. Chem.*, **B32**, 439 (1936).
16. B. A. Thompson, Ph.D. Dissertation, Rensselaer Polytechnic Institute (1962), University Microfilms, Inc., Ann Arbor, Michigan.

The Sulfidation Kinetics of Nickel-Aluminum Alloys at 700°C in Hydrogen Sulfide-Hydrogen Atmospheres

V. S. Bhide¹ and W. W. Smeltzer*

Department of Metallurgy and Materials Science, McMaster University, Hamilton, Ontario, Canada, L8S 4M1

ABSTRACT

The sulfidation kinetics of Ni-Al alloys containing 3-13 atomic percent Al were investigated at 700°C in $\text{H}_2\text{S}-\text{H}_2$ atmospheres at sulfur pressures $10^{-8} \leq P_{\text{S}_2} \leq 10^{-2}$ atm. The reaction product was comprised of three regions: an external NiS or Ni_3S_2 layer, an Al_2S_3 - Ni_3S_2 lamellar layer, and an innermost Al-Ni-S liquid layer. Sigmoidal shaped reaction curves before onset of linear kinetics resulted from the temporally partial protective nature of the oxide films on the metallographically polished specimens. The magnitudes of the linear rate constant for growth of the reaction product layers were predominantly determined by interfacial processes for transfer of reactants at the gas/scale and scale/subscale interfaces.

Aluminum is a commonly used alloying element in Ni-base superalloys for improving their strength and corrosion resistance. These alloys, however, undergo severe degradation by sulfidation. The sulfidation ki-

netics of pure nickel have been studied by several investigators (1-6). At temperatures in the range 300°-600°C, linear kinetics resulting from a gas/scale phase boundary reaction are observed in sulfur pressures $10^{-4} \leq P_{\text{S}_2} \leq 0.1$ atm and parabolic kinetics resulting from reactant diffusion in the nickel sulfide scales are observed at higher sulfur pressures. It has also been

* Electrochemical Society Active Member.

¹ Present address: International Business Machines Corporation, San Jose, California, 95193.

Key words: Ni-Al alloys, sulfidation kinetics.

demonstrated that nickel containing 0.5 atomic percent (a/o) Al sulfidizes at 620°C and 10^{-4} atm sulfur pressure by linear kinetics (2). Since there is a paucity of results for sulfidation of Ni-Al alloys, we have systematically investigated the sulfidation properties of these alloys containing up to 13 a/o Al at 700°C in H_2S-H_2 atmospheres containing sulfur at pressures $10^{-8} \leq P_{S_2} \leq 10^{-2}$ atm.

Experimental

The compositions of the alloys containing 3-13 a/o Al prepared by melting the pure metals in an argon arc furnace are given in Table I. Plates, $1.5 \times 0.8 \times 0.1$ cm, were polished to 600 grit silicon carbide paper using water as lubricant. Following a vacuum anneal at 800°C for 3 days, the specimens were again polished to 600 grit silicon carbide paper and, in several instances, polished to 1 μ m size diamond using kerosene as lubricant. The specimens were successively washed with petroleum ether and methyl alcohol, dried, and stored in acetone.

Sulfidation kinetics using H_2S-H_2 atmospheres were determined gravimetrically at 700°C using a McBain balance assembly which has been described elsewhere (7). The sulfur pressures in the atmospheres at 700°C were calculated from the equilibrium constant $K = 5.29 \times 10^{-3}$ for the reaction $H_2S = H_2 + \frac{1}{2} S_2$ (8-10). The oxygen containing impurities in the ultrahigh purity hydrogen were $O_2 = 1$ ppm and $H_2O = 5$ ppm, and in the 99.5% chemically pure hydrogen sulfide SO_2 and CO_2 equal to 0.05 and 0.13 mole percent. The scales were examined using optical and scanning electron microscopy. The reaction products were identified by electron microprobe, x-ray diffraction, and differential thermal analyses. Several 125 μ m diam Pt markers were spot-welded on a Ni-6 a/o Al alloy specimen before its sulfidation at 10^{-5} atm sulfur pressure.

Results

Sulfidation kinetics.—Results are shown in Fig. 1 and 2 for the alloys containing 6 and 13 a/o Al and with the specimen surfaces subjected to the fine metallographic polish of 1 μ m diamond. The curves are regression fits of the results to a sigmoidal-type rate equation for which the linear rate constants were obtained from observations at long time periods after complete surface coverage of a specimen by a sulfide scale. The irreproducible initial reaction rates were associated with the presence of defective oxide films on these alloy specimens. This characteristic behavior was demonstrated by sulfidizing a Ni-13 a/o Al alloy specimen at $P_{S_2} = 10^{-10}$ atm for 10 hr. The weight gain was less than 0.1 mg/cm² and a thin gray film < 0.5 μ m thick was found to have developed. Its composition was not established conclusively; nevertheless, it consisted primarily of oxide rather than Al_2S_3 because it did not react with water. It is thermodynamically feasible to form Al_2O_3 upon taking into account the impurity oxygen concentration in the H_2S-H_2 gas stream. Results are shown in Fig. 2 for this specimen with the above preformed film sulfidized in pure H_2S ($P_{S_2} = 1.9 \times 10^{-2}$ atm). The more protective nature of this thicker film emphasized the initial sigmoidal shape of

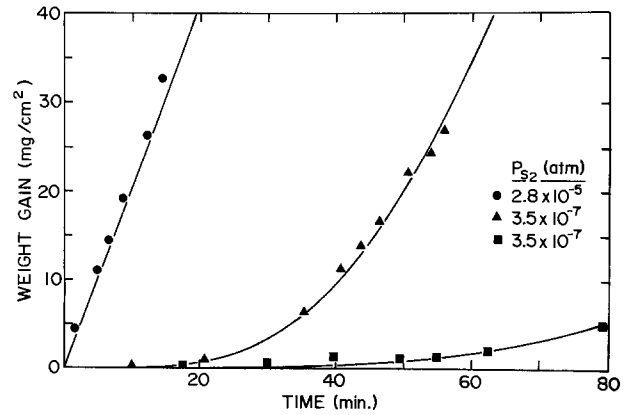


Fig. 1. Sulfidation kinetics at 700°C of the Ni-6 a/o Al alloy subjected to 1 μ m diamond metallographic polish.

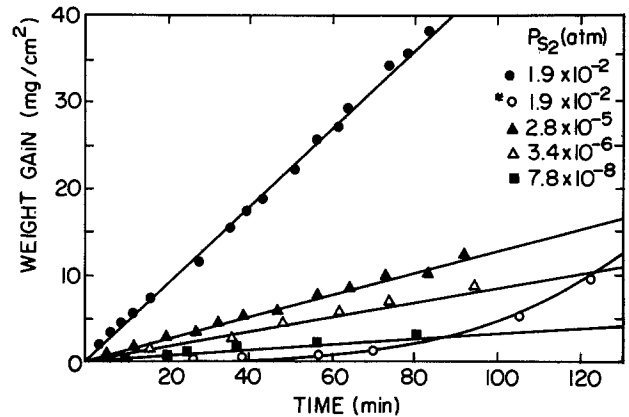


Fig. 2. Sulfidation kinetics at 700°C of the Ni-13 a/o Al alloy subjected to 1 μ m diamond metallographic polish. The run marked with an asterisk refers to sulfidation of a specimen with preformed film.

the reaction curve. The transitory influence of an oxide film was greatly reduced by only coarsely polishing the alloy surface to 15 μ m grit silicon carbide paper. This behavior is illustrated by the sulfidation curves at various sulfur pressures for the alloys containing 3 and 10 a/o Al shown in Fig. 3 and 4. Good reproducibility of each sulfidation curve was obtained and the sigmoidal overtones were significantly reduced in the reaction curves.

Morphologies of the reaction products.—An external scale and subscale were formed in all cases. Isolated nickel sulfide growths, Fig. 5, grew over an alloy specimen surface in the very early reaction stages. Differently sized growths appeared in the same topograph suggesting that they did not nucleate simultaneously. These growths merged together to form a compact scale, Fig. 6, with increasing exposure time at intervals significantly longer in the case of the finely polished specimens, which exhibited pronounced sigmoidal-shaped sulfidation curves. The subscale, which was initially confined to regions beneath the isolated nickel sulfide growths, ultimately penetrated uniformly into the alloy when surface coverage with an external scale was complete.

The subscale in all instances was composed of two distinct regions involving a two-phase lamellar solid layer directly beneath the external scale and an innermost liquid layer sandwiched between the solid lamellae and the alloy. These regions are illustrated by the photomicrographs in Fig. 7. With increasing alloy aluminum content, the thickness of the solid lamellar layer increased at the expense of the liquid layer. Thus, the lamellar layer was only detectable on the Ni-3 a/o Al alloy, but became the predominant layer of the subscale in the Ni-13% Al alloy. Marker observations,

Table I. Chemical analyses of the Ni-Al alloys

| Alloy | (Composition in weight percent) | | | | | |
|---------------|---------------------------------|--------|--------|-------|--------|-----|
| | Al | Co | Fe | Cu | Mn | Ni |
| Ni-3 a/o Al* | 1.35 | <0.003 | 0.020 | 0.032 | <0.004 | Bal |
| | 1.32 | <0.003 | 0.021 | 0.030 | <0.004 | |
| Ni-6 a/o Al | 3.14 | 0.28 | 0.037 | 0.011 | 0.012 | |
| Ni-10 a/o Al* | 4.5 | <0.003 | 0.037 | 0.048 | <0.004 | |
| | 5.1 | <0.003 | 0.056 | 0.043 | <0.004 | |
| Ni-13 a/o Al | 6.38 | 0.044 | -0.164 | 0.042 | 0.04 | |

* Two buttons of same nominal composition were used. There was no significant difference in their sulfidation properties.

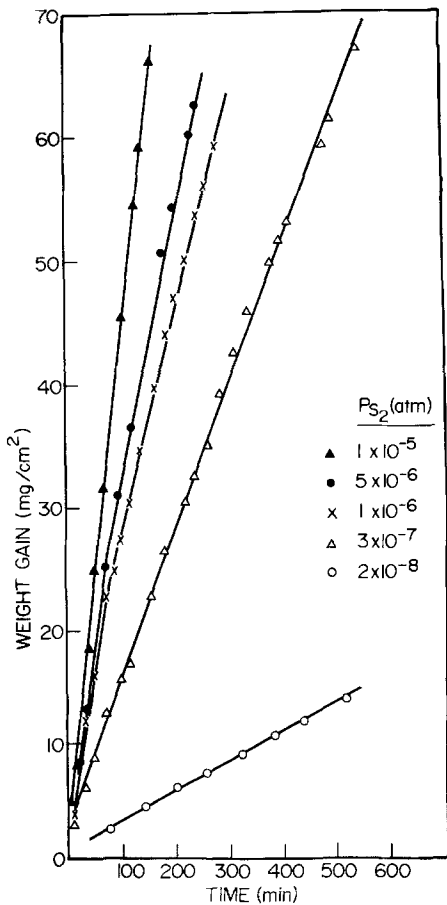


Fig. 3. Sulfidation kinetics at 700°C of the Ni-3 a/o Al alloy subjected to 600 (15 μm) grit silicon carbide metallographic polish.

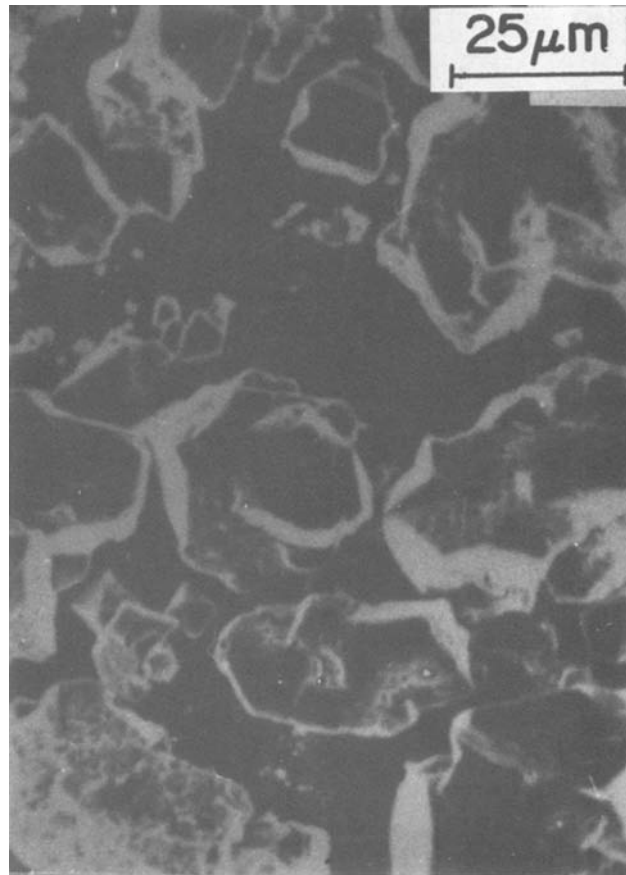


Fig. 5. Top view of Ni-13 a/o Al alloy after sulfidation at $P_{S_2} = 10^{-7}$ atm and 700°C for 12 min.

Fig. 7(a), demonstrated that the Pt marker remained at the external scale/subscale interface consistent with scale growth by outward metal diffusion and subscale growth by inward sulfur diffusion.

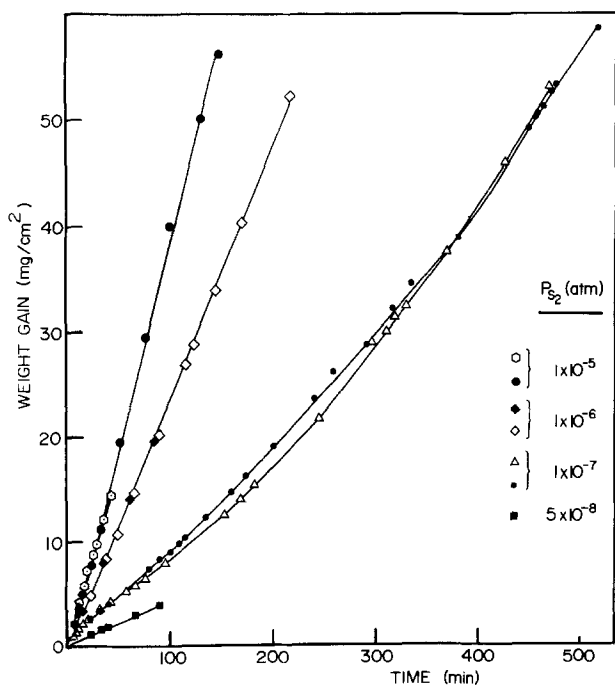


Fig. 4. Sulfidation kinetics at 700°C of the Ni-10 a/o Al alloy subjected to 600 (15 μm) grit silicon carbide metallographic polish.

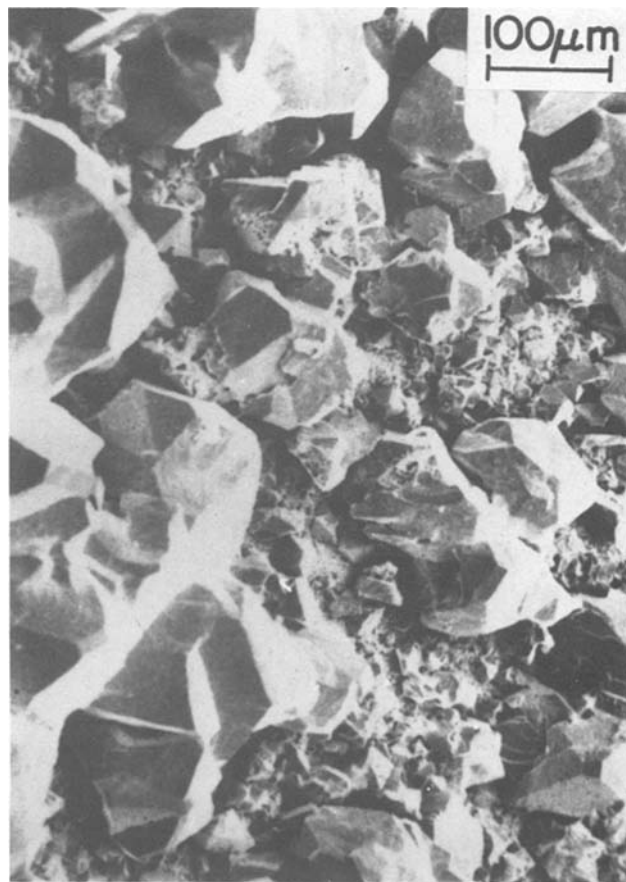


Fig. 6. Top view of a Ni-10 a/o Al specimen after sulfidation at $P_{S_2} = 10^{-7}$ atm for 30 min.

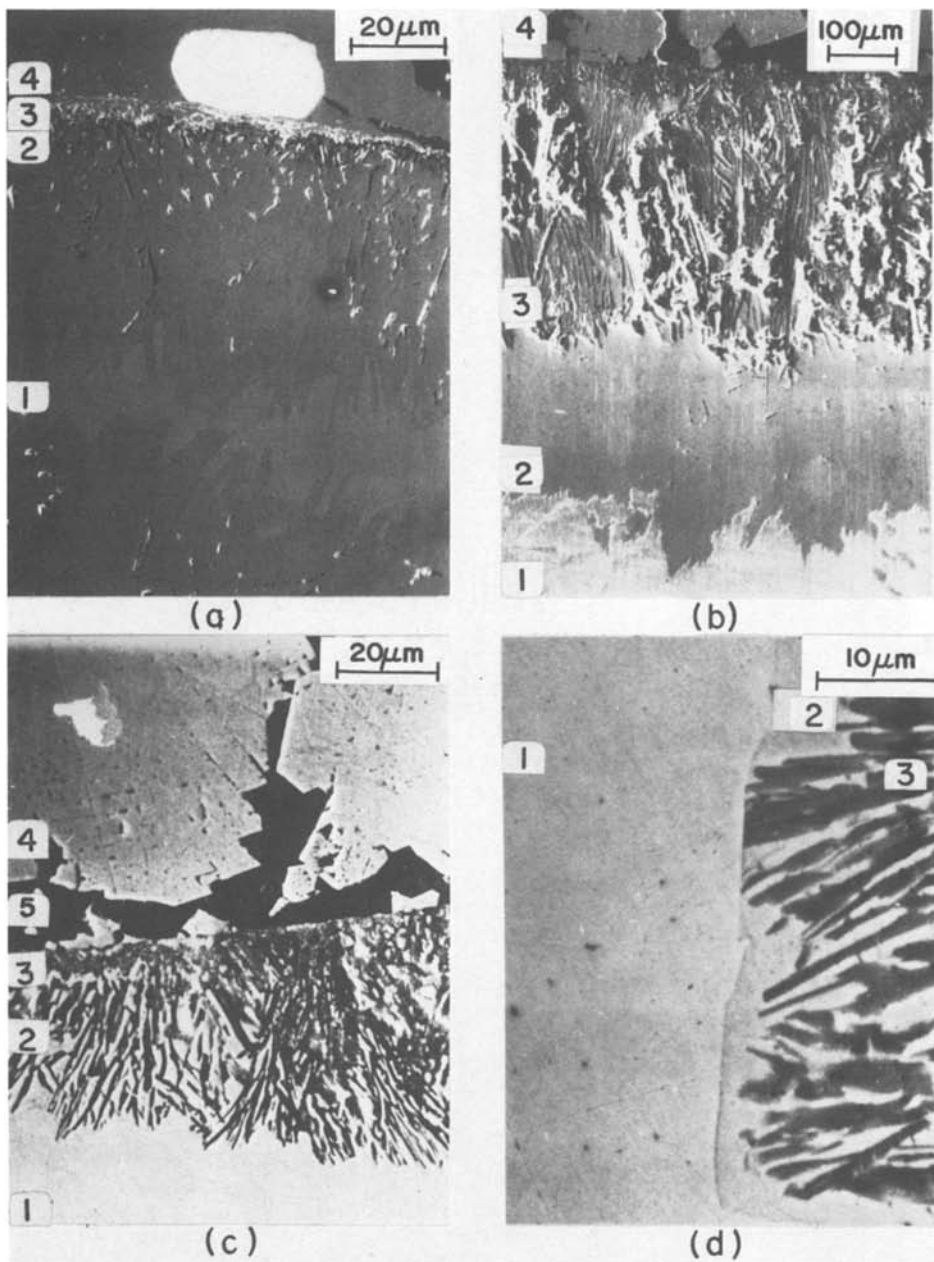


Fig. 7. Cross sections of the sulfide layers formed on the Ni-Al alloys upon sulfidation. Regions 1, 2, 3, 4, refer to bulk alloy, liquid Al-Ni-S layer, lamellar Al_2S_3 - Ni_3S_2 layer, Ni_3S_2 external scale, respectively, and the black areas 5 refer to penetrated plastic mounting material. (a) Ni-6 a/o Al specimen sulfidized at $P_{\text{S}_2} = 10^{-5}$ atm for 75 min illustrating Pt marker positioned between external scale and subscale. (b) Ni-10 a/o Al specimen sulfidized at $P_{\text{S}_2} = 10^{-7}$ atm for 49 hr. (c) Ni-13 a/o Al specimen sulfidized at $P_{\text{S}_2} = 10^{-18}$ atm for 34 hr. (d) Closeup of liquid/alloy interface in cross section (c).

Identification of phases.—It was necessary to obtain samples of the external scale and the two subscale layers. The scale was easily separated from the specimen by mechanical flaking. Samples of the lamellar layer were obtained by scraping a specimen denuded of the external layer and discarding the initial and final portions of the easily scrapable material. A sample of the solidified liquid layer was obtained by further filing of the specimen. In order to confirm that no underlying alloy was mixed with this sample, it was necessary to cold mount this stripped material and examine its cross section.

The x-ray diffraction patterns of the external scales completely indexed as NiS (millerite) when sulfidation was performed at $P_{\text{S}_2} > 10^{-4}$ atm and as β - Ni_3S_2 at lower pressures. The solidified liquid layer was identified as β - Ni_3S_2 . The diffraction pattern of the material from the two-phase lamellar layer could be resolved into that of β - Ni_3S_2 and an extraneous pattern. Although the line positions in this extraneous pattern matched that of the standard Al_2S_3 pattern (11), the line intensities did not match. Attempts to compare calculated and observed line intensities under the assumption of several rational fiber textures were also unsuccessful. Al_2S_3 readily undergoes hydrolysis,

but attempts to identify the extraneous pattern as hydrated alumina structures failed. Since the diffraction pattern of NiAl_2S_4 is not known, the extraneous pattern was compared to standard diffraction patterns of the double sulfides CrAl_2S_4 , ZnAl_2S_4 (cubic-spinel) and MnAl_2S_4 , FeAl_2S_4 , MgAl_2S_4 (rhombohedral), but without success. Accordingly, x-ray diffraction demonstrated that Ni_3S_2 existed in the lamellar layer, but it did not resolve a reasonable ambiguity whether the second phase was Al_2S_3 or NiAl_2S_4 .

Figure 8 represents the differential thermal analyses of the different sulfide layers carried out at a heating rate of $20^\circ\text{C}/\text{min}$. Trace 1 was taken from the solidified liquid layer; the peak at 535°C results from the B'-B transformation of Ni_3S_2 and the peak at 637°C corresponds to the melting point of the Ni_3S_2 -Ni eutectic. Thus the innermost sulfur containing layer adjacent to the alloy was liquid at the reaction temperature of 700°C . Trace 2 was obtained from a sample of the Ni_3S_2 external scale; peaks at 540° and 805°C correspond to β '- β and solid-liquid transformations, respectively (12, 13). In the preliminary analyses of the lamellar layer samples, it was only possible to obtain the above peaks for transformation and melting of Ni_3S_2 . It was therefore suspected that the aluminum-rich phase

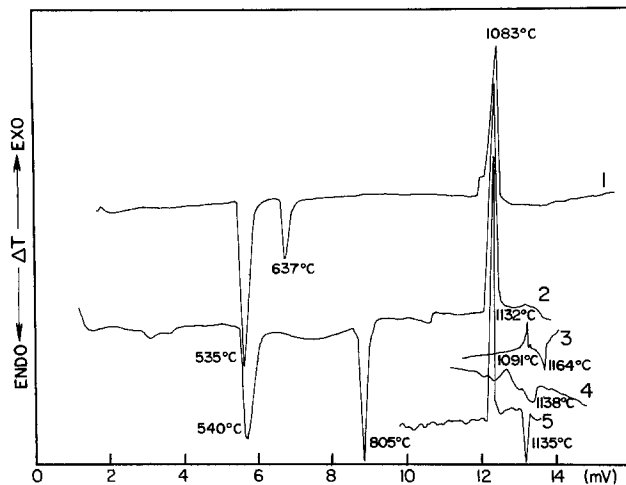


Fig. 8. Differential thermal analyses of the different sulfide layers with the abscissa mV scale corresponding to readings of the Pt-13% Rh thermocouple (the peaks at 1083°C correspond to the melting point of copper standard): curve 1, DTA trace of solidified liquid layer; curve 2, DTA trace of Ni_3S_2 external scale; curves 3, 4, 5, DTA traces of lamellar two-phase solid layer.

was decomposed by hydrolysis during handling of the material or during the course of the test. When freshly prepared samples were analyzed under ultrahigh purity argon, an additional peak at 1135°C was obtained as shown in trace 5. The liquidus temperature of Al_2S_3 varies from 1100° to 1200°C (10). It is reported that an α - γ polymorphic transformation in Al_2S_3 takes place at temperatures higher than 1100°C and that the γ -phase can be retained by fast cooling (11). Upon conducting the analysis using a tin rather than copper standard, the melting point of which interferes with the transformation peak, an exothermic peak was observed prior to the endothermic melting peak as shown in traces 3 and 4. The endothermic peak reappeared as an exothermic peak on cooling, but the exothermic peak did not reappear which can be explained by assuming that the cooling rates of 20°-50°C/min suppressed the above γ - α transformation. Any additional peak which could be attributed to the decomposition of a single phase into lamellar products was not observed below 700°C. Thus, these findings strongly indicate that the aluminum-rich phase is Al_2S_3 and that the two-phase lamellar solid layer was formed during the course of the reaction and not as a result of quenching.

A typical microprobe trace across a sulfidized specimen is shown in Fig. 9. The external scale composition corresponded to NiS at $P_{\text{S}_2} > 10^{-4}$ atm and Ni_3S_2 at the lower sulfur pressures investigated. Aluminum was not detected in these scales at the lower detection limit of 0.5 a/o. Close examination of the trace in the lamellar layer reveals that the increases in Al and S counts correspond to a decrease in the Ni counts, and vice versa. This is taken as substantiating evidence that the phases consist of Ni_3S_2 and Al_2S_3 . It can be further observed from the traces that the compositions change very sharply across interfaces with a large segregation of aluminum concentration in the lamellar layer. Although the average width of individual dark and bright lamellae was of the order 1-3 μm , a few lamellae were slightly larger than the 5 μm probe diameter. Spot probe analyses proved that the bright lamellae were composed of Ni_3S_2 whereas the dark lamellae contained < 1 a/o Ni. However, insufficiently intense S- $k\alpha$ radiation was obtained to establish that they consisted of Al_2S_3 . This latter observation is consistent with the conclusion that the material is hydrated alumina which resulted from hydrolysis of Al_2S_3 lamellae during specimen preparation and analysis. Systematic gradients in the average composition of the

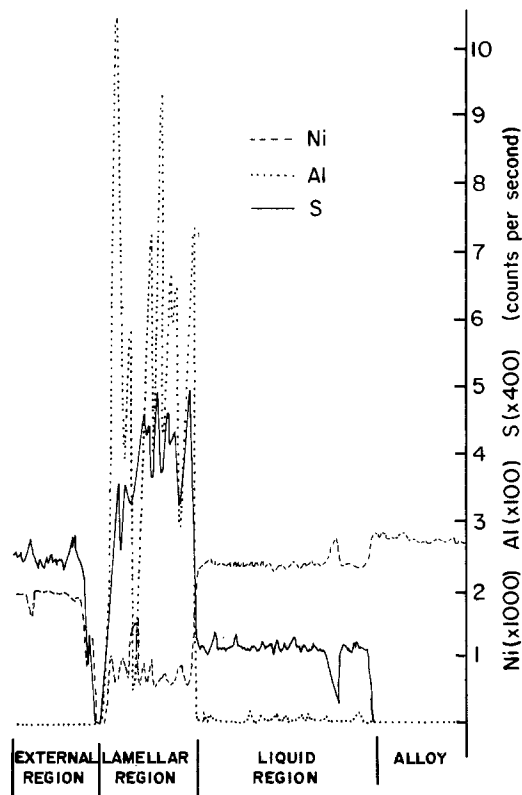


Fig. 9. Microprobe trace for Al, Ni, and S across a sulfidized Ni-6 a/o Al alloy specimen.

innermost solidified liquid layer were not observed but the composition varied to a certain extent from region to region and alloy to alloy. Several compositions are listed in Table II. The variation from an average composition over different analyzed areas on the same specimen arose from solidification of the liquid phase upon cooling into a three-phase structure containing Ni and Al_2S_3 as precipitates in a matrix of Ni_3S_2 .

Discussion and Conclusions

Sulfidation of the Ni-Al alloys led to development of NiS or Ni_3S_2 scales and subscales of Al_2S_3 - Ni_3S_2 lamellae and liquid Al-Ni-S layers. Scales grew by outward nickel diffusion while subscales penetrated into the alloys by sulfur diffusion. Sigmoidal-shaped reaction curves occurred in several instances as a result of nucleation of nickel sulfide which grew laterally and outward with concurrent growth of subscale from sites of imperfections distributed in the oxide films on the metallographically polished alloy surfaces. The sulfidation kinetics and morphological development of the sulfide scales and subscales can be shown to approximate most closely to a model for reaction control by interfacial processes.

Sigmoidal reaction curves upon sulfidizing the 6 and 13 a/o Al alloys subjected to fine metallographic pol-

Table II. Observed compositions in the liquid region

| Alloy | Ni | S | Al |
|--------|----|----|----|
| 10 a/o | 47 | 44 | 9 |
| | 67 | 27 | 6 |
| | 64 | 27 | 9 |
| | 47 | 39 | 14 |
| | 72 | 22 | 6 |
| | 60 | 28 | 12 |
| 3 a/o | 58 | 36 | 6 |
| | 66 | 24 | 10 |
| | 65 | 25 | 10 |
| | 65 | 27 | 8 |
| | 64 | 33 | 3 |
| | 63 | 24 | 13 |
| | 72 | 24 | 4 |
| | 72 | 23 | 5 |

ishing (Fig. 1 and 2) are analyzed by a rate equation in order to determine if the same rate constant governed growth of the isolated nickel sulfide nuclei and the fully developed scales and subscales. An equation of the form

$$\frac{\Delta w}{A} = [1 - \exp - (\beta t)^3] [k_i e^{t^{1/i}} + k_j t^{1/j}] \quad [1]$$

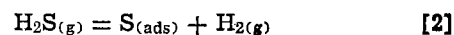
describes this sigmoidal characteristic if the nickel sulfide nuclei are assumed to appear sporadically and the external and internal sulfides grow at linear or parabolic rates. The leading term in Eq. [1], which describes the fractional surface coverage of nickel sulfide, is based upon the derivation given by Evans (14) for nucleation of a phase taking place sporadically in time and position on a substrate and the nuclei subsequently spreading on the surface as expanding circles. Here, $\Delta w/A$, is the weight change per unit area of the reacting specimen, t is the time, β is a parameter having dimension t^{-3} and characteristic of the initial oxide film, and k^e , k^s are the rate constants assigned to vertical growth of the scale and subscale, respectively, where the symbols $i = 1, 2, j = 1, 2$ refer to conditions of linear and parabolic sulfidation, respectively.

It can be concluded that growth of the reaction products proceeded linearly since comparison of the variances of the four possible fits of Eq. [1] to results in Fig. 1 and 2 using the χ^2 test proved that the variance was least at the 95% confidence level for $i = j = 1$. The overall linear sulfidation rate constant is therefore defined as $k_1 = k^e + k^s$. The calculated curves in Fig. 1 and 2 and the kinetic parameters recorded in Table III summarize results of this regression analysis. Note that the irreproducibility of the sulfidation kinetics, which is best evident for two Ni-6 a/o Al specimens sulfidized at $P_{S_2} = 3.5 \times 10^{-7}$ atm, is reflected in the differences for the magnitudes of β whereas the same linear rate constant describes the kinetics. Also the presence of a thicker preformed oxide film, which retarded sulfidation significantly (Fig. 2), did so by affecting β and not by affecting the linear rate constant (Table III).

Occurrence of linear sulfidation kinetics has demonstrated that the sulfide layers were not sufficiently thick to act as rate-controlling diffusion barriers to the reacting species. The reaction rates showed a strong dependence on sulfur pressure but stagnant gas films did not act as effective diffusion barriers since the highest observed reaction rate was lower by an order of magnitude than expected by such calculations (15). Consequently, an attempt was made to determine if a surface reaction involving H_2S dissociative adsorption and sulfur incorporation into nickel sulfide would account for the effect of sulfur pressure on the reaction kinetics. This could be examined because several reaction curves exhibiting linear kinetics were carried out under conditions for growth of Ni_3S_2 scales at $P_{S_2} < 10^{-4}$ atm. Reactant diffusion in the sulfide layers, nevertheless, plays a role in view of the nickel and sulfur activity gradients which exist across the scales. According to the binary equilibrium diagram (12), Ni_3S_2 -NiS and liquid sulfide-Ni exist at P_{H_2S}/P_{H_2}

ratios of 0.9 and 5×10^{-3} , respectively, at 700°C. It was observed that scales consisted of Ni_3S_2 when the alloys were sulfidized in atmospheres up to ratios $P_{H_2S}/P_{H_2} = 1.5$. Thus, at best, 40% of the total sulfur activity drop across a reaction path occurs at the gas/scale interface.

Detailed balancing of two surface reactions is made to obtain the functional dependence of the linear sulfidation rate constant on gas composition



where $S_{(ads)}$ and $S_{(inc)}$ represent sulfur adsorbed and sulfur incorporated into Ni_3S_2 by nickel outward migration. Forward and backward rate constants in this reaction scheme are represented by k and k' . Accordingly, the linear reaction rate constant is

$$k_1 = k_3 \theta_s - k_3' \theta_v a_s = k_3 \theta_v \left[\frac{\theta_s}{\theta_v} - \frac{k_3'}{k_3} a_s \right] \quad [4]$$

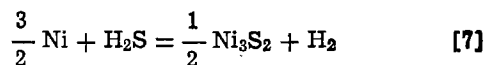
where θ_s and θ_v are the fraction of surface sites covered with sulfur and free of adsorbed species, respectively, and a_s is the sulfur activity in the Ni_3S_2 surface. Under steady-state sulfidation, $d\theta_s/dt = 0$, and

$$\frac{\theta_s}{\theta_v} = \frac{k_2 P_{H_2S} + k_3' a_s}{k_2' P_{H_2} + k_3} \quad [5]$$

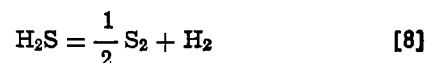
At zero rates of reactions [2] and [3] for equilibrium

$$\frac{\theta_s^*}{\theta_v^*} = \frac{k_2 P_{H_2S}^*}{k_2' P_{H_2}^*} = \frac{k_3' a_s}{k_3} \quad [6]$$

where asterisks assigned to parameters of the adsorbed state and gas refer to equilibrium values. The equilibrium gas ratio is defined by



and its equilibrium constant $K_7 = P_{H_2}^* (a_{Ni_3S_2})^{1/2} / P_{H_2S}^* (a_{Ni})^{3/2}$ where a is an activity. The sulfur activity in the Ni_3S_2 surface can be defined in terms of this equilibrium gas ratio by the reaction



from which $a_s = K_8 P_{H_2S}^* / P_{H_2}^*$ where K_8 is the equilibrium constant. Substitution of [5] and [6] into [4] using relations from [7] and [8] leads to

$$k_1 = \frac{k_2 k_3 \theta_v}{k_2' P_{H_2} + k_3} \left[1 - \frac{a_s}{a_s^{(e)}} \right] P_{H_2S} \quad [9]$$

where a_s has been defined above and $a_s^{(e)}$ is the sulfur activity in the H_2S - H_2 atmosphere during reaction. If $k_3 \gg k_2' P_{H_2}$, Eq. [9] can be placed in the following form for analysis of the reaction kinetics

$$\frac{k_1}{P_{H_2}} = k_2 \theta_v \left[\frac{P_{H_2S}}{P_{H_2}} - \frac{P_{H_2S}^*}{P_{H_2}^*} \right] = A \frac{P_{H_2S}}{P_{H_2}} - A'; \quad \frac{A'}{A} = \frac{P_{H_2S}^*}{P_{H_2}^*} \quad [10]$$

Equation [10] describes the sulfur pressure dependence of the linear sulfidation kinetics for the alloys containing 3, 10, and 13 a/o Al as illustrated by the plots in Fig. 10. The intercepts on the abscissa are small and do not differ from zero at the 95% significance level in agreement with the extremely low value for the dissociation pressure of Ni_3S_2 . This functional dependence has arisen because dissociative adsorption of hydrogen sulfide partially determined the reaction rate.

Table III. Parameters of sigmoidal sulfidation equation (Eq. [1])

| Alloy | P_{S_2} (atm) | β (min ⁻³) | k_1 (mg cm ⁻² min ⁻¹) |
|--------------|----------------------|------------------------------|--|
| Ni-6 a/o Al | 2.8×10^{-5} | $> 1.02 \times 10^3$ | 2.07 |
| | 3.5×10^{-7} | 1.55×10^{-7} | 0.89 |
| | 3.5×10^{-7} | 4.90×10^{-6} | 0.89 |
| Ni-13 a/o Al | 1.9×10^{-2} | $> 1.02 \times 10^3$ | 0.45 |
| | 1.9×10^{-2} | 1.10×10^{-7} | 0.45* |
| | 2.8×10^{-5} | $> 1.02 \times 10^3$ | 0.13 |
| | 3.4×10^{-5} | 4.79×10^{-2} | 0.09 |
| | 7.8×10^{-5} | $> 1.02 \times 10^3$ | 0.03 |

* Specimen with preformed film (Fig. 2).

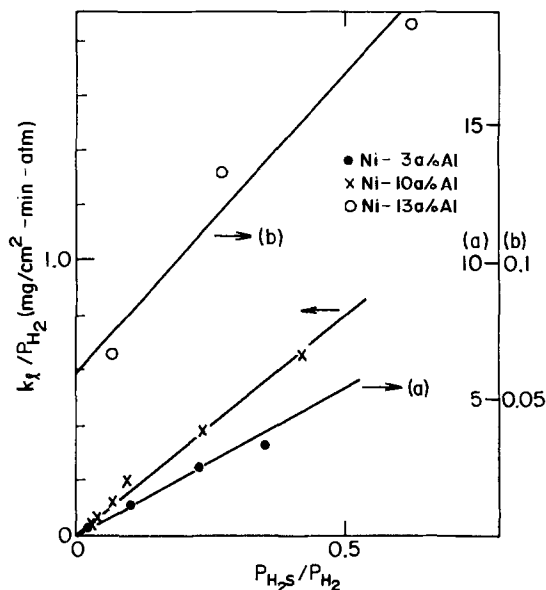


Fig. 10. Graphical representation of the linear sulfidation kinetics of the Ni-Al alloys at 700°C according to Eq. [8].

Equation [1] describing the sigmoidal shape of the reaction curves and Eq. [10] describing the sulfur pressure dependence of the linear reaction rate constant have led only to a cursory description of the sulfidation kinetics. The same linear rate constant did define the growth kinetics of the reaction products as isolated growths or as uniform scales. However, the parameter β in Eq. [1], which determined the nickel sulfide fractional surface coverage exhibited a very large variation of $\sim 10^{10}$ without any correlation to the aluminum alloy contents or to the atmospheric sulfur compositions (Table III). This large variation of β led either to long irreproducible sigmoidal overtones in the reaction curves or to practically immediate onset of linear sulfidation kinetics (Fig. 1 and 2). The model for growth of the sulfide nuclei as expanding circles is only a simple approximation (Fig. 5 and 6). The parameter β , notwithstanding, does qualitatively describe the surface coverage of the alloy by nickel sulfide up to very large sulfur uptakes as illustrated by the reaction curve for the 6 a/o Al alloy at $P_{S_2} = 3.5 \times 10^{-7}$ atm (Fig. 1) where the observed and calculated surface coverage was ~ 0.5 after 50 min exposure. An attempt could not be made to correlate the magnitudes of the linear rate constants to the aluminum contents of the alloys using Eq. [10] because of the irreproducible influence of the initial oxide films on subsequent sulfidation behavior. For example, the reaction curves (Fig. 1 and 3) demonstrate that the Ni-6 a/o Al alloy (1 μ m diamond polish) reacted by linear kinetics at $P_{S_2} = 10^{-5}$ atm five times more rapidly than the Ni-3 a/o Al alloy (15 μ m silicon carbide polish). On the other hand, the alloys containing 3, 10, and 13 a/o Al, which were subjected to different metallographic polishes, sulfidized at rates decreasing with increasing alloy aluminum contents. Irreproducible properties of the initial oxide films on the alloy surfaces, accordingly, influenced all stages of the sulfidation kinetics.

The present findings and analysis indicate that reaction control is largely established by transfer of reactants across at least two interfaces, the gas/scale and scale/subscale interfaces. The same linear rate constant defined development of the corrosion products as isolated growths or complete scales, and the sulfur pressure dependence of the linear reaction kinetics was caused by an interfacial gas/scale reaction. The inert metal marker measurements also demonstrated that outward nickel and inward sulfur migration accounted for scale and subscale growth, respectively. An undefined fraction of the scale/subscale interface, nevertheless, remained partially dormant for transfer of reactants. Although nickel sulfide nuclei spread and grew from imperfections in the initial oxide films on the alloys, oxide film remnants due to incomplete dissolution of oxide into the sulfides or alloy acted as partial diffusion barriers to reactant transfer across the scale/subscale interface. This behavior cannot be quantified since the sigmoidal overtones of the reaction curves were irreproducible and the magnitudes of the linear rate constants did not exhibit a consistent dependence on alloy composition.

Acknowledgments

This research was carried out under the auspices of the National Research Council of Canada. V. S. Bhide wishes to express his appreciation for awards of Noranda and Stelco Research Fellowships to carry out this research as part of his Ph.D. studies program at McMaster University.

Manuscript submitted July 11, 1979; revised manuscript received Oct. 30, 1980.

Any discussion of this paper will appear in a Discussion Section to be published in the December 1981 JOURNAL. All discussions for the December 1981 Discussion Section should be submitted by Aug. 1, 1981.

Publication costs of this article were assisted by McMaster University.

REFERENCES

1. K. Hauffe and A. Rahmel, *Z. Phys. Chem.*, **199**, 152 (1952).
2. I. Pfeiffer, *Z. Metallkd.*, **49**, 267 (1958).
3. J. E. Dutrizac and T. R. Ingraham, *Can. Met. Quart.*, **8**, 119 (1969).
4. L. Czerski, S. Mrowec, and T. Werber, *This Journal*, **109**, 273 (1962).
5. P. Hancock, in Proceedings I, International Conference on Metallic Corrosion, London (1961).
6. A. Bruckman, S. Mrowec, and T. Werber, *Fiz. Metal. Metalloved.*, **20**, 702 (1965).
7. G. Romeo, W. W. Smeltzer, and J. S. Kirkaldy, *This Journal*, **118**, 740 (1971).
8. D. Yuan and F. A. Kroger, *ibid.*, **118**, 841 (1971).
9. J. D. Hager, Ph.D. Thesis, M.I.T., Cambridge, MA (1966).
10. JANAF Thermochemical Tables, U.S. Dept. Commerce, NBS (1964).
11. J. Flahaut, *Ann. Chim. Paris*, **7**, 632 (1952).
12. T. Rosenqvist, *J.I.S.I.*, **37**, 176 (1954).
13. M. Hansen, "Constitution of Binary Alloys," McGraw-Hill, New York (1958).
14. U. R. Evans, *Trans. Faraday Soc.*, **41**, 365 (1945).
15. C. O. Bennet and J. E. Myers, "Momentum, Heat and Mass Transfer," McGraw-Hill, New York (1974).

Computer Simulation in Silicon Epitaxy

R. Reif*

*Department of Electrical Engineering and Computer Science,
Massachusetts Institute of Technology, Cambridge, Massachusetts 02139*

and R. W. Dutton

Integrated Circuits Laboratory, Stanford University, Stanford, California 94305

ABSTRACT

A computer model capable of simulating epitaxial doping profiles resulting from a variety of deposition conditions, including time-varying dopant gas flows during growth, is described. The model takes into account gas-phase dynamics, physicochemical processes at the growing epitaxial surface, and thermal redistribution of impurities during epitaxial growth. The techniques employed to obtain experimentally the values of the parameters in the computer model are described. The numerical implementation of the model in the process simulation program SUPREM is also described. Finally, numerical simulations using the model are compared to epitaxial doping profiles obtained experimentally.

The operation of semiconductor devices is dictated, primarily, by the distribution of impurities in the semiconductor. Therefore, computer programs that simulate the distribution of impurities after a complete integrated circuit fabrication sequence are a necessity. These programs can be used to optimize an IC fabrication sequence by studying the effect of process variations on the final impurity profile.

One such computer program is SUPREM (1). The Stanford University Process Engineering Models program is a computer simulator capable of simulating most typical IC fabrication steps. The input to the program is a set of process specifications for each fabrication step, and the output is a one-dimensional profile of all dopants present in the silicon and silicon dioxide.

SUPREM's capabilities of simulating IC fabrication steps rely on the physical process models that are numerically implemented. As of now, physical models for ion implantation, chemical predeposition, oxidation/drive-in, epitaxy, etching, and oxide deposition have been implemented. Recently, a new model describing the dopant incorporation process in silicon epitaxy has been reported (2, 3). This model considers gas-phase dynamics and the physicochemical processes occurring in the gas phase and at the growing epitaxial surface. By using this model it is possible to calculate the depth-variation of the epitaxial layer dopant concentration that results from any given time-variation of the gas-phase dopant partial pressure during growth (3, 4).

This paper deals primarily with this new epitaxial doping model, and its numerical implementation in the computer program SUPREM. With this new addition, SUPREM's simulation capabilities in the area of silicon epitaxy are considerably enhanced, and epitaxial impurity distributions resulting from either a time-independent or time-varying gas-phase dopant partial pressure can be readily simulated.

It is important to emphasize the relevance of a computer program capable of predicting epitaxial-layer doping profiles. Epitaxial films with uniform impurity distribution are often required in IC fabrication. However, the distribution of impurities near the film-substrate interface is, in general, nonuniform. During the initial stages of growth the dopant incorporation process goes through a transient period, and 2-3 min are required (4) before the steady-state epitaxial doping level is established. As a result, a transition layer cor-

responding to this initial transient develops, and the epitaxial dopant concentration within this layer is either higher or lower than expected, depending on the initial conditions prior to the deposition cycle (e.g., substrate surface concentration, prebake time, prebake temperature, etc.). A special case of this initial transient problem is the commonly known "autodoping" phenomena, which occurs when lightly doped films are deposited on heavily doped buried-layers/substrates. The extent of this transition layer imposes severe limitations on the fabrication of submicron epitaxial films, which will be required with the development of VLSI technology.

Epitaxial films with intentional, nonuniform, impurity distributions are sometimes also required. These can be used to fabricate specialized devices or to optimize device characteristics. Examples of these are the hyperabrupt epitaxial tuning diodes (5), in which precisely controlled impurity distributions are needed in order to obtain the specific C-V characteristics. Nonuniform doping profiles can be fabricated by varying with time the dopant gas flow entering the epitaxial reactor during deposition.

In short, nonuniform epitaxial doping profiles may occur intentionally (e.g., parametric diodes) or unintentionally (e.g., autodoping). The availability of a simulator capable of predicting these nonuniform profiles will allow the integrated-circuit process engineer to assess the importance of any undesired transient phenomena, to optimize the device fabrication sequence, and potentially to open up vistas in the design and fabrication of integrated circuits. Langer and Goldstein (6) have already reported a numerical solution for both front and back autodoping effects as well as for impurity redistribution during epitaxial growth. As mentioned earlier, the autodoping problem is treated in this work as a special case of a more general "initial transient" problem. This approach has the advantage that the same epitaxial doping model is used to describe all transient phenomena occurring during epitaxial deposition, including autodoping.

In this paper, the epitaxial doping model implemented in SUPREM is described in detail. It is based on the model reported earlier (2) with proper modifications to make it suitable for computer implementation and to account for thermal redistribution during epitaxial growth. Following this, the techniques employed to determine experimentally the values of the parameters in the epitaxial doping model are discussed. The numerical implementation of the model in SUPREM is also briefly described. Finally, several

* Electrochemical Society Active Member.

Key words: CVD, doping, integrated circuits, semiconductor.

comparisons between SUPREM simulations and experiments are presented.

Equipment

Unless otherwise stated, the epitaxial reactor used in this work was a horizontal, rf-heated Unipak VI (Sola Basic-Tempres) that operates at atmospheric pressure. The quartz reactor tube has an effective cross section of 26 cm² above the susceptor. The silicon carbide-coated graphite susceptor has the dimensions 56 cm (length) × 11.4 cm (width) and is tilted at an angle of 1.5°. Hydrogen was used as the carrier gas at a velocity of 67 cm/sec above the susceptor (at room temperature). Silane was used as the source of silicon and arsine diluted in hydrogen was used as the dopant source. The corrected deposition temperature at the wafer surface was approximately 1050°C. The experiments shown in Fig. 7 were carried out in a commercially purchased horizontal reactor (Hugle Model HIER II) described elsewhere (4).

General Statement of the Problem

The problem being addressed in this work is that of determining a computer model capable of simulating the epitaxial doping profile resulting from any given time-varying, gas-phase composition during growth. The model must also account for thermal redistribution of dopant atoms in silicon during epitaxial deposition. Because the redistribution of impurities within the solid is controlled by diffusion, the starting mathematical framework is to solve Fick's Second Law throughout the solid silicon, from a plane very deep inside the substrate up to the silicon surface. That is (see Fig. 1)

$$\frac{\delta N(z,t)}{\delta t} = D \frac{\delta^2 N(z,t)}{\delta z^2} \quad \infty > z > z_f \quad [1]$$

where N is the dopant concentration in the solid, D is the diffusion coefficient of the impurity in solid silicon, and z and t are the spatial and time variables, respectively. As shown in Fig. 1, the z -direction goes perpendicular to the silicon surface, and z_f is defined as the location of the moving gas-solid interface.

The solution to the diffusion equation during epitaxial growth must satisfy the following initial and boundary conditions. The initial condition is given by

$$N(z, 0) = f_1(z) \quad [2]$$

where $f_1(z)$ represents the distribution of impurities in the substrate just before epitaxial deposition.

The boundary conditions are

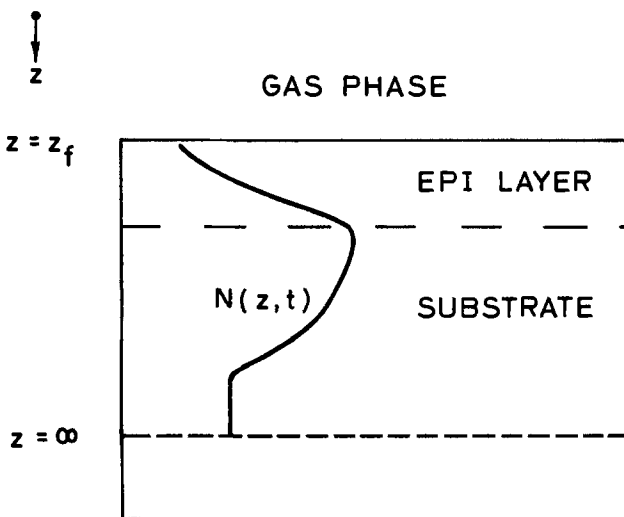


Fig. 1. Schematic cross section of a silicon wafer for the purpose of solving Fick's Second Law.

$$D \frac{\delta N}{\delta z} \Big|_{z \rightarrow \infty} = 0 \quad [3]$$

$$D \frac{\delta N}{\delta z} \Big|_{z=z_f} = f_2(t) \quad [4]$$

Equation [3] indicates that the impurity diffusive flux at a plane very deep in the silicon substrate is zero. This is a reasonable boundary condition because silicon wafer thicknesses are much larger than diffusion lengths in bulk silicon.

Equation [4] indicates that the impurity diffusive flux in the solid at the gas-solid interface is, during epitaxial growth, a function of time. As will be shown later, an expression for $f_2(t)$ can be derived from a basic understanding of the mechanisms controlling the incorporation of impurities in the epitaxial silicon during growth. The time-dependence of Eq. [4] is related to (i) the transients associated with the establishment of a steady-state deposition process, and (ii) the time-variation (if any) of the gas-phase composition in the reactor. Notice that the autodoping problem falls in the first category. The right-hand side of Eq. [4] is a function of dopant partial pressure, epitaxial growth rate, deposition temperature, and to a lesser degree: reactor geometry, hydrogen velocity, etc.

In order to solve Fick's Second Law during epitaxial growth an expression for $f_2(t)$ in Eq. [4] must be obtained. This is accomplished by using the epitaxial doping model described in the next section.

Epitaxial Doping Model

In this section, the behavior of dopant species in each important region of an epitaxial reactor is studied in detail, both in terms of gas-flow dynamics and chemical kinetics. Figure 2 shows schematically a section of the horizontal reactor tube along the length of the susceptor. Three main regions are indicated in Fig. 2: 1) main gas stream, 2) boundary layer, and 3) adsorbed layer. The main gas stream consists of hydrogen mixed with silane and arsine flowing by forced convection. The boundary layer is a thin layer, about 5 mm thick, through which reactants diffuse to the silicon surface. The adsorbed layer consists of a population of hydrogen, silicon-, and dopant-containing species that occupy adsorption sites and are capable of moving on the solid surface. The behavior of dopant species in each of these three regions is now discussed, and equations describing this behavior will be derived. These equations will then be used to obtain an expression for $f_2(t)$ in Eq. [4].

Main gas stream.—In most epitaxial reactors, gas-phase depletion of dopant species in the main gas stream is almost negligible. Therefore, the partial pressure of dopant species in the main gas stream can be assumed to be independent of position, and nearly equal to the partial pressure of dopant species at the reactor input. Moreover, the time constant associated with the transport of dopant species

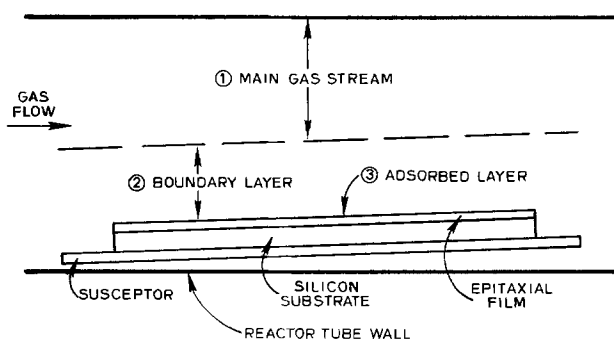


Fig. 2. Schematic section of the horizontal reactor tube along the length of the susceptor.

in the main gas stream by forced convection is of the order of 1 sec (3), while the time constant of the overall doping process in a horizontal reactor is of the order of 40 sec (4). Therefore, it can be assumed that any time-variation of the dopant partial pressure at the reactor input is transmitted "instantaneously" throughout the main gas stream. Consequently, the following expression can be used to describe the behavior of dopant species in the main gas stream region

$$P_D(t) \simeq P_D^\circ(t) \quad [5]$$

in which P_D is the partial pressure of dopant species in the main gas stream region, and P_D° is the input dopant partial pressure. A more detailed discussion of the derivation of Eq. [5] is given in Appendix A.

Boundary layer.—The time constant associated with the transport of dopant species through the boundary layer by diffusion is of the order of 0.1 sec (4), which is much shorter than that of the overall doping process. Therefore, it is reasonable to assume that the flux of dopant species leaving the boundary layer by adsorbing on the silicon surface (F_s) follows closely any time-variation of the dopant flux entering the boundary layer from the main gas stream [$F_z(\bar{z})$, see Fig. 12], i.e.

$$F_s(t) \simeq F_z(\bar{z}, t) \quad [6]$$

A more detailed discussion of the derivation of Eq. [6] is presented in Appendix B.

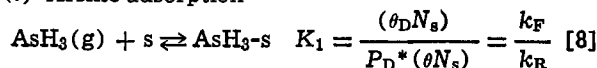
The two fluxes in Eq. [6] can be expressed in terms of deposition parameters. The flux of dopant species leaving the main gas stream toward the wafer surface [$F_z(\bar{z})$] can be approximated by (2)

$$F_z(\bar{z}) = k_m[P_D^\circ - P_D^*] \quad [7]$$

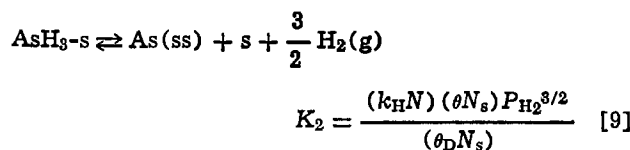
in which k_m is the boundary layer mass transport coefficient of dopant species in hydrogen, and P_D^* is the dopant partial pressure just above the gas-solid interface. k_m is a function of reactor geometry, hydrogen velocity, gas-phase temperature, etc. An expression for $F_s(t)$ is obtained in the next section.

Adsorbed layer.—In order to determine F_s , the sequence of steps taking part in the doping process and occurring at the silicon surface must be considered in detail. These steps are shown in Fig. 3 (2). When an arsine molecule in the gas phase is close to the silicon surface it undergoes a process of adsorption [step (1)]. The arsine molecule, once adsorbed, decomposes chemically yielding elemental arsenic [step (2)] which then diffuses on the surface until it finds an incorporation site and attaches to it [step (3)]. The arsenic atom, now incorporated in the silicon lattice, is quickly covered by subsequently arriving silicon atoms [step (4)], and diffuses into (or out of) the bulk silicon. For the treatment presented here, it is sufficient to select one of the above steps as the rate-limiting step, leaving all other steps in the sequence near thermodynamic equilibrium (2). If step (1) above is assumed to be the slowest in the sequence, the surface steps can be summarized in the following two reactions

(i) Arsine adsorption



(ii) Chemical decomposition, site incorporation, and covering of arsenic by silicon



where s represents a vacant adsorption site on the surface, $\text{AsH}_3\text{-s}$ represents an arsine molecule occupy-

ing an adsorption site, K_1 and K_2 are equilibrium constants, θ_D is the fraction of adsorption sites occupied by arsine, N_s is the surface density of adsorption sites per unit area, k_F and k_R are the forward and reverse reaction rate constants for arsine adsorption, θ is the fraction of adsorption sites which are vacant, k_H is Henry's law constant, and P_{H_2} is the hydrogen pressure (~ 1 atm). An expression for F_s can now be obtained by using Eq. [8] and [9] (see Appendix C)

$$F_s = k_f[P_D^* - N/K_F] \quad [10]$$

where $k_f \equiv k_F(\theta N_s)$ is a kinetic constant associated with arsine adsorption, and $K_F \equiv K_1 K_2 / k_H$ is a thermodynamic constant relating dopant species in the gas phase and the solid silicon. Equations [7] and [10] can now be used to obtain the following expression relating F_s and the input dopant partial pressure P_D°

$$F_s = k_{mf}[P_D^\circ - N/K_F] \quad [11]$$

in which $k_{mf} \equiv [1/k_m + 1/k_f]^{-1}$.

As discussed earlier, the times associated with gas-phase mass transport of dopant species are negligible as compared to the time constants measured for the overall doping process. Therefore, the only mechanisms that could be responsible for these long time constants ought to be associated with the adsorbed layer. This point will become evident in the following discussion of an expression describing the behavior of dopant species in the adsorbed layer.

By considering mass balance of dopant species in the adsorbed layer the following equation is obtained

$$F_s - gN(z_f) + D \left. \frac{\delta N}{\delta z} \right|_{z=z_f} = \frac{d(\theta_D N_s)}{dt} \quad [12]$$

where g is the epitaxial growth rate. In Eq. [12], F_s represents the rate at which the adsorbed layer increases its population of dopant species. The second term in Eq. [12] represents the rate at which the adsorbed layer decreases its population of dopant species due to the silicon covering step (see Fig. 3), and the third term represents diffusive exchanges between dopant atoms in the adsorbed layer and the bulk silicon. The right-hand side of Eq. [12] represents the rate of change of the density of dopant species per unit area in the adsorbed layer, and becomes zero when the overall doping process reaches steady state. By substituting Eq. [11] into Eq. [12], the following expression is obtained

$$k_{mf}[P_D^\circ - N(z_f)/K_F] - gN(z_f) + D \left. \frac{\delta N}{\delta z} \right|_{z=z_f} = K_A \frac{dN(z_f)}{dt} \quad [13]$$

in which Eq. [9] was used with $K_A \equiv k_H(\theta N_s)P_{\text{H}_2}^{3/2}/K_2$. Equation [13] relates the epitaxial dopant concentra-

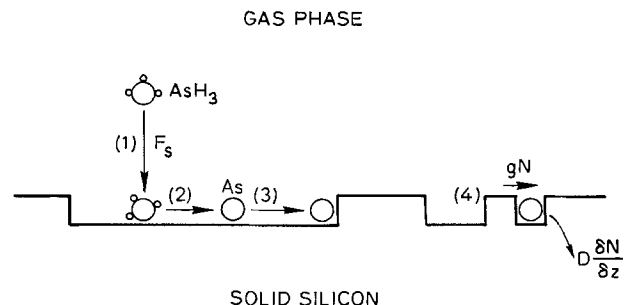


Fig. 3. Steps taking part in the doping process, and occurring at the silicon surface: (1) arsine adsorption, (2) arsine chemical decomposition, (3) arsenic surface diffusion and site incorporation, and (4) covering of incorporated arsenic by subsequently arriving silicon atoms.

tion at the silicon surface $N(z_f)$ and the input dopant partial pressure P_D° . It is clear from Eq. [12] and [13] that any abrupt variation of P_D° with time during epitaxial growth is not transmitted "instantaneously" to $N(z_f)$ because some time is required before the population of dopant species in the adsorbed layer $\theta_D N_s$ accommodates to the new steady-state condition. This storage-like behavior of the adsorbed layer is responsible for the relatively long time constants measured experimentally for the overall doping process. Equation [13] can be rearranged to give the boundary condition $f_2(t)$ needed in Eq. [4], i.e.

$$D \frac{\delta N}{\delta z} \Big|_{z=z_f} = f_2(t) = -k_{mf}[P_D^\circ - N(z_f)/K_P] + gN(z_f) + K_A \frac{dN(z_f)}{dt} \quad [14]$$

Fick's Second Law (Eq. [1]) can now be solved subjected to the initial and boundary conditions given by Eq. [2], and [3] and [14], respectively. This will be carried out numerically in a manner analogous to that described by Langer and Goldstein (6). Before this numerical technique is described, however, values for the parameters in the doping model (i.e., k_{mf} , K_P , K_A) need to be determined. In the next section the technique used to determine the values of k_{mf} and K_P is discussed.

Parameter Determination: k_{mf} and K_P

Numerical values for k_{mf} , K_P , and K_A were determined experimentally. In this section, the technique employed to obtain values of k_{mf} and K_P is described. It consists of comparing the predictions of the epitaxial doping model described in the previous section to experimental results. The values of k_{mf} and K_P are extracted by properly fitting theory to experiments.

The epitaxial doping model is contained mathematically in Eq. [13], which relates $N(z_f)$ to $P_D^\circ(t)$. This equation can be simplified, however, when only "steady-state" deposition conditions are considered. The term steady state is used here to describe deposition conditions for which the gas-phase composition in the reactor has remained unchanged for a time longer than several time constants of the epitaxial system. Under these conditions, the epitaxial dopant concentration is uniform and Eq. [13] can be simplified to

$$0 = k_{mf}[P_D^\circ - N/K_P] - gN \quad [15]$$

in which N is the uniform epitaxial doping level, and P_D° and g are time-independent. Equation [15] can be used to determine the uniform epitaxial dopant concentration that results from deposition conditions in which the total deposition time is much longer than the time constant of the system, and the gas flows entering the reactor are kept constant throughout the whole deposition cycle. Equation [15] can be rearranged as

$$P_D^\circ/N = 1/K_P + g/k_{mf} \quad [16]$$

which indicates that a plot of P_D°/N vs. g generated experimentally under steady-state deposition conditions should yield a straight line from which values of k_{mf} and K_P can be extracted.

Figure 4 shows a plot of P_D°/N vs. g with the circles showing experimental results carried out under steady-state conditions. In these experiments the hydrogen, silane, and arsine flows were unchanged throughout the deposition cycle. The thicknesses of the epitaxial layers were between 7 and 9 μm so as to neglect the influence of the initial transient period. The arsine partial pressure was varied to produce epitaxial doping levels in the 10^{15} - 10^{17} cm^{-3} range, and the silane partial pressure was varied to produce growth rates between 0.07 and 0.42 $\mu\text{m}/\text{min}$. Higher growth rates were accompanied by a loss of growth rate and doping

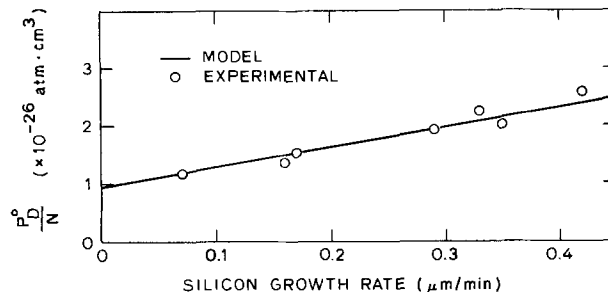


Fig. 4. Plot of P_D°/N vs. silicon growth rate used to determine k_{mf} and K_P .

level uniformity along the length of the susceptor, with downstream wafers having lower growth rates and higher resistivities than upstream wafers. These non-uniformities were apparently caused by a parasitic homogeneous decomposition of silane in the gas phase. The substrates were (100)-oriented silicon wafers, boron-doped, with resistivities ranging from 1 to 4 $\Omega\text{-cm}$. The epitaxial layer thicknesses were measured by a groove and stain technique, and the resistivity of the layers were determined by the four point probe technique. By fitting Eq. [16] to the experimental data in Fig. 4 the following values were obtained: $K_P = 1.05 \times 10^{26}/\text{cm}^3$ atm and $k_{mf} = 4.85 \times 10^{19}/\text{cm}^2$ sec atm, for the experimental conditions described above.

In this section, the technique used to obtain k_{mf} and K_P for a given set of deposition conditions was described. In order to determine the value of K_A a different technique is required. In this case, Fick's Second Law (Eq. [1]) is solved to determine the epitaxial doping profile that results when $P_D^\circ(t)$ is varied with time during epitaxial growth. At this point, the profile depends on the value of K_A (see Eq. [13]), and a family of profiles can be obtained by varying K_A . Next, the deposition conditions simulated above are carried out experimentally, and the resulting epitaxial doping profile is measured. The value of K_A is now determined by selecting, from the family of calculated profiles, that which gives the best match to the measured profile.

Before this exercise can be carried out, however, it is important to describe the numerical method used to solve Fick's Second Law with the initial and boundary conditions given by Eq. [2], [3], and [14]. This is done in the next section.

Numerical Implementation

The built-in capabilities of the computer program SUPREM were employed in the implementation of the numerical technique used to solve Fick's Second Law with the boundary conditions dictated by the epitaxial deposition process. Because SUPREM is a program essentially capable of solving Fick's Second Law with the initial and boundary condition given by Eq. [2] and [3], respectively, the only remaining problem is to couple the surface boundary condition, i.e., Eq. [14], to the main body of SUPREM. This coupling is described in this section. Figure 5 shows the discretization of the simulation space as implemented in SUPREM (1). In Fig. 5a the solid line separates the gas phase and the solid phase. P_D is the dopant partial pressure in the gas phase which, according to Eq. [5], can be approximated by P_D° . The solid silicon is shown partitioned into discrete cells with broken lines delineating the cell boundaries. The dopant concentration within each cell (i.e., N_i , N_{i+1} , N_{i+2} , etc) is considered uniform. The coupling between the surface boundary condition (Eq. [14]) and the main body of SUPREM is carried out in two steps, and is described below.

Step 1.—At time $t = t_0$ (Fig. 5a) the doping profile in the solid silicon is known. This profile is either the initial condition (Eq. [2]) or the result of the simula-

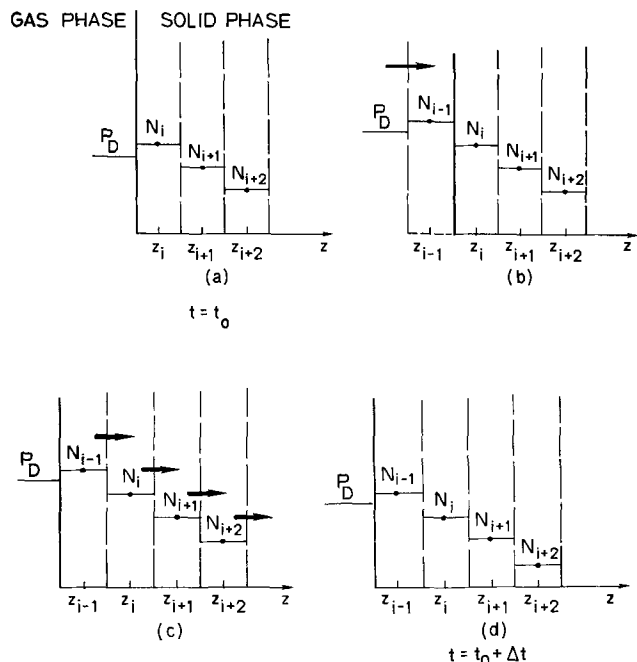


Fig. 5. Implementation of the numerical technique used to solve Fick's Second Law with the surface boundary condition dictated by the epitaxial deposition process. For explanation see text.

tion up to the time t_0 . The cycle now starts by adding a new cell z_{i-1} (Fig. 5b). In order to calculate the dopant concentration N_{i-1} of this new cell a numerical routine is used to solve Eq. [14] with the left-hand side of the equation set to zero, i.e.

$$0 = k_{mf} \left[P_D^\circ - \frac{N_{i-1}}{K_P} \right] - gN_{i-1} - K_A \frac{dN_{i-1}}{dt} \quad [17]$$

This is equivalent to accounting only for dopant introduction into the newly added cell without computing the simultaneous impurity redistribution in the solid silicon. This step is illustrated in Fig. 5b, with the arrow representing the net flux of dopant atoms entering the new cell.

Step 2.—The thermal redistribution of impurities that occurs during the growth of cell z_{i-1} is now computed. This is done by entering the impurity profile shown in Fig. 5b into SUPREM, which then computes the thermal redistribution of impurities during the interval Δt under consideration. This is illustrated in Fig. 5c. The arrows in the figure represent diffusive fluxes crossing cell boundaries. Notice that no flux is shown crossing the gas-solid interface. This is because the net introduction of impurities during this interval Δt was already considered in connection with Fig. 5b and Eq. [17] when N_{i-1} was first determined. After the dopant concentration in each cell is rearranged due to these diffusive fluxes, one time increment Δt has been advanced (Fig. 5d), and the cycle of operations just described is repeated.

Parameter Determination: K_A

In this section, the technique used to determine K_A is described. As mentioned above, it consists of generating a family of doping profiles corresponding to a given $P_D^\circ(t)$ using SUPREM with K_A as a variable, and then comparing these simulated profiles to that obtained experimentally. K_A is obtained from the simulated profile that best fits the measured profile.

Figure 6 shows the results of this experiment. As indicated in the inset, the arsine flow was kept constant for the first 10 min of silicon deposition, at which point it was abruptly decreased and then kept constant at this lower level for the rest of the deposition cycle which lasted 20 min. The corresponding arsine

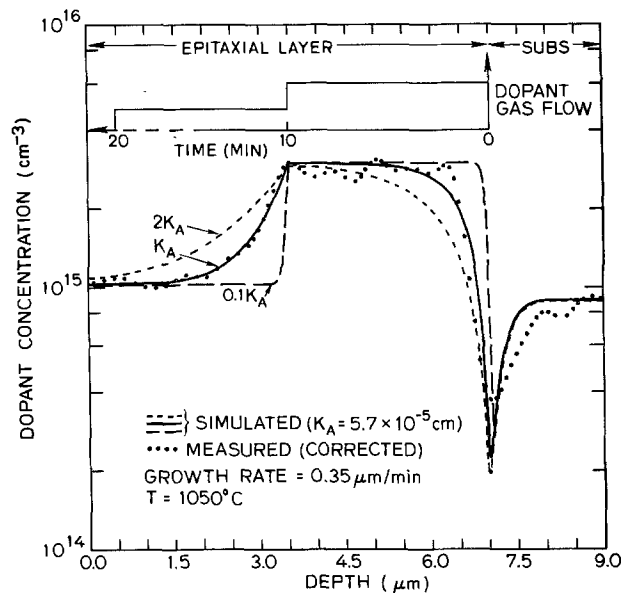


Fig. 6. Measured and simulated doping profiles used to determine K_A .

partial pressures were 7.5 and 2.4×10^{-11} atm, respectively. A silane partial pressure of 8.4×10^{-4} atm was used to obtain a growth rate of $0.35 \mu\text{m}/\text{min}$. In this and the following experiments epitaxial layers were deposited simultaneously on (100) phosphorus and boron-doped substrates. The layers deposited on phosphorus-doped substrates were used to measure the epitaxial doping profile, while the layers deposited on boron-doped substrates were used to measure the epitaxial layer thickness by a groove-and-stain technique. The dotted line in Fig. 6 shows the doping profile that results in the epitaxial film as measured by the spreading resistance technique and corrected using multilayer correction factors (8). (Unless otherwise stated, all measured profiles in this work were determined by the spreading resistance technique and properly corrected.) Capacitance-voltage measurements on planar p-n junctions and deep-depletion MOS structures (9) confirmed the corrected spreading resistance profile shown in Fig. 6. The solid and broken lines in the figure correspond to simulations using SUPREM for three different values of K_A . In order to obtain these simulations the input to SUPREM for the epitaxial step must specify growth rate, deposition time, deposition temperature, doping element, and dopant partial pressure. It is clear from this exercise that the doping profile corresponding to $K_A = 5.7 \times 10^{-5}$ cm shows the best fit to the measured profile.

The dip shown by the measured profile at the epitaxial-substrate interface and predicted by the SUPREM simulations is not an artifact of the measurement technique. It is caused by a combination of phosphorus evaporation from the substrate during the high temperature bake prior to epitaxial growth and the transient in the epitaxial layer associated with the establishment of the steady-state arsenic concentration. Also, notice that the full transition between the two uniform doping levels in the epitaxial film is of approximately $2 \mu\text{m}$. This gradual transition is due to the time required to remove the excess arsenic-containing species present in the adsorbed layer as a result of the decreasing step change in the arsine flow. This removal step occurs by dopant incorporation into the growing film and by desorption (see Eq. [12]).

In this section, the technique used to determine K_A was described. It was also shown that the numerical implementation of the epitaxial doping model described here enabled SUPREM to simulate small doping level changes during epitaxial deposition. In the

next section, the capabilities of SUPREM to simulate more complex doping profiles are demonstrated.

Comparison of SUPREM Simulations and Experiments

Figures 7a and 7b show measured and simulated doping profiles corresponding to the time-varying arsine flows indicated in the insets. In both cases the input to the epitaxial system consisted of an increasing step in arsine flow followed by a decreasing step, the combination simulating a pulse. The epitaxial layer in Fig. 7a was deposited at $0.33 \mu\text{m}/\text{min}$, and the pulse duration was of 8.6 min. The epitaxial layer in Fig. 7b was deposited at $0.59 \mu\text{m}/\text{min}$, and the pulse duration was only 48 sec. The broken line shows the impurity profile simulated by SUPREM. The solid line shows the corresponding majority-carrier distribution obtained by using the SUPREM output and calculating a one-dimensional solution to the Poisson's equation. The computer program SEDAN was used to obtain the Poisson solution (10). The circles indicate the epitaxial doping profile as determined by capacitance voltage measurements on deep-depletion MOS structures (4,9). The agreement between the simulated majority-carrier profile and the measured profile is better than that between the SUPREM output and the measured profile. This is because the profile measured by the capacitance-voltage technique is a closer representation of the majority-carrier distribution than it is of the impurity distribution (11). The experiments shown in Fig. 7 were carried out in a horizontal reactor (Hugle Model HIER II) different than the Unipak system described earlier. The equipment details are reported elsewhere (4). The parameters used to simulate the Hugle reactor were obtained from the data in Ref. (4), and are shown in Table I together with those corresponding to the Unipak unit. Table II shows values of decay time τ and decay length L (3,4) for each reactor at different silicon growth rates, calculated from

$$\tau \equiv \frac{K_A}{g + \frac{k_{mf}}{K_P}} \quad [18]$$

$$L \equiv g\tau \quad [19]$$

It is interesting to observe that τ and L of each reactor (for a given growth rate) are remarkably close, which indicates that the extent of any transient phenomena (including autodoping) is independent of the

Table I. Reactor parameters corresponding to the Unipak and the Hugle units

| | Unipak | Hugle |
|---|-----------------------|-----------------------|
| K_P ($\text{cm}^{-3} \text{atm}^{-1}$) | 1.05×10^{26} | 3.8×10^{25} |
| k_{mf} ($\text{cm}^{-2} \text{sec}^{-1} \text{atm}^{-1}$) | 4.85×10^{19} | 5.26×10^{18} |
| K_A (cm) | 5.7×10^{-5} | 4.1×10^{-5} |

Table II. Decay time τ and decay length L calculated for the Unipak and the Hugle reactors at different silicon growth rates

| | Unipak | | Hugle | |
|-------------------------------|--------------|-----------------------|--------------|-----------------------|
| | τ (sec) | L (μm) | τ (sec) | L (μm) |
| 0.3 $\mu\text{m}/\text{min}$ | 59 | 0.3 | 64 | 0.32 |
| 0.45 $\mu\text{m}/\text{min}$ | 47 | 0.35 | 46 | 0.35 |
| 0.6 $\mu\text{m}/\text{min}$ | 39 | 0.39 | 36 | 0.36 |

horizontal reactor used. These experiments clearly indicate that SUPREM is capable of simulating epitaxial doping profiles corresponding to different time-varying dopant gas flows. Moreover, these experiments demonstrated that the simulation capability of SUPREM is not restricted to one single reactor.

Figure 8 shows measured (dotted line) and simulated (solid line) doping profiles resulting from the decreasing step change in arsine flow indicated in the inset. There are three major differences between this experiment and that described in connection with Fig. 6. These are: (i) the doping level change in the epitaxial film of this experiment, as shown in Fig. 8, is one order of magnitude, in contrast with the 3:1 ratio shown in Fig. 6; (ii) the growth rate in this experiment was $0.07 \mu\text{m}/\text{min}$, much slower than $0.35 \mu\text{m}/\text{min}$; and (iii) the total deposition time in this experiment was 90 min instead of 20 min, with the decreasing step change occurring 40 min after the start of the deposition cycle. The agreement between the simulated and measured profiles is excellent. Notice that the full transition between the two uniform doping levels in this experiment is approximately $1 \mu\text{m}$, in contrast with $2 \mu\text{m}$ as shown in Fig. 6. The reason for this more abrupt transition is related to the rate at which silicon is deposited (3). The dip shown in Fig. 6 at the epi-substrate interface is again present in this experiment. On the other hand, the measured profile in Fig. 8 shows a pronounced peak in the epitaxial layer side of the epi-substrate interface. Careful ex-

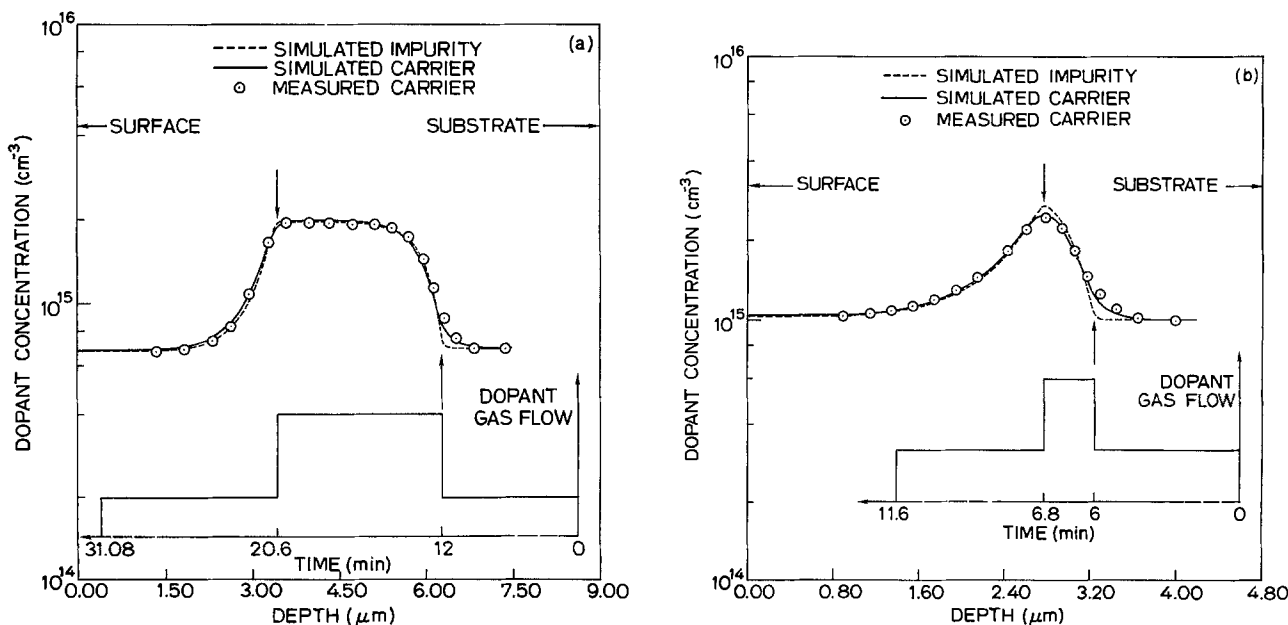


Fig. 7. Measured and simulated epitaxial doping profiles corresponding to the time-varying arsine flows indicated in the insets

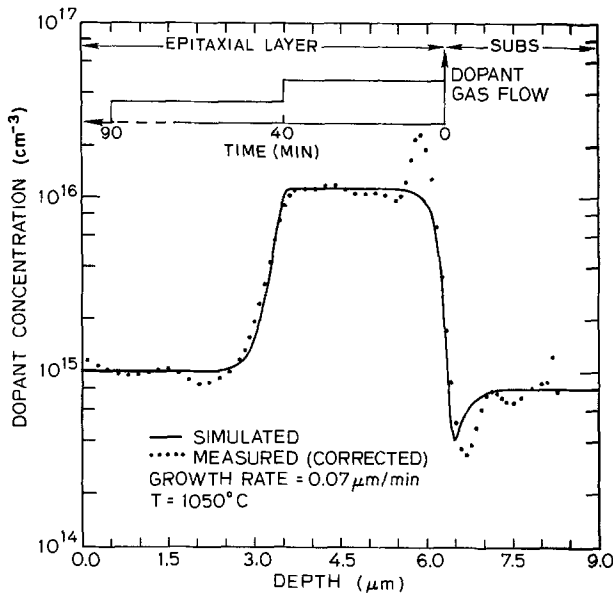


Fig. 8. Measured and simulated doping profiles resulting from the decreasing step change in arsine flow indicated in the inset.

amination of the spreading resistance data indicated that this peak is an artifact created by the computer program used to reduce the spreading resistance profile. The limitation of the program to reduce spreading resistance data for very abrupt transitions creates this artifact. Notice that this peak is also present in Fig. 6, but it is much less evident because the transition is more gradual. The conclusion from this experiment is that SUPREM is also capable of simulating large doping level changes during epitaxial growth.

Figure 9 shows another comparison between the doping profile simulated by SUPREM (solid line) and that measured by the spreading resistance technique (dotted line). In this experiment, two independent and consecutive arsenic-doped epitaxial films were deposited, as indicated in the inset. The arsine flows corresponding to the first and second layers were adjusted to produce epitaxial doping levels of approximately 10^{17} cm^{-3} and 10^{15} cm^{-3} , respectively. The reactor was purged with hydrogen for 8 min at 1050°C between the end of the first deposition cycle and the beginning of the second. The transition between the

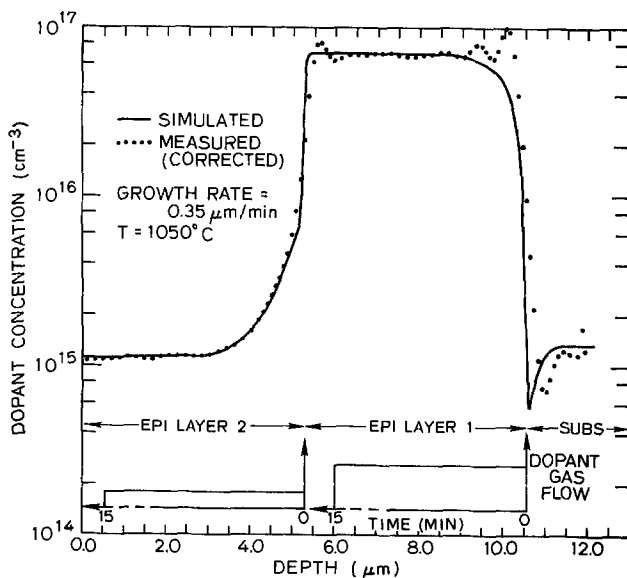


Fig. 9. Measured and simulated doping profiles corresponding to two consecutive epitaxial depositions (see text).

high doping level of layer 1 and the low doping level of layer 2 is typical of that encountered when a lightly doped epitaxial film is deposited on a heavily doped substrate or buried layer. It consisted of a very abrupt transition followed by a more gradual transition until the required impurity concentration is reached. The gradual transition is caused by the "autodoping" phenomena.

The agreement between the simulated and measured profiles in Fig. 9 is excellent. However, in order to simulate this autodoping profile, another parameter must be defined, and its value must also be determined. This new parameter is the concentration of dopant species present in the adsorbed layer prior to the epitaxial deposition step, *i.e.*, $(\theta_D N_s)^\circ$ (see Appendix D). As mentioned earlier, the initial condition of the epitaxial system is given by the distribution of impurities in the solid silicon just before epitaxial deposition. However, in cases like that shown in Fig. 9 in which the substrate doping level is much higher than the required epitaxial doping level, $(\theta_D N_s)^\circ$ is not negligible and must also be taken into account. This is because the dopant species present in the adsorbed layer prior to epitaxial deposition are responsible for the autodoping phenomena (12).

The technique used to determine $(\theta_D N_s)^\circ$ is similar to that used to determine K_A . Several SUPREM simulations, each with a different value of $(\theta_D N_s)^\circ$, were carried out until a good fit was obtained to the measured profile. The simulated doping profile in Fig. 9 was obtained with $(\theta_D N_s)^\circ = 4 \times 10^{11} \text{ cm}^{-2}$. Work is under way to determine the dependence of $(\theta_D N_s)^\circ$ on different experimental conditions, such as substrate impurity concentration, prebake time, prebake temperature, deposition temperature, total pressure, etc.

The mechanisms responsible for the autodoping tail in Fig. 9 and for the gradual transition between the two uniform epitaxial doping levels in Fig. 6 are the same. In both cases, the dopant concentration in the epitaxial film reaches the required steady-state doping level slowly, because some time is required to remove the excess dopant species from the adsorbed layer. In Fig. 6, these excess species are produced by the sudden decrease in arsine flow, while in Fig. 9 they come from the evaporation of dopant atoms from the substrate prior to epitaxial growth. Part of the excess dopant species in the adsorbed layer is incorporated in the growing film and produces the gradual transition shown in Fig. 6 and 9, and the rest is released to the gas-phase by desorption.

Finally, Fig. 10 shows the measured (dotted line) and simulated (solid line) profile of a more typical autodoping case. In this experiment arsenic was implanted ($3 \times 10^{15} \text{ cm}^{-2}$, 100 keV) into a boron-doped, $10 \Omega\text{-cm}$, (100) silicon wafer, and then redistributed for 2 hr at 1250°C . The substrate was vapor etched with HCl (0.5% by volume, 2 min, 1200°C) and then baked in hydrogen (32 min, 1200°C) before the epitaxial deposition step. The epitaxial layer deposited in this experiment was intended to be intrinsic, *i.e.*, no arsine flow was entered into the reactor. The epitaxial growth rate was of approximately $0.27 \mu\text{m}/\text{min}$, and the total deposition time was of 6 min. The simulated profile was obtained using $(\theta_D N_s)^\circ = 4 \times 10^{11} \text{ cm}^{-2}$ and agrees fairly well with the measured profile. In experiments in which different preepitaxial bake times and temperatures were used, the resulting autodoping profile was only slightly affected (13), suggesting that $(\theta_D N_s)^\circ$ is not a strong function of the hydrogen preepitaxial bake cycle. The results shown in Fig. 9 and 10 clearly indicate that SUPREM simulations can be used to estimate the extent of the autodoping phenomena.

Summary and Conclusions

A computer model capable of simulating epitaxial doping profiles resulting from a variety of deposition

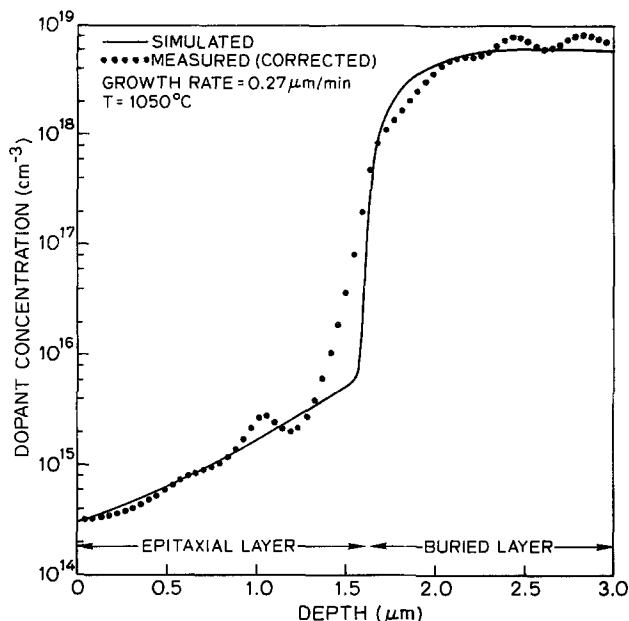


Fig. 10. Measured and simulated doping profiles corresponding to a typical autodoping situation.

conditions was described. The model consists of solving Fick's Second Law throughout the solid silicon with the proper set of initial and boundary conditions. It is necessary to solve Fick's Second Law in order to take into account the thermal redistribution of impurities during epitaxial growth. On the other hand, the boundary condition at the growing silicon surface contains information on the gas-phase dynamics and the physicochemical mechanisms taking part in the doping process. In order to obtain an expression for the surface boundary condition, the epitaxial system was separated into three regions (main gas stream, boundary layer, and adsorbed layer) and equations describing the behavior of dopant species in each of these regions were obtained. These equations were then used to determine the surface boundary condition. According to the model, three parameters are required to completely characterize an epitaxial system: k_{mf} , K_P , and K_A . k_{mf} is a kinetic coefficient associated with the mechanism dominating the dopant incorporation process. K_P and K_A are thermodynamic constants, and relate the epitaxial dopant concentration to the concentration of dopant species in the gas-phase and the adsorbed layer, respectively. A fourth parameter, $(\theta_D N_s)^\circ$, is also required when heavily doped substrates or buried layers are considered. $(\theta_D N_s)^\circ$ is the concentration of dopant species per unit area in the adsorbed layer prior to the epitaxial deposition step, and becomes appreciable for heavily doped substrates, dominating the dopant incorporation process during the first few minutes of growth. The techniques used to determine experimentally the values of these parameters were also described. Finally, the computer model was numerically implemented with the aid of the computer simulator SUPREM, and numerical simulations were carried out and compared to epitaxial doping profiles obtained experimentally. It was concluded that the numerical solution of Fick's Second Law as carried out by SUPREM using the surface boundary condition described here is capable of simulating epitaxial doping profiles corresponding to a variety of deposition conditions, including time-varying gas flows and the autodoping phenomena.

Acknowledgments

M. Vanzi and S. E. Hansen are gratefully acknowledged for their help on the spreading resistance measurements and the numerical implementation in SUPREM, respectively. This work was supported by

the U.S. Army Research Office (Contract No. DAAG-29-77-C-0006) and was conceived and carried out at Stanford University. R. Reif gratefully acknowledges the financial support provided by the National Science Foundation (Grant No. DMR 78-24185) through the M.I.T. Center for Materials Science and Engineering, which made the writing of this article possible.

Manuscript submitted July 7, 1980; revised manuscript received ca. Oct. 8, 1980.

Any discussion of this paper will appear in a Discussion Section to be published in the December 1981 JOURNAL. All discussions for the December 1981 Discussion Section should be submitted by Aug. 1, 1981.

Publication costs of this article were assisted by the Massachusetts Institute of Technology.

APPENDIX A

Figure 11 shows an enlarged view of the main gas stream region. The upper tube wall is at $z = 0$, and the boundary between the main gas stream region and the boundary layer region is at $z = \bar{z}$. In the main gas stream region dopant species travel by forced convection in the x -direction, while in the boundary layer region dopant species travel by diffusion in the z -direction. F_x and F_z will be used to represent the flux of dopant species in the main gas stream and the boundary layer, respectively. F_x is assumed to be only a function of x , while F_z is assumed to be a function of x and z . By considering mass-balance of dopant species within an element of length Δx , height \bar{z} , and unit width in the main gas stream (see Fig. 11), the following equation can be obtained

$$[F_x(x_0) - F_x(x_0 + \Delta x)] \bar{z} - \bar{F}_z(\bar{z}) \Delta x = \frac{\Delta \bar{C}_x}{\Delta t} \Delta x \bar{z} \quad [\text{A-1}]$$

in which $F_x(x_0)$ is the flux of dopant species entering the element at $x = x_0$, $F_x(x_0 + \Delta x)$ is the flux of dopant species leaving the element at $x = x_0 + \Delta x$, $\bar{F}_z(\bar{z})$ is the average flux of dopant species leaving the element at $z = \bar{z}$, and \bar{C}_x is the average concentration of dopant species per unit volume within the element in the main gas stream. C_x is assumed to be only a function of x . In typical horizontal reactors, the susceptor is tilted to improve the uniformity of silicon deposition (7). Therefore, strictly speaking, the location of \bar{z} is also a function of x . This fact has been neglected here. Equation [A-1] is valid only if (i) dopant species do not undergo chemical reactions within the element, and (ii) there is no interchange of dopant species between the upper tube wall and the element. By rearranging Eq. [A-1] and letting $\Delta x \rightarrow 0$, the following equation is obtained

$$-\frac{\delta F_x}{\delta x} \cdot \frac{\bar{F}_z(\bar{z})}{\bar{z}} = \frac{\delta C_x}{\delta t} \quad [\text{A-2}]$$

Equation [A-2] describes the behavior of dopant spe-

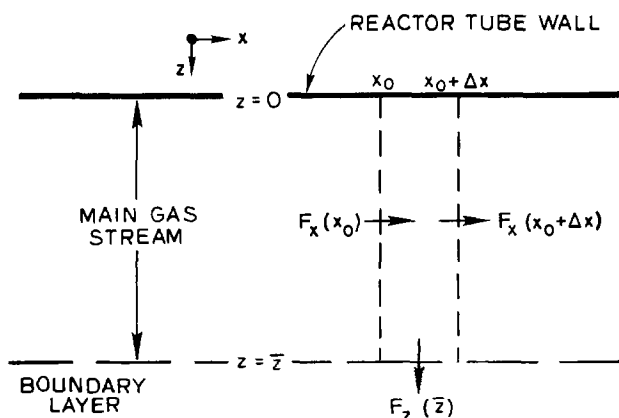


Fig. 11. Enlarged view of the main gas stream region

cies in the main gas stream. As is shown below, this equation can be simplified for most conventional epitaxial reactors.

The time constant associated with Eq. [A-2] is of the order of 1 sec (3). It has been reported, however, that the time constant of the overall doping process in a horizontal reactor is of the order of 40 sec (4). This means that in a transient situation (e.g., an abrupt variation in dopant gas flow during epitaxial growth) the dopant species in the main gas stream reaches steady state long before the new steady-state epitaxial condition is established. By assuming that the main gas stream always reaches steady-state "instantaneously," Eq. [A-2] can be simplified to

$$-\frac{\delta F_x}{\delta x} - \frac{\bar{F}_x(\bar{z})}{\bar{z}} \approx 0 \quad [\text{A-3}]$$

for the epitaxial doping process. Also, for most epitaxial reactors, the second term in Eq. [A-3] may be neglected because gas-phase depletion of dopant species caused by $\bar{F}_x(\bar{z})$ is very small, and Eq. [A-3] can be further simplified to

$$\frac{\delta F_x}{\delta x} \approx 0 \quad [\text{A-4}]$$

Equation [A-4] indicates that F_x varies only slightly with position in a conventional epitaxial system. Because dopant species are transported by forced convection in the main gas stream, F_x can be expressed as

$$F_x = v_{H_2}(x) \frac{P_D(x)}{kT} \quad [\text{A-5}]$$

in which v_{H_2} is the carrier gas (hydrogen) velocity, k is the Boltzmann constant, and T the absolute temperature. By using Eq. [A-5], Eq. [A-4] can be rewritten as

$$\frac{\delta F_x}{\delta x} = \frac{1}{kT} \frac{\delta}{\delta x} [v_{H_2}(x) P_D(x)] = 0 \quad [\text{A-6}]$$

However, when the tilt of the susceptor is neglected, $v_{H_2}(x)$ in Eq. [A-6] can be replaced by a position-independent effective velocity v_{H_2} , i.e.

$$\frac{\delta F_x}{\delta x} = \frac{\bar{v}_{H_2}}{kT} \frac{\delta}{\delta x} [P_D(x)] = 0 \quad [\text{A-7}]$$

Equation [A-7] indicates that the partial pressure of dopant species in the main gas stream (P_D) is nearly independent of x . Consequently, because P_D reaches steady state "instantaneously" and is nearly independent of position, then

$$P_D(t) \approx P_D^\circ(t) \quad [\text{A-8}]$$

in which $P_D^\circ(t)$ is the input dopant partial pressure. In other words, any time-variation of the dopant partial pressure at the reactor input is transmitted "instantaneously" throughout the main gas stream in the epitaxial reactor. Equation [A-8] is sufficient to describe the behavior of dopant species in the main gas stream of most epitaxial reactors.

APPENDIX B

Figure 12 shows an enlarged view of the boundary layer, with the main gas stream on top, and the solid silicon below. F_s in Fig. 12 is the net flux of dopant species leaving the boundary layer by adsorbing on the silicon surface. An expression describing the behavior of dopant species in the boundary layer can be derived using the same technique employed in Appendix A. By considering mass-balance of dopant species within an element of thickness Δz , unit length, and unit width in the boundary layer (see Fig. 12), the following expression can be obtained

$$-\frac{\delta F_x}{\delta z} = \frac{\delta C_z}{\delta t} \quad [\text{B-1}]$$

where C_z is the concentration of dopant species per unit volume in the boundary layer. Equation [B-1] was obtained assuming that (i) dopant species are

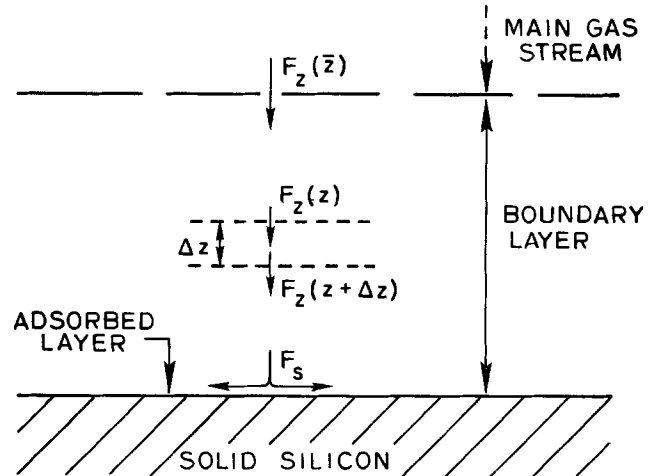


Fig. 12. Enlarged view of the boundary layer region

neither formed nor consumed within the boundary layer, and (ii) dopant species in the boundary layer travel only in the z -direction. C_z is assumed to be only a function of z .

Equation [B-1] can be simplified by considerations analogous to those discussed in Appendix A. The time constant associated with Eq. [B-1] is of the order of 0.1 sec (4), which is much shorter than that of the overall doping process. Therefore, the dopant species in the boundary layer are essentially always at steady state, i.e.

$$\frac{\delta F_x}{\delta z} \approx 0 \quad [\text{B-2}]$$

and F_x can be considered position-independent regardless of whether the overall doping process is at steady state or undergoing a transient. This means that the dopant flux leaving the boundary layer due to surface adsorption always follows closely the time-variation of the dopant flux entering the boundary layer, i.e.

$$F_s(t) \approx F_x(\bar{z}, t) \quad [\text{B-3}]$$

and vice versa. Equation [B-3] is sufficient to describe the behavior of dopant species within the boundary layer.

APPENDIX C

From Eq. [8]

$$F_s = k_F(\theta N_s) P_D^* - k_R(\theta_D N_s) \quad [\text{C-1}]$$

which can be rearranged as

$$F_s = k_F(\theta N_s) \left[P_D^* - \frac{k_R}{k_F} \frac{(\theta_D N_s)}{(\theta N_s)} \right] \quad [\text{C-2}]$$

By using Eq. [8] and [9], Eq. [C-2] can be rewritten as

$$F_s = k_F(\theta N_s) \left[P_D^* - \frac{1}{K_1} \frac{k_H}{K_2} P_{H_2}^{3/2} N \right] \quad [\text{C-3}]$$

or

$$F_s = k_t [P_D^* - N/K_P] \quad [\text{C-4}]$$

in which $k_t \equiv k_F(\theta N_s)$, $K_P \equiv K_1 K_2 / k_H$, and $P_{H_2} \approx 1$ atm was omitted for simplicity.

APPENDIX D

As discussed in the section on Numerical Implementation, the dopant concentration of each new cell is first computed by solving Eq. [17], i.e.

$$0 = k_{mf} \left[P_D^\circ - \frac{N}{K_P} \right] - gN - K_A \frac{dN}{dt} \quad [\text{D-1}]$$

The initial condition of Eq. [D-1] is the dopant concentration of the epitaxial film at $t = 0$, which is given by

$$N(0) = K_A (\theta_D N_s)^\circ \quad [\text{D-2}]$$

REFERENCES

1. D. A. Antoniadis, S. E. Hansen, and R. W. Dutton, Stanford Electronics Labs., Stanford University, Tech. Rep. SEL 78-020, June 1978.
2. R. Reif, T. I. Kamins, and K. C. Saraswat, *This Journal*, **126**, 644 (1979).
3. R. Reif, T. I. Kamins, and K. C. Saraswat, *ibid.*, **126**, 653 (1979).
4. R. Reif, T. I. Kamins, and K. C. Saraswat, *ibid.*, **125**, 1860 (1978).
5. D. N. Jackson, Jr. and T. A. DeMassa, *Solid-State Electron.*, **20**, 485 (1977).
6. P. H. Langer and J. I. Goldstein, *This Journal*, **121**, 563 (1974).
7. F. C. Eversteyn *et al.*, *ibid.*, **117**, 925 (1970).
8. D. C. D'Avanzo, R. D. Rung, A. Gat, and R. W. Dutton, *ibid.*, **125**, 1170 (1978).
9. R. F. Pierret and D. W. Small, *Solid-State Electron.*, **18**, 79 (1975).
10. D. C. D'Avanzo, Stanford Electronics Labs., Stanford University, Tech. Rep. SEL 78-011, February 1978.
11. W. C. Johnson and P. T. Panousis, *IEEE Trans. Electron Devices*, **ed-18**, 965 (1971).
12. M. Tabe and H. Nakamura, *This Journal*, **126**, 822 (1979).
13. J. D. Shott and C. P. Ho, Unpublished results.

Technical Notes



Lift-Off Patterning of Sputtered SiO₂ Films

Tadashi Serikawa and Toshiaki Yachi

*Nippon Telegraph and Telephone Public Corporation,
Musashino Electrical Communication Laboratory, Midori-cho, Musashino-shi, Tokyo, 180 Japan*

Sputtered SiO₂ film is used as an intermediate insulator in multilevel metallization and as a final passivator in large-scale integrated circuits, because good film characteristics can be obtained at low temperature deposition (1, 2). SiO₂ film is usually patterned by wet chemical etching or plasma etching using photoresist patterns as the etching mask. Wet chemical etching and plasma etching in a barrel reactor, however, have the disadvantage of side-etching due to lateral attack by the etchant. The plasma etching method usually called reactive ion sputter etching does not have this disadvantage. In this method, the pattern sidewall taper is obtained only when many factors, such as photoresist sidewall angle, photoresist thickness, and relative etch rates of substrate and photoresist, are precisely controlled (3). On the other hand, lift-off technique is promising for producing a fine pattern in a large-scale integrated circuit. The lift-off method has been employed in aluminum metallization (4), but no study has been reported on sputtered insulating films. In this study, a lift-off method for sputtered SiO₂ film is proposed. An SiO₂ pattern with positive slope sidewalls was successfully produced without pattern width reduction through successively following the steps shown in Fig. 1: (i) photoresist pattern formation, (ii) SiO₂ film deposition, (iii) slight etching with buffered hydrofluoric acid to remove SiO₂ film deposited on photoresist sidewalls, and (iv) removal of the photoresist.

Experimental

Patterns of positive-type photoresist (AZ1370) were formed on a silicon substrate using conventional photolithography. Postbaking was performed at 140°C. These patterns were 1 μm thick and had 60° slope sidewalls. SiO₂ film was deposited on these substrates with a planar rf magnetron sputtering apparatus. The substrates were placed on a rotating substrate holder and were electrically at floating potential during deposition. The smallest spacing between the substrate and the target was 50 mm. The target was a 3 mm thick, 125

mm × 375 mm, 99.99% pure SiO₂ sheet. Film deposition was carried out at 0.3 Pa argon pressure, at a 4 nm/min deposition rate, and at temperatures less than 180°C. SiO₂ film on the photoresist sidewalls was removed by slight etching in buffered hydrofluoric acid [100 ml (50% HF) + 860 ml (40% NH₄F)]. Unwanted SiO₂ film was removed along with photoresist patterns by soaking the substrates in photoresist strip (J-100). After cleaving substrates at various steps, the fractured sections were studied using scanning electron microscopy (SEM).

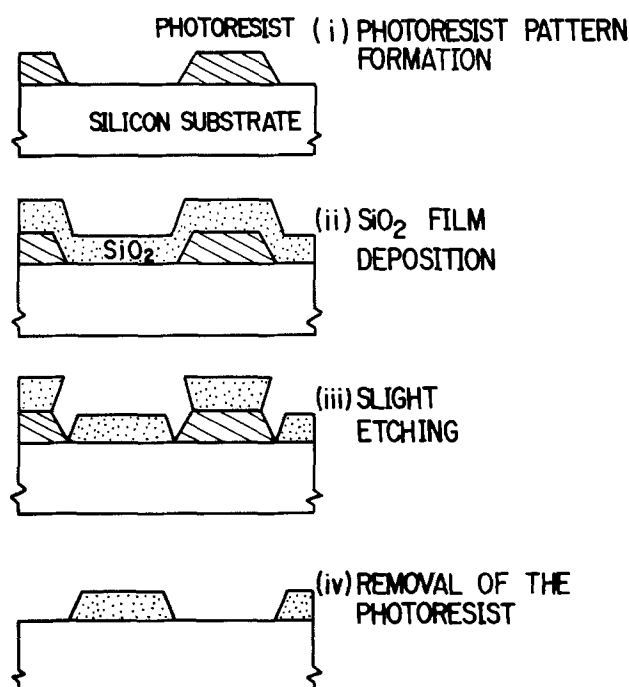


Fig. 1. A diagram of the successive steps for lift-off patterning of sputtered SiO₂ films.

Results

A deposited sample with about 1 μm thick SiO_2 film was lifted off according to the process in Fig. 1. Figure 2 shows SEM photographs at the various steps. The film thickness at photoresist sidewalls is less than the thickness elsewhere, as shown in Fig. 2(a). However, as shown in Fig. 2(b), the film on the photoresist sidewall is completely removed when slightly etched in buffered hydrofluoric acid at 30°C for 30 sec. This is because the

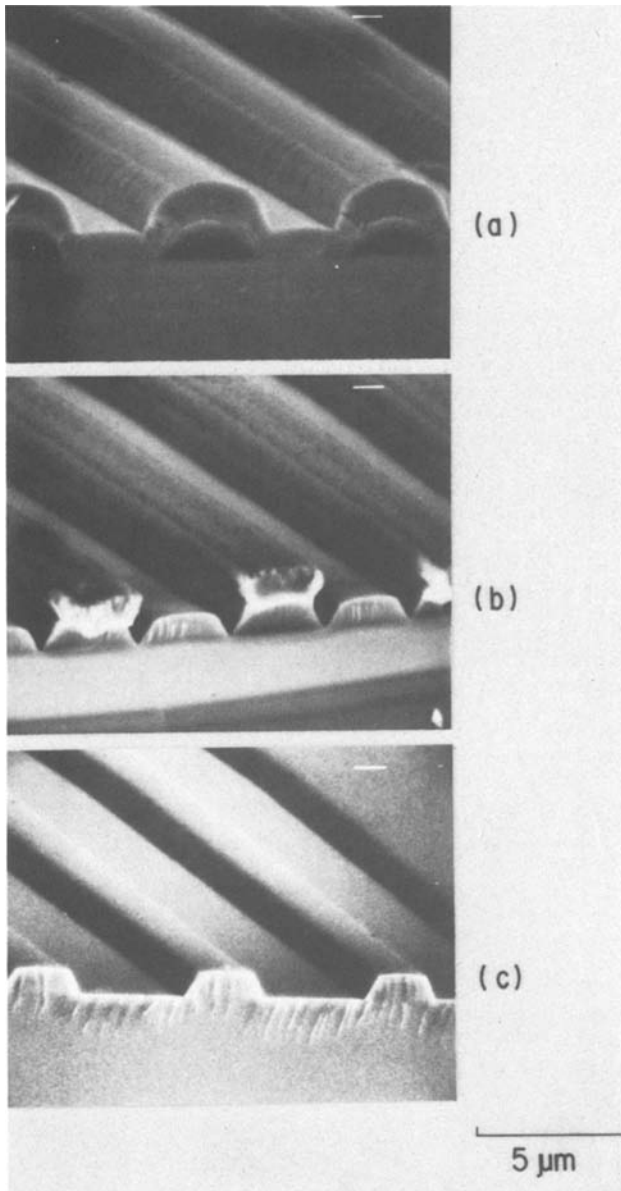


Fig. 2. SEM photographs of lift-off patterning processes. (a) SiO_2 film deposited. (b) After slight etching for 30 sec. (c) After lift-off patterning.

film at the sidewall is porous and has about a 2.0 $\mu\text{m}/\text{min}$ etching rate, which is much higher than the 0.1 $\mu\text{m}/\text{min}$ etching rate elsewhere. Consequently, grooves were formed having tetragonal cross sections on the side of the photoresist pattern sidewall. Soaking the sample in a solution to dissolve photoresist material removed unwanted SiO_2 film along with the photoresist pattern. Thus, an SiO_2 film pattern was formed, as shown in Fig. 2(c). SiO_2 patterns are successfully obtained without pattern width reduction, because a boundary between the porous film and the dense film is formed along a line from the under edge of photoresist pattern to the SiO_2 film edge in the deposited sample. In addition, the SiO_2 lifted-off patterns have sloped sidewalls even when sidewalls of photoresist pattern have positive slopes as shown in Fig. 2.

The porous structure near the photoresist pattern sidewall is the result of shadowing of deposited SiO_2 material in the photoresist pattern step (5-7). The substrate near the step sees less of the target area, hence it receives less incoming SiO_2 material than the surrounding surface. Thus, it has a smaller deposition rate. Also, the SiO_2 film deposition rate on the photoresist pattern top is high enough to result in greater shadowing effect, causing the formation of a porous film structure. Consequently, sputtered SiO_2 film patterns are easily lifted off. However, the detailed formation mechanism of a distinct boundary between the porous structure area and the dense film area near the step is not completely understood.

In conclusion, sputtered SiO_2 film patterns with sloped sidewalls were successfully produced using a lift-off technique without pattern width reduction. Therefore, this method is very useful for patterning SiO_2 films in integrated semiconductor device fabrication.

Acknowledgments

The authors wish to express their sincere thanks to Dr. M. Terajima and Dr. K. Hasegawa for their valuable suggestions and encouragement.

Manuscript submitted June 9, 1980; revised manuscript received Nov. 17, 1980.

Any discussion of this paper will appear in a Discussion Section to be published in the December 1981 JOURNAL. All discussions for the December 1981 Discussion Section should be submitted by Aug. 1, 1981.

Publication costs of this article were assisted by Nippon Telegraph and Telephone Public Corporation.

REFERENCES

1. C. L. Standly, R. E. Jones, and L. T. Maissel, *Thin Solid Films*, **5**, 355 (1970).
2. K. Urbanek, *Solid State Technol.*, **20**, 87 (1977).
3. H. W. Lehmann and R. Widmer, *J. Vac. Sci. Technol.*, **15**, 319 (1978).
4. W. G. Hanse, L. H. Donhue, and A. J. Speth, *IEEE Trans. Electron Devices*, **ed-26**, 360 (1979).
5. L. L. Standley, R. E. Jones, and L. I. Maissel, *Thin Solid Films*, **5**, 355 (1970).
6. J. A. Bleck *ibid.*, **6**, 113 (1970).
7. T. N. Kennedy, *J. Vac. Sci. Technol.*, **13**, 1135 (1976).

A High Resolution Etching Technique for Determining Epitaxial Layer Thickness

C. W. Pearce*

Western Electric Company, Allentown, Pennsylvania 18103

This paper describes the use of Secco etching to develop the thickness topography of an epitaxial layer. The technique is capable of 0.1 micron resolution and could be used as a test method in research or production. A potential application would be the evaluation of material used for bipolar device fabrication where the epitaxial layer thickness is a key parameter, such as the OXIL (1) (oxide isolated logic) technology. The etching method was more reliable in determining epitaxial thickness variation than infrared measurements in the cases studied.

Background

Preferential etching of silicon to reveal defects (or junctions) has become a well-established investigative tool (2). It is widely used because of its convenient and inexpensive nature in research and production applications. A number of etchants have been reported in the literature (3-5), each with particular characteristics. As a guide to potential applications, there have been a number of etchant comparisons made (6, 7). Schimmel (8) in particular examined the characteristics of the hydrofluoric acid, chromic acid, and water etching system to develop an optimum etch for heavily boron-doped silicon. Futagami (9) added a degree of sophistication by distinguishing decorated from undecorated stacking faults using Sirtl etch.

This report describes the application of silicon etching in determining the radial thickness variation in an epitaxial layer. Customarily, this parameter is measured using an infrared reflectance technique (10), although the geometry of epitaxial stacking faults (11) and junction staining (12) have also been utilized. Evaluating radial variation with such methods is customarily limited to a few measurement points, which may not adequately characterize the surface of a large diameter wafer. Here, the staining which occurs on a heavily boron-doped substrate when using Secco's etch (8), and the etch rate are used to measure epitaxial layer thickness. Although destructive, since the whole wafer is etched, contours of constant thickness can easily be generated by step etching.

Experimental

Developing an accurate topography requires precise control of the etch rate, which entails control of etch temperature and composition. These requirements were accomplished for Secco's etch by using the following procedure. A 5.42g wafer was placed in 150 cm³ of solution and left to etch until the reaction was complete, resulting in the dissolution of 0.23g of silicon. It was estimated that approximately 25,000 cm³ of etchant for each gram of silicon to be removed would be of sufficient volume to keep both parameters essentially fixed, yielding a constant etch rate. This estimate was verified by etching 0.22g of silicon in 5300 cm³ of solution and checking the etch rate at the beginning and the end of etching. The silicon to be removed can be calculated from the nominal layer thickness and wafer surface area. The value should be doubled if the rear surface is unmasked, or adjusted if the substrate has a different etch rate from the layer. In the first example, the substrate etched 3.5× as fast as the layer (7), hence we decided to mask the rear surface with wax to keep the etch volume reasonable.

* Electrochemical Society Active Member.
Key words: silicon, etching, defects.

The sensitivity of etch rate to temperature was determined to be nominally 0.02 μm/min/°C by measurements at 32° ± 2°C and at 89° ± 4°C. This parameter is assumed linear over the range of temperatures studied.

To develop a topograph, a 100 mm diam, P/P+, wafer was etched face up in 5300 cm³ of solution. The layer thickness was 11 μm and the substrate resistivity 0.008 Ω-cm. The wafer was first measured at five points by the infrared method using a DIGILAB FTG-12.¹ The initial etch rate was 0.45 μm/min after etching for 20 min the substrate first appeared via the stain. At this point, the etch rate was rechecked and found to be the same. The wafer was then step-etched to develop contours representing 0.23 μm, each step representing 30 sec of etching. After each etch, the outline of the stained region was traced onto paper to develop Fig. 1A. There is some subjectivity in the tracing as the stain demarcation is not always abrupt. Temperature was monitored throughout the etching and found not to vary.

A second example consisted of a 76 mm diam wafer etched in 150 cm³ of etchant. The layer thickness was nominally 2.3 microns and the rear surface was masked with wax. The substrate was patterned and diffused with antimony and boron typical of OXIL processing. The etching time was varied for this wafer based on a visual observation of the developing pattern during the etching. Figure 1B is the resulting topograph.

Discussion

In the case of Fig. 1A, the thickness variation by etching was found to be 1.8 μm, which is three times as great as the variation seen by the five-point infrared measurements. However, the diameter of maximum

¹ Trademark of Digilab Incorporated, Cambridge, Massachusetts.

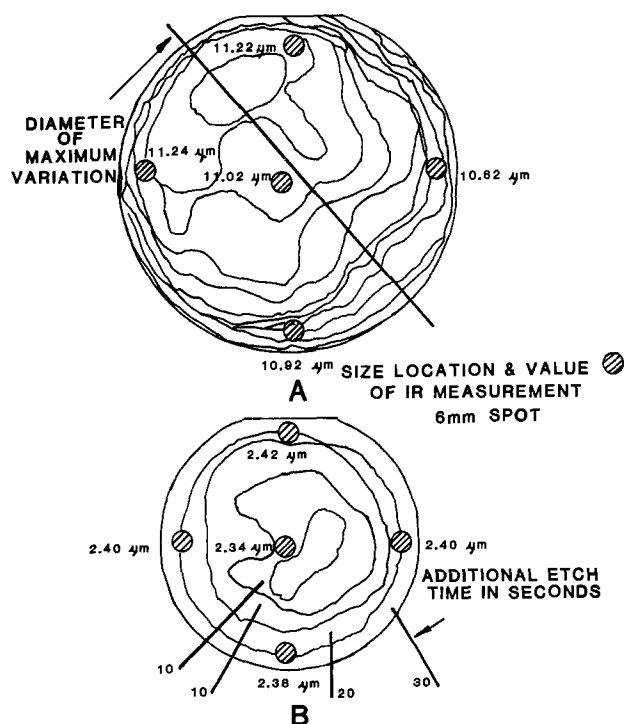


Fig. 1. Two topographs of epitaxial layers by Secco etching

variation did not coincide with any diameter defined by the IR measurements. In terms of absolute values, the center thickness was estimated to be 11.60 μm by etching which compares favorably with the IR value of 11.02 μm .

The second wafer had a topography (Fig. 1B) nominally concentric about the wafer center, but offset from the center IR measurement point. Starting at the first contour the thickness variation was calculated as 0.34 μm . This is substantially greater than the 0.08 μm derived from the IR measurements. Furthermore, the IR measurements predicted the center to be the thinnest region of the wafer. The IR results mainly reflect the measurement scatter of the FTG-12.

The repeatability of the instrument is nominally $\pm 0.1 \mu\text{m}$ (3 sigma). Thus, on a fairly uniform layer measurement scatter is a dominant effect. The etch method would in general be correct with respect to the direction and shape of thickness variation. Changes in etch rate would lead to uncertainty in the position of a given contour, but the correct sense of thickness variation is maintained between contours. In terms of absolute thickness, the extreme edge cleared first at 3 min of etching, after 3½ min the edge near the IR readings was cleared for a thickness of 1.6 μm compared to the 2.4 μm by IR. The difference is not unexpected and is ascribed to the faster outdiffusion of the boron buried layer that stains, relative to the slower diffusing antimony buried layer, the latter diffusion determining the position of the IR reading. SUPREM (Stanford University Process Engineering Models) calculations show a difference of 1 μm between the peak concentration points of the two diffusions.

By using a sufficient volume of solution it is possible to obtain an etching bath for silicon wafers having a constant etch rate. This can be used to determine the total extent of thickness variation in an epitaxial wafer provided the substrate shows some staining. In the examples presented herein five point IR measurements

tended to underestimate the thickness variation for two reasons. The customary five-point measurement often misses high and low points on the wafer and generally excludes some edge variation. Given an etch rate of 0.45 $\mu\text{m}/\text{min}$ and etch times of 10 sec, the resolution achievable is on the order of 0.1 μm . This would be useful for evaluating wafers where layer thickness is a key parameter such as in the OXIL device fabrication technology. Thus, an epitaxial reactor could be profiled by wafer etching to determine the most meaningful places for IR measurements to be made.

Manuscript submitted Aug. 11, 1980; revised manuscript received Nov. 7, 1980.

Any discussion of this paper will appear in a Discussion Section to be published in the December 1981 JOURNAL. All discussions for the December 1981 Discussion Section should be submitted by Aug. 1, 1981.

Publication costs of this article were assisted by Western Electric Company.

REFERENCES

1. J. Agraz-Guerena *et al.*, IEDM-1978, p. 209, December 1978.
2. C. W. Pearce and G. A. Rozgonyi, in "Semiconductor Characterization Techniques," P. A. Barnes and G. A. Rozgonyi, Editors, p. 314, The Electrochemical Society Softbound Proceedings Series, Princeton, N.J. (1978).
3. W. C. Dash, *J. Appl. Phys.*, **27**, 1193 (1956).
4. F. Secco D'Aragona, *This Journal*, **119**, 948 (1972).
5. E. Sirtl and A. Adler, *Z. Metallk.*, **52**, 529 (1961).
6. D. G. Schimmel, *This Journal*, **123**, 734 (1976).
7. M. W. Jenkins, *ibid.*, **124**, 757 (1977).
8. D. G. Schimmel, *ibid.*, **126**, 479 (1979).
9. M. Futagami, *ibid.*, **127**, 1172 (1980).
10. ASTM Annual Book of Standards, Part 43, F95 (1980).
11. *Ibid.*, Part 43, F522.
12. *Ibid.*, Part 43, F110.

Minority Carrier Diffusion Length EBIC Measurements in Cadmium Telluride

P. Gaugash¹ and A. G. Milnes*

Department of Electrical Engineering and Center for the Joining of Materials,
Carnegie-Mellon University, Pittsburgh, Pennsylvania 15213

Diffusion Lengths in CdTe

CdTe is a direct-gap semiconductor (bandgap 1.45 eV) that is used in nuclear particle detectors and for optical modulation purposes. It is a II-VI compound semiconductor that can be doped both n and p-type and the carriers have acceptable mobilities ($\mu_n \sim 500\text{--}1200 \text{ cm}^2/\text{Vsec}$, $\mu_p \sim 50 \text{ cm}^2/\text{Vsec}$) (1).

However, CdTe has potential beyond its present uses. This potential lies in the combination of optical and electrical properties it offers. CdTe is a material of high potential for solar cells with possible efficiencies of npCdTe cells of up to 22-25%, matching that of GaAs. Even heterojunction cells of nCdS/pCdTe are considered to have the potential for 17% efficiency. Ten to 12% efficiency has been achieved in the work of Yamaguchi *et al.* (2) with cells prepared by vapor-phase epitaxy of n⁺CdS on single crystal pCdTe wafers. Among those who have worked with this material there is optimism that heterojunction CdTe/CdS

or homojunction pnCdTe thin film cells offer important alternatives to Cu₂S/CdS and GaAs thin film cells (3-6).

One problem that limits the solar cell performance presently obtained with CdTe is the tendency of the single crystal ingot material to have low minority diffusion lengths. For instance, Bell *et al.* (3) report hole diffusion lengths between 0.4 and 0.8 μm for n-type CdTe with Cl, Br, or I doping in the range $2\text{--}6 \times 10^{17} \text{ cm}^{-3}$. Higher L_p diffusion lengths, such as 1.75-3 μm , may have been observed particularly with "undoped" or In-doped n-CdTe (7). The present work documents such values from EBIC measurements for several ingots and doping levels and reports some unexpected features of the measurements.

Samples and Preparation of Schottky Barrier EBIC Specimens

The specimens available were taken from four n-type ingots and four p-type ingots. All of the ingots, except C, were grown by a modified Bridgman method that used a molten Te zone so that the maximum temperature involved was about 750°C (8). This presum-

* Electrochemical Society Active Member.

¹ Present address: Kishinev State University, Moldavia, USSR.

Key words: semiconductor, II-VI, doping, lifetime, gold, electron beam.

ably results in less pick-up of impurities such as silicon, oxygen, and copper, from the system and quartz growth tube, than when a normal Bridgman growth is made at 1100°C.

For the electron-beam-induced current (EBIC) measurements, slices about 0.030 in. thick were cut and polished with Mirrolux and 0.05 μm Al_2O_3 grit and polish-etched in methanol-bromine (0.5%) solution. The ohmic contact on the reverse side of n-type slices was provided by an indium evaporation and the substrate raised to about 200°C for a few minutes to provide some alloying action. Gold for the Schottky barrier ($\phi \sim 0.85$ eV) was then deposited on one side by gold evaporation. The Schottky barrier area was about 10^{-4} cm^2 . For the p-type slices the procedure was to evaporate Au for the ohmic contact with a short 200°-250°C heat-treatment, and then Al was evaporated for the Schottky barrier.

An hour or so before insertion in the scanning electron microscope (JSM-35) the specimens to be measured were cleaved across the Schottky barrier, mounted in a T05 header, and checked for leakage currents of less than 10^{-9} A at a reverse voltage of 1V. The diffusion length measurement procedure was then as described by Sekela *et al.* (10) or others (11-14) with about 0.1V or less reverse voltage applied to the diode. Most of the measurements were made at a beam voltage of 25 keV and a beam current in the low 10^{-10} A. (This current varies by factors of several times between different measurements, depending on the microscope focus and collimation adjustments.) Some measurements were made with larger beam currents, up to 10^{-7} A, and in these the effects of series-resistance drop in the semiconductor caused by larger beam-induced currents required more reverse voltage across the device. A few measurements were also made with the beam voltage varied between 5 and 25 keV, however no well-behaved data were obtained from which the recombination velocity of the cleaved surface could be inferred (11). In general, the surface was found to be rather insensitive: After many weeks of storage on air the specimens gave almost the same diffusion lengths as just after cleaving. Neither did we see any effects of carbon deposition from the vacuum column or of repeated scanning with the electron beam of the surface track measured (14).

Diffusion Length Results

Table I shows the results for some of the specimens measured. The curves obtained for specimens No. 20 and 22 are shown in Fig. 1. The diffusion length for specimen No. 20 is seen to be 2.8 μm . A specimen No. 22 from the same slice given a heat-treatment in Cd vapor at 750°C for 120 hr in a quartz ampul showed only a slightly lower diffusion length, 2.4 μm , even though

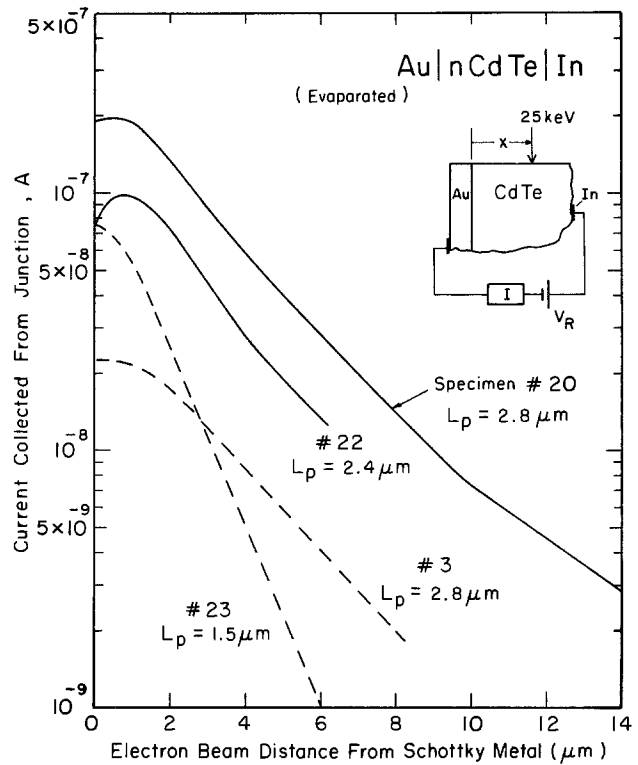


Fig. 1. Diffusion length measurements, L_p , for n CdTe with evaporated Au Schottky barrier.

there was a very large reduction in resistivity. The results for specimens 3, 23, and 49 show a somewhat larger change after Cd vapor treatment.

Specimen No. 27 from a different slice of the ingot A was anomalous since it exhibited an apparent diffusion length of 4.4 μm in the first 5 μm from the barrier surface, followed by 1.3 μm in the next 5 μm . The implication is that lifetime controlling impurities or defects have either entered or been taken from the 5 μm surface region. Annealing of similar material in Cd vapor, at 750°C for 120 hr as before, gave for specimen 30 similarly anomalous results with an initial L_p of 3.3 μm changing into 1.6 μm . If the effect is caused by an impurity entering from the surface during the heat-treatment, it should be noted that a very small surface concentration such as 10^{13} cm^{-2} (about a hundredth of a monolayer) entering to a depth of 5 μm could cause a concentration of 2×10^{16} cm^{-3} if uniformly distributed. This density of defects could have a profound effect on the doping density or on the density of active

Table I. Diffusion lengths and other data for the n and p CdTe specimens

| Ingot (growth type)* (i) | Specimen number (ii) | Conductivity type (iii) | Dopant (iv) | Majority carrier density cm^{-3} (v) | Resistivity $\Omega\text{-cm}$ (vi) | Diffusion length μm (vii) | Treatment (viii) |
|--------------------------|----------------------|-------------------------|-------------|---|-------------------------------------|--------------------------------------|---|
| A (MB) | 20 | n | In | 7×10^{16} | ~ 10 | $L_p = 2.8$ | Grown w/750°C Te meltzone Heat-treated in Cd vapor, 750°C, 120 hr |
| | 22 | n | In | — | 10^{-2} | 2.4 | |
| | 27 | n | In | 5×10^{16} | ~ 10 | Anomalous | |
| | 30 | n | In | — | 10^{-2} | Anomalous | |
| B (MB) C (B) | 13 | n | I | 1×10^{17} | $\sim 10^{-1}$ | 1.05 | Grow w/Te meltzone Grown at 1100°C Heat-treated in Cd vapor, 750°C, 120 hr |
| | 3 | n | Undoped | 2×10^{17} | $\sim 10^{-1}$ | 2.8 | |
| | 23 | n | Undoped | — | 10^{-2} | 1.3 | |
| | 49 | n | Undoped | — | 10^{-2} | 1.5 | |
| D (MB) | 31 | n | Undoped | 3×10^{16} | 10 | $L_p = 1.6 \mu\text{m}$ | Goldfilm, 250°C, 10 min Grown w/750°C Te meltzone Grown w/750°C Te meltzone Grown w/750°C Te meltzone Grown w/750°C Te meltzone |
| E (MB) | 5 | p | Undoped | 2×10^{15} | 10^{-2} | $L_n = 0.58 \mu\text{m}$ | |
| F (MB) | 44 | p | P | 7×10^{15} | $\sim 5 \times 10^1$ | 0.74 | |
| G (MB) | 14 | p | Undoped | 5×6^{14} | 2.4×10^2 | 0.87 | |
| H (MB) | 41 | p | Undoped | 2×10^{15} | 10^{-2} | 0.6 | |

* MB means modified Bridgman growth with Te molten zone (8).
B means normal Bridgman growth.

recombination centers. Alternatively a very thin high-concentration surface skin could develop that might have the effect of gettering recombination defects from the bulk. Defect gettering appears to occur in GaAs as a result of sub-monolayer surface contamination from various etches used, even though the chemicals are of semiconductor grade purity for Si processing (13-15). Further experiments to establish whether similar effects occur for CdTe need to be done.

Cd vapor treatment as applied here certainly did not improve the hole diffusion lengths. The large increase in n-type conduction after such a treatment is presumably a consequence of reduction of V_{Cd} or V_{Cd}^{2-} or V_{Cd} -donor complexes [see Table 3.4 of Ref. (1)].

Comparison of the results for specimens 20 and 3 suggest that growth by the modified Bridgman method (8), involving a Te molten zone and a temperature of about 750°C, does not automatically result in a longer hole diffusion length than the normal Bridgman method at 1100°C. However, the sample comparison is limited and one cannot help feeling that the lower temperature process should allow less contamination from the system (8, 16). Ge and Sn are considered to have adverse effects on lifetimes on CdTe but little is reported about the effects of Si. The iodine-doped specimen, No. 13, is seen to have a lower diffusion length than the indium-doped specimens 20 and 22. This is in agreement with the experience of other workers (3, 4).

The results for L_n in p-type CdTe show low diffusion lengths in the range 0.5-0.9 μm , Fig. 2, again in agreement with other reports (3).

In the course of the studies an attempt was made to obtain an Au Schottky barrier, or thin p region, from a solution known as Goldfilm (manufactured by the Emulsitone Company and described as forming a polymer with gold atoms attached through suitable groupings to a carbon-carbon backbone). This material is supplied as a source of Au for use in lifetime control in silicon. The company also states that on Si wafers

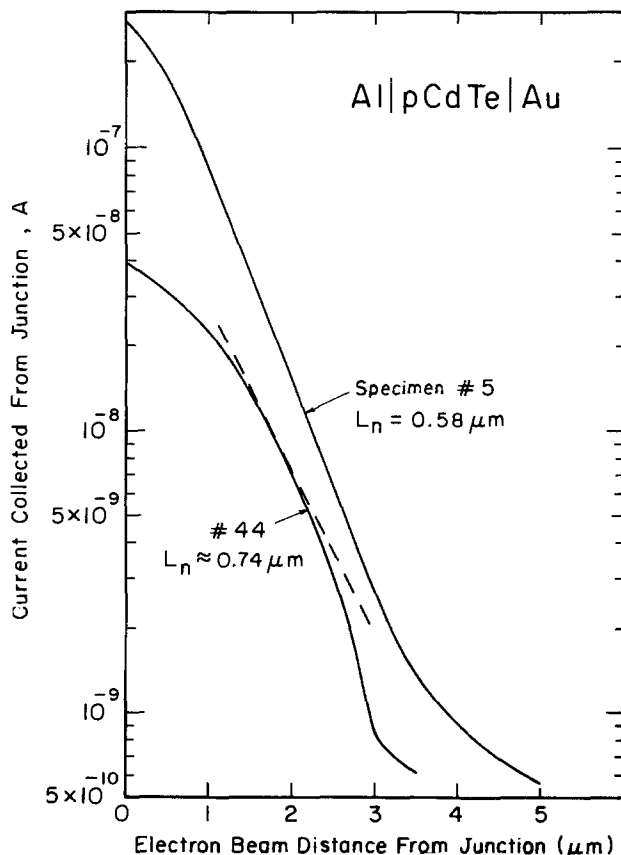


Fig. 2. Diffusion length measurements, L_n , for p CdTe with evaporated Al Schottky barrier.

heated to 250°-300°C, for 5-10 min, film decomposition occurs and a yellow film of 20-100Å of gold is deposited. This Goldfilm was applied to a number of n CdTe specimens prior to the 250°C 10 min heat-treatment for the In ohmic contact. An EBIC curve typical of the results is shown in Fig. 3. It appears that the Au has doped the CdTe p-type to a depth of about 4 μm and both hole and electron diffusion lengths are observed, $L_p = 1.6 \mu\text{m}$ and $L_n = 1.5 \mu\text{m}$. The flat response region between 4 and 8 μm presumably represents a region of high resistivity where field-aided collection of current occurs. Since the junction depth is deep, the diffusion of gold in CdTe must be rapid at 250°C, but no information on this has been found in the literature (17).

Conclusions

Hole diffusion lengths of greater than 2.5 μm are obtainable in n-type CdTe ingot material doped in the high 10^{16} cm^{-3} range. Electron diffusion lengths for p-type ingot material are normally between 0.5 and 0.9 μm .

There is no reason to believe that these represent limiting values that cannot be improved by further attention to purity and crystal perfection and careful handling of the material before heat-treatment.

Acknowledgments

The support of the International Research and Exchanges Board (IREX), New York, in making possible the stay of Professor P. Gaugash at Carnegie-Mellon University is gratefully acknowledged. Also we gratefully acknowledge the supply of specimens from various sources including K. Sutchkievitch of Kishnev State University, and the use of the central facilities of the Carnegie-Mellon Center for the Joining Materials.

Manuscript submitted June 24, 1980; revised manuscript received Nov. 21, 1980.

Any discussion of this paper will appear in a Discussion Section to be published in the December 1981 JOURNAL. All discussions for the December 1981 Discussion Section should be submitted by Aug. 1, 1981.

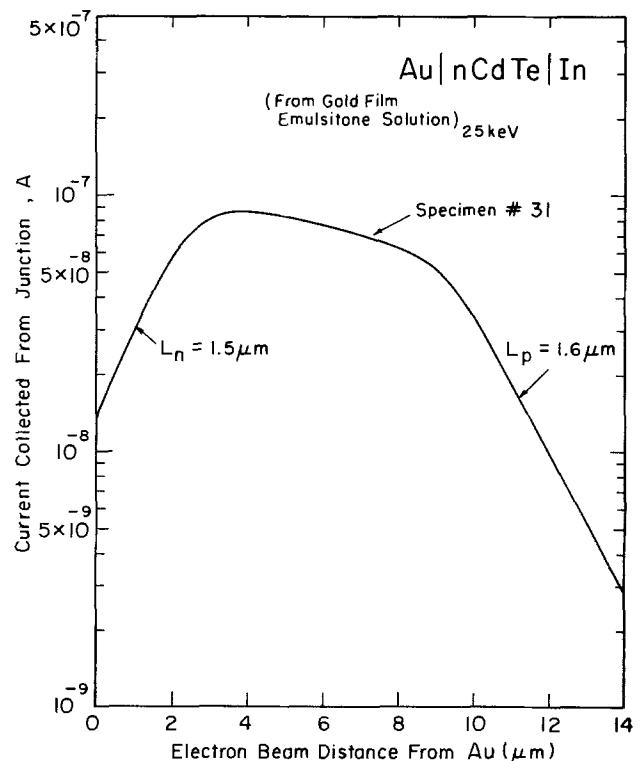


Fig. 3. Electron-beam-induced current in n CdTe treated with a Goldfilm deposit (250°C heat-treatment).

Publication costs of this article were assisted by Carnegie-Mellon University.

REFERENCES

1. K. Zanio, "Cadmium Telluride," Vol. 13 of "Semiconductors and Semimetals," R. F. Willardson and A. C. Beer, Editors, Academic Press, New York (1978).
2. K. Yamaguchi *et al.*, *Jpn. J. Appl. Phys.*, **14**, 1397 (1975); **15**, 1575 (1976); **16**, 1203 (1977).
3. R. O. Bell, H. B. Serreze, and F. V. Wald, Eleventh IEEE Photovoltaic Specialists Conference Record, p. 497 (1975).
4. M. Rodot, *Rev. Phys. Appl.*, **12**, 411 (1977).
5. P. K. Raychaudhuri and D. J. Trevoy, Abstract 431, p. 1122, The Electrochemical Society Extended Abstracts, Atlanta, Georgia, Oct. 9-14, 1977.
6. D. Lincot, J. Mimila-Arrayo, R. Tribouiet, Y. Marfaing, G. Cohen-Solal, and M. Barbé, 2nd EC Photovoltaic Solar Energy Conference Proceedings, p. 424, Reidel Publishing Co., Dordrecht, Holland (1979).
7. A. Lastras-Martinez, P. M. Racciah, and R. Tri-boulet, *Appl. Phys. Lett.*, **36**, 469 (1980).
8. R. O. Bell, N. Hemmat, and F. Wald, *Phys. Status Solidi A*, **1**, 375 (1970).
9. G. M. Martin, E. Fugarassy, and E. Fabre, *J. Appl. Phys.*, **47**, 264 (1976).
10. A. M. Sekela, D. L. Feucht, and A. G. Milnes, "1974 Symposium on GaAs and Related Materials," p. 245, Deauville, France, Inst. of Physics and Phys. Soc., Conference Series No. 24, London (1975).
11. L. Jastrzebski, J. Lagowski, and H. C. Gatos, *Appl. Phys. Lett.*, **27**, 537 (1975).
12. J. J. Oakes, I. G. Greenfield, and L. D. Partain, Eleventh IEEE Photovoltaic Specialists Conference Record, p. 454 (1975).
13. D. L. Partain, A. G. Milnes, and L. F. Vassamillet, *This Journal*, **126**, 1584 (1979).
14. D. L. Partain, A. G. Milnes, and L. F. Vassamillet, *J. Electron. Mater.*, **8**, 493 (1979).
15. D. L. Partain, A. G. Milnes, and L. F. Vassamillet, *This Journal*, **126**, 1581 (1979).
16. N. R. Kyle, *ibid.*, **118**, 1790 (1971).
17. I. Teramoto and S. Takayanagi, *J. Phys. Soc. Jpn.*, **17**, 1137 (1962).

Etching of Cadmium Telluride

P. Gaugash¹ and A. G. Milnes*

Electrical Engineering Department and Center for the Joining of Materials,
Carnegie-Mellon University, Pittsburgh, Pennsylvania 15213

Etching Procedure and Rates

CdTe is a semiconductor of bandgap 1.45 eV that can be doped both n and p-type and also is available in a semi-insulating form (1). It is used in nuclear particle detection and for its electro-optical properties. Interest is also growing in the potential of this material for solar cells.

The slices selected for these etching studies came from ingots grown by a modified Bridgman method with a Te melt zone at 750°C. Details of the material will be found in a companion paper (2). The slices were cut with a diamond saw and lapped with an Al₂O₃ grit and a Mirrolux solution. In general the orientation was (111).

About ten etching solutions were selected from the general literature of etching solutions for semiconductors (4, 8, 9). The experiments were made at room temperature with gently agitated solutions and the

etching rate determined by weight loss. The etchant compositions are shown in column (i) of Table I and the etch rates in column (ii). The rates should be taken as a guide only, since repeated experiments were not made to obtain average numbers or to reveal the effects of starting surface conditions or slight differences in solution temperature or agitation rate. Column (iii) comments on the appearances of the surfaces after etching.

Auger Studies

From previous work it is known that there is a tendency for Te rich layers to be formed on CdTe surfaces by some etches. Presumably this is because the etches cause soluble Cd salts to form and do not react with the Te or form insoluble Te salts.

To determine which of the etches studied produced Te rich layers, the surfaces were examined with a Perkin Elmer Physical Electronics Auger spectrometer. The ratio of the Cd signal peak (at 376 eV) to Te signal peak (at 483 eV) is 1.42 with an input electron beam of 3000 eV according to the handbook supplied

* Electrochemical Society Active Member.

¹ Present address: Kishinev State University, Moldavia, USSR.

Key words: semiconductor, II-VI, Auger, oxide.

Table I. Results of etching and Auger measurements for n CdTe

| Composition of etching solution (by volume)* (i) | Approximate etching rate (~300 K) (ii) | Comments on the appearance of surface (iii) | Auger measurements | |
|---|--|---|---|----------------------------------|
| | | | Ratio Cd _{peak} /Te _{peak} (iv) | Estimated Te layer thickness (v) |
| HCl or H ₂ SO ₄ | None detected | — | — | — |
| HNO ₃ | 3.5 μm/min | Dark precipitate, easily removed mechanically | — | — |
| NaOH | 1.6 | Produces bright surface | — | — |
| 10% NaOH + Na ₂ SO ₄ | 1.2 | Produces bright surface | 1.42 | None |
| 2 HF, 1 HNO ₃ , 1 CH ₃ COOH | 60 | Pits form | 1.42 | None |
| 0.5% Br ₂ in CH ₃ OH (medium red in color) | 2.8 | Pits form | 1.44 | None |
| 50 HNO ₃ + 10 CH ₃ COOH + 1 HCl + 18 H ₂ SO ₄ | 8.0 | Polishes | 1.40 | None |
| 7g K ₂ Cr ₂ O ₇ + 3g H ₂ SO ₄ | 2.3 | Polishes | 0.9 | 50-100A |
| 0.5% Br ₂ + 10 mg AgNO ₃ + CH ₃ OH (medium red in color) | 2.2 | Pits form, p-n junction | 1.1-1.2 | — |
| 2 H ₂ O ₂ , 3 HF, 1 H ₂ O | 3.4 | Polishes one (111) face (5) | 0.2 | 600-800A |
| 2 HNO ₃ , 2 HCl, H ₂ O | 12.5 | Pits form | 0.15 | 500-800A |
| 10 ml HNO ₃ , 20 ml H ₂ O, 4g K ₂ Cr ₂ O ₇ | 4.2 | Mirror polish | 0.08 | 300-600A |

* The concentrations of solutions used in making up these etchants were: HCl 37%; HF 45%; HNO₃ 70%; H₂SO₄ 97%; H₂O₂ 30%; CH₃COOH 100%; NaOH 50%.

with the system (3). This was confirmed for our instrument by separate spectra for pure Cd and pure Te control specimens. Slightly varied ratios, in the range 1.36-1.48, were obtained for fresh CdTe surfaces inserted in the machine shortly after cleaning. The Auger spectrum obtained for such a specimen is shown in Fig. 1. After etching for about 10 min in a solution of $2 \text{H}_2\text{O}_2 + 3 \text{HF} + 1 \text{H}_2\text{O}$ (by volume) the spectrum, Fig. 2, shows a ratio of Cd to Te peak of only 0.2 indicating a great enrichment of Te on the surface. The oxygen peak (at 510 eV) has developed in size a little but is still quite minor. The carbon peak at 270 eV is quite small compared with those seen on other semiconductors, such as GaAs, after comparable handling.

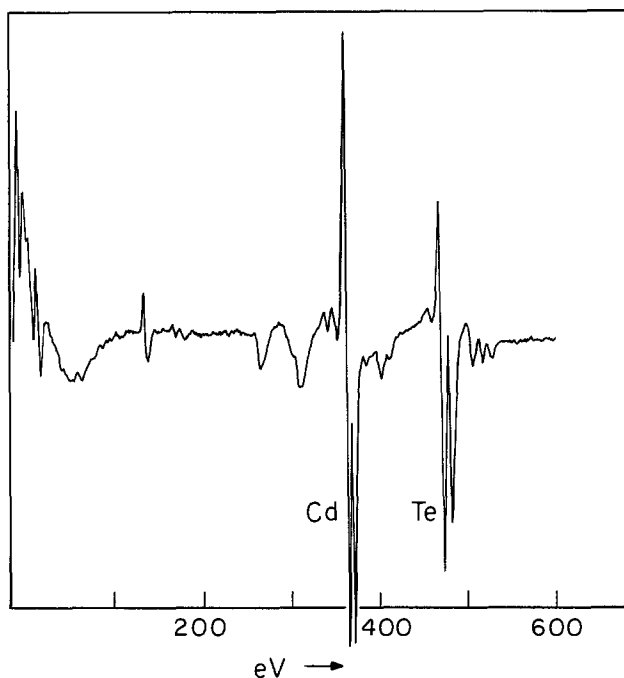


Fig. 1. Auger spectrum for cleaved CdTe to show the normal pattern and Cd/Te peak ratio. (Taken at 3 keV electron input.)

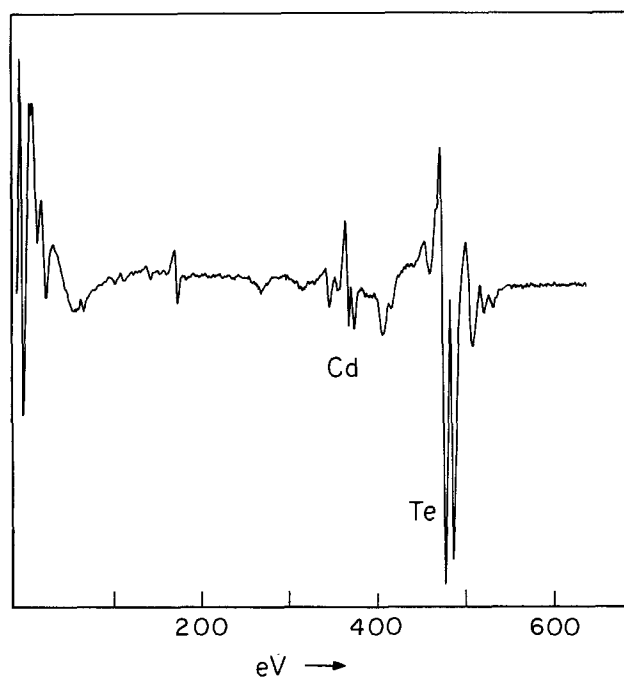


Fig. 2. Auger spectrum of CdTe surface after an etch in $2\text{H}_2\text{O}_2 + 3\text{HF} + 1\text{H}_2\text{O}$. This shows the Cd peak greatly reduced relative to the Te peak.

By Ar ion bombardment at a pressure of 5×10^{-6} Torr until the normal Cd/Te peak ratio was obtained, the thickness of the Te rich layer was inferred to be 600-800 Å (assuming an ion sputter etching rate of 60-80 Å per min).

The results for all the etchants studied may be seen in columns (iv) and (v) of Table I, where the etchants have been listed roughly in order of tendency to form Te rich layers. It is seen that about 4 of the etchants produce no Te enrichment and three produce considerable enrichment. The HNO_3 etchant produces a dark poorly adhering precipitate and the etchant containing AgNO_3 tends to form a p-n junction on n CdTe. No significant difference was observed for Cd and Te (111) faces in these etching studies, except for the rate in Table I.

One question of interest to us was whether the composition of electrolytically grown oxides on the surface of CdTe would be markedly affected by the presence of an initial Te layer produced by one of the Te-enhancing etchants. A number of electrolytic solutions were tried, modeled on those used for native oxide layers on GaAs (6, 7), but the one that was most effective was 1-2 parts of KOH in 100 parts of pure H_2O for a pH value of 9.0. The CdTe specimen of area about 0.4 cm^2 was the anode and the cathode was platinum foil. The currents applied were 10-40 mA and the voltages were 100-250 V. No attempt was made to regulate the temperature of the solution which became moderately warm. The layers that were grown were estimated to be about 0.5-1.5 μm thick and tended to be brown in color. They were well adhering and high in resistivity ($>10^6 \Omega\text{-cm}$).

Although it has been suggested that oxides on CdTe might be predominantly TeO_2 , this was not our experience (9). As Fig. 3 shows, Auger examination of the top surface of our oxides always showed substantial amounts of Cd. Ar-ion sputtering showed that the proportion of Cd to Te to O did not greatly change through the thickness of the oxide. This seemed to be true whether or not the initial etchant was one that produced a Te rich surface or not. The formation of a tellurate such as CdTeO_3 is one possible explanation (9).

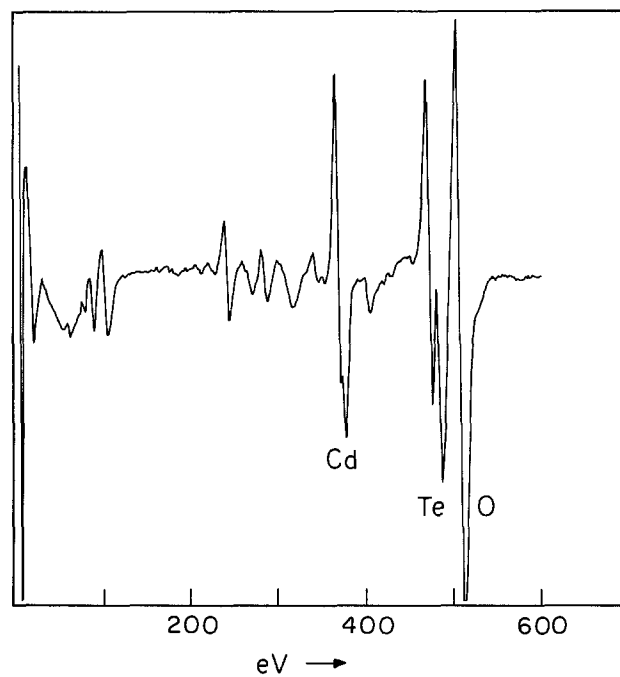


Fig. 3. Auger spectrum for an oxide anodically grown on CdTe. The grown layer is probably a mixture of Cd and Te oxides, possibly in the form of a tellurate such as CdTeO_3 .

Acknowledgments

One of the authors (P.G.) was supported by the International Research and Exchanges Board (IREX), New York. The research made use of the central facilities of the Carnegie-Mellon Center for the Joining of Materials and we appreciate the willing assistance of Professor L. F. Vassamillet with the Auger studies.

Manuscript submitted June 24, 1980; revised manuscript received Nov. 21, 1980.

Any discussion of this paper will appear in a Discussion Section to be published in the December 1981 JOURNAL. All discussions for the December 1981 Discussion Section should be submitted by Aug. 1, 1981.

Publication costs of this article were assisted by Carnegie-Mellon University.

REFERENCES

1. K. Zanio, "Cadmium Telluride," Vol. 13 of "Semiconductors and Semimetals," R. K. Willardson and

- A. C. Beer, Editors, Academic Press, New York (1978).
2. P. Gaugash and A. G. Milnes, *This Journal*, **128**, 921 (1980).
3. L. E. Davis *et al.*, "Handbook of Auger Electron Spectroscopy," 2nd ed., (1976). Perkin Elmer Physical Electronics Division, Eden Prairie, Minnesota.
4. M. Inoue, I. Teramoto, and S. Takayanagi, *J. Appl. Phys.*, **33**, 2578 (1962).
5. E. P. Warekoi, M. C. Lavine, A. N. Mariano, and H. C. Gatos, *J. Appl. Phys.*, **33**, 690 (1962).
6. S. M. Spitzer, B. Schwartz, and G. D. Weigle, *This Journal*, **122**, 398 (1975).
7. H. Hasegawa and H. L. Hartnagel, *ibid.*, **123**, 713 (1976).
8. A. G. Milnes and D. L. Feucht, "Heterojunctions and Metal-Semiconductor Junctions," Chap. 9, Academic Press, New York (1972).
9. M. Hage-Ali, R. Stuck, A. N. Saxena, and P. Siffert, *Appl. Phys.*, **19**, 25 (1979).

Orientation and Implantation Effects on Stacking Faults during Silicon Buried Layer Processing

McD. Robinson,* G. A. Rozgonyi,* T. E. Seidel,* and M. H. Read

Bell Laboratories, Murray Hill, New Jersey 07974

Bipolar integrated circuit processing requires several oxidation steps, any one of which is a potential source of oxidation-induced stacking faults (OSF). The OSF in turn are well known sources of diode leakage (1-5) and emitted-collector shorts (2, 6-8). Approaches which have been shown to reduce the size, density, and leakage current of OSF include preoxidation back side gettering (POGO) (9-12), preoxidation inert gas anneal (13), high temperature dry oxidation (14-18), processing in low oxygen (4, 5, 19-24) or chlorine-containing (17, 25-27) atmospheres, and deliberate misorientation from low index planes (16, 28, 29).

Bipolar IC processing typically starts with the formation of a masking oxide, followed by implantation or diffusion of a buried collector through an etched pattern of windows in the oxide. An earlier paper (30) showed that surface OSF are prevented or annihilated if wafers with appropriate misorientation receive the initial oxidation in dry oxygen at 1150° or 1200°C. The experiments reported here extend the earlier study to show that properly misoriented wafers remain free of OSF through buried layer processing, and that the correct choice of buried layer drive-in temperature can annihilate preexisting OSF.

Experiments

The starting material was 2 in. diam, 4-9 Ω -cm, n-type Czochralski silicon grown by the Western Electric Corporation. Two boules, nominally grown with (100) and (111) orientations, were cut to the misorientations shown in Table I. All wafers were chemically etched to remove saw damage, followed by chem-mechanical polish on one side.

The above lot received the processing sequence shown in Table II. After an initial clean, half of each wafer was given an implanted dose of $1E14 \text{ cm}^{-2}$ boron, in order to introduce a known source of OSF nuclei (4, 31, 32). Boron implantation was followed by 1150°C dry oxidation (3800Å of oxide). Following buried layer pattern definition, the buried layer implant ion and drive-in temperature were split as shown in Tables I and II.

Pieces were cleaved from the wafers and examined after each stage of processing, using Secco etching (33) and optical microscopy with Nomarski interference contrast.

In a separate experiment a wafer oriented 5° from the (100) plane toward the <011> direction was subjected to the first oxidation, then oxide stripped, Secco etched, and compared with the other orientations.

Table I. Wafer orientations; buried layer ion; drive-in time and temperature

| Wafer | Orientation* | Ion | Drive-in | |
|-------|--------------|-----|-----------|-----------|
| | | | Temp (°C) | Time (hr) |
| 00A-1 | 0.0° (100) | As | 1200 | 5 |
| 00A-2 | 0.0° (100) | As | 1270 | 1 |
| 00S-1 | 0.0° (100) | Sb | 1200 | 5 |
| 00S-2 | 0.0° (100) | Sb | 1270 | 1 |
| 05A-1 | 5.0° (100) | As | 1200 | 5 |
| 05A-2 | 5.0° (100) | As | 1270 | 1 |
| 05S-1 | 5.0° (100) | Sb | 1200 | 5 |
| 05S-2 | 5.0° (100) | Sb | 1270 | 1 |
| 12A-1 | 2.5° (111) | As | 1200 | 5 |
| 12A-2 | 2.5° (111) | As | 1270 | 1 |
| 12S-1 | 2.5° (111) | Sb | 1200 | 5 |
| 12S-2 | 2.5° (111) | Sb | 1270 | 1 |
| 19A-1 | 9.0° (111) | As | 1200 | 5 |
| 19A-2 | 9.0° (111) | As | 1270 | 1 |
| 19S-1 | 9.0° (111) | Sb | 1200 | 5 |
| 19S-2 | 9.0° (111) | Sb | 1270 | 1 |

* (100) wafer misorientation is toward <010>. (111) wafer misorientation is toward <112>.

Table II. Process sequence

1. Clean
2. Boron implant: $1E14 \text{ cm}^{-2}$, 50 keV; half of each wafer masked against implant
3. Oxidize: 1150°C, dry oxygen, 6 hr
4. Photoresist, expose pattern, etch buried layer windows
5. Clean
6. Implant buried layer
 - a. $4E15 \text{ cm}^{-2}$ arsenic, or
 - b. $4E15 \text{ cm}^{-2}$ antimony
7. Buried layer drive-in
 - a. 1200°C, 5 hr, or
 - b. 1270°C 1 hr

Results and Discussion

The first (1150°C, dry) oxidation introduced OSF on the boron-implanted sides of the 0° (100) and 9° (111) orientations. Figure 1A illustrates the boundary between the boron-implanted (left) and nonimplanted (right) regions of a 0° (100) wafer after the first oxidation. This piece was Secco etched for 3 min after stripping the oxide in HF. Figure 1B of a cleaved and Secco etched cross section of the same wafer shows the near-surface origin of the boron implant-induced OSF (4, 30). The 5° (100) and 2.5° (111) wafers were completely free of OSF after oxidation, confirming previous observation (16, 28-30).

Figure 2A shows the wafer which was misoriented 5° from the (100) plane toward the <011> direction. This wafer and a 0° (100) wafer (Fig. 2B) received the initial 1150°C dry oxide. They are shown in the figures following an oxide strip and 30 sec Secco etch. OSF appear along surface scratches. On the 5° (100) <011> wafer the OSF intersect the surface in one <011> direction (Fig. 2A), whereas on the 0° (100) wafer there are OSF in two orthogonal <011> directions. These results are consistent with the observations of Sugita *et al.* (28).

After buried layer implant and drive-in, no OSF were observed on any of the wafers which were driven in at 1270°C. Figure 3 shows the 0° (100) sample which received the arsenic buried layer implant and 1270°C drive-in, followed by oxide strip and a 3 min Secco etch. The pairs of dislocation etch pits in Fig. 3 are believed to be the end points of dislocation loops which remained following annihilation of the OSF by an unfauling reaction.

Of those samples which received the 1200°C drive-in, the 5° (100) and 2.5° (111) wafers remained free of OSF. The boron-implanted side of the 0° (100) and 9° (111) wafers retained approximately the same density of OSF ($2-4E4 \text{ cm}^{-2}$) before and after buried layer implant and drive. These results correlate very well with recent work by Pearce and Rozgonyi (34) who found a large increase in device yield following a change from a 1200°C drive-in.

The buried layer drive-in affected the OSF density, but the buried layer ion implants did not. The OSF density on the 0° (100) and 9° (111) wafers after the 1200°C drive-in was the same inside and outside the buried layer regions, for both arsenic and antimony implants. Secco etching created one artifact, in that

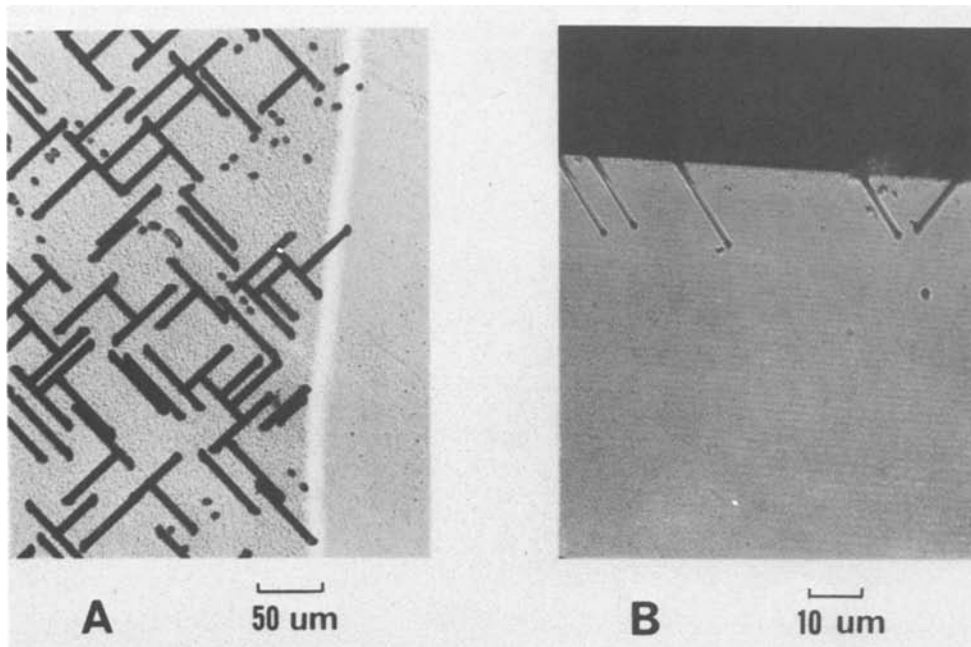


Fig. 1. Wafer 00A1; (100) on-orientation wafer after 1150°C, 6 hr oxidation in 100% O₂. (A) Oxide stripped; Secco etched 3 min. The left half was implanted with $1E14 \text{ cm}^{-1}$ boron ions prior to oxidation. (B) Cleaved cross section of the boron-implanted side; Secco etched 15 sec.

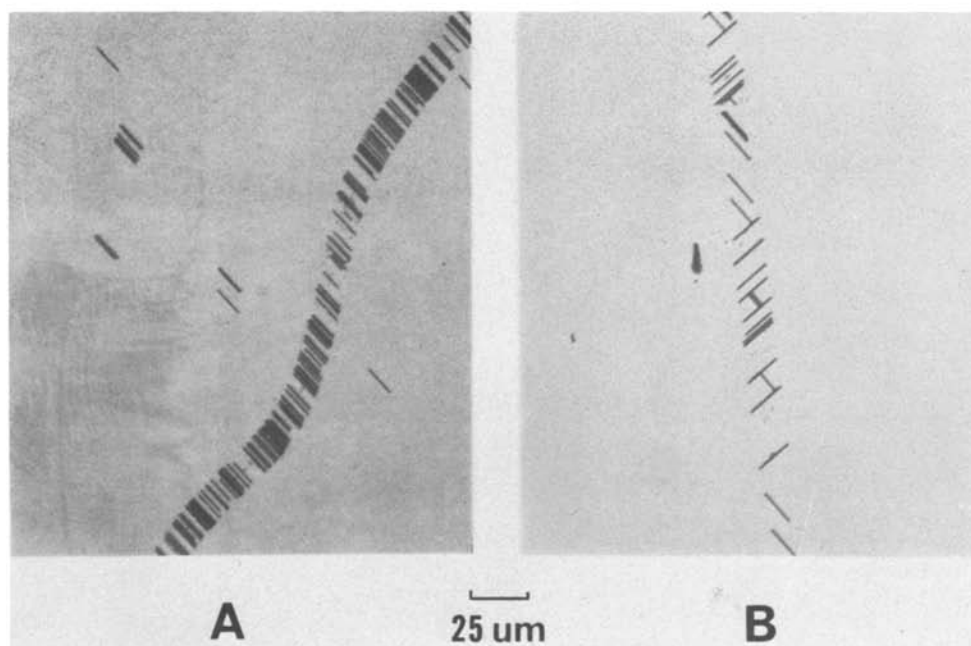


Fig. 2. (100) wafers after first oxidation; oxide stripped; Secco etched 30 sec. (A) Misoriented 5° in the <011> direction. The OSF intersect the surface only in one <011> direction. (B) No misorientation. The OSF intersect the surface in two orthogonal <011> directions.

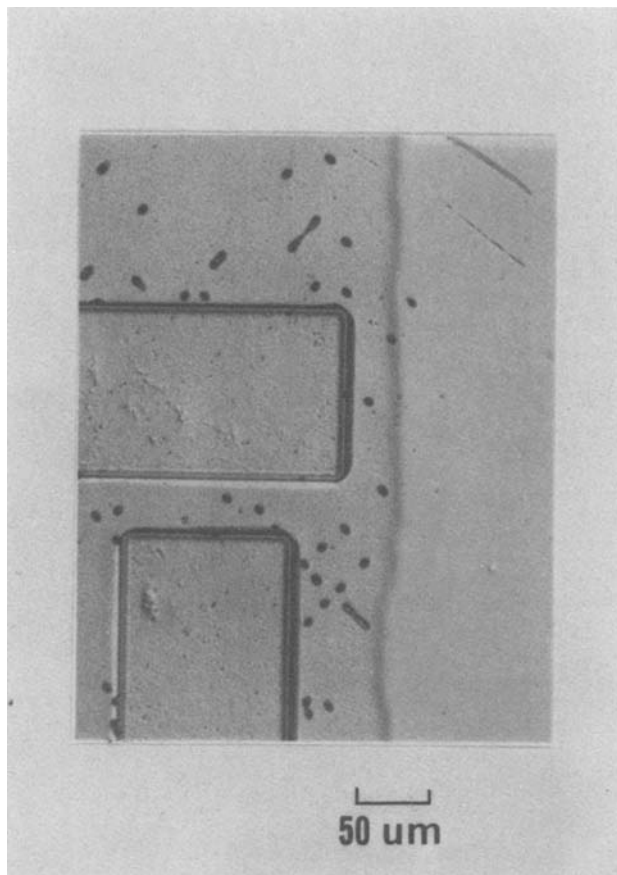


Fig. 3. Wafer 00A2; (100) on-orientation wafer after arsenic buried layer implant and 1270°C drive-in for 1 hr in 100% O₂. Oxide stripped; Secco etched. The dislocation pairs are believed to be remnants of OSF which were annihilated during the 1270°C drive-in. Only the area to the left of the irregular vertical line received the initial boron implant.

etching revealed OSF in all boron implant-nucleated regions except the 0° (100) arsenic-implanted buried layer windows. TEM analysis (Fig. 4) showed, however, that the OSF were present in these windows also.

Conclusions

Several of the results confirm that the proper choice of misorientation and/or oxidation temperature prevents OSF formation during the dry oxidation of silicon:

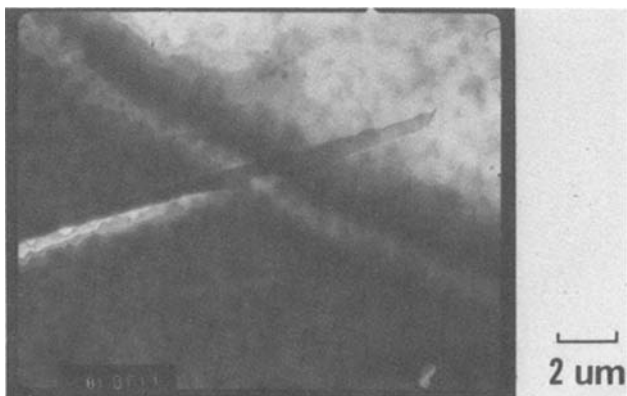


Fig. 4. TEM photograph of a thinned section from wafer 00A1; (100) on-orientation after arsenic implant and 1200°C drive-in. The light region in the upper right half of the photograph is the arsenic-implanted buried layer window. An OSF crosses the boundary into the window.

- Misorientation of 5° from the (100) toward <001> or 2.5° from the (111) toward <112> prevents OSF formation during a 1150°C, 100% oxygen, 6 hr oxidation, even after 1E14 cm⁻² boron implant seeding.

- Wafers oriented on (100) (no deliberate misorientation), and 9° from (111) toward <112>, are subject to OSF formation during the above implant and oxidation.

- The directional dependence of the misorientation effect is confirmed by the formation of stacking faults of only one orientation on a (100) wafer misoriented 5° toward <011>.

Additional results show that proper choice of buried layer drive-in temperature can annihilate already existing OSF:

- Drive-in at 1270°C (100% oxygen) eliminates all OSF. The unfauling reaction leaves behind a dislocation loop.

- Drive-in at 1200°C (100% oxygen) leaves the OSF density essentially unchanged.

Acknowledgments

The authors are grateful to T. T. Sheng for the TEM work.

Manuscript submitted May 7, 1980; revised manuscript received Nov. 14, 1980.

Any discussion of this paper will appear in a Discussion Section to be published in the December 1981 JOURNAL. All discussions for the December 1981 Discussion Section should be submitted by Aug. 1, 1981.

Publication costs of this article were assisted by Bell Laboratories.

REFERENCES

- K. V. Ravi, C. J. Varker, and C. E. Volk, *This Journal*, **120**, 533 (1973).
- J. E. Lawrence, in "Semiconductor Silicon 1973," H. R. Huff and R. R. Burgess, Editors, p. 17, The Electrochemical Society Softbound Proceedings Series, Princeton, N.J. (1973).
- L. E. Katz, *This Journal*, **121**, 969 (1974).
- S. Prussin, *J. Appl. Phys.*, **45**, 1635 (1974).
- R. Komatsu, *Jpn. J. Appl. Phys.*, **14**, 419 (1975).
- W. K. Tice, R. C. Lange, and R. B. Shasteen, in "Semiconductor Silicon 1973," H. R. Huff and R. R. Burgess, Editors, p. 639, The Electrochemical Society Softbound Proceedings Series, Princeton, N.J. (1973).
- D. K. Seto, F. Barson, and B. F. Duncan, in *ibid.*, p. 651.
- C. J. Varker and K. V. Ravi, in "Semiconductor Silicon 1977," H. R. Huff and E. Sirtl, Editors, p. 785, The Electrochemical Society Softbound Proceedings Series, Princeton, N.J. (1977).
- D. Pomerantz, *J. Appl. Phys.*, **38**, 5020 (1967).
- G. A. Rozgonyi, P. M. Petroff, and M. H. Read, *This Journal*, **122**, 1725 (1975).
- P. M. Petroff, G. A. Rozgonyi, and T. T. Sheng, *ibid.*, **123**, 565 (1976).
- S. Prussin, S. P. Li, and R. H. Cockrum, in "Semiconductor Characterization Techniques," P. A. Barnes and G. A. Rozgonyi, Editors, p. 357, The Electrochemical Society Softbound Proceedings Series, Princeton, N.J. (1978).
- S. P. Murarka, H. J. Levinstein, R. B. Marcus, and R. S. Wagner, *J. Appl. Phys.*, **48**, 4001 (1977).
- J. E. Lawrence, *ibid.*, **40**, 360 (1969).
- K. V. Ravi, *Philos. Mag.*, **30**, 1081 (1974).
- S. M. Hu, *Appl. Phys. Lett.*, **27**, 165 (1975).
- H. Shiraki, *Jpn. J. Appl. Phys.*, **15**, 1 (1976).
- H. Shiraki, in "Semiconductor Silicon 1977," H. R. Huff and R. R. Burgess, Editors, p. 546, The Electrochemical Society Softbound Proceedings Series, Princeton, N.J. (1977).
- I. R. Sanders and P. S. Dobson, *Philos. Mag.*, **20**, 881 (1969).
- H. Shiraki, *Jpn. J. Appl. Phys.*, **13**, 1514 (1974).
- H. Shiraki, *ibid.*, **13**, 1859 (1974).
- H. Hashimoto, H. Shibayama, H. Masaki, and H. Ishikawa, *This Journal*, **123**, 1899 (1976).
- Y. Sugita, H. Shimizu, A. Yoshinaka, and T.

- Aoshima, *J. Vac. Sci. Technol.*, **14**, 44 (1977).
24. S. Kishino, S. Isomae, M. Tamura, and M. Maki, *Appl. Phys. Lett.*, **32**, 1 (1978).
 25. H. Shibayama, H. Masaki, H. Ishikawa, and H. Hashimoto, *ibid.*, **29**, 136 (1976).
 26. T. Hattori, *This Journal*, **123**, 945 (1976).
 27. Y. Hokari and H. Shiraki, *Jpn. J. Appl. Phys.*, **16**, 1899 (1977).
 28. Y. Sugita, T. Kato, and M. Tamura, *J. Appl. Phys.*, **42**, 5847 (1971).
 29. S. M. Hu, *ibid.*, **45**, 1567 (1974).
 30. G. A. Rozgonyi and T. E. Seidel, in "Semiconductor Silicon 1977," H. R. Huff and E. Sirtl, Editors, p. 616, The Electrochemical Society Softbound Proceedings Series, Princeton, N.J. (1977).
 31. J. F. Gibbons, *Proc. IEEE*, **60**, 1062 (1972).
 32. M. Tamura, *Appl. Phys. Lett.*, **23**, 651 (1973).
 33. F. Secco D'Aragona, *This Journal*, **119**, 948 (1972).
 34. C. W. Pearce and G. A. Rozgonyi, in "Semiconductor Silicon 1977," H. R. Huff and E. Sirtl, Editors, p. 606, The Electrochemical Society Softbound Proceedings Series, Princeton, N.J. (1977).

Electrical Conductivity of Tetragonal Zirconia below the Transformation Temperature

T. K. Gupta and R. B. Grekila

Westinghouse R&D Center, Pittsburgh, Pennsylvania 15235

and E. C. Subbarao

Indian Institute of Technology, Kanpur 208016, India

Zirconia has three polymorphic modifications: monoclinic up to 1170°C, tetragonal from 1170° to 2350°C, and cubic from 2350°C to the melting point. The tetragonal-monoclinic transformation is martensitic in nature (1), and is accompanied by a large, disruptive volume change. As a result, the properties of the tetragonal phase could not be studied below the transformation temperature. Due to this difficulty of obtaining the tetragonal zirconia at room temperature, the electrical conductivity of tetragonal zirconia has been measured only at high temperatures (2, 3) or at ultrahigh pressure (4) where the tetragonal phase is stable. To conduct measurements below the transformation temperature, the tetragonal phase must first be made stable at room temperature. This has recently been accomplished (5, 6) by taking advantage of fine particle technology and minor doping with Y_2O_3 . As a result of this new development, the opportunity is now available to conduct electrical measurements on tetragonal zirconia below the transformation temperature. This note presents the initial data on the conductivity of tetragonal zirconia from 200° to 900°C. The superior mechanical properties of the tetragonal zirconia below the transformation temperature have also been studied and reported elsewhere (7, 8).

Experimental

The detailed procedure for making tetragonal zirconia disks and their identification by x-ray diffraction analysis have been reported (5, 6) previously. Briefly, the fabrication procedure is as follows. Fine powders¹ (100-300Å particle size) of zirconium oxide alloyed with 1.4 mole percent (m/o) Y_2O_3 were isostatically pressed into disks at a pressure of ~200 MPa. The disks were sintered in air at 1300°-1400°C for 5 hr to obtain specimens which were found to contain 97-98% tetragonal phase as determined by x-ray diffraction, and completely crack-free as observed under the microscope. The disk dimensions were ~2 cm diam and ~0.15 cm thick. The density of the specimens was ~5.6 g/cm³, grain size was about 0.25 μm, and mechanical strength was about 600 MPa (7). It should be emphasized here that there is a critical grain size of about 0.3 μm above which the tetragonal phase starts to convert to the monoclinic phase (7) with the

appearance of microcracks on the surface of the specimen.

Electrical conductivity was measured using a Wayne Kerr Universal Bridge No. B221 at 20 kHz. Platinum electrodes were applied to the disks by coating the two surfaces with Pt paste and heating to 1000°C in air. The specimens were spring loaded between two platinum blocks to which Pt lead wires were attached. The whole assembly was heated in a platinum-wound tube

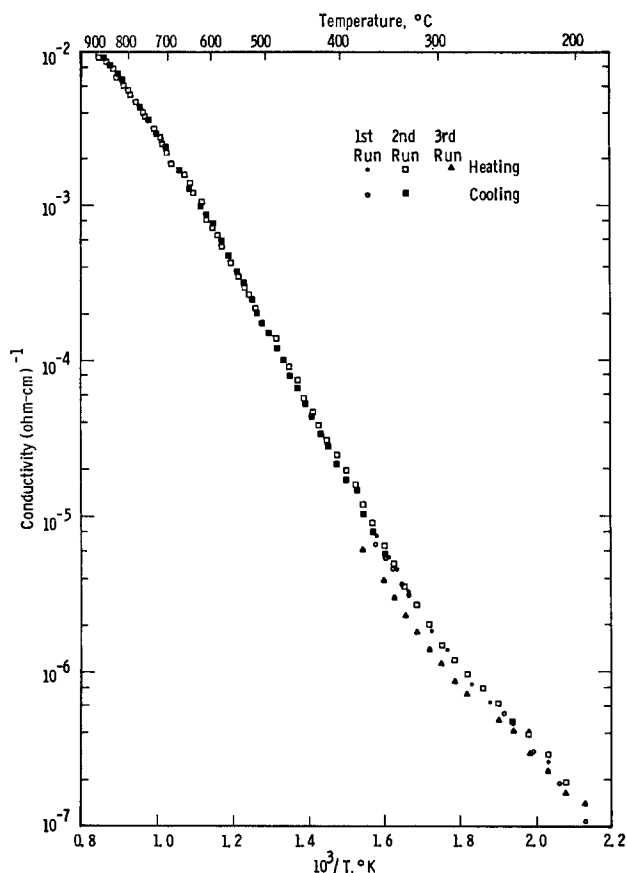


Fig. 1. Temperature dependence of electrical conductivity of 98% tetragonal zirconia.

Key words: tetragonal, zirconia, electrical, conductivity, activation, energy, electrolyte.

¹ Zircor Incorporated, Florida, New York.

furnace at a heating rate of approximately 7°C per minute. The electrical conductivity was measured up to 900°C in air. The data were collected during both heating and cooling, which was accomplished by shutting off the power. Tests were repeated on several specimens to check the reproducibility of the data.

Results and Discussion

The electrical conductivities of tetragonal zirconia (97-98%) as a function of temperature are shown in Fig. 1 and 2 for three different specimens. The results are presented in two figures simply to avoid overlapping of the data. For the data in Fig. 1, the specimen was held at 900°C overnight between each run and the conductivity values are seen to be slightly lower at the third run. Figure 2 shows similar lowering effect (for samples No. 1) at third run during heating (after an overnight hold at 800°C), suggesting perhaps an aging effect at high temperature. During cooling, the values are in close agreement with the other two runs. Above about 400°C, the data in Fig. 1 falls in the middle of that shown in Fig. 2, and below about 400°C, they fall slightly above that shown in Fig. 2. This may be due to slight variation in tetragonal phase between various specimens. The results obtained from other specimens containing 97-98% tetragonal zirconia show agreement with above data, although they are not reported here for redundancy.

The activation energies were calculated by assuming that there is a break in the Arrhenius plots (Fig. 1 and 2) at about 300°C. Actually, there is a region of curvature near this temperature which is, however, ignored for simplicity of calculation. The best fit values for six sets of data gave activation energies between 0.91 and 0.94 eV above 300°C and 0.50 and 0.58 eV below 300°C. The standard deviations are 0.03-0.06 eV in the high temperature region, and 0.04-0.06 eV in the low temperature region. There also appears to be a

region of decreased activation energy above 600°C which is again neglected in the present calculation.

In previous studies (2, 3) it was shown that the electrical conductivity of "pure" tetragonal zirconia is predominantly ionic except at very low oxygen partial pressure ($\sim 10^{-13}$ atm) or at very high temperature ($\sim 1400^\circ\text{C}$). Based on these observations, an ionic conduction mechanism may be suggested for the tetragonal zirconia reported here, although no transference number was measured in the present study. With the above assumption, the high activation energy may be considered as due to transport in the bulk and the low activation energy as that in the grain boundary (grain size $\sim 0.25 \mu\text{m}$) or as impurity controlled.

Figure 3 compares the conductivity data of "pure" and Y_2O_3 containing zirconia for tetragonal and cubic structures. The estimated activation energies are shown in Table I. It is clear from the figure that the present study has extended the range of measurement to well below the transformation temperature. It is also instructive to note that the conductivity tends to increase with increasing concentrations of Y_2O_3 , perhaps due to increasing concentration of oxygen vacancy. The activation energy, however, does not show a similar trend. Furthermore, there is a large discrepancy in conductivity and activation energy for the two reported studies (2, 3) on "pure" zirconia. This discrepancy may be explained partly by the uncertainty of calculation and partly by impurities, grain size, etc. Finally, the conductivity of zirconia containing 1.4 m/o Y_2O_3 is within an order of magnitude of that of zirconia containing 5 and 10 m/o Y_2O_3 , although the structure varied from tetragonal to cubic.

Summary

In summary it can be stated that the conductivity of tetragonal zirconia has been measured at temperatures below the transformation temperature within

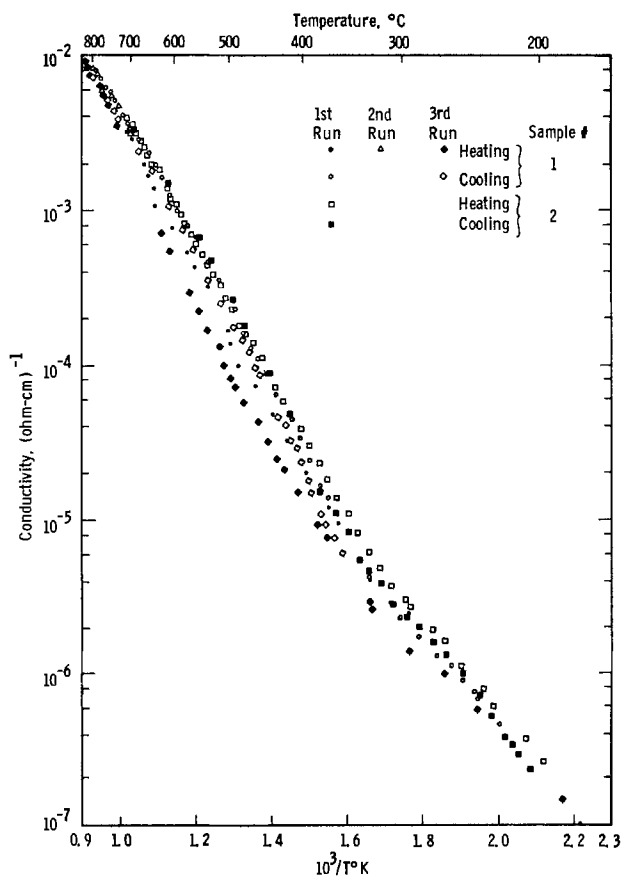


Fig. 2. Temperature dependence of electrical conductivity of 98% tetragonal zirconia.

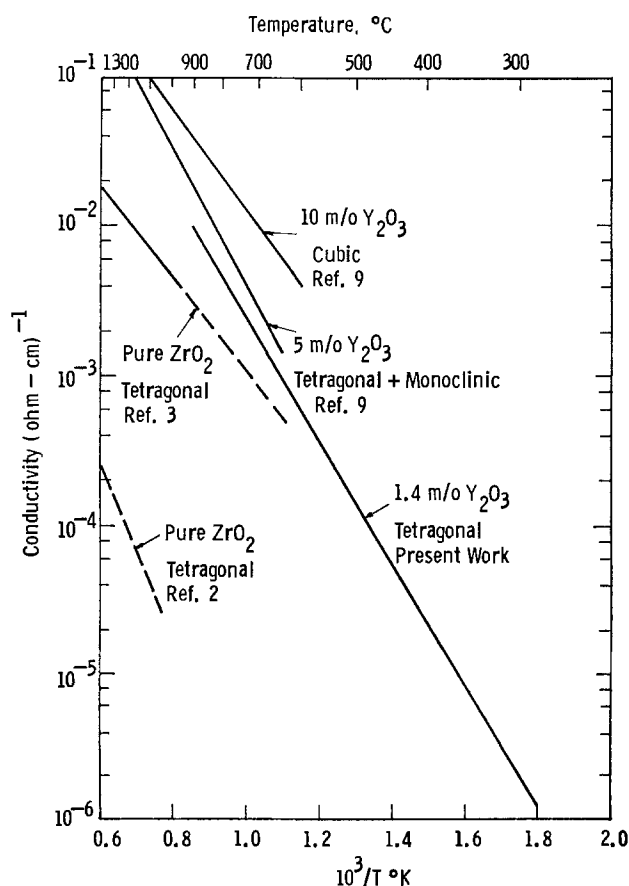


Fig. 3. Temperature dependence of electrical conductivity of tetragonal and cubic zirconia.

Table I. Activation energies of zirconia ceramics

| Material | Structure | Temperature range, °C | Activation energy, eV | Ref. |
|--|--------------------|-----------------------|-----------------------|--------------|
| Pure ZrO ₂ | Tetragonal | 1000-1550 | ~0.86 | (3) |
| Pure ZrO ₂ | Tetragonal | 1227-1330 | ~1.4 | (2) |
| ZrO ₂ + 1.4 m/o Y ₂ O ₃ | Tetragonal | 300-900 | 0.91-0.94 | Present work |
| ZrO ₂ + 1.4 m/o Y ₂ O ₃ | Tetragonal | 200-300 | 0.50-0.58 | Present work |
| ZrO ₂ + 5 m/o Y ₂ O ₃ | Cubic & monoclinic | 600-1300 | ~1.07 | (9) |
| ZrO ₂ + 10 m/o Y ₂ O ₃ | Cubic | 600-1300 | ~0.79 | (9) |

that range. The conductivity has a high temperature region (300°-900°C) with an activation energy of about 0.9 eV and a low temperature region (200°-300°C) with an activation energy of about 0.5 eV. The conductivity values are close to that of Y₂O₃ stabilized cubic zirconia reported in the literature. The high electrical conductivity and the suggestive high ionic transport number combined with high mechanical strength (7) of tetragonal zirconia make it an attractive candidate for solid electrolyte applications.

Manuscript submitted Aug. 18, 1980; revised manuscript received Oct. 27, 1980.

Any discussion of this paper will appear in a Discussion Section to be published in the December 1981 JOURNAL. All discussions for the December 1981 Discussion Section should be submitted by Aug. 1, 1981.

Publication costs of this article were assisted by Westinghouse R&D Center.

REFERENCES

1. E. C. Subbarao, H. S. Maiti, and K. K. Srivastava, *Phys. Status Solidi*, **A21**, 9 (1974).
2. P. Kofstad and D. J. Ruzicka, *This Journal*, **110**, 181 (1963).
3. R. W. Vest and N. M. Tallan, *J. Am. Ceram. Soc.*, **48**, 472 (1965).
4. E. Dow Whitney, *This Journal*, **112**, 91 (1965).
5. T. K. Gupta, J. H. Bechtold, R. C. Kuznicki, L. H. Cadoff, and B. R. Rossing, *J. Mater. Sci.*, **12**, 2421 (1977).
6. T. K. Gupta, *Sci. Sinter.*, **10**, 205 (1978).
7. T. K. Gupta, F. F. Lange, and J. H. Bechtold, *J. Mater. Sci.*, **13**, 1464 (1978).
8. F. F. Lange, in "Fracture Mechanics of Ceramics," Vol. 4, R. C. Bradt, D. P. H. Hasselman, and F. F. Lange, Editors, pp. 877-889, Plenum Publ. Corp., New York (1978).
9. D. W. Stickler and W. G. Carlson, *J. Am. Ceram. Soc.*, **47**, 122 (1964).
10. H. G. Scott, *J. Mater. Sci.*, **10**, 1527 (1975).



Lithium Closoboranes II. Stable Nonaqueous Electrolytes for Elevated Temperature Lithium Cells

Jack W. Johnson and A. H. Thompson*

Exxon Research and Engineering, Corporate Research, Linden, New Jersey 07036

Nonaqueous electrolyte secondary lithium cells are of interest for a variety of potential applications, ranging from such low rate applications as in cardiac pacemakers to the high rate systems needed for electric vehicles and off-peak power storage. In particular, Li cells with cathodes of intercalation and insertion compounds have been shown to have highly desirable properties (1,2). A crucial component of Li battery systems is the electrolyte, which must have extraordinary chemical stability in order to allow long cycle life and have sufficient conductivity to allow cell operation at the desired rates. We have previously reported (3) that Li closoborane/dioxolane/DME electrolytes are stable in the presence of both Li metal and TiS_2 at $70^\circ C$ for extended periods. Herein we report the results of Li- TiS_2 cell tests carried out at elevated temperatures.

The intermediate temperature range ($50-180^\circ C$) in Li batteries has not yet been thoroughly explored because of the absence of suitable electrolytes, although some plating tests have been reported in $LiAsF_6/THF$ in which improved efficiencies are observed over room temperature tests (4). One incentive for testing cells in this regime is the possibility of achieving higher operating rates due to improved mass transport in both the electrolyte and the cathode without requiring the expensive and difficult to fabricate materials for separators and containers needed in high temperature cells (5). In addition, many ambient temperature applications of secondary Li cells such as protection of volatile memory in computers will involve operation at temperatures higher than $25^\circ C$. Operation at higher temperatures, near the melting point of the metal, may also improve Li plating. In this communication we report results on the

rate performance and cycling stability Li- TiS_2 cells using a Li closoborane/DME/dioxolane electrolyte at temperatures to $110^\circ C$.

AC conductivity measurements showed an approximate doubling of the conductivity of $Li_2B_{10}Cl_{10}$ and $Li_2B_{12}Cl_{12}$ /DME/dioxolane solutions upon heating from 25 to $100^\circ C$ (6). In order to test the effect of this conductivity improvement on the rate performance of actual cells, we measured signature curves in Li- TiS_2 cells at various temperatures. The cells contained 2 cm^2 cathodes loaded with 70-90 mg of a 90% TiS_2 /10% Teflon mixture hot pressed into a stainless steel grid and wrapped with polypropylene separator. The anodes were excess Li sheet and the electrolyte was 0.6M $Li_2B_{10}Cl_{10}$ ·6DME/dioxolane. The data were obtained by discharging the cell at a given high rate until the voltage dropped to 1.5 V, then allowing the cell to relax on open circuit to constant potential, and repeating the discharge at a lower rate to the same cut-off voltage. By continuing this process until the cell was totally discharged a plot of cumulative capacity vs. current density was obtained. As can be seen in Figure 1,

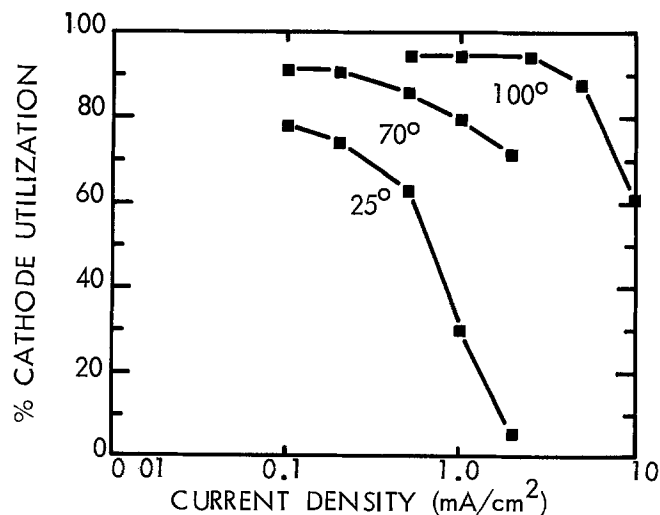


Fig. 1 Signature Curves for Li- TiS_2 Cells

Keywords: closoborane, lithium, electrolyte, battery

*Electrochemical Society Active Member.

a substantial improvement in the rate performance of TiS_2 cells is realized with increasing temperature. At $25^\circ C$ the rate has to be lowered to 0.5 ma/cm^2 in order to reach 60% discharge, while at $100^\circ C$, this level is reached at 10 ma/cm^2 and the cell is fully discharged at 2.5 ma/cm^2 .

The stability of the electrolyte system to continued operation at elevated temperatures was demonstrated in the following experiment. A $Li-TiS_2$ cell constructed like the above cells, but with a cathode made of TiS_2 suspended in a stainless steel mesh bag, was discharged at 0.5 ma and recharged at 0.2 ma at $70^\circ C$ for 19 cycles with no significant capacity fade (Figure 2). The temperature was then raised to $110^\circ C$ and the discharge rate to 1.0 ma and cycling continued for 17 more cycles. During this period, the capacity gradually faded by about 30%. Autopsy of the cell showed a decline

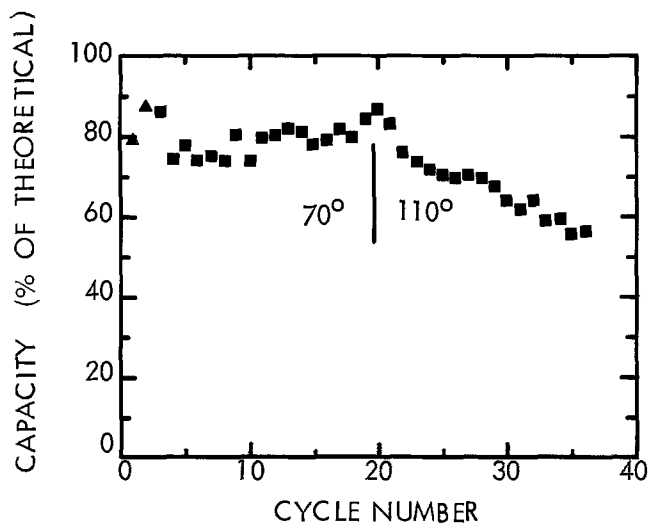


Fig. 2 Elevated Temperature Cell Cycling

in the electrolyte level, so that the entire cathode was no longer immersed. The total duration of the experiment was ten weeks with the cell functioning the entire time at elevated temperatures, thus demonstrating the inherent stability of the Li closoborane electrolyte under these conditions.

In summary, we have shown that Li closoborane electrolytes are stable to the operating conditions of a $Li-TiS_2$ cell at elevated temperatures, and that there are substantial improvements in the rate performance of such cells operated at increased temperatures. Cells using these electrolytes may be

particularly useful where conditions require operating temperatures above $25^\circ C$ or where increased current densities are required.

REFERENCES

1. M. S. Whittingham, *Science* **192**, 1126 (1976).
2. M. S. Whittingham, *Prog. Solid Stat Chem.* **12**, 41 (1978).
3. J. W. Johnson and M. S. Whittingham, *J. Electrochem. Soc.* **127**, 1653 (1980).
4. S. B. Brummer, F. W. Dampier, V. R. Koch, T. F. Reise, and J. H. Young, NSF Report NTIS-PB-290934 (1978).
5. J. E. Battles, J. A. Smaga, and K. M. Myles, *Metallurgical Transactions* **9A**, 183 (1978).
6. J. W. Johnson, A. H. Thompson, and J. F. Brody, submitted to *J. Electrochem. Soc.*

Manuscript received Dec. 31, 1980.

Publication costs of this article were assisted by Exxon Research and Engineering Company.

Promotion by Carbon of the Reactivity of Lithium with SOCl_2 and SO_2 —Effect on Lithium Battery Safety

William P. Kilroy* and Stanley D. James*

Naval Surface Weapons Center, Electrochemistry Branch, Silver Spring, Maryland 20910

We wish to draw the attention of the battery community to what may be a pervasive source of dangerously high reactivity in lithium batteries. This is the strong catalytic power of carbon black which is the substrate for the positive electrodes of most lithium primaries. The presence of carbon causes an intense activation of the direct reaction between Li and the battery oxidant (1). This effect may be at the bottom of many of the dangerous incidents involving Li batteries which have occurred over the last few years since there are plausible scenarios by which the lithium and carbon components can become intimately mixed.

Lithium is quite inert to LiAlCl_4 - SOCl_2 and LiAsF_6 -AN- SO_2 battery electrolytes at room temperature even under conditions of violent mechanical shock. However, prior grinding of the Li with fine carbon black changes this picture dramatically; spontaneous ignition on mixing and explosive energy release on shocking become common, especially with the SOCl_2 electrolyte. We examined various parameters that influence this reactivity; nature and freshness of carbon; freshness, purity and conductive salt of the electrolyte; degree of mixing of Li and carbon; presence of Teflon and moisture; undervoltage deposition onto polarized carbon. Both local cell action and Li dispersion contribute to our observed carbon catalysis of the reaction of Li with battery oxidants. The formation of reactive Li binary compounds with C, O or N does not seem to be a factor with the possible exception of a Li-graphite intercalate.

*Electrochemical Society Active Member

REACTIVITY OF PHYSICALLY PREPARED Li-C MIXTURES

Reactivity was relatively low and quite variable if the Li and C were merely lightly pressed together. However, prior grinding of the Li-C mixture significantly raised both the level and reproducibility of the reactivity. Therefore, we routinely studied ground mixtures. Both grinding and addition of electrolyte were done in standard Pyrex Ignition Tubes. Relative reactivity was then assessed with a qualitative scale of numbers from one to ten.

Traces of carbon are insufficient to activate the Li-oxidant reaction. Only when the carbon content of the Li-C mixes rose above 10 and 30% w/w for the SOCl_2 and SO_2 electrolytes respectively did reactivity commence. Figure 1 shows this trend and illustrates the far higher reactivity of the SOCl_2 electrolyte. For both electrolytes an increase in Li/C mass ratio led to a fall in spontaneous flammability accompanied by a rise in shock-sensitivity.

We studied a variety of carbons (blacks, graphites and charcoal) to correlate Li-C reactivity with the carbon's surface area, graphite crystallinity and purity. For Li-carbon black mixtures reacting with SOCl_2 - LiAlCl_4 , reactivity rose smoothly with carbon specific surface. At a value of about $100 \text{ m}^2/\text{g}$ reactivity had levelled off in the region of 9.5 which means vigorous fires were consistently observed when electrolyte contacted the Li-C mix. Carbon surface area is the biggest factor affecting its ability to promote reactivity with external particle surface being much more active than

internal pore area. The purity and crystallinity of the carbon appear to be of no consequence. Shawinigan acetylene black extensively used as the cathode substrate of Li batteries is one of the most reactive carbons we studied.

REACTIVITY OF CARBON CATHODIZED
BETWEEN +1.0 AND +0.1V VERSUS
A Li REFERENCE ELECTRODE

Several workers have reported intermediate voltage-time plateaus (above 0, V versus Li) when carbon is cathodized in aprotic solvents free of cathode depolarizer (2-5). These plateaus are thought to involve the undervoltage deposition of Li to form Li-C intercalates. Since these Li-C compounds were shown to be much more reactive than pure Li(2) we prepared carbon that had been cathodized under these conditions and tested its reactivity to battery electrolytes. For various preparations involving different electrolytes and current densities, the undervoltage plateau occurred between +1.2 and +0.2V, versus Li. We found that the most reactive preparations were those formed at the high end of this voltage range. These materials were capable of boiling the SOCl_2 electrolyte but appeared to be inert to the SO_2 electrolyte.

RELEVANCE TO LITHIUM BATTERY SAFETY

We observed a very powerful catalysis by carbon of the lithium/battery-oxidant reaction. This effect is important because, in polarized cathodes, Li and C may become intimately mixed (a) by undervoltage deposition to form reactive, Li-C intercalates which react continuously with the electrolyte accumulating heat to possibly dangerous levels (b) by normal overvoltage deposition of passivated Li dendrites. Subsequent shear or shock could then grind dendrites and carbon together causing violent reactivity. Furthermore, severe mechanical distortion of fresh or normally discharged Li batteries could shear Li and C components together with the same dangerous result. With this in mind we are currently testing carbons that have the promise of combining a greatly reduced reactivity in Li-C mixes with unimpaired

efficiency as cathodes.

ACKNOWLEDGEMENT

The authors thank the Independent Research Program of the Naval Surface Weapons Center and the Naval Sea Systems Command in conjunction with the Electrochemistry Technology Block Program for financial support of this work.

REFERENCES

1. S. Dallek, S. D. James and W. P. Kilroy, Submitted to J. Electrochem. Soc.
2. J. O. Besenhard, Carbon, 14, 111 (1976)
3. S. D. James, J. Electrochem. Soc. 122, 921 (1975)
4. J. O. Besenhard, H. P. Fritz, J. Electroanal. Chem., 53, 329 (1974)
5. G. Eichinger, *ibid*, 74, 183 (1976)

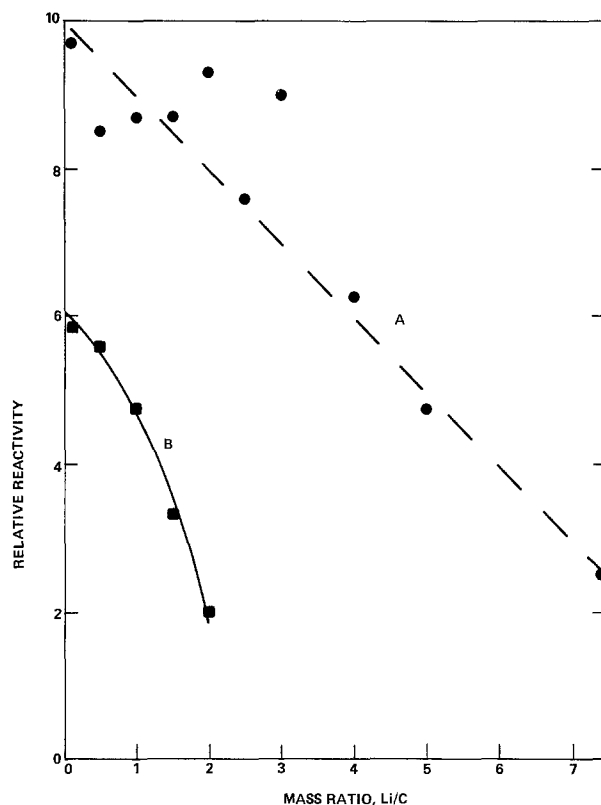


Fig. 1 Reactivity versus carbon content for ground Li-C mixes with A) SOCl_2 -LiAlCl₄ B) SO_2 -AN-LiAsF₆

Publication costs of this article were assisted by the Naval Surface Weapons Center.

Electron Trap-Free Low Dislocation Melt-Grown GaAs

J. M. Parsey, Jr., Y. Nanishi,* J. Lagowski, and H. C. Gatos*

*Department of Materials Science and Engineering,
Massachusetts Institute of Technology, Cambridge, Massachusetts 02139*

Melt growth of electron trap-free GaAs was achieved for the first time, employing the Bridgman method under conditions permitting high precision control of the As vapor pressure over the melt and by doping the melt with minute amounts of Ga₂O₃. Stringent control of both of these parameters was found to be critical as neither alone leads to electron trap-free material.

.

The availability of high quality bulk crystals is critical for realizing the full potential of GaAs in electronic applications. At present, high quality material can be produced only in thin layer form by epitaxial techniques. Presently available bulk GaAs exhibits significant concentrations of structural defects and deep states which act as trapping or recombination centers, precluding most of its direct applications as an active device material. GaAs of this quality when used as a substrate in epitaxial technology often has profound adverse effects on the structural and electronic characteristics of epilayers and devices.

In this communication we report on a melt growth process which leads to significant advancement in the electronic and structural characteristics of GaAs and yields reproducibly electron trap-free, very low dislocation material, which thus far is achieved only in thin layer form by epitaxial techniques.

Growth was performed in a horizontal Bridgman apparatus into which two unique features were incorporated: 1) a sodium heat pipe in the low temperature zone for the stabilization and precise control of the arsenic vapor pressure during growth; and 2) a multi-channel thermal monitoring system which makes seeding possible by thermal monitoring rather than by sight. Elimination of the viewing window leads to enhanced thermal symmetry in the high temperature region. Thus, convection in the melt is reduced and thermal stresses in the growing crystal are also reduced. Details of the growth apparatus and its operation will be presented elsewhere (1).

*Electrochemical Society Active Member.

The ampoule is a two-section quartz tube with a breakable seal between the sections as shown in Fig. 1. A very critical step in the growth process is the surface treatment of the high purity quartz (sand blasting with 50 μ m Al₂O₃ and cleaning with aqua regia).

The section of ampoule containing 6N⁺ polycrystalline arsenic is sealed (under vacuum) after a bake-out at 250°C for 2 hours at a pressure less than 10⁻⁶ torr. The high temperature section contains a seal-breaking weight, a diffusion barrier (2), the boat with a seed crystal (<111> B orientation) and 6N polycrystalline GaAs; it is baked under vacuum of about 3 x 10⁻⁷ torr at 600°C for 2 hrs and then sealed off. The internal seal is broken magnetically completing the preparation for growth.

The sealed growth ampoule is placed in a quartz tube over which a 4-zone furnace rides. To initiate growth, the preheated furnace is positioned over the quartz tube and stabilized at the desired thermal profile. A 5-hour equilibration takes place prior to growth. Typical macroscopic growth velocities of 5 mm/hr are achieved by controlled furnace motion.

From a series of growth experiments in which the As source temperature was systematically varied it was established that the structural and electronic properties of GaAs depend critically on the arsenic source temperature and that they are optimized when the arsenic source temperature is maintained at 616°C. At this As source temperature (optimum As pressure) crystals with low dislocation densities (below 500 dislocations/cm²) were reproducibly grown; in these crystals the deep level concentrations and compensation ratios were significantly decreased (3). It was further discovered that under these optimum arsenic pressure conditions light doping of the melt with Ga₂O₃ (in the weight ratio 1 Ga₂O₃: 10⁵ GaAs) yields GaAs with undetectable concentrations of deep electron traps.

As seen from typical DLTS spectra shown

in Fig. 2, the crystal doped with Ga_2O_3 grown under optimum As pressure exhibits two deep levels near the seed; as growth proceeds the concentrations of these levels decrease to below detectability limits (approximately 10^{-4} of free carrier concentration, 10^{13}cm^{-3} in the present case). It should be noted that only two electron traps are initially present in this material (0.75 eV and 0.40 eV below the conduction band edge) in contrast to three to five deep states typically found in bulk GaAs (4), and also found in the GaAs grown under optimum As pressure without Ga_2O_3 doping. Recently it has been demonstrated that plastic deformation increases the concentration of these states at 0.75 eV suggesting that this level results from native point defects (5).

Photocapacitance measurements confirmed the absence of electron traps. In addition, they revealed a single hole trap at about 0.4 eV above the valence band with a concentration of about $3 \times 10^{15}\text{cm}^{-3}$ (i.e., on the order of 1% of carrier concentration). In contrast, high quality LPE GaAs often exhibits two hole traps of similar relative concentrations.

The striking beneficial effect of Ga_2O_3 doping is further evidenced in Table I where typical properties of GaAs crystals grown under optimum As pressure with and without Ga_2O_3 doping are shown. GaAs grown with Ga_2O_3 exhibits a much larger value of minority carrier diffusion length (as determined from photovoltage (6) and SEM-EBIC measurements, (7)) and its minority carrier lifetime value is close to the radiative recombination limit (8). GaAs grown without Ga_2O_3 doping exhibits significant concentrations of deep states and its minority carrier lifetime is nearly 25 times shorter than that of the electron trap-free GaAs.

The remarkable decrease in dislocation density at the optimum As pressure suggests that under this pressure the density of vacancies is significantly reduced (near stoichiometric growth conditions). This conclusion is corroborated by the corresponding reduction of the densities of deep levels which are believed to result from vacancy-vacancy (9) or vacancy-impurity interactions (10) (the total level of impurity contamination was not affected by the As pressure). The role of oxygen (Ga_2O_3 doping of the melt) in eliminating deep levels (or in decreasing their concentrations below the detection limits) is not understood at present. However, it is reasonable to speculate that oxygen-vacancy interactions are responsible for reducing the

Table I. Materials Properties

| MATERIAL | DISLOCATION DENSITY | CARRIER CONCENTRATION | COMPENSATION RATIO | |
|-------------------------------|--|-----------------------------------|---------------------------|----------------------|
| | (cm^{-2}) | (cm^{-3}) | (N_A/N_D) | |
| Ga_2O_3 added | $\ll 500$ | 1.8×10^{17} | 0.58 | |
| Ga_2O_3 free | $\ll 500$ | 6.2×10^{16} | 0.68 | |
| | MOBILITY | MINORITY CARRIER DIFFUSION LENGTH | MINORITY CARRIER LIFETIME | |
| | ($\text{cm}^2/\text{V-s}$) | (μm) | (sec) | |
| Ga_2O_3 added | 2400 | 5 | 3.2×10^{-8} | |
| Ga_2O_3 free | 3300 | 1 | 1.3×10^{-9} | |
| | ELECTRON TRAP CONCENTRATION (cm^{-3}) | | | |
| | 0.75 | 0.54 | 0.40 | 0.34 (eV) |
| Ga_2O_3 added | N/D | N/D | N/D | N/D |
| Ga_2O_3 free | 2.3×10^{16} | 6.8×10^{14} | 3.1×10^{15} | 6.6×10^{15} |

N/D = Not Detected

already low density of free vacancies. It should be pointed out that according to recent studies (11) oxygen is not responsible for the deep level at ~ 0.8 eV in contrast to earlier prevailing views (9).

In view of the present findings which demonstrate the critical role of the absolute value and control of the As pressure over the melt it is apparent that Czochralski growth, with liquid encapsulation, cannot yield high quality GaAs crystals.

In summary, low dislocation electron trap-free melt-grown GaAs was achieved for the first time. The key contributing factors to the achievement are the addition of minute amounts of Ga_2O_3 in the melt and the precise control of the optimum arsenic vapor pressure attained by the use of a heat pipe (12).

ACKNOWLEDGEMENT

The authors would like to thank Ms. M. Kaminska and Ms. K. Isozumi for assistance in the measurements of our crystals. We are also grateful to the National Aeronautics and Space Administration for financial support of this project.

REFERENCES

1. J.M. Parsey, Y. Nanishi, J. Lagowski, and H.C. Gatos, to be published.
2. J.M. Woodall, Trans. A.I.M.E. 239, 378 (1967).
3. Y. Nanishi, J.M. Parsey, J. Lagowski, and H.C. Gatos, to be published.

4. G.M. Martin, A. Mitonneau, and A. Mircea, *Elec. Lett.* **13**, 191 (1977).
5. T. Ishida, K. Maeda, and S. Takeuchi, *Appl. Phys.* **21**, 257 (1980).
6. A.M. Goodman, *J. Appl. Phys.* **32**, 2550 (1961).
7. C.J. Wu and D.B. Wittry, *J. Appl. Phys.* **49**, 2827 (1978).
8. "GaAs Growth, Properties and Applications," ed. F.P. Kesmanl and D.N. Nasledov, Nauka, Moscow, 1973, pp. 267.
9. J. Blanc, R.H. Bube, and L.R. Weisberg, *J. Phys. Chem. Sol.* **25**, 225 (1964).
10. D.T.J. Hurle, *Inst. Phys. Conf. Ser. No. 33a*, 1977, Chap. 2, pp. 113.
11. A.M. Huber, N.T. Linh, M. Valladon, J.L. Debrun, G.M. Martin, A. Mitonneau, and A. Mircea, *J. Appl. Phys.* **50**, 4022 (1979).
12. T.R. AuCoin, M.J. Wade, R.L. Ross, and R.O. Savage, *Solid State Tech.*, Jan. 1979, pp. 59.

Manuscript received Jan. 19, 1981.

Publication costs of this article were assisted by the Massachusetts Institute of Technology.

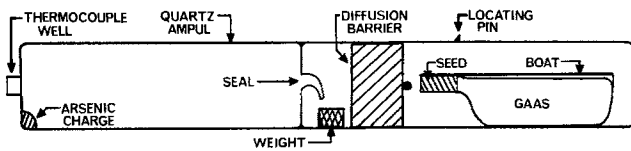


Fig. 1. Cross section of growth apparatus

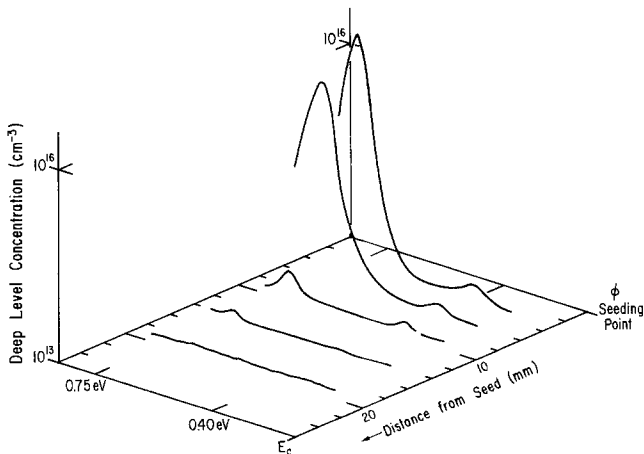


Fig. 2. Deep level concentration and energy position vs. location in crystal, showing reduction of deep level concentration below detection limits



Ernest Yeager

John Yeager*

It is with a feeling of great pleasure that I am speaking to you this afternoon about Ernest Yeager, the recipient of the Edward Goodrich Acheson medal and prize for 1980. I have had good reason to always be proud he is my "big" brother, and thankful to have him as such a close friend.

Ernie was born in 1924 in Orange, New Jersey, and just a few years later my lifelong relationship with him began. Our parents were both Swiss that had immigrated to the United States—our father as a child and our mother in her late teens. They can be best described as dedicated, loving parents committed to raising their sons to the best of their ability. Both had a great respect for the value of education, and from early on instilled that feeling in their sons.

In Ernie's years in the Orange Public Schools, he developed strong interest in the areas that were to be his life's work—the physical sciences and teaching. His choice of career wasn't obvious, however, because he also excelled and had equal interest in mathematics and music. After much hard deliberation, Ernie made his choice, and selected a local college, New Jersey State Teachers College at Montclair, where he did his undergraduate work as a math major with chemistry and physics as minors. The idea of a musical career, however, was very strongly considered. By the time he completed high school, his talent and accomplishment as a classical pianist were considerable, and he was recognized locally as a good dance band musician. The popular music aspect was particularly fortunate because, besides the enjoyment he derived from playing, he was able to help pay for his college education working with local dance bands. With the years, Ernie is a little rusty in his musical skills, but even now when the family is together Ernie's piano playing is a source of real enjoyment for us.

Ernie completed his undergraduate work at Montclair and received the B.A. (summa cum laude) in 1945. Among the faculty there was Dr. Rufus Reed, a chemistry professor that strongly encouraged Ernie to pursue his graduate studies in the Chemistry Department of Western Reserve University. Still interested in math, the choice was difficult, but Ernie elected to carry out his graduate work in physical chemistry and received his M.S. in 1946 and Ph.D. in 1948. At Western Reserve University his thesis professor for both degrees was Dr. Frank Hovorka, an individual, and now a close personal friend, that had a marked effect on development of Ernie's technical career. Ernie was given considerable latitude in selection of his work for his doctoral thesis and, in the course of searching a topic, he came upon an article in the first volume of the *Journal of Chemical Physics* by Dr. Peter Debye. In it was predicted what became known as the Debye effect of ionic vibrating potentials. The work, Ernie undertook and successfully completed in detection of the effect, developed in him a keen interest in ultrasonics

and its application to physical chemistry, particularly its effects on electrolytes. His presently well-recognized interest in electrochemistry developed during this period and blossomed after he remained upon graduation as a faculty member at Western Reserve University. Ernie's work with ultrasonics had led him to consider the effect it might have on electrode processes, and from that entry he became immersed in the study of electrode processes themselves. Ultrasonics and acoustics were not abandoned, however, as evidenced by continuing publications, his being a past vice president and a fellow of the Acoustical Society of America, 14 years as a member of the Committee on Undersea Warfare of the National Research Council, and the two years he served on the Underwater Sound Advisory Committee of the U.S. Navy.

Prior to proceeding further with the technical side of Ernie's career, there are a few personal observations that I want to make to round out your picture of him. I can state he is always busy, but it isn't always in the scientific field. He has a continuing long term involvement with the church from his youth. He has been a Sunday school teacher, and in more recent years, an Elder of the United Presbyterian Church. Ernie is a people person and truly involved with those he contacts. While he has never married, his family is real and big. It includes my wife and I, and our four children who consider him more than just an Uncle; it includes numerous relatives, mostly in Switzerland; and it includes the 54 graduate and 40 post doctoral students that have worked with him and literally been brought into his family over the 30 plus years at Case Western Reserve University. Fortunately, Ernie loves the travel aspect of his technical work, and derives great pleasure on trips visiting with his "family." In fact, for the past twenty or so years he has always managed at least yearly visits to the family in Switzerland. Lastly, to round out the picture of Ernie, he is a very practical guy and quite skilled as a do-it-yourselfer around his home. He does virtually all his own plumbing, painting, gardening, electrical work, and carpentry; and he does it well.

Ernest has been also strongly involved in the necessary operational work at Case Western Reserve University. He has served as Chairman of the Chemistry Department and as Chairman of the University Faculty Senate at the time of the planning and execution of the merger of Case and Western Reserve University. In 1976 he became Director of the newly established Case Laboratories for Electrochemical Studies, a cooperative effort of six departments which, as described by Ernie, is to "push" electrochemistry at Case.

He is a Past President and honorary member of The Electrochemical Society; he has served as chairman of the Theoretical Electrochemistry Division (now Physical Electrochemistry Division) and as chairman of the Cleveland Section of The Electrochemical Society. Further, Ernie is also a past president of the International Society of Electrochemistry.

* Introductory remarks by John Yeager on the occasion of the presentation of the Acheson Medal Award to Ernest Yeager on October 7, 1980 at the Hollywood, Florida, Meeting.

In addition to the prestigious award he is now receiving, he has received Alumni Awards from both Case Western Reserve and New Jersey State College at Montclair, the Biennial Award of the Acoustical Society of America, the Navy Certificate of Commendation the Cleveland Technical Society of America Council Award, and the Heise Award of the Cleveland Section of The Electrochemical Society.

Ernie has served as a member of the IUPAC Commission on electrochemistry, the ARPA Technical Power Panel, and as a representative member of the National Research Council. He is currently serving on the visiting committee for Brookhaven National Laboratories, the Advisory Committee on USSR and

Europe of the Commission on International Relations of the National Academy of Sciences, and the Committee on Battery Materials Technology of the National Material Advisory Board of the National Research Council.

Ernie is editor and co-editor of seven books and 154 publications in electrochemistry. These publications as well as his present research emphasis include electrochemical kinetics, electrocatalysis, the electrochemistry of oxides, optical studies of electrochemical interfaces, and the relaxation properties of electrolytes.

President Pell, it is with the greatest of pleasure that I present to you, Ernest Yeager, the recipient of the Edward Goodrich Acheson Medal and Prize for 1980.

Recent Advances in the Science of Electrocatalysis

Ernest Yeager¹

Case Laboratories for Electrical Studies and the Chemistry Department,
Case Western Reserve University, Cleveland, Ohio 44106

Electrochemistry is experiencing a renaissance. The meetings of The Electrochemical Society and its Journal provide ample evidence of this renaissance, which has been stimulated by the energy problem and the importance of electrochemistry conversion, and conservation. Equally important are indications that electrochemistry has reached a critical stage where especially rapid development of the science is likely to occur over the next decade.

Already early in this century, much of the thermodynamics of electrochemistry was reasonably well in place but electrochemical kinetics and electrocatalysis remained more an art than a science. Reproducibility in kinetic studies has been a particular problem but in recent years electrochemists have gained sufficient control over the various experimental factors, including impurity effects, to achieve reproducible results even with surface demanding reactions. Substantial theoretical developments have also occurred over the last two decades in the areas of electron and proton charge transfer at electrochemical interfaces. Further, the impact of various surface chemical physics techniques, both *in situ* and *ex situ* to the electrochemical environment, is starting to be felt in electrocatalysis studies.

Adsorption on the electrode surface plays a key role in electrocatalysis. Little information is available, however, concerning the chemical nature of the interactions of adsorbed species with the electrode and the adsorption sites. This situation has been detrimental to the development of electrocatalysis as a science. There has been a general lack of good molecular level techniques for examining the chemical structure of electrochemical interfaces, analogous to the various spectroscopic techniques which have had such an impact on the physics and chemistry of bulk phases. In most instances electrochemical techniques provide a sensitive tool for the detection of electrosorption but lack the needed molecular level specificity. Even the charge on electrosorbed species cannot be determined electrochemically in most instances because of the difficulty of resolving what fraction of the externally provided charge is transferred to the adsorbed species rather than just on the metal surface and compensating the charge of the electrosorbed species and the remainder of the ionic double layer.

In this lecture I shall first assess some of the more promising *in situ* and *ex situ* techniques of a more or less nontraditional type for obtaining such information

and then consider the state of our understanding of some important electrocatalytic systems.

In Situ Techniques for the Study of Electrochemical Interfaces

Table I lists the majority of the presently used *in situ* spectroscopic techniques for the study of electrochemical interfaces. Various windows exist for electromagnetic radiation in solvents such as water; *i.e.*, for x-ray, u.v.-visible and, for very short path lengths, certain parts of the infrared. Consequently optical spectroscopy lends itself to *in situ* studies (1). The majority of the u.v.-visible and infrared studies make use of intensity changes upon reflectance from the electrochemical interface in the external or internal attenuated total reflectance modes, the latter with transparent electrodes. With the external mode, both specular and diffuse reflectance techniques have been used. With transparent electrode, transmission techniques have also been used. The optical changes attending the change of electrode potential and the adsorption of various species at mono- and submonolayer levels are small but still easily measured with modern signal detection-processing techniques. Ellipsometric spectroscopy (2-4), using automatic instrumentation (3), is a particularly powerful technique for obtaining information concerning the collective dielectric properties of the interface and adsorbed layers as a function of wavelength and potential.

The various ultraviolet-visible optical measurements have yielded substantial information concerning sur-

Table I. Nontraditional techniques for the study of electrochemical interfaces and adsorption at such interfaces

Presently used techniques

1. Optical
 - a. ultraviolet-visible and infrared spectroscopy
 - specular reflectance (external, internal)
 - diffuse reflectance
 - transmission through optically transparent electrodes
 - ellipsometry—as a spectroscopic tool
 - b. Raman spectroscopy
 - c. photoassisted processes, including photoemission
2. Mössbauer spectroscopy
3. acoustoelectrochemical techniques
4. electron spin resonance

Promising techniques

1. EXAFS
2. NMR
 - broadline
 - high resolution

¹Acheson Medal Address delivered October 7, 1980 at the Hollywood, Florida, Meeting of The Electrochemical Society.

face charge, adsorption isotherms, structural information for adsorbed molecules, the state of water in the compact double layer, structural transitions in underpotential deposited layers, surface roughness, and the electronic properties of anodic films and passivation layers on metals. For the most part, however, these optical techniques have not made as great a fundamental contribution to the understanding of electrochemical interfaces and adsorption at such interfaces as some of us expected at the start of such work in the mid 1960's. In part this is because of limitations on the type of information which can be gained with only ultraviolet-visible spectroscopy. The impact of these measurements, however, has been lessened by the lack of quantitative theoretical treatments of the collective optical properties of the metal-electrolyte interface and adsorbed species to provide a quantitative framework within which to interpret such optical measurements. Only with layers much thicker than monolayer dimensions [e.g., passivation layers on active metals (5)] is a simple three-layer optical model involving two bulk phases with an intermediate thin layer adequate.

Vibrational data for adsorbed species can be very useful. *In situ* infrared studies using internal reflectance have been carried out with semiconductor transparent electrodes. It has been possible to detect the C-H stretched frequency for adsorbed layers of higher molecular weight molecules (6) using D₂O as the solvent to minimize solvent interference. With semiconductor electrodes of sufficient transparency in the infrared, however, most of the potential drop is in the space charge region in the electrode phase and relatively little information is gained concerning the adsorption process. Further, solvent absorption in the infrared imposes very severe restrictions.

Recently Bewick and Pons (7) at the University of Southampton have used external infrared reflectance spectroscopy with very thin electrolyte layers combined with electromodulation techniques to study the water layer adjacent to the interface. This approach is very promising although much care must be exercised to guard against artifacts in the measurements.

Particularly exciting developments have occurred over the past few years in the application of *in situ* Raman spectroscopy to the study of electrochemical interfaces. Since the observation of unusually strong Raman signals for pyridine adsorbed on silver by Fleischmann, Hindra, and McQuillan at Southampton (8, 9) in the early 1970's, great interest has developed in Raman studies of adsorbed species on electrode surfaces. A large number of publications (10, 11) have appeared, mostly concerned with experimental and theoretical studies of possible mechanisms for the extraordinarily large surface enhanced Raman signals observed with most adsorbed molecules on silver and, to a lesser extent, copper.

Several explanations have been offered for the surface enhancement; it is likely that more than one mechanism is involved. Although the Raman signals may only be observable with certain electrode surfaces, this technique is expected to prove of great importance to electrochemistry in providing much needed *in situ* vibrational data. With adsorbed molecules exhibiting strong intrinsic resonance Raman, strong Raman signals can be obtained on other electrodes besides silver and copper (13-15). For example, in our laboratory, we have studied such species as parinitrosodimethyl aniline (14) and the transition metal phthalocyanines (15) adsorbed on platinum as well as silver. Further, Raman spectroscopy has been used in our laboratory to examine the passivation films on iron (16) as well as silver (17).

Aside from the implications of various photoelectrochemical processes for solar energy conversion, they afford interesting information concerning band bending in semiconductor electrodes, surface states, and

other electronic features of the interface of importance to electrocatalysis (11). Photoemission from metals into electrolytes also has been studied by electrochemists [see, e.g., Ref. (18, 19)] but so far has not proven very useful for studies of adsorption and electrocatalysis.

Mössbauer spectroscopy has been applied to *in situ* studies of various layers on electrode surfaces containing appropriate elements to serve as either emitters or absorbers, e.g., iron, cobalt. From the Mössbauer spectra, under favorable conditions it is possible to gain insight into spin states and nearest neighbor interactions. Particularly interesting results have been obtained for electrochemical passivation layers on iron (20) and iron transition metal macrocyclic catalyst layers on electrode surfaces such as carbon (21, 22).

When the potential across an electrochemical interface is a-c modulated, both shear and compressional acoustical waves are generated. The shear waves result from the modulation of the a-c interfacial tension and are detected in the solid electrode phase with a shear sensitive transducer attached to the back side of the electrode (23, 24). The compressional waves are readily detected in the electrolyte phase with a hydrophone (25, 26). With solid metal electrodes, these compressional waves are produced principally by the a-c modulation of the volume of the ionic double layer—particularly the compact double layer. With semiconductor electrodes, intrinsic and field-induced piezoelectric properties may result in large compressional components in the electrolyte phase and both shear and compressional components in the solid electrode phase. Both the shear and compressional acousto-electrochemical effects are quite sensitive to adsorbed species at the electrode surface and can be used to follow the adsorption-desorption of such. Quantitative measurements of the compressional effect on metal electrodes should yield dV/dE (where V is the volume, E is the applied potential) and hence be of special interest in testing double layer models.

Electron spin resonance has been used to detect various free radicals in the electrolyte phase (27-29) and in principal can be used to examine radicals adsorbed on electrode surfaces by proper location and configuration of the electrode in the microwave cavity of the spectrometer.

Two techniques that appear promising for *in situ* studies of electrochemical interfaces and particularly catalyst and passivation layers are extended x-ray absorption fine structure (EXAFS) and nuclear magnetic resonance. In both instances it will probably be necessary to use high area electrodes such as dispersed ultrasmall metal particles on a high area carbon support or metal blacks. With the *in situ* EXAFS, it is worthwhile to consider fluorescence yield as well as the more conventional absorption measurements. With the recent developments in NMR solids, using magic angle spinning and various spin decoupling techniques, it may be possible to obtain the fine line NMR spectra of adsorbed species even at the monolayer level using very high surface area dispersed electrocatalysts.

Ex Situ Techniques

The electron and ion spectroscopies listed in Table II can be used to characterize electrode surfaces including single crystal systems before and after electrochemical measurements. The critical question is whether the electrode surface can be transferred from the ultrahigh vacuum environment to the electrochemical environment and vice versa without substantial restructuring of the surface as well as chemical changes and contamination. Several research groups (30-35) have carried out electrochemical measurements such as hydrogen electroadsorption and lead underpotential electrodeposition on noble metal single crystal surfaces which have been prepared and characterized with LEED or RHEAD in ultrahigh vacuum.

Table II. *Ex situ* electron and ion techniques for the study of electrochemical interfaces

Ex situ

Electron physics
 X-ray photoelectron spectroscopy (XPS)
 Ultraviolet photoelectron spectroscopy (UPS)
 Auger spectroscopy
 Electron energy loss spectroscopy
 Low energy electron diffraction (LEED)
 Reflection high energy electron diffraction (RHEED)
 Inelastic electron tunneling
 Transmission electron microscopy—diffraction

Ion

Ion scattering spectroscopy
 Secondary ion mass spectroscopy

Special precautions have been used to minimize the possibility of restructuring during the transfer into the electrolyte. The approach used in our laboratory for accomplishing such is as follows (30, 31, 36). Clean single crystal platinum or gold surface of known orientation are prepared by repeated sputtering with argon and high temperature annealing in an ultrahigh vacuum chamber on the right in Fig. 1. The surfaces are examined with LEED and Auger spectroscopy in ultrahigh vacuum (10^{-10} – 10^{-11} Torr) and then transferred into a second vacuum chamber on the left in Fig. 1, also at $\sim 10^{-10}$ – 10^{-11} Torr without removal from the vacuum environment by means of a magnetically operated transfer wand. Ultrapure argon is then admitted to this vacuum container. A second parallel electrode surface with a drop of electrolyte on it is next brought close to the single crystal surface to form a thin layer electrochemical cell with a gap of $\sim 10^{-3}$ cm. This second electrode is chosen so as to serve as a combined counter and reference electrode. The use of the thin layer cell technique results in a high area-to-volume of electrolyte ratio and hence much less sensitivity of the single crystal surface to impurities in the electrolyte (e.g., 10^{-6} m of a typical ionic impurity corresponds to 10^{-3} of a monolayer even if all adsorbed on the electrode surface). Following the electrochemical measurements, the electrodes are separated. With an electrolyte such as aqueous dilute HF, the electrolyte can be completely vaporized at room temperature as the argon is pumped out. The single crystal electrode is then retransferred into the LEED-Auger chamber and the surface is re-examined.

This system has been used at Case with some success for studies of underpotential electrodeposition, hydrogen electroadsorption, and anodic film formation on plat-

inum and gold single crystal surfaces. The electrochemical behavior is highly dependent on the particular surface crystal plane. Such information is of critical importance to the understanding of electrocatalysis on a microscopic level.

Complementary *Ex Situ* Experiments

The electrochemical interface cannot be simulated even approximately with solid-vacuum interfaces. Nonetheless, studies of the adsorption of water, hydrogen, oxygen, carbon monoxide, various organic molecules, and other species at metal and semiconductor interfaces can provide information of help in understanding electrochemical interfaces. The interaction of water with such metals as gold and platinum is relatively weak at electrochemical interfaces, and hence, some similarities are expected between the behavior of various adsorbed neutral species such as hydrogen atoms and CO on these metals in the electrochemical and vacuum environments. Such comparisons are more likely to be valid when the electrochemical interface is near the potential of zero charge and the potential gradient at the interface is small.

Particular types of experimental and theoretical information which can prove useful to the electrochemist include the energetics of the adsorption process, types of adsorption sites, configuration, electronic and vibrational properties of the adsorbed species, and chemical modifications of the adsorbate attending the adsorption process. Most electrochemists concerned with various electrocatalysis processes already pay considerable attention to solid-gas catalytic literature and this trend is likely to increase.

Specific Electrocatalytic Processes

Some typical electrocatalytic processes are listed in Table III. By far the most research effort has been applied to the hydrogen and oxygen electrode reactions. The most exciting development in applied electrocatalysis in recent years, however, has been the development of the dimensionally stable anode as a replacement for the carbon electrode for the generation of chlorine in the chlor-alkali industry. The catalyst for this reaction is ruthenium oxide, perhaps with additives, on a titanium substrate. In contrast to carbon anodes, the RuO_2/Ti electrode is not attacked at an appreciable rate and is dimensionally stable over years. Almost all of the Cl_2 produced electrochemically in the United States is generated with this electrode with large savings in energy because of the very low overpotential.

Fig. 1. LEED-Auger-thin layer electrochemical cell system with special transfer system (36).

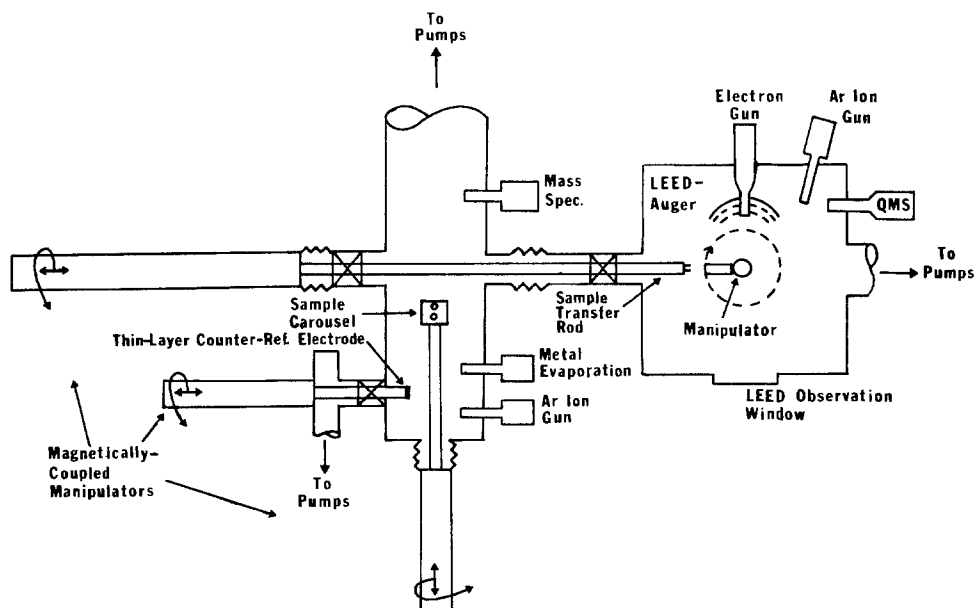
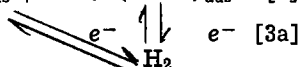
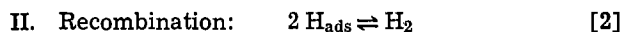
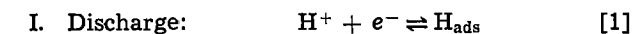


Table III. Typical electrocatalytic reactions

1. The hydrogen electrode reaction
 $H_2 = 2H^+ + 2e^-$
2. The oxygen electrode reaction
 $O_2 + H_2O + 4e^- = 4OH^-$
3. Chlorine generation
 $2Cl^- = Cl_2 + 2e^-$
4. Organic oxidations
 $CH_3OH + H_2O = CO_2 + 6H^+ + 6e^-$
 $C_6H_6 + 6H_2O = 3CO_2 + 20H^+ + 20e^-$
5. Organic synthetic reactions
Kolbe reaction: $R-CO_2^- \rightarrow 2CO_2 + RR + 2e^-$

Our laboratory at Case has directed much attention to the hydrogen and oxygen electrode reactions and I shall emphasize these two areas of electrocatalysis in the remainder of this lecture.

The hydrogen electrode reaction.—Hydrogen generation on various electrode surfaces is generally considered to involve the following steps



In recent years some general insight has been achieved into the relationship of hydrogen electrode kinetics to hydrogen adsorption energies. For a given step the exchange current density is related to the standard free energy of adsorption of the particular type of adsorbed hydrogen involved in this step (ΔG°). This dependence is represented by the familiar volcano-shaped curves (37-39) shown in Fig. 2 according to Parsons (37) for the three reaction steps just listed. The flat portion of the curves corresponds to the Tafel region of the adsorption isotherm. In constructing the volcano curves, the cathodic and anodic transfer coefficients have been taken to be 1/2. This may be open to question for reactions II and III. Arguments have been put forth (40), based on Bond's model of nonactivated adsorption of hydrogen (type C) (41), that the free energy of activation for reaction II approaches the free energy change for this step on some metals. Further, it is likely that the activated state $(H-H)^+$ for reaction III involves the direct interaction of both hydrogens with the surface rather than an end-on interaction of an H—H intermediate. Consequently, the transfer coefficient α for reaction III may also approach unity rather than 1/2. Under such circumstances, the volcano curves take on the form (40) indicated in Fig. 3, using a combination of Breiter's

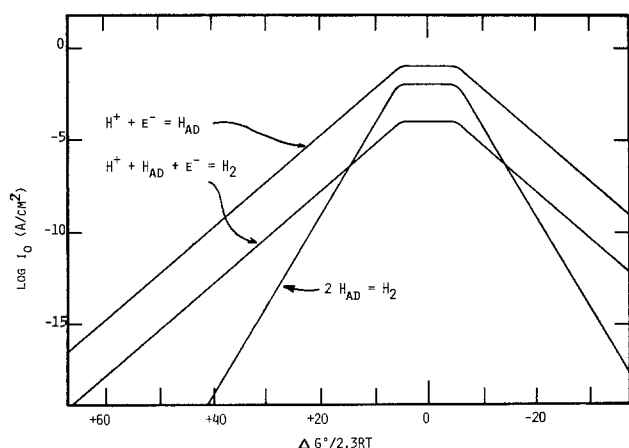


Fig. 2. Volcano curves for the exchange current densities of the hydrogen electrode component steps vs. the standard free energy of adsorption of hydrogen (39). Transfer coefficient for each process: $\alpha = 1/2$.

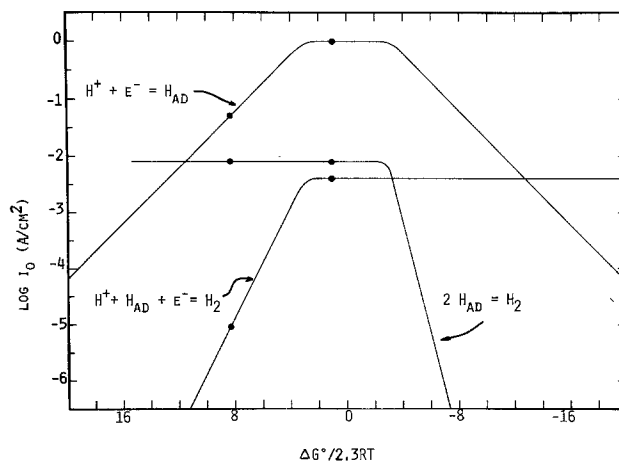


Fig. 3. Volcano curves (40) in 3M HCl with $\alpha_I = 1/2$ for the discharge reaction; $\alpha_{II} = 1$ for the recombination reaction; and $\alpha_{III} = 1$ for the ion-plus-atom reactions.

data (42) and Ludwig's data (40) as a few calibration points.

The experimentally observed behavior of hydrogen overpotential on various metals correlates reasonably well with Fig. 3. Metals such as Hg, Tl, Zn, Cd, and Pb, which adsorb hydrogen only weakly (large positive values of ΔG°), have low values for the apparent exchange current density, Tafel slopes ($dE/d \log i$) of $-2.30 (2 RT/F)$, and reaction I rate controlling. Metals such as Pt and the Pt family with ΔG° values close to 0 have high apparent exchange current densities and kinetics which indicate that reaction II follows reaction I and is rate controlling. Metals such as Mo, Ta, and W, which strongly adsorb hydrogen and have very negative values of ΔG° , again have low exchange current densities and kinetics which indicate region III follows reaction I.

An important implication of the volcano curves is that it is unlikely a catalyst will be found with an overall exchange current density higher than that for Pt since this metal has ΔG° close to 0. The main thrust of applied research on hydrogen electrocatalysts should be the finding of catalysts with higher exchange currents per unit cost and resistance to poisoning and to loss of area when used in high area forms.

Various authors have examined the discharge step I theoretically [for a review, see Ref. (44)]. Bockris, Matthews, and Srinivasan (45, 46) have proposed the model in Fig. 4 in which the proton is transferred over a barrier representing the intersection of two Morse curves. The vertical transition ΔE_0 corresponds to the transfer of an electron from the Fermi level of the metal to the H_3O^+ ion with no change in the reaction coordinate. Radiationless electron transfer by tunneling occurs at the intersection of the two Morse curves, from the metal to the vibrationally excited H_3O^+ . The various electron energy levels in the metal correspond to translation vertically of the Morse curve for the initial state. The principal levels contributing to the discharge current are those within kT of the Fermi level. This model yields reasonable predictions for the kinetics of the discharge step.

Various electrochemists have considered proton tunneling through the potential energy barrier rather than transmission over the barrier. These include Bockris and his co-workers (45, 46); Christov (47-49); Conway and Salomon (50, 51); Dogonadze, Kuznetsov, and Levich (52-54); Kharkats and Ulstrup (55). All of the treatments involve questionable assumptions. The extent to which proton tunneling is involved in the discharge process is very sensitive to the barrier thickness as well as height. Isotopic studies of hydrogen discharge on mercury, however, do provide evidence that proton tunneling is involved (21, 22).

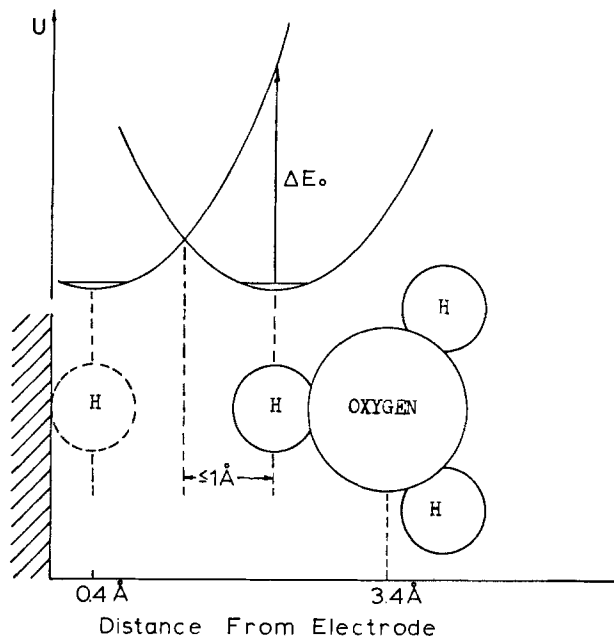


Fig. 4. Potential energy surfaces in the Bockris-Matthews model for proton discharge (110).

Hydrogen electrode kinetics are of special interest on Pt because of its high catalytic activity. Various workers have found a Tafel slope for the cathodic branch of $-2.30(RT/2F)$ or -30 mV/decade and high exchange current densities (e.g., $\geq 10^{-2}$ A/cm²). Two explanations have been advanced for this behavior. Schuldiner (56) and Bockris *et al.* (57) have used a mechanism involving reactions I and II (discharge followed by atomic recombination) with reaction II rate controlling. Breiter has proposed pure diffusion control involving dissolved H₂ (58). On the basis of ultrasonic and rotating disk-ring measurements, Yeager *et al.* (43, 59, 61) have proposed that the cathodic process is controlled by combined H₂ diffusion and recombination kinetics. Parsons (37) and Krishtalik (60) have offered theoretical arguments for desorption by reaction II as rate controlling.

The anodic oxidation of H₂ exhibits first-order dependence on H₂ concentration, and most workers consider the dissociative-adsorption of H₂ (the reverse of the recombination of reaction II) as rate controlling. Here again, however, the high exchange current density makes it difficult to examine the kinetics without transport of dissolved H₂ to the electrode surface being the predominant control, even with the rotating disk electrode technique, particularly with Pt electrodes which have relatively high area, and hence high activity, as a result of repeated cycling to anodic potentials prior to the H₂ oxidation measurements. The current-potential data from rotating disk data are very well fitted with equations involving combined kinetic and molecular H₂ diffusion control with the atomic recombination step rate controlling. With Langmuir behavior, the current potential data for the anodic and cathodic branches is

$$\ln X = -\frac{2F\eta}{RT} + \ln X_0 \quad [4]$$

$$X = i / \left(1 - \exp \frac{2F\eta}{RT} \right) \quad [4a]$$

$$\frac{1}{X_0} = \frac{1}{i_0} + \frac{1}{i_d} = \frac{1}{i_0} + \frac{1}{B\sqrt{\omega}} \quad [5]$$

where η is the overpotential, i_d is the anodic limiting current density for H₂ transport, i_0 is the exchange current density, ω is the rotation rate, B is a constant dependence on the H₂ diffusion coefficient and concen-

tration, and the other symbols have their usual meaning. Equation [5] has been tested for Pt by Ludwig *et al.* (43) using the rotating disk data and fits the data quite well (see Fig. 5). The slope is essentially $-2.30(RT/2F)$ over seven decades. The rotation rate dependence of the function X_0 indicates that i_0 is of the same order as i_d under most circumstances.

A problem associated with H₂ formation with the kinetics controlled by reaction II is that the Tafel linearity with a slope of $-2.30(RT/2F)$ is to be expected only with low H(ads) coverage. On the other hand, various electrochemical measurements, including impedance (66), linear sweep voltammetry (63, 64), and charging curves (66, 67) indicate that the total H(ads) coverage is already close to unity at the reversible potential. This problem can be resolved by assuming that two types of H(ads) are involved in the overall electrode process and that the adsorbed hydrogen involved in reaction II is at low coverage, as suggested by Schuldiner (62).

The question remains open as to what type of adsorbed hydrogen is involved in the desorption reaction II on platinum. It is unlikely that the lower coverage H involved in this step corresponds to any of the hydrogen peaks observed by linear sweep voltammetry and other chemical techniques on Pt. Nonetheless, it will be helpful to understand the various factors contributing to up to several hydrogen peaks observed in the voltammetry curves (63). Figure 6 indicates some of the peaks found for Pt in 0.1M HF and the effects of adding H₂SO₄ (64). Various explanations have been proposed for the several peaks including different adsorption sites on a given single crystal surface, a distribution of crystallographic surfaces, induced heterogeneity associated with hydrogen adsorption itself and anion adsorption which induces heterogeneity by blocking sites to varying degrees and perturbing adjacent sites. The pronounced dependence of the hydrogen electroadsorption on the type and concentration of anion (Fig. 6) indicates that hydrogen ad-

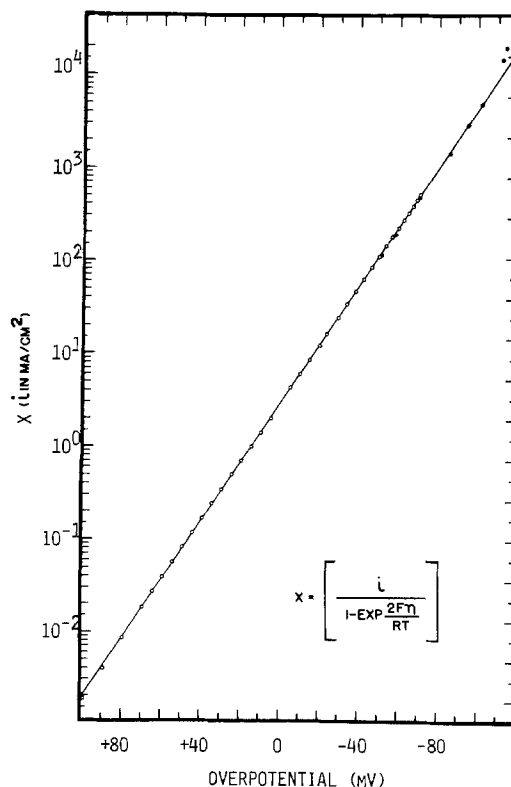


Fig. 5. Hydrogen electrode kinetics on Pt (43). Rotating disk electrode. Rotation rate: 187 Hz; $T = 26^\circ\text{C}$; 6.1M HCl (H₂ saturated).

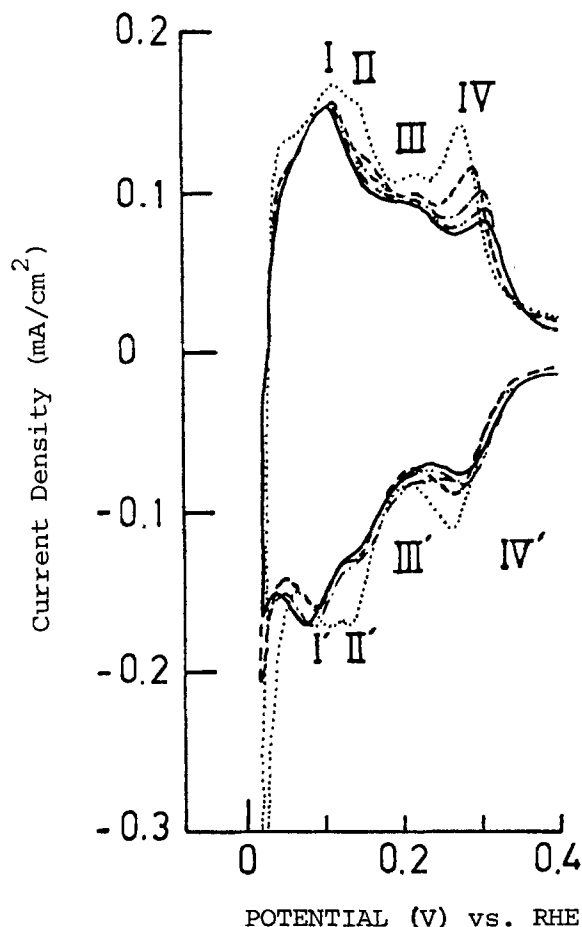


Fig. 6. Voltammograms for Pt in 0.1M HF with various concentrations of H_2SO_4 added. — 0.1M HF, - - - 0.1M HF + $5 \times 10^{-5}\text{M}$ H_2SO_4 , ···· 0.1M HF + $5 \times 10^{-4}\text{M}$ H_2SO_4 , - · - · 0.1M HF + $5 \times 10^{-3}\text{M}$ H_2SO_4 , - - - - 0.1M HF + $5 \times 10^{-2}\text{M}$ H_2SO_4 .

sorption-desorption are coupled to anion desorption-adsorption.

In an attempt to resolve this problem, various electrochemists have examined hydrogen electroadsorption on single crystal Pt. Will (65) examined the low index planes (100), (110), and (111) and found the same two major peaks on these three orientations although the relative heights depended on the crystal orientation. The single crystal Pt electrodes studied by Will probably did not expose a single crystallographic surface. The distribution of crystallographic surface planes depends on the overall orientation and the extent to which the surface has been cycled to anodic potentials. Will arrived at the conclusion that the strongly adsorbed hydrogen peak corresponding to IV, IV' in Fig. 6 is on the (100) plane and the weakly adsorbed peaks I, I' are on the (110) plane. Rather analogous results have been reported by Bronel *et al.* (68) for the (100) and (111) Pt surfaces. These workers used electron microscopy to establish that the surfaces were facet-free. Kinoshita and Stonehart (69) have examined hydrogen adsorption on dispersed Pt as a function of crystallite size and found a dependence which they interpret as further evidence that the multiple peaks result from different surface crystallographic structures.

In contrast, Bagotzky *et al.* (70) and Conway *et al.* (63) have concluded from their single crystal Pt studies that there is little difference in the hydrogen adsorption on the (100), (110), and (111) planes. Conway *et al.* (63) attributed the multiple peaks principally to induced heterogeneity arising from collective long range electronic interactions.

The probability is high in all of the single crystal studies just cited that the surface prevailing during

the electrochemical measurements does not correspond to a single crystal plane. Even if the Pt crystal has only one plane predominant before the electroadsorption measurements, these workers generally cycled their electrodes to anodic potentials in the anodic film region to oxidize or desorb interfering surface contaminants and this procedure is likely to cause restructuring.

Recently several groups have attempted to devise techniques which permit the introduction of a single crystal surface of predominantly one plane and free of impurities into an electrochemical environment with a minimum possibility of restructuring and contamination. In the USA these include A. Hubbard (71, 72) at the University of California at Santa Barbara, J. A. Joebstl (73, 74) at Fort Belvoir, P. Ross (75, 76) at the Lawrence Berkeley Laboratories, and our group (30, 31, 77) at Case Western Reserve University. Each group has turned its attention to the (100), (110), and (111) planes of Pt and first established that the surface is predominantly one plane using low energy electron diffraction (LEED) and free of surface impurities down to a few percent of a monolayer using Auger electron spectroscopy.

The key features of the techniques used in our laboratory by O'Grady *et al.* (30, 31, 77) with the equipment in Fig. 1 are vacuum transfer; thin layer electrochemical cell techniques to avoid contamination; and introduction of the Pt single crystal surfaces into the electrolyte at controlled potentials in the hydrogen adsorption region. In the cyclic voltammetry studies of hydrogen electroadsorption, the potential range is restricted to +0.05-0.50V vs. RHE to reduce any possible restructuring. The voltammetry curves on the single crystal Pt surfaces retract with repeated cycling, starting with the very first sweep. If the voltage sweep is extended into the anodic film formation region to $\cong 1.4\text{V}$ vs. RHE, the hydrogen adsorption region changes significantly with new peaks appearing or very minor peaks becoming major peaks, depending on the original surface. This is probably the result of restructuring although the possibility exists that oxygen has been irreversibly adsorbed into sites within the surface layer.

On the (100) Pt surface, Hubbard *et al.* (72), Ross (75, 76), and our group (30, 31) find one predominant peak (Fig. 7) corresponding to the strongly adsorbed hydrogen peak on polycrystalline Pt in acid solutions. The LEED pattern for the Pt (100) indicates a 5×20 overlayer. This surface probably reverts to (1×1) in contact with the electrolyte. On the (111) surface, our group finds only a minor peak corresponding to weakly adsorbed hydrogen while Ross and Hubbard *et al.* report a major peak. The source of this discrepancy is not fully clear but may be caused by the cycling of the electrode to anodic potentials in the case of Ross's work and possibly also that of Hubbard *et al.* Alternatively our Pt (111) surface may have some of the sites blocked by an impurity such as carbon.

With the sulfuric acid electrolyte, it was not possible to volatilize the residual electrolyte off of the single crystal surface without encountering an oxidizing range of sulfuric acid concentrations. More recently, Arthur Homa, a graduate student in my group, has repeated these studies with 0.1M HF as the electrolyte. This acid is completely volatilizable and does not specifically adsorb. Thus it has been possible to examine the LEED patterns and Auger spectrum following the electrochemical measurements. The postelectrochemical LEED patterns are usually of reasonably good quality with the same symmetry as for the original surfaces. Small amounts of carbon, up to 10%, are usually found with the Auger examination. This carbon is believed to originate from CO released from ion pumps during the pumping out of the ultrapure argon support gas following the electrochemical measure-

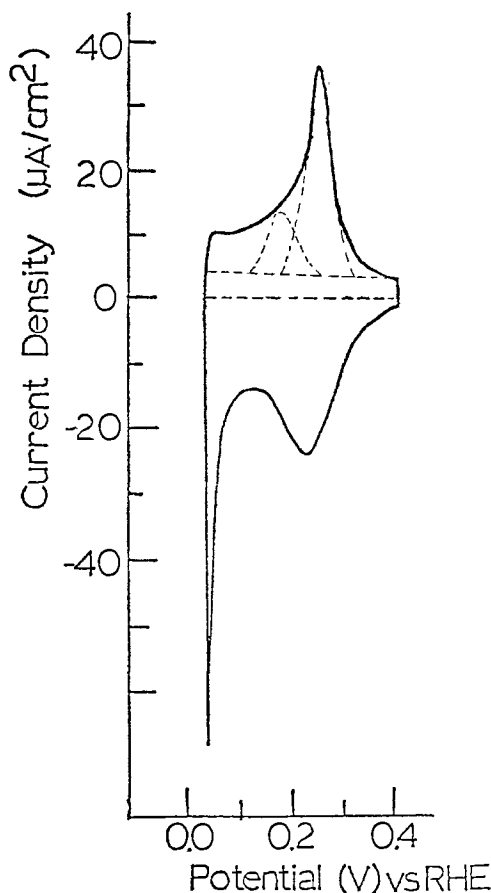


Fig. 7. Voltammogram for Pt (100) — (5 × 20) in 0.05m H₂SO₄. Sweep rate: 50 mV/sec. *T* = 25°C (30).

ments and not to have been present during these measurements.

The voltammetry results in the 0.1m HF are very similar to those in the 0.05m H₂SO₄ on the (111) and (110) (1 × 2) surfaces with only one H adsorption

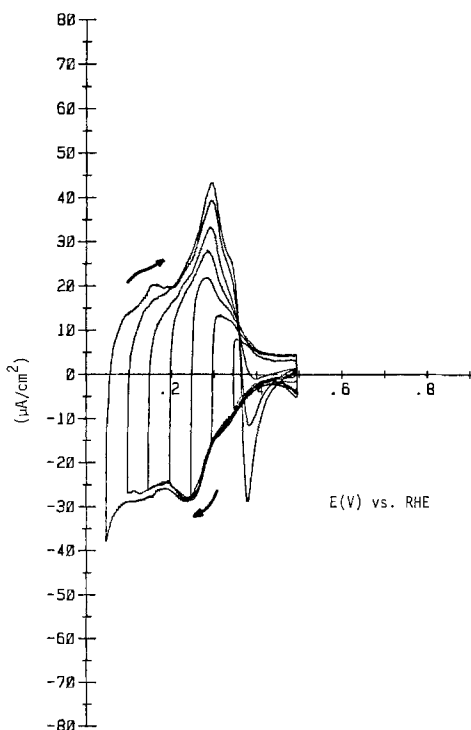


Fig. 8. Voltammogram for Pt (100) — (5 × 20) in 0.1m HF. Sweep rate: 50 mV/sec. *T* = 25°C.

peak on each surface and the H coverage much lower than a monolayer. The (100) (5 × 20) surface also shows only one principal peak but a sharp cathodic spike appears in the anodic sweep (Fig. 8). This spike remains to be explained but may be caused by surface restructuring. Repeated cycling of the three low index surfaces to potentials well in the anodic film region produces large increments in the peaks on these low index surfaces, disappearance of the cathodic spike on (100) surface, and voltammetry curves resembling those of Ross and the Hubbard group. We do not believe that these large changes are the result of the stripping of a minor carbon impurity but rather are related to some special role of oxygen in the hydrogen adsorption process. Rather similar results with cycling for polycrystalline platinum treated in high vacuum have been reported by the Soviet Academy Institute of Electrochemistry in Moscow (78).

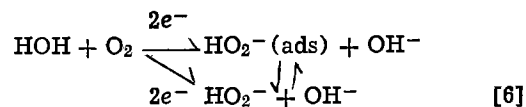
Note is taken of the very unusual results for hydrogen voltammetry curves on Pt (111) found by J. Clavilier *et al.* (79, 80) and described by Roger Parsons in his Palladium Award address before this Society. This strange behavior is difficult to explain either as the true situation or as an artifact.

In perspective, it appears that the question of hydrogen adsorption on single crystal Pt surfaces is still not a settled issue experimentally. Similar anomalous results for hydrogen adsorption on Pt single crystal surfaces are also to be found in the solid-gas phase literature.

The oxygen electrode.—The oxygen electrode reactions are even less well understood than for the hydrogen electrode. The pronounced irreversibility of the oxygen electrode reactions at moderate temperatures has complicated mechanistic studies. The exchange current densities for the oxygen electrode are very low—typically 10⁻¹⁰ to 10⁻¹¹ A/cm² on an effective catalytic surface such as platinum at room temperature. Consequently, the current densities near the reversible potential are generally too low to permit measurements under conditions where the kinetics are sensitive to the reverse as well as forward reactions. Further, the experimentally accessible portions of the cathodic and anodic branches of the polarization curves are sufficiently separated in potential that the surface conditions differ very substantially. Therefore, the cathodic and anodic processes under these conditions are probably not the reverse of each other. To complicate the situation further, the oxygen electrode reactions may proceed through a large number of pathways. This explains why the mechanisms of O₂ generation and reduction are still not fully understood even on platinum, the most extensively used and most studied O₂ electroreduction catalyst. I shall address only the question of the catalysis of the O₂ reduction reactions.

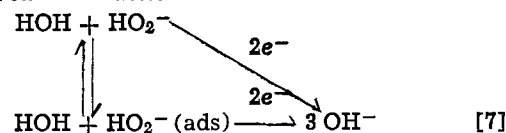
Oxygen reduction is usually considered to proceed by two pathways:

1. *The peroxide pathway (the series process):*

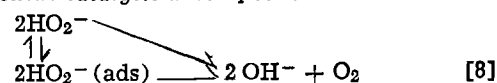


The peroxide is then either electroreduced further to OH⁻ or catalytically decomposed; *i.e.*

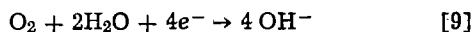
- a. *peroxide reduction*



- b. *peroxide catalytic decomposition*



The overall reaction is the 4-electron reduction reaction



regardless of whether the peroxide elimination occurs via reaction [7] or [8] since the O_2 resulting from reaction [8] is recycled through reaction [6].

2. The direct 4-electron pathway:

This pathway involves a series of steps in which O_2 is reduced to OH^- or water without hydrogen peroxide being produced in the solution phase. This does not mean that the reduction process does not involve an adsorbed peroxide intermediate but rather that the reduction does not involve any adsorbed intermediate which leads to appreciable peroxide in the solution phase. When both pathways are operating on a given electrode surface, the reduction is referred to as involving parallel mechanisms.

The distinction between these two pathways mechanistically can be quite diffuse since the question of whether a peroxide adsorbed intermediate desorbs or not can depend on various impurities in the electrolyte as well as electrode potential and temperature. An adsorbed peroxide state is very likely involved in the direct 4-electron pathway as well as the peroxide pathway. The classification of the pathway as "direct 4-electron" then may depend on whether the peroxide desorption proceeds to a significant extent. This may depend on the type of site. Two sets of sites may each support the reaction through essentially the same surface reaction pathway but differ in the extent to which the peroxide desorbs from each. If the desorption is very slow or thermodynamically unfavorable from one set of sites but not another, the O_2 reduction will proceed by the so-called "parallel" pathways.

Illustrations of catalysts on which the peroxide pathway is clearly predominant include carbon, graphite, and gold in alkaline electrolytes while the direct 4-electron pathway is predominant on clean platinum surfaces and also certain transition metal macrocyclics. In the presence of impurities peroxide pathway *a* can become predominant even on platinum.

Under some circumstances it is possible that the superoxide species O_2^- may be formed in the outer Helmholtz plane by outer sphere electron transfer. This

ion is formed as a reasonably stable entity during O_2 reduction in aprotic solvents [see, e.g., Ref. (81-84)] and probably in carbonate melts (85). The superoxide ion also has been proposed to be formed in aqueous solutions of Hg (85, 86), and amalgamated gold (87) and carbon paste (88) cathodes in the presence of surface active agents. In the absence of adsorbed organic species, however, it does not appear in alkaline solutions that an O_2^- species in the solution phase contributes significantly to the observed current (89).

The specific adsorption of O_2 molecules.—The search for effective 4-electron catalysts is guided by the models in Fig. 9 for the interaction of O_2 and related oxygen species with adsorption sites. O_2 reduction in aqueous solutions requires a strong interaction with the electrode surface for the reaction to proceed at a reasonable rate. Three types of interactions have been proposed. Partial charge transfer is probably involved with each of these models. The Griffiths model (112) involves a lateral interaction of the π -orbitals of the O_2 interacting with empty d_{z^2} orbitals of a transition element, ion, or metal atom with back bonding from at least partially filled d_{xz} orbitals of the transition element to the π^* orbitals of the O_2 . A strong metal-to-oxygen interaction results in a weakening of the O-O bond and an increment in the length of this bond. Sufficiently strong interaction of this type may lead to the dissociative adsorption of O_2 with probably simultaneous proton addition and valency change of the transition element in the manner represented by pathway I in Fig. 9 followed by reduction of the $\text{M}(\text{OH})_2$ to regenerate the catalyst site. Sandstede *et al.* (91, 92) have attempted to explain oxygen reduction with square pyramidal Co(II), Fe(II), and Fe(III) complexes as well as on the thiospinels on the basis of such π bonding.

With most transition metal catalysts, the most probable structure for O_2 adsorption is the Pauling model (93) in which the π^* orbitals of O_2 interact with d_{z^2} orbitals of the transition metal. The square pyramidal complexes of Fe(II) and Co(II), which have good activity for O_2 reduction in acid solutions, appear to involve such an end-on interaction on the basis of ESR and other evidence (94). This adsorption of O_2 is expected to be accompanied by at least a partial charge

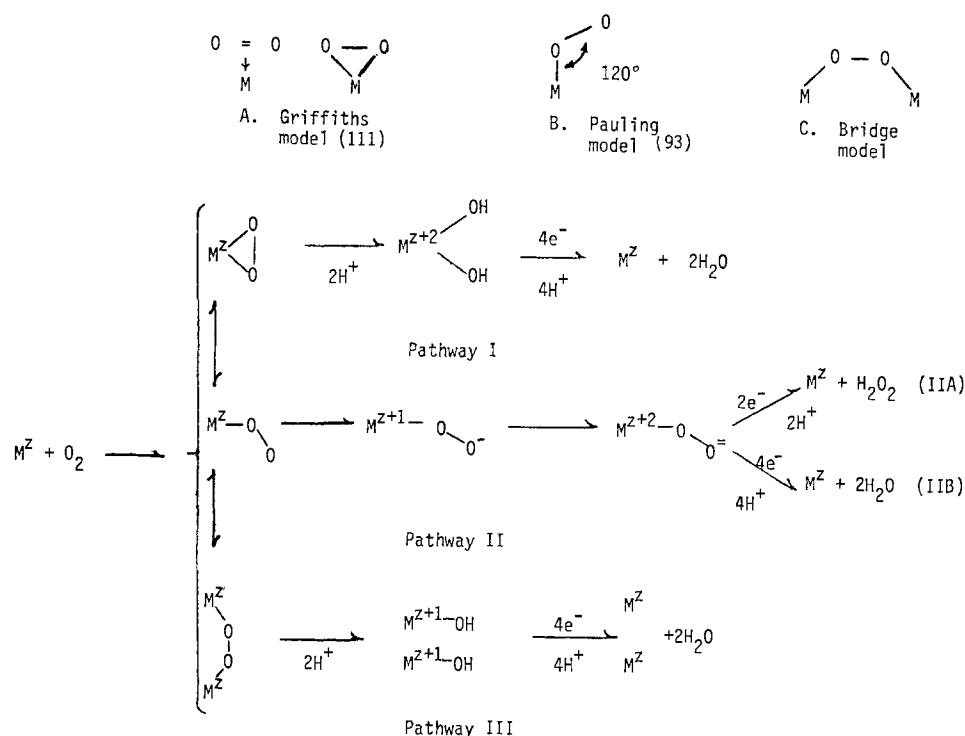


Fig. 9. Reaction pathways for O_2 electroreduction in acid electrolytes [Yeager(111)].

transfer to yield a superoxide and then peroxide state, as represented by pathway II in Fig. 9. The adsorption of the O_2 on the square pyramidal complexes of Fe(II) and Co(II) may lead directly to the superoxide state. With somewhat similar oxyhemoglobin complexes of iron, various workers have proposed that O_2 binding to the iron involves O_2^- or $O_2^=$ states with Fe in the III valent state (95-97). The change in valency state of the transition metal coupled with the change in O_2 oxidation state during formation of the O_2 adduct corresponds in principle to the redox electrocatalyst concept proposed by Beck *et al.* (98, 99).

The further reduction of the O_2 beyond the peroxide state requires rupture of the O-O bond. Such can occur

in pathway IIB through the formation of O^- or $HO\cdot$ free radicals in solution or the simultaneous reduction bond cleavage (electrochemical desorption) to yield H_2O or OH^- . Neither of these processes are likely to be sufficiently fast at practical operating potentials for O_2 cathodes. The free energies of formation of the O^- and $HO\cdot$ free radicals in solution are just too high.

Pathway III in Fig. 9 provides an alternate means for bringing about rupture of the O-O bond through the formation of an O-O bridge. Such a mechanism may come into play with the proper surface spacing of transition metal atoms or ions in a metal, oxide, or thiospinel or in a bimetal complex such as a macrocycle. The formation of the bridge species also requires that the two metal species have partially filled d orbitals to participate in bonding with the π^* orbitals of the O_2 . Bimetal macrocyclic complexes with the proper M-M distance have been synthesized [*e.g.*, see Ref. (100-103)] and appear to occur naturally in heme-thrin.

For any of the pathways in Fig. 9, considerable questions exist as to the reversibility of the O_2 adsorption step at the rather high rates involved with practical O_2 cathodes. For O_2 to bond to M^z will generally require the replacement of a water molecule or anion of the electrolyte—a situation which would normally be expected to be unfavorable to O_2 unless the O_2 adduct has a pronounced dipolar character ($M^z+^1O-O^-$) (104, 105).

Of the various possibilities for catalysts which promote the 4-electron reduction, the transition metal macrocyclics appear particularly promising. In the work in our laboratory these are adsorptively attached to high area conducting substrates, as monolayers.

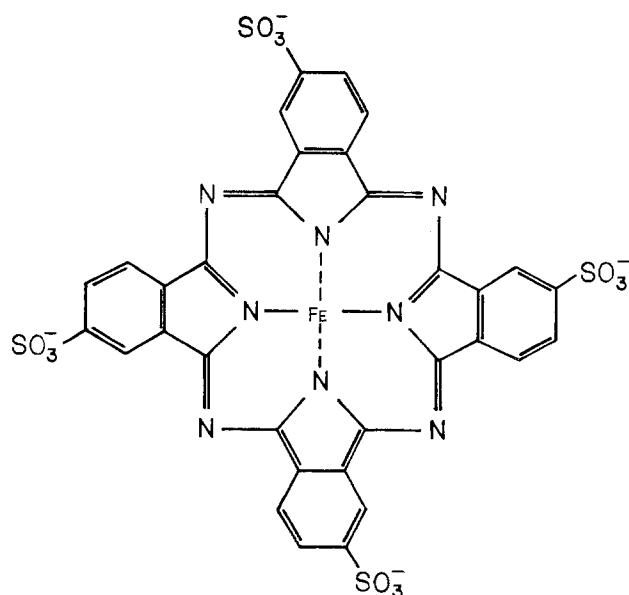


Fig. 10. The molecule: cobalt tetrasulfonated phthalocyanine (CoTSPc).

The water soluble iron tetrasulfonated phthalocyanine (Fe-TSPc) (Fig. 10) strongly adsorbs on graphite and at monolayer levels has high activity for the overall 4-electron reduction of O_2 in neutral and dilute alkaline electrolytes. The catalytic activity per unit surface area is higher than for platinum. Rotating disk-ring electrode measurements indicate no detectable peroxide over a substantial potential range (106). The principal problem is the stability of the iron macrocyclic in concentrated caustic and acid solutions. In contrast to the Fe-TSPc, the adsorbed Co-TSPc catalyzes the reduction of O_2 to the peroxide (106, 107).

The interaction of the adsorbed Co-TSPc and Fe-TSPc with the substrate electrode surface (graphite, Pt, and Au) has been studied using visible reflectance spectroscopy (108) (see Fig. 11). The reflectance spectra of the adsorbed Fe-TSPc and Co-TSPc monolayers undergo substantial changes at constant potential with the introduction of O_2 into the electrolyte. We

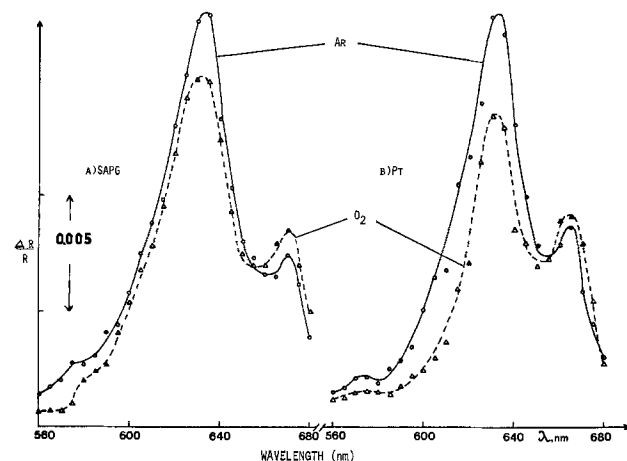


Fig. 11. Reflectance spectra of Fe(III)-TSPc in 0.1M NaOH adsorbed on (a) the basal plane of stress annealed pyrolytic graphite electrode (SAPG) at 0.90V vs. RHE and (b) a Pt electrode at 0.70V with Ar(—) and O_2 (---) saturated solutions. Perpendicular polarization (108).

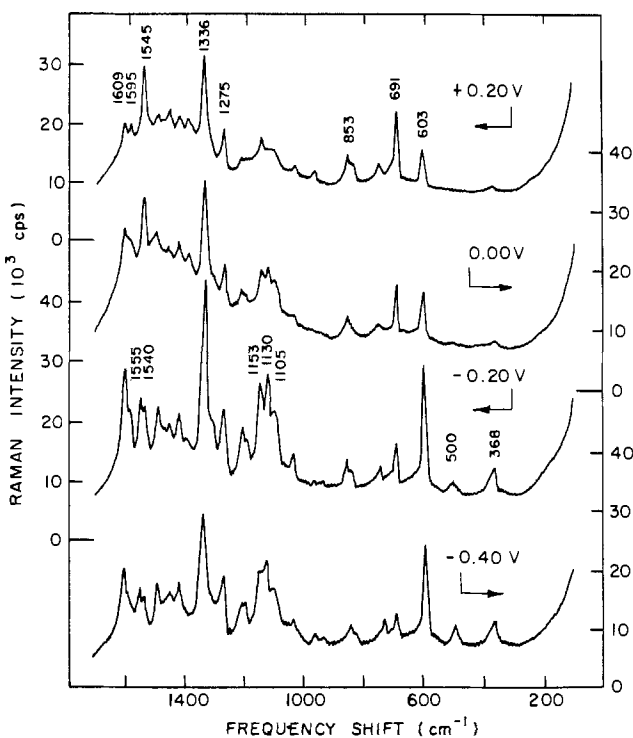


Fig. 12. Raman spectra of CoTSPc adsorbed on an Ag electrode for different electrode potentials in 0.05M H_2SO_4 + $10^{-5}M$ CoTSPc; 514.5 nm; power at the sample 50 mW (15).

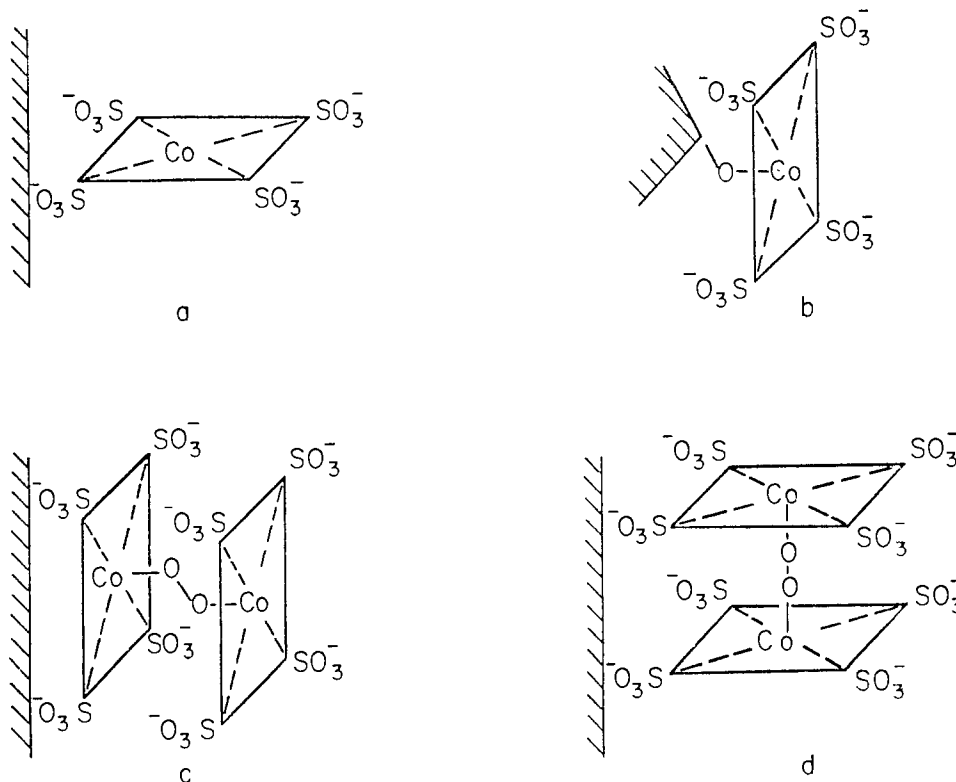


Fig. 13. Possible configurations for CoTSPc adsorbed on an electrode surface (15).

believe this is caused by the formation of an O_2 adduct with the adsorbed species. The Raman spectrum of the Co-TSPc (Fig. 12) has also been obtained with this complex adsorbed on silver, which provides a large surface enhancement of the Raman signal (15). Further work is needed to interpret the Raman spectra and their potential dependence. On the basis of the strong adsorption and the Raman data, we believe that the Co-TSPc is adsorbed on the silver as shown by model C in Fig. 13 with one of the Co-TSPc units in the O_2 bridge dimer interacting directly with the metal substrate. We do not yet have Raman data for the Fe-TSPc but suspect that the adsorption may be in a similar configuration. Dimeric $-O-O-$ complexes have been proposed in aqueous solutions for both the Fe-TSPc and Co-TSPc, principally on the basis of the u.v.-visible absorption spectra. The $-O-O-$ bridged complex would be a likely candidate in the case of the adsorbed Fe-TSPc to explain the 4-electron reduction. The Co-TSPc apparently also forms such a bridge but because of its redox properties or some other factors, does not undergo reduction via a 4-electron pathway (107).

Collman, Anson, and their co-workers (109) have recently synthesized covalently linked face-to-face dicobalt porphyrin dimers with the proper spacing to form a Co-O-O-Co bridge. With relatively thick layers of this complex graphite, rotating disk-ring electrode measurements also indicate a 4-electron reduction in acid electrolytes, verifying that the bridged complex can promote the overall 4-electron reduction. The complexes of Collman *et al.*, however, are expensive to synthesize with many steps while the approach involving adsorbed solubilized complexes is not.

While these are encouraging fundamental developments in O_2 electrocatalysis, it is difficult to translate them into practical electrodes, principally because of catalyst stability problems. Research is in progress at Case to establish whether other macrocyclic catalysts affording M-O-O-M bridging may have greater stability.

Acknowledgment

The research cited in this address in the awardee's laboratory in the field of electrocatalysis has been carried out by a number of former and present gradu-

ate and postdoctoral students, whose names in most instances are in the cited publications. Most of the credit for this work belongs to them.

The Office of Naval Research has supported the awardee's research in the field of electrocatalysis continuously since 1952 and is gratefully acknowledged. The awardee also is pleased to acknowledge support for the research on O_2 electrocatalysis in more recent years from the U.S. Department of Energy, the Electric Power Research Institute, NASA, and several other companies including Diamond Shamrock, General Motors, Union Carbide, and the International Nickel Company.

REFERENCES

1. For a review, see J. D. McIntyre, in "Advances in Electrochemistry and Electrochemical Engineering," Vol. 9, Chap. 2, R. H. Mueller, Editor, Wiley and Sons, New York (1973).
2. R. H. Mueller, *loc. cit.*, Chap. 3.
3. B. D. Cahan and R. F. Spaner, *Surf. Sci.*, **16**, 166 (1969).
4. B. D. Cahan, *ibid.*, **56**, 354 (1976).
5. D. J. Wheeler, B. D. Cahan, C. T. Chen, and E. Yeager, in "Passivity of Metals," R. P. Frankenthal and J. Kruger, Editors, pp. 546-562, The Electrochemical Society, Princeton, N.J. (1973).
6. A. Reed and E. Yeager, *Electrochim. Acta*, **15**, 1345 (1970); see also *J. Appl. Opt.*
7. A. Bewick, K. K. Kumatsu, and B. S. Pons, *Electrochim. Acta*, **25**, 465 (1980); see also A. Bewick and K. Kumatsu, *Surf. Sci.*, In press.
8. M. Fleischmann, P. J. Hindra, and A. J. McQuillan, *J. Chem. Soc. Chem. Commun.*, **3**, 80 (1973); *Chem. Phys. Lett.*, **26**, 163 (1974).
9. A. J. McQuillan, P. J. Hindra, and M. Fleischmann, *J. Electroanal. Chem. Interfacial Electrochem.*, **65**, 933 (1975).
10. R. P. van Duyne, in "Chemical and Biochemical Applications of Lasers," Vol. 4, Chap. 4, C. B. Moore, Editor, Academic Press, New York (1978).
11. A number of papers on the use of Raman spectroscopy and photochemical systems to study electrochemical interfaces were presented at the Symposium on Non-Traditional Approaches to the Study of Solid-Electrolyte Interfaces are scheduled for publication in *Surf. Sci.* in 1980.
12. R. P. van Duyne, F. W. King, and G. C. Schatz, *J. Chem. Phys.*, **69**, 4472 (1978).

13. R. P. van Duyne, *J. Phys.*, **38**, C5-308 (1977).
14. G. Hagans, B. Simic-Glavaski, and E. Yeager, *J. Electroanal. Chem. Interfacial Electrochem.*, **88**, 269 (1978).
15. R. Kötz and E. Yeager, *ibid.*, **113**, 113 (1980).
16. A. Nazri and E. Yeager, Unpublished research.
17. R. Kötz and E. Yeager, *J. Electroanal. Chem. Interfacial Electrochem.*, **111**, 105 (1980).
18. A. M. Brodskii and Yu. V. Pleskov, in "Progress in Surface Science," S. G. Davison, Editor, Pergamon, Oxford (1972).
19. J. K. Sass and H. J. Lewerenz, *J. Phys.*, **38**, C5-277 (1977).
20. W. E. O'Grady, *This Journal*, **127**, 555 (1980).
21. A. J. Appleby and M. Savy, in "Electrocatalysis on Non-Metallic Surfaces," A. D. Franklin, Editor, National Bureau of Standards, Special Publication **455**, 241 (1976).
22. H. Meier, V. Tschirwitz, E. Zimmerhackl, W. Albrecht, and G. Seitler, *J. Phys. Chem.*, **81**, 712 (1977).
23. A. Ya. Gokhshtein, *Elektrokhimiya*, **2**, 1204 (1966).
24. R. E. Malpas, R. A. Fredlein, and A. J. Bard, *J. Electroanal. Chem. Interfacial Electrochem.*, **98**, 339 (1979).
25. F. Borsay and E. Yeager, *J. Acoust. Soc. Am.*, **59**, 596 (1978).
26. F. Borsay and E. Yeager, *Trans. SAEST*, **12**, 179 (1977).
27. C. D. Jaeger and A. J. Bard, *J. Phys. Chem.*, **63**, 3146 (1979).
28. B. Kastening, in "Advances in Analytical Chemistry and Instrumentation," Vol. 10, H. W. Nurnberg, Editor, pp. 421-494, Wiley, New York (1974).
29. T. M. McKenney, in "Electroanalytical Chemistry," Vol. 10, A. J. Bard, Editor, Dekker, New York (1979).
30. E. Yeager, W. E. O'Grady, M. Y. C. Woo, and P. Hagans, *This Journal*, **125**, 346 (1978).
31. W. E. O'Grady, M. Y. C. Woo, P. L. Hagans, and E. Yeager, in "Electrode Materials and Processes for Energy Conversion and Storage," J. D. E. McIntyre, S. Srinivasan, and F. G. Will, Editors, p. 172, The Electrochemical Society Softbound Proceedings Series, Princeton, N.J. (1977).
32. A. T. Hubbard, R. M. Ishikawa, and J. Kalekaau, *J. Electroanal. Chem. Interfacial Electrochem.*, **86**, 271 (1978).
33. R. N. Ross, *ibid.*, **76**, 139 (1977); R. N. Ross, *This Journal*, **126**, 67 (1979).
34. R. M. Ishikawa and A. T. Hubbard, *J. Electroanal. Chem. Interfacial Electrochem.*, **69**, 317 (1976).
35. H. O. Beckmann, H. Gerischer, D. M. Kolb, and Gunter Lehmppohl, in "Faraday Symp. 12, Electrosorption, Nucleation and Phase Formation," p. 51, The Chemical Society, London (1977).
36. P. Hagans, Ph.D. Thesis, Case Western Reserve University, Cleveland, Ohio (1980).
37. R. Parsons, *Trans. Faraday Soc.*, **54**, 1053 (1958).
38. B. Conway and J. O'M. Bockris, *J. Chem. Phys.*, **26**, 532 (1957).
39. L. Krishtalik, *Elektrokhim.*, **2**, 616 (1966).
40. F. Ludwig and E. Yeager, "Hydrogen Overpotential on Platinum," Tech. Report 21, U.S. Office of Naval Research Contract N00014-67-C-0389, Case Western Reserve University, Cleveland, Ohio, 1 February 1968.
41. G. Bond, "Catalysis by Metals," pp. 68-69, 93-98, 174-179, Academic Press, New York (1962).
42. M. Breiter, *Electrochim. Acta*, **7**, 25 (1962).
43. F. Ludwig, R. K. Sen, and E. Yeager, *Elektrokhim.*, **3**, 717 (1977).
44. R. K. Sen, E. Yeager, and W. E. O'Grady, *Ann. Rev. Phys. Chem.*, **26**, 287 (1975).
45. J. O'M. Bockris and D. B. Matthews, *Proc. Roy. Soc. London A*, **292**, 479 (1966).
46. J. O'M. Bockris, S. Srinivasan, and D. B. Matthews, *Disc. Faraday Soc.*, **39**, 239 (1965).
47. S. G. Christov, *Z. Elektrochem.*, **62**, 567 (1958).
48. S. G. Christov, *Electrochim. Acta*, **4**, 306 (1961).
49. S. G. Christov, *J. Res. Inst. Catal., Hokkaido Univ.*, **16**, 169 (1968).
50. B. E. Conway, *Can. J. Chem.*, **37**, 178 (1959).
51. B. E. Conway and M. Salomon, *J. Chem. Phys.*, **41**, 3169 (1964). See also *ibid.*, **68**, 2009 (1964); *Ber. Bunsenges. Phys. Chem.*, **68**, 331 (1964).
52. R. R. Dogonadze, A. M. Kuznetsov, and V. G. Levich, *Elektrokhim.*, **3**, 739 (1967).
53. R. R. Dogonadze, A. M. Kuznetsov, and V. G. Levich, *Electrochim. Acta*, **13**, 1075 (1968).
54. V. G. Levich, in "Physical Chemistry, An Advanced Treatise," Vol. 9B, Chap. 12, H. Eyring, D. Henderson, and W. Jost, Editors, Academic Press, New York (1970).
55. Yu. I. Kharkats and J. Ulstrup, *J. Electroanal. Chem. Interfacial Electrochem.*, **65**, 555 (1975).
56. S. Schuldiner, *This Journal*, **99**, 488 (1952); **106**, 891 (1959); **108**, 985 (1961).
57. J. O'M. Bockris, I. Ammar, and A. Huq, *J. Phys. Chem.*, **61**, 879 (1957).
58. M. Breiter, "Transactions of the Symposium on Electrode Processes," E. Yeager, Editor, pp. 307-324, J. Wiley and Sons, New York (1961).
59. F. Ludwig, E. Yeager, and G. Lozier, *Rev. Polarogr. (Jpn.)*, **14**, 94 (1967).
60. (a) E. Yeager, T. Oey, and F. Hovorka, *J. Phys. Chem.*, **57**, 268 (1953). (b) L. J. Krishtalik, in "Advances in Electrochemistry and Electrochemical Engineering," Vol. 7, P. Delahay, Editor, pp. 283-340, J. Wiley and Sons, New York (1970).
61. M. P. Makowski, E. Heitz, and E. Yeager, *This Journal*, **113**, 204 (1966).
62. S. Schuldiner, *ibid.*, **110**, 332 (1963); **115**, 362 (1968).
63. H. Angerstein-Kozłowska, W. B. A. Sharp, and B. E. Conway, in "Electrocatalysis," M. W. Breiter, Editor, p. 94, The Electrochemical Society Softbound Proceedings Series, Princeton, N.J. (1974).
64. J. C. Huang, W. E. O'Grady, and E. Yeager, *This Journal*, **124**, 1733 (1977).
65. F. Will, *ibid.*, **112**, 451 (1965).
66. M. Breiter, G. Knorr, and W. Volkl, *Z. Elektrochem.*, **59**, 681 (1955).
67. A. N. Frumkin, in "Advances in Electrochemistry and Electrochemical Engineering," Vol. 3, Chap. 5, P. Delahay and C. Tobias, Editors, J. Wiley and Sons, New York (1963).
68. G. Bronel, M. Haim, J. Pesant, and G. Peslerbe, *Surf. Sci.*, **61**, 297 (1976).
69. K. Kinoshita and P. Stonehart, *Electrochim. Acta*, **20**, 101 (1975).
70. V. S. Bagotzky, Yu. B. Vassilyev, and J. I. Pyshnograeva, *ibid.*, **16**, 2141 (1971).
71. R. M. Ishikawa and A. T. Hubbard, *J. Electroanal. Chem. Interfacial Electrochem.*, **69**, 317 (1976).
72. A. Hubbard, R. Ishikawa, and J. Kalekaau, *ibid.*, **86**, 271 (1978).
73. J. A. Joebstl, "Surface Characterization of Electrocatalysts by LEED, Auger Electron Spectroscopy and Related Techniques," First Chemical Congress of North American Continent, Mexico City, Nov. 30-Dec. 5, 1975. Abstract: PHSC-18.
74. J. A. Joebstl, "Surface Research for Development of New Electrocatalysts for Acid Electrolyte Fuel Cells," Army Research Conference, Fort Belvoir (1976).
75. P. Ross, *J. Electroanal. Chem. Interfacial Electrochem.*, **76**, 139 (1977).
76. P. Ross, *This Journal*, **126**, 67 (1979).
77. W. E. O'Grady, M. Y. C. Woo, P. L. Hagans, and E. Yeager, *J. Vac. Sci. Technol.*, **14**, 365 (1977).
78. V. I. Lukyanychzeva, L. A. Fokins, and N. A. Shumilova, *Elektrokhim.*, **15**, 1620 (1979).
79. J. Clavilier, R. Faure, G. Guinet, and R. Durand, *J. Electroanal. Chem. Interfacial Electrochem.*, **107**, 205 (1980).
80. J. Clavilier, *ibid.*, **107**, 211 (1980).
81. See, e.g., D. L. Maricle and W. G. Hodgson, *Anal. Chem.*, **37**, 1562 (1965).
82. D. T. Sawyer and J. C. Roberts, *J. Electroanal. Chem. Interfacial Electrochem.*, **12**, 90 (1966).
83. M. E. Peover and B. S. White, *Electrochim. Acta*, **11**, 1061 (1966).
84. L. N. Nekrasov, L. Pukhanova, N. Dubrovina, and L. Vykhdotseva, *Elektrokhim.*, **6**, 388 (1970).
85. (a) J. Appleby, "Molten Carbonate Fuel Cells" in Conference Proceedings, Fuel Cell Catalysis Workshop, Electric Power Research Institute, Palo Alto, California, EPRI SR-13, Special Report, August 1975, pp. 153-6. (b) B. Kastening and G. Kazemifard, *Ber. Bunsenges. Phys. Chem.*

- Chem.*, **74**, 551 (1970).
86. J. Divisek and B. Kastening, *J. Electroanal. Chem. Interfacial Electrochem.*, **65**, 603 (1975).
 87. N. I. Dubrovina and L. N. Nekrasov, *Elektrokhim.*, **8**, 1503 (1972).
 88. M. Brezina and A. Hofanova-Matejkova, *J. Electroanal. Chem. Interfacial Electrochem.*, **44**, 460 (1973).
 89. I. Morcos and E. Yeager, *Electrochim. Acta*, **15**, 953 (1970).
 90. e.g., J. A. McGinnety, in MTP International Reviews of Science, Inorganic Chemistry Series I, Vol. 5, D. Sharp, Editor, p. 229, Butterworths, London (1972).
 91. H. Behret, H. Binder, and G. Sandstede, in "Electrocatalysis," M. Breiter, Editor, pp. 319-338, The Electrochemical Society Softbound Proceedings Series, Princeton, N.J. (1974).
 92. H. Behret, H. Binder, and G. Sandstede, *Electrochim. Acta*, **20**, 111 (1975).
 93. L. Pauling, *Nature*, **203**, 182 (1964).
 94. See, e.g., B. Hoffman, D. Diemente, and F. Basolo, *J. Am. Chem. Soc.*, **92**, 61 (1970).
 95. J. J. Weiss, *Nature*, **203**, 183 (1964).
 96. J. Wittenberg, B. Wittenberg, J. Persach, and W. Blumberg, *Proc. Nat. Acad. Sci.*, **67**, 1846 (1980).
 97. E. I. Ochiai, *J. Inorg. Chem.*, **36**, 2129 (1974).
 98. F. Beck, W. Dammert, J. Heiss, H. Hiller, and R. Polster, *Z. Naturforsch.*, **28A**, 1009 (1973).
 99. F. Beck, *Ber. Bunsenges. Phys. Chem.*, **77**, 353 (1973).
 100. E. I. Ochiai, *Inorg. Nucl. Chem. Lett.*, **10**, 453 (1974).
 101. T. G. Traylor and C. K. Chang, *J. Am. Chem. Soc.*, **95**, 5810 (1973).
 102. M. J. Bennett and P. B. Donaldson, *ibid.*, **93**, 3307 (1971).
 103. W. P. Schaefer, *Inorg. Chem.*, **7**, 725 (1968).
 104. H. C. Stynes and J. A. Ibers, *ibid.*, **94**, 5125 (1972).
 105. W. Brimgar, C. Chang, J. Gerbel, and T. Traylor, *ibid.*, **96**, 5597 (1974).
 106. J. Zagel, P. Bindra, and E. Yeager, *This Journal*, **127**, 1506 (1980).
 107. J. Zagel, R. Sen, and E. Yeager, *Inorg. Chem.*, **16**, 3379 (1977).
 108. B. Nikolic, R. Adzic, and E. Yeager, *J. Electroanal. Chem. Interfacial Electrochem.*, **103**, 281 (1979).
 109. J. P. Collman, P. Denisevich, Y. Konai, M. Marrocco, C. Koval, and F. Anson, *J. Am. Chem. Soc.*, **102**, 6027 (1980).
 110. D. Matthews and J. Bockris, in "Modern Aspects of Electrochemistry," Vol. 6, Chap. 4, Plenum Press, New York (1971).
 111. E. Yeager, "Mechanisms of Electrochemical Reactions on Non-Metallic Surfaces," in *Electrocatalysis on Non-Metallic Surfaces*, NBS Special Publication 455, 1976, pp. 203-219.
 112. J. S. Griffiths, *Proc. Roy. Soc. A*, **235**, 73 (1956).



Electrochemical Behavior of Copper in Thionyl Chloride Solutions

Wishvender K. Behl*

*U.S. Army Electronics Technology and Devices Laboratory (ERADCOM),
 Power Sources Division, Fort Monmouth, New Jersey 07703*

ABSTRACT

The electrochemical and chemical behavior of copper and copper chlorides was studied in 1.5M LiAlCl₄-SOCl₂ solutions using cyclic voltammetric, controlled potential electrolysis, and x-ray techniques. It was shown that copper metal reacts with thionyl chloride even at ambient temperatures resulting in the formation of cuprous chloride and cupric sulfide. In LiAlCl₄-SOCl₂ solutions, cuprous chloride is further oxidized, chemically as well as electrochemically, to cupric chloride. Cupric chloride was found to be electroactive in these solutions and undergoes reduction in the solid state to cuprous chloride and copper, respectively. It was also found that due to the presence of copper chloride films at the copper metal electrode in these solutions, the electrochemical reduction of thionyl chloride at copper electrodes occurs at more negative potentials than observed at carbon electrodes.

Copper metal has been recently used as a cathode additive (1) to enhance the performance of lithium-thionyl chloride batteries. Thionyl chloride is known (2, 3) to react rapidly with a number of metals at high temperatures and more slowly at ambient temperatures but the chemical literature is devoid of any information on the reaction of copper metal with thionyl chloride. Further, to date, no studies have been reported on the electrochemical behavior of copper metal in thionyl chloride solutions. We have, therefore, investigated the chemical as well as electrochemical behavior of copper metal in 1.5M LiAlCl₄-SOCl₂ solutions using cyclic voltammetric technique and x-ray analysis. This paper summarizes our results.

Experimental

The preparation and purification (4) of thionyl chloride (SOCl₂) and lithium tetrachloroaluminate (LiAlCl₄) and other experimental details (5-7) have been described previously. A three electrode system was used for all measurements. The lithium reference electrode was separated from the lithium counter-electrode and copper working electrode by use of a Pyrex tube (10 mm diam) with a coarse porosity fritted glass bottom. The copper electrode was fabricated by machining a piece of pure copper rod (m5N + purity; Alfa Division, Ventron Corporation) to 4.064 mm diam and threading it to another copper rod of unknown purity. The electrode was then heat sealed in a shrinkable Teflon tubing and the end ground flush with the seal so as to expose the cross section of the pure copper rod.

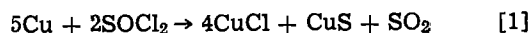
The copper electrodes were mechanically polished on crocus cloth and soft paper before recording each voltammogram. The cross-section area of the copper electrode was 0.13 cm². For controlled potential elec-

trolysis experiments, a strip of pure copper metal foil (m5N purity; Alfa Division, Ventron Corporation, 1 × 5 cm; 0.127 mm thick) was used as the working electrode.

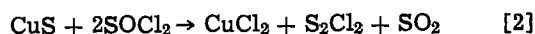
All experiments were performed inside a dry-train, dry-lab (Vacuum Atmosphere Corporation) in a pure dried argon atmosphere.

Results and Discussion

Thionyl chloride was found to react with copper metal (foil or wire) even at room temperature resulting first in the formation of a black film on the copper metal surface followed by its complete disintegration in a few days. The reaction was also accompanied by gassing, presumably due to the formation of sulfur dioxide (see Eq. [1] below). X-ray analysis of the solid product indicated it to be mainly cuprous chloride (CuCl). However, the product was only partially soluble in hydrochloric acid and left behind a small residue after a number of washings with hydrochloric acid. The hydrochloric acid solution was analyzed and gave positive tests (8, 9) for cuprous chloride. The black residue was identified by x-ray analysis to be cupric sulfide (CuS). The reaction of copper with thionyl chloride at ambient temperatures may, therefore, be represented by the equation



Cupric sulfide is known (2, 10) to react with thionyl chloride at 150°C according to the equation



However, it appears that this reaction (Eq. [2]) does not occur at ambient temperatures.

In LiAlCl₄-SOCl₂ solutions, a black film is formed on the copper metal first but it rapidly transforms into a yellow film. After a few hours, the copper metal foil covered with the yellow film was removed, washed

* Electrochemical Society Active Member.
 Key words: cathode, electrolyte, voltammetry.

with thionyl chloride, and vacuum dried. The yellow film was identified by x-ray analysis to be cupric chloride (CuCl_2). It, therefore, appears that in $\text{LiAlCl}_4\text{-SOCl}_2$ solutions, both cuprous chloride and cupric sulfide are at least partially converted to cupric chloride. The reactions may be represented by equations



A reaction similar to Eq. [4] has been shown to occur (11) between lithium sulfide and lithium tetrachloroaluminate in thionyl chloride solutions. Lithium thiochloroaluminate (LiAlSCl_2) is soluble in thionyl chloride and has been proposed (11) as a new electrolyte for lithium thionyl chloride batteries.

The reactions of cuprous chloride and cupric sulfide in $\text{LiAlCl}_4\text{-SOCl}_2$ solutions were independently confirmed by treating reagent grade samples with 1.5M solutions. While the cuprous chloride sample was completely converted to brown cupric chloride in a few hours, the reaction of cupric sulfide was much slower and only a part of the black cupric sulfide sample was converted to brown cupric chloride. The specific role of lithium tetrachloroaluminate in these reactions, however, needs to be further investigated.

Copper metal also reacted with $\text{AlCl}_3\text{-SOCl}_2$ solutions to form an outer layer of cupric chloride film. Since aluminum chloride is known (12) to catalyze the reaction of metals with thionyl chloride, cuprous chloride formed by the reaction of copper metal with thionyl chloride is further oxidized to cupric chloride in $\text{AlCl}_3\text{-SOCl}_2$ solutions. However, in contrast to $\text{LiAlCl}_4\text{-SOCl}_2$ solutions, cupric sulfide does not react with $\text{AlCl}_3\text{-SOCl}_2$ solutions to form cupric chloride.

If the yellow cupric chloride film formed on copper electrodes in $\text{LiAlCl}_4\text{-SOCl}_2$ or $\text{AlCl}_3\text{-SOCl}_2$ solutions is carefully scraped, a thin layer of original mainly cuprous chloride film is found intact next to the copper metal surface and underneath the outer cupric chloride film. This is not surprising since copper metal would be thermodynamically unstable in contact with cupric chloride.

Copper metal electrode momentarily exhibits an open-circuit potential¹ of $\sim 2.85\text{V}$ when first introduced in 1.5M $\text{LiAlCl}_4\text{-SOCl}_2$ solution, but the potential quickly increases to $\sim 3.36\text{V}$. This increase in open-circuit potential can be explained by the chemical transformation of the original mainly cuprous chloride film to cupric chloride film as discussed above. Thus the copper electrode assumes the Cu(I)-Cu(O) couple potential when first introduced in $\text{LiAlCl}_4\text{-SOCl}_2$ solution but as some of the cuprous chloride film is chemically converted to cupric chloride, the electrode assumes a mixed potential involving the two processes.

A typical cyclic voltammogram obtained at the copper electrode by scanning it in the anodic direction from 3.3 to 5.8V at a scan rate of 0.09 V/sec is shown in Fig. 1. The cyclic voltammogram shows an increasing anodic current as the potential becomes more positive and exhibits an anodic peak at $\sim 3.63\text{V}$. After the anodic peak, the electrode is passivated due to the formation of a yellow film on the electrode surface. Thus, due to the passivation of the electrode, the cyclic voltammogram does not show the anodic peaks for the oxidation of $\text{LiAlCl}_4\text{-SOCl}_2$ solutions which are observed (6, 11) at glassy carbon electrodes at potentials above 4.0V. The electrode remains passivated during the reverse scan till the onset of a reduction process at $\sim 3.55\text{V}$.

Cyclic voltammograms similar to those presented in Fig. 1 were obtained at scan rates of 0.01-1.0 V/sec and the anodic peak height increased with increasing scan rate.

¹ All potentials are reported with respect to the lithium reference electrode.

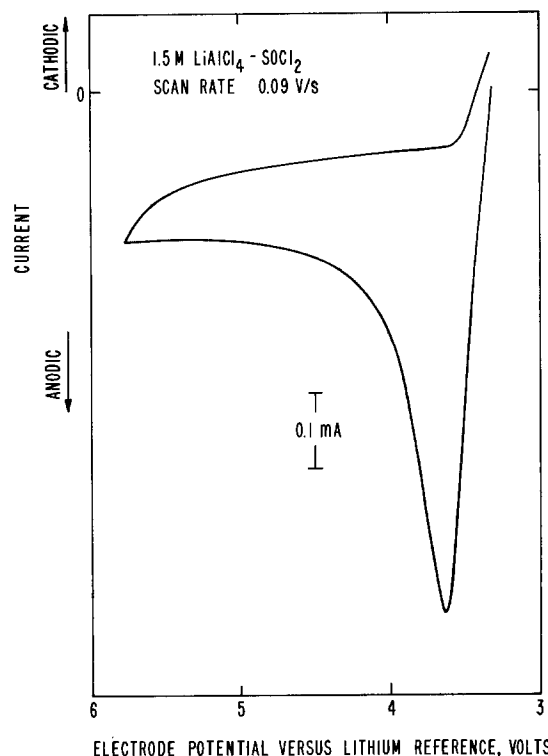
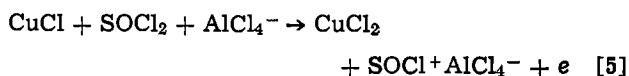


Fig. 1. Typical cyclic voltammogram obtained by scanning the copper electrode between 3.3 and 5.8V.

Controlled potential electrolysis of a strip of copper foil at 4.0V for 16 hr resulted in the formation of a thick yellow film. After the electrolysis, the copper foil covered with the yellow film was removed, repeatedly washed with thionyl chloride, and vacuum dried. The yellow film was then identified by x-ray analysis to be cupric chloride (CuCl_2). Again a thin layer of mainly cuprous chloride film was found intact next to the copper metal surface and underneath the outer cupric chloride film.

Thus, the anodic peak at $\sim 3.63\text{V}$ in the cyclic voltammogram presented in Fig. 1 may be assigned to the oxidation of cuprous chloride to cupric chloride



The anodic peak height in these voltammograms was found to depend to a large extent on the time for which the electrode was held at open circuit before recording the cyclic voltammograms. Thus as the time interval was increased, a larger part of the cuprous chloride-cupric sulfide film converted chemically to cupric chloride (Eq. [3] and [4]) so that only a small anodic peak, due to the electrochemical oxidation of cuprous chloride to cupric chloride, was observed.

In the next series of experiments, the copper metal electrode was held at 4.0V for a few minutes before recording the cyclic voltammograms in the cathodic direction. A large anodic current is initially observed at 4.0V due to the formation of cupric chloride but it quickly decreases to a small steady-state anodic current. A typical cyclic voltammogram obtained by scanning the copper electrode from 4.0 to 2.0V at a scan rate of 0.05 V/sec is shown in Fig. 2. The cyclic voltammogram shows two reduction peaks at ~ 2.7 and $\sim 2.1\text{V}$ and corresponding anodic peaks are observed at ~ 3.7 and $\sim 2.9\text{V}$, respectively, during the reverse scan. If the copper electrode is scanned to 2.5V, only the reduction peak at $\sim 2.7\text{V}$ and the corresponding oxidation peak at $\sim 3.7\text{V}$ are observed in the cyclic voltammograms. Similar cyclic voltammograms were obtained at scan rates of 0.01 to 0.1 V/sec. At higher scan rates, the reduction peak at

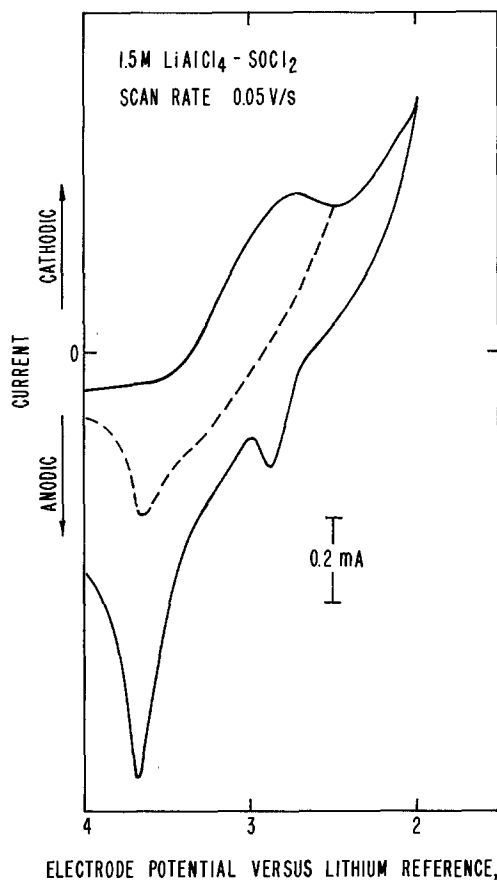


Fig. 2. Typical cyclic voltammogram obtained by scanning the copper electrode between 4.0 and 2.0V (solid curve); broken curve is obtained if the scan is reversed at 2.5V.

$\sim 2.1V$ was indiscernible and only one large anodic peak was observed during the reverse scan.

Controlled potential electrolysis of a strip of pure metal foil at 2.75V for ~ 16 hr resulted in a light blue film on the electrode surface. The copper metal foil was removed, washed with thionyl chloride, and vacuum dried. The light blue film was identified as cuprous chloride ($CuCl$) by x-ray analysis. Thus, the reduction peak in the cyclic voltammograms at $\sim 2.7V$ (Fig. 2) may be ascribed due to the reduction of cupric chloride to cuprous chloride according to the equation

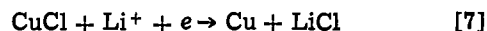


and the corresponding anodic at $\sim 3.7V$ to the oxidation of cuprous chloride to cupric chloride according to Eq. [5] as discussed above.

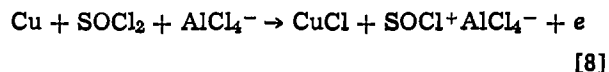
The cell potential for the hypothetical solid-state cell, $Li/LiCl/CuCl_2, CuCl/C$ was calculated to be 3.557V from the free energies of formation of lithium chloride (13a), cupric chloride (13b), and cuprous chloride (13b). It is seen that the electrochemical reduction of cupric chloride to cuprous chloride in $LiAlCl_4-SOCl_2$ solutions occurs at potentials ($\sim 3.5V$) close to the theoretically predicted value.

During the course of these experiments, it was noticed that a thin layer of metallic copper deposited on the lithium counterelectrode. Since cupric chloride was found to have negligible solubility in $LiAlCl_4-SOCl_2$ solutions, it appears likely that during the reduction of cupric chloride to cuprous chloride, part of cupric chloride complexes with chloride ions and goes into solution as $CuCl_4^{--}$ ions. A similar explanation was offered by Rao (14) to account for the increased solubility of cuprous chloride during discharge in $LiAlCl_4$ -propylene carbonate solutions. Copper metal is then plated on the lithium counterelectrode by the reaction of lithium metal with $CuCl_4^{--}$ ions in solution.

The reduction peak at $\sim 2.1V$ in the cyclic voltammograms (Fig. 2) may be ascribed to the reduction of cuprous chloride to copper metal

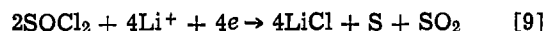


and the corresponding anodic peak at $\sim 2.9V$ to the oxidation of copper metal to cuprous chloride according to the equation



As soon as some cuprous chloride is reduced to copper metal, the cathodic current rapidly increases at $\sim 2.0V$ due to the simultaneous reduction of thionyl chloride at the bare copper metal surface. Thus, the cuprous chloride reduction peak at $\sim 2.1V$ appears only as a small step to the larger reduction peak at $\sim 1.6V$ in the cyclic voltammograms (Fig. 3) at scan rates below ~ 0.1 V/sec and merges with the larger reduction peak at higher scan rates.

Controlled potential electrolysis of a strip of copper metal foil at 1.5V resulted only in a lithium chloride film on the bare copper metal surface. Thus, at potentials negative to $\sim 2.0V$, the copper chloride films as well as any unreacted cupric sulfide on the electrode surface are all reduced to metallic copper. It is also seen that the presence of various films on copper electrodes at potentials positive to $\sim 2.0V$ block the reduction of thionyl chloride. As soon as these films are reduced, the copper metal surface becomes available for the reduction of thionyl chloride. Thus, the electrochemical reduction of thionyl chloride at copper electrodes occurs at more negative potentials than observed at carbon electrodes (6, 7, 11, 15, 16) and may be represented by the generally accepted equation (6, 7, 11, 17-20)



Due to high background currents at copper electrodes in the potential region of 1-2V, other minor reduction peaks (6, 7, 11, 15) observed at carbon electrodes in this potential region are not discernible in the cyclic voltammograms. At more negative potentials ($\sim -0.25V$), a large increase in the cathodic current is observed due to the deposition of lithium metal. On the reverse scan, an anodic peak for the dissolution of deposited lithium metal is observed at $\sim 0.15V$ and at more positive potentials, a minor ox-

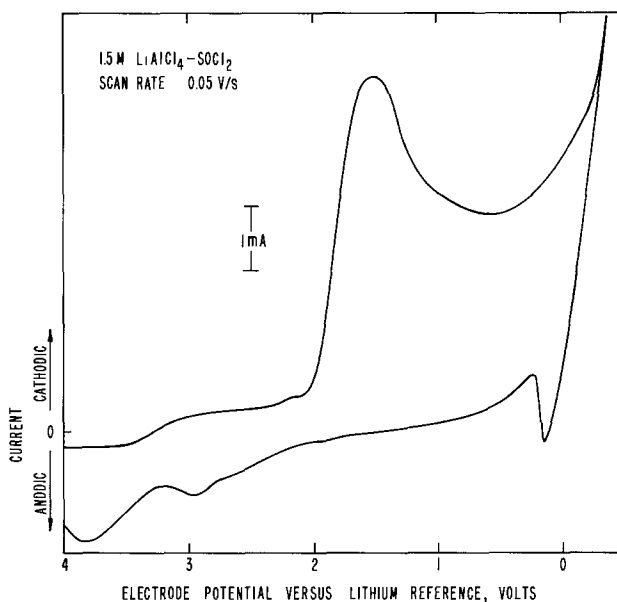


Fig. 3. Typical cyclic voltammogram obtained by scanning the copper electrode between 4.0 and $-0.35V$.

duction peak is observed at $\sim 1.9V$ followed by the anodic peaks for the oxidation of copper to cuprous chloride at $\sim 2.95V$ and cuprous chloride to cupric chloride at $\sim 3.7V$, respectively.

From the results presented above, it is seen that the electrochemical reduction of cupric chloride to cuprous chloride in $LiAlCl_4-SOCl_2$ solutions occurs at about similar potentials as the electrochemical reduction of thionyl chloride at Shawinigan black carbon electrodes (4). It is also seen that the cupric chloride/cuprous chloride redox couple is catalytic in $LiAlCl_4-SOCl_2$ solutions and results in the regeneration of cupric chloride by the reaction of cuprous chloride with thionyl chloride. Cupric chloride, therefore, appears to be a useful cathode additive for lithium-thionyl chloride batteries. Preliminary results (21) with Shawinigan black carbon cathodes containing about 21.7 weight percent of cupric chloride indicate that these electrodes show less polarization, particularly at high current densities, than the Shawinigan black carbon cathodes without the cupric chloride additive.

Acknowledgment

The author wishes to thank D. Eckart of this laboratory for x-ray analyses.

Manuscript submitted Sept. 19, 1980; revised manuscript received Dec. 6, 1980. This was Paper 57 presented at the Hollywood, Florida, Meeting of the Society, Oct. 5-10, 1980.

Any discussion of this paper will appear in a Discussion Section to be published in the December 1981 JOURNAL. All discussions for the December 1981 Discussion Section should be submitted by Aug. 1, 1981.

Publication costs of this article were assisted by the U.S. Army Electronics Technology and Devices Laboratory (ERADCOM).

REFERENCES

1. L. R. Giattino, U.S. Pat. 4,167,608 (1979).
2. J. W. Mellor, "A Comprehensive Treatise of Inorganic and Theoretical Chemistry," Vol. 10, Long-

- mans, Green and Co., London (1930).
3. M. Davis, H. Szkuta, and A. J. Krubsack, in "Mechanisms of Reactions of Sulfur Compounds," Vol. 5, pp. 4-57, Intra-Science Research Foundation, Santa Monica, California (1970).
4. W. K. Behl, J. A. Christopoulos, M. Ramirez, and S. Gilman, *This Journal*, **120**, 1619 (1973).
5. W. K. Behl, *J. Electroanal. Chem. Interfacial Electrochem.*, **70**, 213 (1976).
6. W. K. Behl, in "Proc. 27th Power Sources Symposium," p. 30, Atlantic City, N.J., June 24-26, 1976.
7. W. K. Behl, *J. Electroanal. Chem. Interfacial Electrochem.*, **101**, 367 (1979).
8. R. K. McAlpine and B. A. Soule, "Prescott and Johnson's Qualitative Chemical Analysis," D. Van Nostrand Co., Inc., New York (1933).
9. J. W. Mellor, "A Comprehensive Treatise of Inorganic and Theoretical Chemistry," Vol. 3, Longmans, Green and Co., London (1930).
10. H. B. North and C. B. Conover, *J. Am. Chem. Soc.*, **37**, 2486 (1915).
11. K. M. Abraham and R. M. Mank, *This Journal*, **127**, 2091 (1980).
12. R. A. Hubbard and W. F. Luder, *J. Am. Chem. Soc.*, **73**, 1327 (1951).
13. JANAF Thermochemical Tables, The Dow Chemical Company, Midland, Michigan; (a) June 30, 1962; (b) March 31, 1966.
14. M. L. B. Rao, *This Journal*, **114**, 13 (1967).
15. G. E. Blomgren, V. Z. Leger, M. L. Kronenberg, T. Kalnoki-kis, and R. J. Brodd, in "Proc. 11th Internat. Power Sources Symposium," p. 583, Brighton, England (1978).
16. Yu. M. Povarov, T. D. Nikolaeva, and V. S. Bagot'skii, *Sov. Electrochem.*, **14**, 732 (1978).
17. A. N. Dey and C. R. Schlaikjer, in "Proc. 26th Power Sources Symposium," p. 47, Atlantic City, N.J., April 29-May 2, 1974.
18. A. N. Dey, *This Journal*, **123**, 1262 (1976).
19. J. R. Driscoll, G. L. Holleck, and D. E. Toland, in "Proc. 27th Power Sources Symposium," p. 28, Atlantic City, N.J., June 24-26, 1976.
20. C. R. Schlaikjer, F. Goebel, and N. Marincic, *This Journal*, **126**, 513 (1979).
21. W. K. Behl, U.S. Pat. Application, 171,515, July 23, 1980.

Effect of Sulfur Impurities on Li/TiS₂ Cells

B. M. L. Rao and J. A. Shropshire

Exxon Research and Engineering Company, Advanced Energy Systems Laboratory, Linden, New Jersey 07036

ABSTRACT

Conditions leading to the generation of sulfur and hydrogen sulfide from TiS₂ can occur with uncontrolled handling of the active material during the fabrication of Li/TiS₂ cells. These impurities affect the storage behavior of the ambient temperatures rechargeable organic electrolyte cells. An increase in the lithium anode polarization and self-discharge of the cells is witnessed in the presence of these impurities. A mechanism of Li₂S_n film formation and S_n⁻²/S_{n-x}⁻² redox shuttle is discussed to account for the observed results.

In previous work, operation of high energy density Li/TiS₂ cells in organic electrolytes (1-3), molten salts (4-6), and solid electrolyte (7), has drawn attention to several important chemical reactions which influence the TiS₂ half-cell performance in organic electrolyte cells. These include: (i) the effect of nonstoichiometry in the titanium and sulfur ratio in the active material, and (ii) the intercalation of solvents. The former, leading to the generation of Ti_{1+x}S₂, results in diminished rate capability of the cells, due to a reduction of lithium diffusion rate in

the host lattice (8). The latter, a phenomenon of solvent co-intercalation along with lithium, results in a large expansion of c-axis distance. This event occurs in the presence of trace amounts of water, which is a common impurity in organic electrolytes. For example, co-intercalation of electrolyte solvents, such as propylene carbonate, dimethyl sulfoxide, and diglyme, result (6) in c-lattice expansion of 14-19Å compared to 6.2Å for the intercalation of lithium into TiS₂. Such large lattice expansion causes an excessive volume change during the cell operation. In this study, we have observed that sulfur-based impurities also affect the rate capability and storage life of Li/TiS₂ cells.

Key words: electrolyte cell, discharge, chelation.

Background Information

Origin of sulfur-based impurities, i.e., free elemental sulfur, or hydrogen sulfide in TiS_2 , may be traced to either of the following sources: (i) nonequilibrium conditions of production of TiS_2 (from the elements, or by the reaction of H_2S and TiCl_4), and (ii) uncontrolled treatments and handling of the active material.

Solvent extraction procedures (9) are effective in the removal of impurities from the TiS_2 samples. The purified TiS_2 is stable in a dry, inert environment, as the estimated equilibrium sulfur vapor pressure is $\sim 10^{-6}$ atm at room temperature. However, regeneration of these impurities occurs on contact with moisture and air. Moist air ($\sim 40\%$ RH) reacts with battery grade, high surface area ($\sim 5 \text{ m}^2/\text{g}$) TiS_2 powder and releases hydrogen sulfide. This reaction appears to be gradually retarded by the formation of a TiO_2 surface film. Although TiS_2 may be handled, to a limited extent, in the dry room ($< 1.5\%$ RH), H_2S monitoring systems need to be employed to take precautions against an accumulation or release of toxic levels of the gas. Interaction of TiS_2 with dry air results in the release of free elemental sulfur (7), with the formation of nonstoichiometric TiS_2 , i.e., $\text{Ti}_{1+x}\text{S}_2$ and TiO_{2y} ($y \sim 1$). This reaction is naturally accelerated by an increase in temperature. Combustion of TiS_2 ensues at $> 232^\circ\text{C}$, initiated by the auto-ignition of liberated sulfur. This reaction is of importance in controlling conditions of fabrication (9) of thermal bonded TiS_2 electrodes with plastic binders.

Based on the aforementioned reactions, regeneration of sulfur-based impurities may reoccur in purified TiS_2 during handling of the material for the manufacture of electrodes, cell assembly, and storage conditions. This paper discusses the effect of these impurities on the storage behavior of Li/TiS_2 cells in an organic electrolyte.

Experimental

Cells.—The Li/TiS_2 test cells were of one anode, one cathode, parallel plate, prismatic configuration. The negative electrode was 0.025 cm thick, 6.45 cm^2 lithium foil pressed on copper grid. The positive electrode was a sintered porous cake ($\sim 45\%$ porosity) of $\sim 0.99\text{g}$ TiS_2 and 0.1g polytetrafluoroethylene, which was prepared using solvent-treated TiS_2 and hot-pressed onto a (6.45 cm^2) tantalum grid in a helium dry box. The electrodes were individually enclosed in microporous polyethylene bags and were sandwiched across a 0.04 cm porous fiberglass mat separator. A polyethylene bag served as the cell container. Stack pressure was realized by clamping the cell between metal plates. The cells were assembled with lithium reference electrodes in a dry room ($< 1.5\%$ RH) and placed in suitable jars with leads to exclude atmospheric contamination. The cells were tested after addition of 2.5–3.5 ml of 2.5M $\text{LiSCN}\cdot 1,3$ -dioxolane, an electrolyte previously developed for rechargeable Li/TiS_2 cells (10).

Tests.—Cells assembled, as described above, served as controls for comparison of storage behavior in the presence of sulfur and hydrogen sulfide impurities. Current-potential profiles and the open-circuit voltage behavior were investigated as a function of room temperature storage duration in these experiments. The former was obtained in a galvanostatic polarization for a period of 1 min, measuring the lithium half-cell behavior during the test. The spread in the data indicated in various sets of data in Fig. 1 cover the voltage excursions noted from the start to the end of the polarization experiments.

The effect of elemental sulfur was studied by assembling Li/TiS_2 cells, as above, with deliberate contamination of the TiS_2 electrode with the impurity as different from the use of excess sulfur as cathode ac-

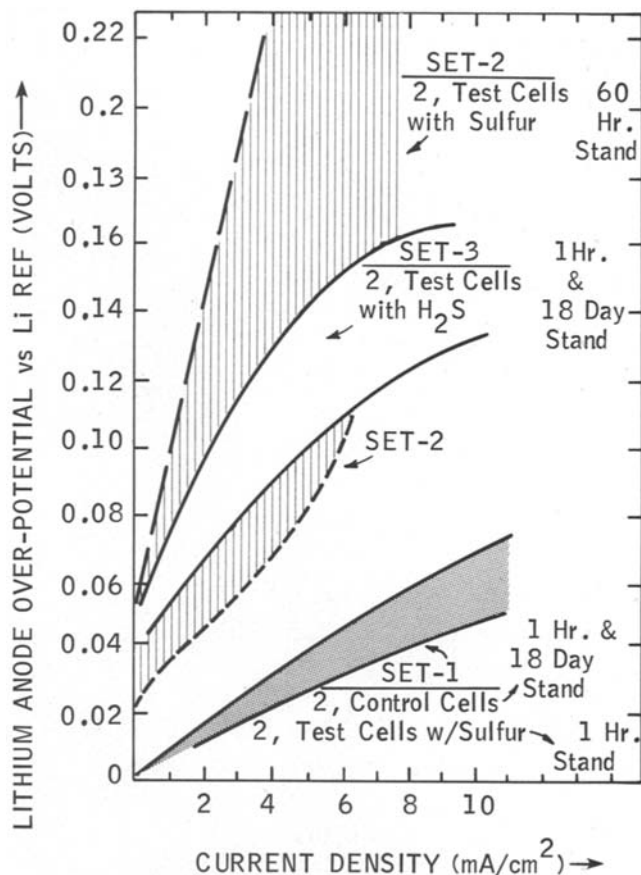


Fig. 1. Anode polarization data on open-circuit stand in the presence of "S" and " H_2S " in Li/TiS_2 cells.

tive material with transition metal chalcogenide by Broadhead (11). For this purpose, TiS_2 electrodes, similar to the ones used in control cells, were smeared with 0.06g of sulfur powder on the 6.45 cm^2 area. Test cells were assembled with the sulfur-containing side facing the lithium electrode. The effect of hydrogen sulfide was examined by using TiS_2 cathodes exposed to laboratory humidity ($\sim 40\%$ RH). The formation of > 200 ppm H_2S under this condition was noted in ~ 20 min of exposure (5), by the tarnishing of lead acetate paper positioned 1 in. away from the electrode.

In supplementary experiments, the solubility of sulfur in 1:3-dioxolane was measured to be 0.02g/100 ml solvent. Chemical analysis of electrode products of self-discharged cells indicated sulfur species in the anode film by x-ray fluorescence and Li_2TiS_2 was detected in the TiS_2 cathode by x-ray diffraction.

Results

Figure 1, set 1, provides the current-potential behavior of the lithium half-cell of the Li/TiS_2 cell observed during discharge of two control cells, at 1 hr and 18 days storage, after the addition of electrolyte. This set also represents the lithium anode polarization data at 1 hr soak, for two cells containing sulfur impurity. After 60 hr of stand, the lithium anode exhibited the behavior represented in Fig. 1, set 2, in the presence of sulfur in the cell. Figure 1, set 3, illustrates lithium anode polarization for two cells, with cathodes containing H_2S , after 1 hr and 18 days of open-circuit stand, at room temperature.

Figure 2 provides a comparison of open-circuit voltage of Li/TiS_2 control cells, with similar data over a 2 month period at $\sim 23^\circ\text{C}$, on cells containing sulfur and hydrogen sulfide impurities at levels of earlier description.

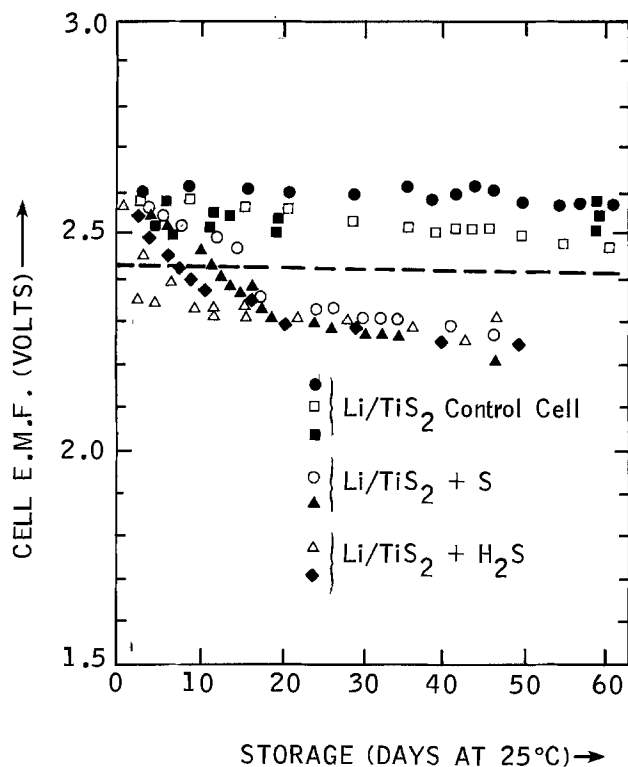
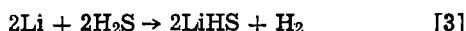


Fig. 2. Open-circuit voltage of Li/TiS₂ cells

Discussion

Data in Fig. 1 and 2 indicate an increase in lithium anode polarization and a self-discharge of Li/TiS₂ cells in the presence of sulfur and hydrogen sulfide. As these impurities originate at the TiS₂ electrode, they are presumably transported to the anode, as dissolved species, and interactions in Eq. [1]-[3] occur



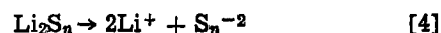
The formation of Li₂S_n, Li₂S, or LiHS films on the anode account for the increase in polarization voltage of the lithium half-cells in Fig. 1. This is plausible, as sulfur and H₂S are observed to be soluble in the electrolyte and sulfur has been detected on the anode by x-ray fluorescence analysis. The differences in the magnitude of the polarization voltage and the time effect variations between sulfur and H₂S containing cells in Fig. 1, sets 1-3, are not only caused by the differences in the quantity of impurities, their solubility, diffusion transport, etc., but also by the film composition, compactness, and other parameters.

Although the reactions in [1]-[3] may account for the increased polarization voltage of the lithium electrode on storage of Li/TiS₂ cells, these reactions alone cannot explain the self-discharge noted in Fig. 2.

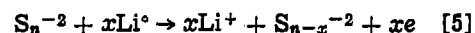
It is noted, in Fig. 2, that control cells exhibit formal potentials of Li/TiS₂ cells above 2.42V measured for fully charged cycled cells. This initial behavior is due to the fact that the TiS₂ half-cell potential is not in equilibrium in the absence of small amounts of Li_xTiS₂. The formal potential is influenced by small quantities of other impurities, such as dissolved oxygen peroxides, or (CNS)_x in the LiSCN-1:3-dioxolane electrolyte. However, emf of the control cells stored in the dry room over a 60 day period do not drift below the expected 2.42V for the Li/TiS₂ system.

In comparison to the data of the control cells, the open-circuit voltage of Li/TiS₂ shows a self-discharge behavior, in that the cell voltage drifts below 2.42V in

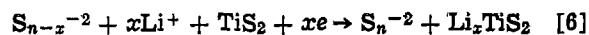
the presence of sulfur and H₂S impurities. It appears that these impurities partially solubilize the films formed in reactions [1]-[3] to generate polysulfides of composition S_n⁻². If the emf of the TiS₂ and Li_xTiS₂ half-cell is favorable for the oxidation of the polysulfide species, then a soluble redox couple may result. Shuttling of these species between the lithium and TiS₂ electrodes could cause the observed self-discharge. Equations [4]-[6] describe this phenomenon



At Li⁺ (-ve) electrode



At TiS₂ (+ve) electrode



Conditions for the reoxidation of S_n⁻²/S_{n-x}⁻² couple is indicated by Rauh *et al.* (12) to be 2.1V in electrolytes with tetrahydrofuran, a cyclic ether solvent similar to 1:3-dioxolane. This, indeed, is noted in Fig. 2, as the emf of the Li/TiS₂ cells is >2.1V. The formation of Li_xTiS₂, as evidenced by x-ray diffraction analysis of the cathode, represents the self-discharge reaction and the drop in cell voltage noted in the presence of the impurities in question. The initial fast drop in the open-circuit voltage noted in Fig. 2 may correspond to a redox shuttle of S₈/S₈⁻² to ~2.3V (12,13), and the remaining slower reactions to S_n⁻²/S_{n-x}⁻² (n = 8, x = 2-4), as observed, to 2.1V in the previous work (12) on the study of the lithium/dissolved sulfur battery. Sulfur and H₂S are likely to generate similar redox shuttles, in reactions [5] and [6] and, hence, the similarity in self-discharge in the presence of these impurities (Fig. 2). Lack of polysulfide formation indicated by Broadhead (11) in Li/NbSe₂ and S cells, appears to be an effect of propylene carbonate medium.

Based on the results of this study, it is indicated that exclusion of sulfur-based impurities is required to minimize the self-discharge of Li/TiS₂ cells operating in cyclic ether solvents.

Acknowledgment

The authors wish to acknowledge helpful discussions with Dr. D. J. Eustace and the laboratory assistance of Mr. R. J. Solarczyk.

Manuscript submitted April 17, 1980; revised manuscript received Dec. 15, 1980.

Any discussion of this paper will appear in a Discussion Section to be published in the December 1981 JOURNAL. All discussions for the December 1981 Discussion Section should be submitted by Aug. 1, 1981.

Publication costs of this article were assisted by Exxon Research and Engineering Company.

REFERENCES

- M. S. Whittingham, Belgian Pat. 819,672 (1975); *Science*, **192**, 1126 (1976).
- G. L. Hollek, F. S. Shuker, and S. B. Brummer, in "Proc. 10th IECEC" (1975).
- L. H. Gaines, R. W. Francis, G. H. Newman, and B. M. L. Rao, "Proc. 11th IECEC" (1976).
- Y. M. F. Marikar and A. D. Inman, Faraday Soc., Brighton Meeting, 1976, Brighton, England.
- Argonne National Lab., Report ANL-76-98.
- M. S. Whittingham, *Prog. Solid State Chem.*, **12**, 41 (1978).
- C. C. Liang, A. V. Joshi, and N. E. Hamilton, *J. Appl. Electrochem.*, **3**, 455 (1978).
- M. S. Whittingham, U.S. Pat. 4,001,005 (1975).
- B. M. L. Rao and J. A. Shropshire, Submitted to *Ind. Eng. Chem.*
- B. M. L. Rao, D. J. Eustace, and J. A. Shropshire, *J. Appl. Electrochem.*, **10**, 757 (1980).

11. J. Broadhead, in "Power Sources 4," D. H. Collins, Editor, Oriole Press, Newcastle upon Tyne, England (1973); U.S. Pat. 3,791,867.
12. R. D. Rauh, K. M. Abraham, G. F. Pearson, J. K.

- Suprenant, and S. B. Bummer, *This Journal*, **126**, 523 (1979).
13. Freeman, Oklahoma State Univ. Research Foundation Report No. 60 (1962).

Semiconductor Electrodes

XXXVI. Characteristics of n-MoSe₂, n- and p-WSe₂ Electrodes in Aqueous Solution

Fu-Ren F. Fan* and Allen J. Bard*

Department of Chemistry, The University of Texas at Austin, Austin, Texas 78712

ABSTRACT

Capacitance and voltammetric measurements were employed to investigate the electrochemical and photoelectrochemical (PEC) behavior of n-WSe₂, p-WSe₂, and n-MoSe₂ single crystal electrodes in aqueous solutions containing various redox couples (Br⁻/Br₂, I⁻/I₃⁻, Fe(CN)₆⁴⁻/Fe(CN)₆³⁻, Fe²⁺/Fe³⁺, HV⁺/HV²⁺, and MV⁺/MV²⁺, where HV is heptyl viologen and MV is methyl viologen). In supporting electrolyte (0.5M Na₂SO₄), the conduction bandedges of MoSe₂ and WSe₂, determined from the capacitance measurement, are at -0.14 and -0.44V vs. SCE, respectively, and the valence bandedge of WSe₂ is at 0.93V vs. SCE. A bandgap of 1.4 eV for WSe₂ was determined either from the photocurrent action spectrum or from the capacitance measurement. The specific effects of iodide on the capacitance and voltammetric behavior of layer-type compounds are compared. The characteristics of several PEC cells are also described.

The application of semiconductor electrode photoelectrochemical (PEC) cells (1) for the utilization of solar energy for the production of electricity or chemical species depends on the discovery of inexpensive and abundant materials with an energy gap which matches the solar spectrum and which are capable of stable operation. Thus there has been an active search for new semiconductor materials for PEC cells which meet these requirements.

Tributsch (2) introduced the concept of using layer-type electrodes (e.g., MoS₂, MoSe₂, WSe₂) for such applications and a number of recent papers (3-8)¹ have described PEC cells based on these materials. These cells show quite good efficiencies and good stability in aqueous and acetonitrile solutions containing redox couples with reasonably positive redox potentials (e.g., I⁻/I₃⁻). Wrighton and co-workers demonstrated that MoSe₂ and MoS₂ can even photo-oxidize chloride in highly concentrated aqueous LiCl solutions (3).

The behavior and efficiencies of these cells depend strongly on the nature of the electrode surface (4-8). A wide range of scatter in the electrochemical parameters (e.g., flatband potential, V_{FB}) and the PEC behavior is reported from different laboratories. These different results are apparently due to the significant sample-to-sample variations in the morphology of crystals. For example, the presence of exposed edges in the van der Waals surface (⊥ C-axis) has been shown to lead to significant dark anodic currents at n-type electrodes and lower photocurrent efficiencies (4c, 8b).

In this report, we describe the voltammetric and impedance measurements of some carefully selected and well-behaved n-MoSe₂, n- and p-WSe₂ single crystals. Some physical properties, e.g., V_{FB} and the bandgap, E_g, of WSe₂, obtained by different techniques are compared. The specific effect of iodide on the onset

photopotentials of layer-type compounds is compared with V_{FB} obtained by capacitance measurements. We also discuss the performance of several solar cells composed of n-MoSe₂ and (halogen/halide) redox couples.

Experimental

The semiconductors used, n-MoSe₂, n- and p-WSe₂, were single crystals generously donated by Dr. Barry Miller and Dr. Frank DiSalvo, Bell Laboratories. The detailed procedures for selecting, mounting, cleaning, and etching the single crystals and preparing the ohmic contacts are similar to those previously reported (4). The electrodes studied here showed mirror-like surfaces with no obvious edges and pits on the surfaces when examined at a magnification of 100×. They produced negligibly small dark oxidation currents (< 1 μA cm⁻²) in 0.5M Na₂SO₄ between -0.5 and 1V vs. SCE. Typically, the electrode areas of the semiconductors were 0.03-0.2 cm². If not otherwise mentioned, the exposed surface is the van der Waals surface (⊥ C-axis).

A conventional three-electrode, single-compartment cell was used for all experiments. The electrochemical cell (volume ~ 25 ml) contained Pt disk and semiconductor working electrodes and was fitted with a flat Pyrex window for illumination of the semiconductor electrode. A platinum foil (~ 40 cm²) was used as the counterelectrode in the voltammetric and impedance measurements. An aqueous saturated calomel electrode (SCE) was used as the reference electrode.

The voltammetric experiments and the solar cell measurements were performed with the same apparatus and procedures as reported previously (4). The light source used in the study of the PEC effect was an Oriol Corporation (Stamford, Connecticut) 450W Xe lamp. Experiments designed for specific wavelengths employed an Oriol 7240 grating monochromator with a 20 nm bandpass. A red filter (590 nm cut-on) was used with the Xe lamp. The radiant intensity was measured with an EG & G (Salem, Massachusetts) Model

* Electrochemical Society Active Member.

Key words: capacitance, voltammetry, impedance, photoelectrochemical behavior, solar cells.

¹ A solar power conversion efficiency of 10.2% has been reported for a cell based on n-WSe₂ and I⁻/I₃⁻ systems (5).

550 Radiometer/Photometer. Neutral density filters were used to vary the intensity of the light.

All impedance measurements were carried out with an aqueous 0.5M Na₂SO₄ solution, if not otherwise mentioned. The electrical circuit allowed the application of a variable potential at the semiconductor electrode with respect to the reference electrode. The impedance was measured between this working electrode and a large (~ 40 cm²) counterelectrode. The applied potential was controlled potentiostatically, and the capacitance was measured as the 90° quadrature signal from a lock-in amplifier (Princeton Applied Research, Model HR-8) with excitation by an external a-c generator via the potentiostat. The amplitude of the sinusoidal wave superimposed on the d-c bias potential was ~ 5 mV. The measured capacitances were calibrated by replacing the electrochemical cell by a set of standard capacitors. The quantity measured was the equivalent series capacitance, C, since the dissipation factor ωRC, where ω is the angular frequency and R is equivalent series resistance, was much smaller than unity for all systems studied here, as shown in the results below. The measured impedance values were not changed when the counterelectrode was partially lifted out of the solution; thus the counterelectrode did not contribute significantly to the reported capacitances. All impedance measurements were performed in the dark.

Reagent grade chemicals were used without further purification. All solutions were prepared from triply distilled water and were deoxygenated for at least 30 min with purified nitrogen before each experiment. All experiments were carried out with the solution under a nitrogen atmosphere.

Results

Impedance measurements.—The capacitance of an electrode as a function of frequency and potential was a useful indicator of the electrode quality. The n-MoSe₂ and n-WSe₂ electrodes were subjected to impedance measurements in supporting electrolyte solutions, if not otherwise mentioned, at d-c bias potentials where the residual currents were negligibly small (< 1 μA cm⁻²). Thus the measured value of C is the equivalent differential capacitance of the interface, with no faradaic contribution. If the presence of the oxidized form of a redox couple was required, its concentration was kept as low as possible to prevent substantial reduction current, which might distort the Mott-Schottky plots.

The value of the flatband potential, V_{FB}, was determined from the intercept of the plot of 1/C² vs. potential according to the Mott-Schottky equation (9)

$$\left(\frac{1}{C}\right)^2 = \frac{2}{\epsilon\epsilon_0 e_0 n} \left(|V - V_{fb}| - \frac{kT}{e_0} \right) \quad [1]$$

In this equation ε is the dielectric constant of the semiconductor, ε₀ is the permittivity of free space, n is the donor density, n_D, for n-type and the acceptor density, n_A, for p-type semiconductors, e₀ is the absolute value of the charge of the electron, T is the absolute temperature, and k is the Boltzmann constant.

n-MoSe₂.—As shown in Fig. 1a, at frequencies between 1 and 10 kHz, a linear C⁻² vs. V relationship was observed over a considerable potential range. Since the capacitance at these potentials is frequency independent, the intercept of the Mott-Schottky plot gives the flatband potential after correction for the thermal term in Eq. [1] and the potential drop across the Helmholtz double layer (i.e., for the contribution of capacitance of the Helmholtz layer). The flatband potential of this n-MoSe₂ electrode was ~0.0V vs. SCE at pH 4.5.

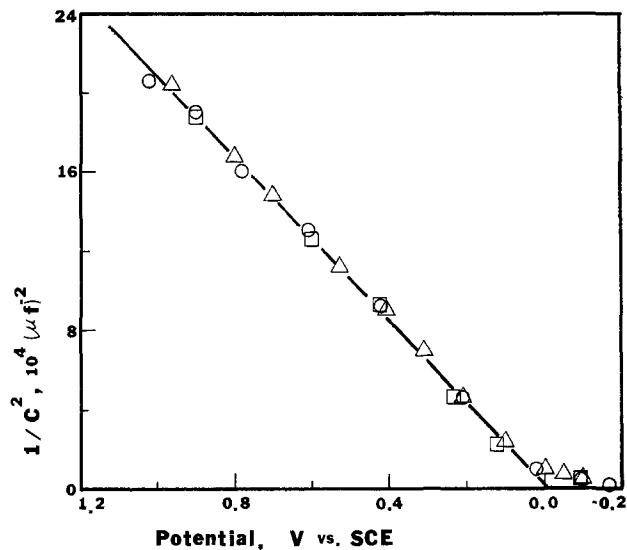


Fig. 1a. C⁻² vs. V at different frequencies for n-MoSe₂ electrode in aqueous solution of 0.5M Na₂SO₄ at pH 4.5: (□) 1 kHz, (○) 3 kHz, (△) 10 kHz. Electrode area, 0.030 cm².

If we take the dielectric constant perpendicular to the C-axis, ε_⊥, as 6.8 (10),² the slope of the Mott-Schottky plot yields n_D ~ 1.2 × 10¹⁷ cm⁻³. With this value of the donor density of the MoSe₂ single crystal, the location of conduction bandedge, E_c, was calculated from Eq. [2] (9), assuming that the donor impurities are completely ionized. Since N_c >> n_D (see below)

$$n_D = N_c \exp [-(E_c - E_F)/kT] \quad [2]$$

in which E_F is the Fermi energy and N_c is the density of the effective states in the conduction band, which is given by

$$N_c = 2 \left(\frac{2\pi M_e^* kT}{h^2} \right)^{3/2} \quad [3]$$

where h is the Planck constant and M_e^{*} is the effective mass of electrons in the conduction band. With the assumption M_e^{*} ≈ M₀ (11),³ in which M₀ is the mass of a free electron, N_c was estimated to be ~ 2.5 × 10¹⁹ cm⁻³. Thus, E_c was ~ 0.14 eV above the V_{FB} Fermi level energy, i.e., the conduction bandedge is located at a potential ~ -0.14V vs. SCE.

The frequency independence of the capacitance implies that no oxide layer was on the surface of MoSe₂. The presence of an oxide layer often leads to frequency dispersion in the measured capacitance values because of dielectric relaxation in this layer.

As shown in Fig. 1b, the flatband potential of the n-MoSe₂ electrode was independent of pH, at least in the range studied (0-8). This finding further confirms the absence of an oxide layer on the electrode surface.

The flatband potential of the n-MoSe₂ electrode shifted to a more negative potential when iodide was present in the solution (Fig. 2a). Moreover, addition of a small amount of triiodide (0.25 mmole) shifted V_{FB} to an even more negative potential. However, bromide had no effect on V_{FB} (Fig. 2b). These results parallel those obtained by the voltammetric measurements which are described later. We can also estimate the resistivity, ρ, of this n-MoSe₂ electrode from the mobility, μ_e, of electrons and the free electron density, n_e, based on Eq. [4]

$$\rho \cong 1/(e_0 n_e \mu_e) \quad [4]$$

Here we neglect the contribution from the minority

²The ε_⊥ value of MoSe₂ was assumed close to that of MoS₂. The ε_⊥ of MoS₂ has been reported by Evans et al. (10).

³Here we assume that electrons in MoSe₂ have similar effective mass to that in WSe₂ (11).

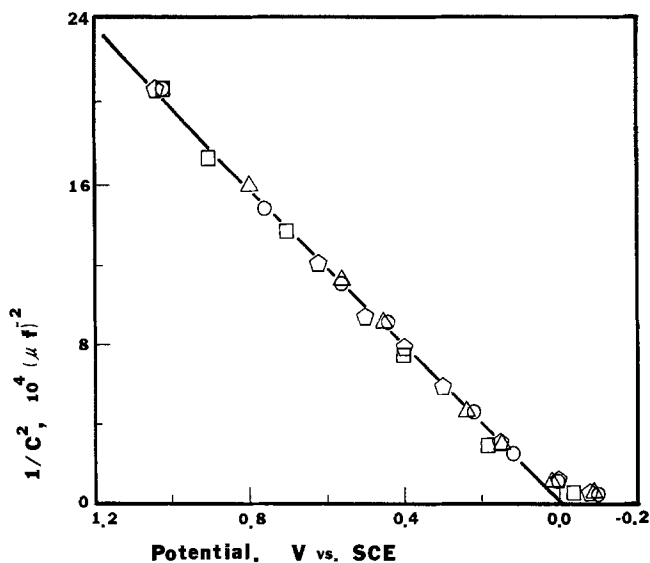


Fig. 1b. C^{-2} vs. V at different pH for n-MoSe₂ electrode in aqueous solution of 0.5M Na₂SO₄ at 2 kHz; (□) pH 0.5, (○) pH 2.5, (△) pH 4.5, (◇) pH 8.0.

charge carriers. With $\mu_e = 10 \sim 50 \text{ cm}^2 \text{ V}^{-1} \text{ sec}^{-1}$ (12) and the assumption that the donors are completely ionized, ρ can be estimated to be $1 \sim 5 \Omega\text{-cm}$.

n-WSe₂.—The general behavior for n-WSe₂ electrodes was similar to that of the n-MoSe₂ electrode described above. At frequencies between 0.2 and 2 kHz, a linear C^{-2} vs. V relationship was obtained over a considerable potential range and the capacitance was essentially frequency independent (see Fig. 3). Thus, V_{fb} of this n-WSe₂ electrode was $\sim -0.32\text{V vs. SCE}$. Assuming that $\epsilon_{\perp} \approx 10$ for WSe₂ (13),⁴ we estimate a donor density of this electrode of $\sim 2.0 \times 10^{17} \text{ cm}^{-3}$. According to Hicks (11), $M_e^* \approx M_h^* \approx M_0$; hence N_c was $\sim 2.5 \times 10^{19} \text{ cm}^{-3}$ and E_c was $\sim 0.12 \text{ eV}$ beyond the V_{FB} Fermi level energy. With $\mu_e = 100 \sim 150 \text{ cm}^2 \text{ V}^{-1} \text{ sec}^{-1}$ for the n-WSe₂ single crystals (12), the resistivity of this n-WSe₂ is $0.1 \sim 0.2 \Omega\text{-cm}$.

p-WSe₂.—As shown in Fig. 4a, p-WSe₂ electrodes show quite different capacitance-potential curves from their n-counterparts. With potentials positive of 0.05V vs. SCE, a linear C^{-2} vs. V relationship was observed at frequencies of 1-10 kHz (Fig. 5a). For potentials more negative than 0.05V vs. SCE, frequency dispersion of capacitance occurs. The capacitance at -0.2V vs. SCE

⁴An approximate value was taken here since the exact dielectric constant at the frequency range studied is unknown (13).

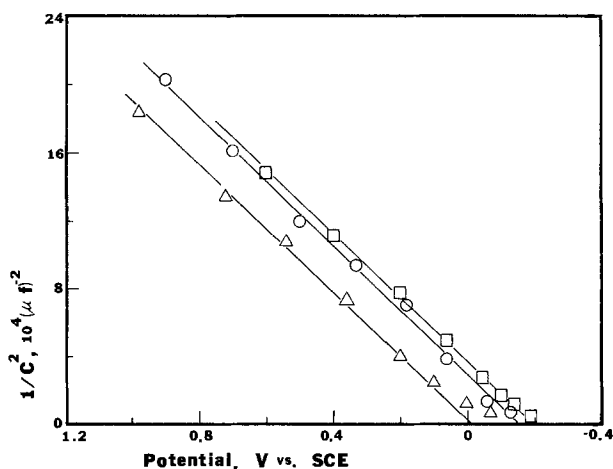


Fig. 2a. C^{-2} vs. V at 2 kHz for n-MoSe₂ electrode in aqueous solution of 0.5M Na₂SO₄ without containing iodide and triiodide (△), in the presence of 1.0M iodide (○), and in the presence of 1.0M iodide and 0.25 mmoles triiodide (□).

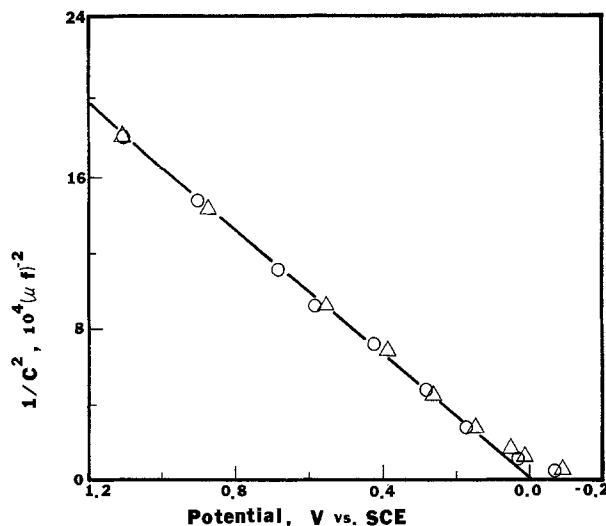


Fig. 2b. The effect of bromide on the Mott-Schottky plots on n-MoSe₂ in aqueous solution of 0.5M Na₂SO₄ at 2 kHz: (△) no bromide, (○) 1.0M bromide.

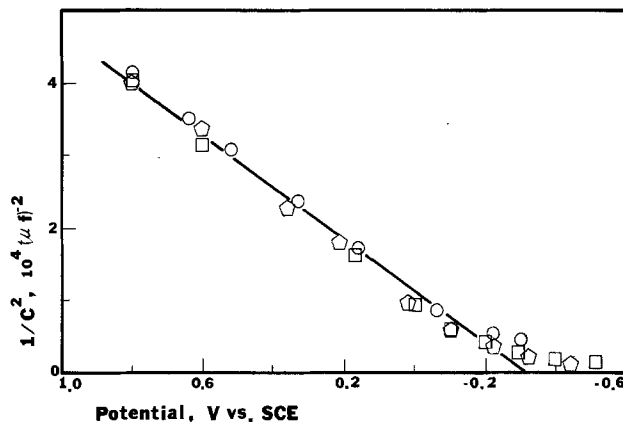


Fig. 3. The Mott-Schottky plots at different frequencies for n-WSe₂ electrode in aqueous solution of 0.5M Na₂SO₄ at pH 4.5: (◇) 200 Hz, (□) 500 Hz, (○) 2 kHz. Electrode area, 0.049 cm².

SCE for p-WSe₂ follows a (frequency)⁻² dependence at frequencies $> 2 \text{ kHz}$. The origin of this frequency dispersion is still not clear, but might involve the presence of interface states or the onset inversion coupled with a faradaic process. Further investigations are required to explain this behavior.

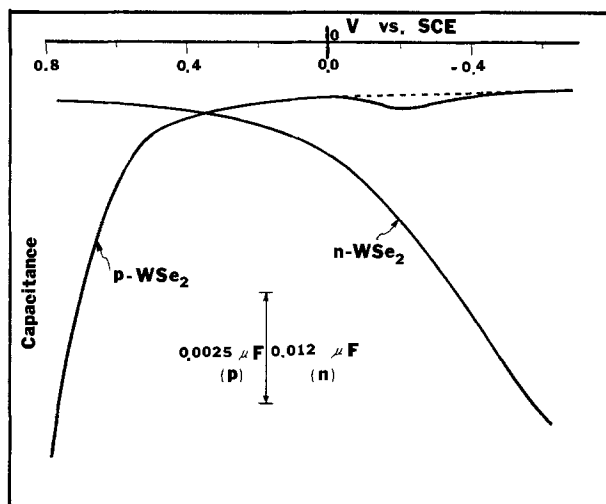


Fig. 4a. The capacitance-potential curves for n- and p-WSe₂ electrodes at 5 kHz in aqueous solution of 0.5M Na₂SO₄ at pH 4.5.

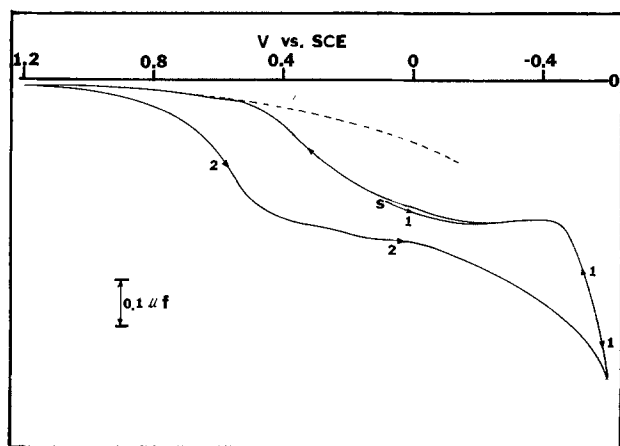


Fig. 4b. Capacitance vs. potential plot for n-WSe₂ electrode, type E. The potential was scanned beginning at point "s" at 5 mV/sec in the direction indicated by the arrows. $f = 200$ Hz. The dotted line indicates the expected capacitance for an electrode following the Mott-Schottky relation.

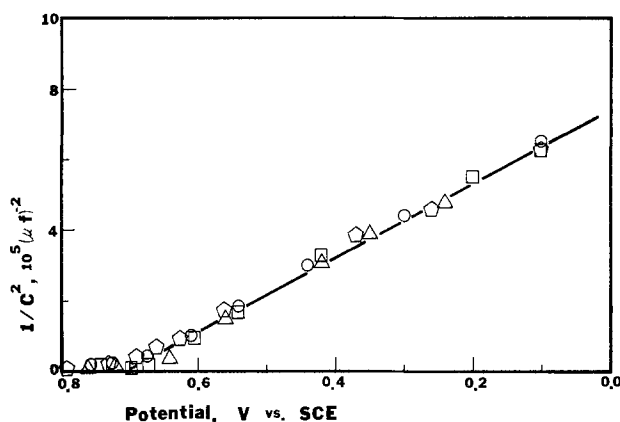


Fig. 5a. C^{-2} vs. V at different frequencies for p-WSe₂ electrode in aqueous solution of 0.5M Na₂SO₄ at pH 4.5: (Δ) 1 kHz, (\circ) 2 kHz, (\square) 5 kHz, (\diamond) 10 kHz. Electrode area, 0.050 cm².

Since frequency dispersion is found only at potentials negative of 0.0V vs. SCE which is well negative of V_{FB} , it has essentially no effect on the Mott-Schottky plots as shown in Fig. 5a. V_{FB} of this p-WSe₂ electrode was thus ~ 0.72 V vs. SCE. If $\epsilon \approx 10$ for WSe₂ (13), the acceptor density of this electrode can be estimated as $\sim 5 \times 10^{15}$ cm⁻³. The density of effective states in the valence band of WSe₂, N_v , the energy of the valence bandedge, E_v , and the resistivity of this p-WSe₂ are shown in Table I. As found with n-MoSe₂, V_{FB} of p-WSe₂ is pH independent (Fig. 5b) in the pH range studied.

The capacitance-potential plots which correspond well to that expected of the semiconductor space charge capacitance (e.g., well-behaved Mott-Schottky plots

Table I. Impurity densities, bandedges, effective densities of states in the conduction, and valence bands and resistivities of MoSe₂ and WSe₂ samples*

| | n-MoSe ₂ | WSe ₂ |
|---------------------------|----------------------|--|
| n (cm ⁻³) | 1.2×10^{17} | 2.0×10^{17} (n) 5×10^{15} (p) |
| E_c (V vs. SCE) | -0.14 | -0.44 |
| E_v (V vs. SCE) | 1.26 | 0.93 |
| N_c (cm ⁻³) | — | 2.5×10^{19} |
| N_v (cm ⁻³) | — | 2.5×10^{19} |
| ρ (Ω -cm) | 1 ~ 5 | 0.1 ~ 0.2 (n) 5 ~ 10 (p) |

* In aqueous solution of 0.50M Na₂SO₄.

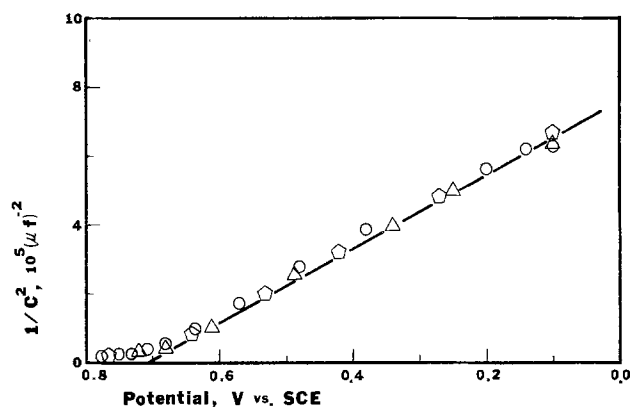


Fig. 5b. The pH effect on the Mott-Schottky plots at 5 kHz for p-WSe₂ electrode in aqueous solution of 0.5M Na₂SO₄: (\circ) pH 1, (Δ) pH 4.5, (\diamond) pH 8.

and frequency independence) found with edge-free electrode material (e.g., Fig. 4a for n-WSe₂) can be contrasted with that found with material which contains some edges and discontinuities on the surfaces [designated "type E" in previous studies (4c)]. For type E n-WSe₂ electrodes, discontinuities are seen in the capacitance plots (Fig. 4b) as well as hysteresis effects and frequency dispersion. Thus capacitance plots are useful in distinguishing electrode material which produces low dark currents and efficient PEC cells from less efficient (type E) material.

Voltammetric behavior.—Electrochemical and PEC behavior of n- and p-WSe₂ electrodes have been reported previously (4). The following results mainly involve n-MoSe₂ electrodes. The voltammetric behavior of iodide at n-MoSe₂ and Pt is shown in Fig. 6. With or without I⁻ in the solution, in the dark a negligibly small background current was observed (curves a and b). Under illumination with slowly chopped red light (wavelength ≈ 590 nm), an anodic photocurrent commencing at 0.5V vs. SCE (curve c) was observed in the supporting electrolyte containing 0.50M H₂SO₄. No cathodic photocurrent was found, as expected for an n-type material. In the presence of 1.0M NaI, the onset photopotential, V_{on} , shifted to a much more negative potential, -0.26V vs. SCE (curve d). The addition of iodine (0.10M) to the solution shifted V_{on} to slightly more negative potentials (~ -0.30 V vs. SCE) (curve e). Note that the specific effects of iodide and triiodide on V_{on} parallel their effects on the V_{FB} determined from impedance measurements. The current-potential curves on Pt (curve f) and n-MoSe₂ in an I⁻/I₃⁻ solution yield an "underpotential" for I⁻ photo-oxidation at n-MoSe₂ $V_{on} - V_{redox}$, of -0.59V. This value agrees fairly well with the experimental open-circuit voltage, V_{oc} , of an n-MoSe₂/I₂, I⁻/Pt PEC cell described below.

The voltammetric data and photopotentials of other redox couples on n-MoSe₂ electrodes are summarized in Table II. For redox couples with standard potentials, V^0 , much more negative than V_{FB} , no photoeffect was observed. The V_{on} for the redox couples with $V_{FB} < V^0 < 0.29$ V vs. SCE (except for I⁻/I₃⁻) are nearly independent of the redox couples and are close to V_{FB} (~ 0.0 V vs. SCE). For redox couples with 0.50 V $< V^0 < 1.0$ V vs. SCE, V_{on} depended on the particular species and varied from ~ 0.25 V for Br⁻ to ~ 0.50 V for background oxidation. The photo-oxidation of compounds with V^0 more positive than for water oxidation is uncertain because of the background photoreaction. It is interesting to compare the reduction of various oxidants on n-MoSe₂ electrodes in the dark. As shown in Fig. 7, reduction of bromine (curve a) and Fe³⁺ (curve b) occurs at potentials negative of 0.5V vs. SCE

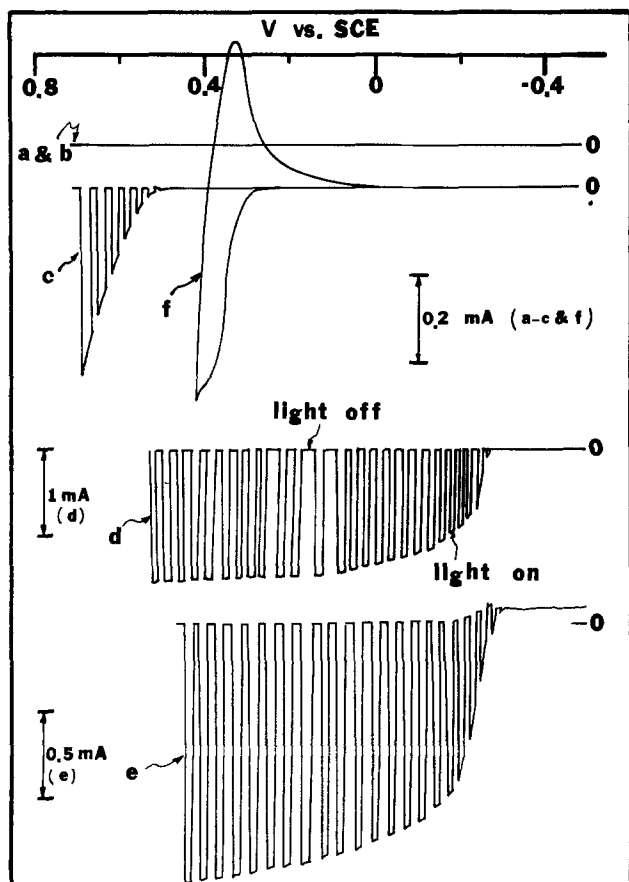


Fig. 6. Voltammetric curves of n-MoSe₂ and Pt in 0.5M Na₂SO₄ and 0.5M H₂SO₄. Scan rate, 10 mV/sec. Light source, 450W Xe lamp with a 590 nm cut-on filter. (a) Dark cyclic voltammogram on n-MoSe₂. (b) Dark cyclic voltammogram on n-MoSe₂. Solution contained 1.0M NaI. (c) Voltammogram curve under illumination by chopped red light on n-MoSe₂. No iodide or iodine in solution. (d) Current-potential curve under illumination by chopped red light on n-MoSe₂. Solution contained 1.0M NaI. (e) Same conditions as in (d) but solution contained 1.0M NaI and 0.10M iodine. (f) Cyclic voltammogram on Pt. Solution contained 0.10M NaI. Initial potential at -0.10V vs. SCE.

(well positive of V_{FB}). However, iodine reduction occurs only at potentials well negative of 0.1V vs. SCE (curve c). The reduction of ferricyanide (curve d) occurs at a potential ~ 0.25 V vs. SCE. Under irradiation these significant cathodic currents would constitute a back-reaction of a photogenerated oxidant which can affect the performance of the solar cells, as described below.

Photovoltaic cell measurements.—Regenerative semiconductor/liquid junction solar cells were fabricated

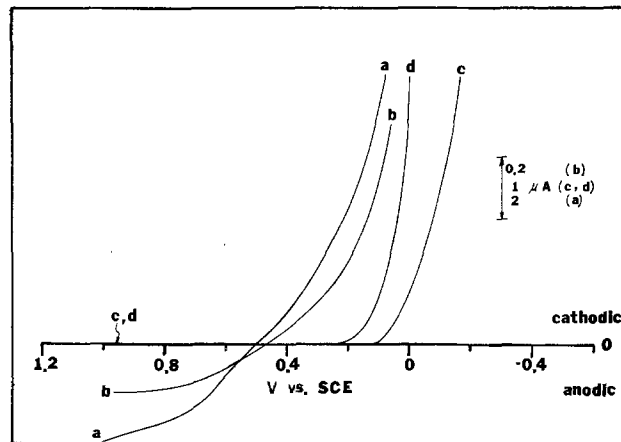


Fig. 7. Voltammetric curves in the dark on n-MoSe₂ electrode in 0.50M Na₂SO₄. Scan rate, 10 mV/sec. (a) Solution contained 1.0M NaBr and 0.02M bromine. (b) Solution contained 0.10M Fe²⁺, 0.02M Fe³⁺, and 0.50M H₂SO₄. (c) Solution contained 1.0M NaI and 0.10M iodine. (d) Solution contained 0.1M Fe(CN)₆⁴⁻ and 0.1M Fe(CN)₆³⁻.

by immersing the semiconductor electrode and a suitable counterelectrode in an aqueous solution containing the appropriate redox couple.

The n-MoSe₂/iodide, triiodide/Pt system.—Photovoltaic cells were set up with an n-MoSe₂ photoanode and a platinum foil cathode immersed in a solution containing 1.0M I⁻, 0.025M I₃⁻, and 1.0M H⁺. The action spectrum of the short-circuit photocurrent, i_{ss} , is shown in Fig. 8. The bandgap of WSe₂ and MoSe₂ can be determined from the $(\eta h\nu)^2$ vs. $h\nu$ plot (for a direct transition) or the $(\eta h\nu)^{1/2}$ vs. $h\nu$ plot (for an indirect transition) near the bandedge region (14). η here is the quantum efficiency (proportional to i_{ss}) and $h\nu$ is the photon energy. As shown in Fig. 9, both $(\eta h\nu)^2$ vs. $h\nu$ and $(\eta h\nu)^{1/2}$ vs. $h\nu$ plots give fairly good straight lines. The nature of the fundamental optical transition is thus ambiguous as simply determined from the action spectrum. However, the determination of E_g from the capacitance measurements, as discussed later, is helpful in deciding on the value of E_g .

The i - V characteristics of this cell under irradiation, shown in Fig. 10, yields a fill factor of 0.53. The light intensity dependence of the open-circuit photovoltage and the short-circuit photocurrent of the cell is shown in Fig. 11. Irradiation of the n-MoSe₂ crystal with the full visible (longer than 590 nm and infrared filtered) output (150 mW/cm²) from a 450W Xe lamp focused onto the photoelectrode surface yielded a constant $i_{ss} \sim 50$ mA/cm² and an open-circuit photovoltage ~ 0.59 V. The photocurrent and photovoltage were essentially the same and the electrode surface showed no apparent change during the experimental period (~ 8 hr).

Table II. Voltammetric data, onset photopotential* and underpotential at n-MoSe₂

| Redox couple | V° (V vs. SCE)** | V_{on} (V vs. SCE) | Experimental underpotential, $\Delta V = V_{on} - V^\circ$ (V) | Theoretical underpotential***, $\Delta V' = V_{FB} - V^\circ$ (V) |
|---|-------------------------|----------------------|--|---|
| Cl ⁻ /Cl ₂ (pH = 0) | 1.12 | — | — | -1.12 |
| H ₂ O/O ₂ (pH = 0) | 0.99 | 0.50 | -0.49 | -0.99 |
| Br ⁻ /Br ₂ (pH = 0) | 0.82 | 0.25 | -0.57 | -0.82 |
| Fe(II)/Fe(III) (1N H ₂ SO ₄) | 0.53 | 0.30 | -0.23 | -0.53 |
| I ⁻ /I ₂ (pH = 0) | 0.29 | -0.30 | -0.59 | -0.59 |
| Fe(CN) ₆ ⁴⁻ /Fe(CN) ₆ ³⁻ (pH = 6) | 0.22 | 0.02 | -0.20 | -0.22 |
| Fe(II)-EDTA/Fe(III)-EDTA (pH = 5) | -0.15 | 0.0 | No | No |
| HV ⁺ /HV ²⁺ † (pH = 5) | -0.48 | No photoeffect | — | — |
| MV ⁺ /MV ²⁺ ‡ (pH = 2.5) | -0.66 | No photoeffect | — | — |

* The onset photopotential V_{on} here is defined as the potential at which 1% of the limiting or maximal photocurrent is observed.

** V° = standard potential.

*** V_{FB} is based on that obtained from the impedance measurement. It is -0.3V vs. SCE for I⁻/I₂ and 0V for other redox couples.

† HV = heptyl viologen (1,1'-diheptyl-4,4'-bipyridyl).

‡ MV = methyl viologen (1,1'-dimethyl-4,4'-bipyridyl).

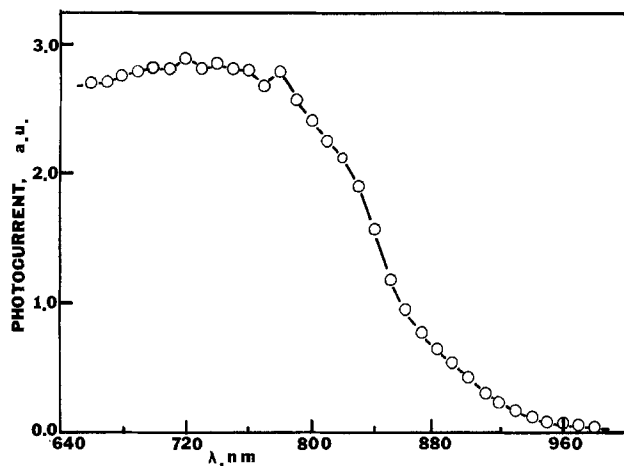


Fig. 8. Action spectrum of the short-circuit photocurrent for an $n\text{-MoSe}_2/1.0\text{M NaI}, 0.05\text{M I/Pt}$ solar cell. The spectrum has been corrected for the solution absorbance.

The $n\text{-MoSe}_2/\text{bromide, bromine/Pt}$ system.—When a solution containing 1.0M Br^- , 0.02M Br_2 , and 1.0M H^+ was used as the electrolyte, a lower open-circuit photovoltage (0.52V), and a lower fill factor (0.25) were found (Fig. 10) (15).⁵ However, the short-circuit photocurrent was higher ($\sim 60\text{ mA/cm}^2$) under the same intensity irradiation. This difference is probably attributable to the lower light absorbance by the Br^- ,

⁵ Solar cells with higher fill factors but lower open-circuit voltages have been reported by Ang *et al.* (15).

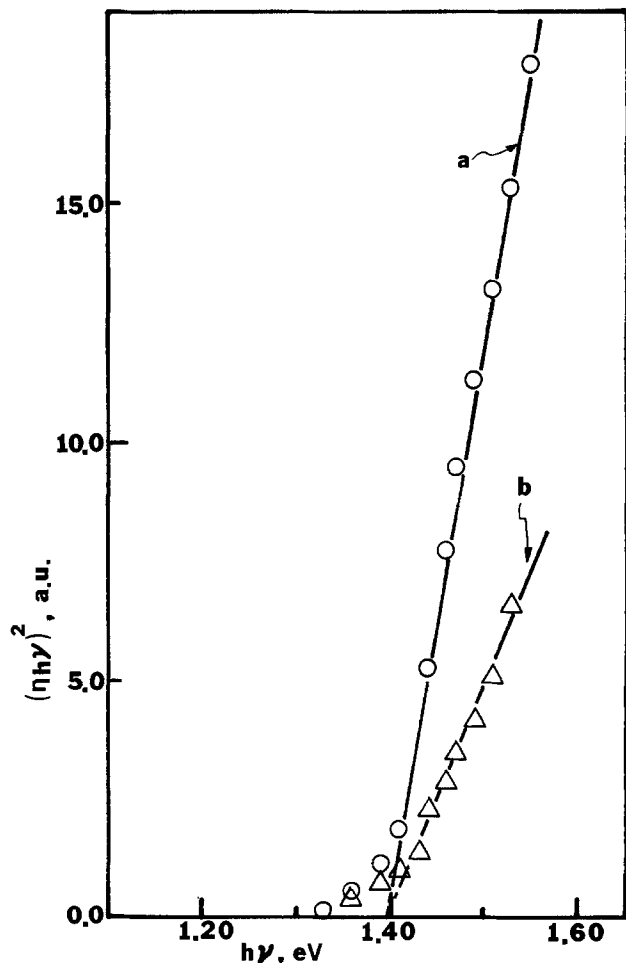


Fig. 9a. $(\eta h\nu)^2$ vs. $h\nu$ in aqueous solution containing $0.5\text{M Na}_2\text{SO}_4$, 1.0M NaI , and 0.05M iodine. Here η is the quantum efficiency and $h\nu$ is the photon energy. (a) $n\text{-MoSe}_2$; (b) $n\text{-WSe}_2$. Electrodes are biased at 0.2V vs. SCE.

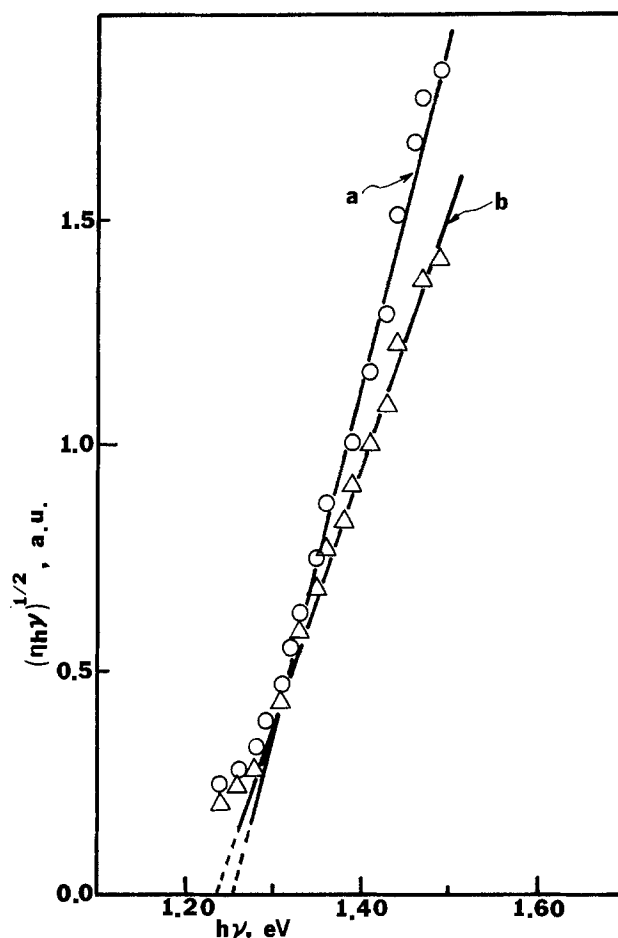


Fig. 9b. $(\eta h\nu)^{1/2}$ vs. $h\nu$ for (a) $n\text{-MoSe}_2$; (b) $n\text{-WSe}_2$. Same conditions as in Fig. 9a.

Br_2 solution. The light intensity dependence of the short-circuit photocurrent and the open-circuit photovoltage is shown in Fig. 12.

Discussion

The ($n\text{-MoSe}_2/\text{solution}$) interface.—A model for the behavior of the $n\text{-WSe}_2/\text{solution}$ interface in aqueous electrolyte has been discussed previously (4). A similar model, *i.e.*, the recombinative model, is applicable to explain the voltammetric behavior of $n\text{-MoSe}_2$ in various redox electrolytes. V_{FB} of the $n\text{-MoSe}_2$ electrode determined from the impedance measurement is $\sim 0.0\text{V}$ vs. SCE. When no specific adsorption occurs, the expected most negative V_{on} value was obtained for redox couples with $0 \leq V^\circ \leq 0.5\text{V}$ vs. SCE. (The I^-/I_3^- couple involves adsorption effects and is discussed later.) For redox couples with V° more positive than 0.5V , however, V_{on} occurs at more positive potentials. This can be ascribed to the effects of dark reduction of the oxidized form of redox couples. Recall that considerable dark reduction of the $\text{Fe}(\text{CN})_6^{3-}$ takes place at a potential $\sim 0.3\text{V}$ positive of V_{FB} (Fig. 7). The reduction of I_3^- occurred at more negative potentials probably because the bandedges shift with specific adsorption as suggested by the impedance measurements and the voltammetric experiments. For the couples with V° more positive than 0.5V vs. SCE, *e.g.*, $\text{Fe}^{2+}/\text{Fe}^{3+}$ and Br^-/Br_2 , the reduction occurred at a potential $\sim 0.5\text{V}$ vs. SCE. This positive shift of the zero current or onset potential might involve induced positive surface charges. The positive shift of V_{on} is attributed to the dark reduction of photogenerated species. There are several different mechanisms by which such dark reduction can occur at an n -type material at potentials significantly positive of that for V_{FB} (*i.e.*, of the energy of the conduction bandedge) in the supporting electro-

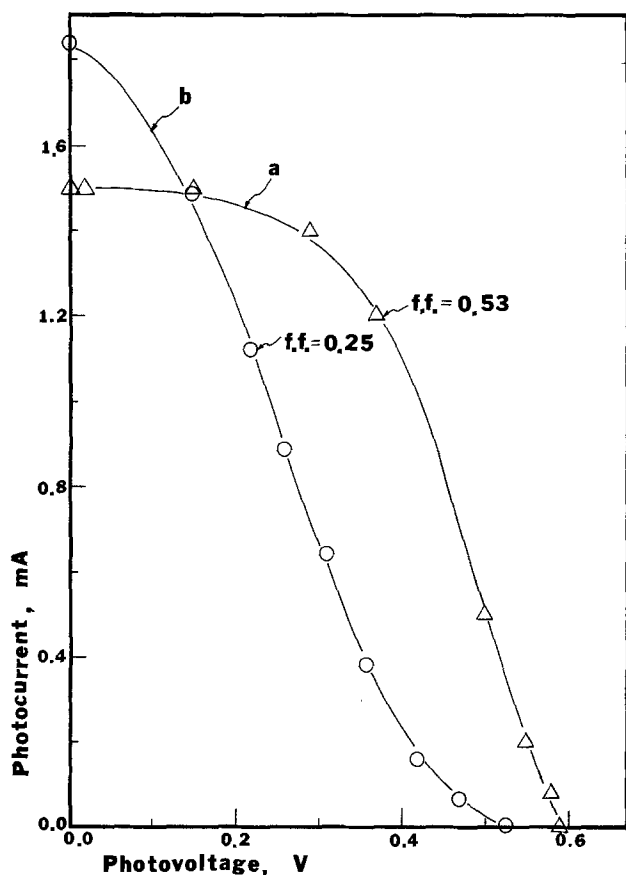


Fig. 10. Performance characteristics of n-MoSe₂ based PEC cells. 450W Xe lamp fitted with a 590 nm cut-on filter was used as the light source. (a) n-MoSe₂/0.50M Na₂SO₄, 0.50M H₂SO₄, 1.0M NaI, 0.05M I⁻/Pt. (b) n-MoSe₂/0.50M Na₂SO₄, 0.50M H₂SO₄, 1.0M NaBr, 0.02M Br⁻/Pt.

lyte solution. One involves a recombination model and the existence of filled surface states or intermediate levels at energies within the bandgap which can be emptied by electron donation to solution oxidants (or by photogenerated holes in the valence band) (16). The lack of detection of such states in the capacitance plots and the lack of significant dark anodic current implies that such states are very "slow" with respect to emptying via the conduction band. An alternative mechanism involves positive charge injection into the surface states (via solution species or photogenerated holes) causing a shift in the conduction bandedge toward more positive potentials and allowing electron transfer directly from the conduction band. This latter mechanism should result in a shift in V_{FB} in the presence of the redox couple; determination of such a shift by capacitance measurements are made difficult by the interference of faradaic reactions in determination of the actual space charge capacitance. Inversion could also cause such a shift in the bandedge (8); however, the location of the Fe³⁺/Fe²⁺ couple is such that inversion would not occur at these potentials. A schematic representation of the energetic situation at the n-MoSe₂/solution interface, neglecting any band bending and specific surface interactions, is shown in Fig. 13. A direct-transition bandgap of 1.4 eV⁶ is taken here based on the agreement of E_g determined from the action spectrum and the capacitance measurements for WSe₂ electrodes, discussed later.

Photovoltaic cells based on n-MoSe₂ electrodes.—The n-MoSe₂/I⁻, I₃⁻/Pt system shows a V_{oc} of 0.59V which is identical to the value predicted either from the experimental, ΔV , or the theoretical, $\Delta V'$, underpotential 0.59V, as shown in Table II. For the n-MoSe₂/Br⁻,

⁶ An indirect transition bandgap of 1.1 eV has been reported (8c). An E_g of 1.4 eV has also been reported (7).

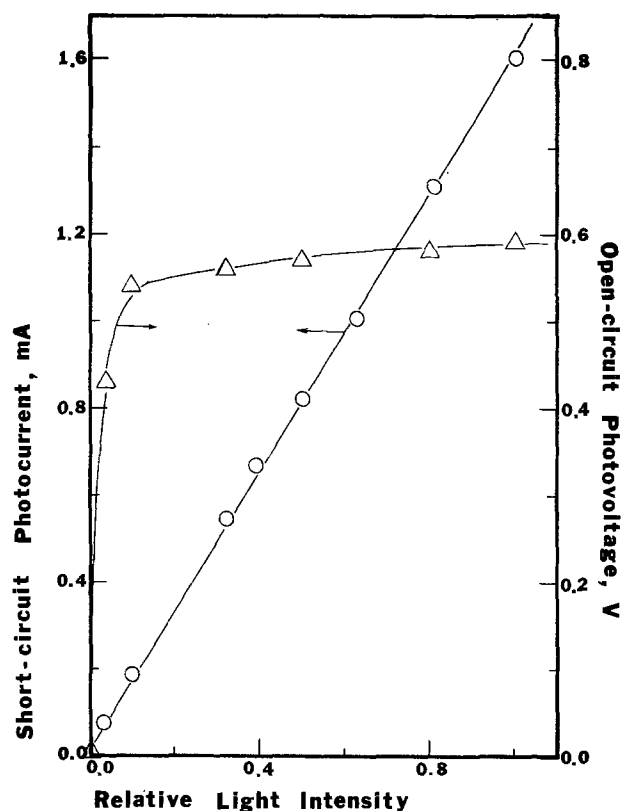


Fig. 11. Open-circuit photovoltage and short-circuit photocurrent as functions of light intensity. Same light source as in Fig. 10. Same solar cell as used in Fig. 10(a).

Br₂/Pt system, the V_{oc} of 0.52V was close to ΔV , 0.57V; however, it was much smaller than $\Delta V'$, 0.82V. This

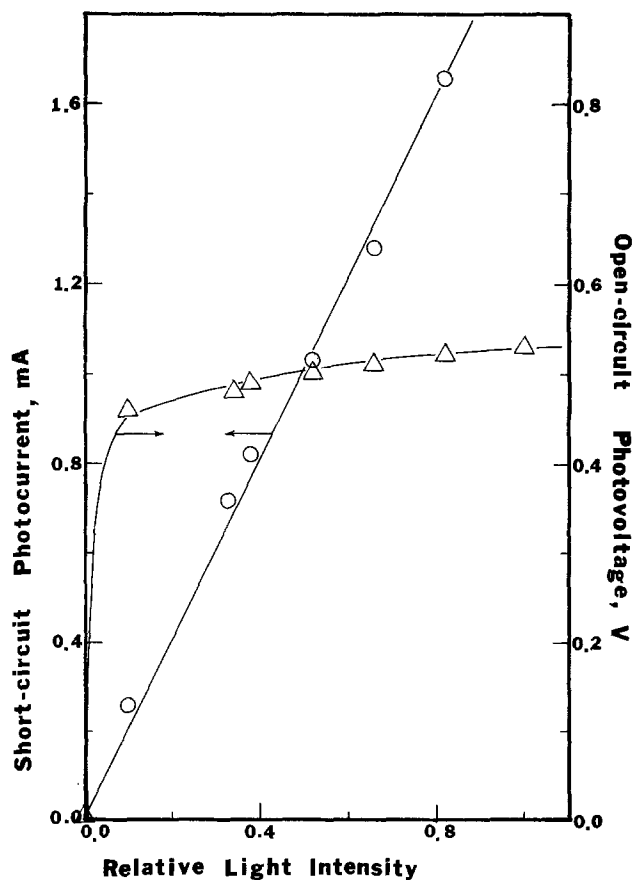


Fig. 12. Open-circuit photovoltage and short-circuit photocurrent as functions of light intensity. Same light source and solar cell as used in Fig. 10(b).

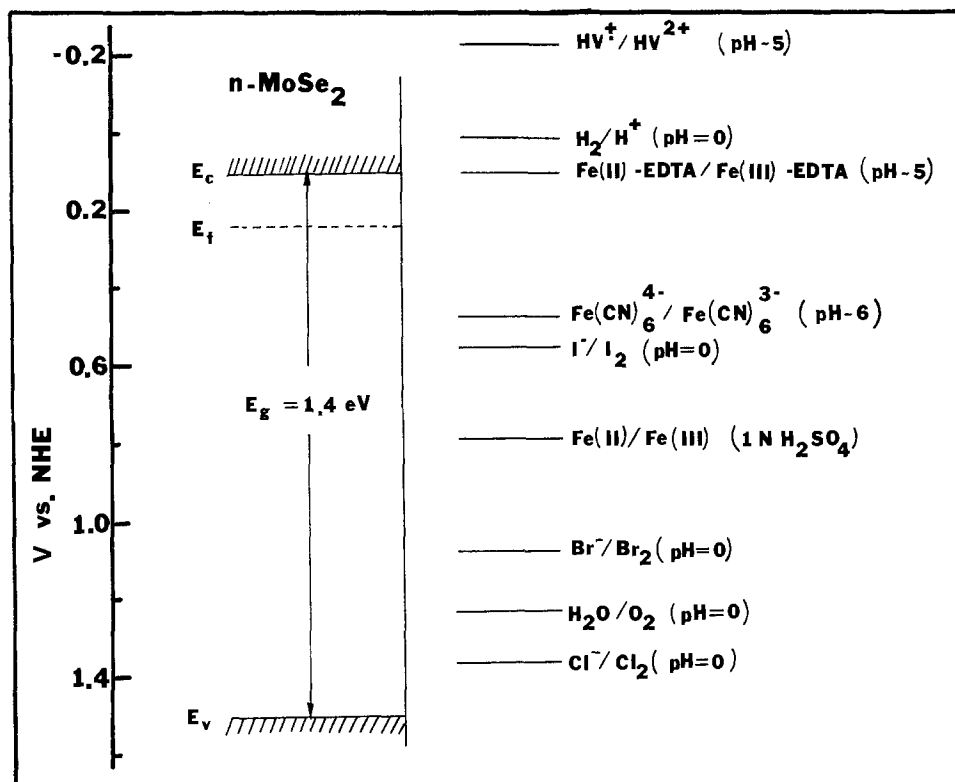


Fig. 13. Schematic representation of the energetic situation at the $n\text{-MoSe}_2$ /solution interface. E_c = conduction band edge; E_f = Fermi energy corresponding to flatband potential; E_v = valence band edge; E_g = bandgap.

discrepancy can be attributed to the dark reduction processes or to a shift in the band edges toward positive potentials because of induced positive surface charges. Besides this striking difference in V_{oc} between I^-/I_3^- and Br^-/Br_2 system, the fill factors for these two systems were also quite different, probably again because of the effects discussed above.

E_g of WSe_2 .—As shown in Table I, E_v and E_c of WSe_2 in aqueous solution correspond to 0.93V and -0.44V vs. SCE, respectively. The uncertainty of E_v and E_c due to the uncertainties in the dielectric constant taken here is less than 20 meV. Thus E_g of WSe_2 is $\sim (1.4 \pm 0.05)$ eV. This agrees fairly well with the direct transition bandgap determined from the action spectrum of the photocurrent.

Acknowledgment

This work was supported by a grant from the Solar Energy Research Institute. We are grateful to Dr. Miller and Dr. DiSalvo for providing the samples of the semiconductor materials.

Manuscript submitted Oct. 17, 1980; revised manuscript received Dec. 29, 1980.

Any discussion of this paper will appear in a Discussion Section to be published in the December 1981 JOURNAL. All discussions for the December 1981 Discussion Section should be submitted by Aug. 1, 1981.

Publication costs of this article were assisted by the University of Texas.

REFERENCES

- (a) A. J. Bard, *J. Photochem.*, **10**, 59 (1979); (b) A. J. Bard, *Science*, **207**, 139 (1980); (c) M. S. Wrighton, *Acc. Chem. Res.*, **12**, 303 (1979); (d) A. J. Nozik, *Ann. Rev. Phys. Chem.*, **29**, 189 (1978).
- (a) H. Tributsch and J. C. Bennett, *J. Electroanal. Chem. Interfacial Electrochem.*, **81**, 97 (1977); (b) H. Tributsch, *Ber. Bunsenges. Phys. Chem.*, **81**, 361 (1977); (c) H. Tributsch, *ibid.*, **82**, 169 (1978); (d) H. Tributsch, *This Journal*, **125**, 1086 (1978); (e) J. Gobrecht, H. Gerischer, and H. Tributsch, *ibid.*, **125**, 2085 (1978); (f) L. F. Schneemeyer and M. S. Wrighton, *J. Am. Chem. Soc.*, **101**, 6496 (1979); (g) L. F. Schneemeyer, M. S. Wrighton, A. Stacy, and M. J. Sienko, *Appl. Phys. Lett.*, **36**, 701 (1980); (h) J. Gobrecht, H. Gerischer, and H. Tributsch, *Ber. Bunsenges. Phys. Chem.*, **82**, 1331 (1978); (i) H. Tributsch, H. Gerischer, C. Clemen, and E. Bucher, *ibid.*, **83**, 655 (1979).
- C. P. Kubiak, L. F. Schneemeyer, and M. S. Wrighton, *J. Am. Chem. Soc.*, In press.
- (a) F-R. F. Fan, H. S. White, B. Wheeler, and A. J. Bard, *J. Am. Chem. Soc.*, **102**, 5142 (1980); (b) F-R. F. Fan, H. S. White, B. Wheeler, and A. J. Bard, *This Journal*, **127**, 518 (1980); (c) H. S. White, F-R. F. Fan, and A. J. Bard, *ibid.*, **128**, 1045 (1981).
- B. A. Parkinson, T. E. Furtak, and D. Canfield, Paper No. 23 in *Faraday Society Discussion, No. 70*, The Royal Society of Chemistry, London (September 1980).
- H. J. Lewerenz, A. Heller, and F. J. DiSalvo, *J. Am. Chem. Soc.*, **102**, 1877 (1980).
- S. Menezes, F. J. DiSalvo, and B. J. Miller, *This Journal*, In press.
- (a) W. Kautek, H. Gerischer, and H. Tributsch, *Ber. Bunsenges. Phys. Chem.*, **83**, 1000 (1979); (b) S. M. Ahmed and H. Gerischer, *Electrochim. Acta.*, **24**, 705 (1979); (c) W. Kautek and H. Gerischer, *This Journal*, **127**, 2471 (1980).
- V. A. Myamlin and Yu. V. Pleskov, "Electrochemistry of Semiconductors," Plenum Press, New York (1967).
- B. L. Evans and P. A. Young, *Proc. R. Soc. London, Ser. A*, **284**, 402 (1965); see also A. R. Beal and H. P. Hughs, *J. Phys. C*, **12**, 881 (1979).
- W. T. Hicks, *This Journal*, **111**, 1058 (1964).
- J. A. Wilson and A. D. Yoffe, *Adv. Phys.*, **18**, 193 (1969).
- A. R. Beal, W. Y. Liang, and H. P. Hughs, *J. Phys. C*, **9**, 2449 (1976).
- (a) M. A. Butler, *J. Appl. Phys.*, **48**, 1914 (1977); (b) J. J. Earnest, in "Semiconductors and Semimetals," Vol. 3, R. K. Willardson and Albert C. Beer, Editors, Chap. 6, Academic Press, New York (1967).
- P. G. P. Ang and A. F. Sammells, Paper No. 11 in *Faraday Society Discussion, No. 70*, The Royal Society of Chemistry, London (September 1980).
- S. N. Frank and A. J. Bard, *J. Am. Chem. Soc.*, **97**, 7427 (1975).

The Detection of Corrosion Phenomena with pH-Sensitive Fluorescent Dyes on Aluminum- and Gold-Metallized IC Devices

L. K. White,* R. B. Comizzoli,* C. A. Deckert,* and G. L. Schnable*

RCA, David Sarnoff Research Center, Princeton, New Jersey 08540

ABSTRACT

Corrosion sites on IC devices are often difficult to detect before a significant amount of metallization deterioration occurs. The identification of corrosion sites in their early stages would be a powerful tool in studies of metallized IC device reliability and of corrosion processes themselves. Recently, this laboratory has been investigating metallization corrosion phenomena on IC devices. During these studies we explored the use of pH-sensitive fluorescent dyes to decorate the IC device surface. After application of pH-sensitive fluorescent dye molecules to the surface of the IC test device, an external d-c bias was applied to the device which activated or deactivated localized fluorescence on the device. We believe this observed behavior relates to corrosion phenomena occurring on the metallization of the IC. Here we report the results of these exploratory experiments conducted on aluminum- and gold-metallized IC test devices.

Experimental Procedures

Test devices used for these studies consisted of interdigitated combs of metal. The dielectric below the metal was 6 kÅ of SiO₂. Four comb pairs were on each test chip. The passivation over each comb pair varied; pair A had continuous passivation over the entire comb, pair B had 7 μm diam openings over every metal line, with the openings spaced 50 μm; pair C had 7 μm diam openings over one comb and 7 μm wide slots over the other; pair D had the passivation completely removed from the metal combs. The passivating layer was 4.9% phosphorus by weight phosphosilicate glass. Electrical bias was applied to each comb pair through bond pads, causing each comb to act essentially like an electrode. The positive bias was applied to one comb, while the other comb of the pair received the negative bias. Figure 1 displays the layout of the two photomasks required to fabricate this test vehicle. The first-level mask is used to define the metallization. The second is used to etch intentional pinholes and vias into the passivating glass overcoat. Metallization consisted of E-beam deposited 99.999% pure aluminum. The linewidth of each tooth of the comb was nominally 12 μm. The gold-metallized test devices consisted only of adjacent positively and negatively bias lines with and without a passivation glass.

Three pH-sensitive fluorescent dyes were used for our experiments: β-methylumbelliferone, β-naphthol, and fluorescein. These dyes were applied directly to the test device surface in a 1 to 2 × 10⁻⁴M solution consisting mainly of ethanol. The ethanol evaporates rapidly, leaving the fluorescent dye molecules behind. We have achieved improved results (i.e., more intense fluorescence) when a small amount of a nonvolatile solvent is added to the ethanol-dye solution. Typically, a 1% glycerol solution by volume was used, with a surfactant added to insure that the solution flowed evenly over the entire device surface. Apparently, the residual glycerol promotes the proton transfer processes necessary to activate or deactivate the pH-sensitive dye molecules on the IC surface.

If the same test device was to be treated with successive dye coatings, an acetone rinse treatment proved adequate to remove the previous coating. The acetone treatment can dry the surface of the IC, and often

moisture has to be restored to the IC surface before the corrosion process can again be studied. We recommend that the test device be exposed to a humid ambient (RH greater than 50%) before applying an initial or successive dye coating.

Aluminum Metallization Test Results

Several test devices with aluminum metallization were coated in humid ambients with the pH-sensitive fluorescent dyes. The application solvent was allowed to evaporate and the device was inspected with and without an external d-c bias in the presence of a long-wavelength u.v. actinic radiation source. A faint fluorescence was detected on and above the aluminum metallization of the β-methylumbelliferone treated de-

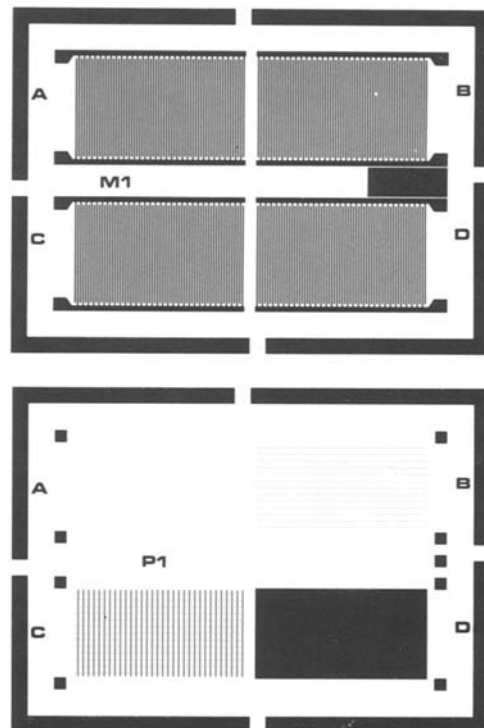


Fig. 1. Layout of photomasks for test vehicle fabrication: Top: metallization level mask; bottom: passivation level mask.

* Electrochemical Society Active Member.

Key words: corrosion, aluminum metallization, gold metallization, fluorescence, integrated circuit.

vice without any d-c bias applied. When a d-c bias was applied to the comb pairs, an intense localized fluorescence was immediately activated at several localized sites and tended to spread out from a central point as the bias was kept on. The site of the fluorescence was not confined to metallized regions on the device, but frequently extended into dielectric regions between the metal lines. After the localized fluorescent site reached a relatively stable size, the perimeter of the localized fluorescent sites continued to fluctuate as the d-c bias remained on. When the d-c bias was turned off, the fluorescent intensity reverted very slowly to its original intensity. In addition, gas bubbles were observed to emanate from the sites exhibiting the localized fluorescence, while the bias was on and shortly after removal of the bias. Evidently, the surface tension of the liquid film on the moist substrate surface tended to trap the bubbles. A similar experiment conducted with the β -naphthol dye yielded the same results, with the localized fluorescent sites occurring in the same regions on each test device. As low as a 0.5V bias was sufficient to activate some localized fluorescence. Figures 2 and 3 display photos of β -methylumbelliferone and β -naphthol decorated devices, respectively.

Fluorescein, although exhibiting a bright green fluorescence when applied to the aluminized IC test device (i.e., before the ethanol solvent evaporates) did not perform well. Its fluorescent intensity is quite sensitive to the amount of solvent present and diminishes drastically with solvent evaporation. However, for a short period of time as the application solvent is evaporating, localized fluorescence can be activated by an external bias. β -methylumbelliferone and β -naphthol apparently exhibit better proton transfer properties in relatively dry environments. Their localized fluorescence can be observed in a humid ambient for long periods of time after application and evaporation of the solvent.

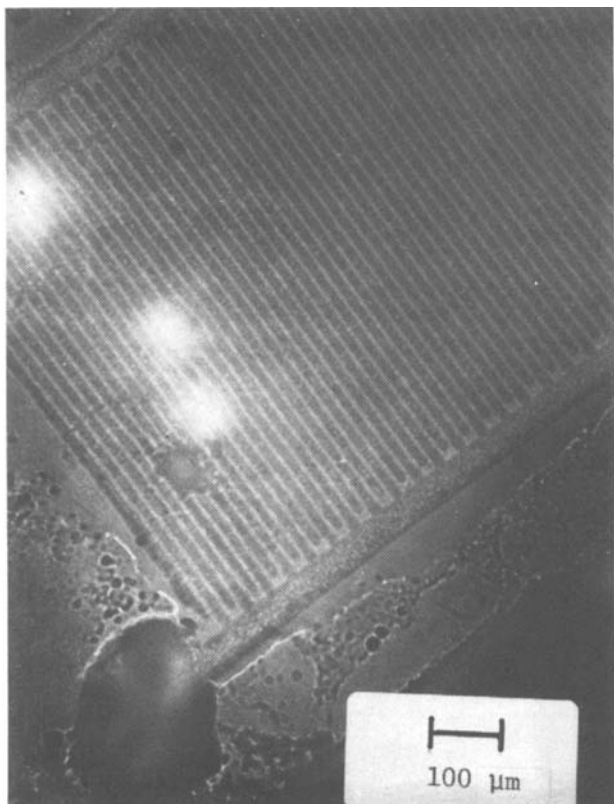


Fig. 2. β -methylumbelliferone decoration of IC: Long-wave u.v. source, 20V bias, humid ambient, room temperature. The width of metal lines in the comb is nominally 12 μm . Spacing between lines is also 12 μm .

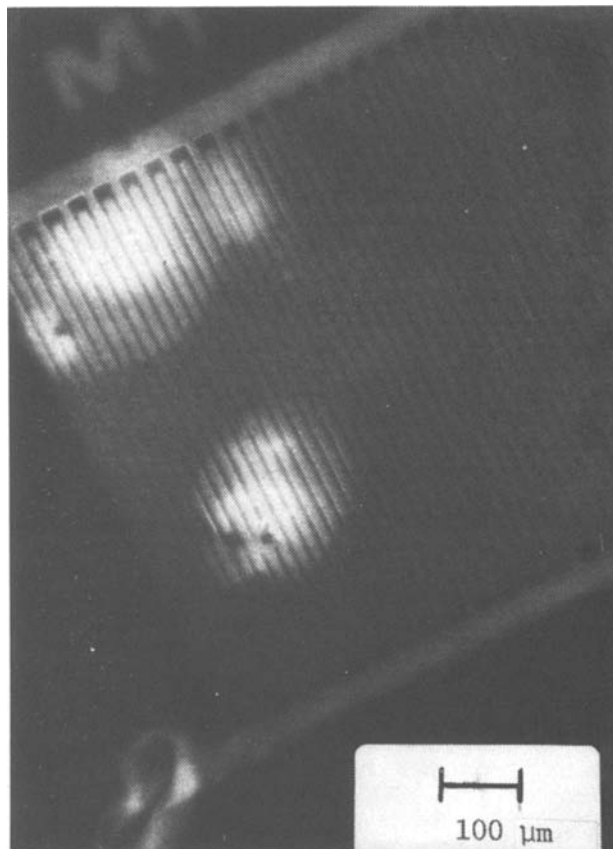


Fig. 3. β -naphthol decoration of IC: Long-wave u.v. source, 20V bias, humid ambient, room temperature. The width of metal lines in the comb is nominally 12 μm . Spacing between lines is also 12 μm .

The reason for formation of the localized fluorescent sites was difficult to characterize from these preliminary studies. Not all visually obvious defects in the passivation layer over the metallization fluoresced, and localized fluorescence was observed where no apparent defect was present. Fluorescence was observed in localized regions on the comb pairs with and without the protective glass passivating layer. We did attempt to correlate the localized fluorescent sites with intentional defects in the passivating overcoat, but localized fluorescence was observed only occasionally at intentional pinholes in the passivation glass. The localized fluorescence was not strictly confined to positively or negatively biased lines. Some test devices had numerous fluorescent sites and others very few.

The production of gas bubbles at fluorescent sites strongly suggests that the pH-sensitive fluorescent dye is detecting corrosion sites of a cathodic nature. The gas bubbles are presumably hydrogen. Other investigators (1-3) have observed H_2 gas bubbles from corrosion on aluminum metal. Theoretical calculations of the corrosion reactions within pits show that the cathodic reaction site can spread outside a pit or defect under certain conditions (4, 5). The reduction of hydronium ion to hydrogen, $2\text{H}_3\text{O}^+ + 2e^- \rightarrow \text{H}_2\uparrow + 2\text{H}_2\text{O}$ or $\text{H}_2\text{O} + 2e^- \rightarrow \text{H}_2\uparrow + 2\text{OH}^-$ is the most likely cathodic reaction accompanying Al corrosion (6-8) and is also the cathodic reaction for the electrolysis of water. The production of hydrogen gas depletes the hydronium ion concentration in regions near the cathodic reaction site. Our pH-sensitive fluorescent dyes have the property of releasing a proton (H^+) with relative ease, ($\text{HM} \rightarrow \text{H}^+ + \text{M}^-$). The deprotonated species (M^-) exhibits fluorescence while the protonated species (HM) does not. The dye molecules can be expected to supply protons for the cathodic reaction, and thus become active fluorescent species in the vicinity of the cathodic reaction site. Different degrees of sol-

vation (hydration) are required to facilitate the release of the protons from certain dye molecules. Hence, some dyes will fluoresce in drier ambients than others.

Although the pH-sensitive fluorescent dye molecules are activated in specific pH ranges in an aqueous solution [i.e., pH \sim 7.6 for β -methylumbelliferone, pH \sim 8.4 for β -naphthol, and pH \sim 4.5 for fluorescein (9)], their behavior on surfaces and in presence of external d-c bias may be somewhat different. Both the dye molecules and water molecules bound to a surface can have significantly different properties than unbound molecules. The d-c bias introduces the possibility of an electrochemical potential bias into the environment which can affect the molecular equilibria. However, the localized fluorescence at a specific site does suggest that the site has a lower hydronium ion concentration than that of its surroundings.

We believe that the cathodic electrolysis sites decorated by the pH-sensitive dye identifies aluminum corrosion sites for two related reasons. The region where the cathodic electrolysis reaction occurs shows an increased pH, according to our pH-sensitive fluorescent dyes. Aluminum-water corrosion reactions are known to be thermodynamically favorable at high pH (10, 11). The electrolysis site identifies or may produce a high pH region where the aluminum corrosion can occur. Also, the reduction of hydronium ion is thought to be a complementary reaction to the oxidation of Al metal. The humid ambient (i.e., water bound to the IC surface) and the electrical bias may accelerate and propagate small corrosion sites already present.

Gold Metallization Test Results

Decorating gold-metallized devices with pH-sensitive dyes produced substantially different results. For these experiments, the pH-sensitive fluorescent dye was deactivated rather than activated. This was observed by coating the device with a fluorescein-ethanol solution and then turning on the u.v. actinic radiation before the solvent had completely dried. Under these conditions, the entire surface of the device fluoresced under u.v. actinic radiation, with no applied bias. When the bias was turned on, fluorescence was quenched locally on exposed metal lines for only the positively biased lines. Reversing the polarity of the bias changed the lines that exhibited a quenched fluorescence at exposed metal, accordingly. A 12V d-c bias was sufficient to quench the fluorescent dye coating on exposed metal at the anodic lines.

The observations are consistent with our corrosion testing of gold-metallized IC's (12). Corrosion was observed only at the anodically biased lines. Recently, Frankenthal and Becker (13) have reported gold corrosion products on anodic portions of IC devices. Previous corrosion studies of gold metal have reported similar results (14). The quenching of fluorescence is the expected result after analyzing the anodic corrosion reaction. Gold hydroxides are formed on the anodically biased metal and these hydroxides generally remain bound to the metal surface. The hydronium ion, (H_3O^+) produced during this reaction is left unneutralized in the water film; generally, $Au + 3H_2O \rightarrow Au(OH)_3\downarrow + 3H^+ + 3e^-$. A substantial pH drop is expected, provided that the gold hydroxide corrosion products remain relatively insoluble. The pH drop induces a quenching of the pH-sensitive fluorescent dye molecules at the anodic corrosion site on the gold metallization.

No localized fluorescence was activated during these experiments, contrary to what was observed for the Al-metallized test device. Although electrolysis of water is certainly possible at these voltages, none was observed on the Au metallization with the pH-sensitive indicators. This observation suggests that the cathodic reaction (i.e., the reduction of hydronium ion) detected on Al metallization is more related to an Al-induced corrosion reaction rather than the electrolysis

of water, per se. Electrochemical bias studies (12) of test electrodes in aqueous solution showed that aluminum metallization produced mainly cathodic reactions and gold metallization only anodic reactions.

Conclusions

We have demonstrated that decorating procedures employing pH-sensitive fluorescent dyes can provide valuable information relating to IC device reliability and corrosion phenomenon in general. The pH-sensitive fluorescent dye decoration behaves differently depending on the metallization of the IC. Our results on aluminum metallization suggest that the technique can be used to identify corrosion sites on IC devices before much metal deterioration has occurred. The technique may facilitate identification of specific defects that produce corrosion sites. The propagation of corrosion reactions may be monitored during or after stress-bias reliability testing. The technique may also offer a procedure for evaluating device design, materials, and processing variables that contribute to corrosion/reliability problems. For example, our test device showed that adjacent negatively and positively biased lines spaced nominally 12 μ m apart on an SiO_2 dielectric may frequently produce a cathodic electrolysis site in a humid ambient.

The decoration of gold metallization with pH-sensitive dyes appears to have different reliability testing applications. Under a sufficiently large bias voltage, all exposed portions of the gold under anodic bias deactivated the pH-sensitive fluorescent dye. This observation suggests that the technique may offer an inspection procedure for detecting pinholes through a passivation glass over a gold-metallized surface.

These studies have supplied information about the corrosion phenomenon themselves, most notably pH differences in the vicinity of a corrosion site. On aluminum metallization, the pH-sensitive fluorescent dyes show an increased effective pH in the vicinity of cathodic electrolysis sites, while on gold metallization the effective pH in the water film above anodic corrosion sites was significantly decreased. In both cases, the pH-sensitive fluorescent dye detects pH differences caused by H_3O^+ or OH^- being effectively removed from the moist surface by a corrosion reaction. Also, the pH-sensitive fluorescent dye continues to be activated or deactivated after the external bias is turned off. The slow return of the fluorescent dye to its pre-bias condition reflects proton transfer processes occurring on the surface of the IC. These processes are related to diffusion rates of H_3O^+ and OH^- on the moist IC surface and the inertia of the corrosion reaction after the bias is turned off. Characterization of these processes may be possible with the fluorescent dye decoration technique.

These experiments were largely of an exploratory nature to demonstrate the potential application of this technique. More detailed studies using this technique could provide additional information relating to IC device corrosion processes and reliability.

Acknowledgment

This work was supported by the Rome Air Development Center under contract No. F30602-78-C-0276 and by RCA Corporation.

Manuscript submitted Sept. 22, 1980; revised manuscript received Nov. 24, 1980.

Any discussion of this paper will appear in a Discussion Section to be published in the December 1981 JOURNAL. All discussions for the December 1981 Discussion Section should be submitted by Aug. 1, 1981.

Publication costs of this article were assisted by RCA.

REFERENCES

1. H. Kaesche, *Z. Phys. Chem. N. F.*, **26**, 138 (1960); *ibid.*, **43**, 87 (1962).

2. H. W. Pickering and R. P. Frankenthal, *This Journal*, **119**, 1297 (1972).
3. C. Edeleanu and U. R. Evans, *Trans. Faraday Soc.*, **47**, 1121 (1951).
4. J. R. Galvele, *This Journal*, **123**, 464 (1976).
5. R. Alkire and D. Siitari, *ibid.*, **126**, 15 (1979).
6. E. P. G. T. van de Ven and H. Koelmans, *ibid.*, **123**, 143 (1976).
7. S. C. Kolesar, "Principles of Corrosion," 12th Ann. Proc. Reliab. Phys., pp. 155-167 (1974).
8. W. M. Paulson and R. W. Kirk, "The Effects of Phosphorus-Doped Passivation Glass on the Corrosion of Aluminum," 12th Ann. Proc. Reliab. Phys., pp. 172-179 (1974).
9. J. DeMent, "CRC Handbook of Chemistry and Physics," 50th ed., R. C. Weast, Editor, pp. D106-D107, Cleveland, Ohio (1969).
10. M. Pourbaix, "Atlas of Electrochemical Equilibria in Aqueous Solutions," Pergamon Press, Oxford, England (1966).
11. M. Pourbaix, "Lectures on Electrochemical Corrosion," translated by J. A. S. Green, Plenum Press, New York (1973).
12. R. Comizzoli, L. White, W. Kern, and G. Schnable, RADC-TR-80-236, Final Report on Contract No. F-30602-78-C-0276 prepared by RCA Labs for Rome Air Development Center, Griffiss Air Force Base, N.Y., July 1980.
13. R. P. Frankenthal and W. H. Becker, *This Journal*, **126**, 1718 (1979).
14. G. M. Schmid and M. E. Curley-Fiorino, "Gold," in "Encyclopedia of Electrochemistry of the Elements," Vol. 4, A. J. Bard, Editor, pp. 87-178, Marcel Dekker, Inc., New York (1975).

Hysteresis in Formation and Reduction of Submonolayer Quantities of Surface Oxide at Pt in an Almost Anhydrous Solvent

B. E. Conway* and D. M. Novak*¹

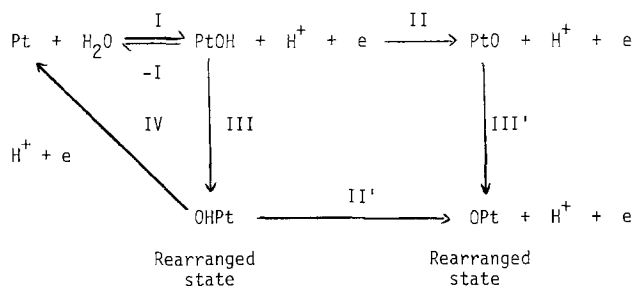
Chemistry Department, University of Ottawa, Ottawa, Ontario, Canada

ABSTRACT

Surface oxidation of Pt at small coverages by O-species has been investigated in trifluoroacetic acid as solvent containing traces of water from which Pt surface oxide species are generated. It is shown that even at quite low, submonolayer coverages, there is a large extent of hysteresis between the potential range for surface oxide formation and that for reduction, comparable with that found in water as solvent only when strong anodic oxidation has taken place. Also the relations between reduction peak potentials in a cyclic-voltammetry experiment and the surface oxide reduction charges are similar to those for extensively formed films in water, rather than to those for submonolayers. The behavior observed is attributed mainly to strong anion (CF₃COO⁻) adsorption in the TFA solvent but the possibility of the surface oxide existing in 2-d phase-oxide islands, stabilized by lateral attractive interactions, is also considered.

In previous potentiodynamic work (1-4), we have investigated the origin of hysteresis effects in the surface oxidation of noble metals (5) and interpreted them in terms of a place-exchange process (6, 7) which takes place as an irreversible postelectrochemical step with respect to an initial anodic electrodeposition reaction, according to a reaction and reconstruction sequence of the following schematic kind

SCHEME I



Step I, in the anodic direction, is a fast process (3) and its reverse, -I, is also rapid but can only be ob-

served at high sweep rates and low temperatures (3) owing to the alternative rearrangement step III. Under such conditions, a cathodic current component in cyclic voltammetry due to reaction (-I) can be resolved (3) from the cathodic pathway III, IV involving a rearranged state of OH on Pt, written as "OHPt," especially at low coverages by chemisorbed OH deposited in I. Steps II, II', and III' represent pathways for formation of a more highly oxidized state of the Pt surface, to "PtO" or "OPt."

In the present communication, we describe some interesting observations on the surface oxidation of Pt itself in anhydrous and almost anhydrous trifluoroacetic acid (TFA) where the degree of surface oxidation normally attained at a given potential (for a given sweep rate) is limited and can be controlled by the water content of the TFA solvent as well as by potential. The point of special interest in this paper is the observation of a quite large degree of hysteresis between the processes of formation and reduction of Pt surface oxide but at extents of coverage far less than a monolayer where, in ordinary aqueous solutions, the behavior would be almost reversible or exhibit only small hysteresis (3).

In other work (8, 9), we have investigated the behavior of Pt in electrooxidation reactions of formic acid (8) and H₂ (9) also in almost anhydrous media with the idea of diminishing the inhibition of these reactions which sets in at potentials where surface

* Electrochemical Society Active Member.

¹ Present address: Eldorado Nuclear Ltd., Research Laboratories, Ottawa, Ontario, Canada.

Key words: surface oxidation, platinum, oxidation in trifluoroacetic acid, hysteresis, in oxidation, anion adsorption.

oxidation of the metal commences on account of the presence of water as solvent.

Experimental

General experimental procedure.—Potentiodynamic experiments were carried out using the programmable system previously described (2, 3) in which linear potential sweeps could be applied to the electrode at various sweep-rates, s , and after various times of holding the potential constant at certain desired values (2). Electrodes and cells used were as described previously (2, 3). An ($\alpha + \beta$) PdH electrode was used as a reference electrode in all the work and behaved satisfactorily in the anhydrous TFA solutions. It was checked periodically against a platinized Pt hydrogen electrode in the same solution but in an external compartment. All potentials are referred to the H_2/H^+ potential and denoted by E_H .

Choice of solvent.—Trifluoroacetic acid (TFA) was used as solvent in this work because (i) it can be made initially almost anhydrous and may be well purified by normal solvent purification and drying procedures; also it can be made very anhydrous (9, 10) by "gettering" any remaining traces of water by addition of a trace of trifluoroacetic anhydride through the reaction $CF_3CO \cdot O \cdot COCF_3 + H_2O(\text{traces}) \rightarrow 2 CF_2COOH$; (ii) it can be made "electrochemically" pure, i.e., no spurious oxidation or reduction currents arise from reaction of any impurities over a wide potential range at Pt; and (iii) it is a good ionizing solvent for a number of salts including potassium trifluoroacetate (KTFA). Also (iv) it is itself, with KTFA as electrolyte, not oxidizable until about $+2.2V E_H$ when it undergoes the Kolbe reaction (10). Thus, there exists a large anodic² potential range over which the solvent is electrochemically inactive. Also, since TFA does not have actively available the "elements of oxygen," there is no possibility of oxidation of the Pt electrode surface by species discharged from the solvent itself over a wide potential range until the carboxylate function is discharged (10). Hence, effects of controlled trace additions of water which lead to limited surface oxidation of the Pt and to underpotential deposition of H (see below) can conveniently be examined.

Chemicals and purification procedures.—All chemicals used were analytical reagent grade. Further purification procedures were performed as described below:

(a) TFA (Eastman Kodak Company) was first gently refluxed over $KMnO_4$ (Fisher Company, Limited) for at least 24 hr. The mixture was then slowly distilled, three successive distillations being performed. Prior to the third distillation, 0.05% of trifluoroacetic anhydride was added to eliminate any residual traces of water in the acid to be used immediately after the distillation in the initial experimental runs in completely anhydrous TFA (Fig. 1).

(b) Trifluoroacetic anhydride (Eastman Kodak Company) was used to diminish water content in the TFA, as mentioned above. It was purified first by distillation from $KMnO_4$ followed by another slow distillation at 312.5 K prior to use in a run.

(c) KTFA, the K^+ salt of TFA, used as electrolyte, was prepared by neutralization of previously purified TFA with 5M potassium carbonate (Fisher ACS analytical grade). The mixture was heated gently until saturation was achieved. The solution was then left to crystallize slowly. The crystals were washed with the mother liquor followed by some of the purified TFA and dried under vacuum at 373 K.

(d) Water used for controlled additions of water in the runs was obtained by the pyrocatalytic distillation procedure previously described (12).

² There is evidence (11) that, in aq. media, cathodic reduction of TFA can occur. However, in the present work, the effects studied were mostly at potentials well positive to those where reduction of the molecule could occur.

(e) H_2 and N_2 gases used for bubbling in the cell were purified and dried as described previously (1-3).

Solutions and solution purity.—The solutions used consisted of 0.5M KTFA dissolved in the pure 100% TFA liquid. The dryness or wetness of each solution was controlled with additions of trifluoroacetic anhydride or of the pyrodistilled water, respectively, as required.

Aqueous solutions of $HClO_4$ and H_2SO_4 were made up from pyrodistilled water, prepared as previously described (12), using the Aristar (B.D.H.) high purity acids. The $HClO_4$ contained no detectable Cl^- ions.

The criteria for solution purity, formulated previously (12), were applied to the experiments in the aqueous media. For the TFA solutions, purity was judged acceptable when a potentiodynamic i - V profile such as that in Fig. 1a, showing virtually no diffusion-controlled residual oxidation or reduction currents, was observed. The cathodic and anodic current profiles at the least positive potentials in the sweep are associated with underpotential deposition of H in a reversible reaction $CF_3COOH + Pt + e \rightleftharpoons CF_3COO^- + PtH_{ads}$, as in aqueous solutions, as indicated by (a) linear dependence of peak currents on s and (b) independence of peak currents on stirring.

Water additions.—After establishing an i vs. V profile for the completely anhydrous TFA solution, such as shown in Fig. 1a, the effects of addition of controlled traces of pyrodistilled water were investigated.

Integration of potentiodynamic i - V profiles.—Charges for surface oxide reduction or formation, and for H deposition and ionization, were evaluated by weighing the cut-out i - V profiles recorded on good quality graph paper of uniform thickness and previously calibrated weight per unit area. Charges thus evaluated were accurate to ca. 1%, i.e., much better than can be achieved using a planimeter for measuring small areas. The double-layer charge contributions were subtracted using the base lines of i - V profiles such as those in Fig. 1a.

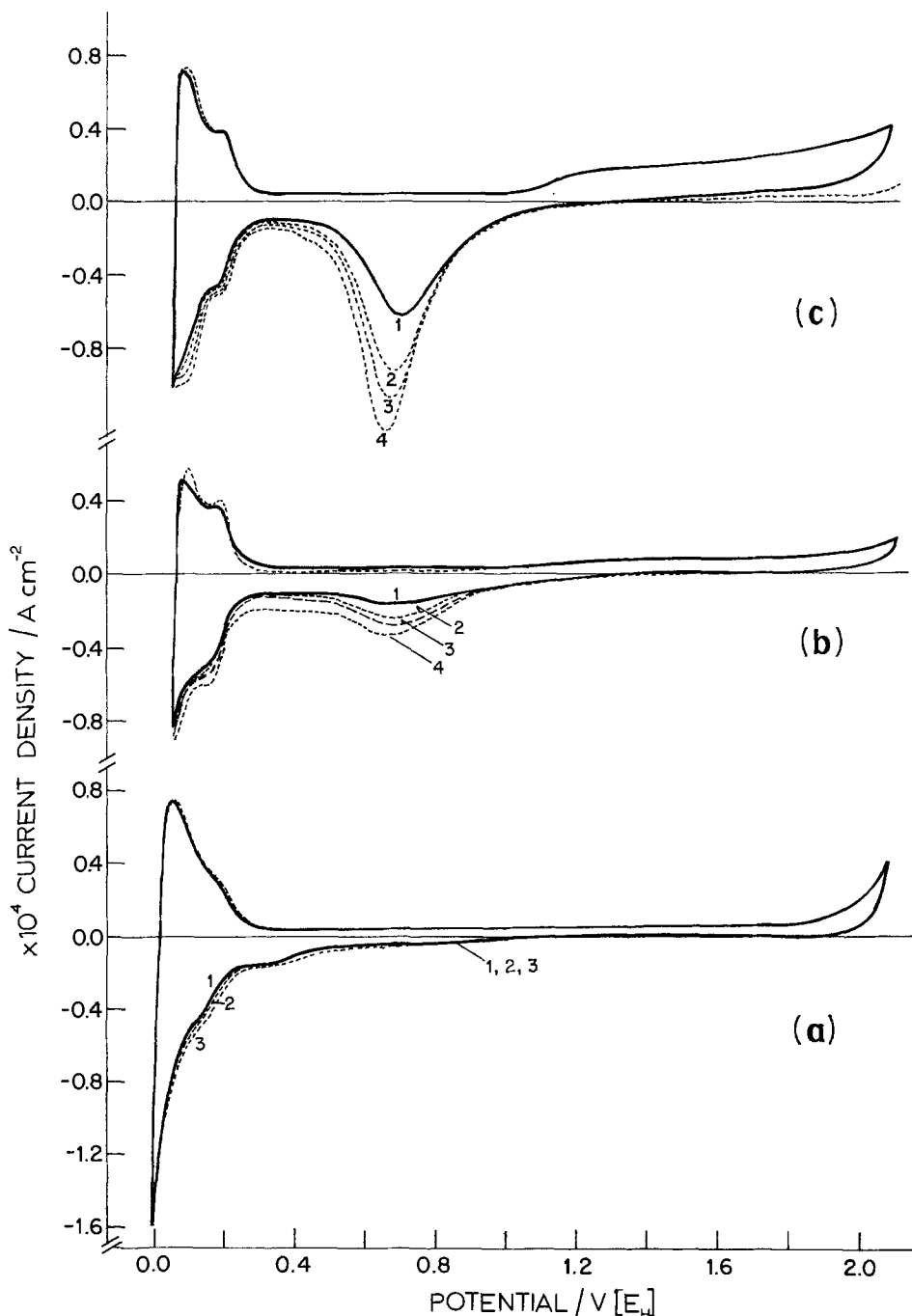
Results

Aims of the experiments.—The aims of the experiments were to evaluate the surface oxidation behavior of Pt which arises when small coverages of surface oxide [the general term is used here since a variety of 2-dimensional lattice states can be formed, leading to "PtOH," "PtO," and corresponding place-exchanged species "OHPt," "OPT" (4)—(see Scheme I)] are generated from traces of water in an excess of the initially anhydrous solvent. The i vs. V profiles for Pt in TFA + KTFA solutions, with and without traces of water present, will be described first.

The current vs. potential profiles for Pt in anhydrous TFA and with added traces of water.—**Behavior in ultradry and slightly aqueous solutions.**—We show first the potentiodynamic i vs. V profiles at Pt for the most anhydrous TFA solutions (Fig. 1a) and then comparatively (Fig. 1b, 1c) those for the same solutions with controlled additions of water. Effects of holding the potential at the positive limit V_a of the anodic sweep for various times are also shown.

If the initial preparation of distilled TFA contains, as it usually does, a residual trace of water, this is indicated by small but significant oxide film formation currents at potentials more positive than ca. $1.05V E_H$ and a small oxide reduction current peak in the cathodic sweep. An ultradry solution can then be obtained by adding controlled traces of trifluoroacetic anhydride until the i vs. V profile takes the form of Fig. 1a with zero surface oxidation current and no oxide reduction peak in the cathodic sweep. Confirmation of ultradryness of the initial solutions is given by holding the potential at the positive end of the sweep for 1-5 min and demonstrating (Fig. 1a, curves 2, 3) no development (<1% coverage) of any signifi-

Fig. 1. Potentiodynamic i vs. V profiles for a Pt electrode in trifluoroacetic acid containing 0.5M potassium trifluoroacetate as electrolyte and with varying, including zero, concentrations of water. Sweep rate 8.2×10^{-2} Vsec $^{-1}$; temperature 298 K. (a) In very dry solution, gettered with trifluoroacetic anhydride. Curves 1, 2, 3 with holding at the anodic end potential of the sweep for 0.120 and 300 sec. (b) With water added to a concentration of 0.19 m/o. Curves 1, 2, 3, 4 with holding at the anodic end potential of the sweep for 0, 30, 60, and 120 sec, respectively. (c) With water added to a concentration of 0.42 m/o. Curves 1, 2, 3, 4 with holding at anodic end potential of the sweep for 0, 30, 60, and 120 sec, respectively.



cant Pt surface oxide reduction peak in a following cathodic sweep.

Surface oxidation behavior.—Three families of potentiodynamic i vs. V profiles for a Pt electrode over the potential range 0.0V to +1.86V E_H electrode in the same solution, are recorded in Fig. 1. Figure 1a shows the behavior in the most anhydrous TFA solution, gettered by addition of a trace of trifluoroacetic anhydride. No surface oxidation currents are detectable but underpotential deposition of H in two distinguishable states is observed (region A). Addition of traces of water (Fig. 1b, 1c) causes development of surface oxide in the anodic sweeps, commencing detectably at 1.05V E_H , and a current profile for its reduction is observed around 0.7–0.6V in the following cathodic sweep.

In order to follow the transition towards aqueous solution behavior and to provide comparisons with surface oxide formation and reduction behavior in largely aqueous solutions, experiments were performed in TFA containing 0.2, 0.5, 0.98, 2.6, and 4.1 mole

percent (m/o) H_2O , in water 0.1 and 1.0M in TFA and in water 0.1, 1.0, and 6.0M in $HClO_4$.

In the absence of significant quantities of water, it is seen from the profiles of Fig. 1a that it is possible to reach quite high positive potentials and thus relatively high interphasial fields without establishing currents either for surface oxidation (as would occur in regular aqueous solutions) or for dissolution of Pt. When traces of water are present, holding the potential for various times (curves 1, 2, 3, 4 in Fig. 1b, 1c) causes an increase in the extent of surface oxidation as occurs (1, 2) under aqueous solution conditions but to much larger extents.

It is found, somewhat surprisingly, that the extent of surface oxidation attained on holding or during a sweep is almost independent of solution stirring (Fig. 1c). This is presumably because the oxide growth process is sufficiently slow and the quantity of H_2O molecules required to produce the submonolayer oxide film is sufficiently small, ca. 4×10^{-10} mole cm^{-2} , in a fairly dry solution, that the process of oxide film growth is not diffusion-controlled with respect to H_2O .

The points of interest to be discussed later are (i) the relation between the charge Q for reduction of the surface oxide formed up to various potentials, V_a , at the positive end of a previous anodic sweep as shown in Fig. 2; (ii) the relation between the peak potential, V_p , of the cathodic i vs. V profile for surface oxide reduction, and the oxide reduction charge, Q , as shown in Fig. 3; (iii) the hysteresis that arises typically in Fig. 1b, 1c for quite small degrees of surface oxidation, down to a relative surface coverage $\theta_{OH} = 0.023$ (i.e., $Q \simeq 5 \mu\text{C cm}^{-2}$); and (iv) the difference of behavior of surface oxide reduction at Pt in aq. and TFA solutions shown in Fig. 2 and 3.

It is to be noted that the potential scales in Fig. 2 and 3 for the results obtained in aqueous and in the TFA solutions are, of course, different on account of the different solvents. However, the potential span between the reversible H_2 -potential in TFA and the onset of surface oxidation of Pt from small concentrations of water in TFA is only a little longer than that from water itself containing small quantities of HClO_4 or H_2SO_4 . Also, for a given solution, it is the relation between Q and V_p or V_a that is of interest.

H adsorption in anhydrous and almost anhydrous TFA.—Before proceeding to the discussion of the surface oxidation behavior, it is interesting to note that even in the driest solution, current peaks for adsorbed H atom deposition and ionization are observed (Fig. 1a) indicating that underpotential deposition of chemisorbed H in at least two states [there are 4 or 5 observable in water (13)] on the Pt surface is possible in a solvent other than water. Comparative experiments in 0.1M aq. HClO_4 on the same electrodes (see below) showed that the H-accommodation at Pt in anhydrous TFA up to the H_2 -reversible potential is about 40% of that in water. This is probably due to displacement of the H deposition region to more negative potentials due to anion adsorption. Similar effects are seen in aq. KTFA + TFA solutions where CF_3COO^- modifies H adsorption.

Absence of impurity effects in TFA was demonstrated by showing that the H charge attains a well-defined value (Fig. 1c) of $109 \pm 10 \mu\text{C cm}^{-2}$, independent of the extents of surface oxide generated from traces of water (Fig. 1b, 1c) by the "holding" experiments, at 2.090V vs. PdH. In 0.1M aq. HClO_4 , the same electrode gave $270 \mu\text{C cm}^{-2}$ for the H charge. This charge was used as a standard of reference for comparative evaluation of extents of surface oxidation of the same Pt electrode in the TFA solutions.

Discussion

The extent of surface oxidation as a function of potential.—Several overlapping states of surface oxidation of Pt can be resolved (3, 17) in an anodic sweep up to ca. 1.1V E_H ; however, the total charge, Q , for surface oxidation is an approximately linear function of V_a , as found, e.g., in aqueous 0.1M HClO_4 or H_2SO_4 , except at quite low coverages, $Q < 30 \mu\text{C cm}^{-2}$.

In TFA solutions containing traces of water, the Q vs. V_a relations have much lower slopes (Fig. 2) than for the aqueous acid solutions, indicating that surface oxidation is more difficult in such almost non-aqueous solutions than in water. The slopes give the average electrochemical capacitance, dQ/dV_a , of the film over various potential ranges for its formation. dQ/dV_a values for aqueous 0.1M HClO_4 and H_2SO_4 are almost the same ($426 \pm 10 \mu\text{F cm}^{-2}$). However, for the TFA solutions containing traces of water, $dQ/dV_a = 91 \mu\text{F cm}^{-2}$, i.e., some 4.7 times smaller. This latter result is not due to restriction of the quantity of oxide that can be grown by diffusion of water, as was shown by the stirring experiments referred to earlier.

The low slope, dQ/dV_a , for surface oxide formation in the TFA solutions may be due (i) to difficulty in displacing strongly adsorbed TFA solvent molecules and CF_3COO^- ions and/or (ii) absence of stabilization of the OH/O layer which can arise in the water solvent through H-bond bridging through H_2O molecules at the oxide film/solution interface.

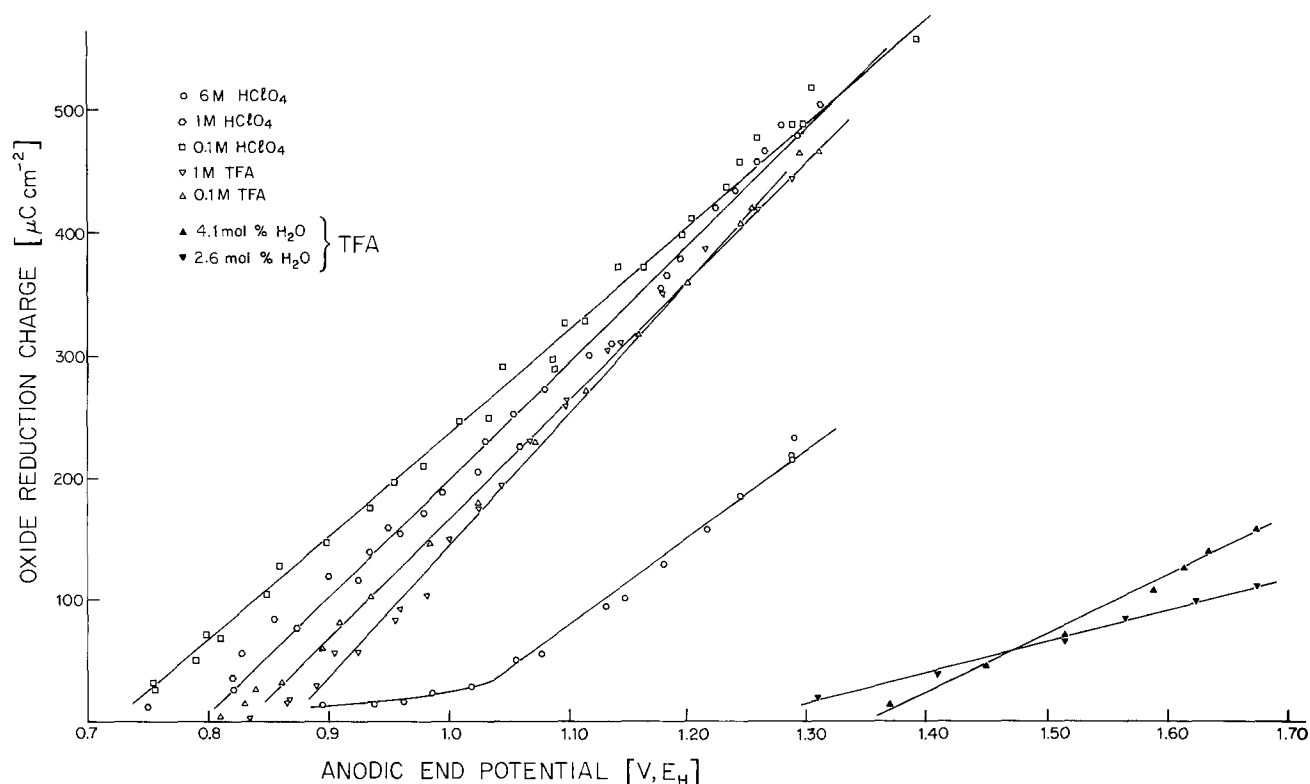


Fig. 2. Comparison of oxide reduction charges, Q , as a function of anodic end potential, V_a , in repetitive sweeps at $8.2 \times 10^{-2} \text{ V sec}^{-1}$ for small quantities of water in TFA, for aq. TFA and for aq. HClO_4 solutions.

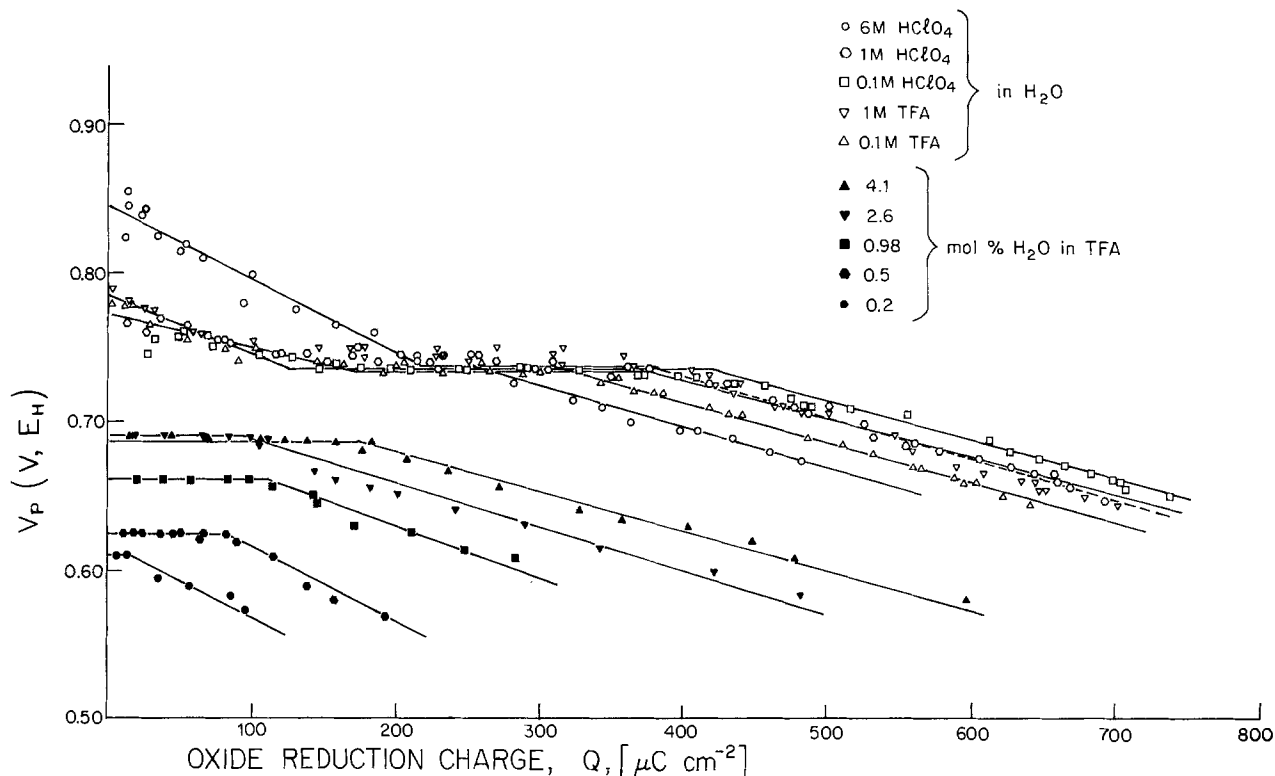


Fig. 3. Oxide film reduction peak potential, V_p , as a function of oxide reduction charge Q for various concentrations of water in TFA, for aq. TFA and for aq. HClO_4 . [The increasing Q values are achieved by holding the potential at various V_a values for controlled periods of time [cf. Ref. (2, 3)]. V_p values are referred, in each solution, to the potential of the H_2/H^+ electrode in that solution.

Hysteresis and irreversibility in surface oxide formation and reduction.—As we have shown previously (2, 3), the state of the oxide film formed up to a given V_a [and for a controlled time (1,2)] is conveniently characterized electrochemically by the peak potential, V_p , of the i vs. V reduction profile in a cathodic potentiodynamic sweep following an anodic sweep to some potential V_a . Usually, with increasing extent of surface oxidation (V_a and/or time increasing), V_p becomes less positive and the peak narrower (2, 3). Thus, in dilute aqueous acid solutions, it is well known (2, 3, 14) that V_p becomes less positive with increasing extent of surface oxidation, measured by Q , but there is an inflection in this relation with a section in which V_p is independent of Q (3). This corresponds approximately to a situation where the full OH monolayer at Pt (completed at ca. 1.1V) is converted to O species by reaction II (or II' from "OHPT") without change of geometrical coverage. Plots of V_p vs. Q are shown in Fig. 3 for water in TFA and for several aqueous solutions of HClO_4 (lines with points marked \square , \circ , Δ , and ∇). In sufficiently strong (6M) aqueous HClO_4 , the region where V_p is independent of Q is much smaller than in dilute aq. acid solution (3) and an almost continuous linear relation (points marked \circ) is seen between V_p and Q .

In the plot of V_p for the reduction profile vs. Q (Fig. 3), these submonolayer quantities of oxide give only continuously decreasing (less positive) values of V_p with increasing Q or, at higher water contents (0.5–4.1 m/o H_2O), an initially flat region (V_p independent of Q) followed by a region where V_p decreases linearly with Q . These regions look like the right-hand side parts of the V_p vs. Q relations for the dilute aqueous solutions [cf. Ref. (3)], also shown in Fig. 3 (results for aq. TFA and HClO_4), where much larger Q values are involved.

Since V_p becomes, in general, less positive with increasing V_a and Q , it is evident that the processes of formation and reduction of the surface oxide become progressively more irreversible with respect to one another, giving rise to the observed hysteresis (1, 2)

between these processes. It is convenient to define this hysteresis arbitrarily as the difference, ΔV , in volts between the potential for detectable onset of surface oxidation in the anodic sweep and the potential, V_p , at the maximum current in the reduction curve.

The striking feature of the i vs. V profiles for small extents of surface oxidation of Pt attained in TFA with traces of water present, is that the hysteresis, ΔV , is much larger than is found for corresponding small Q values in ordinary aqueous media. This is illustrated in Fig. 4 where ΔV is plotted against Q in the series of points for ~0–4.1 m/o H_2O in initially anhydrous TFA.

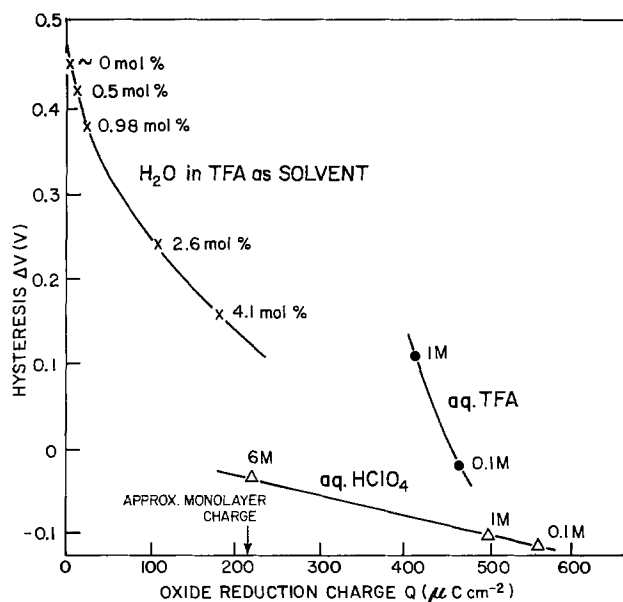


Fig. 4. Hysteresis (ΔV volts) between potential for onset of surface oxidation of Pt and reduction peak potential as a function of oxide reduction charge, Q , for various solutions. End potentials, V_a , in anodic sweeps: for TFA solutions, 1.66V; for aq. solutions of TFA and HClO_4 , +1.35V.

This figure also shows how ΔV depends on Q for aqueous TFA (0.1 and 1.0M) and for aqueous HClO_4 (0.1-6M). Comparison between the ΔV values for the oxide films formed in the various solutions indicated in Fig. 4 shows that there is a large difference between the behavior of the oxide films formed from traces of water in excess TFA and that for films formed in excess water in dilute acid solutions. The small submonolayer quantities of oxide, produced under the former conditions, behave [cf. Ref. (1,2)] like full oxide films, with $Q > 400 \mu\text{C cm}^{-2}$, formed at high V_a values in aqueous solutions.

The fact that the submonolayer films produced in TFA with traces of water are reduced at less and less positive potentials as more surface oxide is generated (Fig. 3, lines for H_2O in TFA), indicates that there is the usual [cf. Ref. (1-3)] progressive stabilization of the oxide film (probably in a rearranged "OPT" state) with increasing coverage, even at low apparent geometrical coverages of the electrode surface. Such films, at low coverages, seem already to be in the so-called "phase-oxide" state (6, 15).

This is quite unlike the situation for irreversible reduction of a randomly deposited film where the reduction peak potential, we have shown (16), should be independent of the quantity of material (below a monolayer) initially existing if interaction effects are absent. However, if attractive interactions are significant, then the reduction peak potential does become less positive with increasing initial coverage, depending on the magnitude of the g factor (4) characterizing these interactions.

The results of the present work show that experiments in TFA containing traces of water allow low coverages of surface oxide to be formed (Fig. 1 and 2) up to substantially higher V_a values than are normally possible in aqueous solutions where the water activity is invariant, *i.e.*, where a given coverage is determined only by V_a and time spent at V_a in that case [cf. Ref. (2)]. Two electrostatic factors can then tend to enhance the extent and velocity of place-exchange: (i) the metal/solution field will be greater for the conditions (high V_a) of surface oxide formation in TFA than for those for surface oxidation in water; such conditions will promote more rapid and extensive field-dependent place-exchange; (ii) the local dielectric constant in the inner region of the double-layer would be smaller in TFA than in water, giving higher surface fields for a given surface charge density on the electrode.

The use of a range of solvents with widely different ϵ would be required to test the role of factor (ii). However, practically, this is difficult as there are few, if any, other nonaqueous solvents that can survive strong anodic polarization at Pt without suffering oxidation; also, the varying solvating power of such solvents for anions of the electrolyte would cause a simultaneous variation of the strength of competitive anion adsorption (see "Anion adsorption effects" below).

Both the factors (i) and (ii) above tend to induce a relatively more facile place-exchange since the place-exchange process is field assisted (the PtOH or PtO surface dipole is presumably of opposite direction to that of place-exchanged OHPT or OPT, so that anodic fields assist the process).

Commentary on the state of the oxide films.—The behavior described above must be examined in the light of previous ideas (2-6) on surface oxidation of Pt involving place-exchange and the role of anion adsorption (17, 18). The results presented above indicate that the characteristics of the submonolayer quantities of surface oxide formed from traces of water in excess TFA [as determined by the V_p vs. Q behavior (Fig. 3) and the ΔV values] are surprisingly similar to those of oxide films formed to much greater coverages, at high V_a values, in excess water.

The unusual behavior of the submonolayer oxide films formed in TFA from traces of water can be considered in terms of two possible effects: (i) the adsorption of the CF_3COO^- anion (cf. Fig. 5) may promote irreversibility in the formation of the oxide film in TFA solutions by assisting (18) the place-exchange and leading to deposition of the film in a rearranged state without observable prior development of the reversibility electroadsorbed OH layer at significant coverage [ca. 15% in dilute aqueous HClO_4 (3) or 30% in dilute KOH (17)]; and (ii) the submonolayer oxide films are deposited as islands within which a large degree of place-exchange and conversion of electrodeposited OH species to O species has taken place, giving rise to the observed irreversibility and hysteresis shown in Fig. 4. This would be facilitated by the relatively large anodic potentials V_a which can be reached in the anhydrous TFA (Fig. 1).

Anion adsorption effects.—In connection with (i), it is to be noted that similar behavior is observed when the Pt surface oxide film is grown in dilute aqueous H_2SO_4 or HClO_4 to which Cl^- ions (that are strongly adsorbed) are added³ (18): For Cl^- concentrations $> ca. 10^{-4}$ M, Pt surface oxidation occurs in a completely irreversible manner with the three partially reversible states (3, 17) normally distinguishable between 0.8 and 1.1V E_H , being eliminated on account of competitive adsorption of Cl^- ions. Figure 5 shows that the surface oxidation of Pt in aqueous solutions of TFA at 0.1 and 1.0M concentrations is much inhibited in comparison with the behavior in aq. HClO_4 . Also the H region is changed in a way characteristic of strong anion adsorption, *e.g.*, as observed with Cl^- . The behavior observed confirms that CF_3COO^- (and/or CF_3COOH) can have a strong effect, like Cl^- ion (18), on the formation and reduction behavior of the monolayer oxide film at Pt. In TFA, the adsorption of CF_3COO^- is likely to be stronger than in water due to its weaker solvation than in the latter medium. However, there are difficulties in seeing how an anion effect alone could cause the hysteresis effects observed if the submonolayer films formed in TFA were dilute random arrays of OH/O species. Hence rearrangement into 2-dimensional condensed island regions has also to be considered.

Island formation.—Here we examine to what extent a 2-dimensional formation of islands of place-exchanged OH or O species could account for the hysteresis behavior as an additional effect to that caused by anion adsorption, indicated above. Two dimensional islands could arise if the place-exchanged OH or O species are sufficiently stabilized by attractive lateral interactions, *i.e.*, with a g -factor [see Ref. (16)] in the ad-

³ In the present work, there is no question of there being traces of Cl^- ion present that might lead to the effects observed: The TFA used was triply distilled and solutions gave no positive test for Cl^- by the sensitive nephelometric method.

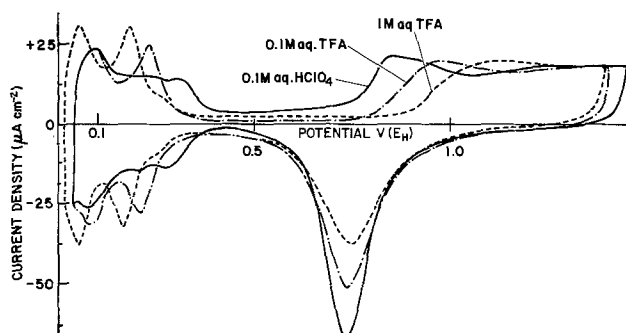
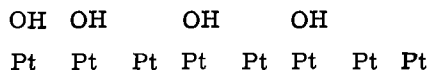
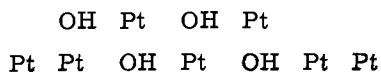


Fig. 5. Cyclic-voltammetry i vs. V profiles for Pt in 0.1M aq. 0.025 V sec^{-1} at 298 K and in 0.1M aq. HClO_4 with addition of CF_3COOH at concentrations of 0.1 and 1.0M causing blocking of surface oxide formation.

sorption isotherm < -4 . This would follow if a random array such as



became restructured into a 2-d phase such as



where PtOH and OHPt dipoles are oriented in attractive configurations, leading to stabilization.⁴ These representations are, of course, highly schematic.

The suggestion that the behavior observed with the submonolayer oxide films formed from water in TFA is associated with formation of islands of the place-exchanged species is not inconsistent with the picture we have given previously (3, 4) for the progressive development of a monolayer of surface oxide on Pt and other noble metals. Place-exchanged species, "OHPT" or "OPT," will tend to be most stable when adjacent to "unexchanged" adsorbed OH or O species on the Pt surface, as shown schematically above (in fact, this is probably part of the driving force for place-exchange), so that the tendency for formation of islands of the place-exchanged species has to be included in mechanisms of surface oxidation. Initially, formation of lattices of electrodeposited OH species up to a monolayer (at 1.1V E_H in water) seems to account (3) for the anodic i vs. V profile in water. Hence, the ultimate formation of the surface oxide film in a state which is reducible only at less positive potentials than those required for its formation [the hysteresis effect; Ref. (1-4)] would seem to require surface diffusion of the initially deposited species coupled with their place-exchange. At any reasonably significant coverage, say 25%, surface diffusion, if involved, would need to be over 2 ~ 3 lattice sites only and would thus be difficult to distinguish from the lattice reconstruction processes. These effects are presumably those which give rise to the time-dependence of oxide film formation (1-3) and the aging effects reported by Arvia (19).

Although the viewpoint examined here on the role of development of submonolayer islands of surface oxide in the process of surface oxidation of Pt from traces of water in TFA is related to the recent treatment of Gilroy (20) in which a nucleation and growth mechanism is advanced for explaining the logarithmic law of growth (1, 15) for increasing degree of oxidation at Pt at constant potential, it must be mentioned that the following type of transient experiment does not indicate a nucleation and growth mechanism that could lead to island formation: If a rapid potential sweep is made to a particular potential V_a in the potential range where surface oxide formation occurs, and the resulting current-time transient is recorded at (this constant) V_a , then only a continuously diminishing $i(t)$ transient is observed, not one in which i at first increases and then decreases with t , which would be characteristic of nucleation and growth of the oxide film. A similar experiment, made in the reduction direction after a monolayer or submonolayer of oxide has been formed anodically, similarly does not indicate

⁴ Island stability will be influenced by edge-to-area ratio. In square arrays of n^2 particles, for example, the number of particles in the edges relative to the number inside the edges is given by $[n^2 - (n-2)^2]/(n-2)^2$, i.e., $4(n-1)/(n-2)^2$. As $n \gg 1$, this ratio approaches $4/n$. Thus, e.g., 40×40 particle squares still contain 10% of particles in their perimeters.

"hole" nucleation and growth as the film reduction mechanism.

Acknowledgments

Grateful acknowledgment is made to the Natural Sciences and Engineering Research Council of Canada, for support of this work. One of us (D.M.N.) acknowledges a Leave of Absence for Specialization from the Ruder Bosković Institute, Zagreb, Yugoslavia. We also acknowledge useful discussions on anion adsorption with Dr. H. Angerstein-Kozłowska of this laboratory.

Manuscript submitted Sept. 17, 1980; revised manuscript received Dec. 1, 1980.

Any discussion of this paper will appear in a Discussion Section to be published in the December 1981 JOURNAL. All discussions for the December 1981 Discussion Section should be submitted by Aug. 1, 1981.

Publication costs of this article were assisted by the University of Ottawa.

REFERENCES

1. D. Gilroy and B. E. Conway, *Can. J. Chem.*, **46**, 875 (1968).
2. P. Stonehart, H. A. Kozłowska, and B. E. Conway, *Proc. Roy. Soc. London A*, **310**, 541 (1969).
3. H. Angerstein-Kozłowska, B. E. Conway, and W. B. A. Sharp, *J. Electroanal. Chem. Interfacial Electrochem.*, **43**, 9 (1973).
4. B. V. Tilak, B. E. Conway, and H. Angerstein-Kozłowska, *ibid.*, **48**, 1 (1973).
5. K. Vetter and W. Schultze, *Ber Bunsenges. Phys. Chem.*, **76**, 920, 927 (1972); *J. Electroanal. Chem. Interfacial Electrochem.*, **34**, 131, 141 (1972).
6. A. K. N. Reddy, M. Genshaw, and J. O'M. Bockris, *J. Chem. Phys.*, **48**, 671 (1968).
7. A. H. Lanyon and B. M. W. Trapnell, *Proc. Roy. Soc., London A*, **227**, 387 (1955).
8. B. E. Conway, B. W. Tilak, J. Wojtowicz, and B. MacDougall, 2nd Intl. Conference on Fuel Cells, S.E.R.A.I., Bruxelles, (1968), pp. 164-170.
9. B. E. Conway and D. M. Novak, *J. Phys. Chem.*, **81**, 1459 (1977).
10. A. K. Vijn and B. E. Conway, *ibid.*, **71**, 3637 (1967).
11. R. Woods, *Electrochim. Acta*, **15**, 815 (1970).
12. B. E. Conway, W. B. A. Sharp, H. Angerstein-Kozłowska, and E. Criddle, *Anal. Chem.*, **45**, 1331 (1973).
13. B. E. Conway, H. Angerstein-Kozłowska, and W. B. A. Sharp, in "Electrocatalysis," M. W. Breiter, Editor, p. 94, The Electrochemical Society Softbound Proceedings Series, Princeton, N.J. (1974).
14. W. Böld and M. W. Breiter, *Electrochim. Acta*, **5**, 145 (1961); see also M. W. Breiter, *ibid.*, **8**, 447 (1963).
15. A. Damjanović, A. T. Ward, and M. O'Jea, *This Journal*, **121**, 1186 (1974); see also A. Damjanović and A. T. Ward, M.T.P. International Reviews of Science, Physical Chemistry, Series II, Butterworths, London, 1976, p. 103.
16. H. Angerstein-Kozłowska, J. Klinger, and B. E. Conway, *J. Electroanal. Chem. Interfacial Electrochem.*, **75**, 45, 61 (1977).
17. H. Angerstein-Kozłowska, B. E. Conway, B. Barnett, and J. Mozota, *ibid.*, **100**, 417 (1979).
18. D. M. Novak and B. E. Conway, *J. Chem. Soc. Faraday Trans. I*, **75**, 2454 (1979) and in press (1981).
19. M. E. Folquer, J. O. Zerbino, N. R. de Tacconi, and A. J. Arvia, *This Journal*, **126**, 592 (1979); and N. R. de Tacconi, J. O. Zerbino, M. E. Folquer, and A. J. Arvia, *J. Electroanal. Chem. Interfacial Electrochem.*, **85**, 213 (1977).
20. D. Gilroy *ibid.*, **71**, 257 (1976).

The Structural Characterization of Cadmium Sulfide Films Grown by Cathodic Electrodeposition

Andrzej S. Baranski, W. Ronald Fawcett,* Alex C. McDonald, and Rosanne M. de Nobriga

The Guelph-Waterloo Centre for Graduate Work in Chemistry (Guelph Campus),
Department of Chemistry, University of Guelph, Guelph, Ontario, Canada N1G 2W1

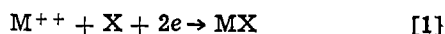
and Jack R. MacDonald

Department of Physics, University of Guelph, Guelph, Ontario, Canada N1G 2W1

ABSTRACT

The structural characteristics of CdS films cathodically electrodeposited from a dimethylsulfoxide solution containing cadmium chloride and elemental sulfur have been studied. The thickness, continuity, smoothness, and the degree of substrate coverage of the CdS films have been examined using stylus-type surface profiling techniques, x-ray diffractometer patterns, and scanning electron microscopy. The composition of the films was examined using Rutherford backscattering spectrometry. It is concluded that high quality films of CdS with a high degree of crystal structure can be electrodeposited in this manner and that minority components may be easily incorporated in the films.

Recently, there has been a great deal of interest in the applications of n-CdS in the conversion of solar energy to electrical energy (1-3). The use of semiconductors in photovoltaic cells is well known; more recently, they have also been employed in photoelectrochemical cells in which they are stabilized by hole consumption reactions involving redox couples in the electrolyte (4, 5). Although the majority of CdS used in these devices is produced by vapor deposition techniques, recent work has described the electrochemical deposition of thin layers of CdS and other semiconductors (6-10). CdS and Bi₂S₃ films may be grown on Cd and Bi metal, respectively, by anodic oxidation of the parent metal in an electrolyte solution containing sulfide ion (6-8). CdSe (9) and CdTe (10) have been deposited cathodically from acidified aqueous solutions containing CdSO₄ and either SeO₂ or TeO₂. The electrode process in which the chalcogen dioxide is reduced to its corresponding dianion is obviously complex since it involves six electrons. However, in the case of CdTe where the structure of the resulting film has been studied (10), the quality of the deposit is quite good. A third method of electrodepositing II-VI compounds involves a cathodic process in a solution containing the desired metal ion and soluble chalcogen (11, 12), the overall reaction being



where M⁺⁺ is a divalent cation and X, the chalcogen. Since the chalcogens are not soluble in water under normal conditions, these reactions were carried out in a variety of nonaqueous solvents.

In the present paper, the structural characteristics and composition of CdS films electrodeposited from dimethylsulfoxide (DMSO) solutions containing cadmium chloride and elemental sulfur are described for a variety of electrodeposition conditions. The electrical properties of the films and the mechanism of film formation will be discussed in future papers.

Experimental

The CdS films were deposited on high purity platinum foil (99.9999%) of thickness 0.05 mm and total exposed area of 2.00 cm². Electrical contact to the platinum squares was made with platinum wire arc-welded to the foil and mounted in a glass tube. A platinum

counterelectrode of similar geometry was used and oriented to provide uniform charge distribution (see Fig. 1). All voltages were measured against a Cd/CdCl₂ reference electrode in DMSO held at the temperature of the electrolyte solution. The electrolyte solution consisted of 0.055M CdCl₂ and 0.19M S in reagent grade DMSO; it was held at constant temperature by immersing the cell in an oil bath whose temperature was maintained by a temperature controller/circulator.

The Pt cathode was etched in concentrated HCl, then rinsed first with triply distilled water, followed by acetone. Electrolysis was carried out at constant current density using a PAR Model 170 programmable potentiostat/galvanostat, the voltage across the cell being monitored on a strip chart recorder. The solution was stirred with a magnetic stirrer during deposition.

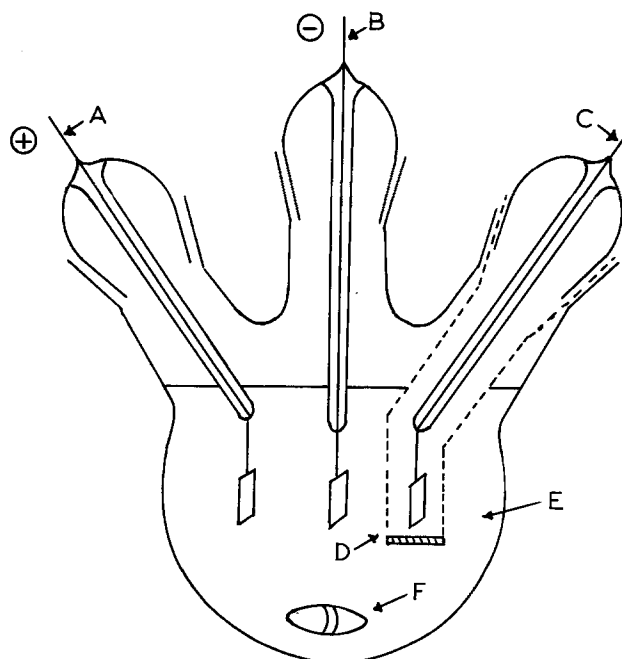


Fig. 1. Diagram of cell used for electrodeposition showing the counterelectrode (A), cathode (B), and reference electrode (C) with the isolating glass sleeve (D). The electrolyte solution (E) was stirred with a magnetic stirrer (F).

* Electrochemical Society Active Member.

Key words: electrodeposition of semiconductors, CdS films, semiconductor films.

The squares of Pt coated with CdS were immediately removed from the electrolyte, rinsed first with hot DMSO, then with acetone. For observation under the scanning electron microscope (SEM), the samples were mounted with silver coagulant on machined aluminum stubs (suitable for insertion into the SEM). The CdS films were examined within 24 hr of electrodeposition with an Etec Autoscan SEM using the backscattered electron technique. All micrographs were taken on Kodak FXP120 film with a Graphex lens and aperture. The procedure was repeated for a series of films varying the time of deposition, the current density, the temperature of the electrolyte solution, the concentration of additives in the electrolyte solution, such as thiourea, potassium iodide, and thallium chloride, and finally the nature of the substrate conductor. In the case that the substrate was not Pt, the required metal (Au or Cd) was first electrodeposited from aqueous electrolytes using standard techniques.

The structure of the CdS films was investigated using a General Electric Model 11GN1 x-ray diffractometer with a cobalt target. The films were also analyzed in a rotating crystal geometry. The stoichiometry and uniformity of selected films were measured using backscattering spectrometry (13) utilizing a 3 MV Van der Graff accelerator.

In order that thickness measurements of the CdS films could be performed, the semiconductor layers were deposited on smooth substrates of Pt sputtered on glass. The thickness of the film was measured with a Sloan Dektak, stylus-type device. The sputtering of the Pt was carried out with an Edwards S150A sputter coater, the resulting metal films being heated for 3 min at 575°C after formation. After electrodeposition of the CdS film by the methods described above, the film was scratched away from the substrate and the thickness was measured at a minimum of 5 positions on the surface.

Results and Discussion

Film smoothness, continuity, grain size, adhesion to substrate, and the percentage of substrate coverage were all considered to be criteria for determining film quality.

Typical plots of voltage during deposition against time for varying current densities are shown in Fig. 2. The initial sharp rise in voltage is attributed to the charging of the double layer and the initialization of the deposition process. This is followed by a 100-200 sec film nucleation step, after which the semiconductor is deposited at a constant rate. Film "breakdown," inferred from the erratic fluctuation at high voltages, occurred independent of current density at $\approx 5V$.

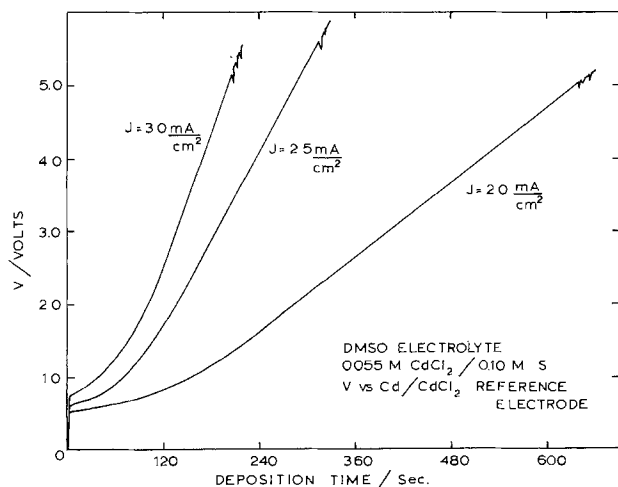


Fig. 2. Plots of voltage against deposition time during the deposition of CdS films at several current densities as indicated.

Electron micrographs of CdS films grown for 50, 150, 500, and 1500 sec at 110°C and a current density of 2.5 mA/cm² are shown in Fig. 3. It is apparent that the films grown for longer than 250 sec at 2.5 mA/cm², that is, for a cell voltage greater than 5V, had significant cracking and defects. The defects, namely undulations and outgrowths, are probably due to charge concentration at the substrate surface caused by macroscopic defects in the substrate. The ridges visible in Fig. 3a and 3b are due to scratches in the underlying Pt. The dependence of the cracking on deposition time, and hence voltage, consistent with the growth curves in Fig. 2, suggests that cracking occurs during deposition.

The x-ray diffractometer pattern shown in Fig. 4 is for a CdS film grown for 500 sec at 110°C and a current density of 2.5 mA/cm². The intense peak at $2\theta = 31.5^\circ$ corresponds to an interplanar distance of 3.34Å and compares well with the theoretical value of 3.36Å for the $\langle 111 \rangle$ planes of β -CdS. The minor peaks in the pattern correspond to the Pt substrate and reflect its limited degree of orientation. It is significant that only one peak associated with CdS was observed. This result indicates a high degree of symmetry along the axis perpendicular to the substrate surface. Rotating-crystal x-ray patterns were typical of single crystal CdS in the β -CdS form. A typical Rutherford spectrum for α -particles backscattered from a CdS film deposited on Pt is illustrated in Fig. 5. The spectrum is shown for the energy ranges where backscattering is due to S⁻ and Cd⁺⁺ ions; the central peak between 0.95 and 11.8 MeV which is due to the Pt substrate has been left out for the sake of clarity. The rise in backscattered intensity at the high energy side of the region corresponding to Cd⁺⁺ at 139 MeV is qualitative confirmation of the presence of this atom and the yield at this energy permits precise determination of the relative amount of Cd in the film. The corresponding high energy intensity for the S peak is obscured by the Pt peak. However, approximate analysis yields an S to Cd ratio of 0.9 ± 0.1 to one. The shape of the Cd and S peaks provides evidence that the film composition is uniform as a function of depth (13). There is some evidence of a peak due to Cl⁻ ions at channel numbers corresponding to lower energies but the intensity was too low with respect to background noise for this element to be positively identified from the Rutherford analysis. However, it is probable that Cl⁻ ions are incorporated into the film to a minor extent during deposition.

The cracking of the thicker film (see Fig. 3c and 3d) has been observed previously in CdS films grown by anodic polarization of Cd in an Na₂S solution (7) and was attributed to water loss. Due to the strong solvation of the Cd²⁺ ion in DMSO, there is probably a small amount of solvent incorporated into the CdS films; however, the above results suggest a secondary, more complex cracking mechanism. Cracking may result during deposition due to tensile stress in the CdS crystal resulting from a strong, secondary piezoelectric effect (14) which is permitted because the $\langle 111 \rangle$ axis has no center of symmetry. Thus, the electric field applied during deposition in this direction may result in the displacement of deposited ions and hence the incorporation of stress during growth. The nonequilibrium positions of the ions in the film would result in stress causing the observed "breakdown" (cracking) when the force was of sufficient magnitude. This conclusion is consistent with the experimental observation of a constant voltage at which "breakdown" occurred, independent of applied current density. It is also reasonable that some cracking may occur after deposition caused by migration of the ions to equilibrium lattice positions.

Figure 6 shows a micrograph of a CdS film grown by decreasing the current density from 2.5 mA/cm² (at $t = 0$ sec) to 0 (at $t = 900$ sec) in equal incre-

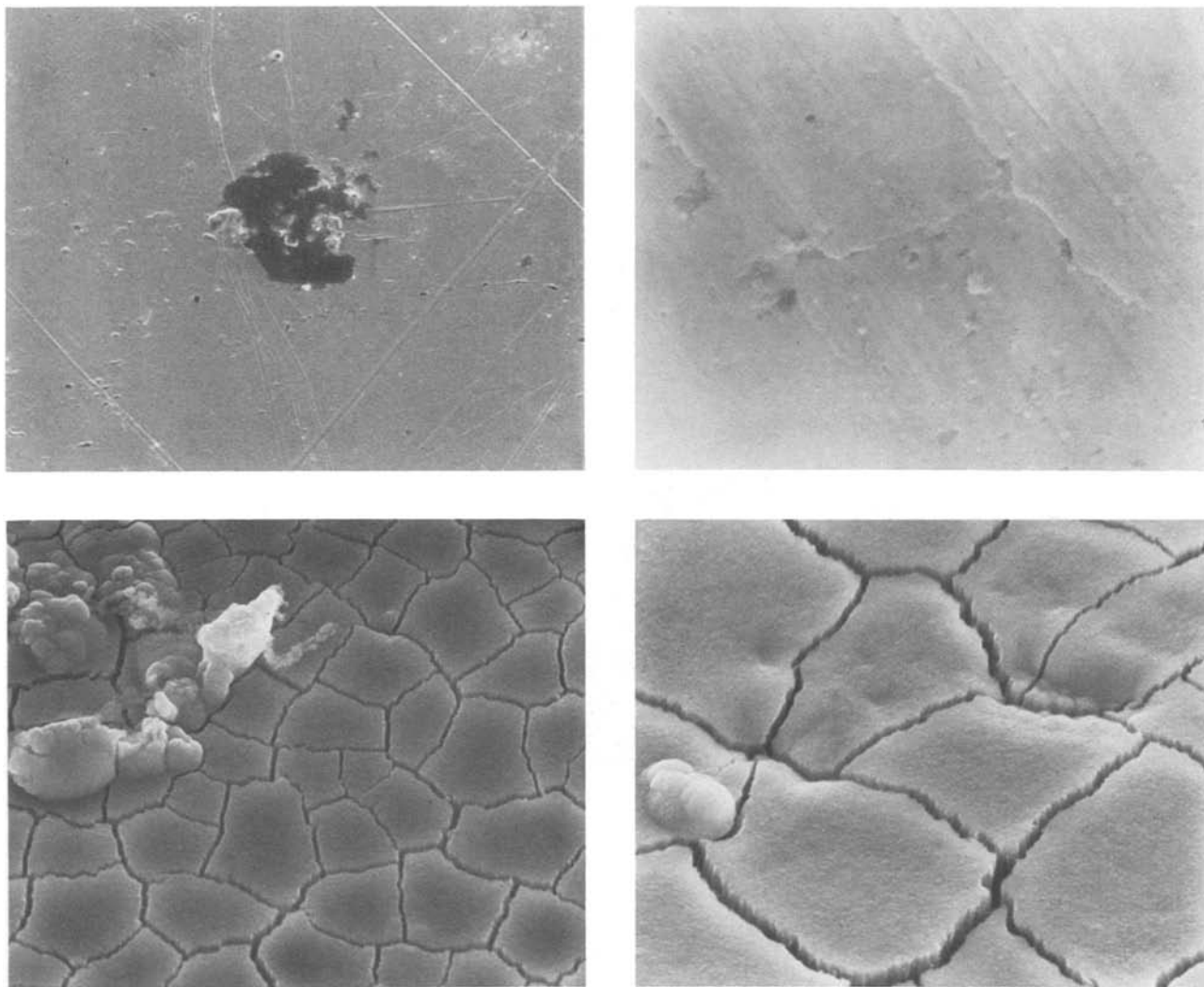


Fig. 3. Electron micrographs of CdS films deposited on Pt at a current density of 2.5 mA/cm^2 for (a, top left) 50 sec (mag $3000\times$); (b, top right) 150 sec (mag $8300\times$); (c, bottom left) 500 sec (mag $6100\times$); (d, bottom right) 1500 sec (mag $6100\times$). The dust particle in (a) was used as a point of focus only.

ments every 180 sec. Although there are significant surface undulations and irregularities in the CdS film, characteristic of thicker films, there is a complete absence of cracks, 100% substrate coverage being achieved. Limiting the applied field by decreasing the current density during deposition may allow a gradual relaxation and migration process to occur. One also notes that in Fig. 6, there is evidence of overlapping

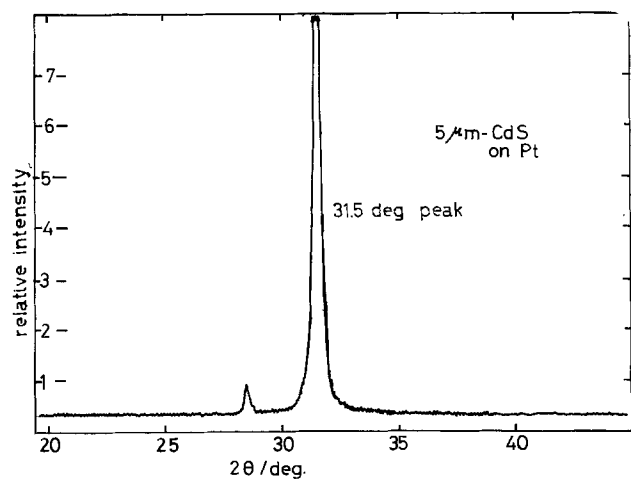


Fig. 4. X-ray diffractometer pattern of a $0.5 \mu\text{m}$ CdS film on Pt (cobalt target).

plates, probably originating from the presence of different nucleating sites on the substrate surface.

A plot of the average film thickness, $\langle d \rangle$ against deposition time is shown in Fig. 7. The dotted line corresponds to the theoretical relationship between thickness and time assuming that the only electrode

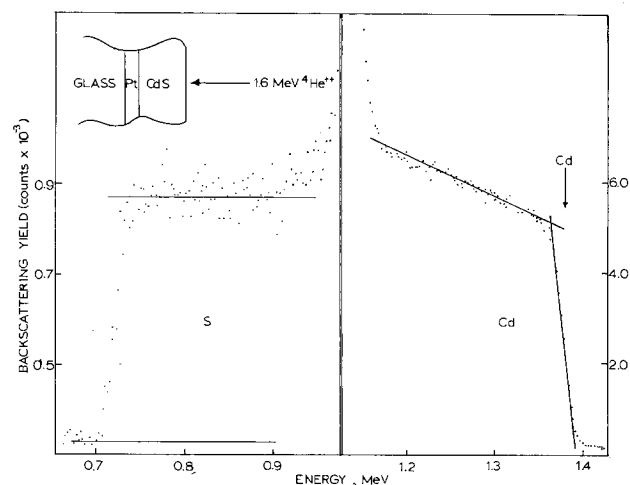


Fig. 5. Rutherford spectrum of backscattered α particles from a CdS film on Pt in the energy ranges 0.65-0.95 MeV and 1.15-1.4 MeV corresponding to scattering from S and Cd atoms, respectively.

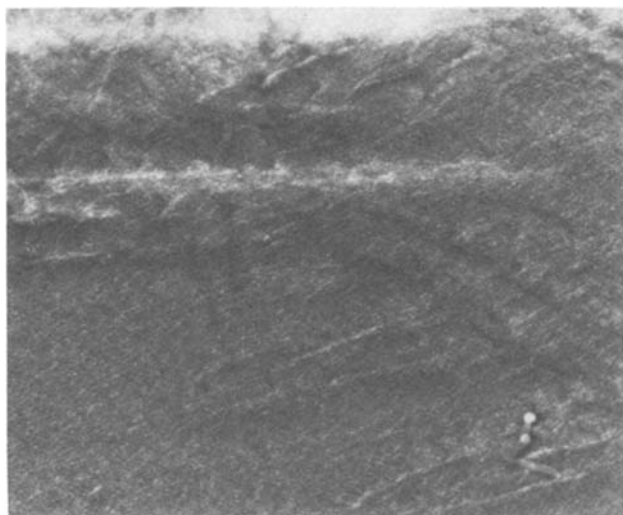
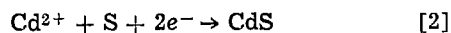


Fig. 6. Electron micrograph of a CdS film deposited on Pt by decreasing the current density from 2.5 mA/cm^2 to zero during deposition in order to prevent the voltage across the cell to exceed 5V (mag 6100 \times).

process is



Accordingly

$$d = \frac{jM}{nF\rho} t \quad [3]$$

where j is the current density, M the molecular weight of CdS (144.46g), n the number of electrons transferred, F the Faraday, and ρ the density of the electro-

deposited material. ρ was assumed to be that for β -CdS, namely, 4.82 g/cm^3 and n was assumed to be 2.

The most notable feature of the experimental data is the linear dependence of film thickness on time. Comparison of the slope observed (Fig. 7) with that predicted for reaction [2] according to Eq. [3] yields an efficiency of 81% for the deposition process. The discrepancy between the experimental and theoretical slopes may be attributed to several factors. Firstly, it may result from the presence in solution of sulfur compounds with sulfur in a higher oxidation state. If sulfur in these forms is involved in the deposition process to a significant extent, the effective number of electrons transferred during the process would be greater than that proposed by the simpler process involving elemental sulfur. Such sulfur compounds are most surely present in DMSO at 110°C due to the oxidation of elemental sulfur by atmospheric oxygen. The presence of sulfur containing impurities is strongly suggested by the distinctive odor of reagent grade DMSO, the pure solvent being odorless. Alternatively, the presence of oxygen and water in the solvent may result in other side reactions.

A plot of average CdS film thickness $\langle d \rangle$ against current density j for a fixed deposition time is shown in Fig. 8. Again, the relationship predicted by Eq. [3] on the basis of Faraday's laws is plotted as a dotted line. Below 3.0 mA/cm^2 , the plot of experimental data is reasonably linear, whereas at higher current densities there is significant deviation from linearity. It is possible that the discrepancies between the experimental data and the theoretical relationships are due to varying composition of the film with current density. At high current density, the interface between the Pt and the CdS was observed to be darker in color than the surface of the CdS layer (the Pt layer was translucent). The darkening may indicate an excess of cadmium in the initial layers of the semiconductor film. The variation of the film composition with cur-

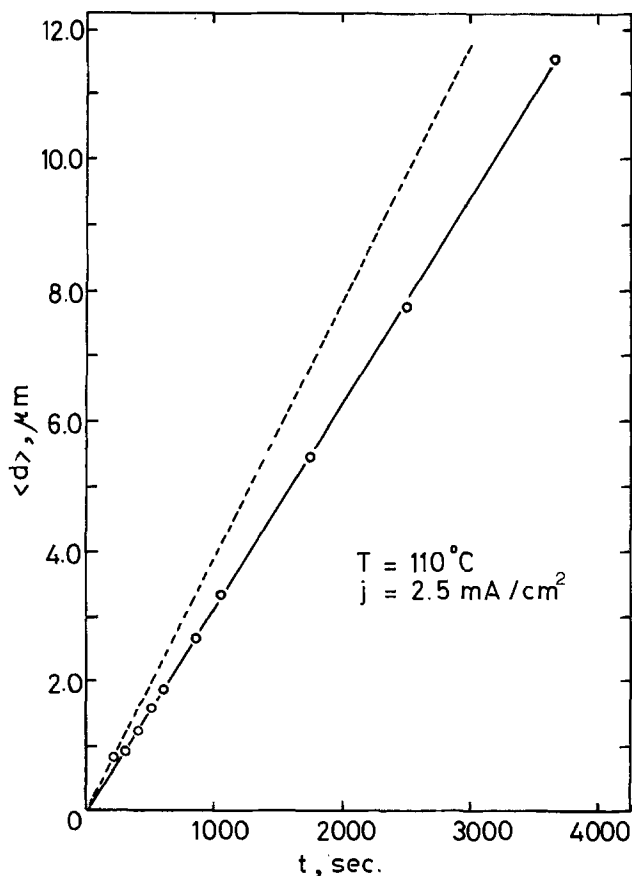


Fig. 7. Average thickness of CdS films deposited on Pt against deposition time. Current density during deposition and electrolyte solution composition and temperature were held constant as indicated.

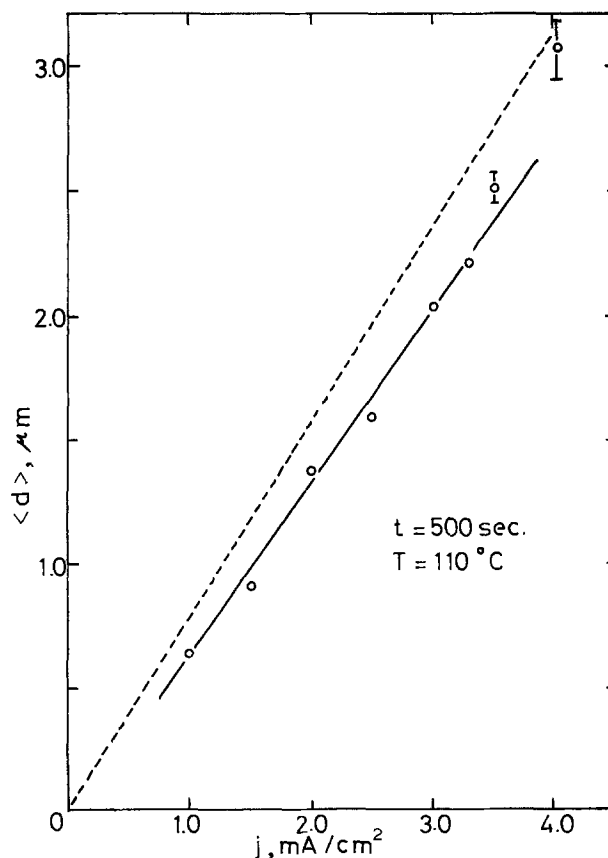


Fig. 8. Average thickness of CdS films deposited on Pt against current density. Deposition time and solution composition and temperature were held constant as indicated.

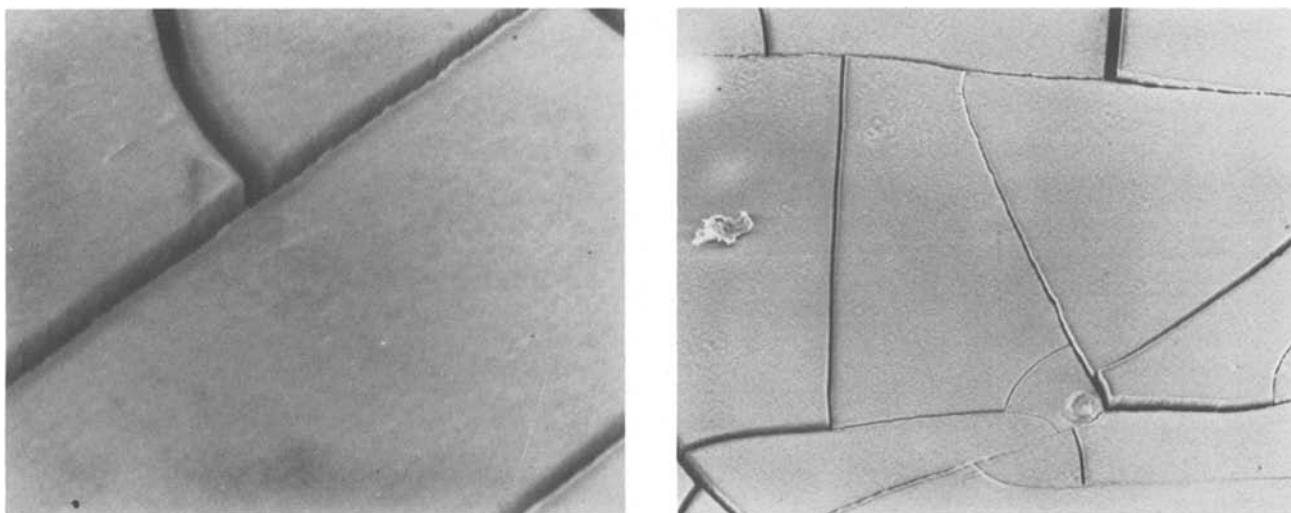


Fig. 9. CdS films deposited on (a, top) gold substrate (mag 4500 \times) and (b, bottom) from electrolyte solution containing $5 \times 10^{-3}\text{M}$ thiourea (mag 1000 \times).

rent density suggests that the stoichiometry of the electrodeposited CdS, and hence its electrical properties, may be altered.

Modifying the substrate surface, prior to depositing the CdS, by adding water or thiourea to the electrolyte solution or by predepositing gold or cadmium had a significant effect on the quality of the deposit. Figure 9a illustrates a characteristic CdS film grown on a gold substrate and Fig. 9b shows a film grown from an electrolyte solution containing thiourea. The films grown on a cadmium substrate and from an electrolyte solution containing water had similar characteristics. These films were much smoother with fewer undulations than films grown from electrolyte solution with no additives; however as can be seen in Fig. 9, such films exhibited poor adhesion to the substrate. The thiourea or water in the DMSO solution is believed to be adsorbed at the electrode surface at sites of high energy (outgrowths). This adsorption may retard film growth at these points and allow growth in "valleys," thus producing a smoother, more uniform deposit. The above results probably illustrate a reduction in the number of points of charge concentration by a smoothing of the substrate surface.

Voltage against deposition time curves for CdS films deposited with TlCl in the electrolyte solution are shown in Fig. 10. It is noted that the slope of voltage against time curves (after the nucleation step) de-

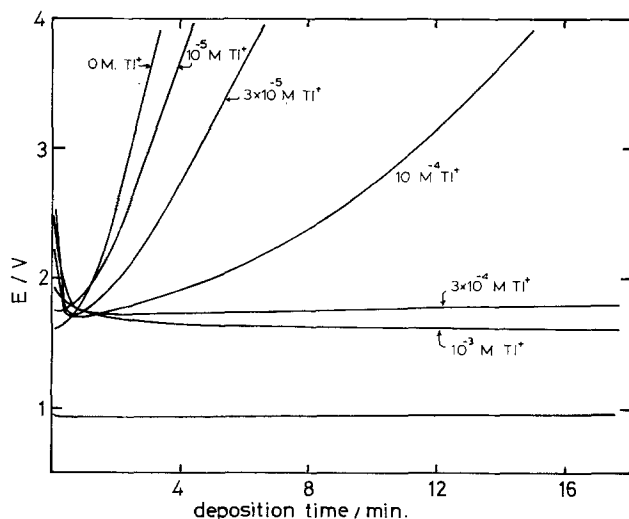


Fig. 10. Voltage against deposition time during deposition of CdS on Pt from electrolyte solution containing various concentrations of TlCl as indicated.

creased with increasing concentration of TlCl in the solution, reflecting a decreased resistivity of the deposited CdS layer due to possible incorporation of Tl⁺ in the film. Selected CdS films deposited from the electrolyte solution containing TlCl were analyzed using the Rutherford backscattering technique. Figure 11 shows a typical spectrum of 2 MeV alpha particles scattered from a CdS film grown for 500 sec from a solution containing 10^{-3}M TlCl. The relative heights H_1 and H_2 due to scattering from Cd and Tl nuclei, respectively, are directly indicative of a 2% abundance of Tl⁺ in CdS. The shape of the spectrum suggests an even distribution of Tl⁺ as a function of depth within the film.

In conclusion, CdS films electrodeposited as described above from DMSO solution are of high quality based on their continuity, adhesion to the substrate, substrate coverage, and degree of crystallinity. The deposition process is technically simple, fast, and has numerous advantages over vapor deposition processes. The observed cracking due to piezoelectric and substrate surface effects is not a serious problem and can be overcome in a straightforward manner. The possibility that minor impurities may be incorporated into the CdS film by electrodeposition is of great significance. This result suggests that CdS films of the desirable electrical properties may be achieved merely by dissolving different doping ions in the deposition solution in suitable concentrations. Preliminary studies have indicated that carrier concentrations on the order of

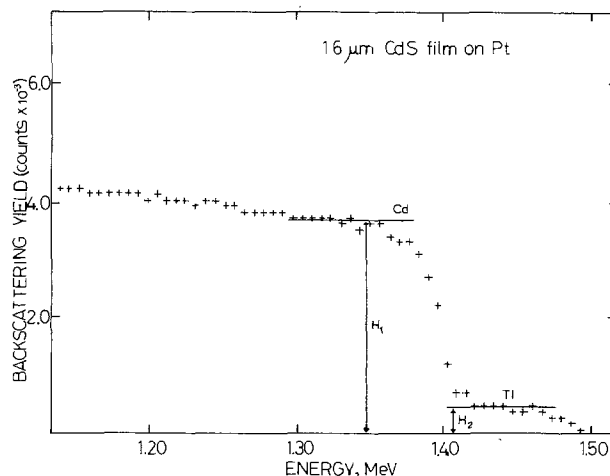


Fig. 11. Rutherford backscattered spectrum of a CdS film deposited from electrolyte solution containing 10^{-3}M TlCl.

10^{14} cm^{-3} and carrier mobilities of approximately $50 \text{ cm}^2 \text{ V}^{-1} \text{ sec}^{-1}$ can be achieved in this manner.

Acknowledgments

WRF and JRM acknowledge the financial support of the Natural Science and Research Council of Canada (NSERC) through operating and equipment grants. ACM also acknowledges the support of NSERC through the award of a postgraduate scholarship.

Manuscript submitted July 31, 1980; revised manuscript received Dec. 11, 1980.

Any discussion of this paper will appear in a Discussion Section to be published in the December 1981 JOURNAL. All discussions for the December 1981 Discussion Section should be submitted by Aug. 1, 1981.

Publication costs of this article were assisted by the National Science and Engineering Research Council (NSERC), Ottawa.

REFERENCES

1. K. Rajeswar, P. Singh, and J. DuBow, *Electrochim. Acta*, **23**, 1117 (1978).
2. H. Gerischer, *J. Electroanal. Chem. Interfacial Electrochem.*, **58**, 263 (1975).
3. T. S. Jayadevaiah, *Appl. Phys. Lett.*, **25**, 399 (1974).
4. A. B. Ellis, S. W. Kaiser, and M. S. Wrighton, *J. Am. Chem. Soc.*, **98**, 6855 (1976); *ibid.*, **99**, 2839 (1977).
5. T. Inoue, T. Watanabe, A. Fujishima, and K. Honda, *This Journal*, **124**, 719 (1977); *Bull. Chem. Soc. Jpn.*, **52**, 1243 (1979).
6. B. Miller and A. Heller, *Nature*, **262**, 680 (1976).
7. L. M. Peter, *Electrochim. Acta*, **23**, 165 (1978).
8. L. M. Peter, *J. Electroanal. Chem. Interfacial Electrochem.*, **98**, 49 (1979).
9. G. Hodes, J. Manassen, and D. Cahan, *Nature*, **261**, 403 (1976).
10. M. P. R. Panicker, M. Knaster, and F. A. Kroger, *This Journal*, **125**, 566 (1978).
11. A. S. Baranski and W. R. Fawcett, *ibid.*, **127**, 766 (1980).
12. W. R. Fawcett and A. S. Baranski, U.S. Pat. 4,192,721 (1980).
13. W. K. Chu, J. W. Mayer, and M. A. Nicolet, "Back-scattering Spectrometry," Academic Press, New York (1978).
14. B. Ray, "II-VI Compounds," Chap. 1, 5, and 6, Pergamon Press, Oxford (1969).

An Admittance Study of the Copper Electrode

S. H. Glarum* and J. H. Marshall

Bell Laboratories, Murray Hill, New Jersey 07974

ABSTRACT

The admittance of a rotating-disk copper electrode in $\text{CuSO}_4/\text{H}_2\text{SO}_4$ has been measured as a function of frequency, potential, and concentration. A theoretical analysis of the Mattson-Bockris model incorporating finite exchange currents for the redox and crystallization reactions and diffusion of both cuprous and cupric ions leads to a simple equivalent circuit representation. Although this basic electrode model provides an adequate explanation for results at the equilibrium potential, substantial deviations occur at anodic potentials due to disproportionation. 10^{-5}M chloride concentrations lead to formation of a surface monolayer which alters relaxation at both anodic and cathodic potentials. No evidence was found for the conventional adatom relaxation process.

The deposition and dissolution of copper in an electrochemical environment is a complex and challenging problem for electrochemistry. Our present understanding of copper electrode kinetics has been recently reviewed by Bertocci and Turner (1, 2), and bears little resemblance to the complexities of practical copper plating. What seems clearly established is the importance of cuprous ions as intermediates in the electrochemical reactions



and



which we shall refer to as the redox and crystallization reactions. As was first demonstrated by Mattson and Bockris (3), and confirmed by others (4, 5), the asymmetry in current-voltage plots is explained by the above reactions with the redox step being rate determining. Given a Butler-Volmer relationship between current and overpotential, equating the steady-state currents of both reactions, and assuming the exchange current, I_{10} of [1] is much less than that of [2], one obtains the Mattson-Bockris results

$$I = 2I_{10} [\exp(2 - \alpha_1) e\eta/kT - \exp(-\alpha_2 e\eta/kT)] \quad [3]$$

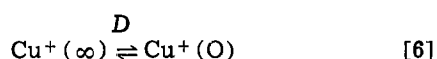
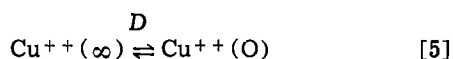
* Electrochemical Society Active Member.
Key words: circuits, relaxation, potential.

$$[\text{Cu}^+] = [\text{Cu}^+]_{\text{eq}} \exp(e\eta/kT) \quad [4]$$

One puzzling aspect of this model, as noted by Bertocci and Turner (1), is that current-voltage response depends only upon the parameters of a redox reaction, making it difficult to rationalize the range of values reported for these parameters and their sensitivity to surface preparation.

Many studies have attempted to probe more deeply into electrode kinetics using either pulse (3, 4, 6, 7) or alternating current modulations (8-14). The former experiments have generally involved large potential excursions ($>10 \text{ mV}$), and the interpretation of non-linear, time-dependent phenomena requires the assumption of a specific model uncomplicated by instrumental or chemical side effects. A-C measurements, although more time consuming, are more readily analyzed by reduction to an equivalent circuit description without recourse to a specific model. Complex-plane analysis provides a powerful tool for unraveling multi-element circuits, and often the shape alone of a complex-plane plot can be a powerful mechanistic discriminator. One might note that, based largely upon the interpretation of pulse experiments, adatom diffusion had been credited with playing an important role in copper electrocrystallization near equilibrium (3, 6, 8, 10). Subsequent a-c work revealed that this dispersion could also be explained by diffusion of cuprous ions from the electrode (11-14).

Clearly any analysis of copper electrode kinetics must consider diffusion of both cupric and cuprous ions



Although these steps constitute a straightforward addition to reactions [1] and [2] if a Nernst diffusion model is adopted, a full treatment has not been previously given. One aspect of this work is the derivation of kinetic results for the steady state and the a-c admittance behavior for the coupled reactions [1], [2], [5], and [6]. This will be referred to as the basic electrode model (BEM).

The majority of a-c measurements on copper electrodes have been confined to equilibrium studies, although Burrows, Harrison, and Thompson have recently published, without interpretation, complex-plane plots at several anodic and cathodic potentials (14). A second objective of our study is the determination of the a-c admittance for copper electrodes over a range of frequencies and potentials. Two basic experiments are involved, frequency-sweep measurements of admittance at fixed potentials, $Y_{\eta}^*(\omega)$, and potential-sweep measurements of admittance at fixed frequencies, $Y_{\omega}^*(\eta)$. The former experiments are more useful for characterizing the response function, while the latter better reveal parameter changes with potential. The need for both experiments is predicated by the difficulty in maintaining a reproducible electrode surface over long periods of time. Using newly developed experimental techniques in conjunction with computer-controlled data acquisition and processing, essentially continuous measurements of $Y_{\eta}^*(\omega)$ and $Y_{\omega}^*(\eta)$ can be made, and complex-plane analyses can be expeditiously carried out with this large data base.

Finally, we are especially interested in detecting and understanding deviations from the simplistic BEM, for these "discrepancies" may reveal the complexities of copper electrode kinetics. As we shall find, careful data analysis shows a variety of differences from BEM predictions. Although definitive interpretations seem premature, accurate and detailed admittance studies can tell us considerably more about electrode processes than has been observed in the past.

Experimental

Cupric sulfate was recrystallized from the anhydrous, analytical-grade compound. Solutions were prepared with Baker Ultratex sulfuric acid and water from a Millipore Super-Q system. A copper wire inserted through rigid glass capillary tubing served as a reference electrode. It was positioned so that the exposed tip lay in the plane of the electrode about 1.5 cm from its center. All experimental potentials reported are with respect to this reference.¹ The cell was thermostated at 25°C and degassed with argon.

The potentiostat and admittance measuring apparatus have been previously described (15). Low frequency sweep measurements were expedited by the addition of four sample-and-hold circuits to the phase-detector outputs. The in-phase voltage was sampled at 90° and 270°, and the two signals added. The out-of-phase voltage was similarly sampled at 0° and 180°. Provided the response or filtering functions for both channels are identical, it may be shown that the complex ratio of unknown and reference input voltages to the phase detector is given by the ratio of the sample-and-hold outputs. Tests on R-C admittances

confirmed the reliability of this procedure. In this fashion the output signal could be updated four times per cycle, and 1 Hz measurements were possible with a time constant of 10 msec.

Platinum disk electrodes with diameters of 1/4 and 1/16 in. were potted in thin epoxy sheaths and surrounded by Teflon mantles. The surface was mechanically polished with alumina powders. The electrodes were plated with copper from the solution under investigation, either in a potential cycling mode or by stepping to a set cathodic potential. Deposit thicknesses were estimated from coulometric measurements. Following a measurement, the deposit was stripped and then reformed. Even 2000Å deposits showed responses dependent upon platinum pretreatment. The d-c equilibrium admittance of copper plated on freshly polished platinum decreased threefold over several hours of continuous plating and stripping. If the electrode was first cycled for several minutes to anodic potentials so that a surface oxide was formed and reduced, this drift was eliminated and the lower admittance values could be maintained for several hours.

After cycling solutions of low chloride concentration for 30 min, a narrow, copper-colored band was often observed adhering to the epoxy insulation near the periphery of the electrode. This band could be seen to grow when the electrode was cathodic, but it was not completely removed at anodic potentials, presumably because of a break in electrical contact. We could not recreate this behavior with a copper electrode, and surmise that chloride removes platinum from the electrode during anodic stripping, and this platinum in some manner sensitizes the epoxy surface to the lateral growth of a copper layer. The working time of an electrode in 10⁻⁴M chloride was about 20 min before results became erratic.

Prior to each type of measurement it was necessary to find conditions which optimized reproducibility. For studies of $Y_{\text{eq}}^*(\omega)$ approximately 600Å were deposited at -150 mV. Eight triangular frequency-sweep measurements were then summed by signal averaging, requiring about 160 sec. A storage oscilloscope monitor ensured that there was no drift of the input data during the measuring period. The deposit was then stripped, reformed, and the reference voltage similarly determined. The nonequilibrium functions, $Y_{\eta}^*(\omega)$, had to be measured in less time because of rapid surface changes, and they were restricted to frequencies above 200 Hz. For these studies the electrode was cycled between -300 and +200 mV. The cycle was halted at a preset potential, a single sweep-frequency measurement requiring 1 sec was taken, and cycling then resumed until eight such sweeps had been accumulated. For $Y_{\omega}^*(\eta)$ measurements the electrode was continuously cycled between -250 and +170 mV at about 18 mV/sec, data storage being triggered at the start of each anodic trace.

For all experiments it was most important to determine as accurately as possible the high frequency cell resistance. Extrapolations of high frequency data on copper surfaces proved unreliable. Best results were given by a sweep-frequency measurement of an oxidized platinum surface, for its double-layer capacitance is comparatively large and shows only a small frequency dispersion (15).

Current-voltage curves were also taken to check reproducibility and to permit subsequent potential corrections for electrolyte IR drop. Tafel plot data were obtained from current-voltage cycling curves with internal IR compensation by the potentiostat.

Results

The majority of experiments were made with 0.25M CuSO₄/1.75M H₂SO₄ solutions. This composition is presently used in commercial plating baths designed for high throwing power, and its high conductivity is especially suitable for high frequency studies. Although

¹If the bulk Cu⁺ concentration is not in equilibrium with copper metal, the reference adopts a mixed potential. This difference may be estimated from the BEM equations to be $(RTD_{\text{Cu}^+}\Delta[\text{Cu}^+]/4I_0\delta)$ where δ is the effective Nernst layer thickness. For the rotating disk electrode $\delta \approx 10^{-3}$ cm and the error is less than 1 mV. At the reference δ is not well defined, but it is certainly larger so that the offset is negligible for our purposes.

we do not intend to explore here additive effects in copper plating, the ubiquitous role of chloride in copper baths prompted several experiments which revealed marked effects for concentrations in the 10^{-6} M to 10^{-3} M range. At these low concentrations precipitation of CuCl or formation of soluble cuprous chloride complexes is unimportant. Because the changes induced by trace amounts of chloride are helpful in understanding the properties of chloride-free solutions, we include these results in this report.

The procedures for a complex-plane analysis are formally straightforward, but we think it beneficial to illustrate one such case in detail, in order to expose the difficulties inherent in the interpretation of any linear experiment, be it a.c. or transient in nature. The data we shall discuss were obtained with an 0.25M $\text{CuSO}_4/1.75\text{M H}_2\text{SO}_4$ solution at the equilibrium potential, 640Å of copper were plated at -150 mV on a 1/4 in. platinum electrode rotating 200 rad/sec.

The initial stage in our analysis is a correction for series lead resistance (0.05Ω) and inductance ($0.28 \mu\text{H}$). The latter is not a negligible value for high frequencies in a 1Ω circuit. Next, correction is made for nonuniform current distributions as discussed in a previous paper (15), and complex admittance plots examined. Figure 1a shows such plots for an oxidized platinum surface and a plated copper surface. Because the platinum data more closely approximate a semicircle or series R-C circuit, Y_∞ was obtained with $\pm 0.5\%$ accuracy from a numerical analysis of $1/Y^*$. Actually

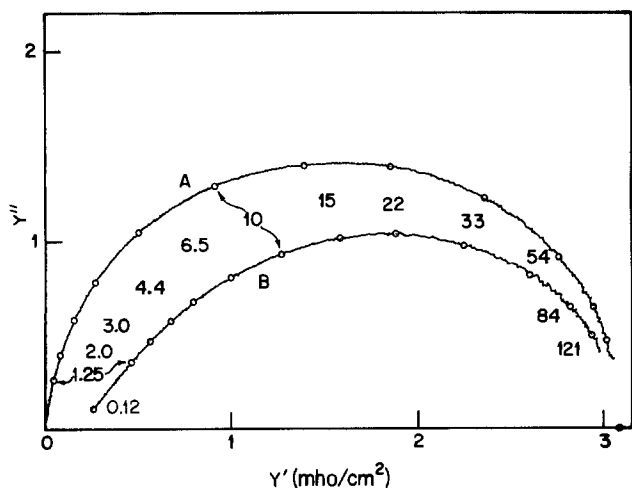


Fig. 1a. Complex admittance plots after lead impedance and current distribution corrections for (A) Pt at $+1.0\text{V}$ and (B) Cu at 0.0V . Frequencies are given in kHz.

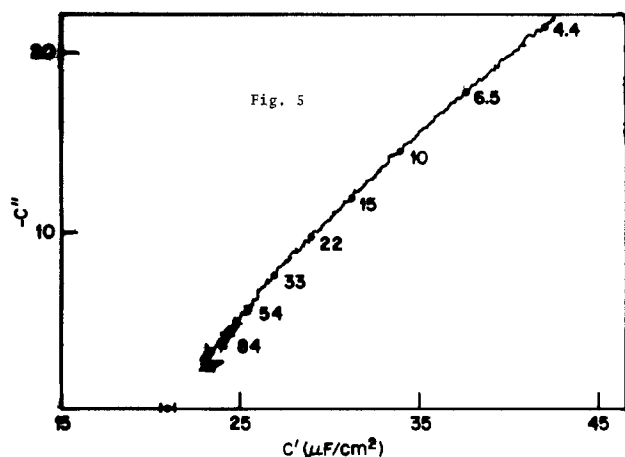


Fig. 1b. Complex capacitance plot of copper data in Fig. 1a after elimination of Y_∞ . The uncertainty in C_∞ in a linear extrapolation appears on the real axis.

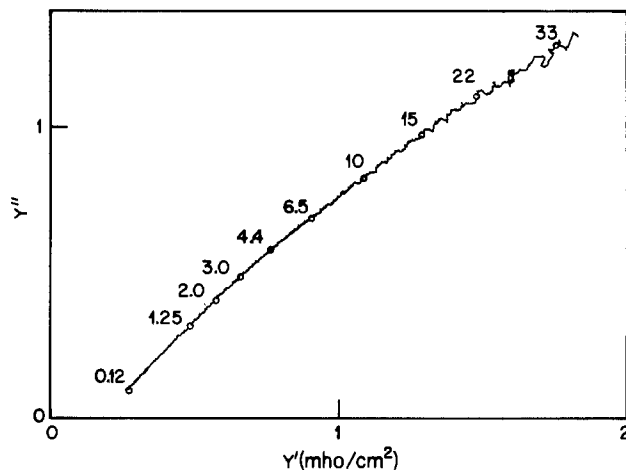


Fig. 1c. Complex surface admittance after elimination of Y_∞ and C_∞ .

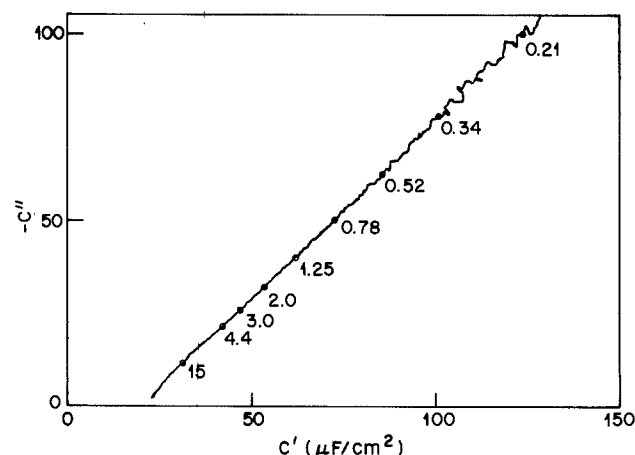


Fig. 1d. Complex surface capacitance after elimination of Y_∞ and G_0 .

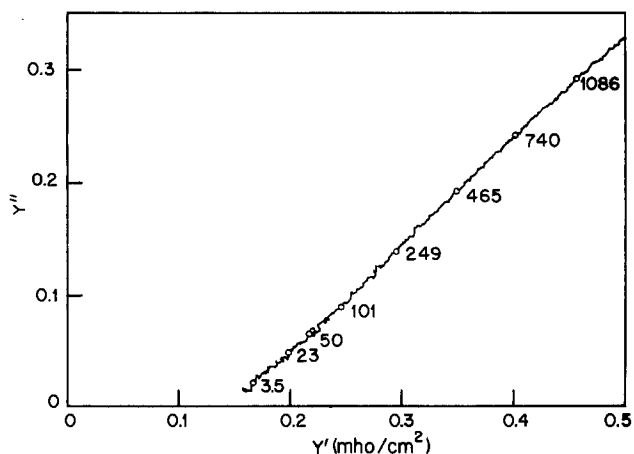


Fig. 1e. Complex surface admittance at low frequencies (c.f. Fig. 1c). Frequencies are given in Hz.

this parameter is needed for the preceding current distribution corrections, but the iteration is rapidly convergent.

Subsequent analysis was made in terms of the circuit depicted in Fig. 2. Formally the surface admittance, Y_e^* , may be resolved into three components

$$G_0 = \lim_{\omega \rightarrow 0} Y_e^*$$

$$C_\infty = \lim_{\omega \rightarrow \infty} (Y_e^*/i\omega)$$

[7]

and Y_x^* includes whatever remains. Given Y_∞ , a com-

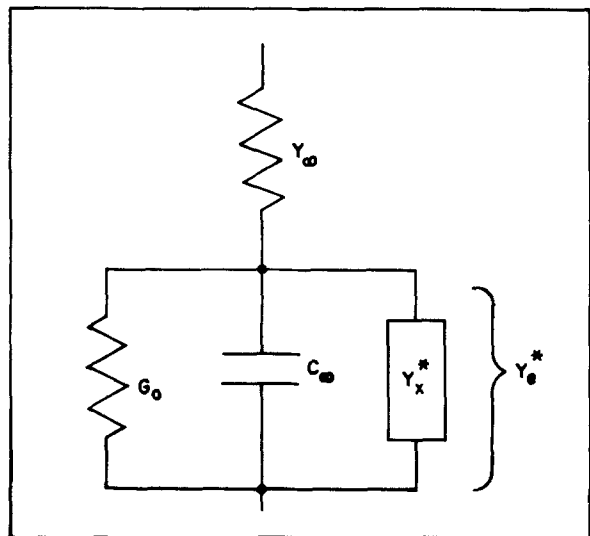


Fig. 2. Equivalent circuit defining deconvolution parameters

plex-plane plot is next made of $Y_e^*/i\omega$, and C_0 evaluated by extrapolation to infinite frequency (Fig. 1b). Assuming the plot retains its general form above our experimental frequency range, $C_0 = 20.9 \pm 0.4 \mu\text{F}/\text{cm}^2$. The greater scatter in high frequency points reflects the fact that these data are largely determined by Y_x .

We then examine plots of $Y_e^* - i\omega C_0$ (Fig. 1c), which will show the presence of time-dependent surface processes. Data are only plotted for frequencies below 35 kHz, for, although the curve continues its apparent course at higher frequencies, the measurement is dominated by Y_x and C_0 , and scatter is much greater. Subtraction of C_0 is necessary to avoid a high frequency divergence in these plots. It is often desirable to also plot $C_e^* = (Y_e^* - G_0)/i\omega$ (Fig. 1d), and G_0 , obtained from a low frequency extrapolation of admittance plots, avoids an analogous low frequency divergence. Although the plots in Fig. 1c and 1d contain similar information, they are complementary in that admittance plots emphasize high frequency behavior while capacitance plots exaggerate low frequency data.

At low frequencies both Y_e^* and C_e^* plots appear linear, indicating an admittance proportional to a power of the frequency, i.e., $(i\omega)^\alpha$, and from the slopes $\alpha = 0.50_5$. A separate 1-1400 Hz sweep measurement is shown in Fig. 1e. A new surface had been formed for this run, and, although comparison with the preceding data at overlapping frequencies shows 5% differences, linear behavior persists down to 1 Hz. From the slope, $\alpha = 0.49_0$. Evidently the low frequency response of a copper electrode is accurately given by an empirical expression

$$Y_e^* = G_0 + \sqrt{i\omega W} \quad [8]$$

Above 5 kHz (Fig. 1c), admittance plots show a slight negative curvature. Mention should also be made that, although not apparent in the data shown, Y_e^* plots sometimes showed a tailing off at low frequencies so that no unambiguous extrapolation to $\omega = 0$ was feasible. Values for G_0 , C , and W are summarized in Table I.

Solutions of CuSO_4 with concentrations ranging 0.001-1.0M in 1M H_2SO_4 were then examined. Deposi-

Table I. Equilibrium relaxation parameters for 600Å deposits from 0.25M $\text{CuSO}_4/1.75\text{M H}_2\text{SO}_4$ solutions

| | 0M Cl ⁻ | 10 ⁻⁴ M Cl ⁻ | 10 ⁻⁵ M Cl ⁻ |
|--|----------------------|------------------------------------|------------------------------------|
| C_0 ($\mu\text{F}/\text{cm}^2$) | 20.9 | 22.6 | 23.7 |
| G_0 (mho/cm ²) | 0.17 | 0.10 | 0.15 |
| W (mho-sec ^{1/2} /cm ²) | 5.0×10^{-3} | 4.7×10^{-3} | 6.8×10^{-3} |

tions conditions were 600Å at -150 mV. Complex-plane plots were similar to those already discussed, although at the highest and lowest concentrations the low frequency asymptotic behavior was not always as close to 45°. Results for G_0 and W are plotted in Fig. 3. The error bars show the range of values calculated from data between 1 kHz and 50 Hz assuming Eq. [8] applies. The capacitances C_0 , ranged 21-25 $\mu\text{F}/\text{cm}^2$, with no evident concentration dependence. Although deposition conditions were chosen to minimize the effects of thickness and deposition potential upon response, the scatter in Fig. 3 indicates the importance of other uncontrolled parameters.

Measurements of $Y_{\eta}^*(\omega)$ were made with a 1/16 in. platinum disk electrode in 0.25M $\text{CuSO}_4/1.75\text{M H}_2\text{SO}_4$. The electrode was cycled between -300 and +200 mV, with data taken at 25 mV intervals between -275 and +100 mV. Subsequently, potentials were recalculated to take into account electrolyte IR drop. The maximum deposit thickness was of order 1000Å at $\eta = 0$. High frequency capacitances varied between 26 and 30 $\mu\text{F}/\text{cm}^2$, with higher values found at higher overpotentials. Figure 4 shows several admittance plots obtained after elimination of Y_x and C_0 . Low frequency intercepts, estimated by linear extrapolation, are comparable with the slope of the current-voltage curve at the corresponding potential.

The dispersion increases with potential, and, above +50 mV, plots approach the real axis perpendicularly

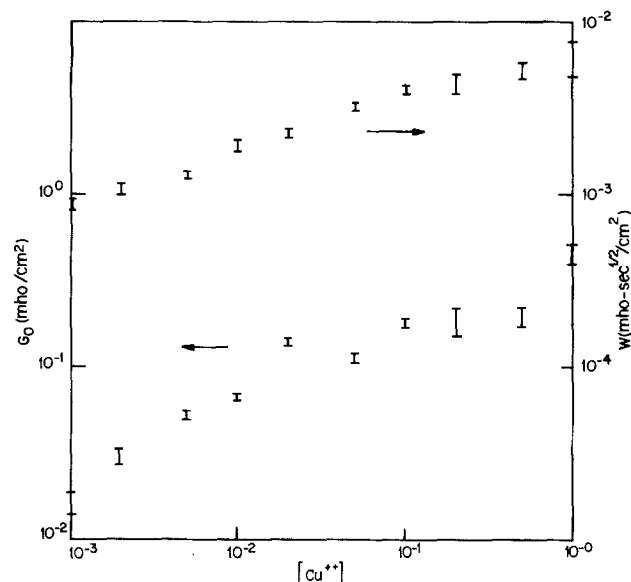


Fig. 3. Concentration dependence of G_0 and W for CuSO_4 in 1M H_2SO_4 .

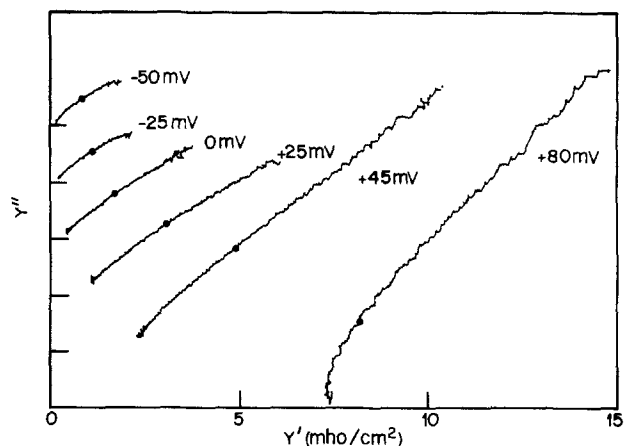


Fig. 4. Complex surface admittance plots at various potentials. 10 kHz points are shown.

at low frequencies. Below -50 mV only a small dispersion remains, and admittance plots also near the real axis at an angle significantly steeper than 45° . C_e^* plots shown in Fig. 5 offer a capacitive interpretation for the residual relaxation of magnitude 50 - 100 $\mu\text{F}/\text{cm}^2$, with the amplitude and relaxation time decreasing with potential. The dispersion is not that of a simple relaxation process, but appears to be better described by a circular-arc function.

When 10^{-4}M chloride was added, $\sqrt{i\omega}$ low frequency response was found at all potentials. The curvature in anodic plots (Fig. 4) was suppressed, and the cathodic capacitive dispersion was reduced to less than 5 $\mu\text{F}/\text{cm}^2$ between -100 and -200 mV. The high frequency capacitance exhibited a greater variation with potential, changing from 20 $\mu\text{F}/\text{cm}^2$ at -250 mV to 27 $\mu\text{F}/\text{cm}^2$ at equilibrium, and rising to over 60 $\mu\text{F}/\text{cm}^2$ above $+50$ mV. These measurements were complicated by an increase in electrode area due to the spreading of copper from the electrode as mentioned previously. The resulting uncertainties in Y_e were reflected in deviant high frequency behavior.

Studies of $Y_e^*(\eta)$ were made with the $1/4$ in. electrode and 0.25M $\text{CuSO}_4/1.75\text{M}$ H_2SO_4 solutions. Because dispersion analysis had shown a tendency towards a $\sqrt{i\omega}$ variation of Y_e^* (Eq. [8]), we show plots of $Y_e''(\eta)/\sqrt{\pi f}$ in Fig. 6. These results were calculated from experimental data by subtraction of Y_e and a fixed value for C_e . One notes a prominent peak at $+50$ mV and a lesser peak at -100 mV. Near 100 Hz Y_e'' dropped reproducibly to negative values at high anodic overpotentials. There is also a definite dispersion at potentials more than ± 25 mV from equilibrium, indicating the limitations of Eq. [8].

Upon addition of 10^{-4}M chloride these plots were dramatically altered (Fig. 7). The maxima disappeared and for frequencies 0.02 - 30 kHz no deviations from Eq. [8] are evident between $+75$ and -100 mV. At more cathodic potentials a new low frequency dispersion appears. Figure 8 compares low frequency plots of $Y_e'(\eta)$ for both solutions. Chloride addition has shifted the minimum 25 mV anodically and raised substantially the curve in the cathodic region. As expected, these plots are comparable to those found by differentiating current-voltage curves.

Discussion

The Mattson-Bockris results (Eq. [3] and [4]) follow from several specific assumptions and it is desirable to test their validity by a more thorough analysis of the BEM. Bertocci has considered this question in some detail (2), but explicit calculations of current-voltage or Tafel plots have not been offered. The Butler-Volmer equations corresponding to reactions [1] and [2] are

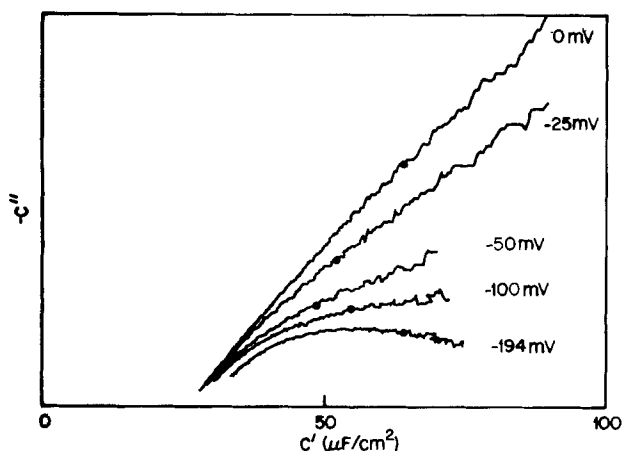


Fig. 5. Complex surface capacitance plots at cathodic potentials. 3.3 kHz points are shown.

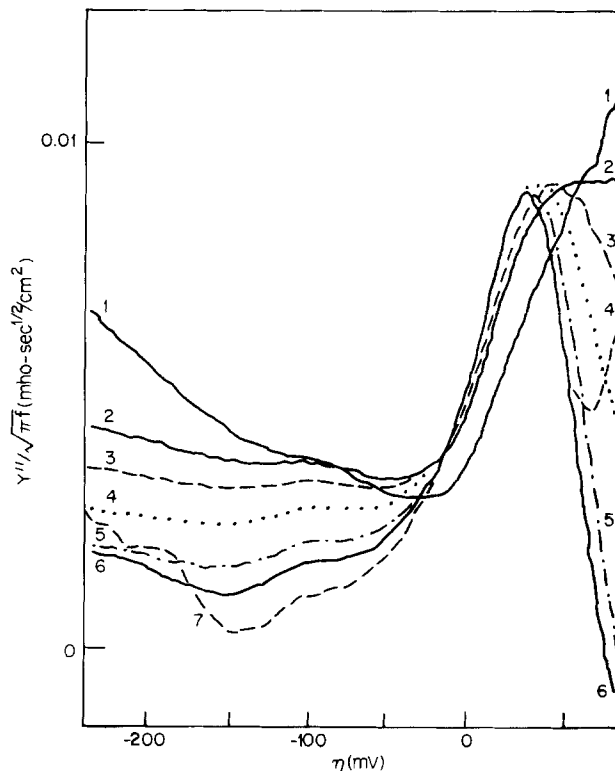


Fig. 6. Variation of $Y_e''(\eta)$ for chloride-free solutions. For curves 1-7 the frequencies are 20 , 2.0 , 1.0 , 0.5 , 0.2 , 0.1 , and 0.05 kHz.

$$I_1 = I_{10} [x_1 \exp((1 - \alpha_1)e\eta/kT) - x_2 \exp(-\alpha_1 e\eta/kT)]$$

$$I_2 = I_{20} [\exp((1 - \alpha_2)e\eta/kT) - x_1 \exp(-\alpha_2 e\eta/kT)] \quad [9]$$

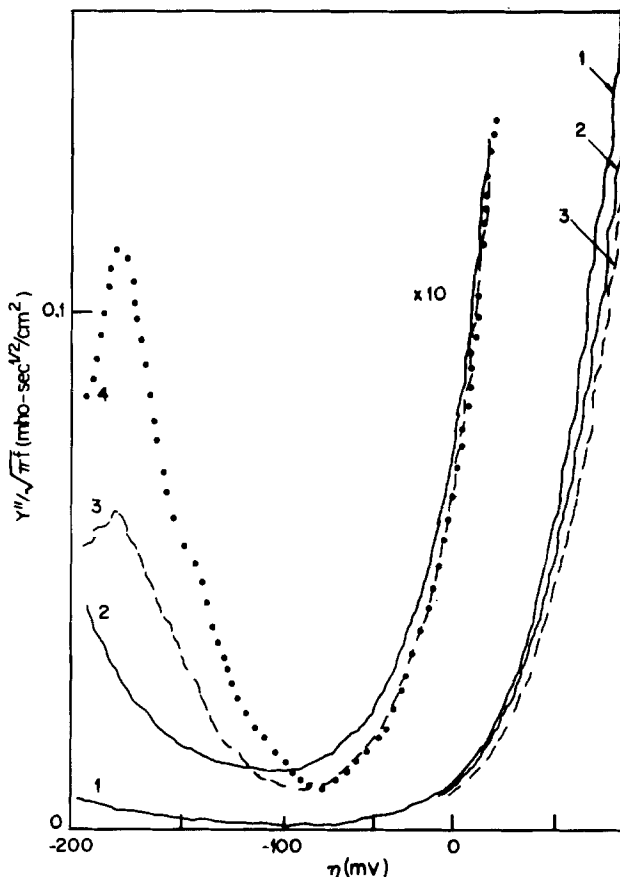


Fig. 7. Variation of $Y_e''(\eta)$ for 10^{-4}M chloride solutions. For curves 1-4 the frequencies are 20 , 1.0 , 0.1 , and 0.05 kHz.

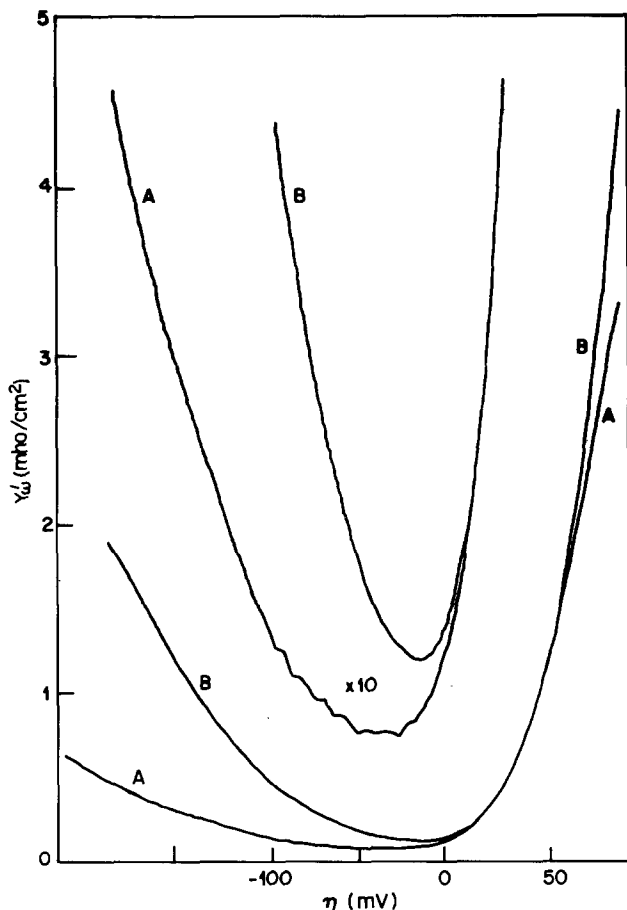


Fig. 8. Variation of $Y_{\omega}'(\eta)$ at 15 Hz for chloride-free (A) and 10^{-4}M chloride (B) solutions.

where

$$x_1 = [\text{Cu}^+(\text{O})]/[\text{Cu}^+]_{\text{eq}}$$

$$x_2 = [\text{Cu}^{++}(\text{O})]/[\text{Cu}^{++}]_{\text{eq}} \quad [10]$$

In the steady state, reactions [5] and [6] yield

$$0 = (FD_2/\delta_2) [\text{Cu}^{++}]_{\text{eq}}(1 - x_2) + I_1$$

$$0 = (FD_1/\delta_1) [\text{Cu}^+]_{\text{eq}}(x_0 - x_1) - I_1 + I_2$$

$$x_0 = [\text{Cu}^+]_{\text{bulk}}/[\text{Cu}^+]_{\text{eq}} \quad [11]$$

In these equations $[\text{Cu}^+(\text{O})]$ and $[\text{Cu}^{++}(\text{O})]$ are concentrations at the electrode surface while $[\text{Cu}^+]_{\text{bulk}}$ and $[\text{Cu}^{++}]_{\text{eq}}$ are actual concentrations in the bulk of the electrolyte. $[\text{Cu}^+]_{\text{eq}}$ is the concentration which would exist in the bulk if the solution were in thermodynamic equilibrium with copper metal.

The four relevant linear equations may now be solved for the four unknowns I_1 , I_2 , x_1 , and x_2 . As we are primarily interested in ascertaining what deviations from simple Tafel behavior occur when both exchange currents are finite and concentration polarization is present, it is expedient to neglect the difference in diffusion coefficients, assume $\alpha_1 = \alpha_2 = 0.5$, and introduce the four reduced parameters

$$\gamma_1 = FD [\text{Cu}^{++}]_{\text{eq}}/\delta I_{10} = I_1^{\text{lim}}/I_{10}$$

$$\gamma_2 = [\text{Cu}^{++}]_{\text{eq}}/[\text{Cu}^+]_{\text{eq}} = ([\text{Cu}^{++}]_{\text{eq}}/K_{\text{eq}})^{1/2}$$

$$\gamma_3 = I_{20}/I_{10}$$

$$\gamma_4 = [\text{Cu}^+]_{\text{bulk}}/[\text{Cu}^+]_{\text{eq}} \quad [12]$$

The calculations can be readily handled by a pocket calculator and current-voltage behavior examined for various choices of the γ parameters. K_{eq} fixes γ_2 , and, according to Tindall and Bruckenstein, equals $5.6 \times 10^{-7}\text{M}$ (16). Nonequilibrium cuprous bulk concentra-

tions, $\gamma_4 \neq 1$, have their principle effect when $\eta \approx 0$, slightly shifting the open-circuit potential (4). Changing γ_1 , corresponding to varying the rotational speed of a disk electrode, shows up most prominently in the limiting current regime at large cathodic overpotentials. We are particularly interested in the kinetics of the second electrochemical step which are reflected in γ_3 . Typical plots in Fig. 9 show that the major changes occur at anodic potentials. When the anodic current exceeds I_{20} by an order of magnitude, Tafel slopes are reduced from 40 to 120 mV/decade. As a practical matter, if data taken below +100 mV show a 40-50 mV/decade slope, a lower limit to γ_3 of about 30 can be set.

This more realistic calculation also indicates that good agreement is expected for exchange currents found from Tafel intercepts and the equation

$$I_0 = (kT/2e) (\partial I/\partial \eta)_{\eta=0} \quad [13]$$

For the parameters used for Fig. 9, the slope of the current-voltage curve near $\eta = 0$ is independent of γ_4 , although the open-circuit potential shifts to -1 mV when $\gamma_4 = 0$. The separate currents I_1 and I_2 agree to within 10%. Because of the slight curvature of the cathodic plot in Fig. 9 for $\gamma_3 = 10^4$, the apparent slope is 135 mV/decade, leading to $\alpha_1 = 0.44$, although 0.5 was assumed in the calculations. Generally we observe no serious pitfalls in using Eq. [3] instead of a more precise calculation unless unrealistically high values are chosen for γ_1 . Major differences between experiment and the BEM must be due to inadequacies of the model, not to the simplifying assumptions made in the derivation of Eq. [3].

Our Tafel results for 0.25M $\text{CuSO}_4/1.75\text{M}$ H_2SO_4 solutions show a 40 mV/decade slope on the anodic

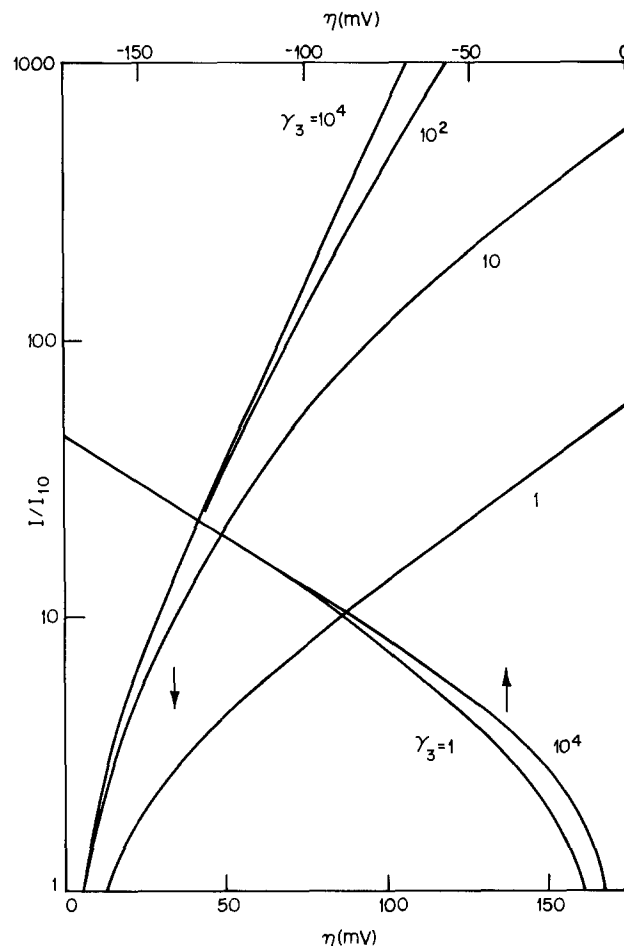


Fig. 9. Theoretical BEM Tafel plots for $\gamma_1 = 100$, $\gamma_2 = 663$, and $\gamma_4 = 1$. Values for γ_3 are shown.

side at 30-40 mV, but the curve bends gradually with increasing potential, showing no truly linear region (Fig. 10). A formal comparison with calculated plots for $\alpha = 0.5$ can give a good fit if $\gamma_3 \approx 25$ and $I_0 = 3.5$ mA/cm². For the cathodic plot a well-defined linear region is fit by $\alpha = 0.33$ and $I_0 = 5.0$ mA/cm², while, from the slope at $\eta = 0$, $I_0 = 2.2$ mA/cm². The magnitude of these currents and their variation with the manner of calculation are similar to those reported by Mattson and Bockris for electrodes prepared by electrodeposition (3). These variations are not explained by model calculations which consider diffusion and finite rates for both electrochemical steps.

Tafel plots were significantly altered upon addition of 10^{-4} M chloride (Fig. 11). The anodic curve remains linear to beyond +100 mV, with a 48 mV/decade slope and an intercept giving $I_0 = 1.5$ mA/cm². The cathodic plots are no longer so nicely linear, but show a slope at -100 mV giving $\alpha = 0.56$ and $I_0 = 2.2$ mA/cm².

These Tafel results are consistent with earlier work (3, 4), and verify the equivalence of our deposits with those of prior studies. We believe it is important to recognize that traces of chloride can seriously influence such measurements. Bearing in mind that we observed major changes with a 10^{-4} M concentration on surfaces freshly formed during continuous potential cycling, much lower levels can affect measurements on "aged" surfaces. The scavenging of chloride ions by a copper surface tends to shift Tafel slopes towards values yielding $\alpha = 0.50$.

Several authors have derived expressions for the a-c response of an electrode reaction equivalent to that represented by Eq. [1], [2], [5], and [6], assuming an infinite diffusion layer (17, 18). In the advent of a finite layer of thickness δ , a Nernst calculation for the gradient of the concentration modulation yields

$$(\partial A^*/\partial x)_{x=0} = -\sqrt{i\omega/D} \coth \sqrt{i\omega\delta^2/D} A^*(O) \quad [14]$$

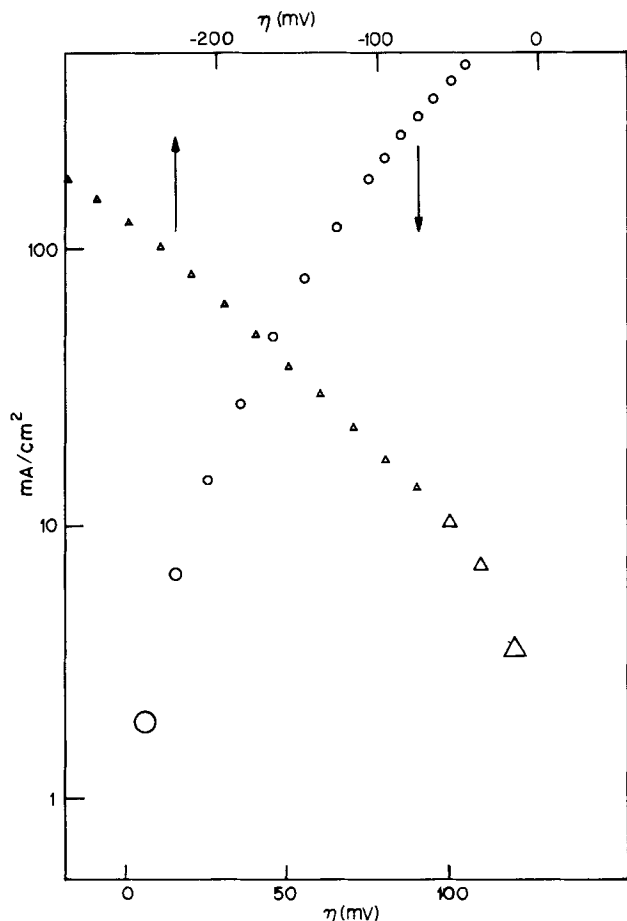


Fig. 10. Experimental Tafel plots for chloride-free solutions

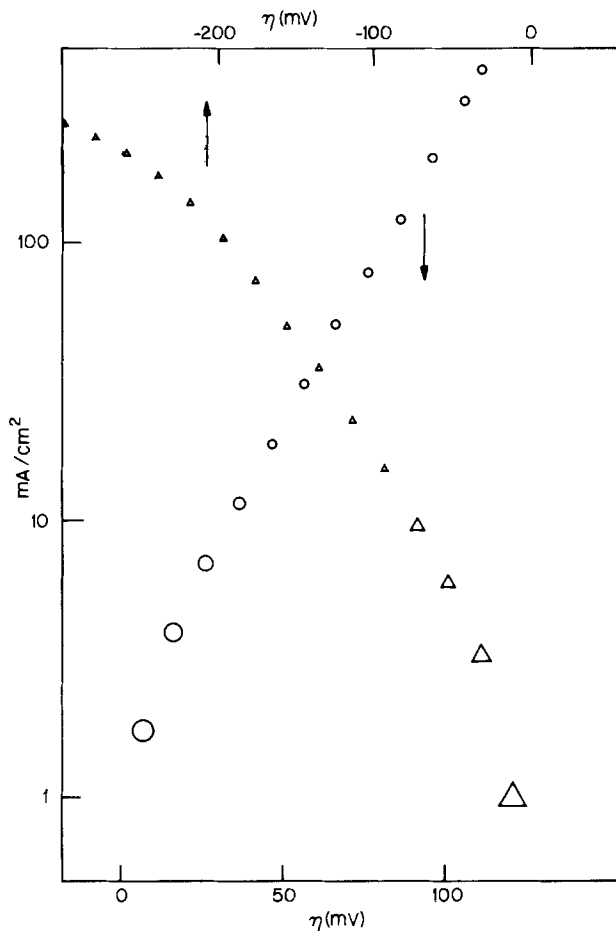


Fig. 11. Experimental Tafel plots for 10^{-4} M chloride solutions

For a disk rotating 200 rad/sec, $\delta^2/D \approx 0.2$ sec, and the high frequency approximation suffices above 1 Hz.

When the results of Armstrong and Firman are applied to the copper problem (18), one obtains

$$\bar{Y}^* = \frac{\frac{\partial(I_1 + I_2)}{\partial \eta} - \frac{1}{\sqrt{i\omega}} \left(2 \frac{\partial I_1}{\partial \eta} \frac{\partial I_2}{\partial \lambda_1} - 2 \frac{\partial I_1}{\partial \lambda_1} \frac{\partial I_2}{\partial \eta} + \frac{\partial I_1}{\partial \lambda_2} \frac{\partial I_2}{\partial \eta} \right)}{1 - \frac{1}{\sqrt{i\omega}} \left(\frac{\partial I_1}{\partial \lambda_2} - \frac{\partial I_1}{\partial \lambda_1} + \frac{\partial I_2}{\partial \lambda_1} \right) + \frac{1}{i\omega} \frac{\partial I_1}{\partial \lambda_2} \frac{\partial I_2}{\partial \lambda_1}} \quad [15]$$

where

$$\lambda_1 = F\sqrt{D_1} [\text{Cu}^+(\text{O})]$$

$$\lambda_2 = F\sqrt{D_2} [\text{Cu}^{++}(\text{O})] \quad [16]$$

This rather formidable expression has a simple complex-plane representation, for it can be factored into

$$Y^* = Y_1/[1 + (i\omega\tau_1)^{-1/2}] + (Y_2 - Y_1)/[1 + (i\omega\tau_2)^{-1/2}] \quad [17]$$

A complex-plane plot of Eq. [17] will therefore consist of the superposition of two 45° circular arcs (32). How well resolved they will appear depends upon the ratio τ_1/τ_2 . The corresponding equivalent circuit is the parallel combination of two partial circuits, each composed of a resistance in series with a Warburg admittance.

For copper kinetics $I_{20} \gg I_{10}$ and $[\text{Cu}^{++}]_{\text{eq}} \gg [\text{Cu}^+]_{\text{eq}}$, so that

$$\partial I_2/\partial \lambda_1 \gg \partial I_1/\partial \lambda_2 \quad [18]$$

Under this condition the dispersions are well resolved and

$$\begin{aligned}
 1/\sqrt{\tau_1} &= -\partial I_1/\partial \lambda_2 \\
 1/\sqrt{\tau_2} &= \partial(I_1 - I_2)/\partial \lambda_1 \\
 Y_1 &= 2 \left(\frac{\partial I_1}{\partial \lambda_1} \frac{\partial I_2}{\partial \eta} - \frac{\partial I_1}{\partial \eta} \frac{\partial I_2}{\partial \lambda_1} \right) / \left(\frac{\partial I_1}{\partial \lambda_1} - \frac{\partial I_2}{\partial \lambda_1} \right) \quad [19]
 \end{aligned}$$

$$Y_2 = \partial(I_1 + I_2)/\partial \eta$$

Assuming the functional relations of Eq. [9], with $I_{20} \gg I_{10}$ and $x_1 = \exp(e\eta/kT)$

$$\begin{aligned}
 1/\sqrt{\tau_1} &= (I_{10}/F\sqrt{D_2}[\text{Cu}^{++}]_{\text{eq}}) e^{-\alpha_1 e\eta/kT} \\
 1/\sqrt{\tau_2} &= (I_{20}/F\sqrt{D_1}[\text{Cu}^+]_{\text{eq}}) e^{-\alpha_2 e\eta/kT} \\
 Y_2 &= (e I_{20}/kT) e^{(1-\alpha_2)e\eta/kT} \\
 Y_1 &= (2e I_{10}/kT) [(2 - \alpha_1) e^{(2-\alpha_1)e\eta/kT} + \alpha_1 e^{-\alpha_1 e\eta/kT}] \quad [20]
 \end{aligned}$$

It should be evident that Y_1 is the derivative of Eq. [3].

Heuristic estimates for a 1M solution at equilibrium with $I_{10} = 2 \text{ mA/cm}^2$ and $I_{20}/I_{10} > 30$ yield $\tau_1 = 2 \times 10^4 \text{ sec}$ and $\tau_2 < 10^{-5} \text{ sec}$. The low frequency dispersion will be quenched by a finite diffusion layer thickness. At sufficiently cathodic potentials, i.e., in the limiting current region, τ_1 will decrease sufficiently for this dispersion to appear. It should be possible to characterize the high frequency dispersion at $\eta = 0$ for the lowest estimate of I_{20} , but increasing I_{20} by an order of magnitude shortens τ_2 by a factor of 100, shifting the high frequency dispersion beyond the accessible experimental range. Best chances for detecting τ_2 would be in concentrated solutions at large anodic potentials. Thus, at +200 mV for $\tau_2 > 10^{-6} \text{ sec}$, $I_{20} < 10 \text{ A/cm}^2$. When $1/\tau_1 \ll \omega \ll 1/\tau_2$, Eq. [17] reduces to

$$Y^* = Y_1 + \sqrt{i\omega} \frac{eF}{kT} \sqrt{D_1}[\text{Cu}^+(\text{O})] \quad [21]$$

This expression is equivalent to Eq. [8] which was found to provide a good description of low frequency data.

Turning now to our experimental results, analyses of numerous runs gave high frequency capacitance values of 20-25 $\mu\text{F/cm}^2$ for deposits grown at a fixed overpotential. While slightly higher values appeared for surfaces formed during potential cycling, no major reproducible dependence of C_e upon deposition conditions, deposit thickness, potential, or chloride concentration was apparent. This limiting capacitance may be attributed to the double layer, and our values are comparable with recent data of Slaiman and Lorenz (8). Variations can be rationalized by minor surface roughness changes, although the narrow range observed indicates that roughness is probably determined by the platinum substrate.

Using Eq. [21] and the results of Tindall and Bruckenstein for D_1 and K_{eq} (16), the BEM predicts $W = 5.2 \times 10^{-3} \text{ mho-sec}^{1/2}/\text{cm}^2$ at equilibrium, in excellent agreement with our measurements (Table I). The values for Y_1 are also commensurate with Tafel results for I_0 , indicating the absence of major additional low frequency dispersions.

Equation [17] suggests that the curvature seen in Fig. 1c may be due to a finite Y_2 . A plot of $1/(Y_e^* - Y_1)$ should then give a 45° line with a high frequency intercept $1/Y_2$. In making this plot (Fig. 12), it is apparent that slight errors in C_e lead to large errors in Y_2 . Given the uncertainty in finding C_e by extrapolation (Fig. 1b), $Y_2 = 10\text{-}25 \text{ mho/cm}^2$, or $I_{20} = 0.25\text{-}0.65 \text{ A/cm}^2$. Corresponding values for τ_2 are $4\text{-}30 \times 10^{-8} \text{ sec}$ and show that even 100 kHz is too low a frequency to furnish a reliable estimate for I_{20} .

No obvious explanation for the effects of chloride ions were evident from these equilibrium studies. The double-layer capacitance showed no shift indicating large roughness changes. The BEM predicts that W

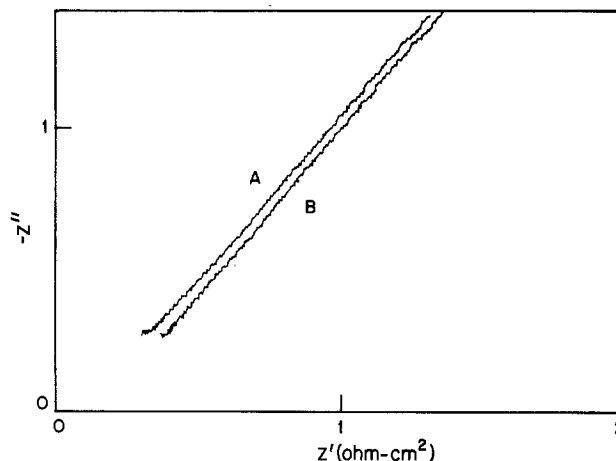


Fig. 12. Complex impedance plot for the estimation of Y_2 (see text). Values for C_e are (A) 20.4 F/cm^2 and (B) 21.4 F/cm^2 .

depends upon equilibrium rather than kinetic parameters, and changes in W were indeed small. The decrease in Y_1 for 10^{-4}M chloride and subsequent rise at 10^{-3}M were reproducible, and a BEM interpretation would suggest an influence upon the exchange current of the redox reaction. Complex capacitance plots were erratic at high frequencies in these solutions and estimates of Y_2 were not feasible. There was no indication in admittance plots, however, of a reduction in Y_2 beyond the uncertainties in its evaluation.

One might conclude from an equilibrium analysis that the BEM provides an excellent explanation for the electrode response function, with no need for the invocation of crystallization or other processes. Such a conclusion was reached by Burrows, Harrison, and Thompson (14). Unfortunately, the problem is not so clear-cut. The equilibrium cuprous ion concentration should vary as $[\text{Cu}^{++}]^{1/2}$, yet the variation of W is significantly less (Fig. 3). That data for an 0.25M CuSO_4 solution agree so well with the Tindall-Bruckenstein diffusion coefficient and equilibrium constant values appears somewhat fortuitous. Despite numerous attempts involving variously formed and aged copper surfaces, we have not been able to obtain a W value greater than 6×10^{-3} in a 1M solution, although, by comparison with 0.25M results, 1×10^{-2} is expected. The intercept Y_1 also varies more as the 0.4 power of concentration than the 0.75 power predicted by the Mattson-Bockris model for $\alpha = 0.50$. This discrepancy has been found in other concentration studies (4, 19). It has been attributed to surface differences for deposits formed under different conditions (4), but what these differences are remains unanswered. They are not apparent in the double-layer capacitance.

For 0.005-1.0M solutions complex admittance plots were linear between 50 and 1500 Hz, making angles of $45^\circ \pm 2^\circ$ with the real axis. Often, but not reproducibly, a deviation with a positive curvature was seen below 50 Hz. This additional dispersion was most evident with surfaces which had remained for some time near $\eta = 0$. It was further noted that current-voltage cycling curves between +5 and -20 mV concurrently developed a slight hysteresis loop with inflection points near 0 mV on anodic traces and -10 mV on cathodic traces. The loop was independent of sweep rate for 1-20 mV/sec rates. The details of the low frequency response changes could not be determined from measurements above 1 Hz, but rough estimates suggest an admittance magnitude of 0.05 mho/cm^2 and a relaxation time $> 0.1 \text{ sec}$. Formally a capacitance of $5 \times 10^{-3} \text{ F/cm}^2$ may be inferred, and, for unit charges, a surface density of 10^{15} cm^{-2} ($C = Ne^2/kT$). Values for W and Y_1 obtained from data above 50 Hz indicated no significant changes as this added dispersion developed.

It is tempting to suppose that this irregular behavior reflects morphological or crystallization processes, for it is difficult to rationalize the surface density estimate and the narrow potential range cited in terms of impurity effects. The equivalent low frequency circuit predicted by the BEM (Eq. [21]) is the parallel combination of resistive and Warburg admittances. The additional low frequency dispersion requires the insertion of a complex admittance in the resistive path, which is tantamount to a modification of the redox reaction. One would have anticipated a crystallization impedance to appear in series with the Warburg path. We can not recreate the shape of the low frequency dispersion by adding plausible elements in this path. The conventional adatom model may be represented by a parallel R-C circuit (20, 21), and leads to deviations in the wrong direction. Previous studies of silver electrocrystallization have found that an admittance proportional to $\sqrt{i\omega}$ also characterizes equilibrium response and is not due to bulk diffusion (22, 23). If such an element were inserted in the deposition portion of the circuit, $\sqrt{i\omega}$ dependence would be retained, but W would be less than predicted for cuprous ion diffusion. This could explain why, at high concentrations, W levels off instead of increasing as expected.

Examination of electrode response as a function of potential offers a more critical test of the BEM. Within ± 25 mV of equilibrium the response function behaved as predicted, approaching the real axis at 45° at low frequencies (Fig. 4). Analysis of the curvature in these plots at high frequencies (c.f. Fig. 12) gave $Y_2 = 18$ mho/cm² at equilibrium, while the variation of Y_2 with potential indicated $\alpha_2 \sim 0.4$ (Eq. [20]). Use of the smaller electrode lessened the importance of electrolyte resistance and increased the accuracy of high frequency results. These are still quite sensitive to errors in C_∞ , but they do support the hypothesis that the curvature in Y^* plots is due to a finite Y_2 .

The predictions of the BEM are not fulfilled at potentials farther from equilibrium. The low frequency curvature appearing at the higher anodic potentials can be simulated by insertion of a capacitance, ~ 200 μ F/cm², in series with the Warburg admittance for cuprous ion diffusion. Below -75 mV a dispersion remains which is not consistent with the BEM. A capacitive interpretation suggests a possible double-layer process, and the dispersion is not unlike that observed in the double-layer region of the Pt/H₂SO₄ interface (15). Both anodic and cathodic deviations from BEM behavior were suppressed upon addition of 10^{-4} M chloride.

Changes in relaxation parameters with potential are seen more clearly in $Y_\omega^*(\eta)$ experiments. When cupric ion concentration polarization is negligible, the BEM predicts that Y^* varies as $\sqrt{i\omega}$ at low frequencies (Eq. [21]) and linearly with the surface cuprous ion concentration. Hence plots of $Y''/\sqrt{\eta f} = W$ should be independent of frequency and increase exponentially with potential. Within ± 25 mV of equilibrium Fig. 6 shows this to be the case. The anodic maximum is clearly inconsistent with the BEM, while the maximum seen at -100 mV is also not explained. Comparison of a log plot of W with BEM theory based on the Tindall-Bruckenstein parameters (Fig. 13) shows agreement only in magnitude near $\eta = 0$.

The variation of Y_e' at 15 Hz is plotted in Tafel fashion in Fig. 14. Anodic and cathodic slopes are 48 and 160 mV/decade, values similar to those found directly from current-voltage measurements. According to Eq. [20], from the minimum at -40 mV, $\alpha = 0.35$, while from the ratio Y_{\min}'/Y_{eq}' one finds $\alpha = 0.45$. These values are consistent with the cathodic Tafel slope, although the agreement is not overly impressive, and Eq. [20] provides only a rough description of this curve.

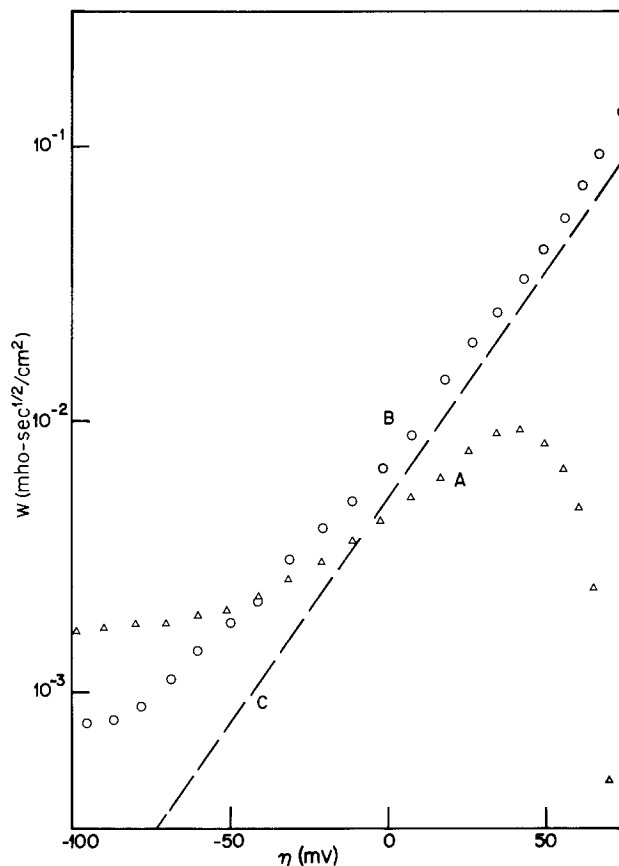


Fig. 13. Log plot of W vs. potential for (A) chloride-free solutions, (B) 10^{-4} M chloride solutions, and (C) a theoretical plot based on Tindall-Bruckenstein parameters.

Addition of 10^{-4} M chloride produces striking changes. A Tafel plot of Y_e' (Fig. 14) agrees with current-voltage measurements having cathodic and anodic slopes of 110 and 45 mV/decade. From either the potential for which Y_e' is a minimum or the ratio

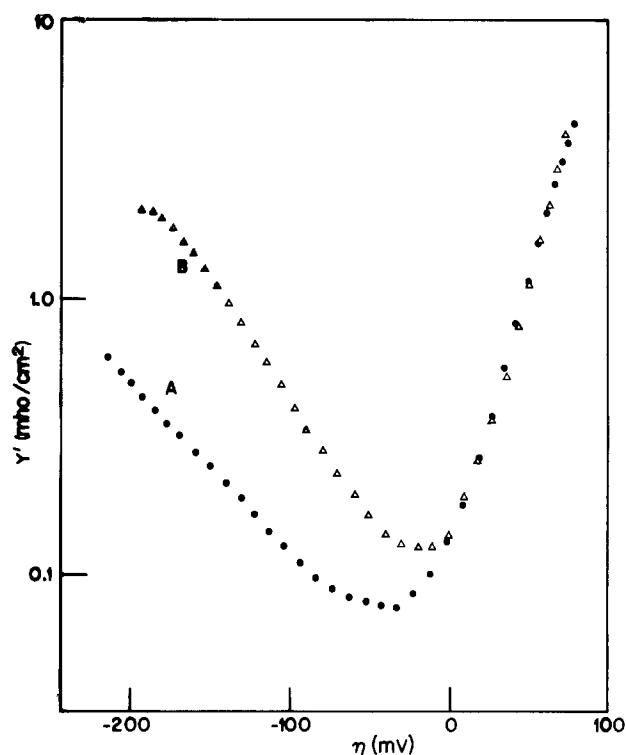


Fig. 14. Log plot of $Y_\omega'(\eta)$ for (A) chloride-free and (B) 10^{-4} M chloride solutions for 15 Hz data.

Y_{\min}'/Y_{eq}' one finds $\alpha = 0.53$, in accord with the cathodic slope and Eq. [20].

Plots of $Y_e''/\sqrt{\pi f}$ also agree quite well with the BEM (Fig. 7). From 17 Hz to 10 kHz they are independent of frequency above -100 mV. A log plot vs. potential is linear with a 61 mV/decade slope (Fig. 13) precisely as expected if the dispersion is due to cuprous ion diffusion. Below -100 mV the plots again rise. For frequencies below 200 Hz the rise varies as $1/\omega$, and may be quantitatively explained by cupric ion diffusion. The d-c currents are significantly larger at these cathodic potentials in chloride solutions because of the increase in α , and the relaxation time, τ_1 , has decreased sufficiently for the low frequency dispersion due to Cu^{++} to appear. Above 200 Hz, however, the cathodic rise requires an alternative explanation.

The ability of dilute chloride solutions to "clean up" the relaxation characteristics of copper electrodes is most evident in measurements of this form. Varying chloride concentrations showed that 10^{-5}M was a critical concentration for an electrode rotational speed of 200 rad/sec. Between 3×10^{-5} and 10^{-3}M , changes were comparatively minor, while above this range an additional hump appeared in $Y_e''(\eta)$ plots which was attributed to precipitation of CuCl . Slight changes could be seen upon addition of 10^{-6}M chloride, but this level could be comparable to residual chloride in solution (35 ppb).

A physical picture of the electrode processes is helpful for discussing changes in relaxation behavior. At the surface, possibly at preferential sites, a rapid exchange occurs between the metal and cuprous ions. On our shortest time scale, 10^{-6} sec, these ions will diffuse about 250Å, and a uniform surface concentration should then be established. Within the solution a diffuse cloud of cuprous ions extends outward through the Nernst layer, which is about 10^{-3} cm thick for our experiments. Following a small anodic change in electrode potential, a new surface concentration is quickly established. The added ions diffuse from the surface and are replaced by further metal dissolution. It is this time-dependent flux which is responsible for the experimental relaxation. A steady-state profile is established after about 0.3 sec, and the relaxation ceases. In this state the cloud continues to be drained by diffusive escape through the Nernst layer and the surface redox reaction. The latter does not contribute to a relaxation if cupric ion concentration polarization is negligible, for it depends only upon the surface density of cuprous ions which very rapidly adjusts to this sink.

The changes seen in chloride-free solutions at high anodic overpotentials occur below 1-3 kHz, or after about 10^{-4} sec. This would indicate a change in those cuprous ions which have been able to diffuse $\sim 3000\text{Å}$ into solution. This distance is comparable with surface roughness, and one might anticipate a change in behavior as the concentration contours shift from the microscopic to the geometric surface. There is no evident reason, however, why $\sqrt{i\omega}$ response should not resume at lower frequencies, with W values decreased by a surface roughness factor.

If one postulates a reactive decay path in solution such that

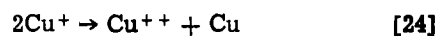
$$\frac{d}{dt} [\text{Cu}^+(x)] = D \frac{\partial^2}{\partial x^2} [\text{Cu}^+(x)] - k[\text{Cu}^+(x)] \quad [22]$$

then Eq. [21] becomes

$$Y_e^* = Y_1 + \sqrt{i\omega + k} \frac{eF}{kT} \sqrt{D_1} [\text{Cu}^+(O)] \quad [23]$$

At low frequencies this expression is equivalent to a parallel R - C circuit. The shape of this function in the complex plane is similar to that observed at large anodic overpotentials, and the capacitances measured are in accord with our estimates for k and $[\text{Cu}^+(O)]$.

Disproportionation



is a possible explanation for the disappearance of cuprous ions under anodic conditions where their concentration exceeds its equilibrium value. This reaction, however, does not occur homogeneously, but only at metallic copper surfaces (24). Practical experience has shown that copper particles are formed at copper anodes (24, 25), and we may postulate that at large anodic overpotentials clusters of copper atoms break away from the surface and diffuse into the Nernst layer, providing nuclei for the disproportionation reaction. The nuclei will grow in size until the local cuprous concentration is reduced to its equilibrium value, and then they may either escape into the bulk electrolyte or, with a greater probability, diffuse back to the anode and dissolve electrolytically. Should they break away before the latter process is completed, a renewable source of nuclei would be established.

An upper limit can be set for the rate constant if disproportionation is limited by diffusive meetings of cuprous ions and spherical clusters

$$k = 4\pi DR_m N_m \quad [25]$$

where R_m is the cluster radius and N_m their number density (26). Setting the particle volume equal to their accrete atomic volume

$$(4\pi/3)R_m^3 N_m = N_{\text{Cu}} + \nu_{\text{Cu}} \quad [26]$$

For $k \simeq 10^4 \text{ sec}^{-1}$, we obtain $R_m = 34\text{Å}$ and $N_m = 2 \times 10^{14} \text{ cm}^{-3}$. These appear to be feasible values for the 3000Å solution layer near the surface. The diffusion coefficient for a particle of this size is $\sim 10^{-6} \text{ cm}^2/\text{sec}$, and re-encounters with the electrode should occur in 10^{-3} sec. There is some indication in the experimental data (Fig. 6) that the negative or inductive low frequency response peaks between 100-200 Hz, and this is consistent with surface fluctuations due to particle re-encounters. We trust it apparent that these heuristics are not a rigorous calculation. A proper treatment considering the spatial and temporal changes in cuprous ion concentration and particle size and diffusion is beyond the scope of this discussion.

The large change in low frequency anodic response following chloride ion addition provides a means to investigate their role in copper electrode kinetics. The most sensitive experiment is a measurement of $Y_e''(\eta)$ near 100 Hz. When the bulk chloride concentration is 10^{-5}M and cycling takes place between -300 and $+200$ mV at 20 mV/sec, only a small effect is noted when the electrode's rotation is less than 10 rad/sec, while at 400 rad/sec the changes approximately equal those in 10^{-4}M to 10^{-3}M solutions. The latter response is seen if plating occurs at 400 rad/sec, the potential scan is halted for 15 sec at $\eta = 0$ with rotation off, and the anodic scan then resumed with no rotation. It also occurs if plating takes place at 0 rad/sec, the scan is halted at $\eta = 0$ for 15 sec and rotation stepped to 400 rad/sec before resuming the sweep. When plating and stripping both occur at 0 rad/sec, but during a hold at $\eta = 0$ rotation is increased, the anodic response depends upon both the holding time and the rotational speed. At 400 rad/sec optimum changes follow a 10-20 sec pause, while at 100 rad/sec a 20-40 sec halt is needed for an equivalent response. These results show that the chloride effect is determined by diffusion and that 10^{15} ions/cm² are involved. Because the effect appears in the absence of a hold with plating at 400 rad/sec, it appears that the accumulation of surface chloride is unimpeded by deposition. The large numbers suggest formation of a full surface layer of chloride, not just preferential adsorption at specific sites, and the layer must be sufficiently tenacious to ride out vigorous surface changes at large anodic and cathodic current densities. The electrostatic energy for such a

high ionic coverage would prevent its formation unless compensating cations are also present, and we suggest that the surface is covered by a monolayer of CuCl. Based on the solubility product of CuCl, 10^{-6} , formation of a bulk surface deposit is only expected for chloride concentrations greater than 10^{-3} M, and a true surface species must be involved.

The presence of a surface chloride layer could affect disproportionation by either impeding the flux of metallic nuclei into solution or retarding the reaction at cluster surfaces. The former explanation is more likely, for there are insufficient ions in solution to mask a growing surface, and the high exchange current of the $\text{Cu}^+ \rightarrow \text{Cu}$ reaction is not greatly reduced by chloride. Whether chloride additions are beneficial in controlling anodic reactions in plating baths is debatable, for while the rate of formation of fines may be reduced, there will be an attendant accumulation of Cu^+ in solution which may disproportionate at undesirable sites.

Near equilibrium and at cathodic potentials, as is evident in Fig. 13, the variation of W with potential in chloride-free solutions is less than predicted by the BEM. Either the apparent surface concentration of Cu^+ is "buffered" by kinetics or W is dependent on other factors. One possible deposition path would be the surface reduction of Cu^{++} to Cu^+ , followed by the diffusion of Cu^+ to lattice incorporation sites. This might create a bottleneck leading to an excess surface accumulation of Cu^+ at cathodic potentials.

We can estimate this effect in the following manner (27). Assume that crystal growth occurs only at linear steps of length L , and that a hemicylindrical diffusion zone exists along the step, with rapid equilibration at a distance a of atomic dimensions. Then, within this zone the cuprous concentration will vary as

$$c(r) - c(a) = (c_\lambda - c_a) \frac{\ln r/a}{\ln \lambda/a} \quad [27]$$

where the distance λ is a measure of the size of the zone, which we assume equals half the step spacing. In the steady state let us equate the inward flux at a with the redox flux which we assume to be generated uniformly on the plane between steps. Making the crude approximation that the surface concentration on this plane is equivalent to c_λ

$$-\frac{\pi DFL(c_\lambda - c_a)}{\ln \lambda/a} = 2\lambda LI_{10}[(c_\lambda - c_a) \exp(1 - \alpha_1)e\eta/kT - \exp(-\alpha_1e\eta/kT)] \quad [28]$$

Upon solving for c_λ and I , with $c_a = c_e \exp(e\eta/kT)$

$$c_\lambda/c_e = \frac{\exp(e\eta/kT) + (I_{10}/I_c) \exp(-\alpha_1e\eta/kT)}{1 + (I_{10}/I_c) \exp[(1 - \alpha_1)e\eta/kT]} \quad [29]$$

$$I = 2I_{10} \frac{\exp(2 - \alpha_1)e\eta/kT - \exp(-\alpha_1e\eta/kT)}{1 + (I_{10}/I_c) \exp[(1 - \alpha_1)e\eta/kT]}$$

where

$$I_c = \frac{\pi D F c_e}{2\lambda \ln \lambda/a} \quad [30]$$

If for estimates we take $\lambda = 10^{-6}$ cm and $a = 2 \times 10^{-8}$ cm, $I_c = 200$ mA/cm².

Anodic Tafel plots will show a negative curvature, shifting to a 60 mV/decade slope above 240 mV if $\alpha_1 = 0.5$, while the surface cuprous concentration should rise at potentials below -90 mV. Provided the value chosen for λ remains feasible under high current density conditions, this bottleneck could explain Tafel curvatures and the frequency-independent rise of W at cathodic potentials in chloride solutions. It does not explain deviations near equilibrium, for the ratio I_{10}/I_c is far too small.

If a hemispherical diffusion zone were postulated, corresponding to diffusion to kinks instead of steps, a similar level of analysis yields

$$I_c = \pi D F a c_e / 2\lambda^2 \quad [31]$$

or $I_c \sim 16$ mA/cm². Even in this more restrictive model one cannot explain the behavior near $\eta = 0$, although much larger changes are predicted at anodic and cathodic potentials than are actually observed.

An alternative possibility is that an additional mechanism is inserting an admittance also varying as $\sqrt{i\omega}$ in series with the Cu^+ diffusional admittance. The required value is of order 10^{-2} mho-sec^{1/2}/cm². Studies of silver deposition revealed such an admittance with $W = 0.03$, and no apparent concentration dependence (23). If such an admittance were present in our copper studies it would explain both the constancy of W values at high cupric concentrations and the reduced potential dependence of W . An analogy between silver and Cu^+/Cu deposition seems reasonable, but unfortunately we lack a satisfying interpretation for the process responsible for the $\sqrt{i\omega}$ relaxation behavior. It is not compatible with the adatom diffusion models which have been analyzed in considerable detail.

The frequency dispersion of W at potentials below -25 mV (Fig. 6) remains unexplained. $W_\omega(\eta)$ plots might be interpreted as showing an adsorption maxima at -100 mV. From C^* plots the equivalent dispersion amplitude is about $50 \mu\text{F}/\text{cm}^2$, equivalent to 10^{13} atoms/cm², and the response time is 10^{-4} sec. A double-layer relaxation involving specific adsorption is the simplest explanation. The potential of zero charge for copper is -240 mV with respect to the equilibrium potential (28), and is not correlated with the -100 mV peak. Chloride adsorption appears to quench this dispersion, but our experimental results are insufficient to justify an interpretation. Morphological investigations have revealed considerable changes in the growth habit of copper deposits between 0 and -200 mV (29-31). It is tempting to suppose that these variations are in some manner reflected in our admittance results, but no connection is obvious. The high frequency double-layer capacitance is independent of potential in this region and offers no evidence for changes in the microscopic surface.

Conclusions

Near equilibrium, the two-step model proposed by Mattson and Bockris for copper electrodes generally agrees with admittance measurements if allowance is made for the diffusion of cupric and cuprous ions and a finite exchange current for the crystallization reaction. Analysis of this model leads to an equivalent circuit description with parallel contributions from the redox and crystallization reactions. The complex-plane reduction of experimental data can reveal which branch is affected when deviations from this model are encountered. At anodic potentials the exponential increase in cuprous ion concentration is quenched, and this has been attributed to disproportionation and the growth of metallic clusters in solution. In the cathodic region only a comparatively small surface dispersion was found, and this could be due to a double-layer relaxation. The addition of low concentrations of chloride leads to the rapid formation of a surface monolayer which increases the cathodic Tafel slope, eliminates anodic disproportionation at the electrode, and reduces the cathodic dispersion.

No clear-cut evidence for crystallization-controlled kinetics was found for freshly formed surfaces. Aged surfaces did exhibit irregularities which might be construed as due to cooperative processes. Other "inconsistencies" begging further explanation are the concentration dependences of the relaxation parameters Y_1 and W , and the potential dependence of W .

Manuscript submitted Nov. 19, 1979; revised manuscript received Oct. 27, 1980.

Any discussion of this paper will appear in a Discussion Section to be published in the December 1981 JOURNAL. All discussions for the December 1981 Discussion Section should be submitted by Aug. 1, 1981.

Publication costs of this article were assisted by Bell Laboratories.

LIST OF SYMBOLS

| | |
|--------------------|--|
| Y^* | the complex admittance function ($Y' + iY''$) which is the reciprocal of a complex admittance, Z^* |
| $Y_\eta^*(\omega)$ | measured values for Y^* as a function of frequency at the potential η |
| $Y_\omega^*(\eta)$ | measured values for Y^* as a function of potential at the frequency ω |
| $Y_{eq}^*(\omega)$ | measured values for $Y^*(\omega)$ at the equilibrium potential |
| Y_∞ | the limiting high frequency value of $Y^*(\omega)$ which is due to electrolyte conductivity |
| Y_e^* | the electrode surface admittance obtained after separation of electrolyte conductance contributions |
| C_∞ | the limiting high frequency value of $Y_e^*/i\omega$ |
| G_0 | the limiting low frequency value of Y_e^* |

REFERENCES

- U. Bertocci and D. R. Turner, "Encyclopedia of Electrochemistry of the Elements," Vol. II, A. J. Bard, Editor, Marcel Dekker, New York (1974).
- U. Bertocci, *Electrochim. Acta*, **11**, 1261 (1966).
- E. Mattson and J. O'M. Bockris, *Trans. Faraday Soc.*, **55**, 1586 (1959).
- O. R. Brown and H. R. Thirsk, *Electrochim. Acta*, **10**, 383 (1965).
- L. I. Andropov, L. E. Sribnyi, and M. I. Donchenko, *Elektrokhimiya*, **13**, 788 (1975).
- J. O'M. Bockris and M. Enyo, *Trans. Faraday Soc.*, **58**, 1187 (1962).
- D. Landolt, R. H. Muller, and C. W. Tobias, *This Journal*, **118**, 40 (1971).
- Q. J. M. Slaiman and W. J. Lorenz, *Electrochim. Acta*, **19**, 791 (1974).
- I. M. Pearson and G. F. Schrader, *ibid.*, **13**, 2021 (1968).
- N. A. Hampson and R. J. Latham, *Trans. Faraday Soc.*, **67**, 1440 (1971).
- Yu. S. Kmitriev, A. A. Murtazina, and A. S. Kolosov, *Elektrokhimiya*, **5**, 106 (1969).
- Z. A. Tkachik, K. M. Gorbunova, and E. S. Sevast'yanov, *ibid.*, **5**, 351, 1125 (1969).
- K. M. Gorbunova and Z. A. Tkachik, *Electrochim. Acta*, **16**, 191 (1971).
- I. R. Burrows, J. A. Harrison, and J. Thompson, *J. Electroanal. Chem. Interfacial Electrochem.*, **58**, 241 (1975).
- S. H. Glarum and J. H. Marshall, *This Journal*, **126**, 424 (1979).
- G. W. Tindall and S. Bruckenstein, *Anal. Chem.*, **40**, 1402 (1968).
- A. R. Despic, D. R. Jovanovic, and S. B. Bingulac, *Electrochim. Acta*, **15**, 459 (1970).
- R. D. Armstrong and R. E. Firman, *J. Electroanal. Chem. Interfacial Electrochem.*, **45**, 3 (1973).
- J. Newman, "Electrochemical Systems," p. 177, Prentice-Hall, Englewood Cliffs, N.J. (1973).
- W. Lorenz, *Z. Naturforsch. Teil A*, **9**, 716 (1954).
- R. D. Armstrong, R. E. Firman, and H. R. Thirsk, *Faraday Discuss. Chem. Soc.*, **56**, 244 (1973).
- T. Vitanov, E. Sevast'yanov, Zdr. Stoinov, and E. Budevski, *Elektrokhimiya*, **5**, 238 (1969).
- S. H. Glarum and J. H. Marshall, Unpublished results.
- A. I. Molodov, G. N. Markosyan, and V. V. Losev, *Electrochim. Acta*, **17**, 701 (1972).
- C. Wagner, *ibid.*, **11**, 971 (1969).
- M. V. Smoluchowski, *Z. Phys. Chem.*, **92**, 129 (1917).
- M. Fleischmann and H. R. Thirsk, *Electrochim. Acta*, **2**, 22 (1960).
- L. Ya. Egorov and I. M. Novosel'skii, *Elektrokhimiya*, **6**, 521 (1970).
- H. J. Pick, G. G. Storey, and T. B. Vaughn, *Electrochim. Acta*, **2**, 165, 179, 195 (1960).
- S. C. Barnes, *ibid.*, **5**, 79 (1961).
- A. Damjanovic, M. Paunovic, and J. O'M. Bockris, *J. Electroanal. Chem.*, **9**, 93 (1965).
- R. D. Armstrong, M. F. Bell, and A. A. Metcalfe, "Electrochemistry—Spec. Period. Rpts.," Vol. 6, Chemical Soc. (1978).

Experimental Study of the Gas Bubble Effects on the IR Drop at Inclined Electrodes

G. Kreysa* and H.-J. Kùlp

Dechema-Institute, 6000 Frankfurt/M. 97, Germany

ABSTRACT

The existence of a gas evolving electrode in industrial electrolysis cells may greatly increase the cell voltage due to the additional IR drop caused by the gas bubbles. The main area of expanded metal electrodes as they are used in the industry consists of inclined planes. It was therefore considered of interest to study the influence of the inclination angle on the IR drop caused by the gas layer at an inclined hydrogen evolving electrode. Evaluation of IR drop measurements at various current densities shows that slightly up-facing oriented electrodes ($\alpha = -15^\circ$) have a gas layer of an optimum state in terms of a minimum IR drop. A simple model of the motion of gas bubbles near the electrode surface allows the dependence of the IR drop on the inclination angle to be calculated. Calculations based on this model show good agreement with experimental results.

In practical electrolysis processes involving gas evolving electrode reactions the effect of the gas bubbles on the electrolyte resistivity is an important factor. Depending on the magnitude of the current density

this bubble effect causes an additional IR drop increasing the cell voltage by about 100-200 mV and thus the specific energy consumption of the chemicals produced. A number of authors have already investigated the effects of gas bubbles on the electrolyte resistivity, cell voltage, and the current density distribution both by experimental studies and theoretical

* Electrochemical Society Active Member.

Key words: gas evolution, theoretical model, optimization, electrolysis.

models. Most of these papers deal with gas bubble *IR* effects in narrow flow channels with planar electrodes (1-6) or the mass transfer enhancement due to the gas bubbles (6-14). However, in industrial electrolysis cells planar electrodes are relatively rare and mainly machined block electrodes, mesh electrodes, and expanded metal electrodes are being used. Investigations of bubble effects on industrial electrodes have been carried out by Müller (15), Kuhn (16), and Jorne (17).

Expanded metal electrodes, as recently studied by Jorne (17), are mainly consisting of inclined electrode planes, the inclination angle being dependent on the degree of expansion. In industrial cells these electrodes are mounted with an up-facing inclination of the metal bands. This configuration allows the evolving gases to divert mainly on the back side of the electrode resulting in a lower *IR* drop.

Many papers have dealt with mass and heat transfer as well as natural convection at inclined gas evolving electrodes (18, 19). Some authors (20-22) have studied also the influence of the inclination angle more extensively. However, there is a lack of knowledge concerning the dependence of the *IR* drop caused by the gas bubbles on the inclination angle. The present work studies the *IR* drop due to the gas bubbles in the electrolyte and its dependence on the inclination angle of the electrode. An attempt was also undertaken to discuss the results in terms of a simple theoretical model.

In the following the sign of the electrode inclination angle is defined as shown in Fig. 1. Positive and negative signs refer to down-facing and up-facing inclinations of the electrode, respectively. Close to the electrode a gas layer with a finite thickness exists as was already assumed in a model proposed by Hine (3). If one considers the vectorial splitting of the rising velocity (u_{ss}) of the bubble swarm into two components, parallel (u_p) and normal (u_n) to the electrode, respectively, it results in an expansion of the gas layer at negative inclination angles and in a compression at positive ones. On one hand, the *IR* drop increases with increasing thickness of the gas layer; on the other hand, the decrease of the gas void fraction due to the gas layer expansion results in a decrease of the resistivity. Therefore, an optimum inclination angle corresponding to a minimum *IR* drop of the gas layer should exist.

The experiments described in this paper are aimed to verify the existence of an optimum inclination angle. The experimental conditions were chosen to allow a certain analogy to commercial expanded metal electrodes and, furthermore, to minimize the effect of the current distribution on the experimental results. Of course, the hydrodynamic conditions in a narrow gap are not the same as the undisturbed free convection which we have investigated.

Experimental

As a model system of a gas evolving electrode the hydrogen evolution on a planar platinum electrode was chosen. A 4M KOH solution with 0.5 g/liter iso-octanol (6) was used as an electrolyte. The addition of this surfactant was important for obtaining reproducible results (6). The conductivity of the gas-free electrolyte was determined to 0.350 mho/cm and the

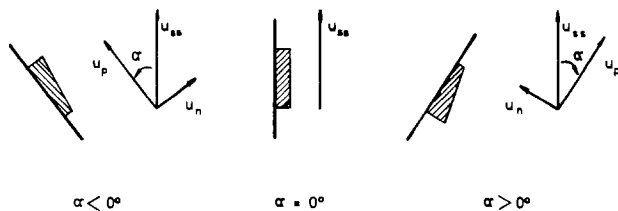


Fig. 1. Angle definitions for inclined electrodes and deformation of the gas bubble layer (shaded area).

kinematic viscosity was $2.23 \cdot 10^{-2} \text{ cm}^2/\text{sec}$. The $1 \times 1 \text{ cm}$ platinum foil electrodes were fixed to a Perspex support. The small electrode size was chosen for two reasons. First, the dimensions of the metal bands of expanded metal electrodes should not be essentially exceeded. Second, the nonuniform current density distribution due to the bubble accumulation as studied by Tobias (1) should be almost avoided.

An inclination of the cathode alone would alter the potential and current density distributions due to the varying interelectrode gap. In order to avoid this complication the cathode and the anode were mounted on a pivoted disk in a fixed parallel position as shown in Fig. 2. Thus, the angle of the cathode could be varied by turning the disk without changing the relative position to the anode. The Luggin probe containing a saturated calomel electrode was mounted in a fixed position at a distance of 5 mm from the electrode. The distance from the electrode to the capillary was always larger than the thickness of the bubble layer. The electrolytic cell was controlled potentiostatically (Potentiostat LB 75M, Bank Elektronik, Göttingen), and between the potentiostat and the working electrode an electronic interrupter unit (Model PU1, Forschungsinstitut Meinsberg) was applied to measure the *IR* drop between electrode and Luggin probe (23). During each measurement the electrode polarization was varied with a scan rate of 1 mV/sec from 0 to -1V and from -1 to 0V using a voltage scan generator (Model VSG 72, Bank Elektronik, Göttingen). During the scanning the *IR* drop between electrode and Luggin probe was plotted on a X-Y-Recorder (Servogor XY, Type RE 551, Metrawatt, Nürnberg) as a function of the current density. Since the shape of these curves was independent of the polarization direction, the equilibrium of dissolution of hydrogen was established. A schematic diagram of the experimental equipment is shown in Fig. 3. For a gas-free electrolyte the *IR vs. i* plot should result in a straight line. Due to the in-

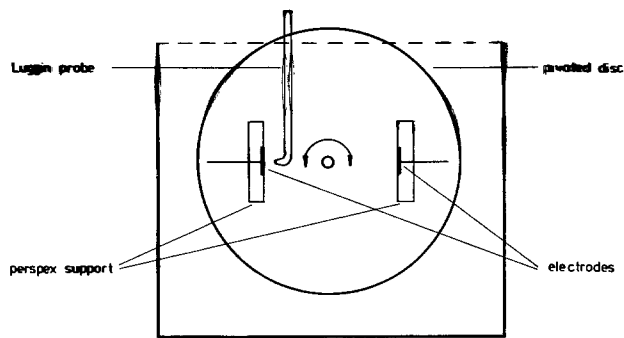


Fig. 2. Schematic view of the electrolysis cell

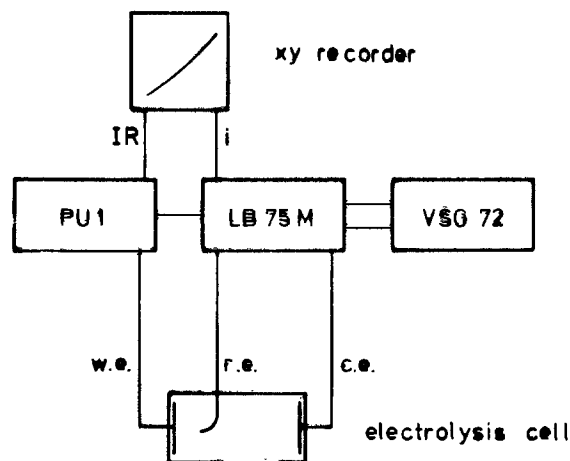


Fig. 3. Schematic diagram of instrumentation (w.e., working electrode; r.e., reference electrode; c.e., counterelectrode).

creasing gas evolution with increasing current density the experimentally obtained IR drop deviates from a linear dependence toward large IR values, e.g., as shown in Fig. 4. A second-order regression polynomial can be fitted to the experimentally obtained IR - i plots.

The described experimental technique for measuring the IR effects of the gas bubbles offers the following advantages:

1. The actual electrode potential and the IR drop in the gas-containing electrolyte can be measured separately.

2. A single potentiokinetic scanning yields IR drop data for the whole current density range applied (up to 1 A/cm^2).

3. IR drop oscillations due to the statistics of gas evolution can easily be equalized by a regression polynomial.

4. The tangent of the IR vs. i curve at $i = 0$ corresponds to the IR drop for the gas-free solution. At any i value the difference between the overall IR drop and this straight line thus represents the additional IR drop caused by the gas bubbles.

It should be noted that the results given in the following do not cover all possibilities offered by this technique. Further investigations into this problem are being carried out.

Results and Discussion

In Fig. 5 the additional IR drop caused by the gas bubbles has been plotted as a function of the current density. The IR drop is obviously strongly dependent on the current density and reaches about 200 mV at 10 kA/m^2 . Measurements similar to those shown in Fig. 4 were carried out at inclination angles ranging from -60 to $+60^\circ$. Figure 6 shows a photograph of the gas-evolving electrode at an inclination angle of -30° . In this figure the expansion of the bubble layer as previously shown schematically in Fig. 1 is quite apparent. Measurements of the angular dependence of the IR drop were performed at current densities of 1, 3, and 5 kA/m^2 thus covering the range usually applied in industrial cells. Comparable results could be obtained for different current densities by applying the normalization

$$\Delta U = IR(\alpha) - IR(0) \quad [1]$$

The ΔU value in [1] represents the part of the IR drop which is dependent on the inclination angle. In Fig. 7 the angular dependence of ΔU values is shown for various current densities. From this figure it is obvious that the IR drop has a minimum at an electrode inclination of about -15° independent of the current density. It is interesting to note that due to the expansion degree the inclination of industrial expanded metal electrodes is usually close to this value. Furthermore, Fig. 7 shows that the angular dependence of the IR drop is clearly asymmetric. A compression of the

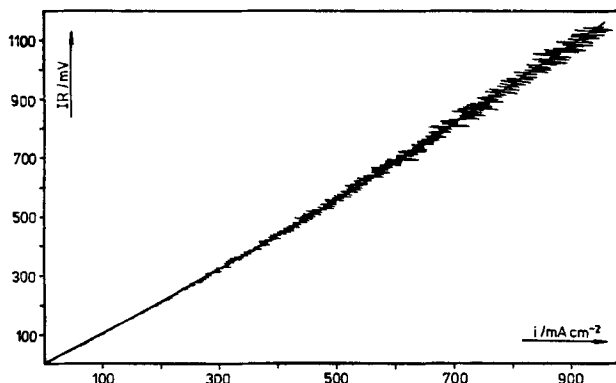


Fig. 4. Experimental plot of the IR drop vs. current density with the regression curve ($\alpha = 0^\circ$).

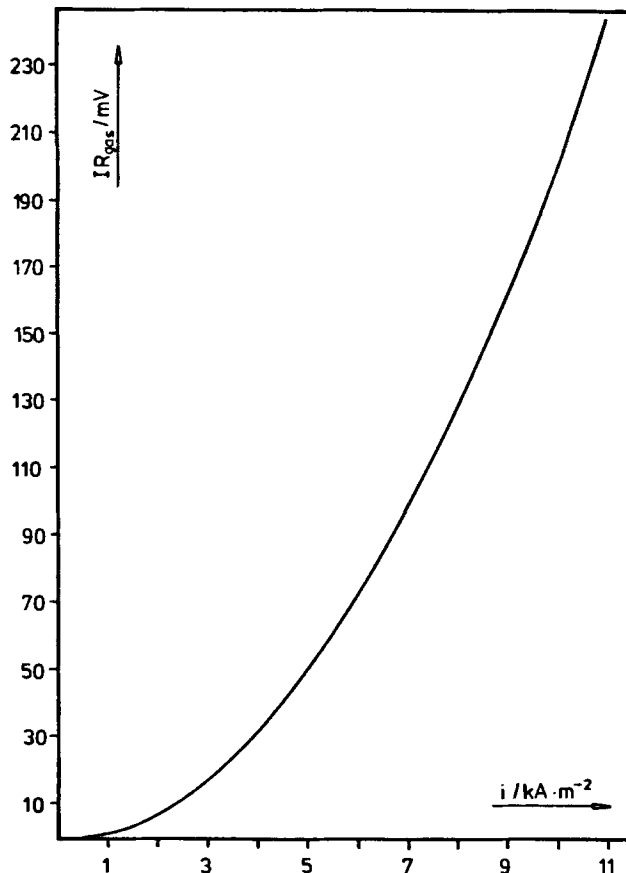


Fig. 5. IR drop due to the gas bubbles as a function of the current density ($\alpha = 0^\circ$).

gas layer thus results in a markedly higher IR drop than an expansion.

In the following a theoretical model based on well-known principles of the gas bubble motion is suggested. This model reflects the experimentally obtained angular dependence of the IR drop if realistic parameter values are assumed. The following assumptions are made:

1. The gas bubbles have a uniform size, i.e., their actual size distribution is disregarded.

2. Instead of the real gas layer expansion and the gas accumulation with height the gas layer is considered to have a defined mean thickness and a mean uniform gas void fraction as a first-order approximation.

3. Shape changes of the bubbles at various angles are ignored as a reasonable simplification of the real physical situation.

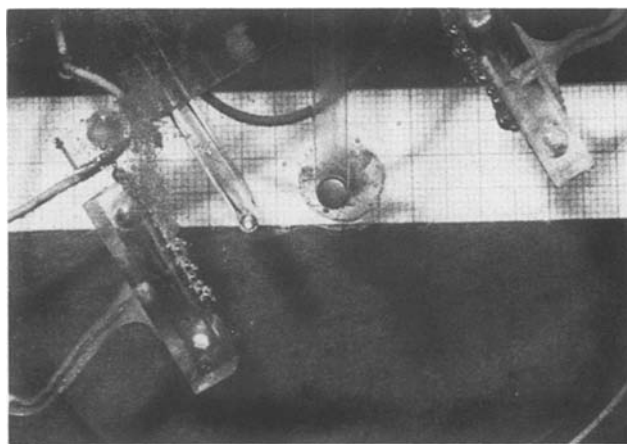


Fig. 6. Photographic picture of the gas evolving electrode at -30° .

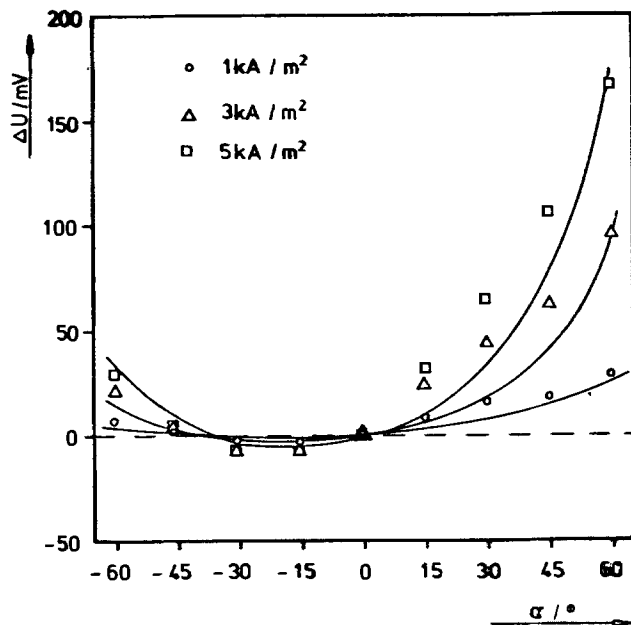


Fig. 7. Relative ΔU values (related to $\alpha = 0^\circ$) vs. the angle of inclination and calculated curves.

4. On vertically positioned electrodes the bubble layer thickness increases with increasing current density, but the gas void fraction remains constant.

5. The gas flow velocity within the bubble layer is constant and equal to the sum of the electrolyte flow velocity due to natural convection and the rising velocity of the swarm of bubbles.

6. The electrolyte flow velocity due to convection depends on the inclination angle of the electrode.

7. The expansion and the compression of the bubble layer results from the vectorial splitting of the vertical rising velocity of the swarm of bubbles.

8. The current density distribution at the electrode is assumed to be uniform.

As the observed bubble diameter is smaller than 0.2 mm the rising velocity of a single bubble can be calculated using the Levich equation (24)

$$u_b = \frac{d_b^2 g}{12\nu} \quad [2]$$

The rising velocity of the swarm of bubbles is then given by Marucci's equation (25)

$$u_{ss}(0) = u_b \frac{(1 - \epsilon(0))^2}{1 - \epsilon(0)^{5/3}} \quad [3]$$

Sigrist (6) has experimentally demonstrated that at gas void fractions up to 0.6 the conductivity of the gas-containing electrolyte can be calculated by the Maxwell equation. For a vertical electrode this equation yields

$$x(0) = x_0 \frac{1 - \epsilon(0)}{1 + \epsilon(0)/2} \quad [4]$$

From the gas flow velocity, u_g

$$u_g = u_1 + u_{ss} \quad [5]$$

and Faraday's law the thickness of the bubble layer can be calculated for a vertical electrode provided that a constant gas void fraction is assumed

$$d(0) = \frac{V_M I}{z F b \epsilon(0) u_g(0)} \quad [6]$$

The electrolyte flow velocity, u_1 , results from natural convection due to the difference in hydrostatic pressure. If h_0 means the height of the vertical electrode then

$$\Delta p_h \sim \epsilon(\alpha) h_0 \cos \alpha \quad [7]$$

If the bubble layer is assumed as a flow channel, the pressure drop must fulfil the relation

$$\Delta p \sim u_1^2 \quad [8]$$

In the steady state the difference in hydrostatic pressure is equal to the pressure drop. Combination of Eq. [7] and [8] leads to the relation between the electrolyte flow velocity parallel to the electrode surface and the inclination angle

$$u_1(\alpha) = C(\epsilon(\alpha) \cos \alpha)^{1/2} \quad [9]$$

For a vertical electrode [9] can be written

$$u_1(0) = C\epsilon(0)^{1/2} \quad [10]$$

Assuming realistic values for $\epsilon(0)$ and $u_1(0)$ Eq. [10] can be applied to calculate the constant C . Due to the compression and expansion of the bubble layer, respectively, an inclination of the electrode results in a change of the gas void fraction and the thickness of the bubble layer. Similar to Eq. [3] the rising velocity of the bubble swarm at a gas void fraction $\epsilon(\alpha)$ can be written as

$$u_{ss}(\alpha) = u_b \frac{(1 - \epsilon(\alpha))^2}{1 - \epsilon(\alpha)^{5/3}} \quad [11]$$

The vectorial splitting of the bubble swarm velocity (see Fig. 1) into two components, one parallel ($u_{ss} \cos \alpha$) and one normal ($u_{ss} \sin \alpha$) to the electrode plane and using Eq. [5] and [9] leads to the equation

$$u_g(\alpha) = C(\epsilon(\alpha) \cos \alpha)^{1/2} + u_{ss}(\alpha) \cos \alpha \quad [12]$$

Using the normal component of the bubble swarm velocity gives the mean thickness of the compressed or expanded gas bubble layer

$$d(\alpha) = d(0) - \frac{h_0}{2u_g(\alpha)} u_{ss}(\alpha) \sin \alpha \quad [13]$$

According to Eq. [6] the gas void fraction of the bubble layer is given by

$$\epsilon(\alpha) = \frac{V_M I}{z F u_g(\alpha) b d(\alpha)} \quad [14]$$

Equations [11] and [14] define $\epsilon(\alpha)$ and $d(\alpha)$ for each α and thus $\epsilon(\alpha)$ can be calculated by common numerical methods (e.g., a uniform search method). The value introduced in Eq. [11] must be fitted in such a way that the value resulting from Eq. [14] yields the same result within the accuracy limits given. The Maxwell equation is again applied to obtain the conductivity of the bubble layer

$$x(\alpha) = x_0 \frac{1 - \epsilon(\alpha)}{1 + \epsilon(\alpha)/2} \quad [15]$$

If a is the distance between electrode and the Luggin probe it follows from Ohm's law

$$IR(0) = \left[\frac{d(0)}{x(0)} + \frac{a - d(0)}{x_0} \right] i \quad [16]$$

and

$$IR(\alpha) = \left[\frac{d(\alpha)}{x(\alpha)} + \frac{a - d(\alpha)}{x_0} \right] i \quad [17]$$

By introducing Eq. [16] and [17] in Eq. [1] and simple algebraic steps one obtains the angle dependence equation of the normalized part of the IR drop of the gas bubbles

$$\Delta U = i \left[\frac{d(\alpha)}{x(\alpha)} - \frac{d(0)}{x(0)} + \frac{1}{x_0} (d(0) - d(\alpha)) \right] \quad [18]$$

In the list of symbols the parameter values defined by the experimental conditions used for the calculation of the ΔU functions are given. The theoretical model

contains three further parameters which must be estimated by assuming realistic values

$$d_b = 0.012 \text{ cm}$$

$$\epsilon(0) = 0.45$$

$$u_1(0) = 2.0 \text{ cm/sec}$$

The assumed bubble diameter is in close agreement with data of other authors (2). Unfortunately, the real bubble diameter cannot be taken from Fig. 6 because large adhering bubbles on the edge of the electrode hide the small bubbles in front of the electrode. However, these small bubbles are detectable in the rising swarm far from the electrode. The electrolyte flow velocity represents the main part (about 90%) of the gas flow velocity and can be estimated by visual observations. Introducing an estimated value of the bubble layer thickness into Eq. [6] yields the gas void fraction given above for a vertical electrode. Theoretical ΔU functions calculated with this model using the above-mentioned data are shown also in Fig. 7. In agreement with the experimental data the theoretical curves also show the minimum at -15° and the asymmetric shape. Considering that the theoretical model was based on several simplifying assumptions the agreement between experiments and theoretical calculations may be regarded as satisfactory. Regarding the IR drop minimum at -15° it should be mentioned here that for a natural convection flow around a plate at nearly the same angle Lloyd (20) has found a transition from wave-type flow disturbances to longitudinal vortices. In a mass transfer study at inclined gas evolving electrodes Wragg (22) also obtained a local minimum of the Sherwood number in the same range of inclination angles. A possible relation between these interesting observations cannot be clarified in the present state.

Conclusions

The present investigation has shown that a change of the state of the gas bubble layer in front of an inclined electrode is accompanied by a marked change of the IR drop which may amount up to 200 mV. This demonstrates that in industrial electrolysis cells the inclination of the metal bands of the electrode is an important factor, especially if expanded metal electrodes are used. Independent of the current density, the gas bubble layer has an optimum structure in terms of a minimum IR drop at an inclination angle of -15° . However, the IR drop minimum shows a flat range between $15^\circ \cong \alpha \cong -45^\circ$. This means that an angle can be chosen within this range relatively freely that is optimum to meet other goals as, e.g., the diversion of the gas bubbles which is also influenced by the hydrodynamic conditions in the electrode membrane gap. There is a need of further detailed investigations. The inclined surfaces of commercial expanded metal electrodes usually have an inclination within the optimum range. Thus, it seems reasonable that the ohmic drop saving of these electrodes is not only caused by enabling the diversion of the gas to the rear of the electrode, but also due to an optimum state of the bubble layer at this inclination angle.

Acknowledgment

The authors acknowledge DECHEMA, Deutsche Gesellschaft für chemisches Apparatewesen e. V., for financial support of this work.

Manuscript submitted Sept. 4, 1980; revised manuscript received ca. Nov. 21, 1980.

Any discussion of this paper will appear in a Discussion Section to be published in the December 1981 JOURNAL. All discussions for the December 1981 Discussion Section should be submitted by Aug. 1, 1981.

Publication costs of this article were assisted by DECHEMA.

LIST OF SYMBOLS

| | |
|--------------------|---|
| a | distance between the electrode and the Luggin probe (cm) |
| b | width of the electrode (cm) |
| C | proportionality constant (cm sec^{-1}) |
| $d(0)$ | thickness of the gas bubble layer at $\alpha = 0^\circ$ (cm) |
| $d(\alpha)$ | thickness of the gas bubble layer at $\alpha \neq 0^\circ$ (cm) |
| d_b | diameter of a single bubble (cm) |
| F | Faraday number (96,487 As mole $^{-1}$) |
| g | gravitational acceleration ($980.66 \text{ cm sec}^{-2}$) |
| h_0 | height of the electrode in vertical position ($\alpha = 0^\circ$) (cm) |
| I | current (A) |
| i | current density (A cm^{-2}) |
| $IR(0)$ | IR drop at $\alpha = 0^\circ$ (V) |
| $IR(\alpha)$ | IR drop at $\alpha \neq 0^\circ$ (V) |
| Δp | hydrostatic pressure drop ($\text{g cm}^{-1} \text{ sec}^{-2}$) |
| R | ohmic resistance (Ω) |
| u_b | rising velocity of a single bubble (cm sec^{-1}) |
| u_g | gas flow velocity (cm sec^{-1}) |
| $u_g(0)$ | gas flow velocity at $\alpha = 0^\circ$ (cm sec^{-1}) |
| $u_g(\alpha)$ | gas flow velocity at $\alpha \neq 0^\circ$ (cm sec^{-1}) |
| u_1 | electrolyte flow velocity (cm sec^{-1}) |
| $u_1(0)$ | electrolyte flow velocity at $\alpha = 0^\circ$ (cm sec^{-1}) |
| $u_1(\alpha)$ | electrolyte flow velocity at $\alpha \neq 0^\circ$ (cm sec^{-1}) |
| u_n | velocity component of u_{ss} normal to the electrode plane (cm sec^{-1}) |
| u_p | velocity component of u_{ss} parallel to the electrode plane (cm sec^{-1}) |
| u_{ss} | rising velocity of the swarm of gas bubbles (cm sec^{-1}) |
| $u_{ss}(0)$ | rising velocity of the swarm of gas bubbles at the vertical electrode ($\alpha = 0^\circ$) (cm sec^{-1}) |
| $u_{ss}(\alpha)$ | rising velocity of the swarm of gas bubbles at an inclined electrode ($\alpha \neq 0^\circ$) (cm sec^{-1}) |
| ΔU | difference between $IR(\alpha)$ and $IR(0)$, see Eq. [1] (V) |
| V_M | molar volume of the evolved gas ($22,414 \text{ cm}^3 \text{ mole}^{-1}$) |
| z | number of electrons (1) |
| α | angle of the inclined electrode (deg.) |
| ϵ | gas void fraction (1) |
| $\epsilon(0)$ | gas void fraction at $\alpha = 0^\circ$ (1) |
| $\epsilon(\alpha)$ | gas void fraction at $\alpha \neq 0^\circ$ (1) |
| κ_0 | conductivity of the gas free electrolyte ($0.350 \text{ mho cm}^{-1}$) |
| $\kappa(0)$ | conductivity of the gas containing electrolyte at $\alpha = 0^\circ$ (mho cm^{-1}) |
| $\kappa(\alpha)$ | conductivity of the gas containing electrolyte at $\alpha \neq 0^\circ$ (mho cm^{-1}) |
| ν | kinematic viscosity ($0.0223 \text{ cm}^2 \text{ sec}^{-1}$) |

REFERENCES

1. C. W. Tobias, *This Journal*, **106**, 833 (1959).
2. J. E. Funk and J. F. Thorpe, *ibid.*, **116**, 48 (1969).
3. F. Hine, M. Yasuda, R. Nakamura, and T. Noda, *ibid.*, **122**, 1185 (1975).
4. Z. Nagy, *J. Appl. Electrochem.*, **6**, 171 (1976).
5. F. Hine and K. Murakami, *This Journal*, **127**, 292 (1980).
6. L. Sigrist, Dissertation No. 6286, ETH Zürich (1978).
7. N. Ibl, *Chem.-Ing.-Tech.*, **43**, 202 (1971).
8. J. Venczel, *Electrochim. Acta*, **15**, 1909 (1970).
9. N. Ibl and J. Venczel, *Metalloberfläche*, **24**, 365 (1970).
10. L. J. Janssen and J. G. Hoogland, *Electrochim. Acta*, **15**, 1013 (1970).
11. L. J. Janssen, *ibid.*, **23**, 81 (1978).
12. H. Vogt, *ibid.*, **23**, 203 (1978).
13. N. Ibl, *ibid.*, **24**, 1105 (1979).
14. L. Sigrist, O. Dossenbach, and N. Ibl, *Int. J. Heat Mass Transfer*, **22**, 1393 (1979).
15. J. Müller, *Chem.-Ing.-Tech.*, **49**, 326 (1977).
16. A. T. Kuhn, J. Bin Yusof, and P. Hogan, *J. Appl. Electrochem.*, **9**, 765 (1979).
17. J. Jorne and J. F. Louvar, *This Journal*, **127**, 298 (1980).
18. M. G. Fouad and A. M. Ahmed, *Electrochim. Acta*, **14**, 651 (1969).
19. T. Fujii and H. Imura, *Int. J. Heat Mass Transfer*, **15**, 755 (1972).
20. J. R. Lloyd and E. M. Sparrow, *J. Fluid Mech.*, **42**, 465 (1970).
21. J. R. Lloyd, E. M. Sparrow, and E. R. G. Eckert,

- Int. J. Heat Mass Transfer*, **15**, 457 (1972).
 22. M. A. Patrick, A. A. Wragg, and D. M. Pargeter, *Can. J. Chem. Eng.*, **55**, 432 (1977).
 23. W. Oelssner, Firmenschrift des Forschungsinstituts Meinsberg (1980).
 24. V. G. Levich, "Physicochem. Hydrodynamics," Chap. 8, Prentice-Hall, New York (1962).
 25. G. Marucci, *Ind. Eng. Chem. Fundam.*, **4**, 224 (1965).

The Polarography of Vitamin B_{12a} in Acidic Media

Ronald L. Birke* and S. Venkatesan*

The City University of New York, Department of Chemistry, The City College, New York, New York 10031

ABSTRACT

The nature of the polarographic reduction wave of vitamin B_{12a} in acidic media (pH 1-5) has been investigated. The wave exhibits a region of negative differential resistance which is due to the blockage of the electrode reaction by adsorption of a reduced species and by a double layer repulsion effect. A protonation step follows the electroreduction of vitamin B_{12a} to vitamin B_{12r} and the protonated vitamin B_{12r} is adsorbed on the dropping mercury electrode. The pK_a for this follow-up protonation step has been measured, and the mechanism of the electrode process is discussed.

Since the oxidation-reduction chemistry of vitamin B₁₂ compounds plays a definite role in many important biochemical processes, there has been much interest in the electrochemistry of these bioinorganic compounds (1). There are many forms of the vitamin which have the so-called Cob(III)alamin structure with a cobalt ion in the 3+ oxidation state as the central atom and various substituted axial ligands in the β position (2). We have studied the electrode processes of the aquo-substituted Cob(III)alamin complex, vitamin B_{12a}, because reduction of any other axial substituted form of Cob(III)alamin and subsequent reoxidation usually gives aquocobalamin, i.e. vitamin B_{12a}. Various features of the polarography and cyclic voltammetry of vitamin B_{12a} have already been studied by several investigators using mercury and other electrodes in acidic to neutral aqueous media (3-11). The reduction process is well established as two separate one-electron transfers yielding two well-separated polarographic waves. The second step representing the reduction of vitamin B_{12r} (Co(II)) to vitamin B_{12s} (Co(I)) is coupled to the opening of the nucleotide side chain in neutral pH and becomes a simple reversible electron transfer reaction if the supporting electrolyte is a strong acid. A good deal of attention had been focused on this process (5, 6). Less attention has been given to the reduction of vitamin B_{12a}, Co(III), to B_{12r}, Co(II), because of its irreversible nature. A recent investigation deals with the B_{12a}/B_{12r} system electrode process on vitreous carbon and gold electrodes (12) over a wide pH range. The nature of the adsorption of vitamin B_{12a} and B_{12r} on mercury has been studied by cyclic voltammetry, chronopotentiometry, and differential double layer measurements (11). Spectroelectrochemical studies (13, 14) have also been made which involve determining the electrode potential of the vitamin B_{12a}/B_{12r} couple, but no attempt has been made to explain the electrode process in the polarographic wave for this couple in the concentration range above 1×10^{-5} M. This electrode process has a rather unusual polarographic behavior which warrants further investigation. In neutral pH the first polarographic wave of vitamin B_{12a} has a depression on the rising portion of the first wave as it slowly rises to a plateau while in more acidic media such as acetate buffer (pH 4.5 in 0.5M NaNO₃) a maximum develops at ca. -0.1V vs. SCE followed by a minimum at ca. -0.18V vs. SCE and then the wave slowly rises to a plateau at -0.4V vs. SCE

(7). Imhoff (7) attributed the depression to adsorption on the dropping mercury electrode (DME). He also found from differential double layer capacity studies that vitamin B_{12r} was strongly adsorbed on the mercury surface in the region of the depression. These results have been confirmed recently (11).

Preliminary investigations in this laboratory indicated that both pH and ionic strength greatly affect the behavior of this polarographic wave. The present investigation is a more detailed study of the polarographic electroreduction mechanism of vitamin B_{12a} in acidic media.

Experimental

Aquocobalamin samples were obtained from Sigma Chemical Company in the form of hydroxycobalamin hydrochloride and their percentage purity was determined spectrophotometrically by calculating the concentration after conversion to dicyanocobalamin (5). For the differential pulse polarographic experiments aquocobalamin samples free of chloride were prepared by the electrolysis of cyanocobalamin in NaNO₃ solution. At sufficiently cathodic potentials it is well known that the cyanide group in the cyanocobalamin gets cleaved (7). The HCN formed was driven away by the current of nitrogen and was absorbed into NaOH solution. After about 10 min the current of nitrogen was replaced by a current of air which was maintained for 10 min. The solution changes to the characteristic red color of vitamin B_{12a}. The B_{12a} in the catholyte solution was extracted using the solvent extraction technique described by Dolphin (15). The purity of the product was tested by paper chromatography in various aqueous-butanol solvent systems. Only one spot showed up with some streaming. The polarograms obtained from this procedure were identical to those of aquocobalamin obtained from Sigma Chemical Company in contrast to those made by the electrochemical procedure of Kenyhercz and Mark (16) which gave aquocobalamin polarograms of an unusual nature unless Triton X-100 was added.

All the other chemicals were Fischer A.C.S. certified grade chemicals. The Triton X-100 and Triton QS-30 were obtained from Sigma Chemical Company. The decyl, octyl, hexyl, and butyl sodium sulfate were obtained from Eastman Organic Chemicals.

A Princeton Applied Research (PARC) Model 173 potentiostat/galvanostat in combination with a PARC Model 175 Universal Programmer was used for polarographic measurements. A commercial fiber plug type saturated calomel electrode (SCE) was used in all

* Electrochemical Society Active Member.

Key words: vitamin B₁₂ compounds, polarography, adsorption, electrode mechanism.

cases. Thus potentials quoted in this paper are always with respect to an SCE. An MFE Model 815 Plotomatic X-Y recorder served for recording the polarograms. Pulse polarograms were obtained with a Tacussel Model PGR-5 pulse polarograph. Cells were of the commercial, Metrohm type with water jacket (EA-76) (Brinkmann Instruments, Incorporated). The temperature of the test solution was varied by circulating hot water from a Haake Model FK thermostat. The accuracy of temperature maintenance was $\pm 0.5^\circ\text{C}$. The dropping mercury electrode had a column height of 86 cm and a mass flow rate of 2.05 mg sec^{-1} .

Cyclic voltammetry experiments were also performed using the PARC potentiostat/galvanostat universal programmer combination. At low scan rates a recorder was used for recording voltammograms. At high scan rates the voltammograms, were recorded with Tektronix 5403 oscilloscope and photographed with Tektronix C12 camera attachment.

pH was measured with a Beckman Zeromatic SS-3 pH meter or an Orion Research digital pH meter Model 801A. In both cases a combination electrode system was used. The pH of the various electrolytes used was adjusted by additions of NaOH solution.

A Metrohm microburette hanging mercury drop apparatus (E410) was used to form drops which were collected in a small glass holder and attached to an amalgamated Pt recessed tip electrode which was then used as the hanging Hg drop electrode. The area of the hanging Hg drop was 0.0403 cm^2 .

The polarographic potential variations were followed with a Keithley Model 160B digital voltmeter.

All solutions were deaerated in a stream of high purity nitrogen gas.

Results and Discussion

Nature of current-potential curves.—Figure 1 shows a typical d-c polarogram of $4.8 \times 10^{-4} \text{ M}$ vitamin B_{12a} in $0.1 \text{ M H}_2\text{SO}_4$ at pH 1.2. This figure has a distinctive peak around 0.06 V and a pronounced dip between 0.0 and -0.4 V similar to that observed by Imhoff in acetate buffer (7). The bottom of the dip shows a narrow range of potentials around -0.2 V where the current *vs.* time oscillations are reminiscent of an inhibited electrode reaction. Following the dip the current slowly rises to a first plateau at about -0.4 V . Another wave with an $E_{1/2}$ value of ca. -0.75 V follows the first one. As mentioned above the diffusion current on the first plateau represents the Co(III) to Co(II) reduction and on the second plateau the diffusion current represents the reduction of the diffusing Co(III) species to Co(II) and then to a Co(I) species.

Figure 2 shows a representative cyclic voltammogram (CV) of vitamin B_{12a} in 0.1 M NaClO_4 at pH 3.8

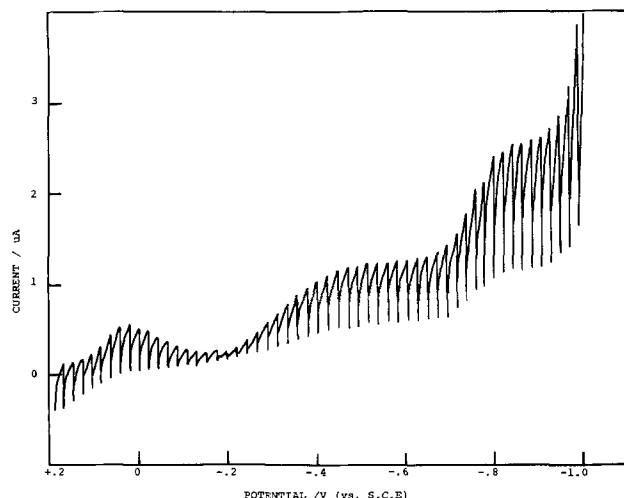


Fig. 1. Polarogram of $4.8 \times 10^{-4} \text{ M}$ vitamin B_{12a} in $0.1 \text{ M H}_2\text{SO}_4$, pH 1.2.

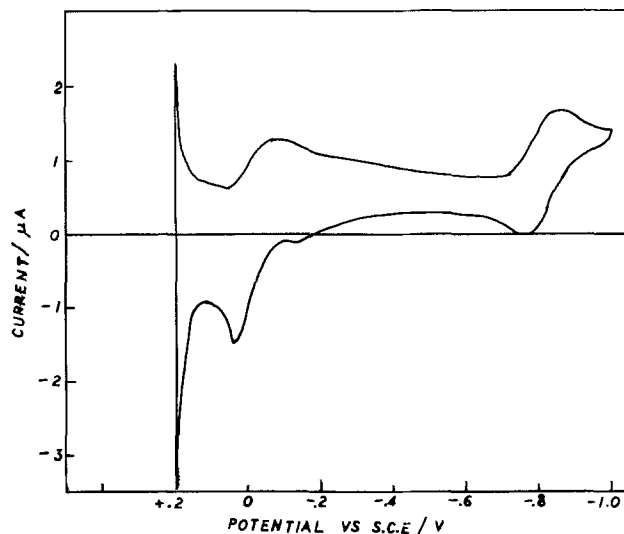


Fig. 2. Cyclic voltammogram of $1.6 \times 10^{-4} \text{ M}$ vitamin B_{12a} in 0.1 M NaClO_4 , pH 3.8, 50 mV sec^{-1} scan rate. Temperature 29°C .

on a hanging drop mercury electrode (HDME). The sharp decaying cathodic and anodic currents at $+0.2 \text{ V}$ are due to adsorption processes difficult to ascertain since they may involve a mercurous chloride species. The cathodic peak at -0.08 V is mainly diffusion controlled at low scan rates since a plot of cathodic current *vs.* the square root of scan rate is linear up to 100 mV sec^{-1} and then the slope of the plot increases at higher scan rates. On the other hand, the sharp anodic current peak at $+0.04 \text{ V}$ is definitely due to the oxidation of adsorbed vitamin B_{12r} since a plot of anodic peak current *vs.* the first power of scan rate is linear over the entire range measured up to 200 mV sec^{-1} . In addition the nearly reversible nature of the vitamin B_{12r} and B_{12s} couple can also be seen in the -0.8 V region of this figure.

Figure 3 shows differential pulse (DP) polarograms of chloride-free vitamin B_{12a} for a series of concentrations in $0.1 \text{ M H}_2\text{SO}_4$, pH 1.07. The peak at ca. $+0.2 \text{ V}$ grows linearly as a function of concentration until about $5 \times 10^{-5} \text{ M}$ where it levels off and then begins to decrease as the concentration is increased further. The peak at ca. $+0.02 \text{ V}$ is an impurity in background current and appears in the DP polarogram of $0.1 \text{ M H}_2\text{SO}_4$. It is noteworthy that the reduction is taking place at a potential quite positive to that of the reversible B_{12a}/B_{12r} couple (13) (-0.040 V) and this reduction appears to involve the adsorption of the product of the electrode reaction (11). Furthermore, although in neutral media the DP detection limits of

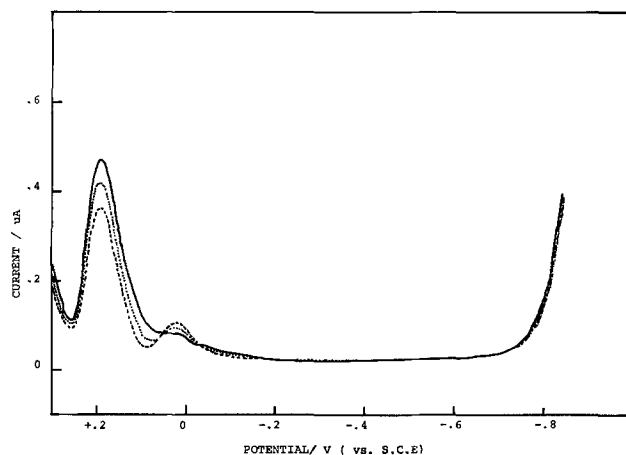


Fig. 3. Differential pulse polarograms of 2.2 , 2.6 , and $3.0 \times 10^{-5} \text{ M}$ vitamin B_{12a} in $0.1 \text{ M H}_2\text{SO}_4$, pH 1.1. Potential pulse is 50 mV , drop time is 1.0 sec , and pulse duration 40 msec .

the vitamin B_{12a} to B_{12r} peak negative to zero volts vs. SCE is about $1.0 \times 10^{-4}M$ (17), the detection limit in acidic media for this peak as can be seen from Fig. 3 is around $1.0 \times 10^{-6}M$. Indeed only at much higher concentration of around $10^{-4}M$ does the diffusion-controlled vitamin $B_{12r}H^+$ to B_{12s} peak at $-0.73V$ appear in DP polarogram in $0.1M H_2SO_4$. The DP polarographic peaks for reduction of diffusing vitamin B_{12a} appear in the potential range of -0.1 to $-0.3V$ and are complicated due to the dip phenomenon in the d-c polarogram.

Effect of ionic strength and the pH.—Figure 4 shows the effect of changing the pH on the vitamin B_{12a} system in an H_3PO_4 medium. Decreasing the pH tends to increase the magnitude of the dip and below pH 4.3 decreasing the pH causes a positive potential shift in the peak potential and the rising part of the wave. It can also be seen from Fig. 4 that the second wave becomes more reversible with a decrease in pH (6). Although only the envelopes of the polarograms are shown in Fig. 4 an examination of the current-time behavior of individual drops in the region of the valley of the dip shows a current which first decreases with time and then increases toward the end of the drop-life indicating highly inhibited currents with possibly a rearrangement of the adsorbed species (7, 11). Identical behavior was found with an H_2SO_4 medium.

Plots of E_{DME} vs. $\log((i_D - i)/i)$ were made in H_2SO_4 buffer media and found to be straight lines for the initial rising part of the curves (0.2 to ca. 0.0V). The slopes of these plots had close to a Nernst value at lower vitamin B_{12a} ($4 \times 10^{-4}M$) concentrations and short drop times, but were not Nernstian at higher B_{12a} ($10^{-3}M$); however, the current-potential curves are complicated by the adsorption process which accounts for the change in slope. The $E_{1/2}$ values obtained

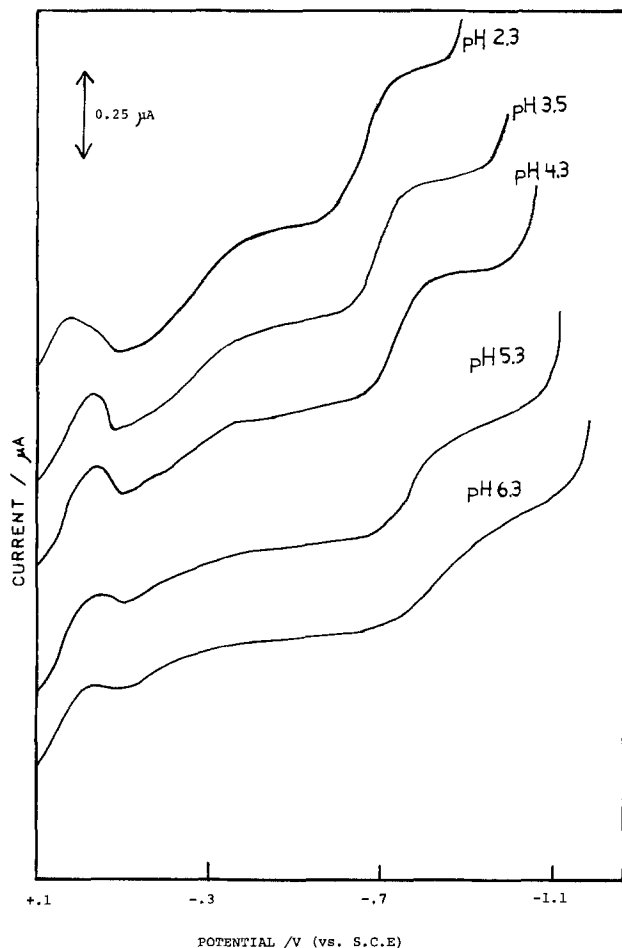


Fig. 4. Effect of pH on the polarographic wave of $1.6 \times 10^{-4}M$ vitamin B_{12a} in $0.1M H_3PO_4$. The pH was adjusted by adding NaOH.

from the logarithmic analysis were plotted against pH for a solution containing $1M Na_2SO_4$. The $\Delta E_{1/2}/\Delta pH$ value was -56.7 mV/pH. The crossing point of the straight line portions in curve A of Fig. 5 is at 2.7 which corresponds to the pK_a for the protonation of the 5,6-dimethylbenzimidazole (DMB) nucleotide base-form of vitamin B_{12r} . The $E_{1/2}$ value of the vitamin B_{12a}/B_{12r} couple found at values above pH 3 on the flat part of the curve is $-0.034V \pm 0.004V$ which is close to the reversible value measured spectroelectrochemically (13). The value of pK_a found lies between the value found by ESR measurements (18) ($pK_a = 2.5$) and the value found by pH titration (6) and cyclic voltammetry (19) ($pK_a = 2.9$). Since the slope of the plot agrees with theory (59 mV) and the E° found is within 6 mV of that measured spectroelectrochemically (13), under the conditions of high ionic strength the polarographic system appears reversible.

If the total ionic strength is reduced by starting with $0.1M H_2SO_4$ medium the $E_{1/2}$ vs. pH plot using a 3.0 sec drop time shows a slope of 59.7 mV/pH with a cross-over point of 2.8 for the pK_a and an $E^\circ = -0.017V$. However, when the drop time is lowered to 0.5 sec for this media, the slope becomes 34.4 mV/pH with a cross-over point of 3.7 and an $E^\circ = -0.003V$ (curve B, Fig. 5). The slopes of the E_{DME} vs. $\log((i_D - i)/i)$ varied somewhat with pH, but were around twice the value of the slope of the $E_{1/2}$ vs. pH plots. This fact is consistent with an electrode process involving a follow-up protonation step. Indeed, on the rising part of the polarographic wave at potentials between 0.04 and 0.10V in the pH range between 1 and 3, the current was found to be directly proportional to $[H^+]^{0.4}$ which is close to $[H^+]^{0.5}$ which would be expected for a postkinetic current.

The ionic strength of the supporting electrolyte was found to have a dramatic effect on the shape of the polarograms of vitamin B_{12a} . When the ionic strength is increased at nearly constant pH, the dip in the polarogram begins to decrease and almost completely disappears at an ionic strength of around $1M$ in pH 3 to 4 media.

Effect of concentration, temperature, and mercury column parameters.—The relationship between current and vitamin B_{12a} concentration was also investigated at various potentials. Figure 6 shows these results for

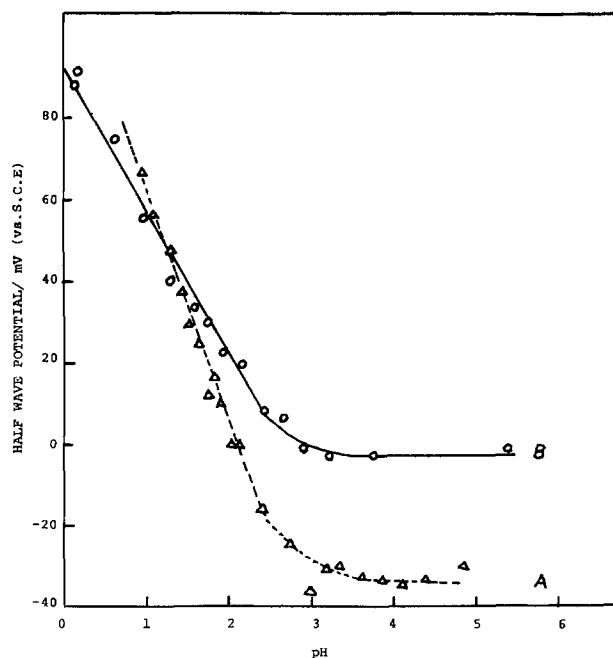


Fig. 5. Plot of $E_{1/2}$ vs. pH for 2.0×10^{-4} vitamin B_{12a} (A) $1M Na_2SO_4$, drop time of 3.0 sec. (B) $0.1M H_2SO_4$, drop time of 0.5 sec.

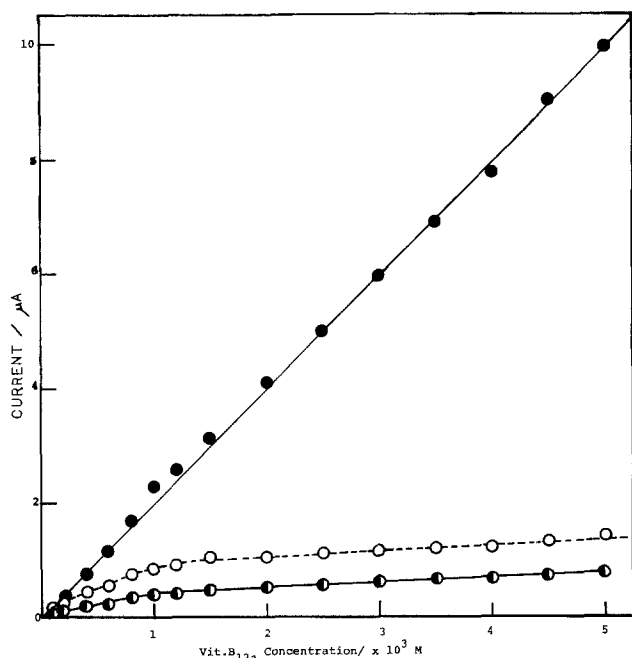


Fig. 6. Current vs. concentration of vitamin B_{12a} at various values of potential: ●—● diffusion limited potential, ○—○ peak potential 0.0V, ●—● valley potential -0.15V. The electrolyte is 0.1M H₂SO₄, pH 1.2.

the potential of the peak current, valley current, and diffusion plateau current. The peak current has a linear increase with concentration up to about 1.5×10^{-3} M and then reaches a steady state. The valley current (i.e., at the bottom of the dip) shows very similar behavior. At -0.5V which is on the diffusion plateau the current increases linearly with concentration throughout the entire concentration range used. These results indicate that the potential range from peak potential through the valley potential and up the ascending branch of the curve is a region of blockage of the electrode reaction by the product of the electrode reaction, vitamin B_{12r}, and its protonated form.

The effect of temperature can be seen in Fig. 7 which shows a series of polarograms recorded from 27° to 75°C. The inhibited nature of the current in the valley is clearly seen at 27° and 40°C, whereas at 56° and 75°C the valley current-time profiles lose their inhibited nature. As the temperature increases the peak becomes more of a plateau region and the dip or valley becomes more pronounced. The most likely cause of the current-time profiles at low temperature is an electrode process blocked by adsorption as concluded by Imhoff (7). The computed temperature coefficients of the current both at the peak and valley potentials are positive (1.0%) so that these currents are not adsorption controlled which would be indicated by a negative coefficient (20).

Further information on the nature of the electrode process was obtained from a study of current as a function of the height of the mercury column, h . This study was made for different potentials on the d-c polarogram of 4×10^{-3} M vitamin B_{12a} in 0.1M H₂SO₄ solution, pH 1.2. The slope of the $\log i$ vs. $\log h$ plot was found in the following regions of the polarograms: on the rising part of the initial peak (+0.2 to 0.06V), near the peak potential (+0.00V), on the descending branch of the current-potential curve, in the valley (-0.14V), on the ascending branch of the curve (-0.18 to -0.3V), and finally on the diffusion plateau (-0.5V). The slope at the most positive potential was close to zero showing the independence of the current on the column height and indicating kinetic control by the follow-up chemical reaction. On the peak, descend-

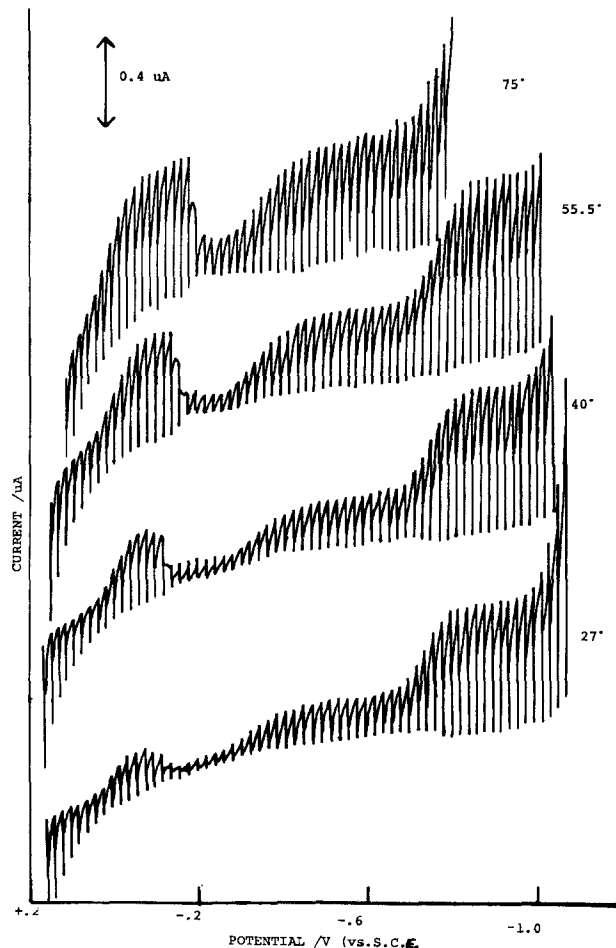


Fig. 7. Polarograms of 1.6×10^{-4} M vitamin B_{12a} in 0.01M Na₂SO₄ (pH 3.0) at various values of temperature.

ing branch, and the ascending curve, the exponent was between 0.37 and 0.16 so that there is a mixed control most likely by slow electron transfer and diffusion until diffusion control takes over on the plateau where the exponent was 0.43. Figure 6 shows that the i vs. c curve reaches a maximum at the peak and valley indicating a blocked electrode reaction, however, the $\log i$ vs. $\log h$ plot shows that these are not adsorption currents. Thus reduction can take place even on a blocked surface (7).

In addition to the independence of h on the polarographic current another criterion for a following chemical reaction (postkinetic current) is the shift in $E_{1/2}$ with drop time. The $E_{1/2}$ value should shift by ca. 30 mV per decade of drop time for a postkinetic current. An irreversible electrode reaction also shows a shift of $E_{1/2}$ with drop time, however, in this case only if the charge transfer coefficient, α , is unity would the shift be 30 mV and for $\alpha = 0.5$ the $E_{1/2}$ shift is 60 mV. Values of $E_{1/2}$ were determined for six drop times in 0.5-4.5 sec range and the plot of $E_{1/2}$ vs. $\log t$ had a slope of 23 mV per log unit. Again this value is additional evidence for a postkinetic current.

Another mercury column parameter which was studied was the drop time as a function of potential. These measurements were performed at various pH values and ionic strengths with the view that the curves would qualitatively resemble surface tension vs. potential curves. Figures 8 and 9 show these drop times vs. potential curves. As can be seen in the presence of vitamin B_{12a} the total curve is lower than the pure supporting electrolyte curve indicating that adsorption is present at all pH values and ionic strengths over a wide potential region. Almost identical drop time vs. potential curves were obtained in 0.1M Na₂SO₄ at various pH values from 2.0 to 8.0.

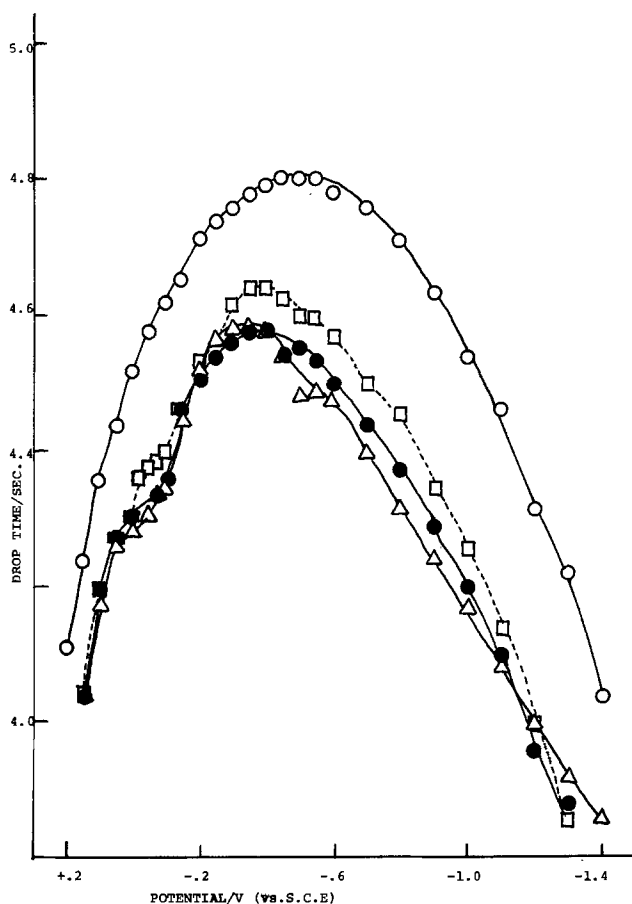


Fig. 8. Drop time vs. potential curves at various values of pH: ○—○ pure electrolyte 0.1M HC₂H₃O₂; □—□ vitamin B_{12a} in acetic acid buffer, pH 5.0; ●—● vitamin B_{12a} in acetic acid buffer, pH 4.2; △—△ vitamin B_{12a} in acetic acid buffer, pH 3.5. All vitamin B_{12a} concentrations are 1.6×10^{-4} M.

Both figures show a peculiar inflection from 0.0 to -0.1 V which is in the same potential region as the peak and dip in the polarographic curves. Also this inflection is found to decrease with an increase in pH (Fig. 8) suggesting that at low pH the protonated vitamin B_{12r} which is the species present at the electrode surface in the potential region of the inflection is the cause of the inflection. This inflection is interpreted as caused by a rearrangement of the adsorbed molecule on the electrode surface. Similar results and interpretation have been recently obtained using differential double layer capacity measurements (11). Furthermore as the pH decreases, the drop time vs. potential maximum shifts in a positive direction indicating cationic adsorption, i.e., of the protonated vitamin B_{12r}. It is seen in Fig. 9 that increasing the ionic strength shifts the maximum to more negative potentials in an NaNO₃ medium at pH 2.1. In addition, the total profile of the curves drops with increasing ionic strength. Both these observations indicate that these changes are due to anionic adsorption which is increasing with increasing electrolyte NaNO₃ or Na₂SO₄ concentration. Although the polarographic dip nearly disappears at high ionic strength in pH 3-4 media the nature of the drop time-potential curve indicates that the vitamin B_{12r} and B_{12H}⁺ are not desorbed at high ionic strengths and that specific anionic adsorption is taking place under these conditions. The insert in Fig. 9 shows the effect of temperature on the drop time vs. potential curve. It is seen that even at an elevated temperature of 76°C the separation of the pure electrolyte curve from that with B_{12a} added is still present indicating that although adsorption decreases at higher temperatures, especially at the potential extremities, it is still present. The curve in the potential region of the inflection

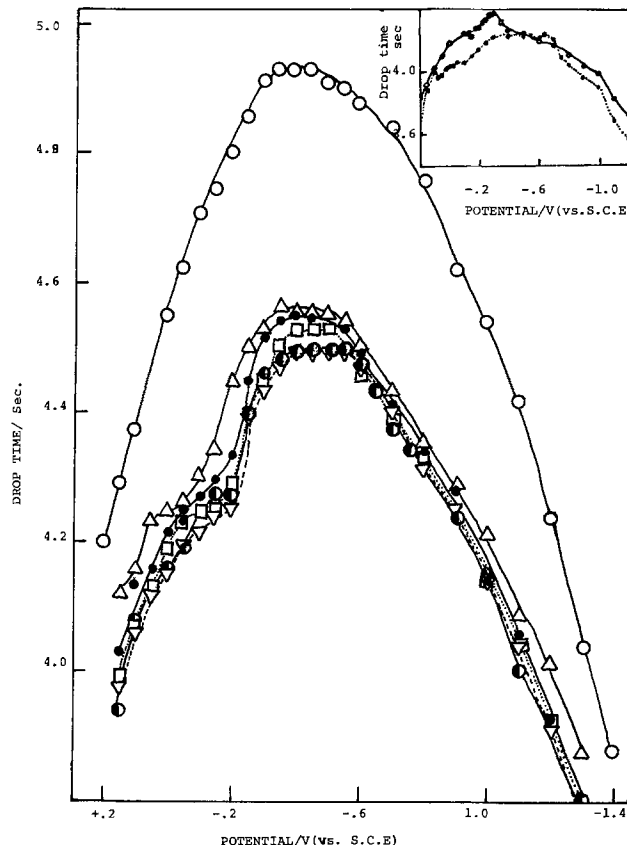


Fig. 9. Drop time vs. potential curves at various values of ionic strength of NaNO₃: △—△ vitamin B_{12a} in 0.1M NaNO₃, ●—● vitamin B_{12a} in 0.3M NaNO₃, □—□ vitamin B_{12a} in 0.5M NaNO₃, ●—● vitamin B_{12a} in 0.7M NaNO₃, ▽—▽ vitamin B_{12a} in 0.9M NaNO₃. Room temperature. Insert: ○—○ 0.1M NaNO₃ at 76°C, ●—● vitamin B_{12a} in 0.1M NaNO₃ at 76°C. All vitamin B_{12a} concentrations are 1.6×10^{-4} M.

still indicates that this effect is present although it is much less pronounced at the higher temperature.

In an effort to decrease adsorption of vitamin B₁₂ compounds, various surfactants were added. This technique proved to be effective in the study of the B_{12r} to B_{12s} system (6). We have tested Triton X-100, a nonionic surfactant, Triton QS30, an anionic surfactant, and several other anionic surfactants (decyl, octyl, hexyl, or butyl) sodium sulfates. The Triton surfactants had no effect on the maximum which was originally taken as evidence that the maximum was not a normal polarographic maximum. The effect of sulfate surfactant on the polarographic wave of 2×10^{-4} M B_{12a} in 0.1M Na₂SO₄ (pH 4.0) did show some interesting effects. At concentrations of the surfactants up to 5×10^{-3} M the peak current was completely suppressed and an irreversible wave developed starting at around 0.0V. On increasing the surfactant concentration the usually observed peak and valley reappeared, but at more positive potentials and with higher concentration the second diffusion current plateau disappeared. Thus, the surfactant which competes for adsorption sites with the protonated vitamin B_{12r} appears to either make the electrode simply irreversible at low surfactant concentrations or produces a similar effect to the protonated vitamin B_{12r} at higher surfactant concentrations with the additional effect of suppressing the second wave completely.

Interpretation of the electrode process.—The cyclic voltammetry and drop time vs. potential curves indicate that B_{12r} and its protonated form are adsorbed on the electrode surface depending on the potential. Weak vitamin B_{12a} adsorption is also indicated since the cathodic peak current rises above a square root dependence on scan rate at scan rates above 100 mV per

sec⁻¹. The nature of the DPP wave at ca. 0.2V, furthermore, shows strong adsorption of the electrode product and this wave is probably related to the Brdicka adsorption waves (21) of d-c polarography.

The inflection on the drop time-potential curve, which mirrors the dip on the polarographic curve, is still present at elevated temperatures, but disappears at pH values above 5.0. We, therefore, conclude that the protonated vitamin B_{12r} is the most effective blocking species. While vitamin B_{12a} and B_{12r} may only differ in structure in a minor way (22), the protonation of the nucleotide base leads to the unfolding of this chain portion of the molecule. A model of the compound shows a doubling of the linear dimensions of the molecule and indicates that the adsorbed state of the protonated molecule would cover much more surface area than the nonprotonated molecule.

The dependence of the current on the square root of the hydrogen ion concentration, the positive shift of $E_{1/2}$ with pH, and the independence of the current on the column height at the beginning of the polarographic curve all indicate that a homogeneous post-kinetic chemical protonation reaction is kinetically coupled to the electrode process. Also, there is no evidence that a prior chemical step involving the protonation of vitamin B_{12a} is taking place at the DME in the pH range investigated (pH 1-3), the pK_a of this reaction is -2.4 (23).

A current-potential expression for the electrode process in the potential region +0.2-0.0V can be obtained using the steady-state approach as illustrated by Guidelli (24). The electron transfer process is given by the expression

$$\frac{i}{nFA} = C_A k_2 - \theta_R \bar{k}_2 \quad [1]$$

where C_A is the volume concentration of vitamin B_{12a} in the reaction layer and θ_R is the fraction of the surface occupied by vitamin B_{12r} in the adsorbed state, the other variables have their usual significance. The volume concentration of vitamin B_{12a} has been used in Eq. [1] since the cyclic voltammetry experiment indicates that the current is due to a diffusing species at slow sweep rates. The anodic current is clearly due to adsorbed species and thus θ_R has been introduced in Eq. [1]. The follow-up chemical reaction is considered to be in a steady state with the electrode reaction. This current is represented by

$$\frac{i}{nFA} = \mu k_1 [H^+] C_R \quad [2]$$

where the backward step in Eq. [2] has been neglected, k_1 is a first-order rate constant, and μ is the Brdicka-Wiesner reaction layer thickness (24). The follow-up protonation is definitely a homogeneous chemical step as shown by the dependence of the current on the square root of the $[H^+]$. For short drop times (0.5 sec), a linear adsorption isotherm $\theta = \beta C$ is assumed to hold with $\beta = \beta_M e^{-\alpha(E-E_M)}$, where β_M is the maximum adsorption constant, α is the adsorption coefficient, and E_M is the potential of maximum adsorption. The linear form of the potential dependence is taken because of the very strong adsorption (25) and because this form fits the data as opposed to a quadratic form. Use of Eq. [1], [2], the adsorption isotherm, and $\mu = \sqrt{D_R/k_1[H^+]}$ yields

$$\frac{i}{nFA} = \frac{k_1 C_A}{1 + [(k_2 \beta_M e^{-\alpha(E-E_M)}) / \sqrt{D_R k_1 [H^+] }]} \quad [3]$$

For the condition $k_2 \beta > \sqrt{D_R k_1 [H^+]}$, one obtains a current which is proportional to $\sqrt{[H^+]}$, and by approximating C_A by the Ilkovic equation, the final result is

$$\frac{i}{i_D - i} = \sqrt{\left(\frac{3\pi}{7}\right) \frac{D_R k_1 [H^+] t}{D_A \beta}} \exp \left[-\frac{nF}{RT} (E - E^\circ) + \alpha (E - E_M) \right] \quad [4]$$

The factor $\sqrt{3\pi/7}$ will be slightly in error as shown by more rigorous derivations in the absence of adsorption (26, 27). Equation [4] when plotted as E_{DME} vs. $\log(i/(i_D - i))$ will have a slope larger than the Nernst factor. Also in agreement with the experimental data, the slope from the $E_{1/2}$ vs. pH plot should be one-half the slope from the E_{DME} vs. $\log(i/(i_D - i))$ plot.

The condition $k_2 \beta > \sqrt{D_R k_1 [H^+]}$ indicates that the electron transfer rate constant for vitamin B_{12a} to B_{12r} should be large, but the condition also depends on β which may also be large. A logarithmic plot of E_{DME} vs. $\log(i/(i_D - i))$ as given by Eq. [4] will be a straight

line with a slope of $-1 \left| \left(\frac{nF}{RT} - \alpha \right) 2.3 \right.$ which will

be larger than the Nernst factor, 59.2 mV, as was found experimentally. The plot of $E_{1/2}$ vs. pH should have a positive slope one-half that of the latter value and this fact was also verified experimentally (Table I). Calculation of k_1 however, depends on knowing β which must be measured independently. The data appear to be consistent with the current-potential relationship derived.

The electrode mechanism giving rise to Eq. [3] involves protonation of a solution vitamin B_{12r} species. Thus the adsorption-desorption equilibrium must be reversible.

In order for the protonation to be the rate-determining follow-up step it must be faster than a protonation mechanism involving side chain opening and subsequent protonation of free dimethylbenzimidazole. The latter step would be diffusion controlled [the k for imidazole protonation (28) is $1.5 \times 10^{10} \text{ M}^{-1} \text{ sec}^{-1}$]. Since the experimental results show that at low pH the reaction is dependent on $[H^+]$ we concluded that the pathway has an initial attack of the proton on the base-on species. If the rate constant for this protonation is also very large a subsequent step of side chain opening of the protonated species would be rate determining.

As the potential is moved into the region of the dip in the polarographic curve, the assumptions of low coverage and rapid adsorption equilibrium for the various cobalamin moieties break down completely. From Fig. 8 the maximum of the drop time vs. potential curve comes at -0.30V for pH 3.5 indicating that the maximum coverage moves to more positive potentials as the pH is decreased. We also conclude that there is high electrode coverage over a broad range of potentials as illustrated by the inflection and the rounded top of Fig. 8 (7, 11). The fact that the plot of current as a function of vitamin B_{12a} concentration in acidic media reaches a plateau for both the peak and valley potentials is in agreement with the concept of electrode blockage at sites covered by the product of the electrode process, protonated base-off vitamin B_{12r}. Since the polarographic dip only occurs at a low pH, this phenomenon must be attributed specifically to adsorption of protonated vitamin B_{12r}.

Table I. Comparison of the slopes of logarithm current vs. potential data and $E_{1/2}$ vs. pH data

| Conditions | $\frac{\Delta E / \Delta \log(i/(i_D - i))}{\text{mV}}$ | $\frac{\Delta E_{1/2} / \Delta \text{pH}}{\text{mV}}$ | pK _a |
|--|---|---|-----------------|
| 1.0M Na ₂ SO ₄ (drop time equals 3.05 sec) | 122 | -56.7 | 2.7 |
| 0.1M Na ₂ SO ₄ (drop time equals 3.05 sec) | 117 | -59.7 | 2.8 |

In the region of the peak and valley of the polarographic curve, the electrode potential is at least 0.1V positive to the point of zero charge (ca. -0.3V) and the electrode should be positively charged. Specifically adsorbed protonated B_{12r} will increase the positive surface charge although specifically adsorbed anions should decrease it. The drop time *vs.* potentials curves, indeed, show that both protonated vitamin B_{12r} and NO_3^- can be simultaneously adsorbed. However, a net positive surface charge would account for retardation of the charge transfer rate in the region of the dip due to charge repulsion of the positively charged vitamin B_{12a} . An increase in ionic strength causes the dip to almost completely disappear. This result can be explained by three phenomena: (i) a decrease in the effective thickness of the diffuse double layer, (ii) a decrease in the net positive surface charge due to increased specific anion adsorption, and (iii) desorption caused by increased ionic strength.

In the region of the dip a linear isotherm can no longer be used since the electrode coverage is high. Once the potential reaches a value where vitamin $B_{12r}H^+$ is adsorbed we can envisage both an electrostatic repulsive effect and a blockage effect due to the adsorbed molecules so that the rate constant for electron transfer on the covered electrode surface would be much lower than that for the uncovered surface. Here the reaction becomes totally irreversible. The inflection on the drop-time *vs.* potential curves (Fig. 8-9) ends around -0.2V which is in the valley of the current *vs.* potential curve. This inflection indicates a rearrangement of the adsorbed molecules and the new configuration could allow electron transfer as the potential is moved negative even though the surface is still covered. As the current rises to the first plateau, between ca. -0.2 to -0.4V the surface coverage has increased to a maximum and then electron transfer must take place on the covered surface. However, now the value of forward heterogeneous rate constant increases because the potential is negative enough to overcome the activation energy barrier. The electrode process in this region is then controlled by slow-electron transfer and diffusion.

Conclusion

The investigation of the electroreduction of vitamin B_{12a} on a dropping mercury electrode in acidic medium (pH 1-5) has led to the conclusion that the structure of the interface dramatically influences the intrinsic rate of the reduction reaction. At potentials positive to the polarographic dip the electrode reaction is either reversible or quasireversible; whereas, at potentials negative to the dip the reaction is completely irreversible. Recently it was reported, by Tacconi, Lexa, and Saveant (12) from the results of a cyclic voltammetry study that the rate of this electron-transfer reaction on a vitreous carbon electrode is always quite irreversible ($k_s \sim 10^{-5}$ cm sec⁻¹). It would appear that the structure of the interfaces of the mercury and vitreous carbon electrodes are quite different which would explain the discrepancy. The latter authors did not investigate the shift in cathodic peak potential with pH. In our experiments the anodic shift in $E_{1/2}$ with decreasing pH definitely shows that electrode process must depend on the reduced species B_{12r} which is the only species that can be protonated in this pH range.

The theory of electron transfer processes (29) shows that the intrinsic rate constant of charge transfer, *i.e.*, the electron transfer probability, depends on the distance of the molecule from the electrode surface. With a large molecule like vitamin B_{12a} it is quite reasonable that the electrode interface structure will effect the orientation of the molecule and the distance of closest approach. Thus it is possible that the interfacial structure could effect the electron-transfer prob-

ability which depends on the molecule having a distance of closest approach.

The homogeneous exchange rate for the vitamin B_{12a}/B_{12r} couple has been measured by an NMR line broadening technique (30) and was found to be around 2.0×10^3 M⁻¹ sec⁻¹ and to be nearly independent of pH. Also this couple has the fastest exchange rate yet reported for a Co(III)-Co(II) couple. The electron transfer theory of Marcus (31) can be used to find a heterogeneous charge transfer rate constant, k_{het} , from the homogeneous exchange rate constant, k_{ex} . The values of k_{het} for B_{12a}/B_{12r} couple turns out to be around 1 cm/sec. On the basis of this calculation one would expect that under certain conditions the electrode reduction of vitamin B_{12a} to B_{12r} could be fast. The conditions under which Eq. [4] reduces to Eq. [3] is only consistent with a fast electron transfer reaction of vitamin B_{12a} to B_{12r} . Thus it can be concluded that when the Hg electrode is not blocked by adsorption the electron transfer rate for the B_{12a}/B_{12r} couple should be fast. The significance of these results for biochemical situations is that the electron transfer rate is very sensitive to the environment of the molecules.

Acknowledgment

The authors wish to thank Jack I. Morrow, Michael Weiner, and Charlotte Russell of this Department for their helpful discussions. This research was supported by the National Institutes of Health under HEW-PHS Grant 5 R01-AM18440 and by the City University under a Faculty Research Award Grant RF 10752N.

Manuscript submitted May 27, 1980, revised manuscript received Dec. 4, 1980.

Any discussion of this paper will appear in a Discussion Section to be published in the December 1981 JOURNAL. All discussions for the December 1981 Discussion Section should be submitted by Aug. 1, 1981.

REFERENCES

1. T. C. Stadman, *Science*, **171**, 859 (1971).
2. B. M. Babior, Editor, "Cobalamin," John Wiley & Sons, Inc., New York (1978).
3. B. Jaselskis and H. Diehl, *J. Am. Chem. Soc.*, **76**, 4345 (1954).
4. H. P. C. Hogenkamp and S. Holmes, *Biochemistry*, **9**, 1886 (1970).
5. R. L. Birke, G. A. Brydon, and M. F. Boyle, *J. Electroanal. Chem. Interfacial Electrochem.*, **52**, 237 (1974).
6. D. Lexa and J. M. Saveant, *J. Am. Chem. Soc.*, **98**, 2652 (1974).
7. D. W. Imhoff, Ph.D. Dissertation, Ohio State University, 1966, University Microfilms, Inc., Ann Arbor, Michigan.
8. J. W. Collat and S. L. Tackett, *J. Electroanal. Chem. Interfacial Electrochem.*, **4**, 59 (1962).
9. S. L. Tackett and T. W. Ide, *ibid.*, **30**, 510 (1971).
10. P. G. Swetik and D. G. Brown, *ibid.*, **51**, 433 (1974).
11. C. L. Schmidt and H. S. Swofford, Jr., *Anal. Chem.*, **51**, 2026 (1979).
12. N. R. de Tacconi, D. Lexa, and J. M. Saveant, *J. Am. Chem. Soc.*, **101**, 467 (1979).
13. D. Lexa, J. M. Saveant, and J. Zickler, *ibid.*, **99**, 2786 (1977).
14. T. M. Kenyhercz, T. P. DeAngelis, B. J. Norris, W. R. Heineman, and H. B. Mark, Jr., *ibid.*, **98**, 2469 (1976).
15. D. Dolphin, "Methods in Enzymology," Vol. XVIII, Vitamins and Coenzymes, Part C, S. P. Colonic and N. D. Caplan, Editors, p. 34, Academic Press, New York (1971).
16. T. M. Kenyhercz and H. B. Mark, *Anal. Lett.*, **7**, 1 (1974).
17. M. Youssefi and R. L. Birke, *Anal. Chem.*, **49**, 1380 (1977).
18. R. A. Firth, H. A. O. Hill, B. E. Mann, J. M. Pratt, and R. G. Thorp, *Chem. Comm.*, 1013 (1976).
19. D. Lexa and J. M. Saveant, *ibid.*, 872 (1975).
20. J. Heyrovsky and J. Kuta, "Principles of Polarography," p. 90, Academic Press, New York (1966).
21. R. Brkicka, *Collect. Czech. Chem. Commun.*, **12**,

- 522 (1947).
22. J. M. Pratt, "Inorganic Chemistry of Vitamin B₁₂," p. 102, Academic Press, London (1972).
 23. R. Brkicka, *Collect. Czech. Chem. Commun.*, **12**, 142 (1947).
 24. R. Guidelli, in "Electroanalytical Chemistry," A. J. Bard, Editor, Vol. 5, p. 149, Marcel Dekker, New York (1971).
 25. P. Delahay, "Double Layer and Electrode Kinetics," p. 106, Interscience, New York (1965).
 26. D. M. H. Kern, *J. Am. Chem. Soc.*, **76**, 1011 (1954).
 27. J. Koutecky, *Collect. Czech. Chem. Commun.*, **20**, 116 (1955).
 28. M. Eigen, G. G. Hammes, and K. Kustin, *J. Am. Chem. Soc.*, **82**, 3482 (1960).
 29. V. G. Levich, in "Advances in Electrochemistry and Electrochemical Engineering," Vol. 4, p. 333, Interscience, New York (1966).
 30. D. P. Rillema, J. F. Endicott, and N. A. P. Kane-Maguire, *J. Chem. Soc. Chem. Comm.*, **9**, 495 (1972).
 31. R. A. Marcus, *J. Chem. Phys.*, **43**, 679 (1965).

The Kinetics of the O₂/CO₂ Reaction in Molten Carbonate: Reaction Orders for O₂ and CO₂ on Porous NiO

Jack Winnick

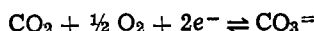
Department of Chemical Engineering, Georgia Institute of Technology, Atlanta, Georgia 30332

and Philip N. Ross, Jr.*

Lawrence Berkeley Laboratory, Materials and Molecular Research Division, University of California, Berkeley, California 94720

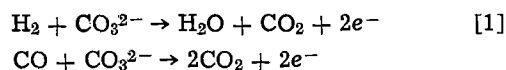
ABSTRACT

A molten carbonate electrolytic cell of the Broers and Ketelaar type was used to study the reaction



in an Li/K carbonate eutectic melt with porous NiO electrodes. A noble gas Au wire reference electrode was used to measure anodic and cathodic polarization during electrolysis. Steady-state polarization curves were obtained at 800-1000 K with a matrix of fifteen CO₂/O₂ mixtures: 0.5, 1, 10, 20, 50% CO₂/1, 19, 50% O₂. Kinetic analysis in the linear overpotential region indicated ($\partial \log i_0 / \partial \log P$) is near zero for CO₂ and 0.5 for O₂. The kinetic Tafel slope was measured from current-potential curves for current densities well below the diffusion limiting current and was found to be *ca.* RT/2F for cathodic polarization and *ca.* 3RT/2F for anodic polarization. The reaction orders are + 1/4 in CO₂ and + 5/8 in O₂ in the cathodic direction, and - 3/4 in CO₂ and + 1/8 in O₂ in the anodic direction.

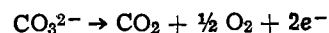
The molten carbonate fuel cell is undergoing extensive research and development (1-3) as a potential option for converting synthesis gas to electric power. In these cells a fuel gas containing principally hydrogen and carbon monoxide is electrochemically oxidized in the fuel cell anode



The carbon dioxide produced is recycled to the air intake for the cathode to form the gas mixture that is electrochemically reduced



This process is somewhat similar to that which occurs in the aqueous alkaline electrolysis cell used by NASA as a CO₂ concentrator (4-6). Ambient levels of CO₂ are removed at the cathode to be rejected at high concentration at the anode. A molten carbonate electrolyte cell also has the promise of use as a CO₂ concentrator, either with a reducing gas at the anode or in an electrolysis mode. In the latter case, application of an external potential produces a concentration gradient across the cell, the cathodic reaction being the evolution of CO₂ from the carbonate melt



Recent work on molten carbonate cells has focused on either the kinetics in free electrolyte on noble electrodes (7) or performance characteristics of subscale commercial cells with paste electrolyte and porous nickel electrodes (2, 3). Development of these cells as gas concentrators requires knowledge of the behavior under both anodic and cathodic polarization with very low CO₂ partial pressures. Fundamentally, observation of the kinetic reaction orders is an essential step in the evaluation of mechanistic sequences proposed for the O₂/CO₂ reaction.

The basic experimental approach we have used in this work is similar to that used in the classic experiments of Broers and Ketelaar (8). Here we employed paste electrolytes and *in situ* oxidized sintered nickel electrodes. For the purposes of measuring reaction kinetics, free-electrolyte cells with either rotating disk electrodes or smooth (nonporous) foil electrodes are preferred, since the transport characteristics of reactants (and products) can be carefully controlled. However, rotating disk electrodes for molten carbonate electrolytes have not yet been perfected even for gold electrodes. Nickel foils oxidized *in situ* are porous and thus present an uncontrolled (nonanalytic) electrode structure to the electrolyte. For kinetic studies of nickel oxide formed by *in situ* oxidation, which is the

* Electrochemical Society Active Member.

• Key words: cell, molten carbonate, polarization.

electrode material of interest for practical devices, the Broers and Ketelaar type cell appears to be the best available. With optimal experimental design, the gas diffusion properties of cells of this type are such that the transport limiting currents are very high, and a region of polarization exists where a kinetically controlled current-potential relation may be observed if the exchange currents are below ca. 1 mA/cm² (9).

In order to minimize the possible effects of diffusion, we have used a two-step approach to the determination of reaction orders. First, exchange currents at various P_{CO_2} and P_{O_2} were measured using the low polarization method. We assume a steady-state current-voltage relationship of the form

$$I = I_0 [\exp(\alpha_+ F\eta/RT) - \exp(-\alpha_- F\eta/RT)] \quad [3]$$

where $\eta = E - E_0$, α_+ is the anodic transfer coefficient, α_- the cathodic transfer coefficient ($\alpha_+ + \alpha_- = 2$). For $\eta \ll \alpha RT/F$, Eq. [3] simplifies to

$$I \approx (2FI_0/RT) \eta$$

so that $I_0 = (RT/2F) (\partial I/\partial \eta)_{T,P}$. The reaction orders can be obtained from the partial pressure dependence of I_0 and the values of the transfer coefficient α_+ and α_- . Let

$$\left(\frac{\partial \log I_0}{\partial \log P_{CO_2}} \right)_T = m \quad [4]$$

$$\left(\frac{\partial \log I_0}{\partial \log P_{O_2}} \right)_T = n \quad [5]$$

Then the reaction orders for the anodic (I_+) and cathodic (I_-) partial currents, after accounting for the Nernst effect (10), are

$$\left(\frac{\partial \log I_{\pm}}{\partial \log p_{CO_2}} \right)_{E,T} = \begin{cases} m - 1 + (\alpha_-/2) & \text{anodic} \\ m + (\alpha_-/2) & \text{cathodic} \end{cases} \quad [6]$$

$$\left(\frac{\partial \log I_{\pm}}{\partial \log P_{O_2}} \right)_{E,T} = \begin{cases} n - 1/2 + (\alpha_-/4) & \text{anodic} \\ n + (\alpha_-/4) & \text{cathodic} \end{cases} \quad [7]$$

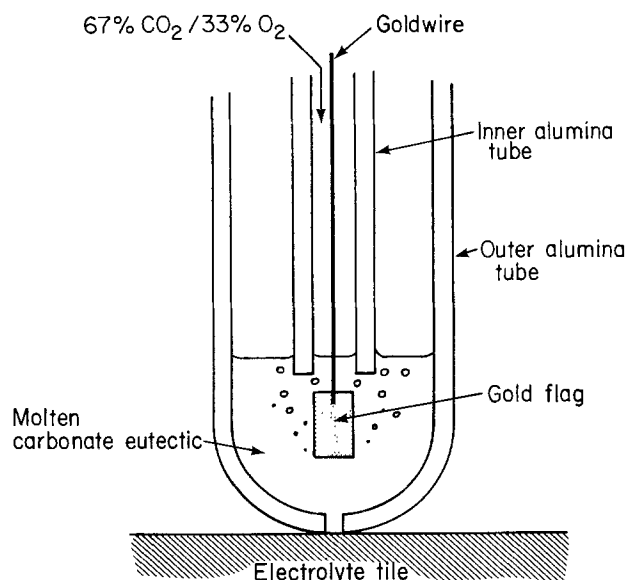
Second, the transfer coefficients were obtained from the slope of the Allen-Hickling plot

$$\ln [I / \{\exp(2F\eta/RT) - 1\}] = \ln I_0 - (\alpha_- F\eta/RT) \quad [8]$$

for current densities low enough so that concentration polarization within the electrode can be neglected.

Apparatus and Procedure

We assembled a molten carbonate test cell using paste electrolyte tiles and porous nickel electrodes typical of those used in current subscale molten carbonate cells. The cell was comprised of two housings of 316 stainless steel which hold the electrolyte tile between them. The electrodes, made of porous nickel, were 0.07 cm in thickness and 1.9 cm in diameter. They fitted snugly in the center of the cavity, in firm contact with the gas distributors (see Fig. 1). The faces of the housings were aluminized to provide a wet-seal against the tile upon melting of the carbonate. The upper housing had a 0.5 cm hole drilled through for the reference electrode, which was a gold flag suspended in the eutectic melt, as in Fig. 2. The noble gas mixture (67% CO₂, 33% O₂) was bubbled slowly through the inner alumina tube past the electrode and then out through the center tube. A small hole in the bottom of the outer tube allowed communication between the free electrolyte in the tube and that in the tile. The upper housing had a well in which was placed an iron-constantan thermocouple, sheathed in a stainless steel tube and mounted with a standard fitting. When assembled, the cell was mounted on a ceramic block, held in place with steel guides, and placed inside a furnace made of two clam-shell heaters. The gas inlet line, of stainless tubing, passed



REFERENCE ELECTRODE

Fig. 1. Schematic diagram of the electrolysis cell assembly

around the outside of the heater allowing the gas to be preheated before entry into the cell. The outlet line, also of stainless, led straight out of the furnace. The furnace was insulated with transite panels and fibrous zirconia felt. The entire apparatus was mounted in a steel frame and a pneumatic cylinder applied pressure to the top of the upper housing to assure firm contact between cell components.

The gases were calibrated mixtures purchased from Matheson. Fifteen binary combinations were used from the matrix 0.5, 1, 10, 20, 50% CO₂; 1, 19, 50% O₂, the balance N₂ in every case. The noble gas mixture 67% CO₂/33% O₂ was used as the reference gas.

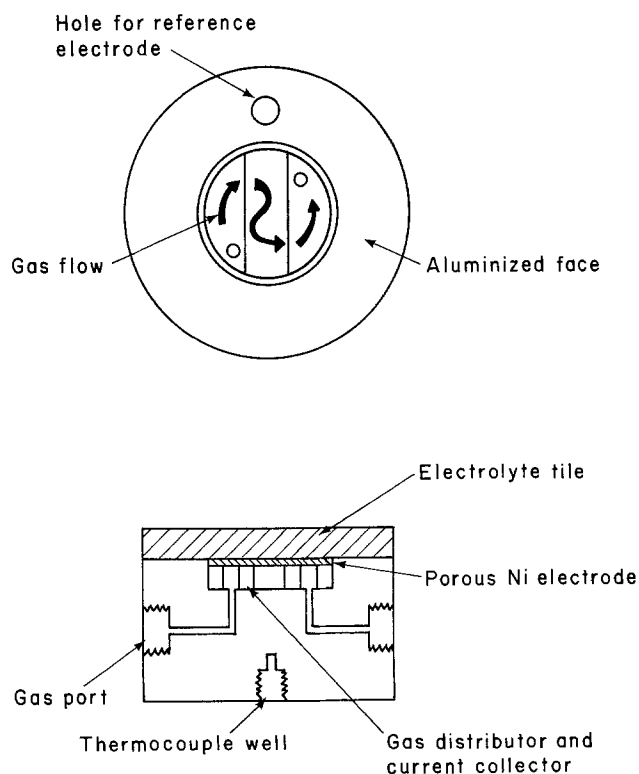


Fig. 2. Schematic diagram of the reference electrode

The experiments were begun by assembling the cell with an electrolyte tile supplied by Argonne National Laboratory. The composition by weight of this tile was 25.6% Li_2CO_3 , 29.4% K_2CO_3 , and 45.0% LiAlO_2 . The porous electrodes were fabricated by Gould for use in molten carbonate fuel cells and were pure nickel when the cell was assembled. The physical characteristics of these electrodes are given in Table I. At start-up, the cell was heated slowly while oxidant gases continually flowed over both electrodes. About 5 hr were necessary to bring the cell to 600°C. The cell was left in this open-circuit condition for 30-50 hr before experiments were begun to assure complete conversion of the electrodes to NiO.

Measurements were made only of the steady-state polarization of the top electrode using a Princeton Applied Research Potentiostat/Galvanostat (Model 371) in the galvanostatic mode. The gas flow to the top electrode was increased until no change in polarization was seen. The voltage reading was taken when apparent steady state was reached although some fluctuation was still seen. A current-interruption technique was occasionally employed to measure the IR drop between reference and top electrode. This loss averaged about 3 mV at 100 mA, as measured on an oscilloscope (Tektronix 5111) and was linear over the range studied. This yields a specific conductivity of $2.1 (\Omega \text{ cm})^{-1}$ for the 0.18 cm thick tile. The current was increased step-wise until the potential was about -0.5V (all potentials are relative to the 67% CO_2 /33% O_2 reference electrode). Larger polarizations were avoided because, in a sacrificial experiment, cyclic voltammetry disclosed that the reduction of NiO to Ni occurred at about -0.6V and cycling through this potential region irreversibly changed the electrolyte/porous electrode structure.

Results

The use of very low polarizations and the linear form of Eq. [3] to measure exchange current requires the absence of interfering reactions near the rest potential of the system, i.e., the observed rest potential is not a mixed potential. The rest potentials we observed were within ± 10 mV of the theoretical open-circuit calculated from the Nernst equation

$$E = E_o + \frac{RT}{2F} \ln P_{\text{CO}_2} P_{\text{O}_2}^{1/2} \quad [9]$$

After anodic or cathodic polarization, the cell returned quickly to the starting rest potential. These observations indicated the only faradaic process occurring at a measurable rate near the rest potential is the O_2/CO_2 reaction. Typical current-voltage curves in the very low polarization region are shown in Fig. 3. These curves were reasonably linear and showed clearly that the CO_2 partial pressure dependence of the exchange current, which is proportional to the slope of these lines, is very nearly zero. More than 100 sets of curves were obtained with varying gas composition and temperature. The correlation that resulted from analysis of the current-potential curves at very low polarization was

$$I_o = (1.5 \times 10^2) P_{\text{CO}_2}^0 P_{\text{O}_2}^{0.5} \exp[-6 \times 10^3 / (T + 273)] \quad [10]$$

where I_o is in A/cm^2 for $T = 550^\circ\text{-}750^\circ\text{C}$ and partial pressures of 0.1-0.5 atm. We can report only the exchange current density per external area of electrode,

since the internal area of the electrode contacted by electrolyte is not known. If all of the internal area were contacted, then about 100 cm^2 of NiO is available per cm^2 external area. At 700°C , this would mean an i_o of about 1.4 mA/cm^2 for 20% CO_2 /20% O_2 , about the same as that found by Appleby and Nicholson for smooth Au in Li/K eutectic melt (11).

The second step necessary for determining reaction orders according to Eq. [6] and [7] is the measurement of the cathodic transfer coefficient, α_- . The current-voltage behavior of these electrodes at polarization $ca. RT/F$ was typically like those in Fig. 4; no reaction limiting current was observed either anodically or cathodically, nor was a cathodic diffusion limiting current observed above -0.6V , where the NiO undergoes reduction to Ni. At current densities an order of magnitude below the diffusion limiting current, the currents are predominantly kinetically controlled. Typical Allen-Hickling plots for cathodic polarizations to $2 RT/F$ are shown in Fig. 5. According to Eq. [8], the intercept is just $\ln I_o$, which Fig. 5 shows corresponds to $I_o \approx 150 \text{ mA}$ (53.5 mA/cm^2 external), in good agreement with the Fig. 3 values. The average values found from analysis of ca. 100 polarization curves were 0.5 ± 0.1 for α_- , 1.6 ± 0.1 for α_+ . Figure 5 also shows the characteristic effect of CO_2 partial pressure on both I_o and α_- and, as in Fig. 3, the exchange current is essentially zero order in CO_2 pressure. From Eq. [6] and [7], the reaction orders are, therefore

$$\left(\frac{\partial \log I_{\pm}}{\partial \log P_{\text{CO}_2}} \right)_{E,T} = \begin{cases} -3/4 & \text{anodic} \\ +1/4 & \text{cathodic} \end{cases} \quad [11]$$

$$\left(\frac{\partial \log I_{\pm}}{\partial \log P_{\text{O}_2}} \right)_{E,T} = \begin{cases} +1/8 & \text{anodic} \\ +5/8 & \text{cathodic} \end{cases} \quad [12]$$

Discussion

It should be emphasized that the reaction orders given by Eq. [11] and [12] represent only apparent reaction orders, and not necessarily the true kinetic reaction orders. The distinction arises because the values of the transfer coefficient (α_-) were determined using porous electrodes, and the possible effects of diffusion on the polarization behavior of these electrodes must either be accounted for or eliminated experimentally. Modeling studies (9) on Ni sinter electrodes like those used here have indicated that diffusion polarization is not significant for total polarizations $ca. RT/F$ if the carbonate melt wets the electrode in an optimal fashion. The very high limiting currents observed with these electrodes (as in Fig. 4) indicate that the ideal thin-meniscus structure was approached with this cell configuration, and that polarization behavior observed here was essentially kinetically controlled. Independent studies (12) utilizing nonporous electrodes and applying transient techniques have indicated the transfer coefficient α_- is 0.6 ± 0.05 , close to that found here. However, while there is some support for a claim that the reaction orders found in this work are the kinetic orders, the determination is certainly not definitive. More properly, one should regard these reaction orders as representative of the polarization behavior of the paste electrolyte-Ni sinter electrode technology represented by our apparatus. As such, they are useful for systems analysis and for the design of large scale hardware based on this representative technology.

The cathodic reaction, of primary interest for fuel cell application, has a low but finite order in CO_2 pressure and the power density of the cell at constant voltage will increase with increasing CO_2 pressure. However, increasing CO_2 partial pressure decreases O_2 pressure, and since the reaction order for O_2 is higher than that for CO_2 , this will result in a power density function that has an optimum CO_2/O_2 ratio, i.e., an

Table I. Physical characteristics of Ni sinter electrodes

| | |
|---|----------------------------|
| Mean pore size, μm | 9 |
| Pore size distribution (80%), μm | 3 to 16 |
| Porosity | 77% |
| BET surface area | 0.15 m^2/g |
| BET area after oxidation | 0.20 m^2/g |

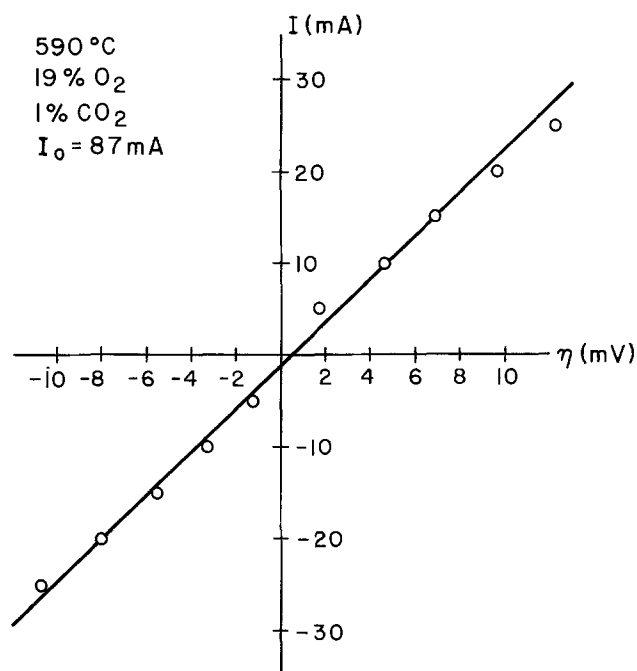
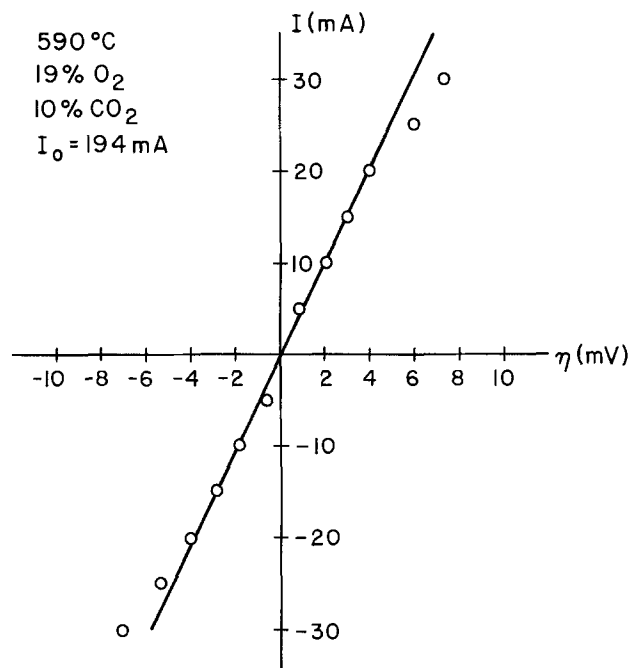
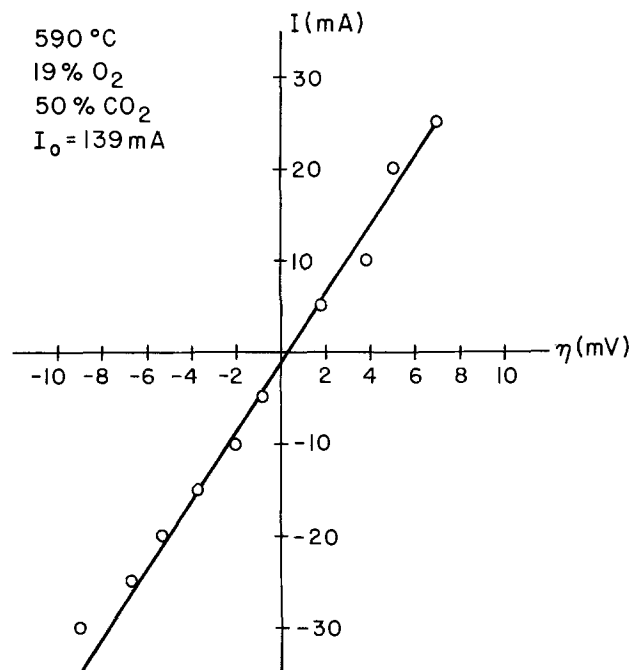


Fig. 3. Polarization curves near the rest potential as a function of CO₂ pressure.

optimum CO₂ recycle ratio subject to the constraint of no net rate of removal of carbonate from the cell.

The reaction orders in CO₂ are ideally suited to the operation of this cell as a gas concentrator. In this application, CO₂ is removed from a CO₂/O₂ mixture with very low (*e.g.*, 0.005 atm) CO₂ partial pressure by cathodic reduction to CO₃²⁻, and transported by anodic evolution to a carrier gas stream where the CO₂ pressure is relatively high. The cathodic reaction has a low order in CO₂, so that the kinetics for CO₂ reduction are high even at very low CO₂ partial pressure.

It is interesting to note that none of the reaction mechanisms yet proposed (7, 11) for the CO₂/O₂ reaction in alkali carbonate melts are consistent with the reaction orders we report here. They are also very different from the values reported by Appleby and Nicholson (7, 11) for Au, which may be indicative of differences in kinetics between Au and NiO electrodes. Since the possible influence of diffusion on the reaction orders has not been eliminated in this work, conclusive statements about reaction mechanisms cannot be made. It is also possible that the NiO electrode surface chem-

istry changes as a function of the CO₂/O₂ ratio by virtue of the Lux-Flood acid-base properties of the carbonate electrolyte, *i.e.*, the equilibrium concentration of oxide ion in the melt. Future mechanistic studies of the CO₂/O₂ reaction should consider the use of (specific) oxide ion electrodes to monitor possible changes in melt basicity with gas composition.

Acknowledgments

This work was done at the Lawrence Berkeley Laboratory with financial support from the National Aeronautics and Space Administration (Research Contract NSG-2193) and the U. S. Department of Energy (Contract W-7405-ENG-48). We thank Dr. Kim Kinoshita of the Argonne National Laboratory for supplying the electrolyte tiles and Mr. Charles Iacovangelo of the General Electric Research Center for valuable assistance in design of the cell.

Manuscript submitted Sept. 24, 1980; revised manuscript received Dec. 4, 1980. This was Paper 129 presented at the Hollywood, Florida, Meeting of the Society, Oct. 5-10, 1980.

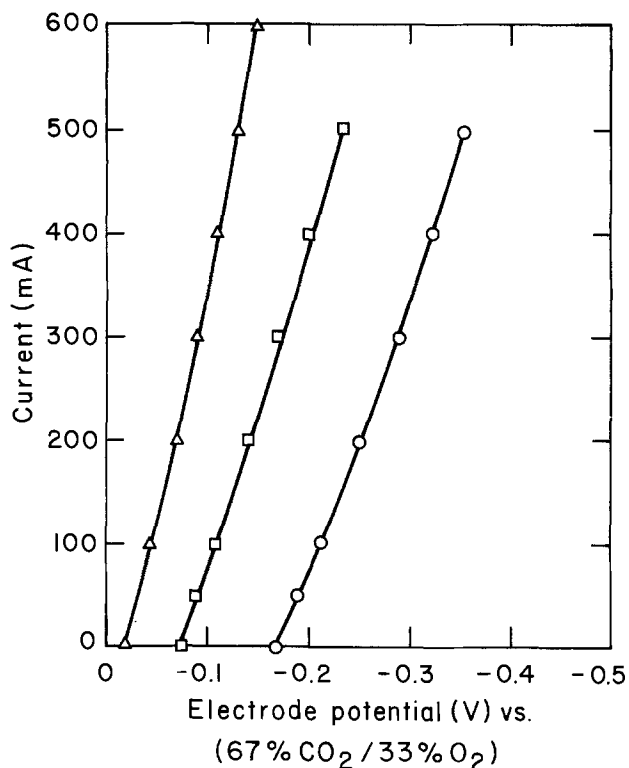


Fig. 4. Cathodic current-voltage behavior for porous Ni electrodes. 590°C. 19% O₂. Δ 50%, □ 10%, ○ 1% CO₂.

Any discussion of this paper will appear in a Discussion Section to be published in the December 1981 JOURNAL. All discussions for the December 1981 Discussion Section should be submitted by Aug. 1, 1981.

Publication costs of this article were assisted by the University of California.

REFERENCES

1. Argonne National Laboratory, Contract No. W-31-109-ENG-38, Report No. ANL78-71, August 1978.
2. United Technologies Corporation, Research Project 114-2, Report EM-956, December 1978.
3. Institute of Gas Technology, Project 9105, Final Report, April 1979.

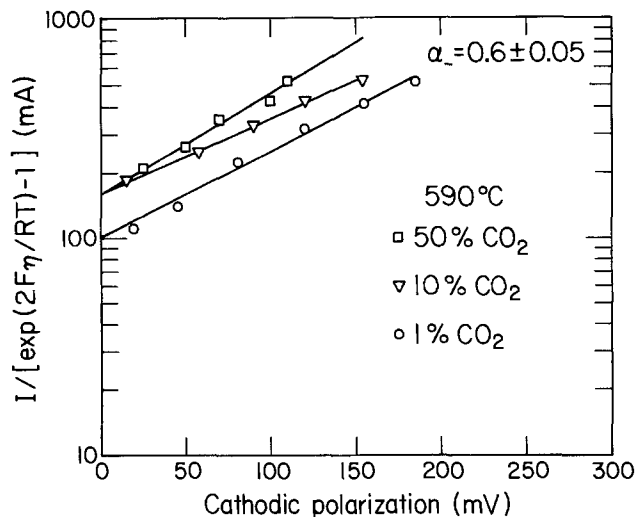


Fig. 5. Allen-Hickling plots of cathodic polarization data for porous Ni electrodes as a function of CO₂ partial pressure.

4. J. Winnick, R. D. Marshall, and F. H. Schubert, *I. E.C. Proc. Des. Dev.*, **13**, 59 (1974); F. H. Schubert, D. B. Heppner, T. M. Hallick, and R. R. Woods, NASA CR152250, Final Report, May 1979.
5. C. H. Lin and J. Winnick, *I. E.C. Proc. Des. Dev.*, **13**, 63 (1974).
6. C. H. Lin, M. L. Heinemann, and R. M. Angus, *I. E.C. Proc. Des. Dev.*, **13**, 261 (1974).
7. A. J. Appleby and S. B. Nicholson, *J. Electroanal. Chem. Interfacial Electrochem.*, **53**, 105 (1974); *ibid.*, **83**, 309 (1977).
8. G. Broers and J. Ketelaar, in "Fuel Cells," G. Young, Editor, pp. 78-94, Reinhold Publishing, New York (1960).
9. J. Selman, H. Mann, V. Sampath, and L. Marianowski, in "Electrode Materials and Processes for Energy Conversion and Storage," J. D. E. McIntyre, S. Srinivasan, and F. G. Will, Editors, pp. 656-81, The Electrochemical Society Softbound Proceedings Series, Princeton, N.J. (1977).
10. K. J. Vetter, "Electrochemical Kinetics," pp. 436-38, Academic Press, New York (1967).
11. A. J. Appleby and S. B. Nicholson, *J. Electroanal. Chem. Interfacial Electrochem.*, To be published.
12. J. Winnick and P. N. Ross, Jr., Abstract 129, p. 351, The Electrochemical Society Extended Abstracts, Hollywood, Florida, Oct. 5-10, 1980.

Electrocatalytic Activity of Cubic Sodium Tungsten Bronze

I. Effects of Platinum Doping, Anodization, and Platinum Pre-Electrolysis of the Electrolyte

Michael Francis Weber,^{*1} A. J. Bevolo, H. R. Shanks, and G. C. Danielson

Ames Laboratory-USDOE and Department of Physics, Iowa State University, Ames, Iowa 50011

ABSTRACT

The electrocatalytic activity of cubic sodium tungsten bronzes, including high purity and platinum-doped crystals, has been measured for oxygen reduction before and after anodization in both fresh and platinum pre-electrolyzed acid solutions. The effects of platinum doping, anodization, and platinum pre-electrolysis have been separately studied for current densities between 10^{-8} and 10^{-3} A/cm². A previously unreported break in the Tafel curve at 4×10^{-5} A/cm² was observed for all clean undoped bronze samples. Below this break the Tafel slope was -110 mV/decade while above it the Tafel slope was -200 mV/decade. Anodization of a pure bronze electrode failed to produce any change in the Tafel curve. Platinum pre-electrolysis of an anodized, undoped bronze produced a general increase in activity for all current densities. The break in the Tafel curve increased to 1×10^{-4} A/cm² while the Tafel slopes above and below this current density were unchanged. Platinum doping to 130 ppm increased the electrode activity at current densities below 1×10^{-6} A/cm², even when measured in platinum-free solutions before anodization of the electrode. The increased activity of an unanodized electrode in fresh solutions could be accounted for by the surface platinum concentration expected from the bulk platinum doping. Anodization of a doped bronze electrode increased the limiting current from 1×10^{-6} to 5×10^{-6} A/cm² even in fresh solutions while subsequent platinum pre-electrolysis increased the limiting current to 5×10^{-5} A/cm². Auger analysis of the anodized, platinum-doped electrode exposed to the platinum pre-electrolyzed solution revealed platinum on the surface of the bronze electrode at a coverage sufficient to account for the increased electrode activity below 5×10^{-5} A/cm². A small but reproducible increase in activity was found at high current densities near 10^{-3} A/cm² after either a pure or platinum-doped bronze electrode was exposed to a platinum pre-electrolyzed solution that lead to the research reported in the following paper (II).

After Sepa *et al.* (1) reported the sodium tungsten bronzes to be excellent electrocatalysts for oxygen reduction, several workers tried to confirm their results. Experiments by Broyde (2) did not reproduce the spectacular results. He reported only limited catalytic activity for oxygen reduction on powdered bronzes, including sodium, cerium, and nickel tungsten bronzes. A subsequent paper by Fishman, Henry, and Tessore (3) observed that traces of platinum on the sodium tungsten bronze surface were needed to produce the high catalytic activity. In their experiments, they found that platinum could be deposited on the bronze by dissolving minute traces of platinum from a large platinum electrode in the test cell. Bockris and McHardy (4) then claimed that only 400 ppm platinum doping of the bronze produced platinum-like behavior for oxygen reduction. They assumed that the surface concentration of platinum was the same as the bulk concentration, which led them to suggest that a synergistic effect for oxygen reduction existed in the platinum-bronze system. However, the findings of Bockris and McHardy (4) on platinum-doped single crystals were disputed by Randin (5) and by Weber and Shanks (6). On the other hand, the results of Bockris and McHardy were reproduced by Appleby and Van Drunen (7). Platinum pre-electrolysis (PPE) was used to clean the solutions used in their experiments, as it was in Bockris and McHardy's experiments, but possibilities of platinum contamination were not considered by either group. Fredlein (8) has recently reported on the effects of PPE on the activity of platinum-doped as well as undoped Na_xWO₃. He observed

only a change in Tafel slope from -240 to -120 mV/decade after his PPE treatment of undoped bronzes. Upon doping he observed increased activity at low current densities of the type reported in Ref. (4 and 7). He concluded that his PPE treatment, which was identical to that of Ref. (4), primarily resulted in the deposition of platinum onto the bronze surface. However the type of increased activity associated with platinum doping was different from that observed after his PPE treatment. The possibility that the change in Tafel slope after his PPE treatment was primarily due to removal of organic impurities from the bronze surface was not eliminated. A number of other papers have dealt with oxygen reduction on pure bronzes (9-11) and on platinum-coated bronze powders (12), but not for platinum-doped single crystals.

Bockris and McHardy (4) platinum pre-electrolyzed their solutions to reduce the organic contamination so that measurements could be made as low as 10^{-9} A/cm². Their interpretation of the enhanced activity as a synergistic effect failed to take into account the possibility of additional platinum contamination of their electrodes. On the other hand, Randin (5), who chose to avoid the possible contaminating effects of PPE, was forced to take measurements above 10^{-5} A/cm² because of the presence of other impurities in the electrolytes. Since nearly all of the results reported by Bockris and McHardy (4) were taken below 10^{-5} A/cm², a comparison of their results with those of Randin (5) necessarily involved extrapolation from one current density to another. As we shall see this proved to be impossible since the Tafel plots are anything but straight lines from 10^{-7} to 10^{-3} A/cm².

Clearly, then, what was required was the ability to take Tafel data below 10^{-5} A/cm² without PPE. By careful attention to the possible sources of contamina-

* Electrochemical Society Active Member.

¹ Present address: Chemistry Department, University of Toronto, Toronto, Canada, M5S 1A1.

Key words: surfaces, fuel cell, current density, Tafel slope.

tion from the gases, the electrolyte, the cell itself, and the bronze crystals we have been able to make Tafel measurements to current densities below 10^{-7} A/cm² without platinum pre-electrolysis. This system allowed reproducible data to be taken so that the effects of bronze surface treatments, anodization, bulk platinum doping, and PPE could be separately studied from 10^{-7} to 10^{-3} A/cm². In addition to the electrochemical studies, Auger electron spectroscopy was used to examine the surface of the treated bronze samples with special regard to the incorporation of Pt after various treatments. This surface analytical tool is especially suited for studies of suspected irreversible contamination of an electrode surface and it proved invaluable in unraveling the complex electrochemistry of the sodium tungsten bronzes.

The results of this investigation are reported in two parts. The first part, presented in this paper (I), concerns the effects of bulk Pt doping, anodization, and platinum pre-electrolysis. The second part, given in the following paper (II), concerns the activation of a pure bronze electrode by intentionally incorporating Pt onto its surface by a variety of electrochemical techniques.

Experimental

Crystal growth.—All measurements in this study were done on single crystals of sodium tungsten bronze, which were prepared by the electrolysis of a fused salt of sodium tungstate and tungsten trioxide as described by Shanks (13). By this method single crystals, approximately 2 cm or more on an edge, were obtained with a composition of Na_{0.7}WO₃. Platinum doping was achieved by the use of a platinum anode in the melt. The doped crystal contained 800 ppm atomic platinum referred to tungsten as determined by mass spectrographic analysis. Referred to Na_xWO₃ this concentration of platinum becomes 130 ppm by weight which is the form used in Ref. (4 and 8).

Sample preparation.—For the electrochemical studies the bronze crystals were either cleaved or cut on a high speed diamond saw into smaller pieces, a typical sample size being 4 × 4 × 6 mm. The cleaved crystals were cleaned in boiling conductivity water, but the crystals cut on the diamond saw required a more elaborate cleaning procedure. Contaminants were removed first by boiling in ethyl acetate, followed by hot concentrated NaOH, and finally by boiling in conductivity water. The samples cut on the diamond saw were then either polished, or one end was cleaved away to ensure a fresh, pure bronze surface. Polishing was performed after the crystal was mounted in Teflon using the method described by Nagy and McHardy (14).

The samples were mechanically polished on micro-cloth with alumina powder down to 0.05 μm particle size. Immediately before insertion into the cell, all samples were washed with acetone, then with isopropyl alcohol. The final cleaning was done with an isopropyl alcohol vapor phase degreaser. The area of each sample was determined from a photograph of the mounted crystal, with no corrections being made for surface roughness. After insertion into the cell, the potential on each electrode was cycled between -0.1 and 1.6V NHE for approximately 20 min to further clean the surface. Only small changes in the cyclic voltammetry curves were observed during this time.

Test cell and distillation unit.—Research in many areas of electrochemistry requires ultrahigh purity experimental conditions before reliable information can be obtained (15). The most notable problem area in this regard is the electrochemistry of oxygen. The correct rest potential of 1.23V HE for oxygen reduction in acid solutions can be obtained only under extremely stringent conditions of purity on carefully prepared electrodes (16-18). Fortunately, a good Tafel plot, with the correct slope and exchange current, can be obtained under somewhat less stringent conditions, although the problems are still serious.

A common practice is that of "pre-electrolyzing" the solution, usually with large platinum electrodes (19). However, it was suspected that trace amounts of platinum were dissolved from these electrodes (20) which could then plate out onto the test electrodes (6). If the electrode being studied is also platinum, then no problem should result, but such a situation limits the use of pre-electrolysis to a minority of experiments. Therefore, a cell of sufficiently high purity had to be constructed which permitted studies of oxygen reduction to be performed without the use of pre-electrolysis. This cell was connected to a high purity water distillation unit that permitted the *in situ* distillation of water and solution preparation. Complete details of this electrochemical test apparatus are given in a separate report (21). A brief description is given here.

The electrochemical cell had three compartments each constructed entirely of quartz and Teflon. The counterelectrode was a gold foil with H₂ gas bubbled over it. A palladium hydride electrode (22) was used as a reference electrode. The Pd-H electrode was constantly checked against a saturated calomel reference electrode since its potential tended to drift for long times after recharging with hydrogen. Thus all potentials given here are referenced to the normal hydrogen electrode using the relation

$$V_{\text{NHE}} = V_{\text{SCE}} + 0.242\text{V}$$

Since the effects of traces of platinum were being investigated, no platinum electrodes touched the solutions used for studies on the bronzes, except for those solutions that were Pt pre-electrolyzed.

Extensive efforts were made to purify the gases bubbled into the cell. "Zero oxygen" with 0.2 ppm total hydrocarbons (THC) was passed through a quartz tube of platinized asbestos at 450°C, then over moist KOH, and finally through two traps containing Linde 13X molecular sieve. When an inert atmosphere was needed "zero helium" (<0.5 ppm THC) was passed over hot copper turnings and through two liquid N₂ cooled cold traps also containing Linde 13X molecular sieve. Zero hydrogen (0.5 ppm THC) was passed through two traps of Linde 13X molecular sieve when a hydrogen atmosphere was required. The gas handling system was constructed entirely of acid-etched stainless steel and Pyrex tubing, with Fischer and Porter glass-Teflon valves and stainless steel Swagelock tubing connectors.

Platinum pre-electrolysis was done with a 20 cm² shiny platinum foil anode and a gold cathode carrying current of 20 mA for 24 hr prior to the exposure of the bronze electrode to the PPE solution.

The degree of cleanliness of the system is indicated in Fig. 1 by a cyclic voltage scan on a high purity platinum electrode. The platinum electrode was mounted in Teflon and polished in the same manner as described above for the bronze samples. No PPE of the solution had been performed. Well-defined hydrogen adsorption and desorption peaks and platinum oxide formation and reduction peaks are observed. No impurity oxidation peaks were observed at lower sweep rates or when the solution was stirred. Rest potentials on the platinum test electrode in fresh solutions were normally near 0.98V NHE. The only solution used in the cell for this study was 0.1N H₂SO₄ (pH 1.2) mixed *in situ* from Apache Chemical 99.9999% pure (distilled in Vycor) sulfuric acid. This pH value permitted comparison to the work of other investigators, particularly, Bockris and McHardy (4), and reduced corrosion currents to a minimum.

The catalytic activity of a sample for the oxygen or hydrogen reaction was determined from the Tafel plots of the current-potential data. The general electrochemical properties of the bronzes were studied by linear sweep cyclic voltammetry and these results were reported in a previous publication (23). Chemical compositional analysis of the electrode surfaces was performed by Auger electron spectroscopy. In addition,

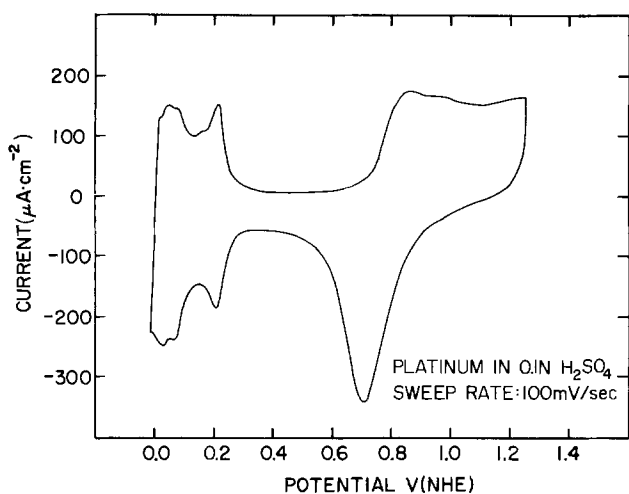


Fig. 1. Cyclic voltammogram for Pt taken in high purity test cell without Pt pre-electrolysis of the acid solution. The well-defined H_2 absorption and desorption peaks near 0.0V and PtO oxidation and reduction peaks near 0.7V indicate very clean experimental conditions in the cell.

scanning electron micrographs helped reveal the surface morphology of the samples.

Data for the Tafel plots on all samples were obtained galvanostatically, in the current density range 10^{-3} – 10^{-8} A/cm². Currents were generated with a very stable, constant current power supply (24). A Keithley Model 640 electrometer was used to measure the potentials, while its output was read on a Dymec Model 2401A five digit integrating DVM. All measurements were made at $25^\circ \pm 2^\circ C$. All samples required from 2 to 5 hr at each data point to reach a steady-state potential, which was defined to be a potential drift of less than 1 mV/10 min. True steady-state conditions were checked by allowing 9 hr for the steady-state condition to occur on approximately 1/6 of all data points. Also, the first point was allowed at least 8 hr to reach steady state. This procedure insured reproducible curves. Data were taken by starting at high currents and decreasing the current by halving it for each succeeding point. No difference in the steady-state data was observed if the data were taken by starting at low current densities. However, the time to reach steady state was longer if the data were taken at low current densities first. A similar effect was reported in Ref. (4 and 8). For a valid comparison to pure platinum, the Tafel plot on the platinum sample was obtained in exactly the same manner. For this reason, the Tafel plot shown for platinum is somewhat different than the data usually seen in the literature. In most figures shown here, a Tafel plot for O_2 reduction in platinum is given for comparison with the bronzes.

A variety of Tafel plots for the platinum can be found in the literature because of different measurement procedures or different solution purities. Most steady-state data on platinum involves a 2-5 min wait between data points. Prolonged cathodic polarization for O_2 reduction may result in the buildup of hydrogen peroxide in the solution, which results in a lowering of the observed potentials (25). Each Tafel plot for the bronzes required 2 or 3 days because of a 3-4 hr wait for steady state to occur at each point. Comparison with the bronze electrodes becomes difficult because platinum is more sensitive than the bronzes to the buildup of impurities in the cell during a 2 day Tafel measurement. Since the cell was rather well sealed, and ultrapure solutions could normally be stored for several weeks in the storage flask, the impurity was either hydrogen peroxide, which was produced during oxygen reduction, or residual impurities from the gas and solution that showed a preferential adsorption on the platinum electrode. In any case, the high rest potentials

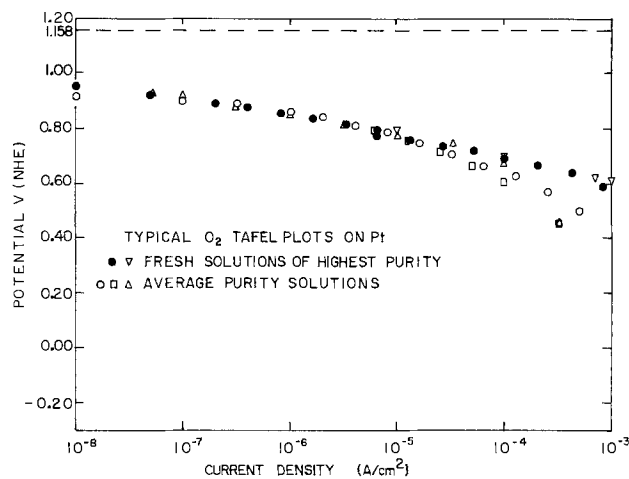


Fig. 2. Oxygen Tafel plots taken on a Pt electrode under the same experimental conditions as used for testing the bronze crystals. This data was taken without Pt pre-electrolysis of the solution.

of 1.00V NHE could not be reproduced after 1 day of measurements, and after 2 days of measurements, large deviations in potential occurred at the higher current densities on platinum. Our Tafel data on platinum are shown in Fig. 2. The solutions were not pre-electrolyzed, so the slope was less than the normal 100 mV/decade due to traces of impurities remaining in the solution. In 0.1N H_2SO_4 , the theoretical rest potential of the oxygen reaction is 1.158V NHE and is $-0.072V$ NHE for the hydrogen reaction.

Auger analysis.—The Auger analysis of the bronze surfaces was performed using a Physical Electronics Model 10-155 cylindrical mirror analyzer with a 5 kV-50 μA integral electron gun. Typically a 4 kV-5 μA electron beam, focused to 50 microns, was incident to the sample normal at an angle of 60° . Figure 3 shows a typical Auger spectrum of a pure Na_xWO_3 crystal before any electrochemical treatment. The most important transitions for each element were labeled by their electron energies. The carbon peak at 272 eV was always present and is due to approximately one monolayer coverage of hydrocarbons picked up by the sample as it was transferred from the electrochemical test station to the surface analysis chamber. Preferential desorption of oxygen by the focused 5 μA electron beam was observed and this resulted in an equilibrium oxygen to tungsten ratio closer to two than the bulk value of three. However, the electron beam current

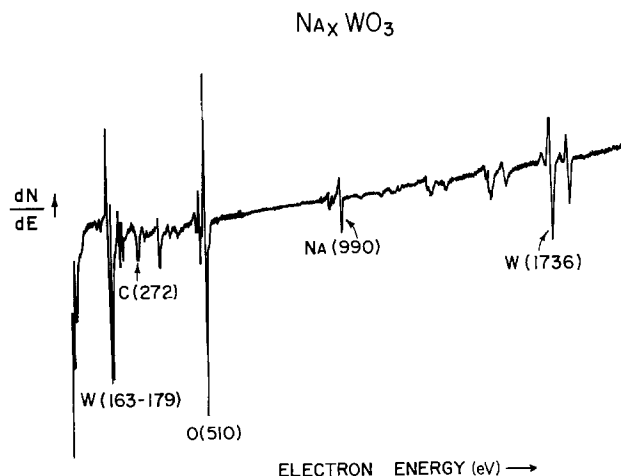


Fig. 3. Auger spectrum of an air cleaved single crystal of $Na_{0.7}WO_3$ prior to any electrochemical treatment showing the prominent Auger peaks of the tungsten bronze and the carbon peak due to the thin hydrocarbon overlayer. The peaks are labeled by their respective electron energies.

density could not be reduced any further without hampering the detection of small amounts of platinum on the bronze surface.

Results

Undoped Na_xWO_3 electrodes.—Figure 4 shows data for undoped Na_xWO_3 crystals before and after our PPE treatment as well as results for pure platinum and an undoped bronze in a helium-saturated solution. Also shown in Fig. 4 are the data from Ref. (5, 6, 8) for undoped bronze electrodes. In the complete absence of platinum, from either bulk doping or possible contamination by our PPE treatment, a pure Na_xWO_3 electrode does exhibit some activity for oxygen reduction when the results are compared to those taken in a helium-saturated solution. However, the exchange current density is estimated to be 10^{-14} A/cm² and the rest potential is near 0.5V (NHE), both of which are very low values. Not shown in Fig. 4 are the data on samples before anodization since the results are essentially unchanged after anodization. Also not shown in Fig. 4 are the data for polished or cleaved samples since there is little difference from that of the polished and NaOH etched sample used to take the data given in Fig. 4.

Two features of the Tafel curve shown in Fig. 4 taken prior to our PPE treatment have not been previously reported. First, we find a break in the Tafel curve at 4×10^{-5} A/cm² which moves to 1×10^{-4} A/cm² after our PPE treatment. This break was observed on all samples that had been thoroughly cleaned and measured in our test cell, but it was not observed in our first report on the bronze electrodes (6) where less stringent cell and sample cleanliness procedures were used. The second new feature is that below 1×10^{-4} A/cm² the Tafel slope is -110 mV/decade, close to -2 RT/F . All previous measurements in this current density range prior to any PPE treatment produced Tafel slopes near -4 RT/F , even our prior measurements (6) performed in a less clean environment.

After our PPE treatment of undoped bronzes slightly higher potentials at all current densities were observed with no change in Tafel slope at low current densities from the -2 RT/F value observed before PPE. The straight line Tafel behavior below 4×10^{-5} A/cm² down to current densities near 1×10^{-7} A/cm² indicates very low corrosion rates for the bronze electrodes.

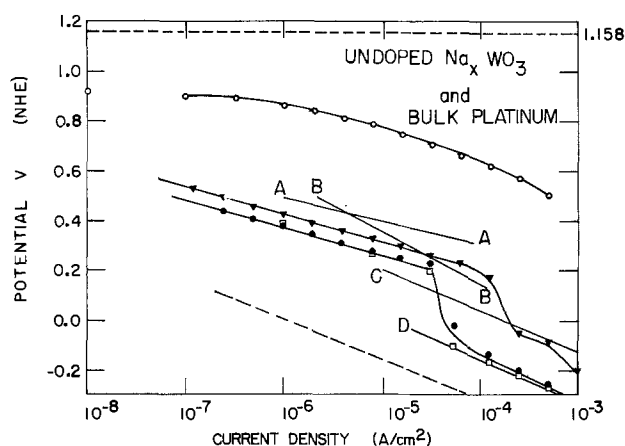


Fig. 4. Oxygen Tafel plots of an undoped bronze sample taken in fresh (\bullet , \square) and platinum pre-electrolyzed (\blacktriangledown) solutions. The dashed line represents the Tafel line for an undoped bronze in a helium-saturated solution. Also shown are Tafel plots of undoped bronzes taken from Ref. (8) before (B) and after (A) platinum pre-electrolysis and from Ref. (6) (C) and Ref. (5) (D) before platinum pre-electrolysis. Only this work (\bullet , \square) shows a slope of nearly -2 RT/F and a break in the Tafel plot at 5×10^{-5} A/cm² prior to platinum pre-electrolysis. All previous results show no break and a Tafel slope of approximately -4 RT/F . Tafel plot for pure platinum is also shown (\circ).

Platinum doped Na_xWO_3 electrodes.—Figure 5 shows data on bronze electrodes doped with platinum as a function of anodization and our PPE treatment. Prior to either anodization or PPE there is an increased activity below 1×10^{-6} A/cm², but no change in the Tafel plot above this current density when compared to an undoped bronze (Fig. 4). The increased activity below 1×10^{-6} A/cm² can only come from the presence of platinum atoms on the bronze surface due to the bulk doping.

Prolonged anodization of this sample at 1 mA/cm² to a potential of 9V prior to our PPE treatment significantly improved its activity for current densities between 1 and 5×10^{-6} A/cm². The rest potential of the anodized, doped bronze electrode reached 0.72V (NHE). No change in the Tafel curve was detected above 5×10^{-6} A/cm².

Our PPE treatment of the anodized, doped bronze electrode shown in Fig. 5, resulted in further increases in potential at all current densities. The rest potential rose to 0.8V (NHE) while increased activity occurred from 5×10^{-6} to 4×10^{-5} A/cm². Also there was an increase in potential above 4×10^{-5} A/cm² similar to that observed for an undoped bronze. It is significant that our PPE treatment of a platinum-doped bronze electrode (Fig. 5) produced a qualitatively different increase in activity from 5×10^{-6} to 4×10^{-5} A/cm² when compared to its effect on an undoped electrode (Fig. 4). This anodized, doped bronze electrode after PPE produced the highest electrocatalytic activity for oxygen reduction of any sample reported in this study. Its overpotential was only 0.1V larger than that of bulk platinum at all current densities below 1×10^{-5} A/cm². It was noted that if the doped samples were anodized for longer periods of time in the PPE solutions their activities would increase.

Auger analysis.—Figure 6 shows the Auger spectrum of a $\text{Na}_{0.7}\text{WO}_3$ sample doped with 130 ppm Pt after cleaving in air. Even at the highest possible gain no platinum signals were observed at 1667 and 2044 eV. It is estimated that the minimum detectable Pt/W ratio, averaged over the 25Å escape depth (26) expected for these high energy Auger transitions, is about 0.003 which is higher than the bulk Pt/W ratio of 0.0008. Figure 7 shows the Auger spectra of an anodized sample after it had been measured in a Pt

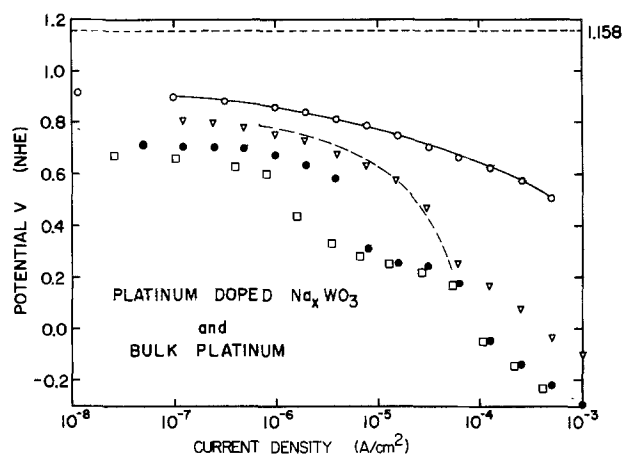


Fig. 5. Oxygen Tafel plots of a platinum-doped Na_xWO_3 electrode before anodization or platinum pre-electrolysis (\square), after anodization but before platinum pre-electrolysis (\bullet), and after both anodization and platinum pre-electrolysis (\blacktriangledown). Both anodization and platinum pre-electrolysis increase the electrode activity at lower current densities, while only platinum pre-electrolysis has any significant affect at high current densities. The increased activity below 10^{-4} A/cm² is believed to be due to increased surface platinum produced by anodization and pre-electrolysis. A Tafel plot for pure platinum (\circ) and that taken from Ref. (8) (- - -) for a doped Na_xWO_3 electrode before platinum pre-electrolysis but after anodization are also shown.

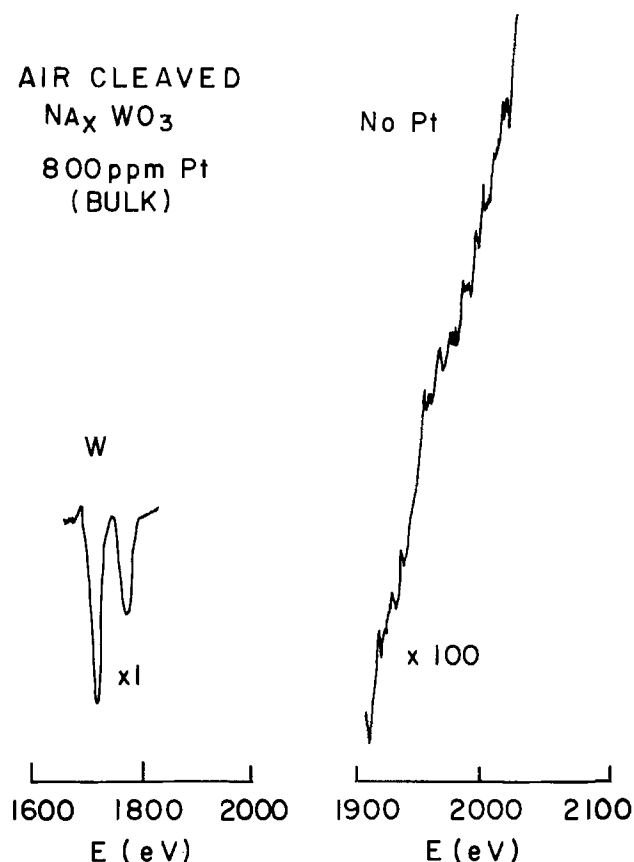


Fig. 6. Auger high energy spectra of a platinum-doped (Pt/W atomic ratio of 800 ppm) bronze crystal cleaved in air. No Pt (1967) Auger signal is evident.

pre-electrolyzed solution which resulted in the enhanced activity previously shown in Fig. 5. The presence of platinum Auger signals at their correct energies and relative intensities confirms that combined anodization and Pt pre-electrolysis results in an increase surface platinum coverage of the bronze electrode over and above the presence due to bulk Pt doping. From the relative sensitivity factors for these tungsten and platinum Auger transitions, measured from bulk metal samples taken under the same experimental conditions, we estimate the Pt/W ratio to be 1%. Assuming a WO_3 surface composition for the bronze sample the Pt concentration is 0.25% referenced to sodium, the most likely site to be occupied by the platinum atoms.

In the Auger spectrum of clean, bulk Pt there is a very intense transition at 64 eV. Because of a very small escape depth of about 4Å (26), this transition proved to be very sensitive to small changes in the surface carbon layer and could not be used to measure reliably the platinum surface coverage. Although considerably weaker than this 64 eV transition, the high energy peaks shown in Fig. 6 and 7 have escape depths of about 25Å so that they were much less sensitive to variations in the thickness of the hydrocarbon layer. In addition, these high energy transitions have nearly the same escape depth so that their intensity ratio is expected to be independent of the thickness of the carbon overlayer. The 0.25% Pt concentration quoted above assumed that the platinum is uniformly distributed over the 25Å escape depth of the Pt and W transitions. If the platinum is confined to the top monolayer (~2.5Å) of the bronze surface then the Pt coverage would be approximately ten times larger or about 3% for the Auger spectra shown in Fig. 7.

Discussion

Undoped Na_xWO_3 electrodes.—Referring to Fig. 4, all three previous investigations (5, 6, 8) in the ab-

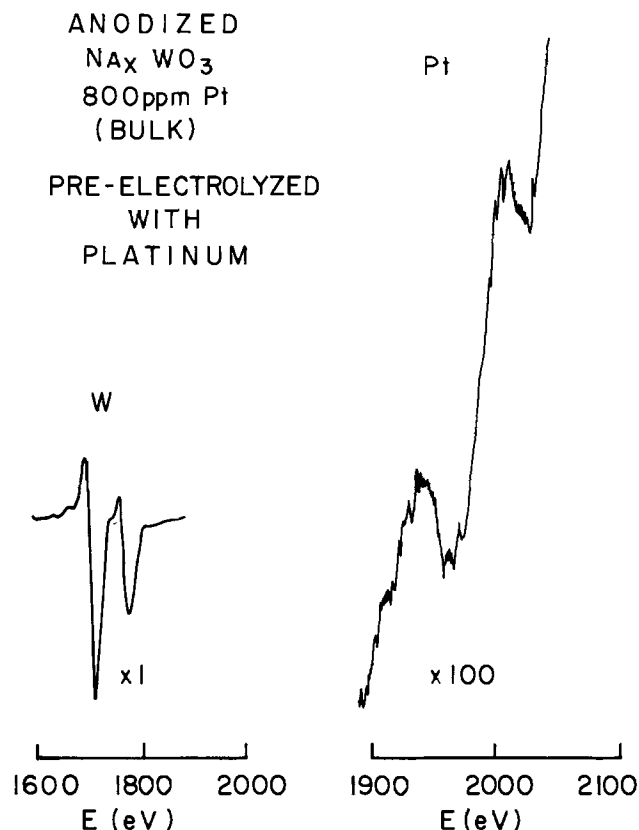


Fig. 7. Auger high energy spectra of platinum-doped (Pt/W atomic ratio of 800 ppm) bronze crystal after anodization and platinum pre-electrolysis treatment resulting in the Tafel plot denoted by ∇ in Fig. 4. The platinum doublet is clearly evident.

sence of PPE have nearly identical slopes of $-4 RT/F$ while our data in the absence of PPE show a slope of $-2 RT/F$ for current densities below $4 \times 10^{-5} \text{ A/cm}^2$. Only above the break in our Tafel plot does the slope change to $-4 RT/F$. A slope of $-2 RT/F$ was obtained even before any PPE treatment so that it cannot be associated with adsorbed platinum on the bronze electrode as Fredlein (8) has proposed. It is our contention that the $-4 RT/F$ slope is due to surface organic contamination of the bronze electrode whose source is either the electrode itself or the solution. Only by using stringent cell design and sample cleaning methods were we able to produce the $-2 RT/F$ in the absence of any PPE. Support for this assumption comes from our prior observations (6) under less stringent conditions that produce a $-4 RT/F$ slope and no break in the Tafel plot at $4 \times 10^{-5} \text{ A/cm}^2$. Also cyclic voltammograms of undoped bronzes in platinum-free solutions showed little change after the first sweep indicating a very clean surface. Fredlein (8) after PPE treatment observed a $-2 RT/F$ slope which suggests to us that the cause of this change in slope is the removal of organic contaminants by PPE of the electrolyte. Fredlein (8) ascribed this change in slope to adsorbed platinum released during PPE treatment. We reject this interpretation on two grounds. First as just discussed we observed a $-2 RT/F$ slope prior to any surface platinum contamination of the electrode by either PPE or bulk doping. Second, the type of changes in Tafel behavior observed after PPE by us, as well as Fredlein (8), is distinctly different than that observed on doped samples measured prior to PPE (see Fig. 4 and 5). We conclude that our samples were nearly free of organic contamination in fresh electrolytes and that the Tafel behavior shown in Fig. 4 with the break at $4 \times 10^{-5} \text{ A/cm}^2$ is a test, along with the $-2 RT/F$ slope, of the cleanliness of the bronze surface. This conclusion is supported by the fact that after our PPE treatment no change in the $-2 RT/F$ slope is evident

below 4×10^{-5} A/cm² while the break at 4×10^{-5} A/cm² increased after our PPE, both of which are readily explained as a further cleaning of the electrodes by the PPE treatment, if we interpret this break as a limiting current for oxygen reduction on a platinum-free bronze surface $i_L(B)$.

It is of some interest to compare our results on undoped bronze electrodes with those of Bockris and McHardy (4) and Randin (5). The data of Ref. (4) (not shown for clarity in Fig. 4) taken after PPE is identical to our data taken after PPE over the complete range in current density from 1×10^{-7} to 1×10^{-4} A/cm² that is available from Ref. (4). The data of Ref. (4) did not extend to current densities above 1×10^{-4} A/cm² where we observed a break in the Tafel slope. However below 1×10^{-4} A/cm² the slopes are identical at $-2 RT/F$ which we interpret to mean that the samples used by Bockris and McHardy (4) are nearly free of organic contamination as a result of PPE treatment. Our data above 4×10^{-5} A/cm² taken prior to any PPE also agree very well with those of Randin (5) who did not use any PPE treatment. Our data showing a break in Tafel slope before and after PPE eliminates PPE as a source of the difference between the results of Bockris and McHardy (4) and those of Randin (5). Rather this difference is due to an intrinsic property of a clean bronze electrode, namely, the break in Tafel slope we have observed.

Platinum doped Na_xWO_3 electrodes.—Results on a platinum-doped electrode prior to either anodization or any PPE are shown in Fig. 5. The break at 1×10^{-6} A/cm² presumably represents a limiting current for oxygen reduction due to surface platinum on the bronze surface, $i_L(BP)$, which is about 10^{-3} times smaller than the limiting current for pure platinum $i_L(P)$ as measured in the same cell. The expected surface concentration of platinum on the doped bronze electrodes is 0.0008 which is also about 10^{-3} times smaller than the surface platinum coverage of a pure platinum electrode. Thus our value of $i_L(BP)$ is readily accounted for by the expected surface platinum concentration of the doped Na_xWO_3 electrode if the activity of a platinum atom is the same for both types of electrodes. This latter point is discussed below.

All previous investigations have reported enhanced activity of platinum-doped Na_xWO_3 electrodes after anodization. We have shown the effects of prolonged anodization to 9V in Fig. 5, prior to any PPE, where the increased activity is confined to current densities below 10^{-5} A/cm². In particular no change in $i_L(B)$ at 10^{-4} A/cm² or any significant increase in potential above $i_L(BP)$ was observed after anodization. This indicates that the enhanced activity in the 10^{-5} A/cm² current density region is not due to surface roughening. The form of the increased activity after anodization suggests additional surface platinum on the bronze electrode that causes $i_L(BP)$ to increase from 1×10^{-6} A/cm² to about 5×10^{-6} A/cm² and the rest potential to rise from 0.65 to 0.72V (NHE). It has been known for some time that anodization removes sodium from the surface of Na_xWO_3 . The heavy anodization used to produce the results shown in Fig. 5 is shown in Part II to produce a sodium depletion layer approximately 1000Å thick. Having eliminated surface roughening and platinum absorption from the solution (*i.e.*, data taken prior to any PPE) and accepting that the form of the increased activity suggests increased platinum surface coverage, a possible source of the additional surface platinum is the electromigration of platinum atoms from the bulk of the crystal. The empty sodium sites provide diffusion paths for the Pt^{++} ions to migrate to the surface under the influence of the anodic potential applied during anodization. In addition, the ionic radius of Pt^{++} is nearly identical to that of Na^+ at 0.96Å so that size effects would not inhibit electromigration. Unfortunately the required fivefold increase in surface platinum coverage is just below the detection limit of our Auger spectrometer, so our hypothesis

of platinum electromigration could not be directly verified.

Our data for anodized, doped platinum bronzes as well as those of Fredlein (8) both taken after PPE are shown in Fig. 5. Our data show increased activity for nearly all current densities after PPE treatment. The increases above 1×10^{-4} A/cm² are similar to those observed for undoped Na_xWO_3 shown in Fig. 4 after PPE. This increase at high current densities following PPE had not been previously reported and formed the basis for the studies reported in the next paper. The increased activity below 1×10^{-4} A/cm² is of the type associated with bulk platinum doping, *i.e.*, increased platinum on the surface of the bronze electrode. Indeed the surface platinum coverage required to explain the observed value of $i_L(BP)$ is very close to that found by Auger analysis. It is proposed that the increased surface platinum on the bronze electrode after the PPE treatment is due to platinum dissolved in the electrolyte during the PPE treatment becoming attached to the bronze surface. Before this assumption can be fully accepted two results have to be explained. First, we did not observe any significant activity for an undoped bronze electrode after PPE. Second, no effect due to PPE was observed by Fredlein (8) on an anodized, doped bronze electrode and yet the activity of his electrode is very similar to ours after PPE treatment.

As shown in Fig. 4 for an undoped bronze electrode our PPE did not produce any significant increase in electrode activity of the type observed for a platinum-doped electrode which we have identified as surface platinum. A clue to the different response of undoped and doped Na_xWO_3 to our PPE is provided by the fact that attempts to intentionally contaminate the bronze surface (as described in II) were more successful at low platinum coverages when the bronze electrode was doped with platinum. This suggests that the platinum present on the bronze surface by virtue of bulk doping provides nucleation sites for those platinum atoms present in the electrolyte after PPE. In the absence of these nucleation sites the activation energy for absorption of platinum on a clean bronze surface is high enough to inhibit the incorporation of platinum onto the undoped bronze surface. Because of the low coverages involved we were unable to verify by Auger analysis whether platinum was present on an undoped bronze electrode after PPE treatment. As a result it is possible that platinum was present, but in an inactive form. Of the two hypotheses presented above it is our judgment that the nucleation hypothesis seems more feasible than the inactive platinum model.

If the nucleation model is accepted it remains to account for the absence of enhanced activity of an anodized, doped bronze electrode observed by Fredlein (8) after PPE treatment. Before addressing this point let us consider the relative $i_L(BP)$ values before PPE of our electrode compared to Fredlein (8). Our value of $i_L(BP)$ is about ten times less than that of Fredlein. Certainly one source of this discrepancy is the threefold increase in bulk platinum used by Fredlein (400 ppm) compared to our 130 ppm platinum concentration. In addition differences in surface roughness or types of anodizations used could be important in explaining the relative difference in the reported activities of the electrodes before any PPE. However, none of these factors are relevant to the fact that Fredlein (8) did not observe any increase after PPE while we certainly did. The explanation lies in the different types of PPE used by the two studies. Fredlein (8) passed a 2 mA current through a cell volume of 100 cm³ with a platinum gauze electrode with a geometric area of 50 cm² for 12 hr. Our PPE treatment passed a 20 mA current through a nearly equal cell volume with a platinum foil of 20 cm² for 24 hr. In addition, our PPE treatment was continued using a 5 mA current during the several days it took to acquire the Tafel data. Assuming equal surface roughness for the platinum electrodes, it would appear that our PPE treatment dis-

solved some twenty times the amount of platinum than the PPE treatment used by Fredlein. This large, additional source of platinum in our solutions is believed to be responsible for the increased activity of a doped, anodized bronze electrode after our PPE treatment.

Since Bockris and McHardy (4) used the same PPE treatment as Fredlein (8) it is evident that the effects they observed on anodized, platinum-doped bronzes were not dominated by adsorbed platinum from their PPE solutions. Rather it appears from our results that the increase in activity was due to anodization which produced an $i_L(\text{BP})$ only two orders of magnitude below $i_L(\text{P})$. It was the approximately three orders of magnitude lower platinum surface coverage, assumed by Ref. (4) to be present due to bulk platinum doping, that required a spillover model to increase the $i_L(\text{BP})$ by a factor of ten. As explained above, before anodization our $i_L(\text{BP})$ was 10^{-3} lower than $i_L(\text{P})$ so that the extra factor of ten must come from the effects of anodization. We have proposed that the primary mechanism is an increased surface coverage of platinum due to electromigration of bulk platinum atoms to the bronze surface during anodization. Certainly no spillover model was required to explain the combined effects of anodization and our PPE treatment since the Auger results show a surface platinum coverage sufficient to explain the observed value of $i_L(\text{BP})$.

Our results and those of Randin (5) for current densities above 5×10^{-5} A/cm² are in full agreement in that no effects due to platinum doping are evident (Fig. 4 and 5). However, in this current density range our PPE treatment did increase the potentials.

Some comments on the role of anodization are in order. Only in the presence of platinum did anodization enhance the bronze electrode activity. The removal of sodium from the surface after anodization provides vacant sites that permit the incorporation of additional platinum onto the bronze surface if there is a supply of platinum available from either the platinum pre-electrolyzed electrolytes or from bulk platinum doping. At very low coverages it seems that bulk platinum doping is required to induce platinum absorption from electrolytes containing platinum.

Simple bulk doping of the bronze crystal to a value of 800 ppm atomic referred to tungsten should result in atomically dispersed platinum atoms at a surface coverage of about 10^{-3} . Our data showing a value of $i_L(\text{BP})$ about 10^{-3} lower than $i_L(\text{P})$, prior to anodization or any PPE treatment, becomes understandable only if the presumably isolated platinum atoms on the bronze surface are just as active as they are when they are on the surface of a piece of platinum metal. It has been long suspected that a major source of platinum's electrocatalytic activity is its electronic structure with its high density of states near the Fermi energy. Recently a calculation of the density of states of Pt_xWO_3 with $x = 1$ has been made (27) which also gives a very high density of states at its Fermi energy. In a manner analogous to Na^+ ions in Na_xWO_3 , the Pt^{++} ion in Pt_xWO_3 donates its outer electrons to the conduction band formed by tungsten d orbitals. Thus although the platinum atoms at sodium sites on the surface of Na_xWO_3 are isolated from each other in a chemical bonding sense, they find themselves in an electronic environment very similar to that of platinum metal. To the extent that electronic properties are important for electrocatalytic activity it seems plausible that a surface coverage of 10^{-3} on a doped bronze electrode would produce an $i_L(\text{BP})$ some 10^{-3} less than that of platinum metal. Thus the role of the bronze electrode, besides providing a corrosion-free substrate, seems to extend to provide a very favorable electronic environment for isolated platinum atoms.

Summary and Conclusions

In agreement with previous studies we find that pure cubic Na_xWO_3 free of any surface platinum is a poor electrocatalyst for oxygen reduction in acid solutions.

Careful attention to cleanliness of the electrolyte and the bronze surface produced two new, reproducible features in the Tafel plot of an undoped bronze electrode measured in platinum-free solutions. A limiting current density, $i_L(\text{B})$, of 4×10^{-5} A/cm² for oxygen reduction on an undoped bronze electrode was observed. Also for the first time, a Tafel slope very near $-2 RT/F$ was measured for current densities below 4×10^{-5} A/cm² prior to any PPE treatment. All previous measurements (5, 6, 8), including our own (6) done under less stringent conditions of purity, produced a Tafel slope near $-4 RT/F$ for a platinum-free bronze electrode. Our ability to observe a $-2 RT/F$ Tafel slope prior to any PPE treatment rules out Fredlein's (8) contention that this slope is due to incorporation of platinum from platinum-contaminated solutions. The presence of the break in the Tafel plot at 4×10^{-5} A/cm² and the $-2 RT/F$ Tafel slope below this current density we believe is a test of the organic cleanliness of a bronze surface and therefore establishes the need for any PPE treatment of the electrolyte to remove this form of contamination.

Anodization of an undoped bronze electrode in platinum-free solutions produced little or no change in the Tafel plot of the electrode.

Our platinum pre-electrolysis treatment of an undoped, anodized bronze electrode did not change the $-2 RT/F$ Tafel slope at current densities below 4×10^{-5} A/cm², but it did increase $i_L(\text{B})$ from 4×10^{-5} to 1×10^{-4} A/cm². These effects along with the overall increase in potential at all current densities are believed to be due primarily to the further cleaning of the bronze electrode with respect to organic impurities rather than any absorption of platinum from the PPE treated electrolyte. These changes are not of the same type observed by bulk platinum doping of the bronze electrode.

Prior to either anodization or any PPE of the electrolyte, a bronze electrode doped with 800 ppm atomic platinum referenced to tungsten produced a significant increase in rest potential and enhanced electrocatalytic activity. However, this enhanced activity was totally confined to current densities below 1×10^{-6} A/cm², which was taken to be a limiting current density for oxygen reduction due to platinum on the surface of the bronze electrode, $i_L(\text{BP})$. This magnitude of $i_L(\text{BP})$ could be accounted for if the surface platinum atoms on the doped electrode had an activity equal to that of platinum atoms on a bulk platinum electrode.

Anodization of a doped bronze electrode even in platinum-free solutions produced increased electrocatalytic activity of the type found by bulk doping. The value of $i_L(\text{BP})$ increased from 1×10^{-6} to 5×10^{-6} A/cm² after anodization of the platinum-doped bronze, but no change in Tafel behavior above 5×10^{-6} A/cm² was observed. The latter observation eliminated surface roughening as a source of the increase in $i_L(\text{BP})$. Since this result was found in platinum-free solutions the only source of additional surface platinum to account for the increase in $i_L(\text{BP})$ was platinum from the bulk of the electrode. We proposed that electromigration of bulk Pt^{++} ions occurs to the surface of the bronze electrode during anodization. The presence of empty sodium sites after anodization, the polarity of the electrode during anodization, and the nearly equal ionic radii of Pt^{++} and Na^+ formed the basis for proposing electromigration as a mechanism to explain the increase in $i_L(\text{BP})$. This mechanism also accounts for the fact that anodization of an undoped bronze electrode does not produce increased activity of the type observed for doped bronze electrodes. The expected increase in surface platinum concentration was below the detection limit of our Auger spectrometer so that direct verification of platinum electromigration in a doped bronze electrode after anodization could not be obtained.

A further increase in electrocatalytic activity of the type associated with surface platinum was observed

when a doped bronze electrode was anodized in a heavily platinum pre-electrolyzed solution. The value of $i_L(\text{BP})$ increased to $4 \times 10^{-5} \text{ A/cm}^2$. The source of this additional surface platinum was clearly the platinum that had been dissolved into the electrolyte following our PPE treatment. The magnitude of the surface concentration of platinum acquired to explain the observed value of $i_L(\text{BP})$ was confirmed by Auger measurements. Previous measurements of Fredlein (8) who found no effect due to PPE of a doped, anodized bronze electrode was consistent with the much less contaminating PPE treatment he used when compared to ours.

Since the PPE treatment used by Fredlein (8) was identical to that of Bockris and McHardy (4) our interpretation of the effects of platinum doping, anodization, and the various PPE treatments has an important bearing on the understanding of their results. Bockris and McHardy (4), as well as Fredlein (8) and us, obtained $i_L(\text{BP})$ about two orders of magnitude less than the limiting current of pure platinum $i_L(\text{P})$ on anodized bronze electrodes doped with platinum when measured in solutions that had been PPE. An $i_L(\text{BP})$ of three orders of magnitude less than $i_L(\text{P})$ could only be expected from bulk platinum doping of the bronze. Since Bockris and McHardy (4) did not consider that other sources of surface platinum might be responsible for the additional tenfold increase in $i_L(\text{BP})$ they observed, they were forced to consider a spillover model that required a synergism between the surface platinum and the Na_xWO_3 lattice. We have shown that anodization of a doped bronze electrode prior to any PPE treatment can produce nearly an order of magnitude increase in $i_L(\text{BP})$, which we have interpreted as being due to electromigration of bulk platinum through the sodium depletion layer to the bronze surface. Also the absence of any effect due to the same PPE treatment used by both Fredlein (8) and Bockris and McHardy (4) on a doped, anodized bronze eliminates PPE as a source of the increased $i_L(\text{BP})$ required by the measurements of Bockris and McHardy (4). Thus we conclude that the additional tenfold increase in $i_L(\text{BP})$, over and above that expected from bulk platinum doping, is accounted for primarily by anodization rather than platinum pre-electrolysis of the electrolyte or a spillover mechanism.

Finally, at current densities above 10^{-5} A/cm^2 our results are in agreement with those of Randin (4) and Weber and Shanks (6) in that no effect due to bulk platinum doping could be formed. However, our PPE treatment did affect the bronze activity even at current densities approaching 10^{-3} A/cm^2 . Although this previously unreported effect was small and independent of bulk platinum doping no sign of a limiting current seemed evident. This result led to a study of various electrochemical schemes to intentionally increase the amount of platinum that could be incorporated onto the bronze surface. This study is reported in the following paper where it is shown that certain platinized Na_xWO_3 electrodes gave overpotentials comparable to those for bulk platinum at current densities as high as 10^{-3} A/cm^2 .

Acknowledgments

The initial stages of this project were funded by the National Science Foundation and the authors would like to extend their thanks for their support. The

authors would like to express their appreciation to Erwin Buck, David Eckels, O. M. Sevde, Harold Hall, and Harry Horner for their assistance during this work as well as Ben Bruns of Physical Electronics for the Auger microprobe results. This research was supported by the Director for Energy Research, Office of Basic Energy Sciences, WPAS-KC-02-02-02.

Manuscript submitted May 12, 1980; revised manuscript received Nov. 12, 1980.

Any discussion of this paper will appear in a Discussion Section to be published in the December 1981 JOURNAL. All discussions for the December 1981 Discussion Section should be submitted by Aug. 1, 1981.

Publication costs of this article were assisted by Iowa State University.

REFERENCES

1. D. B. Sepa, A. Damjanovic, and J. O'M. Bockris, *Electrochim. Acta*, **12**, 746 (1967).
2. B. Brody, *J. Catal.*, **10**, 13 (1968).
3. J. H. Fishman, J. F. Henry, and S. Tessore, *Electrochim. Acta*, **14**, 1314 (1969).
4. J. O'M. Bockris and J. McHardy, *This Journal*, **120**, 61 (1973).
5. J. P. Randin, *ibid.*, **121**, 1029 (1974).
6. M. F. Weber and H. R. Shanks, "Proc. Workshop on Electrocatalysis on Non-Metallic Surfaces," Natl. Bur. Std. Spec. Publ. 455, Alan D. Franklin, Editor, p. 297, U.S. GPO, Washington, D.C. (1976).
7. A. J. Appleby and C. Van Drunen, *This Journal*, **123**, 200 (1976).
8. R. A. Fredlein, *Aust. J. Chem.*, **32**, 2343 (1979).
9. R. D. Armstrong, A. F. Douglas, and D. E. Williams, *Energy Conversion*, **11**, 7 (1971).
10. M. Voinov and H. Tannenberger, "From Electrocatalysis to Fuel Cells," G. Stansted, Editor, p. 101, University of Washington Press, Seattle, Washington (1972).
11. J. Vondrak and J. Belej, *Collect. Czech. Chem. Commun.*, **40**, 3298 (1975).
12. J. Heffler and H. Böhm, *Metalloberflaechen-Angew. Electrochem.*, **27**, 77 (1973).
13. H. R. Shanks, *J. Cryst. Growth*, **13/14**, 433 (1972).
14. Z. Nagy and J. McHardy, *This Journal*, **117**, 1222 (1970).
15. B. E. Conway, H. Angerstein-Kozłowska, and W. B. A. Sharp, *Anal. Chem.*, **45**, 1331 (1973).
16. J. O'M. Bockris, and A. K. M. S. Hug, *Proc. Roy. Soc. London, Ser. A*, **237**, 277 (1956).
17. N. Watanabe and M. A. V. Devanathan, *This Journal*, **111**, 615 (1964).
18. R. Thacker and J. P. Hoare, *ibid.*, **113**, 862 (1966).
19. A. Damjanovic, A. Dey, and J. O'M. Bockris, *Electrochim. Acta*, **11**, 791 (1966).
20. J. P. Randin, A. K. Vijh, and A. B. Chugtai, *This Journal*, **120**, 1174 (1973).
21. N.T.I.S. Report 4437 (High Purity Electrochemical Experimental Station), M. F. Weber (1978).
22. J. McHardy, Ph.D. Thesis, University of Pennsylvania (1972), p. 84.
23. M. F. Weber, H. R. Shanks, A. J. Bevolo, and G. C. Danielson, *This Journal*, **127**, 329 (1980).
24. N.T.I.S. Report 4438 (Wide Range Constant Current Power Supply) M. F. Weber (1978).
25. J. P. Hoare, "The Electrochemistry of Oxygen," p. 122, Interscience, New York (1968).
26. M. P. Seah and W. A. Dench, *Surf. Interface Anal.*, **1**, 2 (1979).
27. S. H. Liu, Private communication.

Electrocatalytic Activity of Cubic Sodium Tungsten Bronze

II. Effects of Intentional Platinization

A. J. Bevolo, Michael Francis Weber,^{*1} H. R. Shanks, and G. C. Danielson

Ames Laboratory-USDOE and Department of Physics, Iowa State University, Ames, Iowa 50011

ABSTRACT

This paper is an extension of the work reported in the preceding paper (I) and concerns the effects of intentional platinization of sodium tungsten bronze electrodes on their electrocatalytic activity for oxygen reduction in an acid electrolyte. Some of these electrodes had activities and stabilities at 10^{-3} A/cm² better than those for bulk platinum electrodes measured in the same solutions. The samples were prepared by three separate techniques and were characterized by SEM, cyclic voltammetry, x-ray dispersive analysis, Auger surface measurements, depth profiles, and microprobe analysis. Two types of platinum morphology were produced. The first type consisted of 1000-3000Å platinum particles attached to a platinum-free bronze surface. For platinum coverages θ_p less than a few percent the activity of the electrodes was proportional to θ_p . The apparent activity per platinum atom was higher than that of bulk platinum although surface roughening effects made it difficult to quantify the specific activity of these electrodes. For θ_p approaching 10% there was a large unexplained increase in activity. The second type of platinum morphology is best viewed as layer of PtWO₃ on top of the bronze surface. These electrodes failed to exhibit any PtO reduction peak even though the Auger results indicated platinum atoms were present. In some cases, it was found that the activity per atom was as good as that of bulk platinum and that these electrodes had better long-term stability than bulk platinum. In all cases the bronze provided: (i) a corrosion resistance support, (ii) a good lattice matrix for either the growth of platinum particles or the incorporation of PtWO₃ layers, and (iii) an electronic environment comparable to bulk platinum with its large density of states near the Fermi level. Techniques used in this study could provide the basis for construction of an economical fuel cell cathode.

This paper is an extension of the research presented in the preceding article (referred to here as I) concerning the electrocatalytic activity of single crystal cubic sodium tungsten bronzes for oxygen reduction in acid electrolytes. As reported in I, a small but reproducible enhancement of the electrode activity near 10^{-3} A/cm² was produced by platinum pre-electrolysis of the electrolyte. Based on this previously unreported result, a series of platinized Na_xWO₃ electrodes were prepared by a variety of methods. The purpose of this experiment was to compare the electrode activity with the surface platinum coverage as determined by SEM and Auger analysis. A significant result of this study was the enormously enhanced activity of the platinized Na_xWO₃ for oxygen reduction, as well as hydrogen reduction and oxidation, when activated by comparatively small amounts of platinum. In some cases activities as high as bulk platinum and electrode stability better than bulk platinum were obtained at current densities approaching 10^{-3} A/cm².

Experiment

Three methods for incorporating platinum onto the Na_xWO₃ surface were attempted. In all cases it was found that platinum would not adhere to a fresh, thoroughly cleaned bronze surface unless it was first anodized to at least 2V (NHE). The first method, denoted as method A, involved platinum plating from a 0.3M HCl solution containing 7.5×10^{-5} M H₂PtCl₆. Cleaved samples were not used because SEM micrographs revealed that micron-sized platinum platelets had formed on the crystal surface. All of the A samples were first polished (see I) and then anodized to 9V (NHE). The bronze electrode was rotated at 900 rpm to insure uniform deposition. The effects of plating

time and potential were investigated. For the second method, method B, a large 20 cm² shiny platinum electrode was used as a counterelectrode for cycling a preanodized bronze crystal from -0.2 to 1.8V (NHE) for approximately 12 hr using a sweep rate of 100 mV/sec. After this treatment the electrolyte was analyzed by an inductively coupled plasma technique (1) and it was found to contain platinum. The third method, method C, was a variation of method B. The 20 cm² platinum electrode itself was cycled between 0.0 and 1.50V (NHE) for 3.5 hr using a gold counterelectrode. Oxygen was then passed into the cell and a bronze electrode was lowered into the electrolyte. An anodic current of 400 μ A/cm² was passed for 1.5 hr followed by an equal cathodic current. Initially the cathodic potentials were low, but after several minutes they increased. For both method B and C the platinizing electrolyte was a helium-saturated 0.1N H₂SO₄ solution. All three methods resulted in platinum deposition on the bronze electrode surfaces as verified by Auger analysis.

Three analytical tools were used to characterize the surfaces of the platinized bronze crystals. First, scanning electron microscopy (SEM) with a 200Å lateral resolution was used to examine the morphology of the platinum deposits. An x-ray energy dispersive analyzer on the SEM was used to probe the composition of the surface features with a depth resolution of approximately one micron. Second, some samples were examined using cyclic voltammograms, especially near the PtO reduction peak at 0.7V (NHE). Third, Auger spectroscopy was used to determine surface composition and depth profiles were taken with a depth resolution of several monolayers. In addition to the Auger spectrometer and measurement conditions as described in I, a Physical Electronics, Incorporated, Model 595 scanning Auger microprobe was also used. This instrument has a lateral resolution of only 500Å compared

* Electrochemical Society Active Member.

¹ Present address: Chemistry Department, University of Toronto, Toronto, Canada, M6S 1A1.

Key words: surfaces, fuel cell, current density, Tafel slope.

to the 40 microns obtained from the other Auger spectrometer described in I, which was used to obtain surface Pt/W ratios and compositional depth profiles.

The electrochemical apparatus and preparation of the bronze electrodes were the same as described in I unless otherwise noted. None of the bronze electrodes had been doped with platinum during their growth. Tafel plots were obtained as described in I.

Results

Electrochemical.—Intentional platinum incorporation into the electrolyte could be used to activate the Na_xWO_3 crystals to a wide variety of electrocatalytic activities. The first such experiment demonstrated the vastly improved activity of an undoped bronze electrode after treatment by method C. Oxygen reduction Tafel plots for sample 4C before and after platinum depositions are shown in Fig. 1, along with the Tafel plots of pure platinum and an 800 ppm platinum-doped Na_xWO_3 taken earlier in a platinum-free electrolyte. The overpotential of sample 4C near 10^{-3} A/cm² is only 0.1V below that of bulk platinum, indicating considerably enhanced activity over any of the bronze electrodes investigated in I.

After this encouraging result, experiments were performed to determine if the increased activity could be quantitatively related to the platinum surface coverage. The three methods of platinizing the bronze samples, described in the experimental section, were used to prepare a series of samples with a wide range of platinum coverages. A true steady-state condition, requiring several hours, was allowed to occur for all the data points presented here since considerably higher potentials, especially at high current densities, were obtained if fast (5 min) measurements were attempted.

The data for six samples platinized by plating at 0.120V (NHE) in chloroplatinic acid (method A) are shown in Fig. 2 along with the Tafel plots for bulk platinum and a pure Na_xWO_3 sample. It is clear that for all current densities the activity of the plated bronze electrodes increases with plating time. Subsequent Auger measurements show an increasing platinum coverage with increasing plating time, except for the slowest plating time which had a platinum coverage below the Auger detection limit. Figure 3 shows the effect of changing the plating potential on the Tafel plots using sample 3A plated at 0.120V (NHE) and sample 8A plated at 0.040V (NHE). Although the activities of these two samples are clearly different the calculated platinum coverage was nearly identical at 4%.

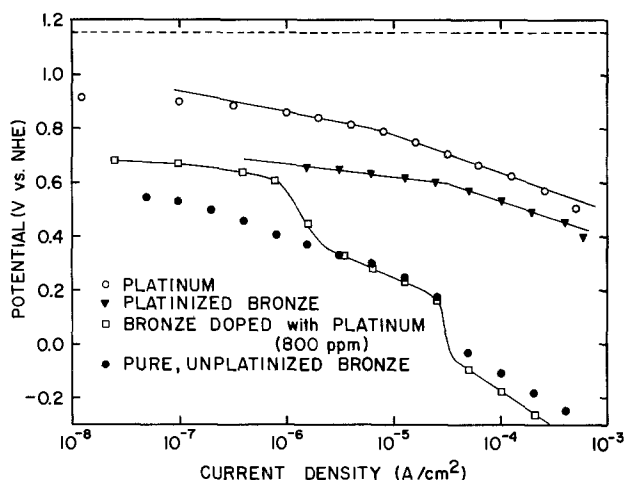


Fig. 1. Comparison of the electrocatalytic activity for oxygen reduction of pure platinum (○), a platinum-doped bronze (□), a pure bronze crystal (●), and the same bronze crystal, 4C, platinized by method C (▼).

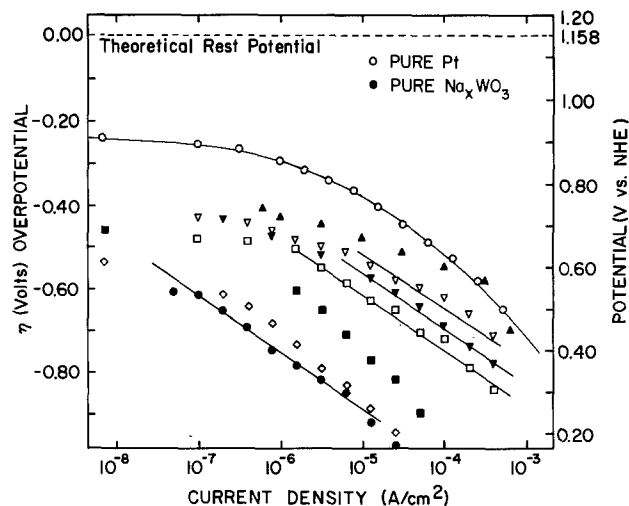


Fig. 2. Oxygen Tafel plots for Na_xWO_3 crystals plated at 0.120V (NHE) in chloroplatinic acid (method A) compared to those for pure platinum (○) and a pure uncontaminated Na_xWO_3 (●). The plated samples are: 1A plated for 8 min (◇), 2A plated for 20 min (■), 4A plated for 60 min (□), 5A plated for 100 min (▼), 7A plated for 160 min (▽), and 9A plated for 240 min (▲). The activity for oxygen reduction increases with platinum plating time.

Figure 4 shows the results for methods B and C for two samples each. As was the case for method A, increasing the surface coverage of platinum increased the electrocatalytic activity for oxygen reduction for all current densities, even those near 10^{-3} A/cm². Of the three methods used, method B produced the highest activity. In fact, these samples showed activities greater than that for bulk platinum at the highest current densities.

Encouraged by the effects of platinizing the bronze electrodes on the oxygen reduction reaction, we investigated other electrochemical reactions using these electrodes. A Tafel plot for hydrogen evolution from an anodized, platinum-free Na_xWO_3 is shown in Fig. 5. The exchange current density of this sample was about 10^{-7} A/cm², which is very low. Figure 6 shows the Tafel plots for hydrogen oxidation and reduction for samples 3A and 8A compared to bulk platinum. One should note the difference in overpotential scale between Fig. 5 and Fig. 6. Figure 6 is a linear plot of overpotential vs. current and the exchange currents are calculated from the slopes. It is interesting that the hydrogen reaction exchange current densities for oxidation and reduction of sample 3A were nearly

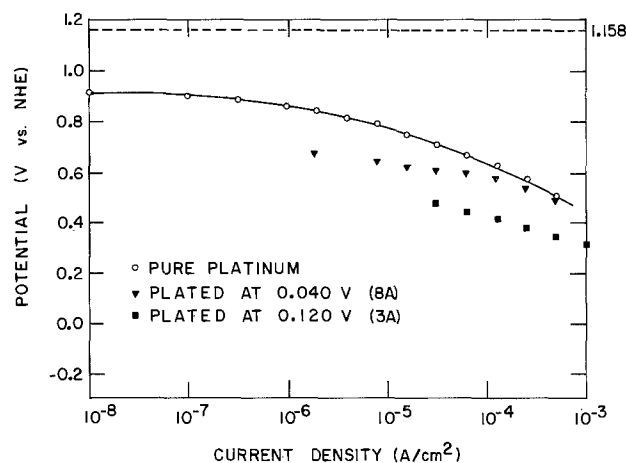


Fig. 3. Oxygen Tafel plots of two bronze crystals plated for equal times (3.5 hr) at different plating potentials; sample 8A (▼) plated at 0.040V (NHE) and sample 3A (■) plated at 0.120V (NHE). The improved performance of electrode 8A is evident, especially when compared to bulk platinum (○) near 10^{-3} A/cm².

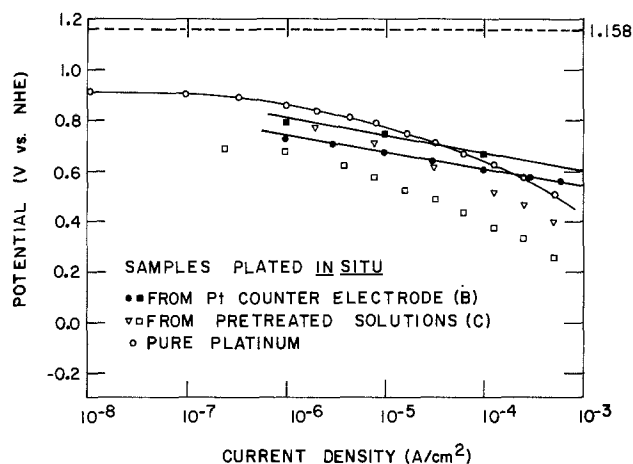


Fig. 4. Tafel plots of samples prepared by method B, 1B (●) and 2B (■) and by method C, 2C (□) and 3C (▽) showing the very high activity of these samples especially those prepared by method B.

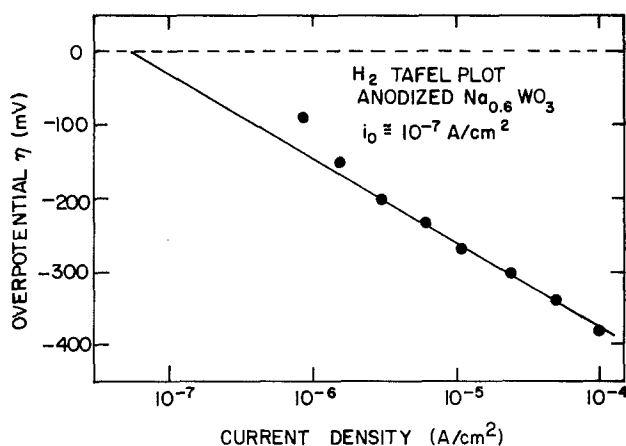


Fig. 5. Typical H₂ Tafel plot for an anodized Na_{0.6}WO₃ crystal. The slope is 120 mV/decade and the exchange current is approximately 10⁻⁷ A/cm². Such a low exchange current is very poor for a hydrogen electrode. The sample had not been platinized.

twice as large as those of 8A, while the current density for oxygen reduction at 0.5V (NHE) was twenty times lower for 3A when compared to 8A.

Platinum morphology.—Vital information on the form of the platinum deposits was provided by SEM, AES, and PtO reduction peaks. Platinum particles were observed by SEM on all samples prepared by method A. This is illustrated using sample 8A in Fig. 7 where the light areas on the surface were found to be platinum by using the x-ray detection capability of the SEM. The average particle in Fig. 7 is 1500Å, uniformly distributed over the bronze surface. The platinum particles on sample 8A covered approximately 10% of the bronze surface. In contrast to method A, samples prepared by methods B and C did not have platinum particles visible within the 200Å lateral resolution of the SEM.

The presence of the platinum particles on the A samples was always detectable *in situ* by monitoring the PtO reduction peak at 0.7V (NHE) in the cyclic voltammograms. As a result the PtO reduction peak was a good indicator of the metallic, bulklike nature of the platinum particles on the bronze surface. No PtO reduction peak was observed on any of the C samples despite the fact that the Auger results indicated that sufficient platinum was present on the surface of these samples to have produced a PtO peak. No cyclic voltammograms were taken of either of the two B samples. However, the B samples were prepared in a

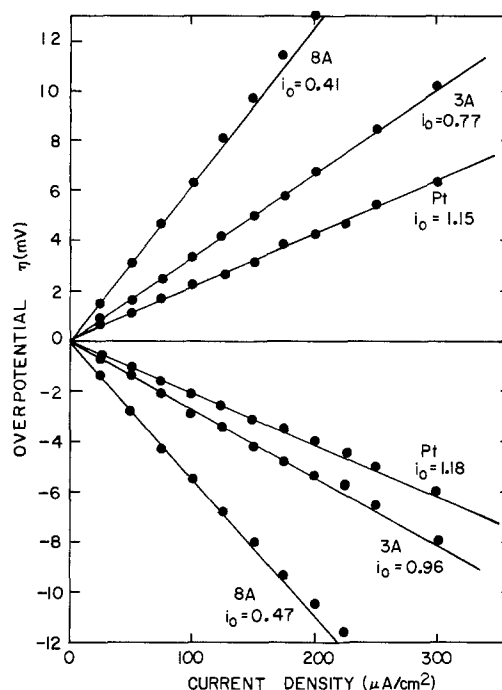


Fig. 6. Current-potential data for the hydrogen reduction and oxidation on two platinized Na_{0.6}WO₃ electrodes, 3A and 8A. The exchange current i_0 are in mA/cm² and show the large improvement after platinization (see Fig. 5) with respect to bulk platinum.

manner identical to that used by Fishman *et al.* (2) to activate Na_{0.6}WO₃ electrodes with platinum. They found no PtO reduction peaks on their samples which they attributed to either the absence of any platinum on the bronze surface or to its presence in a chemical state different from that found on the surface of a bulk platinum electrode.

Auger experiments.—Two types of Auger data were available. The first was an Auger spectrum of the sample surface, while the second consisted of compositional depth profiles obtained during ion bombardment. Nearly all of the Auger spectra of the first type were taken using the 40 micron electron beam of the Physical Electronics Model 10-155 Auger spectrometer. The lateral dimension of the electron beam of this spectrometer was sufficient to provide an average composition of the bronze surface. The 500Å lateral res-

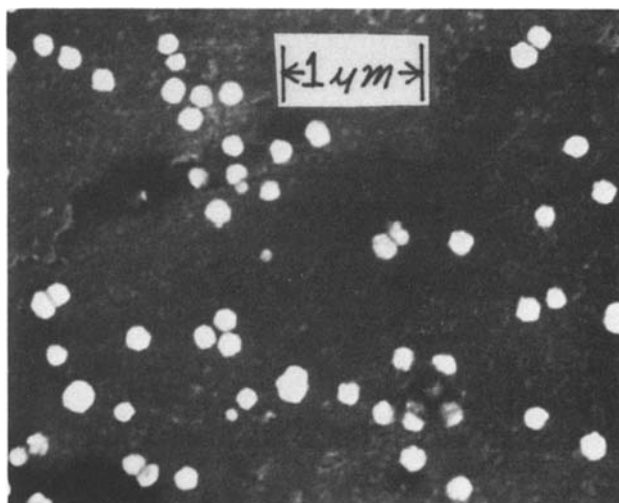


Fig. 7. SEM micrograph of sample 8A which was platinum plated at 0.040V (NHE) in 7.5 × 10⁻⁵M chloroplatinic acid. The platinum particles visible in the photograph are about 1500Å in diameter.

ution of the Physical Electronic Model 595 was used to probe the surface composition of the A samples between the large (>1000Å) platinum particles. All of the depth profiles were taken with the Model 10-155 Auger system.

As explained in I, the Pt(1967) and W(1796) Auger transitions provided the best measure of the platinum concentration on the surface of a bronze sample before any ion bombardment. The 25Å escape depths of these two transitions (3) minimized the attenuating effects of the approximately one monolayer overlayer of carbon always present on the samples. The effects of the carbon overlayer are nearly completely eliminated when the ratio R of the intensity of the Pt(1967) transition to that of the W(1796) transition are used as a measure of the platinum coverage θ_p , since the attenuation of each transition is nearly equal. This effect is a direct consequence of the near identity of the escape depths of these two transitions. The measured values of R for all of the bronze samples, as determined using the Model 10-155 Auger system, are given in Table I. The disadvantage of using these two high energy Auger transitions is that subsurface platinum atoms could contribute significantly to the intensity of the Pt(1967) transition without effecting θ_p , which depends entirely on platinum atoms present on the top monolayer of the electrode. Auger microprobe, SEM, and Pt(64) Auger depth profiles all provided vital information on the subsurface platinum distribution.

Auger depth profiles were obtained in the usual manner by monitoring the peak-to-peak Auger signals from a continuously sputtered surface. In this case we used the Pt(64) Auger transition, which has an escape depth of approximately two monolayers (3), to provide high surface sensitivity. To obtain the exact thickness of the platinum layer required accurate knowledge of the sputter removal rate. No data on the sputter yield of Na_xWO_3 or pure platinum could be found that would permit the exact conversion of sputter time to depth. The ion beam consisted of 2.5 keV Ar^+ ions at normal incidence with a current of 30 nA focused to a diameter of 250 microns. The ion beam was rastered over a 2×2 mm square area to avoid crater edge effects. We have assumed that the sputter yield for $\text{Na}_{0.7}\text{WO}_3$ is 2 atoms per incident ion so that the sputter removal rate for $\text{Na}_{0.7}\text{WO}_3$ becomes 1 Å/min. For bulk platinum, Wehner (4) reported a value of 1.4 atoms/ion for 0.5 keV Ar^+ ions, while Almén and Bruce (5) find 12 atoms/ion for 45 keV Kr^+ ions. Based on these values and knowledge of the general dependence of sputter yields with ion en-

ergy and mass (6), we estimate that for 2.5 keV Ar^+ ions, platinum would have a sputter yield of approximately 5 atoms/ion. For our ion beam flux we calculate a sputter removal rate for pure platinum to be 3.5 Å/min. As we shall discover, for platinum layers in the monolayer range the presence of the carbon overlayer makes it very difficult to obtain exact values for the platinum depth distribution even if the sputter yields were accurately known. However, the Auger depth profiles were very useful in a comparative analysis of the platinum layer thickness and for measuring the extent of the sodium depletion layer after anodization.

Figure 8 shows a depth profile of pure Na_xWO_3 crystal after mechanical polishing but before any electrochemical treatment. There are three regions of interest in this figure. For sputter depths below 15Å the profile is dominated by the removal of the ever present carbon overlayer. As the carbon is removed, the Auger signals coming from the bronze crystal increase in intensity because of their finite escape depths. The second region occurs from 15 to 150Å and shows decreasing oxygen and sodium signals and an increasing tungsten signal. There are two possible explanations for this behavior. First, the concentrations of these elements may actually vary in the manner shown in Fig. 8, that is, oxygen and sodium concentrations are higher in the first 150Å of the bronze surface. Alternatively, the effect may be due to preferential sputtering of oxygen and sodium from the crystal until equilibrium is reached at 150Å. In this case the concentration variations are ion induced. Preferential sputtering of light elements from a compound or alloy is not uncommon. Considering the current state of our knowledge of the sputtering process for compound targets it is difficult to judge the importance of preferential sputtering in Fig. 8. In any case, this profile represents the standard against which the depth profiles of electrochemically treated bronzes will be compared.

Figure 9 shows the Auger depth profile of sample 7A, which had been heavily anodized to 9V (NHE) at 1 mA/cm² prior to platinization by method A. This sample had 1500Å platinum particles present at a coverage of about 6% as confirmed by PtO reduction and SEM

Table I. The measured ratio R of the intensities of the Pt(1967) and W(1796) Auger transitions, the calculated platinum coverages θ_p , and measured current density ($\mu\text{A}/\text{cm}^2$) at 0.5V (NHE) for oxygen reduction I of a series of cubic sodium tungsten bronze electrodes platinized by three (A, B, and C) different electrochemical techniques

| Sample | R | θ_p | I |
|--------|----------|---------------------|--------|
| 1A | — | 0.0007 ^a | 0.47 |
| 2A | — | 0.003 ^a | 3.1 |
| 3A | 0.15 | 0.039 | 17 |
| 4A | 0.08 | 0.008 | 25 |
| 5A | 0.14 | 0.038 | 50 |
| 6A | 0.30 | 0.076 | 120 |
| 6A* | 0.02 | 0.039 | 120 |
| 7A | 0.22 | 0.059 | 150 |
| 8A | 0.16 | 0.042 | 370 |
| 9A | 0.25 | 0.064 | 1,400 |
| 1B | 0.50 | 0.269 | 2,500 |
| 2B | 0.88 | 0.473 | 10,000 |
| 1C | 0.010 | 0.034 | 25 |
| 2C | 0.013 | 0.044 | 25 |
| 3C | 0.050 | 0.168 | 150 |
| 4C | 0.080 | 0.270 | 150 |
| Pt | ∞ | 1.000 | 500 |

* Values determined by plating time.

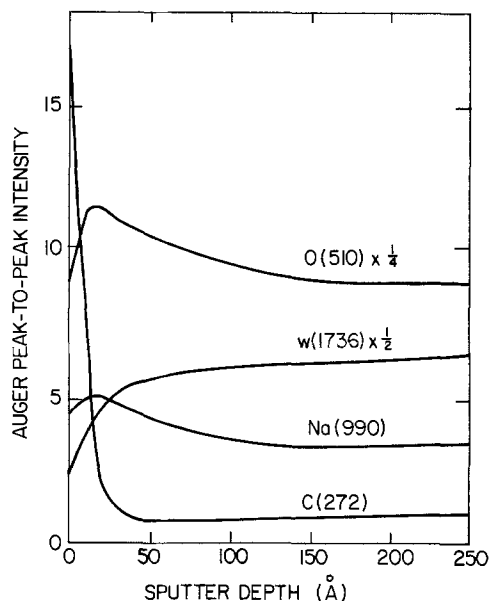


Fig. 8. Auger depth profile of a pure sodium tungsten bronze before any electrochemical treatment, but after mechanical polishing through 0.05 μm alumina. Assuming a sputter yield of 2 atoms/ion the sputter removal rate is 1Å/min. The enhanced oxygen and sodium signals for sputter depths less than 150Å may represent preferential sputtering of the light elements from the nearly carbon-free Na_xWO_3 surface.

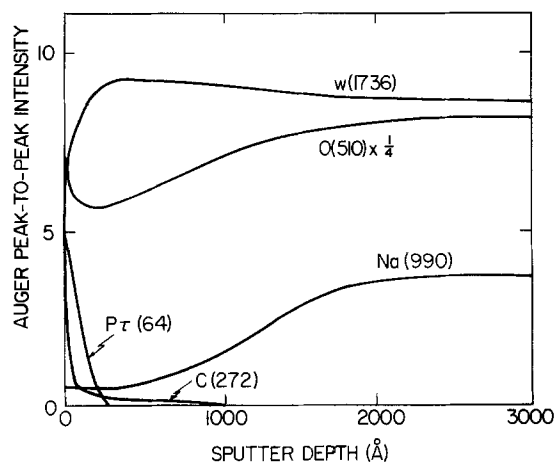


Fig. 9. Auger depth profile of a platinum-plated Na_xWO_3 crystal (sample 7A) that had been heavily anodized prior to platinization. The sodium depletion layer extends nearly 2000 Å into the bronze surface. The Pt(64) signal represents the removal of the platinum particles known to be on the sample surface. As in Fig. 8 the assumed bronze sputter rate is 1 Å/min.

micrographs. As a result the interpretation of this depth profile requires some care. The Auger peaks for sodium, oxygen, and tungsten are the same as for a platinum-free surface because it is shown later that no platinum was present between the platinum particles. The presence of the sodium depletion layer is evident from the behavior of the Na(990) signal and extends about 1500 Å into the sample. With regard to the Pt(64) signal it represents the sputter ion removal of the essentially pure platinum particles. The 300 min required to remove the platinum particles, combined with our estimated 3.5 Å/min sputter rate for pure platinum, gives about 1000 Å as the thickness of the platinum particles. This is reasonable considering their lateral dimension of 1500 Å.

Before leaving Fig. 9 it is interesting to note that the O(510) signal parallels that of the Na(990) suggesting that heavily anodized Na_xWO_3 also loses some oxygen in the sodium depletion layer. Although the oxygen depletion depth is the same as for sodium, the amount of oxygen lost is much less than that of sodium. It should be noted that the decreased O(510) intensity for depths less than 2000 Å is opposite to the behavior of the O(510) transition found in Fig. 8 for an unanodized bronze. This implies that the reduced oxygen Auger signal does represent a reduced oxygen concentration in the sodium depletion layer.

Figure 10 shows a depth profile of sample 4C which had been initially anodized to only 2V (NHE) before platinum deposition. The depth distribution for O(510), W(1736), Na(990), and C(272) are nearly identical to those found for a mechanically polished bronze surface shown in Fig. 8. In particular, anodization to 2V (NHE) did not produce any evidence of a sodium depletion layer. The depth distribution of the Pt(64) transition is important in the determination of the platinum morphology. The initial rise occurs because of the removal of the carbon overlayer. During the next 10 Å the Pt(64) goes to zero. It is evident that the platinum signal completely disappears even before the carbon coverage has reached its equilibrium value. This behavior of the Pt(64) signal for sample 4C is in marked contrast to that shown in Fig. 9 for sample 7A which was known from SEM studies to contain 1500 Å platinum particles over 6% of its surface. No platinum particles were evident in SEM micrographs of sample 4C. The presence of a significant carbon signal during the evolution of the Pt(64) signal complicates the extraction of the exact depth of the platinum composition. Our best estimate is that the platinum is confined to the first few monolayers of the

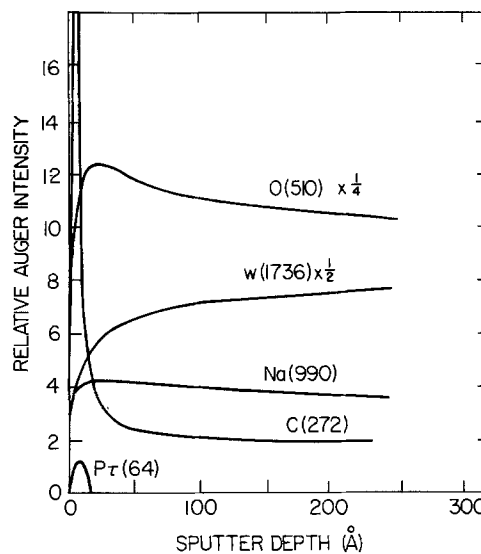


Fig. 10. Auger depth profile of sample 4C which was only lightly anodized to 2V (NHE) prior to platinization. No sodium depletion layer is found. The rapid disappearance of the Pt(64) signal even before the C(272) signal has reached its equilibrium value suggests a platinum coverage of approximately one monolayer.

bronze surface. Auger depth profiles of the other C samples were similar to that shown in Fig. 10 for sample 4C.

Auger depth profiles were also performed using the B samples, which like the C samples did not have any large platinum particles evident in their SEM micrographs. A depth profile of sample 1B produced a Pt(64) depth distribution more like that of sample 7A (Fig. 9) than that of sample 4C (Fig. 10) in that the Pt(64) signal was still strong well after the carbon signal had reached its low equilibrium value. In addition, the oxygen and tungsten Auger peaks were evident even before sputtering began. These results suggest that the platinum-containing layer was hundreds of angstroms thick, but that it did not consist of a pure platinum overlayer, since any pure platinum layer that thick would have completely suppressed the oxygen and tungsten signals from the covered bronze surface. In fact in none of the Auger depth profiles was there any evidence that a bronze surface was uniformly covered by a pure platinum layer thick enough to suppress the oxygen and tungsten signals from the bronze crystal.

It was important to know whether any platinum was deposited between the platinum particles produced by method A. Although the electron microscope had x-ray dispersive analysis capable of chemical identification and sufficient lateral resolution, its depth resolution of about one micron was insufficient to detect a monolayer coverage of platinum between the platinum particles. Using the Model 595 scanning Auger microprobe, an Auger spectrum was taken on and off a platinum particle on the surface of sample 3A. No Pt(64) peak was evident from the bronze matrix. No sputtering was used, so that even a small fraction of a monolayer of platinum was not removed from the surface. As a result, Auger spectra from the platinum particle and the bronze matrix did have some carbon evident. However for the platinum particle, the Pt(64) line was clearly evident, while the W(38), W(48), and W(150-180) lines with their correspondingly small escape depths were observed from the bronze matrix. Correcting for the carbon overlayer and the relative Auger sensitivities (7) we estimate that no more than 1% of the top monolayer of the bronze matrix was occupied by platinum. This result implies that for this sample, and presumably all samples prepared by method A, all of the platinum on the surface of these

bronze electrodes resides in the large platinum particles.

Dependence of electrochemical activity on platinum morphology.—Although platinum particles were observed on all of the samples prepared by method A, the electrocatalytic activity for oxygen reduction was not always proportional to the number of platinum particles observed in the SEM micrographs. This was strikingly demonstrated in the following manner using sample 6A. The platinum particles could be removed from the bronze surface by reanodizing the crystal to 10V (NHE). The disappearance of the platinum particles was confirmed by SEM measurement and the absence of the PtO reduction peak. The oxygen reduction Tafel plots of this sample before (sample 6A) and after (sample 6A*) the particles were removed is shown in Fig. 11. Surprisingly very little change in the relatively high activity of the electrode was observed. A depth profile of sample 6A* (not shown) was performed and a very thin platinum layer was found indicating that the platinum was confined to the top few monolayers of the bronze electrode. The observation that the electrocatalytic activity of samples 6A and 6A* was essentially unchanged even though the platinum morphology was drastically altered, represents one of the most interesting observations made during this study.

Discussion

Platinum coverage.—The ultimate aim of this study is to compare the electrocatalytic activity of platinized Na_xWO_3 electrodes to that of bulk platinum and to the platinum coverage θ_p on the bronze surface. Only by determining the platinum coverage on a bronze surface can the electrocatalytic activity of a platinum atom on the bronze surface be compared to that of a platinum atom on a bulk platinum surface. Once this is known, the role of the bronze in catalyzing the oxygen reduction reaction in the presence of the surface platinum can be clearly elucidated. In I it was shown that a pure bronze surface is a very poor electrocatalyst for oxygen reduction. Even when activated by surface platinum produced by anodization or platinum pre-electrolysis of the electrolyte no clear evidence of synergism was found in I. However the possibility of a synergistic relation between the platinum and the bronze surface may exist for the more heavily platinized bronze electrodes prepared for this study by techniques different from those used in I.

We start from the assumption that only the top monolayer of any electrode actively participates in the oxygen reduction process. This assumption is based on the fact that the absorption of reactants and products occurs only on the top monolayer of the electrode even

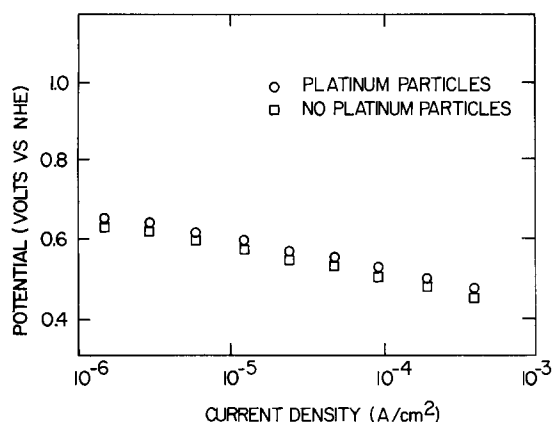


Fig. 11. Oxygen Tafel plots of sample 6A before (○) and after (□) removal of platinum particles by anodization to 10V (NHE). Little difference in the high electrocatalytic activity of the sample was found after removal of the platinum particles.

though electron exchange can occur over several monolayers by electron tunneling. For bulk platinum foils the number of active sites is equal to the surface density of platinum atoms. Platinum has a face-centered cubic structure (fcc) shown in Fig. 12A with a lattice constant $a_{\text{Pt}} = 3.916\text{\AA}$. Let us assume that the polycrystalline foils used in our experiment had predominantly (100) faces exposed to the electrolyte. Assuming no lattice rearrangements at the surface, the surface density of platinum atoms, σ_{Pt} , is given by

$$\sigma_{\text{Pt}} = 2/a_{\text{Pt}}^2 = 1.304 \times 10^{15}/\text{cm}^2 \quad [1]$$

where the factor of two is the number of platinum atoms per unit cell on a (100) face of the fcc structure.

Before the platinum coverage θ_p for a bronze electrode can be calculated, the morphology of the platinum layer must be known. The results we have observed on the presence of a PtO reduction peak on bulk platinum and the A samples as well as the absence of such a peak on the B, C, and 6A* samples are significant. The Auger analysis shows that the absence of a PtO peak on the B, C, and 6A* samples does not occur because of the absence of any platinum. The alternative is that, for those samples which did not produce a PtO reduction peak, the platinum is on the bronze surface in a chemical state different from the platinum on the surface of bulk platinum or the A samples. An appealing hypothesis is that the platinum atoms on the surface of the B, C, and 6A* samples are located at the empty sodium sites of the anodized bronze electrodes, forming a PtWO_3 phase. If the platinum atoms were to reside at the empty sodium sites, then one would expect that they would give up their two 6s electrons to the conduction band formed by the tungsten-oxygen bands forming Pt^{2+} , just as sodium gives up its one 3s electron forming Na^+ . The ionic radius of Na^+ is 0.95Å and that of Pt^{2+} ions is 0.96Å, which is a very good match. In addition, the bronze lattice provides a very good lattice match to that of bulk platinum. A unit cell of the cubic perovskite structure of NaWO_3 is shown in Fig. 12B. The

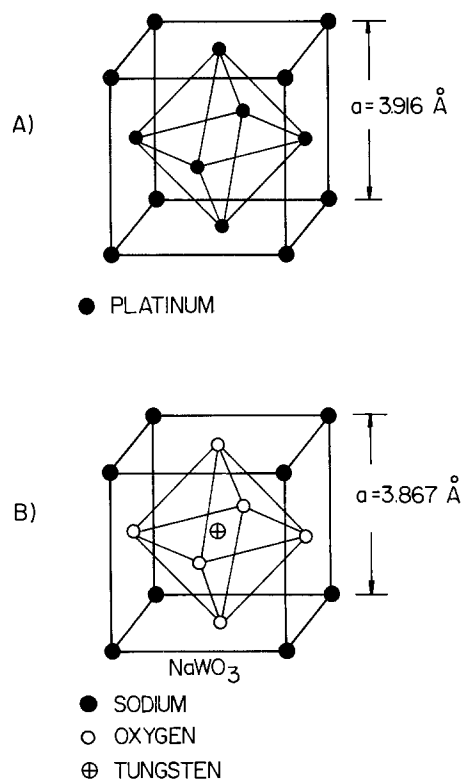


Fig. 12. A. Unit cell of face-centered cubic platinum. B. Unit cell of cubic perovskite structure.

lattice constant for $x = 1$ for NaWO_3 is $a_B = 3.876\text{\AA}$ (8), which is within 1.5% of that for bulk platinum. The sublattice of the empty sodium sites provides a very good matrix for the growth of platinum on the surface of the bronze crystal. Depending on the experimental conditions, there are two possible fates for the arriving platinum atoms after the top monolayer sodium sites of the bronze surface have been filled; either the platinum atoms grow on top of the bronze forming platinum islands as was found for the A samples, or the platinum atoms could diffuse into the sodium depletion region by hopping among the empty sodium sites forming PtWO_3 . We propose that the latter mechanism has probably occurred for the B, C, and 6A* samples. The formation of a PtWO_3 layer would explain the absence of a PtO reduction peak associated with the Pt—Pt bonds of bulk platinum.

Given these two proposed models for the platinum morphology, θ_p can be defined for the various platinized bronze electrodes. For the A samples, which have large, discrete platinum particles, θ_p is simply the percentage of the bronze surface area covered by these platinum particles. The Auger microprobe results ruled out any contribution to θ_p from the bronze surface not covered by the platinum particles. For the other bronze electrodes we assume islands of PtWO_3 covering $\alpha\%$ of the bronze surface. Neglecting the small difference in lattice spacings (see Fig. 12A and 12B), the surface density of potential platinum sites on the bronze surface (i.e., sodium vacancies of the anodized bronze) is one-half that of the platinum sites on bulk platinum so that

$$\theta_p = \frac{1}{2} \alpha \quad [2]$$

We can now calculate $\theta_p(R)$ for the various types of bronze electrodes using the well-known dependence of Auger intensities on the concentration vs. depth and surface coverage (9).

Consider first the A samples. Based on SEM, Auger microprobe, and Auger depth profiles we assume that all of the platinum is confined to islands many times thicker than the 25Å escape depth of the Pt(1967) or W(1796) Auger electrons are those from the bronze surface not covered by the platinum islands, while the only source of Pt(1967) Auger electrons is the platinum islands themselves which cover $\theta_p\%$ of the electrode surface. The intensity of the Pt(1967) transition on the bronze surface $I_{Pt}(B)$ can be written in terms of the intensity of the same transition from a platinum foil $I_{Pt}(Pt)$ as

$$I_{Pt}(B) = \theta_p I_{Pt}(Pt) \quad [3]$$

The intensity of the W(1796) transition from the $1 - \theta_p\%$ of the bronze surface free of any platinum islands $I_W(B)$ can be given in terms of the intensity of the same transition from a tungsten foil $I_W(W)$ as follows

$$I_W(B) = (1 - \theta_p) I_W(W) K_1 \quad [4]$$

where K_1 is the ratio of the volume density of tungsten atoms in the anodized bronze surface ($\sim \text{WO}_3$) to that in a tungsten foil. Tungsten has a bcc structure with two atoms per unit cell and a lattice spacing of $a_W = 3.159\text{\AA}$ so that

$$K_1 = \left[\frac{1}{a_B^3} \right] / \left[\frac{2}{a_W^3} \right] = 0.27 \quad [5]$$

since $a_B = 3.876\text{\AA}$. From the definition of R we write

$$R \equiv \frac{I_{Pt}(B)}{I_W(B)} = \frac{\theta_p I_{Pt}(Pt)}{K_1 (1 - \theta_p) I_W(W)} \quad [6]$$

When measured under the same conditions used to obtain the bronze Auger spectrum we find

$$I_{Pt}(Pt) = I_W(W) \quad [7]$$

Solving Eq. [6] for θ_p using Eq. [5] and [7] we find

$$\theta_p(R) = R / (3.7 + R) \quad [8]$$

for the A samples. It is noted that a measured value of R provides a unique value for θ_p independent of the thickness of the platinum islands assuming that these platinum islands are much thicker than the 25Å escape depth of the W(1796) and Pt(1967) Auger transitions used to calculate $\theta_p(R)$.

Consider now the B samples. The absence of a PtO reduction peak implies no metallic, bulklike platinum is present even below the lateral detection limit (200Å) of the SEM. The Auger depth profiles gave evidence of a platinum distribution many times thicker than the 25Å escape depth. These results lead us to assume a model where $\alpha\%$ of the bronze surface has been converted to a PtWO_3 phase extending many hundreds of angstroms beneath the bronze surface. The appropriate connection between α and θ_p is given by Eq. [2]. The intensity of the Pt(1967) transition from the PtWO_3 phase $I_{Pt}(B)$ can be written in terms of $I_{Pt}(Pt)$ as

$$I_{Pt}(B) = \alpha I_{Pt}(Pt) K_2 \quad [9]$$

where K_2 is defined as the ratio of the volume concentration of platinum in PtWO_3 to that of metallic platinum or

$$K_2 = \left[\frac{1}{a_B^3} \right] / \left[\frac{2}{a_{Pt}^3} \right] = 0.26 \quad [10]$$

The intensity of the W(1796) transition from the PtWO_3 and WO_3 phases $I_W(B)$ is given by

$$I_W(B) = \alpha I_W(W) K_1 + (1 - \alpha) I_W(W) K_1 \quad [11]$$

respectively. In Eq. [11] we have assumed no change in the tungsten concentration on going from the WO_3 to the PtWO_3 phase so that Eq. [11] reduces to

$$I_W(B) = K_1 I_W(W) \quad [12]$$

We find for the B samples that

$$R \equiv \frac{I_{Pt}(B)}{I_W(B)} = \frac{2\theta_p K_2}{K_1} \quad [13]$$

using Eq. [2], [7], [9], and [12]. Solving Eq. [13] for θ_p we get

$$\theta_p = 0.54R \quad [14]$$

using Eq. [5] and [10]. Again as for the A samples, a given measured value of R produces a unique value of θ_p independent of the exact platinum depth distribution as long as it is assumed to be uniform for depths larger than a few escape depths as indicated by the Auger depth profiles.

Consider next the C samples. Like the B samples the absence of a PtO reduction peak allows us to assume no metallic platinum islands are present. However, in contrast to the B samples, the Auger depth profiles indicate a platinum distribution very localized near the top monolayer of the bronze surface (see Fig. 10). For simplicity it will be assumed that all of the platinum atoms of the PtWO_3 phase on the C samples are confined to the top monolayer of the bronze surface covering $\alpha\%$ of the bronze surface. We can then write

$$I_{Pt}(B) = \alpha I_{Pt}(Pt) K_3 (1/l) \quad \text{for } l \gg 1 \quad [15]$$

where l is the escape depth of the Pt(1967) transition in monolayers and K_3 is the ratio of the surface concentration of platinum sites for PtWO_3 to that of platinum metal. Thus

$$K_3 = \left[\frac{1}{a_B^2} \right] / \left[\frac{2}{a_{Pt}^2} \right] = 0.51 \quad [16]$$

referring to Fig. 12A and 12B. Since one monolayer of

PtWO₃ is very nearly equal to $\frac{1}{2} a_B$ we obtain

$$l = 25\text{\AA}/1.94\text{\AA} \simeq 13 \text{ monolayers} \quad [17]$$

For the tungsten Auger intensity from the bronze surface we can use Eq. [12]. From the definition of R we find

$$R \equiv \frac{I_{\text{Pt}}(\text{B})}{I_{\text{W}}(\text{B})} = \frac{\alpha K_3 I_{\text{Pt}}(\text{Pt})}{l K_1 I_{\text{W}}(\text{W})} \quad [18]$$

which reduces to

$$R = \frac{2\theta_p K_3}{K_1} \quad [19]$$

using Eq. [2] and [7]. Solving Eq. [19] for $\theta_p(R)$ we find for the C samples that

$$\theta_p = 3.4R \quad [20]$$

using Eq. [5], [16], and [17]. Again given a measured value of R a unique θ_p is determined if we assume all of the platinum atoms of the C samples are confined to the top monolayer of the bronze surface.

Sample 6A* is unique since it was prepared by removing the platinum particles from sample 6A. From the measured value of $R = 0.30$ we find $\theta_p = 0.076$ for sample 6A using Eq. [8]. If we assume that the platinum remaining on sample 6A* is in the PtWO₃ phase as evidenced by the lack of a PtO reduction peak, then we envision the 6A* surface to be covered by a PtWO₃ layer covering 7.6% of the bronze surface. This gives $\theta_p = 3.8\%$ for 6A* since there are half as many available platinum sites (*i.e.*, sodium vacancies) for PtWO₃ as for bulk platinum. Using $\theta = 0.038$ we find that the thickness of the PtWO₃ layer on 6A* must be about four monolayers to produce the measured R value of 0.02 for 6A*.

It should be noted that for those samples that did not show any PtO reduction peaks (B, C, and 6A* samples), it has been assumed that not even one monolayer of bulk platinum exists on the surface of the bronze crystal. It is not clear how thin a layer of platinum metal would continue to produce a PtO reduction peak at 0.7V (NHE). Let us assume the worst case so that a single monolayer of platinum metal would not produce a PtO reduction peak at 0.7V (NHE). The effect of such a monolayer on our calculated θ_p depends on the sample type considered. For the A samples, the Auger microprobe results rule out any monolayer coverage by platinum in any form. The B samples have sufficient total platinum concentration as evidenced by the Auger depth profiles and R values that a platinum monolayer could be present. If such a layer existed then $\theta_p = 1$ for these samples instead of 0.27 for 1B and 0.47 for 2B. For the C samples we previously had placed all of the platinum on the top monolayer of the bronze surface and still calculated $\theta_p < 1$. Simply rearranging the platinum atoms into submonolayer platinum islands would not change θ_p at all. However, if some of the platinum atoms were stacked into islands more than monolayer thick then θ_p would be reduced. Thus the θ_p calculated for the C samples represents their maximum values. For sample 6A* we calculated a model where the platinum atoms are distributed into PtWO₃ islands about four monolayers thick, so that roughly one-fourth of the platinum atoms contribute to θ_p . If all of the platinum atoms were now placed on the top monolayer of the bronze θ_p would be increased by a factor of four. For this to happen, however, would require that during the 10V anodization, used to remove the platinum particles from 6A, some of the platinum atoms had migrated from those platinum particles onto the bronze matrix. We consider that process to be unlikely. Summarizing, the θ_p values, calculated assuming no metallic platinum whenever

no PtO reduction peak was observed, appear to be good approximations and they will be used to compare the electrocatalytic activity of the bronzes with bulk platinum and each other.

Comparison of platinum coverage to electrocatalytic activity.—The electrocatalytic activity of the platinized bronze electrodes and bulk platinum were obtained from steady-state oxygen reduction Tafel plots as presented in the Results section. Exchange current densities could not be used to compare the relative activities of these electrodes because their low Tafel slopes made extrapolation to zero overvoltage very unreliable. Instead the current density at 0.5V (NHE) was used as a measure of electrode activity because most of the Tafel lines passed through this potential. For those Tafel lines which did not cross 0.5V (NHE) only short extrapolation was required. The values of θ_p and oxygen reduction current density ($\mu\text{A}/\text{cm}^2$) at 0.5V (NHE) are both plotted logarithmically in Fig. 13 for all of the bronze electrodes as well as bulk platinum. For bulk platinum θ_p is of course equal to one. A straight line of slope one passing through the point for bulk platinum is shown in Fig. 13. This line, which we call the platinum line, divides the area in Fig. 13 into two regions, one above the line and one below the line. For a sample to be placed above the line implies that the electrode activity is due to more than just the platinum present on the electrode surface, *i.e.*, the bronze matrix is directly participating in the oxygen reduction reaction. For a sample placed below the line the electrode activity per platinum atom is less than that of bulk platinum and it is very unlikely that the bronze matrix directly contributes to the reaction rate for oxygen reduction. The errors in placing a sample in the $i - \theta_p$ plane are of several types. We have discussed the effects of our assumptions concerning the platinum morphology on the cal-

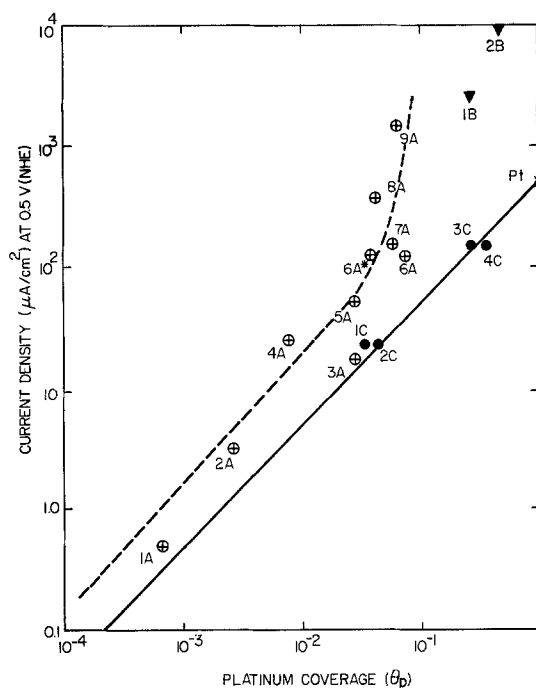


Fig. 13. Log-log plot of platinum coverage θ_p and electrocatalytic activity as measured by the current density at 0.5V (NHE) for all the platinized tungsten bronzes and for a bulk platinum electrode polished and measured in the same manner as the bronze electrodes. The solid line is a straight line of slope one passing through the bulk platinum point. The dashed line passes through those samples prepared by method A and it shows the sharp increase in activity as the platinum coverage approaches 10%. Sample 1B and 2B show anomalously high activity because of the considerably roughened surface they acquired during platinization. Samples 1-4C fall along a solid line of slope one.

culated values of θ_p for the various types of bronze electrodes. For the A and C samples no changes are necessary and for the B samples the θ_p values in Table I are minimum ones while for 6A* θ_p could be four times that plotted in Fig. 13. One other fact, not yet discussed, is surface roughness which could affect current density through the effective surface area of the electrode. For the A samples the SEM micrographs of the platinum particles suggest a microroughness that could increase the atomically smooth surface assumed calculating θ_p . This would have the effect of moving the data points for the A samples lower on the current density scale closer to the platinum line. A definite surface roughening of the B samples, where the bronze electrode was swept in potential, is evident in their SEM micrographs. An order of magnitude increase in surface area is not unreasonable. This would move the points for the 1B and 2B samples much closer to the platinum line. No evidence of surface roughening was present on the C samples which had the platinum counterelectrode swept in potential. In fact the surface roughness of the C sample was comparable to that of the bulk platinum electrodes. As a result no effects due to surface roughness are expected for the four C samples. Sample 6A* showed evidence of surface roughening after the second anodization was used to remove the platinum particles. With these qualifications in mind we can now discuss the significance of the data presented in Fig. 13.

The data for the A samples all fall above the platinum line. The activity is roughly proportional to platinum coverage except near $\theta_p = 0.10$ where the activity rises dramatically with little change in θ_p . The somewhat higher activity for $\theta_p < 0.05$ with respect to the platinum line probably results from the microroughness of the platinum particles rather than any active participation by the bronze matrix. The rapid rise near $\theta_p = 0.10$ is not understood.

The two B samples have the highest activity of any of the bronze samples and they have a specific activity nearly an order of magnitude better than bulk platinum. However the combined effects of surface roughness, which moves the data points toward lower activity, and the possibility of a full monolayer coverage of platinum, which moves the data points toward higher θ_p , leave some doubt as to whether the specific activity of these electrodes is any better than that of bulk platinum. Certainly no definite evidence for direct involvement of the bronze electrode can be deduced from our data on the two B samples.

The four C samples lie directly along the platinum line. As discussed above no significant corrections for surface roughness or platinum coverage are expected for these samples. The results for the C samples suggest that the platinum atoms on the surface of these bronze electrodes are as active per atom as those platinum atoms on the surface of bulk platinum. This conclusion is independent of the location or arrangement of the platinum atoms because the PtWO₃ model used to calculate θ_p had all of the available platinum atoms on the top monolayer of the bronze. If any of the platinum atoms are below that top monolayer, the θ_p for these samples is decreased, moving them above the platinum line. This would lead to the conclusion that either the bronze is an active partner to the platinum or that the top surface platinum atoms are more active than those of a bulk platinum electrode. Samples 1C and 2C have $\theta_p \approx 0.004$ so that only one-tenth of the vacant sodium sites are occupied. The nearest neighbor platinum distance for these samples is therefore about 10Å. In spite of this, each of the platinum atoms on the surface of 1C and 2C is just as active as a platinum atom on the surface of bulk platinum where the nearest neighbor spacing is only 2Å. Our conclusion is that isolated platinum atoms, without any Pt—Pt bonds, still are very active as oxygen reduction catalysts when present on a properly prepared bronze

surface. A similar conclusion was reached in I for a platinum-doped bronze after anodization and treatment in a platinum pre-electrolyzed solution where $\theta_p \approx 3\%$.

One of the important properties of pure platinum as a catalyst is the high density of electron states near the Fermi energy. The band structure of PtWO₃ has been calculated (10) and a larger peak in the density of states occurs at the Fermi level. This peak is due to the highly localized platinum 5d electrons, which are known to be important for the catalytic properties of platinum. The role of the bronze matrix of the C samples seems to extend beyond providing a good lattice match to platinum and a noncorrosive substrate to providing a favorable electronic environment for individual platinum atoms. The bronze matrix may also be involved in providing for the superior stability of these electrodes at high current densities when compared to bulk platinum. It is well known (11) that H₂O₂ builds up in an electrolyte after prolonged oxygen reduction and that its presence contributes to the decreasing activity of a platinum electrode. Randin (12) has shown that a pure bronze electrode is a good electrocatalyst for the reduction of H₂O₂. Thus a potential mechanism for the enhanced stability of the C sample is that the bronze surface is removing the H₂O₂ and thereby preventing the poisoning of the submonolayer platinum layer. In summary, the samples prepared by method C could provide a basis for an economic fuel cell cathode for oxygen reduction in an acid electrolyte with the activity of pure platinum and superior long-term stability.

Sample 6A* lies above the platinum line in Fig. 13. The surface roughening found after the 10V anodization could result in a lower current density. In addition, if all of the platinum atoms are placed on the surface of the bronze electrode, then θ_p would be increased from 3.9% to about 14%. The combined effect of these two assumptions would move the 6A* much closer to the platinum line. Even so, the PtWO₃ model is probably valid and the same conclusion reached for the C samples are valid except for the enhanced stability. Clearly the method used to produce 6A* also is worthy of further investigation as the basis for an economical oxygen reduction cathode.

As described above one of the most interesting and puzzling observations of this study was that found for sample 6A. After platinizing by method A SEM revealed platinum particles present on the surface, a PtO reduction peak was found, and the Auger measurements gave $R = 0.30$. The activity of the electrode was comparatively high (see Fig. 11). After anodization to 10V no platinum particles were evident by SEM, the PtO reduction peak had disappeared while the Auger still gave evidence of platinum with $R = 0.02$. Despite this order of magnitude decrease in Pt/W ratio after anodization to 10V the activity of the electrode, now denoted as 6A*, was essentially unchanged (see Fig. 11).

Several possibilities presented themselves to explain these results. If there was a monolayer of platinum on sample 6A that was responsible for its activity, then the removal of the platinum particles covering only about 7% of the electrode would have little effect on its activity. However the scanning Auger results convincingly showed that all of the platinum on 6A resided in the platinum particles: A second possibility was that the anodization had left some platinum on the electrode despite the removal of the platinum particles and the absence of the PtO peak. This was confirmed by the Auger Pt/W ratio measurement of 6A*. Although the intensity of the Pt(1467) transition was small it was consistent with the idea that after anodization there remained a thin layer of platinum of equal surface area to that of the platinum particles at the former interface between the platinum particles at the bronze surface. The fact that anodization failed

to remove this platinum suggested a different chemical environment as did the absence of a PtO peak. Realizing that the surface platinum is the only platinum that contributes to the electrocatalytic activity it became clear that, despite the order of magnitude decrease in R , the surface coverage of platinum could be nearly the same for 6A and 6A*. If the activity of the isolated platinum atoms on the surface of 6A* could be shown to be nearly the same as for the platinum atoms of bulk platinum, then the near equivalence of the electrode activity of 6A and 6A* could be accounted for. Our analysis of the lattice match of platinum of Na_xWO_3 , the ionic sizes of Pt^{++} and Na^+ , the role of anodization, and the expected electronic structure of PtWO_3 all gave support to the concept of isolated platinum atoms at the empty sodium sites of an anodized bronze electrode having a specific activity similar to that of bulk platinum. It is fair to state that the observation of 6A and 6A* provided a crucial test for our understanding of the role of platinum on the surface of a bronze electrode.

Conclusions

A large number of undoped Na_xWO_3 crystals were plated with platinum by a variety of techniques and tested as cathodes for oxygen reduction. Electrocatalytic activities equal to and higher than bulk platinum electrodes were obtained as well as improved stability for some bronze electrodes over that of bulk platinum. Two types of platinum morphology were postulated. First, there were distinct platinum islands whose minimum sizes were larger than 200Å as determined by SEM micrographs. The activity of these electrodes at low platinum coverages was directly proportional to the platinum coverage and no synergistic effects of the bronze electrode was indicated. Near 10% coverage there was a dramatic increase in electrode activity that has not been explained. The second type of platinum distribution consisted of about a monolayer or less coverage over the bronze surface. Because of the absence of a PtO peak and the lattice match between the crystal structure of Na_xWO_3 and platinum, we have proposed a PtWO_3 layer formed by the diffusion of platinum atoms from the electrolyte into the empty

sodium sites of an anodized bronze surface. Depending on the preparation method, the PtWO_3 layer was either approximately one monolayer thick or several hundred angstroms thick. The activity per platinum atom, taking into account surface roughness and different possible platinum morphologies, is about the same as that of bulk platinum. It is the second form of platinum incorporation that provides a basis for the further development of an economically competitive oxygen reduction fuel cell cathode.

Acknowledgment

This research was supported by the Director for Energy Research, Office of Basic Energy Sciences, WPAS-KC-02-02-02.

Manuscript submitted May 12, 1980; revised manuscript received Nov. 12, 1980.

Any discussion of this paper will appear in a Discussion Section to be published in the December 1981 JOURNAL. All discussions for the December 1981 Discussion Section should be submitted by Aug. 1, 1981.

Publication costs of this article were assisted by Iowa State University.

REFERENCES

1. See for example, V. A. Fassel, *Pure Appl. Chem.*, **19**, 1533 (1977) and references therein.
2. J. H. Fishman, J. F. Henry, and S. Tessore, *Electrochim. Acta*, **14**, 1314 (1969).
3. M. P. Seah and W. A. Dench, *Surf. Interface Anal.*, **1**, 2 (1979).
4. G. K. Wehner, *Phys. Rev.*, **102**, 690 (1956).
5. O. Almen and G. Bruce, *Nucl. Instrum. Methods*, **11**, 257 (1961).
6. P. Sigmund, *Phys. Rev.*, **184**, 383 (1969).
7. "Handbook of Auger Spectra," 2nd ed., Physical Electronics Industries, Eden Prairie, Minn.
8. H. R. Shanks, *J. Cryst. Growth*, **13/14**, 433 (1972).
9. C. C. Chang and D. M. Boulin, *Surf. Sci.*, **69**, 385 (1977).
10. S. Liu, Private communication.
11. J. P. Hoare, "The Electrochemistry of Oxygen," p. 122, Interscience, New York (1968).
12. J. P. Randin, *This Journal*, **121**, 1029 (1974).

Photoelectrochemical Reduction of 2-*t*-Butyl-9,10-Anthraquinone at Illuminated P-Type Si: An Approach to the Photochemical Synthesis of Hydrogen Peroxide

Gary S. Calabrese* and Mark S. Wrighton**

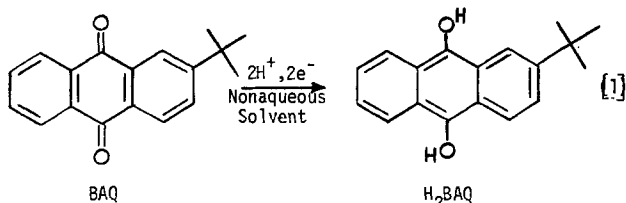
Department of Chemistry, Massachusetts Institute of Technology, Cambridge, Massachusetts 02139

ABSTRACT

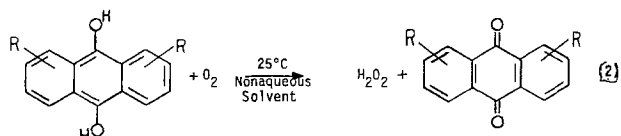
The electrochemical behavior of 2-*t*-butyl-9,10-anthraquinone, BAQ, has been investigated at illuminated (632.8 nm, ~50 mW/cm²) p-type semiconducting Si in CH₃CN/0.1M [*n*-Bu₄N]ClO₄ with and without added CH₃COOH. In the absence of CH₃COOH the BAQ is photoreducible at the photocathode to form BAQ^{•-}. Relative to $E^\circ(\text{BAQ}/\text{BAQ}^{\bullet-}) = -0.95\text{V vs. SCE}$ the photovoltage E_V , at open circuit is ~0.5V. An efficiency for a regenerative photoelectrochemical cell based on the BAQ/BAQ^{•-} is ~4% for the conversion of 632.8 nm light. In the presence of 0.5M CH₃COOH the BAQ is photoreducible to 2-*t*-butyl-9,10-dihydroxyanthracene, H₂BAQ, with a measured current efficiency of >90% when the p-type Si photocathode is held at -0.3V vs. SCE in a two-compartment cell. Preparative, controlled-potential photoelectrochemical reduction of BAQ to H₂BAQ in CH₃CN/0.5M CH₃COOH/0.1M [*n*-Bu₄N]ClO₄ has been demonstrated for >90% conversion of 0.2M BAQ to H₂BAQ. Reaction of the photoelectrochemically generated H₂BAQ (>0.18M) with O₂ from air yields solutions containing >0.18M H₂O₂. The BAQ → H₂BAQ has only ~2% photoelectrochemical energy conversion efficiency. The low efficiency is apparently a consequence of sluggish electrode kinetics or adsorption problems that lead to a low E_V with respect to the $E^\circ(\text{BAQ}/\text{H}_2\text{BAQ}) \approx -0.35\text{V vs. SCE}$ in the presence of 0.5M CH₃COOH.

Much effort has recently been directed toward the use of semiconductor-based photoelectrochemical cells for splitting H₂O to H₂ and O₂ (1-3). While the photoelectrolysis of H₂O is an important objective, there are other worthwhile redox reactions that could, in principle, be photochemically driven by illumination of semiconductors immersed in liquid electrolytes (4). For solar driven processes, it would seem that generation of a reduced or oxidized reagent at the photoelectrode followed by its use in concentrated form at a remote reactor would have practical advantages. For example, rather than direct H₂ production from H₂O in large area devices, it might be best to effect the direct generation of a reducing agent capable of effecting H₂O reduction via a catalyzed process at a reaction remote from the solar device (5-7).

With the long range objective of demonstrating photochemical routes to H₂O₂, we have undertaken a study of the photoelectrochemical reduction of 2-*t*-butyl-9,10-anthraquinone, BAQ, according to Eq. [1]. The relationship to H₂O₂ synthesis is established by



the known process represented by Eq. [2] (8). Indeed, catalytic



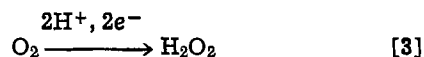
* Electrochemical Society Student Member.

** Electrochemical Society Active Member.

Key words: solar energy, oxygen reduction, photoreduction.

hydrogenation of BAQ-like molecules followed by reaction of O₂ with the H₂BAQ-like reduction product is an industrial process for the production of H₂O₂. Our objective here is to demonstrate that reaction according to Eq. [1] can be sustained in a thermodynamically uphill sense by illumination of a p-type semiconducting photocathode. Photogeneration of H₂BAQ in an uphill sense is an example of the production of a useful redox reagent that can be used in concentrated form at a remote reactor. The BAQ/H₂BAQ redox couple is transparent to the bulk of the visible spectrum and particularly at 632.8 nm, the wavelength employed in these studies. Chemical durability of the BAQ/H₂BAQ couple is sufficiently good that >0.18M H₂O₂ can be generated photoelectrochemically (*vide infra*).

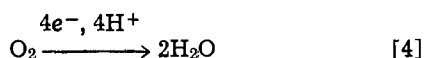
Compared to the direct reduction of O₂ to H₂O₂ in aqueous acid solution, Eq. [3], the cyclic process represented by Eq. [1] and [2]



involving photogeneration of H₂BAQ has a lower theoretical efficiency for energy utilization because $E^\circ(\text{O}_2/\text{H}_2\text{O}_2) \approx +0.45\text{V vs. SCE}$ in acid solution (9), whereas $E^\circ(\text{BAQ}/\text{H}_2\text{BAQ}) \approx -0.35\text{V vs. SCE}$.¹ While the quantitative considerations are clouded by the differences in the media associated with these potentials, it is very clear that H₂BAQ is a far more powerful reductant than required thermodynamically. Thus, a low efficiency for energy utilization in the indirect process is to be expected. However, the indirect process may be desirable in practice on the basis of overall current efficiency, since H₂O₂ is reducible to H₂O at the same

¹ We find that the potential for the BAQ/H₂BAQ is acid strength dependent as would be expected. The -0.35V vs. SCE that we give here is the value we determine from cyclic voltammetry of BAQ in CH₃CN/0.5M CH₃COOH/0.1M [*n*-Bu₄N]ClO₄ at an Hg-drop working electrode. 9,10-Anthraquinone itself has been studied as a function of CH₃COOH concentration in dimethylformamide/0.05M [Et₃N]. The $E_{1/2}$ value varies in a manner similar to that which we find, cf. L. Y. Kheifets, V. D. Bezuglyi, and L. I. Dmitrievskaya, *Zh. Obshch. Khim.*, 41, 68 (1971), and D. H. Evans, in "Encyclopedia of Electrochemistry of the Elements," Vol. XII, Chap. 1, A. J. Bard, Editor, Marcel Dekker, New York (1973).

potential as O_2 is reducible to H_2O_2 ; $E^\circ(H_2O_2/H_2O) \approx +1.54V$ vs. SCE (9). Further, the reduction of O_2 to H_2O , Eq. [4], may compete with H_2O_2 production



since $E^\circ(O_2/H_2O) \approx +1.00V$ vs. SCE (9). Finally, the presence of H_2O_2 in high concentration in the photoelectrochemical device might prove to be incompatible with the cell components, especially the photocathode.

Experimental

Materials—Single crystal p-type Si wafers (0.35 mm thick, 111 face) doped with B and with a resistivity of 3-7 Ω cm were obtained from Monsanto Company, Electronics Division (Palo Alto, California). Ohmic contact to the back side of the Si was made by vapor deposition of Al followed by sintering at 723 K under N_2 for 5 min. The Al-plated surface was then lightly scratched and secured to a coiled Cu wire with conducting silver epoxy. The Cu wire lead was passed through a 4 mm glass tubing. All surfaces were then sealed with ordinary epoxy so as to leave only the front surface (111 face) of the p-type Si single crystal exposed.

Just prior to use, all electrodes were pretreated by etching at 25°C in concentrated HF for 60 sec, rinsed with distilled water followed by acetone, and air dried.

Chemicals—Reagent grade CH_3CN was distilled from P_2O_5 ; $[n-Bu_4N]ClO_4$ (Southwestern Analytical Chemicals) was vacuum dried at 70°C for 24 hr; reagent grade glacial acetic acid (Mallinckrodt), NaCl, and 2-*t*-butyl-9,10-anthraquinone (Aldrich) were all used without further purification.

Equipment and procedures—All experiments employed solutions of $CH_3CN/0.1M [n-Bu_4N]ClO_4$ that were degassed with Ar or N_2 . The Ar or N_2 was first passed through an oxygen scrubber (acidic aqueous solution of $\sim 0.4M Cr^{2+}$) and then over P_2O_5 and $CaSO_4$ to remove H_2O .

Cyclic voltammograms and steady-state current-voltage curves were obtained using a PAR Model 173 potentiostat equipped with a Model 175 programmer. Data were recorded on a Houston Instruments XY recorder, or, for current vs. time plots, on a Hewlett-Packard strip chart recorder. For cyclic voltammograms a single-compartment cell was used employing a standard three-electrode configuration with a p-type Si, Hg, or Pt cathode, a Pt counterelectrode, and reference electrodes being either a saturated calomel electrode (SCE) or a silver wire (Ag/Ag^+) immersed in $0.1M AgNO_3/0.1M [n-Bu_4N]ClO_4$ in CH_3CN (+0.35V vs. SCE). Current vs. time experiments were carried out using the same type of cell except that an Hg pool counterelectrode was used in place of a Pt wire. Current efficiency and exhaustive electrolysis experiments were carried out in two-compartment cells in which the Pt anode was isolated by an ultrafine glass frit.

Electrodes were illuminated using a beam-expanded 632.8 nm He-Ne laser (Coherent Radiation) providing ~ 50 mW/cm². Laser intensity was varied using Corning colored glass filters and monitored using a beam splitter and a Tektronix J16 radiometer equipped with a J6502 probe. The laser beam was masked to match the size of the Si surface.

Optical density measurements were made using 1.00 cm path optical cells with a Cary 17 spectrophotometer that operates in the ultraviolet, visible, and near infrared regions.

Current efficiency determination—The current efficiency for the reduction of BAQ to H_2BAQ at a p-Si photocathode was determined in CH_3CN containing 0.5M CH_3COOH , 0.01M BAQ, and 0.1M $[n-Bu_4N]ClO_4$. First, a similar solution containing a precisely known concentration of BAQ was exhaustively electrolyzed in a two-compartment cell at a Pt electrode such that no

further changes in the optical density of the solution at 380 nm (corresponding to H_2BAQ) were observed. Thus, a molar extinction coefficient of 9600 ± 200 $l\text{mole}^{-1} \text{cm}^{-1}$ at 380 nm was calculated for H_2BAQ in CH_3CN .² The relative current efficiency at irradiated p-Si was then determined by measuring changes in optical density at 380 nm of the cathode compartment of a two-compartment cell containing 20.0 cm³ of the solution described above. The electrode potential of the p-Si was fixed at $-0.3V$ vs. SCE.

Analysis of H_2O_2 —Small volumes of CH_3CN containing H_2O_2 were diluted with H_2O containing an excess of Ti(IV) ions. The optical density at 405 nm corresponding to the Ti(IV)- H_2O_2 complex was used to determine H_2O_2 concentrations (10). Control analyses using authentic samples of H_2O_2 were run to insure the reliability of the technique. Standard solutions of H_2O_2 for preparation of calibration curves for the Ti(IV) analyses were prepared using reagent grade H_2O_2 and their H_2O_2 concentration was determined by titration with standard solutions of $KMnO_4$.

Results

Cyclic voltammetry of BAQ in nonaqueous solution at illuminated p-type Si—P-type Si has been well characterized (5) in $CH_3CN/0.1M [n-Bu_4N]ClO_4$ and the (BAQ/BAQ⁻) system appears to be well behaved. Figure 1a shows the cyclic voltammetry corresponding to the reversible $BAQ \rightleftharpoons BAQ^-$ system at Hg, Pt, and

Si. The $E^\circ(BAQ/BAQ^-)$ falls in a potential regime where the output photovoltage of p-type Si is expected to be $\sim 0.5V$ (5). Consistent with this expectation we find that the photocathodic current peak is $\sim 0.45V$ more positive than at Hg or Pt. The difference in the cathodic current peak positions is one measure of the output photovoltage (5) for the photocathode with respect to the E° of the solution couple.

Figure 1b shows the effect from adding 10 mM CH_3COOH as a source of H^+ . The cathodic current peak in each case is more positive and is \sim twice that found in the absence of H^+ . These facts indicate that the reduction current corresponds to the two-electron reduction process to form H_2BAQ . The reoxidation

$H_2BAQ \xrightarrow{-2e^-, -2H^+} BAQ$ appears to be sluggish, and even the reduction peak positions differ at Pt and Hg suggesting kinetic difficulties there as well. Addition of CH_3COOH to 0.5M gives somewhat sharper cyclic waves and the cathodic current peaks are somewhat more positive, Fig. 1c. Use of Pt in 0.5M CH_3COOH is not useful, since H_2 evolution current obscures the BAQ electroactivity. The presence of small amounts of H_2O does not affect our results. The use of H_2O as a solvent is precluded because the BAQ/ H_2BAQ couple is not soluble.

The $E^\circ(BAQ/H_2BAQ)$ in $CH_3CN/0.5M CH_3COOH/0.1M [n-Bu_4N]ClO_4$ would appear to be about $-0.35V$ vs. SCE. This potential is again in the regime where fast, one-electron redox systems can be reduced with $\sim 0.5V$ output photovoltage at p-type Si (5). Note, however, that the peak at p-type Si is only 0.2V more positive than that at Hg. This indicates that the extent to which the $BAQ \rightarrow H_2BAQ$ reduction can be driven uphill at illuminated p-type Si will be limited to $\sim 0.2V$.

The low output photovoltage for the $BAQ \rightarrow H_2BAQ$ process is disappointing. Previous experiments (5) showing $\sim 0.5V$ output for couples in the same potential regime were done using $CH_3CN/0.1M [n-Bu_4N]ClO_4$ as the solvent/electrolyte system. We thus wondered whether the 0.5M CH_3COOH could deleteriously affect the interface energetics. We find this not to be the

² A similar molar absorptivity has been found for 9,10-dihydroxyanthracene, cf. R. M. Wightman, J. R. Cockrell, R. W. Murray, J. N. Burnett, and S. B. Jones, *J. Am. Chem. Soc.*, 98, 2562 (1976).

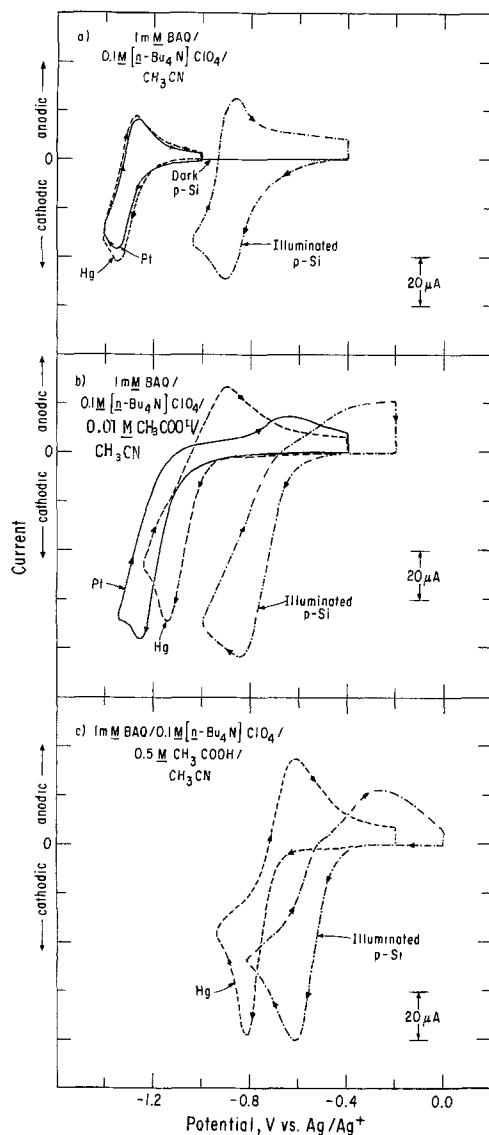


Fig. 1. Cyclic voltammetry at 200 mV/sec for Pt, Hg, and p-Si under the conditions shown. Illumination of the p-Si was at 632.8 nm, 50 mW/cm². The initial potential was the positive limit in all cases.

case, since the output photovoltage (~ 0.5 V) for the reduction of *N,N'*-dimethyl-4,4'-bipyridinium (5, 11) is independent of whether the CH_3COOH is present. We thus conclude that the low photovoltage that can be achieved reflects relatively sluggish kinetics for the $\text{BAQ} \rightarrow \text{H}_2\text{BAQ}$ process. The data in Fig. 1b show that Hg and Pt differ in their behavior with respect to reduction and it is possible that Si has poor kinetics. Kinetics for reduction of quinones is known to be dependent on the electrode material (12). We thus conclude that the poor photovoltage may be improved by altering the photocathode surface to improve the kinetics.

Current efficiency for $\text{BAQ} \rightarrow \text{H}_2\text{BAQ}$ photoreduction.—The current efficiency for the photoreduction of BAQ at illuminated p-type Si has been found to be quite high. The reduction product H_2BAQ has unique visible near ultraviolet absorption spectral properties that allow its concentration to be monitored in a two-compartment cell. Figure 2 shows the results of a determination of moles of H_2BAQ formed as a function of charge passed. Within experimental error the current efficiency is 100%, two moles of electrons passed per mole of H_2BAQ formed.

Steady-state photocurrent-voltage curves and durability of the photocathode.—Figure 3 shows steady-state

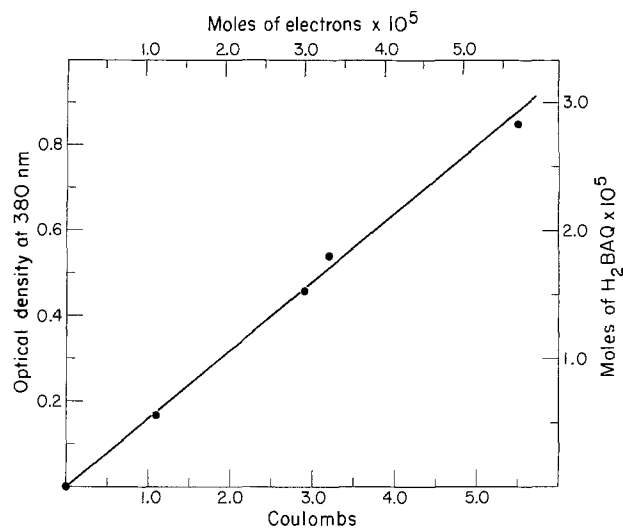


Fig. 2. Plot of increase of optical density at 380 nm associated with H_2BAQ generation from BAQ at a p-Si electrode illuminated with 632.8 nm light in a two-compartment cell. The current efficiency for this electrode is thus $100 \pm 5\%$. The photocurrent density was ~ 5 mA/cm².

photocurrent voltage curves for the reduction of BAQ to H_2BAQ as a function of light intensity. As expected from the cyclic voltammetry results, Fig. 1, the output photovoltage with respect to the E_{redox} ($\text{BAQ}/\text{H}_2\text{BAQ}$) is rather modest. Table I summarizes the efficiency for the photoelectrochemical reduction of BAQ from the curves given in Fig. 2. The maximum energy conver-

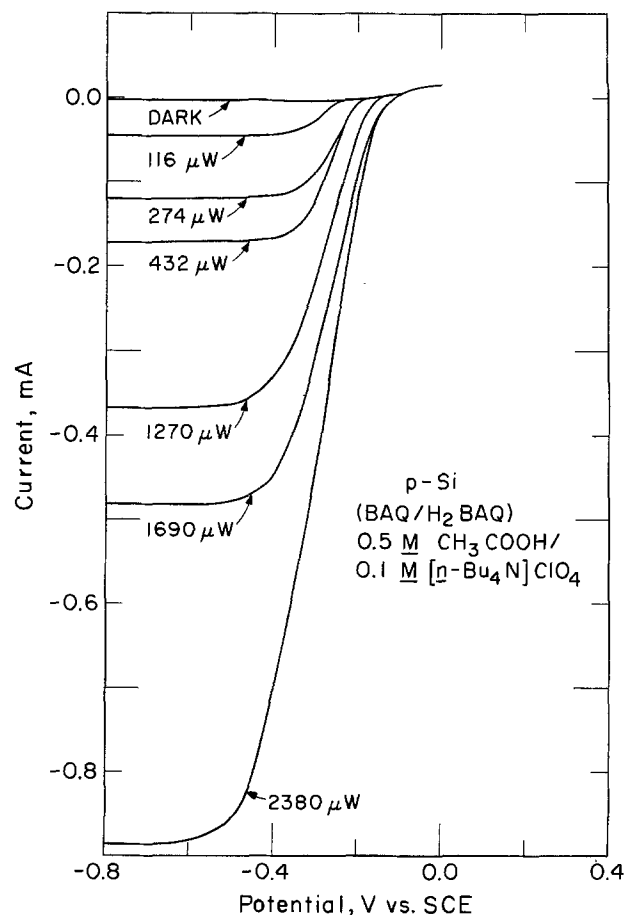


Fig. 3. Representative steady-state current-voltage curves at 10 mV/sec for a 0.03 cm² p-Si electrode in CH_3CN containing 0.2 M BAQ, ~ 1 mM H_2BAQ , 0.5 M CH_3COOH , and 0.1 M $[\text{n-Bu}_4\text{N}]\text{ClO}_4$. Incident 632.8 nm optical power is given in μW . The solution redox potential was measured at an Hg pool to be ~ -0.4 V vs. SCE.

Table I. Output characteristics for a p-Si-based photoelectrochemical cell culled from the current-voltage curves in Fig. 3

| Input power at 632.8 nm, mW ^a | Φ_e^b | Open circuit E_V , mV ^c | η_{max} , % ^d | E_V at η_{max} , mV | Fill factor |
|--|------------|--------------------------------------|-------------------------------|----------------------------|-------------|
| 0.12 | 0.68 | 170 | 2.1 | 85 | 0.3 |
| 0.28 | 0.79 | 210 | 2.6 | 90 | 0.3 |
| 0.43 | 0.73 | 210 | 2.3 | 90 | 0.3 |
| 1.27 | 0.50 | 230 | 1.6 | 100 | 0.3 |
| 1.70 | 0.51 | 270 | 1.6 | 100 | 0.2 |
| 2.37 | 0.55 | 270 | 1.6 | 100 | 0.2 |

^a Input power is from a 632.8 nm He-Ne laser. For power density multiply by $\sim 32 \text{ cm}^{-2}$.

^b Quantum yield for electron flow at E_{redox} ; this corresponds to the short-circuit quantum yield measured as the number of electrons passed per incident photon.

^c Photovoltage at open circuit relative to $E_{redox}(\text{BAQ}/\text{H}_2\text{BAQ}) = -0.4 \text{ V vs. SCE}$.

^d Efficiency for conversion of 632.8 nm light to electricity.

sion efficiency, η , is given by Eq. [5], where E_V is the output voltage in volts at

$$\eta = \frac{(E_V \times i)_{max} \times 100\%}{\text{Input optical power}} \quad [5]$$

the maximum power point; i is the photocurrent in amperes at the maximum power point and the input optical power is the power in watts from a 632.8 nm He-Ne laser source. Thus, we can realize an energy conversion efficiency of $\sim 2\%$ for the uphill reduction of BAQ. As Table I shows, the major loss would appear to be associated with the low open-circuit photovoltage. The quantum yield for electron flow is ≥ 0.50 and much of the inefficiency is reflection loss from the polished Si. In the absence of CH_3COOH we find $\sim 4\%$ efficiency for a photoelectrochemical cell based on

BAQ/BAQ^- converting 632.8 nm light to electricity. This doubled efficiency is about what is expected (5) for a fast, outer-sphere, one-electron redox couple.

The behavior of the p-type Si photocathode is constant in time. Figure 4 shows the photocurrent against time for a BAQ/ $\text{CH}_3\text{CN}/0.5 \text{ M } \text{CH}_3\text{COOH}/0.1 \text{ M } [n\text{-Bu}_4\text{N}]\text{ClO}_4$ solution. As shown, the efficiency for a cell where the photocathode process is according to Eq. [1] and where the anode process is its reverse can be sustained for a 20 hr period. There is no evidence that the photoelectrode undergoes any deterioration. Similar data have been published for the photoreduction of other species in nonaqueous media (5).

Preparative, controlled-potential photoreduction of BAQ.—We have demonstrated that synthetically sig-

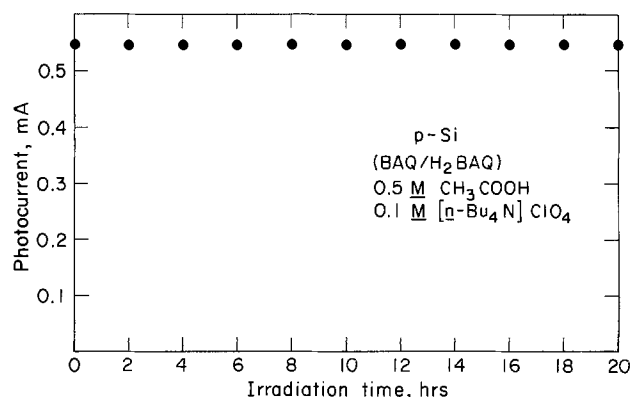


Fig. 4. Plot of photocurrent against time for a 0.1 cm^2 p-Si electrode irradiated with 632.8 nm ($\sim 50 \text{ mW/cm}^2$) light. The run was performed in 5.0 cm^3 of rigorously deoxygenated CH_3CN containing 0.2 M BAQ , $\sim 1 \text{ mM H}_2\text{BAQ}$, $0.5 \text{ M CH}_3\text{COOH}$, and $0.1 \text{ M } [n\text{-Bu}_4\text{N}]\text{ClO}_4$. The electrode was maintained at -0.3 V vs. SCE .

nificant quantities of H_2BAQ can be prepared by photoelectrochemical reduction of BAQ in $\text{CH}_3\text{CN}/\text{CH}_3\text{COOH}$. Irradiation (632.8 nm) of a p-type Si photocathode held at -0.3 V vs. SCE in a two compartment cell containing $0.2 \text{ M BAQ}/0.5 \text{ M CH}_3\text{COOH}$ in the $\text{CH}_3\text{CN}/0.1 \text{ M } [n\text{-Bu}_4\text{N}]\text{ClO}_4$ solution results in the generation of H_2BAQ . Spectrophotometric analysis reveals $>0.18 \text{ M H}_2\text{BAQ}$ generated. The photocurrent in the stirred cathode compartment was constant to $\sim 90\%$ depletion of the BAQ. Exposure of the resulting H_2BAQ solution to air resulted in the generation of a $>0.18 \text{ M H}_2\text{O}_2$ solution as determined by a spectrophotometric analysis by complexation with Ti(IV) (10).

Discussion

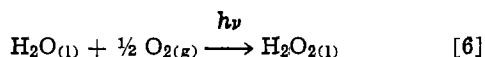
Our data establish that p-type Si photocathodes can be used to sustain the uphill generation of H_2BAQ . Synthetically significant concentrations of H_2BAQ and subsequently H_2O_2 can be generated. However, there is a disappointingly low overall efficiency for the process with respect to the utilization of the light energy in the $\text{BAQ} \rightarrow \text{H}_2\text{BAQ}$ step. Figure 3, for example, represents the photocurrent-voltage curves in what has been termed a regenerative photoelectrochemical cell for the conversion of light to electricity. "Regenerative" refers to the fact that the photoelectrode process is reversed at the counterelectrode. In the present case, the photocathode process is $\text{BAQ} \rightarrow \text{H}_2\text{BAQ}$ and the anode process is the reverse. The 632.8 nm light is converted to electricity with an efficiency of $\sim 2\%$, Table I. This efficiency also represents the efficiency for effecting the uphill reduction of BAQ to H_2BAQ . Such an efficiency is probably far too low to be useful inasmuch as the cost of electricity from conventional sources is significantly less than would be the cost of electricity generated photoelectrochemically when the solar efficiency is $<2\%$. It is widely believed that solar efficiencies for photovoltaic and photoelectrochemical processes must exceed $\sim 10\%$ in order to be practical, even if the cell is free (13). When a chemical such as H_2O_2 is the final product a lower efficiency might be allowable, except that conventional electricity can be generated at low cost. Thus, the photoelectrochemical approach to H_2O_2 , though demonstrated to work, must be improved significantly with respect to efficiency.

The problem of low efficiency for p-type Si-based cells for the $\text{BAQ} \rightarrow \text{H}_2\text{BAQ}$ is apparently associated with a low value of E_V . The low fill factors for the photocurrent-voltage curves in Fig. 3 are misleading because the E_V at open circuit is so low. The low E_V for $\text{BAQ} \rightarrow \text{H}_2\text{BAQ}$, compared to fast, outer-sphere, one-electron reagents like $\text{N,N'-dimethyl-4,4'-bipyridinium}$, appears to be a consequence of sluggish kinetics at the photoelectrode for the $\text{BAQ} \rightarrow \text{H}_2\text{BAQ}$ process. The electrochemical behavior of quinones has been the object of many studies showing that the mechanism is complicated and the interfacial kinetics sluggish (12). Adsorption may contribute to the difficulties associated with the $\text{BAQ} \rightarrow \text{H}_2\text{BAQ}$ reduction.³ We conclude that favorable manipulation of the kinetics of the BAQ reduction in acid medium is an important objective and our present research is directed toward this goal.

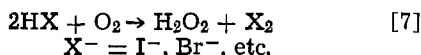
It is gratifying that the p-type Si/BAQ/ H_2BAQ system is durable. The direct reduction of O_2 in the presence of H^+ to form H_2O_2 in the photocathode compartment would very likely lead to fast, chemical deterioration of the p-type semiconductor, since H_2O_2 is a powerful oxidant. Further, most of p-type semiconductors that would be considered viable from the standpoint of solar efficiency are known to be unstable at very positive potentials or in the presence of strong oxidants (14).

³ We note that an earlier study of 9,10-anthraquinone itself at illuminated p-type Si showed little or no photovoltage, cf. D. Laser and A. J. Bard, *J. Phys. Chem.*, **80**, 5 (1976).

A final problem area concerns the overall cell chemistry. In our two-compartment cell the photocathode compartment gives the BAQ \rightarrow H₂BAQ. The BAQ can be regenerated in the H₂O₂ forming step, but 2H⁺ is consumed in the compartment per H₂O₂ molecule formed. The anode compartment in our cell has not been dealt with. Ideally, we would like to effect the overall chemistry represented by Eq. [6] where the only consumables are



truly abundant and inexpensive. Further, the free energy change associated with Eq. [6] is ~ 25 kcal/mole of H₂O₂ (9) and would in these terms represent an excellent match to the solar spectrum. But in order to do the chemistry represented by Eq. [6] the anode must effect the oxidation of H₂O to either H₂O₂ or to O₂. If the anode generates H₂O₂ then O₂ from air could be photoreduced at the cathode. If H₂O is oxidized to O₂ then there is no need for an external O₂ feed. There are photoanode materials, e.g., SrTiO₃, TiO₂, Fe₂O₃, etc., that are known to be able to effect the photo-oxidation of H₂O (1-3, 15). These anodes give poor solar efficiency for production of either O₂ or H₂O₂, from H₂O. More generally, H₂O₂ formation by the chemistry represented by Eq. [7] should be explored. For example



n-type CdS is known to be able to effect photo-oxidation of I⁻ in nonaqueous media to complete the cycle for the anode compartment (16). Further studies of such systems are underway in this laboratory.

Acknowledgments

We thank the Dow Chemical Company for partial support of this research. M.S.W. acknowledges support as a Dreyfus Teacher-Scholar grant recipient, 1975-1980.

Manuscript submitted Nov. 3, 1980; revised manuscript received Dec. 16, 1980.

Any discussion of this paper will appear in a Discussion Section to be published in the December 1981 JOURNAL. All discussions for the December 1981 Discussion Section should be submitted by Aug. 1, 1981.

Publication costs of this article were assisted by the Massachusetts Institute of Technology.

REFERENCES

1. A. J. Nozik, *Ann. Rev. Phys. Chem.*, **29**, 189 (1978).
2. M. S. Wrighton, *Acc. Chem. Res.*, **12**, 303 (1979).
3. M. Tomkiewicz and H. Fay, *Appl. Phys.*, **18**, 1 (1979).
4. A. J. Bard, *Science*, **207**, 139 (1980).
5. (a) A. B. Bocarsly, D. C. Bookbinder, R. N. Dominey, N. S. Lewis, and M. S. Wrighton, *J. Am. Chem. Soc.*, **102**, 3683 (1980); (b) D. C. Bookbinder, N. S. Lewis, M. G. Bradley, A. B. Bocarsly, and M. S. Wrighton, *ibid.*, **101**, 7721 (1979).
6. F.-R. Fan, B. Reichman, and A. J. Bard, *ibid.*, **102**, 1488 (1980).
7. A. Heller, B. Miller, H. J. Lewerenz, and K. J. Bachmann, *ibid.*, **102**, 6556 (1980).
8. "Chemical and Process Technology Encyclopedia," D. M. Considine, Editor, p. 600, McGraw-Hill, New York (1974).
9. W. M. Latimer, "Oxidation Potentials," 2nd ed., Prentice-Hall, New York (1952).
10. W. F. Schumb, C. N. Satterfield, and R. L. Wentworth, "Hydrogen Peroxide," p. 561, Reinhold Publishing Co., New York (1955).
11. D. C. Bookbinder, J. A. Bruce, R. N. Dominey, N. S. Lewis, and M. S. Wrighton, *Proc. Natl. Acad. Sci., U.S.A.*, **77**, 6280 (1980).
12. (a) J. M. Hale and R. Parsons, *Trans. Faraday Soc.*, **59**, 1429 (1963); (b) J. Q. Chambers, in "The Chemistry of Quinonoids," S. Patai, Editor, Chap. 14, John Wiley, New York (1974); (c) P. H. Given and M. E. Peover, *J. Chem. Soc.*, 385 (1960).
13. "Solar Photovoltaic Energy Conversion," The American Physical Society, New York (1979).
14. (a) A. J. Bard and M. S. Wrighton, *This Journal*, **124**, 1706 (1977); (b) H. Gerischer, *J. Electroanal. Chem. Interfacial Electrochem.*, **82**, 133 (1977); (c) S.-M. Park and M. E. Barber, *ibid.*, **99**, 67 (1977).
15. H. Kung, H. S. Jarrett, A. W. Sleight, and A. Ferretti, *J. Appl. Phys.*, **48**, 2463 (1977).
16. K. Nakatani, S. Matsudaira, and H. Tsubomura, *This Journal*, **125**, 406 (1978).

The Variation of Supporting Electrolyte Concentration in Impedance Studies at a Rotating Disk Electrode

Daniel A. Scherson and John Newman*

Department of Chemical Engineering, University of California, Berkeley, California 94720

ABSTRACT

An analytic expression for the flux of the electrolyte cation at the surface of a rotating disk electrode subject to a sinusoidally varying electrical perturbation is presented. The boundary conditions to which this treatment is relevant as well as some advantages of the impedance technique are discussed briefly.

The study of electrode kinetics in the presence of an excess of supporting electrolyte is a common practice in experimental electrochemistry. Solution conductivities can in this way be appreciably increased, thus diminishing the magnitude of the electric field. This represents in certain cases a real advantage in the sense that migration of the reactive species can effec-

tively be ignored. However, the interaction between these and the ions of the inert electrolyte cannot be neglected, if double layer effects are to be considered. Mass transfer equations accounting for this coupling can be derived by separating the flux into diffusion and migration contributions. In particular, if the ratio of reactant to electrolyte concentration is small, a linearization procedure can be applied, thereby reducing the complexity of the governing laws. Based

* Electrochemical Society Active Member.

Key words: convection, diffusion, mass transport.

on the latter, Newman (1) has obtained analytic expressions for steady-state concentration profiles of a system containing three species, for a rotating disk with neglect of radial variations. This communication will examine within the same framework of approximations the system response to sinusoidally varying boundary conditions [see also Ref. (2)]. Following an analysis previously reported by Scherson and Newman (3), a series expansion for the frequency dependence of the flux of the electrolyte ions at the surface will be presented. Krylov and Babak (4) have earlier stated that these series converge in the whole domain; however, a numerical evaluation of the expansion coefficients (5) has given a strong indication that this is not the case. It is important to note that a complete numerical treatment of the impedance of a rotating disk electrode including radial convection and without an *a priori* separation of the current has been recently described by Appel (6) [see also Ref. 7]. Although this is a significant advancement in attempting to account adequately for double layer effects, the time required for computer calculations makes its general use rather impractical.

Mathematical Formulation

The linearized form of the equation of convective diffusion to a rotating disk for the electrolyte cation is given, according to Newman (1) by

$$\frac{\partial c_+}{\partial t_+^*} - 3\xi_+^2 \frac{\partial c_+}{\partial \xi_+} = \frac{\partial^2 c_+}{\partial \xi_+^2} + \frac{1}{D_e} \left\{ \delta_R \left(\frac{D_e}{D_R} \right)^{2/3} \frac{\partial^2 c_R}{\partial \xi_R^2} + \delta_P \left(\frac{D_e}{D_P} \right)^{2/3} \frac{\partial^2 c_P}{\partial \xi_P^2} \right\} \quad [1]$$

where c_i is the concentration of species i . The dimensionless variables t_i^* and ξ_i are related to the time, t , and axial distance, y , by

$$t_i^* = \Omega \left(\frac{D_i}{\nu} \right)^{1/3} \left(\frac{a}{3} \right)^{2/3} t, \quad \xi_i = y \left(\frac{a\nu}{3D_i} \right)^{1/3} \sqrt{\frac{\Omega}{\nu}} \quad i = +, R, P \quad [2]$$

and the parameters D_e and δ_j are defined as follows

$$D_e = \frac{z_+ u_+ D_- - z_- u_- D_+}{z_+ u_+ - z_- u_-}, \quad \delta_j = \frac{u_+ z_j (D_- - D_j)}{u_+ z_+ - u_- z_-} \quad j = R, P \quad [3]$$

The subscripts $-$, $+$, R , and P refer to the anion, cation, reactant, and product, respectively, and other constants are specified in the List of Symbols.

As it becomes clear from Eq. [1], a previous knowledge of the functional dependence of c_R and c_P is necessary in order to solve the differential equation. According to this formalism, the effect of migration on the reactive species is ignored, therefore these functions can be obtained by solving independently the convective diffusion equation for reactant and product subject to appropriate boundary conditions.

If a sinusoidal perturbation is applied to the surface of the electrode, a state will be reached in which all variables involved will oscillate with the same frequency prescribed by the external signal. However, due to the approximations introduced in this analysis, only perturbations of very small amplitude will be considered.

A solution for the transient concentration profiles can be formally expressed as

$$c_i = c_i^{ss} + \tilde{c}_i \quad i = +, R, P \quad [4]$$

where c_i^{ss} and \tilde{c}_i are the steady-state and time dependent solutions, respectively. A procedure to determine c_i^{ss} has been described by Newman (1) and will not be reproduced here. Furthermore, because of the unique character of the perturbing signal, an explicit functional dependence for \tilde{c}_i can be established, namely

$$\tilde{c}_i = \theta_i \exp(jK_i t_i^*) \quad i = +, R, P \quad [5]$$

where θ_i ($i = +, R, P$) are coordinate dependent functions, and K_i are dimensionless frequencies defined by

$$K_i = \omega\nu \left(\frac{3D_i}{a\nu} \right)^{2/3} \left| \Omega D_i \quad i = R, P, \right. \\ \left. K_+ = \omega\nu \left(\frac{3D_e}{a\nu} \right)^{2/3} \left| \Omega D_e \right. \quad [6]$$

Upon substitution of Eq. [5] into Eq. [1], the following differential equation is obtained

$$jK_+ \theta_+ - 3\xi_+^2 \frac{\partial \theta_+}{\partial \xi_+} = \frac{\partial^2 \theta_+}{\partial \xi_+^2} + \frac{1}{D_e} \left\{ \delta_R \left(\frac{D_e}{D_R} \right)^{2/3} \frac{\partial^2 \theta_R}{\partial \xi_R^2} + \delta_P \left(\frac{D_e}{D_P} \right)^{2/3} \frac{\partial^2 \theta_P}{\partial \xi_P^2} \right\} \quad [7]$$

subject to

$$\theta_+ = 1 \text{ at } \xi_+ = 0, \quad \theta_+ \rightarrow 0 \text{ as } \xi_+ \rightarrow \infty \quad [8]$$

As discussed in a previous communication (3), the functions θ_R and θ_P can be determined by a Laplace transformation of the solution for the problem of transient convective diffusion under unit concentration step conditions at the surface of the electrode. Krylov and Babak (4) have analyzed this last problem and arrived at a series expansion in terms of parabolic cylinder functions, denoted hereafter by D_k . Based on this particular solution, the inverse Laplace transform of Eq. [7] and Eq. [8], regarding $jK_+ = p$ as a complex parameter, yields a differential equation in the real space

$$\frac{\partial \tilde{\theta}}{\partial \tau} = \frac{\partial^2 \tilde{\theta}}{\partial \xi^2} + 3\xi^2 \frac{\partial \tilde{\theta}}{\partial \xi} + \sum_{i=R,P} \sum_{n=0}^{\infty} \alpha_i^{-n/2} 2^{2n-1} \tau^{(3n-2)/2} \Theta_i(\eta) \quad [9]$$

where

$$\tilde{\theta}(\xi, \tau) = \mathcal{L}_p^{-1} \{ \theta_+(\xi_+, p) \} \quad [10]$$

and

$$\Theta_i(\eta) = \frac{\delta_i \alpha_i}{D_e} \exp \left(-\frac{\alpha_i}{2} \eta^2 \right) \sum_{k=-3n-1}^{3n-1} b_k^{(n)} D_{k+2}(\alpha_i^{1/2} \eta \sqrt{2}) \quad [11]$$

The similarity variables η and α_i are defined by

$$\eta = \frac{\xi}{2\sqrt{\tau}}, \quad \alpha_i = \frac{D_e}{D_i} \quad i = R, P \quad [12]$$

and the double asterisk in Eq. [11] indicates that k assumes odd values for even n , or even values for odd n . The expansion coefficients $b_k^{(n)}$ are given in Appendix A.

Finally, from Eq. [8]

$$\tilde{\theta} = 1, \text{ at } \xi = 0, \quad \tilde{\theta} \rightarrow 0 \text{ as } \xi \rightarrow \infty \quad [13]$$

Introduction of a new variable $z = 2\tau^{1/2}$ into Eq. [9] yields

$$2z \frac{\partial \tilde{\theta}}{\partial z} - \eta \frac{\partial \tilde{\theta}}{\partial \eta} \{2 + 3z^3 \eta\} = \frac{\partial^2 \tilde{\theta}}{\partial \eta^2} + 2 \sum_{i=R,P} \sum_{n=0}^{\infty} \alpha_i^{-\eta/2} z^{3n} \theta_i(\eta) \quad [14]$$

$$A_{-3n-1}^{(n)} = -\frac{3}{2} n \Gamma\left(\frac{3}{2}n\right) \sum_{k=-3n+1}^{2n-1} \frac{\{A_k^{(n)} + B_k^{(n)} + C_k^{(n)}\}}{\Gamma\left(\frac{1-k}{2}\right)} 2^{(3n+k+1)/2} \quad [22]$$

and a solution can therefore be sought in the form

$$\tilde{\theta}(\eta, z) = \sum_{n=0}^{\infty} \theta_n(\eta) z^{3n} \quad [15]$$

$$-\left. \frac{\partial \tilde{\theta}}{\partial \zeta} \right|_{\zeta=0} = \sum_{n=0}^{\infty} \tau^{1/2(3n-1)} \sum_{k=-3n-1}^{3n-1} \{A_k^{(n)} + \alpha_R^{1/2} B_k^{(n)} + \alpha_P^{1/2} C_k^{(n)}\} \frac{2^{3n+k/2} \tau^{1/4}}{\Gamma\left(-\frac{k}{2}\right)} \quad [23]$$

Substitution of Eq. [15] into Eq. [14], followed by a comparison of terms of identical order in z , generates a recursion relationship for the resulting set of differ-

$$\mathcal{L}_\tau \left\{ -\left. \frac{\partial \tilde{\theta}}{\partial \zeta} \right|_{\zeta=0} \right\} = -\left. \frac{\partial \theta_+}{\partial \zeta_+} \right|_{\zeta_+=0} = \sum_{n=0}^{\infty} \Gamma\left(\frac{3n+1}{2}\right) (jK_+)^{-1/2(3n-1)} \sum_{k=-3n-1}^{3n-1} \frac{2^{3n+k/2} \tau^{1/4}}{\Gamma\left(-\frac{k}{2}\right)} \times \{A_k^{(n)} + \alpha_R^{1/2} B_k^{(n)} + \alpha_P^{1/2} C_k^{(n)}\} \quad [24]$$

ential equations

$$\theta_n'' + 2\eta\theta_n' - 6n\theta_n = -3\eta^2 \theta_{n-1}' - 2 \sum_{i=R,P} \alpha_i^{-\eta/2} \theta_i(\eta) \quad [16]$$

Furthermore, it can be shown that a generalized expression that satisfies Eq. [16] is given by

$$\theta_n(\eta) = e^{-\eta^2/2} \sum_{k=-3n-1}^{3n-1} A_k^{(n)} D_k(\eta\sqrt{2}) + e^{-\alpha_R \eta^2/2} \sum_{k=-3n-1}^{3n-1} B_k^{(n)} D_k(\alpha_R^{1/2} \eta\sqrt{2}) + e^{-\alpha_P \eta^2/2} \sum_{k=-3n-1}^{3n-1} C_k^{(n)} D_k(\alpha_P^{1/2} \eta\sqrt{2}) \quad [17]$$

In particular, for $n = 0^1$

$$\theta_0(\eta) = \sqrt{\frac{\pi}{2}} \{A_{-1}^{(0)} \operatorname{erfc}(\eta) + B_{-1}^{(0)} \operatorname{erfc}(\alpha_R^{1/2} \eta) + C_{-1}^{(0)} \operatorname{erfc}(\alpha_P^{1/2} \eta)\} \quad [18]$$

Based on the assumption that $\theta_0(\eta)$ satisfies the boundary conditions specified in Eq. [10], an explicit form for the zeroth order coefficient is established by substitution of Eq. [18] into Eq. [16]

$$A_{-1}^{(0)} = \sqrt{\frac{2}{\pi}} \{1 - \Delta_R^{(0)} - \Delta_P^{(0)}\} \\ B_{-1}^{(0)} = \sqrt{\frac{2}{\pi}} \Delta_R^{(0)} \text{ and } C_{-1}^{(0)} = \sqrt{\frac{2}{\pi}} \Delta_P^{(0)} \quad [19]$$

where

¹The function $\theta_0(\eta)$ is obtained from Eq. [16] for $n = 0$ under the assumption $\theta_{-1}'(\eta) = 0$.

$$\Delta_i^{(n)} = \frac{\delta_i \alpha_i^{(1-n)/2}}{D_e(1-\alpha_i)} \quad i = R, P \quad [20]$$

Therefore, for n greater than zero

$$\theta_n(\eta) = 0 \text{ at } \eta = 0, \text{ and } \theta_n(\eta) \rightarrow 0 \text{ as } \eta \rightarrow \infty \quad [21]$$

The first relationship in Eq. [21] determines $A_{-3n-1}^{(n)}$

and further substitution of Eq. [17] into Eq. [16] yields after extensive algebraic manipulations recursion formulas for all remaining coefficients. These are given in Appendix B.

Based on Eq. [17], the derivative of $\tilde{\theta}(\zeta)$ evaluated at $\zeta = 0$ is given by

which after a Laplace transformation yields the derivative of the concentration of the electrolyte cation at the surface of the electrode, that is

The effect of the supporting electrolyte on the overall impedance can be obtained by introducing this last expression into the boundary conditions which in turn are to be equated to the specific linearized kinetics that prescribe the system.

Discussion and Conclusions

The individual fluxes corresponding to the electrolyte cation and anion can be reduced to a single equation by elimination of the electric field contributions and further use of the electroneutrality condition

$$\left\{ \frac{z_+ - z_-}{z_-} \right\} \left. \frac{\partial \theta_+}{\partial \zeta} \right|_{\zeta=0} + \frac{z_R}{z_-} \left. \frac{\partial \theta_R}{\partial \zeta} \right|_{\zeta=0} + \frac{z_R}{z_-} \left. \frac{\partial \theta_P}{\partial \zeta} \right|_{\zeta=0} = f(\Gamma_+, \Gamma_-) \quad [25]$$

where $f(\Gamma_+, \Gamma_-)$ corresponds to a linearized form for the kinetics of the particular system under analysis. Moreover Γ_i ($i = +, -$) are functions of a properly defined overpotential and surface concentrations of all ions involved. In addition, similar boundary conditions can be established for reactant and product as outlined elsewhere (6).

The treatment presented above allows individual fluxes of all ions to be expressed in terms of analytic functions, which represents an advantage over strictly numerical techniques. The theoretical interpretation of results obtained through the use of the impedance method will be strongly influenced by the particular model chosen especially in connection with the non *a priori* separation of the current in terms of double layer charging and faradaic reaction. A detailed description of these processes invariably leads to the introduction of certain quantities which may not be easily measured independently. It is precisely in this

respect that this transient technique could prove extremely useful because a large set of experimental data is obtained, therefore allowing a strict test of a general mathematical model.

Acknowledgment

This work was supported by a grant from Sandia Laboratories, Albuquerque, New Mexico.

Manuscript submitted July 14, 1980; revised manuscript received Dec. 16, 1980.

Any discussion of this paper will appear in a Discussion Section to be published in the December 1981 JOURNAL. All discussions for the December 1981 Discussion Section should be submitted by Aug. 1, 1981.

Publication costs of this article were assisted by the University of California.

APPENDIX A

Based on the particular set of dimensionless variables chosen in this work the $b_k^{(n)}$ coefficients are slightly different from those reported by Krylov and Babak (3), namely

$$b_{-1}^{(0)} = \sqrt{\frac{2}{\pi}} \quad [A-1]$$

$$b_2^{(1)} = -\frac{1}{4\sqrt{\pi}}, \quad b_0^{(1)} = -\frac{3}{8\sqrt{\pi}},$$

$$b_{-2}^{(1)} = 0, \quad b_{-4}^{(0)} = \frac{3}{8\sqrt{\pi}} \quad [A-2]$$

The values of $b_k^{(1)}$ given in Eq. [A-2] serve as a basis to generate any higher order coefficients ($n > 1$), through the recursion formulas specified below

$$b_{3n-1}^{(n)} = -\frac{\sqrt{2}}{8n} b_{3n-4}^{(n-1)} \quad [A-3]$$

$$b_{3n-3}^{(n)} = -\frac{3\sqrt{2}}{8(3n-1)} \{b_{3n-6}^{(n-1)} + (6n-5)b_{3n-4}^{(n-1)}\} \quad [A-4]$$

$$b_{-3n+1}^{(n)} = -\frac{9\sqrt{2}}{8} (3n-2)(n-1)b_{-3n+2}^{(n-1)} \quad [A-5]$$

$$b_{-3n+3}^{(n)} = \frac{3\sqrt{2}}{16} \{(6n-7)b_{-3n+2}^{(n-1)} - (3n-5)(3n-4)b_{-3n+4}^{(n-1)}\} \quad [A-6]$$

$$b_k^{(n)} = \frac{-3\sqrt{2}}{4(3n+k+1)} \{b_{k-3}^{(n-1)} + (2k+1)b_{k-1}^{(n-1)} + (k+1)(k+2)b_{k+1}^{(n-1)}\} \quad [A-7]$$

for $-3n+5 \leq k \leq 3n-5$

and

$$b_{-3n-1}^{(n)} = -\frac{3}{2} n \Gamma\left(\frac{3}{2}n\right) \sum_{k=-3n+1}^{3n-1} b_k^{(n)} \frac{2^{1/2}(3n+k+1)}{\Gamma\left(\frac{1-k}{2}\right)} \quad [A-8]$$

APPENDIX B

The first term in the RHS of Eq. [17] can be regarded as the solution for the electrolyte cation behaving as if it were a minor species. Therefore, it is not surprising that the recursion formulas for $A_k^{(n)}$ ($n > 1$) are precisely those specified in Appendix A, Eq. [A-3] through Eq. [A-7]. Moreover, $A_k^{(1)} = b_k^{(1)}$ for $k = 2, 0, -2$, and $A_{-4}^{(1)}$ is determined from Eq. [22], that is

$$A_{-4}^{(1)} = -\frac{3}{2} \Gamma\left(\frac{3}{2}n\right) \sum_{k=-2}^2 \frac{\{A_k^{(1)} + B_k^{(1)} + C_k^{(1)}\}}{\Gamma\left(\frac{1-k}{2}\right)} 2^{1/2}(3+k+1) \quad [B-1]$$

where $B_k^{(n)}$ and $C_k^{(n)}$ are listed below.

Defining

$$i x_k^{(n)} = B_k^{(n)} \text{ for } i = R (= C_k^{(n)} \text{ for } i = P) \quad [B-2]$$

the governing relationships for these coefficients are given as follows

$$i x_2^{(1)} = -\frac{1}{4\sqrt{\pi}} \Delta_1^{(1)} \quad i x_0^{(1)} = -\frac{(7-3\alpha_1)}{8\sqrt{\pi}(1-\alpha_1)} \Delta_1^{(1)} \quad [B-3]$$

$$i x_{-2}^{(1)} = \frac{2}{\sqrt{\pi}(1-\alpha_1)^2} \Delta_1^{(1)}$$

$$i x_{-4}^{(1)} = -\frac{\{16(1-\alpha_1)^3 - 3\}}{8\sqrt{\pi}(1-\alpha_1)^3} \Delta_1^{(1)} \quad [B-4]$$

$$\text{and for } n > 1 \quad i x_{3n-1}^{(n)} = \Delta_1^{(n)} b_{3n-1}^{(n)} \quad [B-5]$$

$$i x_{3n-3}^{(n)} = \Delta_1^{(n)} b_{3n-3}^{(n)} - \Phi_1 i x_{3n-4}^{(n-1)} - \frac{6n}{(1-\alpha_1)} i x_{3n-1}^{(n)} \quad [B-6]$$

$$i x_{3n-5}^{(n)} = -\Phi_1 i x_{3n-6}^{(n-1)} - \frac{(6n-2)}{(1-\alpha_1)} i x_{3n-3}^{(n)} - \Phi_1(6n-5) i x_{3n-4}^{(n-1)} + \Delta_1^{(n)} b_{3n-5}^{(n)} \quad [B-7]$$

$$i x_{k-2}^{(n)} = -\Phi_1 \{i x_{k-3}^{(n-1)} + (2k+1) i x_{k-1}^{(n-1)} + (k+1)(k+2) i x_{k+1}^{(n-1)}\} + \Delta_1^{(n)} b_{k-2}^{(n)} - \frac{(3n+k+1)}{(1-\alpha_1)} i x_k^{(n)} \text{ for } -3n+5 \leq k \leq 3n-5 \quad [B-8]$$

$$i x_{-3n+1}^{(n)} = -\frac{4}{(1-\alpha_1)} i x_{-3n+3}^{(n)} + \Phi_1(6n-7) i x_{-3n+2}^{(n-1)} - \Phi_1(3n-5)(3n-4) i x_{-3n+4}^{(n-1)} + \Delta_1^{(n)} b_{-3n+1}^{(n)} \quad [B-9]$$

$$i x_{-3n-1}^{(n)} = -\frac{2}{(1-\alpha_1)} i x_{-3n+1}^{(n)} - \Phi_1(3n-3)(3n-2) i x_{-3n+2}^{(n-1)} + \Delta_1^{(n)} b_{-3n-1}^{(n)} \quad [B-10]$$

where

$$\Phi_1 = \frac{3\sqrt{2}}{4(1-\alpha_1)} \alpha_1^{-1/2} \quad [B-11]$$

LIST OF SYMBOLS

| | |
|------------|---|
| a | 0.51023 |
| A, B, C | coefficients in series for $\theta_n(\eta)$, Appendix B |
| b | coefficients in series for minor species, Appendix A |
| c_i | concentration of species i /mole cm^{-3} |
| D_i | diffusion coefficient of species i /cm ² sec ⁻¹ |
| D_k | parabolic cylinder function of order k |
| K | dimensionless frequency, see Eq. [6] |
| p | complex parameter |
| t | time/sec |
| u_i | mobility of species i /cm ² mole sec ⁻¹ |
| y | axial distance from disk/cm |
| z_i | charge of ion i |
| z | $2\tau^{1/2}$, see Eq. [14] |
| α_1 | D_e/D_i , see Eq. [12] |
| Γ_i | dimensionless surface concentration of species i |
| Δ_1 | see Eq. [20] |
| ν | kinematic viscosity/cm ² sec ⁻¹ |
| ω | frequency of signal/radians sec ⁻¹ |
| Ω | rotation speed of disk/radians sec ⁻¹ |
| τ | dimensionless time |
| θ_i | dimensionless concentration of species i |
| Θ_1 | see Eq. [11] |
| ξ | dimensionless axial distance |
| x | see Eq. [B-3] |
| η | $\xi/2\sqrt{\tau}$, similarity variable, see Eq. [12] |
| Φ_1 | see Eq. [B-2] |

Suffixes

| | |
|---|--------------------|
| + | electrolyte cation |
| - | electrolyte anion |

e electrolyte
P product
R reactant

REFERENCES

1. J. Newman, "Electrochemical Systems," Section 121, Prentice-Hall, Englewood Cliffs, N.J. (1973).
2. P. Appel and J. Newman, *This Journal*, **124**, 1864 (1977).
3. D. Scherson and J. Newman, *ibid.*, **127**, 110 (1980).
4. V. S. Krylov and V. N. Babak, *Sov. Electrochem.*, **7**, 626 (1971); [*Elektrokhimiya*, **7**, 649 (1971)].
5. D. Scherson, P. F. Marconi, and J. Newman, *This Journal*, **127**, 2603 (1980).
6. P. W. Appel, Ph.D. Thesis, University of California, Berkeley (1976).
7. P. Pierini, P. Appel, and J. Newman, *This Journal*, **123**, 366 (1976).

Method for Kinetic Analysis of a Recombination-Controlled Reaction over a Wide Range of Current-Densities from the Reversible Region up to the Limiting Current

B. E. Conway* and D. M. Novak*¹

Chemistry Department, University of Ottawa, Ottawa, Ontario, Canada

ABSTRACT

Hitherto, the criterion for recombination-control in an electrochemical reaction sequence has been simply the observation of a Tafel slope of $RT/2F$ but applicable only to potential ranges where the coverage of the intermediate concerned is low ($< ca. 15\%$). A new general method is proposed which enables recombination kinetics to be tested over a full range of coverages and corresponding current-densities, up to the saturation limiting value, by means of linear plots of a function in $i^{1/2}$ and $\exp \eta F/RT$. If linear plots are found, both the recombination rate-constant and the quasi-equilibrium constant for the prior ion discharge/chemisorption step can be calculated. The method is illustrated by application to data for Cl_2 -evolution kinetics. The steepness of approach of overpotential *vs.* \log [current] curves to the saturation limiting current is shown to be dependent on interaction effects in the ad-layer, as seems to be indicated experimentally.

In a number of electrochemical gas evolution reactions (e.g., O_2 , H_2 , Cl_2 , C_2F_6 , C_2H_6), the step of recombination of radicals derived from a prior initial discharge of ions has been suggested as the rate-controlling step in the overall reaction. Only at one or two metals, however, has such a step been indicated experimentally, e.g., for H_2 on Pt (1), but then the evidence has been questioned (2). With the anodic Cl_2 evolution reaction, on the other hand, a number of authors (3-9) have proposed the recombination mechanism with various kinds of supporting evidence, e.g., Tafel slope and reaction order information.

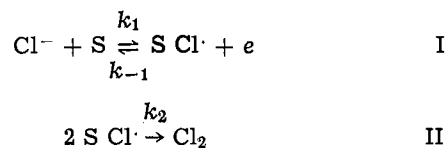
At Pt anodes in aq. Cl^- solutions, the general curved shape of the \log [current-density i] *vs.* potential curves (3) is suggestive of a recombination-controlled mechanism with coverage θ_{Cl} by the intermediate, Cl^\cdot discharged from Cl^- , reaching values near saturation corresponding (1) to the approach of currents to limiting recombination-controlled values as $\theta_{Cl} \rightarrow 1$. At catalytically active electrodes, the curved approach of the Tafel relation towards the reversible potential, at low overpotentials, becomes experimentally accessible and makes an added complication in the interpretation of curved Tafel relations, so that corrections for the back-reaction current component are then desirable.

In terms of analyses of consecutive reactions of heterogeneous multistep electrochemical processes (1, 10), it is well known that a rate-limiting recombination step following an ionic discharge process, producing a chemisorbed reactive intermediate, can lead to a Tafel slope of the potential *vs.* \log [current-density] relation equal to $RT/2F$ for "nonactivated" (11) adsorption or RT/F for "activated" adsorption (11).

Observation of the lower value of $RT/2F$ would usually be a clear indication of a recombination-controlled, 2-stage electrode process. However, such a Tafel slope is only predicted if the coverage θ of the electro-active intermediate has a low value, *viz.* $\theta < 0.1$. The more general case, where $\theta > 0.1$, corresponds to a curved $\log i$ *vs.* overpotential, η , relation with i eventually approaching a limiting value, i_{lim} , as is observed in the anodic Cl_2 evolution reaction at certain electrodes, e.g., Pt, C (3, 8). This implies that θ is already $> ca. 0.1$ at potentials somewhat positive to the reversible potential, so that diagnostic information from a Tafel slope cannot be obtained.

We present here a more general way of examining the kinetics of a reaction, where recombination control may apply, which is not limited by any restrictive assumptions about coverage by the intermediate. For convenience, the anodic Cl_2 evolution reaction is considered as it seems that this is one of the few cases where recombination-controlled kinetics might arise, so that our analysis may be applicable.

A mechanism previously considered [cf. Ref. (3-9)] for Cl_2 evolution is



where k_1 and k_{-1} are the electrochemical rate constants of the forward and backward directions of step I, and k_2 in the heterogeneous chemical rate constant of step II. S represents surface sites on the electrode on which a Cl^\cdot radical is discharged into a presumably chemisorbed state; θ will represent the fractional cov-

* Electrochemical Society Active Member.

¹ Present address, Eldorado Nuclear Ltd., Research Laboratories, Ottawa, Ontario, Canada.

erage of such species on the electrode surface and $1 - \theta$ the free area site fraction. S can be an oxide-free metal surface site or, more usually in aqueous medium, S is a site on an oxidized or partially oxidized Pt electrode surface. The degree of oxidation of the surface at the reversible potential for Cl_2 evolution in H_2O corresponds to about 2e per surface Pt atom in the absence of adsorbed Cl^- , i.e., "PtO," but due to competitive Cl^- ion adsorption (12), Cl_2 evolution must usually occur on an only partially oxide-covered surface. This aspect of the Cl_2 electrode reaction will be considered elsewhere (13). Here we shall concentrate on the kinetics of step II, when rate determining, in relation to the kinetics of step I and its reverse, especially as the current-density i_2 (controlled by II) increases toward its limiting value $i_{2,\text{lim}}$ corresponding to supposed saturation coverage by the intermediate.

Experimental Data

The experimental data to which the treatment given in this paper is applied, were obtained in point-by-point (30 sec at each potential) potentiostatic measurements at 298 K in aq. KCl + 0.05M HCl solutions made up from $3 \times$ recrystallized KCl and pyrodistilled water and in 0.5M RbCl in anhydrous trifluoroacetic acid. In this solvent, Cl_2 evolution can be established at an oxide-free surface over a wide potential range, up to 2.1V, E_{H} . More complete details of the experimental work, where Cl_2 evolution kinetics are related to Cl^- ion adsorption and surface oxide coverage at Pt, are given elsewhere (13, 15).

General Kinetic Analysis for the Recombination Mechanism I, II

The following method enables the kinetic behavior associated with pathways I, II to be represented over the whole range of θ_{Cl} and corresponding currents up to $i_{2,\text{lim}}$, by means of a linear test plot. The procedure applies without any restriction to special conditions (cf., 10, 11) that may lead limitingly to a Tafel slope of $RT/2F$, RT/F , or ∞ (limiting current).

The current-density for II is written as

$$i_2 = 2Fk_2\theta_{\text{Cl}}^2 \quad [1]$$

in the absence of interaction or heterogeneity effects [see Ref. (11), (14), and below]. If II is rate controlling, θ_{Cl} may be represented as $f(\eta)$ in the usual way (employing the quasi-equilibrium hypothesis) approximately by the electrochemical (Langmuir) adsorption isotherm as a first approach to the discussion of the current-potential behavior

$$\theta_{\text{Cl}} = \frac{\bar{K}_1 C_{\text{Cl}^-} \exp[\eta F/RT]}{1 + \bar{K}_1 C_{\text{Cl}^-} \exp[\eta F/RT]} \quad [2]$$

where \bar{K}_1 ($= k_1/k_{-1}$) is the electrochemical quasi-equilibrium constant² for step I and C_{Cl^-} is the chloride ion concentration. Then the i_2 vs. η relation over any range of anodic overpotentials is

$$i_2 = 2Fk_2 \left[\frac{\bar{K}_1 C_{\text{Cl}^-} \exp[\eta F/RT]}{1 + \bar{K}_1 C_{\text{Cl}^-} \exp[\eta F/RT]} \right]^2 \quad [3]$$

It is convenient to rearrange Eq. [3] to the form

$$\frac{\exp[\eta F/RT]}{i_2^{1/2}} = \frac{1}{(2Fk_2)^{1/2} \bar{K}_1 C_{\text{Cl}^-}} + \frac{\exp[\eta F/RT]}{(2Fk_2)^{1/2}} \quad [4]$$

Hence, a plot of $\exp[\eta F/RT]/i_2^{1/2}$ vs. $\exp[\eta F/RT]$ should give a straight line of slope $(2Fk_2)^{-1/2}$ and an intercept $[(2Fk_2)^{-1/2}/\bar{K}_1 C_{\text{Cl}^-}]$, and will be applicable to any range of values of θ_{Cl} . Thus, both the quasi-equilibrium constant \bar{K}_1 and k_2 the rate constant of

the rate-controlling recombination step II can be quantitatively evaluated.

An alternative way of examining experimental results, which provides a more sensitive basis for analyzing the kinetic behavior at high θ_{Cl} , follows by rearranging Eq. [3] to

$$i_2^{-1/2} = (2Fk_2)^{-1/2} + (2Fk_2)^{-1/4} (\bar{K}_1 C_{\text{Cl}^-})^{-1} \exp[-\eta F/RT] \quad [5]$$

which enables again both k_2 and \bar{K}_1 to be evaluated, this time from the slope and intercept of a plot of $i_2^{-1/2}$ vs. $\exp[-\eta F/RT]$.

Application to Some Experimental Results

In the course of examination (13) of the role of surface oxidation of Pt and specific adsorption of Cl^- ions on the kinetics of anodic Cl_2 evolution at that metal, some results for Cl_2 -evolution currents at closely spaced intervals of potential were obtained (15). The currents tended to approach a limiting value at high η suggesting recombination control with $\theta_{\text{Cl}} \rightarrow 1$. Experimentally, by working at a rotating Pt disk electrode, it was shown that the limiting currents were not diffusion controlled, as may also be calculated from the known concentrations and diffusion constant. It is therefore of interest to apply the above analysis to these data.

Application of Eq. [4] to the experimental results expressed as steady-state current-densities for Cl_2 evolution at various η values (Fig.1) gives the plots shown in Fig. 2. Good linearity evidently obtains over almost the whole range of η (except, because of the back-reaction, as $\eta \rightarrow 0$; see below), indicating applicability of the recombination-controlled mechanism. It is of interest that the results of Yokoyama and Enyo (3), obtained from an enlarged photo of their published η vs. $\log i$ curves which show an approach to limiting currents at Pt, also plot out in a similar way (based on Eq. [4]) and thus appear to indicate re-

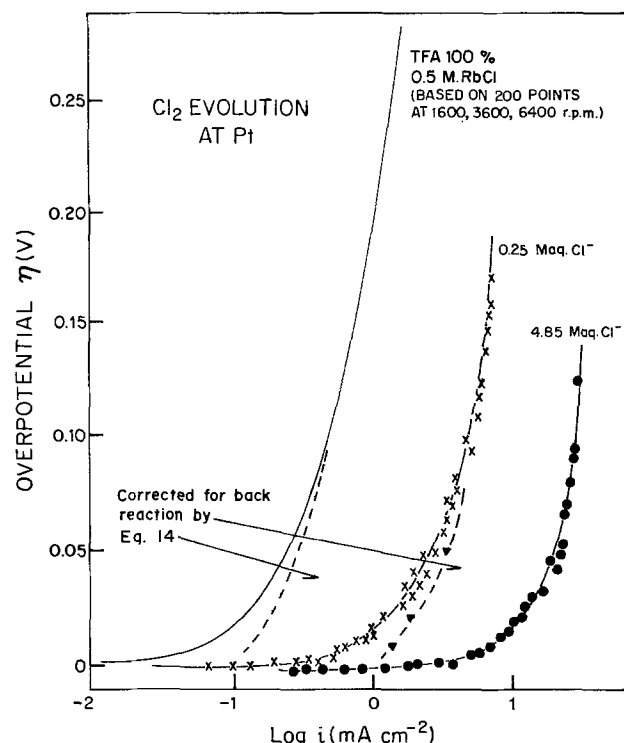


Fig. 1. Overpotential-log[current-density] relations for anodic Cl_2 evolution at rotating Pt disk electrode from 0.5M RbCl in anhydrous trifluoroacetic acid, 0.25M and 4.85M KCl in water at 298 K, showing approaches to kinetically controlled limiting currents. Plots shown are based on iR corrected data and are independent of electrode rotation rate. Back reaction corrections are also shown.

² \bar{K}_1 being an electrochemical equilibrium constant for step I contains the exp factor in $V_{\text{rev}}F/RT$ where V_{rev} refers to the reversible potential for the overall reaction on which the scale of η is based.

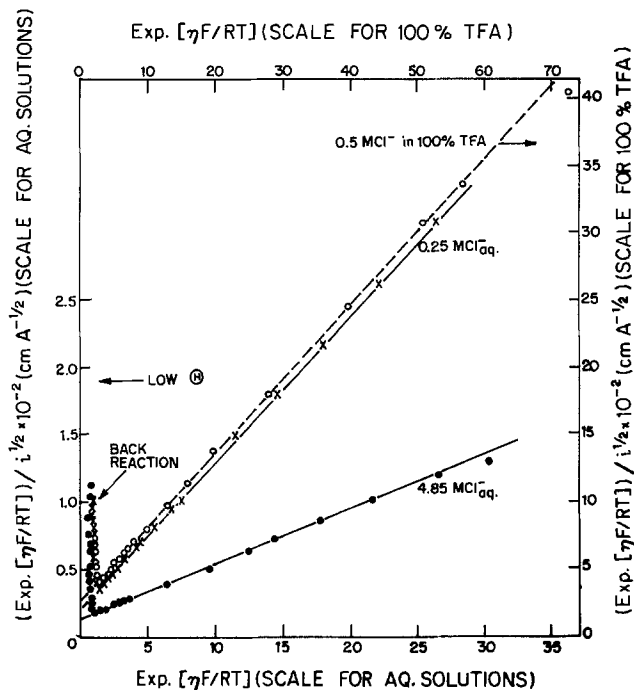


Fig. 2. Plots of the data in Fig. 1 according to Eq. [4]

combination-controlled kinetics. However, only a small number of experimental points are available from that work in order to make the test plot. In the present work, many more were obtained in order to provide a good basis for test of linearity of the plots. Fanta and Fiori's work (9) also led to the conclusion that the recombination reaction was rate controlling, but on the basis of observation of an $RT/2F$ Tafel slope.

Plots according to Eq. [5] may also be made, as shown in Fig. 3. In this method of treating the results, there is some small but significant curvature in the resulting lines for the data at higher current densities as $i \rightarrow i_{2,lim}$ or $\theta_{Cl} \rightarrow 1$. The effect due to neglect of the back-reaction gives the curvature at the other ends of the lines in Fig. 3. For high θ_{Cl} , lateral interactions between adsorbed Cl^- should be taken into account [cf. (11)] and will give rise to deviations from the behavior expected according to Eq. [5]. Such effects may be treated as follows.

When lateral interactions are significant, both the rate equation for recombination and the electrochem-

ical isotherms for Cl^- adsorption must be modified (11, 14) to include interaction terms. Thus Eq. [1] becomes

$$i_2 = 2Fk_2\theta_{Cl}^2 \exp[2g\theta_{Cl}] \quad [6]$$

for "nonactivated" adsorption (11) and the isotherm corresponding to Eq. [2] would be of the form

$$\frac{\theta_{Cl}}{1 - \theta_{Cl}} = \bar{K}_1 \exp[-g\theta_{Cl}] \cdot C_{Cl^-} \exp[\eta F/RT] \quad [7]$$

In these equations, g is a lateral interaction parameter (14) which measures in units of "RT" the assumed linear (17) change of free energy of adsorption of Cl^- with coverage at the electrode surface according to a Frumkin type isotherm.

Following a procedure similar to that for deriving Eq. [4] or [5] by substituting for θ_{Cl} from Eq. [7] into [6], we obtain

$$i_2^{-1/2} = (2Fk_2)^{1/2} \exp[-g\theta_{Cl}] + (2Fk_2)^{-1/2} (\bar{K}_1 C_{Cl^-})^{-1} \exp[-\eta F/RT] \quad [8]$$

This equation shows that when $g \neq 0$, $i_2^{-1/2}$ is no longer proportional to $\exp[-\eta F/RT]$ as is indicated by Eq. [5] since there is an additional term involving $g\theta_{Cl}$ in the function for potential dependence of θ_{Cl} , now given by Eq. [7] rather than Eq. [2]. Equation [8] cannot be explicitly evaluated but numerical treatment for selected reasonable values of g ($= 0, 2, 4$, and -2 units of RT) enables the form of Eq. [8] for the variation of $i_2^{-1/2}$ with θ_{Cl} , and hence η , to be obtained as shown in Fig. 4. The resulting behavior towards $\theta_{Cl} = 1$ may be compared with that based on the experimental results shown in Fig. 3. The evaluation of Eq. [8] is made by choosing a range of θ_{Cl} values up to $\theta_{Cl} \rightarrow 1$ and taking arbitrary values of $k_2 = 1$, $K = 1$, and $C_{Cl^-} = 1$ so that the scales of the plots are relative ones but the four curves are self-consistent ones. The potentials in $\exp[-\eta F/RT]$ are taken on an overpotential scale relative to a reversible potential, V_r , taken as zero, corresponding to $\bar{K}_1 = 1 \exp[-V_r F/RT] = 1$, where V_r is defined in footnote 2.

It will be noted that g -dependent deviations from the (linear) Langmuir plot which arises when g is taken as zero in Eq. [7] appear in a characteristic way, dependent on the sign and magnitude of g ($= 0, 2, 4$, and -2 units of RT). All four curves in Fig. 4 become asymptotic to the $g = 0$ line for sufficiently low η , as expected.

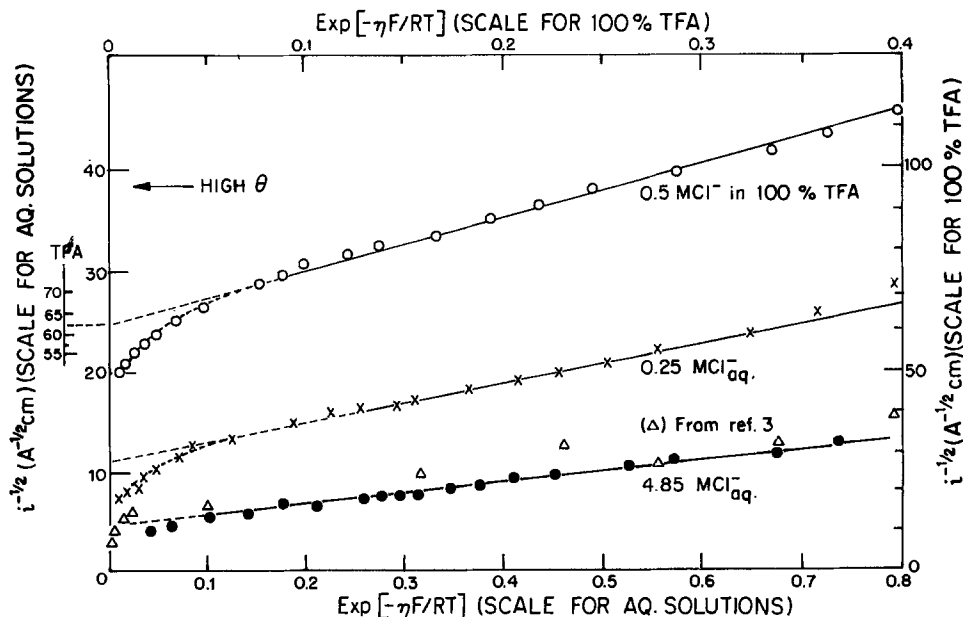


Fig. 3. Plots of the data of Fig. 1 according to Eq. [5].

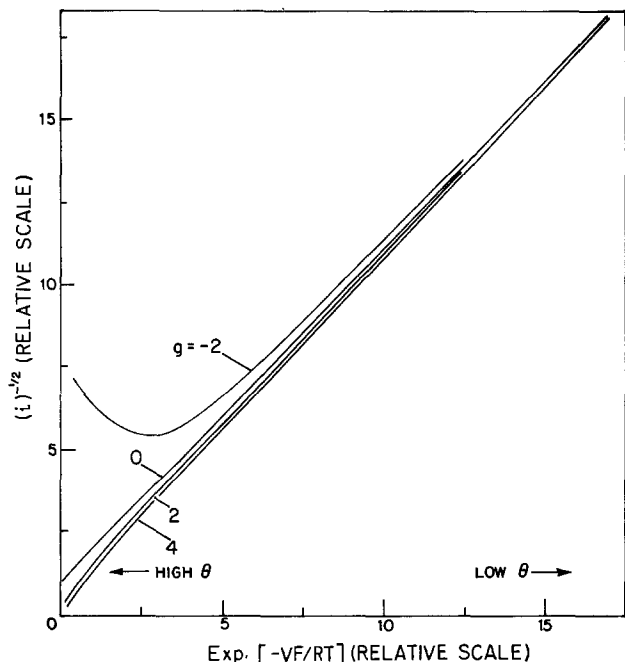


Fig. 4. Simulation of the behavior of a recombination-controlled process according to Eq. [8] with various values of the g factor ($g = 4, 2, 0$, and -2). Langmuir case ($g = 0$) gives a straight line.

The plots of (Fig. 4) of $i^{-1/2}$ vs. $\exp[-\eta R/RT]$ derived by this numerical evaluation of Eq. [8] for values of $g > 0$ have similar directions of curvature to those of Fig. 3, based on the experimental data, as $\theta_{Cl_2} \rightarrow 1$, i.e., as $i^{-1/2} \rightarrow 0$. The Langmuir case ($g = 0$) is indicated as a reference and gives, of course, a linear plot, as for Eq. [5]. A more realistic interaction term for this case of metal-to-Cl surface dipoles would be written with an $\exp[-g\theta_{Cl_2}^{3/2}]$ term or a more complex one if dipole imaging were included (18). Such a term arises from surface dipole repulsion in the nearest-neighbor approximation and gives a somewhat steeper curvature of the plots near $\theta_{Cl_2} \rightarrow 1$. A value of $g \approx 2$ is required to fit the observed experimental behavior in aqueous solutions.

The intercepts and slopes of the almost linear relations of Fig. 2 or 3 give values of the rate constant k_2 and the quasi-equilibrium constant \bar{K}_1 (Table I).

It should be mentioned³ that any exponential relation of the form $i_\eta = i_0 \exp[\beta\eta F/RT]$ for a discharge-controlled process, or a more general one including the back-reaction component, $i_\eta/i_0 = 2 \sinh[\eta F/2RT]$, where $\beta = 0.5$ is the transfer symmetry factor, can give a plot of $(i_\eta)^{-1/2}$ which is an exp function of η ; for example, in the above case for a simple single-stage process, $i^{-1/2}$ would be linear in $\exp[-\beta\eta F/2RT]$ or $\sinh^{-1/2}[\eta F/2RT]$. However, for the present type of case involving recombination control, the linear test plot has to be made in terms of $i_\eta^{-1/2}$ vs. $\exp[-\eta F/RT]$ and not vs. $\exp[-\beta\eta F/2RT]$. A more important point is that a simple exp Tafel relation for a discharge-controlled step cannot give an intercept as in Eq. [5]

³ We are grateful to Professor M. Enyo for remarks in correspondence on this point. [See Ref. (19).]

Table I. Values of \bar{K}_1 and k_2 for the Cl_2 evolution process, I, II, in various solutions

| Solution | \bar{K}_1 $\times 10^{-3}$ cm ³ mol ⁻¹ | k_2 $\times 10^9$ mol sec ⁻¹ cm ⁻² |
|-----------------------------------|--|--|
| 0.5M RbCl in trifluoroacetic acid | 0.764 | 1.96 |
| 0.25M KCl in water | 2.63 | 49.5 |
| 4.85 KCl in water | 0.12 | 290 |

at higher η for the recombination-controlled process. Such an intercept arises, of course, from the form of the adsorption Eq. [2] and hence [3], when $\bar{K}_1 C_{Cl_2} - \exp(\eta F/RT)$ is neither small nor large compared with 1. The results shown above demonstrate that tests of experimental data according to Eq. [4] or [5], corresponding to the mechanism I, II, do, in fact, give (i) good linear relations over most (see above) of the potential range and (ii) significant nonzero intercepts. These are critical aspects of the fit of the experimental kinetic data to the recombination type of mechanism according to Eq. [4] or [5], based on a large number of experimental i, η points in the original measurements.

Role of the Back-Reaction

When the experimental data are treated in terms of Eq. [4], e.g., as shown in Fig. 2, the plots always show a sharp bend-up at low values of η . The Cl_2 evolution reaction is a relatively reversible one at Pt and the measured current-overpotential relations (in the presence of Cl_2 at 1 atm pressure) are always asymptotic to the $\log i$ axis at low η , i.e., participation of the back-reaction sets in at easily accessible current densities (Fig. 1). The bend-up of the lines of Fig. 2 at low η can be accounted for simply by the increasing participation of the back-reaction as the condition $\eta \rightarrow 0$ is approached, corresponding to the observed asymptotic approach of the $\log i$ vs. η curve to the current-density axis as $\eta \rightarrow 0$.

The above method for analysis of recombination-controlled kinetics necessarily applies only to the anodic component, i_a , of the net current density, i . Near the reversible potential, i_a differs from the measured net current i according to $i_a = i + |i_c|$, where $|i_c|$ is the numerical value of the back-reaction component of i . We can write for a general case, with recombination control

$$i = i_a - |i_c| = 2Fk_2\theta^2 - 2Fk_{-2}(1 - \theta)^2 \quad [9]$$

At $\eta = 0$, $i = 0$ and $|i_c| = i_a = i_0$ and $\theta = \theta_r$, the value of θ at the reversible potential. Then i can be written in terms of θ_r , with i_a and $|i_c|$ as

$$i = i_0 \theta^2 / \theta_r^2 - i_0 (1 - \theta)^2 / (1 - \theta_r)^2 \quad [10]$$

where i_0 is defined by comparing the last equation with Eq. [9]. i_a is obtained from Eq. [10], after elementary rearrangements, as

$$i_a = i \left/ \left[1 - \frac{(1 - \theta)^2}{\theta^2} \cdot \frac{\theta_r^2}{(1 - \theta_r^2)} \right] \right. \quad [11]$$

Quasi-equilibrium in step I enables θ and θ_r to be related to the reversible potential V_r and η as follows

$$\frac{\theta_r}{1 - \theta_r} = K_1 C_{Cl_2} - \exp \left[\frac{V_r F}{RT} \right];$$

$$\frac{\theta}{1 - \theta} = K_1 C_{Cl_2} - \exp \left[\frac{V_r + \eta}{RT} \right] \quad [12]$$

so that

$$\frac{\theta}{1 - \theta} = \frac{\theta_r}{1 - \theta_r} \exp \left[\frac{\eta F}{RT} \right] \quad [13]$$

Hence

$$i_a = i \left/ \left[1 - \exp \left(- \frac{2\eta F}{RT} \right) \right] \right. \quad [14]$$

Thus, near the reversible potential, the measured net current-densities have to be corrected by the factor $[1 - \exp(-2\eta F/RT)]^{-1}$ in order to obtain the relevant anodic current-densities controlled by the kinetics of the recombination step. Then Eq. [4] for testing the recombination kinetics is written

$$\exp[\eta F/RT] \cdot (1 - \exp[-2\eta F/RT])^{1/2}$$

$$= \frac{i_2^{1/2}}{(2Fk_2)^{1/2} \bar{K}_1 C_{Cl_2}} + \frac{\exp[\eta F/RT]}{(2Fk_2)^{1/2}} \quad [15]$$

which eliminates the hook at low η values in the plots of Fig. 2. It should also be noted in relation to the recombination-controlled kinetics, indicated by the test plots according to Eq. [4] (or [15]), or [5], that a direct plot of $\log i_2/(1 - \exp[-2\eta F/RT])$ vs. η for the Pt data does not (cf. Fig. 1) give a linear corrected Tafel plot as do corresponding plots for Cl_2 evolution currents on Ir which then exhibit a Tafel slope of $1 RT/2F$ for a variety of conditions. In the latter case, for a process with potential-dependent exp factors in the component currents of $\alpha\eta F/RT$ and $-(1 - \alpha)\eta F/RT$, the correction factor for back-reaction current is $1/(1 - \exp[\eta F/RT])$.

Application of this correction causes the points in the hook of the lines of Fig. 2 at their lower ends to be reduced in magnitude so that they all fall more or less on the line after correction. The hook is therefore due to participation of the back-reaction at low η values. The correspondence of the corrected points at low η values with the line connecting points derived for higher η shows, incidentally, that the mechanism which applies at high η , giving a limiting current, persists down to the reversible potential without change.

Form of η vs $\ln i$ Curves: Steepness of Approach to the Limiting Current

The rate of approach of the current to its limiting value is an easily observable and interesting aspect of the experimental behavior. In the Langmuir case for the adsorption of the intermediate according to Eq. [2], this is determined by the range of potentials over which θ_{Cl} increases from ca. 0.15 (below which a linear Tafel relation is observed) to ca. 0.95, viz. 105 mV. When significant repulsive interaction effects arise in the ad-layer of the intermediate, the adsorption isotherm Eq. [7] applies and the range of potentials over which θ_{Cl} increases from 0.15, for example, to 0.95 increases approximately in proportion to g . Then the range of potentials over which the current increases towards its limiting value (Eq. [6]) correspondingly increases but the value of the limiting current itself also increases with g when $g > 0$ according to the factor $\exp 2g$ (Eq. [6]). Thus g has only to be 1.15 for the limiting current to be increased by a factor of 10 and when $g > 0$ in the general case, the approach of the current to its limiting value is less steep than in the Langmuir case. This is the kind of behavior observed experimentally [Fig. 1 and Ref. (3)].

Thus, by means of the general rate Eq. [6] and the corresponding electroadsorption isotherm (Eq. [7]), the reciprocal slope of the η vs. $\ln i$ relation at any point may be calculated from

$$d \ln i / d \eta = (d \ln i / d \theta) (d \theta / d \eta) \quad [15]$$

where θ here is written for any intermediate in a mechanism of the type I, II. Thus

$$d \ln i / d \theta = 2/\theta + 2g \quad [16]$$

and

$$d \eta / d \theta = \frac{RT}{F} \left[\frac{1 + g\theta(1 - \theta)}{\theta(1 - \theta)} \right] \quad [17]$$

Then

$$d \eta / d \ln i = \frac{RT}{2F} \left[\frac{1 + g\theta(1 - \theta)}{(1 - \theta)(1 + g\theta)} \right] \quad [18]$$

which gives the required limiting values of the Tafel slope as $RT/2F$ as $\theta \rightarrow 0$ and ∞ as $\theta \rightarrow 1$, and the slope of the g -dependent η vs. $\ln i$ curve for any intermediate θ values. The corresponding changes of the limiting current itself when $g > 0$ can be expressed (cf. Eq. [6]) as

$$i_{\text{lim},g}/i_{\text{lim},g=0} = \exp 2g \quad [19]$$

Thus, when $g > 0$, a quasi-catalytic effect arises in recombination control due to lateral interaction effects.

Illustrative values of the gradients, $d\eta/d \ln i$, of the overpotential vs. \ln [current-density] curves near the

Table II. Some values of $d\eta/d \ln i$ near the limiting current-density for various g values

| Coverage | g value/ RT | Slope $\frac{RT}{2F}$ at θ | i/i_{lim} at θ |
|-----------------|-----------------|-----------------------------------|--------------------------------|
| $\theta = 0$ | ~ 0 | $\rightarrow 1$ | $< < 1$ |
| $\theta = 0.95$ | 1 | 20 | 0.903 |
| | 2 | 10.4 | 0.817 |
| $\theta = 0.99$ | 0 | 7.55 | 0.739 |
| | 1 | 100 | 0.980 |
| $\theta = 1$ | 2 | 50.7 | 0.961 |
| | Any value | 32.9 | 0.942 |
| | | ∞ | 1 |

limiting current condition ($i \rightarrow i_{\text{lim}}$ as $\theta \rightarrow 1$) are given in Table II as multiples of $RT/2F$ for $g = 0, 1$, and 2 , and show the trend toward less steep approaches of i to i_{lim} as g is larger than zero; the corresponding i/i_{lim} ratios are given. The slope is given as a multiple of the limiting value $RT/2F$ attained for all g values at sufficiently low θ (Eq. [18]). The experimental behavior in this work and that of Ref. (3) is fitted by a value of $g = 1.5 \sim 2.0$.

Conclusion

A new method for treating electrode-kinetic data for reactions where a recombination-controlled process may be occurring is proposed. It gives linear test plots over the whole range of coverage of the intermediate involved, corresponding to a wide range of current-densities from low values up to the limiting value determined by saturation coverage by the intermediate. If linear behavior is found in such test plots, quantitative evaluation of the rate constant of the recombination step and the quasi-equilibrium constant of the prior discharge/deposition step can be made. Interaction effects cause deviations from linearity.

It is shown how the approach of the current to the recombination-controlled limiting value, i.e., the steepness of the curved η vs. $\ln i$ relation, depends on interactions between the ad-species in the recombination step. Experimental behavior in anodic Cl_2 evolution at Pt corresponds to significant repulsive interactions between Pt-Cl⁻ surface dipoles, dependent on coverage.

Acknowledgments

Grateful acknowledgment is made to the Natural Sciences and Engineering Research Council of Canada for award of a grant in support of this and related work. One of us (D.M.N.) acknowledges the award of the Joseph W. Richards Summer Research Fellowship of The Electrochemical Society (1978). We also thank Dr. B. V. Tilak of Hooker Research for useful discussions.

Manuscript submitted April 18, 1980; revised manuscript received July 30, 1980.

Any discussion of this paper will appear in a Discussion Section to be published in the December 1981 JOURNAL. All discussions for the December 1981 Discussion Section should be submitted by Aug. 1, 1981.

Publication costs of this article were assisted by the University of Ottawa.

REFERENCES

- J. O'M. Bockris and A. M. Azzam, *Trans. Faraday Soc.*, **48**, 145 (1952).
- M. W. Breiter, *This Journal*, **109**, 549 (1962); see also S. Schuldiner, *ibid.*, **109**, 550 (1962).
- T. Yokoyama and M. Enyo, *Electrochim. Acta*, **13**, 1631 (1968); **15**, 1921 (1970).
- R. G. Erenburg, L. I. Krishtalik, and Bystrov, *Electrokhimiya*, **8**, 1740 (1972).
- R. G. Erenburg, L. I. Krishtalik, and I. P. Yaroshvskaya, *ibid.*, **11**, 1068, 1072 (1975).
- E. C. Littauer and L. L. Shrier, *Electrochim. Acta*, **11**, 527 (1966).
- F. T. Chang and H. Wick, *Zeit. Phys. Chem.*, **A172**, 448 (1935).

8. W. E. Triaca, C. Solomons, and J. O'M. Bockris, *Electrochim. Acta*, **13**, 1949 (1968).
9. G. Faita and G. Fiori, *J. Appl. Electrochem.*, **2**, 31 (1972); see also *This Journal*, **117**, 1333 (1970).
10. J. O'M. Bockris, *J. Chem. Phys.*, **24**, 817 (1956).
11. J. G. N. Thomas, *Trans. Faraday Soc.*, **57**, 1603 (1961).
12. M. W. Breiter, *Electrochim. Acta*, **8**, 925 (1963).
13. B. E. Conway and D. M. Novak, *J. Chem. Soc. Faraday Trans. 1*, **75**, 2454 (1979).
14. B. E. Conway and E. Gileadi, *Trans. Faraday Soc.*, **58**, 2493 (1962).
15. D. M. Novak, Ph.D. Thesis, University of Ottawa (1979).
16. B. E. Conway and R. G. Barradas, *Electrochim. Acta*, **5**, 319 (1961).
17. M. Boudart, *J. Am. Chem. Soc.*, **72**, 3556 (1958).
18. J. K. Roberts, *Trans. Faraday Soc.*, **34**, 1342 (1938).
19. T. Yokoyama and N. Enyo, *J. Electroanal. Chem.*, in press.

Diffusion and Solid-Film Formation during Electropolishing of Metals

R. Kirchheim, K. Maier, and G. Tölg

Max-Planck-Institut für Metallforschung, Institut für Werkstoffwissenschaften, 7000 Stuttgart 1, Germany

ABSTRACT

Various metals and electrolytes were used for potentiostatic electropolishing. When measuring the current-time behavior over several orders of magnitude and for the different temperatures, three stages were observed: (i) a short stage I, during which the current density was approximately constant; (ii) during the following stage II saturation of the dissolved metal ions (reaction products) was obtained in the vicinity of the anode surface, and the current density decreased with the reciprocal square root of time; and (iii) after sufficiently long times, during stage III a steady-state current density was approached by an exponential time law. The known theoretical models, based on the work of Elmore, are able to explain the relations between current density, time, and temperature for stage I and II. For stage III a new model is presented which takes convection within the electrolyte into account. The possible formation of a solid film at the transition from stage I to stage II is thought to be responsible for characteristic deviations from the expected current-time behavior. A mathematical treatment of this formation yields film thicknesses of 3-30 nm.

Electropolishing is a well-known method for anodic dissolution of metals and for simultaneous smoothing of the metal surface. Since the first fundamental work of Jaquet (1), many experimental and theoretical contributions have been made in order to explain the process of electropolishing.

In a very important investigation, Elmore (2) could show that the diffusion of a species of the cell reaction determines the rate of dissolution. Kojima and Tobias (3) concluded from diffusion data that the diffusing species for copper/phosphoric acid is some copper phosphate. This contradicts the concept of Edwards (4), who assumed water or phosphoric acid diffusion to be rate controlling.

In this study the current-time behavior is thoroughly examined for different metals and electrolytes with constant cell voltage. The theoretical treatment is extended to describe the influence of natural and forced convection and of the formation of a solid film on the current-time function.

The occurrence of a solid film during electropolishing, its thickness and composition, and its role in brightening are not fully understood (5-9). Direct experimental evidence of the film is difficult to obtain, because the film is dissolved in the electrolyte after switching off the cell voltage (9).

According to theory (2), the product of initial current density and square root of transition time should be proportional to the product of solubility and square root of diffusivity. This was checked for copper in phosphoric acid by measuring the temperature dependence of all quantities.

Experimental Procedure

The cell and the electric circuit used in this study are shown schematically in Fig. 1. This arrangement

Key words: electrolyte, electrode, current density.

has also been used in another study to determine concentration-depth profiles on microsectioning specimens (10).

The apparent area of the portion of the anode exposed to the electrolyte was 1.00 cm². The anodes were prepared from high purity polycrystalline material, both mechanically and electrolytically polished before they were mounted in the cell. The cathode was made of a platinum disk spot welded on a steel cylinder. Analytical grade acids were diluted with bidistilled water to the desired concentration.

Usually the experiments were run with constant cell voltage. A voltage slightly less than necessary for oxygen evolution, just at the end of the so-called polishing plateau (11), was applied. In some cases, a saturated calomel reference electrode was used to achieve potentiostatic conditions (12). For measuring temperature effects, the cell was placed into a thermostated bath.

Theory

The equations derived below should describe the time dependence of the cell current during potentiostatic electropolishing, where diffusion into the elec-

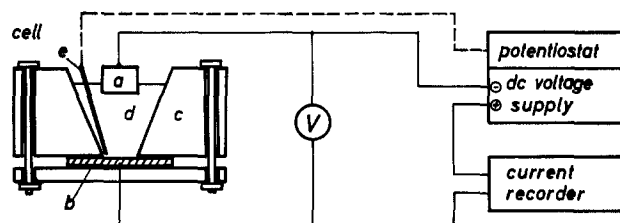


Fig. 1. Schematic view of the experimental cell and the electric circuit. a, Cathode; b, sample (anode); c, Teflon cell body; d, electrolyte; e, reference electrode.

trolyte is the rate-controlling step of the overall cell reaction. Three stages of the current-time function, schematically shown in Fig. 2, are distinguished due to changing boundary conditions.

During stage I from $t = 0$ to $t = t_s$ the concentration of dissolved metal ions at the anode/electrolyte interface increases until the solubility limit is reached. Supersaturation can occur and may cause a solid film to be formed on the anode during stage IIa. Assuming local equilibrium between the solid film and the adjacent electrolyte, the concentration of metal ions is kept constant at that interface for the duration of stage II. If electropolishing times are long or if the electrolyte is stirred, natural or forced convection must be taken into account, thus giving rise to stage III. The diffusion of metal ions in the presence of excess supporting electrolyte obeys Fick's second law

$$\frac{\partial c}{\partial t} = D \frac{\partial^2 c}{\partial x^2} \quad [1]$$

with a constant diffusion coefficient D . Because the boundary conditions are different for each stage, it is convenient to discuss the stages separately. The following mathematical treatment is also applicable for the depletion of a so-called acceptor (4) where $c(0, t_s) = 0$ instead of $c(0, t_s) = c_s$ has to be inserted.

Diffusion during stage I.—At the onset of electropolishing, the concentration c_b of metal ions in the electrolyte, which is zero in this study, should be uniform. The current density i is related to the ion flux if only one electrochemical reaction is taken into account. The initial and boundary conditions on Eq. [1] are, therefore, (2)

$$c_I(\infty, t) = c_b$$

$$c_I(x, 0) = c_b$$

$$\frac{\partial c_I}{\partial x}(0, t) = -\frac{i_I(t)}{nFD}$$

giving the well-known solution (13) for stage I

$$c_I(x, t) = c_b + \frac{1}{nF\sqrt{\pi D}} \int_{t'=0}^{t'} \frac{i(t')}{\sqrt{t-t'}} \exp\left(-\frac{x^2}{4D(t-t')}\right) dt' \quad [2]$$

For constant current density i_0 , the integration yields

$$c_I(x, t) = c_b + \frac{2i_0}{nF} \sqrt{\frac{t}{\pi D}} \exp\left(-\frac{x^2}{4Dt}\right) - \frac{i_0 x}{nFD} \operatorname{erfc}\left(\frac{x}{2\sqrt{Dt}}\right) \quad [3]$$

From the last equation a relation between diffusivity D and solubility limit c_s and the measurable quantities i_0

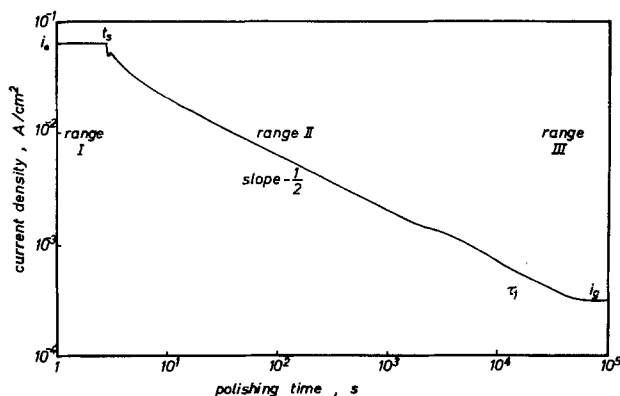


Fig. 2. Double logarithmic plot of current vs. time

and t_s is easily obtained

$$i_0\sqrt{t_s} = \frac{nF}{2} (c_s - c_b) \sqrt{\pi D} \quad [4]$$

where t_s is the time necessary to reach the saturation concentration c_s at the electrode ($x = 0$).

Diffusion during stage II.—For $t \geq t_s$ the concentration at the anode/electrolyte interface is c_s , and Eq. [1] has to be solved with the new boundary condition

$$c_{II}(0, t) = c_s$$

The new initial condition is the concentration profile built up in the electrolyte during stage I (Eq. [2])

$$c_{II}(x, 0) = c_I(x, t_s)$$

For convenience a new zero point at $t = t_s$ is used on the time scale during stage II. Then the concentration distribution is (14)

$$c_{II}(x, t) = c_b + \frac{xc_s}{2\sqrt{\pi D}} \int_{t'=0}^t (t-t')^{-3/2} \exp\left(-\frac{x^2}{4D(t-t')}\right) dt' + \frac{1}{2\sqrt{\pi D}t} \int_{x'=0}^{\infty} \left[c_b + \frac{1}{nF\sqrt{\pi D}} \int_{t'=0}^{t_s} \frac{i_I(t')}{\sqrt{t_s-t'}} \exp\left(-\frac{x'^2}{4D(t_s-t')}\right) dt' \right] \cdot \left[\exp\left(-\frac{(x-x')^2}{4Dt}\right) - \exp\left(-\frac{(x+x')^2}{4Dt}\right) \right] dx' \quad [5]$$

No attempt is made to find an analytical solution for $c_{II}(x, t)$. However, the current density

$$i_{II}(t) = -nFD \frac{\partial c_{II}}{\partial x} \Big|_{x=0}$$

is readily calculated, especially after changing the sequence of integration in the third term of Eq. [5].

Substituting $t_s - t'$ by r^2 one obtains

$$i_{II}(t) = \frac{(c_s - c_b)nF\sqrt{D}}{\sqrt{\pi t}} - \frac{2}{\pi\sqrt{t}} \int_{r=\sqrt{t_s}}^0 \frac{r^2 i_I(r)}{t + r^2} dr \quad [6]$$

where in the first term $c_s - c_b$ and \sqrt{D} can be substituted by i_0 and t_s according to Eq. [4]. For a constant current $i_I = i_0$ during stage I, the analytical solution is

$$\frac{i_{II}(t)}{i_0} = \frac{2}{\pi} \arctan \sqrt{\frac{t_s}{t}} = \frac{2}{\pi} \operatorname{arccot} \sqrt{\frac{t}{t_s}} \quad [7]$$

As an asymptotic approximation for $t \gg t_s$ the following form can be used

$$\frac{i_{II}(t)}{i_0} = \frac{2}{\pi} \sqrt{\frac{t_s}{t}} \quad [8]$$

which is independent of the history of stage I, because it is the solution for the initial condition $c(x, 0) = c_b$ as well. Using Heaviside-Carson operators, Elmore (2) obtained the same results as Eq. [7]. Nevertheless the mathematical treatment of stage I and II was repeated, because the more general Eq. [2] and [6] are better descriptions of electropolishing with constant cell voltage, where the current density i_I usually decreases more or less during stage I. With slight changes the mathematical treatment presented in this section is applied in the following section to demonstrate possible changes of the current density i_{II} caused by the formation of a solid film on the anode.

Formation of a solid film during stage IIa.—The existence of a solid film on the anode is usually assumed

for electropolishing, and there are some experimental studies (6-9) which agree on the thickness of the film, but disagree on the chemical composition.

The necessary material for the film might be supplied by backward diffusion from the supersaturated electrolyte. This process is described by a model which also has been recently used by Alkire *et al.* (15) for the occurrence of salt films during repassivation. In this model the concentration at the anode is raised during stage I from $t = 0$ to $t = t_{ss}$ to a supersaturated value c_{ss} . At $t = t_{ss}$ the solid film appears on the metal surface, and the concentration there instantaneously drops from c_{ss} to the equilibrium value c_s . The concentration distribution following the onset of precipitation is given by Eq. [3] with $t = t_{ss}$, except at the surface where $c = c_s$. Then the solution of Eq. [1] is given again by Eq. [5] where t_s has to be replaced by t_{ss} . Neglecting any charge consumption for the film formation, the electrical current density i is given again by the concentration gradient in the electrolyte, and its evaluation follows the lines shown in the section before. Inserting t_{ss} in Eq. [6], the general solution is obtained. For constant density i_0 during stage I, the following solution is found by using Eq. [4] with c_{ss} and t_{ss} instead of c_s and t_s

$$\frac{i_{IIa}}{i_0} = \frac{(c_s - c_{ss})nF\sqrt{D}}{\sqrt{\pi t}} + \frac{2}{\pi} \operatorname{arccot} \sqrt{\frac{t}{t_{ss}}} \quad [9]$$

where the first term with $c_s - c_{ss}$ describes the amount of supersaturation. This analytical solution is also applicable to the work of Alkire *et al.*, who used numerical solutions of Eq. [5].

For $t \gg t_{ss}$ the perturbation caused by the film formation is negligible, and the asymptotic solution of Eq. [8] can be applied again. For very small times, however, i_{IIa} deviates remarkably from i_{II} as shown in Fig. 3 schematically, where solutions of Eq. [7] and [9] are presented. According to the anticipated backward diffusion i_{IIa} becomes negative during the time interval $0 \leq t \leq t_1$, where t_1 is the only solution of Eq. [9] with $i_{IIa} = 0$. A negative current does not flow through the cell in reality, but it corresponds to an equivalent amount of matter, which diffuses back to the anode to form a solid film. Thus the thickness d of the film can be calculated from the charge flowing back to the metal surface between $t = 0$ and $t = t_1$

$$d = -\frac{V}{nF} \int_{t=0}^{t_1} i_{IIa} dt \quad [10]$$

where V is the mole volume of the solid film. Usually the relation $t_1 \ll t_{ss}$ is valid, and the following approximation can be used

$$d = -V(c_s - c_{ss})^2 nFD \frac{\pi}{i_0}$$

Diffusion and convection during stage III.—For stage I and II diffusion in a semi-infinite electrolyte corresponding to the boundary condition $c(\infty, t) = c_b$ is

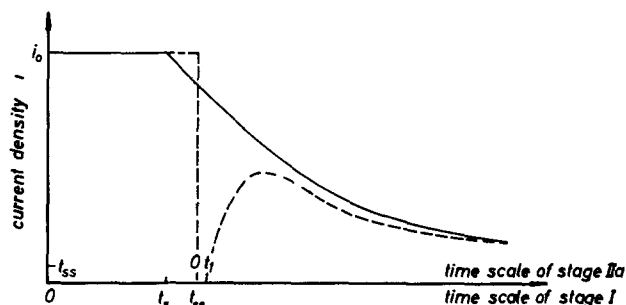


Fig. 3. Schematic current-time plot during stage I and II with and without solid film formation according to Eq. [7] and [9]. Solid lines without, dashed lines with film formation.

considered, and from Eq. [8] it can be concluded that i goes to zero if t goes to infinity. Experimental results (Fig. 2), however, show that a steady-state value i_g is attained, which is attributed in electrochemistry (16) to the influence of convection. In order to take convection into account the following model is frequently used (17).

In front of the electrode an undisturbed layer of thickness δ is assumed in which only diffusion occurs. Adjacent to the layer convection is the rate-controlling phenomenon, rapidly transporting away the ions supplied by diffusion. Thus the concentration is kept at the initial value c_b . The boundary conditions for this model are

$$\begin{aligned} c(0, t) &= c_s \\ c(\delta, t) &= c_b \\ c(x, 0) &= c_b \end{aligned}$$

Here, the simple initial condition $c(x, 0) = c_b$ is used instead of the complex concentration profile caused by stage I and described by Eq. [3]. This is only correct if convection appears a long time after the end of stage I, otherwise the concentration changes caused by stage I have to be considered. The analytical solution of Eq. [1] with the boundary and initial conditions above is

$$c_{III}(x, t) = c_b + \frac{2}{\delta} \sum_{m=1}^{\infty} \frac{(c_s - c_b)}{m\pi} \left[1 - \exp\left(-\frac{t}{\tau_m}\right) \right] \sin \frac{m\pi x}{\delta}$$

where the time constants τ_m are defined as

$$\tau_m = \frac{\delta^2}{m^2\pi^2 D} \quad [11]$$

From $c_{III}(x, t)$ the current density i_{III} can be calculated, and for $t > \tau_1$ all exponential terms except the first one can be neglected. Thus

$$i_{III}(t) = i_g \left[1 + 2 \exp\left(-\frac{t}{\tau_1}\right) \right] \quad [12]$$

with the steady-state current density

$$i_g = \frac{nF(c_s - c_b)\sqrt{D}}{\pi\sqrt{\tau_1}} = \frac{2}{\pi\sqrt{\pi\tau_1}} i_0 \sqrt{t_s} \quad [13]$$

This steady-state current density is approached by the exponential time law in Eq. [12] and corresponds to a linear decrease of concentration from c_s at $x = 0$ to c_b at $x = \delta$.

Experimental Results and Discussion

Pure diffusion (stages I and II).—During stage I the current density i_1 depends on the cell voltage and the resistivity of the cell and, therefore, it depends on arbitrary quantities like geometry, polarization of the cathode, etc. The assumption $i_1 = i_0 = \text{const.}$ frequently made in the theoretical treatment before is not fulfilled for an applied constant cell voltage. With the experimental setup of this study i_1 decreased by about 10-20% of its initial value from $t = 0$ to $t = t_s$. It will be shown in the Appendix that the Eq. [4], [7], and [8] can be applied to this case if the mean value of i_1 is inserted for i_0 . Elmore (2) avoided this complication by using galvanostatic conditions during stage I and switching to potentiostatic conditions at the beginning of stage II. In this work constant cell voltage was applied from the beginning of the whole electropolishing process because this is more important for practical applications.

Another basic assumption necessary for the validity of the derived equations is that diffusion controls the rate of the overall cell reaction, especially during stages I and II. This is fulfilled if the anode potential is

high enough to be within the polishing region (12). The potential drop at the anode was measured with a calomel reference electrode. For appropriate constant cell voltages it increased, and the necessary anode potential was reached at stage II. In some cases the anode potential drop was held constant by a potentiostatic device during the experiment. But even then the desired potential was not achieved during stage I, because the current limit of the potentiostat (4A) was reached as short-time measurements with an oscilloscope revealed. With the onset of stage II, however, the anode potential approached the value set on the potentiostat, which is probably due to the formation of a solid film after stage I and its additional ohmic resistance.

Table I shows results for i_0 , t_s and $i_0\sqrt{t_s}$ of stage I for different metals, electrolytes, and temperatures, where t_s is easily determined from the recorder plot. It is evident as a large change of the slope of the current-time curve.

The current density i_0 was then defined by the equation

$$i_0 t_s = \int_{t=0}^{t_s} i dt$$

corresponding to the arithmetic average during stage I (cf. Appendix). From those values for i_0 and t_s the product $i_0\sqrt{t_s}$ was calculated. The current density during stage II was plotted vs. $t^{-1/2}$ and straight lines cut the origin in excellent agreement with Eq. [8]. A typical example is shown in Fig. 4. From the slopes of the straight lines which are $2/\pi i_0\sqrt{t_s}$, other values of $i_0\sqrt{t_s}$ were obtained and compiled in Table I. They were always in good agreement with the less precise values evaluated from stage I. From the validity of Eq. [8] it can be concluded that during stage II the current density only depends on time and on the product $i_0\sqrt{t_s}$, which is according to Eq. 4 a material constant of the electrolyte. Thus starting with different i_0 values during stage I, due to different cell geometry for instance, the same current densities are obtained during stage II. Deviations from the straight lines in Fig. 4 for long times are caused by convection and are described below.

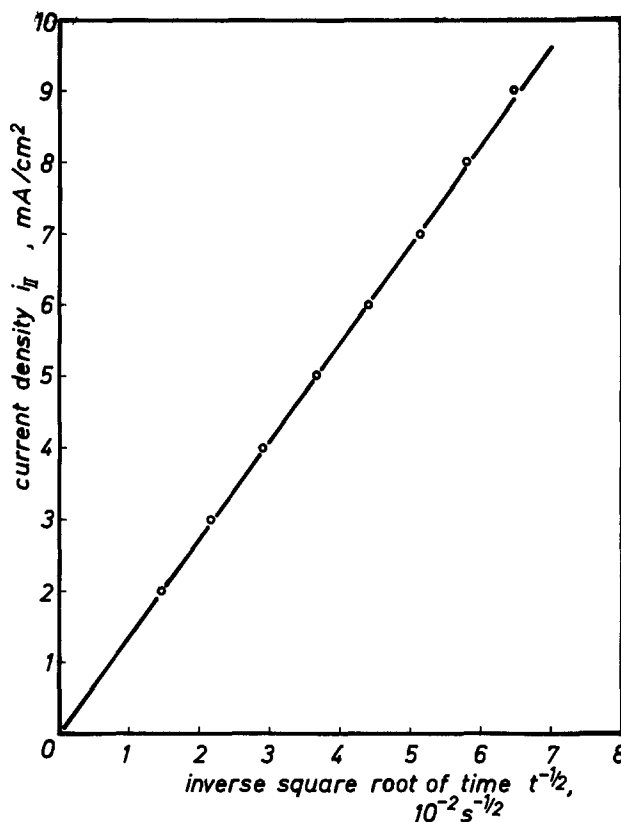


Fig. 4. Current density vs. $t^{-1/2}$

The characteristic product $i_0\sqrt{t_s}$ of the electrolyte depends on the temperature and the composition of the electrolyte. For copper/phosphoric acid, the concentration dependence at 20°C is described in the literature (3), where measurements were made only for stage I. A comparison with the results of this study is shown in Fig. 5. The dependence on temperature is discussed in a separate section.

Deviations from the square root time law for stage II also occur at short times, because then Eq. [7] is

Table I. Experimental data

| Metal | Electrolyte* | Cell voltage (V) | Temperature (°C) | i_0 (A/cm ²) | Stage I | | Stage II | Stage III | |
|-------|--|------------------|------------------|----------------------------|-------------|-----------------|-----------------|----------------|-----------------------------|
| | | | | | t_s (sec) | $i_0\sqrt{t_s}$ | $i_0\sqrt{t_s}$ | τ_1 (sec) | i_e (mA/cm ²) |
| Cu | 14.8M H ₃ PO ₄ | 1.6 | 0 | 0.0071 | 67.8 | 0.058 | 0.069 | 275,000 | 0.033 |
| | | | 20 | 0.016 | 64.5 | 0.13 | 0.14 | 76,000 | 0.13 |
| | | | 40 | 0.047 | 24 | 0.23 | 0.22 | 9000 | 0.81 |
| | | | 60 | 0.047 | 66 | 0.38 | 0.35 | 2380 | 2.6 |
| | | | 80 | 0.071 | 56 | 0.53 | 0.50 | 2800 | 4.0 |
| | 12.3M H ₃ PO ₄ | 1.6 | 20 | 0.12 | 3.4 | 0.28 | 0.26 | 13,700 | 0.6 |
| | | | 20 | 0.16 | 4.5 | 0.35 | 0.32 | 2400 | 1.8 |
| | | | 20 | 0.071 | — | — | 0.14 | — | — |
| | 9.8M H ₃ PO ₄ | 1.6 | 0 | 0.19 | 2.4 | 0.29 | 0.37 | — | — |
| | | | 20 | 0.15 | 14 | 0.55 | 0.56 | 79,000 | 0.6 |
| | 7.4M H ₃ PO ₄ | 1.6 | 40 | 0.051 | 208 | 0.74 | 0.67 | 5300 | 3 |
| | | | 60 | 0.076 | 218 | 1.12 | — | — | — |
| | 4.9M H ₃ PO ₄ | 1.6 | 20 | 0.185 | 19 | 0.80 | 0.80 | 610 | 9.0 |
| | | | A | 0.036 | 8.1 | 0.10 | 0.13 | 4600 | 1.0 |
| | | | B | 0.047 | 8.5 | 0.14 | 0.19 | 2800 | 1.5 |
| C | | | 0.0091 | 36 | 0.055 | 0.052 | 10,700 | 0.13 | |
| 20 | | | 0.016 | 27 | 0.082 | 0.077 | 2600 | 0.55 | |
| Fe | 14.8M H ₃ PO ₄ | 0.4 | 20 | 0.050 | 61 | 0.039 | 0.040 | — | — |
| | | | 20 | 0.030 | 1.4 | 0.35 | 0.52 | 69 | 16.2 |
| Mo | 7.4M H ₃ PO ₄ | 0.4 | 20 | 0.64 | 4.8 | 1.4 | 1.87 | 66 | 96 |
| | | | 20 | 0.26 | 1.7 | 0.34 | 0.35 | 590 | 4.1 |
| Al | D | 40 | 20 | — | — | — | 0.72 | 5000 | 3.2 |
| | | | 20 | 0.095 | 59 | 0.73 | 0.68 | 87 | 22.5 |
| Ti | D | 50 | 20 | 0.046 | 111 | 0.48 | 0.53 | 320 | 9.8 |
| | | | 20 | 0.020 | 94 | 0.19 | 0.17 | 20,000 | 0.33 |
| V | D | 19 | 20 | 0.011 | 155 | 0.13 | 0.14 | 2350 | 0.93 |
| | | | 20 | 0.11 | 1.1 | 0.13 | — | 80 | 7.9 |
| Zn | F | 1.6 | 20 | 0.12 | 3 | 0.55 | — | 5.5 | 84 |
| | | | 20 | 0.11 | — | — | — | — | — |
| Cu | 14.8M H ₃ PO ₄ | 2.0 | 20 | 0.11 | — | — | — | — | — |
| | | | 20 | 0.12 | — | — | — | — | — |
| Cu | 7.4M H ₃ PO ₄ stirring | 2.0 | 20 | 0.11 | — | — | — | — | — |
| | | | 20 | 0.12 | — | — | — | — | — |

* Composition of electrolytes: (volume parts) A, 2 ethanol + 1 phosphoric acid (85%); B, 1 butanol + 1 phosphoric acid; C, 2 glycerol + 1 phosphoric acid; D, 100 acetic acid (99%) + 5 perchloric acid (70%); E, 87 methanol + 13 sulfuric acid (97%); F, 1 ethanol + 1 phosphoric acid; G, 14.8M phosphoric acid, electrode distance 100 mm.

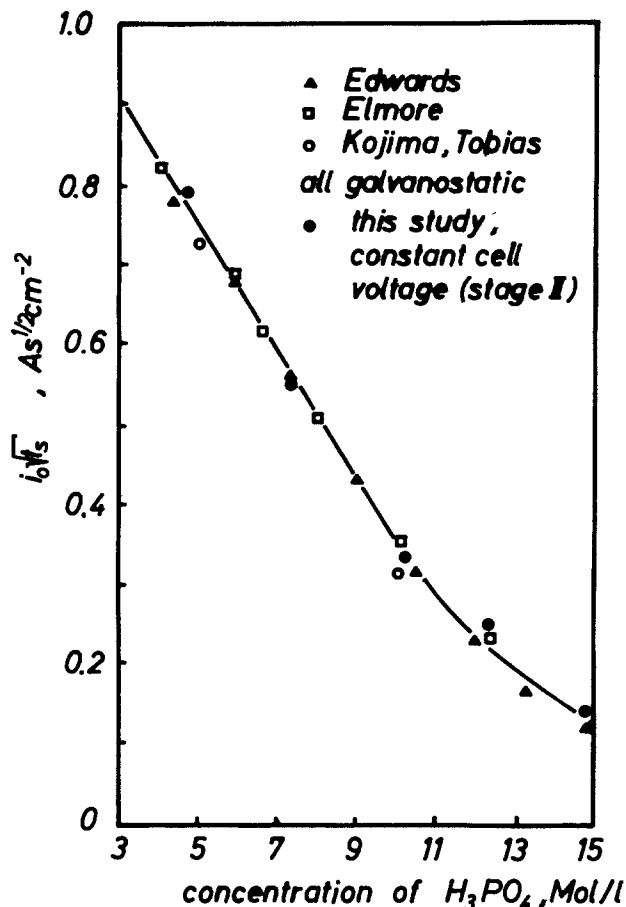


Fig. 5. $i_0\sqrt{t_s}$ plotted vs. concentration of phosphoric acid at room temperature for electropolishing of copper.

the appropriate description of the current-time behavior. Neglecting perturbations by a solid film formation after $t = t_s$, the arccot-function of Eq. [7] was always in good agreement with experimental data, as has been already proved by Elmore (2) for the special system Cu/H₃PO₄. If the cell voltage was chosen to be within the polishing region, no influence of the voltage on the measured product $i_0\sqrt{t_s}$ could be observed. At lower voltages some oscillations of the cell current were seen, which may be due to the formation and solution of solid films (18).

Solid film formation (stage IIa).—Figure 6 shows a typical recorder plot of the current density during stage I and II, which is similar to the schematic plot in Fig. 3. The end of stage I is obvious by a sharp drop of the current. The mathematical solutions ($i = i_0$ for $t < t_s$) and Eq. [7] are presented as dashed lines. Deviations from the anticipated behavior during stage I are shown in the Appendix to be negligible for the solution of stage II. Therefore, solid film formation is assumed to be responsible for the difference between the solid and the dashed line. This difference can be written as

$$i_{II} - i_0 \frac{2}{\pi} \operatorname{arccot} \sqrt{\frac{t}{t_s}}$$

If supersaturation of the electrolyte and subsequent precipitation of a solid film is assumed, Eq. [9] should be valid according to the model used for that process above. In order to check Eq. [9] the difference between the two lines in Fig. 6 was plotted in Fig. 7 vs. $t^{-1/2}$. A straight line is obtained, but it does not go through the origin as predicted by Eq. [9]. From that we may conclude that the model is probably too simple to account for all the experimental effects. Nevertheless Eq. [10], derived within this model, was used to cal-

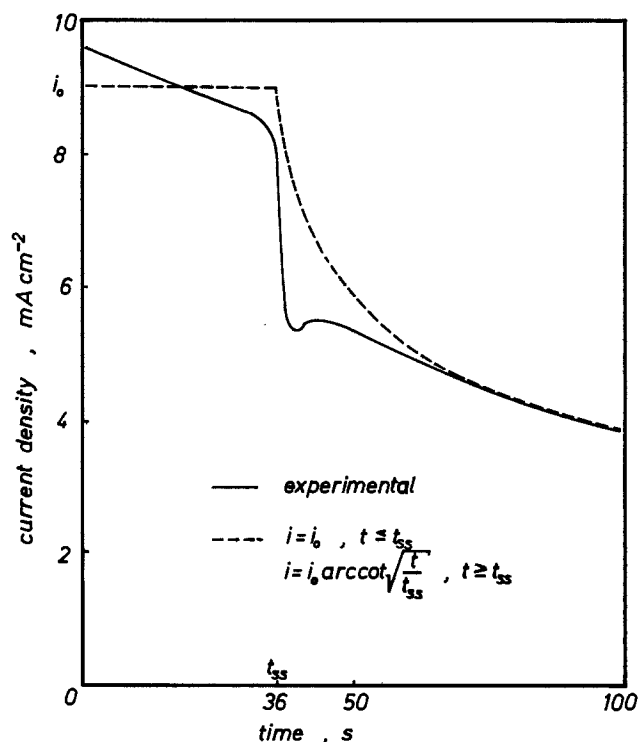


Fig. 6. Recorder plot of the current density for electropolishing of copper in H₃PO₄ (85%)-glycerol (1 + 2). Dashed line calculated from Eq. [7].

culate the thickness of the solid layer. If both the amount of supersaturation from Eq. [9] and the slope of the straight line in Fig. 7 are evaluated, all parameters of Eq. [9] are known, and Eq. [10] can be solved. Such calculations were carried out for various electropolishing experiments of copper in different phosphoric acids, and they gave always the same order of magnitude for the thickness d . A mean value of d was 3–30 nm corresponding to mole volumes of $V = 10$ cm³ for CuO and $V = 100$ cm³ estimated for some copper phosphate. Thicknesses reported in the literature for copper (6–9) are of the same order of magnitude.

In some cases (high temperatures and/or low concentrated phosphoric acids) a salt precipitated onto the electrode forming layers of about 1 mm thickness. The precipitation took place far away from the end of stage I, and it shows that a supersaturated electrolyte is still present in front of the anode. If only a few crystallization nuclei are present on the polishing area and if the crystals grow very slowly, polishing goes on at the uncovered surface regions and is stopped at the covered regions. Therefore, hills are formed at

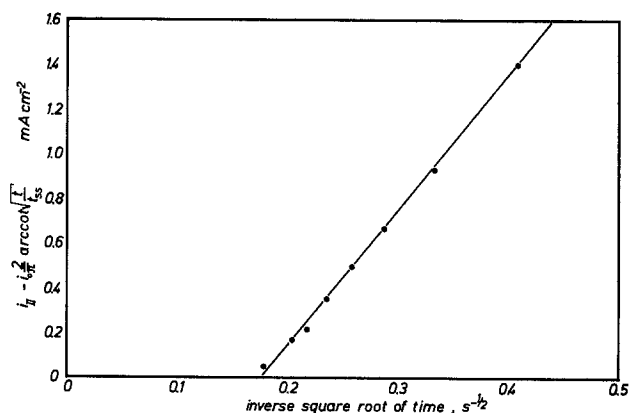


Fig. 7. Results of Fig. 6 plotted as $i_{II} - i_0 \frac{2}{\pi} \operatorname{arccot} \sqrt{t/t_s}$ vs. $t^{-1/2}$.

places where the crystallization starts and valleys are left at places where growing crystals from different nuclei meet each other. Thus the history of crystal growth is sometimes beautifully impressed on the sample surface, as can be seen in Fig. 8, where dendritic growth of the precipitated film must have occurred.

Diffusion and convection (stage III).—For the evaluation of stage III the samples were polished until a constant current density i_g was obtained. The logarithm of the current i_{III} minus the steady-state value i_g was then plotted vs. time. Always straight lines were obtained which cut the current axis more or less exactly at $2i_g$ as predicted by Eq. [12]. A typical result for iron and acetic-perchloric acid is shown in Fig. 9.

From the slope of the straight lines τ_1 was calculated. Values of i_g and τ_1 determined in this way are compiled in Table I. Usually the reproducibility of such measurements was poor because natural convection is strongly influenced by small temperature fluctuations or small vibrations. However, it could be stated that τ_1 increases with increasing viscosity η of the electrolyte for natural convection.

This corresponds, as predicted by some models (16), to an increase of δ (cf. Eq. [11]) and a decrease of diffusivity D according to the Stokes-Einstein equation

$$D = kT/6\pi\eta r$$

(with k = Boltzmann constant, r = molecule radius).

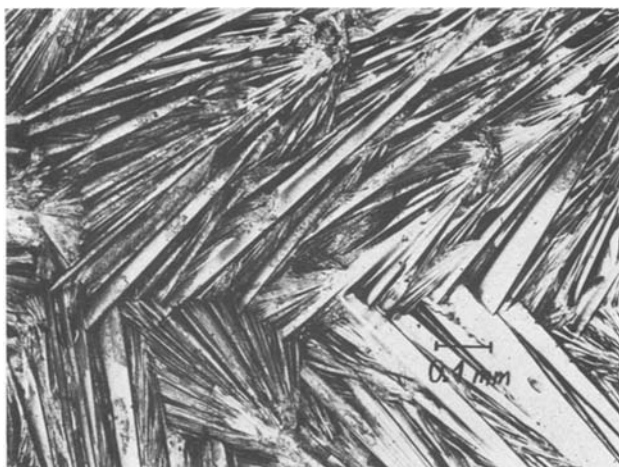


Fig. 8. Copper surface showing the history of salt precipitation

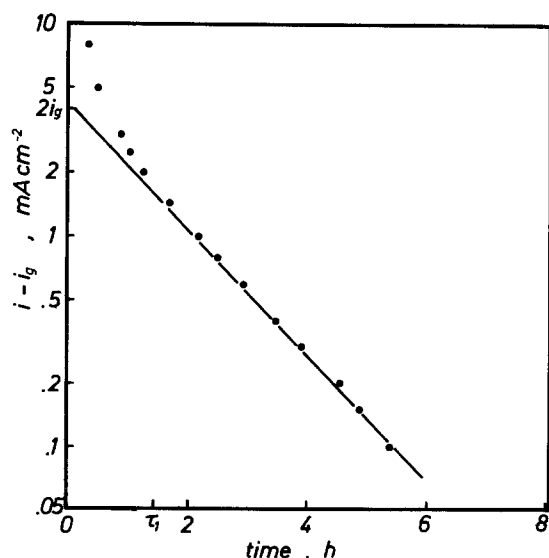


Fig. 9. $\log(i - i_g)$ vs. time for stage III (cf. Eq. [12]) [Fe, 30V, 100 volume parts acetic acid (99%) and 5 volume parts perchloric acid (70%)].

If the electrolyte was stirred, τ_1 could be reduced by about four orders of magnitude. In these cases stage I was immediately followed by stage III. Increasing stirring velocity will reduce δ and τ_1 even more, and for $\tau_1 < t_s$ i_g becomes i_0 before the saturation concentration c_s is reached.

These are reasons why electropolishing becomes ineffective with increasing stirring velocities (19), since one sufficient condition for polishing is that roughness should be smaller than the thickness of the "viscous layer" (20), which may be defined as the layer of thickness δ . With the results of this study δ can be calculated from τ_1 and D . For copper/phosphoric acid values for D at 20°C are available (21, 22) which give a thickness δ of about 1 mm under natural convection.

From the validity of an exponential time law only it cannot be concluded that the model proposed for stage III is useful because diffusion through a solid film yields the same time dependence. The assumption of diffusion through a liquid layer is justified by the good agreement of experimental and calculated (Eq. [13]) values of i_g over four orders of magnitude as shown in Fig. 10.

Temperature dependence.—The temperature dependence of the product $i_0\sqrt{t_s}$ can be predicted by Eq. [4] from that of the solubility c_s and that of the diffusivity D . For a comparison of the copper/phosphoric acid results it is assumed that according to the Stokes-Einstein equation the inverse square root of viscosity shows the same temperature dependence as the square root of diffusivity. Measured values (23) are shown in Fig. 11 in the form of an Arrhenius plot, and straight lines are best fits to the experimental values according to the equations

$$i_0\sqrt{t_s} = 696 \exp\left(-\frac{2550}{T}\right) A \cdot s^{1/2}$$

$$c_s = 7.6 \exp\left(-\frac{840}{T}\right) \text{mole/liter}$$

$$\eta^{-1/2} = 28 \exp\left(-\frac{1580}{T}\right) \text{cp}^{-1/2}$$

From these relationships an activation energy of 21 kJ/mole for $i_0\sqrt{t_s}$ was evaluated in good agreement with the value of 20 kJ/mole for $c_s\sqrt{D} \propto c_s\sqrt{\eta}$ ($c_b = 0$).

The time constant τ_1 , obtained during stage III for copper and 14.8M H_3PO_4 (cf. Table I), decreases

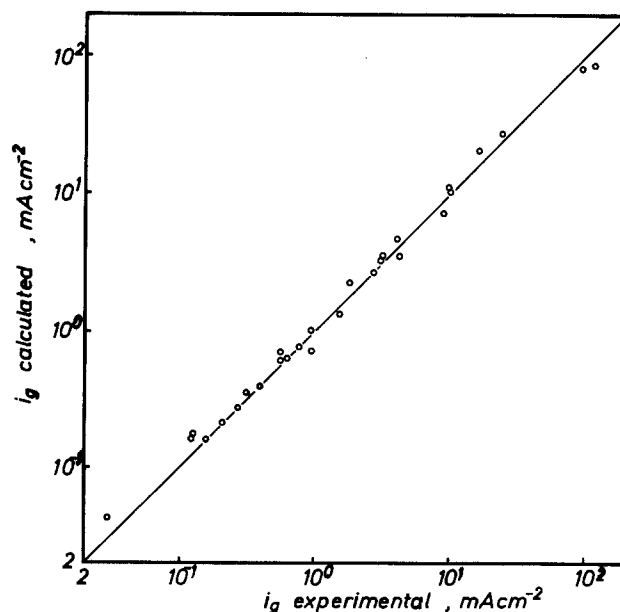


Fig. 10. Comparison of experimental (Table I) and calculated (Eq. [13]) values of the steady-state current density i_g .

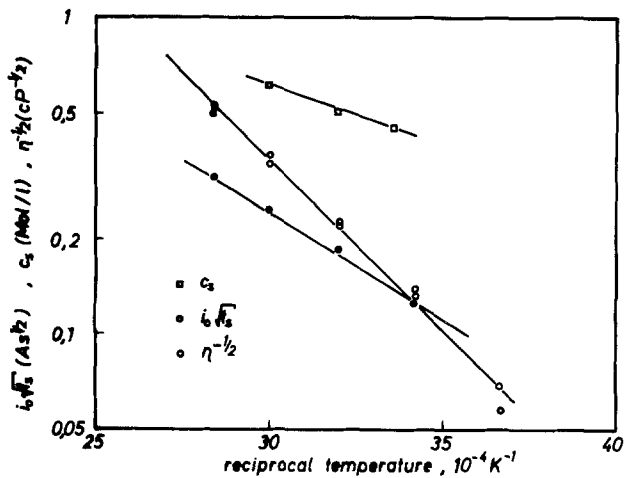


Fig. 11. Arrhenius plot of $i_0\sqrt{t_s}$, solubility c_s , and inverse square root of viscosity for Cu/14.8M H_3PO_4 .

strongly with increasing temperature corresponding to an activation energy of about 50 kJ/mole. For a constant thickness δ of the diffusion layer, Eq. [11] predicts 26 kJ/mole since τ_1 is proportional to D^{-1} and, therefore, to η . The disagreement of the activation energies indicates that δ is temperature dependent, decreasing with increasing temperature.

Concluding Remarks

The results of this study show that the current-time behavior of potentiostatic electropolishing can be completely described with solutions of Fick's second law, assuming that diffusion in the electrolyte is the rate-determining step and different boundary conditions cause the occurrence of three stages. Even the formation of a solid film on the anode and its influence on the current can be described by backward diffusion from a supersaturated electrolyte consistent with experimental findings.

In all three stages of electropolishing the same transport mechanism within the diffusion layer is valid, since it depends in any case on the characteristic parameter $i_0\sqrt{t_s}$. The duration of the particular stages cannot be calculated for a certain material system from first principles, because it is influenced for stage I by the geometry and the cathodic process and for stage II and III by natural and forced convection within the electrolyte.

Therefore, the transport of a species through the solid film cannot be rate determining, in contradiction to the concept of Hoar *et al.* (6). Only at the transition from stage I to II, can deviations from the simple diffusional concept be attributed to solid-film formation.

From the relationships derived it is possible to calculate the thickness of the viscous layer. This layer must be thick enough to reach the saturation concentration and to smooth surface roughness.

Acknowledgment

The authors wish to thank the DECHEMA for financial support and G. Klukas for his skillful experimental assistance.

Manuscript submitted June 14, 1979; revised manuscript received Sept. 15, 1980.

Any discussion of this paper will appear in a Discussion Section to be published in the December 1981 JOURNAL. All discussions for the December 1981 Discussion Section should be submitted by Aug. 1, 1981.

Publication costs of this article were assisted by the Max-Planck-Institut für Metallforschung.

APPENDIX

Variable Current Density during Stage I

The variable current density is represented by a linear decrease of i from a maximum value i_1 at $t = 0$ to i_2 at $t = t_s$

$$i(t) = i_0 + \frac{\Delta i}{2t_s} (t_s - 2t) \quad [A-1]$$

where $i_0 = \frac{1}{2}(i_1 + i_2)$ and $\Delta i = i_2 - i_1$. This is the simplest case for the solution of Eq. [2] and [6], and it is a good description of the experimental behavior of the cell used in this study.

Then the increase of concentration at the anode ($x = 0$) is given by Eq. [2]

$$c_1(0, t) = c_b + \frac{1}{nF\sqrt{\pi D}} \int_{t'=0}^t \frac{i(t')}{\sqrt{t-t'}} dt' \quad [A-2]$$

The saturation c_s is reached for $t = t_s$, and with Eq. [A-1] the relation between i_0 , t_s , and c_s , D corresponding to Eq. [4] is obtained by integrating Eq. [A-2]

$$\left[1 - \frac{\Delta i}{6i_0} \right] i_0\sqrt{t_s} = \frac{nF}{2} (c_s - c_b) \sqrt{\pi D} \quad [A-3]$$

The brackets on the left side of Eq. [A-3] contain a correction coefficient in comparison with Eq. [4], which equals approximately one in this study because the condition $\Delta i/i_0 = 0.1$ was fulfilled throughout the experiments.

In order to describe the influence of a variable current density during stage I on stage II, Eq. [6] has to be solved. This has been done by using Eq. [A-1] and [A-3]. The result can be written in the following form

$$i_{II} = \frac{2i_0}{\pi} \left[1 - \frac{\Delta i}{2i_0} \right] \operatorname{arccot} \sqrt{\frac{t}{t_s}} + \frac{2i_0\Delta i}{\pi} \left[\frac{t}{t_s} \operatorname{arccot} \sqrt{\frac{t}{t_s}} - \sqrt{\frac{t}{t_s}} \right]$$

For $t \gg t_s$ the simple form

$$\frac{i_{II}}{i_0 \left[1 - \frac{\Delta i}{2i_0} \right]} = \frac{i_{II}}{i_2} = \frac{2}{\pi} \sqrt{\frac{t_s}{t}}$$

is obtained as an analogy of Eq. [8].

LIST OF SYMBOLS

| | |
|---------------------------------|---|
| c | concentration (mole/liter) |
| c_b | initial and bulk concentration |
| c_s | saturation concentration |
| c_{ss} | supersaturation concentration |
| c_I, c_{II}, c_{III} | concentrations during stages I, II, and III |
| D | diffusion coefficient (cm^2/sec) |
| d | thickness of the solid film (nm) |
| F | Faraday constant |
| i | current density (A/cm^2) |
| i_0 | constant current density during stage I |
| i_1, i_2 | current densities at the beginning and the end of stage I |
| $i_I, i_{II}, i_{IIa}, i_{III}$ | current densities during stages I, II, IIa, and III |
| i_g | steady-state current density during stage III |
| Δi | current density drop during stage I |
| k | Boltzmann constant |
| m | number of order |
| n | electrochemical valence number |
| r | molecule radius |
| T | temperature (K) |
| t | polishing time (sec) |
| t_1 | time to form the solid film |
| t_s | time to reach c_s |
| t_{ss} | time to reach c_{ss} |
| V | mole volume (cm^3/mole) |
| x | distance from the anode |
| δ | thickness of the diffusion layer (mm) |
| η | viscosity (cp) |
| τ_m | time constant during stage III, m th order |
| τ_1 | time constant during stage III, first order (sec) |

REFERENCES

1. P. A. Jaquet, *Nature*, **135**, 1076 (1935); *Compt. Rend.* **201**, 1473 (1935); *Compt. Rend.*, **202**, 403 (1936); *Trans. Electrochem. Soc.*, **69**, 629 (1936).
2. W. C. Elmore, *J. Appl. Phys.*, **11**, 797 (1940); *ibid.*, **10**, 724 (1939).
3. K. Kojima and C. W. Tobias, *This Journal*, **120**, 1026 (1973).
4. J. Edwards, *ibid.*, **100**, 189C (1953).
5. W. J. McG. Tegart, "The Electrolytic and Chemical Polishing of Metals," Pergamon Press, London (1959).
6. T. P. Hoar, D. C. Mears, and G. P. Rothwell, *Corros. Sci.*, **5**, 279 (1965).
7. E. C. Williams and M. A. Barrett, *This Journal*, **103**, 363 (1956).
8. K. Kojima and C. W. Tobias, *ibid.*, **120**, 1202 (1973).
9. M. Novak, A. K. N. Reddy, and H. Wroblowa, *ibid.*, **117**, 733 (1970).
10. K. Maier, R. Kirchheim, and G. Tölg, *Mikrochim. Acta (Wien)*, Suppl. 8, p. 125 (1979).
11. K. F. Lorking, *Electrochim. Acta*, **7**, 101 (1962).
12. R. W. Powers, *Electrochem. Technol.*, **2**, 274 (1964).
13. M. S. Carslaw and J. C. Jaeger, "Conduction of Heat in Solids," 2nd ed., p. 75, University Press, Oxford (1959).
14. M. S. Carslaw and J. C. Jaeger, *ibid.*, pp. 62, 58.
15. R. Alkire, D. Ernsberger, and T. R. Beck, *This Journal*, **125**, 1382 (1978).
16. K. J. Vetter, "Electrochemical Kinetics, Theoretical and Experimental Aspects," Academic Press, New York-London (1967).
17. W. Nernst, *Z. Phys. Chem.*, **47**, 52 (1904).
18. B. Pointu, *Electrochim. Acta*, **14**, 1207, 1213 (1969).
19. T. P. Hoar and G. P. Rothwell, *ibid.*, **9**, 135 (1964).
20. C. Wagner, *This Journal*, **101**, 225 (1954).
21. S. I. Krichmar, A. Ya. Pronskaya, and K. F. Afendik, *Soviet Electrochem. (Engl. Transl.)*, **2**, 896 (1966).
22. K. Maier, Dissertation, Stuttgart (1978).
23. R. Kirchheim, Unpublished results.

The Soret Effect in Molten Ag-Te Solutions

R. K. Williams

Oak Ridge National Laboratory, Metals and Ceramics Division, Oak Ridge, Tennessee 37830

and W. O. Philbrook

Carnegie-Mellon University, Pittsburgh, Pennsylvania 15213

ABSTRACT

The Soret effect was studied in liquid Te solutions containing 17.5 to 69 at/o Ag. The measurements extended from close to the liquidus temperatures to 1100-1200 K. The factors affecting the experimental uncertainty were examined and used to estimate the accuracy of the data. Thermodynamic data for the liquid solutions and solid Ag₂Te were compiled and used to calculate experimental heat of transport, Q^* , values. These Q^* values were found to have strong negative temperature coefficients; this observation can be explained on the basis of a correlation between the Soret segregation and the thermoelectric properties of the melts.

The results presented in this paper were obtained some years ago, during the course of a study of the thermal conductivity of a series of semiconducting Ag-Te melts (1). The Soret effect is important for these measurements because it can enhance natural convection (2) and must be considered in analyzing experimental data. At the time it was apparent that the Soret results showed some unusual features, but we could not proceed with an analysis of the data because the required theoretical background had not been developed and thermodynamic data needed for computation of the heats of transport were not available. Since that time both of these deficiencies have been at least partially eliminated by other workers, and publication of our results now offer some improved experimental evidence of the connection between mass flow and the electronic transport properties.

The principal components of this paper are: (i) a brief review of the information available on other properties of the melts; (ii) description of the apparatus and an attempt to define the experimental errors; (iii) the experimental results; and (iv) a discussion which also includes a review of the thermodynamic data for the system.

Dancy (3) published the first systematic study of the electronic transport properties of Ag-Te solutions. The electrical conductivity, σ_e , and Seebeck coefficient, S , data showed semiconducting behavior over a wide

range of compositions with high S and low σ_e values associated with compositions near Ag₂Te. The data were interpreted in terms of degenerate semiconduction and the possibility that a bandgap could exist at some composition near Ag₂Te. The thermal conductivity study (1), showed that the conductivities are low and that the relatively weak electronic contribution is roughly consistent with degenerate behavior. Glazov *et al.* (4) showed that the viscosity exhibits a sharp maximum at Ag₂Te and suggested that the compound persists as a stable entity into the liquid phase. Their work also included σ_e values, which differ from those of Dancy for Ag-rich compositions. The Russian data, if correct, would indicate that the thermal conductivity data for Ag rich melts (1) can be explained by the degenerate semiconductor model. Wobst (5) showed that the curve of surface energy vs. composition exhibits an inflection near the stoichiometric ratio whereas the density does not show any unusual behavior. Other related, though not directly relevant, studies include the study of electromigration in Cu₂Te by Glazov and Burkhanov (6) and a study of the Soret effect in Te-Se solutions (7).

Experimental Method

To study the Soret effect, a vertical column of liquid was held in a known, linear temperature gradient until the steady-state composition distribution had been attained. The liquid was then rapidly frozen, and the Ag content of samples taken along the lengths of the ingots was determined. The experimental observations pro-

vide the basic relationship between the increments of temperature, ΔT , and composition, ΔX . With the small (15-30 deg/cm) temperature gradients used, the composition, X , vs. distance, Z , plots could adequately be described by straight lines, so the T - Z and X - Z data were combined to yield the two increments, and experimental Soret coefficients, σ , were calculated from the defining equation (8)

$$\sigma \equiv \frac{\Delta X_{Ag}}{X_{Ag} X_{Te} \Delta T} \quad [1]$$

X_i = atom fraction of component i

The samples were prepared by melting 99.999 purity Ag shot with 99.99 purity Te crystals under argon in a high purity graphite crucible. The resulting ingots were crushed and cast in fused-silica tubes, producing the thermal diffusion samples which were 6 mm diam cylinders and about 38 mm long. Fused-silica tubing was also used for the thermotransport runs because it is inert to the melts. The sample capsules were sealed off under vacuum and attached to a long silica tube for positioning in the furnace. The compositions studied are described in Table I.

The approximately ($\pm 5\%$) linear temperature gradients were produced in a vertical furnace which had two sets of windings. Power to the outer, uniform windings was automatically controlled, and a smaller amount of power was also supplied to an inner, non-uniform winding from a manually adjusted Variac. All of the samples were positioned so that the top of the liquid column would be hotter, thus minimizing convective remixing.

The temperature differences were obtained from two uncalibrated, 0.13 mm diam Chromel-P vs. Alumel thermocouples which were attached to the outside of the sample capsules. The corrosive nature of the melts precluded placing the thermoelements in direct contact with the liquid, but one test with thermocouples inside and outside a capsule showed that this procedure did not introduce a serious error. This was the expected result because the thermal conductivities of the melts are not much different from fused silica (1).

The experiments were begun by positioning the sample capsules in the uniform-temperature zone of the furnace to homogenize the melts. During this 1 hr period the samples were 50-200 K hotter than the average temperature during the run and were also agitated to promote mixing and remove bubbles. Table II shows data for three samples which were water-quenched either after the homogenization treatment or after a short time in the temperature gradient. These results indicate that the homogenization treatment was effective.

Homogenized samples were then lowered into the desired position in the temperature gradient and held there until the steady-state concentration gradients had been established. Some tests with the 32 atomic percent (a/o) Ag melt at 740 K showed that the σ values did not change after 70-80 hr, and 120-hr runs were used at lower temperatures. The experiments

Table I. Compositions of melts used in this study

| Nominal composition (a/o Ag) | No. of samples ^a | Range of mean sample temperatures (K) | Range of mean sample compositions (a/o Ag) |
|------------------------------|-----------------------------|---------------------------------------|--|
| 69 | 2 | 1213-1239 | 0.2 |
| 65.6 | 2 | 1295 | 0.2 |
| 60.4 | 7 | 1012-1239 | 2.5 |
| 48.4 | 9 | 790-1238 | 6.8 |
| 32.4 | 11 | 687-1091 | 6.3 |
| 24.3 | 6 | 741-1095 | 2.8 |
| 17.5 | 1 | 900 | — |

^a Steady-state samples, excluding specimens used in auxiliary tests.

Table II. Data on homogenization test samples

| Average composition (w/o Ag) | Temperature (K) | Time (hr) | Concentration gradients | |
|------------------------------|-----------------|-----------|---|---|
| | | | At indicated time (w/o-cm ⁻¹) | Steady-state ^a (w/o-cm ⁻¹) |
| 29.55 | 935 | 0 | 0.07 | 0.59 |
| 30.16 | 743 | 0.33 | 0.18 | 1.48 |
| 56.47 | 1117 | 0.25 | 0.09 | 0.34 |

^aBased on overall trends of data and a 75° temperature difference.

were terminated by carefully lifting the samples from the furnace and quenching them into an ice-water bath. Water and ice-brine quenches were also used, but the results did not show any sensitivity to quenching rate.

After quenching, the thermocouple positions were rechecked, and the samples were removed from the fused silica capsules, identified, and measured. Each sample was then sawed into five equal segments, and the sections were analyzed for Ag by a standard gravimetric technique. Values of the quantity $\Delta X_{Ag}/\Delta Z$ were then computed from a linear least square analysis and combined with the measured temperature gradient to calculate σ . Two extreme examples of the experimental concentration profiles are shown in Fig. 1.

Experimental Data

For three of the melts (Table I) only one or two samples were run, and these data are shown in Table III. Data for the other four compositions are shown in Fig. 2. The data were not corrected for the effects of differential thermal expansion and the volumetric change on fusion. Presumably (5) this correction would lower all of the σ values by about 5%. For reasons explained in the following section, the overall trend lines for the data shown in Fig. 2 are drawn to favor the higher data points. The general form of the composition dependence is a gradual increase in slope with increasing Ag content, but the results for the 60 a/o Ag melt cannot be distinguished from those for the 48 a/o

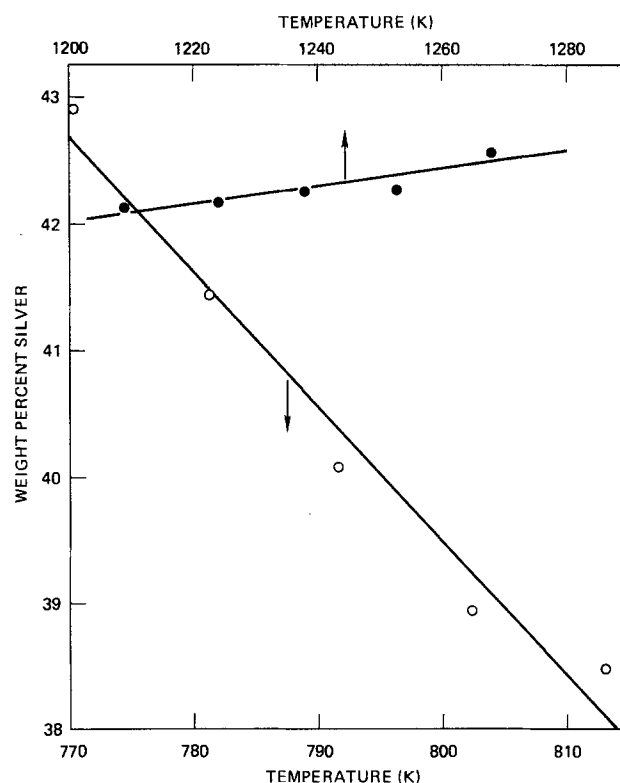


Fig. 1. Experimental composition-temperature curves for the 48 a/o Ag melt at two different average temperatures.

Table III. Experimental Soret coefficients for three melts

| Melt composition (a/o Ag) | Temperature (K) | Soret coefficient, σ^a (K ⁻¹) | Q_{exp}^* (kJ/g at.) |
|---------------------------|-----------------|--|-------------------------------|
| 17.5 | 899 | -1.03×10^{-3} | 5.5 |
| 65.6 | 1295 | -0.27×10^{-3} | |
| | 1295 | -0.40×10^{-3} | |
| 69.0 | 1213 | -0.08×10^{-3} | |
| | 1239 | -0.14×10^{-3} | |

* Defined by Eq. [1].

Ag composition. It should be noted that the σ data do not tend toward zero at infinite temperature.

Experimental Uncertainties

A lower bound for the error can always be obtained from the individual uncertainty limits for the various experimentally determined quantities. This sort of analysis is summarized in Table IV. This table is, in part, based on the assumptions that σ varies at T^{-2} and X_{Ag} in the composition and temperature ranges of interest. Uncertainties calculated in this way are shown with some of the data points in Fig. 3. These estimates should be compared to the σ variation, and this indicates that the σ variation is not obscured by these uncertainties.

A realistic assessment of the systematic experimental errors is generally much more difficult. In the present case, four major possibilities have been considered: (i) the times chosen might have been insufficient for the attainment of a true steady state, (ii) the system might be inherently subject to convective remixing errors, (iii) some runs might have been spoiled through mechanical agitation during the final quench, and (iv) the higher-temperature data might have been more affected by remixing during quenching.

Convective remixing occurs in a Soret experiment when the column is heated from the bottom and the Rayleigh number exceeds some critical value (9). When the column is heated from the top, it is inherently stable unless the Soret segregation causes the heavier component to migrate to the hot end, overcoming the density gradient caused by differential thermal expansion. In these experiments the denser component, Ag, migrates to the cold end and the test columns should always have fallen in Velarde and Schechter's (9) inherently stable quadrant II. The

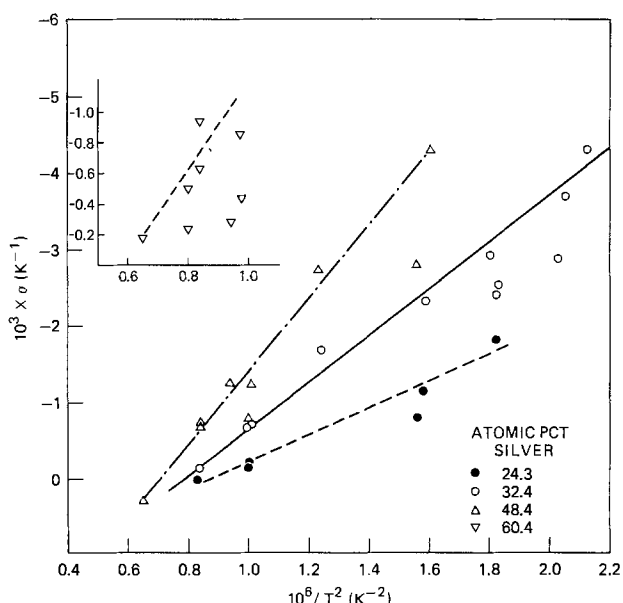


Fig. 2. Soret coefficient data for four Ag-Te melts. Note that the trend lines favor the larger values.

Table IV. Estimates of the minimum uncertainty in the experimental Soret coefficients

| Experimental quantity | Contribution to uncertainty (\pm %) | | Basis for estimation |
|-------------------------------|--|--------|---|
| | 800 K | 1200 K | |
| T | 2 | 2 | 1% temperature accuracy of Chromel P: Alumel thermocouples |
| ΔT | 12.5 | 20.5 | 75° temperature difference, also includes some ΔZ uncertainty |
| ΔX | 10.9 | 24.4 | Scatter in X vs. Z averages about $\pm 5\%$ |
| $X_{\text{Ag}} X_{\text{Te}}$ | 6.4 | 6.4 | Includes sample-to-sample composition variation |
| Total | ~30 | ~50 | |

normal Rayleigh numbers estimated for typical conditions varied from 1×10^7 for the 60 a/o Ag melt to 4×10^6 for the 24 a/o melt.

Horizontal temperature gradients can also produce convective remixing, but experimental data indicate that this is not as serious a problem in a Soret experiment as it is in an isothermal mass diffusion experiment. Agar and Turner (10) who used a 10 mm diam Soret cell showed that horizontal temperature gradients influenced their results when the combined (thermal plus Soret density gradients) yielded Rayleigh numbers less than about 10^6 . The minimum Rayleigh number for our experiments was 4×10^6 and this takes no credit for the large enhancement from the Soret effect. The data of Winter and Drickamer (11) on Pb-Sn, Cd-Sn, and Zn-Sn solutions also support this conclusion. These authors, who used 3 mm diam capillaries, found that their results for the Pb-Sn and Cd-Sn systems were in good agreement with earlier data obtained with 10 mm diam columns. Convective errors became significant for $\sim 2\%$ density differences (Zn-Sn) but the density difference for Ag-Te is comparable to that of Pb-Sn.

It has been shown that convection reduces the steady-state segregation and that σ values calculated from short-time data tend to exceed the apparent steady-state values (12). The usual kinetic equation, which should fit data for times greater than about 0.2 θ , is (12)

$$\frac{\sigma_t}{\sigma_\infty} = 1 - \frac{8}{\pi^2} \exp\left(-\frac{t}{\theta}\right) \quad [2]$$

where σ_t = apparent value of σ calculated from data, σ_∞ = steady-state value, t = time, $\theta = a^2/\pi^2 D_{12}$, a = cell height, and D_{12} = effective diffusion coefficient for the solution. Figure 3 shows that the test data for the 32.4 a/o Ag melt taken at about 740 K fit the equation reasonably well. The diffusivity derived from the data, $\sim 1 \times 10^{-5}$ cm²/sec, also seems reasonable, sug-

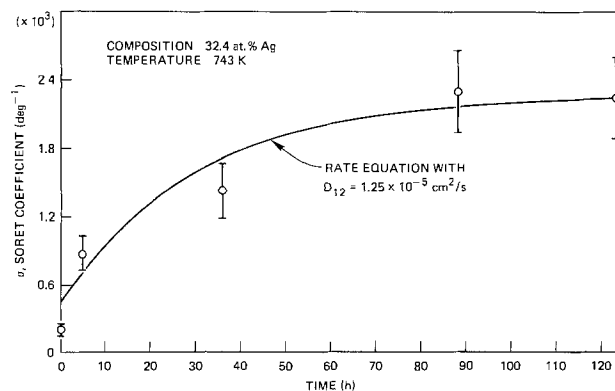


Fig. 3. Variation of the apparent Soret coefficient at the 32 a/o Ag melt with time.

gesting that the times chosen were sufficient for attaining steady-state conditions.

Data from two runs on the 60 a/o Ag composition at 1012 K also support this point of view. The σ values for 6.3 and 88 hr indicate a θ of about 12 hr and a diffusivity of 3.5×10^{-5} cm²/sec. This is similar to the D derived by Glazov and Burkhanov for molten Cu₂Te (6). Other data (Fig. 2) on the 32 a/o Ag composition indicate that the two "steady-state" σ values fall below the general experimental trend, possibly by as much as 30%. Also the two points at 5 and 36 hr seem to show that θ increases with time. This suggests that convection could have influenced some of the experiments.

Inadvertent mechanical agitation of the sample capsules during the final quench could lead to occasional low σ values; this probably happened 10-20% of the time. This intermittent difficulty was compensated by weighing the higher σ values more heavily than the lower ones. A more elaborate experimental apparatus would also have been useful in this regard.

A final point is that data taken at high temperatures may be more subject to convective remixing than those from lower temperatures. At higher temperatures, the thermal diffusivity increases, but this is compensated by the viscosity decrease and the net effect should be to produce a Rayleigh number which does not vary strongly with temperature. On this basis, the test samples should have remained in Velarde and Schechter's (9) stable second quadrant, although moving closer to the unstable third quadrant because the stabilizing influence of the Soret effect is diminished at elevated temperatures. The much higher thermal diffusivity (1, 3) of the low Ag melts would lower their Rayleigh numbers relative to the compositions near Ag₂Te, and thus the low-Ag melts should be less stable. The viscosity variation, which should be smaller than the diffusivity change, is unknown.

Discussion

In the first part of this section, thermodynamic data for the system are critically reviewed and used to derive $d \ln \gamma_{Ag}/d \ln X_{Ag}$ values for calculating the experimental heat of transport, Q_{Ag}^* (8)

$$Q_{Ag}^* = -RT^2 \left(1 + \frac{\partial \ln \gamma_{Ag}}{\partial \ln X_{Ag}} \right) \sigma \quad [3]$$

A fairly extensive examination was required because the two sets of experimental activity data (13, 14) are in conflict. In the second part of the section, the Q_{Ag}^* values are compared with some theoretical formulas to see how well theory can account for the observed temperature and composition variations.

Thermodynamic factor.—Both Zaleska (13) and Predel and Piehl (14) have reported activity data for liquid Ag-Te solutions. Zaleska (13) obtained silver activities from emf measurements on concentration cells, while Predel and Piehl (14) made measurements of the Te pressure over the solutions and obtained Ag activities from a Gibbs-Duhem integration. The agreement is poor for silver concentrations greater than about 10 a/o, and for solutions containing more than about 35 a/o Ag the two sets of data do not even give the same sign for the deviations from Raoult's law. Calorimetric data for the system support the Zaleska (13) values.

Thermodynamic data for the compound Ag₂Te cover a wide temperature range, appear to be internally consistent, and can be used as a valuable check on the measurements for liquid solutions of other compositions. The specific heat data (15-17) cover the range 16-1500 K, and the absolute entropy, S_{298} , given by Mills and Richardson (16) was used in the calculations. The high temperature specific heat data of Blachnik and Gunia (17), which are in good agreement with the Mills and Richardson (16) results at lower temperatures, were employed in calculating H_T-H_{298} and

S_T-S_{298} . These calculations also require values for the two-solid-state enthalpy increments for the (l → i) and (i → h) phase transitions (18) and the enthalpy of fusion. Three values for the (l → i) ΔH are available (16-18) and an average, 2.96 kJ/g atom of alloy, was used in the calculation. Castanet and Bergman (19) have reported ΔH for the (i → h) phase transition and there are two experimental values for the enthalpy of fusion (17, 19). The average of these two values, 3.41 kJ/g atom of alloy, was used in the calculations. Several direct measurements of the heat of formation of the low (20), intermediate (21, 22), and high (19) temperature forms of Ag₂Te have been reported and two values (14, 20) have been published for the enthalpy of formation of the Ag₂Te liquid solution. Kiukkola and Wagner (23) also obtained values for ΔG_f° at 523 and 573 K, and Knudsen cell studies of the vaporization of the solid compound (24, 25) can be extrapolated to make an estimate of the tellurium activity at the melting point.

One convenient way to test the consistency of these results is to use the C_p-T data in combination with the enthalpies of the transitions to convert all of the experimental heats of formation to values corresponding to 1g atomic weight of the low temperature phase. Values for the two elements were taken from the literature (26). Excluding the Predel and Piehl value, and including the two values derived from ΔS° and ΔG° (23), the ΔH_{298} values calculated for the low temperature form range from -12.39 (22) to -11.28 kJ/g atom (21) and the experimental value (20) is -12.01 kJ/g atom. The Predel and Piehl (14) value is about -15.9 kJ/g atom.

The overall compilation of data for Ag₂Te show at least two interesting features. First, the specific heat data for the liquid compound (17), when combined with literature data for the liquid elements (26), indicate that the temperature coefficient of the heat of formation should be only about 1.5%/100°. The results of Castanet and Bergman (19) showed that ΔH is approximately independent of temperature. Second, the absolute S values for Ag, Te, and Ag₂Te indicate that ΔS for formation of the liquid solution, 1.25 J/g atom deg, is much less than the ideal value. This result seems to support the idea (19) that this solution is not a random one. The calorimetric ΔS falls along the trend of the Zaleska (13) values and is considerably greater than the ΔS given by Predel and Piehl (14), -6.6 j/g atom deg.

The calorimetric data for Ag₂Te yield a value for ΔG for formation of the liquid solution from the two liquid components, and the magnitude of this ΔG is about a factor of 2 larger than ΔG calculated from a_{Te} and a_{Ag} as given by Predel and Piehl (14). The Zaleska (13) data do not extend to the Ag₂Te composition. The problem with the activity data (14) seems to arise mostly because there is only one a_{Te} data point for tellurium contents less than 40 a/o, and it appears to be too high. This conclusion is supported by Knudsen cell data (24, 25) which indicate $10^{-3} < a_{Te} < 10^{-2}$ at the melting point of Ag₂Te, and by making a rough estimate of a_{Te} at the miscibility gap. For the assumptions that in silver rich, metallic solutions a_{Ag} follows Raoult's law and a_{Te} obeys Henry's law, the entropy of mixing is ideal, and using the experimental integral heat of mixing (19), one obtains $a_{Te} \sim 4 \times 10^{-3}$ for solutions containing between 9 and 30 a/o Te. The assumptions employed in this estimate are obviously not correct, but the intent is only to demonstrate that a_{Te} must be very low in Ag-rich melts. The Predel and Piehl (14) data indicate $a_{Te} \approx 0.2$ for a 40 a/o solution, and if these two results are even approximately correct, the activities of both components must vary quite rapidly near the Ag₂Te composition. Blachnik and Bolte (27) have noted that this is the case in some selenide systems. This analysis implies that the thermodynamic factor (Eq. [3]) is very

large near the Ag_2Te composition, and Q^* values derived for the two silver-rich melts (Table III) are thus subject to large uncertainties.

The evidence showing that the a_{Ag} values of Predel and Piehl (14) are probably not correct does not establish the validity of the Zaleska (13) values, but further examination of the data for solutions in the 0-60 a/o Ag range at least shows that the results are internally consistent. This test involved using the Predel and Piehl (14) a_{Te} data with the experimental heats of mixing (13, 19, 28) and ΔS values to calculate a_{Ag} . The tellurium activity data are consistent with values calculated from the phase diagram and should not vary much with temperature (14, 28, 29). The enthalpy data are principally due to Castanet *et al.* (19, 28) but Maekawa (30) and Zaleska (13) have reported results which support Castanet *et al.* The Predel and Piehl (14) enthalpy data, which appear to be too large at the Ag_2Te composition, were not used. The ΔS values were chosen by plotting (i) the ΔS values tabulated by Zaleska (13), (ii) the ΔS computed from \bar{S}_{Ag} (13) and \bar{S}_{Te} (28), and (iii) the ΔS values computed from specific heat data for Ag, Te, and Ag_2Te . This produced a curve which is nearly ideal for solutions containing less than 45 a/o Ag. This experimental line then falls well below the ideal values for more silver-rich compositions. The Predel and Piehl (14) ΔS values show this same general variation, but the negative departures from ideal mixing are much larger.

The two sets of activity coefficient values are compared in Fig. 4. The heat of mixing data were used to adjust the Zaleska (13) values to 1281 K. The agreement is excellent, and both sets of values were used in defining the $\gamma_{\text{Ag}}-X_{\text{Ag}}$ variation. The deviative (Eq. [3]) is small (~ -0.2) for the 18, 24, and 32 a/o Ag melts and increases rapidly ($+0.3$ for 48 a/o and $+0.9$ for 60 a/o Ag) at higher silver contents. It should be noted (Fig. 4) that the activity data imply that Henry's law is only valid for very low silver contents. Also the increase which begins at about 45 a/o Ag must lead to a very rapid activity variation in the vicinity of the Ag_2Te composition.

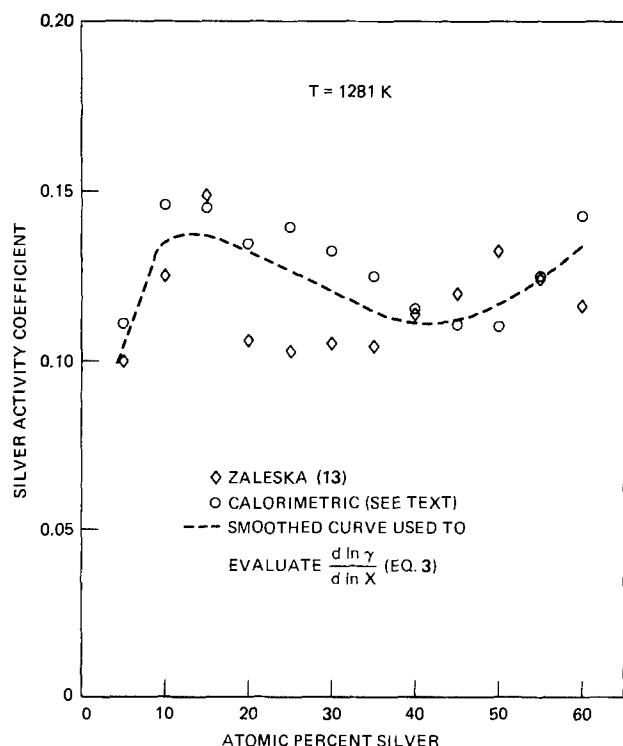


Fig. 4. Silver activity coefficients for Ag-Te solutions at 1281 K. The dotted line was used to evaluate the thermodynamic correction factor (Eq. [3]).

The effects of composition and temperature on the heat of transport.—The data presented here represent a survey of the Soret effect in Ag-Te solutions over an unusually large temperature range. As shown in Fig. 5, Q^* tends to increase with the Ag content of the melts, and the temperature dependence is strong. Measurements on the 26-60 a/o Ag melts show that Q_{exp}^* decreases at higher temperatures and approaches zero at about 0.8 to 0.9 of the normal boiling points. One measurement (Fig. 1) also suggests that Q^* becomes negative at still higher temperatures.

These variations can be discussed by using the theoretical framework presented by Huntington (31). In general, the heat of transport should contain three terms, two of which can be temperature dependent

$$Q_{\text{exp}}^* = Q_{\text{int}}^* + Q_{\text{Th}}^* + Q_{\text{el}}^* \quad [4]$$

where Q_{int}^* = intrinsic, temperature independent term which would be present in all liquids, Q_{Th}^* = contribution from the internal Thompson field to the motion of a charged species, and Q_{el}^* = component due to atom-charge carrier interactions. Detailed calculations for liquid metals (8) show that the electronic and intrinsic terms are usually both significant while the Thomson contribution can be neglected. This is not necessarily the case for semiconducting solutions. The possible magnitudes of the three terms for the semiconducting Ag-Te melts are discussed in the following paragraphs.

Bhat and Swalin (32) have discussed application of various models for calculating Q_{int}^* for liquid metal solutions and concluded that the theory developed for dense gases is more successful than the Wirtz-Brinkman model. There does not seem to be any unique way to making this test in the present case, since diffusion and viscosity data are not available and the dense gas theory should not apply when the molar volumes are greatly different. An earlier theory (11) based on differences in the heats of vaporization does give the sign of the heat of transport, but the calculated Q_{int}^* values are too large. This theory was also modified to include the activation energies, ΔU^\ddagger , for diffusion or viscous flow (11)

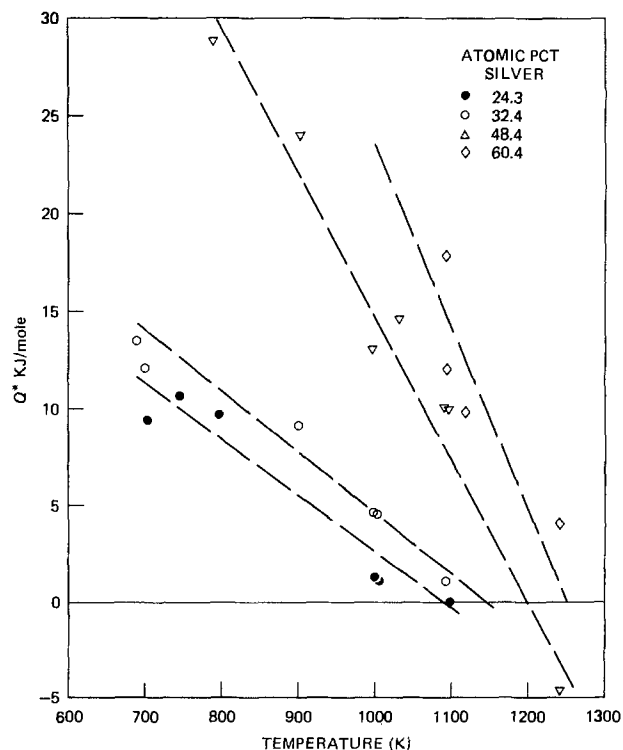


Fig. 5. Temperature dependence of the heats of transfer of four Ag-Te solutions.

$$Q_{\text{int}}^* = \frac{M_{\text{Ag}}\bar{V}_{\text{Te}} + M_{\text{Te}}\bar{V}_{\text{Ag}}}{2M} \left(\frac{\Delta U_{\text{Ag}}^{\pm}}{\bar{V}_{\text{Ag}}} - \frac{\Delta U_{\text{Te}}^{\pm}}{\bar{V}_{\text{Te}}} \right) \quad [5]$$

where \bar{V}_i = partial molar volume of component i and M_i = mass of component i . This formula, which is fairly successful for liquid metals, probably can explain the composition dependence of Q_{int}^* , because the activation energy difference term should be different for Ag-rich and Te-rich solutions. The general trend of this variation is similar to the liquidus curve for the system.

The Thomson field contribution is given by (31)

$$Q_{\text{Th}}^* = eZ_{\text{es}}\zeta_{\text{T}}T \quad [6]$$

where e is the magnitude of the electronic charge, ζ_{T} the Thomson coefficient, and Z_{es} is the effective charge number of the moving ion seen by the electrostatic field. The Seebeck coefficients, S , data of Dancy (3) can be described by equations of the form

$$S = S_0 - \Delta T \quad [7]$$

so that with the Kelvin relationship Eq. [12] becomes

$$Q_{\text{Th}} = -9.6 \times 10^4 Z_{\text{es}}\Delta T^2 \text{ J/g atom} \quad [6a]$$

The chief trouble is in deciding what value to assign to Z_{es} . In a metallic solution, it ought to be positive and Huntington (31) has argued that it should be taken as the full ion charge. This is not so clearly the case for Ag-Te solutions, since one could imagine negatively charged Te ions playing a role. At any rate the potential importance of this term can be seen by assuming that Z_{es} is unity. For the eutectic (33% Ag) melt Δ is about $7 \times 10^{-8} \mu\text{V/deg}^2$, and this leads to a Q_{Th}^* of about -6.7 kJ/mole at 1000 K. The experimental value at this temperature is about $+4.8 \text{ kJ/mole deg}$, so this contribution is large enough to explain the observed negative temperature coefficient.

It is also possible that the third component, Q_{el}^* , could be responsible for the temperature dependence of Q_{exp}^* . For liquid alkali and noble metal solutions, Murarka *et al.* (8) have shown that Q_{el}^* is negative and proportional to temperature, and that the average of the temperature coefficients calculated for seven cases is about -8 J/g atom deg . This kind of calculation would not apply to an Ag-Te solution, but some general guidance can be gained by referring to the two-band treatment which Huntington applied to Pt (31). The analysis shows that Q_{el}^* is larger than for single-band metals and that the coefficient is proportional to, among other factors, the Seebeck coefficient. The sign of the contribution is governed by the Seebeck coefficient and the ratio of elective masses of holes and electrons, and turns out to be positive for Pt. Then, since the transport property data indicate that the Ag-Te melts are hole conductors, Q_{el}^* could have the sign and magnitude required to explain the experimentally observed negative temperature coefficients.

To examine these possibilities in more detail, Q_{Th} was computed by assuming that Z_{es} in Eq. [6a] was unity, and the remaining part of the heat of transport was plotted as a function of temperature. The quantities ($Q_{\text{int}}^* + Q_{\text{el}}^*$) obtained in this fashion can be adequately described by a linear temperature variation and the calculation shows that Q_{Th}^* probably is not responsible for all of the temperature dependence. The linear temperature coefficients obtained in this fashion are larger than those calculated by Murarka *et al.* (8) and increase with the Seebeck coefficients of the melts. This is roughly what was expected from the theory.

The principal conclusion drawn from this work is, therefore, that there is a correlation between the temperature dependence of the Soret segregation and the electronic transport properties of the melts. This correlation involves one or both of the thermoelectric properties, S and ζ_{T} , and the dominant effect could be

experimentally identified if the precision of the results could be improved.

Acknowledgments

K. C. Mills aided us in the area of thermodynamics and R. Castanet furnished some experimental results prior to their publication. P. Carlson and the late J. R. Shegog contributed useful experimental assistance. The manuscript was carefully prepared by Sharon Buhl. This research was sponsored by the U.S. Atomic Energy Commission at Carnegie Institute of Technology, contract AT (30-1) 2360.

Manuscript submitted April 14, 1980; revised manuscript received Dec. 5, 1980.

Any discussion of this paper will appear in a Discussion Section to be published in the December 1981 JOURNAL. All discussions for the December 1981 Discussion Section should be submitted by Aug. 1, 1981.

Publication costs of this article were assisted by Oak Ridge National Laboratory, operated by Union Carbide Corporation for the U.S. Department of Energy.

REFERENCES

1. R. K. Williams, M. Veeraburns, and W. O. Philbrook *Metall. Trans.*, **3**, 255 (1972).
2. R. K. Williams, M. Veeraburns, and W. O. Philbrook, *Rev. Sci. Instrum.*, **39**, 1104 (1968).
3. E. A. Dancy, *Trans. TMS-AIME*, **233**, 270 (1965).
4. V. M. Glazov, N. M. Makhmudova, and A. N. Krestovnikov, *Inorg. Mater.*, **5**, 1008 (1969) (English translation).
5. M. Wobst, *Scr. Metall.*, **4**, 239 (1970).
6. V. M. Glazov and A. S. Burkhanov, *Russ. J. Phys. Chem.*, **49**, 1873 (1975) (English translation).
7. F. L. Konopel'ko and D. K. Belashchenko, *Inorg. Mater.*, **10**, 631 (1974) (English translation).
8. S. P. Murarka, T. Y. Kim, M. Y. Hsieh, and R. A. Swalin, *Acta Metall.*, **22**, 185 (1974).
9. M. G. Velarde and R. S. Schechter, *Chem. Phys. Lett.*, **12**, 312 (1971).
10. J. N. Agar and J. C. R. Turner, *Proc. R. Soc. London, Ser. A*, **255**, 307 (1960).
11. F. R. Winter and H. G. Drickamer, *J. Phys. Chem.*, **59**, 1229 (1955).
12. H. J. V. Tyrreil, "Diffusion and Heat Flow in Liquids," Butterworths, London (1961).
13. E. Zaleska, *Rocz. Chem. Ann. Soc. Chim. Polonorum*, **19**, 1257 (1975).
14. B. Predel and J. Piehl, *Z. Metallkd.*, **66**, 33 (1975).
15. P. N. Walsh, E. W. Art, and D. White, *J. Phys. Chem.*, **66**, 1546 (1962).
16. K. C. Mills and M. J. Richardson, *Thermochim. Acta*, **6**, 427 (1973).
17. R. Blachnik and P. Gunia, *Z. Naturforsch Teil A*, **33**, 190 (1978).
18. F. C. Kracek, C. J. Ksanda, and L. J. Cabri, *Am. Mineral*, **51**, 14 (1966).
19. R. Castanet and C. Bergman, *J. Chem. Thermodyn.*, **11**, 83 (1979).
20. M. J. Pool, *TMS-AIME*, **233**, 1711 (1965).
21. R. Castanet and M. Laffitte, *Rev. int. Htes. Temp. et Refract.*, **11**, 103 (1974).
22. E. Zaleska and J. Terpilowski, "Conf. Ann. of the Soc. Chim. Pol.," Gliwice (1972).
23. K. Kiukkola and C. Wagner, *This Journal*, **104**, 379 (1957).
24. K. C. Mills, *J. Chem. Thermodyn.*, **4**, 903 (1972).
25. V. M. Glazov and N. M. Korenchuk, *Russ. J. Phys. Chem.*, **45**(10), 1520 (1971).
26. R. Hultgren, P. Desai, D. Hawkins, M. Gleiser, K. Kelly, and D. Wagman, "Selected Values of the Thermodynamic Properties of the Elements," Vol. 17, p. 505, American Society for Metals, Metals Park, Ohio (1973).
27. R. Blachnik and G. Bolte, *J. Less-Common Metals*, **57**, 21 (1978).
28. R. Castanet, Y. Claire, and M. Laffitte, *J. Chim. Phys. Physicochem. Biol.*, **68**, 1133 (1971).
29. G. N. Lewis and M. Randall, "Thermodynamics," (revised by K. Pitzer and L. Brewer) p. 392, McGraw Hill, New York (1961).

30. T. Maekawa, Y. Yokokawa, and K. Niwa, in "The Properties of Liquid Metals," S. Takeuchi, Editor, pp. 501-505, Taylor and Francis, Ltd. (1973). Also see *J. Chem. Thermodyn.*, **7**, 505 (1975).
31. H. B. Huntington, *J. Phys. Chem. Solids*, **29**, 1641 (1968).
32. B. N. Bhat and R. A. Swalin, *Acta Metall.*, **20**, 1387 (1972).

Photoelectrochemical Properties of Polycrystalline TiO₂ Doped with 3d Transition Metals

Yasumichi Matsumoto,* Jun-ichi Kurimoto, Tateki Shimizu, and Ei-ichi Sato*

Department of Industrial Chemistry, Faculty of Engineering,
Utsunomiya University, Ishi-icho 2753, Utsunomiya, Japan

ABSTRACT

The photoelectrochemical properties of the polycrystalline TiO₂ doped with 3d transition metals (Cr, Mn, V, Cu, Ni, and Zn) have been investigated. The electrodes doped with Cr, Mn, V, and Cu show the visible light photoreponses. It is concluded that the visible light photoresponse is based on the impurity band formed near the π^* conduction band of the TiO₂ in energy position, in analogy with the Co-doped TiO₂ electrode reported previously. The cathodic photocurrent of the O₂ reduction was also observed for the doped and undoped electrodes. From the good agreement of the spectral dependences of the anodic and cathodic photocurrents, it is judged that both type photocurrents are brought about by the same photoexcitation process. The observed large cathodic photocurrents for the electrodes that give the visible light photoresponse are attributable to the d-orbitals of the doped metal as the active site, by which the impurity band is formed in the bulk. A mechanism for the photosynthesis is also suggested from the simultaneous appearance of the photo-oxidation and photoreduction currents on an electrode.

TiO₂ is suitable for the anode material of the photoelectrolysis of water from the point of view of the stability in aqueous solution, but its large bandgap brings about only small efficiency in using the solar spectra. Recently, it has been reported that the TiO₂ electrode is improved by doping with various elements. Cr and Mn-doped TiO₂ single crystals bring about the visible light response, and the u.v. response increases by doping with Al(1, 2). Polycrystalline TiO₂ doped with Al and Be show the interesting property that the quantum efficiencies to the u.v. light increase like the TiO₂ single crystal electrode doped with Al(3, 4). Moreover, there is a report that Ni, Cr, Cd, and Zn-doped polycrystalline TiO₂ electrodes give the visible light response (5).

In our laboratory, it is found that the polycrystalline TiO₂ prepared at high temperature and the Co-doped polycrystalline TiO₂ show the visible light response (6). The polycrystalline-type electrode is more suitable for the photoanode than the single crystal in preparation cost and in ease of the preparation process. In the present paper, the photoelectrochemical properties of the polycrystalline TiO₂ doped with 3d transition metals are studied. In our results, the visible light response was observed for the Cr, Mn, V, and Cu-doped electrodes, but not for the Zn-doped electrode, and was very small for the Ni-doped electrode. Moreover, the large cathodic photocurrent was also observed for some electrodes. A mechanism for these phenomena is proposed and qualitatively confirmed in the present paper. From the simultaneous appearance of the anodic and cathodic photocurrents, a possible mechanism for the photosynthesis is also suggested.

Experimental

All the electrodes are prepared by the thermal decomposition of the aqueous solutions of 3d metal salts on the Ti metal substrate (99.6%). The nitrates were used for Mn, Cu, and Zn, and the oxide (CrO₃) for Cr.

* Electrochemical Society Active Member.

Key words: photoelectrochemistry, semiconductor electrode, TiO₂.

VOCl₂ dissolved in the diluted HNO₃ was used for V. The preparation method is the same as that described in a previous paper (6), but H₂O₂ was not used in the present study. The samples were prepared at either 500° or 600°C as the final heat-treatment. No oxide other than TiO₂ was observed in x-ray analysis for the electrodes with the coating concentration less than about 2.5×10^{-7} mole/cm². As for the electrodes used in this study, almost all of the metals in the coating metal salts will be doped in the formed TiO₂ layer. All the electrodes are denoted as TiO₂/M in this paper.

The electrolyte was pre-electrolyzed 1M KOH. An Hg/HgO electrode was used as the reference electrode and electrode potentials cited in this paper are referred to this electrode. The spectral dependence of the cathodic photocurrent was measured in the O₂ saturated electrolyte, and that of the anodic photocurrent was done in air. Both photoresponses of the anodic and cathodic currents were fast (<0.3 sec) for all the electrodes used in the present study, analogous to the Co-doped TiO₂ electrode (6). The other measurements were conducted in the same way as in the previous paper (6). The irradiation intensity is not corrected. However, a sequence of measurements is done with the same experimental setup, so that the irradiation intensity has been kept constant during the measurements.

Results

TiO₂/Cr, TiO₂/Mn, TiO₂/V, and TiO₂/Cu electrodes.—The potential sweep voltammograms for the TiO₂/Cr (2.5×10^{-9} mole/cm²) and TiO₂/Mn (2.5×10^{-8} mole/cm²) electrodes are shown in Fig. 1 and 3, respectively. The spectral dependences of the photocurrents for the TiO₂/Cr and TiO₂/Mn electrodes are shown in Fig. 2 and 4, respectively. The photocurrents were determined by the differences between the stable illumination current and the dark current as described in the previous paper (6). The u.v. photocurrents for both electrodes, as the figures show, are based on the original photoexcitation process of the TiO₂. The observed large photocurrents due to the visible light for

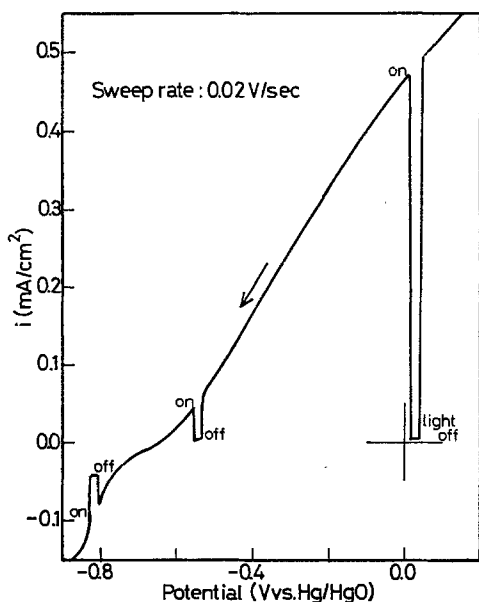


Fig. 1. Potential sweep voltammogram of the TiO₂/Cr (2.5×10^{-9} mole/cm²) electrode prepared at 600°C.

the TiO₂/Cr and TiO₂/Mn electrodes are attributable to the Cr and Mn impurity bands formed in the TiO₂ lattice as described in a later section. Relatively large cathodic photocurrents were also observed for both types of electrodes in the O₂ saturated 1M KOH, but not in the Ar saturated one. The cathodic photocurrents, therefore, are based on the O₂ reduction. This observed cathodic photocurrent is not attributable to the increase of the photoconductivity as described in a later section. Good agreement of the spectral dependences of the anodic and cathodic photocurrents show that photoelectrochemically reactive electrons and holes are produced by the same photoexcitation process.

The spectral dependences of the photocurrents for the TiO₂/V and TiO₂/Cu electrodes are shown in Fig. 5 and 6, respectively. It is concluded that the photo-

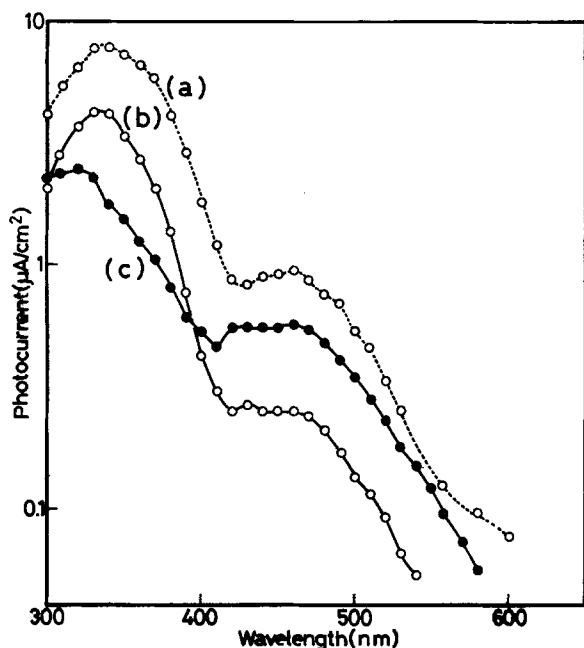


Fig. 2. Spectral dependences of the photocurrents at the TiO₂/Cr (2.5×10^{-9} mole/cm²) electrodes. The cathodic and anodic photocurrents were measured at -0.8 and 0V, respectively. (a) Cathodic photocurrent at the electrode prepared at 600°C, (b) anodic photocurrent at the electrode prepared at 600°C, (c) anodic photocurrent at the electrode prepared at 500°C, (d) cathodic photocurrent at the electrode prepared at 500°C.

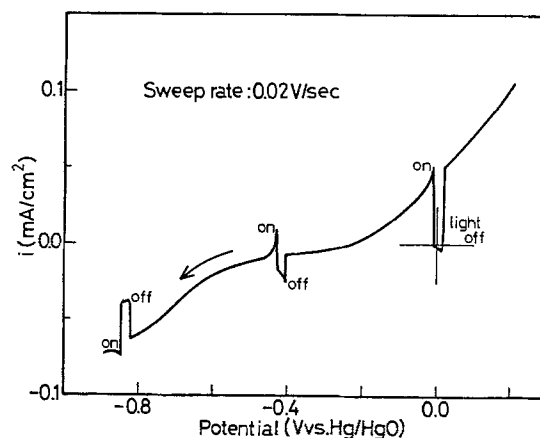


Fig. 3. Potential sweep voltammogram of the TiO₂/Mn (2.5×10^{-8} mole/cm²) electrode prepared at 600°C.

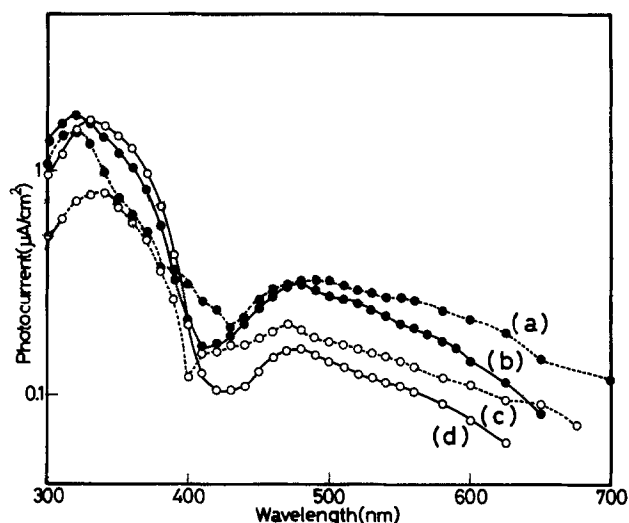


Fig. 4. Spectral dependences of the photocurrents at the TiO₂/Mn (2.5×10^{-8} mole/cm²) electrodes. The cathodic and anodic photocurrents were measured at -0.8 and 0V, respectively. (a) Cathodic photocurrent at the electrode prepared at 500°C, (b) anodic photocurrent at the electrode prepared at 500°C, (c) cathodic photocurrent at the electrode prepared at 600°C, (d) anodic photocurrent at the electrode prepared at 600°C.

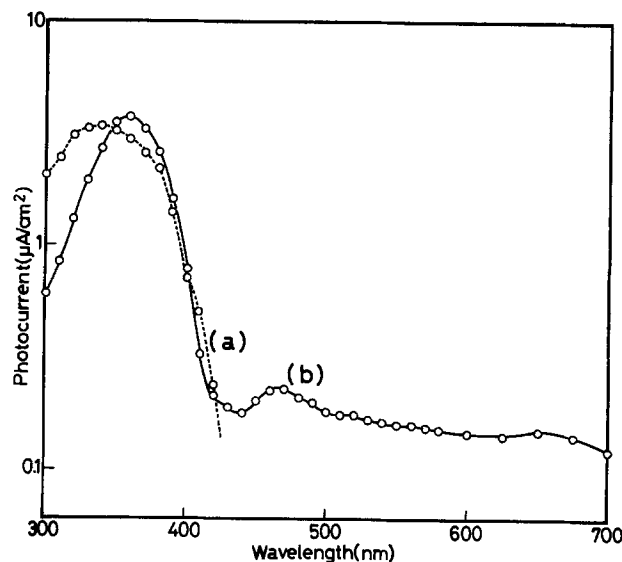


Fig. 5. Spectral dependences of the photocurrents at the TiO₂/V (2.5×10^{-8} mole/cm²) electrode prepared at 600°C. The cathodic and the anodic photocurrents were measured at -0.9 and 0V, respectively. (a) Cathodic photocurrent, (b) anodic photocurrent.

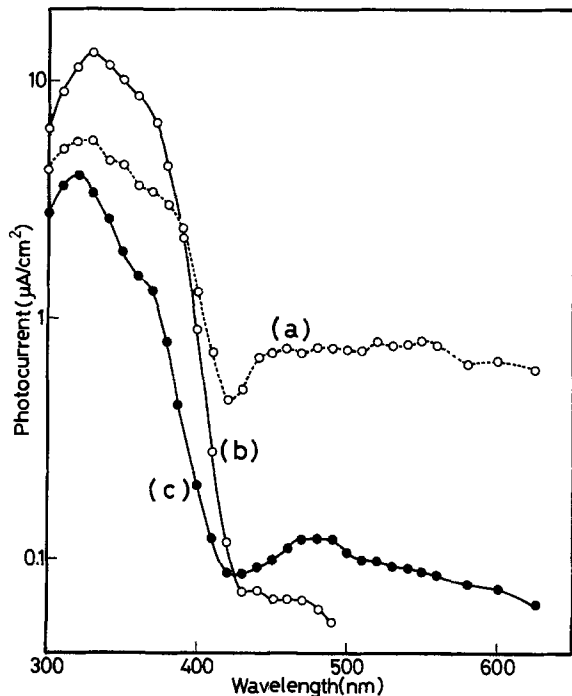


Fig. 6. Spectral dependences of the photocurrents at the TiO_2/Cu (2.5×10^{-7} mole/cm 2) electrodes. The cathodic and anodic photocurrents were measured at -0.8 and 0V , respectively. (a) Cathodic photocurrent at the electrode prepared at 600°C , (b) anodic photocurrent at the electrode prepared at 600°C , (c) anodic photocurrent at the electrode prepared at 500°C .

currents due to the visible light for the TiO_2/V and TiO_2/Cu electrodes are based on the V and Cu impurities doped in the TiO_2 lattice, respectively. The TiO_2/V electrode prepared at 500°C showed no visible light photoresponse. The u.v. light responses for the both electrodes are due to the fact that the photoexcitation process in the original bandgap of the TiO_2 is the same as for the TiO_2/Cr and TiO_2/Mn electrodes.

TiO₂/Ni, TiO₂/Zn, and TiO₂/Fe electrodes.—The TiO_2/Ni electrode shows the very small response to the visible light near the original TiO_2 bandgap energy as well as the variation in the u.v. spectral dependence of the photocurrent, but the TiO_2/Zn electrode shows no visible light response. These results are different from those reported by Monnier *et al.* (5). These differences are probably due to the preparation method of the electrode, but this is not clear.

The visible light response was not observed for the TiO_2/Fe electrode with 2.5×10^{-8} Fe mole/cm 2 , but was observed for the electrode with 2.5×10^{-6} Fe mole/cm 2 as shown in Fig. 7. It is judged that the visible light photocurrents of the latter electrode are not due to the Fe impurities doped in the TiO_2 lattice, but are due to the Fe_2O_3 formed on the top of the surface, since the spectral dependences of the photocurrents agree with that of the Fe_2O_3 electrode reported earlier (7-11). The good agreement of the spectral dependences of the anodic and cathodic photocurrents shows that the photoproduced electron in the conduction band and hole in the valence band of the Fe_2O_3 react with the solution species under the cathodic and the anodic biases, respectively.

Discussion

The large cathodic photocurrent is not attributable to the increase of the conductivity by the photon. This is confirmed by the following result. The TiO_2 (single crystal)/Cr electrode as described in a later section, whose surface layer is only doped, also gives the large cathodic photocurrent as Fig. 11 shows, while non-doped TiO_2 (single crystal) gives no cathodic photocurrent. If the observed cathodic photocurrent is based on the photoconductivity, this doped electrode will not

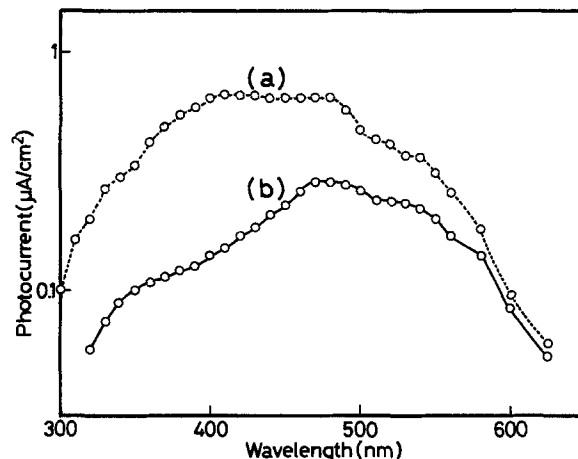


Fig. 7. Spectral dependences of the photocurrents at the TiO_2/Fe (2.5×10^{-6} mole/cm 2) electrodes prepared at 600°C . The cathodic and anodic photocurrents were measured at -0.5 and 0V , respectively. (a) Cathodic photocurrent, (b) anodic photocurrent.

give the cathodic photocurrent, because the impurity band or sites formed only in the surface layer do not affect the photoconductivity.

The electrodes used in this study will contain the surface states and the recombination centers as well as the formed impurity band. The visible light response of the Cr-doped electrode used in this study agrees with that reported by Ghosh *et al.* (1), in which Cr is doped in the bulk of the TiO_2 single crystal. This agreement shows that the visible light responses in the doped electrodes used in this study also are mainly based on the impurity levels in the TiO_2 bulk, but not the surface states. These formed impurity levels are broad in their energy positions as the spectral dependences of the photocurrents show, therefore they seem to form a band, *i.e.*, an impurity band. The surface states will be mainly formed on the surface by these impurity level edges. These will act in the electron transfer from the electrode surface to the solution species. On the other hand, many recombination centers also will be formed by the doping, but will be situated in the deep levels and not participate in the formation of the impurity band. These recombination centers will bring about the relatively small photocurrents at the doped electrodes used in this study.

Table I shows the onset potentials of the anodic photocurrents in air for the various electrodes used in the present study. The onset potentials of the doped electrodes (except for the TiO_2/Fe and TiO_2/Mn electrodes) are almost the same as that of the undoped TiO_2 electrode, as the table shows. Therefore, the electrodes doped with Cr, V, and Cu are favorable for the anode in the photoelectrolysis of water by sunlight from the viewpoint of the high visible light response, but some improvements are necessary in order to obtain the large photocurrent. As stated above, the visible light response is based on the formed impurity band throughout the TiO_2 layer, which is situated near the

Table I. Onset potential of the anodic photocurrent

| Sample | Preparation temp. | Onset potential |
|--|---|-----------------|
| TiO_2 | 500°C , 600°C | -0.70 |
| TiO_2/Cr (2.5×10^{-9} mole/cm 2) | 500°C | -0.65 |
| | 600°C | -0.70 |
| TiO_2/Mn (2.5×10^{-8} mole/cm 2) | 500°C | -0.50 |
| | 600°C | -0.50 |
| TiO_2/V (2.5×10^{-8} mole/cm 2) | 600°C | -0.70 |
| TiO_2/Cu (2.5×10^{-8} mole/cm 2) | 500°C | -0.65 |
| | 600°C | -0.70 |
| TiO_2/Zn (2.5×10^{-8} mole/cm 2) | 600°C | -0.70 |
| TiO_2/Ni (2.5×10^{-8} mole/cm 2) | 600°C | -0.70 |
| TiO_2/Fe (2.5×10^{-8} mole/cm 2) | | -0.50 |
| | 600°C | -0.40 |

π^* conduction band (6) in the energy position as described in detail in a later section.

The spectral dependences of the cathodic and anodic photocurrents for the polycrystalline TiO₂ electrode heated at 600°C are shown in Fig. 8. The cathodic photocurrents for the TiO₂/Zn and TiO₂/Ni electrodes show similar spectral dependences to the TiO₂ electrode, but these are very small, as shown in Table II. The ratios of the maximum cathodic photocurrent (i_{mc}) to the maximum anodic photocurrent (i_{ma}) obtained from the figures of the spectral dependences are listed in Table II for the various electrodes. These photocurrents are brought about by the u.v. light, and therefore based on the photoproduced electron in the π^* conduction band and the photoproduced hole in the π valence band of the TiO₂ (6). The high cathodic photocurrents for the Cr, Mn, V, and Cu-doped electrodes are noteworthy. The flatband potential will give no effect on the cathodic photocurrent, because the onset potentials of the TiO₂, TiO₂/Zn, and TiO₂/Ni electrodes are almost the same as those of the TiO₂/Cr, TiO₂/Cu, and TiO₂/V electrodes, but very different in the above ratio. It is concluded that the high O₂ reduction photocurrent is attributable to many surface states formed on the surface by the dopants, which easily reduces the O₂ molecule. That is, these surface states will be the active sites for the O₂ reduction. The active site will be the d-orbital of the dopant (Cr, Mn, V, and Cu) as discussed previously. The photoproduced electron in the π^* conduction band of the TiO₂ will flow to the O₂ molecule adsorbed at the active site through the impurity band, if the impurity band is formed near the π^* conduction band in the same energy position as the Co-doped TiO₂ (6). This is a reasonable energy position in a theory of electron transfer. Therefore, it is predictable that the impurity band is situated near the π^* conduction band for all the TiO₂/M electrodes which show the visible light response. Figure 9 shows the model for the cathodic and anodic photocurrents on the TiO₂/M electrodes (M: Cr, Mn, V, and Cu).

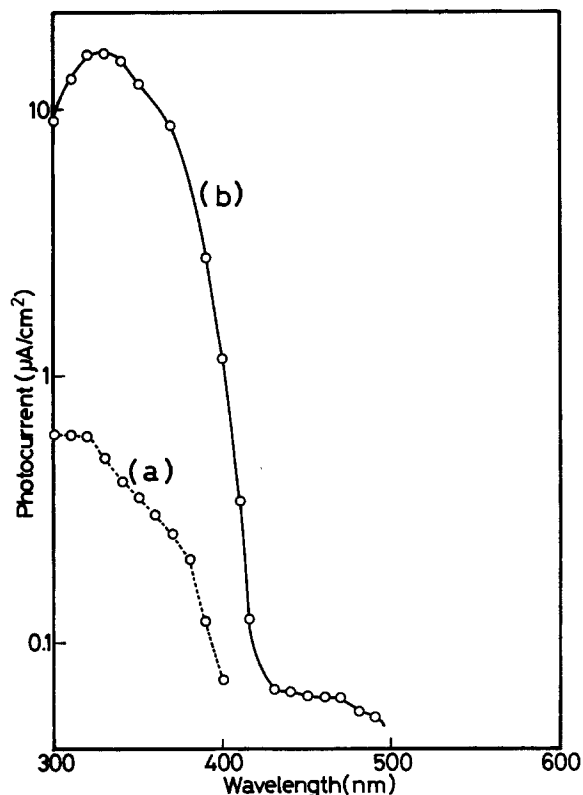


Fig. 8. Spectral dependences of the photocurrents at the TiO₂ prepared at 600°C. The cathodic and anodic photocurrents were measured at -0.8 and $0V$, respectively. (a) Cathodic photocurrent, (b) anodic photocurrent.

Table II. Ratio of the maximum cathodic photocurrent to the maximum anodic photocurrent

| Sample | Preparation temp. | Ratio $i_{mc} (\mu A) / i_{ma} (\mu A)$ |
|--|-------------------|---|
| TiO ₂ | 600°C | 0.6/16 = 0.04 |
| TiO ₂ /Cr (2.5×10^{-9} mole/cm ²) | 600°C | 6.8/4.2 = 1.6 |
| TiO ₂ /Cr (2.5×10^{-8} mole/cm ²) | 600°C | 1.4/1.5 = 0.9 |
| TiO ₂ /Mn (2.5×10^{-8} mole/cm ²) | 500°C | 1.5/1.7 = 0.9 |
| TiO ₂ /Mn (2.5×10^{-8} mole/cm ²) | 600°C | 0.8/1.6 = 0.5 |
| TiO ₂ /V (2.5×10^{-8} mole/cm ²) | 600°C | 3.4/3.6 = 0.9 |
| TiO ₂ /Cu (2.5×10^{-7} mole/cm ²) | 600°C | 5.8/13 = 0.4 |
| TiO ₂ /Zn (2.5×10^{-9} mole/cm ²) | 600°C | 0.09/16 = 0.006 |
| TiO ₂ /Ni (2.5×10^{-7} mole/cm ²) | 600°C | 0.24/2.6 = 0.09 |

It is confirmed by the following experiment for the TiO₂/Cr electrode that the impurity band is situated near the π^* conduction band in energy position. In this experiment, the TiO₂ (single crystal)/Cr electrode, which was prepared by coating the isopropyl alcohol solution with metal oxide and then heating in the same way described in the experimental section, was used. The electrode was heated at 600°C in air as the final heat-treatment. If the impurity band is situated near the π^* conduction band, the visible light photoresponse will be observed for the cathodic current but not for anodic current as illustrated in Fig. 10, because the impurity band is formed only on the electrode surface region. The photoproduced electron by the visible light cannot flow into the bulk under the anodic bias, but into the solution under the cathodic bias. The spectral dependences for this type of electrode are shown in Fig. 11. The clear cathodic photocurrent due to the visible light was observed, but only the small anodic

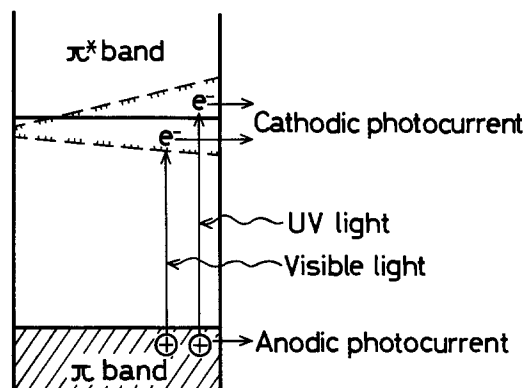


Fig. 9. Model of the photoexcitation process at the electrode giving the visible light photoresponse.

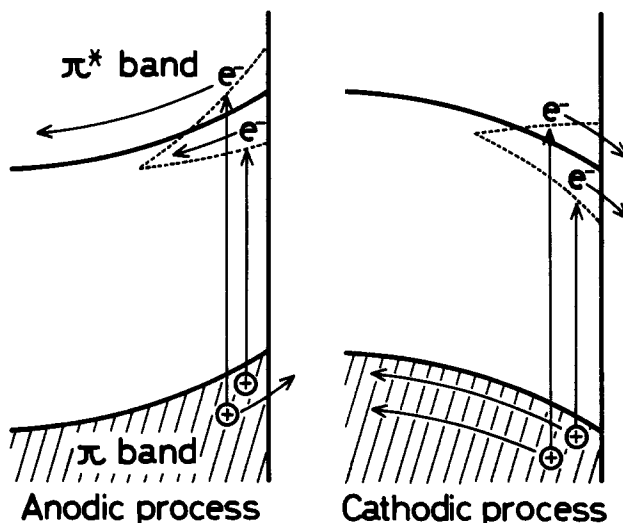


Fig. 10. Cathodic and anodic photoprocess at the TiO₂ (single crystal)/Cr. The larger visible light response for the cathodic photocurrent than the anodic photocurrent is brought about.

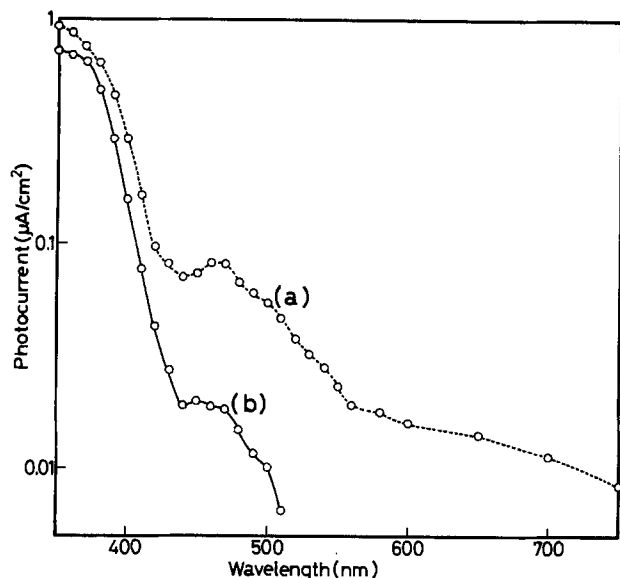


Fig. 11. Spectral dependences of the photocurrents at the TiO_2 (single crystal)/ $\text{Cr}(2.5 \times 10^{-9} \text{ mole/cm}^2)$ electrode prepared at 600°C . (a) Cathodic photocurrent, (b) anodic photocurrent.

photocurrent due to the visible light with the wavelengths near the bandgap energy of the TiO_2 was observed. This result agrees with the expectations as stated above very well. The small visible light response for the anodic current reflects that the impurity band slightly interacts with the π^* conduction band. The same type electrodes doped on their surfaces with the other transition metal (Mn, V, Cu) also gave the similar spectral dependences in which the visible light responses of the anodic photocurrents are small, but not stable. From the energy position of the impurity band, it is estimated that this band will consist mainly of the d-orbital of the impurity transition metal. Therefore, the d-orbital on the top of the impurity band will act as the active site for the O_2 photoreduction on the electrode surface.

The simultaneous appearance of the both cathodic and anodic photocurrents at the TiO_2 electrodes reflects that the photoreduction by the photoproduced electron and the photo-oxidation by the photoproduced hole possibly proceed on the same surface at the same time in the potential region near the flatband potential, and give a photosynthetic mechanism. In particular, the above two reactions will rapidly proceed on the TiO_2 surface doped with Cr, Mn, V, and Cu. This mechanism is essentially different from that of the photosynthesis proposed on the platinized TiO_2 in which the reduction proceeds on Pt and the oxidation on the TiO_2 (12, 13), but similar to that suggested by Schrauzer *et al.* (14) and Inoue *et al.* (15).

Conclusions

In the electrodes used in the present work, the Cr, Mn, V, and Cu-doped TiO_2 electrodes show the visible light response. From the results of the experiment in which the single crystal TiO_2 coated by Cr was used, it is confirmed that the impurity band is formed near the π^* conduction band of the TiO_2 . It is found that TiO_2 electrodes also give the O_2 reduction photocurrent, and that in particular the doped TiO_2 electrodes which show the visible light response bring about the large O_2 reduction photocurrent. The good agreement of the spectral dependences of the anodic and cathodic photocurrents show that both photocurrents are brought about by the same photoexcitation process. The large O_2 reduction photocurrent is based on the d-orbital of the impurity metal by which the impurity band will be formed in the bulk. That a photosynthesis of the photoreduction by the photoproduced electron and the photo-oxidation by the photoproduced hole simultaneously proceed on the same surface is suggested from the simultaneous appearance of the both cathodic and anodic photocurrents.

Manuscript submitted Sept. 11, 1980; revised manuscript received Nov. 15, 1980.

Any discussion of this paper will appear in a Discussion Section to be published in the December 1981 JOURNAL. All discussions for the December 1981 Discussion Section should be submitted by Aug. 1, 1981.

Publication costs of this article were assisted by Utsunomiya University.

REFERENCES

1. A. K. Ghosh and H. P. Maruska, *This Journal*, **124**, 1516 (1977).
2. H. P. Maruska and A. K. Ghosh, *Solar Energy Mater.*, **1**, 237 (1979).
3. J. Augustynski, J. Hinden, and C. Stalder, *This Journal*, **124**, 1063 (1977).
4. C. Stalder and J. Augustynski, *ibid.*, **126**, 2007 (1979).
5. A. Monnier and J. Augustynski, *ibid.*, **127**, 1576 (1980).
6. Y. Matsumoto, J. Kurimoto, Y. Amagasaki, and E. Sato, *ibid.*, **127**, 2148 (1980).
7. K. L. Hardee and A. J. Bard, *ibid.*, **123**, 1024 (1976).
8. L.-S. R. Yeh and N. Hackerman, *ibid.*, **124**, 833 (1977).
9. J. H. Kennedy and K. W. Frese, Jr., *ibid.*, **125**, 709 (1978).
10. L. A. Harris, M. E. Gerstner, and R. H. Wilson, *ibid.*, **126**, 850 (1979).
11. S. M. Wilhelm, K. S. Yun, L. W. Ballenger, and N. Hackerman, *ibid.*, **126**, 419 (1979).
12. B. Kraeutler and A. J. Bard, *J. Am. Chem. Soc.*, **100**, 5985 (1978).
13. H. Reiche and A. J. Bard, *ibid.*, **101**, 3127 (1979).
14. G. N. Schrauzer and T. D. Guth, *ibid.*, **99**, 7189 (1977).
15. T. Inoue, A. Fujishima, S. Konishi, and K. Honda, *Nature*, **277**, 637 (1979).

Semiconductor Electrodes

XXXIII. Photoelectrochemistry of n-Type WSe_2 in Acetonitrile

Henry S. White, Fu-Ren F. Fan, and Allen J. Bard*

Department of Chemistry, The University of Texas at Austin, Austin, Texas 78712

ABSTRACT

The photoelectrochemical behavior of n-type WSe_2 single crystal electrodes in acetonitrile solutions containing several redox couples (I^-/I_3^- , Br^-/Br_2 , Cl^-/Cl_2 , thianthrene $^{0/+}$, $\text{Ru}(\text{bpy})_3^{2+/3+}$) was investigated. Electrodes with discontinuities in the van der Waals' surface show large dark currents and recombination of electrons with photo-oxidized solution species. Pretreatment of such a surface with Cl^- passivates these dark active sites and increases the photocurrent density. The observed photopotentials at WSe_2 for redox couples with potentials, V_{redox} , more positive than 0.5V vs. SCE show behavior consistent with Fermi level pinning; the onset potential of photocurrents increases linearly with increasing V_{redox} while the photopotential remains constant. The energy position at which pinning occurs depends on the density of surface states and the concentration of solution species. The characteristics of a photovoltaic cell based on the n- WSe_2/Cl^- , Cl_2^-/Pt system is also described.

The performance of photoelectrochemical devices for conversion of solar to chemical and electrical energy can be critically limited by processes occurring via intermediate energy levels at the semiconductor/liquid interface (surface states). Surface recombination and Fermi level pinning are two such processes that generally are detrimental to efficient energy conversion. In either case the photoelectrochemical results are somewhat different from expectations based on the idealized model (1) of the semiconductor electrode/solution interface. A number of investigations of the dependence of potential distribution (2) and charge transfer kinetics (3) on surface states have been carried out. The surface pretreatment or modification procedures can influence the distribution and density of surface states at energies located within the band-gap and thus cause changes in the electrochemical behavior (4, 5).

Recently, Tributsch and co-workers have introduced photoelectrochemical cells based on layer-type transition metal dichalcogenides (5). These and later investigations (6-11) have shown that the observed photopotentials in aqueous (5f, 9) and nonaqueous (6-8) solutions are smaller than the expectations based on the ideal junction model. Lewerenz (10) and Tributsch (11) and co-workers have also recently investigated the role of surface morphology on conversion efficiencies of layered semiconductors in aqueous solutions. We report here an investigation of n-type WSe_2 electrodes in acetonitrile (MeCN) solutions. The effect of the nature of the surface and pretreatment procedures on the electrochemical response and a photovoltaic cell based on the photogeneration of chlorine at n-type WSe_2 immersed in an MeCN solution containing Cl^-/Cl_2 is described.

Experimental

Semiconductor electrodes.—N-type WSe_2 single crystals were generously donated by Dr. Barry Miller and Dr. Frank DiSalvo of Bell Laboratories. Electrical contacts were made to the back of each crystal by rubbing In/Ga alloy into the crystal to which a copper lead was contacted with silver epoxy cement (Allied Products Corporation, New Haven, Connecticut). A clean new crystal face (\perp C-axis) was exposed by sticking adhesive tape on the front side and gently pulling off the top surface layer. To obtain electrodes with only

the van der Waal's surface (\perp C-axis) exposed, a very minute surface area was carefully chosen that was free from any edges or face defects; these are known to provide recombination centers (10, 11). Such electrodes are designated "type S" in this paper. No electrodes were prepared with only the surface \parallel C-axis exposed, since the crystals were only ~ 1 -2 mm thick along this plane and are difficult to mount without leaking. Electrodes were prepared from several crystals that had visible edges (discontinuities in the otherwise smooth van der Waal's plane) exposed to the solution. These electrodes are designated "type E." Scanning electron micrographs of type S and type E WSe_2 electrodes are shown in Fig. 1. The surface defects represented roughly 5%-10% of the total surface area of type E electrodes.

The crystal sides and back and the copper lead were completely covered with 5 min epoxy cement; this was then covered with silicone rubber sealant (Dow Corning Corporation, Midland, Michigan). For long-term stability measurements involving strong oxidants, such as Cl_2 , the electrode was covered with a preactivated photo-cure epoxy cement that is used in dental restorative work (Caulk Nuva-Fil, D.A., Milford, Delaware). The exposed areas of the crystal faces in both types of electrodes were between 0.010 and 0.070 cm^2 .

Unless noted otherwise, before each experiment the electrodes were etched in 12M HCl for 15-30 sec, rinsed thoroughly with distilled water, and dried under vacuum for 1 hr. The electrodes were then stored inside an He-filled dry box (Vacuum Atmospheres, Hawthorne, California) and used within one day.

Chemicals.—All electrochemical grade tetraalkylammonium salts were purchased from Southwestern Chemical Company (Austin, Texas). Tetrabutylammonium perchlorate (TBAP), tetrabutylammonium bromide (TBABr), tetramethylammonium chloride (TMACl), and tetrabutylammonium iodide (TBAI) were crystallized at least twice from acetone-ether and dried under vacuum for 2 days. Tetraethylammonium chloride (TEAC) was recrystallized from MeCN-ether and dried as above. Thianthrene (Th) (Aldrich Chemicals) was either sublimed three times or recrystallized from benzene twice. $\text{Ru}(\text{bpy})_3(\text{ClO}_4)_2$ was prepared and purified as previously described (12). After purification the reagents were stored inside the dry box. I_2 (Fisher Scientific Company), Br_2 (MCB), and Cl_2 (Matheson Gas Company) were used without

* Electrochemical Society Active Member.
Key words: capacitance, voltammetry, photopotential, oxidation, solar cells.

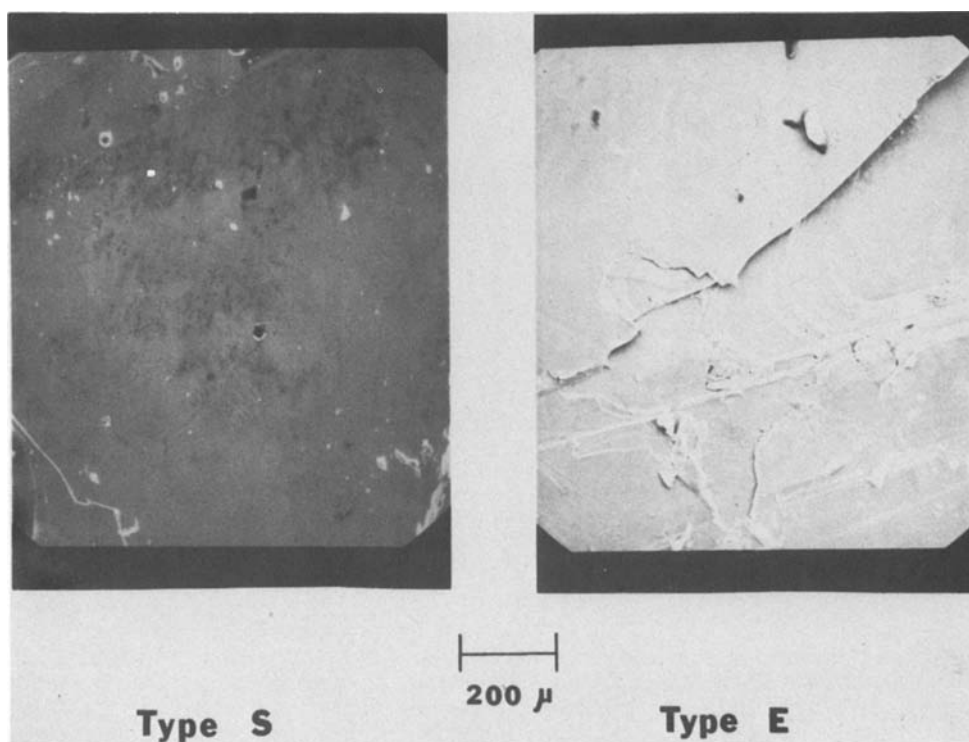


Fig. 1. Scanning electron micrographs of WSe_2 electrodes: (a) type E; (b) type S. Magnification $100\times$.

further purification. MeCN was purified and dried as previously described (13) and stored inside the dry box.

Electrochemical apparatus.—Voltammetric measurements were made in a two-compartment cell (30 ml) equipped with an optically flat Pyrex window. The working and reference electrodes were separated from the auxiliary electrode, a Pt flag ($\sim 8\text{ cm}^2$), by a medium-porosity frit. Along with the semiconductor electrodes the main compartment contained a Pt disk (0.025 cm^2) sealed in glass that was used to check the purity of the electrolyte and to locate the potential of the reference electrode with respect to the potential of a known reversible redox couple. The reference electrode was a polished silver wire inside a glass cylindrical compartment containing only the supporting electrolyte and separated from the main solution by a medium-porosity frit. All potentials reported here are referenced to an aqueous saturated calomel electrode (SCE). Single compartment, two-electrode cells, also equipped with optically flat Pyrex windows, were used as photovoltaic (solar) cells.

The electrochemical cell and solutions were prepared before each experiment within the dry box. All ground glass joints were sealed with silicone-based vacuum grease to permit the cell to be removed from the inert atmosphere for study. When the experiment required opening of the electrochemical cell outside of the dry box, prepurified N_2 was blown over the top of the solution until the cell was reclosed.

The cyclic voltammograms were obtained with a Princeton Applied Research (PAR) Model 173 potentiostat and PAR Model 175 Universal programmer and recorded on a Houston Instruments Model 2000 X-Y recorder. Capacitance measurements were made using a PAR Model HR-8 lock-in amplifier. Solar cell current-voltage curves were made by measuring the voltage across a variable load resistance with a Keithley Model 179 TRMS digital multimeter.

The light source used for photoelectrochemical studies was an Oriel Corporation (Stamford, Connecticut) 450W xenon lamp. A red filter was used to eliminate wavelengths below 590 nm. Neutral density filters (Oriel Corporation) were used to vary the light intensity. The full, filtered xenon lamp power output was $\sim 150\text{ mW/cm}^2$ as measured with an E. G. and G.

(Salem, Massachusetts) Model 550 radiometer/photometer and a Scientech 361 power meter.

Results

Capacitance measurements and cyclic voltammetry in the absence of redox couple.—Capacitance measurements on several n- WSe_2 electrodes in MeCN containing only TBAP (0.2M) resulted in two distinct types of behavior. The capacitance vs. potential curve of a type S electrode, Fig. 2, closely resembles behavior typical of a fairly large bandgap n-type semiconductor, where at potentials positive of the flatband potential, V_{FB} , the space charge region is depleted of electrons and contains ionized donors at some constant concentration (1). This region extends up to potentials of 1.3V vs. SCE. At potentials more negative than -0.4V , the capacitance becomes constant indicating the onset of degeneracy. The voltammetric behavior of the same electrode in MeCN-0.2M TBAP is shown in Fig. 3. In the dark a small current, $\sim 0.2\text{ mA/cm}^2$, begins at 0.6V. Under illumination, the photocurrent begins at $\sim 0.5\text{V}$ and increases steadily at more positive potentials. At $\sim 1.0\text{V}$, the photocurrent is $\sim 1.0\text{ mA/cm}^2$. On the reverse

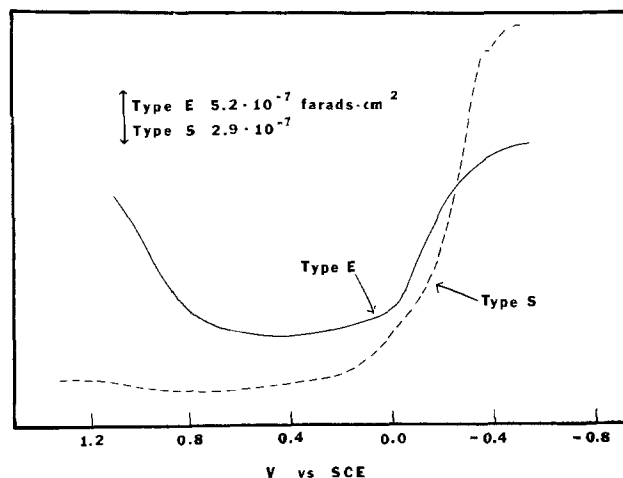


Fig. 2. Differential capacitance curve for type E and type S WSe_2 electrodes in MeCN containing 0.2M TBAP. Scan rate, 5 mV/sec; applied a-c voltage, 5 mV rms. Frequency, 1000 Hz.

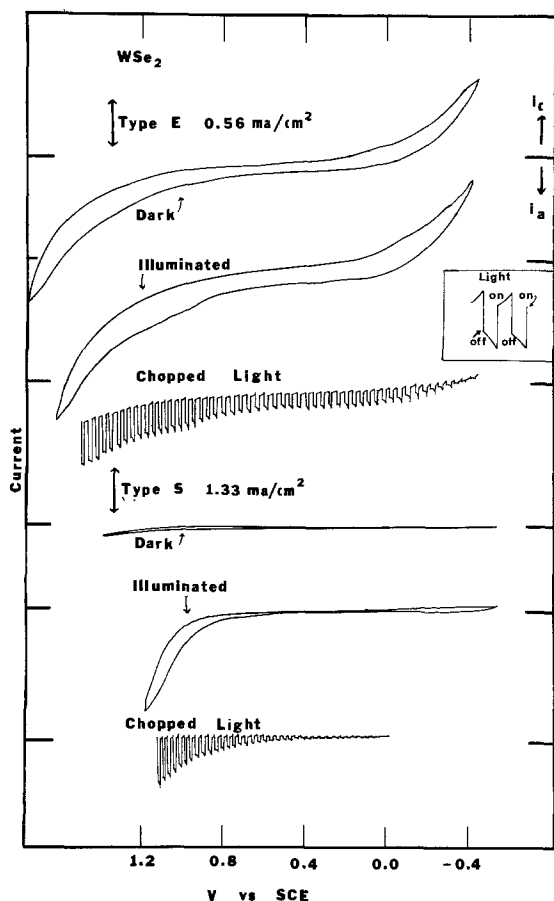


Fig. 3. Voltammetric behavior of type S and type E electrodes in MeCN-0.2M TBAP. Scan rate, 100 mV/sec, except for chopped light scans, 10 mV/sec.

scan, under illumination, a small cathodic current, ~ 0.2 mA/cm², begins at 0.0V. This same cathodic current is observed if the light is turned off on the reverse scan and increases with more positive switching potentials. The anodic photocurrent and induced dark current are probably due to the oxidation and re-reduction of the crystal surface caused by traces of H₂O in the acetonitrile (5e). Further purification of the solvent by addition of Al₂O₃ significantly reduced these currents.

The capacitance behavior of a type E WSe₂ electrode, also shown in Fig. 2, is typical of electrodes with discontinuities in the van der Waal's surface. The branch toward negative potentials is similar in shape to the type S electrodes. However, at potentials more positive than 0.7V, the capacitance increases sharply indicating either deep surface states, inversion of the space charge region, or the occurrence of a faradic process.

As Tributsch has already pointed out (5e), inversion of the space charge region in a semiconductor with a bandgap of 1.4 eV is unlikely within this potential region. If space charge inversion due to thermal activation of electrons into the conduction band were responsible for this increase in capacitance, both type S and type E electrodes should show this behavior. The voltammetric behavior of the same crystal (type E) in a blank solution is shown in Fig. 3. A dark anodic current is observed that is approximately five times larger than on the type S electrode (compare at 1.0V). Under illumination, a photocurrent begins at -0.3V and is fairly constant until 0.7V where a sharp increase in anodic currents begins. The net photocurrent density at 1.0V is ~ 0.6 mA/cm², which is $\sim 60\%$ the current density at the type S electrode. The V_{FB} values and donor densities of these crystals were estimated from the capacitance measurements. Mott-Schottky plots for the two crystals described above are shown in Fig. 4a and 4b. The results for several crystals are summarized in Table I. V_{FB} , for WSe₂ in MeCN, estimated by extrapolating to the potential where $1/C_{sc}^2 = 0$, was always in the range of -0.2 to -0.4V vs. SCE. The apparent donor densities, n_D , for type E electrodes were 3-7 times larger than for type S electrodes. As can be seen in the Mott-Schottky plots, the apparent capacitance values were highly dependent on the frequency of the applied alternating voltage. Frequency dispersion of the capacitance due to dielectric relaxation should be negligible in a covalent-type material like WSe₂. It is possible that the dispersion observed here is due to small changes in the effective electrode surface due to corrosion. The values of n_D listed in Table I are from measurements in the range 500-1000 Hz. A value of 10 for the dielectric constant of WSe₂ was used in all calculations (14).

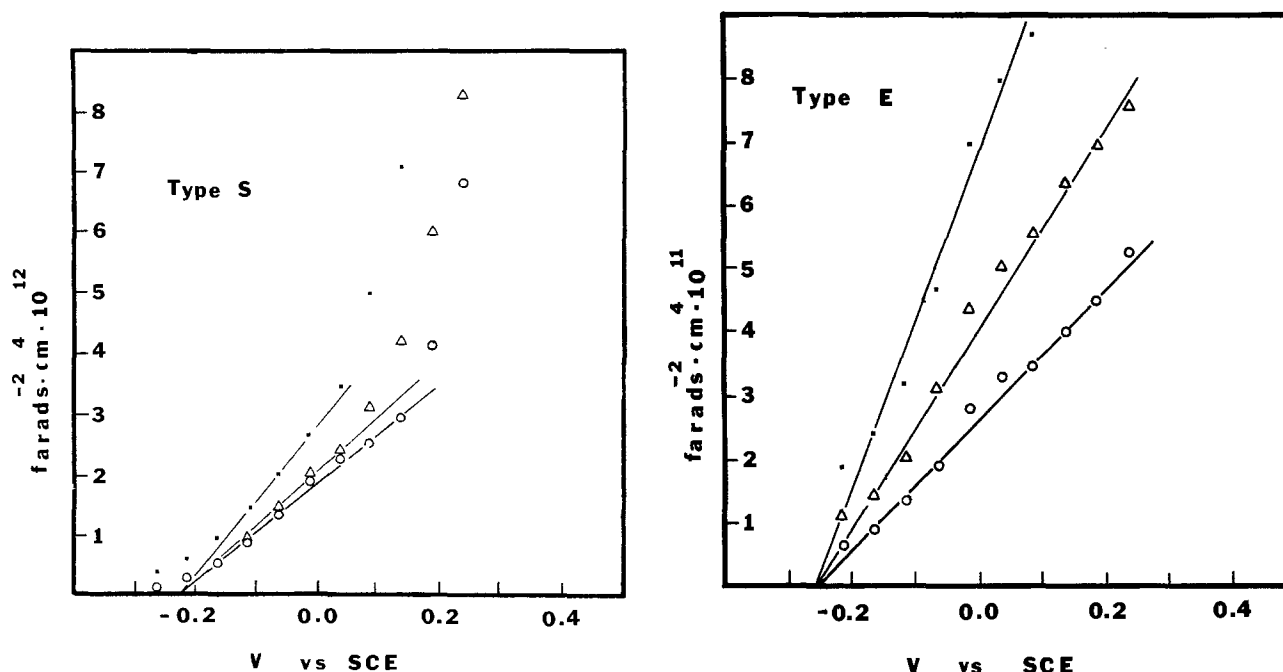


Fig. 4. Mott-Schottky plots of (a) type S and (b) type E WSe₂ electrodes in MeCN-0.2M TBAP. (○) 200 Hz, (△) 500 Hz, (■) 1000 Hz

Table I. Estimates of flatband potentials and donor densities for n-WSe₂

| Crystal, WSe ₂ | V _{FB} (V vs. SCE) | n _D (cm ⁻³) |
|---------------------------|--------------------------------|------------------------------------|
| Type S | -0.22 | 1.3 × 10 ¹⁸ |
| | -0.36 | 2.0 × 10 ¹⁸ |
| | -0.42 | 1.8 × 10 ¹⁸ |
| Type E | -0.26 | 8.5 × 10 ¹⁸ |
| | -0.26 | 8.5 × 10 ¹⁸ |
| | -0.4* | 5.6 × 10 ¹⁸ |

* Measured vs. Ag quasi-reference electrode and corrected to SCE with accuracy of $\sim \pm 0.1V$.

Voltammetric behavior of various redox couples at n-WSe₂.—Types S and E electrodes showed distinctly different voltammetric behavior. Recall that type E electrodes are those that have visible edges or discontinuities in the van der Waal's plane exposed to the solution. These edges have been associated with the face parallel to the main C-axis (|| C-axis) (15) where empty conduction band orbitals are exposed to the solution. The results are summarized in Tables II and III.

Oxidation of I⁻ and Br⁻.—The type S electrode shows negligible dark current in the vicinity of I⁻ oxidation on Pt (Fig. 5a). Upon illumination, the potential for onset of photocurrent, V_{on}, was 0.0V and attains a saturation current at $\sim 0.2V$. The chopped light voltammogram clearly indicates that little back-reaction (reduction of photo-oxidized products) occurs beyond the onset potential. The dark current at the type E electrode in the presence of I⁻ (Fig. 5b) was smaller (i.e., about one-tenth) than in the blank solution (Fig. 3). V_{on} was $\sim 0.07V$ more negative than the V_{on} at the type S electrode. This difference in onset potential is approximately the difference in the measured flatband potentials for these crystals. The maximum photocurrent densities were about the same for both type S and type E electrodes. However, on scan reversal, a much larger reduction peak centered at $-0.07V$ was found with the type E electrode.

The oxidation of Br⁻ (as TBABr) on WSe₂ followed behavior similar to that found for I⁻ (Fig. 6a and 6b).

Table II. Voltammetric data for various redox couples at WSe₂

| Couple | Pt* | | Type S** | | Type E† | |
|---------------------------------------|-----------------|-----------------|--------------------|-----------------|--------------------|-----------------|
| | V _{pa} | V _{pc} | V _{onset} | V _{pc} | V _{onset} | V _{pc} |
| I ⁻ /I ₃ | 0.35 | 0.1 | 0.00 | — | -0.07 | -0.08 |
| Br ⁻ /Br ₂ | 0.69 | 0.25 | 0.05 | -0.35 | 0.02 | -0.12 |
| Cl ⁻ /Cl ₂ | 1.09 | 0.82 | 0.55 | — | 0.21 | -0.02 |
| Th ^{0/+} | 1.26 | 1.20 | 0.60 | 0.76 | 0.67 | 0.75 |
| Ru(bpy) ₃ ^{2+/3+} | 1.33 | 1.27 | 0.91 | 0.96 | — | — |

* All values in V vs. SCE; E_{onset} = potential of photocurrent onset.

** Under illumination; negligible dark anodic currents at type S electrodes.

† Under illumination; no well-defined peaks in dark except for thianthrene oxidation, V_{pa} = 1.35V; V_{pc} = 1.15V.

Table III. Comparison of current densities at type S and type E WSe₂ electrodes in solutions containing various redox couples

| Redox couple | Current, * mA/cm ² | | | |
|-----------------|-------------------------------|-------------|--------|-------------|
| | Type S | | Type E | |
| | Dark* | Illuminated | Dark | Illuminated |
| I ⁻ | <0.1 | 0.66 | <0.1 | 0.71 |
| Br ⁻ | <0.1 | 5.0 | <0.1 | 1.1 |
| Cl ⁻ | <0.1 | 6.0 | 0.1 | 2.0 |
| Th | <0.1 | 3.2 | 2.4 | 2.4 |

* Dark current measured at potential of oxidation peak on Pt. Photocurrent measured at peak potential for type E electrodes. Measured at current plateau for type S electrode except for Br⁻ where i_{photo} was measured at 0.8V.

The V_{on} for the type E electrode was about 30 mV more negative than for the type S electrode. A much larger difference existed, however, in the total photocurrent densities. The current density at the type S electrode was about 4-5 times larger than that at type E.

Oxidation of Cl⁻.—The voltammetric behavior for the oxidation of Cl⁻ at the two WSe₂ electrodes are shown in Fig. 7a and 7b. At the type S electrode, V_{on} is 0.55V. Again, no dark current or back-reaction is seen at this electrode. The oxidation of Cl⁻ on the type E electrode is strikingly different. V_{on} was 0.34V more negative at this crystal. This difference in onset potential cannot be accounted for by the small difference in flatband potential (~ 50 mV). The cyclic voltammogram at the type E electrode shows a large reduction peak centered at 0.17V in the dark on scan reversal. This peak probably corresponds to the reduction of chlorine generated in the dark on the anodic scan. Under illumination, this reduction peak occurred at a potential about 0.2V more negative. No reverse reduction peak was observed in the dark on the type S electrode since no dark anodic current flowed. However, under illumination, a similar cathodic current was observed at potentials more negative than 0.0V.

Thianthrene.—The voltammetric behavior for the oxidation of thianthrene (Th) at the two WSe₂ crystals is shown in Fig. 8a and 8b. While under illumination, the onset potential and waveforms are almost identical at the two electrodes; in the dark a striking difference exists. With the type E electrode, a large quasi-reversible peak is located at approximately the same potential as on Pt. The current density in the dark is equal to the photocurrent density. On the type S electrode, no dark anodic current is observed. On scan reversal following an anodic scan under illumination, a cathodic peak is observed at both type E and S electrodes.

Oxidation of thianthrene in the presence of halide.—The photo-oxidation of Th with small amounts of halide species (10-15 mM) added to the solution was studied to determine the effect of halide ions on the photoelectrochemical behavior of WSe₂. The cyclic voltammograms obtained in the dark at the type E electrode in mixed Th/halide solutions is shown in Fig. 9. The previously observed dark quasi-reversible wave

due to Th oxidation and Th^{•+} reduction is noticeably absent in the presence of I⁻, Br⁻, or Cl⁻. A comparison of the cyclic voltammograms under illumination of thianthrene alone and with either I⁻ or Br⁻ in solution shows little change in the peak potentials due to Th photo-oxidation. In the presence of Cl⁻, however, these peaks, which were centered around 0.75V vs. SCE, are absent (Fig. 10), and instead, a new pair of oxidation and reduction waves centered at 0.52V appeared. These peaks were not present in solutions containing Cl⁻ alone and therefore are assigned to the oxidation and reduction of Th. From these results, it appears that Cl⁻ induces a 230 mV shift in V_{on} for the oxidation of thianthrene. To demonstrate that this effect results from the interaction of Cl⁻ with the surface discontinuities, the experiment illustrated by Fig. 11 was undertaken. A fresh type E electrode was prepared and the dark and photo-oxidation of Th was observed (curves a, b). The electrode was then removed and dipped into an MeCN solution of 7.0 mmoles TEACl in the dark without any external electrical connection. After 30 sec, the electrode was removed, rinsed thoroughly with MeCN, and placed back into the original Th-containing solution. The resulting cyclic voltammograms (curves c and d) showed an immediate decrease in the dark current and a negative shift (~ 180 mV) of the onset potential for photocurrent. The maximum photocurrent for Th oxidation increased by about 25% following this surface treatment. This improved photocurrent-potential curve re-

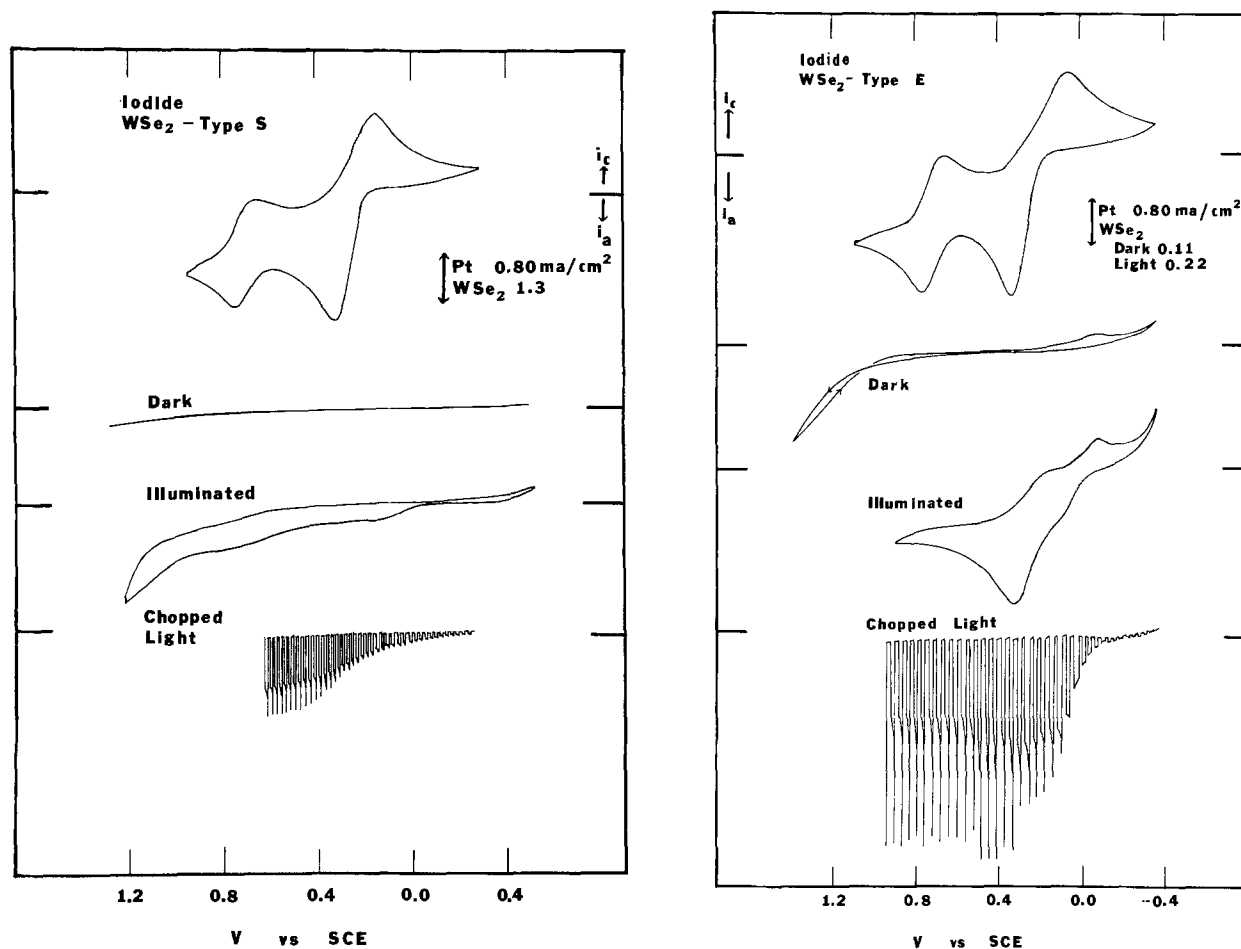


Fig. 5. Voltammetric behavior of iodide in MeCN containing 0.2M TBAP and TBAI. (a) Type S, $[I^-]$, 10 mmole; (b) type E, $[I^-]$, 15 mM. Scan rate, 100 mV/sec, except for chopped light scan at 10 mV/sec.

mained unchanged for at least 30 min of continuous cycling. When a similar experiment was carried out with a type S electrode, no changes in the dark oxidation current (which was negligible) or the photocurrent was found by a Cl^- pretreatment. Note that the decrease in dark current for the type E electrode on treatment with Cl^- takes place without any possibility of photo-oxidation occurring during the exposure of the electrode to Cl^- so that the formation of a light-induced complex between the electrode and Cl^- is unlikely. The observed effect can be ascribed to interactions of the Cl^- with surface discontinuities leading to modification or passivation of these sites.

Photovoltaic cell based on WSe_2/Cl^- , Cl_2 , (MeCN)/Pt.—Schneemeyer and Wrighton have previously reported photovoltaic cells based on the generation of Cl_2 at illuminated MoS_2 (6) and $MoSe_2$ (7) in MeCN. Similar cells employing type S WSe_2 photoanodes were constructed to test the efficiency and stability of this material. The i - V characteristics for several electrodes in cells saturated with TEACl and with Cl_2 bubbled through the solution are shown in Fig. 12. The open-circuit photovoltage, V_{oc} , and short-circuit photocurrents, i_{sc} , for several electrodes are listed in Table IV.

At low photovoltages the photocurrents at several electrodes appear remarkably high, representing quantum efficiencies of 1 (or even more) under short-circuited conditions. A sharp drop in photocurrent ($\sim 30\%$ - 40%) is observed with increasing load resistance in the first 100 mV of the photo i - V curve (Fig. 12). To determine if these unusually high currents are due to a photoinduced corrosion process, a WSe_2 crystal (11.5 mg) was placed in contact with a Pt electrode and immersed in a 2.0M TEAC solution saturated with Cl_2 . After 60 hr under illumination (~ 80 mW/cm 2) the crystal remained unchanged with no weight loss (± 0.1

mg). While this experiment may not reproduce the actual conditions of a PEC cell, photoinduced corrosion does not appear to be the major cause of the high short-circuit currents. Other causes for this result, such as the focusing or scattering of the incident radiation onto the very small area electrode by the surrounding glass or sealant to cause a higher effective light flux on the electrode, have been considered. Probing experiments with the small beam of an He-Ne laser show that this is a small effect. At this time, the actual cause of these anomalous currents is unclear.

V_{oc} depended strongly on the amount of Cl_2 bubbled through the solution. The highest V_{oc} values listed for the 1.9M Cl^- solutions (Table IV) were produced by optimizing the Cl^-/Cl_2 ratio. No attempt was made to measure exactly the amount of Cl_2 dissolved in the solution. As shown in Fig. 13, V_{oc} drops considerably as excess Cl_2 is added to the solution. In a regenerative photocell with an inert metal electrode and without an external power supply the photocurrent can be limited by either processes at the photoanode or at the metal cathode. Thus, at low concentrations of Cl_2 the photocurrent was limited by mass transfer to the platinum cathode, while at high Cl_2/Cl^- ratios, the photovoltage was limited by the solution redox potential (as discussed below). When the photocurrent did not increase with higher concentrations of Cl^- or Cl_2 , addition of Cl^- to the solution increased V_{oc} . The i_{sc} value increased steadily with Cl^- concentration up to 1.6M. Additional increases in Cl^- concentration had no effect on i_{sc} or V_{oc} .

In a 1.9M Cl^- solution, V_{oc} approached a constant maximum value at light intensities ≥ 30 mW/cm 2 . The short-circuit photocurrent increased linearly with light intensity up to 120 mW/cm 2 , where it also reached a saturation value.

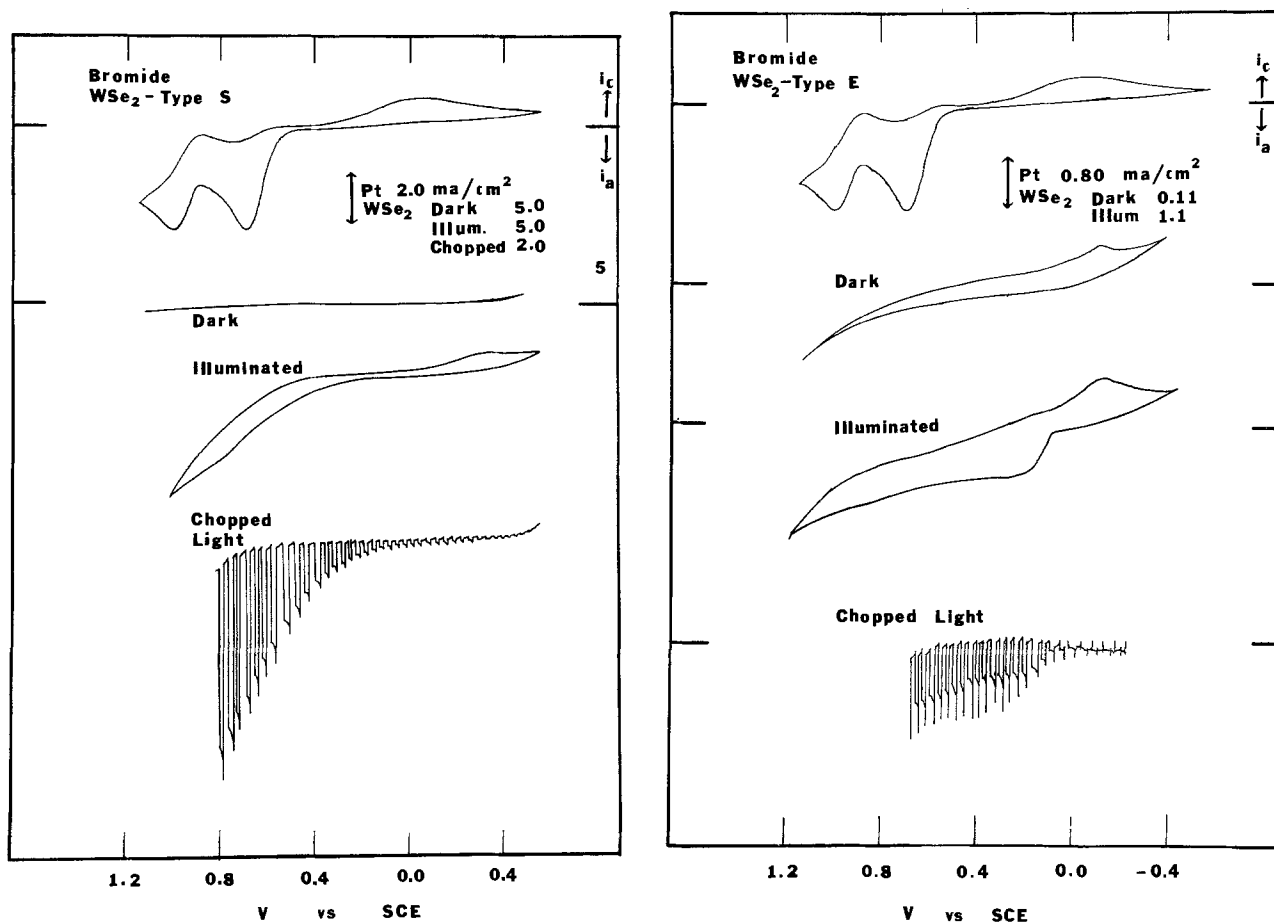


Fig. 6. Voltammetric behavior of bromide in MeCN containing 0.2M TBAP and 10 mM Br⁻. (a) Type S; (b) type E. Scan rate, 100 mV/sec except for chopped light scan at 10 mV/sec.

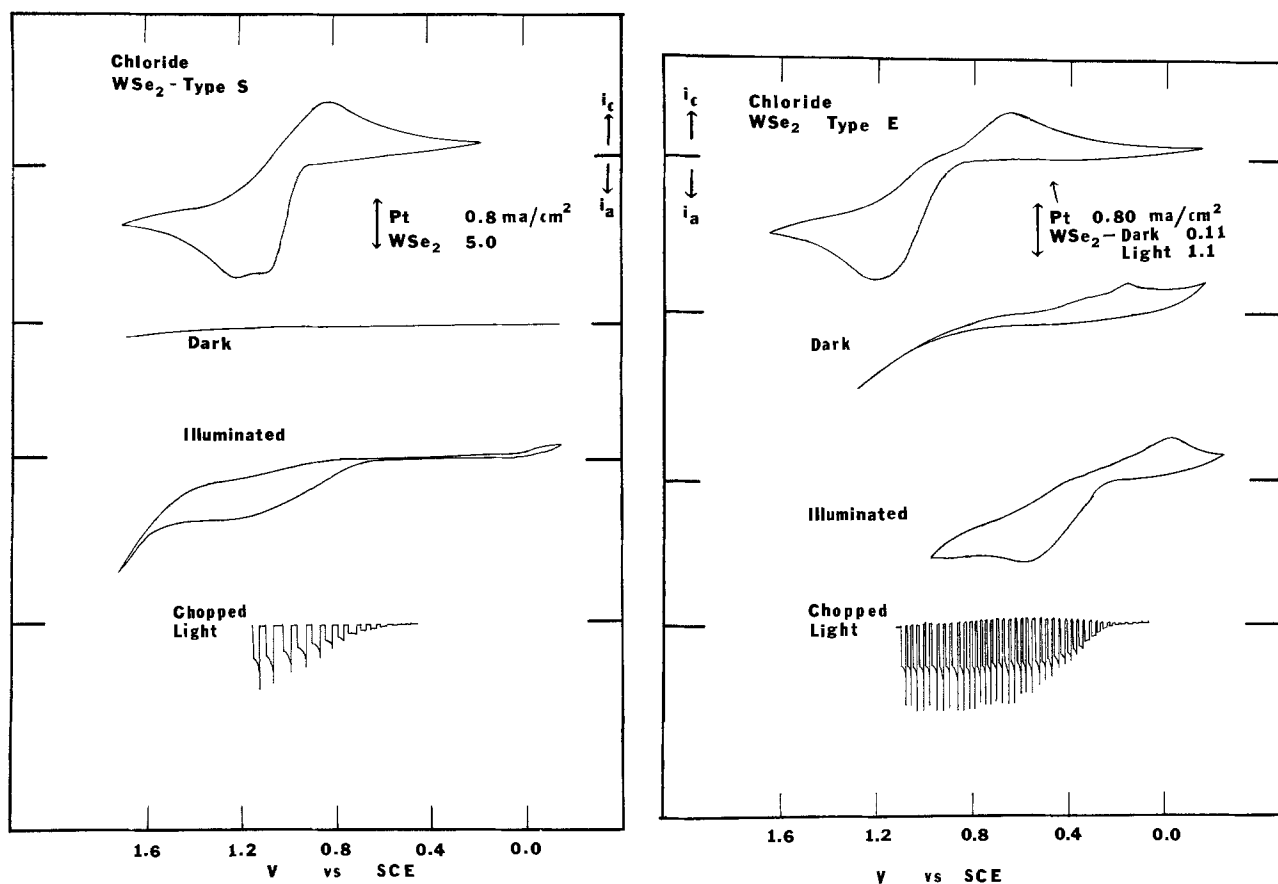


Fig. 7. Voltammetric behavior of chloride in MeCN containing 0.2M TBAP and 10 mM Cl⁻. (a) Type S; (b) type E. Scan rate, 100 mV/sec except for chopped light scan at 10 mV/sec.

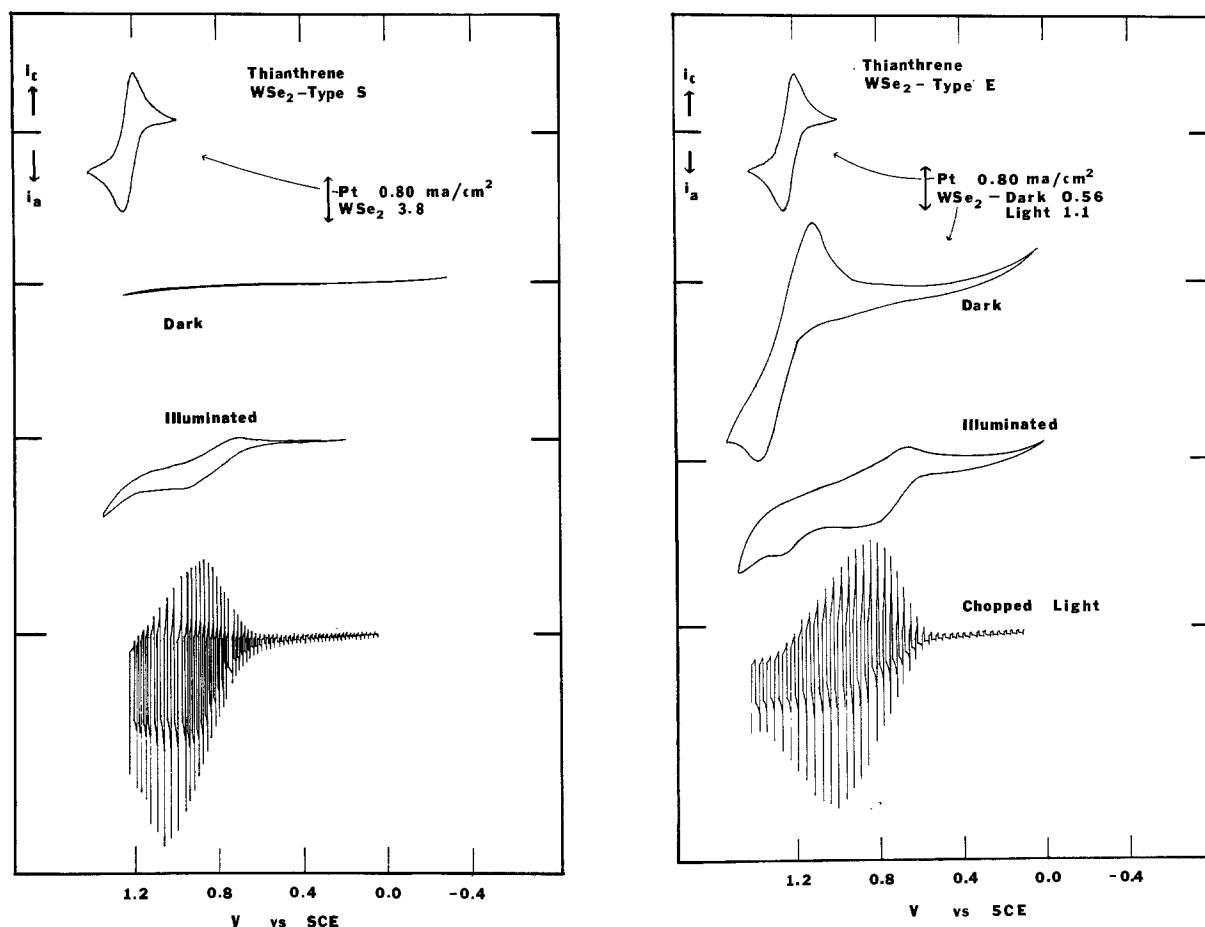


Fig. 8. Voltammetric behavior of thianthrene in acetonitrile solution containing 0.2M TBAP and 5 mM Th. (a) Type S; (b) type E. Scan rate, 100 mV/sec except for chopped light scan at 10 mV/sec.

Irradiation of the WSe_2 photoanode with the full output from a 450W xenon lamp (>590 nm and infrared filtered) focused onto the electrode surface yielded the i_{sc} and V_{oc} values listed in Table IV. Maximum power efficiencies under these conditions were estimated to be 7%–10.5%. No attempts were made to correct for solution absorption or reflections at the cell windows or the electrode surface. However, since the same photocurrent was found at $\sim 80\%$ of this light intensity, the power efficiencies at lower intensities would be $\sim 2\%$ higher.

The stability of n- WSe_2 (type S) against possible attack by Cl_2 generated at the surface was tested by allowing the photovoltaic cell to run for several hours (Fig. 14). After 7 hr, the short-circuit photocurrent had decreased by $\sim 4\%$ from its original stable value of 146 μA . This corresponds to 3.7C of charge passed which represents an amount of charge sufficient to consume an appreciable part of the 10 mg crystal, if corrosion were occurring. The electrode surface appeared unchanged after 7 hr.

Table IV. Characteristics of several photovoltaic cells: n- WSe_2 (type S)/(MeCN), Cl^- , Cl_2/Pt^+

| Electrode** | Conc. TEACl | Fill factor (max) | Power efficiency | i_{sc} (mA/cm ²) | V_{oc} (mV) |
|-------------|-------------|-------------------|------------------|--------------------------------|---------------|
| A | Satd. | 0.27 | 6.4 | 70 | 510 |
| A | 1.9M | 0.24 | 5.6 | 65 | 540 |
| B | Satd. | 0.26 | 10.4 | 125 | 480 |
| C | Satd. | 0.23 | 7.6 | 120 | 410 |
| C | 1.9M | 0.28 | 10.3 | 96 | 575 |
| D | Satd. | 0.20 | 7.3 | 90 | 544 |

* Irradiated with light >590 nm. The power output of the lamp was 150 mW/cm².

** Electrodes A-D were different type S crystals.

Discussion

Dark and photocurrents.—The large differences in dark currents on the type S and type E electrode can be understood by a modified model used by Gerischer *et al.* for dark currents on MoS_2 (15). In this model, the d-orbitals parallel to the C-axis, in addition to forming the conduction band in the bulk material, are assumed to provide surface states at discontinuities of the type E electrode at energies in the upper part of the bandgap (11). Facile electron transfers can take place from the electroactive species into the conduction band via these mediating d-orbitals. When the exposed surface is free from edges, the layer of Se atoms block overlap between the conduction band and molecular orbitals of the species. In this case, electron transfer in the dark via the conduction band is allowed only by thermal excitation or by tunneling. This model seems to fit the behavior found for the oxidation of Th at WSe_2 . In the dark, a small current (<0.2 mA/cm²) is observed on the type S electrodes. This dark current is no larger than the current observed for the same electrode in a solution containing only supporting electrolyte (0.2M TBAP). At the type E electrode, a large, mass transfer limited, dark current is observed for Th oxidation indicating that the current is not controlled by the number of dark oxidation sites on the crystal surface. Under illumination, both electrodes show similar voltammetric responses, with slightly higher photocurrents observed on the type S electrode. Thus for the type E electrode, the existence of the surface states allows Fermi level pinning and electron transfer to occur at potentials close to the standard potential of the redox couple. However, for a type S electrode, there are much lower densities of surface states near the conduction band. Fast electron transfer reactions do not occur in the dark for couples with potentials much more positive than the flatband

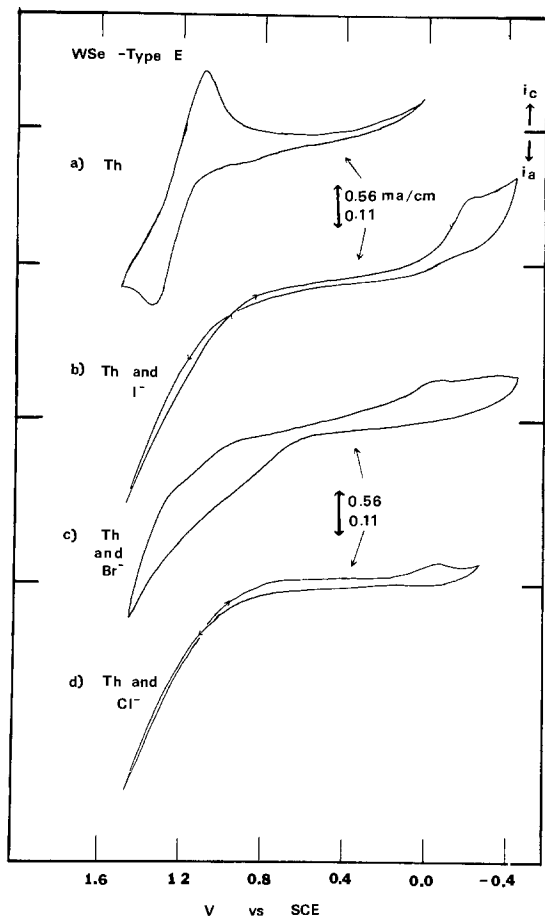


Fig. 9. Effect of bulk halide on dark currents at type E $n\text{-WSe}_2$ electrode. (a) 5 mmoles thianthrene (Th); (b) 5 mmoles Th and 15 mM TBAl; (c) 5 mM Th and 10 mM TBABr; (d) 5 and 10 mM TMACl. Scan rate 100 mV/sec. 0.2M TBAP as the supporting electrolyte.

potential. However, even with type S electrodes, Fermi level pinning at the bottom part of the bandgap may occur, as discussed later.

The photo-oxidation of halide species shows a slightly more complicated behavior. At the type S electrode, the dark anodic current in the presence of halides is about the same as the small dark current observed in a solution containing only supporting electrolyte. However, at the type E electrode, the dark current in the presence of halides is much smaller than that in the blank solution. Tributsch *et al.* have previously proposed an interaction of I^- with the surface in aqueous solutions (5f). The decrease in the dark oxidation currents on the type E electrode on the addition of halide ions similarly suggests a strong interaction of I^- , Br^- , and Cl^- with the surface states, composed of empty d-orbitals along the exposed edges, deactivating these previously dark active sites. This is confirmed by the decrease in the dark currents for Th oxidation (and Th $^+$ reduction) by the addition of I^- , Br^- , or Cl^- .

The total photocurrent densities for the oxidation of Cl^- or Br^- are 3-5 times larger at the type S electrode. Apparently while the dark active sites at the exposed edges are ineffective for the dark oxidation of Br^- or Cl^- , they remain rather efficient at trapping electrons and reducing photogenerated Cl_2 and Br_2 . The total photocurrent density for the oxidation of I^- at the two electrodes was approximately the same.

The difference in behavior between Br^- or Cl^- and I^- probably reflects the stronger interaction of I^- with the electrode surface. The decrease in background current after treatment with halide (compare the dark

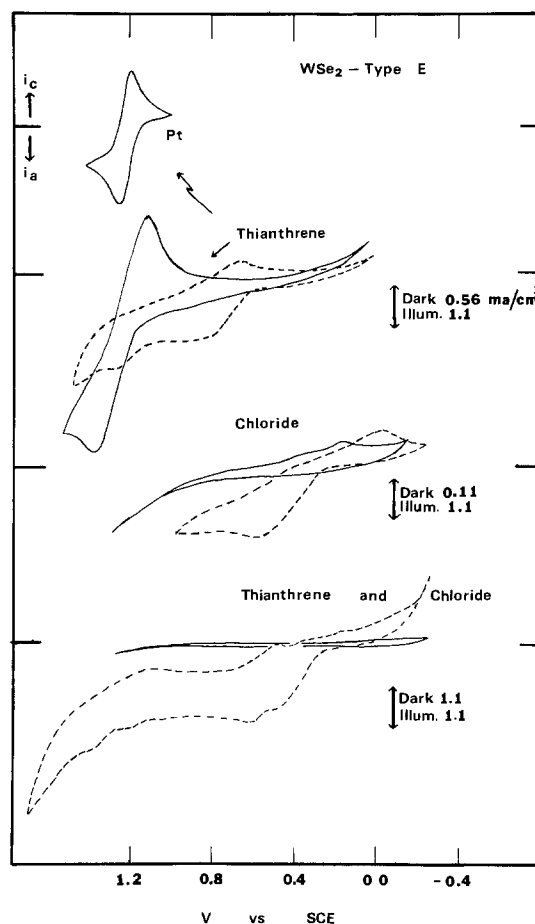


Fig. 10. Effect of chloride on photo-oxidation of thianthrene; 5 mmoles Th, 10 mM TEACl, and 0.2M TBAP in acetonitrile solution. Solid lines indicate dark current; broken lines indicate photocurrent; same conditions of Th and Cl^- in mixed solution.

currents at type E electrode before and after addition of I^- , Br^- , Cl^-) is important, since this current is presumably caused by oxidation of the surface lattice in the presence of trace amounts of H_2O in the acetonitrile (5e). Suppression of the crystal oxidation is equivalent to stabilization of these photoanodes and may be the reason for the stability observed in the aqueous iodide (5e, 9) and nonaqueous chloride (6, 7) cells employing layered materials. Further experiments are necessary to demonstrate if the halide pre-treatments are sufficient for long-term stability.

Photopotentials.—From differential capacitance measurements, V_{FB} of n -type WSe_2 (both type S and E) in MeCN/TBAP alone was $-0.3 \pm 0.1\text{V vs. SCE}$ (Table II). The bandgap of these samples, determined from the action spectrum, is $\sim 1.4\text{ eV}$. After correction for the difference between Fermi level and the conduction band edge, this places the edge of the valence band at $\sim 1.0\text{V vs. SCE}$. This is in good agreement with the flat-band potential of p -type WSe_2 , $+1.0\text{V vs. SCE}$, measured in MeCN (16).

The difference in potential for oxidation at Pt and illuminated WSe_2 (*i.e.*, the photounderpotential) *vs.* the standard potential for several redox couples is shown in Fig. 15. The standard potentials taken for I^- , Br^- , and Cl^- are the average of the reduction and oxidation peak potentials at Pt. The V_{on} for I^- and Br^- is approximately 0.2-0.3V positive of the measured flat-band potential. This positive value of V_{on} suggests recombination is occurring and this can be attributed to the band of surface states lying directly below the conduction band edge.

For couples with standard potentials more positive than 0.5V *vs.* SCE (Cl^-/Cl_2 , Th/Th $^+$, and $\text{Ru}(\text{bpy})_3^{2+}/^{3+}$) the photopotential ($V^\circ - V_{\text{on}}$) be-

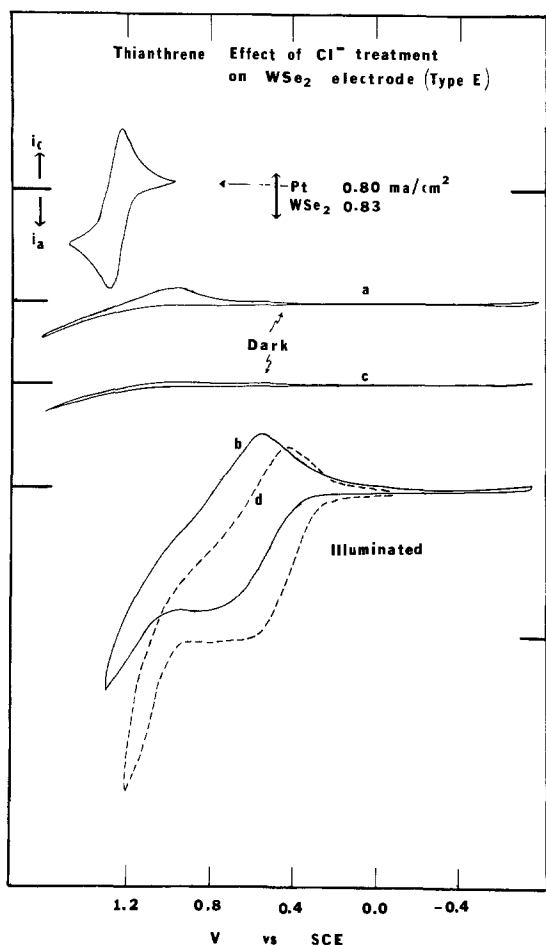


Fig. 11. Effect of dipping type E n-WSe₂ electrode into 7 mM TEACl solution. (a) Dark oxidation of 5 mM Th on untreated electrode. (b) Photo-oxidation of 5 mM Th on untreated electrode. (c) Dark oxidation of Th after Cl⁻ treatment. (d) Photocurrent after Cl⁻ treatment.

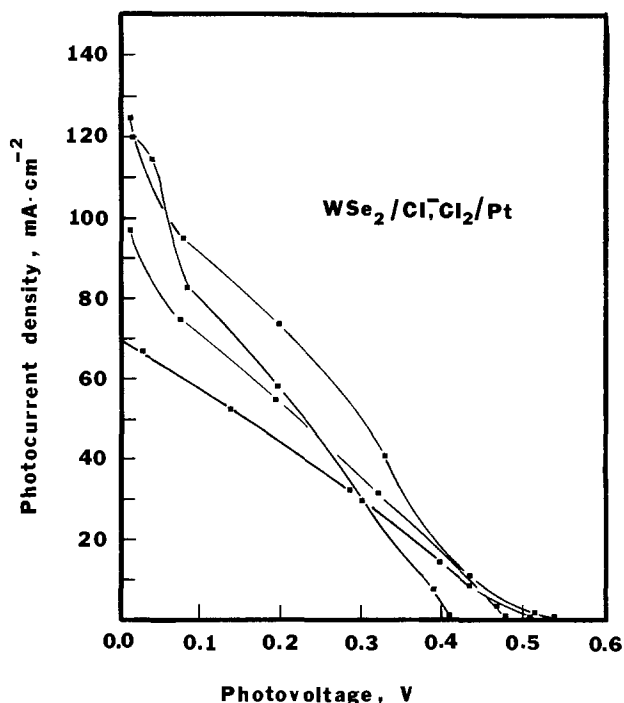


Fig. 12. Performance characteristics of n-WSe₂/Cl⁻ (satd.), Cl₂/Pt photoelectrochemical cells. 450W Xe lamp fitted with a 590 nm cut-on filter used as light source. Power of focused light at electrode surface, 150 mW/cm².

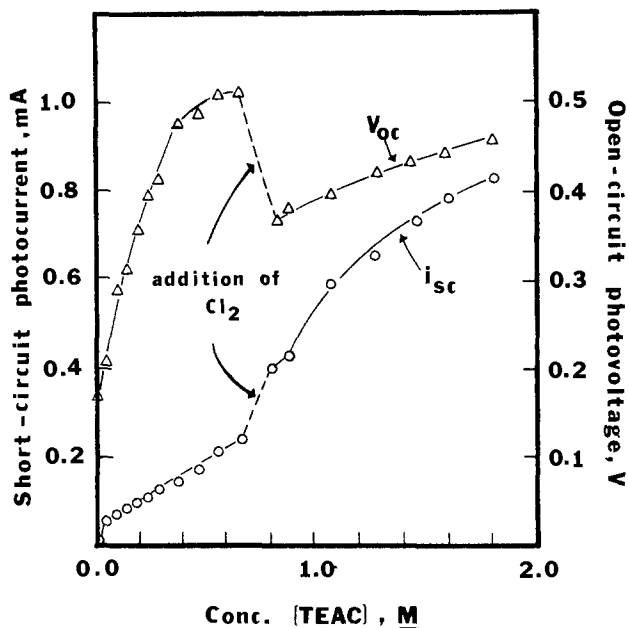


Fig. 13. Effect of Cl⁻ and Cl₂ concentration on open-circuit photovoltage, V_{oc} , and short-circuit photocurrent, i_{sc} . Electrode area, 0.011 cm². Light source as in Fig. 12.

comes almost constant at a value of $\sim 0.4-0.5V$. This limiting value can best be understood by Fermi level pinning (2a) at surface states located approximately 0.5 eV above the valence bandedge. V_{on} for redox couples with V° more positive than 0.5V vs. SCE should increase linearly with increasing V° . For couples with V° at potentials negative of the surface-state level ($<0.5V$), V_{on} is constant and the photopotential should increase as V° becomes more positive, as seen in Fig. 15. Further evidence for the presence of surface states is the highly dependent nature of the photovoltage developed in the n-WSe₂/Cl⁻, Cl₂(MeCN)/Pt cell upon the Cl₂/Cl⁻ ratio (Fig. 13). Based on the ideal model of the semiconductor-solution interface (1), V_{on} should be at V_{FB} and the Pt electrode would be poised by the redox couple so that a higher photovoltage is expected with higher Cl₂/Cl⁻ ratios, i.e., a higher Cl₂/Cl⁻ shifts the solution redox potential to more positive values while the bandedges remain unaffected. However, the experimental results do not conform to this behavior. Upon addition of Cl₂, V_{oc} actually decreases (see Fig. 13). This could be attrib-

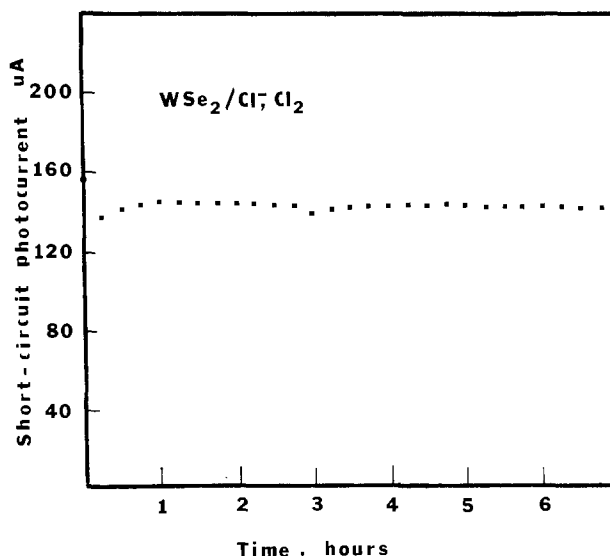


Fig. 14. Short-circuit photocurrent of WSe₂/Cl⁻ (1.9M), Cl₂/Pt PEC cell as function of time. Electrode area, 0.015 cm².

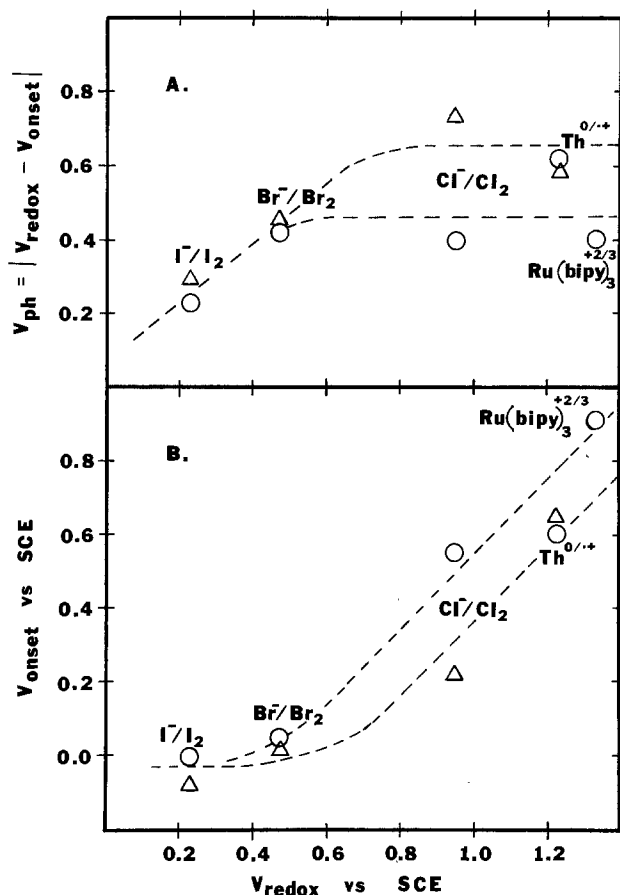
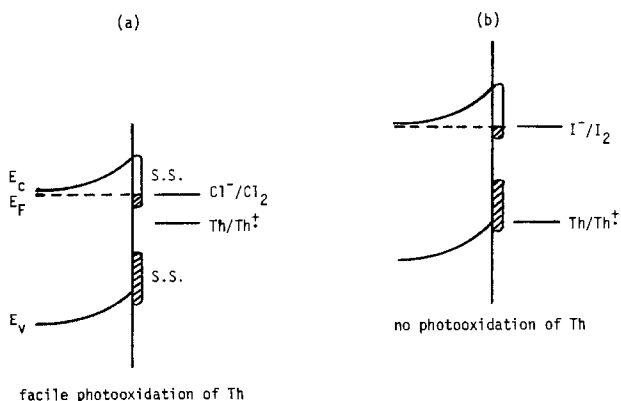


Fig. 15. (a) Comparison of photopotentials developed at type S (O) and type E (Δ) WSe_2 electrode for several redox couples in MeCN. (b) Comparison of onset potential of photocurrent at type S (O) and type E (Δ) electrodes for several redox couples in MeCN.

uted to a higher surface recombination rate at the higher Cl_2 concentration.

The shift in onset potential for Th oxidation at the type E electrode in the presence of Cl^- can also be explained by Fermi level pinning as shown in Scheme I (a). As the applied potential is biased in a positive direction, Cl_2 is initially generated and the Fermi level is pinned at the redox potential of Cl_2/Cl^- or, more likely, somewhat between the V^0 's of the two redox couples. The result should be a more negative onset potential for thianthrene oxidation as is observed in Fig. 10. I^-/I_2 does not affect the onset potential for thianthrene oxidation, since at the potential where the Fermi level is pinned, i.e., at the standard potential of I^-/I_2 , the valence bandedge and the bottom surface



Scheme I. E_C , conduction bandedge; E_F , Fermi level; E_V , valence bandedge; S.S., surface state.

states are well beyond the potential of $\text{Th}^{0/+}$ [see Scheme I (b)].

Conclusion

The results presented here indicate that the surface morphology of WSe_2 single crystals is a critical factor in determining their performance characteristics in photoelectrochemical cells. Both the photocurrent and photovoltage are dependent on the discontinuities in the surface plane. The application of layer-type semiconductors toward efficient solar conversion devices will depend on the ability to passivate recombination centers located at these surface discontinuities. Halide pretreatment can improve the photoresponse for the oxidation of thianthrene. Surface pretreatments with other electron-donating species may passivate recombination to a larger degree and is under investigation. The correlation of the density of surface states (surface discontinuities) with the observed photopotential lends support to the role of Fermi level pinning (2). Further results are required before an unambiguous relationship can be drawn between the density of surface states and the observed photopotential.

The stability and efficiency of the nonaqueous $n\text{-WSe}_2/\text{Cl}^-$, Cl_2/Pt photovoltaic cell confirm the original predictions of Tributsch (5a) on the performance of layered materials.

Acknowledgment

The assistance of Dr. Michael Schmerling in obtaining the electron micrographs is gratefully appreciated. This work was supported by the National Science Foundation, the Office of Naval Research, and by the Solar Energy Research Institute (in a cooperative project with SumX Corporation).

Manuscript submitted Aug. 19, 1980; revised manuscript received Dec. 1, 1980.

Any discussion of this paper will appear in a Discussion Section to be published in the December 1981 JOURNAL. All discussions for the December 1981 Discussion Section should be submitted by Aug. 1, 1981.

Publication costs of this article were assisted by The University of Texas.

REFERENCES

- H. Gerischer, in "Physical Chemistry: An Advanced Treatise," H. Eyring, D. Henderson, and W. Jost, Editors, Vol. 9A, Academic Press, New York (1970).
- (a) A. J. Bard, A. B. Bocarsly, F.-R.F. Fan, E. G. Walton, and M. S. Wrighton, *J. Am. Chem. Soc.*, **102**, 3671 (1980); (b) F.-R.F. Fan and A. J. Bard, *ibid.*, **102**, 3677 (1980); (c) A. B. Bocarsly, D. C. Bookbinder, R. N. Dominey, N. S. Lewis, and M. S. Wrighton, *ibid.*, **102**, 3683 (1980).
- (a) R. Memming and G. Schwandt, *Surf. Sci.*, **5**, 97 (1966); (b) R. A. L. Vanden Berghe, F. Cardon, and W. P. Gomes, *ibid.*, **39**, 368 (1973); (c) P. Kohl and A. J. Bard, *J. Am. Chem. Soc.*, **99**, 7531 (1977); (d) S. Frank and A. J. Bard, *ibid.*, **97**, 7427 (1975).
- (a) B. A. Parkinson, A. Heller, and B. Miller, *J. Appl. Phys.*, **33**, 521 (1978); (b) B. A. Parkinson, A. Heller, and B. Miller, *This Journal*, **126**, 954 (1979).
- (a) H. Tributsch, *Z. Naturforsch. Teil A*, **32**, 972 (1977); (b) H. Tributsch and J. C. Bennett, *J. Electroanal. Chem. Interfacial Electrochem.*, **81**, 97 (1977); (c) H. Tributsch, *Ber. Bunsenges. Phys. Chem.*, **81**, 361 (1977); (d) H. Tributsch, *ibid.*, **82**, 169 (1978); (e) H. Tributsch, *This Journal*, **125**, 1086 (1978); (f) H. Tributsch, H. Gerischer, C. Clemen, and E. Bucher, *Ber. Bunsenges. Phys. Chem.*, **83**, 655 (1979); (g) J. Gobrecht, H. Gerischer, and H. Tributsch, *This Journal*, **125**, 2085 (1978).
- L. F. Schneemeyer and M. S. Wrighton, *J. Am. Chem. Soc.*, **101**, 6496 (1979).
- L. F. Schneemeyer, M. S. Wrighton, A. Stacy, and

- M. J. Sienko, *Appl. Phys. Lett.*, **36**, 701 (1980).
8. L. F. Schneemeyer and M. S. Wrighton, *J. Am. Chem. Soc.*, Submitted.
 9. F.-R. F. Fan, H. S. White, B. Wheeler, and A. J. Bard, *J. Am. Chem. Soc.*, **102**, 5142 (1980); *This Journal*, **127**, 518 (1980).
 10. H. J. Lewerenz, A. Heller, and F. J. DiSalvo, *J. Am. Chem. Soc.*, **102**, 1877 (1980).
 11. W. Kautek, H. Gerischer, and H. Tributsch, *Ber. Bunsenges. Phys. Chem.*, **83**, 1000 (1979).
 12. N. E. Tokel-Takvoryan, R. E. Hemingway, and A. J. Bard, *J. Am. Chem. Soc.*, **95**, 6582 (1973).
 13. S. N. Frank, A. J. Bard, and A. Ledwith, *This Journal*, **122**, 898 (1975).
 14. A. R. Beal, W. Y. Liang, and H. P. Hughes, *J. Phys. C*, **9**, 2449 (1976).
 15. S. M. Ahmed and H. Gerischer, *Electrochim. Acta*, **24**, 705 (1979).
 16. G. Nagasubramanian and A. J. Bard, *This Journal*, **128**, 1055 (1981).

Semiconductor Electrodes

XXXIV. Photoelectrochemistry of p-Type WSe_2 in Acetonitrile and the p- WSe_2 -Nitrobenzene Cell

G. Nagasubramanian and Allen J. Bard*

Department of Chemistry, University of Texas at Austin, Austin, Texas 78712

ABSTRACT

The photoelectrochemical behavior of p-type WSe_2 single crystal electrodes in acetonitrile solutions containing a number of redox couples [e.g., N,N,N',N'-tetramethyl-p-phenylene diamine (+ 1/0), methyl viologen (+ 2/+1), nitrobenzene (0/-1), phthalonitrile (0/-1)] was investigated. For couples with potentials in the bandgap region (ca. -0.4 to +1.0V vs. SCE), a linear increase of the photopotential with V_{redox} was observed. Couples located at more negative potentials (i.e., above the conduction band edge) also showed a photoeffect, with the photopotential pinned at $\sim -0.95\text{V}$; this was ascribed to surface state pinning or inversion. A PEC cell of the form p- $\text{WSe}_2/\text{PhNO}_2$, MeCN/Pt is described. Treatment of the p- WSe_2 electrode with iodide was shown to improve the efficiency of such cells.

In the preceding paper, the behavior of n-type WSe_2 in acetonitrile (MeCN) solutions was discussed (1). WSe_2 and other layer-type semiconductor materials, first proposed by Tributsch for photoelectrochemical (PEC) applications (2), have been extensively investigated recently (3-8). The results with n- WSe_2/MeCN were consistent with a flatband potential of $\sim -0.3\text{V}$ vs. SCE and the existence of surface states which provide sites for surface recombination and lead to Fermi level pinning. Studies of p-type WSe_2 in MeCN were undertaken to confirm the location of the band edges in WSe_2 and to ascertain if the behavior of a number of redox couples at this material was consistent with a pinning model.

A second goal of this work was the construction of a PEC cell for conversion of solar to electrical energy utilizing this material. Past research involving PEC cells in nonaqueous solvents such as MeCN have shown that while high stability can often be attained in such systems, the maximum light intensities that can be utilized are often limited by the low concentrations of the electroactive materials in the solution (9). However, nitrobenzene (PhNO_2) is miscible in all proportions with MeCN and should be a reasonable oxidant at a p-type semiconductor electrode. Cells with p- WSe_2 and PhNO_2 which appear stable and show monochromatic efficiencies $\sim 4\%$ are described here.

Experimental

Chemicals.—Nitrobenzene (PhNO_2) was purified following the procedure of Marcoux *et al.* (10). PhNO_2 was first passed through an activated alumina column and then vacuum distilled. MeCN was purified as previously described (11). The other redox couples were purified by recrystallization. All compounds were stored inside a helium-filled Vacuum Atmosphere Cor-

poration (Hawthorne, California) glove box. Polargraphic grade, tetra-n-butyl ammonium perchlorate (TBAP), dissolved and recrystallized from ethanol, thrice, and dried under vacuum ($<10^{-5}$ Torr) for 3 days was used as supporting electrolyte. The cell employed was a conventional single compartment cell of 25 ml capacity containing the p- WSe_2 , a Pt working and counterelectrode and a quasi-reference electrode, which was an Ag wire immersed inside the solution and separated from it by a medium-porosity glass frit. The potential of this electrode was checked against an aqueous saturated calomel electrode (SCE) at regular intervals and was found to be constant. All potentials, unless specified otherwise, are given in V vs. SCE.

The p- WSe_2 single crystal generously donated by Dr. B. Miller and Dr. F. DiSalvo, Bell Laboratories, was used as the electrode. This was selected, after carefully verifying under microscope that the surface was quite free of exposed edges. A clean new crystal surface (\perp C-axis) was produced by attaching adhesive tape and peeling off the surface layer. Gold was electroplated on one side of the pellet and the contact was found to be ohmic. A copper wire lead for electrical contact was attached to the gold-coated side with silver epoxy cement (Allied Product Corporation, New Haven, Connecticut) and was subsequently covered with 5 min epoxy cement. The assembly was mounted into 7 mm diam glass tubing and was held in position with silicone rubber sealant (Dow Corning Corporation, Midland, Michigan), which also served as an effective seal against the seepage of electrolyte solution to the rear of the semiconductor electrode. The exposed area of p- WSe_2 was 0.05 cm^2 . The surface of the electrode was etched before use with 12M HCl for 5-10 sec and then rinsed thoroughly with distilled water and dried. The area of the Pt cylindrical wire, used as a counterelectrode, was 0.15 cm^2 .

* Electrochemical Society Active Member.

Key words: capacitance, voltammetry, solar cells.

A Princeton Applied Research (PAR) Model 173 potentiostat and PAR Model 175 Universal programmer were used in all experiments, with positive feedback iR -compensation employed to compensate for solution resistance and internal resistance of the electrode. The i - V curves were recorded on a Model 2000 X-Y recorder (Houston Instruments, Austin, Texas). In solar cell experiments, the photovoltage and photocurrent between the working electrode and counterelectrode as a function of load resistance were measured with a Keithley Model 179 TRMS Digital Multimeter. The light sources were an Oriol Corporation (Stamford, Connecticut) 450W xenon lamp and a 2-mW spectrophysics Model 132 He-Ne laser. Differential capacitance was measured with PAR Model HR8 lock-in amplifier. All of the solutions were prepared and sealed in the glove box and removed for the experiments.

Results

Capacitance plots.—The location of the band energies is often estimated from Schottky-Mott plots of $1/C^2$ vs. V , where C is the capacitance of the semiconductor electrode (assumed to be the space charge capacitance) and V is the electrode potential. A typical plot for p-WSe₂ in a 0.1M TBAP/MeCN solution at 10 Hz and 10 kHz is shown in Fig. 1. This behavior was essentially unaffected by the addition of PhNO₂ to the solution. Analysis of the plot yields a flatband potential, V_{FB} , of 0.9V vs. SCE and a doping level of 4×10^{18} cm⁻³. From this value and the bandgap energy, E_g of 1.4 eV, the location of the conduction and valence bandedge energies can be estimated, as shown in Fig. 2.

Cyclic voltammetry of various redox couples.—To study the effect of the redox couple in solution, on the behavior of p-WSe₂, the cyclic voltammetric (CV) response for a number of redox couples, in the dark and under illumination was investigated. The couples investigated and their standard potentials are shown in Fig. 2. From the location of the energy levels of these couples with respect to the bandedges, one would predict that a photocurrent for reduction could only be obtained for those with standard potentials in the range -0.4 to $+1.0V$ vs. SCE (e.g., TMPD/TMPD⁺), if the "ideal" model of the interface applied (12). With this model, dark oxidation of the reduced forms of the couples with potentials above the conduction bandedge ($< -0.4V$ vs. SCE), but not those in the gap, is expected. The experimental results for the different couples are summarized in Table I and details for some of these are discussed below. For TMPD (Fig. 3), a

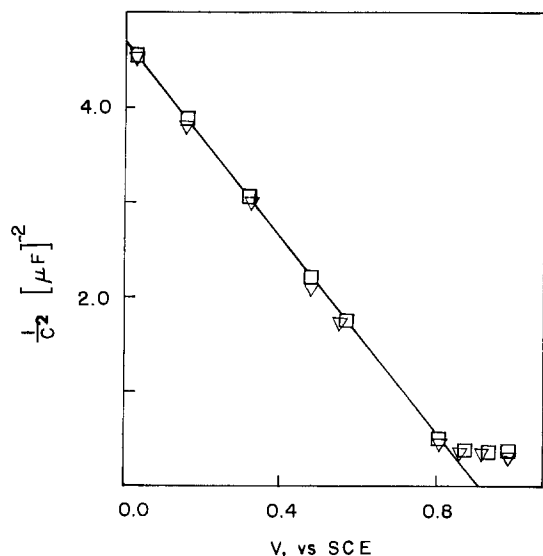


Fig. 1. Mott-Schottky plot of p-WSe₂ in MeCN containing 0.1M TBAP supporting electrolyte: (—□—□—) 10 kHz; (—▽—▽—) 10 Hz.

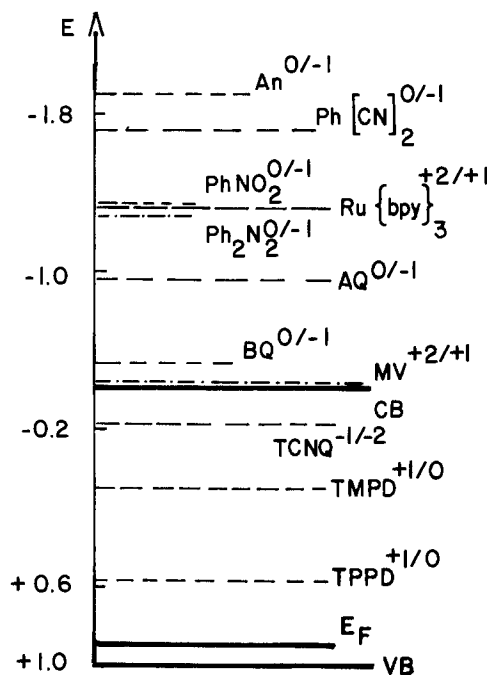


Fig. 2. Schematic representation of the energetic situation at p-WSe₂/solution interface along with V_{redox} of various redox couples investigated in this work. CB = conduction bandedge; E_F = Fermi level; VB = valence bandedge.

dark oxidation current, is observed beginning at $\sim +0.2V$ vs. SCE. The onset of photocurrent under chopped illumination, V_{on} , is $+0.55V$ which is negative of V_{FB} . Similarly for TTPD, a dark two-step oxidation at potentials only slightly more positive than at Pt is observed and V_{on} for the small photocurrent is $+0.55V$. While these results are consistent with the usual semiconductor electrode model, with the presence of some surface states in the gap region accounting for the dark oxidation at energies above E_V , the behavior for couples above E_C requires the assumption of Fermi level pinning (13) or inversion (14). Consider the behavior of the PhNO₂ couple at p-WSe₂. The photoelectrochemical behavior was a function of both the con-

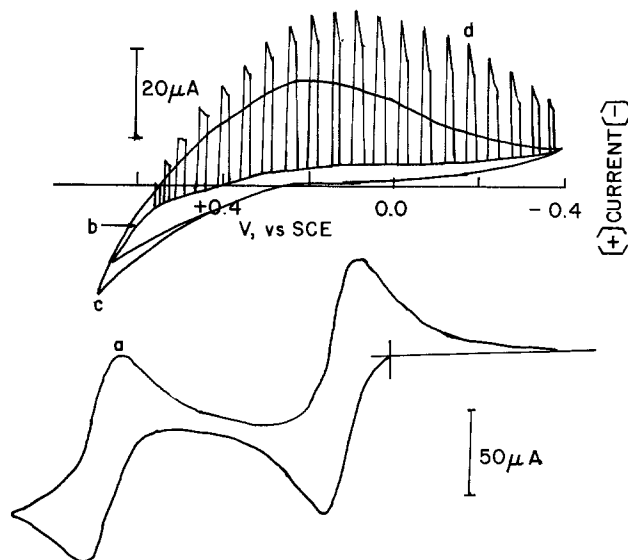


Fig. 3. Voltammetric curves on Pt and p-WSe₂ in MeCN solution containing 2.0 mM TMPD, 0.1M TBAP (supporting electrolyte). Light source 450W Xe lamp. Scan rate 20 mV/sec. (a) Cyclic voltammogram at Pt. (b) Dark voltammetric curve on p-WSe₂. (c) Voltammetric curve on p-WSe₂ under continuous illumination. (d) Current-potential characteristics under chopped light on p-WSe₂.

Table I. Voltammetric data and onset potential of photocurrent*

| Redox couple** | V_{redox} (V vs. SCE) | V_{on} (V vs. SCE) | $V_{ph} =$ $ V_{redox} - V_{on} $ |
|---------------------------------------|----------------------------|-------------------------|--------------------------------------|
| An(0/-1) | -1.90 | -0.95 | -0.95 |
| Ph(CN) ₂ (0/-1) | -1.72 | -0.85 | -0.87 |
| PhNO ₂ (0/-1) | -1.33 | -0.40 | -0.93 |
| Ph ₂ N ₂ (0/-1) | -1.28 | -0.34 | -0.94 |
| BQ(-1/-2) | -1.40 | -0.44 | -0.96 |
| Ru(bpy) ₃ (+2/+1) | -1.30 | -0.35 | -0.95 |
| AQ(0/-1) | -0.96 | 0.00 | -0.96 |
| BQ(0/-1) | -0.53 | +0.38 | -0.91 |
| MV(+2/+1) | -0.43 | +0.52 | -0.95 |
| TCNQ(0/-1) | -0.23 | +0.54 | -0.77 |
| TMPD(+1/0) | +0.11 | +0.53 | -0.44 |
| TPPD(+1/0) | +0.58 | +0.55 | -0.03 |

* V_{on} is defined as the potential at which 1% of maximal photocurrent is observed.

** Abbreviations: An = anthracene; Ph(CN)₂ = phthalonitrile; PhNO₂ = nitrobenzene; Ph₂N₂ = azobenzene; BQ = benzoquinone; Ru(bpy)₃ = ruthenium 2,2'-bipyridine; AQ = anthraquinone; MV = methyl viologen; TCNQ = tetracyanoquinone dimethane; TMPD = N,N,N',N'-tetramethyl-p-phenylene diamine; TPPD = N,N,N',N'-tetraphenyl-p-phenylene diamine.

centration of PhNO₂ and that of PhNO₂⁻. A cyclic voltammogram of PhNO₂ (0.2M) in MeCN at a Pt electrode (0.15 cm² area) (Fig. 4) shows the well-known wave for the reduction to the radical anion at -1.33V vs. SCE while only a small reduction current is found in the dark at p-WSe₂ (Fig. 4b); a small photocurrent is observed during the first scan (Fig. 4c). This photocurrent greatly increases during the second and subsequent scans under continuous illumination (Fig. 4d).

Clearly the presence of PhNO₂⁻ in the solution greatly enhances the photocurrent for the reduction as illustrated in Fig. 5 where the effect of chopped illumination in a solution in which anion radicals were generated at the Pt electrode by the passage of 0.27 and 2.3C, is

demonstrated. The effect of concentration of PhNO₂⁻ (produced by electrogeneration) on the limiting cathodic photocurrent is shown in Fig. 6a. The photocurrent rises sharply at PhNO₂⁻ concentrations up to 0.019 mM and then essentially levels off.

The concentration of PhNO₂⁻ at which this leveling off occurs depends somewhat on the PhNO₂ concentration. The magnitude of the maximum photocurrent at a given concentration of radical anion depends on the PhNO₂ concentration as shown in Fig. 6b. At low concentrations of PhNO₂, the current is limited by mass transfer of PhNO₂ to the electrode surface. At higher concentrations, the current saturates at a level governed by the light intensity. For irradiation with the full unfocused output of the 450W xenon lamp, this saturation

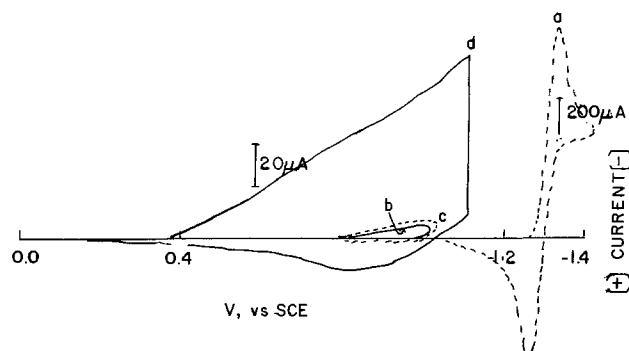


Fig. 4. Voltammetric curves of Pt and p-WSe₂ in MeCN solution containing 0.2M PhNO₂ and 0.1M TBAP supporting electrolyte. Scan rate 50 mV/sec. Light source, 2.0 mW He-Ne laser. (a) Cyclic voltammogram of the reduction of PhNO₂ at Pt. (b) Dark voltammetric curve on p-WSe₂. (c) Voltammetric curve on p-WSe₂ under continuous illumination. (d) Scan in continuous illumination after (c).

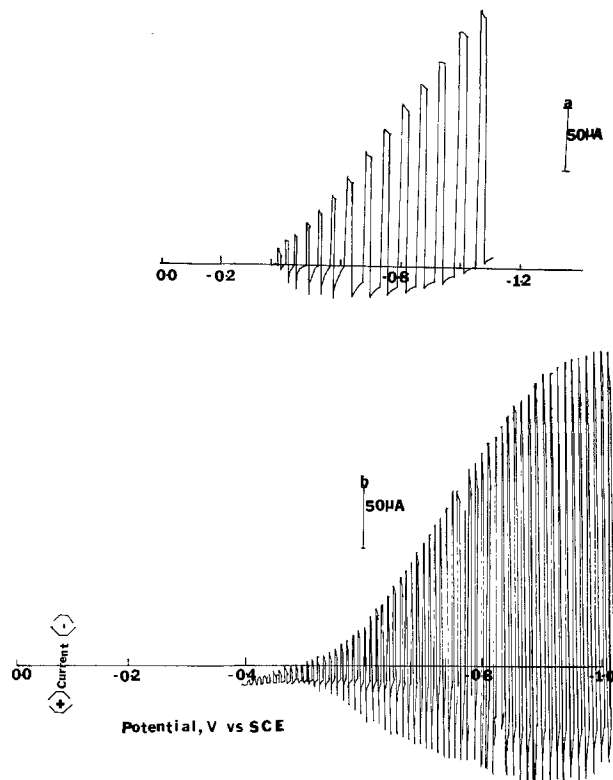


Fig. 5. Current-potential characteristics under chopped light on p-WSe₂ in MeCN containing 0.2M PhNO₂, 0.1M TBAP. Light source, 2.0 mW He-Ne laser. Scan rate 50 mV/sec. (a) After generating PhNO₂⁻ electrochemically by passing 0.27C. (b) After generating PhNO₂⁻ electrochemically by passing 2.30C.

tion occurred at ~0.2M PhNO₂. With PhNO₂ under these conditions, V_{on} was -0.4V vs. SCE; this represents reduction at potentials about 0.9V more positive than those at Pt.

For other couples with standard potentials corresponding to energies above E_C , similar photoeffects and underpotentials are observed (Table I). Note that with these V_{on} shifts more negative, as the standard potential becomes more negative so that the difference $V_{redox} - V_{on}$ is essentially constant at ~0.9V. Such behavior is characteristic of Fermi level pinning or in-

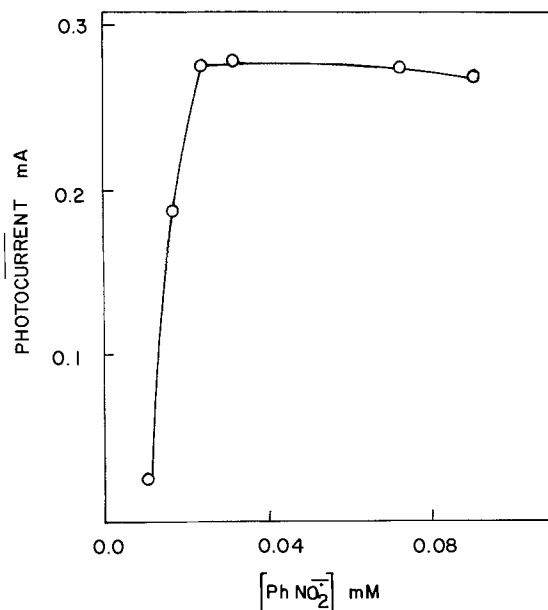


Fig. 6a. Plot of photocurrent as a function of PhNO₂⁻ in MeCN solution containing 0.2M PhNO₂ and 0.1M TBAP. Light source, 2.0 mW He-Ne laser.

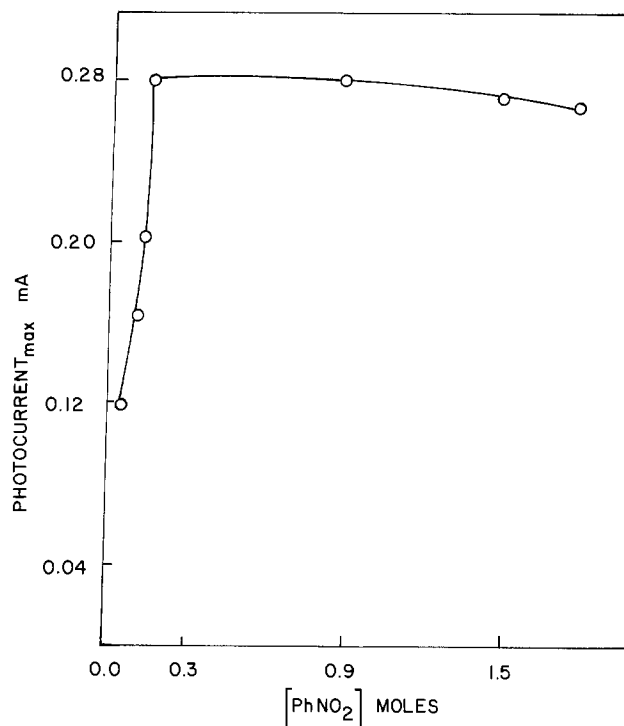


Fig. 6 b. Plot of maximum photocurrent vs. the concentration of PhNO_2 in MeCN. Light source 2.0 mW He-Ne laser. Supporting electrolyte, 0.1M TBAP.

version (13, 14). However, recall that couples at more positive potentials showed a relatively constant value for V_{on} , or a value of $V_{\text{redox}} - V_{\text{on}}$ which was a function of V_{redox} . The behavior for all the couples is illustrated in Fig. 7 and discussed below.

p-WSe₂/PhNO₂, MeCN solar cells.—A number of electrochemical photovoltaic cells based on nonaqueous electrolytes have been described (9). A general problem found with such cells for possible application to

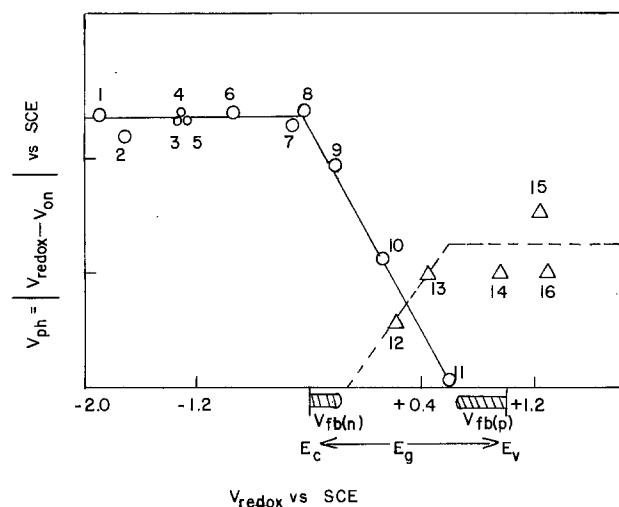


Fig. 7. Plot of $|V_{\text{redox}} - V_{\text{on}}|$ vs. V_{redox} for various redox couples employed in this study. 1 = Anthracene (0/-1); 2 = phthalonitrile (0/-1); 3 = nitrobenzene (0/-1); 4 = ruthenium 2,2'-bipyridine (+2/+1); 5 = azobenzene (0/-1); 6 = anthraquinone (0/-1); 7 = benzoquinone (0/-1); 8 = methyl viologen (+2/+1); 9 = tetracyanoquinone dimethane (+1/0); 10 = N,N,N',N'-tetramethyl-p-phenylene diamine (+1/0); 11 = N,N,N',N'-tetraphenyl-p-phenylene diamine (+1/0); 12 = iodide/iodine; 13 = bromide/bromine; 14 = chloride/chlorine; 15 = thianthrene (+1/0); 16 = ruthenium 2,2'-bipyridine (+3/+2). The values of V_{redox} and V_{on} for couples from 12 to 16 are taken from Ref. (1).

solar to electrical energy conversion is that the solubilities of the reduced or oxidized species in solution are low and mass transfer to either the semiconductor or counterelectrode limits the current at levels appreciably below those corresponding to the incident radiation. Since PhNO_2 can be mixed in all proportions, with MeCN, and as shown in Fig. 6, its concentration can be adjusted so that the saturation current is controlled by the light flux, photoelectrochemical cells of PhNO_2 and p-type semiconductors in nonaqueous solutions are particularly interesting. A two-electrode cell containing a p-WSe₂ photocathode and a Pt gauze (40 cm² area) counterelectrode immersed in a MeCN solution

containing 0.2M PhNO_2 and 0.019 mmoles PhNO_2^- was fabricated. The *i-V* characteristics of such a cell obtained with different load resistances is shown in Fig. 8a. The open-circuit photovoltage was 0.56V and the short-circuit photocurrent was 0.11 mA. From this plot, the fill factor was computed to be 0.56. With this value of fill factor, the overall optical to electrical energy conversion was ~2.0%. The photocurrent as a function of time is shown in Fig. 9. The photocurrent was fairly stable for at least 3 hr, at which time the experiment was terminated. The relatively low efficiency of the cell suggests that recombination processes at the p-WSe₂ surface (e.g., the oxidation of photogenerated

PhNO_2^-) are important. Previous studies of n-WSe₂ have shown that exposed edges on the van der Waals surface of the electrode act as such recombination centers and that treatment with I^- or other halide ions appears to passivate these edges (1). Such an iodide treatment is also effective in improving the performance of the p-WSe₂ cell. If the p-WSe₂ electrode is immersed for ~45 sec in MeCN solution of 4 mM tetra-n-butylammonium iodide (TBAI), then removed, rinsed with MeCN, and immersed into the solar cell

containing 0.2M PhNO_2 and 0.019 mM PhNO_2^- , a much higher photocurrent is observed (vide Fig. 8a). Although the V_{oc} and fill factor are essentially unchanged, this increase in i_{sc} increases the maximum power efficiency (monochromatic) to 4.1%. The effi-

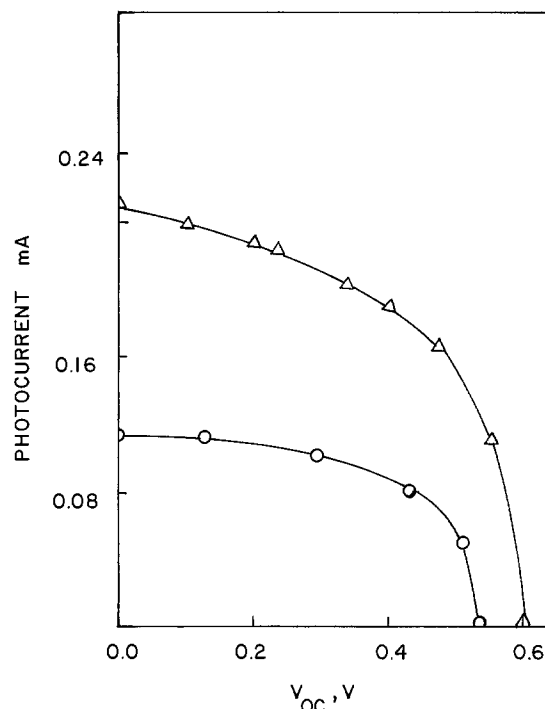


Fig. 8 a. Photocurrent-photovoltage characteristic of the cell p-WSe₂/MeCN, 0.2M PhNO_2 , 0.019 mM PhNO_2^- /Pt. Irradiation source, 2.0 mW He-Ne laser. (— ∇ — ∇ —): The electrode was pretreated with 4 mM I^- in MeCN. (— \circ — \circ —): Not pretreated with iodide.

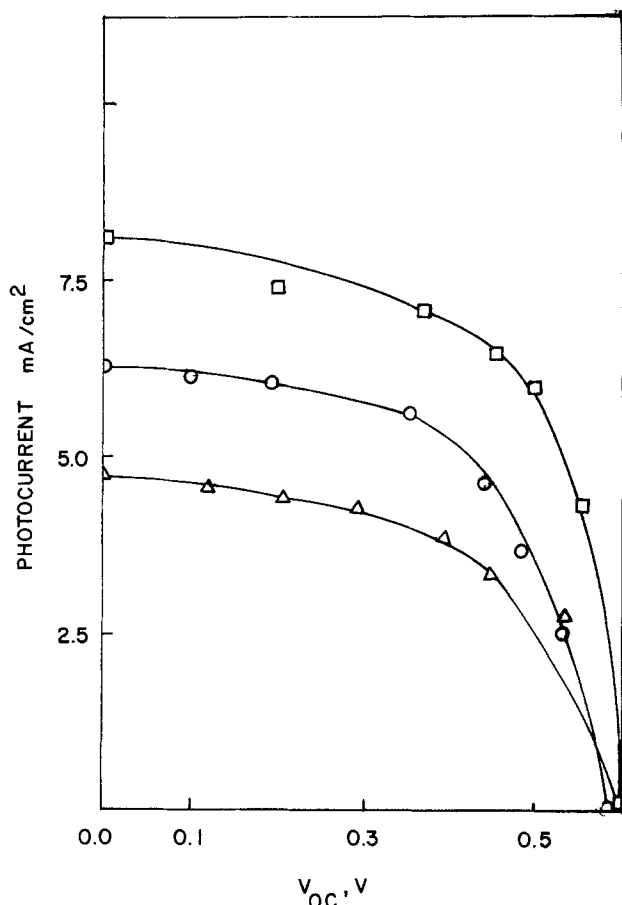


Fig. 8 b. Photocurrent-photovoltage characteristic of the cell p-WSe₂/MeCN, 0.2M PhNO₂, 0.02 mM PhNO₂⁻/Pt. Irradiation sources: (i) 450W Xe lamp with 590 nm cut-on filter. (—□—□—): The electrode treated with 4 mM I⁻ in MeCN. (—△—△—): not treated with iodide. (ii) Direct sun: at Austin, Texas, around noon, in July 1980. (—○—○—): Treated with 4 mM I⁻ in MeCN.

ciency is similarly increased by the direct addition of 3 mM TBAI to the MeCN/PhNO₂ solution in the cell.

The behavior of the PEC cell was also studied at higher light intensities by irradiation with the red-filtered light of a 450W xenon lamp or by direct sunlight. The variation of photocurrent and photovoltage

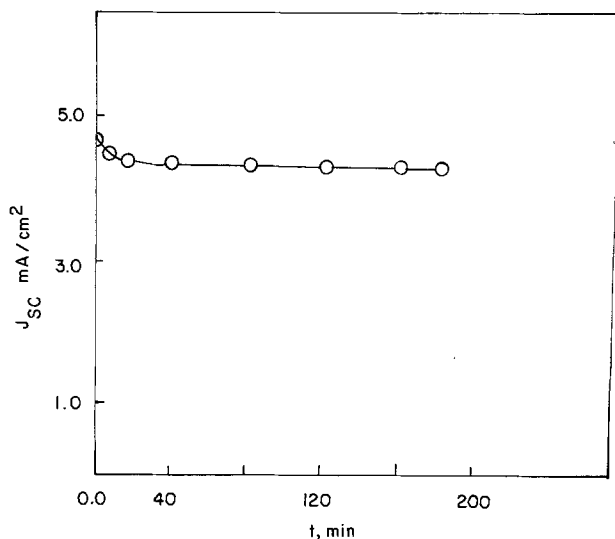


Fig. 9. Plot of photocurrent-output of the cell, p-WSe₂/MeCN, 0.2M PhNO₂, 0.02 mM PhNO₂⁻/Pt as a function of time. Irradiation source: 450W Xe lamp fitted with 590 nm cut-on filter.

as a function of light intensity is plotted in Fig. 10 for a MeCN solution containing 0.2M PhNO₂ and 0.02 mM

PhNO₂⁻. The photovoltage and photocurrent increased sharply at low light intensities, but became essentially saturated at higher intensities. Essentially, the same behavior was observed for solution containing 2.0M

PhNO₂/0.02 mM PhNO₂⁻ (Fig. 10) which suggests that the saturation of photocurrent at higher light intensities was not caused by limited mass transfer of PhNO₂ to the electrode. Hence, the cause of the saturation of short-circuit current is probably recombination at the p-WSe₂ surface. However, treatment with iodide (as in the previous case) produced higher photocurrents and removed the saturation effect. This treatment caused little change in the open-circuit photovoltages. The overall behavior of the intensity of the PEC cell at maximum red-filtered xenon lamp and in sunlight is shown in Fig. 8b. Note that as with irradiation with the He-Ne laser, treatment of the p-WSe₂ with iodide produces a higher photocurrent with only a marginal increase of fill factor and V_{oc}. The overall optical-to-electrical energy efficiency in full sun is ~2% with the iodide-treated electrode.

Discussion

The results of the photoelectrochemical experiments with the various redox couples, shown in Fig. 7, can be summarized as follows. The photopotential, V_{ph}, equal to V_{redox} - V_{on}, increases linearly with a slope near one, and then, at a potential near that corresponding to the conduction band edge (~ -0.4V vs. SCE), it levels off at a constant value near 0.95V. Note that this parallels the behavior found with n-WSe₂/MeCN (1), except that for the n-type material the maximum photopotential was smaller (~0.5V) and that the leveling off occurred at potentials about 0.5V negative of the

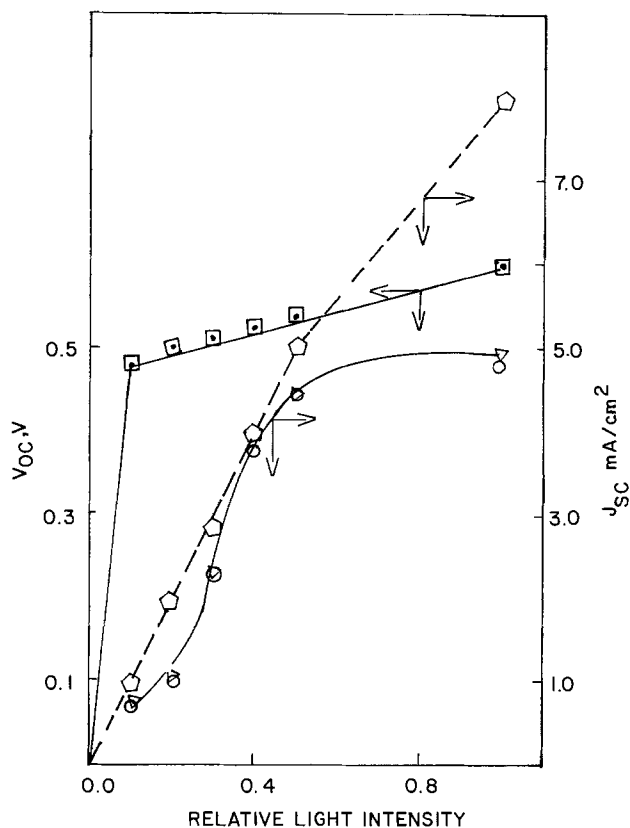


Fig. 10. Plot of V_{oc} and J_{sc} as a function of light intensity. Irradiation source 450W Xe lamp fitted with 590 nm cut-on filter. (—△—△—): 0.2M PhNO₂; 0.02 mM PhNO₂⁻. (—○—○—): 2.0M PhNO₂; 0.02 mM PhNO₂⁻. (◇—◇—): Treated with 4 mM I⁻ in MeCN. (—□—□—): Not treated with iodide. (—○—○—): Treated with 4 mM I⁻ in MeCN.

valence bandedge. The results with n-WSe₂ were consistent with the onset of Fermi level pinning (13) by surface states at energies about 0.5 eV above the valence band. The existence of such states as recombination centers could also explain the low values of V_{ph}

found with p-WSe₂ for TPPD⁺ (i.e., the fact that the line V_{ph} vs. V intersects at +0.6V rather than at V_{FB} for p-WSe₂). The leveling at negative potentials for p-WSe₂ could be ascribed to pinning by surface states just below the conduction bandedge, E_C . Such states were invoked to explain recombination in n-WSe₂/MeCN (1). However, because the onset of this pinning occurs at a potential very close to the V_{FB} value of n-WSe₂ (i.e., the conduction bandedge), the inversion model, proposed by Kautek and Gerischer (14) for n-type layered compounds could also apply. In both cases, the injection of electrons, either into surface states or at the surface at energies corresponding to E_C , causes the development of a negative surface charge which then causes changes in the potential drop across the Helmholtz layer. Thus, the pinning effect should occur in the presence of reductants of energies near or

above E_C . Recall that the addition of $PhNO_2^-$ greatly promoted the photoreduction of $PhNO_2$ at WSe₂, in agreement with this concept. The effect of the introduction of a reduced form with a redox level energy above E_C to shift the bandedges has been seen previously, e.g., in solvated electron production in liquid ammonia at p-GaAs (15), and with a number of couples at p-GaAs (16) and p-Si (17).

Acknowledgment

The support of this research by the Robert A. Welch Foundation and the Solar Energy Research Institute (in a cooperative project with SumX Corporation) is gratefully acknowledged.

Manuscript submitted Aug. 19, 1980; revised manuscript received Dec. 1, 1980.

Any discussion of this paper will appear in a Discussion Section to be published in the December 1981 JOURNAL. All discussions for the December 1981 Discussion Section should be submitted by Aug. 1, 1981.

Publication costs of this article were assisted by The University of Texas.

REFERENCES

- H. S. White, F.-R. Fan, and A. J. Bard, *This Journal*, **128**, 1045 (1981).
- (a) H. Tributsch, *Z. Naturforsch. Teil A*, **32**, 972 (1977); (b) H. Tributsch and J. C. Bennett, *J. Electroanal. Chem. Interfacial Electrochem.*, **81**, 97 (1977); (c) H. Tributsch, *Ber. Bunsenges. Phys. Chem.*, **81**, 361 (1977); (d) H. Tributsch, *ibid.*, **82**, 169 (1978); (e) H. Tributsch, *This Journal*, **125**, 1086 (1978); (f) H. Tributsch, H. Gerischer, C. Clemen, and E. Bucher, *Ber. Bunsenges. Phys. Chem.*, **83**, 655 (1979); (g) J. Gobrecht, H. Gerischer, and H. Tributsch, *This Journal*, **125**, 2085 (1978).
- L. F. Schneemeyer and M. S. Wrighton, *J. Am. Chem. Soc.*, **101**, 6496 (1979).
- L. F. Schneemeyer, M. S. Wrighton, A. Stacy, and M. J. Sienko, *Appl. Phys. Lett.*, **36**, 701 (1980).
- L. F. Schneemeyer and M. S. Wrighton, *J. Am. Chem. Soc.*, Submitted.
- F.-R. F. Fan, H. S. White, B. Wheeler, and A. J. Bard, *J. Am. Chem. Soc.*, **102**, 5142 (1980); *This Journal*, **127**, 518 (1980).
- H. J. Lewerenz, A. Heller, and F. J. DiSalvo, *J. Am. Chem. Soc.*, **102**, 1877 (1980).
- W. Kautek, H. Gerischer, and H. Tributsch, *Ber. Bunsenges. Phys. Chem.*, **83**, 1000 (1979).
- P. A. Kohl and A. J. Bard, *This Journal*, **126**, 603 (1979), and references therein.
- L. S. Marcoux, J. M. Fritsch, and R. N. Adams, *J. Am. Chem. Soc.*, **89**, 5766 (1967).
- P. A. Kohl and A. J. Bard, *ibid.*, **99**, 753 (1977).
- H. Gerischer, in "Physical Chemistry: an Advanced Treatise," H. Eyring, D. Henderson, and W. Jost, Editors, Vol. 9A, Academic Press, New York (1970).
- A. J. Bard, A. B. Bocarsly, F.-R. F. Fan, E. G. Walton, and M. S. Wrighton, *J. Am. Chem. Soc.*, **102**, 3671 (1980).
- W. Kautek and H. Gerischer, *This Journal*, In press.
- R. E. Malpas, K. Itaya, and A. J. Bard, *J. Am. Chem. Soc.*, **101**, 2535 (1979).
- F.-R. F. Fan and A. J. Bard, *ibid.*, **102**, 3677 (1980).
- A. B. Bocarsly, D. C. Bookbinder, R. N. Dorniney, N. S. Lewis, and M. S. Wrighton, *ibid.*, **102**, 3683 (1980).

Technical Notes



Moderate Temperature Na Cells

II. Transition Metal Diselenide Cathodes

K. M. Abraham* and L. Pitts

EIC Laboratories, Incorporated, Newton, Massachusetts 02158

Recently we described (1) a moderate temperature rechargeable Na cell which operates at ~130°C and utilizes a β -Al₂O₃ solid electrolyte in conjunction with a transition metal disulfide cathode. In that study, we investigated the cathodic cycling behavior of TiS₂, VS₂, and Nb_{1.1}S₂. In our continuing search for suitable cathode materials for the moderate temperature Na cell (1-3), we have made a preliminary evaluation of the suitability of the diselenides, VSe₂ and TiSe₂ as rechargeable cathodes. Our findings are presented in

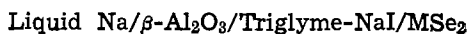
this paper. While there have been prior studies dealing with the structural chemistry of the Na intercalates of TiSe₂ and VSe₂ (4, 5), very little is known about the reversibility of the intercalation reaction. The available data on the structural chemistry of the Na intercalates of TiSe₂ and VSe₂ show that structural changes of the host lattice occur with Na intercalation. An understanding of the effects of these structural changes on cathode rechargeabilities in Na cells is of both scientific and practical interest. Vanadium diselenide has been shown to be a highly reversible cathode in secondary Li cells utilizing nonaqueous solvents (6, 7).

* Electrochemical Society Active Member.

Key words: secondary cell, diselenide cathodes, sodium anode.

Experimental

VSe₂ (99.8%) and TiSe₂ (99.8%), obtained from Cerac, Incorporated, Milwaukee, Wisconsin, were used without further treatment. Their x-ray powder pattern agreed quite well with literature data (6). The electrochemical cell incorporating a β-Al₂O₃ tube was of the same type described previously (1, 2). The metal selenide cathodes were fabricated in the form of pressed electrodes from a cathode mix consisting of ~50 weight percent (w/o) MSe₂, 40 w/o Shawinigan carbon (50% compressed), and 10 w/o Teflon, as described previously (1). The electrolyte was a 1M solution of NaI in 1,2-Bis(2-methoxy-ethoxy) ethane, (triglyme) (1). The assembled cell had the configuration

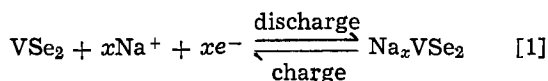


The cells were cycled galvanostatically after thermostating them at 130°C (1-3).

Results and Discussion

Na/VSe₂ cell.—The open-circuit voltage (OCV) of the cell at 130°C was 2.32V. A cell was discharged slowly (0.5 mA/cm²) to determine the capacity of the cathode and the shape of the discharge curve. Typical discharge curves are shown in Fig. 1. Initially, the cell rapidly polarized to 1.7V and the discharge proceeded with a voltage plateau at ~1.6V. The discharge showed a somewhat gradual but definite endpoint to 1.2V when a capacity equivalent to 1 Na/VSe₂ has been achieved. The cell exhibited 100% rechargeability in the first charge performed also at 0.5 mA/cm². With repeated cycling, the cathode utilization of ~1 Na/VSe₂ was maintained with 100% recharge efficiency. The cycling data for 24 cycles are shown in Table I. The cycling current from the fourth discharge onwards was maintained at 8 mA (1.0 mA/cm²) with very little effect on cathode utilization. In some discharges, when the lower cutoff voltage was reduced to 1.0V, an additional capacity was obtained with a second voltage plateau at ~1.15V. While the additional capacity in the lower plateau region was not recharged, the deep discharge did not effect the rechargeability of the capacity in the higher plateau region. Since the electrolyte does not reduce at this lower voltage plateau, the additional capacity may correspond to further discharge of VSe₂ as was observed in the lower voltage discharge of Li/VSe₂ cells (6, 7). We have not investigated this further.

The x-ray powder pattern of the VSe₂ cathode, cycled 24 times and terminated at the end of discharge, exhibited, among others,¹ lines at 7.76 and 6.86Å. These lines agree quite well with the c lattice parameters of Na_xVSe₂ compositions described by Bloembergen *et al.* (5). These authors have identified two structural types in Na_xVSe₂ for 0 < x ≤ 1. In the type I rhombohedral structure, found for 0.5 ≤ x ≤ 0.7, the lattice parameters, in the hexagonal description, were a = 3.48Å and c = 3 × 7.41Å. In the type II rhombohedral structure, found in Na_{1.0}VSe₂, the lattice parameters were a = 3.73Å and c = 3 × 6.88Å. In Na_xVSe₂ for 0.8 ≤ x ≤ 0.9 a mixture of both type I and type II structures was found. In the region 0 < x ≤ 0.5, a two phase mixture of VSe₂ and type I Na_xVSe₂ was present together. The x-ray data of our cycled cathode show the presence of Na_xVSe₂ compositions with both the type I and type II structures. The data indicate also that the cycling reactions involve Na intercalation and deintercalation as shown in Eq. [1]



¹ Many of the expected lines in the x-ray pattern were absent due to interference from the carbon and Teflon present in the electrode. Other lines observed were at 3.41, 3.01, 2.68, 2.63, 2.34, 2.08, and 2.0Å.

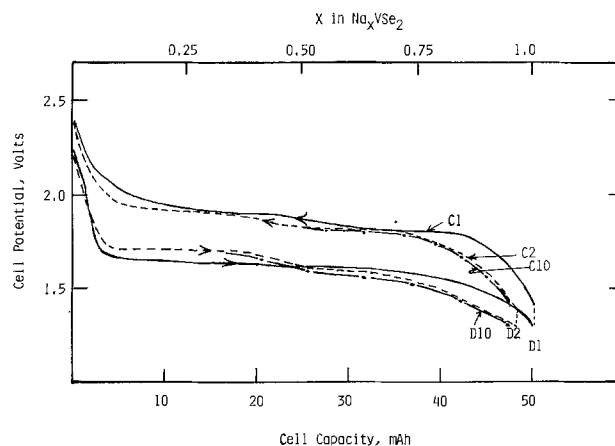


Fig. 1. Galvanostatic discharge and charge curves of the cell, liquid Na/β-Al₂O₃/triglyme, NaI/VSe₂ at 130°C. Curves D1, D2, and D10 are the 1st, 2nd, and the 10th discharges and curves C1, C2, and C10 are the corresponding charges. Current: 4 mA for the 1st and 2nd cycle; 8 mA for the 10th cycle.

A break in the discharge curve, which becomes more pronounced in the second discharge and thereafter, is observed at Na_{0.48}VSe₂. In agreement with the work of Bloembergen *et al.*, the first plateau in the discharge may correspond to the two phase region of VSe₂ and type I Na_xVSe₂. In the second plateau then, the discharge involves further Na intercalation into the Na_xVSe₂ phase(s) and both type I and type II phases may coexist at high values of x. Unlike the VS₂ cathode where the rechargeability was limited to the Na compositional range ~0.3 < x ≤ 1.0 (1), the VSe₂ cathode is reversible for the entire range of 0 < x ≤ 1.0. In Na_xVS₂, the phase at x < 0.3, is a second state compound in which Na occupies every other layer. The Na in this phase becomes irreversible as cycling continues. Such a phase is absent in Na_xVSe₂ and may explain the superior reversibility of VSe₂.

Preliminary data on the rate capability of VSe₂ was obtained from the potentiostatic discharge of a cathode held at 1.3V vs. Na⁺/Na. A capacity of 0.72 Na/VSe₂ was obtained at current densities ≥ 5.0 mA/cm². Since the present work was not aimed at optimization of cathode structure, rates considerably higher than these should be possible. The relatively high rate capability of the VSe₂ cathode in Li cells has already been reported (6).

Na/TiSe₂ cell.—The cell had an OCV of 2.29V at 130°C. Some typical discharge curves are shown in Fig. 2. To 1.1V cutoff, a capacity of 1 Na/TiSe₂ was obtained in the first discharge. The discharge at 0.5 mA/cm² proceeds in two distinct potential plateaus at ~1.75 and ~1.40V. A definite endpoint is reached

Table I. Cycling data for Na/VSe₂ cell at 130°C

| Cycle No. | Discharge* capacity | | Charge capacity | |
|-----------|---------------------|----------------------------------|-----------------|----------------|
| | mA-hr | Utilization, Na/VSe ₂ | mA-hr | % of discharge |
| 1 | 51.0 | 1.0 | 50.5 | 100 |
| 2 | 49.5 | 0.98 | 49.5 | 100 |
| 3 | 49.0 | 0.97 | 49.0 | 100 |
| 4 | 49.0 | 0.95 | 49.0 | 100 |
| 5 | 49.0 | 0.95 | 49.0 | 102 |
| 6 | 48.5 | 0.96 | 48.0 | 99 |
| 7 | 48.5 | 0.96 | 48.0 | 99 |
| 8 | 48.0 | 0.95 | 48.0 | 100 |
| 9 | 48.0 | 0.95 | 48.0 | 100 |
| 10 | 48.0 | 0.95 | 48.0 | 100 |
| 15 | 48.0 | 0.95 | 48.0 | 100 |
| 20 | 47.0 | 0.94 | 46.0 | 100 |
| 23 | 46.0 | 0.93 | 46.0 | 100 |
| 24 | 46.0 | 0.93 | — | — |

* Current: 4 mA (0.5 mA/cm²) for cycles 1-3.
: 8 mA (1.0 mA/cm²) for cycles 4-24.

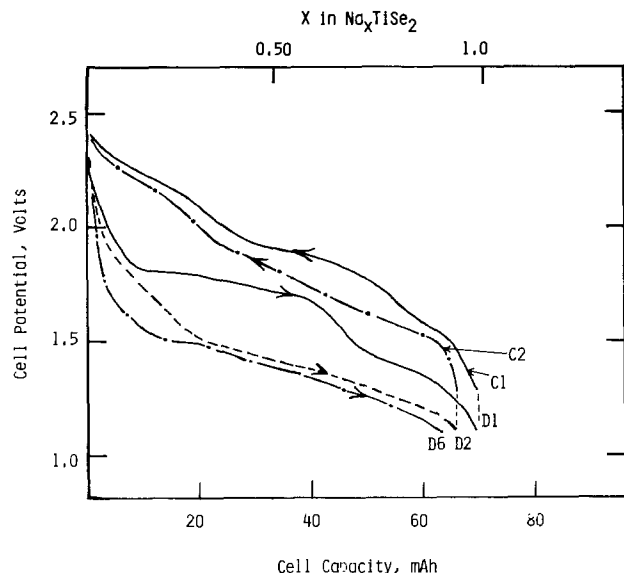


Fig. 2. Galvanostatic discharge and charge curves for the cell, liquid Na/ β -Al₂O₃/triglyme, NaI/TiSe₂ at 130°C. Curves D1, D2, and D6 are the 1st, 2nd, and the 6th discharges and curves C1 and C2 are the 1st and 2nd charges. Current: 4 mA.

after a capacity of 1 Na/TiSe₂. The recharge at 0.5 mA/cm² was 100% efficient in the first charge. The second and subsequent discharges, however, proceeded at lower potentials than in the first discharge, although the capacity in the sixth discharge was still 0.88 Na/TiSe₂ to 1.1V cutoff. Apparently, a structural change of the TiSe₂ host lattice occurs in the first cycle with very little change thereafter. X-ray powder pattern of cycled cathodes showed only broad patterns and no useful information regarding mechanisms of cycling reactions or structural changes during discharge was obtainable this way. Nevertheless, the

cycling data have demonstrated the reversibility of TiSe₂ in Na cells. The discharge of the cathode is accompanied by phase changes and a gross structural change of the host lattice apparently occurs after the first cycle.

In conclusion, we find that VSe₂ is useful as a rechargeable cathode for Na cells. It appears to be suitable for moderate rate applications. The specific energy of the Na/VSe₂ couple based on the observed cell voltage (1.6V) and capacity is 185 W-hr/kg. The performance of TiSe₂ is somewhat inferior to that of VSe₂.

Acknowledgment

This work was supported by The National Aeronautics and Space Administration, under Contract No. NAS3-21726.

Manuscript submitted Aug. 7, 1980; revised manuscript received Dec. 8, 1980.

Any discussion of this paper will appear in a Discussion Section to be published in the December 1981 JOURNAL. All discussions for the December 1981 Discussion Section should be submitted by Aug. 1, 1981.

REFERENCES

1. K. M. Abraham, L. Pitts, and R. Schiff, *This Journal*, **127**, 2545 (1980).
2. K. M. Abraham, R. D. Rauh, and S. B. Brummer, *Electrochem. Acta.*, **23**, 501 (1978).
3. K. M. Abraham, R. D. Rauh, and S. B. Brummer, in "Electrode Materials and Processes for Energy Conversion and Storage," J. D. E. McIntyre, S. Srinivasan, and F. G. Will, Editors, p. 985, The Electrochemical Society Softbound Proceedings Series, Princeton, N.J. (1979).
4. R. Brec, G. Ouvard, J. Ritsma, and J. Rouxel, *Rev. Chim. Miner.*, **13**, 348 (1976).
5. J. R. Bloembergen, R. J. Haange, and G. A. Wieggers, *Mat. Res. Bull.*, **12**, 1103 (1977).
6. M. S. Whittingham, *ibid.*, **13**, 959 (1978).
7. D. W. Murphy and J. N. Carides, *This Journal*, **126**, 349 (1979).
8. J. A. Wilson and A. D. Yoffe, *Adv. Phys.*, **18**, 193 (1969).

Anodic Oxidation of Polysilicon

Pier Luigi Buldini and Quintilio Zini

C.N.R. Istituto LAMEL, Via de' Castagnoli 1, 40126 Bologna, Italy

Donatella Ferri

Istituto Chimico, Facoltà di Ingegneria, Università di Bologna, Bologna, Italy

The electrical characteristics of semiconductor devices are primarily determined by the impurities incorporated into the body of the semiconductor and by their spatial distribution. The widest applied method for determining impurity profiles in semiconductor involves successive measurements following the removal of controlled amounts of semiconductor. Radio-tracer counting (1-2), differential sheet resistivity measurements (1, 3), or chemical methods (4-5) can be used in conjunction with the sectioning to determine the impurity profile.

Semiconductor oxidation followed by etching of the oxide is a very useful technique for sectioning. Removal by anodic oxidation is reproducible, practically does not cause impurity redistribution, and can be carried out in a simple cell without the necessity of any expensive facilities. Several papers appeared dealing with the variables affecting anodic oxidation of silicon (6-8). Due to increasing interest in polysilicon

technology, this paper makes a comparison between mono- and polysilicon anodic oxidation.

Experimental

Mechanically polished n- and p-type silicon slices of different resistivity and orientation were used. In order to obtain a significant comparison between mono- and polysilicon anodic oxidation, a number of slices having the same characteristics were selected from each of the ingots. A number of slices belonging to each selected group were analyzed for monocrystalline data and on the remaining slices, polysilicon was chemical vapor deposited and analyzed. Chemical vapor deposition was performed at 650°C with an hydrogen flux of 62 liters/min and a silane flux (5% in hydrogen) of 280 ml/min, if measured at room temperature and atmospheric pressure. For avoiding polysilicon inhomogeneities, 2000Å layers were deposited and their thickness was checked by masking a small side area in order to provide a reference surface and then measuring

the resulting step. Polysilicon grain size was found to be about 100Å.

The slices were carefully cleaned in trichloroethylene-acetone-methanol (9), and just before anodizing they were etched in 10% hydrofluoric acid for about 10 min, rinsed in running doubly distilled water, and blown dry. A 3000Å thick aluminum layer was evaporated onto the back of the wafer to ensure a good uniform electrical contact.

An Electronic Measurements, Incorporated, Regatron C633CM power supply, capable of delivering 300 mA at 500V, was used to power the cell. A projection lamp was used to provide sufficient and uniform intensity of illumination (15 mW cm^{-2}) of the sample. The cathode was a stainless steel ring situated as shown in Fig. 1 in order not to impede both the continual mixing of the solution and the illumination.

Anodization was carried out at constant current (corresponding to about 4 mA cm^{-2} of slice surface) and variable voltage in an electrolyte of ethylene glycol containing 0.05M potassium nitrate and 10% of water (4, 8). The cell was kept at room temperature ($20^\circ\text{--}23^\circ\text{C}$). The range of oxide layers grown were sufficient to consume 50–400Å of silicon.

After the predetermined net forming voltage was reached, the electrolyte was removed and the cell was rinsed in running doubly distilled water. The wafer surface was scrubbed lightly during the rinse to ensure complete removal of the ethylene glycol. Any ethylene glycol residues prevent uniform removal of the oxide. After the oxide removal as described below, the cell was again rinsed in doubly distilled water and blown dry. Another oxidation step could now take place. During multiple runs, the electrolyte was re-

jected after every oxidation in order to avoid changes in the electrolyte characteristics.

A method for accurately measuring the thickness of silicon removed during anodization was previously reported (4). The method is based on the spectrophotometric determination of silicomolybdc complex when reduced to molybdenum blue and in the described conditions it is not subject to phosphates interference.

Normal precautions for trace analysis were taken throughout and polyethylene vessels and volumetric equipment were exclusively used to avoid any silica contamination.

The oxide removal was obtained by pipetting 1 ml of 0.1M hydrofluoric acid onto the slice surface and after 10 min (in order to assure the complete dissolution of the oxide) 5 ml of sulfuric acid solution, containing 1.25 ml of concentrated sulfuric acid per 100 ml of solution, were added to the cell. The solution was then transferred to a polyethylene volumetric flask and the cell was washed 2–3 times with 5 ml of doubly distilled water each time, and these washings were transferred to the same flask. 5 ml of ammonium heptamolybdate solution, containing 1.6g $(\text{NH}_4)_6\text{Mo}_7\text{O}_{24}\cdot 4\text{H}_2\text{O}$ per 100 ml H_2O , were added to the flask and after 6 min (in order to assure a complete molybdosilicic acid formation) 5 ml of a 10 mg Fe(II) ml^{-1} reducing solution [prepared by dissolving 70g of iron(II) ammonium sulfate in 1000 ml of 1.25% sulfuric acid solution] and 5 ml of sodium fluoride solution, containing 2.4g NaF per 100 ml H_2O , were also added. After diluting to 50 ml with doubly distilled water, the absorbance of this solution was read at 828 nm against water. Spectrophotometric measurements were performed on a Perkin-Elmer Model 554 spectrophotometer.

A calibration curve was prepared by adding aliquots of standard silicon solution to 1 ml of 0.1M hydrofluoric acid solution and proceeding as above. The calibration curve is linear and reproducible from $10 \mu\text{g Si liter}^{-1}$ to $800 \mu\text{g Si liter}^{-1}$. The method permits determinations as low as $10 \mu\text{g Si liter}^{-1}$, with a standard deviation better than $\pm 4\%$. When using a cell having an anodization area of about 5 cm^2 (i.e., 25 mm diam), a thickness of 5Å of silicon can be determined. When using this method it is not necessary to remove the wafer from the cell, so it is possible to easily monitor the progress of the anodization from run to run.

To check the uniformity of oxidation and the removal of the surface layers, the physical profile of the treated surface was tested with a Talysurf 10 (Rank Precision Industries, Leicester, England); the obtained results agree within a few percent with those obtained via the chemical method.

Results and Discussion

The different rates for monocrystalline silicon anodic oxidation as a function of dopant type, resistivity, and crystalline orientation are shown in Fig. 2. Every reported datum represents the mean value with standard deviation of sixty analyses on each of 5–7 samples for net forming voltages of 50, 100, and 150V. Data obtained on "reference" monocrystalline slices (Fig. 2) and those coming from the deep oxidation of the monocrystalline substrate of the polysilicon samples (not shown) were found equal. It can be seen that crystalline orientation does not seem to influence the anodic oxidation, as previously reported (8), while the conductivity type and resistivity (especially for the n-type) do influence anodic oxidation rate.

Figure 3 shows a comparison between mono- and polysilicon anodic oxidation rates. In spite of the fact that the polycrystalline silicon is undoped, the substrate seems to influence anodic oxidation especially at low dopant concentrations. Reported data do not take in account the mono-/polysilicon interface zone, where the anodic oxidation shows intermediate char-

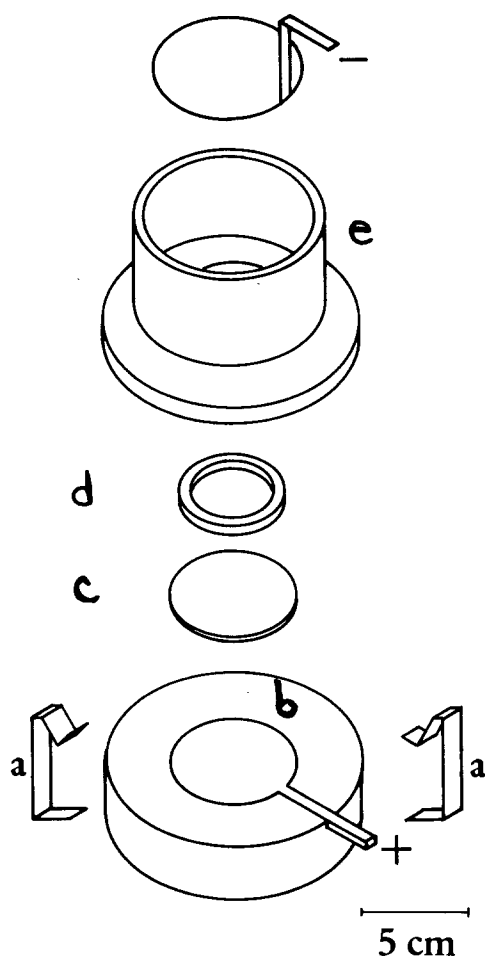


Fig. 1. Anodization cell (a—clamps, b—insulator, c—silicon slice, d—silicone packing, e—Plexiglas upper part of variable size according to the oxidized area).

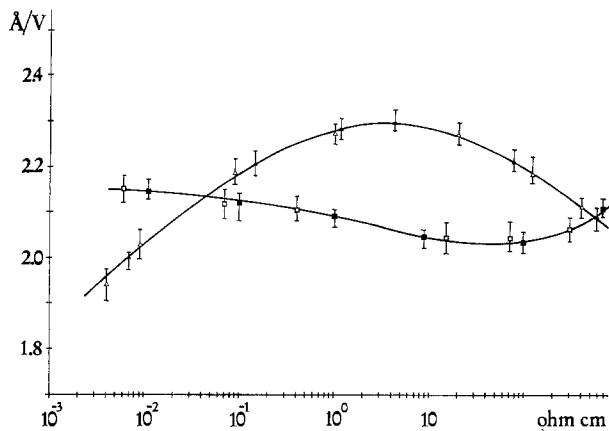


Fig. 2. n- and p-type monocrystalline silicon anodic oxidation rates: \blacktriangle n-type Si(111), \triangle n-type Si(100), \blacksquare p-type Si(111), \square p-type Si(100). Conditions as reported in the text.

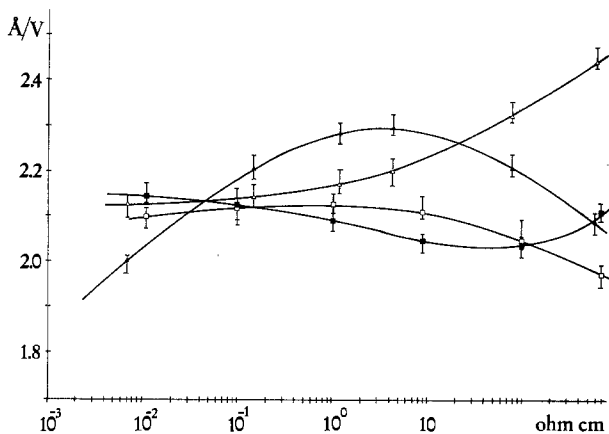


Fig. 3. n- and p-type monocrystalline and polycrystalline silicon anodic oxidation rates: \blacktriangle n-type Si(111), \triangle polysilicon on n-type Si(111), \blacksquare p-type Si(111), \square polysilicon on p-type Si(111). Conditions as reported in the text.

acteristics with respect to poly- and monocrystalline regions.

Another interesting feature, especially when performing automatic anodic oxidation, is the behavior of the initial drop voltage across the cell. Because the initial drop voltage depends on the electrolyte/wafer contact resistance, it is expected to increase with the wafer resistivity. This fact is confirmed for monocrystalline silicon, while polycrystalline silicon is influenced by the substrate resistivity and moreover shows the same behavior both on p- and n-type substrate. Figure 4 shows the initial voltage drop variation both for mono- and for polycrystalline silicon as a function of silicon resistivity.

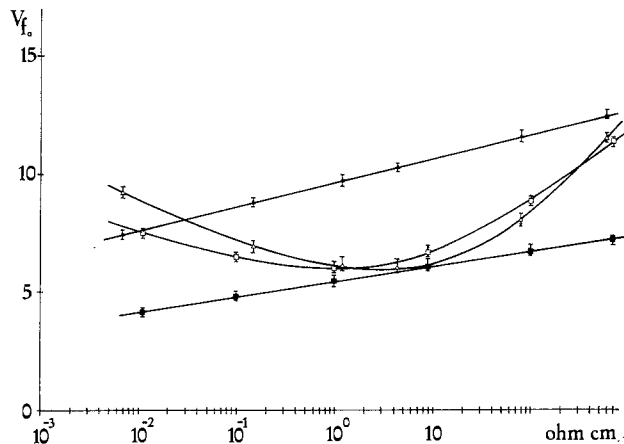


Fig. 4. n- and p-type monocrystalline and polycrystalline silicon initial drop voltage: \blacktriangle n-type Si(111), \triangle polysilicon on n-type Si(111), \blacksquare p-type Si(111), \square polysilicon on p-type Si(111). Conditions as reported in the text.

Preliminary results on amorphous silicon layers, obtained by B⁺ and P⁺ ion implantation at high dose on monocrystalline silicon, show a similar behavior with respect to polysilicon.

Acknowledgments

The authors wish to thank Prof. D. Nobili for his helpful discussions and the MOS Development Labs of SGS-ATES (Agrate Brianza, Italy), for supplying and checking polysilicon samples.

Manuscript submitted April 25, 1980, revised manuscript received Dec. 5, 1980.

Any discussion of this paper will appear in a Discussion Section to be published in the December 1981 JOURNAL. All discussions for the December 1981 Discussion Section should be submitted by Aug. 1, 1981.

Publication costs of this article were assisted by C.N.R. Istituto LAMEL.

REFERENCES

1. E. Tannenbaum, *Solid-State Electron.*, **2**, 123 (1961).
2. G. B. Larrabee and J. A. Keenan, *This Journal*, **118**, 1351 (1971).
3. R. A. Evans and R. P. Donovan, *Solid-State Electron.*, **10**, 155 (1968).
4. P. Lanza and P. L. Buldini, *Anal. Chim. Acta*, **104**, 139 (1979).
5. P. L. Buldini, D. Ferri, and P. Lanza, *ibid.*, **106**, 137 (1979).
6. G. C. Jain, A. Prasad, and B. C. Chakravarty, *This Journal*, **126**, 89 (1979).
7. H. D. Barber, H. B. Lo, and J. E. Jones, *ibid.*, **123**, 1404 (1976).
8. A. Manara, A. Ostidich, G. Pedrioli, and G. Restelli, *Thin Solid Films*, **8**, 359 (1971).
9. P. Lanza and P. L. Buldini, *Anal. Chim. Acta*, **85**, 69 (1976).



All Dry Lithography Processes and Mechanistic Studies with Poly(methacrylonitrile) and Related Polymers

H. Hiraoka*

IBM Research Laboratory, San Jose, California 95193

ABSTRACT

Poly(methacrylonitrile) and related polymers have been found to be uniquely suited for all dry lithographic processes. The polymer patterns are generated by thermal treatment followed by oxygen plasma removal. Poly(methacrylonitrile) and copolymer (acrylonitrile-methacrylic acid) yield patterns with positive tone, while poly(α -chloroacrylonitrile) provides negative tone patterns. Oxygen plasma etch rate differs for the exposed and the unexposed parts. The polymer patterns, after heat-treatment, become highly CF_4 plasma etch resistant, providing well-defined SiO_2/Si patterns. Thus, with 2 μm thick films of poly(methacrylonitrile) exposed to electron dose of 5×10^{-6} C/cm², 1.5-1.8 μm deep SiO_2/Si patterns are generated with high resolution by all dry processes; the resist patterns of 1.5 μm width, depth, and spacing are obtained at 5×10^{-6} C/cm² with the wall angle of 65°. Mechanistic studies including EPR, ESCA, and mass spectroscopic measurements were carried out to provide a mechanism.

A dry development process for photoresists and electron beam resists may be an attractive alternative to resists developed by wet methods from points of view including pollution, safety, high process yields, high throughput, and high resolution. Vapor development of poly(olefin sulfones) exposed to electron beams has been reported (1). It is also noted that even poly(methyl methacrylate) showed very shallow troughs after electron beam exposures at a dose of 10^{-4} C/cm² (2). Poly(olefin sulfones) and poly(methyl methacrylate) are, however, highly susceptible to plasma degradation and provide poor plasma etch resistance. They are, therefore, not suitable for all dry processes. Thermal development of poly(α -cyanoethylacrylate) has been reported (3); at a dose of 10^{-5} C/cm² remaining film thickness of developed areas was about 20% of original film thickness at 160°C. Complete development by oxygen plasma was not attempted, but the wall angle obtained with poly(α -cyanoethylacrylate) was shallow, 35°, making it unsuitable for high resolution work. Recently, Smith and his co-workers reported a plasma developable negative tone photoresist (4). Similarly, Penn reported dry development of a negative tone photoresist (5). However, the nature of their plasma developable photoresists has not been disclosed. Dry development of x-ray resists have also been reported recently (6).

I wish to report here that poly(methacrylonitrile), poly(α -chloroacrylonitrile), and related polymers provide resist patterns, after electron beam exposure, with high sensitivity and high resolution upon dry development. The dry developed resist patterns are highly resistant to CF_4 plasma etching to the same degree as cresol-formaldehyde novolac resin. They thus provide well-defined SiO_2/Si patterns (7). Furthermore, poly(methacrylonitrile) and copolymer (acrylonitrile-

methacrylic acid) can be made photosensitive to u.v. light by addition of photoactive compounds like 2,3,4-trihydroxybenzophenone-tris-[naphthoquinone-(1, 2)-diazide-(2)-5-sulfonate]. Their photoimages can be developed by dry methods, but they have only mediocre photosensitivity (8). EPR, ESCA, and mass spectroscopic studies have been carried out to understand the dry development processes for these materials.

Experimental

Polymeric materials.—Poly(methacrylonitrile) was obtained from Polysciences, Incorporated. Poly(α -chloroacrylonitrile) was prepared from the monomer using potassium persulfate as a catalyst (9). Copolymers of acrylonitrile-methacrylic acid and of acrylonitrile-methyl methacrylate were synthesized from the freshly distilled monomers using benzoyl peroxide as a catalyst.

Resist film preparations.—The polymers were dissolved in their suitable solvents; poly(methacrylonitrile) in cyclohexanone, the copolymers in 2-methoxyethanol, and poly(α -chloroacrylonitrile) in dimethylformamide. For lithographic studies, a photoactive compound like 2,3,4-trihydroxybenzophenone-tris-[naphthoquinone-(1, 2)-diazide-(2)-5-sulfonate], was added to the polymer solutions at concentrations up to about 20 weight percent (w/o) solid. The polymer films were spin-coated onto silicon wafers to a film thickness of 1-3 μm . The resist films of poly(methacrylonitrile) and of copolymer (acrylonitrile-methacrylic acid) were prebaked at 120°-130°C for 30 min, while the resist films of poly(α -chloroacrylonitrile) and copolymer (acrylonitrile-methyl methacrylate) were prebaked at 90°C for 20 min.

Electron beam exposures.—Electron beam exposures were carried out with a Vector Scan electron beam exposure system in our laboratory. For preliminary re-

* Electrochemical Society Active Member.
 Key words: polymers, plasma, etching, integrated circuits.

sults exposures were conducted with an ISI scanning electron microscope used in conjunction with a microammeter and a lab timer. For the mass spectroscopic studies a Varian Auger scanning electron gun was used at a current level of $5 \mu\text{A}$; mass spectra were taken with a UTI quadrupole mass analyzer (10). The gaseous products formed during the thermal treatments were studied with a Hitachi-Perkin Elmer mass spectrometer.

U.V.-light exposures.—U.V.-light exposures for photoimage generation were carried out with a medium pressure mercury lamp and a photomask which cuts off the shorter wavelength light below 3000\AA . The exposure times required for dry development appear to be 3-4 times longer than for the conventional wet development.

Thermal development.—Thermal development of the polymer patterns was carried out both in vacuum and in air at $150^{\circ}\text{--}200^{\circ}\text{C}$ for poly(methacrylonitrile), and at $100^{\circ}\text{--}200^{\circ}\text{C}$ for copolymer(acrylonitrile-methacrylic acid). The copolymer required much shorter times and lower temperature for thermal development than poly(methacrylonitrile). The presence of air during the thermal development did not influence the development at temperatures below 180°C . At higher temperatures some deterioration took place in unexposed parts of the resist films. The exposed samples were kept in air without any appreciable deterioration for a few weeks at room temperature prior to thermal development.

Plasma development and etching.—The wafers with thermally developed polymer patterns were placed in oxygen or CF_4 plasma; in the plasma the gas pressure was about 100 Pa, and the sample holder had a bias potential of -45V . After the plasma development, SEM pictures of polymer patterns were taken with an ISI Super II scanning electron microscope. For SiO_2/Si patterns the wafers with resist patterns were exposed to a CF_4 plasma for several minutes; then, the wafers were again exposed to an oxygen plasma to remove the remaining resist films. The SiO_2/Si patterns thus obtained were photographed with the SEM.

EPR study.—Powders of the polymer samples were sealed in a quartz tube in vacuum for EPR measurements. The electron beam exposures were carried out at liquid nitrogen temperature through a thin aluminum window with a Febetron, pulsed electron beam systems of Field Emission Corporation, which operated at 600 keV. The EPR spectra were taken with a spectrometer operating in the X band.

ESCA study.—ESCA measurements were carried out at room temperature under a vacuum better than 4×10^{-7} Pa using a Hewlett-Packard 5650B ESCA spectrometer which had resolution better than 1 eV. The samples were flooded with thermal electrons during the data collection to neutralize the charge effect. The reported binding energies were referenced to the $\text{Au}_{4f_{7/2}}$ transition at 83.9 eV used to calibrate the instrument.

Results

Lithographic Studies

Poly(methacrylonitrile).—Typical results obtained with poly(methacrylonitrile) are presented in Fig. 1. After electron beam exposures at doses of 1×10^{-5} , 5×10^{-6} , and 1×10^{-6} C/cm^2 , the wafers were heated at $155^{\circ}\text{--}200^{\circ}\text{C}$ for 20 min to 3 hr. Figure 1(a) shows the polymer patterns developed by 3 hr heating at 155°C , and Fig. 1(b) presents the polymer patterns obtained by 20 min heating at 200°C ; in both cases the electron beam dose was 5×10^{-6} C/cm^2 . These pictures demonstrate that the $1.5\text{--}2.8 \mu\text{m}$ deep polymer patterns were obtained from original film thicknesses of $2\text{--}3 \mu\text{m}$ without any appreciable thickness loss of the unexposed parts. Figure 1(a) reveals line patterns of

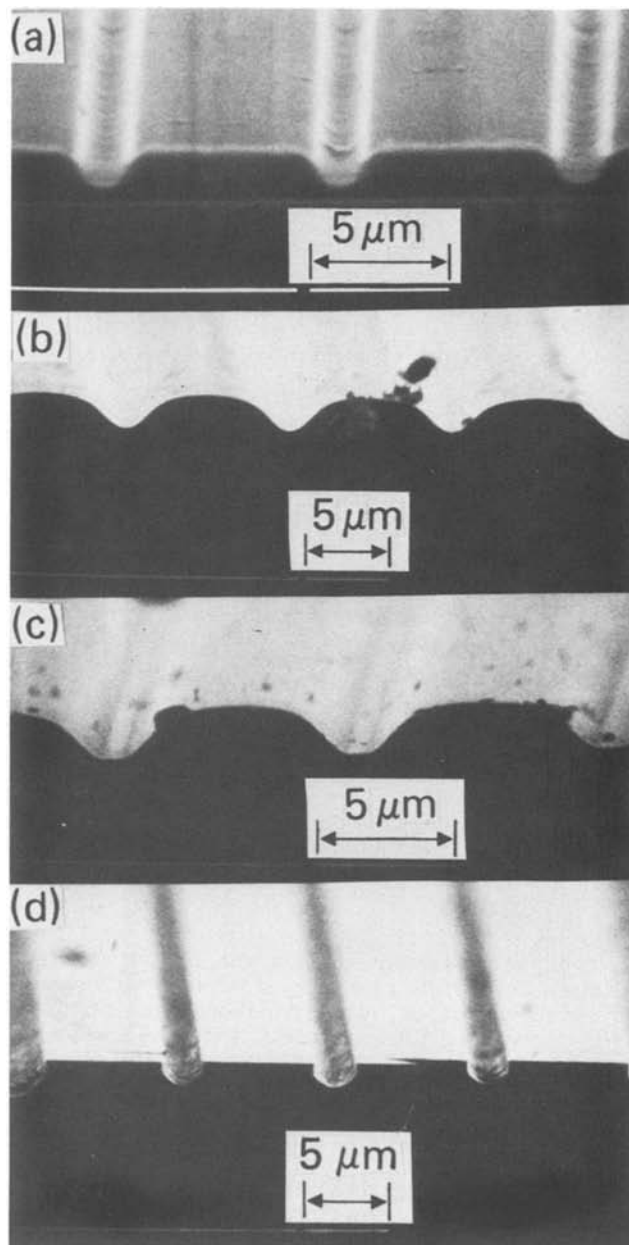


Fig. 1. (a) Thermally developed polymer patterns of poly(methacrylonitrile) after electron beam exposure at a dose of 5×10^{-6} C/cm^2 and heat-treatment at 155°C for 3 hr in vacuum; (b) the same as in (a) except heat-treatment at 200°C for 20 min; (c) oxygen plasma developed polymer patterns of (b); (d) SiO_2/Si patterns obtained by CF_4 plasma etching with (c).

$1.5 \mu\text{m}$ width and depth. Although the lines are $6 \mu\text{m}$ apart, this spacing may be reduced to about $1.5 \mu\text{m}$. The wall angle of the line patterns in Fig. 1(a) is 65° , while the wall angle in Fig. 1(b) is 45° . Clearly high temperature development loses resolution and wall angles. These wall angles obtained with poly(methacrylonitrile) in dry development were steeper than those shown in the SEM pictures reported previously with poly(α -cyanoethylacrylate) (3) and with the plasma developable negative working photoresist (4).

Wafers with thermally developed polymer patterns were placed in the oxygen plasma for about 5 min in order to completely develop the images. The resulting polymer patterns from the ones in Fig. 1(b) are shown in Fig. 1(c). The electron beam exposed area had 1.6 times faster oxygen plasma etch rate than the unexposed area. A similar observation was reported previously (11). The comparison of Fig. 1(b) with Fig. 1(c) indicates that there is no change in the wall angle after the oxygen plasma exposure.

In order to transfer polymer patterns to SiO₂/Si substrate layers, the wafers with completely developed polymer patterns were placed in the CF₄ plasma for about 20 min. In order to remove remaining polymer layers, the wafers were placed again in the oxygen plasma for about 5 min. The SiO₂/Si patterns thus obtained are shown in Fig. 1(d). From the loss of the polymer film thickness and the depth of the substrate patterns obtained the relative etch rate of the silicon to the polymer layers in the CF₄ plasma is calculated to be 1.3. In our CF₄ reactive ion etching condition with -500V bias potential the relative etch rate of the heat-treated poly(methacrylonitrile) to cresol-formaldehyde novolac resin is 1.2. Vertical walls of the SiO₂/Si patterns shown in Fig. 1(d) indicate that the polymer becomes highly etch resistant during the CF₄ plasma exposure.

With a higher dose of electron beams thermally developed polymer patterns have a steeper wall angle, as described in more detail with copolymer(acrylonitrile-methacrylic acid).

Poly(methacrylonitrile) yields positive acting polymer patterns upon conventional wet development after electron beam exposure and has a sensitivity of about 1×10^{-5} C/cm² (12). The wall profiles of the developed polymer patterns of poly(methacrylonitrile) were not vertical with either dry or wet development. This is also apparent in the x-ray exposed films (12).

With addition of a photoactive compound to poly(methacrylonitrile) the polymer films become u.v.-light sensitive. They can be developed in a completely dry process as shown in Fig. 2. Here, the photoactive compound used is a diester of dihydroxybenzophenone with 1,2-diazo-naphthoquinone-5-sulfonic acid. More recent experiments show that the triester is the best suited for this dry development, followed by the diester; the monoester is the least sensitive for the dry development. The photoactive compound was admixed as 20 w/o solid, and the mixture was dissolved in cyclohexanone. The dry developed photoresist is not very sensitive; it took exposure times four times longer than a conventional wet development of AZ 1350J.¹ The thermal image development was carried out at 200°C for 20 min, resulting in 0.5 μm deep patterns as shown in Fig. 2(a). The resulting polymer patterns were completely developed in an oxygen plasma.

These experimental results indicate that the photo-sensitivity for dry development is derived from decomposition of the photoactive compounds exposed to u.v. light. Insofar as host resins do not thermally flow or decompose and are CF₄ plasma etch resistant, any resin making uniform films with the photoactive compound may become a dry developable photoresist. AZ 1350J becomes a dry developable positive working photoresist when the resist films are heated at 180°C for 15 min. AZ 2400¹ did not develop polymer patterns even though the resist films were treated exactly in the same way as AZ 1350J. The difference between AZ 1350J and AZ 2400 is clearly due to different photoactive compounds used. When copolymer(acrylonitrile-methacrylic acid) is admixed with 2,3,4-trihydroxybenzophenone-tris-[naphthoquinone-(1,2)-diazide-(2)-5-sulfonate], the resist films become a dry developable positive tone photoresist like AZ 1350J and poly(methacrylonitrile) admixed with the photoactive compound.

Copolymer(acrylonitrile-methacrylic acid).—Three different monomer ratios were used for the copolymer synthesis; [acrylonitrile]/[methacrylic acid] = 0.13/0.87, 0.5/0.5, 0.65/0.35. The polymerization was carried out at 60°-65°C. The polymer formed was dissolved in 2-methoxymethanol, filtered, reprecipitated in cyclohexane. The resist films were spin-coated from a 2-methoxymethanol solution onto silicon wafers and prebaked at 130°C for 30 min prior to electron beam exposures.

¹ Shipley Company Trademark.

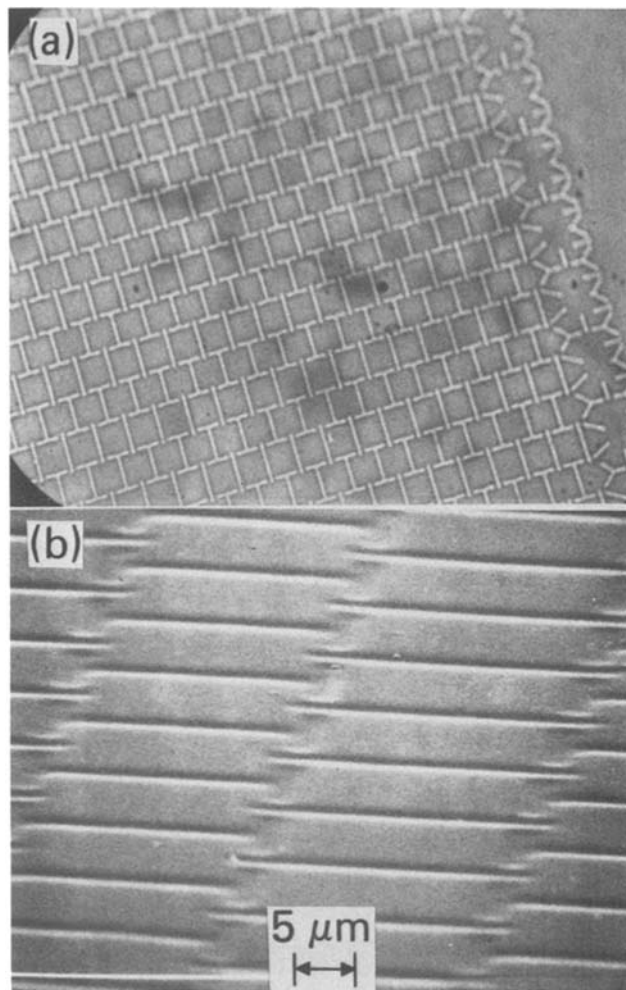


Fig. 2. All dry photolithography with a photo-sensitized poly(methacrylonitrile) which contains a diester of dihydroxybenzophenone with 1,2-diazo-naphthoquinone-5-sulfonic acid; (a) polymer patterns, (b) SiO₂/Si patterns obtained with (a).

Among the copolymers with three different monomer ratios the equimolar copolymer is found to be the best suited for dry development. The copolymer with the higher methacrylic acid fraction does not have sensitivity for dry development, while the copolymer with the excess acrylonitrile fraction tends to have thermal flow in dry development at 100°-200°C. The polymer patterns of the equimolar copolymer shown in Fig. 3 were developed by 10 min heating at 200°C in vacuum. A steep wall angle can be obtained at high electron beam dose but the angle decreases markedly with decreasing dose; 73° at 1×10^{-5} C/cm² [Fig. 3(a)], 45° at 5×10^{-6} C/cm² [Fig. 3(b)], 15° at 1×10^{-6} C/cm² [Fig. 3(c)]. The SiO₂/Si substrate patterns were generated from these polymer patterns in the same way as described for poly(methacrylonitrile).

A copolymer of methyl methacrylate and acrylonitrile with the acrylonitrile content below 14% is reported to have a high electron beam sensitivity for conventional wet development (13). We observed that this copolymer (methyl methacrylate-acrylonitrile) was not suited for all dry processes because the resist films cannot stand in the CF₄ plasma; besides, depth of the developed resist patterns was shallow, although the images were recognizable even at 1×10^{-6} C/cm² due to color change caused by thermal treatment at 150°C.

Poly(α -chloroacrylonitrile).—The resist films of poly(α -chloroacrylonitrile) gave negative working polymer patterns upon electron beam exposure and dry development. For a dose of 6×10^{-6} C/cm² of 25 keV electrons, this material yielded relief images of

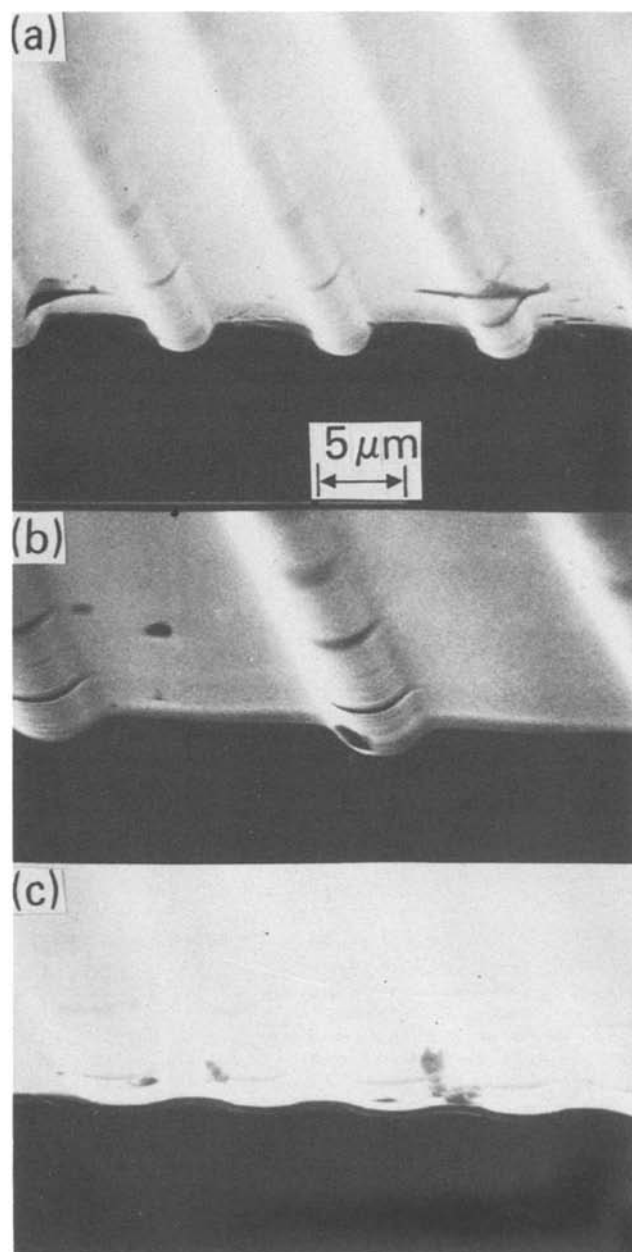


Fig. 3. Thermally developed polymer patterns of copolymer-(acrylonitrile-methacrylic acid) after heat-treatment at 200°C for 10 min; electron beam doses: (a) 1×10^{-5} C/cm², (b) 5×10^{-6} C/cm², (c) 1×10^{-6} C/cm².

0.5 μm height after post-baking at 150°C for 20 min in vacuum. With this relief image of the resist film subsequent CF₄ plasma etching gave SiO₂/Si patterns of 1.5 μm height, as shown in Fig. 4(a). This result indicates either relatively higher etch resistance in the exposed parts than in the unexposed parts, or stronger etch resistance of the resist films over SiO₂/Si substrates.

We have already reported our ESCA studies of structural changes of poly(α-chloroacrylonitrile) and poly(acrylonitrile) upon u.v.-light, heat, and electron beam exposures (14). In unexposed areas both unzipping and hydrogen chloride elimination reactions took place in the thermal development, while in the exposed areas the conjugated double bond polymer chains are already formed in electron beam induced reactions and unzipping reactions play only a minor role in the development. This difference causes the negative tone resist patterns in the thermal development of poly(α-chloroacrylonitrile).

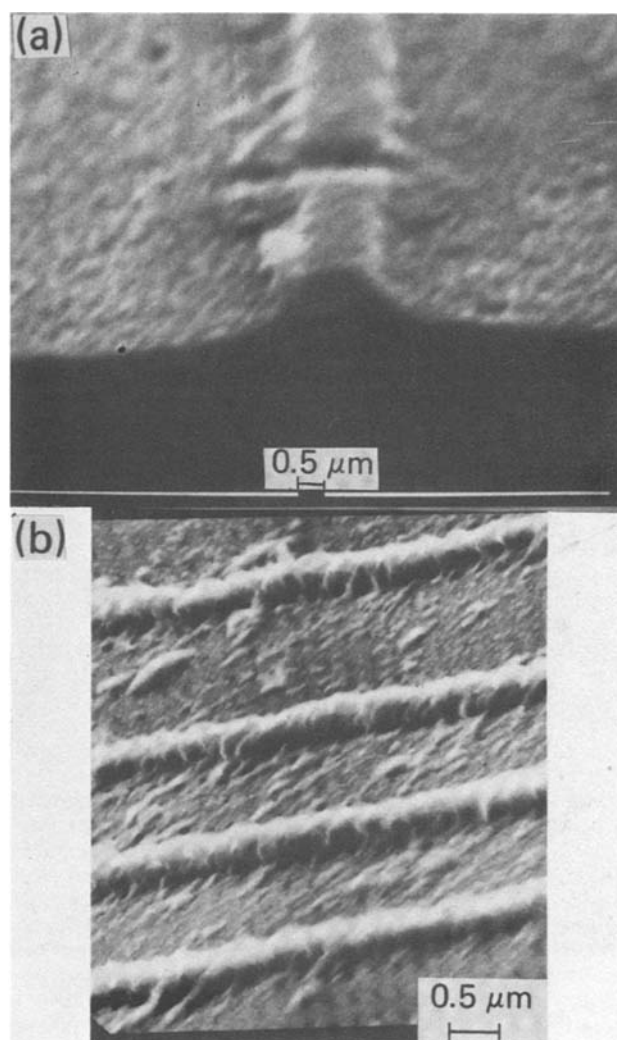


Fig. 4. (a) All dry processed SiO₂-Si patterns with poly(α-chloroacrylonitrile) after electron beam exposure at 6×10^{-6} C/cm², heat-treatment at 150°C for 20 min in vacuum, and subsequent oxygen and CF₄ plasma treatments; (b) polymer lines of poly(α-chloroacrylonitrile) after baking at 800°C for 40 min in vacuum; patterns were generated by wet development in aqueous acetone.

Poly(α-chloroacrylonitrile) also yields negative working images upon electron beam exposure and conventional wet development (15). Once polymer patterns were formed and post-baked, the lines are extremely stable upon thermal treatment because of the structural changes shown in the following

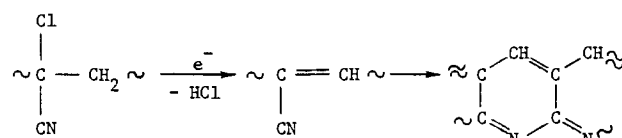


Figure 4(b) demonstrates that the polymer lines thus formed from poly(α-chloroacrylonitrile) are extremely stable even at 800°C. Such high heat resistance and consequent high etch resistance are the result of the conjugated ladder-type structure formed from poly(acrylonitrile) and related polymers (16).

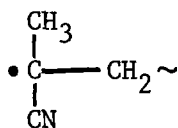
Mechanistic Studies

In order to understand the chemical reactions involved in the dry lithographic processes described in the preceding section, we have carried out some mechanistic studies using mass spectroscopy, EPR, and ESCA.

Mass spectroscopic study.—The gaseous products formed during electron beam exposure were studied with a UTI quadrupole mass spectrometer. The mass

spectrum obtained with poly(methacrylonitrile) is shown in the upper line of Fig. 5, while the lower line of Fig. 5 is the background spectrum; mass peaks at 57, 56, 55, 43, 41, 39 are contamination peaks due to cracked diffusion pump oil. Removal of H₂, CH₃, CN, and HCN have clearly been observed. A small amount of carbon dioxide formed may be due to contamination. The gaseous products formed from poly(α -chloroacrylonitrile) during electron beam exposure are H₂, HCl, CN, and HCN, as already described in our previous report (14).

EPR study.—The powder of poly(methacrylonitrile) was irradiated in vacuum with 600 keV electron beam pulses through an aluminum window at 77 K. The free radicals generated were studied at 77 K with an EPR spectrometer. The EPR spectrum obtained with poly(methacrylonitrile) at 77 K is shown in Fig. 6(a). The features of the spectrum can be simulated by superposition of a 6-line spectrum (10G bandwidth, 20.5G coupling constant) and a broad singlet (13G bandwidth), as shown in Fig. 6(b). The 6-line spectrum belongs to a tertiary free radical shown below



which has an unpaired electron coupled to five hydrogen atoms. The broad singlet spectrum is not due to trapped free electrons; the trapped electrons usually give a sharp singlet signal at $G = 2.0023$. Although its origin is not clear, it may belong to an unpaired electron attached to the cyano group. The electronegativity of cyano groups is well known. Unlike poly(methyl methacrylate), methyl radicals were not observed, indicating that the CH₃ scission from the main chain may not be important; the CH₃ peak found in the mass spectrum may be due to a fragmentation of monomeric products. As long as air was excluded from the sample, the free radicals having the EPR spectrum shown in Fig. 6(a) are fairly stable; the essential features of the spectrum did not change even if the sample were brought to room temperature.

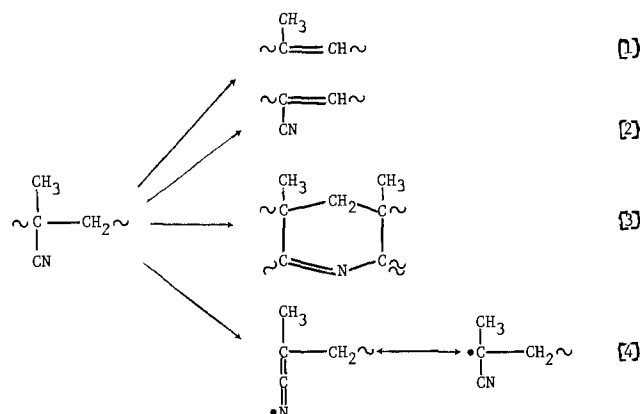
ESCA study.—ESCA measurements were carried out on thin films of poly(methacrylonitrile), which were exposed to electron beams, or u.v. light, and heat-treated. The core level signals of C_{1s} and N_{1s} are shown in Fig. 7 and 8, respectively. The exposure to u.v. light caused only small changes in the core level signals, as expected from the u.v.-absorption spectrum of the polymer. The u.v.-absorption spectra of the poly(methacrylonitrile) sensitized with the photoactive compounds show only the photo-bleaching of the sensitizer at 310-450 nm upon u.v.-light exposure. Electron beam exposures and heat-treatment, however, caused significant changes in both core level signals. Unexposed films of poly(methacrylonitrile) have two distinct C_{1s} core level signals at 286.5 and 285 eV, which belong to the carbon atom of the cyano group and to the main chain carbons and methyl group carbon, respectively. The loss of the cyano group carbon signal upon

electron beam exposure is clearly demonstrated by the C_{1s} core level signals. This is in agreement with the loss of HCN as previously described in the mass spectroscopy study. However, the removal of the cyano group as HCN must be a minor part of its total disappearance, based on the N_{1s} core level signal observed.

The displacement of the C_{1s} core level signals to a lower binding energy indicates an increased electron density on the carbon atom. This is consistent with the formation of olefinic linkages. Electron beam exposure also caused a shift of the N_{1s} core level signal peak to a lower binding energy, although the whole spectrum broadened. As was reported earlier for poly(acrylonitrile) and poly(α -chloroacrylonitrile) (14), the N_{1s} core level signal is shifted to a higher binding energy by 1.5 eV upon cyclization through cyano groups to yield —C=N— linkages. The observed lower binding energy shifts of both core level signals of C_{1s} and N_{1s} indicate enriched electron density on the nitrogen as well as olefinic linkage formation. Subsequent heating of the exposed polymer films caused the shift of the N_{1s} core level signal to higher binding energy as shown in Fig. 8, probably due to cyclization through the cyano groups, while little change of the C_{1s} core level signal of the exposed samples was observed upon subsequent heat-treatment. The broadening of the N_{1s} core level signal at higher energies upon electron beam exposure may indicate an electron beam-induced cyclization to a small degree.

Discussion

The overall reactions of poly(methacrylonitrile) upon electron beam exposure may be summarized below



Reaction [1], [2], and [3] may play only minor roles, and reaction [4] is probably the major reaction of poly(methacrylonitrile) upon electron beam exposure which would lead to an unzipping reaction upon heating. Reactions [1], [2], and [3] result in some residual resist layer in the thermally developed polymer patterns. In Fig. 1 this is about 10%-20% of the original resist thickness.

Different from poly(methacrylonitrile), electron beam exposure of poly(α -chloroacrylonitrile) causes elimination of hydrogen chloride from the main chain

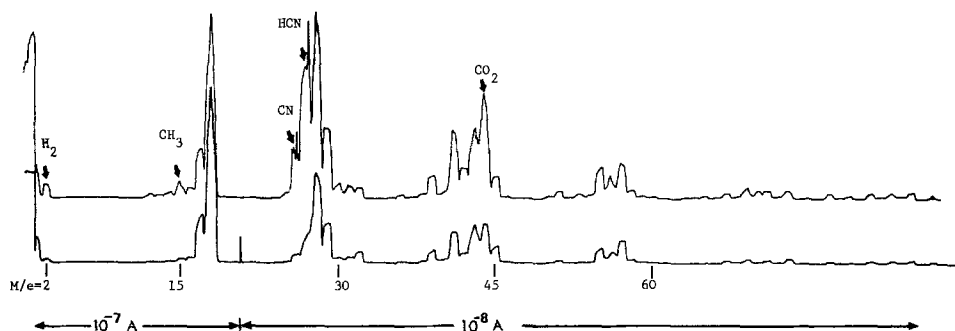


Fig. 5. Mass spectrum of gaseous products formed during electron beam exposure of poly(methacrylonitrile); the upper line is for products, and the background is shown by the lower line.

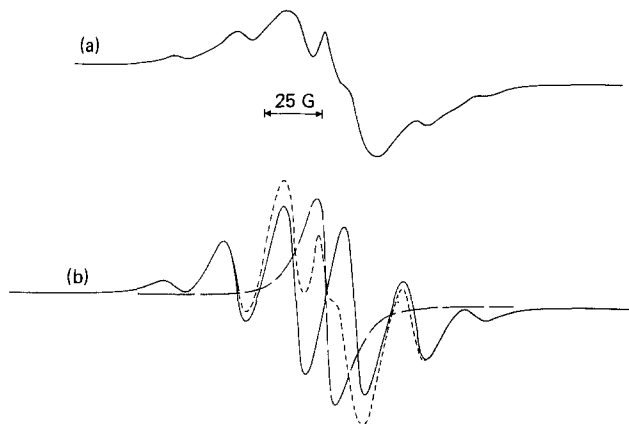


Fig. 6. (a) The EPR spectrum obtained with poly(methacrylonitrile) after electron beam exposure at 77 K in vacuum; (b) the solid 6-line spectrum (10 G bandwidth, 20.5 G coupling constant) and the solid single-line spectrum (13 G bandwidth) are combined together in the dashed line to simulate the experimental spectrum shown in (a).

as the major reaction, resulting in a conjugated double bond main chain; here the main chain scission is a minor reaction. The conjugated main chain thus formed undergoes only cyclization to yield the conjugated ladder-type structure upon subsequent heating. In an unexposed area, however, thermal development causes both elimination of hydrogen chloride and the main chain scission. This difference of the reactions in electron beam exposed areas from unexposed areas causes relief images in the resist films upon thermal development.

Copolymer (acrylonitrile-methacrylic acid) undergoes anhydride formation to a small degree in the pre-baking process, as evidenced by appearance of its new u.v.-absorption band at 240 nm. Upon electron beam exposure the main chain scission takes place in both acid and anhydride sections (10). The subsequent thermal development causes an unzipping reaction in electron beam exposed areas, while in unexposed areas the cyclization suggested by Grassie (17) and anhydride formation may occur, resulting in the generation of polymer patterns as shown in Fig. 3.

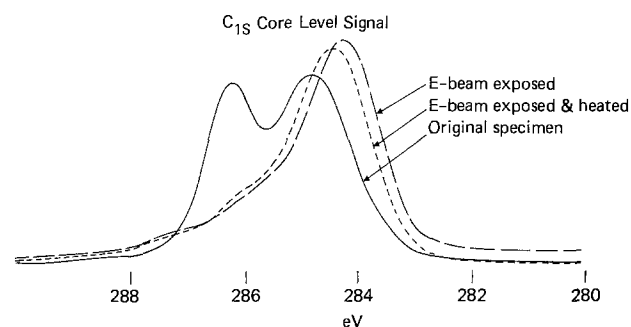


Fig. 7. The C_{1s} core level signals of poly(methacrylonitrile)

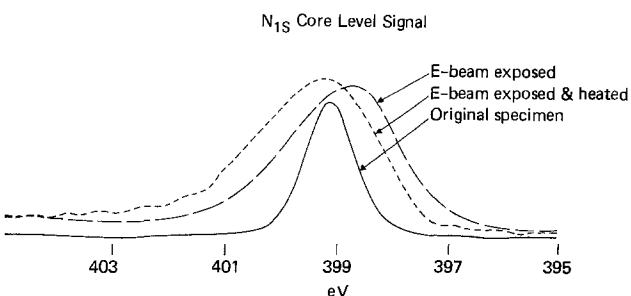


Fig. 8. The N_{1s} core level signals of poly(methacrylonitrile)

With copolymer (methyl methacrylate-acrylonitrile), the main chain scission takes place in the methyl methacrylate section in both electron beam exposed areas and unexposed areas upon heating. This results in only shallow polymer patterns in thermal development. Besides, the methyl methacrylate section suffers severe degradation in a CF_4 plasma.

Conclusions

All dry processes for photo- and electron beam lithography are still in a stage of infancy, although all dry photolithography has been claimed to be in a production stage for specific applications (4). All dry processes are important not only because of possible economic advantages but also because of ecological and safety aspects. Poly(methacrylonitrile) and related polymers appear to have unique properties for use in dry development. After heat-treatment which causes chemical rearrangements of the main polymer chains, the polymer films become highly CF_4 plasma etch resistant and hence are suitable for dry processes. The major problem appears to be the control of the wall profiles of polymer patterns. With high dose and low temperature development steep wall angles can be obtained. The resolution may be limited at present to polymer lines 1.5 μm wide and deep with 1.5-2 μm spacings.

Acknowledgments

The author wishes to thank M. Hatzakis for his useful discussion and W. Lee for his ESCA measurements.

Manuscript submitted July 14, 1980; revised manuscript received Dec. 15, 1980.

Any discussion of this paper will appear in a Discussion Section to be published in the December 1981 JOURNAL. All discussions for the December 1981 Discussion Section should be submitted by Aug. 1, 1981.

Publication costs of this article were assisted by IBM Corporation.

REFERENCES

1. M. J. Bowden and L. F. Thompson, *Polym. Eng. Sci.*, **14**, 525 (1974).
2. I. Haller, M. Hatzakis, and R. Srinivasan, *IBM J. Res. Dev.*, **12**, 251 (1968).
3. T. Asano, T. Tsujimura, G. Nagamatsu, K. Hasegawa, and K. Nakamura, in Proc. Tokyo Symposium '77 on Photo- and Electro-Imaging, Society of Photographic Scientists and Engineers, pp. 241-248, Washington, D.C. (1978).
4. J. N. Smith, H. G. Hughes, J. V. Keller, W. R. Goodner, and T. E. Wood, *Semiconductor Intl.*, **2**, 41 (December 1979); also H. G. Hughes, R. W. Goodner, T. E. Wood, J. N. Smith, and J. V. Keller, in Proc. 8th Reg. Tech. Conf., Mid-Hudson Sect., Society of Plastics Engineers, Ellenville, N.Y., Oct. 12, 1979.
5. T. C. Penn, *IEEE Trans. Electron Devices*, **ed-26**, 640 (1979).
6. G. N. Taylor, *Solid State Technol.*, **23**, 73 (May 1980).
7. M. Hatzakis and H. Hiraoka, *IBM Tech. Discl. Bull.*, **23**, 2948 (1980).
8. H. Hiraoka, *IBM Tech. Discl. Bull.*, **23**, 3354 (1980).
9. W. R. Sorenson and T. W. Campbell, "Preparative Methods of Polymer Chemistry," Interscience Publishers, New York (1961).
10. H. Hiraoka, *IBM J. Res. Dev.*, **21**, 121 (1977).
11. G. N. Taylor and T. M. Wolf, in Proc. 8th Reg. Tech. Conf., Mid-Hudson Sect., Society of Plastics Engineers, Ellenville, N.Y., Oct. 12, 1979.
12. J. N. Helbert, C. F. Cook, Jr., C. Y. Chen, and C. U. Pittman, Jr., *This Journal*, **126**, 694 (1979).
13. Y. Hatano, H. Shiraishi, Y. Taniguchi, S. Horigome, S. Nonogaki, and K. Naraoka, Abs. 380, p. 946, The Electrochemical Society Extended Abstracts, Seattle, Washington, May 21-26, 1978.
14. H. Hiraoka and W. Lee, *Macromolecules*, **11**, 622 (1978).
15. J. N. Helbert, C. U. Pittman, Jr., and J. N. Lai, in Proc. 8th Reg. Tech. Conf., Mid-Hudson Sect., Society of Plastics Engineers, Ellenville, N.Y.,

- Oct. 1979; also, J. N. Helbert, C-Y. Chen, C. U. Pittman, Jr., and G. L. Hagnauer, *Macromolecules*, **11**, 1104 (1978).
16. W. J. Burlant and J. L. Parsons, *J. Polym. Sci.*, **22**, 249 (1956); N. Grassie and J. C. McNeill, *ibid.*, **39**, 211 (1959); N. Grassie and J. N. Hay, *ibid.*, **56**, 189 (1962); M. Becher and H. F. Mark, *Angew. Chem.*, **73**, 641 (1961).
17. N. Grassie, "Kinetics and Mechanism of Polyreactions," IUPAC Intl. Symposium on Macromolecular Chemistry, Akademiai Kiado, Budapest, 1971, p. 725.

Optical Characterization of Tungsten Silicide Thin Films

M. Delfino* and W. I. Lehrer

Fairchild Camera and Instrument Corporation, Research and Development Laboratory, Palo Alto, California 94304

ABSTRACT

The optical constants of tungsten silicide formed by thermally reacting chemically vapor deposited tungsten on $\langle 100 \rangle$, $\langle 111 \rangle$, and polycrystalline silicon substrates are reported. The substrate and thermal annealing temperature, unlike the annealing time, are shown to have a marked effect upon the optical properties of the silicide. The ellipsometric charts necessary for determining the thickness and refractive index of oxides grown or deposited on the silicides are constructed.

Tungsten disilicide (WSi_2) shows considerable promise as a low resistivity electrical interconnect and gate electrode material in integrated circuit technologies. The refractory metal silicide can be obtained by rf diode sputtering (1, 2), E -beam co-depositing (3), or chemically vapor depositing (CVD) (4) the metal onto silicon and its subsequent conversion by thermal annealing. For very large scale integrated circuit (VLSI) applications, it is generally necessary to cover the silicide with an oxide layer for stability and controllability requirements. This necessitates that non-destructive methods such as ellipsometry be used for measuring the oxide thickness and uniformity. Consequently, the optical constants of the silicide must be known.

This paper reports measurements of the optical constants of WSi_2 formed by reacting CVD tungsten on single crystal $\langle 100 \rangle$, and $\langle 111 \rangle$ substrates and polycrystalline silicon films over the temperature range of 600°-900°C. The dependence of the optical properties on the substrate and on the annealing times is investigated. Finally, the ellipsometric charts used in annealing oxide thickness and refractive index are constructed and are shown to be in excellent agreement with thickness measurements made by selective etching and profilometry.

Experimental Procedures

Studies were conducted on 3 in. diam wafers of 4-6 Ω -cm, n-type $\langle 100 \rangle$, and 1-5 Ω -cm, p-type $\langle 111 \rangle$ Czochralski grown silicon. The samples were etched in 1:10 ($\text{HF}:\text{H}_2\text{O}$) for 20 sec, rinsed in deionized water, and blown dry with nitrogen prior to tungsten depositions. Polycrystalline silicon was deposited at 600°C at a rate of 375Å min^{-1} to a thickness of 3000Å on 2000Å of thermal oxide prepared by oxidizing the $\langle 111 \rangle$ material in dry oxygen at 1000°C. Tungsten films were deposited at a rate of 100Å min^{-1} on all three different substrates maintained at 600° \pm 5°C in a Unipak VIII CVD reactor at atmospheric pressure in 80 liter min^{-1} dry hydrogen. For the gaseous tungsten source, a hydrogen flow of 8 liter min^{-1} was passed over resublimed WCl_6 (Alfa) maintained at 170° \pm 5°C with a corresponding vapor pressure of 2.3 to 6.2 $\times 10^{-6}$ atm. The tungsten depositions on the polycrystalline silicon were performed in the same reactor immediately following the silicon deposition, thus minimizing the effects of a native oxide interface between

the tungsten and silicon. Thermal annealing of the films was done in quartz tubes under 3 liter min^{-1} of dry hydrogen for 30 min.

Several methods were employed for characterizing the films. Scanning electron micrographs (SEM) of the cleaved samples and profilometry using a Dektak after etching were employed to estimate film thickness and to evaluate surface topography. Auger electron spectroscopy (AES) depth profiles were used to establish chemical composition and to verify film thickness. Low-angle x-ray diffraction was done with $\text{CuK}\alpha$ radiation using a Phillips diffractometer in order to determine crystal structure. Resistivity was measured by the usual four-point probe method. Ellipsometric measurements were made with a Rudolph Model 436-200E ellipsometer at angles of incidence, $\phi = 70.0^\circ$ and 75.0° . The light source was a 5 mW He-Ne laser ($\lambda = 6328\text{Å}$).

Results and Discussion

The 800Å thick tungsten films were found to form silicide layers which were approximately 2000Å thick. The surfaces exhibited a metallic luster and were free of cracks as examined by SEM. AES depth profiles showed a silicon to tungsten ratio of nominally 2:1 throughout the film thickness. In all samples, some oxide $\lesssim 20\text{Å}$ was detected at the surface, presumably in the form of a native tungsten-silicon oxide. No other contaminants were found. X-ray diffraction did not show any evidence of crystallinity in the 600°C films corresponding to either tungsten or silicide. At 900°C, the silicides formed on all three substances were identified as the tetragonal phase of WSi_2 , space group $I4/mmm$ (D_{4h}^7) with the lattice parameters $a_0 = 3.21$, and $c_0 = 7.83\text{Å}$ (5). The x-ray diffraction results are summarized in Table I. The relative intensities have

Table I. X-ray diffraction data for tungsten silicides annealed at 900°C for 30 min in hydrogen

| d (Å) | hkl | Si $\langle 100 \rangle$ | I/I_0^* Si $\langle 111 \rangle$ | Polycrystalline Si |
|---------|----------|--------------------------|---------------------------------------|--------------------|
| 3.92 | 002 | 20 | 15 | 80 |
| 2.96 | 101 | 40 | 35 | 100 |
| 2.03 | 103 | 40 | 40 | 95 |
| 1.98 | 004, 112 | — | — | 60 |
| 1.61 | 200 | 5 | 5 | 20 |

* Relative intensities are normalized to the (101) reflection of the silicide formed on the polycrystalline silicon substrate.

* Electrochemical Society Active Member.

Key words: ellipsometry, CVD, annealing, resistivity.

been normalized to the most intense peak, *i.e.*, the (101) reflection of the silicide formed on the polycrystalline substance. Interestingly, the (004) reflection is absent in the silicides formed on the single crystal substrates and the other reflections are significantly less intense relative to that of the polycrystalline substrate. Thus the nature of the crystallinity of the silicide depends on that of the silicon substrate and/or the interfacial native oxide.

The resistivity as a function of annealing temperature is shown in Fig. 1. The annealing time is 30 min. At 800°C and below, the resistivity of the silicides formed on the <100> and <111> silicon substrates is essentially identical, whereas the silicide grown on polycrystalline silicon has a lower resistivity. As this temperature is increased, a change in slope is noted in all three samples suggesting the onset of a phase change resulting in similar resistivities at 900°C. Increasing the thermal annealing time to 120 min had a negligible but decreasing effect on the resistivity values. The resistivity minima of $\sim 3 \times 10^2 \mu\Omega\text{-cm}$ at 900°C is slightly lower than that reported for sputtered WSi_2 annealed at 975°C for 30 min in nitrogen (2). The lowest resistivity that we have obtained was $2.2 \times 10^2 \mu\Omega\text{-cm}$ for silicide formed at 900°C on the <100> silicon substrate.

The refractive index n , and the extinction coefficient k , were calculated from the ellipsometric parameters ψ (azimuth angle) and Δ (relative phase difference) from the following equations (6)

$$n^2 - k^2 = \sin^2 \phi + \sin^2 \phi \tan^2 \phi \left[\frac{\cos^2 2\psi - \sin^2 2\psi \sin^2 \Delta}{(1 + \sin 2\psi \cos \Delta)^2} \right] \quad [1]$$

$$2nk = \sin^2 \phi \tan^2 \phi \left[\frac{\sin 4\psi \sin \Delta}{(1 + \sin 2\psi \cos \Delta)^2} \right] \quad [2]$$

where ϕ is the angle of incidence. These equations assume an oxide-free surface, an air ambient, and $k > 1$. For transparent surface films less than $\sim 20\text{\AA}$ these equations are still valid within experimental uncertainties, if both $n > 1$ and $k > 1$. The single surface reflectivity is obtained from n and k by the relation

$$R = \frac{(n - 1)^2 + k^2}{(n + 1)^2 + k^2} \quad [3]$$

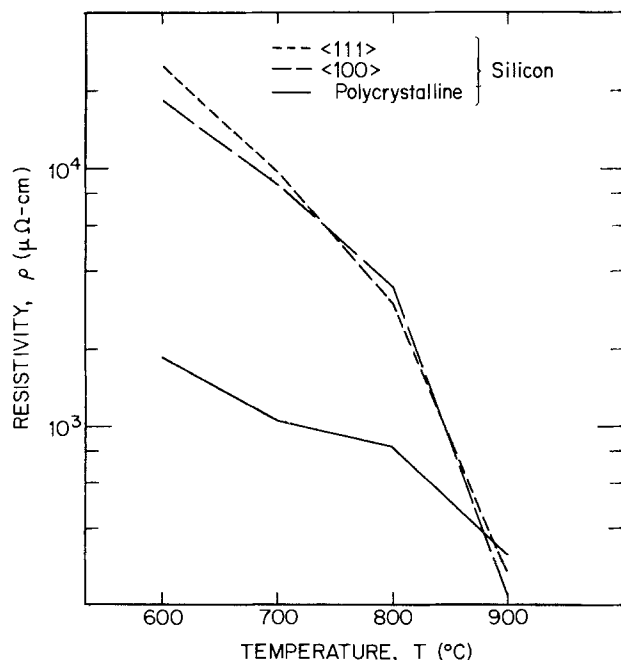


Fig. 1. Dependence of the resistivity, ρ , of tungsten silicide on the annealing temperature.

The dependence of the measured optical constants on annealing temperature is shown in Fig. 2-4. The error bars reflect the reproducibility of a minimum of three measurements at two angles of incidence on a given sample. The measured optical constants of the as-deposited tungsten on thermal oxide are shown for comparison. These values are different than those reported (7) for bulk single crystal tungsten, presumably because our measurements were done on thin amor-

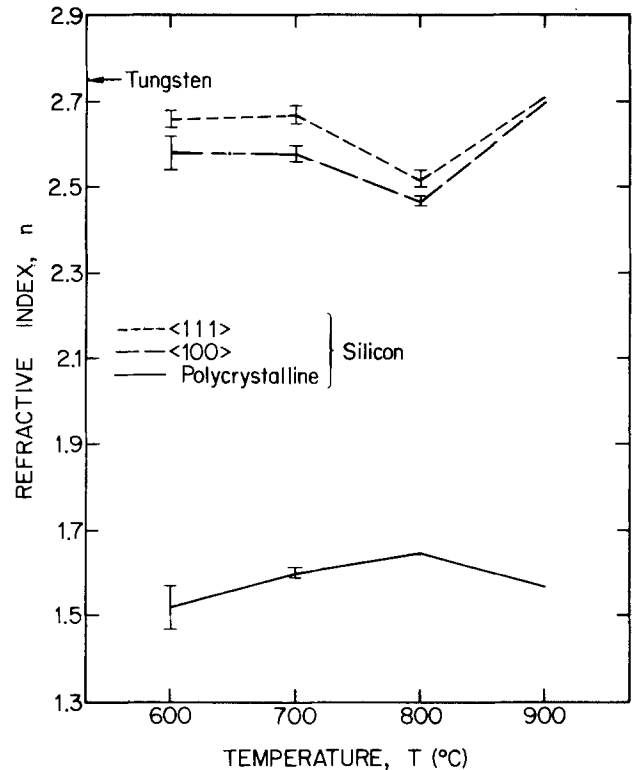


Fig. 2. Dependence of the refractive index, n , of tungsten silicide on the annealing temperature.

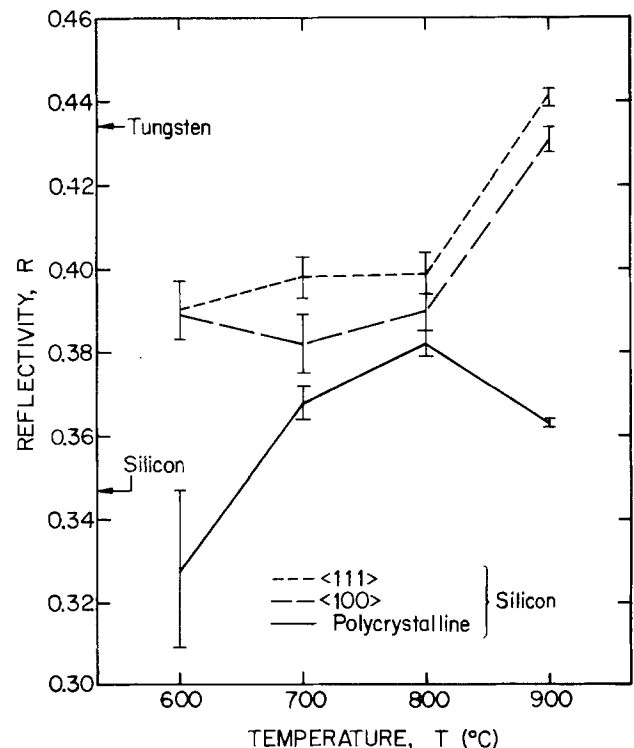


Fig. 3. Dependence of the extinction coefficient, k , of tungsten silicide on the annealing temperature.

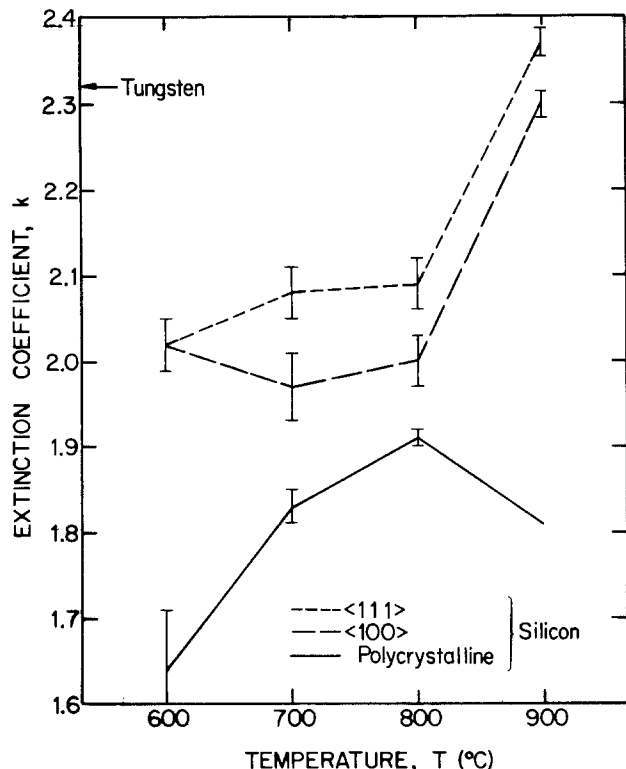


Fig. 4. Dependence of the single surface reflectivity, R , of tungsten silicide on the annealing temperature.

phous films of tungsten. Based on our data, and the value for the complex refractive index for single crystal silicon of $3.862-0.0335i$ (8), a silicide reaction appears to have occurred at 600°C on all three substrates. The dependence of the optical constants of the $\langle 100 \rangle$ and $\langle 111 \rangle$ substrate silicides on annealing temperature is nearly identical, whereas that of the polycrystalline substrate silicide is markedly different. A change in slope is observed as 800°C is exceeded in all three samples, but of opposite sign in the polycrystalline substrate silicide. Increasing the annealing time to 120 min had no effect on the extinction coefficient, and a small essentially negligible decrease on the refractive index. It should be emphasized that these measurements assume homogeneity throughout the film thickness, and are most sensitive to the surface properties, i.e., the light is virtually completely attenuated within the first 200\AA . Furthermore, the measured optical constants are found to be essentially invariant with respect to thickness for film thickness $> 1000\text{\AA}$.

The ellipsometric chart necessary for determining the thickness and refractive index of transparent films on WSi_2 was constructed from the calculated values of $\bar{\psi}$ and $\bar{\Delta}$ from the Leberknight-Lustman relation (9) given as

$$\tan \bar{\psi} \exp(i\bar{\Delta}) = \tan \psi \exp(i\Delta)$$

$$\left\{ 1 - \left[\frac{i4\pi \cos \phi \sin^2 \phi \alpha}{\left(\lambda - \frac{\lambda}{\tilde{n}_2^2} \right) \left(\cos \phi - \frac{\sin^2 \phi}{\tilde{n}_2^2} \right)} \right] \right\} \quad [4]$$

where $\tilde{n}_2 = n_2 - ik_2$ is the complex refractive index of WSi_2 , shown in Fig. 2 and 3, as calculated from the measured ellipsometric parameters ψ and Δ at the wavelength λ . The film property coefficient is

$$\alpha = d^2 - \frac{d^2}{n_1^2} - \frac{n_1^2 d^2}{\tilde{n}_2^2} + \frac{d^2}{\tilde{n}_2^2} \quad [5]$$

where d is the film thickness of refractive index n_1 . If the film is absorbing, then n_1 is complex.

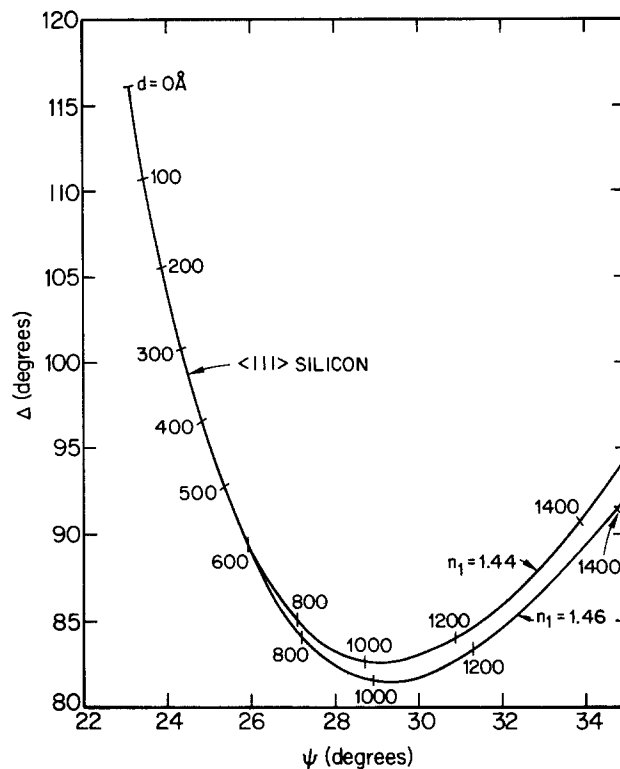


Fig. 5. Dependence of ψ and Δ on the properties of thermal oxide ($n = 1.46$) and vapox ($n = 1.44$ on WSi_2) formed on $\langle 111 \rangle$ silicon annealed at 900°C .

As an example, the dependence of ψ and Δ on the properties of thermal oxide ($n_1 = 1.46$) and vapox (1.44) on WSi_2 annealed at 900°C is shown in Fig. 5. For film thickness less than $\sim 700\text{\AA}$, it is virtually impossible to distinguish between the oxide refractive indexes. The ellipsometric chart when applied to a variety of oxide film thickness was found to be in excellent agreement ($\pm 5\%$) with thickness determination done by selective removal of the oxide followed by profilometry. In cases where a large number of samples of identical silicide characteristics are employed it was found that removal of the oxide and subsequent measurement of the optical constants of the silicide resulted in accuracies as high as $\pm 1\%$ in film thickness.

Summary

It appears that CVD tungsten on $\langle 100 \rangle$, $\langle 111 \rangle$, and polycrystalline silicon substrates react to form silicides at temperatures as low as 600°C . On the basis of the AES and SEM data the extent of silicide film thickness is invariant with respect to thermal annealing conditions. The silicides are amorphous transforming to crystalline WSi_2 at temperatures exceeding 800°C , but the nature of the crystallinity appears to be enhanced for the silicides on the polycrystalline silicon substrate. This may be a result of the absence of a native oxide at the tungsten silicon interface, since the presence of oxide is known to inhibit the silicide reaction kinetics. For native oxide on $\langle 100 \rangle$ silicon, the reaction rate is initially limited to localized nucleation of WSi_2 , whereupon formation of a continuous layer of WSi_2 , the kinetics become diffusion limited (1). An alternate explanation is that the grain size of the silicon substrate plays an active role in the reaction kinetics. The electrical resistivity and optical properties of the silicides are found to depend strongly on the substrate and thermal annealing temperature but not the annealing time. Construction of the ellipsometric charts proved useful for estimating the thickness and refractive index of oxides on silicides by non-destructive means.

Acknowledgments

The authors wish to thank J. Vincak, T. Trujillo, and S. Sekigahama for their excellent technical assistance, and J. M. Pierce, B. E. Deal, and J. M. DeBlasi for many helpful criticisms and suggestions.

Manuscript submitted Sept. 16, 1980; revised manuscript received Dec. 2, 1980.

Any discussion of this paper will appear in a Discussion Section to be published in the December 1981 JOURNAL. All discussions for the December 1981 Discussion Section should be submitted by Aug. 1, 1981.

Publication costs of this article were assisted by Fairchild Camera and Instrument Corporation.

REFERENCES

1. L. D. Locker and C. D. Capio, *J. Appl. Phys.*, **44**, 4366 (1973).
2. F. Mohammadi and K. C. Saraswat, *This Journal*, **127**, 450 (1980).
3. J. Baglin, J. Dempsey, W. Hammer, F. d'Heurle, S. Peterson, and C. Serrano, *J. Electron. Mater.*, **8**, 641 (1979).
4. N. Hashimoto, *Trans. TMS-AIME*, **239**, 1109 (1967).
5. H. Nowotny, R. Kieffer, and H. Schachner, *Met. Chem.*, **83**, 1243 (1952).
6. R. W. Ditchburn, *J. Opt. Soc. Am.*, **45**, 743 (1955).
7. J. J. Carroll and A. J. Melmed, *ibid.*, **61**, 470 (1971).
8. R. J. Archer, *ibid.*, **52**, 970 (1962).
9. C. E. Leberknight and B. Lustman, *ibid.*, 59 (1939).

High Resolution Doping Profiles in $Pb_{1-x}Sn_xTe$ Thin Film Structures

D. L. Partin

General Motors Research Laboratories, Physics Department, Warren, Michigan 48090

ABSTRACT

The fabrication of thin laser structures by molecular beam epitaxy has placed stringent demands upon the techniques for characterizing these structures. An electrochemical etch originally developed by Norr is shown to be capable of well-controlled etching of sub-micron dimensions from $Pb_{1-x}Sn_xTe$ surfaces. This allows material parameters, such as the doping level, to be measured as a function of depth.

The application of molecular beam epitaxy (MBE) techniques to the growth of lead-salt diode laser structures has resulted in attainment of micron-dimensioned structures with improved performance (1, 2). However, characterization of the grown layers becomes increasingly difficult as their dimensions become smaller. It is therefore useful to investigate a chemical etching system which has the capability of removing thin layers of these materials in a well-controlled manner. When used successively, it would then enable depth profiles of a variety of material properties to be measured, such as the doping level, defect density, etc.

The etching system investigated in this work was originally developed for use on PbTe by Norr (3). It consists of 45 ml H_2O , 20 ml ethanol, 35 ml glycerol, and 20g KOH. The sample is the anode and the cathode is platinum. This solution does not attack the sample ($<0.002 \mu m/min$) with no applied potential. At relatively low voltages ($\sim 1V$) it attacks the (100) surface preferentially at defects, and is therefore used to measure dislocation density. At 10V the etching is uniform, producing a polished surface.

This etching system was chosen because it appeared to offer potential for controlling the amount of material removed by controlling the etching time. The other well-known polishing solution for $Pb_{1-x}Sn_xTe$ is a solution of Br_2 in HBr. The material removal rate can be made small ($\sim 0.1 \mu m/min$) by diluting the solutions with water. However, x-ray photoelectron spectroscopy (XPS) studies of PbTe polished with this dilute solution showed that almost all tellurium of the etched layer remains on the surface (4). This makes this etching solution unsuitable for the present purpose.

Experimental Techniques

In this work, 50 ml of Norr etching solution were used in a beaker which was magnetically stirred at 200 rpm. The cell voltage was 10.0V, and the solution temperature was 25°C unless noted otherwise. The samples

Key words: epitaxy, etch, laser, spectroscopy.

were mechanically polished single crystals with a (100) orientation. After Norr etching to obtain damage-free surfaces, Apiezon wax was used to coat part of the sample surface. The sample was then etched for a controlled length of time. After removing the wax, the resulting step height on the sample surface was measured with a Sloan Dektak film thickness profiler. In a few cases an interference microscope was used to check the Dektak results, and agreement within 5% was obtained.

Experimental Results

Figure 1 shows the results of etching studies on PbTe doped p-type with Tl to a level of $1 \times 10^{19} cm^{-3}$. The initial etch rate is rapid followed by a relatively slow, linear etch rate. The graph and the inset table show that etched depths in the range 0.1-2.5 μm are readily obtained, which covers the range of practical interest.

When a voltage pulse is applied to the sample, a blue film appears in a fraction of a second. This film disappears in roughly 1 sec after the cell potential is reduced to zero, indicating that the film dissolves into the etching solution. However, if the sample is removed from the solution while etching and immediately rinsed with deionized water, the film is still present. Examination of the film with Auger electron spectroscopy in combination with Ar-ion sputtering indicated that the film consists of roughly equal amounts of Pb, Te, and O (Fig. 2). The atomic concentrations were obtained by normalizing the Auger signals by the elemental sensitivity factors which is generally accurate within a factor of 2. The depth scale was approximated by assuming that the sputtering rate in the oxide was the same as that in the PbTe substrate, which was separately determined. Some of the oxide may have dissolved before the etching solution was rinsed from the sample. Other elements were looked for in the film, such as potassium or carbon, but none was found within the instrumental sensitivity (typically 1%).

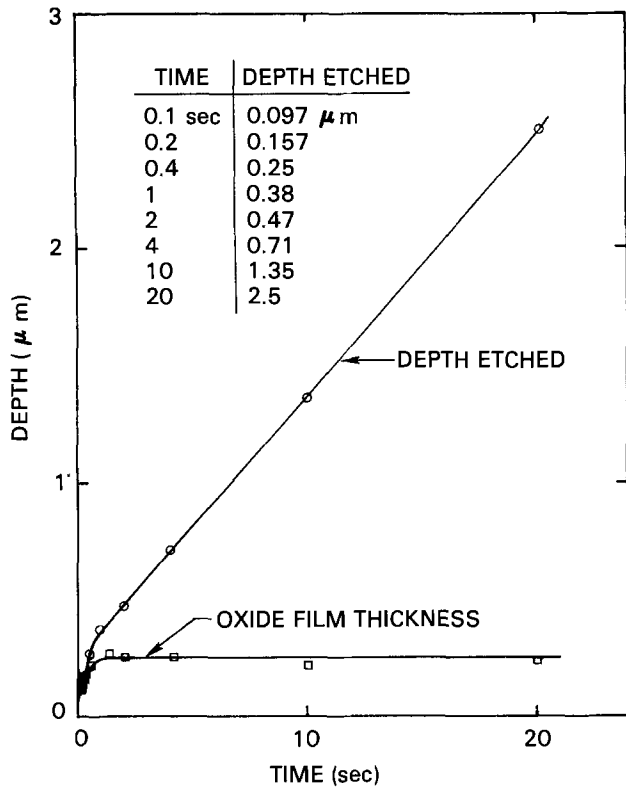


Fig. 1. Calibration curve for PbTe:Tl etched with the Norr etch at 25°C and 10V applied potential.

Thus, when a 10V potential is applied to the film, there appears to be an initial period of rapid oxide film growth. After about 1 sec of film growth, the film interference color observed visually appears to remain constant, implying that the film thickness remains constant. Therefore, growth of the oxide film at the film/substrate interface is occurring at the same rate as dissolution of the film at the film/solution interface.

Film Growth Model

These observations can be made more quantitative with a simple model. The total depth etched, D , after time t is given by

$$D = T + Ct \tag{1}$$

where T is the oxide thickness and C is the rate of dissolution of the oxide film at the film/solution interface (Fig. 3). Differentiating gives

$$\frac{dD}{dt} = \frac{dT}{dt} + C \tag{2}$$

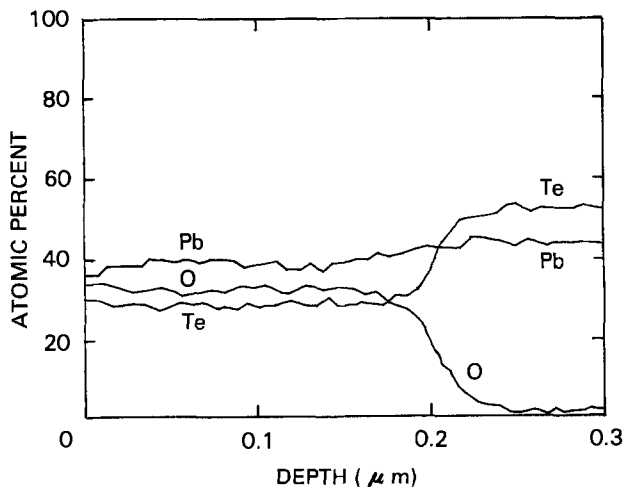


Fig. 2. Auger depth profile of oxide film formed by the Norr etch

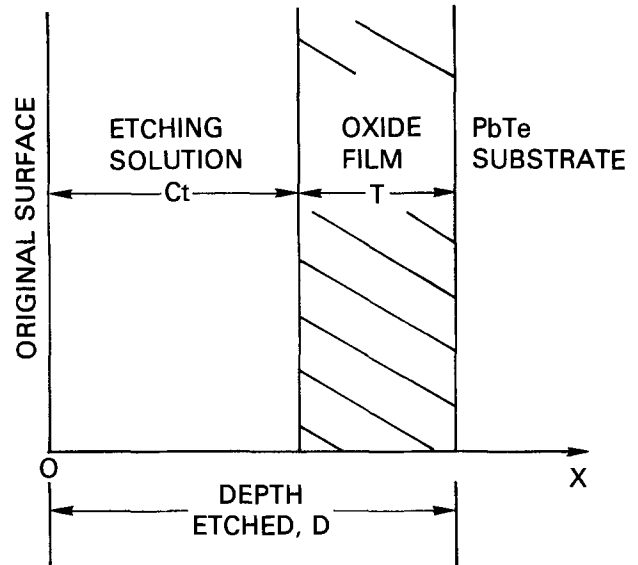


Fig. 3. Schematic showing the total depth etched, D , as the sum of the oxide film thickness, T , and the depth of dissolved material, Ct .

As noted above, the oxide thickness becomes constant after about 1 sec, so that

$$\frac{dD}{dt} = C, \quad t > 1 \text{ sec} \tag{3}$$

Thus, using the linear portion of the "depth etched" vs. time curve in Fig. 1, the constant $C = 1.13 \times 10^{-5}$ cm/sec. Using this value of C in combination with Eq. [1] and the "depth etched" curve of Fig. 1, the oxide film thickness can be calculated as a function of etching time. This data is plotted in Fig. 1, and shows rapid film growth until the thickness stabilizes, as expected. The limiting thickness is 0.25 μm, which is in good agreement with the oxide thickness shown in Fig. 2.

The current which flows through the etching solution is related to the depth etched into the substrate. The number of substrate atoms oxidized per unit area and time is $N_s dD/t$, where N_s is the number density of atoms in PbTe (2.94×10^{22} cm⁻³). Thus, the current density through the oxide, J , is given by

$$J = qBN_s \frac{dD}{dt} \tag{4}$$

where B is the average number of electrons required to oxidize PbTe atoms. The oxide species are known to be PbO and TeO₂ (5, 6). Thus, Pb is formally in the +2 valence state in PbTe and PbO, but Te changes from the -2 state to the +4 state, which requires 6 electrons. This implies a theoretical value of 3 for B . For comparison with experiment, Eq. [4] may be expressed in integral form

$$Q = \int_0^t J dt = qBN_s D \tag{5}$$

where Q is the total charge per unit area which passed through the oxide in time t . Using an oscilloscope, Q was measured vs. etching time t . From the known dependence of D on t (Fig. 1), an experimental value of B could be determined. Over the range of etching times from 0.1 to 20 sec, the value of B obtained was 3.4 ± 0.2 , which is in reasonably good agreement with the theoretical value of 3 determined above.

Sensitivity to Experimental Variables

The etching results shown in Fig. 2 are for PbTe doped p-type with Tl at a level of 1×10^{19} cm⁻³. The lead salts can also be doped n-type or p-type by making them metal-rich or chalcogenide-rich, respec-

tively. The etch rate for Pb-rich PbTe ($n = 6 \times 10^{17} \text{ cm}^{-3}$) or Te-rich $\text{Pb}_{0.86}\text{Sn}_{0.14}\text{Te}$ ($p = 1.5 \times 10^{18} \text{ cm}^{-3}$) was determined for several etching times, and always found to agree with the data for Tl-doped PbTe ($p = 1.0 \times 10^{19} \text{ cm}^{-3}$) (Fig. 1) within about 10%. This implies that the etch rate remains constant through a heterojunction or p-n junction in the $\text{Pb}_{1-x}\text{Sn}_x\text{Te}$ system, at least for x in the range 0-0.14, which covers most of the range used in practical devices.

The sensitivity of the etch rate to variations in etching solution composition or temperature is shown in Table I. All data shown is for a 2 sec etch on Tl-doped PbTe. The addition of 20% extra ethanol or glycerol leaves the etch rate essentially unchanged, while water and KOH change it by $\sim 50\%$. This may imply that OH^- is the species that conducts current through the oxide film and supplies oxygen at the PbTe/oxide interface. It should be noted that hydrogen cannot be observed with Auger electron spectroscopy. Therefore, its presence in the oxide film (Fig. 2) could not be confirmed.

The potassium concentration in the Norr etching solution is very high, and some of it may be left behind on the etched surface. After etching, the samples are rinsed in ethanol, water, dilute nitric acid, and then water. The nitric acid is believed to be effective in getting the potassium from the surface. This was tested by studying the surface concentration of potassium with secondary ion mass spectroscopy (SIMS), which is extremely sensitive to alkali metals. This technique yields only relative concentrations, but it was found that samples cleaned with the Norr etch and rinsed in the above sequence of reagents had only 2-5% as much potassium on their surfaces as samples which were rinsed in ethanol and water only. This was so even when the sample was rinsed for 3 sec in nitric acid diluted to 0.1 volume percent with water.

The nitric acid rinse also affected the thermoelectric voltage measured on the etched surface of lightly doped samples. PbTe samples ($n = 6 \times 10^{17} \text{ cm}^{-3}$) which did not have a nitric acid rinse had thermoelectric voltages which were $\sim 20\%$ lower than samples rinsed in 0.1-1% nitric acid. Since potassium is expected to be an acceptor impurity in PbTe, this probably means that it compensates donors near the surface of PbTe. Thus, the removal of potassium from the surface is necessary if the Norr etch is to be useful for depth profiling of carrier concentrations.

Carrier Concentration Profile

The carrier concentration profile of a diode laser will be shown to illustrate the usefulness of this etching system (Fig. 4). The substrate consisted of PbTe doped p-type with Tl at $2 \times 10^{19} \text{ cm}^{-3}$. A $4.7 \mu\text{m}$ thick Tl-doped PbTe active region was then grown by molecular beam epitaxy. This was followed by a $0.7 \mu\text{m}$ thick Bi-doped region. The growth was carried out at $2 \mu\text{m/hr}$ deposition rate and 350°C substrate temperature. Other aspects of the growth technique are being reported elsewhere (7).

Table I. Sensitivity of etch rate to variations

| Variation | Depth in 2 sec (μm) | Normalized depth |
|---------------------------------|----------------------------------|------------------|
| Standard (25°C) | 0.47 | 1.00 |
| 20% extra water | 0.75 | 1.60 |
| 20% extra ethanol | 0.50 | 1.06 |
| 20% extra glycerol | 0.48 | 1.02 |
| 20% extra KOH | 0.66 | 1.40 |
| 35°C | 0.77 | 1.64 |
| 45°C | 0.91 | 1.94 |

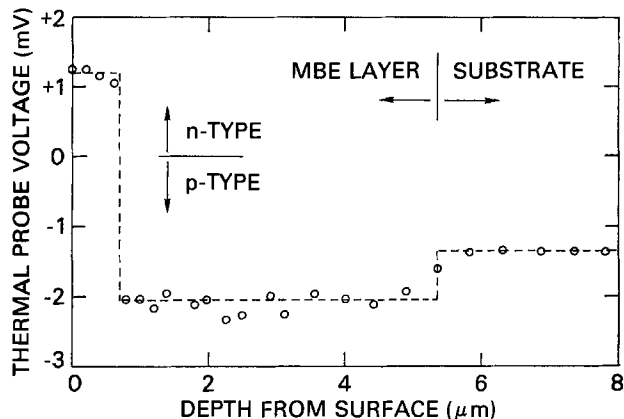


Fig. 4. Thermal probe voltage as a function of depth through a laser structure.

The carrier concentration is determined from the thermoelectric voltage generated by a metal probe held 9°C above a room temperature contact at the back of the sample. The measurement is repeated after each etching step to obtain the profile shown in Fig. 4. The thermoelectric voltage in the active region corresponds to a hole concentration of $\sim 4 \times 10^{18} \text{ cm}^{-3}$ at 77 K. The electron concentration in the Bi-doped region is $1 \times 10^{19} \text{ cm}^{-3}$. Of particular interest is the abrupt change in voltage between depths of 0.6 and $0.8 \mu\text{m}$. This implies that the measurement technique is capable of $0.2 \mu\text{m}$ resolution or better, which is adequate to profile micron-dimensioned structures.

Conclusions

An electrochemical etch is shown to reproducibly remove $\text{Pb}_{1-x}\text{Sn}_x\text{Te}$ to depths in the range $0.1\text{-}2.5 \mu\text{m}$. The etch rate as function of time can be well understood in terms of the formation of an anodic oxide film which is soluble in the etching solution. The etch rate is not sensitive to conductivity type, doping level, or Sn concentration in the range $0 \leq x \leq 0.14$. This makes this etching system useful for depth profiling the doping level of MBE-grown heterostructure diode lasers.

Acknowledgments

Use of the Electronics Department's Sloan Dektak film thickness profiler and growth of PbTe crystals by Don E. Swets is gratefully acknowledged.

Manuscript received Oct. 15, 1980.

Any discussion of this paper will appear in a Discussion Section to be published in the December 1981 JOURNAL. All discussions for the December 1981 Discussion Section should be submitted by Aug. 1, 1981.

Publication costs of this article were assisted by General Motors Research Laboratories.

REFERENCES

1. H. Preier, *Appl. Phys.*, **20**, 189 (1979).
2. D. L. Partin and W. Lo, To be published.
3. M. K. Norr, *This Journal*, **75**, 118 (1962).
4. M. Bettini, G. Brandt, and S. Rotter, *J. Vac. Sci. Technol.*, **16**, 1548 (1979).
5. M. Bettini and H. J. Richter, *Surf. Sci.*, **80**, 334 (1979).
6. H. H. Strehblow and M. Bettini, *This Journal*, **127**, 847 (1980).
7. D. L. Partin, To be published.

Low Energy Ion Beam Etching

J. M. E. Harper, J. J. Cuomo, P. A. Leary, and G. M. Summa

IBM Research Center, Yorktown Heights, New York 10598

H. R. Kaufman

Colorado State University, Fort Collins, Colorado 80523

and F. J. Bresnock

IBM Data Systems Division, Hopewell Junction, New York 12533

ABSTRACT

We present two developments in low energy ion beam etching. First, we have extended the usable ion energy range for broad beam ion etching down to tens of electron volts by using a single extraction grid of very fine aperture size. High ion current densities (up to 1.0 mA/cm²) are achieved below 100 eV ion energy while maintaining a collimated beam with low energy spread (about 10 eV). Second, we have applied this capability to reactive ion beam etching (RIBE) of Si and SiO₂ and we introduce a quantitative parameter which characterizes the effectiveness of ion bombardment in enhancing chemical etching. This parameter is obtained from etch rate measurements using Ar and CF₄ gases over the ion energy range 20-1500 eV. Step edge profiles are also examined.

In this paper we present two developments in low energy ion beam etching. First, we have extended the usable ion energy range for broad beam ion etching down to tens of electron volts by replacing the conventional dual grid ion extraction system with a single grid of very fine aperture size. High ion current densities (up to 1.0 mA/cm²) are achieved at low ion energies (down to 20 eV) while maintaining a collimated beam with low energy spread (about 10 eV). Second, we introduce a quantitative parameter which characterizes the effectiveness of ion bombardment in enhancing chemical etching, the basis of reactive ion etching (RIE). The ion enhancement parameter is obtained from the energy dependence of the etch rates of a material using reactive and inert gases. We have measured the etch rates of Si and SiO₂ with Ar and CF₄ gases over the energy range 20-1500 eV. We find, for example, that in etching SiO₂ with CF₄ at an ion energy of 200 eV, the ion enhancement parameter is about 3, indicating that for each substrate atom removed by physical sputtering, two additional atoms are removed by enhanced chemical etching. Above an ion energy of 500 eV this enhancement parameter decreases to unity, indicating that ion enhancement of chemical etching has reached its maximum effectiveness. These measurements may be used to optimize etch rate selectivity in reactive ion beam etching (RIBE).

We also compared the step edge profiles obtained using CF₄ etching of SiO₂ with those obtained with Ar ion etching. Inert gas ion etching usually leaves sloping walls and may cause trenching and redeposition on mask edges. These problems are minimized by using a reactive ion beam etching process at an energy low enough to cause little physical sputtering. Ion beam systems operate at two orders of magnitude lower pressure than a glow discharge RIE system, reducing the effect of neutrals. The mean free path of ions and etch products exceeds the chamber dimensions, minimizing loading effects, contamination by backscattering, and chemical effects of the sample holder. The ion energy spread is low, and the energy and current density may be independently controlled and measured. These advantages provide an incentive

to extend the useful energy range to below 100 eV and to take advantage of the selectivity available with chemically reactive species. These two topics are addressed here, beginning with the limits encountered when the ion energy is decreased.

Theory—Limit on Ion Current Density at Low Energy

Ion beam etching is usually carried out using broad beam electron bombardment ion sources (1). Figure 1 shows the general configuration. This diagram shows a single extraction grid, whereas typically a dual grid system is used. A low voltage magnetically enhanced discharge is maintained between the thermionic cathode and surrounding anode, and ions are extracted through the grid system to form a directed beam. The ion energy is close to the anode potential V_a . The beam is aimed at the material to be etched, and normally a flow of electrons is supplied from a neutralizer filament to avoid surface charging effects (1). The conventional dual grid configuration is shown in Fig. 2a. In this design the screen grid potential differs from the discharge plasma potential by the magnitude of the discharge voltage V_d , and the accelerator grid is held negative to prevent backstreaming of electrons into the discharge chamber. Further details of operation are given in Ref. (1, 2). These ion sources easily generate ion current densities of 0.5 mA/cm² at 500 eV, but such high ion energies may cause device damage, knock-on penetration of contaminants, or intermixing of layers. Lower ion energies are desirable, but below about 100 eV the ion current density is space charge limited to only a few hundredths milliamperes per square centimeter. Since this current density corresponds to less than one tenth monolayer of bombardment per second, practical ion etching cannot be carried out below 100 eV with a dual grid system.

The space charge limit on current flow may be stated as follows. The maximum current density obtainable from an ion source (1) is related to the ion acceleration voltage V and the acceleration distance d by

$$j_{\max} \propto V^{3/2}/d^2 \quad [1]$$

In a dual grid system (Fig. 2a) V is the potential difference between the discharge plasma and the accelerator grid, and d is approximately the distance between the plasma sheath and the accelerator grid. To

Key words: reactive ion etching, ion bombardment, etch rate ratio, ion current, space charge, extraction.

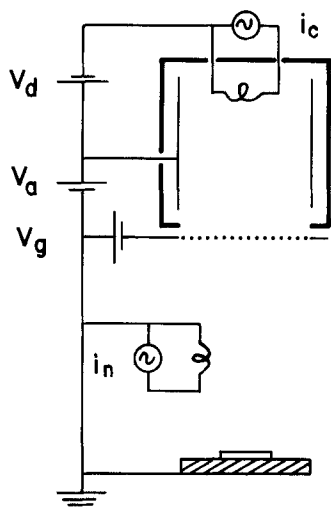


Fig. 1. Diagram of single grid ion source, showing cathode current i_c , discharge voltage V_d , anode voltage V_a , grid voltage V_g , neutralizer current i_n , and sample on a grounded holder.

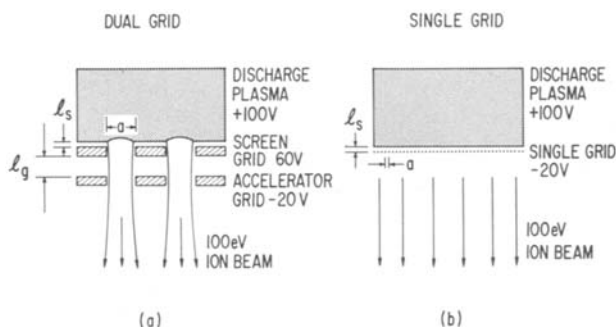


Fig. 2. Comparison of the extraction grid region of (a) dual grid ion source and (b) single ion source, showing the grid aperture diameter a , discharge sheath thickness l_s , grid spacing l_g , and potentials typical for generating a 100 eV ion beam.

generate a low energy ion beam, V must be decreased, and since d is fixed by the grid spacing (typically 1 mm or greater), j_{\max} decreases also. The relationship is shown in Fig. 3, in which the maximum current density obtained from a dual grid ion source is plotted as a function of $V_t^{3/2}$. Therefore, while a current density of 3.0 mA/cm² is obtained at an ion energy of 1500 eV ($V_t^{3/2} = 67,000$), only 0.05 mA/cm² is obtained at 100 eV ($V_t^{3/2} = 1153$). This space charge limitation on ion current density is a ceiling above which a dual grid source cannot operate, even by increasing the ion density in the source.

In order to maintain high current density at low ion energy, we use a single extraction grid (3) (Fig. 2b) which overcomes the space charge limitation of a dual grid system. The single grid is formed from a material with a very fine aperture size a . The aperture size must be comparable to or less than the thickness of the plasma sheath l_s for effective operation. With this condition satisfied, ions leave the discharge plasma in almost parallel trajectories, with a certain fraction passing through the grid as a collimated beam. Although the grid is bombarded by ions, sputtering damage is minimized by operating at low ion energy.

The single grid differs markedly from the dual grid system by maintaining high current density at low ion energy. The acceleration distance d is now equivalent to the sheath thickness l_s , which is on the order of 0.1 mm. As the ion energy is decreased, d is no longer fixed, and the sheath thickness l_s decreases to keep the ion current density equal to the space charge limit. Therefore almost constant current density is maintained down to about 20 eV ion energy.

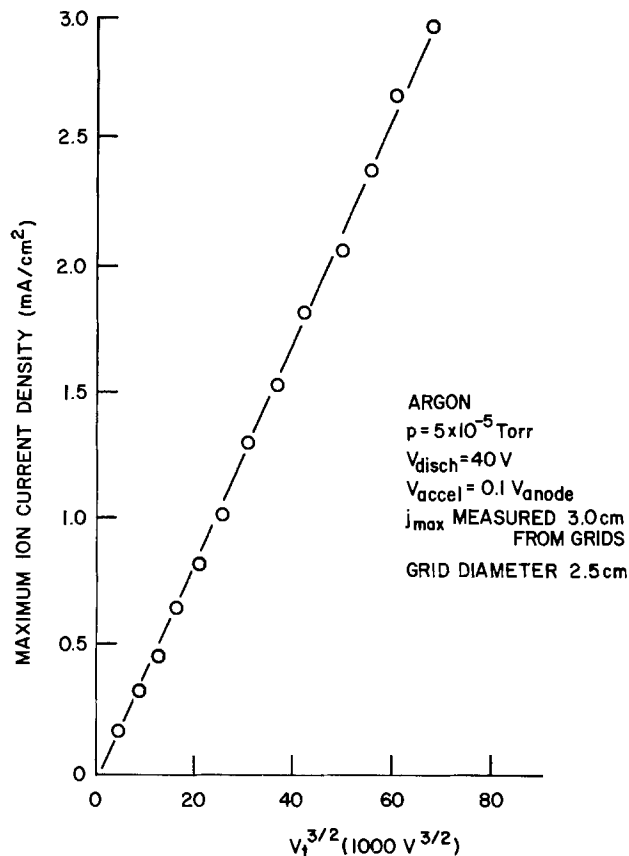


Fig. 3. Maximum current density obtained from a dual grid ion source as a function of $V_t^{3/2}$, illustrating the space charge limit on current density. V_t is the total potential difference between the discharge plasma and the accelerator grid.

Experimental Procedure

Single grid ion source.—We have tested the single grid design on two ion sources of 3.5 and 7.5 cm beam diameter by simply replacing the grid system with a single grid of electroformed nickel mesh of 0.2 mm aperture size and 82% transparency (100 lines per inch). The 3.5 cm source is shown schematically in Fig. 1. Cathode and neutralizer filaments are tungsten. Typical operating parameters which generate a 100 eV argon beam are: sample chamber pressure = 10^{-2} Pa (8×10^{-5} Torr), discharge voltage = 40V, discharge current = 0.2A, anode voltage = 100V, grid voltage = -20V, grid current = 3 mA, beam current = 7 mA, current density at grid = 0.73 mA/cm², current density 14 cm from grid = 0.32 mA/cm², and ion energy = 95 ± 5 eV.

The current density and energy distribution in the ion beam are measured using a retarding grid analyzer. The analyzer measures the ion current which reaches a collector plate after passing through a positively biased mesh grid. The voltage on this retarding grid is swept to trace out the energy distribution of the ions. Another negatively biased grid is used to screen out electrons from the analyzer. Measurements confirm that current densities up to 1.0 mA/cm² can be obtained at ion energies as low as 20 eV. This result demonstrates that the sheath thickness adjusts itself to maintain the beam current density independent of ion energy. The ion current density is now determined by the ion density in the source and is not limited by grid geometry. Thus a wide range of operating conditions is available at low ion energy, as shown in Fig. 4. In this figure the operating range of the dual grid source is shown for ion energies up to 200 eV. This curve is the low energy portion of Fig. 3. Also shown is the operating range of the single grid. With the single grid, ion energies much higher than 200 eV are not suitable be-

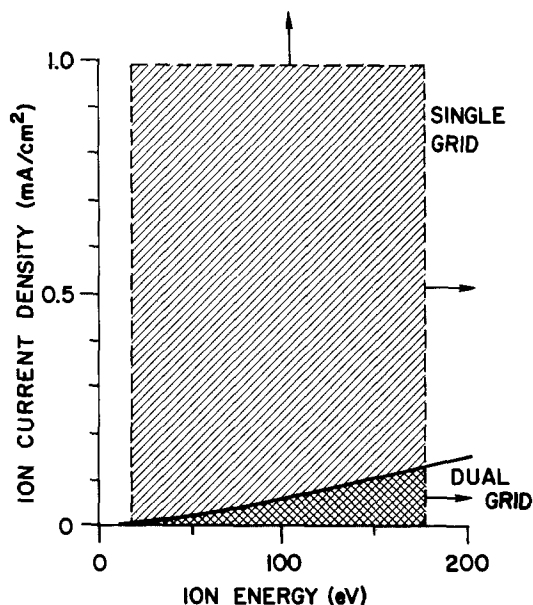


Fig. 4. Comparison of the low energy operating range of the single grid and the dual grid ion source.

cause of ion bombardment of the grid. Current densities above 1.0 mA/cm² can be obtained, but are limited eventually by overheating of the grid. Energy analyzer measurements indicate an energy spread of about 10 eV, similar to that obtained with a dual grid source. We have operated the single grid source as low as 20 eV ion energy, but below this value the ion energy spread becomes comparable to the average ion energy, and the beam can no longer be considered almost monoenergetic. Over the entire operating range shown in Fig. 4, however, the energy spread remains far smaller than the broad energy distributions found in rf glow discharge systems, and the current density is much higher than a dual grid system can generate. Thus quantitative measurements of etch rates can be carried out with current densities on the order of 1.0 mA/cm² over a wide range of low energies by using the single grid design.

A convenient feature of the single grid design is that it may be easily used on an existing dual grid ion source. The discharge chamber remains unchanged, while the low energy performance of the ion source is greatly improved. Finer mesh grids up to 333 lines per inch were also tested, but these developed holes during operation. With care, a 100 mesh grid can be used for 5-10 hr operation including several exposures to air.

Etch rates of Si and SiO₂ with Ar and CF₄.—We have measured the etch rates of Si and SiO₂ using Ar and CF₄ gases in the ion source, over an ion energy range of 20-1500 eV. The 3.5 cm diam single grid source was used for ion energies below about 200 eV, and the 2.5 cm diam dual grids were used on the same ion source for higher ion energies. Ion source parameters were similar to those listed above, except that with CF₄ a discharge voltage of 70V was used. The sample chamber was evacuated to an initial pressure of typically 5×10^{-5} Pa (4×10^{-7} Torr), then raised to an Ar or CF₄ pressure of $1-5 \times 10^{-2}$ Pa ($0.8-4 \times 10^{-4}$ Torr) for etching. Etch rate measurements were made using a coated quartz crystal rate monitor located 14-20 cm from the ion source and were supplemented by step measurements on masked Si and oxidized Si wafers. Several measurements were also made using a larger diameter (7.5 cm) single grid source. Ion current density and energy were measured above the sample using a retarding grid analyzer. Current densities of typically 0.1 mA/cm² were used, with etch times of 10-90 min. These measurement times were longer than

time constants associated with the rate monitor temperature or the establishment of steady etching conditions (4).

Etch rates were divided by the ion current density to calculate the etching yield in atoms/ion for each ion/sample combination. Argon ion current densities were corrected for the resonant charge exchange process (2, 5) which converts a fraction of the energetic beam ions to energetic neutrals. This fraction increases with background pressure and causes the measured ion current density to underestimate the total energetic particle flux striking the sample. Correcting for this process allows measurements at different pressures to be reliably compared. Current density values with CF₄ were not corrected for charge exchange since this process should not be significant for CF₃⁺ ions (the dominant species) passing through mostly CF₄ gas.

To examine the step edge profiles generated by low energy RIBE, several wafers of oxidized Si were coated with a 1 μm thick photoresist pattern. After etching with CF₄ at 200 eV ion energy, the photoresist was removed and the steps were examined by scanning electron microscopy. The step profiles were then compared with steps etched using 500 eV argon ions.

Results

Etching yields are given in Fig. 5 as a function of ion energy, for Si and SiO₂ using Ar or CF₄. To convert these yields to etch rates, in the case of Si a yield of 1 atom/ion means that in an ion beam of current density 1.0 mA/cm², the Si etch rate is 12.5 Å/sec. For SiO₂, a yield of 1 atom (either Si or O) per ion means that in an ion beam of current density 1.0 mA/cm², the SiO₂ etch rate is 9.5 Å/sec. For reference, the asterisk in Fig. 5 indicates the maximum chemical etching yield of SiO₂ by a single CF₃⁺ ion to yield SiF₄ plus CO and CO₂, according to the equation



This maximum yield is 0.75 SiO₂ molecules, or 2.25 atoms (Si or O) per CF₃⁺ ion. The significance of this value is discussed in the next section. The data obtained with the single grid ion source are shown as circles and those taken with the dual grid are shown as triangles. These measurements merge smoothly at 200 eV in the case of Ar/SiO₂, but for CF₄/SiO₂ there is a significant difference in etch rates measured by

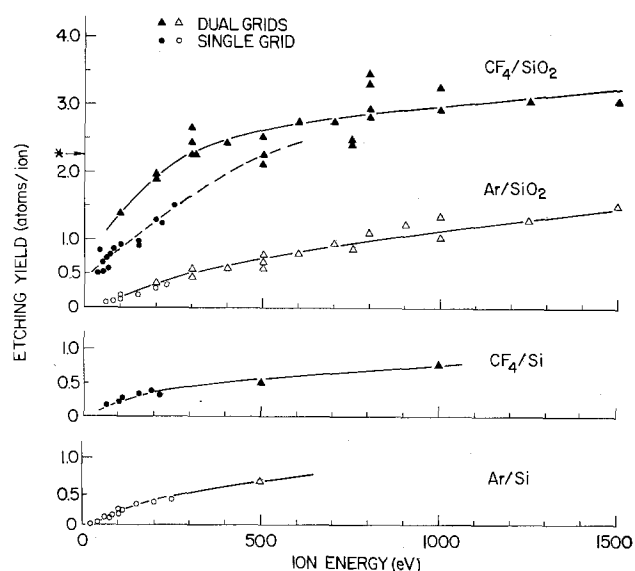


Fig. 5. Etching yields (atoms/ion) as a function of ion energy for four ion/material combinations: CF₄/SiO₂, Ar/SiO₂, CF₄/Si, and Ar/Si. Circles are measurements taken with the single grid ion source, and triangles are taken with the dual grid system. The asterisk indicates the maximum CF₄/SiO₂ chemical etching yield of 2.25 atoms/ion.

these two grid systems. This difference appears to be caused by a mild rate of deposition of polymeric material from the CF_4 discharge, which competes with the etching process, especially at low ion energy. The multiple data points shown at the same ion energy in Fig. 5 were obtained from different samples, using various values of gas pressure and ion current density to assess the overall reproducibility of the process.

Step edge profiles are shown in Fig. 6. The initial photoresist mask shape is shown in Fig. 6a. A $1\ \mu\text{m}$ deep step in SiO_2 etched with CF_4 at 200 eV is shown in Fig. 6b, and a $0.5\ \mu\text{m}$ deep step in SiO_2 etched with Ar at 500 eV is shown in Fig. 6c. The step edge profile obtained with CF_4 has almost vertical walls with no evidence of trenching. This indicates directional, anisotropic etching with mostly volatile products. The wall is not quite vertical because of the sloping mask shape (Fig. 6a) and the slight divergence angle of the ion beam (about 10°). Since the mask is etched at about $1/5$ the rate of the SiO_2 , the lateral movement of the step edge contributes to a slightly sloping wall. The step edge profile obtained with Ar (Fig. 6c) shows a sloping wall with a shallow trench formed by reflected

ions. This shape evolves when etching is by purely physical sputtering, causing partial redeposition on the wall of the step. Although this redeposited material may be simultaneously removed by sputtering, it has the effect of decreasing the etch rate of the sloping wall, contributing to a shallower slope. Also with Ar sputtering, the photoresist mask and the SiO_2 substrate etch at similar rates. The mask edge therefore moves a greater distance laterally than in etching with CF_4 to the same depth, again contributing to a sloping step edge. Trenching can be more severe than shown in Fig. 6c, as shown in Ref. (6). Also redeposition on mask edges can leave unwanted fringes (7,8). These artifacts of inert gas ion etching are minimized by using low energy RIBE.

A fringe is evident in Fig. 6b, but this is not due to redeposited sputtered material. The deposit on the top of the step is the polymer coating obtained when using CF_4 in the ion source. The polymer coated the side of the photoresist and then fell onto the top surface of the SiO_2 when the photoresist was removed. The formation of this polymeric coating on the sample being etched caused wide variations in the measured etch

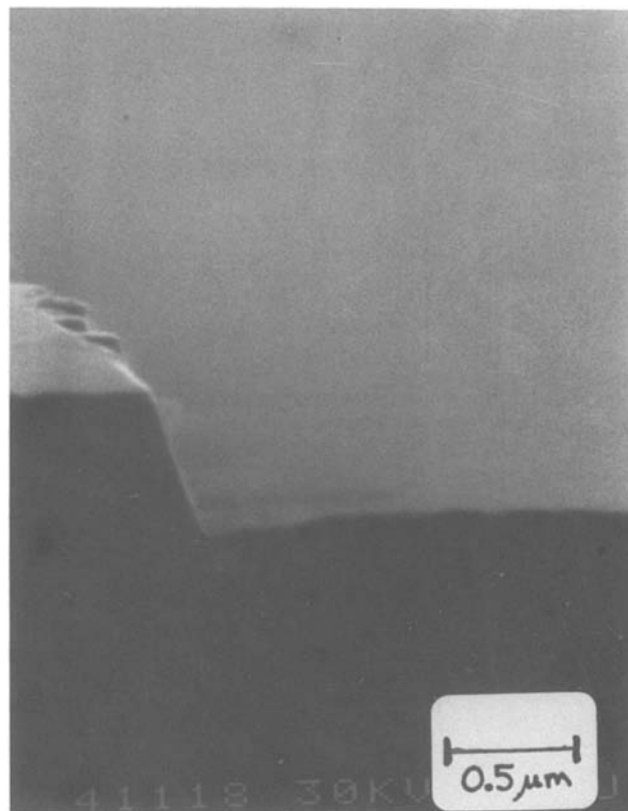
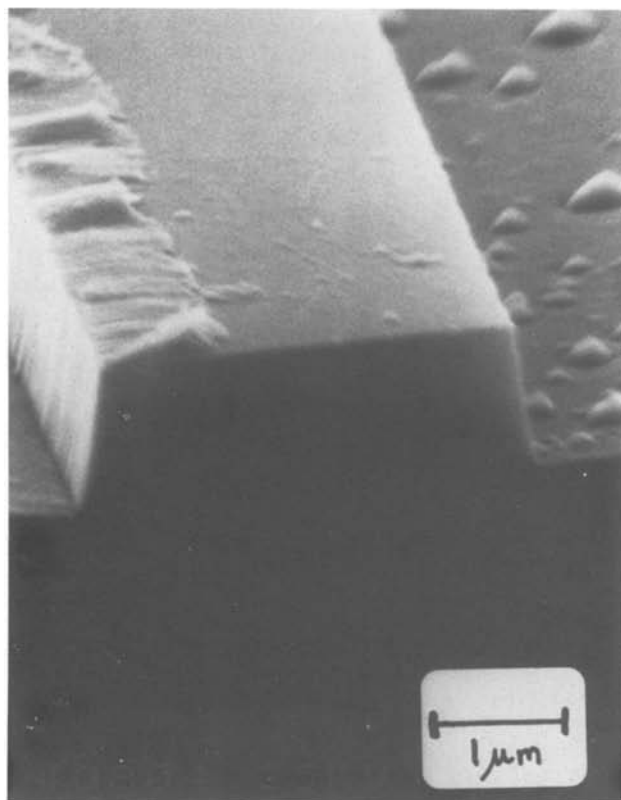
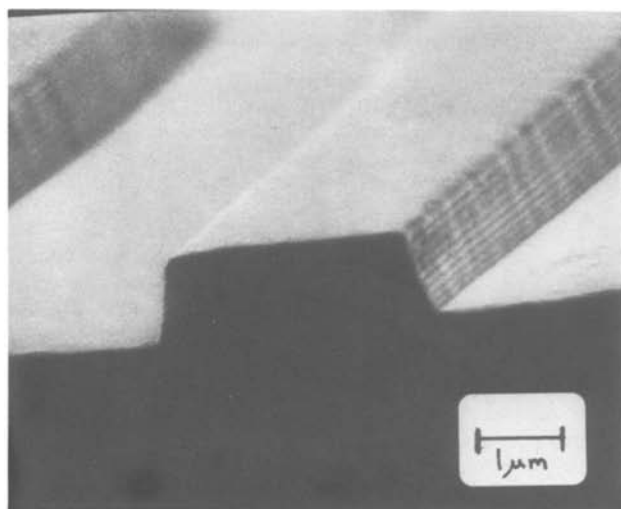


Fig. 6. Scanning electron micrographs showing: (a, upper left) $1\ \mu\text{m}$ thick photoresist pattern on $1\ \mu\text{m}$ thick SiO_2 , prior to ion beam etching. (b, lower left) Etched step in SiO_2 after 200 eV CF_4 etch to a depth of $1\ \mu\text{m}$, after removal of photoresist, showing near-vertical walls and polymer residue. (c, above) Etched step in SiO_2 after 500 eV Ar etch to a depth of $0.5\ \mu\text{m}$, after removal of photoresist, showing sloping walls and shallow trench.

rate of CF_4/SiO_2 at ion energies below 100 eV and probably accounts for the roughness of the etched surface in Fig. 6b. Under certain operating conditions the deposition process dominated and showed a positive deposition rate exceeding the etch rate. Competition from this deposition process was minimized by operating at low gas pressure ($<10^{-2}$ Pa) and large distances from the ion source (>10 cm). Preliminary etch rate measurements using the larger diameter (7.5 cm) ion source were inconclusive because net deposition always occurred below 100 eV ion energy. The larger diameter source acts as a broad area vapor source for deposition on the sample. When CF_4 was used in either ion source, an insulating coating also formed inside the discharge chamber. This coating gradually increased the resistance of the discharge circuit and after several hours operation the discharge would be extinguished. Cleaning the anode surface quickly restored normal operation. The complications which arise from the deposition of polymeric material on both the sample and the discharge chamber surfaces may possibly be eliminated by using a different gas mixture. However, above ion energies of 200-300 eV, etch rates with CF_4 did not seem to be affected by polymer deposition. Also, when using argon the operation of the ion source was straightforward, and reproducible etch rates were obtained at ion energies as low as 20 eV (Fig. 5).

The ratio of etching yields between CF_4/SiO_2 and Ar/SiO_2 is plotted in Fig. 7. Also shown is the ratio of the slope of the CF_4/SiO_2 etch yield curve to the slope of the Ar/SiO_2 curve. This ratio is defined as the ion enhancement parameter p , to be discussed in the following section.

Discussion

Comparison of etching results.—The etch rate measurements (Fig. 5) over the range 20-1500 eV demonstrate several points. The etch rates of Ar/SiO_2 , CF_4/Si , and Ar/Si are very similar. Etching of Si or SiO_2 by Ar is a purely physical sputtering process, and etching of Si by CF_3^+ ions has been shown to be almost entirely by physical sputtering (4). These results also indicate that in RIBE there is a low concentration of

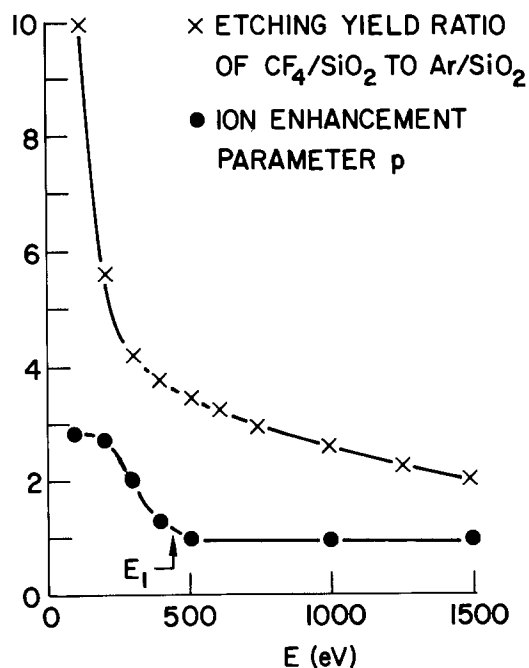


Fig. 7. Ratio of etching yields of CF_4/SiO_2 to Ar/SiO_2 as a function of ion energy, obtained from data of Fig. 5, and the ion enhancement parameter p (the ratio of the slopes of the etching yields of CF_4/SiO_2 to Ar/SiO_2), as a function of ion energy. The energy E_1 is the energy at which the ion enhancement of chemical etching is saturated.

F radicals involved in etching, in contrast to glow discharge systems (9). We find, therefore, that when CF_4 is used in the ion source, the dominant etching species is CF_3^+ ions and that etching by neutral species is less important. This assumption is reasonable in a system which exposes the sample to a collimated ion flux extending far from the ion source, whereas neutral etching species are spread over a wide solid angle upon leaving the source. Since mean free paths are long in the ion beam system, gas phase reactions and loading effects should be negligible.

The CF_4/SiO_2 etch rate curve (Fig. 5) represents the etch rate of SiO_2 by CF_3^+ ions, apart from the undesirable effect of polymer deposition. We can estimate the magnitude of this deposition effect by comparing the etch rates obtained with the single grid (circles) and dual grid system (triangles). Due to differences in open area fraction and beam diameter, the single grid exposes more than three times the area of discharge plasma to substrate line of sight than does the dual grid system. Therefore the deposition flux should differ by at least a factor of three for these two measurements. With this in mind, we can estimate that if polymer deposition were completely absent, the CF_4/SiO_2 etch rate should be only slightly higher than the curve obtained with the dual grids.

In the following discussion we will consider the CF_4/SiO_2 etch rate curve obtained with the dual grids to be an accurate measurement of the SiO_2 etch rate by CF_3^+ ions. The CF_4/SiO_2 etch rates measured here are consistent with SiO_2 etch rates obtained in glow discharge RIE (9) when reasonable assumptions are made for ion energy and current density, which are not directly measurable in RIE. Also, recent etch rate measurements of SiO_2 in ion beams of other fluorocarbon gases are in good agreement with the results presented here. Meusemann (8) reports SiO_2 etch rates in CHF_3 and in $\text{CF}_4 + 4\% \text{O}_2$ giving etching yields of about 3.1 atoms/ion at 1000 eV, in agreement with Fig. 5. Horiike *et al.* (10) report SiO_2 etch rates in C_2F_6 over a range of ion energies, but give no values of ion current density. Using Eq. [1] we can estimate the values used and arrive at etching yields consistent with Fig. 5. The general agreement between etching yields of SiO_2 in different fluorocarbon gases supports our interpretation that the main etching species in these cases is the CF_3^+ ion. Step edge profiles shown in Ref. (8, 10) are also nearly vertical, with no trenching.

Model of ion enhanced chemical etching.—The etch rate of SiO_2 using CF_4 is significantly higher than with argon because of the combined effect of ion bombardment and chemical etching. In RIE, much progress has been made in understanding the etching effects of neutral radicals (F, CF_3), reactive ions (CF_3^+), and the role of ion bombardment (4, 9). However, experiments with finely focused ion beams (4) are not easily extended to low ion energy and large sample areas, and studies in glow discharge RIE systems (9, 11) lack direct measurements of ion energy and current density on which to base a model. Low energy RIBE is a more well-defined process, in which ion energy and flux are easily measured and controlled, allowing us to model the effects of ion bombardment in chemical etching.

In this section we introduce a quantitative parameter which characterizes the effect of ion bombardment in enhancing chemical etching. To describe this parameter, we focus on the CF_4/SiO_2 etching yield curve of Fig. 5. This curve is shown schematically in Fig. 8 as y_n , the net etching yield, which is made up of three components:

1. A physical sputtering yield, y_s : This component is the etching yield due to sputtering by CF_3^+ ions. Since the CF_4/Si , Ar/SiO_2 , and Ar/Si yields are close, we expect the sputtering component of the CF_4/SiO_2 etching yield to be similar to these curves.

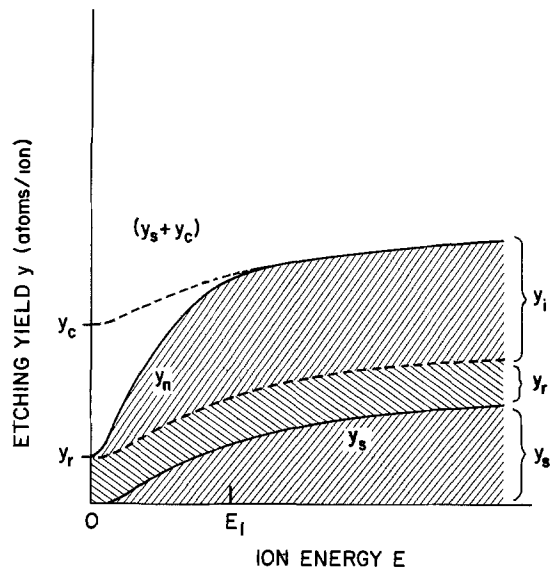


Fig. 8. Schematic diagram of the components involved in RIBE. y_s is the physical sputtering yield, y_r is the residual chemical etching yield, y_i is the ion enhanced chemical etching component, y_c is the maximum chemical etching yield, and y_n is the net etching yield. The energy E_1 is indicated, at which point the ion enhancement of chemical etching is saturated.

2. A residual chemical etching yield, y_r : This component requires only low energy ion impact (< 20 eV) and not sputtering. Its magnitude is given by the extrapolated zero-energy intercept of the CF_4/SiO_2 curve and equals approximately 0.4 atoms/ion. Considering the F atom content of CF_3^+ , the maximum etching yield of SiO_2 by purely chemical etching is 2.25 atoms per CF_3^+ ion, as described earlier. This value is labeled by an asterisk in Fig. 5 and is indicated by y_c in Fig. 8. Therefore the residual chemical etching yield y_r is well below its potential value of y_c . If the residual chemical etch rate were at its maximum, the sum of this value plus the physical sputtering yield would be the curve $(y_s + y_c)$ in Fig. 8. This curve represents the maximum yield possible due to both sputtering and chemical etching, assuming no other etching species are present.

3. An ion enhanced chemical etching yield, y_i : After subtracting the residual chemical etching component y_r and the sputtering component y_s from the net CF_4/SiO_2 etching yield y_n , there remains a component which is the ion enhanced chemical etching yield y_i . This component increases with energy in a manner similar to the sputtering component y_s and is approximately a multiple of y_s at low energy. At an energy E_1 , y_i reaches a value of $(y_c - y_r)$. Above E_1 , y_i remains constant, indicating that ion enhancement of the chemical etching process has saturated. At high energy, therefore, the net etching yield follows the sum of the sputtering yield y_s and the maximum chemical etching yield y_c .

The energy dependence of these etching yields suggests the following interpretation of ion enhanced chemical etching. Ion impact increases the reactivity of the chemical etching process from a low value at low energy (< 20 eV) to its full value at some high energy E_1 . Above this ion energy the CF_4/SiO_2 etching yield should follow the curve $(y_s + y_c)$. The data of Fig. 5 show that below 500 eV the CF_4/SiO_2 etching yield rises rapidly with energy, as does y_n in Fig. 8. Above 500 eV the CF_4/SiO_2 etching yield follows a similar slope to the Ar/SiO_2 curve. Although the Ar/SiO_2 curve cannot be equated directly to the sputtering component y_s of CF_4/SiO_2 etching, they are expected to be very similar. Therefore, above 500 eV the CF_4/SiO_2 etching yield follows the sum of a sputtering component and the maximum chemical etching yield (the asterisk in Fig. 5).

The physical picture is that in CF_3^+ etching of SiO_2 the rate of formation of volatile etch products is limited by the number of active sites available on the SiO_2 surface. This point is confirmed by a low value of the residual chemical etching yield y_r . The creation of more active sites adds to the chemical etching yield, a contribution proportional to the number of additional sites. Physical sputtering creates active surface sites by removing atoms and creating surface defects. We expect the number of additional sites to be approximately proportional to the sputtering yield, or equivalently to the sputtering component of the CF_4/SiO_2 etch rate, y_s . It is therefore reasonable that the ion enhanced chemical etching component y_i be a multiple of the sputtering component y_s , at least at low ion energy where the enhancement has not saturated. The multiplying factor is the ratio of the slope of the net etching yield curve y_n to the slope of the sputtering component y_s . We define this ratio as the ion enhancement parameter p . The parameter p gives a quantitative measure of the ion enhanced chemical etching process. From the CF_4/SiO_2 and Ar/SiO_2 etching yield curves of Fig. 5 we obtain values of the parameter p as a function of energy. These results are shown in Fig. 7. A value of $p = 2$ (at 300 eV, for example) means that in addition to residual chemical etching, each departing sputtered atom (Si or O) leaves behind enough active sites to cause on the average one additional atom to be removed by chemical etching (formation of volatile products). The enhancement parameter p shows a high value at low energy, decreasing to unity above about 500 eV ion energy. Since the shape of the low energy portion of the CF_4/SiO_2 etching yield curve is not precisely known, the energy dependence of p in Fig. 7 should be regarded as a trend. We find that the enhancement of chemical etching by ion bombardment saturates at an ion energy E_1 of approximately 500 eV.

The energy dependence of the ion enhancement parameter p (Fig. 7) illustrates several phenomena. At ion energies below E_1 , ion impact has a multiplicative effect on the etching yield. Ions in the range of 100-200 eV are effective at stimulating additional chemical etching, and the ratio of the net etching yield to the sputtering yield is high. Above E_1 , at 500-1000 eV, chemical etching has been increased to its maximum effectiveness, and individual ions do not have as great a multiplicative effect on the etching yield. The yield becomes the additive sum of sputtering plus maximum chemical etching. The energy E_1 is consistent with CF_3^+ ions penetrating the SiO_2 surface, dissociating and depositing their energy within the top few layers. This process generates maximum chemical reactivity, whereas at lower energies the molecular ion would dissociate on the surface, but active sites may not be available to complete the reaction with the substrate.

Having measured the enhancement parameter p for a given ion/material combination, we can now choose an energy for ion beam etching which optimizes the ratio between chemical etching and sputtering. For example, in etching a vertical structure as shown in Fig. 6b, it is important to minimize the sputtering component of etching to reduce mask erosion and redeposition of sputtered material. Simultaneously, the chemical etching component should be maximized to gain highly anisotropic etching. From Fig. 7 it looks most attractive to carry out the etching at the lowest ion energy, where the enhancement parameter p is maximized. However, at very low energy the net etching rate may be too low for practical applications (Fig. 5). An optimum etching energy would be closer to E_1 , around 300-500 eV for CF_4/SiO_2 . Here the net etching yield is high, and the etching yield ratio between chemical etching and sputtering is still high. Little would be gained by increasing the ion energy above 1000 eV, because the net etching yield does not increase significantly, while the sputtering yield rises by more

than a factor of two. The ratio between the net etching yield and the sputtering yield (Fig. 7) decreases gradually as the ion energy is increased above E_1 . High ion energy sacrifices selectivity while generating more substrate damage. Similar considerations apply to applications in which a reactively etched film is to be removed down to an underlying nonreactive substrate. Here again, the sputtering yield should be minimized to avoid overetching, and an energy near E_1 would be optimum for high selectivity combined with short etching time.

We have demonstrated that low energy ion beam etch rate measurements give quantitative information on the process of reactive ion etching. From the energy dependence of etching yields, an ion enhancement parameter p is obtained which characterizes the effectiveness of ion bombardment in stimulating chemical etching. This parameter guides the choice of the optimum ion energy for practical RIBE applications.

For low energy ion beam etching, the single grid modification to a broad beam ion source can be used to obtain high ion current density at low ion energy. This capability extends practical ion beam etching down to tens of electron volts. In addition to the application to RIBE discussed in this paper, such low energy ion beam etching is appropriate for surface cleaning applications prior to thin film deposition, or in conjunction with analytical techniques where surface damage is to be minimized.

Acknowledgments

The authors thank D. Irmischer, D. L. Goldman, and G. A. Waters for help in carrying out etch rate mea-

surements, J. L. Speidell for preparation of step edge test wafers, and C. F. Aliotta for electron microscopy. We also thank J. W. Coburn for helpful discussions.

Manuscript submitted June 4, 1980; revised manuscript received Dec. 19, 1980. This was Paper 284 presented at the St. Louis, Missouri, Meeting of the Society, May 11-16, 1980.

Any discussion of this paper will appear in a Discussion Section to be published in the December 1981 JOURNAL. All discussions for the December 1981 Discussion Section should be submitted by Aug. 1, 1981.

Publication costs of this article were assisted by IBM Corporation.

REFERENCES

1. H. R. Kaufman, *J. Vac. Sci. Technol.*, **15**, 272 (1978).
2. H. R. Kaufman, J. M. E. Harper, and J. J. Cuomo, *ibid.*, **16**, 899 (1979).
3. P. LeVaguerese and D. Pigache, *Rev. Phys. Appl.*, **6**, 325 (1971).
4. J. W. Coburn, H. F. Winters, and T. J. Chuang, *J. Appl. Phys.*, **48**, 3532 (1977); J. W. Coburn and H. F. Winters, *J. Vac. Sci. Technol.*, **16**, 391 (1979).
5. R. S. Robinson, *ibid.*, **16**, 185 (1979).
6. S. Somekh, *ibid.*, **13**, 1003 (1976).
7. R. E. Lee, *ibid.*, **16**, 164 (1979).
8. B. Meusemann, *ibid.*, **16**, 1886 (1979).
9. G. C. Schwartz, L. B. Rothman, and T. J. Schopen, *This Journal*, **126**, 464 (1979).
10. Y. Horiike, M. Shibagaki, and K. Kadono, *Jpn. J. Appl. Phys.*, **18**, 2309 (1979).
11. J. L. Mauer, J. S. Logan, L. B. Zielinski, and G. C. Schwartz, *J. Vac. Sci. Technol.*, **15**, 1734 (1978).

Amorphous Transparent Conductors: The CdO-SnO₂ System

F. T. J. Smith and S. L. Lyu

Eastman Kodak Company, Research Laboratories, Rochester, New York 14650

ABSTRACT

In the CdO-SnO₂ system both end members and the phases Cd₂SnO₄ and CdSnO₃ have been reported to be useful transparent conductors. The present report concerns amorphous sputtered films having compositions ranging from 20 to 80 mole percent CdO in SnO₂. We have determined the properties of both as-deposited and annealed films as functions of both film composition and sputtering conditions. From these results, the optical and electrical properties of the films have been correlated with film structure and composition. The optimum conditions for obtaining highly conductive and transparent films are described. Films having a transmission of 80%-90% in the visible and a sheet resistance of less than 5 Ω /sq can be deposited under these conditions.

Materials having both a high degree of transparency in the visible and a high electrical conductivity have found a wide variety of applications, usually in the form of thin films (1). The most commonly used materials are based on oxides of Cd, In, Sn, and Sb, with most attention having been paid to SnO₂ and the In₂O₃-SnO₂ system.

In the CdO-SnO₂ system both end members have been reported to be useful transparent conductors. Films of CdO have been used, for example, as transparent electrodes on selenium photovoltaic cells (2), as heating elements (3), and as transparent electrodes on CdS (4). Films of SnO₂ doped with various donors have been used even more widely (1). The phases Cd₂SnO₄ (5) and CdSnO₃ (6) have also been reported

to be transparent conductors. Films of the intermediate phases exhibit the highest ratio of visible-wavelength transmission to sheet resistance, and properties superior to those of the best indium-tin oxide films have been reported for Cd₂SnO₄ films (7). It has been reported that sputtered films having compositions close to that of the phase Cd₂SnO₄ are amorphous when deposited onto amorphous substrates at room temperature and crystalline when deposited onto substrates heated to 400°-500°C (5).

Most of the previous work has been concerned with the properties of crystalline films having compositions close to that of Cd₂SnO₄ (7, 8). About amorphous films, on the other hand, little information exists. Nozik (5) reported the properties of four as-deposited films obtained by using various power levels and oxygen con-

centrations in the sputtering gas. He found electron mobilities in the range $5.8\text{--}24\text{ cm}^2/\text{V sec}$ and resistivities of 2.6×10^{-3} to $10\text{ }\Omega\text{-cm}$. Haacke *et al.* (9) reported a mostly amorphous film to have a mobility of $\sim 27\text{ cm}^2/\text{V sec}$ and a resistivity of $\sim 6.2 \times 10^{-2}\text{ }\Omega\text{-cm}$. Such high mobilities are not generally observed in materials which lack long-range order.

We report in detail the properties of amorphous films and in particular the effects of target composition and sputtering atmosphere on these properties. We will also report the results of post-deposition anneals on film properties. We have observed a minimum resistivity for as-deposited amorphous films of $3.3 \times 10^{-4}\text{ }\Omega\text{-cm}$ compared with a lowest reported value of $4.8 \times 10^{-4}\text{ }\Omega\text{-cm}$ for as-deposited polycrystalline films (8). A resistivity of $1.5 \times 10^{-4}\text{ }\Omega\text{-cm}$ has been reported for polycrystalline Cd_2SnO_4 films annealed and reacted with CdS in an argon atmosphere (9); however, the film composition resulting from this process was not reported.

Experimental Methods

The sputtering system consisted of an rf diode with the target placed horizontally below the substrates as shown in Fig. 1. So that target compositions could be changed easily, the sputtering target used was a shallow dish 20 cm in diameter filled with the powdered oxides mixed in the appropriate ratio. Substrates were loaded through an airlock, thus avoiding exposure of the target to the atmosphere. This avoided the problems of absorption of moisture and oxygen which would have been expected as a result of repeated exposure of a target with a large surface area to the atmosphere between runs. As a result we observed a high degree of reproducibility of film properties after initial outgassing and presputtering of new targets. For example, over several series of 20 runs under the same conditions, all sheet resistance values were within 8% of the mean value. In earlier experiments with indium-tin oxide in this system, we obtained essentially identical properties with films sputtered under the same conditions from either a loose powder or a hot-pressed target. This confirms that the physical form of the target is not a major concern with this equipment.

The sputtering system was enclosed in a stainless steel cylinder pumped by an oil diffusion pump with a cold trap. A pressure of 1×10^{-7} to 5×10^{-8} Torr was measured in this cylinder between runs. During sputtering, a throttle valve of fixed diameter was used to limit pumping speed. Both argon and oxygen of high purity were introduced to the chamber through metering valves to form the sputtering atmosphere. A stainless steel cup could be rotated into position over the target in place of the substrates. Deposition onto this cup was always carried out for 30 min to equilibrate the system before deposition onto the substrates.

The substrates used were 5 cm diam disks of fused quartz 0.5 mm thick and polished on both sides. They were cleaned with ammonia-hydrogen peroxide and hydrochloric acid-hydrogen peroxide mixtures before use. The substrates were clamped into recesses in a

massive aluminum and copper disk which was water cooled. The substrate surface did not exceed $\sim 100^\circ\text{C}$ during a typical deposition procedure.

Optical measurements were made at near-normal incidence by using a Cary 14 two-beam spectrophotometer in the visible and near-infrared range, and a Beckman AR10 spectrometer in the $2\text{--}10\text{ }\mu\text{m}$ range. Measurements were made with an uncoated substrate in the reference beam of the Cary 14 and were corrected for absorption due to the substrate in the case of measurements made with the Beckman instrument. Sheet resistance was measured using a four-point tungsten probe, and both sheet resistance and Hall coefficient were measured by the van der Pauw method. For the van der Pauw measurements the films were etched into a cloverleaf pattern by masking them with photoresist and etching in dilute hydrochloric acid. Silver paste or simple pressure contacts were used, and the measurements were made using an a-c current and a d-c magnetic field of 4.3 k θ e. Film thickness was measured with a mechanical profilometer to determine the average height of an etched film edge.

Results and Discussion

A series of films $5\text{--}10,000\text{ \AA}$ thick were deposited from a target containing 67 mole percent (m/o) CdO and 33 m/o SnO_2 to find sputtering conditions giving a maximum ratio of transmission to sheet resistance. The sputtering power, total gas pressure, oxygen-argon ratio, and target-substrate spacing were systematically varied. For example, Fig. 2 shows the conductivity and transmission at 550 nm as functions of the sputtering power for films deposited using an argon plus 1.2% oxygen atmosphere at a total pressure of 2×10^{-2} Torr. The target-substrate spacing was 3.5 cm. The transmission shown was obtained by averaging interference fringes and is only weakly dependent on sputtering power, whereas the conductivity increases rapidly with increasing power up to 400W and then levels off. Sputtering powers above 2 W/cm^2 were not used because they resulted in arcing, powder levitation, and overheating at the target surface. Similar problems

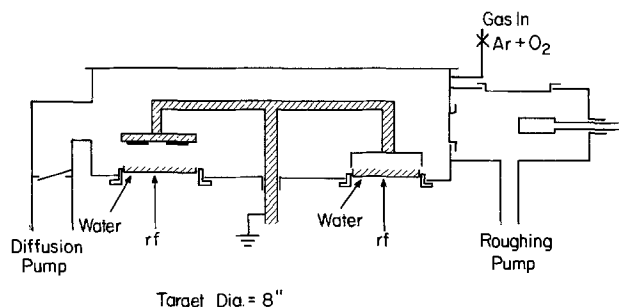


Fig. 1. RF diode sputtering system

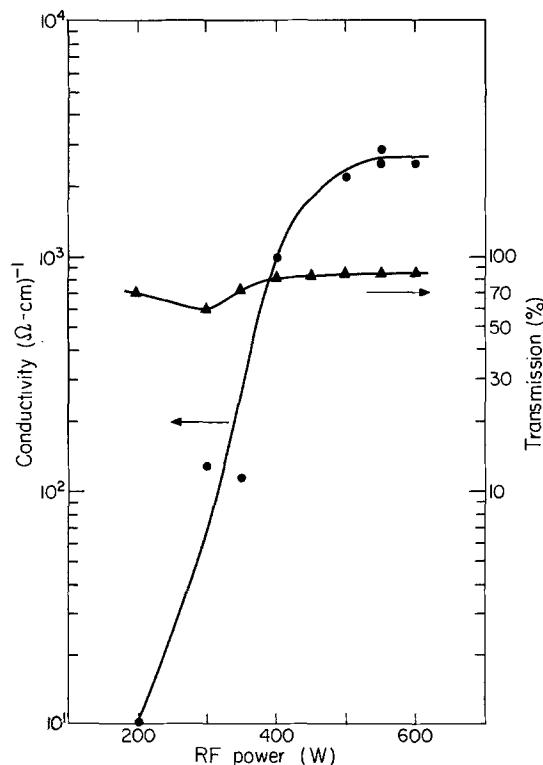


Fig. 2. Dependence of conductivity and optical transmission at 550 nm on the sputtering power. Film thickness $\sim 7000\text{ \AA}$, target 30 m/o SnO_2 , oxygen content of sputtering atmosphere 1.2%.

with powder targets at high power densities have been reported (9), and direct evaporation of CdO at higher powers has been reported to result in changes in film composition (10). From this series of experiments, we found the optimum deposition conditions to be a sputtering power of 500W (1.6 W/cm²), a target-substrate spacing of 3.5 cm, and a sputtering atmosphere of argon plus 0-10% oxygen at a total pressure of 2×10^{-2} Torr. All further experiments were therefore carried out under these conditions; only the compositions of the target and of the sputtering atmosphere were varied.

The deposition rate decreased with increases in the amount of SnO₂ in the target and showed a maximum at 2% oxygen in the sputtering atmosphere. The results for three target compositions are shown in Fig. 3. The deposition rate increased with the amount of CdO in the target, indicating a higher sputtering efficiency for CdO than for SnO₂. This difference apparently increases with oxygen level up to ~3%, since the curves of Fig. 3 diverge up to this point. It would therefore be expected that the target surface would change in composition, becoming depleted of cadmium oxide, during an initial target equilibration process. In support of this we observed that the color of the target surface changed from red-brown to gray during the first few hours of use. Once a steady state has been reached, Cd and Sn must be removed in the ratio in which they are present in the target. On the other hand, because of differences in sticking coefficient between Cd and Sn on surfaces of various types and temperatures, the film composition need not be identical with that of the target. Sputtering was carried out on a new target for at least 8 hr before the films, the properties of which are reported here, were deposited. Also, when changes were made in the oxygen level in the sputtering atmosphere, presputtering was carried out for at least 2 hr under the new conditions. After these conditioning processes, film properties were highly reproducible over a series of more than 50 deposition runs including several changes in sputtering gas composition. This confirms that a steady state had been reached in each case.

To determine film compositions, a series of deposits were made from targets containing 25, 30, and 50 m/o SnO₂ in sputtering atmospheres containing 0-6% oxygen. These were analyzed using an electron microprobe. The results are shown in Fig. 4. Films sputtered from the 30 and 50 m/o SnO₂ targets contained substantially less Cd than the target, whereas films from the 25 m/o SnO₂ target contained somewhat more. In general the Cd/Sn ratio increased with increases in

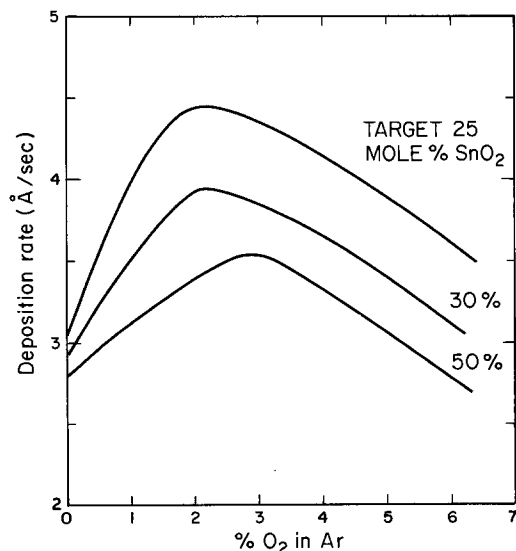


Fig. 3. Deposition rate at 500W power as a function of sputtering atmosphere for three target compositions.

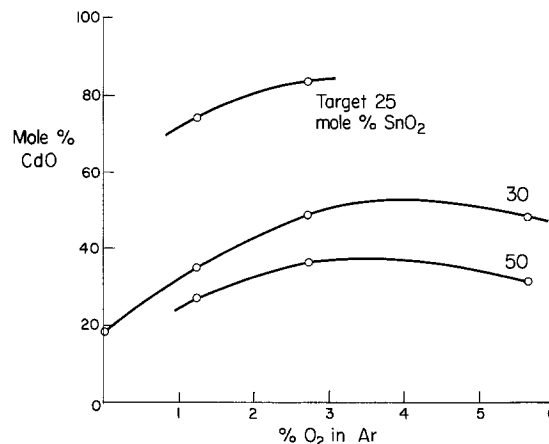


Fig. 4. Results of microprobe analysis of films deposited at 500W from three different target compositions.

the oxygen content of the sputtering atmosphere. These compositions were found to be extremely uniform across each sample. The compositions shown in Fig. 4 cover a range on both sides of the phases CdSnO₃ (50 m/o SnO₂) and Cd₂SnO₄ (33 m/o SnO₂).

With polycrystalline films, significant variations in properties such as conductivity would be expected over such a wide range of compositions. In particular, it has been reported that good conductivity is obtained only from single-phase Cd₂SnO₄ films (7). Lloyd has obtained films having Cd/Sn ratios in the range 0.7-3.5 as a result of heating the target at high powers and thus directly evaporating CdO. It is not reported whether these films were amorphous or crystalline; however, at the power levels used, heating of the substrate would probably have resulted in crystalline films. A distinct downward trend in resistivity was reported at high powers and Cd/Sn ratios. A similar trend has been reported for indium-tin oxide films (11) and attributed to effects of substrate heating on the film structure rather than compositional changes. At a deposition rate of 200 Å/min from argon + 20% oxygen and a Cd₂SnO₄ target, Lloyd obtained Cd/Sn ratios of 1.2-2.3 and conductivities of 5-50 (Ω-cm)⁻¹. Because deposition rates are dependent on geometry and even on substrate, it is difficult to make such a comparison; however, by extrapolation from our results we would expect to obtain a Cd/Sn ratio of 0.5 and a conductivity of 2500 (Ω-cm)⁻¹ for amorphous films deposited from such a target in an argon plus 1.5% oxygen mixture. The conductivity is shown in Fig. 5 for films 5-8000Å thick deposited from the three targets at various oxygen levels. The conductivity decreases rapidly at oxygen levels above 2%, but is not strongly dependent on the target composition itself. Thus, in contrast with these results for polycrystalline films, the conductivity for amorphous films is determined primarily by the oxygen level in the sputtering atmosphere rather than the Cd/Sn ratio in the film. Films deposited from the 50 m/o SnO₂ target at 3% O₂ or from the 30 m/o SnO₂ target at 1% O₂ both contain ~35 m/o CdO; however, their conductivities are 20 and 2000 (Ω-cm)⁻¹, respectively.

X-ray diffraction patterns could not be obtained from any of these films even for film thicknesses of up to 2 μm. This result is consistent with previous reports (9) that films sputtered onto amorphous substrates at temperatures below 400°C are amorphous. In attempts to crystallize the films, they were annealed in nitrogen for 30 min at various temperatures. No crystallization occurred for anneal temperatures up to 600°C. At higher anneal temperatures, the film spalled from the substrate. Both 400°C annealed and as-deposited film surfaces were examined by SEM. They appeared to be smooth even at a magnification of 10,000×, in contrast with sputtered polycrystalline indium-tin oxide films

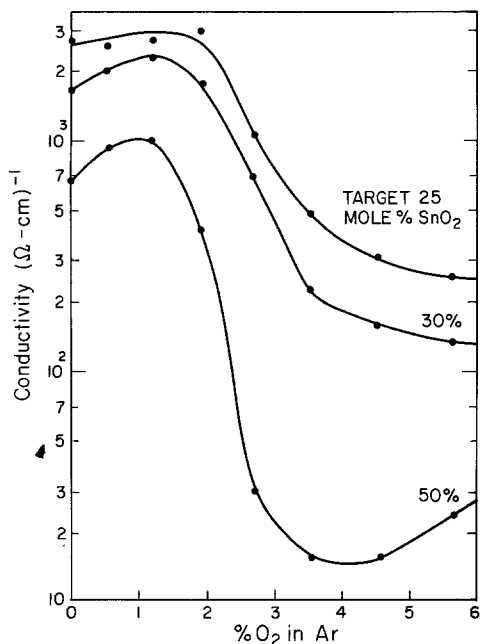


Fig. 5. The conductivity as a function of sputtering atmosphere for films 5-8000Å thick deposited at 500W.

on which a rough dimpled surface could be seen under the same conditions.

Annealing did result in major changes in both electrical and optical properties of the less-conductive films. After the films were annealed in nitrogen at 300°-600°C, the conductivity of films deposited at the highest oxygen levels was drastically increased, but films deposited at below 2% oxygen were much less affected. At 400°C this increase was complete in ~15 min, and no further change occurred with longer anneals of up to 10 hr. The conductivity of films annealed at 400°C for 30 min is shown in Fig. 6. These curves may be compared with the data for as-deposited films shown in Fig. 5. The highest conductivities before annealing were obtained for films sputtered from the 25 m/o SnO₂ target at ~1.5% O₂. A maximum value of 3000 ($\Omega\text{-cm}^{-1}$) was obtained compared with a pre-

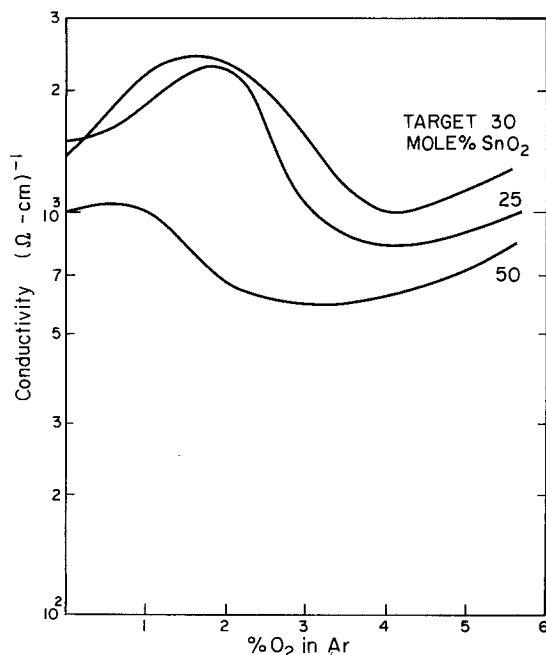


Fig. 6. The conductivity as a function of sputtering atmosphere for films 5-8000Å thick deposited at 500W and annealed in nitrogen at 400°C for 30 min.

viously reported maximum value for as-deposited amorphous films of 385 ($\Omega\text{-cm}^{-1}$) (5). After annealing, the 30 m/o SnO₂ target also sputtered at 1.5% O₂ gave the most conductive films. The large increase in conductivity resulting from nitrogen annealing specimens deposited at a high oxygen level was not reversible by annealing in oxygen. Annealing any of the films in oxygen at 400°C for 30 min after a prior nitrogen anneal at the same temperature resulted in only a 5%-10% reduction in conductivity. Thus, it is unlikely that these large changes in conductivity can be attributed simply to changes in the degree of oxidation of the film.

Since the increase in conductivity on annealing did not result from recrystallization of the films, it could be attributed to an increase in mobility resulting from some more subtle structural change. Alternatively, it could be the result of an increase in carrier concentration due to separation or dissolution of an amorphous second phase. For crystalline films Haacke reported that 750°C anneals reduced the CdO content (9). To discriminate between these two possibilities, Hall-effect measurements were made on the films both before and after annealing.

All of the films were found to be n-type. The Hall mobilities for films deposited at various oxygen levels are shown in Fig. 7. The most unexpected aspect of the results is the relatively high mobility, in the range 15-50 cm²/V sec. These mobilities are as high as or higher than values reported elsewhere for crystalline films (9). Our results are, however, comparable with those reported by the same authors for their amorphous films. Normally electron mobilities of much less than 1 cm²/V sec are measured in amorphous films (12), and the Hall effect is usually anomalous. One possible explanation is that the films are not amorphous, but of extremely small grain size, too small to give an observable x-ray diffraction pattern. The grain size would then, however, have to be less than 20Å. The Hall mobility after a 400°C 30-min anneal in nitrogen is shown in Fig. 8. The values for films from the 25 and 30 m/o SnO₂ targets were not appreciably changed. The shape of the curve for films from the 50 m/o SnO₂ target is, however, quite different. Possibly the changes in these tin-rich films result from dissolution or precipitation of crystalline SnO₂, although no evidence for this was seen in x-ray diffraction patterns.

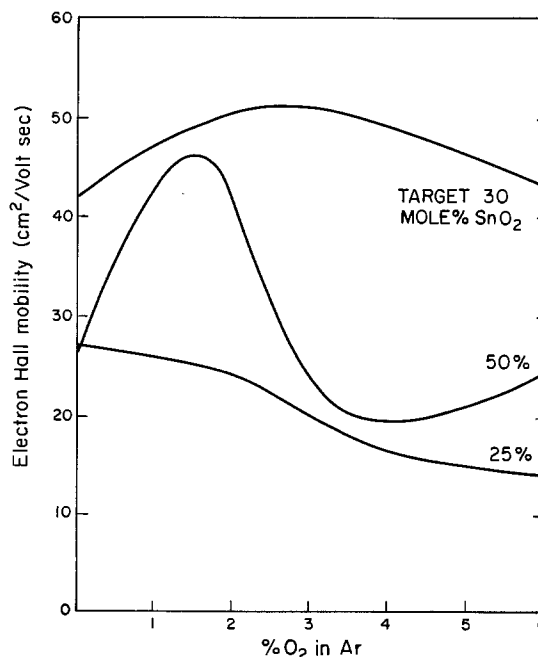


Fig. 7. The electron mobility as a function of sputtering atmosphere for films 5-8000Å thick deposited at 500W.

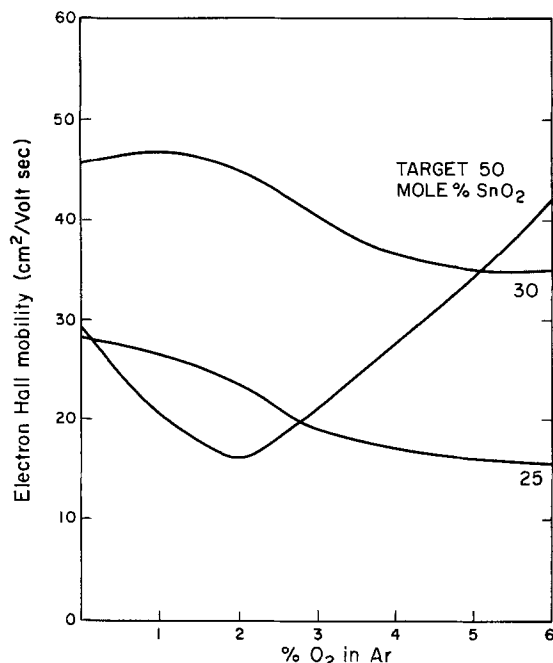


Fig. 8. The electron mobility as a function of sputtering atmosphere for films 5-8000Å thick deposited at 500W and annealed in nitrogen at 400°C for 30 min.

The electron concentrations obtained from Hall measurements, assuming a Hall factor of unity, are shown in Fig. 9. A maximum value of $6.5 \times 10^{20}/\text{cm}^3$ was obtained for the as-deposited films. This is very close to the value $7 \times 10^{20}/\text{cm}^3$ measured for tin-doped indium oxide films deposited in the same sputtering system. The effect of a 400°C anneal in nitrogen on the electron concentration in films deposited from the 30 m/o SnO₂ target is also shown in Fig. 9. After annealing, the electron concentration was only weakly dependent on the oxygen level in the sputtering atmosphere. Similar behavior was seen for films deposited from the

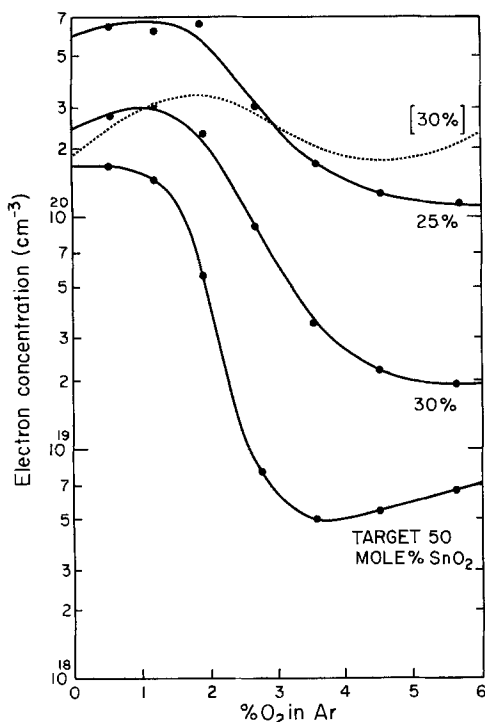


Fig. 9. The electron concentration as a function of sputtering atmosphere for films 5-8000Å thick deposited at 500W. The dashed curve refers to films from the 30 m/o SnO₂ target annealed in nitrogen at 400°C for 30 min.

other targets. Thus, the effect of annealing on the conductivity of films deposited at a high oxygen level results almost entirely from an increase in the electron concentration. As discussed above, this is apparently not simply due to a reduction in oxygen content of these films, since annealing in oxygen instead of nitrogen has little effect.

All of the sputtered films were highly transparent. Their color varied with composition from pale yellow for films of high SnO₂ content to reddish at high CdO level. Transmission spectra are shown in Fig. 10 for a 6950Å thick film sputtered from the 30 m/o SnO₂ target at 2.7% oxygen. This spectrum is similar to that reported previously for amorphous films (5) except that the absorption edge is shifted to somewhat shorter wavelengths. The transmission is 80%-90% throughout most of the visible range, ~10% higher than previously reported for amorphous films (5). Annealing this film in nitrogen at 400°C for 30 min raised its carrier concentration from 8×10^{19} to $3 \times 10^{20}/\text{cm}^3$. The spectrum measured after this anneal is also shown in Fig. 10. At short wavelengths the absorption edge is shifted to higher energies. A similar shift is observed with crystalline indium oxide films (13) and cadmium oxide films (14) and results from the Burstein mechanism. In amorphous materials, however, such shifts have usually been attributed to the effect of annealing in reducing the density of state tailing into the bandgap (15).

Summary

Our results can be summarized as follows.

1. Highly transparent and conductive amorphous films can be deposited onto unheated amorphous substrates from targets consisting of powdered cadmium and tin oxides mixed together. Films having a transmission of 80%-90% in the visible region and a sheet resistance of less than 5 Ω/sq can be deposited under appropriate conditions. These properties are comparable to those achieved with as-deposited crystalline films in the CdO-SnO₂ system. Control of the oxygen level in the sputtering atmosphere is critical to achieving this result.
2. Annealing in nitrogen increases the conductivity of films deposited at high oxygen levels, but does not greatly affect those deposited under optimum conditions. This increase is due to an increase in electron concentration.
3. The target composition is not critical for these amorphous films, but the optimum is 25%-30% SnO₂ in CdO.

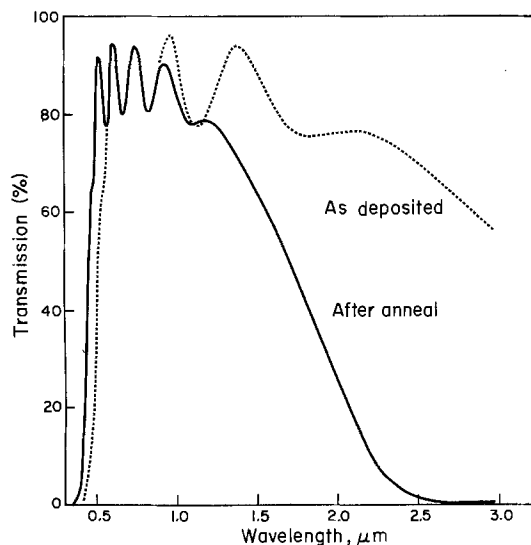


Fig. 10. Optical transmission of a 6950Å thick film deposited at 500W from a 30 m/o SnO₂ target. Dashed curve is for the same film after annealing in nitrogen at 400°C for 30 min.

Acknowledgments

We are grateful for the assistance of L. R. Spaulding in obtaining x-ray data and of R. E. Bice for the microprobe analysis.

Manuscript submitted Jan. 11, 1980; revised manuscript received Dec. 18, 1980. This was Paper 322 presented at the Seattle, Washington, Meeting of the Society, May 21-26, 1978.

Any discussion of this paper will appear in a Discussion Section to be published in the December 1981 JOURNAL. All discussions for the December 1981 Discussion Section should be submitted by Aug. 1, 1981.

Publication costs of this article were assisted by Eastman Kodak Company.

REFERENCES

1. J. L. Vossen, in "Physics of Thin Films," Vol. 9, G. Hass, M. H. Francombe, and R. W. Hoffman, Editors, Academic Press, New York (1977).

2. J. S. Preston, *Proc. R. Soc. London, Ser. A*, **202**, 449 (1950).
3. L. Holland, "Vacuum Deposition of Thin Films," p. 504, John Wiley & Sons, Inc., New York (1956).
4. R. R. Mehta and S. F. Vogel, *This Journal*, **119**, 752 (1972).
5. A. J. Nozik, *Phys. Rev. B*, **6**, 453 (1972).
6. R. D. Shannon, J. L. Gilson, and R. J. Bouchard, *J. Phys. Chem. Solids*, **38**, 877 (1977).
7. G. Haacke, *Appl. Phys. Lett.*, **28**, 622 (1976).
8. N. Miyata, K. Miyake, K. Koga, and T. Fukushima, *This Journal*, **127**, 918 (1980).
9. G. Haacke, W. E. Mealmaker, and L. A. Siegel, *Thin Solid Films*, **55**, 67 (1978).
10. P. Lloyd, *ibid.*, **41**, 113 (1977).
11. J. C. C. Fan and F. J. Bachner, *This Journal*, **122**, 1719 (1975).
12. D. Emin, in "Amorphous and Liquid Semiconductors," W. E. Spear, Editor, University of Edinburgh (1977).
13. H. K. Müller, *Phys. Status Solidi*, **27**, 723 (1968).
14. H. Finkenrath, *Z. Phys.*, **159**, 112 (1960).
15. M. L. Theye, in "Amorphous and Liquid Semiconductors," J. Stuke and W. Brenig, Editors, Taylor and Francis, London (1974).

Thermal Decomposition of InP and Its Influence on Iso-Epitaxy

H. Temkin,* V. G. Keramidas,* and S. Mahajan*

Bell Laboratories, Murray Hill, New Jersey 07974

ABSTRACT

The effects of rapid thermal degradation of InP substrate on the quality of epitaxially grown layers are generally underestimated. Scanning photoluminescence, photocurrent, and etch pitting techniques have been used to evaluate the influence of InP substrate decomposition on the quality of epitaxially grown layers. Growth on substrates protected with an InP cover piece results in epitaxial layers with localized regions of low luminescence and high dislocation density. These are present even in layers with a very good surface morphology. The use of source-piece protection, in conjunction with a shallow In meltback prior to epitaxy, eliminates the deleterious effects of thermal decomposition. The incorporation of these steps into the growth of device wafers greatly improves the yield of InP/InGaAsP light emitting diodes.

The attractiveness of InGaAsP/InP quaternary alloy for use in fiber communications is now well established. In particular, light emitting diodes (LED's) operating in the region of zero dispersion of silica fibers, *i.e.*, between 1.27 and 1.32 μm , can provide much higher data capacity than comparable GaAlAs devices (1). However, liquid phase epitaxy of InP and InGaAsP is not as well established as that of GaAs and its alloys. The recent research effort in this area has been directed mainly towards improvements in the growth of the quaternary alloy (2), without much attention being given to problems related to InP itself.

The rapid thermal degradation of the InP substrate prior to growth appears to be one of the main problems in the reproducible preparation of high quality InP epitaxial layers (3). Among the techniques commonly used to prevent or remove such damage are the use of a polished InP cover piece (4), which protects the substrate before growth and an *in situ* In etch (5, 6). The combination of the two methods, labeled as "perhaps over cautious," has also been reported (7).

In this work, the application of photoluminescence (PL), photocurrent scanning, and etch pitting techniques to evaluate the effectiveness of substrate pro-

tection measures is described. The role of defects caused by the thermal decomposition of InP in device yield and performance will be discussed. We demonstrate that the use of an InP cover piece alone, while assuring an excellent surface morphology of epitaxial layers, results in a large density of macroscopic defects which are not visible by Nomarski-contrast microscopy but clearly seen as areas of lower photoluminescence efficiency. In addition, dislocation pits with the density exceeding that of the underlying substrate are observed. Similarly, it is difficult to achieve good growth reproducibility with a pure In meltback alone.

Experimental Details

Thermal decomposition studies and the liquid phase epitaxy were carried out on {100} oriented InP substrates doped with Sn ($n \approx 1 \times 10^{18} \text{ cm}^{-3}$) and S ($n \approx 1 \times 10^{19} \text{ cm}^{-3}$). The dislocation densities in the respective substrates are $\sim 1 \times 10^4$ and $< \sim 1 \times 10^3 \text{ cm}^{-2}$. All the substrates were polished with 0.5% bromine-methanol to an optically smooth finish. Single layers of InP and double heterostructure (DH) InP/InGaAsP wafers were prepared by conventional techniques (8), with the substrate protected by an InP cover piece prior to growth. The DH wafers consisted of a 5 μm thick buffer layer followed by a 0.8 μm thick

* Electrochemical Society Active Member.

Key words: crystal growth, defects, photoluminescence.

InGaAsP active layer ($\lambda_p = 1.3 \mu\text{m}$) and a $2 \mu\text{m}$ thick confining layer. After the growth, the substrate side of the wafer was thinned to $\sim 100 \mu\text{m}$ by Br-methanol polishing. The contact metallization was subsequently applied through shadow masks. The scanning apparatus used is similar to that recently described by Johnston *et al.* (9) and has a spatial resolution of 5-10 μm , limited by the laser beam size.

Results

As demonstrated in Fig. 1(a), iso-epitaxial layers grown on substrates protected by an InP cover piece show very good surface morphology under Nomarski-contrast microscopy. Only in some isolated areas very small ($< 5 \mu\text{m}$ diam) dissociation pits and associated In droplets with local density of less than $10^4/\text{cm}^2$ can be seen. These shallow pits are probably formed during the short time when the wafer is exposed to high temperature following the termination of growth. Figure 1(b) shows the same area, identified by a "knee" in the lamellae, subjected to the Huber etch for 45 sec to reveal dislocations. The etch pits are either isolated or form pairs, very likely due to the presence of small dislocation half loops. To ascertain whether the dislocations observed in Fig. 1(b) result from the replication of defects present in the bulk of the underlying substrate, the epitaxial layer and the portion of the substrate contiguous to the epi-substrate interface have been removed. The subsequent Huber etching of the substrate indicates significantly lower dislocation density and an absence of very small dislocation half loops.

In addition to the microscopic defects, the PL scan reveals a number of randomly distributed dark spots. Figure 2 shows a picture obtained on a $5 \mu\text{m}$ thick epitaxial layer. The scan covers an area of 0.25 mm^2 , equal in size to a single LED. While the upper right part of the scanned area is uniformly bright, a number of irregularly shaped dark regions can be seen in the remainder of the photograph. The smallest imaged defects are approximately 7-10 μm in diameter, their apparent size limited by the extent of the laser beam. The largest dark feature is about 150 μm long. The difference in PL efficiency between bright and dark areas is no more than a factor of 2. In order to investigate the effects of thermal treatment we have subjected the substrate (protected with InP cover) to a temperature cycle corresponding to melt homogenization prior to the growth. The cycle consists of a rapid rise to 675°C and holding this temperature for 90 min. After this thermal treatment the surface remains flat and featureless under examination at high magnification ($\times 700$) with a Nomarski-contrast microscope. Morphological changes can be seen on intentional scratches, in which fine In droplets appear. The thermal

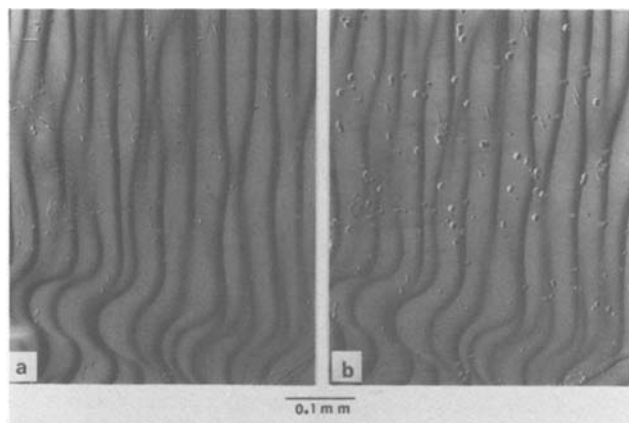


Fig. 1. Optical micrograph of an epi-layer grown with neither the source-piece protection nor the meltback. (a) As-grown surface, and (b) same area as in (a) except that the epi was Huber etched for 45 sec to reveal dislocations.

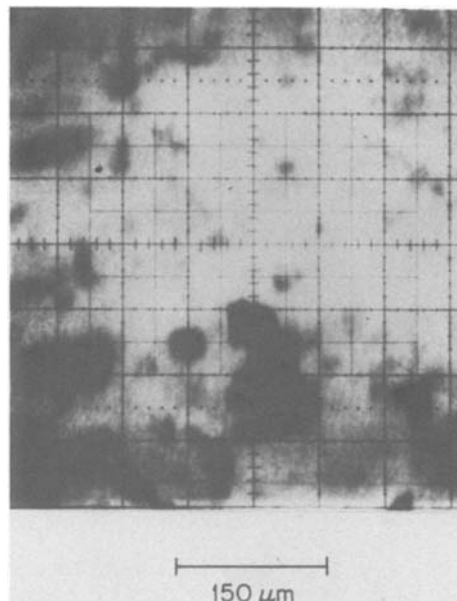


Fig. 2. Photoluminescence scan of the epitaxial layer of InP grown with substrate cover and without In meltback.

etch pits, identical to those described by Lum and Clawson (3), can be found only in a part of the substrate not covered with InP during the high temperature treatment. The PL scan however, reveals a number of dark areas, up to 150 μm in diameter, without corresponding morphological features. These defects, absent in substrate wafers not subjected to an intentional heat-treatment, are similar to those shown in Fig. 2. In addition, the overall PL efficiency (band-edge emission) of the heat-treated substrate decreases by about a factor of 2.

The effects of thermal dissociation on device performance were investigated on single diodes fabricated from different wafers. Since in a DH wafer the buffer layer is covered by other epitaxial layers, it cannot be examined by a PL scan. The defects in the buffer layer can, however, be imaged by a modified photocurrent scan technique, schematically shown in Fig. 3. The photoluminescence generated by the scanning laser beam at the surface of the InP substrate (top of the device) is transmitted through the wafer and is detected by the LED operating as a photodetector. Defects within the substrate and the buffer layer, *i.e.*, in the region above the p-n junction, that act as non-radiative recombination centers, In inclusions, etc., will result in regions of low photocurrent. Unlike the case of conventional photocurrent scan, direct injection of the scanning beam into the depletion region is not required. This photocurrent scan is similar in principle

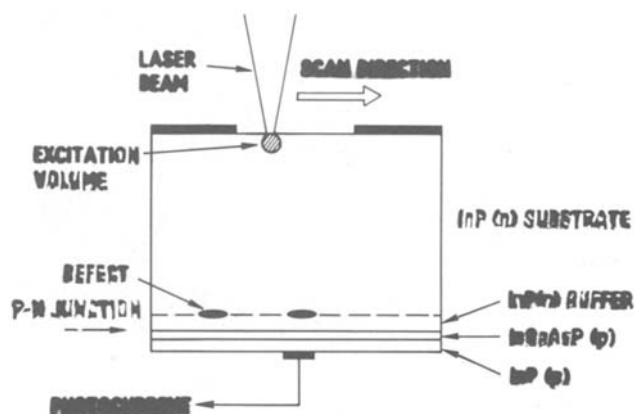


Fig. 3. Schematic diagram of a single chip photocurrent scan. Defects above the p-n junction can be imaged by this technique.

to the recently proposed technique of transmission cathodoluminescence (10). Similar, but not identical, results can be also obtained with the electron beam excitation (11).

Figure 4 shows the result of a photocurrent scan of an individual LED chosen for its low power output from a wafer grown with a cover piece and without In meltback. The bright key-shaped outline is defined by the top metallization. Inside its 200 μm diam opening, in addition to a number of smaller defects, a large and not fully resolved dark feature can be seen. Their dimensions and density are very similar to the defects imaged by PL scan on epitaxially grown InP buffer layers and thermally treated substrates. Examination of the quaternary layer by the PL scan of the epise did not reveal any nonuniformities, suggesting that the observed defects are confined to the InP layers. A large density of defects can be invariably found in diodes with low electroluminescence output. Typically, the power output of these diodes is a factor of 2-5 lower than the best devices obtained from the same wafer.

If the substrate is not covered, a very deep In meltback, up to 25 μm , is required to remove thermal damage. In our experience, however, even with such a deep etch the density of In inclusions exceeds that found in iso-epitaxial layers grown with the substrate cover and a shallow meltback. Once a thermal etch pit which gives rise to an In inclusion is formed, as discussed in Ref. (3), its removal by In etch is very difficult. Furthermore, since the In etch is crystallographic in nature, it is equally difficult to retain the flat surface essential for the growth of uniform epitaxial layers. Finally, the deep meltback frequently results in melt carryover and wipe-off problems. These difficulties of deep In etch become more severe for large area growth ($\cong 1 \text{ cm}^2$).

The defects of the type described above can be eliminated by an *in situ* In meltback, 2-5 μm deep, of the covered InP substrate immediately before growth commences. The PL scan of InP buffer layer and laser-induced current scan of devices grown with this additional In etch do not show any large defects of the type shown in Fig. 2 and 4. In addition, great reduction in the dislocation density is achieved. Figure 5(a) shows the surface of an epitaxial layer grown on low dislocation density S:InP, using the two substrate

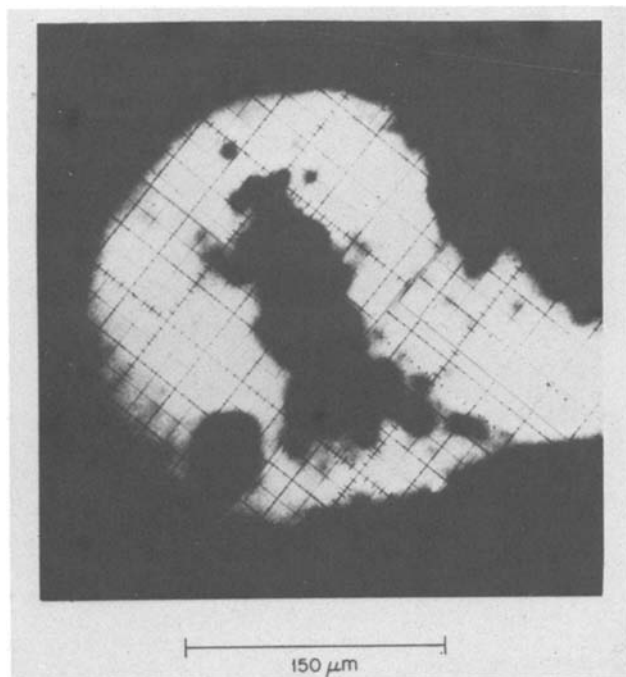


Fig. 4. Photocurrent scan of an LED chip. Bright key-like shape is defined by the n-metallization, as discussed in the text.

protection measures. The surface morphology is somewhat better than that shown in Fig. 1(a). Figure 5(b) shows the same area, indicated by black arrows, Huber etched for 45 sec. The evident microscopic perfection of this iso-epitaxial layer is made possible by the combination of InP cover piece and shallow In meltback. In the growth experiments in which only part of the protected substrate was subjected to a meltback, only that portion did not contain excess dislocations and dislocation loops.

Implementation of these two growth procedures resulted in a large increase of device yields. In the device wafers grown with the substrate cover but without meltback, a very large variation of LED power output was observed, with only about 30% of the diodes clustered at the high power end of the distribution histogram. This percentage increased to 80-90% in devices obtained from wafers grown with the addition of the meltback procedure.

Discussion

The results presented here can be rationalized if it is assumed that a shallow and discontinuous layer of degraded material is formed at the surface of InP on heating. It has been observed that thermal treatment at temperatures higher than 370°C readily degrades the stoichiometry of near-surface InP due to phosphorous out-diffusion (12). When an epitaxial layer is grown on such a surface without meltback, the formation of a degraded layer is expected. The presence of such a thermally degraded layer near the substrate-epitaxial layer interface has been studied in n-GaAs, where the loss of As through thermal annealing has been accompanied by changes in the optical and electrical characteristics of the material. For instance, a reduction in the electron concentration in Se- and Te-doped GaAs has been observed upon annealing (13). Furthermore, photoluminescence studies of thermally degraded layers show great reduction of near bandgap luminescence efficiency and spectral changes associated with formation of As vacancies (14). Since these layers were very shallow, from 0.1 to 0.8 μm , their delineation by etching was not possible. The presence of a similar degraded layer on thermally treated InP is therefore plausible.

Two possibilities exist regarding the origin of dislocations observed in Fig. 1(b). First, the condensation of point defects inherited by an epi-layer during growth may result in formation of dislocations and dislocations loops. Second, thermal decomposition-induced defects in the substrate may aggregate to produce the observed shallow defects, which can then be replicated in the epi-layer. The second mechanism is more likely since it is consistent with the PL scan results and growth experiments in which only a portion of the substrate was etched with In.

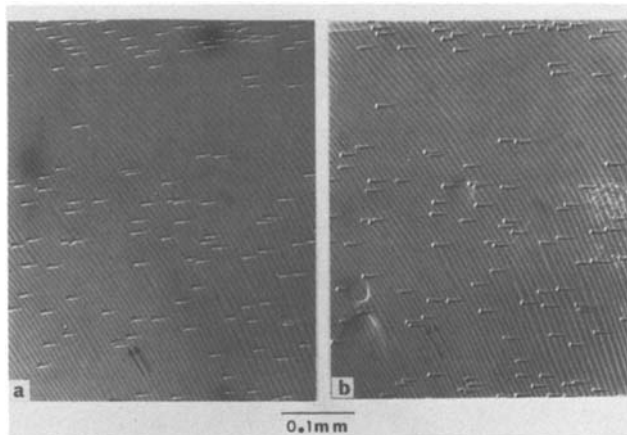


Fig. 5. Optical micrographs of an epi-layer which was protected by a source piece and the substrate melt-back. (a) As-grown surface, and (b) after Huber etching for 45 sec.

The use of substrate cover and In meltback works best when employed together. The InP cover piece greatly reduces the thermal decomposition of the substrate, as shown by the excellent surface morphology, by providing local phosphorus overpressure. However, in spite of good morphology, thermal decomposition is still present as demonstrated by areas of low luminescence in epitaxial layers. This residual shallow layer of dissociated substrate material is subsequently removed by a light In etch.

Manuscript submitted Aug. 6, 1980; revised manuscript received Nov. 26, 1980.

Any discussion of this paper will appear in a Discussion Section to be published in the December 1981 JOURNAL. All discussions for the December 1981 Discussion Section should be submitted by Aug. 1, 1981.

Publication costs of this article were assisted by Bell Laboratories.

REFERENCES

1. J. Conradi, F. P. Kapron, and J. C. Dymant, *IEEE Trans. Electron Devices*, **ed-5**, 180 (1978).
2. M. Feng, L. W. Cook, M. M. Tashima, and G. E. Stillman, *J. Electron Mater.*, **9**, 241 (1980).
3. W. Y. Lum and A. R. Clawson, *J. Appl. Phys.*, **50**, 5296 (1979).
4. P. D. Wright, Y. C. Chai, and G. A. Antypas, *IEEE Trans. Electron. Devices*, **ed-26**, 1220 (1979).
5. V. Wruck, G. J. Scilla, L. F. Eastman, R. L. Henry, and E. M. Swiggard, *Electron Lett.*, **12**, 394 (1976).
6. P. D. Wright, E. A. Rezeke, M. J. Ludowise, and N. Holonyak, Jr., *IEEE J. Quantum Electron.*, **qe-13**, 637 (1977).
7. R. C. Goodfellow, A. C. Carter, I. Griffith, and R. R. Bradley, *IEEE Trans. Electron Devices*, **ed-26**, 1215 (1979).
8. M. A. Pollack, R. E. Nahory, J. C. DeWinter, and A. A. Ballman, *Appl. Phys. Lett.*, **33**, 314 (1978).
9. W. D. Johnston, Jr., G. Y. Epps, R. E. Nahory, and M. A. Pollack, *ibid.*, **33**, 992 (1978).
10. A. K. Chin, H. Temkin, S. Mahajan, W. A. Bonner, A. A. Ballman, and A. G. Dentai, *J. Appl. Phys.*, **50**, 5707 (1979).
11. "Quantitative Scanning Electron Microscopy," D. B. Holt, M. D. Muir, P. R. Grant, and I. M. Boswara, Editors, p. 213, Academic Press, New York (1974).
12. R. F. C. Farrow, *J. Phys. D. Appl. Phys.*, **7**, 2436 (1974).
13. C. S. Fuller and K. B. Wolfstin, *J. Appl. Phys.*, **34**, 2287 (1963).
14. M. Otsubo, H. Miki, and S. Mitsui, *Jpn. J. Appl. Phys.*, **16**, 1957 (1977).

Defect-Revealing Etches on GaAs: A Comparison of the AHA with the A/B and KOH Etches

Wilfried R. Wagner, L. I. Greene, and L. I. Koszi*

Bell Laboratories, Murray Hill, New Jersey 07974

ABSTRACT

AHA etch-revealed features on {100} N⁺ GaAs wafers were compared to defects revealed by the well-characterized A/B and molten KOH etches on the same sample areas. It was demonstrated that the AHA etch technique reveals dislocation line segments, growth striae, and microdefects as does the A/B etch. Unlike the A/B etch the AHA etch did not result in a "memory" effect. A 1:1 correlation between molten KOH-induced dislocation etch pits and AHA-revealed dislocation line segments was demonstrated.

Today, highly doped Bridgeman-grown GaAs represents the most commonly utilized substrate for GaAlAs-GaAs LPE. In this material only line dislocations can presently be characterized with confidence using various defect-revealing etches. A defect microstructure is known to exist (1, 2) in this material but has not been characterized in any detail. Oscillations in the rates of dopant incorporation during growth arising from constitutional supercooling (3) are revealed as the etched striae (4, 5) but the defect microstructure often observed in combination with such striae (5) has not been investigated as well. Defect-revealing etches are useful in determining substrate quality, evaluating the results of epitaxial growth, and monitoring processing steps. However, it is necessary to know and understand the behavior of each etchant thoroughly. Because of the unique characteristics of defect-revealing etches they can only be used with confidence if they have been well calibrated (5) and compared with other etches. The A/B etch (6), now commonly used in the GaAs industry, initially yielded irreproducible results until its "memory" (7) charac-

teristic was understood. This etch determines defects/volume rather than defects/area as do most other etches.

One of us (LIG) reported on a new defect-revealing etch (8) effective on all orientations of conducting GaAs. Ammonium-hydroxide anodic (AHA) etching occurs by anodic electrochemical dissolution in a solution consisting of reagent grade ammonium hydroxide added to distilled water in sufficient quantities to reach a pH level between 10.6 and 13.4. Current densities between 0.1 and 2 mA/cm² and etching times between 1 and 5 min are sufficient to delineate defects. The AHA etch is particularly sensitive to changes in the electronic properties of GaAs such as the impurity atmospheres of dislocations and dopant segregation in growth striae. The simplicity, safety, and ease of use makes this a desirable etching technique. In this paper we present the results of an etch-to-etch calibration of the AHA etch vis-a-vis the A/B (5) and molten KOH (9) etches.

Procedures

Individual defects were mapped by etching a numbered grid on the back of selected {100} substrates by means of a photomask matrix grid. The map on the

* Electrochemical Society Active Member.

Key words: etching, "memory" effect, microdefects.

back of the wafer and the etched wafer front were superimposed by utilizing a Zeiss Universal microscope equipped with a "Photochanger" coupled to an infrared sensitive TV camera. The image on the TV monitor shows the strong image of the transmitted matrix pattern on the bottom surface (Fig. 1) while the photographed image is due to the infrared filtered reflected light from the etched top surface (Fig. 3a). Careful alignment ensured that identical wafer cross sections were viewed in both images. A specific wafer area could then be relocated easily by finding its grid position on the TV monitor. The use of Nomarski interference contrast was found to be essential in resolving etch features.

The etchants used were the AHA etch (8), the A/B etch (6), and the molten KOH (9) etch. All etched surfaces were of the {100} orientation from Si-doped ingots. AHA etching was done at room temperature in an electrolyte consisting of DI water and NH_4OH , usually at a pH of 11.5 and at 25 mA current for 30 sec. Following Stirland (2), A/B etching was done at

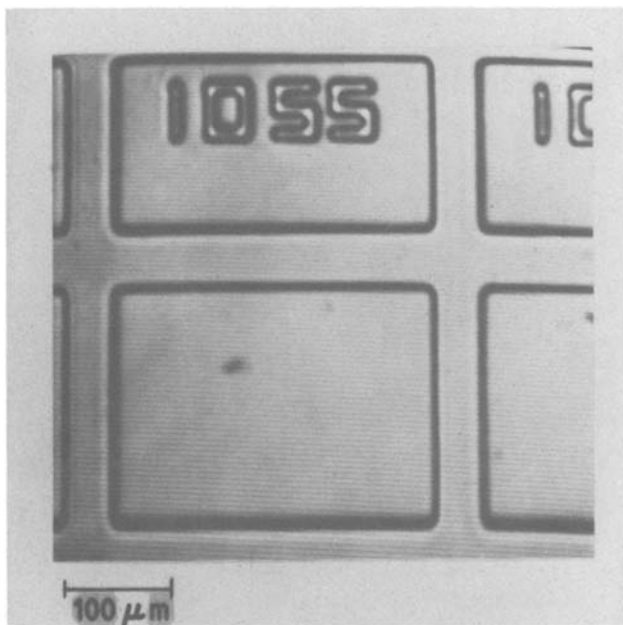


Fig. 1. The TV monitor image of a section of a specimen corresponding to the photomicrograph of an AHA etched surface shown in Fig. 3a.

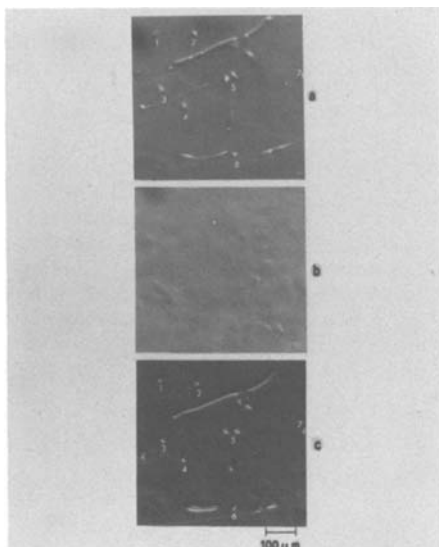


Fig. 2. Photomicrographs of an AHA-A/B etching sequence: (a) the AHA-etched surface; (b) the repolished surface; (c) the A/B-etched surface.

room temperature for a few minutes only. A/B etching was stopped when the Nomarski interference contrast of the first-revealed dislocations was similar to that of the AHA etch-revealed dislocations. In this manner complications arising from the "memory effect" (7) are avoided.

The molten KOH etch was utilized at 300°C for 30 min. A fresh KOH solution was always used and the samples were dipped into the solution as soon as the temperature set point was reached, approximately 15 min after the power was turned on. Experimental problems were common with this technique. Frequently, a solid crust would form over the solution; breaking this crust caused occasional samples to fracture. Defect-revealing etching did not take place on samples that were in contact with the precious metal crucible used to contain this corrosive etch. The exact composition of this etch is ill defined. KOH has a literature melting point of 360°C, yet the anhydrous, reagent-grade KOH we used was liquid already at 250°C. This chemical is extremely hygroscopic, therefore we suspect that this etch actually consists of a concentrated aqueous solution where the water is derived from atmospheric moisture. Defect-revealing etching did not occur in a dry nitrogen atmosphere.

The different etches were successively used on the same samples. The initial surface preparation on each sample consisted of a Syton-Peroxide (S-P) chemo-mechanical polish which had been used satisfactorily for liquid phase epitaxy applications. The subsequent polishing between each etch application was the same but did not result in as fine a surface because polishing was stopped as soon as the etchant-induced morphology was no longer visible.

The occurrence of a "memory" effect resulting from prolonged etching with the AHA etch was investigated by repeated sequential etching on the same area. Initially an array of dislocations was located on an AHA-etched surface by the technique described above. Then, to demonstrate the action of the A/B "memory" effect, the sample was A/B-etched without repolishing and the resultant morphology recorded after 5, 10, and 20 min of cumulative etching time. Next, again without repolishing the sample, the wafer was AHA-etched and the resultant morphology was recorded on the same area after 1, 3, 6, and 12 min of cumulative etching time.

Results

Calibrating the AHA etch against the AB etch.—Figures 2-4 demonstrate the correlation between the AHA and A/B etchant-revealed defects on three types of etch features, namely dislocations, "growth" striae, and microdefects. In Fig. 2a seven similar line features resulted from AHA etching (Fig. 2c). In Fig. 2c all seven defects mapped in Fig. 2a could be identified again. Both etchant-induced defect morphologies are similar. In Fig. 3 the etch features of interest consist of the "growth" striae. Using the defect contrast calibrated in Fig. 2 as location markers, in Fig. 3a the AHA etch reveals a stria superimposed on the sets of line defects at locations 1 and 2. Neither etch induced stria at location 3.

The AHA etchant-revealed defects visible in Fig. 4a are especially complex. In Fig. 4a the AHA-revealed line defects and striae are partially obscured by the dense background of a "microdefect" structure. With this sample, as defect registration was not considered essential, nearly 2 mils of sample thickness were polished off to achieve a specular surface before the A/B etch was applied. The results of the A/B etch are shown in Fig. 4b. A similar microdefect morphology of equivalent density is again found to exist in the same area.

Calibrating the AHA etch against the molten KOH etch.—An elegant correlation of the two etches is presented in Fig. 5. A {100} surface that had been etched

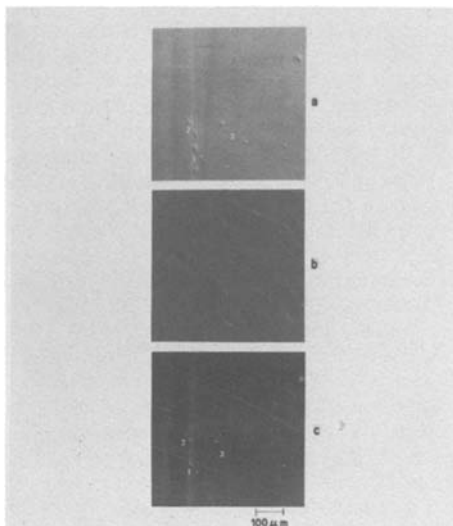


Fig. 3. Photomicrographs of an AHA-A/B etching sequence: (a) the AHA-etched surface; (b) the repolished surface; (c) the A/B-etched surface.

with molten KOH was cleaved, exposing a $\{110\}$ cleavage plane. Then the cleavage plane was etched with the AHA etch. To every KOH-generated etch pit which was (substantially) intersected by the cleavage plane, an AHA-revealed line feature was traced. No other AHA-induced feature could be correlated with the KOH etch. The KOH etch did not reveal striae or microdefects.

Testing for the "memory" effect.—The effects of a series of etch sequences on the same six dislocations are shown in Fig. 6. In Fig. 6a six dislocations that were initially identified with the AHA etch and subsequently etched for 5 min with the A/B etch are shown. In Fig. 6b and c the etch morphology after 10 and 20 min of cumulative room temperature A/B etching is shown. The typical A/B dislocation traces can be seen to extend as a function of total etching time from the AHA-induced pits. Upon changing back to the AHA etch in Fig. 6d, e, and f, a pit can be seen to appear at the end of each A/B-induced dislocation trace. As a function of time, these pits do not elongate as was seen to occur with the A/B etch traces, but simply become more pronounced.

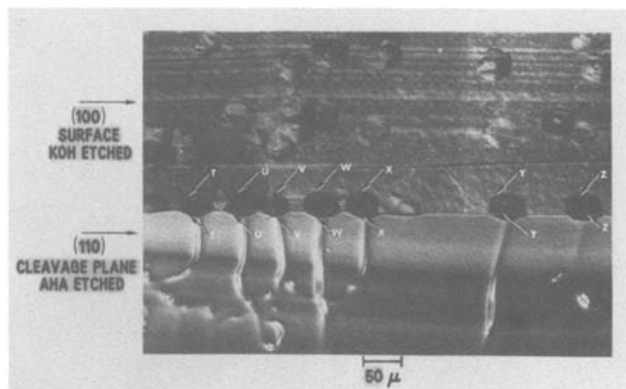
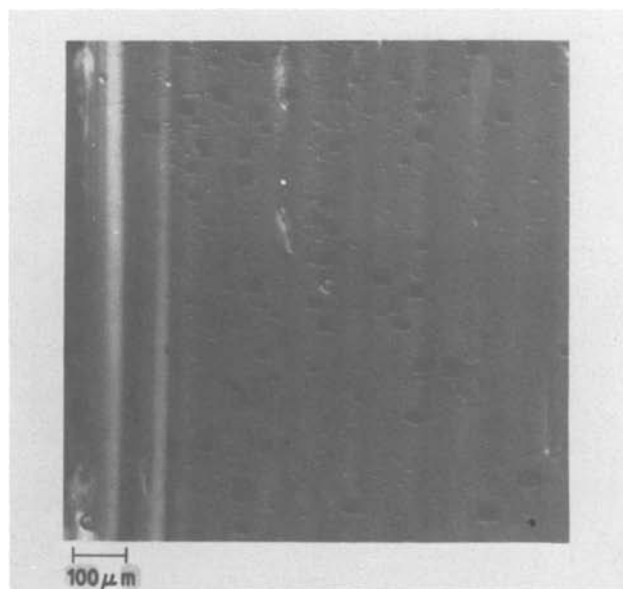


Fig. 5. A photomosaic of a molten KOH-etched specimen with an AHA-etched cleavage face.

Discussion

It is well known that the A/B-induced morphology shown in Fig. 2c is the result of dislocations that existed in the material that was removed by the etch (1, 2, 5, 7). AHA-induced line features, as shown in Fig. 2a, were previously correlated with existing dislocations with an x-ray topograph (8). Molten KOH-induced etch pits, as are illustrated in Fig. 5, have been shown to result from the intersection of a dislocation with a free surface (10). We have demonstrated here that the use of the AHA etch results in a characteristic morphology at the same locations at which the other etches revealed the existence of dislocation line segments. The AHA-induced etch pits that begin to be visible in Fig. 6d prove that the AHA etch reveals dislocations intersecting the surface at the actual point of emergence. Dislocations near the surface are also revealed by the AHA etch. Pits Y and Z in Fig. 5 both have the AHA-revealed dislocations leading to the apex of the pit, but this dislocation "contrast" is different from that associated with pits T-X. The weaker relief suggests dislocation line segments underneath. The electrolytic etches are particularly sensitive to the impurity atmosphere surrounding dislocations (11). Because of this, a faint defect trace can be resolved for a "submerged" dislocation.

It was demonstrated in Fig. 3 that both the AHA and the A/B etch will reveal the same striae, but the relief is not the same, although our setting of the Nomarski contrast made it appear so. Given the nature of the two

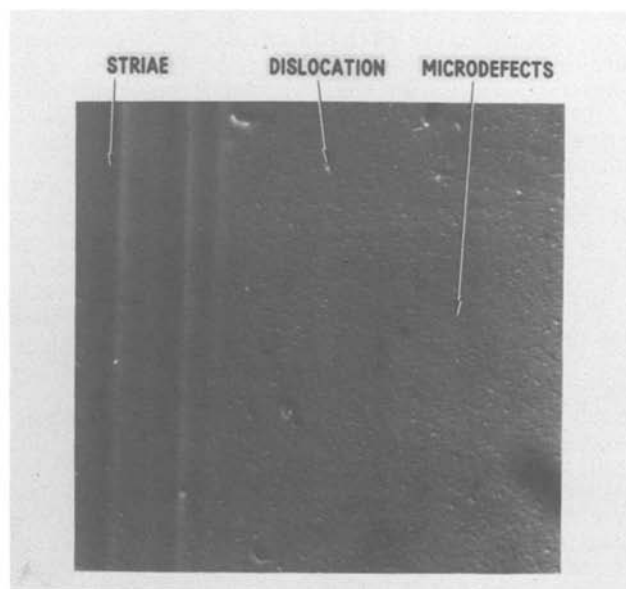


Fig. 4. Photomicrograph of an AHA-A/B etching sequence: (a, left) the AHA-etched surface; (b, right) the A/B etched surface

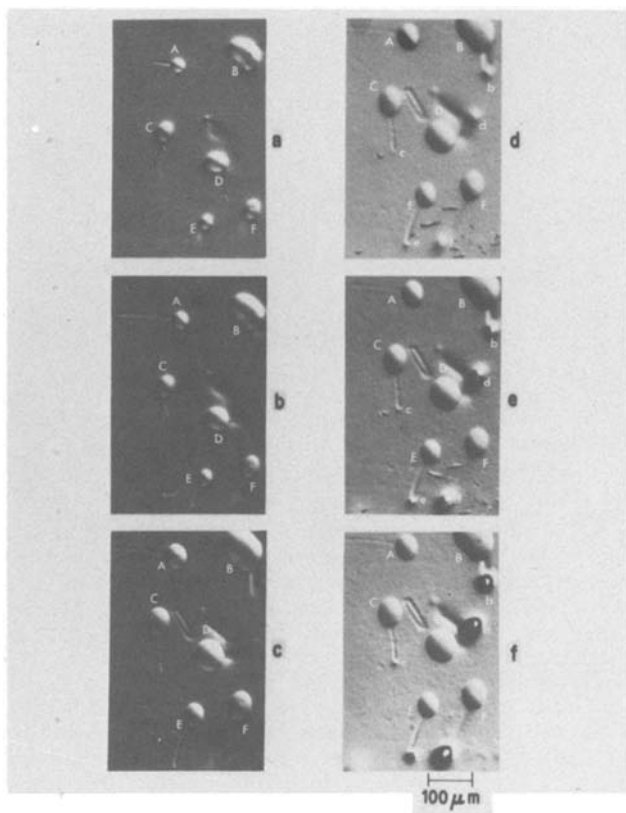


Fig. 6. Photomicrographs of an AHA-A/B-AHA etching sequence: (a) after 1 min AHA and 5 min A/B etching; (b) after 5 more minutes A/B etching; (c) after 10 more minutes A/B etching; (d) after 1 more minute AHA etching; (e) after 3 more minutes AHA etching.

etches, *i.e.*, that the A/B etch preferentially removes perfect material (7) while the AHA etch is thought to be primarily sensitive to the electronic nature of the material (11), the striae relief of both etches is opposite, *i.e.*, AHA-induced ridges were correlated to A/B-induced troughs.

Our data confirms that the KOH etch is only effective in revealing dislocations intersecting the free surface. This suggests that the KOH etch is principally sensitive to strain, while the A/B etch is also sensitive to chemical effects such as the impurity atmosphere near dislocations and impurity segregation or variations in stoichiometry at striae. Similarly, the AHA etch appears to be principally sensitive to variations in the electronic structure of the material. For this reason, dislocations and striae are revealed by the A/B etch in semi-insulating GaAs while this material is not normally etched at all by the AHA etch, but in N^+ GaAs striae are revealed much stronger with the AHA etch than with the A/B etch.

The nature of the defect microstructure revealed by the AHA etch in Fig. 4a and by the A/B etch in Fig. 4b is not understood. It may be composed of small dislocation loops or stacking faults. We do not believe that these microdefects correspond to the "S" pits described by Stirland and Augustus (1) because neither the observed defect morphology nor the wafer doping level correspond to their findings. The large rectangular pits visible in Fig. 4a occur as a result of local accelerated etching possibly at microdefect sites and are found after prolonged etching. These are also not well understood, presumably they are initiated by localized conductivity fluctuations. Prolonged etching was necessary in this particular sample to achieve resolution of both the dislocations and striae in addition to the microdefects.

The growth of the A/B etch-induced dislocation traces as a function of time in Fig. 6a-c is a clear illus-

tration of the A/B "memory" effect. It is not unexpected to observe such relatively long dislocation traces because the A/B etch removes approximately $2.5 \mu\text{m}/\text{min}$ at room temperature. Eventually, these traces form a dense network of lines across the entire sample. With the AHA etch such a "memory" effect does not take place. As AHA etching is continued (Fig. 6e and f) the AHA etch features have become more pronounced but new etch features do not occur. The AHA-induced dislocation etch morphology visible in Fig. 6f is essentially identical to the original AHA-induced morphology still visible in Fig. 6a. (For brevity, a figure depicting the original, AHA-etched surface was omitted.) After 12 min of AHA etching, areas adjacent to the six dislocations shown had already degraded into the large rectangular pits discussed above, indicating that the specimen was completely etched. Nevertheless, prolonged AHA etching did not result in new dislocation traces and therefore a misleading defect determination.

The effect of the AHA etch on p-type (Zn -doped $2 \times 10^{18}/\text{cm}^3$) GaAs is somewhat different. The observed defect morphology was identical to n-type material; dislocations, microdefects, and striae were revealed precisely the same, but accelerated etching effects were never observed on this type of material. Etching could be continued apparently indefinitely, therefore new dislocation traces would eventually appear. This is, of course, a "memory" effect. In practice, only a prolonged etching, continued long after dislocation traces were readily resolved, would result in an erroneous defect determination.

Conclusion

The AHA technique reveals defects on GaAs such as dislocations, growth striae, and microdefects. The resultant defect morphology is similar to that of the A/B etch but the etch is readily effective on conducting GaAs only. All defects revealed by the molten KOH or A/B etches are also revealed by the AHA etch. There is no "memory" effect associated with the AHA etch but prolonged etching may result in large pits at the sites of defects.

Acknowledgments

We are indebted to N. E. Schumaker for many fruitful discussions and his critical review of this manuscript.

Manuscript submitted July 7, 1980; revised manuscript received Dec. 12, 1980.

Any discussion of this paper will appear in a Discussion Section to be published in the December 1981 JOURNAL. All discussions for the December 1981 Discussion Section should be submitted by Aug. 1, 1981.

Publication costs of this article were assisted by Bell Laboratories.

REFERENCES

1. D. J. Stirland and P. D. Augustus, "GaAs and Related Compounds," p. 150, Edinburgh (1976).
2. D. J. Stirland, *Inst. Phys. Conf. Ser.*, **33a**, 150 (1977).
3. D. T. J. Hurle, *Solid State Electron.*, **3**, 37 (1961).
4. C. LeMay, *J. Appl. Phys.*, **34**, 439 (1963).
5. D. J. Stirland and B. W. Straughan, *Thin Solid Films*, **31**, 139 (1976).
6. M. S. Abrahams and E. S. Buiocchi, *J. Appl. Phys.*, **36**, 2855 (1965).
7. D. J. Stirland and R. Ogden, *Phys. Status Solidi (A)*, **17**, K-1 (1973).
8. L. I. Greene, *J. Appl. Phys.*, **48**, 3739 (1977).
9. J. G. Grabmaier and C. B. Watson, *Phys. Status Solidi*, **32**, K-13 (1969).
10. H. Richter and M. Schulz, *Kristall Techn.*, **9**, 1041 (1974).
11. M. M. Faktor and J. L. Stevenson, *This Journal*, **125**, 621 (1978).

Detection of Structural Defects in N-type InP Crystals by Electrochemical Etching under Illumination

A. Yamamoto, S. Tohno, and C. Uemura

Ibaraki Electrical Communication Laboratory, Nippon Telegraph and Telephone Public Corporation, Tokai, Ibaraki 319-11, Japan

ABSTRACT

An experimental study has been made of the detection of structural defects in n-type InP crystals by electrochemical etching under illumination. Under illumination, presence of structural defects such as mechanical damage or grown-in defects on the crystal surface led to a decrease of dissolution rate of the surface. This enabled structural defects to be revealed as etch hillocks. Surface damage introduced during handling processes of the crystal was detected with high sensitivity. By observing etch hillocks, detailed information was obtained regarding fine structure and distribution of dislocations or dislocation clusters in nominally undoped crystals. It was found that novel defects, which were not involved in nominally undoped crystals ($n = 1-5 \times 10^{16} \text{ cm}^{-3}$), were involved in highly sulfur-doped crystals ($n = 4 \times 10^{18} \text{ cm}^{-3}$) with low dislocation densities ($\text{EPD} \lesssim 10^3 \text{ cm}^{-2}$).

The interest in InP has increased recently since InP crystals have been used as substrates for InGaAsP-InP lasers emitting in the 1.0-1.6 μm wavelength region. It is well known that a poor quality substrate is a major source of imperfections in epilayers. Therefore, to enhance the reliability of InP-based devices, it is essential to lower defect content in InP crystals. Simultaneously, it is desirable to evaluate InP crystals accurately by simple and convenient methods.

Chemical etching techniques have been widely used to detect structural defects in III-V compound crystals. For GaAs crystals, it has been found that the chemical etching using the AB etchant (1) or the photoetching using the modified AB etchant (2) produce etch hillocks at defects. Such etch hillocks give us more useful information with regard to the fine structure of defects than the "orthodox" etch pits (3). We have found previously (4) that, in the electrochemical etching of n-type GaAs under illumination, etch hillocks can be produced by employing suitable current density and incident light intensity. The detection of structural defects in n-type GaAs by electrochemical etching has been studied by Factor and Stevenson (5).

For InP crystals, on the other hand, chemical etchants that produce etch hillocks have not been reported. Also, few studies have been made of anodic dissolution or electrochemical etching of InP.

In this work, we studied anodic dissolution of n-type InP under illumination and, on the basis of that, detected structural defects in n-type InP crystals by electrochemical etching under illumination. As a result, it was proved that electrochemical etching under illumination was able to reveal handling damage or grown-in defects as etch hillocks with high sensitivity and high resolution. It was also found that novel defects, which were hardly detected by the conventional chemical etching technique, were involved in highly sulfur-doped InP crystals.

Experimental

The apparatus used for the study of anodic dissolution and electrochemical etching of n-type InP under illumination is schematically illustrated in Fig. 1. The anodic current was pulsed at a frequency of 30 Hz and with a 10% duty cycle. Measurements of potential were made of InP electrodes against a saturated calomel electrode (SCE). The InP sample was illuminated with an incandescent lamp of 60W, and the light

was introduced to the sample surface by using a low-loss quartz rod. For the electrolyte, a solution of 1 mole/liter NaOH (6) was employed. The electrolyte was kept at 25°C and dry N_2 gas was slowly bubbled during experiments.

Most of samples used were InP single crystals with $\langle 100 \rangle$ or $\langle 111 \rangle$ P orientation grown by the liquid encapsulation Czochralski (LEC) method. The nominally undoped crystals with carrier concentration of $1-5 \times 10^{16} \text{ cm}^{-3}$ were grown in our laboratory. The sulfur-doped crystals with carrier concentration of $4 \times 10^{18} \text{ cm}^{-3}$ were purchased from Varian Associates (USA). For the study of carrier concentration dependence of dissolution rate, heavily sulfur-doped crystals ($n = 2 \times 10^{19} \text{ cm}^{-3}$) grown by the synthesis solute-diffusion (SSD) method (7) were also used. The InP wafers of 0.5 mm thickness were cut from the single crystal rods. They were mechanically lapped with SiC slurry

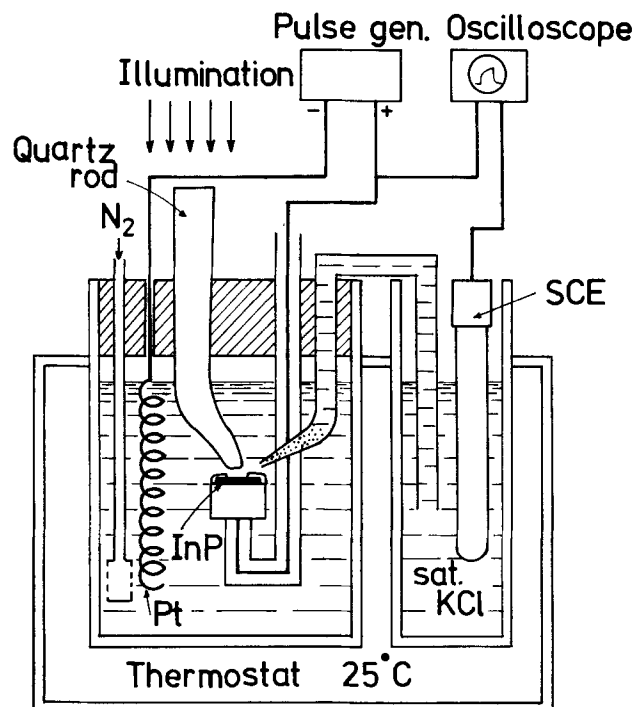


Fig. 1. Apparatus used for the study of anodic dissolution and electrochemical etching of n-type InP under illumination.

Key words: InP, structural defect, anodic dissolution, electrochemical etching.

(No. 4000) and then mechanically polished with fine abrasive alumina ($0.3 \mu\text{m}$ particle size). After being degreased and rinsed with deionized water, they were chemically polished in a 2% Br-methanol solution.

The sample was fixed by the sample holder shown in Fig. 2. The InP wafer was cemented with an adhesive wax to the Teflon electrode holder and coated with Apiezon wax. The exposed area of the InP surface was $5\text{--}10 \times 10^{-2} \text{ cm}^2$. Ohmic contact to the wafer was made by rubbing Ga-In eutectic on the rear surface of the wafer.

To calibrate etch hillocks produced by the electrochemical etching, the sample surface was also chemically etched with a solution of $2 \text{ H}_3\text{PO}_4 + 1 \text{ HBr}$ (Huber etch) (8), which has been currently used to reveal dislocations in InP crystals. Etched patterns were examined by the Nomarski technique. Profiles of etched surface were determined by Dektak (an instrument for mechanical measurement of roughness and waviness, manufactured by Sloan Instruments Corporation).

Results and Discussion

I-V Characteristics of n-Type InP Electrodes

Current density-dissolution potential (*I-V*) characteristics of n-type InP electrodes were studied to understand the anodic behavior and, furthermore, to find conditions for preferential etching for the detection of structural defects. Dissolution potentials of InP electrodes under the dark and illumination conditions were measured as a function of current density. By employing a pulsed current of 10% duty ratio, the potential became completely stable and was measured with high reproducibility.

Figure 3 shows the *I-V* curves for a chemically polished InP sample and a mechanically polished one. The samples are nominally undoped (100) InP crystals with carrier concentration of $1 \times 10^{16} \text{ cm}^{-3}$. In the dark, the surface damaged mechanically exhibits less noble dissolution potential than the undamaged one. This fact indicates that the presence of defects leads to an increase in reactivity of the InP surface. This increase is due to the hole generation at defects introduced by mechanical polishing. From this fact, it is obvious that etch pits are produced at defect sites on the surface when the electrochemical etching is carried out in the dark. By illuminating the surface, dissolution potential of the undamaged surface is drastically shifted to a more active value, whereas that of the damaged one is slightly changed. Under illumination, consequently, the undamaged surface is more reactive than the damaged one. Such smaller dissolution rates

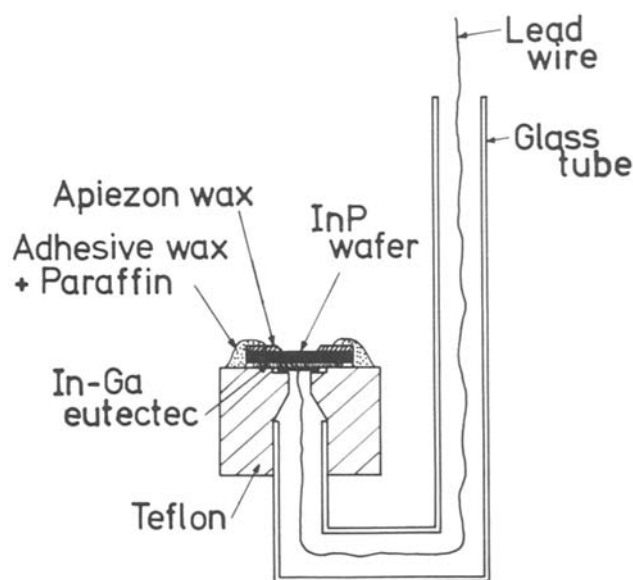


Fig. 2. Cross section of sample holder

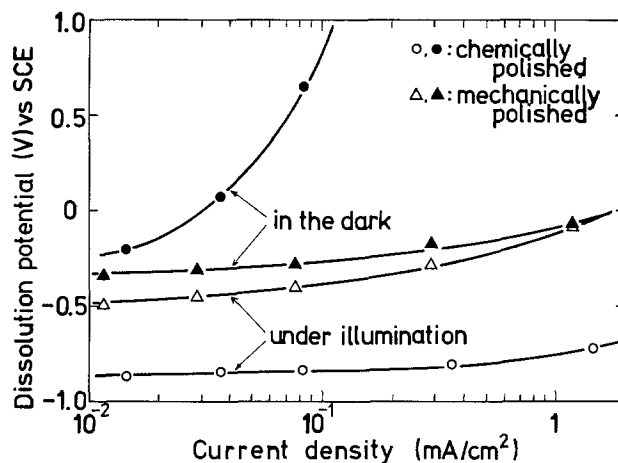


Fig. 3. Dissolution potential-current density curves for $\langle 100 \rangle$ -oriented InP electrodes polished chemically or polished mechanically with abrasive alumina ($0.3 \mu\text{m}\phi$).

of the damaged surface under illumination is due to lower hole concentration at the surface, because defects introduced by mechanical polishing act as recombination centers of holes generated by incident light. This fact suggests that etch hillocks can be produced at defect sites by the electrochemical etching under illumination.

Figure 4 shows the *I-V* curves for $\langle 100 \rangle$ -oriented InP samples with different carrier concentrations. All samples were chemically polished in a Br-methanol solution before measurements. In the dark, the sample with higher carrier concentration shows less noble dissolution potential, i.e., higher dissolution rate. This result is similar to those for other semiconductors (4, 9, 10) and cannot be explained by taking into account only the hole concentration in the bulk of the sample. Under illumination, the sample with higher carrier concentration shows lower dissolution rates because of its smaller increase in dissolution rate by illumination. Such a smaller increase in dissolution rate by illumination, as well as the higher dissolution rate in the dark, for the sample with higher carrier concentration may be explained by the decrease of contribution rate of hole to the anodic dissolution process (9). The sample with carrier concentration of $2 \times 10^{19} \text{ cm}^{-3}$ is electrochemically polished even in the dark, and the *I-V* curve for this sample is scarcely influenced by the introduction of mechanical damage. These facts show that the detection of defects by electrochemical etching is impossible for such heavily doped samples. From the facts mentioned above, it also seems that n-type InP with carrier concentrations of about 10^{19} cm^{-3} needs no holes in the dissolution reaction (10).

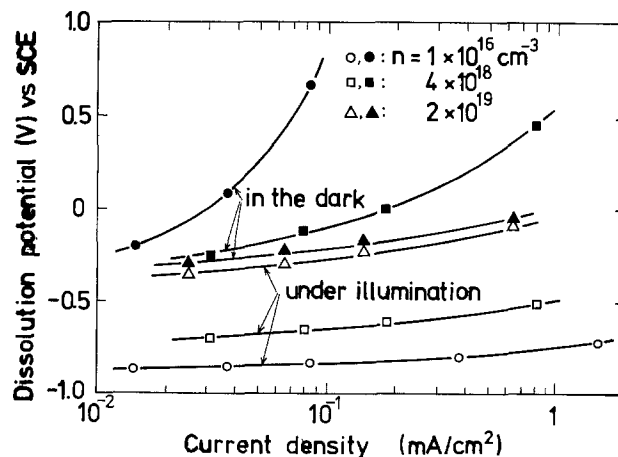


Fig. 4. Carrier concentration dependence of dissolution potential-current density curve for $\langle 100 \rangle$ -oriented InP electrodes.

It can be seen from the carrier concentration dependence of the dissolution rate shown in Fig. 4 that growth striations in the crystal are detected as a rugged feature on the etched surface, because they are due to local fluctuations of carrier concentration in the crystal.

Detection of Handling Damage and Grown-In Defects

Handling damage.—Surface damage introduced during preparation or handling processes of the samples must be completely removed in order to evaluate grown-in defects accurately. It is well known that damage is introduced by cutting, lapping, or mechanical polishing of the crystal (preparation damage). Such damage can be removed by the chemical polishing as a final preparation process. Damage is also introduced in the handling process of the sample after the chemical polishing (handling damage). The handling damage is not so heavy as the preparation damage and, therefore, is considerably difficult to detect. In this work, the detection of handling damage by electrochemical etching under illumination was investigated.

Figures 5 and 6 show the handling damage revealed by electrochemical etching under illumination. The samples are nominally undoped crystals ($n = 1 \times 10^{16} \text{ cm}^{-3}$) with $\langle 100 \rangle$ orientation. Linear and dot-like features are produced when the surface was rubbed with a filter paper [Fig. 5(a)]. These features consist of elevated structures (etch hillocks) as seen from Fig. 5(b). Band-like hillocks are produced when the surface was held with a Teflon tweezer, as shown in Fig. 6(a) and 6(b). Before the electrochemical etching, no features such as scratches are observed on the surface. As can be seen from the results in Fig. 5 and 6, however, the electrochemical dissolution rate at the damaged portions on the surface is remarkably decreased. These results suggest that the recombination velocity of holes at the damaged portions is extremely in-

creased in spite of no changes in the surface morphology. On the other hand, no features are produced by the chemical etching with the Huber etch or a Br-methanol solution. Therefore, it is concluded that the detection sensitivity of electrochemical etching to defects is higher than that of chemical etching.

Detection of the handling damage for the samples of $4 \times 10^{18} \text{ cm}^{-3}$ is successfully performed as in the case of the samples of $1 \times 10^{16} \text{ cm}^{-3}$. For the samples of $2 \times 10^{19} \text{ cm}^{-3}$, on the other hand, the detection is unsuccessful, that is, no etch hillocks are formed and the samples are electrochemically polished. This result agrees with that expected from the I - V curves.

As described above, it is confirmed that etch hillocks can be produced at damaged portions on the n -type InP surface by the electrochemical etching under illumination, and is also found that light damage such as handling damage can be detected with high sensitivity by this technique.

Grown-in defects.—Detection of grown-in defects was carried out for the samples prepared carefully to eliminate any surface damage. The samples investigated are nominally undoped ($n = 1.5 \times 10^{16} \text{ cm}^{-3}$) and sulfur-doped ($n = 4 \times 10^{18} \text{ cm}^{-3}$) crystals grown by the LEC method.

Defects in nominally undoped crystals.—A typical electrochemically etched pattern produced on the (100) surface is shown in Fig. 7(a). Dot-like features are observed and they consist of elevated structures (etch hillocks) as shown in Fig. 7(b). The surface shown in Fig. 7(a) was then chemically etched with the Huber etch to reveal etch pit patterns. The result and the correspondence between the etch hillocks and the etch pits are shown in Fig. 7(c) and 7(d), respectively. Good correspondence between both is evident. Therefore, it is concluded that the etch hillocks are due to dislocations because the Huber etch produces dislocation pits. The correspondence, however, is not completely perfect. A few pits which do not correspond

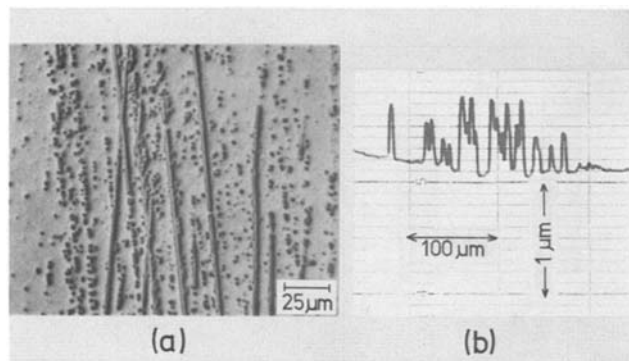


Fig. 5. Surface damage introduced by rubbing with a filter paper: (a) electrochemically etched pattern; (b) profile of the etched surface.

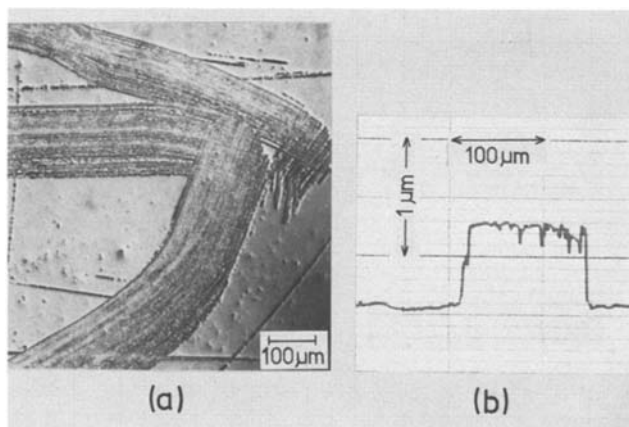


Fig. 6. Surface damage introduced by holding with a Teflon tweezer: (a) electrochemically etched pattern; (b) profile of the etched surface.

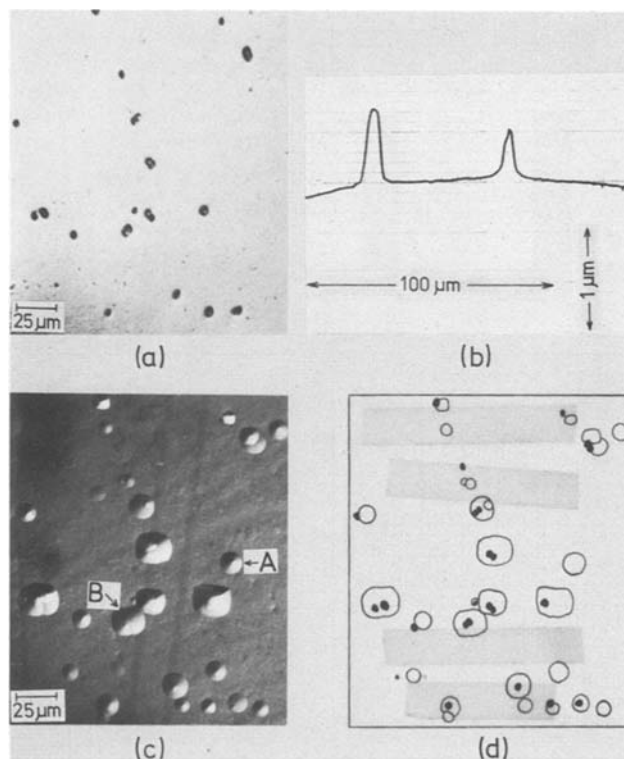


Fig. 7. Detection of dislocations on the (100) surface of nominally undoped crystal: (a) electrochemically etched pattern; (b) profile of the etched surface; (c) etch pit pattern revealed with the Huber etch; (d) correspondence between etch hillocks (a) and etch pits (c).

to the etch hillocks, such as the pit denoted by "A" in Fig. 7(c), are observed. The numbers of such pit were found to increase with increasing the time of the chemical etching. This fact indicates that these pits are due to dislocations laid at deeper portions beneath the original surface. Several rectangular pits are observed in Fig. 7(c) and each pit corresponds to two hillocks lying very close to each other as seen in Fig. 7(d). One of the rectangular pits, denoted by "B" in Fig. 7(c), has no apex and resembles a saucer-pit rather than a dislocation-pit. These facts suggest that the defects responsible for the rectangular pits are not line defects (linear dislocations) but isolated defects such as dislocation loops.

Figure 8 shows the electrochemically etched pattern produced on the (111)P surface. Linear hillocks, which are not found on the (100) surface, are observed on the (111)P surface in addition to dot-like hillocks. This is in contrast with the results for GaAs (2,3) in which dot-like hillocks mainly exist on the (111)As surface and linear hillocks on the (100) surface. The linear hillocks on the (111)P surface show the existence of dislocations comparatively parallel to (111) planes in InP crystals. The straight line denoted by "S" in Fig. 8 is a growth striation. It should be noted that the revelation of growth striations in the crystals of such low doping levels ($\sim 10^{16} \text{ cm}^{-3}$) shows the high detection sensitivity of electrochemical etching to inhomogeneity in the crystal.

In some of the crystals investigated, defects consisted of clustered etch pits, i.e., clustered dislocations were observed when the surfaces were etched with the Huber etch. A typical result is shown in Fig. 9(a). Figure 9(b) shows such defects revealed by electrochemical etching under illumination. Although these defects are observed as mere clusters of pits in Fig. 9(a), it can be seen from Fig. 9(b) that they consist of the following three regions: a ball-shaped nucleus, a region of inseparably concentrated dislocations around the nucleus, and an outermost region in which dislocations are scattered. The nucleus is not always found in all cases. Defect II in Fig. 9(b) is an example in which the nucleus is not found. The region of inseparably concentrated dislocations is star-like and is extended to $[110]$ directions. Seki *et al.*¹ have observed this type of defect in etch pit patterns and found from Auger analysis of the etched surface that the composition of the crystal is In-rich at the portions involving these

¹ M. Seki, Y. Kawamura, and H. Okamoto, Preprint of the 40th Autumn Meeting of the Japan Society of Applied Physics, Sapporo, September, 1979, No. 30aG8 (in Japanese).

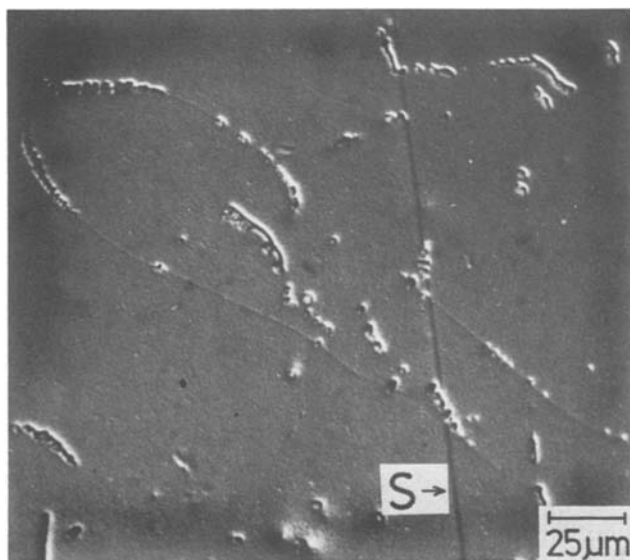


Fig. 8. Electrochemically etched pattern produced on the (111)P surface of nominally undoped crystal.

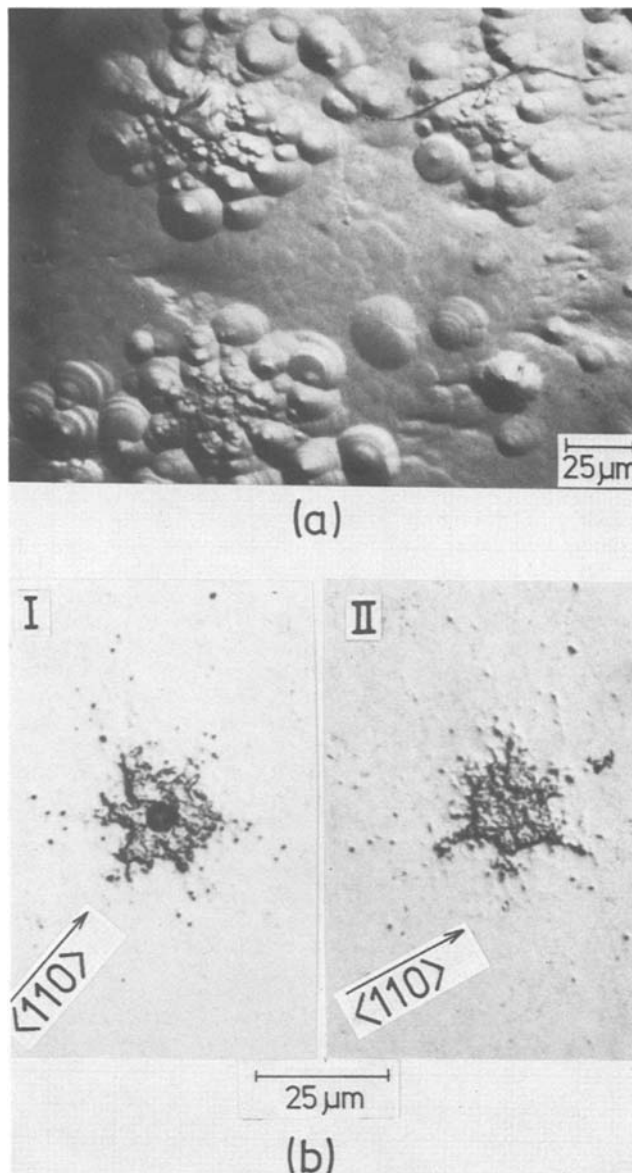


Fig. 9. Clusters of dislocations observed in nominally undoped crystal: (a) chemically etched pattern; (b) electrochemically etched pattern.

defects. On the other hand, similar defects to those revealed here have been observed in GaP crystals pulled from Ga-rich melts and they have been attributed to the defects caused by Ga inclusions (11). From these results, it is reasonable to interpret that the defects shown in Fig. 9 are caused by In inclusions and the ball-shaped nucleus is an In inclusion. The nucleus in the defect II in Fig. 9(b) is thought to either have been already removed during the preparation process of the sample or have been buried below the surface.

As described above, major defects detected in nominally undoped InP crystals are dislocations and dislocation clusters including In inclusions. The observations of etch hillocks produced by the electrochemical etching under illumination give more detailed information on the structure and distribution of these defects than those of etch pits.

Defects in S-doped crystals.—The samples investigated were cut from S-doped wafers having average etch pit density (EPD) of $\leq 10^3 \text{ cm}^{-2}$. The distribution of EPD in the wafer was not uniform, that is, EPD depended largely on the portion of the wafer. The samples having EPD from zero to more than 10^4 cm^{-2} were prepared. Sorts or densities of defects newly detected in

the samples were found to be different depending on EPD in the sample.

The results obtained for the samples having high EPD ($\geq 10^3 \text{ cm}^{-2}$) are described. Figure 10(a) shows a typical pattern produced electrochemically on the (100) surface. Etch pits observed on the surface were formed by using the Huber etch before the electrochemical etching. In this sample, no other defects are observed except for dislocations and growth striations. Figure 10(b) shows the surface profile of the pit-free region in Fig. 10(a) traced perpendicularly to the striae. Growth striations are due to local fluctuations of doping levels in the crystal. From the *I-V* curves in Fig. 4, it can be seen that the dents and bulges in Fig. 10(b) correspond to the regions of lower doping levels and of higher doping levels, respectively.

The results obtained for the samples having EPD of nearly zero are described and discussed. Figure 11(a) shows the electrochemically etched pattern produced on the (100) surface of the dislocation-free sample. In contrast to the result for the higher EPD sample [Fig. 10(a)], ellipse-shaped or dash-like features are observed in this figure. The density of these features was found to drastically decrease with increasing EPD in the sample. The density on the surface shown in Fig. 11(a) is about 10^5 cm^{-2} . These features are distributed parallel to $\langle 110 \rangle$ direction, as seen from Fig. 11(b). When the surface shown in Fig. 11(a) is etched with the Huber etch (etched depth $\approx 2 \mu\text{m}$), these features disappear leaving the vestiges "A"- "D" only for the relatively large features "A"- "D" as shown in Fig. 11(c). Mahajan *et al.* (12) have observed similar features to the ellipse-shaped ones in the transmission cathodoluminescence (TCL) images for highly zinc-doped (100) crystals and have interpreted them as impurity clusters. In the TCL images, however, the fine structure of the ellipse-shaped features and the presence of the dash-like features have not been re-

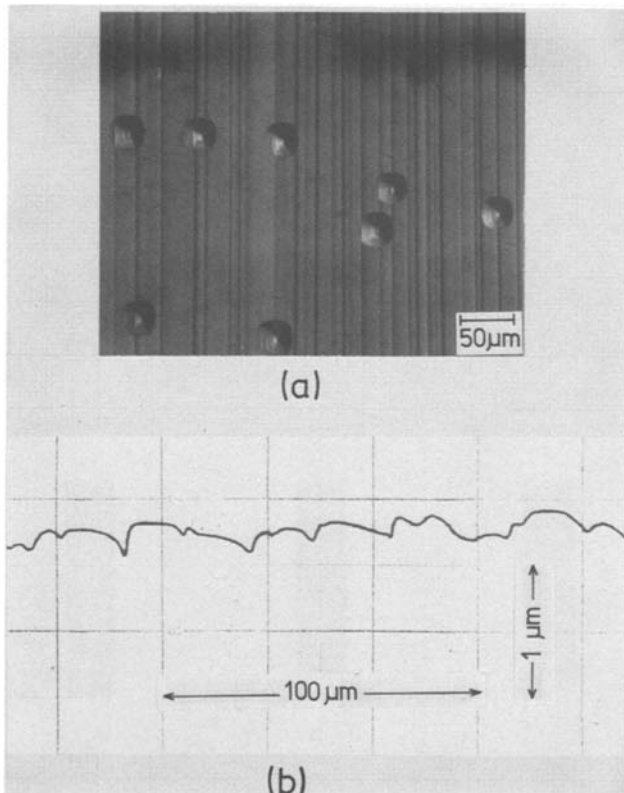


Fig. 10. (100) surface of S-doped crystal ($n = 4 \times 10^{18} \text{ cm}^{-3}$) having dislocation density of about 10^4 cm^{-2} after electrochemical etching: (a) electrochemically etched pattern; (b) surface profile of the pit-free region. The etch pits observed in (a) were produced with the Huber etch before electrochemical etching.

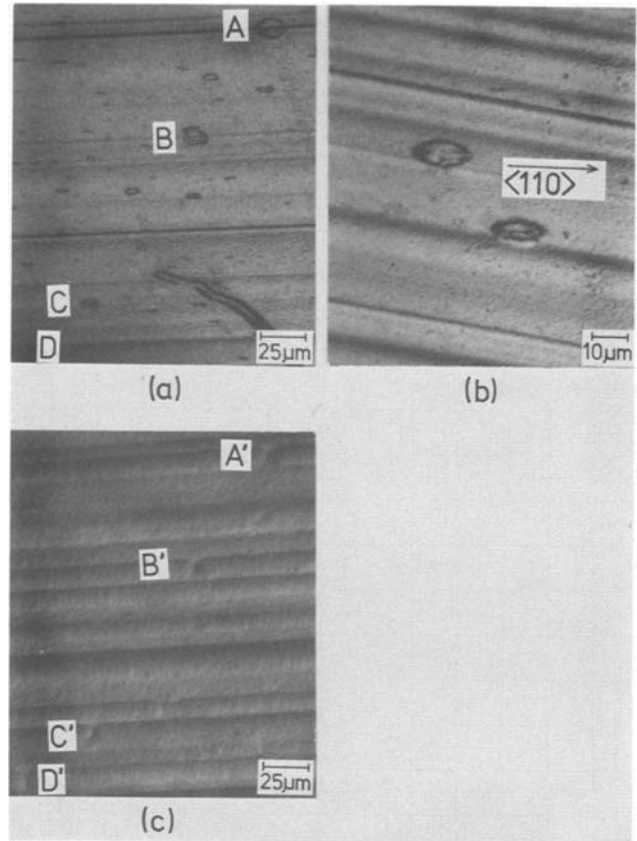


Fig. 11. (100) surface of S-doped crystal ($n = 4 \times 10^{18} \text{ cm}^{-3}$), dislocation-free, after electrochemical etching: (a) electrochemically etched pattern; (b) magnification of (a); (c) variation of the etched pattern (a) by chemical etching with the Huber etch (etched depth is about $2 \mu\text{m}$).

vealed. This may be due to the relatively low resolution of the TCL image.

Figure 12(a) shows the electrochemically etched pattern produced on the (111)P surface of dislocation-free sample. Dot-like features of density about 10^4 cm^{-2} are observed. Figure 12(b) is a magnification of Fig. 12(a). In this figure, relatively large features denoted by "A" and "B" and a small one denoted by "C" are observed. When the surface in Fig. 12(b) is etched with the Huber etch (etched depth $\approx 2 \mu\text{m}$), saucer-pits "A" and "B" are produced at the features "A" and "B," respectively, and, on the other hand, the feature "C" disappears leaving a faint vestige "C," as shown in Fig. 12(c). This result suggests that the features "A" and "B" are due to different origins from that of the "C." The origin of feature "C" seems to be similar to that of the feature observed on the (100) surface [Fig. 11(a)], because both features disappear after the chemical etching.

As described above, it was found, with the assistance of electrochemical etching under illumination, that novel defects, which were not observed in the crystals with high dislocation densities, were involved in the dislocation-free crystals doped with sulfur. Although these defects are somewhat larger in size than the microdefects observed in GaAs:S or GaAs:Te (13), we believe that their presence is closely related with high-impurity doping and/or with reduction of grown-in dislocations. Interpretation of structural defects by electrochemical etching alone is difficult, however. Further investigations to reveal fine structures of the defects detected in this work with transmission electron microscope (TEM), in combination with the detection of the defects by the electrochemical etching, are now in progress.

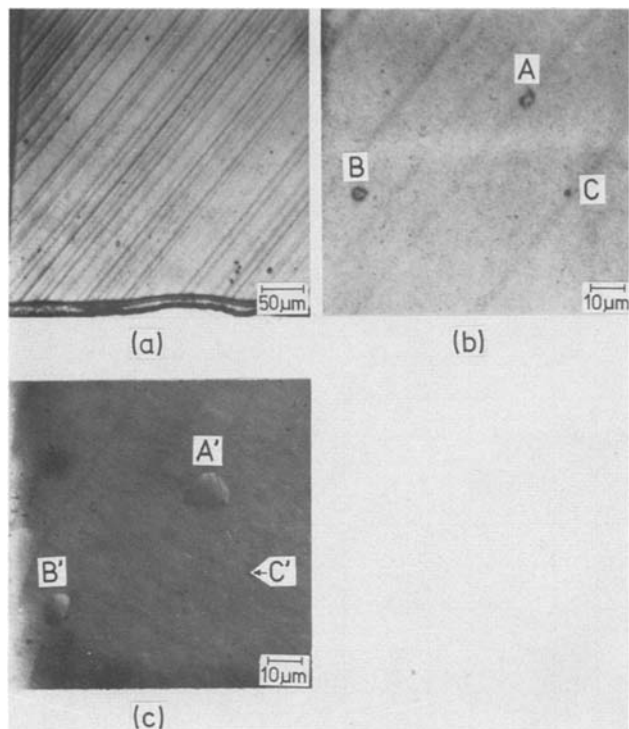


Fig. 12. (111)P surface of S-doped crystal ($n = 4 \times 10^{18} \text{ cm}^{-3}$), dislocation-free, after electrochemical etching: (a) electrochemically etched pattern; (b) magnification of (a); (c) variation of the etched pattern (a) by chemical etching with the Huber etch (etched depth is about $2 \mu\text{m}$).

Summary

Anodic dissolution and electrochemical etching of n-type InP under illumination were studied in order to detect structural defects in n-type InP crystals.

The presence of structural defects led to a decrease of dissolution rates of the crystal surface under illumination. This enabled us to reveal defects as etch hillocks. Surface damage introduced during treatments with a filter paper or a tweezer were detected with high sensitivity. Major grown-in defects detected in nominally undoped crystals ($n = 1\text{--}5 \times 10^{16} \text{ cm}^{-3}$) were dislocations and dislocation clusters caused by In inclusions. By the observations of the etch hillocks, more detailed information was provided regarding the structure and distribution of these defects than by those of the etch pits. In sulfur-doped crystals ($n = 4 \times 10^{18} \text{ cm}^{-3}$) with low dislocation densities (EPD

$\lesssim 10^3 \text{ cm}^{-2}$), ellipse-shaped or dash-like defects were observed on the (100) surface and dot-like defects on the (111)P surface. Such defects were hardly detected by the chemical etching technique. The density of these defects were decreased drastically with increasing dislocation density in the crystal. The presence of these defects was thought to be closely related with high-impurity doping and/or reduction of grown-in dislocations.

Through these investigations, it was demonstrated that electrochemical etching under illumination had the ability to reveal inhomogeneity in n-type InP crystals, including structural defects, with high sensitivity and high resolution.

Acknowledgment

The authors would like to thank Dr. N. Niizeki, Dr. H. Takata, and Dr. K. Kudo for their encouragement and support through this work, and Mr. S. Shinoyama for helpful discussions.

Manuscript submitted July 14, 1980; revised manuscript received Dec. 18, 1980.

Any discussion of this paper will appear in a Discussion Section to be published in the December 1981 JOURNAL. All discussions for the December 1981 Discussion Section should be submitted by Aug. 1, 1981.

Publication costs of this article were assisted by Nippon Telegraph and Telephone Public Corporation.

REFERENCES

1. M. S. Abrahams and C. J. Buiocchi, *J. Appl. Phys.*, **36**, 2855 (1965).
2. T. Saitoh, S. Matsubara, and S. Minagawa, *This Journal*, **122**, 670 (1975).
3. D. J. Stirland, "Gallium Arsenide and Related Compounds 1976," (Inst. Phys. Conf. Ser. No. 33a) p. 150 (1977).
4. A. Yamamoto and S. Yano, *This Journal*, **122**, 260 (1975).
5. M. M. Factor and J. L. Stevenson, *ibid.*, **125**, 621 (1978).
6. A. B. Ellis, J. M. Bolts, and M. S. Wrighton, *ibid.*, **124**, 1063 (1977).
7. S. Tohno, A. Yamamoto, and C. Uemura, *Jpn. J. Appl. Phys.*, **19**, L342 (1980).
8. A. Huber and N. T. Linh, *J. Cryst. Growth*, **29**, 80 (1975).
9. R. L. Meek, *This Journal*, **118**, 427 (1971).
10. R. Gereth and M. E. Cowher, *ibid.*, **115**, 645 (1968).
11. G. A. Rozgonyi, A. R. Von Neida, T. Iizuka, and S. E. Haszko, *J. Appl. Phys.*, **43**, 3141 (1972).
12. S. Mahajan, W. A. Bonner, A. K. Chin, and D. C. Miller, *Appl. Phys. Lett.*, **35**, 165 (1979).
13. T. Kamejima, J. Matsui, Y. Seki, and H. Watanabe, *J. Appl. Phys.*, **50**, 3312 (1979).

Studies of Phosphorus Pile-Up at the Si-SiO₂ Interface Using Auger Sputter Profiling

S. A. Schwarz,¹ R. W. Barton, C. P. Ho,* and C. R. Helms*

Stanford Electronics Laboratories, Stanford University, Stanford, California 94305

ABSTRACT

We have used Auger sputter profiling to investigate in detail the pile-up of phosphorus at the Si-SiO₂ interface, which occurs during thermal oxidation of heavily doped silicon. We find that, in the early stages of oxidation, the interfacial region acts as a sink for phosphorus. As oxidation proceeds, the "pile-up" within 50Å of the interface saturates and the phosphorus concentration in the silicon near the interface begins to rise. High temperature nitrogen anneals had little effect on the pile-up, indicating that existence of the pile-up cannot be explained by a simple diffusion mechanism. We also observed the pile-up to be greatly diminished in a heavily boron-compensated sample. We discuss possible mechanisms which may be responsible for this effect.

During the thermal oxidation of heavily phosphorus-doped silicon, the phosphorus, which is relatively insoluble in SiO₂, is rejected by the oxide and pushed into the silicon where it diffuses away from the interface. This process was first described in detail by Grove *et al.* (1). If oxide growth and diffusive transport are the only operative mechanisms in the process, the phosphorus concentration near the Si-SiO₂ interface should be no more than twice the bulk concentration for typical conditions, as illustrated in Fig. 1. However, a magnified view of the interfacial region, obtained using Auger sputter profiling, shows an anomalous buildup of phosphorus near the interface as illustrated in the inset in Fig. 1. This phosphorus pile-up has been observed by several groups (2-6) and is the subject of this paper.

The pile-up phenomenon has implications for device performance. We will show that the rapid uptake of phosphorus at the interface has a significant effect on the doping level near the interface, especially during the early stages of oxidation. This may be particularly important for VLSI devices in which thin oxides, high doping levels, and shallow junctions may be present. The phosphorus pile-up is also one of a class of related interfacial phenomena which are of current practical interest. Other phenomena include dopant-enhanced oxidation (7-9), oxidation-enhanced diffusion (10), and doped oxide-source diffusion (11).

In this paper, we investigate the evolution of the phosphorus pile-up during oxide growth for a variety of oxidation conditions. We also examine the effects of high temperature N₂ anneals and boron compensation. We find that the driving force for phosphorus pile-up is an equilibrium property of the interface, and is not due to the oxidation process itself. The interface acts as a sink for phosphorus, which may be represented as a sharp minimum in the chemical potential for that region. A vacancy mechanism model is also presented which is consistent with our experimental results and also accounts, to some extent, for the related phenomena mentioned above.

The paper is organized as follows. We begin by describing the Auger sputter profiling (ASP) technique. Experimental details and results appear next, and then we discuss these results and examine several physical mechanisms which could account for our observations. The thermodynamic model is also discussed. A Summary follows. The vacancy mechanism model is discussed in the Appendix.

* Electrochemical Society Active Member.

¹ Present address: Bell Laboratories, Murray Hill, New Jersey 07974.

Key words: interface, oxidation, anneal.

Auger Sputter Profiling

The Auger sputter profiling (ASP) technique has been discussed in detail elsewhere (12). We briefly describe here the details of the ASP technique as it applies specifically to these studies.

Our experiments were performed in a Varian 2730 Spectrometer with a base pressure of $\sim 10^{-9}$ Torr. Electrons from the integral gun of the variable-aperture cylindrical mirror analyzer struck the sample at an angle of 30° to the surface normal. The 4.5 keV electron beam was operated at currents less than 10 μ A rastered over a 200 \times 200 μ m square to minimize effects of electron-stimulated desorption and electron beam-induced diffusion (2, 4, 13). Sputtering was performed using a pseudorandom rastered ion beam at beam energies of 1 keV or less at an angle of incidence of 49°. Neon was used so that a liquid N₂ cryopanel could be employed to minimize the partial pressure of contaminant gases. We have previously shown that, with these experimental parameters, the measured

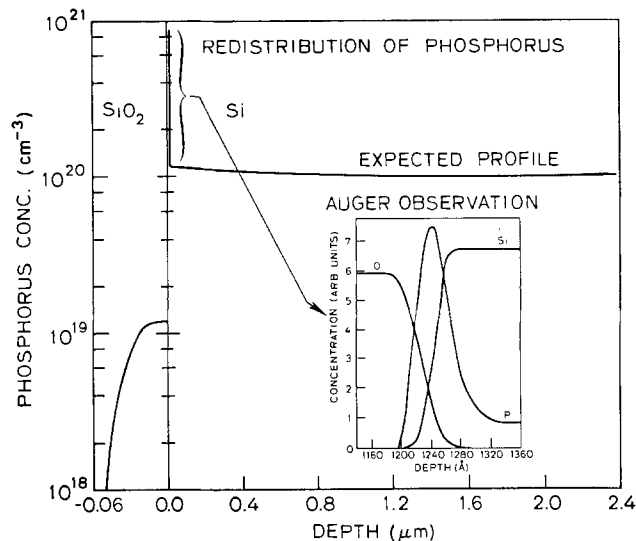


Fig. 1. Illustration of the phosphorus pile-up effect at the Si-SiO₂ interface for a bulk concentration of 10²⁰ cm⁻³ and a sample oxidized at 1150°C for 10 min. Except for the delta-function-like contribution near the interface, the profile shown has been calculated using traditional diffusion redistribution theory. Note, the falloff in phosphorus concentration at the surface of the oxide is due to evaporation of phosphorus. The insert shows an actual measurement from this work of the near interface region, indicating the anomalous pile-up observed.

width of the interface is not seriously affected by electron escape depth broadening (5) or ion knock-on mixing (14).

A typical set of derivative spectra obtained during profiling of the phosphorus-rich Si-SiO₂ interfacial region are illustrated in Fig. 2. As we sputter through the oxide, two peaks appear in the featureless SiO₂ spectrum—a weak elemental Si peak at 108 eV and the P_{LMM} peak at ~120 eV. The phosphorus peak grows rapidly and then decreases to a steady value in the silicon bulk. The phosphorus peak is observed to shift gradually to higher energies during the profile. The phosphorus peak in P₂O₅ is generally found at ~110 eV. The 3 eV energy shift shown in Fig. 2 could be attributed to a single phosphorus-oxygen bond or to a more complex interfacial structure.

Although, generally, the Auger spectroscopy technique can be sensitive to elements in concentrations below 10¹⁹ cm⁻³, the practical sensitivity in these studies is limited by the overlap of the Si 108 eV and P 120 eV spectra. Because the silicon derivative spectrum has a small positive slope in the vicinity of the P (LMM) spectrum, peak-to-peak measurements of this spectrum alone will not detect phosphorus below 4 × 10¹⁹ cm⁻³ (as calibrated by ion implanted standards). In fact, assuming that the silicon background remains the same, all peak-to-peak determinations of phosphorus concentration will be underestimated by the same amount; this is shown in Fig. 3. Most measurements presented here, however, are for concentrations in excess of 10²⁰ cm⁻³, for which the sloping background will add only a small correction to the peak-to-peak concentration.

When the peak-to-peak height of the Si_{LVV} (92 eV), P_{LMM} (120 eV), and O_{KLL} (502 eV) transitions are plotted as a function of depth, a profile (5) similar to that of the inset in Fig. 1 is obtained. The distance over which the Si_{LVV} signal rises from 10% to 90% of its final value is termed the interface width. In lightly doped samples, the interface width is ~25 Å and does not vary with the oxide thickness (15). In heavily doped samples, we have shown that the interface width increases significantly (5).

It is interesting to compare the Auger sputter profile of phosphorus in Fig. 4 with depth profiles of the same sample obtained elsewhere using the SIMS (secondary ion mass spectroscopy) technique. In Fig. 4, we compare the data of Dobrott (16) (20 keV O₂ + sputtered) and Evans (17) (8 keV Cs + sputtered) with our own (1 keV Ar + sputtered). It is observed that the SIMS technique, as applied in their studies, has

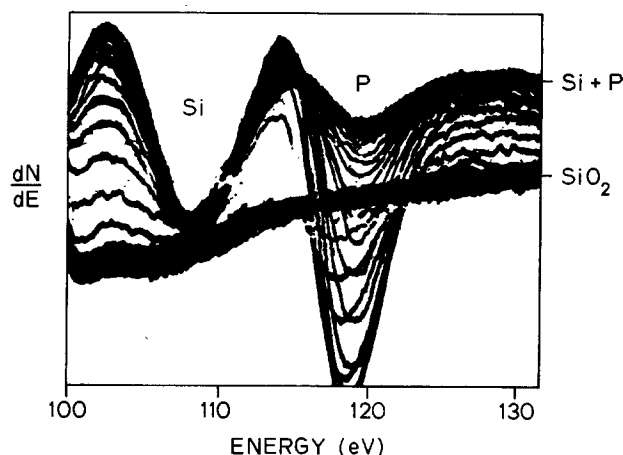


Fig. 2. Oscilloscope photograph of Auger spectra being recorded during profile from an electron energy of 104-134 eV. For elemental silicon, there is a weak LVV peak that is present at ~108 eV, and the phosphorus LMM transition appears at 120 eV. The sloping background in the vicinity of the phosphorus peak causes errors in quantitative analysis that are illustrated in Fig. 3.

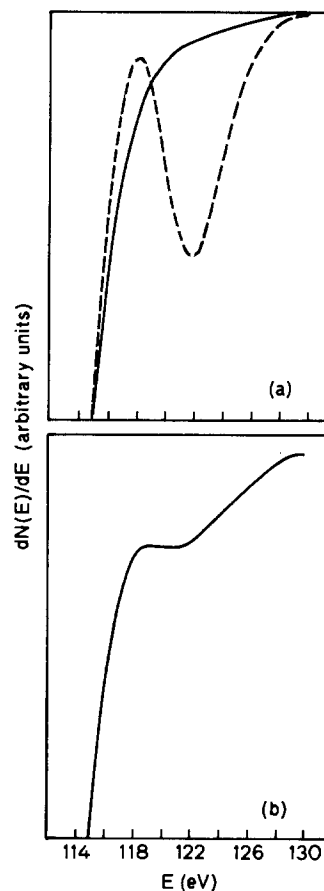


Fig. 3. Examples of phosphorus Auger spectra taken from an implanted standard in silicon. (a) The solid line is the silicon spectrum for a sample without phosphorus, the dotted line is a spectrum for a sample with 1×10^{20} cm⁻³ phosphorus. (b) Auger spectrum for 4.0×10^{19} cm⁻³ phosphorus. Due to the sloping background, a simple peak-to-peak measurement would erroneously indicate zero concentration.

greater sensitivity to phosphorus but poorer depth resolution due to the high ion sputtering energies.

Results

Heavily doped Si (111) and (100) samples were prepared by thermal deposition and drive-in from a POCl₃ source. The resultant phosphorus profiles were flat to within 10% to a distance of 1 μm into the silicon. Oxidations were performed in dry O₂ at 900° and 1150°C with 30 sec push-pulls in O₂.

Three sets of experiments were performed. First, the effect of oxidation time and therefore oxide thickness on the pile-up was measured at an oxidation temperature of 900°C for (100) oriented samples. Second, the effect of subsequent postoxidation N₂ anneals was determined. Finally, the effect of an additional electrically compensating dopant, boron, on the pile-up effect was measured.

A series of experiments were performed to examine the evolution of the pile-up during oxidation. Si (100) samples with bulk phosphorus doping 2×10^{20} cm⁻³ (as measured by ASP calibration from ion-implanted standards) were oxidized in dry O₂ at 900°C for various lengths of time. The oxidation times used in these experiments are tabulated in Table I. Oxide thicknesses were determined from previous calibrations (18) by the time required to sputter to the interface and are also listed in the table. The resultant interface widths, again the 10-90% width of the Si_{LVV} transition, appear in the third column of the table. As previously reported, the interface width appears to increase with oxide thickness. This effect is not observed in undoped samples (17).

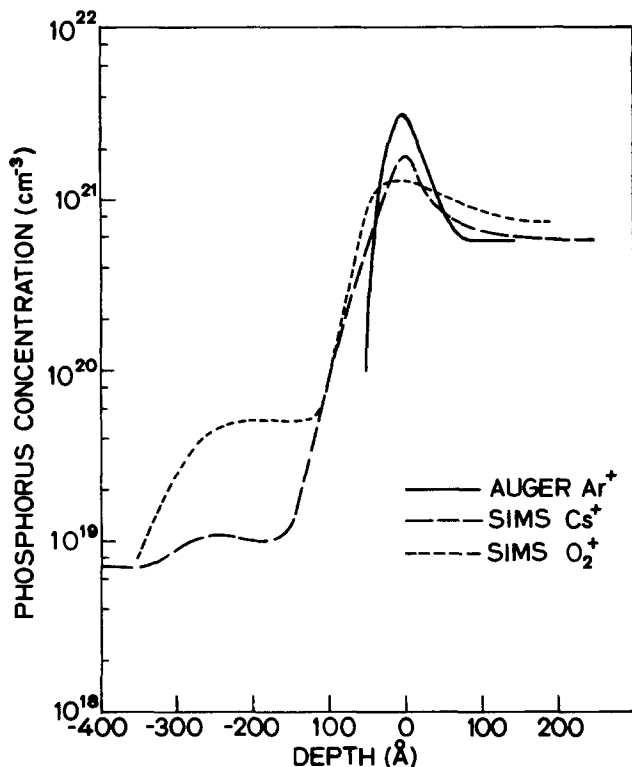


Fig. 4. Comparison of SIMS and Auger profiles of phosphorus pile-up. Auger data are shown as the solid line; SIMS data from Dobrott (13) (20 keV O_2^+ sputtering) are shown as the short dashed line; SIMS data from Evans (14) (8 keV Cs^+ sputtering) are shown as the long dashed line. The broadening observed in the SIMS experiments is due to the higher ion energies used. The SIMS technique does have higher sensitivity to phosphorus; the deviation in the phosphorus levels from the two SIMS profiles in the SiO_2 may be due to the presence of SiH which has the same mass as phosphorus.

The phosphorus profiles from the samples of Table I are collectively illustrated in Fig. 5. This figure shows the phosphorus profiles as a function of depth measured from the outside surface of each sample. Each phosphorus peak is situated at the Si/ SiO_2 interface as shown in Fig. 3. The sample oxidized for 90 min, for example, has an oxide 550 Å thick and so shows the phosphorus peak at a depth of 550 Å. The peak heights shown were reproducible to within $\sim 20\%$.

We see in Fig. 5 that a pile-up is just beginning to form in the 1 min oxide. The next profile, for a 10 min oxidation, illustrates an important phenomenon. Much more phosphorus is present in the pile-up region than can be accounted for by the displacement of phosphorus from 70 Å of oxide. The concentration of phosphorus on the silicon side of the pile-up is observed to dip below the bulk doping level. Thus, we find that the interface is acting as a sink for phosphorus, with phosphorus diffusing from the bulk of the Si to the interface where it is immobilized. Succeeding profiles in Fig. 5 show that, for oxide thicknesses greater than

Table I. Data for 900°C dry oxidation of Si (100) samples with initial P doping of $\sim 2 \times 10^{20} \text{ cm}^{-3}$

| Oxidation time (min) | Oxide thickness (Å) | Interface width* (Å) |
|----------------------|---------------------|----------------------|
| 1 | 22 | 21 |
| 10 | 67 | 23 |
| 20 | 121 | 34 |
| 90 | 548 | 38 |
| 200 | 750 | 40 |
| 750 | 1760 | 51 |

* 10-90% width of the $Si_{L_{VV}}$ (92 eV) profile.

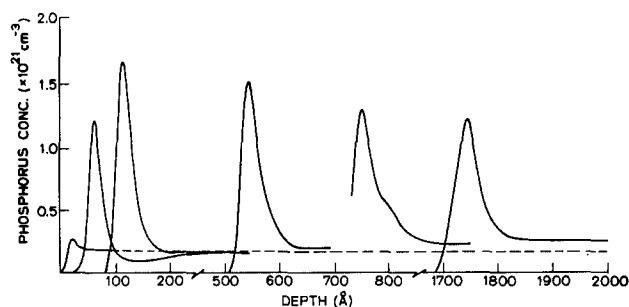


Fig. 5. Evolution of phosphorus pile-up for samples of bulk concentration $2 \times 10^{20} \text{ cm}^{-3}$ oxidized at 900°C. Depth is measured from the surface of the oxide in all cases. From right to left, each profile corresponds to oxidation times of 1, 10, 20, 90, 200, and 750 min, respectively, with oxide thicknesses of 20, 70, 120, 550, 750, and 1760 Å, respectively (see Table I). The peak in phosphorus concentration occurs on the silicon side of the interface for each case.

200 Å, the peak phosphorus concentration is no longer increasing, i.e., the pile-up has saturated. As the oxide thickness increases, the phosphorus level on the silicon side of the pile-up rises above the bulk doping level. Thus, any further phosphorus which is rejected by the growing oxide redistributes in the silicon bulk in a manner consistent with previous models (1) of phosphorus accumulation.

As a further check of the concentration dip effect, we examined a less heavily doped sample ($\sim 5 \times 10^{19} \text{ cm}^{-3}$) which was oxidized concurrently with the 10 min heavily doped ($2 \times 10^{20} \text{ cm}^{-3}$) sample of Fig. 5. A comparison of these two profiles is shown in Fig. 6. The oxide thickness of the heavily doped sample is slightly larger, consistent with the oxidation enhancement model of Ho *et al.* (8). In the less heavily doped

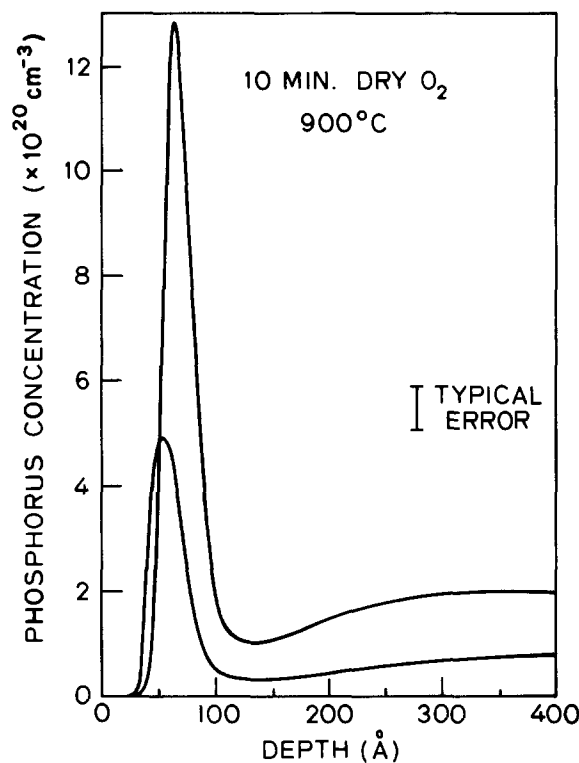


Fig. 6. Illustration of the depletion of phosphorus that occurs in the near interface region for short oxidation times. Two curves are shown for samples of phosphorus concentration $2 \times 10^{20} \text{ cm}^{-3}$ and $8 \times 10^{19} \text{ cm}^{-3}$, with oxides grown at 900°C for 10 min. (The 2×10^{20} curve is identical to the curve with peak second from the left in Fig. 6.) An obvious depletion (dip) in the phosphorus is observed.

sample, we again observe a prominent concentration dip.

In order to determine whether or not the observed phosphorus distribution is related to the motion of the Si/SiO₂ interface, or is instead an inherent property of the interface, we measured the effect of N₂ annealing on phosphorus pile-up. One sample with a bulk doping level of $2 \times 10^{20} \text{ cm}^{-3}$ was oxidized for 10 min at 1150°C (thickness of 450Å) and later annealed for 14 min at the same temperature. Assuming conventional values for the phosphorus diffusion constant (19), the phosphorus that is observed at the interface after oxidation should be able to diffuse back into the bulk of the silicon after only 0.1 sec at 1150°C. As shown in Fig. 7, however, no significant change in the phosphorus distribution was detected after the postoxidation anneal. The diffusion length of phosphorus under the conditions of the anneal was 3300Å.

In a further test, a sample grown at 900°C for 10 min (thickness of 48Å) was annealed at 900°C for 8.75 hr. The sample prior to the anneal showed a depletion of phosphorus on the silicon side of the phosphorus pile-up (see Fig. 5 and 6). After the anneal, the phosphorus pile-up had grown to the height of that in the sample oxidized for 20 min, and the depleted area had redistributed itself into the bulk so as to be undetectable. The diffusion length for this anneal was ~1500Å.

One of the heavily phosphorus doped ($\sim 6 \times 10^{20} \text{ cm}^{-3}$) samples was further subjected to a 60 min boron deposition at 1100°C from a diborane source. The residual oxide was etched, and the sample was oxidized in dry O₂ for 4 hr at 900°C. An Auger sputter profile indicated a bulk boron doping level of $\sim 2 \times 10^{21} \text{ cm}^{-3}$ (5 atomic percent), well above the solid solubility limit. The sputter profile also indicated that the phosphorus pile-up had almost completely disappeared. The peak phosphorus concentration was roughly 10% larger than the bulk concentration. The interface width, as measured by the 10-90% width of the Si_LVV profile, was ~80Å, much broader than the typical width of a similar sample with no boron present. Ho (9) has reported that the oxidation rate of this sample is much

reduced by boron compensation. The possible implications of these results will be discussed in the Appendix.

Discussion

As has been pointed out previously, the measured phosphorus profiles are not consistent with a simple diffusion-redistribution model, as these models would predict a much smaller peak concentration with the pile-up region extending much further into the silicon.

A model put forth in a previous paper from this laboratory suggested that the pile-up may be caused by the formation of a P⁺V=P⁺ complex that would diffuse slowly and therefore cause a high concentration of phosphorus to build up near the interface. Our present data is inconsistent with this model in two ways. First, the depletion of phosphorus in the silicon in the near interface region for short oxidation times (see Fig. 6) clearly cannot be explained by this mechanism. Second, these complexes would tend to diffuse back into the bulk of the silicon during the N₂ anneal; the pile-up, however, does not decrease during the anneal and, in fact, increases for some initial conditions. This mechanism therefore cannot account for the pile-up observed.

Our data can only be explained by considering the interface as a sink for phosphorus during both oxidation and anneal. This behavior is therefore a property of the interface and not a direct consequence of the oxidation process itself. The behavior of the Si-SiO₂ interface as a sink for phosphorus implies that the chemical potential for phosphorus has a sharp minimum at the interface.

There are several mechanisms which can account for this chemical potential sink at the interface. Since the phosphorus is positively charged in the silicon, it might be attracted to a negative electrical potential at the interface. Since the phosphorus is a different size than silicon and will have, in general, a different bonding geometry, it might reduce the interfacial strain energy. The phosphorus might also form a chemical species at the interface (an SiP or a SiP_xO_y) which is not observable in the bulk. And, finally, the phosphorus might accumulate where vacancies, with which it is normally paired, have been depleted. A vacancy mechanism model is described in the Appendix.

Summary

We have used Auger sputter profiling to investigate the pile-up of phosphorus at the Si-SiO₂ interface which occurs during the thermal oxidation of heavily doped silicon. We find that, in the early stages of oxidation, the interfacial region acts as a sink for phosphorus. As oxidation proceeds, the pile-up saturates and the doping level in the silicon near the interface begins to rise. High temperature anneals had little effect on the pile-up, indicating that the existence of the pile-up cannot be explained by a simple diffusion mechanism. We also observed the pile-up to be greatly diminished in a heavily boron compensated sample. A vacancy mechanism model is proposed which is consistent with these results.

Acknowledgment

We are grateful to Professor Bill Spicer, in whose laboratory these studies were performed, for useful discussions and financial support. This work was supported by the Defense Advanced Research Projects Agency Contract DAAB07-77-6-2684.

Manuscript submitted Jan. 14, 1980; revised manuscript received Aug. 25, 1980.

Any discussion of this paper will appear in a Discussion Section to be published in the December 1981 JOURNAL. All discussions for the December 1981 Discussion Section should be submitted by Aug. 1, 1981.

Publication costs of this article were assisted by Stanford University.

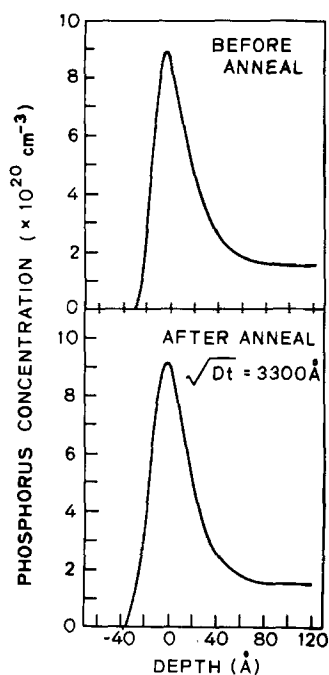


Fig. 7. Illustration of the effect on annealing on the pile-up effect for a sample of concentration $2 \times 10^{20} \text{ cm}^{-3}$ oxidized for 10 min at 1150°C in dry O₂ and annealed at the same temperature for 14 min. The profile before annealing is shown in (a); after the anneal is shown in (b). The annealing has had very little effect on the pile-up.

APPENDIX

A Vacancy Mechanism Model

In the recent work of Fair and Tsai (19), Ho *et al.* (7-9), and Ghoshtagore (11), in which heavily phosphorus-doped samples were investigated, vacancy mechanism models were used in each case to explain experimental results. These models will be considered briefly below. Phosphorus has long been known as a substitutional diffusant, indicating that the redistribution of phosphorus in silicon will certainly be affected by the concentration of vacancies. We find that, given the known pairing tendency of phosphorus with charged vacancies, a localized pile-up at the interface may result if the interface acts as a sink for vacancies. In this section, we first discuss the models just mentioned as they pertain to the phosphorus pile-up. We then describe our vacancy mechanism model and some of its implications.

Recently, Fair and Tsai (19) examined the effect of the phosphorus doping level, or alternatively the Fermi level position, on the phosphorus diffusivity. An increased concentration of vacancies is expected in heavily doped samples due to the production of charged vacancies. Fair and Tsai demonstrated a significant change in phosphorus diffusivity which occurs when the Fermi level crosses a position 0.11 eV below the conduction band edge. They surmised that this level corresponds with the production of doubly charged vacancies $V^{=}$.

Ho *et al.* (7-9) investigated the effect of the phosphorus doping level on the oxidation rate of silicon. They found that the oxidation rate was significantly enhanced when the Fermi level rose above the 0.11 eV position. The oxidation rate correlated well with the expected concentration of vacancies. On the assumption that oxygen moves into vacant sites at the interface, the interface may well be acting as a vacancy sink. As a further test of their model, they compensated several heavily phosphorus doped samples with boron in order to bring the Fermi level down below the $V^{=}$ level. In these samples, the oxidation rate was much reduced, as illustrated in Fig. 8. The rightmost compensated sample in this figure was profiled using ASP, as discussed in the text. While the phosphorus pile-up was absent, the extreme doping levels in this sample render any interpretation suspect.

Ghoshtagore (11) has investigated the redistribution of phosphorus into silicon from a heavily doped oxide as a function of annealing times and temperatures. He showed that the redistribution process could be described using a surface barrier constant K such that the diffusive flux of phosphorus at the interface is balanced by a factor $K C_B$ where C_B is the bulk phosphorus concentration near the interface. The factor K , when plotted as a function of temperature on an Arrhenius plot (11), exhibits an activation energy of ~ 3.8 eV. The diffusion constant of phosphorus exhibits the same activation energy within experimental error. These results indicate that phosphorus entering the silicon from the oxide may be activated by a vacancy mechanism.

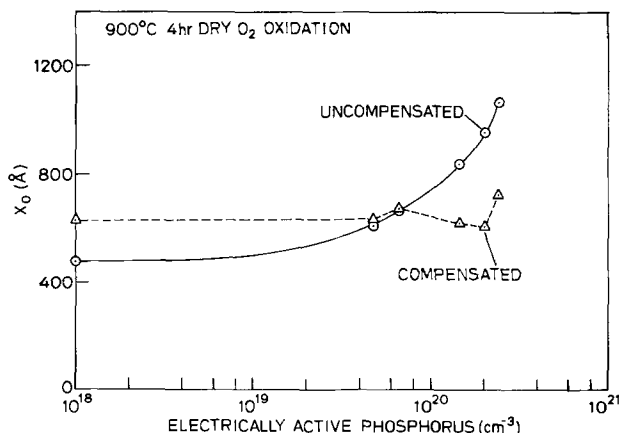


Fig. 8. Oxide thickness (oxidation rate) vs. phosphorus concentration of phosphorus-doped Si compensated and uncompensated by a constant boron diffusion [Ref. (9)].

We now propose a simple extension of these vacancy models which may provide a mechanism for the phosphorus pile-up. Phosphorus atoms, positively charged in the silicon lattice, are expected to pair up with negatively charged vacancies (19) due to coulombic attraction. These PV pairs then travel in tandem through the crystal. If the interface acts as a sink for vacancies or as a preferential binding site for phosphorus, PV pairs arriving at the interface may lose their vacancy, thus immobilizing the phosphorus atom. This could account for the concentration dip effect (Fig. 6) which occurs during the initial stages of oxidation. Immobilized phosphorus atoms at the interface may be activated, as in Ghoshtagore's work, by a vacancy mechanism and hence escape from the interface. In fact, activation may simply occur when an unpaired vacancy contacts the phosphorus atom.

As the oxidation proceeds, a steady-state condition will be reached where the immobilization of phosphorus is balanced by its activation. A detailed calculation would have to account for the immobilization site density at the interface, the probabilities associated with vacancy consumption and activation, the altered vacancy concentrations near the interface, as well as any other chemical or field effects which may be operating. Thus, a generalized thermodynamic model (20) may provide a simpler description of these effects. However, the vacancy mechanism model may provide some qualitative insight into a variety of experimental results. One implication of the model is that the pile-up should be greatly diminished when the Fermi level is a distance kT or greater below the $V^{=}$ level. This could account for the absence of the pile-up in the boron compensated sample. In a previous study by Johannessen *et al.* (4), the pile-up ratio was monitored as a function of the bulk doping level. This ratio showed an apparent decrease as the Fermi level dropped below the $V^{=}$ level. (This level crossing occurs at a phosphorus concentration of $\sim 1 \times 10^{20} \text{ cm}^{-3}$ at 900°C according to Fair and Tsai.) These results are somewhat questionable, however, as the low concentration data may have been affected by the peak-height measurement error discussed in the text. Further annealing experiments as well as investigations of other dopants will help to clarify the mechanisms involved.

REFERENCES

1. A. S. Grove, O. Leisteko, Jr., and C. T. Sah, *J. Appl. Phys.*, **35**, 2695 (1964).
2. C. C. Chang, A. C. Adams, G. Quintana, and T. T. Sheng, *ibid.*, **45**, 252 (1974).
3. N. J. Chou, R. Hammer, Y. J. Van der Meulen, and J. Cahill, *Appl. Phys. Lett.*, **24**, 200 (1974).
4. J. S. Johannessen, W. E. Spicer, J. F. Gibbons, J. D. Plummer, and N. J. Taylor, *J. Appl. Phys.*, **49**, 4453 (1978).
5. S. A. Schwarz, C. R. Helms, W. E. Spicer, and N. J. Taylor, *J. Vac. Sci. Technol.*, **15**, 227 (1978).
6. T. H. DiStefano, in "ARPA/NBS Workshop: Surface Analysis for Silicon Devices," A. G. Lieberman, Editor, NBS Special Publication **400-23**, pp. 197-210 (1976).
7. C. P. Ho, J. D. Plummer, J. D. Meindl, and B. E. Deal, *This Journal*, **125**, 665 (1978).
8. C. P. Ho and J. D. Plummer, *ibid.*, **126**, 1516 (1979).
9. C. P. Ho, Ph.D. Thesis, Stanford University, Stanford, Calif. (1978).
10. D. A. Antoniadis, A. M. Lin, and R. W. Dutton, *Appl. Phys. Lett.*, **33**, 1030 (1978).
11. R. N. Ghoshtagore, *Solid State Electron.*, **17**, 1065 (1974).
12. C. C. Chang, in "Characterization of Solid Surfaces," P. F. Kane and G. B. Larrabee, Editors, pp. 509-576, Plenum Press, New York (1979).
13. J. S. Johannessen, W. E. Spicer, and Y. E. Struasser, *Appl. Phys. Lett.*, **27**, 452 (1975).
14. S. A. Schwarz and C. R. Helms, *J. Vac. Sci. Technol.*, **16**, 781 (1979).
15. C. R. Helms, N. M. Johnson, S. A. Schwarz, and W. E. Spicer, in "The Physics of SiO₂ and Its Interfaces," S. T. Pantalides, Editor, pp. 366-372, Pergamon Press, New York (1978).
16. R. D. Dobrott, Materials Characterization Report, Texas Instruments, Inc., Dallas, Tx (1976), Unpublished.

17. C. A. Evans, Jr., Technical Report, Univ. of Ill., Urbana, Ill. (1977), Unpublished.
 18. C. R. Helms, N. M. Johnson, S. A. Schwarz, and W. E. Spicer, *J. Appl. Phys.*, To be published.

19. R. B. Fair and J. C. C. Tsai, *This Journal*, **124**, 1107 (1977).
 20. R. W. Barton, C. R. Helms, and W. A. Tiller, To be published.

An X-Ray Lithography System

W. D. Buckley and G. P. Hughes

Perkin-Elmer Corporation, Norwalk, Connecticut 06856

ABSTRACT

A full field, short exposure time x-ray lithography system which is capable of submicron lithography on silicon wafers is described. The optimum system configuration is determined and a new high flux x-ray lithography source is identified. The overall system performance is summarized including resolution, exposure time, overlay capability, mask stability and technology, experimental x-ray resist evaluation, and evaluation of source radiation effects on silicon MOS integrated circuits.

X-ray lithography is a candidate technology for the fabrication of silicon integrated circuits with submicron minimum feature size. The lithographic performance of an x-ray lithography system is determined by the interaction of the exposure source, the aligner, the mask technology, and the photoresist (Fig. 1). This paper discusses an approach to one such system and reports its performance including evaluation of radiation damage.

The system is based on an electron beam generated x-ray source with a water-cooled rotating anode. Since exposures are performed in helium at atmospheric pressure, a thin Be window separates the source vacuum chamber from the exposure chamber. A compatible mask technology has been developed based on titanium mask membranes and gold absorbers. The fabrication, patterning, and stability of these masks is described in Ref. (1). Similarly, an optical aligner has

been developed compatible with optically opaque or transparent masks. The principle and performance of this aligner is described in Ref. (2).

System Considerations

In any lithography system, the parameters of practical interest are the resolution, linewidth control, exposure time, and overlay capability. In an x-ray lithography system the dependent parameters are controlled by the independent parameters, source diameter (s), mask to wafer distance (d), exposure distance (D), and source power (P). System design consists of optimizing the geometric factors to satisfy the conflicting requirements of high resolution and short exposure time.

Table I lists typical system parameters for a 3 in. wafer exposure system. The mask-to-wafer separation of $50\ \mu\text{m}$ is chosen so as to minimize the possibility of mask damage during exposure and is large enough to ensure an effectively infinite mask life.

Key words: x-ray, lithography, tungsten source.

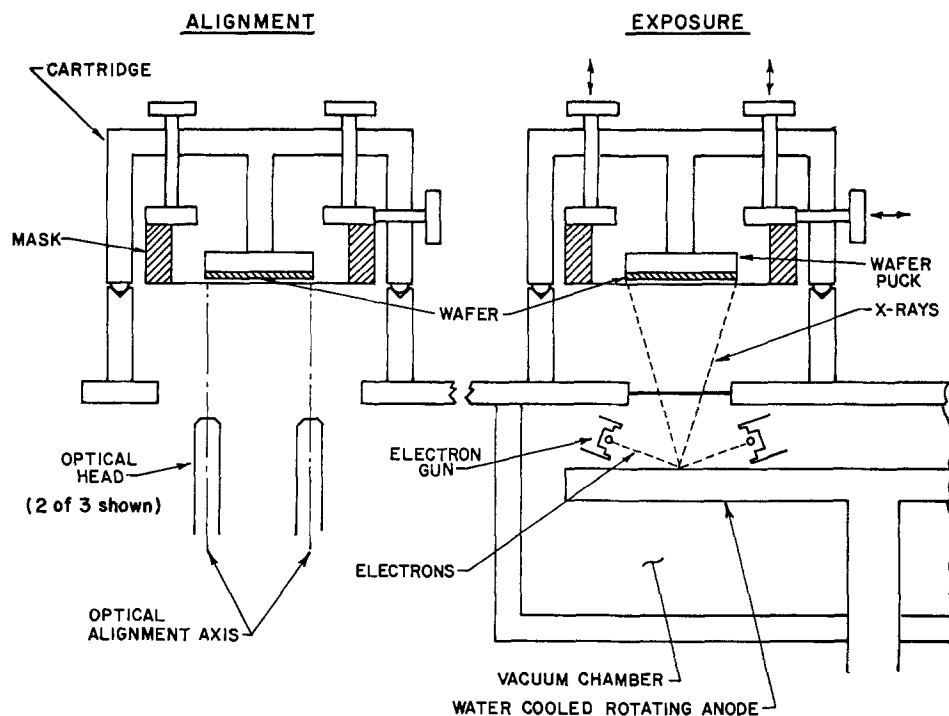


Fig. 1. X-ray lithography system (schematic). The mask and wafer are carried in a cartridge which fits in turn over the alignment and exposure system.

Table I. System parameters: geometric limitations

| Parameter | Has impact on | Control parameters | Limiting value |
|---|---|---|---|
| d = Mask to wafer gap D = Wafer to source distance | Mask life Exposure uniformity ($\pm 5\%$) Minimum exposure time | $D \geq 3 \times$ wafer radius D , window thickness, resolution | $50 \mu\text{m}$ $D \geq 12 \text{ cm}$ $D = 15 \text{ cm}$ |
| S = X-ray source diameter | Resolution ($0.5 \mu\text{m}$) Linewidth variation ($>5\%$) Variation in d ($1 \mu\text{m}$) Temperature corrections ($\pm 1^\circ\text{C}$) Wafer Out of flat $5 \mu\text{m}$ | Penumbral $\frac{S}{D} d$ $\frac{S}{D} \Delta d$ $\frac{S}{D} \Delta d$ $\frac{S}{D} \Delta d$ | $S \leq 0.15$ $S \leq 0.15 \text{ cm}$ |

The optimum exposure distance ($D = 15 \text{ cm}$) is determined by the consideration of exposure flux uniformity and the exposure time. Since the wafer is illuminated by a quasi-point source of x-rays, the exposure flux at the wafer decreases radially. In order to ensure an exposure uniformity within $\pm 5\%$ across the wafer, it is necessary that the exposure distance be greater than three times the wafer radius. For the 15 cm exposure distance used here, the flux uniformity is $\pm 3\%$.

The exposure time is determined by the radiation flux and absorption in the vacuum window, mask membrane, helium atmosphere, and photoresist, and by the photoresist sensitivity. In addition two other factors are important.

First, for a fixed wafer diameter, as the exposure distance increases the diameter of the vacuum window can be reduced. In principle a thinner window can be used and, because of reduced absorption, the exposure time is decreased.

Second, it is usual to consider the effects of exposure distance variations at constant source power. However, it is more useful to examine these effects at constant resolution. This perspective has a major effect on the permissible power since the electron beam diameter can vary with exposure distance.

The exposure time (τ) relation can be written [Ref. (3)]

$$\tau = \tau_0 \frac{D^2}{P_B} \exp(\mu_1 t + \mu_2 D) \quad [1]$$

where τ_0 is independent of P_B and D . The absorption coefficients of the vacuum window and helium atmosphere are μ_1 and μ_2 , respectively, and t is the thickness of the vacuum window.

The required thickness (t) of a vacuum window is related to its diameter (V) by the relation

$$t = AV \quad [2]$$

where A is a constant, characteristic of the window material. The diameter of a circular window required to expose a circular area of diameter W is given by

$$(V - S) = \frac{x}{D} (W - S) \quad [3]$$

where x is the source to window distance. Combining Eq. [2] and [3] we may substitute

$$t = \frac{x}{D} (W - S) + S \quad [4]$$

in Eq. [1].

It is usual to consider the effects of variations in the source-to-wafer distance D while maintaining the beam power, P_B , constant. It is more useful to examine the variation of exposure time at constant resolution. This innovation has a major effect on the permissible

power since the electron beam spot size can vary with the exposure distance.

The source diameter is related to the resolution (p) by the relation

$$p = \frac{Sd}{D} \quad [5]$$

For a high power rotating anode x-ray source, the maximum power is related to the spot diameter (s) by a relation of the form [Ref. (5, 6)]

$$P_B = BS^{3/2} \quad [6]$$

where B is a constant, characteristic of the anode material.

Combining Eq. [1], [4], [5], and [6], it can be shown that the exposure time is given by

$$\tau = \frac{\tau_1}{B} \left(\frac{d}{p}\right)^{3/2} D^{1/2} \exp\left(\mu_1 A \frac{x}{D} (W - S)\right) \exp \mu_2 D \quad [7]$$

where $\tau_1 = \tau_0 \exp(\mu_1 AS)$.

The situation is summarized in Fig. 2. In calculating these curves, use was made of the experimentally determined exposure time and sensitivity for COP photo-

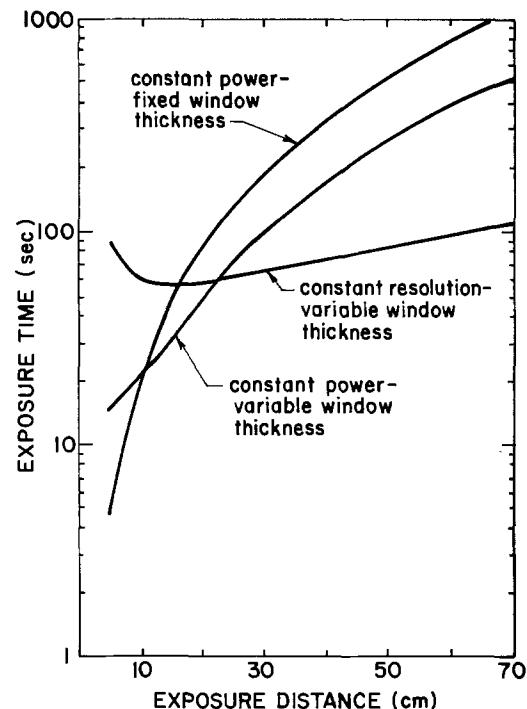


Fig. 2. Various relationships between exposure time and source-to-wafer distance. The conventional model assumes a constant window thickness and derives the exposure time for constant power.

resist. For all the curves, a 5 μm Mylar mask, a helium exposure atmosphere, and a 5 cm source-to-vacuum window distance were assumed. A source power of 10 kW was used for constant power calculations and a Be window of thickness 25 μm for constant window thickness. Similarly, 1 μm resolution was assumed for the constant resolution curve. A value of 5×10^{-4} was used for the constant A based on our experimental data and a recent publication (5). The value of the constant B was based both upon theoretical considerations and upon the specifications of commercially available rotating anode sources (Fig. 3).

The constant power, constant window thickness curve is dominated by the inverse square law term and, over most of the range, the exposure time is proportional to D^2 . This is the basis of the conventional exposure time curve. When the window thickness variation is included, the square law term is significantly modified. Over most of the range illustrated, the exposure time is approximately proportional to D . Finally, for the constant resolution curve, an entirely different conclusion is apparent. An optimum exposure distance exists for which the exposure time is at a minimum. For greater distances the exposure time is approximately proportional to $D^{1/2}$ in agreement with Eq. [7]. In addition, the exposure time is only a weak function of exposure distance and, over the distance range illustrated, the increase is less than 50% above the minimum.

The optimum exposure distance can be derived from Eq. [7]. If the effect of the helium atmosphere is ignored, the optimum exposure distance (D_{opt}) is given by

$$D_{\text{opt}} = 2 A a \lambda^3 (W - S) \quad [8]$$

where $\mu_1 = a\lambda^3$ and λ is the exposure wavelength.

The minimum exposure time is obtained at the optimum exposure distance which, for an aluminum source and a 3 in. wafer, is approximately 15 cm.

Because the exposure time is insensitive to exposure distance, other system requirements will determine the distance. However, in general, a shorter distance is preferred in order to minimize power requirements.

The optimum source spot diameter is determined by the desired resolution and by the maximum permissible linewidth variation. In order to provide process latitude for 1 μm lithography, and to have the capability of extending to the sub-micron regime, a penum-

bral resolution limit of 0.5 μm was selected. This requires a 1.5 mm spot diameter, a 15 cm exposure distance, and 50 μm mask-to-wafer separation.

Linewidth variations can arise from variation in the wafer surface and from uncontrolled or controlled variations in mask-to-wafer separation. For a 1.5 mm spot linewidth variations are 80 \AA per μm variation in gap.

Deliberate variations in the gap are part of the alignment procedure. These variations cause linear magnification changes at the image plane due to the inherent nature of point source imaging. The magnitude of the change, at a radius R , is given by the relation $\Delta R/R = \Delta d/D$. For the system geometry chosen this results in a magnification change of about 0.25 μm per μm of gap variation at the periphery of a 3 in. wafer. This effect can be used to compensate for linear magnification changes in the mask or wafer which can occur due to thermal or wafer processing effects (4). It can also compensate for linear magnification changes in the mask and, in so doing, considerably relax mask stability requirements.

Uncontrolled variations in the gap between exposures can result in image distortions which will limit the overlay precision. The magnitude of these distortions is given by the relation above and amounts to about 0.25 μm per μm of uncontrolled gap variation at the periphery of a 3 in. wafer. In order to minimize this effect a "bed of nails" wafer chuck was used. This reduces the chance of particle entrapment by simultaneously reducing the total contact area between the chuck and wafer and distributing this area over an array of small studs. The chuck surface was polished flat and served as a reference surface for the back of the wafer. In this manner the front surface profile of the wafer was controlled.

As a result of the discussion above one defines the geometrical parameters of the system as $d = 50 \mu\text{m}$, $D = 15 \text{ cm}$, and $S = 0.15 \text{ cm}$. The source power is the only unspecified independent parameter. Its value is determined by the maximum permissible power input to the specified source size for the anode material chosen.

The maximum power dissipation P of a rotating anode can be expressed as a function of the maximum allowable temperature rise, ΔT , (5, 6) by

$$P = \pi^2 (\rho C_v K s^3 v)^{1/2} \frac{\Delta T}{16} \quad [9]$$

where v is the surface velocity of the anode, K is the thermal conductivity, C_v is the specific heat, ρ is the density, and s is the spot diameter. The quantity (ΔT) is limited by melting or by the fatigue failure limit.

The equation predicts that the maximum power is proportional to the 3/2 power of the spot diameter. This relationship has been confirmed in the literature and by commercially available Al_K rotating anode sources. In Fig. 3, the data points are for x-ray sources available from Rigaku. The line labeled Rigaku-Al obeys the theoretical power law. The highest power commercial source uses a 250 mm diam Al target rotating at 8000 rpm. A projection for this source is also shown in Fig. 3. Also shown in Fig. 3 is the calculated power dissipation for a Pd anode (7).

It is apparent (Fig. 3) that the maximum power dissipation for an Al source and a 0.15 cm spot diameter is about 3.5 kW. Reference to Fig. 2 indicates an exposure time of approximately 100 sec. This consideration led us to evaluate alternate anode materials with the objective of increasing the power and reducing the exposure time. It was confirmed experimentally that a tungsten source is as efficient as aluminum in exposing both COP and PMMA resist. However, as shown in Fig. 3, the tungsten source can dissipate about six times more power than either the aluminum or pal-

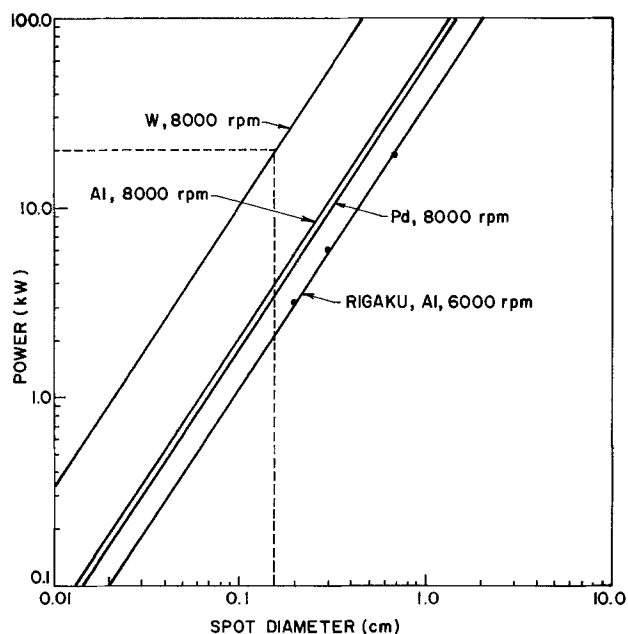


Fig. 3. Input power vs. spot diameter for water-cooled, rotating anode x-ray anodes.

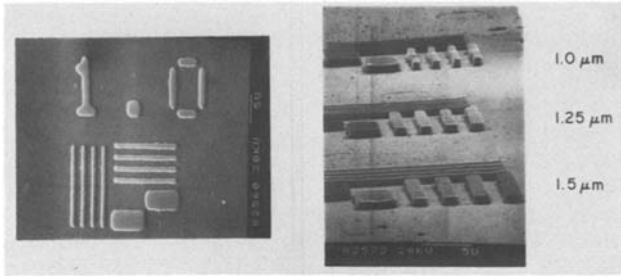


Fig. 4. X-ray lithography in PMMA [$1 \mu\text{m}$ using a tungsten M-line ($W_m = 7\text{\AA}$) irradiation source. Resolution is not limited by photoelectron range.

ladium source (for a constant spot size) and results in a projected exposure time of less than 20 sec.

The lithographic capability of a tungsten M line (7\AA) source is illustrated by Fig. 4, a scanning electron micrograph of resolution patterns with $1 \mu\text{m}$ thick PMMA film. One micron resolution in COP was also demonstrated and reported previously (8).

Table II summarizes the projected characteristics of an x-ray lithography system based on a tungsten source and a resist with the sensitivity of COP. For this system exposure time is not a limiting parameter. The table specifies a 3 in. wafer although the performance parameters are relatively insensitive to wafer size.

It is informative at this point to compare this system with conventional lithographic tools. It is customary to describe the performance of lithographic tools by the vague term resolution. However, King and Goldrick (9) have shown that the modulation transfer function (MTF) is a useful concept in describing the performance of photolithographic tools. MTF is a plot of the image modulation as a function of the spatial frequency of the mask pattern. Current practice is to associate an MTF value of 60% with the minimum feature size achievable in production.

For an x-ray lithography exposure system the modulation of the aerial image at the wafer plane is determined by the system penumbra and the mask contrast. The "system" MTF is the product of the MTF of the imaging system and the MTF of the mask.

Rao has shown how to calculate the MTF of an x-ray lithography system (10). Figure 5 compares the MTF of an F3 projection aligner and the x-ray lithography system described above. The large improvement in MTF obtained with the x-ray system is apparent. However, it is important to remember that the overall system MTF is determined by the product of the MTF of the imaging system and the MTF of the mask. For an optical system, with a high contrast mask, the mask MTF is essentially 100% and the system MTF dominates. For the x-ray system the mask contrast is less and dominates for features larger than about $0.5 \mu\text{m}$.

Figure 6 illustrates the measured mask contrast and MTF for a gold absorber and a tungsten source. As can be seen the contrast depends on the accelerating voltage of the electron beam x-ray source due to continuum radiation. For 20 kV accelerating voltage the contrast is degraded by continuum radiation and W_L radiation generated by the source. Experimental mea-

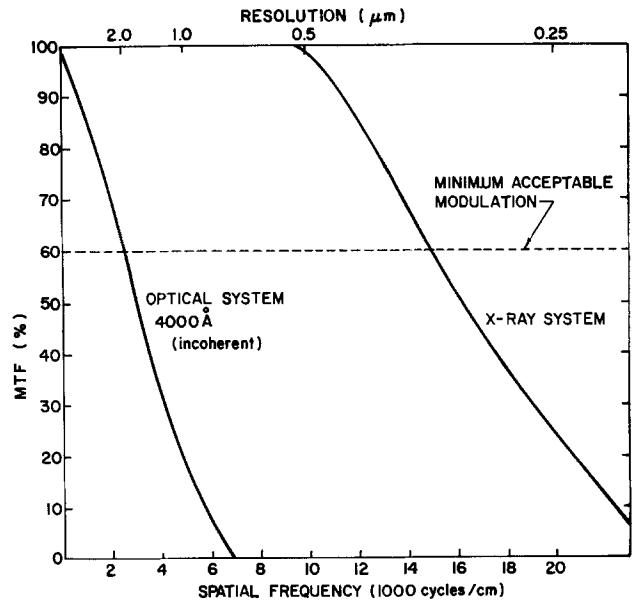


Fig. 5. A comparison of MTF of an optical lithography system (F3 projection aligner) with the MTF of the proposed x-ray lithography system.

surements indicate that continuum radiation is the predominant source of contrast reduction. For an 8 kV source a gold thickness of $0.5 \mu\text{m}$ results in an MTF of 60% and at 20 kV $0.7 \mu\text{m}$ of gold is necessary. For these masks, linewidths of $0.5 \mu\text{m}$ and greater have an MTF of 60%, limited by the absorber since the imaging system MTF is 100% (Fig. 4). Thicker gold increases the mask contrast and reduces the minimum feature size toward $0.3 \mu\text{m}$. Clearly, the higher MTF possible with an x-ray system should result in better linewidth control in the presence of exposure nonuniformities. In addition, the absence of the multiple reflections characteristic of optical systems (11) should also aid in linewidth control.

System Performance

An experimental system has been constructed (Fig. 7) consisting of a tungsten anode x-ray source with a

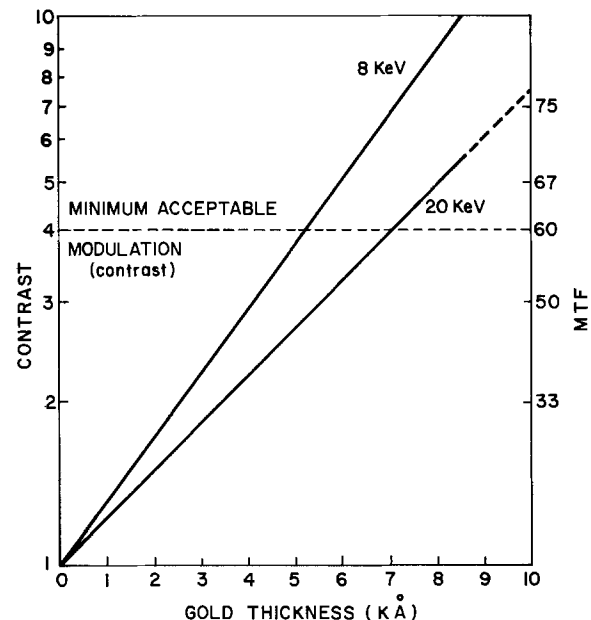


Fig. 6. The contrast of an x-ray mask using a gold absorber and a tungsten M line source. The lower energy excitation reduces bremsstrahlung radiation and produces approximately theoretical contrast.

Table II. Theoretical performance characteristics of an optimized x-ray system

| | |
|--|---------------------|
| Wafer diameter | 3 in. |
| Exposure distance | 15 cm |
| Exposure time | 17 sec |
| Power | 20 kW |
| Spot size | $1.5 \mu\text{m}$ |
| Resolution (penumbral) | $0.5 \mu\text{m}$ |
| Printing capability | $<1.0 \mu\text{m}$ |
| Linewidth variations | |
| Nonflatness ($\pm 5 \mu\text{m}$) | $0.04 \mu\text{m}$ |
| d Variation ($\pm 1 \mu\text{m}$) | $0.068 \mu\text{m}$ |
| Temperature correction ($\pm 1^\circ\text{C}$) | $0.006 \mu\text{m}$ |

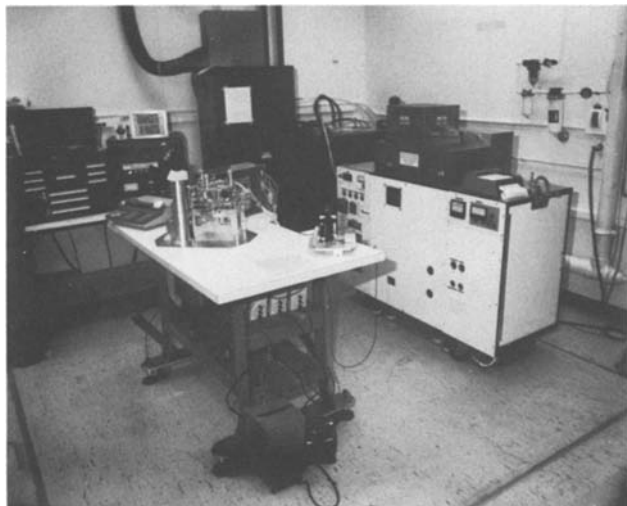


Fig. 7. An experimental x-ray lithography system. The alignment system with the removable cartridge is on the left and the exposure system on the right.

ring cathode electron gun. For this system the source power is limited to 10 kW by a low anode rotational speed (2000 rpm). This system has operated reliably at Perkin-Elmer for more than a year. A similar system at a customer facility has experienced less than 2% down time and has exhibited no evidence of flux output degradation in this time period. The exposure time is longer than predicted since a nonoptimum system configuration was used. For COP resist an exposure time of about 1 min is typical.

The use of a tungsten anode simplifies the electron gun design. Since tungsten deposition on the anode from the gun filament is not an issue, direct line of sight from the filament to the anode is acceptable. Consequently, we have constructed a ring cathode electron gun by adapting the design of a linear cathode electron gun from a conventional x-ray tube. This configuration is not optimized for x-ray lithography and is presently limited to a minimum spot size of about 2.5-3 mm. Although larger than our ultimate goal of 1.5 mm, this spot size results in an overall system MTF of 60% for linewidths greater than 0.7 μm which is quite adequate for sub-micron lithography.

The PBS resist is somewhat slower than COP but appears capable of developing finer features. Patterns consisting of 0.75 μm lines and spaces and isolated 0.5 μm geometries of either polarity can be replicated (Fig. 8). A statistical comparison of 1 μm features on a mask and patterns printed on a wafer indicates a

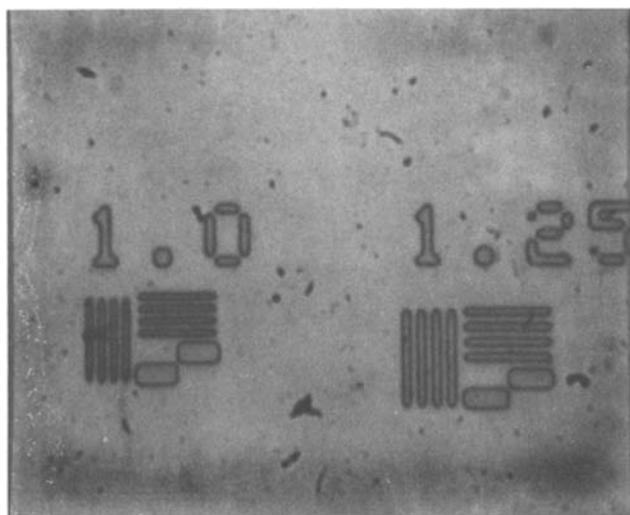


Fig. 8. X-ray lithography in PBS resist using a tungsten source

100% yield as measured at 50 locations. Extensive determination of critical linewidth control has not yet been undertaken. Preliminary measurements on COP resist indicate a linewidth standard deviation of about 0.1 μm for a 2 μm feature.

We have evaluated the exposure characteristics (Fig. 9) of several conventional u.v. and experimental photoresists. Experimental resist EK88 prepared by Eastman Kodak is attractive. This negative resist is almost twice as sensitive as COP with better resolution in thicker layers. The resist γ is about 1.25 compared to $\gamma = 1$ for COP. Figure 10 is a scanning electron micrograph of 1 μm lines and spaces in EK88. The initial resist thickness of 1 μm was exposed and developed to a final thickness of about 0.5 μm .

Radiation damage evaluation has been performed by a major semiconductor manufacturer using both discrete MOS devices and MOS integrated circuits. X-ray lithography was simulated by exposing completed MOS devices to 1, 3, and 10 times the PBS exposure dose. All devices exhibited parametric changes but the differences for the different doses were small. Discrete device results indicate that radiation effects are removed by a conventional aluminum alloy process for all exposure doses. Similar experiments were performed on an integrated circuit chosen for its expected sensitivity to radiation damage. Radiation effects were removed by an additional aluminum anneal of the finished circuits. No significant behavior difference was observed between the irradiated devices and a control group.

The mask technology utilizes a titanium membrane (1). Experiments so far indicate that this material is stable to better than 0.2 μm (the measurement precision) over at least 5 months. An optical aligner has been evaluated (2) using these masks. In its present form this experimental system has achieved an overlay error standard deviation of less than 0.5 μm . Data analysis indicates that $\frac{1}{8}$ μm overlays are achievable in a reconfigured system.

Conclusion

An x-ray proximity lithography system with a well-developed source, mask, and alignment system has been described. The fundamental problems of x-ray lithography have been addressed and shown to be tractable. The use of a high brightness x-ray source with conventional E-beam resist has reduced exposure times to less than a minute. Experimental resists result in exposure times comparable to optical lithography systems. The use of ductile titanium mask substrates with gold absorber layers has yielded high contrast, low distortion masks. The mask and bright exposure source in conjunction with an optical alignment system have been used to demonstrate the feasibility of x-ray lithography as a high resolution tool.

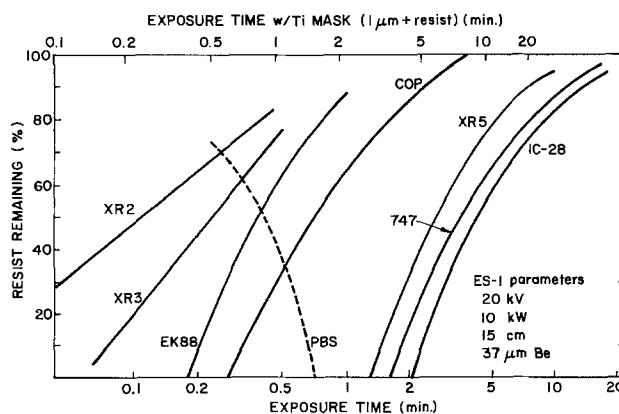


Fig. 9. Exposure characteristics of a selection of commercial and experimental resists. The high gamma and sensitivity of Eastman Kodak experimental resist EK88 is notable.

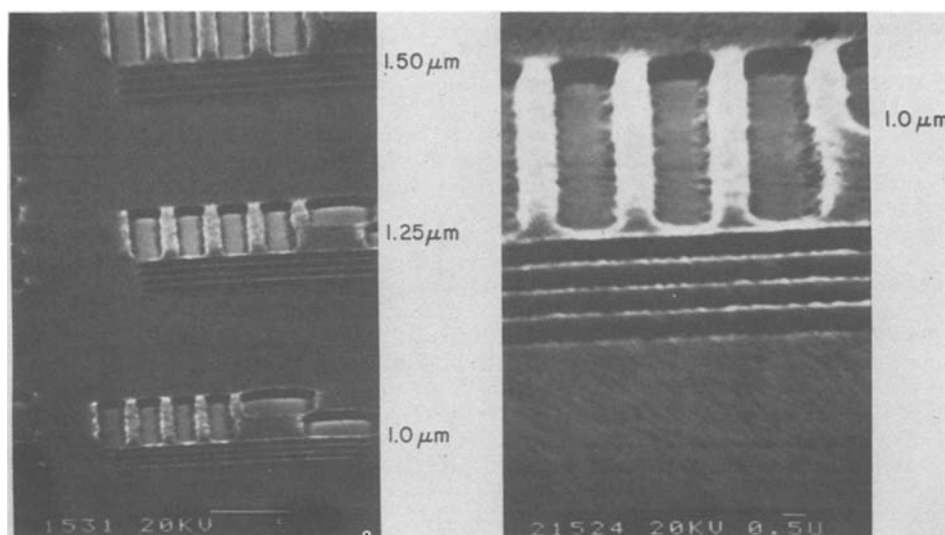


Fig. 10. X-ray lithography in Eastman Kodak Experimental Resist EK88. The smallest features are $1\ \mu\text{m}$ lines and spaces.

Manuscript submitted Aug. 12, 1980; revised manuscript received Dec. 18, 1980. This was Paper 276 presented at the St. Louis, Missouri, Meeting of the Society, May 11-16, 1980.

Any discussion of this paper will appear in a Discussion Section to be published in the December 1981 JOURNAL. All discussions for the December 1981 Discussion Section should be submitted by Aug. 1, 1981.

Publication costs of this article were assisted by The Perkin-Elmer Corporation.

REFERENCES

1. W. D. Buckley, J. F. Nester, and H. Windischmann, Paper 278 presented at The Electrochemical Society Meeting, St. Louis, Missouri, May 11-16, 1980.
2. W. D. Buckley, M. P. Eisenberg, G. P. Hughes, D. H. Kittell, and J. L. Kruezer, Paper 277 presented at The Electrochemical Society Meeting, St. Louis, Missouri, May 11-16, 1980.
3. W. D. Buckley, in "Electron and Ion Beam Science and Technology," R. Bakish, Editor, pp. 453-463, The Electrochemical Society Softbound Proceedings Series, Princeton, N.J. (1976).
4. N.-H. Tsai and C. N. Alquist, "Semiconductor Microlithography V," SPIE, San Jose, California (1980).
5. W. J. Oosterkamp, *Phillips Res. Rep.*, **3**, 303 (1948).
6. G. A. Wardly, E. Munro, and R. W. Scott, International Conference on Microlithography, SEE, Paris, France (1977).
7. J. R. Maldonado, M. E. Poulsen, T. E. Saunders, F. Vratny, and A. Zacharias, *J. Vac. Sci. Technol.*, **16**, 1942 (1979).
8. W. D. Buckley and J. A. DalleAve, Paper 383 presented at The Electrochemical Society Meeting, Seattle, Washington, May 21-26, 1978.
9. M. C. King and M. R. Goldbrick, *Solid State Technol.*, **2**, 37 (1977).
10. G. U. V. Rao and A.-L. Soong, *Med. Phys.*, **1**, 204 (1974).
11. C. N. Alquist, W. G. Oldham, and P. Schoen, "Microcircuit Engineering 1979," Institute of Semiconductor Electronics, Aachen, p. 339 (1979).

An X-Ray Lithography Alignment System

W. D. Buckley, M. P. Eisenberg, G. P. Hughes, D. H. Kittell, and J. L. Kruezer

The Perkin-Elmer Corporation, Norwalk, Connecticut 06856

ABSTRACT

The design, operation, and performance of an experimental alignment system which is suitable for use with an x-ray lithography exposure system will be described. The system consists of optical, mechanical, and electronic subsystems and permits alignment of either opaque or transparent masks by means of an optical alignment detection and transfer system. A computer assisted procedure permits mask to wafer overlay with a mean plus standard deviation of less than $0.5\ \mu\text{m}$. The alignment algorithm automatically compensates for linear magnification changes in the mask or wafer by varying the mask to wafer separation. A data reduction scheme is described which identifies the major sources of misalignment and permits the analysis of wafer overlay data in terms of rigid body alignment errors in six degrees of freedom. The component evaluation of the system along with the system data analysis indicate that a second generation system should have overlays of less than one-third that of the prototype.

In another publication (1) we have described an x-ray lithography exposure system capable of sub-micron lithography. In order to fully exploit this capability, an alignment system with an overlay ac-

Key words: x-ray, lithography, alignment.

curacy of one-half to one-third the minimum feature size is required. In addition, the alignment system must be compatible with the overall lithography system and mask technology. A mask technology based on titanium membranes has been described (2). The use

of this mask technology mandates that the aligner be capable of aligning optically opaque masks.

Since x-ray lithography is based on point source projection imaging, the gap between the mask and wafer results in a magnification of the mask pattern. The image on the wafer is enlarged by an amount $\Delta = Rd/D$ where d is the mask-to-wafer gap, R is the radial distance from the wafer center, and D is the exposure distance. Consequently, in order to minimize magnification changes between consecutive exposures the mask-to-wafer separation must be controlled.

The cumulative overlay error of one level to another will be influenced by in plane wafer distortions. However, recent studies (3-6) have shown that these changes manifest themselves principally as a linear change in wafer dimensions. Similar changes will result from thermal differences between exposures. Consequently, the magnification of an x-ray system can be used to advantage if the proximity gap can be fine-tuned to compensate these effects.

Alignment System

An alignment system based on optical detection and an optical alignment transfer standard can satisfy all of the requirements defined above.

The basis of the approach is illustrated in Fig. 1. The center of the wafer alignment target is located in space on the axis of an optical alignment channel by means of precise lateral and vertical alignment positioners. The wafer is then displaced a known distance, typically 50 μm , in order to provide the mask-to-wafer separation. Next the mask is inserted and the alignment procedure is repeated. Since the location of the wafer alignment target is retained in the transfer standard at the optical axis location, it is not necessary to view the wafer during mask alignment. Therefore either transparent or opaque masks can be aligned. In order to locate the mask parallel to the wafer, three alignment channels are used.

The overall alignment system consists of an optical detection system, a mechanical positioning system, a mensuration system, and a computer assisted alignment algorithm.

The optical system detects both lateral and vertical position of the alignment target simultaneously by means of a combined interferometer objective. A point in space is thus defined along the optic axis which serves as an alignment transfer standard and permits the alignment of opaque masks.

Lateral alignment is accomplished by means of a microscope ($NA = 0.60$) and prism assembly. As shown in Fig. 2 the prism assembly includes a beamsplitter and the overall effect is to generate two images rotated 180° relative to each other. When the center of the alignment target is not coincident with the axis of the optical system, a double image is seen. If the alignment target center is brought into coincidence with the optic axis, the two images coincide and a single image is

seen, as illustrated in Fig. 3. The subsequent insertion of an opaque mask prevents viewing of the wafer alignment target directly, however, mask-to-wafer alignment is then accomplished by aligning the mask to the viewing optics.

A white light interferometer is used to define the position of the alignment mark in the z direction, i.e., along the optic axis. The interferometer is operated in a null fringe mode in which a single interference fringe fills the entire viewing field. This interferometer yields a unique signature, characteristic of the surface being viewed when the two path lengths are nearly equal, and a minimum signal at the point of precise equality. The axial location of the alignment target can be determined to a small fraction of a micron.

In the experimental alignment system a Leitz "Mirau" interference objective is used to implement the white light interferometer. In this device the beamsplitter and reference mirror are combined in an assembly that mounts directly on the objective. Consequently, the same optical channel can be used for both lateral and vertical alignment.

In order to evaluate the alignment scheme, a single channel optical alignment system was established using conventional microscope components and interference objectives. Experimental repeatability tests were run for both alignment axes. The test involved performing the appropriate alignment, then displacing the stage an unknown amount and repeating the alignment without viewing the position sensor readout. The position of the stage after each alignment was recorded and the alignment procedure was repeated ten or more times. The mean and standard deviations were computed for each data set. This repeatability experiment was performed both on an x-ray mask and on ten substrates which were supplied by a commercial silicon device manufacturer and represented different stages of circuit fabrication. Each of the silicon devices was coated with 1.0 μm of photoresist in order to simulate a realistic alignment situation. The results are shown in Table I. In all cases the precision of the system was 0.25 μm or better.

The mechanical positioning mechanism is capable of positioning the mask and wafer at the required point in space defined by the optical channel. It is necessary to control both mask and wafer with six degrees of freedom. The basic building block of the mechanical positioning system is the lever reduction machine. It consists of a differential screw mechanism in conjunction with a lever. The differential screw is loaded against the long side of the lever, which is mounted to a base by two rotary flexures. Fine adjustment is obtained by directly turning the differential screw, whereas coarse adjustment is obtained by turning a knob threaded about the screw. The threads are selected so that one complete turn of the fine adjustment results in a 25 μm displacement at the short end

TRANSFER ALIGNMENT PRINCIPLE

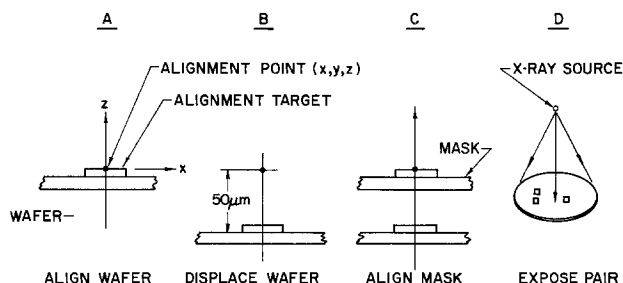


Fig. 1. Simplified single channel alignment procedure. Three channels are needed to set the mask and wafer parallel as shown on the right.

Table I. Single channel visual alignment repeatability

| | Standard deviation (μm) | |
|---|--------------------------------------|------|
| | z | x |
| A—X-ray mask | 0.10 | 0.06 |
| B—Resist-coated wafers | | |
| 1. Thick/oxide/metal*/protective overcoat | 0.12 | 0.26 |
| 2. Thick oxide/multilevel*/metal | 0.18 | 0.24 |
| 3. Thick oxide/poly Si*/metal | 0.17 | 0.16 |
| 4. Gate oxide*/metal | 0.14 | 0.18 |
| 5. Resist oxide*/multilevel | 0.08 | 0.15 |
| 6. Gate oxide/poly Si*/multilevel | 0.12 | 0.12 |
| 7. Thick oxide*/multilevel | 0.12 | 0.16 |
| 8. Thick oxide*/poly Si | 0.18 | 0.08 |
| 9. Thick oxide*/gate oxide | 0.20 | 0.11 |
| 10. Thick oxide/poly Si*/poly Si | 0.13 | 0.10 |

* z target level.

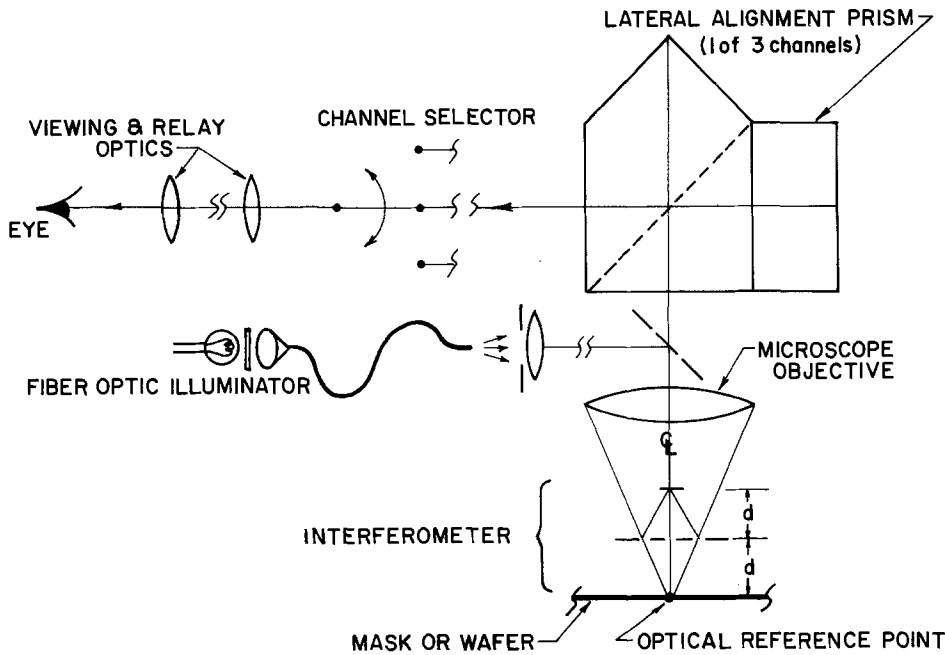


Fig. 2. Mask-or-wafer aligner optical schematic. It uses an image shearing prism to define the optical axis for both mask and wafer levels along with an interferometer to define the vertical plane of the alignment.

of the lever. The total range is about 600 μm . The lever pivot flexure bearing was selected for its ability to pivot with minimal lost motion or stick-slip effects. (The average backlash is less than 0.03 μm .) At the short end of the lever is a push rod. This assembly is axially stiff but flexible in all other directions. It is designed to provide axial motion with minimal cross-coupling to other directions.

A mensuration system is included in order to permit full characterization and control of the mask or wafer position. Each control axis has a corresponding position sensor. This is an eddy current, noncontacting proximity-positioning-detecting device,¹ which exhibits good linearity over the design range of $\pm 300 \mu\text{m}$. The combination of a lever reduction machine and gauge permits deliberate movements as small as 0.01 μm for each control axis.

¹ Kaman Proximity Gauge Model I.U., Kaman Sciences Corporation, Colorado Springs, Colorado.

The temporal stability of a single control axis was measured at a fixed knob setting by recording the gauge reading as a function of time. The results obtained are illustrated in Fig. 4. The experiment was performed in a laboratory environment over a period of about 30 min. The results obtained represent cumulative drift due to mechanical and thermal effects as well as the stability of the gauge and gauge control and readout circuits. Approximately 26 min elapsed before the accumulated drift read 0.1 μm .

As a general conclusion, the mechanical positioning mechanism gauge combination exhibited excellent linearity, backlash, and temporal stability characteristics and has been used for all the mechanical motions required for alignment.

The alignment system was divided into an optical subsystem and a mechanical subsystem as shown schematically in Fig. 5. The mechanical subsystem or cartridge mounts on top of the optical subsystem and is located by means of a ball bearing and groove arrangement.

The optical assembly contains the three optical channels required to provide the overall alignment capability. This assembly, referred to as the optical head, contains a total of six mechanical positioning mechanisms. Three are used to move the optical channels in order to locate the individual channels over their respective alignment targets. The other three change the position of the cartridge relative to the optical head by moving the mounting grooves in which the bearings rest.

VISUAL ALIGNMENT

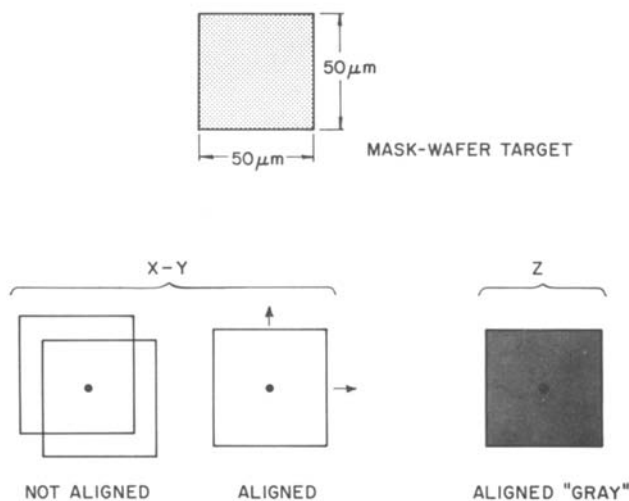


Fig. 3. An alignment target as seen through an optical channel. The left-hand side illustrates lateral alignment relative to the optic axis indicated by the dot. The right-hand target illustrates the axial alignment signal. Correct positioning along the optic axis is achieved when a minimum brightness fringe is observed.

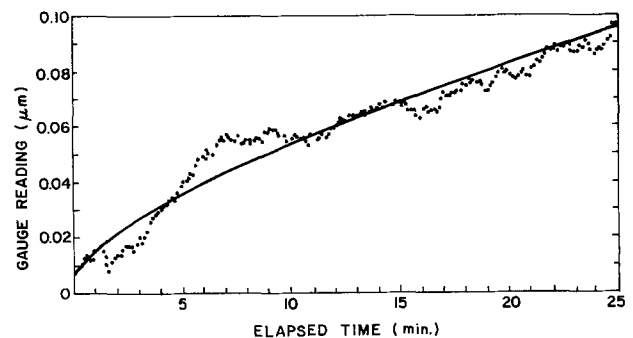


Fig. 4. Temporal stability of the positioning mechanism as measured by an eddy current sensor. The drift is representative of the entire system including the gauges and thermal effects.

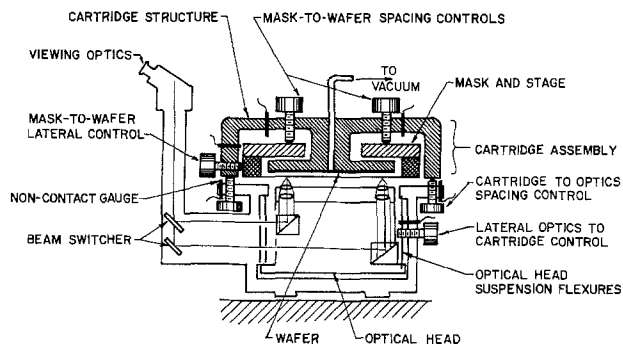


Fig. 5. Schematic diagram of the alignment cartridge. Mask and wafer are aligned separately to three optical channels (two of which are shown). In order to expose, the cartridge is removed together with the mask and wafer, and placed over the exposure source.

The cartridge contains a fixed wafer stage and a mask stage. The mask stage is mounted on three vertical and three horizontal mechanical positioning mechanisms and is kinematically constrained. Auxiliary clamps are not required to maintain the position of the mask after alignment.

The alignment procedure requires that the optical head be first aligned to the wafer. Next, the cartridge is removed to permit installation of the mask, and the mask is then aligned to the optical channels. Since the alignment transfer standard is the axis of the optical channels, they are not disturbed after the first alignment. Subsequent alignments are by means of the mask stage position controls. Successful alignment requires accurate replacement of the cartridge after loading the mask. This can be done within an rms error of less than $0.05 \mu\text{m}$. Exposures are performed by placing the cartridge containing the mask and wafer over the exposure source.

Alignments are performed with calculator assistance. The calculator interrogates the gauges and aids the operator through the alignment procedure. The alignment algorithm compensates for mask-to-wafer scale differences and determines the appropriate mask-to-wafer separation. The system is designed so that all alignment steps consist of nulling a digital voltmeter readout. Figure 6 is a photograph of the complete alignment system.

Aligner Evaluation

The aligner evaluation was performed using oxidized silicon wafers and a titanium x-ray mask. A double exposure technique was used. The wafer was first coated with COP resist and the aligner was used to set the mask to wafer spacing and center the mask over the wafer. After exposure by means of the x-ray source, the resist image was developed and the underlying oxide was etched. The resist was then stripped and the wafer was recoated. In subsequent experiments, the mask was aligned to the image defined in the oxide and then exposed. After development, the position of the resist image relative to oxide image was used to determine the overlay performance of the aligner.

Since the same mask was used for the overlay, the evaluation was independent of mask-to-mask distor-

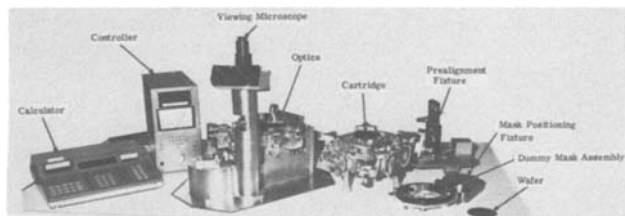


Fig. 6. Mask/wafer aligner system

tions. In addition, since the wafer was not subject to high temperature processing after the oxide etch, wafer distortions did not affect the results. In order to read the overlay errors a vernier mask pattern was used. Overlay was achieved by shifting the mask laterally $300 \mu\text{m}$ to produce an overlay image. The central vernier pattern had a resolution of $0.2 \mu\text{m}$.

Figure 7 is an example of a double exposure overlay on a 3 in. wafer. The dots on the wafer represent the location on the wafer where the vernier patterns were read and the vectors represent (to the scale drawn) the magnitude and direction of the measured misalignment. In this example, the mask was misaligned toward the lower left, however, the displacement vectors lie on diameters with a common center to within the measuring accuracy. This is an indication that the mask is undistorted and stable. Figure 8 summarizes

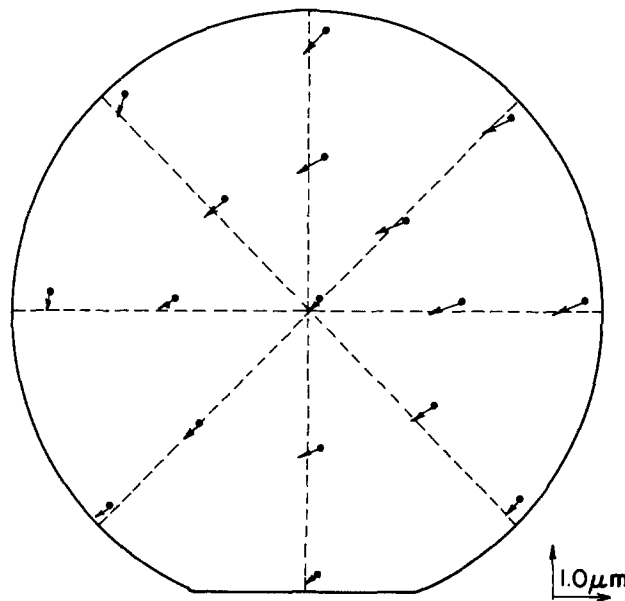


Fig. 7. Overlay performance using titanium mask. The arrows represent (to scale) the displacement vector at each location. The dashed lines are diameters with a common center. All the vectors lie in the lines indicating that the mask is stable, i.e., behaving as a rigid body.

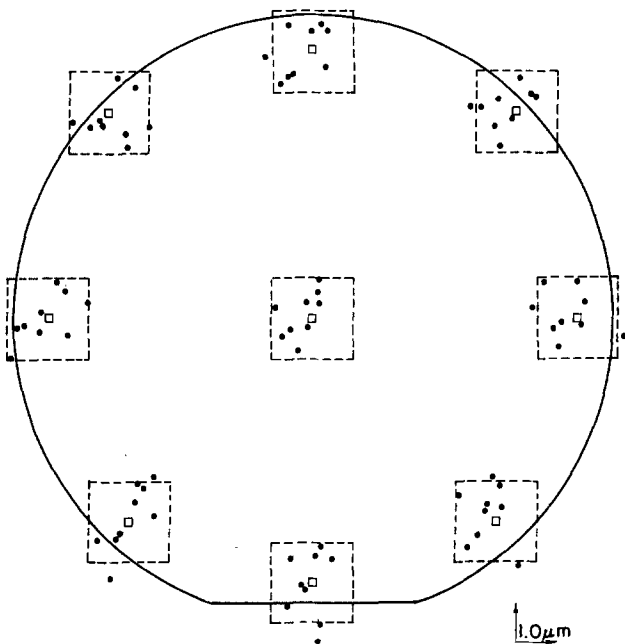


Fig. 8. Composite of double exposure overlays for 9 wafers. The dots represent a single wafer. The boxes are consistent with an alignment error with a standard deviation of less than $0.5 \mu\text{m}$.

the results for 8 wafers. The data points represent the heads of all of the displacement vectors. The boxes are $\pm 1.0 \mu\text{m}$ misalignment limits.

The alignment precision can be estimated from Fig. 9 which is a histogram of the overlay errors at 17 data points on each of nine wafers. The curve illustrates the percentage of data points within a particular overlay error.

Both the histogram and the curve indicate that the alignment accuracy has a standard deviation of about $0.5 \mu\text{m}$. In these initial experiments no attempt was made to control the temperature or to vary the mask-to-wafer gap to compensate for scale changes. This simplification permitted data analysis and overlay error source determination.

Alignment Error Analysis

X-ray lithography alignment consists of aligning a mask relative to a wafer in six degrees of freedom. Assuming the mask and wafer are rigid bodies, errors in alignment can be represented by a set of rigid body alignment error terms as shown in Fig. 10. These errors include translational errors ($\epsilon X, \epsilon Y$), mask-to-wafer spacing error (ϵZ), in-plane rotational errors ($\epsilon \theta_x, \epsilon \theta_y$), and mask-to-wafer tilt ($\epsilon \theta_x, \epsilon \theta_y$). The rigid body errors act in combination to produce overlay errors ($\Delta X, \Delta Y$) on the wafer. In order to relate the rigid body errors to the displacement errors the coordinate system of Fig. 11 has been adopted. At any coordinate (X, Y) the total displacement error on the wafer due to the rigid body error terms is given by

$$\Delta X = \epsilon X + \left(\frac{X}{D}\right) \epsilon Z + \left(\frac{XY}{D}\right) \epsilon \theta_x + \left(\frac{X^2}{D}\right) \epsilon \theta_y + (Y) \epsilon \theta_z \quad [1]$$

and

$$\Delta Y = \epsilon Y + \left(\frac{Y}{D}\right) \epsilon Z + \left(\frac{XY}{D}\right) \epsilon \theta_y + \left(\frac{Y^2}{D}\right) \epsilon \theta_x + (X) \epsilon \theta_z \quad [2]$$

Using these equations and the overlay displacement errors, a best fit set of rigid body terms can be computed for each overlay wafer. Figure 12 represents the result of subtracting the vectors determined by the best fit overlay data from the measured overlay error vectors. The standard deviation of the X and Y

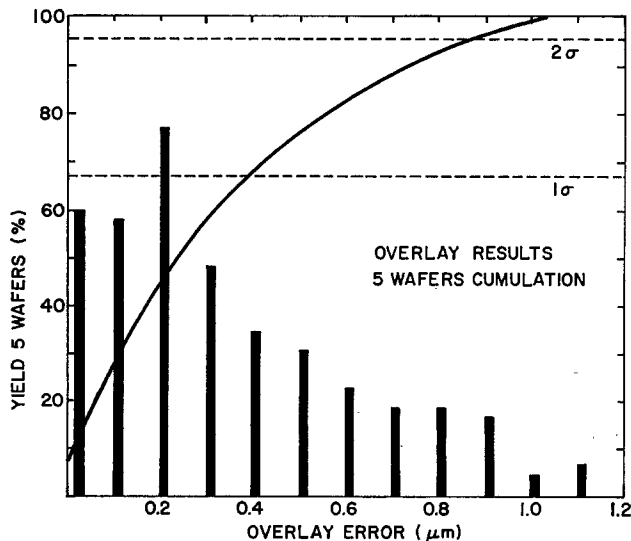


Fig. 9. Histogram of the alignment data. Alignment has been achieved with a $0.5 \mu\text{m}$ standard deviation in a nontemperature-controlled environment.

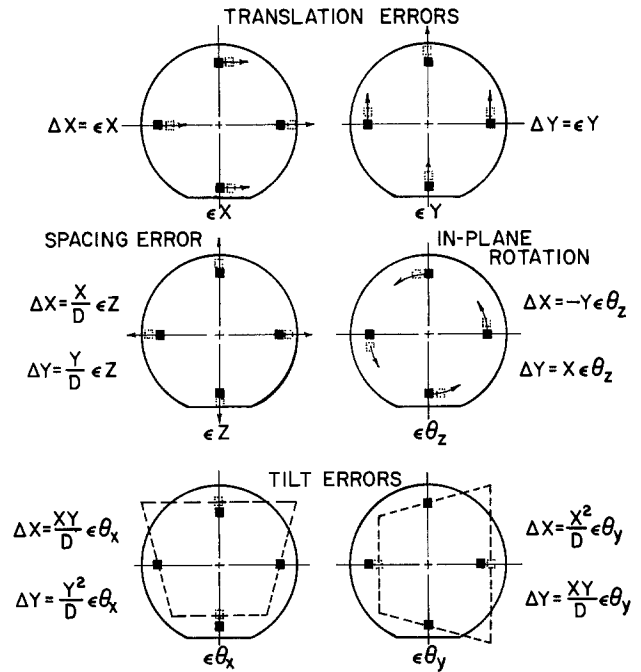


Fig. 10. Rigid body misalignment errors. These terms are used to evaluate aligner performance.

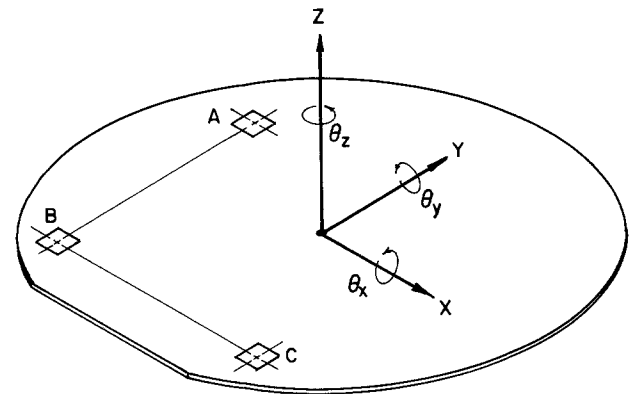


Fig. 11. The coordinate system used for overlay data reduction. Alignments are made by an optical channel located at each of point A, B, and C.

components of these residuals is $\pm 0.1 \mu\text{m}$ which is the reading error of the vernier targets. Thus the alignment errors as shown in Fig. 7 can be represented, within our measuring accuracy, by the rigid body error terms implying that there is no measurable wafer or mask distortion.

Another measure of the alignment performance can be represented by Table II which details the mean and standard deviation of the rigid body error for the wafer overlays in Fig. 8. The effect of these rigid body

Table II. Alignment performance of nine wafers

| | Rigid body error terms | | Calculated error on wafer at 1.5 in. radius | |
|----------------------------|------------------------|------|---|-------------------|
| | Mean | S.D. | Mean | S.D. |
| Translation | | | | |
| $\epsilon X (\mu\text{m})$ | -0.17 | 0.37 | -0.17 | 0.37 |
| $\epsilon Y (\mu\text{m})$ | 0.03 | 0.53 | 0.03 | 0.53 |
| $\epsilon Z (\mu\text{m})$ | -1.08 | 4.8 | -0.12 | 0.53 ^a |
| Rotational | | | | |
| θ_x (arc-sec) | 0.74 | 8.6 | 0.01 | 0.15 |
| θ_y (arc-sec) | 3.45 | 12.0 | 0.06 | 0.21 |
| θ_z (arc-sec) | 0.55 | 1.6 | 0.08 | 0.26 |

^a Includes temperature variation contribution.

RESIDUAL OVERLAY DISPLACEMENTS

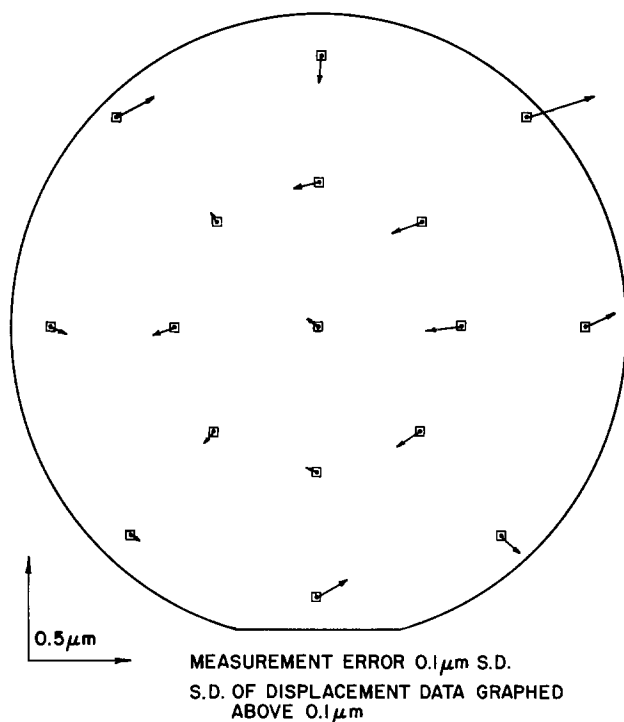


Fig. 12. Residual misalignment vectors for one wafer after rigid body error compensation. These residuals have the same standard deviation as the measuring error indicating that there is no measurable mask instability.

terms on the edge of a 3 in. wafer is also included. Note that the mean values are all small and thus represent no systematic alignment error. The standard deviation is consistent with the histogram of Fig. 9. The standard deviation of the axial alignment term (ϵz) is a major contributor to the overall alignment error. This result is not surprising since these data were obtained without correcting for magnification changes which result

from the poorly controlled thermal environment. The use of the linear scale change capability should significantly reduce this term.

Conclusion

The basic concept, approach, and elements of an optical alignment system suitable for x-ray lithography have been described. An experimental alignment system has demonstrated overlay performance with a standard deviation of less than $0.5 \mu\text{m}$, using optically opaque x-ray mask and 3 in. silicon wafers. This performance is limited by the aligner and not by mask or wafer stability. Readily implemented improvements including a temperature controlled environment, high resolution viewing optics, and linear magnification change compensation should result in an overlay standard deviation of better than $\frac{1}{8} \mu\text{m}$.

Manuscript submitted Aug. 12, 1980 revised manuscript received Dec. 18, 1980. This was Paper 277 presented at the St. Louis, Missouri, Meeting of the Society, May 11-16, 1980.

Any discussion of this paper will appear in a Discussion Section to be published in the December 1981 JOURNAL. All discussions for the December 1981 Discussion Section should be submitted by Aug. 1, 1981.

Publication costs of this article were assisted by The Perkin-Elmer Corporation.

REFERENCES

1. W. D. Buckley and G. P. Hughes, Paper 276 presented at The Electrochemical Society Meeting, St. Louis, Missouri, May 11-16, 1980.
2. W. D. Buckley, J. F. Nester, and H. Windischmann, Paper 278 presented at the Electrochemical Society Meeting, St. Louis, Missouri, May 11-16, 1980.
3. N.-H. Tsai and C. N. Alquist, *Semiconductor Micro-lithography*, V, San Jose, California (1980).
4. L. D. Yan, *Appl. Phys. Lett.*, **33**, 756 (1978).
5. J. D. Cuthbert, "Microcircuit Engineering 1979," pp. 190-197, Aachen, Germany (1979).
6. J. D. Cuthbert, Paper presented at the IEEE Solid State Technology Workshop on Scaling & Micro-lithography, April 22, 1980, New York.

X-Ray Lithography Mask Technology

W. D. Buckley, J. F. Nester, and H. Windischmann

The Perkin-Elmer Corporation, Norwalk, Connecticut 06856

ABSTRACT

A high yield process will be described for fabricating large area free-standing membranes of thickness down to $0.5 \mu\text{m}$ for use as an x-ray lithography mask substrate. The choice of material, method of preparation, and technique for separating the membrane from its substrate will be discussed. Techniques for generating x-ray absorber patterns with submicron feature size are reported. These methods result in absorber geometries which are uniquely suited to x-ray lithography mask applications. Measurements of the mask patterning distortion and the temporal dimensional stability of a completed x-ray mask are reported.

X-ray lithography is a proximity mask replication technique that permits the definition of submicron features on silicon wafers or other substrates. Like its counterpart, u.v. proximity printing, it utilizes a patterned photomask. However, because soft x-rays are the exposing radiation there are significant differences in the photomask technology (1, 2). The ideal x-ray mask support should meet many difficult, seemingly

Key words: x-ray, titanium mask, electroplating.

contradictory, criteria. It should be relatively thin, yet rugged, flat and dimensionally stable, have a low atomic number and a favorably located absorption edge relative to the source wavelength; be fabricable in large area with low defect density and uniformly thin; have isotropic mechanical properties, be optically transparent, relatively inexpensive, and impervious to process chemicals commonly encountered in the semiconductor industry. In addition the absorber must be

deposited with low intrinsic stress so as not to induce pattern distortions.

Since x-ray lithography permits the choice of a range of exposing wavelengths the mask technology must be selected in the context of the overall system selection. In this paper a mask technology is described which is compatible with the x-ray exposure system described in Ref. (3) and the alignment approach described in Ref. (4). The x-ray lithography mask chosen consists of a thin ($\sim 1 \mu\text{m}$) titanium membrane stretched on a support ring. The desired pattern is defined on the membrane by a gold absorber.

In order to be useful for submicron lithography the membrane must be dimensionally stable in order to permit overlay of sequential mask patterns. In addition, the membrane must have a smooth surface morphology to permit submicron absorber definition and to avoid defects. These requirements constrain the choice of fabrication process and pattern definition technology. In the following discussion, membrane fabrication, tensioning, patterning, and dimensional stability are described.

Membrane Fabrication

Titanium membranes are produced by electron beam evaporation onto a glass substrate. In order to ensure membrane dimensional stability the deposition conditions are chosen to produce bulk strength films (5) of uniform thickness with isotropic physical characteristics, zero intrinsic stress, and smooth surface morphology.

Films are deposited onto 12.5 cm diam photomask quality soda lime glass. This glass is chosen because of the close match of its thermal expansion coefficient with titanium and because the high quality surface minimizes defects. The combination of high rate (100 A/sec), high deposition temperature (350°C), and matched expansion coefficient produces large area bulk strength films with low intrinsic stress. The evaporation system geometry is chosen to ensure membrane thickness variations of less than 2% across a 8.6 cm active diameter.

A gold parting agent is used to facilitate separation of the titanium membrane from the glass substrate. The choice of parting agent, its thickness, and deposition temperature are critical to the membrane fabrication process and to the membrane surface morphology. Because gold has a relatively low recrystallization temperature (150°C) it must be deposited at low temperature to minimize grain growth which has a deleterious effect on the titanium surface morphology. Similarly a thin gold film ($< 500\text{\AA}$) is used to minimize the effect of grain growth during titanium deposition. A titanium surface with features smaller than $0.2 \mu\text{m}$ is obtained by minimizing the heat cycle. The lower limit of gold parting layer thickness is determined by the interdiffusion kinetics of the Au-Ti system. It has been observed (6, 7) that the Au-Ti system is susceptible to significant intergranular diffusion at temperatures above 300°C. Furthermore, the diffusion rate is ambient dependent. Faster diffusion occurs in vacuum than in air possibly due to oxide formation at the titanium grain boundaries which act as interdiffusion barriers (8). Therefore, to assist peeling, it is necessary to minimize the elapsed time in vacuum after the completion of titanium deposition. The use of a gold parting layer results in a peeling yield of greater than 90% for $1 \mu\text{m}$ thick titanium films 12.5 cm in diameter. We have demonstrated that films as thin as $0.4 \mu\text{m}$ can be peeled successfully by this technique.

Table I presents a comparison of the transmission characteristics of various materials for the tungsten M-line (6.983Å). As can be seen the titanium must be significantly thinner than other materials to transmit 50% of the W_m radiation. On the other hand, titanium is fabricable in large area, free-standing form

Table I. Comparison of the x-ray transmission of various membrane materials at the W_m line (6.983Å)

| Membrane material | Thickness required for 50% transmission at W_m line (μm) |
|--------------------------------|---|
| Titanium | 1.1 |
| Beryllium | 41.8 |
| Silicon | 9.6 |
| SiO ₂ | 5.0 |
| Si ₃ N ₄ | 5.7 |
| SiC | 6.8 |
| BN | 7.9 |
| Polyimide | 9.0 |
| Mylar | 8.6 |

and can be tensioned to any desired value independent of the fabrication process parameters and are tough.

The titanium film is removed from the glass by mechanical peeling as illustrated in Fig. 1. A thin flexible ring is attached to the titanium by means of double-sided adhesive tape. Peeling proceeds under water until the membrane is free-standing on the flexible ring. The water acts as a surfactant to reduce peeling forces at the film-glass interface. Separation occurs at the weakly bonded gold glass interface and a titanium-gold film is obtained. The gold surface replicates the original glass substrate and is featureless at 10 KX magnification in an SEM. This surface is used for subsequent lithography and patterning. After separation the membrane is slack on its mounting ring, indicative of the absence of intrinsic stress.

The peeled membrane is tensioned and attached to a support ring. Figure 2 is a photograph of a $1 \mu\text{m}$ thick tensioned membrane and support ring with an 8.6 cm unsupported diameter suitable for exposing 7.5 cm diam silicon wafers. Figure 3 illustrates schematically the tensioning procedure. The membrane (M) mounted on its peeling ring (P) is placed symmetrically over the smoothly machined rim (A). Weights (W) are added at the periphery to apply a known tension to the membrane and the permanent support ring (T) is epoxied in place. Membranes are typically tensioned to approximately 10^4 psi. The tension in the membrane probably is not uniform since pinholes, a thickness nonuniformity (of $\sim 2\%$) from center to edge and differentially friction along the bearing edge, A in Fig. 3, would result in an anisotropic tension field.

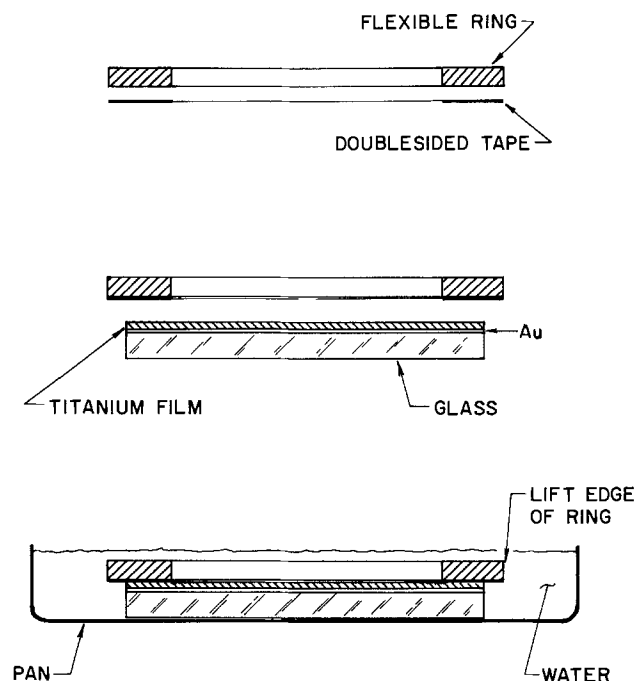


Fig. 1. Mechanical peeling of a titanium membrane from a glass substrate.

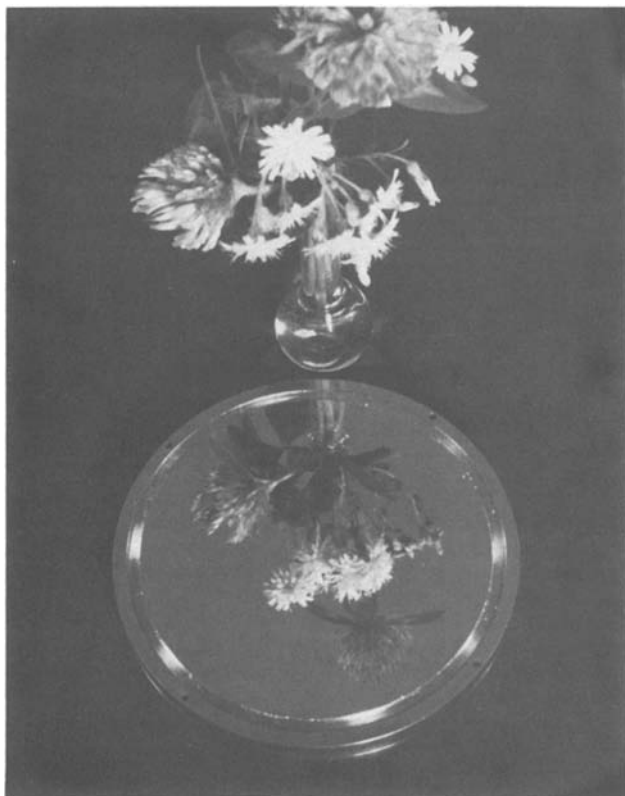


Fig. 2. 1 μm titanium membrane mounted on a rigid ring ready for patterning.

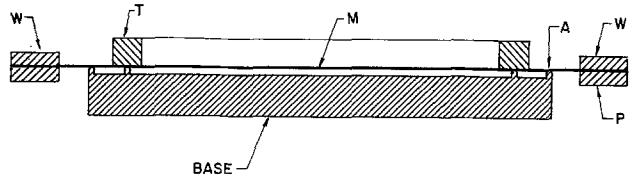


Fig. 3. Titanium membrane tensioning procedure. The support ring (T) is epoxied to the membrane (M).

However, within a ±2% precision (which represents a nonlinear in-plane distortion of <0.1 μm), our long-term stability tension measurements indicate that the dimensional stability does not appear to be compromised by these factors.

Mask Patterning

The tensioned membranes described above serve as substrates for the subsequent generation of a completed mask with the desired absorber pattern. Unlike optical photomasks, the absorber in an x-ray mask may have significant transmission. The x-ray transmission may be minimized by increasing the absorber thickness. However, the patterning process becomes progressively more difficult as the absorber thickness increases. Therefore, a practical compromise is necessary between the conflicting requirements of thick absorbers to produce high contrast and thin absorbers to facilitate high resolution patterning.

The choice of absorber thickness is influenced by the overall system configuration. For a tungsten-source M line (W_m) lithography system a contrast of 4:1 (analogous to that achieved by an optical system operating at 60% MTF) mandates a gold absorber thickness of at least 0.5 μm as shown in Fig. 4. In practice, a gold thickness of about 8000Å is used corresponding to an 8:1 contrast.

Submicron patterning of the absorber has been achieved by both additive and subtractive processing. Both of these processes require a photoresist thickness comparable to the absorber thickness. Submicron resist

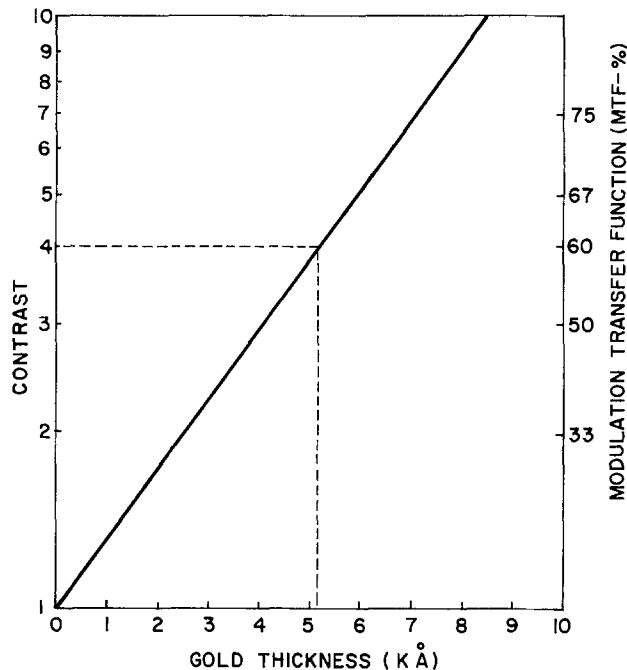


Fig. 4. Contrast and MTF dependence on gold absorber thickness. The dashed line indicates an MTF of 60% a value generally used to define the minimum feature size for practical lithography using optical systems.

pattern generation was achieved by electron beam lithography using an MEBES instrument.

Since it is difficult to achieve submicron pattern features in thick electron resist we have used tri-level or stencil processes. The additive stencil process is shown in Fig. 5. The tri-levels consist of 1 μm of PMMA on the membrane which is coated by 0.1 μm of evaporated Cr (or Al) on top of which is a 0.4 μm layer of electron resist (PBS). The PBS is electron beam patterned and the developed resist serves as an

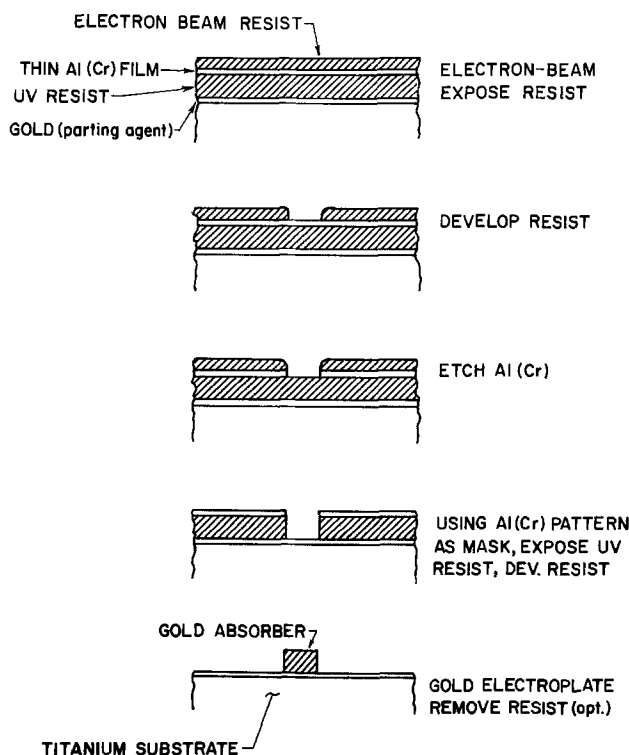


Fig. 5. Additive absorber definition process. The pattern is defined in the upper resist by electron beam lithography. This pattern is transferred to the thick lower resist by u.v. exposure. Subsequent absorber definition is by low stress gold plating.

etch mask for patterning the metal layer. The PBS is then stripped in an oxygen plasma and the metal stencil is transferred to the PMMA by deep u.v. exposure. After developing the PMMA in MIBK, and removing the masking metal by etching, the gold absorber is electroplated onto the thin parting layer which is used as a plating base. The final process step is removal of the PMMA in acetone. This process is attractive when Cr is used as the metal stencil since the electron beam resist patterning and metal etching use established photomask fabrication technology.

The electroplating process takes advantage of the conductivity of the titanium membrane. The plating apparatus is shown schematically in Fig. 6. In this scheme the entire mask is surrounded by an insulated housing with both surfaces of the membrane exposed to a conducting liquid solution. An internal electrode is placed in close proximity to the back-surface of the membrane. In this configuration gold plating occurs onto the front surface of the membrane through openings in the PMMA resist pattern. Since the current flow is perpendicular to the membrane plane, current distribution problems are avoided and uniform absorber thickness is obtained independent of position on the membrane surface. Figure 7 is a scanning electron micrograph of $1\ \mu\text{m}$ lines and spaces produced by this process.

For an x-ray exposure system using a relatively short source to mask distance and a thick absorber, geometrical shadowing effects may result in linewidth variations as illustrated in Fig. 8. However, in the process described above, if a point deep u.v. source is located at the same source to mask distance as in the x-ray exposure system, then a leaning pattern is produced in the PMMA. Electroplating faithfully reproduces this profile in the absorber and eliminates the shadowing effects as illustrated in Fig. 8.

During exposure, x-rays absorbed in the titanium membrane produce photoelectrons which can cause spurious exposure of the x-ray resist. In order to minimize this effect of $1\ \mu\text{m}$ thick coating of low atomic number material, such as PMMA, is applied to the unpatterned surface of the membrane. Figure 9 is a photomicrograph of a finished patterned x-ray mask.

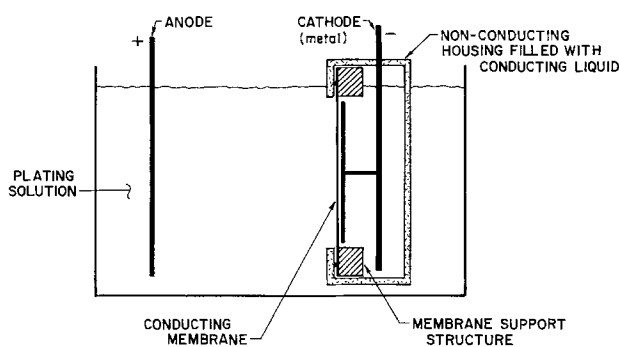


Fig. 6. Apparatus for electroplating a titanium mask membrane

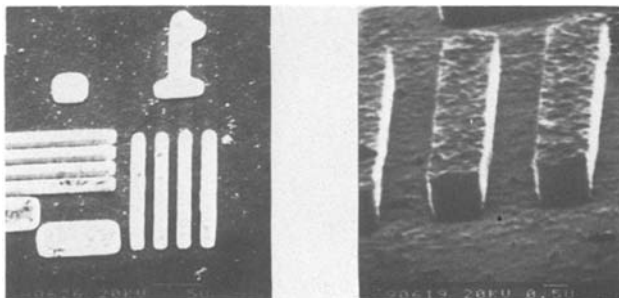


Fig. 7. $1\ \mu\text{m}$ features $\times 1\ \mu\text{m}$ thick electroplated gold test patterns on titanium x-ray mask.

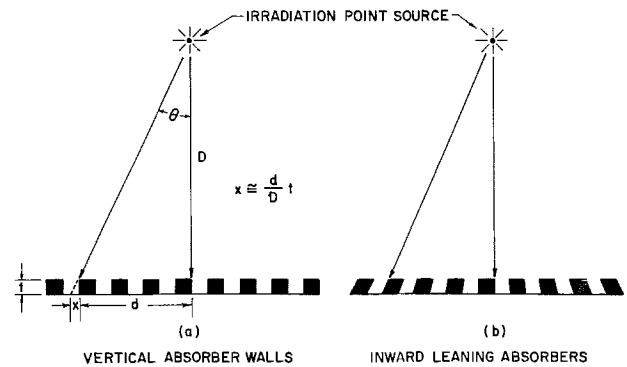


Fig. 8. Absorber definition technique which eliminates shadowing effects.

The subtractive version of the mask patterning process is similar to that described above except that a thick layer of absorber is deposited before stenciling layers are applied. Absorber patterning proceeds by sputtering or ion etching.

In its present state of development a finished mask has an optically visible defect density of less than $20\ \text{cm}^{-2}$ for defects greater than $0.5\ \mu\text{m}$. Straightforward improvements in cleanliness and process techniques are expected to lead to a notable improvement.

Mask Dimensional Stability

A practical x-ray lithography system mask must permit accurate overlay of successive mask layers. The dimensionless stability of the overall mask structure is thus critical. Dimensional instabilities include distortions introduced by the mask patterning process as well as those associated with the membrane itself.

In order to measure these distortions we have fabricated x-ray masks with vernier test patterns. These masks were patterned by means of a Micralign™ projection printer using a quartz master photoplate. The x-ray mask was subsequently compared with the original photoplate by using the optomechanical alignment system of the projection printer to read the vernier patterns. A patterned silicon wafer was also measured periodically to insure against changes in the measurement system. Using these methods the precision of our measurement technique was estimated to be $\pm 0.25\ \mu\text{m}$.

The x-ray alignment system (4) permits the detection and compensation of small linear scale changes in the x-ray mask by adjustment of the mask-to-wafer distance. Therefore, our major concern is with random or nonlinear dimensionless changes remaining after a single linear magnification correction. We have ana-

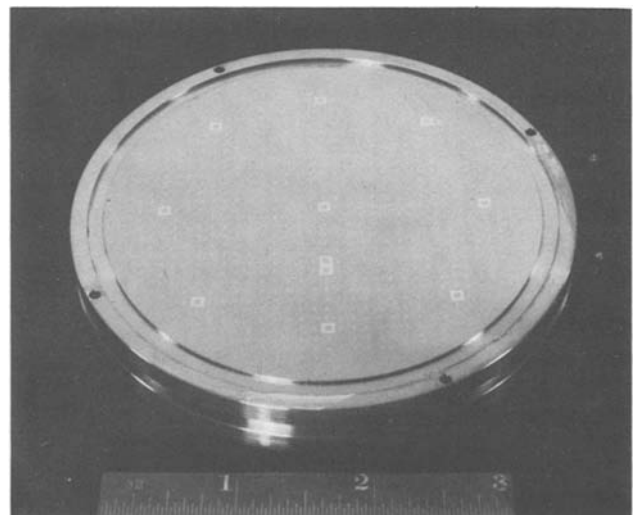


Fig. 9. Titanium x-ray mask with gold absorber pattern

lyzed our dimensional stability data in terms of linear and nonlinear distortions.

Figure 10 illustrates the average linear scale change of a 7.5 cm diam mask with time. The data indicates a small continuous shrinkage of the mask pattern with time. However, most of the shrinkage occurs in the first 1000 hr. This suggests that patterning of the stretched membrane after an initial aging could result in no further scale change (although the small scale change illustrated in Fig. 10 is, in fact, well within the compensating capability of the system).

Figure 11 illustrates the temporal variation of the residual nonlinear distortion term. It can be seen that this random term is small and within our measuring uncertainty at all times. It is important to note that these data include pattern distortions introduced by the fabrication process.

An x-ray multiple exposure technique was also used to measure the temporal stability of the x-ray mask. The x-ray lithography system was used to expose a silicon wafer and the pattern was etched in silicon dioxide. A second exposure using the same mask created an image in a new resist coating. (Unlike the Micralign measurement, these data do not include the pattern distortion since the mask is compared to itself rather than the master mask from which it was made.) The second exposure was offset from the first so that a vernier mask pattern could be used to measure misregistration. The vernier measurement uncertainty was approximately $0.1 \mu\text{m}$. Misregistration was measured at seventeen locations in the wafer. The linear alignment errors were removed mathematically and the residual nonlinear errors are shown in Fig. 12. This figure summarizes the data for 8 wafers with an elapsed time of three weeks between exposures. The data shows that to within 1 standard deviation there is no nonlinear error, within the measuring precision.

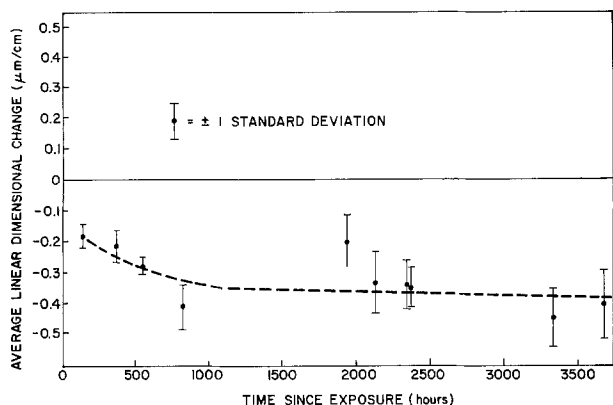


Fig. 10. Average linear magnification change as a function of time for a $1 \mu\text{m}$ thick titanium mask membrane.

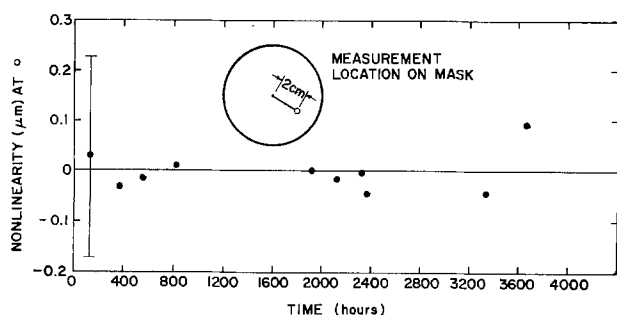


Fig. 11. Nonlinear dimensional change as a function of time at a fixed location on a titanium mask membrane.

x - REFERENCE LOCATION AT $t=0$
 • - NEW LOCATION AFTER 3 WEEKS

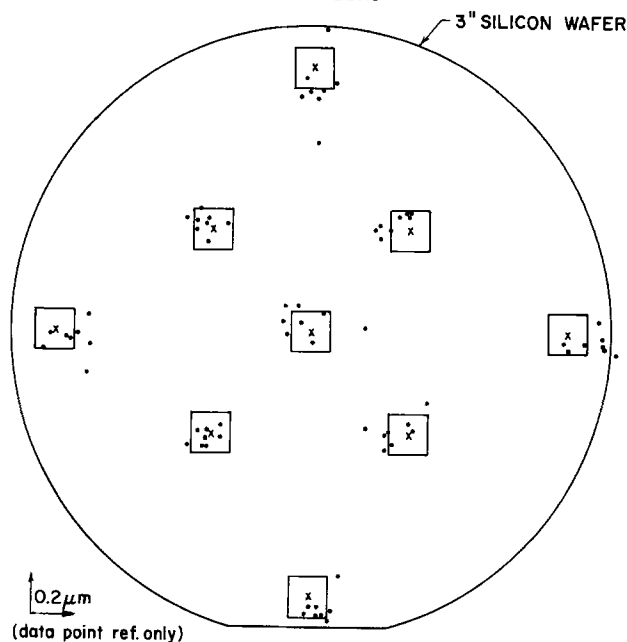


Fig. 12. Nonlinear dimensional change after 3 weeks for 8 wafers and a single mask. The data scatter is of the same magnitude as the measuring uncertainty.

Conclusion

Using a unique combination of materials and novel processing techniques we have developed a full field x-ray mask fabrication process. The masks are rugged, have a relatively high x-ray transmittance, are stable, and sufficiently blemish-free to be suitable for device fabrication.

Manuscript submitted Aug. 12, 1980; revised manuscript received Dec. 18, 1980. This was Paper 278 presented at the St. Louis, Missouri, Meeting of the Society, May 11-16, 1980.

Any discussion of this paper will appear in a Discussion Section to be published in the December 1981 JOURNAL. All discussions for the December 1981 Discussion Section should be submitted by Aug. 1, 1981.

Publication costs of this article were assisted by The Perkin-Elmer Corporation.

REFERENCES

- H. I. Smith, D. L. Spears, and S. E. Bernacki, *J. Vac. Sci. Technol.*, **10**, 913 (1973).
- D. Maydan, G. A. Coquin, J. R. Maldonado, S. Somelch, D. Y. Lou, and G. N. Taylor, *IEEE Trans. Electron Devices*, **ed-22**, 429 (1975).
- W. D. Buckley and G. P. Hughes, Paper 276 presented at The Electrochemical Society Meeting, St. Louis, Missouri, May 11-16, 1980.
- W. D. Buckley, G. P. Hughes, D. H. Kittell, J. L. Kreuzer, and M. P. Eisenberg, Paper 277 presented at The Electrochemical Society Meeting, St. Louis, Missouri, May 11-16, 1980.
- B. A. Movchan and A. V. Demshishin, *Fiz. Metall.*, **28**, 83 (1969).
- J. M. Poate, P. A. Turner, and W. J. BeBonte, *J. Appl. Phys.*, **46**, 4275 (1975).
- W. D. Sylwestrowicz, H. A. Elkholy, and G. W. Kammlott, *J. Mater. Sci.*, **14**, 873 (1979).
- R. S. Nowicki and I. Wang, *J. Vac. Sci. Technol.*, **15**, 253 (1978).

The Growth of Oxidation Stacking Faults and the Point Defect Generation at Si-SiO₂ Interface during Thermal Oxidation of Silicon

A. Miin-Ron Lin^{*,1} and Robert W. Dutton

Integrated Circuits Laboratory, Stanford University, Stanford, California 94305

Dimitri A. Antoniadis^{*}

*Department of Electrical Engineering and Computer Science,
Massachusetts Institute of Technology, Cambridge, Massachusetts 02139*

and William A. Tiller

Department of Materials Science and Engineering, Stanford University, Stanford, California 94305

ABSTRACT

A general relation for the growth and retrogrowth of oxidation-induced stacking faults (OSF) has been developed with three key observations from OSF experiments: (i) the growth rate of OSF is independent of their size and density, (ii) the ambient, pressure, and time dependences are explained by an oxidation rate dependence of the supersaturation of silicon self-interstitials in silicon which induces the fault growth, and (iii) the shrinkage of the faults in inert or oxidizing ambients is controlled by the same mechanism with activation energy of ~ 4.8 eV. To explain the oxidation rate dependence of interstitial supersaturation, a two-step oxidation model is proposed. In the first step, the lattice silicon atoms near the Si-SiO₂ interface oxidize to form SiO₂, but leave a substantial number of silicon atoms as interstitials near the interface. In the second step, these excess silicon atoms flow interstitially mostly into the oxide where they react with oxygen atoms until the oxidation is essentially complete, while a small fraction flows into the bulk silicon. The balance of the reactions in the two steps determines the silicon interstitial supersaturation in silicon which controls the growth rate of OSF. The correlation between the OSF and other oxidation-induced phenomena, e.g., oxidation-enhanced diffusion (OED), and oxide fixed charge, Q_f , formation is also discussed based on the model. The correlation supports the postulate that these phenomena are caused by oxidation via the same point defect mechanism.

Thermal oxidation of silicon is known to induce growth of stacking faults in silicon (1). The presence of stacking faults has been found to cause adverse effects on the performance of integrated circuits, e.g., current leakage in junction diodes and bipolar transistors, storage time degradation in MOS devices, dark current nonuniformity in CCD's, etc. (2-4). There have been successful efforts to reduce the density and size of oxidation-induced stacking faults (OSF), resulting in significant improvement in yield and performance of integrated circuits (5, 6). Understanding the OSF growth kinetics and its relation to processing steps is fundamental to further optimization of IC processes. More importantly, since OSF growth is induced by the oxidation process, a detailed understanding of OSF growth as well as of other oxidation-related process phenomena, e.g., oxidation-enhanced diffusion (OED) and the formation of interface charges, may shed new light on oxidation kinetics.

From the abundant experimental data reported in literature (1), many important characteristics of OSF growth can be inferred. The density of OSF is influenced strongly by imperfections in the silicon wafer and is generally not affected by the oxidation process, exceptions result from the chlorine-assisted gettering oxidations (6). The size of OSF following oxidation, on the other hand, is essentially determined by the oxidation conditions. The growth of OSF consists of

two different regimes, commonly referred to as growth and retrogrowth regimes. In the growth regime, in short oxidations at low temperatures, OSF expand with time. In the retrogrowth regime, in long oxidations at high temperatures, OSF shrink. The shrinkage of OSF is also observed when the wafers with OSF are annealed in neutral ambients at high temperatures (7, 8). It is shown in later sections that the shrinkage of OSF in both neutral and oxidizing ambients is similar and appears to be controlled by the same mechanism. The growth of OSF follows a time dependence of $t^{0.8}$ and an activation energy of 2.3 eV for most oxidation conditions (1). The OSF growth rate varies strongly with different oxidation ambients including different oxygen and steam pressures as well as chlorine-containing ambients (6, 9, 10).

This paper proposes a general equation relating the growth/retrogrowth of OSF to oxide growth rate. The basis of the general relationship is a model of point defect generation at the Si-SiO₂ interface during oxidation. The general relationship is shown to explain experimental results under a wide range of oxidation conditions. In later sections, the details of the point defect generation model and its implications to other oxidation-induced phenomena, e.g., oxidation-enhanced diffusion and the formation of oxide fixed charges, are discussed.

Growth of Oxidation-Induced Stacking Faults

TEM analysis shows that OSF are two-dimensional extrinsic defects lying in $\langle 111 \rangle$ planes and are bounded by Frank partial dislocations (11, 12). The

^{*} Electrochemical Society Active Member.

¹ Present address: Bell Laboratories, Allentown, Pennsylvania 18103.

Key words: oxidation, stacking faults, point defects, interface.

extrinsic nature of OSF suggests that the faults grow by the climb of Frank partials via emission of silicon vacancies or absorption of silicon interstitials. In a first attempt to model the growth of OSF, Hu (13) postulated that thermal oxidation of silicon is not a complete process and thus produces excess interstitial silicon atoms near the Si-SiO₂ interface. More recently, Tiller (14-16) has shown that oxidation of silicon requires the creation of free volume at the Si-SiO₂ interface. The free volume can be generated in part by the flux of silicon interstitials away from the interface. In both cases, a supersaturation of silicon interstitials occurs in the silicon substrate near the Si-SiO₂ interface and OSF grow by absorbing these interstitials. The rate of absorption determines the growth rate of OSF. In equation [13] of Ref. (13), Hu gave the growth rate as

$$\frac{dr}{dt} = \pi a_0^2 D_1 (C_I - C_I^*) \quad [1]$$

where r is the radius of the stacking faults, a_0 the capture distance of interstitials by the faults, D_1 the diffusivity of self-interstitials in silicon, and C_I and C_I^* the extrinsic and intrinsic interstitial concentrations in silicon, respectively.

Equation [1] states that at a given temperature the stacking fault growth rate depends only on the excess interstitial concentration. Since it is reasonable to assume that identical oxidation conditions yield identical excess interstitial concentration, they should also yield identical stacking fault growth irrespective of the initial size of the faults. This growth behavior of OSF is in agreement with Shiraki's experiments (9) described below and will prove to be an important difference between Hu's model and a recent model proposed by Murarka (1).

In Shiraki's experiments, silicon wafers were oxidized in dry oxygen ambient. OSF of $\sim 65 \mu\text{m}$ length were observed on the wafers after oxidation. The oxide was then completely etched away and these wafers together with similar wafers, which were not oxidized, thus having no visible OSF, were oxidized in dry oxygen ambients containing different concentrations of HCl. The change in length of OSF after oxidation is replotted in Fig. 1(a-d). As can be seen from the figures, OSF of different initial lengths (0 and $65 \mu\text{m}$) grow with similar rates throughout the same oxidation step, indicating that the growth rate of OSF is nearly independent of size and is determined only by the oxidation conditions as implied by Eq. [1]. This is particularly true during the early growth. For long oxidations, there appears to be some size dependence, which is probably caused by the overlapping of large faults or other secondary factors not known at present.

In his recent model, Murarka (1) considered the OSF growth analogous to the three-dimensional crystalline growth at the surface of kinks. He adapted a model developed by Kahlweit (17) and derived an expression for the OSF growth as a function of time.

$$r = \frac{4}{\sqrt{3b}} (\Omega D \Delta C_I)^{3/4} t^{3/4} \quad [2]$$

where b is the magnitude of the Burger's vector of the partials bounding the faults, Ω is the atomic volume of silicon, D is the self-diffusion coefficient of silicon, and ΔC_I is the supersaturation of silicon interstitials in silicon.

Recently, Leroy (19) has criticized Murarka's use of Kahlweit's model to explain the growth of OSF. We will not repeat Leroy's arguments, but we would like to make here two additional points against Murarka's model. (i) In Kahlweit's original model the growth rate of the three-dimensional nuclei is inversely proportional to the diameter of the growing nuclei. Following Murarka's adaptation of the model, the growth rate of OSF is expected to vary with size. This is in

disagreement with Shiraki's experiments described above. (ii) At a given temperature and ambient, the supersaturation of interstitials, ΔC_I , is constant according to Murarka's original paper (1), or varies inversely with oxidation rate, following a power law, according to a more recent presentation by the same author (20). Both of these arguments are contradicted by observations of oxidation enhanced diffusion, OED, which also results from interstitial supersaturation (21, 22). Indeed, OED experiments indicate that ΔC_I varies proportionately with oxidation rate, following a power law, in agreement with the one proposed later in the present paper.

Retrogrowth and Shrinkage of Oxidation-Induced Stacking Faults

As mentioned earlier, OSF shrink during long oxidations (23) and neutral ambient annealing (7, 8) at high temperatures. This section will show that in both the neutral and oxidizing ambients, the shrinkage is controlled by the same mechanism.

Sugita *et al.* (7) have observed that OSF shrink with constant rate when the wafers are annealed at high temperatures in N₂ ambient. Claeys *et al.* (8) reported similar shrinkage, with the shrinkage rate slightly dependent on annealing ambient (N₂, H₂, or Ar). These data are compared to the results of Shiraki's experiments shown in Fig. 1(a-d). Shiraki's data indicate that the addition of HCl to the oxidation ambient reduces the rate of OSF growth. When the added HCl content is high enough, the OSF growth is totally suppressed and the initial faults shrink with a rate similar to that of the shrinkage in N₂ ambients observed by Sugita *et al.* (7) and Claeys *et al.* (8). The activation energy of the shrinkage is also very similar for various cases and is independent of ambient. In fact, all shrinkage data follow an Arrhenius temperature dependence with an activation energy of approximately 4.8 eV. This strongly suggests that the retrogrowth of OSF for long oxidations and the shrinkage during neutral ambient annealing are controlled by the same activated process.

A Model for the OSF Growth/Retrogrowth

Following the discussion in the previous two sections two important characteristics of the OSF growth in silicon must be emphasized: (i) the growth rate of the oxidation stacking faults is nearly independent of their size and density, and (ii) retrogrowth of OSF during oxidation is similar to shrinkage during annealing in neutral ambients.

To explain both the growth and retrogrowth, we consider that the Frank loop partial bounding the faults act as a sink or a source of interstitials. During oxidation, silicon interstitials are produced at the Si-SiO₂ interface and diffuse quickly into the bulk silicon, supersaturating the interstitial concentration to a level higher than the interstitial concentration in equilibrium with the faults, C_I^S , which is defined as the concentration at which the faults neither grow nor shrink. The partial dislocation, acting as a sink, captures the interstitials within a domain of radius, a_0 , and causes the fault to grow (Fig. 2). For neutral ambients or when the oxidation rate is small and the interstitial generation is negligible, the interstitial concentration in the bulk returns to the equilibrium level, C_I^* , which is lower than C_I^S . The dislocation then acts as a source of interstitials and the interstitials diffuse away from the faults causing the faults to shrink. Although the importance of interstitials in OSF growth/retrogrowth is widely recognized, the detailed mechanism of the interstitials absorption and emission is still controversial. Leroy (19) advocates a diffusion controlled model, while Hu (24) favors a reaction control model. As the present paper is focused on the general macroscopic behavior of OSF in differ-

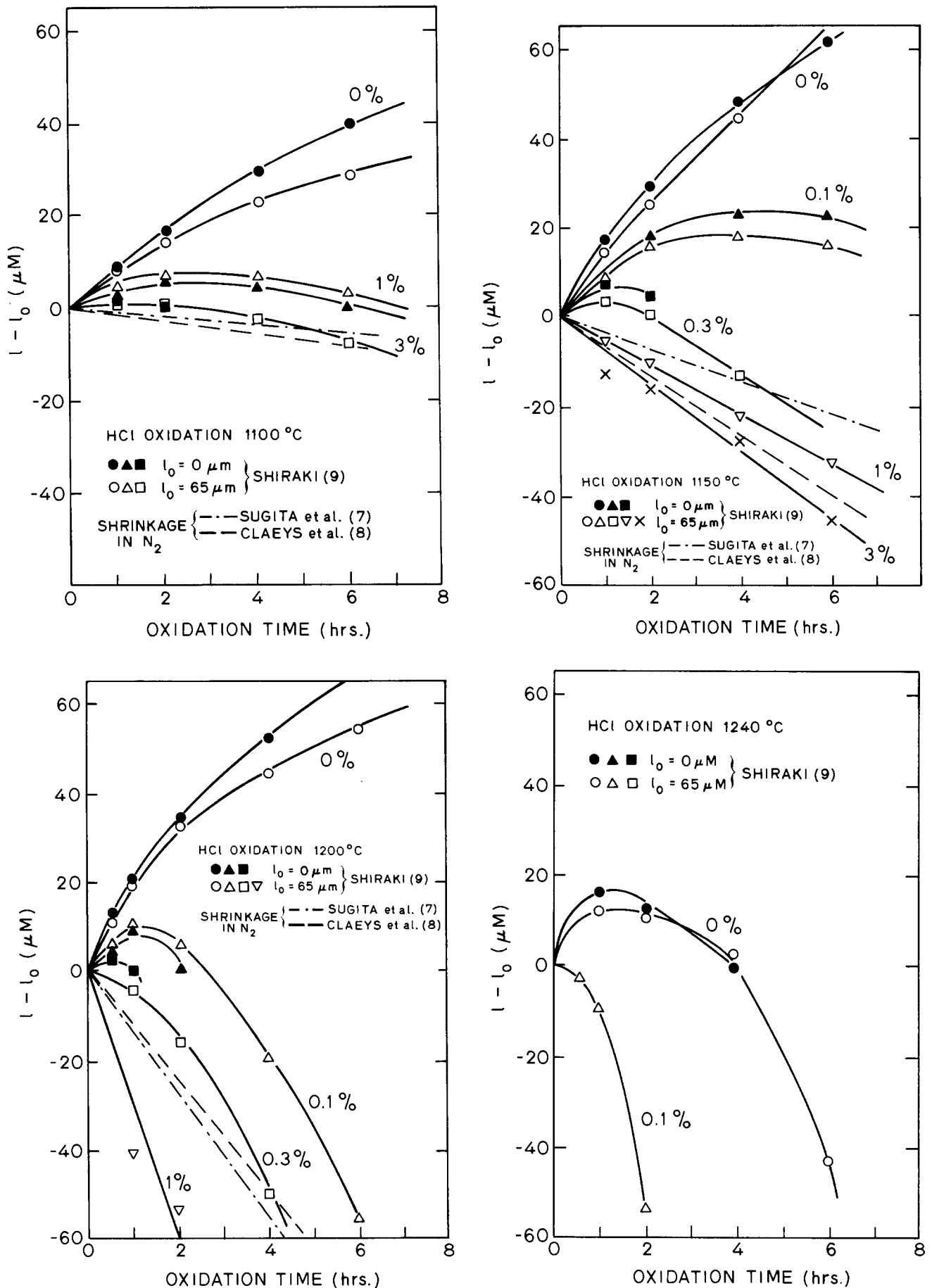


Fig. 1. Stacking faults of different initial lengths grow with similar rates in $\langle 100 \rangle$ silicon oxidations with different HCl concentrations at (a, top left) 1100°C, (b, top right) 1150°C, (c, bottom left) 1200°C, and (d, bottom right) 1240°C. Also shown are results of OSF shrinkage in N_2 ambient from Refs. (7, 8).

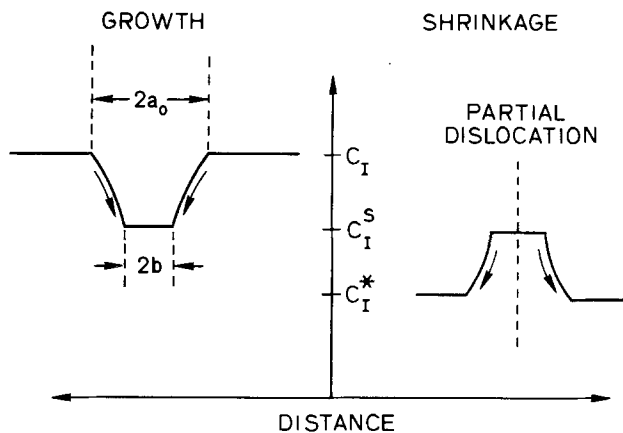


Fig. 2. The silicon interstitial distribution near the partial dislocation bounding the stacking faults during the growth and shrinkage of OSF.

ent processing ambients, readers interested in more details on the microscopic models are referred to the above references. Both models, nevertheless, agree on the basic formulation of the OSF growth as follows

$$\frac{dr}{dt} = P(C_I - C_I^S) \quad [3]$$

where P is a proportionality factor, involving the diffusion of self-interstitials and the reaction energy barrier (19, 24).

The growth of OSF and, thus by implication, the interstitial supersaturation occurs only when the silicon is oxidized. In a later section, we discuss the possible mechanisms leading to the generation of interstitials at the Si-SiO₂ interface. It is also demonstrated later that the interstitial supersaturation can be related to the rate of oxide growth by the expression

$$C_I - C_I^* = K \left(\frac{dX}{dt} \right)^n \quad [4]$$

where K is a reaction constant related to the point defect generation process at the interface, and X is the oxide thickness.

Combining Eq. [3] and [4] gives a general relationship for the growth of OSF in silicon

$$\frac{dl}{dt} = K_1 \left(\frac{dX}{dt} \right)^n - K_2 \quad [5]$$

$$K_1 = 2PK \quad [5a]$$

$$K_2 = 2P(C_I^S - C_I^*) \quad [5b]$$

where $l = 2r$ is the diameter of stacking fault, generally taken as the length of the fault.

A linear dependence ($n = 1$) in Eq. [4] was initially proposed by Hu (13) for OSF growth. However, as Hu pointed out later (23), the predicted time dependence of OSF growth based on the linear dependence disagrees with experimental results. Detailed comparison of Eq. [5] with experimental results shown in the next section gives the value of n to be 0.4. We believe that this sublinear dependence results from a particular point defect generation mechanism at the Si-SiO₂ interface. A model for the generation mechanism is discussed in a later section.

Comparison with Experiments

Figure 3 shows experimental data from Hu (23) and Murarka (25) for the OSF growth in dry oxygen at different temperatures in <100> silicon. At low temperatures (1050°-1150°C), only growth is observed

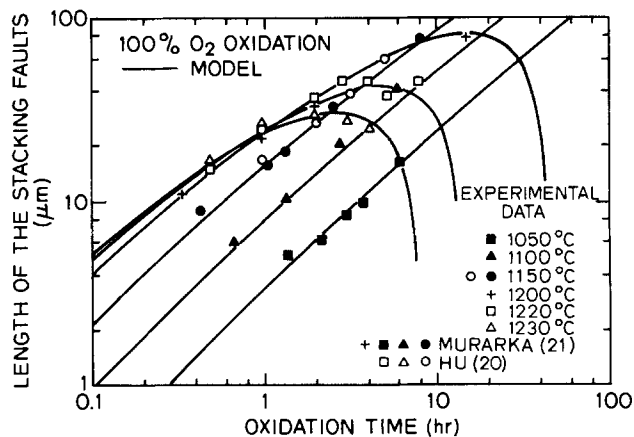


Fig. 3. Experimental data for OSF growth in 100% O₂ oxidation and comparisons with the model.

while at higher temperatures both growth and retro-growth occur. The length of OSF grown at low temperature shows a time dependence of $t^{0.3}$ which gives a dependence of $t^{-0.2}$ for OSF growth rate. The coefficient K_2 is insignificant at these temperatures and OSF growth is governed by the oxide growth, following Eq. [5]. For the temperatures and times shown in Fig. 3, oxidation is in the so-called parabolic oxide growth regime where dX/dt follows a $t^{-0.5}$ dependence (18). Thus, Eq. [5] yields a value of $n = 0.4$. With the known oxidation rate at these temperatures, K_1 is directly obtained from the data in Fig. 3. At higher temperatures, however, K_2 becomes significant and retrogrowth occurs during oxidation. K_1 and K_2 are then simultaneously obtained by a least squares fit. The extracted values for K_1 and K_2 are plotted in Fig. 4 as a function of temperature. Both appear to follow an Arrhenius temperature dependence with different activation energies

$$K_1 = 1.58 \times 10^{10} \exp(-2.4 \text{ eV}/kT) (\mu\text{m/hr})^{0.6} \quad [6]$$

$$K_2 = 6.45 \times 10^{17} \exp(-4.8 \text{ eV}/kT) (\mu\text{m/hr}) \quad [7]$$

These data are for OSF growth in <100> silicon in dry O₂ ambient and will be different for other orientations. The calculations using Eq. [5] with the now known n , K_1 and K_2 show good agreement with the experimental data in the complete range of temperatures and times as demonstrated in Fig. 3.

In the absence of oxidation, the interstitial concentration returns to the equilibrium level, C_I^* , and the stacking faults shrink with the rate

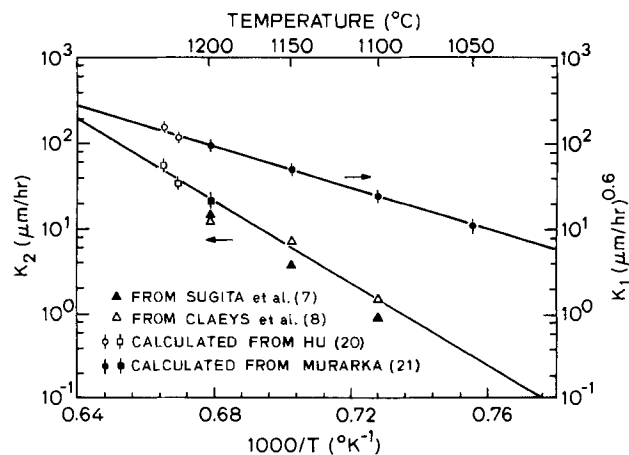


Fig. 4. The extracted data for the OSF growth constant K_1 and retrogrowth constant K_2 from the data in Fig. 3. Note the good agreement between the extracted K_2 and the measured shrinkage rates in N₂ from Refs. (7, 8).

$$\frac{dl}{dt} = -K_2 \quad [8]$$

This allows an independent calculation of K_2 . In Fig. 4 the OSF shrinkage rates in N_2 ambient from Sugita *et al.* (7) and Claeys *et al.* (8), are compared with the calculated K_2 from the dry O_2 experiments. Claeys *et al.* (8) also observed that the OSF shrinkage is different in different neutral ambients (Ar and H_2 as compared with N_2), which suggests that C_1^* is affected by the annealing gas ambients. They attributed the effect to nitridation possibly occurring at the interface during the N_2 annealing.

The difference in the activation energies of K_1 and K_2 is significant and can explain the strong temperature dependence of OSF retrogrowth. Figure 5 plots separately the growth and retrogrowth rates. At low temperature, the growth rate is seen to dominate. As the temperature increases, because of the larger activation energy of K_2 , the retrogrowth rate increases more rapidly than the growth rate and, at sufficiently high temperatures, the retrogrowth dominates. This is in agreement with experimental findings (23, 25).

The 2.4 eV activation energy of K_1 includes the energy of interstitial generation at the Si-SiO₂ interface and of interstitial migration in silicon. Assuming an interstitial self-diffusion mechanism for silicon Seeger *et al.* (26) obtained 2.0 eV for the interstitial migration energy which leaves 0.4 eV for the activation energy of interstitial generation at the Si-SiO₂ interface.

The activation energy of K_2 involves the formation and migration of interstitials near the stacking faults. The calculated 4.8 eV activation energy of K_2 is close to that of silicon self-diffusion, which lies between 4.78 and 5.13 eV (27-29) and suggests the same formation and migration energies of the interstitial near the faults as in the bulk away from the faults.

Since K_1 involves only the migration of interstitials and the interstitial generation at the Si-SiO₂ interface, whereas K_2 involves only the formation and migration of interstitials near the faults, both are expected to

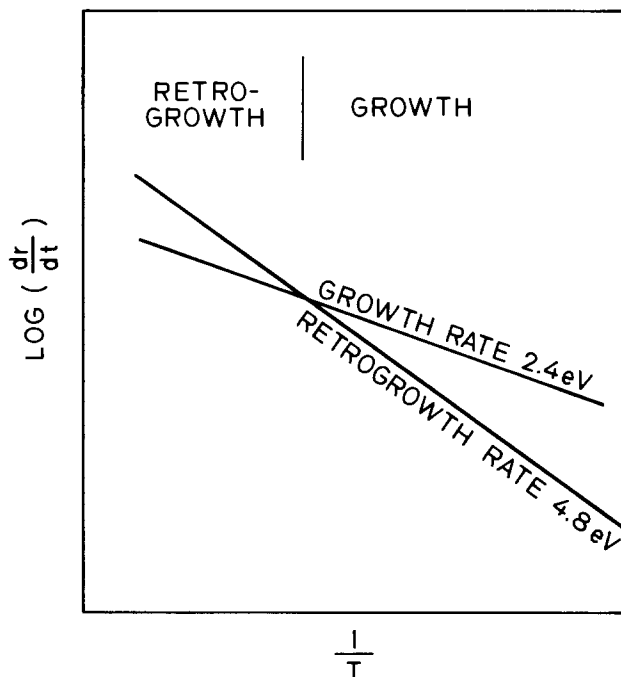


Fig. 5. At low temperatures, OSF growth rate is larger than retrogrowth rate. As the temperature increases, because of its larger activation energy, retrogrowth rate increases more rapidly and becomes dominant at high temperatures.

be rather independent of oxidation ambients.² Hence Eq. [5]-[7] form a general relationship and can be readily applied to OSF growth under any different oxidation conditions. In the following subsections, we discuss the growth/retrogrowth of OSF for oxidations with different oxygen and steam pressures and compare the proposed general model to the experimental results available in the literature.

Oxygen partial pressure oxidations.—The growth of OSF is found to vary with different partial pressures of oxygen for otherwise similar oxidation conditions (25, 30). The partial pressure of oxygen results in different oxidation rates whereas the oxidizing species and interface kinetics are the same regardless of the pressure. Hence the different OSF growth at different oxygen pressures should provide an important test for the generality of Eq. [5].

For long oxidations, such as those used in OSF experiments, the oxide growth is dominated by a parabolic growth regime (18), in which the oxidation rate follows a $t^{-0.5}$ time dependence with actual value determined by the oxidant's partial pressure. The stacking fault growth rate at different oxygen pressures will then have a $t^{-0.2}$ time dependence, but different overall value, following Eq. [5] with $n = 0.4$ and assuming K_2 is negligibly small. Thus the length of OSF grown in different oxygen pressures will vary, but the same $t^{0.8}$ time dependence will always be observed. This is consistent with experimental data reported by Murarka (25) as shown in Fig. 6. The different lengths are also explained by the specific dependence of oxidation rate on oxygen pressure. Figures 7a, b, and c show more complete comparisons with data of OSF growth and retrogrowth during oxidations in different pressures at various temperatures and times. Calculations utilizing the present model show generally good agreement with these experimental data that come from many workers (9, 23, 30).

Atmospheric and high pressure steam oxidations.—OSF grow to a greater size in steam ambients than in dry oxygen ambients for the same oxidation temperature and time (23, 31). Figure 8 shows a comparison between experimental data from Ref. (23, 31) and calculations by Eq. [5]. Since the values of K_1 and K_2 used in Eq. [5] are obtained from data for dry oxidation only, the good agreement between experimental and calculated data shown in Fig. 8 suggests that the basic point defect process at the interface is the same for dry and steam ambients and is controlled primarily by the rate of oxide growth as postulated earlier in Eq. [4].

² One exception is chlorine-containing oxidation in which Cl atoms possibly affect the silicon point defect generation at the Si-SiO₂ interface.

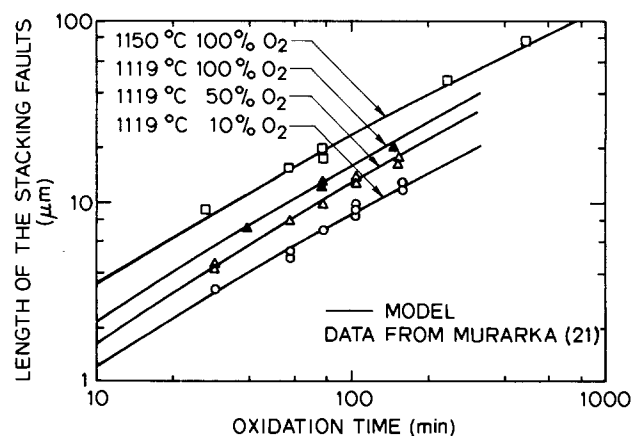


Fig. 6. The stacking faults growth in different O_2 partial pressures. These curves show the same time dependence, $t^{0.8}$, illustrating the same oxidation rate dependence of OSF growth.

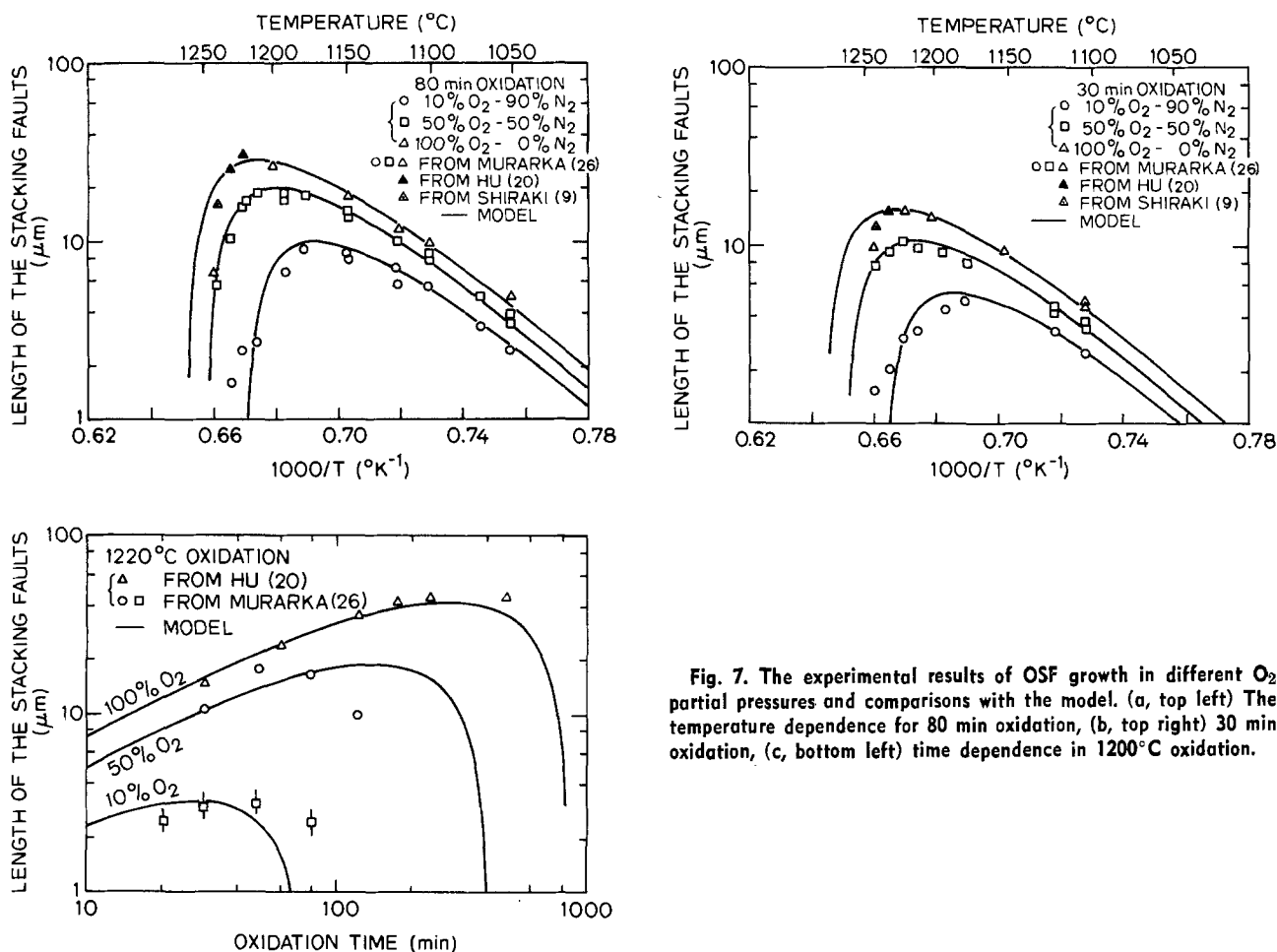


Fig. 7. The experimental results of OSF growth in different O₂ partial pressures and comparisons with the model. (a, top left) The temperature dependence for 80 min oxidation, (b, top right) 30 min oxidation, (c, bottom left) time dependence in 1220°C oxidation.

Tsubouchi *et al.* (32) reported that much smaller OSF result when the same thickness of oxide is grown in high pressure steam than in atmospheric steam (Fig. 9a and b). This supports strongly the sublinear oxidation rate dependence in Eq. [5]. It is rather obvious that if the oxidation rate dependence was linear, similar sizes of OSF would grow for the same thickness of oxide regardless of different ambients used at the same temperature. Calculations using the proposed model again show good agreement with experimental data both at atmospheric and high pressures.

Chlorine-containing oxidations.—The addition of HCl in the oxidation atmosphere suppresses the growth

of OSF (Fig. 1). A similar effect has been observed for oxidations with other chlorine-containing atmospheres, *e.g.*, TCE (33) and C33 (6).

It can be seen from Fig. 1 that the presence of chlorine primarily reduces the growth rate of OSF while leaving the retrogrowth rate generally unaffected. This can be understood by considering a reaction of chlorine with silicon interstitials at the interface (forming silicon chlorides), which reduces the supersaturation of silicon interstitials in silicon during oxidation. The reaction at the interface, acting as a sink for both chlorine and excess silicon atoms, may partly explain the experimentally observed chlorine pile-up at the interface during oxidation (34).

Retrogrowth time (t_R) and temperature (T_R).—As mentioned in the earlier sections, there exists a time during oxidation at certain temperature when OSF begin to shrink with time instead of growing; this retrogrowth time is denoted as t_R . Also for a fixed duration of oxidation there exists a temperature at which OSF grow to a maximum length, this temperature is defined as retrogrowth temperature, T_R . It can be seen from Fig. 3 and 7 that both t_R and T_R are strong functions of oxidation temperature, time, and ambient.

At a given temperature, T , the retrogrowth begins during oxidation when the OSF growth rate decreases to 0, *i.e.*, $\partial r/\partial t|_T = 0$. Hence t_R can be calculated from Eq. [5] by deriving the oxide growth rate at which the above condition is obtained, as follows

$$\begin{aligned} \frac{dX}{dt_R} &= \left(\frac{K_2}{K_1} \right)^{1/n} \\ &= \left(\frac{K_2}{K_1} \right)^{2.5} \\ &= 1.06 \times 10^{19} \exp(-6.0 \text{ eV}/kT_R) (\mu\text{m}/\text{hr}) \quad [9] \end{aligned}$$

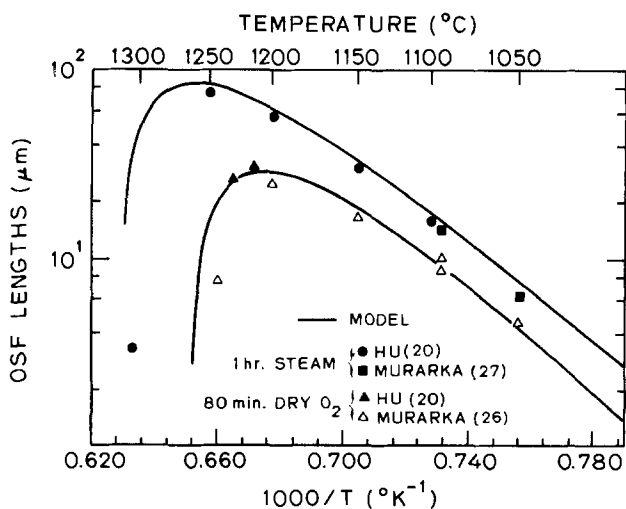


Fig. 8. The OSF growth in steam ambient as compared to that in dry O₂ ambient. The larger size of faults grown in steam ambients is explained by the oxidation rate dependence of OSF growth.

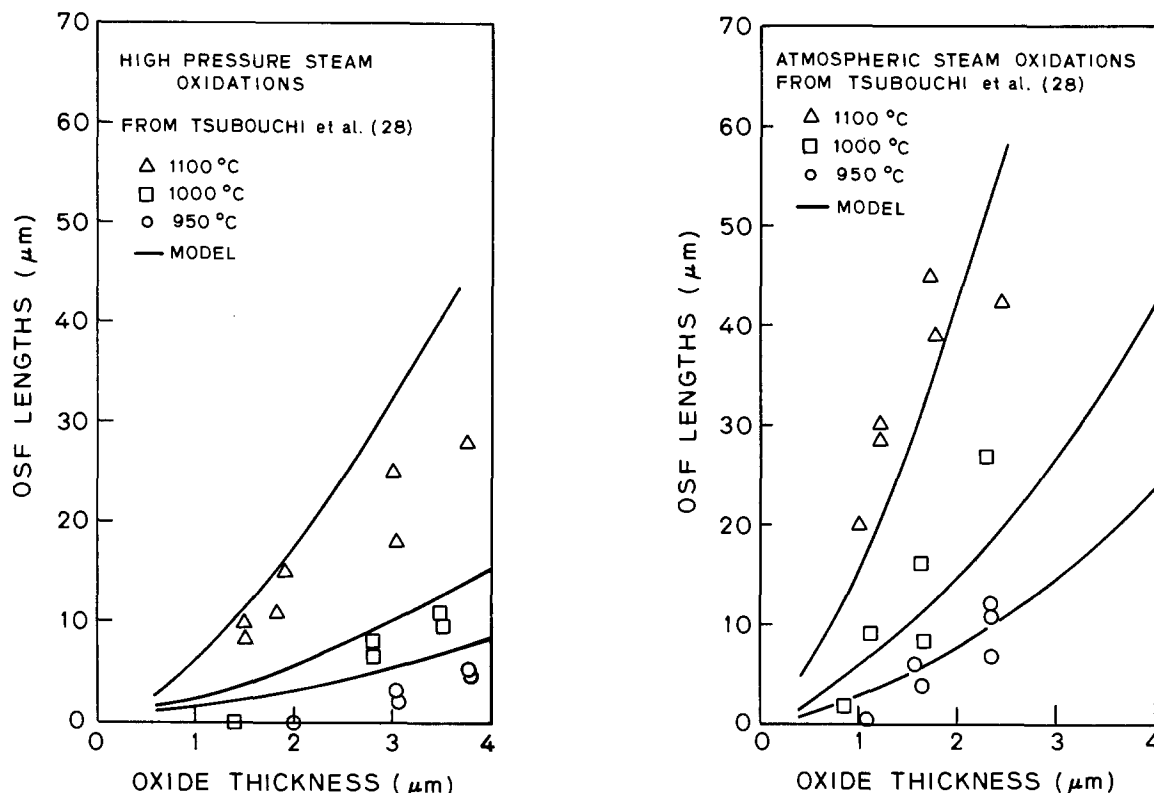


Fig. 9. The OSF growth in steam oxidations at (a, left) atmospheric pressure and (b, right) high pressure. Note the reduction of OSF sizes when the same oxide thickness is grown at high pressures instead of atmospheric pressure.

for $\langle 100 \rangle$ silicon. K_1 and K_2 are independent of oxidation ambient while the oxidation rate is strongly ambient and time dependent. Thus, from Eq. [9], t_R is expected to vary at different oxidizing ambients. Equation [9] can also be used for the calculation of T_R . An example graphical solution of this equation, for a 1 hr oxidation at different ambients, is shown in Fig. 10. While dX/dt at a fixed time is strongly ambient dependent, K_1 and K_2 are not. Thus, the temperature at which retrogrowth begins, defined by the intersection of the $(K_2/K_1)^{2.5}$ and $(dX/dt)_t$ curves, increases with increasing $(dX/dt)_t$. A certain similarity between Fig. 10 in the present paper and Fig. 10 in Ref. (25) should be noted here. The similarity, however, is only superficial since the plotted quantities and the theory behind them are different in the two cases. Since we have discussed our objections to Murarka's theory earlier in this paper, we will make no further comment at this point.

T_R can also be calculated utilizing Eq. [5] with the condition for maximum OSF growth for a given oxidation time, $\partial r/\partial T|_t = 0$. The calculations are compared in Fig. 11 with experimental results from Ref. (23 and 25) with generally good agreement.

Point Defect Generation at the Si-SiO₂ Interface

From the fact that stacking faults grow during oxidation, it is clear that the oxidation reaction is a source of point defects, assumed here to be self-interstitials, that induce the fault growth. While the Deal-Grove model (18) for oxidation explains very well the basic phenomenology of oxide growth, it provides little insight into its relationship with point defect generation process. In this section we discuss a model for the generation of interstitial point defects near the Si-SiO₂ interface and the subsequent distribution of these defects. This model is based on two key postulated mechanisms: (i) a two-step oxidation reaction and (ii) a segregation of excess silicon at the interface (16).

Two-step oxidation.—The average spacing between silicon atoms in SiO₂ is about 1-3 times the average spacing of silicon atoms in the Si lattice. If the Si-

SiO₂ interface moves into the bulk Si with a velocity, V , during oxidation, the oxide thickens at a rate of $2.25V$, which means that free volume must be created at a rate of $1.25V$ per unit area, otherwise the interface would be severely strained and oxidation would be retarded (14). The free volume may be supplied by a flux of vacancies from the bulk silicon to the interface, a flux of silicon interstitials from the interface to the bulk oxide or silicon, or a viscous flow of the oxide. If the free volume is to be entirely supplied by point defect fluxes, extremely large fluxes would be needed, which is unlikely. However, if less than 45% (1/1.25) of the silicon at the interface is oxidized and the rest of the silicon (55%) is placed at interstitial sites in the oxide, free volume would not be immediately needed. Since oxidation is experimentally found

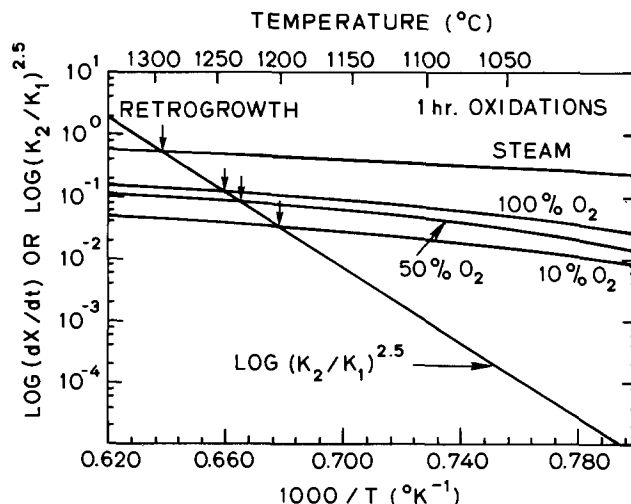


Fig. 10. The arrows indicate the temperature at which retrogrowth will occur for 1 hr oxidation in different ambients, calculated using Eq. [9]. The retrogrowth temperature increases for oxidations with increasing oxidation rates.

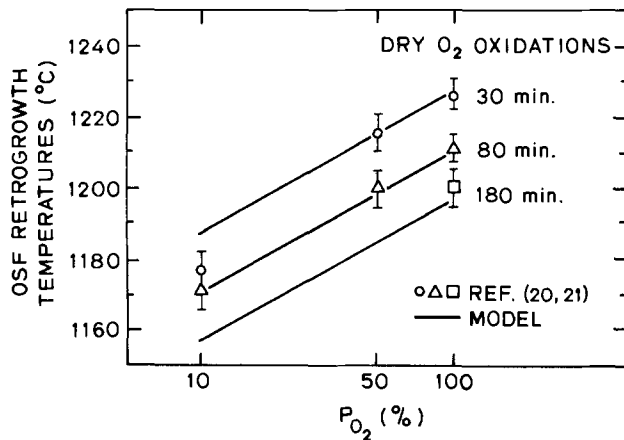


Fig. 11. For the same duration of oxidation, the retrogrowth of stacking faults occurs at lower temperatures at lower O_2 partial pressures. The calculations are from Eq. [5] with the condition, $d\tau/dT|_t = 0$.

to be more than 99% complete (35), the majority of these interstitial silicon atoms have to be oxidized in other reactions. Hence, the postulated initial oxidation and boundary motion reflect a localized intermediate mechanism for interstitial generation rather than a macroscopic observable fact.

The formation of interstitials at the interface can also be understood from the interface match between the Si and SiO_2 phases. It is pointed out by Tiller (16) that for low temperature oxidation, α -cristobalite is the preferred form for SiO_2 to initially form during thermal oxidation. The $\langle 100 \rangle$ α -cristobalite phase matches the $\langle 100 \rangle$ silicon quite well if 4 silicon atoms per unit cell (1/2 of total) become interstitials and diffuse either into bulk silicon or into the oxide. Based on observed results of OSF growth and the near completeness of oxidation, it seems most likely that the dominant fraction of these interstitials are consumed in subsequent oxidation rather than moving into bulk silicon.

From both the consideration of free volume and interface match at the Si- SiO_2 interface, it appears unlikely that the oxidation reaction immediately consumes all the silicon atoms in place at the interface. During oxidation, a substantial number of excess silicon atoms move away from the interface and become excess Si atoms near the interface; the fraction in the oxide is not directly observable whereas those which flow into bulk silicon affect OSF growth. Subsequent reactions of excess silicon with oxygen in the oxide then determine the silicon point defect distribution both in the oxide and in the silicon near the interface. In essence, oxidation of silicon is visualized as a two-step reaction in which point defects play an important role. In the first step, lattice silicon atoms located at the interface react with oxygen and form SiO_2



where Si_L and Si_I represent the lattice silicon and the excess silicon at the interface, respectively, and γ indicates the fraction of excess silicon at the interface. We expect γ to range between approximately 0 and 0.55 based on considerations of free volume and interface mismatch. As oxidation proceeds, the concentration of excess silicon at the Si- SiO_2 interface builds up rapidly; some atoms can escape into bulk silicon and become silicon self-interstitials while others flow into the bulk oxide and quickly react with incoming oxygen near the interface. To avoid continuous buildup of excess silicon at the interface, the total flux away from the interface should equal the rate of generation of excess silicon. Thus

$$G = J_1 + J_2 \quad [11]$$

where G is the generation rate and J_1 and J_2 are the interstitial fluxes into bulk silicon and oxide, respectively. Based on the previously mentioned physical observations it is expected that G and J_2 are considerably larger than J_1 and the dimensions over which the fluxes persist differ by orders of magnitude. Specifically, J_2 being the intermediate reaction product persists only for a few monolayers. On the other hand, J_1 represents the flux which reaches deep into bulk silicon (Fig. 12).

From the reaction [10], the rate of generation of interstitials per unit area at the Si- SiO_2 interface is proportional to the velocity of interface movement, V , as given by

$$G = \frac{\gamma V}{\Omega} = \frac{a\gamma}{\Omega} \left(\frac{dX}{dt} \right) \quad [12]$$

where Ω is the unit volume of silicon. The interface velocity is related to the overall oxidation rate through the well-known ratio $a = 0.44$.

The extrinsic silicon interstitials in silicon may recombine with vacancies or may be absorbed by stacking faults and other defect structures existing in the silicon substrate. These effects are approximated by an infinite sink of interstitials at an effective distance L_S from the interface.³ Then

$$J_1 = D_I \frac{(C_I - C_I^*)}{L_S} - C_I \left(\frac{dX}{dt} \right) \quad [13]$$

where D_I is the diffusion coefficient of silicon interstitials in bulk silicon and C_I is the concentration of silicon interstitials near the interface in bulk silicon. $C_I(dX/dt)$ is the convective flux due to the interface movement and is generally negligible. Since the excess silicon that flows from the interface into bulk silicon would be lost for further oxidation, J_1 should be much smaller than G and J_2 , because oxidation is experimentally found to be more than 99% complete (35). This is further supported by the calculation of the flux of interstitials from the interface to the faults during a typical growth of OSF. For 1 hr oxidation at 1200°C OSF grow with an average rate of $\sim 20 \mu\text{m/hr}$ and absorb interstitials at a rate of $[d(N_0\pi r^2)/dt]/\pi r^2 \sim 6 \times 10^{15} \text{ atoms/hr-cm}^2$, for OSF of 10 μm size. Here,

³ This distance L_S is of the order of 25 μm based on the work of Taniguchi *et al.* (36) on oxidation-enhanced diffusion.

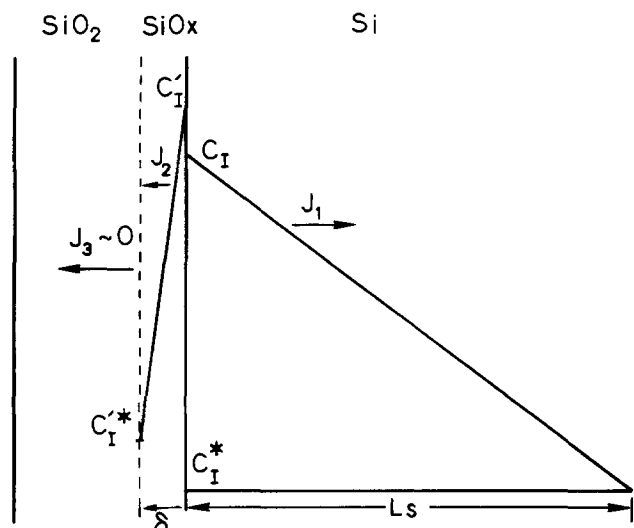
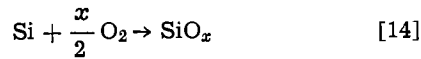


Fig. 12. Interstitial fluxes at the Si- SiO_2 interface during oxidation. J_1 reaches deep into bulk silicon, while J_2 is determined by the re-oxidation of excess silicon in oxide and persists only for a few monolayers.

$N_0 = 1.5 \times 10^{15} \text{ cm}^{-2}$ is the number of atoms per unit area of OSF. The oxidation rate, on the other hand, is $\sim 2 \text{ } \mu\text{m/hr}$, which produces excess silicon atoms at the interface at a rate of $\sim 2.6 \times 10^{18} \text{ atoms/hr-cm}^2$, from Eq. [12] with $\gamma = 0.55$. The detailed form of J_1 is thus not important for determining the interstitial generation at the Si-SiO₂ interface.

Experimentally, excess silicon atoms are found in bulk oxide only very near the interface (37, 38), which indicates that the excess silicon atoms generated during oxidation are quickly oxidized near the interface. This reaction determines the flux J_2 into the bulk oxide. The oxidation of these excess silicon atoms in the oxide is important for determining the net interstitial generation. Without it, the interstitial supersaturation would be linearly dependent on oxidation rate as proposed by Hu (13). The existence of the second oxidation reaction reduces the exponent of the power law dependence, as empirically found from the OSF data described in earlier sections. The reaction of the excess silicon with oxygen in the first layers of the oxide is assumed to follow a general reaction of the form



where x is a parameter to be determined and may represent a mixture of several different SiO_x-type reactions. The postulated SiO_x, if different from SiO₂, is further oxidized later to SiO₂. J_2 can now be expressed as

$$J_2 = k' [\text{O}_2]^{x/2} (C_1' - C_1'^*) \quad [15]$$

where k' is the SiO_x reaction constant, $(C_1' - C_1'^*)$ the concentration of excess silicon interstitials in the oxide near the interface and $[\text{O}_2]$ the concentration of oxygen at the interface. J_2 can be directly related to the overall oxidation rate through the experimentally observed relation involving the oxygen concentration at the Si-SiO₂ interface (18)

$$\frac{dX}{dt} = k [\text{O}_2] \quad [16]$$

where k is the overall reaction coefficient of silicon oxidation at the interface. It then follows that

$$J_2 = \frac{k'}{k^{x/2}} \left(\frac{dX}{dt} \right)^{x/2} (C_1' - C_1'^*) \quad [17]$$

Neglecting J_1 , Eq. [11] is reduced to

$$\frac{a\gamma}{\Omega} \left(\frac{dX}{dt} \right) = \frac{k'}{k^{x/2}} \left(\frac{dX}{dt} \right)^{x/2} (C_1' - C_1'^*) \quad [18]$$

and thus

$$C_1' - C_1'^* = \frac{a\gamma k^{x/2}}{\Omega k'} \left(\frac{dX}{dt} \right)^{1-x/2} \quad [19]$$

Segregation of Excess Silicon at Si-SiO₂ Interface

Equation [19] gives the concentration of excess silicon interstitials in the oxide immediately adjacent to the silicon-oxide interface. During oxidation, silicon interstitials exist in both bulk oxide and silicon near the interface. Because of the different chemical potential of silicon atoms in the two phases, segregation of excess silicon atoms should result, leading to different concentrations at the respective sides of the interface (16). Since oxidation is a relatively slow process, the segregation is assumed to be near equilibrium and the interstitial concentrations are related by an equilibrium segregation m_I

$$m_I = \frac{C_1 - C_1^*}{C_1' - C_1'^*} \quad [20]$$

Combining Eq. [19] and [20], the concentration of extrinsic interstitials in bulk silicon near the Si-SiO₂ interface during oxidation is obtained as

$$C_1 - C_1^* = \frac{a\gamma m_I k^{x/2}}{\Omega k'} \left(\frac{dX}{dt} \right)^{1-x/2} \quad [21]$$

which is in the same form as Eq. [4]. In an earlier section, the value of n was obtained from experiments as 0.4, which gives a value of x equal to 1.2. Then

$$C_1 - C_1^* = \frac{a\gamma m_I k^{0.6}}{\Omega k'} \left(\frac{dX}{dt} \right)^{0.4} \quad [22]$$

and

$$C_1' - C_1'^* = \frac{a\gamma k^{0.6}}{\Omega k'} \left(\frac{dX}{dt} \right)^{0.4} \quad [23]$$

SiO_x represents several different possible phases in the transition region between Si and SiO₂. The value of 1.2 determined here for x suggests that SiO is possibly the more dominant phase in this region.

Orientation dependence.—The growth of OSF depends strongly on the crystalline orientation of the silicon substrate surface. Under the same oxidation conditions, OSF grow more than two times faster in $\langle 100 \rangle$ than in $\langle 111 \rangle$ silicon (23). A significant decrease in OSF growth rate is also observed for off-axis orientation (39).

In Eq. [21] we expect the segregation coefficient, m_I , to vary with different orientations (16), in a way similar to impurity segregation at the Si-SiO₂ interface (40, 41) and thus be partly responsible for the orientation dependence of OSF growth. Indeed, the OSF data imply that $m_{\langle 100 \rangle} > m_{\langle 111 \rangle}$, which is the same as that of measured impurity segregation coefficient (40, 41).

Relation to Other Oxidation-Related Phenomena

The diffusion of commonly used impurities in silicon, i.e., B, P, and As, is enhanced by oxidation (40, 42, 43). Oxidation-enhanced diffusion (OED) of impurities shows dependence on temperature (40, 42, 43), ambient (43), and orientation (40), similar to that of the OSF growth and is believed to be also caused by the supersaturation of silicon interstitials in bulk silicon. Assuming that the enhancement of impurity diffusivity is proportional to the interstitial supersaturation, in a separate paper (21), we demonstrate that the enhancement is directly related to oxidation rate in the manner expressed by Eq. [22]. The oxidation rate dependence of OED also explains the variation of OED in different ambients, temperatures, and times. The similar orientation dependence of OED and OSF further supports that both are caused by the same point defect mechanism.

The formation of oxide-fixed charges, Q_f , at the Si-SiO₂ interface during oxidation is mostly believed to be related to the excess unoxidized silicons in the bulk oxide (44). From Eq. [23], it is then expected that even at the same temperature, different Q_f will form in different oxidation conditions. Murarka (45) recently reported that different Q_f indeed result from oxidations at different oxygen partial pressures at the same temperatures (the higher the pressure, the larger the Q_f). This is in qualitative agreement with Eq. [23] which predicts higher concentration of interstitials in bulk oxide for oxidations with higher oxidation rates.

Conclusion

Thermal oxidation of silicon induces growth of stacking faults in silicon. A general relationship between OSF growth rate and oxidation rate has been developed which quantitatively explains the different growth and retrogrowth of oxidation stacking faults under various oxidation conditions, namely, temperature, time, ambient, and orientation.

The growth of oxidation stacking faults is caused by the supersaturation of silicon interstitials in bulk silicon during oxidation. The driving force for the genera-

tion of point defects at the Si-SiO₂ interface is thought to be the free volume requirement and interface mismatch. A model has been proposed for the point defect generation at the Si-SiO₂ interface in which oxidation is visualized as a two-step reaction involving generation, re-oxidation, and segregation of excess silicon. This point defect generation model forms the physical basis for the general relationship between OSF growth and oxidation rates.

Acknowledgments

The authors would like to thank Professor J. D. Plummer for helpful discussions. The critical reading of the manuscript and the useful comments by Professor G. J. Declerck and Dr. C. L. Claeys are highly appreciated. This research has been supported through ARO Contract No. DAAG-29-77-C-006 and through DARPA Contract No. DAAB07-77-C-2684.

Manuscript submitted June 19, 1980; revised manuscript received Nov. 11, 1980. This was Paper 539 presented at the Los Angeles, California, Meeting of the Society, Oct. 14-19, 1979.

Any discussion of this paper will appear in a Discussion Section to be published in the December 1981 JOURNAL. All discussions for the December 1981 Discussion Section should be submitted by Aug. 1, 1981.

Publication costs of this article were assisted by Stanford University.

REFERENCES

1. S. P. Murarka, *Phys. Rev. B*, **16**, 2849 (1977) and references therein.
2. K. V. Ravi, C. J. Varker, and C. E. Valk, *This Journal*, **120**, 553 (1973).
3. G. H. Schwuttke, K. Brock, and E. W. Hearn, *Microelectronics Reliability*, **10**, 467 (1971).
4. Y. Hokari and H. Shiraki, *Jpn. J. Appl. Phys.*, **45**, 263 (1974).
5. S. Prussin, S. P. Li, and R. H. Cockrum, in "Semiconductor Characterization Techniques," P. A. Barnes and G. A. Rozgonyi, Editors, p. 352, The Electrochemical Society Softbound Proceedings Series, Princeton, N.J. (1978).
6. C. L. Claeys, E. E. Laes, G. J. Declerck, and R. J. Van Overstraeten, in "Semiconductor Silicon 1977," H. R. Huff and E. Sirtl, Editors, p. 773, The Electrochemical Society Softbound Proceedings Series, Princeton, N.J. (1977).
7. Y. Sugita, H. Shimizu, A. Yoshinaka, and T. Roshina, *J. Vac. Sci. Technol.*, **14**, 44 (1977).
8. C. L. Claeys, G. J. Declerck, and R. J. Van Overstraeten, *App. Phys. Lett.*, **35**, 796 (1979).
9. H. Shiraki, *Jpn. J. Appl. Phys.*, **15**, 1 (1976).
10. T. Hottori, *This Journal*, **123**, 945 (1976).
11. G. R. Booker and W. J. Tunstall, *Philos. Mag.*, **13**, 71 (1966).
12. R. J. Jaccodine and C. M. Crum, *Appl. Phys. Lett.*, **8**, 29 (1966).
13. S. M. Hu, *J. Appl. Phys.*, **45**, 1567 (1974).
14. W. A. Tiller, *This Journal*, **127**, 619 (1980).
15. W. A. Tiller, *ibid.*, **127**, 625 (1980).
16. W. A. Tiller, *This Journal*, **128**, 689 (1981).
17. M. Kahlweit, in "Progress in Solid State Chemistry," Vol. 2, H. Reiss, Editor, p. 134, Pergamon, New York (1965).
18. B. E. Deal and A. S. Grove, *J. Appl. Phys.*, **16**, 3770 (1965).
19. B. Leroy, *ibid.*, **50**, 7996 (1979).
20. S. P. Murarka, *Phys. Rev. B*, **21**, 692 (1980).
21. A. M. Lin, D. A. Antoniadis, and R. W. Dutton, *This Journal*, **128**, 1131 (1981).
22. A. M. Lin, R. W. Dutton, and D. A. Antoniadis, Abs. 133, p. 356, The Electrochemical Society Extended Abstracts, Boston, Massachusetts, May 6-11, 1979.
23. S. M. Hu, *Appl. Phys. Lett.*, **27**, 165 (1975).
24. S. M. Hu, in "Defects in Semiconductors," J. Narayan and T. Y. Tan, Editors, North-Holland Publishers, Amsterdam, in press.
25. S. P. Murarka, *J. Appl. Phys.*, **48**, 5020 (1977).
26. A. Seeger, H. Foll, and W. Frank, *Inst. Phys. Conf. Ser.*, **31**, 12 (1977).
27. R. N. Ghoshtagore, *Phys. Rev. Lett.*, **16**, 890 (1966).
28. R. F. Peart, *Phys. Status Solidi*, **15**, K119 (1966).
29. J. M. Fairfield and B. J. Masters, *J. Appl. Phys.*, **38**, 3148 (1967).
30. S. P. Murarka, *ibid.*, **49**, 2513 (1978).
31. S. P. Murarka and G. Quintana, *ibid.*, **48**, 46 (1977).
32. N. Tsubouchi, H. Miyoshi, and H. Abe, in Proceedings of 9th Conference on Solid State Devices, *Jpn. J. Appl. Phys.*, **17**, Supplement 17-1, 223 (1978).
33. T. Hattori, *Appl. Phys. Lett.*, **30**, 312 (1977).
34. B. E. Deal, A. Hurrle, and M. J. Schulz, *This Journal*, **125**, 2024 (1978).
35. B. E. Deal, *ibid.*, **110**, 527 (1963).
36. K. Taniguchi, K. Kurisawa, and M. Kashiwagi, Abs. 134, p. 360, The Electrochemical Society Extended Abstracts, Boston, Massachusetts, May 6-11, 1979.
37. W. L. Harrington, R. E. Honig, A. M. Goodman, and R. William, *Appl. Phys. Lett.*, **27**, 644 (1975).
38. J. S. Johannessen and W. E. Spicer, *J. Appl. Phys.*, **47**, 3028 (1976).
39. Y. Sugita and T. Kato, *ibid.*, **42**, 5847 (1971).
40. D. A. Antoniadis, A. G. Gonzalez, and R. W. Dutton, *This Journal*, **125**, 813 (1978).
41. R. B. Fair, *ibid.*, **125**, 2050 (1978).
42. D. A. Antoniadis, A. M. Lin, and R. W. Dutton, *Appl. Phys. Lett.*, **33**, 1030 (1978).
43. G. Masetti, S. Solmi, and G. Soncini, *Philos. Mag.*, **33**, 613 (1976).
44. B. E. Deal, *ibid.*, **121**, 199C (1974).
45. S. P. Murarka, *Appl. Phys. Lett.*, **34**, 587 (1979).

The Oxidation Rate Dependence of Oxidation-Enhanced Diffusion of Boron and Phosphorus in Silicon

A. Miin-Ron Lin,^{*1} Dimitri A. Antoniadis,^{*2} and Robert W. Dutton

Integrated Circuits Laboratory, Stanford University, Stanford, California 94305

ABSTRACT

Oxidation-enhanced diffusion (OED) of boron and phosphorus has been found to vary with oxidation rate. The measurement technique uses a grating pattern of parallel nitride and oxide stripes on the silicon surface, which allows three different drive-in conditions to be achieved on the same wafer, namely, inert and oxidizing conditions with two different oxidation rates. Because of the close proximity of the profiles diffused under different conditions on the wafers, the relative change in the diffusivity of dopants could be accurately determined by means of spreading resistance measurements. The results show that impurity diffusion in oxidizing ambients is enhanced and the enhancement clearly depends on oxidation rates, the higher the rate, the larger the enhancement. Oxidation-enhanced diffusion is caused by the supersaturation of extrinsic point defects generated at the Si-SiO₂ interface during oxidation. The present work indicates that the supersaturation is directly related to oxidation rate by a sublinear power-law dependence, similar to that observed for the growth of oxidation-induced stacking faults. The oxidation rate dependence is used as a basis to formulate a general model which explains the variation of OED under different oxidation conditions, namely, temperature, time, ambient, and pressure.

It has been well established (1, 2) that diffusion of boron, phosphorus, and arsenic is enhanced during thermal oxidation of silicon. The oxidation-enhanced diffusion (OED) has been shown to depend on oxidation ambient (3) and temperature (1) as well as on orientation of the silicon substrate (1). It is generally accepted that thermal oxidation of silicon results in the generation of excess silicon point defects in the Si-SiO₂ interface during oxidation (4, 5). Some of these extrinsic point defects flow into the bulk silicon and supersaturate the point defect population there. Since substitutional impurities are known to diffuse by interactions with lattice point defects (6), the supersaturation results in the enhancement of impurity diffusivity.

Because the supersaturation of point defects is a direct result of oxidation, the level of supersaturation is expected to vary under different oxidation conditions, particularly with the rate of oxidation. In the present paper, we report experimental results on oxidation-enhanced diffusion of boron and phosphorus in dry oxygen ambient and demonstrate that OED of both impurities varies with oxidation rate. A quantitative model is presented that relates OED to the rate of oxidation by expressing the supersaturation point defects as a power law of oxidation rate.

The supersaturation of lattice point defects (self-interstitials) was originally suggested by Hu (4) as also causing the growth of oxidation stacking faults (OSF) in silicon during oxidation. The OSF growth shows dependence on oxidation ambient and temperature as well as substrate orientation (7), similar to that observed for OED. In a separate paper (8), we demonstrate that the OSF dependence can be explained by an oxidation rate dependence of point defect supersaturation, similar to that reported here.

Experiments

The starting materials for the experiments are p- and n-type 2 in. wafers of Czochralski <100>-oriented silicon with a resistivity of 10-20 Ω-cm. The wafers

were oxidized in steam at 1000°C for 27 min to grow about 1900Å of oxide. Boron and phosphorus were implanted through the oxide into p- and n-type silicon wafers, respectively, to avoid the formation of the junctions. The dose for both impurities was low (6×10^{13} atoms/cm² at 60 keV for B and 8.5×10^{13} atoms/cm² at 160 keV for P) to avoid diffusion enhancement by high carrier concentration effects (9). The implanted wafers were annealed at 900°C for 30 min to activate the implanted dopants and 500Å of CVD silicon nitride was then deposited on the wafers at low temperature. Another layer of CVD oxide was used to pattern the nitride and oxide into parallel stripes (Fig. 1), which define three different regions repeated across the silicon wafer: (i) the first region labeled I with the nitride and oxide layers, (ii) the second region labeled II with only oxide, and (iii) the final region labeled III with the silicon surface directly exposed. Each of the three regions has a width of 500 μm and extends along the entire wafer. When the patterned wafers are thermally processed in dry oxygen ambient at high temperatures (900°-1200°C), the surface pattern allows three different drive-in conditions to be achieved on the same wafer. In region I, because of the nitride, the silicon surface is not oxidized and the impurities in the region diffuse under nonoxidizing conditions during the thermal process. In the other two regions, silicon is oxidized, but the rate is different because of the presence of the initial oxide in region II. The diffusion of impurities in both regions is enhanced, but by a different magnitude owing to the different oxidation rates. These different diffusivities result in different impurity profiles in the three regions on the same wafer.

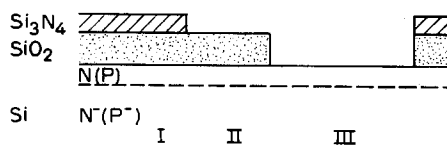


Fig. 1. The surface pattern of parallel nitride and oxide stripes that allows three different drive-in conditions on the same wafer; nonoxidizing in region I, and oxidizing in other regions with faster oxidation rate in region III. Each region has a width of 500 μm.

* Electrochemical Society Active Member.

¹ Present address: Bell Laboratories, Allentown, Pennsylvania 18103.

² Present address: Massachusetts Institute of Technology, Cambridge, Massachusetts 02139.

Key words: point defects, interstitialcy, spreading resistance.

The impurity profiles were characterized by means of spreading resistance measurements. Small samples (5×5 mm) were cut from the processed wafers and beveled on a block of 16 or 34 min angle so that the bevel edge was perpendicular to the surface stripes (Fig. 2). Because of the small stripe width, each bevel contains all three regions and thus the different impurity profiles are exposed side by side on the same bevel surface.

The probes used in the spreading resistance measurement have a small separation ($25 \mu\text{m}$) and thus the probe tracks can be located well within each stripe. The accurate control of both the lateral and transverse movement of the probes (better than $3 \mu\text{m}$) allows one to match the three neighboring profiles measured on the same bevel surface to within $150\text{-}300\text{\AA}$, depending on the bevel angle. As a result, a small difference in the diffusion of impurities can be accurately determined. This measurement technique has been successfully used to study the OED of phosphorus and arsenic (2).

Figure 3 shows a series of measured spreading resistance profiles in phosphorus-implanted silicon. The profiles in the two oxidized regions (II and III) show different locations of the silicon surface which is expected, because different oxide thickness has been grown in the two regions. Also shown in the plots is the initial profile measured on a separate sample. The difference between the initial and diffused profiles indicates the extent of the impurity diffusion during the thermal oxidation. At all temperatures, both profiles in the oxidized regions (II and III) are farther apart from the profile in region I, clearly showing enhanced impurity diffusion in the oxidized regions. The data also indicate that the enhancement increases with decreasing temperature, consistent with the results of our previous works (1, 2).

At the two higher temperatures (1100° and 1200°C), the diffusion enhancement in the two oxidized regions is different, as evidenced from the different profiles in regions II and III. The difference becomes small at 1000°C and is almost nonexistent at 900°C . This follows closely the ratio of average oxidation rates in the two oxidized regions deduced in Table I from the ratio of the oxide thickness grown in these regions.

Analysis

Measured spreading resistance profiles have been analyzed by the process simulation program SUPREM (10) and a computer program (11) which converts impurity profiles into spreading resistance profiles. The advantage of comparing directly spreading resistance profiles instead of extracting impurity profiles is discussed elsewhere (2). The technique allows the accurate determination of very small differences in diffusivity. Figure 4 shows the comparison between measured and calculated spreading resistance for the initial and diffused phosphorus profiles at 1100° and 1200°C . Because of the effects of probe penetration and bevel edge rounding in spreading resistance measurements

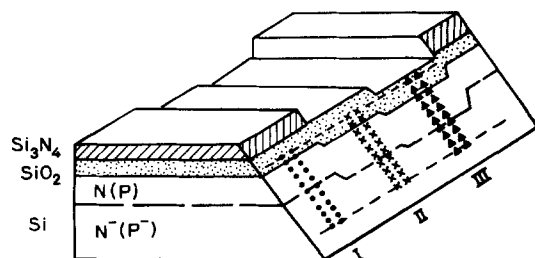


Fig. 2. The beveled spreading resistance measurement sample, which contains all three different regions. The close proximity of the profiles on the same bevel surface allows the relative depth of the neighboring profiles to be matched accurately.

Table I. The thickness of additional oxide grown during oxidation in oxidized regions II and III for phosphorus experiments

| | 900°C, 22 hr | 1000°C, 5 hr | 1100°C, 45 min | 1200°C, 10 min |
|--------|-----------------|-----------------|-------------------|-------------------|
| II, Å* | 1225 | 911 | 468 | 160 |
| III, Å | 1634 | 1632 | 1158 | 798 |
| Ratio | 1.33 | 1.79 | 2.47 | 4.99 |

* Region II has an initial oxide of thickness 1981Å.

(12), the agreement near the tail and the surface of the profiles is rather poor. However, to determine the relative change in the impurity diffusivity, it is adequate to match the profiles within the resistance window, $1 \times 10^4\text{-}13 \times 10^4\Omega$ shown in Fig. 4.

Table II lists the extracted diffusivities and the enhancement factors for boron and phosphorus in the three diffused regions for the processing temperatures, $900^\circ\text{-}1200^\circ\text{C}$. The extracted diffusivities in region I agree well with the generally accepted low concentration (intrinsic) diffusivities in neutral ambients (13, 14). The diffusivity in the two oxidized regions (II and III) is enhanced with larger enhancement in region III where the oxidation rate was higher.

Since the same initial oxide thickness ($\sim 1900\text{\AA}$) was used in all experiments to achieve two different oxidation rates, the difference of oxidation rate in the two regions is small at low temperatures, where oxidation is dominated by linear growth, and increases at high temperatures where parabolic growth dominates. Results presented in Fig. 3 and Table II for the difference of impurity diffusivity in the two regions suggest that the oxidation-induced diffusion enhancement is related to the oxidation rate.

The diffusion enhancement during oxidation of silicon was originally explained by Hu (4) by a dual diffusion mechanism in which impurities are assumed to diffuse with vacancies and interstitials. Thus an increase in the concentration of either vacancies or interstitials would cause the enhancement of impurity diffusion. For the purpose of this paper we assume that the impurity diffusivity, D , is generally given by direct superposition of the two mechanisms. Then

$$D = D_{AV} + D_{AI} \quad [1]$$

where D_{AV} and D_{AI} are the vacancy and interstitialcy motivated impurity diffusivities. These are respectively related to the concentrations of vacancies, C_V , and self-interstitials, C_I , by

$$\begin{aligned} D_{AV} &= d_{AV}C_V \\ D_{AI} &= d_{AI}C_I \end{aligned} \quad [2]$$

Denoting intrinsic values by "*", the proportionality factors, d , can be related to the intrinsic diffusivities and point defect concentrations by

$$\begin{aligned} d_{AV} &= \frac{D_{AV}^*}{C_V^*} \\ d_{AI} &= \frac{D_{AI}^*}{C_I^*} \end{aligned} \quad [3]$$

The above equations are valid only if the intrinsic point defect concentration is nonzero. However, Eq. [2] are always valid.

During oxidation, the silicon self-interstitial concentration is supersaturated and impurity diffusion is enhanced via the interstitialcy mechanism by a magnitude proportional to the supersaturated interstitial concentration. Thus the total diffusivity of impurity during oxidation is simply

$$D = D^* + d_{AI}(C_I - C_I^*) \quad [4]$$

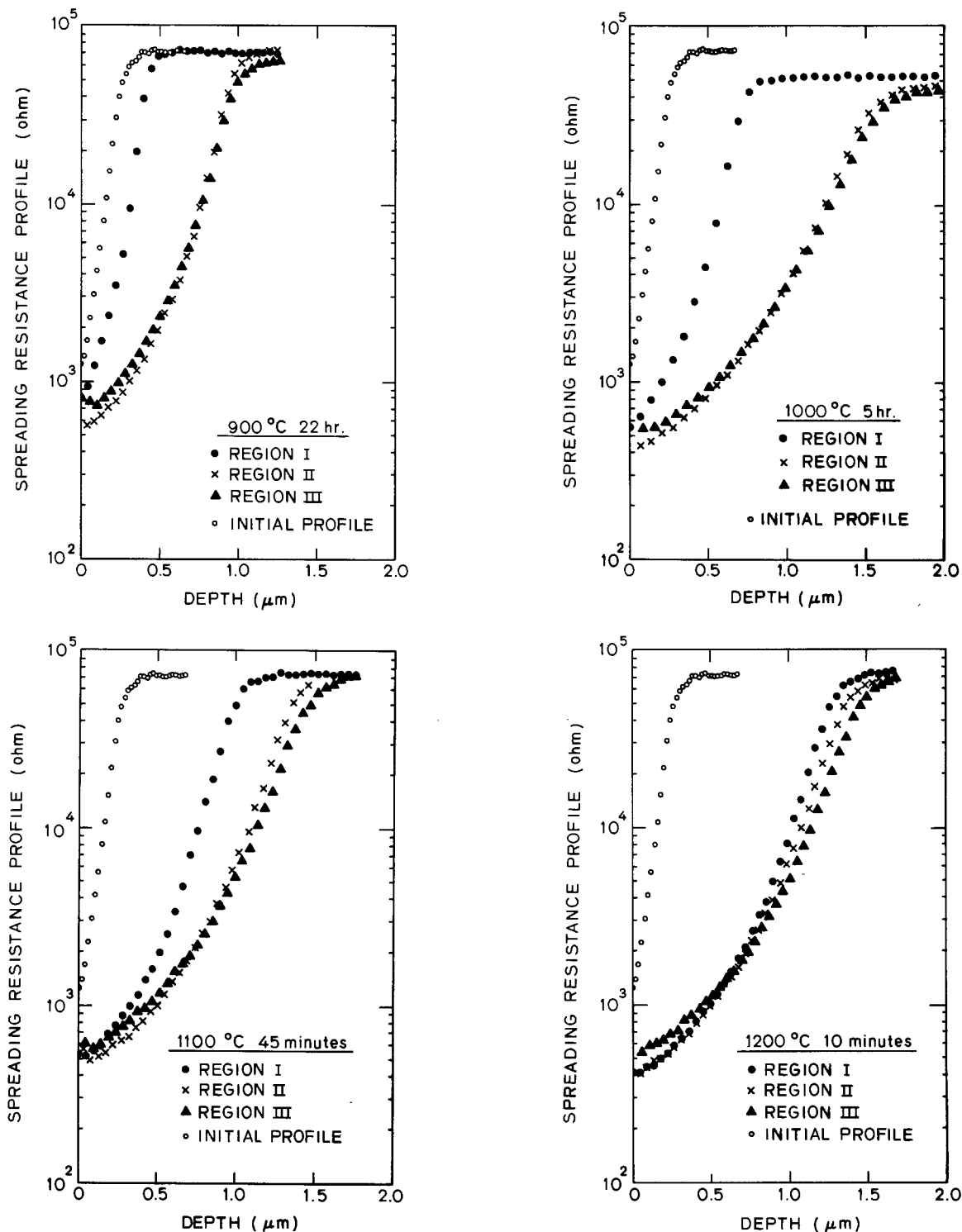


Fig. 3. The matched spreading resistance profiles of phosphorus in silicon at (a, upper left) 900°C, (b, upper right) 1000°C, (c, lower left) 1100°C, and (d, lower right) 1200°C, measured on the same beveled sample. The initial profile is measured on a separate sample. The depth resolution of the measurements is $\sim 200\text{\AA}$. Only every other three measurement points are shown.

where D is the total diffusion coefficient, and $D^* = D_{\text{AV}}^* + D_{\text{AI}}^*$, is the intrinsic diffusivity in the neutral ambient.

In the absence of oxidation the interstitial concentration is probably low and the impurity diffusion is probably dominated by the vacancy mechanism. During oxidation excess silicon is produced at the Si-SiO₂ interface, part of which flows into the bulk silicon and raises the interstitial concentration above its equilibrium value, thus increasing the impurity diffusivity. The generation of the excess silicon at the interface is a result of the incompleteness of oxidation suggested by Hu (4), or of the free volume requirement and Si-SiO₂ interface mismatch suggested by Tiller (5). In

both cases, the supersaturation of interstitials in silicon is related to the oxidation rate. The relation is assumed to be a power-law dependence of the form (15)

$$C_1 - C_1^* = K \left(\frac{dX}{dt} \right)^n \quad [5]$$

where dX/dt is the rate of oxide growth, and the reaction constant, K , and the power exponent, n , are related to the point defect generation process at the Si-SiO₂ interface. Combining Eq. [4] and [5], one obtains

$$D = D^* + d_{\text{AI}} K \left(\frac{dX}{dt} \right)^n \quad [6]$$

for the impurity diffusivity during oxidation.

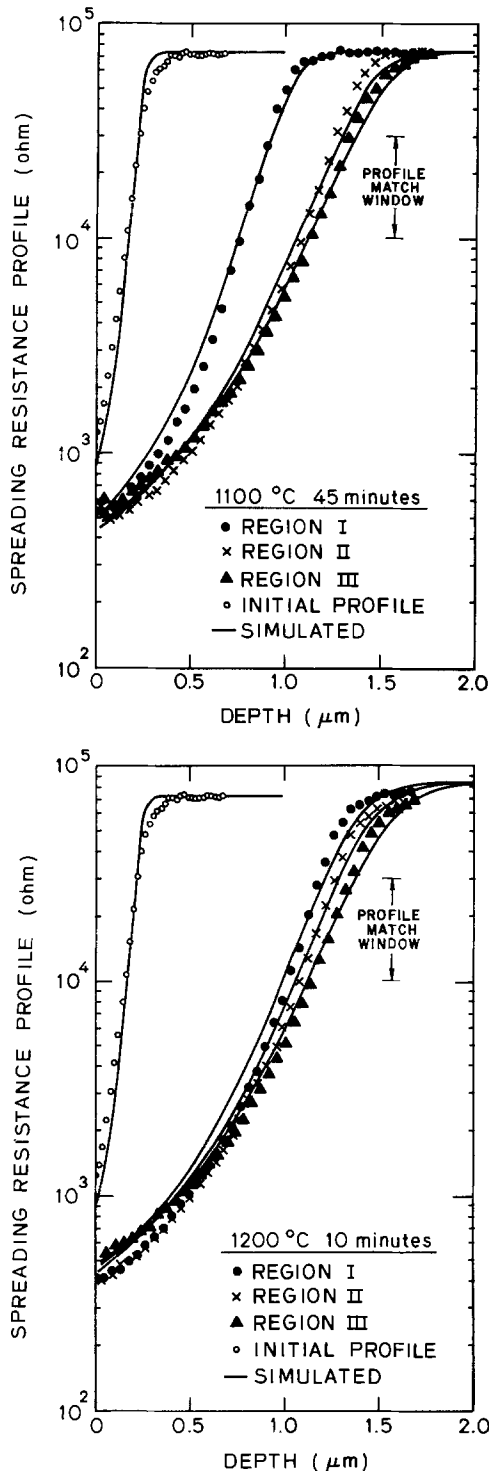


Fig. 4. The measured and calculated spreading resistance profiles of phosphorus-doped samples: (a) at 1100°C and (b) at 1200°C. The match between the measured and calculated spreading resistance profiles is emphasized within the resistance window, $1 \times 10^4 - 3 \times 10^4 \Omega$ (see text).

The above equation implies that generally D will be a function of time because dX/dt is time dependent. On the other hand, our experiments yield only an average diffusivity over the time of each experiment. However, as is shown in the Appendix, an average diffusivity, $\langle D \rangle = 1/t \int_0^t D(\tau) d\tau$ produces exactly the same impurity profile as a time-varying $D(\tau)$ over the same time period, if $D(\tau)$ is independent of impurity concentration. Thus, the extracted diffusivities can be related to the oxidation rate by

$$\frac{\langle D \rangle}{D^*} - 1 = \frac{d_{AI}K}{D^*t} \int_0^t \left(\frac{dX}{d\tau} \right)^n d\tau \quad [7]$$

Assuming that the growth of oxide can be described by the Deal-Grove equation (16)

$$X^2 - X_0^2 + A(X - X_0) = Bt \quad [8]$$

where X_0 is the initial oxide thickness, and B and B/A are the parabolic and linear growth rates, Eq. [7] gives

$$\frac{\langle D \rangle}{D^*} - 1 = \frac{d_{AI}K}{D^*t} \frac{B^{n-1}}{2(2-n)} [(2X + A)^{2-n} - (2X_0 + A)^{2-n}] \quad [9]$$

We define the diffusion enhancement ratio, DER , between regions III and II by

$$DER = \left(\frac{\langle D \rangle}{D^*} - 1 \right)_{III} / \left(\frac{\langle D \rangle}{D^*} - 1 \right)_{II} \quad [10]$$

Then using Eq. [9] and [10] we obtain

$$DER = \frac{(2X_{III} + A)^{2-n} - A^{2-n}}{(2X_{II} + A)^{2-n} - (2X_0 + A)^{2-n}} \quad [11]$$

where X_{III} and X_{II} are the final thicknesses in regions III and II. Comparison of Eq. [7] with the experimental results in Fig. 5 gives values of n between 0.4 and 0.6. Although the data in Fig. 5 are considerably scattered and do not allow accurate determination of n , the key fact that the value of n is less than 1 is easily deduced.

Recently, Tsukamoto *et al.* (17) reported that if the same thickness of oxide is to be grown at a given temperature, high pressure steam oxidation results in a much shorter impurity diffusion length than atmospheric pressure. At 950°C, one of the temperatures used in their experiments, the total diffusion enhancement can be estimated from our work to be larger than 4 and the diffusion is thus dominated by the extrinsic diffusion component. At high pressure the oxidation rate increases and the time needed to grow the same amount of oxide is reduced. But following Eq. [7], we expect the diffusion enhancement to increase also. If the diffusion enhancement was linearly proportional to the oxidation rate, instead of exhibiting sublinear dependence found in the present work, the increase in diffusion enhancement at high pressure would be the same as the reduction in oxidation time. Hence, the resultant impurity diffusion length would be almost independent of the pressure used. The fact that the impurity diffusion length is significantly reduced in higher pressure oxidation fur-

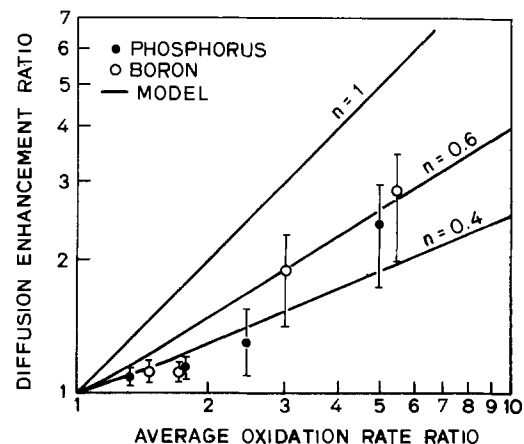


Fig. 5. The correlation between diffusion enhancements and average oxidation rates. The average oxidation rate is defined as the oxide thickness grown divided by the oxidation time.

Table II. Diffusivities in cm²/sec for boron and phosphorus in regions I, II, and III

| | | 900°C, 22 hr | 1000°C, 5 hr | 1100°C, 45 min | 1200°C, 10 min |
|---|-----|---------------------------------|-------------------------------|-------------------------------|-------------------------------|
| B | I | 1.5 × 10 ⁻¹⁵ (1.0) * | 1.5 × 10 ⁻¹⁴ (1.0) | 1.8 × 10 ⁻¹³ (1.0) | 1.7 × 10 ⁻¹² (1.0) |
| | II | 9.7 × 10 ⁻¹⁵ (6.4) | 5.7 × 10 ⁻¹⁴ (3.7) | 3.2 × 10 ⁻¹³ (1.7) | 2.2 × 10 ⁻¹² (1.2) |
| | III | 1.1 × 10 ⁻¹⁴ (7.0) | 6.1 × 10 ⁻¹⁴ (4.0) | 4.4 × 10 ⁻¹³ (2.4) | 3.0 × 10 ⁻¹² (1.7) |
| P | I | 6.7 × 10 ⁻¹⁶ (1.0) | 1.3 × 10 ⁻¹⁴ (1.0) | 1.4 × 10 ⁻¹³ (1.0) | 1.1 × 10 ⁻¹² (1.0) |
| | II | 4.7 × 10 ⁻¹⁶ (7.0) | 5.3 × 10 ⁻¹⁴ (4.3) | 2.8 × 10 ⁻¹³ (2.0) | 1.3 × 10 ⁻¹² (1.1) |
| | III | 5.0 × 10 ⁻¹⁶ (7.5) | 5.8 × 10 ⁻¹⁴ (4.7) | 3.3 × 10 ⁻¹³ (2.3) | 1.5 × 10 ⁻¹² (1.3) |

* The data in parentheses are the diffusion enhancement factors, $\langle D \rangle / D^*$.

ther supports the generality of the sublinear dependence found here.

Discussion

The growth of stacking faults during oxidation varies under different oxidation conditions, namely, temperature, time, ambient, and substrate orientation (18), in a manner similar to that observed for oxidation-enhanced diffusion. This strongly supports the hypothesis that both phenomena are caused by the same point defect mechanism (4, 19, 20). The OSF growth rate is proportional to the capture rate of interstitials, which is determined by the excess interstitial concentration in the bulk silicon during oxidation. We have demonstrated (8) that the variation of OSF growth under different oxidation conditions can be explained by a dependence of interstitial supersaturation on oxidation rate of the same form as Eq. [5] with the power exponent, $n = 0.4$, which is consistent with the value of n obtained from diffusion enhancements in Fig. 5. This provides another strong indication of the close correlation between stacking fault growth and oxidation-enhanced diffusion. The value of n , 0.4, is obtained from experimental data of OSF growth in a wide range of oxidation conditions (8) and will be used to represent oxidation rate dependence of OED for further discussion.

Using $n = 0.4$, the diffusion enhancement, $\langle D \rangle / D^*$ - 1, in Eq. [7] becomes

$$\frac{\langle D \rangle}{D^*} - 1 = \frac{d_{AI}K}{D^*t} \int_0^t \left(\frac{dX}{d\tau} \right)^{0.4} d\tau \quad [12]$$

The oxidation rate decreases as oxidation time increases. It is thus expected from Eq. [12] that the diffusion enhancement will also decrease with oxidation time. Using the Deal-Grove oxidation equation (16) and assuming no initial oxide, Eq. [12] can be expressed as

$$\frac{\langle D \rangle}{D^*} - 1 = G_E F(t) \quad [13]$$

$$G_E = \frac{d_{AI}K}{D^*} \left(\frac{B}{A} \right)^{0.4} \quad [13a]$$

$$F(t) = \frac{A^2}{3.2Bt} \left\{ \left(1 + \frac{4Bt}{A^2} \right)^{0.8} - 1 \right\} \quad [13b]$$

Here G_E represents the maximum diffusion enhancement and $F(t)$ expresses the reduction with time.

$F(t)$ is plotted in Fig. 6 to show the sensitivity of diffusion enhancement to oxidation time at different temperatures. From the figure, the reduction of diffusion enhancement for the oxidation times used in the experiments are to 88%, 74%, 68%, and 66% for temperatures, 900°, 1000°, 1100°, and 1200°C, respectively. The maximum enhancement factor G_E can then be determined by dividing the measured enhancement by the reduction factor. The results are shown in Fig. 7 which indicates essentially the same OED for boron and phosphorus, suggesting a similar diffusion mechanism for both impurities. The data also indicate a negative activation energy of ~ -1.2 eV, which suggests a continuous increase of diffusion enhancement

at low oxidation temperatures. As the trend of integrated circuit technology is toward lower processing temperatures, oxidation-enhanced diffusion should continue to play an important role in impurity profile control.

An implication of the oxidation rate dependence of diffusion enhancement is that oxidation ambients having different oxidation rates result in different diffusion enhancements. For example, oxidation in wet and steam ambients is faster than in dry oxygen ambient and thus impurity diffusion is expected to be enhanced more in those ambients. On the other hand, in partial oxygen pressure ambients, the oxidation rate is reduced and diffusion enhancement should decrease accordingly. The ambient dependence of OED has been experimentally observed (3, 21) with the results in qualitative agreement with Eq. [12]. Detailed quantitative comparisons cannot be made at present, pending more comprehensive experimental data. On the other

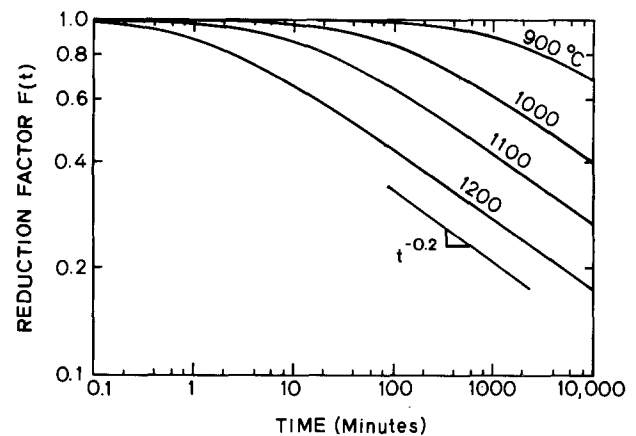


Fig. 6. The reduction factor $F(t)$ is calculated as a function of oxidation time. Oxidations used in the calculations start without initial oxide.

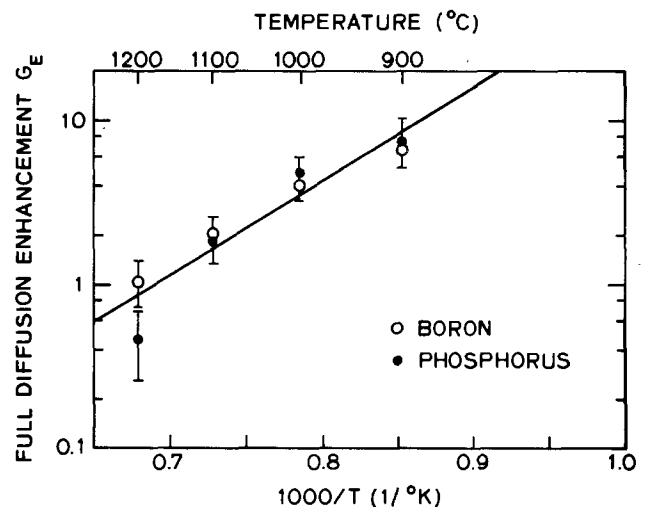


Fig. 7. The maximum diffusion enhancement factors G_E for boron and phosphorus at different oxidation temperatures.

hand, it has been demonstrated (8) that the sublinear oxidation rate dependence quantitatively explains the growth of OSF in a wide range of oxidation conditions. Thus, since oxidation-enhanced diffusion is closely related to OSF growth by the same point defect mechanism, we expect Eq. [5] and hence Eq. [12] to also largely explain the OED under different oxidation conditions.

An Example of Application

Today's integrated circuit technology is very much into VLSI (very large scale integration) where the lateral device dimensions are rapidly approaching micro- or submicrometer range. In order to optimize devices, the vertical dimensions need to be scaled accordingly. The vertical dimensions are, in most cases, dominated by impurity diffusion. This is particularly true in the formation of the oxide isolation commonly used in both the MOS and bipolar technologies, where long oxidations are used to produce sufficient oxide thickness to separate the active devices. These oxidations are increasingly done at low temperatures and high pressures to minimize the impurity diffusion. At these conditions, the oxidation-enhanced diffusion is clearly important.

Consider a case where 5000Å of oxide is to be grown. Equation [6] is used to calculate the impurity diffusion length, $2\sqrt{Dt}$, when the oxide is grown in dry oxygen, steam, or high pressure steam where the oxidation rate is further increased by a factor of 6, at different temperatures. The results plotted in Fig. 8 clearly show the reduction of impurity diffusion length in the two fast oxidizing steam ambients. Also shown in the figure is the diffusion length calculated with only intrinsic diffusivity. At high temperatures ($>1100^\circ\text{C}$), the diffusion length is dominated by intrinsic diffusion and the reduction in diffusion length in the two steam ambients is mainly due to reduction in oxidation time. At low temperatures ($<1000^\circ\text{C}$), however, extrinsic diffusion dominates and the reduction results from the sublinear oxidation rate dependence of the diffusion enhancement. It is important to also note in Fig. 8 that the reduction of the diffusion length toward decreasing temperatures is only gradual at low temperatures as compared to the rapid decrease when only intrinsic diffusion is considered. This is a result of the negative activation energy of oxidation-enhanced diffusion and emphasizes the importance of OED in impurity profile control at these temperatures.

Conclusion

The diffusion of ion-implanted boron and phosphorus in near-intrinsic $\langle 100 \rangle$ silicon has been studied ex-

perimentally in nonoxidizing and oxidizing conditions. The measurement technique uses a grating pattern of parallel nitride and oxide stripes on the silicon surface which allows three different diffusion conditions (inert and oxidizing with two different oxidation rates) to be achieved on the same wafer. Because of the close proximity of impurity profiles diffused under different conditions on the same wafer, the small relative change of impurity diffusivity was accurately determined by means of spreading resistance measurements. Results indicate that impurity diffusion is enhanced by oxidation and the enhancement is directly related to oxidation rate with higher enhancements at higher oxidation rates. The diffusion enhancement has a negative activation energy and consequently slows down the reduction of impurity diffusion length at low temperature processing.

Oxidation-enhanced diffusion is caused by supersaturation of lattice point defects during oxidation. The present work indicates that the point defect supersaturation depends on oxidation rate. The dependence is approximated by a power-law relation with an exponent ranging between 0.4 and 0.6 which is consistent with the oxidation rate dependence of the growth of oxidation stacking faults. The sublinear oxidation rate dependence of the diffusion enhancement explains the reduction of impurity diffusion length when growing the oxide in high pressure steam oxidation at low temperatures. It is also in qualitative agreement with the dependence of oxidation-enhanced diffusion in wet oxidation and reduced oxygen pressure oxidations, observed elsewhere (21).

Acknowledgment

The helpful discussions with Professors J. D. Plummer and W. A. Tiller are highly appreciated. The authors are also grateful for the assistance by the staff of Stanford Integrated Circuits Laboratory in wafer processing. This research was sponsored through ARO Contract No. DAAG-29-77-C-006.

Manuscript submitted June 19, 1980; revised manuscript received Oct. 27, 1980. This was Paper 133 presented at the Boston, Massachusetts, Meeting of the Society, May 6-11, 1979.

Any discussion of this paper will appear in a Discussion Section to be published in the December 1981 JOURNAL. All discussions for the December 1981 Discussion Section should be submitted by Aug. 1, 1981.

Publication costs of this article were assisted by Stanford University.

APPENDIX

In the present experiments, the impurity concentration is kept below the intrinsic carrier concentration at the processing temperatures. The impurity diffusivity is thus independent of concentration and the impurity diffusion equation is

$$\frac{\partial C(x, t)}{\partial t} = D(t) \frac{\partial^2 C(x, t)}{\partial x^2} \quad [\text{A-1}]$$

with boundary conditions

$$\frac{\partial C}{\partial x} \Big|_{x=0} = 0 \quad \text{for neutral ambient drive-in} \quad [\text{A-2}]$$

or

$$D \frac{\partial C}{\partial x} \Big|_{x=0} = \left(\frac{1}{m} - \alpha \right) \frac{dX}{dt}$$

for oxidizing ambient drive-in [A-3]

where $C(x, t)$ is the impurity concentration, m the segregation coefficient, and α the ratio of the consumed silicon to the thickness of oxide grown. dX/dt is the oxide growth rate.

Since D is a function of t only, by changing the variable t to $t' = \int_0^t D(t) dt$, the above equations are simplified to

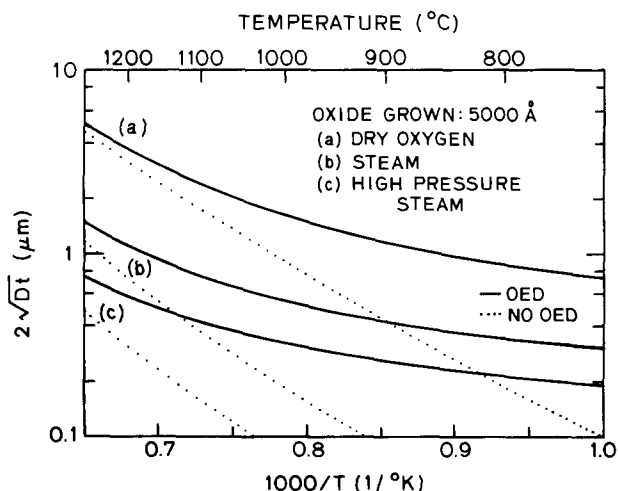


Fig. 8. Boron diffusion length during oxidation to grow 5000Å of oxide in dry oxygen, steam, or high pressure steam ambients at different temperatures.

$$\frac{\partial C(x, t')}{\partial t'} = \frac{\partial^2 C(x, t')}{\partial x^2} \quad [\text{A-4}]$$

with

$$\frac{\partial C}{\partial x} \Big|_{x=0} = 0 \quad [\text{A-5}]$$

or

$$\frac{\partial C}{\partial x} \Big|_{x=0} = \left(\frac{1}{m} - \alpha \right) \frac{dX}{dt} \quad [\text{A-6}]$$

The solution to the above equations is a function of x and t' only. Hence the concentration, C , at a given x is determined by the value of $t' = \int_0^t D(\tau) d\tau$ and is independent of the detailed form of $D(\tau)$. In other words, a constant diffusivity, $\langle D \rangle = 1/t \int_0^t D(\tau) d\tau$ will produce exactly the same profile as the time-varying $D(\tau)$ over the same time period.

REFERENCES

1. D. A. Antoniadis, A. G. Gonzalez, and R. W. Dutton, *This Journal*, **125**, 813 (1978) and references therein.
2. D. A. Antoniadis, A. M. Lin, and R. W. Dutton, *Appl. Phys. Lett.*, **33**, 1030 (1978).
3. G. Masetti, S. Solmi, and G. Soncini, *Philos. Mag.*, **33**, 613 (1976).
4. S. M. Hu, *J. Appl. Phys.*, **45**, 1567 (1974).
5. W. A. Tiller, *This Journal*, **127**, 625 (1980).
6. S. M. Hu, in "Atomic Diffusion in Semiconductor," D. Shaw, Editor, Chap. 5, Plenum Press, New

- York (1973).
7. S. M. Hu, *Appl. Phys. Lett.*, **27**, 165 (1975).
 8. A. M. Lin, R. W. Dutton, D. A. Antoniadis, and W. A. Tiller, *This Journal*, **128**, 1121 (1981).
 9. R. B. Fair, in "Semiconductor Silicon 1977," H. R. Huff and E. Sirtl, Editors, p. 968, The Electrochemical Society Softbound Proceedings Series, Princeton, N.J. (1977).
 10. D. A. Antoniadis and R. W. Dutton, *IEEE J. Solid State Circuits*, **sc-14**, 412 (1979).
 11. A. M. Lin, Unpublished.
 12. D. C. D'Avanzo, R. D. Rung, and R. W. Dutton, Technical Report No. 5013-2, Stanford Electronics Labs., Stanford University (unpublished).
 13. A. D. Kurtz and R. Yee, *J. Appl. Phys.*, **31**, 303 (1960).
 14. S. Maekawa, *J. Phys. Soc. Jpn.*, **17**, 1592 (1962).
 15. A. M. Lin, R. W. Dutton, and D. A. Antoniadis, Abs. 133, p. 356, The Electrochemical Society Extended Abstracts, Boston, Massachusetts, May 6-11, 1979.
 16. B. E. Deal and A. S. Grove, *J. Appl. Phys.*, **16**, 3770 (1965).
 17. K. Tsukamoto, Y. Akasaka, Y. Miyoshi, N. Tsubouchi, Y. Horiha, K. Kijima, and H. Nakata, 1979 International Electronics Devices Meeting, Washington, D.C., Abs. 14.5.
 18. S. P. Murarka, *Phys. Rev. B*, **16**, 2849 (1977) and references therein.
 19. R. Francis and P. S. Dobson, *J. Appl. Phys.*, **48**, 46 (1977).
 20. B. Leroy, *ibid.*, **50**, 7996 (1979).
 21. S. P. Murarka, *Phys. Rev. B*, **12**, 2502 (1975).

An Efficient Integration Technique for Use in the Multilayer Analysis of Spreading Resistance Profiles

H. L. Berkowitz* and R. A. Lux

U.S. Army Electronics Technology and Devices Laboratory, ERADCOM, Fort Monmouth, New Jersey 07703

ABSTRACT

The efficiency of multilayer analysis in calculating resistivity profiles from spreading resistance measurements depends on the rapid numerical evaluation of the well-known correction factor integral first introduced by Schumann and Gardner. We present a new approximate form for the correction factor which allows its numerical evaluation with only 22 integrand values for each evaluation of the integral. When this technique is used in our multilayer analysis program, we unfold spreading resistance profiles at the real time rate of less than 3 sec/point on a desktop computer. Its results match those of analytic evaluations of special two layer cases or with more elaborate numerical evaluations of graded structures to within 1%.

Two-probe spreading resistance measurement has become a widely used technique for determining impurity profiles in semiconductors (1-4). The conductivity of the material contacted by the probes is given by

$$R = C/(2a\sigma) \quad [1]$$

where R is the measured spreading resistance, a is the contact radius, and C is a correction factor which is a function of the conductivity profile of the material. The multilayer analysis technique of evaluating this correction factor was originally proposed by Shumann and Gardner (1) and later developed in more easily calculated forms (2-4); complete derivations are given in Ref. (2, 3). In this technique the correction factor is

$$C = \frac{8}{I} \int_0^\infty dx \left[\frac{J_1(x)}{x} - \frac{J_0(Dx)}{2} \right] I(x) F(tx) \quad [2]$$

I is the total current flowing between the probes, where J_1 and J_0 are Bessel functions of the first kind, D and t are, respectively, the probe separation and layer thickness measured in probe radii, F (sometimes denoted by $1 + 2\theta$) is a function of all conductivities deeper than the contacted layer, and $I(x)$ is the Hankel transform of the normal component of the current density $I(r)$ at a probe. F can be expressed by a recursion relation

$$F_{i+1} = \frac{F_i \sigma_{i+1} + \sigma_i \tanh(tx)}{\sigma_i + F_i \sigma_{i+1} \tanh(tx)} \quad [3]$$

which is equivalent to a form given by Choo (3). $I(x)$ is given by

* Electrochemical Society Active Member.
Key words: resistivity profiles, spreading resistance measurements.

$$\underline{I}(x) = \int_0^a J_0(xr/a) I(r) r dr$$

Two forms of $\underline{I}(x)$ are found in the literature

$$\underline{I}(x) = \frac{I \sin(x)}{2\pi x} \quad [4]$$

which was first used by Shumann and Gardner (1) and

$$\underline{I}(x) = \frac{I J_1(x)}{\pi x} \quad [5]$$

which was suggested by Severin (5) and used by Choo (6); the latter is used in the remainder of this paper. A complete discussion of the consequences of using either form is given in Ref. (7).

The calculation of a conductivity profile from a set of measured spreading resistances proceeds as follows. Starting at the deepest point, the value of the conductivity (and the resulting correction factor) is adjusted until the calculated spreading resistance agrees with the measured spreading resistance to the required accuracy. When this is achieved, the process is repeated at the next point, continuing until the entire set of measurements has been exhausted. The trial conductivity enters the calculation of the correction factor only through the function F . Hence during a numerical evaluation of C only the function F need be recalculated, the remainder of the integrand in Eq. [2] having been calculated once and stored as a numerical array.

Because the multilayer analysis scheme may require several evaluations of the correction factor per point an efficient technique for its evaluation is desirable. In this paper we introduce an approximation to the correction factor integral which can be evaluated rapidly. We then develop a numerical method which evaluates the approximate integral by sampling the integrand at only 22 points. We then compare this method with an analytic evaluation for special cases and with other numerical methods for a full multilayer case.

Approximation of the Correction Factor

The correction factor integral in Eq. [2] contains a term proportional to $J_0(Dx)/2$ which describes the voltage reduction at one probe due to the other probe. On physical grounds its effect can be significant only when the conductivity of the contacted layer is very high or when the spacing between probes is small, for which case Choo (3) showed that the primary effect of the J_0 term is to assure that the integrand vanishes at $x = 0$, even when F is singular at the origin.

In this section we show that it is possible to approximate the correction factor integral by an integral without a J_0 term by integrating from a nonzero lower limit

$$C_a = \frac{8}{\pi} \int_L^\infty dx \left(\frac{J_1(x)}{x} \right)^2 F(tx) \quad [6]$$

where L is given by

$$L = 2e^{-\gamma/D} \quad [7]$$

Here γ is Euler's constant, 0.577... We demonstrate this by direct calculation of C and C_a in three cases which are amenable to analytic methods, namely (a) a conducting layer over an insulating substrate, (b) a conducting layer over a perfect conductor, and (c) a uniform semi-infinite slab. The appropriate forms of F are, respectively

$$F_A = \coth(tx), \quad F_B = \tanh(tx), \quad F_C = 1$$

For any multilayer case F must be within the envelope $\coth(tx)$ and $\tanh(tx)$. The test cases therefore represent the extreme cases and one intermediate case.

For thin conducting layers (i.e., in the limit $t \rightarrow 0$), the first two forms can be approximated by

$$F_A = 1/(tx), \quad F_B = tx$$

allowing the integral in Eq. [2] to be evaluated analytically. For case (a) the function F_A has a pole at $x = 0$; the lower limit L is chosen so as to minimize the difference between C and C_a for this case. Equation [2] written as

$$C = \frac{8}{\pi t} \lim_{\epsilon \rightarrow 0} \int_0^\infty \frac{J_1(x)}{x} \left[\frac{J_1(x)}{x} - \frac{J_0(Dx)}{2} \right] \frac{dx}{x^{1-\epsilon}}$$

a special case of the Weber Schafheitlin integral (8), yields

$$C = \frac{2}{\pi t} (\ln(D) + 1/4) \quad [8]$$

The corresponding value of C_a is obtained by evaluating Eq. [6]

$$C_a = \frac{8}{\pi t} \lim_{\epsilon \rightarrow 0} \left[\int_0^\infty \frac{J_1^2(x)}{x^{3-\epsilon}} dx - \int_0^L \frac{J_1^2(x)}{x^{3-\epsilon}} dx \right]$$

which yields

$$C_a = \frac{2}{\pi t} [\ln(2e^{-\gamma}/L) + 1/4 + L^2/8 \dots] \quad [9]$$

where γ is Euler's constant, 0.577...

With L set at

$$2e^{-\gamma}/D = 1.12292/D$$

the fractional difference between C and C_a in this case is minimized; its magnitude can be estimated by evaluating the term of order L^2 , namely

$$\frac{C - C_a}{C} \approx 0.14 / ((\ln D + 0.25) D^2) \quad [10]$$

Using this value of L , both C and C_a were evaluated for cases (b) and (c); results are shown in Table I. These three cases represent very different physical situations. The fact that the errors introduced by using C_a rather than C are smaller than 1% when D is greater than 10 suggests that the approximation is generally useful: in most probe arrangements D is greater than 30. The numerical procedure for evaluating C_a is much simpler than that necessary to evaluate C . The latter involves calculating the integrand at enough points to follow the rapid oscillations of the function $J_0(Dx)$. For example, when D is equal to 30, $J_0(Dx)$ has more than 30 zeros at values less than the first zero of $J_1(x)$.

The Numerical Integrator

In this section we describe a numerical integrator which has been tailored to take advantage of the properties of the integrand of [6] in order to minimize the required evaluations of F .

Our objective is to choose a set of numbers x_i and weights w_i such that C_a can be well represented by a numerical approximation.

$$C_n = \sum w_i F(tx_i) \quad [11]$$

The appropriate numerical integration technique was selected so as to accommodate the most singular case, $F = \coth(tx)$ taking care that other cases were treated with sufficient accuracy.

Based on properties of $(J_1/x)^2$, we divide the domain of integration into four regions

$$(A) \quad L \leq x \leq 0.1$$

$$(B) \quad 0.1 \leq x \leq 1$$

$$(C) \quad 1 \leq x \leq j_{1,1}$$

$$(D) \quad j_{1,1} < x$$

where $j_{1,i}$ is the i th zero of the Bessel function J_1 and $j_{1,0} = 0$, $j_{1,1} = 3.83171$. In cases of practical significance

Table I. Functional forms of correction factors with $L = 1.12292/D$

| F | C | C_a | $ 1 - C_a/C $ |
|-------|--|---|-----------------------------------|
| $1/x$ | $\frac{2}{\pi t} (\ln D + 0.25)$ | $\frac{2}{\pi t} \left(\ln D + 0.25 + \frac{L^2}{8} + \dots \right)$ | $\frac{0.14}{D^2 (\ln D + 0.25)}$ |
| 1 | $\frac{8}{\pi} \left(\frac{4}{3\pi} - \frac{1}{4D} \left(1 + \frac{1}{8D^2} + \dots \right) \right)$ | $\frac{8}{\pi} \left(\frac{4}{3\pi} - \frac{L}{4} \right)$ | 0.072/D |
| x | $4t/\pi$ | $t(4 - L^2)/\pi$ | 0.03/D ² |

L is restricted to the domain $0.001 \leq L \leq 0.1$. In each region we choose a numerical integrator which will assure adequate convergence of the integrals.

In region (A) we replace $(J_1/x)^2$ by $1/4$. In this region the most difficult integrand that can arise will be proportional to $\coth(tx)$, which approaches $1/(tx)$ for small x . To treat the pole at $x = 0$, we choose $\ln x$ to be the integration variable; this segment of C_a is then

$$\frac{8}{\pi} \int_{x=L}^{x=0.1} \frac{x}{4} F(tx) d(\ln x)$$

We then apply a nine point Newton-Cotes integrator to the integrand. The nine points, equally spaced in $\ln x$, are given by

$$x_i = L (0.1/L)^{(i/8)}, \quad 0 \leq i \leq 8$$

This segment of C_n is

$$\frac{1}{4\pi} \ln(0.1/L) \sum_0^8 w_{9,i} x_i F(tx_i) \quad [12]$$

The weights $w_{9,i}$ for a nine point Newton-Cotes integrator are given in Ref. (9).

In region (B) the slowly varying $(J_1/x)^2$ is explicitly calculated. Again the most difficult integrand is proportional to $1/(tx)$, and we make the same transformation as in region (A). To achieve the same density of points in (B) as in (A), with $L = 0.001$, we use a five-point Newton-Cotes integration formula. This segment of C_n is then

$$\frac{2}{\pi} \ln(10) \sum_0^4 J_1^2(x_i) F(x_i) w_{5,i}/x_i \quad [13]$$

The weights $w_{5,i}$ are given in Ref. (9) and $x_i = 0.1(10)^{(i/4)}$.

In region (C), $(J_1/x)^2$ is falling rapidly; a five-point Newton-Cotes integrator in x rather than $\ln x$ provides adequate coverage. This segment of C_n is

$$\frac{2}{\pi} (j_{1,1} - 1) \sum_0^3 (J_1(x_i)/x_i)^2 F(x_i) w_{5,i} \quad [14]$$

Only four of the five points need be calculated, as $J_1(j_{1,1})$ is by definition zero.

In region (D), the rapid decrease in $(J_1/x)^2$ guarantees that the integral beyond the first zero, $j_{1,1}$, will make only a small contribution to the correction factor. Using the mean value theorem

$$\int_{x=a}^{x=b} F(x) du(x) = F(\xi) (u(b) - u(a)) \quad [15]$$

where $a \leq \xi \leq b$ and $du = (J_1/x)^2 dx$, we approximate the integral between successive zeros of J_1 by choosing ξ to be the centroid of $(J_1/x)^2$ between zeros

$$\xi = \frac{\int_a^b J_1^2(x) dx/x}{\int_a^b (J_1(x)/x)^2 dx} \quad [16]$$

The approximation is exact if F varies at most linearly with x . We took five subintervals between successive zeros of J_1 to $j_{1,6}$, $x = 19.616$, and found that the integral truncated at this point was adequate for most integrands. [Albers (10) truncates at $x = 20$ and Choo (6) truncates at $x = 20.8$.] However, in cases where F is small in region (A) (for example when $F = \tanh(tx)$), an error of as much as 4% can be made due to this truncation. By using one additional point at the centroid of $(J_1/x)^2$ taken between 19.616 and infinity, this error can be reduced to below 1%.

This segment of C_n is then

$$\frac{8}{\pi} \sum w_{D,i} F(\xi_i) \quad [17]$$

where the weights $w_{D,i}$ and ξ_i are shown in Table II. As the points at the region boundaries need be calculated only once, the complete integration requires only 22 evaluations of F .

Testing Procedures

The integration technique has been tested in the range $0.001 \leq t \leq 1$ and $10 \leq D \leq 1000$ for two layer cases where analytic results can be obtained and for representative multilayer distributions. We present the results of the two layer calculation and a sample multilayer case.

Test 1.—In the first test we compared C_n calculated using the 22 point integrator with C_a calculated analytically in the section Approximation of the Correction Factor.

$F(x)$ is replaced by tx , 1, and $1/(tx)$ in the cases now under consideration.

We evaluated C_n at 12 values of D between $D = 10$ and $D = 1000$ and list the maximum deviations in Table III. Maximum errors were found on comparing C with C_a and C_a with C_n . In all cases the maximum error occurs at $D = 10$.

In all cases we find agreement between the approximation and the numerical integrator to be better than 0.3%.

Table II. Centroids and weights used in region (D)

| i | $a = j_{1,i}$ | $b = j_{1,i+1}$ | Centroid ξ_i | Weight $w_{D,i}$ |
|-----|---------------|-----------------|------------------|------------------|
| 1 | 3.83171 | 7.01558 | 5.23853 | 0.688546E-2 |
| 2 | 7.01558 | 10.1735 | 8.48093 | 0.163592E-2 |
| 3 | 10.1735 | 13.3237 | 11.6681 | 0.627777E-3 |
| 4 | 13.3237 | 16.4706 | 14.829 | 0.305139E-3 |
| 5 | 16.4706 | 19.6159 | 17.9861 | 0.173318E-3 |
| 6 | 19.6159 | ∞ | 39.3 | 0.4119E-3 |

Table III. Maximum deviations

| F | $ C - C_a $ | $ C_a - C_n $ |
|--------|-------------|---------------|
| | C | C_a |
| tx | 0.003 | 0.002 |
| 1 | 0.007 | 0.0008 |
| $1/tx$ | 0.0006 | 0.0009 |

Test 2.—To measure the performance of our 22 point integrator for cases where analytic techniques were unavailable we constructed a Simpson integrator of 1597 points constructed as shown in Table IV.

This integrator was programmed in three versions to accommodate the various tests needed:

SIM which numerically integrates

$$\text{SIM} = \frac{8}{\pi} \int_0^{20} \left(\frac{J_1(x)}{x} - \frac{J_0(Dx)}{2} \right) \frac{J_1(x)}{x} F dx$$

SIMSG which evaluates the Schumann and Gardner correction factor

$$\text{SIMSG} = \frac{4}{\pi} \int_0^{20} \left(\frac{J_1(x)}{x} - \frac{J_0(Dx)}{2} \right) \frac{\sin(x)}{x} F dx$$

SIMT which corrects SIM for truncation error as described in the section The Numerical Integrator.

Truncating the integral at $x = 20$ allows us to compare our results with those of Albers (10), who generated spreading resistance data (MD in Table V) from model resistivity profiles by using the integration scheme of D'Avanzo *et al.* (4) over the interval $0 \leq x$

Table IV. The 1597 point integrator

| x , min. | x , max | Weights | Number of points |
|------------|-----------|-------------|------------------|
| 0 | 0.001 | Trapezoidal | 2 |
| 0.01 | 0.01 | Simpson | 199 |
| 0.01 | 0.1 | Simpson | 199 |
| 0.1 | 1 | Simpson | 199 |
| 1 | 20 | Simpson | 999 |

Table V. Summary of results calculating resistance as a function of depth in a layered medium using the various integrators mentioned in text. All calculations are based on the conductivity profile plotted in Fig. 1 and excerpted in this table for the case $a = 2 \mu\text{m}$, $D = 25$, $t = 0.015$.

A. Comparison of our large Simpson integrators SIM and SIMSG with the integration scheme of D'Avanzo

A.

| Alber's model data | | | | |
|--------------------|-----------------------|--------------------------------------|----------------------|------------|
| Layer No. | Conductivity (mho-cm) | MD spreading resistance (Ω) | Fractional deviation | |
| | | | 1-SIMSG/MD | 1-SIM/MD |
| 1 | 7.975E-03 | 1.744E+04 | 1.121E-05 | -1.153E-01 |
| 4 | 1.940E-02 | 3.420E+03 | 1.144E-05 | -1.054E-01 |
| 7 | 7.050E-01 | 3.895E+02 | 1.310E-04 | -4.691E-02 |
| 10 | 9.775E+00 | 3.044E+02 | 1.780E-04 | -2.769E-02 |
| 13 | 4.000E+01 | 3.101E+02 | 1.740E-04 | -2.534E-02 |
| 16 | 1.010E+02 | 3.630E+02 | 1.924E-04 | -2.478E-02 |
| 19 | 1.351E+02 | 5.639E+02 | 1.186E-04 | -2.475E-02 |
| 22 | 8.547E+01 | 1.331E+03 | 9.739E-05 | -2.487E-02 |
| 25 | 3.040E+01 | 4.756E+03 | 1.051E-04 | -2.557E-02 |
| 28 | 6.203E+00 | 2.737E+04 | 5.895E-05 | -2.982E-02 |
| 31 | 3.110E-01 | 1.840E+05 | 5.066E-06 | -5.994E-02 |
| 34 | 1.177E-03 | 3.022E+05 | -2.861E-06 | -8.439E-02 |
| 37 | 7.926E-03 | 3.072E+05 | -9.537E-06 | -8.499E-02 |
| 40 | 7.908E-03 | 3.072E+05 | -2.289E-05 | -8.501E-02 |

B. Comparison of the results of our 22 point integrator and the Gauss Laguerre integrator with SIMT and SIM, respectively

B.

| Layer No. | SIMT-OHMS | 1-SIM/SIMT | Fractional deviation | |
|-----------|-----------|------------|----------------------|------------|
| | | | 1-(22)/SIMT | 1-GL/SIM |
| 1 | 1.976E+04 | 1.568E-02 | 2.388E-03 | -6.939E-02 |
| 4 | 3.871E+03 | 2.332E-02 | 2.225E-03 | -6.798E-02 |
| 7 | 4.103E+02 | 6.247E-03 | -3.461E-04 | -4.640E-02 |
| 10 | 3.130E+02 | 6.092E-04 | -1.259E-03 | -3.891E-02 |
| 13 | 3.180E+02 | 1.796E-04 | -1.380E-03 | -3.802E-02 |
| 16 | 3.720E+02 | 6.694E-05 | -1.457E-03 | -3.782E-02 |
| 19 | 5.779E+02 | 3.421E-05 | -1.642E-03 | -3.761E-02 |
| 22 | 1.364E+03 | 2.933E-05 | -2.220E-03 | -3.796E-02 |
| 25 | 4.878E+03 | 2.241E-05 | -3.438E-03 | -3.874E-02 |
| 28 | 2.819E+04 | 1.830E-05 | -7.906E-04 | -4.469E-02 |
| 31 | 1.951E+05 | 6.187E-05 | 4.389E-03 | -6.807E-02 |
| 34 | 3.279E+05 | 7.526E-04 | 3.595E-03 | -7.096E-02 |
| 37 | 3.336E+05 | 9.924E-04 | 3.570E-03 | -7.095E-02 |
| 40 | 3.336E+05 | 9.953E-04 | 3.573E-03 | -7.095E-02 |

≤ 20 . Table V and Fig. 1 show one such data set calculated to represent the conductivity profile of a silicon wafer containing a Gaussian implant. Simulated spreading resistances were calculated from these conductivities for the case $a = 2 \mu\text{m}$, $D = 25$, $t = 0.015$ using SIMSG. We compared these to the set of resistances supplied by Albers. The largest fractional deviation found between the two data sets was less than 2 parts in 10^4 . Spreading resistances were then calculated for the same data using the 22 point integrator, SIM, and SIMT. We find that agreement between the 22 point integrator and SIMT to be better than 5 parts in 10^3 . This represents the total deviation between C and C_n for this case. A comparison between SIM and SIMT results indicate that the maximum relative deviation due to truncating at $x = 20$ for this case is about 2%.

The Gauss Laguerre Integrator

To demonstrate the value of the lower limit cutoff approximation, we repeated the tests performed on the 22 point integrator using another sparse point numerical integrator the Gauss Laguerre integrator (GL in Table V) of Choo *et al.* (11). This integrator retains the term in $J_0(Dx)$.

In Fig. 2 we plot the fractional deviation between C and the Gauss Laguerre integrated correction factors in the cases of the section Testing Procedures, Test 1.

We find that the deviations for these cases tend to cluster in a band of $\pm 5\%$ with occasional excursions to 10% or 20%. This is due principally to the fact that for D greater than 10, $J_0(Dx)$ has more than 60 zeros in the interval of $0 \leq x \leq 20$. The 33 points used for the GL integrator cannot hope to cover it adequately.

Discussion and Conclusions

We have presented a new approximate form for the correction factor integral of Schumann and Gardner which facilitates the rapid and accurate evaluation of

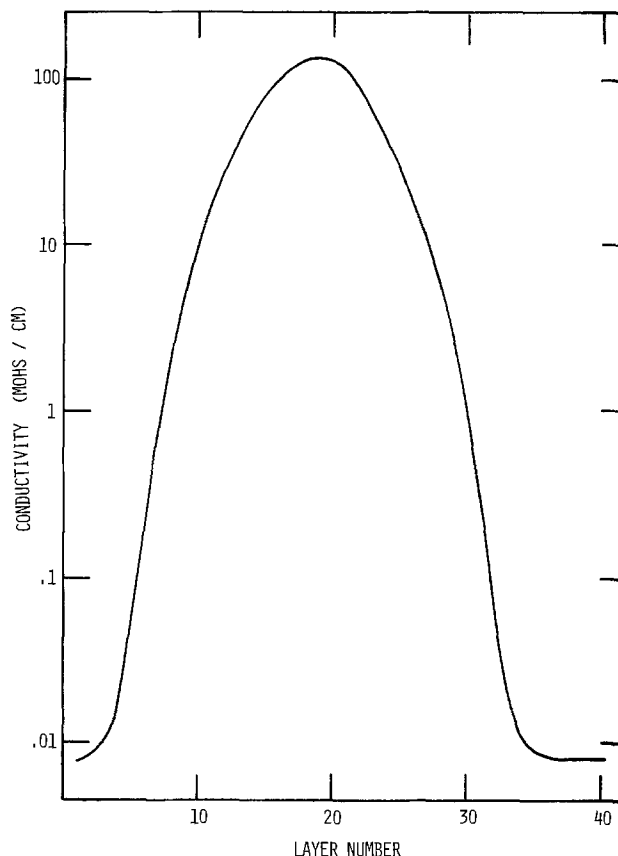


Fig. 1. Displays data supplied to us by Albers (10)

Fig. 1A. Plot of conductivity vs. depth for a model Gaussian implant.

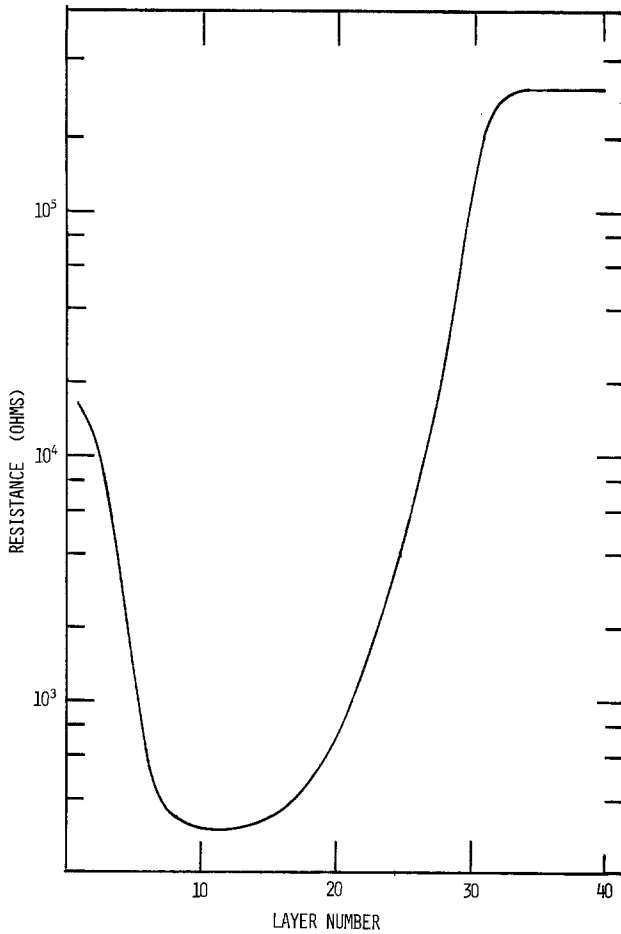


Fig. 1B. Plot of spreading vs. depth calculated by Albers using the integration scheme of D'Avanzo (4). The set shown here was calculated for $a = 2 \mu\text{m}$, $D = 25$, $t = 0.015$.

spreading resistance correction factors. This has been accomplished by eliminating the rapidly varying $J_0(Dx)$ term from the usual correction factor integral, Eq. [2].

Although we have presented the approximate integral of Eq. [2] only for $I(x)$ satisfying

$$\underline{I}(x) = \frac{IJ_1(x)}{\pi x}$$

the approximation remains valid with the lower limit, L , given by Eq. [7] for all current density profiles whose Hankel transform satisfies Eq. [4b] of (5)

$$\underline{I}(x) = \frac{I \Gamma(\nu + 1) J_\nu(x)}{2\pi(x/2)^\nu}$$

All of the commonly used forms of $\underline{I}(x)$ are special cases of the above.

The integrator of the section The Numerical Integrator was incorporated into a multilayer analysis program described elsewhere (12). The program was written in BASIC for an HP system 9845. The time to

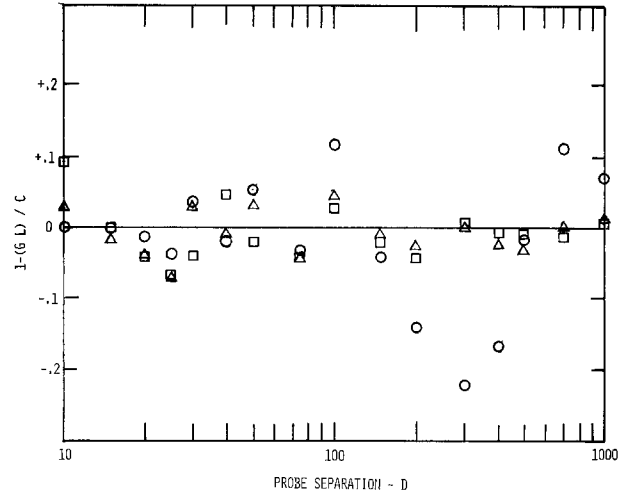


Fig. 2. Correction factors, GL , were calculated using the Gauss Laguerre integrator (11) for the Shumann and Gardner function, F , replaced by tx , 1 , $1/tx$ and $10 \leq D \leq 1000$. Figure 2 shows a plot of the fractional deviation of GL from the analytically calculated correction factors, C of Table I. The squares, triangles, and circles refer to cases where F is set equal to tx , 1 , $1/(tx)$, respectively.

calculate one point was generally less than 3 sec. As the time to measure a spreading resistance on modern equipment (e.g., an ASR-100 probe) is about 6 sec the complete conductivity profile can be corrected as measurements are made.

Manuscript submitted April 14, 1980; revised manuscript received Nov. 6, 1980.

Any discussion of this paper will appear in a Discussion Section to be published in the December 1981 JOURNAL. All discussions for the December 1981 Discussion Section should be submitted by Aug. 1, 1981.

Publication costs of this article were assisted by the U.S. Army Electronics Technology and Devices Laboratory (ERADCOM).

REFERENCES

1. P. A. Schumann and E. E. Gardner, *Solid State Electron.*, **12**, 371 (1969).
2. Y. Iida, H. Abe, and M. Kondo, *This Journal*, **124**, 1118 (1977).
3. S. C. Choo, M. S. Leong, H. L. Hong, L. Li, and L. S. Tan, *Solid State Electron.*, **20**, 839 (1977).
4. D. C. D'Avanzo, R. D. Rung, A. Gat, and R. W. Dutton, *This Journal*, **125**, 1170 (1978).
5. P. J. Severin, Spreading Resistance Symposium, NBS. Special Publication 400-10, p. 27 (1974).
6. S. C. Choo, M. S. Leong, H. L. Hong, L. Li, and L. S. Tan, *Solid State Electron.*, **21**, 769 (1978).
7. H. L. Berkowitz and R. A. Lux, *This Journal*, **126**, 1479 (1979).
8. M. Abramowitz and I. A. Stegun, Editors, "Handbook of Math. Functions," NBS Applied Math Series 50, Third printing (1965), see Chap. II especially Eq. 11.4.34.
9. M. Abramowitz and I. A. Stegun, Editors, *ibid.*, Chap. 25, Eq. 25.4.14 and Eq. 25.4.18.
10. J. Albers, To be published in *Solid State Electron.*
11. S. C. Choo and M. S. Leong, *ibid.*, **22**, 405 (1979).
12. H. L. Berkowitz and R. A. Lux, To be published.

Low Temperature CVD Growth of Epitaxial HgTe on CdTe

T. F. Kuech* and J. O. McCaldin†

California Institute of Technology, Pasadena, California 91125

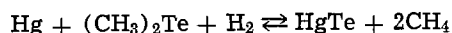
ABSTRACT

Epitaxial layers of HgTe on CdTe substrates have been grown by a low temperature metal organic CVD technique at temperatures of 325°-350°C. Thin films of HgTe exhibiting good crystalline perfection were formed by the reaction of Hg vapor and dimethyl telluride. Similar techniques may provide an alternative growth method for the epitaxial growth of Hg_xCd_{1-x}Te at low temperatures.

The semiconducting alloy system, Hg_xCd_{1-x}Te, is an important material for use in infrared detectors and imaging arrays. The bandgap of the material may be varied with composition over a wide spectral range from the visible ($x \simeq 0$) to over 30 μm ($x > 0.80$). Since the lattice parameters of HgTe and CdTe are nearly equal ($\Delta a/a = 0.003$), lattice matched epitaxial growth of Hg_xCd_{1-x}Te for all values of x may be obtained on CdTe substrates. Epitaxial layers of Hg_xCd_{1-x}Te on CdTe substrates have been grown by a variety of methods including vacuum deposition (1), sputter deposition (2), ion implantation (3), vapor deposition (4-5), close-spaced transport (6), and liquid-phase epitaxy (LPE) (7-9). Overall, LPE has proved to be the most useful of these methods. Epitaxial layers have been grown by LPE from both Hg and Te solutions. Recently, growth from Te solutions has produced good epitaxial layers with a minor amount of compositional variation across the layer (8). A change in composition can lead to undesirable variations in the spectral response of the material particularly in the long wavelength (high Hg content) regime. The relatively high temperatures used in Te solution LPE growth can also lead to the interdiffusion of the growing layer with the underlying substrate causing a vertical compositional grading in the Hg_xCd_{1-x}Te layer. The extent of the interdiffusion increases rapidly with temperature making a low temperature growth technique desirable.

The use of chemical vapor deposition techniques, which have been very successful in silicon processing and the growth of III-V and some II-VI semiconductors, has previously not been reported in the case of Hg_xCd_{1-x}Te. The CVD growth of both HgTe and Hg_xCd_{1-x}Te is difficult due to the large vapor pressures of the constituent elements, in particular Hg, required to be present to prevent thermal decomposition of the growing layer. In the case of pure HgTe at 500°C, the vapor pressure of Hg must remain between 0.16 and 7.0 atm to prevent decomposition or two-phase formation (10). The high Hg pressures required at these temperatures (500°C) for the growth and stability of the deposited layer have prevented the use of conventional open tube CVD reactors which operate at pressures less than or equal to 1 atm. If the substrate temperature is lowered, however, the required Hg pressures also decrease such that growth of HgTe at 325°C requires the Hg pressure to remain between 5×10^{-4} and 0.6 atm.¹ These pressures can be easily maintained by a source consisting of elemental Hg held at an appropriate temperature. However, the use of elemental Hg as a source does require the use of a hot wall reactor to prevent Hg condensation.

We are investigating CVD growth in the HgTe-CdTe system and present here the results for the CVD growth of epitaxial layers of HgTe on CdTe substrates. Epitaxial layers of HgTe were formed by the reaction of Hg vapor and the organic compound dimethyl telluride (DMT) according to the reaction



Dimethyl telluride has been used previously, together with other metal-organic compounds, in the formation of CdTe, ZnTe, and a variety of IV-VI compounds (11, 12). DMT has been used instead of H₂Te, which is a preferred source of Te. H₂Te is commercially unavailable probably due to its unstable nature. The use of DMT may introduce carbon as an impurity into the growing films.

The crystal growth was undertaken in a horizontal silica hot wall reactor, heated in a two-zone resistance furnace. This is shown schematically in Fig. 1. The left zone of the furnace was used to control the temperature of a boat of elemental Hg (triple distilled) which served as the source of Hg vapor. The Hg vapor pressure in the reactor was regulated by controlling the Hg source temperature. The right zone controlled the substrate temperature. DMT vapor was supplied by bubbling hydrogen through liquid DMT held at room temperature. The DMT vapor was introduced downstream from the mercury source to prevent surface contamination of the Hg. Typical H₂ flow rates through the DMT were 10-40 cm³/min. Quartz baffles were installed in the reactor to insure good mixing of the Hg and DMT vapors prior to reaction. The hydrogen used as a carrier gas was purified in a Pd purifier and passed through a liquid nitrogen cold trap before entering the reactor. The apparatus operated at atmospheric pressure with total hydrogen flow rates of 0.4-0.6 liter/min.

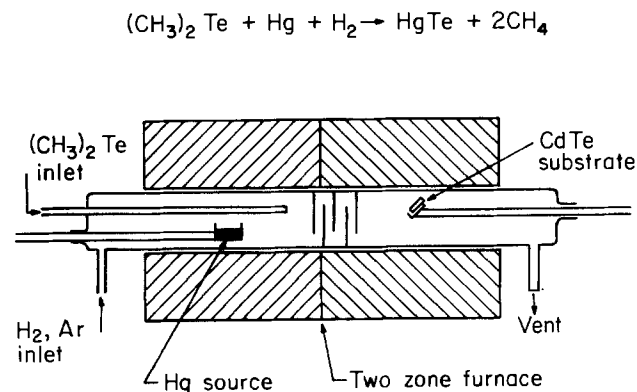


Fig. 1. A schematic diagram of the CVD reactor used in this study. The mercury source and substrate holder may be moved inside the reactor.

* Electrochemical Society Student Member.

† Electrochemical Society Active Member.

Key words: epitaxy, metal organic-chemical vapor deposition, mercury cadmium telluride.

¹ These values are extrapolated from data given in Ref. (10).

Substrates of $\langle 110 \rangle$ CdTe were prepared by cleaving bulk single crystals of CdTe in air. The $\langle 110 \rangle$ CdTe substrate was used in most of this study due to the ease of sample preparation. However, substrates of $\langle 111 \rangle$ A CdTe etched in 1% bromine in methanol were also used.

The CdTe substrate was annealed in the reactor under an H_2 atmosphere for 30-60 min at 325° - 350° C prior to the growth of the HgTe. This step was found necessary to insure good epitaxial growth of the HgTe. The growth of the HgTe was initiated by heating the Hg source to 270° - 300° C followed by the introduction of DMT into the reactor. The substrate temperature was typically 325° - 350° C during the growth period which lasted 10-120 min. This procedure gave growth rates of 0.3 - $0.6 \mu\text{m/hr}$. After the growth period, the sample was quickly pulled from the furnace hot zone to prevent thermal decomposition of the HgTe layer. The growth procedure used here should not be considered to be optimal without further experimentation. Higher growth rates may be possible.

The growth morphology of the HgTe layers was examined by scanning electron microscopy (SEM). A variety of growth morphologies were observed depending on substrate crystal orientation and growth conditions. A typical HgTe growth on a $\langle 110 \rangle$ cleaved CdTe surface is shown in Fig. 2.

Figure 2(a) shows an HgTe layer grown over a tilt boundary in the CdTe substrate. This is evident in the surface morphology of the HgTe layer. Small terraces are found to be oriented along specific crystal directions in the substrate. Figure 2(b) shows an enlarged view of the HgTe surface. This reveals the faceting

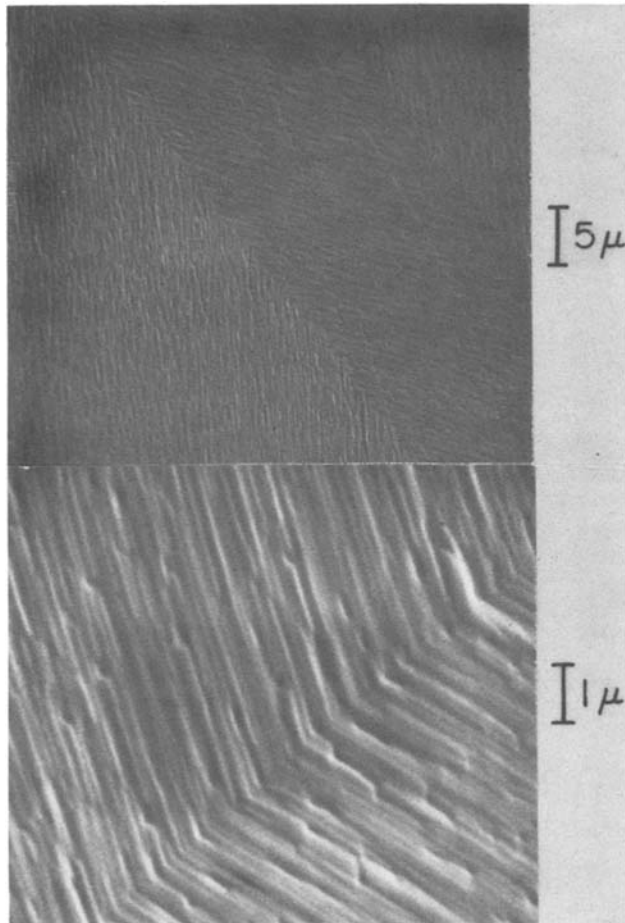


Fig. 2. HgTe layer grown on a $\langle 110 \rangle$ cleaved CdTe surface. (a, top) HgTe layer grown over a tilt boundary in the substrate. (b, bottom) A higher magnification view reveals the faceting which occurs on the growing layer. The small terraces are orientated along specific crystal directions in the substrate. The SEM views are inclined 60° from the normal.

which occurs on the growing layer. This faceting may imply that the cleaved crystal face may not be the preferred growth direction. In LPE studies, the $\langle 111 \rangle$ A CdTe surface has been found to be the optimal surface for growth of $Hg_xCd_{1-x}Te$ (9), while previous vapor phase growth studies found the highest growth rate on the $\langle 111 \rangle$ B CdTe surface (4).

We have also obtained smoother growth morphologies than shown in Fig. 2 on the $\langle 110 \rangle$ cleaved surface as seen in Fig. 3. The HgTe layer shown growing over a cleavage step on the substrate surface is very smooth with little or no surface relief. The occurrence of different growth morphologies was found to be partly dependent on the quality of the substrate material.

The growth morphology on the $\langle 111 \rangle$ A surface of the CdTe is shown in Fig. 4. On this surface, the HgTe exhibits a triangular relief, characteristic of the symmetry of the underlying substrate. The $\langle 111 \rangle$ B face was not investigated.

The HgTe layers were also examined by helium backscattering and channeling measurements and glancing angle x-ray diffraction. In the helium backscattering experiment, a beam of 1.5 MeV helium ions impinges on the substrate and the energy distribution of the backscattered particles is measured at 170° from the direction of the incident beam. A typical backscattering spectrum of an HgTe layer is shown in Fig. 5. The curve labeled random corresponds to the case where the substrate is randomly aligned with respect to the ion beam. The high energy peak in the spectrum is due to scattering off the HgTe layer while the broad

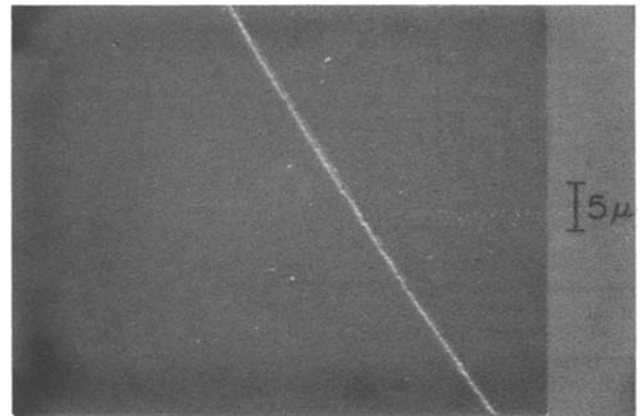


Fig. 3. HgTe layer on a $\langle 110 \rangle$ CdTe substrate possessing a smooth growth morphology. This layer was grown over a cleavage step in the substrate surface. Growth morphology was found to be partly dependent on substrate quality.

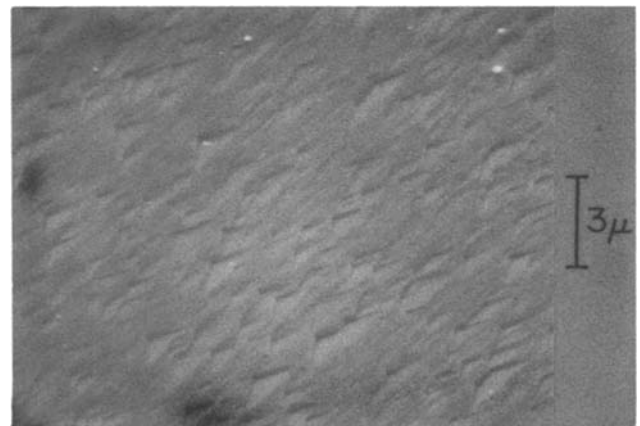


Fig. 4. HgTe layer grown on a $\langle 111 \rangle$ A CdTe substrate. The growing layer exhibits a triangular relief, characteristic of the underlying substrate. The polarity of the substrate was determined by chemical etching techniques.

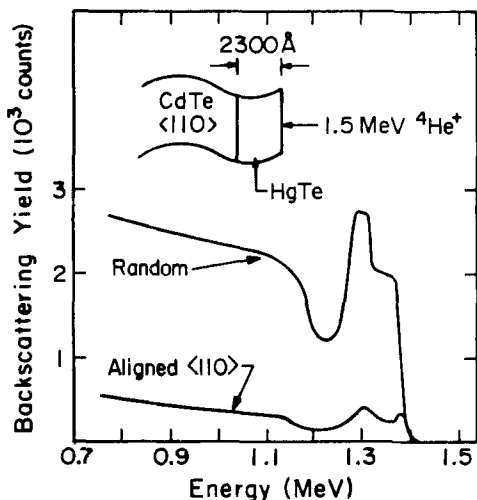


Fig. 5. The 1.5 MeV He^+ backscattering spectra of epitaxial HgTe layers. The random spectrum was used to determine the thickness of the HgTe layer. The aligned $\langle 110 \rangle$ spectrum indicates good epitaxial growth.

low energy part of the spectrum corresponds to scattering off the CdTe substrate. The thickness of the HgTe layer is easily obtained from the energy width of the HgTe peak (13). The curve labeled "aligned $\langle 110 \rangle$ " in Fig. 5 is the channeling spectrum of the HgTe layer. In this case, the ion beam is aligned along the $\langle 110 \rangle$ axis of the CdTe substrate. The ratio of the height of the HgTe peak in the channeled spectrum to random spectrum (χ_{min}) gives an indication of the crystal perfection of the HgTe layer which in this case is very good with $\chi_{\text{min}} = 10\%$ -15% and indicates epitaxial growth.

The thickness and hence the growth rate of the epilayer can be monitored by this technique. In Fig. 6, the HgTe peak from the random backscattering spectrum taken on two different growths is shown. The thicker film was grown with twice the vapor pressure of DMT in the reactor than in the case of the thinner layer. The growth rate was found to be proportional to the DMT pressure under the growth conditions used here. The variation of Hg pressure obtained by changing the Hg source temperature did not change the growth rate of the HgTe

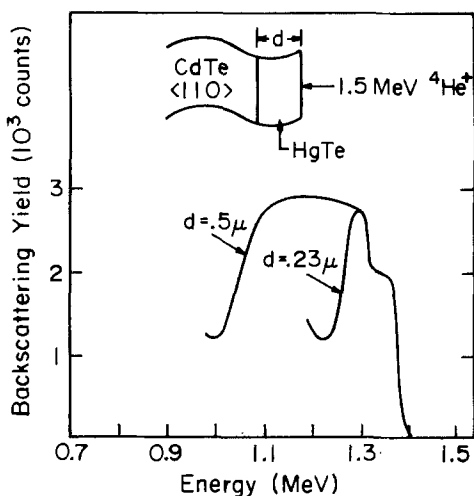


Fig. 6. The HgTe peak of the random backscattering spectrum taken on two different growths. The growth rate was obtained from the energy width of the HgTe peak.

for a given DMT pressure. The Hg source temperature was varied from 250°-300°C.

HgTe grown at temperatures greater than 350°C yielded poor results. At these temperatures the Hg and DMT vapors begin to react in the gas phase leading to undesirable film growth. Many metal organic compounds react easily at low temperatures, a fact which has necessitated the use of cold wall CVD reactors. This gas phase reaction sets an upper limit on the temperature range used in a hot wall reactor. The lower limit on the substrate temperature was found in this case to be 325°C. At temperatures below 325°C, the reaction between Hg and DMT is very slow leading to little or no HgTe growth.

In this study, we have demonstrated the use of a CVD technique for the low temperature growth of high quality HgTe epitaxial layers on CdTe substrates. However, the straightforward extension of this work to the growth of $\text{Hg}_x\text{Cd}_{1-x}\text{Te}$ is not possible in the present arrangement. The reaction of dimethyl tellurium and dimethyl cadmium, the desired source of Cd, proceeds rapidly at low temperatures preventing the use of a hot wall reactor. The use of elemental mercury as a source of mercury vapor requires a hot wall arrangement. Dimethyl mercury could serve as an alternative source of mercury for use in a cold wall reactor. We are presently investigating the extension of this technique to the low temperature CVD growth of $\text{Hg}_x\text{Cd}_{1-x}\text{Te}$.

Acknowledgment

The authors would like to thank J. Best for his helpful discussions, and S. S. Lau and M. Grimaldi for performing the backscattering experiments. The work was supported in part by the Office of Naval Research (L. R. Cooper).

Manuscript submitted Aug. 14, 1980; revised manuscript received ca. Dec. 1, 1980.

Any discussion of this paper will appear in a Discussion Section to be published in the December 1981 JOURNAL. All discussions for the December 1981 Discussion Section should be submitted by Aug. 1, 1981.

Publication costs of this article were assisted by the California Institute of Technology.

REFERENCES

1. S. A. Ignatowicz, *Thin Solid Films*, **6**, 81 (1970).
2. R. H. Connelly, L. Suchow, D. DeRidder, and T. Gabara, Paper 145 presented at The Electrochemical Society Meeting, Boston, Massachusetts, May 6-11, 1979.
3. N. Foss, *J. Appl. Phys.*, **39**, 6029 (1968).
4. G. A. Antcliff and H. Kraus, *J. Phys. Chem. Solids*, **30**, 243 (1969).
5. P. Vohl and C. M. Wolf, *J. Electron. Mater.*, **7**, 659 (1978).
6. O. N. Tufte and E. L. Stelzer, *J. Appl. Phys.*, **40**, 4559 (1969).
7. S. G. Konnikov, V. K. Ogovodnikov, and P. G. Sydoruk, *Phys. Status Solidi A*, **27**, 43 (1975).
8. J. Schmidt and J. Bowers, *Appl. Phys. Lett.*, **35**, 457 (1979).
9. M. Chu and C. C. Wang, *J. Appl. Phys.*, **51**, 2255 (1980).
10. R. F. Brebrick and A. J. Strauss, *J. Phys. Chem. Solids*, **26**, 989 (1965).
11. H. M. Manasevit and W. I. Simpson, *This Journal*, **118**, 644 (1971).
12. H. M. Manasevit and W. I. Simpson, *ibid.*, **122**, 444 (1975).
13. W. K. Chu, J. W. Mayer, and M.-A. Nicolet, Editors, "Backscattering Spectrometry," Chap. 3 and 4, Academic Press, New York (1978).

Photoelectrochemical Behavior of n-GaAs Electrodes in Ambient Temperature Molten Salt Electrolytes: Device Characterization and Loss Mechanisms

P. Singh,* R. Singh,** K. Rajeshwar, and J. DuBow*

Department of Electrical Engineering, Colorado State University, Fort Collins, Colorado 80523

ABSTRACT

The use of molten-salt electrolytes in photoelectrochemical (PEC) devices is demonstrated by the n-GaAs|AlCl₃-BPC (1:1M ratio), ferrocene/ferricenium chloride|C system. Both single crystal and polycrystalline n-GaAs electrodes were employed. The performance parameters under illumination with a tungsten halogen lamp at 100 mW/cm² for PEC devices based on single crystal material were: Short-circuit current density (J_{SC}) = 4.9 mA/cm², open-circuit voltage (V_{oc}) = 611 mV, fill factor (FF) = 0.39, and conversion efficiency (η) = 1.2%. The corresponding values for the polycrystalline devices were: J_{SC} = 3.8 mA/cm², V_{oc} = 580 mV, FF = 0.33, and η = 0.7%. A marginal improvement in the performance parameters was observed on addition of benzene and methylene chloride. The factors limiting conversion efficiency in these PEC devices are J_{SC} and fill factor. The major loss mechanisms leading to poor J_{SC} and fill factors and thereby degrading cell output are identified as surface-state assisted carrier recombination and sluggish charge transfer at the n-GaAs/AlCl₃-BPC interface possibly arising from Cl⁻ ion adsorption on the n-GaAs electrode. Electrostatic means of minimizing surface state effects by inverting the semiconductor surface are discussed with the aid of energy band diagrams. It is shown that for n-type GaAs, inversion may be achieved by choosing a redox system such that its equilibrium potential lies positive of 0.59V vs. NHE. The use of molten-salt electrolytes and non-aqueous media in general, offers a greater flexibility in the choice of redox couples in this regard, since the onset potentials for electrode decomposition are more positive than values observed for aqueous media. The excellent PEC stability of n-GaAs electrodes in AlCl₃-BPC electrolytes is another manifestation of this effect.

Much attention has been focused in recent years on the prospect of utilizing photoelectrochemical (PEC) devices for conversion and storage of solar energy (1). An outstanding problem in PEC research is the photocorrosion undergone by the semiconductor electrode. The tendency of small bandgap semiconductors to undergo photocorrosion imposes severe limitations on their performance and lifetime in a PEC cell. The use of nonaqueous electrolytes has offered an attractive alternative in this regard (2). In a previous paper, we reported on the PEC characterization of n-GaAs electrodes in an aprotic room temperature molten salt electrolyte consisting of a mixture of AlCl₃ and n-butyl pyridinium chloride (BPC) (3). Cyclic voltammetry and capacitance-voltage measurements revealed that the semiconductor bandedges are optimally placed with respect to the stability limits of the electrolyte containing AlCl₃ and BPC in the 1:1M ratio. Photogenerated holes on n-GaAs electrodes were also seen to be utilized effectively in the ferrocene/ferricenium ion (Fe(Cp)₂/Fe(Cp)₂⁺) redox reaction at the expense of the parasitic electrode dissolution process.

In the present paper, we describe the performance parameters of regenerative PEC cells based on the n-GaAs|1:1 AlCl₃-BPC, Fe(Cp)₂/Fe(Cp)₂⁺|C system. Both single crystal and polycrystalline n-GaAs electrodes were examined in this study. Our results show that the above PEC system is capable of generating significantly high open-circuit potentials. Photopotentials as high as 680 mV have been observed under illumination with a tungsten halogen lamp at 100 mW/cm². The current densities (~2-7 mA/cm²), however, were rather low compared to values typical of PEC cells based on aqueous electrolytes.

* Electrochemical Society Student Member.

** Electrochemical Society Active Member.

Key words: surface states, specific ion adsorption, surface inversion.

In an effort to probe the origin of the low current density, a systematic study of the various loss mechanisms in the n-GaAs|1:1 AlCl₃-BPC, Fe(Cp)₂/Fe(Cp)₂⁺|C cell was carried out. Factors relating to the effect of electrolyte conductivity, specific ion adsorption, hindrance to charge transfer at the semiconductor/electrolyte interface, and surface states, were of particular relevance in this regard. The deleterious effect of surface states on the photovoltaic performance was unequivocally demonstrated by a comparison of the dark and illuminated current-voltage characteristics of the above PEC system.

Finally, conclusions based on the present experimental data are extended to encompass aspects related to the design and operation of PEC systems in general. Ways in which the relative positions of semiconductor bandedges and redox couples may be optimized and the deleterious influence of surface states minimized by electrostatic means, are discussed with the help of energy band diagrams. It is proposed that carrier recombination via surface states, which is likely to be a major loss mechanism in PEC devices, may be reduced considerably by inverting the semiconductor surface.

Experimental

PEC devices were fabricated using single crystal (Te-doped, $\langle\bar{1}\bar{1}\bar{1}\rangle$ and $\langle 100 \rangle$ orientations) and polycrystalline (average grain size 0.1-0.5 mm) n-GaAs wafers obtained from commercial sources. The wafers were degreased with xylene, rinsed with methanol, and dried under nitrogen. They were then given a chemomechanical polish with 1% solution of bromine in methanol. Individual electrodes were scribed from these wafers after providing them with ohmic contacts consisting of thermally evaporated Ge-Au alloy on the back surface which was subsequently annealed in nitrogen at 450°C for 15 min. A Teflon-coated copper

wire was attached to the contacts using conducting silver epoxy. The entire back surface and the edges of the electrodes were covered with nonconducting epoxy resin. The electrodes were etched in 10% HCl for 15 min to remove any native oxide and the damaged surface layers. This was followed by etching in $\text{H}_2\text{SO}_4\text{:H}_2\text{O}_2\text{:H}_2\text{O}$ (3:1:1) for 15 sec. The electrodes were rinsed with deionized water and etched for 30 sec in 6M HCl. After rinsing with deionized water and ethyl alcohol the electrodes were dried under vacuum and then transferred into the dry box. The geometric area of the electrodes was nominally 0.10-0.25 cm^2 . A vitreous carbon plate (nominal dimensions: $1.5 \times 15 \times 30$ mm) was used as the counterelectrode in the PEC devices.

Molten salt electrolytes consisting of AlCl_3 -BPC in the 1:1M ratio were prepared according to procedures described elsewhere (3). Ferrocene ($\text{Fe}(\text{Cp})_2$) was obtained from commercial sources and purified by extraction with petroleum ether and subsequent recrystallization. Ferricenium chloride ($\text{Fe}(\text{Cp})_2\text{Cl}$) was prepared using standard procedures (4). Nominal concentrations of $\text{Fe}(\text{Cp})_2$ and $\text{Fe}(\text{Cp})_2\text{Cl}$ in the electrolyte were 0.2M and 20 mM, respectively. All manipulations with the electrolytes and redox chemicals were carried out in a dry box.

A 300W tungsten halogen lamp was used to illuminate the n-GaAs electrodes. The intensity of the light source was calibrated using a radiometer/photometer. The light intensities reported herein are not corrected for reflection and absorption losses in the cell and in the electrolyte.

Dark current-voltage measurements were performed using a PAR 173 potentiostat (Princeton Applied Research Corporation, Princeton, New Jersey) equipped with PAR 179 coulometer accessory. Three-electrode geometry was employed for these measurements. An aluminum wire immersed in the AlCl_3 -BPC electrolyte (2:1M ratio) and separated from the main cell compartment by a fine-porosity glass frit was employed as the quasi-reference electrode. Photocurrent vs. potential data were obtained by using a Hewlett-Packard 721 A power supply in series with the PEC cell. The cell current was monitored by measuring the potential drop across a 10 $\text{k}\Omega$ resistor in series with the cell.

Results

Illuminated current-voltage characteristics.—Figure 1 illustrates the illuminated current-voltage characteristics for n-GaAs (single crystal) |1:1 AlCl_3 -BPC, $\text{Fe}(\text{Cp})_2/\text{Fe}(\text{Cp})_2\text{Cl}|C$ PEC cells. Corresponding data obtained on polycrystalline n-GaAs wafers are also illustrated. The relevant performance parameters for these cells are assembled in Table I.

The relationship between short-circuit current density (J_{sc}) and light intensity is illustrated in Fig. 2a. A linear correlation is observed for light intensities up to approximately 1 sun ($100 \text{ mW}/\text{cm}^2$). The variation of open-circuit voltage (V_{oc}) with light intensity is also shown in Fig. 2a. After an initial sharp increase, the rate of increase of V_{oc} with light intensity slows down in accordance with the behavior predicted by the equation (5)

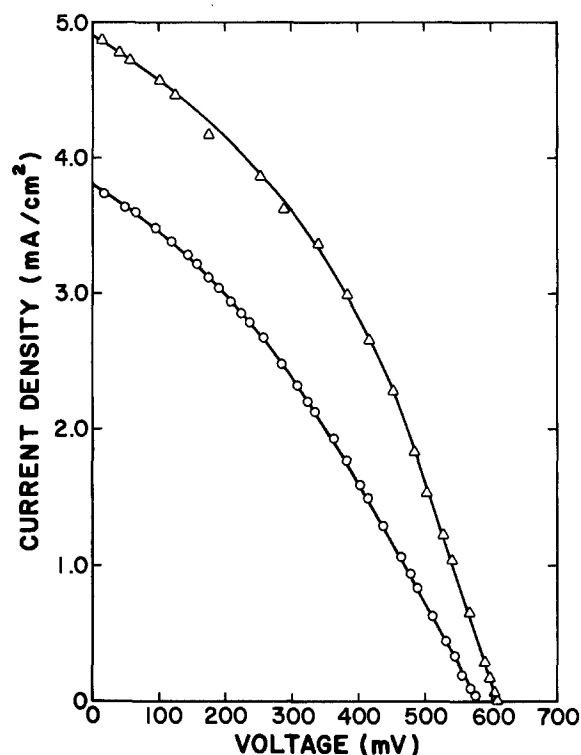


Fig. 1. Current voltage characteristics of n-GaAs| AlCl_3 -BPC, $\text{Fe}(\text{Cp})_2/\text{Fe}(\text{Cp})_2\text{Cl}|C$ system. (Δ)—single crystal n-GaAs, (\circ)—polycrystalline n-GaAs. The light intensity in these experiments was $100 \text{ mW}/\text{cm}^2$.

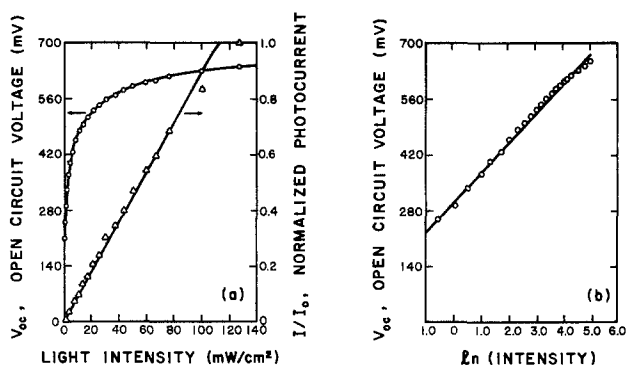


Fig. 2. (a) Relationship of open-circuit voltage and photocurrent with light intensity and (b) correlation of V_{oc} with logarithm of light intensity for the n-GaAs (single crystal)| AlCl_3 -BPC, $\text{Fe}(\text{Cp})_2/\text{Fe}(\text{Cp})_2\text{Cl}|C$ system.

$$V_{oc} = (n kT/q) \ln [(J_{sc}/J_0) + 1] \quad [1]$$

where n is the junction "ideality factor," J_0 is the reverse saturation current density of the device, and the other terms assume their usual significance. The relationship between V_{oc} and logarithm of light intensity is illustrated in Fig. 2b. Values of n in the range 1.8-3.0

Table I. Photoelectrochemical behavior of n-GaAs of different doping and orientation in 1:1 AlCl_3 -BPC electrolyte containing $\sim 0.2\text{M}$ ferrocene and 20 mM ferricenium chloride under $100 \text{ mW}/\text{cm}^2$ illumination

| Donor density | Orientation | Additive | V_{oc} (mV) | J_{sc} (mA/cm^2) | Fill factor | Efficiency (%) |
|----------------------------------|-------------|----------|---------------|--------------------------------------|-------------|----------------|
| 2.17×10^{17} (unetched) | 111 | None | 680.0 | 1.9 | 0.44 | 0.60 |
| 4.5×10^{16} (unetched) | 100 | None | 595.0 | 1.9 | 0.41 | 0.46 |
| 5.13×10^{17} (unetched) | 111 | None | 493.0 | 2.2 | 0.38 | 0.41 |
| 2.17×10^{17} (etched) | 111 | None | 611.0 | 4.9 | 0.39 | 1.17 |
| 2.5×10^{16} (etched) | Poly | None | 580.0 | 3.8 | 0.33 | 0.70 |
| 2.17×10^{17} (etched) | 111 | Benzene | 625.0 | 6.7 | 0.40 | 1.70 |
| 2.5×10^{16} (etched) | Poly | Benzene | 608.0 | 4.9 | 0.38 | 1.13 |

were extracted from the slopes of such plots for the devices examined in this study.

Effect of organic additives.—The illuminated current-voltage characteristics of the n-GaAs|1:1 AlCl₃-BPC, Fe(Cp)₂/Fe(Cp)₂Cl|C system are shown in Fig. 3 in the presence of benzene (50% by volume) in the electrolyte. A comparison of the data, with and without the presence of benzene, is presented in Table I for single crystal and polycrystalline material. A slight improvement in J_{SC} values is apparent for the electrolyte containing benzene, although these values are still below current levels in n-GaAs PEC cells based on aqueous electrolytes (6, 7). The enhancement of J_{SC} values in the presence of benzene is consistent with recent work which shows that addition of benzene to AlCl₃-BPC molten salt electrolytes, results in an increase in the conductivity of the medium due to a sharp reduction in the viscosity (8). The slight improvement in fill factors for the devices utilizing mixtures of AlCl₃-BPC and benzene (Table I) is again consistent with a reduction in the series resistance brought about by the above effect.

Effects similar to those obtained with benzene were observed on addition of methylene chloride (50% by volume) to the 1:1 AlCl₃-BPC electrolyte.

Cell stability.—Long-term irradiation of n-GaAs electrodes was carried out in the 1:1 AlCl₃-BPC electrolyte and the photocurrents were monitored under short-circuit conditions. Figure 4 illustrates typical results. The incident light intensity in this experiment was 57 mW/cm². The constancy of the observed photocurrents indicates the excellent PEC stability of n-GaAs electrodes in the 1:1 AlCl₃-BPC electrolyte. (The slight fluctuations in the photocurrent in Fig. 4 are attributed to electrolyte stirring effects and variations in light intensity as a function of time.) Further confirmation is provided by stoichiometric data. For example, in the results shown in Fig. 4, a total amount of charge of 7776 C/cm² was passed through the elec-

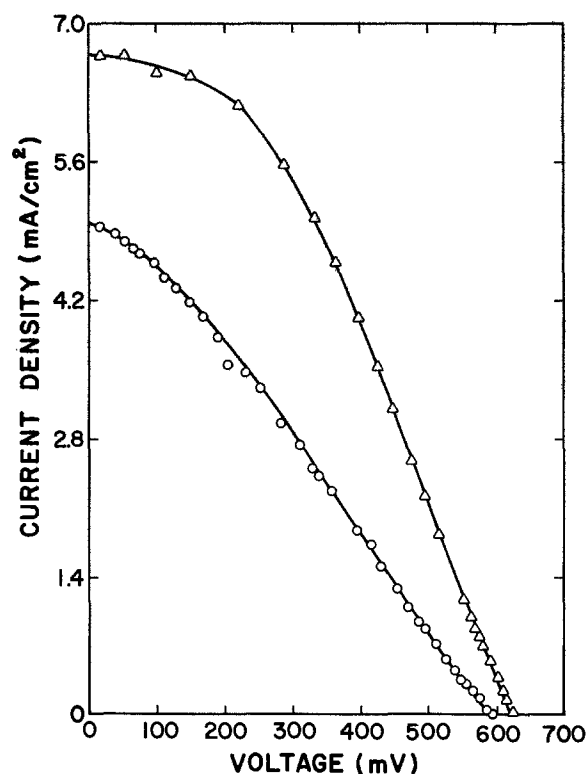


Fig. 3. Current voltage characteristics of n-GaAs|AlCl₃-BPC, Fe(Cp)₂/Fe(Cp)₂Cl|C system in the presence of benzene (50% by volume) in the electrolyte. (Δ)—single crystal, (○)—polycrystalline n-GaAs. The light intensity was 100 mW/cm².

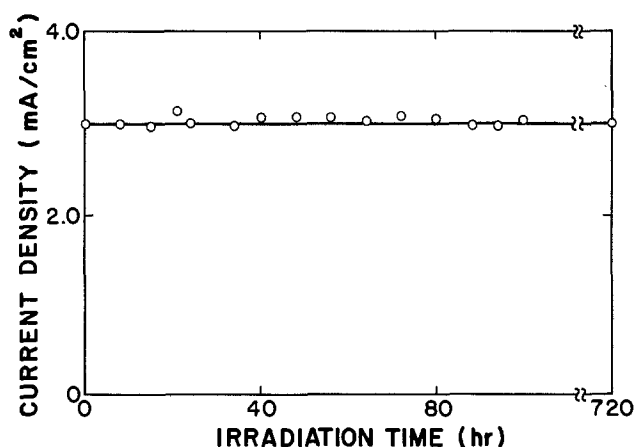


Fig. 4. Time dependence of short-circuit current density for n-GaAs (single crystal)|AlCl₃-BPC, Fe(Cp)₂/Fe(Cp)₂Cl|C system. The light intensity was 57 mW/cm² and the 1:1 AlCl₃-BPC electrolyte contained 200 mM ferrocene and 20 mM ferricenium chloride.

trode. This corresponds to 3.9g of GaAs decomposed per unit area assuming a decomposition reaction involving the transfer of three electrons. Since the electrode mass in this experiment was ca. 20.3 mg, even 5% of the total current that was passed would have resulted in complete consumption of the electrode. The enhanced stability of n-GaAs electrodes in the aprotic AlCl₃-BPC system may be understood if we note that the onset potentials for photocorrosion currents lie significantly positive of the values observed in aqueous electrolytes (3). This point is further illustrated by a comparison of the two cases as shown in Fig. 5.

Discussion

The V_{oc} values observed for the n-GaAs|AlCl₃-BPC, Fe(Cp)₂/Fe(Cp)₂Cl|C system in the present study, compare favorably with those observed by previous authors for PEC devices based on the n-GaAs/aqueous electrolyte interface (6, 7). Even higher V_{oc} values than

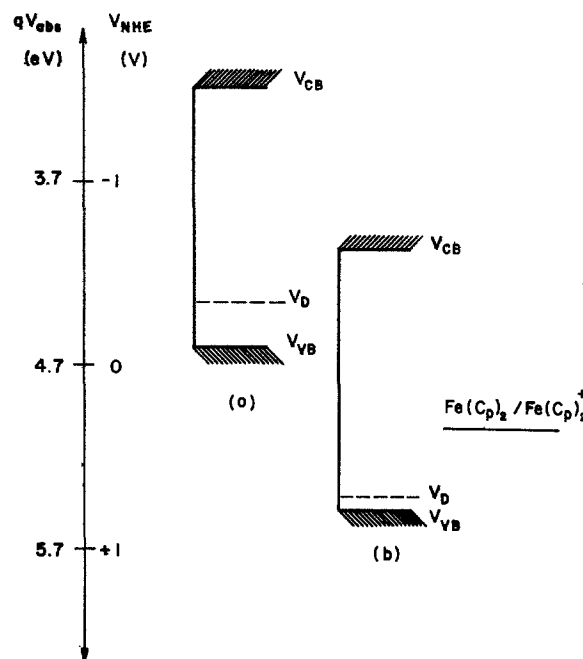


Fig. 5. Relative positions of potentials corresponding to n-GaAs bandedges (V_{CB} and V_{VB}) and onset potentials (V_D) for electrode decomposition for (a) aqueous electrolytes (pH = 12) and (b) AlCl₃-BPC (1:1M ratio) electrolyte. Relevant data were obtained from Ref. (3), (9), and (14). The redox level refers to the AlCl₃-BPC electrolyte only.

those shown in Table I were observed for some n-GaAs electrodes (750-800 mV) although difficulties were experienced in consistently reproducing this behavior. The overall conclusion from the present data is that high V_{oc} values can be realized with n-GaAs|AlCl₃-BPC, Fe(Cp)₂/Fe(Cp)₂Cl|C devices and the main factors limiting conversion efficiency are fill factor and short-circuit current density. Mass transfer of electroactive species [Fe(Cp)₂ and Fe(Cp)₂⁺] in the bulk electrolyte does not seem to be a limiting factor in the observed J_{SC} values as indicated by the linear correlation observed for J_{SC} with light intensity (Fig. 3a). The relatively minor effects noted above on addition of organic additives also seem to support this interpretation. Therefore, the factors limiting the magnitude of J_{SC} and fill factor are to be sought elsewhere. The following paragraphs amplify the possible role of surface states and specific ion adsorption effects in this regard.

Surface states.—Surface states have been implicated in previous studies on the semiconductor/electrolyte interface (2a, 10). A brief examination of their role in impairing PEC performance, however, would be relevant to the following analysis of the experimental data. Surface states at the semiconductor electrode/electrolyte interface, manifest themselves in the following ways:

(i) They act as charge storage centers and thereby modify the electrostatics (*i.e.*, the amount of band bending) and consequently the barrier height in the system. In the extreme case of high surface-state densities, Fermi level pinning ensues (11).

(ii) Surface states provide charge transfer paths between the charge carriers in the semiconductor and the electrolyte species in cases where there is not sufficient overlap between the semiconductor bandedges and the redox levels. For an n-type semiconductor, electron transfer from the semiconductor conduction band to the oxidized redox species represents a leakage current which detracts from the overall PEC performance of the electrode. The net result is that any change in the occupancy of the surface states on illumination, may result in a reduced anodic current flow (for an n-type semiconductor).

(iii) Surface states act as recombination-generation centers by interacting with the valence and conduction bands of the semiconductor. Sluggish charge transfer at the semiconductor/electrolyte interface, which leads to an accumulation of charge carriers at the surface (under illumination), may cause recombination losses via surface states to be significantly larger under illumination than in the dark.

It may be noted that in the preceding discussion no distinction has been made between "intrinsic" surface states (*e.g.*, dangling bonds, Tamm levels) and those brought about by interaction of electrolyte species with the semiconductor surface (11). Let us now examine the data in Fig. 6 in the light of the above discussion. Figure 6 is a comparison of the dark current-voltage characteristics and the current-voltage curves obtained by subtracting J_{SC} from the illuminated current-voltage data for the n-GaAs|1:1 AlCl₃-BPC, Fe(Cp)₂/Fe(Cp)₂Cl|C system. For cases where carrier losses (for example, via recombination) are unchanged upon illumination, the two curves in Fig. 6 are expected to coincide (12). The large separation of the two curves in Fig. 6 is taken as direct evidence for the active participation of surface states as leakage current paths and recombination centers in the n-GaAs|AlCl₃-BPC system [effects (ii) and (iii) noted above]. Consequently, the rather poor short-circuit current densities observed in the present study for the n-GaAs|AlCl₃-BPC, Fe(Cp)₂/Fe(Cp)₂Cl|C system may be partially attributed to the deleterious effect of surface states (*vide infra*).

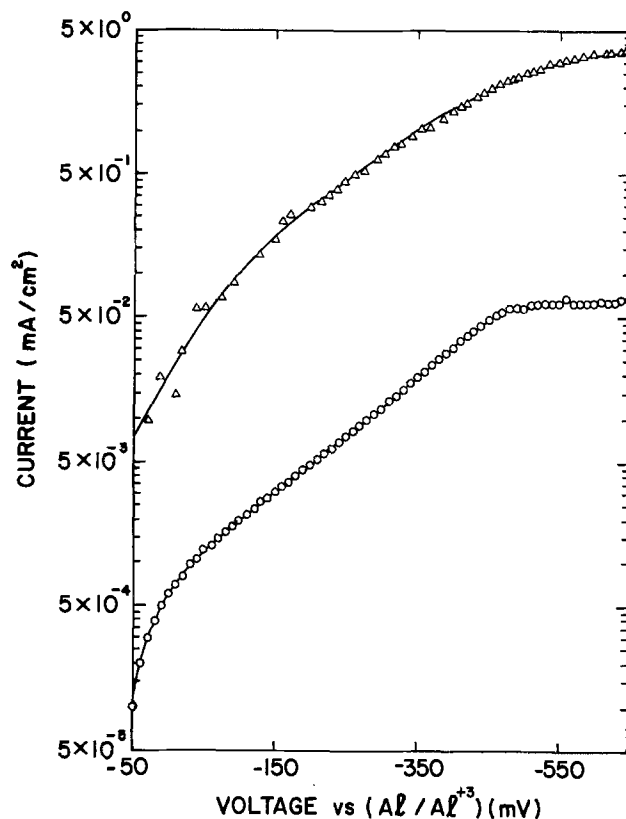


Fig. 6. Comparison of the dark current-voltage characteristics (0) and current-voltage behavior obtained by subtracting J_{SC} from illuminated current-voltage characteristics for the n-GaAs (single crystal) AlCl₃-BPC, Fe(Cp)₂/Fe(Cp)₂Cl|C system. The illuminated current-voltage data were obtained at a light intensity of 100 mW/cm².

Further evidence for the effect of surface states on the photovoltaic performance of the n-GaAs|AlCl₃-BPC, Fe(Cp)₂/Fe(Cp)₂Cl|C system is found in the magnitude of the slope of V_{oc} vs. $\ln I$ plots (Fig. 2b). Ideal junctions with $n = 1$ should yield a slope of 25 mV (*cf.*, Eq. [1]). Slopes consistently greater than this value were observed for the present PEC system (the data shown in Fig. 3b yield a slope of ~ 75 mV). This behavior implies an n -value of greater than unity which in turn is indicative of recombination-generation dominated current-voltage behavior (13).

Specific ion adsorption.—Specific adsorption of electrolyte species on the semiconductor surface often leads to rather dramatic effects on the electrostatics at the semiconductor/electrolyte interface (14). The negative shift observed in flatband potentials with increasing pCl ($= -\log [Cl^-]$) for the n-GaAs|AlCl₃-BPC interface (3, 15) is consistent with specific adsorption of Cl⁻ ions on the n-GaAs surface. This adsorption effect could lead to sluggish charge transfer at the electrode/electrolyte interface by partially blocking close approach of Fe(Cp)₂ molecules to the n-GaAs surface. This in turn enhances the carrier recombination losses as discussed above.

Adsorption of electronegative species on an n-type semiconductor surface, however, can also have a beneficial effect. For example, adsorbed Cl atoms may function as efficient electron traps and thereby induce an effective positive charge on the semiconductor surface at equilibrium. In the extreme case, the semiconductor surface may become inverted (*vide infra*) and thereby lead to an enhancement of the barrier height in the system. Such effects are well known in metal-insulator-semiconductor (MIS) devices (16). It is doubtful, however, whether Cl⁻ ion adsorption has such a favorable effect in the n-GaAs|AlCl₃-BPC, Fe(Cp)₂/

Fe(Cp)₂Cl|C system; the V_{oc} values are only 65-75% of the theoretical maximum output (3).

In the light of the present experimental data and recent studies on PEC systems in general (2a, 10), it appears that a major loss mechanism in these devices involves surface states. How can their effect be ameliorated? Previous studies on solid-state devices (17) have shown that for an inverted semiconductor interface, the electrostatic effect of surface states remains virtually independent of the cell potential (*i.e.*, no change in surface-state occupancy) over a wide range of applied bias. This contrasts the situation obtaining with a depleted semiconductor surface. The key to minimizing the deleterious influence of surface states, then, is to ensure the presence of an inversion layer on the semiconductor surface. The conditions to be fulfilled by semiconductor/electrolyte interfaces in general and by n-GaAs/electrolyte systems in particular, for the formation of an inversion layer, are analyzed below with the help of energy band diagrams.

Figure 7 illustrates the energy band diagram for an n-type semiconductor in contact with the electrolyte. The vacuum level is chosen as the reference in this diagram. V_{redox} is the redox (equilibrium) potential of the redox couple in the PEC system with respect to the reference level. V_{redox} may be converted to normal hydrogen electrode (NHE) or saturated calomel electrode (SCE) electrochemical scale by the equations (18)

$$V_{redox} = V_{redox}^{NHE} + 4.70 \quad [2]$$

$$V_{redox} = V_{redox}^{SCE} + 4.94 \quad [3]$$

The Helmholtz layer at the semiconductor/electrolyte interface is nominally 2-6Å thick. Inversion layers cannot usually be sustained on the semiconductor surface under these conditions which accounts for the relatively rare occurrence of inversion layer formation by effects similar to those noted above for specific ion adsorption (19). Deliberate introduction of an oxide layer or any other dielectric of tunelable dimensions (~15-30Å depending on the semiconductor) is therefore necessary to ensure inversion layer formation. The interphase region shown in Fig. 7, therefore, represents a composite of the Helmholtz layer and the dielectric region. The total potential drop across the interphase, ΔV , then consists of two components: (i)

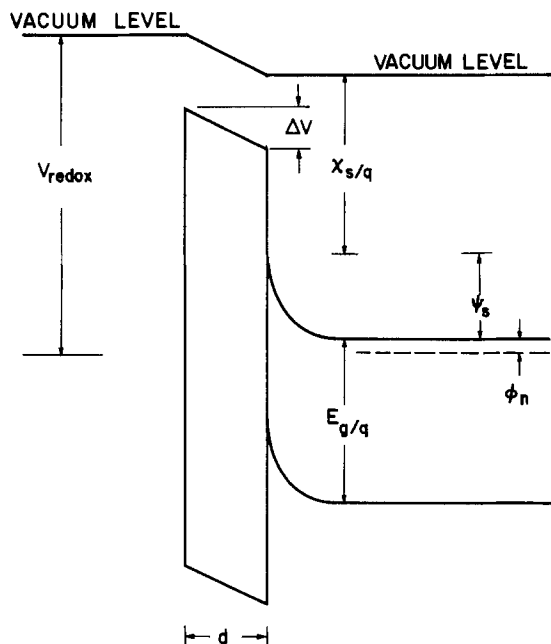


Fig. 7. Energy band diagram for an n-type semiconductor in contact with the electrolyte. See text for description of symbols.

ΔV_1 , potential drop across the interphase region of thickness, d and dielectric constant, ϵ_1 , and (ii) ΔV_2 , potential drop across the interphase states and any fixed charges in the interfacial layer, *i.e.*

$$\begin{aligned} \Delta V &= \Delta V_1 + \Delta V_2 \\ &= E_s d + \frac{q(Q_{ss} + Q_i)d}{\epsilon_1} \end{aligned} \quad [4]$$

E_s is the electric field at the semiconductor surface, and Q_{ss} and Q_i are the charge densities in the surface states and in the interphase region, respectively.

An inspection of Fig. 7 leads to the equation

$$V_{redox} = \Delta V + \frac{x_s}{q} + \psi_s + \phi_n \quad [5]$$

x_s is the electron affinity of the semiconductor, ψ_s is the surface potential of the semiconductor, and ϕ_n is the potential difference between the Fermi level and the conduction band edge. For the semiconductor surface to be under inversion, the following condition must be satisfied (20)

$$\psi_s > 2 \frac{kT}{q} \ln \left(\frac{N_D}{n_i} \right) \quad [6]$$

N_D is the donor density in the semiconductor, n_i is the intrinsic carrier concentration, and T is the temperature in °K. To ensure inversion at the semiconductor surface

$$V_{redox} > \Delta V + \frac{x_s}{q} + \phi_n + 2 \frac{kT}{q} \ln \left(\frac{N_D}{n_i} \right) \quad [7]$$

For cases where ΔV is negligible, the condition for inversion at the semiconductor surface can be written as

$$\begin{aligned} V_{redox} &> \frac{x_s}{q} + \phi_n + 2 \frac{kT}{q} \ln \left(\frac{N_D}{n_i} \right) \\ &> 2 \frac{kT}{q} \ln \left(\frac{N_D}{n_i} \right) + V_{FB} \end{aligned} \quad [8]$$

V_{FB} is the flatband potential of the n-type semiconductor.

An analogous treatment for the case of a p-type semiconductor yields

$$\begin{aligned} V_{redox} &< \frac{x_s}{q} + \frac{E_g}{q} - \frac{2kT}{q} \ln \left(\frac{N_A}{n_i} \right) - \phi_p - \Delta V \\ &< V_{FB} + \frac{E_g}{q} - 2 \frac{kT}{q} \ln \left(\frac{N_A}{n_i} \right) - \Delta V \end{aligned} \quad [9]$$

N_A is the acceptor density and ϕ_p is the potential difference between the Fermi level and the valence band edge of the semiconductor.

For the case of n-GaAs with a carrier concentration of $2 \times 10^{17}/\text{cm}^3$ and an electron affinity of 4.06 eV (21), the condition expressed in Eq. [8] reduces to

$$V_{redox} > 5.29V \quad [10]$$

Therefore the redox potential needed to invert the n-GaAs surface must lie more positive than 0.59V on the NHE scale, provided the net potential drop across the interphase region is zero. (It may be noted in this regard that V_{redox}^{NHE} of the Fe(Cp)₂/Fe(Cp)₂⁺ system is only 0.42V.) Two effects may impose restrictions on the choice of conditions for the formation of an inversion layer: (i) V_{redox} must lie at potentials more negative than the decomposition potential of the semiconductor (22) and (ii) in the presence of high surface-state densities and concomitantly high potential drops across the interphase region (14, 23), the Fermi level may become pinned at the interphase. It may not be then possible to obtain inversion on the

semiconductor surface. The first restriction is rather severe for aqueous electrolytes since the decomposition potentials tend to be rather negative. On the other hand, for nonaqueous electrolytes in general and for molten salt electrolytes in particular, a greater degree of flexibility is rendered in the choice of V_{redox} by the favorable location of decomposition potentials (cf. Fig. 5).

Summary and Conclusions

1. Open-circuit voltages as high as 680 mV have been obtained with the n-GaAs|AlCl₃-BPC, Fe(Cp)₂/Fe(Cp)₂Cl|C system. These values are close to the highest observed to date on PEC systems in general. The overall solar conversion efficiencies in this system are admittedly low (~2%) relative to values observed for PEC systems based on aqueous electrolytes. No attempts, however, were made towards optimizing cell design. It is also worth noting that the performance parameters of PEC cells based on molten salt electrolytes are comparable to those observed for other nonaqueous electrolyte systems (24).

2. The cells demonstrate good PEC stability under short-circuit conditions. The electrode decomposition potentials in AlCl₃-BPC electrolytes lie significantly positive of values observed for aqueous media.

3. The main factors currently limiting conversion efficiency in the n-GaAs|AlCl₃-BPC, Fe(Cp)₂/Fe(Cp)₂Cl|C system are poor short-circuit current densities and fill factors. Addition of organic additives to the AlCl₃-BPC electrolyte marginally improves J_{SC} and fill factors.

4. The major loss mechanism leading to poor J_{SC} and fill factors have been identified as surface-state assisted recombination of charge carriers coupled with sluggish charge transfer at the n-GaAs/AlCl₃-BPC interface, presumably because of Cl⁻ ion adsorption on the electrode surface.

5. Electrostatic conditions for minimizing the deleterious influence of surface states have been analyzed with the help of energy band diagrams. Recombination losses of photogenerated carriers may be reduced by inverting the semiconductor surface. For n-type GaAs, inversion may be achieved by choosing a redox couple such that its equilibrium potential lies more positive than 0.59V on the NHE scale. Similar considerations are presented for PEC systems in general, based on n- and p-type semiconductors.

6. A wider range of redox potentials satisfying the above conditions for inversion layer formation would be available with nonaqueous electrolytes such as AlCl₃-BPC molten salts because of (2) above.

Acknowledgment

This research program received financial support from the U.S. Department of Energy and Solar Energy Research Institute (Grant XP-9-8002-9).

Manuscript submitted May 19, 1980; revised manuscript received ca. Dec. 8, 1980.

Any discussion of this paper will appear in a Discussion Section to be published in the December 1981

JOURNAL. All discussions for the December 1981 Discussion Section should be submitted by Aug. 1, 1981.

Publication costs of this article were assisted by Colorado State University.

REFERENCES

1. K. Rajeshwar, P. Singh, and J. DuBow, *Electrochim. Acta*, **23**, 1117 (1978).
2. (a) S. N. Frank and A. J. Bard, *J. Am. Chem. Soc.*, **97**, 7427 (1975); (b) M. Miyake, H. Yoneyama, and H. Tamura, *Electrochim. Acta*, **22**, 319 (1977); (c) K. Nakatani and H. Tsubomura, *Bull. Chem. Soc. Jpn.*, **50**, 783 (1977).
3. P. Singh, K. Rajeshwar, J. DuBow, and R. Job, *J. Am. Chem. Soc.*, **102**, 4676 (1980).
4. D. N. Hendrickson, Y. S. Sohn, and H. B. Gray, *Inorg. Chem.*, **10**, 1559 (1971).
5. H. J. Hovel, "Semiconductors and Semimetals," Vol. 11, p. 176, Academic Press, New York (1975).
6. B. A. Parkinson, A. Heller, and B. Miller, *This Journal*, **126**, 954 (1979).
7. R. Noufi and D. Tench, *ibid.*, **127**, 188 (1980).
8. J. Robinson, R. C. Bugle, H. L. Chum, D. Koran, and R. A. Osteryoung, *J. Am. Chem. Soc.*, **101**, 3776 (1979).
9. P. A. Kohl and A. J. Bard, *This Journal*, **126**, 59 (1979).
10. (a) R. N. Noufi, P. A. Kohl, S. N. Frank, and A. J. Bard, *This Journal*, **125**, 246 (1978); (b) P. A. Kohl and A. J. Bard, *ibid.*, **126**, 598 (1979); (c) R. A. Fredlein and A. J. Bard, *ibid.*, **126**, 1892 (1979); (d) B. Pettinger, H. R. Schappel, and H. Gerischer, *Ber. Bunsenges Phys. Chem.*, **77**, 960 (1973); (e) T. Yamase, H. Gerischer, M. Lübke, and B. Pettinger, *ibid.*, **82**, 1041 (1978); (f) W. Kautek, H. Gerischer, and H. Tributsch, *ibid.*, **83**, 1000 (1979).
11. S. R. Morrison, "The Chemical Physics of Surfaces," p. 206, Plenum Press, New York (1977).
12. (a) P. Panayotatos and H. C. Card, *Solid State Electron.*, **23**, 41 (1980); (b) S. Kar, *J. Appl. Phys.*, **49**, 5278 (1978).
13. S. M. Sze, "Physics of Semiconductor Devices," p. 104, John Wiley & Sons, New York (1969).
14. K. Rajeshwar, R. Singh, P. Singh, R. Gale, and J. DuBow, *J. Appl. Phys.*, **51**, 6286 (1980).
15. R. Gale, P. Singh, K. Rajeshwar, and J. DuBow, Unpublished data (1979).
16. R. B. Godfrey and M. A. Green, *IEEE Trans. Electron Devices*, **ed-27**, 737 (1980).
17. M. A. Green, *Appl. Phys. Lett.*, **33**, 178 (1978).
18. H. Gerischer, *J. Electroanal. Chem. Interfacial Electrochem.*, **58**, 263 (1975).
19. S. R. Morrison, in "Treatise on Solid State Chemistry," Vol. 6B, Chap. 3, N. B. Hannay, Editor, pp. 228-229, Plenum Press, New York (1976).
20. S. M. Sze, "Physics of Semiconductor Devices," p. 432, John Wiley & Sons, New York (1969).
21. S. M. Sze, "Physics of Semiconductor Devices," p. 57, John Wiley & Sons, New York (1969).
22. (a) H. Gerischer, *J. Electroanal. Chem. Interfacial Electrochem.*, **82**, 133 (1977); (b) A. J. Bard and M. S. Wrighton, *This Journal*, **124**, 1706 (1977).
23. S. Kar, K. Rajeshwar, P. Singh, and J. DuBow, *Solar Energy*, **23**, 129 (1979).
24. P. A. Kohl and A. J. Bard, *This Journal*, **126**, 603 (1979).

Lateral Epitaxial Recrystallization of Deposited Silicon Films on Silicon Dioxide

T. I. Kamins,* T. R. Cass, and C. J. Dell'Oca*

Hewlett-Packard Laboratories, Palo Alto, California 94304

and K. F. Lee,* R. F. W. Pease, and J. F. Gibbons*

Stanford Electronics Laboratory, Stanford, California 94305

ABSTRACT

A scanning cw argon laser has been used to epitaxially recrystallize silicon films deposited over exposed regions of single crystal silicon substrates and cause the lateral extension of these epitaxial regions into the portions of the silicon film deposited over oxide-covered regions of the substrate. Planar and cross-sectional transmission electron microscopy were used to investigate the microstructure, which is consistent with melting and liquid-phase regrowth.

In a recent report, Tamura *et al.* (1) have demonstrated the possibility of "bridging epitaxy" in which a single crystal silicon substrate is used as a seed for the laser recrystallization of a silicon film over silicon dioxide. The regrowth of the deposited film starts where the film contacts the substrate and extends laterally into the portion of the silicon film on top of the insulating oxide layer. Such a single crystal film would find many applications in integrated circuit technology.

In their experiments, Tamura *et al.* used a Q-switched ruby laser to melt the silicon layer deposited on the single crystal silicon wafer which was partially covered with oxide stripes. Using planar transmission electron microscopy, they observed the vertical epitaxial growth of the deposited silicon as it solidified over the exposed silicon substrate and some lateral extension of the single crystal material over the oxide-coated areas.

A pulsed laser, however, melts a large region of material which then solidifies in a manner primarily determined by heat transfer away from the molten areas. In this manner, Tamura *et al.* proposed that the regions over the exposed single crystal substrate crystallized before the silicon over the oxide because the low thermal conductivity of the oxide layer kept the film in these regions above the melting point for a longer time.

The use of a scanning cw laser would appear to be an attractive alternative to the pulsed laser for this application. The epitaxial regrowth process could start over the exposed silicon substrate, and then the molten zone could be moved into the film over the oxide-covered regions in a more controlled manner.

In this report we describe the use of a cw argon laser to epitaxially recrystallize silicon films over exposed regions of a single crystal silicon substrate and the lateral extension of these epitaxial regions into the deposited silicon film over oxide-covered regions of the substrate. Planar and cross-sectional transmission electron microscopy were used to reveal the structure both in the plane of the film and perpendicular to it.

Sample Preparation

Silicon wafers with (100) orientation were oxidized at 1000°C in a TCE/O₂ atmosphere to form a 1000Å thick oxide layer. The oxide was then patterned using a mask containing rectangles of varying sizes from 50 × 50 μm to 150 × 300 μm, and the oxide was removed from the orthogonal, 12 μm-wide grid lines separating the oxide rectangles. Silicon films were then deposited in a low pressure, chemical vapor deposition reactor onto both exposed substrate and the oxide-

covered regions. (The wafers were cleaned with dilute HF no longer than 5 min before insertion into the LPCVD reactor.) Two different deposition temperatures were used: 550° and 625°C. Films deposited at 625°C have been shown to have a columnar, polycrystalline structure, while those deposited at 550°C are initially amorphous (2). Both types of film were deposited to a thickness of approximately 2000Å. For comparison with the regrown structure to be discussed below, Fig. 1 shows a cross-sectional TEM of an unrecrystallized area of 625°C polysilicon from one of the same wafers as the laser-recrystallized samples. The expected columnar, (110)-oriented grains are apparent (2, 3).

In an attempt to make the deposited layer and the surface region of the underlying single crystal substrate amorphous and facilitate regrowth, some of the structures were then implanted with a dose of 3×10^{15} cm⁻² silicon ions while the substrate was held on a liquid-nitrogen-cooled support. The implant energy of 135 keV placed the peak of the implant close to the substrate-film interface.

After implantation, the deposited films were recrystallized with a cw argon laser at Stanford (4). The laser beam was moved by galvanometer-controlled mirrors. A 135 mm focal length lens was used, and the spot size on the wafer surface was 40 μm. The retrace was blanked so that the trace of the laser beam on the wafer surface was always in one direction. The scan speed was 12 cm/sec, and a power of 9.5W was used. With the given scan speed and spot size, this power appears to be optimum. At significantly lower powers, the

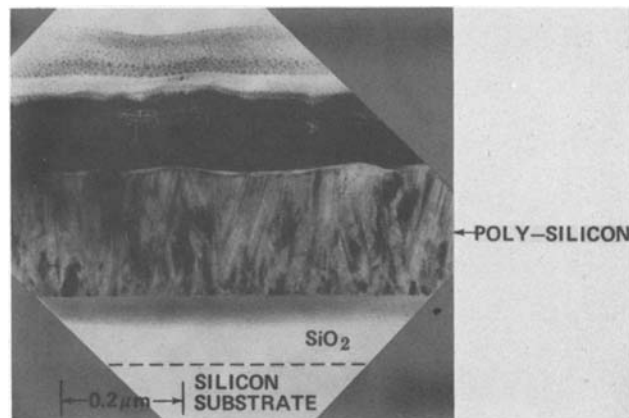


Fig. 1. Cross-sectional TEM of unrecrystallized polysilicon film deposited on silicon dioxide.

* Electrochemical Society Active Member.

Key words: laser recrystallization, silicon film, epitaxial growth.

large-grained regions do not overlap, especially over the single crystal silicon with its high thermal conductivity. At much higher laser powers, the silicon over the oxide tends to agglomerate, and the substrate may be damaged. Other satisfactory combinations of laser parameters are, of course, possible.

After completion of the recrystallization, the wafers were returned to Hewlett-Packard for analysis. Suitable control wafers were thermally annealed for comparison with laser-recrystallized samples. These wafers were inserted into a standard diffusion furnace at 550°C and annealed for 5 hr before the temperature was ramped to 650°C for 2 hr and then to 950°C for 1 hr.

After preliminary observation with optical and scanning electron microscopes, planar and cross-sectional samples were prepared (5) from the various wafers and examined in a Siemens Model 101 transmission electron microscope. Some samples were also chemically etched using Secco etch to reveal grain boundaries.

Results and Discussion

Optical microscopy and SEM analysis of the re-grown material showed regions of varying thickness over the oxide-covered areas of the substrate (deduced from interference colors) and also surface ripples, especially over the exposed substrate, probably due to optical interference effects, as has been described previously (6). The silicon film extending into the oxide-covered regions in the direction of the laser scan appeared to be especially smooth. Etching to delineate grain boundaries revealed fewer boundaries near the oxide step than farther onto the oxide-coated rectangles. These preliminary observations support the more detailed TEM analysis, although they cannot be considered definitive. A scanning electron micrograph of an unetched sample is shown in Fig. 2 to place the transmission electron micrographs to be discussed next in context. The laser scanned the sample from left to right. Thickness nonuniformities perpendicular to the scan direction are seen at the trailing edge (left side of oxide cut).

Cross-sectional TEM's of one sample are shown in Fig. 3. This sample contained a deposited layer of initially polycrystalline silicon and was implanted with silicon to disrupt any barrier to recrystallization at the film-substrate interface. The scan direction was again from left to right. Figure 3c shows the deposited film directly over the exposed single crystal substrate, and

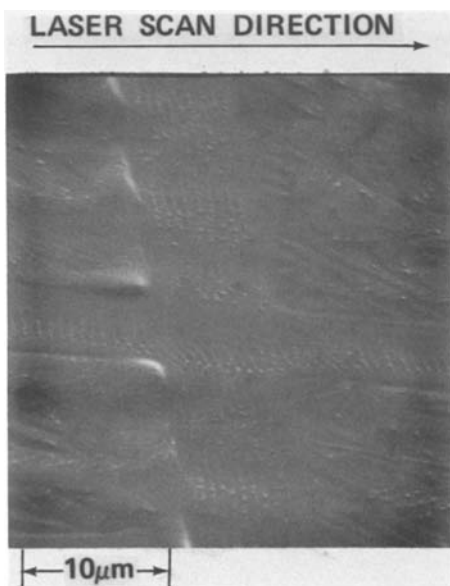


Fig. 2. Scanning electron micrograph of laser-recrystallized silicon film deposited over exposed silicon lines and oxide-covered rectangles. The laser beam scanned the sample from left to right.

the other portions of the figure show the silicon film extending over the oxide steps. (The speckled region above the deposited film is the epoxy used in preparing the cross-sectional TEM's). Figure 3 and detailed comparison of the relevant electron diffraction patterns confirm that the film directly over the single crystal substrate has recrystallized epitaxially; the crystal orientation is the same in the film as in the substrate, and the film contains few defects. The planar TEM of Fig. 3d reveals that the defects at the substrate-film interface seen in Fig. 3d are an orthogonal array of misfit dislocations propagating from the oxide step. These misfit dislocations were not observed in all regions, suggesting that they can be avoided by proper processing conditions. Occasionally, twins and inclined dislocations were seen extending from the substrate-film interface, as schematically indicated in Fig. 3f.

Figure 3e shows the silicon film extending onto the oxide layer. Detailed examination in the TEM reveals that the crystal orientation of the film is the same as that of the substrate, although variation of the thickness of the cross section makes comparison of the orientations directly from the photomicrographs difficult. Although some defects are seen in the film, no grain boundaries are visible within the portion of the film seen in the micrograph. Since this is the leading edge of the laser scan, where the laser moves from the part of the film over the substrate onto that over the oxide, the scanning beam is expected to extend the single crystal region of the film significantly in the lateral direction. Optical microscopy after grain boundary etching does, indeed, suggest that the single crystal region extends farther on this side of the oxide cut than on the other side, although the asymmetry is not clearly revealed by the cross-sectional TEM's, which sample only one isolated area. This observation suggests that two different mechanisms may dominate on the two sides of the oxide cut.

These cross-sectional TEM's reveal several other important features. Most obvious is the mass transport caused by the laser recrystallization. Since the deposited film initially has a uniform thickness of approximately 2000Å, a 1000Å-high step should appear at the top of the deposited film, replicating the oxide step. This step is not seen in Fig. 3e. On the thermally annealed samples, which remained solid during the recrystallization, the expected step of 1000Å was observed.

The opposite side of the oxide cut is seen in Fig. 3a and b. As on the right side, the crystal extends continuously over the oxide step. In this case the grain is seen to terminate at the left approximately 0.5 μm from the edge of the oxide step. Because the laser beam approaches this region from the area which contains a buried oxide layer, rather than from the region with the exposed substrate, the recrystallization mechanism may be quite different than on the opposite side. On the trailing edge there should be no marked tendency of the laser beam to "drag" a single crystal region away from the oxide edge. The controlling mechanism on this side could be similar to that described in experiments with the pulsed laser (1) where the low thermal conductivity of the oxide causes the silicon above it to remain molten longer than that over the exposed substrate. If the major heat loss is by lateral heat transfer toward the oxide cut, the solid silicon would propagate from the oxide edge, and lateral single crystal growth is possible. Although a step is seen at the top of the silicon film where it crosses the edge of the oxide, the step is much less abrupt and of less height than the oxide step. For comparison, the shape seen on the thermally annealed sample is shown by the dashed line superimposed on Fig. 3a. The silicon film on top of the oxide is also seen to be much thinner than that directly over the substrate, indicating significant mass transport, as is shown by the SEM of Fig. 2.

Near both edges of the oxide cut, defects are seen in the substrate. One might speculate that these defects

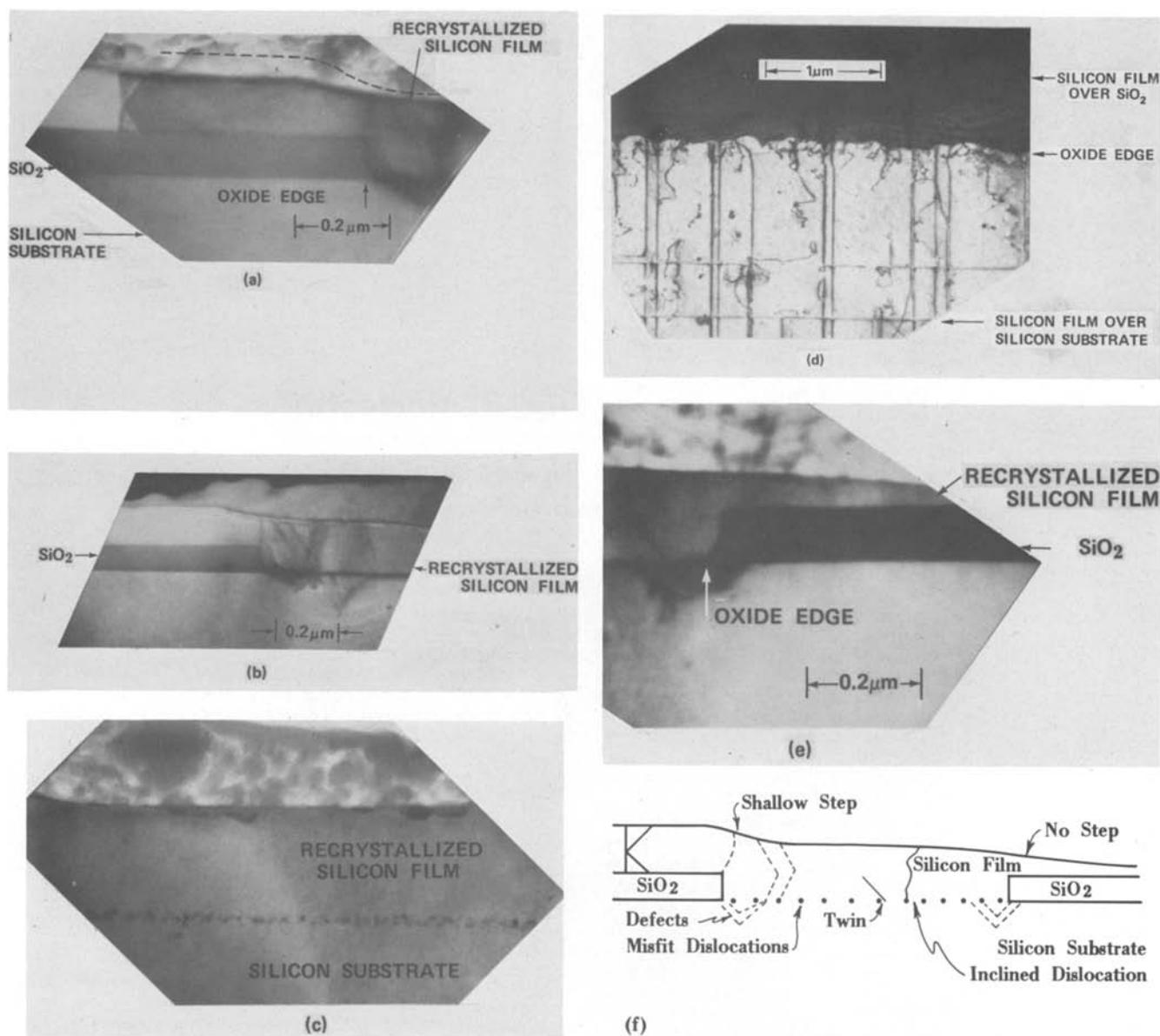


Fig. 3. Cross-sectional and planar TEM's of laser recrystallized silicon film: (a) and (b) over oxide steps at left of oxide cut (b is a dark-field micrograph); (c) over exposed single-crystal substrate; (d) planar section, primarily over exposed substrate; (e) over oxide step at right. (f) Schematic representation of features observed. The scan direction was from left to right in all except (d).

arise from relaxation of stress discontinuities caused by the different thermal expansion coefficients of silicon and silicon dioxide (3×10^{-6} compared to $0.5 \times 10^{-6}/^\circ\text{C}$), as well as by temperature differences over silicon- and oxide-covered regions. Not only are defects observed extending into the substrate, but slip dislocations parallel to the wafer surface have also been seen several microns beneath the surface of the substrate. These have been observed both under the oxide and under the oxide cuts. These deep-lying dislocations are probably caused by thermal stresses associated with scanned beam recrystallization.

The regrowth of the initially amorphous films was similar to that of polycrystalline films in the regions which were melted. Surrounding the melted regions, of course, were regions where the initially amorphous film was converted to polycrystalline silicon, probably by solid-phase crystallization.

Observation of laser-recrystallized samples with and without the silicon implant showed little difference, with epitaxial regrowth over the single crystal substrate and defects at the interface. This suggests that the implantation is not needed in the case of liquid-phase recrystallization. The lack of epitaxial regrowth in the case of the thermally annealed sample indicates

that the implant dose was insufficient to disrupt the interfacial layer present because of the deposition conditions and to allow solid-phase regrowth, even though the dose was sufficient to amorphize the surface regions of the silicon substrate beneath the interface. We speculate that a dose of 10^{16} cm^{-2} might produce the necessary disruption of the interfacial layer to allow solid-phase regrowth.

The different behavior on the two sides of the oxide cut leads us to suggest the following modification of the experimental structure. If the polysilicon is etched from part of the oxide cut and the laser scanning direction is such that laser-assisted growth is started where the polysilicon contacts only the underlying single crystal and proceeds over a gradually beveled oxide step, superior results might be achieved, including the possibility of solid-phase regrowth.

Conclusion

A scanning cw argon laser has been used to epitaxially regrow deposited silicon films over exposed regions of a single crystal silicon substrate and cause the lateral extension of these epitaxial regions into the deposited silicon film over oxide-covered regions of the substrate.

This process occurred by melting and liquid-phase re-growth.

Acknowledgment

The authors would like to thank Dr. J. L. Moll for his encouragement during the course of this investigation and Frank Perlaki for the scanning electron micrograph.

Manuscript submitted Aug. 25, 1980; revised manuscript received Dec. 1, 1980.

Any discussion of this paper will appear in a Discussion Section to be published in the December 1981 JOURNAL. All discussions for the December 1981 Discussion Section should be submitted by Aug. 1, 1981.

Publication costs of this article were assisted by Hewlett-Packard Laboratories.

REFERENCES

1. M. Tamura, H. Tamura, and T. Tokuyama, *Jpn. J. Appl. Phys.*, **19**, L23 (1980).
2. T. I. Kamins, *This Journal*, **127**, 686 (1980).
3. T. I. Kamins, J. Manoliu, and R. N. Tucker, *J. Appl. Phys.*, **43**, 83 (1972).
4. A. Gat and J. F. Gibbons, *Appl. Phys. Lett.*, **32**, 142 (1978).
5. e.g., T. T. Sheng and R. B. Marcus, *This Journal*, **127**, 737 (1980).
6. H. J. Leamy, G. A. Rozgonyi, T. T. Sheng, and G. K. Cellar, *Appl. Phys. Lett.*, **32**, 535 (1978).

Donor Densities in TiO₂ Photoelectrodes

J. Schoonman,* K. Vos, and G. Blasse

Solid State Department, Physics Laboratory, State University, 3508 TA Utrecht, The Netherlands

ABSTRACT

Mechanical polishing and etching in acids or molten NaOH of TiO₂ electrodes frequently lead to nonlinear Mott-Schottky plots. These surface treatments are discussed in relation to surface roughness effects and the occurrence of nonuniform donor distributions. Modified Mott-Schottky equations are presented and discussed. They account quantitatively for surface roughness and nonuniform donor distributions, which can be induced not only by etching, but also by anodical aging, surface doping, reoxidation effects, and cathodical loading with hydrogen.

Semiconducting TiO₂ (rutile) has attracted widespread attention as photoanode for the photoelectrolysis of water. Its surface properties are of paramount importance and their determination has received considerable effort. Usually, key parameters such as flat-band potential V_{FB} , and donor density N_D , are obtained from capacitance measurements, when the semiconductor in contact with an aqueous electrolyte is in the depletion mode. The space-charge capacitance C_{sc} then varies with the potential drop ϕ_{sc} over the depletion layer according to the Mott-Schottky equation (1, 2)

$$C_{sc}^{-2} = \frac{2}{\epsilon_0 \epsilon N_D A^2} \left(\phi_{sc} - \frac{kT}{e} \right) \quad [1]$$

where ϵ is the relative dielectric constant, ϵ_0 the permittivity of free space, e the electronic charge, N_D the donor density, and A the interfacial surface area. The potential drop ϕ_{sc} can be expressed as $\phi_{sc} = V - V_{FB}$, V being the electrode potential, provided that the potential drop ϕ_H over the Helmholtz layer at the semiconductor/electrolyte interface is constant. The flat-band potential and donor density are then obtained from a linear Mott-Schottky plot, C_{sc}^{-2} vs. V .

Nonlinear Mott-Schottky plots for TiO₂/electrolyte junctions have been reported frequently (3-10). Nonlinearity can be attributed to nonhomogeneous donor distributions in the depletion layer, or to surface roughness effects. Surface states on a TiO₂ surface can change the potential of the Helmholtz layer, thereby leading to nonlinearity. The latter model has been described quantitatively by Tomkiewicz (6).

It has become quite apparent that surface preparations are of crucial importance in the determination of V_{FB} and N_D (7, 8, 10). It is the purpose of the present paper to discuss some effects which lead to nonlinear Mott-Schottky plots in relation to surface preparations.

Polishing and Etching

The plane parallel capacitance approach for the depletion layer leads with Eq. [1] to

$$L_D = \left(\frac{2\epsilon\epsilon_0}{eN_D} \right)^{1/2} \left(\phi_{sc} - \frac{kT}{e} \right)^{1/2} \quad [2]$$

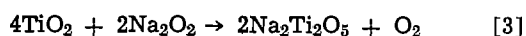
With donor densities of the order of $10^{18}/\text{cm}^3$, and ϵ (//c axis) = 173, the width L_D of the depletion layer varies between 0.1 to 0.2 μm for potentials ranging from 0.5 to 2.0V. Larger donor densities will further decrease L_D .

Vos and Krusemeijer (4, 5) reported a deformation layer of 0.5 μm thickness for a TiO₂ electrode with a donor density of about $10^{18}/\text{cm}^3$ polished to 0.3 μm finish. The recent data of Wilson *et al.* (7) are very well in line with this observation. Although mirror-like surfaces are obtained using 1-0.3 μm grade diamond pastes (4, 10), the deformation layer may extend far beyond the depletion layer into the bulk of the electrode. As reduction procedures induce larger donor densities in the deformation layer (4, 5, 7), differential capacitance measurements need to be performed up to potentials of about 30V, i.e., much larger than usually employed in order to establish not only the thickness of the deformation layer, but also the difference between the donor density in the bulk and in the deformation layer. In addition, L_D values of 0.1-0.2 μm compare unfavorably with 1-0.3 μm grade polishing pastes. Hence, surface roughness needs to be taken into consideration in order to obtain the true donor density in the deformation layer from Mott-Schottky plots. This will be further dealt with in detail in the next section.

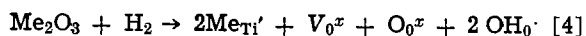
It is common practice to remove the deformation layer by etching polished nonconducting TiO₂ crystals in molten NaOH at about 500°C (4-6, 9, 11, 12), in 1:1 mixtures of ammonium sulfate and sulfuric acid at 240°C (7), or in concentrated sulfuric acid at 250°-260°C (10). The amphoteric character of TiO₂ is illus-

* Electrochemical Society Active Member.
Key words: etching, doping, photoelectrodes.

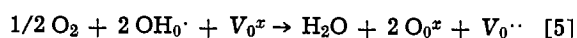
trated by these etchants, which lead to the formation of Na_2TiO_3 and TiOSO_4 , respectively (13). However, these etchants do not always lead to smooth surfaces (7, 9), and do not necessarily lead to linear Mott-Schottky plots (6-10). Nonlinearity for potentials up to 3V has been ascribed to a change in the potential of the Helmholtz-layer due to surface states on the TiO_2 crystal (6), or to different donor densities in individual areas of the surface region (9), or to donor densities which vary with depth (7, 8, 10). Side reactions during the etching process in molten NaOH may provide a rationale for varying donor densities. Usually, employed etching times are 1 hr. Cardon (14) has observed that under these circumstances a layer of 50 μm is removed. For TiO_2 surfaces polished to a 0.25 μm finish, etching periods of 2-5 min are sufficient. In our experience, etching for periods longer than 5 min sometimes results in the formation of a white porous layer on parts of the crystal's surface. This layer can be removed in boiling HCl, in which it does not dissolve. However, the surface in contact with the layer reveals severe pitting after etching. The formation of the layer is ascribed to a reaction between TiO_2 and sodium peroxide (15), inherently present in sodium hydroxide melts



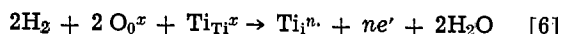
This reaction may also account for the white layer of colloidal titanates formed during etching as reported by Barber and Farabough (16), and may have other implications for the surface region. Commercial Verneuil-grown crystals contain as residual impurities, among others, Al, Fe, and Sb (Me_2O_3). In addition, residual hydrogen is present in Verneuil-grown crystals (17-19). This hydrogen has been found to compensate for the residual impurities Me_2O_3 (17). Following the defect notation of Kröger (20), and taking into account that OH stretch vibrations have been recorded (19) we can write for such extrinsic crystals



These crystals can lose hydrogen when heated in O_2 at about 600°C (17, 19). If, in addition to etching, reaction [3] occurs the following interfacial reaction would produce charged oxide ion vacancies



The OH_0 centers can dissociate throughout the crystal, thereby producing regular lattice oxide ions O_{O}^x and protons. As protons are more mobile than oxide ion vacancies the density of these vacancies will increase towards the surface. A subsequent hydrogen reduction will introduce titanium interstitials as multiple donors (21), the reaction being



where n is found to be 3 (22). Usually donor densities range from 10^{18} to $10^{20}/\text{cm}^3$ in reduced TiO_2 electrodes. Residual impurity contents (Me_2O_3) can be as high as $\sim 3 \times 10^{18}/\text{cm}^3$ (~ 100 ppm) (17) in commercial crystals. The reduced crystals exhibit the characteristic blue-black color, while the crystals with Me_2O_3 , even for concentrations greater than 100 ppm, remain light yellow. This indicates that the neutral vacancy V_{O}^x as present in proton compensated crystals does not act as a donor. Von Hippel *et al.* (18) already indicated that charged oxide ion vacancies will readily trap two electrons. Hence, a surface layer with a lower conductivity may be present after surface treatments in the sequence NaOH etching-reduction. In view of reaction [3], reversing the sequence can lead to reoxidation effects



Extensive reoxidation has been observed by Wilson *et al.* (7) and by Dare-Edwards and Hamnett (10). In fact, reoxidation also takes place when the reduced

crystal is stored in air at ambient temperature. Again a low-conductive layer will result.

The acidic etchants (7, 10) are preferential for several crystallographic planes (23-25). Dislocation densities and etch pits have been studied. The nonshiny faceted surfaces as reported by Wilson *et al.* (7) after etching in mixtures of ammonium sulfate and sulfuric acid generate nonlinear Mott-Schottky plots. However, their shape does not indicate surface roughness to be the cause, as will be shown in the next section. Instead, donor densities seem to decrease towards the surface. This would be consistent with proposed reoxidation effects in acidic etchants (10). Moreover, when anodically aged under illumination, TiO_2 electrodes show nonlinear Mott-Schottky plots which closely resemble in shape the plots obtained with acid-etched surfaces (7, 8). Butler (26) has established indeed that donor densities strongly decrease upon anodical aging, due to electromigration of the donors in the depletion layer. Besides the nonlinearity, an important difference is to be noted. The measured capacitances are much smaller for the aged electrodes, while acid treatments lead to capacitances that are larger than the initial capacitances (6, 8). It should be mentioned in passing that the initial capacitances also lead to nonlinear Mott-Schottky plots, which indicate decreasing donor densities towards the surface (8). These initial capacitances were measured on NaOH-etched surfaces (8), of which defect chemical aspects have been discussed above. It has been proposed that during acid treatments of NaOH-etched and subsequently H_2 -reduced TiO_2 electrodes protons cross the interface as hydrogen atoms. Once inside the crystal they donate their electron to the conduction band (8). As electrons in the conduction band at the surface are assumed to cause some reduction of the protons in the electrolyte, the net effect is the introduction of protons on interstitial sites in the crystal, leaving the net n-type semi-conductivity unaltered (8). This in fact violates the condition for electroneutrality for both the crystal and the electrolyte solution. It is known that the flatband potential of oxidic semiconductors varies with about 60 mV/pH unit. This variation is to be related with chemically bonded OH-groups on the surface of the semiconductor in contact with an aqueous electrolyte. The dissociation of these surface hydroxyl groups is pH dependent (6). This also indicates that the mechanism underlying the capacitance increase upon acid treatment could be more complicated than proton injection from the electrolyte. Irrespective of the mechanism, acid treatment does not restore the linearity to the Mott-Schottky plots in the studies reported by Harris and co-workers (7, 8), while it does in the study reported by Tomkiewicz (6). This author ascribes the nonlinearity to a change in the potential of the Helmholtz layer due to the presence of surface states on a matte, NaOH-etched TiO_2 surface. The smaller slope of the linear Mott-Schottky plot, and consequently the larger capacitances after acid treatment, were ascribed to a different roughness factor due to mild etching effects. This approach suggests a relation between the density of the surface states, and the surface roughness, but this has not been explored in the reported study (6). Recently, Ullman (27) has shown that the surface-state model needs some revision. Instead, a plausible alternative would be a thin surface layer with a smaller donor density, thus bringing about a general concordance between the results reported by Wilson *et al.* (7) and Tomkiewicz (6).

Modified Mott-Schottky Equations

From the preceding section it is apparent that rough surfaces and nonuniform donor densities may be inherently related with chemical etching and mechanical polishing procedures. Even smooth TiO_2 surfaces appeared matte after hydrogen reduction due to thermal etching (28).

Rough electrodes have actual interfacial areas ($A = A_0 + \Delta A$) which are greater than the geometrically determined surface areas (A_0). The edge of the depletion layer inside the crystal follows the surface roughness for small values of the electrode potential. For large values the edge of the depletion layer will approach A_0 . Following Goodman (29) it can be shown that under these circumstances the following Mott-Schottky equation holds

$$C_{sc}^{-2} = \frac{2(1 - 2\Delta A/A_0) \left(\phi_{sc} - \frac{kT}{e} \right)}{\epsilon\epsilon_0 e N_D A_0^2} + \frac{4\alpha \left(\phi_{sc} - \frac{kT}{e} \right)^2}{\epsilon\epsilon_0 e N_D A_0^3} \quad [8]$$

where α represents $[dA/d(\phi_{sc} - kT/e)]_{V=V_{FB}+kT/e}$.

The Mott-Schottky plot will be concave upward. However, for small $(\phi_{sc} - kT/e)$ values the plot will be linear, and may be used to determine V_{FB} . A reliable value for N_D will be hard to obtain. Tomkiewicz (9) reported a practically linear Mott-Schottky plot for a TiO_2 electrode polished to $0.3 \mu m$ finish for potentials up to 3V. With Eq. [1] he obtained the value $5.9 \times 10^{19}/cm^3$ for N_D . In this situation $L_D \ll 0.3 \mu m$. Consequently, the surface roughness is considerable. A small value for α , and $d\Delta A/d(\phi_{sc} - kT/e) \approx 0$ are reasonable assumptions. The Mott-Schottky plot will be virtually linear indeed with a slope $2(1 - 2\Delta A/A_0)/\epsilon\epsilon_0 e N_D A_0^2$. The donor density as calculated with Eq. [1] need then be multiplied by a factor $(1 - 2\Delta A/A_0)$ in order to obtain a correct though smaller donor density. This may, as stated before, not be the electrode's bulk donor density as reduction induces a greater donor density in the deformation layer (4, 5, 7) Concave curves have also been reported (9).

The aging experiments reported by Butler (26) reveal a rather sharp edge to exist between the surface layer with smaller donor density and the bulk of the electrode. Figure 1 shows a schematic representation of the nonuniform donor distribution in aged TiO_2 (26). Here $N_{D,s}$ is the donor density in a surface layer with thickness δ_1 , while $N_{D,l}$ is the donor density for $x > \delta_1$. If a deformation layer with depth $\delta_2 (> \delta_1)$ is present, $N_{D,l}$ will not be equal to the bulk donor density $N_{D,b}$, i.e., $N_{D,l} > N_{D,b}$. For small potentials $L_D < \delta_1$. Equation [1] can then be used to calculate $N_{D,s}$. For $\delta_1 < L_D < \delta_2$ the following modified Mott-Schottky equation holds, where the surface at $x = 0$ is assumed to be flat (30)

$$C_{sc}^{-2} = \frac{2}{\epsilon\epsilon_0 e N_{D,l} A^2} \left(\phi_{sc} - \frac{kT}{e} \right) - \frac{N_{D,s} - N_{D,l}}{N_{D,l}} \left(\frac{\delta_1}{\epsilon\epsilon_0 A} \right)^2 \quad [9]$$

For still larger potentials the situation $L_D > \delta_2$ may occur. The Mott-Schottky equation is then given by (30)

$$C_{sc}^{-2} = \frac{2}{\epsilon\epsilon_0 e N_{D,b} A^2} \left(\phi_{sc} - \frac{kT}{e} \right) - \frac{N_{D,s} - N_{D,l}}{N_{D,b}} \left(\frac{\delta_1}{\epsilon\epsilon_0 A} \right)^2 - \frac{N_{D,l} - N_{D,b}}{N_{D,b}} \left(\frac{\delta_2}{\epsilon\epsilon_0 A} \right)^2 \quad [10]$$

The relations hold provided that Helmholtz layer, and Gouy-layer effects, and the capacitance of the counter-electrode need not be taken into consideration.

In Fig. 2 we have plotted calculated Mott-Schottky plots using $N_{D,s} = 5 \times 10^{19}/cm^3$, $N_{D,l} = 2 \times 10^{19}/cm^3$, $N_{D,b} = 8 \times 10^{18}/cm^3$, $\epsilon = 173$, $\epsilon_0 = 8.8542 \times 10^{-14} F/cm$, $\delta_1 = 48 nm$, and $\delta_2 = 70 nm$. The lower linear curve in Fig. 2 has been calculated using Eq. [1], and

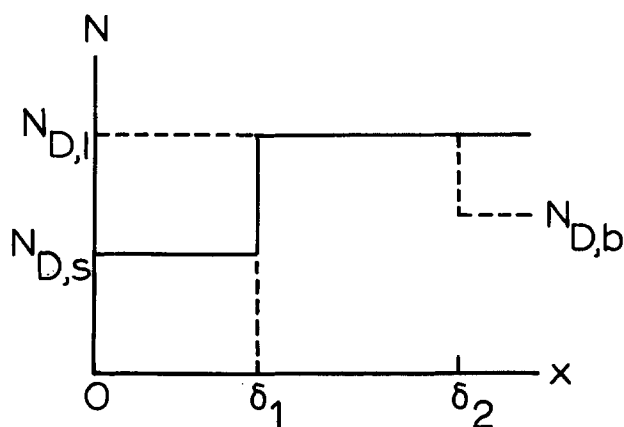


Fig. 1. Schematic nonuniform donor density in aged TiO_2 . See text.

$N_D = N_{D,l}$ and represents the uniform doping level situation. The nonlinear curve in Fig. 2 (solid line) has been calculated using Eq. [1] with $N_D = N_{D,s}$ for $L_D \leq \delta_1$ and Eq. [9] for $L_D \geq \delta_1$. If the situation as depicted also in Fig. 1 were to occur, i.e., $N_{D,s} < N_{D,l}$ and $N_{D,s} < N_{D,b} < N_{D,l}$ we find three linear portions in the curve, for which the slopes are governed with increasing potential by $N_{D,s}$, $N_{D,l}$ and $N_{D,b}$, respectively. In this case ($L_D \geq \delta_2$); Eq. [10] was used to calculate the (dotted) line in Fig. 2.

Taking into account Ullman's (27) discussion on the low C_{sc} values reported by Tomkiewicz (6), the solid lines in Fig. 2 represent the TiO_2 data before and after

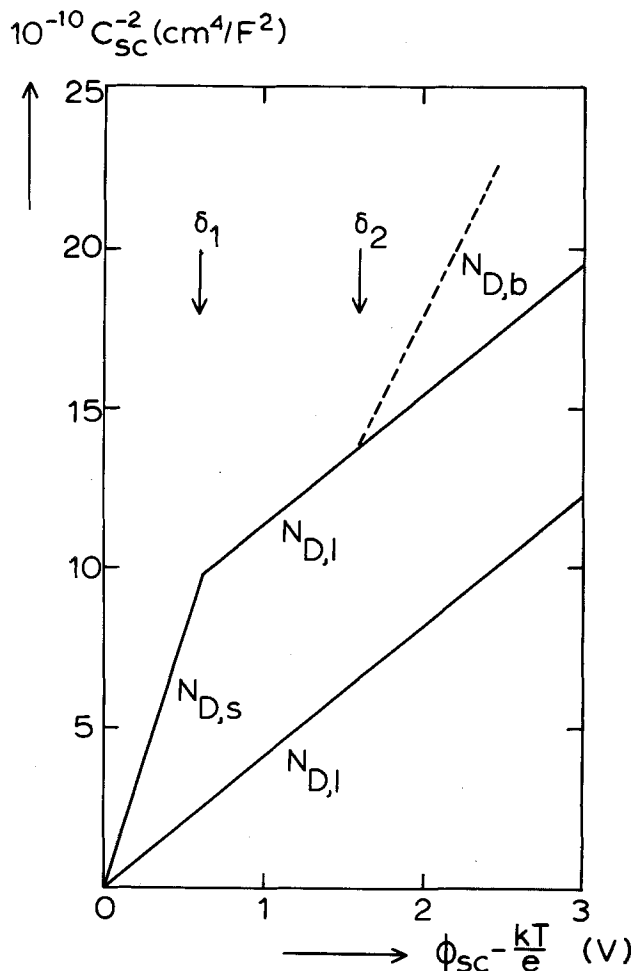


Fig. 2. Mott-Schottky plot for uniform doping level ($N_{D,l}$), and for nonuniform doping level ($N_{D,l} > N_{D,s}$; $N_{D,s} < N_{D,b} < N_{D,l}$). See text.

treatment with a mild etchant (6). Upon using $N_D = 3.8 \times 10^{19}/\text{cm}^3$ (6) and Eq. [2] we arrive at the removal of a surface layer of only 22 nm in order to account for the observed data (6) on the basis of the present nonuniform donor-density model. This model provides a reasonable alternative for the nonlinearity as being due to surface states, and linearity after acid treatment as being caused by different roughness factors (6). In fact, Eq. [8] reveals that the surface roughness would have increased after the acid treatment in order to account for the larger C_{sc} values, and this is not to be expected when TiO_2 is washed with a mild acid etchant.

Harris and co-workers (7, 8) obtained nonlinear Mott-Schottky plots as given by the solid line in Fig. 2 only after prolonged etching in $(\text{NH}_4)_2\text{SO}_4\text{:H}_2\text{SO}_4$ mixtures at 240°C, or after anodical aging, while other nonlinear Mott-Schottky plots [Fig. 7 in Ref. (7)] indicate a situation $N_{D,s} > N_{D,b}$ and $N_{D,l} < N_{D,b}$. This latter situation leads to nonlinearity which is also observed in the C_{sc} data reported by Tomkiewicz (9) for a smooth NaOH-etched TiO_2 electrode [Fig. 9 in Ref. (9)], whereby it must be noted that side reactions during etching in molten NaOH as discussed in the preceding section do account for the opposite situation, i.e., $N_{D,s} < N_{D,l}$. Nonlinearity which would be concordant with a situation $N_{D,s} > N_{D,b}$ and $N_{D,l} < N_{D,b}$ can also be accounted for by assuming nonuniform surface potentials as already indicated by Vos and Krusemeijer (4,5). This will be dealt with in more detail in a forthcoming paper (30).

Nonlinearity indicating $N_{D,s} < N_{D,l}$, $N_{D,b}$ is frequently encountered. Although several of the discussed defect chemical aspects may provide a rationale for having these nonuniform donor densities it must be noted that, in general, experimenting with TiO_2 photoanodes will cause electromigration of the donors (26), thereby contributing to the situation $N_{D,s} < N_{D,l}$, $N_{D,b}$. Equations [9] and [10] cannot only be used in clarifying anodical aging experiments quantitatively, they can also contribute to our insights into deformation layers having donor densities different from the bulk, reoxidation influences, cathodical loading of TiO_2 electrodes with hydrogen (4, 5, 8, 19), or TiO_2 electrodes modified by surface dopants (31).

Acknowledgment

The authors gratefully acknowledge Dr. A. Mackor for discussions and critically reading of the manuscript.

Manuscript submitted Aug. 21, 1980; revised manuscript received Dec. 1, 1980.

Any discussion of this paper will appear in a Discussion Section to be published in the December 1981

JOURNAL. All discussions for the December 1981 Discussion Section should be submitted by Aug. 1, 1981.

Publication costs of this article were assisted by the State University, Utrecht.

REFERENCES

1. W. Schottky, *Z. Phys. Chem.*, **113**, 367 (1939); **118**, 539 (1942).
2. N. F. Mott, *Proc. Roy. Soc. London, Ser. A*, **171**, 27 (1939).
3. P. J. Boddy, *This Journal*, **115**, 199 (1968).
4. K. Vos, Thesis, State University, Utrecht (1976).
5. K. Vos and H. J. Krusemeijer, *J. Phys. C.*, **10**, 3893 (1977).
6. M. Tomkiewicz, *This Journal*, **126**, 1505 (1979).
7. R. H. Wilson, L. A. Harris, and M. E. Gerstner, *ibid.*, **126**, 844 (1979).
8. L. A. Harris, M. E. Gerstner, and R. H. Wilson, *ibid.*, **126**, 850 (1979).
9. M. Tomkiewicz, *ibid.*, **126**, 2220 (1979).
10. M. P. Dare-Edwards and A. Hamnett, *J. Electroanal. Chem. Interfacial Electrochem.*, **105**, 283 (1979).
11. E. C. Dutoit, F. Cardon, and W. P. Gomes, *Ber. Bunsenges. Phys. Chem.*, **80**, 475 (1976).
12. R. H. Wilson, *J. Appl. Phys.*, **48**, 4292 (1977).
13. "Gmelin Handbuch der Anorganischen Chemie," Vol. 41, 8th ed., p. 391, Weinheim (1951).
14. F. Cardon, *J. Appl. Phys.*, **33**, 3358 (1962).
15. H. Lux, K. Renauer, and L. Betz, *Z. Anorg. Allg. Chem.*, **310**, 306 (1961).
16. D. J. Barber and E. N. Farabough, *J. Appl. Phys.*, **36**, 9, 2803 (1965).
17. G. J. Hill, *Brit. J. Appl. Phys. (J. Phys. D.)*, **1**, 1151 (1968).
18. A. von Hippel, J. Kalnajs, and W. B. Westphal, *J. Phys. Chem. Solids*, **23**, 779 (1962).
19. D. S. Ginley and M. L. Knotek, *This Journal*, **126**, 2163 (1979).
20. F. A. Kröger, "The Chemistry of Imperfect Crystals," North Holland, Amsterdam (1964).
21. G. A. Acket and J. Volger, *Physica*, **32**, 1680 (1966).
22. P. F. Chester, *J. Appl. Phys.*, **32**, 2233 (1961).
23. Y. Nakazumi, K. Suzuki, and T. Yagina, *J. Phys. Soc. Jpn.*, **17**, 1806 (1962).
24. W. M. Hirthe and J. O. Brittain, *J. Am. Ceram. Soc.*, **45**, 546 (1962).
25. O. W. Johnson, *J. Appl. Phys.*, **35**, 3049 (1964).
26. M. A. Butler, *This Journal*, **126**, 339 (1979).
27. D. L. Ullman, *ibid.*, **127**, 1321 (1980).
28. R. U. E. 't Lam, J. Schoonman, and G. Blasse, *Ber. Bunsenges. Phys. Chem.*, Submitted for publication.
29. A. M. Goodman, *J. Appl. Phys.*, **34**, 329 (1963).
30. K. Vos and J. Schoonman, To be published.
31. P. de Korte, R. U. E. 't Lam, J. Schoonman, and G. Blasse, *J. Inorg. Nucl. Chem.*, In press.

Technical Notes



Luminescence of Silica Glasses Containing Copper

J. M. Brownlow and I. F. Chang*

IBM Thomas J. Watson Research Center, Yorktown Heights, New York 10598

This note reports the conditions under which monovalent copper imparts photoluminescence to silica glass. A strong permanent luminescence is produced

by Cu paired with Al. Cu paired with OH imparts a moderate activity which fades with time of heating at 1200°C. The activity with Cu and Ga together is weak but permanent. No activity was found when each of 20 other potentially active dopants was paired with Cu.

* Electrochemical Society Active Member.
Key words: copper, photoluminescence, dopants.

Samples for a composition survey of the Cu-Al-Si oxide system were made by mixing silicic acid with Cu and Al nitrates in water, drying, and reacting at 1200°C in wet nitrogen gas for 15 min. The compositions with the greatest activity were near 0.5 mole percent (m/o) Cu₂O and bridged a range of Al₂O₃ content from 1 to 10 m/o. Heating beyond 1 hr at 1200°C did not cause intensity loss. The light output of the brightest compositions in this ternary was enhanced by a factor of 2 by the addition of 10% B₂O₃.

The intensity of the emitted light under 254 nm excitation was comparable to that of commercial P15 (ZnO) phosphor. The emission spectrum is given in Fig. 1. This curve is similar to the results of Claffy and Schulman (1) who added Cu, Na, and Ca oxides to several alumina-silica mixtures. They suggested that crystalline phases may be the seat of the luminescence. This was not supported by experiments in which the bright luminescence of 1200°C reaction products was

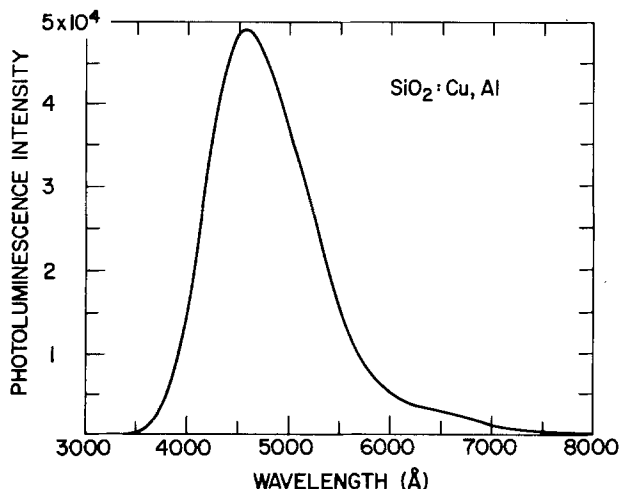


Fig. 1. Photoluminescence intensity (arbitrary units) vs. wavelength (Å) for SiO₂ glass containing 0.5 m/o Cu₂O, 10% Al₂O₃.

found to be preserved when they were melted to a clear glass in an oxy-propane flame. This glass has a broad absorption band at 250 nm.

The conjecture that monovalent copper is part of the active center was supported by two findings. First, reactions carried out under neutral or slightly reducing conditions (wet N₂ or wet N₂ with 1-2% H₂) which minimize divalent copper produced brighter samples than reactions carried out in air. Second, a bright phosphor was produced when some of the Na⁺ in Vycor¹ brand glass (96% SiO₂) was replaced by Cu⁺ by electrolysis at 730°C.

The cooperative effect of bound water with Cu⁺ was the focus of the following trials. Products of the initial reaction between silicic acid and cuprous oxide were moderately luminescent. However, this activity and that of Cu-doped Vycor nearly vanished after holding one or two days at 1200°C. Silica glass laboratory ware made from natural quartz exhibits a similarly fugitive weak blue luminescence which could be imitated in glasses synthesized from silicic acid with about 50 ppm Cu₂O. Anhydrous silica and cuprous oxide did not produce active products with or without addition of B₂O₃.

It remains to be explained why Al, Ga, or OH ions must be present to enable Cu⁺ to impart luminescence to silica glass.

Manuscript received Oct. 17, 1980.

Any discussion of this paper will appear in a Discussion Section to be published in the December 1981 JOURNAL. All discussions for the December 1981 Discussion Section should be submitted by Aug. 1, 1981.

Publication costs of this article were assisted by IBM Corporation.

¹ Corning Glass Company.

REFERENCE

1. E. W. Claffy and J. H. Schulman, *This Journal*, **119**, 400 (1952).

A Method for Rapidly Screening Polymers as Electron Beam Resists

Robert G. Brault* and Leroy J. Miller*

Hughes Research Laboratories, Malibu, California 90265

The search for new, improved electron resists could be greatly facilitated by having methods available for rapidly determining sensitivity (Q) and contrast (γ). Improved sensitivity is necessary to obtain desirable throughput, and good contrast is a necessary (although not a sufficient) condition for achieving high resolution (1). Such a rapid test would be useful not only for screening candidate resists, but also for accelerating subsequent process development, such as the optimization of developer composition, development time, and bake conditions. To evaluate Q and γ accurately, it would be desirable to have a large number of areas exposed at different doses, as many as 50 per decade, in the dose range of interest. The exposed areas should be as small as practical to minimize exposure time. Finally, a rapid, accurate method for measuring the thickness of each area on the developed wafer is

needed. This paper describes a test method in which writing the test pattern takes about 30 min and making the required thickness measurements takes about another 30 min.

Test Method

The test pattern consists of a 10 × 10 matrix of squares each 25 μm on a side (see Fig. 1) and separated from other squares by 50 μm. The dosage received by each square is varied systematically by increasing the dwell time linearly along one axis of the matrix and increasing the point spacing linearly along the other. The squares are large enough to eliminate the proximity effect as a variable if the thickness measurement is made at the center, where the losses due to electron scattering are compensated for by scattering contributions from the surrounding area. Each matrix covers a range of dosages extending over more than two orders of magnitude. By writing two, three, or four such matrices at different beam cur-

* Electrochemical Society Active Member.

Key words: electron resists, sensitivity, contrast, positive resists, negative resists.

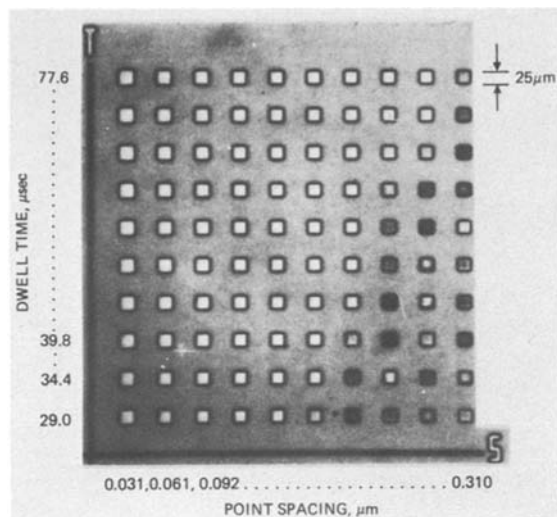


Fig. 1. Image of the test matrix in resist. At 3×10^{-11} A, the exposures range from 2.42×10^{-4} C/cm² at upper left to 9.05×10^{-7} C/cm² at lower right.

rents, an extremely wide range of exposures can be obtained with very small dose increments. When different processing procedures are to be tested, several such sets of matrices can be exposed on a single wafer with a single pump-down to achieve further time savings.

After the exposed image has been developed, the sensitivity can be estimated by examining the matrix under a microscope. With positive resists, the squares that are developed out cleanly can easily be identified, and the sensitivity is estimated as the minimum dose required to produce a cleaned-out square. In the case of negative resists, a distinct value for the sensitivity cannot be determined by simple visual examination, since the sensitivity is generally taken as the dose required to produce an image with a thickness that is some specific fraction of the thickness of the undeveloped resist.

A plot of the normalized thickness (t_N) vs. the log of the exposure ($\log E$) is a more convenient and accurate method for determining both sensitivity and contrast of both positive and negative resists. This plot requires knowing the thickness of the residual resist in underexposed squares. But since the squares are too small to allow the thickness to be measured easily by a mechanical stylus technique, we investigated using a Nanospec AFT microarea film thickness gauge for this purpose.¹ This instrument measures thickness by recording the spectrum of visible light reflected from the coated silicon wafer and comparing it with standard data previously recorded for similar films and stored in memory. Its unique advantage is that it can measure the thickness of extremely small areas, the minimum spot size being $3.5 \mu\text{m}$ in diameter. For our purposes, a spot diameter of $9 \mu\text{m}$ was most suitable.

Among the programs currently available with the Nanospec are some for measuring the thickness of resist on both oxidized and unoxidized silicon surfaces. Since these programs had been prepared for positive photoresists, the validity of applying them to the measurement of other polymeric coatings was open to question. Therefore, 17 silicon wafers coated with poly(methyl methacrylate) (PMMA) in thicknesses ranging from 150 to 19,500Å were prepared and measured using the mechanical stylus technique with a Sloan Dektak surface profile measuring system as well as with the Nanospec photoresist-on-silicon program. As shown in Fig. 2, the Nanospec values are linear with the Dektak thicknesses. The linear-regression plot has

¹ Available from Nanometrics, Incorporated, Sunnyvale, California.

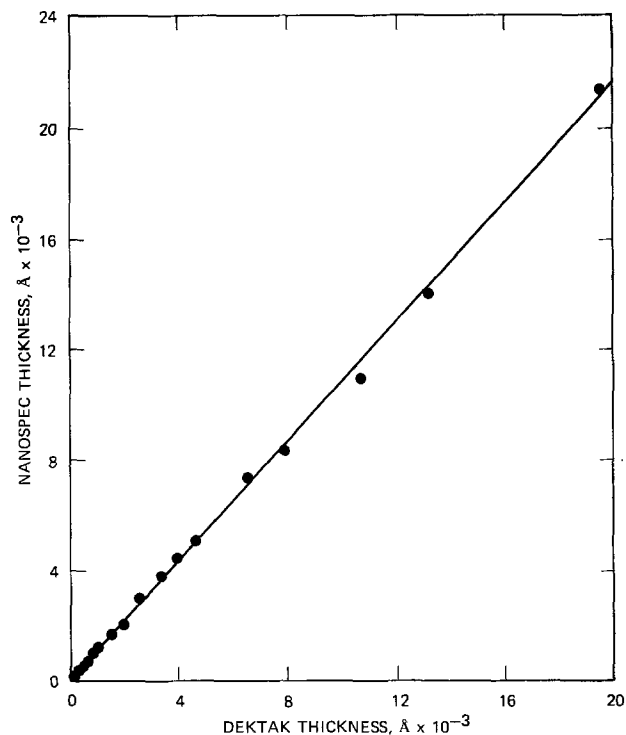


Fig. 2. Correlation of PMMA thickness measurements using the Sloan Dektak and the Nanospec AFT with the program for photoresist on silicon. The anticipated error in Dektak measurements is about $\pm 2.5\%$.

a slope of 1.078 and a y intercept of 83.4Å. We are interested primarily in the normalized thickness t_N , which can be determined accurately from the formula $t_N = (t - b)/(t_0 - b)$, where t and t_0 are the thicknesses obtained with the Nanospec program for the exposed and unexposed resist, respectively, and b is the reading obtained in an area of the same wafer with no resist.

To obtain the data reported in this paper for positive resists, we routinely determined t_0 as the average value for the unexposed areas at the four corners of the developed image of the matrix. Consequently, whenever there was any thinning of the unexposed resist during development, t_N was based on the thinned resist. Values for b were the averages of about four individual measurements on squares that received substantially different, but obviously excessive, doses and that clearly were developed completely and cleanly. For negative resists, we used a t_0 value obtained before the image was developed, and the values for b were the average of several readings on cleaned areas of the developed wafer.

The surface of underexposed and partially developed resist coatings is often quite nonuniform, being uneven in thickness or having a bubbly appearance. In spite of this, the Nanospec generally yields internally consistent data that can be plotted to form smooth curves. Occasionally there are some exceptions, however, where the Nanospec measurement is obviously faulty. The overall quality is illustrated by the plot of t_N as a function of $\log E$ for poly(*tert*-butyl methacrylate) (PtBMA) shown in Fig. 3. In most cases, it is a simple matter to ignore the results that are clearly erroneous. Frequently, other areas that received approximately the same exposure to radiation are satisfactory for Nanospec measurements.

Screening Results

These methods were used to determine the electron beam sensitivity and contrast for 10 polymethacrylate positive resists and 14 negative resists, half of which were polystyrene derivatives. Many of the development conditions used in this study were previously re-

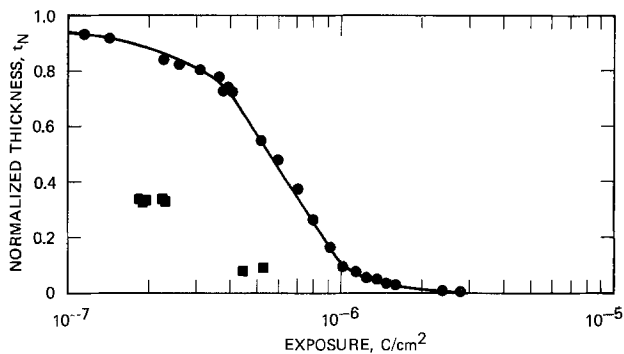


Fig. 3. Typical plot of normalized thickness as a function of the log of the exposure to 20 keV electrons. Resist is poly(*tert*-butyl methacrylate), 0.5 μm thick on silicon, baked 4 hr at 147°C *in vacuo*, and developed with 33% methyl ethyl ketone: 67% acetonitrile for 30 sec.

ported in the literature. In the case of positive resists, conditions were chosen to produce a limited amount of thinning of the unexposed resist (about 5%, but up to about 20% in one case). No attempt was made to optimize the development procedure. Tables I and II provide pertinent data on the polymethacrylates, the methods of development, and the results. Usually, the sigmoidal curves that were obtained from the t_N vs. $\log E$ plots were similar to those of PMMA and PtBMA shown in Fig. 4. No effort was made to eliminate the "toe" at the higher doses just short of those resulting in clean development. Additional rinses with weak solvents, particularly spray rinses, are sometimes useful in minimizing the size of the toe. The sensitivity (Q) determined by simple inspection of the matrix corresponded to the end of the toe. A second value for the sensitivity (Q_{ext}) could be obtained by extrapolating the approximately linear, descending portion of the sigmoidal curve to the baseline. Q_{ext} may be assumed to be the limiting value for the sensitivity if one is completely successful in removing the toe with appropriate rinses or a light plasma etch. The size of the toe varied with the resist and the development method.

Table I. Source and molecular weights of polymethacrylates evaluated as positive electron resists, $[\text{CH}_2\text{C}(\text{CH}_3)(\text{COOR})]_n$

| RESIST | SOURCE ^a | $\bar{M}_W \times 10^{-5}$ ^b | \bar{M}_W/\bar{M}_N ^b |
|---|---------------------|---|------------------------------------|
| CH ₃ | DuP | 4.00 | 2.86 |
| C ₂ H ₅ | SPP | 3.42 | 2.05 |
| <i>n</i> -C ₃ H ₇ | Pos | 13.0 | 3.27 |
| <i>i</i> -C ₃ H ₇ | Pos | 6.58 | 3.12 |
| <i>n</i> -C ₄ H ₉ | HRL | 2.52 | 1.19 |
| <i>s</i> -C ₄ H ₉ | Pos | 0.89 | 2.47 |
| <i>t</i> -C ₄ H ₉ | | | |
| HIGH \bar{M}_W | HRL | 30.7 | 1.48 |
| LOW \bar{M}_W | Pos | 1.17 | 2.05 |
| ϵ -C ₆ H ₁₁ | HRL | 6.81 | 3.23 |
| C ₆ H ₅ CH ₂ | HRL | 15.0 | 3.04 |
| C ₆ H ₅ | HRL | 13.9 | 3.28 |
| CF ₃ CH ₂ | HRL | 0.44 | 1.68 |

^a Ald = ALDRICH CHEMICAL CO., MILWAUKEE, WI
 DuP = DUPONT CO., PLASTICS DEPT., WILMINGTON, DE
 HRL = SYNTHESIZED AT HUGHES RESEARCH LABORATORIES
 Pos = POLYSCIENCES, INC., WARRINGTON, PA
 SPP = SCIENTIFIC POLYMER PRODUCTS, INC., WEBSTER, NY

^b DETERMINED BY GEL PERMEATION CHROMATOGRAPHY ON MICROSTYRAGEL COLUMNS USING TETRAHYDROFURAN SOLUTIONS.

Table II. Processing parameters, sensitivity, and contrast of polymethacrylate electron resists

| RESIST | PREBAKE | | DEVELOPMENT | | | SENSITIVITY ^a | | γ |
|--|-----------|----------|--------------------------------|-----------|-------------------------------------|--------------------------|------------------|----------|
| | TIME, hr | TEMP, °C | DEVELOPER SOLVENT ^b | TIME, sec | PERCENTAGE THINNING (OR THICKENING) | Q | Q _{EXT} | |
| CH ₃ | 1/3 (AIR) | 145 | 3:1 IPA: MIBK | 30 | 0 | 198 | 184 | 7.59 |
| C ₂ H ₅ | 4 (VAC) | 160 | 2:1 IPA: MA | 15 | 5 | 55.1 | 47.3 | 2.98 |
| <i>n</i> -C ₃ H ₇ | 4 (VAC) | 160 | 2:1 IPA: MA | 30 | 2 | 49.5 | 24.2 | 11.6 |
| <i>i</i> -C ₃ H ₇ | 4 (VAC) | 160 | 2:1 IPA: MA | 15 | (6) | 46.1 | 39.1 | 3.30 |
| <i>n</i> -C ₄ H ₉ (ON SiO ₂) | 0.5 (AIR) | 110 | 30:1 IPA: MIBK | 60 | 21 | 2.99 | | |
| <i>s</i> -C ₄ H ₉ | 4 (VAC) | 160 | MA | 15 | 6 | 197 | ~34 | ~15 |
| <i>t</i> -C ₄ H ₉ | | | | | | | | |
| HIGH \bar{M}_W | 15 (VAC) | 160 | CARB | 180 | (3) | 31.6 | 22.0 | 11.3 |
| LOW \bar{M}_W (ON SiO ₂) | 4 (VAC) | 160 | CARB | 180 | (3) | 14.2 | 13.5 | 5.76 |
| ϵ -C ₆ H ₁₁ (ON SiO ₂) | 4 (AIR) | 115 | 1:1 IPA: MIBK | 60 | 4 | 45.8 | 40.5 | 1.68 |
| C ₆ H ₅ CH ₂ | 4 (VAC) | 155 | 2:1 MEK: IPA | 30 | 0 | 299 | 147 | 1.68 |
| C ₆ H ₅ | 4 (VAC) | 155 | DIOXANE | 30 | 2 | 38.0 | 36.0 | 3.91 |
| CF ₃ CH ₂ (ON SiO ₂) | 1 (AIR) | 115 | 3:1 IPA: MIBK | 15 | 6 | 30.7 | 24.0 | 1.34 |

^a TESTED ON SILICON OR, WHERE INDICATED, ON SiO₂-COATED SILICON WAFERS.

^b CARB = CARBITOL OR 2-(2-ETHOXYETHOXY)ETHANOL
 IPA = ISOPROPYL ALCOHOL
 MA = METHYL ALCOHOL
 MEK = METHYL ETHYL KETONE
 MIBK = METHYL ISOBUTYL KETONE

^c SENSITIVITY Q WAS OBTAINED BY INSPECTION OF THE MATRIX WITH THE OPTICAL MICROSCOPE; Q_{EXT} WAS OBTAINED BY EXTRAPOLATION OF THE LINEAR PORTION OF THE t_N VERSUS LOG E CURVE TO THE BASELINE WHERE $t_N = 0$.

This is also illustrated in Fig. 4 with the curves for poly(*iso*-propyl methacrylate) and poly(*sec*-butyl methacrylate). The particularly prominent toe in the curve for the latter resist was due to a discontinuous coating of polymer droplets that remained on the incompletely developed surface. The tendency to leave this type of residue was responsible for the large but poorly defined value for the contrast γ .

Values for γ were generally obtained as the absolute value of the slope of a least squares plot of "acceptable" data points. The subjective selection of the points that were acceptable was made from an examination of the graph, and it excluded the obviously erroneous readings previously discussed as well as those points clearly belonging to the regions in which the plot curves away from the straight-line, descending portion of the plot. Usually, the acceptable points were for t_N values ranging from 0.1 at the lower end to 0.4-0.8 at the upper end, depending on how quickly the curve deviated from a straight line at decreasing exposures.

Data for four of the resists included in Table II were derived from coatings on oxidized silicon wafers. The Nanospec measurements on these wafers were made using a program designed for photoresist on SiO₂-coated silicon, where the thickness of the SiO₂ was determined separately on a clean wafer and entered as a constant into the memory. The procedure used and

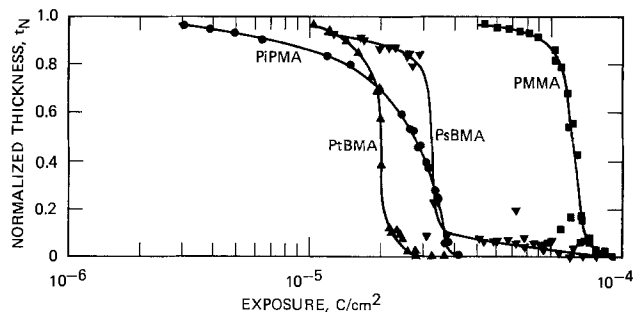


Fig. 4. Illustrative plots of t_N vs. $\log E$ for poly(alkyl methacrylates). The alkyl groups are: PtBMA, *tert*-C₄H₉; PIPMA, *iso*-C₃H₇; PsBMA, *sec*-C₄H₉; and PMMA, CH₃.

Table III. Source and molecular weights of polymers evaluated as negative electron resists

| RESIST | MATERIAL SOURCE ^a | $\bar{M}_W \times 10^{-5}$ ^b | \bar{M}_W/\bar{M}_N ^b |
|--|------------------------------|---|------------------------------------|
| POLY (DIALLYL PHTHALATE) | Pos | 0.99 | 3.5 |
| POLY (METHYL VINYL KETONE) | SPP | 2.05 | 2.50 |
| POLY (VINYL ACETATE) | Pos | 2.83 | 3.07 |
| POLY (VINYL CINNAMATE) | Pos | 1.42 | 2.77 |
| POLY (VINYL CHLORIDE) | UCC | 0.60 | 1.66 |
| POLYVINYLPIRROLIDONE | Pos | ($\bar{M}_N = 4 \times 10^4$) | — |
| POLY (GLYCIDYL METHACRYLATE-CO-ETHYL ACRYLATE) | Mead | — | — |
| POLYSTYRENE | Ald | 3.21 | 3.80 |
| POLY (4-CHLOROSTYRENE) | Pos | 2.90 | 2.97 |
| POLYVINYLTOLUENE (MIXED ISOMERS) | Pos | 2.77 | 4.76 |
| POLY (VINYL BENZYL CHLORIDE) (60/40 MIXTURE OF ORTHO/PARA) | Ald | 1.24 | 3.74 |
| POLY (4-BROMOSTYRENE) | Ald | 5.34 | 2.01 |
| POLY (4-ISO-PROPYLSTYRENE) | Ald | — | — |
| POLY (4-TERT-BUTYLSTYRENE) | Pos | 0.6 | 2.03 |

^a Ald = ALDRICH CHEMICAL CO., MILWAUKEE, WI
HRL = SYNTHESIZED AT HUGHES RESEARCH LABORATORIES
Mead = MEAD CHEMICAL CO., ROLLA, MO
Pos = POLYSCIENCES, INC., WARRINGTON, PA
SPP = SCIENTIFIC POLYMER PRODUCTS, INC., WEBSTER, NY
UCC = UNION CARBIDE CORP., NEW YORK, NY

^b MOLECULAR WEIGHTS WERE DETERMINED BY GEL PERMEATION CHROMATOGRAPHY AT HUGHES, EXCEPT FOR THE VALUE IN PARENTHESIS, WHICH WAS THE VENDOR'S CHARACTERIZATION.

Table IV. Processing parameters, sensitivity, and contrast of negative electron resists

| RESIST | BAKE | | DEVELOPMENT | | SENSITIVITY, C/cm ² (Q _{0.5}) | γ |
|--|-------------|-------------|----------------------|--------------|--|------|
| | TEMP, °C | TIME, hr | SOLVENT ^a | TIME, sec | | |
| POLY (DIALLYL PHTHALATE) | 50 (VAC) | 16 | 1:1 CB:AA | 30 | 3.0×10^{-6} | 0.83 |
| POLY (METHYL VINYL KETONE) | 50 (VAC) | 16 | MIBK | 30 | 1.7×10^{-4} | 1.29 |
| POLY (VINYL ACETATE) | 150 | 0.5 | TOL | 30 | 4.4×10^{-5} | 0.94 |
| POLY (VINYL CINNAMATE) | 50 (VAC) | 60 | MEK | 30 | 3.0×10^{-6} | 1.15 |
| POLY (VINYL CHLORIDE) | 50 (VAC) | 60 | CB | 30 | 7.4×10^{-5} | 0.86 |
| POLYVINYLPIRROLIDONE | 150 | 0.5 | WATER | 30 | 4.1×10^{-5} | 0.66 |
| POLY (GLYCIDYL METHACRYLATE-CO-ETHYL ACRYLATE) | 90 | 0.25 | COP DEV | 15 | 4.2×10^{-7} | 0.72 |
| POLYSTYRENE | 60 (VAC) | 16 | CB | 30 | 4.6×10^{-5} | 1.43 |
| POLY (4-CHLOROSTYRENE) | 50 (VAC) | 16 | CB | 30 | 4.6×10^{-6} | 1.82 |
| POLYVINYLTOLUENE | 50 (VAC) | 1 | CB | 30 | 4.6×10^{-5} | 1.43 |
| POLY (VINYL BENZYL CHLORIDE) | 50 (VAC) | 1 | CB | 30 | 2.0×10^{-6} | 2.1 |
| POLY (4-BROMOSTYRENE) | 60 (VAC) | 1 | CB | 15 | 1.7×10^{-6} | 1.89 |
| POLY (4-ISO-PROPYLSTYRENE) | 90 (VAC) | 1 | TOL | 5 | 8.1×10^{-5} | 1.20 |
| POLY (4-TERT-BUTYLSTYRENE) | 90 (VAC) | 1 | TOL | 5 | 2.9×10^{-4} | 2.88 |

^a AA = AMYL ACETATE
CB = CHLOROBENZENE
COP DEV = COP DEVELOPER, INCLUDING 2 RINSES
MEK = METHYL ETHYL KETONE
MIBK = METHYL ISOBUTYL KETONE
TOL = TOLUENE

the results obtained were otherwise normal in all respects.

One resist, poly(*n*-butyl methacrylate), was so un-even after development that we could not obtain

enough acceptable points to prepare a plot of t_N vs. $\log E$. This was true for tests on both oxidized and unoxidized silicon wafers.

The results from screening a series of negative resists are presented in Tables III and IV. Some of the data in these tables were previously reported for comparative purposes (2). In the case of negative resists, we report Q_{50} , the dose required to give a film thickness of 50% of t_0 , as the sensitivity. Although other values have also been used to represent sensitivity, this value seems reasonable to us for comparing experimental resists since the contrast curve of some resists starts to turn over soon after that value. The contrast is the maximum slope of the ascending portion of the curve and is usually the same as the tangent to the curve at $t_{0.5}$. It is sometimes impossible to obtain as many closely spaced points at the low dose end of negative resist plots as one would desire, because these squares do not adhere and frequently are removed during development.

The test method described is a quick and convenient method for screening polymers as resist materials. It can also be used in the preliminary stages of process development to help establish reproducible conditions for such processing variables as baking time and temperature, developer composition, and development time. We have found that the reproducibility in measuring the thicknesses of individual squares with the Nanospec AFT is about 5-20Å. The measurements of four different matrix sets of PMMA made over a period of a week gave sensitivity measurements that range from 1.84 to 1.91×10^{-4} C/cm², and γ values from 7.01 to 7.59.

Acknowledgments

We thank Mr. Vincent Coates and Mr. Russell Lewis of Nanometrics, Incorporated for their assistance and hospitality in permitting us to use the Nanospec AFT microarea film thickness gauge in their facility. We also wish to acknowledge the help of Mr. Philip Coane and Ms. Judi Thompson for making the electron beam exposures, the consultation of Dr. Edward Wolf and Dr. Faik Ozdemir, and the technical assistance of Mrs. Camille Van Ast and Mr. Willis Smith.

Manuscript submitted Oct. 7, 1980; revised manuscript received Dec. 10, 1980. This was Paper 265 presented at the St. Louis, Missouri, Meeting of the Society, May 11-16, 1980.

Any discussion of this paper will appear in a Discussion Section to be published in the December 1981 JOURNAL. All discussions for the December 1981 Discussion Section should be submitted by Aug. 1, 1981.

Publication costs of this article were assisted by Hughes Research Laboratories.

REFERENCES

1. K. Murase, M. Kakuchi, and S. Sugawara, "Newly Developed Electron and X-Ray Resist Materials," International Conference on Microlithography, pp. 261-269, Paris, France, June 21-24, 1977.
2. R. G. Brault and L. J. Miller, Regional Technical Conference, Society of Plastics Engineers, Ellenville, N.Y., Oct. 10-12, 1979; *Poly. Eng. Sci.*, **20**, 1064 (1980).

Anodic Dissolution Technique for Preparing Large Area GaAs Samples for Transmission Electron Microscopy

Jack P. Salerno,* John C. C. Fan,** and Ronald P. Gale**

Lincoln Laboratory, Massachusetts Institute of Technology, Lexington, Massachusetts 02173

This paper describes a novel technique that uses anodic dissolution for thinning relatively large, selected areas of single crystal or polycrystalline GaAs to prepare self-supporting, uniformly thin foils for transmission electron microscopy (TEM). Samples containing low-angle grain boundaries have been prepared by this technique from poly-GaAs grown by the horizontal Bridgman method. By TEM examination of these samples we have obtained the first electron micrographs showing the structure of grain boundaries in bulk GaAs.

Development of the new technique was motivated by our investigation of GaAs photovoltaic solar cells. Although we have achieved conversion efficiencies exceeding 20% (AM1) for single crystal GaAs cells (1), these devices will be too costly for large-scale applications unless much less expensive fabrication techniques are developed. Lower fabrication costs should be possible for cells utilizing polycrystalline GaAs thin films deposited on low cost substrates, but the efficiencies so far obtained for such cells are too low to permit their practical use. Consequently, there is considerable interest in achieving a detailed understanding of the role played by grain boundaries in reducing photovoltaic efficiency, with the objective of developing passivation techniques for minimizing their adverse effects on cell performance. While the electronic properties of grain boundaries in GaAs have been investigated in some detail (2), there has been little study of grain boundary microstructure, although this structure should have an important influence on the electronic properties (3). Furthermore, our investigations of electroluminescence and cathodoluminescence in poly-GaAs have shown variations in radiative recombination emission from different grain boundaries and, in some cases, along a particular boundary. Similar effects have been reported for polycrystalline Ge (4) and Si (5).

For these reasons it is desirable to study the structure of selected grain boundaries in conjunction with an analysis of their electronic properties. The new preparation technique was developed to facilitate this type of investigation by permitting TEM observation of preselected areas containing the boundary regions of interest. Since foils produced by this technique appear to be of uniform thickness over areas significantly greater than the boundary regions, they should also be suitable for direct analysis of compositional variations among grain boundaries by high spatial resolution ($\sim 50\text{\AA}$) x-ray and electron-energy-loss spectroscopy (6).

Before giving a detailed description of the foil preparation procedure, we will review the more conventional thinning techniques, chemical etching and ion-beam milling. Chemical (or electrochemical) etching, which is usually performed by a jet process (7-9), is very rapid, generally taking only a few minutes. However, this technique yields a perforated foil with a tapered thickness profile. Usually only the region very close to the perforation is transparent to the electron

beam, and control of the lateral position of this region is very difficult. This combination of small sample area and poor lateral positioning makes chemical etching unsatisfactory for the types of grain boundary studies described above. Chemical etching in conjunction with mechanical processing has produced small area foils at preselected locations in single crystal Si (10) but has not been applied to polycrystalline samples of brittle compound semiconductors.

Ion milling (11) is generally performed at very slow rates to avoid sample heating and thermal dissociation. The systems generally available produce a small foil area in an uncontrolled location. These problems were encountered in preparing TEM samples of GaAsP (12). It might be possible to produce large area foils by ion milling, but this would require elaborate equipment.

In contrast to chemical etching and ion milling, the anodic dissolution technique is moderately fast, readily controlled, and capable of producing uniformly thin foils over large preselected areas. The method is simple to use with both single crystal and polycrystalline samples.

To use the anodic dissolution technique, a GaAs wafer is first lapped with 2 μm grit, mechanochemically polished in Clorox to a thickness of 80-100 μm , and diamond sawed into square samples 2.5 mm on a side. The wafers used in this investigation were doped with Zn at concentrations of $\sim 10^{18}\text{ cm}^{-3}$. A sample selected for thinning is electroplated on one face (except for the region to be examined) with a layer of Au about 5 μm thick, then heated to 300°C for 1 sec to form an ohmic contact (1). A Pt wire is attached to the Au contact with conductive adhesive, and the sample is mounted contact-side-down on a glass slide with transparent wax. The area to be thinned is defined by covering the exposed surface with wax except for a circle, typically about 0.5 mm in diameter, opposite the region not plated with Au. The sample configuration is shown schematically in Fig. 1. Dissolution proceeds from the exposed surface toward the contact surface.

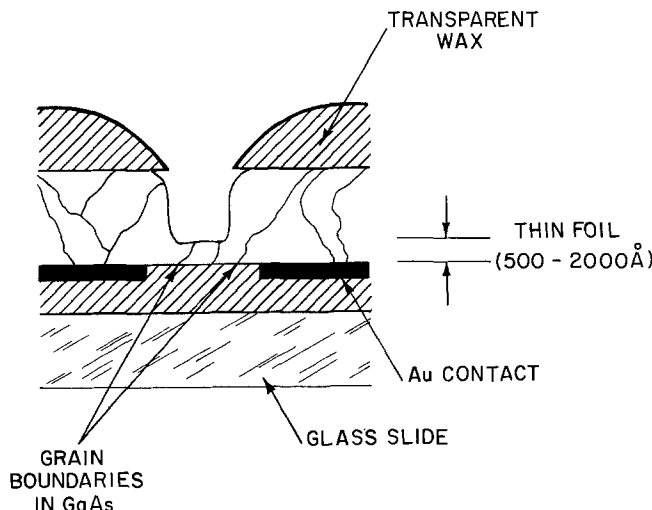


Fig. 1. Schematic diagram showing GaAs sample mounted for anodic dissolution.

* Electrochemical Society Student Member.
** Electrochemical Society Active Member.
Key words: anodic dissolution, grain boundaries, photovoltaics.

The sample forms the anode of an electrochemical cell with a large area Pt-mesh cathode. The electrolyte is the disodium salt of 0.1M 4-5-dihydroxy-m-benzenedisulfonic acid, which is very similar in composition to the Tiron solution used by Faktor and Stevenson (13) for characterization of GaAs by anodic dissolution but is preferred because of its lower cost and better availability. Measured polarization curves for the two solutions are virtually identical. Dissolution is performed at a constant current density of 15 mA/cm² with an etch rate of approximately 0.3 μm/min, so that 4-5 hr is usually required to achieve the desired sample thickness. It was observed that lower currents delineate crystal defects while higher currents tend to result in nonuniform etching unrelated to such defects.

The transmission of a low power (2 mW) He-Ne (6328Å) laser through the foil is monitored to determine when the dissolution process should be terminated. To reduce background noise the laser beam is chopped mechanically at 400 Hz, and the transmitted radiation is detected by using a lock-in amplifier to measure the output of an Si photodiode across a 1Ω load resistor. The circuit of the electrochemical cell is interrupted as soon as transmission is detected, which occurs when the foil is about 2000Å thick. The measurements are made intermittently, and the laser is shuttered between measurements, since the dissolution rate is increased by light so that continuous laser exposure would therefore result in nonuniform thinning.

During the dissolution process the GaAs surface becomes coated with a brown-black film, which has been shown by Auger analysis to be composed of As and O without detectable Ga. Unlike films formed by anodic oxidation of GaAs, this coating is not soluble in HCl. To remove the coating, after dissolution is complete the GaAs surface is anodically oxidized in a tartaric acid/propylene glycol solution (1, 14) and the oxide formed is dissolved in dilute HCl. The sample is then removed from the glass slide by dissolving the wax and cleaned in successive acetone and methanol baths.

Self-supporting thin foils of both single crystal and polycrystalline GaAs have been prepared by the procedure described. The single crystal samples usually can be thinned uniformly without perforation. Figure 2 is an optical transmission micrograph of such an unperforated sample with a thin region approximately 0.2 mm² in area and 2000Å thick. Although the transmitted intensity varies strongly within this region, TEM examination shows that the foil is essentially uniform in thickness, and Nomarski contrast microscopy of the etched surface reveals the same features as the optical transmission micrograph. Therefore, we attribute the observed variation in transmitted light intensity to scattering resulting from the roughness of the foil sur-

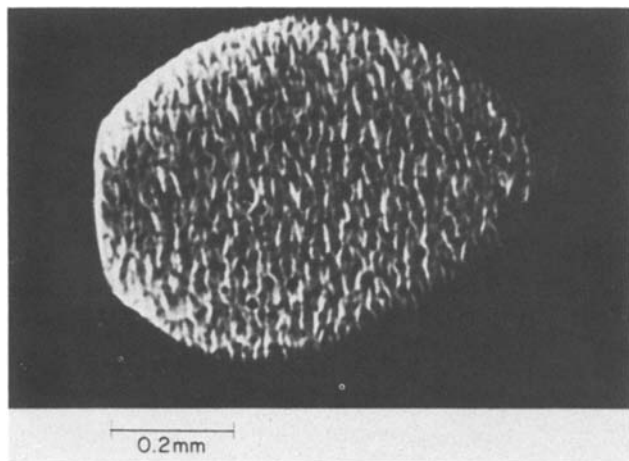


Fig. 2. Transmission optical micrograph of single crystal GaAs foil.

face. Samples given a better polish before anodic dissolution do not exhibit such scattering.

While foils prepared by anodic dissolution of polycrystalline GaAs are frequently perforated, they contain relatively large, uniformly thin areas. Micrographs of two grain boundaries in GaAs foils examined by TEM are shown in Fig. 3 and 4. The micrographs were taken using a two-beam condition and an accelerating potential of 125 kV. The structure of the grain boundary shown in Fig. 3, with dislocations separated by approximately 325Å, is indicative of a low-angle boundary with a misorientation angle of 0.7° for a Burgers vector of $a/2 \langle 110 \rangle$. This structure is similar to that of grain boundaries observed in cast Si (15). A grain boundary with a smaller misorientation angle ($<0.2^\circ$) is shown in Fig. 4. In this case the individual dislocations are separated by approximately 1470Å in a continuous matrix. This type of defect structure has been observed in heteroepitaxial GaAs/GaAlAs films where there is a lattice mismatch between substrate and epilayer (16). While grain boundaries observed in the present study were formed during melt growth of bulk GaAs, they should be similar in structure to grain boundaries in GaAs epitaxial layers grown on polycrystalline GaAs substrates, a class of materials with potential application in high efficiency/low cost photovoltaics. Polycrystalline GaAs solar cells fabricated from such layers have achieved efficiencies of 13% (AM1) (17).

In summary, an anodic dissolution technique has been developed for the preparation of relatively large area, uniformly thin foils of single crystal or polycrystalline bulk GaAs. Use of this technique has made

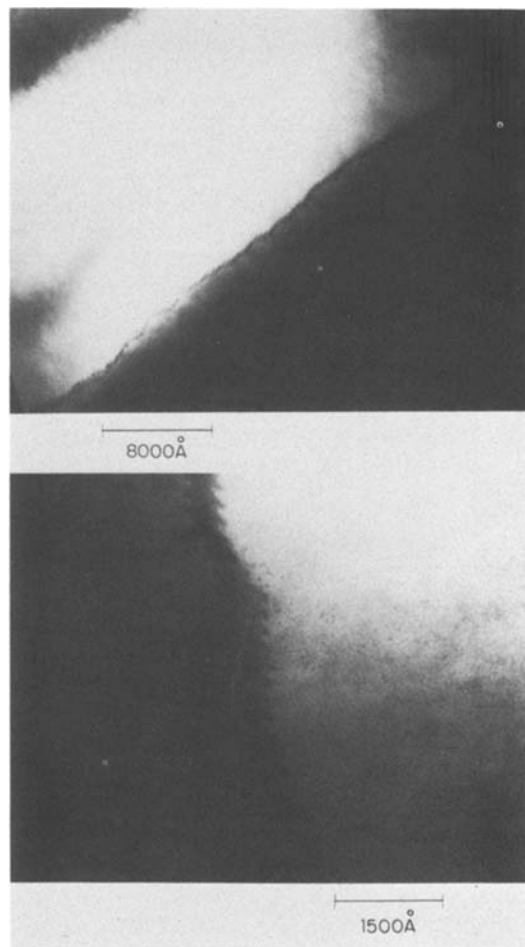


Fig. 3. TEM micrographs (two beam condition) of GaAs grain boundary with misorientation angle of 0.7°. Discrete dislocations composing the boundary are evident in the lower micrograph, which was taken at higher magnification.

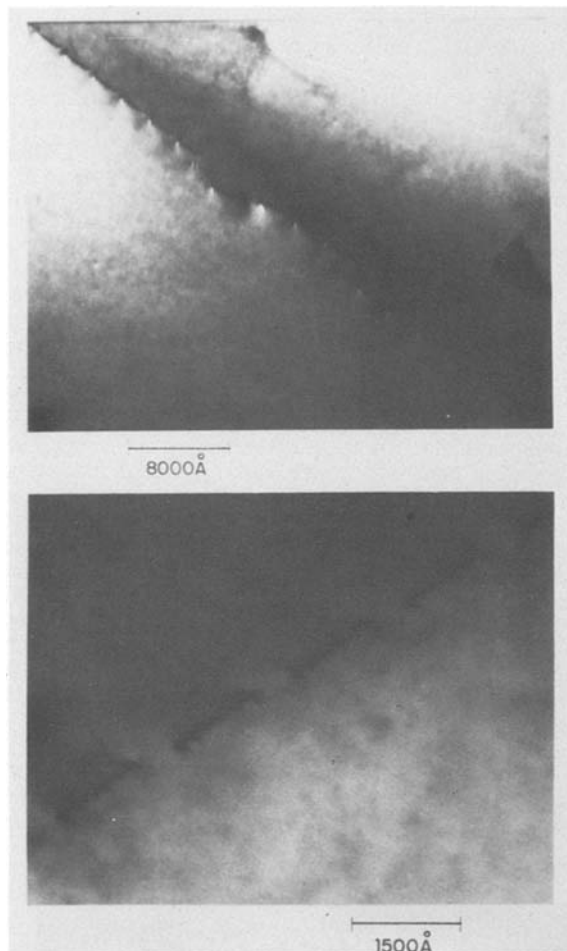


Fig. 4. TEM micrographs (two beam condition) of GaAs grain boundary with misorientation angle of $<0.2^\circ$.

it possible to carry out the first TEM observations of grain boundaries in GaAs. With appropriate modifications, the technique should be applicable to other semiconductors. Development of this technique is significant in that it permits TEM examination of selected grain boundaries, facilitating the investigation of relationships between the structural, compositional, and electronic properties of grain boundaries in photovoltaic materials.

Acknowledgments

We are grateful to A. F. Witt, J. G. Mavroides, A. J. Strauss, and H. J. Zeiger for many valuable discussions,

to M. C. Finn for performing the Auger analysis, and to O. Hurtado, S. Duda, and B. DiGiorgio for technical assistance. This work was supported by the Department of the Air Force.

Manuscript submitted Sept. 9, 1980; revised manuscript received Dec. 9, 1980.

Any discussion of this paper will appear in a Discussion Section to be published in the December 1981 JOURNAL. All discussions for the December 1981 Discussion Section should be submitted by Aug. 1, 1981.

Publication costs of this article were assisted by the Massachusetts Institute of Technology.

REFERENCES

1. J. C. C. Fan, C. O. Bozler, and R. L. Chapman, *Appl. Phys. Lett.*, **32**, 390 (1978).
2. For example, M. J. Cohen, J. S. Harris, Jr., and J. R. Waldrop, *Inst. Phys. Conf. Ser.*, **45**, 263 (1979); M. Spencer, R. Stall, L. F. Eastman, and C. E. C. Wood, *J. Appl. Phys.*, **50**, 8006 (1979).
3. H. F. Matare, "Defect Electronics in Semiconductors," Wiley, New York (1971).
4. For example, W. E. Taylor, N. H. Odell, and H. Y. Fan, *Phys. Rev.*, **38**, 867 (1952); R. K. Mueller, *J. Appl. Phys.*, **32**, 635 (1961).
5. For example, C. H. Seager and T. G. Castner, *J. Appl. Phys.*, **49**, 3879 (1978); D. Helmreich and H. Seiter, in "Proc. of 2nd European Community Photovoltaic Solar Energy Conf.," Berlin (1979).
6. J. B. Vander Sande and E. L. Hall, *J. Am. Ceram. Soc.*, **62**, 246 (1979).
7. G. R. Booker and R. Stickler, *Br. J. Appl. Phys.*, **13**, 446 (1962).
8. E. Biedermann and K. Brack, *This Journal*, **113**, 1088 (1966).
9. E. S. Meieran, *J. Appl. Phys.*, **36**, 2544 (1965).
10. A. Bohg, E. Mirboch, and L. Schneider, *J. Phys. E.*, **11**, 166 (1978).
11. M. S. Abrahams, C. J. Buiocchi, and M. D. Coutts, *Rev. Sci. Instrum.*, **39**, 1944 (1968).
12. J. S. Ahearn and C. Laird, *J. Mater. Sci.*, **12**, 699 (1977).
13. M. M. Faktor and J. L. Stevenson, *This Journal*, **125**, 621 (1978).
14. H. Hasegawa and H. L. Hartnagel, *ibid.*, **123**, 712 (1976).
15. T. F. Cizek, G. H. Schwuttke, and K. H. Yang, *IBM J. Res. Dev.*, **23**, 270 (1979).
16. C. H. Olsen and M. Ettenberg, "Crystal Growth," Vol. 2, C. H. L. Goodman, Editor, p. 44, Plenum, New York (1978).
17. G. W. Turner, J. C. C. Fan, R. P. Gale, and O. Hurtado, "Conf. Record of the 14th IEEE Photovoltaics Specialists Conference, 1980," p. 1530, IEEE, New York (1980).



Anodization and Sulfation of Tetrabasiclead sulfate in Sulfuric Acid: *In Situ* Monitoring of Electrode Surface Phases by Laser Raman Scattering

R. Varma,* G. Cook,* and N. P. Yao*

Argonne National Laboratory, Chemical Engineering Division, Argonne, Illinois 60439

The morphology of lead-dioxide prismatic crystallites in freshly "formed" positive plates of lead-acid batteries has been reported⁽¹⁾ to evolve to a coralloid state and subsequently degrade during continued charge-discharge cycling. Since tetrabasiclead sulfate, $4\text{PbO}\cdot\text{PbSO}_4$, (TBLS) had been observed⁽²⁾ to crystallize as large elongated prisms and undergo anodic conversion to a mechanically strong PbO_2 microstructure, which maintains a crystallite form similar to the original, the suggestion was made⁽³⁾ that the use of TBLS as the active material on positive plates may help increase the cycle life of lead-acid batteries.

During electrolytic formation of TBLS-pasted lead plates in H_2SO_4 , concomitant chemical sulfation reactions are anticipated, since TBLS has been shown⁽⁴⁾ to react readily with sulfuric acid. Therefore, the morphology of "formed" active material in such electrodes will depend directly on the continuously changing phase compositions of the sulfate active material as well as the kinetics of anodization reactions of the various single phase components. If rapid chemical sulfation reactions result in the formation of lead-sulfate, PbSO_4 , as a major component when the TBLS-pasted electrode is put in the electrolyte, the advantage of TBLS as a precursor of mechanically strong PbO_2 microstructure might be lost. A few experimental results identifying intermediates and products

of the sulfation as well as anodic oxidation reaction are described in this communication.

The surface-layer composition was monitored continuously in-situ⁽⁵⁾ by laser Raman scattering during anodization and open circuit stand of tetrabasiclead sulfate electrodes in $0.1\text{N H}_2\text{SO}_4$ in a 3-compartment spectroelectrochemical cell, shown in Figure 1. In order to suppress the interfering spectra due to H_2SO_4 and HSO_4^- specie 0.1N sulfuric acid was used as the electrolyte. Raman spectral transitions were observed ex-situ for $4\text{PbO}\cdot\text{PbSO}_4$ and a 1:1 mixture of $3\text{PbO}\cdot\text{PbSO}_4\cdot\text{H}_2\text{O}$ and $\text{PbO}\cdot\text{PbSO}_4$. These results and the published⁽⁵⁾ data for PbSO_4 are given in Table 1 for use as references in the interpretation of the experimental in-situ spectral data. The spectra in all cases were reproduced in duplicate runs. Analysis of electrode surface layers by ex-situ techniques, such as scanning electron microscopy and X-ray diffraction, provided additional supporting evidence for characterizing the phase compositions.

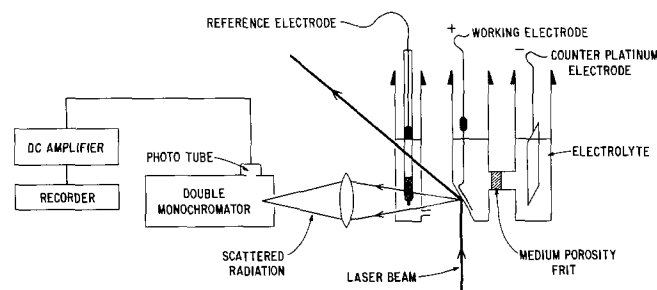


Figure 1. Experimental Setup for In-Situ Laser Raman Spectroscopy of Electrochemically Formed Surface Phases at Electrodes

*Electrochemical Society Active Member
Key words: In-Situ Raman Spectroscopy, Anodization of Tetrabasiclead-sulfate, Lead Cathode Formation, etc.

Table 1
Raman Spectrum* Observed Ex-Situ for Basic Leadsulfates

| Compound | Band Frequency, $\nu(\text{cm}^{-1})$ | Relative Intensity | Comment |
|---|---------------------------------------|--------------------|------------|
| Tetrabasicleadsulfate, $4\text{PbO} \cdot \text{PbSO}_4$ | 132 | W(sh) | unresolved |
| | 142 | VS | |
| | 969 | VS | |
| | 461 | W(sh) | |
| | 444 | M | |
| Tribasicleadsulfate Hydrate, $3\text{PbO} \cdot \text{PbSO}_4 \cdot \text{H}_2\text{O}$ | 132 | W | |
| | 142 | VS | |
| | 429 | M | |
| | 444 | M | |
| | 974 | S | |
| Monobasicleadsulfate $\text{PbO} \cdot \text{PbSO}_4$ | 132 | W | unresolved |
| | 142 | S | |
| | 962 | S | |
| | 444 | M | |
| | 434 | M | |
| Leadsulfate | 420 | VW(sh) | |
| | 977 | VS | |
| | 434 | M | |
| | 447 | M | |

Note: VS = Very Strong; S = Strong; M = Medium; W = Weak; VW - Very Weak
Sh = Shoulder

*The frequency recorded is average of observed frequencies extending over a range of $\pm 2 \text{ cm}^{-1}$

The spectrometer parameters such as the intensity of exciting laser light, scattering angle, scan rate, slit width, etc., were maintained at approximately the same level during each experimental run. In spite of these efforts the relative intensity of the Raman bands could not be used to estimate quantitatively the relative abundance of various phases in the surface layers. More sophisticated equipment would be required to obtain these estimates.

In-situ Raman spectra recorded at different time intervals during the anodization of TBLs-pasted lead electrode in 0.1N H_2SO_4 at 1.5 V vs. a $\text{Hg}/\text{Hg}_2\text{SO}_4$ reference are shown in Figure 2. Tetrabasicleadsulfate, characterized by Raman bands at 132, 142, 435, 444, 461, and 969 cm^{-1} (see Table 1), was observed to be converted partially, through the sulfation reaction into PbSO_4 , as shown by the appearance of a shoulder at 977 cm^{-1} on the 969 cm^{-1} band in the spectra obtained at 18 and 130 minutes (see Figure 2).

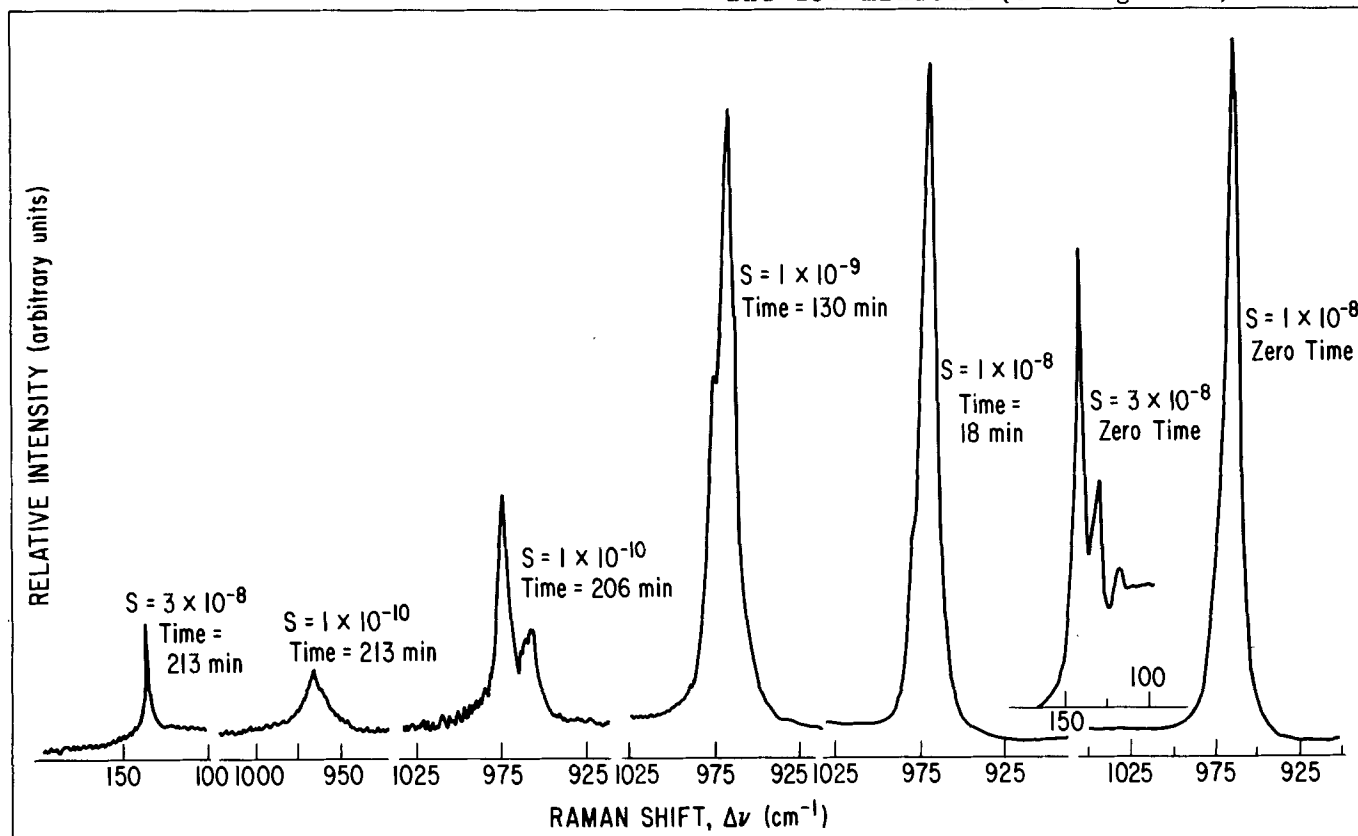


Figure 2. Laser Raman Scattering; In-Situ Spectra Observed on Tetrabasicleadsulfate Electrode During Anodization in 0.1N H_2SO_4 at 1.5 V vs. $\text{Hg}/\text{Hg}_2\text{SO}_4$

When compared with assigned spectra for $\text{PbO}\cdot\text{PbSO}_4$ and $3\text{PbO}\cdot\text{PbSO}_4\cdot\text{H}_2\text{O}$ (see Table 1), the Raman Bands observed at 142, 960, and 973 cm^{-1} at end of 206 minutes strongly suggest the presence of these compounds in the surface layers of the PbO_2 which was formed as a blackened mass. The entire electrode active material was observed to turn black by the end of 213 minutes. In-situ Raman spectra recorded at this time showed very weak bands at 142 cm^{-1} and 958 cm^{-1} suggesting the presence of $\text{PbO}\cdot\text{PbSO}_4$. No PbSO_4 band was observed. The black mass was found to be primarily $\beta\text{-PbO}_2$ by ex-situ X-ray analysis. In addition to providing an unambiguous identification of sulfate phases in the presence of $\beta\text{-PbO}_2$, these investigations also provided an indication of changes in composition of surface layers during anodization. The observed production of $\beta\text{-PbO}_2$ during "formation" in $0.1\text{N H}_2\text{SO}_4$ (specific gravity = 1.002) contrasts with the previous observation that (6) $\alpha\text{-PbO}_2$ was the major product from formation in $0.2\text{N H}_2\text{SO}_4$.

Tribasicleadsulfate, $3\text{PbO}\cdot\text{PbSO}_4\cdot\text{H}_2\text{O}$, monobasicleadsulfate, $\text{PbO}\cdot\text{PbSO}_4$ and leadsulfate, PbSO_4 , were observed in electrode surface layers during anodizations. Leadsulfate was observed to be the major product while $3\text{PbO}\cdot\text{PbSO}_4\cdot\text{H}_2\text{O}$ and $\text{PbO}\cdot\text{PbSO}_4$ were minor constituents. Close examination of the spectral data also suggests that the various leadsulfates are oxidized at different rates, at least for the particular experimental conditions a tentative ranking being $\text{TBLs} > \text{PbO}\cdot\text{PbSO}_4 > \text{PbSO}_4$.

Any pre-soak proceeding the "formation" process must invariably involve the chemical sulfation process. Therefore, Raman bands were continuously observed for 20 hours, during the open circuit acid-soaking of a tetrabasiclead-sulfate electrode. The continuous generation of PbSO_4 in the electrode surface layers, was observed as shown (see Figure 3) by the growth of Raman bands in the region of $975\text{-}977\text{ cm}^{-1}$ as well as at 436 and 444 cm^{-1} .

Since the height of the TBLs band at the end of 20 hours is still $\sim 50\%$ of the original height a significant proportion of tetrabasicleadsulfate apparently remains unreacted. Spectral representation of the dynamic sulfation process showing changes in composition over a period of time is shown in Figure 3. The spectrum recorded after 2 hours and 20 hours, showed definite shoulders, at $\sim 960\text{ cm}^{-1}$ on the $975\text{-}977\text{ cm}^{-1}$ band and at $\sim 420\text{ cm}^{-1}$ on the unresolved band in the region of $430\text{-}460\text{ cm}^{-1}$. It is likely that $\text{PbO}\cdot\text{PbSO}_4$ phase is present along with TBLs. The presence of this compound was confirmed by ex-situ X-ray diffraction analysis. It is possible that tribasicleadsulfate, $3\text{PbO}\cdot\text{PbSO}_4\cdot\text{H}_2\text{O}$, may be generated in the surface layers during the sulfation process. However, the spectral evidence for this intermediate is merely suggestive.

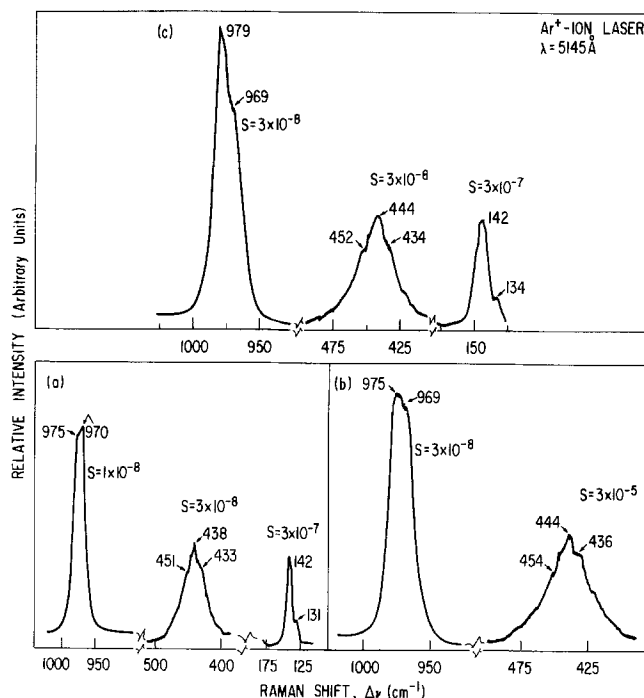


Figure 3. Laser Raman Scattering; In-Situ Spectra, Observed on Tetrabasicleadsulfate Electrode Immersed in $0.1\text{N H}_2\text{SO}_4$; After (a) 1 hour, (b) 2 hours, and (c) 20 hours

We have shown that tetrabasicleadsulfate is partially transformed

through chemical sulfation reactions in 0.1N H₂SO₄ into a mixture of PbSO₄ and PbO·PbSO₄, in the surface layers. This sulfation process seems to stop within 2-3 hours. The generation of PbO·PbSO₄ as a reaction intermediate during electrolytic "formation", at 1.5 V vs. Hg/Hg₂SO₄, of tetrabasic lead sulfate in 0.1N H₂SO₄ (specific gravity 1.002) is clearly established. The essential features of the spectra were found to be reproducible in replicate experiments.

The observance of PbO·PbSO₄ and 3PbO·PbSO₄·H₂O reaction intermediates in the surface layers during chemical sulfation and potentiostatic anodization is consistent with the Pourbaix diagram⁽⁷⁾ reported in literature only for conditions of high PH (PH > 8.0). Therefore, these conditions must prevail in the underlayers at the electrode and are due to electrolyte starvation. These results also show the multiphase structure of the surface layer. This structure must be considered when studying the kinetics of "formation" and the microstructure of PbO₂ active materials. The mechanisms of the conversion of the several sulfates into a PbO₂ matrix during plate "formation" should be understood to achieve durability for the positive plate active material during cycling, since it is likely that the PbO₂ microstructure depends upon the starting material. Further studies required to accomplish this work, are in progress.

ACKNOWLEDGEMENT

Financial support by the Division of Electrochemical Systems, Department of Energy, is hereby acknowledged. The authors extend their thanks and appreciation to the Chemistry Division at Argonne for allowing the use of their Raman spectrometer. Donation of samples of tetrabasic lead sulfate by C&D Battery Company is gratefully acknowledged. We acknowledge contributions made to this work by John Englert of Northwestern University as an undergraduate research participant.

REFERENCES

1. A. C. Simon, S. M. Caulder, and J. T. Stemmlie, *J. Electrochem. Soc.* 122, 461 (1975).
2. J. Burbank, *J. Electrochem. Soc.*, 113, 10 (1966).
3. R. V. Biagetti and M. C. Weeks, *The Bell System Technical Journal*, 149, 1305 (1970).
4. Y. B. Kamenev and A. I. Rusin, *Zh. Priklad. Khim*, 51, No. 7, 1481-1485 (1978).
5. R. Varma, C. A. Melendres, and N. P. Yao, "In-Situ Identification of Surface Phases on Lead Electrodes by Laser Raman Spectroscopy", *J. Electrochemical Society*, 127, 1416 (1980).
6. C. F. Yarnell and M. C. Weeks, *J. Electrochem. Soc.*, 126, 7 (1979).
7. P. Reutschi and R. T. Angstadt, *J. Electrochem. Soc.*, 105, 555 (1979).

Manuscript submitted Nov. 19, 1980;
revised manuscript received Jan. 28, 1981.

Publication costs of this article were
assisted by Argonne National Laboratory.

Initiation of Single Corrosion Pits by Focused Laser Illumination

Richard K. Ulrich* and Richard C. Alkire**

*Materials Research Laboratory and Department of Chemical Engineering,
University of Illinois, Urbana, Illinois 61801*

An experimental method has been developed for selective depassivation of small regions on an otherwise passive metal surface with use of focused laser radiation. Techniques for generating bare metal surfaces on passive metals have, to date, included scraping, straining, abrading, shearing, and fracturing (1). Each of these involves uncertainties in the initial active condition of the surface and/or gross mechanical disturbances. With the laser method, these uncertainties still exist but are confined to regions of time and/or distance which are orders of magnitude smaller than other methods.

Because the laser depassivation method allows generation of fresh metal surfaces under controlled and reproducible conditions, it should prove useful in fundamental studies on metal repassivation and localized corrosion. Preliminary results on pitting for example, are presented below.

While the corrosion behavior of laser modified surfaces has received some attention (2), no reports are known which use focused lasers for localized depassivation, although similar applications have been made previously to promote rates of maskless pattern electroplating (3).

APPARATUS

A tunable dye laser (Molelectron DL-II, Exiton dye type BBQ, 390nm) was pumped by a pulsed nitrogen laser (Molelectron UV-24) and provided a beam which was focused with an ordinary compound microscope lens (Bausch & Lomb) fitted with a 32 mm objective lens. The working distance between lens and (immersed) specimen was about 4 cm.

The metal specimen was held under conditions of controlled potential vs. SCE (Princeton Applied Research, 173-175-176 system). Flow of current after laser illumination was recorded either on a storage oscilloscope (Tektronix, 5103) or an X-Y recorder (Houston, 2000), depending upon the speed of the transient behavior under study.

*Electrochemical Society Student Member.

**Electrochemical Society Active Member.

The electrolytic cell was fabricated from Plexiglas in a manner which avoided crevice corrosion at the edges (4). The only materials in contact with the electrolyte were the specimen and the Plexiglas cell.

Post-electrolysis examinations were made with a scanning electron microscope (JEOL JSM-35C).

PROCEDURE

Iron specimens were cut from 2.54 cm stock (99.99%, Leico), polished with alumina down to 0.3 μm powder, and rinsed with acetone. Electrodes were passivated in 0.1 M $\text{Na}_2\text{B}_4\text{O}_7$ at 500 mV vs. SCE for one hour, whereupon the potential was changed to a value in the passive region (-300 to +860 mV vs. SCE) and sodium chloride solution was added to make $[\text{Cl}^-] = 0.01 \text{ M}$. Under these conditions of potential and chloride concentration, the surface would remain passive for long periods (hours) unless otherwise disturbed.

Pulsed laser radiation (15 ns duration, 30 μJ energy, 20 hz repetition rate) was focused to about 5 μm diameter. Usually, a single pulse was sufficient to initiate a single pit.

Pit growth could be arrested by interrupting the power supply. After a short time, the surface would repassivate, and a fresh pit could be initiated at a new site on the specimen.

Post-electrolysis examination of pits with an SEM included measurement of pit shape and volume. Pit depth was determined as a function of radial position by measurement of parallax movement of features inside the pit based on photomicrographs taken at 0° and 30° tilt.

RESULTS AND DISCUSSION

The diameter ascribed to a focused laser beam cannot be precisely defined, and depends on the gaussian energy profile across the beam (5). Also some pulse energy may be lost in focusing optics, by reflection from the metal surface, and from the plasma cloud which

develops. Based on a 5 μm beam diameter, this system produced 10^{10} W/cm^2 for 15 ns, or $150 \text{ J}/\text{cm}^2$.

Preliminary laser-pulse experiments were carried out with a specimen immersed in chloride-free borate solution, and held at potentials where corrosion did not occur. SEM photomicrographs indicated that the damaged area was a smooth crater of 5 to 10 μm diameter, and 1 to 2 μm depth. These observations are in reasonable agreement with others (6) who studied laser damage of iron in air.

Focused laser illumination causes locally chaotic events which include heating, melting, evaporation, and cavitation; these events may interfere with corrosion processes within microenvirons of time and space during repassivation. Also, the microscope lens eventually requires replacement owing to damage to the coating.

In the pitting results reported below, the pit volumes were appreciably larger than the original cavity created by the laser pulse. For example, within two seconds after pulsing, the pit volume had increased by more than 100 times the original laser cavity volume.

By comparing measurements of pit volume with the coulombs which passed during pit growth, it was found that the current efficiency during the pitting was $130 \pm 10\%$ based on $n=2$.

Figure 1 illustrates typical results for a series of six experiments repeated under identical conditions. The results indicate that data were reproducible to within a bandwidth of 5% of the average value. By using the least-squares method, these data were found to obey the empirical equation

$$I = 18 t^{0.53}$$

with an $r^2=0.998$, where I is the measured current (μA) and t is the time since initiation (s). As seen in Fig. 1, the above relation was obtained over the range of 20 to 400 seconds after pit initiation.

CONCLUSIONS

Focused laser illumination can trigger localized depassivation and subsequent pitting at pre-selected sites on an otherwise passive surface. The method creates damage in the vicinity of the beam impaction region, and creates chaotic events which briefly influence local events on a micro-scale. For corrosion processes which occur over large scales of time and distance in comparison with these initial events, the method gives highly reproducible results.

The depassivated region has a well

defined area which is orders of magnitude smaller than that produced by other depassivating techniques (1). The ohmic resistance associated with flow of current to the damaged region can be calculated accurately based on knowledge of the radius of the damaged region. The specimen remains immersed throughout an experiment, and there is ample working room in the vicinity of the specimen to place additional hardware nearby.

Investigations based on this method are in progress on metal repassivation and localized corrosion, and will be reported in future publications.

ACKNOWLEDGMENT

Research support was provided by the U.S. Department of Energy (Contract DE-AC02-76ER01198) and by an industrial fellowship from the IBM Corporation. J. Wehmer assisted in use of the Laser Laboratory of the School of Chemical Sciences.

REFERENCES

1. T. R. Beck, in "Electrochemical Techniques for Corrosion," R. Baboian, ed., p. 27, NACE, Houston (1977).
2. C. Draper, R. Woods and L. Meyer, *Corrosion*, **36**, 405 (1980).
3. R. J. von Gutfeld, et al., *Appl. Phys. Lett.*, **35**, 651 (1979).
4. R. K. Ulrich, M.S. Thesis, University of Illinois, in progress.
5. D. Maydan, *Bell Syst. Tech. J.*, **50**:6, 1761 (1971).
6. I. Kolalev, et al., *Int. J. Mass Spec. and Ion Physics*, **27**, 101 (1978).

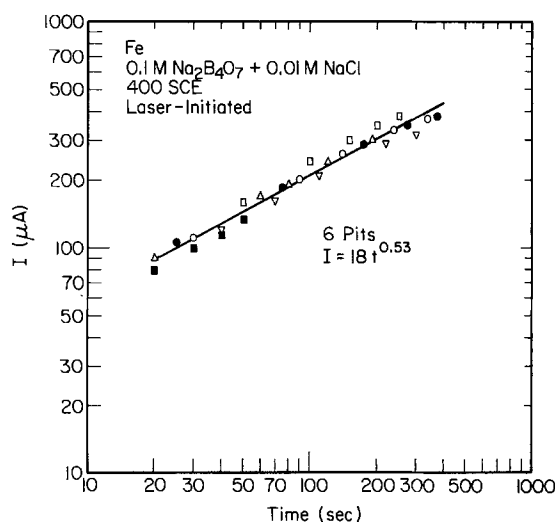


Figure 1: Reproducibility of measured corrosion current from six single pits produced under identical conditions.

Manuscript received Jan. 16, 1981.

Publication costs of this article were assisted by the University of Illinois.

A Modified Approach to Isothermal Growth of Ultrahigh Quality HgCdTe for Infrared Applications

P. Becla,* J. Lagowski,* H. C. Gatos,* and H. Ruda*

*Department of Materials Science and Engineering,
Massachusetts Institute of Technology, Cambridge, Massachusetts 02139*

Epitaxial layers of $\text{Hg}_{1-x}\text{Cd}_x\text{Te}$ on CdTe substrate were isothermally obtained with mirror-like surface morphology, high radial compositional uniformity, and outstanding electronic characteristics (e.g., electron mobility of the value of $500,000 \text{ cm}^2/\text{V-sec}$ for x in the vicinity of 0.15). The novel feature of the growth process was the utilization of Te-rich HgCdTe as a source material rather than HgTe (or stoichiometric $\text{Hg}_{1-x}\text{Cd}_x\text{Te}$) previously employed. Desired values of x were obtained by varying the composition of the source material and the growth temperature. Temperature high precision control and minimization of convection in the liquid (source) and vapor phases were achieved by employing a heat pipe.

.

HgCdTe is ideally suited for infrared detection and imaging, particularly in monolithic systems, such as charge coupled devices. Because of its broad phase diagram this material cannot be obtained by the standard growth techniques with a compositional uniformity and electronic properties required for high performance devices. This problem has to a great extent been resolved by the isothermal crystal growth method (1) also referred to as the "isothermal evaporation-condensation-diffusion" method. In this method CdTe is used as substrate and HgTe (or $\text{Hg}_{1-x}\text{Cd}_x\text{Te}$) as the source. Both substrate and source, x in a closed ampul, are brought to an elevated temperature (but below the melting point of the source). Isothermal growth occurs because the equilibrium vapor pressure of Hg and Te over the source is higher than over the substrate (1-8).

As discussed in a recent publication (9), upon stringent control of temperature and Hg pressure in the processing ampul, HgCdTe of a very good quality suitable for IR applications has been obtained by the standard isothermal growth method. In this communication a modified approach to isothermal growth is reported in which (through the utilization of tellurium-rich solution as a source material) the

control of the growth process and thus that of the composition, the morphology and electronic properties of the grown layers is enhanced.

Single crystal CdTe substrates of (111) orientation were polished and etched using standard procedures (5,6). Growth was carried out utilizing a spectral purity graphite boat with a rectangular well; the source material was placed at the bottom of the well on a sapphire plate, and the CdTe substrate on the top, closing the well. In this way, a confined space with the desired volume (typically a few cm^3) is defined for the growth system and free volume is minimized. The assembled graphite boat was placed in a quartz ampul which was then evacuated (below 10^{-5} torr) and sealed off. The ampul was positioned inside a heat pipe, which was placed in the constant temperature zone of a gold reflection-coated, resistance-heated furnace. The heat pipe maintained the temperature constant to within 0.02°C and the temperature gradients to within $10^{-2}^\circ\text{C}/\text{cm}$ in the growth system.

The source material utilized in the present study contained excess tellurium and varying amounts of Hg and Cd; thus, its composition can be expressed by $(\text{Hg}_{1-z}\text{Cd}_z)_{1-y}\text{Te}_y$, where z and y vary between 0 and 1. It should be noted that the source material utilized in previous studies (1-8) was characterized by $y = 0.5$.

The source material of the desired composition was prepared by carefully weighing the components and placing in a quartz ampul, which was evacuated to 10^{-5} torr, sealed, and heated to a temperature 20°C above the melting point of the selected composition; after homogenization at this temperature the solution was quenched rapidly to room temperature. The compositions employed were $0 < z < 0.2$ and $0.5 < y < 0.6$, which correspond to an energy gap of the grown layer in the vicinity of 0.1 eV, most desirable for IR applications ($\sim 10 \mu\text{m}$).

*Electrochemical Society Active Member.

Isothermal growth on CdTe substrates was carried out at two temperatures, 530°C and 575°C, for a period ranging between 20 and 48 hours. Typically the thickness of the grown layers ranged from 50 to 250 μm (the highest value corresponding to 48 hours' growth at 575°C). The layers were characterized with respect to crystallographic orientation, composition, compositional homogeneity, surface morphology, free carrier concentration, and mobility.

It was found that the surface composition of the layers grown at a given temperature was determined by the composition of the source material. However, in contrast to earlier findings (1-4), the surface composition of the grown layer was not identical to that of the source. The surface composition of the $\text{Hg}_{1-x}\text{Cd}_x\text{Te}$ layers grown with $(\text{Hg}_{1-z}\text{Cd}_z)_{1-y}\text{Te}_y$ sources is shown in Fig. 1a. Growth was performed at 575°C for 48 hours. The composition of the layers was determined with an Electron Microprobe and Energy Dispersive X-ray Analyzer.

Compositional profiles were determined on cross sections of the layers employing an electron microprobe; the results are shown in Fig. 1b. Consistent with the growth mechanism involving solid state diffusion, the grown layers exhibit composition gradients in the growth direction; however, no detectable compositional variations were found parallel to the surface.

Growth from a Te-rich source resulted in monocrystalline epitaxial layers with the same orientation as the substrate. On precisely oriented (111) substrates the layers exhibited high quality surfaces with a mirror-like appearance (Fig. 2). Deviations from (111) orientation affect adversely surface quality. Some of the macro- and microscopic defects in the substrate (grain boundaries, inclusions) usually propagate into the grown layer, although the surface quality of the grown layer is invariably superior to that of the substrate. The reasons for the superior surface morphology of the layers grown with a source containing excess tellurium are not clearly understood at present. It should be noted, however, that excess tellurium leads to noticeably slower growth rates than stoichiometric sources. Apparently, this change in growth kinetics has a highly beneficial effect on surface morphology. As seen from the Hall mobility data of Fig. 3, the as-grown layers with x values between 0.15 and 0.3 were intrinsic at room temperature; however, they became p-type at lower temperatures. Their

corresponding hole concentration ($N_A - N_D$) was between 10^{17}cm^{-3} and 10^{16}cm^{-3} , and the hole mobility between 215 and 600 $\text{cm}^2/\text{V-s}$ at 77 K.

In as-grown layers p-type conductivity is due to Hg vacancies which act as acceptor centers; their presence is unavoidable at growth temperatures exceeding 500°C. Standard annealing in an Hg atmosphere at temperatures below 300°C reduces vacancy concentration ($N_A - N_D$) and leads to n-type conduction. Typical carrier concentrations ($N_D - N_A$) at 77 K are as low as 10^{15}cm^{-3} in annealed layers. The high quality of these annealed layers is manifested by their high electron mobility which was found to be routinely as high as 500,000 $\text{V}/\text{cm}^2\text{s}$ at 77 K for $x = 0.15$; the temperature dependence of the Hall mobility for annealed layers of different compositions is shown in Fig. 3. It should be noted that HgCdTe layers grown by liquid phase epitaxy, now extensively employed, exhibit carrier mobilities about an order of magnitude smaller (10-12) than the isothermally grown layers with similar values of x .

Advanced IR applications (e.g., detector arrays) require HgCdTe layers of uniform surface composition and with as large surface dimensions as possible. The heat pipe employed ensures a perfectly constant temperature over a distance of about 2 inches, which in principle makes possible isothermal growth of the layers exceeding 2 square inches. A practical limitation encountered in the present study was the unavailability of large area CdTe substrates. The available melt-grown CdTe substrates contain large amounts of twins. The largest single crystal twin-free substrates available for this study were 1 inch \times 0.5 inch; these dimensions defined the largest dimension of isothermally grown HgCdTe layers.

ACKNOWLEDGEMENT

The authors are grateful to DARPA for financial support.

REFERENCES

1. Y. Marfaing, F. Bailly, G. Cohen-Solal, M. Rodot; United States Patent Office, No. 3,472,685, U.S. CL. 156-612 patented October 14, 1969.
2. G. Cohen-Solal, Y. Marfaing, F. Bailly, and M. Rodot, C.R. Acad. Sci. Paris 261, 931 (1965).
3. G. Cohen-Solal, Y. Marfaing, and F. Bailly, Rev. Phys. Appl. 1, 11 (1966).
4. Y. Marfaing, G. Cohen-Solal, and F. Bailly, J. Phys. Chem. Solids Suppl. 1, 549 (1967).

5. G.S. Almasi and A.C. Smith, J. Appl. Phys. 39, 233 (1968).
6. O.N. Tufte and E.L. Stelzer, J. Appl. Phys. 40, 4559 (1969).
7. F. Bailly, L. Svob, G. Cohen-Solal, and R. Triboulet, J. Appl. Phys. 46, 4244 (1975).
8. L. Svob, Y. Marfaing, R. Triboulet, F. Bailly and G. Cohen-Solal, J. Appl. Phys. 46, 4251 (1975).
9. T. Nguyen-Duy, J.C. Morand and G. Cohen-Solal, in Technical Digest 1980 Int'l Electron. Devices Meeting December 1980, Washington, D. C., I.E.E.E. New York 1980.
10. J.L. Schmit and J.E. Bowers, Appl. Phys. Lett. 35, 457 (1979)
11. M. Chu and C.C. Wang, J. Appl. Phys. 51, 2255 (1980).
12. C.C. Wang, S.H. Shin, M. Chu, M. Lanir, and A.H.B. Vanderwyck, J. Electrochem. Soc. 127, 175 (1980).

Manuscript received Feb. 6, 1981.

Publication costs of this article were assisted by the Massachusetts Institute of Technology.

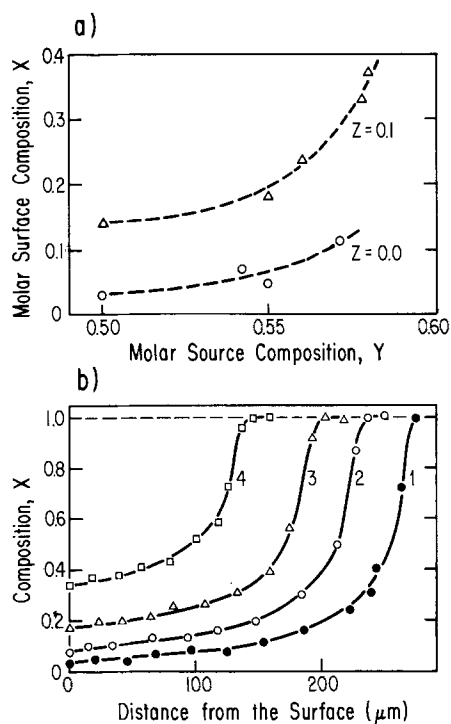


Fig. 1. Composition of $\text{Hg}_{1-x}\text{Cd}_x\text{Te}$ layers grown isothermally at 575°C for 48 hours; a) surface composition as a function of the source composition; b) compositional depth profiles; 1, 2, 3 and 4 correspond to source materials HgTe , $\text{Hg}_{0.45}\text{Te}_{0.55}$, $(\text{Hg}_{0.9}\text{Cd}_{0.1})_{0.45}\text{Te}_{0.55}$, and $(\text{Hg}_{0.9}\text{Cd}_{0.1})_{0.41}\text{Te}_{0.59}$, respectively.

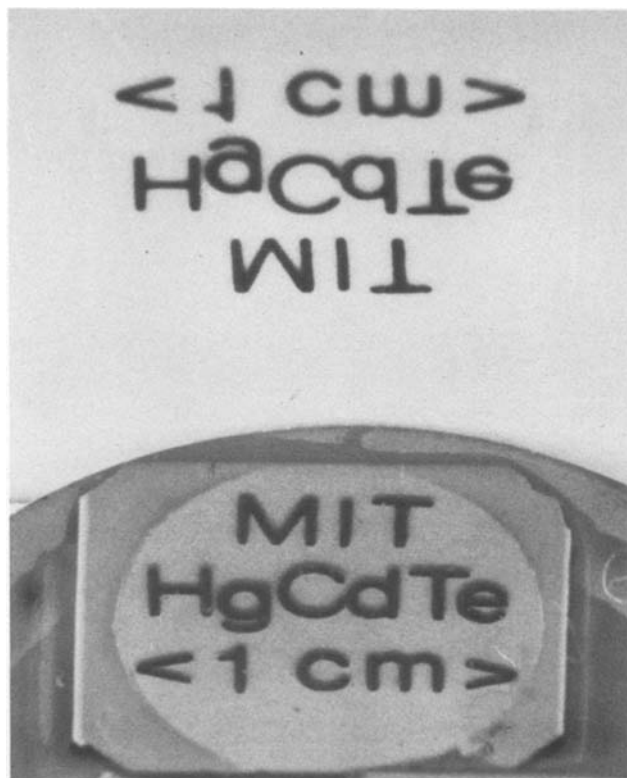


Fig. 2. A typical HgCdTe layer ($\text{Hg}_{0.8}\text{Cd}_{0.2}\text{Te}$); the reflection of an inverted sign demonstrates its specular characteristics.

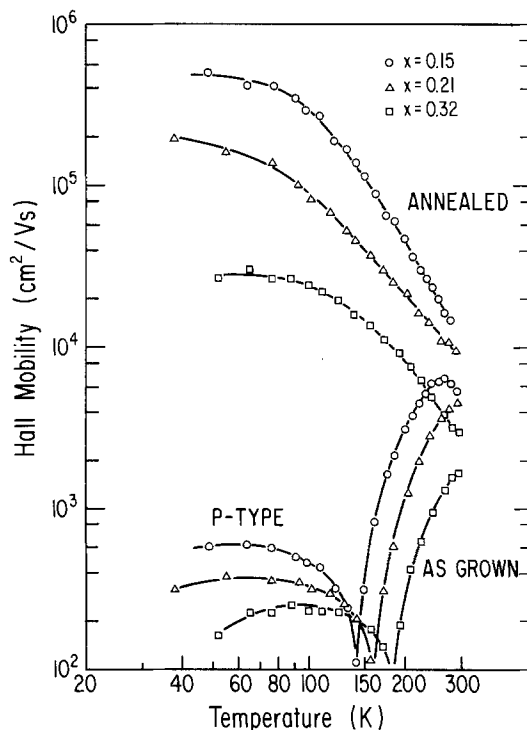


Fig. 3. Temperature dependence of the Hall mobility of as-grown (p-type) and annealed (n-type) layers of $\text{Hg}_{1-x}\text{Cd}_x\text{Te}$.

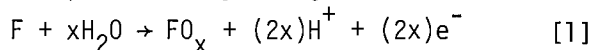
Hydrogen Generation from Glucose Depolarized Water Electrolysis

Michael R. St. John,* Alan J. Furgala, and Anthony F. Sammells*

Institute of Gas Technology, Chicago, Illinois 60616

With presently available technology, the only non-fossil fuel method of hydrogen generation is water electrolysis. Hydrogen produced by water electrolysis is restricted to specific application where variable high-quality hydrogen is required because its cost is typically several times more expensive than hydrogen obtained using fossil fuels. As is well known, the high cost of the electrolytic hydrogen is largely a consequence of the electrical power requirements which provides an obvious incentive to reduce the electrolysis cell voltage. Approaches for cell voltage reduction have been directed at either enhancing electrode kinetics resulting in reduced overpotential losses, particularly at the oxygen electrode, or by "depolarizing" the oxygen evolution reaction. The latter approach involves substitution of a reaction with a more cathodic reversible potential than that for oxygen.

Recent attempts exploring suitable depolarizing reactions have concentrated on the oxidation of fuel-like substances such as coal (1-4), SO_2 (5-7), and methanol (6). All such reactions can be represented by the general reaction -



where F is a fuel-like molecule which becomes oxidized to FO_x with the generation of hydrogen ions and electrons. The oxidation of a fuel-like molecule insures favorable thermodynamics in the form of a reversible potential more negative than oxygen evolution.

It is the purpose of this communication to suggest that materials derivable from biomass possess attractive properties as the depolarizer F in Equation 1 and to present cyclic voltammetric data on the biomass derivable material, glucose, which indicate its potential as a depolarizer. Possible advantages that biomass derived materials have are renewability and in many instances availability as waste products.

*Electrochemical Society Active Member

Key Words: Hydrogen, Glucose, Oxidation Depolarizer

In the course of a program to survey biomass materials for their depolarizing ability, glucose was chosen because of its abundance in the biosphere.

Cyclic voltammograms obtained in 12 w/o H_2SO_4 with and without 0.51 molal glucose are compared in Figure 1 over the potential range available to the electrolyte, at 23°C. A platinumized platinum working electrode was used with a sweep rate of 5 mV/s to approximate steady-state reaction conditions. In the absence of glucose, the 12 w/o H_2SO_4 electrolyte exhibits the well-documented surface reactions occurring on a platinum electrode upon cycling between these voltage limits (8). When the 12 w/o H_2SO_4 is made 0.51 molal in glucose, new anodic peaks were observed in the cyclic voltammograms as designated by the solid line in Figure 1. At ambient temperature the principal oxidation peaks observed in the anodic sweep are a sharp peak at +50 mV and large shoulder peak at around +510 mV, all potentials being measured versus $\text{Hg}/\text{Hg}_2\text{SO}_4$ in 12 w/o H_2SO_4 (+670 mV versus the reversible hydrogen electrode for comparison). These features are essentially the same as those reported for the oxidation of glucose on platinum foil in 1M H_2SO_4 (9). Not observed on the platinum foil was the broad anodic peak found upon sweeping cathodically, centered at -200 mV versus the $\text{Hg}/\text{Hg}_2\text{SO}_4$ reference.

Substantial changes in the cyclic voltammogram occur both qualitatively and quantitatively upon increasing the electrolyte temperature. Figure 2 compares the cyclic voltammograms under the same conditions as Figure 1, but at 92°C. The most striking qualitative change observed is transformation of the relatively sharp anodic peak at +50 mV found at 22°C, into a broad band spanning the potential range -50 mV to +200 mV at the higher temperature. In addition, the oxidation observed in the cathodic sweep has effectively coalesced with this band. The shoulder at +510 mV versus $\text{Hg}/\text{Hg}_2\text{SO}_4$ remains much the same at the higher temperature.

The anodic peak or band near +50 mV versus $\text{Hg}/\text{Hg}_2\text{SO}_4$ would, of course, be the most attractive for lowering the overall cell voltage for depolarized water electrolysis. Under ambient

conditions peak current densities of 15 mA/cm^2 were found, whereas at 92°C peak current densities increased to 140 mA/cm^2 . Correspondingly the shoulder at $+510 \text{ mV}$ versus $\text{Hg/Hg}_2\text{SO}_4$ increased from 20 mA/cm^2 to 215 mA/cm^2 over this temperature range.

Continued oxidation of glucose past the well known gluconic acid state (10-12) would be desirable for anode depolarization. To investigate this property, cyclic voltammetry on the anticipated oxidation products, gluconic and glucaric acids, was performed. Figure 3 compares the cyclic voltammograms of glucose and gluconic acid in H_2SO_4 at 60°C . The intensity of the anodic bands centered around 0 mV versus $\text{Hg/Hg}_2\text{SO}_4$ and are very similar, but the shoulder current $+510 \text{ mV}$ is substantially reduced suggesting that it arises from oxidation of glucose to gluconic acid.

Cyclic voltammograms of glucaric acid and the H_2SO_4 electrolyte at 56°C are compared in Figure 4. Although there still remains an oxidation centered around $+50 \text{ mV}$ versus $\text{Hg/Hg}_2\text{SO}_4$, it is substantially reduced in intensity from either glucose or gluconic acid. These cyclic voltammograms of gluconic and glucaric acids indicate that continued electrochemical degradation of glucose occurs at potentials negative of the oxygen potential. The actual oxidation products formed are not known, and the possibility of the formation of useful organic compounds at the anode exists. In this event, the depolarizing scheme presented would become even more attractive.

In conclusion, it has been demonstrated that glucose and some of its oxidation products are possible candidates for depolarizing the water electrolysis reaction capable of affecting a large reduction in cell voltage. Compared to coal, water soluble biomass is logistically more convenient to introduce into an electrochemical cell. Equally significant is the short term renewable nature of biomass. Successful development of this approach could provide hydrogen at costs below those available with existing electrolytic technologies.

REFERENCES

1. R.W. Coughlin and M. Farooque, *Nature*, 279, 301 (1979).
2. M. Farooque and R.W. Coughlin, *Fuel*, 59, 705 (1979).
3. R.W. Coughlin and M. Farooque, *Ind. Eng. Chem. Process Res. Dev.*, 19, 211 (1980).
4. R.W. Coughlin and M. Farooque, *J. Appl. Electrochem.*, 10, 729 (1980).
5. P.W.T. Lu and R.L. Ammon, Abs. No. 653, p. 1639, Ext. Abs., Electrochem. Soc., Los

Angeles, California, October 14-19, 1979.

6. S. Srinivasan, *et al.*, Abs. No. 348, Ext. Abs., Electrochem. Soc., St. Louis, Mo., May 11-16, 1980.
7. A.J. Appleby and B. Pinchon, *Int. J. Hydrogen Energy*, 5, 253 (1980).
8. S. Gilman, *Electroanal. Chem.*, 2, 111 (1967).
9. E. Skou, *Electrochim. Acta*, 22, 313 (1977).
10. C.G. Fink and D.B. Summers, *Trans. Electrochem. Soc.*, 74, 625 (1938).
11. H.S. Isbell, H.L. Frush and F.J. Bates, *Ind. Eng. Chem.*, 24, 375 (1932).
12. M. Fedoronko, *Adv. Carbohyd. Chem. Biochem.*, 29, 107 (1974).

Manuscript submitted Feb. 5, 1981;
revised manuscript received Feb. 26, 1981.

Publication costs of this article were assisted by the Institute of Gas Technology.

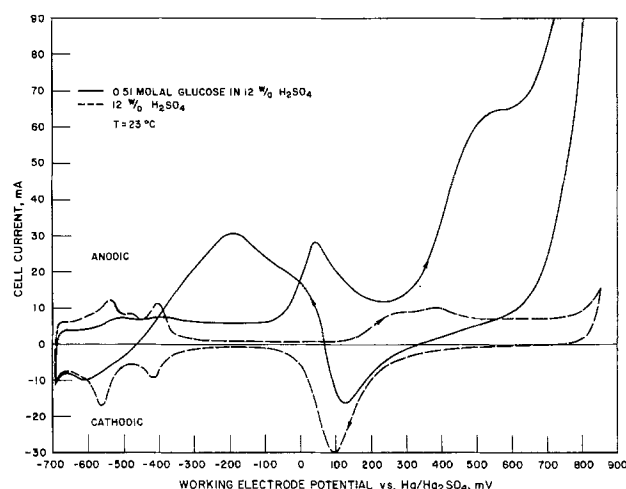


Fig. 1. Comparative cyclic voltammograms of 12 w/o H_2SO_4 and 0.51 molal glucose in 12 w/o H_2SO_4 . Sweep rate, 5 mV/sec ; temperature, 23°C ; working electrode, 1 cm^2 platinized platinum flag.

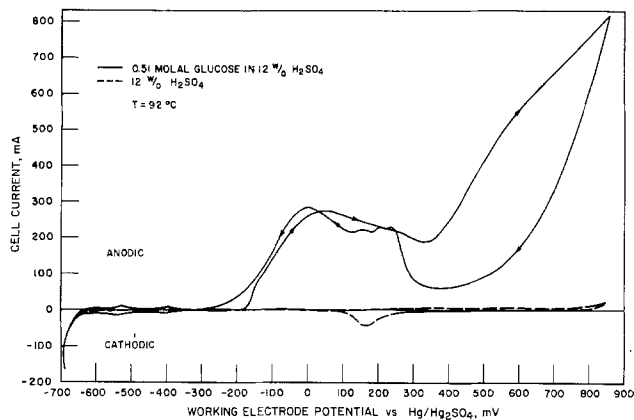


Fig. 2. Comparative cyclic voltammograms of 12 w/o H_2SO_4 and 0.51 molal glucose in 12 w/o H_2SO_4 . Sweep rate, 5 mV/sec; temperature, 92°C ; working electrode, 1 cm^2 platinized platinum flag.

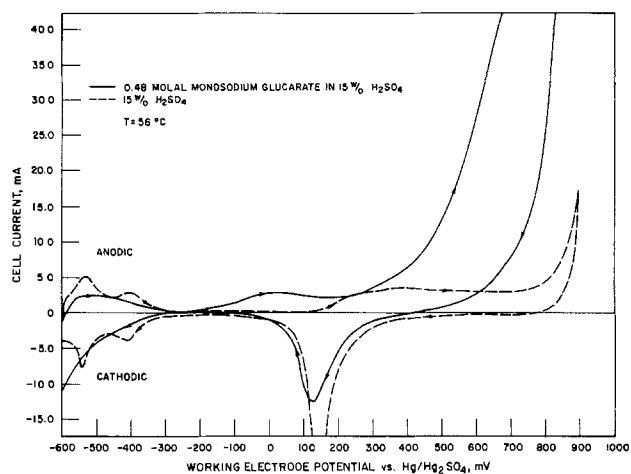


Fig. 4. Comparative cyclic voltammograms of 15 w/o H_2SO_4 and 0.48 molal monopotassium glucarate in 15% H_2SO_4 . Sweep rate, 5 mV/sec; temperature, 56°C ; working electrode, 1 cm^2 platinized.

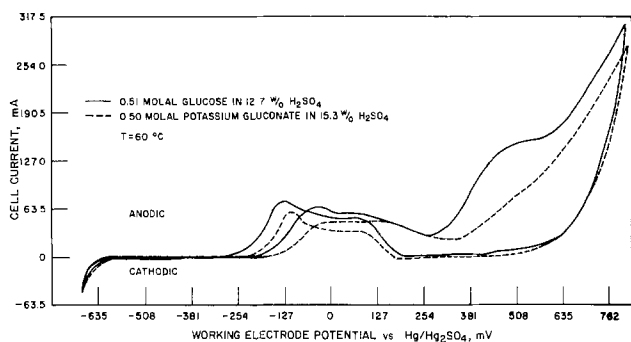


Fig. 3. Comparative cyclic voltammograms of 0.51 molal glucose in 12.7 w/o H_2SO_4 and 0.50 molal potassium gluconate in 15.3 w/o H_2SO_4 . Sweep rate, 5 mV/sec; temperature, 60°C ; working electrode, 1 cm^2 platinized platinum flag.



The Physics and Chemistry of the Lithographic Process

Murrae J. Bowden

Bell Laboratories, Murray Hill, New Jersey 07974

ABSTRACT

The object of the lithographic process is to delineate a pattern in a resist by means of some form of exposing radiation and to subsequently transfer that pattern to the underlying substrate. The faithful replication of the pattern originally described by the device designer is limited by the physical and chemical processes involved in both stages of pattern transfer. In this review discussion is confined to the first stage of the lithographic process, *viz.*, pattern delineation in the resist and in particular to the fundamental physical and chemical limitations of each of the exposure technologies as they relate to sensitivity and resolution.

At the heart of the ongoing revolution in the field of microelectronics is the silicon integrated circuit. This tiny modular silicon chip contains all the active elements of an electronic circuit such as transistors, capacitors etc., inseparably associated and connected to each other by metallic interconnects on the surface of the chip. The packing density and complexity of circuit components has increased enormously with the number of components per circuit approximately doubling every year since 1959. This exponential growth of complexity has been provided by increased chip size, decreased feature size, and improved device design (1).

Circuit fabrication requires the selective diffusion of tiny amounts of impurities into specific regions of the silicon to produce the desired electrical characteristics of the circuit (2). These regions are defined by lithographic processes in which the desired pattern is defined in a resist layer (usually a polymeric film which is spin-coated onto a substrate) and then transferred via processes such as etching to the underlying substrate. Currently photolithography is used to delineate patterns in the resist but future device designs will demand resolution beyond the capability of conventional photolithography.

There are a number of potentially high resolution technologies being pursued, *viz.*, deep u.v. photolithography, electron beam lithography, x-ray lithography, and ion beam lithography. Each of these technologies involves the common feature of causing chemical changes in the resist system which enable the exposed regions to be differentiated from the unexposed regions either by solubility differences or by differences in plasma etch rate. The ultimate objective of these technologies is the economic production of submicron devices. Hence it is important to understand the implication of physics and chemistry to resist sensitivity and resolution for each of these processes coupled with their engineering limitations in order to make an objective assessment of each technology.

The lithographic process falls into two distinct areas: (i) definition of the pattern in the resist layer and (ii) transfer of this pattern to the underlying substrate. In this paper we will confine our discussion of the litho-

graphic process to the former and concern ourselves with the fundamental physical and chemical limitations on pattern definition for each of the exposure technologies. It is important to distinguish between the fundamental limit of resolution of an exposure tool and its practical or achievable limit in fabricating devices in a manufacturing environment. The latter takes into account the variations in feature size due to errors in the system. Factors such as alignment tolerances and resist characteristics usually result in practical minimum feature sizes somewhat larger than theoretically expected.

Physical Limitations

Photolithography.—There are a variety of methods for producing photoresist patterns on semiconductor wafers. These include contact and proximity printing, both of which are shadow printing techniques and projection printing which can be performed on a 1:1 scale or with varying scales of reduction such as 5:1 or 10:1. With shadow printing, only 1:1 replications are possible.

Historically, shadow printing techniques have been the mainstay of device lithography. The primary factor limiting resolution is diffraction of light as it passes through the clear areas of the mask. Figure 1 shows a typical distribution of the u.v. light intensity incident on the photoresist surface for light passing through a mask consisting of a periodic grid of opaque and transparent spaces with equal linewidths b . The period of the grid is $2b$ and $\frac{1}{2}b$ is its fundamental spatial frequency ν . If a gap of width s is maintained between the mask and the photoresist surface, then from diffraction theory and experimental evaluations, the practical minimum period $2b_{\min}$ of the grid which can be replicated by shadow printing using collimated light for exposure is found to be (3)

$$2b_{\min} = 3\sqrt{\lambda(s + d/2)} \quad [1]$$

where λ is the wavelength and d the photoresist thickness. Conventional photoresists operate in the $0.4 \mu\text{m}$ wavelength region for which the practical minimum linewidth obtainable in the contact printing mode ($s = 0$) is around $0.7 \mu\text{m}$ for a $1 \mu\text{m}$ thick organic resist film.

Key words: lithography, x-ray, E-beam.

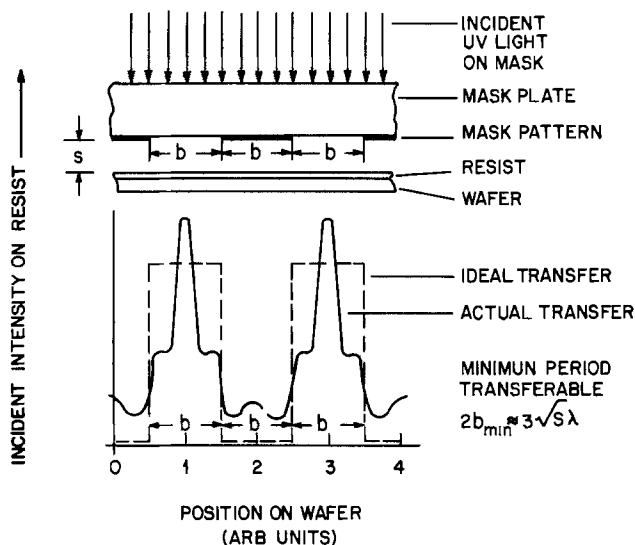


Fig. 1. Schematic representation of pattern transfer by projection printing [from D. Widmann and K. U. Stein, *Solid State Circuits, Proc. 2nd Eur. Solid State Circuits Conf.*, 1976 pp. 29-47 (pub. 1977)].

The principal drawback to these shadow printing techniques stems from practical considerations. Contact between mask and wafer transfers debris from the wafer to the mask resulting in damage to both. A decrease in resolution in contact printing can also arise from lack of intimate contact between the mask and wafer due to such effects as process-induced wafer deformation, mask bowing, contamination, etc. These problems are reduced in the proximity printing mode but only at the expense of resolution. A small constant spacing requires flatness of both mask and wafer to a combined tolerance which is less than the gap in order to avoid contact. Proximity printers generally operate with a gap width of $\sim 10 \mu\text{m}$ and are most useful in the 2-4 μm resolution range. Resolution at a fixed gap width can be improved by reducing the wavelength since resolution is proportional to $\lambda^{1/2}$ (cf. Eq. [1]). Using light in the spectral range 2000-2600 \AA , Lin (4) has obtained 0.5 μm Y-I bars separated by 0.25 μm gaps in 1.78 μm of photoresist.

The major development thrust in exposure hardware technology has been in the area of projection printing. Modern projection printers employ optics which are essentially diffraction limited. This implies that the design and fabrication of the optical elements are perfect enough that their imaging characteristics are dominated by diffraction effects associated with fine apertures in the condenser and projection optics rather than by aberrations.

The concept of a modulation transfer function (MTF) has been applied successfully to describe and predict the resolution capability of projection aligners. Consider the same mask pattern as before consisting of a periodic grid of opaque lines and transparent spaces with equal linewidths b . Due to diffraction considerations, the light pattern projected onto the photoresist surface exhibits gradual transitions of the light intensity (illustrated schematically in Fig. 2) instead of abrupt transitions from bright to dark regions. Even in the center of the dark lines there is a considerable amount of light when the width of b approaches 1 μm . If we denote the light intensity in the center of the dark line as I_{min} and in the center of the bright line as I_{max} , then we define modulation M of the image as

$$M = \frac{I_{\text{max}} - I_{\text{min}}}{I_{\text{max}} + I_{\text{min}}} \quad [2]$$

The MTF is the ratio of the modulation in the image plane to that in the object plane of an exposure sys-

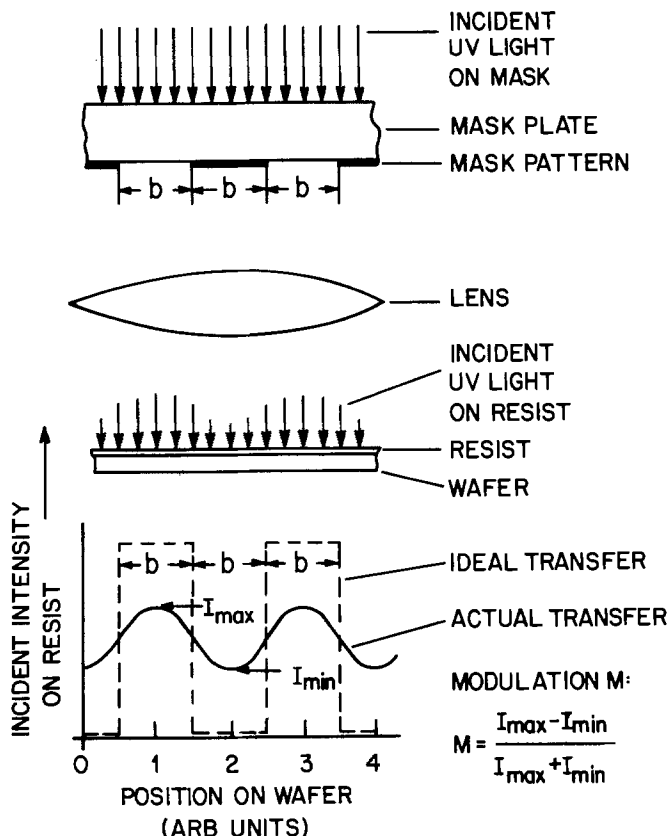


Fig. 2. Schematic representation of pattern transfer by 1:1 projection printing [from D. Widmann and K. U. Stein, *Solid State Circuits, Proc. 2nd Eur. Solid State Circuits Conf.*, 1976, pp. 29-47 (pub. 1977)].

tem. It is a function of the frequency of the object to be imaged as well as the numerical aperture (NA) of the optical system. The NA is given by $n \sin \alpha$ where n is the refractive index in image space and 2α is the maximum cone angle of rays reaching an image point on the optic axis of the projection system. Thus the frequency dependence of the MTF characterizes the exposure system under given conditions of illumination, focus, and wavelength of the exposing radiation and is a quality criterion for projection systems.

The shape of the MTF vs. frequency curve depends on the spatial coherency of the illuminating system (5). Spatial coherency refers to the effective size of the source relative to the aperture of an optical system. In a projection system, Köhler-type illumination is used which means that the exposure source is imaged through a condenser in the entrance pupil of the projection lens. This source image is the effective size source. The degree of coherency can be quantified by the ratio $s = (NA)_c / (NA)_o$, where $(NA)_c$ and $(NA)_o$ are the numerical apertures of the condenser and objective, respectively. This parameter describes the degree of filling of the entrance pupil of the lens by the source and specifically is the ratio of the diameter of the imaged source at the pupil to the pupil diameter. An incoherent source is rigorously a source of infinite extent ($s = \infty$) whereas a coherent source ($s = 0$) is a point source. The fully incoherent case is only of academic interest because all light collected from the finite source is always deliberately imaged within the entrance pupil and hence $s \leq 1$. We refer to this case as partial coherence.

An appreciation of how the degree of illumination coherence will affect the MTF curve can be gained from Fig. 3. The solid lines show a plane wave front ($s \rightarrow 0$) incident normally on a mask (object) which contains a grating pattern of frequency ν equal to $1/2b$. The undiffracted or (d-c) component of light emerg-

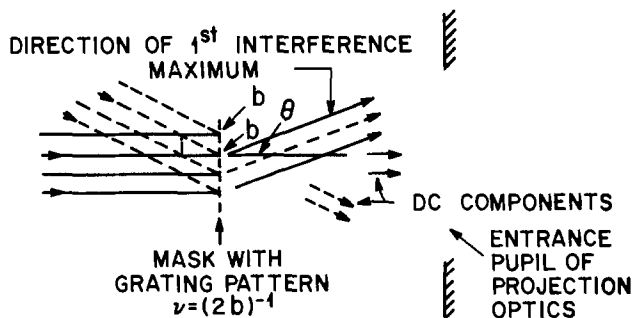


Fig. 3. Diffraction of coherent and incoherent light by a grating pattern [from J. D. Cuthbert, *Solid State Technol.*, 20, 59 (1977)].

ing from the mask contains no information about ν . This information is contained only in the diffracted light. The direction of the first diffraction peak is given by the grating formula

$$n_o(2b)\sin\theta = N\lambda \quad (N = 1) \quad [3]$$

so that

$$\nu = n_o \sin\theta / \lambda \quad [4]$$

Clearly if the light diffracted into direction θ is to reach the image plane, then θ must be $\leq \alpha_o$ where α_o is defined by $NA_o = n_o \sin\alpha_o$, the numerical aperture of the projection optics. Therefore the highest grating frequency which can be imaged by an optical system with coherent illumination is

$$\nu_{max} = n_o \sin\alpha_o / \lambda = NA / \lambda \quad [5]$$

For incoherent illumination (shown by dotted lines in Fig. 2) incident at a general angle ϕ , the direction of the first maxima is given by

$$n_o(2b)(\sin\phi + \sin\theta) = \lambda$$

In order for both the d-c beam and the first diffraction peak to reach the image plane, both ϕ and θ must be $\leq \alpha_o$, i.e.

$$\nu_{max} = 2NA / \lambda \quad [6]$$

The MTF curve can be described mathematically in terms of these variables. For example, the MTF ($H(\nu)$) of a lens system employing incoherent illumination and a circular exit pupil is given by (6)

$$H(\nu) = \frac{2}{\pi} [\cos^{-1}(\nu/\nu_{max}) - \nu/\nu_{max} \sqrt{1 - (\nu/\nu_{max})^2}] \quad [7]$$

where ν_{max} is $2NA/\lambda$ (cf. Eq. [6]).

The MTF vs. spatial frequency curves provide a convenient description of the variation of image quality since the higher the value of the MTF for a given frequency, the greater the contrast in the projected image. Figure 4 shows plots of MTF vs. spatial frequency for different degrees of coherency s . The figure shows that the MTF of a fully coherent optical system has a spatial frequency cutoff which is half that of an incoherent system (cf. Eq. [5] and [6]). With partially coherent illumination ($0 < s < \infty$) the MTF is higher for spatial frequencies $0 < \nu < \frac{1}{2} \nu_o$ and lower for $\frac{1}{2} \nu_o < \nu < \nu_o$ where $\nu_o = 2NA/\lambda$. This cross-over occurs at an MTF of ~ 0.4 for $s \approx 1$. From this we can conclude that partial coherence will be beneficial for recording media which require an MTF > 0.4 as is typical of most organic-based positive photoresists.

The best illumination for image reproduction is spatially partially coherent with $s \approx 0.7$ (5, 8). Although values of $s < 0.7$ result in even higher values of the MTF for a given frequency, other factors must be considered. For example increased coherence is achieved by narrowing the illumination slit and hence is obtained at the expense of longer exposure times.

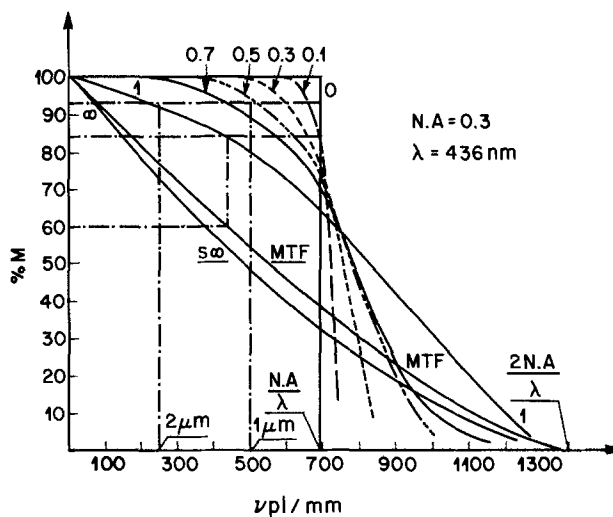


Fig. 4. Modulation M of the image intensity vs. spatial frequency ν of a sinusoidal amplitude transmission grating for different values of the coherency factor s . [from M. Lacombat, J. Massin, G. M. Dubroeuq, and M. Brevignon, *Solid State Technol.*, 23, 115 (1980)].

The image characteristics of isolated edge features also degrade for values of s below 0.7 due to phenomena such as ringing (8) shown in the intensity distribution curve in Fig. 5. For degrees of coherency > 0.7 , it becomes difficult to maintain linewidth control in such features since the intensity of the low portion of the intensity distribution curve increases with increasing s (cf. Fig. 5). There is also decreased tolerance to focus error for $s > 0.7$ for focus errors $< 4 \mu\text{m}$ (8). Thus a partial coherency of $s = 0.7$ represents an acceptable trade-off between these various factors.

Resolution can be improved by using lenses with higher numerical apertures or using shorter wavelengths. For example, Fig. 6 shows the MTF curves for 1X and 10X reduction lenses for exposure at 4360Å. It is seen that for a given spatial frequency, projection with the 10X reduction lens provides a larger modulation than 1:1 projection, the reason for this being the larger numerical aperture of the 10X reduction lens (0.33 for 10X vs. 0.125 for 1X). It will be noted however that the image field diameter of the 10X reduction lens is ten times smaller than that for the 1X reduction lens. This reflects an important constraint in

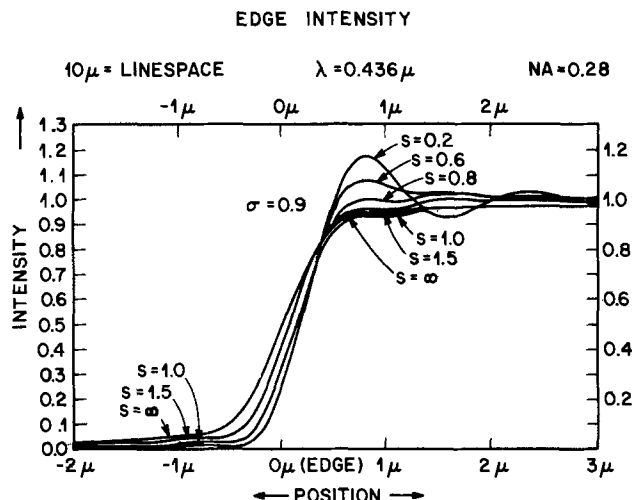


Fig. 5. Image intensity profile near the edge of a mask pattern consisting of $10 \mu\text{m}$ lines and spaces. The mask pattern was imaged at 4360\AA with a lens of $NA = 0.28$ [from M. M. O'Toole and A. R. Neureuther, *SPIE Developments in Semiconductor Microlithography IV*, 174, 22 (1979)].

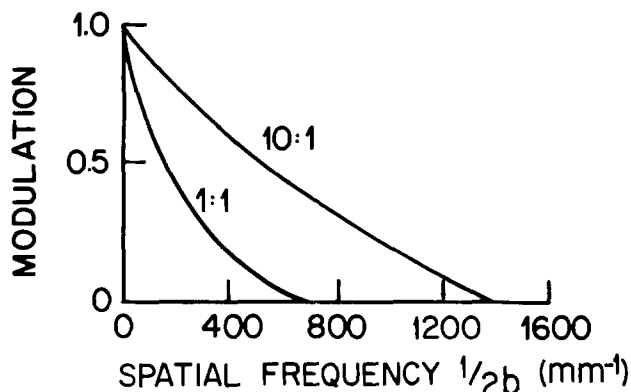


Fig. 6. Modulation transfer functions (MTF) for two different lenses. Lens 1: 1 \times reduction, $NA=0.125$, image field—75 mm diam; lens 2: 10 \times reduction, $NA=0.33$, image field—7.5 mm diam; the wavelength λ is 436 nm [from D. Widmann and K. U. Stein, *Solid State Circuits, Proc.*, 2nd Eur. Solid State Circuits Conf., 1976, pp. 29-47 (pub. 1977)].

lens design, *viz.*, that higher resolution via higher NA is obtained at the expense of image field diameter. The current state-of-the-art in the design of refractive microcircuit lenses permits placement of $\sim 10^8$ resolved spots within the image field (9). With refractive lenses, this number depends little on field size or resolution. Thus for a given NA and λ , the limiting resolution ν_{max} will be obtained over a square field approximately given by $10^8/\nu_{max}^2$. For example, a lens system whose NA and λ enable resolution of 1 μm lines and spaces ($\nu_{max} = \frac{1}{2}, \mu m^{-1}$), could only exhibit such resolution over a square field $4 \times 10^8 \mu m^2$, *i.e.*, 2 cm on the side. Higher resolution can only be obtained at the expense of field in a manner which keeps the total number of resolved elements within the field fixed. This relationship is shown in Fig. 7 as a line connecting points representing lenses of similar design and complexity. Such reduction in field size requires a step and repeat approach to pattern an entire wafer.

The other alternative for obtaining higher resolution for a fixed NA is to decrease λ . Usually mono-

STATE-OF-THE-ART LENSES FOR PHOTOLITHOGRAPHY

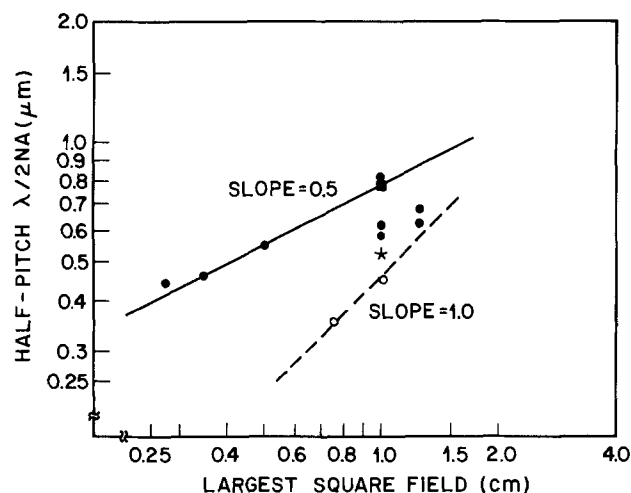


Fig. 7. Limiting resolution vs. field size for state-of-the-art refractive lenses for photolithography. Points indicated by closed circles are refractive designs which, for the same complexity have a constant number of resolution elements as field is traded for resolution. Open circles indicate scaling of a BTL reflective design which yields more resolution elements at smaller fields. Zeiss, 10 \times lens, 0.28 NA , CERCO Lippia 5 \times [from J. Bruning, *J. Vac. Sci. Technol.*, 17, 1147 (1980)].

chromatic light is used in refractive projection systems in order to eliminate chromatic aberration effects. Such refractive lenses are designed to operate typically at $\lambda > 4000\text{\AA}$. Shorter wavelengths are precluded by difficulties in lens design resulting from high absorption of optical glasses. On the other hand, resolution in an all reflecting optical system (10) can in principle be increased by reducing the wavelength provided that wave aberrations are suitably low at the reduced wavelength. For example, by using a modified optical design of the 1:1 Perkin-Elmer printer Bruning (7) demonstrated significant resolution improvement using 3100 \AA over 4000 \AA for the exposure.

There are several other important physical limitations on image quality in projection systems. Clearly one would like as large a depth of focus δ as possible in order to compensate for aberrations, wafer distortions, and variable resist thickness due to topography. The depth of focus in an optical system is given by

$$\delta = \lambda/2NA^2 \quad [8]$$

Thus improvements in resolution resulting from an increase in NA or a decrease in λ provide for a smaller depth of focus or, put another way, less defocusing tolerance. For example, the Lippia 5 \times reduction lens of CERCO which achieves a 0.35 NA at 4047 \AA over a 1 cm square field provides a depth of focus of $\sim 1.5 \mu m$. Such a shallow depth of focus requires focusing at each chip during step and repeat operation in order to maintain linewidth control. We may note that since resolution is proportional to λ/NA , the fall-off in depth of focus will be less severe for resolution improvement gained by decreasing λ since there is only a first power dependence of both parameters on λ .

Step and repeat exposure systems use demagnifying optics to project the image of a reticle onto a wafer. Reduction ratios vary typically between 2 \times and 10 \times . The resolution capability of a lens depends only on its numerical aperture and not on its reduction ratio although a higher reduction ratio permits a higher NA (11). Considerations of the optimal reduction ratio appear to revolve around practical considerations such as defect densities associated with reticle size (9).

The other major factor which limits resolution and linewidth control is the standing wave phenomenon. When photoresist films are exposed using monochromatic radiation as in optical projection printing, standing waves are formed in the resist (5; 12). These are caused by coherent interference effects due to a reflecting substrate which result in periodic intensity distributions in the direction perpendicular to the plane of the resist with a period $\lambda_r/2$ (typically 1300 \AA) where λ_r is the exposure wavelength in the resist. This problem has been considered by several authors with the work of Dill *et al.* (12, 13) being especially comprehensive. Figure 8 shows the image intensity distribution as a function of depth in the resist determined from the model of Dill *et al.* using Fourier optical theory. It is noted that the average intensity decreases with increasing depth. This is due to the strong optical absorption of the resist which attenuates the light as it passes through the film. This intensity pattern changes in magnitude during exposure due to changes in absorption resulting from photo bleaching but the positions of the interference maxima and minima do not move.

Exposure of a positive photoresist under this condition destroys more inhibitor at the intensity maxima than at the minima. Thus the periodicity in the exposure profile as a function of depth into the film results in a similar variation in the rate of development of exposed regions of the resist and produces edge fringes or contours in the positive photoresist wall profile. Such fringes calculated by the Dill model which also takes development of the resist into ac-

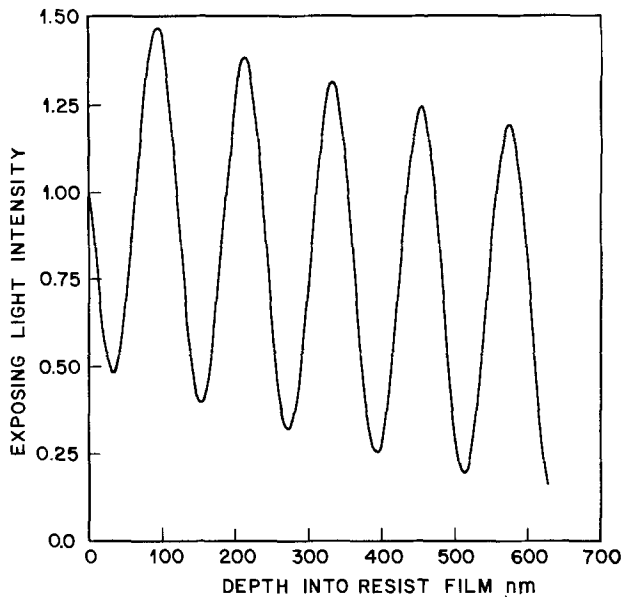


Fig. 8. Plot of intensity of exposing light within a 630 nm AZ1350 photoresist film on bare silicon at the beginning of exposure at a 4047 Å wavelength [from F. H. Dill, *IEEE Trans. Electron Devices*, ed 22, 440 (1975)].

count are shown in Fig. 9 with experimental verification shown in Fig. 10. These fringes give rise to variations in linewidth that can obliterate lines or close up gaps at the 1 μm level.

A further disadvantage of standing wave effects is the linewidth variations over topography. Figure 11 shows the linewidth variation of an AZ1350H photoresist stripe running across a 0.5 μm vertical step. These linewidth variations stem from the fact that the resist thickness is not uniform across a step. Since reflectivity maximizes for even quarter wavelength multiples of resist thickness (lowering the energy coupled into the resist) and minimizes for odd quarter wavelength multiples (maximizing energy coupling), then the time to develop through a photoresist film becomes periodic with resist thickness for a fixed exposure flux (12). Thus the exposure variations resulting from variations in resist thickness in the vicinity of a step are manifested as linewidth variations.

Standing wave effects are more pronounced in systems employing monochromatic radiation than in those employing broad band illumination. The latter results in a smoothing of the distribution of light intensity within the resist layer. Correcting the projection optics for exposure at two wavelengths rather than a single wavelength appears to reduce the standing wave effect (16). This is seen in Fig. 12 which compares patterns in 1.2 μm thick HPR204 photoresist exposed using the CERCO 5X reduction lens designed for the Philips wafer stepper at 4050 and 4360 Å (Fig. 12a and b) with

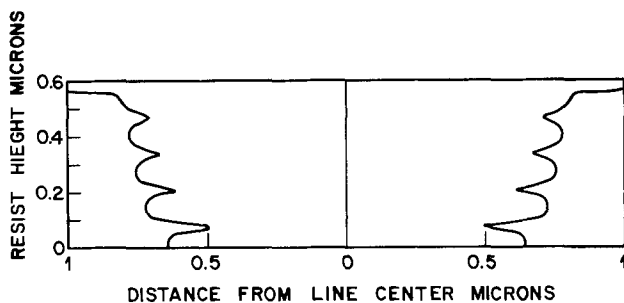
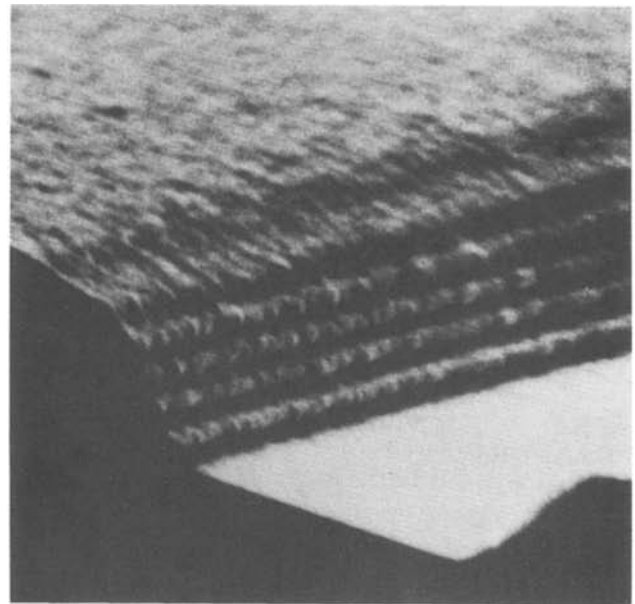
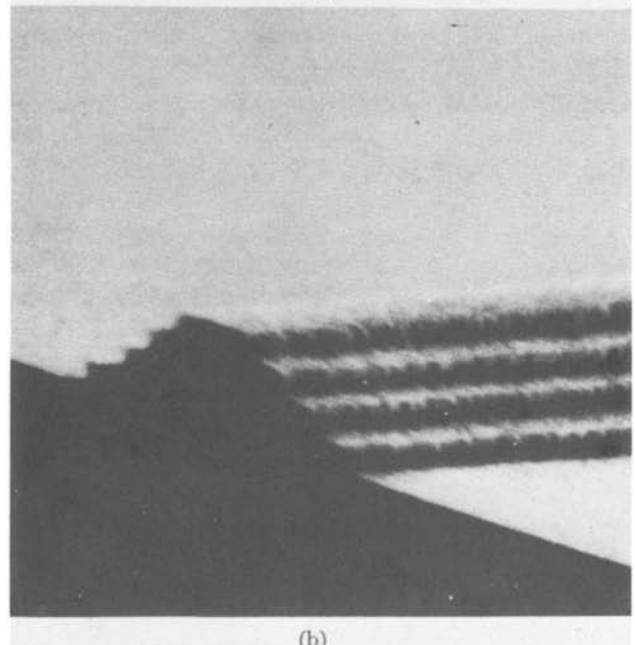


Fig. 9. Edge profile for a nominal 1 μm line in AZ1350 photoresist developed for 85 sec in 1:1 AZ developer:water [from F. H. Dill, A. R. Neureuther, J. A. Tuttle, and E. J. Walker, *IEEE Trans. Electron Devices*, ed 22, 456 (1975)].



(a)



(b)

Fig. 10. Scanning electron micrograph of a 1.2 μm line AZ13505 photoresist exposed with a nominal 1 μm image [from F. H. Dill, A. R. Neureuther, J. A. Tuttle, and E. J. Walker, *IEEE Trans. Electron Devices*, ed 22, 456 (1975)].

patterns obtained by a single wavelength exposure at 4050 Å (Fig. 12c and d).

Other approaches to reducing standing wave effects include optimizing resist and oxide thicknesses (5) as well as postexposure baking schedules (14) and using concentrated developers (13). It should be noted that the latter two approaches do not eliminate the sensitivity of the line size to the resist and dielectric layer thicknesses since the exposure is still monochromatic. Another approach utilizes a tri-level process (15) in which a planarizing polymeric layer is applied to the circuit at a thickness sufficient to smooth out all the topography (~ 1.5 - $2.5 \mu\text{m}$). After a bake step at $\sim 210^\circ\text{C}$ to harden the film and render it opaque at the exposure wavelength, a layer of plasma-deposited SiO_2 $\sim 1000\text{Å}$ thick is applied on top of the planarizing layer followed by a thin layer of the desired photoresist (3000-5000 Å). This structure permits the image to be recorded in a thin resist on a planar, reflectionless sub-

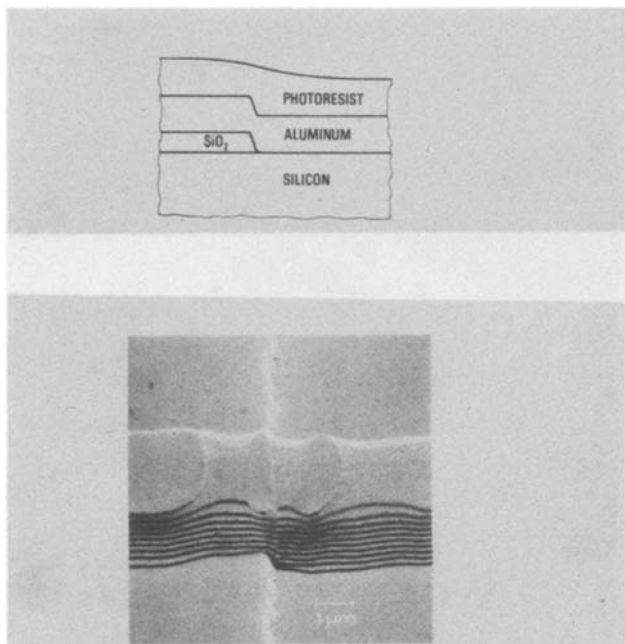


Fig. 11. Scanning electron micrograph of an AZ1350H photoresist stripe running across a $0.5 \mu\text{m}$ vertical step showing line width variation across the step [from D. W. Widmann and H. Binder, *IEEE Trans. Electron Devices*, ed 22, 467 (1975)].

strate. Following exposure and development, the SiO_2 layer is etched. The top photoresist layer thus only

serves as an etch mask for the SiO_2 layer which in turn serves as an etch mask for reactive etching of the underlying thick polymer layer. It is the anisotropically patterned thick resist which serves as the "resist" layer for the underlying circuit. Since the primary lithographic patterning step is accomplished in thin resist with no reflection from the substrate excellent resolution and linewidth control can be maintained even over topography.

As was indicated earlier, the overall practical resolution is determined by a number of factors such as registration, alignment, and alignment control in addition to diffraction considerations and given the advances in lithographic technology and in design of photolithographic hardware, one is forced to speculate on the maximum practical resolution with some degree of uncertainty. Markle (17) has suggested that some combination of NA , short λ (summarized in Table I) combined with a high contrast resist may permit $0.5 \mu\text{m}$ resolution to be realizable. Bruning (9) also considers the end of the road for photolithography to lie somewhere between 0.4 and $0.8 \mu\text{m}$ depending on how fully deep u.v. and image partitioning are exploited.

Electron beam lithography.—The past 10 years have seen an enormous effort in developing electron beam lithography as a viable technology. Although electron projection (18, 19) and shadow printing methods (20) have been developed for full image exposure, these techniques have not gained major importance. The following considerations are therefore limited to electron beam scanning (21-23) in which an electron beam of defined shape is controllably deflected in order to

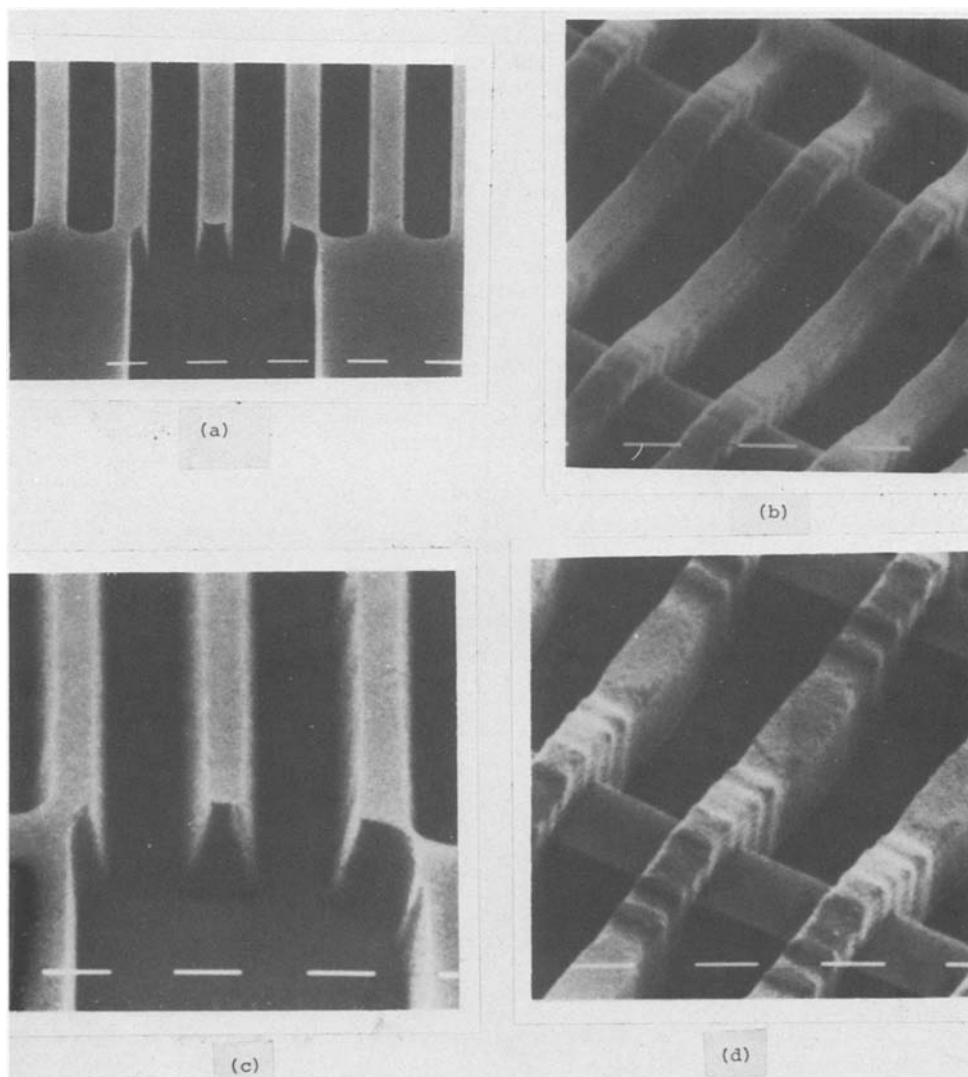


Fig. 12. Patterns in $1.2 \mu\text{m}$ thick photoresist (HPR 209) on silicon wafers. (a) and (b) exposed at 4050 \AA ; (c) and (d) exposed at 4360 \AA [from S. Wittekoek, *Solid State Technol.*, 23, 80 (1980)].

Table I. Dependence of minimum feature size on NA and λ (17)

| NA | λ (μm) | Minimum feature (μm) |
|------------|-----------------------------|-----------------------------------|
| 0.164 (F3) | 0.39 | 1.78 |
| 0.164 | 0.25 | 1.14 |
| 0.242 (F2) | 0.25 | 0.775 |

expose the desired areas of the resist film. Since the wavelength of an electron is only on the order of a few tenths of an angstrom, the resolution limitation due to diffraction considerations is not important. However, although an electron beam can be focused to spot sizes of 1000Å or less, the minimum feature size may be considerably greater than the beam diameter because of electron scattering in the resist. When an electron beam enters a thin polymer film the electrons lose energy by elastic and inelastic collisional processes known collectively as electron scattering. This results in a transverse or lateral electron flux $J(z,y)$ normal to the incident beam direction (see Fig. 13). The magnitude of this flux which has scattering contributions from within the resist (forward and lateral) and from within the substrate (backscattering) depends upon the energy, current, and geometry of the beam, film thickness, and the atomic number of the polymer and substrate. The existence of this transverse flux of electrons results in energy dissipation at points remote from the point of entry of the beam and thus the developed contour of the exposed area in the resist is reflective of the energy dissipated in that region. In particular it may be considered that the developed contour represents a contour of constant absorbed energy density and measurement of exposure profiles can yield valuable information concerning energy dissipation profiles of electrons in the resist. Thus electron scattering provides the fundamental limitation to resolution in electron lithography.

In the past, the dose required to obtain a given relief structure in the resist has been determined experimentally. While an empirical approach permits one to write patterns and fabricate devices, it provides neither a basic understanding of the physical mechanism involved in polymer film exposure nor a means for predicting quantitatively how changing a given parameter will effect the polymer relief structure. As illustrated in Fig. 14, when a positive resist such as poly(methyl methacrylate) PMMA is exposed in a line by a scanned electron beam, developed in a solvent to remove the exposed regions, and viewed in cross section, undercut contours are observed whose dimensions

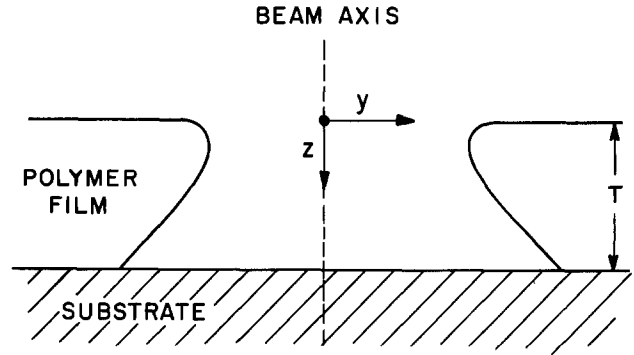


Fig. 14. Schematic diagram illustrating the undercut contours typically obtained in PMMA film of thickness T on top of a substrate after exposure by a scanned electron beam and developing [from R. J. Hawryluk, A. M. Hawryluk, and H. I. Smith, *J. Appl. Phys.*, **45**, 2551 (1974)].

depend on the line charge density. Similarly, if the beam is held at a fixed position and turned on for a time interval τ , a radially symmetric contour is obtained which is termed a dot exposure. These contours as already mentioned are identified as surfaces of equal energy dissipation per unit volume. Quantitatively, the contour $z(r)$ can be obtained from (24, 25)

$$qi\tau I(r, z) = D_{crit} \text{ (erg/cm}^3\text{)} \quad [9]$$

where r is the radial distance from the beam axis, z is the depth in the polymer film, and D_{crit} is the energy dissipated per unit volume required to expose the polymer adequately for development. The azimuthally symmetric two-dimensional function $I(r,z)$ is the energy dissipated per unit volume per electron. The term preceding $I(r,z)$ is the product of the beam current i , the exposure time τ , and the number of electrons per coulomb q and is therefore the total number of electrons incident at the surface. Thus by determining the locus in the resist of the critical value of absorbed energy, we have in fact determined the contour of the developed line.

In similar fashion, the contour $z(y)$ of a line scan exposure obtained by scanning the beam along the x direction at a velocity \dot{x} cm/sec (Fig. 15) can also be obtained. For adequate exposure the contour corresponds to the locus where the energy dissipated per unit volume equals D_{crit}

$$\int_{-\infty}^{\infty} qiI(r, z) dt = D_{crit} \quad [10]$$

The input line dose (linear charge density) $D^0_x = i/\dot{x}$. Transposing variables we thus obtain

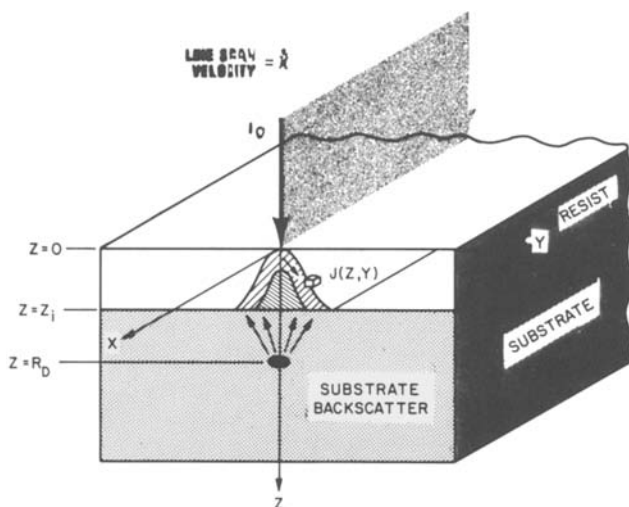


Fig. 13. Three dimensional electron scattering model for a polymer resist film on a substrate [from L. F. Thompson, *Solid State Technol.*, **17**, 27 (1974)].

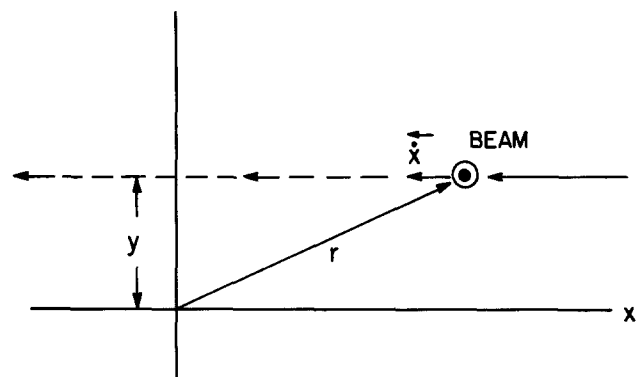


Fig. 15. Electron beam scanned past a point with velocity \dot{x} at a lateral displacement y viewed normal to the sample surface [from R. J. Hawryluk, A. M. Hawryluk, and H. I. Smith, *J. Appl. Phys.*, **45**, 2551 (1974)].

$$\int_{-\infty}^{\infty} qI(r, z) dx \cdot D^{\circ}_x = D_{\text{crit}} \quad [11]$$

which may be abbreviated to

$$E(y, z) D^{\circ}_x = D_{\text{crit}} \quad [12]$$

where

$$E(y, z) = \int_{-\infty}^{\infty} qI(r, z) dx \quad \text{and} \quad r^2 = x^2 + y^2$$

$E(y, z)$ is the energy dissipated per unit volume per coulomb per centimeter. Thus from $E(y, z)$ and D_{crit} , one can calculate the linear charge density D°_x required to obtain a given contour.

We should note that the proper exposure for an array of closely spaced lines is different than that for a single isolated line. This is because even a highly focused beam contributes to the exposure several micrometers away. This is referred to as the proximity effect (26) and will be discussed later. A careful evaluation of $E(y, z)$ for a single line permits one to calculate this cooperative exposure effect.

Both analytic (24, 27, 28) and Monte Carlo models (24, 29-31) have been used to calculate $I(r, z)$ and $E(y, z)$. The Monte Carlo method attempts to simulate via a digital computer the trajectories of the incident electrons within the resist/substrate system. This involves following the electron trajectory through a succession of distinct scattering events. Most approaches employ a single scattering model. The angular deflections suffered by the incident electrons are assumed to occur via elastic scattering with the target nuclei with the angle of scattering for each event being calculated in accordance with the differential scattering cross section for a nucleus in a screened atomic field. In between elastic scattering events, the incident electrons are assumed to travel in straight lines (given by the mean-free path) undergoing energy loss. This energy loss process is modeled via the continuous slowing down approximation in which the electron loses energy continuously along each free flight segment according to the Bethe energy loss formula (32)

$$\frac{dE}{dx} = \frac{-2\pi e^4 n_e}{E} \ln \left[\frac{E}{I} \left(\frac{e}{2} \right)^{1/2} \right] \quad [13]$$

where n_e is the density of atomic electrons and I the mean excitation energy. Figure 16 shows 100 simulated trajectories projected onto the x - y plane for a 10 and 20 kV point source. This figure qualitatively shows the degree of forward and lateral scattering within the film as well as the degree and position of backscattering. We can also make a number of other qualitative deductions from the results of these simulated trajectories. Clearly the range of a 20 kV electron is greater than that of a 10 kV electron. But although scattering of 20 kV electrons occurs over a greater lateral distance, it is apparent that the absorbed energy density in regions transverse to the beam falls off

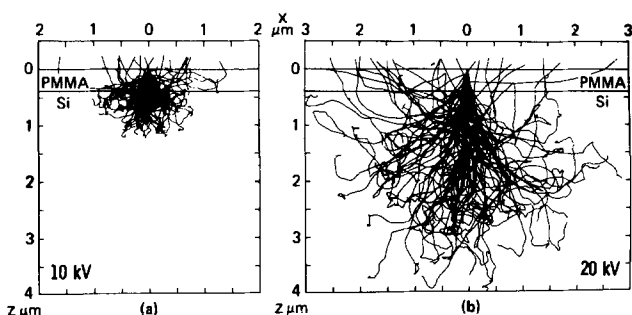


Fig. 16. Monte Carlo simulated trajectories of 100 electrons in PMMA resist on silicon [from D. Kyser and N. S. Viswanathan, *J. Vac. Sci. Technol.*, **12**, 1305 (1975)].

more rapidly in this case than for 10 kV electrons suggesting that higher resolution can be obtained at 20 kV than at 10 kV. Of course for overexposure, the greater lateral spread at 20 kV will eventually result in broader lines. Heidenreich *et al.* (33) used Monte Carlo methods to calculate the effects of film thickness and operating voltage on the contour width. Their results are summarized in Fig. 17. This figure also shows the computed range of electrons in the resist calculated from the Bethe expression for energy loss as a function of electron energy. The data indicates two clear trends. For a given resist thickness, the linewidth, as expected, decreases with increasing incident electron energy up to some electron energy beyond which there is no further significant reduction. The decrease in linewidth continues over a wider range of incident electron energy for thick films. Hatzakis and Broers (34) generated experimental profiles in thick PMMA (Fig. 18) which confirm this conclusion. It would be difficult to make a quantitative comparison between theory and experiment here since the calculations of Heidenreich *et al.* include the effects of substrate backscattering while the data of Broers and Hatzakis do not. The second trend shown by the data indicates that for a given operating voltage, the linewidth decreases with decreasing resist thickness.

In order to determine spatial profiles, the distribution of electrons in the incident beam has to be taken into account. It is usually assumed that the beam has a Gaussian profile

$$J(r) = J_0 \exp(-r^2/\bar{r}^2) \quad [14]$$

where J_0 is the current density at the spot center ($r = 0$) and \bar{r} is the Gaussian radius. If the total current of the incident beam is i_0 , then

$$J(r) = \frac{i_0}{\pi \bar{r}^2} \exp(-r^2/\bar{r}^2) \quad [15]$$

Thus for a given exposure dose, one can calculate equi-energy density contours. Figure 19 shows a comparison

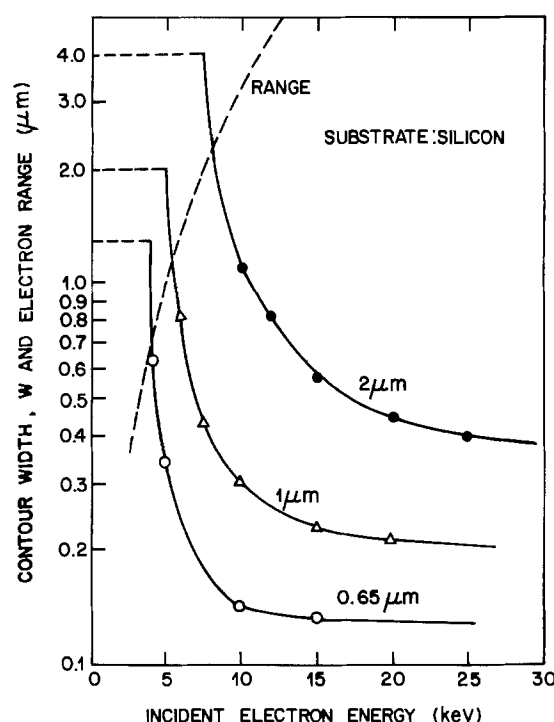


Fig. 17. Computed variation of contour width W as a function of incident electron energy for three resist thicknesses. The computed Bethe range of electrons in the resist material is also shown [from R. D. Heidenreich, J. P. Ballantyne, and L. F. Thompson, *J. Vac. Sci. Technol.*, **12**, 1284 (1975)].

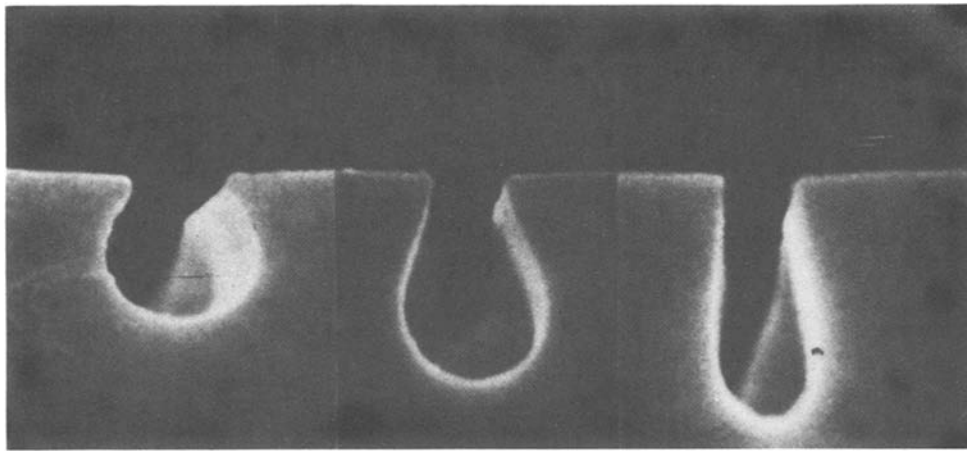


Fig. 18. Composite photomicrograph of the cross sections of three lines exposed at 10^{-4} C/cm² at varying beam voltages: left to right 10, 15, and 25 kV [from M. Matzakakis, C. H. Ting, and N. Viswanathan, in "Electron and Ion Beam Science and Technology," R. Bakish, Editor, p. 542, The Electrochemical Society Softbound Proceedings Series, Princeton, N.J. (1974)].

of the Monte Carlo results obtained by Kyser and Murata (30) with the experimental results of Wolf *et al.* (35) for thick PMMA at 10 kV. The Monte Carlo calculations were arbitrarily matched to the experimental contour for $D^0_x = 0.3 \times 10^{-8}$ C/cm at $x = 0$, i.e., on axis. This was achieved with a contour of $D_{crit} = 1.1 \times 10^{22}$ eV/cm³ and this same contour value was then calculated for the remaining values of 0.7, 1.0, and 2.0 D^0_x . The agreement between theory and experiment shown in Fig. 19 is generally good in spite of the neglect in the theory of developer effects. The most obvious discrepancy occurs at the surface where the experiment shows a significant width for the contour and theory predicts a small width. This discrepancy may be due to (i) surface tension in the film after irradiation or (ii) finite etching rate of the polymer in regions where $D < D_{crit}$.

The major disadvantage of the Monte Carlo method is that it is necessary to calculate the trajectories of several thousand electrons in order to obtain meaningful results. This implies a great deal of computer time and expenditure. Thus for practical as well as heuristic reasons analytic models to predict the energy dissipation are useful.

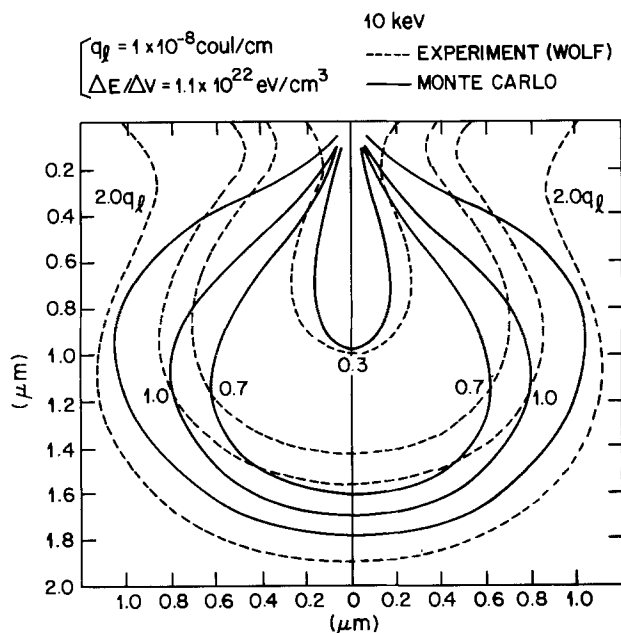


Fig. 19. Comparison of profiles calculated by Monte Carlo simulation with those determined by experiment for thick PMMA resist at 10 kV [from D. Kyser and K. Murata, in "Electron and Ion Beam Science and Technology," R. Bakish, Editor, p. 205, The Electrochemical Society Softbound Proceedings Series, Princeton, N.J. (1974)].

In the analytical models, the energy dissipated by an electron beam is considered to be composed of three contributions, (i) small angle forward scattering of the incident beam in the polymer, (ii) large angle backscattering from the substrate, and (iii) large angle backscattering of the incident beam within the polymer.

We have seen that the cumulative effects of small angle scattering events determine the spatial distribution of electrons inside the resist film. By assuming those scattering events to be elastic and small angle, the spatial probability distribution of scattered electrons can be expressed as (28)

$$H(r, z) = \frac{3\lambda}{4\pi z^3} \exp\left(-\frac{3\lambda^2}{4z^3}\right) \quad [16]$$

where r is the radial distance from the axis of the incoming electron, z is the vertical distance along the axis of electron penetration, and λ is the transport mean-free path which in the nonrelativistic approximation is given by

$$\lambda(\text{\AA}) = \frac{5.12 \times 10^{-3} E^2 A}{\rho Z^2 \ln(0.725 E^{1/2}/Z^{1/3})} \quad [17]$$

where A = mass number, E = electron energy, ρ = film density, and Z = atomic number.

Equation [16] shows that the spatial distribution of electrons is Gaussian at any depth for an impulse input function. When the impinging electrons have a Gaussian distribution $J(r)$ defined by Eq. [15], then the resulting density distribution inside the solid will be given by the convolution of the integral of the input function $J(r)$ and the response function $H(r, z)$

$$J(r, z) = \int_0^{2\pi} \int_0^\infty H(r, z) J(r) r dr d\theta \quad [18]$$

This integration cannot be carried out rigorously in closed analytical form and thus requires numerical integration. However, a very good approximation is obtained using the approximation that in a Gaussian distribution the value of \bar{r} is the root-mean-square uncertainty in the radial position of an electron. If scattering now occurs, an additional uncertainty is introduced [in this case $(4z^3/3\lambda)^{1/2}$] and if the two uncertainties are random or independent they can be combined in quadrature to yield the minimum dispersion of the Gaussian. This dispersion \bar{s} is the minimum uncertainty in electron radial position and is simply

$$\bar{s} = (\bar{r}^2 + 4z^3/3\lambda)^{1/2} \quad [19]$$

for a spreading Gaussian profile. The Gaussian profile of the beam as it penetrates the resist is therefore given by

$$J(r) = \frac{i_0}{\pi s^2} \exp \left[- \left(\frac{r^2}{s^2} \right) \right] \quad [20]$$

The energy loss per cm³ per electron due to the forward scattered electrons can be calculated as

$$I(r, z)|_{FS} = \frac{dE}{dx} \times \frac{J(r)}{i_0} \quad [21]$$

The contributions of large angle backscattering from the substrate and polymer are obtained by following the approach of Everhart (36) which assumes that electrons undergo only one large-angle Rutherford scattering. The reflection coefficient is calculated on this basis and one parameter in the model is adjusted to obtain a good fit to experimental reflection coefficient data for atomic numbers $Z < 50$. Alternatively, the backscatter contribution may be calculated empirically. Heidenreich (37), for example, has developed an empirical backscatter model for thin resist films based on the direct observation of chemical change produced by backscattered electrons at different accelerating voltages on several substrates. The model is independent of scattering, trajectory, and energy dissipation calculations and is essentially a radial exponential decay of backscatter current density out to the backscatter radius determined by electron range.

The total electron flux per unit area at a given point is calculated as the sum of the individual components. One can then determine the total energy absorption from the integral over all space of the product of electron flux and the rate of energy loss. Figure 20 shows a comparison of developed profiles for line dose charges of 0.3×10^{-8} and 1.0×10^{-8} C/cm for PMMA on an aluminum substrate at different accelerating voltages. Comparison of the theoretical contours calculated from the model of Greeneich and Van Duzer (27) with the

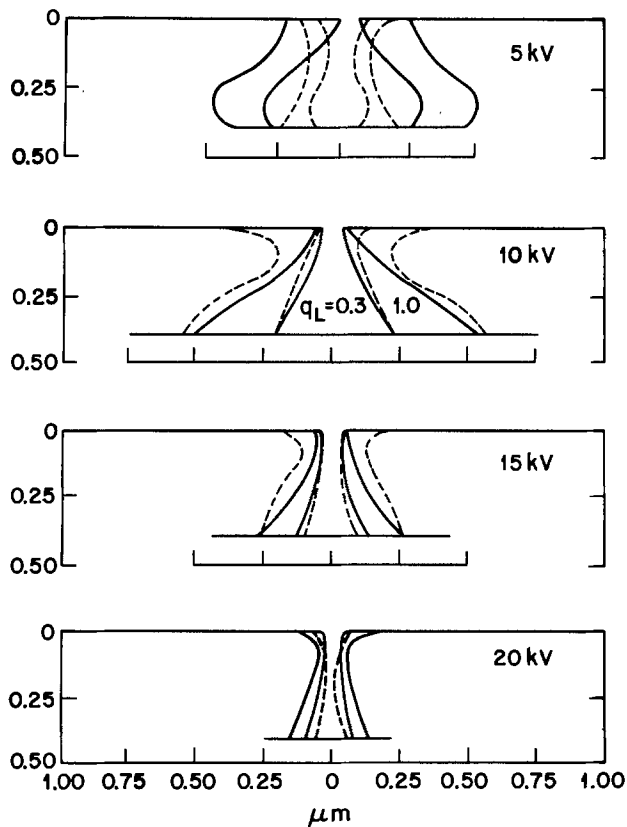


Fig. 20. Comparison of developed profiles for charges per unit length of 0.3×10^{-8} C/cm and 1.0×10^{-8} C/cm for PMMA on an aluminum substrate. The solid lines are from theory; the broken lines are the experimental contours of Wolf *et al.* [from J. S. Greeneich and T. Van Duzer, *IEEE Trans. Electron Devices*, ed 21, 286 (1974)].

experimental contours of Wolf *et al.* (35) also shows reasonable agreement except at 5 kV. Greeneich and Van Duzer attribute this to a lack of validity of the plural scattering theory for primary electrons at 5 kV.

Heidenreich *et al.* (33, 38) developed an empirical or phenomenological model for determining gel energies and profiles in negative resists. For the case of a uniform large area exposure such as one encounters in the determination of the contrast curve, the incident electron energy dissipation density depends only on the depth z into the resist. The rate of energy deposition at penetration depth z is given by

$$\frac{dE}{dt} = \frac{J_0}{e} \frac{\partial V}{\partial z} \text{ eV/cm}^3/\text{sec} \quad [22]$$

where J_0 is the incident current density and $\partial V/\partial z$ the specific energy dissipation in eV/cm. The specific dissipation can be written as

$$\partial V/\partial z = \frac{V_a}{R_G} \Lambda(f) \text{ eV/cm} \quad [23]$$

for beam voltage V_a with R_G , the Grün range, given by

$$R_G = (0.046/\rho) V_a^{1.75} \mu\text{m} \quad [24]$$

and $\Lambda(f)$ the depth dose function in terms of normalized penetration ($f = z/R_G$). The density is ρ and is approximately unity for polymeric resists. From Eq. [22] it is seen that the minimum electron dose $D_g^0 = J_0 \tau$ for exposure time τ required to gel the resist at the substrate interface is related to the gel energy E_g^i by

$$E_g^i = \frac{D_g^i}{e} \left(\frac{\partial V}{\partial z} \right)_i \text{ eV/cm}^{-3} \quad [25]$$

The value of $(\partial V/\partial z)_i$ the energy dissipation at the interface, is obtained from Eq. [23] for a resist of initial thickness z_i . Heidenreich incorporated backscatter from the substrate by means of a backscattered coefficient η which is used to modify the forward scattered beam density as $J_0(1 + \eta)$.

The effects of backscatter are readily seen when we examine the lithographic response curves for negative resists supported on a variety of substrates. Figure 21 shows the response curves for $\sim 6600\text{\AA}$ COP on three different substrates. In this figure curves 1 and 2 are for a thin Si_3N_4 substrate ($\sim 1000\text{\AA}$ thick) and the same Si_3N_4 film supported by a bulk silicon substrate, respectively. Curve 3 pertains to a substrate consisting of a layer of gold approximately 4000\AA thick on top of a silicon wafer. The backscatter coefficient from Si_3N_4 is less than 3% so that the contrast curve for the thin Si_3N_4 substrate can be considered to be an acceptable approximation of that corresponding to an unsupported resist film. Such experiments provide a means of

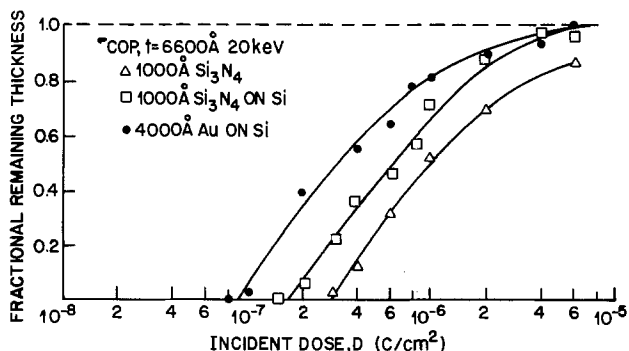


Fig. 21. Measured contrast curves for COP on three different substrates. Exposure conditions are as given in the figure [from M. C. Chung and K. L. Tai, in "Electron and Ion Beam Science and Technology," R. Bakish, Editor, p. 242, The Electrochemical Society Softbound Proceedings Series, Princeton, N.J. (1978)].

evaluating the backscattered coefficient (39). We consider $\partial V/\partial z$ to be the sum of two terms, i.e.

$$\partial V/\partial z = (\partial V/\partial z)_{FS} + (\partial V/\partial z)_{BS} \quad [26]$$

where $(\partial F/\partial z)_{FS}$ is the energy dissipation due to forward scattering and $(\partial V/\partial z)_{BS}$ is the energy dissipation due to electrons backscattered from the underlying substrate material. Equation [26] can be rewritten as

$$\partial V/\partial z = (\partial V/\partial z)_{FS} \{1 + (\partial V/\partial z)_{BS}/(\partial V/\partial z)_{FS}\} \quad [27]$$

$$= (\partial V/\partial z)_{FS} \{1 + \eta\} \quad [28]$$

where η is defined as the backscatter coefficient. For the case of the thin Si_3N_4 substrate, $\eta = 0$ so that from Eq. [25] we have

$$E_g^i = \frac{(D_g^i)_0}{e} \left(\frac{\partial V}{\partial z} \right)_{FS}^i \quad [29]$$

where $(D_g^i)_0$ is the incident interface gel dose for the zero backscatter contribution. For any other substrate

$$E_g^i = \frac{D_g^i}{e} \left\{ \left(\frac{\partial V}{\partial z} \right)_{FS}^i + \left(\frac{\partial V}{\partial z} \right)_{BS}^i \right\} \quad [30]$$

Thus from Eq. [29] and [30] we obtain

$$(D_g^i)_0/D_g^i = 1 + \eta^i \quad [31]$$

where η^i is the effective backscattering coefficient evaluated at the interface.

The depth dose model thus allows the gel energy E_g^i of a resist to be calculated from an observed interface dose D_g^i and predicts a dependence of D_g^i on accelerating voltage going as $V_a^{(-0.75)}$ which agrees reasonably well with experiments.

The depth-dose model can also be used to determine energy profiles in the resist when convolved with the spreading Gaussian treatment of Nosker described earlier (28). Heidenreich *et al.* (33) simplified this even more by convolving the spreading Gaussian beam treatment with the experimentally determined relationship between resist thickness remaining after development and input electron dose (see Fig. 37). Backscattering was again included as $J_0(1 + \eta)$, i.e., as a modification of the incident current. For a beam scanning along the x direction at line speed x , the dose at distance y from the line center at penetration z is given by

$$D(y) = \frac{(1 + \eta)D_0^x}{\bar{s}\sqrt{\pi}} \exp(-y^2/\bar{s}^2) \text{ C/cm}^2 \quad [32]$$

where $D_0^x = i_0/x$. The area input dose at the line center $y = 0$ is thus

$$D(0) = \frac{(1 + \eta)D_0^x}{\bar{s}\sqrt{\pi}} \text{ C/cm}^2 \quad [33]$$

It should be noted that Eq. [32] is a quasi-monoenergetic approximation applying only for penetration z such that the loss in electron energy is about $0.1 V_a$.

The significant amount of swelling that accompanies the removal of uncross-linked polymer during development of a negative resist renders the development process in these resists much more difficult to treat. In particular, the surface-limited etching hypothesis that has been found suitable for positive resists like PMMA (40) is completely inapplicable to negative polymer resists in general. Nevertheless, convolution of the input Gaussian with the resist response curve (Fig. 37) yields single line profiles which agree well with experimental profiles for widths down to about $0.18 \mu\text{m}$ below which interface distortion of the gel becomes dominant. Discrepancies can be attributed to the lack of mechanical integrity of the gel. Ge! interactions can take place between neighboring features leading to distortion and errors in the experi-

mentally developed profiles. Such results show the importance of good gel rigidity and high contrast for negative resists used in high resolution applications.

The simplified phenomenological model of Heidenreich was also used by Hatzakis *et al.* (41) to determine resist profiles in PMMA. These authors also took into account the effect of the developing process. The assumption that the developed profiles can be approximated by contours of equal absorbed energy density is a good approximation at high-exposure densities where development is time independent. As pointed out by Hatzakis *et al.* and Greeneich (42), such a model is not adequate for time-dependent developers. Using the phenomenological model, Hatzakis *et al.* obtained contour lines for equal absorbed energy in the resist and expressed it as an energy matrix $E(r, z)$ from the product of the electron intensity distribution and the energy dissipation function. Knowing the change in molecular weight for a given exposure level and the dependence of solubility rate on fragmented molecular weight, they were able to transform the two-dimensional energy density matrix into a solubility rate matrix. Greeneich (42) used a similar model based on a more rigorous analytical analysis of absorbed energy density. He used an empirically determined formula for solubility rate in the form

$$R = R_0 + \frac{\beta}{M_f^\alpha} \quad [34]$$

where R_0 , β , and α are constants for a given developer. Hatzakis *et al.* concluded that the developed resist profiles are dominated by the developing process at low-exposure densities, but at high-exposure densities, the developed resist profiles are dominated by scattering inside the resist. Their results are summarized in Fig. 22. Experimental verification of these three profiles was presented by Hatzakis (43) using PMMA resist. The resulting resist profiles are shown in Fig. 23. By careful control of exposure conditions, Hatzakis was able to obtain a 2500\AA wide line in $1 \mu\text{m}$ of resist

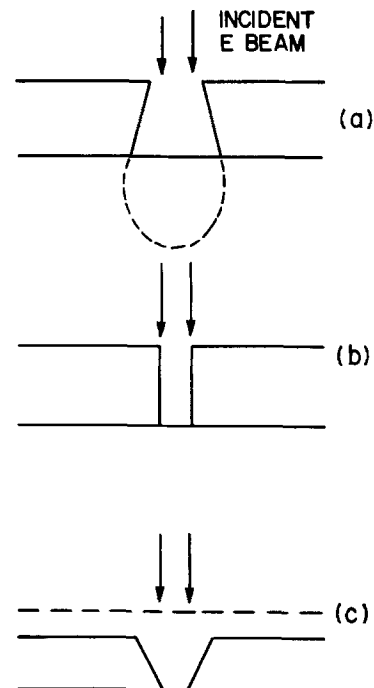


Fig. 22. Positive resist profiles for (a) high charge density (developed resist profile dominated by the electron penetration profile); (b) medium charge density (developed resist line shape results from combination of electron penetration profile and development process); (c) low charge density (developed resist line shape dominated by development process) [from M. Hatzakis, *J. Vac. Sci. Technol.*, 12, 1276 (1975)].

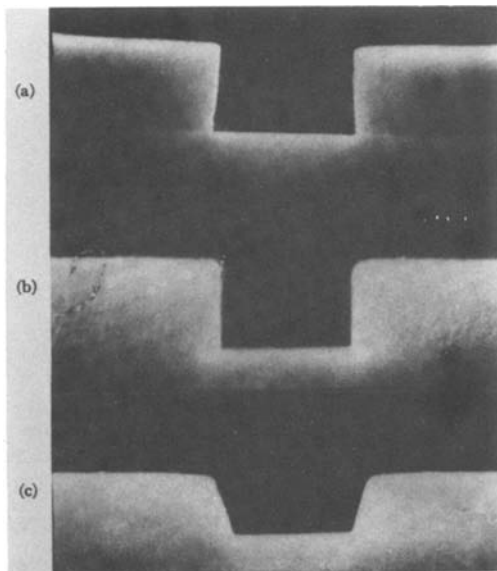


Fig. 23. Actual PMMA resist profiles at an incident charge density of (a) 10^{-4} C/cm², (b) 8×10^{-5} C/cm², and (c) 5×10^{-5} C/cm² [from M. Hatzakis, *J. Vac. Sci. Technol.*, **12**, 1276 (1975)].

with vertical walls using a 1000Å diam beam at 20 kV. Greeneich presented his results in terms of time evolution of developed contours. He also found the incident dose to be particularly important, as was the particular developer chosen. A typical time-developed profile observed for a low-incident dose is shown in Fig. 24. Overall, the results are qualitatively similar to those of Hatzakis *et al.*

In summary, both analytic and Monte Carlo methods calculate the spatial distribution of energy dissipation in a polymer film. Since the development of the image can be related to energy dissipation, such calculations provide a means of determining line profiles. In general the Monte Carlo model is more precise whereas the analytic models do show some discrepancies with experiment. Both methods have several disadvantages. The Monte Carlo approach involves a great deal of computer time and the results are difficult to adapt for various experimental conditions. The analytic models are mathematically complex, even with simplifying assumptions. The phenomenological model of Heidenreich is the simplest approach and has been used to determine profiles of both positive and negative resists.

Figure 25 represents an important result of the electron scattering effect. Although the incident charge density is the same for each of the five lines in Fig. 25, the outer two lines are underexposed because these two lines have only one neighboring line while each of

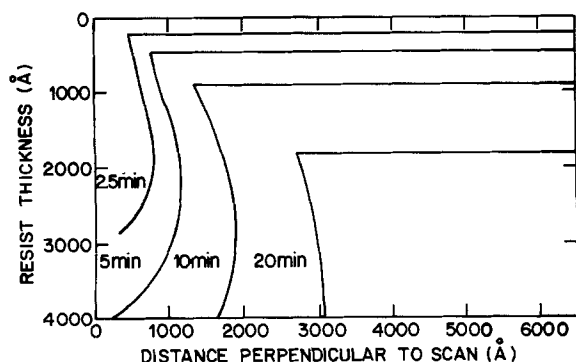


Fig. 24. Time evolution of developed contours in PMMA developed in MIBK at 22.8°C. $V = 10$ kV, $D = 5 \times 10^{-10}$ C/cm, and $M_n = 2 \times 10^5$ [from J. Greeneich, *J. Appl. Phys.*, **45**, 5264 (1974)].

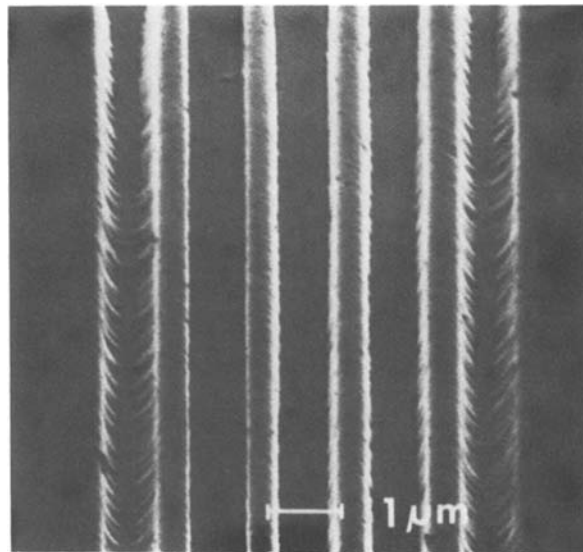


Fig. 25. Scanning electron micrograph of a line pattern in 0.8 μ m PMMA on SiO₂. The incident charge density was 10^{-4} C/cm² for each of the five lines. The incomplete development of the outer two lines is due to the smaller number of electrons scattered during exposure of neighboring lines [from D. Widmann and K. U. Stein, *Solid State Circuits, Proc., 2nd Eur. Solid State Circuits Conf.*, 1976, 29-47 (pub. 1977)].

the inner three lines has two neighboring lines from which electrons are scattered. This proximity effect which was alluded to earlier may be partially compensated by proper control of the beam scanning speed. However the lateral spread of the dissipated energy at the line edges remains and both the resist parameters and the development conditions must be carefully controlled in order to arrive at the desired linewidths.

If we define resolution as the smallest line-space pattern we can generate (as opposed to the width of an isolated line) we find that positive resists give much higher resolution than negative resists. Further, it is found that the calculated values of minimum grating spacing for a rigid negative resist are 2-5 times better than can be obtained experimentally (44). The gratings fail prematurely because the cross-linked lines swell and deform in the developer. The exact shape of a free standing line is determined also by the strength of the solvent used to develop it.

Thus the faithful production in the resist of a feature written by the electron beam does not depend exclusively on electron scattering and molecular parameters of the polymer but also on factors such as solvent-induced swelling, competitive wetting of the substrate by the solvent and the polymer, and gel rupture by forced-development (45). Solvent-induced swelling limits line space resolution in negative resists to about 1 μ m for about 0.5 μ m residual film thickness and a beam diameter of 0.5 μ m. Somewhat higher resolution could be obtained for smaller residual film thickness (lower exposure dose). The developing process in certain positive resists such as PMMA is akin to a surface etching in which there is negligible swelling (46). Minimum line space resolution is therefore determined more directly by absorbed energy density and using the same 0.5 μ m diam beam as above, one can easily resolve the beam address structure.

Another important physical limitation follows from the statistics of electron beam exposure (47). If we divide the electron resist surface to be exposed into a configuration of densely packed identical square elements of width a μ m, then the average number of primary electrons per element \bar{n} is given by

$$\bar{n} = \frac{a^2 D}{q 10^8} \quad [35]$$

where D is the exposure dose in C/cm^2 and q is the electronic charge. The actual number n of electrons per resolution element has a Poisson distribution and if we assume that a resolution element is exposed if it receives an exposure at or above a fraction r of the average dose \bar{n} , then a certain fraction $(1 - r)$ of the resolution elements will receive a dose which is below the exposure dose and hence will print as a defect. The statistics of the exposure can be treated mathematically and the results are summarized as a set of curves in Fig. 26. The figure shows as a function of resolution element size the exposure flux in C/cm^2 required to achieve a fixed average number of defective elements per cm^2 . There are three pairs of curves. One pair pertains to situations in which an element is regarded as defective if it receives an exposure that is not within $\pm 25\%$ of the nominal level; the second pair applies if an exposure error is defined as a deviation of $\pm 50\%$ or more from the nominal level; the third pair considers exposure errors of exactly 100%, i.e., elements which receive no electron hits at all. Within each pair, one curve pertains to a fixed average defective element rate of 1 defect/ cm^2 and the other to a rate of 100 defective elements/ cm^2 . In Fig. 26 we see that by going from the upper to the lower curve of any pair, the defect rate increases by a factor of 100 with a flux decrease of only about 30%. Given that resist sensitivities are on the order of 10^{-6} C/cm^2 , we are not yet in a regime where we are becoming statistically limited.

We have seen that the fundamental limit to resolution is due to electron scattering considerations. The extent of scattering is in turn determined by a variety of parameters discussed previously which determine the maximum resolution. The optimum resolution for a given resist thickness is best determined in those positive resists which do not swell during development, e.g., PMMA, and whose profile is thus primarily determined by scattering considerations. The resolution can be obtained by exposing lines with a single beam spot of very small diameter and varying the exposure density. Figure 27 shows a plot of the ratio of beam

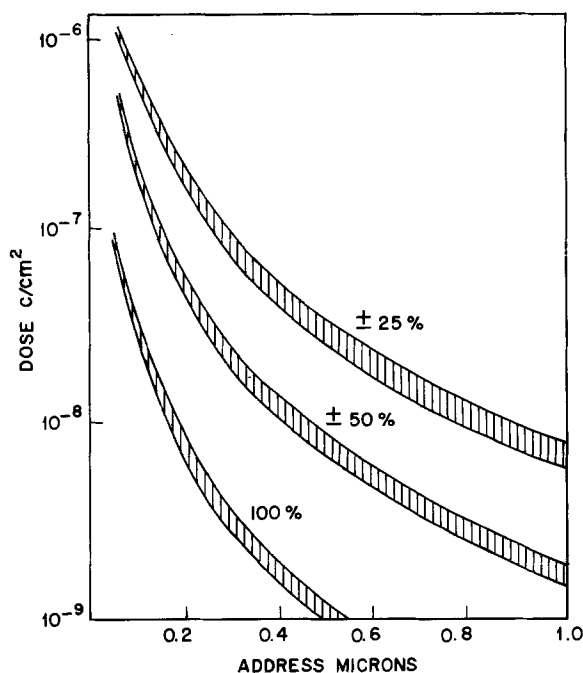


Fig. 26. Minimum required exposure to obtain a given defect probability as a function of element size (from M. Feldman, Private communication).

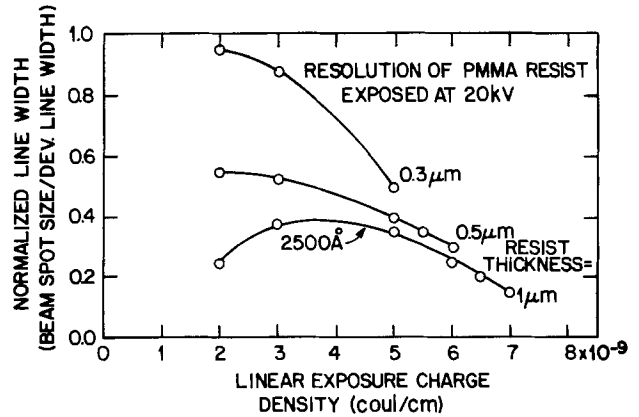


Fig. 27. Curves of normalized linewidth vs. linear exposure charge density for PMMA at 1.0, 0.5, and 0.3 μm [from M. Hatzakis, *J. Vac. Sci. Technol.*, 12, 1276 (1975)].

spot size to developed linewidth in PMMA at the point of complete line development vs. the linear exposure charge density. The figure shows the results for resist thickness of 0.3, 0.5, and 1.0 μm , respectively, for a 1000Å diam beam. We can see that for thin films on the order of 0.3 μm , it is possible to obtain linewidth comparable to the beam diameter at linear charge densities of about 2×10^{-9} C/cm . Of course at higher charge densities the line starts to broaden considerably. Figure 28 is a scanning micrograph of one sample on the curve which exhibits an aspect ratio of 4. It shows a 2500Å wide line in 1 μm thickness resist with vertical walls and represents the optimum resolution that can be obtained in PMMA 1 μm thick exposed with a 1000Å wide beam (43).

In order to obtain even finer resolution, one has to resort to special techniques to minimize electron scattering effects. Two main approaches (48) have been used. Firstly the sample substrate is made so thin that electron backscattering is minimized. Secondly, the electron resist in which the pattern is initially formed is made so thin that forward scattering is also reduced. Broers *et al.* (49) for example have defined 250Å wide lines and spaces in 225Å thick films of $Pd_{40}Au_{60}$ using PMMA resist. The initial resist thickness was 1100Å and the resist was exposed in a high resolution scanning transmission electron microscope (STEM) at a charge density of 5×10^{-4} C/cm^2 , a beam potential of 56 kV, and a beam diameter of 10Å. Thus 200-300Å would appear to be the range of the secondary electrons produced by passage through the resist of the primary electron. Using contamination techniques (a technique in which a line is built up by *in situ* poly-

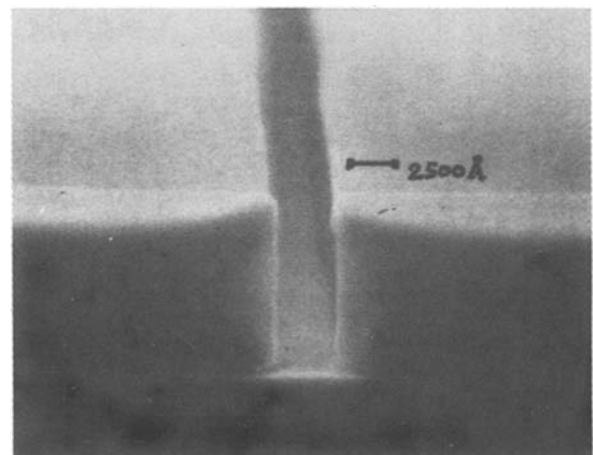


Fig. 28. Profile of a 2500Å wide line exposed and developed in 1 μm thick PMMA at 4×10^{-9} C/cm at 20 kV [from M. Hatzakis *J. Vac. Sci. Technol.*, 12, 1276 (1975)].

merization of mobile monomers adsorbed on the substrate surface), Broers *et al.* (50) have fabricated 80Å wide and 100Å thick Pd₄₀Au₆₀ lines. In this case resolution was not limited by electron scattering but by the grain size of the metal films.

X-ray lithography.—X-ray lithography was established as a viable fabrication technique by Spears and Smith in 1972 (51). The essential ingredients of this process include: (i) a mask consisting of a device pattern made of x-ray absorbing material on a thin membrane of x-ray transmitting material, (ii) an x-ray source of sufficient brightness in the soft x-ray region to expose the resist through the mask, and (iii) an x-ray resist.

For all practical purposes, x-rays travel in straight lines through matter with resolution being primarily determined by the effective range δ of the photoelectrons produced in the resist following absorption of an x-ray photon (52). Energy absorption follows an exponential dependence on μ_m the mass absorption coefficient, on ρ the density, and on z the thickness of the absorbing film according to

$$I = I_0 e^{-\mu_m \rho z} \quad [36]$$

where I_0 and I are the intensities of x-rays before and after passage through the absorbing film. Photoelectrons lose energy by the same elastic and inelastic collisional processes discussed earlier producing secondary electrons which are responsible for nearly all changes in the resist. Each location of an absorption event is therefore surrounded by a small volume of dimension δ where the resist has been modified. The energy of photoelectrons ejected during absorption of 4Å x-rays for example is on the order of 3 keV for which the range is on the order of 0.3 μm . The range will be smaller [$\sim 50\text{Å}$ for C_K x-rays ($\lambda = 44.8\text{Å}$)] and hence potential resolution will be higher for longer wavelength x-rays.

Resolution is further limited by two types of geometrical distortion (Fig. 29). The opaque parts of the mask cast shadows onto the wafer below. The edge of the shadow is not absolutely sharp because of the finite extent of the x-ray source (diameter of focal spot of electrons on the anode) at distance D from the mask. If the gap between mask and wafer is g , this effect which is referred to as penumbral blur σ_p , limits resolution to

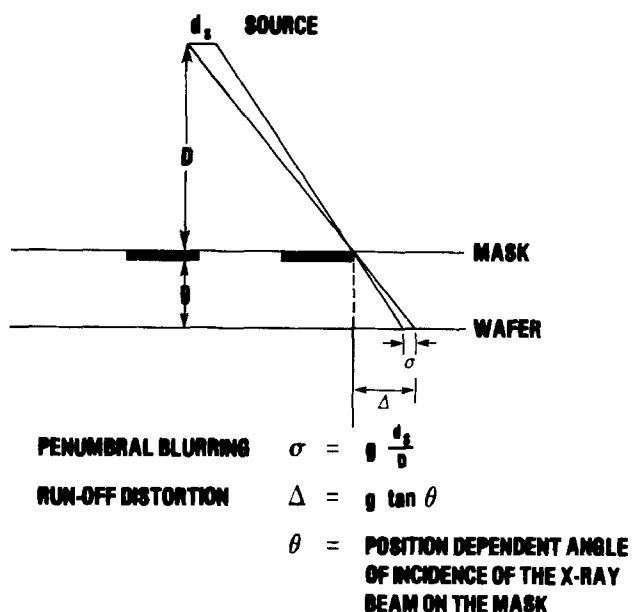


Fig. 29. Schematic diagram of an x-ray exposure system showing the types of geometric distortion encountered.

$$\sigma_p = g(d_s/D) \quad [37]$$

The angle of incidence of the x-rays on the wafer varies from 90° at the center of the wafer to $\tan^{-1}(D/R)$ at the edge of a wafer of radius R . The shadows are slightly longer at the edge by an amount Δ which is given by

$$\Delta = g(R/D) \quad [38]$$

This small magnification is generally of no concern but for multilevel devices it must have the same value for each level or at least its variation must be within the registration tolerance. This implies stringent control of the gap g . These geometric distortions can be reduced by increasing the distance between mask and source but since the intensity is inversely dependent on the square of the distance, the exposure times become too long. One way out of this dilemma is to use synchrotron radiation (53, 54). Synchrotron radiation arises as the major loss mechanism from electrons in motion at relativistic energies. The radiation consists of an intense continuous spectral distribution from the infrared out to x-ray wavelengths. It is highly collimated and is confined near the orbital plane of the circulating electrons thereby requiring spreading in the vertical direction or moving the mask wafer combination with constant speed through the fan of synchrotron radiation to expose the entire wafer surface. The high power output offers the advantage of reasonable resist exposure times and the fact that the radiation is produced over a few milliradians divergence means that run-out error and penumbral distortion are significantly reduced.

A further factor which can degrade resolution is mask contrast. Figure 30 shows the linear absorption coefficient α of some of the most absorbing and some of the most transparent materials available. Except for discontinuities at absorption edges, the absorption increases with increasing wavelength. It should be noted that the most absorbing materials are only about a factor of 50 higher in their absorption coefficient than the most transparent materials. Thus mask substrates have to be relatively thin to have sufficient transmission and the absorber pattern has to be relatively thick

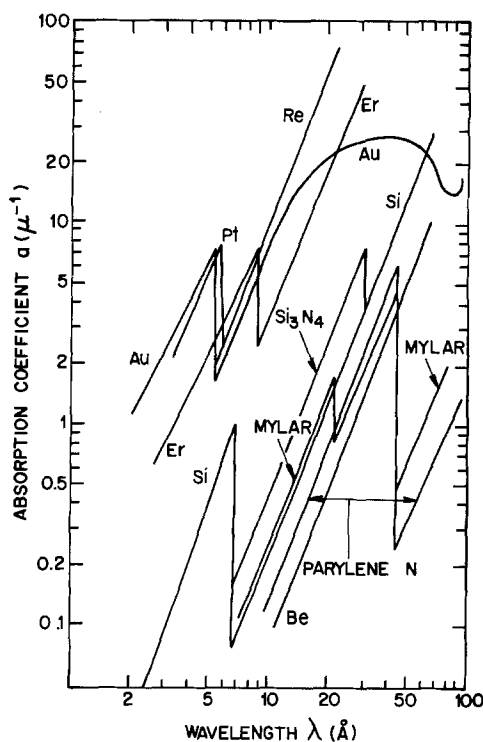


Fig. 30. Absorption coefficient of some of the most absorbing and most transparent materials for soft x-rays.

to attenuate x-rays sufficiently. Contrast is the ratio of the transmission of the "clear" area to the transmission of the "opaque" area. A low contrast mask will give rise to some additional spurious exposure of the resist (55) as shown in Fig. 31. The additional exposure is caused by (i) continuous x-rays, (ii) secondary electrons and Auger electrons ejected from the x-ray mask, and (iii) secondary electrons ejected from the resist substrate. As an example of the effect of continuous radiation, for an 8:1 contrast ratio in an x-ray resist exposed with a Pd x-ray source, 7000Å of gold is required for the absorber pattern on the mask. In comparison, if the exposure were done by 4.4Å characteristic radiation only, 4500Å of gold would give the same contrast ratio. Likewise the secondary electrons and Auger electrons contribute to the exposure of the resist in the regions underneath the gold layers and therefore decrease the resolution and contrast of the exposed pattern.

The fact that absorption coefficients for x-rays vary roughly as λ^3 between absorption edges favors the use of short wavelengths to penetrate the mask substrate and long wavelengths to be absorbed by the patterned areas. The selected wavelength is therefore a compromise between the desire to obtain as much transmission as possible and as much contrast as possible. For patterns with dimensions around 1 μm , the wavelength region between 4 and 50Å represents an acceptable compromise.

Mask contrast is also important in determining the shot noise limitation for the sensitivity of the resist (56). The shot noise in the absorption of photons defines a limitation for the sensitivity of any detector. Consider the average number \bar{n} of x-ray photons absorbed in a small volume of resist (Fig. 32) to be given by

$$\bar{n} = \frac{E}{h\nu} A\delta^2 \quad [39]$$

where E is the incident exposure density, $h\nu$ is the energy of each x-ray photon, and A is the fraction of the incident energy which is absorbed in the resolution element of resist with lateral dimension δ and a thickness d . It is assumed that the resist is ideal, i.e., there are no other limitations on its performance; the resist contrast is infinite. The absorption is given by

$$A = 1 - e^{-\alpha d} \quad [40]$$

$$A \approx \alpha d \text{ for } \alpha \ll 1 \quad [41]$$

where α is the linear absorption coefficient. Since photons actually arrive at random, the actual number of photons absorbed in different resolution elements will deviate from the average value. These deviations

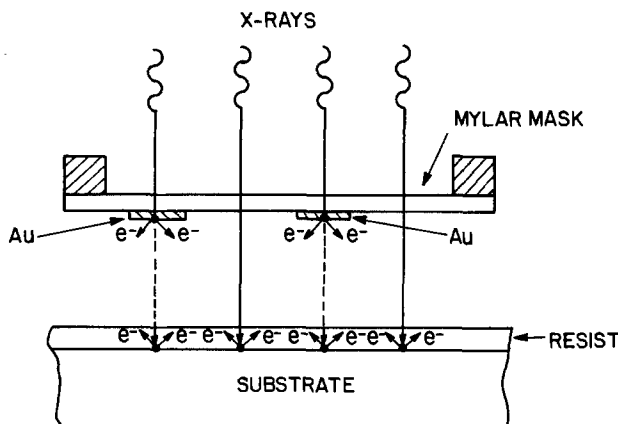


Fig. 31. Schematic representation of spurious exposure effects affecting the x-ray exposure [from J. R. Maldonado, G. A. Coquin, D. Maydan, and S. Somekh, *J. Vac. Sci. Technol.*, 12, 1329 (1975)].

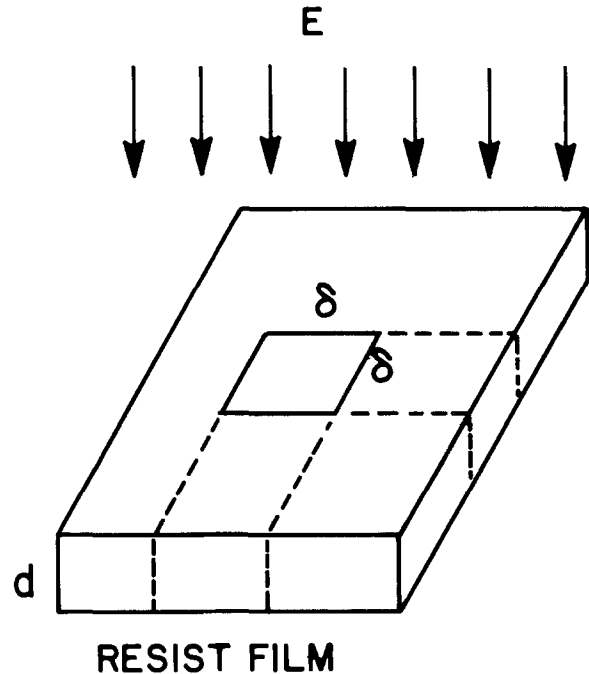


Fig. 32. Schematic resolution element in a resist film

from the average value are responsible for the performance limitations of an ideal resist. The probability of absorbing photons in one resolution element for which the average number of absorbed photons per resolution element is \bar{n} is determined by the Poisson distribution

$$p(n, \bar{n}) = \frac{\bar{n}^n}{n!} e^{-\bar{n}} \quad [42]$$

Which for large \bar{n} can be approximated by

$$p(n, \bar{n}) \approx \frac{1}{\sqrt{2\pi\bar{n}}} \exp\left[-\frac{(n - \bar{n})^2}{2\bar{n}}\right] \quad [43]$$

The Poisson distribution has a width defined by its standard deviation

$$\sigma = \sqrt{\bar{n}} \quad [44]$$

Let us now assume that the "clear" areas of the x-ray mask have a transmission of 1 and that the "opaque" areas have a transmission of T . The average exposure in the "opaque" area is then reduced to $\bar{n}_T = T\bar{n}$ as compared to the value \bar{n} in the "clear" parts of the mask.

The probability $p(n)$ of observing n photons in a resolution element is plotted in Fig. 33 for areas under the clear and opaque parts of the mask for an exposure in which $\bar{n} = 15$ in the clear part and $\bar{n}_T = 7.5$ in the opaque part ($T = 0.5$). It can be seen from Fig. 33 that the two distributions overlap. Thus there is no way of knowing from the exposed resist copy whether the mask was transparent or opaque in a special area for observed photon absorptions which are in the overlap region. For an ideal resist we might define an optimum threshold value n_{opt} such that all elements which received $n \leq n_{opt}$ photons are developing as if not exposed and all resist areas with $n \geq n_{opt}$ are recognized as exposed areas and then choose n_{opt} in such a way as to minimize the probability for an error. Whenever we observe $n \leq n_{opt}$ photons in the clear sections of the mask or $n > n_{opt}$ photons in the opaque sections, we have made an error and produced a defect. The probability P_{def} for such a defect is

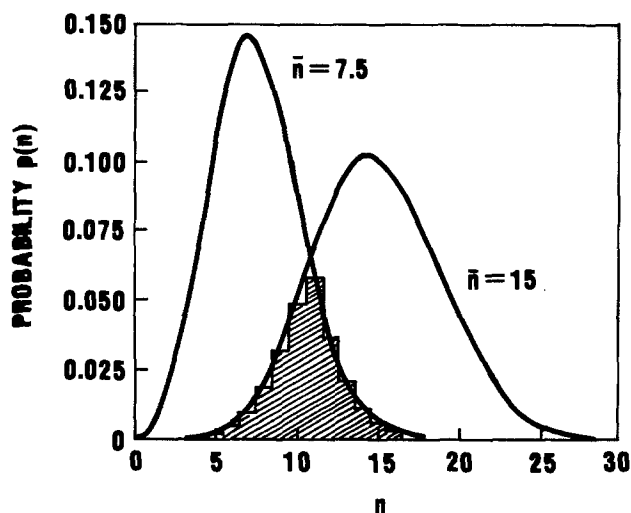


Fig. 33. Poisson distribution for an exposure $\bar{n} = 15$ in the clear and $\bar{n} = 7.5$ in the opaque areas of the mask ($T = 0.5$). The shaded area represents the probability for a defect which occurs when more than $n_{\text{opt}} = 11$ photons are observed in opaque areas or $n_{\text{opt}} = 11$ or less photons for the clear areas of the mask [from E. Spiller and R. Feder, Topics in Applied Physics, Vol. 22, "X-Ray Optics, Applications to Solids," Chap. 3, H. J. Queisser, Editor, Springer Verlag, Berlin (1977)].

$$P_{\text{def}} = \sum_{n=0}^{n_{\text{opt}}} p(n, \bar{n}) + \sum_{n=n_{\text{opt}}}^{\infty} p(n, T \cdot \bar{n}) \quad [45]$$

In Fig. 33, P_{def} is represented by the shaded area under the two Poisson distributions. The defect probability becomes smaller for a larger separation of the two Poisson distributions which can be achieved by increasing the exposure and/or by increasing the contrast of the mask.

Figure 34 is a plot of P_{def} as a function of exposure for various transmission values of the absorber pat-

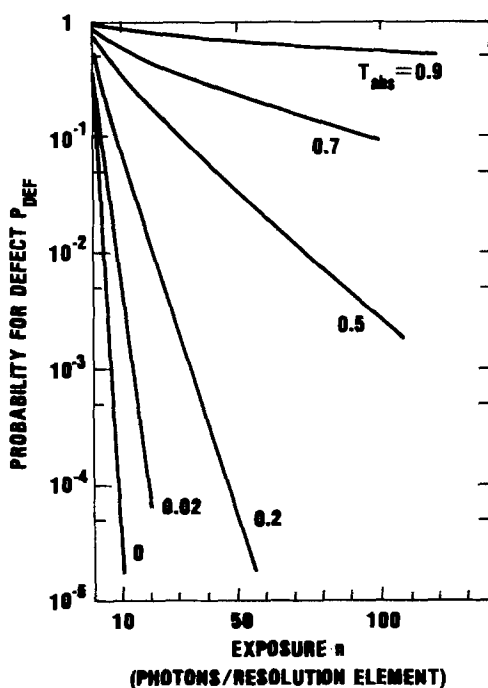


Fig. 34. Probability for a defect P_{def} as a function of exposure in the clear areas of a mask for an ideal resist for different transmission values in the opaque areas of the mask [from E. Spiller and R. Feder, Topics in Applied Physics, Vol. 22, "X-Ray Optics, Applications to Solids," Chap. 3, H. J. Queisser, Editor, Springer Verlag, Berlin (1977)].

tern. For high contrast masks ($T < 0.02$) practically defect-free resist copies ($P_{\text{def}} < 10^{-6}$) can be obtained with exposures $\bar{n} > 30$. For masks of low contrast ($T \approx 1$) the exposure has to be increased drastically to obtain a similar performance. The 3σ criterion is a widely used measure for an acceptable low error probability. This requires that the overlap of the two Poisson distributions should only occur outside the 3σ limit of each distribution. The separation of the two distributions should be three times the standard deviation of each distribution

$$\bar{n} - T \cdot \bar{n} = 3\sigma_{\text{clear}} + 3\sigma_{\text{opaque}} \quad [46]$$

combining Eq. [44] and [46] we obtain for the required exposure

$$\bar{n} = 9/(1 - \sqrt{T})^2 \quad [47]$$

Thus, low contrast masks require higher exposures, i.e., less sensitive resists, to obtain a predetermined defect density. The minimum value of \bar{n} required to expose the resist is given by Eq. [39]. Equation [47] then gives the mask contrast required to meet the 3σ defect limit.

As mentioned already, the intrinsic resolution attainable with x-ray lithography is determined by the effective range of the primary photo-electrons and is as low as 50Å for a C_K x-ray ($\lambda = 44.7\text{Å}$). In order to test the resolution capability of x-ray lithography, one needs a mask. High-resolution test masks have been fabricated by electron beam lithography and have allowed replication of 0.1 μm geometries with x-ray lithography (52). The technique allows sharp vertical sidewalls and large aspect ratios to be obtained. Figure 35 shows a scanning electron micrograph of the cross section of a 1600Å linewidth grating pattern exposed in an 8500Å thick PMMA film on an SiO_2/Si substrate using Cu_L x-ray radiation at 13.3Å. The slight curvature of the grating lines are believed caused by overdevelopment which led to softening of the PMMA.

Ion beam lithography.—Resolution in ion beam lithography is determined by ion scattering and scattering of the resultant secondary electrons (57). The contribution of each to the overall transverse energy distribution is a function of the energy and atomic number Z of the ions. For ions of high Z and high energy for which the range may be considerably greater than the resist thickness, resolution is primarily determined by the range of the secondary electrons. For a large Z ion, e.g., O^+ at 1.5 MeV, the velocity of the scattered electron is relatively small and so they have a relatively short range. In addition, the cross section for electron scattering from a heavy ion is greater so

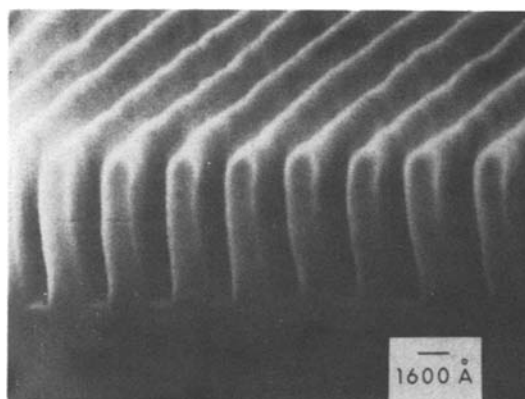


Fig. 35. Scanning electron micrograph of the cross section of a 1600Å linewidth grating pattern exposed in 8500Å thick PMMA on an Si/SiO_2 substrate using Cu_L x-rays at 13.3Å [from D. C. Flanders, H. I. Smith, H. W. Lehmann, R. Widmer, and D. C. Shaver, *Appl. Phys. Lett.*, 32, 112 (1978)].

the deposited energy density is high in the center of the particle track extending out to perhaps 100Å. For a lighter particle at the same energy, the secondaries have much higher velocities and hence a larger range. This situation is schematically represented in Fig. 36 which shows the radial distribution of deposited energy by secondary electrons for 1.5 MeV O⁺, He⁺, and H⁺.

On the other hand, the range of secondary electrons for ions of low Z and energy, e.g., 50 keV H⁺ is very small (≅50Å) and resolution is primarily determined by ion scattering. Thus the practical resolution can be varied depending on choice and energy of the ion.

The amount of energy deposited by an ion per unit track length (dE/dx) as it passes through a resist is considerably greater than for electrons. The dissipation for 1.5 MeV O⁺ is about 800 eV/nm, for 1.5 MeV He⁺ is about 200 eV/nm, and for 1.5 MeV H⁺ is about 20 eV/nm. The dissipation for 10 keV electrons is about 4 eV/nm and for 20 kV electrons is about 2 eV/nm. Thus the resist sensitivity in terms of incident dose (C/cm²) is considerably greater [about one to two orders of magnitude (58)] for an ion beam exposure than for an electron beam exposure. One might expect that on the basis of absorbed energy, resists would have the same sensitivity. Preliminary results indicate however that the amount of deposited energy to achieve the same degree of exposure is not constant as one goes from electrons through light ions to heavy ions (57). Thus the resist chemistry is a function of the energy transfer function, i.e., dose rate.

Chemical Limitations

We have seen that several factors contribute to inherent loss of resolution depending on the particular exposure technology. Diffraction of light, scattering of

primary, secondary, and photo electrons, scattering of ions, and mask-related problems all contribute to energy deposition in areas remote from the point of entry of the impinging radiation. The scattered energy can cause chemical changes in the resist thereby leading to resolution loss. Thus an understanding of resist response, which has common elements for all exposure technologies, is important in determining the maximum resolution attainable with a given set of process conditions. The resist response function which primarily determines resolution is the contrast (γ). Contrast in the case of negative resist is related to the rate of cross-linked network (gel) formation and may be conveniently measured by exposing pads of known area to varying radiation doses. Gel is not formed until a certain dose, termed the interface gel dose (D_gⁱ), has been reached. Thereafter, the gel content increases with increasing dose; consequently the thickness remaining after development increases until, ultimately, the thickness of the developed pad is equal to the original film thickness (in practice it is slightly less due to volume contraction during cross-linking). This situation is shown schematically in Fig. 37a. Resist contrast (γ_n) is then defined as (59)

$$\gamma_n = 1 / (\log D_g^0 - \log D_g^i) = \left[\log \frac{D_g^0}{D_g^i} \right]^{-1} \quad [48]$$

where D_g⁰ is the dose required to produce 100% initial film thickness and it is determined by extrapolating the linear portion of the thickness vs. dose plot to a value of 1.0 normalized film thickness. We may also note here that the sensitivity of a negative resist is usually taken as the dose (D_g^{0.5}) required to cross-link the film so that 50% of the initial film thickness

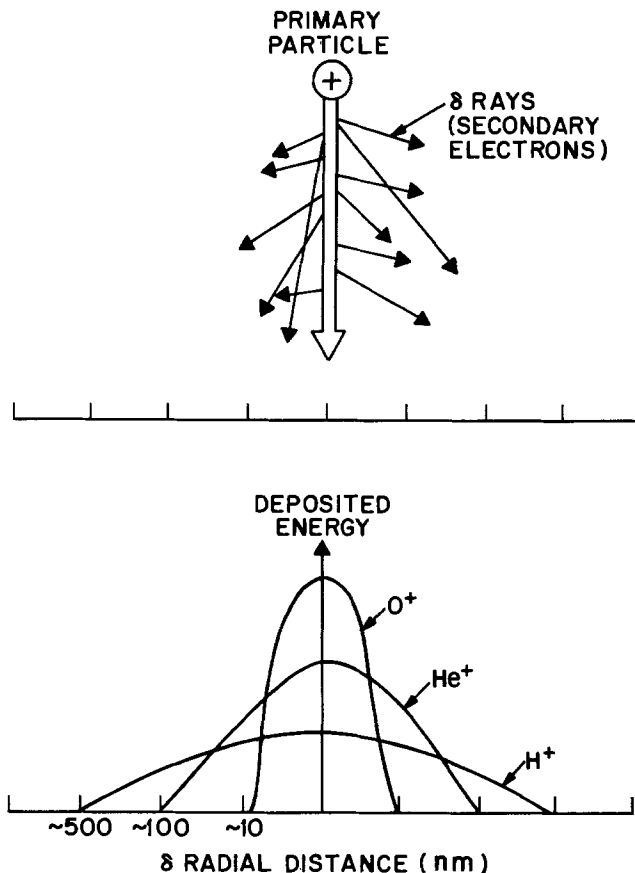


Fig. 36. Schematic representation of radial distribution of deposited energy by secondary electrons for O⁺, He⁺, and H⁺ [from T. M. Hall, A. Wagner, and L. F. Thompson, *J. Vac. Sci. Technol.*, 16, 1889 (1979)].

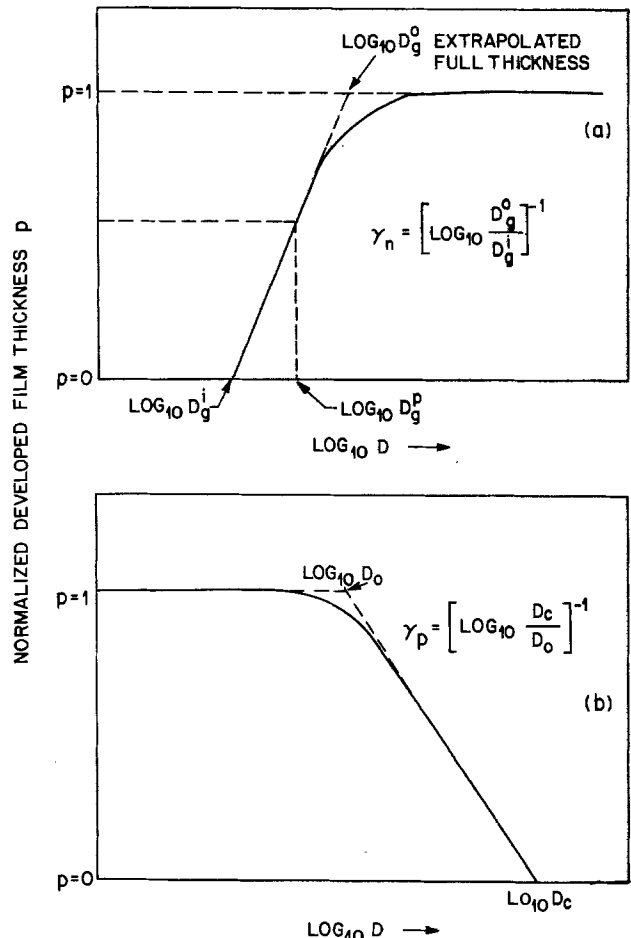


Fig. 37. Typical response or contrast curves for (a) negative resists and (b) positive resists.

remains after development. A residual film thickness 50% of the original film thickness is chosen somewhat arbitrarily as representing that thickness required for the resist to serve as a lithographically useful etch mask (60). Other considerations may dictate different thicknesses.

For a positive resist, the film thickness of the irradiated region remaining after development decreases, until eventually a dose D_c is reached, which results in complete removal of the film on development (Fig. 37b). This value also represents the sensitivity of a positive resist. Contrast (γ_p) is related to the rate of degradation of molecular weight and is defined as

$$\gamma_p = 1/(\log D_c - \log D_0) = \left[\log \frac{D_c}{D_0} \right] \quad [49]$$

where D_0 is the dose at which the developer begins to attack the irradiated film and is determined by extrapolating the linear portion of the film thickness remaining vs. dose plot to a value of 1.0 normalized initial film thickness.

Most negative resists operate on a cross-linking principle and most positive resists operate on a chain scission principle to achieve differential solubility. These mechanisms will be assumed for the purpose of the following discussion although it is recognized that other mechanisms like those operative in positive resists for photolithography at conventional wavelengths do exist. The reader is referred to the pertinent references for discussion of these mechanistic differences (61, 62).

Regardless of mechanism, it is the resist contrast which determines the response of the resist in regions remote from the point of entry of the exposing radiation. The contrast of positive resists such as PMMA or poly(butene-1 sulfone) PBS, is greater than 2 and is much higher than that of negative resists whose contrasts lie in the range between 0.5 exemplified by epoxidized polybutadiene to about 2 for monodisperse polystyrene. Positive resists accordingly show a higher resolution than negative resists although as we have already noted, resolution in negative resists is also determined by other factors such as swelling. Within negative resists, resolution is directly proportional to contrast.

Optical projection printing provides an excellent example of the importance of contrast. We saw earlier that the modulation transfer function provides a convenient measure of the range of exposure or light intensity levels achievable with a given pattern. Although the cut-off frequency of the MTF curve (cf. Fig. 4) indicates the resolution limit for the exposure tool, it is the resist contrast which determines the minimum MTF for acceptable imaging. For a given resist system, image development requires that the optically determined MTF exceeds some critical value related to the contrast characteristic of the resist material. This critical value has been defined as (63)

$$(\text{CMTF})_{\text{resist}} = \frac{I_{100} - I_0}{I_{100} + I_0} \quad [50]$$

where I_{100} is the minimum exposure energy for 100% exposure and I_0 is the maximum exposure energy for zero exposure (I_{100} is equivalent to D_g^0 or D_c in Eq. [48] and [49]; likewise I_0 is equivalent to D_g^1 or D_0). The contrast of the resist is related to the (CMTF)_{resist} as shown in Fig. 38. The minimum sized printable feature using any combination of resist and lens is then determined by the condition $(\text{MTF})_{\text{optical}} \cong (\text{CMTF})_{\text{resist}}$. The (CMTF)_{resist} for polymer resists is commonly quoted to be 0.6. Some newly developed negative inorganic resists exhibit contrasts three to four times greater than that of polymeric resists thereby facilitat-

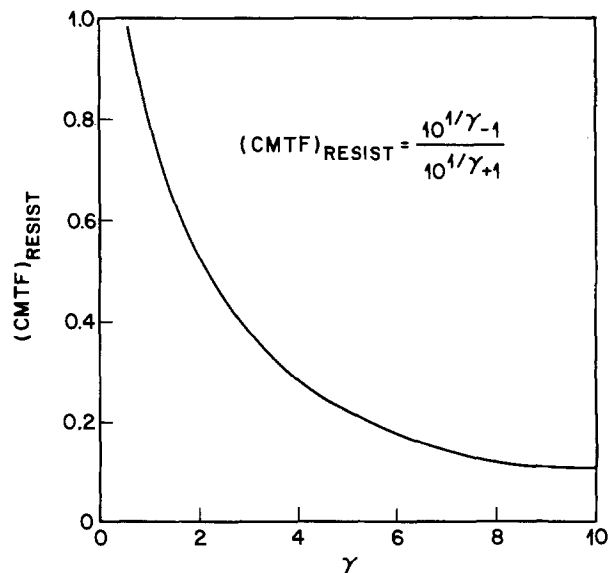


Fig. 38. $(\text{CMTF})_{\text{resist}}$ as a function of resist contrast [from K. L. Tai R. G. Vadimsky, C. T. Kemmerer, J. S. Wagner, V. E. Lamberti, and A. G. Timko, *J. Vac. Sci. Technol.*, 17, 1169 (1980)].

ing imaging at higher frequencies than is possible with polymer-based resists (63).

There is very little quantitative information on those factors which determine resist contrast. Attempts (64) have been made to describe the lithographic response curves in terms of physical-chemical processes particularly those accompanying cross-linking in sol-gel behavior in bulk samples. These processes include: (i) changes in molecular weight distribution; (ii) competition between cross-linking and degradation of polymer chains, and (iii) chemical amplification of the cross-linking process. In general though, theoretical arguments have only guided discussions of contrast (65).

The other major factor limiting resolution, particularly in negative resists, is swelling of the exposed areas during developing. Neighboring exposed areas swell during the development process and when those areas are close together, the swollen regions can fuse giving rise to "stringers" between exposed regions (Fig. 39). Swelling can also occur in positive resists such as poly(isobutylene) giving rise to poor resolution (61).

Nevertheless, in spite of the lack of a quantitative understanding of many of these factors, there is considerable body of information which can be applied to resist design in order to maximize sensitivity and contrast. Clearly, positive resists which operate on the chain scission principle should possess a high susceptibility to degradation (high G -value for scission) with negligible concurrent cross-linking (low G -value for cross-linking). [The G -value is a measure of radiation sensitivity and is the number of events (scission on cross-linking in this case) per 100 eV of energy absorbed]. Optimum sensitivity and contrast for a given system usually requires high molecular weight and narrow molecular weight distribution. Negative resists operating on the cross-linking principle should possess high G (cross-linking) and negligible G (scission), high initial molecular weight, and narrow molecular weight distribution. The implications of these design features to actual polymeric resist systems have been extensively reviewed (59, 61).

Polymers generally dissolve by first imbibing solvent to produce a swollen gel followed by disintegration of the gel into a true solution (54). In the case of negative resists, the swollen gel is insoluble and development involves leaching the soluble uncross-

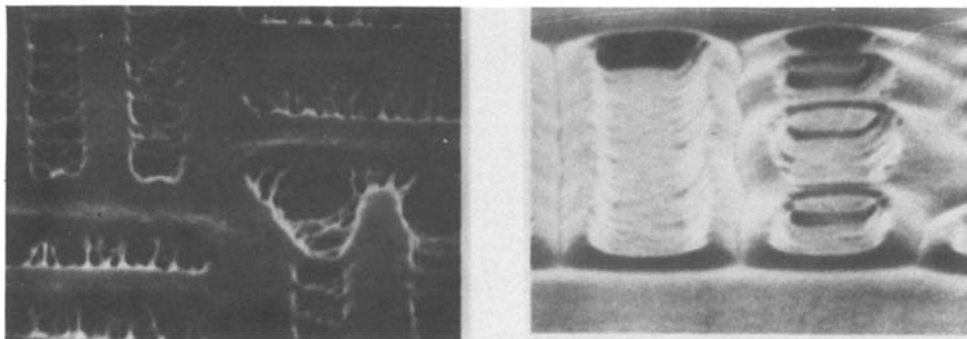


Fig. 39. Photomicrograph showing bridging between adjacent features caused by swelling during development [from D. W. Johnson, SPIE Vol. 174, *Developments in Semiconductor Microlithography IV*, 108 (1979)].

linked material from the gel. Positive resists form a swollen gel layer between the solvent and virgin polymer. Development involves dissolution of the gel portion as the solvent front moves through the polymer. The degree of swelling in both cases can be minimized by choice of developer (66, 67). Also, the glass transition temperature of the polymer should be greater than the dissolution temperature. PMMA appears unique among the positive resists (indeed among polymers in general) in that its dissolution mechanism effectively does not involve the formation of a swollen gel layer (54). By proper choice of solvent and temperature, swelling can be minimized in other positive resists such as PBS but unfortunately there is no clear cut understanding of just why PMMA exhibits this unique dissolution mode over the normal room temperature range.

Conclusions

For the near future, it appears that advanced optical lithography systems will be adequate to produce most of the next generation of microcircuits, but below 0.4-0.8 μm some alternative exposure technology will be required. Each of the other technologies is capable of submicron resolution with electron beam and x-ray systems being most advanced with respect to technological development. Electron beam lithography on thin substrates has opened up a new regime of dimensions below 100 nm that is of particular scientific rather than technological interest. The major driving force though in today's electronic industry is cost rather than performance so smaller and smaller dimensions are only desirable if they can be obtained without a large increase in cost. Thus, although the resolution capability of each technology is sufficient for the foreseeable future, the particular technology chosen will be on the basis of cost effectiveness.

Manuscript submitted Aug. 21, 1980; revised manuscript received Dec. 4, 1980.

Any discussion of this paper will appear in a Discussion Section to be published in the December 1981 JOURNAL. All discussions for the December 1981 Discussion Section should be submitted by Aug. 1, 1981.

Publication costs of this article were assisted by Bell Laboratories.

REFERENCES

1. See issue devoted to microelectronics in "Scientific American," 237 (3), 62 et seq. (1977).
2. M. Fogiel in "Modern Microelectronics," Research and Education Association, N.Y. (1972).
3. D. Widmann and K. U. Stein, in "Semiconductor Technologies With Reduced Dimensions, Solid State Circuits," Proc. 2nd Eur. Solid State Circuits Conf., 1976, 29 (pub. 1977).
4. B. J. Lin, *J. Vac. Sci. Technol.*, **12**, 1317 (1975).
5. J. D. Cuthbert, *Solid State Technol.*, **20**, 59 (1977).
6. J. W. Goodman, in "Introduction to Fourier Optics," McGraw Hill, New York (1968).
7. J. H. Bruning, *J. Vac. Sci. Technol.*, **16**, 1925 (1979).
8. M. M. O'Toole and A. R. Neureuther, "Influence of Partial Coherence on Projection Printing, SPIE, *Developments in Semiconductor Microlithography IV*," **179**, 22 (1979).
9. J. H. Bruning, *J. Vac. Sci. Technol.*, **17**, 1147 (1980).
10. D. Markle, *Solid State Technol.*, **17**, 50 (1974).
11. D. A. Doane, *ibid.*, **17**, 101 (1980).
12. F. H. Dill, *IEEE Trans. Electron Devices*, **ed-22**, 440 (1975).
13. F. H. Dill, A. R. Neureuther, J. A. Tuttle, and E. J. Walker, *ibid.*, **ed-22**, 456 (1975).
14. E. J. Walker, *ibid.*, **ed-22**, 464 (1975).
15. J. M. Moran and D. Maydan, *J. Vac. Sci. Technol.*, **16**, 1620 (1979).
16. S. Wittekoek, *Solid State Technol.*, **6**, 80 (1980).
17. D. Markle, "Limits of Optical Lithography," Paper presented at Semicon East, Boston (1979).
18. T. W. O'Keefe, *IEEE Trans. Electron Devices*, **ed-17**, 465 (1970).
19. J. P. Scott, *ibid.*, **ed-22**, 409 (1975).
20. H. Bohlen, P. Greschner, and P. Nehmiz, *J. Vac. Sci. Technol.*, **16**, 1834 (1979).
21. D. R. Herriott, R. J. Collier, D. S. Alles, and J. W. Stafford, *IEEE Trans. Electron Devices*, **ed-22**, 385 (1975).
22. A. J. Speth, A. D. Wilson, A. Kern, and T. P. H. Chang, *J. Vac. Sci. Technol.*, **12**, 1235 (1975).
23. G. L. Varnell, D. F. Spicer, and A. C. Roger, *J. Vac. Sci. Technol.*, **10**, 1048 (1973).
24. R. J. Hawryluk, A. M. Hawryluk, and H. I. Smith, *J. Appl. Phys.*, **45**, 2551 (1974).
25. R. J. Hawryluk, H. I. Smith, A. Soares, and A. M. Hawryluk, *ibid.*, **46**, 2528 (1975).
26. T. H. P. Chang, *J. Vac. Sci. Technol.*, **12**, 1271 (1975).
27. J. S. Greeneich and T. Van Duzer, *IEEE Trans. Electron Devices*, **ed-21**, 286 (1974).
28. R. W. Nosker, *J. Appl. Phys.*, **40**, 1872 (1969).
29. R. M. Shimizu and T. E. Everhart, *Optik Stuttgart*, **36**, 59 (1972).
30. D. F. Kyser and K. Murata, in "Electron and Ion Beam Science and Technology," R. Bakish, Editor, p. 205, The Electrochemical Society Softbound Proceedings Series, Princeton, N.J. (1974).
31. D. F. Kyser and N. S. Viswanathan, *J. Vac. Sci. Technol.*, **12**, 1305 (1975).
32. R. D. Birkhoff, in "Handbuch der Physik," Vol. 23, E. Fluegge, Editor, p. 53, Springer Verlag, Berlin (1958).
33. R. D. Heidenrich, J. P. Ballantyne, and L. F. Thompson, *J. Vac. Sci. Technol.*, **12**, 1284 (1975).
34. M. Hatzakis and A. N. Broers, in "Proc. 11th Symp. on Electron, Ion and Laser Beam Technol.," R. F. Thornley, Editor, p. 337, San Francisco Press, San Francisco, Calif. (1971).
35. E. D. Wolf, F. S. Ozdemir, W. E. Perkins, and P. J. Coane, in "Proc. 11th Symp. on Electron, Ion and Laser Beam Technol.," R. F. Thornley, Editor, p. 331, San Francisco Press, San Francisco, Calif. (1971).
36. T. E. Everhart, *J. Appl. Phys.*, **31**, 1483 (1960).
37. R. D. Heidenreich, *ibid.*, **48**, 1418 (1977).
38. R. D. Heidenreich, L. F. Thompson, E. D. Feit, and C. M. Melliar-Smith, *ibid.*, **44**, 4039 (1973).
39. M. C. Chung and K. L. Tai, Paper 382 presented at The Electrochemical Society Meeting, Seattle, Washington, May 21-26, 1978.
40. J. S. Greeneich, *This Journal*, **122**, 970 (1975).
41. M. Hatzakis, C. H. Ting, and N. Viswanathan, in "Electron and Ion Beam Science and Technology," R. Bakish, Editor, p. 542, The Electrochem-

- ical Society Softbound Proceedings Series, Princeton, N.J. (1974).
42. J. S. Greeneich, *J. Appl. Phys.*, **45**, 5264 (1974).
 43. N. Hatzakis, *J. Vac. Sci. Technol.*, **12**, 1276 (1975).
 44. R. D. Heidenreich and G. W. Kammlott, Three Dimensional Behavior of Negative Electron Resists, Proc. 4th Regional Tech. Conf. SPE, p. 94 (1976).
 45. E. D. Feit, M. E. Wurtz, and G. W. Kammlott, *J. Vac. Sci. Technol.*, **15**, 944 (1978).
 46. Y. Tu and A. C. Ouano, *IBM J. Res. Dev.*, **21**, 131 (1977).
 47. M. Feldmann, Private communication.
 48. W. W. Molzen, A. N. Broers, J. J. Cuomo, J. M. E. Harper, and R. B. Laibowitz, *J. Vac. Sci. Technol.*, **16**, 269 (1979).
 49. A. N. Broers, J. M. E. Harper, and W. W. Molzen, *Appl. Phys. Lett.*, **33**, 392 (1978).
 50. A. N. Broers, W. W. Molzen, J. J. Cuomo, and N. D. Wittels, *ibid.*, **29**, 596 (1976).
 51. D. L. Spears and H. I. Smith, *Electron. Lett.*, **8**, 102 (1972).
 52. R. Feder, E. Spiller, and J. Topalian, *J. Vac. Sci. Technol.*, **12**, 1332 (1975).
 53. B. Fay, J. Trotel, Y. Petroff, R. Pinchaux, and P. Thiry, *Appl. Phys. Lett.*, **29**, 370 (1976).
 54. S. Doniach, I. Lindau, W. F. Spicer, and H. Winick, *J. Vac. Sci. Technol.*, **12**, 1123 (1975).
 55. J. R. Maldonado, G. A. Coquin, D. Maydan, and S. Somekh, *ibid.*, **12**, 1329 (1975).
 56. E. Spiller and R. Feder, in "X-Ray Optics Applications to Solids," Topics in Applied Physics, Vol. 27, Chap. 3, H. J. Queisser, Editor, Springer Verlag, Berlin (1977).
 57. T. M. Hall, A. Wagner, and L. F. Thompson, *J. Vac. Sci. Technol.*, **16**, 1889 (1979).
 58. M. Komuro, N. Atoda, and H. Kawakatsu, *This Journal*, **126**, 483 (1979).
 59. L. F. Thompson, *Solid State Technol.*, **17**, 27 (1974).
 60. J. P. Ballantyne, *J. Vac. Sci. Technol.*, **12**, 1257 (1975).
 61. M. J. Bowden, *CRC Crit. Rev. in Solid State Sci.*, **8**, 223 (1979).
 62. M. J. Bowden and L. F. Thompson, *Solid State Technol.* **22**, 72 (1979).
 63. K. L. Tai, R. G. Vadimsky, C. T. Kemmerer, J. S. Wagner, V. E. Lamberti, and A. G. Timko, *J. Vac. Sci. Technol.*, **17**, 169 (1980).
 64. O. Saito, Statistical Theories of Crosslinking in "The Radiation Chemistry of Macromolecules," Vol. 1, Chap. 2, M. Dole, Editor, Academic Press, New York (1972).
 65. E. D. Feit, L. F. Thompson, C. W. Wilkins, M. E. Wurtz, E. M. Doerries, and L. E. Stillwagon, *J. Vac. Sci. Technol.*, **16**, 1997 (1979).
 66. K. Ueberreiter, The Solution Process in "Diffusion Polymers," Chap. 7, J. Crank and G. S. Park, Editors, Academic Press, New York (1968).
 67. M. J. Bowden, L. F. Thompson, and J. P. Ballantyne, *J. Vac. Sci. Technol.*, **12**, 1294 (1975).



Structural Effect of Formic Acid in Electrolytic Solutions of Lithium Perchlorate in Tetrahydrofuran, at 298.15 K

E. T. de Almeida and A. A. Inocência*

Departamento de Química, Fundação Universidade de Brasília, 70910, Brasília, D.F., Brazil

ABSTRACT

The structural changes of electrolytic solutions of LiClO_4 in tetrahydrofuran (THF), caused by addition of HCOOH at 298.15 K, have been studied. The conductance data at different solvent composition showed the presence of ion pairs, triple ions, and quadrupoles in the solution. The measured viscosity, dielectric constant, electric conductance, and density values were used to calculate the equivalent conductivity at infinite dilution for simple ions Λ^∞ , the association constant for the ion pairs, K_a , and the formation constant for the triple ions, K_t .

Interest in studying the physical properties of organic electrolytic solutions arises mainly from the likely application of the results to the improvement of lithium batteries in organic solvents. The knowledge of the physical parameters such as Δ , ϵ , η , ρ , and the constants of ionic association K_a , K_t , and K_q , becomes particularly important in connection to lithium batteries in organic solvents that use liquid catholytes such as H_2O , HCOOH , CH_3OH , etc., owing to the structural effect of those cathodic reactants in the organic electrolytic solution itself, e.g., a solution of LiClO_4 in tetrahydrofuran or propylene carbonate (1-3). The results obtained in the present work may help the lithium cell manufacturers to choose optimum composition of the electrolyte in order to get minimum internal ohmic drop, using a minimum amount of the rather expensive electrolyte (LiClO_4), and maximum energetic capacity of the cell. This paper deals with the results obtained for HCOOH in an electrolytic solution of LiClO_4 in THF.

Experimental

A Leeds and Northrup bridge (Cat. No. 4866-60), and a Beckman pipette-type conductivity cell were used in all the conductance measurements. The cell constant L was obtained according to Jones and Bradshaw (4), with 0.01D solutions of KCl. A mean value of $L = 1.013 \pm 0.003 \text{ cm}^{-1}$ was found for 5 measurements. A Sargent oscillometer Model V, calibrated with standards of known dielectric constant, was used. The expression, $\epsilon = 2.107 + 2.646 \cdot 10^{-4}S$, obtained by the least squares method, relates the dielectric constant ϵ , with the scale reading of the instrument S . Two Ostwald viscosimeters were used, calibrated with conductivity water $\eta_{\text{H}_2\text{O}} = 0.8903 \text{ cp}$ (5) and THF, $\eta_{\text{THF}} = 0.4583 \text{ cp}$ (6), as standards and utilizing the Jones and Stauffer equation (7), $\eta = A\rho t - B$ (ρ/t). All calibrations and measurements were carried out at 298.15 (± 0.02) K. The

chemicals used were: tetrahydrofuran (THF), Merck p.a., density at 298.15 K, $\rho_{\text{THF}} = 0.8820 (\pm 0.001) \text{ g cm}^{-3}$, measured with a 25 cm^{-3} picnometer and a Metler balance Model H20-T, compares well with the values found in the literature: 0.880 and 0.883 (8, 9). The measured dielectric constant $\epsilon_{\text{THF}} = 7.39$ also agreed with the values found in the literature (8, 9). Critchfield (10), by measuring the dielectric constant of THF as a function of water concentration, reported a value $\epsilon_{\text{THF}} = 7.39$ for 100% THF. The NMR and infrared spectra did not show the presence of water and consequently, it was used without any further purification. Anhydrous lithium perchlorate (LiClO_4) used was FLUKA, A.G., pure grade. The product showed no weight loss in an oven test after being heated at 463.15 K for 2-3 days. The reagent was carefully stored in a desiccator over CaCl_2 . While preparing the solutions the bottle was left opened for the shortest possible time. In this way, the water content was always maintained below the limit of sensibility of the physical constants to be measured (Δ , η , ϵ , ρ), and therefore its influence in the experimental results cannot be significant. Formic acid (HCOOH), Merck p.a., was used without further purification. Potassium chlorite (KCl), Merck p.a., was dried at 443.15 K and low pressure in an oil bath to constant weight and stored in a desiccator over CaCl_2 . Conductivity water was prepared according to Morita (11) using a borosilicate glass condenser. The mixtures of THF and HCOOH and the solutions of LiClO_4 in these mixtures, were prepared separately by weighing, and were used within 4 hr after being prepared.

Results and Discussion

Table I shows some physical properties of the THF + HCOOH mixtures. The density of 6-8 solutions of LiClO_4 in this mixture, at constant composition, was measured and the results fit a quadratic equation, of the type $\rho = a + bm + cm^2$. A plot of this equation was employed to get the density of any other solution

* Electrochemical Society Active Member.

Key words: formic acid, electrolytic solutions, organic solvents, tetrahydrofuran, lithium perchlorate.

Table I. Physical properties of the solvent (THF + HCOOH)

| Mass percent HCOOH | $\rho/\text{kg dm}^{-3}$ | ϵ/D | η/cp | $k/\text{S cm}^{-1}$ |
|--------------------|--------------------------|--------------|------------------|-----------------------|
| 0.0 | 0.8820 | 7.39 | 0.4583 | — |
| 1.5 | 0.8885 | 7.60 | 0.4696 | 4.6×10^{-10} |
| 3.0 | 0.8907 | 7.80 | 0.4906 | 2.9×10^{-9} |
| 5.0 | 0.8970 | 8.00 | 0.4857 | 1.1×10^{-8} |
| 10.0 | 0.9046 | 8.90 | 0.5270 | 7.1×10^{-8} |
| 15.0 | 0.9196 | 9.75 | 0.5526 | 2.1×10^{-7} |

of the same solvent composition, Table II. In the equation above m is the molality, a , b , and c are constants.

The viscosity of the solutions becomes greater as the concentration of the HCOOH increases, because $\eta_{\text{HCOOH}} = 1.61 \text{ cp}$ (5) is greater than $\eta_{\text{THF}} = 0.4583 \text{ cp}$ (6). For each solvent composition the viscosity becomes greater too, as the concentration of LiClO_4 increases. The relative viscosity, η/η_0 , η and η_0 being the viscosity of the solution and of the solvent, respectively, fit a curve, whose analytical expression was found to be $\eta/\eta_0 = 1 - 0.5776 \sqrt{c} + 1.590c$.

It was also found that the logarithm of the electrical specific conductivity for solvent mixtures of THF and HCOOH $\log k$, is a linear function of the logarithm of the mass percent of HCOOH, $\log(100w)$, according to the equation $\log k = 2.65 \log(100w) - 9.80$; this expression was used to extrapolate the values of k for low values of the mass percent of HCOOH, when k went out of the scale of the conductance bridge. Figure 1 shows plots of $\log \Lambda$ vs. the logarithm of the concentration of the electrolyte (LiClO_4) in the solvent mixture, $\log c$. The electrical conductance of the solutions increases with the percentage of the HCOOH (w/w) in the solvent mixture, Table III. This can be explained, partly, by the increase of the dielectric constant. With the increase in dielectric constant the ionic interactions become weaker and the ionic dissociation easier.

Table II. Physical properties of the electrolytic solutions

| Mass percent HCOOH | $\text{LiClO}_4/\text{mol dm}^{-3}$ | $\rho/\text{kg dm}^{-3}$ | η/cp | η/η_0 |
|--------------------|-------------------------------------|--------------------------|------------------|---------------|
| 0 | 0 | 0.8820 | 0.4583 | 1.0000 |
| | 0.0400 | 0.8865 | 0.4809 | 1.0493 |
| | 0.0967 | 0.8920 | 0.4929 | 1.0755 |
| | 0.2342 | 0.9022 | 0.5405 | 1.1794 |
| | 0.3323 | 0.9123 | 0.5796 | 1.2647 |
| | 0.4952 | 0.9245 | 0.6549 | 1.4290 |
| | 0.5882 | 0.9317 | 0.7007 | 1.5289 |
| | 0.9304 | 0.9604 | 0.9254 | 2.0192 |
| | 0 | 0.8855 | 0.4696 | 1.0000 |
| | 0.1549 | 0.8972 | 0.5090 | 1.0839 |
| 1.5 | 0.3322 | 0.9127 | 0.5786 | 1.2321 |
| | 0.6758 | 0.9424 | 0.8125 | 1.7302 |
| | 0.8639 | 0.9577 | 0.8780 | 1.8696 |
| | 1.0801 | 0.9762 | 1.0419 | 2.2187 |
| | 0 | 0.8907 | 0.4806 | 1.0000 |
| | 0.0648 | 0.8958 | 0.5008 | 1.0420 |
| | 0.1587 | 0.9045 | 0.5365 | 1.1163 |
| | 0.2983 | 0.9151 | 0.5923 | 1.2324 |
| | 0.5038 | 0.9339 | 0.6935 | 1.4430 |
| | 0.7171 | 0.9502 | 0.8085 | 1.6767 |
| 0.9347 | 0.9664 | 0.9516 | 1.9798 | |
| 3.0 | 0 | 0.8970 | 0.4857 | 1.0000 |
| | 0.0862 | 0.9030 | 0.5110 | 1.0521 |
| | 0.2180 | 0.9144 | 0.5633 | 1.1598 |
| | 0.3354 | 0.9237 | 0.6116 | 1.2592 |
| | 0.5191 | 0.9377 | 0.7006 | 1.4425 |
| | 0.7089 | 0.9541 | 0.8143 | 1.6795 |
| | 0.9224 | 0.9706 | 0.9651 | 1.9870 |
| | 0 | 0.9046 | 0.5270 | 1.0000 |
| | 0.0859 | 0.9139 | 0.5638 | 1.0698 |
| | 0.1780 | 0.9227 | 0.6065 | 1.1509 |
| 10.0 | 0.2624 | 0.9288 | 0.6472 | 1.2281 |
| | 0.4546 | 0.9445 | 0.7458 | 1.4152 |
| | 0.7027 | 0.9643 | 0.9078 | 1.7226 |
| | 0.9765 | 0.9853 | 1.1363 | 2.1562 |
| | 0 | 0.9196 | 0.5526 | 1.0000 |
| | 0.0932 | 0.9277 | 0.5959 | 1.0784 |
| | 0.1749 | 0.9344 | 0.6304 | 1.1408 |
| | 0.2252 | 0.9468 | 0.6727 | 1.2173 |
| | 0.4446 | 0.9560 | 0.7792 | 1.4101 |
| | 0.6457 | 0.9734 | 0.9177 | 1.6607 |
| 0.9628 | 0.9977 | 1.1828 | 2.1404 | |

Table III. Conductance of the LiClO_4 solutions in THF + HCOOH

| Mass percent HCOOH | $\text{LiClO}_4/\text{mol dm}^{-3}$ | $k/\text{S cm}^{-1}$ | $\Lambda/\text{S cm}^2 \text{ mol}^{-1}$ |
|------------------------|-------------------------------------|-----------------------|--|
| 0 | 9.304×10^{-1} | 3.16×10^{-3} | 3.40 |
| | 5.882×10^{-1} | 1.67×10^{-3} | 2.84 |
| | 4.952×10^{-1} | 1.25×10^{-3} | 2.52 |
| | 3.323×10^{-1} | 6.34×10^{-4} | 1.91 |
| | 2.342×10^{-1} | 3.42×10^{-4} | 1.46 |
| | 9.669×10^{-2} | 7.99×10^{-5} | 0.827 |
| | 3.999×10^{-2} | 2.38×10^{-5} | 0.595 |
| | 1.987×10^{-2} | 1.20×10^{-5} | 0.633 |
| | 1.551×10^{-2} | 1.03×10^{-5} | 0.664 |
| | 9.164×10^{-3} | 6.96×10^{-6} | 0.759 |
| | 6.639×10^{-3} | 5.17×10^{-6} | 0.779 |
| | 3.916×10^{-3} | 3.87×10^{-6} | 0.988 |
| | 2.458×10^{-3} | 2.89×10^{-6} | 1.18 |
| | 1.884×10^{-3} | 2.47×10^{-6} | 1.31 |
| | 1.278×10^{-3} | 1.91×10^{-6} | 1.49 |
| | 9.738×10^{-4} | 1.69×10^{-6} | 1.74 |
| | 1.080 | 4.03×10^{-3} | 3.73 |
| | 8.639×10^{-1} | 3.14×10^{-3} | 3.63 |
| | 6.758×10^{-1} | 2.31×10^{-3} | 3.42 |
| | 3.322×10^{-1} | 7.58×10^{-4} | 2.28 |
| 1.459×10^{-1} | 1.91×10^{-4} | 1.31 | |
| 5.729×10^{-2} | 4.09×10^{-5} | 0.715 | |
| 2.183×10^{-2} | 1.64×10^{-5} | 0.751 | |
| 5.411×10^{-3} | 5.66×10^{-6} | 1.05 | |
| 5.278×10^{-3} | 5.55×10^{-6} | 1.05 | |
| 3.416×10^{-3} | 4.47×10^{-6} | 1.31 | |
| 1.762×10^{-3} | 2.76×10^{-6} | 1.57 | |
| 6.355×10^{-4} | 1.48×10^{-6} | 2.33 | |
| 3.397×10^{-4} | 9.62×10^{-7} | 2.83 | |
| 1.5 | 9.347×10^{-1} | 3.83×10^{-3} | 4.10 |
| | 7.171×10^{-1} | 2.83×10^{-3} | 3.95 |
| | 5.038×10^{-1} | 1.98×10^{-3} | 3.93 |
| | 2.983×10^{-1} | 8.47×10^{-4} | 2.84 |
| | 1.587×10^{-1} | 3.19×10^{-4} | 2.01 |
| | 6.479×10^{-2} | 7.97×10^{-5} | 1.23 |
| | 5.440×10^{-2} | 6.23×10^{-5} | 1.15 |
| | 2.435×10^{-2} | 2.99×10^{-5} | 1.23 |
| | 1.040×10^{-2} | 1.45×10^{-5} | 1.39 |
| | 5.865×10^{-3} | 9.88×10^{-6} | 1.68 |
| | 3.804×10^{-3} | 6.94×10^{-6} | 1.82 |
| | 1.728×10^{-3} | 4.40×10^{-6} | 2.55 |
| | 1.075×10^{-3} | 3.06×10^{-6} | 2.85 |
| | 5.149×10^{-4} | 2.63×10^{-6} | 5.11 |
| | 2.684×10^{-4} | 1.86×10^{-6} | 6.93 |
| | 9.224×10^{-1} | 4.30×10^{-3} | 4.66 |
| | 7.089×10^{-1} | 3.15×10^{-3} | 4.44 |
| | 5.191×10^{-1} | 2.19×10^{-3} | 4.22 |
| | 3.354×10^{-1} | 1.14×10^{-3} | 3.40 |
| | 2.180×10^{-1} | 5.96×10^{-4} | 2.73 |
| 4.034×10^{-2} | 1.52×10^{-4} | 1.51 | |
| 8.618×10^{-2} | 6.10×10^{-5} | 1.76 | |
| 2.922×10^{-2} | 4.35×10^{-5} | 1.49 | |
| 1.790×10^{-2} | 2.85×10^{-5} | 1.60 | |
| 1.335×10^{-2} | 2.30×10^{-5} | 1.72 | |
| 9.219×10^{-3} | 1.77×10^{-5} | 1.92 | |
| 4.233×10^{-3} | 9.92×10^{-6} | 2.34 | |
| 2.224×10^{-3} | 6.60×10^{-6} | 2.97 | |
| 1.431×10^{-3} | 4.91×10^{-6} | 3.43 | |
| 8.915×10^{-4} | 4.23×10^{-6} | 4.74 | |
| 3.523×10^{-4} | 2.09×10^{-6} | 5.93 | |
| 3.0 | 9.765×10^{-1} | 5.88×10^{-3} | 6.02 |
| | 7.027×10^{-1} | 4.39×10^{-3} | 6.24 |
| | 4.546×10^{-1} | 2.76×10^{-3} | 6.07 |
| | 2.624×10^{-1} | 1.45×10^{-3} | 5.53 |
| | 1.780×10^{-1} | 8.96×10^{-4} | 5.03 |
| | 1.075×10^{-1} | 4.97×10^{-4} | 4.62 |
| | 8.589×10^{-2} | 3.78×10^{-4} | 4.40 |
| | 6.128×10^{-2} | 2.52×10^{-4} | 4.11 |
| | 3.903×10^{-2} | 1.62×10^{-4} | 4.15 |
| | 2.303×10^{-2} | 9.83×10^{-5} | 4.27 |
| | 1.587×10^{-2} | 7.29×10^{-5} | 4.59 |
| | 5.755×10^{-3} | 2.82×10^{-5} | 4.90 |
| | 3.096×10^{-3} | 2.00×10^{-5} | 6.46 |
| | 2.141×10^{-3} | 1.52×10^{-5} | 7.10 |
| | 1.439×10^{-3} | 1.18×10^{-5} | 8.20 |
| | 8.537×10^{-4} | 8.42×10^{-6} | 9.86 |
| | 4.725×10^{-4} | 5.51×10^{-6} | 11.66 |
| | 9.628×10^{-1} | 6.87×10^{-3} | 7.13 |
| | 6.457×10^{-1} | 4.92×10^{-3} | 7.62 |
| | 4.446×10^{-1} | 3.41×10^{-3} | 7.67 |
| 2.252×10^{-1} | 1.79×10^{-3} | 7.95 | |
| 1.749×10^{-1} | 1.18×10^{-3} | 6.72 | |
| 9.317×10^{-2} | 6.10×10^{-4} | 6.55 | |
| 6.580×10^{-2} | 3.92×10^{-4} | 5.96 | |
| 5.351×10^{-2} | 3.20×10^{-4} | 5.98 | |
| 4.600×10^{-2} | 2.78×10^{-4} | 6.04 | |
| 3.666×10^{-2} | 2.22×10^{-4} | 6.06 | |
| 2.061×10^{-2} | 1.36×10^{-4} | 6.60 | |
| 1.342×10^{-2} | 9.34×10^{-5} | 6.96 | |
| 8.631×10^{-3} | 6.75×10^{-5} | 7.82 | |
| 6.640×10^{-3} | 4.33×10^{-5} | 9.33 | |
| 2.402×10^{-3} | 2.76×10^{-5} | 11.49 | |
| 9.473×10^{-4} | 1.57×10^{-5} | 16.57 | |
| 5.202×10^{-4} | 1.08×10^{-5} | 20.76 | |
| 2.893×10^{-4} | 6.00×10^{-6} | 20.74 | |

Equivalent conductivity at infinite dilution (Λ^∞).—The equivalent conductivity at infinite dilution Λ^∞ cannot be obtained by extrapolating the curves $\Lambda =$

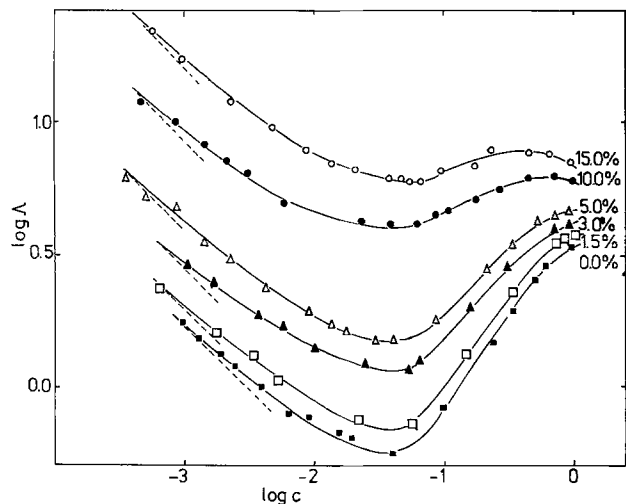
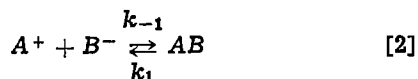


Fig. 1. Logarithm of the equivalent conductivity of LiClO_4 in THF + HCOOH ($\log \Lambda$), vs. logarithm of the concentration of LiClO_4 ($\log c$) at 298.15 K and different solvent composition (mass percent HCOOH).

$\Lambda(\sqrt{c})$, by Onsager's method (12), because Onsager's equation is not obeyed at the low concentrations at which the measurements were carried out. The plots of F/Λ against $c\Lambda\gamma_{\pm}^2/F$, which are straight lines with intercept $1/\Lambda^{\infty}$ and slope $1/K_a \Lambda^{\infty 2}$ for concentrations less than $3 \cdot 10^{-7} \epsilon^3$, cannot be used either, because the concentrations here were much higher (12, 14). The expression

$$K_a = 4\Lambda^{\infty 2}/(c\Lambda^2)_{\min.} \quad [1]$$

obtained from the condition for a minimum of $\Lambda = \Lambda(\sqrt{c})$ (15), cannot be used either because the mass action constant K_a , for the equilibrium



is unknown. Therefore, the Walden's rule $\Lambda^{\infty} \cdot \eta_0 = \text{const.}$ must be tried, where η_0 is the viscosity of the solvent. If the dielectric constant ϵ does not vary much and one of the components of the binary mixture is predominant, this rule is accurate enough as to be applied. In the present work, the concentration of HCOOH in the THF did not exceed 15%, and the value of the dielectric constant laid between 7.39 and 9.75. The ionic equivalent conductivity for Li^+ and ClO_4^- are known from the literature: $\lambda_{\text{Li}^+}^{\infty} = 36.6 \text{ S cm}^2 \text{ eq}^{-1}$ (17) and $\lambda_{\text{ClO}_4^-}^{\infty} = 119.5 \text{ S cm}^2 \text{ eq}^{-1}$ (18), giving $\Lambda^{\infty}_{\text{LiClO}_4} = 156.1 \text{ S cm}^2 \text{ eq}^{-1}$, in THF (6). The results in Table IV were obtained with this value for $\Lambda^{\infty}_{\text{LiClO}_4}$. Out of this value λ_{+}^{∞} and λ_{-}^{∞} were calculated assuming that the transport number at infinite dilution does not vary too much with the concentration of formic acid.

Ionic association.—The shape of the plots $\log \Lambda$ vs. $\log c$ (Fig. 1) shows the existence of different types of ionic association in the electrolytic solution. At low concentration of LiClO_4 , the slope of the curves, $d \log \Lambda/d \log c \approx -1/2$, with small $K_a^{-1} = k_1/k_{-1}$, is char-

Table IV. Equivalent conductivity at infinite dilution (Λ^{∞})

| Mass percent HCOOH | $\eta/c\mu$ | $\Lambda^{\infty}/\text{S cm}^2 \text{ mol}^{-1}$ | $\lambda_{+}^{\infty}/\text{S cm}^2 \text{ mol}^{-1}$ | $\lambda_{-}^{\infty}/\text{S cm}^2 \text{ mol}^{-1}$ |
|--------------------|-------------|---|---|---|
| 0.0 | 0.4583 | 156.1 | 36.6 | 119.5 |
| 1.5 | 0.4696 | 152.6 | 35.7 | 116.6 |
| 3.0 | 0.4806 | 148.9 | 34.9 | 114.0 |
| 5.0 | 0.4857 | 147.3 | 34.5 | 112.8 |
| 10.0 | 0.5270 | 135.8 | 31.8 | 103.9 |
| 15.0 | 0.5526 | 129.5 | 30.4 | 99.1 |

acteristic for ion association in strong electrolytes (17-19). As $\log c$ increases, the slope $d \log \Lambda/d \log c$ tends to zero, taking this value at the minimum of the curves. This minimum shows the existence of triple ions, which are electrically charged and therefore contribute to the electrical conduction. At some distance after the minimum $d \log \Lambda/d \log c$ diminish and the curves tend to a maximum. This shows the existence of quadrupoles, that being electrically neutral, cause the decrease of the electrical conductance. As the concentration of the HCOOH in the solution increases, a shift of the maximum of the curves toward lower values of $\log c$ is noted. For concentrations of HCOOH higher than 10%, the maximum of the curves is found at concentrations of the electrolyte lower than 1 eq dm^{-3} . The electrolyte concentration at the minimum of the curves obeys the empirical rule of Walden, $\epsilon^3/c_{\min.} = \text{constant}$, wherein ϵ is the dielectric constant of the solvent (Table V). The main source of error in calculating the constant is perhaps the difficulty in localizing the minimum of the curve.

Ion pair association.—The plot of F/Λ against $c\Lambda\gamma_{\pm}^2/F$, γ_{\pm} being the mean ionic activity coefficient and F a continued fraction, gives, according to Fuoss and Kraus, good straight lines at low concentrations (Fig. 2), but the values of Λ^{∞} obtained from the intercept ($1/\Lambda^{\infty}$) are too low ($5-7 \text{ S cm}^2 \text{ mol}^{-1}$). This shows the influence of ion associations of higher order, as it is expected at concentrations larger than $3.2 \cdot 10^{-7} \epsilon^3$ at 298.15 K (14). The presence of triple ions rather than the slope of a Fuoss-Kraus plot seems to affect the intercept and therefore the determination of Λ^{∞} (6). With the values of Λ^{∞} obtained by using Walden's rule, the association constant K_a can be obtained from the slope (Table VIA). Only the first value in this table can be compared with those values known from the literature. It is rather low when compared with $K_a = 4.84 \cdot 10^7 \text{ mol}^{-1} \text{ dm}^3$ found by Jagodzinski and Petrucci (6), with $K_a = 3.60 \cdot 10^{-7} \text{ mol}^{-1} \text{ dm}^3$ given by Nicolas and Reich at 293.15 K (20) and with $K_a = 1.56 \cdot 10^{-7} \text{ mol}^{-1} \text{ dm}^3$, obtained here using Eq. [1] (Table VIB). Consequently, it may be postulated that the K_a values in column B of Table VI are more reliable than those in column A, at least up to a concentration of 5% HCOOH in the solvent mixture, since the first value (mass percent HCOOH = 0) compares well with the one reported in Ref. (6) and (20). After a concentration of 5% HCOOH the error in localizing the minimum of the curves in Fig. 1 becomes greater. In both cases the K_a values decrease with increasing HCOOH concentration or with the permittivity of the medium, which is quite reasonable.

Table V. Minima of the curves $\log \Lambda$ vs. $\log c$ and the Walden's rule $\epsilon^3/c_{\min.} = \text{const.}$

| Mass percent HCOOH | ϵ/D | $10^2 c_{\min.}/\text{mol dm}^{-3}$ | $\Lambda_{\min.}/\text{S cm}^2 \text{ mol}^{-1}$ | $10^{-1} \epsilon^3/c_{\min.}$ |
|--------------------|--------------|-------------------------------------|--|--------------------------------|
| 0.0 | 7.39 | 2.5 | 0.50 | 1.61 |
| 1.5 | 7.60 | 2.9 | 0.70 | 1.51 |
| 3.0 | 7.80 | 3.2 | 1.10 | 1.48 |
| 5.0 | 8.00 | 3.3 | 1.50 | 1.55 |
| 10.0 | 8.90 | 4.6 | 4.05 | 1.53 |
| 15.0 | 9.75 | 6.0 | 5.95 | 1.55 |

Table VI. Triple ion analysis

| Mass percent HCOOH | $K_a/\text{dm}^3 \text{ mol}^{-1}$ | | | $K_t/\text{dm}^3 \text{ mole}^{-1}$ |
|--------------------|------------------------------------|-------------------|-------------------|-------------------------------------|
| | A | B | C | |
| 0.0 | $7.25 \cdot 10^8$ | $1.56 \cdot 10^7$ | $1.06 \cdot 10^7$ | $0.73 \cdot 10^2$ |
| 1.5 | $4.30 \cdot 10^8$ | $6.56 \cdot 10^8$ | $8.64 \cdot 10^8$ | $1.02 \cdot 10^2$ |
| 3.0 | $1.36 \cdot 10^8$ | $2.29 \cdot 10^8$ | $3.29 \cdot 10^8$ | $1.33 \cdot 10^2$ |
| 5.0 | $8.47 \cdot 10^8$ | $1.16 \cdot 10^8$ | $2.01 \cdot 10^8$ | $1.52 \cdot 10^2$ |
| 10.0 | $1.99 \cdot 10^8$ | $9.78 \cdot 10^4$ | $3.55 \cdot 10^5$ | $2.83 \cdot 10^2$ |
| 15.0 | $6.89 \cdot 10^4$ | $3.16 \cdot 10^4$ | $1.58 \cdot 10^5$ | $14.50 \cdot 10^2$ |

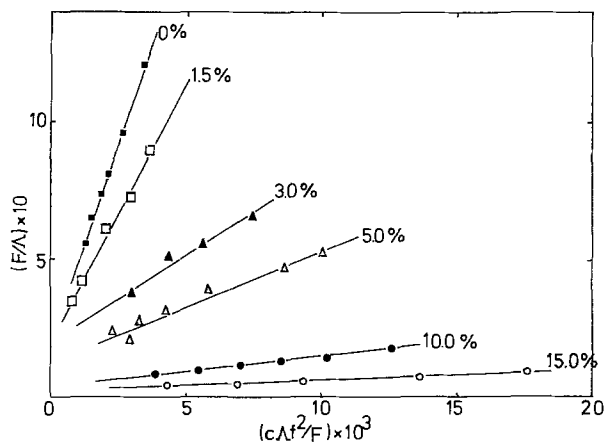


Fig. 2. Ion pair analysis, according to Fuoss and Kraus

Triple ion analysis.—The minimum of the curves in Fig. 1 shows the presence of triple ions in the electrolytic solution. The shape of the same curves at higher electrolytic concentrations shows the presence of quadrupoles too. If the influence of these quadrupoles could be neglected, a plot of $\Lambda \sqrt{c} g(c)$ against $(1 - \Lambda/\Lambda^\infty)c$ should give a straight line. Except for low concentrations (Fig. 3a and b) this is not so and this may be due to the influence of the quadrupoles. Using Λ^∞ from Table IV and taking $\Delta_t/\Lambda^\infty = 1/3$ (15, 21), K_a and K_t can be calculated from the plots of Fig. 3b (Table VIC). The K_a value of this table from 0.0% HCOOH, is now of the same order of magnitude as those known from the literature and of that obtained here using Eq. [1]. It can be assumed that the K_a values for the concentrations 1.5, 3.0, 5.0, 10.0, and 15% HCOOH have also the correct order of magnitude and they are perhaps more reliable than those of Table VIB considering the concentration at which the minimum appears. This is especially so at higher concentration because of the difficulty in localizing the mini-

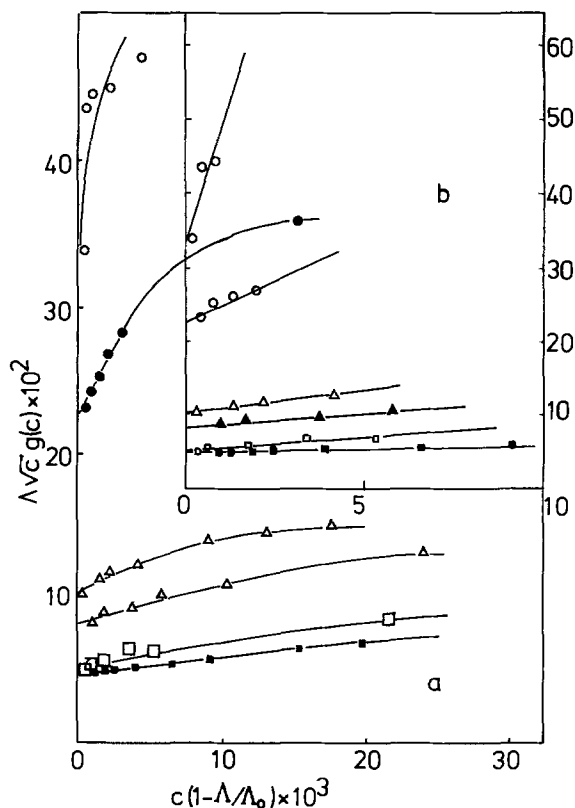


Fig. 3. (a) Triple ion analysis, according to Fuoss and Kraus. (b) Amplification of (a) at low concentrations.

mum of the curves in Fig. 1. Although these K_a values were obtained using a mathematical analysis for the case where aggregates up to the third order existed while the experimental results showed the presence of aggregates of higher order, this fact does not invalidate them at all, because they were calculated taking only the electrolyte concentrations where the influence of quadrupoles is not decisive.

The change of the K_t values with increasing percentage of HCOOH, that in our opinion cannot be attributed to the error from applying Walden's rule, is rather surprising. As a matter of fact, an increase of dielectric constant would hinder the triple ion formation, but the experimental results showed that the contrary was true: The constant for the triple ion formation K_t had a value of $73 \text{ dm}^3 \text{ mol}^{-1}$ for LiClO_4 in $\text{THF} + 0\% \text{ HCOOH}$, and reaches $1,450 \text{ dm}^3 \text{ mol}^{-1}$ in $\text{THF} + 15\% \text{ HCOOH}$. This fact leads to the assumption that the formic acid shares the triple ion formation. It seems that the dissociation of the formic acid is favored by the presence of ionic species in the solution. The H^+ and HCOO^- ions seem to associate with the perchlorate ion pairs to give rise to triple ions. The apparent equivalent conductivity at infinite dilution $(\Lambda^\infty_{\text{LiClO}_4})_{\text{app}}$ would be the sum of the actual equivalent conductivity at infinite dilution $(\Lambda^\infty_{\text{LiClO}_4})_{\text{act}}$ plus the equivalent conductivity of the triple ions Δ_t : $(\Lambda^\infty_{\text{LiClO}_4})_{\text{app}} = (\Lambda^\infty_{\text{LiClO}_4})_{\text{act}} + \Delta_t$.

Conclusion

The experimental results discussed above showed that the addition of HCOOH to the electrolytic solution of LiClO_4 in THF changes their physical properties and microscopic structure as well. The increase of the HCOOH concentration is not favorable to the ion pair formation (the K_a values decrease) but is favorable to the triple ion formation (K_t increases). The quadrupole association becomes important at lower LiClO_4 concentrations as the HCOOH concentration in the solvent mixture increases.

Acknowledgments

Part of this paper has been realized with a grant of CNPq, to which we are grateful. We thank Dr. G. East for the revision of the English text.

Manuscript submitted Aug. 5, 1980; revised manuscript received Jan 5, 1981.

Any discussion of this paper will appear in a Discussion Section to be published in the December 1981 JOURNAL. All discussions for the December 1981 Discussion Section should be submitted by Aug. 1, 1981.

Publication costs of this article were assisted by the Fundação Universidade de Brasília.

REFERENCES

1. A. A. Inocência, Pat. DE 25 27 903 C3, Deutsches Patentamt (1980).
2. A. A. Inocência, *This Journal*, **124**, 1729 (1977).
3. A. A. Inocência, *Electrochim. Acta*, **23**, 977 (1978).
4. G. Jones and C. Bradshaw, *J. Am. Chem. Soc.*, **55**, 1780 (1933).
5. "Handbook of Chemistry and Physics," 49th ed., The Chemical Rubber Co. (1968-1969).
6. P. Jagodzinski and S. Petrucci, *J. Phys. Chem.*, **78**, 917 (1974).
7. G. Jones and R. E. Stauffer, *J. Am. Chem. Soc.*, **59**, 1630 (1937).
8. D. J. Metz and A. Glines, *J. Phys. Chem.*, **71**, 1158 (1967).
9. C. Carvajal, K. L. Tolle, J. Smid, and M. Szwarc, *J. Am. Chem. Soc.*, **87**, 5548 (1965).
10. F. E. Critchfield, J. A. Gibson, and J. L. Hall, *ibid.*, **75**, 6044 (1953).
11. R. M. V. Assumpção and T. Morita, "Manual de Soluções, Reagentes e Solventes," 1st ed., Edgar

- Blucher Ltda., São Paulo, Brazil (1968).
12. R. M. Fuoss and C. A. Kraus, *J. Am. Chem. Soc.*, **55**, 1019 (1933).
 13. R. M. Fuoss, *J. Chem. Ed.*, **32**, 527 (1955).
 14. R. M. Fuoss, *J. Am. Chem. Soc.*, **57**, 488 (1935).
 15. R. M. Fuoss and C. A. Kraus, *ibid.*, **55**, 2387 (1933).
 16. "Nonaqueous Electrolytes Handbook," Vol. I, G. J. Janz and R. P. Tomkins, pp. 108, 384, Academic Press, New York (1972).
 17. M. Szwarc *et al.*, *J. Phys. Chem.*, **69**, 608 (1965).
 18. J. C. Justice and C. Treiner, *C.R. Acad. Sci.*, **269**, 1364 (1969).
 19. R. Fuoss and C. A. Kraus, *J. A. Chem. Soc.*, **55**, 476 (1933).
 20. M. Nicolas and R. Reich, 27th Meeting of ISE, Abstract No. 243, Zurich, Switzerland (1976).
 21. P. Beronius and T. Lindbäck, *Acta Chem. Scand.*, **A32**, 423 (1978).

Thermodynamic Study of the Lithium-Tin System

C. John Wen*¹ and R. A. Huggins*

Department of Materials Science and Engineering, Stanford University, Stanford, California 94305

ABSTRACT

A thermodynamic study of the lithium-tin system was made using galvanic cells of the type

Al, "LiAl"/LiCl-KCl (eut.)/Li-Sn

over the temperature range from 360° to 590°C. The composition of the alloy was varied from pure tin to 86 a/o Li using the coulometric titration technique. Coulometric titration curves showed that six intermediate phases exist, with nominal stoichiometric compositions LiSn, Li₇Sn₃, Li₅Sn₂, Li₁₃Sn₅, Li₇Sn₂, and Li₂₂Sn₅. At low lithium concentrations, the activity of lithium in molten lithium-tin alloys follows Henry's law behavior. The partial and integral molar thermodynamic properties of the lithium-tin system were evaluated as a function of composition from emf measurements at 415°C. The temperature dependence of the standard Gibbs free energies of formation for the six intermediate phases was also determined. The experimental results were used to map out parts of the phase diagram of the lithium-tin system. The homogeneity ranges of the six solid phases are all quite narrow. The phase LiSn congruently melts at about 488°C and the phase Li₇Sn₃ peritectically decomposes at 500°C. These two phases form an eutectic mixture of 57 a/o Li at 470°C. The liquidus line on the tin-rich side of the binary phase diagram was found to agree with data reported in literature.

Solid lithium-aluminum (1, 2) and lithium-silicon (3-5) alloys are currently being utilized instead of pure lithium as anode materials in high performance rechargeable lithium batteries being developed for use as power sources for electric vehicles and as energy storage devices for electric utility load leveling. As they are solid at the operating temperatures (400°-500°C), the retaining problems encountered with molten Li are avoided. Also, since they have lower Li activities, the solubility of Li in the molten salt electrolytes, which causes self-discharge due to increased electronic conduction and diffusion of Li to the other electrode, is significantly reduced. Furthermore, corrosion problems associated with molten lithium are avoided, resulting in less difficult materials selection and cell design problems.

The development of other new lithium battery systems should be aided by the investigation of other solid lithium alloys which might perform better than the lithium-aluminum and lithium-silicon alloys presently used as anode materials. In order to evaluate the suitability of other alloys as active materials for use in negative electrodes, the compositional variations of the lithium activity and the chemical diffusion coefficient within them is required. The former parameter determines both the potential and the capacity of an alloy anode, and thus influences the specific energy when coupled with an appropriate cathode. The electrode potential range must also lie within the stability window of the electrolyte in order to avoid interface reactions. The power is related to the rate processes in-

involved in the electrode reaction. The charge transfer reaction at the electrode-electrolyte interface is generally very rapid in elevated temperature molten salt cells, and is seldom rate limiting. On the other hand, mass transport of the electroactive species within solid electrode phases by chemical diffusion is often quite important.

The properties of lithium-tin alloys relating to their possible use as anode materials have been examined. The results of the thermodynamic studies are reported here. Information about kinetic properties will be reported in a separate publication.

The lithium-tin system was first investigated by Masing and Tammann (6) using thermal and microscopic analysis, and the existence of the compounds Li₄Sn, Li₃Sn₂, and Li₂Sn₅ was claimed. Later, careful thermoresistometric and thermal analysis experiments on 58 alloys by Grube and Meyer (7) revealed a rather more complicated phase diagram. In 1964, structural work (8) showed that the phase originally thought to be Li₄Sn is actually Li₂₂Sn₅. Later structural investigations by Hansen and Chang (9) showed that the most tin-rich phase is Li₂Sn₅. Recently, the existence of the phases LiSn (10), Li₅Sn₂ (11), and Li₇Sn₂ (12), which also appear in Hansen's diagram, was confirmed by x-ray diffraction studies. In addition, new phases with nominal compositions of Li₇Sn₃ (13) and Li₁₃Sn₅ (14) have also been reported.

The thermodynamic properties of liquid lithium-tin alloys were measured by several investigators at elevated temperatures (15-17). Foster, Crouthamel, and Wood (15) carried out emf measurements on cells of the type

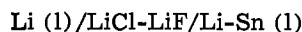
Bi, Li₃Bi/LiCl-LiF (30 m/o)/Li-Sn (1)

* Electrochemical Society Active Member.

¹ Present address: Shell Development Company, Houston, Texas 77001.

Key words: alloy, cell, phases, current.

where the alloy composition varied from 10 atomic percent (a/o) Li to tin saturated with the phase Li_5Sn_2 . The temperature range was 800-1050 K. The standard Gibbs free energies of formation for solid Li_5Sn_2 at 800, 850, 900, 950, and 1000 K were determined to be -61.4, -59.8, -57.9, -55.3, and -52.4 kcal/mole, respectively, with an estimated error of 1 kcal/mole. EMF measurements were also made on cells of the type



at 550°C by Morachevskii and co-workers (17), who calculated the partial and integral molar Gibbs free energies from 4 to 50 a/o Li. Liquid-vapor equilibrium data for the molten lithium-tin system were obtained from vapor pressure measurements using the transpiration technique by Fischer and Johnson (16).

The thermodynamic properties of the liquid lithium-tin alloys show negative deviations from ideal behavior. However, there is no information about the thermodynamic properties of the other phases in the lithium-tin system. Since this type of information is necessary to evaluate the potential use of materials in this system as electrode reactants, experiments were undertaken using techniques developed earlier for such purposes (18-22).

Experimental Details

Coulometric titrations and emf measurements were made using galvanic cells of the type



where LiCl-KCl (eut.) represents the liquid electrolyte, which was the eutectic mixture of LiCl [58.8 mole percent (m/o)] and KCl (41.2 m/o) with a melting point of 352°C. The above cell was in a three-electrode configuration and it was set up in a controlled atmosphere glove box filled with high purity helium gas. Both counter and reference electrodes were made of two-phase mixtures of the α and β phases, Li-saturated Al and "LiAl," with an overall composition of 40 a/o Li. Pure tin (99.9% Baker Reagent Grade) was used as the starting material for coulometric titration and was placed in a small molybdenum bucket because it is molten at the experimental temperatures (from 360° to 590°C). Alumina crucibles were used to contain the molten salt electrolyte. Molybdenum was earlier shown to be suitable as an electrical lead material at all lithium activities (18-22). Furthermore, the solubility of lithium in molybdenum is negligibly small in the temperature range used in these experiments (23).

The LiCl-KCl eutectic salts were purchased from Lithcoa (Lithium Corporation of America). They were heated in an alumina crucible at 420°C in the glove box for 12 hr before use. Without further purification, these molten salts were clear and colorless.

The reference electrodes were made of cold-pressed pellets of two-phase lithium-aluminum alloy powder (40 a/o) and were held in molybdenum holders. They were prepared by melting preweighed lithium ribbons (99.9% Foote Mineral) and aluminum wires (99.9999% Cominco) together in a molybdenum cup with a cover at 750°C. The temperature was then slowly reduced to about 500°C and maintained there for 12 hr. The resultant solid alloys were crushed and ground to fine powder in a porcelain mortar and pestle. The powder was then cold-pressed into pellets of 3/8 in. diam at a pressure about 8×10^4 psi under a helium atmosphere. The emf of these two-phase reference electrodes relative to pure lithium may be expressed as a function of temperature as (1, 4, 20, 24)

$$E_{\text{Al, "LiAl"}} = 451 - 0.220 T (\text{K}) \text{ mV}$$

The counterelectrodes were prepared either by casting into molybdenum buckets under the conditions described above or by an electrochemical method. In

the latter case, lithium was titrated into pure aluminum wires up to a composition of 40 a/o Li using molten lithium as the anode and the same eutectic molten salt as an electrolyte.

The use of these two-phase lithium-aluminum alloys as both reference and counterelectrodes offers several advantages over molten lithium. Because they have a lower lithium activity than pure lithium, the solubility of lithium (whose magnitude is not quantitatively known) in the LiCl-KCl eutectic salt is significantly reduced, thus decreasing the electronic leakage current through the electrolyte (25). The displacement reaction to produce potassium vapor (26) is also reduced.

In addition to the many (over 150) compositions produced by the coulometric titration technique, measurements were also made on 31 individually prepared lithium-tin alloys. These alloys were synthesized by use of the fusion technique in the glove box. EMF measurements were made after the synthetic alloys had been equilibrated in cells for at least 24 hr.

The electrochemical measurements were made using a PAR potentiostat/galvanostat (Model 173) with a plug-in digital coulometer (Model 179). The cell temperature was determined by means of two Chromel-Alumel thermocouples sheathed with 304 stainless steel.

Results and Discussion

Figure 1 shows the measured coulometric titration curve for the lithium-tin system at 415°C. The data are depicted by a solid line, as the resolution in such a figure is not sufficient to show the actual points from the more than 150 individual measurements. The emf measurements made on the 31 alloys of various compositions that were individually prepared are also included, as shown by the data points in Fig. 1, for comparison. It is seen that the results for compositions prepared in these two ways show excellent agreement. At that temperature, the solubility of lithium in liquid tin is 36.4 a/o Li, and on the lithium-rich side of this composition there are six intermediate phases within which the voltage varies with composition, and seven two-phase voltage plateaus at which the emf is independent of composition. The homogeneity ranges of the intermediate phases are all quite narrow, and their nominal compositions are LiSn , Li_7Sn_3 , Li_5Sn_2 , $\text{Li}_{13}\text{Sn}_5$, Li_7Sn_2 , and $\text{Li}_{22}\text{Sn}_5$. The ranges of stoichiometry and data on the (very high) chemical diffusion coefficients within these six phases will be presented in a separate publication (27). Due to the high chemical diffusion coefficients in these phases, equilibrium could be reached easily in minutes to a few hours for

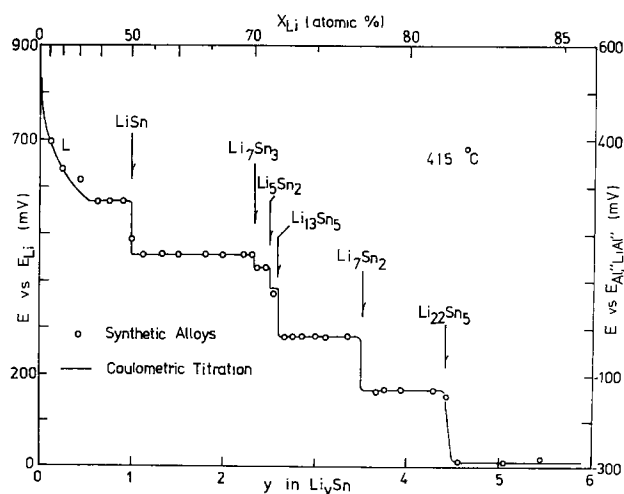


Fig. 1. Coulometric titration curve for the lithium-tin system at 415°C.

all compositions. Data taken by both adding and deleting lithium gave consistent results.

It was found that the activity of lithium, a_{Li} , in the liquid lithium-tin alloy obeyed Henry's law, so that the emf can be expressed by

$$E = -\left(\frac{RT}{F}\right) \ln a_{Li} = -\left(\frac{RT}{F}\right) \ln \gamma_{Li} X_{Li} \quad [1]$$

where the activity coefficient of lithium γ_{Li} is constant at a specific temperature. X_{Li} is the mole fraction Li. The experimental results at 415°C are shown in Fig. 2. It is seen that E varies linearly with the logarithm of X_{Li} to a composition of about 10 a/o Li. The slope, expressed as $dE/d \ln X_{Li}$, is $5.92 \times 10^{-2} V$, which is equal to the numerical value of (RT/F) at 415°C. The activity coefficient of lithium, γ_{Li} , in this range is 6.44×10^{-5} . The liquid alloys of lithium-cadmium (28), lithium-gallium (29), lithium-indium (30), lithium-lead (31), and lithium-bismuth (32) all exhibit Henry's law behavior at low lithium compositions, and experimental results for these systems are summarized in Table I. In all cases, the activity coefficients of lithium in these liquid alloys are very low, showing negative deviations from Raoult's law.

Although the activity coefficient of lithium in the liquid alloys is independent of composition at low lithium concentrations at a constant temperature, it varies with temperature at a fixed composition. The emf at a constant composition varies approximately linearly with temperature. At the composition of 0.9 a/o Li, the activity coefficient of lithium was found to increase from 3.23×10^{-5} at 372°C to 4.70×10^{-4} at 589°C.

Figures 3 and 4 present typical emf measurements as a function of temperature at a number of compositions. The compositions were fixed by coulometric titration. Over the temperature range of 360°-590°C the measured emf was a linear function of temperature as long as no phase transitions occurred. For those compositions where phase transformations took place as the temperature was varied, the emf curves have changes in slope.

Figure 5 shows the derivative of the emf across the lithium-tin system with respect to temperature. The partial molar entropy of lithium, $\Delta \bar{S}_{Li}$, is also shown in the same plot, but with a different scale, since

$$\Delta \bar{S}_{Li} = F \left(\frac{\partial E}{\partial T} \right) \quad [2]$$

The partial molar entropy of lithium is seen to vary with composition in the single-phase regions and to be independent of composition in two-phase regions.

Both the relationship between the emf and the temperature in the two-phase regions of the lithium-tin

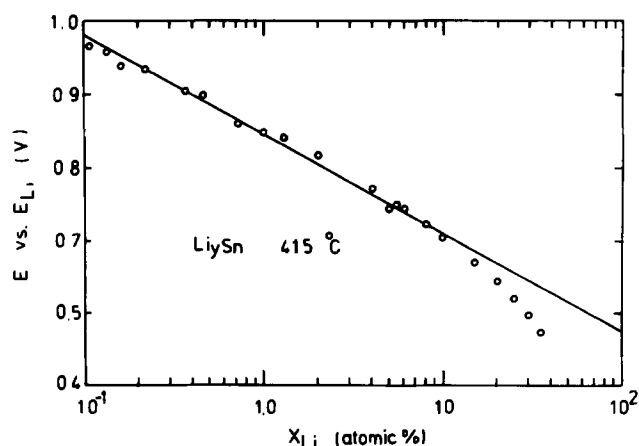


Fig. 2. Semi-logarithmic plot of the emf vs. mole fraction of lithium at 415°C.

Table I. Activity coefficients of lithium in various liquid lithium alloys

| System | T (K) | γ_{Li} | Composition | Ref. |
|--------|-------|-----------------------|---------------------|-----------|
| Li-Cd | 688 | 6.85×10^{-4} | $X_{Li} \leq 0.077$ | (27) |
| Li-Ga | 688 | 4.49×10^{-4} | $X_{Li} \leq 0.083$ | (28) |
| Li-In | 688 | 7.12×10^{-4} | $X_{Li} \leq 0.071$ | (29) |
| Li-Sn | 688 | 6.44×10^{-5} | $X_{Li} \leq 0.100$ | This work |
| Li-Pb | 800 | 7.80×10^{-4} | $X_{Li} \leq 0.117$ | (31) |
| Li-Bi | 800 | 3.20×10^{-5} | $X_{Li} \leq 0.144$ | (32) |

system and the related values of the partial molar entropy of lithium are presented in Table II.

The partial molar enthalpies of lithium, $\Delta \bar{H}_{Li}$, in the lithium-tin alloys relative to pure lithium were calculated from the expression

$$\Delta \bar{H}_{Li} = F \left[-E + T \left(\frac{\partial E}{\partial T} \right) \right] \quad [3]$$

The compositional variation of the partial molar enthalpy of lithium in the lithium-tin system at 415°C is shown in Fig. 6. Up to the composition 85.7 a/o Li, the partial molar enthalpy of lithium is negative. This is no longer true for the two-phase mixture of the most lithium-rich phase $Li_{22}Sn_5$ and the liquid alloy of lithium saturated with tin. The partial molar enthalpy of lithium in the single-phase lithium-tin liquid alloys was found to be essentially composition-independent. Values of the partial molar enthalpy of lithium in the two-phase regions at 415°C are presented in Table III.

The activity, a_{Sn} , and the chemical potential or the partial molar Gibbs free energy, $\Delta \bar{G}_{Sn}$, of tin were calculated as a function of composition for the lithium-tin system according to the relation (20)

$$\Delta \bar{G}_{Sn} = RT \ln a_{Sn} = F \left(yE - \int_0^y E dy \right) \quad [4]$$

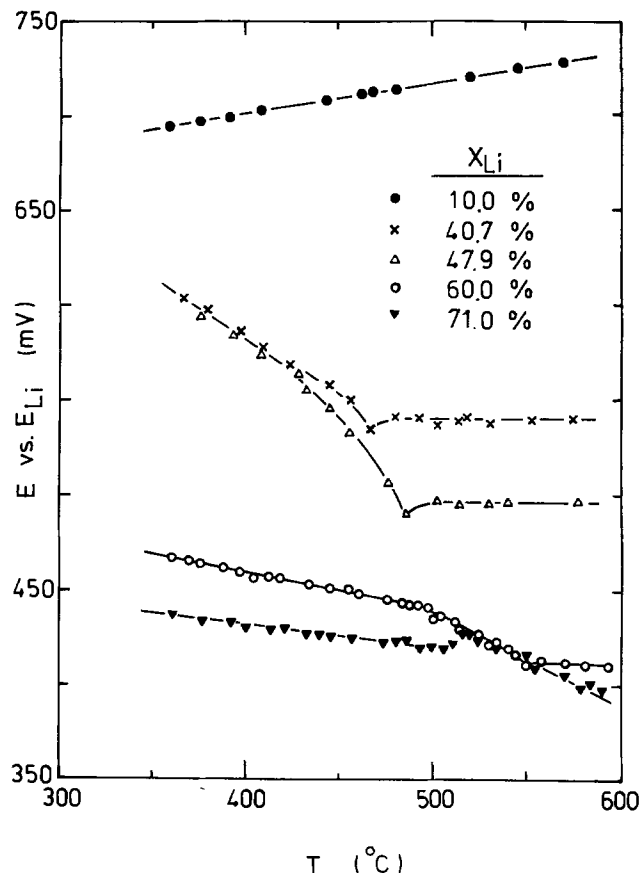


Fig. 3. Temperature variation of the emf at various compositions

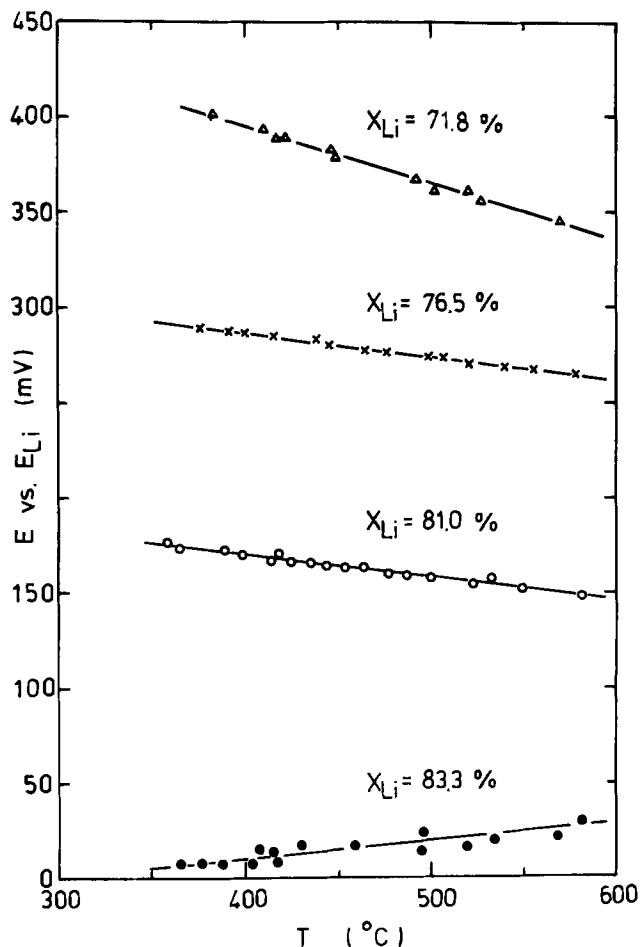


Fig. 4. Temperature variation of the emf at various compositions

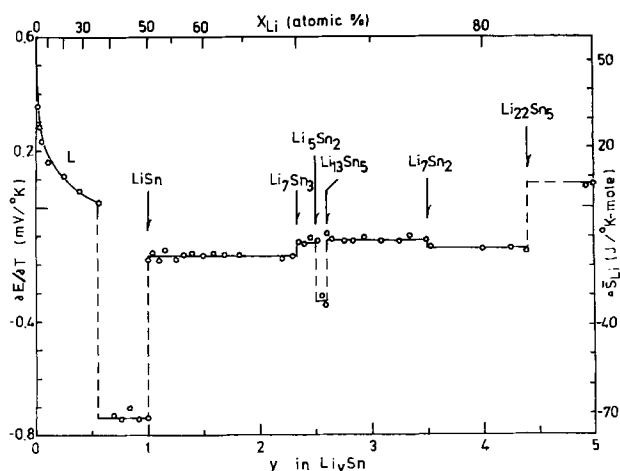


Fig. 5. Temperature derivative of the emf or the partial molar entropy of lithium at various compositions.

where y is the composition parameter in Li_ySn . The results at 415°C are shown in Fig. 7. It is seen that the

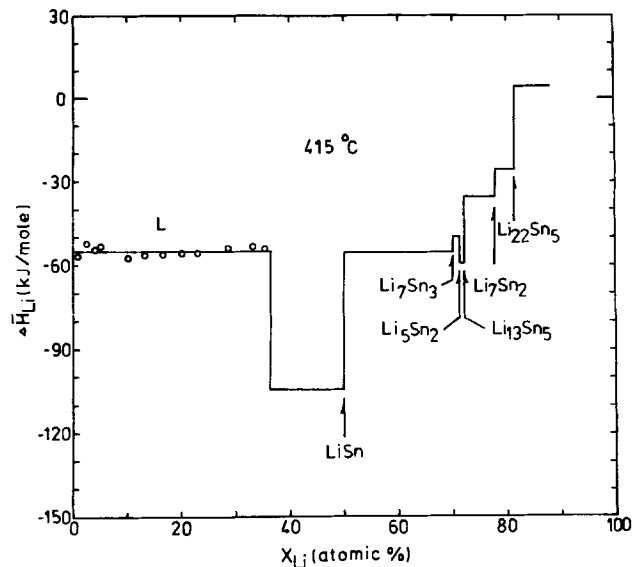


Fig. 6. Compositional variation of the partial molar enthalpy of lithium at 415°C .

activity of tin in the lithium-tin alloy system initially follows Raoult's law, i.e., $a_{\text{Sn}} = X_{\text{Sn}}$ or $(1 - X_{\text{Li}})$, and then has a negative deviation as more lithium is added. The values of the activity of tin in the two-phase regions at 415°C are included in Table III.

The partial molar entropies of tin, $\Delta\bar{S}_{\text{Sn}}$, were evaluated from the expression

$$\Delta\bar{S}_{\text{Sn}} = -yF\left(\frac{\partial E}{\partial T}\right) + F\int_0^y\left(\frac{\partial E}{\partial T}\right)dy \quad [5]$$

The partial molar entropy of tin is positive and slowly increases to a value of 5.6 J/deg mole with increasing lithium concentration in the tin-rich terminal liquid phase. The values of $\Delta\bar{S}_{\text{Sn}}$ in the two-phase regions are included in Table II.

The partial molar enthalpies of tin, $\Delta\bar{H}_{\text{Sn}}$, were calculated from the definitional expression

$$\Delta\bar{H}_{\text{Sn}} = \Delta\bar{G}_{\text{Sn}} + T\Delta\bar{S}_{\text{Sn}} \quad [6]$$

It was found that $\Delta\bar{H}_{\text{Sn}}$ is essentially zero in tin-rich molten lithium-tin alloys. The values of $\Delta\bar{H}_{\text{Sn}}$ in the two-phase regions at 415°C are included in Table III.

The integral molar Gibbs free energy of mixing, ΔG_m , was determined by graphically evaluating the area under the coulometric titration curve using the equation (20)

$$\Delta G_m = -\frac{F}{1+y}\int_0^y E dy \quad [7]$$

The results at 415°C are shown in Fig. 8. It is seen that the values are negative over the entire range of composition, with a minimum (-35.7 kJ/mole) at approximately the nominal composition of the phase $\text{Li}_{13}\text{Sn}_5$. In the two-phase regions, ΔG_m is, of course, a linear function of the mole fraction of lithium, as expected.

Table II. Temperature dependence of the emf and the partial molar entropy of lithium and tin in two-phase lithium-tin alloys

| Phases present | Temperature dependence of the emf (mV) | Partial molar entropy of Li (J/deg mole) | Partial molar entropy of Sn (J/deg mole) | Temperature range ($^\circ\text{C}$) |
|--|--|--|--|--|
| Liq. + LiSn | $E = 1078 - 0.740 T \text{ (K)}$ | -71.4 | +45.6 | 360-480 |
| LiSn + Li ₇ Sn ₃ | $E = 573 - 0.170 T \text{ (K)}$ | -16.4 | -9.4 | 360-480 |
| Li ₇ Sn ₃ + Li ₅ Sn ₂ | $E = 517 - 0.120 T \text{ (K)}$ | -11.6 | -19.5 | 360-500 |
| Li ₅ Sn ₂ + Li ₁₃ Sn ₅ | $E = 616 - 0.330 T \text{ (K)}$ | -31.8 | +29.9 | 360-590 |
| Li ₁₃ Sn ₅ + Li ₇ Sn ₂ | $E = 365 - 0.1100 T \text{ (K)}$ | -10.6 | -23.4 | 360-590 |
| Li ₇ Sn ₂ + Li ₂₂ Sn ₅ | $E = 268 - 0.145 T \text{ (K)}$ | -14.0 | -14.1 | 360-590 |
| Li ₂₂ Sn ₅ + Liq. | $E = -46 + 0.085 T \text{ (K)}$ | +8.2 | -112.0 | 360-590 |

Table III. Thermodynamic data for two-phase equilibria in the lithium-tin system at 415°C

| Phases present | EMF vs. .Li (mV) | Activity of Li | Partial molar enthalpy of Li (kJ/mole) | Activity of Sn | Partial molar enthalpy of Sn (kJ/mole) |
|--|------------------|-----------------------|--|------------------------|--|
| Liq. + LiSn | 569 | 6.79×10^{-5} | -104.0 | 4.67×10^{-1} | +27.0 |
| LiSn + Li ₇ Sn ₃ | 456 | 4.57×10^{-4} | -55.3 | 6.94×10^{-2} | -21.7 |
| Li ₇ Sn ₃ + Li ₅ Sn ₂ | 430 | 7.08×10^{-4} | -49.8 | 2.49×10^{-2} | -34.5 |
| Li ₅ Sn ₂ + Li ₁₃ Sn ₅ | 390 | 1.39×10^{-3} | -59.3 | 4.06×10^{-3} | -10.9 |
| Li ₁₃ Sn ₅ + Li ₇ Sn ₂ | 284 | 8.31×10^{-3} | -35.4 | 4.85×10^{-5} | -72.9 |
| Li ₇ Sn ₂ + Li ₂₂ Sn ₅ | 170 | 5.88×10^{-2} | -25.8 | 4.57×10^{-5} | -106.0 |
| Li ₂₂ Sn ₅ + Liq. | 10 | 8.40×10^{-1} | +4.4 | 4.61×10^{-28} | -239.0 |

The integral molar entropy of mixing, ΔS_m , was calculated from the relation (20)

$$\Delta S_m = \frac{F}{1+y} \int_0^y \frac{\partial E}{\partial T} dy \quad [8]$$

The results given in Fig. 9 were obtained by graphical integration. ΔS_m is positive at low lithium compositions and becomes negative for lithium concentrations greater than 39 a/o Li, and thus for all the intermediate phases, in the temperature range investigated. It has a maximum value (4.2 J/deg mole) near the com-

position of 36 a/o Li and a minimum (-14.7 J/deg mole) at the composition of 72.2 a/o Li.

The integral molar enthalpy of mixing, ΔH_m was calculated from the expression

$$\Delta H_m = \Delta G_m + T \Delta S_m \quad [9]$$

and the experimental results at 415°C are shown in Fig. 10. Like ΔG_m , ΔH_m is negative over the whole composition range studied and it has a maximum negative value (-45.8 kJ/mole) near the stoichiometric composition of the phase Li₁₃Sn₅.

The standard molar Gibbs free energy of formation, ΔG_f° (Li_ySn), for the intermediate phases per mole of tin were obtained from the relation (20)

$$\Delta G_f^\circ (\text{Li}_y\text{Sn}) = -F \int_0^y E dy \quad [10]$$

and the results are shown as functions of temperature in Fig. 11. For all phases, ΔG_f° (Li_ySn) shows a linear dependence upon temperature. The standard entropies of formation, ΔS_f° (Li_ySn), were obtained from the slopes of best-fit straight lines, and the values are tabulated in Table IV.

The corresponding standard enthalpies of formation, ΔH_f° (Li_ySn), were evaluated from the extrapolated intercepts at $T = 0$. Those values are also included in Table IV.

Two types of emf measurements were undertaken to provide an independent check on portions of the binary phase diagram of the lithium-tin system reported by Grube and Meyer (7). The first kind was carried out at fixed alloy compositions, varying the temperature. Representative results were shown in Fig. 3. The temperatures at which phase transitions occur are evidenced by changes of slopes in the emf vs. temperature plots. The second set of measurements was made at constant temperatures, with the composition varied by use of the coulometric titration technique. Since the lithium activity is independent of composition in two-phase regions and varies with com-

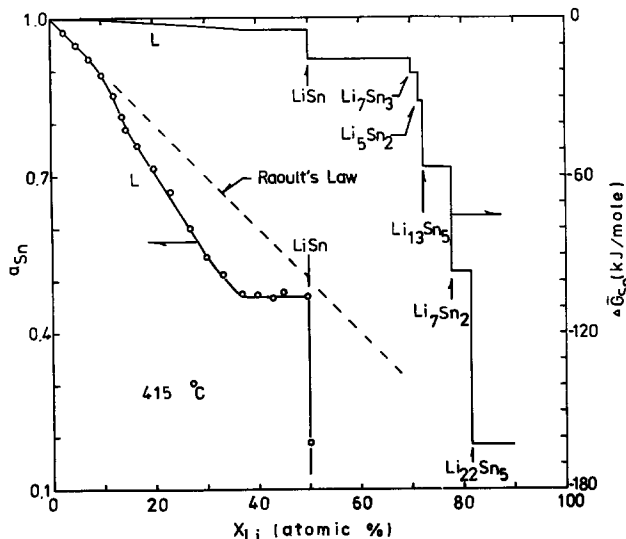


Fig. 7. Compositional variation of the activity and partial molar Gibbs free energy of tin at 415°C.

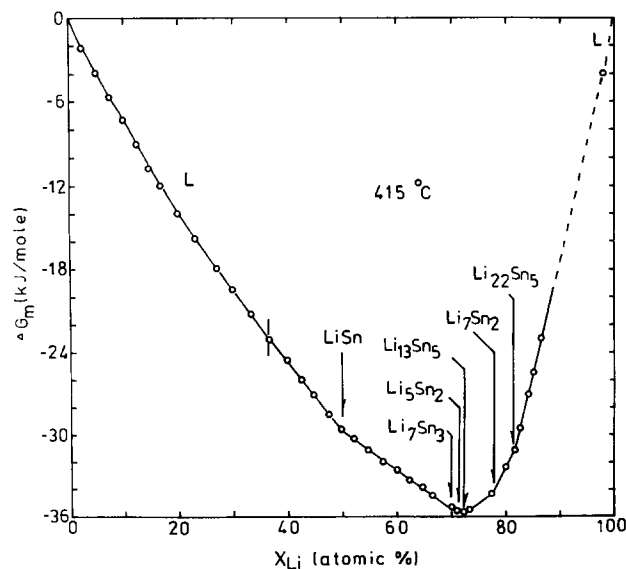


Fig. 8. Compositional variation of the integral molar Gibbs free energy of mixing at 415°C.

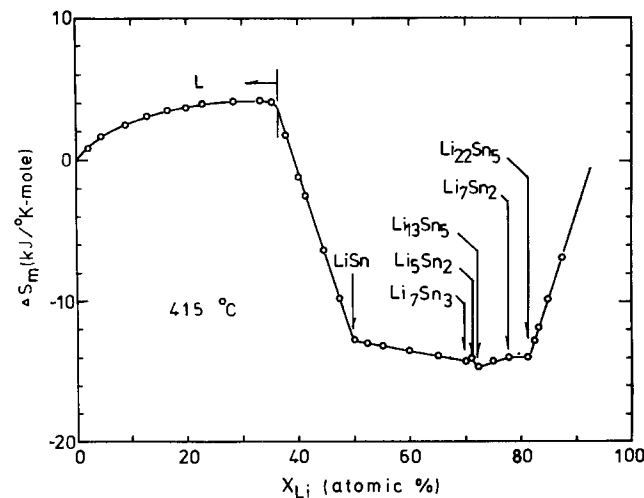


Fig. 9. Compositional variation of the integral molar entropy of mixing at 415°C.

Table IV. Thermodynamic data for the intermediate phases (Li_ySn) in the lithium-tin system at 415°C

| y in Li_ySn | Standard entropy of formation (J/deg mole) | Standard enthalpy of formation (kJ/mole) |
|-------------------------------|--|--|
| 1 | -25.8 | -70 |
| 7/3 | -47.7 | -151 |
| 2.5 | -49.7 | -159 |
| 2.6 | -52.8 | -165 |
| 3.5 | -63.1 | -197 |
| 4.4 | -75.6 | -220 |

position in single-phase regions, coulometric titration curves such as that in Fig. 1 can be used to locate phase boundaries.

On the basis of these results, a partly revised phase diagram has been deduced for the lithium-tin system. The results are shown in Fig. 12. The liquidus line is in good agreement with that determined by Grube and Meyer (7). The eutectic composition and temperature were found to be 57 a/o Li and 470°C , respectively. The phase LiSn melts congruently at about 488°C , close to the value reported by Grube and Meyer (485°C). In the present work, however, it was found that the phase Li_7Sn_3 , rather than Li_2Sn , peritectically decomposes at about 500°C .

The new phase $\text{Li}_{13}\text{Sn}_5$, first discovered by Frank and Muller (14), was confirmed in this work by use of the coulometric titration technique as well as x-ray diffraction analysis. The equilibrium conditions for the existence of the phase $\text{Li}_{13}\text{Sn}_5$ have been recently examined by Balley, Skelton, and Smith (33) using thermal analysis and metallography. They reported that the peritectic melting of Li_5Sn_2 at 716° , or 720°C as reported by Grube and Meyer (7), is in fact the peritectic melting of $\text{Li}_{13}\text{Sn}_5$, and that Li_5Sn_2 melts peritectically at a temperature about 18 degrees lower, i.e., 698°C . That the most lithium-rich phase is $\text{Li}_{22}\text{Sn}_5$,

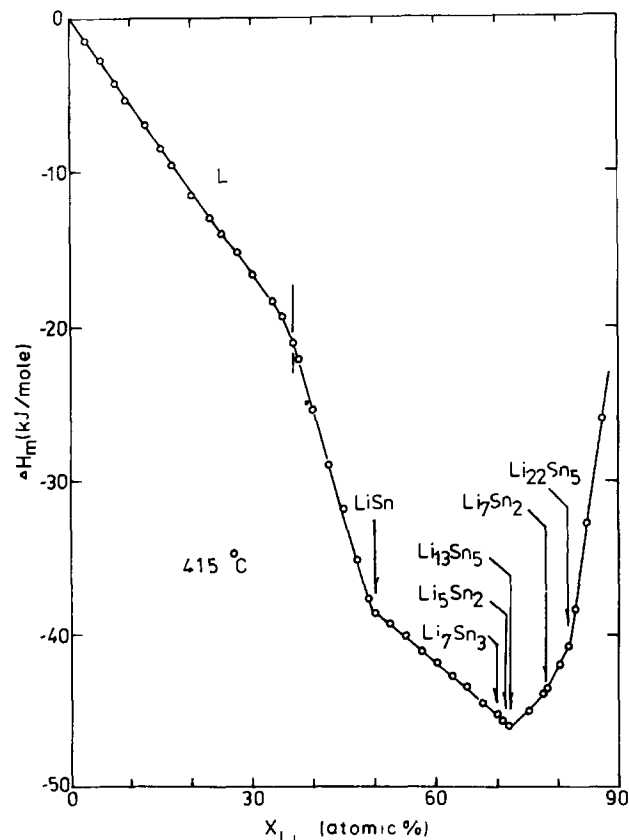


Fig. 10. Compositional variation of the integral molar enthalpy of mixing at 415°C .

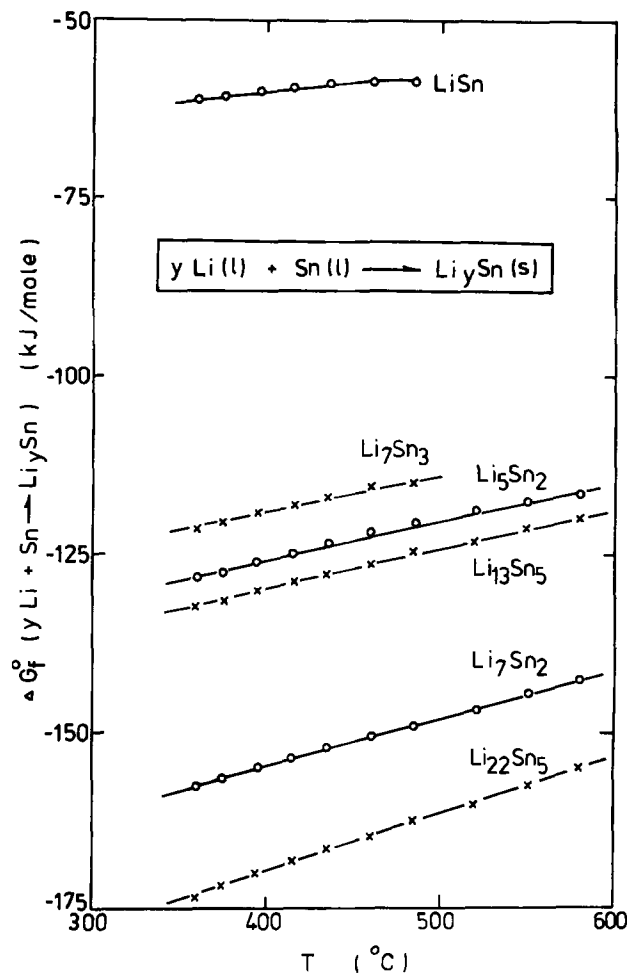


Fig. 11. Standard Gibbs free energy of formation of the intermediate phases in the lithium-tin system as a function of temperature.

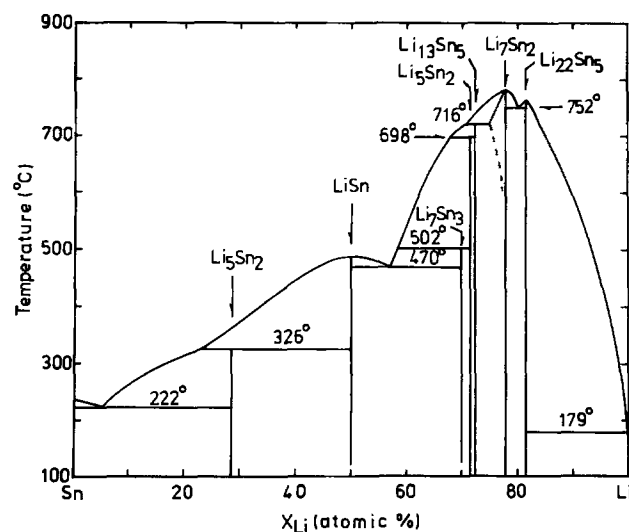


Fig. 12. Revised phase diagram of the lithium-tin system

instead of Li_4Sn , was also substantiated in the current investigation.

Acknowledgment

This work was supported by the U.S. Department of Energy under Contract No. EC-77-S-02-4506 and LBL Subcontract No. 4503110.

Manuscript submitted Dec. 9, 1979; revised manuscript received Jan. 4, 1981.

Any discussion of this paper will appear in a Discussion Section to be published in the December 1981 JOURNAL. All discussions for the December 1981 Discussion Section should be submitted by Aug. 1, 1981.

Publication costs of this article were assisted by Stanford University.

REFERENCES

1. N. P. Yao, L. A. Heredy, and R. C. Saunders, *This Journal*, **118**, 1039 (1971).
2. E. C. Gay, D. R. Vissers, F. J. Martino, and K. E. Anderson, *ibid.*, **123**, 1591 (1976).
3. S.-C. Lai, *ibid.*, **123**, 1196 (1976).
4. R. A. Sharma and R. N. Seefurth, *ibid.*, **123**, 1763 (1976).
5. R. N. Seefurth and R. A. Sharma, *ibid.*, **124**, 1207 (1977).
6. G. Masing and Tammann, *Z. Anorg. Chem.*, **67**, 190 (1910).
7. G. Grube and E. Meyer, *Z. Elektrochem.*, **40**, 771 (1934).
8. E. I. Gladyshevskii, G. I. Oleksiv, and P. I. Kripyakovich, *Kristallografiya*, **9**, 338 (1964); *Sov. Phys. Cryst.*, **9**, 269 (1964).
9. D. A. Hansen and L. J. Chang, *Acta Cryst.*, **B25**, 2392 (1969).
10. W. Müller and H. Schäfer, *Z. Naturforsch.*, **28b**, 246 (1973).
11. U. Frank, W. Müller, and H. Schäfer, *ibid.*, **30b**, 1 (1975).
12. U. Frank, W. Müller, and H. Schäfer, *ibid.*, **30b**, 6 (1975).
13. W. Müller, *ibid.*, **29b**, 304 (1974).
14. U. Frank and W. Müller, *ibid.*, **30b**, 316 (1975).
15. M. S. Foster, C. E. Crouthamel, and S. E. Wood, *J. Phys. Chem.*, **70**, 3042 (1966).
16. A. K. Fischer and S. A. Johnson, *J. Chem. Eng. Data*, **17**, 280 (1972).
17. A. G. Morachevskii, L. N. Gerasimenko, A. I. Demidov, and O. A. Drozdova, *Elektrokhimiya*, **8**, 1622 (1972).
18. W. Weppner and R. A. Huggins, *This Journal*, **124**, 1569 (1977).
19. W. Weppner and R. A. Huggins, *J. Solid State Chem.*, **22**, 297 (1977).
20. W. Weppner and R. A. Huggins, *This Journal*, **125**, 7 (1978).
21. B. E. Liebert, Ph.D. Dissertation, Stanford University (1977).
22. B. E. Liebert, W. Weppner, and R. A. Huggins, in "Electrode Materials and Processes for Energy Conversion and Storage," J. D. E. McIntyre, S. Srinivasan, and F. G. Will, Editors, p. 821, The Electrochemical Society Softbound Proceedings Series, Princeton, N.J. (1977).
23. F. A. Shunk, "Constitution of Binary Alloys," Second Supplement, p. 479, McGraw-Hill, New York (1969).
24. C. J. Wen, W. Weppner, B. A. Boukamp, and R. A. Huggins, *This Journal*, **126**, 2258 (1979).
25. R. J. Heus and J. J. Egan, *J. Phys. Chem.*, **77**, 1989 (1973).
26. R. N. Seefurth and R. A. Sharma, *This Journal*, **122**, 1049 (1975).
27. C. J. Wen, B. A. Boukamp, and R. A. Huggins, *Solid State Chem.*, **26**, 887 (1981).
28. C. J. Wen, Ph.D. Dissertation, Stanford University (1980).
29. C. J. Wen, B. A. Boukamp, and R. A. Huggins, *This Journal*, **128**, 1251 (1981).
30. C. J. Wen, B. A. Boukamp, and R. A. Huggins, *Mater. Res. Bull.*, **16**, 786 (1981).
31. A. I. Demidov, A. G. Morachevskii, and L. N. Gerasimenko, *Elektrokhimiya*, **9**, 848 (1973); *Sov. Electrochem.*, **9**, 813 (1973).
32. A. I. Demidov and A. G. Morachevskii, *Elektrokhimiya*, **9**, 1393 (1973); *Sov. Electrochem.*, **9**, 1321 (1973).
33. D. M. Bailey, W. H. Skelton, and J. F. Smith, *J. Less-Common Metals*, **64**, 233 (1979).

A Point Defect Model for Anodic Passive Films

I. Film Growth Kinetics

C. Y. Chao,* L. F. Lin,** and D. D. Macdonald*

Department of Metallurgical Engineering, The Ohio State University, Columbus, Ohio 43210

ABSTRACT

A model based on the movement of point defects in an electrostatic field is proposed to interpret the growth behavior of a passive film on a metal surface. This model results in a logarithmic growth law. The theoretical equations derived from the model readily account for experimental data for the growth of a passive film on iron. It is found that the field strength of the film is 1.11×10^6 V/cm. The dependence of film/solution interface potential difference on the applied potential (α) was found to be 0.743, and is independent of the identity of the anion in solution. However, the dependence of the potential difference across the film/solution interface on the solution pH (β) is strongly dependent on the identity of the solution anion.

It is generally believed that passivity is due to the formation of a three-dimensional film (usually an oxide film) on a metal surface. Experimentally, it is found that the film growth kinetics may follow one of the two following laws

$$L = A + B \ln t \text{ (logarithmic law)} \quad [1]$$

$$1/L = C - D \ln t \text{ (inverse logarithmic law)} \quad [2]$$

where L is the film thickness and t is time. A , B , C , and D are constants. However, many cases are known

where the experimental data may fit both laws equally well (1-3). This dual behavior is not unexpected, since the logarithmic law and inverse-logarithmic law are almost mathematically equivalent when the change in thickness is small, as illustrated by Lukac *et al.* (2).

Over the last forty years, several models have been proposed to explain the form of either Eq. [1] or Eq. [2] (see the next section). However, as shown in the following section, none of the existing models are completely satisfactory from a physical viewpoint, nor are they in complete agreement with the experimental data. Accordingly, it is necessary to develop an alternative model that can account for all of the ex-

* Electrochemical Society Active Member.

** Electrochemical Society Student Member.

Key words: metals, passivity, films, growth.

perimental observations. The purpose of the present paper is to develop such a model and to demonstrate that the model is in substantial agreement with the data that are currently available.

Review of the Existing Models

Mott-Cabrera model.—One of the earliest models for the growth kinetics of passive films was proposed by Mott (4) in 1947 and was later extended by Cabrera and Mott (5) in 1948. This model assumes: (i) Film growth is due to the transport of metal cations across the oxide film to the film/solution interface where they react with the electrolyte; (ii) the penetration of cations through film is assisted by the high electric field strength which is assumed to exist within the oxide (field strength, $\epsilon = -d\phi/dx$, where ϕ is the electrical potential and x is the distance); (iii) the field strength is constant throughout the film, i.e., $\epsilon = -d\phi/dx = \phi_f/L$, where ϕ_f is the total potential drop across the film of thickness L ; (iv) ϕ_f is a constant and hence is independent of film thickness; (v) the rate-limiting step for film growth is the emission of metal cations from metal into film at the metal/film interface.

These assumptions lead to the following rate law for film growth

$$dL/dt = N\Omega\nu \exp \left[\left(-W + \frac{qa\phi_f}{2L} \right) / kT \right] \quad [3]$$

where N is the number of mobile ions per unit surface area, Ω is the molecular volume per cation, ν is the vibrational frequency, W is the activation energy for the rate-controlling step, q is the charge that the cation carries, a is the jump distance, and kT is the thermal energy.

An approximate solution to Eq. [3] can be obtained by integrating by parts and neglecting higher terms in $2LkT/qa\phi_f$. This approximation yields an inverse logarithmic rate law

$$1/L = C - D \ln t \quad [4]$$

where

$$C = \frac{2}{qa\phi_f} \left\{ W - kT \ln \left[\frac{2(W - 39kT)^2 N\Omega\nu}{\phi_f a q k T} \right] \right\} \quad [5]$$

and

$$D = 2kT/qa\phi_f \quad [6]$$

Sato and Cohen's model.—From their study of iron in pH 8.4 borate buffer solution, Sato and Cohen (6) found that the relationship between external current, i , the applied potential, V_{app} , and the accumulated charge in the oxide film, Q_T , can be expressed by the following empirical equation

$$i = k' \exp (mV_{app} - Q_T/n) \quad [7]$$

where k' , m , and n are parameters.

The authors then used the so-called "place-exchange" mechanism to explain their results. According to this model, a layer of oxygen is adsorbed onto the surface which then exchanges places (possibly by rotation) with underlying metal atoms. A second layer of oxygen is then adsorbed and the two M—O pairs rotate simultaneously. This process is repeated and results in oxide film thickening. A schematic representation of this mechanism is given in Fig. 1.

From the "place-exchange" mechanism model, Sato and Cohen obtained analytical expressions for the parameters in Eq. [7]

$$k' = \frac{2FkT}{h} \sqrt{N_s^{a/\nu} (nN_{Fe})^{2/\nu}} \exp \left[\frac{qE_o F}{2\nu RT} - \frac{W_M - W_o + 0.5 qW_s}{\nu RT} \right] \quad [8]$$

$$m = \frac{qF}{2\nu RT} \quad [9]$$

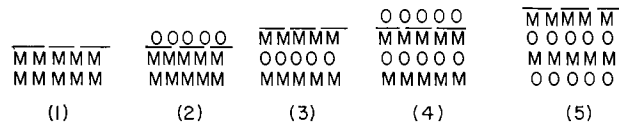


Fig. 1. Oxide film growth by the "place-exchange" mechanism. M and O represent metal and oxygen atoms, respectively. The dashed line is the solid-electrolyte interface. (1) A film-free metal; (2) oxygen adsorption on the metal surface; (3) "place-exchange" between oxygen and metal; (4) second oxygen layer is adsorbed; (5) "place-exchange" between two M—O pairs simultaneously.

$$n^{-1} = l^2 W_o / 4qRT \quad [10]$$

where F is Faraday's constant, h is Planck's constant, ν is defined as the number of times that a rate-controlling step occurs when the overall reaction occurs once, N_s is the total number of adsorption sites, and nN_{Fe} is the number of iron ions per unit area of oxide at the metal surface, and E_o is a constant. W_M is the chemical activation energy for the formation of the first layer of oxide, W_o is the chemical activation energy of subsequent layers, and W_s is the chemical activation energy for the incorporation of adsorbed oxygen into the growing film. R , T , and q have their usual meanings.

Later, Sato and Notoya (7) pointed out that under potentiostatic conditions, the integration of Eq. [7] results in the logarithmic law

$$L = A + B \ln (t + t_o) \quad [11]$$

with

$$A = \frac{l\nu RT}{W_o} \left[\ln \frac{W_o \beta T}{l\nu RT} + \frac{\sigma}{T} \right] + \frac{l\nu FV_{app}}{2W_o} \quad [12]$$

and

$$B = \frac{l\nu RT}{W_o} \quad [13]$$

Fehlner and Mott's model.—As early as 1960, Eley and Wilkinson (8) pointed out that the logarithmic growth law could be obtained by assuming any mechanism whose activation energy increased linearly with film thickness. Based on this argument, they preferred the "place-exchange" model, since it is the only model that gives a linear dependence of the activation energy on film thickness. The theory was fully developed by Sato and Cohen four years later (see "Sato and Cohen's model" above).

However, the "place-exchange" mechanism does not provide a very convincing description of the growth of a film whose thickness is more than one or two monolayers. Thus, in 1970, Fehlner and Mott (9), modified the earlier Mott-Cabrera model to provide an alternative to the "place-exchange" mechanism. The modifications involve the following assumptions: (i) Anion diffusion is responsible for film growth; (ii) the rate-limiting step (rls) is the emission of an anion from the environment into the film at the film/environment interface; (iii) the field strength in the film is independent of thickness, i.e., $\epsilon = \phi_f/L = \text{constant}$; (iv) the activation energy, W , of the rls increases linearly with thickness by, as the authors stated, "whatever the mechanism is." (Fehlner and Mott did not provide details of how this might occur.) Accordingly

$$W = W_o + \mu L \quad [14]$$

where W_o and μ are constants.

Based on these new assumptions, Eq. [3] becomes

$$\frac{dL}{dt} = N\Omega\nu \exp \left[\left(-W_o - \mu L + \frac{qa\epsilon}{2} \right) / kT \right] \quad [15]$$

This yields another logarithmic law

$$L = A' + B' \ln (t + t_o) \quad [16]$$

with

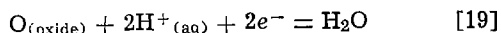
$$A' = \frac{kT}{\mu} \left[\ln \frac{\mu}{kT} + \ln N\Omega v - \frac{W^0}{kT} + \frac{qa\epsilon}{2kT} \right] \quad [17]$$

and

$$B' = kT/\mu \quad [18]$$

Several comments regarding existing growth models.—Over the past four decades, the growth models reviewed above have been used to interpret experimental data with only minor challenges [e.g., see Ref. (10-12)]. Recently, Lukac *et al.* (2) used ellipsometry to systematically investigate the growth kinetics of the passive film on iron in pH 8.6 borate buffer solution over a range of temperatures and potentials. Their data largely dispute some of the predictions of the existing models. Thus, the authors concluded “none of the existing models for film growth were found to be completely consistent with the temperature and potential dependence of the growth constants.” Macdonald and Roberts (13) also found that none of the existing models are able to account for the potentiostatic transients observed during the growth of anodic films on iron in sodium hydroxide solution.

Further, there are a number of fundamental arguments that tend to discredit the existing models. (i) The inverse logarithmic growth law has been observed for solutions of low pH (14-17), where passive film dissolution is significant. The Mott-Cabrera model, however, does not take this phenomenon into consideration. (ii) Recent studies at the Chalk River Nuclear Laboratories (18-21) have used radioactive markers to identify mobile species in anodic films. These studies showed that, for all the metals investigated (Al, Nb, Ta, W, Zr, Hf, U, Si), anion transportation is largely, if not exclusively, responsible for film growth. This observation tends to discredit the Mott-Cabrera model, which assumes that metal cation diffusion is responsible for film growth. (iii) Transient phenomena resulting from sudden changes of the applied potential or the pH of the solution have been investigated (14, 15). The results showed that at the film/solution interface, the following equilibrium is established rapidly



This observation contradicts the Fehlnner-Mott model which assumes that the rate-limiting step is located at the film/solution interface.

A New Model for the Growth of Passive Films under Anodic Polarization

In this section, a new model is presented to account for the growth kinetics of a passive film on a metal surface. Initially, the assumptions involved are clearly stated and the growth law is derived. Subsequently, it is demonstrated that the new model is in substantial agreement with many experimental observations that have been reported in the literature.

Basic features of the model.—This model is based on the following assumptions: (i) Whenever the external potential, V_{ext} , is more noble than the Flade potential, a continuous passive film will form on the surface of a metal. For the present purpose, the film is assumed to be an oxide of composition $MO_{x/2}$. However, the model developed below is perfectly general and can be applied to other (oxide and non-oxide) films as well. (ii) It is assumed that the passive film contains a high concentration of point defects. High temperature studies indicate that the major point defects that exist in an oxide film are $V_M^{x'}$, $V_O^{\cdot\cdot}$, e' , and h^{\cdot} .¹ The same species are expected to be present

¹The Kroger-Vink notation is adopted here for designating point defect species. According to the notation, X_i means that a species X occupies a Y lattice site (e.g., V_M means a vacancy occupies a metal site in the oxide, i.e., a metal vacancy); e and h are electrons and holes. The superscript gives the number and the sign of the charge. Thus, “ $\cdot\cdot$ ” means two positive charges. “ x' ” means x negative charges (e.g., $V_M^{x'}$ means a metal vacancy which carries x negative charge).

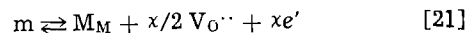
in a passive film. (iii) It is well known that passive films are characterized by high electrical fields ($\sim 10^6$ V/cm) and we assume that the field strength is of the same order as that required for dielectric breakdown.² Accordingly, the passive film behaves as an “incipient semiconductor” because it exists on the verge of dielectric breakdown. Consequently, the field strength is a function of the chemical and electrical characteristics of the film and therefore is independent of thickness even for potentiostatic conditions. (iv) Since passive films are regarded to be “incipient semiconductors,” it is assumed that electrons (e') and electron holes (h^{\cdot}) in the film matrix are in their equilibrium states, and that the electrochemical reactions involving electrons (or electron holes) are rate controlled at either the metal/film (m/f) or the film/solution (f/s) interfaces. On the other hand, the rate-controlling step for those processes which involve metal vacancies ($V_M^{x'}$) and oxide vacancies ($V_O^{\cdot\cdot}$), (i.e., film growth) is assumed to be the transport of the vacancies across the film. This assumption implies that metal and oxide vacancies are in their equilibrium states at the m/f and the f/s interfaces.

Additional assumptions will be given later, as necessary.

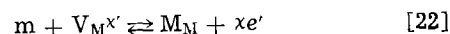
Kinetic growth law.—Figure 2 shows schematically the relationship between the working electrode and reference electrode in an electrochemical cell, and the corresponding potential-position relationships. The parameters $\phi_{m/f}$, $\phi_{f/s}$, and ϕ_R represent the potential drops at the metal/film, film/solution, and solution/reference electrode interfaces, respectively. ϕ_f is the potential drop across the film and V_{ext} is the external position. The potential drops in the solution as well as that in the external circuit are neglected in the present treatment. From Fig. 2 we obtain

$$V_{\text{ext}} + \phi_R = \phi_{m/f} + \phi_f + \phi_{f/s} \quad [20]$$

Two reactions occur at the metal/film (m/f) interface



and



where m represents the metal atom in the metal, and M_M is metal cation in the film. Since equilibrium is established at the m/f interface, then

$$\mu_m = \mu_{M_M} + \frac{x}{2} \mu_{V_O^{\cdot\cdot}} + xF\phi_f' + x\mu_{e'} - xF\phi_m \quad [23]$$

where ϕ_f' and ϕ_m are the flatband potentials of the film and metal at the m/f interface, respectively, and μ_i is the chemical potential of species i . Furthermore, the standard Gibbs energy of reaction [21], ΔG_{21}° , is defined as

$$\Delta G_{21}^\circ = \mu_{M_M}^\circ + \frac{x}{2} \mu_{V_O^{\cdot\cdot}}^\circ + x\mu_{e'}^\circ - \mu_m^\circ \quad [24]$$

By selecting appropriate standard states³

$$\mu_m = \mu_m^\circ, \mu_{M_M} = \mu_{M_M}^\circ, \mu_{e'} = \mu_{e'}^\circ, \phi_m - \phi_f = \phi_{m/f} \quad [25]$$

and

$$\mu_{V_O^{\cdot\cdot}} = \mu_{V_O^{\cdot\cdot}}^\circ + RT \ln a_{V_O^{\cdot\cdot}}(m/f) \quad [26]$$

²Very little dielectric breakdown data for oxides have been reported. Furthermore, wide variations exist in these values which have been reported. For impure sintered Al_2O_3 plates (25), breakdown has been reported to occur at 50 kV/cm. For higher purity Al_2O_3 , breakdown was reported at 200 kV/cm. It seems reasonable to expect that the “intrinsic” breakdown for pure Al_2O_3 is of the order of 10^8 V/cm. Recently, a value of 1.1×10^7 V/cm has been reported for SiO_2 (26).

³The standard state for each species is defined as follows: m = a metal which is in equilibrium with the metal oxide; M_M = metal cation which occupies a normal cation site in the oxide lattice which is in equilibrium with the metal; e' = electron in the metal; and $V_O^{\cdot\cdot}$ = hypothetical “pure” $V_O^{\cdot\cdot}$ which possesses the same properties as if they were the species that are present in the metal oxide that is in equilibrium with metal.

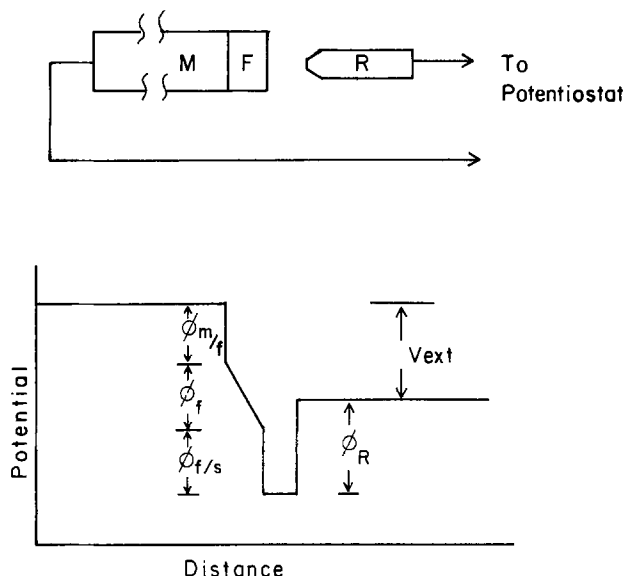


Fig. 2. Schematic of the working and reference electrodes in a typical electrochemical cell (upper figure), and the corresponding potential-distance relationships (lower figure). M represents metal, F represents film, and R represents reference electrode.

where $a_{V_{O^{2-}}(m/f)}$ represents the activity of $V_{O^{2-}}$ at the m/f interface.

Combining Eq. [23] and [24] yields

$$a_{V_{O^{2-}}(m/f)} = \exp\left(\frac{2F\phi_{m/f} - (2/\chi)\Delta G_{21}^\circ}{RT}\right) \quad [27]$$

Similar treatment for Eq. [22] will result in

$$a_{V_{M^{x+}}(m/f)} = \exp\left(\frac{\Delta G_{22}^\circ - xF\phi_{m/f}}{RT}\right) \quad [28]$$

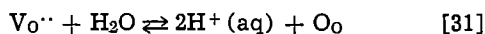
where ΔG_{22}° is the standard Gibbs energy of reaction [22].

At this time, it is necessary to assume that the interaction between point defects is negligible, i.e., the point defects behave as an ideal solution. Accordingly, the activity coefficient is unity and we estimate the number of $V_{O^{2-}}$ and $V_{M^{x+}}$ at the m/f interface as

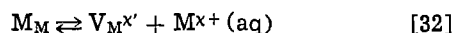
$$\begin{aligned} C_{V_{O^{2-}}(m/f)} &= \frac{N_v}{\Omega} a_{V_{O^{2-}}} \\ &= \frac{N_v}{\Omega} \exp\left(\frac{2F\phi_{m/f} - (2/\chi)\Delta G_{21}^\circ}{RT}\right) \end{aligned} \quad [29]$$

$$C_{V_{M^{x+}}(m/f)} = \frac{N_v}{\Omega} \exp\left(\frac{\Delta G_{22}^\circ - xF\phi_{m/f}}{RT}\right) \quad [30]$$

where N_v is Avogadro's number and Ω is the molecular volume of oxide. C_i is the concentration of species i in units of No. of species/cm³. At the film/solution (f/s) interface, two other reactions occur



and



where $M^{x+}(aq)$ is the hydrated metal cation in the electrolyte solution. Because of local equilibrium at the f/s interface, the number of oxide vacancies at this interface, $C_{V_{O^{2-}}(f/s)}$, can be calculated easily by equating the electrochemical potentials on both sides of Eq. [31]

$$\mu_{V_{O^{2-}}} + 2F\phi_f'' + \mu_{H_2O} = 2\mu_{H^+} + 2F\phi_s + \mu_{O_o} \quad [33]$$

where ϕ_f'' and ϕ_s are flatband potentials for the film and solution at the f/s interface, respectively. Furthermore, the change in standard Gibbs energy for reaction [31] is given by

$$\Delta G_{31}^\circ = 2\mu_{H^+} + \mu_{O_o} - \mu_{V_{O^{2-}}} - \mu_{H_2O} \quad [34]$$

where

$$\mu_{H_2O} = \mu_{H_2O}^\circ, \mu_{O_o} = \mu_{O_o}^\circ, \phi_f'' - \phi_s = \phi_f/s \quad [35]$$

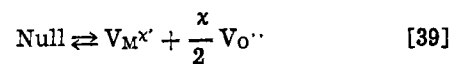
$$\mu_{V_{O^{2-}}} = \mu_{V_{O^{2-}}}^\circ + RT \ln a_{V_{O^{2-}}}(f/s) \quad [36]$$

$$\mu_{H^+} = \mu_{H^+}^\circ - 2.303 RT \times pH \quad [37]$$

These relationships lead to

$$C_{V_{O^{2-}}(f/s)} = \frac{N_v}{\Omega} \exp\left[\left(\frac{\Delta G_{31}^\circ - 2F\phi_f/s}{RT}\right) - 4.606 pH\right] \quad [38]$$

The number of $V_{M^{x+}}$ at the f/s interface, $C_{V_{M^{x+}}}(f/s)$, can be calculated from the Schottky-pair reaction



Therefore

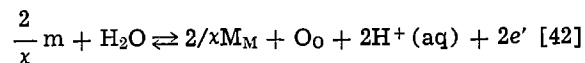
$$C_{V_{M^{x+}}}(f/s) \cdot [C_{V_{O^{2-}}}(f/s)]^{x/2} = \left[\frac{N_v}{\Omega}\right]^{1+x/2} \exp\left(-\frac{\Delta G_s^\circ}{RT}\right) \quad [40]$$

where ΔG_s° is the standard Gibbs energy change for the Schottky-pair reaction and the multiplier on the right-hand side arises because of the use of concentrations rather than activities. From Eq. [38] and [40], it is possible to obtain $C_{V_{M^{x+}}}(f/s)$

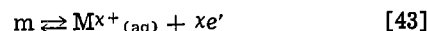
$C_{V_{M^{x+}}}(f/s)$

$$= \frac{N_v}{\Omega} \exp\left[\frac{xF\phi_f/s - \Delta G_s^\circ - x/2\Delta G_{31}^\circ}{RT} + 2.303 x pH\right] \quad [41]$$

It is apparent (see Eq. [21] and [31]), that oxide ion vacancies are produced at the m/f interface but are consumed at the f/s interface. As a result, oxide ion vacancies diffuse from the m/f to the f/s interfaces. Similar arguments show that $V_{M^{x+}}$ diffuses from the f/s to the m/f interfaces or equivalently, metal cations diffuse from the m/f to the f/s interfaces. The net result of $V_{O^{2-}}$ migration can be seen by combining reactions [21] and [31] to yield



Similarly, combining Eq. [22] and [32] shows that the net result of $V_{M^{x+}}$ migration can be expressed as



It is clear that the diffusion of $V_{O^{2-}}$ (or equivalently, oxygen anion) results in oxide growth, whereas the diffusion of $V_{M^{x+}}$ (or equivalently, metal cation) results in metal dissolution only. This conclusion is opposed to the assumption of accepted theories that cation diffusion is responsible for oxide growth (4, 5, 22, 23). However, this conclusion is subject to experimental verification (18-21).

Since $V_{O^{2-}}$ diffusion results in film growth, the problem of calculating film growth kinetics is equivalent to calculating the $V_{O^{2-}}$ diffusional rate. Thus

$$\frac{dL}{dt} = \frac{\Omega}{N_v} J_{V_{O^{2-}}} \quad [44]$$

where dL/dt is the film growth rate, Ω is the molar volume per cation, and $J_{V_{O^{2-}}}$ is the flux of $V_{O^{2-}}$ per unit area per unit time. In the Appendix, we show that it is possible to calculate the diffusional rate of a charged species in the presence of both concentration and potential gradients. The result is given by

$$J_{V_{O^{2-}}} = 2KD_{V_{O^{2-}}} \frac{C_{V_{O^{2-}}(m/f)} \exp(2KL) - C_{V_{O^{2-}}(f/s)}}{\exp(2KL) - 1} \quad [45]$$

where K , as defined in Appendix, is equal to $F\epsilon/RT$.

Now, it is necessary to introduce an additional assumption that the potential drop at the film/solution interface, $\phi_{f/s}$, is a function of applied potential and solution pH, but is independent of anodic film thickness. Accordingly, we may express $\phi_{f/s}$ in the form

$$\phi_{f/s} = \alpha V_{\text{ext}} + \beta \text{pH} + \phi_{f/s}^{\circ} \quad [46]$$

The assumption that $\phi_{f/s}$ is independent of thickness seems reasonable, because the film growth results from a reaction at the m/f interface (i.e., oxygen anions diffuse to the m/f interface and react with metal). The potential- and pH-dependent assumptions for $\phi_{f/s}$ also seem justified, since the f/s interface is polarizable.

From Eq. [20] and [46], it is possible to derive an expression for $\phi_{m/f}$

$$\phi_{m/f} = (1 - \alpha) V_{\text{ext}} - \beta \text{pH} - \phi_{f/s}^{\circ} + \phi_{\text{R}} - \phi_{\text{f}} \quad [47]$$

According to the assumption [4], $\phi_{\text{f}} = \epsilon L$, so that

$$\phi_{m/f} = (1 - \alpha) V_{\text{ext}} - \beta \text{pH} - \phi_{f/s}^{\circ} + \phi_{\text{R}} - \epsilon L \quad [48]$$

where ϕ_{R} is treated as a constant because the reference electrode is nonpolarizable. Substituting Eq. [29], [38], [45], [46], and [48] into Eq. [44] yields

$$\frac{dL}{dt} = \frac{A(B-1)}{\exp(2KL) - 1} \quad [49]$$

where

$$A = 2KD_{\text{VO}} \cdot \exp \left[-\frac{2F}{RT} (\alpha V_{\text{ext}} + \beta \text{pH} + \phi_{f/s}^{\circ}) + \frac{\Delta G_{31}^{\circ}}{RT} - 4.606 \text{pH} \right] \quad [50]$$

and

$$B = \exp \left[\frac{2F}{RT} (V_{\text{ext}} + \phi_{\text{R}}) - \frac{2\Delta G_{21}^{\circ}}{xRT} - \frac{\Delta G_{31}^{\circ}}{RT} + 4.606 \text{pH} \right] \quad [51]$$

Note that A and B are functions of external potential, V_{ext} . When experiments are conducted potentiostatically, V_{ext} is equal to the applied potential (V_{app}) and is independent of the film thickness (L). Thus Eq. [49] can be integrated directly since

$$\int_0^L [\exp(2KL) - 1] d(2KL) = \int_0^t 2KA(B-1) dt \quad [52]$$

which therefore yields

$$\exp(2KL) - 2KL - 1 = 2KA(B-1)t \quad [53]$$

For most anodic films, the field strength (ϵ) is of the order of 10^6 V/cm (or 10^{-2} V/Å) at room temperature. Thus, $2KL = 2F\epsilon/RT L \approx 0.76L$. This means that whenever $L \approx 5\text{Å}$, $\exp(2KL) \gg 2KL \gg 1$ and Eq. [53] can be simplified to

$$\exp 2KL = 2KA(B-1)t \quad [54]$$

or

$$L = \frac{1}{2K} [\ln 2KA(B-1) + \ln t] \quad [55]$$

Equation [55] has the form of the logarithmic growth law. Furthermore since current, i , is equal to $2F \frac{N_{\text{v}}}{\Omega} \frac{dL}{dt}$, Eq. [55] gives

$$i = \frac{FN_{\text{v}}}{K\Omega} t^{-1} \quad [56]$$

On the other hand, when the film thickness is small, Eq. [53] can be expanded using

$$\exp(2KL) = 1 + 2KL + 2K^2L^2 + \frac{4}{3} K^3L^3 + \dots \quad [57]$$

to yield

$$2K^2L^2 + \frac{4}{3} K^3L^3 + \dots = 2KA(B-1)t \quad [58]$$

For very small values for L (designated by subscript "s") the third and higher order terms may be neglected so that Eq. [53] reduces to

$$L_s = \left[\frac{A(B-1)}{K} t \right]^{1/2} \quad [59]$$

This gives a current transient of

$$i_s \propto \frac{dL_s}{dt} = \frac{1}{2} \left[\frac{A(B-1)}{K} \right]^{1/2} t^{-1/2} \quad [60]$$

where L_s and i_s represent the film thickness and current, respectively, for extremely thin films.

Under galvanostatic conditions, $i = 2F \frac{N_{\text{v}}}{\Omega} \frac{dL}{dt}$ is constant, and Eq. [49] becomes

$$i \frac{\Omega}{2FN_{\text{v}}} [\exp(2KL) - 1] = A(B-1) \quad [61]$$

Whenever $L \geq 5\text{Å}$ and hence $\exp(2KL) \gg 1$ Eq. [61] becomes

$$i \frac{\Omega}{2FN_{\text{v}}} \exp(2KL) = A(B-1) \quad [62]$$

Justification of the new model.—The newly developed model contains four unknown parameters: α (the potential dependence of $\phi_{f/s}$), β (the pH dependence of $\phi_{f/s}$), $\phi_{f/s}^{\circ}$ (an intrinsic constant), and ϵ (the field strength). The best way to verify the model would be to determine (by some independent means) these parameters, and then to substitute the values into Eq. [55], [59], [60], and [62] for direct comparison with experiment. Unfortunately, it does not seem possible to determine values for these parameters by completely independent means. Accordingly, we will attempt to justify the model in a reverse manner, i.e., by determining numerical values of these parameters from experimental data and demonstrating that the values obtained are physically reasonable. This analysis will be performed using experimental data for iron.

Before doing this, it is important to note that Eq. [49], [54], and [55] and Eq. [59], [60], and [62] involve a "(B-1)" term. The equations should become much simpler if one can prove that B is much larger than 1 so that $B-1 \approx B$. Since

$$B = \exp \left[\frac{2F}{RT} (V_{\text{ext}} + \phi_{\text{R}}) - \frac{2\Delta G_{21}^{\circ}}{xRT} - \frac{\Delta G_{31}^{\circ}}{RT} + 4.606 \text{pH} \right] \quad [63]$$

the criterion for $B \gg 1$ is that

$$\frac{2F}{RT} (V_{\text{ext}} + \phi_{\text{R}}) - \frac{2\Delta G_{21}^{\circ}}{xRT} - \frac{\Delta G_{31}^{\circ}}{RT} + 4.606 \text{pH} > 4 \quad [64]$$

Further, $2/x \Delta G_{21}^{\circ} + \Delta G_{31}^{\circ}$ is equal to the standard Gibbs energy for reaction [42], which is -2.33 kcal for $\text{Fe}/\gamma - \text{Fe}_2\text{O}_3$. Thus, whenever $V_{\text{ext}} > -0.06 \text{pH} - \phi_{\text{R}}$, B is much larger than 1. Unfortunately, we do not know the exact value for ϕ_{R} , so that it is not possible to specify the V_{ext} value which will ensure that $B \gg 1$. Nevertheless, we may conclude that at not-too-negative potentials, $B-1 \approx B$. In the following treatments, it is always assumed that $B \gg 1$ unless otherwise specified. Thus, under potentiostatic condition

$$\frac{dL}{dt} = \frac{C}{\exp(2KL) - 1} \quad [65]$$

$$\exp(2KL) - 2KL - 1 = 2KCt \quad [66]$$

$$L = \frac{1}{2K} [\ln 2KC + \ln t] \quad [67]$$

$$L_s = \left(\frac{C}{K}\right)^{1/2} t^{1/2} \quad [68]$$

$$i_s = \frac{1}{2} \left(\frac{C}{K}\right)^{1/2} t^{-1/2} \quad [69]$$

under galvanostatic condition

$$i \frac{\Omega}{2FN_v} \exp(2KL) = C \quad [70]$$

where

$$C = 2KD_{VO} \cdot \exp \left\{ \frac{2F}{RT} [(1 - \alpha)V_{\text{ext}} - \beta \text{pH} - \phi_{f/s}^\circ + \phi_R] - \frac{2\Delta G_{21}^\circ}{\chi RT} \right\} \quad [71]$$

Calculation of α and ϵ .—Equation [67] shows that in a given solution (i.e., fixed pH and $\phi_{f/s}^\circ$) the film thickness is proportional to V_{ext} and $\ln t$. Therefore

$$\left. \frac{dL}{dV_{\text{ext}}} \right)_{t, \text{pH}, \phi_{f/s}^\circ} = \frac{1 - \alpha}{\epsilon} \quad [72]$$

and

$$\left. \frac{dL}{d \ln t} \right)_{V_{\text{ext}}, \text{pH}, \phi_{f/s}^\circ} = \frac{RT}{2F\epsilon} \quad [73]$$

Goswami and Staehle (1) have determined the growth kinetics of the passive film on iron in pH 8.4 borate buffer solution over a wide range of potential ($0.05V_{\text{she}} \leq V_{\text{ext}} \leq 1.05V_{\text{she}}$). They found that their data could be fitted to both logarithmic and inverse-logarithmic functions equally well. Disregarding this dual nature, G-S's data yield

$$\left. \frac{dL}{d \ln t} \right)_{V_{\text{ext}}, \text{pH}, \phi_{f/s}^\circ} = 1.16 \text{ (\AA)} \quad [74]$$

and

$$\left. \frac{dL}{dV_{\text{ext}}} \right)_{t, \text{pH}, \phi_{f/s}^\circ} = 28.1 \text{ (\AA/V)} \quad [75]$$

Substitution of these experimental values into Eq. [72] and [73] yields $\epsilon = 1.11 \times 10^{-2} \text{ V/\AA}$ (or, equivalently, $1.11 \times 10^6 \text{ V/cm}$) and $\alpha = 0.69$. The calculated value for ϵ is of the correct order.

Lukac, Lumsden, Smialowska, and Staehle (2) conducted a systematic investigation of the effects of temperature and potential on the growth kinetics of the passive film on iron in borate buffer solution (pH 8.6 at room temperature). The calculated α and ϵ values⁴ at various temperatures are shown in Table I. It can be seen that the field strength, ϵ , and α decrease and increase, respectively, with increasing temperature.

Calculation of β and of the effect of anion type on α and β .—Sato, Noda, and Kudo (24) studied the formation of anodic films on iron in borate and phosphate solutions over a range of pH. Their data provide an excellent opportunity to evaluate β and/or the anion effect on α and β (assuming ϵ is independent of solution pH).

S-N-K's results are reproduced in Fig. 3 and 4. Figure 3 shows the film thickness after 1 hr of polarization in borate solution as a function of applied potential and pH. Figure 4 shows the film thickness for iron after polarization for 1 hr in phosphate solution.

From Fig. 3 and Eq. [72], one finds that for borate buffer solution

$$\left. \frac{dL}{dV_{\text{ext}}} \right)_{t, \text{pH}, \phi_{f/s}^\circ} = \frac{1 - \alpha}{\epsilon} = 23.33 \text{ (\AA/V)} \quad [76]$$

⁴The small pH changes due to the variation in temperature were not taken into consideration in the calculation.

Table I. Calculated α and ϵ values at various temperatures using L-L-S-S's data (2) for the growth of passive films on iron in borate solution

| Temperature (°C) | Calculated α | Calculated ϵ (V/\AA) |
|------------------|---------------------|-------------------------------|
| 0 | 0.747 | 1.12×10^{-2} |
| 20 | 0.728 | 1.10×10^{-2} |
| 35 | 0.812 | 9.37×10^{-3} |
| 50 | 0.841 | 8.10×10^{-3} |
| 80 | 0.853 | 7.57×10^{-3} |

for all pH values. If one assumes that ϵ is independent of pH, and is equal to $1.11 \times 10^{-2} \text{ V/\AA}$, then α is equal to 0.743 for all pH values. This value for α agrees with G-S's result within experimental error.

From Fig. 4, it is found that for the high pH range (pH ≥ 6.15), $1 - \alpha/\epsilon$ is also equal to 23.33 for iron in phosphate solutions. These data suggest that α is independent of pH and identity of anion. Figure 4 also shows that when pH ≤ 3.02 , $1 - \alpha/\epsilon$ deviates from 23.33. However, at such low pH's, it is very possible that phosphate anions are incorporated into the passive film (the well-known Parker Process utilizes this fact to produce a conversion coating). Accordingly, the calculated α values no longer refer to a pure oxide film.

S-N-K's result can also be used to calculate a value for β . From Eq. [67], one obtains

$$\left. \frac{dL}{d \text{pH}} \right)_{V_{\text{ext}}, t, \phi_{f/s}^\circ} = -\beta/\epsilon \quad [77]$$

The data plotted in Fig. 3 demonstrate that $(dL/d \text{pH}) = 0$ for all potentials. This indicates that β is equal to zero in borate buffer solution. On the other hand, Fig. 4 also shows that, whenever pH ≥ 6.15 , $(dL/d \text{pH}) = 1.3$ at constant V_{ext} . This indicates that $\beta = -(1.3 \times \epsilon) = -1.44 \times 10^{-2}$ and suggests that β depends on the identity of the anion in the solution.

Current-voltage characteristics under galvanostatic conditions.—Equation [70] shows that, under galvanostatic conditions

$$i = k' \exp \left\{ 2K \left[\frac{1 - \alpha}{\epsilon} V_{\text{ext}} - L \right] \right\} \quad [78]$$

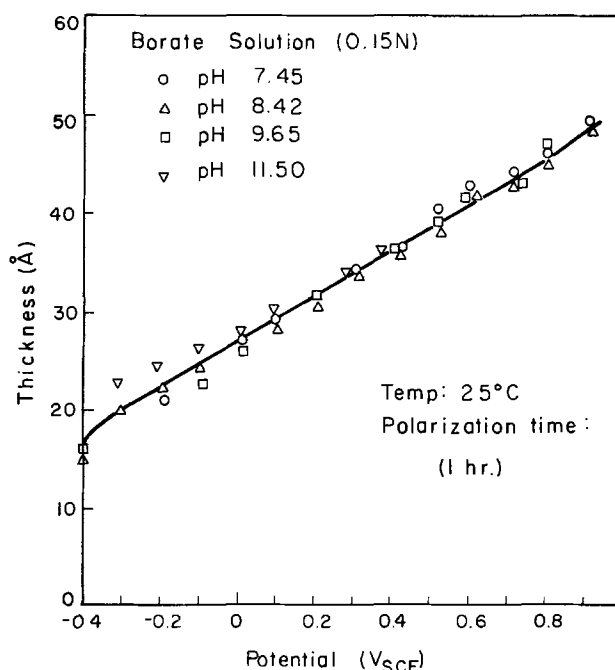


Fig. 3. Film thickness as a function of potential for iron that was polarized at passive potentials for 1 hr in borate solutions. [Figure 2 of Ref. (24)].

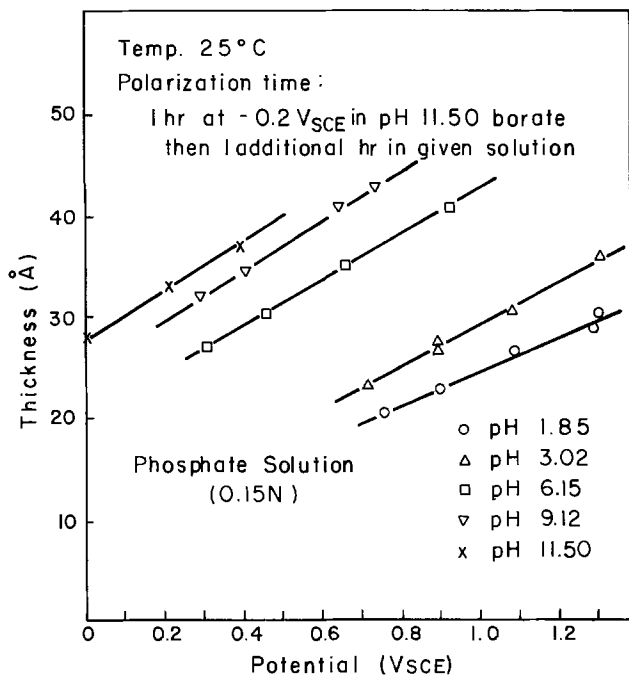


Fig. 4. Film thicknesses as a function of potential for iron that was polarized at passive potentials for 1 hr in phosphate solutions. [Figure 4 of Ref. (24).]

According to the previous calculation $\alpha = 0.743$ and $\epsilon = 1.11 \times 10^{-2}$ V/Å. Substitution of these values into Eq. [78] yields

$$i = k' \exp [19.97 V_{\text{ext}} - 0.86 L] \quad [79]$$

Sato and Cohen (6) have shown that, at constant anodic currents ranging from 0.3 to 23 $\mu\text{A}/\text{cm}^2$, $i \propto \exp\{\beta V_{\text{ext}}\}$ at any given thickness. Furthermore, they found that $\beta = 19.19$ which is in excellent agreement with the value ($\beta = 19.97$) predicted by the model developed in this paper.

Current-time transients for extremely thin film.—Equation [69] shows that for extremely thin films

$$i_s = \left(\frac{D_{V_{O^{2+}}}}{2}\right)^{1/2} \exp\left\{\frac{F}{RT} [(1-\alpha)V_{\text{ext}} - \beta pH - \phi_{t/s} + \phi_R] - \frac{\Delta G_{21}^\circ}{xRT}\right\} t^{-1/2} \quad [80]$$

or

$$i_s = k'' \exp\left\{\frac{F}{RT} (1-\alpha)V_{\text{ext}}\right\} t^{-1/2} \quad [81]$$

Since $\alpha = 0.743$, as determined previously

$$i_s = k'' \exp\left\{\frac{0.257FV_{\text{ext}}}{RT}\right\} t^{-1/2} \quad [82]$$

Usually, an extremely thin film is formed during the first few tenths of a second (*i.e.*, the transient period) during a potential jump between cathodic and passive potentials. Recently, Macdonald and Roberts (13) published a study of the potentiostatic transient behavior of carbon steel in 1M NaOH solution. They demonstrated that the transient current-time relationships follow an empirical equation of the form

$$i = k''' \exp\left\{m \frac{FV_{\text{ext}}}{RT}\right\} t^{-n} \quad [83]$$

where n and m depend on the initial and the final potentials of the jump. Their data at high anodic potentials, where $\gamma\text{-Fe}_2\text{O}_3$ is expected to form (note that α refers to this oxide), indicate that $n = 0.5$ and

m is equal to 0.21-0.23; this latter value is close to the value of 0.257 predicted by the new growth model. The success of the present model in interpreting the transient period growth kinetics should not be overemphasized, however, because the thickness of the "film" formed during this period is frequently smaller than the lattice parameter of film lattice. Therefore, attempts to model the film as a compact, continuous medium appears should be treated with caution.

Film growth due to reprecipitation of the cations from solution.—We have assumed that metal cations at the film/solution interface are in their equilibrium state. That is, the metal cations in the solution are in equilibrium with the metal cations in the highly defected film. Since the defected film has a more positive free energy of formation than a perfectly crystalline film, the concentration of metal cations in solution is greater than that for the perfectly crystalline oxide (or even hydroxide). Accordingly, metal cations will tend to reprecipitate back onto the surface to form a highly crystalline oxide (or hydroxide) upper layer. It should be pointed out that this deposit, or "secondary" layer, may not readily form because of the difficulties associated with the nucleation of a highly crystalline (low defect) phase. However, once it is formed, its thickness should be potential independent, as observed by Sato (27), provided that no change in oxidation state occurs during the deposition process and its structure may be porous. Finally, the formation of a secondary layer explains why radioactive marker experiments (18-21) indicate that the transport number of oxygen in a growing anodic passive film is less than one.

Conclusions

A point defect model has been developed to account for the kinetics of growth of passive films on metal surfaces. The model leads to a number of important generalizations concerning the kinetics of film growth.

1. The migration of oxygen anions or oxide ion vacancies ($V_{O^{2+}}$) is essential for passive film growth. On the other hand, the diffusion of metal cations or cation vacancies (V_M^x) results only in metal dissolution.

2. The integrated rate law for film growth is of the form

$$\exp(2KL) - 2KL - 1 = 2KA(B-1)t$$

For thick films, this expression reduces to a logarithmic expression and yields a current transient which varies inversely with time. For very thin films, a current transient which varies inversely with the square root of time is indicated.

3. The validity of the model has been demonstrated by use of experimental data from the literature for the growth of anodic films on iron.

4. It is found that for the formation of $\gamma\text{-Fe}_2\text{O}_3$ on iron, the dependence of the potential difference across the film-solution interface on the applied potential (α) is equal to 0.743 and is independent of the identity of the anion in solution. On the other hand, the dependence of this potential difference on the pH of the solution (β) is a strong function of the identity of the anionic species in solution.

Acknowledgments

The authors wish to thank the Electric Power Research Institute, Palo Alto, California, for support of this work under Contract RP1166-1.

Manuscript submitted Oct. 8, 1980; revised manuscript received Jan. 12, 1981.

Any discussion of this paper will appear in a Discussion Section to be published in the December 1981 JOURNAL. All discussions for the December 1981 Discussion Section should be submitted by Aug. 1, 1981.

Publication costs of this article were assisted by The Ohio State University.

APPENDIX

Calculation of the Diffusional Rate of a Charged Species

The rate of diffusion of a charged species i under the influence of concentration and potential gradients can be calculated from the generalized Fick's first law

$$J_1 = -D_1^* \frac{\partial C_1}{\partial x} - D_1^* \frac{C_1}{RT} q_1 F \frac{\partial \phi}{\partial x} \quad [\text{A-1}]$$

where $\partial C_1/\partial x$ is the concentration gradient, $\partial \phi/\partial x$ is the potential gradient, D_1^* is the electrochemical diffusivity of i , q_1 is the charge of the species under consideration, and F is Faraday's constant.

According to assumption [4] in the text, the field strength, ϵ , is independent of distance so that

$$\epsilon = \frac{\phi_f}{L} = -\frac{\partial \phi}{\partial x} - \epsilon_{in} \quad [\text{A-2}]$$

where ϵ_{in} is the induced electrical field due to the presence of space charge. Since ϵ is of the order of 10^6 V/cm, we may assume that $\epsilon \gg \epsilon_{in}$ and thus $\epsilon = \phi_f/L = -\partial \phi/\partial x$.

Substituting this result into Eq. [A-1] yields

$$\frac{dC_1}{dx} = -\frac{J_1}{D_1^*} + \frac{C_1}{RT} q_1 F \epsilon = -\frac{J_1}{D_1^*} + q_1 K C_1$$

where K is defined as $F\epsilon/RT$. Therefore

$$\int_{C_1(m/f)}^{C_1(f/s)} \frac{dC_1}{q_1 K C_1 - J_1/D_1^*} = \int_0^L dx \quad [\text{A-3}]$$

Here $C_{1(f/s)}$ and $C_{1(m/f)}$ are the concentrations of i at the f/s and m/f interfaces, respectively.

Under steady-state conditions, J_1 is a constant throughout the film. The integration of Eq. [A-3] then becomes

$$J_1 = q_1 K D_1^* \frac{C_{1(m/f)} \exp(q_1 K L) - C_{1(f/s)}}{\exp(q_1 K L) - 1} \quad [\text{A-4}]$$

REFERENCES

1. K. N. Goswami and R. W. Staehle, *Electrochim. Acta*, **16**, 1895 (1971).
2. C. Lukac, J. B. Lumsden, S. Smialowska, and R. W. Staehle, *This Journal*, **122**, 1571 (1975).
3. C. Chao and S. Smialowska, *Surf. Sci.*, **96**, 426 (1980).
4. N. F. Mott, *Trans. Faraday Soc.*, **43**, 429 (1947); *J. Chim. Phys.*, **44**, 172 (1947).
5. N. Cabrera and N. F. Mott, *Rep. Prog. Phys.*, **12**, 163 (1948-1949).
6. N. Sato and M. Cohen, *This Journal*, **111**, 512 (1964).
7. N. Sato and T. Notoya, *ibid.*, **114**, 585 (1967).
8. D. D. Eley and P. R. Wilkinson, *Proc. Roy. Soc. (London) Ser. A*, **254**, 327 (1960).
9. F. P. Kehner and N. F. Mott, *Oxid. Met.*, **2**, 59 (1970).
10. J. F. Dewald, *This Journal*, **102**, 1 (1955).
11. D. A. Vermilyea, *Acta Met.*, **1**, 282 (1953).
12. R. Ghez, *J. Chem. Phys.*, **58**, 1838 (1973).
13. D. D. Macdonald and B. Roberts, *Electrochim. Acta*, **23**, 557 (1978).
14. K. J. Vetter, *Z. Elektrochem.*, **58**, 230 (1954).
15. K. G. Weil, *ibid.*, **59**, 711 (1955).
16. N. Sato and T. Noda, *Electrochim. Acta*, **22**, 839 (1977).
17. M. Zamin and M. B. Ives, *This Journal*, **126**, 470 (1979).
18. J. A. Davis, B. Domeij, J. P. S. Pringle, and F. Brown, *ibid.*, **112**, 675 (1965).
19. J. L. Whitton, *ibid.*, **115**, 58 (1968).
20. F. Brown and W. D. Mackintosh, *ibid.*, **120**, 1096 (1973).
21. W. D. Mackintosh and H. H. Plattner, *ibid.*, **123**, 523 (1976); *ibid.*, **124**, 396 (1977).
22. K. J. Vetter, *Electrochim. Acta*, **16**, 1923 (1971).
23. K. J. Vetter and F. Gorn, *ibid.*, **18**, 321 (1973).
24. N. Sato, T. Noda, and K. Kudo, *ibid.*, **19**, 471 (1974).
25. A. A. Bauer and J. L. Bates, "An Evaluation of Electrical Insulators for Fusion Reactors," Battelle-Columbus Report No. BMI-1930, p. 23 (1974).
26. D. W. Ormond, *This Journal*, **126**, 162 (1979).
27. N. Sato, "Passivity and Its Breakdown of Iron and Iron Alloys," R. W. Staehle and H. Okada, Editors, NACE (1976).

A Point Defect Model for Anodic Passive Films

II. Chemical Breakdown and Pit Initiation

L. F. Lin,* C. Y. Chao,* and D. D. Macdonald**

Department of Metallurgical Engineering, The Ohio State University, Columbus, Ohio 43210

ABSTRACT

The point defect model that was previously developed (1) to explain the growth kinetics of a passive film has been extended to account for chemical breakdown. This model provides quantitative explanations of the dependence of breakdown potential on halide concentration, and of the incubation time-breakdown overpotential relationships that have been observed for iron and nickel in aqueous solutions. Limitations of the model are identified and discussed.

It is generally recognized that passivity is due to the formation of a thin film on the metal surface. Four basic questions arise as to the nature of the film: (i) What is the composition of the film? (ii) How fast does it grow? (iii) Why do some specific anions (e.g., Cl^- , Br^- , etc) result in local breakdown and hence in the initiation of pitting? (iv) What is the ionic and electronic structure of the film? Any reasonable model for

the film should provide satisfactory answers to these four questions.

Recently, Chao, Lin, and Macdonald (1) proposed a point defect model for the growth of a passive film. This model readily provides answers to the first two questions: (i) The passive film is a crystalline compound (e.g., an oxide) which contains a high concentration of point defects (note that in an extreme case, where the concentration of point defects is large enough, the passive film may be regarded as amor-

* Electrochemical Society Student Member.

** Electrochemical Society Active Member.

Key words: metals, passivity, corrosion, films.

phous in structure), and (ii) the kinetics of film growth can be described by a linear logarithmic law of the form

$$\exp(2KL) - 2KL - 1 = 2KA(B - 1)t$$

where L is the film thickness and t is time. The other parameters are defined in Ref. (1).

The present paper provides an answer to the third question. A clear-cut explanation of the film breakdown phenomenon not only makes the model more acceptable, but also unifies two important processes in corrosion science—passivation and localized corrosion.

Experimental Observations and Existing Models

Due to extensive studies over the last five decades, a great deal of experimental data now exists concerning film breakdown and subsequent corrosion (e.g., pitting). Although not all of the experimental data are in agreement, it is generally recognized that:

1. Film breakdown occurs only above some critical potential, V_c (the critical breakdown potential).
2. For a given material, V_c is a function of halide activity (e.g., Cl^- or some other halide) of the form

$$V_c = A - B \log a_{x^-} \quad [1]$$

where A , B are constants and a_{x^-} is the activity of the halogen anion.

3. Breakdown occurs at highly localized sites.
4. There exists an incubation time between the addition of halide and the appearance of pits on the surface. This incubation time is potential dependent.
5. Ellipsometric work by Kruger *et al.* (3) reveals that during the incubation period the ellipsometric readings for the passive film undergo a sudden change which might be attributed to the incorporation of Cl^- anion into the oxide film.

Several models have been proposed to account for the breakdown of the passive film. The more popular models are briefly discussed below.

Competitive ion adsorption theory.—Uhlrig (4) and Kolotyrlkin (5) proposed that both O^{2-} and Cl^- anions can be adsorbed onto metal surfaces. When O^{2-} is adsorbed, the metal passivates whereas adsorption of chloride does not produce a passive surface. Thus, above a critical potential, where Cl^- adsorption is favored over O^{2-} adsorption, breakdown of passivity occurs.

Complex ion formation theory.—Hoar and Jacob (6) assumed that a small number of Cl^- ions jointly adsorb around a cation in the film surface to form a high energy complex. Once formed, this complex will readily dissolve into the solution. The film is thus made thinner locally. The stronger anodic field at this site will rapidly transfer another cation to the surface where it will meet more Cl^- , complex with them, and thereby enter the solution. This process will result in "auto-accelerated" breakdown.

Ion penetration theory.—This theory suggests that Cl^- incorporates into and migrates through the passive film, and, upon reaching the metal/film interface, results in film breakdown. This theory has strong support from the ellipsometric work of Kruger *et al.* (3). However, theoretical calculations (7) reveal that the time required for Cl^- to penetrate through a film is much longer than the induction time measured experimentally.

Chemico-mechanical theory.—Hoar (8) postulated that the adsorption of Cl^- onto the film/solution interface results in "peptization" due to the mutual repulsion of the adsorbed charged species. When the repulsive forces are sufficiently high, the film cracks. Later, Sato (9) suggested that thin films always contain a "film pressure"

$$P = P_0 + \frac{\delta(\delta - 1)\epsilon^2}{8\pi} - \gamma/L \quad [2]$$

where P is the film pressure, P_0 is the atmospheric pressure, δ is the film dielectric constant, ϵ is the electric field, γ is the surface tension, and L is the film thickness. Sato proposed that adsorption of chloride ion greatly reduces the surface tension γ which in turn, increases P . When P exceeds some critical value, the film breaks down.

Although, these models can account for most of the experimental data qualitatively, no quantitative treatment has been developed so far. A quantitative model for film breakdown is presented below.

Mechanism for the Breakdown of a Passive Film

This section is divided into two parts. The first part describes the basic concepts behind the model and the second part presents a mathematical treatment which yields analytical expression for the critical breakdown potential and the incubation time.

Basic concepts.—In a previous study (1), the authors proposed a model for the growth of a passive film which involves transport of both anions (oxygen ion) and cations (metal ion) or their respective vacancies. Furthermore, the model concludes that anions diffuse from the film/solution (f/s) interface to the metal/film (m/f) interface and subsequently result in film thickening. On the other hand, cation diffusion, while not excluded, results only in dissolution and not in the growth of the primary passive film. This model has successfully accounted for a number of previously unexplained experimental observations (1).

One consequence of the diffusion of metal cations from the m/f to the f/s interfaces is that metal vacancies (or "metal holes")¹ are created at the metal/film interface. These metal "holes" will tend to submerge into the bulk of the metal and hence to "disappear." However, when the cation diffusion rate (i.e., the metal hole production rate) is higher than the rate of "metal hole" submergence into the bulk, the metal holes will start piling up and hence will form a void at the metal/film interface (this is the process of pit incubation). When the void grows to a certain critical size, the passive film suffers local collapse which then marks the end of pit incubation period. Subsequently, the collapsed site dissolves much faster than any other place on the surface thereby leading to pit growth. According to this argument, the criterion for pit initiation can be expressed as follows

$$(J_{ca} - J_m) \times (t - \tau) \geq \xi \quad [3]$$

where J_{ca} is the cation diffusion rate in the film, J_m is the rate of submergence of the metal holes into the bulk metal, t is the time required for metal holes to accumulate to a critical amount, ξ (i.e., t is the incubation time), and τ is a constant whose meaning will become clear in the following discussion.

Up to this point, we have described a process for film breakdown without incorporating a specific role for halide ion in the breakdown phenomenon. In the next part of this section, we will demonstrate that the presence of halide ions will greatly enhance J_{ca} and hence will accelerate film breakdown.

Mathematical expression for the critical breakdown potential and incubation time.—In the Appendix of Ref. (1), it was demonstrated that J_{ca} is given by

$$J_{ca} = xKD_{VM}x^* \left[\frac{C_{VM}x^*(m/f) \exp(-xKL) - C_{VM}x^*(f/s)}{\exp(-xKL) - 1} \right]$$

where, as defined in Ref. [1], x is the charge on a

¹The metal vacancy that is referred to here is a vacancy that is in the metal. In order to distinguish this from the metal vacancy that is in the film, we shall designate the former vacancy as a "metal hole."

cation, K is equal to $F\epsilon/RT$, ϵ is the field strength in the film, $D_{VMX'}$ is the diffusivity of the cation vacancy, L is the film thickness, and $C_{VMX'}(m/f)$ and $C_{VMX'}(f/s)$ are the concentrations of cation vacancies at the metal/film and film/solution interfaces, respectively. Cation vacancies in the film are produced at the f/s interface but are consumed at the m/f interface so that one should expect $C_{VMX'}(f/s) > C_{VMX'}(m/f)$. Moreover, since the passive films on many metals and alloys are of the order of 10 ~ 40 Å thick, then $\exp(-\kappa KL) \ll 1$, and the above equation can be simplified to

$$J_{ca} = \kappa K D_{VMX'} C_{VMX'}(f/s) \quad [4]$$

If the f/s interface achieves local equilibrium, consideration of the Schottky-pair reaction leads to the following relationship

$$[C_{VO\cdot}(f/s)]^{\kappa/2} [C_{VMX'}(f/s)] = \left[\frac{N_v}{\Omega} \right]^{1+\kappa/2} \exp\left(-\frac{\Delta G_s^\circ}{RT}\right) \quad [5]$$

where N_v is Avogadro's number, Ω is the molecular volume per cation, and ΔG_s° is the change in Gibbs energy for the Schottky-pair reaction. Combining Eq. [4] and [5], one obtains

$$J_{ca} = J^\circ [C_{VO\cdot}(f/s)]^{-\kappa/2} \quad [6]$$

where $J^\circ = \kappa K D_{VMX'} [N_v/\Omega]^{1+\kappa/2} \exp(-\Delta G_s^\circ/RT)$

Equation [6] shows that J_{ca} can be enhanced by decreasing $C_{VO\cdot}(f/s)$. Kruger *et al.* (3) have shown that Cl^- ions are capable of being incorporated into passive films. It is reasonable to assume that this is due to the occupation by Cl^- ions of oxygen vacancies,² that is



where $V_{O\cdot}$ is an oxygen vacancy in the film, and $Cl_{O\cdot}$ is a chloride anion occupying an oxygen lattice site. Thus, as the concentration of chloride is increased, the number of vacancies that are occupied also increases. This gives rise to a concomitant decrease in the $V_{O\cdot}$ concentration at the f/s interface. Quantitatively, Eq. [7] leads to the following expression (see derivation in the Appendix)

$$C_{VO\cdot}(f/s) \times a_{Cl^-} = u \exp\left(-\frac{F\alpha V_{app}}{RT}\right) \quad [8]$$

Substitution of Eq. [6] and [8] into Eq. [3] yields the criterion for pit initiation as

$$\left[J^\circ u^{-\kappa/2} \exp\left(\frac{\kappa F\alpha V_{app}}{2RT}\right) (a_{Cl^-})^{\kappa/2} - J_m \right] \times (t - \tau) \cong \xi \quad [9]$$

Equation [9] shows that pit initiation will not occur if

$$J^\circ u^{-\kappa/2} \exp\left(\frac{\kappa F\alpha V_{app}}{2RT}\right) (a_{Cl^-})^{\kappa/2} < J_m$$

and that the critical pitting potential, V_c , is given by the equality

$$J^\circ u^{-\kappa/2} \exp\left(\frac{\kappa F\alpha V_c}{2RT}\right) (a_{Cl^-})^{\kappa/2} = J_m \quad [10]$$

Equation [10] is easily rearranged to yield

$$V_c = \frac{4.606RT}{\kappa F\alpha} \log \frac{J_m}{J^\circ u^{-\kappa/2}} - \frac{2.303RT}{\alpha F} \log a_{Cl^-} \quad [11]$$

The form of Eq. [11] coincides with experimental observation³ (Eq. [1]) with

² Kruger has proposed a slightly different reaction from reaction [7].

³ J_m is the rate of submergence of metal holes into the metal. Accordingly, it can be related to the bulk diffusion rate for holes in the metal and is independent of applied potential.

$$A = \frac{4.606RT}{\kappa F\alpha} \log \frac{J_m}{J^\circ u^{-\kappa/2}}$$

and

$$B = 2.303RT/\alpha F$$

In Ref. (1), we have demonstrated that α is equal to 0.743 for iron and Ref. (10) reveals that $\alpha = 0.878$ for Ni at 25°C. These data enable us to calculate the theoretical value for constant B in Eq. [1], i.e., $B = 2.303RT/\alpha F = 0.080$ (V) for iron, and $B = 0.067$ (V) for nickel. The calculation for constant A in Eq. [1] is not possible at the present time because it involves a number of unknown parameters.

Table I lists the experimental values for B as compiled by Galvele (11). It can be seen that the experimental value for Ni (0.071V) agrees very well with the theoretical value (0.067V) computed above. The experimental data for iron are badly scattered, indicating that the experimental determination of B is anything but easy. Nevertheless, the experimental data scatter around the theoretical value of 0.080V. Thus, it is concluded that the theoretical values are physically reasonable.

Although Eq. [11] was derived for Cl^- -containing solutions, the same arguments can be extended to Br^- - and I^- -containing systems. For brevity, the derivation is omitted. Interested readers can do it themselves by following the same steps from Eq. [7] to Eq. [11]. The extended treatment leads to two conclusions: (i) The constant B is independent of the identity of the anion which is present in the system and (ii) constant A increases with the energy of incorporation of an anion into an oxygen vacancy. Accordingly, values for A are expected to lie in the order $I^- > Br^- > Cl^-$.

Figure 1 shows the experimental result of Janik-Czachor (14) for the critical pitting potential for iron in iodide, bromide, and chloride-containing solutions. It can be seen that the experimental data are in excellent agreement with the theoretical predictions.

The analysis presented above also yields an analytical function for another important parameter in pitting corrosion—the incubation time. Substitution of Eq. [10] into Eq. [9] therefore gives

$$J^\circ u^{-\kappa/2} (a_{Cl^-})^{\kappa/2} \left[\exp\left(\frac{\kappa F\alpha V_{app}}{2RT}\right) - \exp\left(\frac{\kappa F\alpha V_c}{2RT}\right) \right] (t - \tau) \cong \xi \quad [12]$$

or

$$J^\circ u^{-\kappa/2} (a_{Cl^-})^{\kappa/2} \exp\left(\frac{\kappa F\alpha V_c}{2RT}\right) \left[\exp\left(\frac{\kappa F\alpha \Delta V}{2RT}\right) - 1 \right] (t - \tau) \cong \xi \quad [13]$$

where $\Delta V = V_{app} - V_c$ is the breakdown overpotential.

Equation [13] shows that when the chloride concentration in the solution is fixed (i.e., a_{Cl^-} and V_c are constants), the incubation time, t , is a function of the

Table I. Values for constant B in Eq. [1] for iron and nickel [Reproduced from Ref. (11)]

| Metal | Buffer | Value of B (V) | Ref. |
|-------|------------------|------------------|------|
| Fe | None (pH 10) | 0.058 | (12) |
| Fe | Borate (pH 8) | 0.13 | (13) |
| Fe | Phthalate (pH 5) | 0.08 | (13) |
| Fe | Borate (pH 8.4) | 0.10 | (14) |
| Fe | Borate (pH 8.4) | 0.15-0.20 | (15) |
| Fe | Various | 0.03-0.08 | (2) |
| | | Mean 0.10 ± 0.05 | |
| Ni | None | 0.071 | (16) |

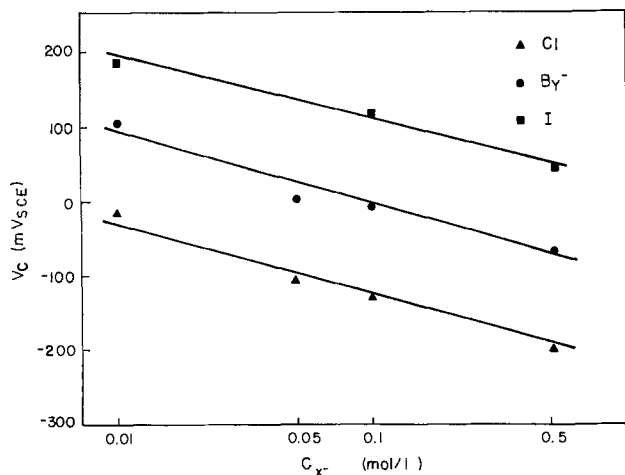


Fig. 1. Critical pitting potential V_c , vs. halide concentration (14).

breakdown overpotential. Mathematically, this can be expressed as

$$t = \xi' \left[\exp \left(\frac{x F \alpha \Delta V}{2RT} \right) - 1 \right]^{-1} + \tau \quad [14]$$

where

$$\xi' = \xi / J^\circ u^{-x/2} (a_{Cl^-})^{x/2} \exp \left(\frac{x F \alpha V_c}{2RT} \right) \quad [15]$$

Furthermore, when $\Delta V \cong 0.05V$, $\exp(x F \alpha \Delta V / 2RT) \gg 1$, so that Eq. [14] can be simplified to yield

$$t = \xi' \left[\exp \left(- \frac{x F \alpha \Delta V}{2RT} \right) \right] + \tau \quad [16]$$

At this point it is necessary to digress somewhat to discuss the significance of τ . Equations [9] and [12] were obtained by substituting Eq. [4] into Eq. [3]. However, Eq. [4] is valid only for steady-state diffusion, so that diffusion that takes place during the initial transient period is not properly included. The parameter τ is therefore introduced to account for diffusion during the transient period and it is a measure of the time over which transient diffusion is significant compared with steady-state diffusion.

Equation [16] shows that for very large values for ΔV , the incubation time, t , is dominated by the transient time, τ . On the other hand, for small values for ΔV (but that are still larger than $0.05V$), t is proportional to $\exp(-x F \alpha \Delta V / 2RT)$. It is interesting to note that Heusler and Fischer (2) obtained an empirical equation for the relationship between t and ΔV of the form

$$\log t / t_0 = V_0 / \Delta V \quad [17]$$

where t_0 and V_0 are constants.

Figure 2 shows the experimental data of Heusler and Fischer plotted in accordance with Eq. [17]. Replotting of the same data as $\log t$ vs. ΔV (Fig. 3), however, shows that Eq. [16] is also valid. Thus, for large values for ΔV , t approaches the value for the constant (τ), which is apparently of the order of a few seconds. However, for small values for ΔV , $\log t$ is inversely proportional to ΔV with a slope of -18.5 . This value is in excellent agreement with the theoretical value of

$$\text{gradient} = - \frac{x F \alpha}{4.606RT} = -18.8V^{-1}$$

which is obtained from Eq. [16] with $x = 3$ and $\alpha = 0.743$ for iron [see Ref. (1)].

Discussion

The analyses presented above demonstrate that the model developed in this paper for halide (in particular chloride) induced breakdown of passive films is in

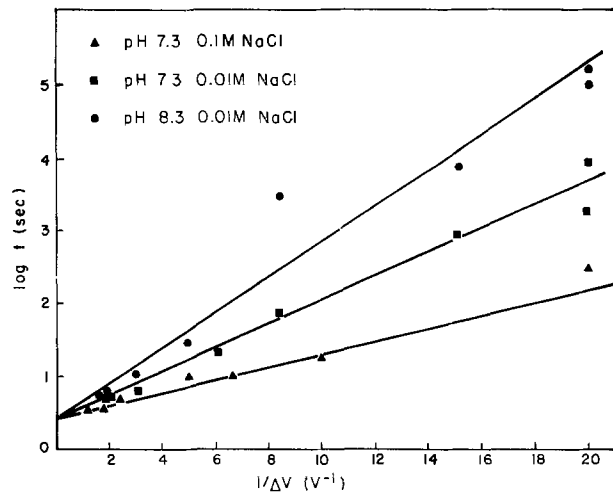


Fig. 2. Times t_i incubation for pitting of passive iron in borate buffer solution, $25^\circ C$, as a function of the reciprocal value of the potential difference, $\Delta V = V - V_c$ vs. the critical pitting potential, V_c . \blacktriangle : pH 7.3, 0.1M NaCl; \blacksquare : pH 7.3, 0.01M NaCl; \bullet : pH 8.3, 0.01M NaCl (17).

quantitative agreement with experimental data for the pitting of iron and nickel in halide-containing aqueous solutions. To our knowledge, no other model has demonstrated the same level of precision—in terms of both the functional and analytical dependencies of the critical pitting potential on halide concentration, and of the incubation time on breakdown overpotentials.

A limitation of the model in its present stage of development is that no surface "structure" (e.g., inclusions, grain boundaries, etc.) is specifically taken into account, although we believe that the model is readily extended to the heterogeneous case. For example, because heterogeneities in the passive film are also likely to be sites of high defect concentration, the model presented here provides a qualitative explanation for the tendency for pits to nucleate at inclusions, grain boundaries, and other macroscopic defects. Also, the model may not be directly applicable to those cases in which the anion in solution forms strong soluble cation complexes, rather than incorporating into the outer layer(s) of the film. Finally, to our knowledge no direct observations of void formation have been made, although it is possible that this is due to a lack of incentive in the past to examine in detail the nature of the metal/film interface prior to formation of a pit.

Acknowledgments

The authors gratefully acknowledge the financial support of this work by the Electric Power Research Institute, Palo Alto, California, under Contract No. RP1166-1.

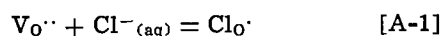
Manuscript submitted Oct. 8, 1980; revised manuscript received Jan. 12, 1981.

Any discussion of this paper will appear in a Discussion Section to be published in the December 1981 JOURNAL. All discussions for the December 1981 Discussion Section should be submitted by Aug. 1, 1981.

Publication costs of this article were assisted by The Ohio State University.

APPENDIX

The reaction that is proposed to occur at the film/solution interface is



Since local equilibrium is established at this interface, the sum of the electrochemical potentials of the reactants should be equal to the electrochemical potential of the product. Therefore

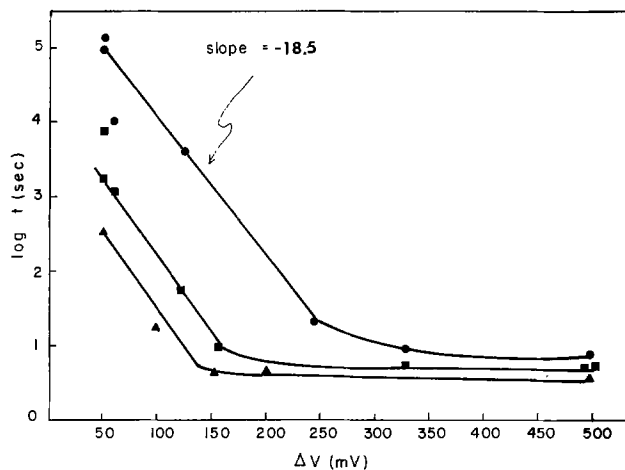


Fig. 3. Plot of $\log t$ vs. ΔV in accordance with Eq. [16]. Data taken from Fig. 2.

$$\mu_{\text{Cl}^-} - F\phi_s + \mu_{\text{VO}_2} + 2F\phi_f = \mu_{\text{ClO}_2} + F\phi_f \quad [\text{A-2}]$$

where μ is the chemical potential, ϕ_s and ϕ_f are the flatband potentials of the solution and film, respectively. Furthermore

$$\phi_f - \phi_s = \phi_{t/s}$$

and Eq. [A-2] becomes

$$\mu_{\text{Cl}^-} + \mu_{\text{VO}_2} - \mu_{\text{ClO}_2} + F\phi_{t/s} = 0 \quad [\text{A-2}']$$

The standard Gibbs energy of reaction [A-1] is

$$\mu_{\text{ClO}_2}^\circ - \mu_{\text{Cl}^-}^\circ - \mu_{\text{VO}_2}^\circ = \Delta G_{\text{A-1}}^\circ \quad [\text{A-3}]$$

where $\mu_{\text{ClO}_2}^\circ$ is the standard chemical potential of ClO_2 and $\Delta G_{\text{A-1}}^\circ$ is the standard Gibbs energy of reaction [A-1]. Since

$$\mu_{\text{Cl}^-} = \mu_{\text{Cl}^-}^\circ + RT \ln a_{\text{Cl}^-}$$

$$\mu_{\text{ClO}_2} = \mu_{\text{ClO}_2}^\circ + RT \ln a_{\text{ClO}_2}$$

and

$$\mu_{\text{VO}_2} = \mu_{\text{VO}_2}^\circ + RT \ln a_{\text{VO}_2}$$

then combining Eq. [A-2'] and [A-3] results in

$$\frac{a_{\text{VO}_2} a_{\text{Cl}^-}}{a_{\text{ClO}_2}} = \exp \left[\frac{\Delta G_{\text{A-1}}^\circ - F\phi_{t/s}}{RT} \right] \quad [\text{A-4}]$$

Now, in most of metal-oxygen-chloride ternary systems, the mutual dissolution of MO-MCl is very small, so that once a " ClO_2 " species is formed, it can be regarded as a precipitate of MCl in the MO matrix. Accordingly $a_{\text{ClO}_2} = 1$ in all cases and Eq. [A-4] becomes

$$a_{\text{VO}_2} a_{\text{Cl}^-} = \frac{\Omega}{N_V} C_{\text{VO}_2} a_{\text{Cl}^-} = \exp \left[\frac{\Delta G_{\text{A-1}}^\circ - F\phi_{t/s}}{RT} \right] \quad [\text{A-5}]$$

In Ref. (1), the authors have demonstrated that

$$\phi_{t/s} = \alpha V_{\text{app}} + \beta \text{pH} + \phi_{t/s}^\circ$$

Thus, for a given solution, Eq. [A-5] becomes

$$C_{\text{VO}_2} (t/s) \times a_{\text{Cl}^-} = u \exp \left(- \frac{F\alpha V_{\text{app}}}{RT} \right) \quad [\text{A-6}]$$

where

$$u = \frac{N_V}{\Omega} \exp \left(\frac{\Delta G_{\text{A-1}}^\circ - F\beta \text{pH} - F\phi_{t/s}^\circ}{RT} \right)$$

REFERENCES

1. C. Y. Chao, L. F. Lin, and D. D. Macdonald, *This Journal*, **128**, 1187 (1981).
2. K. E. Heusler and L. Fischer, *Werkst. Korros.*, **27**, 551 (1976).
3. C. L. McBee and J. Kruger, in "Localized Corrosion," R. W. Staehle *et al.*, Editors, p. 252, NACE, Houston (1974).
4. H. Bohni and H. H. Uhlig, *This Journal*, **116**, 906 (1969); H. P. Leckie and H. H. Uhlig, *ibid.*, **113**, 1262 (1966).
5. Y. M. Kolotyrkin, *ibid.*, **108**, 209 (1961).
6. T. P. Hoar and W. R. Jacob, *Nature*, **216**, 1299 (1967).
7. H. H. Strehblow, *Werkst. Korros.*, **27**, 792 (1976).
8. T. P. Hoar, *Corros. Sci.*, **7**, 355 (1967).
9. N. Sato, *Electrochim. Acta*, **19**, 1683 (1971).
10. C. Y. Chao, *J. Electroanal. Chem. Interfacial Electrochem.*, To be published.
11. J. R. Galvele, "Passivity of Metals," R. P. Frankenthal and J. Kruger, Editors, p. 285, The Electrochemical Society, Inc., Princeton, N.J. (1978).
12. M. G. Alvarez and J. R. Galvele, To be published.
13. H. H. Strehblow and B. Titz, *Corros. Sci.*, **17**, 461 (1977).
14. M. Janik-Czachor, *Br. Corros. J.*, **6**, 57 (1971).
15. Y. M. Kolotyrkin and L. I. Freiman, *Dokl. Akad. Nauk SSSR*, **162**, 376 (1965).
16. T. Koizumi and H. H. Uhlig, *This Journal*, **121**, 1137 (1974).

Measurement of pH and Redox Potential in Boric Acid/Lithium Hydroxide Buffer Solutions at Elevated Temperatures

T. Tsuruta and D. D. Macdonald*

Department of Metallurgical Engineering, The Ohio State University, Columbus, Ohio 43210

ABSTRACT

A palladium-hydride electrode (Pd black on Pt) was used for the measurement of pH in high temperature aqueous systems (25°-275°C). The electrode potential was calibrated against boric acid/lithium hydroxide buffer solutions, whose pH_T vs. temperature profiles have been calculated (1) using known dissociation constants for the components. The plateau potential for the $\alpha + \beta$ phase was observed up to 150°C, but was not observed above 200°C. The potential measured above 200°C was identified to be the redox potential and to correspond to the hydrogen electrode potential in the case of a hydrogenated system. The redox potential measured in hydrogenated systems were found to exhibit linear Nernstian responses to temperatures up to 275°C, but deviations of the measured potentials from equilibrium values were detected at temperatures above 200°C. The deviations are most probably due to uncertainties in the thermal and isothermal liquid junction potentials associated with the external reference electrode, and to uncertainties in the thermodynamic properties of high temperature aqueous solutions.

The importance of pH and redox potential measurements in high temperature aqueous systems, such as BWR and PWR (primary, secondary) nuclear systems, geothermal brines, chemical industries process waters, and for characterizing the solutions which have been used extensively in high temperature electrochemical studies, is widely recognized. A major obstacle to the measurement of pH at elevated temperatures is the lack of a reliable and generally applicable method for measuring the activity of hydrogen ion in these hostile environments. The precise pH measurements using concentration cells, which have been described by Mesmer *et al.* (2-5) and Macdonald and co-workers (6-8), and the use of single hydrogen electrodes, require the presence of molecular hydrogen in the system. Accordingly, these techniques are applicable only to those systems that are stable to reduction by molecular hydrogen. Many metal ions and anions are stable in hydrogenated systems and hydrogen electrodes have been shown to function at elevated temperatures. However, the problems involved with these electrodes are the precise determination of hydrogen fugacity and the difficulty of application for *in situ* pH measurements.

The potential decay of palladium-hydride electrodes has been used for the measurement of pH in high temperature aqueous systems by a number of workers (1, 9-12). The work of Dobson and co-workers (9-12) on this system has indicated that palladium-hydride electrodes exhibit Nernstian responses up to 195°C. However, their work was restricted to highly acidic or basic solutions, and no data were obtained for the technologically important pH range from 5 to 13. Recently, the palladium-hydride electrode has been used by Macdonald *et al.* (1) for the measurement of pH in various boric acid/lithium hydroxide buffer solutions ranging in pH (25°C) between 5 and 13 at temperatures to 275°C. Although linear potential vs. pH correlations were observed for all temperatures studied, the measured potentials deviated significantly from the equilibrium values calculated on the assumption that the

potential determining reaction is $H^+ + e^- = H$ (Pd, $\alpha + \beta$). In this report, we discuss the applicability of the palladium-hydride electrode for pH measurements at temperatures above 200°C.

Experimental

The high temperature recirculating loop used for this study is shown in Fig. 1. Briefly, the aqueous solution was pumped from a reservoir through a heat exchanger and into the autoclave using a positive displacement diaphragm pump. The exiting solution was heat exchanged with the input solution and then discharged back to the reservoir via a back pressure regulator. The pressure in the circuit was maintained at 10 kg/cm² above the saturated vapor pressure in order to maintain a single liquid phase.

Schematic diagrams of the measurement cell and the external reference electrode are shown in Fig. 2 and 3, respectively. Details of the construction, operation, and calibration of the external reference electrode have been recently given by Macdonald, Scott, and Wentreck (6).

Palladised platinum electrodes were employed. The Pd/Pt electrode was palladised cathodically in acidified

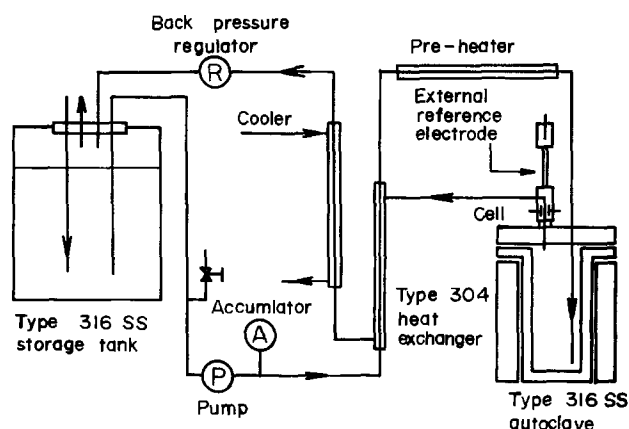


Fig. 1. Schematic diagram of recirculating loop

* Electrochemical Society Active Member.

Key words: pH, redox potential, hydrogen electrode, buffer solution, elevated temperature.

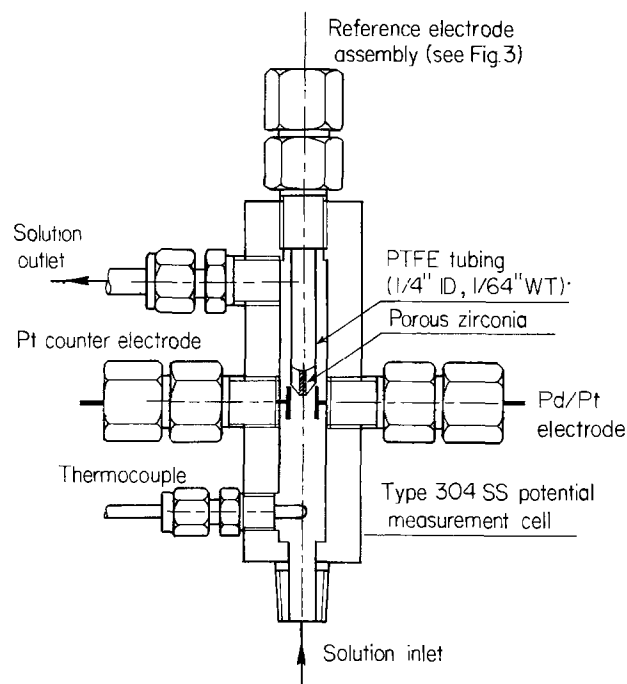


Fig. 2. Design of cell for the measurement of pH in aqueous solution at elevated temperatures (25°-275°C).

PdCl_2 solution (2 weight percent PdCl_2 in 1N HCl) at a current density of 160 mA/cm^2 for 2 min.

The solution in the reservoir was purged with pre-purified argon or with hydrogen-nitrogen mixtures to remove oxygen and to maintain the desired concentration of hydrogen in the system. At all temperatures from 25° to 275°C, the Pd/Pt electrodes were cathodically charged at a current density of 12 mA/cm^2 for 6 min, prior to measurement of the potential decay.

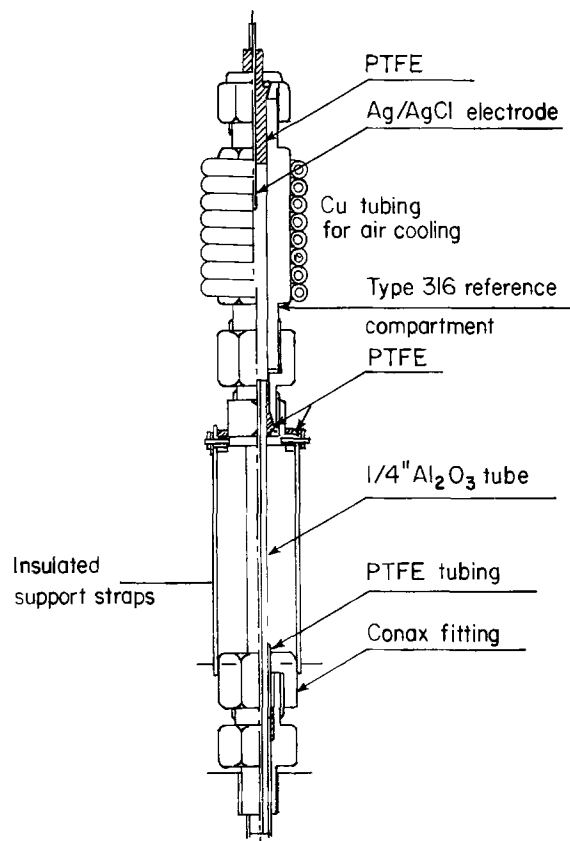


Fig. 3. External reference electrode assembly

Results and Discussion

Potential decay.—Typical potential decay curves for the Pd/Pt electrode in 0.01M LiOH at 25°C (pH 12.0) deaerated by argon or hydrogen are shown in Fig. 4. The $\alpha + \beta$ phase plateau potential (-659 mV vs. SHE) was observed in argon deaerated solution, and the pH was calculated as 12.01 using known data for $P_{\text{H}_2, \beta\alpha}$ (0.0194 atm) (1). Since the measured steady-state potential (-710 mV vs. SHE) in the hydrogen deaerated solution was 51 mV more negative than the $\alpha + \beta$ phase plateau potential, it was suspected that the Pd/Pt electrode was acting as a normal hydrogen electrode in this system (i.e., one which involves equilibrium between H^+ and dissolved H_2 in the aqueous phase). This was confirmed by briefly anodizing the electrode as shown in Fig. 4. After brief anodization the potential decayed rapidly to the plateau at -659 mV , but then later decayed to the redox potential at -710 mV . It is apparent that anodization is necessary in order to observe the palladium-hydride plateau potential in highly hydrogenated systems, even at ambient temperature.

Potential decay curves for the Pd/Pt electrode in 0.01M LiOH over the temperature range 25°-275°C are shown in Fig. 5 and 6. The $\alpha + \beta$ phase plateau potentials were observed up to 150°C in argon deaerated solutions and those saturated with 5% H_2 in nitrogen, but not in the case of those systems purged with pure hydrogen. In this latter case, the stable potential was found to be several tens of millivolts more negative than the palladium-hydride plateau potentials and is attributed to equilibrium between H^+ and H_2 , both in the aqueous phase (i.e., the normal hydrogen electrode reaction). At higher temperatures ($>200^\circ\text{C}$) no palladium-hydride plateau potentials were observed even for argon deaerated systems. This behavior is attributed to the rapid decrease in plateau lifetime with temperature, a trend which is well illustrated by the data at lower temperatures ($\leq 150^\circ\text{C}$, Fig. 5). Since the thickness of the plated Pd layer on Pt employed in these measurements was thought to be insufficient to maintain the $\alpha + \beta$ phase for a significant time above 200°C, the potential decay measurements were repeated at 150° and 200°C using a thickly plated Pd/Pt electrode (160 $\text{mA}/\text{cm}^2 \times 30 \text{ min}$) and a palladium wire electrode (0.5 mm diam, bright and palladised conditions). However, an improvement of plateau lifetime was observed only at 150°C and no plateau potential was exhibited at 200°C with either electrode.

The phase diagram for the palladium hydrogen system has been extensively studied by many workers (9-16), and the average of their data is shown in Fig. 7 together with the diffusion coefficients for hydrogen in

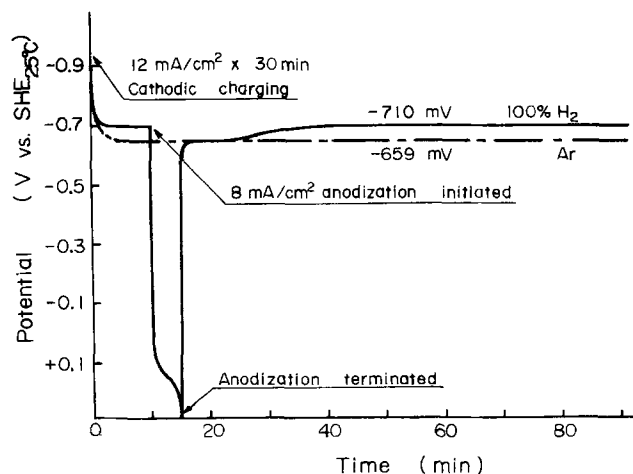


Fig. 4. Potential decay curves for a palladised platinum electrode in 0.01M LiOH deaerated by Ar or H_2 at 25°C.

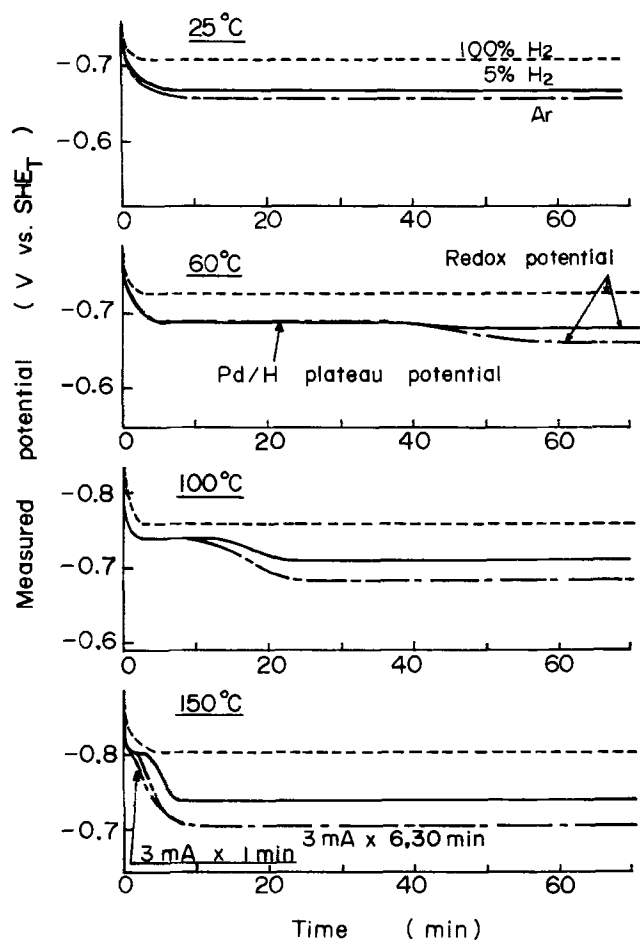


Fig. 5. Potential decay curves for palladised platinum electrodes in 0.01M LiOH. Cathodic charging: $12 \text{ mA/cm}^2 \times 6 \text{ min}$. - - - - 100% H_2 ; — 5% H_2 ; - · - · Ar.

α -Pd, as calculated using the following expression (17)

$$D = 4.5 \times 10^{-3} \exp(-5750/RT) \quad (\text{cm}^2/\text{sec}) \quad [1]$$

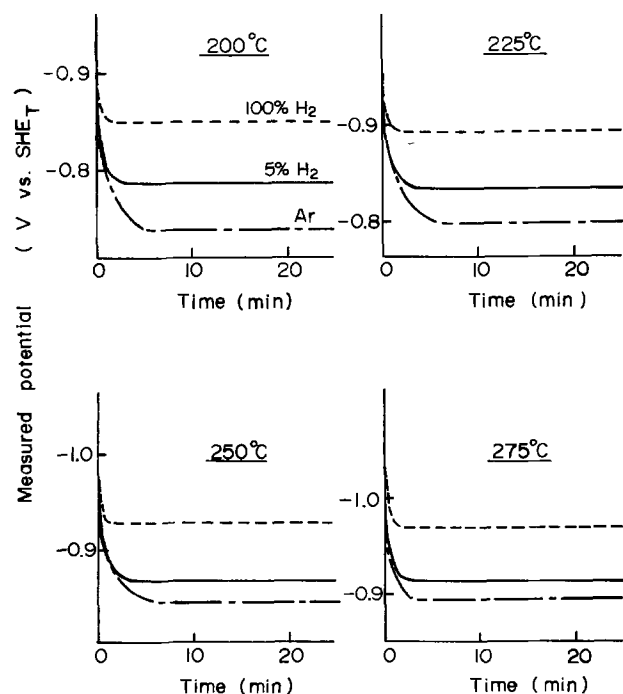


Fig. 6. Potential decay curves for palladised platinum electrodes in 0.01M LiOH. Cathodic charging: $12 \text{ mA/cm}^2 \times 6 \text{ min}$. - - - - 100% H_2 ; — 5% H_2 ; - · - · Ar.

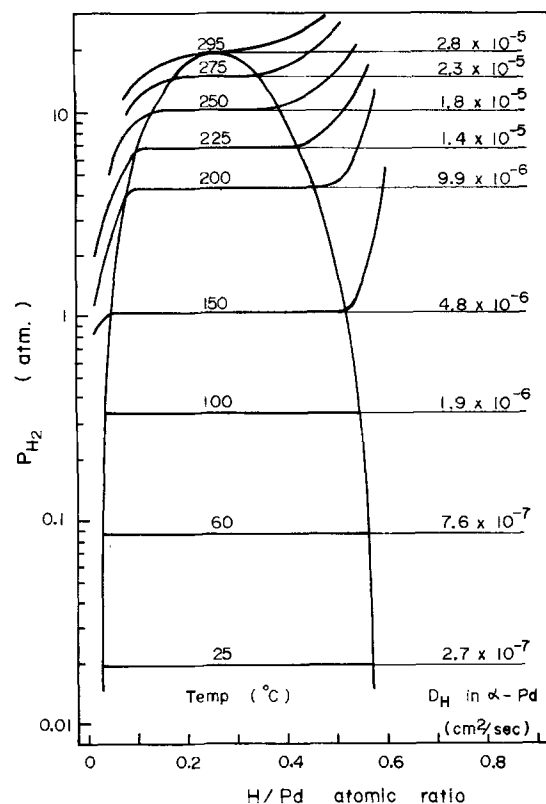


Fig. 7. Phase diagram for the palladium-hydrogen system

According to the data shown in Fig. 7, the width of the $\alpha + \beta$ phase region decreases moderately, but the diffusion coefficients for hydrogen in α -Pd increase rapidly, with increasing temperature. Therefore, it is apparent that the reason that no plateau is observed above 200°C is that hydrogen escapes so rapidly from the surface that the $\alpha + \beta$ phase cannot be maintained at the interface. A drastic decrease in plateau lifetime is also reported by Dobson and co-workers (12) who showed that unless the entry of hydrogen to Pd is restricted, the plateau lifetime observed during absorption of hydrogen from solution (*i.e.*, the reverse of the present case) is very short.

A second factor which must be considered in assessing the viability of the palladium-hydrogen electrode is the relative magnitude of the partial pressure of hydrogen in the aqueous phase and the dissociation pressure of palladium-hydride. For example, if the partial pressure of hydrogen in the aqueous phase is greater than the dissociation pressure of palladium-hydride, the potential will decay only as far as the normal hydrogen electrode potential and no plateau potential will be observed (unless anodization is employed, see Fig. 4). This is apparently the case at 25°C since the partial pressures of hydrogen for both the 5% and 100% H_2 systems are greater than the dissociation pressure of Pd_xH as indicated in Fig. 7. At higher temperatures (60°C - 150°C), however, the dissociation pressure of palladium-hydride is greater than the partial pressure of hydrogen for the argon deaerated and 5% H_2 sparged systems so that palladium-hydride plateau potentials are observed. It is not until a temperature of 150°C is attained that the dissociation pressure of palladium-hydride exceeds the partial pressure of hydrogen in the 100% H_2 sparged environment. In principle, therefore, plateau potentials should be observed in this system at high temperatures. However, the plateau lifetime decreases so rapidly with temperature that no distinct plateaus were observed in these experiments at 200°C and above.

Redox potential measurement.—It was argued from the data presented in Fig. 4-6 that the measured redox

potentials in hydrogenated systems correspond to the normal hydrogen electrode potentials. This view was confirmed by calculation, in that the redox potentials at elevated temperatures were found to correspond approximately to the hydrogen electrode potentials. Since the hydrogen electrode is an effective means for measuring the pH of the solution (at least under ambient conditions), the redox and plateau potentials were measured in various boric acid/lithium hydroxide buffer solutions, whose pH_T vs. temperature profiles have been computed by Macdonald and co-workers (1).

Corrections for the liquid junction potential and the partial pressure of hydrogen were made in order to compare the measured potentials with the theoretical values for the hydrogen electrode. Approximate values for the liquid junction potential between the internal KCl solution of the reference electrode and the $\text{B}(\text{OH})_3/\text{LiOH}$ buffer systems at each composition and temperature have been given by Macdonald *et al.* (1) and are used in this analysis. The hypothetical partial pressure of hydrogen in the high temperature solution has been also calculated by Macdonald *et al.* (18) from the known concentration of hydrogen in the reservoir at 25°C and the Henry's law constants (19) up to 275°C. Briefly, the equivalent partial pressure of hydrogen at the operating temperature for x ppm H_2 in the reservoir at 25°C is

$$P_{\text{H}_2} = x/1000M_{\text{H}_2} \cdot B_{\text{H}_2,T} \quad [2]$$

where M_{H_2} is the molecular weight of hydrogen and $B_{\text{H}_2,T}$ is the Henry's law constant at temperature T .

The observed difference between the measured and calculated hydrogen electrode potentials (both the palladium-hydride and redox electrodes) in boric acid/lithium hydroxide buffer solutions are shown in Fig. 8 as a function of temperature. The measured normal hydrogen (redox) electrode potentials in 0.01m $\text{B}(\text{OH})_3/10^{-2}$ - 10^{-4} m LiOH buffer solutions were in good agreement with the calculated values (within 5 mV up to 200°C and 15 mV at 275°C) and in all cases the deviations at elevated temperatures ($T > 200^\circ\text{C}$) were positive.

The results of the hydrogen electrode potential measurements are summarized in Fig. 9 and 10 together with the theoretical Nernstian responses calculated using the estimated pH values (1) for boric acid/lithium hydroxide systems. Linear Nernstian responses were observed over the temperature range between 25° and

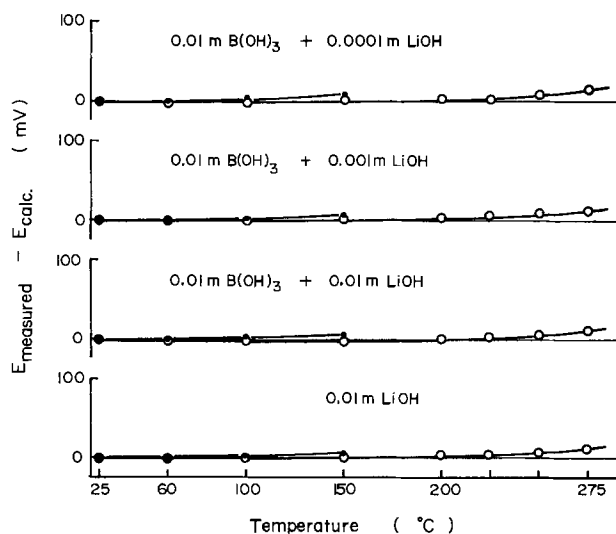


Fig. 8. Difference between calculated and measured potentials for hydrogen electrodes as a function of temperature. — Pd/H plateau potential (palladium hydride electrode); —○— Pd/Pt hydrogen electrodes (redox potential).

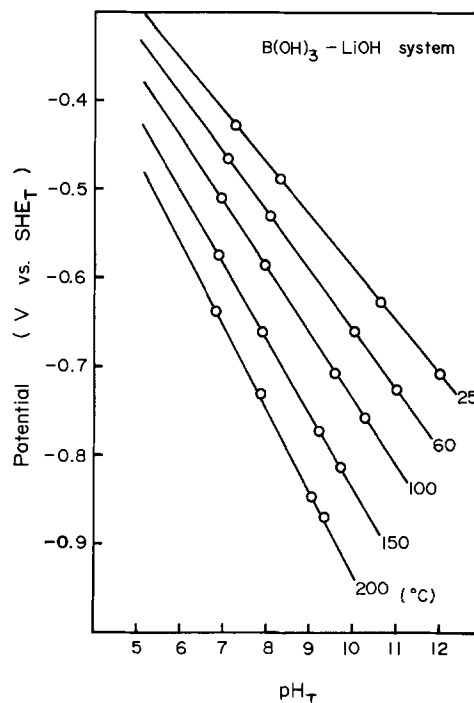


Fig. 9. Potential/pH correlations for the Pd/Pt hydrogen electrode. — theoretical; ○ measured.

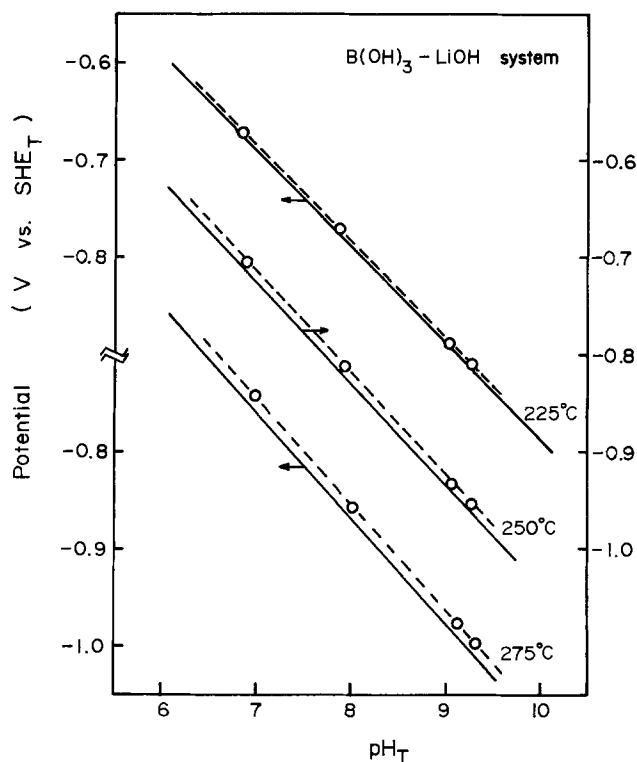


Fig. 10. Potential/pH correlations for the Pd/Pt hydrogen electrode. — theoretical; --○-- measured.

275°C. However, the positive deviations of the measured values from the calculated potentials above 200°C are again apparent.

The origin of this error has not been established unequivocally. Three sources are possible: (i) uncertainty in the isothermal liquid junction potential, (ii) error in the calculated pH values, and (iii) uncertainty in the calculated equilibrium potential for the H_2/H^+ couple. Because the error between the measured and calculated equilibrium potentials amounts to no more than 10-15 mV, it is difficult to assess which of the possible sources of error dominates. However, it should

be noted that the chemical potential of the hydrogen ion at elevated temperatures was computed using estimated entropy values (19) and that uncertainties from this source alone could easily account for the observed deviations.

Conclusions

1. A necessary condition for the appearance of a plateau in the cathodic potential decay for a palladium-hydride electrode in aqueous solution is that the partial pressure of hydrogen in the aqueous phase be less than the dissociation pressure of the hydride phase. If this condition is not satisfied, the stable potential corresponds to that for the normal hydrogen electrode. However, this limitation may be overcome by brief anodization immediately after cathodically depositing hydrogen into the metal phase.

2. The lifetime of the potential plateau for a palladium-hydride electrode was found to decrease sharply with increasing temperature, such that at 200°C and above no plateau could be discerned in the potential decay curves obtained in these studies even though the necessary condition stated in (1) above was satisfied.

3. Positive deviations of the measured hydrogen electrode potentials from the true equilibrium values were observed at temperatures above 200°C. The deviations are possibly due to uncertainties in the isothermal liquid junction potential, the calculated pH values for the buffer solution at elevated temperatures, and in the calculated equilibrium potential for the H_2/H^+ couple at elevated temperatures. This latter source arises because the chemical potential of the hydrogen ion at elevated temperatures is estimated using an entropy extrapolation technique.

Acknowledgment

The authors wish to thank the Electric Power Research Institute, Palo Alto, California, for financial support of this work under Contract RP 1166-1.

Manuscript submitted Oct. 12, 1980; revised manuscript received Jan. 23, 1981.

Any discussion of this paper will appear in a Discussion Section to be published in the December 1981

JOURNAL. All discussions for the December 1981 Discussion Section should be submitted by Aug. 1, 1981.

Publication costs of this article were assisted by The Ohio State University.

REFERENCES

1. D. D. Macdonald, P. R. Wentreck, and A. C. Scott, *This Journal*, **127**, 1745 (1980).
2. R. E. Mesmer, C. F. Baes, and F. H. Sweeton, *J. Phys. Chem.*, **74**, 1937 (1970).
3. R. E. Mesmer, C. F. Baes, and F. H. Sweeton, *Inorg. Chem.*, **10**, 537 (1972).
4. R. E. Mesmer and C. F. Baes, *ibid.*, **10**, 2290 (1971).
5. R. E. Mesmer and C. F. Baes, *J. Soln. Chem.*, **3**, 307 (1974).
6. D. D. Macdonald, P. Butler, and D. Owen, *J. Phys. Chem.*, **77**, 2474 (1973).
7. D. D. Macdonald and D. Owen, *Can. J. Chem.*, **51**, 2747 (1973).
8. D. D. Macdonald, *Corrosion*, **34**, 75 (1978).
9. J. V. Dobson, M. N. Dagless, and H. R. Thirsk, *J. Chem. Soc., Faraday Trans. 1*, **68**, 749 (1972).
10. J. V. Dobson, M. N. Dagless, and H. R. Thirsk, *ibid.*, **68**, 764 (1972).
11. J. V. Dobson, B. R. Chapman, and H. R. Thirsk, in "High Temperature High Pressure Electrochemistry in Aqueous Solutions," R. W. Staehle, D. de G. Jones, and J. E. Slater, Editors, p. 341, NACE, Houston (1976).
12. J. V. Dobson, *J. Electroanal. Chem. Interfacial Electrochem.*, **35**, 129 (1972).
13. D. J. G. Ives and G. J. Jans, "Reference Electrodes. Theory and Practice," Academic Press, New York (1961).
14. F. A. Lewis, "The Palladium-Hydrogen System," Academic Press, London (1967).
15. W. Mueller, J. P. Blackledge, and G. G. Libowitz, "Metal Hydrides," Academic Press, New York (1968).
16. E. M. Wise, "Palladium," Academic Press, New York (1968).
17. H. K. Birnbaum and C. A. Wert, *Ber. Bunsenges. Phys. Chem.*, **76**, 806 (1972).
18. D. D. Macdonald, A. Scott, and P. Wentreck, To be published.
19. G. B. Naumov, B. N. Ryzhenko, and I. L. Khodakovskiy, "Handbook of Thermodynamics Data," USGS Transl., USGS-WRD-74-001 (1974).

Thin Platinum Films on Silicon

L. A. Harris and J. A. Hugo

General Electric Corporate Research and Development, Schenectady, New York 12301

ABSTRACT

Smooth continuous films of platinum, as little as 20Å thick, may be sputter deposited on silicon that is sufficiently ion etched beforehand. The n-Si contact with Pt is ohmic, but on p-Si there is a small electronic barrier. The films display the electrochemical characteristics of platinum metal and are very stable under strongly oxidizing conditions.

Recent proposals for a new type of solar collector and electrolyzer have stimulated interest in the properties of silicon as an electrode in aqueous media (1). It is well known that silicon is unstable under these conditions owing to its tendency to form an insulating layer of SiO_2 on its surface (2, 3). Modification and protection of the Si surface by addition of a transparent, stable electrode material is necessary if the use of Si as the active light absorber within the electrochemical cell is to be retained.

Key words: catalyst, thin films, semiconductor metallization, oxygen electrodes, platinum.

While examining the properties of platinum coatings, chosen for the catalytic properties of this material, it was discovered that, if properly deposited, remarkably thin continuous layers of Pt on Si could be formed and that these films had interesting properties. The films were characterized by transmission electron microscopy and by electrochemical measurements, primarily by cyclic voltammetry and photoresponse. These measurements were useful in providing some information regarding the electrical nature of the interface between the platinum film and its silicon substrate. In this paper

we report and discuss some of the observations made in this study.

Experimental Procedures

The samples used were polished single-crystal, semiconductor grade wafers of silicon. Both n- and p-type wafers, having resistivities from 1 or 2 to about 50 Ω -cm, and with (100) or (111) faces exposed, were used. The wafers were degreased in acetone and methanol, then rinsed in distilled water, and finally cleaned in dilute HF to remove much of their native oxide coatings before they were mounted in a vacuum system for further treatment.

The crucial steps in preparation of the thin Pt films were ion cleaning of the Si substrate and sputter deposition of the Pt. In some initial work these steps were done in an rf sputtering system, but all later work reported here was done, with similar results, in a Veeco Microetch system¹ (4) owing to the lower base pressure and more reproducible conditions achievable in this system.

The vacuum system was pumped to about 2×10^{-6} Torr before argon gas was admitted to a pressure of about 8×10^{-5} Torr. At this pressure an argon plasma could be maintained in the ion-beam source and a beam of ions with a current density of about 0.95 mA/cm² at 500V acceleration was produced. The argon ion beam could be intercepted by a manually controlled shutter.

To ion etch (backsputter) the Si surface, the wafer was placed in the path of the beam under the closed shutter and then exposed to the beam for specific periods of time. The wafer was then immediately moved through a 90° arc so that it was no longer in the beam path, but was placed to receive Pt atoms sputtered from a diagonally mounted Pt target placed in the beam path. The shutter was then opened until the desired amount of Pt was deposited, as indicated by a quartz crystal thickness monitor mounted beside the sample holder.

The accuracy of the crystal thickness monitor was checked for indicated film thicknesses up to 1000Å by means of electron-backscatter (Betascopes) measurements² (5), x-ray absorption measurements, and by colorimetric analysis of platinum films dissolved in aqua regia. The Betascopes measurements showed excellent proportionality with the thickness monitor readings, within a few percent, while the other methods agreed within about 20%. We have therefore assumed that the thickness monitor readings are reliable indications of the mass of Pt deposited. This assumption may not be entirely valid for the extremely thin films discussed here because of possible initial differences in sticking coefficients on the sample and monitor. These differences would tend to disappear as the coatings become thicker.

After removal from the vacuum system, the completed wafers were cut into pieces suitable for electrochemical tests or for examination of the films in a transmission electron microscope. Those pieces to be used electrochemically had ohmic contacts of a Ga-Ag paste applied to the back (uncoated) side after a local etch with a drop of HF to remove any SiO₂ (6).

The electrochemical tests were done in a specially constructed, three-compartment Pyrex cell shown in Fig. 1. The sample was pressed against a Viton gasketed opening in the central working compartment, opposite a flat window through which the sample could be illuminated. This arrangement defines the exposed area ($\frac{1}{2}$ cm²) of the electrode and permits quick and easy replacement of test electrodes (6).

To provide for effective stirring of the electrolyte and to prevent bubble accumulation at the electrode

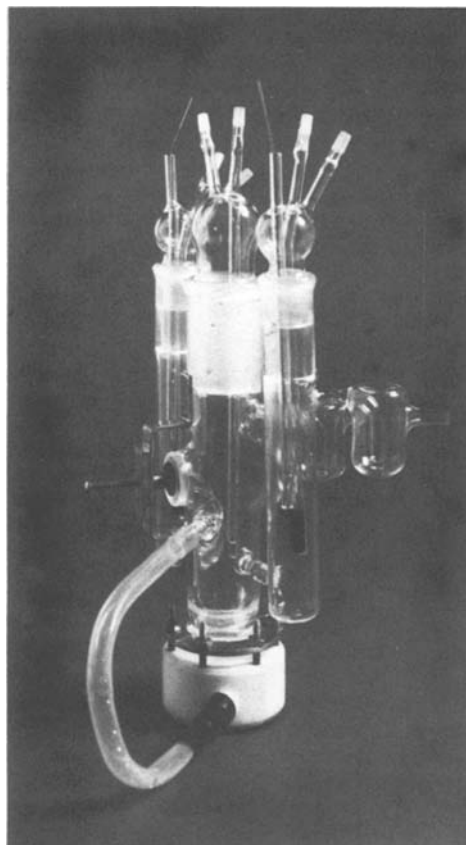


Fig. 1. The electrochemical test cell showing the pump at the bottom, the sample pressed against the black gasket by the screw clamp on the left, and the curved jet aimed at the sample recess.

surface a centrifugal pump, shown in Fig. 2, was incorporated at the base of the working compartment (7). This pump directed a stream of electrolyte through a glass jet aimed across the working electrode face. The pump consists of a Teflon polymer Star-HeadTM stirrer³ enclosed in a Teflon polymer housing and is driven by a conventional magnetic stirrer.

The remainder of the cell was of conventional design, with a Luggin capillary connecting the reference (hydrogen) electrode chamber to the electrolyte near the working electrode and a fine capillary diffusion barrier connecting the counterelectrode chamber to the working electrode chamber.

Most of the tests were done with 1N H₂SO₄ made from analytical reagent (J. T. Baker Chemical Com-

³ Nalge Company.

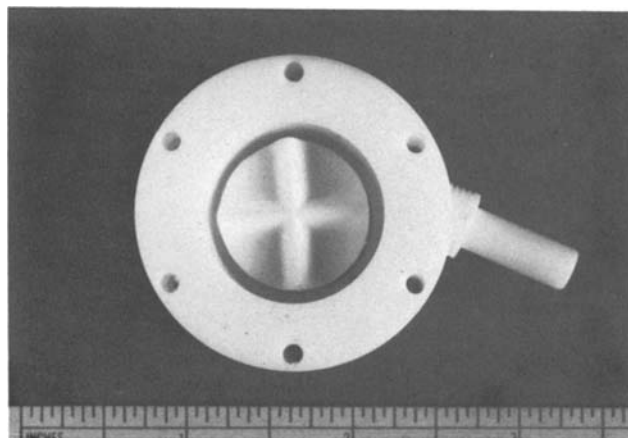


Fig. 2. Top view of the centrifugal pump. Stirrer is centered by a circumferential step on the bottom of the housing.

¹ Veeco Instruments Incorporated, Plainfield, New Jersey 11803.

² Twin City Testing Corporation, North Tonawanda, New York 14120.

pany) diluted with quartz-distilled water. Purified H_2 or He could be bubbled through each chamber of the cell or maintained as an atmosphere over the electrolyte. Before each experiment the electrolyte was purged by bubbling H_2 gas in all three compartments of the cell, and then He was flowed over the electrolyte in the working and counterelectrode compartments, while H_2 continued to bubble over the reference electrode. Electrochemical characteristics were measured with a potentiostat (Pine Instrument Company RDE 3) and recorded with an X-Y recorder (Hewlett-Packard 7046A).

For electron microscopic examination, the films, in some cases coated with carbon and in others uncoated, were separated from the Si substrates by exposure to a mixture of HNO_3 and HF or to their vapors and then floated off on quadruple-distilled water. They were picked up on fine lacey carbon supporting films for insertion in the microscope.⁴ The instrument used was a Siemens Elmiskop 101, operated at 120 kV.

Any particular experimental procedures associated with individual tests are given with the results in the next section.

Results

The tendency of Si to oxidize in aqueous electrolytes is clearly demonstrated in the voltammograms of Fig. 3. The curves represent a series of single sweeps. Each run, displayed below its predecessor, carried the Si electrode to an increasingly positive voltage before the negative excursion and the final return to the starting voltage. Results for n-type Si only are shown, but similar results differing only in detail were obtained with p-Si.

As little as 20Å of Pt on Si radically alters the electrochemical properties of the substrate. On n-Si with Pt, the hydrogen overvoltage is extremely low, characteristic of Pt, and quite insensitive to operation of the

⁴EH Fullam Incorporated Catalog item 1457, Schenectady, New York 12301.

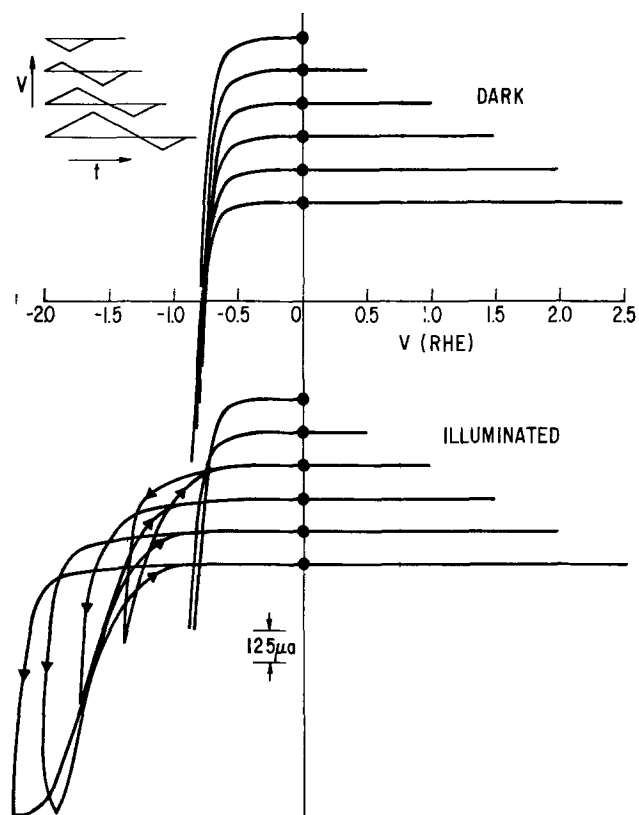


Fig. 3. Illustrating the oxidation of n-Si during single sweeps to positive voltages while illuminated. The pattern of successive sweeps is indicated at the top left.

electrode at positive voltages. The cyclic voltammograms are also unaffected by illumination with photons having energy exceeding the bandgap of Si. Figure 4 shows stable cyclic voltammograms for the thin Pt film on n-Si and for Pt metal sheet tested under similar conditions. Although the similarity of these voltammograms is striking, there are some notable differences. The characteristic oxidation and reduction peaks are more prominent with the bulk Pt than with the thin-film specimen. On the thin-film voltammogram the platinum oxide reduction peak is shifted negatively by about 50 mV from that obtained on bulk Pt, and the oxygen evolution current at the maximum voltage (1.65V) is smaller in relation to the oxide reduction peak than it is for bulk Pt.

If the substrate is p-type Si the voltammograms, though stable toward oxidation, are quite different for the dark and illuminated cases, as Fig. 5 shows. Appreciable reduction currents are not obtained in the dark, but under illumination the Pt-like characteristics are again obtained, though shifted positively in voltage, and the cathodic current due to hydrogen evolution is limited by the light intensity. The extent of the positive shift is somewhat variable with different samples, but it is generally from 0.1 to 0.3V in magnitude.

The stability of these thin films under strongly oxidizing conditions is shown in Fig. 6 which displays

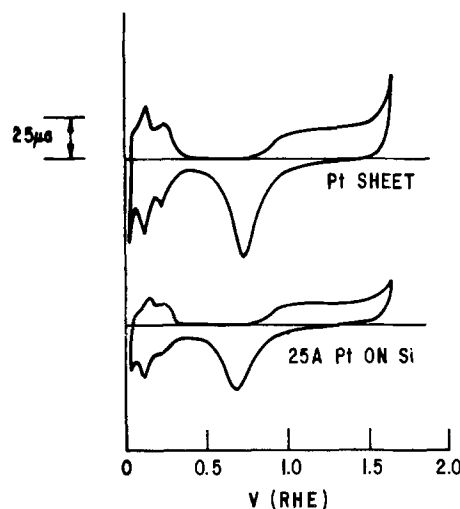


Fig. 4. Comparison of cyclic voltammograms from Pt sheet and from 25Å Pt on n-Si. The electrolyte was 1N H_2SO_4 and the sweep rate was 100 mV/sec.

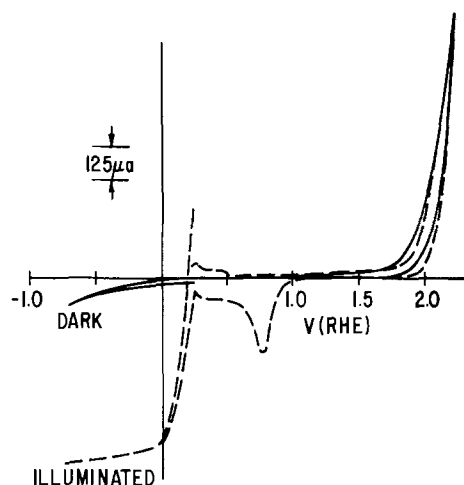


Fig. 5. Single-sweep voltammograms of 20Å Pt on p-Si showing different behavior in the dark and under illumination. Sweep rate was 100 mV/sec.

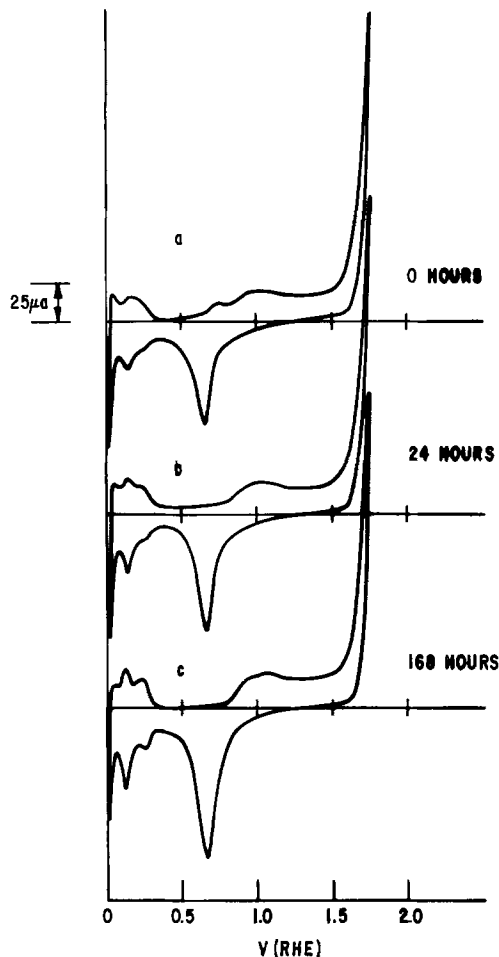


Fig. 6. Cyclic voltammograms of 20Å Pt on n-Si showing stability to oxidation. Sweep rate was 100 mV/sec. a, Initial response; b, after 24 hr at 1.75V, c, after 168 hr at 1.75V.

cyclic voltammograms of a 20Å Pt film on n-Si taken before, during, and after operation at 1.75V. The changes evident in the first 24 hr of operation were complete after 48 hr, when the voltammogram (not shown) was identical to the final one shown.

Despite this stability to oxidation, the films do not retain their catalytic activity when subjected to repeated cycling. Earlier tests, similar to those of Fig. 6, showed the characteristic peaks of the voltammogram reduced to less than half of their original value after 2900 cycles between 50 and 1605 mV, though there was no evidence of increasing overvoltages like those shown for uncoated Si.

Transmission electron micrographs of films taken from wafers similar to the samples used for Fig. 4-6, and some others, are shown in Fig. 7. The large circular features in these pictures are due to the lacey carbon films on which the Pt films rest. The micrographs show that the 20Å films are continuous and virtually free of detectable pinholes, while the 10Å films have many pinholes, but nevertheless are continuous, conducting films.

Electron diffraction patterns from these films, not shown here, are characteristic of Pt with a very fine-grain polycrystalline structure. This structure is also revealed by the partial dark-field micrograph of Fig. 8, where only those crystallites of suitable orientation show up as bright spots in the image.

Figure 9 is a micrograph of a film, like that used for Fig. 6, after it had been repeatedly cycled to degrade its catalytic performance. It is evident that the apparently smooth continuous film indicated by Fig. 7 has been seriously affected by the electrochemical cycling, probably due to dissolution and rearrangement.

In order to assess the importance of the ion-etching step before Pt deposition, a series of 20Å films was deposited on n-Si substrates after differing exposures to the argon ion beam. Figure 10 shows the cyclic voltammograms obtained from these specimens. The Pt-like behavior is not well established until at least 10 sec of ion etching are used, though there is still further improvement if this time is increased to 20 sec or more. For comparison, the 25Å film used in Fig. 4 was sputter deposited on a silicon surface ion etched for 30 sec, while that used for Fig. 6 was 20Å with the same ion-etch time.

The electron micrographs of comparison pieces taken from the same wafers as those used for the tests of Fig. 10 are shown in Fig. 11. They show that with little or no ion etching the film growth is in the familiar island structure, and that film continuity increases with the duration of ion etching. Even with 10 sec of ion etching, the film is not entirely continuous as are the films of Fig. 7a and b which were deposited after 30 sec of ion etching.

It is also of interest to determine how thick the deposited film has to be to obtain the effective catalytic properties of the metal, assuming that sufficient ion etching has been used to prepare the substrate. A series of films of increasing thickness was deposited on n-Si substrates, after 20 sec of ion etching, by passing the ion beam through a rotating shutter. Exposure for each film was controlled by allowing the opening of the shutter (90°) to pass the ion beam different integral numbers of times.

Figure 12 shows a series of voltammograms obtained from some of the members of this series. They indicate that the transition occurs between 16 and 20Å of deposited material. Those substrates with thinner films display some instability toward oxidation and relatively large hydrogen and oxygen overvoltages, with few of the features characteristic of platinum. It is important to note that these last results are not entirely consistent with earlier good results obtained with films only 10Å thick, but deposited in one continuous exposure. Furthermore the electron micrographs of these films (not shown) indicated persistent island structures even in films more than 20Å thick. Indeed one film 21Å thick removed from its Si substrate, without a carbon coating, retained its integrity as a continuous film, but displayed an island structure of Pt particles on an unidentified continuous background film.

These results call for further investigation, but they show nevertheless that some critical thickness of Pt, perhaps determined by vacuum conditions and sputtering rates, is necessary to achieve the useful catalytic properties of this metal.

In these experiments one is led to consider the possible formation of platinum silicides, so it was considered desirable to observe the electrochemical behavior of such silicide films. The compound was deliberately formed by heating n-Si samples with approximately 15Å of deposited Pt in argon at 350°C for 15 min. Comparison samples from the same wafer, without heat-treatment, had been previously shown to give results comparable to those of the 25Å films shown in Fig. 4. Figure 13 shows the single-sweep voltammograms obtained from the Pt-Si surface in the manner described in connection with the tests of Fig. 3. The final (lowest) curve was essentially unchanged when swept cyclically and no effects of illumination could be observed.

Although these samples were quite stable to oxygen or hydrogen generation for periods of several minutes, they did not display any of the electrochemical characteristics of platinum metal.

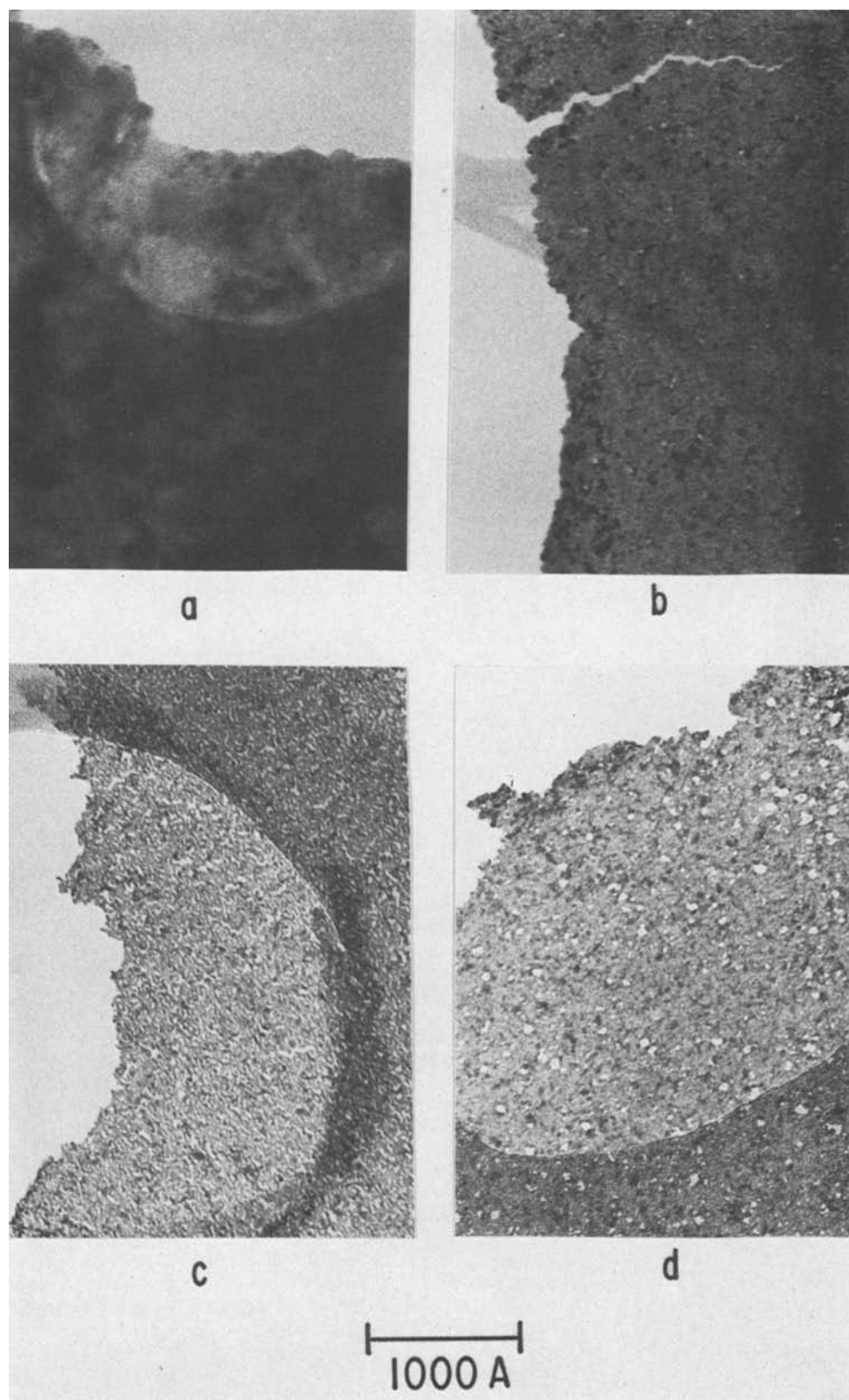


Fig. 7. Transmission electron micrographs of thin Pt films removed from Si substrates. a, 20Å film from n-Si; b, 20Å film from p-Si; c, 10Å film from n-Si; d, 10Å film from p-Si.

Discussion

The electrochemical behavior of bare Si in the dark is explicable in terms of the large negative flatband voltage (high electron energy) of this material with respect to the H^+/H_2 potential in the electrolyte (3, 8). This condition implies that the energy bands of n-Si are bent up strongly near the electrolyte interface so that there is normally an appreciable energy barrier for the transfer of electrons into or out of the conduction band (9). The large hydrogen overvoltage results from the need to flatten the bands (by applying nega-

tive voltage to the Si) so that conduction band electrons can reach the surface where H^+ ions can be reduced.

This situation is unaffected by positive voltage excursions because oxidation of the electrolyte is prevented by the energy barrier. At very high positive voltages the bands are bent so strongly that electrons can tunnel from the electrolyte through the thinned barrier and allow the oxidation of water with the accompanying formation of SiO_2 (10). This thin insulating layer serves to increase the hydrogen overvoltage,

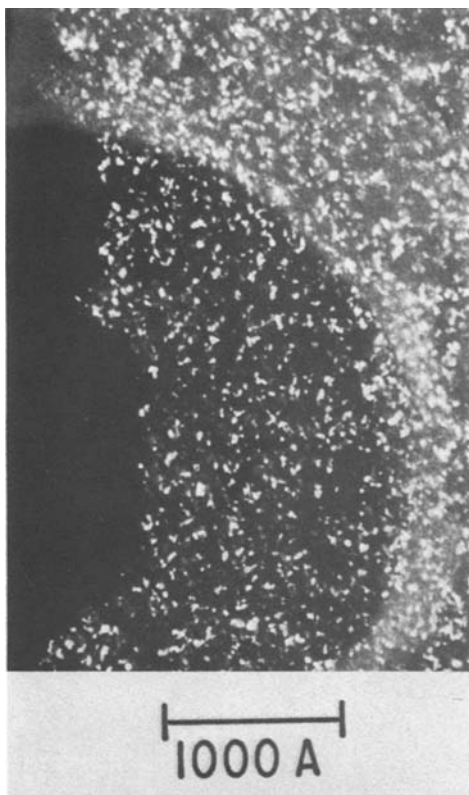


Fig. 8. Dark-field micrograph corresponding to Fig. 7c

an effect just visible in the lowest curves of the top part of Fig. 3.

When light shines upon the Si, oxidation is much more readily accomplished by the holes created in the valence band and moved toward the interface by the surface field (9). The resultant growth of a barrier layer (anodization) is clearly shown by the rapid suppression of positive oxidation current within a

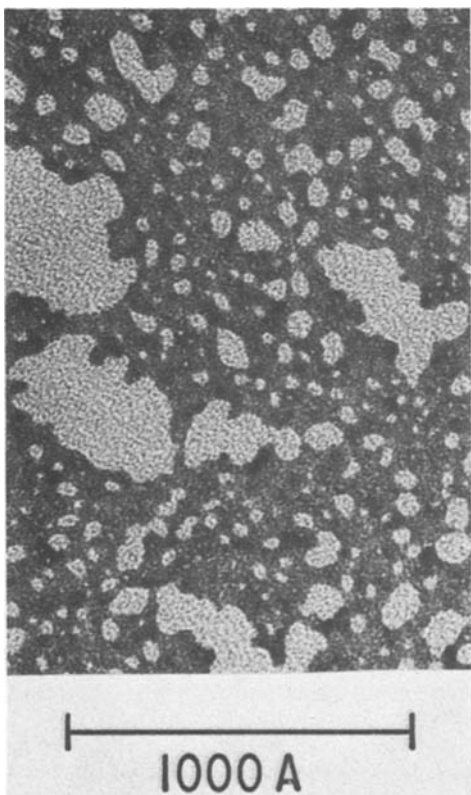


Fig. 9. Electron micrograph of film after prolonged cycling

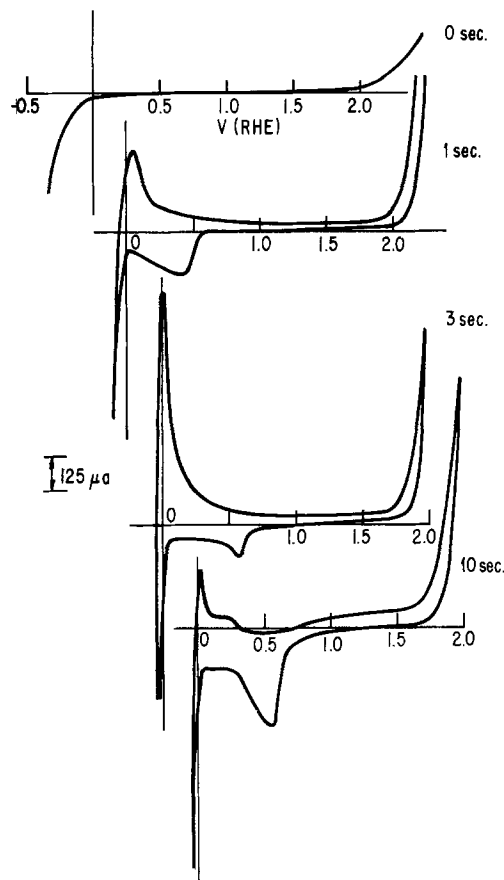


Fig. 10. Cyclic voltammograms from 20Å Pt films deposited on n-Si after varying degrees of ion etching. Sweep rate was 100 mV/sec.

single sweep and by the corresponding increase of hydrogen overvoltage to extremely high values.

The appropriate deposition of Pt on n-Si radically alters the situation described above. The voltage correspondence in the cyclic voltammograms for the test sample and the Pt sheet, shown in Fig. 4, indicates that the Pt film effectively makes an ohmic contact with its semiconducting substrate, a conclusion confirmed by the absence of any observed photoeffect. The more prominent characteristic features obtained on the bulk platinum, noted earlier, may fairly be attributed to its larger effective surface area (11), since the thin films are deposited on extremely smooth single crystal substrates. On the thin films the more negative potential of the platinum oxide reduction peak and the lower oxygen evolution current at maximum positive voltage, also noted earlier, suggest that oxygen atoms are bound more strongly to these films which must be thin enough to still show some effect of the substrate underlying the metallic platinum surface.

The photoeffects and voltage shift observed when Pt is deposited on p-type Si (Fig. 5) indicate the presence of an electronic barrier, shown schematically in Fig. 14. In this case, reduction of H^+ can occur only if electrons are promoted to the normally empty conduction band of p-Si by illumination with photons of sufficient energy. For this reason, the hydrogen reduction current is limited by light intensity.

The voltage shift with illumination allows H_2 to be generated at a voltage more positive than it would be on a bulk Pt electrode. Similar shifts have been observed on Si and other p-type semiconductors with electrodeposited metal layers (12). This undervoltage for reduction is accompanied by an overvoltage for all oxidation processes, though not necessarily of the same magnitude. When the p-Si is part of a photoexcited

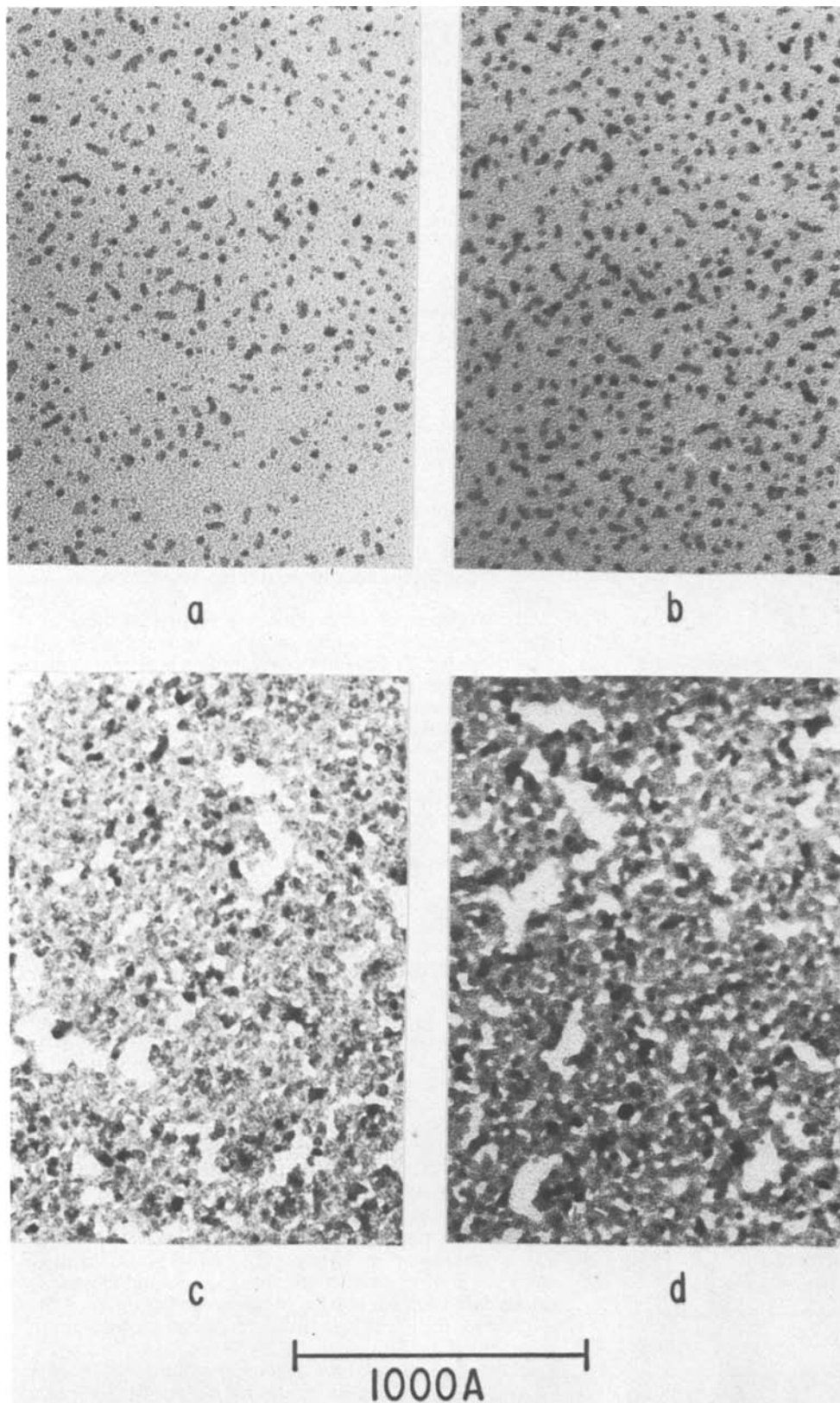


Fig. 11. Electron micrographs of the films of Fig. 10 untested electrochemically. a, No ion etching; b, 1 sec ion etching; c, 3 sec ion etching; d, 10 sec ion etching.

n-p junction device used to drive electrochemical reactions, it is the p-type surface at which oxidations should occur (1). The voltage shift due to the Schottky barrier can represent a significant loss of available electrochemical potential.

The importance of ion etching in obtaining the extremely thin metallic films is demonstrated by the effects shown in Fig. 10 and 11. Insufficient ion etching results in the island structure more usually observed with such thin films (13). The smoothness and uni-

formity of properly deposited Pt films may be attributed to the immobility of the first Pt atoms arriving at the chemically clean and active Si surface. Since Pt and Si interact to form distinct compounds (14, 15), the initial Pt atoms are likely to be chemisorbed with sufficient binding energy to prevent their subsequent migration over the surface.

In addition to removing any residual contaminants, some extra ion etching may be necessary to introduce sufficient disorder (16, 17), and even tighter binding

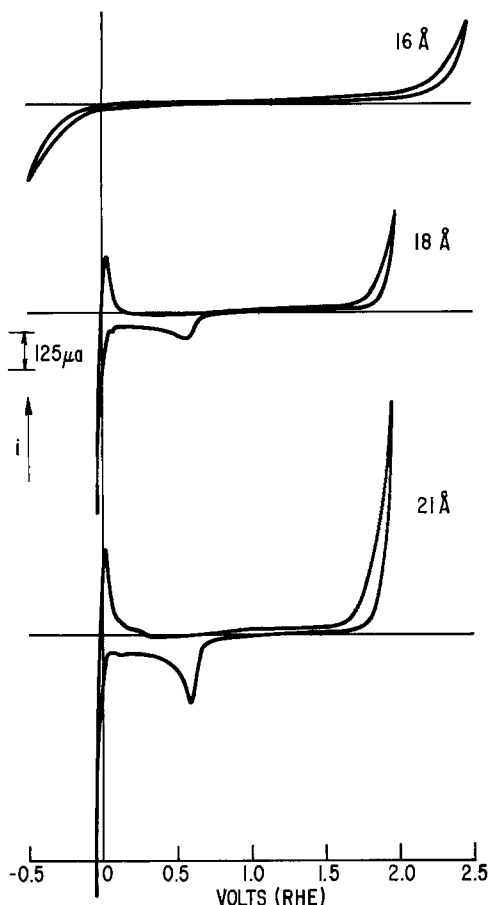


Fig. 12. Cyclic voltammograms of Pt films of various thicknesses deposited on n-Si after 20 sec ion etching. Sweep rate was 100 mV/sec.

sites, in the Si surface. The rate at which SiO_2 is removed from the surface may be estimated from the ion current density, ion voltage, and sputtering rate of Si by argon ions, assuming the rate for SiO_2 approximates that for Si (18). The estimated rate is 5.35 Å/sec so 4 sec of ion etching should be sufficient to remove

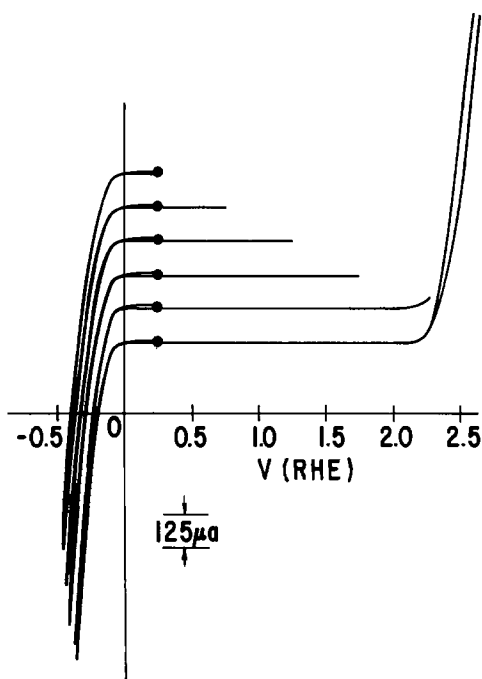


Fig. 13. Single-sweep voltammograms from approximately 15 Å Pt on n-Si after heating in argon at 350°C for 15 min.

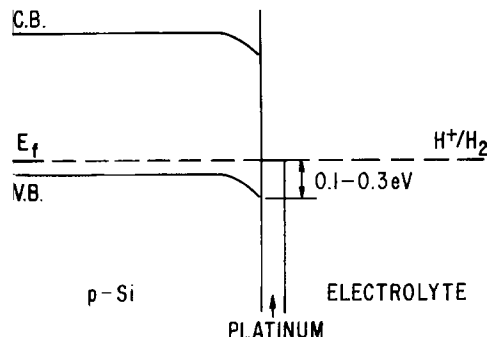


Fig. 14. Suggested energy diagram of p-Si coated with Pt in contact with acid electrolyte, showing Schottky barrier at Pt-Si interface.

an assumed 20 Å of SiO_2 . But in practice we find that about 20 sec of ion etching are required for good results. It is thus reasonable to assume that the surface disorder in the substrate is also an important factor in the adhesion and stability of the deposited films. This assumption is consistent with recent observations of the growth of thin Pt films on single crystal and on amorphous Si done under ultrahigh vacuum conditions (19).

If one thinks of applying these results to metallization of semiconductor devices, as in integrated circuits, this need for surface disorder, if it exists, would be a serious drawback. For electrochemical applications, however, where catalytic coatings with extremely light loading of the expensive catalyst is desired, considerations of surface disorder are not so serious. Of course, in these applications it is also unnecessary that the catalyst metal be disposed in a continuous film, but it must make intimate electrical contact with the substrate. It appears, however, that the conditions which promote this good contact also promote the continuity of the film.

The chemisorption view of Pt film deposition implies the formation of a layer of Pt-Si compound, perhaps only 1 or 2 monolayers thick followed by the addition of Pt metal. The results of Fig. 13 show that deliberately formed platinum silicide is a stable electrode, but has relatively poor catalytic properties. When insufficient Pt is deposited, as in the series of Fig. 12, most of the deposited material may have been consumed in formation of the compound interlayer, leaving little metallic platinum to function as a good catalyst. The continuous unidentified film on which islands of Pt were observed may indeed be evidence of this compound. Such considerations must play a part in determining the least amount of catalyst that can be used to obtain effective catalytic properties. The results of Fig. 12 show that such a minimum amount exists, but, as noted earlier, the quantitative aspects are presently in doubt because the results are influenced by rates of deposition and by vacuum conditions.

The instability of an initially active platinum film to repeated cycling is shown by Fig. 9 to be related to dramatic structural changes in the film. Aside from its relative smoothness, there would appear to be no reason why these thin films should not be subject to the same forces of dissolution that affect other catalytic deposits (20, 21). Although some of the Pt that dissolves in one part of the electrochemical cycle may be redeposited in another, the redeposited material may lose its intimate contact with the substrate and thus much of its catalytic activity.

The stability of the films toward oxidation must be due to the passivation of any exposed areas of Si by formation of SiO_2 which is chemically stable and prevents any undercutting of the intimate metal-semiconductor contact.

Conclusions

The work reported here is not intended to throw any new light on the processes of catalysis. It is well known that minute deposits of Pt on other substrates impart the catalytic properties of the metal to the combination (22). The electrochemical measurements reported here serve merely to characterize the nature of the Pt films on Si and the nature of the electrical contact at the Pt-Si interface.

The continuity of the metal films in such low thickness ranges is of unusual interest, however, as is the effective ohmic contact with the n-type substrate. It is hoped that these observations may contribute to the understanding of the nature of some substrate-deposit interactions.

The ultimate utility of deposits of this sort for electrocatalysis remains to be seen. In view of the excellent material utilization already reported with other methods, the motivation for using this more complex and costly process may depend on whether improved stability can be achieved with it. This, along with other aspects of the problem needs more study at present.

If our present ideas about the film formation are correct, it seems likely that there are many material variations on this theme. Silicon, because it reacts with so many different metals, should be a useful substrate for a variety of catalytic metals. The high purity, electronic grade, single crystal silicon used in these experiments should not be necessary; the cheaper technological grades of polycrystalline Si, provided it is n-type, should serve well as a conducting catalyst support.

Conversely, many of the noble metals might equally well be supported by other materials with which they form compounds and that form stable, chemically resistant oxides. Examples of such supports are the valve metals, Ti, Ta, Nb, and others. Indeed, preliminary experiments show that Pt can be deposited in 20Å amounts onto ion-etched Ti to impart its catalytic properties as it does on n-Si.

Acknowledgment

Significant contributions were made to this work by M. Garbaskas, W. Balz, S. Young, and E. Siwek. Particular thanks are due to F. G. Will for valuable discussions and guidance in the electrochemical aspects of this study.

Manuscript submitted Sept. 9, 1980; revised manuscript received Jan. 18, 1981.

Any discussion of this paper will appear in a Discussion Section to be published in the December 1981 JOURNAL. All discussions for the December 1981 Discussion Section should be submitted by Aug. 1, 1981.

Publication costs of this article were assisted by General Electric Company.

REFERENCES

1. J. S. Kilby, J.W. Lathrop, and W. A. Porter, U.S. Pat. 4,021,323 (1977); 4,100,051 (1978); and 4,136,436 (1979).
2. J. I. Carasso and M. M. Faktor, in "The Electrochemistry of Semiconductors," P. J. Holmes, Editor, pp. 234-238, Academic Press, New York (1962).
3. J. van Muylder, J. Besson, W. Kunz, and M. Pourbaix, in "Atlas of Electrochemical Equilibria in Aqueous Solutions," M. Pourbaix, Editor, 1st English ed., Sec. 17.2, p. 458, Pergamon Press, New York (1966).
4. S. Somekh, *J. Vac. Sci. Technol.*, **13**, 1003 (1976).
5. B. B. Jaffe and R. S. Modjeska, *Metal Finishing*, **61**, (12), 44 (1963).
6. L. A. Harris, D. R. Cross, and M. E. Gerstner, *This Journal*, **124**, 839 (1977).
7. G. H. Brilmeyer and A. J. Bard, *ibid.*, **127**, 104 (1980).
8. D. Laser and A. J. Bard, *J. Phys. Chem.*, **80**, 459 (1976).
9. L. A. Harris and R. H. Wilson, *Ann. Rev. Mater. Sci.*, **8**, 99 (1978).
10. P. J. Boddy, D. Kahng, and Y. S. Chen, *Electrochim. Acta*, **13**, 1311 (1968).
11. F. G. Will, *This Journal*, **112**, 451 (1965).
12. Y. Nakato, S. Tonomura, and H. Tsubomura, *Ber. Bunsenges. Phys. Chem.*, **80**, 1289 (1976).
13. R. S. Sennett and G. D. Scott, *J. Opt. Soc. Am.*, **40**, 203 (1950).
14. J. A. Borders and S. T. Picraux, *Proc. IEEE*, **62**, 1224 (1974).
15. I. Abbati, L. Broicovich, and B. DeMicheliis, *Solid State Commun.*, **36**, 145 (1979).
16. E. Grussel, S. Berg, and L. P. Anderson, *This Journal*, **127**, 1573 (1980).
17. F. Ohira and M. Itakura, *Appl. Phys. Lett.*, **37**, 398 (1980).
18. N. Laegreid and G. K. Wehner, *J. Appl. Phys.*, **32**, 365 (1961).
19. B. Goldstein and D. J. Szostak, *J. Vac. Sci. Technol.*, **17**, 718 (1980).
20. D. A. J. Rand and R. Woods, *Electroanal. Chem. Interfacial Electrochem.*, **35**, 209 (1972).
21. D. F. Untereker and S. Bruckenstein, *This Journal*, **121**, 360 (1974).
22. K. Kinoshita, J. Lundquist, and P. Stonehart, *J. Catal.*, **31**, 325 (1973).

Volume Changes Induced by the Electrochromic Process in Sputtered Iridium Oxide Films

S. Hackwood,* W. C. Dautremont-Smith,* G. Beni,*

L. M. Schiavone,* and J. L. Shay*

Bell Laboratories, Holmdel, New Jersey 07733

ABSTRACT

We report volume changes induced by the electrochromic process in sputtered iridium oxide films (SIROF's). We show that SIROF's expand on incorporation of water. The rate of water uptake is greatly increased by initial potential cycling, *i.e.*, coloring and bleaching. Hydration increases the kinetics of electrochromism by about an order of magnitude. We show also that electrochromic coloring and bleaching reversibly modulates the thickness of partially hydrated SIROF's. As-deposited SIROF's significantly contract upon initial cathodic bleaching which supports the anion mechanism of electrochromism in iridium oxide films.

Several recent papers have described the properties of electrochromic iridium oxide films (1-12). Initial studies were based on iridium oxide films anodically grown on a metallic iridium substrate (AIROF's). It has recently been reported (5) that electrochromic iridium oxide films can be prepared by sputtering from an iridium target in a reactive oxygen discharge. Such sputtered iridium oxide films (SIROF's) have the fast coloring and bleaching kinetics previously reported for AIROF's, and are considerably more resistant to degradation. Operation for more than 10^7 cycles in 0.5M H_2SO_4 leads to no detectable deterioration. Prototype seven-segment digit display cells with ≤ 100 msec response time have recently been demonstrated (12).

The mechanism of the electrochromic reaction has been extensively studied. Early speculations (13) were based on a proton extraction-insertion mechanism, as proposed for ruthenium oxide, and similar to the cation insertion-extraction process of tungstic oxide (14-16). There is evidence, however, that the electrochromism of iridium oxide films is fundamentally different (7-9) from that of WO_3 . For iridium oxide an anion mechanism has been proposed which is supported by considerable experimental evidence (7-9).

The purpose of this paper is fourfold: (i) to demonstrate that SIROF's consist of a structure, which expands on incorporation of water; (ii) to show that the rate of incorporation of water into an as-deposited SIROF can be increased greatly by a few initial color/bleach cycles; (iii) to show that the uptake of water increases the kinetics of electrochromism by about an order of magnitude; and (iv) to show that, until fully hydrated, electrochemical coloring and bleaching reversibly modulates the film thickness. An as-prepared SIROF undergoes a contraction upon initial bleaching, which strongly supports the anion mechanism of electrochromism.

Experimental

To investigate the volume changes induced by the electrochromic process in SIROF's we have measured the thickness of the iridium oxide film on quartz substrates, (i) as deposited, (ii) after immersion in 0.5M H_2SO_4 , (iii) after successive coloring and bleaching, and (iv) on further immersion after two color/bleach cycles.

A seven-segment digit of SIROF was deposited through a 2 μm thick photoresist mask. Dissolution of the photoresist in acetone removed the SIROF from surrounding areas leaving each segment with well-defined sharp edges along its length. The data reported

are average segment thicknesses measured over many up and down steps. Thickness was measured *ex situ* using a stylus instrument, either an Alpha-step or a Talysurf. The electrode was rinsed in distilled water and blown dry with nitrogen before each measurement.

Both the colored and bleached states of SIROF's show significant electronic conductivity. Contact was made to a corner of a segment with silver paint, which was then covered with insulating varnish. Coloring or bleaching of each segment was accomplished by applying +1V or 0V, respectively (*vs.* SCE reference electrode) to the SIROF in the 0.5M H_2SO_4 electrolyte. The coloring or bleaching resulting from anodic or cathodic voltages was monitored by measuring the charge transferred. As previously demonstrated (10), the induced optical density change is essentially linear in the charge transferred.

SIROF's deposited on tantalum were used to measure the electrochromic response time, since in this case the rate of response is not limited by the low sheet conductivity of the iridium oxide film. Bleach/color cycles were performed by applying 1 sec pulses of 1V amplitude (*vs.* SCE), with compensation to the applied potential for IR drop in the electrolyte using a Princeton Applied Research potentiostat and programmer. The charge transferred was monitored by a digital coulometer, with the analog output recorded on a strip chart recorder or photographically from an oscilloscope.

Results and Discussion

We show in Fig. 1(a) the time dependence of the thickness of a SIROF having an initial thickness of 700Å upon immersion in 0.5M H_2SO_4 . There is negligible change in thickness in 5 hr. On the other hand, if a film is first subjected to two color/bleach cycles, and subsequently kept immersed in the same electrolyte, it rapidly increases in thickness to a maximum of 950Å in 2 hr as shown in Fig. 1(b).

No change in coloration results from this increase in thickness, suggesting that the expansion is solely due to water uptake within the SIROF. It is surprising that two initial color/bleach cycles condition the SIROF to take up large amounts of water. Although we have not rigorously demonstrated the porous nature of SIROF's, a porous structure is probable since the electrochromic kinetics are similar to those of AIROF's, which are known to be porous films (11) with a high water content. Throughout this work "pores" is used in a generalized sense which includes microscopic channels. Preliminary thermogravimetric analysis (TGA) and evolved gas analysis (EGA) of SIROF's show (17) that these films, as prepared, contain some unbound (pore) water. In addition, it may be noted that the final thick-

* Electrochemical Society Active Member.
Key words: electrochromism, potential, kinetics.

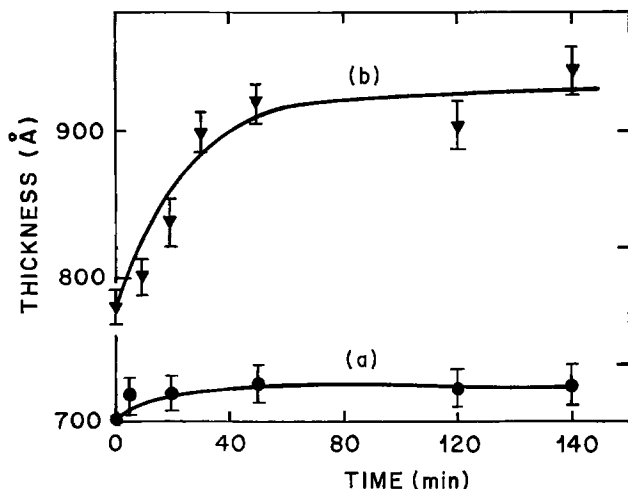


Fig. 1. Increase in thickness of a SIROF, initial thickness 700Å, (a) on immersion in 0.5M H₂SO₄, and (b) on immersion after two color/bleach cycles.

ness of a fully hydrated SIROF is approximately the same as that of an AIROF having the same charge density for the same potential step. For example, for a SIROF of final thickness 1800Å, coloration charge transfer (for 0-1V potential step vs. SCE) is ≈ 30 mC/cm², and that for an equal thickness AIROF is ≈ 27 mC/cm².

We have also investigated the electrochromic response time of SIROF's as a function of hydration. We show in Fig. 2 the electrochromic response of a SIROF for 1 sec voltage pulses stepping between 0 and 1V (vs. SCE) in an aqueous 0.5M H₂SO₄ electrolyte. The data in Fig. 2(a) and (b) were measured within the first 10 sec and after 40 min, respectively, of continuous cycling. Taken together, the data in Fig. 1 and 2 suggest that the film expands from the progressive incorporation of water into the film pores, and the speed of response increases due to the faster diffusion of ions along the pores. The total charge transferred during coloration and bleaching increases from 11.0 mC/cm² [Fig. 2(a)] to 12.6 mC/cm² [Fig. 2(b)] possibly due to a slight increase in the number of accessible iridium sites. The increase is not a kinetic effect; equilibrium values show the same charge increase.

For AIROF's which are known to be highly hydrated, a model of porous films with most of the oxide sites

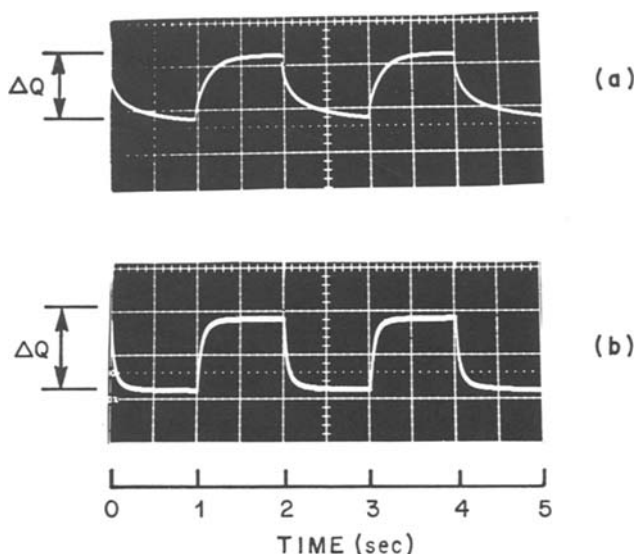


Fig. 2. SIROF electrochromic response (6.8 mC/cm²/div) for 1 sec voltage pulses stepping between 0 and 1V vs. SCE in an aqueous 0.5M H₂SO₄ electrolyte; (a) recorded within the first 10 sec, and (b) after 40 min of color/bleach cycling.

accessible to the electrolyte has been postulated (18) and experimentally verified (11). Such a model is in agreement with the observations reported here for SIROF's. The latter may thus be regarded as porous structures which can expand on water uptake. However, as shown in Fig. 1, expansion is only possible after the film has been subjected to a few color/bleach cycles. Apparently, as-prepared SIROF's have a "closed" structure, i.e., impervious to water, which can be "opened" by potential cycling.

The effect of potential cycling on the structure of a SIROF is more clearly seen from the data in Fig. 3. We find that electrochemical coloring or bleaching produces a significant increase or decrease, respectively, in the film thickness. Data are shown for two different sets of SIROF samples deposited on quartz in an oxygen partial pressure of 20 μm. The data represented by squares refer to thick samples (≈ 1500 Å as prepared); the circles refer to thinner samples (≈ 410 Å as prepared). Full and open symbols designate completely colored and completely bleached SIROF's, respectively. The initial data (half-open symbols) represent measurements on as-deposited, partially colored samples before immersion in the 0.5M H₂SO₄ electrolyte.

It is evident from Fig. 3 that during the first few cycles the films contract upon bleaching and expand upon coloring. This effect has been observed not only for the two sets of samples reported in Fig. 3 but also for other samples of various thicknesses. Particularly significant is the contraction following the first cathodic (i.e., bleaching) voltage pulse. Although not shown in Fig. 3, if the first applied pulse is anodic (i.e., coloring), then the film expands. Since expansion of the film results also from immersion in the electrolyte [Fig. 1(b)], it is difficult to separate the effect of the voltage pulse from that of hydration. Nonetheless, the initial contraction observed upon bleaching clearly shows that the electrochromic effect *per se* causes a significant modulation in film thickness. Following the first few potential cycles in Fig. 3, the thickness modulation associated with coloring and bleaching diminishes. The SIROF's continue to expand until they reach their maximum thickness, approximately following the same behavior as shown in Fig. 1(b). Thus Fig. 3 shows that SIROF's can change their thickness because of two distinct effects: (i) a continuous uptake of water during immersion following a few color/bleach cycles [Fig. 1(b)], and (ii) a thickness modulation directly related to the electrochromic process, which decreases as the film hydration increases.

Conclusions

As previously noted, the porous nature of anodic iridium oxide films has been recognized for some time. The necessity of "pore" water within the structure for fast response times has also been postulated (1, 4). We

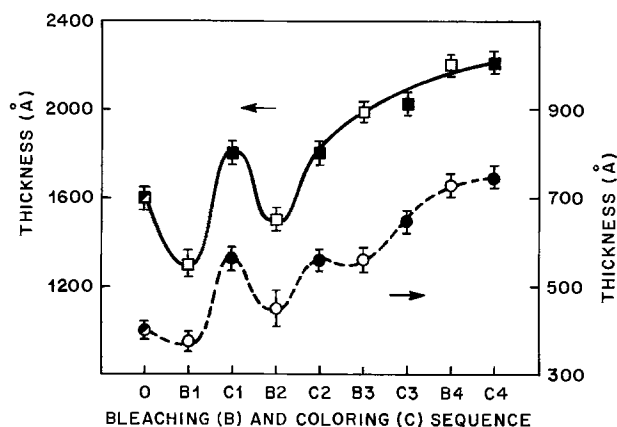


Fig. 3. Initial thickness (0) of SIROF films, and after successive bleaching (B) and coloring (C) for two films of different initial thicknesses.

have shown here that SIROF's have an expandable, porous structure and that water uptake expands the structure. More importantly we have also shown that, for as-deposited films, an expansion occurs upon coloring, and a contraction upon bleaching. The latter observation provides considerable insight into the nature of the mechanism of ion-insertion in electrochromic iridium oxide.

It is now accepted that the coloration reaction in iridium oxide films proceeds by anodic removal of electrons coupled with charge neutralization via ion transfer between the film and the electrolyte. For charge neutrality in aqueous electrolytes, models based on proton extraction or hydroxide ion injection have been postulated. Which of these models is operative is still controversial. Our results, however, suggest that a hydroxide ion mechanism is operative. Contraction of the film upon bleaching indicates removal of ions from the film, and thus precludes a model based on H⁺ insertion.

Although the data in Fig. 3 provide convincing evidence that the ion exchange at the SIROF/bulk-electrolyte interface involves exchange of OH⁻, in principle it is possible that the ion exchange at the iridium oxide grain/pore interface within the SIROF involves H⁺ exchange. However, were H⁺ to dominate the charge transport at the iridium oxide grain/pore interface, it is difficult to understand why OH⁻ would be inserted into the film from the bulk electrolyte in view of (i) the superior mobility of H⁺ over OH⁻ in the pores, and (ii) the abundance of H⁺ available from the acidic bulk electrolyte.

Exchange of OH⁻ at the iridium oxide grain/pore interface provides an explanation for the diminishing amplitude of the thickness modulation observed in Fig. 3 with increasing hydration. In an as-deposited dry film, coloring causes expansion by ion-insertion into the grains directly from the bulk electrolyte; this can only be in a direction normal to the substrate, otherwise loss of adhesion of the SIROF would occur. Once the film has become hydrated and swollen to a volume in excess of that of the colored state in the first coloration of the dry film, expansion of a grain on coloration is no longer constrained to be normal to the film but can also occur laterally by expansion from the pores. It should be noted that there is evidence (19) that AIROF's show a 10-15% thickness increase, measured by *in situ* ellipsometry, during electrochemical coloration in 0.5M H₂SO₄. The latter observation suggests that anion insertion is also responsible for the electrochromic properties of AIROF's. However, our observation that a thickness modulation no longer occurs in SIROF's after full hydration could explain the superior cycle lifetime of SIROF's relative to AIROF's, and be indicative of a different microstructure or H₂O distribution within the films.

In summary, we have measured volume changes in SIROF's and shown that these films: (i) have a sponge-like structure which expands by incorporating large amounts of water following electrochromic cycling; (ii) have electrochromic response times that decrease by an order of magnitude as more water is incorporated within their pores and their structure has expanded; and (iii) as-deposited, expand upon coloring and contract upon bleaching thus supporting the anion mechanism of electrochromism in iridium oxide.

Acknowledgments

We are grateful to Ms. S. P. Lyman for the Alpha-step measurements, and to Mrs. A. A. Pritchard for expert technical assistance.

Manuscript submitted July 24, 1980; revised manuscript received Dec. 16, 1980.

Any discussion of this paper will appear in a Discussion Section to be published in the December 1981 JOURNAL. All discussions for the December 1981 Discussion Section should be submitted by Aug. 1, 1981.

Publication costs of this article were assisted by Bell Laboratories.

REFERENCES

1. S. Gottesfeld, J. D. E. McIntyre, G. Beni, and J. L. Shay, *Appl. Phys. Lett.*, **33**, 208 (1978).
2. G. Beni and J. L. Shay, *ibid.*, **33**, 567 (1978).
3. J. L. Shay, G. Beni, and L. M. Schiavone, *ibid.*, **33**, 942 (1978).
4. S. Gottesfeld and J. D. E. McIntyre, *This Journal*, **126**, 742 (1979).
5. L. M. Schiavone, W. C. Dautremont-Smith, G. Beni, and J. L. Shay, *Appl. Phys. Lett.*, **35**, 823 (1979).
6. W. C. Dautremont-Smith, G. Beni, L. M. Schiavone, and J. L. Shay, *ibid.*, **35**, 565 (1979).
7. C. E. Rice, *ibid.*, **35**, 563 (1979).
8. G. Beni and J. L. Shay, *Phys. Rev. B*, **21**, 364 (1980).
9. G. Beni, C. E. Rice, and J. L. Shay, *This Journal*, **127**, 1342 (1980).
10. S. Hackwood, G. Beni, W. C. Dautremont-Smith, L. M. Schiavone, and J. L. Shay, *Appl. Phys. Lett.*, **37**, 965 (1980).
11. J. D. E. McIntyre, W. F. Peck, and S. Nakahara, *This Journal*, **127**, 1264 (1980).
12. W. C. Dautremont-Smith, L. M. Schiavone, G. Beni, and J. L. Shay, *SID 1980 Digest*.
13. D. N. Buckley and L. D. Burke, *J. Chem. Soc. Faraday Trans. 1*, **71**, 1447 (1975).
14. B. W. Faughnan, R. S. Crandall, and P. M. Heyman, *RCA Rev.*, **36**, 177 (1975).
15. H. N. Hersh, W. E. Kramer, and J. H. McGee, *Appl. Phys. Lett.*, **27**, 646 (1975).
16. M. Green, W. C. Smith, and J. A. Weiner, *Thin Solid Films*, **38**, 89 (1976).
17. S. Hackwood, P. A. Gallagher, and G. Beni, To be published.
18. S. H. Glarum and J. H. Marshall, *This Journal*, **127**, 1467 (1980).
19. S. Gottesfeld and S. Srinivasan, *J. Electroanal. Chem. Interfacial Electrochem.*, **86**, 89 (1978).

The Influence of the Anion on Copper Electrocrystallization

G. Carneval and J. Bebczuk de Cusminsky

*Laboratorio de Investigaciones de Metalurgia Física, Facultad de Ingeniería,
Universidad Nacional de La Plata, 1900 La Plata, Argentina*

ABSTRACT

Structural studies of copper electrodepositions from pyrophosphate, chloride, cyanide, and citrate solutions were carried out on highly polished (001) copper surfaces at a wide range of current densities under galvanostatic conditions. The study was performed by means of x-ray diffraction. The deposition morphology was observed with a scanning electron microscope. Correlation among internal structure, surface morphology, solution composition, and plating conditions were examined. The results were compared with previous studies from sulfate solutions. Epitaxial growth was observed in the early stage of deposition. The effect of the anion on the change from single crystalline to polycrystalline growth at further stage was analyzed. A specific adsorption of the different anions in relation to their ionic size was considered as a critical feature. As a comparative study the action of an addition agent was also considered.

Copper electrodeposition from sulfate solutions has been studied from different points of view and a considerable amount of data on its properties are now available. Electrodeposition of copper from other types of solutions, however, has been less extensively studied and the general picture of the anion effect on the growth mode is not clear. A knowledge of the magnitude of the influence of the anion on the different steps of the electrocrystallization process is desirable for the fundamental understanding of electrodeposition.

In studies on the mechanism and kinetics of copper deposition, Bockris and Enyo (1) assumed that one of the factors which influences growth is the blocking of deposition sites by adsorption of anions. Studies of the surface morphologies (2-3) and of the physical and mechanical properties of electrodeposited copper from different electrolytes were made by various workers (4-5).

Previous studies in this laboratory (6-9) dealt with the effect of the base metal characteristics of single crystalline surfaces on epitaxial growth of copper deposits from sulfate solutions. Most of the epitaxial growth features are explained in the literature (10-23). The change to nonepitaxial growth and a mechanism for the formation of polycrystalline deposits (7-9, 23) is less clearly understood and it is with this purpose that the present contribution was made. The work is a continuation of that mentioned in preceding studies, the structural aspects of deposition having been discussed with the aim of emphasizing how the growth is affected by the anion of the solution.

Experimental

Electrodeposition was carried out on as-grown OFHC (99.98%) copper single crystals of (001) orientation. Experimental details are given in previous communications (7-9); the preparation of the surfaces was considered as one of the very important factors. A 99.999% copper sheet was used as an anode. Depositions of copper were performed from copper solutions of the following anions: pyrophosphate, cyanide, chloride, and citrate, the chemicals being of "Analar" grade and the water triple distilled. Some depositions from sulfate solution, and others from amine-sulfate solution, were also made. The composition of the solutions is specified in Table I. A routine procedure for purifying the solutions (15) was used. Gentle stirring of the solutions was maintained by a glass-coated stirring magnet. In

some cases stirring was made by slight bubbling with high purity nitrogen. Under these conditions the deposits under study usually had an optically smooth appearance and a good adherence to the substrate. The experiments were carried out galvanostatically between 5 and 90 mA/cm², while the potential was recorded continuously on a Honeywell X-t recorder. Each deposition was performed without any interruption to a predetermined thickness. The deposit thicknesses were calculated as detailed elsewhere (7). After a desired time of deposition, the cell was disassembled and the working electrode washed first with doubly distilled water and then with ethyl alcohol. After necessary studies the deposit was removed by mechanical polishing and electropolishing before plating again.

The structural studies were carried out with Philips x-ray equipment (P.W. 1140/00). Laue backreflection method with white chromium radiation was used in order to get a low penetration of the beam. Morphological observations were made, some by optical microscopy of low magnification (Reichert MeF Microscope), but most with a scanning electron microscope (JSM-U₃ JEOLCO Japan) because of a high resolution required.

Results and Discussion

Structural results by x-ray diffraction of the copper deposits from pyrophosphate, cyanide, chloride, and citrate solutions are plotted in Fig. 1, deposit thickness *vs.* current density, where each curve defines the initiation of the polycrystalline structure from the corresponding electrolyte. Previous results of copper deposits from sulfate copper solution on (001) OFHC copper surfaces (9) were also included. Details of the results from the citrate solution were plotted separately in Fig. 2. The characteristic surface morphologies are shown in Fig. 3-7 and are summarized in Table II.

It is observed in Fig. 1 that the structural results point to an essential difference in the action of the different copper solutions on the process of electrodeposition of copper. In the early stage of deposition, the structure from all the solutions used is single crystalline, that is, the copper deposits grew parallel to the substrate, but at further deposition, a polycrystalline structure was developed at a thickness depending on the type of the solution and the current density applied. Thus a critical thickness at which the breakdown of epitaxy occurs is different for the type of solution used.

It is known that during the process of electrodeposition of a metal, certain inevitable foreign species

Key words: copper electrodeposition, anion effect, x-ray study.

Table I. Composition of the deposition solutions

| Sulfate solution | | Chloride solution | | Citrate solution | |
|--|-------------|---------------------------------|------------|---|-------------|
| CuSO ₄ ·5H ₂ O | 0.5 mol | Cu ₂ Cl ₂ | 0.5 mol | Copper citrate | 0.5 mol |
| H ₂ SO ₄ | 0.5 mol | HCl | 0.5 mol | Citric acid | 0.5 mol |
| Pyrophosphate solution | | Cyanide solution | | Amine-sulfate solution | |
| CuSO ₄ ·5H ₂ O | 30 g/liter | CuCN | 32 g/liter | CuSO ₄ ·5H ₂ O | 0.5 mol |
| Na ₂ P ₂ O ₇ ·10 H ₂ O | 120 g/liter | NaCN | 24 g/liter | (NH ₄) ₂ SO ₄ | 0.5 mol |
| Na ₂ HPO ₄ ·12H ₂ O | 90 g/liter | Na ₂ CO ₃ | 15 g/liter | Ethylenediamine | 80 ml/liter |
| | | | | NH ₃ conc | 4 ml/liter |

generally present in an electrolyte as well as the anion may be codeposited or adsorbed at the cathode (1-5, 10-23). The growth during the process of electro-deposition can be seriously affected by these codeposited materials and may eventually influence the physical and mechanical properties of the deposits. On a relatively pure electrolyte, however, the anion must be considered as the main important component of the solution, owing to its large quantity. Codeposition of anions has been reported in the early studies of electro-deposition (24). Some workers (1) assumed that the specific adsorption of the anions may influence the electrochemical kinetic parameters.

If an adsorption mechanism of the anion is considered, all the evidence in the present experiments points to a possible correlation between the breakdown of the epitaxy of the deposits and some property of the anion, the size or spatial content of the anion being a relevant one. A remarkable relationship between the anion size and the deposit thickness at which the polycrystalline structure starts in each solution is stressed in Table III.

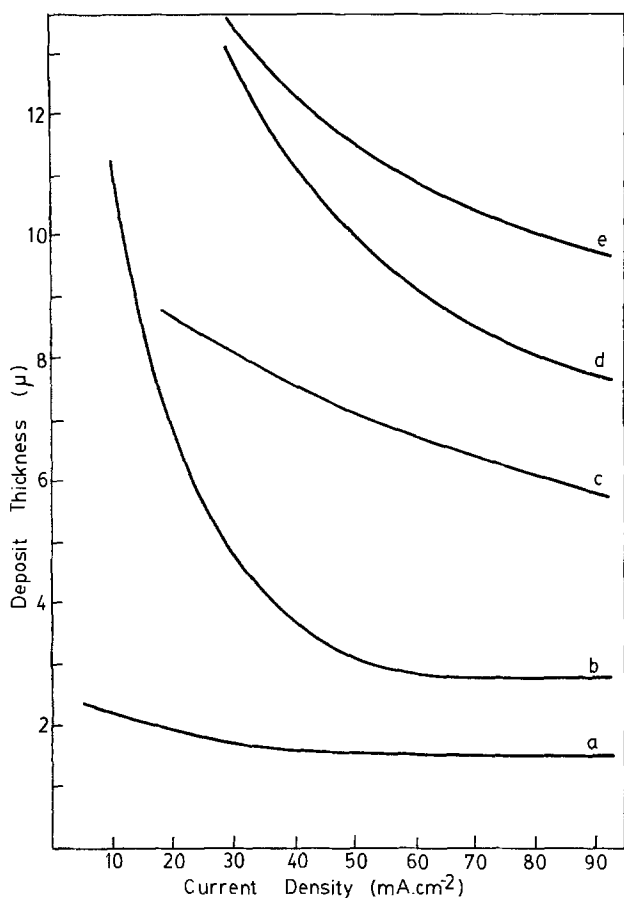


Fig. 1. Initial stage of polycrystalline structure of copper electrodeposit on single crystal substrate surfaces from: a, pyrophosphate solution; b, sulfate solution; c, cyanide solution; d, citrate solution; e, chloride solution. Plots of thickness of copper deposits vs. C.D. An x-ray diffraction study.

Table II. Morphological observations of copper deposits from different solutions

| |
|--|
| Sulfate: layers, square base pyramids (truncated or stepped), dendrites, cauliflower |
| Chloride: square base stepped pyramids, stepped boulders |
| Citrate: square base pyramids, balls, cauliflowers |
| Pyrophosphate: balls, cauliflowers, dendrites |
| Cyanide: small nuclei without any characteristic shape |
| Amine-sulfate ($T = 25^{\circ}\text{C}$): spheres or balls, cauliflowers |
| Amine-sulfate ($T = 55^{\circ}\text{C}$): approx. stepped pyramids |

The size of the anions of the solutions is taken to be the values of the anion radius (interionic distances) (25), as well as the specific volumes of the anions. These last have been calculated from the molecular volumes (mol weight/ ρ) found for copper salts by subtracting the space increment of the cation. The molecular volumes of the anions given by Hückel (26) were also listed. Although the figures represent approximate values only, they provide a clear comparative picture of the spatial relationship between the anions. The correlation observed between the spatial content of the anion and the deposit thickness is quite significant: the greater the size of the anion, the lower is the thickness of the deposit at which the change to polycrystalline structure occurs. This fact is observed at all current densities from approximately 10 mA/cm². At lower C.D.'s the number of anions and other particles adsorbed at the cathode is in a very small

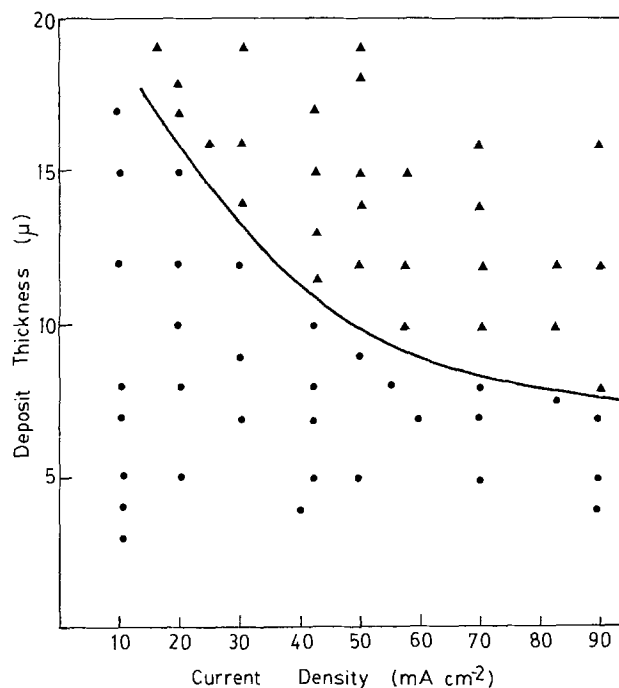


Fig. 2. Initial stage of polycrystalline structure of copper electrodeposits from copper citrate solution. Detailed structural results by x-ray diffraction: ● single crystalline, ▲ polycrystalline. Thickness of copper deposits vs. C.D.

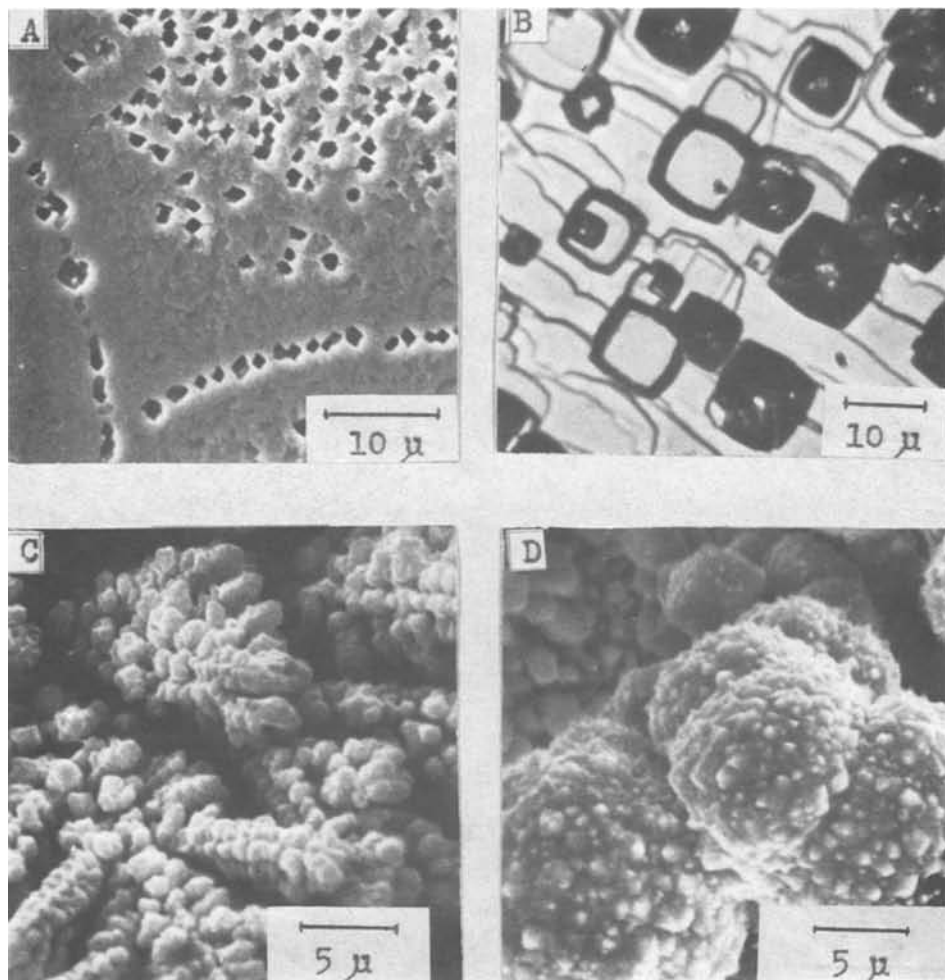


Fig. 3. SEM pictures of copper depositions from sulfate solution. A, 5 mA/cm²; 2 μm thickness. B, 20 mA/cm²; 6 μm thickness. C, 60 mA/cm²; 2 μm thickness. D, 80 mA/cm²; 2 μm thickness.

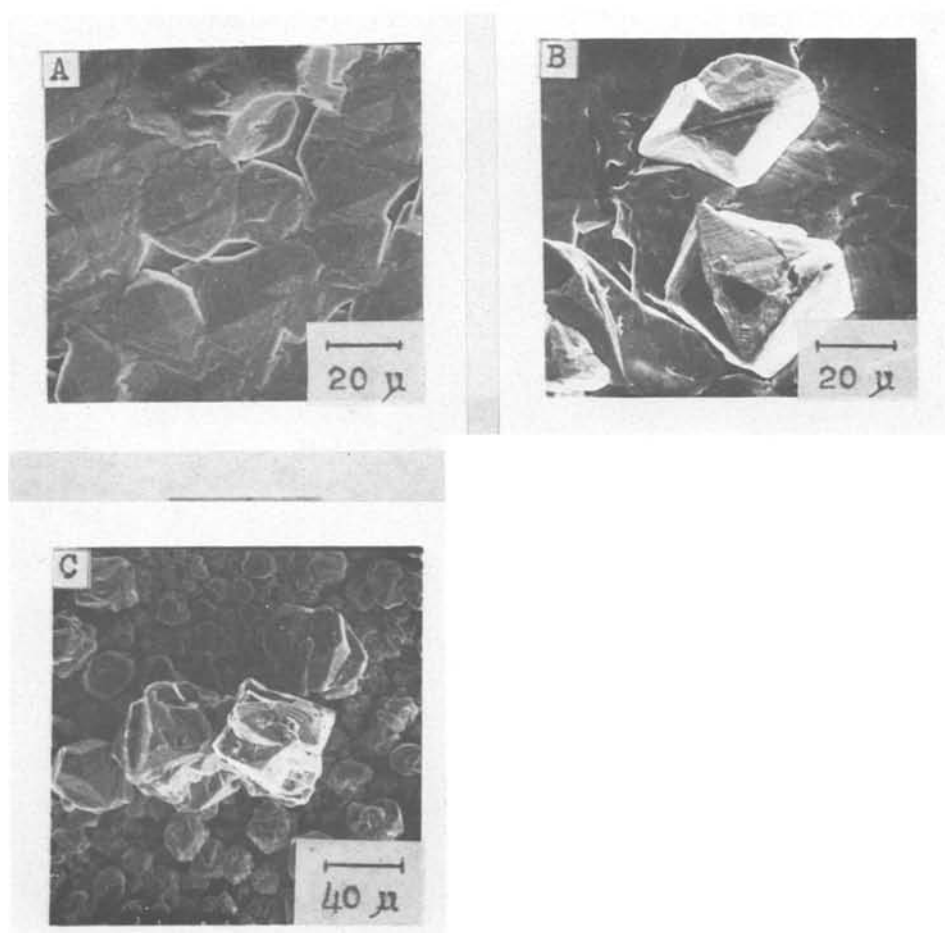


Fig. 4. SEM pictures of copper depositions from chloride solution. A, 20 mA/cm²; 5 μm thickness. B, 30 mA/cm²; 12 μm thickness. C, 50 mA/cm²; 10 μm thickness.

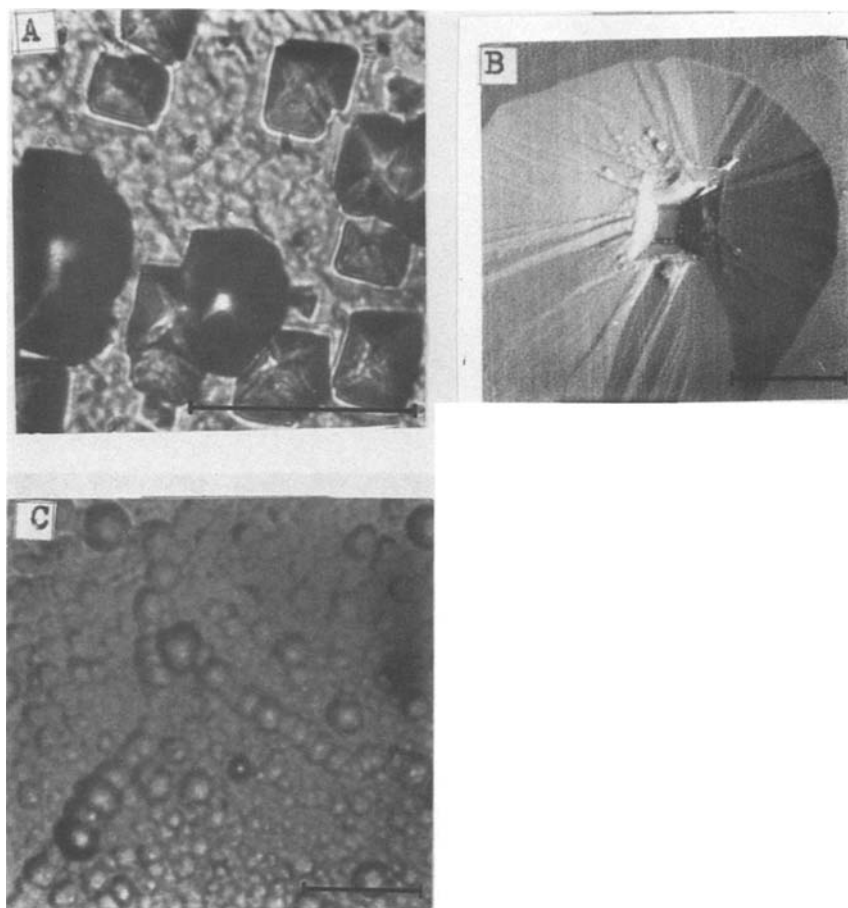


Fig. 5. Optical and SEM pictures of copper depositions from citrate solution. A, 10 mA/cm²; 4 μm thickness. B, 20 mA/cm²; 8 μm thickness. C, 50 mA/cm²; 10 μm thickness. The marks represent 30 μm.

amount and thus their influence in the structural results is less noticeable, as is observed in Fig. 1.

The values taken into account in Table III are at 50 mA/cm² C.D. An outstanding evidence of the effect of

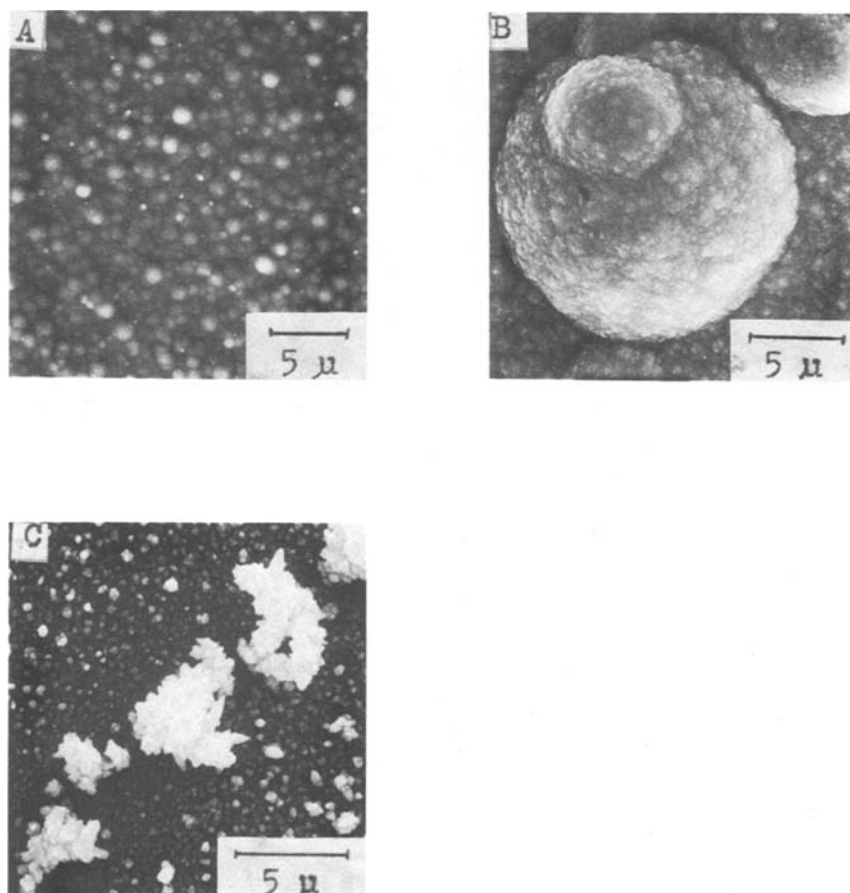


Fig. 6. SEM pictures of copper depositions from pyrophosphate solution. A, 5 mA/cm²; 2 μm thickness. B, 10 mA/cm²; 2 μm thickness. C, 30 mA/cm²; 1 μm thickness.

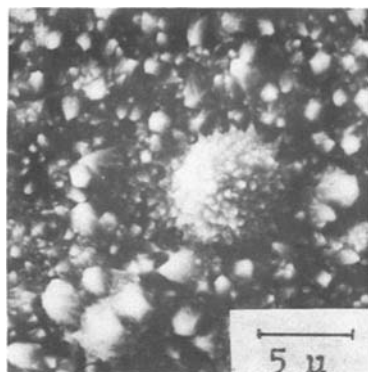


Fig. 7. SEM picture of copper deposition from cyanide solution. 10 mA/cm²; 8 μm thickness.

the size of the anion on the results is the comparison of the values obtained from sulfate and chloride solutions. These solutions are the most representatives of the present experiments, where only copper, the respective anion, and the inevitable adventitious impurities are present. It is observed that the Cl⁻ ion volume is quite reasonably smaller than that of the SO₄⁼ ion (Table III), and thus the electrodeposited copper from the Cl⁻ bath grows in epitaxial form until very high thicknesses (Fig. 1e) in relation to that from the SO₄⁼ solution (Fig. 1b). Therefore the assumption that very small components may be buried into the deposit is implicit here.

The structural results of copper deposits from pyrophosphate and from cyanide solutions are also of interest to compare. In addition to their respective anion, both solutions have Na cations as the main extra components which may also codeposit (Table I). The differences in the results observed at all C.D.'s (Fig. 1) give evidence of the effect of the anion, the difference in size is quite prominent (Table III).

With the purpose of extending this study to deposits of copper from an organic solution, a copper citrate bath was used (Table I). The results are presented in Fig. 1 and detailed in Fig. 2 which show an epitaxial growth until very high thicknesses at all C.D.'s. As is seen in Fig. 1, the initiation of the polycrystalline structure occurs at deposit thicknesses very close to that from chloride solution. It seems that the anions from both solutions must have some characteristics in common that if adsorbed on the copper cathodes they produce similar effects on the surface structure. Both solutions are simple acidic solutions (Table I), but neither the anion size, nor the shape, solubilities of salts, etc. are similar. However, it is probable that the citric anion is decomposed before or during copper deposition, because of its carboxylic acid groups, giving radicals (C-H) of low radius, approximately 0.94–1.06 Å (25). These values are in effect of the order of the Cl⁻ anion radius 0.99 Å. Copper is able to form strain-free attachments with such small components due to the octahedral interstices of approximately 1.06 Å in its

lattice. On the other hand, a low effect of carboxyl groups was also observed, studying the cathode overpotential of copper deposits from solutions with additives having this kind of groups (27).

As a result it may be assumed that the basic action of an anion is similar to that of an addition agent which arises from the adsorption on the surface electrode (21, 27, 28) and affects somehow the elementary processes of electrocrystallization.

In order to observe the effect of an addition agent on the mode of growth, copper was deposited from an amine-sulfate solution. The solution contains together with the SO₄⁼ anion (Table I), a more complex component (ethylenediamine) which may also be adsorbed. The experimental results were represented in Fig. 8. It is observed that the copper polycrystalline structure starts at lower thickness (Fig. 8b) than in copper deposits from the CuSO₄-H₂SO₄ solution (Fig. 8a). It seems that the amino groups play an important effect in the crystalline growth, in the sense that they "inhibit" the free mode of the single crystalline growth. A remarkable effect of these groups was observed also in copper deposition, from the electrochemical point of view by certain investigators (27).

However by heating the amine-sulfate solution at 55°C, the deposition of copper follows the single crystalline structure of the substrate up to higher thicknesses even than that from the CuSO₄-H₂SO₄ solution (Fig. 8c). Presumably ethylenediamine and the ammonium salt of the solution hydrolyze by heating, giving smaller components, some of which are evaporated or adsorbed and others may have the ability to make difficult the transport of the SO₄⁼ ions to the cathode and thus allow the growth in single crystalline form. A pH effect could also be involved in the results. These changes observed in the structural aspect have certain similarities with the morphological observations. A square pyramidal growth was observed mostly at low C.D. in copper deposits from the CuSO₄-H₂SO₄ solution (Fig. 3), but if the solution contained also ethylenediamine and ammonium salt, no pyramids were observed, but rounded forms and cauliflowers (Fig. 9A and B). By heating the solution during deposition, nearly stepped pyramids appeared again (Fig. 9C).

Relating the habit of the crystal growth, the morphologies observed in the present experiments from the simple acidic copper solutions: sulfate, chloride, and citrate, are of a similar overall shape at low C.D.'s and under conditions which allow epitaxial growth to occur. They are mainly square pyramids or square blocks, with slight differences from one solution to the other, as observed in Fig. 3A, 4A, and 5A. As the size and geometry of the anions and most of the properties of their salts are different, these results confirm at first the strong influence of the atomic configuration of the substrate in copper deposits at low C.D. or low overpotential, as was observed in previous investigations from sulfate solutions (7-10, 15-19).

The differences of the surface topographies are more remarkable at increasing C.D.'s and thicknesses, i.e., at 50 mA/cm² and under single crystallinity, the forms

Table III. Relation between the size of the anion and the thickness of the initial stage of polycrystalline structure of the electrodeposited copper

| Anion | Radius of the anion (interionic distance) (Å) (approx. values) | Specific volume of the anion (cm ³ /mol) | | Thickness to initiate polycrys- talline structure† (μm) |
|--|---|--|-------------------------|--|
| | | Calculated | Given by Huckel (26) | |
| Cl ⁻ | 0.99 | 20.873 | 20 | 11.4 |
| CN ⁻ | 1.30 | 23.553 | 23 | 7.0 |
| SO ₄ ⁼ | 1.70 | 37.177 | 39 | 3.0 |
| PO ₄ ⁼ | 1.76 | 37.560 | 39 | — |
| P ₂ O ₇ ⁼ | 3.52 | 75.120 | — | 1.5 |

* The values calculated of P₂O₇⁼ were considered as twice the values of PO₄⁼.

† The values considered here are at 50 mA/cm².

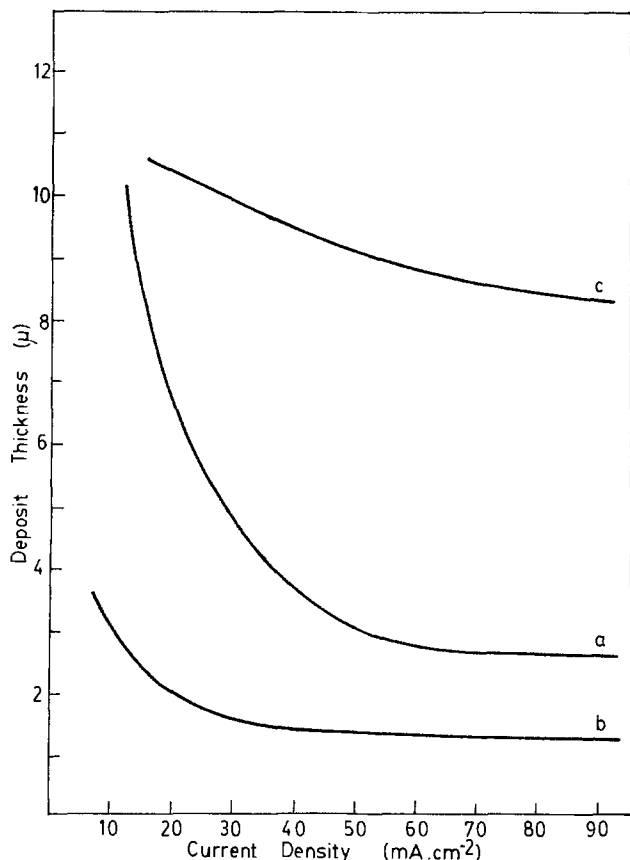


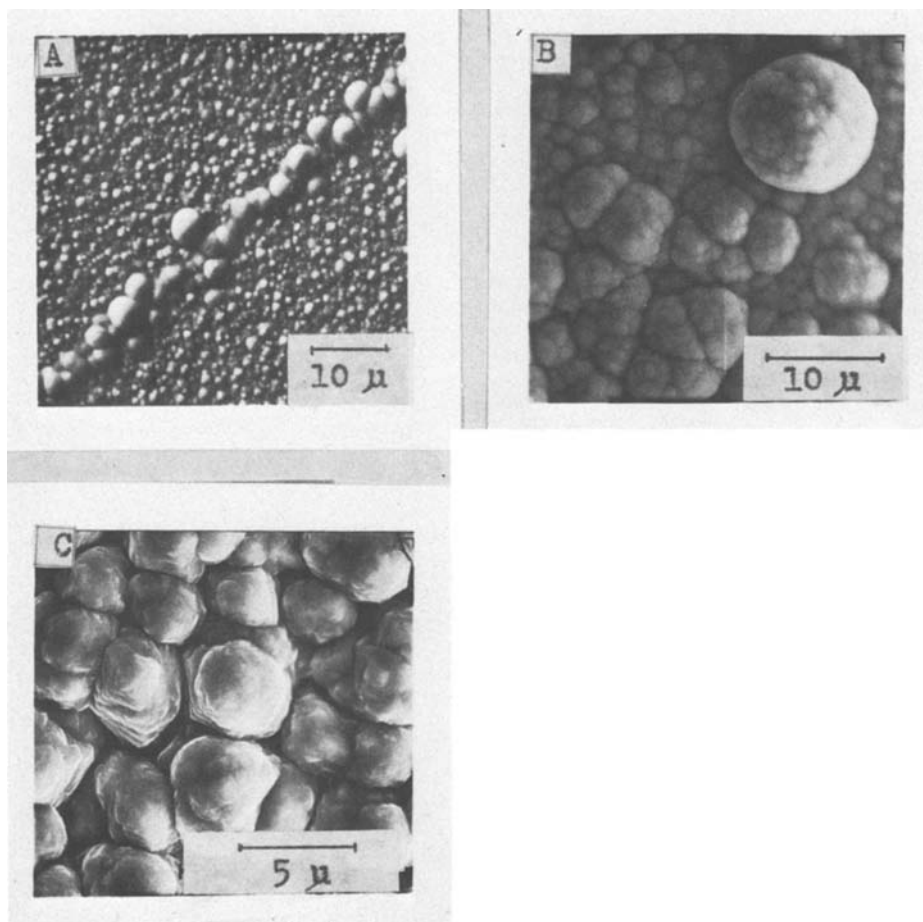
Fig. 8. Comparison between the initial polycrystalline structure of copper deposits from sulfate solution and amine-sulfate solution. a, Amine-sulfate solution at room temperature; b, sulfate solution at room temperature; c, amine-sulfate solution at 55°C. Plots of thickness of copper deposits vs. C.D. An x-ray diffraction study.

observed from Cl^- anion solutions are boulders of certain geometrical shape, Fig. 4B. On the other hand, a cauliflower growth is observed from the sulfate and citrate solutions: Fig. 3B and 5B. A dendritic growth was observed also from the sulfate solution, but not from the other anion solutions. When the x-ray observation was polycrystalline, no defined forms were observed. Nevertheless, how the anion affects the surface morphology is difficult to elucidate due to the high sensitivity of the crystal habit with respect to very small amounts of adsorbed materials. Damjanovic, Paunovic, and Bockris (18) have found that amounts of certain organic substances in solution, as low as 10^{-12} mol/cm² produce visible changes in the morphology of the growing crystal. Taking into account that water molecules and adventitious impurities are always present and may also be adsorbed, the explanation of the different morphologies observed from one solution to the other is much more difficult than that of the crystallographic aspect where the x-ray observations involve a statistical result of the total geometrical area. So when deposition was carried out from more complex solutions, that is, pyrophosphate, cyanide, and aminosulfate, where together with the anion, the other components are present also in great quantity, pyramidal forms were not observed even at low C.D., but spheres or balls, cauliflowers, dendrites, and nuclei without any characteristic shape: Fig. 6 and 9, indicating a predominant influence of the adsorbed components.

Conclusions

1. The x-ray diffraction study of copper deposition shows a critical thickness of breakdown of epitaxy with C.D. This thickness is different for the type of the anion solution used.
2. A correlation between the anion size and deposit thickness at which the polycrystalline structure starts is observed: the greater the anion size, the lower is the thickness of breakdown of epitaxy.

Fig. 9. SEM pictures of copper depositions from amine-sulfate solution; A and B at room temperature; C at 55°C. A, 10 mA/cm²; 4 μm thickness; B, 20 mA/cm²; 10 μm thickness; C, 20 mA/cm²; 10 μm thickness.



3. The basic action of an anion is similar to that of an addition agent.

4. The morphologies from simple acidic copper solutions at low C.D. and thickness are of a similar overall shape, the differences are more remarkable at increasing C.D.'s and thicknesses and in deposits from complex solutions. No specific evidence of an anion effect is observed.

Acknowledgment

J. B. de C. is very grateful to the Consejo Nacional de Investigaciones Científicas y Técnicas of Argentina for financial support.

Manuscript submitted Oct. 21, 1980; revised manuscript received ca. Jan. 16, 1981.

Any discussion of this paper will appear in a Discussion Section to be published in the December 1981 JOURNAL. All discussions for the December 1981 Discussion Section should be submitted by Aug. 1, 1981.

Publication costs of this article were assisted by Universidad Nacional de La Plata.

REFERENCES

1. J. O'M. Bockris and M. Enyo, *Trans. Faraday Soc.*, **58**, 1187 (1962).
2. S. C. Barnes, *Electrochim. Acta*, **5**, 79 (1961).
3. D. W. Hardesty, *This Journal*, **117**, 167 (1970).
4. V. A. Lamb and D. R. Valentine, *Plating*, **1289** (1965).
5. V. A. Lamb, Ch. E. Johnson, D. R. Valentine, *This Journal*, **117**, 291C (1970).
6. J. Bebczuk de Cusminsky, *Metalurgia* (Asoc. Brasileira de Metales), **24**, 605 (1968).
7. J. Bebczuk de Cusminsky, *Electrochim. Acta*, **15**, 73 (1970).
8. J. Bebczuk de Cusminsky, *Anal. Assoc. Quím. Argentina*, **60**, 81 (1972).
9. J. Bebczuk de Cusminsky, *J. Cryst. Growth*, **41**, 330 (1977).
10. F. C. Frank, in "Growth and Perfection of Crystals," R. H. Doremus, B. W. Roberts, and D. Turnbull, Editors, p. 411, John Wiley & Sons, Inc., New York (1958).
11. N. Cabrera and D. A. Vermilyea, *ibid.*, p. 393.
12. R. Kaishev, E. Budevski, and S. Malinowski, *Z. Phys. Chem.*, **204**, 348 (1955).
13. H. Fischer, *Electrochim. Acta*, **2**, 50 (1960).
14. H. Seiter, H. Fischer, and L. Albert, *ibid.*, **2**, 97 (1960).
15. N. A. Economou, H. Fischer, and D. Trivich, *ibid.*, **2**, 207 (1960).
16. H. J. Pick, G. G. Storey, and T. B. Vaughan, *ibid.*, **2**, 165 (1960).
17. S. C. Barnes, G. G. Storey, and H. J. Pick, *ibid.*, **2**, 195 (1960).
18. A. Damjanovic, M. Paunovic, and J. O'M. Bockris, *J. Electroanal. Chem. Interfacial Electrochem.*, **9**, 93 (1965); *Electrochim. Acta*, **10**, 111 (1965).
19. A. Damjanovic, T. H. U. Setty, and J. O'M. Bockris, *This Journal*, **113**, 429 (1966).
20. M. Fleischmann and H. R. Thirsk, in "Advances in Electrochemistry," Vol. 3, P. Delahay and C. W. Tobias, Editors, Chap. 3, Interscience, New York (1963).
21. J. O'M. Bockris and G. A. Razumney, in "Fundamental Aspects of Electrocrystallization," Plenum Press, New York (1967).
22. L. Peraldo Bicelli and G. Poli, *Electrochim. Acta*, **11**, 289 (1966).
23. J. Bebczuk de Cusminsky, *Anal. Asoc. Quím. Argentina*, **59**, 387 (1971).
24. M. Schlotter, *Trans. Faraday Soc.*, **31**, 1177 (1935).
25. L. Pauling, "The Nature of the Chemical Bond," p. 224, Cornell University Press, Ithaca, New York (1960).
26. W. Hüchel, "Structural Chemistry of Inorganic Compounds," p. 316, Elsevier Publishing Co., Inc., New York (1950).
27. H. Schneider, A. J. Sukava, and W. J. Newby, *This Journal*, **112**, 568 (1965).
28. A. J. Sukava and C. A. Winkler, *Can. J. Chem.*, **33**, 961 (1955).

Cathodic Deposition of Amorphous Silicon from Tetraethylorthosilicate in Organic Solvents

Yasuo Takeda, Ryoji Kanno, and Osamu Yamamoto*

Department of Chemistry, Faculty of Engineering, Mie University, Tsu, 514, Japan

and T. R. Rama Mohan, Chia-Hao Lee, and F. A. Kröger*

Department of Materials Science, University of Southern California, Los Angeles, California 90007

ABSTRACT

A blue thin film of amorphous silicon has been deposited on a nickel cathode by the electrolysis of a solution of tetraethylorthosilicate in acetic acid. The maximum thickness of the film obtained was about 0.5 μm . The deposit was confirmed to be amorphous silicon by IR reflection spectra, RHEED, and nondispersive x-ray analysis in the scanning electron microscope.

Amorphous silicon containing hydrogen, a-Si, is a promising material for the manufacture of low-cost large area solar cells with medium efficiency. Amorphous materials not containing hydrogen appear to have large concentrations of dangling bonds, producing levels in the forbidden gap which give the material a high resistance and make a change of the semiconducting properties by doping virtually impossible (1). In materials made in a glow discharge in silane, how-

ever, these bonds are saturated by hydrogen, the levels disappear, and doping to n- and p-type with appreciable conductivity becomes possible (2, 3). Conversion efficiencies as high as 6% have been measured in sunlight (4). The theoretical limit for the efficiency of a thin film a-Si solar cell is estimated to be around 15% (5).

Materials made in different ways have different properties. Amounts of H larger than required to saturate the dangling bonds lead to (SiH)_n polymer formation with less favorable electrical properties. It is, therefore, important to regulate the hydrogen

* Electrochemical Society Active Member.

Key words: amorphous silicon, electrodeposition, tetraethylorthosilicate, nonaqueous electrolyte.

content of the material. Electrodeposition as a method of preparation is attractive for various reasons: It is easy to regulate the hydrogen content of a-Si; it does not involve vacuum equipment or furnaces and is therefore convenient; doped material can be made by adding compounds of the dopant to the electrolyte. It is therefore attractive to apply this method to amorphous silicon. However, the strong affinity of silicon for oxygen makes electrodeposition from aqueous electrolytes impossible. The use of organic solvents removes this difficulty.

Amorphous germanium (together with hydrogen) was plated from ethylene glycol (6). There are a few indications in the literature for a-Si electrodeposition. Warren reported electrodeposition of Si on Hg from a solution of SiF₄ in alcohol (7). Zyazev and Ezrielev described the cathodic deposition of Si on Pt (but not on Cu) from a solution of SiCl₄ or SiF₄ and KI in propylene glycol (8). Recently, Austin reported the electrodeposition of a-Si from SiX₄ (X: halogen) in various organic solvents (9).

In this study, cathodic deposition of a-Si from tetraethylorthosilicate (Si(OC₂H₅)₄) in acetic acid is presented.

Experimental

Commercial grade organic solvents and tetraethylorthosilicate (TEOS) were used without further purification.

The electrodeposition was carried out in an H-shaped vessel. The anode and cathode compartments were separated by a diaphragm of porous polytetrafluoroethylene. The solution of tetraethylorthosilicate in the organic solvents investigated in this study has a high resistance; reduction of the resistivity is achieved by adding tetramethylammonium chloride (TMAC) or tetraethylammonium chloride (TEAC), a usual additive for such purpose. TMAC and TEAC were dried under vacuum at 100°C. A cylindrical graphite rod was used as the anode and a nickel plate (99.99% pure) as the cathode. The effective area of the cathode was 2.3 cm². D-C current of 0.2 mA/cm² ~ 20 mA/cm² was supplied by a constant current power supply. In some cases, power was provided by a potentiostat, cathodic potential being measured relative to a silver-silver chloride electrode, which consisted of a mixture of silver powder and silver chloride powder in acetic acid with TMAC: Ag, AgCl/CH₃COOH, TMAC (0.12 mole/liter).

The electrode potential was 0.22V vs. SCE at 22°C. All experiments were carried out in flowing dry nitrogen. The deposits were investigated by reflection IR analysis, reflection high-energy electron diffraction (RHEED), and dispersive x-ray analysis in the scanning electron microscope.

Results and Discussion

Cathodic deposits were obtained on a nickel cathode from solutions of TEOS in acetic acid, propylene carbonate, and 1-chloropropane.

Table I shows typical experimental results of the electrodeposition from TEOS in acetic acid with TMAC at room temperature at a current density of 1 mA/cm². From this solution, bright blue deposits were obtained,

which were tightly adhering to the nickel cathode. Acetone is effective to make the deposit homogeneous and also to decrease the resistivity of the solution. As shown in Table I, about a 20% increase in conductivity was observed by adding 2 cm³ acetone to the solution of 60 cm³ acetic acid, 4 cm³ TEOS, and 2g TMAC. No deposit, however, was obtained from a solution with concentrations of acetone above 20 volume percent (v/o). A white precipitate became noticeable in the solution after passing a current for about 15 min. The formation of the precipitate was retarded by using distilled acetic acid. The white precipitate may be a product of hydrolysis of TEOS; IR spectra showed it to be a silica gel-like material. Table I indicates that the electrolysis from the solutions with higher concentration of TEOS gives lower weight gain (low current efficiency) (see 1st, 2nd, and 3rd lines). These solutions had the largest amounts of white precipitate, which adhered to the nickel cathode, preventing silicon deposition. The concentration of the supporting electrolyte affects the weight gain of the nickel cathode: There is an optimum concentration of TMAC to obtain the highest current efficiency (see 4th, 5th, and 6th lines). The highest current efficiency of about 60% calculated on the basis of a four-electron change was obtained from the solution consisting of 60 cm³ acetic acid, 4 cm³ TEOS, 2 cm³ acetone, and 2g TMAC. The current efficiency decreases with increasing temperature; above 50°C no precipitate is formed in the solution and no deposit on the cathode is obtained; the evolution of hydrogen was observed.

Relations between the weight gain of the nickel cathode and coulombs passed at various current densities are shown in Fig. 1 for solutions containing 60 cm³ acetic acid, 4 cm³ TEOS, 2 cm³ acetone, and 2g TMAC. As shown in this figure, the cathode increases its weight initially, but no change in weight is observed with further electrolysis. The weight gain and saturation by electrolysis were also observed on an n-type single crystal silicon cathode with relatively low resistivity. The saturation of the weight gain of nickel cathodes may be due to the low current efficiency on the pure silicon layer built on the nickel cathode. As can be seen from Fig. 1, the current efficiency decreases with increasing current density. Maximum weight gain of around 0.5 mg, which corresponds to 0.5 μm in thickness, is obtained at lower current density. No appreciable deposition was observed at current densities of 0.35 mA/cm² or less. Current vs. potential curves shown in Fig. 2 suggest that in this experimental condition hydrogen evolution begins to occur at 0.4 mA/cm². The potentials plotted were measured at the end of a 30 sec period of supplying the constant cathodic current. The electrode potential at 0.4 mA/cm² measured against the Ag/AgCl, acetic acid, TMAC reference electrode, was -0.85V vs. NHE. Therefore, hydrogen evolution on the cathode may play an important role for the cathodic deposition on nickel. Low current efficiencies at higher current densities may be due to the co-evolution of hydrogen.

Nondispersive x-ray analysis in the scanning electron microscope showed that the deposits contain larger concentration of silicon. The intensity ratio of

Table I. Electrodeposition from solutions of Si(OEt)₄ in acetic acid

| Acetic acid (cm ³) | Si(OEt) ₄ (cm ³) | (CH ₃) ₄ NCl (g) | Acetone (cm ³) | Conductivity of the solution (S cm ⁻¹) | Current density (mA/cm ²) | Coulombs passed | Weight gain (mg) | Current efficiency (%) |
|--------------------------------|---|---|----------------------------|--|---------------------------------------|-----------------|------------------|------------------------|
| 60 | 1 | 2 | 2 | 1.2 × 10 ⁻³ | 1 | 11 | 0.5 | 6 × 10 |
| 60 | 4 | 2 | 2 | 1.0 × 10 ⁻³ | 1 | 11 | 0.5 | 6 × 10 |
| 60 | 10 | 2 | 2 | 0.7 × 10 ⁻³ | 1 | 11 | 0.2 | 3 × 10 |
| 60 | 4 | 0.5 | 2 | 0.9 × 10 ⁻³ | 1 | 15 | 0.1 | 1 × 10 |
| 60 | 4 | 2 | 2 | 1.0 × 10 ⁻³ | 1 | 15 | 0.5 | 5 × 10 |
| 60 | 4 | 4 | 2 | 2.3 × 10 ⁻³ | 1 | 15 | 0.2 | 2 × 10 |
| 60 | 4 | 2 | 0 | 0.8 × 10 ⁻³ | 1 | 11 | 0.4 | 5 × 10 |

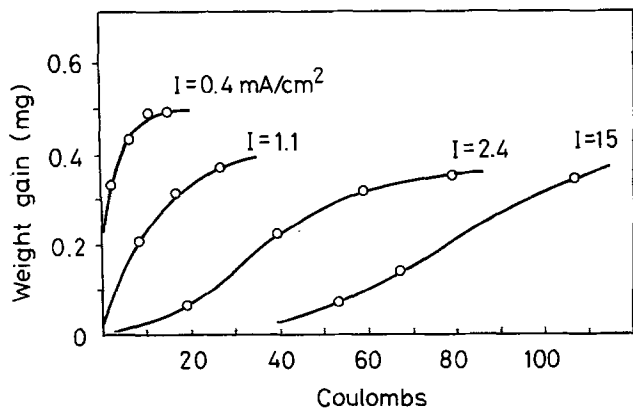


Fig. 1. The relation between the weight gain of the nickel cathode and coulombs passed for a solution containing 60 cm³ acetic acid, 4 cm³ Si(OEt)₄, 2 cm³ acetone, and 2g (CH₃)₄NCl at room temperature.

SiK α and NiK α , I_{Si}/I_{Ni} , of the nickel coated with silicon of about 0.5 μ m thickness was 3.5. As shown in Fig. 3(A), IR reflection spectra of the deposits exhibit no absorption in the wave number range of 4000-600 cm⁻¹. X-ray diffraction patterns showed only those due to the nickel substrate. A RHEED investigation using Hitachi HU-12 A showed no reflection ring or spot from crystallization. It can be concluded from these results that the deposits consist of amorphous silicon.

As shown in Table I, the weight gain (current efficiency) on the cathode depends strongly on the concentration of TMAC in the solution. Attempts were made to plate silicon from a solution with a different supporting electrolyte, tetrabutylammonium chloride and tetrabutylammonium perchlorate. The results were similar to those obtained with TMAC. The conductivity of the solution of TEOS in acetic acid is markedly increased by the addition of pyridine. Pyridine reacts with acetic acid to produce a quaternary amine, which is effective as the supporting electrolyte. From the solution of TEOS, acetic acid, pyridine, and acetone, a whitish-gray deposit was obtained on the nickel cathode. A typical relation between the weight gain of the nickel cathode and coulombs passed at room tempera-

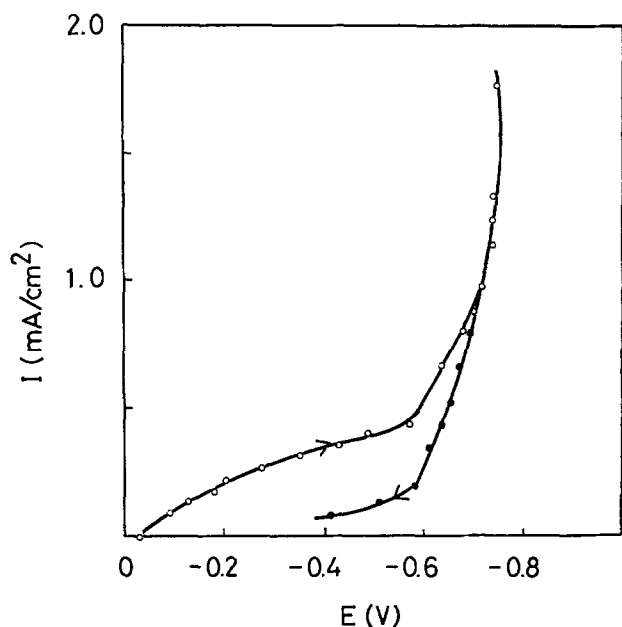


Fig. 2. Current density, I , vs. potential, E , (vs. Ag/AgCl, CH₃COOH, TMAC (0.12 mole/liter) curve for the solution containing 60 cm³ acetic acid, 4 cm³ Si(OEt)₄, 2 cm³ acetone, and 2g (CH₃)₄NCl at room temperature.

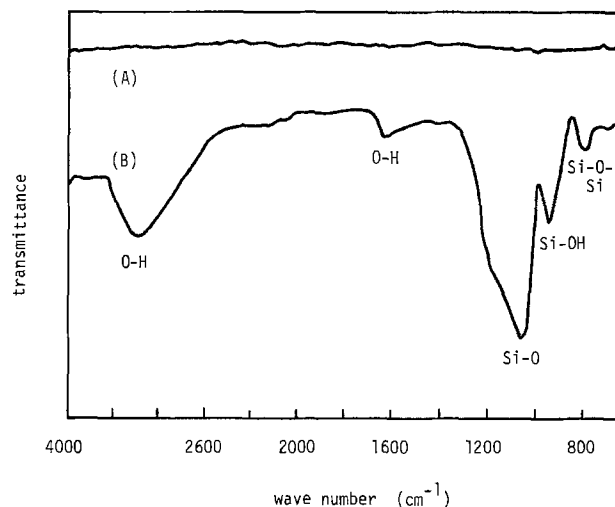


Fig. 3. IR reflection spectra. (A) Blue deposit obtained from the solution containing 4 cm³ Si(OEt)₄, 60 cm³ acetic acid, 2g TMAC, and 2 cm³ acetone at a current density of 1 mA/cm². The thickness of the film is about 0.5 μ m. (B) White deposit obtained from the solution containing 30 cm³ acetic acid, 2 cm³ Si(OEt)₄, 10 cm³ acetone, and 0.05 cm³ pyridine at a current density of 4 mA/cm². The thickness of the film is about 0.7 μ m.

ture is shown in Fig. 4. The composition of the solution was 30 cm³ acetic acid, 10 cm³ acetone, 0.05 cm³ pyridine, and 2 cm³ TEOS, and the current density was about 4 mA/cm². In this case, the weight gain of the cathode increases approximately linearly with the number of coulombs passed. The current efficiency decreased with increasing current density; efficiencies of about 20 and 5% were obtained at 0.8 and 10 mA/cm², respectively.

Nondispersive x-ray analysis showed the deposits to contain silicon. The ratio, I_{Si}/I_{Ni} , of the sample 0.5 μ m in thickness was 0.8. IR reflection spectra of the deposits were similar to those of silica gel and of the white precipitate in the solution as shown in Fig. 3(B). A deposit of silica gel should lose its weight upon annealing in inert gas at 400°C. However, no weight change was observed after heating the sample at 400°C for 2 hr in flowing argon. These results suggest that the deposits from the solution with pyridine contain only a small amount of silica gel-like materials.

A white deposit was obtained on the nickel cathode from the solutions of TEOS in 1-chloropropane with TMAC as the supporting electrolyte. In a dry atmo-

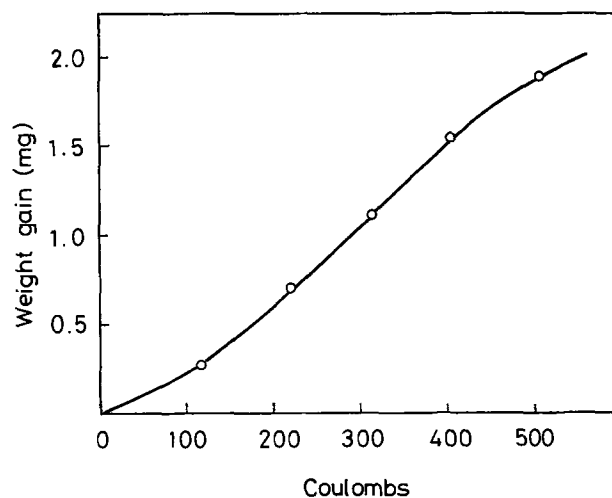


Fig. 4. The relation between the weight gain of the nickel cathode and coulombs passed for a solution containing 30 cm³ acetic acid, 2 cm³ Si(OEt)₄, 10 cm³ acetone, and 0.05 cm³ pyridine at room temperature.

sphere, no deposit was observed; in a wet atmosphere, a white precipitate was formed in the solution and a white deposit was obtained, with a maximum weight gain of about 0.5 mg. Nondispersive x-ray analysis showed that the deposit contained silicon, and I_{Si}/I_{Ni} of the sample 0.5 μm in thickness was 0.56. The IR reflection spectra exhibited peaks of Si-O modes; evidently, the white deposits contained silicon-oxygen compounds. Similar white deposits were obtained from a solution of TEOS in propylene carbonate.

In all cases of electrodeposition from solutions containing TEOS as a silicon source, the deposits were observed after the white precipitate of a silica gel-like material appeared in the solution. Yet the deposit on the cathode is only partly SiO_2 . It is possible that hydrogen evolved on the cathode breaks Si-O bonds in the silica gel-like material and some ions containing silicon are reduced electrochemically on the nickel cathode. No deposit was obtained on copper, gold, and platinum used as cathodes. Clarification of the electrodeposition mechanism requires further study.

Summary

White, whitish-gray and blue deposits were obtained on the nickel cathode by the electrolysis of the solution of TEOS in organic solvents. Nondispersive x-ray analysis showed the deposits to contain silicon. However, it is doubtful whether the white and whitish-gray deposits are amorphous silicon or a silicon-oxygen compound, because IR spectra of these deposits were similar to those of silica gel, and the intensity ratios of $\text{SiK}\alpha$ to $\text{NiK}\alpha$ of these deposits were considerably lower than the ratio for the blue deposit. On the other hand, the blue deposits, which were obtained from the solution of TEOS in acetic acid, did not show the absorption due to Si-O and O-H modes, and had a high intensity ratio of $\text{SiK}\alpha$ to $\text{NiK}\alpha$. The electrodeposi-

tion of thin films of amorphous silicon from the solution of TEOS in acetic acid seems promising, but problems such as the control of hydrogen content and the doping with donors or acceptors remain to be investigated before it can be put in practical use.

Acknowledgments

The authors wish to thank Dr. T. Kaneda for the RHEED measurement. This work was partially supported by U.S. Department of Energy under Contract No. EY-76-S-03-0113.

Manuscript submitted Aug. 28, 1980; revised manuscript received Jan. 19, 1981.

Any discussion of this paper will appear in a Discussion Section to be published in the December 1981 JOURNAL. All discussions for the December 1981 Discussion Section should be submitted by Aug. 1, 1981.

Publication costs of this article were assisted by Mie University.

REFERENCES

1. A. E. Owen and W. E. Spear, *Phys. Chem. Glass*, **17**, 174 (1976).
2. C. R. Wronski and D. E. Carlson, 7th Internat. Conf. on Amorphous and Liquid Semiconductor, Edinburgh, Scotland, June 1977.
3. D. E. Carlson and C. R. Wronski, *J. Electron. Mater.*, **6**, 95 (1977).
4. D. E. Carlson, Abstract 295, p. 791, The Electrochemical Society Extended Abstracts, Atlanta, Georgia, Oct. 9-14, 1977.
5. D. E. Carlson and C. R. Wronski, *Appl. Phys. Lett.*, **28**, 671 (1976).
6. G. Szekely, *This Journal*, **98**, 318 (1951).
7. H. N. Warren, *Chem. News*, **67**, 303 (1893).
8. Y. A. Zyazev and A. I. Ezrielev, *Sib. Trudy Agronomi Fiz.*, **13**, 32 (1966).
9. A. E. Austin, U.S. Pat. 3,990,953 (1976).

Photoactivation of CdSe Films for Photoelectrochemical Cells

Chin-hsin J. Liu, Judith Olsen, David R. Saunders, and Jui H. Wang*

Department of Chemistry, State University of New York, Buffalo, New York 14214

ABSTRACT

The efficiency of photoelectrochemical cells with thin-film CdSe electrodes can be enhanced by illuminating the semiconductor electrode in salt solution under closed-circuit condition. The photoactivation mechanism involves the photooxidation of CdSe to elemental selenium with concomitant release of cadmium ions into the salt solution and subsequent reductive dissolution of the resulting layer of elemental selenium. This method can be controlled more precisely than acid etching and hence is more suitable for large scale application.

The conversion of solar to electrical energy with moderate efficiency has been demonstrated by means of photoelectrochemical (PEC) cells with CdSe photoanodes (1-4). The performance of these semiconductor electrodes can often be greatly improved by limited acid etching. Heller *et al.* (2) showed an inverse correlation between the presence of surface states within the forbidden gap of the semiconductor and the efficiency of PEC cells. They suggested that acid etching of single crystals of CdSe removes the surface states which act as barrier traps and recombination centers.

A more easily controlled activation method particularly suitable for thin-film II-VI semiconductor electrodes is a photoactivation process developed in our work on PEC cells (5). In this process, the thin-film CdSe electrode was immersed together with a platinum counterelectrode in a salt solution (e.g., NaCl) and illuminated under closed-circuit condition. When the photoactivated CdSe thin-film electrode was subsequently used as the photoanode in a photoelectrochemical cell with polysulfide solution, both the photocurrent and the fill factor were enhanced. Recently Hodes (6) reported a "photoetching" effect of 0.1M H_2SO_4 on $\text{CdSe}_{0.65}\text{Te}_{0.35}$ electrodes which could be of

* Electrochemical Society Active Member.

Key words: semiconductor, photovoltaic, cell.

similar nature. The present paper presents some results of our recent studies on the molecular mechanism of this photoactivation process.

Experimental

CdSe film was prepared by spray pyrolysis on titanium substrate (0.25 mm thick, Alfa Division, Ventron Corporation). The substrate was put on a hot-plate maintained at 235°C and a mixture of aqueous solutions of CdCl₂ (0.01M) and N,N-dimethylselenourea (0.01M), respectively, was sprayed onto the heated substrate through a chromatographic spray nozzle with a flow rate of 1-2 ml of the liquid mixture per minute at a constant excess air pressure of 5 psi. The spray apparatus was enclosed in a chamber and the spray nozzle was kept in reciprocating motion during the spraying to assure film uniformity. The CdSe film thus formed was subsequently annealed in the air at 400°-450°C for 20 min, and epoxy resin was applied to insulate the exposed titanium surface.

Photoactivation was conducted by immersing the CdSe electrode together with a platinized platinum counterelectrode in a neutral or weakly acidic salt solution and illuminating the CdSe electrode under closed-circuit condition for a few minutes with a projector light. The CdSe electrode was subsequently rinsed with deionized water and dried in a stream of nitrogen. In a few cases, the CdSe electrode and Pt counterelectrode were immersed in separate cell compartments connected by a salt bridge so that the pH of each cell compartment could be varied independently. The current passed through the system during photoactivation was measured with a Bausch and Lomb VOM-7 chart recorder.

The current-voltage characteristics of the resulting CdSe/polysulfide solution/Pt PEC cells were measured in the standard way. The composition of the polysulfide solution was 1M NaOH + 1M Na₂S + 1M S. A 12 cm² piece of platinized platinum was used as the counterelectrode in all the I-V measurements. The cell was made of Pyrex glass with a flat window. Light was admitted through this window and passed through a 1-2 mm layer of the polysulfide solution to reach the CdSe surface. A projector (Kodak Carousel 750 H) was used as the light source, and the intensity of light was measured with a YSI-Kettering Model 65A radiometer. The electrical measurements were made by means of an operational amplifier I-V plotter.

The photoactivated CdSe electrodes were analyzed by constant current cathodic reduction with a Pt wire as the anode and a saturated calomel electrode as the reference electrode. The current density was set at about 2 mA · cm⁻², and the progress of cathodic reduction was monitored by recording the potential of the CdSe electrode as a function of time.

The concentration of Cd²⁺ ions released into the solution during photoactivation was determined by atomic absorption by means of a Perkin-Elmer 303 Atomic Absorption Spectrometer with an HGA-2100 graphite furnace.

Results and Discussion

The effect of photoactivation of CdSe electrode on the current-voltage characteristics of the resulting PEC cell is shown in Fig. 1. While the photoactivation process did not affect the open-circuit voltage (V_{oc}), it increased the short-circuit current density (J_{sc}) from 8.88 to 16.50 mA/cm² and the fill factor (FF) from 0.27 to 0.40, resulting in a substantial improvement in energy conversion efficiency. The CdSe surface turned from dark gray to blue as a result of photoactivation. But the blue color disappeared after the electrode was immersed in polysulfide solution, and the surface became darker and less reflective. Hodes (6) pointed out that the increase in J_{sc} he observed could not be fully accounted for by the lowering of reflectivity.

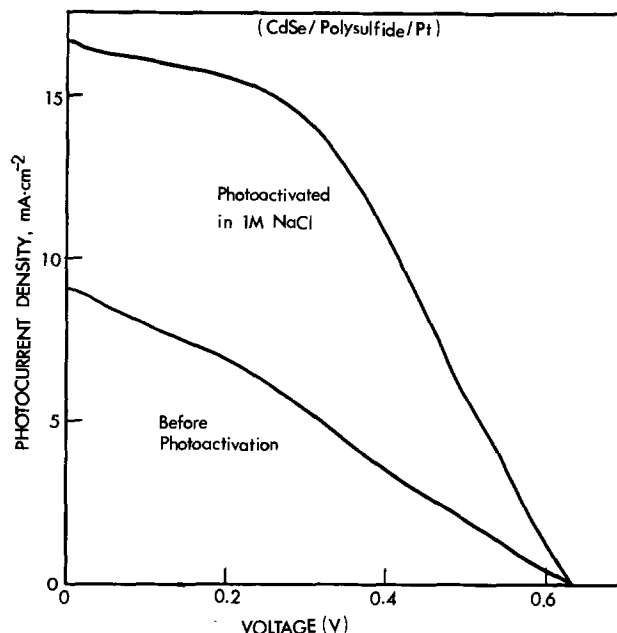


Fig. 1. Effect of photoactivation of the thin-film CdSe photoanode on the current-voltage characteristics of a CdSe/1M NaOH, 1M NaOH, 1M Na₂S, 1M S/Pt photoelectrochemical cell. The CdSe electrode was photoactivated in a 1M NaCl solution at pH 2.85. The light intensity for I-V measurements was 71 mW/cm².

Table I shows that photoactivation process is effective only when the CdSe electrode is illuminated under closed-circuit condition. These observations suggest that the CdSe electrode could be oxidized anodically during the photoactivation process. This possibility is also supported by the data in Fig. 2 which show that the observed enhancement in J_{sc} of the resulting PEC cell increases with the total amount of electricity passed through the CdSe electrode during photoactivation until saturation values are reached when the pH of the electrolyte solution was between 1.6 and 11.6. However at pH = 12.1, the CdSe electrode deteriorated as a result of the same treatment.

Figure 3 shows that the photoactivation process does not require specific anions in the electrolyte solution, and hence the observed increase in J_{sc} cannot be due to the adsorption or incorporation of those anions in the semiconductor. Figure 4 shows the dependence of photoactivation on electrolyte concentration. The observed higher J_{sc} values for CdSe electrodes photoactivated in more concentrated NaCl solutions are apparently due to ionic strength effect rather than due to the direct involvement of chloride ions.

In order to study the molecular mechanism of this photoactivation process, we measured the current during photoactivation under different experimental conditions instead of the characteristics of the finished PEC cells. Consistent with the data in finished PEC cells, Fig. 5 shows that between pH 1 and 10, the

Table I. Effect of various treatments of CdSe electrodes in 1M NaCl solution on their performance as photoanode

| Treatment* | J_{sc} (mA/cm ²) † | |
|--|----------------------------------|-----------------|
| | Before treatment | After treatment |
| In the dark | 7.2 | 7.2 |
| Illuminated under open-circuit condition | 8.2 | 8.5 |
| Illuminated under closed-circuit condition | 7.7 | 18.7 |

* The CdSe electrode was immersed in 1M NaCl solution at pH 6 under the various indicated conditions for 45 sec at about 20°C.
† Measured in the PEC cell CdSe/1M NaOH, 1M Na₂S, 1M S/Pt under a projector light of intensity 71 mW/cm².

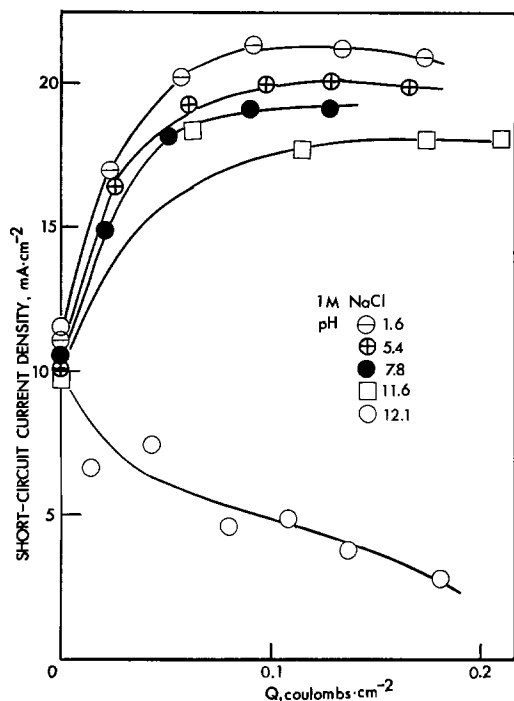


Fig. 2. Effect of pH and extent of electrode reaction during photoactivation on the short-circuit current of the resulting PEC cell CdSe/1M NaOH, 1M Na₂S, 1M S/Pt. Photoactivation was conducted in 1M NaCl solution. The J_{sc} measurements were made under white light intensity of 71 mW/cm².

photoactivation current increases with time to a steady-state value. But at pH 12, drops rapidly from an initial value to a much lower steady-state value.

In Fig. 6a, the observed steady-state activation current is plotted against the pH of the NaCl solution. Comparison with Fig. 2 shows that the photoactivation current and the J_{sc} of the finished PEC cell depend in the same way on the pH of the NaCl solution during the photoactivation process. In order to decide whether this observed pH dependence is due to that of the anodic reaction or cathodic reaction, the same photoactivation process was repeated with the CdSe photoanode and Pt cathode immersed in separate cell compartments connected by an agar salt bridge. Figure 6b

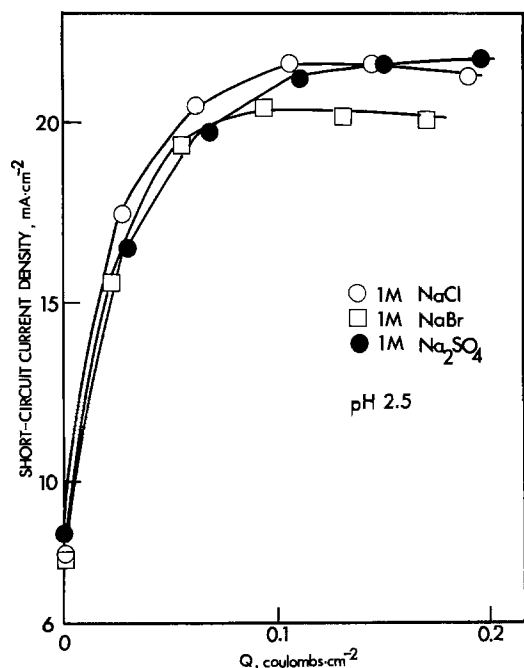


Fig. 3. Photoactivation in different electrolyte solutions

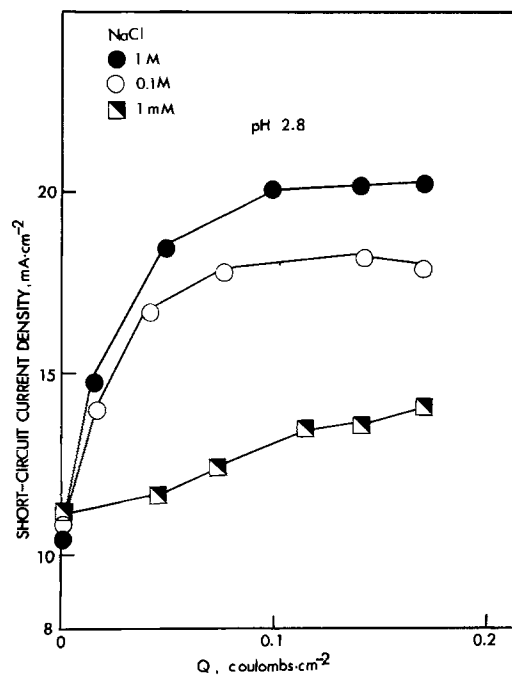


Fig. 4. Effect of NaCl concentration on photoactivation

shows the dependence of photoactivation current on the pH of anolyte (1M NaCl in the CdSe electrode compartment) when the catholyte (1M NaCl in the Pt-electrode compartment) was maintained at pH 2 with HCl. Figure 6c shows the dependence of the photoactivation current on the pH of the catholyte when the anolyte (1M NaCl) was maintained at pH 2. The similarity of pH dependence shown in Fig. 6a and 6b indicates that the rate-limiting step in the photoactivation process is the photooxidation at the CdSe electrode.

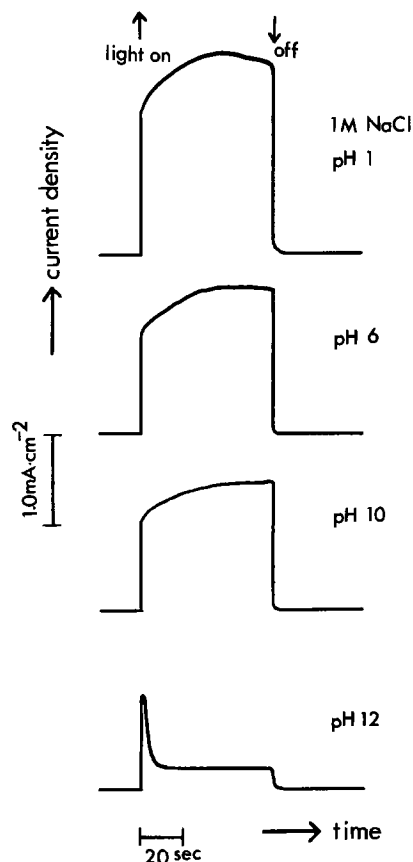


Fig. 5. Photoactivation current in a single-compartment cell containing 1M NaCl solution at different pH values.

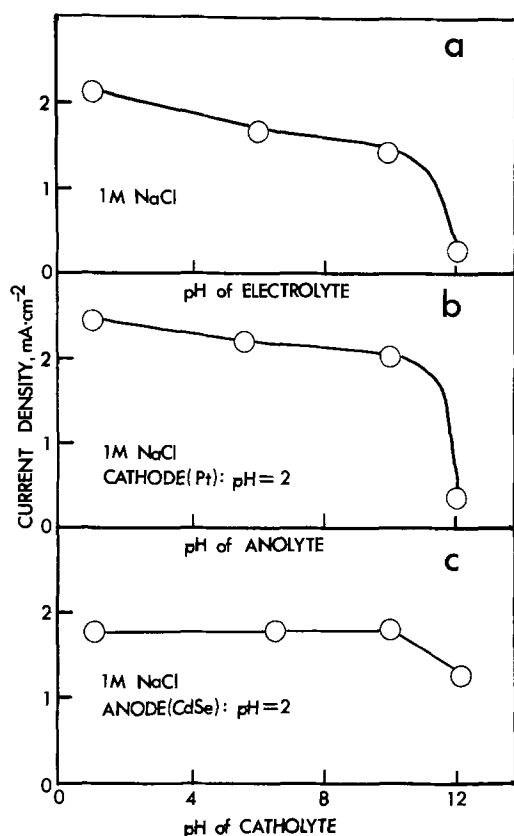
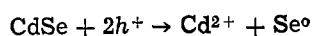


Fig. 6. (a) Photoactivation current as a function of pH in a one-compartment cell. (b) Photoactivation current as a function of pH of the anolyte in a two-compartment cell. (c) Photoactivation current as a function of pH of the catholyte in a two-compartment cell. The principal electrolyte in all three cases was 1M NaCl. These are all three separate series of experiments the slight differences in absolute photoactivation current densities between Fig. 6b and 6c are due to different illumination conditions employed.

But what is oxidized at the photoanode—the electrolyte in solution or the semiconductor film? Figure 7a shows that after the CdSe electrode has been photoactivated in 1M NaCl solution at pH 6 and subsequently reduced electrolytically at constant current density of 1.9 mA/cm² in the dark, the following constant current reduction curves are obtained: (i) The first $V-t$ curve at constant current, which showed electrode reaction(s) occurring at fairly low applied voltage, is the same whether the reduction is conducted in the solution used for photoactivation or a fresh solution of the same composition. (ii) Immediately after the first reduction, a second $V-t$ scan at the same current density shows no reduction wave. These observations show that the product of photoactivation is a reducible substance on the semiconductor electrode, not in the electrolyte solution. The photoactivation reaction is probably



where h^+ represents a photogenerated hole in the semiconductor. The release of Cd^{2+} ions into solution by this reaction is confirmed by the data in Table II which show that two electrons are extracted from the CdSe electrode for every Cd^{2+} ion released into solution by the photoactivation process.

The two plateau regions of the first electrolytic reduction curve in Fig. 7a at -0.98 and -1.16 V, respectively, appear to have the same length on the time scale, an observation which suggests that the blue selenium layer may be formed by two one-electron oxidation steps during the photoactivation process.

When the photoactivated CdSe electrode was immersed in polysulfide solution, the blue color due to the

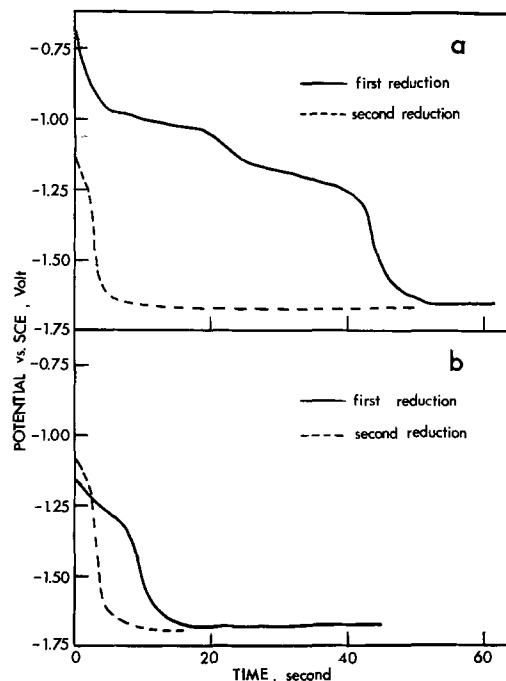


Fig. 7. Constant current cathodic reduction curves in the dark. (a) CdSe electrode was photoactivated in 1M NaCl solution at pH 6 and subsequently reduced electrolytically in the dark at constant current density. Solid curve, first reduction; broken curve, second reduction. (b) An identical photoactivated CdSe electrode was immersed in 1M NaOH + 1M Na₂S + 1M S solution for a few minutes and subsequently reduced electrolytically in the dark in 1M NaCl solution at pH 6. Solid curve, first reduction; broken curve, second reduction.

thin layer of selenium disappeared. Figure 7b shows that subsequent electrolytic reduction of this treated CdSe electrode at constant current density in NaCl solution in the dark did not show a similar reduction wave.

These observations show that the photoactivation process takes place in two steps. In the first step, the photogenerated holes in the semiconductor oxidize CdSe to elementary Se with the concomitant release of Cd^{2+} ions into solution. The observed sharp drop in current density at the early stage of the photoactivation process as shown in Fig. 5 and Fig. 8a at high pH is probably due to the formation of an insoluble thin coating of cadmium hydroxide which retards further oxidation of Se^{2-} to Se^0 with concomitant release of Cd^{2+} into solution. As expected, Fig. 8b shows that the addition of ammonia facilitates the release of Cd^{2+} at the same pH and consequently restores normal current density during photoactivation.

In the second step, immersion of the photoactivated electrode in $\text{Na}_2\text{S} + \text{Na}_2\text{S}_2 + \text{NaOH}$ solution removes the selenium layer from the surface of the electrode

Table II. Correlation between quantities of electricity passed and the amounts of Cd^{2+} ions released into solution during photoactivation

| Faradays passed* | Moles of Cd^{2+} released into solution† | $(e^-)/(\text{Cd}^{2+})$ ratio |
|-----------------------|---|--------------------------------|
| 0 (dark control) | 0.07×10^{-7} | — |
| 2.03×10^{-7} | 1.05×10^{-7} | 2.07 |
| 3.93×10^{-7} | 1.91×10^{-7} | 2.14 |

* Photoactivation was conducted in 0.2M NaCl solution at pH 8.5.

† Samples were assayed by atomic absorption. The amount of Cd^{2+} released in the dark control was independent of immersion time and this value was subtracted from the total assayed amount of Cd^{2+} in the photoactivation samples.

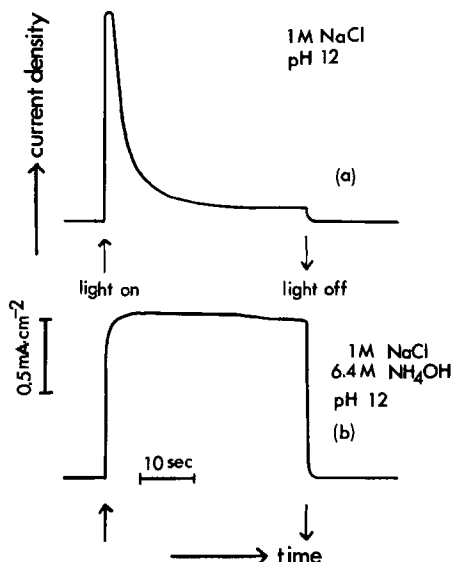


Fig. 8. Photoactivation current observed in (a) 1M NaCl solution at pH 12, (b) 1M NaCl + 6.4M NH_4OH solution at pH 12.

and exposes a new surface of the semiconductor with higher electrochemical activity.

Since the above described photoactivation process can be precisely controlled, it can be safely applied to enhance the efficiency of sprayed thin-film CdSe photoanodes on a large scale. A detailed study of the photoactivation mechanism may help to improve further

the photoelectrochemical properties of semiconductor thin-film electrodes and increase the efficiency of the resulting PEC cells.

Acknowledgment

We thank Professor Robert A. Osteryoung for helpful discussion. This work was supported in part by a research grant from the National Science Foundation (PCM 7755002).

Manuscript submitted Oct. 8, 1980; revised manuscript received Dec. 22, 1980.

Any discussion of this paper will appear in a Discussion Section to be published in the December 1981 JOURNAL. All discussions for the December 1981 Discussion Section should be submitted by Aug. 1, 1981.

REFERENCES

1. A. B. Ellis, S. W. Kaiser, and M. S. Wrighton, *J. Am. Chem. Soc.*, **98**, 6855 (1976).
2. A. Heller, K. C. Chang, and B. Miller, *This Journal*, **124**, 697 (1977).
3. M. A. Russack, J. Reichmann, H. Witzke, S. K. Deb, and S. N. Chen, *ibid.*, **127**, 725 (1980).
4. C. J. Liu and J. H. Wang, *Appl. Phys. Lett.*, **36**, 852 (1980).
5. C. J. Liu, D. R. Saunders, J. Olsen, and J. H. Wang, in "Third International Conference on Photochemical Conversion and Storage of Solar Energy, Boulder, Colorado, Aug. 3-8, 1980, Abstracts, p. 385.
6. G. Hodes, *Nature*, **285**, 29 (1980).

On the Mechanism of Sodium Chlorate Formation

B. V. Tilak,* K. Viswanathan,* and C. G. Rader

Hooker Research Center, Grand Island, New York 14072

ABSTRACT

Sodium chlorate is formed from the chemical combination of HOCl and OCl^- ions. It is reported to be a third-order reaction involving 2 moles of HOCl and 1 mole of OCl^- . Contrasting literature data depict this reaction as bimolecular, involving 2 moles of HOCl only. Experimental results presented here clearly resolve the ClO_3^- formation reaction to be apparent third order. Dichromate, added in concentrations of 2-5 g/l during brine electrolysis to achieve high current efficiency, fulfills two key functions: (i) enhancement of buffer action in the pH region of 5-7; and (ii) prevention of adverse OCl^- and ClO_3^- electrochemical reduction reactions. Experimental evidence is presented elucidating the above observations.

In an electrolytic chlorate cell, the key chemical constituents are hypochlorous acid and hypochlorite ions. These species react chemically to form chlorate. However, the reactants and products involved in this reaction, namely HOCl, OCl^- , and ClO_3^- , are thermodynamically favored to react at the electrodes, resulting in inefficient operation of the cells. Nevertheless, industrial cells operate at high efficiencies (e.g., >93%) by adept choice of operating variables and additives, e.g., $\text{Na}_2\text{Cr}_2\text{O}_7$ (commonly called "chrome" in the industry).

The purpose of this communication is to elucidate the interaction of hypochlorous acid and hypochlorite ion, and to define the purpose of addition of "chrome" during electrolysis.

* Electrochemical Society Active Member.

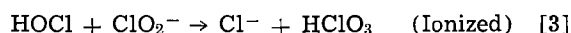
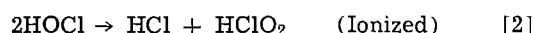
Key words: chlorate, limiting currents, rotating disk electrodes.

A Brief Literature Survey

Two mechanisms are proposed in the literature to describe the formation of chlorate. The reaction sequence proposed by Foerster (1) and confirmed by many others (2-4) is a third-order reaction involving 2 moles of HOCl and 1 mole of OCl^- as



However, according to Lister (5), who examined the decomposition kinetics of hypochlorite in alkaline solutions, chlorate formation follows a bimolecular sequence



Eq. [2] being the slower of the above reactions.

Sodium dichromate is a conventional and multifunctional additive used routinely in the commercial production of sodium chlorate. Several roles are attributed to chrome which include: (i) suppressing the corrosion of the Fe cathode (6-9), (ii) buffering (2, 10) the electrolyte in the pH range of 5-7 where the chlorate formation rate is optimum, (iii) preventing the cathodic reduction of OCl^- and ClO_3^- ions by the " Cr_2O_3 " film formed by chromate reduction (11, 12), and (iv) inhibiting the O_2 evolution reaction at the anode (13, 14). It is of interest to note that the fluoride ion (15) is believed to play a similar role as dichromate during chlorate electrolysis with PbO_2 anodes.

Experimental

All the solutions stated here were prepared from Analar grade chemicals and distilled water. The required hypochlorite concentration was achieved by passing chlorine through the solution (maintained alkaline) and bringing the pH to the desired value.

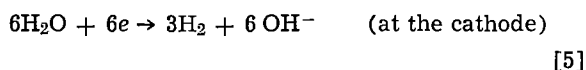
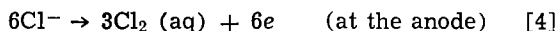
Titrations were performed with an accuracy of ± 0.01 cm^3 —the pH being measured using a Corning pH meter at an accuracy of ± 0.05 units. Hypochlorite and chlorate concentrations were analyzed by standard analytical procedures (16) involving sodium arsenite and iodine. Experiments were conducted by maintaining pH within ± 0.02 units by dropwise addition of 10N NaOH.

Polarization studies were carried out using conventional (17) potentiostatic (Wenking ST72 potentiostat) and galvanostatic techniques. The rotating Pt disk electrode assembly by Pine Instruments Company was also used in this investigation.

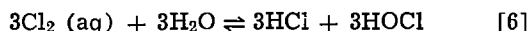
Kinetic studies were performed in a batch reactor at about 25°C in 4M NaCl solutions at various pH values. Care was taken to exclude interaction of light during the course of the reaction. Electrochemical studies were conducted in solutions containing 450 g/l NaClO_3 and 150 g/l NaCl unless otherwise stated.

Results and Discussion

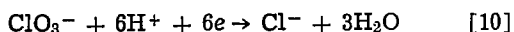
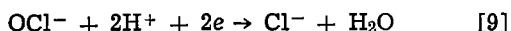
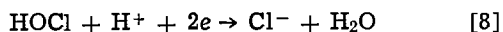
In a typical chlorate cell, the principal electrochemical reactions are as follows



In the bulk the following reactions take place, resulting in the formation of chlorate either by pathways described earlier by Eq. [1] or alternately by Eq. [2]



However, the species involved in chlorate formation and the product formed, i.e., ClO_3^- , may get reduced at the cathode as described by reactions [8]-[10]



Current efficiency losses result from any or all of the above reduction reactions. In this section, experimental results relating to the mechanism of chlorate formation and to the role of dichromate in suppressing the rates of reactions [8]-[10] are stated and discussed.

Mechanism of Chlorate Formation

Two reaction pathways are described in the literature for the chemical formation of chlorate: one proposed by Foerster (reaction [1]) and the other by Lister (reaction [2]). If the kinetics are controlled by reaction [1], then the integrated form of the rate expression may be shown to be

$$\frac{1}{C_o^2(t)} - \frac{1}{C_o^2(O)} = 6k_1t \times (1+x)^{-3} \quad [11]$$

whereas the corresponding expression for reaction [2] would be

$$\frac{1}{C_o(t)} - \frac{1}{C_o(O)} = 3k_2t(1+x)^{-2} \quad [12]$$

In the above equations k_1 and k_2 refer to third order and second order rate constants for reactions [1] and [2], respectively, the units for k_1 being $\text{liter}^2 \cdot \text{mol}^{-2} \text{sec}^{-1}$, and k_2 being $\text{liter} \cdot \text{mol}^{-1} \text{sec}^{-1}$. $C_o(t)$ refers to the total hypo concentration (i.e., concentration of $\text{HOCl} + \text{OCl}^-$) at time, t , expressed in $\text{g} \cdot \text{mol}/\text{liter}$. $C_o(O)$ refers to the initial hypo concentration, x to the ratio of $K/10^{-\text{pH}}$ (i.e., ratio of the concentration of OCl^- to HOCl) and K to the "conditional" equilibrium constant for reaction [7].

Thus, the diagnostic criterion for distinguishing between the reaction pathways 1 and 2 would be the constancy of k_1 and k_2 with pH. Values of k_1 and k_2 can be obtained from the slopes of the linear plots (see Fig. 1 and 2) of $1/C_o^2(t)$ and $1/C_o(t)$ vs. t using a K value of $10^{-7.18}$. This value of K for reaction [7] was determined in 4M NaCl solutions at $\sim 25^\circ\text{C}$. Under these conditions H^+ ions are generated only by reaction [7] and not by the chlorate formation reaction—be it Eq. [1] or Eq. [2]. It must be stressed here that the K values published in the literature (18) for reaction [7], especially those obtained at high temperature ($>40^\circ\text{C}$) and at high OCl^- concentrations, are not precise because of neglect of the H^+ contribution from Eq. [1] or Eq. [2].

Values of reaction rate constants presented in Table I show that while k_1 is constant over a wide range of pH values, k_2 varies significantly with pH. This confirms that the chlorate formation reaction is apparent third order involving 2 moles of HOCl and 1 mole of OCl^- —the third order rate constant being $0.025 \text{ liter}^2 \cdot \text{mol}^{-2} \cdot \text{sec}^{-1}$ at 25°C in 4M NaCl solutions. This conclusion is supported by the results of Taniguchi and Sekine (2) in which an alternate third order reaction mechanism, involving 2 moles of OCl^- and 1 mole of HOCl , was shown to be of negligible importance.

The present results raise questions regarding Lister's mechanism, as opposed to Foerster's mechanism, which was accepted by several investigators. The discrepancy

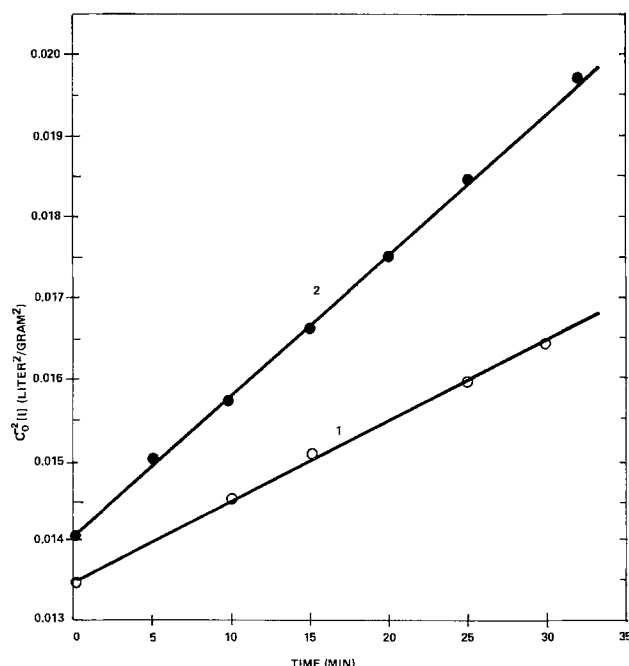


Fig. 1. Plot of $C_o^{-2}(t)$ with time. Curve 1: pH = 6; temp: 24°C ; $k_1 = 0.0275 \text{ liter}^2/\text{g} \cdot \text{mole}^2 \cdot \text{sec}$. Curve 2: pH = 6.5; temp: 23°C ; $k_1 = 0.0230 \text{ liter}^2/\text{g} \cdot \text{mole}^2 \cdot \text{sec}$.

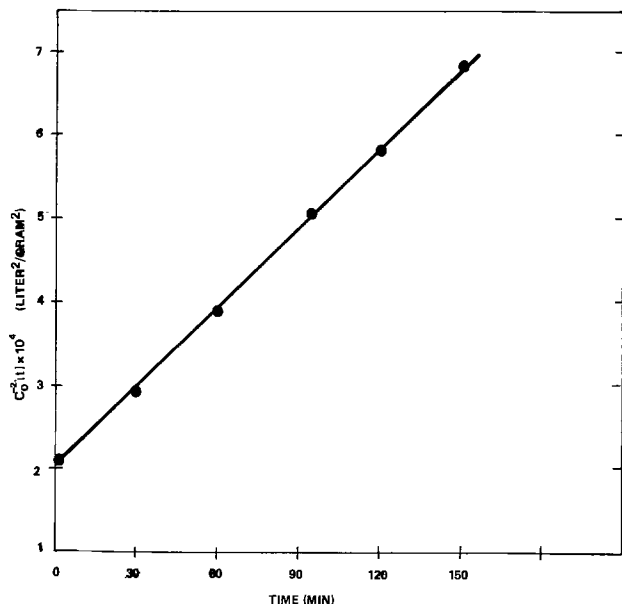
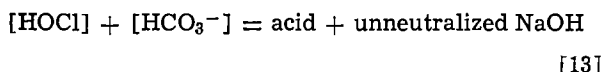
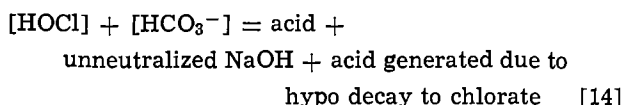


Fig. 2. Plot of $C_0^{-2}(t)$ with time ($\text{pH} = 8.5$); temp: 25°C ; $k_1 = 0.0244 \text{ liter}^2/\text{g}\cdot\text{mole}^2\cdot\text{sec}$.

may be traced to the method of determination of HOCl concentration described by Lister (5), which was subsequently used in the estimation of the rate constant. The concentration of HOCl was determined by solving the material balance equation



This relationship is valid only for short periods when the H^+ generated from chemical chlorate formation is insignificant. However, Lister applied the above method to experiments wherein the chemical chlorate formation was significant and where the appropriate material balance equation is represented as follows



Thus Lister's method of calculating the hypochlorous acid concentration, and hence the mechanism of chlorate formation, seems to be in error. From the present work it is evident that the rate of chlorate formation is proportional to the product of the square of the hypochlorous acid concentration and the hypochlorite concentration, and attains a maximum at a pH equal to $(\text{pK} - \log 2)$. This result has been experimentally verified by Jaksic (19). It may be noted that if Lister's mechanism were to hold, one would not anticipate a maximum rate in the pH range of 5-7. The reader is referred to Ref. (3) for a discussion of other possible mechanisms of chlorate formation of overall third order character.

Role of Dichromate during Chlorate Electrolysis

The functions attributed to dichromate that is added during chlorate electrolysis were noted earlier, and the

Table I. Rate constants for chlorate formation reactions [1] and [2] as a function of pH

| pH | k_1 ($\text{liter}^2\cdot\text{g}\cdot\text{mole}^{-2}\cdot\text{sec}^{-1}$) | k_2 ($\text{liter}^2\cdot\text{g}\cdot\text{mole}^{-1}\cdot\text{sec}^{-1}$) |
|-------------|--|--|
| 6.0 | 2.75×10^{-2} | 1.93×10^{-4} |
| 6.5 | 2.30×10^{-2} | 4.15×10^{-4} |
| 7.0 | 2.76×10^{-2} | 1.06×10^{-3} |
| 7.5 | 2.20×10^{-2} | 1.39×10^{-3} |
| 8.5 | 2.44×10^{-2} | 1.53×10^{-2} |

relative importance of these roles are critically discussed and evaluated in this section.

Inhibition of corrosion of steel cathode.—Cathodes made of steel are generally used in electrolytic chlorate cells—the electrolyte under operating conditions analyzing 450 g/l NaClO_3 , 150 g/l NaCl , 4-7 g/l OCl^- , and 2-6 g/l $\text{Na}_2\text{Cr}_2\text{O}_7$ at 70°C ($\text{pH} \sim 5-6$). If the role of dichromate is indeed one of suppressing the corrosion of steel under open-circuit conditions, then the open-circuit potential (E_{ocp}) should show significant differences in the presence and absence of dichromate. However, experimental measurements in the above solutions show the E_{ocp} to be -0.30 to -0.32V vs. SCE in the presence and absence of dichromate, suggesting that the major role of $\text{Cr}_2\text{O}_7^{--}$ is not one of offering protection to steel from corrosion.

Enhancement of buffer capacity.—It was mentioned earlier that the preferred pH range of operation of a typical chlorate cell is in the range of 5.75-6.75 to achieve optimal conversion of hypochlorite to chlorate. The system has a natural buffer capacity in this range due to HOCl/OCl^- equilibrium represented by Eq. [7]. Taniguchi and Sekine (2) mentioned that chrome addition enhances the buffer capacity in this critical pH range due to the equilibrium reaction



Figure 3 shows the pH titration data obtained in the presence of dichromate in solutions containing 150 g/l NaCl and 450 g/l NaClO_3 at 70°C in the absence of hypo. It is obvious from these results that dichromate indeed buffers in the pH range of 5.75-6.75. During chlorate electrolysis, OCl^- and $\text{Cr}_2\text{O}_7^{--}$ are present in the electrolyte. Hence pH titrations were carried out in mixtures containing varying amounts of hypochlorite and dichromate. The results indicate that the buffer capacity is directly proportional to the concentration of OCl^- and $\text{Cr}_2\text{O}_7^{--}$ and that the buffer capacity of solutions containing OCl^- and $\text{Cr}_2\text{O}_7^{--}$ is a sum of the individual contributions from OCl^- and $\text{Cr}_2\text{O}_7^{--}$. Thus, it is definitively established that dichromate enhances the buffer capacity in the pH region of 5-7. However, the exact buffer requirements of a chlorate system are yet to be quantified especially for cases where chlorate formation is attempted by reacting Cl_2 and NaOH in the pH range of 5-7.

Suppression of parasitic cathodic reactions.—In an electrolytic chlorate cell, there are two parasitic cathodic reactions (Eq. [9] and [10]) arising from the cathodic reduction of negatively charged ions— OCl^- and ClO_3^- . If these negatively charged ions are to be reduced cathodically, they have to approach the cathode by diffusion and convection against an adverse

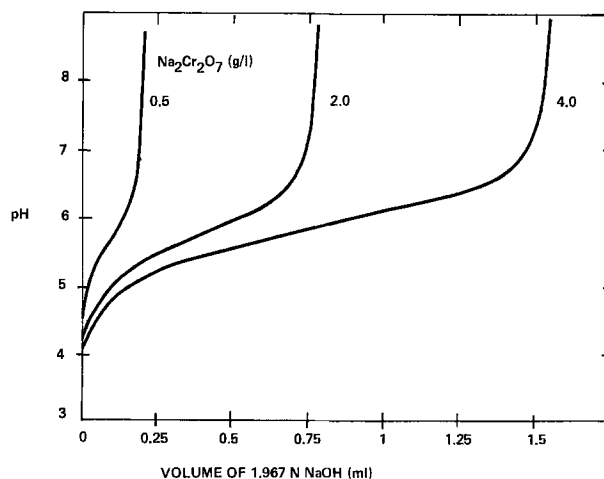


Fig. 3. pH titration curves in solutions containing 450 g/l NaClO_3 and 150 g/l NaCl (volume: 100 ml; temp: 70°C).

potential gradient. If the solution contains a large excess of supporting electrolyte, the adverse potential gradient is small and the transport of anions is affected only slightly. However, if an inert porous diaphragm is formed on the cathode that greatly counteracts the effect of convection, the approximate material balance equation for the species may be written as (20)

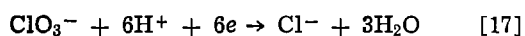
$$N_i = -Z_i U_i F C_i \nabla \phi - D_i \nabla C_i \quad [16]$$

where N_i refers to the flux of species i , Z_i to the valence of the species, U_i to mobility, C_i to concentration, $\nabla \phi$ to the potential gradient, and D_i to the diffusivity of species i .

The first term on the right-hand side of Eq. [16] accounts for transport by migration (away from the cathode surface for anions) and the second term to the contribution from diffusion. If the potential gradient term is increased by increasing the local current density, then the transport of anions to a cathode can be completely suppressed. This may be achieved by forming an inert film with low porosity on the cathode. These facts were clearly expounded in an excellent paper by Wagner (12).

Dichromate is known to be cathodically reduced to form a "Cr₂O₃" film on the cathode surface, which creates an adverse potential gradient that prevents the reduction of OCl⁻ and ClO₃⁻ ions. Polarization studies were performed in the presence and absence of dichromate to examine the influence on the electrochemical behavior of a steel cathode and the results are presented in Fig. 4. In the absence of dichromate, H₂ evolution was not observed even at a current density at 200 mA/cm² in solutions containing 450 g/l NaClO₃, 150 g/l NaCl, and ~2 g/l NaOCl. In addition, the surface was covered by a tenacious brown film (Fe₂O₃??). This is suggestive of chlorate reduction as such high currents cannot be sustained by either O₂ or OCl⁻ reduction. In the absence of hypochlorite and dichromate, the cathode assumed high potential values and H₂ evolution was moderate on a "patchy" brown film on the cathode surface. However in the presence of dichromate, the film disengaged followed by vigorous H₂ evolution.

To contest Wagner's hypothesis, further studies were carried out using 100 g/l NaClO₃ solution as electrolyte and steel cathodes coated with Kalgard¹ and Cr₂O₃ films. If ClO₃⁻ is indeed reduced according to Eq. [17]



then the product of the reaction would be Cl⁻ ions. The chlorate and chloride concentrations were determined using standard volumetric procedures and the results are presented in Table II. It is clear from this data that the inert film on the steel cathode almost completely suppressed the chlorate reduction reaction.

The results presented above have important implications for the chlorate industry as they would provide a potential means of eliminating "chrome" from the

¹Kalgard is a Teflon-based polymer composite obtained from Heany Industry.

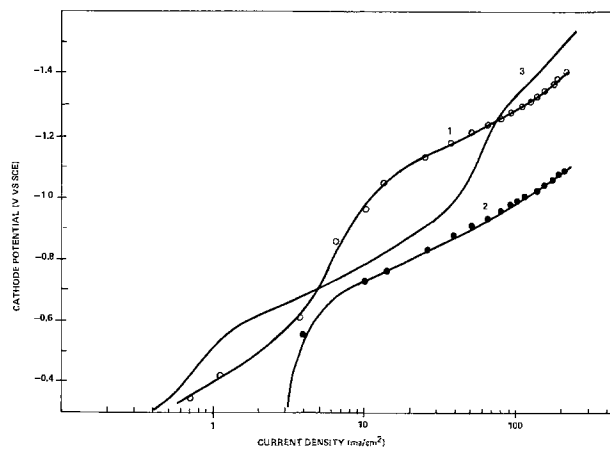


Fig. 4. Cathodic polarization behavior of A-36 steel in solutions containing 450 g/l NaClO₃ and 150 g/l NaCl at 70°C (pH ~4-5). Curve 1: In the absence of NaOCl and Na₂Cr₂O₇; curve 2: in the presence of 1.8 g/l NaOCl; curve 3: in the presence of 1.8 g/l NaOCl and 2 g/l Na₂Cr₂O₇.

product liquor stream which is primarily used as a raw material for ClO₂ generation.

HCC patent application (21) describes the "permanent film" concept described above. Studies on the optimization of the thickness and porosity of the film required for minimizing ohmic drops across the film are in progress.

According to Wagner (12), cathodic reduction of anions is suppressed by the adverse potential gradient generated by the surface film, whereas the cathodic reduction of cations is unhindered under the same conditions. These predictions were verified by limiting current measurements using the ferro-ferricyanide system (0.1N of each) in 1M KCl using a platinum rotating disk electrode. Results in Fig. 5 show that addition of as little as 0.1 g/l of Na₂Cr₂O₇ lowers the limiting current values to an insignificant level. This result further strengthens the "film concept" which effectively serves to repel the anion away from the cathode. Figure 6 shows similar experiments conducted in 1M KCl containing 0.1N FeCl₂ and 0.1N FeCl₃. It is seen that chromate has little effect on the limiting current for Fe³⁺ reduction which is in accordance with Wagner's theory (12).

These results conclusively demonstrate that the primary role of dichromate is in the suppression of the cathodic reduction of OCl⁻ and ClO₃⁻. Further studies are required to characterize the compositional and structural features of the dynamically formed "Cr₂O₃" film.

Inhibition of oxygen evolution.—One of the parasitic anodic reactions during chlorate electrolysis is oxygen evolution from either the discharge of H₂O molecules (Eq. [18]) or oxidation of OCl⁻ to ClO₃⁻ (Eq. [19])

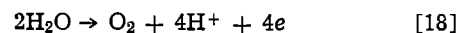


Table II. Reduction of ClO₃⁻ on "permanent film" cathodes

| Cathode | NaClO ₃ (g/l)* | | NaCl (g/l) | | Remarks |
|---|---------------------------|-------|------------|-------|--|
| | Initial | Final | Initial | Final | |
| Steel cathode | 98.5 | 80.5 | 0 | 11.47 | 80% current efficiency assuming reaction [11]** |
| Steel (electrolyte contained 2.5 g/l Na ₂ Cr ₂ O ₇) | 106.3 | 104.1 | 0 | <0.5 | |
| Steel coated with Kalgard (10 mils) | 101.4 | 100.3 | 0 | <0.5 | 0% current efficiency for chlorate reduction reaction (Eq. [10]); based on Na ₂ Cl analysis |
| Steel coated with Cr ₂ O ₃ (10 mils) | 102.0 | 100.6 | 0 | <0.5 | |

Conditions: temp: 70°C; pH ~ 6.5 (adjusted with HClO₄); duration of experiment: 4 hr; current density: 1.67 ASI; anode: Pt/Ir anode; volume: 1.5 liters.

* Accuracy: ±0.5 g/l.

** Reaction [11]: ClO₃⁻ + 6H⁺ + 6e → Cl⁻ + 3H₂O [10]

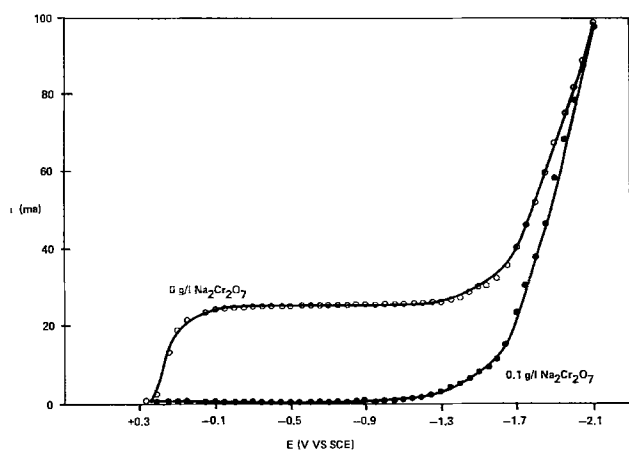


Fig. 5. Influence of $\text{Na}_2\text{Cr}_2\text{O}_7$ on the polarization data on platinum rotating disk electrode in $1\text{M KCl} + 0.1\text{M K}_4\text{Fe}(\text{CN})_6 + 0.1\text{M K}_3\text{Fe}(\text{CN})_6$ at 20°C (electrode area: 0.46 cm^2 ; rpm: 1600).

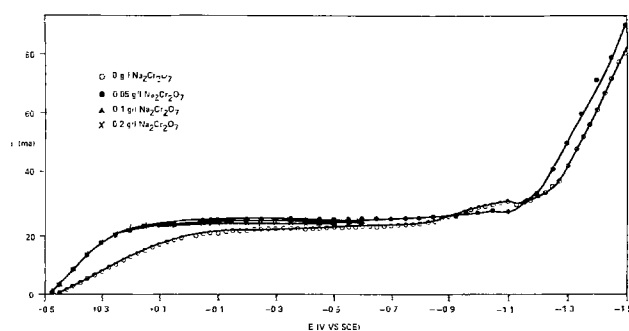
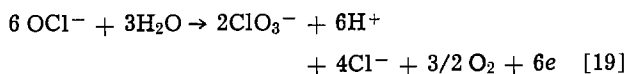


Fig. 6. Influence of $\text{Na}_2\text{Cr}_2\text{O}_7$ on the polarization data on platinum rotating disk electrode in $1\text{M KCl} + 0.1\text{M FeCl}_2 + 0.1\text{M FeCl}_3$ at 20°C (electrode area: 0.46 cm^2 ; rpm: 1600).



It is stated in the literature (13, 14) that $\text{Cr}_2\text{O}_7^{--}$ suppresses the amount of oxygen generated during chlorate electrolysis. While one may rationalize this observation in terms of blocking of sites for oxygen evolution by dichromate and/or complexation of hypochlorite-decomposing catalysts (e.g., Fe, Co, Ni) by $\text{Cr}_2\text{O}_7^{--}$ (and/or CrO_4^{--}) further investigations are needed to understand the mechanistic aspects involved in this phenomenon.

Conclusions

1. Sodium chlorate formation is an apparent third order reaction involving 2 moles of HOCl and one mole of OCl^- . The "second order" mechanism proposed by Lister appears to be incorrect because of errors involved in his method of determining the HOCl concentration.

2. The primary function of dichromate added during chlorate electrolysis is the formation of an inert film which suppresses the ClO_3^- and OCl^- reduction reactions via the establishment of an adverse potential

gradient. Wagner's film theory is further substantiated using steel cathodes coated with Kalgard and Cr_2O_3 films in chlorate solutions, and by rotating disk electrode studies wherein $\text{Fe}(\text{CN})_6^{3-}$ reduction was hindered by $0.1\text{ g/l Cr}_2\text{O}_7^{--}$, while Fe^{3+} reduction was unaffected. Secondary functions which chrome performs include enhanced buffer capacity in the critical pH range of 5.75 and 6.75 and suppression of the undesirable oxygen evolution reaction.

Acknowledgments

The authors wish to thank Miss J. L. Wendt and Mr. R. Kiszewski for performing the experiments and Hooker Chemical Company for permission to publish this work.

Manuscript submitted Oct. 8, 1980; revised manuscript received Jan. 5, 1981.

Any discussion of this paper will appear in a Discussion Section to be published in the December 1981 JOURNAL. All discussions for the December 1981 Discussion Section should be submitted by Aug. 1, 1981.

Publication costs of this article were assisted by Hooker Research Center.

REFERENCES

1. F. Foerster and E. Muller, *Z. Electrochem.*, **9**, 171 (1903); F. Foerster, *Trans. Electrochem. Soc.*, **46**, 23 (1924); *J. Prakt. Chem.*, **59**, 53 (1899).
2. I. Taniguchi and T. Sekine, *Denki Kagaku Oyobi Kogyo Butsuri Kagaku*, **43**, 715 (1975).
3. H. Imagawa, *Denki Kagaku*, **21**, 520 (1953).
4. D. V. Kokouline and L. I. Kristalik, *Sov. Electrochem.*, **7**, 346 (1971).
5. M. W. Lister, *Can. J. Chem.*, **30**, 879 (1952); **31**, 479 (1956).
6. D. M. Brasher and A. D. Mercer, *Trans. Faraday Soc.*, **61**, 803 (1965).
7. H. Kerst *Corrosion*, **16**, 523t (1960).
8. H. Oranowska and Z. Szklarska-Smialowska, *Zasch. Metal.*, **8**, 523 (1972).
9. S. Kowamura, N. Tanaka, and M. Nagayama, *Boshoku Gijutsu*, **22**, 500 (1973).
10. M. M. Jaksic, A. R. Despic, and B. Z. Nikolic, *Sov. Electrochem.*, **8**, 1533 (1972).
11. I. E. Veselovskaya, E. M. Kuchinskii, and L. V. Morochko, *J. Appl. Chem. USSR*, **37**, 76 (1964).
12. C. Wagner, *This Journal*, **101**, 181 (1954).
13. J. Cormier, in "Proc. Oronzio DeNora Symp: Chlorine Technology," O. DeNora, Editor, pp. 237 (1979).
14. F. Greiveldinger, in "Proc. Oronzio DeNora Symp: Chlorine Technology," O. DeNora, Editor, pp. 261 (1979).
15. A. T. Kuhn, "Industrial Electrochemical Processes," Elsevier Publishing Co., Amsterdam (1971).
16. A. I. Vogel, "A Text book of Quantitative Inorganic Analysis," 3rd ed., Longman, London (1961).
17. E. Gileadi, E. Kirowa-Eisner, and J. Penciner, "Interfacial Electrochemistry—An Experimental Approach," Addison-Wesley Publ. Co. Inc., London (1975).
18. D. J. Skojkovic, M. M. Jaksic, and B. Z. Nikolic, *Glasnik Hemijskog Društva.*, **34**, 171 (1969).
19. M. M. Jaksic, *This Journal*, **121**, 70 (1974).
20. J. Newman, "Electrochemical Systems," Prentice Hall, New York (1973).
21. B. V. Tilak, T. H. Dexter, and C. G. Rader, Filed Patent Application (1980).

The Electrochemical Activity Determination of Trypsin-Like Enzymes

V. A Comparative Study of the Electrochemical Oxidation of the Marker, p-aminodiphenylamine, and of Electrogenic Substrates in Human Plasma, Whole Blood, and Aqueous Solutions

M. Daraio de Peuriot, J. M. Nigretto,* and M. Jozefowicz

Department of Chemistry, Université Paris-Nord, 93430 Villetaneuse, France

ABSTRACT

Easily oxidizable aromatic amines can be conveniently used as electrogenic markers for the evaluation of enzymatic activities in whole blood and human plasma dilution. The analytical procedure is based on the cyclic voltammetric detection of the amine released by thrombin (the tested blood coagulation factor) through an amidolytic cleavage from specific substrates. The relevance of parameters susceptible of interfering with the electrochemical signal have been reviewed using carbon paste and smooth platinum disk electrodes. Results obtained in blood and plasma dilutions are compared with aqueous solutions of the enzyme.

Since the early seventies, the use of chromogenic substrates started a rapid development in the field of the assay of trypsin-like enzymes and of their natural inhibitors. Several enzymes of this type are involved along the overall blood coagulation process. The final step in the blood clotting cascade is the conversion of fibrinogen to fibrin, which leads to the formation of the thrombus. The latter catalytic decomposition is mediated by a protease, thrombin. While thrombin induces the thrombosis, it is normally only present in the precursor form, prothrombin. Beside the clotting enzymes, plasma carries components fated to inhibit their action; thus, the most potent antiprotease associated with thrombin is antithrombin III, which has been definitely shown to play a role in the body's defence against thrombosis.

Therefore the quantitative evaluation of antiprotease levels in physiological media is determinant for clinical purposes. From that point of view, the availability of chromogenic substrates provides an access to thrombin and antithrombin activity assay. The principle of the photometric procedure lies in the following: the enzyme is added to a mixture containing the synthetic substrate. Since its chemical structure more or less mimics the C-terminal part of the fibrinopeptide A at the sequence preceding the fibrinogen bond cleaved, thrombin catalyzes the splitting of the chromogenic moiety. The activity of thrombin, or remaining thrombin when antithrombin III levels are assayed, is then proportional to a photometric variable (1).

Most substrates commercially available are designed to release p-nitroaniline (pNA) through amidolytic digestion, which is conveniently monitored photometrically in the visible spectrum region at 405 nm. However, severe limitations restrict the scope of the procedure to colorless, diluted, and homogeneous solutions. Human plasma dilutions fulfill these requirements, but not whole blood; accordingly, antithrombic assays need to be achieved following a centrifugation procedure.

In order to avoid such a more or less traumatic handling of the samples, an electrochemical technique has been recently proposed, so as to permit the assay

of trypsin-like enzymes (*e.g.*, trypsin, factors IXa, Xa, kallikrein, thrombin, plasmin, and their inhibitors) in human whole blood. This technique involves the electroanalytical detection of electroactive markers in place of the chromogenic pNA. Several substrates of various specificity have been tested (Fig. 2). D,L benzoylarginyl p-aminodiphenylamide (D,L BAPADA) has been conceived for the assay of trypsin, S-2421, and S-2497 for thrombin and, accordingly, antithrombin III. Each of these substrates bears an easily oxidizable amine, p-aminodiphenylamine (pADA) (2-5).

While the electroanalytical detection of pADA in physiological media can be speculatively thought to be perturbed with respect to aqueous solutions, the aim of this paper is to investigate the influence of parameters which may mediate the electrochemical redox signal in the conditions for an actual assay. Therefore, the results obtained in whole blood and plasma are compared with those of aqueous solutions exempted from physiological fluids. The following variables of potential relevance are examined in the light of the shape and the position of the cyclic voltammogram of the amine: electroactivity of the substrates that have been tested, redox character of the enzymes, pH, and the effect of plasma and blood levels.

Experimental

Instrumentation, cells, and electrodes.—The instrument used for the electroanalytical studies was a standard amplifier-based potentiostat/galvanostat PAR Model 173 (Princeton Applied Research) provided with a three electrode configuration. Current-voltage and current-time curves were monitored with a Sefram TGM X-Y recorder and generated with a function generator PAR Model 175. For electroanalytical experiments, a one-compartment cell containing a carbon paste electrode (CPE), platinum wire auxiliary, and aqueous SCE reference was employed. Before each individual run, the carbon paste surface was renewed. The working electrode circuitry was buffered with a high impedance electrometer PAR Model 178. The smooth platinum disk electrode was embedded in Teflon (area: 0.0314 cm²). Its pretreatment is detailed in the next section. Coulometric *n* values were obtained with a PAR Model 179 digital coulometer. The vessel consisted of a two-compartment cell in which the

* Electrochemical Society Active Member.

Key words: electrochemistry, trypsin-like enzymes, thrombin, blood, plasma.

platinum wire auxiliary electrode was in one compartment and the platinum gauze working electrode and aqueous SCE reference were in the other; the two were separated by a porous glass frit. Experiments were conducted in 0.2-7*N* H₂SO₄ aqueous solutions, in the presence of 5% added methanol or in buffered solutions. These conditions proved to facilitate the dissolution of the reactants. The analytical concentration range for pADA was in all cases 0.1-0.4 mmol.

Solvents and reagents.—Aqueous solutions were prepared from doubly distilled water and reagent grade H₂SO₄ or standard buffer reagents. The p-aminodiphenylamine (pADA) was a commercial product from Fluka (Switzerland), puriss. p.a., which was purified by successive recrystallizations from water/ethanol mixtures. The amine was stored under vacuum in the dark and was no longer used after one week storage. All other materials were reagent grade and were used without further purification.

Enzymes, plasma, and blood sampling.—Lyophilized thrombin (51 NIH-U/mg, Lot No. A 3133) was purchased from Hoffman-LaRoche, Basel, Switzerland, and stored in the freezer. Its activity was measured either with chromogenic substrates or with the clotting time method. Before use, aliquots of thrombin were dissolved in tris/NaCl buffer pH 7.45 to a concentration of about 50 NIH-U/ml and preincubated for 30 min in an ice bath. Stock solutions were no longer utilized after 60 min following dissolution. Pipettes and syringes were saturated with the thrombin solution before use. Whole blood was taken from a donor under usual conditions at the Centre National de Transfusion Sanguine (Paris, France): 92 ml blood and 25 ml of a citric acid/monosodium phosphate/glucose solution (3.27g citric acid monohydrate, 2.63g trisodium citrate dihydrate, 1.93g anhydrous monosodium phosphate, and 2.32g anhydrous glucose in 100 ml). The haematocrit was 0.48. Human plasma was prepared by centrifugation at 2000g for 20 min at 4°C and kept frozen at -20°C before use.

Results and Discussion

The electrochemical behavior of pADA in aqueous solutions and in dilutions of plasma and whole blood has been investigated with two kinds of electrodes. Mechanistic information has been collected using the carbon paste electrode for the range of potentials attainable with it is fairly extended anodically. It also provides almost zero residual currents. For optimizing the practical purposes, the use of smooth platinum electrodes was studied.

Aqueous Solutions (Results Obtained with the Carbon Paste Electrode)

Influence of pH.—In the moderate pH range, from 2 to 10, the cyclic voltammogram shows a marked pH dependence. The variation of the peak potential is given by the relation

$$E_{p^a} = 0.06 \text{ pH} + 0.53 \text{ V vs. SCE at } 20^\circ\text{C}$$

which holds up to pH 7.5. The slope accounts for the global transfer of an equal number of electrons and protons. The voltammetric analysis of the signal shows the pADA molecule yields the parabenzoquinonediimine form (6). Whereas it is practically constant below pH 7.5, the anodic-to-cathodic peak separation increases as a result of increasing irreversibility (Fig. 1). In coincidence, the current ratio i_{p^c}/i_{p^a} decreases. It must be noted that the break occurring in the potential/pH relationship does not arise at the p*K* for acid-base dissociation of pADA (*ca.* 5), but two units above, instead. This indicates that the nature of the diffusing species (the protonated pADA) differs from those undergoing the electrochemical oxidation at the electrode surface (the neutral amine). The apparent p*K*

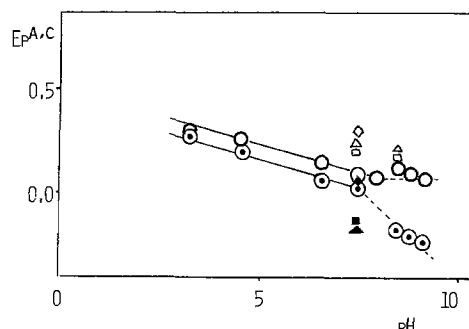


Fig. 1. Anodic and cathodic peak-pH relationship of the pADA redox couple at the carbon paste electrode. (Scan rate = 0.2 V/sec.)

| Anodic | Cathodic | Aqueous solutions NaCl 0.12/tris 0.025M/ Gly 0.05 M/DMSO 5% 1/10 plasma dilutions 1/10 whole blood dilutions Undiluted whole blood |
|--------|----------|--|
| ○ | ⊙ | |
| □ | ■ | |
| △ | ▲ | |
| ◇ | ◆ | |

involved would be that of the adsorbed form. Since the irreversibility more markedly affects the cathodic run than the anodic half-cycle, as shown on Fig. 1, it is suggested that the oxidant anodically formed undergoes a chemical conversion becoming preponderant above pH 7.5. The hydrolysis of the diimine may reasonably account for this trend (7).

The increasing irreversibility of the electrochemical signal, however, does not prevent utilizing it as a marker for enzymatic activity determinations; this was checked with amperometric titrations of the amine in solutions covering the pH range mentioned above. As a result, the endpoint procedure can be applied, for example, after blocking the enzymatic kinetic with the addition of acid (5).

Influence of the sweep rate.—Simplest voltammetric curves were obtained when scanning rates of 0.2 V/sec were used. At this scanning rate, the peak current (i_p) was found to be a linear function of p-aminodiphenylamine concentration with an accuracy of $\pm 5\%$ between 10^{-6} and 10^{-3} M. At lower scanning rates, faradaic and adsorption oxidation peaks of decomposition products of the radicals formed in the first electron uptake (6) were observed at potentials more positive than the oxidation peak of the parent compound.

Influence of the substrate.—Adequate substrates for electrochemical determinations should not be electroactive, at least in the potential span where the marker itself is detected. Three peptides were tested: D,L benzoylarginyl p-aminodiphenylamide, S-2497, and S-2421. The benzoylarginyl-p-aminodiphenylamide and S-2497 yielded p-aminodiphenylamine and S-2421 yielded 4-methoxy-2-naphtylamine (Fig. 2). The first peptide differed from S-2497 and S-2421 by bearing a benzoylarginyl group instead of the phenylalanyl-pipecolylarginyl group of the latter two.

The results of the electrochemical behavior of these substrates are presented in Fig. 3 and Table I. The study was performed in tris/NaCl buffered solutions at pH 7.45. The cyclic voltammograms of the three substrates are similar; they show two anodic peaks for the 10^{-6} M level, which gradually merge into one unique symmetrical peak above the 10^{-3} M range of concentrations. The associated cathodic peaks are not present in each case. Otherwise, the anodic peak current amplitudes are not linearly related to the concentrations of the depolarizer in the studied range. Rough calculation of the apparent diffusion coefficients leads to values above five times larger than that of the released amine. As concerns a relative insight, the data suggest that the ratio i_{p^c}/i_{p^a} for the three sub-

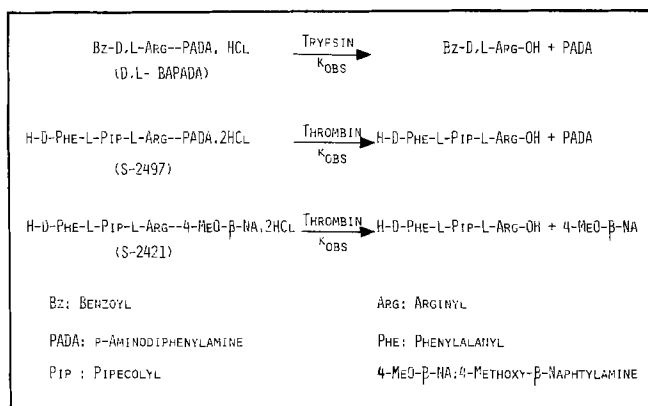


Fig. 2. Reaction schemes for the amidolytic decomposition of the specific substrates by proteases.

strates vary in the order of increasing molecular weight and/or adsorption ability, inasmuch as naphthyl groups are more capable of adsorbing than p-diphenylamine groups (8).

These observations indicate that preponderant adsorption controlled processes accompany the irreversible charge transfer reaction, in such a way that the whole peak only reflects a minor contribution of the faradaic component. This is best shown at low concentrations where the second peak ascribed to the faradaic reaction is gradually overlapped in favor of the preceding adsorption peak, in proportion the concentration is increased.

The potentials of the faradaic peaks were compared to those of the respective amines, in solutions of identical composition. The results are reported in Table I. The constant differences which are obtained provide the indication that the loss of the electrons is in each case promoted by the amine linked up with the peptide chain. It may be concluded that the electron withdrawing ability of the latter is essentially equivalent for the three substrates, whichever group substitutes the arginyl radical.

Due to the final levels at which the substrate is required to allow a pseudo first order kinetic to proceed (at least $10^{-4}M$), adsorption affects the electrochemical signal of the amine when the potential exploration is pursued past the oxidation peak. This holds especially when consecutive sweeps are effectuated with the same electrode surface. In the case of the carbon paste electrode, however, the surface is renewed before each run. Therefore, although wide potential spans are attainable with this kind of electrodes, many determinations are excluded within the duration of the kinetic. Actually, this technique is essentially restricted to endpoint procedures. From this point of view, solid electrodes such as platinum electrodes provide a more suitable tool for continuous determinations. This point is examined below.

Influence of dimethylsulfoxide and of glycine.—DMSO has to be incorporated with the solutions to ensure a sufficient dissolution of the substrates, even at the $10^{-4}M$ level. Glycine, which is known to stabilize protein solutions, was also used at the 0.05M concen-

Table I. Observed oxidation peak potentials of various electrogenic substrates compared to those of the corresponding free amines in aqueous solutions (tris/NaCl pH 7.45 buffer). Concentrations fall in the 0.1 mM range. Mean deviation ± 5 mV.

| Substrates | E_p^a (V) substrate | E_p^a (V) free amine | E_p^a (S) - E_p^a (f.a) |
|------------|-----------------------|------------------------|-----------------------------|
| D,L BAPADA | 0.44 | 0.10 | 0.34 |
| S-2497 | 0.46 | 0.10 | 0.36 |
| S-2421 | 0.97 | 0.62 | 0.35 |

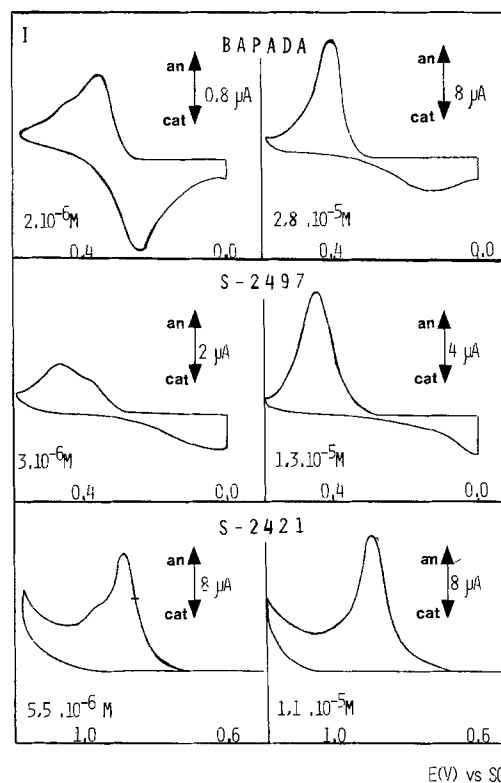


Fig. 3. Cyclic voltammograms of the substrates at the carbon paste electrode (scan rate: 0.2 V/sec; in tris/NaCl/Gly/DMSO solutions at pH 7.45).

tration. The effects of these compounds are described in light of the features of the amine oxidation signal: $E_p^a - E_p^a(1/2)$, the peak to half-peak potential difference, E_p^a , the peak potential, and the i_p^a/C ratio (Table II).

The addition of DMSO markedly reduces the i_p^a/C ratio and hinders the reversibility of the charge transfer, as illustrated by increasing $E_p^a - E_p^a(1/2)$ values. As the increase in the viscosity of the solutions cannot itself explain the importance of the observed effect, it is envisaged that DMSO combines to dissolve superficially the paraffin used to elaborate the electrode material. Thus, the increasing irreversibility would account for an etching phenomenon of the electrode surface by diminishing its catalytic properties rather than for an electrokinetic effect occurring in the double layer.

Per se, glycine does not inhibit the reversibility of the voltammetric peak since the $E_p^a - E_p^a(1/2)$ variation remains the same as for acidic solutions; the observed 40 mV correspond to a number of exchanged electrons intermediate between one and two, which is compatible with the mechanism described elsewhere for the actual sweep rate (6). Although glycine shows no significant effect on the reversibility of the electronic transfer, it nevertheless affects the position of the peak potential, rendering it more anodic. Increasing the amount of DMSO acts likewise. In the case of glycine instead, it is probable that the amino acid modifies the structure of the solvent-electrode interface, presumably through local adsorption. Hence, the transfer of the electrons likely occurs under different local pH conditions which would be responsible for the anodic shift. On the other hand, adsorption of glycine molecules might also restrict the effectiveness of the electrode surface. It is thus not surprising to note a correlative decrease in the i_p^a/C values.

From these partial results, it can be concluded that accurate determinations of peak heights require precise experimental conditions. The potential shift is unimportant with regard to amperometric procedures unless a fixed potential detection is used. The current

Table II. Electroanalytical data for the cyclic voltammograms of pADA in aqueous tris/NaCl pH 7.45 solutions. Influence of the glycine and dimethylsulfoxide content on the anodic peak function, the peak potential, and the peak-to-peak differences. Concentration of the depolarizer: 0.4 mmol. Mean deviation ± 5 mV.

| Ionic strength (M) | Glycine (M) | DMSO (w/w%) | I_p^a/C (A.l./mol) | E_p^a (V) | $E_p^a - E_p^c$ (1/2) (V) | $E_p^a - E_p^c$ (V) |
|--------------------|-------------|-------------|----------------------|-------------|---------------------------|---------------------|
| 0.15 | 0 | 0 | 0.163 | 0.100 | 0.040 | 0.060 |
| 0.15 | 0 | 5 | 0.138 | 0.150 | 0.060 | 0.200 |
| 0.15 | 0 | 10 | 0.115 | 0.180 | 0.080 | 0.280 |
| 0.15 | 0.05 | 0 | 0.144 | 0.100 | 0.040 | — |
| 0.15 | 0.05 | 5 | 0.127 | 0.100 | 0.040 | — |

function i_p^a/C , however, reflects the additive influences of the DMSO and glycine content. A calibration curve must therefore be assessed prior to the titration. In the following, the results will be referred to 5% v/v DMSO and 0.05M glycine solutions.

Influence of thrombin.—Similarly, the influence of the thrombin content is studied through the modification of the anodic half-cycle of pADA oxidation. Results are presented in Table III for pH 7.45 and 8.47.

Proteins, especially thrombin (9) and albumin, are known to readily adsorb on synthetic surfaces. The anodic shift shown by the peaks in proportion to the added amount of protein probably accounts for that phenomenon, in the same way as glycine does. In the activity range in which the electrochemical assay is monitored, ca. 0.1 NIH unit, the disturbance caused by thrombin can be neglected. The electrochemical characteristics of the voltammograms are not drastically modified by the adsorption of proteins, provided that the concentrations fall below a given limit (Table III). For example, the reversibility of the charge transfer rate depicted by the $E_p^a - E_p^c$ (1/2) values is maintained in aqueous solutions along the range for the activity determination of thrombin. Although the i_p^c/i_p^a ratio offers no analytical exploitation, it can be remarked that it does not vary past a given amount of thrombin. This should be relevant for a protein coverage of the electrode surface reaching saturation. After its occurrence, it will likely slow down the chemical reversibility of the cycle, without affecting the electrochemical kinetic.

Human Plasma and Whole Blood Dilutions

Study with the carbon paste electrode.—Results are presented in Fig. 4 and 5 and Table III.

The comparison with voltammogram a of Fig. 4 traced at the reference pH 7.45 (the enzymatic assays are actually conducted at the latter pH) leads to the following remarks:

The dependence of the peak potentials with the pH of the solution is illustrated by voltammograms f, e, and a in Fig. 4, traced in H_2SO_4 0.7N, pH 3.29 and 7.45, respectively. The cathodic shift with increasing pH is relevant to the thermodynamics.

The background voltammograms of blood solutions up to 50% dilutions show no evolution electrochemically detectable up to at least 30 min. At the latter concentration, the anodic width of potential reaches 0.4V vs. SCE. This indicates that the protein content remains electrochemically inactive at the carbon paste electrode, at least with respect to charge transfer reactions.

It is worthy to note that as much as a 10% plasma or blood content reduces the peak current function i_p^a/C by less than 10%, see Table III and voltammograms b, c, and d in Fig. 4. This result is of great interest, keeping in mind that the antithrombin III (or thrombin) content usually estimated this way is included in few microliters of pure sample; therefore, there is no need to set up accurate calibration curves with respect to the final amount of proteins, prior to the assay.

Lowering the dilution of blood or plasma still maintains linear relationships in the amperometric determination of pADA. Figure 5 gives the i_p^a/C values as a function of the plasma or blood dilution. Once the data are corrected by taking into account the viscosity changes, there is no significant difference between these biological fluids. In particular, the presence of a heterogeneous phase brought by the figurative elements of blood (the haematocrit is about 45%) does not affect the applicability of the method. When undiluted blood or plasma samples are tested, it is just necessary to adjust the calibration curve to the conditions for the actual assay. This feature definitely marks the advantage of the electrochemical assay over the photometric one for trypsin-like enzymes in heterogeneous

Table III. Electroanalytical data from the cyclic voltammograms of pADA solutions in the presence of thrombin, plasma, and blood dilutions.

| | | E_p^a (V) | $E_p^a - E_p^c$ (V) | $E_p^a - E_p^c$ (1/2) (V) | I_p^c/I_p^a | I_p^a/C (A.l./mol) |
|---------|--------------|-------------|---------------------|---------------------------|---------------|----------------------|
| pH 8.47 | 0 NIH-U/ml | 0.070 | 0.210 | 0.050 | 0.74 | 0.165* |
| | 1 NIH-U/ml | 0.090 | 0.240 | 0.060 | 0.75 | 0.149* |
| pH 7.45 | 0 NIH-U/ml | 0.100 | 0.060 | 0.040 | 0.91 | 0.162* |
| | 0.1 NIH-U/ml | 0.100 | 0.070 | 0.040 | 0.74 | 0.162* |
| | 1 NIH-U/ml | 0.130 | 0.100 | 0.050 | 0.74 | 0.136* |
| Plasma | 0% | 0.100 | | 0.040 | | 0.144** |
| | 10% | 0.200 | | 0.060 | | 0.135** |
| | 20% | 0.220 | | 0.070 | | 0.110** |
| | 40% | 0.230 | | 0.070 | | 0.091** |
| | 100% | 0.290 | | 0.110 | | 0.061** |
| Blood | 0% | 0.100 | | 0.040 | | 0.127† |
| | 10% | 0.230 | | 0.060 | | 0.121† |
| | 20% | 0.220 | | 0.060 | | 0.103† |
| | 100% | 0.280 | | 0.080 | | 0.074† |

* Without glycine and without DMSO.

** With 5% DMSO.

† With 5% DMSO and glycine 0.05M.

Concentration of the depolarizer 0.4 mM. Mean deviation ± 5 mV.

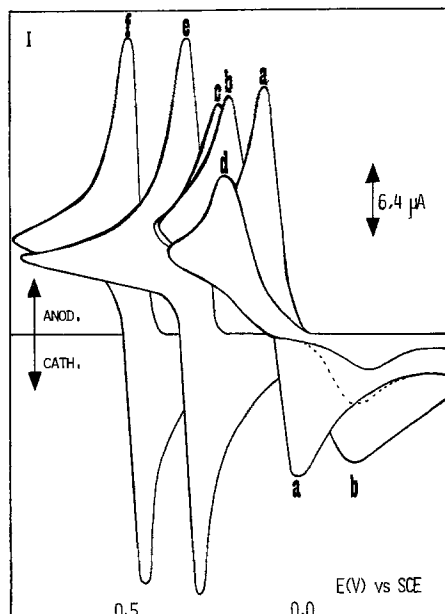


Fig. 4. Cyclic voltammograms of pADA at the carbon paste electrode (scan rate 0.2 V/sec, pADA = 0.26 mM). a, Tris/NaCl/Gly/DMSO pH 7.45; b, 1/10 human plasma (tris/NaCl/Gly/DMSO; pH 7.45); c, 1/10 whole blood (tris/NaCl/Gly/DMSO; pH 7.45); d, 1/5 whole blood (tris/NaCl/Gly/DMSO; pH 7.45); e, Britton-Robinson buffer pH 3.29 (NaCl/Gly/DMSO); f, 0.70N H_2SO_4 .

fluids such as blood, without turning to preliminary centrifugation.

In concentrated fluids and immediately following the mixing, the peak amplitude for pADA oxidation decreases up to ca. 50% of the original amplitude. Because the decrease is in relation to the dilution of the fluid and not to the analytical concentration of pADA, this trend cannot be attributable to macrophagic activity. It more probably concerns a modification of the electrode surface. This point will be discussed further, in light of the results obtained with the platinum electrode. The data presented here account for voltammograms traced passed this transient evolution.

Study with the smooth platinum disk electrode.—For practical purposes, it is obvious that solid electrodes potentially provide a very useful tool, easily applicable to automated or semi-automated analytical titrations, provided that several requisites are fulfilled:

1. The active surface of the electrode shall be sensitive enough and show evidence for reproducible peak currents, including constant background currents.

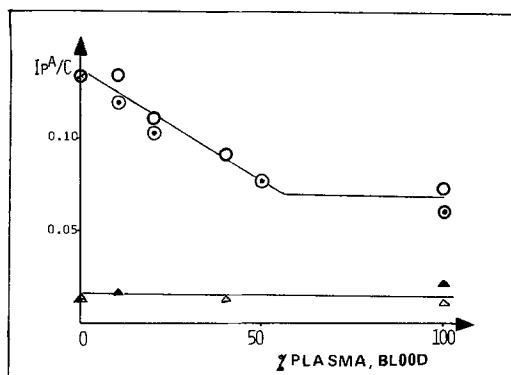


Fig. 5. Peak amplitudes vs. blood or plasma dilution relationships (with viscosity correction; scan rate 0.2 V/sec).

| | Aqueous | Plasma | Blood |
|---------------------------|---------|--------|-------|
| Carbon paste electrode | ○ | ○ | ⊙ |
| Smooth platinum electrode | △ | △ | ▲ |

2. To attain this purpose, it may be essential to elaborate a precise protocol of pretreatment.

3. The amperometric titration shall be effectuated as frequently as possible during the course of the amidolytic hydrolysis of the substrate. Thus, the same electrode surface shall operate several times while the potential is multicycled, without showing hysteresis, i.e., the weakening of its catalytic properties and without restriction of its effective area (with respect to adsorbed species, for example).

The following results have been obtained in aqueous tris/NaCl/glycine/DMSO solutions buffered at pH 7.45. Blood and plasma dilutions were prepared just by mixing the biological fluids with the aqueous buffer.

Pretreatment procedure.—The background trace of metallic electrodes in aqueous solutions is quite sensitive to the chemical state of the surface and to adsorbed oxides. Therefore, the electrodes are often subjected to rather cumbersome prepolarizations, destined to obtain reproducible background voltammograms of the solvent. Inasmuch as the potential region of the amine undergoing oxidation is restricted to few hundred millivolts, it would be suitable to apply a pretreatment procedure inside of this span. Results show that an interrupted triangular sweep of potential between -0.1 and $+0.4$ V promotes the rise of a steady-state background cycle, whatever solvent is used, aqueous or biological. In the latter case, the duration of the pretreatment is even shortened. The integrated currents of the limiting voltammogram is always smaller than the initial trace. It is assumed that the gradual charging of the double layer is responsible for the decrease. After the application of the described prepolarization, the background currents superpose quite reproducibly, within a 10^{-2} μA dispersion. In particular, no current increase or decrease develops on prolonged cycling over a period of time of at least 30 min. Here, the narrowness of the explored potentials and the gradual abrasion of the oxide peaks avoid some time-dependent effects related to the presence of proteins in the solution (9).

Refinements for the detection of pADA.—The optimum anodic and cathodic limits for the triangular sweep were analyzed in the light of the shape of the resulting anodic half-cycle. Results showed the relative unimportance of the potential bounds provided that the pretreatment procedure is applied before and provided that the limits coincide with those of the pre-cycling. Of some importance instead is the rest time separating two consecutive runs, for the adsorbed material formed during the electrochemical conversion somewhat reduces the amplitude of the consecutive voltammograms. The optimum rest time could not be less than 45 sec.

Electrocatalytically speaking toward aromatic hydrocarbons or amines, platinum surfaces are known to behave poorly, in any event less than the carbon paste material. It is therefore not surprising that the pADA voltammograms show irreversible profiles. Although the criteria for electrochemical reversibility are far from being met, the amperometric detection gives nevertheless straight and proportional $i_p^A/C \cdot pADA$ relationships, in any point comparable to those obtained using the carbon paste electrode. The amplitudes are in correspondence with the respective geometrical areas (Fig. 5).

Calibration of the platinum electrode in plasma and blood dilutions.—As was observed with the carbon paste electrode, the peak amplitudes recorded with the platinum electrode show little weakening in blood and plasma dilutions (voltammograms b and c, Fig. 6) up to 10%, if compared against a voltammogram on the reference (voltammogram a) in aqueous medium. It is also typical to note that the peak separation $E_p^a - E_p^c$

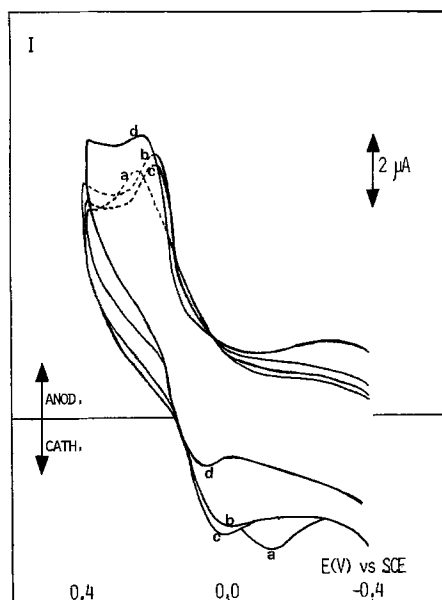


Fig. 6. Cyclic voltammograms of pADA at the pretreated smooth platinum electrode. (Scan rate 0.2 V/sec; tris/NaCl/Gly/DMSO pH 7.45). a, Aqueous solution; b, 1/10 diluted whole blood; c, 1/10 diluted plasma; d, undiluted whole blood.

decreases with the biological mixtures. Probably, the occurrence of the coated proteins favors the chemical reversibility of the redox couple by slowing down the propensity to migrate away (as might occur with more effective adsorption in the presence of coated proteins), although without interfering with the diffusion rate toward the electrode surface.

The more interesting result concerns the peak height for pADA oxidation which fairly well compares in aqueous buffers with even pure blood (voltammogram d in Fig. 6). These findings give rise to the data plotted in Fig. 5 for the platinum electrode in correspondence with those referring to the carbon paste electrode. The comparison is quite attractive inasmuch as it shows the neglectable influence of the blood or plasma content of the solution onto the calibration. In turn, these results indicate that the transient decrease of the peaks traced with the carbon paste electrode

are to be related to surface effects, but not to the consumption of the depolarizer by the biological fluids.

It is obvious that the insensitivity to the biological environment confers to the pretreated platinum electrode a definite advantage over the other electrode systems. It also affords a substantial relief in the practical procedure preceding the enzymatic assay.

On the other hand, calibration curves proving that the measured signal is a linear function of concentration have been published in other papers of this series (3); the function is essentially identical for aqueous solutions, human plasma, and whole blood dilutions.

Conclusion

An electroanalytical method for the study of enzymatic kinetics is proposed. The use of modified electrode surfaces through the adsorption of proteins affords a new insight into the behavior of clotting enzymes in the presence of insoluble materials or into whole blood dilutions.

Manuscript submitted Sept. 18, 1980; revised manuscript received Jan. 5, 1981.

Any discussion of this paper will appear in a Discussion Section to be published in the December 1981 JOURNAL. All discussions for the December 1981 Discussion Section should be submitted by Aug. 1, 1981.

Publication costs of this article were assisted by the Université Paris-Nord.

REFERENCES

1. M. F. Scully and V. V. Kakkar, in "Chromogenic Substrates. Chemistry and Clinical Usages," Churchill Livingstone, Edinburgh, London, New York (1979).
2. J. M. Nigretto and M. Jozefowicz, *Thrombos. Res.*, **17**, 611 (1980).
3. M. Daraio de Peuriot, J. M. Nigretto, and M. Jozefowicz, *ibid.*, **19**, 647 (1980).
4. M. Daraio de Peuriot, J. M. Nigretto, and M. Jozefowicz, *ibid.*, In press (Part III).
5. M. Daraio de Peuriot, J. M. Nigretto, and M. Jozefowicz, *ibid.*, In press (Part IV).
6. J. M. Nigretto, *This Journal*, **128**, 1239 (1981).
7. J. F. Corbett, *J. Chem. Soc.*, 213 (1969).
8. R. N. Adams, "Electrochemistry at Solid Electrodes," p. 344, M. Dekker Inc., New York (1969).
9. L. Duic, S. Srinivasan, and P. N. Sawyer, *This Journal*, **120**, 348 (1973).

The Electrochemical Activity Determination of Trypsin-Like Enzymes

VI. The Electrochemical Oxidation of the Marker, p-aminodiphenylamine in Aqueous Solutions

Jean-Maxime Nigretto*

Department of Chemistry, E.R.A. 607, Université Paris-Nord, 93430 Villetaneuse, France

ABSTRACT

The electrochemical oxidation of p-aminodiphenylamine was investigated in the 0.1 mmol concentration range and in H₂SO₄ aqueous solutions. Cyclic voltammetry with slow scan rates at the carbon paste electrode and controlled potential step electrolysis were the techniques followed. Results suggest that the initial oxidation stage produces p-quinodiimine via an ECE process. This two-electron oxidation product further undergoes addition reactions involving the depolarizer. The hydrolysis of the adduct is assumed to yield a quinoidal derivative, aniline and ammonia, as deduced from step coulometry and visible spectroscopy experiments. The sequence of the decomposition which is proposed integrates most of the results available elsewhere. No polymerization of the starting material occurs in the used working conditions.

p-Aminodiphenylamine (pADA) appears to be a convenient marker for the electrochemical determination of enzymatic activities. The electroanalytical procedure is based on the periodical detection of the amine concentration level in the assay solution using its oxidation signal. The amine is released through a hydrolytic cleavage from a specific substrate by the enzyme (1-4).

This paper is aimed at gathering some mechanistic information on the electrochemical behavior of the marker. The electroanalytical data available in the literature are more concerned with the pADA as an intermediate in the general oxidation pattern of aniline and its related derivatives than per se. In the proposed reaction pathways, pADA is generated from the head-to-tail coupling of aniline with the anilinium radical after it has been formed at the electrode surface. Strong acid solutions favor this reaction scheme, whereas weaker acidities favor the alternate formation of tail-to-tail products, the benzidines (5, 6). The pADA oxidation was described as producing N-phenyl p-benzoquinonediimine, via the transfer of two electrons. Compounds of this series are known to undergo readily a hydrolytic decomposition reaction leading to p-quinone formation with aniline as side product. The intermediate for the proposed pathways, N-phenyl p-quinoneimine has, however, never been characterized, neither in the solution following macroscale electrolysis nor voltammetrically at the electrode surface (7).

Product isolation work in aqueous solution met only with mixed success. Leedy and Adams (8) have isolated and fully identified p-benzoquinone as the ultimate product of the decomposition stages. Hand and Nelson (6) have terminated the preparative electrolysis of pADA at 1.0V with *n* values of 6. Cyclic voltammetry runs on the solution showed that essentially all the parent material had been consumed. The *I-E* curves were identical with those obtained from a solution of hydroquinone. No other peak was observed. In other studies, various coupling derivatives, such as Willstätter blue and Willstätter red imines as the intermediates, have been evidenced electrochemically. On the other hand, the final product of the oxidation of aniline in aqueous solutions was depicted, nearly a century ago, as being an oligomer of aniline, called aniline black, usually supposed in the form of a linear

octamer named emeraldine. Isolation experiments indicated that at least a major constituent of this precipitate is a quinone-hydroquinone mixture, although the full composition thereof has not been completely elucidated. Results show that it is actually composed of many adducts of unspecified structure, depending on the electrolysis parameters: parent to intermediate ratio, concentration range, current density, etc.

The aim of this work is to provide additional insights into the mechanism of the pADA oxidation in solutions initially exempted from the parent aniline molecule and in the tenth millimolar concentration range. In order to detect the possible intermediates issued from the decomposition reactions, slow scan cyclic voltammetry and step coulometry experiments have been used. The results reported herein show that additional features ought to be taken into account to describe the electrochemical behavior of pADA. Also some new indications are given with respect to the redox content of the solution following partial electrolysis.

Experimental

Instrumentation, cells, and electrodes.—The instrument used for the electroanalytical studies was a standard amplifier-based potentiostat/galvanostat PAR Model 173 (Princeton Applied Research) provided with a three electrode configuration. Current-voltage and current-time curves were monitored with a Sefram TGM X-Y recorder and generated with a function generator PAR Model 175. For electroanalytical experiments, a one-compartment cell containing a carbon paste electrode (CPE), platinum wire auxiliary, and aqueous SCE reference was employed. Before each run, the carbon paste surface was renewed. The working electrode circuitry was buffered with a high impedance electrometer PAR Model 178.

Coulometric *n* values were obtained with a PAR Model 175 coulometer. The vessel consisted of a two-compartment cell in which the platinum wire auxiliary electrode was in one compartment and the platinum gauze working electrode and aqueous SCE reference were in the other; the two were separated by a glass frit. In aqueous H₂SO₄ solutions, experiments were conducted in the presence of 5% added methanol; these conditions proved to facilitate the dissolution of the reactants. The analytical concentration range for pADA was in all cases 0.1-0.4 mmol.

* Electrochemical Society Active Member.
Key words: p-aminodiphenylamine, aromatic amines.

Solvents and reagents.—Aqueous solutions were prepared from doubly distilled water and reagent grade H_2SO_4 or standard buffer reagents. The pADA was a commercial product from Fluka (Switzerland), puriss. p.a., which was purified by successive recrystallizations from water/ethanol mixtures. The amine was stored in the dark and was not used after one week storage. All other materials were reagent grade and were used without further purification.

Results

The electrochemistry of this compound in aqueous H_2SO_4 solutions can be broadly characterized as involving an initial reversible charge transfer followed by a series of hydrolysis reactions including the parent material. A typical cyclic voltammogram is represented in Fig. 1. At low scan rates, a maximum number of three anodic peaks and four major cathodic peaks can be detected. In order to avoid confusion, since some couples behave irreversibly (when the cathodic counterpart of the half-cycle is missing or shifted), the half-cycles are numbered separately. Anodically, they will conveniently be labeled in the order of appearance from the right to the left: i_p^{a1} , i_p^{a2} , and i_p^{a3} ; with respect to the cathodic peaks, i_p^{c1} is assigned to the reversible redox couple and associated to i_p^{a1} . The others are referenced as indicated in the figures. In the following, the label i_p indifferently refers to the nature of the couple or to the peak height. The decomposition sequence can be revealed by cyclic voltammetry by applying different pH and sweep rate conditions for the kinetics are pH dependent.

Thermodynamic Features

In buffered aqueous solutions from pH 8 to H_2SO_4 5.6N, the cyclic voltammogram of pADA, restricted to the first system, exhibits a reversible redox couple, $i_p^{a1} - i_p^{c1}$ (Fig. 1), followed by other irreversible systems. The features of this couple are markedly dependent on the acidity level and on the scan rate.

The position of the first anodic peak lies in pH dependence according to the relation (1)

$$E_p^{a1} = -0.06 \text{ pH} + 0.53 \text{ V vs. SCE} \quad [1]$$

At 0.2 V/sec sweep rate, the anodic-to-cathodic peak separation is close to 60 mV up to ca. pH 7.5, whereupon the peaks separate and the system behaves irreversibly. Variations in absolute i_p^{a1} values result in increases in the viscosity of the solutions as the H_2SO_4

content is increased. Except for strong acid solutions for which the pH definition is meaningless, no break occurs in coincidence with the acid-base constant for pADA dissociation ($pK_a'(pADA, H^+/pADA) = 5$). With respect to the Nernst equation, that slope predicts that an equal number of electrons and protons are globally lost by the species undergoing the electrochemical oxidation.

Electroanalytical Features

The reversible i_p^{a1}/i_p^{c1} couple.—The electrochemical behavior of the first couple is described by the data reported in Table I. The extent to which filming effects affect the electroanalytical data is unknown; however, the data presented are reproducible within the 5% dispersion normally attributed to the reproducibility of the CPE. It is found that E_p^{a1} values are constant with slow sweep rates. A slight trend to shift anodically becomes apparent with increasing scan rates, the magnitude thereof being globally inferior to 20 mV with a tenfold increase in the rate of the potential sweep. On the other hand, the anodic peak-to-half-peak potential differences show that the slowing down of the potential sweep favors a reversible two-electron transfer, as indicated by values close to the theoretically predicted 28 mV. With slow scan rates, the S-shaped cathodic cycle and the limiting value attained by the i_p^{c1}/i_p^{a1} ratio at a given acidity level show evidence for a reversible conversion. That limiting value cannot be lowered by using scan rates slower than 0.050 V/sec in strong acid solutions. It remains likewise constant by varying the switching potential E_λ up to the foot of peak i_p^{a3} at 0.9V. The reversibility of the follow-up reaction is also corroborated by applying multiple potential scans at 0.010 V/sec scan rate to the first peak, i.e., from 0.0V up to 80 mV past the peak maximum: the cathodic amplitude i_p^{c1} remains unchanged whereas the anodic one decreases slightly, but tends to a steady-state profile after few runs; it is probably originated from minor side-reactions and cannot be ascribed to filming effects since in that case the global amplitudes are expected to decrease gradually and significantly. Increasing the sweep rate ν , the system apparently evolves to show a mono-electronic charge transfer as indicated by larger $E_p^{a1} - E_p^{a1}(1/2)$ potential separations. Increasing the acidity of the solution acts likewise. These data are corroborated by the plot of the function (2) for increasing scan rates and acidities ranging from H_2SO_4 5.6N to pH 8

$$i_p^{a1}/C \cdot \nu^{1/2} = f(\nu^{1/2}) \quad [2]$$

where C and ν are the analytical concentration of the depolarizer and the sweep rate, respectively. Results show decreasing slopes in a manner similar to that described by Nicholson and Shain for a follow-up reaction after the primary electron transfer (9). This suggests a classic ECE mechanism, in which the species formed after the initial oxidation step undergo a chemical reaction and lead to more oxidizable species.

The test for chemical reversibility is best demonstrated by the current ratio i_p^{c1}/i_p^{a1} (Table I). Results show the faster the sweep rate and the lower the proton availability (below pH 8), the best the reversibility is achieved. In contrast, more anodic switching potentials reinforce this trend. Thus, i_p^{c1}/i_p^{a1} ratios vary from 0.52 to 0.97 with ν ranging from 0.01 to 1.0 V/sec in H_2SO_4 5.6N solutions and from 0.52 to 0.94 if the acidity decreases from H_2SO_4 5.6N to pH 3.17 at a constant 0.010 V/sec sweep rate. On the other hand, with a given H_2SO_4 2.64N level and slow sweep rates, the i_p^{c1}/i_p^{a1} ratio remains constant at 0.52 when E_λ keeps inferior to 0.9V; beyond the potential of i_p^{a3} at 1.0V, i_p^{c1}/i_p^{a1} increases significantly.

The irreversible i_p^{a2} redox peaks.—The ill-defined peaks i_p^{a2} can only be detected voltammetrically with

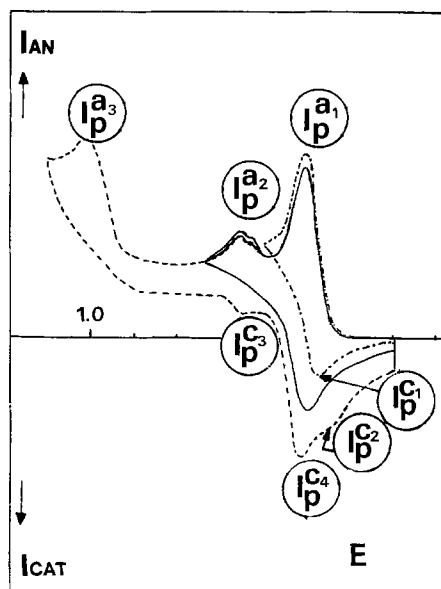


Fig. 1. CPE cyclic voltammograms of pADA in aqueous H_2SO_4 2.64N solutions. pADA 0.24 mmol; ν 0.075 V/sec.

Table I. Cyclic voltammetric data of the first reversible redox couple i_p^{a1}/i_p^{c1} as a function of the acidity, scan rate ν and the switching potential E_λ

| H ₂ SO ₄ or pH level | ν (V/sec) | $E_{p^{a1}} - E_{p^{a1}}(1/2)$ (V) | $E_{p^a} - E_{p^c}$ (V) | E_λ (V) | i_p^{c1}/i_p^{a1} | $E_{p^{a1}}$ (V) | $E_{p^{c1}}$ (V) | |
|--|---------------|------------------------------------|-------------------------|-----------------|---------------------|------------------|------------------|--|
| 0.1N | 0.010 | 0.030 | 0.030 | 0.75 | 0.76 | 0.450 | 0.420 | |
| | 0.020 | 0.030 | 0.030 | | 0.89 | 0.452 | 0.422 | |
| | 0.050 | 0.032 | 0.032 | | 0.97 | 0.452 | 0.420 | |
| | 0.100 | 0.034 | 0.037 | | 0.98 | 0.452 | 0.415 | |
| | 0.200 | 0.037 | 0.040 | | 1.00 | 0.455 | 0.415 | |
| | 0.400 | 0.039 | 0.046 | | 1.00 | 0.458 | 0.412 | |
| | 0.600 | 0.045 | 0.050 | | 1.00 | 0.460 | 0.410 | |
| | 0.800 | 0.052 | 0.060 | | 1.00 | 0.470 | 0.410 | |
| 0.67N | 0.010 | 0.030 | 0.032 | 0.75 | 0.58 | | | |
| | 0.100 | 0.032 | 0.032 | | 0.83 | | | |
| | 0.500 | 0.035 | 0.035 | | 0.92 | | | |
| 2.64N | 0.010 | 0.028 | 0.025 | 0.75 | 0.52 | 0.500 | 0.485 | |
| | 0.020 | 0.028 | 0.025 | | 0.50 | 0.508 | 0.485 | |
| | 0.050 | 0.030 | 0.032 | | 0.52 | 0.510 | 0.485 | |
| | 0.100 | 0.032 | 0.032 | | 0.60 | 0.512 | 0.480 | |
| | 0.200 | 0.030 | 0.036 | | 0.78 | 0.512 | 0.480 | |
| | 0.400 | 0.038 | 0.037 | | 0.89 | 0.516 | 0.480 | |
| | 0.600 | 0.037 | 0.037 | | 0.94 | 0.517 | 0.480 | |
| | 0.800 | 0.044 | 0.040 | | 0.95 | 0.517 | 0.480 | |
| | 0.010 | | | | 0.60 | 0.50 | | |
| | | | | | 1.10 | 0.85 | | |
| | 0.020 | | | | 0.60 | 0.50 | | |
| | | | | | 1.10 | 0.83 | | |
| | 0.050 | | | | 0.60 | 0.50 | | |
| | | | | | 1.10 | 0.74 | | |
| | 0.100 | | | | 0.60 | 0.78 | | |
| | | | 1.10 | 0.83 | | | | |
| 5.60N | 0.010 | 0.025 | | 0.75 | 0.52 | 0.532 | | |
| | 0.100 | 0.032 | 0.030 | | 0.66 | 0.542 | 0.512 | |
| | 1.000 | 0.046 | 0.039 | | 0.97 | 0.546 | 0.505 | |
| 0.17 | 0.010 | 0.032 | 0.032 | 0.50 | 0.94 | 0.327 | 0.295 | |
| | 0.020 | 0.033 | 0.035 | | 0.95 | 0.330 | 0.295 | |
| | 0.050 | 0.033 | 0.035 | | 0.97 | 0.330 | 0.295 | |
| | 0.100 | 0.036 | 0.043 | | 1.00 | 0.335 | 0.292 | |
| | 0.200 | 0.039 | 0.049 | | 1.00 | 0.339 | 0.290 | |
| | 0.400 | 0.045 | 0.050 | | 1.00 | 0.343 | 0.287 | |
| | 0.600 | 0.044 | 0.059 | | 1.00 | 0.344 | 0.285 | |
| | 0.800 | 0.048 | 0.062 | | 1.00 | 0.345 | 0.280 | |
| 4.62 | 0.010 | 0.033 | 0.035 | 0.50 | 0.91 | 0.245 | 0.210 | |
| | 0.020 | 0.034 | 0.040 | | 0.94 | 0.250 | 0.210 | |
| | 0.050 | 0.035 | 0.046 | | 0.95 | 0.251 | 0.205 | |
| | 0.100 | 0.037 | 0.051 | | 0.96 | 0.254 | 0.203 | |
| | 0.200 | 0.039 | 0.059 | | 0.96 | 0.255 | 0.196 | |
| | 0.400 | 0.045 | 0.070 | | 0.95 | 0.266 | 0.196 | |
| | 0.600 | 0.051 | 0.083 | | 0.96 | 0.269 | 0.186 | |
| | 0.800 | 0.051 | 0.084 | | 0.94 | 0.272 | 0.188 | |

slow sweep rates if the acid content of the solution exceeds 2N. In these conditions, the amplitude remains inferior to 15% if compared to i_p^{a1} . i_p^{a2} should actually be considered as a complex system since it is composed of two bumps.

The irreversible i_p^{a3} redox peak.—The corresponding voltammetric data are compiled in Table II. At potentials ca. 0.5V more anodic than the first i_p^{a1}/i_p^{c1} , the anodic run gives a second major redox peak i_p^{a3} which has apparently not been taken into account in the literature so far. Slow sweep rates and strong acid levels contribute to increasing the peak height i_p^{a3} (it is hardly detected above 0.1 V/sec; compare for example Fig. 1 and 2). An indicative plot of i_p^{a3} as a function of the pH variation gives an S-shaped trend, the larger variation being centered around pH 0.3. Thus, the i_p^{a3} peak amplitudes are no longer affected by acidity changes above H₂SO₄ 1M, at constant ν . Results also show that the peak

Table II. Cathodic-to-anodic current ratios as a function of the acidity and the scan rate for the half-cycles i_p^{a2} and i_p^{a3}

| H ₂ SO ₄ | ν (V/sec) | i_p^{a3}/i_p^{a1} | i_p^{a2}/i_p^{a1} |
|--------------------------------|---------------|---------------------|---------------------|
| 0.10N | 0.010 | 0.06 | — |
| | 0.100 | 0.05 | — |
| | 0.500 | 0.03 | — |
| 0.67N | 0.010 | 0.40 | — |
| | 0.100 | 0.06 | — |
| | 0.500 | 0.05 | — |
| 2.64N | 0.010 | 0.50 | 0.15 |
| | 0.100 | 0.28 | 0.09 |
| | 0.500 | 0.080 | — |
| | 0.010 | — | 0.16 |
| | 0.050 | — | 0.05 |

height i_p^{a3} increases linearly with the analytical pADA level. The function intersects the axis origin whereby the faradaic nature of the peak can be assessed. Otherwise, in given solution conditions, i_p^{a3} is also linearly related to the time gate measured past peak i_p^{a1} as shown by the straight function intersecting the origin of the i/t axis. This holds with time gates shorter than ca. 30 sec, thereafter a saturation profile takes place.

Cathodic peaks.—The cathodic features are related to the position of the switching potential E_λ . When E_λ precedes peaks i_p^{a2} , one unique cathodic peak i_p^{c1} rises up, the characteristics of which are compared to those of the associated i_p^{a1} in Table I. As soon as E_λ is reversed past i_p^{a2} , the cathodic half-cycle is displaced anodically by about 30 mV and the resulting peak i_p^{c2} is significantly increased if compared to the previous i_p^{c1} (Fig. 1). Finally, the effect of setting the E_λ potential back at 1.2V, i.e., after i_p^{a3} , is to promote new cathodic peaks of minor importance, on each side of i_p^{c1} , i_p^{c3} at 0.65V, and the shouldered-peak i_p^{c2} at 0.43V, the latter bearing some importance as is mentioned later on in the step coulometry studies. It must be noticed that in the same conditions authentic aniline samples oxidized voltammetrically at 1.0V exhibit three cathodic peaks located at 0.65, 0.51, and 0.43V, matching up in position and amplitude with i_p^{c3} , i_p^{c1} , and i_p^{c2} , respectively. It may be concluded that these additional systems are, at least partially, promoted by the species issued from the i_p^{a3} oxidation peak.

Step Coulometry Experiments with the Platinum Anode

The pADA oxidation mechanism was investigated using step coulometry at the 0.8V controlled potential

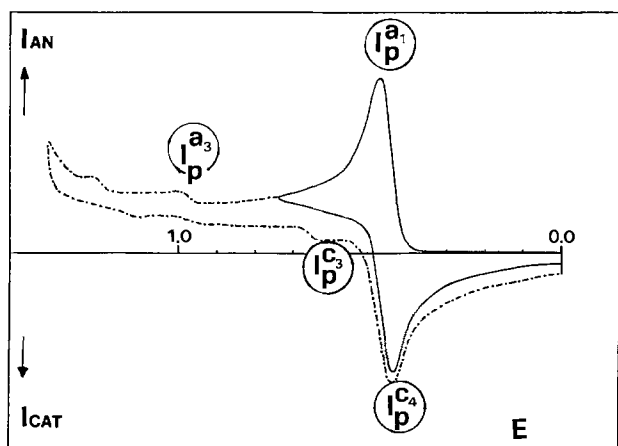


Fig. 2. CPE cyclic voltammograms of pADA in H_2SO_4 0.67N aqueous solutions. pADA 0.39 mmol; ν 0.100 V/sec.

in order to avoid interference with the i_p^{a3} system. Our results thus complete the data published previously in the literature and concerned with the exhaustive electrolysis of pADA at 1.0V for which $n = 6$ values have been collected. The data are reported on the diagram in Fig. 4; the voltammetric curves accounting for partially electrolyzed solutions up to one electron per pADA molecule are represented in Fig. 3; those for beyond that amount in Fig. 5.

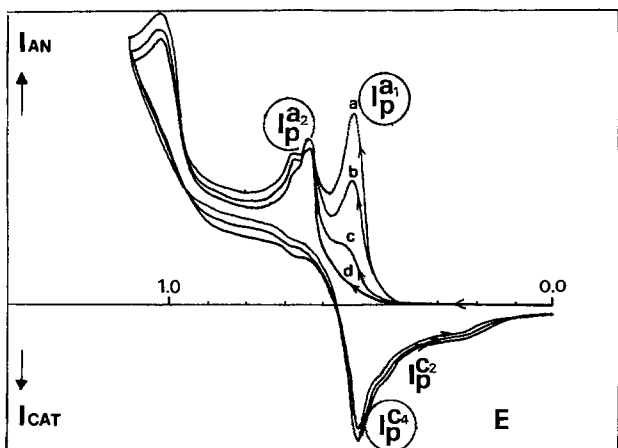


Fig. 3. CPE cyclic voltammograms of pADA in H_2SO_4 2.64N aqueous solutions partially electrolyzed at 0.8V. pADA 0.4 mmol; ν 0.010 V/sec. a, 0.25; b, 0.54; c, 0.85; d, 1.0 Cb/pADA.

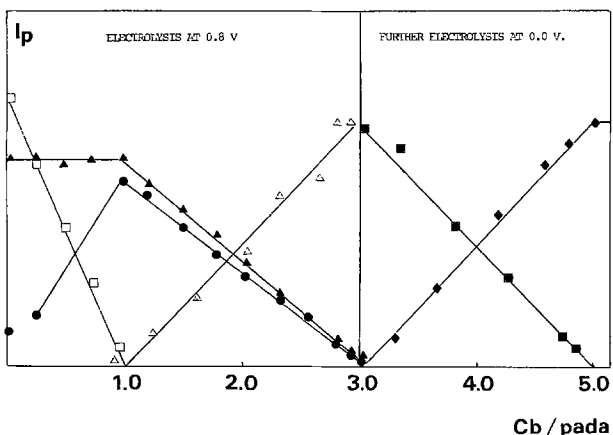


Fig. 4. Voltammetric peak amplitude variations as a function of the transferred coulombs. CPE electrode in H_2SO_4 2.64N at $\nu = 0.010$ V/sec. \square i_p^{a1} ; \bullet i_p^{a2} ; \blacklozenge i_p^{a3} ; \triangle i_p^{c1} ; \blacksquare i_p^{c2} .

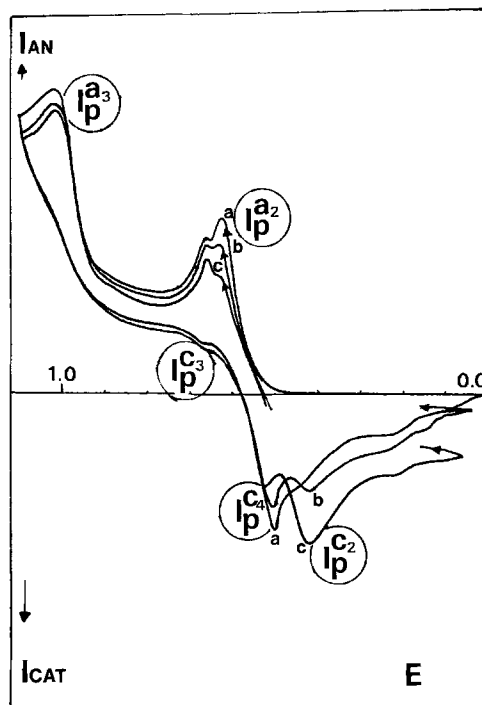


Fig. 5. CPE cyclic voltammograms of pADA in H_2SO_4 2.64N aqueous solutions partially electrolyzed at 0.8V. pADA 0.4 mmol; $\nu = 0.010$ V/sec. a, 1.0; b, 1.15; c, 1.50 Cb/pADA.

One electron step coulometric oxidation.—A break in the charge/time curve indicates first a fast transfer of 1.00 ± 0.05 electron per depolarizer molecule. A transient deep-blue coloration results before the solution turns gradually deep-green. Voltammograms traced while the electrolysis is performed show a correlative decrease of peak i_p^{a1} . This peak vanishes when the faradaic equivalency is attained, whereas the associated cathodic trace remains unaltered (if compared to the unelectrolyzed solution) if E_λ is reversed past i_p^{a2} . When E_λ is reversed just after i_p^{a1} , the decrease of i_p^{c1} parallels that of i_p^{a1} . The limitation of the anodic exploration to past the first peak i_p^{a1} also results in constant i_p^{c1}/i_p^{a1} values. As shown in Fig. 3 and 4, i_p^{a2} increases while i_p^{c1} remains constant with increasing electrolysis. This suggests that i_p^{a2} is relevant for the oxidation of relatively stable products being formed during the initial step of the electrochemical oxidation, while i_p^{c1} is promoted by the reduction of products generated via i_p^{a1} and i_p^{a2} .

Over one-electron step coulometry oxidation.—At this time, the voltammograms have to be started from the rest potential of the solution located in the region of the disappeared first peak. After the transfer of the first electron, two additional charges are necessary to ensure the consummation of peaks i_p^{a2} ; meanwhile, a gradual lightening of the deep-green coloration can be observed in the solution. At the end of the experiment, the only remaining anodic feature is represented by the peak i_p^{a3} , not concerned with the electrolysis conducted at 0.8V; when the used scan rates are slow, the peak amplitude remains constant and reflects the sum of the bulk and electrode concentrations of the species undergoing oxidation at 1.0V.

The major change in the cathodic features rises up with the extension of peak i_p^{c2} at 0.43V, which gradually overlaps i_p^{c1} (Fig. 5). It must be noted that peak i_p^{c2} originally exists as a shoulder promoted by the precursor oxidation at i_p^{a1} (Fig. 1) or by the use of industrially purified (atmospherically oxidized) pADA samples. The decrease of peak i_p^{c1} (i_p^{c1} merges with i_p^{c2} on the cathodic back runs traced from 1.2V) occurs in proportion to the increase of peak i_p^{c2} (Fig. 4).

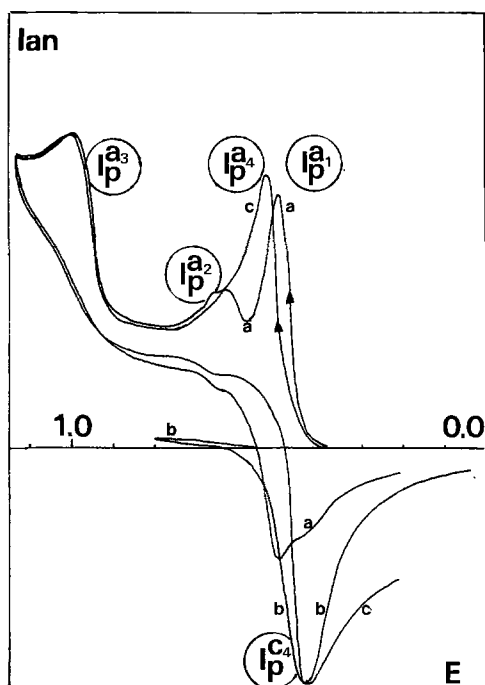


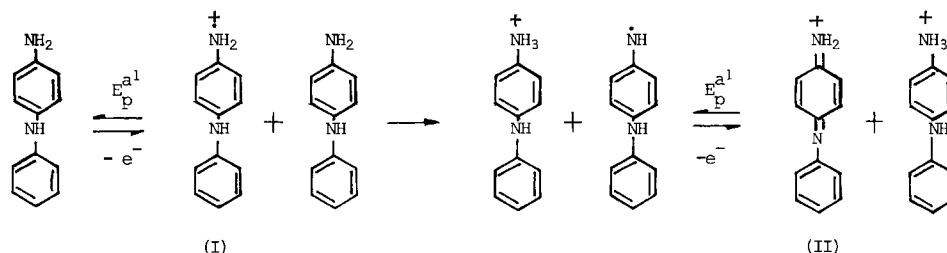
Fig. 6. CPE cyclic voltammograms of pADA in H_2SO_4 2.64N aqueous solutions partially electrolyzed. pADA 0.30 mmol; $\nu = 0.010$ V/sec. a, Initial solution; b, following 3 Cb/pADA electrolysis at 0.8V; c, after the 2 Cb/pADA electrolysis at 0.0V following b.

These observed changes operate within the two-electron coulometric transfer in proportion to the charge balance exceeding one equivalent; thereafter, the solution is no longer oxidizable at 0.8V and the cathodic peak heights remain constant.

Reverse step coulometry at 0.0V following that conducted at 0.8V.—After the exhaustive three-electron electrolysis carried out at 0.8V, the controlled potential was set at 0.0V in order to integrate the oxidative capacity of the resulting solution. The Q /time function indicates the rapid proceeding of a two-electron reduction per original pADA molecule. The final voltammogram consists in an anodic peak i_p^{a4} (Fig. 6) at $E_p^{a4} = 0.53\text{V}$ (slightly more anodic than the disappeared i_p^{a1} peak), exempted from the i_p^{a2} peaks characteristic of the pADA basic system and preceding the still remaining and unchanged i_p^{a3} peak. Thus, the reverse electrolysis conducted alternatively at 0.8 and 0.0V apparently operates the irreversible change from the original pADA reducer to a mixture composed of two electroactive reducers able to undergo two oxidations, at 0.53V (reversible) and at 1.0V (totally irreversible), respectively.

Visible Spectroscopy

Visible spectral curves recorded for partially electrolyzed solutions of pADA in 2.64N H_2SO_4 are shown in Fig. 7 a-b. Whereas the initial curve and the final



curve following the exhaustive 3 Cb/pADA electrolysis are characteristically weak and ill-defined, intermediate solutions exhibit one intense and transient absorp-

tion band in the pADA region around 750 nm (6) and a weak band at 420 nm, in the quinone absorption region; another transient absorption band, not attributed, occurs at 500 nm. The increase of the major absorption band, related to the number of transferring coulombs, reaches a maximum value for one equivalent, thereafter it decreases gradually as shown in Fig. 7b.

Discussion

Electroanalytical Results

Since no apparent break produces on the E_p^{a1} vs. pH plots and since the i_p^{a1} values are mediated by viscosity changes rather than by changes in the diffusion coefficients, it can be postulated that in the studied pH range the same reacting species undergo oxidation at the electrode surface. It follows that fast deprotonation reaction(s) ought to precede the electron transfer, with rates unable to compete with the potential sweeps that have been used. Such a conclusion is in agreement with comparative chronopotentiometric (10) and voltammetric (11) studies performed with numerous aromatic amines in aqueous H_2SO_4 solutions. For example, as opposed to *N,N*-dimethyl *p*-phenylenediamine and *p*-phenylenediamine, the oxidation pathway of pADA and of diphenylamine were found to behave quite differently. In particular, no region of kinetic control occurred in the studied pH range. Likewise, the mechanism for the electrochemical oxidation of anilinium solutions involved a fast precursor deprotonation step following adsorption onto the electrode (12). It will therefore be postulated that the oxidation peak i_p^{a1} involves the same form, whatever acidity level condition prevails. This form is supposed to be the uncharged depolarizer molecule, for another assumption would less easily explain the ease of the oxidative attack and the stability of the multicharged species that would result from the oxidation as well. Above pH 7.5-8, the anodic-to-cathodic peak separation splits, as a result of a hydrolysis reaction affecting the oxidized species under mild alkaline conditions (13a).

To keep constancy with the coulometric results, it is necessary to envisage that two neutral molecules of the depolarizer participate globally in the oxidation step, thus transferring an equal number of electrons. These two charge transfers are separated by a chemical conversion, as indicated by the slope of the $i_p^{a1}/C \cdot \nu^{1/2} = f(\nu^{1/2})$ function. Slow scan rates allow the reaction to proceed without interfering with the second charge transfer. Accordingly, with reference to the $E_p^{a1} - E_p^{c1}$ and $E_p^{a1} - E_p^{a1}$ (1/2) values, two electrons are kinetically exchanged successively. Conversely, applications of faster scan rates show only the transfer of one electron, owing to the competitive chemical reaction. Hence, just one parent molecule loses apparently one electron, the second species merely serves as a neutralizing organic base, all the more effectively as it would exist under the uncharged form.

In the framework of the aforementioned assumptions, it is obvious that the cation radical I is formed after the primary electron transfer (scheme 3)

The involvement of radicals in the follow-up reaction was indirectly assessed. Hydroquinone is normally oxidized at 0.65V using the same solution conditions.

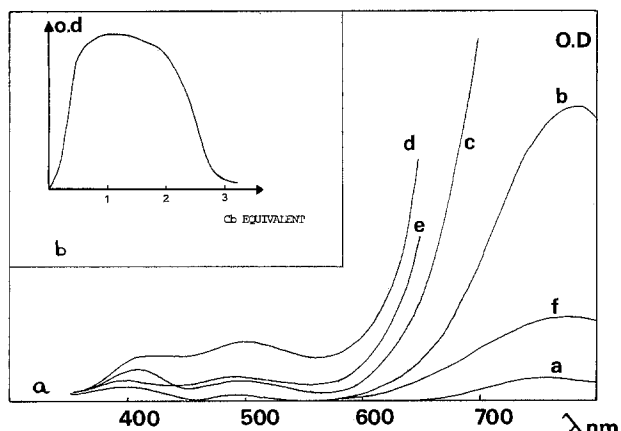
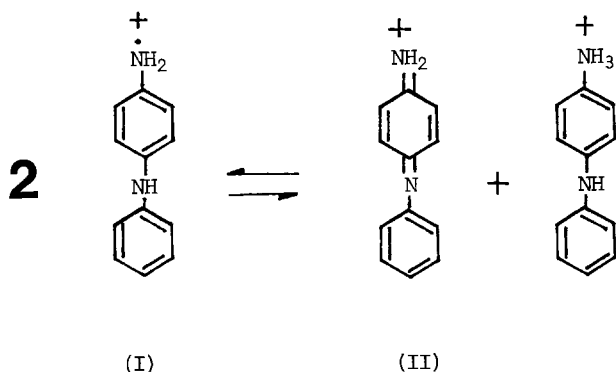


Fig. 7. a. Visible absorption spectra of partially electrolyzed pADA solutions in H_2SO_4 2.64N. a, Initial solution; b, after the transfer of 0.25; c, 0.50; d, 1.0; e, 2.0; f, 3.0 Cb/pADA. b. Variation of the absorption maximum at 780 nm as a function of the extent of the electrolysis.

Since it is known to form stable radicals in acid solutions, mixtures with pADA solutions were prepared. The cyclic voltammograms resulted in the enhancement of the first peak in proportion to the added amount of hydroquinone. Otherwise, another evidence is brought by the involvement of free radical steps in the oxidation mechanism of related compounds with peroxidase (14).

The fate of the cation radical will depend both on the acidity conditions close to the electrode surface and on the scan rate. Since low acidities prove to facilitate the proton loss in favor of another parent molecule, the transient formation of the neutral semiquinone radical must be postulated. The latter species is presumably much more oxidizable than the original reducer or than its protonated form. This would explain the occurrence of the second electron transfer at the same working potential, accounting for an ECE-type sequence.

In fact, the stability of the semiquinone radical cation I is mediated by the disproportionation reaction (4), which is pH-dependent



Spectrophotometric determinations conducted on p-phenylenediamine confirm the involvement of this charged radical in the solution on mixing solutions of the amine with chemical oxidants, such as bromine (15) or ferricyanide (13b). In acid solutions at $\text{pH} < 4$, the equilibrium is almost completely displaced to the left, as was shown in the bulk.

Turning back to the pADA system, it is clear that an analogous qualitative conclusion, ruling out the thermodynamics of these species, may be drawn out. Although pADA shows a less symmetrical structure, its resonance ability will expectably be enhanced due to the presence of the additional aromatic ring. At the electrode surface, however, where deprotonation con-

ditions are locally operating, the stability of this charged radical would be hindered and its existence mediated by an acid-base conversion involving, as deduced above, the deprotonated pADA acting as a strong base. Therefore, the alternate mechanism setting into play the disproportionation reaction of the radical cation as the follow-up reaction will not be preferred. As a result, two monoprotated species are kinetically assumed to form at the electrode surface, in two limit oxidation levels, the acid pADA form, on the one hand, and the charged p-quinonediimine II (pQDI), on the other.

Follow-up Reactions

It has been previously deduced from chemical oxidation experiments conducted with similar compounds that the diimine forms offer a weak resistance to irreversible changes when exposed to solvents such as water (16) or acetic acid (15). However, the reactions are not known for certain to be hydrolyses in any case. The results presented herein show that a fast electroanalytical technique, such as cyclic voltammetry combined with step coulometry at controlled potential, will give some insight into the preliminary stages of the hydrolysis.

There is no question as to the possible occurrence of 1,4 addition reactions in the oxidation of aromatic amines, as outlined in Feiser's study (17). The 1,4 addition (Michael) reaction of a nucleophile with quinoid systems is well established and is assumed to play a predominate role in the follow-up reactions. The rates of these reactions are pH dependent, since they involve reactions of the free base forms of the attacking nucleophile on the partially positively charged 2 position of the quinoid. Results presented elsewhere (13c,d) have shown that the chemical oxidation of p-phenylenediamine, a model compound for pADA, gives Bandrowski bases as major product under mild pH conditions. The mechanism accounting for the formation involves the 2,5 coupling of two protonated diimine molecules to the unoxidized amine, followed by the oxidation of the resulting trimer in the 2,5 p-diimine p-phenylenediamine form. Although the proposed kinetic scheme could not be extended to acid solutions, it was nevertheless clearly indicated that the addition products require monoprotated reacting species to be formed, even in the used mild pH conditions. Keeping in mind that the oxidative coupling of p-anisidine has been similarly realized in hydrochloric solutions (14), the viability of such coupling reactions in acidic media cannot be disregarded, irrespective of the charge status of the reacting species. From that point of view, the partial positive charge at the 2 site should be more facilitated in the p-quinone form than in pQDI, and in the protonated diimine form than in the neutral pQDI (18).

Another mechanism has been proposed to account for the oxidation of aniline in acidic solutions, based on the linear coupling (dimerization) of one pQDI and one pADA molecule to form an adduct called Willstätter blue imine (WBI). Through several oxidation steps combined with further additions of the parent molecule, the sequences are assumed to explain the formation of the octamer, emeraldine. Willstätter red imine (WRI), the oxidized counterpart of WBI, has been intermediately postulated. Under mild pH conditions, additions of the initial material in the 2,5 position on the pQDI have also been envisaged and characterized using thin layer chromatography analysis at the preparative scale (19).

First redox couple.—Our results outline the relative chemical resistance of the first redox couple, as shown by the constancy of the i_p^{c1}/i_p^{a1} ratio, regardless of the number of consecutive cycles when they are strictly applied to the first oxidation peak. Upon step electrol-

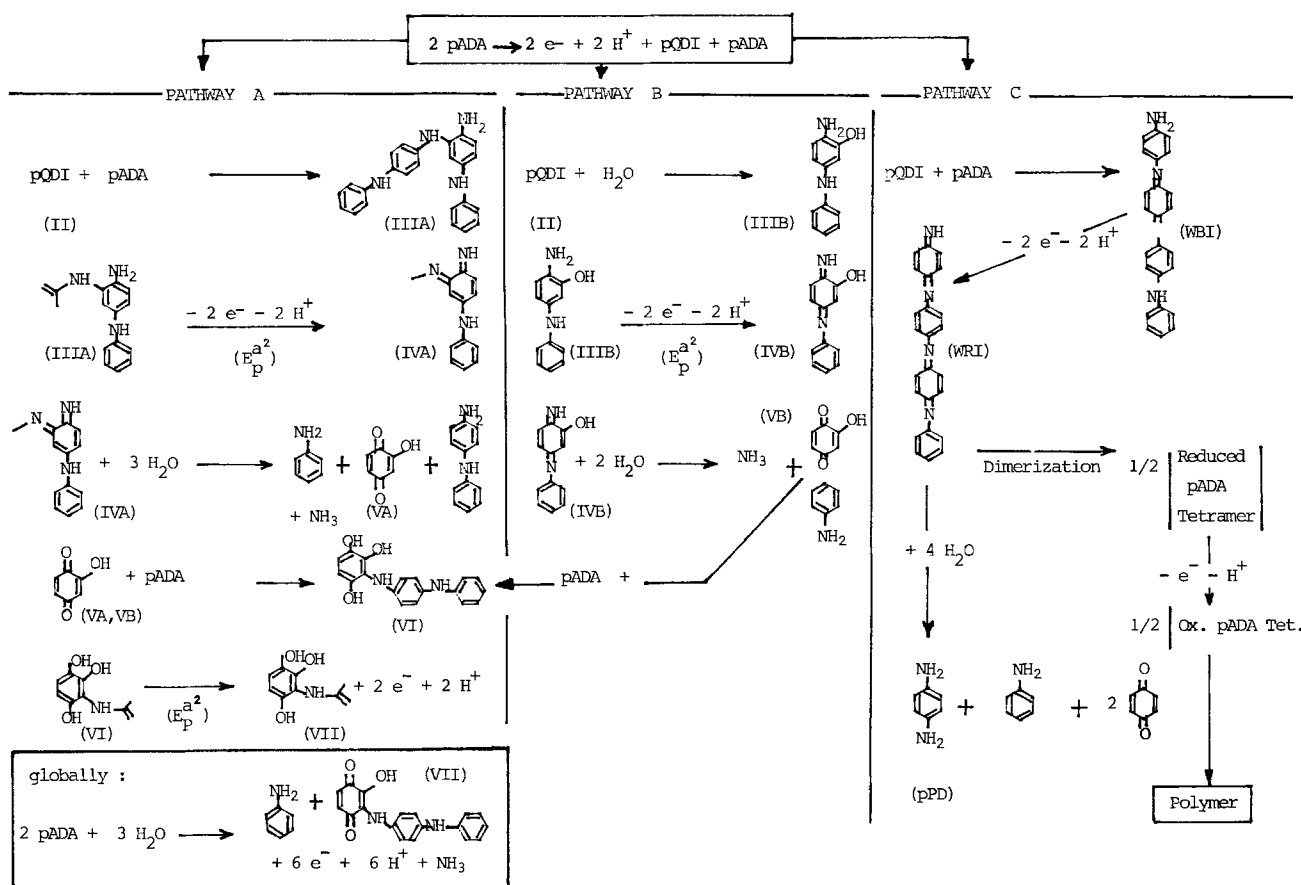
ysis, the wave height $i_{p^{a1}}$ is always proportional to the analytical amount of the depolarizer still remaining in the solution and the reverse half-cycle corresponds only to the reducible pQDI diffusing in the vicinity of the electrode. Thus, within the potential span ruling out the first redox couple, no material consuming irreversible conversion of significant importance can be electrochemically detected. This suggests that in turn the oxidized pQDI product, originated by the partial electrolysis and escaped in the bulk, is irreversibly involved in a follow-up reaction, yielding species that undergo a further oxidation at the $i_{p^{a2}}$ potential.

Second redox couples $i_{p^{a2}}$.—The potential controlled electrolysis cannot be circumscribed about the first peak for $i_{p^{a1}}$ is only separated by few tenths of a volt from $i_{p^{a2}}$. Therefore, the voltammetric features following the partial electrolysis of the solution at 0.8V actually integrate the reactions occurring at peak $i_{p^{a2}}$ too. With respect to the magnitude of the peak heights, $i_{p^{a2}}$ appears rather as a side-system if compared to the amplitudes of the major redox couples $i_{p^{a1}}$ and $i_{p^{a3}}$. As indicated previously, the kinetic requires strong acid conditions and develops irreversibly for being solely detectable with scan rates slower than 0.05 V/sec. For these reasons, the voltammetric contribution of this system remains minor. In contrast, this system becomes preponderant in the electrolysis balance, i.e., under long term conditions. In a similar manner, when the potential is multicycled over the span including $i_{p^{a2}}$, the

sated by the increase of new reducible species, the sum of the cathodic peaks remaining constant.

The occurrence of the peaks $i_{p^{a2}}$ marks the existence of new species present at the electrode surface in an intermediate level of oxidation, obviously comprised between those of pADA and pQDI, since both are no longer oxidizable at this potential. This may suggest that the charged pQDI and pADA molecules, being actually present simultaneously at the electrode surface, interact to form an oxidizable adduct, in proportion of increasing $i_{p^{a2}}$ values. Of interest in these experiments are the colors of the solutions. In the case of the dimethylaniline system (11), the solutions containing only the diimine form are green, whereas the solutions of the diimine plus the amine appeared pale blue. This observation has been attributed to addition compounds of the amine with oxidation products.

Inasmuch as an addition reaction is envisaged between the pQDI and the pADA species with the support of the aforementioned features, several mechanisms can be tentatively formulated to describe the fate of the adduct. Among those proposed in the literature so far, the following ones are retained for they integrate the coulometric results obtained in this study. The data reported in Fig. 4 indicate that two electrons per molecule are further transferred. These exchanges follow the precursor reaction producing pQDI and the chemical conversion of the latter. The mechanisms differ from each other in the nature of that irreversible reaction (scheme 5)



cyclic voltammograms show an increase of peak $i_{p^{a2}}$. In the cathodic part, the global content of reducible material remains constant when the potential is switched beyond peak $i_{p^{a2}}$. This can be interpreted in the following manner: the reduction of the material produced in the $i_{p^{a2}}$ steps occurs irreversibly at 0.51V ($i_{p^{c1}}$), close before the true reduction peak of the pQDI produced at the electrode surface at $E_p^{c1} = 0.48\text{V}$; as a result, the loss of reducible pQDI is gradually and fully compen-

Pathway A: the addition of one pQDI onto one pADA molecule in the ortho position leads to a dimeric Bandrowski-type reduced base (IIIA).

Pathway B: the bulk hydrolysis of pQDI produces the o-hydroxy pADA form (IIIB).

In each case, the resulting product being easily oxidized would release electrons at the potential ascribed to $i_{p^{a2}}$.

Third anodic redox system.—In studying the acid hydrolysis of the Bandrowski bases, ammonia, aniline, and the original amine have been identified, aside from a quinoidal derivative, the structure of which is related to that of the starting amine (13c). The extension of that behavior to either possible pathway A or B would yield the same compound, the 2 hydroxy p-quinone ($VA = VB$), as depicted in scheme 5. The fit with the coulometric data implies that two depolarizer molecules react within the global kinetic sequence. Thereby, the typical 1,4 addition reaction can be postulated again involving the resulting p-quinone with aromatic amines, *i.e.*, the starting material. The products of these reactions are now substituted hydroxy-quinones, which are also oxidizable below 0.8V, species VI.

The following arguments have supported the proposed mechanisms:

1. Since the 1,4 addition involves the nucleophilic nature of the attacking molecule, substitution reactions of nucleophilic groups by the hydroxyl moiety will not be assumed to occur, especially under mild electrolysis and pH conditions.

2. All the mechanisms, even those suggested elsewhere, result in the formation of aniline, in a $\frac{1}{2}$ theoretical ratio with the pADA concentration. This leads us to discuss the nature of the third major redox peak $i_{p^{as}}$ detected at 1.0V. The oxidation of species existing in the solution, in initial thermodynamic equilibrium with the depolarizer, can be disregarded for in that case the redox couple would not be observable at all after the coulometric consumption of the first. Accordingly, the irreversible system $i_{p^{as}}$ must account for the oxidation of stable (the corresponding wave appears after the electrolysis and on the voltammogram traced at 0.01 V/sec with the same intensity) species issued from the first stages. The hypothesis that peak $i_{p^{as}}$ results from the oxidation of new species issued from irreversible conversions is supported by the following observation: the amplitude of peak $i_{p^{as}}$ is proportionally related to the peak height $i_{p^{a1}}$ and only depends on the time gate (or on the scan rate); this holds for a given acidity level. There is no doubt that the position and the shape of peak $i_{p^{as}}$ match those of aniline in the same working conditions. This was shown on the cyclic voltammogram on mixing authentic samples. If this compound is supposed to form upon a proton-catalyzed decomposition of the adducts, it follows that the cathodic half-cycle initiated once the aniline oxidation has been achieved should integrate the behavior of both the oxidized aniline and the remaining pADA. Inspection of the data for the $i_{p^{c1}}/i_{p^{a1}}$ ratio as a function of E_{λ} indicates an increase in the amount of reducible material at the electrode with increasing E_{λ} (Table I). This is due to an accumulation of reducible pQDI provoked by direct pADA oxidation at the working potential and indirectly after the head-to-tail coupling of the aniline oxidation products. Moreover, the peak $i_{p^{c3}}$ also matches in position with that of oxidized benzidine, the alternate tail-to-tail coupling product of the aniline cation radicals (6). This is confirmed by the appearance of peak $i_{p^{c3}}$ solely when the potential is reversed after the aniline oxidation peak (Fig. 2). On this basis, the estimation of the decomposition rate in aniline leads to the value $k_1 = 0.0027 \text{ sec}^{-1}$ in H_2SO_4 0.1N in agreement with values evaluated for model compounds (8). Thus, postulating the hydrolytic generation of aniline and quinones supports the fact that no significant decrease in magnitude affects peak $i_{p^{c1}}$, although $i_{p^{as}}$ reaches in optimal conditions up to 50% of peak $i_{p^{a1}}$. As a result it seems that the appearance of $i_{p^{as}}$ is neither determined by the charge status of the species [as observed in acidic acetonitrile solutions (20)], nor by the oxidation levels. The amplitude of peak $i_{p^{as}}$ reflects the full extent of the decomposition reaction in the solution or,

with slow scan rates, at the electrode surface, instead; in the latter case, the measurement of the final aniline concentration level gives in any case a $\frac{1}{2}$ estimate in good agreement with what might be expected from the pathways proposed. The conversion of $i_{p^{as}}/i_{p^{a1}}$ values in terms of concentrations was effectuated with the aid of aniline calibration curves.

3. pADA possesses a more pronounced nucleophilic character than aniline. Therefore, the chemical addition of pADA to the hypothetical quinone will always be preferred to that of aniline. This assumption is actually supported experimentally by the constancy of peak $i_{p^{as}}$ ascribed to the amount of aniline (not affected in that experiment) issued from the preceding decomposition reactions.

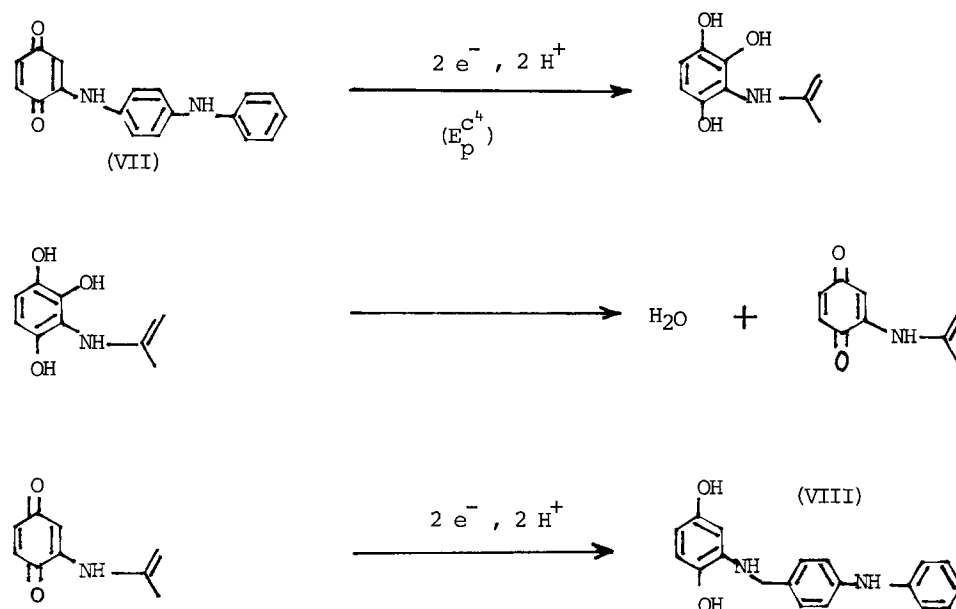
4. The addition of two pQDI molecules on the initial parent molecule instead of one as is figured in pathway A would disagree with the coulometric data.

5. In accordance with these data instead, three electrons are globally exchanged in pathways A and B, if the third irreversible stage is limited to the addition of one parent molecule onto the quinone (this may reasonably be envisaged with respect to the saturation of the quinone).

6. According to the hypothesis of a linear dimer formation involving the head-to-tail dimerization of pADA with pQDI, the net effect of the hydrolysis reaction would, after the oxidation of the products, generate p-phenylenediamine (pPD) (see pathway C in scheme 5). However, the multicycling of the potential does not show evidence for the superimposition of a new depolarizer system on the initial pADA system. On the other hand, the coupling reaction followed by oxidation would form another imine form able to couple again with the starting material. This was the basis of the proposed mechanism accounting for the formation of emeraldine (19). As a result, the number of exchanged electrons would probably be odd and not reproducible experimentally speaking, as might be expected from an oligomerization reaction producing insoluble products, which ought to deposit on the electrode. We actually did not observe such an electrochemical behavior nor the occurrence of red color formation during the electrolysis experiment which would be due to WRI formation. The divergence in the experimental observations may account for the differences in the analytical concentrations used. This effect shall be determinant in the product distribution; low levels inhibiting the polymerization pathway. Therefore, the latter pathway C will not be preferred. In fact, insoluble green polymers have been observed in more concentrated depolarizer solutions.

The assignment of the pathways A and B for the possible mechanism would be fully supported by the identification of the substituted 2 hydroxy 3 pADA p-quinone. However, the voltammetric behavior in the cathodic part does not allow drawing unambiguous conclusions with respect to this point. Indeed, the cathodic behavior of quinones appears to be severely modified when the reduction is carried out in the presence of oxidized amines. For example, with mixtures of authentic aniline and p-quinone, the potential of the p-quinone reduction peak is shifted *ca.* 0.15V anodically when it is preceded by the oxidation of aniline. The apparent increase in the reversibility of the electrochemical transfer would be induced by the formation of amine radicals during the cathodic half-cycle. Therefore, quinones in mixture with oxidized amines cannot be voltammetrically identified on the simple basis of the matching of the peak potentials. This observation indicates that the electrochemical behavior of quinones and of quinoneimines exhibits some resemblance, especially in the presence of unoxidized amine, thus justifying *a posteriori* the viability of the quinone/amine and pQDI/amine coupling reaction.

However, an experimental indication evidencing these pathways is brought by the result of reverse electrolysis. The experiment was conducted discontinuously in two steps: first at 0.8V until three electrons have transferred, then back at 0.0V. The voltammograms indicated the gradual increase of an oxidation peak i_p^{a4} associated with the decrease of the reduction peak produced upon the three electron oxidation, i_p^{c4} (Fig. 4). The found balance of two additional electrons per pADA molecule is compatible with the reduction of the last reducible product remaining in the solution after the exhaustive electrolysis at 0.8V, the hypothetical 2 hydroxy 3 pADA p-quinone, according to the following reaction scheme



The first two-electron reduction would produce the 3 substituted 2 hydroxyhydroquinone, which in turn is known to undergo a second reduction step following the abstraction of one water molecule (7). At this time, the voltammogram indicates that the intermediate chemical reaction operates the removal of water rather than pADA as shown by the unaffected i_p^{a3} peak height, which would increase instead, in proportion to the reductive electrolysis. This illustrates again the nucleophilic character of the addition reaction, neutral pADA being a base much weaker than the hydroxyl anion.

Qualitatively, the effect of the reverse electrolysis is to denature the chemical nature of the initial reducer, pADA, since the final and unique reduction half-cycle only reflects the presence of one species, probably the 2 hydroxy 3 pADA p-quinone and the remaining aniline. In particular, peaks i_p^{a3} no longer appear on the resulting voltammograms (Fig. 6). Thus, the free pADA, abstracted from the solution through the electrolysis, ought to substitute one species, for example the quinoidal VII or VIII. As a result of the three-electron electrolysis conducted at 0.8V, the final redox couple ought to involve a substituted quinone/hydroquinone system, aside from aniline, and not an unsubstituted one, not compatible with the two-electron re-oxidation data.

Visible spectroscopy experiments were performed during the step electrolysis to furnish some support for discriminating between the proposed mechanisms. Results showed that unsubstituted p-quinone samples absorb negligibly and that aniline does not absorb at all in the used conditions. However, the large increase affecting the broad band for pADA absorption (around 780 nm) following the first one-electron transfer and the residual maximum at the same position after the extensive three-electron electrolysis may testify for

the strong resonating species IIIA and IVA and for the existence of the pADA radical substituting the quinone VII, respectively, rather than for the detection of species IIIB and IVB, of much less resonating ability. The development of the latter absorption band is clearly related to the blue coloration affecting partially electrolyzed pADA solutions. By analogy with studies concerned with model compounds (11), it may account for the formation of disproportionation products (IIIA or IVA), derived from the pQDI/pADA coupling. It must be emphasized that the reconstituted aniline and p-quinone mixtures are pale yellow, as also are the pADA solutions fully electrolyzed at 0.8V upon standing overnight; while the solutions freshly

oxidized electrochemically are pale green. This shows, at least qualitatively, that the product distribution resulting from short-term experiments differs somewhat from that obtained with other duration conditions or with atmospheric oxygen as the oxidant. Another fact may account for pathway A. During the one-electron step electrolysis experiment, the position of the peak maximum i_p^{a2} , if projected onto the ordinates, remains constant whereas the global peak height increases. When it reaches its maximum value, i_p^{a2} is about half i_p^{a1} (Fig. 3). Inasmuch as peak amplitudes are correlated to concentrations, this observation might indicate, through the changes of the diffusion coefficients, the oligomeric structure of the diffusing species, i.e., IIIA rather than IIIB. Unaffected two-electron peak amplitudes in the cathodic half-cycle would also corroborate the aforementioned assumptions.

Conclusion

The proposed mechanism A for the pADA first stages of oxidation has been distilled from the electroanalytical and spectroscopic data discussed in the preceding section. It must however be emphasized that mutual exclusion cannot be claimed in the proposed pathways. For example, free radical formation with sufficient lifetime should indeed be possible in the solution. As suggested by slow scan cyclic voltammetry and step coulometry experiments, the electrolysis at 0.8V appears to convert the pADA system into a mixture of aniline and of the proposed quinoidal derivative, via the hydrolysis of the intermediate species. Under the employed working conditions, any loss of the global redox content of the initial material has not been observed in the solution phase, indicating thus that the formation of insoluble (nonelectroactive) heavy molecular weight compounds would not be favored, at

least in the low concentration range and in the earlier stages of the oxidation. Thereby, the electroanalytical behavior of pADA appears to differ from that being described in more concentrated solutions (as in the preparative scale, for example), in which insoluble products result.

The two techniques employed do not support pathway A unequivocally. In particular, the coulometric data just furnish a global balance of the charges transferred, regardless of the structure of the species being formed. Thus, species VII, aside from aniline as the possible product, conveniently translates the redox content of the solution under a unique and concise form, although several other tautomeric forms can be formulated.

This depicted mechanism lacks from more convincing evidence as might be provided by direct product identification. However, the complexity of the system, with the involvement of the original species and the difficulty of characterizing products in the 0.1 mmol concentration range, prevents the somewhat speculative arguments presented in the discussion. From this point of view, however, it is typical to notice that the foregoing attempts described in the literature failed to isolate the possible intermediates and even to detect them in the electrolyzed solutions. The results presented in this work yet give an indicative new insight in the nature of the hydrolytic sequence.

Manuscript submitted Sept. 18, 1980; revised manuscript received Jan. 5, 1981.

Any discussion of this paper will appear in a Discussion Section to be published in the December 1981 JOURNAL. All discussions for the December 1981 Discussion Section should be submitted by Aug. 1, 1981.

Publication costs of this article were assisted by the Université Paris-Nord.

REFERENCES

1. J. M. Nigretto and M. Jozefowicz, *Thrombos. Res.*, **17**, 611 (1980).
2. M. Daraio de Peuriot, J. M. Nigretto, and M. Jozefowicz, *ibid.*, **19**, 647 (1980).
3. M. Daraio de Peuriot, J. M. Nigretto, and M. Jozefowicz, *ibid.*, Part III, In press.
4. M. Daraio de Peuriot, J. M. Nigretto, and M. Jozefowicz, *ibid.*, Part IV, In press.
5. J. Bacon and R. N. Adams, *J. Am. Chem. Soc.*, **90**, 6596 (1968).
6. R. L. Hand and R. F. Nelson, *ibid.*, **93**, 850 (1974).
7. R. L. Hand and R. F. Nelson, *This Journal*, **125**, 1059 (1978).
8. D. W. Leedy and R. N. Adams, *J. Am. Chem. Soc.*, **92**, 1646 (1970).
9. R. S. Nicholson and I. Shain, *Anal. Chem.*, **37**, 178 (1965).
10. H. B. Mark, Jr., and F. C. Anson, *ibid.*, **35**, 722 (1963).
11. T. Mizoguchi and R. N. Adams, *J. Am. Chem. Soc.*, **84**, 2058 (1962).
12. D. M. Mohilner, R. N. Adams, and W. J. Argeringer, Jr., *ibid.*, **84**, 3618 (1962).
13. J. F. Corbett, (a) *J. Chem. Soc.*, 213 (1969); (b) *ibid.*, 207 (1969); (c) *ibid.*, 818 (1969); (d) *ibid.*, 71 (1969).
14. D. G. H. Daniels and B. C. Saunders, *ibid.*, 2112 (1951).
15. L. Michaelis and E. S. Hill, *J. Am. Chem. Soc.*, **55**, 1481 (1933).
16. L. Michaelis, M. P. Schubert, and S. Granick, *ibid.*, **61**, 1981 (1939).
17. L. F. Feiser, *ibid.*, **52**, 4915, 5204 (1930).
18. R. N. Adams, "Electrochemistry at Solid Electrodes," M. Dekker Inc., New York (1969).
19. L. Dunsch, *Electroanal. Chem. Interfacial Electrochem.*, **61**, 61 (1975).
20. T. M. H. Saber, G. Farsang, and L. Ladanyi, *Microchem. J.*, **17**, 220 (1972).

Spectroelectrochemistry of N-Retinylidene-n-butylamine

Kenneth J. Stutts, Linda A. Powell, and R. Mark Wightman

Department of Chemistry, Indiana University, Bloomington, Indiana 47405

ABSTRACT

The electroreduction of N-retinylidene-n-butylamine (NRBA) has been examined in acetonitrile and dimethylformamide solvents with tetra-n-butylammonium perchlorate as the supporting electrolyte. In dimethylformamide with small amounts of water and in acetonitrile, NRBA is reduced in a two-electron process to form the enamine of 5,6-dihydro-NRBA. In dimethylformamide dried with alumina, the radical anion ($\lambda_{\max} = 615$ nm) and dianion ($\lambda_{\max} = 550$ nm) of NRBA can be observed in an optically transparent thin layer electrochemical cell. The protonated form of NRBA is reduced in acetonitrile at a potential 1080 mV positive of NRBA in a one-electron process. Radical intermediates have not been spectrally observed in this reduction, since the electrogenerated products dimerize rapidly.

N-retinylidene-n-butylamine (NRBA) has been widely employed as a model for the chromophore of rhodopsin (1-11). In the protein, the aldehyde of vitamin A is thought to form a protonated Schiff's base linkage with lysine (12, 13) and is responsible for the first stage of the visual transduction process. The initial photochemical excitation of rhodopsin has been extensively studied and several theories including photoreduction (2, 7, 14-20) have been considered to explain the observed spectroscopic changes. However, the reductive electrochemistry of NRBA has not been

previously reported although an ESR active species has been observed following uncontrolled potential electrolysis (2).

Electrochemical studies of retinal, the aldehyde of vitamin A, have been numerous (20-23). Recently, we showed that an optically transparent thin layer electrochemical cell is an ideal tool for examining the spectra of the reduction intermediates of retinal and for determining the reaction pathways of the retinal radical anion (23). In this paper we report a spectroelectrochemical study of the reduction intermediates and products of NRBA in its neutral and protonated form.

Key words: vision, aprotic solvents, radicals.

Experimental

Chemicals.—All-trans retinal (Eastman) was used as received and was stored in the dark in a desiccator under nitrogen at 5°C. N-butylamine (Matheson Coleman and Bell) was distilled immediately prior to use. Acetonitrile (Burdick and Jackson) was dried over 4Å molecular sieves (Fisher) beneath a nitrogen atmosphere. N,N-dimethylformamide (DMF, Matheson Coleman and Bell) was vacuum distilled onto 4Å molecular sieves. Subsequent drying was accomplished by passing this solvent through a column containing neutral aluminum oxide (Woelm, activity grade 1) which had been dried at 450°C for at least 10 hr (24, 25). Tetra-n-butylammonium perchlorate (TBAP, G. F. Smith) and tetraethylammonium perchlorate (TEAP, G. F. Smith) were dried at 60°C in a vacuum oven for several hours. Rhodamine 6G (Matheson Coleman and Bell) and anthraquinone (Eastman) were recrystallized from ethanol. Perchloric acid (70%, Mallinckrodt) and acetic acid (Mallinckrodt) were used as received, and stock solutions of the acids were prepared in the appropriate solvents. The perchloric acid stock solution was standardized vs. 0.2N sodium hydroxide (Certified, Fisher). Phenol (Liquified, Fisher) was vacuum pumped to dryness and then fractionally distilled. (The liquified form was utilized as it contains no H₃PO₂ preservative.) A stock solution in acetonitrile was then made by the appropriate dilution and stored over 4Å molecular sieves at 5°C in darkness. Diethyl malonate (DEM, Fisher) was distilled prior to use. Deoxygenation of all solutions was accomplished with a nitrogen or argon purge.

Synthesis.—All-trans-NRBA was synthesized by a method similar to that of Nakanishi *et al.* (26). Approximately 0.5g of retinal was dissolved in 20 ml n-butylamine (containing 4Å molecular sieves) which had been cooled to -41°C in an acetonitrile slush bath. The reaction was allowed to proceed for approximately 2 hr after which the mixture was filtered and the excess n-butylamine removed via vacuum. The pale yellow crystals were three times dissolved in hexane and pumped to dryness. The product absorbed at 358 nm in acetonitrile (364 nm in ethanol) with a molar absorptivity of $57,600 \pm 1,200$ liter mol⁻¹cm⁻¹. The melting point of 61°C was slightly lower than that previously reported for NRBA (3). IR, NMR, and mass spectra of the product were consistent with the structure of NRBA. Due to the extreme sensitivity of this and similar compounds to CO₂ (1), O₂ (27), light, and H₂O (11, 28b) the above synthesis was carried out in a glove bag containing N₂ in semi-darkness. NRBA was stored under N₂ in the dark at -20°C.

Polarography and cyclic voltammetry.—Polarography was carried out with a polarographic analyzer (Model 174A, Princeton Applied Research Corporation) using a drop timer. A locally constructed three-electrode potentiostat and a Universal Programmer (Model 175, Princeton Applied Research Corporation) were utilized in conjunction with either a hanging mercury drop electrode (HMDE, Metrohm) (geometric area = 0.0136 cm²) or a gold-disk electrode (geometric area = 0.0208 cm²) for cyclic voltammetric experiments. The gold-disk electrode was fabricated by polishing the end of a flush-cut, 14-gauge gold wire with emery cloth and then with 5.0, 0.3, and 0.05 micron polishing aluminas (Buehler) in succession. Heat shrinkable Teflon (Small Parts, Incorporated, Miami, Florida) encased the wire and extended approximately 1 mm past the end of the disk to decrease convective effects. Convection was further minimized by supporting the electrochemical cell on a platform suspended from rubber tubing.

The electrochemical cell (~20 ml in volume) contained a coiled Pt wire auxiliary electrode concentric to the working electrode. A ground-glass joint was sealed to the top of the cell to accommodate the HMDE or the gold-wire electrode. An aqueous SCE reference electrode (saturated with NaCl rather than KCl)

probed through a Luggin capillary and all potentials herein are reported vs. this electrode. The SCE was immersed in solution separated from the working electrode compartment by a fine frit to minimize water contamination.

Acetonitrile and DMF solutions were 0.1M or 0.5M in supporting electrolyte. IR compensation was used to decrease the effects of ohmic drop in the cell. During detailed studies of E_p as a function of sweep rate further correction for i -R effects was made using anthraquinone as a standard reversible compound (29, 30). A 30 sec pre-electrolysis at the base of the electrochemical wave was performed while bubbling the solution with N₂ to minimize adsorptive effects.

Large-scale electrolysis.—Large-scale electrolyses employed a mercury pool cathode (area ~3 cm²) polarized at a potential 300 mV negative of the half-wave potential using the polarographic analyzer as the potentiostat. An SCE reference electrode was separated from the solution by a fine frit and the Pt auxiliary was isolated in similar fashion. Magnetic stirring and bubbling with N₂ accompanied the electrolysis. Polarographic monitoring of the electrolysis was performed at a DME in quiescent solution under N₂.

Approximately 35 ml of acetonitrile containing 0.1M TBAP was pre-electrolyzed at the potential at which the NRBA electrolysis was to be performed. DEM (100-500 μmol) was added before pre-electrolysis when a moderately weak proton donor was desired. Typically 50 μmol NRBA would then be added to the solution and electrolyzed.

Thin layer spectroelectrochemistry.—Two of the optically transparent thin layer electrochemical cells (OTTLE's) employed were of similar design to that described previously (23). One of the OTTLE's was 0.0109 cm thick with an electroactive volume of 3.34 μl and the other possessed corresponding dimensions of 0.00475 cm and 2.52 μl. A third OTTLE was modified especially for application at low temperatures. The sandwiched quartz plates forming the walls of the thin layer cavity were milled out with a diamond-tipped bit so that a cavity 0.25 cm wide extended to within 0.05 cm of the nearest edge of the gold foil. This modification of the previous design improves current distribution to the working electrode; however potential gradients across the working electrode are still apparent with the 0.5M TBAP/DMF solvent system employed in this work. A ground-glass top with inlet and outlet ports for argon bubbling was incorporated in the auxiliary compartment of the OTTLE. The cell was immersed in an acetonitrile-slush bath (-41°C) which was contained in a T-shaped, insulated, copper shell designed to fit into a Cary 14 spectrophotometer. Onto this shell were attached two quartz windows allowing spectral observation through the narrow (approximately 1 in.) arm of the acetonitrile bath encompassing the minigrid portion of the OTTLE. No serious absorptive, dispersive, or reflective problems occurred with this mode of observation. Frosting of the outer quartz windows was prevented with a gaseous nitrogen jet. The optical pathlength of this OTTLE was 0.00493 cm and its electroactive volume 1.95 μl.

Pathlengths of all OTTLE's were determined by the ratio of the absorption of solutions of rhodamine 6G in the OTTLE to that in a 1 cm cell. The one-electron reduction of a known concentration of anthraquinone to the radical anion was used to determine the electroactive volume of the cells. Other experimental procedures are as previously described (23).

Results

Polarography and cyclic voltammetry.—The polarography of NRBA at a DME in acetonitrile containing 0.1M TBAP exhibits a reduction wave at -1.68V. The height of the diffusion-limited current is 1.81 ± 0.19 times that of the first wave of retinal, a known one-electron reduction (21, 23). A second wave of variable

height is seen at -2.6V , near the breakdown of supporting electrolyte. Addition of a 1:1 stoichiometry of HClO_4 results in a new polarographic wave at -0.60V which is one-half the height of the wave produced by NRBA alone. A second wave (of equal height to the first) and a third wave (of variable height) are observed at potentials equal to the first and second half-wave potentials of unprotonated NRBA. A change in the absorption maximum from 358 to 445 nm ($\epsilon = 43,200 \pm 3,600 \text{ liter mol}^{-1}\text{cm}^{-1}$) through an isosbestic point evidences the protonation of NRBA upon the addition of HClO_4 . Addition of a 2:1M excess of HClO_4 reveals the sustained existence of the monoprotonated species although other workers (8) have noted the decomposition of NRBA upon addition of excess acid.

Cyclic voltammetry of NRBA at an HMDE at 0.1 Vsec^{-1} in acetonitrile solution containing 0.5M TBAP also reveals two reduction waves (1 and 2, Fig. 1). An oxidation wave at -0.95V (wave 3) is observed following scan reversal after the first wave. This wave is associated with a small reductive wave ($E_p = -1.01\text{V}$) which is only apparent during the second scan (not shown). At 1.00 Vsec^{-1} a new oxidation wave appears with a peak potential approximately 100 mV positive of that for the primary reduction (wave 1). The ratio of i_{pa}/i_{pc} for this couple increases at higher sweep rates while the relative size of the oxidation wave at -0.95V decreases. Addition of small amounts of water to the solution causes only minor changes in the observed electrochemistry—the reduction wave moves to slightly more positive potentials (*vide infra*) and the two oxidation waves diminish in height. In the presence of weak acids (water or DEM) a small prewave ($<5\%$ of the diffusion-limited current of NRBA) at approximately -1.4V is occasionally observed and is believed to be retinal formed by hydrolysis. Spectral evidence for hydrolysis was noted only at high (1000-fold molar excess) concentrations of water or DEM.

The reduction potential for 1:1 HClO_4 protonated Schiff's base under the above solution conditions and scan rate (0.1 Vsec^{-1}) is -0.60V (wave 4, Fig. 1). At 50 Vsec^{-1} a very slight oxidation wave was noticed approximately 90 mV positive of the peak reduction potential. At 500 Vsec^{-1} a significant oxidation wave was observed for the reduction product although the waves were badly skewed. Two additional irreversible reduction waves (not shown) are located at potentials equivalent to those of the first and second waves of NRBA, respectively. The first of these is equal in height to wave 4 (Fig. 1) while the second is approximately 2.8 times this height (indicating twice the number of electrons transferred).

Greater than stoichiometric amounts of phenol or acetic acid are required to completely protonate the Schiff's base. Spectral titration curves for NRBA in

acetonitrile containing 0.1M TEAP with phenol or acetic acid are best interpreted by assuming that the titration product is a complex of NRBA and the acid rather than assuming proton transfer. For phenol the association constant with NRBA is $0.27 \pm 0.05\text{M}^{-1}$, and for acetic acid it is $16.8 \pm 2.5\text{M}^{-1}$. Reduction of NRBA in the presence of a tenfold molar excess of acetic acid or phenol results in a larger reduction current for protonated NRBA than expected from equilibrium considerations; apparently the greatly enhanced current results from the formation of additional protonated NRBA prior to reduction (a classical CE reaction). Protonation with large excesses of acetic acid or phenol results in cyclic voltammograms similar to those of NRBA protonated with HClO_4 , but the background current obscures the second and third reduction waves.

In DMF containing 100 mM water and 0.1M TBAP, cyclic voltammetry at an HMDE at 0.1 Vsec^{-1} gives qualitatively identical results to those observed in acetonitrile. The two-electron reduction wave corresponding to wave 1, Fig. 1, has a peak potential of -1.55V in DMF and the only oxidation wave observed corresponds to wave 3, Fig. 1. However, in dry DMF with 0.1M TBAP the two-electron cyclic voltammetric wave separates into two distinct waves both with gold (Fig. 2) and mercury electrodes. Scan reversal after the first wave ($E_p = -1.79\text{V}$) results in a spike-shaped oxidation wave at mercury electrodes. This oxidation wave ($E_p = -1.69\text{V}$) is well defined at gold electrodes, and the peak current ratio for this couple approaches unity ($i_{pa}/i_{pc} = 0.8$) at 0.1 Vsec^{-1} . The normalized current for the first wave increases as the scan rate is decreased with a concurrent diminution in the second wave. The apparent peak potential difference for these two waves also decreases with decreasing scan rate in dry DMF. A slight oxidation wave coupled with the second reduction wave is observed at 50 Vsec^{-1} at a gold electrode. At slow scan rates, reduction past the second wave results in an increase in oxidation current at -1.06V .

The shift in the observed peak potential as a function of various parameters was investigated in an effort to elucidate viable reaction pathways. For NRBA in acetonitrile with 0.5M TBAP the observed $\delta E_p/\delta \log V$ is -19 mV/decade . A positive slope of 99 mV/decade is obtained for $\delta E_p/\delta \log [\text{H}_2\text{O}]$. In DMF with 0.5M TBAP and added water the corresponding values were -21 mV/decade and 58 mV/decade . A 0.1 Vsec^{-1} scan rate was used in the water addition studies.

These cyclic voltammetric results are consistent with the following schemes for the initial reduction process of NRBA. In acetonitrile or moist DMF the first reduc-

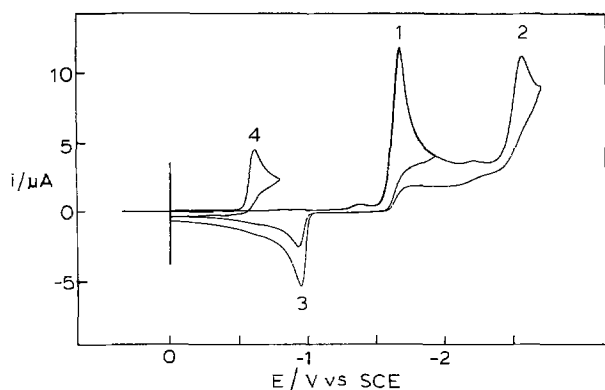


Fig. 1. Cyclic voltammograms of 2.18 mM NRBA in acetonitrile containing 0.1M TBAP at a hanging mercury drop electrode (wave 1, 2, and 3). Wave 4 is a cyclic of the same solution to which a 1:1 stoichiometry of HClO_4 :NRBA has been added. The scan rate is 0.1 Vsec^{-1} .

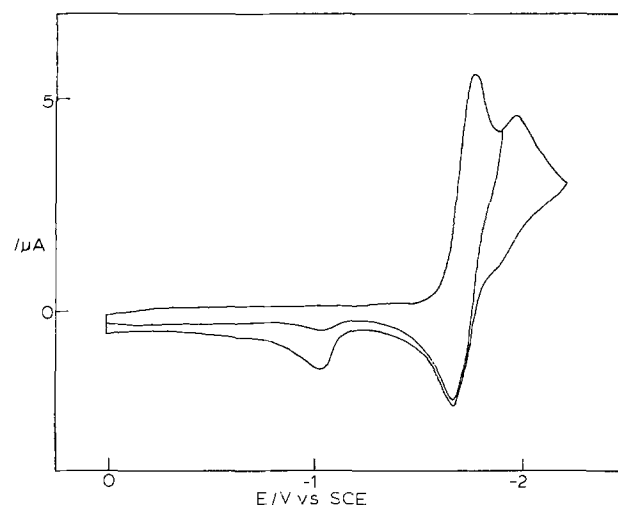
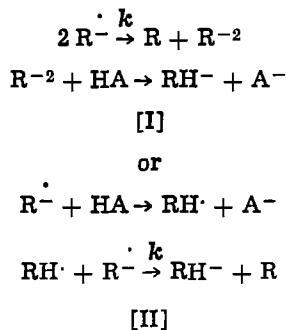


Fig. 2. Cyclic voltammogram of 1.66 mM NRBA in dry DMF containing 0.1M TBAP at a gold-disk electrode. The scan rate is 0.05 Vsec^{-1} .

tion wave generates a two-electron reduction product. The dependence of the peak potential on sweep rate indicates that either of two reduction-protonation

mechanisms involving the radical anion (R^-) and a proton donor (HA) may be apparent following the initial electron transfer (28a and b)



where k indicates the rate-determining step and RH^- is the assumed product (*vide infra*). The dependence of the peak potential on water concentration indicates the importance of solvation (in the case of scheme [I]) or protonation (in the case of scheme [II]) on the overall rate of formation of the two-electron product. The appearance of two distinct waves in dry DMF, both of which are reversible at sufficiently high sweep rates, confirms that the radical anion is an intermediate in the reaction. The formation of dianion from radical anion is presumably the electrochemical process occurring during the second reduction as will be shown. However, the dependence of the cyclic voltammetric peak height (first reduction wave, Fig. 2) and potential on scan rate demonstrate that, even under dry conditions, subsequent reactions are occurring. To determine the products and mechanism of this reduction, we have employed large scale electrolysis and thin layer spectroelectrochemistry. We have also examined the reduction of the protonated Schiff's base with these techniques; however, as is apparent from the cyclic voltammetry, its reduction intermediates are far less stable.

Large scale electrolysis.—Large scale electrolysis of NRBA at a mercury pool electrode in acetonitrile solutions with 0.1M TBAP as supporting electrolyte consumes 1.97 ± 0.08 electrons/molecule. In polarograms of the reduced solutions, the reduction wave at $-2.6V$ is still present. Following two-electron electrolysis with DEM, a well-defined polarographic wave is observed for the oxidation of diethyl malonate anion at $-0.36V$. The height of this polarographic wave and titration with standard $HClO_4$ indicate that 1.93 ± 0.11 diethyl malonate anions are formed per NRBA molecule reduced. Attempts to isolate the product for further characterization have not been successful. The product rapidly decomposes when removed from the electrolysis cell to a mixture of products as determined by u.v.-visible spectroscopy and subsequent polarography. Notable, however, is that the products obtained from the reduction of NRBA in the presence or absence of DEM have absorption bands at 350 and 328 nm in the visible region while the main absorption occurs at wavelengths less than 300 nm.

Thin layer spectroelectrochemistry.—Reduction of NRBA (0.5M TBAP/acetonitrile) at $-2.00V$ in an OTTLE produces an n -value of approximately 1.6. The low result arises because of inadequate potential control in an OTTLE (23). The slow electrode-solution polarization leads to a condition where the homogeneous coupling rate exceeds the rate of heterogeneous reduction to dianion. During electrolysis at this potential the 358 nm absorption band for NRBA decreases and the predominant product of the electrolysis absorbs at 352 nm (Fig. 3). Spectra taken during the electrolysis (dashed line) indicate the presence of an intermediate ($\lambda_{max} \approx 500$ nm) which decays with an increase of

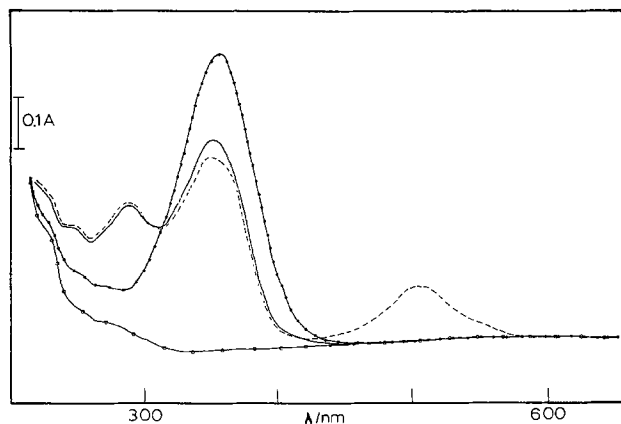


Fig. 3. Spectra of the reduction of 2.05 mM NRBA at $-2.0V$ in acetonitrile containing 0.5M TBAP in an OTTLE. ●—●—●—●— Prior to electrolysis; — — — — during electrolysis (scan started at 650 nm concurrent with onset of reduction); — — — — immediately following electrolysis (scan started at 650 nm approximately 250 sec after onset of reduction); ○—○—○—○— blank (0.5M TBAP/acetonitrile). Spectral scan rate was 2.5 nm sec^{-1} .

the final product. The product which absorbs at 352 nm is also formed via reduction in the presence of diethyl malonate with a concurrent increase in the strong absorbance (255 nm) of the anion of DEM.

In dry DMF (0.5M TBAP) only one reduction wave ($E_p = -1.80V$) is observed for the reduction of NRBA at the 0.005 Vsec^{-1} scan rate employed with the OTTLE. We attribute this to the decreased potential resolution of the OTTLE, as well as the chemical reactions outlined in schemes [I] and [II]. The reduction corresponds to 1.5-1.8 electrons/molecule of NRBA. (The low n -value can be explained as above.) There is no electrochemical evidence for stable reduction intermediates under these conditions. Electrolysis results in a relatively stable product absorbing at 498 nm with an absorbance 1.16 ± 0.08 times that of NRBA (Fig. 4). This species disappears slowly (minutes) with a simultaneous increase in the 350 nm region either with the applied potential 300 mV past the peak potential for the reduction of NRBA, or when the working electrode is disconnected, indicating a purely chemical decay mechanism. The 498 nm absorption band decays rapidly following a step positive of the $-1.0V$ oxidation wave and the oxidation product absorbs at approximately 290 nm. The charge on oxidation is 0.48 ± 0.07 times that obtained during reduction.

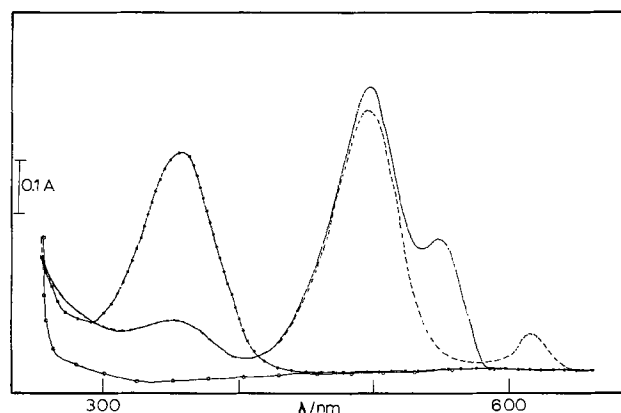


Fig. 4. Spectra of the reduction of 1.53 mM NRBA at $-2.0V$ in dry DMF containing 0.5M TBAP in an OTTLE. ●—●—●—●— Prior to electrolysis; — — — — during electrolysis (scan started at 600 nm concurrent with onset of reduction); — — — — during electrolysis (scan started at 650 nm concurrent with onset of reduction); ○—○—○—○— blank (0.5M TBAP/DMF). Spectral scan rate was 2.5 nm sec^{-1} .

Two transient absorption bands (615 and 550 nm) were first noted when wavelength scanning began at the same time as the potential step (dashed and solid lines, Fig. 4). By utilizing the temperature controlled OTTLE described in the experimental section and monitoring individual wavelengths during the potential step, absorbance vs. time curves such as those shown in Fig. 5 were obtained. During a reductive potential step at ambient temperature ($\sim 25^\circ\text{C}$) neither the rate of growth nor the rate of decay of the 550 nm band is significantly different from the corresponding rates of the 615 nm band when the 0.9 sec/full-scale time constant of the Cary 14 is considered (traces C and D, Fig. 5, upper half). However, when the working electrode is disconnected after production of these intermediates, it is found that the 550 nm moiety is less stable and the 615 nm species more stable than when the potential is left on.

At -41°C (traces C and D, Fig. 5, lower half), the 550 nm species rate of growth is 1.45 times slower than that of the 615 nm species and the absorbance at 550 nm is greatly increased with respect to that at 615 nm. The increase in absorbance at 498 nm (trace A) correlates in time with the decay of the 550 nm transient and follows first-order kinetics. The half-life of the 550 nm transient is 1.75 times longer than that of the 615 nm species with the potential on. Disconnecting the working electrode after production of these species at -41°C again decreases the half-life of the 550 nm intermediate and increases that of the 615 nm intermediate. A potential dependence is also noted when the voltage is stepped further negative. Under these conditions, the 550 nm species has a longer half-life and greater amounts are produced. The 615 nm intermediate's half-life decreases only slightly with increasing overpotential with no noticeable changes in the amount formed.

Thin layer reduction of 1:1 HClO_4 protonated Schiff's base (0.5M TBAP/acetonitrile) consumes 0.91 electrons/molecule following a potential step over the first

irreversible wave. The initial absorbance at 445 nm decreases rapidly with a concomitant increase in the absorbance in the 270 nm region. No intermediates are apparent even at low temperatures. A potential step over both waves yields significantly less 270 nm absorbance with the main absorption band occurring at 352 nm.

Discussion of Results

Reduction products.—Both polarographic and coulometric results indicate that NRBA is reduced with two electrons in CH_3CN containing 0.5M TBAP as is typical of imines (28b). Large-scale electrolysis and thin layer spectroelectrochemical results where DEM is present demonstrate that two protons per NRBA molecule are consumed in the reduction. From these results we denote the final product RH_2 . The fact that we have not been able to isolate RH_2 is not surprising—the instability of the reduced forms of NRBA as well as the molecule itself is well documented (1, 11, 27, 28b, 31). However, the spectra of several of these reduced forms have been reported (4, 31-34) and those pertinent to this work are summarized in Fig. 6. Of the previously reported compounds, our spectral data best agree with the reduction of the 5,6-double bond (structure B). In all-trans-NRBA the ring is out of the plane of the remainder of the conjugated system (4, 35) and thus its contribution to the absorbance maximum location is minimized. However, if 5,6-dihydro-NRBA was the product, remaining an imine, we would expect it to be reduced at approximately -2.0V . Instead the observed product is reduced at much more negative potentials (-2.6V). The most likely candidate for RH_2 is the enamine of 5,6-dihydro-NRBA (structure C). While HMO calculations of the π -electron density predict that the first electron should reduce either the 13-14 double bond or the imine bond (8), apparently the electron

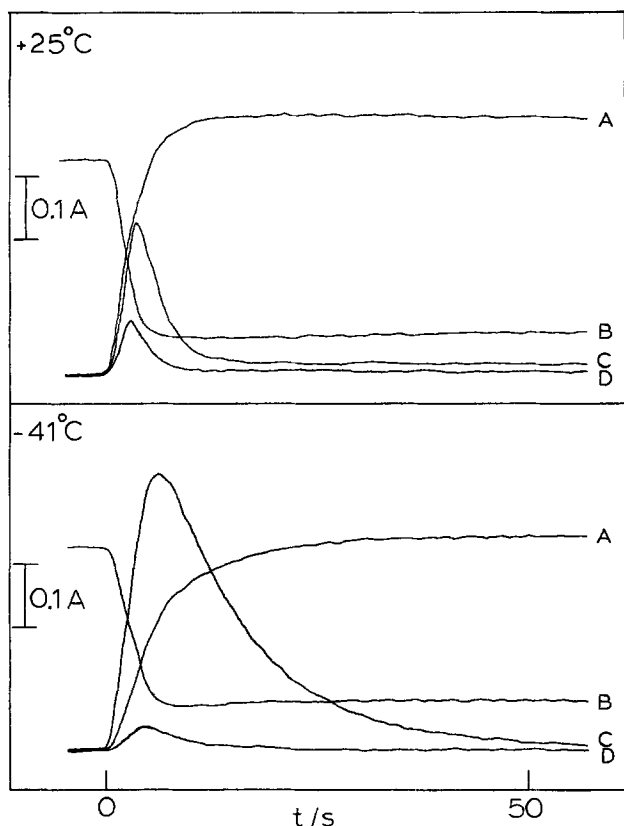


Fig. 5. Absorbance-time measurements of the reduction of 1.23 mM NRBA at -2.0V in dry DMF containing 0.5M TBAP in a jacketed OTTLE at 25°C (upper) and -41°C (lower). (A) 498 nm; (B) 362 nm; (C) 550 nm; (D) 615 nm.

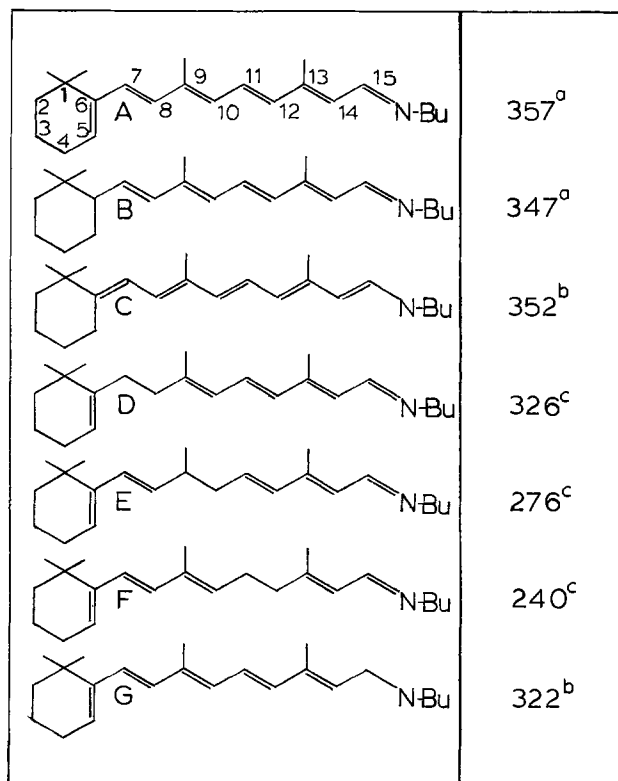


Fig. 6. Absorption maxima of various dihydroretinals and the corresponding n-butyl Schiff's bases obtained from: (a) Ref. (4); (b) Ref. (32); (c) Ref. (33). Spectra were recorded in methanol or ethanol with the exception of C which was obtained in acetonitrile. Although maxima are tabulated for various geometric isomers (trans, 11 cis, and 9 cis) the differences in λ_{max} between these have been shown to be small (34) with respect to those between different dihydroretinals.

density of the radical anion (or protonated radical anion) formed electrochemically favors the second electron reduction in the ring under our solution conditions.

The one-electron reduction of the protonated Schiff's base leads to a mixture of dimeric products as observed spectroscopically. The expected shift in the reduction product distribution from the dimeric form to the dimeric form (29) is found upon reduction past the second wave.

Reduction intermediates.—The spectroelectrochemical observation of a 500 nm transient during the reduction of NRBA in CH_3CN which chemically decays to produce the final product, RH_2 , indicates that this intermediate is RH^- . The enhanced stabilization of the anion in DMF reflects that water is a much poorer proton donor in this medium (28b) and that DMF is a weaker acid than acetonitrile. The observation of decreased anodic current for the oxidation of this species and the decreased absorbance at 500 nm in the presence of the weak acid DEM or H_2O and at higher scan rates is further confirmation of this hypothesis. The one-electron oxidation of RH^- leads to an increase in absorbance at 270 nm and implies that a dimerization of the electrogenerated free radical species (RH^\cdot) occurs. This species has not been observed spectrally though there is some electrochemical evidence for its existence: Sweep reversal after oxidation of RH^- produces a small reduction wave separated 60 mV from the anodic counterpart at scan rates as slow as 0.1 Vsec^{-1} in acetonitrile.

The 615 nm transient seen for NRBA reduction in DMF is the initial reduction product as shown by absorbance vs. time studies. Since a reversible couple is observed in cyclic voltammetry under these conditions

we assign this intermediate as the radical anion (R^\cdot). The increased half-life at -41°C is in agreement with the measurements of Lang *et al.* (2) who have observed an ESR signal for this species in tetrahydrofuran. Since only one two-electron wave is present in the OTTLE,

the observation of R^\cdot is fortuitous; it can undergo protonation and homogeneous electron transfer (disproportionation) as well as obtaining a second electron from the gold-minigrid. The radical anion can be observed as a transient because of the imperfect characteristics of the OTTLE. Both the finite thickness, allowing

R^\cdot to diffuse away from the electrode before being reduced, and the nonuniform potential-gradient across the face of the OTTLE contribute to this anomaly. The increased half-life of this transient when the working electrode is disconnected is most plausibly explained by the elimination of one of the "decay" mechanisms, specifically that of heterogeneous electron transfer from the electrode.

The 550 nm moiety observed in dry DMF is tentatively assigned to the dianion of NRBA rather than the protonated radical anion. Although one would predict R^{2-} to be very unstable with respect to protonation (only in very fast cyclic voltammetry experiments have we evidence for an oxidation wave for this species) there are several facts which lead to this designation. The decay of the 550 nm intermediate coincides with the growth of RH^- which could be true for both R^{2-} and RH^\cdot . However, the half-lives of the 615 and 550 nm species are distinctly different and therefore obviate the possibility of scheme [II]. The first-order decay of the 550 nm species at low temperatures is indicative of the protonation of the dianion. The transient is longer lived at more reducing potentials, which is in agreement with the assignment of dianion since RH^\cdot should be easily reduced. The dianion appears to be more stable with the working electrode at reducing potentials than when disconnected because in the former case its consumption by protonation is accompanied by its formation at the electrode. Furthermore, this species

Table I. Spectroelectrochemical comparison of results for retinal, NRBA, and protonated-NRBA (p-NRBA). p-NRBA results are in 0.5M TBAP/ acetonitrile. All other results are in 0.5M TBAP/DMF. $E_{1/2}$ values for RH^- are for oxidation.

| | Retinal | | NRBA | | p-NRBA | |
|------------------|--------------------|----------------------------------|--------------------|----------------------------------|--------------------|----------------------------------|
| | $E_{1/2}/\text{V}$ | $\lambda_{\text{max}}/\text{nm}$ | $E_{1/2}/\text{V}$ | $\lambda_{\text{max}}/\text{nm}$ | $E_{1/2}/\text{V}$ | $\lambda_{\text{max}}/\text{nm}$ |
| R | -1.28 | 381 | -1.68 | 362 | -0.60 | 445 |
| R^\cdot | -1.71 | 526 | -1.83 | 615 | — | — |
| RH^- | -0.68 | 418 | -1.02 | 498 | — | — |
| RH_2 | — | — | — | 352 | — | 352 |

exhibits no ESR signal (2). All of this evidence supports scheme [I] as the primary reductive pathway for NRBA. (For dry conditions the rate-determining step is the protonation of dianion.)

Comparison of the spectroelectrochemistry of retinal and NRBA.—Our results demonstrate that the protonated form of NRBA is much more easily reduced than retinal or NRBA. In fact, protonated NRBA is reduced at a potential similar to that of quinones, compounds known to be involved in biological redox processes. Therefore, protonated NRBA is a better model for the visual chromophore than retinal or NRBA when theories concerning photoinduced reduction are considered. However, we have not been able to determine the spectrum of the key intermediate for the photoreduction-visual transduction theory—the protonated radical anion.

The spectroelectrochemical data obtained during the reduction of NRBA are compared to results from retinal in Table I. The two-electron reduction product of retinal has only been observed as the anion, while RH^- for NRBA is more readily protonated to form the neutral RH_2 . However, for both retinal and NRBA, the two-electron reduction product in acetonitrile/TBAP solutions is not the corresponding alcohol or amine. Electrolysis in the presence of weak proton donors results in dimer formation in the case of retinal, and a two-electron reduction for NRBA. While this presumably reflects differences in the equilibrium constants for disproportionation of these two compounds, a measurement of these constants is not possible since the dianion of both of these compounds is a very strong base and exhibits a short lifetime. For retinal reduction, we have demonstrated that the addition of weak oxygen acids results in a solvated or hydrogen bonded radical anion which subsequently dimerizes (36). Here, we have demonstrated that the oxygen acid, water, promotes disproportionation of the radical anion of NRBA through a solvated (rather than protonated) intermediate since the dianion is a distinct intermediate under conditions of very low water concentration. The dimeric products found after electroreduction of NRBA in the presence of strong proton donors exhibit u.v. spectroscopic features that are similar to those found following dimerization of retinal induced by oxygen acids. Since the reduction of protonated Schiff's base results in a neutral radical which dimerizes very quickly, disproportionation is disfavored. These results support the proposal of Savéant (28b)—the general features of imine reduction in aprotic solvents parallel those of carbonyl compounds.

Acknowledgment

Financial support of this research by the National Science Foundation under Grant No. BNS 77-28254 is gratefully acknowledged.

Manuscript submitted Oct. 2, 1980; revised manuscript received Jan. 10, 1981. This was Paper 476 presented at the St. Louis, Missouri, Meeting of the Society, May 11-16, 1980.

Any discussion of this paper will appear in a Discussion Section to be published in the December 1981 JOURNAL. All discussions for the December 1981 Discussion Section should be submitted by Aug. 1, 1981.

REFERENCES

- P. E. Blatz, R. H. Johnson, J. H. Mohler, S. K. Al-Dilaimi, S. Dewhurst, and J. O. Erickson, *Photochem. Photobiol.*, **13**, 237 (1971).
- C. M. Lang, J. Harbour, and A. V. Guzzo, *J. Phys. Chem.*, **75**, 2861 (1971).
- P. E. Blatz, J. H. Mohler, and H. V. Navangul, *Biochemistry*, **11**, 848 (1972).
- P. E. Blatz and P. A. Liebman, *Exp. Eye Res.*, **17**, 573 (1973).
- M. M. Fisher and K. Weiss, *Photochem. Photobiol.*, **20**, 423 (1974).
- A. Alchalel, B. Honig, M. Ottolenghi, and T. Rosenfeld, *J. Am. Chem. Soc.*, **97**, 2161 (1975).
- D. Huppert, P. M. Rentzepis, and D. S. Kliger, *Photochem. Photobiol.*, **25**, 193 (1977).
- Y. Inoue, Y. Tokito, R. Chûjô, and Y. Miyoshi, *J. Am. Chem. Soc.*, **99**, 5592 (1977).
- W. H. Waddell, A. M. Schaffer, and R. S. Becker, *ibid.*, **99**, 8456 (1977).
- P. C. Mowery and W. Stoeckenius, *ibid.*, **101**, 414 (1979).
- D. S. Kliger, S. J. Milder, and E. A. Dratz, *Photochem. Photobiol.*, **25**, 277 (1977).
- D. Bownds, *Nature (London)*, **216**, 1178 (1967).
- M. Akhtar, P. T. Blossie, and P. B. Dewhurst, *Biochem. J.*, **110**, 693 (1968).
- B. D. Polis and J. Wyeth, *Fed. Proc. Fed. Am. Soc. Exp. Biol.*, **23**, 384 (1964).
- T. Rosenfeld, B. Honig, M. Ottolenghi, J. Hurley, and G. Ebrey, *Pur. Appl. Chem.*, **49**, 341 (1977).
- F. J. Grady and D. C. Borg, *Biochemistry*, **7**, 675 (1968).
- R. Sack, D. C. Borg, and S. Freed, *Nature (London)*, **235**, 224 (1972).
- K. Shirane, *ibid.*, **254**, 722 (1975).
- J. Simons, *Proc. Natl. Acad. Sci. USA*, **74**, 3375 (1977).
- B. Czochralska, M. Szweykowska, N. A. Dencher, and D. Shugar, *Bioelectrochem. Bioenerg.*, **5**, 713 (1978).
- V. G. Mairanovskii and G. I. Samokhvalov, *Sov. Electrochem. (Engl. Transl.)*, **2**, 53 (1966).
- S. Park, *This Journal*, **125**, 216 (1978).
- L. A. Powell and R. M. Wightman, *J. Electroanal. Chem. Interfacial Electrochem.*, **106**, 377 (1980).
- B. S. Jensen and V. D. Parker, *J. Chem. Soc. Chem. Commun.*, **167**, 367 (1974).
- M. M. Baizer, Personal communication.
- M. Arnaboldi, M. G. Motto, K. Tsujimoto, V. Balogh-Nair, and K. Nakanishi, *J. Am. Chem. Soc.*, **101**, 7082 (1979).
- E. I. Finkel'shtein, S. M. Dolotov, and E. I. Kozlov, *J. Org. Chem. USSR (Engl. Transl.)*, **14**, 486 (1978).
- (a) L. Nadjo and J. M. Savéant, *J. Electroanal. Chem. Interfacial Electrochem.*, **33**, 419 (1971); (b) C. P. Andrieux and J. M. Savéant, *ibid.*, **33**, 453 (1971).
- C. P. Andrieux and J. M. Savéant, *ibid.*, **26**, 223 (1970).
- C. P. Andrieux, L. Nadjo, and J. M. Savéant, *ibid.*, **26**, 147 (1970).
- K. Nakanishi, V. Balogh-Nair, M. A. Gawinowicz, M. Arnaboldi, M. G. Motto, and B. Honig, *Photochem. Photobiol.*, **29**, 657 (1979).
- This work.
- V. Balogh-Nair, Personal communication.
- P. E. Blatz, P. B. Dewhurst, V. Balasubramanian, P. Balasubramanian, and M. Lin, *Photochem. Photobiol.*, **11**, 1 (1970).
- B. Honig, B. Hudson, B. D. Sykes, and M. Karplus, *Proc. Natl. Acad. Sci. USA*, **68**, 1289 (1971).
- L. A. Powell and R. M. Wightman, *J. Electroanal. Chem. Interfacial Electrochem.*, **117**, 321 (1981).

U.V.-Visible and Electron Spin Resonance Spectroelectrochemical Studies of Sulfur Oxidation in $\text{AlCl}_3\text{-NaCl}$ (63/37 m/o) Melt

V. E. Norvell,* K. Tanemoto, G. Mamantov,* and L. N. Klatt

Department of Chemistry, University of Tennessee, Knoxville, Tennessee 37916, and Oak Ridge National Laboratory, Analytical Chemistry Division, Oak Ridge, Tennessee 37830

ABSTRACT

The electrooxidation of sulfur in molten $\text{AlCl}_3\text{-NaCl}$ (63-37 mole percent) has been investigated by means of u.v.-visible and electron spin resonance spectroelectrochemistry in the temperature range 132°-250°C. The electrode reaction sequence for the oxidation of S_8 to SCl_3^+ that was proposed previously based solely on electrochemical results has been modified to include several other intermediates, such as S_{16}^{2+} , S_5^+ , S_4^{2+} , and S(II) .

Tetravalent sulfur is a promising positive electrode in a secondary molten salt battery using chloroaluminates (mixtures of AlCl_3 and alkali halides) as solvents (1-3). The electrochemistry of sulfur in $\text{AlCl}_3\text{-NaCl}$ melts has been studied by this group (4-7) as well as by others (8). In acidic [>50 mol percent (m/o) AlCl_3] chloroaluminate melts, it has been shown (7) that elemental sulfur can be electrochemically oxidized in three steps. Coulometric (7) and spectroelectrochemical (9) studies indicate that at least two species are formed during the first oxidation step, and a preliminary mechanism involving the formation of S_{16}^{2+}

and S_8^{2+} was proposed (7, 9). The second and third oxidation steps yield S(I) and S(IV) , respectively, as products.

Fehrmann *et al.* (10) and Bjerrum (11) have performed constant current oxidation of sulfur in $\text{AlCl}_3\text{-NaCl}$ (63-37 m/o), followed by spectral measurements. A number of absorption bands due to oxidized sulfur species were observed in the 200-2000 nm spectral region. Evidence for the existence of S_{16}^{2+} , S_3^{2+} , S_4^{2+} , S(II) , and S(IV) at various stages of the electrolysis was presented by these authors.

Preliminary ESR experiments with melts containing either chemically or electrochemically oxidized sulfur (12) indicated that free radicals are present both in the molten and frozen solutions. Sulfur radical cations

* Electrochemical Society Active Member.

Key words: electrooxidation, spectroelectrochemistry, oxidation.

have previously been studied in several inorganic media (13-15), but the presence of such species in molten chloroaluminates has not been reported.

In order to obtain a better understanding of the nature of these sulfur species and the reactions by which they are formed, we chose to employ the technique of spectroelectrochemistry using an optically transparent electrode (OTE). This technique has been successfully coupled to several spectroscopic techniques in both aqueous and nonaqueous solvents (16). We have recently reported the use of OTE's in molten chloroaluminates (9). In this paper, an extensive study of sulfur spectroelectrochemistry in $\text{AlCl}_3\text{-NaCl}$ (63-37 m/o) is reported for the temperature range 132°-250°C.

Experimental

The melt preparation and related experimental procedures have been published (17, 18). Elemental sulfur (Alfa Inorganics, t5N5 grade) was used without further purification. Sulfur monochloride (Pfaltz and Bauer, Incorporated) was purified by repeated vacuum distillations in the presence of sulfur and activated charcoal (19). Sulfur dichloride (Pfaltz and Bauer, Incorporated) was purified by repeated vacuum distillations in the presence of PCl_5 (20). The purities of the distilled SCl_2 and S_2Cl_2 were checked by Raman spectroscopy. SCl_2 or S_2Cl_2 was added to the spectroscopic cell by vacuum distillation. $\text{SCl}_3\text{AlCl}_4$ was prepared as previously described (21).

U.V.-visible absorption spectroelectrochemical experiments were carried out at Oak Ridge National Laboratory with a Tektronix Model J20 silicon-based vidicon rapid-scanning spectrometer interfaced to a PDP-8/I computer. The noise level for these measurements is in the range 0.003-0.005 absorbance units. The accuracy of the wavelength axis is ± 4 nm. Details of the spectrometer operation and the computer interface have been published (22). An ORNL Model Q-2943B controlled-potential and controlled-current cyclic voltammeter (23) was also interfaced to the system enabling electrochemical experiments to be synchronized with the acquisition of spectral data. A xenon arc lamp or a deuterium lamp served as u.v. light sources, and a tungsten lamp was used for the visible region. Some u.v.-visible measurements were made using a Cary 17 spectrophotometer.

The cell and furnace designs used for u.v.-visible spectroelectrochemistry have been previously described (9). Optically transparent working electrodes were prepared either from 80 mesh platinum screen or from 80 or 100 pore per inch reticulated vitreous carbon (RVC-4, The Fluorocarbon Company, Anaheim, California) (24) which was cut into thin slices (1-2 mm thick) of appropriate dimensions. The RVC was pre-cleaned by soaking in 6M HCl, then rinsed and dried before use. Electrical contact to the RVC was made by pressing a cleaned 0.5 mm diam tungsten wire into the RVC to a depth of about 1 cm after the RVC had been inserted into the optical cell.

ESR spectroelectrochemical experiments were carried out at the University of Tennessee with a Varian E-Line Model E-109 spectrometer equipped with a Model E-257 Variable Temperature Accessory. The cell design is similar to that used for u.v.-visible spectroelectrochemistry. A platinum screen OTE was used inside a quartz ESR cell with a pathlength of approximately 1 mm. An auxiliary furnace consisting of a Pyrex tube wrapped with heating tape was used above the ESR cavity to maintain the solution molten and to prevent AlCl_3 condensation in the top of the cell. The electrode potential was controlled by a Princeton Applied Research, Model 173/179 potentiostat/coulometer.

The magnetic field was calibrated by using a sample of 2,2-diphenyl-1-picrylhydrazyl (DPPH, $g = 2.0036$)

inside the microwave cavity but outside the electrochemical cell. A modulation amplitude of 4G and a modulation frequency of 100 kHz were employed. The microwave frequency was approximately 9.12 GHz and the microwave power was 3.5 mW. The scan speed was 200 G min^{-1} .

The melt used was $\text{AlCl}_3\text{-NaCl}$ (63-37 m/o \equiv 63/37) in all cases, and potentials are reported vs. the Al(III)/Al reference electrode in this melt.

Results

ESR spectroelectrochemistry.—In preliminary experiments (12), sulfur was dissolved in the 63/37 chloroaluminate melt and then oxidized to formal oxidation states ranging from $+\frac{1}{2}$ to +1 either electrochemically or chemically using stoichiometric amounts of $\text{SCl}_3\text{AlCl}_4$. Most of these solutions produced ESR spectra consisting of two, and sometimes three, signals, both in the molten and in the frozen state. The strongest line in most cases had a g -value of ~ 2.0275 , and weaker lines were observed at $g \sim 2.016$, $g \sim 2.013$ -2.014, and $g \sim 2.0075$. These spectra were obtained at 132°-136°C.

ESR spectra were also obtained for pure S_8 , S_2Cl_2 , SCL_2 , and $\text{SCL}_3\text{AlCl}_4$ dissolved in the melt at 132°C. These represent sulfur with formal oxidation states of 0, +1, +2, and +4, respectively. The latter two solutions produced no signal, S_2Cl_2 produced a weak signal at $g = 2.0277$ and stronger signals at $g = 2.0155$ and $g = 2.013$. Sulfur dissolved in the melt produced only a weak signal at $g = 2.0155$.

In order to study these radicals as a function of potential, a solution of $8.20 \times 10^{-3}\text{m}$ sulfur was oxidized at a platinum OTE at potentials ranging from 1.3 to 1.9V. Figure 1 summarizes the resulting spectra at 132°C. Four lines are observed, labeled A, B, C, and D; the g -values and linewidths are summarized in Table I. Signal D was shown to be due to the quartz ESR cell.

A plot of relative signal intensity vs. potential for lines A, B, and C (Fig. 2) shows that signal A is observed at potentials less positive than signal C and that it reaches a maximum around 1.60V, whereas C reaches a maximum at 1.70-1.75V. It is reasonable to conclude from these results that radical A is due to a sulfur species in a lower formal oxidation state than radical C. The intensities shown in Fig. 2 were calculated from the first derivative spectra by correcting for the signal linewidths. Since line B is very narrow compared to A or C, its intensity is low. These corrected

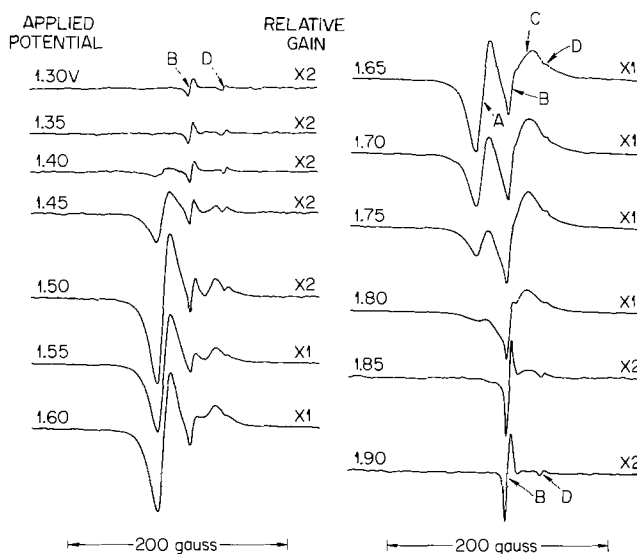


Fig. 1. ESR spectra of sulfur oxidation products in the 63/37 melt at 132°C. Sulfur concentration (as monomer): $8.20 \times 10^{-3}\text{m}$.

Table I. Observed g-values and linewidths for sulfur radicals produced in the 63/37 melt at 132°C

| Signal | g-value† | ΔH_{msl} , g |
|--------|------------------------------|----------------------|
| A | 2.0277 ± 0.0005 | 9.6 |
| B | 2.0155 ± 0.0005 | 3.4 |
| C | $(2.013 \pm 0.001) \ddagger$ | (16)† |
| D* | 2.0007 ± 0.0005 | 2.4 |

* Due to quartz cell.

† Uncertainties represent the limit of confidence in reading line positions from the recorded spectra.

‡ Estimated due to overlap with signal B.

intensities should be directly proportional to the concentrations of the respective radicals in the melt, however, the actual concentrations cannot be calculated since the values of the parameters involved in the proportionality constants are unknown.

An increase in temperature to 150° produced a loss in intensity for all the lines, but the intensity *vs.* potential curves remained unchanged. When the temperature was increased to 225°C, the intensities of all signals decreased considerably. Lines A and C became broader, and A was only barely detectable due to overlap with B. The linewidth of B remained the same at the higher temperature.

The behavior of species B differs from that of A and C in several ways. The fact that it is present over the entire potential range is unexpected assuming that it is due to a species containing sulfur in a formal oxidation state between 0 and 4. In fact, it is present at the open-circuit potential ($\sim 1.3V$) where only S(O) should be present. Furthermore, the same signal was observed when elemental sulfur was dissolved in the melt. The line width of B is small and remains unchanged with temperature, whereas lines A and C are broadened at higher temperatures. A lineshape analysis of signals A, B, and C indicates that signals A and C approximate the Lorentzian function, but B is closer to the Gaussian function.

An experiment was carried out using ^{33}S enriched elemental sulfur as the solute in an attempt to obtain hyperfine splitting of the radical lines. We were unable to observe the hyperfine splitting; thus, the nature of these radicals can only be inferred by comparison with sulfur radicals previously studied in other media (13-15) and by correlation with the u.v.-visible spectroelectrochemical data which are discussed below.

U.V.-visible spectroelectrochemistry.—The various sulfur cations have several absorption bands in the 250-1100 nm region which are useful for determining which species are present in solution. In a previous paper (9) we reported some preliminary results con-

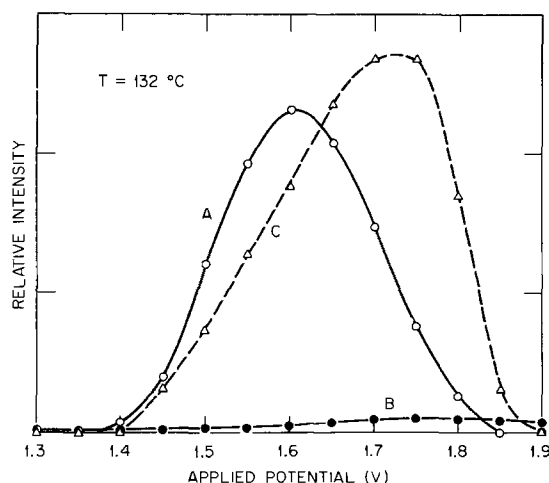


Fig. 2. Potential dependence plot for radicals A, B, and C

cerning the oxidation of sulfur at OTE's, covering the potential range from 1.3 to 1.85V and the 250-1100 nm spectral region. In order to obtain a better understanding of the effects of temperature, potential, and concentration on the sulfur species produced in the melt, a more comprehensive investigation has been conducted.

The first oxidation step for sulfur has not been completely characterized, primarily because the oxidation involves a small number of electrons resulting in a broad cyclic voltammetric oxidation wave (7). This step covers the potential region from 1.3 to $\sim 1.7V$. Figure 3 illustrates spectra acquired at an RVC-OTE for four potentials at temperatures of 150° and 250°C. As previously reported (9), three absorption bands appear at ~ 600 , ~ 730 , and ~ 960 nm for potentials between 1.5 and 1.7V. In addition, a shoulder is observed around 450 nm. Although not shown in this figure, a shoulder is also seen in the ~ 330 -350 nm region. The 600 nm band has previously been attributed to S_3^{2+} and the latter two bands to S_16^{2+} (9-11). The absorbance *vs.* potential behavior for these bands, shown in Fig. 4, supports the assignment of the 600 nm band to the species of a higher formal oxidation state.

Similar absorption bands have been observed when sulfur was oxidized in HSO_3F and oleum (13). After the completion of the present work, a paper by Burns, Gillespie, and Sawyer (15) appeared describing the oxidation of sulfur by AsF_5 in SO_2 . Visible spectra similar to those described above were obtained, and a band at 585 nm was attributed to S_3^+ species. The two longer wavelength bands were assigned to an unknown sulfur radical cation which was previously identified as S_3^+ (13). A somewhat different interpretation of these absorption bands is given in the Discussion section.

The 730 and 960 nm bands have approximately equal absorbances, in agreement with other published spectra (11, 15), however, at potentials greater than $\sim 1.55V$,

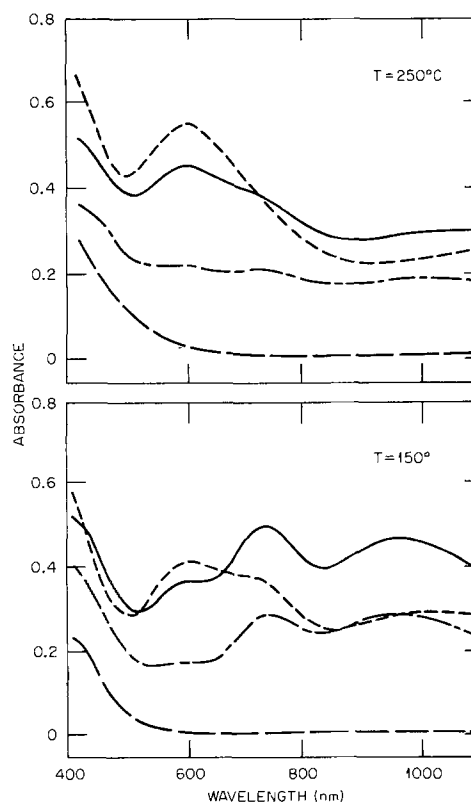


Fig. 3. Absorption spectra of the products of the first sulfur oxidation step for two temperatures. Applied potentials: 1.30V (—), 1.50V (---), 1.60V (— — —), 1.70V (- · - · -). Sulfur concentration: $1.50 \times 10^{-2}m$.

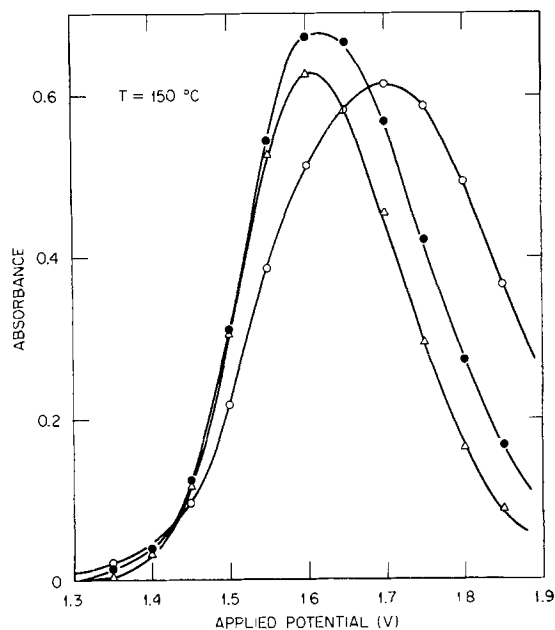


Fig. 4. Potential dependence plot for the absorption bands shown in Fig. 3 at 150°C. O, 600 nm; ●, 730 nm; △, 960 nm.

the absorbance at 730 nm becomes greater than that at 960 nm. The cause apparently lies in the overlap of the 600 and 730 nm bands, such that, as the 600 nm band begins to increase, it contributes to the observed absorbance at 730 nm. This effect is also evident in the spectra of Gillespie and co-workers (15). The 960 nm band is sufficiently separated from the other bands to avoid this problem.

The temperature dependence of these bands, as shown in Fig. 3, indicates that the higher oxidation state species is favored at higher temperatures. This temperature effect is also evident in bulk coulometric results (7) and is further supported by the thin-layer coulometric experiments summarized in Table II. These data were obtained by integrating the current-time curve produced by exhaustively electrolyzing a sulfur solution at a platinum OTE. The increasing n_{app} value at higher temperatures indicates a shift in the equilibrium ratio favoring the higher oxidation state.

Absorbance vs. time profiles for the three absorption bands were obtained by stepping the potential of an OTE from 1.3V (rest potential) to various potentials on the current-limited region of the first oxidation wave. Figure 5 illustrates the results for the 600 and 730 nm bands at potentials of 1.60V (middle of current-limited plateau) and 1.70V (near the beginning of second oxidation wave) at 150°C. The higher potential results in a greater rate of increase in absorbance vs. time for both wavelengths, and a greater absorbance plateau value for the 600 nm band. The maximum and subsequent decrease in the absorbance at 730 nm at 1.70V is expected based on the absorbance vs. potential relationships shown in Fig. 4.

In the spectroelectrochemical experiments described thus far the sulfur concentration ranged from 1.3 to 1.5

Table II. Thin-layer coulometric n_{app} obtained at a platinum OTE for the first sulfur oxidation step. Potential was stepped from 1.30 to 1.65V.

| t (°C) | n_{app} * |
|----------|---------------|
| 150 | 0.157 ± 0.004 |
| 200 | 0.167 ± 0.002 |
| 250 | 0.181 ± 0.006 |

* Uncertainties represent standard deviation of measurements.

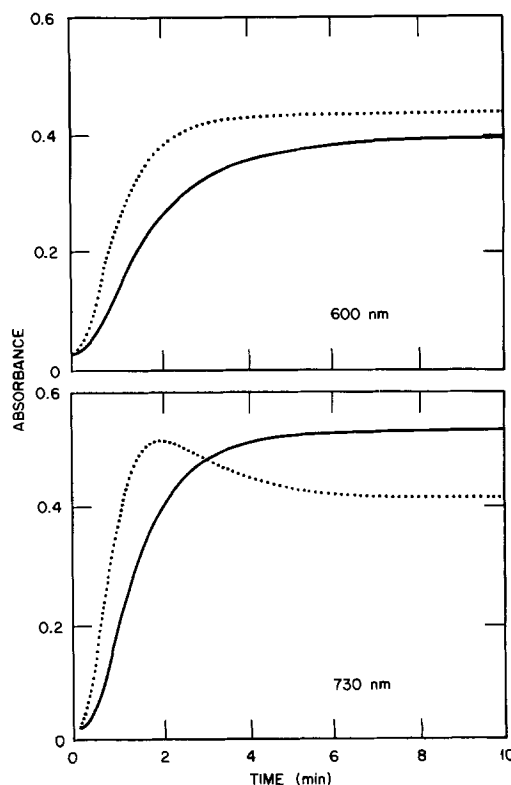


Fig. 5. Absorbance-time profiles for the 600 and 730 nm absorption bands following potential steps from 1.30 to 1.60V (—) and 1.70V (····). Sulfur concentration: $1.50 \times 10^{-2}m$.

$\times 10^{-2}m$ (as monomeric sulfur). To study the effect of sulfur concentration, a $1.75 \times 10^{-1}m$ sulfur solution was examined at a platinum OTE. Temperatures $\geq 200^\circ C$ were necessary to avoid precipitation of molten sulfur from the melt, therefore, these spectra were acquired at $250^\circ C$.

The absorbance vs. potential relationships for the 600 and 730 nm bands for the higher sulfur concentration show a substantial increase in the concentration of the lower oxidation state species relative to the higher oxidation state species. The absorbance value at 730 nm now is greater than that at 600 nm for potentials as positive as 1.70V. This may be contrasted with the lower concentration case where the 600 nm absorbance predominates at 1.70V even at $150^\circ C$ (Fig. 4), and to an even greater extent at $250^\circ C$. Attempts to analyze thin-layer coulometric data for this solution were unsuccessful due to the ill-defined nature of the charge vs. time curves. This is due to the large continuous faradaic current resulting from diffusion of sulfur from the bulk solution to the OTE contact region.

The potential region of interest for the second sulfur oxidation step extends from about 1.70 to 1.85V. This oxidation step was also studied spectroelectrochemically using a $1.35 \times 10^{-2}m$ sulfur solution. As shown by previous coulometric results (7), the product of this oxidation is S(I). A spectrum of S(I) was obtained by dissolving S_2Cl_2 in the 63/37 melt. The resulting spectrum shows a strong band at 263 nm and two weak shoulders around 320-330 nm and 375-380 nm. Figure 6 illustrates spectra obtained at a platinum OTE for several potentials in this region. The correlation between the final spectrum (at 1.85V) and that obtained for S_2Cl_2 is good. Fehrmann *et al.* (10) have published a "calculated" spectrum for S(I) (as S_2^{2+}), indicating bands at 262 and 376 nm. There is also some indication of a shoulder near 320 nm, but this is more predominant in the calculated spectrum for the S_4^{2+} species, and it appears that this band is more properly

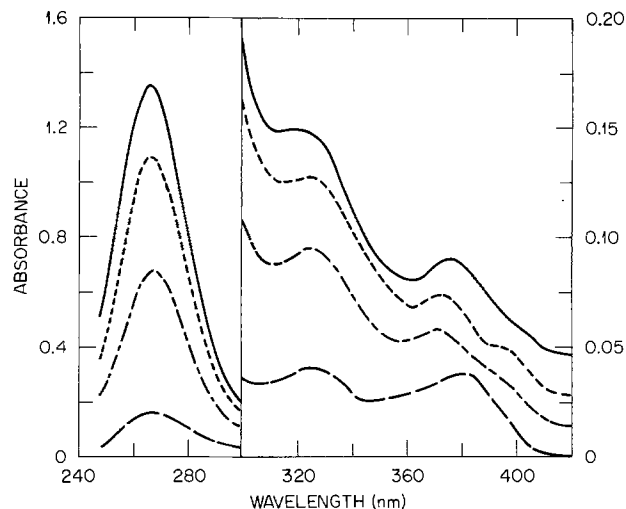


Fig. 6. Absorption spectra of the products of the second sulfur oxidation step at 250°C. Applied potentials: 1.70V (—), 1.775V (---), 1.825V (- - - -), 1.85V (— — —). Sulfur concentration: $1.35 \times 10^{-2}m$.

assigned to S_4^{2+} . The position of the major band in the spectroelectrochemical experiment was approximately 265 nm, and the molar absorptivity was calculated to be ~ 3200 . Fehrmann's calculated spectrum for S(I) has a molar absorptivity of ~ 3700 at the 262 nm band maximum.

An increase of the potential of the OTE past 1.85–1.95V results in the eventual disappearance of all absorption bands at wavelengths longer than ~ 260 nm. There is an indication of a strong absorption at wavelengths less than 260 nm, but this was beyond the dynamic range of our instrumentation. At potentials between 1.85 and 1.90V, there is evidence that the band at ~ 325 nm disappears at a faster rate than the band at ~ 377 nm. This would require the presence of at least two species in this potential region. Since S(I) is known to be a product of the second oxidation step, S(II) might be expected to exist upon oxidation at potentials between the second and third oxidation steps. Fehrmann *et al.* (10) have proposed the existence of S(II) in the melt and have calculated an absorption spectrum showing a single band at 380 nm. The observation that the bands at ~ 325 and ~ 377 nm are seen at 1.85V, and only the ~ 377 nm band is seen at 1.90V supports the existence of an oxidation state between S(I) and S(IV), and S(II) is reasonable.

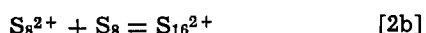
Discussion

The spectroelectrochemical results support the complexity of the first oxidation step indicated by the electrochemical results previously reported (7). These data also suggest a more complex oxidation path than previously proposed for the second and third oxidation steps. In the following discussion these three steps will be discussed separately.

First oxidation step (1.30–1.70V).—A reaction sequence was previously proposed (7) for the first oxidation step based on electrochemical results and some preliminary spectroscopic data. This is summarized by reactions [1a]–[2b]



and



Reactions [1] and [2] assume that both S_8^+ and S_8^{2+} are formed at approximately the same potentials. This reaction sequence, however, is not adequate to account for the presence of at least one other species which has been observed by us in this potential region.

Sulfur radical cations have been studied in HSO_3F , oleum, and SO_2 by several investigators (13–15), and, in most cases, two radical species, R_1 and R_2 , were observed with g -values of approximately 2.013 and 2.027, respectively. Gillespie and co-workers (15) have observed an additional sulfur radical, R_3 , with a g -value of 2.008. The radicals R_2 and R_1 appear to correspond to radicals A and C, respectively, in the present work. The linewidths of the ESR signals for these radicals in chloroaluminate melts (see Table I) are about a factor of two greater than those observed by Gillespie and co-workers (15), but this may be attributed to the difference in solvents and the higher temperatures of the chloroaluminate studies. Volkov *et al.* (25) have reported radicals giving similar ESR signals in $AlCl_3-S_2Cl_2$, however, their interpretation of the nature of species in these media is highly questionable.

The radical denoted as R_3 by Gillespie *et al.* was not observed when sulfur was oxidized in chloroaluminate melts at the OTE; however, its g -value of 2.008 is in good agreement with the signal at $g = 2.0075$ which was observed in preliminary nonelectrochemical experiments (12). In most cases, this signal was observed in solutions initially containing only elemental sulfur or very slightly oxidized sulfur. Also, whenever this signal was present, radical A was present. The relative intensity of signal A with respect to the signal at $g = 2.0075$ was approximately constant and equal to ~ 9 . Gillespie and co-workers (15) also note a relationship between this radical (R_3) and radical R_2 , although the ratio of the intensities appears to be greater than 9 in their case. It seems likely that this radical contains sulfur in a very low oxidation state since it is seen predominantly in weakly oxidized solutions. This observation is in agreement with Gillespie and co-workers (15) who propose the possibility of S_{12}^+ for this species. It is not clear as to why this radical was not observed at the OTE. Further studies will be required to characterize this species as well as radical B; therefore, they will not be considered in the proposed reaction sequence.

Radicals R_1 (C) and R_2 (A) were earlier believed to be S_4^+ and S_8^+ , respectively (13), and monomer-dimer equilibria were introduced to account for their presence as shown below



The existence of S_8^{2+} was confirmed by x-ray diffraction (13), however, no such data were available for S_{16}^{2+} . The stoichiometries of the radical cations were not proved, but rather proposed on the basis of above equilibria.

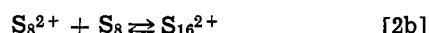
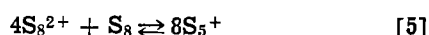
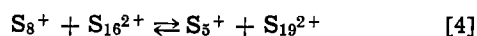
Gillespie and co-workers (15) have recently obtained x-ray diffraction data for a salt thought to contain S_{16}^{2+} ; the cation S_{19}^{2+} was found instead. The structure of this species was shown to consist of two different seven-membered rings linked by a five-membered bridge. Earlier Low and Beaudet (14) determined that radical R_1 , which was thought to be S_4^+ , is S_5^+ based on analysis of hyperfine splitting data. The nature of radical R_2 has not been definitely established. Clearly it is important to consider this information along with the spectroelectrochemical data in order to arrive at a reasonable reaction sequence for the oxidation of sulfur in chloroaluminate melts.

A comparison of the spectroelectrochemical data shown in Fig. 2 and 4 suggests a relationship between

the radical species A and C and species producing the absorption bands at 600, 730, and 960 nm. Both the 730 and 960 nm absorbances and signal A reach their maximum values around 1.60V; this is also true for the 600 nm band and signal C around 1.70-1.75V. The temperature dependence data yield further information on this relationship. An examination of the absorption bands in Fig. 3 for a potential of 1.60V shows that the 600 nm band increases at higher temperature, whereas the 730 and 960 nm bands decrease. For the same potential and a temperature increase from 132° to 225°, the ESR signals A and C both decrease considerably. The relative differences in the amount of change in the absorption bands as compared to the ESR signals indicate that the absorption bands are due, at least primarily, to diamagnetic species which are probably in equilibrium with the radical cation species. Contributions to the absorption bands by the radicals cannot be ruled out completely based on the data available.

The 600 nm absorption band may be attributed to S_8^{2+} (9, 11, 13), which is related to radical C through one or more chemical reactions. Radical C is probably S_5^+ based on the study by Low and Beaudet (14). The formation of S_8^+ by a one-electron oxidation of S_8 (reaction [1a]) is supported by electrochemical data (7) and reasonably accounts for radical A. It also provides a simple pathway to the formation of S_8^{2+} by an additional one-electron step. The originally proposed reaction [1b] appears to best explain the presence of the diamagnetic species in equilibrium with this radical. Bjerrum (11) has presented potentiometric evidence for the existence of S_{16}^{2+} in chloroaluminates melts, and the 730 and 960 nm absorption bands have previously been attributed to this species (9, 11). The existence of S_{19}^{2+} in these melts has not been previously considered, however, the spectroelectrochemical data show a shoulder in the region ~330-350 nm for the early stages of sulfur oxidation. This may be attributed to S_{19}^{2+} on the basis of the assignment by Gillespie and co-workers (15). It was not possible to study this shoulder quantitatively by spectroelectrochemistry due to overlapping absorption bands attributed to higher oxidation state sulfur species (see below).

One set of reactions which may account for the relationships between these various species is shown below



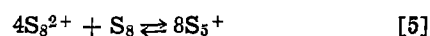
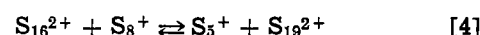
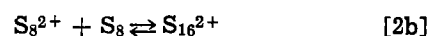
Reactions [1b] and [4] provide a pathway for the formation of S_5^+ and S_{19}^{2+} using S_8^+ as the starting material. Reaction [5] is based on a similar reaction proposed by Low and Beaudet (14), but modified to take into account the presence of S_8 as the likely form of elemental sulfur in chloroaluminates melts (26). These reactions can also be used to explain the dominance of the lower oxidation state species (i.e., formal sulfur oxidation state ≤ 0.20) at higher sulfur concentration as observed from the absorption spectra. This effect was also reflected in bulk coulometric measurements (7). It should be noted that these equations only attempt to represent the reaction sequence and should not be construed to be actual mechanisms.

Additional information concerning the electrochemical reactions involved in the first sulfur oxidation step can be obtained from the absorbance-time plots shown in Fig. 5. These data indicate that the initial rate of formation of the lower oxidation state species (i.e., S_{16}^{2+} formed through reaction [1b]) is faster than that for the higher oxidation state species (i.e., S_8^{2+}). This result favors an electron transfer sequence yielding

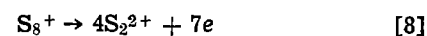
S_8^+ initially, which is oxidized further to S_8^{2+} . Thus the originally proposed reaction [2a] is considered less likely.

Bulk coulometry data (7) as well as thin-layer coulometry (Table II) and spectroelectrochemical measurements indicate that the higher oxidation state of sulfur is favored at higher temperatures. This effect has been observed for other systems in chloroaluminates melts (27) and is probably caused by the increase in chloride ion activity as the temperature is increased (28), which, in turn, favors the higher oxidation state (29).

An overall reaction sequence for the first sulfur oxidation step under the experimental conditions studied (e.g., highly acidic chloroaluminates melts) can be summarized as follows



Second oxidation step (1.70-1.85V).—The spectrum of the oxidation product of the second oxidation step agrees well with that expected for S(I) based on the spectrum of chemically prepared S_2Cl_2 dissolved in the melt. By assuming that the oxidation was complete at 1.85V and that no oxidation to S(I) had proceeded at 1.65V, the concentrations of the reduced form, [R], and the oxidized form, [O], were calculated from the absorbance spectra at each applied potential. This was possible by using the known bulk sulfur concentration. These oxidation reactions have been considered for this step



Nernst plots for these reactions are shown in Fig. 7; essentially straight lines are observed in both cases. The line for reaction [6] has a slope of 14.1 mV, giving an n -value of 7.36. Reactions [7] and [8] have a single Nernst plot, and it yields a slope of 18.6 mV and an n -value of 5.58. This n -value is closer to that expected for reaction [7] than for reaction [8] suggesting that reaction [7] is more likely. The n -values calculated from these slopes suggest that, under the experimental conditions, most of the sulfur in the R form is present as $S^{+1/4}$ or $S^{+1/5}$ rather than $S^{+1/8}$. Since these mea-

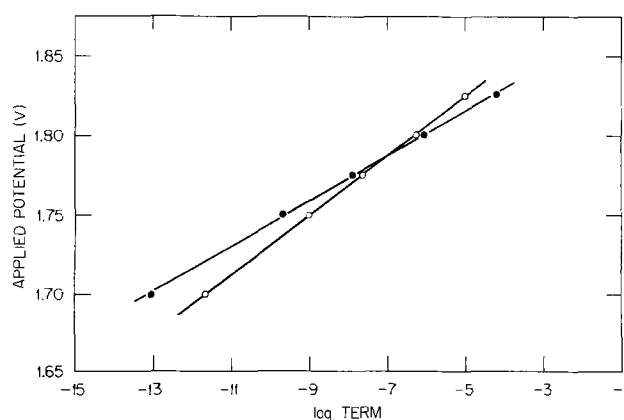


Fig. 7. Nernst plots for reactions [6]-[8] based on the spectroelectrochemical data shown in Fig. 6. Log term. ●, $[O]^{5/2}/[R]$; ○, $[O]^{4/3}/[R]$.

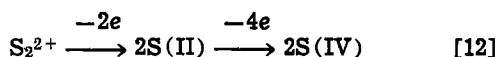
measurements were carried out at 250°, this result is in agreement with spectroelectrochemical data indicating a shift in the A(600 nm)/A(730 nm) ratio to larger values with increasing temperature. Since the spectroelectrochemical data indicate that both S_8^{2+} and S_5^+ are present at 1.65V, reactions [7] and [6] may be occurring simultaneously.

Fehrmann *et al.* (10) have postulated the existence of S_4^{2+} in the melt. Gillespie and Passmore and others (13) have studied this species in oleum and superacid solvents. Some correspondence with bands attributed to S_4^{2+} by Fehrmann *et al.* has been observed at OTE's in the 1.70-1.85V potential range, but some of the proposed bands overlap bands attributed to S(I) and a proposed S(II) species (see below) making a clear assignment of S_4^{2+} difficult. If S_4^{2+} does exist, it is likely that it is formed as an intermediate product between $S^{+1/4}$ and S(I).

The second oxidation step is clearly more complex than originally proposed based solely on electrochemical data. These earlier measurements did not indicate the presence of S_4^{2+} , so it was not considered in the mechanism. Two sets of proposed reactions may now be formulated for this oxidation depending on whether S_4^{2+} is included in the sequence. If it is not included, reactions [7] and [6] are possible. A more complex reaction sequence involving an S_4^{2+} intermediate product is given below



Third oxidation step (1.85-2.0V).—The final product of this oxidation has been shown (7) to be S(IV), present as SCl_3^+ . Assuming that S_2^{2+} is the major product of the second oxidation, the most likely possible intermediate product in the oxidation to S(IV) would be S(II). Fehrmann *et al.* (10) have proposed the existence of S(II) in chloroaluminate melts with a single absorption band around 380 nm. Spectroelectrochemical results indicate the presence of more than one species in the potential region between 1.85 and 1.90V, based on absorbance bands at ~ 325 and ~ 377 nm. Since S(IV) is known to have no bands in this spectral region, then S(II) is a possible candidate for the unknown species. This, however, is in disagreement with spectrum of pure SCl_2 dissolved in the melt, which does not possess any absorption bands at wavelengths longer than 300 nm and has a sharply increasing absorbance at wavelengths shorter than 300 nm. A Raman spectrum of this solution showed the presence of SCl_3^+ , indicating disproportionation of S(II) to S(IV) and some unidentified lower oxidation state. Further study is required to address this problem, therefore we can only tentatively assign S(II) as an intermediate product in the oxidation to S(IV). The originally proposed reaction [7], then, can be modified to



Conclusions

The oxidation of sulfur in chloroaluminate melts is clearly very complex, more so than originally thought based solely on electrochemical measurements. It is convenient to picture this oxidation in terms of a decreasing number of S-S bonds and increasing Cl-complexation as the formal sulfur oxidation state increases. Each sulfur oxidation wave, then, probably consists of a series of closely spaced sequential oxidation steps rather than single multi-electron steps.

At this point we cannot propose a detailed overall mechanism, but we have demonstrated the value of

spectroelectrochemical techniques in enabling us to better understand the sulfur oxidation in these melts.

Acknowledgments

We would like to acknowledge the collaboration of R. Livingston, H. Zeldes, M. Conradi, Chemistry Division, ORNL and J. P. Wiaux, University of Tennessee, in obtaining preliminary electron spin resonance spectra of sulfur radicals, as well as useful discussions with R. Marassi throughout this work. We would also like to thank Professor J. Q. Chambers for the use of his ESR spectrometer. This work has been supported by the Department of Energy, Contract EY-76-S-05-5053, University of California Subcontract 4502810, and the NSF Grant CHE 77-21370. Support by the U.S. Department of Energy, Basic Energy Sciences is also acknowledged. VEN acknowledges receipt of an Oak Ridge Associated Universities Fellowship. Oak Ridge National Laboratory is operated for the U.S. Department of Energy by Union Carbide Corporation under Contract W-7405-eng-26.

Manuscript submitted July 8, 1980; revised manuscript received Dec. 18, 1980.

Any discussion of this paper will appear in a Discussion Section to be published in the December 1981 JOURNAL. All discussions for the December 1981 Discussion Section should be submitted by Aug. 1, 1981.

Publication costs of this article were assisted by The University of Tennessee.

REFERENCES

- G. Mamantov and R. Marassi, U.S. Pat. 4,063,005 (1977).
- G. Mamantov, R. Marassi, J. P. Wiaux, S. E. Springer, and E. J. Frazer, Abstract 89, p. 243, The Electrochemical Society Extended Abstracts, Atlanta, Georgia, Oct. 9-14, 1977.
- G. Mamantov, R. Marassi, M. Matsunaga, Y. Ogata, J. P. Wiaux, and E. J. Frazer, *This Journal*, **127**, 2319 (1980).
- G. Mamantov, R. Marassi, and J. Q. Chambers, Technical Report ECOM-0060-F, April 1974.
- R. Marassi, G. Mamantov, and J. Q. Chambers, *Inorg. Nucl. Chem. Lett.*, **11**, 245 (1975).
- R. Marassi, G. Mamantov, and J. Q. Chambers, *This Journal*, **123**, 1128 (1976).
- R. Marassi, G. Mamantov, M. Matsunaga, S. E. Springer, and J. P. Wiaux, *ibid.*, **126**, 231 (1979).
- K. A. Paulsen and R. A. Osteryoung, *J. Am. Chem. Soc.*, **98**, 6866 (1976).
- G. Mamantov, V. E. Norvell, and L. Klatt, *This Journal*, **127**, 1768 (1980).
- R. Fehrmann, N. J. Bjerrum, and F. W. Poulsen, *Inorg. Chem.*, **17**, 1195 (1978).
- N. J. Bjerrum, in "Characterization of Solutes in Non-Aqueous Solvents," G. Mamantov, Editor, pp. 251-271, Plenum Press, New York (1978).
- R. Livingston, G. Mamantov, J. P. Wiaux, H. Zeldes, M. Conradi, and R. Marassi, Unpublished work.
- R. J. Gillespie and J. Passmore, in "Advances in Inorganic Chemistry and Radiochemistry," Vol. 17, H. J. Emeleus and A. G. Sharpe, Editors, pp. 49-89, Academic Press, New York (1975), and references therein.
- H. S. Low and R. A. Beaudet, *J. Am. Chem. Soc.*, **98**, 3849 (1976).
- R. C. Burns, R. J. Gillespie, and J. F. Sawyer, *Inorg. Chem.*, **19**, 1423 (1980).
- W. R. Heineman, *Anal. Chem.*, **50**, 390A (1978), and references therein.
- G. Torsi, K. W. Fung, G. M. Begun, and G. Mamantov, *Inorg. Chem.*, **10**, 2285 (1971).
- R. Marassi, J. Q. Chambers, and G. Mamantov, *J. Electroanal. Chem. Interfacial Electrochem.*, **69**, 345 (1976).
- R. E. Dodd and P. L. Robinson, "Experimental Inorganic Chemistry" p., 218, Elsevier Publishing Co., New York (1954).
- F. A. Cotton and G. Wilkinson, "Advanced Inorganic Chemistry," 3rd ed., p. 440, Interscience Publishers, New York (1972).

21. G. Mamantov, R. Marassi, F. W. Poulsen, S. E. Springer, J. P. Wiaux, R. Huglen, and N. R. Smyrl, *J. Inorg. Nucl. Chem.*, **41**, 260 (1979).
22. L. N. Klatt, *J. Chromatogr. Sci.*, **17**, 225 (1979).
23. T. R. Mueller and H. C. Jones, *Chem. Instrum.*, **2**, 65 (1969).
24. V. E. Norvell and G. Mamantov, *Anal. Chem.*, **49**, 1470 (1977).
25. S. V. Volkov, I. V. Matyashchuk, V. V. Trachevskii, and Z. A. Fokina, *Ukr. Khim. Zh.*, **44**, 5 (1978).
26. R. Huglen, F. W. Poulsen, G. Mamantov, R. Marassi, and G. M. Begun, *Inorg. Nucl. Chem. Lett.*, **14**, 167 (1978).
27. G. Mamantov and R. A. Osteryoung, in "Characterization of Solutes in Non-Aqueous Solvents," G. Mamantov, Editor, pp. 223-249, Plenum Press, New York (1978).
28. G. Torsi and G. Mamantov, *Inorg. Chem.*, **10**, 1900 (1971).
29. J. D. Corbett, in "Progress in Inorganic Chemistry," Vol. 21, S. J. Lippard, Editor, pp. 129-158, John Wiley & Sons, Inc., New York (1976).

Photoelectrochemistry of Layer-Type Zirconium Disulfide

Helmut Tributsch

Laboratoire d'Electrochimie Interfaciale du C.N.R.S., 1, Place A. Briand, 92190 Meudon-Bellevue, France

ABSTRACT

Semiconducting zirconium compounds have never before been considered for solar energy applications, although Zr is more abundant than most commercially interesting metals and, as opposed to Cd, nontoxic. Reasonably high photocurrent densities (mA/cm^2) which were observed in ZrS_2 ($E_g = 1.68 \text{ eV}$) suggest that it could possibly be developed as a material for solid-state solar cells. Its photoelectrochemical behavior is especially interesting from theoretical points of view. Although ZrS_2 has a layer-type structure very similar to that of MoS_2 or WS_2 , its anodic photoproducts are very different. Sulfur and not sulfate is formed and there is no specific photoinduced surface interaction with iodide. Since photoreactive holes are generated on an energy band derived from sulfur p-orbitals (as in CdS) and not from d-orbitals (like MoS_2), the results are considered as further evidence for the advantage of d-bands for the photoreaction of water with visible light. Possible molecular reasons are discussed and a model is proposed which emphasizes the importance of kinetic factors for photoelectrochemical stability of electrodes and their reactivity with water. ZrS_2 does not seem to provide any advantage as a photoelectrode in regenerative redox solar cells, but some of its peculiar properties such as its high ability to form energy storing intercalation compounds still have to be evaluated.

ZrS_2 is a semiconductor with a layer structure of the cadmium iodide type. It consists of stacked composite layers comprising single sheets of metal cations sandwiched on either side by sheets of anions (Fig. 1). Since primary valency is limited within each multiple sandwich, adjacent layers are held together only by relatively weak van der Waals forces. The resulting structure is markedly anisotropic, exhibiting pronounced cleavage perpendicular to the c-axis of the octahedrally coordinated crystals. Crystal-chemical, optical, and electrical properties of ZrS_2 have been studied (1-5) and reviewed (6). Optical measurements (3-5), photoemission studies (7), and band structure calculations (8, 9) have shown that the lowest d-band of ZrS_2 (and HfS_2) is empty and separated from a bonding p-like valence band by about 2 eV. The theoretical values for the bandgap, 1.74 and 1.84 eV (8), are in good agreement with the experimental result (1.68 eV) (1). The electronic transition was found to be indirect. Calculations with the empirical tight binding (ETP) method (8, 10) indicate that the d-band which is acting as the conduction band is between 1.74 eV (3) and 2.25 eV (8) wide and might be viewed as an antibonding band, formed by the t_{2g} triplet of d-bands. The band configuration indicates considerable ionic character in the bonding. The fractional ionic bond character of ZrS_2 has been estimated to be 0.26, as compared with 0.12 in 2H- MoS_2 . When the applied electric field is perpendicular to the c-axis, the effective charge for a polar lattice vibration in ZrS_2 is found to be $e_T^*/e = 4.6$ (e : electric charge) as compared to $e_T^*/e = 0.78$ in 2H- MoS_2 . The force constants

within the layers for MoS_2 is, on the other hand, considerably bigger ($c_w = 1.7 \cdot 10^5 \text{ dyne cm}^{-1}$) than that for ZrS_2 ($c_w = 0.36 \cdot 10^5 \text{ dyne cm}^{-1}$) (11). When ZrS_2 is grown by iodine vapor transport from a charge in which the ratio S:Zr = 2:1, a crystal composition $\text{ZrS}_{1.98 \pm 0.03}$ results. When the charge composition is varied between the limits Zr:S = 1:3 to 3:1, the di-

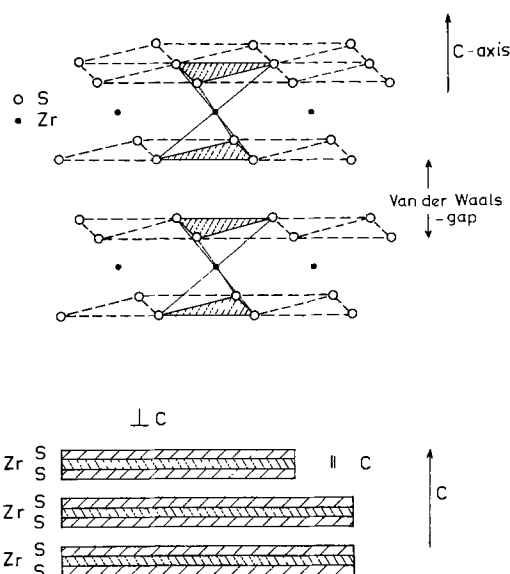


Fig. 1. Crystal structure and schematic arrangement of layers in ZrS_2 .

Key words: photoelectrochemistry, oxygen evolution, photo-corrosion.

sulfide phase is found to shift within a narrow homogeneity range between $ZrS_{1.93 \pm 0.02}$ to $ZrS_{1.94 \pm 0.03}$ (12). Zirconium is thus always present in excess. It can easily be taken up into vacant sites in the van der Waals gap. Nonintentionally doped ZrS_2 will therefore always show n-type character.

Since only weak van der Waals forces act between layers of ZrS_2 , it is possible to intercalate a wide variety of atoms and molecules. The resulting ZrM_yS_2 ($0 < y \leq 1$) intercalation compounds exhibit markedly altered solid-state properties. Interestingly, they seem to remain semiconducting when the intercalated species are Cu or Fe with $0 < y \leq 0.22$ (13). Since intercalation compounds of ZrS_2 can readily be formed electrochemically (14, 15), a certain knowledge of their properties (16, 19) will be essential for understanding electrochemical and photoelectrochemical mechanisms.

There were three reasons which motivated us to start an investigation of the photoelectrochemical properties of ZrS_2 , which has not yet been considered as a possible solar energy material. These are:

1. Zirconium is the eleventh most abundant element on earth, more abundant than Zn, Cu, or Pb. In addition it is, which is most important, practically nontoxic (20). Since zirconium has turned out to be a very valuable structural material for nuclear reactors, its technology is rapidly developing and it is becoming commercially interesting for other applications.

2. ZrS_2 is a layer-type transition metal compound with a crystal lattice almost identical with that of MoS_2 . The only difference is that the cations have an octahedral arrangement (Fig. 1) and not a trigonal prismatic one. The MoS_2 structure can be obtained from that of ZrS_2 by just replacing the dashed octahedrons by prisms in Fig. 1. This close similarity of the crystal structures in combination with a similar chemical behavior of Zr and Mo is especially interesting with respect to a pronounced difference of the electronic structure found in MoS_2 as compared to ZrS_2 (Fig. 2). The trigonal prismatic symmetry in MoS_2 causes the t_{2g} triplet of d-bands found in layer compounds of octahedral symmetry (ZrS_2) to split into a lower d_{z^2} band and a higher d_{xy} , $d_{x^2-y^2}$ energy band. The consequence is that the valence band of ZrS_2 is an energy band derived from sulfur 3p orbitals and the "valence band" of MoS_2 , which is a group VI transition metal compound, is the lower d_{z^2} energy band. Light absorbed in ZrS_2 will therefore produce holes in a sulfur 3p energy band as in CdS while light absorbed in MoS_2 will generate holes in the d_{z^2} energy band. Since layer-type molybdenum- and tungsten-dichalcogenides which permit photoreactions over d-bands have been shown to provide reasonably stable photoelectrodes for regenerative electrochemical solar cells and are able to photoreact with water (21, 22), com-

parison of ZrS_2 and MoS_2 will allow interesting conclusions with respect to the influence of the electronic state of a reactive hole on the quality of photoelectrochemical reactions. Figure 2 represents the approximate relative energetic position of these two compounds (see later) which also shows that the reactive holes have comparable energies. It should, however, also be pointed out that the energy scheme in Fig. 2 contains some degree of arbitrariness. For ZrS_2 the experimentally determined indirect gap of 1.68 eV (1) is, as already mentioned, well in agreement with theoretical results. The theoretical values for the indirect energy gap of MoS_2 , however, scatter between 0.25 and 1.23 eV according to the theoretical model used (10). A weak transition corresponding to $\Delta E = 0.2$ eV has also been attributed to the d-d gap (3). The main optical transitions start to occur at 1.75 eV. Photopotentials as high as 420 mV, which were found when MoS_2 was in contact with an iodide solution, suggest a photoelectrochemically effective energy gap of at least 1 eV. Experimental values for the indirect energy gap of MoS_2 vary from 1.13 eV [optical measurements (23)] to 1.6 eV [conductivity measurements (24)]. As long as the actual value of the indirect energy gap in MoS_2 and its significance for photoelectrochemistry is not established we prefer to use the largest experimental value for the indirect ($E_g = 1.6$ eV) transition. The actually effective gap might be somewhat smaller, placing the "valence band" edge of MoS_2 to somewhat more negative potentials.

3. A third reason for us to start an investigation of the photoelectrochemical properties of ZrS_2 was the possible utilization of layer-type dichalcogenides of group IV.B as electrodes for energy storing batteries (25). Energy densities of up to 480 W-hr/kg and excellent reversibility were obtained with the Li-TiS₂ battery system. Semiconductors of group IV.B such as ZrS_2 , $ZrSe_2$, HfS_2 , and $HrSe_2$ offer the potentiality of cathodic photoreactions suitable for a combined conversion and storage of solar energy. A detailed analysis of this possibility has been provided in a separate publication (26).

Experimental and Materials

Single crystals of ZrS_2 with dimensions between a few mm² and 50 mm² were available for the investigation.¹ Their appearance was violet and metallic. As very thin sheets and viewed against the light they were reddish and transparent. Electrical contacts were made with copper wires attached to the semiconducting crystals (||c) by means of platinum paint (Emetron, Hanau). The crystals were embedded into a Teflon mounting exposing a van der Waals surface (⊥c) to the electrolyte. The renewal of the interface was achieved by removing an attached adhesive tape. Microscopic analysis of the cleaved surface regularly showed a considerable concentration of step sites (||c) and crystalline imperfections. Electrochemical experiments were performed in a standard glass cell containing the semiconductor electrode, a Pt counter-electrode, and a saturated calomel electrode. A potentiostatic circuit and a wave generator for dynamic recordings were used. The light source was a 150W XB0 xenon lamp, the monochromator a Jobin Yvon HRS 2 model. For phase sensitive (lock-in) measurements a PAR 121 lock-in amplifier and a PAR 125 A chopper were employed.

Experimental Results

When undoped ZrS_2 is used as an electrode in an electrochemical cell it behaves like an n-type material exhibiting rectifying behavior and photoeffects in the anodic potential region. Figure 3 shows the anodic photo- and dark-currents of ZrS_2 for two different pH values (1 and 13). It can be seen that the limiting current behavior of the material in the dark is not very

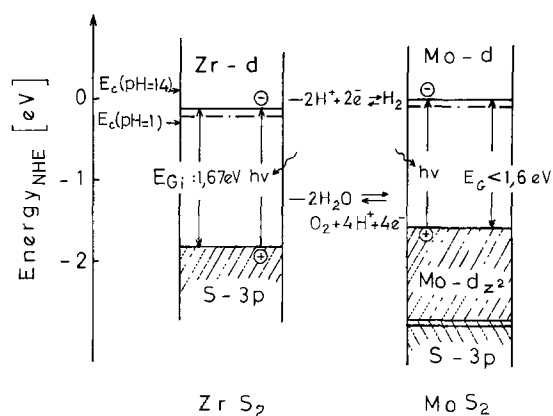


Fig. 2. Energy schemes and approximate relative energetic positions of ZrS_2 and MoS_2 .

¹ We would like to thank Professor Nietsche, Freiburg, for the samples.

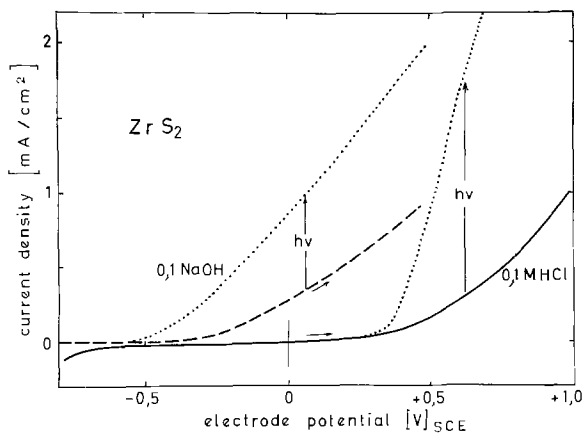


Fig. 3. Electrode photocurrent and dark current of ZrS_2 at two different pH values (pH 1 and 13).

pronounced. The magnitude of dark currents depends on the crystalline quality of the ZrS_2 interface and, like in layer-type transition metal dichalcogenides of group VI (Mo, W) (27), appears to depend on the fraction of surface areas ||c. It increases after anodic polarization of the electrode (corrosion of the surface) or addition of reducing agents (e.g., I^-). In the visible spectral region, the main contribution to the photocurrent comes from photons with wavelengths between 400 and 600 nm. The photocurrent spectrum is in reasonable agreement with the absorption spectrum of the material (Fig. 4). It appears that the $M_1^- \rightarrow M_1^+$ transition near $\Delta E = 2.73$ eV, which is theoretically (8) and experimentally (1, 4) well established, can be distinguished. When photocurrents are separated from dark currents by means of a lock-in technique, their characteristic voltage dependence and limiting current behavior can be recognized (Fig. 5). Limiting photocurrent densities of several mA/cm² have been observed (150W xenon, $400 \leq \lambda < 600$ nm). Their dependence on the light intensity is linear, but reaches a saturation value at high photon densities (Fig. 6). Cyclic current voltage dependencies of ZrS_2 in absence and during illumination are reproduced in Fig. 7 (sweep rate 40 mV/sec). It can be observed that a higher anodic photooxidation is followed by an enhanced cathodic reduction.

ZrS_2 shows considerable electrochemical reactivity both anodically and cathodically. As a consequence of an anodic (photo) current flow, the ZrS_2 electrode loses its metallic brightness and a layer of molecular sulfur is formed on its surface. The principal mechanism of the anodic photoreaction has been determined by our experiments to be

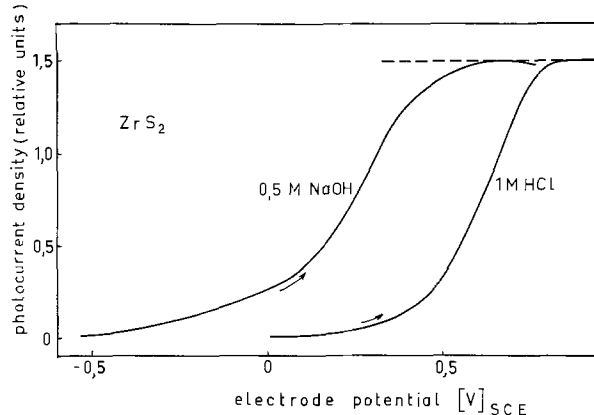
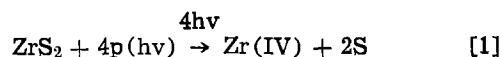


Fig. 5. Voltage dependence and limiting behavior of anodic photocurrents of ZrS_2 for two electrolytes with different pH values (dashed line: normalized limiting value).



In absence of light the same reaction products are formed at a lower rate. In this case, holes are generated by a still undetermined potential dependent surface reaction in the dark. As a consequence of the formation of a sulfur layer on the ZrS_2 surface, the anodic photocurrents are unstable and, depending on the light intensity, decrease more or less rapidly with time. Cathodically, three electrode mechanisms are possible: intercalation of positive ions (e.g., H^+), at somewhat more negative potentials their deposition (e.g., evolution of H_2), and reduction of ZrS_2 leading to lower valent zirconium and H_2S . These electrode reactions cause profound changes of the electrode ma-

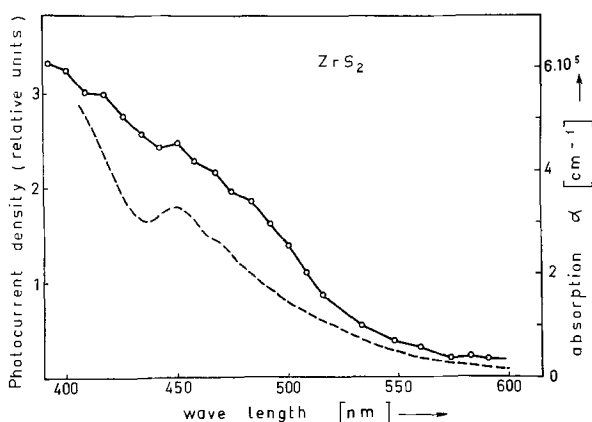


Fig. 4. Spectral dependence of electrode photocurrents and light absorption (dashed line) in ZrS_2 (electrode potential 0.85V, electrolyte 1M HCl).

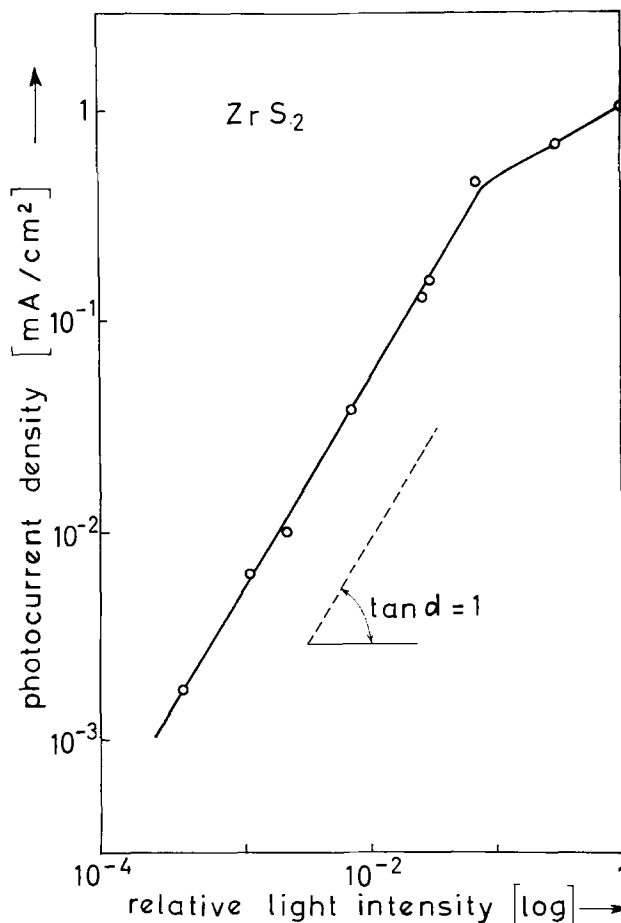


Fig. 6. Dependence of photocurrent density on the intensity of incident light (relative units) (electrode potential: 1V; electrolyte: 0.5M KCl; lock-in technique: 150 cps).

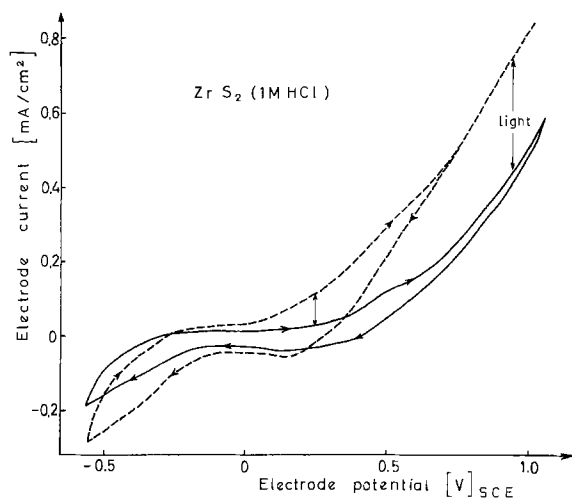


Fig. 7. Cyclic current-voltage curves for ZrS₂ in the absence of, and during, illumination (sweep 40 mV/sec; 1M HCl).

terial. Polarization of ZrS₂ at -2V in 1M HCl for 30 sec leads, for example, to the formation of a gold-yellow surface dotted with many tiny crystal scales, which no longer shows an anodic photoeffect. Cathodic polarization in the presence of NH₄Fe(SO₄)₂, pyridinium ions (in ethanol), Cu²⁺, or Li⁺ (in acetonitrile) similarly affects the electrode material in a way characteristic for intercalation reactions (changes of optical properties, volume changes, alteration of the crystalline macrostructure—small crystal fragments appear on the surface).

The different anodic (photo) behavior of ZrS₂ as compared to MoS₂ which reacts with water to form molybdenum sulfate is also evident from its electrochemical behavior in contact with acetonitrile. While the anodic dark and photocurrents of MoS₂ are drastically reduced in the presence of acetonitrile as compared to an aqueous electrolyte and are dependent on traces of water or other oxidizable species, those of ZrS₂ retain a comparable order of magnitude. In this respect the behavior of ZrS₂ is more similar to that of CdS than that of MoS₂ or WS₂. In order to detect further differences between the photoelectrochemistry of ZrS₂ and MoS₂ we studied the effect of reducing agents on the voltage dependence of the photocurrent across the layer-type interface. As reported in some detail in preceding publications (21c, d, e) the presence of reducing agents (e.g., I⁻, Br⁻, Fe²⁺, hydroquinone) in the electrolyte considerably shifts the photocurrent across molybdenum and tungsten dichalcogenides in the negative direction. The largest shift was observed in the presence of I⁻. It amounts to approximately 0.6V in the case of MoS₂ (Fig. 8). This very pronounced effect of I⁻, which is essential for the operation of reasonably stable regenerative solar cells based on Mo- and W-dichalcogenides, is absent with ZrS₂ in spite of the very similar crystal structure and chemistry of layer compounds of group IV.B and VI.B transition metals (Fig. 8). Shifts of the current voltage characteristic were not observed, but only changes in the magnitude of the currents.

We made some efforts to understand the photocurrent characteristic of ZrS₂. Figure 4 shows that between 400 and 600 nm the absorption coefficient of ZrS₂ changes by a factor of approximately 30. Since the depth of the space charge layer, in which holes are collected and drawn toward the electrode surface, depends on the applied electrode potential, the voltage dependence of photocurrents should therefore change characteristically with the wavelength of the incident light. The photocurrent under reverse bias in a semiconductor electrolyte junction has been calculated to be (28)

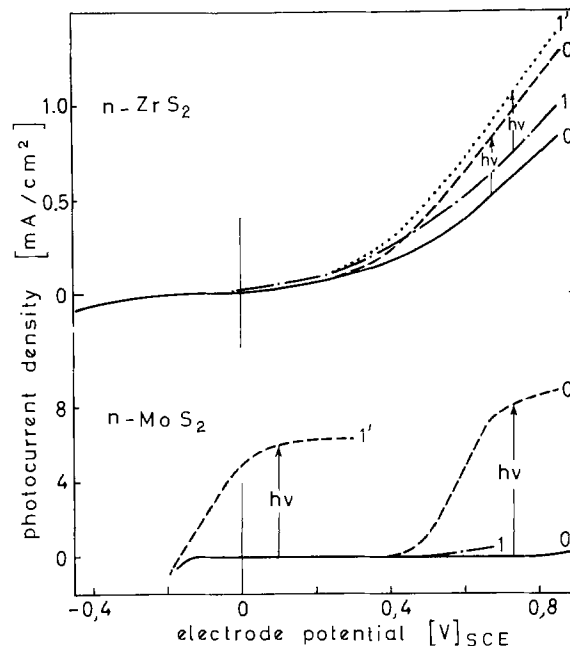


Fig. 8. Effect of addition of I⁻ (1M) to an aqueous electrolyte in contact with n-ZrS₂ and n-MoS₂ [0, 1 and 0', 1' dark currents and photocurrents, respectively, in the absence (0) and the presence (1) of I⁻].

$$I_{ph} = eA I_L \left\{ 1 - \frac{e^{-\alpha W}}{1 + \alpha L_p} \right\} \quad [2]$$

where e = electronic charge, A = constant factor, I_L = light intensity, α = absorption coefficient, L_p = diffusion length, and W = the depth of the space charge, which depends on the electrode potential according to

$$W = \left(\frac{\epsilon \Delta V}{2\pi e N} \right)^{1/2} = B(\Delta V)^{1/2} \quad [3]$$

where ϵ = dielectric constant, N = density of donors, $\Delta V = V - V_{FB}$ = potential drop in the electrode surface (V_{FB} = flatband potential). At the beginning it seemed to be reasonable to assume that the diffusion length L_p of holes perpendicular to the electrode surface ($\parallel c$) is small since their transport across the layers will depend on some hopping mechanism. (A mobility for electrons of only 4.3 cm²/Vsec has been reported for ZrS₂ parallel to the layers (2) where the carrier mobility should be 2-3 orders of magnitude higher than perpendicular to the layers.)

Assuming that $\alpha L_p \ll 1$, which should be expected for smaller values of α , and $\alpha W \gtrsim \alpha L_p$, relation [2] can be simplified and the exponential term expanded. With $e A I_L = I_{ph-lim}$ (= limiting photocurrent) and considering [3] it can be rewritten as

$$(I_{ph}/I_{ph-lim})^2 = B^2 \alpha^2 \Delta V \quad [4]$$

If we plot the square of the normalized photocurrent as a function of the electrode potential we should (at least in certain potential regions) expect straight lines with inclinations proportional to α^2 , the absorption coefficient for the incident light. The results of such plots obtained with light of wavelengths between 400 and 600 nm (corresponding to a change of α by a factor of 30) are shown in Fig. 9 for two different pH values of the electrolyte. Although their inclination would be expected to vary by a large factor, all curves are actually found to be quite similar. Suspicions that the observed limiting currents are masked by concurring anodic electrode reactions have been discarded due to reasonable agreement between the spectral dependence of limiting photocurrents and absorption in ZrS₂ (Fig. 4). In order to understand the ob-

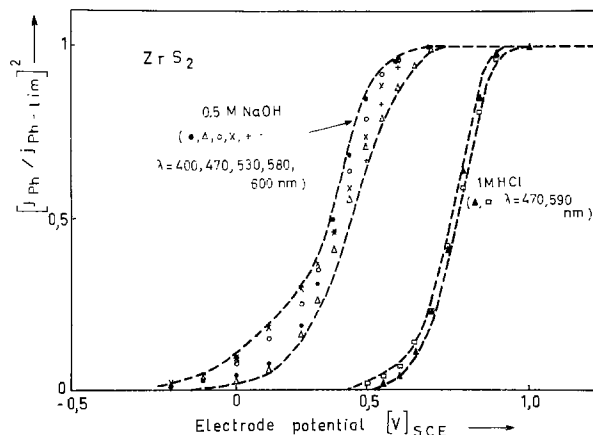


Fig. 9. Square of the normalized photocurrent of ZrS_2 at various wavelengths and two different pH values of the electrolyte plotted as a function of the electrode potential.

served contradiction we have to conclude that the diffusion length of holes L_p in ZrS_2 is much bigger than the depth of the space charge layer W .

In this situation a relation of the type

$$\frac{eAl_L}{I_{ph}} = \frac{1}{\alpha L_p} + 1 \quad [5]$$

should be expected, which seems to be approximately satisfied. More work will be needed to understand the surprisingly high diffusion length of holes in ZrS_2 and to exclude possible contributions by other energy transfer mechanisms (e.g., exciton migration).

Capacity measurements have been attempted with ZrS_2 , but simple and interpretable Mott-Schottky plots have not been obtained, possibly because of complications arising from intercalation. A preliminary estimation of the flatband potential has therefore been made by examining the potential region of the photocurrent onset. Experimental evidence indicates that (in the absence of redox systems), the flatband potential determined by capacity measurements in layer compounds (MoS_2 , $MoSe_2$, WS_2 , WSe_2) is usually situated a few hundred millivolts more negative than the photocurrent onset [compare also data in Ref. (28)]. We have accordingly shifted the flatband position of ZrS_2 into the negative direction so as to be able to explain complementary data on electron transfer reactions (Fig. 2).

Discussion

Experimental differences between ZrS_2 and MoS_2 .—The most important result of our investigation of ZrS_2 is that its photoelectrochemical reaction behavior is entirely different from that of MoS_2 (or WS_2) in spite of a very similar chemical reactivity of its constituents and a largely identical crystal structure. Illuminated and anodically polarized ZrS_2 shows neither the ability to photoreact with water nor the property of specifically interacting with electron donors (e.g., I^-) in the electrolyte. Since bandgaps of ZrS_2 and MoS_2 and the position of energy bands are comparable (Fig. 2) there is little doubt that the reason for the different photoelectrochemical behavior originates from the different electronic nature of photogenerated holes. When comparing the anodic light-induced liberation of molecular sulfur which occurs at ZrS_2 with the light-induced formation of sulfate or molecular oxygen, which was found with MoS_2 (30) we must conclude that the latter reaction is energetically much more demanding. At the energetic position at which holes are available in MoS_2 for electrochemical reactions, the oxidation of water cannot be initiated by a one-electron transfer reaction. Such a reaction would produce a radical and needs an oxidation potential near 2.85V (NHE). The upper edge of the $Mo-d_{2z}$ -energy band, however, might even be

more negative than depicted in Fig. 2 since the indirect energy gap of this compound, which is effective for photoelectrochemical reactions, could be smaller than the value assumed [an indirect gap of $\Delta E = 1.6$ eV has more recently been derived from high temperature conductivity in MoS_2 (24), one of $\Delta E = 1.13$ eV from optical measurements (25); earlier work places it between $\Delta E = 1.4$ eV (31) and 1.7 eV (32)]. A photoelectrochemical reaction with water can therefore only proceed if electron transfer is coupled with the formation of a suitable chemical bond to the electrode surface which avoids the formation of a radical. The problem of understanding the difference in the photoelectrochemical reaction behavior with water at MoS_2 and ZrS_2 is therefore reduced to the question why OH^- ions are able to form a bond suitable for electron transfer with a layer type semiconductor in the presence of a hole on a d_{2z} -energy band, but not in the presence of a hole on a p-energy band. Remarkably, a surface hole on a $Mo-d_{2z}$ orbital of MoS_2 which is centered at Mo atoms protruding perpendicular to the monolayer of sulfur that forms the van der Waals surface but does not penetrate it, is less exposed to reactive species in the electrolyte than a hole on a sulfur p-band in the top-most sulfur monolayer of ZrS_2 (Fig. 10). A steric hindrance for the photoreaction of holes with OH^- or I^- on ZrS_2 electrodes can therefore not be made responsible for the different mechanism.

Considerations on energetic conditions for water oxidation.—In order to estimate what kind of chemical or electrochemical interaction on an electrode surface is sufficient for the electrochemical reaction of OH^- or water on semiconductor electrodes, we must extend our energetic considerations on the reactivity of these reactants. Since the thermodynamic redox potentials of water $E_{redox}(O_2/H_2O) = 1.23V$ in an acid electrolyte and that of OH^- ions $E_{redox}(O_2/OH^-) = 0.40V$ in a basic electrolyte are only defined for a simultaneous transfer of more than one electron, they do not de-

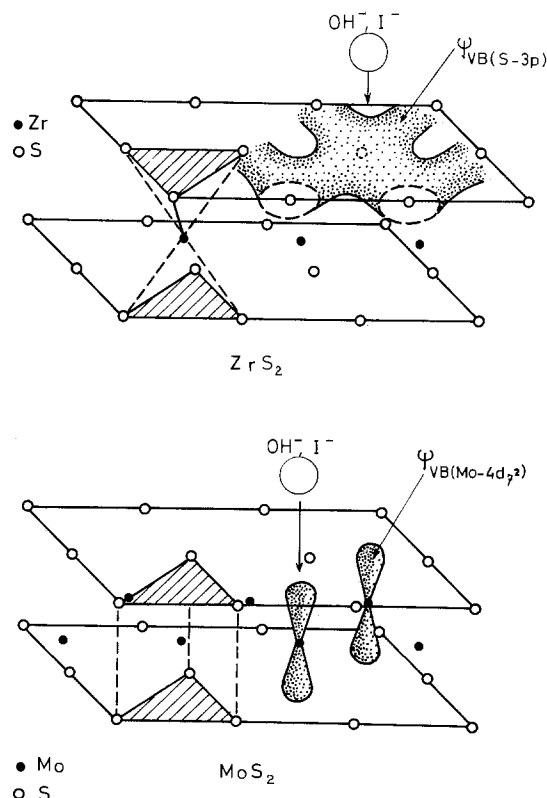


Fig. 10. Simplified schematic drawings characterizing the valence band orbitals responsible for photoelectrochemical reactivity in ZrS_2 (above) and MoS_2 (below).

scribe the actual energetic conditions which have to be met during the experiment. The distribution functions of the electronic states of OH⁻ and H₂O from which electrons have actually to be transferred to the electrode during the oxidation reaction are situated at much more positive energies (electrochemical energy scale). They center around 2.0V for the oxidation of OH⁻ to OH radicals (33) and around 2.85V (vs. NHE) for the oxidation of water to OH radicals (34). The most easily oxidizable species are therefore OH⁻ ions. When there is a chemical bonding interaction between OH⁻ in an electrolyte and an electrode surface, OH⁻ ions will adsorb and, as a consequence, their distribution function of electronic states will considerably change due to the interaction of the manifold electronic states of the solid and the electronic states of the adsorbate. It should be emphasized here that these adsorbed states of OH⁻ which form on the surface of oxides which are suitable for water photoelectrolysis (e.g., TiO₂, SrTiO₃, Fe₂O₃, KTaO₃, SnO₂) would still largely be situated above the edge of the valence band of these large-gap semiconductors. If OH⁻ ions behaved like Br⁻ ions or other simple negative ions they could be readily oxidized. From water electrolysis on metallic electrodes we know, however, that water can be oxidized with electrode potentials which exceed its thermodynamic redox potential by only a few hundred millivolts (e.g., RuO₂). This catalytically favorable behavior has been ascribed to the specific chemical interaction between OH⁻ ions and the electrode surface but few details are known about the molecular energetic conditions which have to be met.

On both photoconductors, ZrS₂ and MoS₂, OH⁻ ions can adsorb. This is evident from the fact that the current voltage curves are pH-dependent for each system and from the fact that a photoreaction with water actually occurs in the case of MoS₂. However, only in the case of MoS₂ is the interaction sufficiently strong or specific to provide electronic states at reasonably positive energy levels for electron transfer. Several questions arise. What is the difference between a kinetically favorable and an unfavorable chemisorption of OH⁻, or its reaction product? What is the contribution of the electrical field in the electrode-electrolyte interface? Is there a minimum interaction energy needed to transform a merely adsorbed OH⁻ ion into a transition complex which can provide electrons at a considerably more negative redox potential?

Theoretical criteria for stability and reactivity.—Thermodynamic criteria for the stability or instability of photoelectrodes have been developed by Gerischer (35) and Bard (36). According to Gerischer, the energy positions of the redox Fermi levels for decomposition with respect to the position of the bandedges and the Fermi levels of competing redox reactions determine the susceptibility of a semiconductor for decomposition. The same author has already emphasized the possibility that kinetic parameters modify thermodynamic conclusions. The difference in the photoelectrochemical reactivity of ZrS₂ and MoS₂ can only be understood in terms of kinetic parameters. There is no thermodynamic reason why illuminated MoS₂ should react with water and ZrS₂ should not. Figure 2 shows that the valence bandedge of ZrS₂ is situated at more positive redox potentials than that of MoS₂. Such an energy position is also indicated by the experimental threshold for photoemission. It is bigger for ZrS₂ (≈ 6 eV) than for MoS₂ (≈ 5 eV) (37). More energy to extract electrons from water would therefore be available at illuminated ZrS₂. MoS₂ would be thermodynamically unstable against electrochemical decomposition but does not decompose into molybdenum ions and molecular sulfur. ZrS₂ would also be thermodynamically unstable, but is photooxidized to zirconium ions and molecular sulfur, although it has a

similar layer structure as MoS₂ and even a higher molar enthalpy of formation ($\Delta H^\circ = -138 \text{ kcal}\cdot\text{mol}^{-1}$) than that of MoS₂ [$\Delta H^\circ = -65.8 \text{ kcal}\cdot\text{mol}^{-1}$ (38)].

It seems that most semiconductors which absorb visible light are thermodynamically unstable and kinetic quantities will therefore finally decide on whether a material will be useful for regenerative or fuel producing solar cells. The understanding of their role appears therefore to be of fundamental importance for the further development of photoelectrode systems. The pronounced difference of photoelectrochemical behavior between layer-type ZrS₂ and MoS₂ could help us to find clues to the parameters which have to be considered.

Research on oxygen evolution on metal electrodes [see the summary in (39, 40)] is much older and much more developed than research on oxygen evolution on illuminated semiconductor electrodes (41). Interestingly, little attempt has been made to evaluate and transfer valuable information on kinetic and catalytic parameters involved in the discharge of OH⁻ ions or water molecules. It is, for example, well known that the nature of electrode material has a profound influence on the kinetics of oxygen evolution from water. The oxygen overvoltage of different metals can vary by as much as 1V depending on their chemical interaction with OH⁻ ions (39). If the chemical bonding is weak, a higher potential drop in the Helmholtz layer can make up for the difference. It generates an electric field (10⁷ V/cm) which facilitates the discharge of OH⁻ ions. Now it has to be considered that the electrode potential applied to a metal electrode practically drops entirely in the Helmholtz layer where it can affect the energy factor of the electron transfer reaction. In contrast, there is little variation of the electric field strength in the Helmholtz layer of a semiconductor since the main potential drop will occur in the space charge layer. A potential applied to a semiconductor will therefore control the entropy factor of a reaction by controlling the concentration of electronic carriers rather than the energy factor. A high field will therefore not be present to assist the discharge of OH⁻ ions. The question arises to what extent other quantities can compensate for this disadvantage.

In order to get a qualitative understanding of those factors which are critical for the discharge of OH⁻ ions at illuminated semiconductor electrodes, we can start a calculation from a kinetic equation derived for metals, correct it for the smaller potential drop in the Helmholtz layer, and supplement it by considering the additional overpotential arising from the generation of reactive holes in the valence band. According to Ruettschi and Delahay (39), Frumkin, and others who treated the discharge of protons (42), the overvoltage for oxygen evolution on metals can be written in the form

$$\eta = \frac{RT}{\alpha z F} \ln \xi + \frac{\Delta H^\ddagger}{\alpha z F} - \left(1 - \frac{1}{\alpha z}\right) \psi_0 \quad [6]$$

In this relation α is the transfer coefficient for the discharge process, z is the number of charges discharged during the rate-determining reaction, ΔH^\ddagger is the energy of activation for the discharge process, ψ_0 the difference of potential across the diffuse part of the double layer, and ξ represents a group of terms, which includes the entropy of activation for the discharge process. The explicit form of ξ will not be needed here.

The overpotential η needed to drive the discharge of OH⁻ ions at metal electrodes (relation [6]) would now have to be substituted by a modified function in order to account for the situation at an illuminated semiconductor electrode. The first thing to be considered is that the electrical potential drop at the semiconductor-electrolyte interface (in the double layer)

Φ_{SE} is much smaller than the electrode potential which is applied. The second is that an additional source of a potential difference will arise at the interface due to the photogeneration of energetically favorable holes. As proposed by Gerischer (35) a reasonable function which describes their free energy would be their quasi Fermi level (${}_pE_{F^*}$) rather than the position of the valence bandedge which would provide no measure of the entropy. The light-induced contribution to the overpotential, for which they are responsible, $\eta_{pE_{F^*}}$, should correspond to the difference between the quasi Fermi level for holes and the standard redox potential for the hydroxyl ion discharge.

$$\eta_{pE_{F^*}} = \frac{{}_pE_{F^*} - {}^{\circ}E_{Redox}}{zF} = \frac{{}_pE_{F^*} - E_F}{zF} + \frac{E_F - {}^{\circ}E_{Redox}}{zF} = -\frac{kT}{zF} \cdot \ln\left(1 + \frac{\Delta_p^*}{p_0}\right) + \frac{E_F - {}^{\circ}E_{Redox}}{zF} \quad [7]$$

In this relation Δ_p^* represents the change of the hole concentration when the semiconductor is illuminated and E_F is the Fermi level in the bulk. p_0 , which is the equilibrium concentration of holes, can be expressed in terms of the bandgap of the semiconductor (n-type)

$$p_0 = \frac{N_c N_v}{N_D} \cdot \exp^{-E_G/kT} \quad [8]$$

(N_c , N_v are the densities of states in the conduction and valence band, respectively, N_D is the donor concentration, and E_G the energy gap.)

For larger energy gaps ($E_G \gtrsim 1$ eV) which corresponds to a situation in which $\Delta_p^* \gg p_0$, relation [7] can be rewritten with relation [8] to give

$$\eta_{pE_{F^*}} = -\frac{kT}{zF} \ln \frac{\Delta_p^* N_D}{N_c N_v} - \frac{E_G}{zF} + \frac{E_F - {}^{\circ}E_{Redox}}{zF} \quad [9]$$

In order to get a kinetic equation for the photoinduced discharge of hydroxyl ions on semiconductor electrodes, we substitute in Eq. [6] (e_0 is an energy depending on the work function)

$$\eta = \Phi_{SE} + \frac{e_0}{F}; \quad e_0 \rightarrow e_0 - F\eta_{pE_{F^*}}$$

We obtain the equation

$$\Phi_{SE} - \frac{\Delta H^\ddagger}{\bar{a}zF} + \frac{E_G}{zF} - \frac{E_F - {}^{\circ}E_{Redox}}{zF} - \frac{RT}{\bar{a}F} \ln \xi - \left(1 - \frac{1}{\bar{a}z}\right) \psi_0 - \frac{e_0}{F} - \frac{kT}{zF} \ln \frac{\Delta_p^* N_D}{N_c N_v} \quad [10]$$

We can simplify it by comparing electrodes with similar work functions (contained in e_0), similar densities of states, and similar donor concentrations, in which light produces a comparable concentration of holes which may initiate an equivalent photoelectrochemical reaction (\bar{a} and z can be assumed to be 1). In this case the right side of Eq. [10] becomes a constant which is characteristic for a specific reaction (different for OH⁻ oxidation and photocorrosion) and a criterion for the photodischarge of hydroxyl ions or the onset of another photooxidation may be seen in the condition

$$F\Phi_{SE} - \Delta H^\ddagger + E_G - (E_F - {}^{\circ}E_{Redox}) > \text{Const} \quad [11]$$

with

$$\text{Const} = \frac{RT}{\bar{a}} \ln \xi - \left(1 - \frac{1}{\bar{a}z}\right) F\psi_0 - e_0 - \frac{kT}{z} \ln \frac{\Delta_p^* N_D}{N_c N_v}$$

It is interesting that this relates the potential dependent electrical energy which is provided at the interface $F\Phi_{SE}$, and the potential dependent difference between Fermi level and redox potential ($E_F - {}^{\circ}E_{Redox}$) with the energy of activation of an oxidation reaction (ΔH^\ddagger) and the energy gap (E_G). It should therefore be possible to utilize it for the discussion of kinetic factors affecting an electrode's photoelectrochemical stability and reactivity with water. A comparison of magnitudes which are to be expected for the different quantities in relation [11] is instructive. The energy gap of photoelectrodes may vary between 4 and 1 eV. The difference between the Fermi level and the redox level is between ~ 1.5 eV (photoelectrolysis) and 0 eV (photoassisted electrolysis). The energy of activation for the discharge of OH⁻ ions or water molecules is more difficult to estimate. For platinum surfaces which show a relatively high overpotential, the activation energies obtained in acid solutions vary between 0.53 and 0.61 eV, in alkaline solutions between 0.36 and 1.1 eV (40). They are much lower for catalytically very active ruthenium-, osmium-, or iridium-electrodes. We estimate a practical variability of ΔH^\ddagger between 0.1 and 1.2 eV. The potential drop in the semiconductor-electrolyte interface Φ_{SE} in [11] may be expressed by the simplified relation (43)

$$\Phi_{SE} \approx \delta_H \frac{\epsilon}{\epsilon_H} \left(\frac{d\Phi}{dx}\right)_s - \chi_{dipole} \quad [12]$$

δ_H is the thickness of the Helmholtz double layer, ϵ and ϵ_H are the effective dielectric constants of the semiconductor and of the Helmholtz double layer, respectively; χ_{dipole} is the contribution of oriented dipoles in the Helmholtz layer and of the electric momentum in the surface of the semiconductor, and $(d\Phi/dx)_s$ is the field strength at the semiconductor surface. The latter can be written down in terms of the potential drop $\Delta\Phi$ in the space charge region and the Debye length L (n_0 is the bulk concentration of electrons) (44)

$$\left(\frac{d\Phi}{dx}\right)_s = \frac{\Delta\Phi}{L} = \Delta\Phi \sqrt{\frac{4\pi e^2 n_0}{\epsilon kT}} \quad [13]$$

The electrical energy $F\Phi_{SE}$, which is available at the semiconductor electrolyte interface for the support of electrochemical reactions, is thus composed of a largely potential independent term due to the dipole orientation and a potential dependent one which is strongly affected by the Debye length and the dielectric constant of the semiconducting material. Between intrinsic semiconductors ($n_0 \approx 10^{14}$ cm⁻³) and metallic solids ($n_0 \approx 10^{22}$ cm⁻³) the Debye length varies from $L \approx 10^{-4}$ to $L \approx 10^{-8}$ cm. For moderately doped semiconductors ($n_0 < 10^{18}$ cm⁻³), the electrical field (13) in the surface ($\Delta\Phi = 1$ V) will stay below 10^{+6} V/cm (43) but it could reach 10^7 V/cm in degenerate semiconductors ($n_0 \approx 10^{20}$ cm⁻³). At suitable photoelectrodes the contribution $F\Phi_{SE}$ may thus be systematically increased by controlling solid state parameters. Layer-type transition metal compounds which have very high absorption coefficients and apparently also high diffusion lengths for holes could, for example, be made highly conducting (provided surface recombination does not become a problem). If photodecomposition is kinetically inhibited (holes on d-energy bands) an electrical field could build up at the interface until water molecules can participate in the photoreaction. We estimate the possible contribution of $F\Phi_{SE}$ between 0 and 0.4 eV. If these values are inserted into relation [11]

$$(0 \text{ to } 0.4) - (0.1 \text{ to } 1.2)$$

$$+ (1 \text{ to } 4) - (0 \text{ to } 1.23) > \text{Const}$$

one immediately realizes the importance of the energy gap. If the gap is between 3 and 4 eV as in u.v.-

absorbing oxides used for photoelectrolysis of water (41), contributions from the electric energy in the interface and from the activation energy are of secondary importance. As long as the discharge of OH⁻ ions can efficiently compete with the photocorrosion there is no difficulty in obtaining oxygen evolution. If one, however, intends to utilize visible light ($E_G \lesssim 2$ eV) the first two terms become important. In order to accomplish an oxidation of water, one will have to choose systems which are especially catalytic, thus requiring a low activation energy ΔH^\ddagger . If possible, a reasonably high electrical field should be created at the semiconductor surface. Simultaneously the activation energy for the photodecomposition of the semiconductor itself should be made as high as possible to suppress corrosion.

It seems to be possible to understand the different electrochemical behavior of MoS₂ and ZrS₂ in terms of relation (11). Since bandgaps and flatband potentials of these systems are comparable, the first two quantities become decisive for the path of the photoelectrochemical reaction. Since the generation of holes does not mean a disruption of chemical bonds in MoS₂, the activation energy for photocorrosion into molybdenum ions and sulfur is so high that an electrical field may build up at the electrode surface (a positive displacement of the photocurrent onset from the flatband potential could be an indication). A low activation energy for the discharge of hydroxyl ions may cooperate to accomplish a photoreaction with water. At ZrS₂ interfaces, where holes are equivalent to breaking essential bonds, a low activation energy for the photodecomposition into zirconium ions and molecular sulfur determines the overall reaction.

Some words might be added to further explain the complete Eq. [10] from which the simplified relation [11] has been derived. Like Eq. [6] for metals it is a relation defining the overpotential needed for the discharge of OH⁻ ions at semiconductor electrodes and could also be used for the discharge of other species, including the oxidation of the surface itself. It can be seen that it depends on a larger number of quantities, including the entropy of activation, the transfer coefficient for the discharge process, the work function of the material, and its density of states. Most probably it could further be elaborated. The photoinduced discharge of OH⁻ ions (or photocorrosion) will proceed when the overpotential is trespassed, this is when condition [11] is met. In the general case the quantity taken as "Const" will vary from system to system, but could have a comparable value for the same reaction proceeding at different semiconductors with a similar density of states and work function. If one intends to learn about conditions which have to be met during light-induced oxygen evolution, such a relation could be an interesting subject for testing and improving.

Conclusions

The analysis of the photoelectrochemical behavior of ZrS₂ and its comparison with that of MoS₂ have emphasized the importance of considering kinetic quantities when searching for low-gap photoelectrodes which should be stable or react with water. Differences in the activation energies for electrochemical reactions can drastically change the reaction mechanism. In addition, the study suggests an energetic advantage of providing an electrical field at the semiconductor-electrolyte interface for the purpose of stimulating photoelectrochemical reactivity with water. At ZrS₂ interfaces there is, in contrast to MoS₂, neither a specific photoelectrochemical interaction between the crystalline solid and OH⁻ or I⁻ ions which decreases the activation energy for oxidation, nor is there a kinetic inhibition for the anodic release of metal ions which leads to the corrosion of the material. ZrS₂ behaves similarly to CdS and appears not to be an especially

interesting material for conventional electrochemical solar cells. However, as discussed elsewhere (26), it might be possible to exploit its electrochemical property of forming energy storing intercalation compounds at low electrode potentials and to develop solar powered intercalation batteries. The comparison of ZrS₂ with MoS₂ has clearly underlined the peculiar nature of photoelectrochemical mechanisms involving holes on d-orbitals of transition metal compounds and their advantage in accomplishing energetically demanding oxidation reactions.

Relation [11] suggests two different strategies for achieving a photodecomposition of water with electrodes absorbing visible light. One is to make ΔH^\ddagger for the photocorrosion mechanism high (holes on d-bands, semiconductors containing insoluble cations), the other one is to make ΔH^\ddagger for the discharge of hydroxyl ions as low as possible (semiconductors containing catalytic metals such as Ru, Os, Ir). Any possibility for creating a supporting electric field at the site of OH⁻ discharge should be exploited. It might be more reasonable to accomplish photoelectrolysis with a small supporting electrical potential than to do it without externally supplied electrical energy at a much lower efficiency.

Acknowledgments

The author thanks Dr. Parsons for helpful criticism of the work and Mr. Rudelle for the numerical computation. He also thanks the Deutsche Forschungsgemeinschaft, Bonn, for support through a Heisenberg fellowship.

Manuscript submitted April 22, 1980; revised manuscript received Jan. 16, 1981.

Any discussion of this paper will appear in a Discussion Section to be published in the December 1981 JOURNAL. All discussions for the December 1981 Discussion Section should be submitted by Aug. 1, 1981.

REFERENCES

1. D. L. Greenaway and R. Nitsche, *J. Phys. Chem. Solids*, **26**, 1445 (1965).
2. L. E. Conroy and K. CH. Park, *Inorg. Chem.*, **7**, 459 (1968).
3. J. A. Wilson and A. D. Yoffe, *Adv. Phys.*, **18**, 193 (1969).
4. A. R. Beal, J. C. Knights, and W. Y. Liang, *J. Phys. C. Solid State Phys.*, **5**, 3531 (1972).
5. H. P. Hughes and W. Y. Liang, *ibid.*, **10**, 1079 (1977).
6. "Physics and Chemistry of Materials with Layered Structures," E. Mooser, Editor, 5 volumes, D. Reidel Publishing Co., Dordrecht, Boston, London (1979).
7. F. R. Shepherd and P. M. Williams, *J. Phys. C. Solid State Phys.*, **7**, 4416 (1974).
8. R. B. Murray, R. A. Bromley, and A. D. Yoffe, *ibid.*, **5**, 746 (1972).
9. L. F. Mattheiss, *Phys. Rev.*, **B8**, 3719 (1973).
10. C. Y. Fong and M. Schlüter, in "Electrons and Phonons in Layered Crystal Structures," T. J. Wieting and M. Schlüter, Editors, D. Reidel Publishing Co., Dordrecht, Boston, London (1979).
11. T. J. Wieting and J. L. Verble, in "Electrons and Phonons in Layered Crystal Structures," T. J. Wieting and M. Schlüter, Editors, p. 398, D. Reidel Publishing Co., Dordrecht, Boston, London (1979).
12. C. R. Whitehouse and A. A. Balchin, *Phys. Stat. Solidi A*, **47**, K173 (1978).
13. B. G. Yacobi, F. W. Boswell, and J. M. Corbett, *J. Phys. C. Solid State Phys.*, **12**, 2189 (1979).
14. G. V. Subbor Rao and J. C. Tsang, *Mater. Res. Bull.*, **9**, 921 (1974).
15. M. S. Whittingham, U.S. Pat. 4,040,917 (1977).
16. L. Trichet, J. Cousseau, and J. Rouxel, *C. R. Acad. Sci. Paris 274 (Série C)*, 394 (1972).
17. L. Trichet and J. Rouxel, *ibid.*, 1040 (1969).
18. F. W. Boswell, B. G. Yacobi, and J. M. Corbett, *Mater. Res. Bull.*, **14**, 1111 (1979).
19. C. Moreau, M. Spiesser, and J. Rouxel, *C. R. Acad.*

- Sci. Paris 280 (Série C)* 1203 (1975).
20. P. Pascal, "Nouveau Traité de Chimie Minérale," Tome IX, p. 216; p. 421.
 21. H. Tributsch, (a) *Z. Naturforsch.*, **32a**, 972 (1977); (b) *Ber. Bunsenges. Phys. Chem.*, **81**, 361 (1977); (c) *ibid.*, **82**, 168 (1977); (d) *This Journal*, **125**, 1086 (1978); (e) *Solar Energy Mater.*, **1**, 257 (1979).
 22. J. Gobrecht, H. Gerischer, and H. Tributsch, *Ber. Bunsenges. Phys. Chem.*, **82**, 1331 (1978).
 23. A. M. Goldberg, A. R. Beal, F. A. Levy, and E. A. Davis, *Philos. Mag.*, **32**, 367 (1979).
 24. A. J. Grant, T. M. Griffiths, P. D. Pitt, and A. D. Yoffe, *J. Phys. C. Solid State Phys.*, **8**, L17 (1975).
 25. M. S. Whittingham, *Science*, **192**, 1126 (1976).
 26. H. Tributsch, *Appl. Phys.*, **23**, 61 (1980).
 27. W. Kautek, H. Gerischer, and H. Tributsch, *Ber. Bunsenges. Phys. Chem.*, **83**, 1000 (1979).
 28. M. A. Butler, *J. Appl. Phys.*, **48**, 1914 (1977).
 29. J. Gobrecht, Thesis, Technical University, Berlin (1979).
 30. H. Tributsch and J. C. Bennett, *J. Electroanal. Chem. Interfacial Electrochem.*, **81**, 97 (1977).
 31. J. Lagremaudie, *J. Phys., Paris*, **15**, 299 (1954).
 32. B. L. Evans and P. A. Young, *Proc. Roy. Soc. A*, **284**, 402 (1965).
 33. H. Gerischer, "Electron Transfer and Electrocatalysis in Electrocatalysis on Non-Metallic Surfaces," Proceedings of a Workshop held at NBS, Gaithersburg, Md. (1975), *Nat. Bur. Stand. Spec. Publ.* 455 (1976).
 34. A. J. de Bethune and N. A. Swendeman, "Standard Electrode Potentials and Temperature Coefficients at 25°C," Clifford A. Hampel, Ill. (1964).
 35. H. Gerischer, *J. Vac. Sci. Technol.*, **15**, 1422 (1978).
 36. A. J. Bard and M. S. Wrighton, in "Semiconductor Liquid-Junction Solar Cells," A. Heller, Editor, p. 195, The Electrochemical Society Softbound Proceedings Series, Princeton, N.J. (1977).
 37. R. B. Murray and R. H. Williams, *J. Phys. C*, **6**, 3643 (1973).
 38. K. C. Mills, "Thermodynamic Data for Inorganic Sulphides, Selenides and Tellurides," Butterworths, London (1974).
 39. P. Rüetschi and P. Delahay, *J. Chem. Phys.*, **23**, 556 (1955).
 40. A. J. Appleby in "Modern Aspects of Electrochemistry," Vol. 9, B. E. Conway and J. O'M. Bockris, Editors, Plenum Press, New York (1974).
 41. M. Tomkiewicz and H. Fay, *Appl. Phys.*, **18**, 1 (1979).
 42. G. Kortüm and J. O'M. Bockris, "Textbook of Electrochemistry," Vol. II, p. 430, Elsevier Publ. Co., Houston, Texas (1951).
 43. H. Gerischer, in "Physical Chemistry," Vol. IX, H. Eyring, Editor, p. 463, Academic Press, New York (1970).
 44. V. A. Myamlin and Y. V. Pleskov, "Electrochemistry of Semiconductors," p. 33, Plenum Press, (1967).

Current Limited by Transport Through the Space-Charge Region of a Semiconductor Electrode

David L. Ullman*

Littleton, Colorado 80161

ABSTRACT

Recently, work was published in *This Journal* on the observation of cathodic current saturation with respect to oxidant species concentration, on the wide-gap, low mobility, n-type semiconducting oxides TiO_2 and SrTiO_3 . These results were interpreted in terms of a kinetic model involving electron transfer through surface states. In the present paper, an alternative explanation is put forward, as suggested by the title, and a detailed comparison made with the trapping kinetic model. The transport-limited model is quantitatively developed, using the simple depletion-region approximation, and to the extent the published data allow, comparison made with the experimental results. The relative strengths and weaknesses of the two competing theories are clearly shown. A quantitative test for distinguishing between the two mechanisms is suggested.

Recently, an experimental study was published in *This Journal* concerning the mechanism of faradaic reaction at semiconductor electrodes by Vandermolen *et al.* (1). These authors observed that, at constant pH and electrode potential, the cathodic current through TiO_2 and SrTiO_3 electrodes would initially rise with increasing concentration of solution oxidant species, and then reach a limiting value. From this, they inferred the presence of a discrete energy level in the bandgap on the surfaces, mediating charge transfer to solution species. This is a quite rational mechanism, and one yielding a solid fit to the experimental data. However, these results seem to be unique, in that such current saturation with respect to reactant solution species concentration has not, to our knowledge, been observed before.

There is considerable indication from experiments, both electrochemical (2, 3) and high vacuum (4), that

surface states occur on semiconductors and may play a role in faradaic reaction. However, while discrete levels apparently can mediate current flow at "reverse biased" semiconductor-electrolyte Schottky barriers (5), Vandermolen's results are apparently the first indication that they might also govern "forward" faradaic currents.

For this and other reasons to be discussed below, it seems worthwhile to test this interpretation against an alternative hypothesis that seems able to explain the experimental results at least equally as well. This hypothesis is that the actual faradaic kinetics are simple first order (6), and current limitation is due to transport resistance in the space-charge region. This possibility seems all the more likely when we recall that TiO_2 and SrTiO_3 are characterized by quite low carrier mobilities, while nearly every other material so investigated has charge carriers with mobilities of at least $100 \text{ cm}^2/\text{Vsec}$, and no such saturation is observed. In fact, this possibility did occur independently to Vandermolen, and was also suggested by a reviewer

* Electrochemical Society Active Member.
Key words: photoelectrochemical cells, semiconductor electrode, space-charge region, SrTiO_3 , TiO_2 .

when the paper was submitted for publication, but this interpretation was rejected for the reason to be described later (7). In the present paper, we provide an analytic technique for distinguishing between the two mechanisms, and provide a possible, testable solution to the objection that led originally to rejection of the transport-limited model.

The Models

The central result of Vandermolen's analysis is (1)

$$-j = e_0 N_{ts} \frac{k_1 n_s c_{ox} - (k_{-1} k_{-2} / k_2) c_{red}}{(k_{-1} + k_1 n_s + k_{-2} c_{red}) / k_2 + c_{ox}} \quad [1]$$

which may be restated as

$$j = j_{sat} c_{ox} / (A + c_{ox}) \quad [2]$$

where

$$-j_{sat} = e_0 N_{ts} k_1 n_s = e_0 N_{ts} k_1 N_D e^{-\phi} \quad [3]$$

$$A = [k_1 (n_1 + n_s) + k_{-2} c_{red}] / k_2 \quad [4]$$

In Eq. [4], we have written n_1 for k_{-1}/k_1 . For brevity, all terms are defined in the List of Symbols. We use the convention that cathodic current is negative.

It was also noted that experimentally, j_{sat} had the following potential dependence

$$\ln |j_{sat}| = \{\ln |j_{sat}|\}_{V=0} - \alpha FV/RT \quad [5]$$

with α close to unity.

For the transport-limited model, we begin with a fairly general expression for simple first-order faradaic kinetics

$$-j = e_0 (k_c c_{ox} n_s - k_a c_{red}) \quad [6]$$

Then, writing the equation for electron flux in a semiconductor, and using the simple depletion approximation for potential in the space-charge region, as suggested in MacDonald (8), we find the expression for net current at the interface, including transport resistance

$$-J = (e^{-\phi} - e^{-\phi_0}) / (1/\sigma_t + \text{Daw}(\sqrt{\phi})) \quad [7]$$

where, again, terms are defined in the List of Symbols. Details of the derivation and definition of the Daw function are given in the Appendix, where, for generality, dimensionless variables are used. Since it involves the depletion region approximation, we term this analysis depletion region transport theory, or DRTT.

Inspection of tabulated values of Dawson's integral shows that it may be well approximated by (9)

$$\text{Daw}(\sqrt{\phi}) = (0.500 + 0.40/\phi) / \sqrt{\phi} \quad [8]$$

with an error of no more than 3% for $\phi \geq 2.50$.

Equations [1] and [7] may be written in the same form, showing the rather strong mathematical similarity between these two physically very different models. Since they play no significant role, we neglect any terms involving c_{red} or anodic current

$$-j/e_0 = \frac{k_1 N_{ts} N_D e^{-\phi} \cdot k_2 c_{ox}}{k_1 (n_1 + N_D e^{-\phi}) + k_2 c_{ox}} \quad [9]$$

$$-j/e_0 = \frac{(D_n N_D e^{-\phi} / \lambda \text{Daw}(\sqrt{\phi})) \cdot k_c c_{ox}}{D_n / \lambda \text{Daw}(\sqrt{\phi}) + k_c c_{ox}} \quad [10]$$

where we have written $N_D \exp(-\phi)$ for n_s and $k_1 n_1$ for k_{-1} in the trapping model, and used dimensional variables in the DRTT expression. Upon comparison of Eq. [10] with Eq. [2], we may write for the DRTT

$$-j_{sat} = (e_0 D_n N_D / \lambda) (e^{-\phi} / \text{Daw}(\sqrt{\phi})) \quad [11]$$

$$A = D_n / (k_c \lambda \text{Daw}(\sqrt{\phi})) \quad [12]$$

It is seen that each model may be represented as two resistances in series, which may be approximately described as a conduction band-to-surface resistance, followed by a surface-to-solution resistance. In the models, the latter are practically identical; to distinguish the mechanisms, it is necessary to determine observable differences in predicted behavior of the former resistances.

We may use Eq. [11] to find α for this case, $= -d \ln |j_{sat}| / d\phi$

$$\alpha = \frac{1}{2} \sqrt{\phi} \text{Daw}(\sqrt{\phi}) \quad [13]$$

We see that, at constant potential, the j vs. c_{ox} behavior predicted by both models is essentially identical and also that j_{sat} depends only on space-charge potential and not on the identity of the redox species, as was seen experimentally. That the trapping kinetic model predicts α equal to unity is seen immediately from Eq. [3]. Comparison of Eq. [8] and [13] shows that the DRTT yields values of α slightly less than unity for large ϕ . From Eq. [3] and [11] we see that there should be no dependence of j_{sat} on pH, other than through the variation of ϕ resulting from pH-induced changes in V_{FB} . Since the dependence of j_{sat} on ϕ is qualitatively quite similar for the models, the j_{sat} vs. pH behavior should be indistinguishable.

For nonadsorbed solution species, charge exchange must occur across the Helmholtz layer, so we expect pH-induced Helmholtz potential variations (manifesting as variation in V_{FB}) to influence the process, as Butler-Volmer type behavior on metallic electrodes is attributed to changes in Helmholtz potential. Then, using the same reasoning as is used to derive the Butler-Volmer equation (10), we find

$$k_c = k_c^0 \exp(-(1 - \alpha_H)(\phi_H - \phi_H^0)) \quad [14]$$

Myamlin and Pleskov (11) arrive at a similar conclusion. An essentially identical expression may be written for k_2 , which in the trapping kinetic model also describes electron transfer directly to solution species.

Comparing Eq. [4] and [12], we see that the dependence of A on k_c in the DRTT is identical to its dependence on k_2 in the trapping kinetic model. Thus, at least at constant space-charge potential (constant $V - V_{FB}$), the models predict identical dependence of A on pH; that is, plots of $\log A$ at constant ϕ against V_{FB} or pH should test the validity of Eq. [14], regardless of which mechanism is the actual one.

Contrasts Between the Models

In contrast to the trapping kinetic model, the DRTT yields an expression for j_{sat} having no adjustable parameters, and is thus fairly readily tested in this respect, provided that reasonably reliable values of the input can be measured independently. As we shall see below, this may be a problem with respect to V_{FB} .

If n_1 is not too large, the trapping kinetic model predicts that current saturation with respect to n_s (like that observed with c_{ox}) should be observed at sufficiently negative electrode potentials. That such behavior was not reported suggests that the surface states must be taken as energetically rather close to the conduction band, that is, that $n_s \ll n_1$ at all investigated potentials. This is because if the ratio n_s/n_1 was at any given potential even a few percent, making the electrode only a fraction of a volt more negative would induce the condition $n_s \gg n_1$, which, at low c_{ox} , would give current saturation.

This poses no problem for the DRTT, which predicts that no such saturation should be observed. But this makes the observed potential dependence of A rather difficult to account for by the trapping model, since we have ruled out as insignificant the only explicitly potential dependent term appearing in the expression for A , Eq. [4]. It is still conceivable, admittedly, that

the trapping parameters may change as a result of interaction with the charge carriers, whose concentration varies with potential.

On the other hand, the potential dependence of A is quite explicit in the DRTT expression Eq. [12], and readily lends itself to experimental test even in the face of uncertainty in V_{FB} , by the following rearrangement

$$[A\sqrt{\phi}\text{Daw}(\sqrt{\phi})]^2 = (D_n/\lambda k_c)^2 (e_0/kT) (V - V_{FB}) \quad [15]$$

This form is of interest to us because, as seen from Eq. [8], $\sqrt{\phi}\text{Daw}(\sqrt{\phi})$ is rather insensitive to the value of ϕ for $\phi \gtrsim 10$. It is apparent that plots of lhs against V (at constant pH and constant identity of oxidant species) should yield a straight line, from whose slope and intercept we extract k_c and a new value of V_{FB} . This iterative process ultimately yields an optimum value of V_{FB} . Because of the rather weak dependence of lhs on V_{FB} , convergence should be fairly rapid. Depending on the accuracy warranted, approximation [8] or interpolations from tabulated values of Dawson's integral (9) may be used.

There are other implications of the DRTT interpretation that are of interest. One of these is the clear implication of first-order faradaic kinetics, which is demonstrated as follows. If we neglect the term in c_{red} of Eq. [6], and use this as the definition of k_c

$$k_c = -j/e_0 c_{ox} n_s \quad [16]$$

then the mathematical development leading to Eq. [7] is just as valid, only now k_c is dependent on n_s and/or c_{ox} if the reaction is not simple first order. In particular, we see from Eq. [12] and [16]

$$A \propto n_s^{1-\alpha_n} c_{ox}^{1-\alpha_o} \quad [17]$$

where α_n and α_o are the true reaction orders. Thus, plots such as the authors' Fig. 4 (1) clearly demonstrate that $\alpha_o = 1$, since otherwise the slope could not be constant. Since n_s depends on j as well as on ϕ (Eq. [A-5]), the apparent value of A would have to change (as n_s changes) unless α_n also equals 1.

Such simple first-order reactions have been observed, as noted by the authors, on ZnO (12). We note here that the electron mobility of ZnO is about 180 cm²/Vsec (13), about 30 times that for SrTiO₃, and at least 10² times that for TiO₂ (below), thus relegating transport resistance in this case to insignificance.

Another, and for us a more critical implication of the model, is that j_{sat} is actually a limiting current, corresponding to zero n_s (Eq. [A-5]) or infinite $k_c c_{ox}$ (Eq. [7]), and, being analogous to the Levich limiting current for a rotating disk electrode, cannot under any circumstances of fixed space-charge potential be exceeded, regardless of the assumed kinetic model. Thus, observed values of current greater than the computed j_{sat} must imply some error in the input data, or some violation of the assumptions under which the model is derived.

Comparison of DRTT Values of j_{sat} with Experiment

We find sufficient data in the article to allow at least approximate comparison between theoretical and experimental values of j_{sat} . We begin with the case for TiO₂ in Fig. 3 and 4 of Vandermolen *et al.*

V_{FB} at pH 0 is reported as $-0.30V$ vs. SHE; this was probably extrapolated from a measurement at pH 2 at the rate of 60 mV/pH. Thus V_{FB} at pH 2 is probably close to $-0.42V$. We have shown, theoretically, that a rate of flatband potential variation with pH less than 59 mV/pH is more reasonable than otherwise (14); published data from the Gent laboratory (15) fairly clearly imply a rate of variation close to 50 mV/pH for hydrogen-doped TiO₂. Using this slope, we estimate a V_{FB} at pH 4.7 of $-0.555V$ vs. SHE. With $V = 0.056$, $V_{sc} = 0.611V$ and $\phi = 23.9$.

For the (001) of TiO₂, $\epsilon = 173$ (16). N_D is reported to lie in the range 10^{18} - 10^{19} cm⁻³. Wilson (3) quotes a value of μ_n for TiO₂ of about 1 cm²/Vsec; a more recent measurement yields a Hall mobility of 0.24 cm²/Vsec (17).

With this data, we may calculate maximum and minimum values for the limiting current, using Eq. [A-2], [A-3], [8], and [11]. We find 2.4×10^{-5} and 1.8×10^{-7} A/cm², corresponding to the high and low values of N_D and μ_n , respectively. These compare with the value in Fig. 3 of 2.0×10^{-5} A/cm² (1).

For SrTiO₃, V_{FB} at pH 0 was determined to be $-0.60V$ vs. SHE, although considerable uncertainty in this value is admitted to. We infer a V_{FB} at pH 2 of about $-0.72V$. For $V = 0$, $V_{sc} = 0.72$ and $\phi = 28.1$.

Again N_D is in the range 10^{18} - 10^{19} cm⁻³; literature values for ϵ and μ_n are 307 (18) and 6 cm²/Vsec (19), respectively. These inputs imply high and low values for j_{sat} of 1.7×10^{-6} and 5.2×10^{-8} A/cm², for which the common logarithms are -5.8 and -7.3 , respectively. Comparing these with points 1 and 2 on curve b of the authors' Fig. 5, we see that even the high computation appears well over an order of magnitude below the curve. Recalling that current cannot exceed the DRTT value of j_{sat} , this result seems to corroborate the unreliability of the measured V_{FB} .

Acknowledging this uncertainty, we recalculate using a V_{FB} 0.20V more positive than the above, as recommended by the authors both in the article under discussion and in Ref. (18). We obtain values of $\log |j_{sat}|$ between -2.5 and -4.0 , and this time, the smaller value appears to lie quite close to curve b of Fig. 5.

While we cannot draw hard conclusions from these calculations, it is nonetheless interesting that the experimental values of j_{sat} lie within the range computed with DRTT. It is of course needless to point out the desirability of calculations using more accurate input, but we point out that it may be more consistent to use V_{FB} values found from Eq. [15].

The Weakness of the DRTT

The limiting-current concept brings us, finally, to a fundamental discrepancy between the DRTT and experiment, evident particularly in Vandermolen's Fig. 1, curve a. According to the DRTT, when the current is near j_{sat} , it must change with electrode potential at a rate close to 1 decade/60 mV, and this is presumably the rate in the high-current portion of the curve. However, the lower portion has a rate of change obviously much shallower than this.

It is stated that the curve was obtained in "sufficiently concentrated" oxidant, implying that the upper portion is in fact reasonably close to j_{sat} ; but if the upper portion is extrapolated at 1 decade/60 mV to more positive potentials, it is immediately apparent that the experimental points are at least an order of magnitude above the extrapolation. As we pointed out, this is impossible for the case of transport limitation. But since these currents are observed, a logical inference is that all currents observed are below their transport-limited values, and it is another effect, trapping kinetics, that yields the observed saturation with respect to c_{ox} .

Because of the lack of data, and the hazard of extrapolation values of V_{FB} over several units of pH, any attempt to quantitative comparison seems rather futile. But the qualitative evidence seems sufficient to make the point. These curves were rather highly reproducible on several different samples (7), and, considering also the long experience of the Gent group in making these measurements, this would seem to rule out artifactual origins of the lower part of the curve.

Another explanation for the lower part of the curve suggested by the authors (1), besides surface states, was hole injection by the oxidant species. However, it

may be shown that the surface hole concentration in TiO_2 in equilibrium with an equimolar solution of each of these redox couples is quite small, and in the case of the $\text{Fe}(\text{CN})_6^{3-/4-}$, vanishing. This would appear to rule out significant participation by holes.

However, an interesting possibility put forward by Tomkiewicz (20) involves a mechanism of flatband potential change due to a high concentration of surface states, which capture electrons as the electrode is made more negative, thus changing their charge. This causes a change in the Helmholtz potential, manifesting as a shift in V_{FB} .

We criticized Tomkiewicz's work on the basis of the fact that when this shift occurred, there were practically no electrons at the surface in his case (21). In the present case, the surface electron concentration is much more substantial. These states, of course, do not directly participate in faradaic reaction.

If such a shift does occur, it should be apparent in Mott-Schottky measurements. We see that Mott-Schottky plots reported by the Gent laboratory on TiO_2 (22) and SrTiO_3 (18) are shown only for potentials 1V or more positive of apparent V_{FB} ; on the other hand, values of V_{sc} involved here in the computation of j_{sat} are less than 1V. It is possible that impedance measurements made at more negative potentials than previously would reveal such a shift.

Summary

In summary, we find four reasons that we feel merit the investigation of possible transport (as opposed to kinetic) limitation of the current on TiO_2 and SrTiO_3 , as observed by Vandermolen *et al.*: (i) Absence of similar observations on other, and in particular, high-mobility materials; (ii) absence of current saturation with respect to n_s ; (iii) experimental values of j_{sat} that lie within the range estimated using the DRTT; and (iv) the dependence of A on potential. In short, with the exception of the lower portion of the j - V curves, the published data imply electrode behavior highly consistent with the predictions of the DRTT. We feel that a good fit of the data to Eq. [15], yielding values of V_{FB} reasonably close to those obtained by impedance measurements, would almost conclusively prove the transport-limited mechanism, since it would really be expecting too much of coincidence for a mysterious potential dependence of trap behavior to occur in such a manner that it mimics transport limitation.

Clearly, we welcome discussion and criticism from these workers, and hope they see fit to investigate our interpretation with a reasonably open mind. We are not insensitive to the amount of labor involved in measuring even a single value of A , but it was remarked that several of these had already been computed, and considering the novelty of these results, it may be worthwhile to expend the necessary effort to compute more, if needed.

Whichever theory proves correct, it is clear that these are extremely novel results with important implications for the theory of operation of semiconductor photoelectrochemical cells. Finally, we wish to remark that this episode should demonstrate the wisdom of entertaining all reasonable interpretations of experimental work when publishing, even if a particular one is favored over the others.

Acknowledgment

The study on which this work is based was done at the University of California, Berkeley, Dept. of Chemical Engineering, under a U.S. Dept. of Energy grant.

Manuscript submitted June 24, 1980; revised manuscript received Dec. 23, 1980.

Any discussion of this paper will appear in a Discussion Section to be published in the December 1981

JOURNAL. All discussions for the December 1981 Discussion Section should be submitted by Aug. 1, 1981.

APPENDIX

Current Flow Through a Space-Charge Region

From the simple depletion-region approximation (23), we find the potential profile in the space-charge region

$$\Phi = -y^2 e_0 N_D / 2\epsilon\epsilon_0$$

where we choose $y = 0$ at the boundary between the space-charge region and the quasi-neutral bulk. In dimensionless form

$$\phi = -(y/\lambda)^2 = -x^2 \quad [\text{A-1}]$$

$$\lambda^2 = 2\epsilon\epsilon_0 kT / e_0^2 N_D \quad [\text{A-2}]$$

The one-dimensional equation for electron current is

$$j/e_0 = D_n dn/dy - \mu_n n d\phi/dy$$

This may, with the aid of the Nernst-Einstein relationship

$$\mu_n = D_n e_0 / kT \quad [\text{A-3}]$$

also be written in dimensionless form

$$J = dN/dx - Nd\phi/dx$$

Using the integrating factor $\exp(-\phi)$ for rhs, this becomes

$$J e^{-\phi} dx = d(N e^{-\phi}) \quad [\text{A-4}]$$

Substituting [A-1] into [A-4], and integrating with the boundary conditions

$$N = 1, \quad \phi = 0 \quad \text{at} \quad x = 0$$

$$N = N_s, \quad \phi = -\phi_{\text{sc}} \quad \text{at} \quad x = \sqrt{\phi_{\text{sc}}}$$

and recalling that J is constant, we find, after rearrangement

$$J = (N_s - e^{-\phi_{\text{sc}}}) / \text{Daw}(\sqrt{\phi_{\text{sc}}}) \quad [\text{A-5}]$$

where Dawson's integral

$$\text{Daw}(x) = e^{-x^2} \int_0^x e^{t^2} dt$$

is tabulated in Ref. (9).

Equation [6] of the text may be restated as

$$-j = e_0 k_c c_{\text{ox}} (n_s - n_{\text{so}})$$

and written in dimensionless form

$$-J = \sigma_t (N_s - e^{-\phi_0})$$

since clearly $N_{\text{so}} = e^{-\phi_0}$. We may use this to eliminate N_s in [A-5], and obtain Eq. [7] of the text. We have dropped the subscript on ϕ_{sc} for brevity.

Upon examining the mathematical properties of the Daw function, we uncover some rather interesting implications of the model. First, we note that the function has a maximum of about 0.54 occurring at about $\phi = 0.85$, and rather slowly, but monotonically, decreases from this point, approaching zero as ϕ approaches infinity. At rather large space charge potential, $\phi = 60$ ($V_{\text{sc}} \approx 1.5\text{V}$), $\text{Daw}(\sqrt{\phi}) = 0.065$. It is apparent, then, that the Daw function is rather slowly varying, much more so than $\exp(-\phi)$, which explains the result $\alpha \approx 1$ (Eq. [11] and [13]).

We see from Eq. [7] that three basic regimes are implied, namely, transport limited ($1/\sigma_t \ll \text{Daw}$), kinetically limited ($1/\sigma_t \gg \text{Daw}$, by far the most common case), and intermediate, in which the terms are roughly equal.

We have tested Eq. [7] against exact numerical solution of the transport equations (24) and found, not surprisingly, that the largest errors occur for transport limitation. For $1/\sigma_t = 0$, Eq. [7] predicts J about 45% too large at $\phi = 4$, but this error decreases to 7% for $\phi = 9$, and decreases with increasing ϕ . Since we deal with j on a logarithmic basis, we shall rather arbitrarily take $\phi > 4$ ($V_{\text{sc}} > 0.10\text{V}$) as the condition for model validity. In this domain, $\text{Daw}(\sqrt{\phi})$ has a maximum of 0.30 at $\phi = 4$.

Because of this slow variation of the Daw function, it is apparent that, for the case of simple first-order kinetics, transition from one regime to another solely as a result of electrode potential variation is quite unlikely. In fact, if we take 0.15 as a representa-

tive value of the Daw function, we can compare $1/\sigma_t$ with this value to determine the approximate extent to which an electrode is transport limited.

If the kinetics are not simple first order, $1/\sigma_t$ must be evaluated as

$$1/\sigma_t = e_0 D_n n_s / \lambda |j| \quad [\text{A-6}]$$

In most such cases, $|j| \propto n_s^{\alpha_n}$, with $0 < \alpha_n < 1$. This means that transport limitation is more likely at low current densities, and can undergo a transition to kinetic limitation at higher currents. This should manifest as a Tafel slope variation from about 60 mV/decade at low C.D.'s to some higher value at high C.D.'s.

It is apparent that it is chiefly the quantity $\mu_n n_s / |j|$ that determines whether a particular case will be transport limited or otherwise. Unfortunately, because of the difficulty of placing an upper limit on $|j|/n_s$, it is not possible to determine a value for μ_n , above which transport limitation cannot occur. However, it appears from experience that significant transport effects are at least unlikely for materials with carrier mobilities of at least 100 cm²/Vsec. For example, our examination of Morrison's (12) data for first-order cathodic reaction on ZnO ($\mu_n = 180$ cm²/Vsec) indicates that, even if the Daw function takes on its maximum value (= 0.54), the maximum error incurred by neglect of transport effects is 3%, for the case of smallest $1/\sigma_t$.

A similar investigation of transport in illuminated electrodes is under way.

LIST OF SYMBOLS

Terms not defined here or in the text have their usual meaning.

| | |
|------------|--|
| A | empirical parameter appearing in j vs. c_{ox} plot; see Eq. [2], mol/liter |
| c_{ox} | concentration of oxidizing species of redox couple, mol/liter |
| c_{red} | concentration of reducing species of redox couple, mol/liter |
| e_0 | elementary charge, 1.602×10^{-19} C |
| j | current density, negative when cathodic, A/cm ² |
| j_{sat} | limiting value that current reaches as c_{ox} increases indefinitely; see Eq. [2], A/cm ² |
| J | dimensionless current, $= \lambda j / e_0 D_n N_D$ |
| kT/e_0 | $= RT/F = 0.0256$ V |
| k_1 | electron capture rate constant for surface states, cm ³ /sec |
| k_{-1} | rate of electron emission by traps, sec ⁻¹ |
| k_2 | parameter for transfer of electrons from occupied surface states to solution oxidant species, 1/mol sec |
| k_{-2} | parameter for oxidation of reduced solution species by vacant surface states, 1/mol sec |
| k_a | anodic rate constant, 1/mol cm ² sec |
| k_c | cathodic rate constant, cm ³ /mol sec |
| n_1 | trap parameter, $= N_C \exp((E_t - E_C)/kT)$. In the present case, it equals k_{-1}/k_1 . See Ref. (23), p. 129-134, cm ⁻³ |
| n_{so} | surface equilibrium electron concentration at zero current flow, $= k_a c_{red} / k_c c_{ox}$, cm ⁻³ |
| N | dimensionless electron concentration, $= n/N_D$ |
| N_{ts} | density of surface states, cm ⁻² |
| V_{sc} | space-charge potential, $= V - V_{FB}$, volts |
| α | empirical parameter governing the experimental current-voltage behavior, Eq. [5], dimensionless |
| α_H | Butler-Volmer coefficient, having a value between 0 and 1, governing variation of faradaic reaction kinetic parameters due to change in Helmholtz potential, dimensionless |
| ϕ | dimensionless space-charge potential, $= e_0 V_{sc} / kT$, text; dimensionless electrostatic potential in space-charge region, $= e_0 \phi / kT$, Appendix |
| ϕ_0 | dimensionless space-charge potential corresponding to zero current flow, $= \ln(n_{so}/N_D)$ |
| ϕ_H | dimensionless Helmholtz potential; $\phi_H - \phi_H^0 = e_0(V_{FB} - V_{FB}^0)/kT$; the superscript o denotes arbitrary reference |

| | |
|------------|---|
| Φ | electrostatic potential in space-charge region, volts |
| λ | space-charge region Debye length, Eq. [A-2], cm |
| σ_t | dimensionless electron transfer coefficient, $= \lambda k_c c_{ox} / D_n$ |

REFERENCES

- J. Vandermolen, W. P. Gomes, and F. Cardon, *This Journal*, **127**, 324 (1980).
- V. A. Tyagai and G. Ya. Kolbasov, *Surf. Sci.*, **28**, 423 (1971); M. D. Krotova and Yu. V. Pleskov, *Sov. Electrochem.*, **2**, 312 (1966) [*Elektrokhimiya*, **2**, 340 (1966)].
- R. H. Wilson, *J. Appl. Phys.*, **48**, 4292 (1977).
- G. M. Guichar, C. A. Sebenne, and C. D. Thualt, *J. Vac. Sci. Technol.*, **16**, 1212 (1979); *Surf. Sci.*, **86**, 789 (1979); G. M. Guichar, M. Balkanski, and L. A. Sebenne, *ibid.*, **86**, 874 (1979); G. Dorda and S. Koc, *ibid.*, **2**, 120 (1964); S. Simov, M. Kalitsova, E. Nikolova, and I. Baltov, *Surf. Sci.*, **59**, 115 (1976); L. J. Brillson, *ibid.*, **51**, 45 (1975); J. Lagowski, C. L. Balestra, and H. C. Gatos, *ibid.*, **29**, 203 (1972).
- H. Gerischer and I. Mattes, *Z. Phys. Chem. N. F.*, **52**, 60 (1967); R. Memming and G. Schwandt, *Electrochim. Acta*, **13**, 1299 (1968); A. M. Baticle and J.-L. Sculfort, *C. R. Acad. Sci. Paris*, **284**, C-103 (1977).
- H. Gerischer, in "Advances in Electrochemistry and Electrochemical Engineering," Vol. 1, P. Delahay and C. W. Tobias, Editors, Chap. 4, Interscience Publishers, New York (1961); H. Gerischer, in "Physical Chemistry: An Advanced Treatise," Vol. IXA, Eyring, Henderson, and Jost, Editors, Chap. 5, Academic Press, New York (1970); J. F. Dewald in "Semiconductors," A.C.S. Monograph #140, N. B. Hannay, Editor, p. 727, Reinhold Publishing Co., New York (1959).
- W. P. Gomes, Private communication.
- J. R. MacDonald, *Solid State Electron.*, **5**, 11 (1962).
- M. Abramowitz and I. A. Stegun, "Handbook of Mathematical Functions" AMS 55, p. 319, Nat'l. Bur. Stds., Washington, D.C. (1964).
- J. S. Newman, "Electrochemical Systems," pp. 171-176, Prentice-Hall, Englewood Cliffs, N.J. (1973).
- V. A. Myamlin and Yu. V. Pleskov, "Electrochemistry of Semiconductors," pp. 159-171, Plenum Press, New York (1967).
- S. R. Morrison, *Surf. Sci.*, **15**, 363 (1969).
- R. C. Weast, Editor, "CRC Handbook of Chemistry and Physics," 51st ed., p. E-91, Chemical Rubber Co., Cleveland, Ohio (1971).
- D. L. Ullman, Paper presented to the Div. of Colloid and Surface Chemistry at the 179th A.C.S. National Meeting, Houston, Texas, March 24-27, 1980; to be submitted to *J. Electroanal. Chem. Interfacial Electrochem.*
- F. Cardon and W. P. Gomes, *J. Phys. D: Appl. Phys.*, **11**, L63 (1978); W. P. Gomes and F. Cardon, in "Semiconductor Liquid-Junction Solar Cells," A. Heller, Editor, p. 120, The Electrochemical Society Softbound Proceedings Series, Princeton, N.J. (1977).
- R. De Gryse, W. P. Gomes, F. Cardon, and J. Vennik, *This Journal*, **122**, 711 (1975).
- C. H. Seager, *Solid State Commun.*, **20**, 539 (1976).
- F. Vanden Kerchove, J. Vandermolen, W. P. Gomes, and F. Cardon, *Ber. Bunsenges. Phys. Chem.*, **83**, 230 (1979).
- H. P. R. Frederikse, W. R. Thurber, and W. R. Hosler, *Phys. Rev.*, **134**, A442 (1964).
- M. Tomkiewicz, *This Journal*, **126**, 1505 (1979).
- D. L. Ullman, *ibid.*, **127**, 1321 (1980).
- E. C. Dutoit, R. L. Van Meirhaeghe, F. Cardon, and W. P. Gomes, *Ber. Bunsenges. Phys. Chem.*, **79**, 1206 (1975); *ibid.*, **80**, 475 (1976).
- A. S. Grove, "Physics and Technology of Semiconductors," pp. 152-163, John Wiley, New York (1967).
- D. L. Ullman and J. S. Newman, Work in progress.

Transient Natural Convection near a Plane Vertical Electrode Surface after Reversing the Electrolytic Current

Y. Fukunaka, T. Minegishi, N. Nishioka, and Y. Kondo*

Department of Metallurgy, Kyoto University, Sakyo-ku, Kyoto 606 Japan

ABSTRACT

Time variations of the concentration profile of CuSO_4 and of the velocity profile of laminar natural convective flow were measured near the electrode surface during the transient electrolysis after reversing the current. A symmetrical transient variation of natural convection was observed after anodic and cathodic current reversions. It was found that the concentration profile possesses an extreme value, and the inverted flow appears near the electrode surface. The effects of current density and vertical location on the natural convection were discussed. Based on the experimental results, the space-time structure of the transient natural convection was considered.

Among numerous works (1-3) in the past on the natural convective flow along the surface of a plane vertical electrode installed in unstirred electrolyte, only a few works concerned the transient natural convection encountered in the unsteady electrolysis. This is in spite of its importance in the practical operation of unsteady electrolysis, such as periodic current reversal in copper refining, as well as in the study of the nature of transient natural convective flow itself.

Tvarusko *et al.* (4, 5) studied the transient natural convection at the start of electrolysis by applying a technique of Mach-Zehnder interferometry and showed that both the concentration difference of CuSO_4 between bulk electrolyte and cathode surface and the thickness of the cathodic diffusion layer increase in proportion to the square root of time elapsed from the start. However, they were not successful in photographing the concentration profile of CuSO_4 in the diffusion layer which develops downstream. This is supposed to be due to the severe optical restriction in two-beam interferometry.

Only after the application of a technique of holographic interferometry, it became possible to precisely measure the concentration profile in the diffusion layer near the electrode surface, and the transient cathodic diffusion layer (6, 7) was studied by applying this technique. In addition, the corresponding transient velocity profile was measured by recording the motion of colophonium particles suspended in the cathodic hydrodynamic boundary layer (7, 8).

Following these studies, it is intended in the present work to study the transient natural convection after the direction of electrolytic current is reversed. Time variations of the concentration profile of CuSO_4 and of the velocity profile of natural convective flow are measured during the time period from reversing the current until the steady natural convection in reversed direction is established.

Experimental Procedures

The inner dimensions of the glass electrolytic cell were 0.6 cm (thickness), 7.5 cm (width), and 19.7 cm (height). Both tough pitch copper electrodes were 0.5 cm square and 26 cm long. They were insulated with PVC resin except for the working surface of 0.5×8.0 cm² between the vertical distance of 4 and 12 cm from the lower edge. Each electrode was vertically installed in the electrolytic cell at a distance of 4.8 cm. Ana-

lytical reagent grade CuSO_4 and deionized water were used to make up aqueous 0.6M CuSO_4 solution. The solution was poured into the electrolytic cell until its surface was positioned at a height of 16 cm from the lower edge of electrodes. With this configuration, equal vertical lengths of insulated surface of 4 cm were maintained on the lower and upper sides of each working electrode, respectively, and the effect of circulating flow of electrolyte was avoided during the measurement. The distance of the electrode surface traversed by the incident beam was 0.5 cm.

The electrolysis was carried out at $23^\circ \pm 1^\circ\text{C}$ at the current densities of 1.0, 2.0, and 4.0 mA/cm², respectively. The electrolytic current was supplied by a galvanostat. The applied current densities were far lower than the cathodic limiting current which was measured at about 45 mA/cm² from the current-potential curve. Thus the uniform distribution of current density along the electrode height was ensured (9). The measuring positions of concentration and velocity profiles at the working electrode surface were, respectively, 2, 4, and 6 cm from the lower edge.

After it was confirmed that the bulk electrolyte was at rest, the electrolysis was started and continued for 10 min to attain the steady state. Then the current was reversed to the same absolute value, and the measurements of concentration and velocity profiles were started. They were made at appropriate time intervals until the reverse steady state was attained.

A technique of holographic interferometry was used for measuring the concentration profile (3). The focal plane was set at the center of the electrode. When the cathodic current was reversed, the interference fringes started to shift upward as shown in Fig. 1, and an extreme value of concentration appeared adjacent to the electrode surface. The steady anodic concentration profile was gradually attained in which the interference fringes were deflected upward.

The horizontal interference fringes in the bulk electrolyte were extended to the electrode surface, and the number of intersecting points with the shifted fringes, N , was counted. The concentration was calculated by the following equations

$$(n^* - n)d = N\lambda \quad [1]$$

$$n = 1.3332 + 27.89c \quad (0.19\text{M} < c < 0.72\text{M at } 23^\circ\text{C}) \quad [2]$$

The latter Eq. [2] is the regression of the refractive index upon CuSO_4 concentration in the above concentration region. The deflection of the incident beam in the boundary layer was corrected by the procedure

* Electrochemical Society Active Member.
Key words: natural convection, laminar flow, mass transfer, holographic interferometry, CuSO_4 .

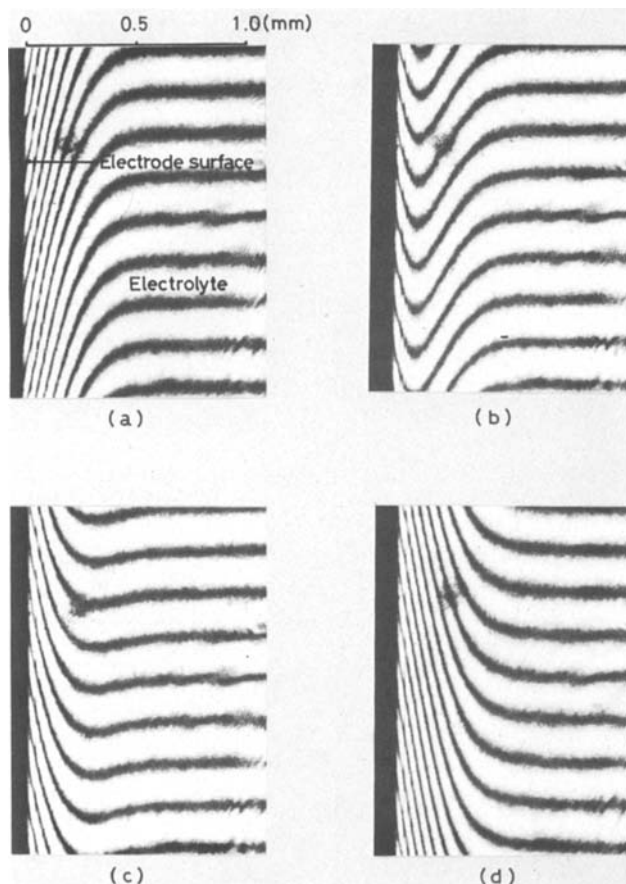


Fig. 1. Holographic interferograms. (a) $t = 0$ sec, (b) $t = 20$ sec, (c) $t = 60$ sec, (d) $t = 600$ sec elapsed after reversing the direction of current (cathodic to anodic) ($0.6M$ $CuSO_4$ solution, $i = 2.0 mA/cm^2$, $x = 4$ cm).

mentioned before (10). The reproducibility in the measurement of concentration profile at the same height was excellent because of the same optical configuration. On the other hand, due to a slight difference in the configuration which was inevitable in the adjustment of electrode surface parallel to the incident beam, the reproducibility in the measurement at various heights was slightly lower. However, this error was less than about 8% to the total variation and was negligible as far as the transient behavior of the concentration profile was concerned.

The measurement of velocity profile was described in a previous paper (11). An aqueous suspension of colophonium particles of $5-10 \mu m$ size was prepared by sedimentation and poured into the electrolyte. Before recording the motion of colophonium particles dragged along with the natural convective flow, a thin nylon fiber was vertically hung along the center of the working electrode, on which the incident beam was focused. The electrode was adjusted to be parallel to the beam by rotating it around the vertical axis. The drift of colophonium particles on the cinefilm was measured by using a NAC DF-1613/MB film motion analyzer.

Results and Discussion

The transient concentration profile at $x = 4$ cm after reversing the cathodic current of $2 mA/cm^2$ is shown in Fig. 2. As seen in this figure, an extreme value appeared adjacent to the anode surface after the current was reversed and moved toward the bulk electrolyte. The remaining cathodic diffusion layer almost disappeared at 90 sec from the current reversal, and the anodic concentration profile gradually grew to the steady profile.

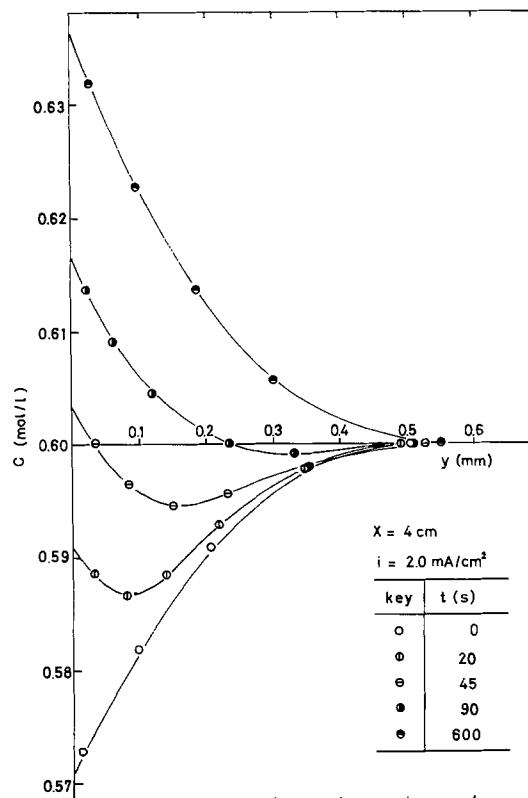


Fig. 2. Concentration profiles during the unsteady process after reversing the direction of current (cathodic to anodic).

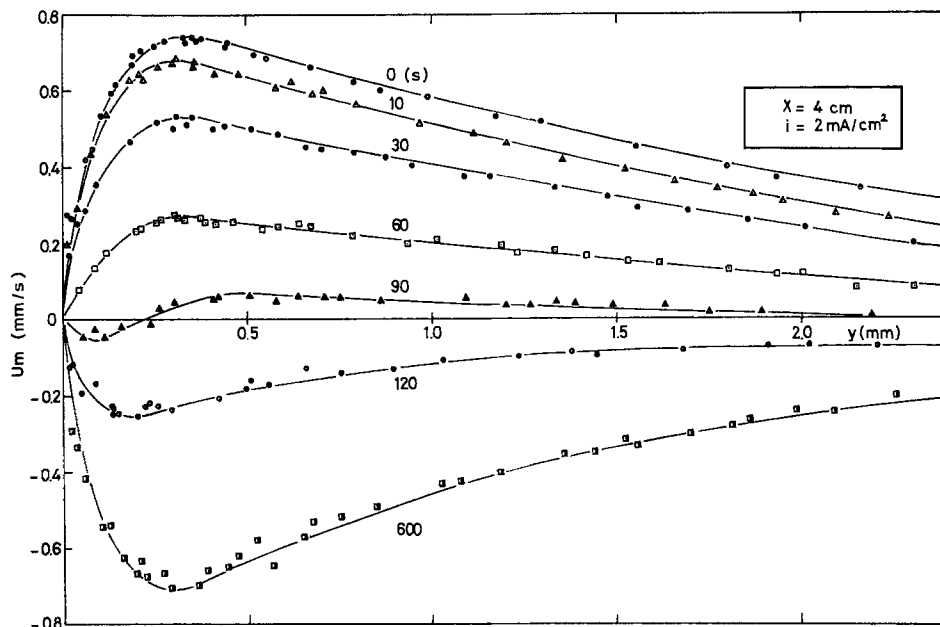
Time variation of velocity profile of natural convective flow is shown in Fig. 3. The experimental conditions were the same as above. It is seen that the velocity of natural convection uniformly decreased in the whole region of hydrodynamic boundary layer during the initial 60 sec. A downward flow appeared in the vicinity of anode surface at 90 sec, while the remaining flow was still upward in the region apart from the surface. Along with further elapsed time, it gradually converged to the downward steady velocity profile.

In order to represent the time variation of concentration and velocity profiles, several parameters were used. They are as follows: the concentration difference between the electrode surface and bulk electrolyte, Δc_s ; the thickness of concentration boundary layer, δ ; the concentration difference between the extreme value and bulk electrolyte, Δc_e ; the distance between the electrode surface and the position of the extreme value, ξ ; the maximal velocity of natural convection, u_m ; and the horizontal distance between the electrode surface and the position of u_m , τ .

They are schematically illustrated in Fig. 4. Dual u_m and τ values were observed in the so-called inverted flow which appeared at 90 sec from the current reversal as shown in Fig. 3.

In the first place, the transient natural convection after the cathodic current reversal was compared with that after the anodic current reversal. An excellent symmetry is seen in Fig. 5 between the time variations of Δc_s after the cathodic current reversal at $x = 6$ cm and after the current reversal in the opposite direction at $x = 2$ cm. Both vertical positions correspond to 2 cm from the leading edge of anodic and cathodic natural convective flow, respectively. Similar symmetry was also observed in the time variation of u_m . Based on this symmetrical nature of the natural convection, the following discussion is concentrated on the cathodic current reversal.

Fig. 3. Time variation of velocity profile (cathodic to anodic).



Time variation of concentration profile.—The time variation of Δc_s at different current densities is shown in Fig. 6. All measurements were made at $x = 4$ cm. It is seen that the rate of change of Δc_s is affected by the applied current density: the required time before Δc_s diminishes to zero is shorter at higher current densities, and Δc_s attains the steady value more rapidly at higher current densities. This is due to the combined effect of higher dissolution rate of Cu^{2+} ion on the anode surface and the broader range of concentration between initial and final steady Δc_s values.

In view of the decrease in velocity of natural convection after the current reversal shown in Fig. 3, it is supposed that the effect of convective mass transfer of Cu^{2+} ion is reduced. Presuming that the effect of convective mass transfer is minor (12), the following diffusional equations approximately hold

$$\frac{\partial c}{\partial t} = D \frac{\partial^2 c}{\partial y^2} \quad (0 \leq y < \infty) \quad [3]$$

at

$$t = 0, c = f(y) \quad \begin{cases} f(y) = c^* + (c^* - c^s)(1 - y/\delta)^\omega & (0 \leq y \leq \delta) \\ f(y) = c^* & (y > \delta) \end{cases} \quad [4]$$

$$y = 0, -D \frac{\partial c}{\partial y} = \frac{i(1 - t_1^*)}{z_1 F} \quad [5]$$

From these equations, we have

$$\Delta c_s = \frac{1}{\sqrt{\pi D t}} \left[\frac{2i(1 - t_1^*)}{z_1 F} t - \theta \int_0^\delta \left(1 - \frac{\eta}{\delta}\right)^\omega e^{(-\eta^2/4Dt)} d\eta \right] \quad [6]$$

where

$$\theta = 1.49 \frac{(1 - t_1^*)}{D z_1 F} \left\{ \frac{z_1 F \nu D^2}{g \alpha (1 - t_1^*)} \right\}^{1/5} \cdot i^{4/5} \cdot x^{1/5} \quad [7]$$

Equation [6] was used to calculate the required time from current reversal to a moment where the concentration at the anode surface becomes equal to bulk electrolyte ($\Delta c_s = 0$) and the time from current reversal to anodic steady state ($\Delta c_s = -\theta$), respectively. The calculated time was compared with the measurement. As seen in Fig. 7(a) and (b), the variation of the calculated and measured times before attaining $\Delta c_s = 0$ and $\Delta c_s = -\theta$ due to the applied current

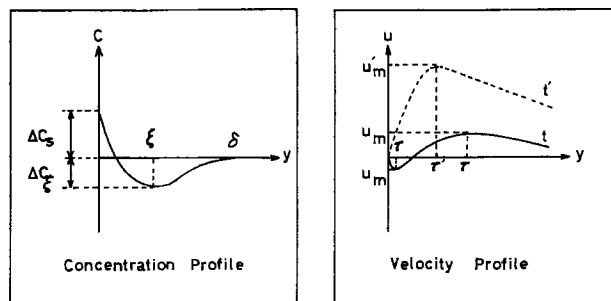


Fig. 4. Schematic illustration of concentration and velocity profiles.

density is very similar, though the calculated time is shorter than the measurement due to the assumption of neglecting convective mass transfer in Eq. [6]. It is also interesting to note that these current density de-

pendences are roughly approximated to a power of -0.4 under the present experimental conditions.

The theory of transient natural convection was developed in the field of heat transfer where the rate of heat transfer on the surface of a vertical plate was studied (13, 14). Gebhart (14) obtained the result that the rise of a dimensionless temperature which is defined as the rise of the mean temperature along the height divided by the total rise of temperature up to the steady value is described by a function of the dimensionless time of

$$T = \alpha' t / \bar{\delta}^2 \quad [8]$$

It is also clarified in a wide range of Prandtl number that the effect of transient natural convection can be neglected until almost 80% of the steady value is reached and the steady state is virtually realized at 0.4 of the dimensionless time.

From the analogy between heat and mass transfer, the required time before the steady natural convection is attained in the present unsteady electrolysis is given by

$$t = 0.4 \bar{\delta}^2 / D \quad [9]$$

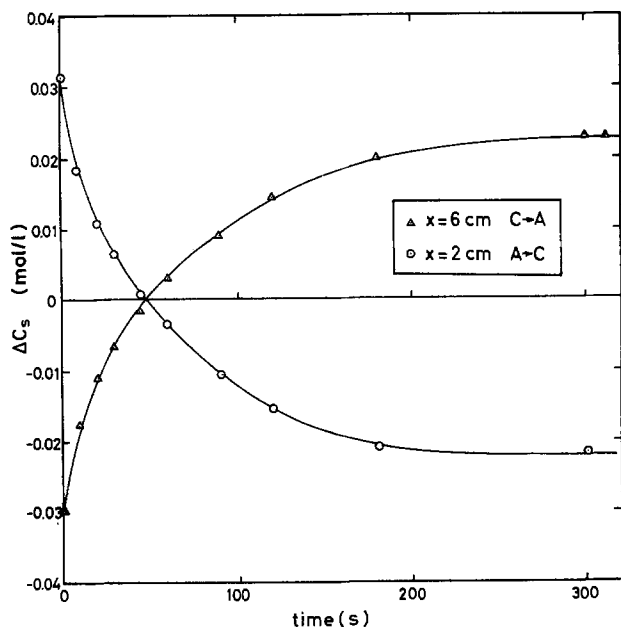


Fig. 5. Symmetrical transient variation of concentration difference at the electrode surface.

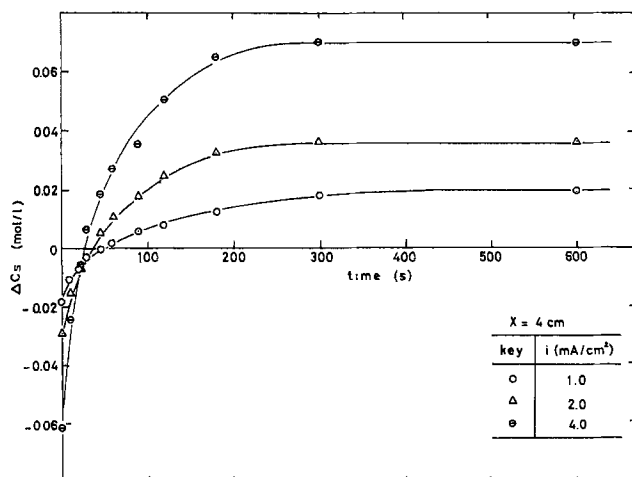


Fig. 6. Time variation of ΔC_s along the elapsed time at $x = 4$ cm.

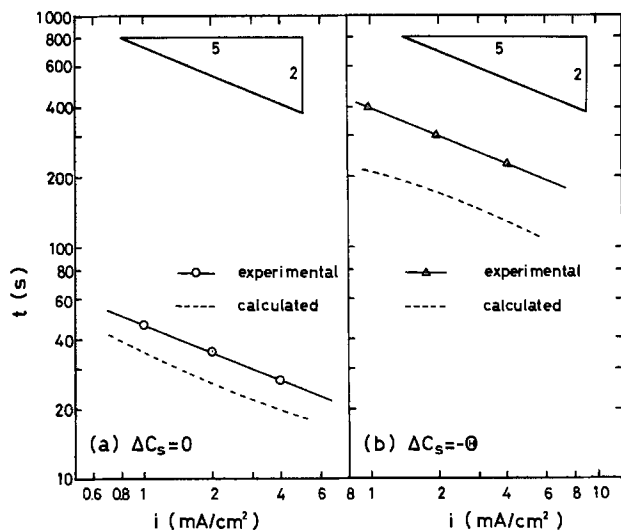


Fig. 7. Current density dependence of the time before ΔC_s reaches zero value and $-\theta$.

On the other hand, it is known that the thickness of the concentration boundary layer is proportional to

$i^{-1/5}$ at the steady state (3). Then the relationship of

$$t \propto i^{-2/5} \quad [10]$$

is obtained, which was shown in Fig. 7.

It should also be noticed that Eq. [8] was derived from the consideration of a vertical plate which is placed in a stagnant fluid and is suddenly heated up with a uniform heat flux along the vertical plate and that the analysis was carried out by applying the similarity of velocity and temperature profiles in the vertical direction, respectively. Though these conditions are not directly applied to the present system of current reversal as seen in Fig. 2 and 3, the same dependence on the driving force was shown in both cases of heat and mass transfer. This may be related to the insensitiveness of the adopted profiles in the analysis using the integral method.

The natural convective flow develops downstream. The time variation of ΔC_s at different vertical locations is shown in Fig. 8. When the initial and final ΔC_s values at various vertical locations are compared, it is seen that they are the same at $x = 4$ cm and that the initial ΔC_s value at $x = 2$ and 6 cm is equal to the final value at $x = 6$ and 2 cm, respectively. It is due to the symmetrical character of natural convection mentioned before.

No significant difference was found among the elapsed time before attaining the anodic steady state. The initial ΔC_s value at lower vertical locations is smaller (3), and the anodic natural convection affects earlier because of the uniform dissolution rate of Cu^{2+} ion. On the other hand, the anodic natural convection develops downward from the upper edge, and the above-mentioned earlier effect of anodic natural convection is compensated.

This explanation is further supported by the time variation of ξ shown in Fig. 9. It is seen that ξ advances toward the bulk electrolyte and that no evident difference was found among the vertical locations during the initial 100 sec. The effect of natural convection is minor near the anode surface during the inversion of natural convective flow; diffusion and migration are the prevailing mechanisms of Cu^{2+} ion transfer. Due to the virtually uniform dissolution rate of Cu^{2+} ion in the vertical direction on the electrode surface, ξ has no significant dependence on vertical location.

Time variation of velocity profile.—The time variation of u_m at different current densities is shown in Fig. 10. After the current reversal, it linearly changes until the anodic steady value is attained. Corresponding to the time variation of ΔC_s shown in Fig. 6, the

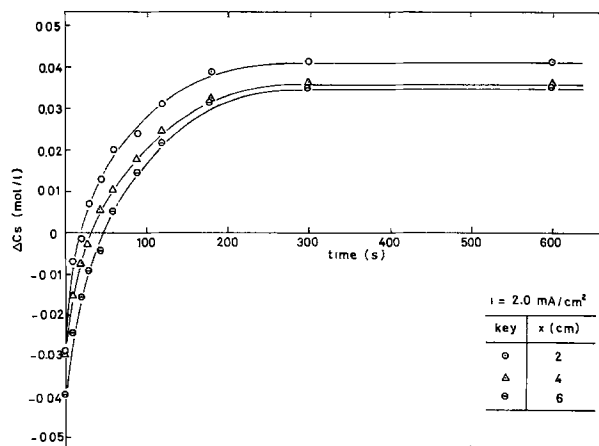


Fig. 8. Time variation of ΔC_s along the elapsed time at a current density of 2 mA/cm^2 .

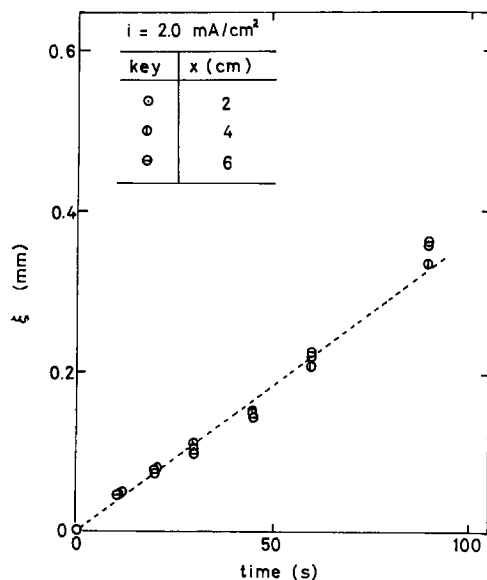


Fig. 9. Time variation of ξ at a current density of 2 mA/cm^2

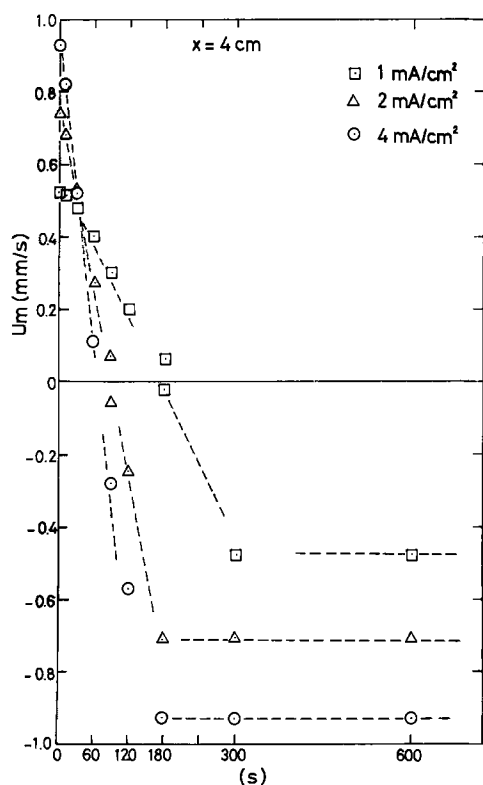


Fig. 10. Time variation of u_m at $x = 4 \text{ cm}$

rate of change of u_m is higher at higher current densities.

Time variation of τ at different current densities is shown in Fig. 11. During the initial period immediately after the current reversal, τ is maintained at the initial

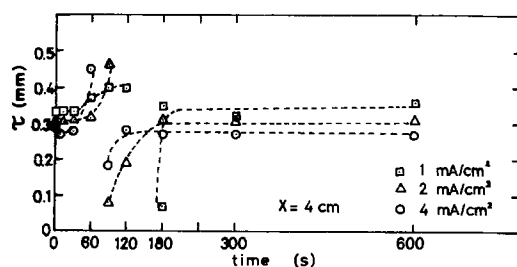


Fig. 11. Time variation of τ at $x = 4 \text{ cm}$

value. After attaining the maximal value, it suddenly falls to the minimal value. Then it again increases to the anodic steady value. This apparently strange variation of τ is simply due to the appearance of inverted natural convective flow during the transition; the newly formed anodic natural convective flow starts to develop from the anode surface, while the remaining cathodic flow is pushed away to the bulk electrolyte where it disappears.

Space-time structure of transient natural convective flow.—We have tried to visualize the transient variation of natural convection after the current reversal. First, the transient concentration profile near the lower edge of working electrode is shown in Fig. 12. Before the current is reversed, the cathodic diffusion layer is observed on the working cathode surface, while no concentration gradient is observed on the insulated surface below the lower edge. An extreme value appears at 10 sec after the current reversal, but no change is observed on the insulated surface: it is indicated that the direction of natural convection is still upward. After more than 30 sec are passed, a concentration gradient is clearly observed on the surfaces of the working anode and the insulated portion; it is shown that the anodic natural convection starts to flow downward.

Next, the transient concentration profile near the upper edge of the working electrode is shown in Fig. 13. Even before current reversal, a concentration gradient is observed on the upper insulated surface. It is due to the convective mass transfer of Cu^{2+} ion by the upward natural convective flow. After the current is reversed, an extreme value appears on both the sur-

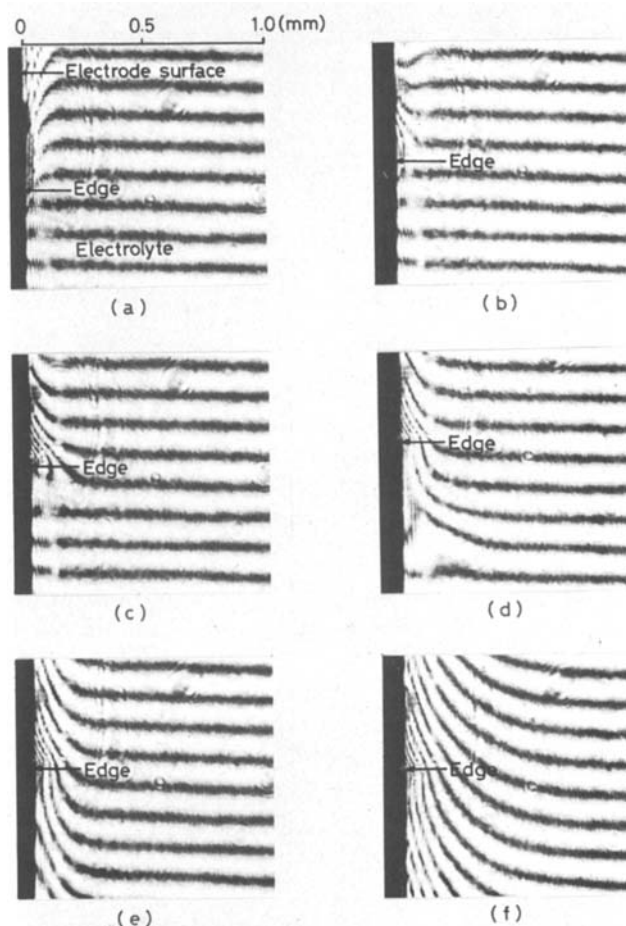


Fig. 12. Holographic interferograms (cathodic to anodic) (a) $t = 0 \text{ sec}$, (b) $t = 10 \text{ sec}$, (c) $t = 20 \text{ sec}$, (d) $t = 30 \text{ sec}$, (e) $t = 45 \text{ sec}$, (f) $t = 600 \text{ sec}$ elapsed after reversing the electrolytic current (0.6M CuSO_4 , $i = 2.0 \text{ mA/cm}^2$, $x = 0 \text{ cm}$).

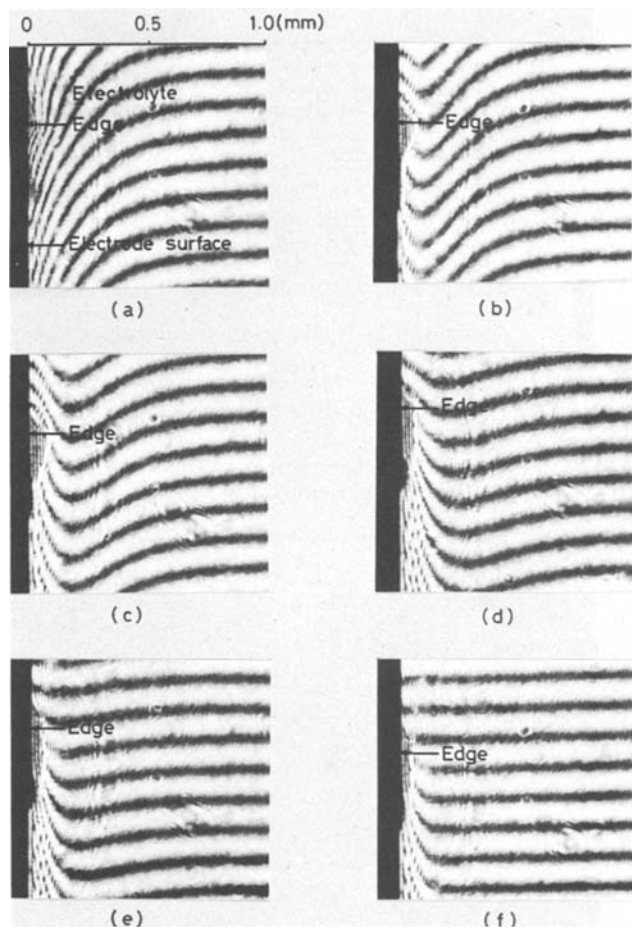


Fig. 13. Holographic interferograms (cathodic to anodic) (a) $t = 0$ sec, (b) $t = 20$ sec, (c) $t = 45$ sec, (d) $t = 90$ sec, (e) $t = 120$ sec, (f) $t = 600$ sec elapsed after reversing the electrolytic current ($0.6M$ $CuSO_4$, $i = 2.0$ mA/cm^2 , $x = 8$ cm).

faces of the working anode and the insulated portion. One may also note that the latter concentration profile has zero gradient at the surface. The extreme value moves toward the bulk electrolyte, and the anodic natural convection develops. At 600 sec the steady anodic convective flow is established. It is seen that the natural convection originates from the upper edge of the working anode, and no concentration gradient is observed on the insulated surface.

The foregoing observations and consideration lead to a presentation of the space-time structure of transient natural convective flow. It is shown in Fig. 14. In this diagram, the time variation of the velocity profile at different vertical locations is shown in the

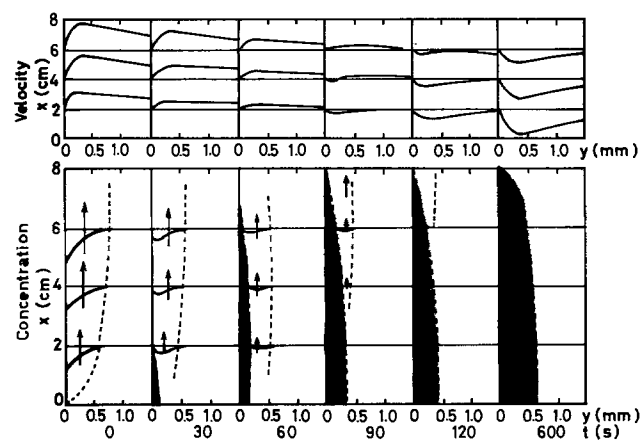


Fig. 14. Transient behavior of natural convection at various heights of electrode (cathodic to anodic).

upper part, and the corresponding time variation of the concentration profile is illustrated in the lower part. The arrows shown in the diagram demonstrate the direction of cathodic natural convective flow.

After 30 sec are passed from the current reversal, an anodic diffusion layer has formed at the lower portion of anode. It continues to grow, though the direction of convective flow is still upward. At 60 sec, this anodic diffusion layer extends to a height of 6 cm from the lower edge, and the direction of natural convective flow starts to turn downward at a height of 2 cm. Along with further elapsed time, this downward natural convection covers the whole surface of the working anode and pushes the remaining upward convective flow away to the bulk electrolyte. At 120 sec, the whole natural convective flow is downward, and the anodic steady state is attained at 600 sec.

Summary

Transient natural convection after reversing the electrolytic current was studied by measuring the concentration and velocity profiles at various vertical locations on the electrode surface. The applied current density was also varied.

When the current is reversed, the concentration profile starts to shift from its original steady, approximately parabolic, shape: an extreme value appears, and it moves from the electrode surface to the bulk electrolyte. Thus the concentration profile evolves to the steady state. Momentum transfer is caused by the convective mass transfer of electrolyte, and thus the velocity of convective flow is decelerated. A new natural convective flow is formed in the reverse direction. It develops in the horizontal direction from the electrode surface toward the bulk electrolyte, until the steady velocity profile is established.

Symmetry between anodic and cathodic transient natural convection was observed. The rate of change of both the concentration at the electrode surface and the maximal velocity of natural convection are higher at higher current densities. The former effect was explained by a simplified mass balance calculation of Cu^{2+} ion near the electrode surface assuming that the convective mass transfer is neglected; while the inversion of natural convection is occurring, the convective mass transfer of Cu^{2+} ion is minor near the electrode surface, and diffusion and migration are the prevailing mechanism of Cu^{2+} ion transfer. It was shown that the required time before attaining the steady state is proportional to a power of -0.4 of the applied current density.

From these observations, a diagram of the space-time structure of transient natural convection was developed.

Acknowledgment

Part of this work was performed under financial aid given to the authors by the Ministry of Education (Project Number 147056), and by the Kurata Foundation, to which they are grateful.

Manuscript submitted July 14, 1980; revised manuscript received *ca.* Dec. 22, 1980.

Any discussion of this paper will appear in a Discussion Section to be published in the December 1981 JOURNAL. All discussions for the December 1981 Discussion Section should be submitted by Aug. 1, 1981.

Publication costs of this article were assisted by Kyoto University.

LIST OF SYMBOLS

| | |
|------------------|---|
| c | concentration (mol/cm^3) |
| c^s | concentration at electrode surface (mol/cm^3) |
| c^* | concentration in bulk electrolyte (mol/cm^3) |
| Δc_{ξ} | concentration difference at extreme value point from c^* (mol/cm^3) |
| Δc_s | concentration difference at electrode surface from c^* (mol/cm^3) |

| | |
|---------|---|
| D | diffusivity of CuSO_4 (cm^2/sec) |
| d | width of electrode (cm) |
| F | Faraday constant (= 96,500 C/g-equiv.) |
| g | gravitational acceleration (= 980 cm/sec^2) |
| i | current density (A/cm^2) |
| N | number of shifted interference fringe |
| n | refractive index |
| n^* | refractive index of bulk electrolyte |
| T | dimensionless time defined by Eq. [8] |
| t | elapsed time (sec) |
| t_1^* | transference number of Cu^{2+} ion in the bulk electrolyte |
| u | velocity (cm/sec) |
| u_m | maximal velocity (cm/sec) |
| x | vertical location from lower edge of electrode (cm) |
| y | distance from electrode surface (cm) |
| z_1 | valency of Cu^{2+} ion (= 2g-equiv./mole) |

Greek Letters

| | |
|----------------|--|
| α | densification coefficient of CuSO_4 , $1/\rho$ ($\partial\rho/\partial c$) (cm^3/mol) |
| α' | thermal diffusivity (cm^2/sec) |
| δ | concentration boundary layer thickness (cm) |
| $\bar{\delta}$ | averaged value of steady concentration boundary layer thickness along vertical plate (cm) |
| θ | concentration difference ($c - c^*$) (mol/cm^3) |
| Θ | concentration difference at electrode surface (mol/cm^3) |
| η | numerical parameter |

| | |
|-----------|---|
| λ | wavelength (\AA) |
| ν | kinematic viscosity (cm^2/sec) |
| ξ | distance between electrode surface and the position of the extreme value (cm) |
| τ | distance between electrode surface and maximal velocity point (cm) |
| ω | numerical parameter |

REFERENCES

1. C. Wagner, *This Journal*, **95**, 161 (1949).
2. N. Ibl and R. H. Müller, *ibid.*, **105**, 346 (1958).
3. Y. Awakura and Y. Kondo, *ibid.*, **123**, 1184 (1976).
4. A. Tvarusko and L. S. Watkins, *ibid.*, **118**, 248 (1971).
5. A. Tvarusko and L. S. Watkins, *Electrochim. Acta*, **14**, 1109 (1969).
6. H. Urano and Y. Kondo, *Denki Kagaku*, **46**, 330 (1978).
7. Y. Fukunaka, M. Inuzuka, A. Tsuboi, and Y. Kondo, *ibid.*, **47**, 471 (1979).
8. H. Tsukada and Y. Kondo, *ibid.*, **46**, 337 (1978).
9. Y. Awakura, A. Ebata, and Y. Kondo, *This Journal*, **126**, 23 (1979).
10. Y. Awakura, M. Okada, and Y. Kondo, *ibid.*, **124**, 1050 (1977).
11. Y. Awakura, Y. Takenaka, and Y. Kondo, *Electrochim. Acta*, **21**, 789 (1976).
12. Y. Fukunaka and Y. Kondo, *ibid.*, To be published.
13. R. Siegel, *Trans. ASME*, **80**, 347 (1958).
14. B. Gebhart, *J. Heat Transfer*, **83**, 61 (1961).

Electroactive Coatings of Tris(bipyridyl)- and Tris(o-phenanthroline)-Ruthenium(II) Attached to Electrodes via Hydrosilylation or Electropolymerization of Vinyl Derivatives

Pushpito K. Ghosh and Thomas G. Spiro*

Department of Chemistry, Princeton University, Princeton, New Jersey 08544

ABSTRACT

Synthetic methods are given for the introduction of a vinyl group into α,α -bipyridine (bipy) and o-phenanthroline (phen). These groups have been employed to attach $\text{Ru}(\text{bipy})_3^{2+}$ and $\text{Ru}(\text{phen})_3^{2+}$ to Pt electrodes by (i) hydrosilylation followed by polycondensation with the electrode, or (ii) cycling the electrode to negative potentials to induce anionic polymerization at the surface. The thickness of silanized films increased linearly with contact time, after an induction period, and also increased with increasing temperature. $\text{Ru}(\text{bipy})_3^{2+}$ coatings prepared in this way showed reversible cyclic voltammograms up to about 20 layers. For thicker films the electrode kinetics became increasingly slow, and the amount of electroactive material actually decreased. Silanized $\text{Ru}(\text{phen})_3^{2+}$ coatings showed sluggish behavior even at lower coverages. The films were stable upon anaerobic storage (exposure to air reduced stability), but showed electrochemical instabilities. Scanning to potentials sufficiently negative to reduce Ru^{2+} produced immediate loss of electroactivity. Holding the electrode at a potential sufficiently positive to produce Ru^{3+} led to a slow loss of electroactivity, while continuous scanning of the $\text{Ru}^{3+/2+}$ wave led to much faster losses (time scale of minutes), the rate increasing with scan rate. A still more rapid loss was observed after scanning the redox wave of ferrocene dissolved in the electrolyte, although the amplitude of the ferrocene wave was nearly undiminished with respect to that observed at an uncoated electrode. Thus the silanized film is permeable to counterions and solution redox species, but is also fragile, and susceptible to disruption by the ion fluxes. Electropolymerization gave a $\text{Ru}(\text{phen})_3^{2+}$ coating which was much more stable, showing very little loss upon continuous cycling. However the cathodic peak, but not the anodic peak, gradually became less reversible. A slow conformation change resulting in inhibited counterion efflux from the film upon reduction is suggested. When electropolymerized at a TiO_2 electrode, the $\text{Ru}(\text{phen})_3^{2+}$ film, in contact with an aqueous solution containing hydroquinone as mediator, supports a steady photocurrent which is stable for at least 15 hr.

We have previously shown (1) that attachment of $\text{Ru}(\text{bipy})_3^{2+}$ (bipy = α,α -bipyridine) to SnO_2 electrodes can be accomplished via hydrosilylation of a vinyl group on one of the bipy rings. Contact with the SnO_2 electrode produces a water-stable coating that shows both electroactivity and photoelectroactivity, albeit with low quantum efficiency. In order to better define the characteristics of this attachment method, we have investigated the electrochemistry of coated platinum electrodes under a variety of conditions. (To avoid complications due to the H_2O oxidation and reduction waves, the measurements were carried out in acetonitrile.) The studies were extended to $\text{Ru}(\text{phen})_3^{2+}$ (phen = o-phenanthroline) via a vinyl group attached to phen by a new synthetic route. Finally we have explored the use of electropolymerization, following the recent report by Murray and co-workers (2) that this method also produces stable coatings when applied to complexes with pendant vinyl groups.

Experiment

Synthesis.—The syntheses of 4,4'-dimethyl-2,2'-bipyridine (I) and 4-hydroxyethyl-4'-methyl-2,2'-bipyridine (II) as well as the synthesis of 4-vinyl-4'-methyl-2,2'-bipyridine (III) from (I) via the alcohol (II) (Fig. 1A) have been described previously (1). The preparation of (III) employing the reaction sequence

reported below for the synthesis of 4-vinyl-1,10-phenanthroline (Fig. 1B) was also tried, but gave a lower yield.

4-Formyl-1,10-phenanthroline (IV)¹.—3.68g (3.31×10^{-2} mol) SeO_2 in 35 ml dioxane (4% H_2O) was placed in a 500 ml flask and the temperature gradually raised until all the SeO_2 dissolved (50°C). 4.5g (2.32×10^{-2} mol) of 4-methyl-1,10-phenanthroline (G. F. Smith Chemical Company) in 180 ml dioxane was slowly added to the SeO_2 solution while its temperature was steadily raised to reflux (25 min). Vigorous stirring was maintained during the reaction. After an additional 20 min of refluxing, the solution turned clear and the bottom of the flasks was coated with metallic selenium. The solution was filtered hot and on removal of solvent yielded a solid compound which was laced with colloidal selenium. By redissolving the solid in chloroform, centrifuging to remove the selenium, and subsequently stripping off the solvent (this procedure was repeated four times), all of the unwanted selenium was separated out.

Weight of product = 3.45g (yield 71%); IR: 1710 cm^{-1} (carbonyl stretch); NMR (60 MHz, CDCl_3): 10.55 δ (s, 1H, $-\text{CHO}$), 9.55 – 7.45 δ (7H, aromatic protons).

4-Vinyl-1,10-phenanthroline (V).—2g (9.6×10^{-3} mol) of (IV) in 450 ml dry tetrahydrofuran (THF)

* Electrochemical Society Active Member.
Key words: modified electrodes, surfaces, photosensitization.

¹ The use of selenium dioxide in the preparation of quinoline aldehydes has been previously reported (3).

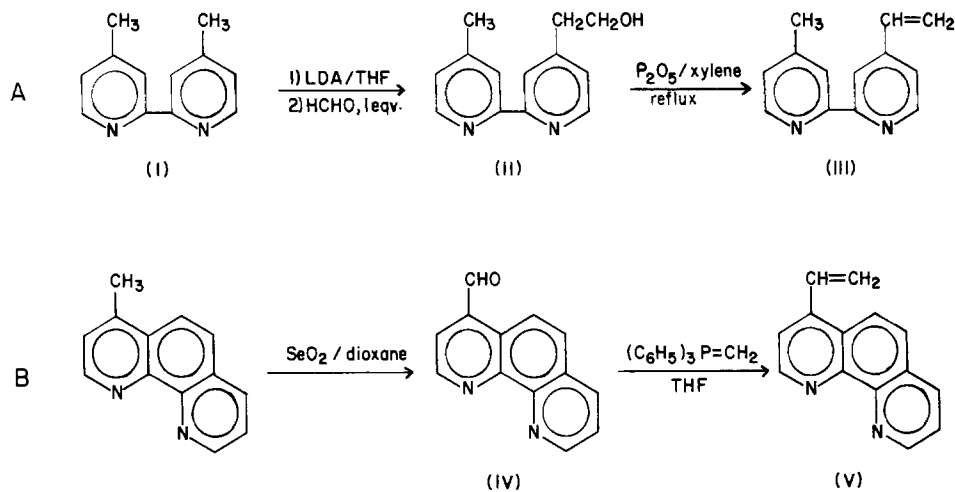


Fig. 1. Synthetic schemes for the preparation of (A) 4-vinyl-4'-methyl-2,2'-bipyridine and (B) 4-vinyl-1,10-phenanthroline.

was placed in a predried 1000 ml three-neck flask equipped with a stirring bar. One neck was closed with a septum and the other two were used for flushing with nitrogen. 3.42g (9.6×10^{-3} mol) of dry (methyl) triphenyl phosphonium bromide (Aldrich) suspended in 10 ml of THF was placed in a separate airless flask and to this was added a solution of *n*-butyl lithium (9.6×10^{-3} mol). An orange solution resulted almost immediately and this was then syringed into the flask containing (IV). The solution slowly turned milky; after stirring for ~ 5 hr the reaction was quenched with 30 ml of cold water. The resulting transparent solution was extracted three times with a total of ~ 900 ml ether. The ether solution was washed once with 100 ml water and then extracted with 350 ml of 1M HCl. The aqueous layer was neutralized (pH 8-10) and extracted with ~ 750 ml ether. The ether layer was washed once with 100 ml water and dried with anhydrous sodium sulfate. The olefin was recovered from the ether layer.

Weight of product, 1.08g (yield 54%); NMR (60 MHz, CDCl_3): 9.1 δ (m, 2H, aromatic), 8.2-7.35 δ (5H, aromatic), 7.6-5.4 δ (3H, vinylic, AMX spin system).

$\text{Ru}(2,2'\text{-bipy})_2(4\text{-vinyl-4'-methyl-2,2'-bipy})^{2+}$ (VI) was prepared as reported previously (1) from $\text{Ru}(2,2'\text{-bipy})_2\text{Cl}_2 \cdot 2\text{H}_2\text{O}$. $\text{Ru}(1,10\text{-phen})_2\text{Cl}_2 \cdot 2\text{H}_2\text{O}$ (VII) was prepared by a procedure analogous to that for $\text{Ru}(2,2'\text{-bipy})_2\text{Cl}_2$.

$\text{Ru}(4\text{-vinyl-1,10-phen})(1,10\text{-phen})_2^{2+}(\text{PF}_6^-)_2$ (VIII) was prepared by heating a solution of ethanol/water (1:1) containing (V) (6×10^{-4} mol) and (VII) (5×10^{-4} mol) for 8 hr at reflux under nitrogen. The hot solution was filtered and the complex was precipitated by the addition of a saturated solution of NH_4PF_6 . The solid was collected, washed first with a total of 25 ml H_2O and then with 20 ml ether. Yield 80%. λ max ~ 450 nm; NMR indicative of both vinylic and aromatic protons.

Hydrosilylation of (VI) and (VIII) to give (IX) and (X), respectively.—A typical procedure is as follows: 1.12×10^{-4} mol of (VI) 1.12×10^{-4} mol of trichlorosilane (HSiCl_3), and 2.5×10^{-6} mol of triethylamine (Et_3N) were dissolved in a total of 3 ml acetonitrile (silylation grade, Pierce Chemicals) and was syringed into a flame dried Pyrex tube. The tube was sealed and then heated for 5 hr in an oil bath maintained at 155°-160°C. It was then stored in a refrigerator until ready for use.

Preparation of modified electrodes.—**Electrode mounting.**—Pt electrodes were prepared by spot-welding a foil of Pt onto one end of a short piece of Pt wire, the other end of which was sealed into a 6 mm OD soft glass tubing. The seal was covered with silicone rubber (Dow) to avoid thin-layer effects. Contact to

the external circuit was made with the help of a mercury pool. TiO_2 electrodes² were mounted by attaching a Cu wire onto the back side of the electrode and passing the wire through Pyrex tubing. The contact was first fastened with a drop of epoxy cement and then all exposed metal was insulated with silicone rubber.

Pretreatment.—Pt electrodes were anodized in 0.5M H_2SO_4 by holding the potential at 1.9V vs. SCE for 5 min, cycling between 1.23 and -0.25 V for 2 hr (100 mV/sec) and then letting the dark current decay to $< 1 \mu\text{A}/\text{cm}^2$ at 1.1V. The electrodes were then rinsed successively with distilled water and methanol and finally dried under vacuum. The true surface area of Pt electrodes was estimated from the area under the hydrogen adsorption waves in the voltammetric scans. TiO_2 electrodes were etched for 30 sec in conc HCl and rinsed with distilled water before being dried under vacuum.

Silanization.—The electrodes were placed in air-tight tubes maintained under inert atmosphere and containing 2-3 ml of (IX) or (X) (10^{-2} M) in acetonitrile. The reaction temperature was maintained between 25° and 70°C and the reaction time varied from a few hours to a few days. The electrodes were then removed from solution, rinsed several times with dry acetonitrile, dried, and stored under vacuum.

Electrochemical polymerization.—Clean Pt foils and etched TiO_2 electrodes were cycled between 0 and -1.6 V vs. SCE in an acetonitrile solution containing 5×10^{-4} M (VIII) and 0.1M tetrabutyl-ammonium perchlorate (TBAP, MC/B). After cycling for 30 min at 200 mV/sec, the electrode was removed, rinsed with acetonitrile, and dried under vacuum. Polymer deposition was evident from the yellowish-orange appearance of the electrodes.

Electrochemical and photoelectrochemical measurements were made in an air-tight cell constructed with O-ring joints. The reference electrode (saturated calomel) was placed in a side arm extending into a Luggin capillary. The working electrode and counterelectrode (Pt) were placed in a parallel configuration in the same solution. Two stopcocks allowed the cell to be flushed with nitrogen and light was focused onto the working electrode through an optical window glued onto one side of the cell. The volume of solution in the cell was ~ 50 ml.

All nonaqueous electrochemistry was carried out using 0.1M TBAP as electrolyte. Cyclic voltammetry was carried out with a PAR Model 175 Programmer, Model 173 Potentiostat, and Model 179 coulometer. Voltammograms were recorded on an X-Y recorder.

²The electrode, which was a TiO_2 coating on a titanium metal substrate, was a gift from Pacific Northwest Laboratories.

Photocurrents were generated with a chopped (PAR 125A) Ar⁺ laser (Spectra Physics 166) and were measured with a lock-in amplifier (PAR 124).

Results and Discussion

Vinyl groups on heterocyclic ligands.—A vinyl group attached to a heterocyclic ligand provides a convenient functionality for relatively stable attachment of transition metal complexes to electrode surfaces. We found previously (1) that hydrosilylation of vinyl-bipy bound to Ru(bipy)₂²⁺, and subsequent condensation with an SnO₂ electrode, produced a water-stable coating, whereas ester or amide links to the electrode were rapidly hydrolyzed. Murray and co-workers (2) have recently shown that this complex, and others that contain vinyl heterocycles, can form stable coatings at electrodes which are simply scanned to potentials negative enough to induce anionic polymerization of the vinyl groups.

In our procedure the ethylene group was introduced (scheme A of Fig. 1) by lithiating 4,4'-dimethyl-bipy, condensing with formaldehyde, and dehydrating the resulting alcohol. The same procedure fails with o-phenanthroline, however, possibly because the Li⁺ ions are chelated by the N atoms of phen more effectively than bipy. An alternative route (scheme B, Fig. 1) involving SeO₂ oxidation of 4-methyl-phen, followed by a Wittig reaction, was found to be effective. This procedure did not, however, work as well with

bipy, for which scheme A remains the preferred synthetic route.

Hydrosilylation of coordinated vinyl-bipy or vinyl-phen proceeded smoothly to products which formed durable multilayer coatings on anodized Pt electrodes upon prolonged contact in dilute solution. The thickness of the coating could be controlled via the time and temperature of contact, and the results were reproducible, provided the electrodes were anodized by the same procedure. We also found that stable coatings with either species could be obtained by the electropolymerization method.

Silanized film characterization.—Figures 2 and 3 show cyclic voltammograms at the Ru^{3+/2+} redox step for Pt electrodes coated with Ru(bipy)₃²⁺ and Ru(phen)₃²⁺, respectively, via the silanization procedure. The amount of electroactive material is given by the area under the voltammograms and corresponds to 21 and 16 equivalent layers for Ru(bipy)₃²⁺ and Ru(phen)₃²⁺, respectively, assuming that a monolayer contains 9×10^{-11} mol/cm², the maximum concentration estimated from space-filling models (4). The Ru(bipy)₃²⁺ electrode behaved nearly ideally, with small peak-to-peak separations, 34 mV, and a linear response of the peak current to sweep rate (5). The Ru(phen)₃²⁺ electrode gave significantly larger peak-to-peak separations and negative deviations from current linearity at higher sweep rates. Increased re-

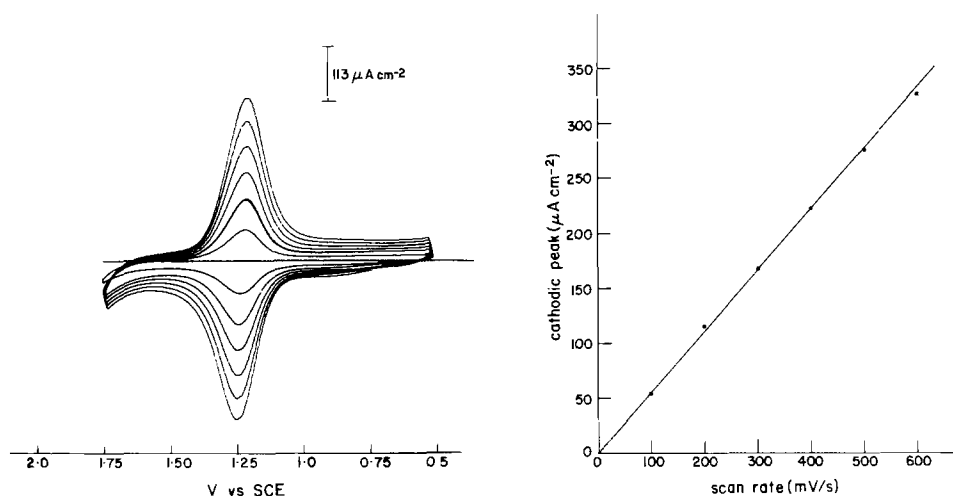


Fig. 2. Voltammograms for a platinum electrode silanized with Ru(bipy)₃²⁺ and cycled at various scan rates (electroactive coverage is ~21 equivalent layers); also shown is the corresponding plot of peak current vs. scan rate. The electrolyte was 0.1M TBAP in acetonitrile.

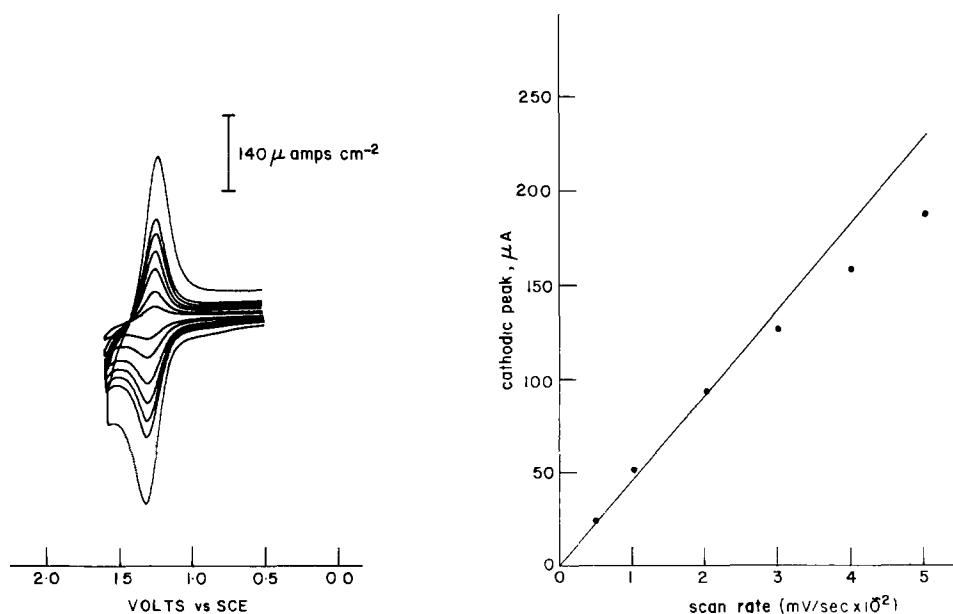


Fig. 3. Voltammograms for a platinum electrode silanized with Ru(phen)₃²⁺ and cycled at various scan rates (electroactive coverage is ~16 equivalent layers); also shown is the corresponding plot of peak current vs. scan rate. The electrolyte was 0.1M TBAP in acetonitrile.

sistance to counterion movements (6) by the bulkier and more rigid $\text{Ru}(\text{phen})_3^{2+}$ complexes might be a factor.

The $\text{Ru}(\text{bipy})_3^{2+}$ film is quite porous, as evidenced by Fig. 4. The peak current density for the redox wave of ferrocene in solution is only 15% smaller for a coated than for an uncoated Pt electrode. $\text{Ru}(\text{bipy})_3^{2+}$ cannot mediate electron transfer from ferrocene, since the redox waves do not overlap. Consequently ferrocene must find its way to the electrode surface to be oxidized. Either the coating, estimated in this experiment to be 14 equivalent layers thick, contains pinholes, or the molecular framework is flexible enough that diffusion of ferrocene to the electrode surface is unimpeded on the voltammetric time scale. This behavior is reminiscent of that observed for polyvinyl ferrocene films on Pt electrodes (6, 7).

The thickness of the silanized $\text{Ru}(\text{bipy})_3^{2+}$ film increases with the length of time the electrode is exposed to the silylated complex, and with increasing temperature, as illustrated by the data in Table I. At a given temperature the amount of electroactive material in the coating increases linearly with time, as shown in Fig. 5. There is, however, an induction period, of about 5 hr at 25°, indicating a preliminary reaction preceding the process. This might involve pre-reaction of the silylated complex, perhaps oligomerization, required for effective coating.

The linearity of Fig. 5 requires that all of the $\text{Ru}(\text{bipy})_3^{2+}$ in the coating is electroactive, or, less plausibly, that the fraction of electroactive material is constant with increasing thickness. For films thicker than about 20 equivalent layers, the electroactivity

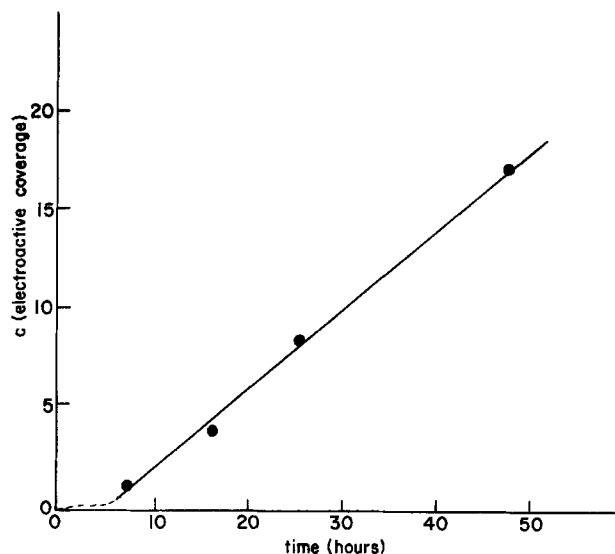
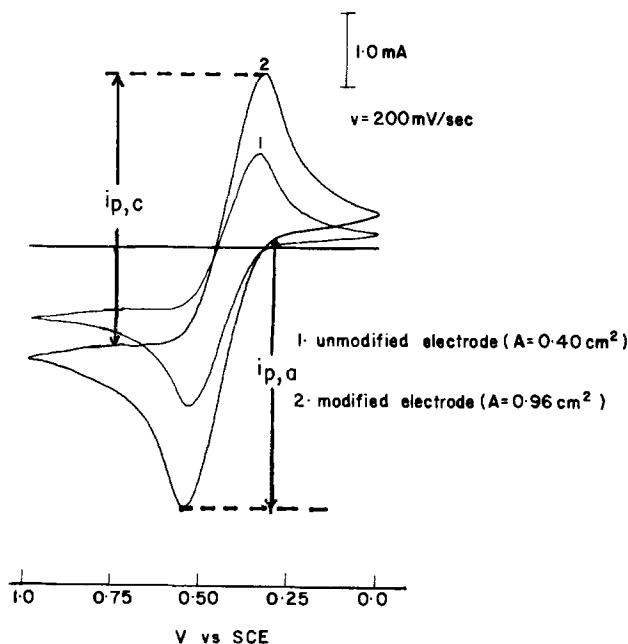


Fig. 5. Electroactive coverage, c (in equivalent layers), of $\text{Ru}(\text{bipy})_3^{2+}$ on anodized platinum electrodes vs. the time of contact, at 25°C, of the electrodes with a solution ($8 \times 10^{-3}\text{M}$) of the silylated complex.

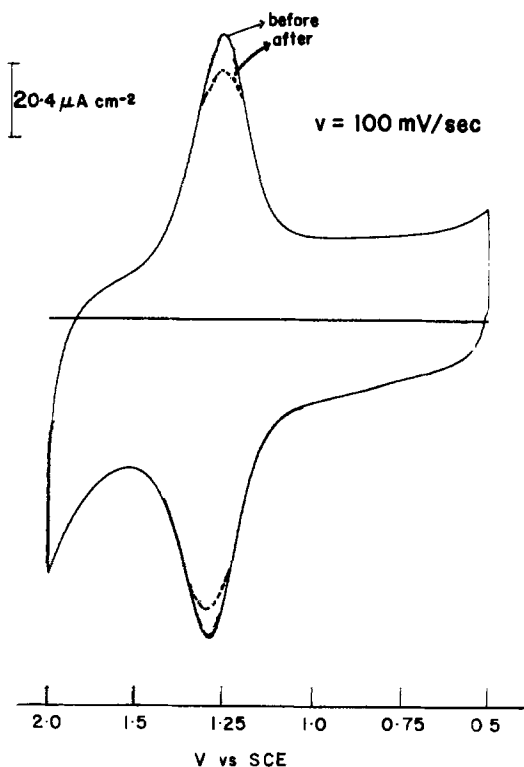
(measured at a given scan rate) begins to decrease, and indeed the absolute amount of electroactive material decreases at higher temperatures and longer contact times, as illustrated in the last three lines of Table I, although the films continue to thicken as evi-

CYCLIC VOLTAMMOGRAMS OF FERROCENE
AT MODIFIED AND UNMODIFIED Pt/PtO₂ ELECTRODES



(a)

CYCLIC VOLTAMMOGRAMS OF MODIFIED ELECTRODE
BEFORE AND AFTER FERROCENE EXPERIMENT



(b)

Fig. 4. (a) Cyclic voltammograms for ferrocene in solution with anodized platinum electrodes, 1, unmodified and 2, modified through silanization with $\text{Ru}(\text{bipy})_3^{2+}$. (b) Voltammograms of the modified electrode in inert electrolyte (0.1M TBAP/acetonitrile) before and after voltammetry (2 cyclic scans) with ferrocene.

Table I. Cyclic voltammetric parameters of silylated Ru(bipy)₃²⁺ films on Pt for different coating times and temperatures

| t (hr) ^a | T (°C) ^b | Film description | v (mV/sec) ^c | E _o ' (vs. SCE) ^d | i _p (μA/cm ²) ^e | ΔE _p (mV) ^f | δ (mV) ^g | c ^h |
|---------------------|---------------------|------------------|-------------------------|---|---|-----------------------------------|---------------------|----------------|
| 7 | 25 | Not visible | 200 | 1.23 | 14.5 | 35 | 137 | ~1 |
| 16 | 25 | Not visible | 200 | 1.23 | 41.3 | 22 | 140 | 3.7 |
| 25 | 25 | Not visible | 200 | 1.23 | 71.8 | 31 | 126 | 8.5 |
| 47 | 25 | Not visible | 200 | 1.23 | 156.0 | 38 | 128 | 17.4 |
| 28 | 65 | Faint yellow | 5 | 1.23 | 18.2 | 43 | 130 | 35 |
| 28 | 65 | Faint yellow | 200 | 1.23 | 365 | 76 | 154 | 35 |
| 38 | 70 | Pale yellow | 200 | 1.23 | 270 | 105 | 162 | 30 |
| 64 | 75 | Bright yellow | 200 | 1.23 | 158 | 140 | 196 | 22 |

^a Time of electrode exposure to hydrosilylated Ru(bipy)₃²⁺ (10⁻²M) in acetonitrile.

^b Solution temperature.

^c Scan rate.

^d Ru^{2+/2+} potential.

^e Cathodic peak current.

^f Peak-peak separation.

^g Cathodic half-width.

^h Electroactive coverage: area under the voltammogram, expressed in equivalent layers, assuming 1 layer = 9 × 10⁻¹¹ mol/cm².

denced qualitatively by the deepening color of the electrode surface. For these thick films the electrode kinetics are slow, as shown by the greatly increased peak separations (ΔE_p) and widths (δ). Presumably the movement of counterions across the increasingly thick films is slowed to the extent that the total number of electrons transferred at a given sweep rate actually decreases. This trend might account for the fact that the ~1000 layer thick coatings deposited on SnO₂ were found to show electroactivity corresponding only to a few layers (1). Since in that case the redox wave appeared to be reversible, this remnant electroactivity might have been due to film heterogeneity, allowing a few counterions rapid access to the electrode.

Table I also shows that the electrode kinetics actually improve somewhat with increasing coverage for the first ten or so equivalent layers (4) contrary to theoretical expectation (8). The electrode with about a monolayer showed significantly broader peaks, and larger peak-to-peak separation, suggesting some heterogeneity at this low coverage.

Film instabilities.—While the silanized films were stable indefinitely under anaerobic storage (exposure to air produced irregularities in the subsequent voltammograms), they were subject to electrochemically induced losses. Figure 6 shows that scanning cathodically past the Ru(bipy)₃^{2+/1+} and Ru(bipy)₃^{1+/0} waves of the silanized Ru(bipy)₃²⁺ films leads to immediate loss of the Ru(bipy)₃^{3+/2+} wave. Similar results were observed with Ru(phen)₃²⁺ films. Evidently,

the reduced forms of the complex are unstable. On the hypothesis that the resulting electrode surface might still contain bound but uncoordinated bipy, we tried reconstituting the film with Ru(bipy)₂(DME)²⁺ (DME = dimethoxyethane) which reacts with bipy in solution to form Ru(bipy)₃²⁺ (9). The film was not regenerated by this procedure, however. The source of the reductive instability is not presently understood.

For the silanized Ru(bipy)₃²⁺ films, moderately rapid loss of electroactive material was also observed on repeated scans of the Ru(bipy)₃^{3+/2+} wave, the rate increasing with the scan rate, as shown in Fig. 7. The curves are not first order, but show a continuous slowing of the loss rate with time. While reactive species might have been generated in the course of the scans, their effect should have been the same for a given exposure time, independent of the sweep rate. A plausible hypothesis to account for the dependence on sweep rate is that the film is disrupted by the movement of counterions accompanying the flow of current, the rate being proportional to the total counterion flux. The flux increases with scan rate, and the slopes of the curves in Fig. 7, at a given coverage, are roughly proportional to the scan rate. On this model the loss of the first 20% of the film electroactivity is accounted for by the disruption of one Ru(bipy)₃²⁺ center per 145 counterion transits (round trip), while the corresponding number for the first 45% of loss is ~190. The slowing of the loss rate is expected if there is a distribution of Ru(bipy)₃²⁺ attachment modes in the film, with varying susceptibility to disruption induced

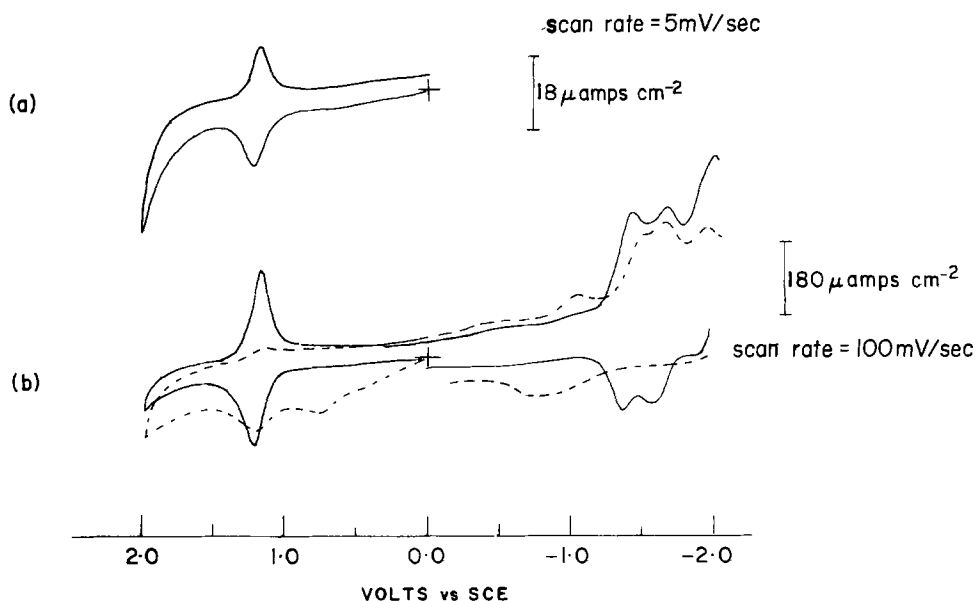


Fig. 6. (a) Single scan of the Ru(bipy)₃^{3+/2+} wave of a moderately thick silanized film on platinum. (b) Successive scans of the same electrode extended to the region of the Ru(bipy)₃^{2+/1+} reduction waves. (—) First scan (---) fourth scan.

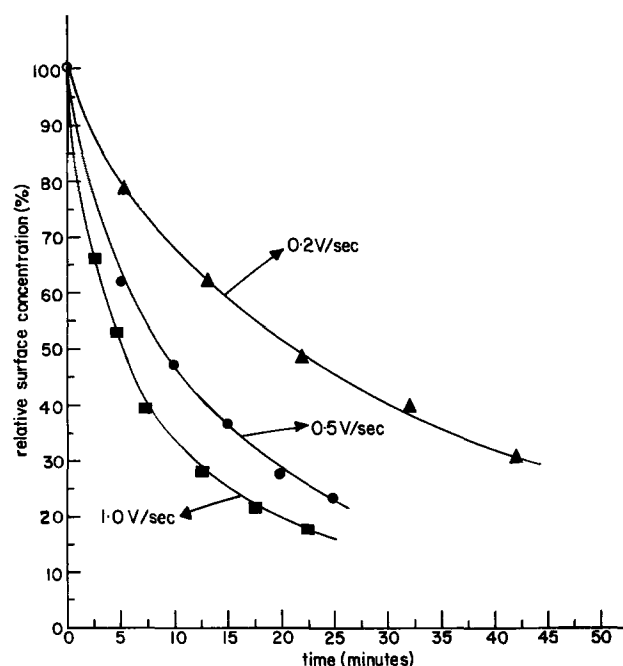


Fig. 7. Electroactive coverage, as percent of original electroactivity, vs. total cycling time, for different values of the scan rate. All three electrodes were identically prepared and had initial coverages of ~ 5 equivalent layers. They were continuously cycled between 0.5 and 1.75V.

by the passage of ions. Space filling models suggest that the silylated $\text{Ru}(\text{bipy})_3^{2+}$ ($1\times$) cannot form highly cross-linked polysiloxane networks due to steric crowding. Weak interactions, susceptible to ion induced disruption may be involved in multilayer film formation.

An additional observation supporting this model is that when the electrode was placed in contact with a ferrocene (Fc) solution and cycled over the $\text{Fc}^{+/0}$ wave, a rapid loss of $\text{Ru}(\text{bipy})_3^{3+/2+}$ activity was again noted (see Fig. 4), even though no electrons passed from $\text{Ru}(\text{bipy})_3^{2+}$ during the cycling. While the film did not impede the diffusion of Fc to the electrode surface on the voltammetric time scale (see above), this diffusion, or more probably the outward diffusion of Fc^+ , did damage the film. The disruption rate was one $\text{Ru}(\text{bipy})_3^{2+}$ per ~ 20 $\text{Fc}^{+/0}$ transits over the first 10% of electroactivity loss.

A slower loss of electroactivity was observed when the film was maintained in the Ru^{3+} state. Figure 8 shows that holding the coated electrode at +1.5V led to two successive first-order decay processes, as measured by the $\text{Ru}^{3+/2+}$ voltammetric peak area, sampled periodically. The fast process, with $t_{1/2} = 72$ min corresponds to a 15% loss of electroactivity; the slower process has $t_{1/2} = 296$ min. Similar decays have been seen for $\text{Ru}(\text{bipy})_3^{2+}$ films by Murray and co-workers (4) and attributed to the chemical instability of $\text{Ru}(\text{bipy})_3^{3+}$, which has been demonstrated in aqueous solution (10). In view of the present results, however, an alternate explanation is that the slow decay at +1.5V might be due to ion transport associated with the significant background currents observed at this potential. In line with this hypothesis, we observed that the loss of electroactivity is qualitatively higher when the electrode was held at +1.75V, where the oxidation state is still $\text{Ru}(\text{bipy})_3^{3+}$ but the background current is higher than at +1.5V.

Electropolymerized $\text{Ru}(\text{phen})_3^{2+}$ films.—Pursuant to the demonstration by Murray and co-workers (2) that stable electrode films could be prepared by electropolymerization of $\text{Ru}(\text{bipy})_3^{2+}$ with attached vinyl groups, we were able to obtain similar results with

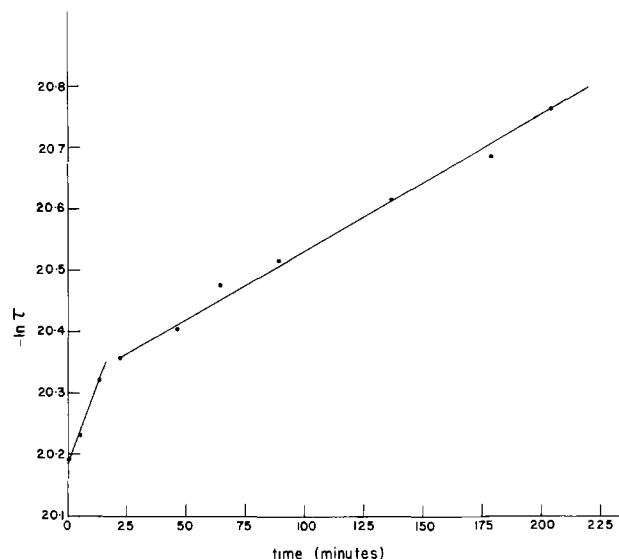


Fig. 8. First-order decay plots (decreasing electroactivity) for a platinum electrode silanized with $\text{Ru}(\text{bipy})_3^{2+}$ (~ 15 equivalent layers) and potentiostated at +1.5V (except to obtain sample voltammograms at various times). ($\tau = \text{mols/cm}^2$ of electroactive material.)

$\text{Ru}(\text{phen})_3^{2+}$. In our hands the method worked in acetonitrile, but not in dimethylsulfoxide (DMSO). Since vinyl pyridine is subject to anionic polymerization in DMSO (11) we presume that electropolymerization of vinyl- $\text{Ru}(\text{phen})_3^{2+}$ may have taken place, but that the resulting polymer was soluble enough in DMSO not to adhere to the electrode. On the other hand, we found that the electropolymerized coating, once formed in acetonitrile, did not subsequently wash off in DMSO.

Like the silanized film, the electropolymerized coating was unstable when the voltage was scanned to sufficiently negative values to reduce the $\text{Ru}(\text{phen})_3^{2+}$. Repeated cycling of the $\text{Ru}(\text{phen})_3^{3+/2+}$ wave produced a small initial loss in electroactivity (10% during the first 20-30 scans), but very little loss thereafter, in contrast to the silanized films (Fig. 7). The repeated scanning did, however, produce a curious asymmetry in the voltammetric waves, as shown in Fig. 9. The cathodic peak gradually broadened and shifted to less negative potentials, although the anodic peak remained essentially unchanged. Thus there was a progressive slowing of electron transfer from the electrode to the Ru^{3+} , but not from the Ru^{2+} to the electrode. The likeliest explanation is that under the influence of repeated counterion movements the film underwent a slow change of molecular conformation, to a framework appropriate for $\text{Ru}(\text{phen})_3^{3+}$. The mobility of anions out of, but not into, the film might thereby have been reduced. It is possible that a similar rearrangement took place in the silanized films, described above, but that the resulting molecular conformation strained the framework too much, producing the observed loss of electroactive material.

Films with >35 equivalent layers of electroactive material imparted a distinct yellow color to the electrodes, which decolorized when the voltage was stepped to values sufficient to oxidize $\text{Ru}(\text{phen})_3^{2+}$ to $\text{Ru}(\text{phen})_3^{3+}$ (which has much weaker visible absorption). Films of this character might find use in electrooptic devices.

Photostability.—We have previously shown (1) that the silanized $\text{Ru}(\text{bipy})_3^{2+}$ coating on n-type SnO_2 supported a steady, albeit low efficiency, photoanodic current when illuminated in the $\text{Ru}(\text{bipy})_3^{2+}$ visible absorption band. A gradual ($\sim 25\%$ in 2 hr) decay in the photocurrent was observed with continuous illumi-

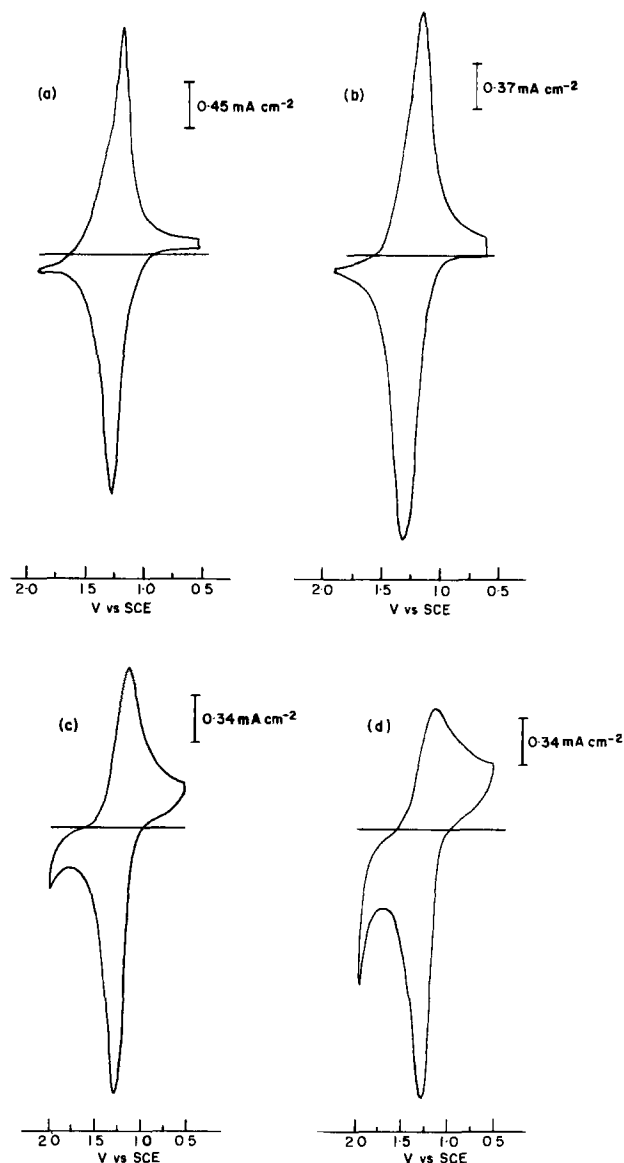


Fig. 9. Time evolution of the shapes of the anodic and cathodic voltammetric waves for electropolymerized $\text{Ru}(\text{phen})_3^{2+}$ on platinum, cycled between 0.5 and 1.9V. The voltammograms were recorded at a scan rate of 200 mV/sec; initial electroactive coverage was ~ 80 equivalent layers.

nation. In view of the present results, a contributing factor might have been reductive quenching of $\text{Ru}(\text{bipy})_3^{2+}$ via back electron transfer from the heavily doped SnO_2 , to produce unstable $\text{Ru}(\text{bipy})_3^+$ (1).

As shown in Fig. 10, a very stable photocurrent is observed for $\text{Ru}(\text{phen})_3^{2+}$ electropolymerized at n-type TiO_2 . In this case hydroquinone was added to the electrolyte to discharge the $\text{Ru}(\text{bipy})_3^{3+}$ formed on photooxidation. The 476.5 nm Ar^+ laser wavelength is close to the $\text{Ru}(\text{phen})_3^{2+}$ absorption maximum, 452 nm. As in the SnO_2 experiments, quantum efficiency was very low (calculated as $\sim 1\%$ if a monolayer was photoactive), but the photocurrent shows no decay during 15 hr of steady illumination. Thus the coating shows no intrinsic photoinstability.

Conclusion

A new synthetic approach to introducing a vinyl group into a heterocyclic ligand has been developed and applied to phen. Both $\text{Ru}(\text{bipy})_3^{2+}$ and $\text{Ru}(\text{phen})_3^{2+}$, with a pendant vinyl group, can be attached to anodized Pt or TiO_2 in films of controlled

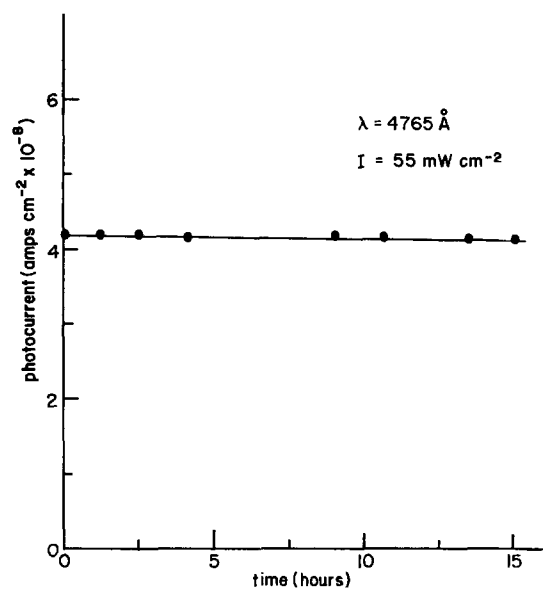


Fig. 10. Anodic photocurrent vs. time for a TiO_2 electrode coated with electropolymerized $\text{Ru}(\text{phen})_3^{2+}$, in contact with 0.1M hydroquinone in 0.5M H_2SO_4 .

thickness, via hydrosilylation or electropolymerization. The films are stable on storage or to illumination, and support steady, low level photoanodic currents on TiO_2 . They show nearly reversible $\text{Ru}^{3+/2+}$ redox behavior, but decay slowly upon repeated cycling, and sometimes show evidence of slow conformation change. Immediate decay occurs upon reduction of Ru^{2+} . It can be concluded that while $\text{Ru}(\text{bipy})_3^{2+}$ and $\text{Ru}(\text{phen})_3^{2+}$ can be stably attached to electrodes, the films remain stable only if the ruthenium is maintained in the 2+ state, through rapid regeneration with solution redox agents.

Acknowledgments

This work was supported in part by Grant EG-77-S-01-4023 from the U.S. Department of Energy. We thank Professors Royce W. Murray and Allen J. Bard for communicating results of their work prior to publication.

Manuscript submitted Sept. 22, 1980; revised manuscript received Dec. 20, 1980.

Any discussion of this paper will appear in a Discussion Section to be published in the December 1981 JOURNAL. All discussions for the December 1981 Discussion Section should be submitted by Aug. 1, 1981.

REFERENCES

1. P. K. Ghosh and T. G. Spiro, *J. Am. Chem. Soc.*, **102**, 5543 (1980).
2. H. D. Abruña, P. Denisevich, T. J. Meyer, and R. W. Murray, *J. Am. Chem. Soc.*, **103**, 1 (1981).
3. H. Kaplan, *J. Am. Chem. Soc.*, **63**, 2654 (1941).
4. H. D. Abruña, T. J. Meyer, and R. W. Murray, *Inorg. Chem.*, **18**, 3233 (1979).
5. E. Laviron, *J. Electroanal. Chem. Interfacial Electrochem.*, **39**, 1 (1972).
6. P. J. Peerce and A. J. Bard, *J. Electroanal. Chem. Interfacial Electrochem.*, **112**, 97 (1980).
7. A. Merz and A. J. Bard, *J. Am. Chem. Soc.*, **100**, 3229 (1978).
8. A. P. Brown and F. C. Anson, *Anal. Chem.*, **49**, 1589 (1977).
9. J. A. Connor, T. J. Meyer, and B. P. Sullivan, *Inorg. Chem.*, **18**, 1388 (1979).
10. C. Creutz and N. Sutin, *Proc. Natl. Acad. Sci., U.S.A.*, **72**, 2858 (1975).
11. R. Kalir and A. Zilkha, *Euro. Poly. J.*, **14**, 557 (1978).

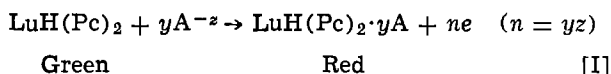


Kinetics of Color Reversal in Lutetium Diphthalocyanine Oxidation Products Formed with Different Anions

F. A. Pizzarello and M. M. Nicholson*

Rockwell International, Anaheim, California 92803

Lanthanide diphthalocyanines are of increasing interest as multicolor electrochromic display materials (1). Recent work in this laboratory has shown that the anodic oxidation of a lutetium diphthalocyanine film in contact with an aqueous electrolyte occurs with fast migration of anions from the solution into the organic solid to compensate for the loss of electrons (2-4). Reaction I



is accompanied by a color change of the film from green to red. Experimental n values of approximately 2 were found with chloride and sulfate electrolytes. Measurements on moving color boundaries in alumina-supported dye films led to the suggestion of predominant charge transport by the corresponding anions in the oxidation products (2). A radiotracer study then confirmed that stoichiometric quantities of chlorine and sulfur were incorporated in the red forms of the dye (3). Galvanostatic transients in lutetium diphthalocyanine films on tin oxide were interpreted with the same moving-boundary model, although the direction of current flow was then perpendicular, rather than parallel, to the surface of the film (4). The rate-controlling factor for the transients was a space charge in the red phase. Meanwhile, the anion reaction mechanism was proposed independently by Yamana to account for anodically induced color changes in erbium diphthalocyanine films (5).

Red colors persist in oxidized films of lutetium diphthalocyanine for minutes to days, depending on experimental conditions. It was observed in the tracer study that the chloride product on alumina gradually lost its red color and its chlorine content while in contact with ambient air (3). The sulfate film remained red, however, and lost no sulfur in a month. On a tin oxide substrate, the bright red is easily regenerated by application of anodic potentials, and electrical cycling between the red and green states has been repeated many thousands of times (1).

This paper reports a spectrophotometric investigation of the anodic oxidation products formed by lutetium diphthalocyanine films with seven different anions in aqueous solutions. These products differed chemically and spectroscopically from the oxidized diphthalocyanines PcLnPcO_x of lanthanide elements (Ln) isolated by Moskalev *et al.* at a platinum anode in a dimethylformamide-hydrazine hydrate solution (6).

Experimental

Green films of lutetium diphthalocyanine were vacuum-sublimed onto 1.25×6 cm strips of single crystal sapphire or Mylar plastic. Details of the specimen preparation were described previously (2). The

electrolytes were air-saturated 1M solutions of NaOAc (sodium acetate), KF, KCl, NaBr, KI, Na_2SO_4 , and $\text{NaOOC}\Phi$ (sodium benzoate).

The dye films were converted to red forms by the boundary-propagation technique used earlier (2, 3). For the present study, however, the cell was mounted in a Perkin-Elmer Model 202 dual-beam spectrometer instead of a viewing device. The reference and counter-electrodes were silver foil anodized in samples of the cell electrolytes; lead foil was used in Na_2SO_4 . The first absorption spectrum was recorded on the green film with no liquid present. Electrolyte was then added to immerse the lower end of the film, and the red color was propagated upward from the meniscus by application of a constant anodic current through a gold contact at the top of the specimen. When the red area intercepted all of the incident light beam, the current was turned off, and spectra were recorded at intervals for about 24 hr. Since the red film extended only several millimeters above the liquid, it was in contact with moist air throughout the experiment.

Results and Discussion

Yamana noted spectral differences in anodic oxidation products of erbium diphthalocyanine films obtained with various anions on a glass substrate but did not report these differences in detail (5). We observed no significant differences in the initial absorption spectra from 350 to 750 nm for lutetium diphthalocyanine oxidation products containing different anions. The rates of spectral changes that occurred on standing in moist air were dependent on the anion, however, and so were the voltages required to propagate the red color. Three types of behavior that were distinguished are discussed below.

Low propagation voltage and relatively fast reversal from red to green.—These characteristics were observed with acetate and fluoride solutions. Representative absorption spectra for the acetate are shown in Fig. 1, where isosbestic points are clearly evident at 571 and 686 nm. Such common intersection points are a necessary, but not a sufficient, condition for a two-component absorption system (7).¹ As a first approach, it was appropriate to examine the results in terms of a first-order reaction with respect to the red dye species

$$\ln(C/C_0) = -kt \quad [1]$$

In Eq. [1], C represents the concentration of the red species in the film at a time t , C_0 is its initial concentration, and k is the first-order rate constant for the red-to-green chemical reaction. The data were analyzed for reactant and product components from the film absorbances at 645 and 690 nm. It was assumed that Beer's law held; that the initial spectrum recorded after boundary propagation was that of the oxidation prod-

* Electrochemical Society Active Member.

Key words: diphthalocyanines, oxidation, anions, kinetics.

¹ Isosbestic points would occur, for example, with $A \rightarrow B$, $A \rightarrow 2B$, or $A \rightarrow B + C$.

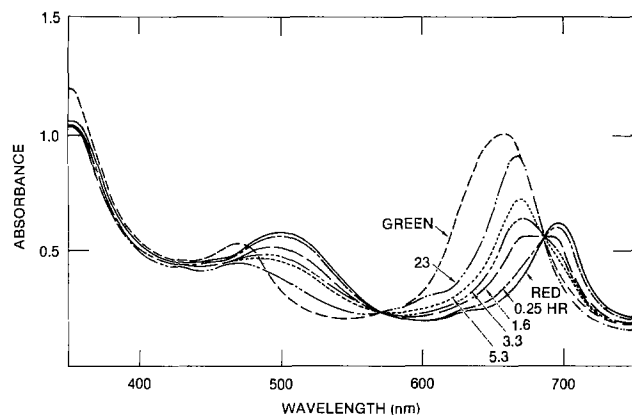


Fig. 1. Absorption spectra of lutetium diphthalocyanine film anodically oxidized in 1M NaOAc. Green denotes original dye film on sapphire; red denotes freshly oxidized film.

uct only; and that a completely reversed film would have the same spectrum as the initial green at the selected wavelengths. Figure 2 includes plots of $\log_{10}(C/C_0)$ vs. t for the acetate and fluoride films. The relationships are linear, in conformity with Eq. [I]. Rate constants evaluated from the slopes are given in Table I. The propagation of the red areas with acetate and fluoride solutions began at about 10V with applied currents of a few microamperes. The final voltage, at a propagation distance of approximately 1 cm, was some 60-70V. Thus, the propagating field was of the order of 50 V/cm.

Low to moderate propagation voltage and stable red film.—Propagation of the red color from chloride, bromide, and sulfate solutions also required fields below 100 V/cm. The oxidation products were much more stable than those containing acetate or fluoride ion, however. The absorption spectrum of the sulfate product in moist air was constant for 20 hr. The spectral changes of the chloride films were too small to determine a rate constant in the 24 hr spectrophotometric experiments, but a value of 0.0039 hr^{-1} was evaluated from the earlier tracer data for films in ambient air (3). With bromide ion, the absorption spectrum changed enough in 18 hr that a rate constant of 0.003 hr^{-1} could be estimated from a large-scale linear plot.

High applied voltage and insufficient color propagation.—With iodide and benzoate ions, the color boundary was again initiated at about 10V, but it required nearly 100V to travel 1 mm. Hence, the applied field was of the order of 1000 V/cm, and it was impractical to obtain absorption spectra of red areas propagated in contact with the gas phase. The very large size of the benzoate ion probably hindered the anodic color

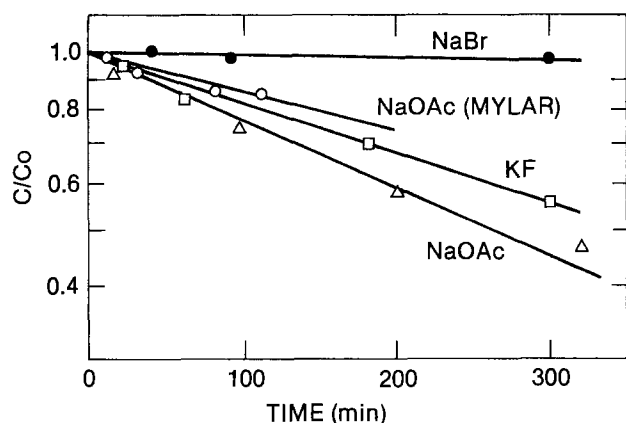


Fig. 2. Plots for determination of first-order rate constants for oxidized films containing different anions. Ordinate is on logarithmic scale.

Table I. Reaction rates of red films containing different anions^a

| Electrolyte ^b | A_{max} (initial) ^c | Current (μA) | k (hr^{-1}) | Comments |
|---------------------------------|---|---------------------------|--------------------------|--|
| NaOAc | 1.01 | 2 | 0.16 | |
| NaOAc | 1.37 | 4 | 0.09 | Mylar substrate |
| KF | 0.86 | 5 | 0.12 | |
| KCl | 1.00 | 3 | — | Red form stable >18 hr |
| KCl | 1.00 | 1 | 0.0039 | Propagated from 0.011M KCl; rate measured in ambient air with tracer (3) |
| NaBr | 0.83 | 2 | 0.003 | Estimated at 18 hr |
| KI | 0.88 | 5 | — | No propagation above liquid |
| Na ₂ SO ₄ | 1.11 | 1-3 | — | Red form stable >20 hr in this study; stable >30 days in ambient air (3) |
| NaOOC ⁺ | 0.64 | — | — | Slight propagation above liquid |

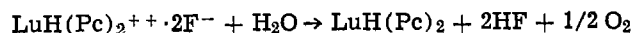
^a Dye film on sapphire unless noted.

^b 1M unless noted.

^c Maximum absorbance of initial green film.

propagation, and this may have occurred with iodide. It is of interest in this context that Moskalev and Kirina were able to extract iodine anodically from an aqueous iodide solution with a lutetium diphthalocyanine/tin oxide electrode (8). The current flow was then perpendicular to the dye film, however, and with a thickness of 3000Å a field of 1000 V/cm would have caused an overvoltage of only 0.03V.

From the spectral changes such as those in Fig. 1, it is inferred that the organic product of the color reversal was the original green dye or a closely related form such as a hydrate of that compound. Therefore, an oxidized species such as a halogen or oxygen also must have been produced. For the red film containing fluoride, the color change was relative fast, and formation of the elemental halogen may be ruled out thermodynamically. Slow oxidation of water by the organic cation is plausible, however



[II]

Corresponding reactions may be suggested to account for the red-to-green color changes that occurred in the cases of other anions on standing in moist air.

Factors that may determine the rate of color reversal include volatility of the acid formed, mobility of the anion in the organic solid, and the morphology of the film in the red and green states. Red films containing halide and acetate ions, which form volatile acids, were found to be less stable than those containing sulfate. However, the chloride film was more stable than the acetate, even though HCl is more volatile than HOAc. Although the mobility of the anion should depend on its size, the paths available for ionic or molecular transport within the organic solids are also influenced by water and oxygen. We have found, for example, that oxygen is required to propagate the red color from a sulfate solution but not from chloride, while ambient water vapor is needed in both cases (9). Further investigations of these systems are in progress.

Acknowledgment

This research was sponsored by the Air Force Office of Scientific Research (AFSC), United States Air Force, under Contract No. F49620-79-C-0104.

Manuscript submitted July 28, 1980; revised manuscript received Dec. 23, 1980.

Any discussion of this paper will appear in a Discussion Section to be published in the December 1981 JOURNAL. All discussions for the December 1981 Discussion Section should be submitted by Aug. 1, 1981.

Publication costs of this article were assisted by Rockwell International.

REFERENCES

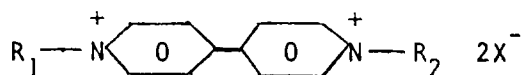
1. M. M. Nicholson and R. V. Galiardi, "SID International Symposium Digest," IX, 24 (1978).
2. M. M. Nicholson and F. A. Pizzarello, *This Journal*, **126**, 1490 (1979).
3. F. A. Pizzarello and M. M. Nicholson, *J. Electron. Mater.*, **9**, 231 (1980).
4. M. M. Nicholson and F. A. Pizzarello, *This Journal*, **127**, 821 (1980).
5. M. Yamana, *Oyo Butsuri*, **48**, 441 (1979).
6. P. N. Moskalev, G. N. Shapkin, and A. N. Darovskikh, *Russ. J. Inorg. Chem.*, **24**, 188 (1979).
7. R. P. Bauman, "Absorption Spectroscopy," p. 419, Wiley, New York (1962).
8. P. N. Moskalev and N. I. Kirina, *J. Appl. Chem. USSR*, **48**, 370 (1975).
9. M. M. Nicholson and F. A. Pizzarello, *This Journal*, **127**, 2617 (1980).

An Improved Electrochromic Display Using An Asymmetrical Viologen

Gabriel G. Barna* and John G. Fish*

Texas Instruments Incorporated, Dallas, Texas 75265

During the past decade there has been a concentrated effort (1-7) to develop a passive electrochromic display (ECD) based upon the reversible reduction and oxidation of viologens. The basic structure of these 4,4'-dipyridinium salts is shown below



where X^- is typically bromide or dihydrogen phosphate. While there has been an investigation of a variety of these compounds with symmetrical alkyl end groups, the majority of the development work has been with salts of 1,1'-diheptyl-4,4'-dipyridinium, that is, where $R_1 = R_2 = (n - C_7H_{15})$. The ability to deposit a uniform purple film onto a transparent electrode (SnO_2) by the one electron reduction of this dipyridinium cation, has been well established (6). However, it has been demonstrated (3, 7) that while this crystalline film is on open circuit, it reorients into a phase with a higher degree of ordering. This reorientation is postulated to be the cause of the ultimate failure of the display, which is the formation of a visible residue on the segments. The proposed mechanism of this failure mode is that the reoriented film does not completely erase, hence leaving a visible deposit after a certain number of cycles.

The driving force for this open-circuit reorientation of the deposited film has been postulated (7) to be the intermolecular interaction between adjacent viologen molecules. It was therefore assumed that by working with an asymmetrical viologen, with at least one bulky end group, the driving force for the intermolecular stacking would be decreased. This should thus decrease the open-circuit reorientation of the deposited film and hence improve the erase characteristics. While there have been other attempts to develop modified viologens (3), all these species were still symmetrical, i.e., $R_1 = R_2$. This difference is not simply fortuitous; it is more difficult to synthesize an asymmetrical viologen molecule. This paper will describe the preparation of one such molecule, benzyl-heptyl-viologen (BHV), its electro-optical properties, and the improved device performance that it provides.

Synthesis

An equimolar amount of 1-bromoheptane dissolved in acetonitrile (ACN) was added to a $-10^\circ C$ solution of 4,4'-dipyridyl. This mixture was refluxed at $85^\circ C$ for 2 hr, then cooled to room temperature. The solvent

* Electrochemical Society Active Member.

Key words: crystallization, organic, electrode.

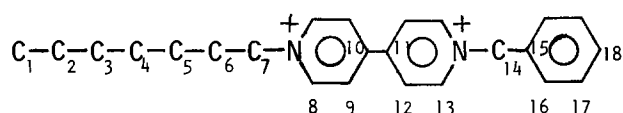
was evaporated off, and the residue washed with cold xylenes. It was then dissolved in chloroform and the 1-heptyl-4, 4'-dipyridinium bromide was recrystallized by the addition of xylenes. The product was a pale yellow powder with a yield of 51%. This intermediate was redissolved in ACN, and was slowly combined with an equimolar amount of α -bromotoluene, also dissolved in ACN. This solution was purged with N_2 then stirred over the weekend at room temperature. The bright yellow precipitate was filtered, washed with ACN and $CHCl_3$ (to eliminate any reactants), and dried in a vacuum desiccator. The purity of the product was established by the single peak seen in a liquid chromatogram. The yield for this second reaction was 79% providing an overall yield of 40% for the synthesis of the BHV.

The structure of the product was confirmed by both proton and C^{13} NMR, obtained on a JEOL FX60Q FTNMR, with the sample dissolved in D_2O . The peak positions are referenced to the 2.040 ppm H peak and the 206.00 ppm C^{13} peak of acetone. The peak positions are listed in Table I, with assignments made where possible. It should be noted that the 4.569 ppm proton peak is partially hidden under the H_2O (in the D_2O) peak. Its identification was made possible only by

Table I. Proton and C^{13} NMR peaks and assignments

| ppm | H | | C^{13} | | | |
|-------------------------------|----------|------------------------|----------|-----------|------------|------|
| | No. of H | Assigned to H on C No. | ppm | Intensity | C No. | |
| 0.645 } 1.122 } 1.910 } | 13 | 1-6 | 4.544 | 1835 | 1 | |
| | | | | 12.986 | 2160 | 2 |
| | | | | 16.362 | 3131 | 3 |
| | | | 18.894 | 3018 | 4 | |
| 4.569 (t) | 2 | 7 | 21.686 | 4063 | 5 | |
| | | | 21.881 | 3077 | 6 | |
| 5.773 | 2 | 14 | 53.373 | 1641 | 7 | |
| | | | 55.905 | 1978 | 14 | |
| 7.361 | 5 | 15-18 | 118.174 | 7749 | (a) | |
| | | | 120.444 | 5657 | | |
| 8.354 } 8.432 } 8.917 } | 8 | 8-13 | 120.833 | 5576 | 16, 17, 18 | |
| | | | | 121.290 | | 2831 |
| | | | | 123.368 | 581 | 15 |
| | | | | 136.547 | 3336 | (a) |
| | | | 140.769 | 419 | 10, 11 | |
| | | | 141.351 | 568 | | |

(a) This peak is assigned to one or more of the pyridine ring C atoms number 8, 9, 12, or 13.



selectively decoupling the protons while observing the carbon spectrum. The assignment of the carbon peaks to the benzene and pyridine rings was also achieved through selective decoupling of the protons on the benzene ring.

Experimental

The benzyl-heptyl-viologen bromide was ion exchanged with NaH_2PO_4 , as previously described (6). A saturated solution of $\sim 0.045\text{M}$ BHV phosphate/ 1M dihydrogenphosphate was then prepared under nitrogen.

Sealed cells were fabricated as before (7). Electro-optical tests were run in these patterned cells, in the potentiostatic mode, under crossed polarizers (7). A given electrode was first turned on by applying -1 VDC between it and the counterelectrode. This segment was then employed as the internal reference electrode for the subsequent experiments. The electrical and optical response of segments to potentiostatic cycling is shown in Fig. 1, where the mechanical offset between the two pens has been left unchanged. In addition to these photometric measurements, the films were also examined visually. This was done with the cell between 80° crossed polarizers. This configuration allowed enough light to leak through to be able to see the amorphous phase (as dark spots), while it was polarizing enough to resolve the crystalline phase (as bright areas).

Experiments to check the residue problem were performed both within the sealed cells as well as in a typical 3-necked flask inside an N_2 purged glove box. In the latter case, the working electrode was a cleaned and treated (6) piece of Nesatron 20 (PPG Industries), identical to the electrodes within the sealed cells; the counter and reference electrodes were a Pt-disk and a double junction Ag/AgCl (10% KNO_3 outer solution) electrode, respectively.

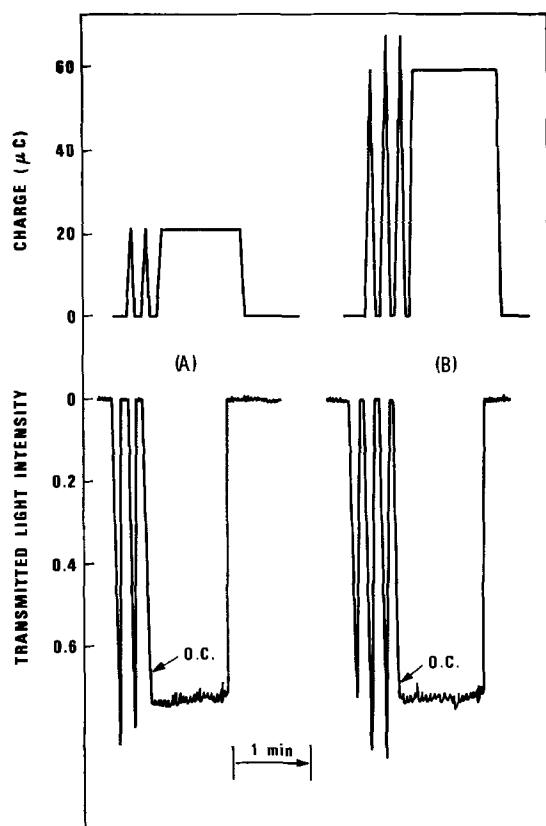


Fig. 1. Electro-optical response of a BHV film, under crossed polarizers, during cycling and open-circuit (O.C.) conditions: (A) $-25/+400$ mV and (B) $-100/+400$ mV pulsing at 0.1 Hz.

Results and Discussion

A cyclic voltammogram of the BHV solution shows the typical one electron reversible waves seen with all viologens. The open-circuit potential of the BHV solution is -50 mV from that of the diheptyl viologen ($n\text{-C}_7$) solution; the reduction and oxidation peaks are at $\eta = -45/+45$ mV, respectively, at a 5 mV/sec scan rate. The deposited film is violet.

Visual examination, under 80° crossed polarizers, of a film deposited at -50 mV, shows it to be significantly different from that of an $n\text{-C}_7$ film. While the $n\text{-C}_7$ film deposits in a birefringent, crystalline form, the BHV deposit is a mixture of amorphous and crystalline phases. When placed on open circuit, these is a brief period of ~ 3 sec (see next paragraph) when some of the amorphous form continues to reorient into the crystalline, optically anisotropic form. The "particle" size of both forms is in the $5\text{-}10$ μm range with an $\sim 10:1$ ratio between amounts of the amorphous and crystalline phases. Upon the application of a positive erase potential, both forms seem to erase at the same rate.

Photometric measurements, under 90° crossed polarizers, were also performed. The electrical and optical response of a single segment, to potentiostatic pulsing, is shown in Fig. 1. In contrast to the behavior of the $n\text{-C}_7$ film, the BHV film (i) increases in crystallinity for only ~ 3 sec after being put on open circuit, and (ii) after this time, there is no subsequent, continuous reorientation of the deposit into a more crystalline form, for films formed at any potential.

The effect of the stable morphology of the open-circuited film, on the subsequent erasure of this film, was tested both in sealed patterned cells as well as with unpatterned Nesatron 20 inside the glove box. In this latter configuration, a transparent electrode was cycled between $\eta = -75/+400$ mV, at 10 sec/cycle. After $41,500$ cycles, there was absolutely no visible residue on the electrode. The electrode was then rinsed off and replaced in an identical setup containing the 0.1M diheptylviologen/ 1M dihydrogenphosphate solution. After less than 50 cycles, a portion of the deposit would not erase at all. This phenomenon was confirmed in the opposite sense also. A freshly cleaned and treated piece of Nesatron 20 was placed in the $n\text{-C}_7$ solution. After 1000 cycles, a large number of residual spots were formed on the electrode. This electrode was then cleaned ultrasonically in the phosphate buffer solution and placed into a solution of BHV. It was then cycled 6100 times, with no visible deposit formed.

Similar improvements were observed in sealed patterned cells. All segments of an "1888" display were driven, in a constant voltage driving mode, in a WRITE/HOLD/ERASE cycle at 5 cycles/min. The first visible residue was seen only after $11,400$ cycles. An identical cell filled with the $n\text{-C}_7$ viologen solution, cycled in a similar fashion, gave rise to a greater amount of residue after only 375 cycles. In both cases, the buildup of the residue was at the edges of the segments, *i.e.*, where the current density is the greatest.

To summarize, several assumptions have been proven. First, looking at the viologen film reorientation problem from the viewpoint of intermolecular interaction is valid. The large majority of the asymmetrical BHV film is deposited in an amorphous phase, in contrast to the complete crystallinity of the symmetrical $n\text{-C}_7$ film. After a brief (3 sec) rearrangement on open circuit, neither the amorphous phase, nor the small amount in the crystalline phase, undergoes a subsequent continuing reorientation. This must be a consequence of the decreased intermolecular forces, *i.e.*, the greater steric hindrance caused by the bulky end group. Second, the data confirm what previously was only a hypothesis, that the open-circuit reorientation of the deposited film is a cause of the subsequent erasure problems, since the stable, nonreorientating BHV is much easier to erase. It is anticipated that further developments

along these lines might yield displays with even longer practical lifetimes.

Acknowledgment

The author wishes to thank P. G. Fields for the synthesis and analysis of the BHV, and Dr. R. A. Owens for the extensive NMR work.

Manuscript submitted Oct. 6, 1980; revised manuscript received Dec. 20, 1980.

Any discussion of this paper will appear in a Discussion Section to be published in the December 1981 JOURNAL. All discussions for the December 1981 Discussion Section should be submitted by Aug. 1, 1981.

DISCUSSION SECTION



This Discussion Section includes discussion of papers appearing in the *Journal of The Electrochemical Society*, Vol. 127, No. 7, 8, 9, 10, 11, and 12, July, August, September, October, November, and December 1980.

Primary Li/SOCl₂ Cells XI. SOCl₂ Reduction Mechanism in Supporting Electrolyte

W. L. Bowden and A. N. Dey (pp. 1419-1426, Vol. 127, No. 7)

Clifton A. Young:¹ In this paper the authors have reported on the electrochemical reduction of thionyl chloride in the supporting organic solvents, N,N-dimethylformamide and dimethyl sulfoxide. This paper is one of a series of lithium-thionyl chloride batteries by Dey.² The work in N,N-dimethylformamide has been previously reported in *This Journal*³ and elsewhere.⁴ The studies in dimethyl sulfoxide have also been reported elsewhere.⁵ It was reported that these and other results suggested a new approach to solving the explosion problem in lithium-thionyl chloride batteries.⁶

Thionyl chloride, along with phosgene and phosphorus oxychloride, reacts with N,N-dimethylformamide to form the Vilsmeier-Haack reagent which has been identified to be [(CH₃)₂N=CHCl]⁺Cl⁻.^{7,8} Dimethyl sulfoxide reacts with thionyl chloride to form chloromethyl methyl sulfide.⁹ This compound was isolated.⁹ Dimethyl sulfoxide has been reported to decompose violently when in contact with thionyl chloride and acid chlorides.¹⁰ The reaction of thionyl chloride with dimethyl sulfoxide has also been reported in the battery literature.¹¹

In my opinion as a result of these reported reactions the electrochemical reduction of thionyl chloride in N,N-dimethylformamide and dimethyl sulfoxide cannot be used as a model of the electrochemical reduction of thionyl chloride at an electrode or in a lithium-thionyl chloride battery. Furthermore, the reported results¹² may apply to the reaction products^{7,9} instead of to thionyl chloride.

¹ Department of Chemistry, Tufts University, Medford, Massachusetts 02155.

² A. N. Dey, *This Journal*, 126, 2052 (1979).

³ W. Bowden and A. N. Dey, *ibid.*, 126, 2035 (1979).

⁴ A. N. Dey, W. Bowden, J. Miller, and P. Witalis, DELET-TR-78-0563-1 April 1979.

⁵ A. N. Dey, W. Bowden, J. Miller, and P. Witalis, DELET-TR-78-0563-2 July 1979.

⁶ A. N. Dey, N. Hamilton, W. Bowden, and P. Witalis, DELET-TR-78-0563-3 November 1979.

⁷ G. J. Martin and S. Poignant, *J. Chem. Soc. Perkin Trans. 2*, 1964 (1972).

⁸ G. J. Martin, S. Poignant, M. L. Filleux, and M. T. Quemeneur, *Tetrahedron. Lett.*, 5061 (1970).

⁹ F. G. Bordwell and B. M. Pitt, *J. Am. Chem. Soc.*, 77, 572 (1955).

¹⁰ S. A. Heininger and J. Dazzi, *Chem. Eng. News*, 35 (9), 87 (1957); *Chem. Abstr.*, 51:10907e (1957).

¹¹ D. R. Cogley, M. J. Turchan, and G. L. Holleck, ECOM-74-0030-3 September 1974.

¹² W. L. Bowden and A. N. Dey, *This Journal*, 127, 1419 (1980).

Publication costs of this article were assisted by Texas Instruments Incorporated.

REFERENCES

1. H. T. van Dam and J. J. Ponjée, *This Journal*, 121, 1555 (1974).
2. J. Bruinink and P. van Zanten, *ibid.*, 124, 1232 (1977).
3. J. Bruinink, C. G. A. Kregting, and J. J. Ponjée, *ibid.*, 124, 1854 (1977).
4. R. J. Jasinski, *ibid.*, 124, 637 (1977).
5. J. Bruinink and C. G. A. Kregting, *ibid.*, 125, 1397 (1978).
6. R. J. Jasinski, *ibid.*, 125, 1619 (1978).
7. G. G. Barna, *ibid.*, 127, 1317 (1980).

W. L. Bowden and A. N. Dey:¹³ We have proposed a mechanism for reduction of thionyl chloride, SOCl₂, in dilute solution with a supporting electrolyte. Since numerous aspects of this mechanism mirror the behavior of LiSOCl₂ cells, we have extended this reduction mechanism to the discharge of Li/SOCl₂ cells.

During our investigations we were particularly concerned with the possibility of reactions between thionyl chloride and the supporting solvent. Accordingly we tried a wide variety of solvents of widely different characteristics, such as CH₂Cl₂, CH₃CN, HCON(CH₃)₂ (dimethylformamide, DMF), SO(CH₃)₂ (dimethylsulfoxide, DMSO). We found similar reduction behavior in these four solvents, of widely different structure and reactivity. The techniques we used, cyclic voltammetry and constant potential coulometry, are both techniques which operate on bulk of the sample and are thus insensitive to relatively small amounts of impurities so that a substantial amount of reaction must occur to have a noticeable effect on results. Both CH₃CN and CH₂Cl₂ are unreactive to SOCl₂.¹⁴⁻¹⁶ Although both DMSO and DMF are known to react with SOCl₂, the reactions were run in refluxing solvent for substantial periods^{14,15} and gave rather disparate products. While the results in DMF and DMSO are by no means central to our conclusions, the similarity to behavior in CH₂Cl₂ and CH₃CN demonstrates the validity of the results. As stated in our paper, we also took samples of partly discharged SOCl₂ electrolytes and examined them by cyclic voltammetry in dilute solution. These voltammograms were identical to voltammograms of partly reduced dilute SOCl₂ solutions, which also demonstrates that reaction of SOCl₂ with solvent was not a serious problem in this work.

Structure-Reactivity Relationships of Methylated Tetrahydrofurans with Lithium

J. L. Goldman, R. M. Mank, J. H. Young, and V. R. Koch
(pp. 1461-1467, Vol. 127, No. 7)

M. H. Miles:¹⁷ This paper shows that the position of the methyl group greatly affects the stability of methylated tetrahydrofurans toward corrosion reactions with lithium metal. Although tetrahydrofuran

¹³ P. R. Mallory & Company, Incorporated, Laboratory for Physical Science, Burlington, Massachusetts 01803.

¹⁴ M. Davis, H. Szkuta, and A. J. Krubsack, "Chemistry of the Thionyl Halides" in "Mechanisms of Reaction of Sulfur Compounds V," p. 16 (1970).

¹⁵ G. J. Martin and S. Poignant, *J. Chem. Soc. Perkin*, 1964 (1972).

¹⁶ F. G. Bordwell and B. M. Pitt, *J. Am. Chem. Soc.*, 77, 572 (1955).

¹⁷ Naval Weapons Center, Chemistry Division, China Lake, California 93555.

(THF) and 3-methyl THF in contact with Li show observable corrosion within a few days at 71°C, it was found that 2-methyl THF was stable for over 10 months under similar conditions. The authors postulate a reduction mechanism involving an initial electron transfer from Li to the lowest unfilled molecular orbital centered on the oxygen atom of THF. They suggest that the location of an electron donating methyl group in the 2-position adjacent to the oxygen atom raises the activation energy by localizing additional electron density on that oxygen atom. An alternative explanation that should be considered involves the quantum mechanical tunnel effect for the transfer of the electron in this reaction. Tunneling through the barrier is generally much more probable than the overcoming of the activation energy barrier for such electron transfer reactions.^{18,19} For the simplest assumption of a rectangular energy barrier, the probability of electron transfer

$$W \approx \exp[-4\pi ah^{-1}(2m(E_a - E_o))^{1/2}] \quad [1]$$

is more sensitive to changes in the tunneling distance (a) than to changes in the activation energy (E_a). Assuming $E_a = 20$ kcal/mol and $a = 5\text{\AA}$, then a decrease in the tunneling probability by a factor of about 100 would require a fourfold increase in E_a while the tunneling distance would only need to increase by a factor of two to give the same effect. Electron tunneling from lithium metal cannot occur until the structure of the THF molecule is modified in such a way that the transfer of the electron leaves the total energy unchanged. The reaction rate will be determined by a compromise between the tunneling probability, W , and the free energy of rearrangement,^{20,21} ΔG_r^\ddagger , thus the rate constant, k_r , for the electron transfer step is given by

$$k_r = kT h^{-1} \cdot W \cdot e^{-\Delta G_r^\ddagger/RT} \\ = kT h^{-1} \cdot W \cdot e^{\Delta S_r^\ddagger/R} \cdot e^{-\Delta H_r^\ddagger/RT} \quad [2]$$

The experimental heat of activation measures only the rearrangement energy required for tunneling to occur, i.e., ΔH_r^\ddagger . In general, ΔH_r^\ddagger is considerably smaller than the actual height of the energy barrier (E_a) for reactions involving tunneling. It is therefore doubtful that the change in the activation energy produced by a methyl group adjacent to the oxygen atom is the major factor for the corrosion reaction of 2-methyl THF with lithium being much slower than the THF or 3-methyl THF reactions with this metal. The location of the methyl group in the 2-position, however, may significantly increase the tunneling distance between the adjacent oxygen atom and the electron in the lithium metal. Adsorption of the methylated THF molecule could be the key factor determining the rate of this corrosion reaction, and this adsorption at the lithium surface might be hindered by steric effects of the methyl group when it is adjacent to the oxygen atom. In accord with a corrosion model proposed elsewhere,^{22,23} the polar oxygen atom end of the THF molecule would be attracted to the film/solution interface by excess positive ions present within the passivating film.

Regarding the mechanistic role of Li^+ , the strong electric field of this ion exerts major effects on many reactions such as the electrode reduction of molten

nitrate,^{24,25} the decomposition of oxyhalides,²⁶ the degradation of pyrophosphate,²⁷ and the reduction of propylene carbonate by lithium.²⁸ The association of Li^+ with electronegative elements in a reacting molecule or ion facilitates electron transfer and bond breaking processes. For the THF molecule, however, the affinity of Li^+ for the sole electronegative oxygen atom is competitive with the attraction and adsorption of this molecule at the positively charged film. With propylene carbonate, lithium ions can interact with the two oxygen atoms in the ring in addition to the terminal oxygen atom that is the likely adsorption site. In fact, the ring oxygen atoms in propylene carbonate are apparently involved in the bond breaking process in the reaction with lithium judging from the reaction products of propylene gas and carbonate ions. In all of the reactions cited above that show strong Li^+ effects, there is more than one oxygen atom present in the reacting molecule or ion. Perhaps Li^+ effects are diminished in heterogeneous reactions involving adsorption when only one electronegative element is present in the molecule. Adsorption involving that lone electronegative element would likely result in a reduced affinity for lithium ions in the solution.

V. R. Koch:²⁹ We thank M. H. Miles for bringing the quantum mechanical tunneling argument to our attention. Without doubt, the energetics of heterogeneous electron transfer mechanisms include contributions from adsorption and tunneling phenomena in addition to the activation energy of the solvent molecule itself. Weighting these contributions in terms of relative importance is a difficult task given the reactivity and nonuniform character of the Li-electrolyte interface.

With regard to the possibility that methyl groups α to the oxygen atom of THF increase the tunneling distance between the lowest unfilled molecular orbital (LUMO) and Li, we report on the following recent stability experiments. A 50:50 mixture of *cis/trans* 2,5-dimethyltetrahydrofuran (2,5-di-Me-THF) (Aldrich) was fractionally distilled until two fractions enriched (80:20) in each isomer were obtained. When these solvents were stored with Li foil at 71°C, the *cis*-fraction manifested superior stability over the *trans*-fraction. Electrolytes of each fraction were prepared 1.5M in LiAsF_6 . When subjected to our usual Li on Li cycling regime³⁰ at 1 mA/cm², the *cis*-enriched electrolyte afforded 56 "100%" cycles while the *trans*-enriched electrolyte gave 35 "100%" cycles. The 50:50 *cis-trans* mixture prepared under identical conditions gave 47 "100%" cycles.

Space filling models of the *cis* and *trans* isomers show that the oxygen atom of the *cis* isomer may more closely approach and thereby more readily interact with a solid surface. Were the electron tunneling argument operational, one would expect the *cis* isomer to react faster than the *trans* isomer. In the 2,5-di-Me-THF system, however, the reverse is observed.

That there is a difference in reactivity between two electronically equivalent LUMO's is of great interest. The results suggest that those molecules which interact strongly with Li^+ are more stable toward Li metal. Since we have shown from ¹³C NMR measurements that 2-methyltetrahydrofuran and 2,5-di-Me-THF (*cis/trans* mixture) interact more strongly with Li^+

²⁴ A. N. Fletcher, M. H. Miles, and M. L. Chan, *This Journal*, 126, 1496 (1979).

²⁵ M. H. Miles and A. N. Fletcher, *ibid.*, 127, 1761 (1980).

²⁶ F. Solymosi, "Structure and Stability of Salts of Halogen Oxyacids in the Solid Phase," pp. 48, 55, 174-176, John Wiley and Sons, New York (1977).

²⁷ J. L. Copeman, A. S. Metcalf, and B. R. Hubble, *J. Phys. Chem.*, 80, 236 (1976).

²⁸ A. Soifer and E. Yeager, Paper 547 presented at The Electrochemical Society Meeting, Seattle, Washington, May 21-26, 1978.

²⁹ Covalent Associates, Framingham, Massachusetts 01701.

³⁰ J. L. Goldman, R. M. Mank, J. H. Young, and V. R. Koch, *This Journal*, 127, 1461 (1980).

¹⁸ K. J. Vetter, "Electrochemical Kinetics," pp. 121-128, Academic Press, New York (1967).

¹⁹ J. O'M. Bockris and A. K. N. Reddy, "Modern Electrochemistry," Vol. 2, pp. 947-990, Plenum Press, New York (1970).

²⁰ R. J. Marcus, B. J. Zwolinski, and H. Eyring, *J. Phys. Chem.*, 58, 432 (1954).

²¹ M. H. Miles and W. S. Harris, *This Journal*, 121, 459 (1974).

²² M. H. Miles, Paper 36 presented at The Electrochemical Society Meeting, St. Louis, Missouri, May 11-16, 1980.

²³ M. H. Miles, *J. Appl. Electrochem.*, To be published.

than THF,³⁰ Dr. Miles' speculation regarding a solvent's Li⁺ affinity competing with adsorption is particularly noteworthy.

Impedance Measurements of the Anodic Iron Dissolution

H. Schweickert, W. J. Lorenz, and H. Friedburg
(pp. 1693-1701, Vol. 127, No. 8)

M. Keddum, O. R. Mattos, and H. Takenouti;³¹ Schweickert *et al.* mentioned extensively our studies on the anodic dissolution of iron. Most of the author's criticisms are answered in our recent paper.³² We note with satisfaction that, according to an opinion we have been claiming for the last ten years, a-c data are now recognized as more selective than d-c ones for elaborating and testing intricate kinetic models. As a very illustrative example, the interpretation of results on the basis of impedance measurements is in entire contradiction with previous and even parallel³³ papers by one of them (W.J.L.): The authors withdraw the two-step consecutive mechanism which has been considered for years as unquestionably proven by the 40 mV Tafel slope. As shown below, essentially because of a number of self-inconsistencies, experimental data excepted, it seems difficult to acquiesce in conclusions drawn in this paper. In particular, the meaning of surface relaxation is not clarified, and no original argument is brought in favor of a delimitation between kinetic and surface effects.

1. On p. 1695, it is stated that at steady state, a plateau is found in the transition range in contrast with a maximum in earlier findings under potentiodynamic conditions. This is not compatible with the negative real part of the impedance in the transition range mentioned [p. 1696 (iii) and Fig. 5] since as stressed by the authors themselves, the low frequency limit of the impedance is identical to the polarization resistance (the slope of the steady-state polarization curve about which the electrode impedance is measured). In solutions of pH \geq 5, the reproducibility of results is declined even if it can be improved by the buffering effect of a large volume of electrolyte.³⁴ In fact, the difference between a plateau and a maximum is of poor significance.

2. The assumption $v_{0,3} \ll v_{0,4} E_4$ (Eq. [4]) is a violation of Table II, in which the step [3] is presented at equilibrium and the step [4] rate determining. Under the conditions of Eq. [4], the step [3] is no longer in pseudo-equilibrium.

3. On p. 1639, the authors claim, "A complete correspondence of all experimental results with the model proposed can be achieved for this set of parameters only." Not only is this correspondence far from being complete (see below), but also such a statement is, at least, nonsense. In fact, even if a fitting program (not mentioned for this particular purpose) were applied for nonlinear equation, a minimal distance between model and experiments cannot prove to be absolute but only local. In the present case, the set of parameters is the best one among those tested on a trial-and-error procedure, nothing more.³²

4. According to the conclusion, "The impedance measurements show clearly that the impedance behavior is determined... also by the influence of electrocrystallization step and surface relaxation phenomena." It seems to us that such a viewpoint is seriously misleading with respect to the very nature of the information provided by impedance or by any

other experimental approach. Surface and kink sites contribution to the impedance is a theoretical possibility which cannot by any means be borne out from the looking of an impedance loci on its own. As a rule, the value of this interpretation should have been founded on its compatibility with commonly accepted physico-chemical laws (e.g., a crystallographic balance for kink sites) and its ability to explain experimental findings. Contrary to the authors' statement on p. 1699, fitting parameters are not restricted to Eq. [19]-[26], but are needed also in the description of surface relaxation. In other words, the authors introduced a hypothesis of surface relaxation with a formal model in such a manner to show an inductive loop in low frequency range. No experimental proof was made in the paper under discussion and thus that remains a pure assumption.

5. All through this paper it is assumed that the high frequency capacitive loop contains two capacitive contributions: The double layer at higher frequencies and a faradaic pseudo-capacitance at lower frequencies. This assumption is very central to the paper since it leads to the value of the charge transfer resistance, crucial in the subsequent deductions, lower than the intercept of this loop on the real axis. Moreover, it brings up to five the number of time constants in the system. This interpretation is certainly supported by the seriously depressed shape of this semi-circle with respect to the true one corresponding to a single R-C circuit. According to the paper, this view is also corroborated by a fitting of the experimental impedance to a fifth order broken-rational function. Unfortunately, Fig. 3 is erroneously mentioned, and no fitting data are provided to substantiate seriously this result of outstanding importance. Can the authors supply further information such as estimated standard deviation and statistic parameters showing the absence of systematic deviations, and proving that higher order function does not result in better fitting as usual with distributed impedance? A-C measurements being limited to 10 kHz, an accurate fitting in the high frequency domains is rather doubtful. In the authors' mind, additional argument is given by the GDP technique. We have recently established³⁵ that this technique cannot be used for resolving an apparently distributed impedance into overlapping R-C time constants except in those cases where the impedance is independently proved to obey such a circuit. This can be performed, for instance, by a fitting calculation, which provides the values of R and C components. The GDP is thus fully redundant. Even though not clearly understood, frequency distribution is a general feature of solid electrodes.³⁶ That holds for the whole frequency spectrum as clearly shown by experiments, but surprisingly, only the high frequency range is considered by the authors. Distribution of the surface properties at a microscale mentioned in the course of the paper is able to give rise to this effect. Is the theoretical meaning of step [1] (Table II) at equilibrium so strong as to require such an effort to find a lower R_t value? It can be remarked, furthermore, that the R_t value, calculated according to the model (see Fig. 10), is of the same order of magnitude as the size of the capacitive loop. Thus no electrochemical step seems to be at fast equilibrium.

6. Though the paper is apparently devoted to impedance, d-c arguments are of predominant value in the more critical mechanistic considerations, in particular for transition and prepassive ranges. Dynamic behaviors, in terms of $R_t I_s$ and b_t , based on the postulated processing of high frequency data (see 5 above) are favored compared to obvious and undoubtful low frequency results. Five time constants exist, in the

³¹ Groupe de Recherche No. 4 du CNRS "Physique des Liquides et Electrochimie," associé à l'Université P & M Curie, 4, Place Jussieu, 75230 Paris Cedex 05, France.

³² M. Keddum, O. R. Mattos, and H. Takenouti, *This Journal*, 128, 257 and 266 (1981).

³³ P. Lorbeer and W. J. Lorenz, *Corros. Sci.*, 20, 405 (1980).

³⁴ I. Epelboin, M. Keddum, O. R. Mattos, and H. Takenouti, *ibid.*, 19, 1105 (1979).

³⁵ C. Gabrielli, M. Keddum, O. R. Mattos, and H. Takenouti, *J. Electroanal. Chem. Interfacial Electrochem.*, 117, 147 (1981).

³⁶ S. H. Glarum and J. H. Marshall, *This Journal*, 126, 424 (1979).

view of the authors, but only three of them are considered in the simulation, i.e., a pseudo-capacitance at high frequency (from θ_1), an inductive loop about 100 Hz (from θ_{k1}), and finally, one more inductive loop about 160 mHz (from $\tau = 1$ sec). The latter is simulated by dropping a convenient value for representing the so-called surface relaxation (Eq. [43]). The simulation concerns only pH 0 solution, and the impedance diagram in Fig. 6 is disregarded since its explanation is completely beyond the possibility of the model: A capacitive loop is observed about 160 mHz in Fig. 6. The process leading to this loop is revealed by an inductive loop in the active range,³² unfortunately, in spite of the formal parameters involved (α_ψ and τ can be varied at will) it cannot predict capacitive effects, *a fortiori* the change of inductive to capacitive behavior or vice versa. Intricate behaviors evidenced in pH 3-5³² are also not explained by the model. Can the authors propose an interpretation of the diagram in Fig. 6?

7. Equations [33] and [39] are proposed as valid in the whole potential range. (Equation [39] is erroneous: read + instead of - at the numerator, and $\nu_{0,6}W_4$ instead of $\nu_{0,6}$ in the denominator.) Subsequently, these equations are simplified in Eq. [41] and [42] for the active range, and the same for Eq. [44]. With the set of parameters used [values of some of them by Ref. (31) of the paper under discussion], this procedure is not correct. Figure 1 shows the diagrams obtained when the simulations (Fig. 10) are repeated by using the complete impedance expression in θ_1 , θ_2 , θ_{k1} , θ_{k2} , and τ .

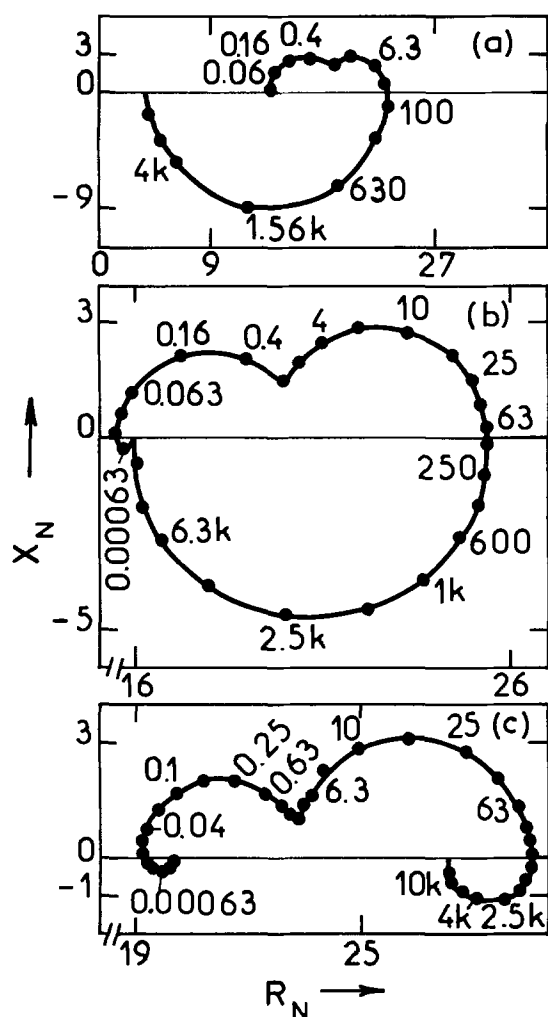


Fig. 1. Simulated transfer loci of the faradaic impedance with complete impedance expression: (a) $\eta = 0.33V$, (b) $\eta = 0.37V$, and (c) $\eta = 0.44V$. For details see Fig. 10 of the paper under discussion.

By comparison with Fig. 4 and 10 of the paper, it can be seen that in addition to the preceding remarks, the model is not satisfactory, since an additional time constant (from θ_{k2}) arising from the prepassive dissolution path, contributes to the impedance in the active range at the low frequency extremity of the diagrams. Inequality $\nu_{0,7a} > \nu_{0,7b} E_7$ assumed in the paper makes this contribution capacitive in contradiction with the inductance shown by experiments. Can the authors explain their interpretation of this inductance in terms of "cosorption"?

We limited our discussion to the basic aspects of their contribution, and tried to keep our questions precise. We hope the authors will reply to each item.

H. Schweickert,³⁷ W. J. Lorenz,³⁷ and H. Friedburg:³⁸

First of all, we agree with Keddum *et al.* that a-c impedance measurements represent a powerful tool for determining the kinetics and mechanisms of electrode reactions. However, this experience is much older than the work of Epelboin *et al.* during the last decade. It is entirely due to the important work of the French group that a-c impedance measurements down to very low frequencies have been introduced in this field. Many complicated electrochemical systems can be analyzed in more detail using this modern technique. This has been attempted in the paper under discussion as well as in the very recently published papers by the authors³⁹ concerning the iron dissolution mechanism. Most of the discussion remarks and questions of the authors deal with the interpretation of very similar experimental results in both papers. Therefore, the different basic concepts of interpretation should be considered first.

In both papers, the common idea is that the iron dissolution at the corrosion potential and in the active, transition, and prepassive polarization ranges occurs via different intermediates called $Fe(I)_{ad}$, $Fe^*(I)_{ad}$, $Fe(II)_{ad}$, and $Fe^*(II)_{ad}$, where Fe^* stands for an adsorbed intermediate at an active surface site. However, different assumptions lead to different interpretations of the experimental data in terms of models.

In both papers, a basic assumption was made that iron dissolution can occur in consecutive and/or parallel paths including "catalyzed" charge transfer processes with a two-electron exchange. It is very interesting to note that the concept of such a catalyzed charge transfer of iron, which was originally established by Heusler,⁴⁰ has been rejected by the French group for a long period, in contrast to our previous interpretations.⁴¹ Furthermore, in both papers it is proposed as a first approximation that the adsorbed intermediates follow Langmuir isotherms.

Only one additional assumption was made in the paper under discussion, namely that the surface concentration of active sites is strongly potential-dependent and leads to surface relaxation phenomena. This assumption seems to be justified by several investigations⁴²⁻⁴⁸ even by the French group.⁴⁹

³⁷ Institute of Physical Chemistry and Electrochemistry, University of Karlsruhe, Karlsruhe, Germany.

³⁸ Institute of Microwave-Technics and Electronics, University of Karlsruhe, Karlsruhe, Germany.

³⁹ M. Keddum, O. R. Mattos, and H. Takenouti, *This Journal*, 128, 257 and 266 (1981).

⁴⁰ K. E. Heusler, *Z. Elektrochem., Ber. Bunsenges. Phys. Chem.*, 62, 582 (1958).

⁴¹ F. Hilbert, Y. Miyoshi, G. Eichkorn, and W. J. Lorenz, *This Journal*, 118, 1919 and 1927 (1971).

⁴² W. Allgaier, Doctoral Thesis, University of Clausthal (1975).

⁴³ W. Allgaier and K. E. Heusler, *Z. Phys. Chem. NF*, 98, 161 (1975).

⁴⁴ W. Allgaier and K. E. Heusler, *Z. Metallk.*, 67, 766 (1976).

⁴⁵ W. Allgaier and K. E. Heusler, *J. Appl. Electrochem.*, 9, 155 (1979).

⁴⁶ I. R. Burrows, J. A. Harrison, and J. Thompson, *J. Electroanal. Chem. Interfacial Electrochem.*, 58, 241 (1975).

⁴⁷ I. R. Burrows, J. A. Harrison, and J. Thompson, *ibid.*, 53, 283 (1974).

⁴⁸ J. A. Harrison and W. J. Lorenz, *Electrochim. Acta*, 22, 205 (1977).

⁴⁹ C. Cachet, I. Epelboin, M. Keddum, and R. Wiert, *J. Electroanal. Chem. Interfacial Electrochem.*, 100, 745 (1979).

On the other hand, the authors introduce the following *a priori* assumptions for the interpretation of a-c impedance results:

(i) The hydrogen evolution reaction on the iron electrode follows a Volmer-Heyrovski mechanism with the Heyrovski reaction as the rate-determining step.^{50,51} The degree of coverage of adsorbed hydrogen is assumed to be nearly unity at the corrosion potential and is supposed to be responsible for an inductive loop in the a-c impedance diagram which can be observed at this potential as well as at low anodic polarization. This inductive loop is completely discarded in the mechanistic interpretation of iron dissolution.

This assumption seems to be in contradiction to hydrogen permeation experiments on iron electrodes (footnote 52 and previous papers cited therein) which show that the Volmer reaction is always rate determining and the degree of coverage of adsorbed hydrogen should be very small. This discrepancy is also very important for different interpretations of a-c impedance results at the corrosion potential in terms of corrosion rates.⁵³

(ii) The steady-state behavior of the iron electrode in the active range is assumed to be strongly influenced by a slow adsorption-desorption process of hydrogen surface coverage. Only a "real" steady-state Tafel slope of +60 mV at $T = 298$ K is accepted in the model of the authors.

The steady-state Tafel slope of the active iron dissolution reaction is well known from many studies under different conditions and values either +40 or +30 mV have been measured independent of the polarization direction and of the rotation speed in disk experiments.

(iii) The deviation of the high frequency capacitive loop in complex a-c impedance diagrams from a true semicircle is assumed to be caused by frequency-dispersion of the system studied. The arguments of the authors³⁹ in order to exclude pseudo-faradaic parts in this high frequency capacitive loop are based on both a rough estimation of the adsorption capacitance and the constancy of the product of the so-called charge-transfer resistance (which should correspond to the intercept of the extrapolated capacitive loop with the real axis) and the steady-state current density.

It can easily be shown that the first argument does not hold for a decision on frequency-dispersion or pseudo-faradaic contributions. On the other hand, the constancy of the product $R_t \cdot i_s$ has not been observed in our experiments up to $i_s \approx 30 \text{ mA} \cdot \text{cm}^{-2}$.⁵⁴

(iv) The authors accept electrochemical charge-transfer coefficients very close to zero or unity in order to explain the experimental results by their proposed model. Furthermore, nonelectrochemical steps are assumed to be potential dependent.

Although not in contradiction with quantum mechanical treatment, strong deviations from the usual value of 0.5 for the electrochemical charge-transfer coefficients have been measured only in few systems under extreme conditions.

Using these additional assumptions [(i)-(iv)], the authors were able to interpret the a-c impedance data measured over wide potential and pH ranges. This impressive work seems to be more complete and self-consistent than the paper under discussion which tried only to explain the d-c and a-c behavior in the active range and the d-c behavior in the transition and pre-

passive ranges but by using less crucial assumptions in comparison to the paper of the authors.³⁹

Now we would like to answer with respect to the points of the authors as follows:

1. There is no contradiction between the results shown in Fig. 1 and 5 because of the extremely slow attainment of the steady state at the current density plateau.

2. As can be seen from Table II, step [4] becomes faster with increasing potential while step [3] is potential-independent. According to Eq. [40], it is assumed that step [3] will be rate determining in the active iron dissolution range studied instead of step [4]. However, the reaction scheme in Table II holds for lower anodic potentials or at the Fe/Fe^{2+} -equilibrium potential in strong acid solutions because $v_{0,3}/v_{0,4}$ has been calculated to be about 10^2 at $\text{pH} = 0$.⁵⁴

3. The α_1 values calculated from experimental data and using the proposed model seem to be quite reasonable (p. 1699).

4. Measurements on iron single crystal faces have been interpreted in terms of a physical model with a very similar analytic expression for the concentration dependence of kink sites.^{42,44,45}

5. There is no physical background for assuming a frequency dispersion to such an extent as observed in the iron system. In the paper under discussion, only one additional time constant was sufficient to obtain a statistically significant fit of the distorted high frequency capacitive loop. Therefore, it seems to us more reasonable to include this behavior into the kinetic model of the system studied.

From the value of R_t , it cannot be concluded that step [1] must be irreversible because in the proposed model (Table II) this step is in parallel with the iron dissolution reaction steps [3], [4], and [5]. Under steady-state conditions it follows that $v_1 = 0$, i.e., step [1] is in pseudo-equilibrium.

6. Figure 6 has only been analyzed with respect to the d-c behavior of the system studied because of the absence of an explicit surface relaxation model.

7. The simulation carried out by the authors does not allow any decision on the validity or nonvalidity of the proposed model, because the appearance of very small capacitive loops at extremely low frequencies are outside of experimental reproducibility.

We thank the authors for the indication of typing errors in Eq. [39] where + instead of - should read in the numerator, and $v_{0,6} \cdot W_4$ instead of $v_{0,6}$ in the denominator. Furthermore, in footnote 6 on p. 1699 it should read $\alpha_{\text{Fe}^{2+}} \approx 10^{-4}$ instead of 10^{-7} .

Finally, at the present state of knowledge one should ask for sufficient experimental and theoretical criteria for or against the different assumptions made in the paper under discussion and in the papers of the authors.³⁹ It seems to be more reliable to study simpler systems than the complicated iron dissolution process in order to check the basic assumptions for the interpretation of a-c impedance measurements.

Ellipsometry and Auger Analysis of Chromium Surfaces Passivated in Acidic and Neutral Aqueous Solutions

M. Seo, R. Saito, and N. Sato (pp. 1909-1912, Vol. 127, No. 9)

G. Dubpernell:⁵⁵ This is a noteworthy communication on an important subject. The authors report their electrode potential measurements as " E_{HESS} " (referred to a hydrogen electrode in the same solution). It is indicated that they make their measurements with a saturated calomel electrode. Since several different methods of converting from one electrode potential scale to another have been used in the past, it would be helpful if they would give the exact method

⁵⁰ I. Epelboin, Interfinish 1972, Forster-Verlag, Zürich, 1973, p. 84.

⁵¹ A. Caprani, I. Epelboin, P. Morel, and H. Takenouti, 4th European Symposium on Corrosion Inhibitors, Ferrara, 1975, Proceedings, III, p. 517 (1975).

⁵² E. G. Dafft, K. Bohnenkamp, and H. J. Engell, *Corros. Sci.*, 19, 591 (1979).

⁵³ W. J. Lorenz and F. Mansfeld, *ibid.*, In press.

⁵⁴ H. Schweickert, Doctoral Thesis, University of Karlsruhe (1978).

used in calculating the electrode potentials at each of the four pH's studied.

M. Seo:⁵⁶ The electrode potential, E_{HESS} , referred to a hydrogen electrode in the same solution was converted from the electrode potential, E_{SCE} , actually measured with a saturated calomel electrode by using the following equation

$$E_{\text{HESS}}(\text{Volt}) = E_{\text{SCE}}(\text{Volt}) + 0.241 \\ + 0.059 \text{ pH (at } 25^\circ\text{C)}$$

The electrode potential scale expressed in terms of E_{HESS} is convenient in dealing with electrochemical behavior of metal electrodes covered with thin oxide films in different pH solutions, as the equilibrium electrode potential of metal/metal oxide systems changes by 0.059V for a unit pH change of solution.

Electrical Conductivity of the LiI-H₂O-Al₂O₃ System

S. Pack, B. Owens, and J. B. Wagner, Jr.
(pp. 2177-2179, Vol. 127, No. 10)

J. Bradley Phipps and D. H. Whitmore:⁵⁷ The general trends reported in the paper by Pack, Owens, and Wagner are in agreement with those observed by us in a recent study⁵⁸ of the LiI-H₂O system; however, we do not agree with several of their conclusions. Those points made by the authors with which we take some issue are discussed below.

1. The authors of this paper suggested that the sudden increase in conductivity at 130°C was due to the formation of a highly conductive solid phase, possibly the half-hydrate, LiI · ½ H₂O. We found that the sharp increase in conductivity at 130° was simply due to the formation of a liquid phase (arising from a eutectic reaction at that temperature) which, not surprisingly, has an ionic conductivity many orders of magnitude greater than the solid-state material that exists below 130°C. In addition, our LiI/H₂O phase diagram work suggests that the compound LiI · ½ H₂O does not actually exist.

2. Pack, Owens, and Wagner state that "(their) results suggest that the presence of a few mole percent of the hydrate-phase in the LiI-Al₂O₃ material increases the conductivity by one to two orders of magnitude." Our work on hydrated lithium iodide, in contrast, suggests that the presence of a few mole percent of the hydrated phase increases the conductivity by only a few percent. In fact, for overall water contents ranging between the compositions LiI and LiI · H₂O, the observed conductivity was closely approximated by that predicted with the aid of the effective-medium theory (developed by Landauer),⁵⁹ if it was assumed that the microstructure consisted of randomly distributed grains of anhydrous lithium iodide and the monohydrate.

One might argue that the monohydrate phase, instead of existing as isolated grains, may actually form an interconnected network in LiI(Al₂O₃) composites due to the influence of the alumina particles. For such a case, the monohydrate phase would act as a highly conductive, parallel path for ion transport and the overall conductivity, σ_c , would be given by

$$\sigma_c = X_m \sigma_m + X_a \sigma_a$$

where X_m and X_a represent the volume fractions of the monohydrate and anhydrous phases and σ_m and σ_a are the corresponding conductivities. However, even

for this situation (which would optimize the composite conductivity) the presence of, say, 2 mole percent (m/o) of the monohydrate would only result in a composite conductivity about three times larger than the conductivity of an anhydrous LiI(Al₂O₃) composite and not the one or two orders of magnitude increase suggested by Pack, Owens, and Wagner. It should be stressed that we do not disagree with the general conclusion of the authors of this paper that the presence of water in lithium iodide is an important consideration. However, we do disagree with their contention that a *small amount* of water, as may be present on the surface of alumina particles, can increase the ionic conductivity of the composite sample by two orders of magnitude.

3. Liang *et al.*⁶⁰ reported that the room temperature conductivity of lithium iodide containing about 50 m/o alumina particles was about 500 times larger than that found for lithium iodide alone. Liang also noted that the activation energy for lithium ion migration in the LiI(Al₂O₃) composite was 0.4 eV which is equal to the activation energy for extrinsic conduction in lithium iodide. Pack and co-workers suggest that "it is possible that some moisture in (Liang *et al.*'s) samples affected their results." It is worthwhile in this connection to point out that Pack, Owens, and Wagner observed (as did we) that the activation energy increased substantially when water was present in LiI(Al₂O₃) composites. We found that as water was added to anhydrous lithium iodide, the activation energy increased from the anhydrous value of 0.39 eV to 0.68 eV for the monohydrate. More specifically, we found that the presence of about 5 m/o of the monohydrate phase caused the activation energy to increase by 20%. Even if only a small amount of moisture was present in Liang's samples, the activation energy should have been greater than 0.4 eV.

In summary, we have suggested that a small amount of monohydrate phase, even if present as an interconnected network, cannot cause an increase of two to three orders of magnitude in the conductivity reported for some LiI(Al₂O₃) composites. We also found that the presence of even a small amount of the monohydrate phase substantially increased the activation energy. In contrast, no increase in the activation energy was observed by Liang for LiI(Al₂O₃) nor by us for LiI(SiO₂) composites which suggests that the enhanced conductivity observed for these materials is not due to the presence of the monohydrate phase. We have evidence that fast ionic transport along microstructural imperfections, arising from the presence of the inert particles, may account for a substantial amount of the enhancement in conductivity observed for LiI(Al₂O₃) and LiI(SiO₂) electrolytes.⁶¹

S. Pack,⁶² **B. Owens,**⁶³ and **J. B. Wagner, Jr.:**⁶² We thank the discussors for their contribution and reply as follows. Point 1: Our paper stated (page 2178), "... that a highly conducting solid LiI · ½ H₂O phase is formed or a fusion process occurs. Further study of the phase diagram is needed." The phase diagram cited in footnote 58 was unavailable. We are pleased that the behavior has been shown to be a fusion process, *i.e.*, a eutectic, thus ruling out one of our two suggested possible mechanisms.

Point 2: We showed that the introduction of moisture increased the conductivity of initially anhydrous LiI regardless of whether the source of moisture was from a hydrate or from moisture sorbed on the Al₂O₃ par-

⁵⁶ Corrosion Research Group, Faculty of Engineering, Hokkaido University, Sapporo, 060 Japan.

⁵⁷ Department of Materials Science and Engineering, Northwestern University, Evanston, Illinois 60201.

⁵⁸ J. B. Phipps and D. H. Whitmore, Paper 371 presented at The Electrochemical Society Meeting, Hollywood, Florida, Oct. 5-10, 1980. To be published.

⁵⁹ R. Landauer, *J. Appl. Phys.*, 23, 779 (1952).

⁶⁰ C. C. Liang, A. V. Joshi, and N. E. Hamilton, *J. Appl. Electrochem.*, 8, 445 (1978).

⁶¹ J. B. Phipps and D. H. Whitmore, Paper 4-JII-80 presented at the American Ceramic Society Meeting, Chicago, Illinois, April 27-30, 1980. To be published.

⁶² Center for Solid State Science, Arizona State University, Tempe, Arizona 85281.

⁶³ Medtronics, Incorporated, Minneapolis, Minnesota 55418.

ticles. The work of Skarstad, Merritt, and Owens⁶⁴ on lithium halides containing dispersions of SiO₂ or Al₂O₃ show that although the monohydrate is more conductive than the anhydrous LiI by a factor of about 10², this alone does not account for the highest conductivities observed in the LiI-Al₂O₃-H₂O systems. The water contents corresponding to each conductivity are presented in that paper which also appeared after our earlier one. In other systems⁶⁵⁻⁶⁷ such as AgI and HgI₂ in which hydrates do not form, the introduction of moist Al₂O₃ particles enhances the conductivity more than the introduction of predried Al₂O₃ particles of the same particle size and volume fraction.

The discussors' equation

$$\sigma_c = x_m \sigma_m + x_a \sigma_a$$

is apparently not applicable to the ternary systems containing the dispersion.

Point 3: We agree that the activation energies reported by Liang did not change and this is evidence against our suggestion that "some moisture in (Liang's *et al.*'s) samples affected their results." Our data show that the introduction of predried, 0.3 micron Al₂O₃ particles to anhydrous LiI did not enhance the conductivity (See Fig. 1 and 2 of Pack, Owens, and Wagner).

To their summary, we reply that our paper reported a one to two orders of magnitude increase not a two to three orders of magnitude change.

We appreciate the interest of the discussors and look forward to reading their work cited in footnotes 58 and 61.

Simultaneous Discharge of Two Reacting Species under Pulsed Current Conditions

K. Viswanathan, M. A. Farrell Epstein, and H. Y. Cheh
(pp. 2383-2385, Vol. 127, No. 11)

Richard Haynes:⁶⁸ Several points should be mentioned regarding the paper under discussion and related works,^{69,70} namely:

1. There is a need for a more quantitative description of both the thermodynamics and the electrode kinetics of the model, otherwise apparent contradictions may arise from the conditions imposed by the model for irreversible reactions, diffusion control, and the requirement that the total current is zero during the off time. It is difficult to conceive, without further quantitative limits, that the current would be zero during the off time for all values of δ , D , τ_1 , i_0 , E_0 , β . A mixed potential may be reached, thus polarizing reaction [1] cathodically and reaction [2] anodically. The relaxation of the processes may not occur during the off time for all parameters. Therefore, this model may not allow the use of calculated values of $(i_p)_{l,1}$ and $(i_{int})_{l,1}$ by Cheh⁶⁹ and Viswanathan *et al.*⁷⁰ since boundary condition for mass transport may not be met during the off time.

2. The efficiencies of the reactions under certain conditions are a function of the on and off times (see Haynes)⁷¹ and are restricted by time constants for the processes. This concept should be incorporated in a complete model and its limits defined.

⁶⁴ P. M. Skarstad, D. M. Merritt, and B. B. Owens, Abstract C-217 in "Third International Meeting on Solid Electrolytes—Solid State Ionics and Galvanic Cells," September 15-19, 1980, Tokyo, Japan; in press in *Solid State Ionics*.

⁶⁵ K. Shahi and J. B. Wagner, Jr., Paper 369 presented at The Electrochemical Society Meeting, Boston, Massachusetts, May 6-11, 1979; *This Journal*, 128, 6 (1981).

⁶⁶ S. Pack, Paper 133 presented at The Electrochemical Society Meeting, Los Angeles, California, Oct. 14-19, 1979.

⁶⁷ J. Bruce Wagner, Jr., *Mater. Res. Bull.*, 15, 1691 (1980).

⁶⁸ Western Electric, Engineering Research Center, Princeton, New Jersey 08540.

⁶⁹ H. Y. Cheh, *This Journal*, 118, 551 (1971).

⁷⁰ K. Viswanathan, H. Y. Cheh, and G. L. Standart, *J. Appl. Electrochem.*, 10, 37 (1980).

⁷¹ R. Haynes, *This Journal*, 126, 881 (1979).

3. The calculations of Cheh⁶⁹ and Viswanathan *et al.*⁷⁰ have not incorporated influences of the pulse on diffusion layer thickness although increased limiting current densities⁷²⁻⁷⁴ have been observed in magnitudes greater than predictable by the present authors (but see Haynes⁷⁵).

A theory of pulse plating should be able to, when necessary, incorporate the effects of the products of the reaction (such as gas bubbles) on diffusion layer thickness. Such effects have been investigated in direct current electrolysis.⁷⁶ If such an enhancement of mass transport occurs during the pulse due to the field effects,⁷²⁻⁷⁴ bubble formation,⁷⁶ etc., then the rates and quantity of metal deposited in pulse plating can be greater than in direct current plating. The relative effects of gas bubbling on diffusion layer thickness in the pulse and direct current cycles are important with respect to the relative rates. The quantity of the metal deposited is seen to be effected by this enhanced efficiency in the model of Haynes.⁷¹ In this model the effect of gas bubbling is eliminated in the pulse cycle but not necessarily in the direct current cycle. If field effects in the pulse cycle enhance the mass transport rates more than gas bubbling in the d-c cycle than $E_p > E_{D-C}$ and $Q_p > Q_{D-C}$.

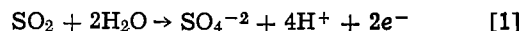
K. Viswanathan,⁷⁷ **M. A. Farrell Epstein,**⁷⁸ and **H. Y. Cheh:**⁷⁸ We agree with Haynes that there is a need for a more quantitative description for simultaneous reactions under pulsed current conditions. Our calculations are strictly valid under the assumption stated in our note. The situation is approached in practice when the exchange current density for reaction [2] is much smaller than that for reaction [1].

The statement that our work has not incorporated influences of the pulse on diffusion layer thickness is not valid. A quantitative analysis on this effect has been presented thoroughly in a paper by us.⁷⁹

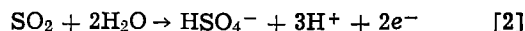
An Investigation of Electrode Materials for the Anodic Oxidation of Sulfur Dioxide in Concentrated Sulfuric Acid

P. W. T. Lu and R. L. Ammon (pp. 2610-2616, Vol. 127, No. 12)

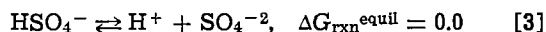
Hassane Saab and Robert Spotnitz:⁸⁰ The authors claim that the reversible potential for the anodic oxidation of sulfur dioxide cannot be determined unambiguously because it is "highly uncertain whether the overall electrochemical reaction for SO₂ oxidation is represented by"



or



However, at the reversible potential, the following chemical equilibrium can be assumed to take place



Therefore calculation of the reversible potential using either reaction [1] or reaction [2] leads to the same value, although reactions [1] and [2] do lead to different values of the *standard state* potentials.

⁷² E. Z. Gak, E'Kh. Rokhinson, and N. F. Bondarenko, *Elektronnaya Obvabotka Materialov*, 6, 24 (1973).

⁷³ E. Z. Gak, E'Kh. Rokhinson, and N. F. Bondarenko, *Elektronkhimiya*, 11, 535 (1975).

⁷⁴ R. Sunderman and T. Z. Fahidy, *J. Appl. Electrochem.*, 6, 89 (1976).

⁷⁵ R. Haynes, Paper 79 presented at The Electrochemical Society Meeting, Las Vegas, Nevada, Oct. 17-22, 1976.

⁷⁶ For example: (a) L. J. Janssen and E. Barendrecht, *Electrochem. Acta.*, 24, 693 (1979); (b) N. Ibl, *Chem. Ing. Tech.*, 43, 202 (1971); (c) S. Mohanta and T. Z. Fahidy, *J. Appl. Electrochem.*, 7, 235 (1977).

⁷⁷ Hooker Development Center, Niagara Falls, New York 14302.

⁷⁸ Department of Chemical Engineering and Applied Chemistry, Columbia University, New York, New York 10027.

⁷⁹ K. Viswanathan, M. A. Farrell Epstein, and H. Y. Cheh, *This Journal*, 125, 1772 (1978).

⁸⁰ Department of Chemical Engineering, University of Wisconsin, Madison, Wisconsin 53706.

The difficulty in determining the reversible potential stems, not from the ambiguity of the overall reaction, but rather from the lack of thermodynamic data for the system $\text{SO}_2\text{-H}_2\text{SO}_4\text{-H}_2\text{O}$. The authors reference the paper of Appleby and Pichon⁸¹ in which it is stated

⁸¹ A. J. Appleby and B. Pichon, *J. Electroanal. Chem. Interfacial Electrochem.*, 95, 59 (1979).

⁸² R. S. Nicholson and I. Shain, *Anal. Chem.*, 36, 706 (1964).

that there was little possibility of extracting rate constants from linear potential sweep data because of the difficulties in defining the reversible potential, since analysis of linear potential sweep data requires knowledge of the standard state potential [e.g., footnote 82]. Appleby and Pichon⁸¹ did report an approximate exchange current density based on their steady-state potentiostatic data.

Erratum

In the paper "Properties of $\text{LiAlCl}_4\text{-SOCl}_2$ Solutions for Li/ SOCl_2 Battery" by H. V. Vankatasetty and D. J. Saathoff which appeared on pp. 773-777 of the April 1981 JOURNAL, Vol. 128, No. 4, Fig. 8, 9, and 10 should appear as follows:

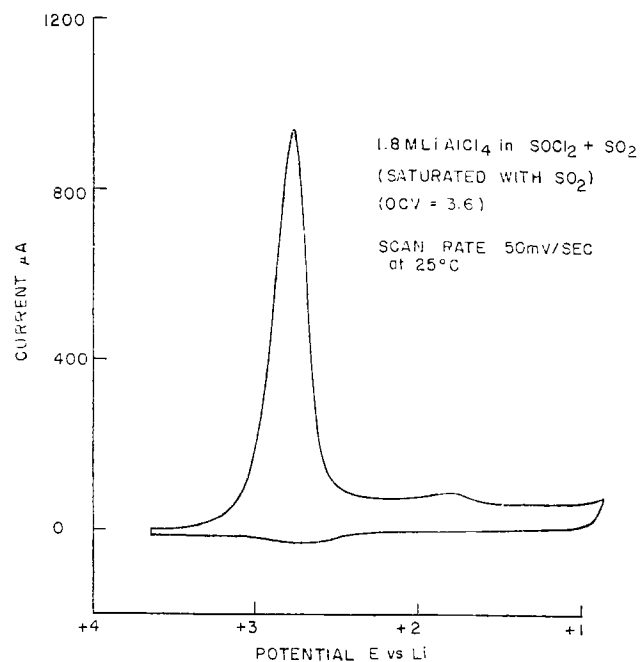


Fig. 8. Cyclic voltammery of $\text{LiAlCl}_4\text{-SOCl}_2$ solution saturated with SO_2 .

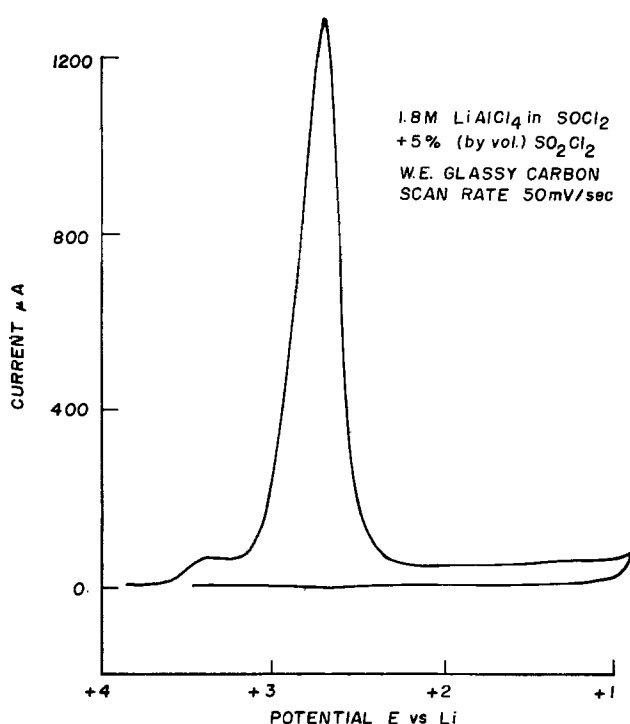


Fig. 9. Cyclic voltammery of $\text{LiAlCl}_4\text{-SOCl}_2$ solution with 5% (by volume) of SO_2Cl_2 .

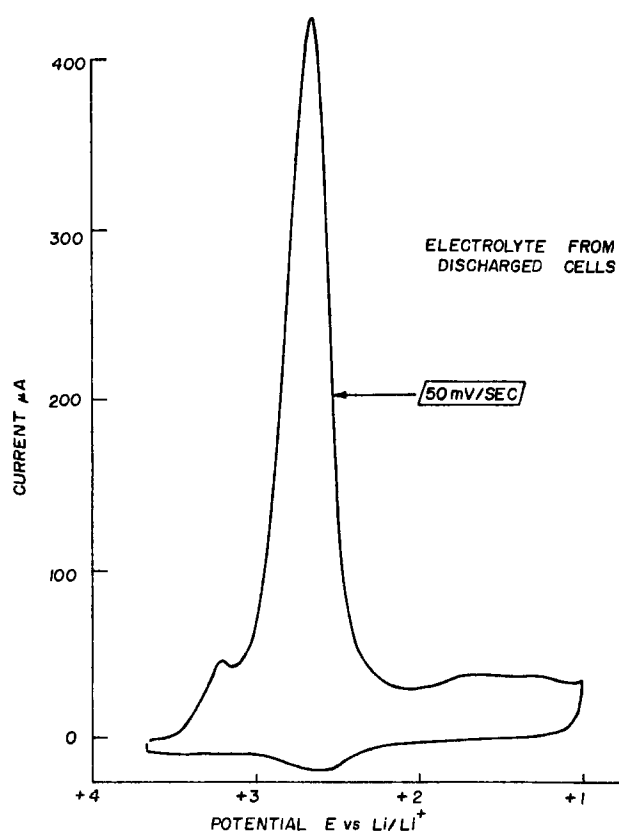


Fig. 10. Cyclic voltammery of $\text{LiAlCl}_4\text{-SOCl}_2$ solution from cell discharge to 0.0V.



Surface Intermediates of an n-Type Gallium Phosphide Electrode as Related with the Shifts of the Surface Band Energy Induced by Oxidants in Solution

Yoshihiro Nakato, Akira Tsumura, and Hiroshi Tsubomura*

Department of Chemistry, Faculty of Engineering Science, Osaka University, Toyonaka, Osaka 560, Japan

ABSTRACT

The energy of the electronic band at the surface of an n-GaP electrode shifts downward, that is to say, to more negative, by the addition of oxidizing agents. Although the surface band energy of GaP for the (111)-face changes linearly with pH, it stays constant in an intermediate pH range in the presence of the $[\text{Fe}(\text{CN})_6]^{4-}/[\text{Fe}(\text{CN})_6]^{3-}$ couple. This result is explained by assuming a "surface-trapped hole" formed by oxidative interaction with the solute. It is also assumed that this surface-trapped hole is acting as an electronic surface state in electronic equilibrium with the redox couple in solution, its energy being estimated to lie about 0.5 eV above the valence bandedge. At higher pH, or in the case of the $(\bar{1}\bar{1}\bar{1})$ -face, the surface band energy interacting with the redox couple increases with pH. The shift in this case is mainly attributed to the accumulation of oxide- or hydroxide-type surface intermediates. It is suggested that these surface intermediates effectively mediate the electron transfer from the conduction band to the oxidizing agents in solution.

It is well known that the energy of the semiconductor electronic band at the surface measured as the potential at minimum capacitance is changed by adsorption of ions in electrolyte solutions onto the electrode surface (1-5). It is also known that it changes sometimes with the electrode potential by the change in the chemical structures at the electrode surfaces, e.g., from an oxidized structure to a reduced one (2).

We have reported in a previous paper (5) that the surface band energy of an n-GaP electrode is shifted by electrode illumination under anodic polarization. The shift was explained from the accumulated surface intermediates formed by photogenerated holes. Similar shifts are therefore expected to occur at dark when holes are injected by oxidizing agents in solutions. Several reports were published on the hole injection from redox couples into the GaP electrode (6-9). In the present paper we report and discuss the shift of the surface band energy caused by interaction with the redox couple.

Experimental

Single crystals of n-type GaP from Yamanaka Chemical Industries, Limited were used as electrodes. The (111)-face (Ga-face) and the $(\bar{1}\bar{1}\bar{1})$ -face (P-face) were distinguishable by microscopic inspection of the etched surface (5). The current-potential curve was obtained by use of a Hokutodenko HA 101 potentiostat. The differential capacitance was measured with

a Yokogawa-Hewlett-Packard Universal Bridge 4265B, together with a function generator. The solutions were deaerated by nitrogen bubbling and were stirred magnetically during the measurements. Further experimental details were described elsewhere (5). The concentration unit, mol/dm³, is abbreviated as M in the present paper.

Results

Figure 1 shows current-potential (*i*-*U*) curves for the (111)-face of an n-GaP electrode at dark. It is seen that the onset potential of the cathodic current (*U*_c) is shifted largely to the positive by the addition of the $[\text{Fe}(\text{CN})_6]^{4-}/[\text{Fe}(\text{CN})_6]^{3-}$ couple. A similar result was obtained with heavily etched electrodes. This current-potential behavior is therefore independent of defects or dislocations at the surface produced by mechanical polishing. Similar shifts were reported by some authors for other semiconductor-redox systems (6, 10, 11).

Figure 2 shows examples of Mott-Schottky plots for the (111)-face of the n-GaP electrode in the presence of the $[\text{Fe}(\text{CN})_6]^{4-}/[\text{Fe}(\text{CN})_6]^{3-}$ couple. Very good straight lines are obtained, like those in the absence of the redox couple (5). In solutions of high pH, relatively high dark anodic currents, of the order of 1-10 μA/cm², were observed, increasing with pH and the redox concentration, in agreement with the results reported previously (6, 10). In spite of such currents, the capacitance measurements could be done independently. The *U*_s value was determined from the intercept of the Mott-Schottky plot with the abscissa. As de-

* Electrochemical Society Active Member.

Key words: semiconductor, hole injection, surface state, surface-trapped hole.

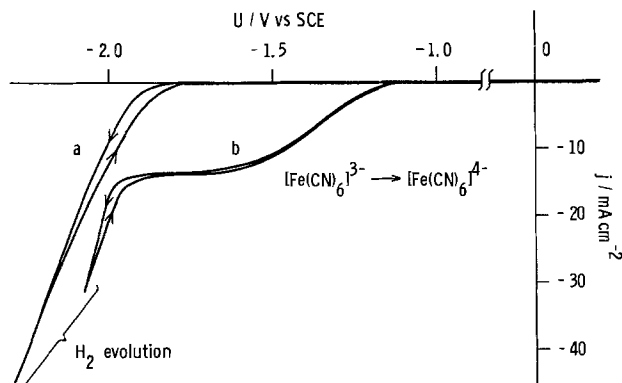


Fig. 1. Current-potential curves for the (111)-face of an n-GaP electrode in a 0.1N NaOH solution, in the absence (a) and the presence (b) of 0.05M $K_4[Fe(CN)_6]$ and 0.05M $K_3[Fe(CN)_6]$. The scan rate is 120 sec/V.

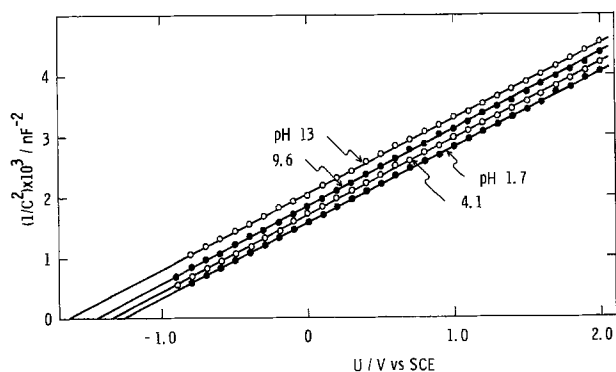


Fig. 2. Mott-Schottky plots for the (111)-face of an n-GaP electrode in solutions containing 0.05M $K_4[Fe(CN)_6]$ and 0.05M $K_3[Fe(CN)_6]$.

scribed previously (5), the U_s value is related to the lower energy limit of the conduction band at the surface, E_c^s , as shown below

$$E_c^s = -eU_s + \Delta \quad [1]$$

if E_c^s and $-eU_s$ are measured with respect to the same reference electrode. Δ refers to a small energy difference between the Fermi level and the lower energy limit of the conduction band in the interior of the semiconductor.

The U_s values for the (111)-face of the n-GaP electrode thus obtained, together with those of U_c , which has been taken as a potential at which the dark cathodic current exceeds $4 \mu A/cm^2$, are shown in Fig. 3, where U_s and U_c designate the values for solution lacking the redox couple (5) and U_s (redox) and U_c (redox) designate those in the presence of the $[Fe(CN)_6]^{4-}/[Fe(CN)_6]^{3-}$ couple. It is seen that the U_s (redox) is kept close to the U_s in the range of $pH \leq 4$, but deviates more to the positive at $pH > 4$. It is also seen that the U_c (redox) changes with pH , nearly in parallel with U_s (redox). This indicates the validity of the U_s (redox) values obtained from the Mott-Schottky plots. It is to be noted that U_s (redox) is kept nearly constant, in parallel with the redox potential of the redox couple (ϵ_{redox}) in the range of $pH 5-10$, while it moves upward with pH in the range of $pH > 10$.

Figure 4 shows the pH dependence of U_s (redox) for the (111)-face at various concentrations of the redox couple. The concentrations of $[Fe(CN)_6]^{4-}$ and $[Fe(CN)_6]^{3-}$ were made equal so as to keep the redox potential unchanged. It is seen that the U_s (redox) value remains nearly constant at the intermediate pH region. The constancy of U_s (redox) was maintained in a wider pH range, as the redox concentration increases.

Figure 5 shows the effect of the redox concentration on U_s (redox) and U_c (redox) at $pH 6.8$ and 13. The

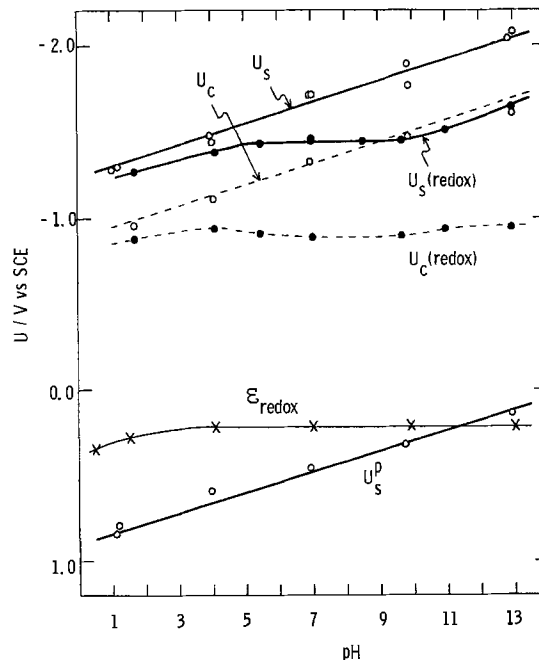


Fig. 3. U_s and U_c for the (111)-face of an n-GaP electrode, measured in the presence and the absence of 0.05M $K_4[Fe(CN)_6]$ and 0.05M $K_3[Fe(CN)_6]$. ϵ_{redox} is the redox potential of the redox couple determined by the cyclic voltammetry. U_s^p is the U_s of a p-GaP electrode (5).

concentrations of $[Fe(CN)_6]^{4-}$ and $[Fe(CN)_6]^{3-}$ were kept equal also in this case. It is seen that the U_s (redox) and U_c (redox) curves are again parallel to each other. The U_s (redox) value for $pH 6.8$ remains nearly constant at least in the range of the redox concentration higher than 3×10^{-3} mol/dm³, whereas U_s (redox) for $pH 13$ shifts to the positive with the concentration.

Figure 6 shows the U_s values for the (111)-face in the presence and absence of the $[Fe(CN)_6]^{4-}/[Fe(CN)_6]^{3-}$ couple. In contrast to the case of the (111)-face (Fig. 3), the U_s (redox) value for the (111)-face changed with pH throughout the pH range measured.

Similar experiments were made for other redox couples. As shown in Fig. 7, the shifts of U_s and U_c were observed by addition of an Fe^{2+}/Fe^{3+} couple and $[Cu(NH_3)_4]^{2+}$. In the latter case the reduced form, $[Cu(NH_3)_2]^+$, is unstable in solutions and was not added in the solutions. The redox potential for $[Cu(NH_3)_4]^{2+}$ was determined by cyclic voltammetry. By adding a V^{2+}/V^{3+} couple at $pH \leq 3$, the U_s shifted very little and the U_c only slightly shifted. The redox potential for this couple is highly negative, about $-0.5V$ vs. SCE.

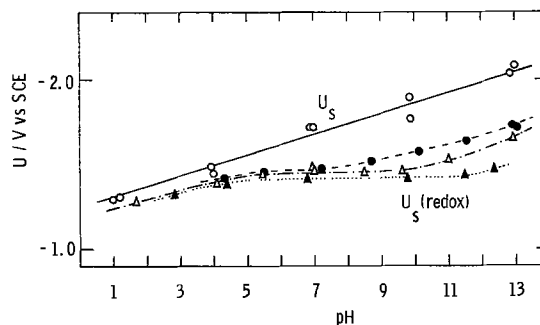


Fig. 4. pH dependences of U_s (redox) for the (111)-face of an n-GaP electrode at various concentrations of the $[Fe(CN)_6]^{4-}/[Fe(CN)_6]^{3-}$ couple (equal concentrations): \circ 0M, \bullet 0.005M, \triangle 0.05M, \blacktriangle 0.4M.

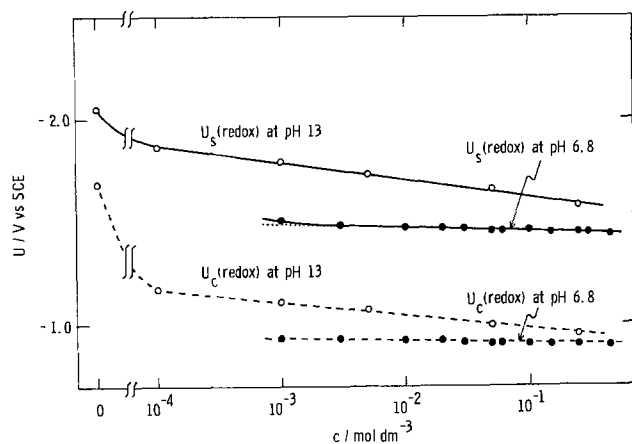


Fig. 5. Effects of the concentration, c , of the $[\text{Fe}(\text{CN})_6]^{4-}/[\text{Fe}(\text{CN})_6]^{3-}$ couple (equal concentrations) on U_s (redox) and U_c (redox) for the (111)-face of an n-GaP electrode.

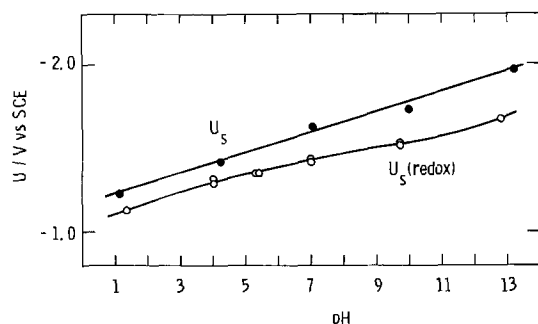


Fig. 6. U_s for the (111)-face of an n-GaP electrode in the presence and the absence of 0.05M $[\text{Fe}(\text{CN})_6]^{4-}$ and 0.05M $[\text{Fe}(\text{CN})_6]^{3-}$.

Figure 8 shows dark cathodic currents observed at a p-type GaP electrode in the presence of a $[\text{Fe}(\text{CN})_6]^{4-}/[\text{Fe}(\text{CN})_6]^{3-}$ couple. Similar cathodic currents were observed for $[\text{Cu}(\text{NH}_3)_4]^{2+}$ or $\text{Fe}^{2+}/\text{Fe}^{3+}$. Almost no cathodic current was observed in the absence of these redox couples.

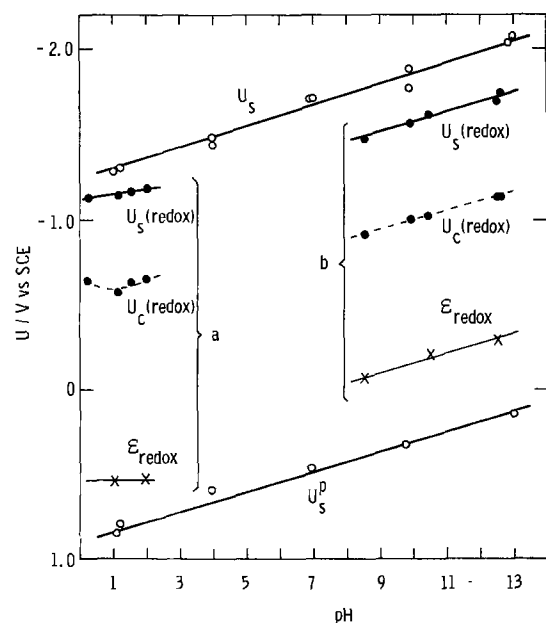


Fig. 7. Shifts in U_s and U_c for the (111)-face of an n-GaP electrode by redox couples. Electrolyte: (a) 0.05M $\text{FeSO}_4 + 0.05\text{M Fe}_2(\text{SO}_4)_3 + 0.005 \sim 0.5\text{M H}_2\text{SO}_4$, and (b) 0.05M $[\text{Cu}(\text{NH}_3)_4]^{2+}(\text{NO}_3)_2$, including 0.1M $(\text{NH}_4)_2\text{SO}_4 + \text{ammonia}$ for pH 8-11 and 0.1M NaOH for pH ~ 13 .

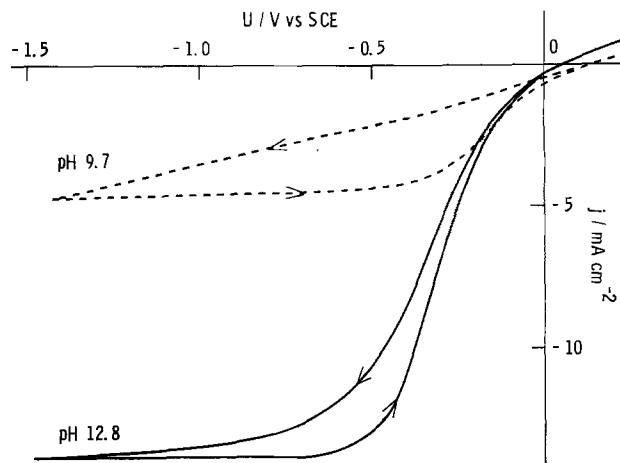


Fig. 8. Dark cathodic currents at a p-GaP electrode in solutions containing 0.05M $[\text{Fe}(\text{CN})_6]^{4-}$ and 0.05M $[\text{Fe}(\text{CN})_6]^{3-}$. The scan rate is 120 sec/V.

Discussion

The dark cathodic currents observed at the p-GaP electrode (Fig. 8) show that holes can be injected into the GaP electrode by the redox couples used in the present work, except $\text{V}^{2+}/\text{V}^{3+}$. The redox potentials of these redox couples are a little higher than the U_s of the p-GaP electrode (U_s^p), as is seen from Fig. 3 and 7. This means that the holes are injected by thermally activated oxidizing agents.

The shift of U_s of the n-GaP electrode caused by the addition of the redox couples is explained most probably by injected holes, similar to the interpretation given previously for the shifts in U_s by electrode illumination (5). The Mott-Schottky plots for solutions containing the redox couples show good straight lines in the potential range where the band bending is large (Fig. 2), indicating that U_s is kept nearly constant in this potential range. The electrode surface in contact with the redox solutions is thought to be in a stationary state in a range of potential where the band bending is large.

As mentioned before, the U_s for the (111)-face of the n-GaP electrode in the presence of the $[\text{Fe}(\text{CN})_6]^{4-}/[\text{Fe}(\text{CN})_6]^{3-}$ couple remains nearly constant in the intermediate pH range (pH 5 \sim 10), if the redox concentration is sufficiently high (Fig. 3, 4, and 5). In analogy to the Bardeen barrier in metal-semiconductor contacts (12, 13), these results suggest that the U_s value in such a pH range is determined by an electron transfer equilibrium between the redox couple in solution and electronic surface states at the electrode. We may assume that such surface states imply electron deficient surface Ga-P bonds. These species, which can be called a "surface-trapped hole," may be stabilized by the distortion of the surface Ga-P framework and also by the orientation of electric dipoles of solvent (water) molecules, their energy being a little above the valence band edge at the surface (E_{v^s}). The nucleophilic attack of bases such as H_2O on these species leads to the electrode decomposition (5, 14). Such species can also accept electrons from reducing agents in solution, recovering to the normal Ga-P bonds. Hence, these species, together with the surface Ga-P bonds, can be regarded as making up a surface redox system, when the nucleophilic attack of H_2O is slow.

The above-mentioned constancy of U_s in the intermediate pH range can be explained as follows. The redox potential for the surface-trapped hole, e_h , with respect to a certain reference electrode, can be described approximately in a form

$$e_h = e_h^\circ + (kT/e) \ln c_h + \psi + \text{const} \quad [2]$$

where c_h means the density of the surface-trapped hole,

which is assumed to be much less than the density of the surface Ga-P bonds. ψ is the surface potential at the electrode. The electronic equilibrium between the surface redox system and the redox couple in solution is established at $e_h = \epsilon_{\text{redox}}$, ϵ_{redox} being the redox potential of the redox couple in solutions (Fig. 9).

It is to be noted that e_h shifts with c_h through both the second and the third term on the right-hand side of Eq. [2], since the change in ψ arises from the electrical double layer due to the surface-trapped hole and therefore varies with c_h . The shift in ψ by the surface-trapped hole, $\Delta\psi$, can be expressed approximately as $\Delta\psi = ec_h/C$, where C is the capacitance for the electrical double layer at the interface. Accordingly, by differentiating the second and third term of Eq. [2] with respect to c_h , we can see that the third term changes with c_h much more steeply than the second in the range of $c_h > (CkT/e^2)$. Let us define $c_h^0 = (CkT/e^2)$. It is calculated to be $5 \times 10^{12} \text{ cm}^{-2}$ when C is assumed to be of the order of $30 \mu\text{F}/\text{cm}^2$, as generally done (15). This concentration corresponds to about one surface-trapped hole per two hundred outermost Ga-P bonds. The condition, $c_h > c_h^0$, can therefore be achieved rather easily.

With this condition, the energy difference between $-e_h$ and the conduction or the valence bandedge at the surface (E_c^s or E_v^s in Fig. 9) is kept nearly constant, since E_c^s and E_v^s also change with ψ in the same manner as ($-e_h$). We can therefore see that, when $e_h = \epsilon_{\text{redox}}$, E_c^s (or U_s) is determined solely by ϵ_{redox} in such a case, in agreement with the experimental results (Fig. 3 and 4).

The shift in ψ (or U_s) may also be caused partly by the hydroxide- or oxide-type surface intermediates (5) formed by the nucleophilic attack of H_2O on the surface-trapped hole. Even in such a case, the same conclusion as above can be derived as far as the electronic equilibrium ($e_h = \epsilon_{\text{redox}}$) is established under the condition of $c_h > c_h^0$.

Based on the above interpretation and the results of Fig. 3, the electronic equilibrium in the intermediate pH range is accomplished when U_s is about -1.45 V vs. SCE, that is, about 1.65 V above ϵ_{redox} . By estimating Δ in Eq. [1] to be ca. 0.1 eV and from the bandgap of GaP (2.26 eV), we can see that e_h is about 0.5 eV above E_v^s , as is shown in Fig. 9. This value, called ΔE , reasonably corresponds to the stabilization energy for the surface-trapped hole due to the distortion of the surface Ga-P framework and the solvation, mentioned before.

It is to be pointed out here that an electroluminescence is observed when the n-GaP electrode is under a

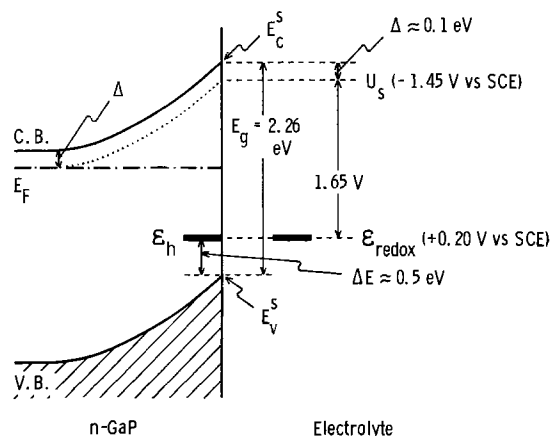


Fig. 9. A model of an electronic equilibrium at an n-GaP/electrolyte interface. For simplicity, the energy such as E_c^s , E_v^s , etc. and the potential such as U_s , ϵ_{hr} , etc. are both used. These can be compared with each other by using a relation, (energy) = $(-e) \times$ (potential), if they are measured with respect to the same reference electrode.

slightly cathodic potential in solutions containing the $[\text{Fe}(\text{CN})_6]^{4-}/[\text{Fe}(\text{CN})_6]^{3-}$ couple (16). The luminescence spectrum ranges from 1.9 to 1.3 eV, with a peak at about 1.6 eV. The similar luminescence was reported in the literature (7, 9) and interpreted to be due to the hole injection by the oxidizing agents in solution. Since a sum of the energy of the luminescence peak and the ΔE value above is 2.1 eV, very close to the bandgap of GaP, it is highly probable that the electroluminescence is caused by a recombination between the surface-trapped hole and the electron in the conduction band.

In the discussion made so far, we assumed that the rate of the nucleophilic attack of H_2O on the surface-trapped hole (R_3) can be neglected as compared to the rates of the hole injection (R_1) and the reverse process (R_2). The very small R_3 value assumed here implies the presence of a fairly large activation energy for the nucleophilic attack of H_2O , which may be understood from three dimensionally bound surface Ga-P bonds of a high covalent character (17), since the attack of H_2O on one Ga-P bond must induce large steric strain in the surrounding Ga-P bonds.

Figures 3 and 4 show that a parallel relation between U_s (redox) and ϵ_{redox} is broken at pH higher than a certain value. The break point becomes higher, the higher the redox concentration. These results can be explained by assuming that the rate of the nucleophilic attack of H_2O , R_3 , increases with pH and exceeds R_2 at a certain pH value. In that case, the electronic equilibrium is broken and e_h is no longer equal to ϵ_{redox} at a high pH region. Figure 5 shows that the constancy of U_s (redox) at pH 6.8 is also broken when the redox concentration is too low. This can be explained by taking into account the low rate R_2 at a low redox concentration.

In both cases, namely, in the range of high pH and in the case of low redox concentration at $\text{pH} \gtrsim 5$, the electrode dissolution occurs predominantly by the hole injection ($R_1 \cong R_3 \gg R_2$). The density of the surface-trapped hole (c_h) must be very small in such cases. The observed shift in U_s can then be attributed mainly to the accumulation of highly polar Ga-O or P-O bonds present in the oxide- or hydroxide-type surface intermediates mentioned before.

The U_s (redox) value for the $(\bar{1}\bar{1}\bar{1})$ -face of the n-GaP electrode does not show any parallelism with ϵ_{redox} throughout the pH range measured (Fig. 6). This suggests that the surface-trapped hole at this face is less stable than that at the (111) -face.

It may be pointed out here that the difference between U_s (redox) and U_c (redox) is considerably larger than that between U_s and U_c in the absence of the redox couple (Fig. 3, 5, and 7). This can be explained by assuming that the capture of electrons in the conduction band by the surface intermediates is very efficient. It was reported previously (5) that a potential at which the photoanodic current deviates from the saturation value (U_{sat}^a) shifts largely from U_s under illumination [U_s (illum.)]. The shift was attributed, in the same way as above, to the effective capture of the electrons by photoanodically formed surface intermediates (5).

Manuscript received April 28, 1980.

Any discussion of this paper will appear in a Discussion Section to be published in the December 1981 JOURNAL. All discussions for the December 1981 Discussion Section should be submitted by Aug. 1, 1981.

Publication costs of this article were assisted by Osaka University.

REFERENCES

1. F. Lohmann, *Ber. Bunsenges. Phys. Chem.*, **70**, 428 (1966).
2. H. Gerischer, H. Hoffmann-Perez, and W. Mindt, *ibid.*, **69**, 130 (1965).
3. D. S. Ginley and M. A. Butler, *This Journal*, **125**, 1968 (1978).

4. H. Tributsch, *ibid.*, **125**, 1086 (1978); J. Gobrecht, H. Gerischer, and H. Tributsch, *Ber. Bunsenges. Phys. Chem.*, **82**, 1331 (1978).
5. Y. Nakato, A. Tsumura, and H. Tsubomura, *This Journal*, **127**, 1502 (1980).
6. R. Memming and G. Schwandt, *Electrochim. Acta*, **13**, 1299 (1968).
7. K. H. Beckmann and R. Memming, *This Journal*, **116**, 368 (1969).
8. R. Memming, *ibid.*, **116**, 785 (1969).
9. B. Pettinger, H.-R. Schöppel, and H. Gerischer, *Ber. Bunsenges. Phys. Chem.*, **80**, 849 (1976).
10. M. J. Madou, F. Cardon, and W. P. Gomes, *ibid.*, **81**, 1186 (1977).
11. H. Gerischer, in "Physical Chemistry," Vol. 9A, H. Eyring, Editor, p. 643, Academic Press, New York (1970).
12. J. Bardeen, *Phys. Rev.*, **71**, 717 (1947).
13. E. H. Rhoderick, *J. Phys. D: Appl. Phys.*, **3**, 1153 (1970).
14. H. Gerischer and W. Mindt, *Electrochim. Acta*, **13**, 1329 (1968); H. Gerischer, *Surf. Sci.*, **13**, 265 (1969).
15. D. C. Grahame, *J. Am. Chem. Soc.*, **70**, 4819 (1954); **79**, 2093 (1957); D. E. Yates, S. Levine, and T. W. Healy, *J. Chem. Soc. Faraday Trans. I*, **70**, 1807 (1974).
16. Our unpublished results.
17. S. Kurtin, T. C. McGill, and C. A. Mead, *Phys. Rev. Lett.*, **22**, 1433 (1969).

A Sensitive Novolac-Based Positive Electron Resist

M. J. Bowden, L. F. Thompson, S. R. Fahrenholtz, and E. M. Doerries

Bell Laboratories, Murray Hill, New Jersey 07974

ABSTRACT

A positive electron resist has been developed which appears to operate on a different mechanism from conventional positive electron resists. Resists in the latter category such as PBS or PMMA achieve differential solubility primarily as a result of scission of the main chain. In the case of the new resist, differential solubility appears to be achieved by the removal of a polymeric dissolution inhibitor. The resist is a composite system consisting of a novolac resin similar to that used in most positive photoresists in solid solution with poly(2-methyl-1-pentene sulfone) which functions as a dissolution inhibitor of the novolac resin in aqueous base. The process operates by spontaneous depolymerization of the polymeric dissolution inhibitor, a process which is initiated by electron irradiation. The sensitivity of this resist (called NPR) is $3 \mu\text{C cm}^{-2}$ at 20 kV and the contrast is 1.0. Submicron features have been delineated in $1.0 \mu\text{m}$ resist films. The resist withstands Al, poly-Si, SiO_2 , doped SiO_2 , and Si_xN_y plasma etching environments and has been used as a plasma etch mask to transfer submicron features into these film substrates.

Positive resists are characterized by increased solubility of the resist film after exposure to radiation. This increase in solubility is achieved by one of two mechanisms, viz., simple chain scission of individual bonds in the main chain (1, 2) or decomposition of a dissolution inhibitor (3, 4). Resists of the former type are high molecular weight polymers which undergo main chain scission under irradiation resulting in a decrease in molecular weight. This process leads to enhanced solubility of the irradiated region which may be developed by fractional solution. Resists which operate on the second principle consist of a mixture of a low molecular weight polymer, e.g., a novolac resin, which is soluble in a given solvent (usually an aqueous base) and a material which inhibits the dissolution of the composite film in that solvent. The dissolution inhibitor is converted to an acidic species during irradiation and as a result of this chemical change, the composite becomes soluble in the aqueous base.

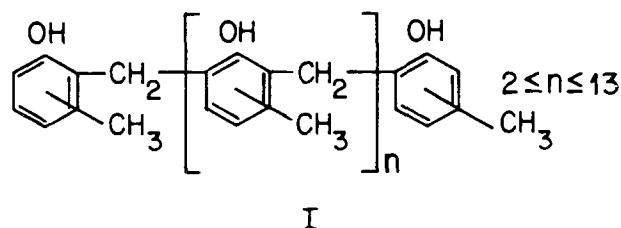
Most positive electron resists are of the first type (5). For example, poly(butene-1-sulfone) (2) and poly(methyl methacrylate) (6) are chain degrading polymers which are used primarily as resists for liquid etching. However, these polymers are thermally unstable and are also unstable to other forms of ionizing radiation; hence they are not very resistant to dry etching environments such as found in plasma etching, ion beam milling, and sputter etching.

The next generation of electron exposure machines will have high-throughput for direct exposure of VLSI silicon devices with submicron features. The high resolution requirement will almost certainly necessitate

dry etching processes for pattern transfer. This requirement places an additional constraint on the resist other than the sensitivity and resolution requirements commensurate with machine design.

Clearly the etch resistance requirements would appear to preclude the positive electron resists which are currently available. Positive photoresists, on the other hand, exhibit excellent resolution and dry etch resistance particularly those positive photoresists based on novolac resins. These resists operate by the second mechanism alluded to earlier and a more detailed description of this mechanism will be helpful in understanding the new concept to be proposed in this paper.

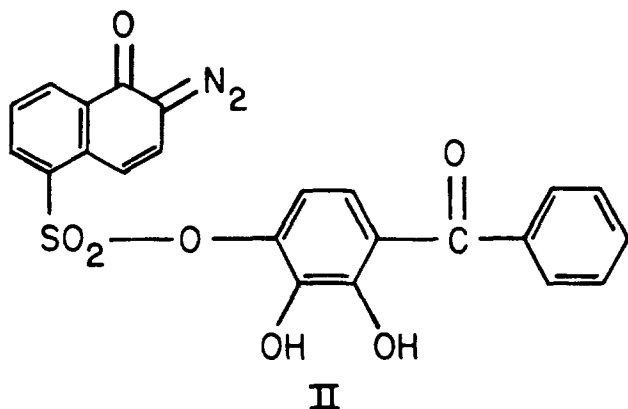
Positive-acting photoresists are composed of three components: a resin, a photoactive compound (dissolution inhibitor), and a solvent system. All positive photoresists utilize the same basic photochemical mechanism, but they may be split into two families on the basis of the resin systems employed. The Shipley and Hunt resist formulations employ low molecular weight novolac resins (I) of this general formula



A novolac resin (in connection with nomenclature, the

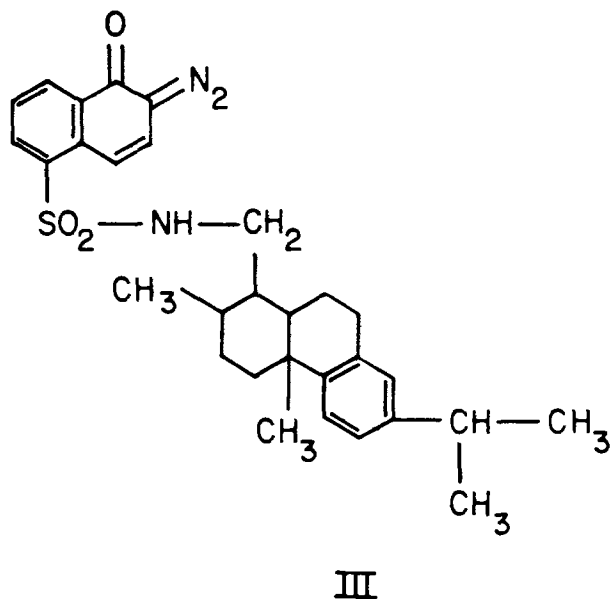
term novolak is sometimes used; following more popular usage and the recommendations of the "Encyclopedia of Polymer Science and Technology," (7) we use the term novolac) is an acid-catalyzed condensation product of a phenol and an aldehyde (usually formaldehyde). The resins have number average molecular weights in the range 600-2000 and are soluble in organic solvents and basic aqueous solutions. The properties of a novolac depend on the structure of the phenols and/or aldehydes used as well as the molecular weight and degree of branching (7, 8).

These resist formulations employ substituted naphthoquinone diazides (II) as the photosensitive dissolution inhibitor



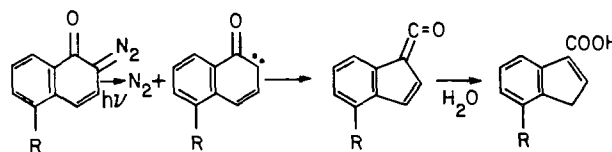
the solvents are mixtures of cellosolve acetate, xylene, and n-butyl acetate (9).

The GAF positive resists (10) utilize a terpolymer of ethyl acrylate, styrene, and methacrylic acid in the approximate ratio 10:5:2 as the resin. Their photoactive component is also a substituted naphthoquinone diazide (III)



The photoactive component:resin ratio is approximately 1:1 and the solvent system is a mixture of xylene and methyl ethyl ketone (9). This particular system will not be discussed further since the dry etch resistance of these resins is inferior to that of novolac-type resins.

The positive working photoresist systems become soluble in aqueous alkaline developers after exposure to u.v. light. This change in solubility depends on the photochemical decomposition of the diazide followed by rearrangement and hydrolysis



There is a synergistic solubility effect between the decomposed diazide and the novolac since the solubility of an exposed resist is greater than that of the pure novolac (11). This is an important point of comparison to the new electron resist and is discussed later.

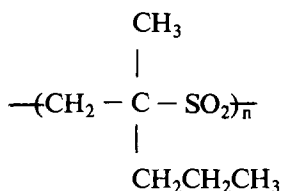
The resistance of these resists to dry etching processes is due to the excellent radiation and thermal stability of the novolac resin. The diazide dissolution inhibitor probably has no effect or even a detrimental effect on resistance to dry etching.

Electron Resist Considerations

It has been shown by several workers that positive photoresists can also be exposed by an electron beam (12, 13). The sensitivity is reported to be $\sim 100 \mu\text{C cm}^{-2}$ at 20 kV. Resolution and processing characteristics are excellent. The sensitivity is low compared with other resists such as PBS and is attributed to the fact that the resist contains 20-30% of the low molecular weight quinone diazide dissolution inhibitor which must be largely decomposed in order to achieve complete differential solubility. The high percentage of functional groups necessitates a large number of photon (electron) interactions per unit volume.

The sensitivity of these systems is more than an order of magnitude too low for direct wafer exposure. In order to enhance the sensitivity, it would be necessary to incorporate some chemical amplification into the dissolution inhibitor decomposition. An alternative and somewhat novel approach would be to use a polymeric dissolution inhibitor which undergoes spontaneous depolymerization (unzipping) during irradiation (14). This can occur when a polymer exists above its ceiling temperature T_c , the latter being the highest temperature at which polymerization is possible for the prevailing conditions of monomer concentration and pressure. Above T_c the polymer is thermodynamically unstable but kinetically stable. Radiation-induced cleavage of a single bond in the main chain results in the production of propagating-type radicals with concomitant extensive depolymerization along the polymer chain. The volatile monomers produced by depolymerization evaporate from the film, a process we have called vapor development (15). A dissolution inhibitor of this type would thus be vaporized, i.e., removed, resulting in an increase in solubility of the remaining film. The polymeric dissolution inhibitor should have the following properties: (i) phase compatibility with the novolac to allow uniform film formation, (ii) kinetic stability (as opposed to thermodynamic stability) at normal ambient conditions both in solution and in bulk, (iii) rapid rate of depolymerization during irradiation at room temperature resulting in adequate electron sensitivity ($< 10 \mu\text{C cm}^{-2}$ at 20 kV), and (iv) dissolution inhibition of novolacs with concentrations of less than 30 weight percent (w/o).

Certain poly(olefin sulfones) are known to meet the above requirements. Factors that affect the rate of depolymerization are dose rate, temperature, olefin structure, molecular weight, and molecular weight distribution with the best combination of properties being shown by poly(2-methyl-1-pentene sulfone) (IV). This material has been extensively studied by Bowden and Thompson (16-18). These polymers do not absorb above 2000Å and can be handled without special care



IV

The use of a degrading polymer as a dissolution inhibitor represents a clear difference between this resist system and positive photoresist systems. The dissolution inhibitor in the photoresist is converted to a carboxylic acid whereas the polysulfone dissolution inhibitor in the resist described here is removed. There is no synergistic solubility effect with the polysulfone/novolac system.

The physical and chemical properties of the novolac are also important to resist performance. Not only must the solubility be within a certain range, but also the thermal and radiation stability and the adhesion must be optimum since the novolac will determine final resist performance. The desired properties are summarized as follows: (i) phase compatibility with the polysulfone to allow uniform film formation, (ii) solubility in aqueous alkaline solutions at pH 9-13, (iii) thermal and radiation stability sufficient for dry etching techniques and process bakes, and (iv) adhesion to film substrates used in device and mask fabrication.

Experimental

Novolac preparation.—An experimental novolac¹ (N64C) was evaluated as the base polymer. The polymer was prepared by an acid catalyzed condensation of substituted phenols with formaldehyde (7, 8).

PMPS preparation.—The dissolution inhibitor used in this work was poly(2-methyl-1-pentene sulfone) PMPS. This is an alternating copolymer of sulfur dioxide and 2-methyl-1-pentene and was prepared by free radical polymerization in excess SO₂ using *t*-butyl hydroperoxide as the initiator. The procedure has been reported elsewhere (15). The polymer is quite stable (up to ~130°C) (18) as the ends are "capped" (protected from degradation) by initiator fragments and/or fragments resulting from transfer reactions.

Resist preparation.—Resist solutions were prepared by dissolving the novolac with PMPS in a solution of methyl cellosolve acetate (80%) and cyclohexanone (20%). The solutions were then filtered several times through a 0.2 μm Teflon filter.

Spin coating.—Films were spin-coated using a Headway EC-101 spinner equipped with a 15 in. bowl. The novolac spun good uniform films from methyl cellosolve acetate. Difficulties were sometimes encountered, however, in spinning uniform films from resist solutions containing PMPS. First, phase separation tended to occur with some novolacs in films spun from pure methoxyethyl acetate. This problem was eliminated by the addition of 10-20% cyclohexanone to the resist solution. Second, the excess liquid which is spun off the substrate during spin coating had a tendency to form fibers (cotton candy) that deposited on the wafer resulting in poor quality films. This problem was reduced by covering the sample with a large beaker during the first 10-20 sec of spinning, then removing the beaker for the final 50 sec drying period. This problem could also have been eliminated by using a different exhaust configuration on the spinner.

¹ The novolac was prepared by Polychrome Corporation to Bell Laboratories specifications.

Baking.—The resist and novolac films were prebaked either in vacuum or a forced air oven in a conventional manner.

Developing.—The developer used in this study was Shipley AZ developer. This is an aqueous alkaline solution with a pH of 12.9. Temperature has a strong influence on dissolution rate and was controlled at 21° ± 0.1°C. Developing was carried out by immersion in a bath without agitation. Samples were removed after a given time, rinsed with deionized water, and dried. Developer strength was varied by dilution with distilled water, the proper strength being that which did not thin or attack the unirradiated film.

Exposure.—Electron beam exposure was carried out using either a modified Cambridge Mark II scanning electron microscope or EBES-I. Relevant exposure conditions are given in the discussion.

Plasma etching.—Films spun from a resist solution containing a weight ratio of PMPS to novolac of 1:10 (9% PMPS) were evaluated as plasma etching masks for SiO₂, polysilicon, and aluminum. The resist thickness removed during plasma etching was measured with a Dectack.

Image evaluation.—The quality of images in both resist patterns and etched patterns were evaluated with an ETEC Autoscan scanning electron microscope.

Results and Discussion

Solubility characteristics of the novolac resin.—Positive resist action depends on a differential solubility between exposed and unexposed regions. The electron resist principle described in this paper requires that the dissolution inhibitor be removed by irradiation; hence, solubility of the irradiated film cannot be greater than that of the pure novolac. Accordingly, it is important to determine the solubility rate of the pure novolac.

The rate of dissolution of a novolac resin in aqueous alkaline solution is dependent on molecular structure and molecular weight of the novolac, base strength (pH), dissolution temperature, and prebake temperature and conditions. Some representative dissolution curves for the particular novolac studied are shown in Fig. 1. Initially we chose a developing temperature of 21° ± 0.1°C and a prebake treatment consisting of 2 hr in an air oven at 120°C. It was observed, however, that the dissolution rate at constant pH decreased with increasing prebake time (Fig. 2) until ultimately the film became totally insoluble, even in organic solvents. The infrared spectrum of a film prior to baking is shown in Fig. 3 (spectrum a) together with the spectrum of the same film after 24 hr at 120°C in air (spectrum b). The infrared spectra of another film which had been baked at 120°C in vacuum for (a) 2.5 hr and (b) 24 hr are shown in Fig. 4. Whereas there is no difference between the spectra before and after heating in vacuum, there is a significant change in the case of the film heated in air. A carbonyl band appears at 1650 cm⁻¹ whose intensity increases with time indicating oxidative degradation. This process appears to give rise to cross-linking so that eventually the film becomes insoluble. The absence of spectral changes for the film heated in vacuum suggests that the dissolution rate should be unaffected. Figure 5 shows that the dissolution rate for films baked 1 hr and 4 hr in vacuum is identical. The slight induction period for the sample prebaked for 4 hr may be due to a small amount of surface degradation resulting from trace oxygen, or removal of unreacted monomer from the film.

Solubility characteristics of novolac/PMPS films.—Not all novolacs appeared to spin uniform films with PMPS. Qualitative observations of the cosmetic ap-

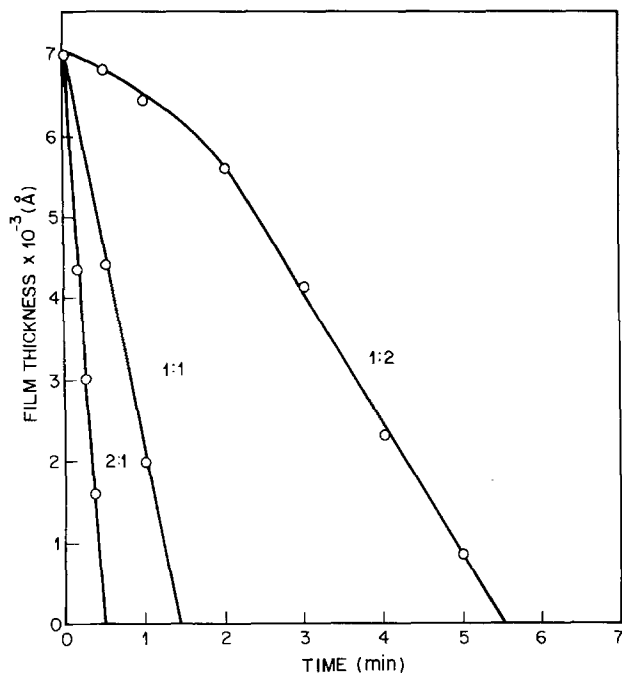


Fig. 1. Effect of developer strength on the rate of dissolution of N64C. The ratio of AZ developer to H₂O in each developing solution is shown in the diagram.

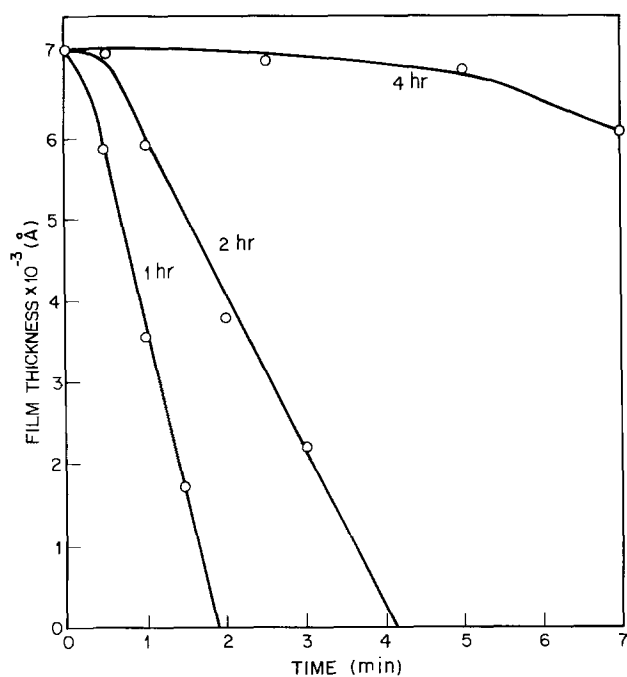


Fig. 2. Effect of varying prebaking time in air on the dissolution rate of N64C. The developer was 1 part AZ: 1 part H₂O.

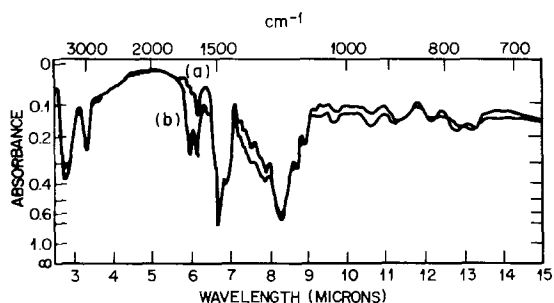


Fig. 3. Infrared spectrum of N64C baked in air at 120°C for (a) 0 hr (b) 24 hr.

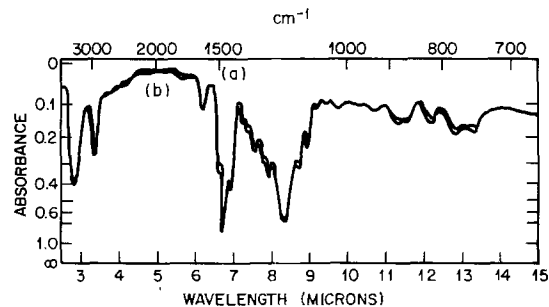


Fig. 4. Infrared spectrum of N64C baked in vacuum at 120°C for (a) 2.5 hr and (b) 24 hr.

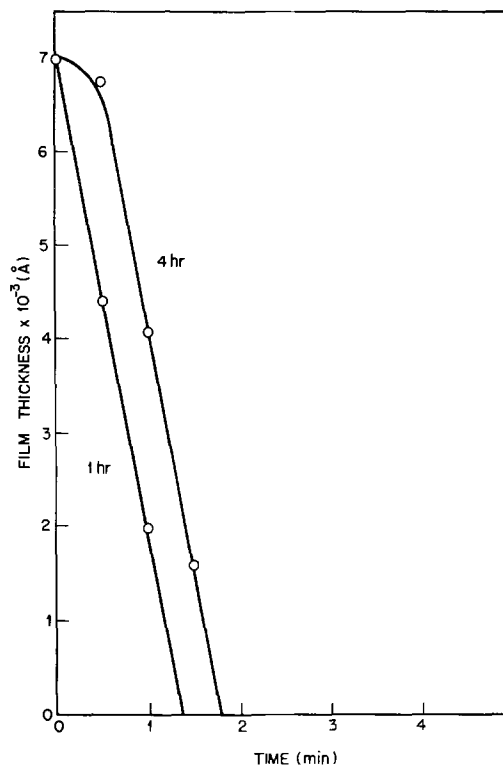


Fig. 5. Dissolution rate for novolac films baked 1 and 4 hr at 120°C in vacuum. The developer was 1 part AZ:1 part H₂O.

pearance of spun films indicated that novolacs based on phenol-formaldehyde are incompatible with PMPS (Fig. 6A). Novolacs based on substituted phenols usually appear to be compatible with PMPS (Fig. 6C) although in some circumstances, depending on the particular substituent and spinning solvent, partial phase separation may be observed (Fig. 6B).

The novolac used in the present study gave uniform, single phase films with PMPS. The presence of PMPS in the novolac film greatly increased the pH required to affect the film. Unlike the films containing quinone diazide dissolution inhibitors which do dissolve at measurable rates in high pH solutions, novolac/polysulfone (NPS) films often do not dissolve uniformly, but rather become extremely pitted (Fig. 7). However, this type of surface attack only occurs at a pH greater than that required for development of the resist so that within the pH range of interest, PMPS does totally inhibit dissolution. The actual pH such films can withstand before pitting depends on the amount of PMPS in the film. Table I shows the maximum pH which the film will withstand for 5 min without pitting as a function of PMPS content.

Exposure characteristics of pure PMPS.—The exposure characteristics of pure PMPS films have been extensively studied (16, 17). A typical plot of the frac-

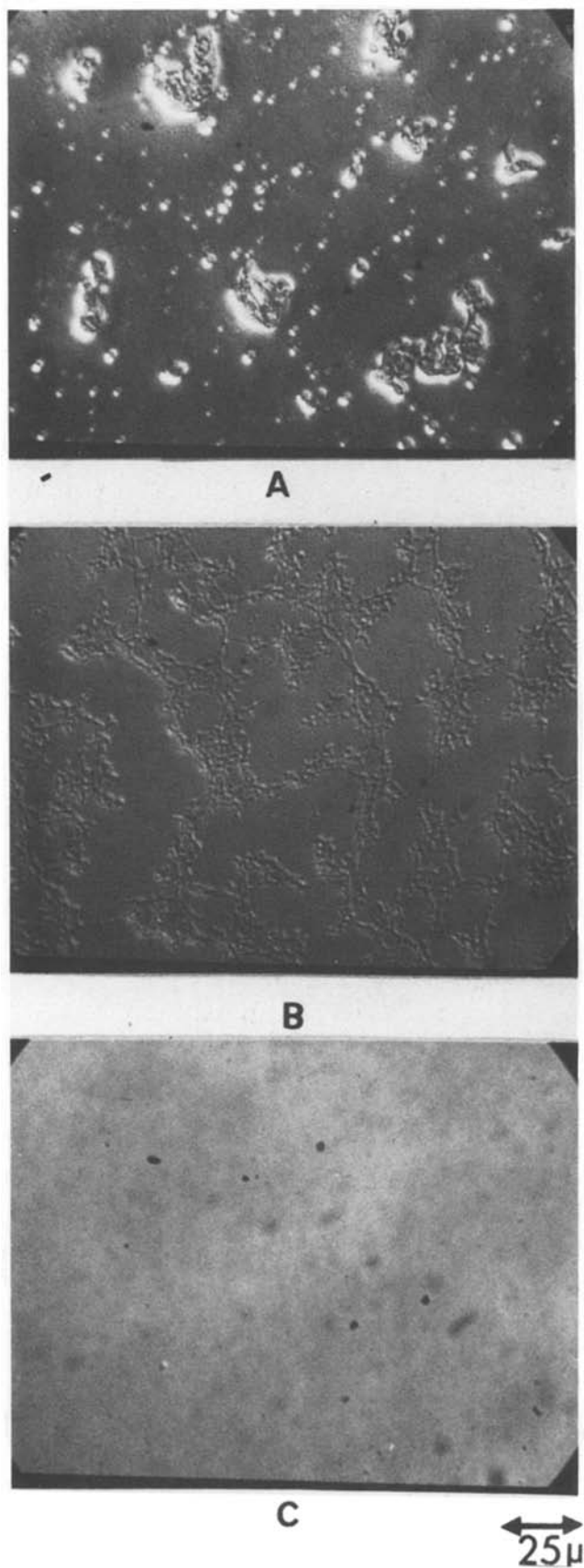


Fig. 6. Optical micrographs ($500\times$) showing the effect of novolac structure on the phase structure of NPR films containing 9 w/o PMPS. A. Phenol-formaldehyde novolac. B. A cresol-formaldehyde novolac supplied by Philip A. Hunt Company. C. N64C.

tion of film remaining against dose is shown in Fig. 8. The exposure was carried out at 20 kV. The film removal rate is an exponential function of dose. Clearly, if it were required to remove all the PMPS, i.e., re-

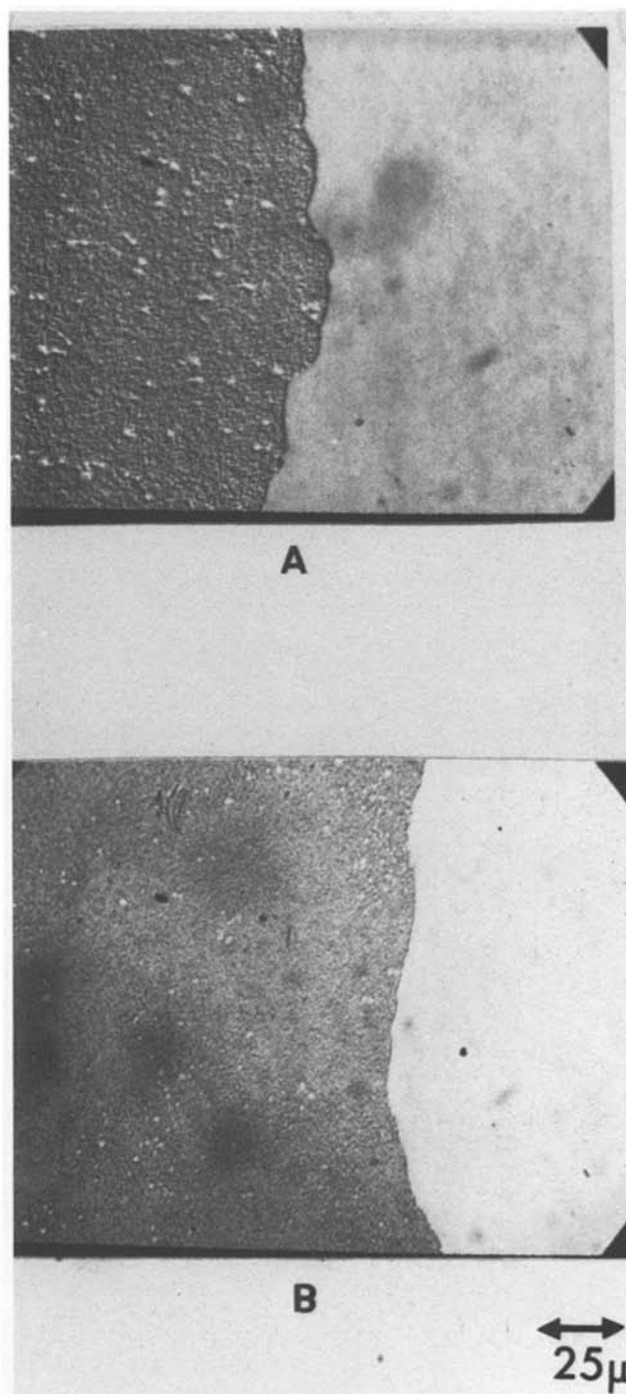


Fig. 7. Optical micrographs ($500\times$) showing pitting of NPR films caused by too strong a developer solution. A. Interference contrast micrograph. B. Normal reflection image.

duce the residual film thickness to zero, a very large dose would be required. It is also apparent from Fig. 8 that the contrast, as determined from the slope of the line, is extremely low, being only 0.3. One might be led to conclude, *a priori*, that the low contrast of the

Table I. Developer resistance (pH) as a function of the weight ratio of PMPS to novolac

| PMPS:novolac (wt ratio) | Developer concentration* | pH |
|----------------------------|-------------------------------------|-------|
| 0.5:10 | 1 part AZ: 2 parts H ₂ O | 12.58 |
| 1:10 | 1 part AZ: 1 part H ₂ O | 12.70 |
| 2:10 | AZ | 12.93 |

* Denotes developer concentration which the film will withstand for at least 5 min without pitting at $21^\circ \pm 0.1^\circ\text{C}$.

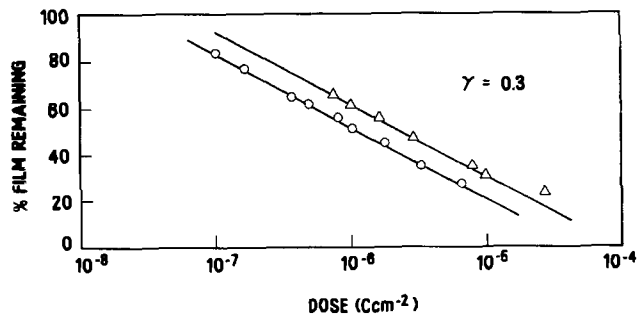


Fig. 8. Rate of film removal as a function of electron dose (20 kV) for PMPS. (Δ) $M_w = 6 \times 10^5$ ($M_w/M_n > 10$), (\circ) $M_w = 1.4 \times 10^6$ ($M_w/M_n = 3.8$).

vapor development process would result in poor resolution. However, the contrast of importance is that obtained on development of the resist and as we shall see, it is significantly higher. Also shown in Fig. 8 is the vapor development curve for a PMPS sample of lower molecular weight. As expected, the dose to remove a given fraction of the film is higher (lower sensitivity), but the contrast is unchanged.

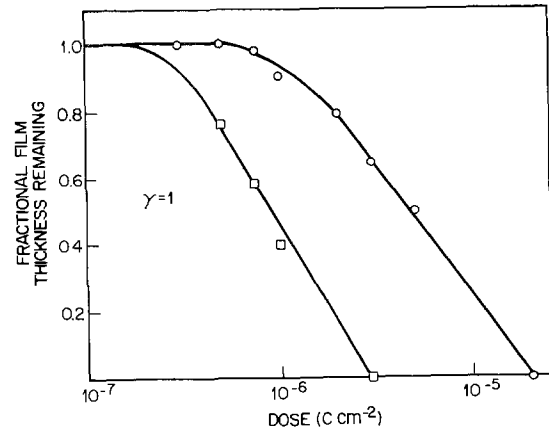


Fig. 9. Developed NPR resist film thickness as a function of electron dose at 20 kV. (\circ) NPR film as exposed. (\square) NPR film exposed and baked at 120°C for 15 min prior to developing.

Exposure characteristics of NPR films.—The exposure characteristics of NPR films were determined by exposing known areas to varying electron doses at 20 kV followed by development in a standard develop-

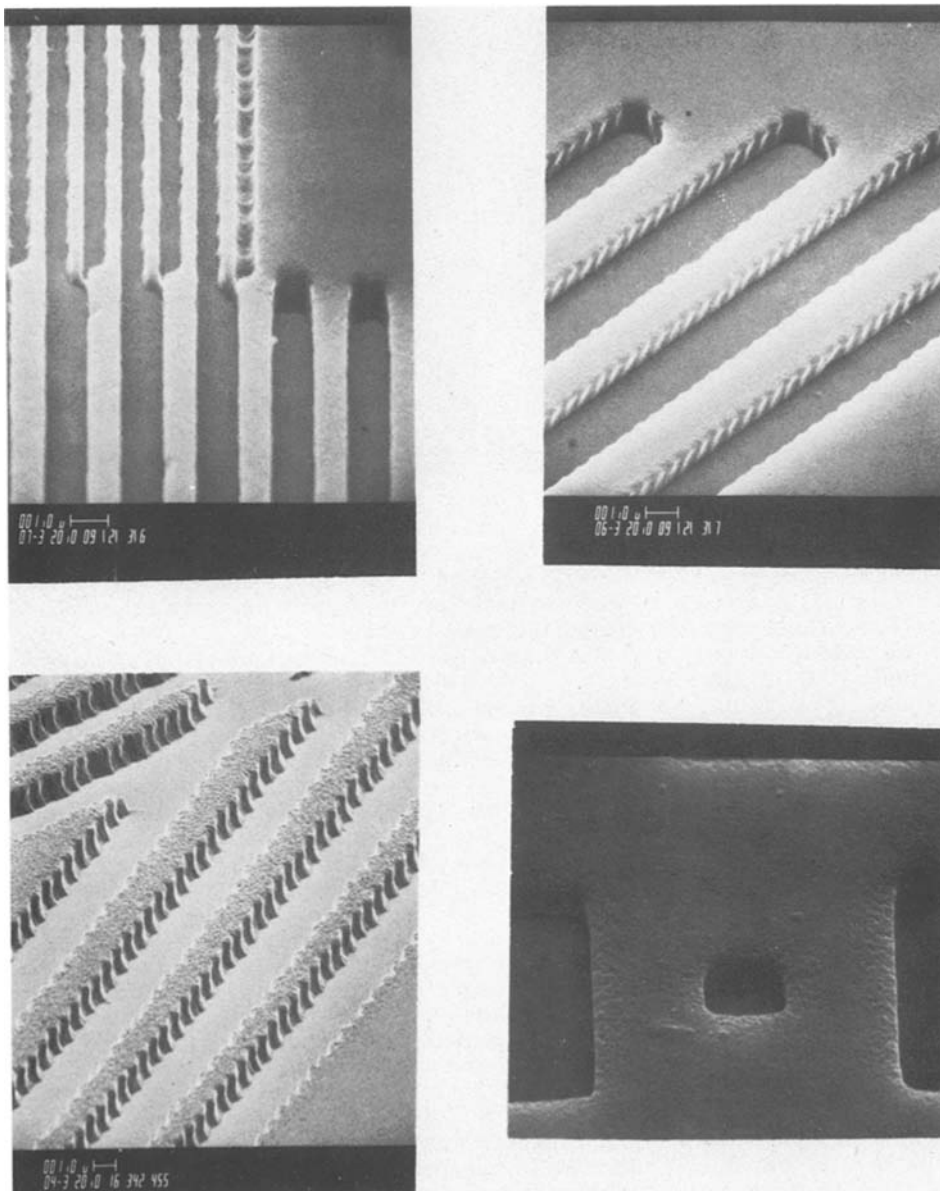


Fig. 10. SEM micrograph of developed pattern in NPR resist. Exposed at 10 kV on EBES I with a dose of $3 \mu\text{C cm}^{-2}$.

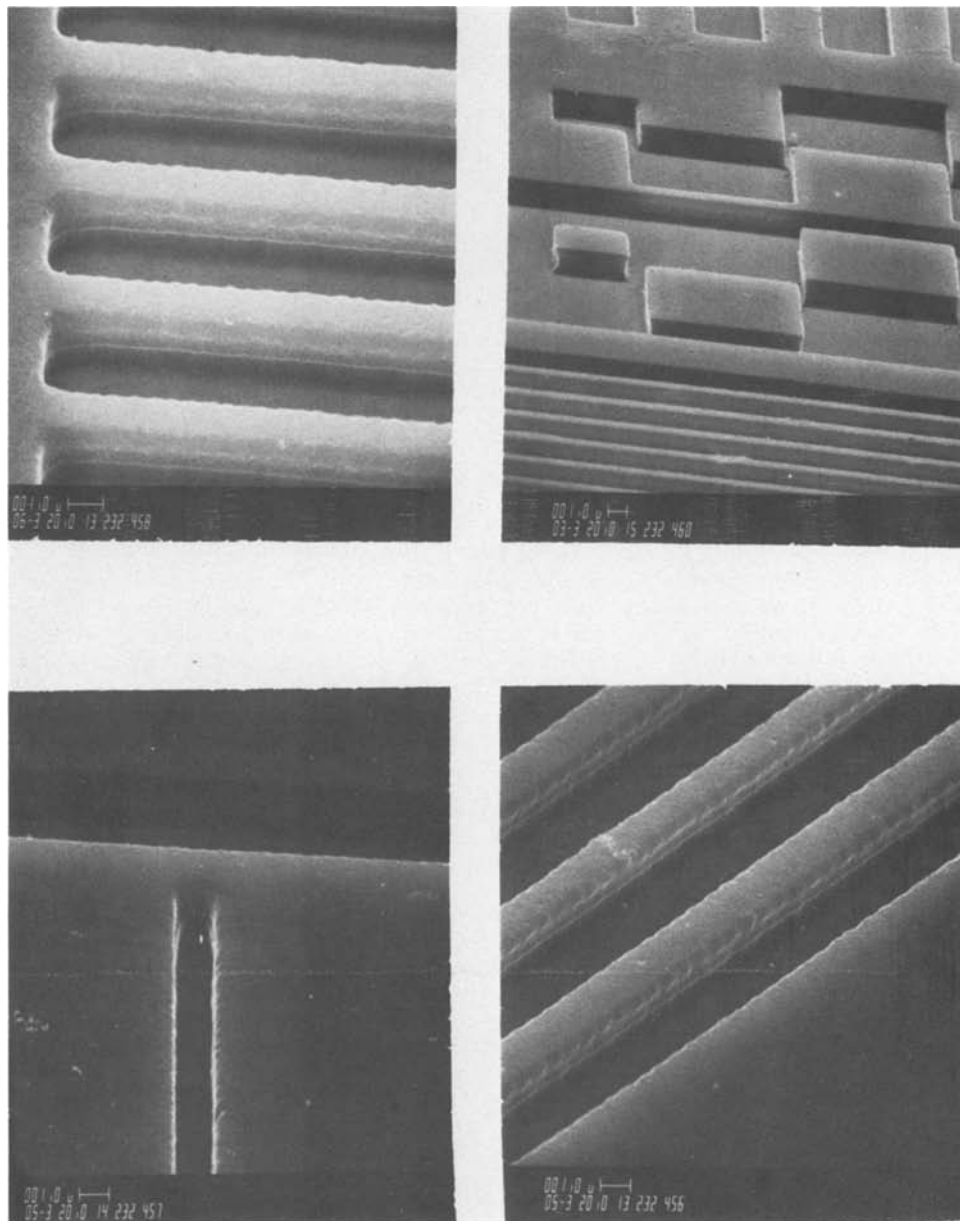


Fig. 11. SEM micrograph of plasma-etched SiO_2 ($0.5 \mu\text{m}$) patterns without the resist removed.

ing solution of sufficient strength to develop the pattern in a reasonable period of time (≤ 5 min). A typical contrast curve generated for the resist containing 9 w/o PMPS is shown in Fig. 9 from which a contrast of 1.0 is obtained. The sensitivity is $16 \mu\text{C cm}^{-2}$ at 20 kV.

The sensitivity can be increased to $3 \mu\text{C cm}^{-2}$ by subjecting the irradiated resist to a postexposure bake at 120°C for 15 min prior to development as shown in Fig. 9. We have attributed this result to additional depolymerization during postexposure baking. Under normal irradiation conditions at room temperature, active radicals becomes trapped thus halting depolymerization. By subjecting the sample to elevated temperatures following exposure, the radicals acquire sufficient energy to escape from the trap giving rise to additional depolymerization, *i.e.*, material loss. Studies on the nature of the trapped radicals are in progress.

Infrared studies (19) have shown that the depolymerization kinetics of PMPS in solid solution with novolac are the same as in a film of pure PMPS. Thus the development dose of $3 \mu\text{m cm}^{-2}$ at 20 kV reflects a loss of about 60% of the PMPS leaving about 3.6 w/o PMPS in the NPR film. This residue still has an inhibiting effect on the dissolution rate so that the developer

strength required to develop the image is greater than would be necessary to dissolve the pure novolac in a comparable period of time.

The contrast for the resist system of 1.0 is improved by a factor of three over that of the vapor development process. This higher contrast presumably reflects the ability of the developer to distinguish small differences in the amount of PMPS remaining in the film.

We speculate that the increase in solubility results directly from the removal of the dissolution inhibitor. Admittedly the depolymerization process produces large amounts of gaseous by-product with subsequent void formation which in turn would enhance the solubility rate ratio between exposed and unexposed film (20, 21). We have noted however that postexposure baking above the glass transition temperature of the novolac results in an increase in sensitivity. Under these conditions one would expect the voids to collapse and this is indeed observed in practice as a surface relief caused by reduction in the film thickness in the exposed areas during postexposure baking. Since void collapse would, on the above premise, result in a decrease in sensitivity it seems reasonable then to attribute the increase in solubility solely to the removal

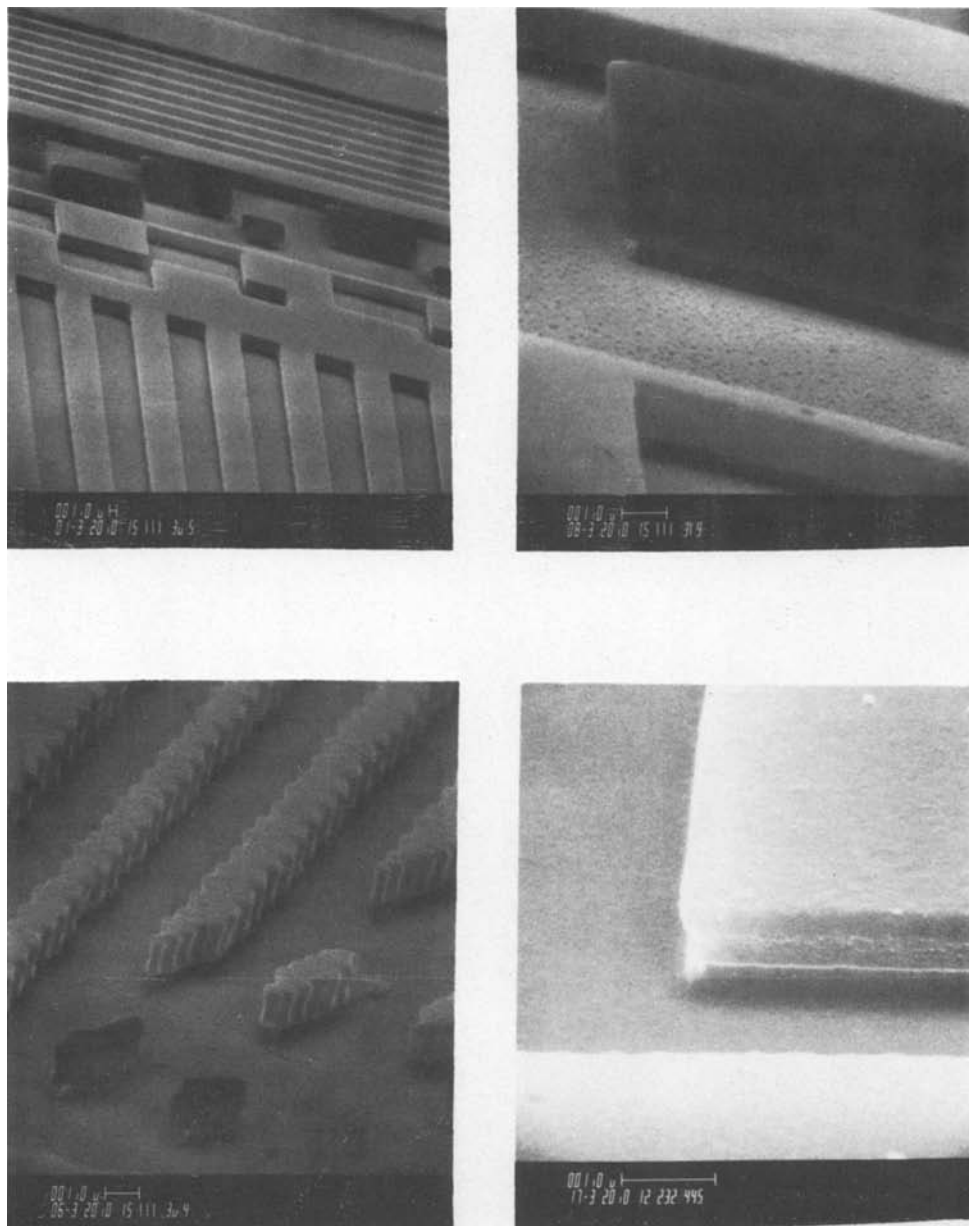


Fig. 12. SEM micrograph of plasma etched polysilicon ($0.75\ \mu\text{m}$) patterns without the resist removed.

of the PMPS. Further evidence is needed to corroborate this point.

Image quality and resolution.—A number of factors such as material and processing parameters determine the reproducibility of image quality obtained. Not all of these are completely understood and further work is required to elucidate these effects. Nevertheless we have been able to obtain patterns with excellent image quality. There is no pattern distortion due to swelling. Line width control is, however, extremely susceptible to overdevelopment and/or overexposure and these difficulties are further compounded by poor adhesion. Nevertheless, with careful development, we have been able to develop $0.5\ \mu\text{m}$ lines and spaces in $0.8\ \mu\text{m}$ resist. The high resolution of this resist system is also reflected in the EBES address structure which is resolved on all oblique lines. Some micrographs showing the pattern quality and resolution are shown in Fig. 10.

Plasma etching resistance.—Test patterns were written on a variety of resist-coated substrates with EBES-I. The substrates and the various plasma etching conditions for those substrates are listed in Table II. The resist withstood all plasma environments, even the Al etch which is considered to be the most reactive of all. Photomicrographs of test patterns plasma etched in

SiO_2 , poly-Si, and Al are shown in Fig. 11, 12, and 13, respectively.

Conclusions

1. We have described a new resist system in which differential solubility appears due to the removal of a polymeric dissolution inhibitor.
2. The sensitivity of this resist system is approximately $3\ \mu\text{C cm}^{-2}$ at 20 kV with a contrast of 1.0.
3. Submicron features have been delineated in $1\ \mu\text{m}$ thick resist films.
4. The resist system withstands Al, poly-Si, SiO_2 , p-SiO₂, and Si_xN_y plasma etching environments and

Table II. Substrates and plasma etching conditions used to evaluate etch resistance of NPS films

| Substrate | SiO_2 | p-glass | Poly-Si | Al |
|---|--|--|------------------------|--|
| Plasma | C_2F_6 (60%) CHF_3 (40%) | C_2F_6 (60%) CHF_3 (40%) | CF_3Cl | CCl_4 , BCl_3 , He |
| Substrate etch rate ($\text{\AA}/\text{min}$) | 600-800 | 1200 | 1000 | ~1000 |
| Resist etch rate ($\text{\AA}/\text{min}$) | ~0 | 100 | ~100 | ~300 |

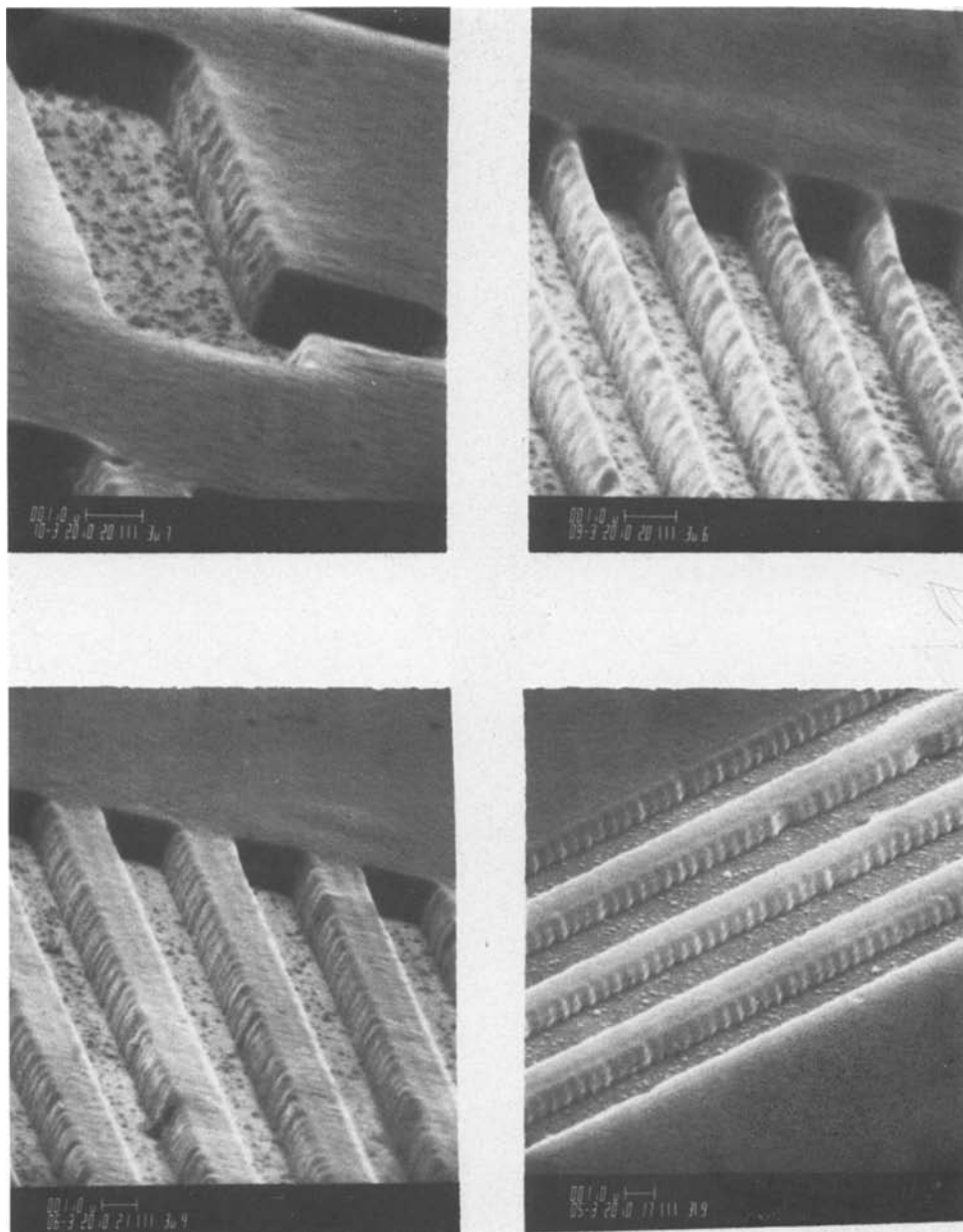


Fig. 13. SEM micrographs of plasma etched Al ($1.0\ \mu\text{m}$) patterns without the resist removed.

has been used to delineate submicron features in the above substrates.

Acknowledgments

The authors gratefully acknowledge C. J. Mogab and D. Fraser for plasma etching work and R. F. Pease and R. D. Heidenreich for many helpful discussions. L. E. Stillwagon is acknowledged for molecular weight determinations.

Manuscript submitted Aug. 12, 1980; revised manuscript received Jan 10, 1981.

Any discussion of this paper will appear in a Discussion Section to be published in the December 1981 JOURNAL. All discussions for the December 1981 Discussion Section should be submitted by Aug. 1, 1981.

Publication costs of this article were assisted by Bell Laboratories.

REFERENCES

- H. Y. Ku and L. C. Scala, *This Journal*, **116**, 980 (1969).
- L. F. Thompson and M. J. Bowden, *ibid.*, **120**, 1722 (1973).
- W. S. DeForest, in "Photoresist Materials and Practices," McGraw-Hill Book Co., New York (1975).
- J. Pacansky and J. R. Lyster, *IBM J. Res. Dev.*, **23**, 42 (1979).
- M. J. Bowden, *CRC Crit. Rev. Solid State Sci.*, **8**, 223 (1979).
- M. Hatzakis, *This Journal*, **116**, 1033 (1969).
- W. A. Kentzen, in "Encyclopedia of Polymer Science and Technology," Vol. 10, N. M. Bikales, Editor, pp. 1-73 (1969).
- S. R. Fahrenholtz, M. R. Goldrink, M. Y. Hellman, D. T. Long, and R. C. Pitetti, *Am. Chem. Soc. Div. Org. Coat. Plast. Chem. Prepr.*, **35**, 306 (1975).
- L. F. Thompson and R. E. Kerwin, *Ann. Rev. Mater. Sci.*, **6**, 267 (1976).
- A. S. Deutsch and F. J. Loprest, U.S. Pat. 3,637,384 (1972).
- J. B. Lounsbury and M. A. Narasimham, *Am. Chem. Soc. Div. Org. Coat. Plast. Chem. Prepr.*, **37**, 125 (1977).
- M. Hatzakis and J. M. Shaw, Paper presented at Microcircuit Engineering '78 Cambridge, U.K., April 11-13, 1978.
- R. F. W. Pease, L. F. Thompson, J. P. Ballantyne, C. J. Mogab, and J. Frackoviak, Paper presented at Microcircuit Engineering '78 Cambridge, U.K., April 11-13, 1978.
- L. F. Thompson, M. J. Bowden, E. M. Doerries, and S. R. Fahrenholtz, Paper 000 presented at The Electrochemical Society Meeting, Seattle, Washington, May 21-26, 1978.
- M. J. Bowden and L. F. Thompson, *J. Appl. Polym.*

- Sci., **17**, 3211 (1973).
16. M. J. Bowden and L. F. Thompson, *Polymer Eng. Sci.*, **14**, 525 (1974).
17. M. J. Bowden and L. F. Thompson, *ibid.*, **17**, 269 (1977).
18. M. J. Bowden, *J. Polymer Sci., Polymer Chem. Edition*, **12**, 499 (1974).
19. M. J. Bowden, D. Allara, and J. Frackoviak, To be published.
20. A. C. Ouano, *Polymer Eng. Sci.*, **18**, 306 (1978).
21. L. E. Stillwagon, *Am. Chem. Soc. Div. Org. Coat. Plast. Chem.*, **43**, 236 (1980).

Electrical Properties and Stability of Supersaturated Phosphorus-Doped Silicon Layers

M. Finetti, P. Negrini, S. Solmi, and D. Nobili

CNR-Istituto LAMEL, Via Castagnoli, 1, 40126 Bologna, Italy

ABSTRACT

Supersaturated solutions of phosphorus in silicon were obtained by ion implantation and pulsed ruby laser annealing. The dependence of electron mobility and electrical resistivity on carrier density was accurately determined by Hall effect and resistivity measurements. Maximum dopant concentration was 5×10^{21} atom/cm³, corresponding to a resistivity of $110 \mu\Omega \cdot \text{cm}$ and to an electron mobility of $11 \text{ cm}^2/\text{V} \cdot \text{sec}$. The stability of these alloys was analyzed by isochronal and isothermal annealing. In the more heavily doped samples a remarkable deactivation of the dopant was verified also for thermal treatments of 1 hr at 300°C. TEM examinations showed a large amount of precipitates with density and size depending on supersaturation. Finally it was observed that the electron mobility depends only on the carrier density and is unaffected by the electrically inactive phosphorus, even when present at very high concentrations.

Many recent papers have indicated laser irradiation as an interesting technique for the recovery of radiation damage in implanted layers (1-8). It was also observed by some authors (6-8) that dopant concentrations in excess of the solid solubility values can be dissolved in silicon by these techniques. The possibility of obtaining higher conductivities, both in monocrystalline silicon slices and in polysilicon films, is of great importance in microelectronics in order to further reduce device geometries as required by the very large scale integration.

In this paper supersaturated silicon layers obtained by Q-switched ruby laser annealing after heavy phosphorus implantation were accurately characterized and the dependence of resistivity and electron mobility on carrier concentration was determined. In addition, the stability of these metastable alloys was studied by isochronal and isothermal annealing; these experiments provided information on the precipitation phenomena of excess dopant.

Experimental

For our experiment we used p-type, <100> oriented, CZ pulled, dislocation-free silicon slices of nominally $1 \Omega \cdot \text{cm}$ resistivity. Wafers were about 300 μm thick and mirror finished on one side.

The crystals were phosphorus implanted in a random direction with an energy of 100 keV and at doses ranging between 2×10^{15} and 5×10^{16} atoms/cm².

Before annealing a thin silicon layer, about 400Å thick, was removed by anodic oxidation to eliminate the contamination of carbon atoms introduced by the implantation process.

Laser annealing was carried out by a 20 nsec single pulse delivered by a Q-switched ruby oscillator ($\lambda = 0.69 \mu\text{m}$) operating in multimode regime. An optical guide was used to yield a uniform 14 mm diam light spot with an energy density of 1.8 J/cm^2 .

Key words: phosphorus implantation, laser annealing, electron mobility in silicon, stability of supersaturated layers, phosphorus precipitation.

For the determination of the electrical profile, the van der Pauw geometry was etched on the specimen's surface by a photolithographic process, or alternatively by using an ultrasonic drill. Sheet resistance and Hall effect measurements were performed after anodic oxidation in steps of 200Å and oxide stripping.

The stability of these metastable layers was analyzed by isothermal annealing at 450° and 550°C, from 15 min to 1500 hr, and by 1 hr isochronal heating in steps of 25° from 300° to 750°C. The processes were carried out in an open tube furnace in nitrogen atmosphere.

After each treatment resistivity and Hall effect measurements were performed to determine the total amount of carrier concentration and the average mobility.

The recovery of the radiation damage and the effects of the successive heat-treatments were checked by transmission electron microscopy (TEM) observations and Rutherford backscattering (RBS) analysis.

Results and Discussion

Electrical characterization of the supersaturated layers.—In Fig. 1 are reported the carrier concentration profiles obtained on samples implanted at 100 keV with doses of about 5, 0.8, and 0.3×10^{16} atoms/cm² and successively laser annealed. In any case the total amount of implanted phosphorus was electrically active. At the highest dose a carrier concentration of about $5 \times 10^{21} \text{ cm}^{-3}$ (corresponding to 10 atomic percent) was obtained, more than one order of magnitude higher than the maximum value of phosphorus solid solubility in silicon (9).

TEM and RBS examinations showed that the above-defined laser annealing completely restored the crystal lattice which was found free of observable defects. This behavior was confirmed also for the most heavily doped specimens.

The dopant was localized in an extremely shallow surface region and the typical high diffusivity tail associated with phosphorus profiles was not present

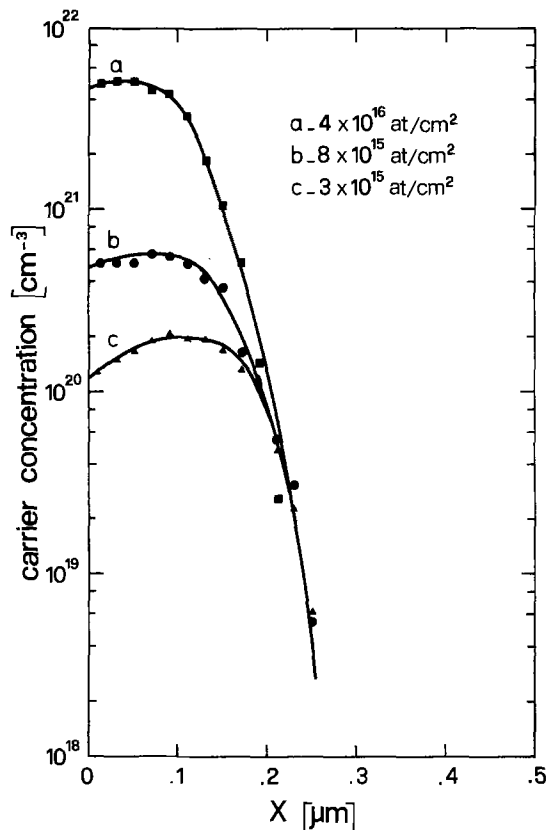


Fig. 1. Carrier concentration profiles of phosphorus-implanted laser annealed samples.

(9-10). The junction depth was lower than $0.3 \mu\text{m}$ and the corresponding sheet resistance was about $8 \Omega/\square$. The quality factor ($q.f. = (\rho_s \cdot x_j)^{-1}$) of this layer is about $0.45 \mu\text{m}^{-1} \cdot \Omega^{-1}$, higher by a factor of four than the one obtainable by the traditional furnace processing.

In Fig. 2 we report the electron mobility *vs.* carrier concentration as determined by resistivity and Hall effect measurements. The experimental points refer not only to the profiles reported in Fig. 1, but also to other implanted doses annealed in the same conditions. The dotted curve represents the behavior followed by thermally diffused samples (11). It stops at about

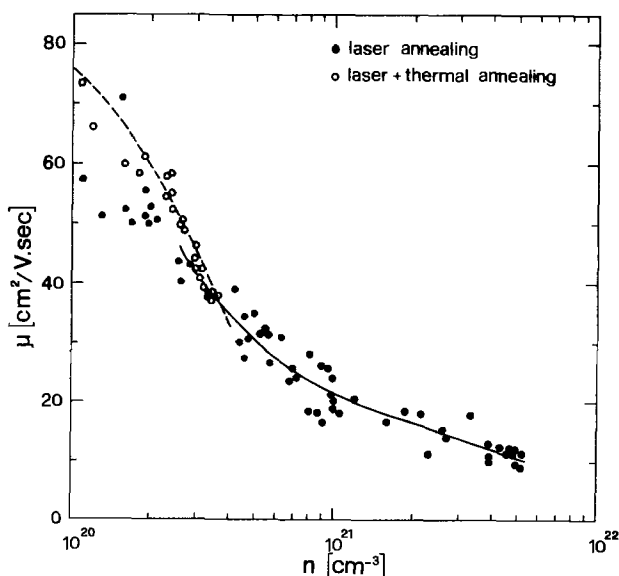


Fig. 2. Electron mobility *vs.* carrier concentration. The dotted curve represents the behavior of mobility in diffused samples (11).

$4 \times 10^{20} \text{ cm}^{-3}$, corresponding to the highest concentration obtainable by the traditional techniques.

The curve of mobility in laser annealed samples joins to the Masetti-Solmi data (11) and decreases with increasing carrier concentration, down to values of $11 \text{ cm}^2/\text{V}\cdot\text{sec}$ corresponding to an electron concentration of $5 \times 10^{21} \text{ cm}^{-3}$.

At carrier densities lower than $3 \times 10^{20} \text{ cm}^{-3}$ the laser annealed samples present mobility values about 10-20% lower than in diffused samples. This effect was attributed to a high concentration of electrically active point defects introduced in the crystal by the laser treatment (12-13). The influence of these defects on mobility is significant only at relatively high μ values ($> 50 \text{ cm}^2/\text{V}\cdot\text{sec}$) and becomes gradually negligible with decreasing mobility. It has been observed that after a thermal treatment at 700°C these defects are completely annealed (12). This behavior is confirmed by our results obtained on supersaturated samples thermally annealed at 850°C for 30 min (open circles in Fig. 2); in this case the mobility values fall on the Masetti-Solmi curve (11).

The data from laser annealed samples, reported in Fig. 3, allow the empirical resistivity *vs.* carrier density curve of n-type silicon to be extended to higher concentrations. By this technique it is possible to obtain resistivities as low as $110 \mu\Omega\cdot\text{cm}$, a factor of three lower than the minimum values presented by thermally predeposited samples and comparable to those characteristic of the transition metal (Mo, W, ...) silicides (14). In this figure we have also shown, for comparison, two experimental curves (dotted lines) of ρ *vs.* n already reported in the literature (9, 15). Irvin data have not been considered here because, as the author himself points out (16), for concentrations in excess of $2 \times 10^{20} \text{ cm}^{-3}$ they are not reliable due to the possible differences between dopant and electron concentrations.

Stability of the supersaturated layers.—These highly supersaturated solutions are far from the equilibrium conditions, therefore their thermal stability, a necessary condition for practical applications, depends on the kinetics of precipitation of the silicon phosphide phase.

The occurrence of precipitation was extensively studied in a companion paper (17). Here we report the results of the observations of the stability as a function of the implanted dose.

Isothermal annealing of four different compositions was performed at 450°C for 1500 hr and at 550°C for 1000 hr. The initial carrier concentration in the top of the profile was 5×10^{21} , 2×10^{21} , 5×10^{20} , and $2 \times$

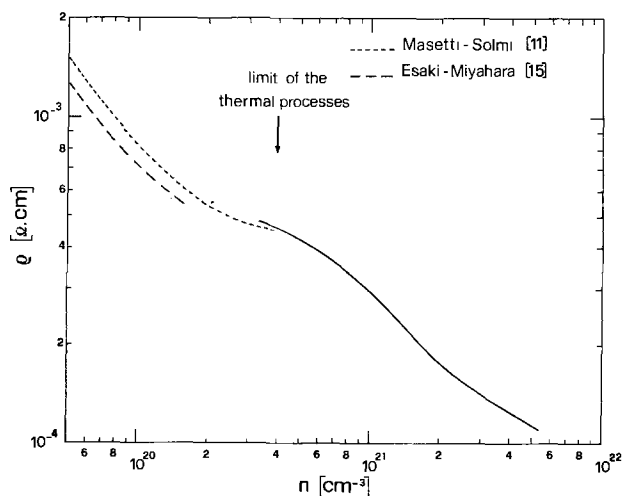


Fig. 3. Resistivity *vs.* carrier concentration in phosphorus-doped silicon.

10^{20} cm^{-3} , respectively. In Tables I and II we report, at increasing annealing times, the phosphorus precipitated fraction f , as defined by

$$f = [C_i - C(t)]/[C_i - C_e]$$

where C_i is the implanted dose, $C(t)$ the time dependent electrically active dose as determined by Hall measurements, and C_e the equilibrium dose.

The calculations of C_e were performed by using phosphorus solubilities of $2.2 \times 10^{19} \text{ atoms} \cdot \text{cm}^{-3}$ at 450°C and $3.8 \times 10^{19} \text{ atoms} \cdot \text{cm}^{-3}$ at 550°C . These data were determined by Ekstrom *et al.* (18) by analysis of the kinetics of P precipitation in $\text{Si}_{10.7}\text{Ge}_{0.3}$ thermoelectric alloys and are significant in our case as silicon and germanium form ideal solutions. Moreover, they are in very good agreement with the solubility values, that we will discuss in a subsequent paper, deduced by the concentration profiles at the end of our isothermal treatments.

Examination of these results puts in evidence the marked dependence of the extent of precipitation on the initial supersaturation; this behavior is foreseen by the models of the precipitation kinetics (18-20). For low concentrations ($2 \times 10^{20} \text{ cm}^{-3}$), comparable to the ones obtained by thermal processes, an appreciable precipitation is observed only after significant annealing times ($t > 100 \text{ hr}$ at 450°C and $t > 1 \text{ hr}$ at 550°C). The extent of the process increases rapidly with supersaturation and at $5 \times 10^{20} \text{ cm}^{-3}$ we obtained a significant precipitation just after 15 min.

TEM observations of the samples showed a very high density of precipitated particles, which is connected to a very high nucleation frequency. Precipitate size decreases with increasing concentration; this is in agreement with the classical model of nucleation (21)

$$I_n = A \exp - B/[RT(\ln i)]^2$$

where I_n is the nucleation frequency, A and B are constants at constant temperature, and i is the supersaturation defined as the ratio of the actual and the equilibrium solute concentration.

In Fig. 4 are reported two examples of TEM micrographs taken on specimens phosphorus implanted with dose of $2 \times 10^{15} \text{ atoms/cm}^2$ (Fig. 4a) and $8 \times 10^{15} \text{ atoms/cm}^2$ (Fig. 4b) after 1500 hr annealing at 450°C .

The less doped sample, which corresponds to an initial concentration of $2 \times 10^{20} \text{ atoms/cm}^3$, presents precipitates of about 200\AA in diameter with a density of about 10^{10} cm^{-2} . Conversely in the more doped specimen (initial concentration $5 \times 10^{20} \text{ atoms/cm}^3$) the

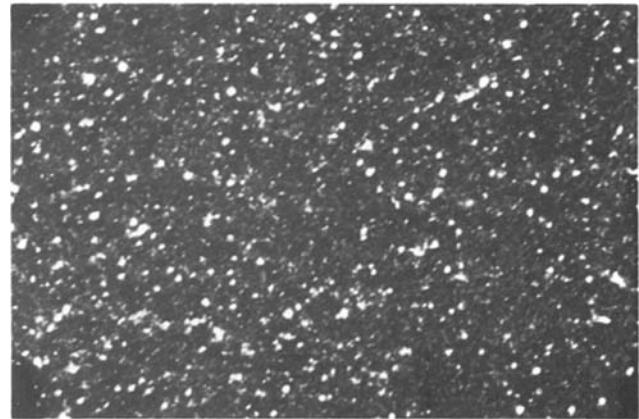
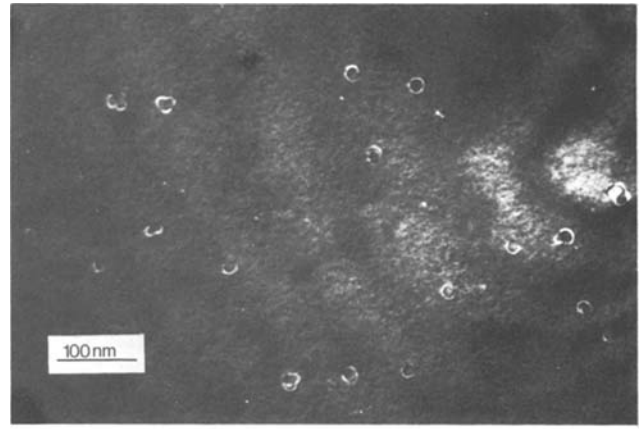


Fig. 4. Weak-beam (g, -g) TEM micrographs of $2 \times 10^{15} \text{ atom/cm}^2$ (a) and $8 \times 10^{15} \text{ atom/cm}^2$ (b) phosphorus-implanted, laser annealed specimens successively treated at 450°C for 1500 hr (g = 220). Magnification $\times 200,000$.

size of the precipitates is smaller ($50\text{-}80\text{\AA}$ in diameter), and their density is higher (10^{12} cm^{-2}). The micrographs were taken in the weak beam geometry in order to have image widths very close to the true particles size. From the density of precipitates (per unit volume), which was obtained by taking into account the geometrical effect of the overlapping (22), and from their average diameters we deduced that the amount of the silicon phosphide phase is consistent with that of the electrically inactive dopant.

Thermal stability as a function of temperature was investigated by isochronal annealing in the range $300^\circ\text{-}750^\circ\text{C}$ in steps of 25°C . Heating time per step was 1 hr. We report in Fig. 5 and 6, respectively, the electrically active dose C and the average mobility μ vs. temperature for three different implanted doses. As expected the stability decreases with increasing supersaturation, in particular a remarkable decrease in C is observed in the most heavily doped specimens where about 40% of the dopant is precipitated after 1 hr at 300°C . The less doped composition is fairly stable and shows a monotonic trend, while those more heavily doped present a minimum active concentration followed by redissolution. The temperature for reverse annealing decreases with increasing initial dopant concentration.

As we discussed in detail (17), this reverse annealing phenomenon is due to the Gibbs-Thomson effect (21). The solubility of the dopant increases with decreasing size of the precipitates; this enhancement is important only for precipitates of very small size. When temperature is raised enough, small particles redissolve and the process takes place at lower temperatures and higher dopant concentrations, the

Table I.

| Isothermal 450°C annealing time (hr) | Precipitated fraction, f (%) | | | |
|---|--|--|--|--|
| | 5×10^{21} (atoms/ cm^3) | 2×10^{21} (atoms/ cm^3) | 5×10^{20} (atoms/ cm^3) | 2×10^{20} (atoms/ cm^3) |
| 0.25 | 82.4 | 45.4 | 28.7 | 6.1 |
| 1 | 86.6 | 54.1 | 40.0 | 6.8 |
| 10 | 92.3 | 69.5 | 55.9 | 6.7 |
| 100 | 95.5 | 80.7 | 71.8 | 12.2 |
| 1500 | 97.2 | 88.9 | 83.7 | 36.5 |

Table II.

| Isothermal 550°C annealing time (hr) | Precipitated fraction, f (%) | | | |
|---|--|--|--|--|
| | 5×10^{21} (atoms/ cm^3) | 2×10^{21} (atoms/ cm^3) | 5×10^{20} (atoms/ cm^3) | 2×10^{20} (atoms/ cm^3) |
| 0.25 | 89.3 | 60.0 | 41.5 | 8.9 |
| 1 | 91.6 | 69.5 | 53.9 | 13.3 |
| 10 | 94.3 | 81.5 | 70.7 | 22.1 |
| 100 | 96.4 | 88.3 | 81.2 | 39.8 |
| 1000 | 98.1 | 94.4 | 89.7 | 92.9 |

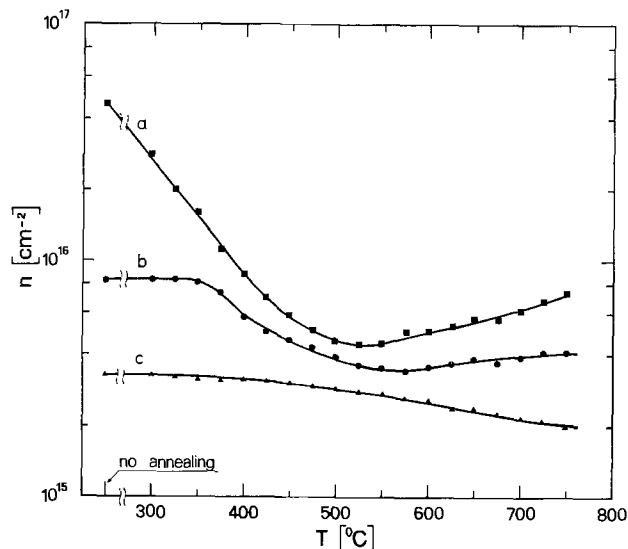


Fig. 5. Electrically active dose vs. 1 hr isochronal annealing temperature for three different implanted doses.

smaller the particle size. This is clearly shown in Fig. 5 where, as it was observed previously, the higher the initial supersaturation the smaller is the particle size.

Finally we point out that this large density of small particles does not influence the carrier mobility. In fact, the average mobility data (Fig. 6) show a behavior depending essentially on the electrically active concentration and lie on the same curve when plotted vs. C .

This phenomenon is demonstrated clearly by measurements performed on specimens implanted at doses of 4×10^{16} atoms/cm² (profile a in Fig. 1), laser annealed, and successively thermally treated at 850°C for 30 min. The mobility values (open circles in Fig. 2), in spite of the large amount of inactive phosphorus, fit very well with the experimental curve reported in the literature (11). This experiment excludes the formation of a significant amount of point defects which compensate or make the excess dopant electrically inactive (10, 23), since their presence would considerably affect carrier mobility.

Conclusions

The following conclusions can be drawn from this study:

1. Silicon n⁺ layers with electron concentration up to 5×10^{21} cm⁻³ can be obtained by high dose phosphorus implantation and pulsed laser annealing.

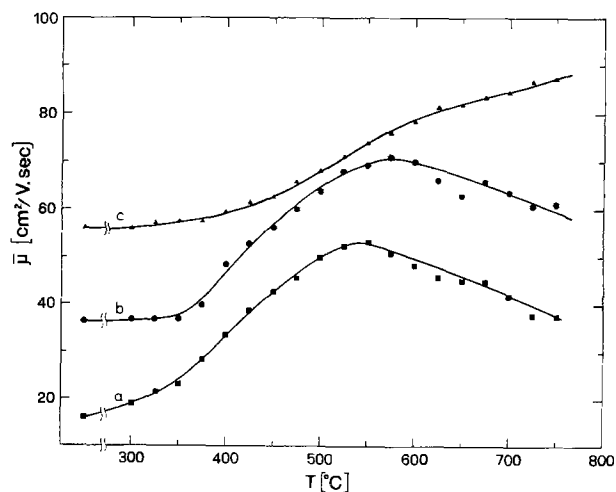


Fig. 6. Average electron mobility vs. 1 hr isochronal annealing temperature for three different implanted doses.

2. Electron mobility decreases monotonically with increasing dopant concentration from ~ 45 cm²/V-sec at 3×10^{20} to ~ 11 cm²/V-sec at 5×10^{21} atoms/cm³. Silicon resistivities as low as $110 \mu\Omega \cdot \text{cm}$, comparable to those presented by the refractory metals silicides, can be obtained.

3. The thermal stability of these alloys, determined by isochronal and isothermal annealing, is strongly dependent on the supersaturation. Even short processes at low temperature, such as metal sintering or die bonding or packaging, can produce a marked precipitation of dopant in the more heavily doped samples.

4. The electrically inactive phosphorus is present in the form of small precipitates, with densities and mean diameter depending on supersaturation.

5. The electrically inactive phosphorus, even when present in concentration about 15 times higher than the carrier density, does not affect the electron mobility, which depends only on carrier concentration.

Acknowledgments

The authors wish to thank Dr. E. Jannitti of the CNR Centro Studi Gas Ionizzati (Padova), for the setting up of the laser apparatus. Thanks are also due to A. Armigliato for TEM observations, F. Cembali for RBS analysis, P. De Luca, E. Gabilli, A. Garulli, R. Lotti, and G. Ruffini for help in sample preparation. This work was supported by CNR, Progetto Finalizzato Energetica, and E.E.C. (European Economic Community).

Manuscript submitted Aug. 12, 1980; revised manuscript received Jan. 12, 1981.

Any discussion of this paper will appear in a Discussion Section to be published in the December 1981 JOURNAL. All discussions for the December 1981 Discussion Section should be submitted by Aug. 1, 1981.

Publication costs of this article were assisted by CNR-Istituto LAMEL.

REFERENCES

- C. W. White, W. H. Christie, B. R. Appleton, S. R. Wilson, P. P. Pronko, and C. W. Magee, *Appl. Phys. Lett.*, **33**, 662 (1978).
- R. T. Young, C. W. White, J. Narayan, G. J. Clark, and W. H. Christie, in "Semiconductor Characterization Techniques," P. A. Barnes and G. A. Rozgonyi, Editors, p. 456, The Electrochemical Society Softbound Proceedings Series, Princeton, N.J. (1978).
- G. L. Miller, J. L. Benton, L. C. Kimerling, D. A. H. Robinson, J. W. Rodgers, and G. K. Celler, in *ibid.*, p. 502.
- F. Zignani, R. Galloni, L. Pedulli, G. G. Bentini, M. Servidori, F. Cembali, and A. Desalvo, in 2nd E.C. Photovoltaic Solar Energy Conference, Berlin, p. 213 (1979).
- C. Hill, in "Laser and Electron Beam Processing of Electronic Materials," C. L. Anderson, G. K. Celler, and G. A. Rozgonyi, Editors, p. 26, The Electrochemical Society Softbound Proceedings Series, Princeton, N.J. (1980).
- B. R. Appleton, B. C. Larson, C. W. White, J. Narayan, S. R. Wilson, and P. P. Pronko, in "Laser-Solid Interactions and Laser Processing," S. D. Ferris, H. J. Leamy, and J. M. Poate, Editors, p. 291, American Institute of Physics, New York (1978).
- M. Tamura, N. Natsuaki, and T. Tokuyama, in "Laser and Electronic Beam Processing of Materials," C. M. White and P. S. Percy, Editors, p. 247, Academic Press, New York (1980).
- A. Lietoila, J. F. Gibbons, and T. W. Sigmon, *Appl. Phys. Lett.*, **36**, 765 (1980).
- G. Masetti, D. Nobili, and S. Solmi, in "Semiconductor Silicon 1977," H. R. Huff and E. Sirtl, Editors, p. 648, The Electrochemical Society Softbound Proceedings Series, Princeton, N.J. (1977).
- R. B. Fair and J. C. C. Tsai, *This Journal*, **124**, 1107 (1977).
- G. Masetti and S. Solmi, *IEEE Solid State Electron*

- Devices*, ed-3, 65 (1979).
12. L. C. Kimerling and J. L. Benton, in "Laser and Electron Beam Processing of Materials," C. W. White and P. S. Peercy, Editors, p. 385, Academic Press, New York (1980).
 13. J. L. Benton, C. J. Doherty, S. D. Ferris, L. C. Kimerling, H. L. Leamy, and G. K. Celler, in *ibid.*, p. 430.
 14. S. P. Muraka, in Intern. Electron Devices Meeting (IEDM) Washington, p. 454, 1979.
 15. L. Esaki and Y. Miyahara, *Solid-State Electron*, **1**, 13 (1960).
 16. J. C. Irvin, Silicon Device Processing, NBS Special Publication 387, p. 99 (1970).
 17. D. Nobili, A. Armigliato, M. Finetti, and S. Solmi, To be published.
 18. L. Ekstrom and J. P. Dismukes, *J. Phys. Solids*, **27**, 857 (1966).
 19. F. S. Ham, *J. Phys. Chem. Solids*, **6**, 355 (1958).
 20. I. M. Lifshitz and V. V. Slyozov, *ibid.*, **19**, 35 (1961).
 21. J. W. Christian, "The Theory of Transformations in Metals and Alloys," Pergamon Press (1975).
 22. J. E. Hilliard, *Trans. Met. Soc. AIME*, **224**, 906 (1962).
 23. D. L. Kendall and R. Carpio, Proc. of the IEEE Sectional Meeting, Monterey, p. 1 (1977).

Anomalous Arsenic Diffusion in Silicon Dioxide

Yasuo Wada^{*1} and Dimitri A. Antoniadis^{*}

Department of Electrical Engineering and Computer Science,
Massachusetts Institute of Technology, Cambridge, Massachusetts 02139

ABSTRACT

The diffusion of ion-implanted arsenic in thermally grown silicon dioxide is examined as a function of temperature, arsenic concentration, and ambient. Diffusion coefficients are calculated from profiles obtained by secondary ion mass spectroscopy (SIMS) analysis. At relatively low concentrations—below approximately $5 \times 10^{20} \text{ cm}^{-3}$ —the activation energy of the diffusion coefficient in nitrogen atmosphere between 1000° and 1200°C is 4.7 eV. At high concentrations—above $5 \times 10^{20} \text{ cm}^{-3}$ —it is found that arsenic practically does not diffuse under the above conditions. This phenomenon might be attributed to arsenic-silicon-oxygen complex formation. However, if annealed in a dry oxygen atmosphere, arsenic diffuses at both high and low concentrations with an activation energy of 3.7 eV. It is determined that it is necessary that oxidation of underlying silicon must be taking place for such an enhanced diffusion to occur. The mere presence of oxygen in the annealing ambient, without silicon oxidation, does not have any effect.

Large-scale integration of silicon MOS circuits is partly accomplished via the scaling principle (1), in which vertical as well as horizontal dimensions of MOSFET's are reduced simultaneously. Because of its low diffusivity, arsenic is thus becoming increasingly important as an n-type dopant. Arsenic ion implantation has become a key process for fabricating self-aligned shallow source and drain regions (2) in scaled polysilicon gate circuits. The diffusion coefficient of arsenic (As), in silicon (Si), has been determined accurately (3), and clustering models have been proposed (4), so that chemical and electrically active profiles of arsenic, as well as residual defect penetration (5), resulting from a wide variety of ion implantation based processes are quite predictable. However, diffusion coefficients in silicon dioxide (SiO_2), reported to date, are scattered by more than an order of magnitude (6-8). As SiO_2 layers become thinner, control of impurity profiles increasingly requires better knowledge of impurity diffusion characteristics in SiO_2 .

The present work presents a study of As diffusion in thermally grown SiO_2 at temperatures between 1000° and 1200°C in inert-nitrogen- and oxidizing-dry oxygen-ambients. Arsenic was ion implanted into SiO_2 at two doses, 10^{15} cm^{-2} for relatively low concentration study and 10^{16} cm^{-2} for high concentration study. Diffusion coefficients were calculated directly from the as-implanted and diffused profiles in SiO_2 observed by secondary ion mass spectroscopy. This direct observation of profiles eliminates uncertainties introduced by assumed models when As diffusion is extracted by electrical characterization of Si doped via the SiO_2 .

SIMS is a very powerful tool in determining impurity profiles both in Si and in SiO_2 (9, 10). However, in analysis of SiO_2 or insulating materials in general, a major problem is the electrostatic charge-up of the sample during sputtering. Another problem, of lesser importance, is the redeposition effect from the high concentration edges of the sputtered crater. Here a new sample structure is introduced to avoid these two problems, and is used to analyze the As-doped SiO_2 . The results of this study indicate that in inert ambients detectable diffusion takes place at arsenic concentrations less than about $5 \times 10^{20} \text{ cm}^{-3}$. At higher concentrations diffusion appears to stop, suggesting some form of As complexing. In oxidizing ambients, diffusivity is enhanced and the complexing effect is not observed. Further it is determined that the enhancement results from the oxidation of underlying silicon, which clearly suggests an oxidation enhanced diffusion (OED), rather than oxygen enhanced diffusion. Interestingly, the change of activation energy of diffusivity under OED in SiO_2 is similar to that observed under OED in silicon (13).

Experimental Procedures

Sample preparation and SIMS measurements.—A 0.5 μm thick SiO_2 layer was thermally grown on a p-type, <100> oriented silicon wafer. As ions were implanted into the oxide layer at 120 keV to doses of between 10^{15} and 10^{16} cm^{-2} . The samples thus prepared were annealed in either dry nitrogen or dry oxygen atmosphere at temperatures between 1000° and 1200°C for times between 15 min and 64 hr. Then the SiO_2 layer was etched to define mesas of 500 μm diam.

SIMS analysis was carried out to measure the As profile in SiO_2 . The mesa structure avoids not only the charge-up of the SiO_2 layer but also the redeposition of

* Electrochemical Society Active Member.

¹ Present address: Central Research Laboratory, Hitachi, Limited, Kokubunji, Tokyo 185 Japan.

Key words: dielectrics, integrated circuits, ion implantation, SIMS.

sputtered atoms from the high impurity concentration edge of the conventional crater, as schematically shown in Fig. 1. Thus, it makes possible to obtain accurate depth profiles by SIMS analysis. The detection limit was around 10^{18} cm^{-3} , which is sensitive enough to allow determination of the diffusion coefficient in more than 10^{19} cm^{-3} arsenic concentrations. The possible error of the concentration determination was $\pm 30\%$. Residual oxide thickness was measured by laser ellipsometry and by surface profilometer (Dektak), and the possible error in this thickness measurement was around $\pm 5\%$. The sputtering rate was calculated from the thickness measurement and was typically 1.5-3.5 nm/min. Ion current signal of Si^+ was quite stable during the measurement, and the variation was typically less than 10% in 6 hr.

Typical sample structures before and after SIMS analysis measured by Dektak are shown in Fig. 2. The

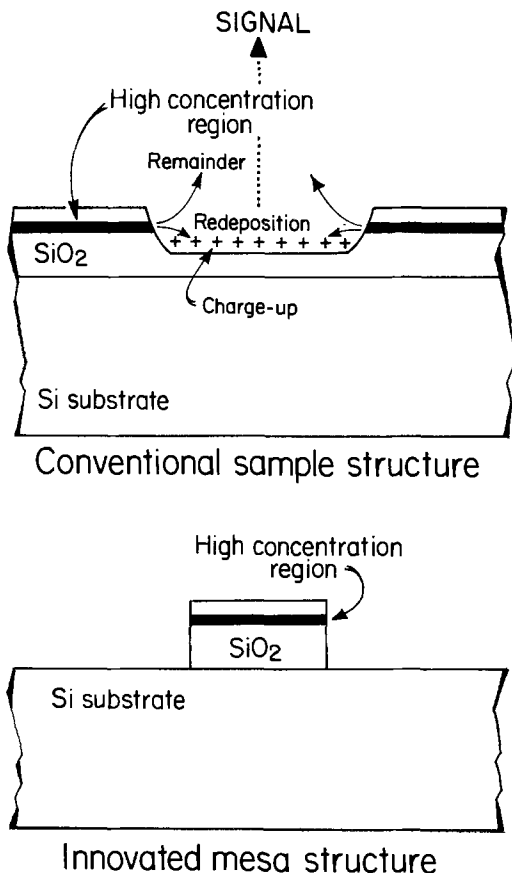


Fig. 1. Schematic cross section of the mesa structure used in the SIMS analysis.

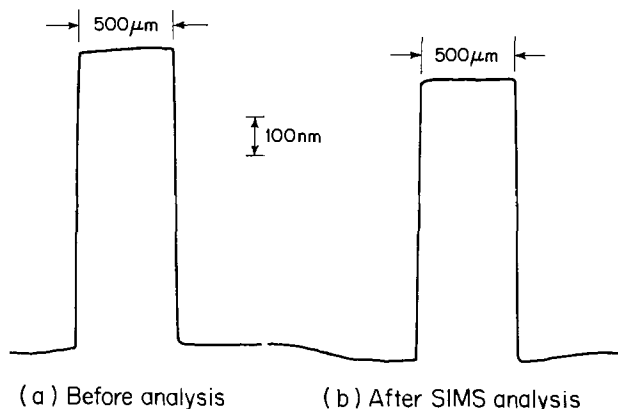


Fig. 2. Typical example of the sample structure (A) before and (B) after SIMS analysis, measured by Dektak.

protrusion represents the mesa-etched SiO_2 region. Negative oxygen (O^-) ions were used as the primary ion beam, and were scanned over more than a $700 \mu\text{m}$ square region. Data acquisition area was $150 \mu\text{m}$ square at the center of the primary ion beam scanned area, and the raggedness of this area was less than 2.5 nm. The rate of sputtering ratio between Si and SiO_2 is approximately 1:2, as depicted in Fig. 2(b).

Diffusion coefficient determination.—The concentration of As atoms in SiO_2 was determined from the signal ratio between $^{75}\text{As}^+$ and $^{28}\text{Si}^+$. The As concentration of the as-implanted sample was determined quantitatively from the experimentally obtained signal ratio by adjusting the integral of the concentration to the actual implanted dose. The sputtered depth, measured by the previously mentioned method, was used to determine the distance of the peak position from the surface. The diffusion coefficient of As in SiO_2 was derived by fitting calculated profiles to the obtained As profiles by SIMS. Simple gaussian-type diffusion was assumed.

Results and Discussion

Anomalous diffusion of arsenic in silicon dioxide.—Typical As profiles in SiO_2 after annealing at 1100°C for 16 hr in nitrogen are shown in Fig. 3 by broken lines. The fluctuation of $^{28}\text{Si}^+$ signal, shown by a chain line, was less than $\pm 10\%$ during the analysis, which usually took 2 hr. In the figure, as-implanted As profiles in SiO_2 are also shown by solid lines to indicate the differences between different As concentrations. The projected range derived from these as-implanted profiles coincide well with the theoretical value (11) within experimental error.

It was found that if the As concentration exceeds about $5 \times 10^{20} \text{ cm}^{-3}$, arsenic atoms practically do not diffuse even after this high temperature treatment. On the other hand, As atoms diffuse with a diffusion coefficient of $3.9 \times 10^{-16} \text{ cm}^2/\text{sec}$ at 1100°C , if the concentration is lower than this value. In Fig. 3, the surface low concentration region which appears after annealing is probably due to the evaporation of As atoms from the SiO_2 surface. As can be seen, As atoms have diffused significantly deep into the layer under both low and high concentration implantation conditions.

The cause of the nondiffusing high As concentration region could be complexing of As-Si-O to form a

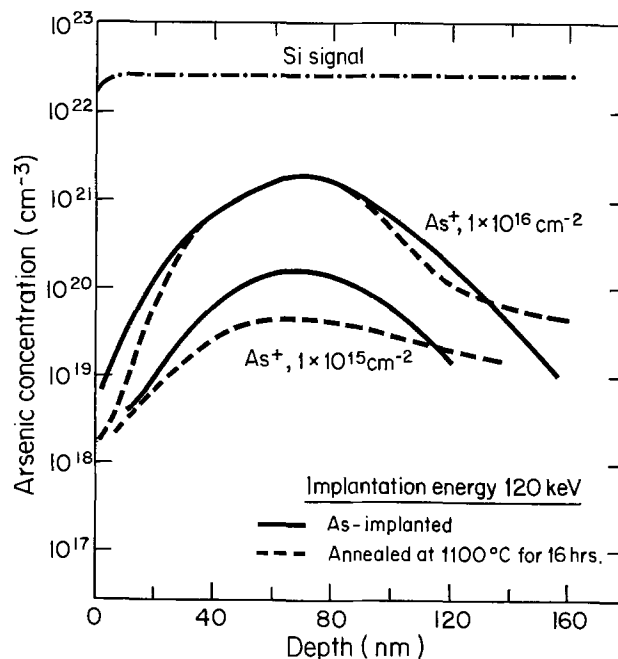


Fig. 3. Arsenic profiles in silicon dioxide measured by SIMS;— as-implanted, --- annealed at 1100°C for 10 hr in dry nitrogen atmosphere.

stable phase. The experimentally obtained critical As concentration is around 1 atomic percent ($5 \times 10^{20} \text{ cm}^{-3}$), which is probably low enough to form solid solutions for $\text{SiO}_2\text{-As}_2\text{O}_3$. However, the segregation effect (sinusoidal decomposition) of the impurity in the matrix (12) could cause the formation of a complex. A more detailed understanding of the $\text{SiO}_2\text{-As}_2\text{O}_3$ system is required before this issue can be settled.

Temperature dependence of diffusion coefficient in inert ambient.—Annealing temperature dependence of the diffusion coefficient was measured in the temperature range of 1000°C – 1200°C in dry nitrogen. Diffusivity of As in SiO_2 was calculated in the low As concentration region, and the results are shown in Fig. 4. The activation energy derived from the Arrhenius plot is 4.7 eV, and is in general agreement with former results (6–8).

Regions with more than a $5 \times 10^{20} \text{ cm}^{-3}$ As concentration yield a diffusion coefficient of at least two orders of magnitude smaller than that of low concentration regions in the same temperature range. In other words, the Si-As-O complex of the high concentration arsenic region is stable up to 1200°C .

Ambient dependence of diffusion coefficient.—The preceding experiments were performed in a dry nitrogen atmosphere. It has been reported that annealing in a dry oxygen atmosphere retards the As diffusion in SiO_2 (7, 13). Therefore, the samples were annealed in a dry oxygen atmosphere in order to examine the ambient effect on the nondiffusing high concentration As region as well as on the low concentration regions.

The samples implanted with 10^{16} cm^{-2} arsenic ions were annealed in a dry oxygen ambient. The resulting As profile is shown by a dotted line in Fig. 5, together with the results of annealing in nitrogen atmosphere at 1200°C for 4 hr. The ambient dependence of As diffusion is clearly shown. The high concentration As region exhibited a marked diffusion in the oxygen atmosphere, which contrasts the nondiffusing As region annealed in nitrogen atmosphere. Also, in the low concentration region, As atoms diffuse faster in SiO_2 under oxygen ambient ($1 \times 10^{-15} \text{ cm}^2/\text{sec}$ at 1100°C), than in a nitrogen atmosphere ($3.9 \times 10^{-16} \text{ cm}^2/\text{sec}$ at 1100°C), as shown in Fig. 6. The diffusion coefficient of As in SiO_2 in the high concentration region was almost the same as that of the low concentration regions.

The temperature dependence of the diffusion coefficient shown in Fig. 7 indicates that the activation energy of As diffusion in SiO_2 in oxygen atmosphere is 3.7 eV, which is 1 eV less than that in nitrogen atmosphere. Therefore, the As diffusion mechanism is

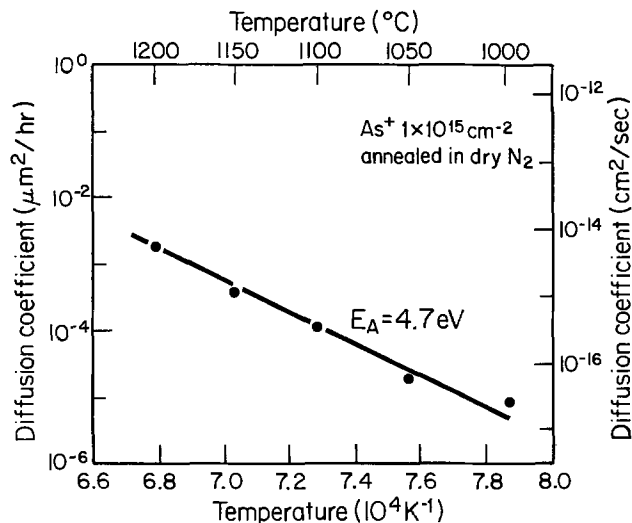


Fig. 4. Temperature dependence of arsenic diffusion coefficient in silicon dioxide in low concentration ($<5 \times 10^{20} \text{ cm}^{-3}$) region, annealed in dry nitrogen.

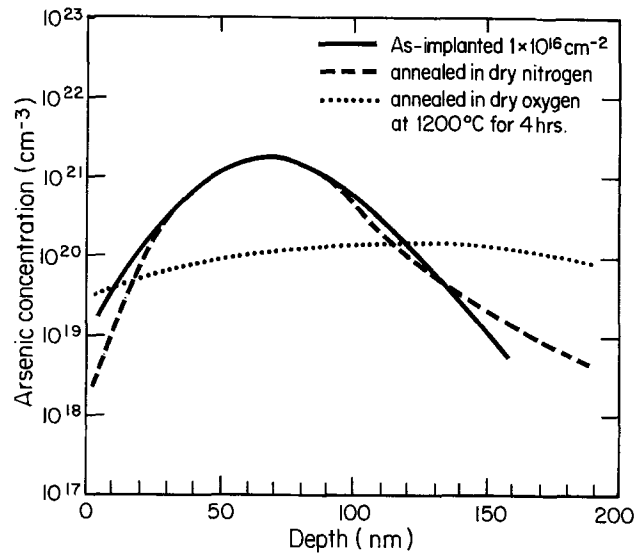


Fig. 5. High concentration arsenic profiles in silicon dioxide annealed at 1200°C for 4 hr; — as implanted, annealed in oxygen, --- annealed in nitrogen.

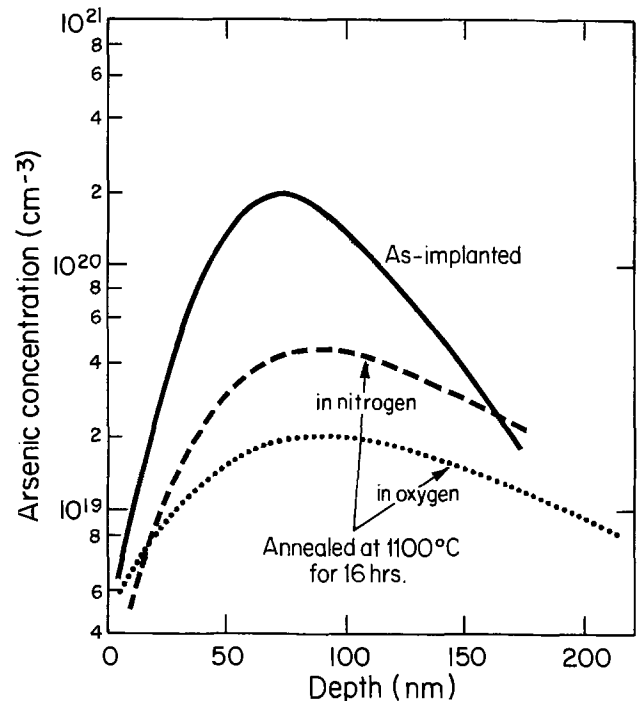


Fig. 6. Low concentration arsenic profiles in silicon dioxide annealed at 1100°C for 16 hr. — as-implanted, annealed in oxygen, --- annealed in nitrogen.

possibly different, or at least is affected by some extrinsic phenomena. In the figure, the reported values of diffusion coefficient (6–8) are also shown, and are generally in agreement with the present results, considering the differences in sample preparation and measuring method.

The activation energy as well as the relative enhancement of the oxidation enhanced diffusion (OED), reported here are similar to those reported for low concentration arsenic, phosphorus, and boron diffusion in Si by Antoniadis *et al.* (14). The mechanism of OED in Si has been proposed as interstitialcy diffusion (15), and the degree of OED has been related to the rate of oxidation (16). In the case of the As- SiO_2 system, there are three possible causes of OED. One is the presence of excess oxygen ions in the SiO_2 network. Another is the transport of oxygen through SiO_2 and

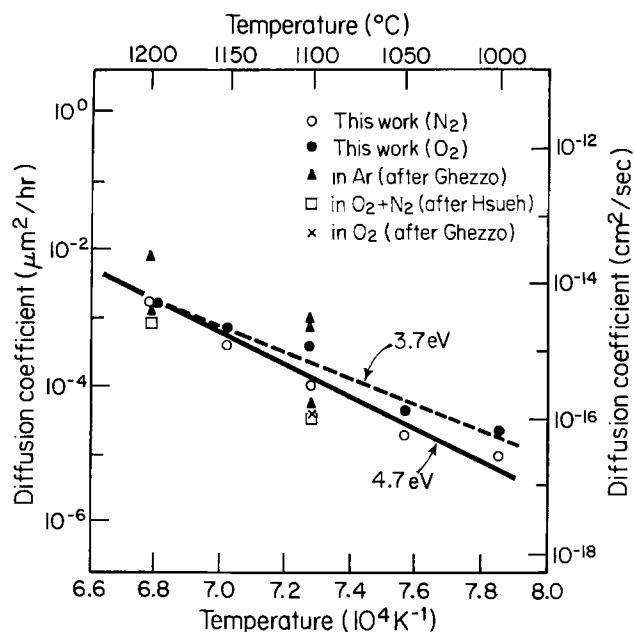


Fig. 7. Temperature of diffusion coefficient, \circ annealed in dry nitrogen, \bullet annealed in dry oxygen, \times Δ after Ghezzeo, \square after Hsueh.

the last is excess point defect generation (perhaps vacancy), at the SiO_2 -Si interface during oxidation.

The following experiment was carried out to shed some light on the mechanism of OED of As in SiO_2 . Annealing of As-doped thermal SiO_2 in oxygen ambient without attendant oxidation of underlying silicon was achieved by using samples prepared by completely oxidizing 250 nm of polysilicon deposited on Si_3N_4 . These samples were implanted with As and were annealed as described previously in both oxygen and nitrogen. Typical results of SIMS analysis have revealed no ambient related difference in the diffused profiles. It can thus be concluded that the presence of excess oxygen in SiO_2 , which would be present at solid solubility levels during oxygen ambient annealing, is not the reason for OED. However, on the basis of the present experiments it is not possible to discriminate between the remaining two possible causes of OED. If transport of oxygen is indeed responsible, one would expect some form of nonuniform diffusivity with the profile shape skewing towards the deep end. Such an effect cannot be concluded from the present data.

The results shown here suggest that it might be difficult to control high concentration arsenic layer diffusion from a doped oxide source. Doped oxide source concentration above $5 \times 10^{20} \text{ cm}^{-3}$ is ineffective if the annealing atmosphere is nitrogen. Oxygen atmosphere would increase the diffusivity of higher concentration As in SiO_2 , however, the SiO_2 layer formed between doped oxide and silicon during annealing (oxidation) would hinder the diffusion of As into Si. Such an effect has been observed by Reindl (13), who noted that a doped oxide source is more effective at 100% O_2 than

100% N_2 , but an optimum efficiency, better than at 100% O_2 , is achieved for a 60-40% mixture of O_2 - N_2 .

Conclusions

Anomalous diffusion phenomena of As in SiO_2 were studied by SIMS using mesa structured samples, which eliminates charge-up and peripheral effect of insulator sample and enables accurate measurements. The results are summarized as follows.

1. At more than a $5 \times 10^{20} \text{ cm}^{-3}$ concentration arsenic does not diffuse between 1000° and 1200°C, probably because of complex formation in SiO_2 .
2. The activation energies of low concentration ($< 5 \times 10^{20} \text{ cm}^{-3}$), As diffusion in SiO_2 are 4.7 and 3.7 eV in dry nitrogen and dry oxygen atmosphere, respectively.
3. In dry oxygen atmosphere, the high As concentration region does diffuse. The cause of the oxidation enhancement is the oxidation of the underlying silicon.

Acknowledgments

This work was supported by the NSF grant DMR 78-21485. The authors wish to express their thanks to Prof. S. R. Hart, Dr. N. Shimizu, and Dr. Ken Burrhus for their valuable discussions on SIMS analysis.

Manuscript submitted Sept. 2, 1980; revised manuscript received Dec. 16, 1980. This was Paper 566 RNP presented at the St. Louis, Missouri, Meeting of the Society, May 11-16, 1980.

Any discussion of this paper will appear in a Discussion Section to be published in the December 1981 JOURNAL. All discussions for the December 1981 Discussion Section should be submitted by Aug. 1, 1981.

Publication costs of this article were assisted by the Massachusetts Institute of Technology.

REFERENCES

1. G. E. Moore, Paper 1-3 presented at IEEE International Electron Device Meeting, Washington, D.C., December 1975.
2. Y. Wada and S. Nishimatsu, *Jpn. J. Appl. Phys. Suppl.*, **18**, 247 (1979).
3. B. J. Masters and J. M. Fairfield, *J. Appl. Phys.*, **40**, 2390 (1969).
4. M. Y. Tsai, F. F. Morehead, J. E. E. Baglin, and A. E. Michel, *ibid.*, **51**, 3230 (1980), and references therein.
5. Y. Wada and N. Hashimoto, *This Journal*, **127**, 461 (1980).
6. M. Ghezzeo and D. M. Brown, *ibid.*, **120**, 146 (1973).
7. M. Ghezzeo and D. M. Brown, *ibid.*, **120**, 110 (1973).
8. Y. W. Hsueh, *ibid.*, **6**, 361 (1968).
9. C. W. Magee and W. L. Harrington, *Appl. Phys. Lett.*, **33**, 193 (1978).
10. K. Wittmaak, *J. Appl. Phys.*, **50**, 493 (1979).
11. J. F. Gibbons, W. S. Johnson, and S. W. Myloie, "Projected Range Statistics," Dowder, Hutchinson and Roth, Inc., Stroudsburg, Pa. (1975).
12. P. G. Shewmon, "Diffusion in Solids," p. 130, McGraw-Hill, New York (1963).
13. K. Reindl, *Solid State Electron.*, **16**, 181 (1973).
14. D. A. Antoniadis, A. M. Lin, and R. W. Dutton, *Appl. Phys. Lett.*, **33**, 1030 (1978).
15. S. M. Hu, *J. Appl. Phys.*, **45**, 1567 (1974).
16. A. M. Lin, D. A. Antoniadis, and R. W. Dutton, *This Journal*, **128**, 1131 (1981).

The Nature and Rate of Creepage of Copper Sulfide Tarnish Films over Gold

V. Tierney*

Bell Laboratories, Murray Hill, New Jersey 07974

ABSTRACT

Tarnish films that form on copper surfaces at high humidity can creep over adjoining gold surfaces, causing increases in the contact resistance of the gold. In many cases, however, when gold-plated contacts having exposed areas of copper are removed from equipment used for extended periods of time in environments known to contain sulfiding compounds, there has been little or no evidence of creepage. This protection against tarnish is caused by a naturally formed oxide and has been duplicated in the laboratory. When copper sulfide tarnish films do creep over gold surfaces, distinctive periodic bands are formed. The humidity dependence of the rate and maximum distance of the creepage have been studied.

When freshly cleaned copper is exposed to an environment containing sulfur, a tarnish film composed of copper oxide and copper sulfide forms. This film can migrate over gold surfaces with which the copper is in contact, causing increases in the contact resistance of the gold. This phenomenon is frequently called creep in the literature.

Gold-plated copper or copper alloy electrical contacts having exposed areas of copper are frequently used in electronic equipment that may be stored, shipped, or used in environments where sulfiding compounds are present.

Plating smaller areas of gold with thinner layers of gold is the result of today's soaring gold prices, increasing the importance of creep as a contact failure mechanism. Since gold contact is now dependent on smaller contact areas, even a slight amount of creepage from pores, which are more likely on thin films, or from the edges of the plating, which are now closer to the contact point, can cause failure.

Since the diffusion of copper through the gold to the gold/air interface is too slow at the temperatures and gold thicknesses under consideration, the degradation of the surface due to the tarnishing of copper is not a likely failure mechanism (1).

In harsh indoor environments, migration of base metal corrosion products over gold can proceed at significant rates (2). Indeed, Antler has observed creepage in an environment that contained both sulfur and chlorine compounds, where a 1.27 cm (0.5 in.) wide gold stripe on CDA 725 was completely covered with tarnish products from the base metal in only 35 days (3). Not surprisingly, this formation of tarnish films, followed by their creepage over adjoining gold surfaces, can result in contact resistance failures. On the other hand, Grau (4) has reported that there is little or no evidence of creepage when gold-plated contacts, having exposed areas of copper, were removed from equipment that had been used for extended periods of time in telephone offices. Thus, we began our study by investigating the reasons for this difference.

In 1926 Vernon (5, 6) showed that an oxidized copper surface tarnishes at a much slower rate than a freshly cleaned surface. More recently, Tierney (2) found that small amounts of cupric oxide (CuO) were responsible for low tarnish rates. Frankenthal has observed that in dry atmospheres, the oxide films on copper protect the copper from sulfidation in flowers of sulfur environments (7). Chessari and Blessington (8) showed that thermal aging could prevent tarnishing in pores.

Copper oxide is thermodynamically more stable than Cu₂S or CuS [the standard free energies of formation at 25°C for Cu₂O, Cu₂S, and CuS are -34.98, -20.6, and -11.7 kcal/mole, respectively (9)] and therefore forms more readily on a copper surface. We suspected that the lack of tarnish film creepage in operating equipment is due to the natural formation of a protective oxide that is present on copper before exposure to the sulfiding environment. To test this hypothesis, a thermally produced oxide was investigated to determine if it acted as the natural oxide produced with time and served as a protection against growth of sulfide/oxide films and inhibited their creepage across adjoining gold-plated surfaces.

Experimental

Since Vernon (5) had reported that the tarnish rate could be affected by variation of the surface condition, we paid careful attention to sample preparation. Our samples were 2.54 × 1.27 cm (1 × 0.5 in.) OFHC copper coupons cut from rolled copper strip. The coupons were immersed in 1:1 HNO₃ at room temperature for about 45 sec to remove sufficient copper to eliminate the surface defects caused by rolling operations. To obtain relatively smooth reproducible surfaces, the coupons were then immersed for 2 min in a chemical etch.¹

Tarnish film thicknesses were determined by electrolytic reduction. In this method the amount of each species present is determined from the durations of the potential plateaus exhibited during a constant current reduction. To minimize the problem of film solubility in the electrolyte, 0.1N KCl was used. The reduction of sulfide occurs at a potential between that for the reduction of oxide and that for hydrogen evolution. The reduction potential is a function of the current density as well as the reference electrode. The reference electrode used in these investigations was silver/silver chloride and most of the work was done at a current density of 0.25 mA/cm².

Under these conditions, copper oxide is reduced at about -0.9V and copper sulfide at -1.2V. In KCl, cupric and cuprous oxides are reduced at the same potential. In NH₄Cl, the two oxide reduction potentials are far enough apart that the separate species can be determined, but this electrolyte was not considered because of its solvent action on copper oxide. Oxygen was excluded from the system by purging the electrolyte with nitrogen both prior to and during reduction in order to minimize errors due to the reduction of dissolved oxygen. Inert platinum anodes completed the cell components.

* Electrochemical Society Active Member.
Key words: contact resistance, humidity, oxidation.

¹ The chemical etch was 100 ml nitric, 275 ml phosphoric, and 125 ml acetic acids at 75°C.

Since Vernon's earlier work did not contain sufficient data to relate copper oxide thickness to a decrease in tarnish rates, the thermal oxidation rate of copper at 100°C and 125°C was first investigated (10). This resulted in the development of reproducible cuprous oxide tarnish films, which were then evaluated for their ability to protect the underlying surface from further attack. It was found that the 225Å cuprous oxide film that formed during an 18 hr exposure to air at 125°C significantly inhibited the formation of sulfide films during subsequent exposures, and this was therefore established as a standard preoxidizing treatment.

Copper coupons having this standard oxide and freshly cleaned coupons were exposed to flowers of sulfur at 50°C under humidity conditions that were controlled using saturated salt solutions. The resulting concentration of sulfur vapor was much higher than is normally found in most service environments.

Several investigators have discussed the significance of relative humidity. Baker (10) has studied the migration of corrosion products over gold surfaces and shown that the rate of migration increases with increasing relative humidity. Sigsbee (11) has reported that relative humidities in excess of 35% are necessary for appreciable sulfide creepage to occur. Sharma (12) has reported that relative humidity is one of the important parameters in the atmospheric corrosion of copper. He found that copper oxide grown in air (several hundred angstroms thick) provided good protection against H₂S at low relative humidity but little protection at high relative humidity.

The relationship between relative humidity and the degree of protection is shown in Fig. 1. The high humidity tests were carried out at 75% RH. At 25°C, saturated air contains 24 g/m³ of water. At 50°C, air at 75% RH contains 61 g/m³ of water, which is equivalent to a relative humidity well in excess of 100% at room temperature. In this extremely severe test environment, the thermally produced oxide did not protect copper from sulfiding. After 71 hr of exposure, 750Å of cuprous sulfide was found in the Cu₂O/Cu₂S tarnish films on both the preoxidized sample and the control.

To test a more realistic humidity, additional samples were exposed to sulfur at 17% RH and 50°C. (This is 14 g/m³ of water, which would be equivalent to 58% RH at 25°C.) While 300Å of cuprous sulfide was found in the tarnish film on the freshly cleaned copper after the 24 hr exposure, less than 25Å formed on the preoxidized copper in the same period. During more extended exposures the amount of sulfide increased on both the preoxidized copper and the control, but the growth rate on the preoxidized surface was much slower at 71 hr, 100Å compared to 700Å and at 168 hr,

900Å compared to more than 2000Å. This last film, with more than 2000Å of sulfide, was nonadherent and much of it flaked off during cathodic reduction, so that accurate thicknesses could not be determined.

For tests under dry conditions, the saturated salt solution used for humidity control was replaced by a desiccant. After 24 hr exposure under this condition, there was no measurable amount of Cu₂S formed on the preoxidized copper, while 500Å of Cu₂S was present on the control. This difference can be seen in Fig. 2, which shows the samples after 10 weeks exposure in this moisture-free sulfiding environment. The copper surface that was not preoxidized, on the left, is completely blackened indicating a very thick Cu₂S film, but the preoxidized copper surface, on the right, shows only a slight trace of darkening. Subsequent analysis by Auger electron spectroscopy showed the amount of sulfide on the preoxidized surface to be about 25Å.

From this work, we conclude that a thermally produced cuprous oxide film, 225Å thick, greatly reduces the rate of copper oxide/sulfide tarnish at low relative humidities even when the sulfur vapor level is much higher than found in some of the worst field environments. Long time protection is achieved in the absence of moisture. No appreciable protection occurs under conditions of extremely high relative humidity.

These results confirm Vernon's earlier observations and appear to explain why sulfide tarnish formation on copper surfaces and subsequent creepage over adjoining gold surfaces has not been a problem in field environments. The natural oxide formed with the passage of time appears, like the laboratory produced thermal oxide, to provide surface protection.

The samples for creepage studies were prepared on flat ceramic substrates. After vapor deposition of Pd, Ti, and Au, 10 microns of copper followed by 3 microns of gold were plated over the entire surface. A photoresist mask was applied, and portions of the gold deposit were etched away, leaving a sample that had straight boundaries between the gold and copper. Figure 3 shows such a sample. Just before testing, the gold-copper specimens were dipped into a 1:1 HCl solution to remove the small amount of oxide that naturally forms on the copper surface. These samples were then exposed to flowers of sulfur at various humidities at 50°C. The distance the tarnish crept over the gold surface was measured at 12 identifiable points along the Cu/Au interface after various exposure times.

The uppermost picture in Fig. 4 shows four distinct bands in the tarnish film that had crept over the gold during a 22 hr exposure to sulfur at 75% RH and 50°C. The average creepage distance was 0.47 mm, giving an average rate of 0.021 mm/hr (0.00082 in./hr). After measurement the sample was returned to the test environment and subsequently removed for additional readings at 46, 113, 229, and 536 hr. The three remain-

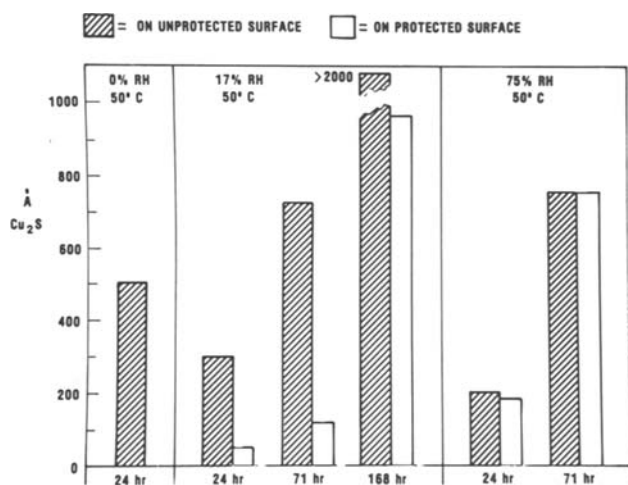


Fig. 1. Effect of protective oxide and relative humidity on sulfide film growth. Time of exposure to sulfiding environment given at bottom.

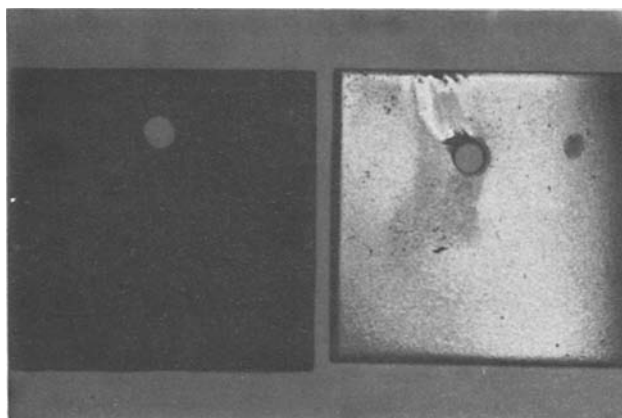


Fig. 2. Copper panels exposed to a moisture-free sulfiding environment for 10 weeks. Panel on the right was preoxidized; panel on the left was not.

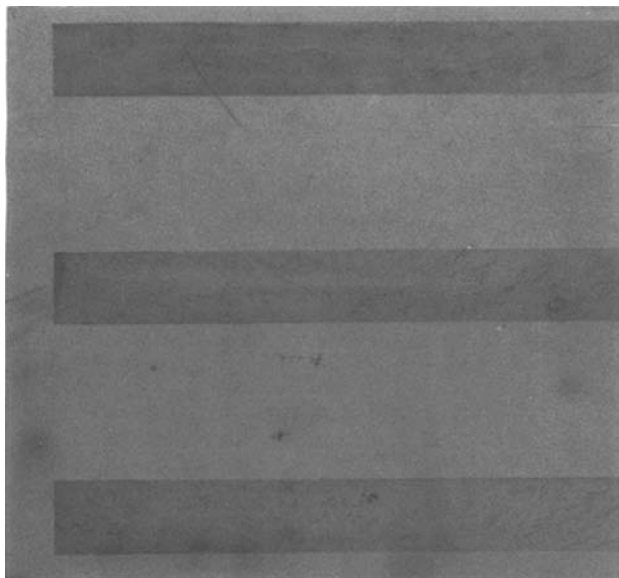


Fig. 3. Gold-copper specimens used for the creepage study. Narrow bands are copper.

ing pictures show that each time the sample was removed, new bands had been formed but the existing bands had not changed either their width or the shape of their leading edges. The bands did, however, darken with increasing exposure time, indicating vertical as well as horizontal growth. In the second picture in Fig. 4, five distinct bands are seen after 46 hr. The next two pictures show six bands after 113 hr and seven bands after 229 hr. At the final reading of 536 hr, the bands were so dark that it was difficult to see them. Table I summarizes the numerical results.

To establish the initial growth rate, measurements were made at shorter times, with the results shown in Table II. After 4 hr most of the gold at the Au/Cu in-

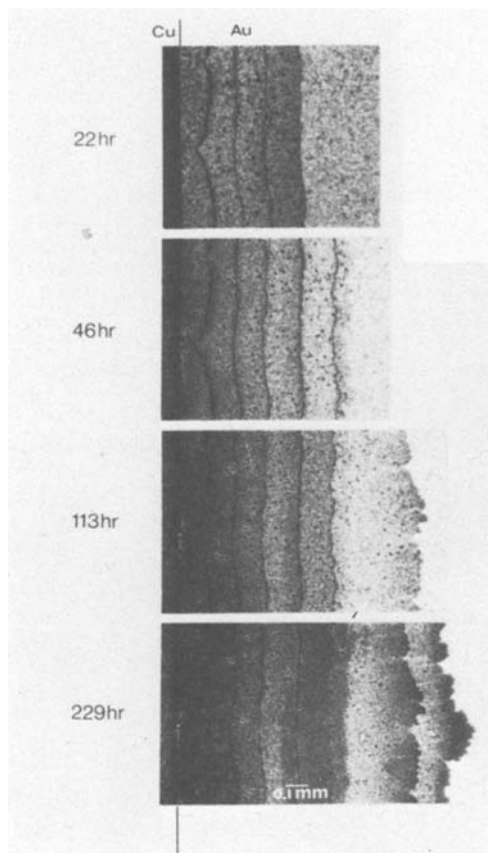


Fig. 4. Copper sulfide creep over gold. Each picture shows same area after different exposure times to sulfur at 75% RH and 50°C.

Table I. Copper sulfide creepage over gold for extended exposure (50°C 75% RH)

| Time (hr) | Average rate (mm/hr) | Average distance (mm) | Average No. of bands |
|-----------|----------------------|-----------------------|----------------------|
| 22 | 0.020 | 0.44 | 4 |
| 46 | 0.013 | 0.61 | 5 |
| 113 | 0.0080 | 0.90 | 6 |
| 229 | 0.0046 | 1.06 | 7 |
| 536 | 0.0018 | 0.98 | * |

* Too dark to be clear.

Table II. Copper sulfide creepage over gold for short exposure (50°C 75% RH)

| Time (hr) | Average rate (mm/hr) | Average distance (mm) | Average No. of bands |
|-----------|----------------------|-----------------------|----------------------|
| 4 | 0.055 | 0.22 | 1-2 |
| 8 | 0.034 | 0.27 | 2-3 |
| 22 | 0.020 | 0.43 | 3-4 |

terface had one distinct band of tarnish present, with a second band just beginning to form.

The creepage distance increased linearly with the square root of time for approximately the first 100 hr of exposure. After 229 hr, as shown in Fig. 5, the creepage stopped and the tarnish product grew only in thickness. To be sure that the removal of the samples from the test environment for measurement had no effect on the creepage rate, one sample was run continuously for 68 hr. As shown in Fig. 5, the creepage distance for this sample lies just slightly above the previously determined curve.

Each data point on the curve represents the average of the 12 identifiable sites that were measured. The number is large enough to make the average significant. No attempt was made to evaluate the reproducibility of the 12 measurements since creepage can be inhibited by random impurities on the surface. Our purpose was to illustrate that creepage can cause failure.

There were, on the average, six bands, but at four of the twelve measuring points, there were only five

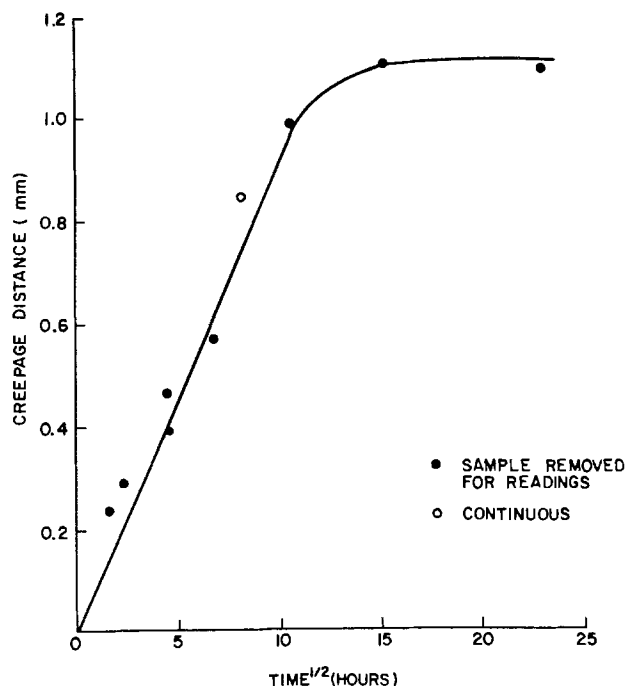


Fig. 5. Creepage distance of copper sulfide over gold as a function of time of exposure to sulfur at 50°C and 75% RH.

bands while at one point there were seven. These results show that the banding effect is not a function of the frequency with which the sample is removed from the test chamber. The bands are discussed later in more detail.

Under the conditions of 17% RH at 50°C, tarnish film creepage was still observed after only 4 hr of exposure.

However, as shown by samples 1 and 2 in Fig. 6, the maximum creep distance was reached after only a short time. Sample 3 shows again that there is no significant difference when the sample is not continuously removed from the oven for testing. Sample 4 on Fig. 6 shows the effect of temperature. When the sample was kept at 17% RH and 70°C, a creep asymptote was reached similar to that for the 50°C samples. However, the creepage film on this 70°C was much darker than that on the 50°C samples, indicating a thicker tarnish film. Cathodic reduction of a copper coupon exposed to these conditions confirmed this.

It was shown above that thermally produced oxide prevents the formation of copper sulfide tarnish film under humidity conditions that might be reasonably expected in a controlled indoor environment and reduces the rate of sulfiding even under severe conditions of relative humidity. Figure 7 shows that a protective oxide significantly reduces creepage. The sample on the left shows tarnish creepage over gold from a freshly cleaned copper surface that had been exposed to flowers of sulfur for 75 hr at 17% RH and 50°C. The sample on the right received a thermal oxide before being exposed to these conditions.

Both a freshly cleaned sample and a preoxidized sample were exposed to flowers of sulfur for 68 hr at 50°C and 75% RH. Copper sulfide from the freshly

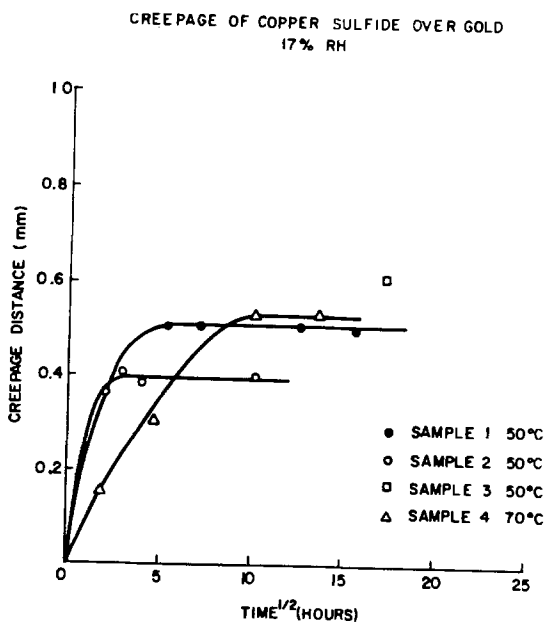


Fig. 6. Creepage distance of copper sulfide over gold as a function of time of exposure to sulfur at 17% RH at both 50°C and 70°C.

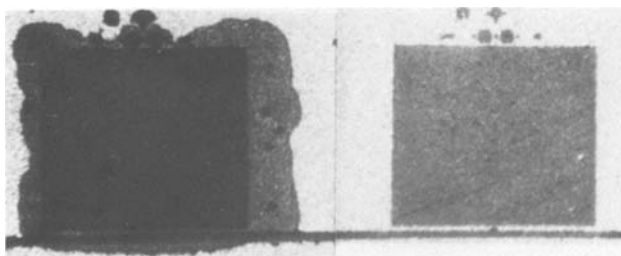


Fig. 7. Effect of preoxidation on copper sulfide creepage after 75 hr exposure to sulfur at 17% RH and 50°C. Specimen on right was preoxidized.

cleaned copper crept over the gold at an average rate of 0.013 mm/hr (0.0005 in./hr), while the average rate of creepage from the preoxidized sample was only 0.005 mm/hr (0.0002 in./hr), as shown in Table III. This is a significant decrease in creepage rate under severe humidity conditions. Another preoxidized sample showed no sign of creepage after 255 hr of exposure to flowers of sulfur at 50°C and 17% RH, while an average creepage rate of 0.02 mm/hr (0.0008 in./hr) over total distance of 0.62 mm (0.0244 in.) was observed after a 28 hr exposure under the same conditions, as shown in Table IV.

There is some question as to whether creepage can take place in the absence of moisture. When the saturated salt solution used for humidity control was replaced by a desiccant, no creepage occurred for the first 100 hr. However, creepage to a distance of 0.33 mm (0.0130 in.) was observed at 215 hr, which gives an average rate of 0.0015 mm/hr (0.00006 in./hr). Although this is a low rate, it shows that creepage is, in fact, possible in the absence of moisture.

All of the studies described thus far have been at elevated temperatures. To investigate the importance of temperature, a test sample was exposed to flowers of sulfur at 80% RH at room temperature. After 5 weeks (over 800 hr), the first signs of creepage were observed (0.01 mm or 0.0004 in.). This is in sharp contrast to the 0.23 mm (0.0091 in.) of creepage measured after only 4 hr at 50°C and 75% RH.

A freshly cleaned copper sample was put in a sulfur-free environment under the most severe test conditions (*i.e.*, 50°C and 75% RH) to determine whether a Cu_2O tarnish film, in the absence of Cu_2S , would creep. After 1750 hr, the exposed copper had darkened due to the formation of Cu_2O , but there was no creepage of the oxide film over the gold surface. It therefore appears that Cu_2S must be present in the tarnish film in order for creepage to occur.

In all of the creepage studies discussed above, the source of sulfur was flowers of sulfur. Experiments have also been carried out using hydrogen sulfide as the sulfur source. The first such experiment was run at 22°C and 88% RH, with air containing 4 ppm H_2S passed through the test chamber in a gas generation system described by Franey (13). Copper coupons exposed to this environment for 24 hr were cathodically reduced and found to have tarnish consisting of 4000Å of Cu_2S and 225Å of Cu_2O . With 4 ppm H_2S , measured in the manner described by Franey (13), at 50°C and 16% RH, the tarnish consisted of 7500Å of Cu_2S and 140Å of Cu_2O . At a more realistic concentration of H_2S , 8 ± 2 ppb, at 25°C and 81% RH, only 24Å of Cu_2S and 50Å of Cu_2O were found. Table V shows these results compared to those for the tarnish formed from flowers of sulfur during a 24 hr exposure.

An even more striking difference in the tarnish films generated by the two sulfur sources was found in the

Table III. Effect of preoxidation on copper sulfide creepage over gold (50°C 75% RH)

| | Time (hr) | Average rate (mm/hr) | Average distance (mm) |
|-------------|-----------|----------------------|-----------------------|
| No oxide | 68 | 0.013 | 0.87 |
| Preoxidized | 68 | 0.005 | 0.35 |

Table IV. Effect of preoxidation on copper sulfide creepage over gold (50°C 17% RH)

| | Time (hr) | Average rate (mm/hr) | Average distance (mm) |
|-------------|-----------|----------------------|-----------------------|
| No oxide | 28 | 0.17 | 0.48 |
| Preoxidized | 255 | 0 | 0 |

Table V. Composition of tarnish product after 24 hr

| %RH | T (°C) | A Cu ₂ O | A Cu ₂ S | Source of sulfur |
|-----|--------|---------------------|---------------------|------------------------|
| 88 | 22 | 225 | 4000 | 4 ppm H ₂ S |
| 16 | 50 | 140 | 7500 | 4 ppm H ₂ S |
| 81 | 23 | 50 | 24 | 8 ppb H ₂ S |
| 75 | 50 | 530 | 200 | Flowers of sulfur |
| 17 | 50 | 300 | 290 | Flowers of sulfur |

Table VI. Creepage distance

| Time (hr) | RH (%) | T (°C) | Source of sulfur | Creepage distance (mm) |
|-----------|--------|--------|------------------------|------------------------|
| 49 | 88 | 22 | 4 ppm H ₂ S | 0.1 |
| 24 | 16 | 50 | 4 ppm H ₂ S | 0.5 |
| 24 | 81 | 23 | 8 ppb H ₂ S | 0 |
| 24 | 17 | 50 | Flowers of sulfur | 0.5 |

nature of the creepage. When viewed with an optical microscope, the film creepage due to an H₂S sulfur source appeared to have bands like those observed with creepage films formed in the flowers of sulfur environment. However, scanning electron microscopy revealed that this creepage was a very thin film, with no indications of raised bands. Thus, the bands seen in the H₂S test are only an optical phenomenon. The creepage distances from these two sulfide sources are shown in Table VI.

The banded creepage that resulted when flowers of sulfur was the sulfur source was examined in detail. It was hoped that this would reveal the mechanism responsible for limiting the creepage distance at various humidities. Figure 4 shows that each of the bands is terminated by a dark edge. As previously discussed, after 536 hr at 75% RH, the tarnish product was too thick to distinguish the bands optically. However, when this sample was examined with the SEM, it was found that the bandedges were actually vertical growth of the tarnish product, as can be seen in Fig. 8. In this picture, the copper surface is on the right and the bands of creepage have grown to the left. The first three bands are shown in Fig. 9a at higher magnification. Figure 9b is an x-ray line scan for copper

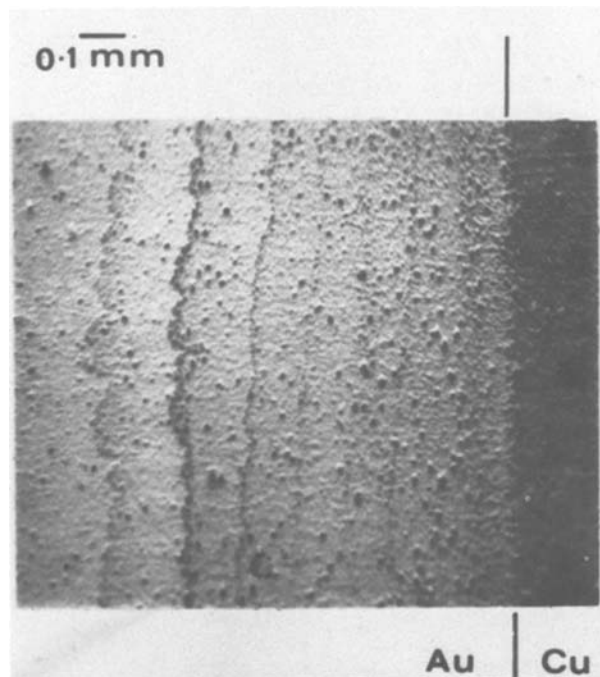


Fig. 8. Vertical copper sulfide growth at bandedges during exposure to sulfur at 50°C and 75% RH.

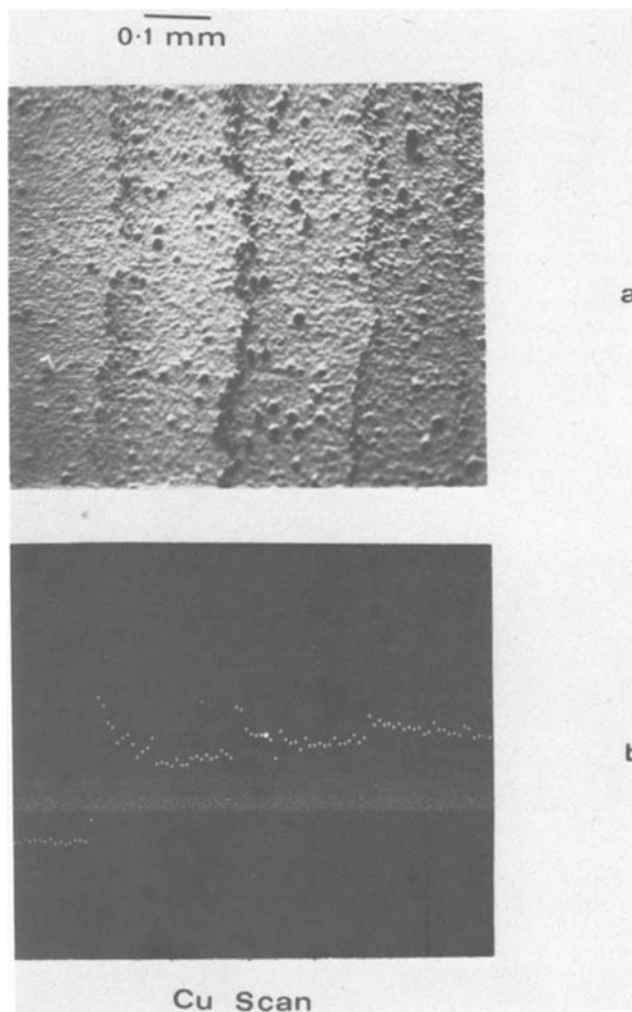


Fig. 9. (a) Higher magnification of the three bands at the left of Fig. 8. (b) X-ray line scan for copper across bands.

through the area shown in Fig. 9a. The scan over the gold is at background level, showing that no copper is seen through the gold. The copper x-ray intensity increases greatly at each bandedge and falls to a plateau along the main body of each band, and the copper signals from the individual bands increase as they approach the copper-gold interface.

To further illustrate this phenomenon, copper x-ray counts in 50 micron windows were taken in a line across the width of the tarnish creepage. The results are plotted in Fig. 10. The bandedges are copper rich

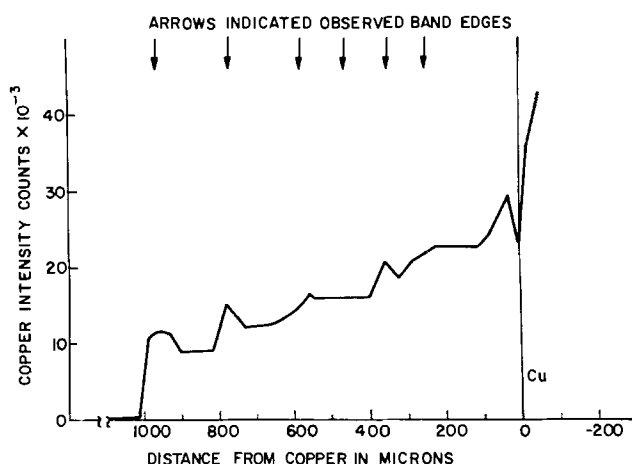


Fig. 10. Copper x-ray counts across width of creepage. Counts taken in 50 micron windows.

and the plateaus of the bands increase in copper toward the metallic copper.

Figure 11 shows two magnifications of the most prominent edge, which was the second from the untarnished gold surface. The small bumps shown near the bands in Fig. 11 are shown in enlargement in Fig. 12. The copper counts within the areas of the bumps were found to be no higher than in the areas surrounding them, showing that the bumps are not vertical copper tarnish film growth but rather the normal thickness of tarnish product following a contour of the underlying gold surface.

All of the bands near the copper/gold interface have about the same width. At present we have no satisfactory explanation for the periodic increase in vertical growth. However, the vertical growth does explain why the band, when formed, does not move across the gold surface. All of the bands pictured were grown at 75% RH. Although creepage was observed at lower humidities, the films never became thick enough to

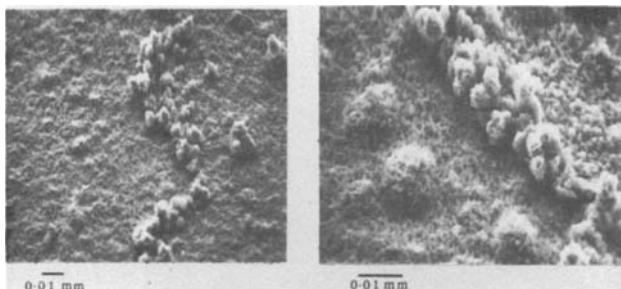


Fig. 11. Two magnifications of most prominent edge—second from untarnished gold surface.

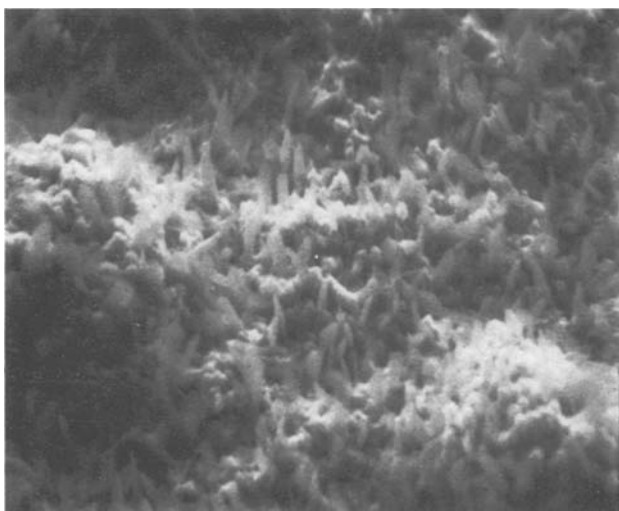


Fig. 12. Small bumps near bands in Fig. 11

form bands. More recent work has shown that bands form at 17% RH if the temperature is 70°C because under these conditions the thickness of the creepage is increased.

Conclusions

1. Thermally produced Cu_2O films can greatly reduce further tarnish of copper surfaces under realistic humidity and temperature conditions.

2. $\text{Cu}_2\text{S}/\text{Cu}_2\text{O}$ tarnish products creep over adjoining gold surfaces in a distinct band structure, the edges of which are characterized by vertical growth.

3. On exposure to flowers of sulfur at 75% RH and 50°C, tarnish creepage increases with the square root of time but reaches a limit of 1.1 mm (0.0433 in.) in 229 hr.

4. With flowers of sulfur at 17% RH and 50°C, creepage did not continue after samples were temporarily removed for measurement, but at a temperature of 70°C, the creepage continues and its behavior is more like that at high humidity.

5. When H_2S is the source of sulfur, the tarnish product is richer in Cu_2S , but the creepage at ordinary temperatures does not exhibit periodic vertical growth.

Acknowledgments

The author gratefully acknowledges the efforts of G. W. Kammlott, who performed the detailed SEM investigations. The author also wishes to thank R. G. Baker and P. C. Milner for their guidance and encouragement.

Manuscript submitted Sept. 18, 1980; revised manuscript received Jan. 27, 1981.

Any discussion of this paper will appear in a Discussion Section to be published in the December 1981 JOURNAL. All discussions for the December 1981 Discussion Section should be submitted by Aug. 1, 1981.

Publication costs of this article were assisted by Bell Laboratories.

REFERENCES

1. R. P. Frankenthal, Private communication.
2. V. Tierney, in "Proc. of the Ninth International Conference on Electrical Contact Phenomena," p. 123, Illinois Institute of Technology, Chicago (1978).
3. M. Antler, Private communication.
4. T. G. Grau, on "Proc. 28th Electronics Components Conference, p. 102 (1978).
5. W. H. J. Vernon, *Trans. Faraday Soc.*, **23**, 113 (1927).
6. W. H. J. Vernon, *ibid.*, **27**, 255 (1931).
7. R. P. Frankenthal, Abstract 8, p. 29, The Electrochemical Society Extended Abstracts, Philadelphia, Pennsylvania, May 8-13, 1977.
8. R. J. Chessari and D. R. Blessington, Private communication.
9. U. S. National Bureau of Standards Circular 500.
10. R. G. Baker, "Ann. Conf. Marine Tech. Soc.," Vol. 2, p. 1265 (1970).
11. R. A. Sigsbee, Unpublished results.
12. S. P. Sharma, *This Journal*, **127**, 21 (1980).
13. J. P. Franey, *ibid.*, **126**, 2159 (1979).

Luminescence of the Bi³⁺ Ion in Compounds LiLnO₂ and NaLnO₂ (Ln = Sc, Y, La, Gd, Lu)

A. C. van der Steen, J. J. A. van Hesteren, and A. P. Slok

Physical Laboratory, Solid State Chemistry Department, State University, 3508 TA Utrecht, The Netherlands

ABSTRACT

The luminescence properties of the Bi³⁺ ion as an activator in the series of compounds LiLnO₂ and NaLnO₂ (Ln = Sc, Y, La, Gd, Lu) vary considerably with the host lattice composition. The Stokes shift of the emission varies from 1500 cm⁻¹ in the case of NaScO₂-Bi³⁺ to 12,800 cm⁻¹ in the case of LiYO₂-Bi³⁺. The large variation of the position of the emission band is ascribed to a Jahn-Teller effect in the excited state of the Bi³⁺ ion resulting in different kinds of minima on the ³P APES. The internal pressure on the Bi³⁺ ion, caused by the differences in the ionic radii of the trivalent cations, can explain the variation in the relative depths of the minima. The Stokes shift of the emission is inversely proportional to the energy difference between the ³P₁ and the ³P₀ excited levels. For small Stokes shifts we observed vibrational structure in the spectra. The vibrational modes involved are ascribed to more or less localized modes of the BiO₆⁹⁻ octahedron.

The luminescence properties of the Bi³⁺ ion (6s²) as an activator in oxidic host lattices have been reported by many investigators (1-7). Excitation occurs from the ¹S₀ ground state to the ³P₁ or ¹P₁ excited state. The emission transition ³P₁ → ¹S₀ yields, usually, a single broad band without structure. At relatively low temperatures, however, the lower-lying ³P₀ level acts as an optical trap and the ³P₀ → ¹S₀ transition is observed (5). This latter transition is strongly forbidden. The temperature dependence of the decay time of the ³P₁, ³P₀ → ¹S₀ transition can, therefore, deliver the energy difference (ΔE) between the ³P₁ and ³P₀ levels. This energy difference can vary considerably: e.g., LaPO₄-Bi³⁺: ΔE = 16.5 cm⁻¹ (8, 9) and MgO-Bi³⁺: ΔE = 1380 cm⁻¹ (6).

A relation was found between the trap depth ΔE and the Stokes shift of the emission transition. A small Stokes shift corresponds to a large energy difference between the ³P₁ and ³P₀ levels and vice versa (8). Consequently, vibrational structure is observed in the Bi³⁺ spectra of those compounds where the trap depth is relatively large: MO-Bi³⁺ (M = Mg, Ca, Sr): ΔE = 1030-1380 cm⁻¹ (6, 7); YAl₃B₄O₁₂-Bi³⁺: ΔE = 1080 cm⁻¹ (10); Cs₂NaYCl₆-Bi³⁺: ΔE = 1150 cm⁻¹ (11), and CaS-Bi³⁺: ΔE = 880 cm⁻¹ (12). In almost all of these cases the Bi³⁺ ion is six coordinated and replaces a smaller cation. This suggests a relatively small Bi³⁺-anion separation. In the case of MO-Bi³⁺ and CaS-Bi³⁺ this is probably even more reduced by the effective charge of the Bi³⁺ ion in the lattices.

The luminescence spectra of Tl⁺ (6s²)-activated alkali halides can show two emission bands (A_T and A_X) due to a combined effect of spin-orbit coupling and electron-lattice interaction (Jahn-Teller effect). The interaction with the ε_g and τ_{2g} vibrational modes of the TlX₆⁵⁻ octahedron (X = Cl, Br, I) results in different kinds of minima on the adiabatic potential energy surface (APES) of the ³T_{1u} (= ³P₁) relaxed excited state (RES) of the Tl⁺ ion (13).

In this paper we report on the luminescence properties of the Bi³⁺ ion in NaLnO₂ and LiLnO₂ (Ln = Sc, Y, La, Gd, Lu). In these compounds the Bi³⁺ ion is substituted for the trivalent cation. These compounds are very suitable for varying the space available for the Bi³⁺ ion without changing the site symmetry. Except for LiGdO₂ these compounds have crystal structures which can be described as ordered variants of the rocksalt structure. The Ln³⁺ ion is octahedrally co-

ordinated by oxygen ions and the site symmetry is determined by the ordering of the monovalent and trivalent cations (Table I). The α-LiFeO₂ and α-NaFeO₂ structures are presented in Fig. 1. The β-LiFeO₂ structure has two different sites for the Ln³⁺ ion.

In these series of compounds the bands in the Bi³⁺ luminescence spectra are either structureless or contain vibrational structure depending on the chemical composition. Also an indication is found for a Jahn-Teller effect in the RES of the Bi³⁺ ion. The Gd³⁺ compounds behave anomalously in certain aspects.

Experimental

Sample preparation.—Starting materials were: Na₂O₂ (Merck, p.a.), Li₂CO₃ (Merck, p.a.), Sc₂O₃ (Highways, 99.99%), Y₂O₃ (Fluka AG, puriss. C), La₂O₃ (Highways, 99.999%), Gd₂O₃ (Highways, 99.999%), Lu₂O₃ (Highways, 99.999%), and Bi₂O₃ ("Baker Analyzed" reagent).

NaLn_{0.995}Bi_{0.005}O₂ powders were prepared by firing intimate mixtures of Ln₂O₃, Na₂O₂ (40% excess), and Bi₂O₃ in a dry nitrogen atmosphere for 3-4 hr at 850°C. Samples LiLn_{0.995}Bi_{0.005}O₂ were prepared by firing intimate mixtures of Li₂CO₃ (10-20% excess), Ln₂O₃, and Bi₂O₃ for about 3 hr at 900°C in a nitrogen atmosphere. The alkaline excess is added to compensate for the sublimation losses from the reaction sample. The samples were checked by x-ray diffraction using CuKα radiation and were kept in a desiccator because they are slightly hygroscopic. We abandoned a study of LiLaO₂-Bi³⁺ in view of the marked hygroscopic character of the host lattice. Those samples which, according to their luminescence spectra, contained a small amount

Table I. Crystallographic data of the compounds studied

| Compound | Crystal structure | Site symmetry Ln ³⁺ ion | Radius ^{*,**} Ln ³⁺ ion (pm) | References |
|--------------------|------------------------|------------------------------------|--|------------|
| LiScO ₂ | α-LiFeO ₂ | D _{2d} | 75 | (15) |
| LiYO ₂ | α-LiFeO ₂ † | D _{2d} | 90 | (15) |
| LiGdO ₂ | α-HAlO ₂ | C _s | 94 | (16) |
| LiLuO ₂ | α-LiFeO ₂ | D _{2d} | 86 | (15) |
| NaScO ₂ | α-NaFeO ₂ | D _{2d} | 75 | (17) |
| NaYO ₂ | β-LiFeO ₂ | D _{2d} + D _{3d} | 90 | (18) |
| NaLaO ₂ | α-LiFeO ₂ | D _{2d} | 103 | (15) |
| NaGdO ₂ | α-LiFeO ₂ | D _{2d} | 94 | (19) |
| NaLuO ₂ | α-NaFeO ₂ | D _{2d} | 86 | (17) |

* The effective ionic radius in six coordination, see Ref. (14).

** The radius of the Bi³⁺ ion is 103 pm (14).

† Slightly distorted.

Key words: inorganic, luminescence, synthesis.

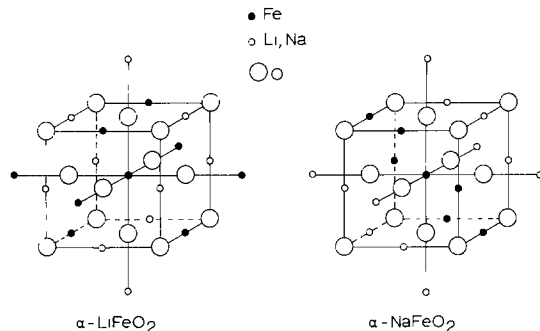


Fig. 1. The α -LiFeO₂ and α -NaFeO₂ crystal structures (schematic). To make the relation between the two structures clear, the unit cell of the rocksalt structure is drawn. Deviations from the ideal structure are not represented.

of Bi³⁺-activated sesquioxide were discarded. According to our experience luminescence is more sensitive in this aspect than x-ray diffraction. High purity Ln₂O₃ is needed, because the luminescence of other rare earth ions (e.g., Pr³⁺, Tb³⁺, and Eu³⁺) will otherwise disturb the measurements (20). Subsequent heating of the samples did not improve their quality. It is realized that samples may be somewhat inhomogeneous due to the single firing procedure.

Apparatus.—The spectra without vibrational structure were recorded on a Perkin-Elmer spectrofluorimeter (MPF-3L) equipped with an Oxford Instruments CF 100 liquid helium flow cryostat and Hamamatsu R928 photomultipliers (spectral resolution ~ 1 nm). The spectra with vibrational structure were recorded on equipment described in Ref. (11) (spectral resolution 0.1–0.2 nm). The decay experiments were performed using an EG&G 108AU Xe flash lamp (pulse width ~ 1 μ sec). The detection apparatus has been described in detail elsewhere (21). Emission spectra were corrected for photomultiplier sensitivity. The excitation spectra were corrected for the intensity distribution of the excitation monochromator, using lumogen as a standard (22). For the emission spectra, the photon flux per constant energy interval (Φ) is obtained by multiplying the radiant power per constant wavelength interval by λ^3 .

Results

NaLnO₂-Bi³⁺.—The Bi³⁺-activated NaLnO₂ compounds emit in the ultraviolet and blue spectral region, except for NaLaO₂-Bi³⁺ which has a red emission. The luminescence has a medium to high intensity. The corresponding excitation spectra consist of two bands with maxima at about 39,000 cm⁻¹ and about 28,400 cm⁻¹ (Table II). It is assumed that the former is the C absorption band and the latter the A absorption band of the Bi³⁺ ion. These correspond to the ¹S₀ \rightarrow ¹P₁ and

Table II. Maxima of the excitation and emission bands (cm⁻¹) of the luminescence of NaLnO₂-Bi³⁺ and LiLnO₂-Bi³⁺ at room temperature

| Host lattice | Excitation | | Emission | Stokes shift |
|--------------------|---------------|---------|----------|--------------|
| LiScO ₂ | $\sim 39,500$ | 31,600 | 24,700 | 6,900 |
| LiLuO ₂ | | 30,300 | 19,500 | 10,800 |
| LiYO ₂ | | 30,800 | 18,000 | 12,800 |
| LiGdO ₂ | $\sim 38,900$ | 30,200 | 21,700 | 8,500 |
| NaScO ₂ | $\sim 38,700$ | 29,800 | | |
| | | 27,700 | | |
| NaLuO ₂ | $\sim 39,100$ | 28,400* | 26,200 | 1,500 |
| NaYO ₂ | $\sim 39,400$ | 28,300* | 26,000 | 2,300 |
| NaGdO ₂ | $\sim 39,500$ | 29,100 | 26,000 | 3,100 |
| NaLaO ₂ | | 28,500 | 18,000 | 10,500 |

* Asymmetric.

the ¹S₀ \rightarrow ³P₁ transition, respectively. In this paper we only consider A band excitation. The emission spectra under C band excitation do not differ from those under A band excitation. At low temperatures vibrational structure is observed in all spectra except those of NaLaO₂-Bi³⁺ (Fig. 2 and 3).

The intensity of the low-energy part of the emission of NaGdO₂-Bi³⁺ is sample dependent. For that reason this part of the emission curve is dashed in Fig. 3. Analysis of the spectra excludes the presence of Gd₂O₃-Bi³⁺. Perhaps this part of the emission is due to Bi³⁺ pairs or to Bi³⁺ centers in inhomogeneous parts of the samples. At higher temperatures this part of the

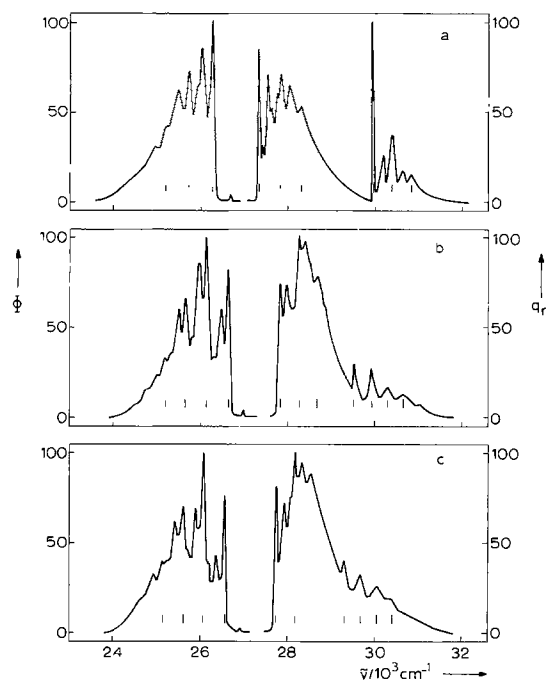


Fig. 2. The emission and excitation spectra of the luminescence of NaScO₂-Bi³⁺ (a), NaLuO₂-Bi³⁺ (b), and NaYO₂-Bi³⁺ (c) at 5 K. The emission spectra are recorded upon excitation into the maximum of the A band. The excitation spectra are obtained by recording the maximum intensity of the emission band. The peak intensities are normalized to unity. The progressions in the mode ν_2 upon the electronic origins (in excitation) and upon the one-phonon origin (in emission) are indicated. Φ denotes the photon flux per constant energy interval in arbitrary units. q_r denotes the relative quantum output in arbitrary units.

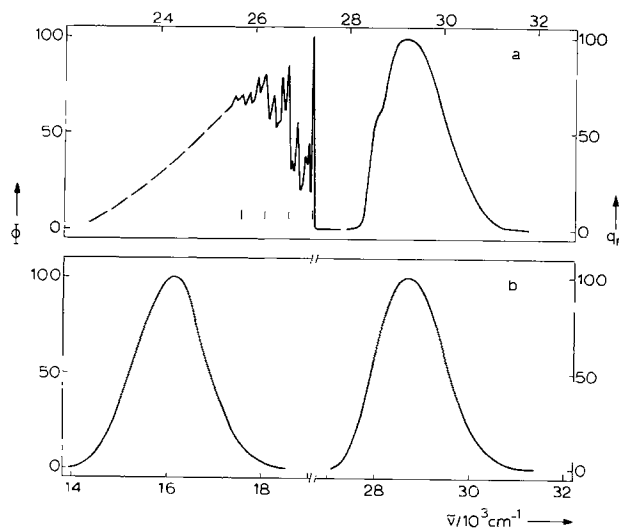


Fig. 3. The emission and excitation spectra of the luminescence of NaGdO₂-Bi³⁺ (a) and NaLaO₂-Bi³⁺ (b) at 5 K. Note the change in energy scale. See also Fig. 2.

spectrum gains intensity suggesting energy transfer. This was not studied any further.

At low enough temperatures the A excitation band of $\text{NaYO}_2\text{-Bi}^{3+}$, $\text{NaLuO}_2\text{-Bi}^{3+}$, and $\text{NaScO}_2\text{-Bi}^{3+}$ consists of two components. The energy difference between the electronic origins of both bands increases in the order $\text{Y} < \text{Lu} < \text{Sc}$. At 5 K this difference is 1558, 1710, and 2606 cm^{-1} , respectively.

The electronic origin in the emission spectrum is very weak in the case of $\text{NaLnO}_2\text{-Bi}^{3+}$ ($\text{Ln} = \text{Sc}, \text{Y}, \text{Lu}$; see Fig. 2). The electronic origin of the emission transition and that of the lowest excitation transition do not coincide; their energy difference is tabulated in Table III. No indication for an origin with a very low intensity has been found in the emission spectrum of $\text{NaGdO}_2\text{-Bi}^{3+}$. The interpretation of the more intense vibronic features in the spectra is given in Tables IV and V and are discussed later. The emission intensity of all compounds starts to quench above room temperature, except for the emission of $\text{NaLuO}_2\text{-Bi}^{3+}$ which quenches above 200 K.

$\text{LiLnO}_2\text{-Bi}^{3+}$.—The emission intensity of all compounds $\text{LiLnO}_2\text{-Bi}^{3+}$ is medium to high and does not

Table III. Parameters deduced from the fit of the temperature-dependent decay times to Eq. [1]

| Host lattice | $\tau_1/\mu\text{sec}$ | τ_2/nsec | | $\Delta E/\text{cm}^{-1}$ | $\Delta E^*/\text{cm}^{-1}$ |
|------------------|------------------------|----------------------|--|---------------------------|-----------------------------|
| | | g | | | |
| LiScO_2 | 380 | 45 | | 520 | |
| LiLuO_2 | 750 | 240 | | 280 | |
| LiGdO_2 | 10 | 200 | | 300 | |
| NaScO_2 | 210 | 25 | | 610 | 635 |
| NaLuO_2 | 650 | 15 | | 760 | 827 |
| NaYO_2 | 730 | 20 | | 740 | 830 |
| NaGdO_2 | 7† | ~100 | | ~600 | |
| NaLaO_2 | 750 | 150 | | 320 | |

* ΔE^* denotes the energy difference between the origins of the emission and the lowest excitation transition.
† The decay time changes below ~18 K from 7 to 5.5 μsec .

Table IV. The vibronic features in the excitation and emission spectra of $\text{NaLnO}_2\text{-Bi}^{3+}$ ($\text{Ln} = \text{Sc}, \text{Lu}, \text{Y}$)

| NaScO_2 | | NaLuO_2 | | NaYO_2 | | Ass.† |
|--|---------------------------------------|--------------------------------|---------------------------------------|--------------------------------|---------------------------------------|--------------------------|
| $\tilde{\nu}/\text{cm}^{-1}$ * | $\Delta\tilde{\nu}/\text{cm}^{-1}$ ** | $\tilde{\nu}/\text{cm}^{-1}$ * | $\Delta\tilde{\nu}/\text{cm}^{-1}$ ** | $\tilde{\nu}/\text{cm}^{-1}$ * | $\Delta\tilde{\nu}/\text{cm}^{-1}$ ** | |
| Excitation $^3\text{S}_0 \rightarrow ^3\text{P}_1$ | | | | | | |
| 27,330 | 0 | 27,832 | 0 | 27,755 | 0 | 0-0 |
| 27,427 | 97 | | | 27,933 | 178 | ν_b |
| 27,544 | 214 | 27,988 | 156 | | | |
| 27,632 | 302 | | | 28,094 (sh) | 339 | ν_a |
| 27,774 | 444 | 28,280 | 448 | 28,200 | 445 | $\nu_b + \nu_a$ |
| 27,847 | 517 | 28,409 | 129 | 27,352 | 148 | |
| 28,054 | 207 | | | 28,555 (br) | 355 | $2\nu_a$ |
| 28,317 (br) | 470 | 28,699 (br) | 419 | 29,313 | 0 | 0-0' |
| 29,936 | 0 | 29,542 | 0 | | | |
| 30,202 | 266 | | | 29,682 | 369 | ν_a' |
| 30,404 | 468 | 29,940 | 398 | | | |
| 30,637 | 233 | | | 30,057 | 375 | $2\nu_a'$ |
| 30,836 | 432 | 29,320 (br) | 380 | 30,395 (br) | 338 | $3\nu_a'$ |
| | | 30,684 (br) | 364 | | | $4\nu_a'$ |
| | | 31,048 (br) | 364 | | | |
| Emission $^3\text{P}_0 \rightarrow ^3\text{S}_0$ | | | | | | |
| 26,695 | 0 | 27,005 | 0 | 26,925 | 0 | 0-0 |
| 26,274 | 421 | 26,638 | 367 | 26,578 | 347 | ν_c |
| 26,040 | 234 | 26,483 | 155 | 26,369 | 189 | $\nu_c + \nu_b$ |
| 25,940 (sh) | 334 | | | 26,219 (sh) | 359 | |
| 25,747 | 527 | 26,147 | 491 | 26,103 | 475 | $\nu_c + \nu_a$ |
| 25,487 | 260 | 25,994 | 153 | 25,917 | 186 | $\nu_c + \nu_b + \nu_a$ |
| | | | | 25,733 (sh) | 370 | |
| 25,230 (br) | 517 | 25,664 | 483 | 25,621 | 482 | $\nu_c + 2\nu_a$ |
| 24,960 (br) | 270 | 25,510 | 154 | 25,440 | 181 | $\nu_c + \nu_b + 2\nu_a$ |
| | | | | 25,275 | 346 | |
| | | 25,200 (br) | 464 | 25,157 | 464 | $\nu_c + 3\nu_a$ |
| | | | | 24,959 | 198 | $\nu_c + \nu_b + 3\nu_a$ |

* sh, shoulder. br, broad.

** Emission transition: $\Delta\tilde{\nu} = (0-0) - \tilde{\nu} - i\nu_a$. Excitation transition: $\Delta\tilde{\nu} = \tilde{\nu} - (0-0) - i\nu_a$.
† The electronic origins are denoted by 0-0 and 0-0'. The phonon symbols are discussed in the text.

Table V. The vibronic features in the emission spectrum of $\text{NaGdO}_2\text{-Bi}^{3+}$

| $\tilde{\nu}/\text{cm}^{-1}$ | $\Delta\tilde{\nu}/\text{cm}^{-1}$ * | Assignment† |
|------------------------------|--------------------------------------|------------------|
| 27,233 | 0 | 0'-0 |
| 27,163 | 70 | ν_1 |
| 27,091 | 142 | ν_6 |
| 26,909 | 324 | ν_8 |
| 26,827 | 406 | $\nu_2 + \nu_1$ |
| 26,731 | 502 | ν_1 |
| 26,584 | 147 | $\nu_5 + \nu_1$ |
| 26,401 | 330 | $\nu_2 + \nu_1$ |
| 26,226 | 505 | $2\nu_1$ |
| 26,081 | 145 | $\nu_5 + 2\nu_1$ |
| 25,906 | 320 | $\nu_2 + 2\nu_1$ |
| 25,733 | 493 | $3\nu_1$ |
| 25,591 | 142 | $\nu_5 + 3\nu_1$ |

* $\Delta\tilde{\nu} = (0'-0) - \tilde{\nu} - i\nu_1$.

† The electronic origin is denoted by 0'-0. The phonon symbols are discussed in the text.

quench below 300 K. The positions of the excitation and emission bands are given in Table II. These spectra do not show vibrational structure, not even at low temperatures (Fig. 4 and 5). $\text{LiScO}_2\text{-Bi}^{3+}$ emits in the blue, whereas $\text{LiYO}_2\text{-Bi}^{3+}$ has a green emission. Two emission bands are observed for $\text{LiLuO}_2\text{-Bi}^{3+}$ (green and blue). The intensity ratio of the blue and green emission varies with temperature. The relative intensity of the blue emission has decreased to 50% of the low temperature value at about 70 K and vanishes at about 100 K. The excitation spectrum of $\text{LiLuO}_2\text{-Bi}^{3+}$ depends on the emission energy. The excitation band of $\text{LiScO}_2\text{-Bi}^{3+}$ is split into three components.

Decay times.—For all compounds the decay time of the emission is temperature dependent as is illustrated for two cases in Fig. 6. The decay curves were exponential within the limitations of the apparatus.

This temperature dependence of the decay time can be treated within the framework of a three-level

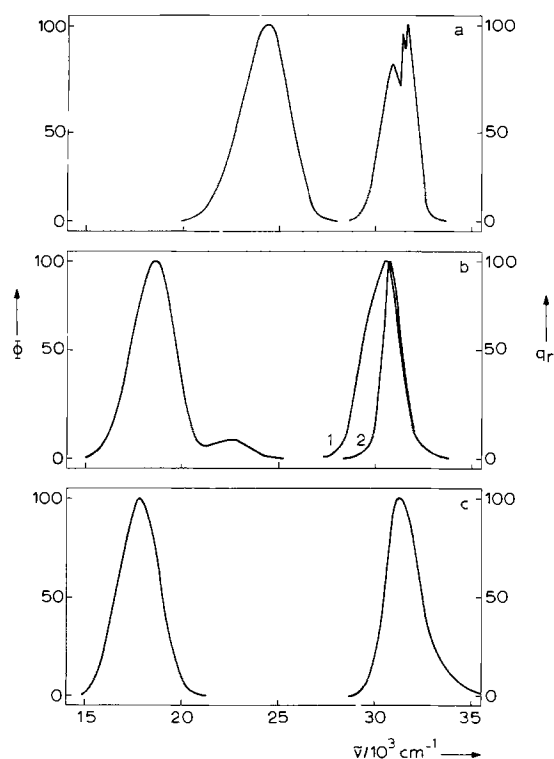


Fig. 4. The emission and excitation spectra of the luminescence of $\text{LiScO}_2\text{-Bi}^{3+}$ (a), $\text{LiLuO}_2\text{-Bi}^{3+}$ (b), and $\text{LiYO}_2\text{-Bi}^{3+}$ (c) at 5 K. For $\text{LiLuO}_2\text{-Bi}^{3+}$ the excitation spectra refer to an emission energy of 18,200, curve 1, and 22,600, curve 2, cm^{-1} . Excitation occurs at 31,000 cm^{-1} . See also Fig. 2.

scheme (see insert Fig. 6) (5, 23, 24). Levels 0, 1, and 2 correspond to the $^1\text{S}_0$, $^3\text{P}_0$, and $^3\text{P}_1$ electronic states of the Bi^{3+} ion. Excitation takes place into level 2. Emission is observed from both levels 1 and 2 to level 0 with probabilities $k_1 = \tau_1^{-1}$ and $k_2 = \tau_2^{-1}$. Further, gk_{12} and k_{21} denote the nonradiative transition probabilities between levels 1 and 2, $k_{12} = k_{21} \exp(-\Delta E/kT)$. The degeneracy of level 2 is called g . In this model two decay times are found. The long decay time can be expressed as follows, assuming $k_2 + k_{21} \gg k_1 + k_{12}$

$$\frac{1}{\tau} = k_1 + g \left(\frac{1}{k_{21}} + \frac{1}{k_2} \right)^{-1} \exp(-\Delta E/kT) \quad [1]$$

We fitted our experimental results to Eq. [1] with the parameters k_2 and ΔE . k_1 is obtained from the low temperature limit of the decay time and k_{21}^{-1} is assumed to be negligible compared to k_2^{-1} . The temperature dependence of the radiative transition probabilities and the temperature dependence of the nonradiative transitions have been neglected in this model. The parameters deduced from these fits are presented in Table III. The decay parameters of $\text{LiLuO}_2\text{-Bi}^{3+}$ relate to the green emission, the blue emission being too weak to measure its decay time. The decay time of $\text{LiGdO}_2\text{-Bi}^{3+}$ and $\text{NaGdO}_2\text{-Bi}^{3+}$ was relatively short, even at 10 K.

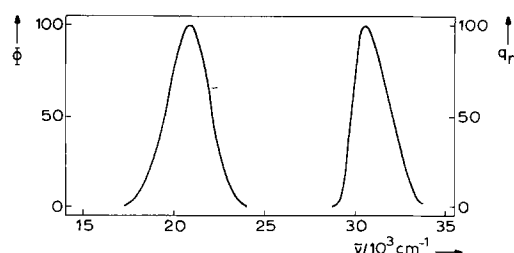


Fig. 5. The emission and excitation spectra of the luminescence of $\text{LiGdO}_2\text{-Bi}^{3+}$ at 5 K. See also Fig. 2.

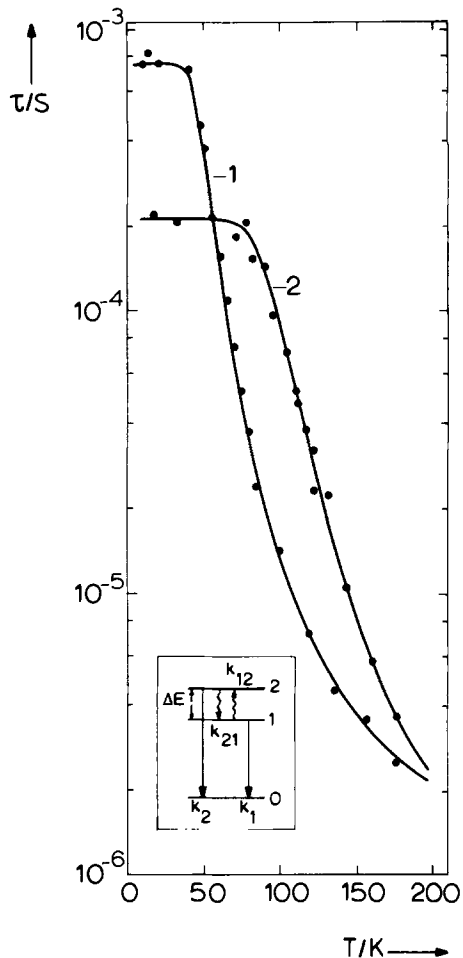


Fig. 6. The decay times of the emission of $\text{LiLuO}_2\text{-Bi}^{3+}$, curve 1, and $\text{NaScO}_2\text{-Bi}^{3+}$, curve 2, as a function of temperature. The solid lines give the best fit to the experimental data with Eq. [1]. The schematic representation of the three-level scheme (insert) is discussed in the text.

Discussion

$\alpha\text{-NaFeO}_2$ structured compounds.—There are two different sites available for the Bi^{3+} ion in NaYO_2 ($\beta\text{-LiFeO}_2$ structure, see Table I). The resemblance between the spectra of $\text{NaLuO}_2\text{-Bi}^{3+}$ and $\text{NaYO}_2\text{-Bi}^{3+}$ suggests that the Bi^{3+} ion is mainly substituted on the site with D_{3d} symmetry in the $\beta\text{-LiFeO}_2$ structure. For this reason we discuss the optical properties of $\text{NaYO}_2\text{-Bi}^{3+}$ together with those of $\text{NaScO}_2\text{-Bi}^{3+}$ and $\text{NaLuO}_2\text{-Bi}^{3+}$.

Comparison with other work on the Bi^{3+} luminescence in oxidic host lattices confirms that the higher energy excitation band ($\sim 39,000 \text{ cm}^{-1}$) corresponds to the $^1\text{S}_0 \rightarrow ^1\text{P}_1$ transition and the lower energy excitation band ($\sim 28,400 \text{ cm}^{-1}$) to the $^1\text{S}_0 \rightarrow ^3\text{P}_1$ transition (2, 4). The two components of the $^1\text{S}_0 \rightarrow ^3\text{P}_1$ excitation band are due to the crystal-field splitting of the $^3\text{P}_1$ excited state. The layered $\alpha\text{-NaFeO}_2$ structure causes a trigonal crystal field on the Bi^{3+} ion which splits the $^3\text{P}_1$ ($^3\text{T}_{1u}$) level in an orbital doublet ($^3\text{E}_u$) and an orbital singlet ($^3\text{A}_{2u}$). The intensity ratio of the two excitation bands suggests that the doublet lies lower in energy than the singlet. In a simple model this corresponds to a situation in which two 6p orbitals are situated in the layer of trivalent cations. They point to the Ln^{3+} ions, whereas the third orbital points to the Na^+ ions which results in a less favorable energy for the latter. The increase of the crystal-field splitting in the sequence $\text{NaYO}_2 < \text{NaLuO}_2 < \text{NaScO}_2$ can be related to the decrease of the radius of the Ln^{3+} ion.

The long decay time indicates that the emission transition at low temperatures is the forbidden $^3\text{P}_0 \rightarrow$

1S_0 transition. In spite of the forbidden character of this transition the zero-phonon line is observed in the emission spectrum. At elevated temperatures the 3P_1 (3E_u) level is also populated and the $^3P_1 \rightarrow ^1S_0$ transition is observed. The agreement between the ΔE values derived from the temperature dependence of the decay time of the emission transition 3P_0 , $^3P_1 \rightarrow ^1S_0$ and those obtained from the excitation and emission spectra is reasonable (Table III).

α -LiFeO₂ structured compounds.—The position of the $^1S_0 \rightarrow ^3P_1$ excitation band does not depend on the crystal structure, but on the monovalent cation. All sodium compounds (with α -LiFeO₂ and α -NaFeO₂ structure) have their $^1S_0 \rightarrow ^3P_1$ excitation band at about 28,400 cm⁻¹ and all lithium compounds at about 31,000 cm⁻¹. This agrees with the higher polarizing power of the Li⁺ ion (3). No crystal-field splitting is observed in the excitation spectra of NaGdO₂-Bi³⁺ and NaLaO₂-Bi³⁺. In the lithium series of compounds a splitting of the excitation band is only observed in the case of LiScO₂-Bi³⁺, *viz.*, 680 cm⁻¹ (compare NaScO₂-Bi³⁺ 2600 cm⁻¹). From this we conclude that the magnitude of the noncubic crystal-field component is much smaller in the α -LiFeO₂ than in the α -NaFeO₂ structured compounds. This is confirmed by the crystal-field splitting of the 7F_1 energy level of the Eu³⁺ ion in these lattices (25). The small splitting of the higher energy component in the excitation spectrum of LiScO₂-Bi³⁺ (Fig. 4) is not discussed here.

The emission spectra of the α -LiFeO₂ structured compounds can be interpreted assuming a Jahn-Teller effect in the excited state of the Bi³⁺ ion (26). Fukuda pointed out that an s² ion in cubic site symmetry can show two emission bands due to a Jahn-Teller interaction in the RES of the ion (13). The noncubic crystal field in the α -NaFeO₂ structured compounds is too large to expect such a Jahn-Teller distortion (27). However, the noncubic crystal field in the α -LiFeO₂ structured compounds is much smaller. In that case, the Jahn-Teller effect may exceed the effect of the noncubic crystal field. This suggests that: (i) the ultraviolet emission of NaGdO₂-Bi³⁺ originates from another kind of minimum (A_T) on the 3P_1 APES than the red emission of NaLaO₂-Bi³⁺ (A_X). This seems to be the only way to understand the pronounced difference between the position of the emission band of the Bi³⁺ ion in NaGdO₂ and NaLaO₂; (ii) the blue emission of LiScO₂-Bi³⁺ originates from a T minimum, the green emission of LiYO₂-Bi³⁺ from an X minimum; both emissions (A_T + A_X, blue + green) can be observed in the spectra of LiLuO₂-Bi³⁺.

Drickamer *et al.* showed that in the case of s² ion activated alkali halides, the occurrence of A_T and/or A_X emission depends also on the external pressure on the crystal (28). An increase of the pressure on the crystal destabilizes the X minimum and favors the emission from the T minimum. The change of external pressure can be compared with a change of the "internal pressure" on the Bi³⁺ ion in our series of compounds. The Bi³⁺ ion has to experience a larger internal pressure in NaGdO₂ than in NaLaO₂, since the ionic radius of the substituted Gd³⁺ ion is smaller than the ionic radius of the La³⁺ ion. The larger internal pressure in the case of NaGdO₂-Bi³⁺ results in an ultraviolet emission (A_T), contrary to the red emission (A_X) in the case of NaLaO₂-Bi³⁺, with a relatively low internal pressure. The same observations hold for the lithium series of compounds. The A_T emission is observed when the Bi³⁺ ion is substituted for the smallest ion (blue emission of LiScO₂-Bi³⁺) and the A_X emission is observed when the Bi³⁺ ion replaces the Y³⁺ ion (green emission of LiYO₂-Bi³⁺). An intermediate case is LiLuO₂-Bi³⁺ where both emissions can be observed at low enough temperatures. The excitation spectra of LiLuO₂-Bi³⁺ (Fig. 4), however,

do not agree with this model. We have no explanation for this discrepancy. We tried to find the green emission for LiScO₂-Bi³⁺ at higher temperatures, but at room temperature only the blue emission is present. The internal pressure on the Bi³⁺ ion is obviously lower in the lithium compounds than in the sodium compounds, because the variation of the Ln³⁺ ionic radius alone cannot explain the differences between cases (i) and (ii) mentioned above. Probably the Li⁺ ions have a stronger polarizing action on the oxygen anions than the Na⁺ ions. This results in a lower pressure on the Bi³⁺ ion in the lithium compounds and explains why the A_X emission is observed in the lithium compounds for smaller Li³⁺ ions than in the sodium compounds.

The interpretation of the emission bands as originating from different kinds of minima on the 3P_1 APES is supported by the decay experiments. The radiative decay time of the A_X emission has to be longer than that of the A_T emission because the 3P_2 wavefunctions are mixed with the 3P_1 wavefunctions near the X minimum (13). The decay time of the $^3P_1 \rightarrow ^1S_0$ emission (τ_2 in Table III) in the case of LiScO₂-Bi³⁺ (A_T emission) is substantially shorter than the corresponding decay times of LiLuO₂-Bi³⁺ and NaLaO₂-Bi³⁺ (A_X emission).

Our interpretation is in line with model calculations by Masunaga *et al.* for tetragonal and trigonal distortions of the 3P_1 and 3P_0 APES of an s² ion on a cubic lattice site (29). If we consider the normalized configurational coordinates bQ_3/Δ (cQ_5/Δ) [$b(c)$ is the linear coupling constant with the ϵ_g (τ_{2g}) mode and $\Delta = E_C - E_A$] to be proportional to the Stokes shift of the emission, their results can be reformulated as follows: (i) the Stokes shift is inversely proportional to the trap depth of the 3P_0 level [Fig. 9 of Ref. (29)]; (ii) the Stokes shift is proportional to the radiative decay time of the 3P_1 level [Fig. 10 of Ref. (29)]. The first relation has already been shown to be valid (8). Both relations are in accordance with our observations on the luminescence properties of the Bi³⁺ ion in α -LiFeO₂ and α -NaFeO₂ structured compounds (see Tables II and III). The fact that NaScO₂-Bi³⁺ with the smallest Stokes shift does not have the largest trap depth must be due to the large crystal-field splitting in this case. This lowers one of the 3P_1 components considerably and shows at the same time that the relation between Stokes shift and trap depth can only be used as a rule of thumb. The validity of the relations is another indication that, especially in the α -LiFeO₂ structured compounds, we can consider a Jahn-Teller interaction in the 3P RES of the Bi³⁺ ion to be effective. This is the first observation of such an effect in oxidic host lattices as far as we are aware.

There is some resemblance between the optical spectra of the Bi³⁺-activated α -LiFeO₂ structured compounds and those of 6s² ion activated alkali halides. In the latter compounds the position of the excitation band also does not vary with the monovalent cation, while the position of the emission band can vary considerably [see *e.g.*, Ref. (30)]. Recently a similar phenomenon has been observed for the Pb²⁺-activated fluorites MF₂ [M = Ca, Sr, Ba; Ref. (31)]. In view of the emission data it cannot be excluded that BaF₂-Pb²⁺ shows A_X and CaF₂-Pb²⁺ and SrF₂-Pb²⁺ A_T emission.

Bi³⁺-activated LiGdO₂ and NaGdO₂.—The compound LiGdO₂ has a different structure, *viz.*, the α -HALO₂ structure (16). The Gd³⁺ ions occupy octahedral sites. In fact the spectral properties of LiGdO₂-Bi³⁺ are not strikingly different from the other lithium compounds (see Table II and Fig. 5), although they do not fit in the Sc, Lu, Y series (note the relatively small Stokes shift). The most striking property of LiGdO₂-Bi³⁺ and NaGdO₂-Bi³⁺ is the short decay time at low temperatures (Table III). The temperature dependence of

the decay time can be described with a three-level scheme. The fitted parameters are similar to those found for the other compounds. Recently a similar short decay time was observed for monoclinic $\text{Gd}_2\text{O}_3\text{-Bi}^{3+}$ (32). For cubic $\text{Gd}_2\text{O}_3\text{-Bi}^{3+}$ Boulon has reported the (normal) long decay times (5), but this could not be confirmed in our laboratory (32).

There seems to be no special reason why in the Gd^{3+} compounds either the $^3\text{P}_0$ level would not be the lowest level or $^3\text{P}_1 \rightarrow ^3\text{P}_0$ relaxation would be very slow. An obvious possibility may be the following. The Gd^{3+} ions surrounding the Bi^{3+} ion may cause a magnetic field at the Bi^{3+} ion site. As a consequence the $^3\text{P}_1$ and $^3\text{P}_0$ levels will be mixed (33). This results in an increase of the $^3\text{P}_0 \rightarrow ^1\text{S}_0$ transition probability and a shorter decay time. Further investigations are necessary to check the feasibility of this possibility.

Vibrational structure.—The vibrational structure in the luminescence spectra of the Bi^{3+} ion in cubic symmetry has been interpreted several times (6, 11, 34, 35). Recently, one of us has analyzed successfully the vibrational structure in the luminescence spectra of $\text{Cs}_2\text{NaYCl}_6\text{-Bi}^{3+}$ by comparing the frequencies found in these spectra with those found from the Raman spectrum of $\text{Cs}_2\text{NaYCl}_6$. The following coupling mechanism, using the $k = 0$ internal modes of the BiCl_6^{3-} octahedron was proposed (11). The electric dipole allowed $^3\text{T}_{1u} \rightleftharpoons ^1\text{A}_{1g}$ ($^3\text{P}_1 \rightleftharpoons ^1\text{S}_0$) transition can be electric dipole vibronically allowed with the enabling vibrations of E_g and T_{2g} symmetry (ν_2 and ν_5). The $^3\text{T}_{1u} \rightleftharpoons ^1\text{A}_{1g}$ emission and excitation bands consist, therefore, of a progression involving the totally symmetric mode (A_{1g} , ν_1) based on the electronic origin (0-0) and on two vibronic origins (ν_2 and ν_5). The emission transition $^3\text{A}_{1u} \rightarrow ^1\text{A}_{1g}$ ($^3\text{P}_0 \rightarrow ^1\text{S}_0$) is electric dipole forbidden, but vibronically allowed by vibrations of T_{1g} symmetry. The τ_{1g} mode is not an internal vibration of the BiCl_6^{3-} octahedron. Vibrational coupling to modes of A_{1g} , E_g , and T_{2g} symmetry, based on the vibronic origin due to coupling with the τ_{1g} mode, is observed.

We realize that this approach will be less successful for the $\text{NaLnO}_2\text{-Bi}^{3+}$ compounds. The BiO_6 octahedra share edges with LnO_6 octahedra, there is possibly more than one type of Bi^{3+} center and the site symmetry of the Bi^{3+} ion is lower than cubic. In the following discussion we nevertheless analyze the main vibronic features of the spectra on the basis of a BiO_6^{9-} octahedron assuming that the symmetry of the BiO_6^{9-} group is the same as for the LnO_6^{9-} group and restricting ourselves to those features which are common to all compounds considered.

The excitation transition has two electronic origins (0-0 and 0-0') corresponding to the $^1\text{A}_{1g} \rightarrow ^3\text{E}_u$ and $^1\text{A}_{1g} \rightarrow ^3\text{A}_{2u}$ electronic transitions, respectively (Table IV). The former transition couples with two modes: ν_a and ν_b . A progression occurs in the mode ν_a , whereas ν_b is an enabling vibration (the modes can be compared with the ν_1 and ν_5 vibrational modes in the octahedral case). A progression (ν_a') is also observed for the latter transition, but the frequency is less than in the former case.

The zero-phonon line of the forbidden emission transition $^3\text{A}_{1u} \rightarrow ^1\text{A}_{1g}$ has a very weak intensity (Table IV, Fig. 2). The first intense line corresponds to coupling with a mode ν_c (compare the τ_{1g} mode in octahedral symmetry). The remainder of the vibrational structure is based on this one-phonon line. Coupling with the vibrational modes as found in the excitation spectra occurs: a progression involving the ν_a mode is observed on two vibronic origins (ν_c and $\nu_c + \nu_b$). The vibrational frequencies are summarized in Table VI. The frequency of the ν_a mode increases in the order $\text{NaYO}_2 < \text{NaLuO}_2 < \text{NaScO}_2$, which is in line with the expectation that a smaller bond length results in a

Table VI. The phonon frequencies (cm^{-1}) as observed in the excitation and emission spectra of $\text{NaLnO}_2\text{-Bi}^{3+}$ ($\text{Ln} = \text{Sc, Lu, Y, Gd}$)

| | Excitation | | | Emission | | | |
|----------|------------|------|------|----------|-----|-----|-----|
| | Sc | Lu | Y | Sc | Lu | Y | Gd |
| ν_a | 515 | 450 | 445 | 525 | 490 | 475 | 500 |
| ν_b | 210 | 155 | 175 | 240 | 155 | 185 | 145 |
| ν_c | — | — | — | 420 | 367 | 347 | — |
| ν_a' | ~465 | ~390 | ~370 | | | | |

higher frequency for the vibrational mode. The frequency of the ν_a' mode which couples with the $^1\text{A}_{1g} \rightarrow ^3\text{A}_{2u}$ transition is lower than that of the ν_a mode which couples with the $^1\text{A}_{1g} \rightarrow ^3\text{E}_u$ transition. This reflects the stronger bonding in the doublet.

Let us now turn to the Raman spectra of the host lattices. A factor-group analysis of the $\alpha\text{-NaFeO}_2$ structure (D_{3d^5} , $\text{R}\bar{3}\text{m}$) shows that there are two modes of even symmetry, viz., $\text{A}_{1g} + \text{E}_g$ (36). Both modes are Raman active. Our Raman spectra of these compounds contain two intense features at about 90 cm^{-1} and about 380 cm^{-1} (NaScO_2 : 390 cm^{-1} ; NaLuO_2 : 385 cm^{-1} ; NaYO_2 : 370 cm^{-1}). A broader and weaker structure is observed at about 530 cm^{-1} .

From these data it is hard to assign the vibrational modes with certainty. The 90 cm^{-1} feature can be recognized in the vibrational pattern of $\text{NaScO}_2\text{-Bi}^{3+}$, but is not general. If we consider the variation of the frequency of the ν_a mode, it seems probable that a model considering more or less localized modes will account for the features observed. The ν_a mode is then the totally symmetric vibration of the BiO_6^{9-} octahedron. The vibrational mode ν_c which makes the emission transition partially allowed will be more delocalized and may be correlated to the 380 cm^{-1} feature in the Raman spectra.

Due to the partially $^3\text{P}_1$ character of the $^3\text{P}_0$ level, the electronic origin is the most intense line in the emission spectrum of $\text{NaGdO}_2\text{-Bi}^{3+}$. The interpretation of the vibronic features (Table V) is very much like the $^3\text{P}_1 \rightarrow ^1\text{S}_0$ transition in the octahedral case of $\text{Cs}_2\text{NaYCl}_6\text{-Bi}^{3+}$ (11). This suggests that the treatment of the BiO_6^{9-} group as an isolated octahedron is more successful in the $\alpha\text{-LiFeO}_2$ structure than in the $\alpha\text{-NaFeO}_2$ structure.

Acknowledgments

The authors wish to thank Professor Dr. G. Blasse for stimulating this work and for the valuable criticism during the preparation of the manuscript. The investigations were performed as a part of the research program of the "Stichting voor Fundamenteel Onderzoek der Materie" (FOM) with financial support from the "Nederlandse Organisatie voor Zuiver Wetenschappelijk Onderzoek" (ZWO).

Manuscript submitted Sept. 16, 1980; revised manuscript received Jan. 19, 1981.

Any discussion of this paper will appear in a Discussion Section to be published in the December 1981 JOURNAL. All discussions for the December 1981 Discussion Section should be submitted by Aug. 1, 1981.

Publication costs of this article were assisted by the State University.

REFERENCES

1. F. A. Kröger, J. Th. G. Overbeek, J. Goorissen, and J. van den Boomgaard, *J. (and Trans.) Electrochem. Soc.*, **96**, 132 (1949).
2. G. Blasse and A. Brill, *J. Chem. Phys.*, **48**, 217 (1968).
3. G. Blasse, *J. Solid State Chem.*, **4**, 52 (1972).
4. G. Boulon, *J. Physique*, **32**, 333 (1971).
5. G. Boulon, C. Pedrini, M. Guidoni, and Ch. Pannel, *ibid.*, **36**, 267 (1975).
6. A. E. Hughes and G. P. Pells, *Phys. Status Solidi B*, **71**, 707 (1975).

7. A. F. Ellervee, *ibid.*, **82**, 91 (1977).
8. G. Blasse and A. C. van der Steen, *Solid State Commun.*, **31**, 993 (1979).
9. R. Moncorgé, G. Boulon, and J. Denis, *J. Phys. C: Solid State Phys.*, **12**, 1165 (1979).
10. F. Kellendonk, M. A. van Os, and G. Blasse, *Chem. Phys. Lett.*, **61**, 239 (1979).
11. A. C. van der Steen, *Phys. Status Solidi B*, **100**, 603 (1980).
12. N. Yamashita and S. Asano, *J. Phys. Soc. Jpn.*, **40**, 144 (1976).
13. A. Fukuda, *Phys. Rev. B*, **1**, 4161 (1970).
14. R. D. Shannon, *Acta Crystallogr., Sect. A*, **32**, 751 (1976).
15. Landbölt-Börnstein, "Numerical Data and Functional Relationships in Science and Technology," New Series, Group III, Volume 7, Crystal structure data of inorganic compounds (1976).
16. M. Gondrand and E. F. Bertaut, *Bull. Soc. Fr. Mineral. Cristallogr.*, **LXXXVI**, 301 (1963).
17. H. Brunn and R. Hoppe, *Z. Anorg. Allg. Chem.*, **430**, 144 (1977).
18. M. Gondrand, M. Brunel, and F. de Bergevin, *Acta Crystallogr., Sect. B*, **28**, 722 (1972).
19. R. Hoppe and L. Hoffmann, *Rev. Chim. Miner.*, **10**, 215 (1973).
20. G. Blasse, A. Roos, and A. C. van der Steen, *J. Solid State Chem.*, **24**, 233 (1978).
21. W. van Loo and D. J. Wolterink, *Phys. Lett. A*, **47**, 83 (1974).
22. A. Brill and A. W. de Jager-Venis, *This Journal*, **123**, 396 (1976).
23. Le Si Dang, R. Romestain, D. Simkin, and A. Fukuda, *Phys. Rev. B*, **18**, 2989 (1978).
24. B. di Bartolo, in "Optical Interactions in Solids," p. 442, John Wiley & Sons, Inc., New York (1968).
25. G. Blasse and A. Brill, *J. Chem. Phys.*, **45**, 3327 (1966).
26. A. C. van der Steen, J. J. A. van Hesteren, and A. Roos, *J. Lumin.*, **18/19**, 235 (1979).
27. W. D. Drotning and H. G. Drickamer, *Phys. Rev. B*, **13**, 4576 (1976).
-li>
28. D. Klick and H. G. Drickamer, *ibid.*, **17**, 952 (1978).
29. S. Masunaga, N. Goto, A. Matsushima, and A. Fukuda, *J. Phys. Soc. Jpn.*, **43**, 2013 (1977).
30. S. Masunaga and R. Takaue, *ibid.*, **43**, 1929 (1977).
31. V. A. Arkhangelskaya, N. E. Lushchik, V. M. Reiterov, Kh. A. Soovik, and L. M. Trofimova, *Opt. Spectrosc.*, **47**, 393 (1979).
32. O Boen Ho and G. Blasse, *J. Lumin.*, In press.
33. W. A. Runciman, N. B. Manson, and M. Marshall, *J. Lumin.*, **12/13**, 413 (1976).
34. G. S. Zavyt and A. F. Ellervee, *Phys. Status Solidi B*, **94**, 757 (1979).
35. A. C. van der Steen and L. T. F. Dijcks, *ibid.*, **104**, 283 (1981).
36. R. K. Moore and W. B. White, *J. Am. Ceram. Soc.*, **53**, 679 (1970).

A Self-Aligned Contact MOS Process for Fabricating VLSI Circuits

M. K. Khan* and G. C. Godejahn, Jr.*

Rockwell International, Microelectronics Division, Newport Beach, California 92663

ABSTRACT

A novel technique is described for fabricating silicon gate NMOSFET's having self-aligned contacts to source, drain, gate, polysilicon line, and diffused line. By employing silicon nitride as a mask in various steps of the process, contact holes were formed by selective oxidation instead of the conventional technique of etching contacts. Diffusion techniques were employed for doping the conductive regions. Electrical properties of the devices are described. The reduction obtained in the size of the individual FET's and the chip area of VLSI circuits by employing this technique are illustrated.

The MOS/VLSI technology requires higher packing density of both transistor elements and interconnect lines. The common approach to achieve higher packing density is to scale down the transistor size and interconnect lines, however, the major limitation to the scaling approach is the mask alignment tolerances which cannot be easily scaled down. The widely used 1:1 projection aligners have an alignment tolerance of typically 1 μm per layer. Because of this limitation and etch tolerance requirements, it is extremely difficult to keep the contact regions less than 3.5 μm away from the nearest active elements in a typical HMOS design as illustrated in Fig. 1.

Tanigaki *et al.* (1) developed a self-aligned contact technique for the source and drain of a silicon gate MOSFET, however, their approach does not allow for self-aligned contacts to the polysilicon gates or to the interconnect lines.

In reality the interconnect lines with the associated contact regions occupy major portions of the chip area and there has been a tendency to waste contact area to the diffused and polysilicon interconnects because of the above-mentioned mask alignment and etching tolerance requirements. A process has been developed

to form self-aligned contacts (SACMOS) to source, drain, gates, polysilicon lines, and diffused lines to achieve higher packing density of both active devices and interconnect circuitry.

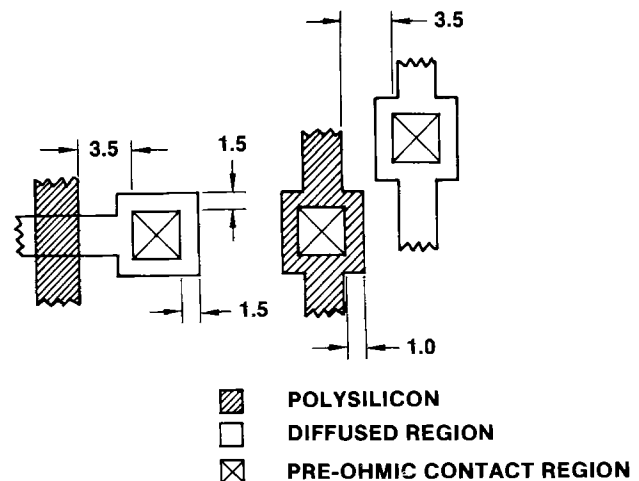


Fig. 1. Design rules for contact mask in a typical HMOS process. All dimensions are in microns.

* Electrochemical Society Active Member.

Key words: oxide-nitride dielectric, selective oxidation, polysilicon interconnects, high density circuitry.

Process Description

The process utilizes silicon nitride in various steps of the process to form self-aligned contact regions. By a combination of selective oxidation and etch techniques, contact holes are formed in the oxide grown simultaneously over polysilicon and diffused regions. In this respect, the process is different from the conventional method of etching contact holes in the thermal or deposited oxides.

The basic process steps and the cross-section of a device and interconnect poly and diffused lines are illustrated in Fig. 2(a)-(i). The starting wafers were $15\ \Omega\text{cm}$, (100) oriented, p-type silicon. An initial oxide of 500\AA was thermally grown and a silicon nitride film 500\AA thick was deposited by low pressure CVD technique. The active area was patterned with photoresist and the silicon nitride was etched off the field region. After a boron implant in the field region, a 9000\AA oxide was grown over field regions. The initial oxide and nitride were retained as the gate dielectric [Fig. 2(a)]. Next, a 7500\AA polysilicon film was deposited by low pressure CVD technique. A 500\AA oxide layer was grown on polysilicon followed by deposition of a second layer of 600\AA silicon nitride. Another 300\AA of polysilicon film was deposited over the nitride II layer and thermally converted to oxide. The intended contact regions to polysilicon (PC) were delineated by photoresist masking as shown in Fig. 2(b). The top oxide and nitride were etched using wet techniques [Fig. 2(c)]. Note that the PC mask (and later NC mask) have enlarged contact areas to allow for noncritical alignment tolerance and insure overlap on polysilicon lines. Next, the gate mask (G) was delineated and the overlapping oxide and silicon nitride edges of the PC region were etched off followed by selective etching of polysilicon. Thus the PC and G mask combination were used to define self-aligned contacts to poly lines

[Fig. 2(e)]. A similar technique was used to define a self-aligned contact region directly on the top of the gate where required. Next, a noncritical NC masking was performed to define self-aligned contact regions to the source, drains, and the N-lines [Fig. 2(f)]. The silicon nitride and underlying oxide was etched off from the N-lines. The poly oxide over poly lines and gates was also etched off simultaneously with the oxide over N-lines. During the NC mask etching, the PC nitride was protected by poly oxide II. At this step, all contact regions were covered by self-aligned nitride buttons whereas the polysilicon lines and N-lines were exposed for phosphorus diffusion or ion implantation. In this work, the phosphorus deposition was done using POCl_3 at 900°C to dope the polysilicon and N-lines [Fig. 2(g)]. Next, the structure was oxidized to grow an isolation oxide of 5000 and 6000\AA over polysilicon and N-lines, respectively. During the oxidation, the SAC regions are protected by silicon nitride buttons. The silicon nitride buttons were next removed by a plasma etch technique and the underlying 500\AA of oxide was etched off in buffered HF. Finally, phosphorus was diffused into the source, drain, NC, and PC contact regions [Fig. 2(h)].

To enhance metal step coverage and reduce crossover capacitance, a phosphorus-doped CVD SiO_2 layer was deposited on the top of the structure and a non-critical contact mask was used to etch vias to the underlying SAC's. The process was completed by sputtering Al-1% Si film followed by conventional masking and metal etching [Fig. 2(i)].

Device Characteristics

Using the foregoing process MOSFET devices having two and three-micron electrical channel lengths have been manufactured and characterized. The electrical parameters for a typical MOSFET are given in Table I. As the gate dielectric in these devices consists of silicon dioxide and silicon nitride sandwich, they were tested for threshold voltage stability. Several devices from different lots were packaged and subjected to extensive bias temperature tests at 125°C , 10V for 2000 hr. The threshold voltage shift as a function of B-T stress time is shown in Fig. 3 which indicates that the threshold voltage shift is about $40 \pm 15\ \text{mV}$ for the total time of 2000 hr. Furthermore, the slope of the curve indicates that the major shift occurs within 600 hr of the B-T stress. The formation of oxynitride film over the silicon nitride during the high temperature field oxidation was found to be an important factor in achieving the threshold stability.

Gain in Circuit Density

By virtually eliminating the contact to gate spacing of $3.5\ \mu\text{m}$ in a typical HMOS process, the length of a

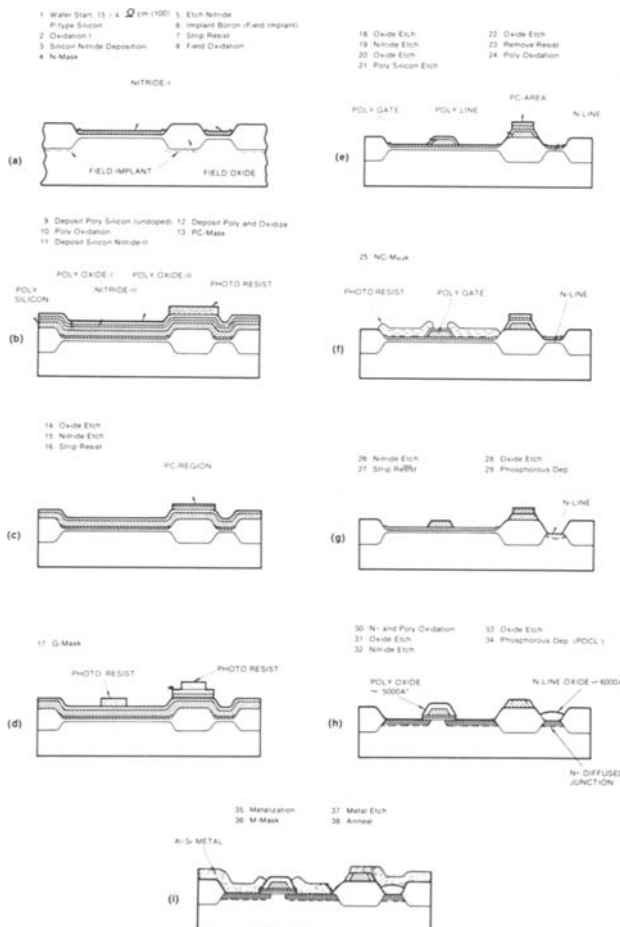


Fig. 2. SAC process flow

Table I. Typical device parameters

| | |
|----------------------------|------------------------------------|
| Equivalent Gate Oxide | $800\ \text{\AA}$ |
| Field Oxide | $8000\ \text{\AA}$ |
| Gate Width | $4.0\ \mu\text{m}$ |
| Gate Length | $4.5\ \mu\text{m}$ |
| Effective Channel Length | $3.0\ \mu\text{m}$ |
| Threshold Voltage | 0.4V |
| Conduction Factor | $30\ \mu\text{A}/\text{V}^2$ |
| Body Effect Coefficient | $0.5\ \text{V}^{-1/2}$ |
| Drains to Source Breakdown | 10V |
| Gate Dielectric Breakdown | 80V |
| Field Inversion Voltage | 8.0V |
| Junction Depths | $0.7\ \text{to}\ 0.9\ \mu\text{m}$ |

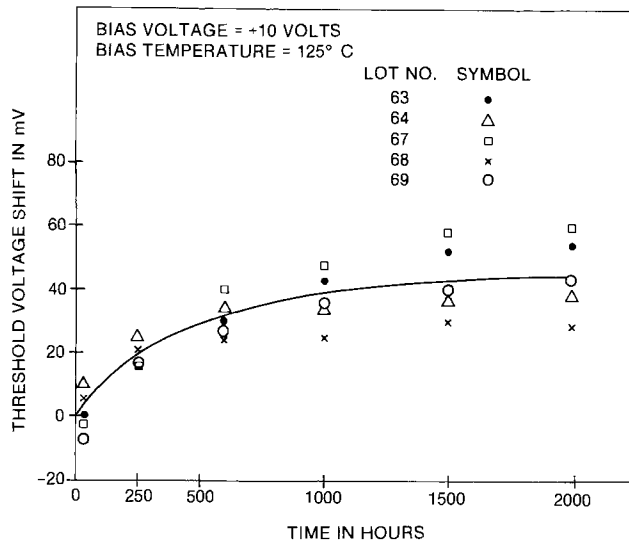


Fig. 3. Bias-temperature stability of a typical $4 \times 4 \mu\text{m}$ MOSFET's fabricated with SACMOS process.

MOSFET is reduced by $8.0 \mu\text{m}$ in the SACMOS process as shown in Fig. 4. The SAC's to interconnect polysilicon and N-lines provide additional savings in interconnect area. A 32K ROM was designed and fabricated using the SACMOS process which had a chip area of $18,800 \text{ mil}^2$. Compared to a 32K ROM chip designed to typical HMOS design rules, the SACMOS process chip was about 30% smaller, thus giving a packing density ratio of 1.3:1. It is, therefore, concluded that SACMOS

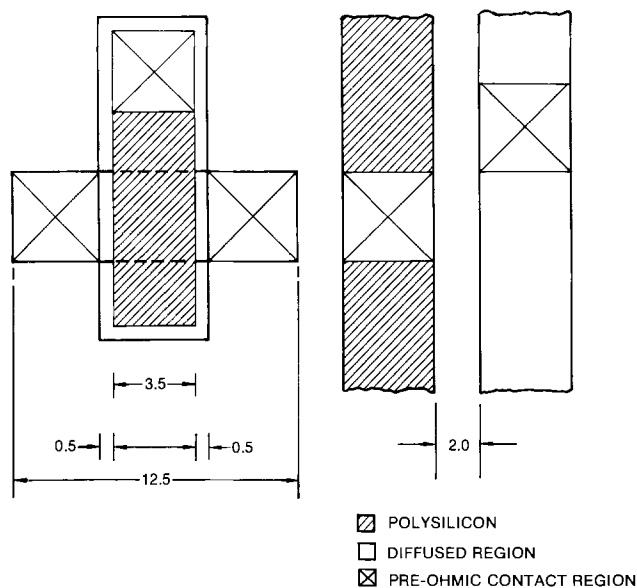


Fig. 4. Layout of a transistor and interconnect lines designed to the SACMOS process. All dimensions are in microns.

process is very effective for achieving higher packing density required for VLSI.

Discussion

During the course of this work it was discovered that retention of the thin $\sim 125\text{\AA}$ oxide layer grown on top of the silicon nitride during the field oxidation process was of paramount importance in achieving gate stability as shown in Fig. 3. Devices made without this thin oxide layer on the top nitride-oxide gates exhibited large threshold shifts due to charge trapping. An analysis of this layer by computer-aided ellipsometry indicated a refractive index of 1.46. From this data we conclude that the film was silicon dioxide rather than oxynitride as thought earlier. We think that the thin oxide layer on the top of nitride prevents charge injection from polysilicon gate into the nitride, while the charge injection from the substrate is inhibited by the thermal oxide below the nitride.

It is recognized that the SACMOS process described above is more complex than conventional NMOS but the attendant advantages of self-aligned contacts to achieve higher circuit density with relaxed alignment tolerance requirements offsets this trade-off. For example, a $4 \mu\text{m}$ NMOS process with self-aligned contacts is equivalent to a $3 \mu\text{m}$ process as far as circuit density is concerned. However, the SACMOS process has some limitations as far as scalability of the devices are concerned. The scaling principle requires thinning of gate dielectric in proportion to the horizontal shrinking of the device. As the oxide/nitride gate dielectric is made thinner the device will be more susceptible to charge trapping at oxide/nitride interface. Some preliminary work indicates that 300\AA oxide and 400\AA nitride gate structures could be made stable using the technique of oxidation of nitride described above.

Metal step coverage, was initially a major problem until sputter metallization was introduced and oxide etch process was optimized. Several complex and large circuits having approximately 6 mm on the side have been fabricated using this technology.

Acknowledgment

The authors acknowledge the contributions of N. A. Aghishian, H. G. Claudius, and G. Heimbigner in various phases of the process development and device analysis.

Manuscript submitted Feb. 11, 1980; revised manuscript received Dec. 15, 1980. This was Paper 586 presented at the Los Angeles, California, Meeting of the Society, Oct. 14-19, 1979.

Any discussion of this paper will appear in a Discussion Section to be published in the December 1981 JOURNAL. All discussions for the December 1981 Discussion Section should be submitted by Aug. 1, 1981.

Publication costs of this article were assisted by Rockwell International.

REFERENCE

1. Y. Tanigaki, S. Iwamatsu, and K. Hirobe, *This Journal*, 125, 471 (1978).

Optical and Electrical Characterization of Chemical Defects in GaAs Layers Grown by MBE

W. H. Koschel, R. S. Smith, and P. Hiesinger

Fraunhofer-Institut für Angewandte Festkörperphysik, D-7800 Freiburg, West Germany

ABSTRACT

Careful control of UHV conditions during molecular beam epitaxial growth of thin crystalline gallium arsenide layers has to be accomplished to avoid undesired incorporation of chemical defects. Residual acceptor impurities in the MBE GaAs films were detected through their characteristic photoluminescence spectra, and the effect of these compensating acceptor centers on electron mobility in n-type MBE GaAs was analyzed. A useful procedure for an accurate determination of the residual acceptor concentration in MBE GaAs is presented.

Thin gallium arsenide layers grown by molecular beam epitaxy (MBE) have the advantage of controlled thickness, composition, and doping profile (1). In particular, very thin layers ($<0.3 \mu\text{m}$) can be prepared by MBE, and successful experiments to obtain abrupt changes in doping profiles have been reported (2,3). However, the quality of MBE layers depends strongly on the conditions of the UHV system used (4-6). Sensitive methods are required to characterize the electrical and optical properties of the residual chemical defect levels (10^{13} - 10^{16} cm^{-3}) in MBE GaAs. The objective of such a characterization is to gain better control of the MBE growth process and to obtain a better understanding of the effect of compensating acceptor centers on electron mobility in n-type MBE GaAs.

This paper reports on the luminescence properties of MBE GaAs layers containing residual acceptor centers, as well as on the information that can be provided on compensation and total impurity concentration by analysis of mobility values as a function of charge carrier concentration. A useful procedure for an accurate determination of the residual acceptor concentration in n-type MBE GaAs is developed.

Experimental

Substrates used for the growth of the MBE GaAs layers were doped with either Cr (semi-insulating), Si, or Te (n^+). The substrates were lapped, then polished using a sodium hypochloride solution, and finally etched for 2 min in hot $\text{H}_2\text{SO}_4:\text{H}_2\text{O}_2:\text{H}_2\text{O}$ (7:1:1) immediately prior to transfer to the MBE growth chamber. The MBE system used was a modified commercial RIBER system with a quadrupole mass spectrometer for residual gas analysis and RHEED and Auger for surface analysis. The base pressure of the system after bakeout and with cryopanel cooling was in the 10^{-10} Torr range and during growth the pressure increased to about 10^{-7} Torr.

Etching the substrates left the surface covered with an oxide layer which was removed in the growth chamber by heating for a few minutes at 560°C in an arsenic atmosphere. The complete removal of the oxide layer was monitored by observing the development of a streaked RHEED pattern due to an As-stabilized, reconstructed (2×4) surface. After the removal of the oxide, the substrate temperature was reduced to 540°C and growth was started by opening the shutter covering the gallium oven. The gallium temperature was adjusted to give a gallium flux of about 6×10^{14} atoms/ cm^2 sec which resulted in a growth rate of about $1 \mu\text{m}/\text{hr}$. The typical growth conditions corresponded to a high As_4/Ga flux ratio. Temperatures were 900° -

1000°C for the gallium oven, 350°C for the arsenic oven, and 640° - 840°C for the tin oven which was used for n-type doping of the MBE GaAs films. A variety of characterization methods were applied to assess the effect of residual chemical defect levels on the electrical and optical properties of the MBE GaAs layers. Photoluminescence was measured with krypton laser excitation and a McPherson 1m spectrometer using a cooled S1 photocathode for detection of the near band-edge infrared emission of the MBE GaAs films. Cathodoluminescence was recorded using a commercial SEM at electron energies from 5 to 30 keV. Electrical properties of the MBE GaAs films were obtained by standard Hall effect techniques. The free electron mobilities were analyzed in n-type MBE GaAs with respect to the effect of compensating acceptor scattering centers.

Results and Discussion

MBE GaAs layers were grown with thicknesses from 1 to $10 \mu\text{m}$. A surface cleaved perpendicular to the growth direction was analyzed using an SEM in the cathodoluminescence mode. A considerable luminescence contrast is obtained at infrared wavelength 865 nm using an 8 nm bandpass (Fig. 1). The increased

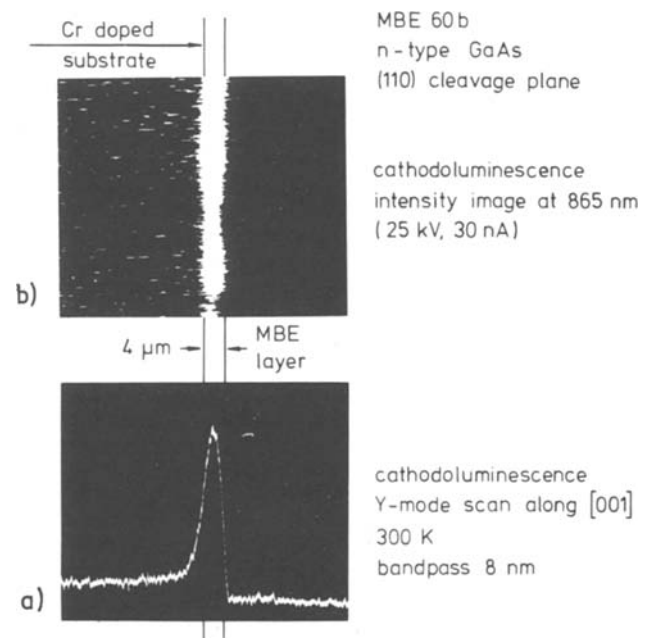


Fig. 1. SEM micrograph and cathode luminescence of an MBE GaAs layer on a GaAs:Cr substrate. (a) Cathodoluminescence (Y-mode); (b) cathodoluminescence (image).

Key words: defects, photoluminescence, MBE.

luminescence efficiency in the MBE GaAs layer is due to the doping level of 10^{15} - 10^{16} cm^{-3} in contrast to the low efficiency of the heavily compensated Cr-doped substrate. Thickness of the layers was obtained either directly from the cathodoluminescence image or by etching the cleaved surface and inspection with an optical microscope.

The residual impurity concentration of GaAs layers of the first MBE experiments in a newly installed system usually ranges from 1×10^{15} to 5×10^{16} cm^{-3} . A sensitive method to assess impurities in this concentration range is low temperature photoluminescence (PL). Figure 2 shows typical luminescence spectra of an n⁺ GaAs substrate and an MBE GaAs layer. The MBE layer exhibits the PL lines of the optically active shallow C and deeper Mn acceptors (C: $E_A = 26$ meV (7), Mn: $E_A = 110$ meV (8,9), and of the bound exciton (BE) recombination. The acceptor band of carbon, as the dominant residual impurity, is always present in the PL spectra of MBE GaAs films since for the small growth rate of $1 \mu\text{m/hr}$ a very low partial pressure (dependent on the sticking coefficient) of carbon compounds would be required in the UHV system to obtain an impurity concentration below 10^{13} cm^{-3} (4).

Hot steel parts in the original MBE system have been found to be the origin of the Mn contamination. After rebuilding the system with all hot stainless steel parts replaced by molybdenum ones, the Mn contamination was reduced to a value below the detection limit of the PL experiments ($<10^{14}$ cm^{-3} , Fig. 3). One of the main requirements for obtaining high quality n-type MBE layers is the avoidance of such undesired acceptors, which compensate shallow donor impurities and reduce the electron mobility by ionized impurity scattering. At 1.479 eV (838 nm), a further

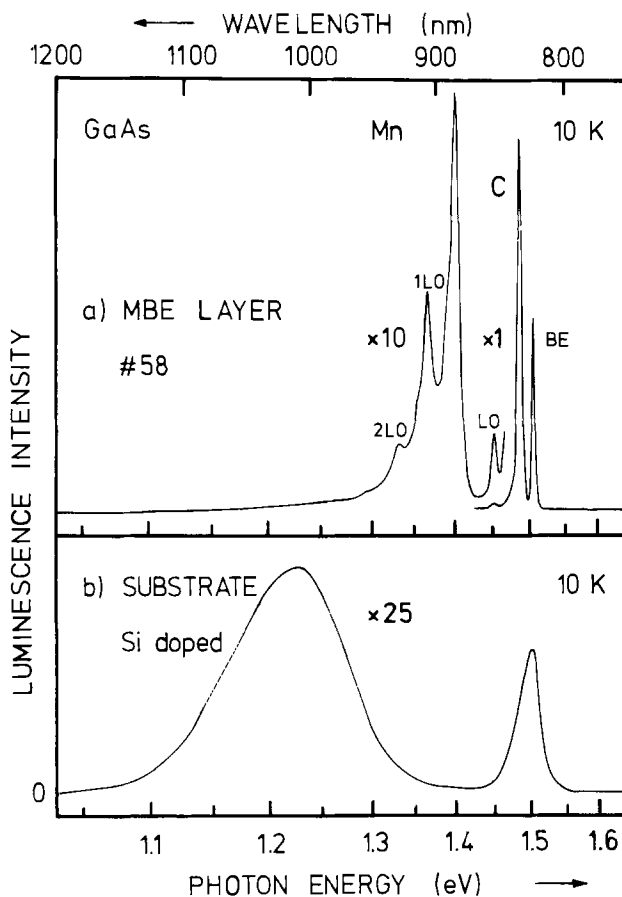


Fig. 2. (a) Photoluminescence spectrum of an MBE GaAs layer showing Mn, C, and bound exciton (BE) peaks. (b) Photoluminescence spectrum of the Si-doped substrate (n⁺).

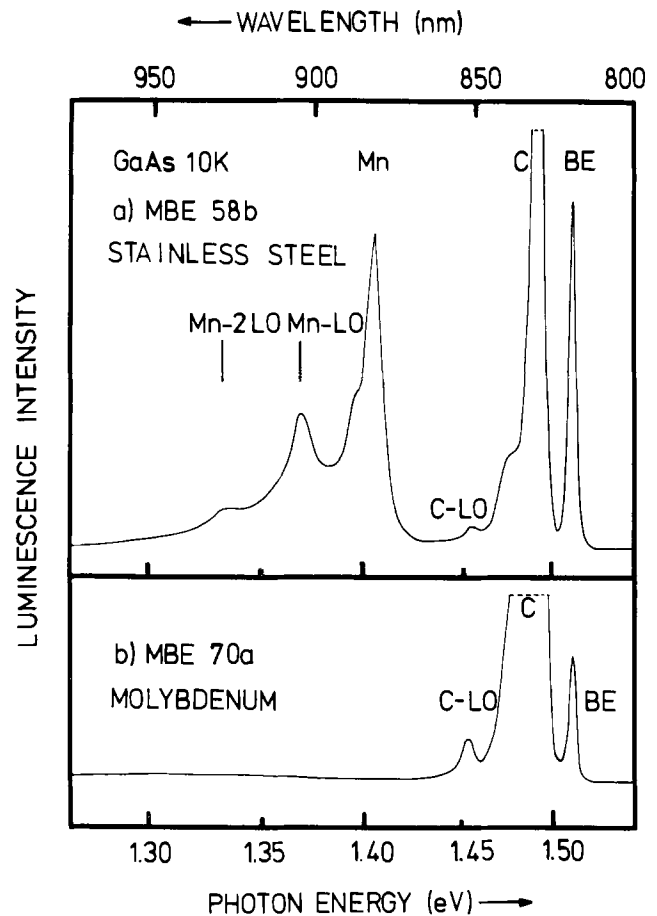


Fig. 3. (a) Photoluminescence spectrum of the Mn acceptor in an MBE GaAs layer prepared with a stainless steel sample holder. (b) Corresponding photoluminescence spectrum of an MBE GaAs layer prepared with a molybdenum sample holder.

typical PL emission in MBE GaAs material appears in Fig. 3 between the carbon line (C) and its phonon replica (C-LO). Usually, this structure is ascribed to band-acceptor recombination at Ge_{As} acceptors ($E_A = 40$ meV) (7). Since Ge is an amphoteric dopant (10, 11) it can also occupy Ga sites in the GaAs lattice (Ge_{Ga}) and become a shallow donor level. This behavior has been demonstrated in intentionally Ge-doped MBE GaAs where the donor or acceptor character of the Ge dopant was controlled through the As_4/Ga flux ratio or the substrate temperature (10, 11).

Reducing the As_4/Ga flux ratio in our MBE experiments indeed resulted in an increase of the 838 nm PL emission (Fig. 4). However, the source of the possible Ge contamination in the growth chamber could not be located.

Therefore, there is still some doubt whether or not the 1.479 eV PL emission in our MBE GaAs samples is due to Ge. The PL emission could also be due to another defect center (simple vacancy V_{As} or vacancy-related defect). The assignment to such an intrinsic defect center is supported by the fact that this PL emission has been found in most of our MBE GaAs samples and also in control samples of other laboratories independent of the As and Ga source materials and the evaporation cells (graphite, pyrolytic boron nitride) used. Since the shallow C acceptor was identified in the same MBE GaAs samples, the 1.479 eV PL emission could also be due to another C related defect center which occurs in addition to the simple C acceptor.

Electrical properties of the MBE GaAs samples were determined by van der Pauw measurements. Results for 300 K are shown in Fig. 5, where the electron mo-

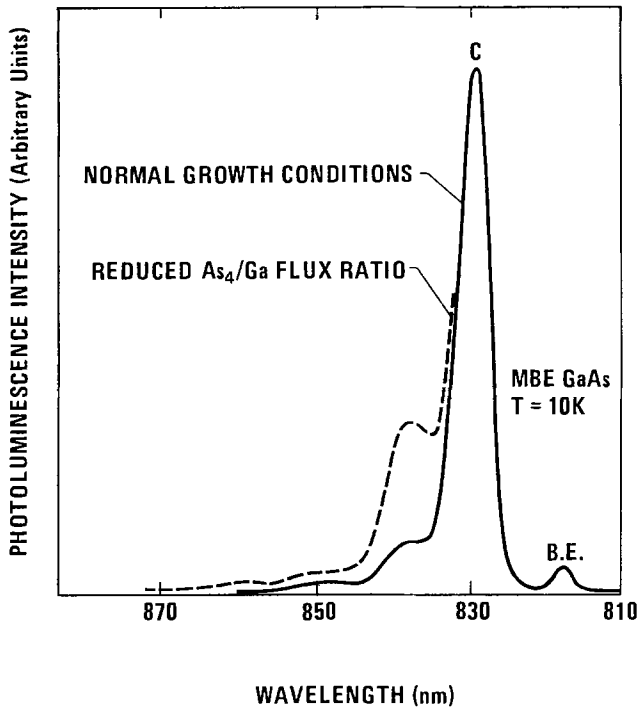


Fig. 4. Photoluminescence spectrum of MBE GaAs layers showing an additional shallow acceptor band under our normal growth conditions and under growth conditions with reduced As_4/Ga flux ratio.

bility values in n-type MBE GaAs are plotted together with the frequently used estimate of the upper mobility limit given by Rode and Knight (12). In the carrier concentration range from 1×10^{15} to $1 \times 10^{16} \text{ cm}^{-3}$, the samples were not intentionally doped, indicating the presence of donor impurities originating from the growth system. If Ge is assumed to be one of the contaminants as discussed above, Ge_{Ga} could be the donor impurity. Another possibility would be the presence of Te or Se donors in our MBE GaAs samples. However, a chemical identification of donor centers in GaAs requires the application of far infrared spectroscopy techniques (13). It is not possible to identify the donors through near infrared PL donor-acceptor spectra since the chemical shifts of the donor levels are too small to be detected.

Additional doping with Sn donors resulted in electron concentrations from 10^{16} - 10^{18} cm^{-3} . The 300 K electron mobility values of Fig. 5 are lower than the theoretical limit, indicating a considerable degree of compensation in the n-type MBE GaAs samples. In order to assess the effect of compensating acceptor scattering centers, a careful analysis of the mobility data was performed at a sample temperature of 77 K where the influence of polar optical phonon scattering

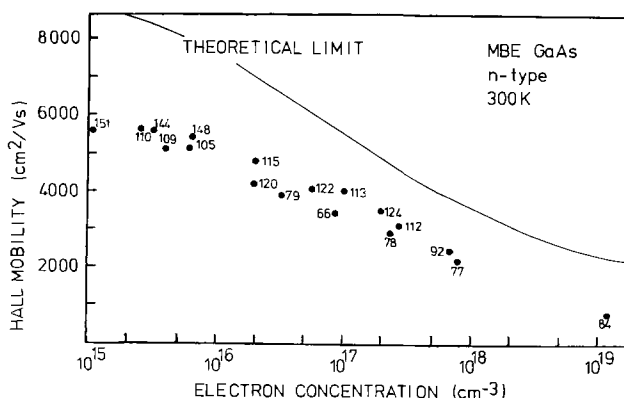


Fig. 5. Electrical properties of n-type MBE GaAs layers at 300 K (Hall mobility vs. free electron concentration).

is small. The mobility data (77 K) of Fig. 6 allow an estimate of the total acceptor concentration for each individual sample. Theoretical curves given in Fig. 6 are different from the usually used treatment by Rode and Knight (12). For higher electron concentrations ($>10^{16} \text{ cm}^{-3}$) we give a physically more realistic estimate of electron mobilities and include the pair correlation of the scattering factors of compensated semiconductors. Therefore, our determination of low temperature mobility values according to the number of ionized impurity scattering centers is similar to the theoretical treatment by Falicov and Cuevas (14).

The experimental mobility data of Fig. 6 can be evaluated with respect to the total number of acceptor centers (N_A). At low electron concentration N_A approaches a value of $5 \times 10^{15} \text{ cm}^{-3}$. The number of donor centers N_D is easily obtained since the net charge carrier concentration is $n = N_D - N_A$. For $N_D < N_A = 5 \times 10^{15} \text{ cm}^{-3}$ we therefore expect a change from n-type to p-type which was indeed observed experimentally. In Fig. 7 the net charge carrier concentration is plotted vs. the donor concentration N_D .

From the PL experiments the dominant shallow acceptor was identified as C_{As} . Our evaluation gives an accurate value of the number of these shallow C acceptors namely $5 \times 10^{15} \text{ cm}^{-3}$ for the series of growth experiments considered here. More recent series of growth experiments with improved vacuum conditions and increased area of the liquid nitrogen shroud made it possible to reduce the C contamination to a value below 10^{15} cm^{-3} . Indeed, the C concentration in the MBE GaAs layers was found to be dependent on the vacuum conditions. In recent experiments a more quantitative correlation of the CO partial pressure during growth, the C_{As} acceptor PL intensity, and the number of compensating C_{As} scattering centers in MBE GaAs has been established (15).

Conclusion

Residual shallow acceptor centers were identified in n-type MBE GaAs. The dominant shallow acceptor was found to be C_{As} in concentrations between 5×10^{14} and $5 \times 10^{15} \text{ cm}^{-3}$. The C_{As} concentration was found to be correlated with the CO partial pressure during MBE growth. C_{As} was also identified as the dominant species of compensating acceptor scattering, and is responsible for the reduced electron mobility in n-type MBE GaAs. Contamination with deeper Mn acceptors during MBE growth of GaAs was easily avoided by replacing hot stainless steel parts in the MBE system by molybdenum ones.

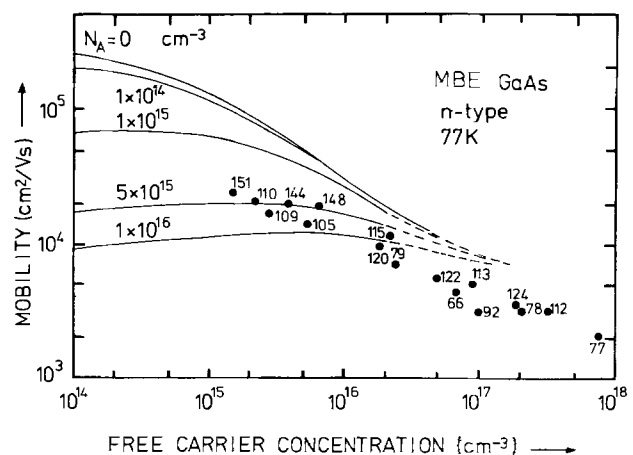


Fig. 6. Electrical properties of n-type MBE GaAs layers at 77 K (Hall mobility vs. free electron concentration). Solid lines correspond to the results of the theoretical evolution for different numbers of compensating acceptors ($N_A = 0$ to $1 \times 10^{16} \text{ cm}^{-3}$).

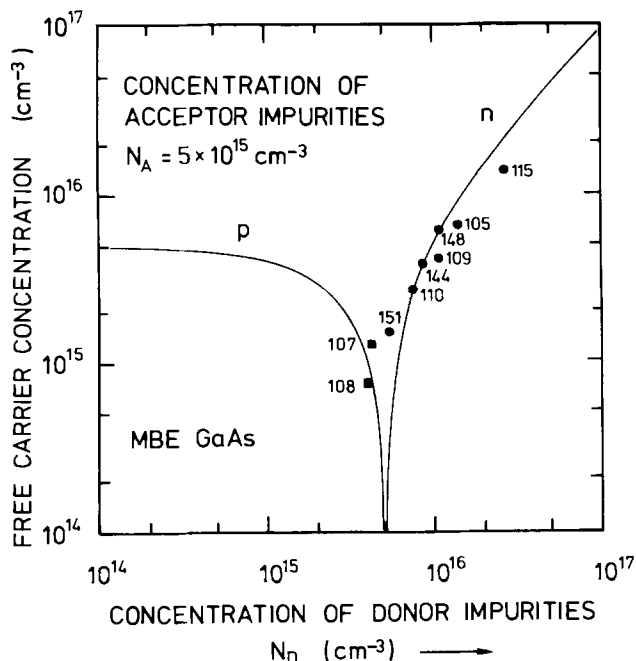


Fig. 7. Free carrier concentration of MBE GaAs layers as a function of donor concentration. The solid lines correspond to the expected behavior for a total acceptor concentration of $N_A = 5 \times 10^{15} \text{ cm}^{-3}$. A change from n-type to p-type is experimentally observed for $N_D < 5 \times 10^{15} \text{ cm}^{-3}$.

Acknowledgments

The authors would like to thank P. Ganser and H. Braun for technical assistance with MBE growth and measurements.

Manuscript received Nov. 18, 1980.

Any discussion of this paper will appear in a Discussion Section to be published in the December 1981 JOURNAL. All discussions for the December 1981 Discussion Section should be submitted by Aug. 1, 1981.

Publication costs of this article were assisted by Fraunhofer-Institut für Angewandte Festkörperphysik.

REFERENCES

1. A. Y. Cho and J. R. Arthur, Jr., *Prog. Solid State Chem.*, **10**, 157 (1975).
2. D. M. Collins, *Appl. Phys. Lett.*, **35**, 67 (1979).
3. C. E. C. Wood and B. A. Joyce, *J. Appl. Phys.*, **49**, 4854 (1978).
4. P. E. Luscher and D. M. Collins, *Prog. Crystal Growth Char.*, **2**, 15 (1979).
5. D. W. Covington and E. L. Meeks, *J. Vac. Sci. Technol.*, **16**, 847 (1979).
6. A. R. Calawa, *Appl. Phys. Lett.*, **33**, 1020 (1978).
7. D. J. Ashen, P. J. Dean, D. T. J. Hurle, J. B. Mullin, A. M. White, and P. D. Greene, *J. Phys. Chem. Solids*, **36**, 1041 (1975).
8. M. Illegems, R. Dingle, and L. W. Rupp, Jr., *J. Appl. Phys.*, **46**, 3059 (1975).
9. T. C. Lee and W. W. Anderson, *Solid State Commun.*, **2**, 265 (1964).
10. C. E. C. Wood, J. Woodstock, and J. J. Harris, in "Proc. of the Conference on GaAs and Related Compounds," St. Louis, Inst. Phys. Conf. Ser. 45, p. 28 (1978).
11. A. Y. Cho and I. Hayashi, *J. Appl. Phys.*, **42**, 4422 (1971).
12. D. L. Rode and S. Knight, *Phys. Rev. B*, **3**, 2354 (1971).
13. R. A. Cooke, R. A. Hault, R. F. Kirkman, and R. A. Stradling, *J. Phys. D. Appl. Phys.*, **11**, 945 (1978).
14. L. M. Falicov and M. Cuevas, *Phys. Rev.*, **164**, 1025 (1967).
15. G. B. Stringfellow, R. Stall, and W. Koschel, *Appl. Phys. Lett.*, **38**, 156 (1981).

Improved Electrochromic Behavior of Reactively Sputtered Iridium Oxide Films

L. M. Schiavone,* W. C. Dautremont-Smith,* G. Beni,* and J. L. Shay*

Bell Laboratories, Holmdel, New Jersey 07733

ABSTRACT

We report deposition parameters for improved electrochromic behavior of reactively sputtered iridium oxide films (SIROF's). When operated in 0.5M H_2SO_4 electrolyte, SIROF's deposited under these conditions may be bleached to a state exhibiting, to within experimental error (<0.4%), zero transmission loss in the visible. SIROF's which can be fully colored to an optical density (OD) of 0.45 (single pass), show a response time for coloring or bleaching (through a ΔOD of 0.3) of 40 msec under constant voltage address. This may be reduced to 20 msec in each direction if IR compensation is employed. Preliminary data show no difference in color/bleach cycle lifetime from that of SIROF's deposited under slightly different conditions. No change in contrast is perceivable after 2×10^7 cycles at room temperature.

Iridium oxide films, anodically grown, (AIROF's) have received much recent attention (1-4) by virtue of their many desirable electrochromic properties, in particular their short response time and good corrosion resistance in the appropriate aqueous electrolyte (3). It is accepted that electrochromism in iridium oxide thin films occurs by a reversible ion insertion mechanism, although the nature of the ion responsible for charge transport across the iridium oxide/aqueous electrolyte

interface is not agreed upon. Coloration occurs anodically by electron extraction accompanied either by H^+ extraction (3) or OH^- insertion (4). For display applications we have prepared AIROF's on transparent, electronically conducting substrates by complete anodization of a previously evaporated thin film of Ir (5). We have reported the fabrication and performance of a solid-state cell utilizing such a display electrode (6). However, the nature of the anodic growth process restricted the choice of employable solid electrolyte to a material which could be compressed between previously grown iridium oxide films, i.e., an iridium film

* Electrochemical Society Active Member.

Key words: electrochromism, ion-insertion electrode, passive displays.

deposited on an electronically insulating solid electrolyte cannot be completely converted to iridium oxide.

A further limitation of the anodic growth process is the difficulty encountered in obtaining a uniform growth rate for all display elements, even in a simple seven-segment digit. Thirdly, AIROF's may only be grown from a thin film of Ir deposited on a highly conducting substrate, thus preventing measurement of their fundamental electronic transport properties.

All of the above limitations are overcome by a direct deposition technique, and therefore, we attempted to deposit the electrochromic iridium oxide film by reactive sputtering from an iridium target. Since AIROF's are known to be highly hydrated (7), and it was believed that their rapid electrochromic kinetics were dependent on this high degree of hydration, initial attempts utilized a humidified oxygen plasma (8). However, it was determined that the electrochromic response time on subsequent immersion in aqueous electrolytes was independent of the partial pressure of H₂O in the sputtering atmosphere during deposition. Initial results (8) were very encouraging in that these reactively sputtered iridium oxide films (SIROF's) were found to have the same rapid response time as AIROF's. Furthermore, these films were found to have superior stability against both chemical and electrochemical corrosion. In fact, these films (deposited on Ta substrates) have been operated at high oxygen evolution overpotentials, i.e., potentials much higher than those applied for electrochromic behavior, for long periods of time without detectable corrosion (9). SIROF's exhibit the same low oxygen evolution overpotential behavior as do AIROF's, which however, corrode rapidly at these potentials, and are therefore being investigated for use as the anode in water electrolyzers (9). It may be noted that the cyclic voltammograms recorded for these early SIROF's were somewhat different from that of an AIROF, in particular, in their lack of distinct features and their greater current densities at low potentials (in the range 0 + 0.5V vs. RHE). From the electrochromic viewpoint, the major disadvantage of these SIROF's was a perceivable residual coloration which could not be electrochemically bleached.

In this paper we report the film deposition parameters we have successfully utilized to deposit films which could be completely electrochemically bleached to a state exhibiting effectively zero visible transmission loss. Equilibrium and kinetic behavior of these electrodes is described.

Experimental

Iridium oxide films were deposited by reactive rf sputtering in a commercial, conventional diode rf sputtering system (Cooke Vacuum Company). The 7.6 cm diam Ir target was presputtered for 20 min at an rf power density of 0.7 W cm⁻² in pure O₂ at 20 μm pressure. O₂ pressure was reduced to 2 μm and deposition commenced. A target power density of 0.7 W cm⁻² was again utilized, with a corresponding target bias of ~700V. Of importance was that the substrates were maintained in good thermal contact with the water-cooled platform. A miniature thermocouple attached to the substrate surface indicated that the substrate surface temperature did not exceed 40°C during deposition. However, in the absence of good thermal contact, or in the absence of water cooling, the substrate surface temperature achieved a maximum value of 100°C, which was found to impart some degree of haze to the as-deposited film and to reduce adhesion of at least the upper layer of the film. A deposition rate of approximately 10 Å min⁻¹ was obtained, requiring a deposition time of 90 min for a film with an available single pass optical density modulation (ΔOD) in the visible of ~0.4. As deposited, the SIROF is in a close to fully colored state.

The overall display electrode fabrication was as follows. Glass substrates previously coated with a trans-

parent, electronically conducting film of either indium-tin oxide (ITO) or tin oxide, in which the appropriate pattern (10) has been etched if a seven-segment digit was being fabricated, were cleaned with detergent and rinsed in hot water, followed by ultrasonic cleaning in distilled water and isopropyl alcohol, and a final vapor degrease in isopropyl alcohol. Photoresist (AZ 1350J) was spun on, dried, exposed, developed, well rinsed in distilled water, and again dried, to leave transparent conductor exposed in the required display electrode pattern. Since this exposed surface could not be cleaned with organic solvents before SIROF deposition, a dry etch process was used to clean this surface of photoresist residue. Preferably, sputter etching of the substrate *in situ* in the rf sputtering system prior to SIROF deposition was performed, but it was found that when ion beam etching was performed in a different vacuum system, short exposure to atmosphere was not detrimental to subsequent SIROF adhesion. The extent of etching of the transparent conductor coating was generally ~300Å. A further advantage of etching the transparent conductor is that the depth of etching may be chosen so that the combined optical thickness of the bleached SIROF on top of the etched transparent conductor is equal to, or $\lambda/2$ greater than (λ = wavelength = 550 nm), the unetched transparent conductor, whose thickness has generally already been chosen for minimum reflection. Thus, interference contrast between a bleached display segment and its surrounding is eliminated, and display brightness is maximized. Dry etching is followed by deposition of the SIROF as described, and SIROF removed from the areas in which it is not required by dissolution in acetone of the underlying photoresist. An alternative technique has been to cause the SIROF deposited onto the photoresist to lose adhesion to the photoresist by immersion in an aqueous electrolyte combined with potential pulsing between the potential limits used for the electrochromic effect. This technique leaves an insulating, protective photoresist film over the exposed transparent conductor.

Electrochemical measurements were performed in 0.5M H₂SO₄ electrolyte, and the potential applied to the SIROF electrode relative to a saturated calomel electrode (SCE) controlled by a PAR potentiostat, incorporating a coulometer, and programmer. Transmission through the electrode of an He/Ne (633 nm) laser beam was measured using an Si photodiode. Transmission and charge inserted into the electrode were monitored simultaneously on an oscilloscope and recorded photographically. Current vs. electrode potential during electrode potential triangular sweeping (cyclic voltammograms) were recorded simultaneously to transmission on a 2-pen X-Y recorder.

Results

Figure 1(a) shows a cyclic voltammogram and corresponding transmission variation of a typical SIROF/ITO electrode, recorded in 0.5M H₂SO₄ electrolyte at 10 mV sec⁻¹ scan rate. The data shown is quasi-equilibrium, i.e., is not a function of the potential scan rate (except for the current density scale). The transmission of the SIROF/ITO electrode at -0.2V vs. SCE can be seen to be 92%, equal to that of the surrounding ITO alone immersed in the aqueous electrolyte. Sweeping the potential to +1.05V continuously reduces the electrode transmission to 31% as shown, giving a 3:1 contrast ratio between the bleached and colored states equivalent to a 9:1 ratio in a device double pass configuration. In comparison to those of our early SIROF depositions (8), the voltammogram has more structure, tending towards the shape of an AIROF voltammogram (1) with, however, the major peak occurring at a potential ~0.23V less anodic than that for an AIROF. Figure 1(b) reshows this voltammogram with those of SIROF's from two other depositions. Each SIROF is of approximately the same thickness but of different area, so that for clarity of presentation absolute current, rather than current density (which

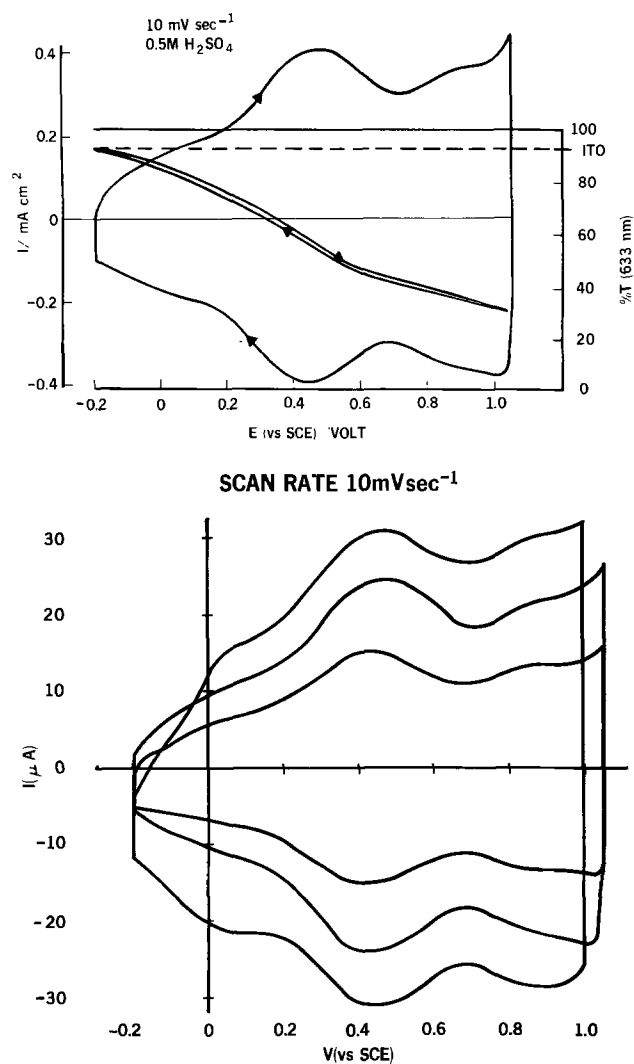


Fig. 1. (a, top) Voltammogram with simultaneous variation in optical transmission of a SIROF, ITO electrode. (b, bottom) Voltammogram of the same SIROF (middle curve) and of SIROF's for two other depositions. All as-deposited film thicknesses were $\sim 900\text{\AA}$. The voltammogram of the largest area sample (with the highest absolute current) was an initial cycle, recorded within a few minutes after immersion. The other two voltammograms were recorded after a number (>30) of color/bleach cycles.

is almost the same in each case), has been plotted. In all cases the main peak occurs at about $+0.44\text{V}$ (vs. SCE), and a higher potential peak can be observed at $\sim 0.84\text{V}$ as well as a lower potential shoulder around 0.0V . However, the shape of the largest amplitude voltammogram is characteristic of the initial color/bleach cycles of an as-deposited SIROF, whereas the other two are the "steady-state" voltammograms achieved in this case after a number (>30) of color/bleach cycles. The difference is due to hydration of the as-deposited film (11).

The relationship between the SIROF electrode potential E , the charge density inserted ΔQ , and the resultant optical density change ΔOD (633 nm) for a SIROF deposited as described is shown in Fig. 2. The thickness of this SIROF as deposited is $\sim 900\text{\AA}$; the number of electrons extracted and ions inserted (31 mC cm^{-2}) when the electrode potential is stepped from -0.200 to $+1.050\text{V}$ (vs. SCE) corresponds to $\sim 0.80/\text{Ir atom}$. The information displayed in the E vs. ΔQ curve, although recorded as a number of discrete points at equilibrium, may be obtained by integration of the voltammogram of Fig. 1(a). The right-hand curve shows an almost linear increase in optical density with inserted charge density, with an optical efficiency ($\eta = \Delta OD/\Delta Q$) of $17.9\text{ cm}^2\text{C}^{-1}$ at low insertion levels.

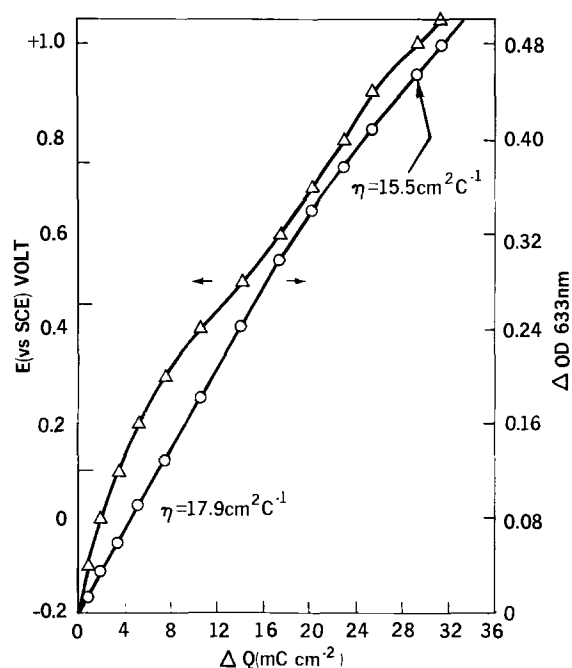


Fig. 2. Relationship between electrode potential E , inserted charge density ΔQ , and induced optical density ΔOD at 633 nm, for the SIROF of Fig. 1(a).

Over the overall voltage range of -0.200 – $+1.000\text{V}$, an average optical efficiency of $15.5\text{ cm}^2\text{C}^{-1}$ is exhibited. This is the same as the effective optical efficiency of an AIROF (10). The absorption spectrum of the induced coloration is featureless over the visible range, other than for interference effects, i.e., the colored state is black, and therefore, this optical efficiency curve, although recorded at 633 nm, applies equally to any visible wavelength.

The kinetics of the electrochromic response of a SIROF are shown in Fig. 3. The SIROF has been deposited on ITO coated glass, to facilitate the transmission measurement recorded in the upper trace, but in a geometry such that the rate of response to a potentiostatic pulse is not restricted by the sheet resistance of the transparent conductor. The lower trace records the charge insertion and extraction from the SIROF electrode, in response to an applied 1.0 Hz square wave potential with limits of -0.250 and $+1.050\text{V}$ vs. SCE. A ΔOD of 0.45 between the bleached state (of zero absorbance) and the colored state, equivalent to 0.9 in a device configuration utilizing a diffuse backscatterer, is indicated. If one arbitrarily defines the response time of the process as that during which the first two-thirds of the total (equilibrium) ΔOD occurs, in this case the first 0.3, a reasonable practical value equivalent to a 2:1 contrast, then both the coloration and bleaching process have a response time of 40

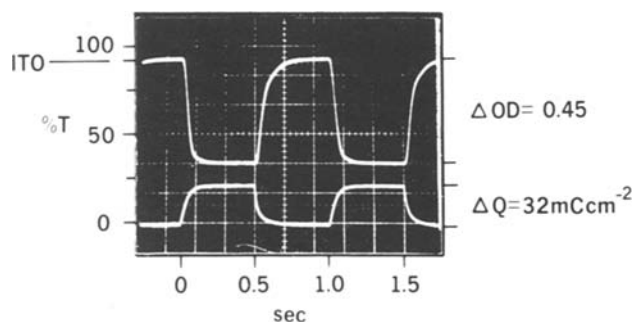


Fig. 3. Optical ($\%T$) and electrical (ΔQ) response of a SIROF electrode (900\AA as-deposited thickness) to a 1.0 Hz square wave potential with values of -0.250 and $+1.05\text{V}$ (vs. SCE) in $0.5\text{M H}_2\text{SO}_4$.

msec. However, complete (to within 1% of the final transmission) coloration and bleaching occur within 150 and 280 msec, respectively. From a perceived contrast point of view for a black-on-white display, coloration and bleaching times are about 50 and 200 msec, respectively. It should be noted that the response shown is not obtained immediately on operation of a freshly deposited SIROF, but only after the film has swelled by hydration (11). The temperature dependence of the response time of a SIROF, deposited under slightly different conditions from those described here, has been reported elsewhere (12).

Conclusions

Electrochromic iridium oxide films have been deposited by reactive sputtering from an Ir target in a pure O₂ plasma. Under the deposition conditions described here, films which could be completely bleached to zero absorbance (at $-0.2V$ vs. SCE in 0.5M H₂SO₄) have been prepared. The colored state of these films is black, and a continuous charge or voltage selectable gray scale is available. These films could be switched through an optical density change of 0.3 in either direction in 40 msec under potentiostatic address; use of IR compensated potentiostatic address (10) can reduce this response time to 20 msec in either direction. Useful low temperature response times are also shown, e.g., 0.25 sec at $-10^{\circ}C$, when IR compensation is used to eliminate the effect of increased electrolyte resistivity. The energy requirement per color/bleach cycle for films as described here which show a single pass ΔOD of 0.48 (0.96, or a contrast ratio of 9:1, in a device configuration) is 38 mJ cm⁻² cycle⁻¹ at a response time down to 40 msec. Although this energy requirement is 20% greater than that for an AIROF (due to the 20% larger voltage window utilized with the same charge density for the same contrast), it is close to the requirement of a stable (nonaqueous) WO₃ half-cell for the same contrast but at a slower response time (~ 0.3 sec). Of course, in many applications a lower contrast is acceptable, permitting the use of a thinner film, with the energy requirement linearly dependent on the required ΔOD . SIROF's deposited under conditions close, but not identical, to those described here have undergone cycle lifetime testing both at room temperature and at elevated temperature in 0.5M H₂SO₄ electrolyte. At room temperature 2×10^7 full color/bleach cycles (with approximately 50% of that time with the SIROF

having reached either the fully colored or fully bleached state) were obtained without perceived change in contrast, although a decrease in ΔQ and ΔOD of about 3% was recorded. Under the same conditions at 73°C, 2.5×10^6 cycles were obtained with a 5% decrease in ΔQ and ΔOD . Although similar life-testing of SIROF's deposited exactly as described in this work has not been performed, preliminary data show no significant difference.

Acknowledgment

We wish to acknowledge the expert assistance of Mrs. A. A. Pritchard, particularly in the SIROF deposition and electrode fabrication and the continued technical support of J. J. Wiegand.

Manuscript submitted Sept. 25, 1980; revised manuscript received Jan. 8, 1981.

Any discussion of this paper will appear in a Discussion Section to be published in the December 1981 JOURNAL. All discussions for the December 1981 Discussion Section should be submitted by Aug. 1, 1981.

Publication costs of this article were assisted by Bell Laboratories.

REFERENCES

1. S. Gottesfeld, J. D. E. McIntyre, G. Beni, and J. L. Shay, *Appl. Phys. Lett.*, **33**, 208 (1978).
2. G. Beni and J. L. Shay, *ibid.*, **33**, 567 (1978).
3. S. Gottesfeld and J. D. E. McIntyre, *This Journal*, **126**, 742 (1979).
4. G. Beni, C. E. Rice, and J. L. Shay, *ibid.*, **127**, 1342 (1980).
5. J. L. Shay, G. Beni, and L. M. Schiavone, *Appl. Phys. Lett.*, **33**, 942 (1978).
6. W. C. Dautremont-Smith, G. Beni, L. M. Schiavone, and J. L. Shay, *ibid.*, **35**, 565 (1979).
7. J. D. E. McIntyre, W. F. Peck, and S. Nakahara, *This Journal*, **127**, 1264 (1980).
8. L. M. Schiavone, W. C. Dautremont-Smith, G. Beni, and J. L. Shay, *Appl. Phys. Lett.*, **35**, 823 (1979).
9. G. Beni, L. M. Schiavone, J. L. Shay, W. C. Dautremont-Smith, and B. S. Schneider, *Nature*, **282**, 281 (1979).
10. W. C. Dautremont-Smith, L. M. Schiavone, G. Beni, and J. L. Shay, *SID 1980 Digest*, p. 122.
11. S. Hackwood, W. C. Dautremont-Smith, G. Beni, L. M. Schiavone, and J. L. Shay, *This Journal*, **128**, 1212 (1981).
12. S. Hackwood, G. Beni, W. C. Dautremont-Smith, L. M. Schiavone, and J. L. Shay, *Appl. Phys. Lett.*, **37**, 965 (1980).

Chemical Etching Characteristics of (001)InP

Sadao Adachi and Hitoshi Kawaguchi

*Nippon Telegraph and Telephone Public Corporation,
Musashino Electrical Communication Laboratory, Musashino-shi, Tokyo 180, Japan*

ABSTRACT

The chemical etching characteristics of (001)InP are studied through an SiO₂ mask in the solutions of various etching systems: (i) HCl, (ii) HCl:HNO₃, (iii) HBr, (iv) H₂SO₄:H₂O₂:H₂O, and (v) Br₂:CH₃OH. The etched depth is evaluated by using a calibrated optical microscope. The etching profiles are examined by cleaving the wafer in orthogonal directions along the (110) and $(\bar{1}10)$ planes. Various etching profiles, such as V-shaped, reverse mesa-shaped ones, and nearly vertical walls, are formed by stripes being etched on the (001) planes. The indexes of the etch-revealed planes are identified by making a comparison with the calculated angle between the (001) surface and etch-side plane. The utility of these etching solutions is also discussed for a variety of InP device applications.

Chemical etching of single crystal semiconductors plays an essential role in microelectronic solid-state

Key words: chemical etching, InP, etching profile.

device technology. Of the compound semiconductors, GaAs is most widely used in solid-state devices for specialized applications. Most of the data on etching of

GaAs that one can find in the literature (1) involve studies of the mechanisms and kinetics of the dissolution processes. Tarui *et al.* (2) have reported in detail preferential etching characteristics of GaAs in the $\text{Br}_2:\text{CH}_3\text{OH}$ system and have then demonstrated geometrically etched profiles produced in the $\{001\}$ and $\{111\}$ planes by employing this system. They have also reported a few examples of practical applications of preferential etching (etching profile) for the device-structure design and fabrication.

InP and its related compounds, such as InGaAsP, are thought to be promising materials for high-speed transistors (IC's) and electrooptical devices. There have been a few reports on the etching characteristics of InP (3-7). Tuck and Baker (4) have studied etching characteristics of InP from crystallographic aspects, *e.g.*, orientation effects on etching rates, shapes of pits and hillocks, and dissolution processes. Huber and Linh (5) have studied defect delineation in InP by using specific etchants. However, to our knowledge, there has been no report on device shaping for InP using preferential etching.

In the present paper, we report chemical etching characteristics of the (001) surface of InP in the solutions of various systems: (i) HCl, (ii) HCl:HNO₃, (iii) HBr, (iv) H₂SO₄:H₂O₂:H₂O, and (v) Br₂:CH₃OH systems. The etching profiles are examined by cleaving the (001) InP wafer in orthogonal directions along the (110) and $\bar{1}\bar{1}0$ planes and are discussed in detail from a crystallographic aspect. The profiles applicable to device-structure design and fabrication are also discussed.

Experimental

Sample.—The InP crystals employed were undoped single crystals grown by the liquid encapsulated Czochralski method. All wafers used were of (001) surface orientation with an uncertainty of 1° or less. These wafers were lapped and polished with fine abrasive alumina (0.05 μm particle size). After being degreased and rinsed in deionized water, they were chemically polished to a mirrorlike finish in a Br₂:CH₃OH solution at room temperature. The thickness of these wafers was about 100 μm to permit cleavage for the observation of etching profiles.

Masking pattern.—Etching studies were performed for the etching-selected regions of (001) surface InP through windows in an SiO₂ mask (see Fig. 1). The SiO₂ masks used were approximately 2000 Å thick and were prepared with conventional sputtering equipment. The desired geometries, in this case the window width of 30 μm wide, were defined by standard photolithography technique using AZ-1350 and an SiO₂ etchant of the HF:NH₄F:H₂O system.

Etching solution.—The etching solutions employed can be classified into the following five groups: (i) HCl system (HCl, HCl:CH₃COOH, etc), (ii) HCl:HNO₃ system, (iii) HBr system (HBr, HBr:CH₃COOH, etc),

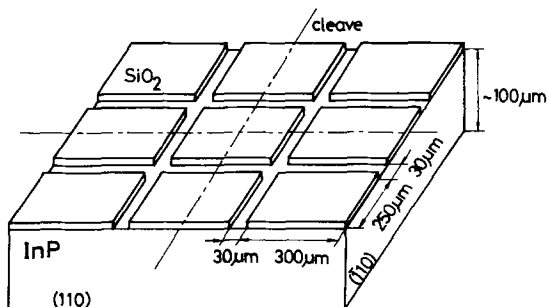


Fig. 1. An SiO₂ masking pattern on (001)InP wafer for chemical etching. The etching profiles are obtained by cleaving the wafer in orthogonal directions along the (110) and $\bar{1}\bar{1}0$ planes.

(iv) H₂SO₄:H₂O₂:H₂O system, and (v) Br₂:CH₃OH system. The chemicals used were all of reagent grade. They were as follows: HCl (12N), H₂O₂ (30%), CH₃COOH (17N), H₃PO₄ (15N), HNO₃ (14.5N), HBr (9N), H₂SO₄ (36N), K₂Cr₂O₇ (purity \geq 99.8%), Br₂ (purity \geq 99%), CH₃OH (purity 99.5%), and H₂O (deionized water). A large quantity of solution was prepared to prevent the etching temperature from rising and the etch-solution composition from varying during the experiments. Etching was carried out in a temperature-controlled water vessel without illumination. The etchant was freshly mixed prior to each experiment. Etching experiments were done by stirring by hand.

Etched depth and etching profile.—After etching, removing the SiO₂ mask, and rinsing in deionized water, the $\{110\}$ plane perpendicular to the etched one was cleaved with a razor blade and the etched depths of samples were measured with a calibrated optical microscope. The etched depths were also measured from a step height between the etched and unetched surfaces using an interference microscope. Etching profiles were observed on the (110) and $\bar{1}\bar{1}0$ cleavage planes perpendicular to the wafer surface under an optical microscope.

Etching Profile

Etch figure.—Figure 2 includes a photograph of etch figures developed on the (001) plane of InP in the H₂SO₄:H₂O₂:H₂O system, where the etch figures were

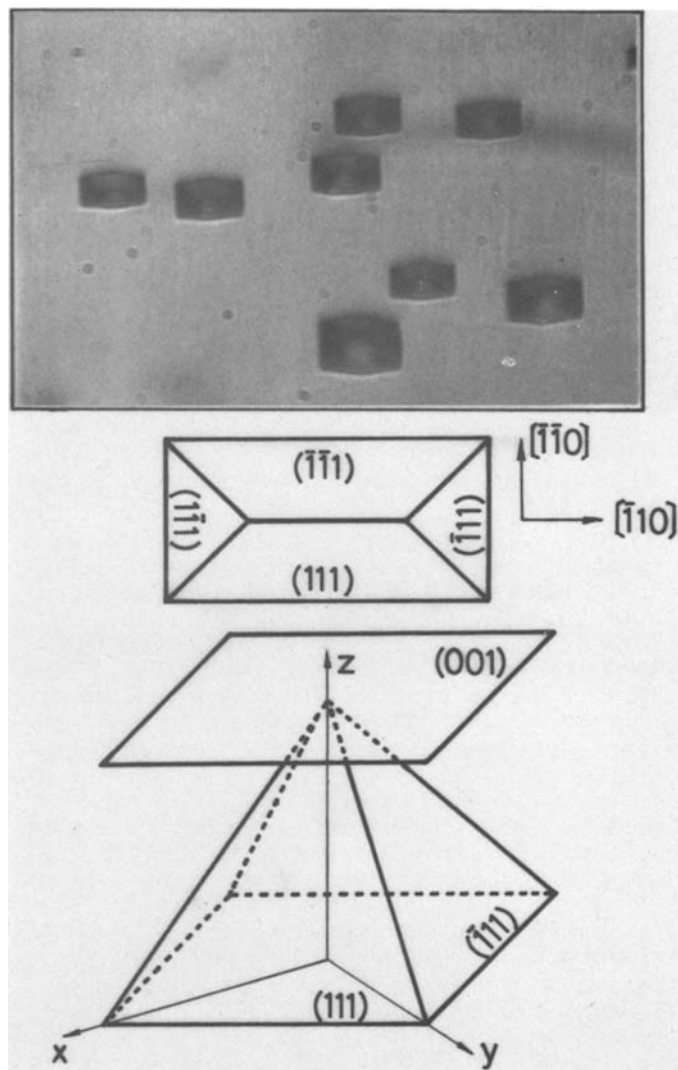


Fig. 2. Etching figures produced on the (001) plane of InP and schematic diagram of the individual etch figures.

produced by etching in the solution through pin-hole windows in an SiO_2 mask. A schematic diagram of the individual etch figures is also shown in the figure. The etch figures exhibit a rectangle-like (elongated) shape.

An important aspect of the arrangement of zincblende type crystals such as InP is the absence of a center of symmetry or inversion. Let the two sublattices of III-V compounds be labeled A^{III} and B^{V} . The A^{III} - B^{V} layers have unique orientations along the $\langle 111 \rangle$ crystal direction. The opposed (111) and $(\bar{1}\bar{1}\bar{1})$ faces and opposed $[111]$ and $[\bar{1}\bar{1}\bar{1}]$ directions may have different physical and chemical properties. Such different properties are known to arise from crystallographic polarity. If a unit cell is chosen such that the B^{V} atoms are situated at its corner, then the $\text{B}\{111\}$ planes may be referred to as $(\bar{1}\bar{1}\bar{1})$, $(11\bar{1})$, $(\bar{1}\bar{1}1)$, and $(\bar{1}11)$, while the $\text{A}\{111\}$ planes will be the corresponding negatives, i.e., (111) , $(\bar{1}\bar{1}1)$, $(1\bar{1}\bar{1})$, and $(1\bar{1}1)$. The pit figures can be successfully interpreted by a geometry constructed from the $\{111\}$ planes, as shown in the middle and lower parts of Fig. 2. The elongated pits, similar to those of Fig. 2, have also been found in III-V compounds such as GaAs (2, 8), InSb (9), and InP (4). Gatos and Lavine (9) have revealed after geometric examination that the etch figures on $(001)\text{InSb}$ are truncated (flat-bottomed) tetragonal pyramid structures, the four sides being $\{111\}$ planes. The top plane of the truncated pyramid is either flat $\{100\}$ or has higher order planes ($\{411\}$) forming a shallow angle with the $\langle 100 \rangle$ direction ($\approx 19^\circ$). Olsen *et al.* (8) have also observed in SEM photographs the truncated tetragonal pyramid etch figures on $(100)\text{GaAs}$. Tuck and Baker (4), on the other hand, have observed untruncated tetragonal pyramid etch pits on $(100)\text{InP}$, where the $(11\bar{1})$ and $(\bar{1}\bar{1}1)$ planes meet in a ridge at the bottom of the pit. From careful inspection using a differential interference microscope, we have also found that the pit figures on $(001)\text{InP}$ have untruncated tetragonal pyramid structures, as shown schematically in the middle part of Fig. 2. The elongated etch figures demonstrate the nonequivalence of $\langle 110 \rangle$ and $\langle \bar{1}\bar{1}0 \rangle$ type directions lying in a $\{001\}$ plane in the III-V intermetallic compounds. As mentioned before, this nonequivalence is known to arise from the $\langle 111 \rangle$ crystallographic polarity of zincblende type crystal. Elongated etch figures, thus, provide us a means for the unique determination of crystallographic directions between the $\langle 110 \rangle$ and $\langle \bar{1}\bar{1}0 \rangle$ type directions.

HCl system.—The etching profiles of $(001)\text{InP}$ etched in the solutions of the HCl system are shown in Fig. 3: (a) HCl (25°C , 1 min), (b) $1\text{HCl}:1\text{H}_2\text{O}_2$ (25°C , 1 min), (c) $1\text{HCl}:1\text{CH}_3\text{COOH}$ (25°C , 1 min), (d) $1\text{HCl}:1\text{H}_3\text{PO}_4$ (25°C , 1 min), (e) $1\text{HCl}:1\text{CH}_3\text{COOH}:1\text{H}_2\text{O}_2$ (25°C , 1 min), and (f) $1\text{HCl}:1\text{H}_3\text{PO}_4:1\text{H}_2\text{O}_2$ (25°C , 1 min). The cross sections are obtained by cleaving the wafers in orthogonal directions along the (110) and $(\bar{1}\bar{1}0)$ planes (see Fig. 1). The determination of crystallographic directions was made by means of the above-mentioned etch-figure test. It is clear from the figure that the etching profiles change in shape with a crystallographic rotation of 90° about the $[001]$ axis and that they exhibit crystal habits. In the case of the (110) cleavage planes, the etching profiles indicate planes are nearly perpendicular to the (001) surface and inclined planes slope downward away from the SiO_2 mask. In the case of the $(\bar{1}\bar{1}0)$ cleavage planes, the profiles indicate only the inclined planes whose sides form angles of about 35° [(a), (c), and (d)] or 55° [(b), (e), and (f)] with respect to the (001) surface. Consequently, the etching profile of the $(\bar{1}\bar{1}0)$ cleavage plane [Fig. 3(a)] clearly shows a V-

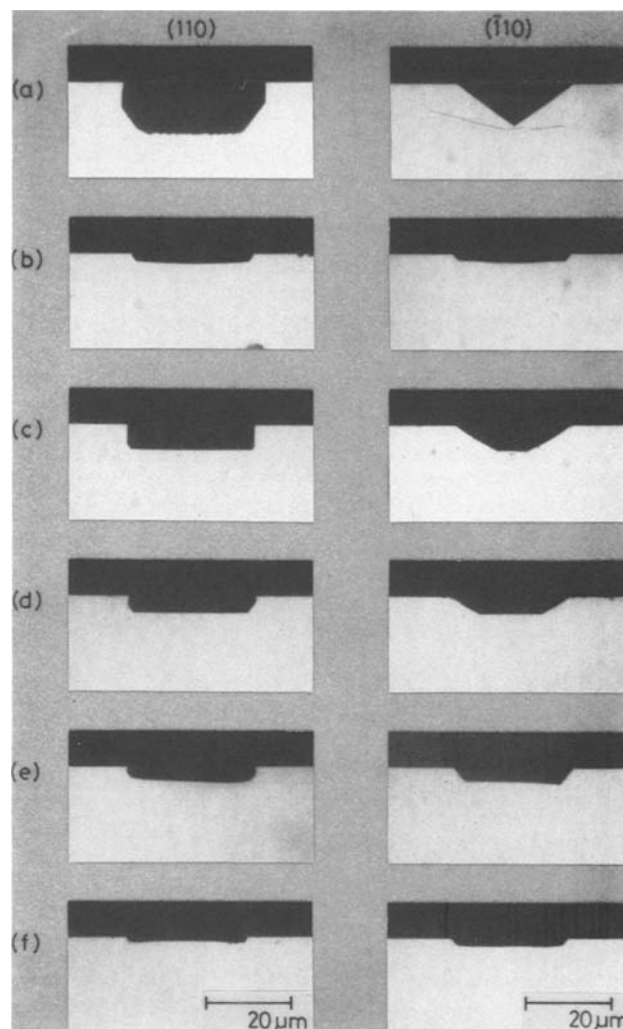


Fig. 3. Etching profiles of $(001)\text{InP}$ etched in the solutions of the HCl system: (a) HCl (25°C , 1 min), (b) $1\text{HCl}:1\text{H}_2\text{O}_2$ (25°C , 1 min), (c) $1\text{HCl}:1\text{CH}_3\text{COOH}$ (25°C , 1 min), (d) $1\text{HCl}:1\text{H}_3\text{PO}_4$ (25°C , 1 min), (e) $1\text{HCl}:1\text{CH}_3\text{COOH}:1\text{H}_2\text{O}_2$ (25°C , 1 min), and (f) $1\text{HCl}:1\text{H}_3\text{PO}_4:1\text{H}_2\text{O}_2$ (25°C , 1 min).

shaped groove profile forming a V-groove angle of 110° (angle between two inclines). If the etching time is properly chosen according to the V-groove width, depth, and corresponding etching rate, one can also easily fabricate the V-shaped groove in the $\langle \bar{1}\bar{1}0 \rangle$ direction on $(001)\text{InP}$ by chemical etching in solutions such as $1\text{HCl}:1\text{H}_2\text{O}_2$ and $1\text{HCl}:1\text{CH}_3\text{COOH}:1\text{H}_2\text{O}_2$ (V-groove angle of 70°).

HCl:HNO₃ system.—The etching profiles of $(001)\text{InP}$ etched in the solutions of the HCl:HNO₃ system are shown in Fig. 4: (a) $1\text{HCl}:1\text{HNO}_3$ (25°C , 1 min), (b) $1\text{HCl}:2\text{HNO}_3$ (25°C , 1 min), (c) $2\text{HCl}:1\text{HNO}_3$ (25°C , 1 min), (d) $1(1\text{HCl}:1\text{HNO}_3):1\text{H}_2\text{O}_2$ (25°C , 1 min), (e) $1(1\text{HCl}:1\text{HNO}_3):1\text{H}_2\text{O}_2$ (25°C , 1 min), and (f) $1(1\text{HCl}:1\text{HNO}_3):1\text{CH}_3\text{COOH}$ (25°C , 1 min). The etching profiles of the (110) cleavage planes [Fig. 4(a), (b), (c), and (f)] indicate the planes are nearly perpendicular to the (001) surface, similar to those of the HCl system. The profile of the $(\bar{1}\bar{1}0)$ cleavage plane [Fig. 4(c)] indicates the inclined planes forming an angle of 35° with respect to the (001) surface, but those of Fig. 4(a) and (b) do not exhibit clear crystal habits. If one chooses proper etching time, the $2\text{HCl}:1\text{HNO}_3$ solution also makes it possible to fabricate a V-shaped groove whose sides form an angle of 110° (i.e., an angle of V-shaped groove). As one can see in Fig. 4(d), (e), and (f), the etching rate reduced abruptly with

an addition of H_2O , H_2O_2 , or CH_3COOH in the solution of the $HCl:HNO_3$ system [see also Table I].

HBr system.—The etching profiles of (001)InP etched in the solutions of the HBr system are shown in Fig. 5: (a) HBr (25°C, 1 min), (b) 1HBr:1H₂O₂ (25°C, 1 min), (c) 1HBr:1CH₃COOH (25°C, 1 min), (d) 1HBr:1H₃PO₄ (25°C, 1 min), (e) 1HBr:1HNO₃ (25°C, 1 min), and (f) 1HBr:1HNO₃:5H₂O (25°C, 1 min). The profiles of Fig. 5(a) indicate the inclined planes for both the (110) and (110) cleavage planes forming an angle of 55° with respect to the (001) surface. The side-etch speed of the (110) cleavage plane is faster than that of the (110) cleavage plane. The cross sections demonstrated in Fig. 5(b) exhibit a reverse mesa-shaped and mesa-shaped profiles for the (110) and (110) cleavage planes, respectively. The etched sides for the (110) and (110) cleavage planes form angles of 125° and 55°, respectively, with respect to the (001) surface. Such profiles are quite similar to those on (001)GaAs etched with H₂SO₄:H₂O₂:H₂O (10) and Br₂:CH₃OH solutions (2). The profile shown in Fig. 5(c) [(110) cleavage plane] exhibits the reverse mesa-shaped and mesa-shaped structures in addition to the flat-bottomed plane. The reverse mesa-shaped and mesa-shaped planes form angles of 110° and 55°, respectively, with respect to the (001) surface. The profile of the (110) cleavage plane [Fig. 5(c)], on the other hand, exhibits only the inclined planes forming an angle of 55° with respect to the (001) surface. Similar etching profiles have also been obtained by Otsubo *et al.* (11) on (001)GaAs with etching in a solution of the C₃H₄(OH)(COOH)₃·H₂O:H₂O₂:H₂O system. The etching profiles of Fig. 5(d) are the same as those of Fig. 5(a). The profiles of Fig. 5(e) and (f) are also quite similar to those of Fig. 5(b), but they do not reveal clear crystallographic planes.

H₂SO₄:H₂O₂:H₂O system.—The etching profiles of (001)InP etched in the solutions of the H₂SO₄ system are shown in Fig. 6: (a) 1H₂SO₄:1H₂O₂ (60°C, 20 min), (b) 3H₂SO₄:1H₂O₂:1H₂O (60°C, 20 min), (c) 1H₂SO₄:1H₂O₂:1H₂O (60°C, 20 min), and (d) 3(2N-K₂Cr₂O₇):1H₂SO₄:1HCl (60°C, 20 min). The profiles of the (110) cleavage planes [Fig. 6(a)-(c)] indicate the planes are nearly perpendicular to the (001) surface, while those of the (110) cleavage planes indicate the inclined sides that slope downward away from the SiO₂ mask. The profiles of the (110) cleavage planes [Fig. 6(a) and (b)] exhibit the mesa-shaped structure, but they do not indicate clear crystal habits, in contrast to that of Fig. 6(c).

The H₂SO₄:H₂O₂:H₂O system is known to be one of the most commonly employed etchants for GaAs (11). Chemical polishing by using this system also gives high-quality GaAs surfaces of low-index orientations except for the Ga{111} surface. However, the etching rates of this system for InP are two or three orders smaller than those for GaAs. The system, moreover, sometimes produces elliptical etch pits on the (001) surface of InP. The photograph of the elliptical etch pits are demonstrated in the lower part of Fig. 6(c). The long- and short-axis directions of the ellipsoid correspond to the [110] and [110] directions, respectively. The profile of the (110) cleavage plane of (001)InP etched in the solution of 3(2N-K₂Cr₂O₇):1H₂SO₄:1HCl [Fig. 6(d)] exhibits the mesa-shaped structure, in contrast to those of the H₂SO₄:H₂O₂:H₂O systems. The profile of the (110) cleavage plane also exhibits the mesa-shaped structure (revealing clear crystal habits), as similar to those found in Fig. 6(a)-(c). This etchant system produces etch-pit free surfaces and moreover provides high-quality InP surfaces. It was found that the etching rates of this system were increased by increasing HCl at a constant ratio of

Table I. The composition of the etchants in parts by volume, etching condition, etched depth, and identified crystallographic planes revealed by etching

| Etchant | Etching condition | | Etched depth (μm) | Identified planes | |
|--|-------------------|------------------|-------------------|-------------------|-------|
| | Time (min) | Temperature (°C) | | (110) | (110) |
| HCl | 1 | 25 | 12.0 | {110}, {111} | {112} |
| 1HCl:1H ₂ O | 1 | 25 | 0.07 | | |
| 1HCl:1H ₂ O ₂ | 1 | 25 | 2.3 | {110}, {111} | {111} |
| 1HCl:1CH ₃ COOH | 1 | 25 | 6.0 | {110} | {112} |
| 1HCl:1H ₃ PO ₄ | 1 | 25 | 4.0 | {110}, {111} | {112} |
| 1HCl:1H ₂ O ₂ :1H ₂ O | 1 | 25 | 0.1 | | |
| 1HCl:1CH ₃ COOH:1H ₂ O ₂ | 1 | 25 | 4.0 | {110}, {111} | {111} |
| 1HCl:1H ₃ PO ₄ :1H ₂ O ₂ | 1 | 25 | 2.0 | † | {111} |
| 1HCl:1HNO ₃ | 1 | 25 | 6.5 | {110} | † |
| 1HCl:2HNO ₃ | 1 | 25 | 7.0 | {110} | † |
| 2HCl:1HNO ₃ | 1 | 25 | 8.5 | {110}, {111} | {112} |
| 1(1HCl:1HNO ₃):1H ₂ O | 1 | 25 | 0.15 | | |
| 1(1HCl:1HNO ₃):1H ₂ O ₂ | 1 | 25 | 0.5 | † | {111} |
| 1(HCl:1HNO ₃):1CH ₃ COOH | 1 | 25 | 1.0 | {110} | {112} |
| HBr | 1 | 25 | 6.5 | {111} | {111} |
| 1HBr:1H ₂ O ₂ | 1 | 25 | 23 | {111} | {111} |
| 1HBr:1CH ₃ COOH | 1 | 25 | 3.0 | {111}, {221} | {011} |
| 1HBr:1H ₃ PO ₄ | 1 | 25 | 2.0 | {111} | {111} |
| 1HBr:1HNO ₃ | 1 | 25 | 11.0 | † | {111} |
| 1HBr:1HNO ₃ :5H ₂ O | 1 | 25 | 9.0 | † | † |
| 1H ₂ SO ₄ :1H ₂ O ₂ | 20 | 60 | 4.0 | {110} | † |
| 3H ₂ SO ₄ :1H ₂ O ₂ :1H ₂ O | 20 | 60 | 3.5 | {110} | † |
| 1H ₂ SO ₄ :1H ₂ O ₂ :1H ₂ O | 20 | 60 | 2.5 | {110} | {111} |
| 3(2N-K ₂ Cr ₂ O ₇):1H ₂ SO ₄ :1HCl | 20 | 60 | 2.0 | † | {111} |
| 4% Br ₂ :CH ₃ OH | 1 | 25 | 25 | {111} | {111} |
| 2% Br ₂ :CH ₃ OH | 1 | 25 | 18 | {111} | {111} |
| 1% Br ₂ :CH ₃ OH | 1 | 25 | 12 | {111} | {111} |
| 0.2% Br ₂ :CH ₃ OH | 2 | 25 | 7.0 | {111} | {111} |
| 0.1% Br ₂ :CH ₃ OH | 4 | 25 | 8.0 | {111} | {111} |

† Etching profile does not exhibit clear crystal habits.

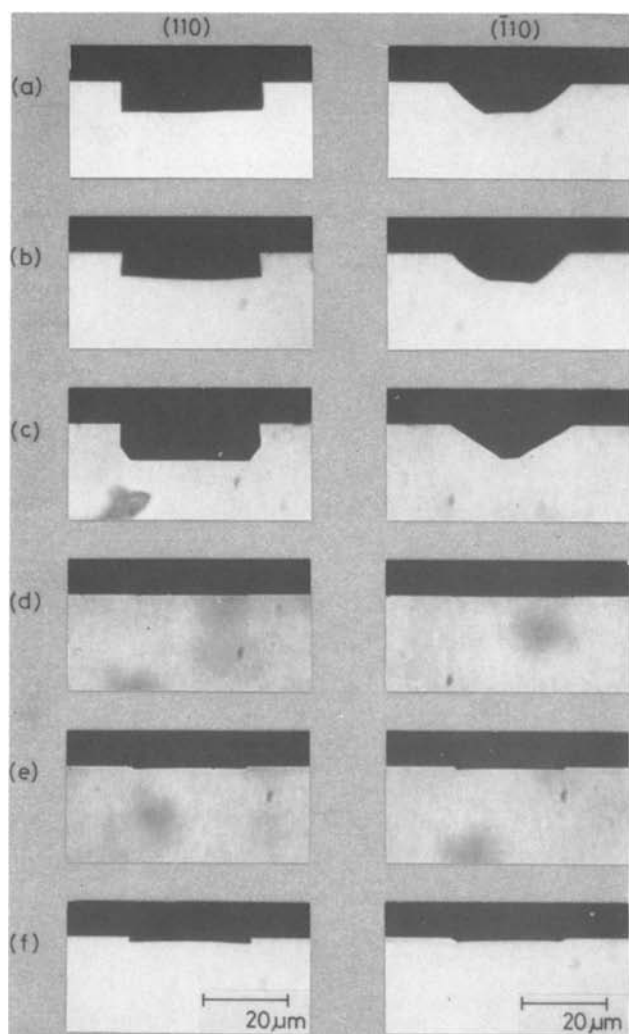


Fig. 4. Etching profiles of (001)InP etched in the solutions of the HCl:HNO₃ system: (a) 1HCl:1HNO₃ (25°C, 1 min), (b) 1HCl:2HNO₃ (25°C, 1 min), (c) 2HCl:1HNO₃ (25°C, 1 min), (d) 1(1HCl:1HNO₃):1H₂O (25°C, 1 min), (e) 1(1HCl:1HNO₃):1H₂O₂ (25°C, 1 min), and (f) 1(1HCl:1HNO₃):1CH₃COOH (25°C, 1 min).

2N-K₂Cr₂O₇ and H₂SO₄ without any change of the surfaces states; $\approx 0.1 \mu\text{m}/\text{min}$ [3(2N-K₂Cr₂O₇):1H₂SO₄:1HCl], $\approx 1.0 \mu\text{m}/\text{min}$ [3(2N-K₂Cr₂O₇):1H₂SO₄:2HCl], and $\approx 2.0 \mu\text{m}/\text{min}$ [3(2N-K₂Cr₂O₇):1H₂SO₄:3HCl] at 60°C. Details of these etching solutions will be presented in the near future.

Br₂:CH₃OH system.—It is well known that the Br₂:CH₃OH systems give good results for preferential etching of GaAs(2). The etching rates can be easily controlled by varying the Br₂ concentrations in CH₃OH. These systems are also usually employed as the etchants, capable of producing highly polished surfaces on GaAs. Figure 7 shows the etching profiles of (001)InP etched in the solutions of the Br₂:CH₃OH system: (a) 4% by volume Br₂:CH₃OH (25°C, 1 min), (b) 2% by volume Br₂:CH₃OH (25°C, 1 min), (c) 1% by volume Br₂:CH₃OH (25°C, 1 min), (d) 0.2% by volume Br₂:CH₃OH (25°C, 2 min), and (e) 0.1% by volume Br₂:CH₃OH (25°C, 4 min). The profiles of the (110) cleavage planes exhibit the reverse mesa-shaped structure forming an angle of 125° with respect to the (001) surface, while those of the (110) cleavage planes exhibit the mesa-shaped structure forming an angle of 55° with respect to the (001) surface. Such features are quite similar to those of (001)GaAs etched with the Br₂:CH₃OH (2) and H₂SO₄:H₂O₂:H₂O systems (10). The profiles are also the same as those of InP etched with the 1HBr:1H₂O₂ solution [see Fig. 5(b)].

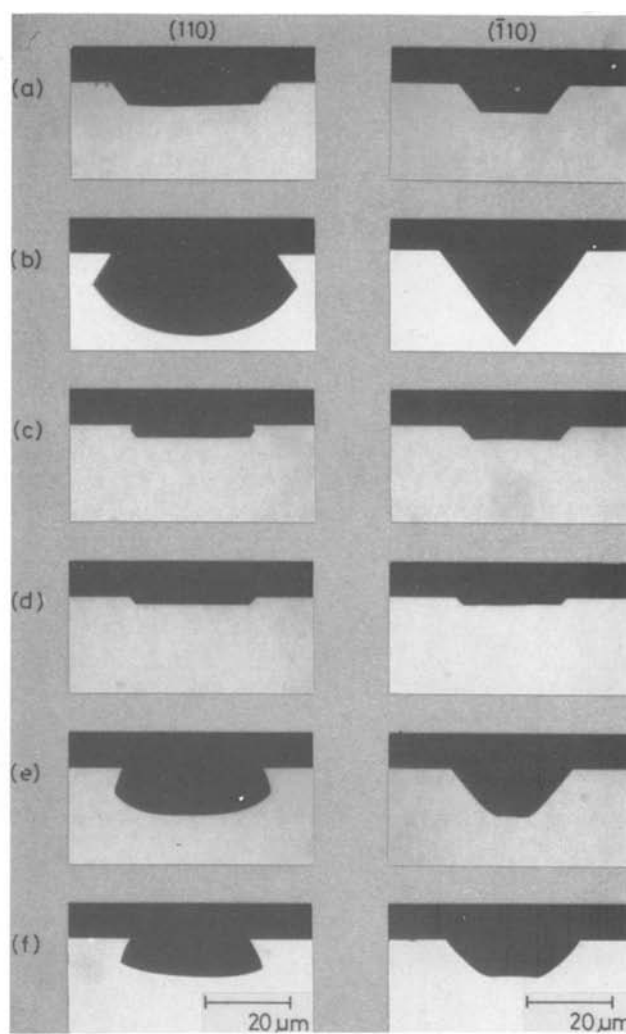


Fig. 5. Etching profiles of (001)InP etched in the solutions of the HBr system: (a) HBr (25°C, 1 min), (b) 1HBr:1H₂O₂ (25°C, 1 min), (c) 1HBr:1CH₃COOH (25°C, 1 min), (d) 1HBr:1H₃PO₄ (25°C, 1 min), (e) 1HBr:1HNO₃ (25°C, 1 min), and (f) 1HBr:1HNO₃:5H₂O (25°C, 1 min).

The etching rates are found to vary from 2 $\mu\text{m}/\text{min}$ (0.1% by volume) to 25 $\mu\text{m}/\text{min}$ (4% by volume) with the Br₂ concentrations in CH₂OH.

Crystallographic aspect.—In this subsection, we discuss the etching profiles of (001)InP demonstrated in Fig. 3-7 from a crystallographic aspect. Figure 8 shows two-dimensional schematic representations of two orthogonal (110) and (110) planes of a (001)InP layer. The open and solid circles indicate the In and P atoms, respectively. The (110) and (110) planes, thus, represent the interchange of In-P atomic species of the zinc-blende type crystal InP upon a rotation of 90° about the [001] axis. The {001} surfaces, in principle, consist either of the In or P atoms. However, neither is preferred since both types are doubly bonded to the crystal lattice at the surface, and real {001} surfaces consist of a mixture of the In and P atoms. On the other hand, the intermetallic compound InP has two types of {111} surfaces, i.e., In{111} and P{111} surfaces, resulting from the crystallographic polarity of the {111} directions. The outermost atom layer in each surface consists of either In or P atoms which are triply bonded to the crystal lattice. The In and P atoms have three and five bonding electrons per atom, respectively. The {111} surface In atoms have no spare electrons because they are all used up in hanging on to the crystal lattice. The {111} surface P atoms, on the other hand, have two electrons per atom available

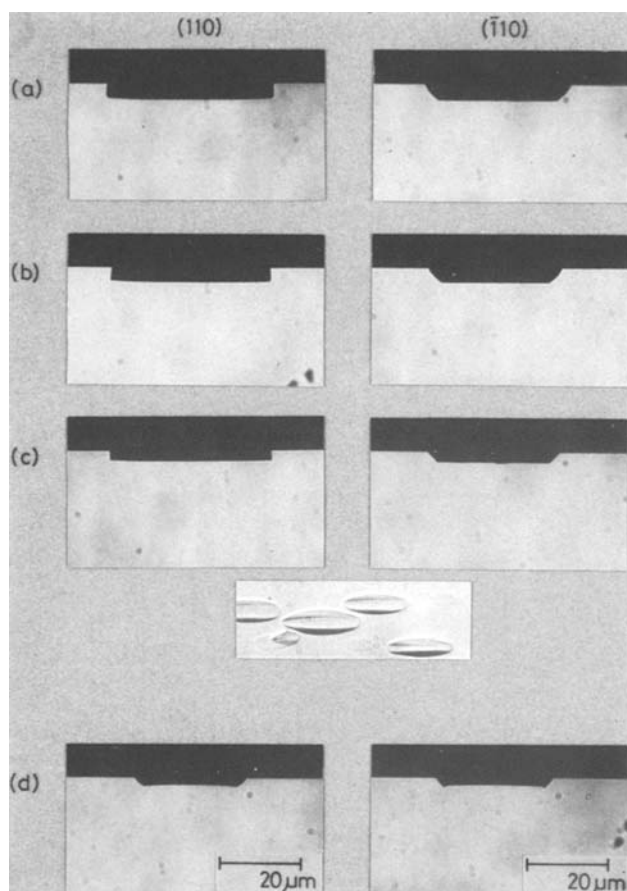


Fig. 6. Etching profiles of (001)InP etched in the solutions of the H_2SO_4 system: (a) $1H_2SO_4:1H_2O_2$ (60°C, 20 min), (b) $3H_2SO_4:1H_2O_2:1H_2O$ (60°C, 20 min), (c) $1H_2SO_4:1H_2O_2:1H_2O$ (60°C, 20 min), and (d) $3(2N-K_2Cr_2O_7):1H_2SO_4:1HCl$ (60°C, 20 min).

to take part in a reaction. Thus, the $P\{111\}$ planes are very reactive compared with the $In\{111\}$ planes.

From a viewpoint of crystallography, we can classify the etching profiles shown in Fig. 3-7 into the four individual groups, as demonstrated in Fig. 9. Details of two-dimensional schematic diagrams corresponding to Fig. 9(d) are also shown in Fig. 8. The etch-revealed walls perpendicular to the (001) surface, observed on the (110) cleavage plane in the solutions of the HCl , $HCl:HNO_3$, and $H_2SO_4:H_2O_2:H_2O$ systems, correspond to the $\{1\bar{1}0\}$ crystallographic planes. The inclined planes forming an angle of 55° with respect to the (001) surface [see, e.g., Fig. 5(a)] correspond to the $In\{\bar{1}11\}$ [(110) cleavage plane] and $In\{111\}$ crystallographic planes [($\bar{1}10$) cleavage plane], where the $\{\bar{1}11\}$ or $\{1\bar{1}1\}$ planes, in principle, form an angle of $54^\circ 44'$ with respect to the $\{001\}$ planes. The inclined plane forming an angle of 35° with respect to the (001), shown in Fig. 9(a), correspond to the $In\{\bar{1}\bar{1}2\}$ crystallographic planes [see, e.g., Fig. 3(a)]. The $\{\bar{1}\bar{1}2\}$ planes, in principle, form an angle of $35^\circ 16'$ with respect to the $\{001\}$ planes. The etching profile of the (110) cleavage plane, shown in Fig. 5(c), is composed of two individual planes, forming angles of 109° and 55° with respect to the (001) surface, while that of the ($\bar{1}10$) cleavage plane exhibits only the mesa-shaped structure forming an angle of 45° with respect to the (001) surface. As shown in Fig. 9(c), the most probable planes deduced from these angles are $In\{\bar{2}2\bar{1}\}$ and $In\{111\}$ planes for the (110) cleavage plane and $\{0\bar{1}1\}$ planes for the ($\bar{1}10$) cleavage plane. The reverse mesa-shaped and V-shaped groove structures were formed on

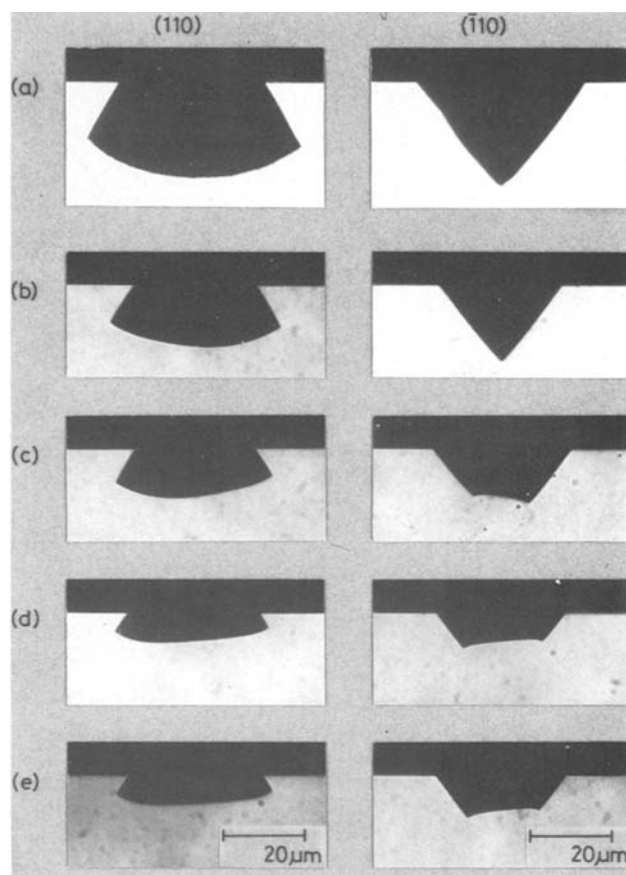


Fig. 7. Etching profiles of (001)InP etched in the solutions of the $Br_2:CH_3OH$ system: (a) 4% by volume $Br_2:CH_3OH$ (25°C, 1 min), (b) 2% by volume $Br_2:CH_3OH$ (25°C, 1 min), (c) 1% by volume $Br_2:CH_3OH$ (25°C, 1 min), (d) 0.2% by volume $Br_2:CH_3OH$ (25°C, 2 min), and 0.1% by volume $Br_2:CH_3OH$ (25°C, 4 min).

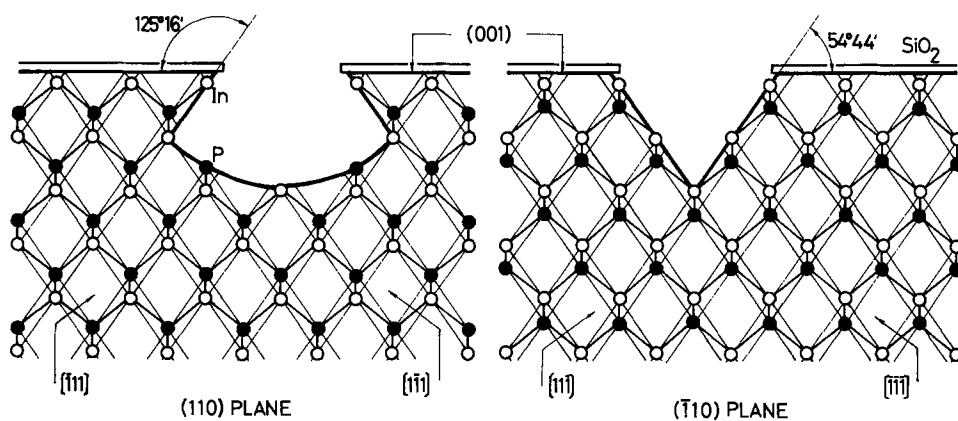
the (110) and ($\bar{1}10$) cleavage planes, respectively, with etchants such as $1HBr:1H_2O_2$ [Fig. 5(b)] and $Br_2:CH_3OH$ solutions (Fig. 7). These structures form angles of 125° (reverse mesa-shaped) and 55° (mesa-shaped) with respect to the (001) surface [Fig. 9(d)], which agree reasonably with angles between the $\{001\}$ and $\{\bar{1}\bar{1}1\}$ planes. The etch-side planes can, thus, be identified to be the $In\{\bar{1}\bar{1}1\}$ planes (see Fig. 8). The etching proceeds up to the $In\{111\}$ planes, because the $P\{111\}$ planes are very reactive compared with the $In\{111\}$ planes. Consequently, the reverse mesa-shaped and V-shaped groove structures are formed on the (110) and ($\bar{1}10$) cleavage planes, respectively, whose sides in principle form angles of $125^\circ 16'$ and $54^\circ 44'$ with respect to the (001) surface.

The dissolution process under consideration is far too complex and the available information rather limited to allow a quantitative development of the dissolution mechanism. Moreover, it is difficult to obtain a complete explanation of the difference in the etching profiles with various etching solutions. However, we suggest that this difference is due to the differences of the etching rates in the various crystallographic planes (i.e., the slowest-etching-rate planes will play an important role on the etching profiles. The etch-side planes identified are summarized in Table I along with the etching time, temperature, and etched depth.

Proposed Device Application

The etching profiles obtained here should be very useful for the design and fabrication of electron and electrooptical devices. Comerford and Zory (12) have used selective etching techniques to fabricate V-groove

Fig. 8. Two-dimensional schematic representations of two orthogonal (110) and $(\bar{1}\bar{1}0)$ planes of a (001) InP layer. The open and solid circles indicate the In and P atoms, respectively. The round hole bottom on the left side is not necessarily the precise atomic configuration.



diffraction grating on the (001) surfaces of GaAs using the $\text{Br}_2:\text{CH}_3\text{OH}$ solution as the preferential etchant. Tsang and Wang (13) have also fabricated the diffraction grating on the (001) surface of GaAs, where the $\text{H}_2\text{SO}_4:\text{H}_2\text{O}_2:\text{H}_2\text{O}$ system has been used as the preferential etchant. The results demonstrated in this paper also indicate that the V-groove diffraction grating on the (001) surface of InP should be fabricated by chemical etching with proper choice of direction of grating-mask groove openings and controlling the width of the groove openings and/or etching time.

Gannon and Nuese (14) have discussed the utility of the $\text{NH}_4\text{OH}:\text{H}_2\text{O}_2$ preferential etchant for GaAs device preparation and have demonstrated its application to the fabrication of integrated GaAs bipolar transistors. The $\text{NH}_4\text{OH}:\text{H}_2\text{O}_2$ etchant has been found to provide a flat etching bottom and a slow etching rate for (001) GaAs, which led to the success of the transistor fabrication procedure. The etchants, such as the $1\text{HCl}:\text{1CH}_3\text{COOH}$ [Fig. 3(c)], $1\text{HCl}:\text{1H}_3\text{PO}_4$ [Fig. 3(d)],

$1\text{HBr}:\text{1CH}_3\text{COOH}$ [Fig. 5(c)], and $1\text{HBr}:\text{1H}_3\text{PO}_4$ solutions [Fig. 5(d)], also provide a flat etching bottom and a relatively slow etching rate for (001) InP. These etchants should, therefore, be useful for producing high-quality InP transistors and IC's. The lateral definition, which is especially required and important in a number of passive optical components such as waveguides and directional couplers, can also be achieved by a chemical etching technique employing these solutions as the etchant.

Realization of monolithic integration of optical circuits will require a conventional means of routing optical signals on integrated chips (15). The fabrication of double heterostructure lasers, which incorporate chemically etched mirrors, has been reported to realize the monolithic fabrication of integrated optical devices (16, 17). In such works, much attention has been paid to produce smooth-mirror Fabry-Perot resonator by chemical etching because it improves the characteristics of laser diodes such as threshold current density, quantum efficiencies, and lasing modes. Therefore, in the fabrication of etched-mirror laser diodes, it is important to produce the vertical walls which give a high value of the mirror reflectivity. The etching solutions, such as the HCl (Fig. 3) and $\text{H}_2\text{SO}_4:\text{H}_2\text{O}_2:\text{H}_2\text{O}$ systems (Fig. 6), are thought to be useful for the monolithic fabrication of etched-mirror laser diodes. Recently, Miller and Iga (17) have successfully fabricated InGaAs/InP laser diodes emitting at $1.3\ \mu\text{m}$ by wet chemical etching with a solution of $1\text{HCl}:\text{2CH}_3\text{COOH}:\text{1H}_2\text{O}_2$ [see Fig. 3(e)]. The geometric profiles are also applicable to the fabrication of lateral-confinement laser diodes such as the buried-heterostructure laser and channeled-substrate laser diodes (18).

Conclusion

In summary, we have studied chemical etching characteristics of (001) InP in the solutions of various systems: (i) HCl , (ii) $\text{HCl}:\text{HNO}_3$, (iii) HBr , (iv) $\text{H}_2\text{SO}_4:\text{H}_2\text{O}_2:\text{H}_2\text{O}$, and (v) $\text{Br}_2:\text{CH}_3\text{OH}$ systems. The etch figures developed on (001) InP have indicated that it has untruncated tetragonal pyramid structure, in contrast to that on (001) GaAs or (001) InSb [truncated (flat-bottomed) tetragonal pyramid structure]. The etching profiles exhibiting crystal habits, e.g., V-shaped groove, reverse mesa-shaped ones, and nearly vertical walls, have been found to be formed by stripes parallel to the $[110]$ and $[\bar{1}\bar{1}0]$ directions being etched on the (001) planes. The indexes of the etch-revealed planes have been identified by making a comparison with the calculated angle between the (001) surface and etch-side plane. The etching profiles applicable to the device-structure design and fabrication have also been discussed.

Acknowledgment

The authors wish to thank Drs. M. Watanabe, T. Suzuki, M. Fujimoto, and G. Iwane for their en-

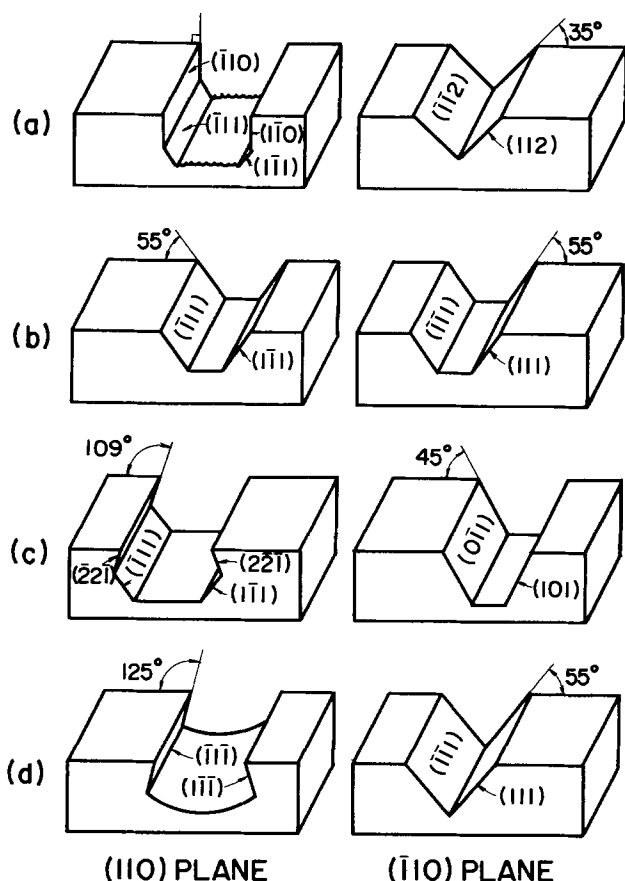


Fig. 9. Schematic diagrams of the etching profiles produced in the (001) planes of InP by the various etching solutions (see text).

couragement throughout this work. They also thank Mr. Y. Suzuki for useful advice.

Manuscript submitted Oct. 6, 1980; revised manuscript received Dec. 22, 1980.

Any discussion of this paper will appear in a Discussion Section to be published in the December 1981 JOURNAL. All discussions for the December 1981 Discussion Section should be submitted by Aug. 1, 1981.

Publication costs of this article were assisted by Nippon Telegraph and Telephone Public Corporation.

REFERENCES

1. W. Kern, *RCA Rev.*, **39**, 227 (1978), and references therein.
2. Y. Tarui, Y. Komiya, and Y. Harada, *This Journal*, **118**, 118 (1971).
3. H. C. Gatos and M. C. Lavine, *ibid.*, **107**, 427 (1960).
4. B. Tuck and A. J. Baker, *J. Mater. Sci.*, **8**, 1559 (1973).
5. A. Huber and N. T. Linh, *J. Cryst. Growth*, **29**, 80 (1975).
6. D. Lubzens, *Electron. Lett.*, **13**, 171 (1977).
7. T. Kambayashi, C. Kitahara, and K. Iga, *Jpn. J. Appl. Phys.*, **19**, 79 (1980).
8. G. H. Olsen, M. S. Abrahams, and T. J. Zamerowski, *This Journal*, **121**, 1650 (1974).
9. H. C. Gatos and M. C. Lavine, *ibid.*, **107**, 433 (1960).
10. S. Iida and K. Ito, *ibid.*, **118**, 768 (1971).
11. M. Otsubo, T. Oda, H. Kumabe, and H. Miki, *ibid.*, **123**, 676 (1976).
12. L. Comerford and P. Zory, *Appl. Phys. Lett.*, **25**, 208 (1974).
13. W. T. Tsang and S. Wang, *ibid.*, **28**, 44 (1976).
14. J. J. Gannon and C. J. Nuese, *This Journal*, **121**, 1215 (1974).
15. J. L. Merz, R. A. Logan, and A. M. Sergent, *IEEE J. Quantum Electron.*, **qe-15**, 72 (1979).
16. P. D. Wright, R. J. Nelson, and T. Cella, *Appl. Phys. Lett.*, **36**, 518 (1980), and references therein.
17. B. I. Miller and K. Iga, *ibid.*, **37**, 339 (1980).
18. H. C. Casey, Jr., and M. B. Panish, "Heterostructure Lasers," Part B, pp. 156-276, Academic Press, New York (1978).

Auger Depth Profile Studies of Diffusion at Iron Phthalocyanine/Copper Phthalocyanine Interfaces

Robert E. Davis* and Larry R. Faulkner**

Department of Chemistry and Materials Research Laboratory, University of Illinois, Urbana, Illinois 61801

ABSTRACT

Elemental depth profiles of thin molecular films have been obtained using Auger electron spectroscopy in conjunction with ion etching by reducing the average electron current density and using a conducting substrate. The minimum observed interface width of CuPc (800Å thick)/FePc (800Å thick) in unannealed samples was approximately 300-400Å. Evidence is presented that this broad interface is due to the microcrystalline morphology of these physically vapor-deposited molecular solids. Annealing under various conditions has provided insight into the diffusion and consequent degradation of these assemblies, apparently through a grain boundary mechanism.

Thin molecular films have been utilized recently as means for organizing a variety of chemical systems, including modified electrodes and photoelectrochemical devices (1-8). Although surface analysis techniques such as x-ray photoelectron spectroscopy (XPS or ESCA) have been used effectively to characterize the surfaces of such systems (5, 7, 9, 10), there is a crippling lack of knowledge about the validity of methods for characterizing them as a function of depth. Auger electron spectroscopy, with ion-beam etching, and secondary ion mass spectrometry have been widely employed for that purpose in dealing with multilayer assemblies of thin films of conventional materials, such as metals and semiconductors (11, 12). However, with molecular materials there is added concern over artifacts resulting from molecular degradation (13) and diffusional mixing (14) under the beams of charged particles.

In this paper, we communicate the successful Auger depth profiling of phthalocyanine (Pc) thin films, which are interesting for their electrocatalytic (15-18) and photovoltaic (6, 19, 20) properties. The results suggest that accurate profiles, without artifacts from beam damage, can be obtained. Data from annealed samples provide information about diffusional degradation of the film assemblies.

Experimental

The samples were prepared by physical vapor deposition in a vacuum of less than 10^{-6} Torr using a commercially available bell jar (Varian Model 3117). First, silver (3000Å) was deposited onto 1×1 in. microscope cover glasses (Corning No. 2) held at room temperature. This layer was intended to provide for thermal and electrical conduction away from the semiconducting thin layers (~ 800 Å each) of two different metal phthalocyanines, which were vapor deposited next at rates from 0.5 to 1 \AA-sec^{-1} from quartz or alumina crucibles heated to $\sim 400^\circ$. Changing of the deposition source necessitated exposure of the samples to the atmosphere between each step. Film thickness and deposition rate were monitored by a quartz crystal balance (Sloan DTM-200) and verified by interferometry (Varian A-scope).

Analysis was done at a typical background pressure of 2×10^{-9} Torr with a scanning Auger microprobe (Physical Electronics Model 545). Excitation was by a coaxial 3 keV electron beam, typically of $2.0 \mu\text{A}$. The electron beam of 20-40 μm diam was rastered over an area approximately $167 \times 167 \mu\text{m}$ to reduce the average current density. Ion etching was obtained with $60 \mu\text{A/cm}^2$ of 1 keV argon from a single, 20.7° off-normal ion gun at a rate of approximately 20 $\text{\AA}/\text{min}$. We will use the term sputtering with caution in the current context of molecular solids. Argon ion etching of polymers has been shown to be a very complex process, involving

* Electrochemical Society Student Member.

** Electrochemical Society Active Member.

Key words: analysis, organic, films, sputtering.

mechanisms of fragmentation, cross-linking, and desorption (13), in addition to hard-sphere collisions.

Results and Discussion

A typical depth profile of a freshly prepared, unannealed sample is shown in Fig. 1, without smoothing or background subtraction. (The nitrogen profile was omitted from Fig. 1-4 for clarity.) The initial ratio of the nitrogen peak-to-peak amplitude to that for carbon was 0.30 ± 0.05 , averaged over several samples. This figure is equivalent to the value of 0.29 ± 0.015 reported earlier by Buchholz (21) for oxygen-saturated CoPc films with a 2 keV primary beam. He predicted an amplitude ratio of 0.254 for an atomic ratio of 8/32 on the basis of relative cross sections at 2 keV and the estimated electron escape depths. Buchholz vapor-deposited and Auger-analyzed his samples *in situ*, whereas ours had to be exposed to air.

No iron is detected at the surface of the unannealed sample (Fig. 1), and there is no additional broadening of the CuPc/FePc interface for samples stored at room temperature for over a week, compared to samples stored below -20° . A similar FePc/CuPc sample does, however, show traces of copper on the surface after 53 days at room temperature. For several CuPc/FePc samples (including that of Fig. 1), the surface Cu/C amplitude ratio is 0.078 ± 0.011 , while unannealed FePc/CuPc or FePc-only samples have surface Fe/C ratios of 0.060 ± 0.005 . Iron and copper become detectable at metal/carbon amplitude ratios just below 0.01. While oxygen is observed in relatively large amounts at the surface (O/C peak-to-peak amplitude ratios as high as 0.4) and, to a much lesser extent (typically O/C ratios of 0.015) evenly throughout both Pc layers, there is no oxygen excess at the CuPc/FePc interface. Since the FePc was exposed to air between depositions, such an excess might be expected. Its absence may be due to desorption by the impinging, thermally excited CuPc during vapor deposition, or to a leveling of the oxygen concentration by diffusion after assembly. Using Buchholz's values for a 2 keV primary beam, one can calculate an O/C amplitude ratio of approximately 0.18 for a monolayer coverage of oxygen on phthalocyanine. The minimum detectable amount of oxygen corresponds to an O/C ratio less than 0.005.

Figure 2 shows data for an equivalent CuPc/FePc sample that was annealed at 200°C for 24 hr in a rotary-pumped vacuum oven; it offers clear evidence of mass transport between the two phthalocyanine layers.

Artifacts of the Auger depth profiling technique were not found to be severe. In every case the carbon

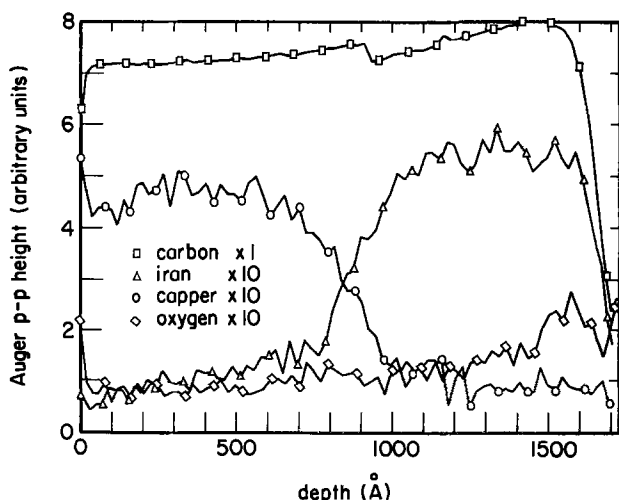


Fig. 1. Auger depth profile of a CuPc (800Å)/FePc (800Å)/Ag (3000Å)/glass sample with no annealing, other than storage for 5 days at room temperature. Etching was obtained with $55 \mu\text{A}/\text{cm}^2$ of 1 keV Ar^+ . Traces connect consecutive data points. Symbols are inserted only at every fourth point.

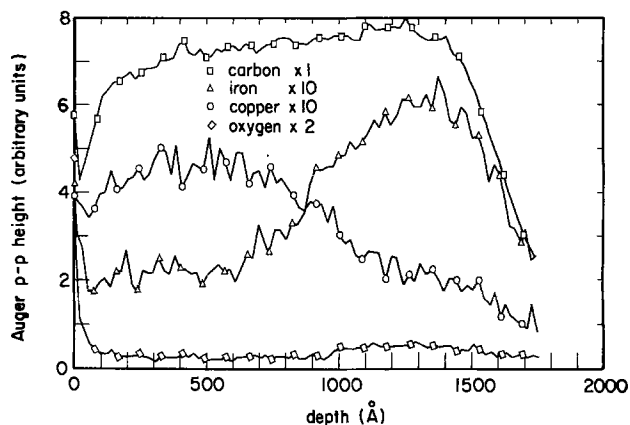


Fig. 2. Auger depth profile of a CuPc/FePc/Ag sample equivalent to that of Fig. 1, but annealed *in vacuo* for 24 hr at 200°C (in addition to storage for 11 days at room temperature).

signal shows a very rapid initial decrease followed by gradual recovery to a steady value, which is maintained through the Pc/Pc interface. The initial decrease in carbon signal may be due to adsorbed hydrocarbon contaminants. During the subsequent increase in carbon signal, the nitrogen signal (not shown) decreases, and the N/C ratio reaches an average steady-state value of 0.2. This coincidence leads us to suspect what might be described loosely as a "preferential sputtering" mechanism, involving molecular degradation. We cannot rule out changes in the Auger line shape of carbon as contributing to the fluctuations in the peak-to-peak signal, since the negative dN/dE peak of carbon near 265 eV initially, is shifted by ~ 3 eV to higher energy by ion bombardment. At the same time the positive peak remains unshifted. Broadening of peaks in the integral $N(E)$ spectrum would lead directly to decreases in peak-to-peak height in the dN/dE spectrum.

Electron beam damage is not a severe problem for these studies, although some chemical damage undoubtedly occurs, as evidenced by changes in the secondary and backscattered electron emission and the optical properties of the assemblies. The net absorbed sample current, when used to obtain an SEM-like picture, reveals the Auger-analyzed area to be slightly darkened, due to increased secondary and backscattered electron yields, which have been demonstrated to be a sensitive criterion for beam damage (22). Also, visual examination of the sample after exposure to electron and/or ion beam reveals qualitatively changes from the initial blue or blue-green to green. However, under the conditions described above (minimum current density, maximum sample stability), the Auger spectrum remains constant for well over 1000 sec, without an initial transient, in the absence of ion etching. Furthermore, the electron beam does not appear to contribute to interface broadening, since the minimum interface width is approximately constant over a wide range of electron current densities and dosages (Table I). In addition, compared to other organic compounds such as aliphatic hydrocarbons, CuPc has been shown to be greater than two orders of magnitude more stable to electron radiation damage (23).

Contributions to the observed width of the CuPc/FePc interface were expected from many sources. Several factors, whose contribution is expected to vary with the depth of the interface and the electron and ion beam parameters, may properly be considered artifacts in that they do not reflect the true composition of the sample before analysis. First, the phenomenon of cascade or atomic mixing has been shown to cause interface broadening due to penetration and resulting collision cascades by the ions (24, 25). Based on the

Table I. Typical interface widths for unannealed samples

| Sample (thickness Å) | Interface width, 10-90% (Å) | Primary electron current (μA) | Etch rate (Å/min) | Ion |
|------------------------------------|-----------------------------|--|-------------------|---|
| ZnPc (170)/MnPc (670) | 275 | 2.0 | 22 | 1 keV Ar ⁺ at 41 $\mu\text{A}/\text{cm}^2$ |
| ZnPc (670)/MnPc (670) | 270 | 1.0 | 15 | 1 keV Ar ⁺ at 38 $\mu\text{A}/\text{cm}^2$ |
| FePc (670)/CuPc (>2000) | 350 | 1.0 | 28 | 1 keV Ar ⁺ at 45 $\mu\text{A}/\text{cm}^2$ |
| FePc (670)/CuPc (>2000) | 390 | 1.0 | 24 | 1 keV Ar ⁺ at 45 $\mu\text{A}/\text{cm}^2$ |
| FePc (670)/CuPc (>2000) | 310 | 1.0 | 25 | 1 keV Ar ⁺ at 45 $\mu\text{A}/\text{cm}^2$ |
| FePc (670)/CuPc (>2000) | 390 | 2.0 | 20 | 1 keV Ar ⁺ at 41 $\mu\text{A}/\text{cm}^2$ |
| FePc (800)/CuPc (800) | 220 | 2.0 | 15 | 1 keV Ar ⁺ at 61 $\mu\text{A}/\text{cm}^2$ |
| FePc (800)/CuPc (800) | 230 | 2.0 | 25 | 3 keV Ar ⁺ at 61 $\mu\text{A}/\text{cm}^2$ |
| FePc (800)/CuPc (800) | 230 | 2.0 | 23 | 1 keV Ar ⁺ at 51 $\mu\text{A}/\text{cm}^2$ |
| H ₂ Pc (800)/FePc (800) | 210 | 2.0 | 18 | 1 keV Ar ⁺ at 51 $\mu\text{A}/\text{cm}^2$ |
| CuPc (800)/FePc (800) | 260 | 2.0 | 21 | 1 keV Ar ⁺ at 55 $\mu\text{A}/\text{cm}^2$ |

available data on ion implantation ranges (26), one would expect penetration by the relatively low energy 1 keV argon beam to be substantially less than the observed CuPc/FePc interface width. This expectation was confirmed by depth profiling equivalent samples with 1 and 3 keV argon beam energy, with no observable changes other than sputter rate (Fig. 3 and 4).

Sputter-induced roughness has also been known to degrade interface resolution. However, if this were the case one would expect the interface width to increase approximately as the square-root of depth (27). Clearly this is not observed experimentally in Fig. 1, where the CuPc/FePc interface is broader than the deeper FePc/Ag interface.

Electron and ion beams have also been observed to cause mass transport via thermal diffusion (28) or electrostatic migration (29). However, these observations were under rather extreme conditions, such as

low thermal or electrical conductivity samples, high power and current densities, and highly mobile species. For the samples that we have constructed and the beam parameters that we use, we have seen no evidence of this type of transport phenomenon. Poor electrical conductivity would be manifested by charging and subsequent shifting of the Auger electron energies. Beam heating would cause the bottom layer to diffuse to the surface with long electron beam exposure.

The inelastic mean-free path (IMFP) of electrons also contributes to the observed interface width of Auger depth profiles, but in a manner which is independent of beam parameters or sample history, and depends principally on the characteristic electron energy and, to a greater or lesser extent, the sample matrix. The value of the inelastic mean-free path for molecular materials has been the subject of debate (30, 31). We can conclude from the lower FePc/Ag interface width of approximately 100Å (measured from 90% to 10%) of the carbon signal, that for electrons of 271 eV energy traveling through FePc (albeit damaged by electron and ion bombardment), the IMFP is less than 50Å, since a distance twice the mean-free path would cause attenuation by 86%.

Another factor contributing to the CuPc/FePc interface width in Fig. 1, independent of analysis conditions or sample history, is expected to be the microcrystalline dimensions of the vapor-deposited phthalocyanines. Electron microscopic examination of Pc films evaporated under similar conditions indicate that the microcrystalline dimensions are typically on the order of 200Å (32, 33). This evidence, coupled with our observation of the relative sharpness of the FePc/Ag interface leads us to conclude that the unannealed CuPc/FePc interface width is dominated by this microcrystallinity.

The original goal of this research was to develop the capability of directly monitoring the integrity of interfaces in these organic thin film assemblies, as a function of sample history. Thus, we were encouraged to find that when sample preparation, history, and analysis parameters were held constant, the interface depth profiles were reproducible. When these samples were compared to identically prepared samples that received different annealing treatments, dramatic changes resulted from chemical, as well as physical, phenomena. The chemical changes, which took place during annealing in air, have been reported orally (34), and will be described in detail at a later date. The physical changes, which were observed following annealing in a vacuum oven that was repeatedly purged with argon and rotary-pumped before heating, evident in Fig. 2, can be explained by diffusion and changes in morphology.

These morphology changes may take place in either the molecular or metallic layers of these assemblies. Phthalocyanines are known to vapor deposit onto a room temperature substrate in the α -("tile") form. The transition to the β -("herringbone") form has been reported to occur at temperatures as low as 60°C (35).

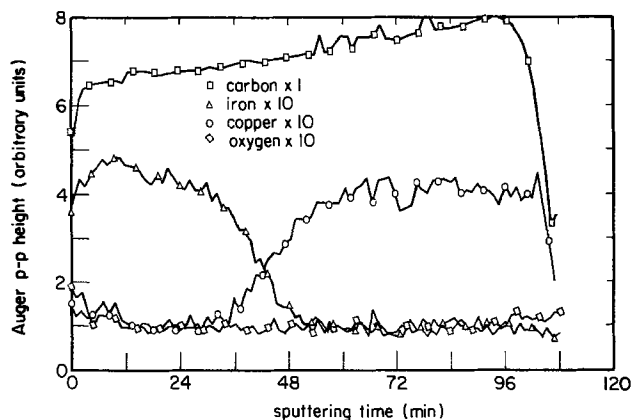


Fig. 3. Auger depth profile of FePc (800Å)/CuPc (800Å)/Ag (3000Å), after storage at room temperature for 18 days, etched with 61 $\mu\text{A}/\text{cm}^2$ of 1 keV Ar⁺ ions.

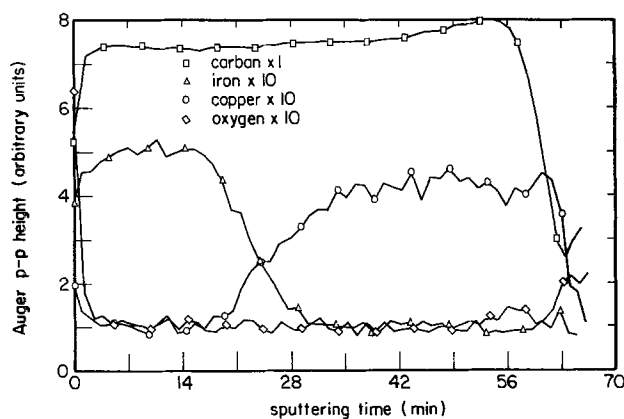


Fig. 4. Auger depth profile of a sample equivalent to that in Fig. 3, etched with 61 $\mu\text{A}/\text{cm}^2$ of 3 keV Ar⁺ ions.

Consequently, any detailed explanation of the mechanism of mass transport during annealing may need to involve morphology. It was our intention in this preliminary report to use higher temperatures and longer times, such that any mass transport due to morphological change is small in comparison to that due to diffusion.

Figure 2 clearly shows degradation of the FePc/Ag, as well as the CuPc/FePc, interface, although the Pc/Ag interface of comparable samples annealed for 14 hr at 175°C show no degradation. This observation, coupled with the absence of any detectable Ag accumulation at any MPC/MPc interface or at the surface of any Pc layer is strongly indicative of a change in the topography of the Ag layer. This change may be the result of a variety of mechanisms. The silver microcrystals could coalesce into larger crystallites, or the silver might migrate to fill voids occurring in the Pc layers. Filaments of metal, observed by electron microscopy of sectioned, vapor-deposited metal/Pc/metal assemblies have been ascribed to this mechanism (32). Scanning electron microscopy of the craters remaining after the Auger depth profiles reveals the sputtered silver surface of an annealed sample to be anisotropically irregular (Fig. 5), while an unannealed sample had a flat-bottomed crater (Fig. 6). This observation leads us to assume that both thermal and ion beam effects are involved in these changes in the silver surface and the consequent Pc/Ag interface broadening.

The nature of the mass transport of FePc through the CuPc was expected to be by a grain boundary mechanism, due to the microcrystalline nature of the Pc. The surface excess of FePc could be accounted for either by a predominantly grain boundary mechanism, or by a bulk diffusion mechanism coupled with a thermodynamic preference for FePc over CuPc at the residual vacuum/Pc interface or surface. This latter possibility is ruled out, since comparably annealed FePc/CuPc samples show a surface excess of CuPc.

Further details of the diffusion mechanism are at this point not completely clear. Two possibilities are molecular diffusion of intact metal phthalocyanines or demetallation and atomic diffusion of the metal atoms from molecule to molecule. A comparison of H₂Pc/FePc samples to CuPc/FePc samples shows roughly comparable diffusion upon identical annealing conditions, which supports, but does not prove, the former hypothesis. Further experiments utilizing secondary ion mass spectrometry are underway to resolve this question.

In conclusion, we have described the successful use of Auger depth profiling, traditionally an atomic anal-

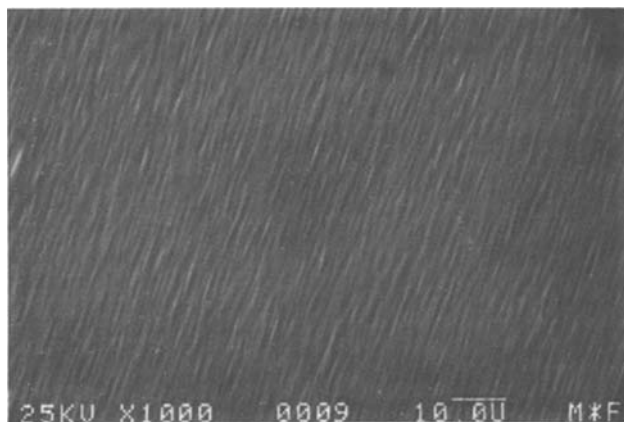


Fig. 5. Scanning electron micrograph of the crater bottom remaining after an Auger depth profile of an air-annealed sample, comparable to the sample of Fig. 2. The sample was over-coated with 500Å of vapor-deposited silver, to improve contrast.

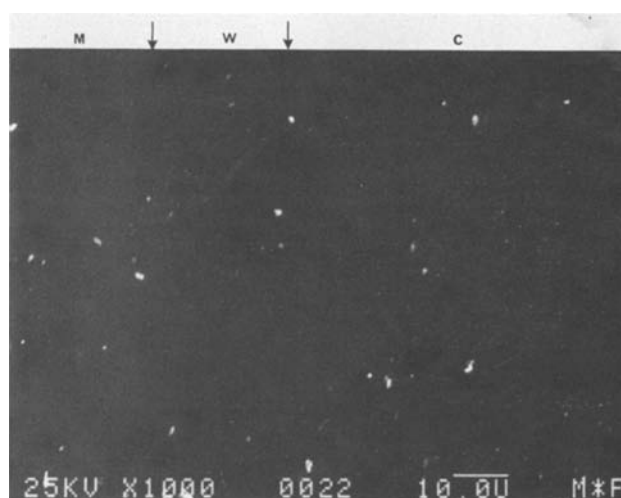


Fig. 6. Scanning electron micrograph of the crater remaining after the profile of Fig. 1, showing (left to right) the masked, unetched sample (M), the crater wall (W), and the flat-bottomed crater (C), over-coated with 500Å of silver. Note the absence of features other than charging dust particles (white), compared to Fig. 5.

ysis technique, applied nontraditionally to molecular thin solid films to investigate diffusion. We have clearly demonstrated that any future applications of such molecular solid assemblies intended for long-term or high temperature use must give careful consideration to grain boundary diffusion as a mechanism of aging or failure.

Acknowledgment

The authors wish to thank P. Williams and E. A. Sammann of the Materials Research Laboratory for technical assistance. This research was supported by the Department of Energy under Contract DE-AC02-76ER01198, administered by the Materials Research Laboratory of the University of Illinois.

Manuscript submitted Sept. 18, 1980; revised manuscript received Jan. 5, 1981. This was Paper 62 presented at the St. Louis, Missouri, Meeting of the Society, May 11-16, 1980.

Any discussion of this paper will appear in a Discussion Section to be published in the December 1981 JOURNAL. All discussions for the December 1981 Discussion Section should be submitted by Aug. 1, 1981.

Publication costs of this article were assisted by the University of Illinois.

REFERENCES

1. D. L. Morel, A. K. Ghosh, T. Feng, E. L. Stogryn, P. E. Purwin, R. F. Shaw, and C. Fishman, *Appl. Phys. Lett.*, **32**, 495 (1978).
2. A. B. Fischer, M. S. Wrighton, M. Umaná, and R. W. Murray, *J. Am. Chem. Soc.*, **101**, 3442 (1979).
3. J. A. Mercer-Smith and D. G. Whitten, *ibid.*, **101**, 6620 (1979).
4. S. N. Chen, A. J. Heeger, Z. Kiss, A. G. MacDiarmid, S. C. Gau, and D. L. Peebles, *Appl. Phys. Lett.*, **36**, 96 (1980).
5. M. S. Wrighton, Editor, "Interfacial Photoprocesses," ACS Adv. Chem. Ser., Vol. 184 (1980); Chap. 4 (D. G. Whitten, J. A. Mercer-Smith, R. H. Schmehl, P. R. Worsham), Chap. 7 (L. R. Faulkner, H. Tachikawa, F.-R. Fan, and S. G. Fischer), Chap. 8 (C. D. Langford, B. R. Holleb, and T. Vandermost), Chap. 14 (H. O. Finklea, H. Abruna, and R. W. Murray), Chap. 15 (M. S. Wrighton, A. B. Bocarsly, J. M. Bolts, M. G. Bradley, A. B. Fischer, N. S. Lewis, M. C. Palazzotto, and E. G. Walton).
6. C. D. Jaeger, F.-R. Fan, and A. J. Bard, *J. Am. Chem. Soc.*, **102**, 2592 (1980).

7. R. W. Murray, *Accounts Chem. Res.*, **13**, 5 (1935).
8. N. Oyama and F. C. Anson, *Anal. Chem.*, **52**, 1192 (1980).
9. N. R. Armstrong, A. W. C. Lin, M. Fujihira, and T. Kuwana, *ibid.*, **48**, 741 (1976).
10. C. M. Elliott and R. W. Murray, *ibid.*, **48**, 1247 (1976).
11. P. F. Kane and G. B. Larrabee, Editors, "Characterization of Solid Surfaces," Plenum, New York (1974).
12. C. A. Evans, Jr., *Anal. Chem.*, **47**, 818A (1975).
13. D. M. Ullevig and J. F. Evans, *ibid.*, **52**, 1462 (1980).
14. J. M. Poate, K. N. Tu, and J. W. Mayer, Editors, "Thin Films—Interdiffusion and Reactions," Wiley, New York (1978).
15. H. Meier, W. Albrecht, V. Tschirwitz, and E. Zimmerhackl, *Ber. Bunsenges Phys. Chem.*, **77**, 843 (1973).
16. A. J. Appleby and M. Savy, in "Electrode Materials and Processes for Energy Conversion and Storage," J. D. E. McIntyre, S. Srinivasan, and F. G. Will, Editors, p. 321, The Electrochemical Society Softbound Proceedings Series, Princeton, N.J. (1977).
17. H. Tachikawa and L. R. Faulkner, *J. Am. Chem. Soc.*, **100**, 4379 (1978).
18. F.-R. Fan and L. R. Faulkner, *ibid.*, **101**, 4779 (1979).
19. A. K. Ghosh, D. L. Morel, T. Feng, R. F. Shaw, and C. A. Rowe, Jr., *J. Appl. Phys.*, **45**, 230 (1974).
20. F.-R. Fan and L. R. Faulkner, *J. Chem. Phys.*, **69**, 3334, 3341 (1978).
21. J. C. Buchholz, *Appl. Surf. Sci.*, **1**, 547 (1978).
22. C. LeGressus, D. Massignon, A. Mogami, and H. Okuzumi, *Scanning Electron Microsc.*, **1**, 161 (1979).
23. J. R. Fryer, "Chemical Applications of Transmission Electron Microscopy," p. 44, Academic Press, London (1979).
24. Z. L. Liau, B. Y. Tsaur, and J. W. Mayer, *J. Vac. Sci. Technol.*, **16**, 121 (1979).
25. P. Williams, *Appl. Phys. Lett.*, **36**, 758 (1980).
26. H. H. Andersen, *Appl. Phys.*, **8**, 131 (1979).
27. R. Shimizu, *ibid.*, **18**, 425 (1979).
28. S. Hofman and A. Zalar, *Thin Solid Films*, **46**, 337 (1979).
29. D. V. McCaughan and R. A. Kushner, in "Characterization of Solid Surfaces," P. F. Kane and G. B. Larrabee, Editors, Chap. 22, pp. 627-640, Plenum, New York (1974).
30. D. T. Clarke, *CRC Crit. Rev. Solid State Mater. Sci.*, **8**, 1 (1978).
31. S. Evans, *Faraday Discuss. Chem. Soc.*, **60**, 197 (1976).
32. W. Katz, C. A. Evans, Jr., D. R. Eaton, and L. R. Faulkner, *J. Vac. Sci. Technol.*, **15**, 1561 (1978).
33. G. S. Zhdanov and Yu. M. Vorona, *Izv. Akad. Nauk SSSR, Ser. Fiz.*, **27**, 1239 (1963).
34. R. E. Davis and L. R. Faulkner, Paper 62 presented at The Electrochemical Society Meeting, St. Louis, Missouri, May 11-16, 1980.
35. J. R. Fryer, "Chemical Applications of Transmission Electron Microscopy," p. 200, Academic Press, London (1979).

The Nucleation of CVD Silicon on SiO₂ and Si₃N₄ Substrates

III. The SiH₄-HCl-H₂ System at Low Temperatures

W. A. P. Classen and J. Bloem*

Philips Research Laboratories, Eindhoven, The Netherlands

ABSTRACT

The growth of polycrystalline silicon layers on SiO₂ and Si₃N₄ substrates can be hampered in the early stages of growth by the presence of different species adsorbed on the surface. In this article nucleation experiments with silicon on SiO₂ and Si₃N₄ are described in the SiH₄-H₂-HCl system at temperatures between 600° and 900°C. In this temperature regime (and without HCl addition) the saturation nucleus density of silicon clusters on SiO₂ substrates shows a decrease in density with decreasing temperature, whereas on Si₃N₄ substrates the opposite occurs. Experiments with nitrogen as a carrier gas, however, give almost the same saturation nucleus densities of silicon clusters on SiO₂ and Si₃N₄ substrates. Additions of HCl to the SiH₄-H₂ system produce a decrease in the nucleus saturation density on SiO₂ and Si₃N₄ substrates, and the density also decreases with decreasing temperatures below 900°C. It is further shown that selective growth of silicon on partly coated silicon substrates becomes more difficult at lower growth temperatures. Adsorption of different surface species (H, Cl, SiCl₂, and SiH₂) on SiO₂ and Si₃N₄ substrates is discussed and it is concluded that a strong adsorption of atomic hydrogen, notably on SiO₂ surfaces, may explain the difference in nucleus densities on SiO₂ and Si₃N₄ substrates at temperatures below 900°C.

In two preceding papers (1, 2) (referred to in the following as Part I and Part II) nucleation experiments are described on SiO₂ and Si₃N₄ substrates. Part I contains experimental data on the SiH₄-HCl-H₂ system at temperatures between 925° and 1200°C, while Part II describes the nucleation behavior in the SiH₂Cl₂-H₂-N₂ system at temperatures between 800°

and 1100°C. In Parts I and II it was demonstrated that nucleation of silicon on a foreign substrate involves the presence of free silicon adatoms, acting as nucleation centers, whereas on a silicon substrate growth proceeds via the incorporation of adsorbed species (SiH₂, SiCl₂) at surface steps. As long as this layer growth is possible there is no need for separate nucleation between the steps, and therefore growth can proceed at low supersaturations. This effect also

* Electrochemical Society Active Member.
Key words: semiconductor, CVD, masking, chemisorption.

explains the selective growth found under conditions of low supersaturations (3, 4). It is not known in what way the nucleation of silicon proceeds at lower temperatures, where an increased surface adsorption could change the nucleation behavior. For this reason nucleation and growth experiments were performed for the $\text{SiH}_4\text{-H}_2\text{-HCl}$ system at temperatures between 600° and 900°C, on SiO_2 and Si_3N_4 substrates.

Experimental and Experimental Results

The nucleation experiments were performed in a horizontal air-cooled, rf heated reactor. The experimental conditions have been described in Parts I and II, but some additional information is given below. The carrier gases hydrogen and nitrogen were purified to water and oxygen concentrations below 1 ppm. The flow rates of the carrier gases, silane (5% in hydrogen) and hydrogen chloride, both electronic grade, were controlled by means of automatic mass-flow controllers. The temperature was measured with the aid of a calibrated radiation pyrometer on an uncoated silicon slice. Silicon slices covered with an amorphous 1500Å thick LPCVD layer of SiO_2 or Si_3N_4 were used as substrates. Because of the relatively high temperatures used and the small partial pressures of oxygen and water present it can be assumed that the Si_3N_4 surface is free of oxygen in contrast with Si_3N_4 which is exposed to air (5). After the nucleation experiments SEM and TEM photomicrographs were used to count the density of the nuclei formed.

Just as in the $\text{SiH}_4\text{-HCl-H}_2$ system at high temperatures (Part I), it is found that after an incubation period the concentration of stable clusters very quickly reaches a saturation density with respect to exposure time. This incubation period becomes longer with decreasing temperature and high hydrogen chloride concentrations combined with low silane concentrations. Furthermore, these periods are longer for SiO_2 substrates than for Si_3N_4 substrates, notably when hydrogen is the carrier gas. Figure 1 shows TEM photomicrographs for an input of 0.1 volume percent (v/o) silane in hydrogen as a carrier gas at 800°C on SiO_2 substrates and different exposure times. As noted

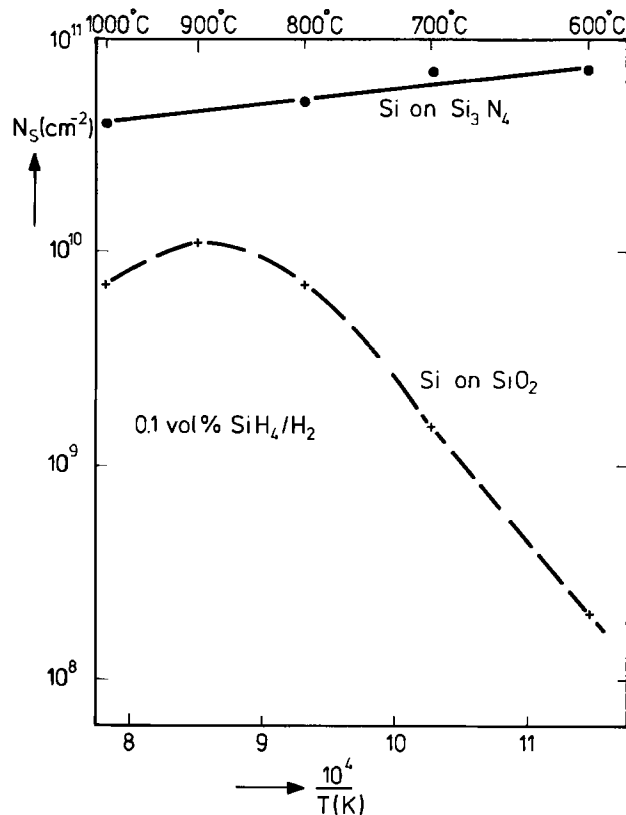


Fig. 2. The saturation density of silicon clusters (N_s) as a function of temperature for an input of 0.1 v/o silane in hydrogen as a carrier gas on SiO_2 and Si_3N_4 substrates.

before, the nucleus density of silicon clusters, after the incubation period, remains almost constant until coalescence occurs. In the following, therefore, only saturation nucleus densities of silicon clusters (referred to as N_s) will be used. Figure 2 gives N_s values as a function of temperature on SiO_2 and Si_3N_4 sub-

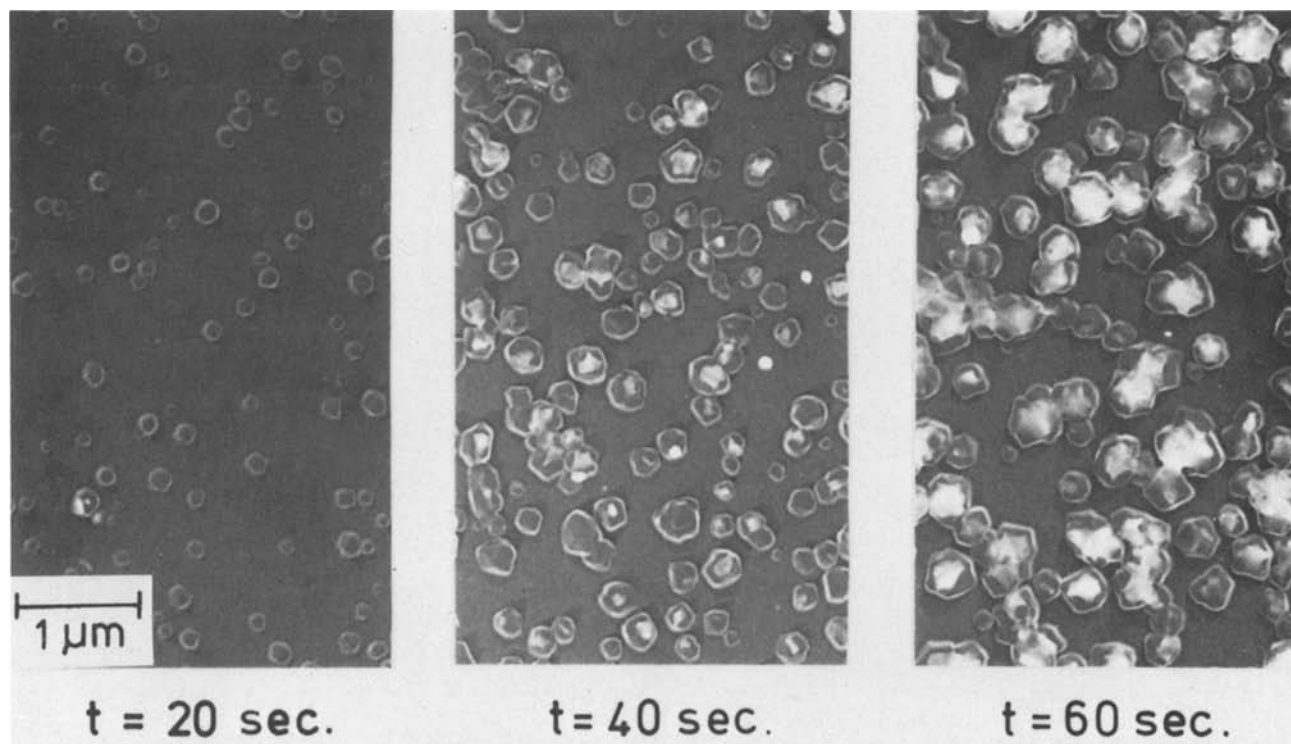


Fig. 1. TEM photomicrographs of the nucleus density on an SiO_2 substrate for an input of 0.1 v/o silane in hydrogen at 800°C as a function of the exposure time.

strates and an input of 0.1 v/o silane in a hydrogen ambient. The experimental data at temperatures above 925°C are discussed in Part I and are only given here for comparison. As will be noticed, N_s decreases with decreasing temperature on SiO_2 substrates at temperatures below 900°C, while at temperatures above 900°C the opposite occurs. On Si_3N_4 substrates N_s varies only slightly with temperature; in the temperature region under discussion no maximum in N_s is observed. It was expected that hydrogen adsorption would strongly reduce the saturation nucleus density of silicon clusters, notably for SiO_2 substrates, in analogy with the $\text{SiH}_2\text{Cl}_2\text{-H}_2\text{-N}_2$ system (Part II). Such an effect is indeed observed: for 0.01 v/o SiH_4 in hydrogen at 700°C the nucleus density is extremely low and is estimated at $2 \times 10^7/\text{cm}^2$, whereas when nitrogen is the carrier gas (0.2 v/o H_2 is present from the silane source, being 5 v/o SiH_4 in H_2) the nucleus density rises to $1.2 \times 10^{11}/\text{cm}^2$. The corresponding TEM photomicrograph for the SiO_2 substrate after an exposure time of 30 sec is shown in Fig. 3. From the N_s values in hydrogen and nitrogen a variation of N_s proportional to $p_{\text{H}_2}^{-3/2}$ can be deduced. Figure 4 shows the influence of hydrogen pressure on N_s for Si_3N_4 substrates and an input of 0.01 v/o SiH_4 . It can be observed that N_s decreases with increasing hydrogen pressure: by plotting N_s^{-1} vs. p_{H_2} a linear relationship can be obtained. Figure 5 gives N_s values on SiO_2 and Si_3N_4 substrates at 700°C as a function of input concentrations of silane. For the input concentrations used in these experiments, N_s is linearly proportional to the silane input pressure in a first approximation. Addition of HCl to the $\text{SiH}_4\text{-H}_2$ mixtures greatly reduces the number of stable silicon clusters as can be seen from Fig. 6. In this figure N_s is plotted as a function of the input concentration of HCl at 800°C on SiO_2 substrates and for an input of 0.1 v/o SiH_4 . For higher input concentrations of hydrogen chloride than those given in Fig. 6 no nucleation is observed. Figure 7 shows the influence of the addition of various amounts of HCl to the $\text{SiH}_4\text{-H}_2$ mixture on the density of nuclei as a function of temperature, both for SiO_2 and for Si_3N_4 substrates. At 900°C N_s shows a distinct maximum, for both SiO_2 and Si_3N_4 substrates.

Another point appears from the observation that silicon layers can be grown selectively on partly oxide-coated or nitride-coated silicon slices (3, 4). The selectivity is explained on the basis of a more difficult nucleation on foreign substrates. In Fig. 8 this selectivity is shown as a function of temperature for the

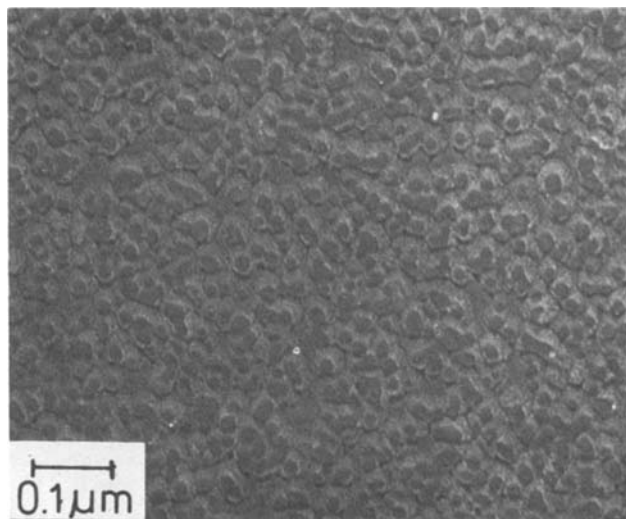


Fig. 3. TEM picture of the nucleus density for an input of 0.01 v/o silane and 0.2 v/o hydrogen in nitrogen as a carrier gas on an SiO_2 substrate at 700°C.

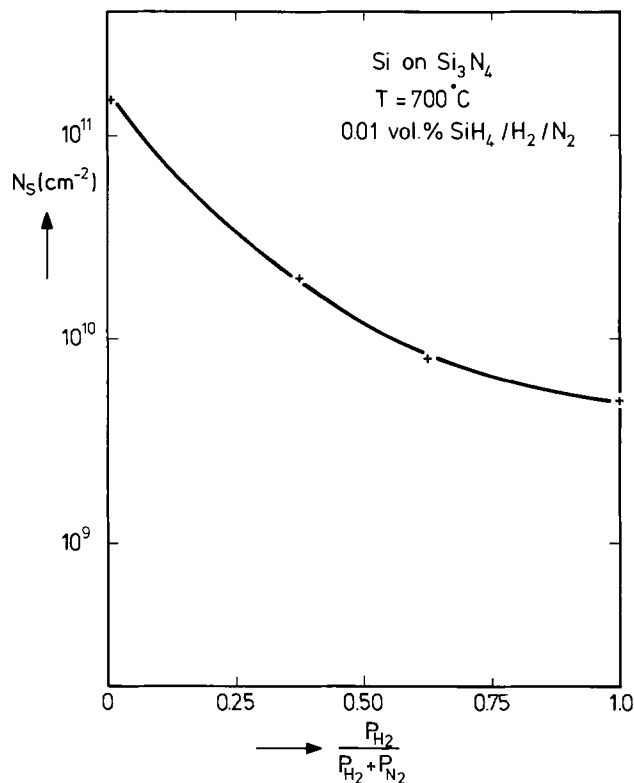


Fig. 4. The saturation density of silicon clusters (N_s) for 0.01 v/o silane and some hydrogen-nitrogen mixtures on Si_3N_4 substrates at 700°C.

$\text{SiH}_4\text{-HCl-H}_2$ system in which the ratio $p_{\text{SiH}_4}/p_{\text{HCl}}^2$ is used as a measure of the supersaturation. Three regions can be distinguished: I, no selective growth; II, selective growth; and III, etching of the silicon slices. It will be seen that with decreasing temperatures the region where selective growth can take place becomes smaller, and at temperatures below 800°C the selectivity between silicon and SiO_2 or Si_3N_4 has disappeared.

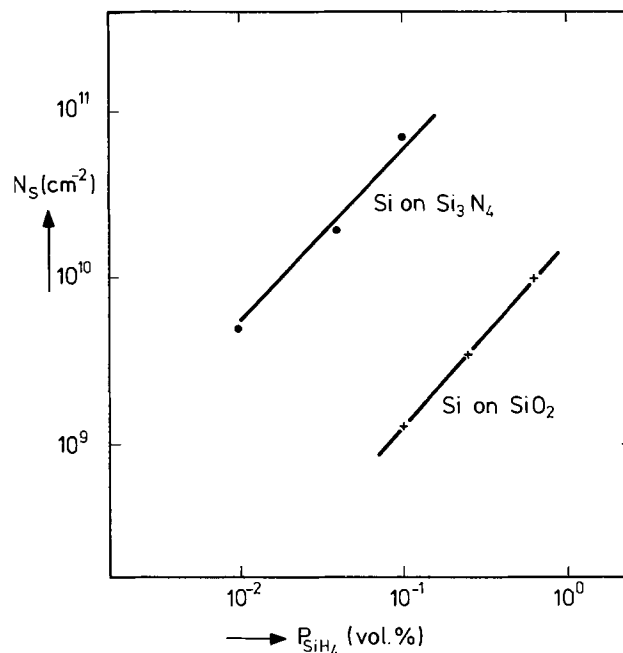


Fig. 5. The saturation nucleus density on SiO_2 and Si_3N_4 substrates at 700°C as a function of the input concentration of silane in a hydrogen ambient.

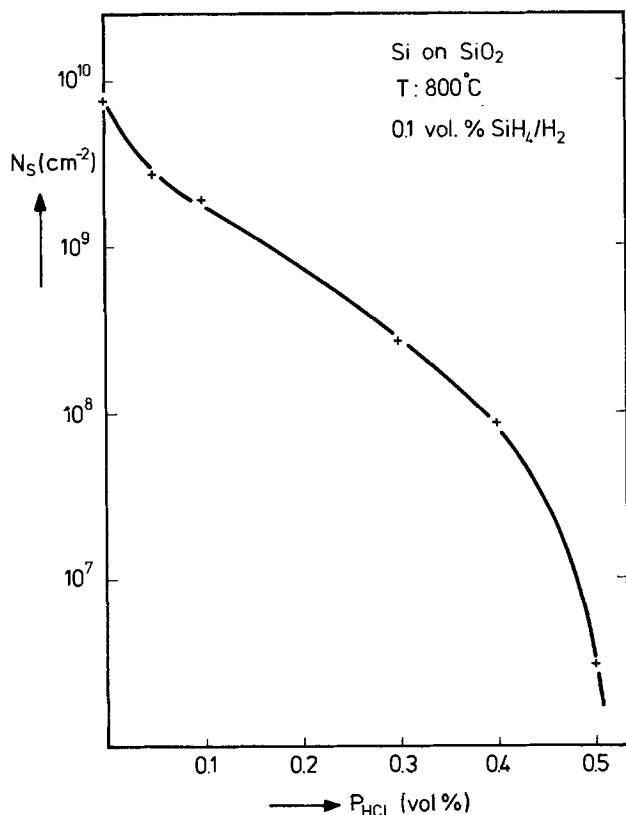


Fig. 6. N_s for SiO_2 substrates for an input of 0.1 v/o silane and different input concentrations of hydrogen chloride in hydrogen as a carrier gas at 800°C .

Discussion

In Part I it was concluded that an expression given by Venables (6) could be used to characterize the saturation density of silicon clusters (N_s) in the present case where incomplete condensation has to be assumed. Venables' expression for the case of mobile clusters can be rewritten as

$$\frac{N_s}{n_0} \cong \left(\frac{n_1}{n_0} \right)^{(i+1)/2} \exp [(E_1 + E_m - E_d)/2kT] \quad [1]$$

where i is the number of atoms in the initial cluster, E_1 the heat of formation of a cluster consisting of i atoms, E_m is the activation energy for surface diffusion of mobile clusters, E_d the activation energy for surface diffusion of adatoms, n_1 the concentration of adatoms per unit area, and n_0 the total number of surface sites per unit area. If only small clusters are mobile at low temperatures Eq. [1] has to be replaced by

$$\frac{N_s}{n_0} \cong \left(\frac{n_1}{n_0} \right) \exp [(E_m - E_d)/2kT] \quad [2]$$

In the Appendix we give reaction schemes in order to arrive at expressions for n_1/n_0 .

Interpretation of the results.—The expression as obtained by Venables (Eq. [1]) for the saturation nucleus density of silicon clusters can be compared with the experimental data in the $\text{SiH}_4\text{-H}_2$ system on SiO_2 and Si_3N_4 substrates in the temperature range under discussion. In the Appendix an expression has been found for the concentration of SiH_2 monomers (Eq. [A-12]), with Eq. [1] this then leads to

$$\frac{N_s}{n_0} = \left(\frac{K_1 K_3 P_{\text{SiH}_4}}{P_{\text{H}_2}} \right)^{(i+1)/2} \exp [(E_1 + E_m - E_d)/2kT] \quad [3]$$

In order to arrive at an expression describing the experimental data, the following remarks can be made:

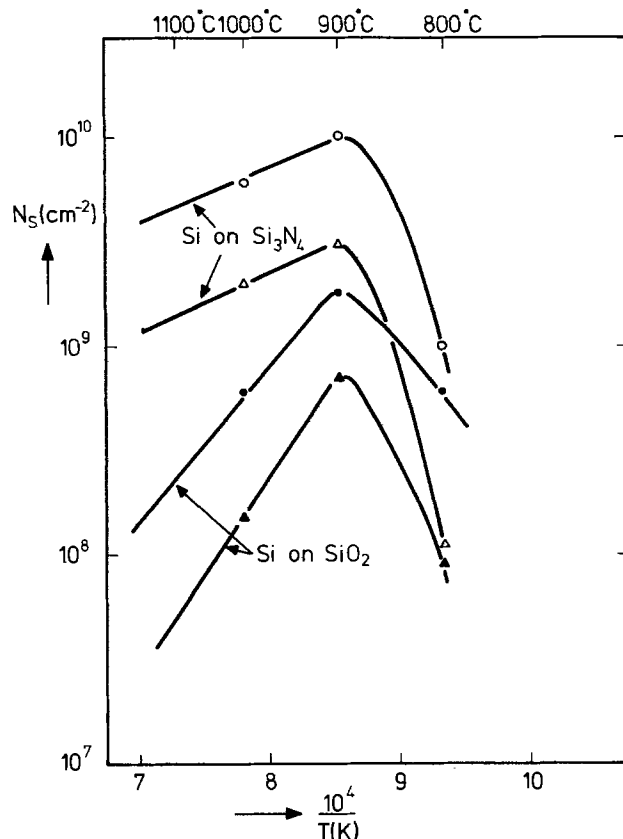


Fig. 7. The saturation nucleus density (N_s) as a function of temperature for two $\text{SiH}_4\text{-HCl}$ mixtures in hydrogen on SiO_2 and Si_3N_4 substrates (\circ , \bullet 0.1 v/o SiH_4 and 0.2 v/o HCl ; \triangle , \blacktriangle 0.1 v/o SiH_4 and 0.4 v/o HCl).

1. N_s is almost equal for SiO_2 and Si_3N_4 substrates in the $\text{SiH}_4\text{-N}_2$ system at 700°C , as discussed before. Be-

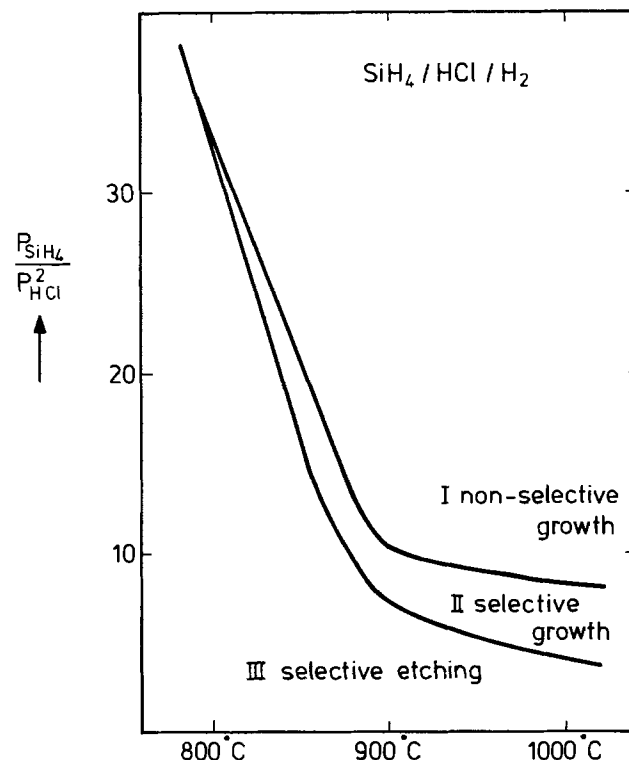


Fig. 8. The temperature dependence of selective growth of silicon on silicon slices partly coated with oxide or nitride as a function of temperature and supersaturation, expressed as $P_{\text{SiH}_4}/P_{\text{HCl}}^2$ in hydrogen as a carrier gas.

tween 800° and 1100°C the SiH₂Cl₂-N₂ system showed the same behavior (Part II), giving comparable results on SiO₂ and Si₃N₄ substrates.

2. The saturation nucleus density of silicon clusters on Si₃N₄ substrates is in a first approximation inversely proportional to p_{H₂} ($N_s \propto p_{H_2}^{-1}$) (Fig. 4). In the case of SiO₂ substrates the hydrogen pressure is observed to have a stronger influence on N_s ($N_s \propto p_{H_2}^{-3/2}$). In Part II it was concluded that adsorption of atomic hydrogen could explain the differences in N_s between SiO₂ and Si₃N₄ in the SiH₂Cl₂-H₂ system ($N_s \propto p_{H_2}^{-1/2}$).

3. The saturation density of silicon clusters on SiO₂ and Si₃N₄ substrates is in a first approximation linearly proportional to the input concentration of silane (Fig. 5).

The remarks made above lead to the conclusion that the experimental data on Si₃N₄ substrates ($N_s \propto p_{SiH_4}/p_{H_2}$) can be described by Eq. [3], leading to a critical cluster with $i = 1$ and SiH₂ as the predominant surface species. The differences in nucleation behavior between SiO₂ and Si₃N₄ substrates at temperatures below 900°C can be explained by a strong hydrogen adsorption on SiO₂ substrates. As is discussed in the section on adsorption, this is due to a large difference in the bond strength between the NH and the OH bonds. In that case a competition between the adsorption of atomic hydrogen and SiH₂ monomers occurs and the simplification made in Eq. [A-10] of the Appendix is no longer valid. For $K_4 p_{H_2}^{1/2} > (1 + K_1 K_2 p_{SiH_4}/p_{H_2})$ (Eq. [A-8]) this then leads to a decrease in the saturation density proportional to $p_{H_2}^{3/2}$ in agreement with the experimental data on SiO₂ below 900°C.

If HCl is introduced to the SiH₄-H₂ system SiH₂ will be converted to SiCl₂ (7, 8) and the SiH₂ monomer concentration decreases with increasing HCl concentrations

$$n_1 = [SiH_2^*] \propto p_{SiH_4}/p_{HCl}^2 \quad [4]$$

In Part I an extensive discussion is devoted to experimental data on the SiH₄-HCl-H₂ system on SiO₂ and Si₃N₄ substrates at temperatures above 925°C. From plots of log N_s vs. log p_{SiH_4}/p_{HCl}^2 it was shown that, if the input concentrations of hydrogen chloride are not too high N_s is linearly proportional to p_{SiH_4}/p_{HCl}^2 , indicating that $i = 1$ and [*] is constant at those temperatures. At higher HCl concentrations the initial cluster size changes from $i = 1$ to $i = 4$. At temperatures below 925°C, N_s decreases with decreasing temperatures in contrast to the situation at higher temperatures where the opposite occurs (Fig. 7). In order to interpret the experimental data below 900°C growth rate measurements for silicon on silicon in the SiH₄-HCl-H₂ system are helpful (7). At temperatures above 900°C the growth rate is gas phase diffusion-controlled and is relatively high compared with the etch rate given by the presence of HCl for not too high input concentration of HCl. As discussed in Part I, N_s is linearly proportional to p_{SiH_4}/p_{HCl}^2 ($i = 1$) for $p_{SiH_4}/p_{HCl}^2 > 50$ (p in bars) at temperatures above 925°C. At lower values of p_{SiH_4}/p_{HCl}^2 the critical cluster size increases and for $p_{SiH_4}/p_{HCl}^2 < 8$ no nucleation is observed at these temperatures. At temperatures below 900°C the growth rate of silicon on silicon is kinetically or surface-controlled in the SiH₄-H₂ system and a strong decrease in the growth rate with decreasing temperatures is apparent. Addition of HCl to this system at temperatures below 900°C leads to an additional lowering of the growth rate as measured in the SiH₄-H₂ system, due to the conversion of SiH₂ into SiCl₂ which easily desorbs (7, 8). At 800°C no nucleation is observed on SiO₂ and Si₃N₄ substrates for $p_{SiH_4}/p_{HCl}^2 < 30$ (Fig. 7 and 8) as is discussed later in connection with selective growth. In the regime where the growth of silicon on silicon is surface-controlled ($T < 900^\circ\text{C}$) N_s is linearly proportional to p_{SiH_4}/p_{HCl}^2 ($i = 1$) only for relatively high values of this parameter

(> 100 as obtained from Fig. 6). Or, in other words, when hydrogen chloride is added to a certain amount of silane the critical cluster size deviates from $i = 1$ for much smaller hydrogen chloride concentrations at 800°C than at temperatures above 900°C. This leads to a decrease in N_s , the term between the brackets in Eq. [3] being smaller than unity (n_1/n_0). A second possibility which could explain the decrease in N_s below 900°C as shown in Fig. 7 for the SiH₄-HCl-H₂ system is given by a strong adsorption of atomic chlorine. As is discussed in the section on adsorption, chlorine will be preferentially adsorbed on the silicon surface atoms of the SiO₂ and Si₃N₄ substrates, but there is evidence that above 700°C the interaction between chlorine and the silicon surface atoms is only weak, leading to a small concentration of chlorine surface atoms ($[Cl^*] \ll n_0$).

According to Fig. 8 silicon can be grown selectively on silicon slices partly coated with oxide or nitride at temperatures above 800°C. As the growth of silicon on silicon in the SiH₄-HCl-H₂ system can be given by $R = k_a p_{SiH_4} - k_b p_{HCl}^2$ leading to $R = 0$ for $p_{SiH_4}/p_{HCl}^2 = k_b/k_a$, this relation is used as a parameter in Fig. 8. In the gas phase diffusion-controlled regime of the growth of silicon on silicon above 900°C, as discussed above, surface diffusion and incorporation of silicon at the atomic steps are relatively fast compared to the diffusion of reactants toward the surface. In the same temperature regime the nucleation of silicon on silicon is surface controlled (Part I), leading to desorption of SiCl₂ if no growth centers are present. Consequently a selective growth can become apparent. At temperatures below 900°C the growth of silicon on silicon becomes surface controlled, the reduction of SiCl₂ at the atomic steps being rate limiting (8). Nucleation of silicon on SiO₂ and Si₃N₄ in the SiH₄-H₂-HCl system below 900°C is also surface controlled, as discussed before. At low temperatures, therefore, nucleation and growth are both limited by the reduction of SiCl₂ by hydrogen. This explains the loss of selectivity at lower temperatures in the Si-H-Cl system. According to Fig. 2 some selectivity in the growth of silicon on SiO₂ and Si₃N₄ can be expected in the SiH₄-H₂ system at low temperatures and low input concentrations of silane.

Adsorption on SiO₂ and Si₃N₄ substrates.—In this section we discuss adsorption of H, Cl, SiH₂, and SiCl₂ in connection with the nucleation experiments on SiO₂ and Si₃N₄ substrates. We also give a comparison with adsorptions of the same compounds on silicon. The concentration of free surface sites on a SiO₂ substrate, $[^*] = [^*_{ox}] + [^*_{si}]$ (where the subscripts ox and si refer to the surface atoms oxygen and silicon), can be given by

$$[^*_{ox}] = n_{ox} - [H^*_{ox}] - [SiH^*_{2,ox}] - [Cl^*_{ox}] - [SiCl^*_{2,ox}] \quad [5]$$

$$[^*_{si}] = n_{si} - [H^*_{si}] - [SiH^*_{2,si}] - [Cl^*_{si}] - [SiCl^*_{2,si}] \quad [6]$$

where $n_0 = n_{ox} + n_{si}$ is the total number of surface sites per unit area. The concentration of free surface sites on Si₃N₄ can be given in a similar way. Making use of the equilibrium partial pressures of the various species in the gas phase, one can calculate the surface concentrations of the different compounds if values for the adsorption energies of these species are known (8). If no direct measurements are available, an upper limit of these adsorption energies (E_a) can best be given by the dissociation energy (D) of the corresponding diatomic molecules. Table I gives accepted values for D , according to the JANAF tables (9) for most of the bonds. D values for Si—O, O—Cl, and N—Cl have been reported by Roberts and Caserio (10), who give average values for polyatomic molecules. Since, as far as

Table I. Accepted adsorption energies in kcal/mol (9, 10)

| Adsorbed atoms | Substrate atoms | | |
|----------------|-----------------|-----|----|
| | Si | O | N |
| Si | 73 | 108 | 92 |
| H | 70 | 102 | 83 |
| Cl | 90 | 52 | 46 |

the authors are aware, no dissociation energy for the single bond of Si—N is known, an estimate of $D_{\text{Si-N}}$ can be given by equating $D_{\text{Si-N}}/D_{\text{Si-O}} = D_{\text{C-N}}/D_{\text{C-O}}$. Using values for the single bonds derived from measurements on polyatomic molecules (10), this yields $D_{\text{Si-N}} = 92$ kcal/mol (Table I).

Adsorption of monoatomic hydrogen.—As discussed before, the nucleation experiments on SiO_2 and Si_3N_4 substrates indicate a strong adsorption of atomic hydrogen on SiO_2 and a weak hydrogen adsorption on Si_3N_4 . According to Table I this could be due to the differences in bond strengths between OH and NH. It is therefore also to be expected that adsorption of atomic hydrogen on silicon will be relatively weak, leading to a small coverage with hydrogen atoms (8). More evidence of a strong hydrogen adsorption on SiO_2 comes from the work of Morterra and Low (11) and of Lawrenko *et al.* (12). Morterra and Low studied the reaction between porous silica and molecular hydrogen. They found that this silica reacts with molecular hydrogen. Infrared studies have shown that if molecular hydrogen reacts with porous SiO_2 at temperatures above 650°C , silanols (Si—OH) are formed while SiH groups are totally absent. Lawrenko *et al.* studied the adsorption of hydrogen on monocrystalline SiO_2 . Measuring the weight changes of the samples by means of a microbalance they found that at temperatures below 900°C measurable quantities of hydrogen are adsorbed on the SiO_2 substrates, indicating the formation of SiOH groups. They also observed that the adsorption is reversible. Stein and Wegener (13) found that CVD Si_3N_4 contains chemically bonded hydrogen.

Annealing experiments showed that the SiH bonds are annealed out more easily than the NH bonds. It can therefore be concluded that adsorption of atomic hydrogen on SiO_2 substrates blocks adsorption sites, leading to a decrease in the saturation density of silicon clusters, whereas in the case of Si_3N_4 and silicon surfaces this adsorption is only weak at temperatures exceeding 600°C .

Adsorption of atomic chlorine.—According to Table I, chlorine does not adsorb preferentially on oxygen or nitrogen, and it may therefore be assumed that adsorption of chlorine on SiO_2 and Si_3N_4 can be treated as adsorption on the silicon surface atoms. Adsorption of atomic chlorine on silicon has been discussed previously in connection with growth rate measurements of silicon on silicon (8). It was concluded there that at temperature above 700°C the fractional surface concentration of atomic chlorine is much smaller than unity, in agreement with evolution measurements reported by Miyamura *et al.* (14).

Adsorption of SiH_2 and SiCl_2 .—Because of the relatively high values of $D_{\text{Si-N}}$ and $D_{\text{Si-O}}$ in contrast to $D_{\text{Si-Si}}$ (Table I) it can be assumed that the surface species SiH_2 and SiCl_2 adsorb predominantly on top of oxygen or nitrogen atoms of the SiO_2 or Si_3N_4 substrates. After adsorption of the first monolayer of silicon the surface mobility of further SiH_2 or SiCl_2 monomers will be enhanced. This postulation could explain the similarity in nucleation densities on SiO_2 and Si_3N_4 with sapphire and spinel substrates as observed by Cullen and co-workers (15). As discussed before, N_5 is linearly proportional to the input concentration of silane on SiO_2 and Si_3N_4 substrates, indicating a small cover-

age of SiH_2 monomers. As discussed previously, the surface concentrations of SiCl_2 on silicon in the SiH_4 -HCl- H_2 systems are considered to be small (8). A strong adsorption of SiCl_2 on SiO_2 or Si_3N_4 substrates cannot be ruled out completely, but according to the experimental data as described in Part II (the SiH_2Cl_2 - H_2 system) the surface coverage of SiCl_2 is much smaller than that of atomic hydrogen, notably for SiO_2 substrates.

Conclusions

In our study of the nucleation of silicon on SiO_2 and Si_3N_4 substrates at temperatures between 600° and 900°C in the SiH_4 -HCl- H_2 system, it was observed that the saturation nucleus density on SiO_2 substrates in the SiH_4 - H_2 system shows a maximum at approximately 900°C , whereas for Si_3N_4 substrates this density increases slightly with decreasing temperatures. Addition of nitrogen to the SiH_4 - H_2 systems produces a strong increase in the saturation density of silicon clusters, notably on SiO_2 substrates. Analysis of the experimental data suggests that atomic hydrogen is strongly adsorbed on SiO_2 because of the formation of OH bonds, whereas on Si_3N_4 substrates adsorption of atomic hydrogen leads to only small coverages. The introduction of HCl strongly reduces the nucleus density, notably at temperatures below 900°C . It is concluded that this additional reduction at temperatures below 900°C is comparable to the decrease in growth rate in the case of silicon on silicon. The adsorption of H, Cl, SiCl_2 , and SiH_2 on SiO_2 and Si_3N_4 substrates is discussed and compared with the adsorption of these species on silicon surfaces. It is concluded that only adsorption of atomic hydrogen on SiO_2 is needed to explain the experimental results: this adsorption blocks the adsorption sites, leading to a decrease in the saturation density of silicon clusters.

Manuscript received Nov. 21, 1980.

Any discussion of this paper will appear in a Discussion Section to be published in the December 1981 JOURNAL. All discussions for the December 1981 Discussion Section should be submitted by Aug. 1, 1981.

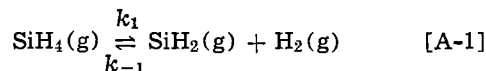
Publication costs of this article were assisted by Philips Research Laboratories.

APPENDIX

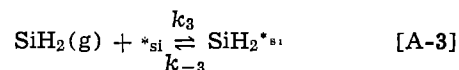
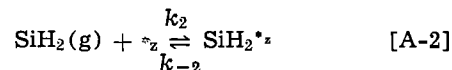
In order to describe the nucleation experiments in the SiH_4 -HCl- H_2 system at temperatures below 900°C it is necessary to consider a number of possible reactions that can take place at or near the surface. The reaction scheme as proposed for the SiH_4 -HCl- H_2 system at temperatures above 925°C (Part I) can be used with some additional assumptions concerning the species present on the surface. The reaction between silicon adatoms and SiO_2 to give volatile SiO can be neglected below 1000°C (16).

If no HCl is present in the gas phase the following reaction scheme will be used:

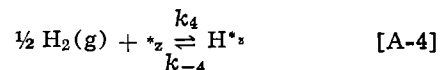
a. Gas phase dissociation of SiH_4 near the surface (17)

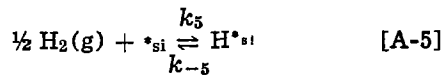


b. Adsorption of SiH_2 on a free surface site (the latter denoted by *). On an SiO_2 or Si_3N_4 substrate, $[*] = [*_z] + [*_{\text{si}}]$, where the subscripts z and si refer to the surface atoms oxygen (or nitrogen) and silicon, respectively



c. Adsorption of atomic hydrogen





The concentration of free surface sites on SiO_2 and Si_3N_4 substrates [n_z] and [n_{Si}] can be given by

$$[n_z] = n_z - [\text{H*}_z] - [\text{SiH}_2^*] \quad [\text{A-6}]$$

$$[n_{\text{Si}}] = n_{\text{Si}} - [\text{H*}_{\text{Si}}] - [\text{SiH}_2^*] \quad [\text{A-7}]$$

where $n_o = n_z + n_{\text{Si}}$ is the total number of surface sites per unit area. The concentrations of the surface species [SiH_4^*], [SiH_3^*], [SiH^*], and [Si^*] are assumed to be small compared with the concentration of [SiH_2^*], according to the experimental data concerning the growth of silicon on silicon in the $\text{SiH}_4\text{-H}_2\text{-N}_2$ system at 700°C (8). In a steady-state situation the concentration of SiH_2 admolecules reaches a constant value, which before the onset of silicon cluster formation can be expressed by

$$[\text{SiH}_2^*] = \frac{K_1 K_2 p_{\text{SiH}_4}}{p_{\text{H}_2}} \times \frac{n_z}{(1 + K_4 p_{\text{H}_2}^{1/2} + K_1 K_2 p_{\text{SiH}_4} / p_{\text{H}_2})} \quad [\text{A-8}]$$

$$[\text{SiH}_2^*] = \frac{K_1 K_3 p_{\text{SiH}_4}}{p_{\text{H}_2}} \times \frac{n_{\text{Si}}}{(1 + K_5 p_{\text{H}_2}^{1/2} + K_1 K_3 p_{\text{SiH}_4} / p_{\text{H}_2})} \quad [\text{A-9}]$$

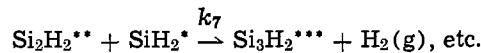
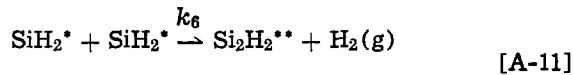
As the SiO and SiN bonds are strong compared with the Si-Si bond (Table I), it is likely that nucleation on SiO_2 and Si_3N_4 substrates starts with the adsorption of SiH_2 on oxygen and nitrogen atoms of the substrate. For an adsorption of SiH_2 exceeding that of atomic hydrogen, i.e.

$$K_1 K_2 p_{\text{SiH}_4} / p_{\text{H}_2} > (1 + K_4 p_{\text{H}_2}^{1/2})$$

this then leads to

$$[\text{SiH}_2^*] = n_z \quad [\text{A-10}]$$

After adsorption of this monolayer of silicon the surface mobility of further SiH_2 monomers will be enhanced and silicon clusters can be formed, according to



The mobile SiH_2 concentration is then given by Eq. [A-9] in which n_{Si} is now equal to the total number of surface sites ($n_{\text{Si}} = n_o$). For a small surface coverage we have

$$n_1 = [\text{SiH}_2^*] = \frac{K_1 K_3 p_{\text{SiH}_4} \cdot n_o}{p_{\text{H}_2}} \quad [\text{A-12}]$$

REFERENCES

1. W. A. P. Claassen and J. Bloem, *This Journal*, **127**, 194 (1980).
2. W. A. P. Claassen and J. Bloem, *ibid.*, **127**, 1836 (1980).
3. L. J. M. Bollen, Unpublished results.
4. E. Sirtl and H. Seiter, in "Semiconductor Silicon 1969," R. R. Haberecht and E. L. Kern, Editors, p. 189, The Electrochemical Society Softbound Proceedings Series, New York (1969).
5. S. I. Raider, R. Flitsch, J. A. Aboaf, and W. A. Pliskin, *This Journal*, **123**, 560 (1976).
6. J. A. Venables, *Philos. Mag.*, **27**, 697 (1973).
7. J. Bloem and W. A. P. Claassen, *J. Cryst. Growth*, **49**, 435 (1980).
8. W. A. P. Claassen and J. Bloem, Submitted to *ibid.*
9. JANAF Thermochemical Tables, 2nd ed., June 1971, NSRDS-NBS-37.
10. J. D. Roberts and M. C. Caserio, "Modern Organic Chemistry," W. A. Benjamin, Inc. (1967).
11. C. Morterra and M. J. D. Low, *J. Catal.*, **28**, 265 (1973).
12. W. A. Lawrenko, W. L. Tikusch, W. S. Senkov, W. A. Krawez, K. W. Nasarenko, and W. M. Werestschak, *Z. Phys. Chem. Leipzig*, **259**, 129 (1978).
13. H. J. Stein and H. A. R. Wegener, *This Journal*, **124**, 908 (1977).
14. M. Miyamura, Y. Sakisaka, M. Nishijima, and M. Onchi, *Surf. Sci.*, **72**, 243 (1978).
15. G. W. Cullen, J. F. Corboy, and J. T. McGinn, in "Semiconductor Silicon 1977," H. R. Huff and E. Sirtl, Editors, The Electrochemical Society Softbound Proceedings Series, Princeton, N.J. (1977).
16. J. Bloem and L. J. Giling, in "Current Topics in Materials Science," Vol. 1, E. Kaldis, Editor, Chap. 4, North-Holland Publishing Co. (1978).
17. C. G. Newman, H. E. O'Neal, M. A. Ring, F. Leska, and N. Shipley, *Int. J. Chemical Kinetics*, **XI**, 1167 (1979).

Oxidation, Impurity Diffusion, and Defect Growth in Silicon—An Overview

R. B. Fair*

Bell Laboratories, Reading, Pennsylvania 19604

ABSTRACT

As a result of a large body of literature on oxidation, impurity diffusion, and defect growth in silicon, a consistent picture has emerged of oxidation-enhanced diffusion (OED) and oxidation-induced stacking fault growth (OISF). It is believed that silicon self-interstitials can be generated at an oxidizing Si/SiO₂ interface as a result of an incomplete half-cell reaction involving silicon and oxygen. Those interstitials that do not participate in surface regrowth participate in raising the steady-state concentration of self-interstitials in the surface region. OED can be explained in terms of a partial interstitialcy mechanism involving the surface-generated self-interstitials. The growth of OISF will occur if the relative steady-state self-interstitial concentration around the fault exceeds the emitted concentration of interstitials from the fault line. It is shown that this model predicts that OISF growth is limited by the production rate of self-interstitials at the Si/SiO₂ interface. The retrogrowth of OISF and the reduction of OED both occur when the concentration of generated self-interstitials decreases. The introduction of chlorine-bearing compounds into the oxidation tube can also cause retrogrowth. The reaction of chlorine with silicon at the interface creates vacancies which can recombine with generated self-interstitials and reduce their concentration. Calculations show that the chlorine compound formed at the interface is SiCl.

Thermal oxidation of silicon is known to promote the growth of stacking faults (1-18) and dislocations (19). The stacking faults may be extrinsic or intrinsic. Extrinsic faults are formed by the insertion of an additional layer of atoms in the atom plane stacking sequence and are the type normally observed in oxidized silicon (6, 8). Stacking fault nuclei lie in the wafer prior to oxidation. Several causes of the nuclei have been observed, including mechanical damage, impurity centers, crystal growth defects, and ion implantation damage. During oxidation the stacking faults grow as two-dimensional structures lying on inclined (111) planes bounded by partial dislocations.

Also occurring during oxidation is the enhanced diffusion of dopant impurities in silicon (20-25). The growth of stacking faults and the enhancement of impurity diffusion during oxidation have some similarities:

1. Both the growth of oxidation-induced stacking faults (OISF) and oxidation-enhanced diffusion (OED) depend upon crystal orientation of surface planes. The rates of these effects increase in the order of (111), (110), and (100) (7, 20, 23, 26).

2. Both phenomena occur more rapidly in steam than in dry oxygen (5, 9, 23). This correlates with the higher oxidation rate in steam.

3. Both phenomena are the consequences of a long-range process. The density of bulk OISF decreases with increasing depth from the Si/SiO₂ interface (27). The effect of OED has been observed to reach ~10 μm below the interface (23).

4. Both OED and OISF phenomena are suppressed in the presence of HCl gas during oxidation (28).

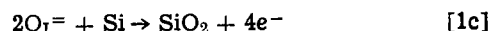
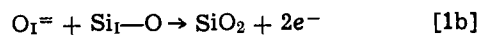
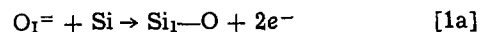
5. Mechanical damage on the back side of a wafer eliminates stacking faults but does not affect OED (29).

Several models have been proposed to explain these results (2, 30, 31). Leroy (30) has shown that stacking fault growth models involving either the absorption of

self-interstitials or emission of vacancies favor the model of interstitial absorption. It will be shown in this paper that by considering OED, OISF, oxidation and its doping dependence, retrogrowth of stacking faults, and the role of HCl gas in OED and OISF, a similar conclusion can be drawn. The model we favor is that of a super-saturation of silicon self-interstitials generated at the oxidizing Si/SiO₂ interface as a result of incomplete oxidation (2). The way in which these interstitials are generated and contribute to OED and OISF are described in the following sections. The role of chlorine in these phenomena is also discussed.

Oxidation

During silicon oxidation two types of reactions can occur at the Si/SiO₂ interface involving the diffusing oxidant species (presumably O_I⁼ — interstitial oxygen ions). One involves O_I⁼ and silicon, and this reaction dominates in lightly doped material (31)



Ionized oxygen reacts with lattice-bound silicon and displaces the silicon to an interstitial position (reaction [1a]) to form Si_I-O. Presumably, reaction [1b] occurs a short time later. The net result is reaction [1c]. These reactions involving interstitial silicon are consistent with the results of Feldman *et al.* (32) who found from backscattering-channeling studies that the silicon atoms in the interface layer have a displacement from the bulk position between 0.1 and 1.0 Å.

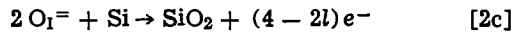
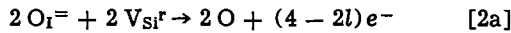
The possibility of creating a free self-interstitial would be greatest for the Si_I-O pair, were it to dissociate before SiO₂ is formed. It has been estimated that such an incomplete oxidation step occurs for 1 silicon atom out of 1000 (2).

The other reaction occurring at the Si/SiO₂ interface involves vacancies and O_I⁼. Ho and Plummer (33, 34)

* Electrochemical Society Active Member.

Key words: silicon oxidation, stacking faults, diffusion, chlorine.

have modeled the enhanced oxidation of heavily doped silicon by correlating oxidation rate with the vacancy concentration dependence on doping. For vacancies generated at the interface in the r^{th} charge state, V_{Si}^r , the primary reactions are (31) (see Fig. 1)



In these reactions the charge state multiplicity of the vacancy is l , where $l = -2, -1, 0, \text{ or } +1 (+2)$ corresponding to $V^=, V^-, V^z, \text{ or } V^+ (V^{++})$ vacancies. Since there are no silicon interstitials generated in these reactions, one would not expect any concentration dependence in the phenomena of oxidation-enhanced diffusion. This agrees with initial experimental evidence (26), but additional data are needed for verification.

Silicon Self-Interstitial Generation

From the interface reaction [1a] we see that the concentration of $\text{Si}_I\text{—O}$ pairs created is proportional to $[O_1^-]$. From the ionization reaction at the SiO_2 surface (see Fig. 1), $[O_1^-] \propto P_{\text{O}_2}^{1/2}$, where P_{O_2} is the O_2 partial pressure in the gas phase (14, 30). Since the oxidation rate is proportional to P_{O_2} , then, assuming a parabolic oxidation rate, the generation rate of silicon self-interstitials is

$$R_{\text{gen}} = \theta K_{\text{Si}}(T) \left(\frac{B^{1/2}}{2v_m} \right)^{1/2} t^{-1/4} = K_{\text{gen}} t^{-1/4} \quad [3]$$

where $K_{\text{Si}}(T)$ is a complex equilibrium and proportionality constant, B is the parabolic rate constant, v_m is the molecular volume of SiO_2 , and θ is the fraction of $\text{Si}_I\text{—O}$ bonds which dissociate to form self-interstitials, Si_I . Equation [3] differs from the assumption of Hu (2) that the generation rate of Si_I was directly proportional to the oxidation rate. Hu's assumption leads to $R_{\text{gen}} \propto t^{-1/2}$ and stacking fault length $\propto t^{1/2}$. This assumption has also been criticized by Leroy (30).

Silicon interstitials may be captured at surface kink sites and contribute to surface regrowth at a rate (2)

$$R_{\text{reg}} = (\pi r \alpha_0 D_{\text{Si}}) (C_I - C_I^0) = K_{\text{reg}} (C_I - C_I^0) \quad [4]$$

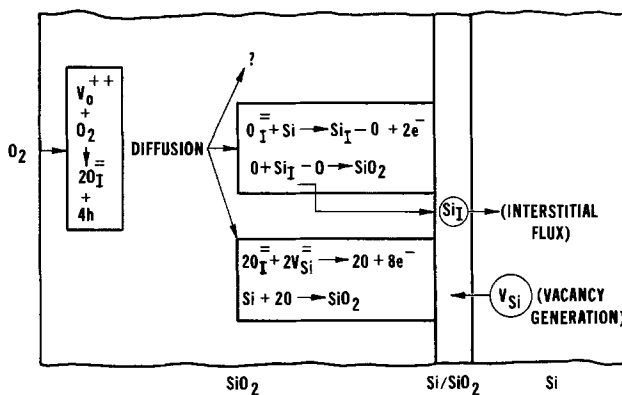


Fig. 1. Detailed reactions in the linear-parabolic oxidation model. Oxygen reacts at the oxide surface to create interstitial oxygen, O_1^- , and holes. O_1^- ions drift to the Si/SiO_2 interface to react with either (i) silicon to form interstitial silicon and atomic oxygen which can combine to form SiO_2 , or (ii) a silicon vacancy to form bound atomic oxygen which can react with silicon to form SiO_2 . In the former process a silicon interstitial flux can occur if all of the interstitial silicon does not combine to form SiO_2 . The latter process will only be significant if sufficient numbers of vacancies are present in the silicon (heavy doping case).

where ρ is the density of surface kinks ($\sim 10^{12} \text{ cm}^{-2}$), D_{Si} is the silicon interstitial diffusivity, $C_I = [\text{Si}_I]$ is the concentration of self-interstitials, C_I^0 is the equilibrium concentration, and α_0 is the capture radius of interstitials by kinks.

Following the arguments of Hu (2) and knowing that the rate of self-interstitial formation is

$$h_t \frac{dC_I}{dt} = R_{\text{gen}} - R_{\text{reg}} \quad [5]$$

where h_t is the wafer thickness, it can be shown that for $t \gtrsim 6/K_{\text{reg}}$ ($t \cong 0.1$ sec for typical numbers)

$$\int_0^t (C_I - C_I^0) dt = \frac{4K_{\text{gen}}}{3K_{\text{reg}}} t^{3/4} \quad [6]$$

The rate of growth of stacking faults is given by

$$\frac{dr}{dt} = \pi \alpha_0^2 D_{\text{Si}} (C_I - C_I^0) \quad [7]$$

and the time-dependent stacking fault length becomes

$$r = \frac{4\alpha_0 K_{\text{gen}} t^{3/4}}{3\rho} \quad [8]$$

Equation [8] predicts a $t^{3/4}$ growth of stacking faults. Most of the reported data on stacking fault growth show a t^n dependence with n varying between 0.62 and 0.9 (4, 5, 7, 9, 16, 35).

In Eq. [8] the only temperature-dependent parameter is K_{gen} . Contained in K_{gen} is (from Eq. [3]) $K_{\text{Si}}(T)$ which has the exponential of the $\text{Si}_I\text{—O}$ binding energy, and $B^{1/4}$. The parabolic rate constant has an activation energy, E_{par} , (36), so the total activation energy for stacking fault growth is

$$Q_{\text{SF}} = E_b (\text{Si}_I\text{—O}) + \frac{E_{\text{par}}}{4} \quad [9]$$

Equation [4] predicts that stacking fault growth is only limited by the generation of self-interstitials at the oxidizing Si/SiO_2 interface, and is not diffusion limited as assumed by Leroy (30). The energy of the silicon-oxygen bond is ~ 2.2 eV (37). However, a large strain is likely to exist at the interface as a result of the molecular size mismatch. This strain should influence self-interstitial production. Tiller (38) has proposed that in the initial stages of oxidation silicon atoms form SiO bonds which are highly strained. He estimates that ≤ 2.6 eV elastic energy is stored in the interface which drives the flux of silicon self-interstitials so as to provide the free volume space for the SiO_2 . Therefore, if we take $E_b(\text{Si}_I\text{—O}) \cong 2.2$ eV and $E_{\text{par}} = 1.23$ eV for dry O_2 oxidation and $E_{\text{par}} = 0.78$ eV for wet O_2 oxidation (36), we find from Eq. [9]

$$Q_{\text{SF}} (\text{dry oxidation}) = 2.51 \text{ eV}$$

$$Q_{\text{SF}} (\text{wet oxidation}) = 2.4 \text{ eV}$$

This result agrees well with the measurements of Murarka and Quintana (16) who found Q_{SF} (dry oxidation) = 2.55 eV and Q_{SF} (wet oxidation) = 2.37 eV.

Stacking Fault Retrogrowth

An anomalous temperature effect has been observed in the growth of OISF (35). For a given oxidation time the size of the OISF first increases with temperature with an activation energy of ~ 2.5 eV, reaches a peak length at some temperature, and then decreases with temperature. The temperature above which retrogrowth occurs is dependent upon the crystal orientation as well as oxidation ambients. Examples of the growth vs. temperature of OISF in dry oxygen for 3 hr (35) are shown in Fig. 2.

In order to account for growth and retrogrowth, Eq. [7] needs to be modified. If we define C_I^L as the con-

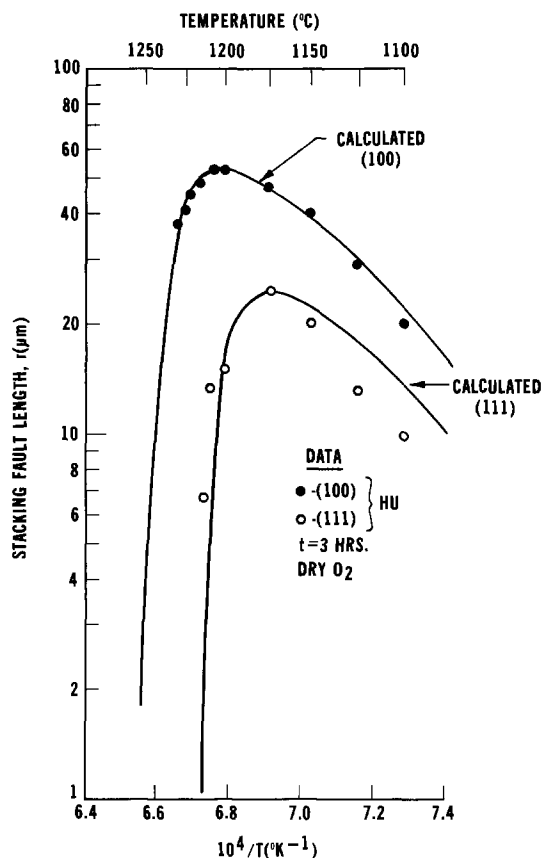


Fig. 2. The growth vs. temperature of oxidation-induced stacking faults in dry O_2 for 3 hr.

centration of self-interstitials at the dislocation line, then a stacking fault will grow if the steady-state interstitial concentration surrounding the dislocation is greater than C_I^L . Figure 3 represents the boundary conditions of this model. Thus

$$\frac{dr}{dt} = \pi\alpha_0^2 D_{\text{ISI}} (C_I - C_I^L) \quad [10]$$

Referencing these concentrations to C_I^0 , the equilibrium concentration, then (39, 40)

$$\frac{C_I^L}{C_I^0} = \exp(\Delta F_L/kT) \quad [11]$$

where ΔF_L is the change in dislocation loop free energy per additional incorporated atom. The silicon interstitial supersaturation, C_I/C_I^0 , can be estimated by integrating Eq. [6]. The result is

$$\frac{C_I}{C_I^0} = 1 + \frac{\theta K_{\text{Si}}(T) B^{3/4}}{\sqrt{2v_m} \pi \rho \alpha_0 D_{\text{ISI}} C_I^0 t^{3/4}} \quad [12]$$

Little is known about the term $(D_{\text{ISI}} C_I^0)$. Therefore it will be assumed that the flux of self-interstitials is some fraction of the flux of silicon atoms diffusing via the vacancy mode of self-diffusion (24, 31)

$$D_{\text{ISI}} C_I^0 = f_I n_H D_{\text{Si}} \quad [13]$$

where f_I is the fractional interstitial contribution, n_H is the number of host lattice sites, and D_{Si} is the self-diffusion coefficient of silicon. Finally, Eq. [10] becomes

$$\frac{dr}{dt} = \pi\alpha_0^2 \left[-n_H D_{\text{Si}} f_I \left\{ \exp\left(\frac{\Delta F_L}{kT}\right) - 1 \right\} + \frac{\theta K_{\text{Si}}(T) B^{3/4}}{\sqrt{2v_m} \pi \rho \alpha_0 t^{3/4}} \right] \quad [14]$$

By using the relations above we have separated the growth rate expression into two parts. The first term in brackets is always negative since $\Delta F_L > 0$. This term is related to the emission of interstitials from the fault line (or absorption of vacancies). The second term is the relative steady-state concentration of generated interstitials under oxidizing conditions. The relative magnitudes of these two terms will determine whether dr/dt is positive (growth) or negative (retrogrowth).

Equation [14] has been fitted to OISF growth data in order to estimate f_I and θ . The surface kink density for $\langle 100 \rangle$ silicon was taken to be $\rho \approx 10^{12} \text{ cm}^{-2}$ and the atomic volume is $v_m \approx 2 \times 10^{-23} \text{ cm}^3$. Hu (2) estimated the capture cross section of a kink for an interstitial to be $\sim \pi\alpha_0^2$, where α_0 is on the order of the surface step height ($3.85 \times 10^{-8} \text{ cm}$). ΔF_L is the sum of the dislocation line energy and the stacking fault energy, γ . Since the line energy varies inversely with the line length, we consider only large interstitial-type stacking faults in which the line energy can be neglected. For silicon, $\gamma \approx 3 \times 10^{13} \text{ eV/cm}^2$ (40). For an atomic cross section in the $\langle 111 \rangle$ plane of $12.77 \times 10^{-16} \text{ cm}^2$ (39), $\Delta F_L = 0.04 \text{ eV}$. It will be shown later that a better fit to OISF shrinkage data occurs when $\Delta F_L = 0.15 \text{ eV}$, so that this value will be used in our calculations.

The two terms in Eq. [14] are plotted vs. temperature in Fig. 4. It can be seen that at $T \approx 1210^\circ\text{C}$, $dr/dt = 0$. Above this temperature the emission of silicon interstitials exceeds their generation at the silicon surface, and $dr/dt < 0$. This result is also shown in Fig. 2 where at $T \approx 1210^\circ\text{C}$, stacking fault growth has stopped for $\langle 100 \rangle$ silicon.

By integrating Eq. [14] we can obtain the time dependence of OISF growth. Thus, substituting in the appropriate numbers for $\langle 100 \rangle$ silicon we find for dry O_2 oxidation in 100% O_2

$$r = 4017t^{3/4} \exp\left(\frac{-2.51 \text{ eV}}{kT}\right) - 3.6 \times 10^{10} t \exp\left(\frac{-5.02 \text{ eV}}{kT}\right) \left[\exp\left(\frac{0.15 \text{ eV}}{kT}\right) - 1 \right] \quad [15]$$

This equation is similar to the result obtained by Leroy (30), even though some of his assumptions and analyses were different. Also, Lin *et al.* (41) arrived at a similar result empirically. The major differences between the model described here and Leroy's model are: (i) we assume OISF growth is limited by the generation of self-interstitials at the Si/SiO₂ interface, rather than limited by diffusion, (ii) we calculate C_I^L from the dislocation free energy, (iii) we assume silicon self-diffusion occurs via a fractional interstitialcy mechanism as proposed by Antoniadis *et al.* (24).

Equation [15] is plotted in Fig. 2 for 3 hr oxidations performed at various temperatures in dry O_2 (35). An excellent fit to the data is obtained. The calculation for $\langle 111 \rangle$ silicon was made by increasing the kink density, ρ , 1.5 times over the $\langle 100 \rangle$ case. This reduces the growth term in Eq. [14] and [15]. From the fitted coefficients in Eq. [15] we find $f_I = 0.19$ and $\theta = 0.043$.

Doping Dependence of OISF Shrinkage

In the retrogrowth term, D_{Si} is doping dependent. The shrinkage of stacking faults in doped layers annealed in dry N_2 becomes (31, 42)

$$\frac{dr}{dt} = -\pi\alpha_0^2 n_H f_I \left[D_{\text{Si}}^x + D_{\text{Si}}^- \left(\frac{n}{n_i}\right) + D_{\text{Si}}^+ \left(\frac{p}{n_i}\right) \right] \left[\exp\left(\frac{\Delta F_L}{kT}\right) - 1 \right] \quad [16]$$

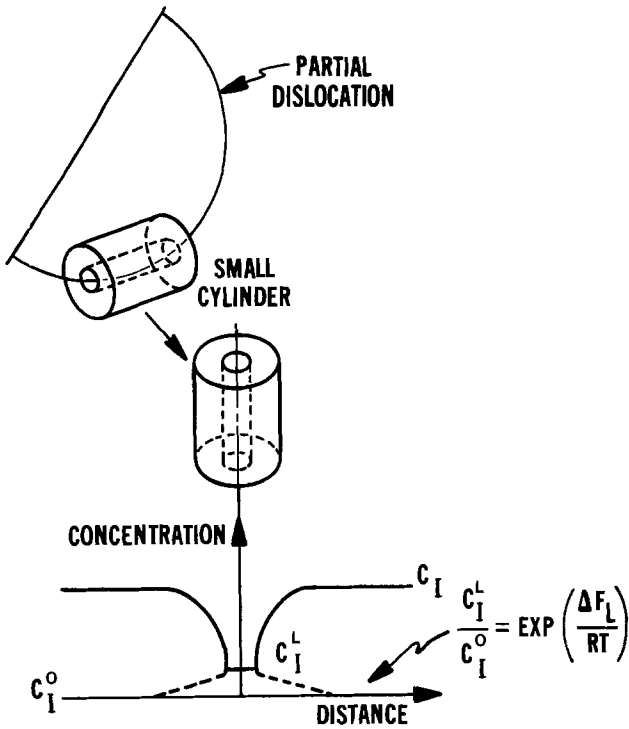


Fig. 3. A model of self-interstitial diffusion from the bulk to the partial dislocation bounding a stacking fault. Under nonoxidizing conditions, the concentration of self-interstitials at the fault line, C_I^L , is greater than the equilibrium bulk interstitial concentration C_I^O . Under oxidizing conditions, $C_I > C_I^L$ until the retrogrowth temperature is reached.

where D_{Si} is the silicon diffusivity via vacancies in the r^{th} charge state. Using the empirically determined values of D_{Si^x} , D_{Si^-} , and D_{Si^+} , (42), dr/dt is shown plotted in Fig. 5 vs. n and p at 1100°C . For this calculation $\alpha_0 = 3.85 \times 10^{-8} \text{ cm}^{-2}$, $f_I = 0.19$, and $\Delta F_L = 0.04 \text{ eV}$. Also shown are 1100°C estimated OISF shrinkage rates from the data of Hashimoto *et al.* (43) for both n and p-type silicon. The calculated curves show a similar dependence on doping for both n and p-type silicon. By setting $\Delta F_L \approx 0.15 \text{ eV}$ we can make the data and calculations agree well (dashed curves in

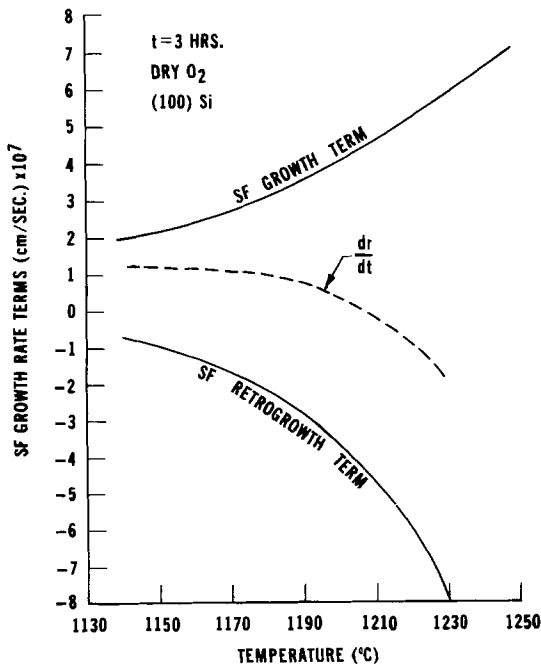


Fig. 4. Stacking fault growth rate term and retrogrowth rate term summed to give the net rate.

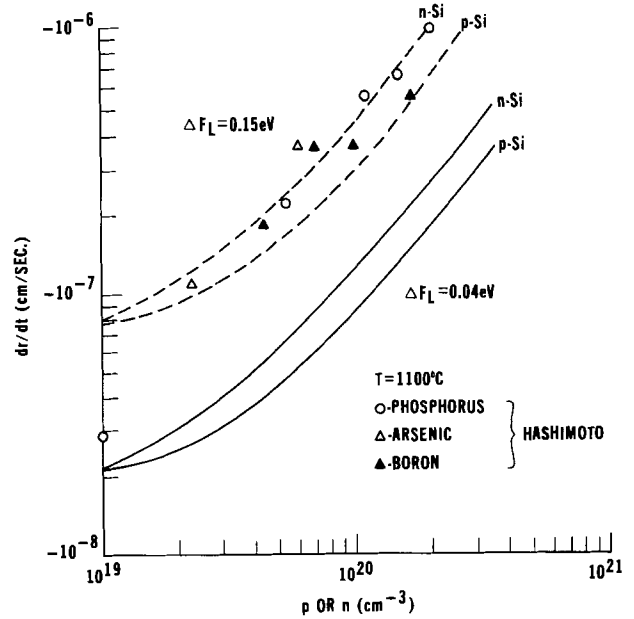


Fig. 5. Donor and acceptor doping effect on stacking fault shrinkage rate at 1100°C .

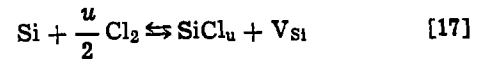
Fig. 5). However, the data are not sufficiently accurate in absolute value to decide if this larger stacking fault energy is real.

The implication here is that the emission of silicon atoms from a stacking fault is enhanced at large doping concentrations by the presence of additional vacancies, as proposed by Hashimoto *et al.* (43). It has been shown how additional vacancies generated near the surface can account for the doping-enhanced oxidation rate (linear rate constant only) (33, 34). Likewise, in a heavily doped layer that is not being oxidized, the increase in the equilibrium vacancy concentration with doping can account for the enhanced migration of silicon atoms away from the stacking fault or for increased absorption of vacancies by the fault.

Effect of Chlorine on OISF Growth

It has been reported that the introduction of small amounts of chlorine or chlorine-containing compounds during silicon oxidation in dry O_2 causes the retarded growth or annihilation of OISF (44-47). The higher the chlorine concentration, the more rapid is the OISF retrogrowth. Also, the temperature at which retrogrowth occurs decreases with increasing chlorine concentration.

Because chlorine atoms localize at the Si/SiO₂ interface, Murarka (48) has proposed a two-step mechanism that can reduce the number of silicon interstitials that flow into the silicon substrate. In the first step, chlorine reacts with silicon atoms on lattice sites to form SiCl_u by the reaction



In the process a silicon vacancy is generated. This vacancy then is available to recombine with a silicon interstitial produced due to oxidation



The condition for retrogrowth would then depend upon whether the chlorine concentration was sufficient to produce enough vacancies to cause $dr/dt = 0$.

Reaction [17] is consistent with the observation that the presence of HCl during dry O_2 oxidation increases the linear rate constant, B/A (49-51). The doping dependence of B/A has also been described as a vacancy enhancement effect.

In terms of Eq. [14] then, the effect of chlorine at the Si/SiO₂ interface is to increase B , but also to decrease θ . From published data (50) $B \propto p_{\text{HCl}}^{1/2}$. From Eq. [17] and [18], (48)

$$[\text{Si}_I] \propto p_{\text{Cl}_2}^{-u/2} \quad [19]$$

Thus, since $\theta \propto [\text{Si}_I]$ we have

$$\theta B^{1/4} \propto p_{\text{Cl}_2}^{(1/32-u/2)} \quad [20]$$

since $p_{\text{HCl}} \propto p_{\text{Cl}_2}$ (48). Substituting Eq. [20] into Eq. [14] and integrating for stacking fault length for a 2 hr, 1100°C dry O₂/HCl oxidation we find for $p_{\text{Cl}_2} > 0$

$$r = K_c p_{\text{Cl}_2}^{(1/32-u/2)} (\mu\text{m}) \quad [21]$$

At $p_{\text{Cl}_2} = 1\%$, $r = 6.0 \mu\text{m}$ after 2 hr. Using this boundary condition, Eq. [21] is plotted with $u = 1$ in Fig. 6 vs. percent HCl in oxygen. Also plotted are data of Shiraki (46) obtained under these same conditions. The agreement is quite good. This result implies that only one chlorine atom is involved in the reaction at the Si/SiO₂ interface which generates a vacancy. On the other hand, Murarka's analysis (48) yields $u = 2$, implying that a Cl₂ molecule is involved. The difference is a result of our assumption that the generation of self-interstitials is proportional to $P_{\text{O}_2}^{1/2}$ rather than P_{O_2} as Murarka assumed.

We can conclude that the model of chlorine combining with silicon to form SiCl and a vacancy is consistent with the observed increase in the linear rate constant, B/A . Also, the subsequent reduction in stacking fault growth rate is consistent with the reduction in the number of silicon interstitials which are generated during oxidation. This reduction is brought about by the trapping of interstitials by excess vacancies created when SiCl is formed (48).

Oxidation-Enhanced Diffusion

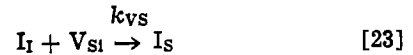
A model explaining orientation-dependent diffusion has been proposed by Hu (2). Briefly, this model is based upon the super-saturation of silicon interstitials at concentrations dependent on the oxide growth rate and silicon orientation. These interstitials are responsible for the growth of stacking faults, and by invoking a partial interstitialcy diffusion mechanism, also influence impurity diffusion enhancement.

To show how the enhancement of impurity diffusion by self-interstitials can act while the dominant diffusion mechanism is a vacancy-assisted process (31, 42), it will be assumed that exchanges can take place between the various species in the silicon lattice (vacancies, self-interstitials, interstitial impurities, and substitutional impurities). Interstitial impurities, I_I , can be created by the exchange between a self-interstitial,

Si_I , and a substitutional impurity, I_S (the Watkins replacement mechanism) (52)



Interstitial impurities can return to substitutional sites primarily by recombination with vacancies



These processes are illustrated in Fig. 7. If it is assumed that vacancies and self-interstitials are very mobile compared to impurities, and if we assume a steady-state concentration of these point defects, then we can write down a set of coupled equations following the work of Baruch (53)

$$\frac{\partial C_{\text{II}}}{\partial t} = D_{\text{II}} \frac{\partial^2 C_{\text{II}}}{\partial x^2} - \frac{C_{\text{II}}}{\tau_I} + k_{\text{SI}} C_I C_{\text{SI}} \quad [24]$$

$$\frac{\partial C_{\text{SI}}}{\partial t} = D_{\text{SI}} \frac{\partial^2 C_{\text{SI}}}{\partial x^2} + \frac{C_{\text{II}}}{\tau_I} - k_{\text{SI}} C_I C_{\text{SI}} \quad [25]$$

In the above equations C_{II} is the concentration of interstitial impurities, C_{SI} is the concentration of substitutional impurities, C_I is the self-interstitial concentration, k_{SI} and k_{VS} are the rate constants of reactions [22] and [23], respectively, and

$$\tau_I^{-1} = k_{\text{VS}} C_V \quad [26]$$

If we define the total impurity concentration as $C_T = C_{\text{II}} + C_{\text{SI}}$, then it can be shown that by adding Eq. [24] and [25], the resulting continuity equation is (31)

$$\frac{\partial C_T}{\partial t} = D_{\text{SI}} \left(1 + f_{\text{II}} \frac{C_I}{C_I^0} \right) \frac{\partial^2 C_{\text{SI}}}{\partial x^2} \quad [27]$$

where C_I^0 is the equilibrium self-interstitial concentration, f_{II} is the fractional partial-interstitialcy contribution to impurity diffusion, and C_I/C_I^0 is the self-interstitial supersaturation given by Eq. [12].

In Eq. [27] we have defined an effective diffusivity of doping impurities for the case where vacancy-dominated diffusion is supplemented by a partial interstitialcy diffusion process. The fraction of the substitutional flux that occurs by this latter mechanism is f_{II} . Values of f_{II} for boron, phosphorus, and arsenic have been obtained by fitting the effective diffusivity to OED data (31). For example, the diffusivity of boron in $\langle 100 \rangle$ silicon in dry O₂ is shown plotted in Fig. 8 (54). Also shown is the diffusivity of boron, $D = D_{\text{SI}}$, under a nonoxidizing surface. Good agreement with the measured data occurs when $f_{\text{II}} = 0.17$ in the equation for effective diffusivity (Eq. [27]). Thus, under nonoxidizing conditions, $C_I/C_I^0 = 1$ and ~17% of the flux of boron is due to the proposed partial interstitialcy process driven by the equilibrium self-intersti-

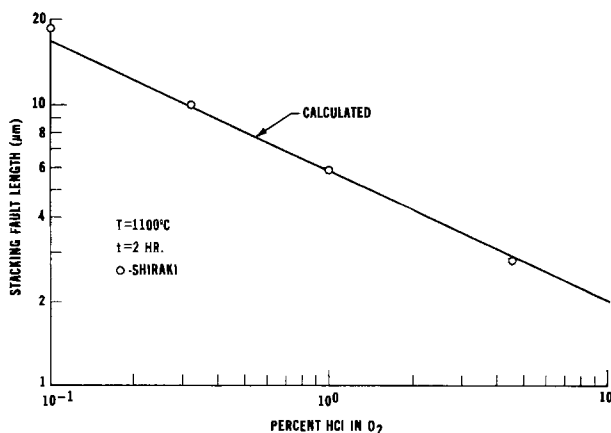


Fig. 6. Length of an oxidation-induced stacking fault formed in HCl-O₂ oxidations as a function of HCl concentration in the ambient.

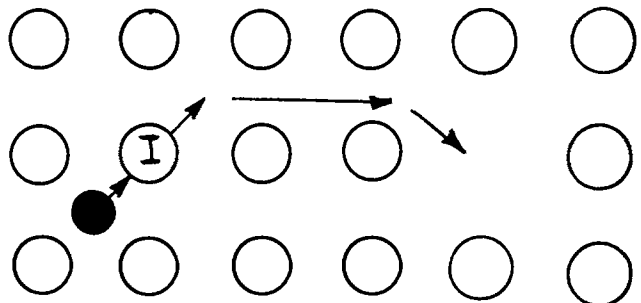


Fig. 7. Schematic diagram of the partial interstitialcy diffusion model (Watkin's replacement mechanism). A silicon self-interstitial replaces a substitutional impurity atom. The interstitial impurity migrates until it combines with a vacancy.

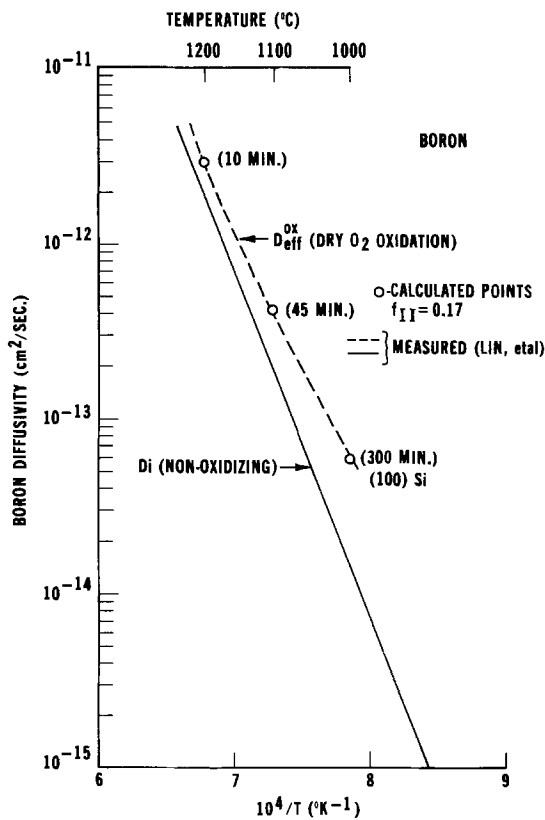


Fig. 8. Boron diffusivity in $\langle 100 \rangle$ silicon in nonoxidizing and dry O_2 oxidizing ambients. The solid and dashed curves were measured [Ref. (54)], and the points are calculated from Eq. [27].

tial concentration. For phosphorus, $f_{II} = 0.12$ and for arsenic, $f_{II} = 0.09$. These factors correlate with the energy required to create an interstitial impurity (31).

An additional observation of OED was recently made by Taniguchi *et al.* (55). They found that OED decreased as the concentration of the diffusing impurity increased beyond the point where normal concentration dependent diffusion occurs. This effect was explained in terms of the reduction of oxidation-produced self-interstitials by recombination with the increasing concentration of vacancies. If we assume that the equilibrium vacancy concentration is unaffected by the self-interstitials generated at the interface, but that the quasi-steady-state value of C_I/C_I^0 is inversely proportional to the vacancy concentration, then the effective diffusivity in Eq. [27] can be written generally as

$$D_e \approx D_n + \Delta D_o \\ \approx D_{SI} \left(\frac{C_v}{C_v^i} \right) + D_{SI} f_{II} \left(\frac{C_I}{C_I^0} \right)_i \left(\frac{C_v^i}{C_v} \right) \quad [28]$$

where $(C_I/C_I^0)_i$ is the self-interstitial supersaturation under intrinsic doping conditions, and C_v/C_v^i is the vacancy enhancement that occurs when $n > n_i$ or $p > n_i$. Equation [28] has been divided into the contribution to diffusion under nonoxidizing conditions, D_n , and the OED enhanced contribution.

The data of Taniguchi *et al.* (55) are shown in Fig. 9 for OED of phosphorus and boron vs. the total number of impurities/cm², Q_T . For the boron data in Fig. 9a, D_n becomes concentration dependent at $Q_T \approx 4 \times 10^{15} \text{ cm}^{-2}$, corresponding to prediffused layers ($X_J = 3.2 \mu\text{m}$) which were subsequently diffused at 1100°C in wet O_2 . According to Eq. [28], ΔD_o should decrease when $C_v > C_v^i$ or when $p > n_i$. For extrinsic boron diffusion we know that $Q_T \propto C_s^{3/2}$ (56), where $C_s \approx p_s$ is the surface concentration. Thus, we expect that $\Delta D_o \propto Q_T^{-2/3}$ for $p_s > n_i$. Similarly, since $D_n \propto p/n_i$, then

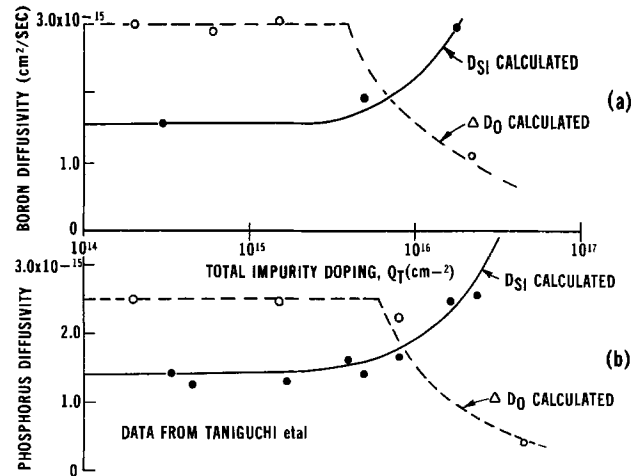


Fig. 9. Diffusivities of (a) boron and (b) phosphorus during wet O_2 oxidation at 1100°C , vs. the total amount of impurity.

$D_n \propto Q_T^{2/3}$ for $p_s > n_i$. These results are plotted in Fig. 9a, and the agreement with the data is reasonable.

For the phosphorus case diffusion is controlled primarily by $V =$ vacancies which form $P^+V =$ pairs in the high concentration region, and which subsequently dissociate and flood the bulk. This increase in the steady-state vacancy concentration raises the diffusivity of phosphorus and creates a tail on the profile (57). If it is assumed that diffusion in the tail dominates, then $D_n \approx D_i^x + D_{TAIL}$, where D_i^x is the intrinsic phosphorus diffusivity via neutral vacancies. It can be shown (58) that since $n_s \propto Q_T^{1/2}$, where n_s is the surface electron concentration, then

$$D_n \approx D_i^x + K_i(T) Q_T^{3/2} \quad [29]$$

$K_i(T)$ is a collection of terms from the Fair-Tsai model (57) that can be directly calculated. Equation [29] is shown plotted in Fig. 9b and agrees well with the D_n data (55) for phosphorus. It can also be shown then that for $n \gg n_i$ this model predicts

$$\Delta D_o \propto Q_T^{-1} \quad [30]$$

This result is also plotted in Fig. 9b starting at $Q_T = 6 \times 10^{15} \text{ cm}^{-2}$. This total doping corresponds to $n_s \approx 6 \times 10^{19} \text{ cm}^{-3}$. It is known (57) that at 1100°C , D_{TAIL} begins to show a strong concentration dependence at this surface concentration.

In summary it has been shown that Taniguchi's model (55) of self-interstitial recombination with vacancies is consistent with the high concentration diffusion models for boron and phosphorus. In addition, the observed decrease in OED with increasing concentration lends support to the notion of two separate but interdependent diffusion mechanisms operating during oxidation.

The Effect of Chlorine on OED

If chlorine or chlorine-bearing compounds are added to oxygen in sufficient concentrations that the resulting mixture in a furnace will cause stacking fault retrogrowth in silicon, oxidation-enhanced diffusion will also become negligible (28). In order to understand the effect of chlorine compounds on OED, recall that the concentration of generated silicon interstitials depends on the partial pressure of HCl through the relation (from Eq. [19])

$$C_I \propto (p_{HCl})^{-1/2} \quad [31]$$

Thus, the effective impurity diffusivity during HCl oxidation is

$$D_{eff}^{ox} = D_{SI} (1 + K_H (p_{HCl})^{-1/2}) \quad [32]$$

where K_H is temperature and orientation dependent. This equation has been adjusted through K_H to fit the

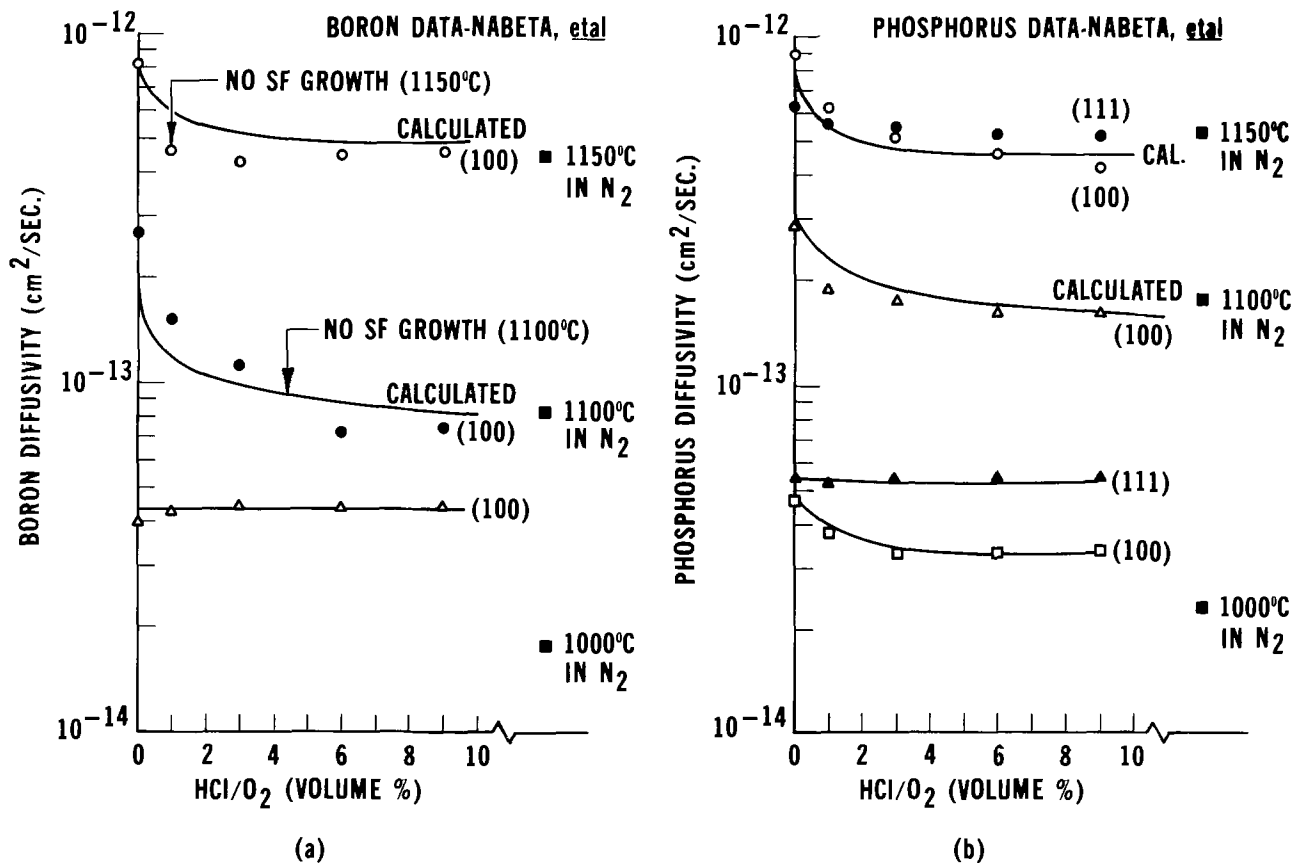


Fig. 10. Diffusivities of (a) boron and (b) phosphorus during HCl-O₂ oxidations vs. HCl concentration in the ambient

data of Nabeta *et al.* (28) shown in Fig. 10. The agreement with the data is reasonable for the case of boron.

The OED of phosphorus shown in Fig. 10b has some anomalies which appear to contradict the model presented here. It can be seen that at 1150°C phosphorus diffuses more rapidly in <100> silicon as compared to <111> when the HCl volume ratio is <2%. At higher HCl flow the diffusivity in <111> silicon is greater. At 1000°C the OED of phosphorus is greater in <111> than <100> for HCl volume ratios >0%. However, the reduction of OED to the neutral ambient case does not occur over the range of HCl flows investigated.

In order to understand these results we need to be aware of the concentration of phosphorus used in the experiments as well as the diffusion times and temperatures. Nabeta *et al.* (28) whose data are shown in Fig. 10b started with prediffused phosphorus layers whose surface concentrations were greater than $2 \times 10^{20} \text{ cm}^{-3}$. Masetti *et al.* (59) who also saw significant OED in <111> silicon at 1000°C prediffused their wafers with highly doped phosphorus (final C_s after OED drive-in was $\sim 5 \times 10^{19} \text{ cm}^{-3}$ and $X_J \approx 5 \mu\text{m}$). Similar results were obtained by Francis and Dobson (60) who observed OED in <111> silicon epitaxial layers doped to $\sim 5 \times 10^{17} \text{ cm}^{-3}$. However, their results have been put into question because the OED enhancement was referenced to diffusion under an Si₃N₄ mask deposited directly on the silicon surface. It has been shown that the compressive stress in the silicon due to the Si₃N₄ overlayer can reduce the diffusion of low concentration profiles (61).

It has been shown that phosphorus diffusion at high concentrations in nonoxidizing ambients is greater in <111> silicon than in <100> (62). An example is shown in Fig. 11 where measured profiles are plotted of 60 min 900°C POCl₃ diffusions. At low concentrations the diffusivities in <100> and <111> silicon are the same with nonoxidizing furnace ambients.

The effective diffusivities plotted by Nabeta *et al.* (28) can be estimated as

$$D_e = D_n + \frac{K_H'}{\rho_{\text{HCl}}^{1/2} \rho} \left(\frac{C_v^{\downarrow}}{C_v} \right) \quad [33]$$

where ρ is the surface kink density and K_H' \propto

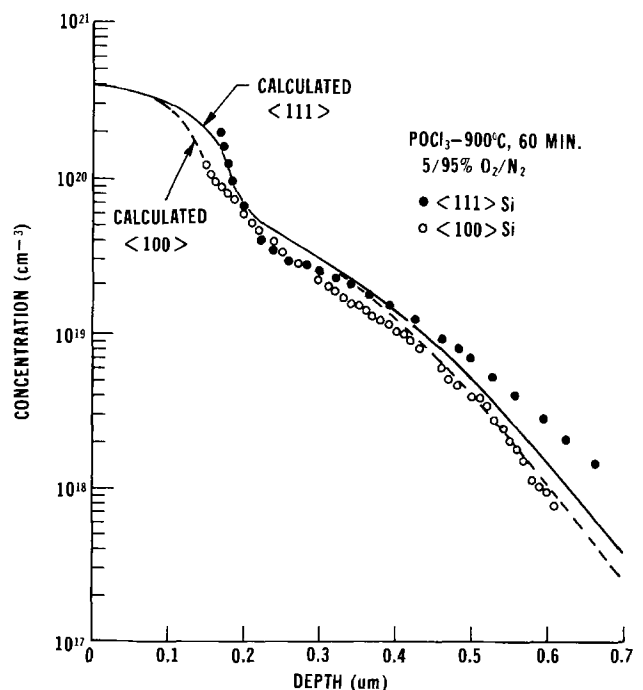


Fig. 11. Measured (62) and calculated profiles of phosphorus diffused for 60 min at 900°C in <111> and <100> silicon in a POCl₃ in N₂ furnace ambient. Calculations are based on the Fair-Tsai model (57) with orientation-dependent strain distribution.

exp (2.5 eV/kT) D_{Si} . At high phosphorus concentrations [$n_s > n_e$ where n_e increases from 10^{20} cm $^{-3}$ at 900°C to 2×10^{20} cm $^{-3}$ at 1150°C (57)] diffusion in oxidizing ambients is such that $D_e \simeq D_n$ (see Fig. 9b). Then

$$\frac{D_e(111)}{D_e(100)} \sim \frac{D_n(111)}{D_n(100)}$$

and $D_e(111) > D_e(100)$. From Fig. 11 this ratio is $\simeq 1.4$. From Fig. 10b the 1000°C data show $D_e(111)/D_e(100) \simeq 1.3$. At low phosphorus concentrations ($n_s < n_i$) and 0% HCl/O $_2$

$$\frac{D_e(111)}{D_e(100)} \simeq \frac{\rho(100)}{\rho(111)} \simeq \frac{2}{3}$$

From Fig. 10b the 1150°C data show $D_e(111)/D_e(100) \simeq 2/3$ at $p_{HCl} = 0$. As p_{HCl} increases the OED term in Eq. [33] becomes smaller relative to D_n . And $D_e(111)/D_e(100) = > D_n(111)/D_n(100) \simeq 1.4$. This reversal in the relative enhancement of $D_e(111)$ to $D_e(100)$ can be seen to occur at 1150°C in Fig. 10b as p_{HCl} increases. However, further discussion of these data would require more complete knowledge of the diffusion profiles.

The only remaining question regarding the orientation dependence of phosphorus diffusion concerns the question of why $D_n(111) > D_n(100)$ at high doping levels. This has not been observed for other dopants, and it is believed to be due to the unusual way in which phosphorus diffuses in the presence of its own strain distribution. It has been observed that the misfit tensile stress of phosphorus at $C_s \gtrsim 3 \times 10^{20}$ cm $^{-3}$ is sufficient to retard diffusion significantly due to narrowing of the silicon bandgap (63). Bandgap narrowing can reduce the number of P+V= pairs which dominate diffusion at high doping levels (57). Fukuhara et al. (64) have calculated the strain distributions of diffused phosphorus layers in $\langle 100 \rangle$ and $\langle 111 \rangle$ silicon. They have shown that the strain component parallel to the $\langle 100 \rangle$ surface is 1.23 times larger than the corresponding strain in $\langle 111 \rangle$ silicon. As a result, the amount of bandgap narrowing in $\langle 100 \rangle$ is also 1.23 times as large as in $\langle 111 \rangle$. Then, the ratio of diffusivities in the phosphorus tail region can be written as (63)

$$\frac{D_{TAIL}(111)}{D_{TAIL}(100)} = \exp \frac{3(\Delta E_g(111) - \Delta E_g(100))}{kT} \quad [34]$$

Using $\Delta E_g(100) = 1.23 \Delta E_g(111)$ and for tensile stress (63)

$$\Delta E_g(111) = -0.7 \times 10^{-22} C_s \quad [35]$$

we find that for $C_s = 5 \times 10^{20}$ cm $^{-3}$ and $T = 900^\circ\text{C}$

$$\frac{D_{TAIL}(111)}{D_{TAIL}(100)} \simeq 1.3$$

This result is in good agreement with the data in Fig. 11. Further illustration that the strain effect can account for high concentration, orientation-dependent diffusion is shown in Fig. 11 where computer-generated profiles are compared with the data. The agreement is good.

We can conclude then that studies of the effect of HCl on OED of phosphorus should be conducted with $C_s \lesssim n_e$ in order to avoid complications in interpreting the results. However, from the preceding analysis it is believed that the phosphorus data in Fig. 10b are consistent with the proposed model of HCl reducing the extent of OED.

Summary and Conclusions

We have presented a consistent picture which ties together numerous observations and models of the oxidation process, the growth of stacking faults, en-

hanced diffusion, and the effects of chlorine compounds on these processes. Silicon self-interstitials generated at the Si/SiO $_2$ interface as a result of incomplete oxidation (Hu's model) (2) raise the concentration of self-interstitials in the silicon surface region. Some of these interstitials participate in surface regrowth which is orientation dependent. The number of surface kinks or regrowth sink sites increases with the order (100), (110), and (111). Thus, the number of self-interstitials that are available for OED and OISF growth decreases in the same order. OED can be explained in terms of a partial interstitialcy mechanism which kicks impurities into the silicon interstices so that interstitial diffusion occurs until recombination of the impurity with a vacancy takes place (Watkin's replacement model) (52).

Retrowth of stacking faults and reduced OED both occur when the concentration of generated self-interstitials decreases. We view OISF growth as a dynamic process whereby growth will occur if the relative steady-state self-interstitial concentration around the fault exceeds the emitted concentration of interstitials from the fault line. Retrowth occurs when the reverse is true. The introduction of chlorine-bearing compounds into the oxidation tube can bring about retrowth and reduced OED if the chlorine concentration is large enough. The reaction of chlorine with silicon at the interface creates vacancies which can combine with generated self-interstitials and reduce their concentration (Murarka's model) (48).

Manuscript received Dec. 1, 1980.

Any discussion of this paper will appear in a Discussion Section to be published in the December 1981 JOURNAL. All discussions for the December 1981 Discussion Section should be submitted by Aug. 1, 1981.

Publication costs of this article were assisted by Bell Laboratories.

REFERENCES

1. R. J. Jaccodine and C. M. Drum, *Appl. Phys. Lett.*, **8**, 29 (1966).
2. S. M. Hu, *J. Appl. Phys.*, **45**, 1567 (1974).
3. I. R. Sanders and P. S. Dobson, *J. Mater. Sci.*, **9**, 1987 (1974).
4. D. J. D. Thomas, *Phys. Status Solidi*, **3**, 2261 (1963).
5. H. J. Queisser and P. G. G. van Loon, *J. Appl. Phys.*, **35**, 3066 (1964).
6. G. R. Booker and W. J. Tunstall, *Philos. Mag.*, **13**, 71 (1966).
7. W. A. Fisher and J. A. Amick, *This Journal*, **113**, 1054 (1966).
8. I. R. Sanders and P. S. Dobson, *Philos. Mag.*, **20**, 881 (1969).
9. A. Mayer, *RCA Rev.*, **31**, 414 (1970).
10. Y. Sugita and T. Kato, *J. Appl. Phys.*, **42**, 5847 (1971).
11. T. Kato, Y. Sugita, and A. Yoshinaka, *Jpn. J. Appl. Phys.*, **11**, 1066 (1972).
12. C. M. Drum and W. van Gelder, *J. Appl. Phys.*, **43**, 4465 (1972).
13. C. M. Hsieh and D. M. Maher, *ibid.*, **44**, 1302 (1973).
14. S. P. Murarka, *ibid.*, **48**, 5020 (1977).
15. S. M. Hu, *J. Vac. Sci. Technol.*, **14**, 17 (1977).
16. S. P. Murarka and G. Quintana, *J. Appl. Phys.*, **48**, 46 (1977).
17. R. Conti, G. Corda, R. Mattucci, and C. Ghezzi, *J. Mater. Sci.*, **10**, 705 (1975).
18. S. P. Murarka, *J. Appl. Phys.*, **49**, 2513 (1978).
19. S. Prussin, *ibid.*, **45**, 1635 (1974).
20. G. N. Wills, *Solid State Electron.*, **12**, 133 (1969).
21. T. C. Chen and C. C. Mai, *Proc. IEEE*, **58**, 588 (1970).
22. L. E. Katz in "Silicon Device Processing," Natl. Bur. Stand. Special Publication 337, p. 192, U.S. GPO, Washington, D.C. (1970).
23. H. Higuchi, M. Maki, and Y. Takano, Paper 78 presented at The Electrochemical Society Meeting, Washington, D.C., May 9-13, 1971.
24. D. A. Antoniadis, A. G. Gonzalez, and R. W. Dutton, *This Journal*, **125**, 813 (1978).
25. D. A. Antoniadis, A. M. Lin, and R. W. Dutton,

- Appl. Phys. Lett.*, **33**, 1030 (1978).
26. W. G. Allen and K. V. Anand, *Solid State Electron.*, **14**, 397 (1971).
 27. S. I. J. Ingre and S. Maniv, Paper 540 presented at The Electrochemical Society Meeting, Los Angeles, California, Oct. 14-19, 1979.
 28. Y. Nabeta, T. Uni, S. Kubo, and H. Takamoto, *This Journal*, **123**, 1416 (1976).
 29. S. M. Hu, Unpublished.
 30. B. Leroy, *J. Appl. Phys.*, **50**, 7996 (1979).
 31. R. B. Fair, in "Processing Technologies," Vol. II, *Applied Solid State Science*, To be published.
 32. L. C. Feldman, I. Stensgaard, P. J. Silverman, and T. E. Jackson, in "The Physics of SiO₂ and Its Interfaces," S. T. Pantelides, Editor, p. 344, Pergamon, New York (1978).
 33. C. P. Ho and J. D. Plummer, *This Journal*, **126**, 1516 (1979).
 34. C. P. Ho and J. D. Plummer, *ibid.*, **126**, 1523 (1979).
 35. S. M. Hu, *Appl. Phys. Lett.*, **27**, 165 (1975).
 36. B. E. Deal and A. S. Grove, *J. Appl. Phys.*, **36**, 3770 (1965).
 37. JANAF Thermochemical Tables, 2nd ed., Nat. Bur. Std. (U.S.), **37** (June 1971).
 38. W. A. Tiller, *This Journal*, **127**, 625 (1980).
 39. I. R. Sanders and P. S. Dobson, *J. Mater. Sci.*, **9**, 1987 (1974).
 40. J. Friedel, "Dislocations," pp. 104-127, Pergamon Press, New York (1964).
 41. A. M. Lin, D. A. Antoniadis, R. W. Dutton, and W. A. Tiller, Paper 539 presented at The Electrochemical Society Meeting, Los Angeles, California, Oct. 14-19, 1979.
 42. R. B. Fair in "Semiconductor Silicon 1977," H. R. Huff and E. Sirtl, Editors, p. 968, The Electrochemical Society Softbound Proceedings Series, Princeton, N.J. (1977).
 43. H. Hashimoto, H. Shibayama, H. Masaki, and H. Ishikawa, *This Journal*, **123**, 1899 (1976).
 44. H. Shiraki, *Jpn. J. Appl. Phys.*, **15**, 1 (1976).
 45. H. Shiraki, *ibid.*, **14**, 747 (1975).
 46. H. Shiraki, *ibid.*, **15**, 83 (1976).
 47. T. Hattori, *This Journal*, **123**, 945 (1976).
 48. S. P. Murarka, *Phys. Rev. B*, **21**, 692 (1980).
 49. B. R. Singh and P. Balk, *This Journal*, **125**, 453 (1978).
 50. D. W. Hess and B. E. Deal, *ibid.*, **124**, 735 (1977).
 51. B. R. Singh and P. Balk, *ibid.*, **126**, 1288 (1979).
 52. G. D. Watkins, in "Radiation Damage in Semiconductors," p. 97, Dunod, Paris (1964).
 53. P. Baruch, in "Radiation Effects in Semiconductors, 1976", p. 126, Inst. Phys. Conf. Ser. No. 31 (1977).
 54. A. M. Lin, R. W. Dutton, and D. A. Antoniadis, Paper 133 presented at The Electrochemical Society Meeting, Boston, Massachusetts, May 6-11, 1979.
 55. K. Taniguchi, K. Kurosawa, and M. Kashiwagi, *This Journal*, **127**, 2243 (1980).
 56. R. B. Fair, *ibid.*, **122**, 800 (1975).
 57. R. B. Fair and J. C. C. Tsai, *ibid.*, **124**, 1107 (1977).
 58. R. B. Fair, *ibid.*, **125**, 323 (1978).
 59. G. Masetti, S. Solmi, and G. Soncini, *Solid State Electron.*, **16**, 1419 (1973).
 60. R. Francis and P. S. Dobson, *J. Appl. Phys.*, **50**, 280 (1979).
 61. R. B. Fair, Paper 137 presented at The Electrochemical Society Meeting, St. Louis, Missouri, May 11-16, 1980.
 62. J. C. C. Tsai and A. W. Rhoads, Unpublished results.
 63. R. B. Fair, *J. Appl. Phys.*, **50**, 860 (1979).
 64. A. Fukuhara and Y. Takano, *Acta Crystallogr., Sect. A*, **33**, 137 (1977).

Interaction of CVD Silicon with Molybdenum Substrates

M. J. Rice, Jr.* and K. R. Sarma*

Motorola Incorporated, Solar Energy R&D Department, Phoenix, Arizona 85008

ABSTRACT

The interaction of CVD silicon with bulk molybdenum substrates was studied as part of a project to grow thin sheets of polysilicon. Deposited silicon sheets separate from the substrate by the thermal expansion shear separation (TESS) technique. The silicide formation was found to play an essential role in the shear separation mechanism. Two silicide phases were formed and identified as MoSi₂ and Mo₅Si₃. The diffusive processes were studied and growth rates of MoSi₂ determined. Void formation was observed and concluded to be necessary for shear separation to occur. Silicon was the primary diffuser in MoSi₂ leading to the void formation at the Si-MoSi₂ interface. The presence of oxygen in the process gases decreased the growth rate of MoSi₂. It is postulated that oxygen inhibits silicon diffusion which in turn affects void formation and reliable shear separation. Silicon nucleation characteristics with various substrate surface preparations were investigated.

The formation of transition metal silicides has been the subject of many papers and symposia in recent years (1-3). The great interest has been generated from the use of transition metals for ohmic or rectifying contacts to single crystal silicon for electronic applications. Another area of interest has been the formation of silicides on refractory metals to protect the metal against high temperature oxidation (4-6). Whether dealing with a thin metal film on a silicon substrate or bulk metal substrates reacting with silicon, it is important to understand the diffusive processes taking place during silicide formation. The present study is concerned with the interaction of chemical vapor deposited silicon with bulk molyb-

denum. This work was part of a project to grow silicon in the form of thin sheets for low-cost solar cells.

The process for producing self-supporting polysilicon films consists of depositing silicon on temporary substrates and separating the silicon from the substrate by the thermal expansion shear separation (TESS) technique (7). The silicon is deposited from a silicon bearing gas at a high temperature, 1000°-1200°C. Subsequent cooling of the substrate and silicon film releases the deposited silicon from the substrate. The shear stresses generated at the substrate-silicon interface due to differences in their thermal expansion coefficients, coupled with a weak bond across the interface, make the separation process feasible. It will be shown that void formation plays an important role in the separation. Molybdenum, as well as the chemically

* Electrochemical Society Active Member.

Key words: diffusion, interfaces, nucleation, semiconductor.

similar tungsten, have proven to be reliable and re-usable temporary substrates.

The silicide formation was found to play an essential role in the shear separation mechanism of silicon from molybdenum substrates. The diffusive processes were studied and pictures of Kirkendall voids (9) were obtained. They are not only necessary for the shear separation observed in this work but could have significance in thin film contact adhesion on silicon. Silicon nucleation characteristics with various substrate surface preparations and growth conditions were also investigated.

Experimental

Molybdenum substrates were cut from 0.040 in. thick sheets with a class 300 finish. Typical analyses showed <15 ppm Fe and Ca and other impurities <10 ppm. The substrates were cleaned by washing in a detergent solution, rinsed in DI water, and degreased in organic solvents unless otherwise noted.

Depositions were carried out in a conventional, horizontal, induction heated CVD reactor using SiCl_4 and H_2 process gases. The hydrogen was withdrawn from a liquid source and contained <2 ppm H_2O and <1 ppm O_2 . The SiCl_4 was semiconductor grade used in epitaxial growth. Temperatures were measured with a disappearing filament pyrometer which had been calibrated to account for emissivity, absorption by the quartz reaction tube, and the mirror used to view the susceptor and substrate. Substrates were placed on a silicon carbide-coated graphite susceptor, and a mask cut from 0.015 in. thick molybdenum was placed on top to mask the edges so that silicon did not deposit over the edges of the substrate. In this way a rectangular sheet of silicon would shear from the substrate without cracking. After purging the furnace with nitrogen, the substrate was heated to the deposition temperature (1150°C) in hydrogen and the temperature allowed to stabilize for 15 min. SiCl_4 was then added to the gas stream as well as dopant gas, B_2H_6 or PH_3 . Microcrystalline silicon sheets 150-250 μm thick were grown in 90 min with areas from 75 to 210 cm^2 . Upon completion of the deposition, the rf power was turned down so that the cooling rate was about $30^\circ\text{C}/\text{min}$. Under these conditions, the silicon separated from the MoSi_2 layer on the substrate in the range of 700°C - 1000°C . Special experiments were carried out in similar fashion except for substrate size, cooling rate, deposition temperature, or process gases as noted in the results and discussion. Silicide layer thicknesses were measured microscopically by averaging ten observations. Samples were mounted and polished by standard metallographic techniques. It was found that staining the samples with an FeCl_3 solution (10g FeCl_3 , 2 ml HCl , 95 ml H_2O) for a few seconds aided in identifying phase boundaries and various layers.

Results

In Fig. 1 and 2 are presented the data for the growth of MoSi_2 . The plot of the thickness squared vs. time in Fig. 1 indicates that the kinetics follow a parabolic law for long times but not in the initial portion of the reaction since the extrapolated curve does not pass through the origin. The experimental points for short times are high because it was not possible to quench the samples in the apparatus used and the small amount of growth which continued during cool-down would be a significant amount of the total growth for short times. It should be pointed out that the data for times longer than 90 min are the result of repeated 90 min runs on the same substrates. A normal run to produce silicon sheets was 90 min so that cross sections were made on substrates used for consecutive depositions, with the silicon shearing off after each run. The data of Gage and Bartlett (8) are shown in Fig. 2, with their growth rates considerably higher. However, they packed molybdenum rods in silicon and NaF to form MoSi_2 at high temperatures and obtained only

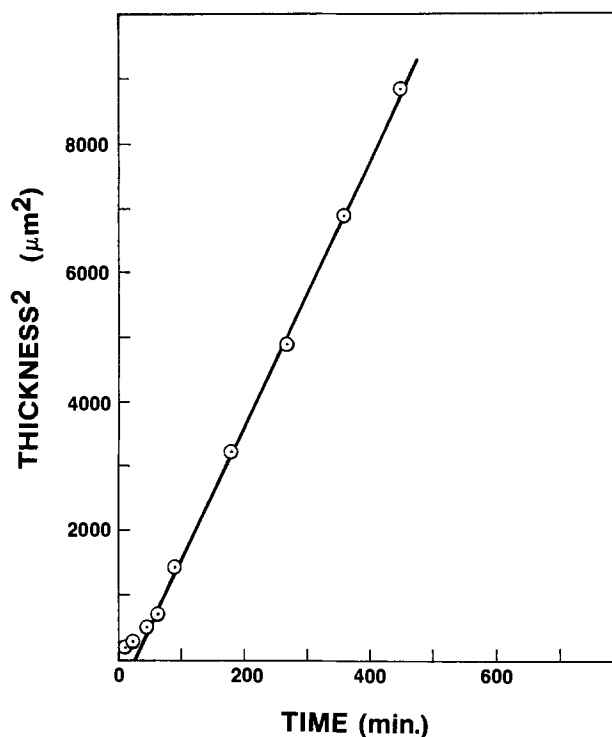


Fig. 1. Growth rate of MoSi_2 layer as a function of time at 1150°C , indicating parabolic behavior.

the disilicide phase. In the CVD method, two silicide phases were always found, although the molybdenum-rich silicide was very thin, on the order of 2-4 μm . The thin layer appeared to grow to a maximum thickness of approximately 4 μm and stay at that thickness. Figure 3 shows a typical cross section with a thick MoSi_2 layer and a thin molybdenum-rich silicide. Samples of molybdenum with an adherent silicon layer were prepared by deposition at 1000°C for short times. After a further anneal at 1150°C in argon for 1 hr, half the samples were quenched by withdrawing from the furnace and dropping them into water. The other half were left in the furnace and cooled at a rate of $10^\circ\text{C}/\text{min}$. In each case two silicide phases were present with the thin molybdenum rich silicide slightly thicker in the slow cooled samples.

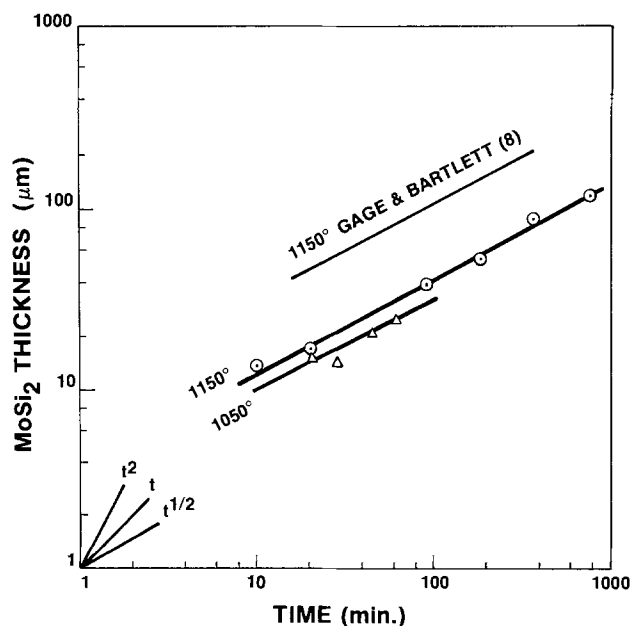


Fig. 2. Effect of temperature on the growth rate of MoSi_2 layer. Note the difference in the growth rate from our measurements and the ones from Gage and Bartlett (8).

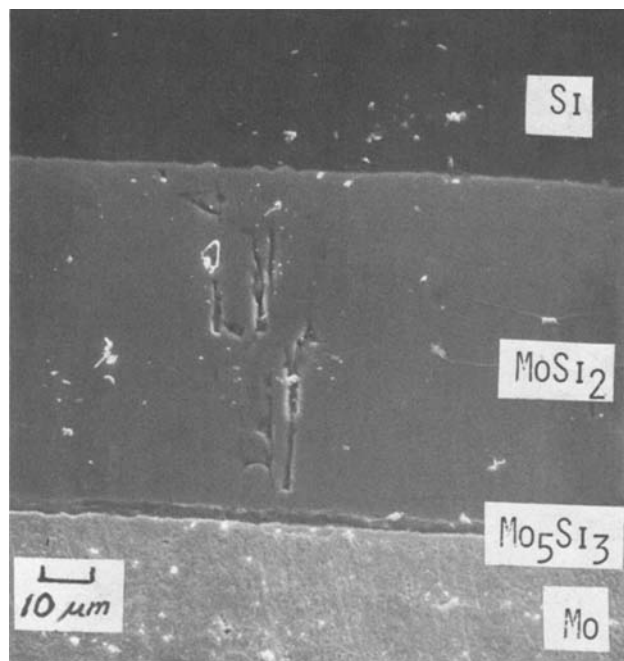


Fig. 3. Cross-sectional view of a substrate showing the interfacial layers; Mo-rich silicide and MoSi_2 .

The effect of impurities, particularly oxygen, in the process gases was studied. Small amounts of oxygen were added to the process gas stream. The growth rate of MoSi_2 was markedly decreased by the addition of oxygen, as shown in Fig. 4. It has been found that thin layers (1000-2000Å thick) of SiO_2 deposited on the substrate prior to deposition impede silicon diffusion so that MoSi_2 formation is drastically decreased. It is possible that the thin layers were not continuous, with many pinholes, and therefore did not act as a barrier. Thick layers of SiO_2 (5000-10,000Å thickness) acted as a barrier preventing interdiffusion. The SiO_2 layers were deposited on the substrates in the CVD furnace by reaction of O_2 with SiCl_4 in H_2 at 1000°C . Then the silicon deposition was carried out without having to remove the substrate from the furnace. Figure 5 shows a barrier layer in cross section with no evidence of silicide formation.

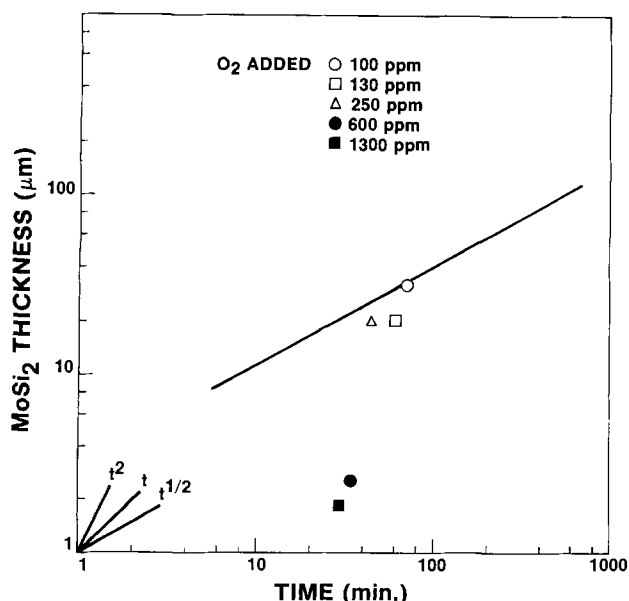


Fig. 4. Effect of presence of oxygen in the process gases during silicon film deposition on the growth rate of MoSi_2 .

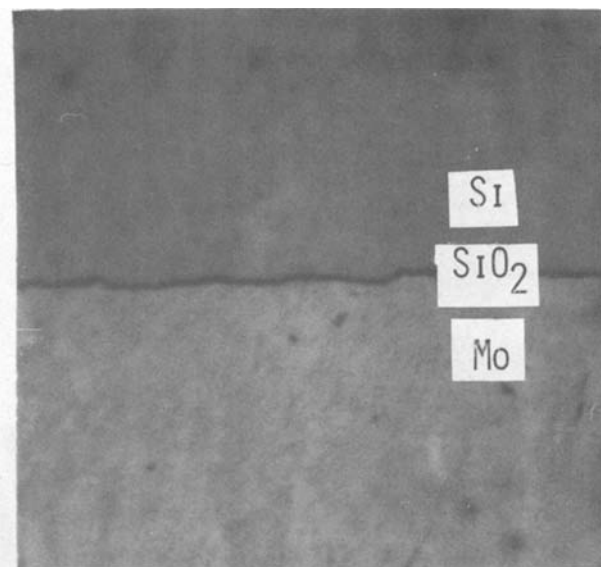


Fig. 5. Cross-sectional view of an SiO_2 coated Mo substrate with an adherent silicon film. Absence of silicide interfacial layers indicates the effectiveness of SiO_2 as a diffusion barrier, $400\times$.

An electron probe x-ray microanalysis of the thick silicide layer indicated a 1:2 atom ratio for Mo:Si and approximately 1:1 for the thin molybdenum-rich silicide layer. To confirm this observation, an x-ray diffraction scan was taken of the thin silicide layer. The sample was prepared by etching the molybdenum substrate away from the silicide layers with solution B (5% HNO_3 , 5% CH_3COOH , 80% H_3PO_4 , 10% H_2O , 60°C). In this way the x-ray beam could be directed onto the thin silicide layer. Table I shows the results of the diffractometer scan obtained from this sample. All peaks could be attributed to be due to MoSi_2 or Mo_5Si_3 , thus identifying the thin molybdenum-rich silicide as Mo_5Si_3 , and thick silicon rich silicide as MoSi_2 .

Discussion

Growth rate.—The growth rate for MoSi_2 obtained in this investigation is lower than that observed by Gage and Bartlett (8) who used a pack cementation method for silicide formation. In their method, molybdenum rods were packed in a mixture of NaF and silicon held at temperature for varying periods of time. By this method, the only silicide observed was MoSi_2 and a parabolic growth rate was obtained. This was interpreted as indicating a diffusion-controlled reac-

Table I. X-ray diffraction patterns of Mo-silicides

| Observed | | MoSi_2 (11) | | | Mo_5Si_3 (12) | | |
|----------|------------------|----------------------|------------------|----------|-------------------------------|------------------|----------|
| d | I/I ₀ | d | I/I ₀ | hkl | d | I/I ₀ | hkl |
| 3.92 | 12 | 3.92 | 45 | 002 | 3.23 | 20 | 211 |
| | | | | | 3.04 | 20 | 310 |
| 2.96 | 20 | 2.96 | 95 | 101 | 2.443 | 10 | 002 |
| 2.45 | 100 | | | | 2.406 | 10 | 400 |
| | | | | | 2.342 | | 110 |
| 2.26 | 88 | 2.26 | 70 | 110 | 2.174 | 20 | 202 |
| | | | | | 2.149 | 60 | 420 |
| | | | | | 2.102 | 50 | 411 |
| 2.02 | 8 | 2.02 | 100 | 103 | 1.986 | 100 | 222 |
| 1.96 | 21 | 1.96 | 40 | 004, 112 | | | |
| 1.60 | 8 | 1.60 | 30 | 200 | 1.522 | 10 | 620 |
| 1.48 | 13 | 1.49 | 20 | 114, 202 | 1.491 | 10 | 512 |
| 1.44 | 11 | | | | 1.437 | 7 | 541 |
| 1.41 | 7 | 1.41 | 25 | 105, 211 | 1.395 | 10 | 323 |
| | | | | | 1.376 | 10 | 631 |
| | | | | | 1.363 | 10 | 532 |
| | | | | | 1.339 | 20 | 602, 413 |
| 1.31 | 7 | 1.308 | 16 | 006 | | | |
| 1.26 | 25 | 1.257 | 45 | 213 | | | |
| | | 1.241 | 10 | 204 | 1.169 | 10 | 642 |

tion with the diffusion of silicon through the silicide the rate-controlling factor. In the present work a parabolic growth rate for MoSi_2 was obtained for reaction times of more than a few minutes. The initial stage of the reaction is controlled by the nucleation of silicon, island formation, and surface coverage before the diffusion of silicon becomes the rate-determining factor. Figure 6 shows the initial stage of nucleation and island formation on several surfaces. In the surfaces studied, MoSi_2 showed complete coverage while Mo, SiO_2 , and Si_3N_4 were not completely covered in the first 5 min. Nuclei were counted from the $100\times$ SEM photographs with the results listed in Table II.

Two effects were observed when oxygen was added to the reactant gases; the rate of formation of MoSi_2 was reduced and the silicon did not shear from the substrate on cooling when greater than 100 ppm of oxygen was added. This indicates that silicide formation is a necessary part of the shear separation mechanism. It is posulated that oxygen impeded silicon diffusion through the MoSi_2 layer. The addition of oxygen for the first 2-5 min of deposition also very significantly reduced the rate of MoSi_2 formation.

Separation mechanism.—It is essential to have an accurate understanding of the shear separation mechanism for reliably producing thin polysilicon sheets using temporary and reusable Mo substrates. Several factors are found to contribute to the shear separation mechanism as discussed below.

The thermal expansion of silicon and molybdenum are significantly different (18) as shown in Fig. 7 which

Table II.

| Surface | N (No./cm ² sec) |
|---------------------------------|-----------------------------|
| SiO_2 | 19 |
| Mo (virgin) | 34 |
| Si_3N_4 | 111 |
| Mo (N_2 added to gas) | 283 |
| MoSi_2 | General coverage |

can generate large stresses upon cooling from the deposition temperature. Calculated values (13) of the stresses developed in a simple silicon-molybdenum couple on cooling from 1100° to 700°C are shown in Fig. 8. The stresses in the silicon film and the molybdenum substrate were calculated using a computer program, LAMIN 1, which is based on linear composite theory (14). The following assumptions were made in the analysis.

1. The silicon film and temporary substrate adhere to each other and comprise a laminated composite with no slip at their interface.
2. A zero stress state exists at the deposition temperature and cooling of the composite is uniform.
3. The strain variation through the thickness of the composite is linear.
4. The material properties are isotropic.
5. While the material properties are temperature dependent, the computations were made using the average values over the temperature range.

The stresses were found to vary strongly with the thicknesses of the silicon and the substrate, but the

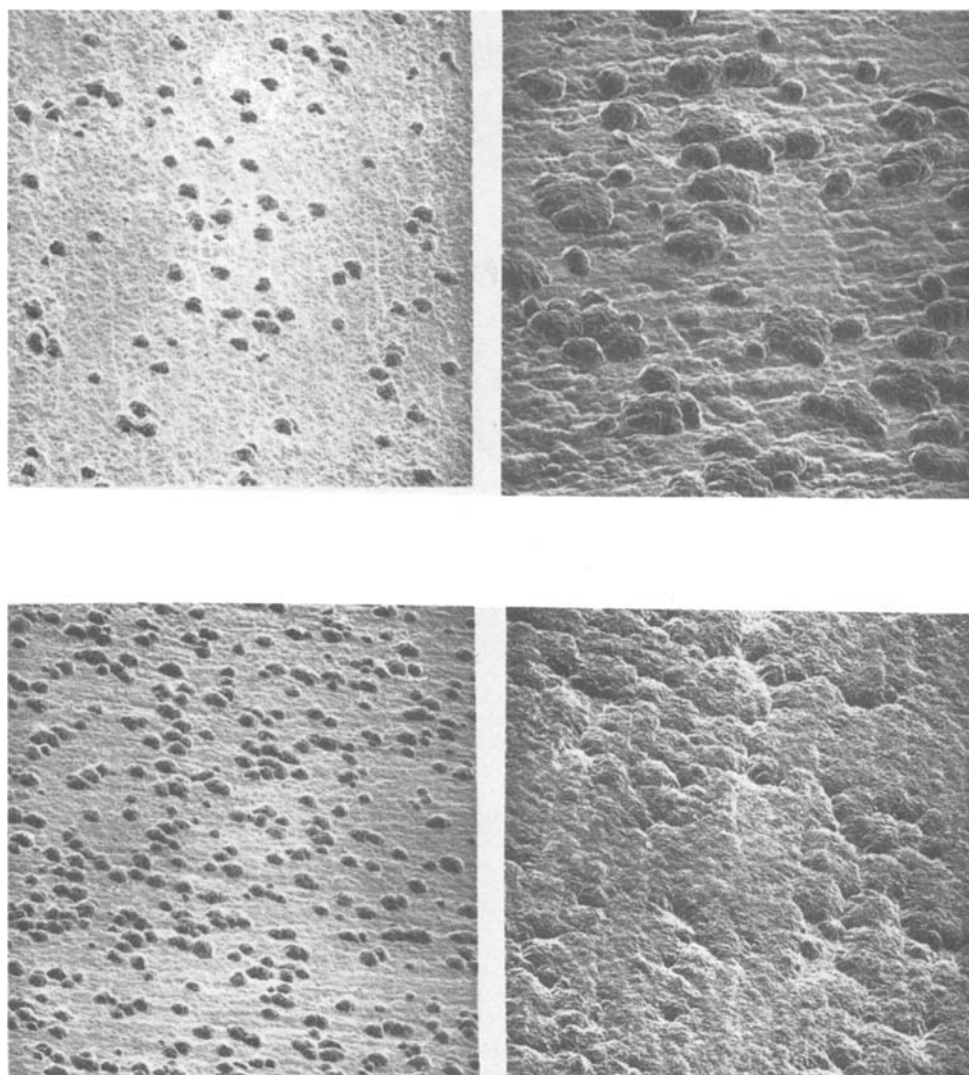


Fig. 6. Silicon nucleation characteristics. (a, top left) Regular Mo substrate, (b, top right) SiO_2 coated Mo substrate, (c, bottom left) Si_3N_4 coated Mo substrate, (d, bottom right) MoSi_2 coated Mo substrate.

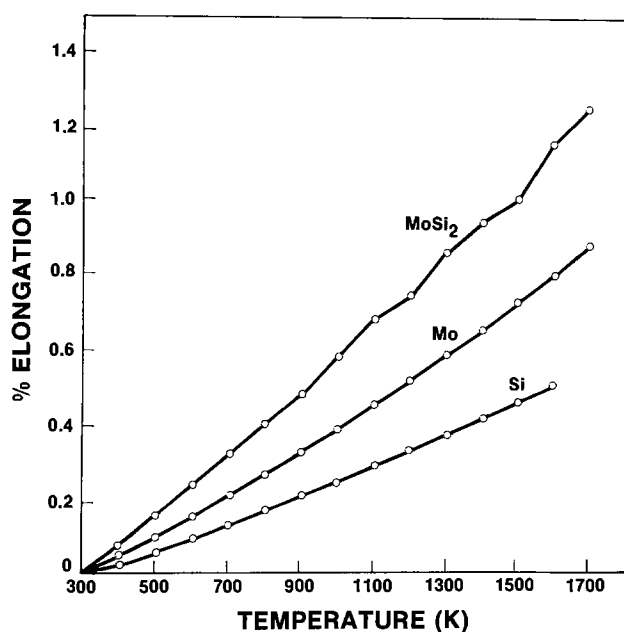


Fig. 7. Thermal expansion of Si, Mo, and MoSi₂ (18)

example shown serves to illustrate the very high stresses developed. This in itself is found not to be sufficient to cause shear separation. Silicon films deposited at 1000°C tended to adhere while deposition temperatures higher than 1100°C always resulted in shear separation. Even when higher stresses were developed in "stuck" ribbons deposited at 1000°C, by cooling them to liquid nitrogen temperature, no shearing took place. As expected, the calculated stress levels were found to increase as the composite is cooled to lower temperatures from deposition temperature (13). Also, while the calculated stresses in the composite were found to be dependent on the relative thicknesses of the Mo substrate and the silicon ribbon, they were not found to correlate well with the shear separation observations. Polysilicon ribbons of very large (>100 cm²) areas with thickness in the range of 0.003-0.020 in. have been separated from Mo substrates with thickness in the range of 0.005-0.050 in. (However, Mo substrates with a thickness greater than 0.030 in. were found to be desirable, since they are less flexible and retain their flatness with repeated silicon deposition-separation cycles.) We believe that, while the stresses generated in the composite are necessary for shear separation, they are not sufficient. A second condition for shear separation was found to be the creation of discontinuities (voids) at the substrate-silicon interface which act as stress raisers as discussed below.

An important factor involved in shear separation is found to be the formation of Kirkendall voids in the silicon adjacent to the MoSi₂ layer. An SEM photograph of such a void is shown in Fig. 9. The formation of

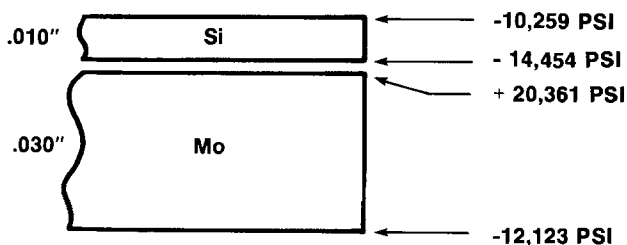


Fig. 8. Calculated stress levels in an Si (0.010 in. thick)/Mo (0.030 in. thick) couple due to cooling from silicon deposition temperature (1100°C) to a temperature of 700°C. — compression, + tension.

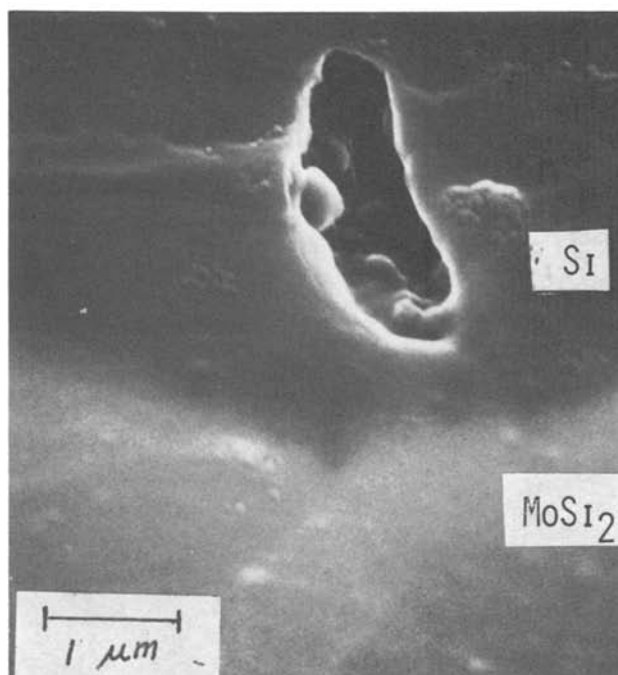
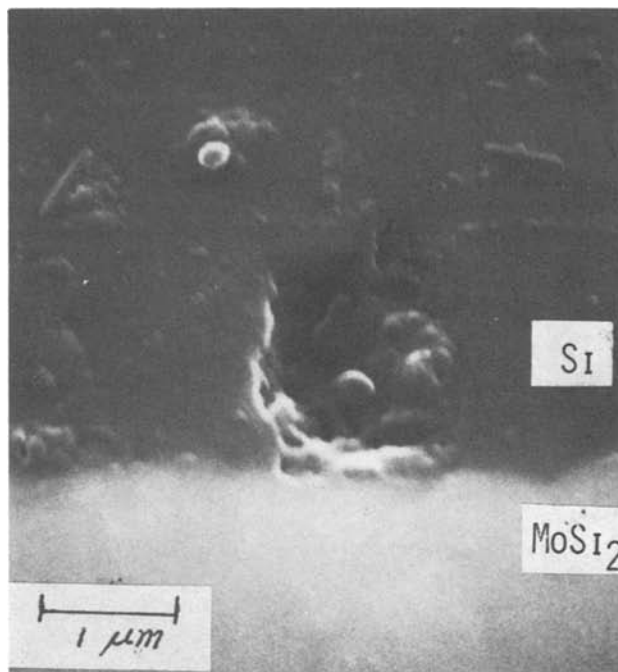


Fig. 9. SEM photographs of a cross-sectional view of the MoSi₂-Si interface showing a Kirkendall void. 18000×.

these voids can be explained if Si is the major diffusing species in MoSi₂, forming vacancies in the silicon which agglomerate to form voids. Borders and Sweet (15) also observed such voids in Si-Ge alloys and W couples where Si was the diffusing species. In a material under stress, any hole or discontinuity acts as a stress concentrator (16) with stress at the edge of the hole many times greater than the average stress. Thus very high stress regions result in the silicon adjacent to the MoSi₂ layer due to the presence of voids. The shear separation appears to occur in this region. Energy dispersive x-ray analysis in an SEM of the separated silicon films in this region showed no Mo. A SIMS analysis (7) of the separated silicon film showed Mo present only in ppm levels while Auger analysis of the MoSi₂ surface after shear separation showed Si in a thin layer of about a few hundred angstroms. Thus it

is clear that the shear separation occurs in the deposited silicon film and the formation of the silicide, in which Si is a faster diffuser than the metal, and formation of Kirkendall voids is essential for reliable shear separation. Further experiments were performed to confirm that silicon diffusion and Kirkendall void formation are essential for reliable shear separation by testing the time-temperature dependence of shear separation. It was found that shear separation occurred when a 1000°C deposition for 90 min was carried out followed by an anneal at 1200°C for 20-30 min. Further, when a "stuck" ribbon on the substrate was annealed for 80 hr at 800° and cooled, over ¾ of the silicon ribbon separated. After 40 hr of additional annealing at 800°C the remainder of the silicon separated from the substrate.

Experiments carried out using SiO₂ diffusion barriers clearly indicate the requirement of silicon diffusion and Kirkendall void formation for shear separation to occur. With SiO₂ diffusion barriers, silicon strongly adhered to the substrate and resulted in a sharply bent bimetallic couple of silicon and molybdenum.

From these results, one would predict that as a substrate is used again and again the MoSi₂ growth becomes less and less with each succeeding run. A point would be reached where silicon diffusion becomes less and insufficient voids are formed so that shear separation does not occur. This is actually observed in practice so that substrates can only be used a few times. Then the MoSi₂ layer must be removed or the time at deposition temperature extended to allow sufficient silicon diffusion to occur, to ensure shear separation.

It has indeed been found that substrates can be used for repeated deposition cycles until the increasing thickness of the silicide layer limits the layer growth to 9 μm during one cycle. Thus, for the growth conditions being used, the MoSi₂ must be removed after seven cycles. Considering a safety factor and assuming substrate resurfacing following every six depositions a 100 μm layer of MoSi₂ must be removed. This corresponds to 30 μm of consumed Mo. Allowing for grinding tolerances and cost of grinding, the Mo substrate cost contribution was estimated to be about \$0.08/peak watt (in 1980 dollars) as an upper limit. The continued shear separation from a given substrate with periodic substrate resurfacing has been observed experimentally.

Conclusions

The interaction of molybdenum and silicon has been investigated by depositing silicon on molybdenum substrates at 1000°-1200°C. Upon cooling the thin silicon sheets sheared from the substrates. Several factors were found to be important in the shear separation mechanism: (i) The thermal expansion mismatch of silicon and molybdenum (or tungsten) generates large stresses upon cooling; (ii) Kirkendall void formation occurs because silicon is the primary diffuser in MoSi₂; and (iii) Voids formed in the silicon film at the MoSi₂-Si interface act as stress raisers.

Two silicides were formed, a thick layer of MoSi₂ and a thin layer of Mo₅Si₃. The growth rate of MoSi₂ was found to be parabolic, after an initial nucleation period, indicating a diffusion-controlled reaction.

Oxygen in the reactant gases, at levels greater than 100 ppm, decreased the growth rate of MoSi₂ and void formation, which caused failure of the shear separation mechanism.

Acknowledgments

This research was supported in part by DOE/SERI under Contract ET-78-C-03-2207. The authors would like to express their appreciation to G. Thome for the SEM work. The stress calculations were performed by L. Moore and L. Harrel of the Motorola Government Electronics Division.

Manuscript submitted Sept. 16, 1980; revised manuscript received Jan. 9, 1981. This was Paper 182 presented at the St. Louis, Missouri, Meeting of the Society, May 11-16, 1980.

Any discussion of this paper will appear in a Discussion Section to be published in the December 1981 JOURNAL. All discussions for the December 1981 Discussion Section should be submitted by Aug. 1, 1981.

Publication costs of this article were assisted by Motorola, Incorporated.

REFERENCES

1. G. J. van Gorp, in "Semiconductor Silicon 1977," H. Huff and E. Sirtl, Editors, p. 342, The Electrochemical Society Softbound Proceedings Series, Princeton, N.J. (1977).
2. K. N. Tu and J. Mayer, in "Thin Films: Interdiffusion and Reactions," J. M. Poate, K. N. Tu, and J. W. Mayer, Editors, p. 359, J. Wiley and Sons, New York (1978).
3. J. Baglin, J. Dempsey, W. Hammer, F. d'Heurle, S. Peterson, and C. Serrano, *J. Electron. Mater.*, **8**, 641 (1979).
4. E. A. Beidler, C. F. Powell, I. E. Campbell, and L. F. Yntema, *This Journal*, **98**, 21 (1951).
5. A. S. Berezoni, "Silicon and its Binary Systems," Transl. from Russ., p. 173, Consultants Bureau, New York (1960).
6. "Refractory Molybdenum Silicides," Bulletin Cdb-6A, p. 9, Climax Molybdenum Co. (May 1963).
7. K. R. Sarma and M. J. Rice, Jr., *IEEE Trans. Electron. Dev.*, **ed-27**, 651 (1980).
8. P. R. Gage and R. W. Bartlett, *Trans. Met. Soc. AIME*, **233**, 832 (1965).
9. A. S. Guy, "Introduction to Materials Science," p. 268, International Student Edition, McGraw-Hill, New York (1972).
10. R. W. Bower and J. W. Mayer, *Appl. Phys. Lett.*, **20**, 359 (1972).
11. ASTM Powder Diffraction Patterns, Card 6-0681.
12. ASTM Powder Diffraction Patterns, Card 17-415.
13. K. R. Sarma, R. W. Gurtler, A. Baghdadi, and M. Cota, 4th Quarterly Report, Dec. 1977, Contract No. EY-76-C-03-1287, ERDA.
14. R. M. Jones, "Mechanics of Composite Materials," McGraw-Hill, New York (1975).
15. J. A. Borders and J. N. Sweet, *J. Appl. Phys.*, **43**, 3803 (1972).
16. G. E. Dieter, Jr., "Mechanical Metallurgy," McGraw-Hill Metallurgy and Metallurgical Engineering Series, p. 46, McGraw-Hill, New York (1961).
17. "Thermophysical Properties of Matter," Vol. 12, Y. W. Touloukian *et al.*, Editors, IFI/Plenum, New York (1975).
18. "Handbook of Thermophysical Properties of Solid Materials," A. Goldsmith, T. E. Waterman, and H. J. Hirseshorn, Editors, Pergamon Press, New York (1962).

Electrical Properties of Divalent Europium Niobium Bronzes Eu_xNbO_3

Kenji Ishikawa, Gin-ya Adachi, Masatake Hasegawa, Kazunao Sato,
and Jiro Shiokawa

Department of Applied Chemistry, Faculty of Engineering,
Osaka University, Yamadakami, Suita-shi, Osaka-fu, Japan

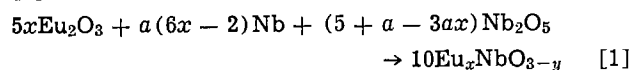
ABSTRACT

The electrical resistivity and thermoelectric power of the europium (II) niobium bronzes, Eu_xNbO_3 , were measured as a function of europium concentration from $x = 0.51$ - 0.92 over temperatures of 4.2 - 373 K. All samples in tetragonal form ($x = 0.51$ - 0.65) showed semiconducting conduction, while the samples in cubic form ($x = 0.65$ - 0.92) exhibited metallic conduction. A Goodenough model for the tungsten bronze, Na_xWO_3 , was employed for the difference in the electrical conduction behavior between the two bronzes. Residual drift mobility for the cubic bronze decreased with x except for $x = 0.76$ and on this point an irregularly high value was obtained. The temperature-dependent part of the drift mobility for the cubic one was found to be describable by the perturbation theory of Howarth and Sondheimer. An effective mass of the electron for each cubic bronze was about $2m_0$ (m_0 is the electronic rest mass), and the quasi-free electron model was roughly applicable.

Only a few metal oxide systems have metallic properties. Most of them are lower oxides of transition metals, e.g., ReO_3 , NbO , and VO (1). Some of the tungsten bronze type oxides, their general formula A_xBO_3 , also exhibit metallic conduction (1). Especially, a number of experimental and theoretical works were done to describe the electrical properties of the cubic sodium tungsten bronze. A strontium niobium bronze, which was first prepared by Ridgley *et al.* (2), also has the cubic structure and has a metallic character (1). The ionic radius of Eu^{2+} ion is analogous to that of Sr^{2+} ion (3), and the analogy leads to preparation of Eu^{2+} compounds which are isostructural with Sr^{2+} compounds (4). Fayolle *et al.* (5) first reported the preparation of a europium niobium oxide Eu_xNbO_3 and showed that this oxide was isostructural with Sr_xNbO_3 . Studer *et al.* (6) reported the electrical properties of the bronzes, although their study was limited to the semiconducting tetragonal bronzes ($x = 0.5$ and 0.6). Work covering a wider range of x is desirable. In this paper, the electrical resistivities and the Seebeck coefficients of Eu_xNbO_3 are reported as a function of europium concentration from $x = 0.51$ - 0.92 over a temperature range of 4.2 - 373 K.

Experimental

Preparation and Analysis.—A mixture of Eu_2O_3 , Nb_2O_5 , and Nb powder was ground together in an agate mortar and pressed into pellets and then heated in vacuo (10^{-2} Pa) at 1173 K for 2 hr. After cooling, the pellets were ground and again pressed into pellets. They were packed into an Mo box, sealed under vacuum (10^{-3} Pa) in a silica capsule, and heated at 1473 K for 48 hr. The reaction was completed during the procedure and was assumed to occur according to reaction [1]



Niobium metal was used " a " times the amount needed to prepare Eu_xNbO_3 in order to compensate for a slight oxidation loss of the bronzes during the course of synthesis, and $a = 1.05$ was adopted for all samples. The deviation of oxygen content from $\text{O/Nb} = 3$ was represented by " y ," and the actual value of $3 - y$ used for each sample is given in Table I. The electrical

measurements were performed on sintered polycrystalline pellets. The pellets were prepared by pressing the powder sample and then sintering them at 1473 K for 10 hr in sealed silica capsules.

The phase purities and structural type of the sintered sample were characterized by x-ray powder analysis, using a Rigaku Denki Rotor-flex diffractometer. The atomic ratios (Eu:Nb) were determined with a Rigaku Denki energy dispersion type x-ray fluorescent spectrograph unit, ultra trace systems, and the oxygen compositional states were determined by a gravimetric technique. The magnetic moments were obtained with a Shimadzu MB-11 magnetic balance. The pycnometric densities of the pellets were also obtained.

Electrical resistivity measurements.—The electrical resistivity measurements for the sintered samples were carried out in a helium atmosphere from 4.2 to 373 K. A simple four-probe d-c method was employed for the resistivity measurements of the samples. Rectangular samples of about 2 mm² in cross section and 8 - 12 mm long were taken for the measurements with the four-probe method. The samples were cut from the sintered pellets of 13 mm in diameter and 1 mm in thickness, and the surfaces of the samples were finished with No. 1000 carborundum paper. Electrical leads were attached to the faces of each sample with Ag paste. The resistivity measurements were performed in the potential region in which the samples behaved ohmically. Furthermore, to avoid any contributions to the measured potential from thermally generated emf's, readings were taken in both forward and reverse directions and the averaged values were recorded.

Thermoelectric power measurements.—Thermoelectric power measurements were carried out in a helium atmosphere from 100 to 373 K. A rectangular sample of about 2 mm² in cross section and about 4 mm long was attached to two copper blocks with Ag paste. A thermal gradient was produced across the sample by small heaters attached to the copper blocks, and the temperature difference across the sample was regulated so as to fall within 10 K. The Seebeck coefficient of the sample was determined according to the relation

$$S = S_{\text{Cu}} - \Delta V / \Delta T \quad [2]$$

Key words: niobates, electrical resistivity, thermoelectric power.

Table I. Lattice constants, magnetic moments, and activation energy of conduction for $\text{Eu}_x\text{NbO}_{3-y}$

| $\text{Eu}_x\text{NbO}_{3-y}$ | | Lattice constants* | | | Magnetic moments† | | E_a (300 K)‡ |
|-------------------------------|-------|--------------------|-----------------|-----------------|-------------------|------------------|-------------------|
| x | $3-y$ | $a(c)/\text{Å}$ | $a(t)/\text{Å}$ | $c(t)/\text{Å}$ | Obs/ μ_B | Calc/ μ_B | E_a/eV |
| 0.51 | 3.02 | | 12.355 | 3.901 | 5.47 | 5.67 | 0.099 |
| 0.58 | 3.02 | | 12.363 | 3.892 | 5.89 | 6.07 | 0.084 |
| 0.60 | 3.03 | | 12.361 | 3.885 | 6.04 | 6.18 | 0.033 |
| 0.68 | 3.05 | 3.978 | | | 6.46 | 6.61 | |
| 0.70 | 3.09 | 3.980 | | | 6.34 | 6.69 | |
| 0.76 | 3.03 | 3.985 | | | 6.80 | 7.03 | |
| 0.82 | 3.03 | 4.002 | | | 7.16 | 7.31 | |
| 0.88 | 3.03 | 4.009 | | | 7.36 | 7.58 | |
| 0.90 | 3.10 | 4.012 | | | 7.42 | 7.65 | |
| 0.92 | 3.13 | 4.013 | | | 7.58 | 7.75 | |

* a, cubic; t, tetragonal.

† μ_{eff} (theoretical) = $\sqrt{x\mu^2(\text{Eu}^{2+}) + (\text{Nb}^{4+}/\text{Nb})\mu^2(\text{Nb}^{4+})}$
 $\mu(\text{Eu}^{2+}) = 7.94 \mu_B$ $\mu(\text{Nb}^{4+}) = 1.73 \mu_B$.

‡ Activation energies of conduction are determined from the equation, $\rho = \rho_0 \exp(E_a/kT)$.

where S_{Cu} is the absolute Seebeck coefficient of copper (7), ΔV is the thermoelectric voltage of the sample, and ΔT is the temperature difference across the sample.

Results and Discussion

The compositional, crystal, and magnetic data for the sintered samples are given in Table I. It is seen that the samples ranging in europium concentration from $x = 0.51-0.65$ have a tetragonal form, while the samples ranging from $x = 0.65-0.92$ have a cubic form. Each of the observed magnetic moments is close to the calculated value, and most of the europium in the sample is considered to be in a $2+$ state.

Results of the resistivity measurements are shown in Fig. 1 and 2. The resistivities are found to decrease with decreasing reciprocal temperature for the samples of low europium concentration ($x = 0.51-0.65$) (Fig. 1), and the changes are expressed by the well-known equation

$$\rho = \rho_0 \exp(E_a/kT) \quad [3]$$

where E_a is related to the activation energy for conduction. The activation energy of each sample is tabulated in Table I. Thermoelectric power measurements reveal that the samples are n-type semiconductors. However, the resistivities are found to decrease on decreasing the temperature for the samples of high

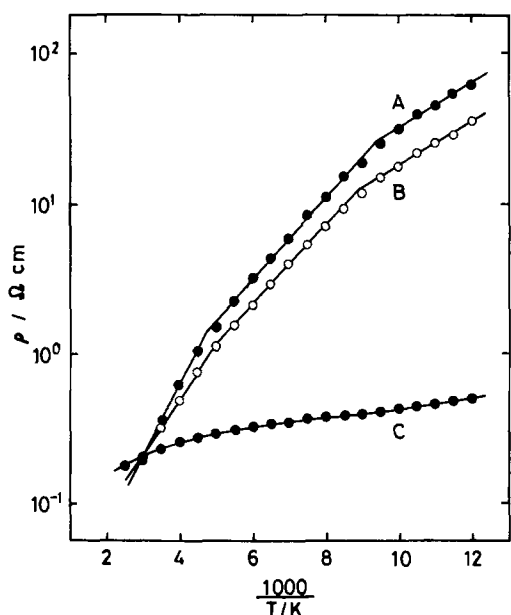


Fig. 1. Specific resistivities of Eu_xNbO_3 . A, $\text{Eu}_{0.60}\text{NbO}_{3.03}$; B, $\text{Eu}_{0.58}\text{NbO}_{3.02}$; C, $\text{Eu}_{0.51}\text{NbO}_{3.03}$.

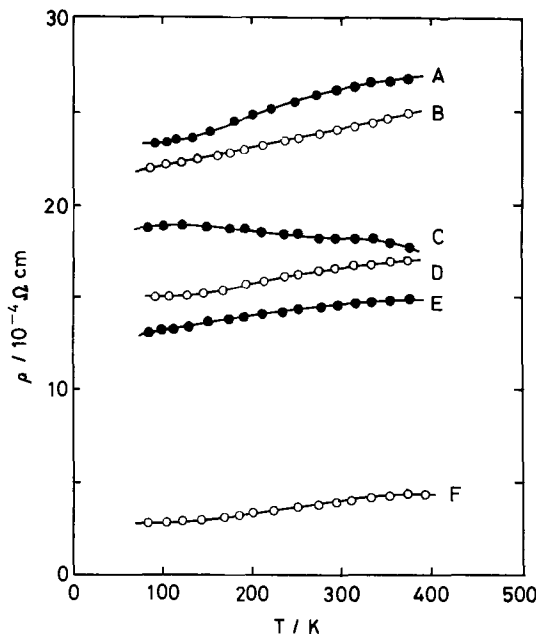


Fig. 2. Specific resistivities of Eu_xNbO_3 . A, $\text{Eu}_{0.90}\text{NbO}_{3.10}$; B, $\text{Eu}_{0.70}\text{NbO}_{3.09}$; C, $\text{Eu}_{0.68}\text{NbO}_{3.05}$; D, $\text{Eu}_{0.82}\text{NbO}_{3.03}$; E, $\text{Eu}_{0.88}\text{NbO}_{3.03}$; F, $\text{Eu}_{0.76}\text{NbO}_{3.03}$.

europium concentration ($x = 0.65-0.92$). In other words, the tetragonal samples are n-type semiconductors and the cubic samples are metallic conductors. An interpretation of the electrical resistivity data for the tetragonal and cubic samples is given on the basis of Goodenough's model (1) for the tungsten bronze. The schematic band models for both cubic and tetragonal phases are formed by the 4d orbitals of niobium and the 2p orbitals of oxygen. All the 4d (t_{2g}) orbitals of niobium are considered to be degenerate for the cubic samples [Fig. 3(a)], and the number of conduction electrons is the same as the number of Nb^{4+} in this case. The number of Nb^{4+} in the general formula $\text{Eu}_x\text{NbO}_{3-y}$ can be provided by the relation

$$n = 2(x + y) - 1 \quad [4]$$

The equation suggests that some conduction electrons exist in the conduction band of the cubic samples ($x > 0.65$), giving all the cubic samples metallic properties. On the other hand, the 4d (t_{2g}) orbitals of niobium in the tetragonal phase split into two states [Fig. 3(b)] and a localized nonbonding level ($4d_{xy}$) is formed below the bottom of the conduction band. The conduction electrons are considered to be trapped by the level, and the tetragonal bronzes exhibit semiconducting properties. From the analysis of the resistivity curve, the level is determined to be 0.1 eV below the bottom of the conduction band.

The resistivity of a metallic compound can be separated into two components. One of them is a residual

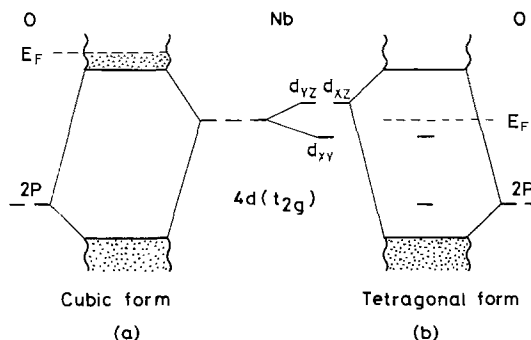


Fig. 3. Energy-level diagram for Eu_xNbO_3

component ρ_0 which is ascribed to electron scattering by impurities and the scattering is temperature independent. The other one, ρ_T , is temperature dependent and is due to electron scattering by lattice vibrations. The total resistivity is therefore the sum of the temperature-independent, or residual, and temperature-dependent, or thermal, components

$$\rho = \rho_0 + \rho_T \quad [5]$$

Figure 4 shows the drift residual mobilities as a function of europium concentration for the cubic samples. On determination of the drift mobility, the carrier concentration is assumed to be equal to the Nb^{4+} concentration and is derived from the following relation

$$N = \frac{dL}{M} [2(x + y) - 1] \quad [6]$$

where d is the pycnometric density of the sample, L is Avogadro's number, M is the formula weight of the sample, and x and y are defined by the formula $\text{Eu}_x\text{NbO}_{3-y}$. The drift mobility is calculated from the following relation

$$\mu_0 = 1/Ne\rho_0 \quad [7]$$

The drift residual mobility decreased with increasing europium concentration of $x = 0.68-0.92$ except for a range around $x = 0.75$. At $x = 0.75$ an irregularly high value was found. The values of mobility for these samples are considerably lower than the value for single crystals of other metallic compounds, e.g., Na_xWO_3 (8-10). A degree of sintering will be a dominant factor for determining the value, and the degree is considered to decrease with europium concentration. An irregularly high mobility at $x = 0.7$ was also found in the studies of Na_xWO_3 (11, 12). Ellerbeck *et al.* (13) pointed out that the electrical homogeneity of the sample was an influential factor in the value of mobility and showed that there was no minimum in resistivity near $x = 0.7$ for electrically homogeneous Na_xWO_3 . The homogeneity of the sample is an important factor for determining the value of resistivity, and the homogeneity should be maximum at $x = 0.76$.

Figure 5 shows the temperature dependence of the thermal part for $\text{Eu}_{0.76}\text{NbO}_{3.03}$. The thermal part of the resistivity is proportional to $T^{3.5}$ below 49 K, indicating that the mobility of electrons increases proportional to $T^{-3.5}$. Bardeen and Shockley (14) have proved that the mobility follows $T^{-1.5}$ dependence when the conduction electrons are scattered by the lattice vibrations for an acoustic mode. On the other hand, Greener *et al.* (15) suggest that a mobility of a polar semiconductor, in which the conduction electrons are scattered by the optical mode lattice vibrations, can be approximated by the relation at low

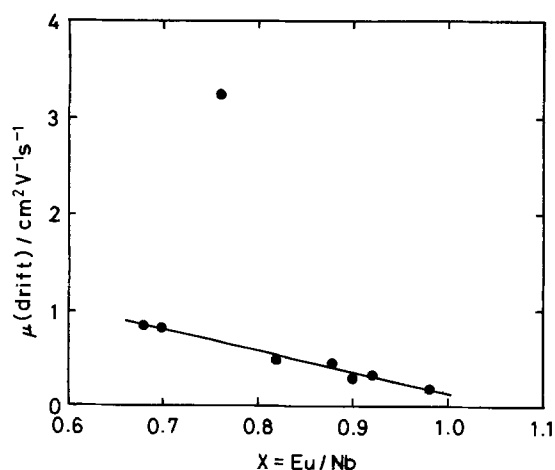


Fig. 4. Drift residual mobility vs. composition (x) for Eu_xNbO_3

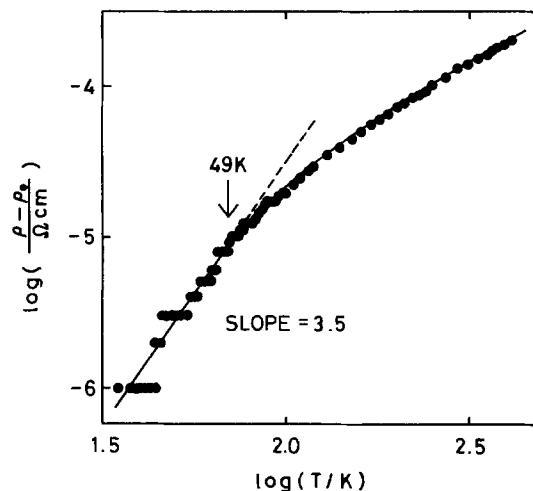


Fig. 5. Temperature dependence of the thermal part of resistivity for $\text{Eu}_{0.76}\text{NbO}_{3.03}$.

temperature

$$\mu \propto T^{-n} \quad [8]$$

where n is a constant of magnitude 2-3.5. It is apparent that the conduction electrons of the niobium bronze are scattered by the optical mode lattice vibrations. The interaction between electron and phonon is describable by the perturbation theory of Howarth and Sondheimer (16) in which the conduction electrons were assumed to degenerate and to be scattered by polarization waves in the crystal. Crowder and Sienko (17) successfully applied the perturbation theory to the tungsten bronze. The thermal part of the electrical resistivity for the metallic compound is given in the relation

$$\rho_T = AT^{-1} \sinh^{-2}(\theta/2T) \quad [9]$$

where A is a constant and θ is the Debye factor. The Debye temperature is conventionally estimated by a method proposed by Kunder and Sienko (18). That is the transition temperature of resistivity from T^n to T^1 dependence in the resistivity curve (Fig. 5) is approximately $\theta/7$. The constant A is evaluated from the measured value of the thermal part at 250 K and from an estimated θ . The Debye temperature and the constant are evaluated as 343 K and $1.41 \times 10^{-2} \Omega\text{K}$, respectively. Figure 6 shows the results. The agreement between the observed and calculated values is satisfactory.

The Seebeck coefficients of the cubic samples are given as a function of the temperature in Fig. 7. For

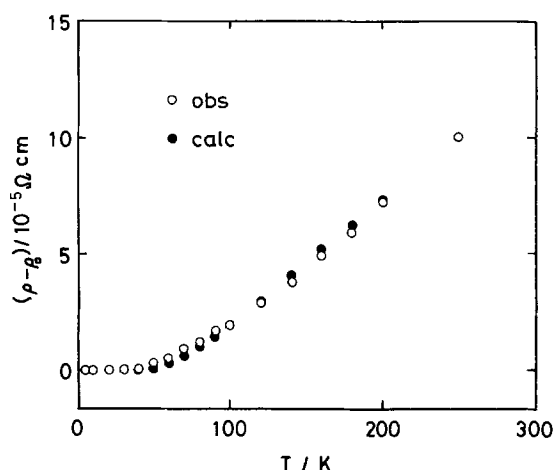


Fig. 6. Comparison of the observed thermal part of resistivity with the calculated one.

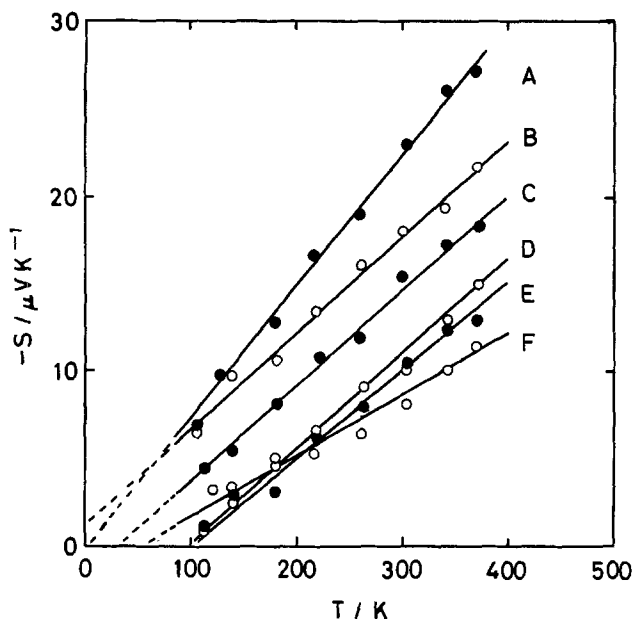


Fig. 7. Temperature dependence of the Seebeck coefficient for Eu_2NbO_3 in cubic form. A, $\text{Eu}_{0.68}\text{NbO}_{3.05}$; B, $\text{Eu}_{0.70}\text{NbO}_{3.09}$; C, $\text{Eu}_{0.76}\text{NbO}_{3.03}$; D, $\text{Eu}_{0.82}\text{NbO}_{3.03}$; E, $\text{Eu}_{0.90}\text{NbO}_{3.10}$; F, $\text{Eu}_{0.88}\text{NbO}_{3.03}$.

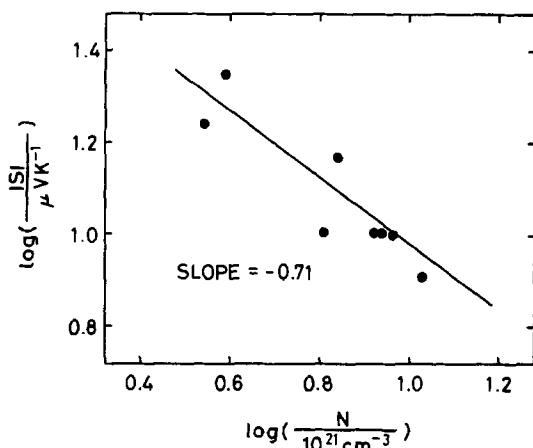


Fig. 8. Seebeck coefficient of Eu_2NbO_3 at 300 K vs. Nb^{4+} concentration.

the free-electron approximation, the Seebeck coefficient is given by the relation

$$S = \frac{2}{3} \left(\frac{\pi}{3} \right)^{2/3} \frac{m^* k^2 T}{e (\hbar/2\pi)^2} N^{-2/3} \quad [10]$$

An almost linear dependence of the Seebeck coefficient with temperature (Fig. 7) suggests that the conduction electrons are close to free electrons. The Seebeck coefficients at 300 K are plotted in Fig. 8 as a function of the carrier concentration given by Eq. [6]. The Seebeck coefficients vary as $N^{-0.71}$ and this is close to $N^{-0.67}$ predicted by the free-electron model (Eq. [10]). Therefore, the conduction electrons of the cubic samples are considered to be close to free electrons. An effective electronic mass for each cubic sample is also evaluated by comparison of the observed Seebeck coefficients with the calculated values ($m^* = m_0$). The effective mass is about $2m_0$ for each sample.

Manuscript submitted June 24, 1980; revised manuscript received ca. Dec. 1, 1980.

Any discussion of this paper will appear in a Discussion Section to be published in the December 1981 JOURNAL. All discussions for the December 1981 Discussion Section should be submitted by Aug. 1, 1981.

Publication costs of this article were assisted by Osaka University.

REFERENCES

1. J. B. Goodenough, in "Progress in Solid State Chemistry," Vol. V, H. Reiss, Editor, Pergamon Press, Inc., Oxford and New York (1972).
2. D. H. Ridgley and R. Ward, *J. Am. Chem. Soc.*, **77**, 6132 (1955).
3. R. D. Shannon and C. T. Prewitt, *Acta Crystall., Sect. B*, **25**, 295 (1969).
4. G. J. McCarthy and J. E. Greedan, *Inorg. Chem.*, **14**, 772 (1975).
5. J. P. Fayolle, F. Studer, and G. Desgardin, *J. Solid State Chem.*, **13**, 57 (1975).
6. F. Studer, J. P. Fayolle, and B. Raveau, *Mater. Res. Bull.*, **11**, 1125 (1976).
7. N. Cusack and P. Kendall, *Proc. Phys. Soc.*, **72**, 898 (1958).
8. E. J. Huibregste, D. B. Barker, and G. C. Danielson, *Phys. Rev.*, **84**, 142 (1951).
9. W. R. Gardner and G. C. Danielson, *ibid.*, **93**, 46 (1954).
10. L. P. Muhlestein and G. C. Danielson, *ibid.*, **158**, 158 (1967).
11. B. W. Brown and E. Banks, *ibid.*, **84**, 609 (1951).
12. W. R. Gardner and G. C. Danielson, *ibid.*, **93**, 46 (1954).
13. L. D. Ellerbeck, H. R. Shanks, P. H. Sidles, and G. C. Danielson, *J. Chem. Phys.*, **35**, 298 (1961).
14. J. Bardeen and W. Shockley, *Phys. Rev.*, **80**, 72 (1952).
15. E. H. Greener, D. H. Whithmore, and M. E. Fine, *J. Chem. Phys.*, **34**, 1017 (1960).
16. D. J. Howarth and E. H. Sondheimer, *Proc. R. Soc. London, Ser. A*, **219**, 53 (1953).
17. B. L. Crowder and M. J. Sienko, *J. Chem. Phys.*, **38**, 1576 (1963).
18. D. R. Kundrak and M. J. Sienko, *Inorg. Chem.*, **6**, 880 (1967).



Characterization of Films Formed by Pyrolysis of Borazine

A. C. Adams*

Bell Laboratories, Murray Hill, New Jersey 07974

A previous publication describes the deposition and characterization of films containing boron, nitrogen, and hydrogen formed by the reaction of diborane and ammonia at 300°-400°C and at about 0.4 Torr (1). The films, which have a composition of approximately B_xNH_x with $7 < x < 10$ (2), are used in the fabrication of masks for x-ray lithography (3). The film deposition rate is related to the concentration of the reactants and is limited by the concentration of the diborane starting material that is readily usable, about 15% diborane in an inert carrier gas. Pure diborane is available and has been used for the deposition of boron coatings (4), but requires refrigerated storage at temperatures below -20°C to prevent decomposition. Pure boron trichloride has been investigated as the starting material for the reaction with ammonia, but the resulting films react with atmospheric moisture to form crystalline boron oxide, possibly by hydrolysis of residual chlorine in the film (1).

An alternate starting material which may provide a high deposition rate is borazine, $B_3N_3H_6$. Borazine, a liquid at room temperature with a vapor pressure given by $\log P$ (mm) = $7.714 - 1609/T$ (5), is prepared by the controlled reaction between diborane and ammonia or by the thermal decomposition of the solid ammonia borane, NH_2BH_3 (6). Borazine is known to thermally decompose by condensation reactions to produce less volatile products (7). In this note, the films formed by the pyrolysis of borazine are compared to the material produced by reacting diborane and ammonia.

The depositions occur in the hot wall, low pressure CVD reactor described previously (1). The substrates are 75 mm diam silicon wafers. Borazine, obtained from Callery Chemical Company, Callery, Pennsylvania, is stored and used in a constant temperature bath at 0°C. The pressure in the reactor is controlled by a needle valve between the borazine container and the reactor. All depositions use pure borazine to obtain high deposition rates; no diluent gas or reactive gases are present. Pressures and temperatures are varied from 0.1 to 0.8 Torr and 300°-650°C.

The deposition rate and refractive index (measured at a wavelength of 0.5461 μ m) are shown for different deposition temperatures in Fig. 1. Data for films formed from the reaction of diborane and ammonia are shown for comparison (1). The deposition rate for the borazine reaction is low at all temperatures in spite of the relatively high pressure of borazine. The deposition rate increases with increasing temperature and goes through a maximum followed by a rapid decrease caused by depletion due to reaction on the hot reactor walls. This is similar to the behavior observed with diborane and ammonia except the maximum occurs at about 550°C instead of 450°C. The apparent activation

energy at the lower temperatures is 9.6 kcal/mole, much lower than the values measured for the diborane and ammonia reaction, 20-25 kcal/mole (1). The deposition rate increases with increasing partial pressure of borazine and appears to follow a square-root dependence.

At deposition temperatures greater than 550°C, the refractive index is the same as observed for films deposited from diborane and ammonia. However, at lower deposition temperatures the refractive index is much lower. This is a strong indication that the films formed at low temperature from the two reactions are not the same. The refractive index increases linearly with borazine pressure at 500°C, ranging from 1.75 at 0.1 Torr to 2.15 at 0.8 Torr.

Films deposited at temperatures greater than 550°C have infrared spectra that are similar to those observed for the diborane-ammonia reaction. However, at lower deposition temperatures, there are considerable differences. Films deposited from borazine still have B-N adsorptions at about 1360, 900, and 750 cm^{-1} , and a B-H absorption at 2520 cm^{-1} . However, the strong NH_2 absorptions previously observed at 3220 and 1540 cm^{-1} have been replaced by a single N-H

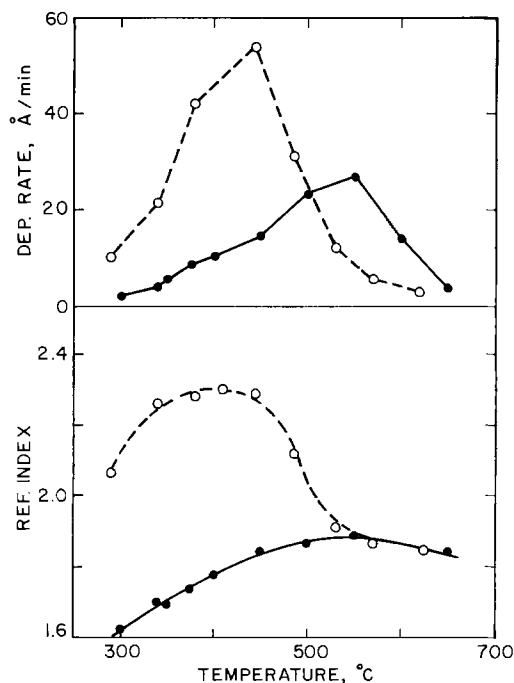


Fig. 1. Deposition rate and refractive index for different deposition temperatures. The partial pressures are: solid points, borazine, 0.3 Torr; open points, diborane, 0.005 Torr, ammonia, 0.006 Torr, and argon, 0.49 Torr.

* Electrochemical Society Active Member.
Key words: deposition, films, masks.

stretching mode at 3420 cm^{-1} . The replacement of the NH_2 groups by NH shows that large differences in the chemical bonding exist between the films from the two reactions.

These differences are also indicated by the increased reactivity of the material formed by pyrolysis of borazine. The films formed from diborane and ammonia at $300^\circ\text{--}400^\circ\text{C}$ do not change after long times at room ambient, and the films are inert towards water and aqueous solutions (1). In contrast, the films formed by borazine pyrolysis at $300^\circ\text{--}450^\circ\text{C}$ react with atmospheric moisture. After a few weeks, the intensity of the B-N absorption at 1360 cm^{-1} has decreased by at least 50%, a broad absorption appears at about 3400 cm^{-1} , probably OH, and a H_2O absorption at 1630 cm^{-1} is observed. In addition a B-O absorption at 1410 cm^{-1} is observed in many samples. These changes are probably caused by hydrolysis of the B-N bond to form B-OH. The films formed from borazine also dissolve in water with dissolution rates at room temperature of $100\text{--}500\text{ \AA}/\text{min}$.

In conclusion, significant differences in the films formed by reacting diborane and ammonia and by pyrolyses of borazine at $300^\circ\text{--}500^\circ\text{C}$ have been observed. The films formed from borazine have NH groups instead of NH_2 , have a lower refractive index, and are more reactive. The low deposition rate and the reaction with water make these films unsuitable for fabrication of masks for x-ray lithography. The films formed by pyrolysis of borazine at temperatures greater than 500°C have not been thoroughly investigated, primarily due to the low deposition rate caused by the reactions on the hot walls. The limited amount

of data available indicate that these films are identical to the films formed at similar temperatures by reacting diborane and ammonia. However, a complete investigation of these high temperature films will require depositions in a cold wall reactor.

Manuscript submitted Oct. 15, 1980; revised manuscript received Dec. 9, 1980.

Any discussion of this paper will appear in a Discussion Section to be published in the December 1981 JOURNAL. All discussions for the December 1981 Discussion Section should be submitted by Aug. 1, 1981.

Publication costs of this article were assisted by Bell Laboratories.

REFERENCES

1. A. C. Adams and C. D. Capio, *This Journal*, **127**, 399 (1980).
2. B. G. Bagley, R. E. Benenson, and A. C. Adams, Unpublished data.
3. D. Maydan, G. A. Coquin, H. J. Levinstein, A. K. Sinha, and D. N. K. Wang, *J. Vac. Sci. Technol.*, **16**, 1959 (1979).
4. H. O. Pierson and A. W. Mullendore, in "Proceedings of the Seventh International Conference on Chemical Vapor Deposition," T. O. Sedgwick and H. Lydtin Editors, p. 360, The Electrochemical Society Softbound Proceedings Series, Princeton, N.J. (1979).
5. W. V. Hough, G. W. Schaeffer, M. Dzurus, and A. C. Stewart, *J. Am. Chem. Soc.*, **77**, 864 (1955).
6. L. F. Honstedt and G. W. Schaeffer, *Adv. Chem. Ser.*, **32**, 232 (1961).
7. A. W. Laubengayer, P. C. Moews, Jr., and R. F. Porter, *J. Am. Chem. Soc.*, **83**, 1337 (1961).

Evaluation of the Pinhole Density in SiO_2 Film by Plasma Etching

Takashi Meguro, Hidekazu Kurita, and Tadatsugu Itoh

School of Science and Engineering, Waseda University, Shinjuku-ku, Tokyo 160, Japan

It has been reported that various radicals are generated in the case of CF_4 plasma etching. Among them, fluorine radical F^* and fluorocarbon ion such as CF_3^+ selectively etch silicon and silicon dioxide, respectively (1). Also it has been observed that the addition of oxygen to CF_4 causes the etch rate of silicon to increase because of the increase of F^* (2). We obtained the high Si-to- SiO_2 etch rate ratio of 130 using a $\text{CF}_4 + \text{O}_2$ mixture gas in rf plasma etching and applied this technique to the detection of the pinhole density in the SiO_2 film by the etching of underlying Si substrate with F^* .

To detect pinholes in SiO_2 films, the Cu-decoration method and the PAW (pyrocathecol-amine-water) method are most commonly used. In the Cu-decoration method (3) an electroplating technique is utilized. If there are pinholes in the SiO_2 film, dissolved Cu from the anode in the form of oxysalts precipitates on the pinhole. In this method, a localization of decorated Cu can be seen when a nonuniform electric field is applied to the SiO_2 film, and a dissolved Cu precipitates on the contamination when the SiO_2 film surface is not clean.

In the case of the PAW method (4), a solution of pyrocathecol and amine can etch Si but not SiO_2 . If a sample is kept in the solution at $110^\circ\text{--}115^\circ\text{C}$ for 1-2

hr, Si is etched through pinholes in the SiO_2 film. After the removal of SiO_2 film, the pinhole density can be measured by counting the number of etch pits formed on Si substrate. The disadvantages of this method are as follows: (i) ventilation is necessary to exhaust H_2 gas generated from the solution, and (ii) N_2 ambient is necessary to prevent oxidation of amine.

The plasma etching method acts the same as the PAW method in principle. The fluorine radical in the

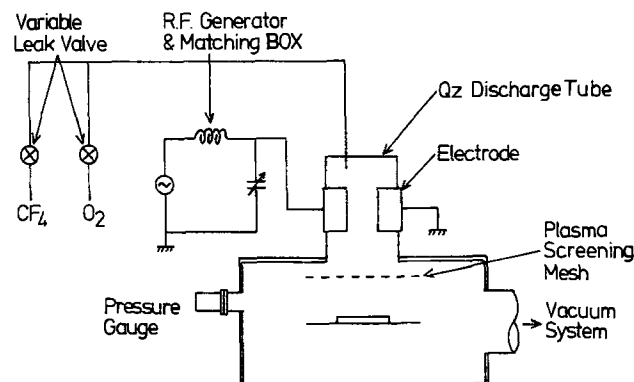


Fig. 1. Schematic diagram of the plasma etching apparatus

$\text{CF}_4 + \text{O}_2$ plasma etches the Si surface. Figure 1 shows a schematic diagram of the plasma etching apparatus used in this experiment. The reactor is made of a quartz tube 100 mm in diameter and 150 mm in height. The distance between the bottom of the discharge column and the surface of the sample is 70 mm, where the plasma screening mesh is set up to confine the plasma. This reactor is similar to the downstream-type reactor (2). RF power of 13.56 MHz is coupled capacitatively by electrodes around the quartz tube. The etching gas, a mixture of CF_4 and O_2 , is introduced into the discharge column through variable leak valves after evacuating the chamber below 5×10^{-6} Torr.

First, we studied the etching conditions so as to maximize the Si-to- SiO_2 etch rate ratio by varying the gas pressure, rf power, and the fraction of O_2 in the etching gas. Unless the ratio is large, the SiO_2 film is also etched off before etch pits become of measurable size. The maximum value of the ratio was obtained at total pressure of 0.25 Torr, rf power of 50W, and the O_2 fraction of 10% in volume. In these conditions, the etch rates of Si and SiO_2 are 400 and 3 nm/min, respectively; therefore, the Si-to- SiO_2 etch rate ratio reaches 130. The reason for the so large ratio is considered as follows: (i) the increase of F^* by oxygen released from the etching of the quartz wall and additional O_2 (ii) the etching of an extremely small area of Si substrate masked by the SiO_2 film which has many pinholes.

To measure the pinhole density, the SiO_2 film on (100) Si substrate was formed by rf sputtering with 200-700 nm and the films with a large number of pinholes were especially prepared for the comparison between the plasma etching method and the PAW method. The number of etch pits measured by these methods decreases with increasing the thickness of the SiO_2 film, as shown in Fig. 2. It also shows that the number of etch pits detected by the plasma etching method is 10-15% less than those by the PAW method. It is considered that active species recombine to stable gases such as CF_4 and COF_2 because of the small conductance of pinholes. On the other hand, pinhole density detected by the Cu-decoration method was about 50% less than those by the PAW method. The decorations grow in size as a function of time, but do not increase in number, because excessive decorations give rise to the coalescence of Cu.

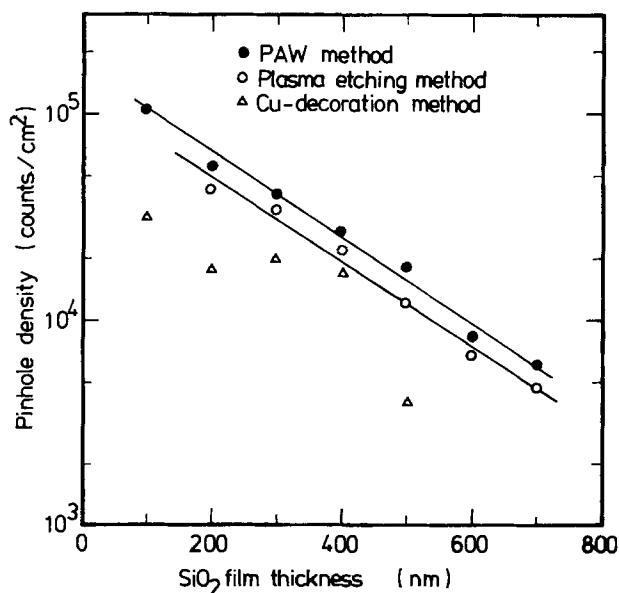


Fig. 2. Pinhole density detected by plasma etching method (○), PAW method (●), and Cu-decoration method (△).

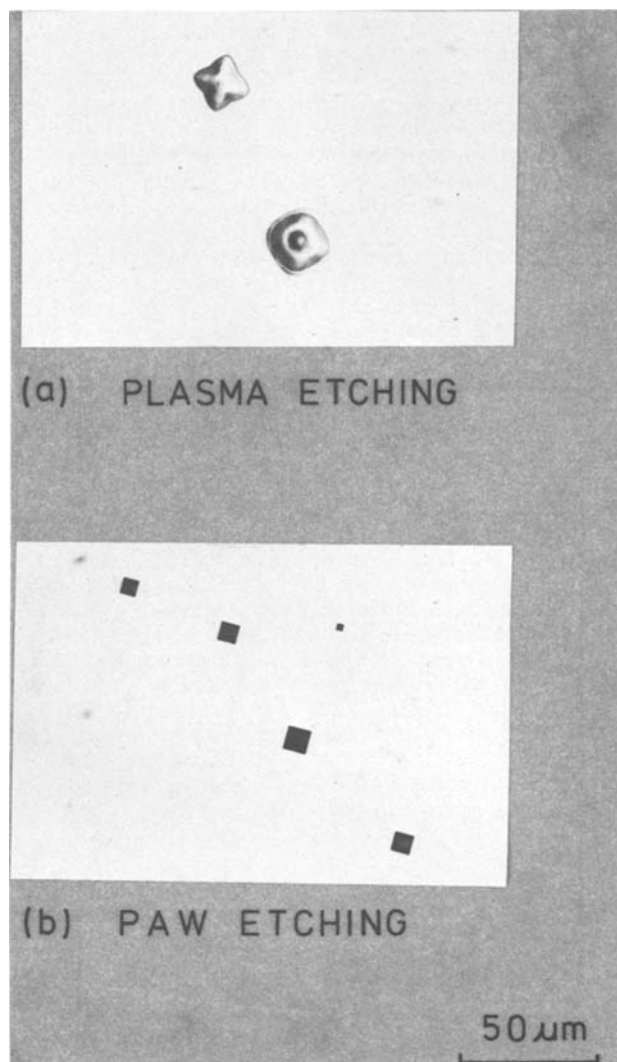


Fig. 3. Figures of etch pits formed by plasma etching method and PAW method.

The present etch rate ratio of 130 is not large enough compared with the ratio of 1000 in the PAW method. Therefore the SiO_2 films thinner than 100 nm are etched off before the etch pits grow to a measurable size in the plasma etching method. The plasma etching method is, however, very useful for the pinhole detection of the SiO_2 film even under the present conditions. The advantages of this method are as follows: (i) identification of pinholes is very easy because of clear etch pits as shown in Fig. 3, (ii) the process is very simple, and (iii) etching time of about 45 min is less than that by the PAW method.

In conclusion, the pinhole detection in SiO_2 films deposited on Si can be carried out rapidly by the $\text{CF}_4 + \text{O}_2$ plasma etching, and the measured value of the pinhole density is considered to be reliable. The plasma etching method is also profitable for evaluating SiO_2 films because of its simplicity.

Manuscript submitted Aug. 22, 1980; revised manuscript received Dec. 16, 1980.

Any discussion of this paper will appear in a Discussion Section to be published in the December 1981 JOURNAL. All discussions for the December 1981 Discussion Section should be submitted by Aug. 1, 1981.

Publication costs of this article were assisted by Waseda University.

REFERENCES

1. R. H. Heinecke, *Solid State Technol.*, 104 (April 1978).
2. Y. Horiike and M. Shibagaki, *Suppl. Jpn. J. Appl. Phys.*, 15, 13 (1976).
3. W. J. Shannon, *RCA Rev.*, 31, 431 (1970).
4. R. M. Finne and D. L. Klein, *This Journal*, 114, 965 (1967).

The Quenching of $Y_2O_3:Eu$ Luminescence by Cerium

Martin J. Fuller

Thorn Lighting Limited, Enfield, Middlesex, EN1 1UL, England

The effect on plaque brightness of doping all the naturally occurring lanthanide elements into $Y_2O_3:Eu$ phosphor is shown in Fig. 1. All these and subsequently described rare-earth doped Y_2O_3 preparations were obtained by oxalate coprecipitation from neutral nitrate solutions followed by air firing at $1550^\circ C$. The preparations shown in Fig. 1 were white after this treatment, with the exception of the praseodymium and terbium-doped samples, which required subsequent treatment at $1000^\circ C$ in 10% H_2 in N_2 to remove a pale yellow body color. This treatment, which has no significant effect on either the luminescence intensity or emission spectrum of undoped $Y_2O_3:Eu$, presumably reduces the Pr and Tb species from oxidation states >3 to the trivalent state.

The existence of significant quenching by the trivalent ions praseodymium, neodymium, dysprosium,

Key words: inorganic, luminescence, energy transfer.

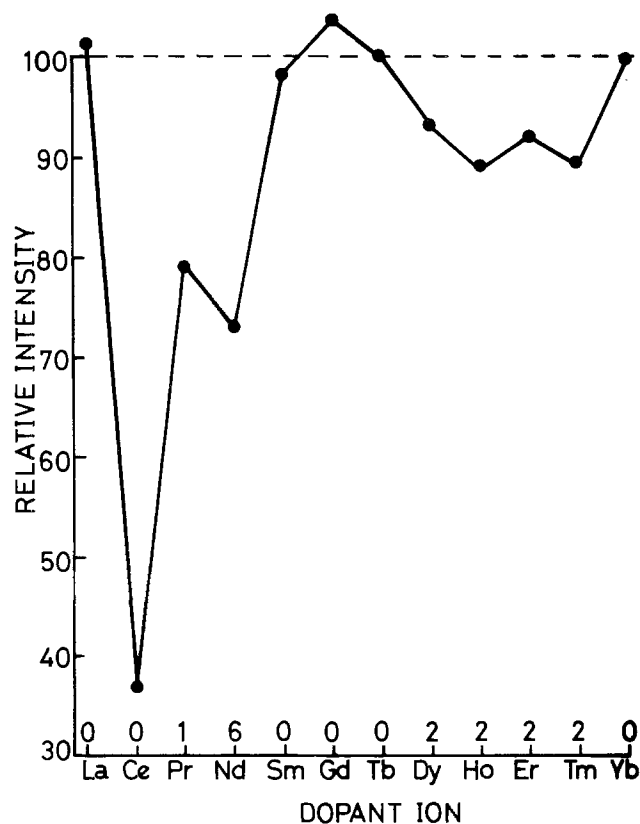


Fig. 1. The effect of incorporation of lanthanide ions at 0.067 m/o on $^5D_0 \rightarrow$ luminescence from $Y_2O_3:5.0$ m/o Eu excited at 254 nm. Numerals above the dopant ions indicate their numbers of energy levels relative to ground state approximately resonant with $^5D_0 \rightarrow ^7F_n$ ($n = 0-6$) transitions in Eu^{3+} .

holmium, erbium, and thulium can be qualitatively related to the presence of at least one 4f-4f transition in the quenching ion at an energy above ground state approximately resonant with a $^5D_0 \rightarrow ^7F_n$ ($n = 0-6$) transition in Eu^{3+} (1). This suggests nonradiative multipolar energy transfer from the 5D_0 level of the Eu^{3+} to the killer ion as being the process responsible for quenching by these ions.

The extensive quenching of $Y_2O_3:Eu$ luminescence by cerium, which has also been reported by other workers (2), can obviously not be ascribed to a similar 4f-4f energy transfer scheme. However, the effect does have particular industrial relevance to the combined preparation and use of $Y_2O_3:Eu$ with cerium and terbium coactivated phosphors as the respective red and green components in the multiphosphor approach to white light production in fluorescent lamps (3). For this reason it would be beneficial to gain more insight into the killer mechanism of cerium.

An interesting aspect of the quenching of $Y_2O_3:Eu$ luminescence by cerium is a time-dependent and cerium concentration-dependent photolytic quenching as shown in Fig. 2. In this experiment the samples were exposed in a double monochromator spectrophotometer (Perkin-Elmer MPF-44A) to the 250-270 nm radiation from a 150W high pressure xenon discharge, and the red luminescence monitored as a function of exposure time. In addition to the initial quenching there is, par-

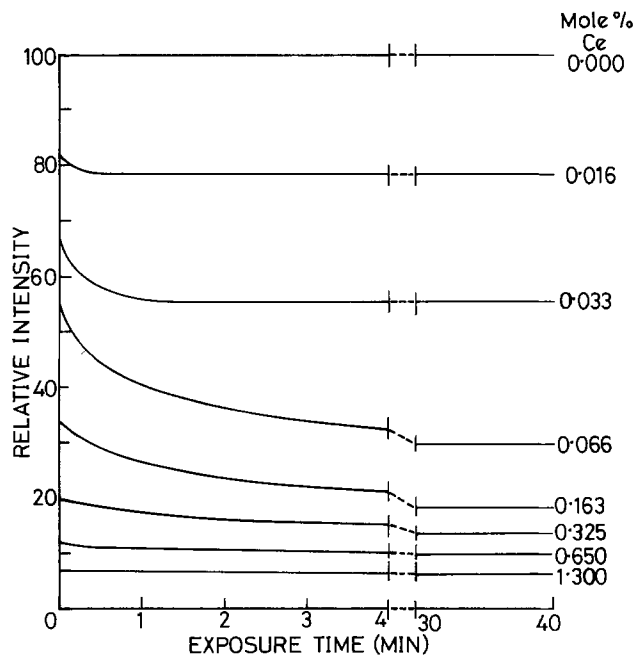


Fig. 2. The time-dependent quenching by Ce of $^5D_0 \rightarrow$ luminescence from $Y_2O_3:5.0$ m/o Eu excited at 250-270 nm.

REFERENCES

1. R. H. Heinecke, *Solid State Technol.*, 104 (April 1978).
2. Y. Horiike and M. Shibagaki, *Suppl. Jpn. J. Appl. Phys.*, 15, 13 (1976).
3. W. J. Shannon, *RCA Rev.*, 31, 431 (1970).
4. R. M. Finne and D. L. Klein, *This Journal*, 114, 965 (1967).

The Quenching of $Y_2O_3:Eu$ Luminescence by Cerium

Martin J. Fuller

Thorn Lighting Limited, Enfield, Middlesex, EN1 1UL, England

The effect on plaque brightness of doping all the naturally occurring lanthanide elements into $Y_2O_3:Eu$ phosphor is shown in Fig. 1. All these and subsequently described rare-earth doped Y_2O_3 preparations were obtained by oxalate coprecipitation from neutral nitrate solutions followed by air firing at $1550^\circ C$. The preparations shown in Fig. 1 were white after this treatment, with the exception of the praseodymium and terbium-doped samples, which required subsequent treatment at $1000^\circ C$ in 10% H_2 in N_2 to remove a pale yellow body color. This treatment, which has no significant effect on either the luminescence intensity or emission spectrum of undoped $Y_2O_3:Eu$, presumably reduces the Pr and Tb species from oxidation states >3 to the trivalent state.

The existence of significant quenching by the trivalent ions praseodymium, neodymium, dysprosium,

Key words: inorganic, luminescence, energy transfer.

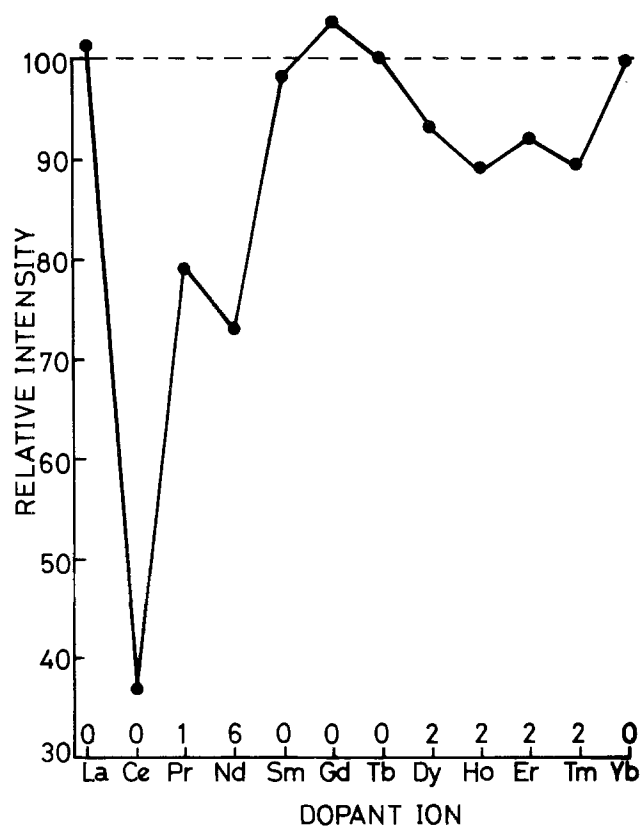


Fig. 1. The effect of incorporation of lanthanide ions at 0.067 m/o on $^5D_0 \rightarrow$ luminescence from $Y_2O_3:5.0$ m/o Eu excited at 254 nm. Numerals above the dopant ions indicate their numbers of energy levels relative to ground state approximately resonant with $^5D_0 \rightarrow ^7F_n$ ($n = 0-6$) transitions in Eu^{3+} .

holmium, erbium, and thulium can be qualitatively related to the presence of at least one 4f-4f transition in the quenching ion at an energy above ground state approximately resonant with a $^5D_0 \rightarrow ^7F_n$ ($n = 0-6$) transition in Eu^{3+} (1). This suggests nonradiative multipolar energy transfer from the 5D_0 level of the Eu^{3+} to the killer ion as being the process responsible for quenching by these ions.

The extensive quenching of $Y_2O_3:Eu$ luminescence by cerium, which has also been reported by other workers (2), can obviously not be ascribed to a similar 4f-4f energy transfer scheme. However, the effect does have particular industrial relevance to the combined preparation and use of $Y_2O_3:Eu$ with cerium and terbium coactivated phosphors as the respective red and green components in the multiphosphor approach to white light production in fluorescent lamps (3). For this reason it would be beneficial to gain more insight into the killer mechanism of cerium.

An interesting aspect of the quenching of $Y_2O_3:Eu$ luminescence by cerium is a time-dependent and cerium concentration-dependent photolytic quenching as shown in Fig. 2. In this experiment the samples were exposed in a double monochromator spectrophotometer (Perkin-Elmer MPF-44A) to the 250-270 nm radiation from a 150W high pressure xenon discharge, and the red luminescence monitored as a function of exposure time. In addition to the initial quenching there is, par-

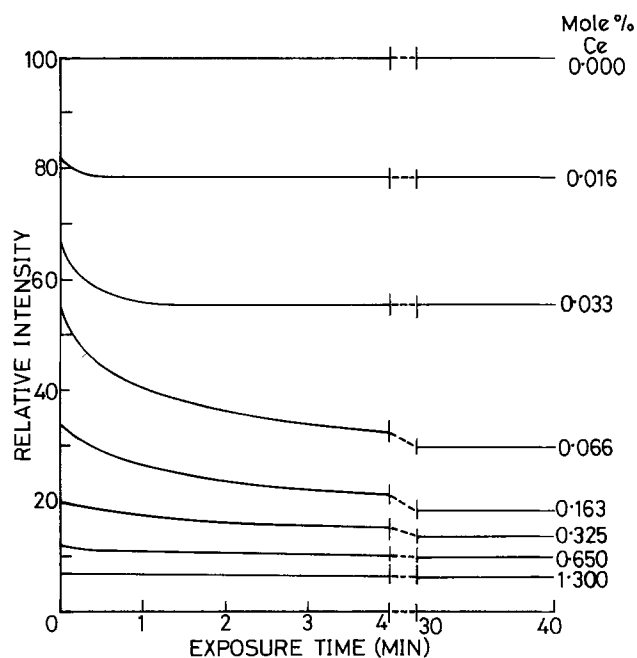


Fig. 2. The time-dependent quenching by Ce of $^5D_0 \rightarrow$ luminescence from $Y_2O_3:5.0$ m/o Eu excited at 250-270 nm.

ticularly at the intermediate cerium concentrations investigated, a significant additional time-dependent quenching effect accompanied by a proportionate photochromic darkening of the initially white phosphor to a pinkish color. This u.v. photochromism is only slowly reversible on removal from the u.v. irradiation and exposure to ambient light, but is rapidly bleached by high intensity visible light. An indication of the contribution of this photochromic quenching is shown in the solid curves of Fig. 3, where the overall equilibrium quenching has been resolved into its initial and time-dependent photochromic components. This clearly shows the photochromic effect to peak at about 0.1 mole percent (m/o) cerium.

Thermal reduction of the cerium-containing phosphors at 1000°C in N₂-10% H₂ results in an increasing darkening to a yellow-brown color with increasing cerium concentration. At cerium concentrations below about 0.1 m/o, where this discoloration is relatively weak, there is no evidence of further darkening by photochromism, which is consistent with the fact that no time-dependent quenching is observed in these reduced samples. The quenching characteristics of these reduced samples, together with the corresponding curve for Y₂O₃:Eu doped with neodymium are shown in the dotted curves of Fig. 3. These S-shaped quenching curves obtained on these axes and over these concentration ranges are typical for trivalent lanthanide ion quenching of Eu³⁺ luminescence in Y₂O₃ (4, 5) and can be correlated with the r^{-n} ($n = 6-10$) dependence expected for nonradiative multipolar energy transfer from the excited Eu³⁺ center over a distance r to the killer ion (5). The curves obtained both for the initial and the overall quenching effect of cerium in the nonreduced samples are not characteristic, suggesting the possibility that an alternative killer mechanism is coming into play.

Insight into this is given by diffuse reflectance spectra obtained on Y₂O₃:Ce samples without Eu³⁺, as shown in Fig. 4. These clearly show that in the nonreduced samples the cerium species present give rise

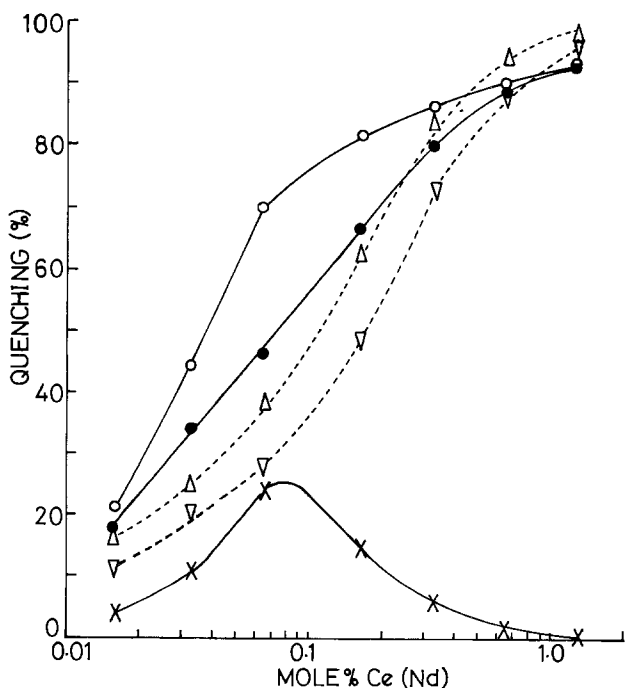


Fig. 3. The quenching by Ce and Nd of ⁵D₀ → luminescence from Y₂O₃:5.0 m/o Eu excited at 250-270 nm. —○—, Ce overall quenching; —●—, Ce initial quenching; —×—, Ce photochromic quenching; ---△---, thermally reduced Ce samples; ---▽---, Nd.

to a very strong u.v. absorption band at <230-300 nm. This absorption, which is not accompanied by any detectable luminescence, causes photochromic darkening to about the same extent as in europium-containing samples with the same amount of cerium. Thus the photochromism is not attributable to redox interactions between the cerium and europium species. Further evidence for the nonparticipation of Eu³⁺ in redox reactions in the systems investigated in this work is the fact that in no case was Eu²⁺ band emission observed.

In contrast to the nonreduced cerium-containing samples, the reduced samples show relatively much less strong absorption of 230-300 nm radiation, but do show an absorption band beginning at about 350 nm and extending up to about 500 nm, which can fairly confidently be assigned to a 4f-5d transition in trivalent cerium. This obviously accounts for the yellow-brown color of the reduced samples. There is no evidence of this band in the nonreduced samples, and the inference must be that the cerium exists in the tetravalent form in these samples.

The presence of this tetravalent cerium causes a very strong absorption band at <230-300 nm, and it is this absorption competing with the O-Eu charge transfer absorption (Fig. 4) responsible for europium excitation in Y₂O₃:Eu (6), which accounts for the initial quenching. We have found no evidence to suggest that a multipolar quenching mechanism between excited europium and "tetravalent" cerium occurs. For example, if the europium in the nonreduced Y₂O₃:Eu,Ce samples is directly excited into its ⁵D₁ (535 nm) and ⁵D₂ (466 nm) levels, then no quenching of the ⁵D₀ Eu luminescence occurs over the range of cerium concentrations investigated. Excitation into the ⁵D₃ (395 nm) level does give rise to slight quenching, but this can be attributed to some residual competitive absorption at this wavelength, as shown in Fig. 4. Direct excitation into these europium ⁵D levels does not result in photochromism.

The additional time-dependent and cerium-concentration dependent quenching, however, is not due to further competitive absorption of the u.v. radiation since the onset of photochromism has been found not to be accompanied by more extensive u.v. absorption. Thus the photochromic quenching occurs by a different mechanism.

Substitution of tetravalent cerium into yttrium sites in a Y₂O₃ lattice would be expected to produce a defect

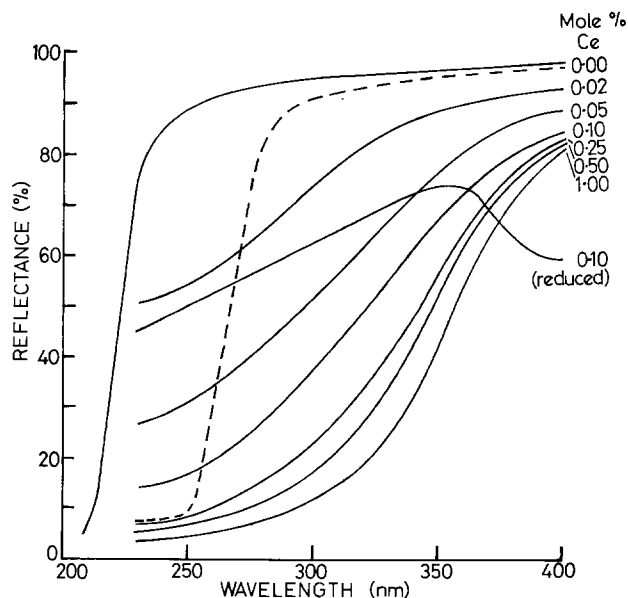


Fig. 4. Diffuse reflectance spectra of Y₂O₃:Ce samples and (dotted) Y₂O₃:5 m/o Eu.

structure in order to maintain electroneutrality. The most likely defect is an yttrium vacancy, *i.e.*, for every three substitutional Ce^{4+} ions introduced a cation vacancy is produced. Cation vacancies are not normally color centers, which is consistent with the fact that the nonreduced cerium samples are white. In addition, these defects are not traps for luminescence from the 3D manifold of europium since no quenching by cerium is observed upon direct excitation into this manifold. However, if it is assumed that upon u.v. irradiation the Ce^{4+} in the defect lattice shows a tendency to photochemically reduce, then the creation of other defect sites such as anion vacancies, O^- sites, or F centers could be envisaged. Defects of this type are well-recognized color centers and luminescence traps and could thus account for the photochromism and its accompanying quenching. The cerium concentration dependence of this photochromism is presumably due to the fact that the Y_2O_3 lattice will only tolerate a limited concentration of defects before structural rearrangement occurs in order to eliminate these.

Manuscript submitted Oct. 7, 1980; revised manuscript received Jan. 27, 1981. This was Paper 579 RNP

presented at the St. Louis, Missouri, Meeting of the Society, May 11-16, 1980.

Any discussion of this paper will appear in a Discussion Section to be published in the December 1981 JOURNAL. All discussions for the December 1981 Discussion Section should be submitted by Aug. 1, 1981.

Publication costs of this article were assisted by Thorn Lighting Limited.

REFERENCES

1. G. H. Dieke, "Spectra and Energy Levels of Rare Earth Ions in Crystals," Fig. 35, Interscience, New York (1968).
2. P. Lavéant, *Rev. Chim. Minérale*, **10**, 329 (1973).
3. J. M. P. J. Versteegen, D. Radielović, and L. E. Vrenken, *This Journal*, **121**, 1627 (1974).
4. M. J. Fuller, Unpublished data.
5. J. D. Axe and P. F. Weller, *J. Chem. Phys.*, **40**, 3066 (1964).
6. G. Blasse, in "Luminescence of Inorganic Solids," B. Di Bartolo, Editor, p. 457, Plenum, New York (1978).

Achievement of High Lifetime by a Combination of HCl Oxidation and POGO Gettering Techniques

Jacobus W. Swart* and E. Charry**

Microelectronics Laboratory, University of Sao Paulo, 05508 Sao Paulo, Brazil

Many devices or integrated circuits such as CCD's and MOS dynamic circuits require, for better performance, that their crystal presents, after completion of the fabrication process, a high lifetime. This means that the crystal must have a very low density of defects, *e.g.*, dislocations, stacking faults, and metal impurities. These crystal defects can also reduce device yield dramatically in bipolar and MOS devices. To reduce or eliminate them, many methods have been described, known as gettering techniques, which promote an increase in lifetime due to the capture of metal impurities and native defects and the suppression of stacking faults. The most usual techniques are: phosphorus gettering (1), back-side abrasion (2), ion implantation damage gettering (3), POGO by misfit dislocations due to phosphorus diffusion (4), POGO by strain gradient due to a silicon nitride layer deposited directly on the silicon substrate's back side (5), and oxidation in an atmosphere of oxygen added by an appropriate amount of chlorine (6-8). The POGO technique by misfit dislocations has been shown (4, 9) to be very efficient in suppressing nucleation centers for stacking faults in addition to capturing impurities introduced in the wafer before and during processing. In addition, the gettering technique by HCl oxidation at high temperature is very efficient in removing stacking fault nucleation centers (8) and metallic impurities (10).

We present in this article an experimental work utilizing a combination of the gettering techniques by HCl oxidation together with POGO by misfit dislocations and also utilizing them separately for the purpose of comparison. For practical reasons the gettering by oxidation is done before the POGO, since an oxide (thermal + silox) on the frontal side of the wafer is

needed for masking against the phosphorus diffusion, and in addition thermal oxide is very clean and passivated.

It has been shown that at 1200°C there is a gettering effect of the S.F. nucleation centers without etching the silicon surface, depending on the HCl/O₂ ratio and the oxidation time (8). We used 1200°C, 0.6% as the HCl/O₂ ratio, and 3 hr as the oxidation time. With these oxidation parameters, etching of the silicon will not occur and we are clearly within the conditions where gettering occurs.

With reference to the conditions necessary to introduce misfit dislocations by phosphorus diffusion, Rozgongi *et al.* (4) have shown that the deposition temperature has to be higher than 1050°C and suggest times longer than 1 hr be used. We choose the temperature of 1150°C and time varying from 90 to 150 min.

For the wafers which were processed by POGO only as the gettering step, the initial oxidation was done at 1000°C for 4 hr in an atmosphere of O₂ plus 5% HCl, since during this oxidation S.F.'s do not grow and a gettering effect does not occur (8).

Besides the study of these two gettering techniques we investigated the influence on the lifetime of thermal processes after the gettering steps. We also present the effect of a steam atmosphere thermal treatment on the wafers submitted to the HCl oxidation gettering process.

Experimental Procedures

To study and evaluate the gettering techniques, we performed three different runs fabricating MOS capacitors using the sequence described below.

1. Oxidation at 1200°C in O₂ + 0.6% HCl for 3 hr or at 1000°C in O₂ + 5% HCl for 4 hr.
2. Silox deposition at 410°C on the wafer's front side to achieve 1 μm thickness oxide.
3. Silox densification at 1000°C, 20 min, in dry O₂ or in steam.

* Electrochemical Society Student Member.

** Electrochemical Society Active Member.

Key words: silicon defects, S.F. nucleation centers, silicon surface etching, thermal stress.

4. Back-side oxide etching.
5. Phosphorus deposition at 1150°C for 90, 130, or 150 min, using POCl_3 as the doping source.
6. 1 μm thickness silox deposition on the wafer's back side.
7. High temperature treatment in a dry O_2 atmosphere.
8. Frontal oxide etching by "buffered HF."
9. Oxidation at 1000°C, in $\text{O}_2 + 3\% \text{HCl}$, obtaining a 100 μm oxide layer.
10. PSG deposition for Al-gate wafers only.
11. Annealing at 1000°C, 30 min in an argon atmosphere.
12. Aluminum deposition using a tungsten crucible or a polysilicon deposition followed by a phosphorus deposition.
13. Definition by photolithography of circular capacitors with $1.32 \times 10^{-3} \text{cm}^2$ area and guard ring as shown in Fig. 1.
14. Back-side oxide etching.
15. Aluminum deposition on the wafers back side.
16. Annealing at 450°C, 30 min in forming gas.

The fabrication process parameters and variables of the three runs are outlined in Tables I, II, and III. The objectives of each run and the description of the wafers used are as follows.

First run: This run had as its objective to compare, by means of wafers with the silox densified in a steam atmosphere, the gettering by the combination of the two techniques with the gettering by HCl oxidation alone. The second objection was to investigate the difference on the interface quality by obtaining the gate oxide by stripping off the initial oxide and reoxidizing, or by chemically thinning the initial oxide. The wafers used were n-type, (100), 1.5 Ωcm , CZ, and made at our laboratory. They were cut in halves and numbered N_{5r} , N_{5l} to N_{8r} , N_{8l} .

Second run: The objectives of this run were to observe the influence of the phosphorus deposition time (POGO); high temperature treatment after the gettering stages; and the silox densification atmosphere. The wafers were n-type, (100), 4.5 Ωcm , CZ, and made at our laboratory. They were also cut in halves and numbered N_{9r} , N_{9l} to N_{13r} , N_{13l} .

Third run: This run had the same objectives as the second run as well as to study in a comparative form the two gettering steps separately and the combination of the two. The wafers were p-type, (100), CZ. Two wafers with $\rho \approx 25 \Omega\text{cm}$ and 3 in. diam made by Wacker were used. They were cut into four pieces each and numbered W_1 to W_4 and W_5 to W_8 . Two other wafers made at our laboratory, with $\rho \approx 12 \Omega\text{cm}$ were cut in halves and numbered L_{1r} , L_{1l} , L_{2r} , and L_{2l} .

In the first and second runs the electrode material used was aluminum while in the third run it was polysilicon.

With reference to the third run, in all the thermal stages the entrance and exit of the wafers were done with the furnace at 800°C. The heating of the furnace and wafers from 800°C to the desired temperature was done at a rate of 10°C/min and the cooling down to 800°C was done at a rate of 3°C/min.

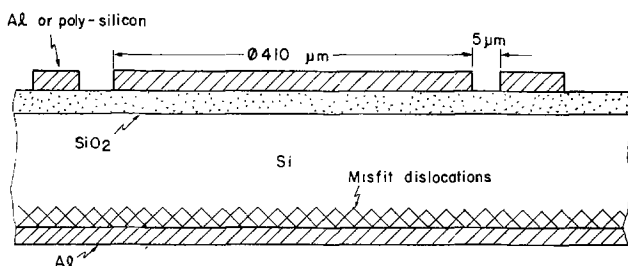


Fig. 1. Sketch of the MOS capacitor

During the third run (initial oxidation), the wafers marked with W were laid horizontally on a quartz susceptor and were supported only at their edges by the quartz bars of the susceptor, while the wafers marked with L were placed vertically on the susceptor.

Measurements.—Storage time, t_f , was measured (at least on ten samples per wafer) by the C-t technique using pulses with 6V amplitude and going from the inversion region into stronger inversion. During these measurements, the guard ring was polarized in the strong accumulation region. For some representative samples, relative to the wafer's mean t_f value, we plotted the C-t curve and using the Zerbst method we got the shielded surface recombination velocity, s , and the generation lifetime, τ_g , where τ_g is twice the value of the bulk lifetime, τ_0 (11).

After these measurements, the electrode material and the oxide were stripped off and the crystallographic defects were revealed by a 5 min etching with Wright solution (12).

Results and Discussion

The experimental results of the three runs are shown in Tables I, II, and III. In these tables we have also specified a classification in accordance with the results obtained by the capacitors' C-t measurements, with a lower number representing a higher quality structure.

The wafers marked W and having the initial oxidation at 1200°C showed many structural defects due to bending caused by the manner in which they were supported during the initial oxidation. We arrived at this conclusion by comparing the results of group L with M or O_1 with O_2 . We can see from our results that although W_7 was within the gettering condition, the result was worse than for W_8 which was not treated within these conditions. The comparison of O_1 with O_2 indicates the same tendency using the same parameters for the two groups. These defects, produced by stress and strain, were substantially eliminated during the POGO stage as the comparison of the results of the group M with O_2 indicates.

Comparing the results of group A with B or C with D, we observe that the combination of the two gettering techniques presents a more powerful gettering action than the HCl oxidation gettering alone. Analogously, comparing group O with N, we observe the same relation between the gettering action of the combination of the two techniques and gettering by POGO alone. These facts indicate that the two techniques have gettering actions at least partially distinct. This means that they complement each other.

Another fact we observed was that the final quality of the wafers was adversely affected by increasing the number of thermal steps after the gettering steps. This can be seen comparing the results of group F with G, H, and I; O with Q; or R with S. Also, longer phosphorus deposition times decrease the crystal quality. This appears to be similar to the former situation, since after a certain time the charge deposition rate or the misfit-dislocation generation rate becomes very small and in this way the process is transformed into an annealing process. To see this, compare the results of group F with J, O with R, or Q with S. These observations suggest that the device fabrication processes, after the gettering stages, have to be as cool as possible.

The wafers with their silox densified in a steam atmosphere presented a grainy appearance. This phenomenon is caused by the silicon etching due to the reaction of the steam with the high amount of chlorine contained in the initial oxide. This event is in accordance with the observations of Claeys *et al.* (13). These wafers also gave worse results than the wafers which had their silox densified in a dry O_2 atmosphere, where this phenomenon did not occur. To see this, compare

Table I. First run wafers' process parameters and variables and experimental results

| Group | Wafer | Main thermal treatments | | | | | Experimental results | | |
|-------|------------------------------------|------------------------------------|--------------------------------|--------------------|--|----------------|--------------------------------|--|----------------|
| | | Initial oxidation temperature (°C) | Silox densification atmosphere | Time of POGO (min) | High temperature treatment in O ₂ | Gate oxidation | $\bar{t}_t \pm \sigma$ | Average total etch pit density (10 ⁴ cm ⁻²) | Classification |
| A | N _{7c} N _{8r} | 1200 | Steam | 90 | No | Yes | 5'10" ± 1'20" 4'20" ± 1'20" | <0.5 <0.5 | I |
| B | N _{7i} N _{8i} | 1200 | Steam | No | No | Yes | 1'50" ± 20" 2'40" ± 3'00" | <0.5 <0.5 | III |
| C | N _{5r} N _{6r} | 1200 | Steam | 90 | No | No | 3'20" ± 1'10" 4'50" ± 1'10" | <0.5 <0.5 | II |
| D | N _{5i} N _{6i} | 1200 | Steam | No | No | No | 20" ± 29" 10" ± 6" | <0.5 <0.5 | IV |

Table II. Second run wafers' process parameters and variables and experimental results

| Group | Wafer | Main thermal treatments | | | | Experimental results | | | | | |
|-------|--|------------------------------------|--------------------------------|--------------------|--|-------------------------|-------------------------|-------------------|----------------------|--|----------------|
| | | Initial oxidation temperature (°C) | Silox densification atmosphere | Time of POGO (min) | High temperature treatment in O ₂ | \bar{t}_t | t_{tMAX} | τ_g (μsec) | S (cm/sec) | Average total etch pit density (10 ⁴ cm ⁻²) | Classification |
| E | N _{12r} N _{13r} | 1200 | Steam | 90 | No | 1'20" 50" | 1'30" 1'10" | 98 108 | 1.10 1.13 | <1 <1 | V |
| F | N _{10i} N _{11i} N _{12i} | 1200 | O ₂ | 90 | No | 4'30" 4'00" 5'50" | 5'00" 4'10" 7'30" | 312 266 332 | 0.10 0.14 0.11 | <1 <1 <1 | I |
| G | N _{10r} | 1200 | O ₂ | 90 | 5 hr, 1000°C | 3'50" | 4'00" | 240 | 0.11 | <1 | II |
| H | N _{6i} | 1200 | O ₂ | 90 | 2 hr, 1150°C | 3'10" | 3'30" | 222 | 0.13 | <1 | III |
| I | N _{11i} | 1200 | O ₂ | 90 | 5 hr, 1000°C + 2 hr, 1150°C | 2'10" | 2'40" | 134 | 0.34 | <1 | IV |
| J | N _{6r} N _{11r} | 1200 | O ₂ | 130 | No | 3'20" 3'00" | 3'40" 4'00" | 214 228 | 0.18 0.10 | <1 <1 | III |

Table III. Third run wafers' process parameters and variables and experimental results

| Group | Wafer | Main thermal treatments | | | | Experimental results | | | | | |
|----------------|------------------------------------|------------------------------------|--------------------------------|--------------------|--|----------------------|------------|-----------------|--------------|--|----------------|
| | | Initial oxidation temperature (°C) | Silox densification atmosphere | Time of POGO (min) | High temperature treatment in O ₂ | \bar{t}_t | t_{tMAX} | τ_g (msec) | S (cm/sec) | Average total etch pit density (10 ⁴ cm ⁻²) | Classification |
| L | L _{1i} W ₈ | 1000 | O ₂ | No | No | 6' 11' | 17' 17' | — 2.6 | — 0.12 | 0.4 0.3 | IV |
| M | W ₇ | 1200 | O ₂ | No | No | 2' | 5' | 0.2 | 0.10 | 1.4 | VI |
| N | W ₈ | 1000 | O ₂ | 90 | No | 16' | 19' | 3.2 | 0.10 | 0.2 | III |
| O ₁ | L _{1r} L _{2r} | 1200 | O ₂ | 90 | No | 35' | 46' | — | — | 0.4 | I |
| O ₂ | W ₅ W ₄ | | | | | 17' 20' | 23' 26' | 4.4 4.2 | 0.07 0.07 | 0.3 0.2 | |
| P | L _{2i} | 1200 | Steam | 90 | No | 4' | 7' | — | — | 0.4 | VII |
| Q | W ₃ | 1200 | O ₂ | 90 | 5 hr, 1000°C | 15' | 22' | 3.4 | 0.09 | 0.1 | II |
| R | W ₂ | 1200 | O ₂ | 150 | No | 13' | 25' | 3.2 | 0.12 | 0.2 | III |
| S | W ₁ | 1200 | O ₂ | 150 | 5 hr, 1000°C | 6' | 10' | 2.6 | 0.12 | 0.2 | V |

the results of group E with F or O with P. The SiO₂/Si interface that had been etched due to the chlorine had its quality improved by removing the first oxide and oxidizing again, this fact being more evident in the case where a POGO step was not done. This observation can be seen by comparing the results of group A with C or B with D.

Comparing the results of the second run with the third run, one observes that the last ones are better. The factors that must have contributed to this are: (i) the method used for the wafer's entrance and exit from the furnace in the thermal steps, (ii) the use of polysilicon as an electrode material which brings about a cleaner process, as can be seen by the average interface charge, Q_{ss}/q , of the two runs, which are 6×10^{10} and 1×10^{10} cm⁻², respectively, (iii) the n-type wafers used may have a lower initial quality.

As to the total number of etch pits, it is interesting to note that the third run wafers presented the lowest numbers, except wafer W₇ which maintained the defects acquired by the bending during the HCl oxidation

at 1200°C. Also, the revealing of etch pits shows the absence of stacking faults, as was expected by the oxidations employed.

Conclusion

We obtained a minority carrier generation lifetime of some milliseconds (4-8 msec) on silicon substrates in large-area structures using a basic procedure described in this work. Besides this fact, the contributions that this work adds to this subject are the following.

1. The combination of the two gettering techniques gives better results than one alone, which indicates that the gettering action of the two techniques complement each other.

2. In the fabrication of devices or IC's with high yield and good performance, the thermal processes after the gettering stages have to be as cool as possible.

3. After carrying out the initial oxidation at 1200°C for the conditions described, any thermal treatment in a steam atmosphere should not be done without the removal of this first oxide layer.

4. It is important not to inflict mechanical damage or contamination in the wafer. In addition, precautions should be taken to not introduce defects caused by the manner in which the wafers are supported during thermal treatment or due to thermal stresses.

Manuscript submitted July 22, 1980; revised manuscript received ca. Jan. 2, 1981. This was Paper 684 RNP presented at the Hollywood, Florida, Meeting of the Society, Oct. 5-10, 1980.

Any discussion of this paper will appear in a Discussion Section to be published in the December 1981 JOURNAL. All discussions for the December 1981 Discussion Section should be submitted by Aug. 1, 1981.

Publication costs of this article were assisted by the University of Sao Paulo.

REFERENCES

1. J. E. Lawrence, in "Semiconductor Silicon," R. R. Haberecht and E. L. Kern, Editors, p. 596, The Electrochemical Society Softbound Proceedings Series, Princeton, N.J. (1969).
2. E. J. Metz, *This Journal*, **112**, 420 (1965).
3. T. E. Seidel, R. L. Meek, and A. G. Cullis, *J. Appl. Phys.*, **46**, 600 (1975).

4. G. A. Rozgonyi, P. M. Petroff, and M. H. Read, *This Journal*, **122**, 1725 (1975).
5. P. M. Petroff, G. A. Rozgonyi, and T. T. Sheng, *ibid.*, **123**, 565 (1976).
6. H. Shiraki, in "Semiconductor Silicon 1977," H. R. Huff and E. Sirtl, Editors, p. 546, The Electrochemical Society Softbound Proceedings Series, Princeton, N.J. (1977).
7. C. L. Claeys, E. E. Laes, G. J. Declerck, and R. J. Van Overstraeten, in "Semiconductor Silicon 1977," H. R. Huff and E. Sirtl, Editors, p. 773, The Electrochemical Society Softbound Proceedings Series, Princeton, N.J. (1978).
8. T. Hattori, *J. Appl. Phys.*, **49**, 2994 (1978).
9. G. A. Rozgonyi and R. A. Kushner, *This Journal*, **123**, 570 (1976).
10. C. Hashimoto, S. Muramoto, N. Shiano, and O. Nakajima, *ibid.*, **127**, 129 (1980).
11. D. K. Schroder and J. Guldberg, *Solid State Electron.*, **14**, 1285 (1971).
12. M. Wright Jenkins, *This Journal*, **124**, 757 (1977).
13. C. L. Claeys, G. J. Declerck, and R. J. Van Overstraeten, Paper 487 presented at The Electrochemical Society Meeting, Los Angeles, California, Oct. 14-19, 1979.

DISCUSSION SECTION



This Discussion Section includes discussion of papers appearing in the *Journal of The Electrochemical Society*, Vol. 127, No. 6, and 11, June and November 1980.

GaAs Oxidation and the Ga-As-O Equilibrium Phase Diagram

C. D. Thurmond, G. P. Schwartz, G. W. Kammlott, and B. Schwartz
(pp. 1366-1371, Vol. 127, No. 6)

V. I. Belyi, A. N. Golubenko, T. P. Smirnova, and K. P. Lelkin:¹ The paper under discussion concerns an important problem: The investigation of phase composition of GaAs oxide films.

The investigation deals with the experimental data obtained by modern analytical techniques and with theoretical consideration by taking into account Ga-As-O ternary phase diagram. In our investigation² we also came to the conclusion that such a combined approach is the most informative one and allows us to clear up the layer by layer distribution of the oxide phases in the oxide films on InSb, which is the same type of chemical formation as the oxide films on GaAs.

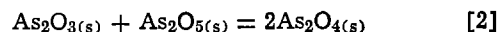
But from our point of view there are some uncertainties in the paper in question which may ultimately lead to some wrong conclusions.

The authors of the paper have taken into account seven individual phases of the Ga-As-O system: Ga(l,s), Ga₂O₃(s), GaAs(s), As(s), As₂O₃(s), As₂O₅(s), GaAsO₄(s) but for some unaccountable reason they have not considered the individual substance arsenic tetroxide, As₂O₄. According to Long and Sackman, arsenic tetroxide may be obtained from a mixture of As₂O₃ + As₂O₅ and does exist at room temperature up to 400°C.³

The enthalpy of formation change of As₂O₄ from individual elements by the reaction



is equal to $\Delta H_{298}^{\text{of}} = -191.1 \text{ kcal} \cdot \text{mol}^{-1}$ according to footnote 4 or $\Delta H_{298}^{\text{of}} = -189.7 \text{ kcal} \cdot \text{mol}^{-1}$ according to footnote 5. The calculated standard enthalpy change of As₂O₄ for the reaction



according to 4 is equal to $\Delta H_{298}^{\circ} = -3.3 \text{ kcal}$ with As₂O₃-claudetit and $\Delta H_{298}^{\circ} = -2.5 \text{ kcal}$ with As₂O₃-arsenolite.

As a rule for solid-state chemical processes, the change of entropy ΔS is close to zero and hence it is possible to judge a process taking in consideration the change of enthalpy only. However, the lack of the entropy meaning does not allow us to calculate the change in the Gibbs energy and to make an absolutely correct conclusion.

On the base of the change enthalpy for reaction [2], we suggest the phase equilibrium diagram which is shown in our Fig. 1. In this diagram the two new phase fields are plotted in.

In the paper under discussion, the mixture of As₂O₃ and GaAs in the mole ratio 2:1 was heated at 600°C during 48 hr and by means of Raman scattering it was shown that the products of the reaction are GaAsO₄ and As₂O₃. But the mole ratio of the initial substances equal to 2:1 does not give the possibility of getting into the phase field As₂O₃-As₂O₅-GaAsO₄ of the diagram (see Fig. 2 in the paper under discussion). In order to reach that field and to have the possibility of detecting arsenic tetroxide, the initial mole ratio of As₂O₅ and GaAs has to be $\geq 4:1$. We have to point out that arsenic tetroxide is unstable above 400°C.³

¹Institute of Inorganic Chemistry, Siberian Branch of the Academy of Sciences of the USSR, 3, Novosibirsk, 630090, USSR.

²T. P. Smirnova, A. N. Golubenko, N. F. Zacharchuk, V. I. Belyi, G. A. Kokovin, and N. A. Valisheva, *Ref. Zh. Chim.*, 9, 1008 (1980) (Russ.).

³L. H. Long and J. E. Sackman, *J. Inorg. Nucl. Chem.*, 25, 79 (1963).

⁴V. P. Glushko, Editor, "Termicheskie Constanti Veschestv, Spravochnik," Vol. III, AN SSSR, Moskva (1968) (Russ.).

⁵"Selected Values of Chemical Thermodynamic Properties," NBS Technical Note, 270-3, Washington, D.C. (1968).

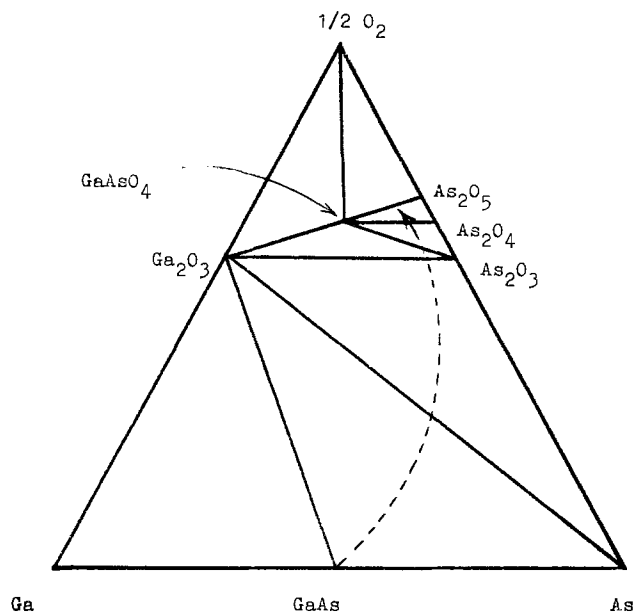


Fig. 1. The Ga-As-O ternary diagram in 25°C-400°C temperature region and $p_{O_2} = 1.01 \times 10^3$ hPa.

We repeated the experiment according to footnote 3 with the mixture of $As_2O_3 + As_2O_5$ taken in mole ratio 1:1, and by means of x-ray diffraction technique detected the As_2O_4 phase.

In our works^{2,6,7} we showed that in the case of oxygen oxidation of the InSb process the spatial distribution of indium and antimony oxides and elemental antimony in oxide film corresponds to the theoretical distribution which may be obtained from In-Sb-O equilibrium diagram. By the experimental method developed in our Institute,⁶ we also found that oxide films on InSb have multilayer composition. For example, when the mole ratio In:Sb is equal to 1:1, we detected the following phase complexes alternating from the InSb-oxide film interface up to the top of the film: InSb, InSb + $In_2O_3 + Sb$, $In_2O_3 + Sb_2O_3 + Sb$, $In_2O_3 + Sb_2O_3 + Sb_2O_4$, $In_2O_3 + Sb_2O_4 + InSbO_4$.⁷

It seems to us that on the basis of the ternary diagram it is possible to reach more varied conclusions than were offered in the paper under discussion. For instance, it is possible to predict the alternating phase composition when the Ga:As ratio differs from 1:1. When an oxidation of GaAs process takes place in the $As_2O_3 + O_2$ mixture, the Ga:As ratio is ≤ 1 and the phase composition change along the route given in Fig. 1 by a dotted line (the line is drawn arbitrarily) is: GaAs, GaAs + $Ga_2O_3 + As$, $Ga_2O_3 + As_2O_3 + As$, $Ga_2O_3 + As_2O_3 + GaAsO_4$, $As_2O_3 + As_2O_4 + GaAsO_4$, $As_2O_4 + As_2O_5 + GaAsO_4$.

In conclusion, we should like to emphasize that the good agreement between the final results of the paper under discussion on the Ga-As-O system and our results on In-Sb-O system makes it possible to claim that there exists some general approach to the understanding of the mechanism of A^{III}B^V semiconductor compounds oxidation processes.

C. D. Thurmond and G. P. Schwartz:⁸ The authors of the comment have pointed out that As_2O_4 as evidenced by the investigations of Long and Sackman⁹⁻¹¹ was not

⁸ N. F. Zacharchuk, N. A. Valisheva, K. P. Lelkin, T. P. Smirnova, I. G. Judelevich, V. I. Belyi, and G. A. Zenkovets, *Izv. SO AN SSSR, ser. chim. nauk., vipusk 2*, 39 (1980) (Russ.).

⁷ T. P. Smirnova, A. N. Golubenko, N. F. Zacharchuk, V. I. Belyi, G. A. Kokovin, and N. A. Valisheva, *Thin Solid Films*, 76, 11 (1981).

⁶ Bell Laboratories, Murray Hill, New Jersey 07974.

⁹ L. H. Long and J. F. Sackman, *J. Inorg. Nucl. Chem.*, 25, 79 (1963).

¹⁰ L. H. Long and J. F. Sackman, *ibid.*, 25, 89 (1963).

¹¹ L. H. Long and J. F. Sackman, *ibid.*, 25, 93 (1963).

included in an article on the Ga-As-O phase diagram which entailed the specification of the condensed phases in that system. Although we were aware of some earlier (1933) data by Brityke, Kapustinskii, and Chentzova,¹² we must acknowledge having overlooked the more current references by Long *et al.* and failure to comment on our reservations concerning the existence of As_2O_4 as a stable oxide phase.

Whereas the data by Long and Sackman⁹⁻¹¹ clarifies many of the inconsistencies present in the earlier literature on As_2O_4 , we remain cautious in our acceptance of their conclusion concerning the existence of this compound. The following comments express the basis for our concern.

1. The authors use a thermodynamic argument in support of their conclusion that As_2O_4 is stable. The Gibbs energy change of the reaction $As_2O_3 + As_2O_5 = 2 As_2O_4$ is obtained from the enthalpy change. The entropy contribution was assumed to be negligible since, in general, the entropy change for a reaction among solids is small. However, when the enthalpy change is small, as it is for this reaction, the sign of ΔG° will be sensitive to small values of ΔS° (i.e., $T\Delta S^\circ$). Thus the use of ΔH° for ΔG° does not provide significant support for the conclusion that As_2O_4 is stable with respect to As_2O_3 and As_2O_5 .

A related aspect of this problem also suggests that the stability of As_2O_4 is not yet known. The authors do not give uncertainties for the enthalpies of formation used in their calculation. If we use the uncertainties recommended by Kubaschewski, Evans, and Alcock,¹³ ± 0.8 kcal/mol for both forms of As_2O_3 and ± 1.5 kcal/mol for As_2O_5 , and assume no uncertainty in the enthalpy of formation of As_2O_4 , a lower limit to the magnitude of the reaction enthalpy uncertainty can be estimated. The uncertainty is ± 2.3 kcal and is seen to be very close to the two calculated enthalpies of -3.3 kcal (claudetite) and -2.5 kcal (arsenolite). With the inclusion of an uncertainty in the enthalpy of formation of As_2O_4 , the possibility arises that the reaction enthalpy, and, with the authors assumption, the Gibbs energy, may be positive rather than negative. It is possible, then, that As_2O_4 is not stable.

2. Long and Sackman demonstrated that As_2O_4 could not be produced as a pure, single phase product from an anhydrous reaction of $As_2O_3 + As_2O_5$. Some water is evidently necessary in order to produce the assigned product in high yield. However, it was stated in footnote 9 that the hydrated form of the tetroxide of formula $6As_2O_4 \cdot 5H_2O$ produced the same diffraction lines as anhydrous As_2O_4 . By "anhydrous" the authors mean dried to constant weight. One might reasonably ask if the diffraction technique is in fact sensitive to distinguishing between As_2O_4 and materials of the form $As_2O_4 \cdot xH_2O$, where x might take on values of 1-4 for hydroxides or oxy-hydroxides, or higher values for incompletely hydrated products. These compounds, of course, would not be part of the Ga-As-O ternary phase diagram.

3. Rather complete synthetic and structural data exist for the formation of two claudetite modifications of As_2O_3 .¹⁴⁻¹⁷ These structures are layer like and quite distinct in their x-ray diffraction patterns from octahedral As_2O_3 (arsenolite). They are also distinctive in that they require approximately 1% of H_2O in order to stabilize. Although Long and Sackman demonstrated that the diffraction pattern of As_2O_4 did not replicate

¹² E. V. Britzke, A. F. Kapustinskii, and L. G. Chentzova, *Z. Anorg. Chem.*, 213, 58 (1933).

¹³ O. Kubaschewski, E. L. Evans, and C. B. Alcock, "Metallurgical Thermochemistry," 4th ed., Pergamon Press, New York (1967).

¹⁴ K. A. Becker, K. Plieth, and I. N. Stranski, *Z. Anorg. Allg. Chem.*, 266, 293 (1951).

¹⁵ K. A. Becker, H. Karge, and I. N. Stranski, *Z. Phys. Chem.*, 44, S1 (1965).

¹⁶ K. A. Becker, H. Karge, and I. N. Stranski, *ibid.*, 44, S7 (1965).

¹⁷ F. Pertlik, *Monatsh. Chem.*, 106, 755 (1975).

the lines of either As_2O_3 (octahedral) or As_2O_5 , they do not appear to have excluded the possibility that the compound generated involved a claudetite modification of As_2O_3 .

4. The question of whether claudetite or some other hydrogen-bearing compound might be involved deserves careful consideration. We intend to study these questions in more detail using infrared and Raman scattering. The latter technique has already been used to characterize claudetite.¹⁷ Until those studies are complete, we remain cautiously skeptical of the existence of As_2O_4 .

The authors make several points about the interpretation of the Ga-As-O phase diagram with the phase As_2O_4 included. One of these points, however, is incorrect, namely that to form As_2O_4 the initial mole ratio of As_2O_5 to GaAs must be ≥ 4 . This statement overlooks the As_2O_4 - As_2O_3 -GaAsO₄ field. The proper criterion for the formation of As_2O_4 from ratios of As_2O_5 to GaAs is that the ratio be > 2 .

Finally, we wish to concur in the conclusions of Belyi *et al.* that the phase diagram approach is a useful tool in studying the oxidation and reaction patterns of certain semiconductors. We would point out for the readers, however, that the form of the In-Sb-O diagram clearly differs from that of Ga-As-O as indicated by the observed phase fields listed by the authors of the comment. The "good agreement" mentioned by these authors should not be construed to mean that the form of the phase fields is identical for the two systems.

On High Temperature Oxidation of Chromium

I. Oxidation of Annealed, Thermally Etched Chromium at 800°-1100°C

II. Properties of Cr_2O_3 and the Oxidation Mechanism of Chromium

K. P. Lillerud and P. Kofstad (pp. 2397-2410 and 2410-2419, Vol. 127, No. 11)

D. Caplan and G. I. Sproule:¹⁹ In these two papers on the oxidation of Cr, Lillerud and Kofstad examine the effect of temperature and pressure, the properties of Cr_2O_3 , and the oxidation mechanism. We would like to comment on the following points.

1. In comparing the parabolic rate constants obtained with their thermal-etch oxidation procedure to our results²⁰ for monocrystalline Cr_2O_3 scales, the authors indicate that our much lower values are in error because no correction was made for volatilization of Cr_2O_3 . In fact, we guarded against oxide evaporation by providing a Cr_2O_3 crucible in the hot zone so that the specimens hung in essentially stagnant oxygen saturated with Cr oxide vapor.²⁰ Additional evidence that our low values of K_p are not caused by oxide volatilization is that, as the authors show in their Fig. 1 (page 2398), our results for polycrystalline scales, similar in structure to their blistered and wrinkled scales, show comparably high K_p values.

2. In the oxidation procedure used by the authors, hot, oxide-free Cr is exposed abruptly to oxygen gas. As a result, very many randomly oriented oxide nuclei form on the metal and produce a fine-grained scale with many oxide grain boundaries to act as preferential diffusion paths. The consequent rapid oxidation rate and high rate of stress generation within the oxide promote separation of the scale from the metal and the wrinkling and lateral growth seen in the authors' illustrations. Values of K_p calculated for such scales are too high because (i) the effective specimen area is larger than the geometric area used to calculate

the weight gain; (ii) the larger area means that the real thickness of the layer is less and diffusion is therefore faster; and (iii) in multilayered scaling, the oxide formed before the failure of a layer by perforation is no longer part of the protective diffusion layer. The authors' assumption that the initial scale is dense, plane-parallel, uniform, and adherent is not supported by the photomicrographs. Previous work would indicate that separation and buckling begin early [Ref. (1), Fig. 5] when the vacancy flux is highest.

Hot-bare oxidation also maximizes the overtemperature effect²¹ which further increases the initial flux of cation vacancies and the compressive stress. Comparable oxidation conditions were found in our experiments with electropolished Cr on which fine-grained, blistered scale also developed.²⁰ When this separated layer failed by cracking, oxygen gas rushed into the vacuum gap between scale and metal, contacted the hot, bare Cr (equivalent to the authors' thermal-etch conditions), and formed a second blistered layer. Electropolishing was judged to be an unsuitable preparation method for Cr oxidation because of these defects in scale structure. Because of fine oxide grain size, hot-bare oxidation was also found to have a large effect on Ni oxidation;²² oxidation constants were as much as 10,000 times higher than for oxidation procedures which formed coarse-grained NiO scales.

3. The authors compare the experimentally determined parabolic rate constants with K_p values calculated from diffusion data for Cr in Cr_2O_3 . They consider the approximate agreement between the two sets of data to be evidence of the validity of their high measured K_p values. Such correspondence is to be expected, however, since the diffusion coefficients used for the comparison are themselves high, having been measured on polycrystalline specimens of hot-pressed Cr_2O_3 (Fig. 5, page 2413). It seems probable that the true oxidation constants and diffusion constants are both orders of magnitude lower.

4. When oxidation runs were discontinued by pumping off the oxygen, the specimens were found to lose weight for as long as they were held at temperature in vacuum. The authors conclude that the weight loss is due to the loss of Cr metal which "may penetrate the scale by lattice diffusion and by transport along grain boundaries, easy diffusion paths, and microcracks." Weight loss via microcracks is probable since Cr evaporating from the bare metal surface could migrate through pores or cracks in the separated scale as Cr vapor. In the absence of an oxygen atmosphere, however, there will be no concentration gradient as a driving force for cation diffusion through the oxide whether by lattice or other diffusion paths.

5. The authors observe that oxygen pressure has a major effect on oxidation rate and on whether "logarithmic," "parabolic," or "linear" kinetics are followed. Because of the structural irregularities in the scales the probability is that these changes are from the effect of pressure on the physical structure of the scale. With dense uniform adherent scale the effect of pressure would be minor.

6. The authors observe apparently cubic crystallites of oxide under the blistered scale and attribute them to CrO. Elsewhere they report cubic crystallites of Cr metal under the scale. Perhaps the "cubic" oxide crystals are Cr crystals (formed by evaporation and condensation in the gap between scale and metal), which oxidized to Cr_2O_3 while preserving their former topography.

To conclude, in our view specimen preparations such as the authors' thermal-etch and our electropolishing technique are unsatisfactory for studying the

¹⁹ E. J. Flynn and S. A. Solin, *Phys. Rev. B.*, 13, 1752 (1976).

²⁰ National Research Council of Canada, Division of Chemistry, Ottawa, Canada K1A 0R9.

²¹ D. Caplan and G. I. Sproule, *Oxid. Metal.*, 9, 459 (1975).

²² D. Caplan, *This Journal*, 107, 359 (1960).

²³ M. J. Graham, G. I. Sproule, D. Caplan, and M. Cohen, *ibid.*, 119, 883 (1972).

oxidation of Cr in that they produce fine-grained oxide and promote loss of adhesion and blistering. The major structural irregularities in the scale invalidate the oxidation constants deduced and the subsequent interpretation of oxidation mechanisms. We believe that the Caplan-Sproule parabolic rate constants, which the authors refer to as "extremely low," reliably describe the growth of monocrystalline Cr_2O_3 scales on Cr. Theoretical modeling, such as the mechanism of Cr transport through Cr_2O_3 , should be based on "ideal" scales of this type rather than on structurally irregular scales.

P. Kofstad and K. P. Lillerud:²³ We appreciate the interest by D. Caplan and G. I. Sproule on our paper.

Chromium exhibits a complex oxidation behavior. Large growth stresses develop in the scale and cause cracking, plastic deformation, and detachment of the scales. Depending upon the microstructures of the scales important transport processes comprise lattice, grain boundary, and "easy" diffusion and vapor transport in microcracks. Other aspects to be considered are CrO_3 evaporation (at high oxygen pressures and temperatures), vapor transport of chromium from the underlying metal to the detached scale, etc. In view of the complexity it is not surprising that the reaction kinetics and behavior may vary considerably with experimental conditions.

Previous work has demonstrated that the behavior of chromium is highly dependent on specimen, and particularly, surface preparation. In our opinion the reason for these large differences has not been adequately explained. In our work the chromium was thermally etched. This gives an oxide-free surface at the start of the reaction and a reproducible reaction behavior under the various conditions. It is not surprising that this surface preparation may, at least initially, exhibit different reaction behavior compared to surface preparations or experimental procedures whereby an oxide film is established on the metal surface at lower temperature prior to the recorded experiments. No method of surface preparation is more "correct" than other ones. The important point is to demonstrate what takes place under different conditions and to obtain an overall consistent interpretation. We believe that our work has provided additional information on the reaction behavior of chromium.

In our work we have found that specimens lose weight when oxidation runs at high temperatures are discontinued by pumping high vacuum on the system. This has been concluded to be due to loss of Cr metal through the scale. Caplan and Sproule claim that such loss can only take place by Cr vapor transport via microcracks and state that there can be no loss by solid-state chromium diffusion through Cr_2O_3 scales in high vacuum as there will be no concentration gradient as a driving force. Let us analyze their comments. The driving force for chromium transport can, for instance, be considered in terms of the chromium potential gradient through the scale. During oxidation or the high vacuum treatments of oxidized specimens there is a chromium potential gradient through the scale: At the inner scale surface the chromium vapor pressure can be considered equal to that of the vapor pressure of chromium metal; at the outer surface the chromium vapor pressure is smaller. This chromium potential gradient (which will depend upon the chromium potential at the inner and outer surface and the thickness of the scale) is the driving force for the chromium transport regardless of whether this takes place by vapor transport or solid-state diffusion processes. Caplan and Sproule apparently agree that

such a driving force is present when chromium is transported as vapor species through the scale, but claim that this driving force is no longer present if the transport takes place by solid-state diffusion. We fail to understand the consistency in their comment. The other important point to consider as regards chromium transport is the mobility (*i.e.*, the diffusion coefficients) involved in the different transport processes. The mobility of the chromium atoms is considerably higher for vapor transport, but chromium is also transported outward through solid-state diffusion processes. If there is no oxygen available at the outer surface to react with the outwardly moving chromium, chromium will evaporate.

Ideal, diffusion-controlled growth of Cr_2O_3 can be correlated with the proper self-diffusion coefficients of the reactants in Cr_2O_3 . For ideal parabolic oxidation of metals, it is always of interest to correlate the transport processes with other defect-dependent properties of Cr_2O_3 . One should be able to correlate these properties in an overall consistent model for the system. In our work we have attempted to do so by evaluating available data on Cr_2O_3 . In this respect there is, however, a very large inconsistency as regards the measured self-diffusion coefficients and the lowest reported values for the apparent parabolic rate constant for oxidation of chromium. These rate constants were estimated from the oxide thickness on some single grains in oxidized Cr specimens. Caplan and Sproule believe that the true self-diffusion coefficients are "orders of magnitude lower" than the measured values. Their reason is that the tracer diffusion studies were done on polycrystalline Cr_2O_3 (hot-pressed specimens, Hagel and Seybolt). However, they fail to quote that Hagel and Seybolt's results are in essential agreement with those of Walters and Grace on single crystal Cr_2O_3 at 1300°C (see our paper II). Furthermore, if grain boundary diffusion were the important process for the hot-pressed specimens, this would be expected to be noted in the tracer penetration profiles.

We believe there is need for further studies. But in general: Polycrystalline material should not necessarily be disqualified for studies of lattice diffusion; the relative importance of lattice and grain boundary diffusion will be a function of grain size, temperature, and ambient partial pressure of oxygen (*i.e.*, bulk defect concentration in the oxide samples).

In our publication we speculated if the large discrepancy between the diffusion data and oxide thicknesses measured in local areas on some oxidized Cr specimens could be due to CrO_3 evaporation or that diffusion in Cr_2O_3 is highly dependent on crystal orientation. We do not have an explanation for the discrepancy at this stage. But in an attempt to contribute to a clarification of the matter we are presently studying chromium transport through dense Cr_2O_3 scales with the aim of delineating the contribution due to lattice diffusion. This work will be submitted for publication in the near future.

We would like to emphasize that from our analysis of defect-dependent properties of Cr_2O_3 it seems most probable that the important defects in Cr_2O_3 at low partial pressures of oxygen are chromium interstitials. Correspondingly we do not believe that chromium diffuses by the vacancy mechanism and that there are vacancy fluxes as suggested by Caplan and Sproule. Also, if chromium interstitials are important, the ideal parabolic rate constant should be independent of the ambient partial pressure of oxygen. This is not the case if vacancy diffusion predominates (see paper II).

In our work we have demonstrated large differences in oxidation behavior when individual runs are made at different oxygen pressures. We conclude that this is related to the microstructures of the scale, and that

²³ Department of Chemistry, University of Oslo, Blindern, Oslo 3, Norway.

transport can take place both by solid-state diffusion and vapor transport through microcracks. As we point out in our publication (II) the larger activation energy of our work compared to several earlier studies is presumably "related to a higher amount of easy diffusion paths and microcracks in the Cr_2O_3 scales when specimens are pretreated through thermal etching."

Caplan and Sproule suggest that overtemperature effects may be important in our work. For the relatively slow rate of reaction, specimens with a thickness of 1 mm, and high temperatures employed in our work any such effects are of no or but minor significance as regards the overall oxidation behavior.

In conclusion we may mention that we are also currently studying other aspects of oxidation of chromium such as the effect of cold-work and oxidation of pre-oxidized Cr with dense Cr_2O_3 scales. These results will be published in due time.

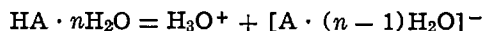
Electrochromism in Solid Phosphotungstic Acid

B. Tell (pp. 2451-2454, Vol. 127, No. 11)

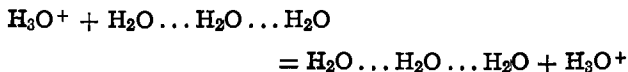
P. G. Dickens and R. H. Jarman:²⁴ In this discussion we propose a simple electrochemical explanation for the salient phenomena observed by Tell in his recent investigation of $\text{H}_3\text{PO}_4 \cdot \text{W}_{12}\text{O}_{36} \cdot 29\text{H}_2\text{O}$ (PWA) as a self-contained electrochromic cell. Schematically the cell consists of



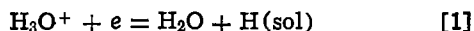
Both the SnO_2 coated glass and graphite electrodes are good electronic conductors. The PWA is a fast proton conductor in which acid dissociation occurs



and the presence of a connected pathway of H_2O molecules facilitates proton transfer through a Grotthus-type mechanism



(Here and subsequently the symbols H_3O^+ and H_2O imply hydronium and H_2O molecules in a mobile phase of the solid hydrate.) The cathodic reaction (coloration process) which occurs at the SnO_2/PWA interface is

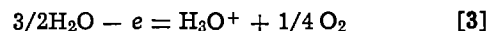
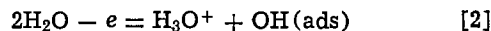


where H(sol) represents H chemically attached to a polytungstate anion (most probably as $-\text{OH}$). This chemical attachment is associated with the creation of a formal W(V) oxidation state and a blue coloration

²⁴ Inorganic Chemistry Laboratory, Oxford OX1 3QR, England.

(c.f., H_xWO_3 -hydrogen tungsten bronze²⁵). By analogy with the values measured for H_xWO_3 and heteropoly "blues,"^{26,27} we estimate a standard electrode potential for reaction [1] in the range 0.1-0.4V. This is effectively the same coloration process as described by Tell.

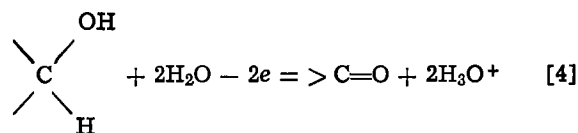
At the graphite/PWA interface, a balancing proton injection reaction is necessary. Possible candidates for this, which would occur at increasing anodic potentials, are



where OH(ads) represents hydroxyl groups attached to the carbon surface. Alternatively, oxidizable surface

groups such as $\begin{array}{c} \text{OH} \\ | \\ \text{C} \\ | \\ \text{H} \end{array}$ could be involved as suggested

by Tell²⁸

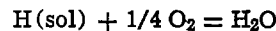


The overall cell reaction



will clearly be associated with a positive free energy change, since reactions [2]-[4] will, so far as can be reasonably estimated, have standard electrode potentials in excess of 0.8V.²⁹ The observed bleaching of the cells with graphite electrodes under short-circuit conditions confirms this (see paper under discussion).

Moreover, for each proposed anodic reaction there is a strong possibility that free oxygen will be evolved, either by direct reaction [3] or by subsequent chemical recombination of $-\text{OH}$ or $-\text{O}$ groups. This will certainly be so if high coloring voltages are employed. This in turn could lead to a slow bleaching effect on open circuit, even within a totally encapsulated cell, when oxygen evolved at the anode during coloration subsequently diffuses to and reacts with reduced PWA in the cathode region



²⁵ P. G. Dickens and R. J. Hurditch, *Nature*, 215, 1266 (1967).
²⁶ R. S. Crandall, P. J. Wojtowicz, and B. W. Faughnan, *Solid State Commun.*, 18, 1409 (1976).
²⁷ P. Stonehart, J. C. Koren, and J. S. Brinen, *Anal. Chim. Acta.*, 40, 65 (1968).
²⁸ B. Tell and F. Wudl, *J. Appl. Phys.*, 50, 5944 (1979).
²⁹ J. P. Hoare, "The Electrochemistry of Oxygen," New York (1968).



Passivation of Fe/Cr Alloys Prepared by Laser-Surface Alloying

P. G. Moore and E. McCafferty*

Naval Research Laboratory, Washington, D.C. 20375

Laser-surface alloying is a relatively new technique for modifying the chemical composition of metal surfaces (1-4). In this process, a metallic coating and the underlying metal substrate are rapidly melted using a high power, continuous wave CO₂ laser. This rapid melting and concomitant mixing followed by rapid resolidification serves to alloy the metals contained in the coating and the substrate. The depth of the laser-surface alloyed region is typically 10 to 100 μm .

The manufacture of chromium steel surface alloys has been previously reported (1-4). These surface alloys have been characterized by metallography, microprobe analysis and hardness tests, but to our knowledge, the electrochemical behavior of such alloys has not yet been published. The purpose of this communication is to describe briefly the preparation of iron/chromium surface alloys, and to report initial results regarding their electrochemical behavior.

PROGRESS

Specimens of AISI 1018 steel (0.18% C, 0.8% Mn) were coated with electroplated or sputter deposited chromium layers ranging in thickness from 10 to 20 μm . These specimens were irradiated with a CO₂ continuous laser ($\lambda = 10.6 \mu\text{m}$) at power outputs up to 7.5 kw. The laser was focused to a spot approximately 0.15 mm in diameter, so that power densities as high as 10^7 w/cm^2 were obtained. The specimens were mounted on a turntable and were swept into the laser beam at linear velocities of 10 to 375 cm/sec. The depth of melting, and hence the alloy composition, was controlled by varying the sweep velocity. Samples were laser-processed in a helium gas shield to minimize oxidation of the metal surface.

*Electrochemical Society Active Member
Key words: Lasers, surfaces, alloy, passivity

For a typical processing speed of 50 cm/sec, a point on the surface is illuminated by the laser for less than 0.5 msec. and the metal remains molten for less than about 1 msec. At the edge of the melt where only the fringe of the beam is seen, these times approach zero while near the center of the molten zone the times are longer. The molten metal is quenched by the cold substrate at cooling rates of 10^6 - 10^7 K/sec. This rapid resolidification is the central feature of laser processing.

Figure 1 shows a micrograph of a cross section through an Fe/Cr surface alloy produced by a single pass of the

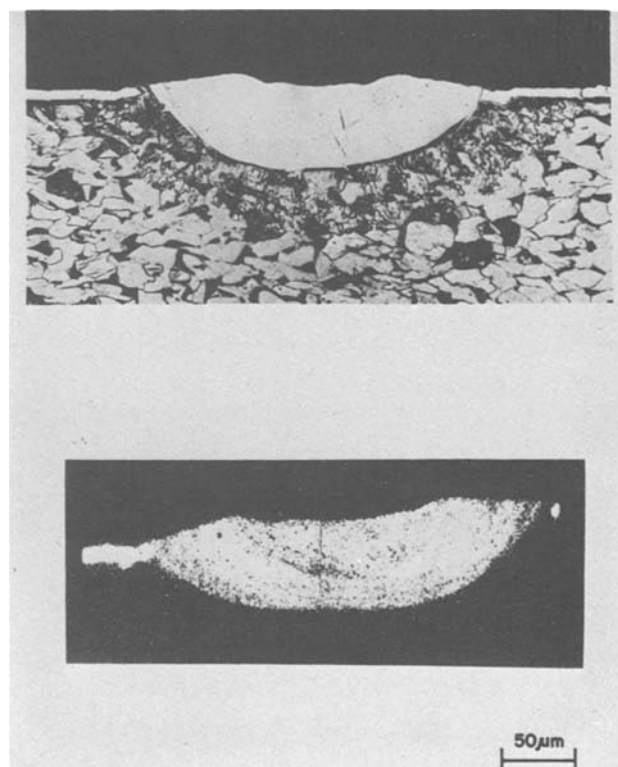


Fig. 1. A transverse cross section of an Fe/Cr laser-surface alloy with average Cr content of 20% shown at the top. Below is a chromium x-ray display of the same melt.

laser. The cross sectioned sample has been etched with Nital. This etchant attacks the steel substrate but does not bring out the metallurgical structure of the surface alloy. Figure 1 also shows a Cr x-ray display of the melt as determined with an electron microprobe. As is evident from the x-ray display, substantial mixing has taken place throughout the depth of the melt even though the laser interaction time was only 0.5 msec and the material was molten for less than 1 msec. The effects of surface tension gradients and fluid flow in the mixing process have been considered by various investigators (5,6). To produce a surface alloy over an extensive area, successive laser passes, spaced a fraction of a melt width apart, have been employed. A cross section of such a surface alloy is shown in Fig. 2. Electron microprobe analysis indicates that the distribution of components is similar to that observed for individual melts.

Figure 3 shows anodic polarization curves for 1018 steel and three different Fe/Cr laser-surface alloys in deaerated 0.1M Na_2SO_4 . Each sample was immersed for 30 minutes and then held cathodically at -1.0V vs. S.C.E. for 5 minutes. Following this cathodic treatment, steady state open circuit corrosion potentials were attained by each sample after an additional 30 minute

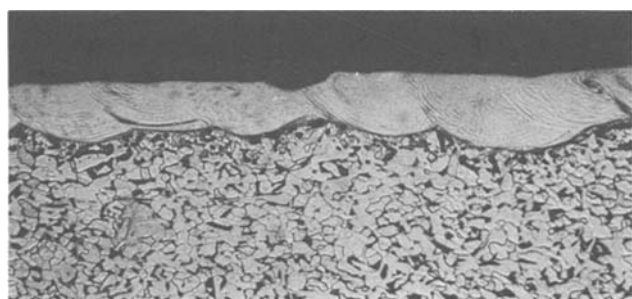


Fig. 2. Transverse cross section of a laser surface alloy, with average Cr content of 16%, produced by successive, overlapping laser passes.

immersion period. Anodic polarization curves were determined potentiodynamically at a scan rate of 10 mV/min.

As seen in Fig. 3, 1018 steel undergoes extensive dissolution at all anodic potentials, but the Fe/Cr surface alloys passivate. With increasing Cr content, there are decreases in both the critical current density for passivation and the current density in the passive region. The laser surface alloy with the highest Cr content passivates without undergoing an active-passive transition. However, it should be noted that the current densities in the passive region are higher than those usually observed for the corresponding Fe/Cr bulk alloys. For example, the passive current density for the 20% Cr surface alloy is about 5 times that observed by Lumsden (6) for bulk Fe-18 Cr and about 50 times the value observed by Lislovs and Bond (7) for bulk Fe-25 Cr in 1N sulfuric acid.

SUMMARY

Laser-surface alloys containing chromium passivate in 0.1M Na_2SO_4 , with the ease of passivation increasing with increasing Cr content. Optical microscopy and electron microprobe analysis show that chromium is dispersed uniformly through the melt region.

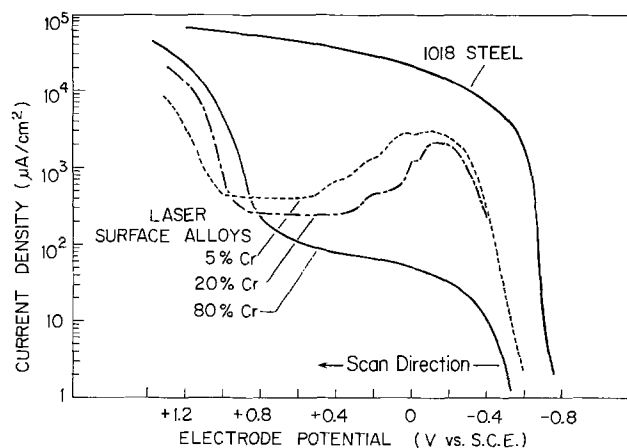


Fig. 3. Anodic polarization curves in de-aerated 0.1M Na_2SO_4 .

REFERENCES

1. L.S. Weinman, J.N. DeVault, and P. Moore in "Application of Lasers in Materials Processing", E.A. Metzbower ed., p.259. American Society for Metals, Metals Park, Ohio (1979)
2. L.S. Weinman and J.N. DeVault in "Laser-Solid Interactions and Laser Processing - 1978", S.D. Ferris, H.J. Leamy and J.M. Poate eds., p.239, American Institute of Physics, New York (1979)
3. P.G. Moore and L.S. Weinman in "Laser Applications in Materials Processing", J.F. Ready, ed., p.120, Society of Photo-Optical Engineers, Bellingham, Washington (1980)
4. D.S. Gnanamuthu, ref. 1, p. 177
5. T.R. Anthony and H.E. Cline, J. Appl. Phys., 48, 3888 (1977)
6. P. Moore, C. Kim, and L.S. Weinman, ref. 3, p.221
7. J.B. Lumsden in "Passivity of Metals," R.P. Frankenthal and J. Kruger, eds., p. 730, The Electrochemical Society, Princeton, N.J. (1978)
8. E.A. Lizlovs and A.P. Bond, J. Electrochem. Soc., 118, 22 (1971)

Manuscript submitted Jan. 23, 1981;
revised manuscript received March 31, 1981.

Publication costs of this article were
assisted by the Naval Research Laboratory.

Poly p-Substituted Phenyl Isopropenyl Ketones for Positive Photoresists

K. Nate and T. Kobayashi

Hitachi Limited, Production Engineering Research Laboratory, Yoshida-machi, Totsuka-ku, Yokohama-shi, Japan

Positive photoresists for photolithography divide roughly into, (I) an alkaline-soluble UV resist composed of phenolic novolac - quinonediazide type and, (II) ketone polymers such as poly methyl isopropenyl ketone (PMIPK) and poly methyl methacrylate (PMMA) for deep UV lithography. One problem with a positive alkaline-soluble UV resist is lack of resistance to chemical agents. On the other hand, positive deep UV resists are excellent in resistance to chemical agents, but are not sufficient in photosensitivity to achieve practical photolithography. In this paper, highly photosensitive positive resists consisting of poly p-substituted phenyl isopropenyl ketones, which are excellent in resistance to chemical agents, are reported.

Ketone polymers undergo severe degradation when exposed to ultraviolet light, and it is shown that the photolysis could be explained on the basis of the Norrish type I and type II reactions (1). PMIPK is a ketone polymer which is highly photosensitive to deep UV radiation, having a wavelength for maximum absorption of 285 nm (2). In this paper, the photolysis of the copolymers of p-substituted phenyl isopropenyl ketone (p-X-PhIPK, X=H, CH₃, and CH₃O), which has an aromatic ring conjugated to a carbonyl group in order to shift the absorption of copolymers to the longer wavelength region, and MMA, is discussed.

The monomers were synthesized by ordinary methods, and identified by nuclear magnetic resonance spectra. The copolymers were prepared by free-radical polymerization in sealed tubes under vacuum using azobisisobutyronitrile as an initiator. The purified copolymers were dissolved to 15 weight percent in methyl isobutyl ketone. The resist films were coated using a spinner on silicon

wafers with a thickness of about 1 μm , and prebaked at 150 °C for 30 minutes. All exposures were carried out with a Xe - Hg lamp. After exposure, the resist films were developed by dipping them in a mixture of methyl isobutyl ketone - xylene (70 : 30 by vol. %) for 2 minutes at 23 °C, and then rinsing them in xylene - isopropyl alcohol (50 : 50 by vol. %) for 1 minute.

The sensitivity and the spectral sensitivity of P(p-X-PhIPK - MMA) are shown in Table I and Figure 1, respectively, compared with PMIPK and PMMA. The spectral sensitivity was measured using Koana's apparatus, whose UV source consisted of a Xe lamp (3). As shown in Table, the resists consisting of P(p-X-PhIPK -MMA) have a higher sensitivity than those of PMIPK and PMMA, and the sensitivity of P(p-X-PhIPK - MMA) greatly depends on the molecular weight and the initial

Table I. Sensitivity of Positive Photoresists

| Polymer* | MW | t_0^{**} (μm) | Sensitivity*** |
|--------------------------|-------------------|------------------------------|----------------|
| A P(PhIPK(6.4)-MMA) | 7.6×10^4 | 0.6 | 600 |
| B P(PhIPK(16)-MMA) | 3.2 | 0.9 | 550 |
| C P(PhIPK(24)-MMA) | 2.0 | 0.9 | 250 |
| D P(PhIPK(28)-MMA) | 1.4 | 0.6 | 100 |
| E P(p-Me-PhIPK(34)-MMA) | 0.5 | 0.4 | 150 |
| F P(p-MeO-PhIPK(10)-MMA) | 4.6 | 1.4 | 330 |
| G P(p-MeO-PhIPK(15)-MMA) | 2.6 | 1.2 | 66 |
| H P(p-MeO-PhIPK(30)-MMA) | 1.1 | 1.1 | 80 |
| PMIPK | 9.3 | 1.2 | 1000 |
| PMMA | 9.4 | 0.6 | 11000 |

* () : Content of p-X-PhIPK in copolymer, mol %.

** t_0 : Initial thickness of resist.

*** Minimum irradiation dose (mJ/cm^2) required for no resist film to remain.

Key words: Positive photoresist, Ketone polymer, UV lithography

thickness of resist films. P(p-MeO-PhIPK - MMA) has a higher sensitivity than other polymers. As shown in Figure, it is obvious that P(p-X-PhIPK - MMA) undergoes photo-degradation in a longer wavelength region compared with deep UV resists, and the sensitivity at a longer wavelength increases with the content of p-X-PhIPK in copolymers.

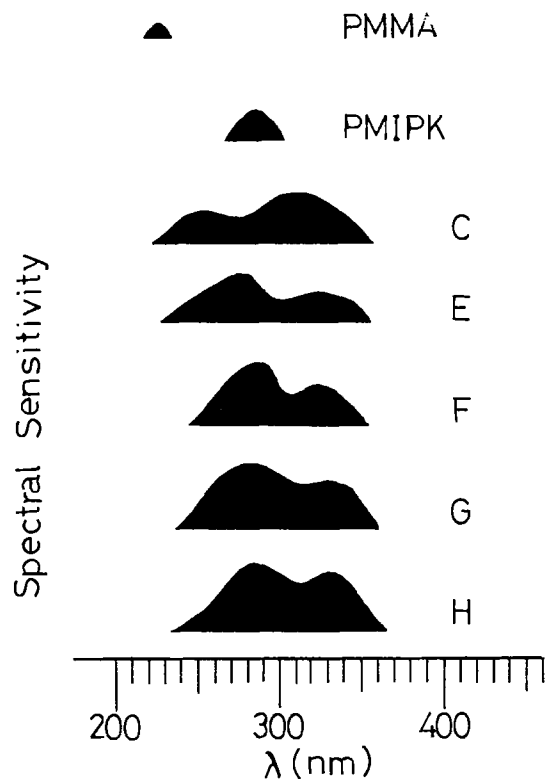


Fig. 1. Spectral sensitivity of positive photoresists.

It was ascertained by gel permeation chromatography that the molecular weight of these resists decreased with UV radiation, in analogy with PMIPK and PMMA. Infrared (IR) evidence showed that the peak of the carbonyl group at 1720 cm^{-1} decreased in the case of PMIPK with UV radiation. But a change in IR spectrum was hardly visible in the case of P(p-X-PhIPK - MMA). It was ascertained that the Norrish type I reaction occurred in the photolysis of PMIPK (4, 5), and that the polymer containing pendant chromophoric groups of $\text{C}_6\text{H}_5\text{C}(=\text{O})-$ behaved differently from

those containing aliphatic carbonyl groups in the polymer backbone.

The detailed photolithographic performance and the characteristics of electron beam exposure of poly p- substituted phenyl isopropenyl ketones will be described in a subsequent paper.

REFERENCES

1. J. E. Guillet and R. G. W. Norrish, Proc. Roy. Soc., Ser. A, 233, 153 (1955).
2. Y. Nakane, T. Tsumori, and T. Mifune, Semiconductor International, Jan.- Feb., 45 (1979).
3. Z. Koana, International Congress of Photographic Science in Tokyo, September (1967).
4. S. K. L. Li and J. E. Guillet, J. Polym. Sci., Part A-1, 18, 2221 (1980).
5. Y. Namariyama, H. Takao, T. Fujiki, and K. Nakamura, Kobunshi Ronbunshu, 37, 261 (1980).

Manuscript received March 11, 1981.

Publication costs of this article were assisted by Hitachi Limited.

Estimation of Series Resistance Losses and Ideal Fill Factors for Photoelectrochemical Cells

P. Singh,* K. Rajeshwar, R. Singh,**¹ and J. DuBow

Department of Electrical Engineering, Colorado State University, Fort Collins, Colorado 80523

ABSTRACT

A simple method is presented for estimating series resistance losses and ideal fill factors for a given photoelectrochemical device from current-voltage measurements at varying light intensity. This method is demonstrated on a model PEC device comprising the n-GaAs|AlCl₃-n-Butyl Pyridinium Chloride, Ferrocene/Ferricenium ion couple |C system. The extent to which the photovoltaic output is degraded by high series resistance losses can be directly estimated using the present approach.

INTRODUCTION

There has been much discussion in recent years on photoelectrochemical (PEC) methods of solar energy conversion (1,2). Two key factors which may dictate the feasibility of PEC devices for terrestrial applications are electrode stability and energy conversion efficiency. The problem with photoanodic dissolution of n-type small band-gap semiconductors in contact with aqueous electrolytes, has been effectively tackled by the use of aprotic, nonaqueous solvents (3-5). On the other hand, fabrication of efficient devices based on nonaqueous electrolytes, requires minimization of the series resistance losses in the system. The manner in which a high series resistance degrades PEC performance may be understood with reference to Fig. 1 which shows a simplified equivalent circuit for a PEC cell under operating conditions. The photocurrent, J_{ph} is represented by a constant current generator (6) opposite in direction to the dark current, J_{dark} of the device. The faradaic resistance, R_f denotes the resistance associated with leakage currents flowing across the semiconductor/electrolyte interface and in an ideal device should be infinitely large. R_L is the external load resistor and J_{out} and V_{out} represent the current and voltage output

generated by the device. The series resistance, R_s comprises the contributions from the back metal contact, semiconductor bulk and the interfacial and bulk resistances of the electrolyte. R_s should be minimized to obtain a high device efficiency.

In this paper, we present a simple method whereby the magnitude of R_s and the maximum fill factor may be estimated for a given PEC device from current-voltage measurements at varying light intensity. A model system comprising the n-GaAs/Aluminum Chloride-n Butyl Pyridinium Chloride (BPC) molten salt electrolyte interface, was chosen for the present analyses. The Ferrocene/Ferricenium ion couple was used as the redox system.

EXPERIMENTAL

Electrodes were fabricated from single-crystal n-GaAs ($\langle 111 \rangle$ orientation, donor density: $2.17 \times 10^{17}/\text{cm}^3$) obtained from commercial sources. Details on electrode preparation and electrolyte handling are given elsewhere (5,7). The electrolyte was adjusted to be slightly basic of the neutral 1:1 (relative molar ratio of AlCl₃ and BPC) composition for the present measurements. Nominal concentrations of ferrocene and ferricenium chloride were 200 mM and 20 mM respectively. Short-circuit currents (I_{sc}) and open-circuit voltages (V_{oc}) were measured under illumination with a tungsten-halogen lamp using instrumentation previously described (5,7).

RESULTS AND DISCUSSION

The equivalent circuit shown in Fig. 1 leads to the following relationship between the output current, J_{out} and voltage output, V_{out} (6):

Key words: equivalent circuits, open-circuit voltage, short-circuit current density.

* Electrochemical Society Student Member.

**Electrochemical Society Active Member.

¹Present address: Energy Conversion Devices, Troy, Michigan 48084

$$J_{\text{out}}(1+R_s/R_f) = J_{\text{ph}} - (V_{\text{out}}/R_f) - J_{\text{dark}} \quad [1]$$

The dark current is given by the equation:

$$J_{\text{dark}} = J_o [\exp (qV_j/nkT) - 1] \quad [2]$$

where J_o is the reverse saturation current density, V_j is the voltage appearing across the junction and n is the junction ideality factor. If we assume a device such that R_f is very large (i.e., $V_{\text{out}}/R_f \approx 0$ and $R_s/R_f \ll 1$), we get on substituting Eq. [2] in Eq. [1]:

$$J_{\text{out}} = J_{\text{ph}} - J_o [\exp (qV_j/nkT) - 1] \quad [3]$$

In the above expression, note that V_j is given by $(V_{\text{out}} + J_{\text{out}}R_s)$ (cf. Figure 1). For small R_s , however, $V_j \approx V_{\text{out}}$. The maximum power output, P_m ($P_m = J_m V_m = (J_{\text{out}} V_{\text{out}})_{\text{max}}$) may be found by differentiating the product $J_{\text{out}} \times V_{\text{out}}$ and setting it equal to zero. The fill-factor, FF which is equal to the ratio $J_m V_m / J_{\text{sc}} V_{\text{oc}}$ is given by the expression (8):

$$FF = \frac{V_m}{V_{\text{oc}}} \left\{ 1 - \frac{[\exp (q V_m / nkT) - 1]}{[\exp (q V_{\text{oc}} / nkT) - 1]} \right\} \quad [4]$$

According to Eq. [4], FF should improve with increasing values of V_{oc} and with decreasing values of n ($n = 1$ for an ideal device, Ref. 7).

In the presence of high R_s and low R_f , the approximations leading to Eq. [3] break down. The current-voltage relationship in the presence of a high R_s may be written as (9)

$$J_{\text{out}} = J_{\text{ph}} - J_o \left\{ \exp \left(\frac{q(V_{\text{out}} + J_{\text{out}}R_s)}{nkT} \right) - 1 \right\} \quad [5]$$

The fill-factor now is decreased below the value given by Eq. [4] and is equal to (9):

$$\begin{aligned} FF &= \frac{(V_{\text{out}} J_{\text{out}})_{\text{max}}}{V_{\text{oc}} J_{\text{sc}}} \\ &= \frac{J_{\text{out}}}{J_{\text{sc}}} \left\{ \left(1 - \frac{J_{\text{out}}}{J_{\text{sc}}} \frac{R_s}{V_{\text{oc}}} \right) + \frac{nkT}{q V_{\text{oc}}} \right. \\ &\times \ln \left[1 - \frac{J_{\text{out}}}{J_{\text{sc}}} \times \left(1 - \exp \left(-\frac{q V_{\text{oc}}}{nkT} \left(\frac{J_{\text{sc}} R_s}{V_{\text{oc}}} - 1 \right) \right) \right) \right] \left. \right\}_{\text{max}} \quad [6] \end{aligned}$$

The deleterious influence of high R_s on cell performance manifests in the effect on FF (Eq. [6]) and overrides the influence on J_{sc} as given by the expression:

$$J_{\text{sc}} = J_{\text{ph}} - J_o \left(\exp \left(\frac{q J_{\text{sc}} R_s}{nkT} \right) - 1 \right) \quad [7]$$

Equation [6] may be used to calculate the ideal FF for a particular device in the absence of any series resistances. $J_{\text{out}}/J_{\text{sc}}$ is varied to find the maximum value for the ratio $V_{\text{out}} J_{\text{out}} / V_{\text{oc}} J_{\text{sc}}$. The ideal FF thus determined should correspond to those estimated directly from J_{sc} versus V_{oc} plots for the particular device at varying light intensity. Figure 2 illustrates a typical plot for the n-GaAs|AlCl₃-BPC, Ferrocene/Ferricenium | C system. An ideal FF of 0.74 was calculated from the data in Fig. 2. This calculation follows the usual procedure of estimating FF from J-V plots (once the values on the current axis in Fig. 2 are transposed so that the maximum V_{oc} value corresponds to the "current zero") and is consistent with the value obtained by iterative procedures using Eq. 6.

To obtain R_s , the ratio $V_{\text{out}} J_{\text{out}} / V_{\text{oc}} J_{\text{sc}}$ is calculated for various values of $J_{\text{out}}/J_{\text{sc}}$ using R_s as a variable parameter in Eq. [6]. The maximum value of $V_{\text{out}} J_{\text{out}} / V_{\text{oc}} J_{\text{sc}}$ is then compared with the experimentally observed FF values. For the model PEC system in the present study, the ratio $V_{\text{out}} J_{\text{out}} / V_{\text{oc}} J_{\text{sc}}$ was found to peak at 0.43

for $J_{\text{out}}/J_{\text{sc}} = 0.75$ when a series resistance of 225Ω was assumed. The experimental FF values (0.44) and the current ratio $J_{\text{out}}/J_{\text{sc}}$ at an incident light intensity of 100 mW/cm^2 for the n-GaAs|AlCl₃-BPC, Ferrocene/Ferricenium ion | C (7) are in good agreement with the above values. The R_s value computed above may be compared with that reported for the resistivity of the AlCl₃-BPC electrolyte by previous authors ($125 \Omega\text{-cm}$, Ref. 10). For the electrode spacing employed in the present case ($\sim 0.5 \text{ cm}$) and within the limits of error introduced by neglecting the influence of redox species on electrolyte resistivity and the other contributions to the R_s term (e.g., Ohmic contact resistance, semiconductor bulk resistance, interfacial effects), agreement between the two values is considered satisfactory.

To summarize, the present method enables an estimation of series resistance losses and the maximum fill-factor for a given PEC device from measurement of J_{sc} and V_{oc} at varying light intensity.

ACKNOWLEDGMENT

The authors thank the Solar Energy Research Institute for financial support of this program under Grant XP-9-8002-9.

REFERENCES

- 1) K. Rajeshwar, P. Singh, and J. DuBow, *Electrochim. Acta* **23**, 1117 (1978).
- 2) S. Kar, K. Rajeshwar, P. Singh, and J. DuBow, *Solar Energy* **23**, 129 (1979).
- 3) S. N. Frank and A. J. Bard, *J. Am. Chem. Soc.* **97**, 7427 (1975).
- 4) K. D. Legg, A. B. Ellis, J. M. Bolts, and M. S. Wrighton, *Proc. Natl. Acad. Sci. USA* **74**, 4116 (1977).
- 5) P. Singh, K. Rajeshwar, J. DuBow, and R. Job, *J. Am. Chem. Soc.* **102**, 4676 (1980).
- 6) H. J. Hovel, "Semiconductors and Semimetals, Vol. 11: Solar Cells," p. 58, Academic Press, New York (1975).
- 7) P. Singh, R. Singh, K. Rajeshwar, and J. DuBow, *This Journal*, in press.
- 8) H. J. Hovel, "Semiconductors and Semimetals, Vol. 11: Solar Cells," p. 60, Academic Press, New York (1975).
- 9) M. Green, *Solid State Electron.* **20**, 266 (1977).
- 10) R. A. Carpio, L. A. King, R. E. Lindstrom, J. C. Nardi, and C. L. Hussey, *This Journal* **126**, 1644 (1979).

Manuscript submitted Nov. 3, 1980;
revised manuscript received Feb. 23, 1981.

Publication costs of this article were assisted by the Research Institute of Colorado.

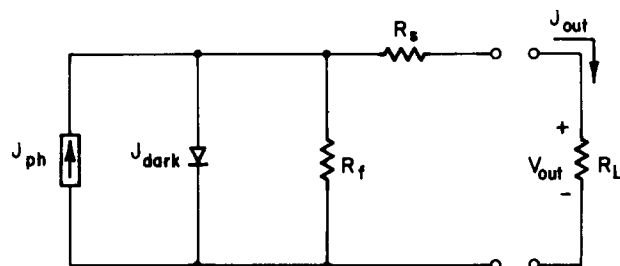


Fig. 1. Simplified equivalent circuit for a PEC cell for conversion of sunlight into electricity. See text for description of symbols.

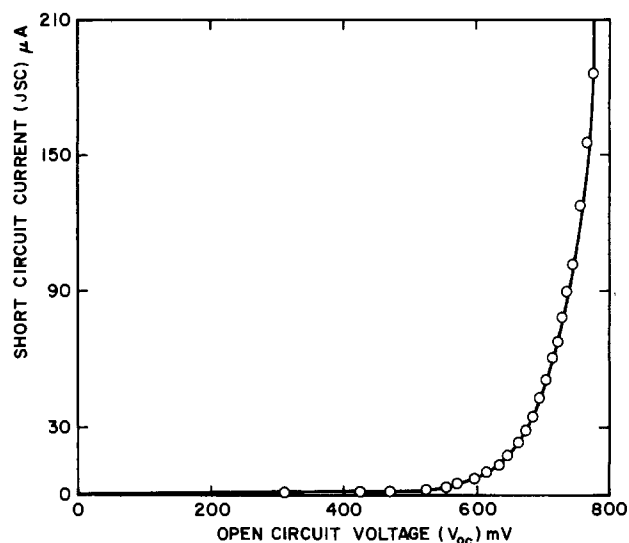


Fig. 2. Plots of short-circuit current vs. open-circuit voltage at various light intensities for the n-GaAs|AlCl₃-BPC, Ferrocene/Ferricenium ion | C system.



Sodium Thiochromite—A New Material for Cathodes in Secondary Li Batteries

R. V. Moshtev, V. Manev, and A. Nassalevska

Central Laboratory of Electrochemical Power Sources, Bulgarian Academy of Sciences, Sofia 1040, Bulgaria

G. Pistoia

*Centro di Studio per la Elettrochimica e la Chimica Fisica delle Interfasi, C.N.R.,
 Via del Castro Laurenziano 7, Rome, Italy*

and M. Icovi

Istituto di Chimica Fisica, Università di Roma, Rome, Italy

ABSTRACT

By electrochemical oxidation of NaCrS_2 in Li cells, phases of the type Na_xCrS_2 ($x \cong 0.1$) have been prepared, which provide host structures for Li^+ intercalation. More than 1 eq. Li^+ /mole NaCrS_2 may be reversibly intercalated at sufficiently high rates. The three-dimensional layered structure of these phases proves to be particularly rugged, thus allowing repeated cycling with minor performance losses. The high potentials of $\text{Li}/\text{Na}_x\text{CrS}_2$ couples allow high energy densities to be obtained. Starting from a theoretical value of 518 W-hr/kg, a calculation based on the performance at 1.0 mA/cm² and on the real battery weight still gives a value of 142 W-hr/kg for an 8 hr discharge rate. Values of the Li^+ chemical potential in Na_xCrS_2 and of the free energy of intercalation have large negative values typical of efficient chalcogenide cathodes. Nonlinearly and continuously decreasing E - x plots seem to indicate the formation of a single phase through Li^+ occupation of energetically different lattice sites.

Among the group IVb to VIb transition metals, Cr is the only one which cannot form the corresponding CrS_2 or CrSe_2 stable chalcogenides. Schöllhorn (1) has reported on the possibility of oxidizing ternary phases ACrX_2 ($A = \text{Li, Na, K; X} = \text{S, Se}$) in aqueous solutions, thus obtaining $\text{A}_x^+(\text{H}_2\text{O})_y(\text{CrX}_2)^{-x}$ phases which could be reversibly oxidized/reduced in the range $0.1 < x < 0.5$. For $x < 0.1$ the metastable CrX_2 could be formed.

The closest approach to CrS_2 was obtained by Murphy (2, 3) who was able to prepare $\text{Cr}_{0.75}\text{V}_{0.25}\text{S}_2$ by partial substitution of V by Cr in VS_2 . This mixed chalcogenide has fairly high voltages and improved capacity over VS_2 . However, as also pointed out by Whittingham (4), both its capacity and current capability are still unsatisfactory and undergo further decrease on cycling.

Attempts to prepare CrS_2 by oxidation of LiCrS_2 with I_2 in CH_3CN solutions only allowed the formation of $\text{Li}_{0.7}\text{CrS}_2$ (2). Indeed, I_2 allows one to obtain VS_2 from LiVS_2 but is not strong enough to oxidize LiCrS_2 to CrS_2 (3). Efforts to synthesize CrS_2 with the stronger oxidant Br_2 gave a substantial amount of chromium dissolution (3). The use of LiCrS_2 as a cathode in an Li cell assembled in the discharged state (4), only permitted 20-30% Li removal at C.D. $\cong 1$ mA/cm²,

this matching the result obtained by chemical oxidation.

LiCrS_2 is a hexagonal compound with Li^+ octahedrally coordinated by S atoms arranged in hexagonally close-packed layers (5). It is isostructural with LiTiS_2 but, unlike the latter, is characterized by high ionicity (4, 5). Indeed, its paramagnetic moment, 3.83 magnetons, corresponds to a number of unpaired electrons of 2.96, i.e., the degree of ionization of Cr^{+3} is 99%. The Li-S distance is 2.62Å (5).

NaCrS_2 has a rhombohedral structure formed by CrS_2^- layers with Na^+ layers intercalated in between (5, 6) (Fig. 1). The succession of layers is that of a cubic close-packing and leads to an octahedral coordination for both Cr and Na. This structure can be considered as a layered three-dimensional one (7). From Rüdorff's data (6) a value of 3.63 magnetons was calculated for the paramagnetic moment, thus giving 2.81 for the number of unpaired electrons. This means that NaCrS_2 is still characterized by high ionicity but shows, unlike LiCrS_2 , weak covalent bonds as also may be inferred by the Cr-Cr distance of 3.53Å (8) vs. 3.46Å in LiCrS_2 (5). The Na-S distance is 2.77Å (6).

As pointed out by Whittingham (4), a reduced ionicity of the lattice is beneficial for chemical ion diffusion due to charge shielding. The c/a ratio in NaCrS_2 is higher than in LiCrS_2 [1.84Å (6) vs. 1.74Å (5)]

Key words: NaCrS_2 , Li secondary batteries, Li^+ intercalation in host structures.

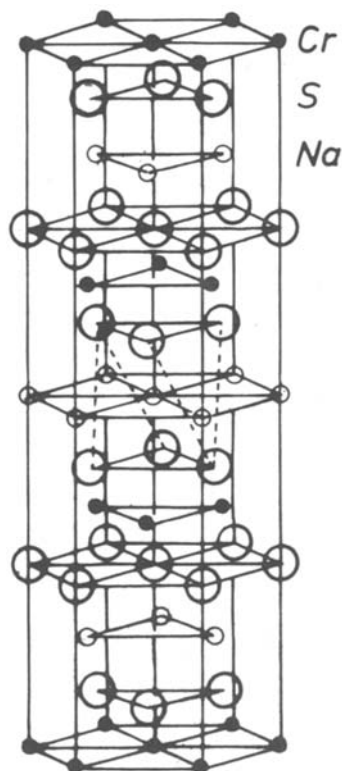


Fig. 1. Crystal structure of NaCrS_2 [Ref. (6)]

due to increased ionic distances along the *c*-axis. This allows one to foresee wider pathways through which alkali ions can move.

Further, as noted by Murphy *et al.* (3) the emf's of Li/MX_2 cells are expected to increase in the order $\text{Ti} < \text{V} < \text{Cr}$, based on the oxidation potentials of the respective $M_{\text{ox}}/M_{\text{red}}$ couples, leading to a corresponding increase of the theoretical energy density. This assumption was corroborated by the finding of the same authors (3) that the emf's at $x = 0.5$ eq. of Li are: 2.30V for $\text{Li}/\text{Li}_{0.5}\text{VS}_2$ and 2.65V for $\text{Li}/\text{Li}_{0.5}\text{Cr}_{0.75}\text{V}_{0.25}\text{S}_2$, while it is only 2.10V for $\text{Li}/\text{Li}_{0.5}\text{TiS}_2$.

Preliminary tests with $\text{Li}/\text{LiClO}_4\text{-PC}/\text{NaCrS}_2$ cells have indeed shown the possibility of removing consistent amounts of Na^+ ($\sim 70\%$ at 1 mA/cm^2). On the subsequent cycling, it was seen that alkali ions could enter/leave the CrS_2^- layers with high efficiency, thus encouraging a more extended investigation.

In the preliminary reports of Basu and Worrell (9) on $\text{Li}/\text{Na}_{0.18}\text{TS}_2$ cells ($\text{T} = \text{Ta}$ or Ti), it was shown that these cathodes could intercalate up to 3 eq. Li as a result of an increased *c* lattice parameter over that of TiS_2 or TaS_2 . This result supports our expectation of good performance by NaCrS_2 .

Experimental

NaCrS_2 was initially prepared according to a method described by Rüdorff (6). Basically, K_2CrO_4 was mixed with Na_2CO_3 and S in 1:30:30 weight ratio and heated in an alumina crucible at $650^\circ\text{-}700^\circ\text{C}$ for 30-60 min. The synthesized material was verified to be single phase by x-ray diffractometry. Chemical analyses showed compositions close to the stoichiometric, and emission spectral analysis revealed no appreciable amounts of potassium in the product. The brick-red crystal powder had 1.0-1.6 m^2/g specific surface area (BET) and the SEM pictures exhibited the typical hexagonal platelets (Fig. 2).

Initial electrochemical experiments showed, however, that cathodes prepared from this product have low coulombic efficiencies which were assigned to the low specific surface area. Indeed, a marked improve-

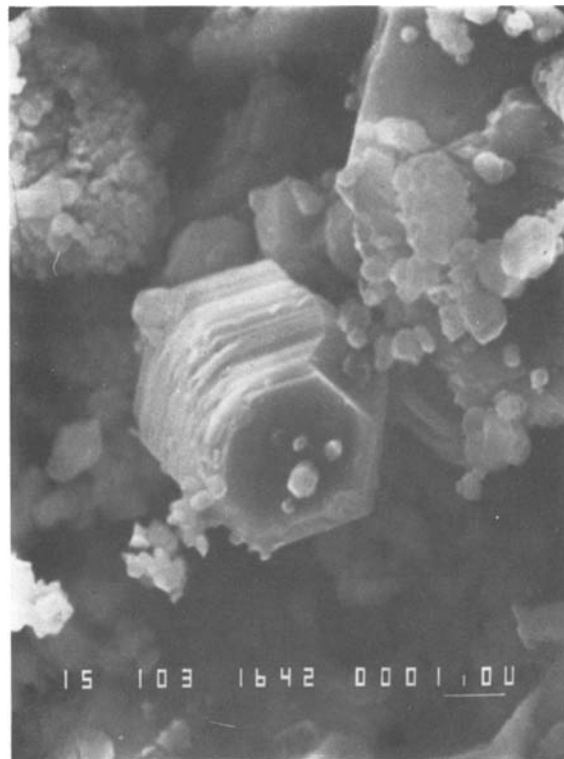


Fig. 2. SEM picture of NaCrS_2 crystals

ment was achieved with NaCrS_2 samples having higher specific surface area. The highly dispersed NaCrS_2 powder was synthesized by a modification of Rüdorff's method (to be disclosed in a subsequent paper), whereby NaCrS_2 powder with a specific surface area up to $20 \text{ m}^2/\text{g}$ could be obtained.

Since NaCrS_2 is not a good electronic conductor ($\rho \approx 10^5 \Omega\cdot\text{cm}$) it appeared necessary to use cathode formulations with conductive additives. Good results were obtained by adding to NaCrS_2 a 2:1 carbon black Teflon mixture (30%) and then intimately dry mixing these components. The cathodes (exposed geometric area 1-5 cm^2), prepared by pressing the mixture on an Ni exmet grid at $500 \text{ kg}/\text{cm}^2$, had a mean porosity of 30%.

The cathode thickness was varied from 0.3 to 2.5 mm corresponding to 50-400 mg/cm^2 of the cathode mixture.

In the experimental cells the Li anode, wrapped in a polypropylene nonwoven separator, had a surface area exceeding that of the cathode by a factor of 5-8. The electrolyte solution, 1M LiClO_4 in PC with a water content less than 60 ppm (as determined with the Fischer method), was also in a great excess. All operations for the cell assembly were performed in a dry box ($\text{H}_2\text{O} < 50 \text{ ppm}$, monitored by an electrochemical sensor based on phosphoric acid as a hygroscopic substance).

In the cyclic voltammetry experiments and the preliminary diffusion coefficient experiments, NaCrS_2 without additives was used. In the first case this was justified by the observation that better shaped curves with very limited background currents were obtained. In the second case, this allowed us to obtain cathodes which, by virtue of the high compacting pressure ($8500 \text{ kg}/\text{cm}^2$), had a real surface area close to the geometric one. *D* values are currently being investigated as a function of cathode composition using the current pulse technique described by Worrell (10, 11).

The *E*-*x* plot was obtained with a galvanostatic technique which allowed the determination of quasi-thermodynamic *E* values. A thin NaCrS_2 cathode (50

mg/cm²) was charged at low rate (0.1 mA/cm²) until the Na_{0.1}CrS₂ composition was reached. After OCV stabilization, the cathode was discharged at 0.1 mA/cm² down to 1V and then recharged at the same C.D. The average of the *E* values during second charge and discharge for a given composition was taken. This technique, which allows a faster determination of the *E*-*x* characteristics in comparison with real OCV determination, is in a way similar to the potentiostatic technique described by Thompson (12).

After assembling, the Li/NaCrS₂ cells (initial OCV, 2.8-2.9V) were charged to 3.5V, at 0.5 mA/cm², whereby oxidation degrees corresponding to formulas in the range Na_{0.2}CrS₂-Na_{0.3}CrS₂ were attained.

Results of Discussion

Quasi-thermodynamic studies.—By oxidizing a thin cathode (50 mg/cm²) up to 3.5V at a low rate (0.1 mA/cm²) we were able to reach Na_{0.1}CrS₂. This material, representing so far the closest approach to CrS₂, was used to obtain the quasi-thermodynamic *E*-*x* plot in Fig. 3. In spite of the low voltage at the end of discharge (1.15V at *x* = 1.1) the hysteresis during the subsequent charge was limited and allowed us to put some confidence on the *E*-*x* curve thus plotted. Preliminary OCV-*x* measurements with NaCrS₂ charged up to Na_{0.3}CrS₂ have allowed us to ascertain that the quasi-thermodynamic plot coincides well with the OCV-*x* plot.

It is seen in Fig. 3 that the emf of Li/Li_{*x*}Na_{0.1}CrS₂ with *x* up to 0.75 is higher than that of TiS₂. It exceeds also that of VS₂ as anticipated in the introduction.

The right-hand ordinate in Fig. 3 presents the values of μ_{Li^+} , i.e., the chemical potential of the intercalated cation in kJ/mole.

The data in Fig. 3 can also be used to estimate the free energy of intercalation ΔG by the expression

$$\Delta G = -F \int_0^x E dx$$

as recently proposed by Nagelberg and Worrell (13). The value of ΔG for Li_{1.0}Na_{0.1}CrS₂ is -56.0 kcal/mole which compares well with those of other Li dichalcogenides: -57.4 for Li_{1.0}TiS₂, -53.1 for Li_{1.0}VS₂, and -50.5 for Li_{1.0}TaS₂ (13).¹

As found for TiS₂ (see Fig. 3) and other layered dichalcogenides (4) the *E*-*x* plot of Li_{*x*}Na_{0.1}CrS₂ falls nonlinearly with the increase of *x*. The absence of true voltage plateaus is indicative of the formation of

¹ Whittingham (4) reports -49.3 kcal/mole for TiS₂.

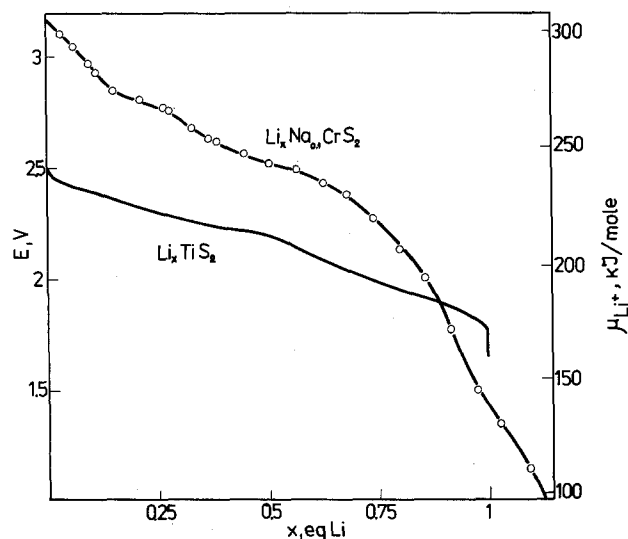


Fig. 3. *E*-*x* plot of an Li/Li_{*x*}Na_{0.1}CrS₂ cell [curve for TiS₂ from (Ref. 12)].

a single phase all over the intercalation range. Preliminary x-ray data substantiate this assumption. Both upon charge (Na⁺ removal) and upon discharge (Li⁺ intercalation) no new peaks appear, thus excluding the nucleation of new phases. Instead, NaCrS₂ peaks are slightly shifted, so indicating minor lattice parameters variations.

In the crystal lattice of NaCrS₂ (Fig. 1) (6) the octahedral positions of the alkali metal atoms are not equivalent. The top and bottom Na layers are made each of 3 Na atoms which are below 3 and above 6 S atoms. The middle Na layer is made of 6 Na atoms placed between two layers of S atoms each comprising 3 atoms. It might be supposed that the occupancy of the middle Na layer would require different energy than the 2 remaining Na layers. This could be the reason for the changes in the slope of the *E*-*x* curve. Rouxel (14) had explained similarly a knee found in the *E*-*x* curve of NiPS₃.

There is little doubt that Li⁺ ions occupy the vacant octahedral sites in Na_{*x*}CrS₂. However, tetrahedral sites are also available. It is known that in TiS₂ Li⁺ is inserted in octahedral positions which are energetically more favorable than the tetrahedral ones (4). Indeed, the radii of the two sites are 0.89Å and 0.64Å, respectively (radius of Li⁺, 0.7Å). However, as Li⁺ diffuses in TiS₂ on its way between two octahedral sites, it has to pass through a tetrahedral one (4, 14). NaS₆ octahedra are larger than LiS₆ octahedra (Li-S distance, 2.57Å; Na-S distance, 2.77Å) so that the corresponding tetrahedra are also larger. This is to say that temporary occupation of tetrahedral sites by Li⁺ in Na_{*x*}CrS₂ is even more probable than in Li_{*x*}TiS₂.

Furthermore, as the ratio between intercalated Li⁺ and deintercalated Na⁺ may well exceed one, it is highly probable that, at high *x*, some reorganization of Li⁺ coordination might take place, i.e., tetrahedral sites could also be permanently occupied. The sum of ionic radii of Li and S (2.49Å)² does not exclude the existence of Li⁺ in tetrahedral sites. The Li-S distance is shortened by about 0.3Å when passing from octahedral to tetrahedral coordination (4, 15). If we suppose that a similar decrease occurs for Na_{*x*}CrS₂, the tetrahedral Li-S distance should be near to 2.45Å, which is not too far from 2.49Å. Tetrahedral coordination has already been found for Cu⁺ and Ag⁺ in CuCrS₂ and AgCrS₂ (5).

Li⁺ may occupy the empty positions in the lattice of NaCrS₂ in an ordered way. The formation of an ordered Li⁺ superlattice in transition metal dichalcogenides has been already observed (12-14). Thompson (12) has investigated this phenomenon in TiS₂ in depth, reaching the conclusion that Li⁺ occupies preferential positions in the layers as a function of *x* in Li_{*x*}TiS₂. According to this author, the *E*-*x* plot and the related (- $\Delta x/\Delta V$) vs. *x* plot are indicative of such ordering. In particular, the "incremental capacity" (- $\Delta x/\Delta V$) would show maxima at compositions corresponding to ordered structures. This view was strongly criticized by Berlinsky (15) who, on the basis of statistical mechanics considerations, has concluded that minima, rather than maxima, should be found at the composition, corresponding to ordering.

The "incremental capacity" vs. *x* plot (Fig. 4) of Li_{*x*}Na_{1-*x*}CrS₂ reveals two maxima at *x* ~ 0.25 and *x* ~ 0.5 and two minima at *x* ~ 0.3 and *x* ~ 0.9. Presently, we are not in a position to interpret more closely the significance of the maxima and minima. We can only observe that, since the structure of NaCrS₂ is an ordered one, Li_{0.9}Na_{0.1}CrS₂ is expected also to be ordered. The minimum at *x* ~ 0.9, although rather flat, could be related to this situation.

² Average of best literature values.

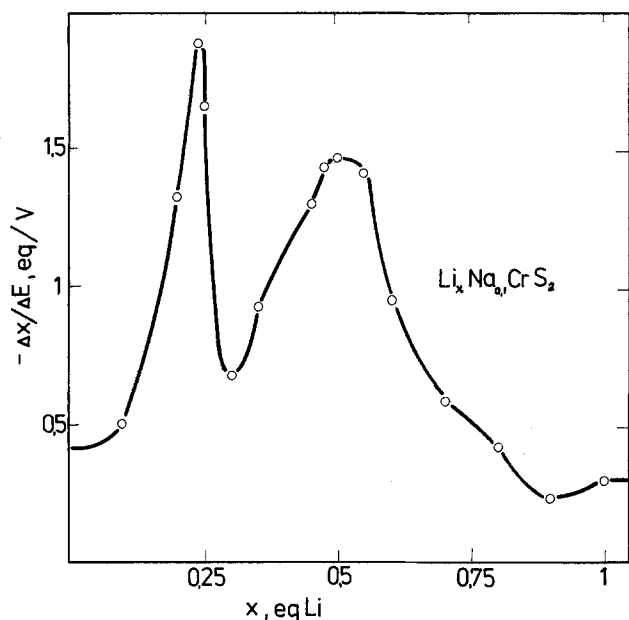


Fig. 4. The incremental capacity vs. composition plot obtained from data in Fig. 3.

We have been supposing throughout this discussion on Li^+ intercalation that the structure and lattice parameters of Na_xCrS_2 do not differ significantly from those of NaCrS_2 . Our first results from x-ray analysis confirm that the NaCrS_2 structure is maintained and limited variations (few unit percent) of the a and c parameters occur during both charge and discharge. This was in a way expected on the basis of the rigid crystal structure of NaCrS_2 brought about by its high ionicity.

Initial performance of Na_xCrS_2 cathodes.—Preliminary experiments proved that performance of Na_xCrS_2 cathodes can be significantly improved by increasing the specific surface area of the initial NaCrS_2 material. The results of a more systematic study in this respect is shown in Fig. 5, where the specific capacity of comparatively thick electrodes (2.5 mm, 400 mg/cm²) obtained at three C.D.'s and 1.5V cutoff is plotted vs. the surface area (BET) of NaCrS_2 . At the lower and medium C.D. there is an initial steep rise of the specific capacity, whereafter a saturation is attained. The almost linear plot at the higher C.D. (2.0 mA/cm²) suggests that a further improvement could be expected

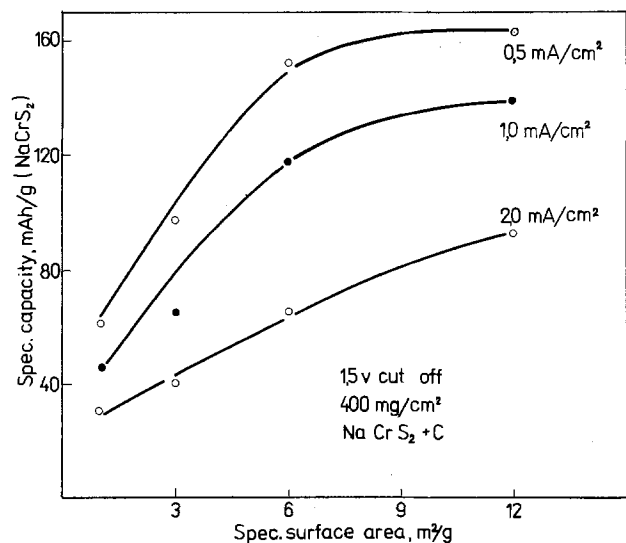


Fig. 5. Effect of specific surface area (BET) on the specific capacity of $\text{Li}/\text{Li}_x\text{Na}_{0.2}\text{CrS}_2$ cells at various C.D.

in cathodes prepared with a higher dispersity ($> 12 \text{ m}^2/\text{g}$) NaCrS_2 . Samples with BET area higher than $20 \text{ m}^2/\text{g}$ are now available and will be shortly investigated.

The effect of particle size on performance of chalcogenide cathodes has been pointed out by various authors. Chianelli (16) has shown that in a small TiS_2 crystal ($5.6 \mu\text{m}$ between opposite edges in the hexagonal layers) the intercalation flux of Li^+ is $18 \times 10^{-8} \text{ g}/\text{cm}^2 \text{ sec}$, whereas in a larger crystal ($40 \mu\text{m}$) it is only $1.3 \times 10^{-8} \text{ g}/\text{cm}^2 \text{ sec}$. This behavior was related to the higher strain induced by intercalation of Li^+ in the larger crystal due to the reduced layer flexibility. Whittingham (17) has shown that $2.7 \text{ m}^2/\text{g}$ TiS_2 has a higher capacity and discharge voltage in comparison with $0.3 \text{ m}^2/\text{g}$ TiS_2 . Atlung (18) has related the cathode efficiency of porous cathodes to the radius r of the particles through the characteristic ratio $Q = TD/r^2$, where T is the stoichiometric discharge time and D the chemical diffusion coefficient. It is obvious from the above ratio that a low r can offset low diffusion coefficients.

We have ascertained the relation between cathode performance and thickness at various C.D.'s. Figure 6 shows that with $12 \text{ m}^2/\text{g}$ NaCrS_2 , good specific capacities are obtained also with thick cathodes. We are inclined to relate the flat maxima observed around 1.8 mm (more evident at higher C.D.) to the competition between two opposite effects. By increasing the thickness of the porous electrode the true volumetric C.D. decreases. On the other hand, the electrolyte diffusion resistance grows, due to the increased length of the pores in the thicker cathode and the cutoff voltage is attained earlier.

The cell discharge voltage is plotted in Fig. 7 as a function of composition at various current drains. The pattern observed at the lower load ($0.5 \text{ mA}/\text{cm}^2$) allows some considerations. First, the potential decreases below the value one would expect if NaCrS_2 were formed again upon discharge. Secondly, 1 eq. Li^+ may be intercalated, although the cathode composition at the beginning of discharge, i.e., $\text{Na}_{0.2}\text{CrS}_2\text{-Na}_{0.3}\text{CrS}_2$, would lead one to expect no more than 0.7-0.8 eq. Li^+ intercalated. The first result indicates that the alkali ion entering the empty positions created in the NaCrS_2 lattice by Na^+ removal is essentially Li^+ . In view of the considerable electrolyte excess in the experimental cells, the probability of Na^+ reentering the Na_xCrS_2 lattice is very small.

From the second result it is evident that the compound $\text{Li}_{1-x}\text{Na}_x\text{CrS}_2$ may be further reduced. Whittingham (4) has observed the same behavior with an LiCrS_2 cathode. As $\text{Li}_{1-x}\text{Na}_x\text{CrS}_2$ can be reoxidized

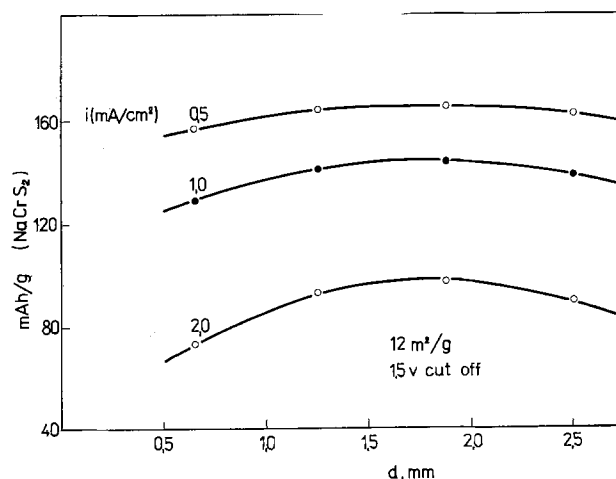


Fig. 6. Effect of cathode thickness on the capacity of $\text{Li}/\text{Li}_x\text{Na}_{0.2}\text{CrS}_2$ cells.

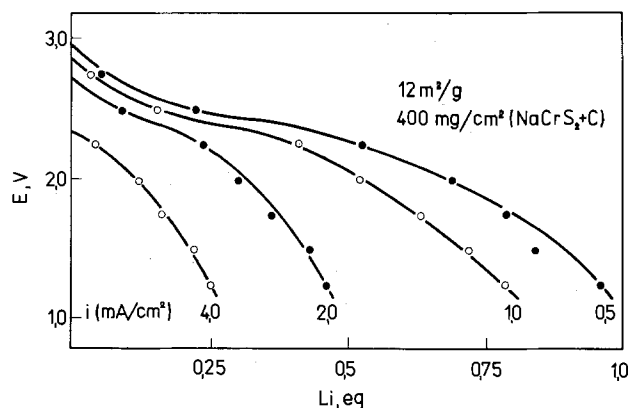


Fig. 7. Discharge voltage of $\text{Li}/\text{Li}_x\text{Na}_{0.2}\text{CrS}_2$ cells as a function of composition (x) at various C.D.

after accepting more than 1 eq. Li^+ , we suppose that even excess Li^+ could enter lattice positions without causing structural degradation.

Figure 7 shows the moderate ability of Li/NaCrS_2 cells to sustain high current drains. Power density in chalcogenide cathodes primarily depends on the diffusion coefficient of the alkali ion in the host lattice and on the possibility of accommodating an electron in the conduction band. As is well known, TiS_2 fulfills both these requirements, thus explaining its very high rate capability (4). Our preliminary measurements of Li^+ diffusion in Na_xCrS_2 gave D values in the range 10^{-10} – 10^{-11} cm^2/sec [for TiS_2 $D = 1.2 \cdot 10^{-8}$ (19, 20) – $5.6 \cdot 10^{-9}$ (11)]. This is sufficient to explain the modest performance of Na_xCrS_2 at high C.D.

This is also evident from the curves of Fig. 8, where the cathodic volumetric energy density is seen to decay with volumetric C.D. This decay, more pronounced for thick cathodes, does not hinder achieving comparatively good energy values, as will be later confirmed.

The high temperature performance of NaCrS_2 as a cathode material was exhibited in a preliminary experiment in an $\text{Li, Al}/\text{LiCl, KCl}/\text{Na}_x\text{CrS}_2$ cell at 430°C . A coulombic efficiency of ca. 20% was achieved at a high C.D., 0.2 A/cm^2 .

Cycling performance.—The intrinsic reversibility of the phases Na_xCrS_2 obtained by electrochemical oxi-

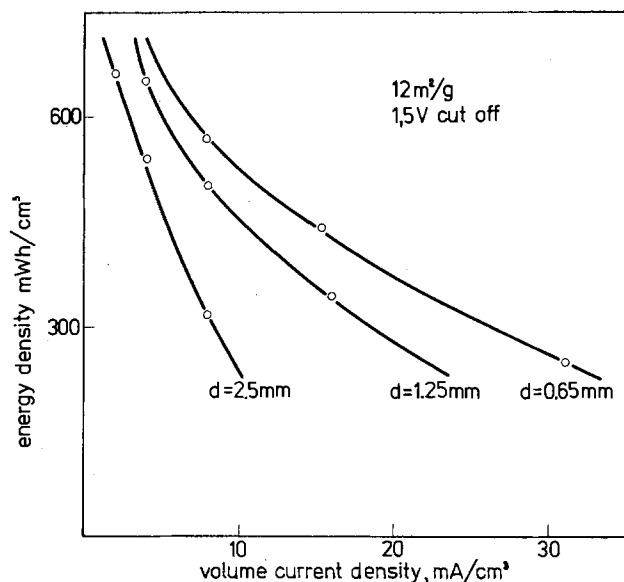


Fig. 8. Volumetric specific energy of $\text{Li}/\text{Li}_x\text{Na}_{0.2}\text{CrS}_2$ cells as a function of volumetric current density.

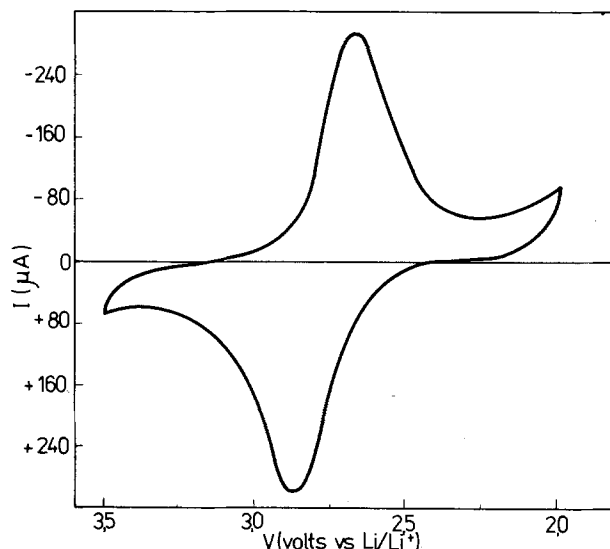


Fig. 9. Cyclic voltammetry of a thin film NaCrS_2 cathode. Scan rate 25 mV/min .

ductive deintercalation of NaCrS_2 is demonstrated by the typical voltammetric curve in Fig. 9. A thin film cathode prepared by pressing NaCrS_2 powder without carbon black on an Ni grid was used for this measurement. Both the small peak-voltage separation and the equality of the cathodic and anodic area are characteristic of a reversible cathode material. Repeated cycling did not exhibit any appreciable alterations in the curves.

The cycling capability of NaCrS_2 was explored also in experimental cells with porous cathodes. The first experiment was carried out with cathodes (1.5 mm) prepared with the low dispersity NaCrS_2 ($1.5 \text{ m}^2/\text{g}$). The charge and discharge C.D. was $0.5 \text{ mA}/\text{cm}^2$ provided by a galvanostat. The cycles were time limited (3 hr for each half-cycle) so that the d.o.d. was 22% in all cycles (Fig. 10). The initial decay of the average discharge voltage up to 200 cycles was stronger, whereafter it diminished at a lower rate. The overall decrease in the discharge voltage during the 500 cycles in over 4 months was 0.22V. This result provided the first evidence for the good cycling capability of $\text{Li}/\text{Na}_x\text{CrS}_2$ cell.

The next experiments were carried out with cathodes prepared with a more dispersed NaCrS_2 (12

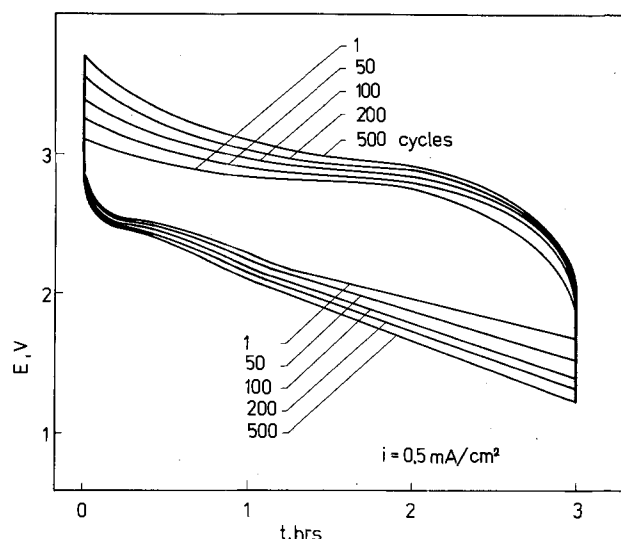


Fig. 10. Charge-discharge curves obtained on cycling of an $\text{Li}/\text{Li}_x\text{Na}_{0.2}\text{CrS}_2$ cell at $0.5 \text{ mA}/\text{cm}^2$. D.o.d. = 22%.

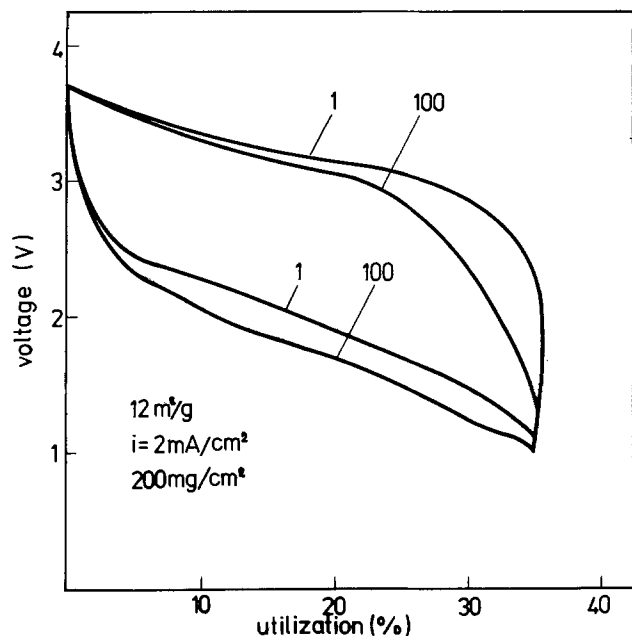


Fig. 11. Charge-discharge curves obtained on cycling of an Li/ $\text{Li}_x\text{Na}_{0.2}\text{CrS}_2$ cell at 2 mA/cm^2 cathode prepared with dispersed NaCrS_2 ($12 \text{ m}^2/\text{g}$).

m^2/g) synthesized by the improved technique. Figure 11 presents the 1st and 100th cycle of a cell with a cathode 1.25 mm thick cycled at 2 mA/cm^2 between 1.1 and 3.5 V with the aid of automatic equipment with voltage control. The initial practical energy density (referred to the weight of anode and cathode only) of 134 W-hr/kg decreased to 120 W-hr/kg after 100 cycles, i.e., by only 10%. The cycling was terminated due to failure in the equipment.

The comparison between the discharge curves in Fig. 10 and 11 reveals the beneficial effect of the increased surface area of the NaCrS_2 cathodes on the energy and power capabilities under cycling conditions as well. Indeed, the discharge curves of the 1st and the 100th cycles in Fig. 11 are only slightly lower than the respective curves in Fig. 10 in spite of the fact that they are obtained at a C.D. 4 times higher and at a d.o.d. 13% larger than those in Fig. 10.

The energy storage capabilities of the $\text{Li}/\text{Na}_x\text{CrS}_2$ cell are reviewed in Table I in comparison with those of well-known ambient temperature Li secondary cells with dichalcogenide cathodes: TiS_2 and $\text{V}_{0.25}\text{Cr}_{0.75}\text{S}_2$. The semi-theoretical energy densities for the $\text{Li}/\text{Na}_x\text{CrS}_2$ cell, estimated from the data in Fig. 7, are referred to weights of the active materials only. The energy densities of real cells can be acquired by multiplying this figure by the packaging coefficient (18), which represents the ratio of the weight of the

Table I.

| | TiS_2 | $\text{V}_{0.25}\text{Cr}_{0.75}\text{S}_2$ | $\text{Na}_{0.1}\text{CrS}_2$ |
|---|------------------------------------|---|-------------------------------|
| ΔG intercalation (kcal/mole) | -49.3 | — | -56.0 |
| Initial emf (V) | 2.47 | 2.8 | 3.15 |
| emf at $x = 1$ (V) | 1.87 | 2.4 | 1.35 |
| Theoretical energy density (W-hr/kg) | 481 | 550 | 518 |
| Semi-theoretical energy density (W-hr/kg) (1st cycle) | 420 ^a /350 ^b | 360 ^c | 410/315/190 ^d |

^a 1.0 mA/cm^2 , 1.5 V cutoff [Ref. (17)].

^b 2.5 mA/cm^2 , 1.5 V cutoff [Ref. (21)].

^c 0.4 mA/cm^2 , 2.0 V cutoff [Ref. (2)].

^d $0.5, 1.0,$ and 2.0 mA/cm^2 , 1.5 V cutoff (This paper).

active materials to the weight of all materials in the cell. A realistic evaluation for the packaging coefficient yields 0.50, from which a 10% reduction is made for the container and terminals. The expected energy density of a real Li cell with an Na_xCrS_2 cathode 0.7 mm thick at a C.D. of 1 mA/cm^2 (8 hr discharge rate) will be 142 W-hr/kg . This compares well with the evaluation of Gaines (22) for an Li/ TiS_2 cell at the 1-6 discharge rate, 1.34 W-hr/kg .

In view of the promising energy storage characteristics of the Na_xCrS_2 cathode in Li secondary cells, further work is in progress aimed to improving its energy and power density mainly by using high dispersity NaCrS_2 material.

Other areas of research include: compositional variation of the diffusion coefficient, structural investigation of $\text{Li}_{1-x}\text{Na}_x\text{CrS}_2$ phases by SEM and x-ray analysis, cycling at high rates, and temperature dependence of cell performance.

Further investigation on NaCrS_2 is justified not only by the reported performance of $\text{Li}/\text{Na}_x\text{CrS}_2$ cells³ but also by economic considerations. Indeed, NaCrS_2 is prepared in the air from very cheap chemicals unlike other transition metal dichalcogenides which have to be prepared in evacuated quartz ampuls from very pure elements.

Acknowledgment

This work was carried out within the framework of the agreement between Consiglio Nazionale delle Ricerche of Italy (C.N.R.) and Bulgarian Academy of Sciences (B.A.S.).

Manuscript submitted Oct. 15, 1980; revised manuscript received Feb. 12, 1981.

Any discussion of this paper will appear in a Discussion Section to be published in the June 1982 JOURNAL. All discussions for the June 1982 Discussion Section should be submitted by Feb. 1, 1982.

Publication costs of this article were assisted by the Consiglio Nazionale delle Ricerche.

³ Patents pending in Italy and Bulgaria.

REFERENCES

1. R. Schöllhorn, *React. Solids*, **8**, 719 (1976).
2. D. W. Murphy, J. N. Carides, F. J. Di Salvo, C. Cros, and J. V. Waszczak, *Mater. Res. Bull.*, **12**, 825 (1977).
3. D. W. Murphy, F. J. Di Salvo, and J. N. Carides, *J. Solid State Chem.*, **29**, 339 (1979).
4. M. S. Whittingham, *Prog. Solid State Chem.*, **12**, 41 (1978).
5. B. Van Laar and D. J. W. Ijdo, *J. Solid State Chem.*, **3**, 590 (1971).
6. W. Rüdorff and K. Stegemann, *Z. Anorg. Allgem. Chem.*, **251**, 376 (1943).
7. F. Hulliger, in "Structural Chemistry of Layer-Type Phases," Vol. V, F. Levy, Editor, p. 86, Reidel Dordrecht (1976).
8. W. Rüdorff, W. R. Ruston, and A. Scherhafer, *Acta Crystallogr.*, **1**, 196 (1948).
9. S. Basu and W. L. Worrell, Papers 24 and 25 presented at The Electrochemical Society Meeting, Los Angeles, California, Oct. 14-19, 1979.
10. A. S. Nagelberg and W. L. Worrell, in "Electrode Materials and Processes for Energy Conversion and Storage," J. D. E. McIntyre, S. Srinivasan, and F. G. Will, Editors, p. 847, The Electrochemical Society Softbound Proceedings Series, Princeton, N.J. (1977).
11. S. Basu and W. L. Worrell, in "Fast Ion Transport in Solids," P. O. Vashista, J. N. Mundy, and G. K. Shenoy, Editors, p. 149, Elsevier, New York (1979).
12. A. H. Thompson, *This Journal*, **126**, 608 (1979).
13. A. S. Nagelberg and W. L. Worrell, *J. Solid State Chem.*, **29**, 345 (1979).
14. J. Rouxel, *Rev. Inorg. Chem.*, **1**, 245 (1979).

15. A. J. Berlinsky, W. G. Unruh, W. R. McKinnon, and R. R. Haering, *Solid State Commun.*, **31**, 135 (1979).
16. R. R. Chianelli, J. C. Scanlon, and B. M. L. Rao, *J. Solid State Chem.*, **29**, 323 (1979).
17. M. S. Whittingham, U.S. Pat. 4,084,046 (1978).
18. S. Atlung, K. West, and T. Jacobsen, *This Journal*, **126**, 1311 (1979).
19. M. S. Whittingham, in "Electrode Materials and Processes for Energy Conversion and Storage," J. D. E. McIntyre, S. Srinivasan, and F. G. Will, Editors, p. 784, The Electrochemical Society Softbound Proceedings Series, Princeton, N.J. (1977).
20. D. A. Winn, J. M. Shemilt, and B. C. H. Steele, *Mater. Res. Bull.*, **11**, 559 (1976).
21. L. Gaines, U.S. Pat. 4,091,191 (1978).
22. L. Gaines, R. Francis, G. Newman, and B. Rao, Paper presented at the 11th Internat. Confer. Energy Convers. Engng., Stateline, Nevada, Sept. 1976.

Current Density and Electrolyte Distribution in Motive Power Lead-Acid Cells

Won G. Sunu* and Brian W. Burrows*

Gould Incorporated, Gould Laboratories, Rolling Meadows, Illinois 60008

ABSTRACT

Current density and electrolyte distributions were investigated in a lead-acid cell of the industrial motive power type. The current density distribution was calculated from the measured potential distribution using a treatment based on the terminal effect. Results show that the current density is strongly nonuniform and dependent on plate height. The acid density distribution was measured directly under both stationary and circulating electrolyte conditions over a range of discharge rates. Analysis of the data confirms that, under stationary conditions, stratification develops due to natural convection and shows that the electrode capacity is limited by the availability of electrolyte within the electrode pores.

Lead-acid cells designed for industrial motive power use are relatively tall (400-800 mm) with a small cross-sectional area. This design is dictated by the need to assemble cells into batteries of a variety of voltages and capacities in a restricted area as in forklift trucks, underground mining vehicles, and diesel-electric submarines.

For some time it has been recognized that tall cells of this type will have a nonuniform distribution of current density in the vertical direction during cycling (1-3). At the beginning of discharge, the current density in the upper part of the electrodes, near the current collecting tab, will be higher than in the lower part. The distribution will vary with time depending on the factors that limit the utilization of active material. As Bagshaw *et al.* (4) have shown, increasing the grid conductivity in tall plates, while keeping the current density constant, results in an increase in capacity and in energy per plate. This effect is especially marked at high discharge rates.

The influence of electrode resistance on current density distribution is called the terminal effect. This effect describes the nonequipotential condition of the electrode resulting from ohmic potential drops in the electrode (1). Tobias and Wijnsman (2) developed a theoretical treatment of the terminal effect and showed that for plane parallel electrode systems with small interelectrode-electrode length ratios, parallel current flow can be assumed, resulting in an expression in closed form for current density distribution. Despite the availability of the theoretical tools, no experimental measurements of potential distribution in lead-acid cells have previously been reported with the aim of using the theory to calculate current density distribution.

Not only is the current density in tall cells nonuniform during cycling, the electrolyte concentration is

also nonuniformly distributed. This vertical gradient of concentration, or stratification as it is commonly called, is a well-known phenomenon in lead-acid batteries. The authors recently reported some detailed measurements of acid stratification in 400 A-hr motive power cells (5). In the present work, the investigation of acid density gradients was extended to cover several discharge rates and the effect of electrolyte circulation. The aim was to elucidate further the influence of acid density gradients on active material utilization, and hence on capacity, and to determine, if possible, the effect of nonuniform current density distribution on the extent of stratification.

Our interest in obtaining a better internal characterization of motive power lead-acid cells arose from our involvement in the development of and experience with semi-industrial cells used in battery-powered vans in the U.S. Postal Service fleet (6). It was recognized that the current density and electrolyte distribution would be nonuniform over the height of the cells during discharge and that this nonuniformity would influence the cell performance; however, no data were available. Thus, the aim of this work was to determine the current density distribution and electrolyte distribution as a function of distance from the top of the electrodes. To this end we measured, during cycling, (i) the ohmic potential losses in the grids and the electrode polarization, and (ii) the variation of acid density (and capacity) both without and with electrolyte circulation.

Experimental

A five-plate cell was built for this work using production plates (Gould 66E type) and a clear PVC container. The two positives and three negatives were separated by microporous rubber separators. The positive and negative grids were 3.8 and 3.0 mm thick, respectively. Both grids were 142 mm wide and 432 mm long. The plate separation was 4.1 mm compared to 3.5 mm in the production cell. The positives were wrapped

* Electrochemical Society Active Member.

Key words: potential distribution, natural convection, stratification.

with the usual fiberglass mat and perforated PVC retainer to minimize the shedding of active material.

Measurements of ohmic potential losses, electrode polarization, and acid density were made via probes placed equidistantly along the length of the cell. The location of these probes is indicated in Fig. 1. Ohmic potential losses in the current collector were measured via insulated lead wires soldered to the grids at five, equally spaced, vertical locations. Five wires were soldered to the surface of the positive grid and five to the negative grid. In addition, wires were attached to the tops of the terminal posts. Plate polarization during cycling was measured using ten Luggin capillary probes from individual $\text{Hg}/\text{Hg}_2\text{SO}_4$ reference electrodes. The capillaries were positioned on either side of a separator at the same five vertical locations as the wires attached to the grids. Acid density was measured via five sampling tubes placed vertically between the separator and the wrapping of one of the positive plates. The tubes were of flexible polyethylene of 0.9 mm internal diameter.

The test cell was equipped with a pump for electrolyte circulation with removal of electrolyte at the base of the cell and addition at the top. The cell element fitted snugly into the cell case with a clearance of 1 mm between the outside negatives and the container. The cured plates were formed in conventional fashion and the final acid density adjusted to 1.290 g-cm^{-3} . The total volume of acid in the cell was 1800 cm^3 .

The rated capacity of the positives is 66 A-hr per plate at the C/6 rate. In the test cell containing two positives, the actual capacity was 140 A-hr at the C/5.5 rate. This increase was due to the fact that the acid was circulated prior to each half-cycle to ensure an initially uniform acid distribution from top to bottom of the cell. Furthermore, to provide sufficient space for the probes, the plate separation was slightly greater than normal.

Discharges were run manually at three different currents, namely; 26, 50, and 100A, corresponding to

discharge times of 5.5, 2.5, and 1 hr, respectively. A two-step, constant-current, charge regime was used. A 30A current was applied until about 85% of the discharged capacity had been replaced, followed by a finishing rate of 10A with an overcharge of between 10 and 20%. All experiments were carried out at room temperature.

During cycling, values of grid potentials and electrode potentials were monitored by a data logger (Fluke 2240B). At intervals small volumes of acid (1 cm^3) were withdrawn from each of the five positions with syringes for measurement of density with a digital density meter (Mettler/PAR). After each density measurement, the withdrawn acid was returned to the cell.

Results

Potential distribution.—The internal potential losses were first measured along a current path through the center of the cell. The current path is shown schematically in Fig. 1 as a resistance network and the measured values are plotted in Fig. 2. The following potential differences were measured during a discharge-charge cycle: cell polarization (E_o); positive electrode polarization (E_p); negative electrode polarization (E_n); sum of ohmic drops between the terminals and the grid centers ($E_g^+ + E_g^- + E_t^+ + E_t^-$). The potential drop across the separator (E_s) was calculated as a residual on the assumption that the sum of the internal potential differences must equal the potential difference at the terminals. The term "polarization" as used here refers to the difference between the measured voltage during discharge or charge and the initial open-circuit voltage.

Figure 2 shows that the cell was positive-limited on discharge with the positive electrode polarization being 70% of the total cell polarization at the voltage cutoff (1.7V per cell). The combined positive and negative electrode polarization accounted for 94% of the polarization at the end of discharge. On charge, the polarization losses at the positive again account for most of the cell polarization except toward the end of the charge steps (near 4 and 7 hr) where the negative electrode polarization increases sharply. This sharp increase corresponds to the onset of hydrogen evolution, indicating that the negative electrode is almost fully charged.

A more complete characterization of the internal potential losses is shown in Fig. 3 and 4 for discharge and charge, respectively. The current paths between

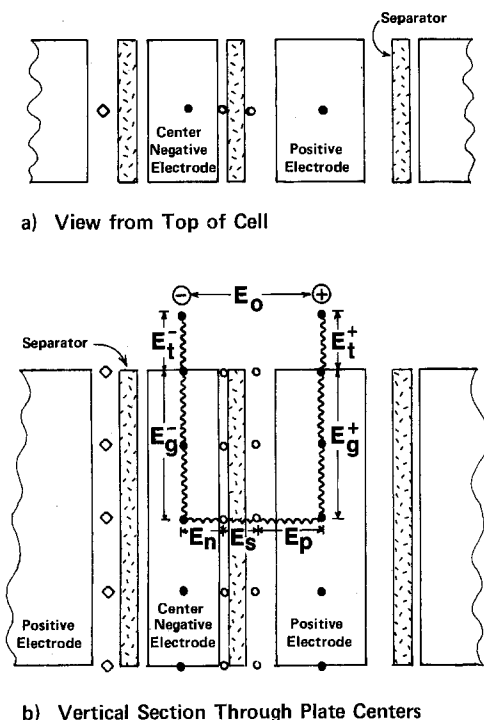


Fig. 1. Schematic diagram showing the location of potential-measuring probes between the plates (○) and on the grids (●) and a representation of the potential drops and polarization losses as a resistance network. ◇ indicates location of probes for measurement of acid density.

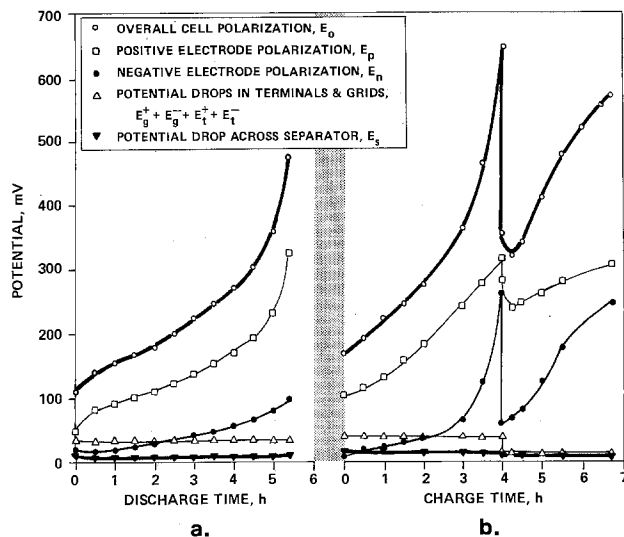


Fig. 2. Polarization and potential drops measured in a five-plate motive power cell; (a) during discharge at 26A and (b) during charge at 30A for 4 hr followed by 3 hr at 10A.

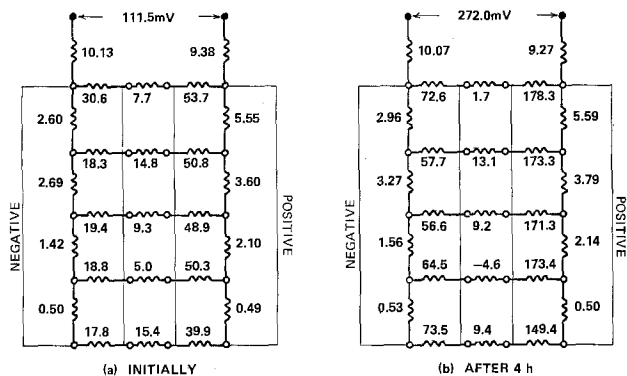


Fig. 3. Polarization and potential drops (in mV) measured in a five-plate motive power cell during a 26A discharge; (a) at the start of discharge, (b) after 4 hr. Electrolyte distribution was uniform prior to start of discharge.

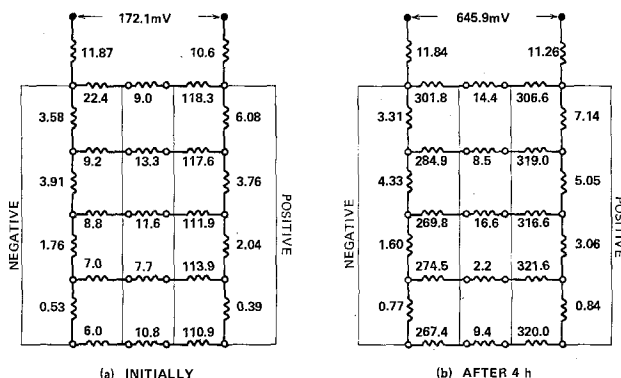


Fig. 4. Polarization and potential drops (in mV) measured in a five-plate motive power cell during charge at 30A; (a) at the start of charge, (b) after 4 hr. Electrolyte distribution was uniform prior to start of charge.

the probes are indicated as a resistance network with the potential differences between the probe locations indicated in millivolts. The potential differences across the separator are residuals and the experimental uncertainty was such that these values cannot be considered meaningful due to the errors in the electrode polarization measurements.

Figure 3 shows that at the start of discharge, the electrodes are more polarized at the top, near the terminal, than at the bottom. This nonuniform polarization and, hence current distribution, is due to the terminal effect as there was no vertical gradient of acid concentration or of temperature at the start of discharge. After 4 hr, the nonuniformity of the potential distribution is reduced. On charge, Fig. 4 shows that the terminal effect is still evident at the negative, even after 4 hr of charge, but the positive electrode was more uniformly polarized both initially and after charging for 4 hr.

For both discharge and charge, the negative electrode polarization was always less than that at the positive. This was due to the three negative/two positive electrode arrangement which results in a lower apparent current density at the central negative plate. It is also clear that the ohmic drops in the grid were smaller for the negative even though the negatives were thinner and contained less lead than the positive grids (380 vs. 510g). This observation can be attributed in part to the electrode arrangement, as discussed above, and partly to the role that the negative active material plays as an electronic conductor. Further evidence of this latter effect is clearly shown in Fig. 5 where the grid potentials at different locations, measured with respect to the top of the plate, are plotted as a function of the discharge time. The potential loss of the negative plate increases with time;

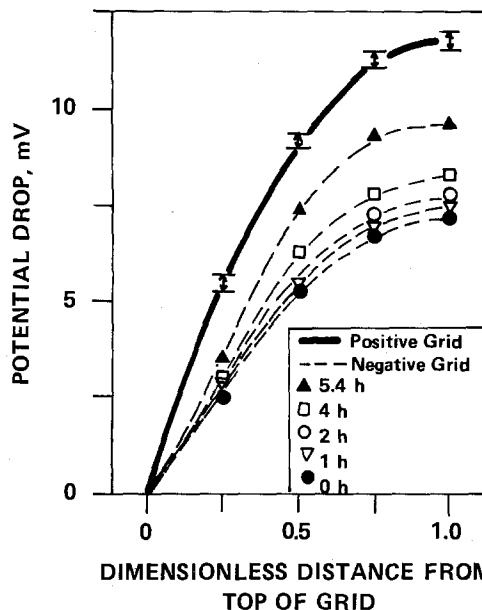


Fig. 5. Potential drops in grids of motive power cell vs. position on grid for various times during a discharge at 26A.

namely, from 7.2 mV initially (at the bottom) to 9.7 mV at the end of discharge, due to the increasing degree of conversion of Pb into PbSO₄. On the other hand, potential losses in the positive grid essentially remained constant during discharge, indicating that the positive active mass, PbO₂, has no significant effect on the grid resistance.

Electrolyte distribution and capacity.—The acid stratification that developed during discharge at the C/5.5, C/2.5, and C/1 rates is shown in Fig. 6. The extent of the stratification, i.e., difference between the density at the bottom and top of the cell, at the end of the discharge was not strongly dependent on the discharge rate being 0.08 g-cm⁻³ at the end of the 5.5 hr discharge and 0.06 g-cm⁻³ at the end of the 1 hr discharge. On the other hand, the absolute values of the acid densities increase with increase in the discharge rates from 1.13 to 1.21 g-cm⁻³ at the top of the cell at the end of the 5.5 and the 1 hr discharges, respectively. This behavior is expected in view of the decreasing utilization of active material, and hence, decreasing consumption of H₂SO₄, as the discharge rate increases. On open-circuit stand, following the end of discharge, it should be noted that the absolute values of acid density continue to decline for several hours before stabilizing, while the extent of stratification remains relatively constant. The continued decline on open-circuit stand is due to the diffusion of more concentrated acid between the plates into the acid-depleted pores of the electrodes.

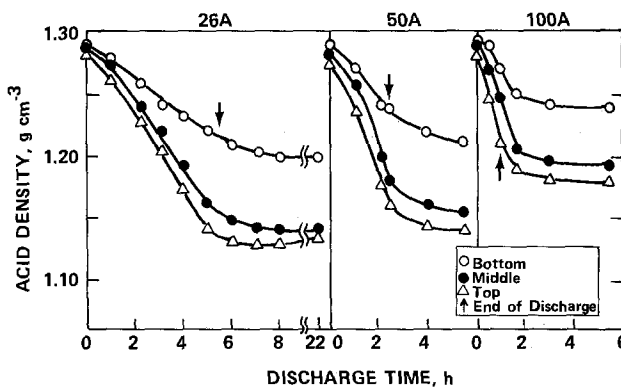


Fig. 6. Acid density vs. discharge time for three discharge rates as measured in a motive power cell.

The effect of electrolyte circulation on the distribution of acid density at the 5.5, 2.5, and 1 hr rates is shown in Fig. 7. It should be noted that the acid densities measured at five different heights, at any given time, formed single data points. In other words, circulation resulted in a uniform mixing of the acid with the elimination of stratification. Two cases are shown in Fig. 7, *viz.*, circulation with and without an external 1400 ml reservoir of acid. As expected, the acid density at the end of discharge was higher with an external reservoir except at the 1 hr rate where no difference was observed. This high-rate behavior suggests that only the acid in the pores of the electrodes is effectively utilized during discharge.

The effect of electrolyte circulation on cell capacity at the 5.5, 2.5, and 1 hr rates is shown in Fig. 8. Electrolyte circulation without an external reservoir had only a small effect on capacity, increasing it by about 4% over the range of rates from 5.5 to 1 hr. This increase is attributed to the absence of acid stratification (see Fig. 7). The inclusion of an external reservoir of 1400 ml further increased the capacity by 15% at the 5.5 hr rate and by 9% at the 2.5 and 1 hr rates. The larger increase in capacity at the 5.5 hr rate can be attributed to the increased time during which higher density acid is available in relation to the rate of acid consumption during discharge. At higher discharge rates, the denser acid is still available between the plates, but the imbalance between the faster rate of consumption of acid and the rate of mass transfer of acid through the plate wrapping into the pores of the electrodes limits the increase in capacity to only 9%. An increase in capacity beyond what was observed could be achieved by forcing electrolyte to flow through the porous electrode.

Discussion

Current density distribution.—The vertical variation in potential as measured during discharge and charge (see Fig. 3 and 4) indicates that the current density distribution is nonuniform over the height of the plates. Potential data were also obtained for discharges at 50 and 100A (see Table I). This nonuniform distribution of current density can be caused by the terminal effect and, to some extent, by the development of acid stratification.

The theoretical treatment of the terminal effect developed by Tobias and Wijsman (2) was simplified by Shepherd (7). We have used a variation of Shepherd's treatment to analyze our potential distribution data to calculate current density distribution.

Following the previous authors (2, 7), we assume (i) linear polarization and (ii) that current flow in the electrolyte is perpendicular to the electrodes. Both of these assumptions are reasonable since the apparent current densities were relatively low and the

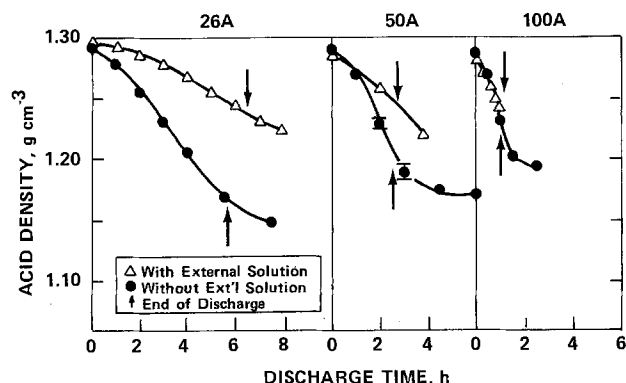


Fig. 7. Acid density vs. discharge time for three discharge rates showing effect of acid circulation (at 92 ml/min) both with and without an external reservoir.

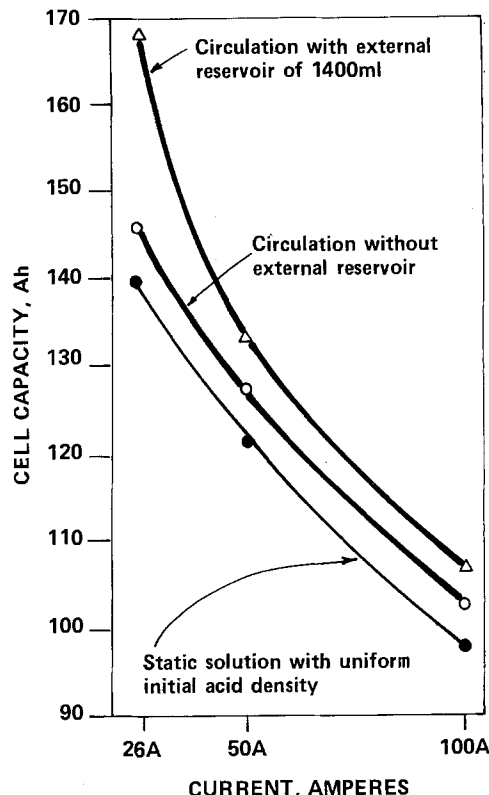


Fig. 8. Capacity vs. discharge current for three electrolyte circulation conditions. Circulation rate was 92 ml/min.

small separation between the plates was significantly less than their height. Other assumptions are discussed by Shepherd (7).

The second assumption greatly simplifies the analysis as it assumes that the current density distribution is the same in both negative and positive electrodes. Under this condition, the apparent current density, $i(y)$, the potential drops across the negative and positive grids, $E_g^-(y)$ and $E_g^+(y)$, and those across the horizontal component, $E(y)$, can be written as a function of the vertical distance y as shown below

$$\frac{dE_g^-(y)}{dy} = R_g^- i_g(y) \quad [1]$$

$$\frac{dE_g^+(y)}{dy} = -R_g^+ i_g(y) \quad [2]$$

$$i(y) = -\frac{1}{W} \frac{di_g(y)}{dy} \quad [3]$$

$$E(y) = E_g^+(y) - E_g^-(y) = (R_s + R_n + R_p) i(y) \quad [4]$$

where y is the distance from the top of the plate in centimeters, $i_g(y)$ is the vertical current across the electrode section of one-half the thickness of the actual electrodes in amperes, R_s is the resistance across the electrolyte and separator in the interplate space in $\Omega\text{-cm}^2$, R_n and R_p are the polarization resistances of the negative and positive electrodes in $\Omega\text{-cm}^2$, respectively, R_g^+ and R_g^- are the resistances, measured vertically, of the positive and negative electrode sections of unit length and one-half the thickness of the actual electrodes in $\Omega\text{-cm}^{-1}$, respectively, and W is the width of the electrode.

The boundary conditions are $y = 0$, $i_g = I$, $E_g^- = 0$, $E_g^+ = E_0$, $y = H$, $i_g = 0$ where H is the height of the plate in cm, E_0 is the voltage loss at the top of the positive plate when that of the negative is taken as zero, and I is one-half of the applied current per plate in amperes. The total discharge current is $2NI$ amperes where N is the number of the positive plates per cell.

Table I. Calculated (observed) potentials in mV as a function of dimensionless distance from top of plate for various discharge and charge rates.

| Discharge and charge rate | Dimensionless distance from top of plate | | | | |
|---------------------------|--|--------------|--------------|--------------|--------------|
| | 0 | 0.25 | 0.50 | 0.75 | 1.00 |
| Discharge, 26A | | | | | |
| E_g^- | 0(0) | 3.2(2.6) | 5.4(5.3) | 6.7(6.7) | 7.2(7.2) |
| E_g^+ | 0(0) | 5.3(5.6) | 9.1(9.2) | 11.2(11.3) | 11.9(11.7) |
| $E_n + E_p + E_s$ or E | (92.0)(92.0) | 83.5(83.8) | 77.6(77.6) | 74.1(74.0) | 72.9(73.0) |
| Charge, 30A | | | | | |
| E_g^- | 0(0) | 4.3(3.6) | 7.3(7.5) | 9.1(9.3) | 9.7(9.8) |
| E_g^+ | 0(0) | 5.6(6.1) | 9.5(9.8) | 11.9(11.9) | 12.6(12.3) |
| $E_n + E_p + E_s$ or E | 149.9(149.7) | 140.0(140.0) | 133.1(132.4) | 129.0(128.6) | 127.6(127.6) |
| Discharge, 50A | | | | | |
| E_g^- | 0(0) | 6.7(5.5) | 11.3(11.1) | 13.9(13.9) | 14.8(15.1) |
| E_g^+ | 0(0) | 10.5(11.0) | 17.7(17.9) | 21.9(22.3) | 23.3(23.3) |
| $E_n + E_p + E_s$ or E | 160.2(160.2) | 143.1(143.7) | 131.3(131.2) | 124.4(124.1) | 122.2(121.9) |
| Discharge, 100A | | | | | |
| E_g^- | 0(0) | 12.0(10.7) | 20.2(19.6) | 24.9(24.5) | 26.5(26.4) |
| E_g^+ | 0(0) | 20.0(20.6) | 33.7(34.3) | 44.7(42.0) | 44.3(43.6) |
| $E_n + E_p + E_s$ or E | 259.0(258.9) | 227.1(227.5) | 205.2(205.0) | 192.4(192.4) | 188.3(188.9) |

The solutions of Eq. [1] to [4] are as follows

$$\frac{i(y)}{i_{avg}} = \frac{Q \cosh Q \left(1 - \frac{y}{H}\right)}{\sinh Q}; \quad i_{avg} = \frac{I}{WH} \quad [5]$$

$$E_g^-(y) = -R_g^{*-} \left(\frac{H}{Q}\right)^2 [i(y) - i(0)] \quad [6]$$

$$E_g^+(y) = -R_g^{*+} \left(\frac{H}{Q}\right)^2 [i(y) - i(0)] + E(0) \quad [7]$$

$$E(y) = (R_s + R_n + R_p) i_{avg} \left[\frac{Q \cosh Q \left(1 - \frac{y}{H}\right)}{\sinh Q} \right] \quad [8]$$

with

$$Q = H \sqrt{\frac{R_g^{*+} + R_g^{*-}}{R_s + R_n + R_p}} \quad [9]$$

where R_g^{*+} and R_g^{*-} are resistances of the positive and negative electrode sections of unit length, unit width, and one-half the thickness of the actual electrodes; namely, $R_g^{*+} = R_g^+ W$ and $R_g^{*-} = R_g^- W$. The parameter Q above depends on the ratio of the sum of grid resistances to the resistance of the horizontal components and on the height of the plates.

To avoid the complications that arise from the development of electrolyte stratification during discharge (see Fig. 6), the analysis can only be applied to the data at the start of discharge, or of charge, for the case where there is no stratification.

The values of the resistances in Eq. [5]-[9] were selected to give the best fit between measured potentials and the calculated values of $E_g^-(y)$, $E_g^+(y)$, and $E(y)$ (see Table I). These best fit values were used in Eq. [5] to predict the current density distribution as a function of distance from the top of the plates. Figure 9 shows the normalized current density distribution for discharge at 26, 50, and 100A and for charge at 30A. As expected, the current density distribution becomes more nonuniform with increase in the discharge rate. For discharge at 100A, the initial current density at the top of the plates is 22% higher than the average current density whereas near the bottom it is 11% lower than the average. For discharge at 26A, the current density at the top is 16% higher and at the bottom it is 9% lower than the average. Thus, the nonuniformity is skewed toward the top of the plates where current is entering or leaving via the current-collecting tabs. The current density distribution on charge at 30A is more uniform compared

to that on discharge at 26A. This is due to the large horizontal polarization loss on charge, especially at the positive electrode, which results in a smaller value of Q .

The dimensionless parameter, Q , depends on the plate height as shown in Eq. [9]. As the plate height increases so does Q and hence, the nonuniformity of current density distribution. In view of this, it was of interest to compare the current density distribution for three plate heights. To facilitate the comparison, the grid resistances and plate thicknesses were kept constant. Figure 10 shows the normalized current density distribution for (i) motive power plates used in this work ($H = 432$ mm), (ii) a tall plate such as is used in submarine propulsion or in standby power applications ($H = 800$ mm), and (iii) a short plate of similar height to automotive battery plates ($H = 120$ mm). Examination of Fig. 10 shows the effect of plate height on current density distribution. Increasing the plate height to 800 mm results in the current density at the top of the plate being 50% higher than average at 10.4 mA cm^{-2} and 70% higher than average at 40 mA cm^{-2} . At the plate bottom, the current density is 25% less than the average at 10.4 mA cm^{-2} and 35% less at 40 mA cm^{-2} . In the case of the short plate, the current density distribution is essentially uniform. Cells with plates of 120 mm in height are used in automotive batteries. Such plates are very much thinner than motive power plates and are discharged at very high rates (100C) during engine

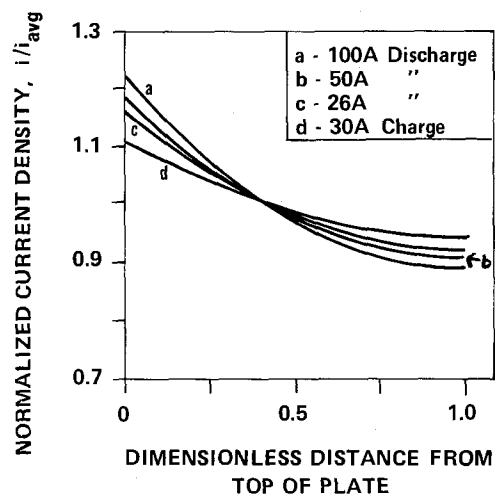


Fig. 9. Normalized current density in the y -direction determined at the start of discharge and charge. i_{avg} is 40 mA/cm^2 for 100A discharge.

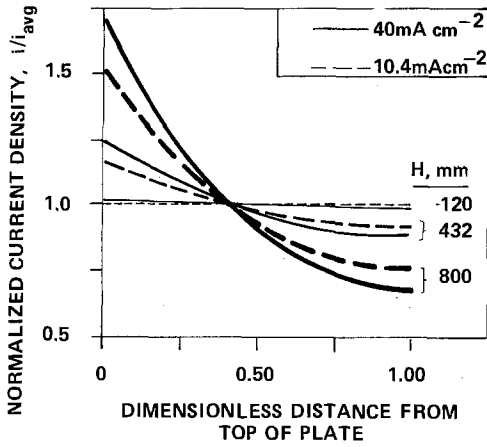


Fig. 10. Normalized current density in the y-direction at two discharge rates for three different plate heights. Current was 100 and 26A for 432 mm high plate.

starting. In these plates, the terminal effect can be expected to be significant. In order to retain a given or acceptable degree of nonuniformity in the current density distribution, the scale-up or scale-down from a particular plate design should be made by varying the value of $(R_{g^{*+}} + R_{g^{*-}})/(R_n + R_p + R_s)$ such that Q remains constant.

Electrolyte distribution.—The acid density distribution was measured directly and is shown for various times, as a function of distance from the top of the plates in Fig. 11. During discharge, a nonuniform distribution develops that is heavily skewed toward the bottom of the plates. On charge (with an initially uniform acid density), a nonuniform distribution develops but, in contrast to the discharge case, is skewed toward the top of the plates. Near the end of charge, the nonuniformity is markedly reduced by gas evolution at the electrodes.

The development of a nonuniform acid density distribution in the vertical direction can be qualitatively explained in terms of a natural convection mechanism (5): during discharge, the dilute acid in

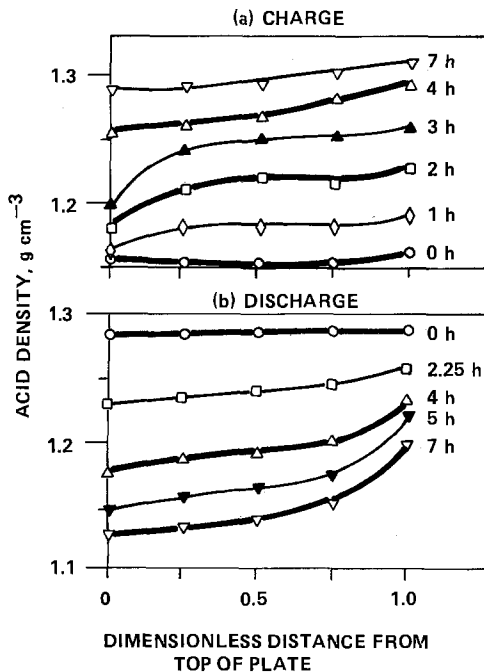


Fig. 11. Acid density distribution in the y-direction for various times during (a) discharge at 26A and (b) charge (4 hr at 30A followed by 3 hr at 10A). Electrolyte distribution was made uniform through circulation prior to charging or discharging.

the pores of the positive and negative plates flows to the top of the cell while the denser acid in the interplate space flows to the bottom.

In addition to the natural tendency of the acid to stratify on discharge due to gravitational forces, the nonuniform current density distribution (see Fig. 9) will favor a rapid consumption, and hence dilution, of acid at the top of the cell. This will amplify the tendency for stratification to develop and Fig. 11 shows that the rate of decrease of acid density is higher at the top of the cell than at the bottom.

On charge, the situation is reversed with the more dense acid that is formed in the pores flowing toward the cell bottom and displacing the more dilute acid in the space between the plates to the top of the cell. On the other hand, the nonuniform current density distribution present during charge (due to the terminal effect) will minimize this tendency for stratification as the plates will be accepting more ampere hours and producing denser acid at the top than at the bottom. The observation that the acid density increases more rapidly at the bottom than at the top during charge (see Fig. 11) indicates that stratification develops primarily due to natural convection: the counter-effect of a nonuniform current density distribution is dominated by convection. Near the end of charge, gas evolution at the plates stirs the electrolyte and causes a rapid rise in the acid density at the top of the plates.

During discharge with circulation, the acid density is uniformly distributed over the height of the plates independent of the discharge rate (see Fig. 7). On open-circuit stand, the acid density continues to decline (see Fig. 6 and 7), indicating that dilute acid in the electrode pores is mixing with the denser acid between the plates. Thus, at the end of discharge, there must be a large, horizontal gradient of acid density from the interior of the porous electrodes to the bulk electrolyte. To better understand this phenomenon, the acid density distribution under uniform circulating electrolyte conditions (as shown in Fig. 7) was analyzed further.

In Fig. 12, three acid density distributions are plotted: the observed acid density, the theoretical acid density, and the density in the pores of the electrodes. The experimental data are taken from Fig. 7. The theoretical acid density was estimated from the actual ampere hours discharged and is the average density of the total 1800 ml of acid within the cell. Clearly, the acid density as measured in the interplate space (1300 ml volume) was higher than the theoretical

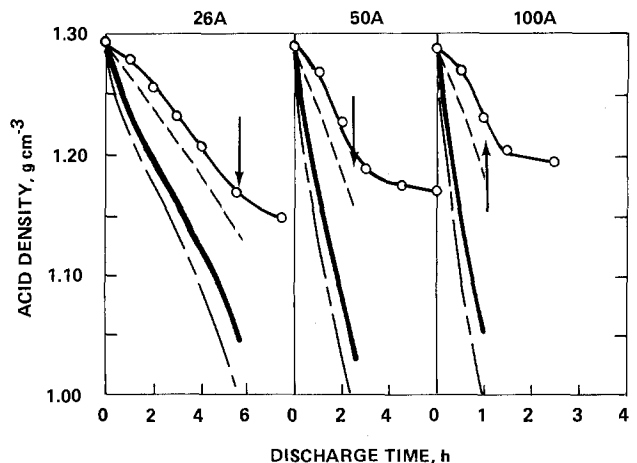


Fig. 12. Variation in acid density during discharge at three discharge rates. \circ — \circ , measured value in the interplate space; --- calculated average value; — predicted value in the pores assuming a 500 ml pore volume; ——— predicted value in the pores assuming a 400 ml pore volume (arrows indicate end of discharge).

average density. Based on these two curves, acid densities in the electrode pores were estimated by assuming that the densities were uniform over the length of the plates.

Two cases were considered; namely, pore volumes of 500 and 400 cm³. These pore volumes were chosen to represent a range of likely pore volumes. Using data on plate porosities and allowing for the volumes occupied by the grids, it was estimated that the total pore volume of both negative and positive electrodes was 610 cm³ while that of the positives was 250 cm³.

Figure 12 shows that the acid densities in the pores decreased to 1.01, 1.00, and 1.00 g-cm⁻³ at the end of discharge at 26, 50, and 100A, respectively for a volume of pore solution of 400 ml. At all three rates, the densities in the pores were much lower than the measured values of 1.17, 1.20, and 1.23 g-cm⁻³. These results suggest that plate capacity is limited by the depletion of electrolyte in the porous electrode structure. The discrepancy between the observed densities and the estimated pore densities become larger with increasing rate of discharge. At high rates, the time for replenishment of electrolyte in the pores by diffusion is reduced and the capacity declines accordingly as shown by the results in Fig. 8. In practice, electrolyte diffusion is also impeded by the wrapping around the positive plates. The limited rate of diffusion of electrolyte into the porous electrodes explains the results in Fig. 7 and 8. In Fig. 7, for example, the difference in acid density for discharge with and without an external reservoir is negligible at the 100A rate, since at this high rate only the acid in the pores is being utilized. In Fig. 8, the capacities corresponding to the discharges in Fig. 7 were not of the magnitude expected from the measured acid densities. Only by forcing electrolyte through the porous structure would the capacity be increased.

The deduction that capacity is limited by the availability of electrolyte in the pores was subsequently verified experimentally and a model developed that predicts positive plate capacity as a function of discharge rate, acid concentration, temperature, plate thickness, plate porosity, interplate space, and the characteristics of the wrapping material (8).

Conclusions

Discharge or charge of a motive power cell, *i.e.*, a cell with relatively tall, narrow plates is accompanied by the development of a nonuniform current density and electrolyte distribution in the vertical direction.

The current density distribution was determined indirectly from measurement of grid potentials and electrode polarization. A treatment based on the terminal effect was used. Calculation showed that the current density was significantly higher at the top of the electrode than at the bottom and that the overall nonuniformity was strongly dependent on the plate height.

Electrolyte or acid density distribution is also nonuniform over the height of the cell. During discharge under stationary electrolyte conditions, stratification develops due to natural convection and is not notably influenced by the nonuniform distribution of current density. Under circulating electrolyte conditions stratification is eliminated and capacity is increased. Analysis of the data shows that capacity is limited by the availability of electrolyte within the pores and that a strong horizontal gradient of acid density must exist at the end of discharge with the acid density in the pores approaching 1.00 g-cm⁻³.

Manuscript submitted Jan. 21, 1981; revised manuscript received Feb. 23, 1981. This was Paper 59 presented at the Los Angeles, California, Meeting of the Society, Oct. 14-19, 1979.

Any discussion of this paper will appear in a Discussion Section to be published in the June 1982 JOURNAL. All discussions for the June 1982 Discussion Section should be submitted by Feb. 1, 1982.

Publication costs of this article were assisted by Gould Incorporated.

REFERENCES

1. C. Kaspar, *Trans. Electrochem Soc.*, **77**, 355 (1940).
2. C. W. Tobias and R. Wijnsman, *This Journal*, **100**, 459 (1953).
3. J. Euler and L. Horn, *Arch. Electrotechnik*, **50**, 85 (1965).
4. N. E. Bagshaw, K. P. Bromelow, and J. Eaton, "Power Sources 6," D. H. Collins, Editor, p. 1, Academic Press (1977).
5. W. G. Sunu and B. W. Burrows, "Power Sources 8," J. Thompson, Editor, Academic Press, New York (1981).
6. B. W. Burrows, W. J. Wyszor, and R. J. Hartman, Proc. Fifth International Electric Vehicle Symposium, Philadelphia, Electric Vehicle Council, New York (1979).
7. C. M. Shepherd, *This Journal*, **112**, 252 (1965).
8. W. G. Sunu and B. W. Burrows, Abs. 15, p. 49, The Electrochemical Society Extended Abstracts, Hollywood, Florida, Oct. 5-10, 1980.

The Behavior of the Zinc Electrode in Alkaline Solutions

V. Supersaturated Zincate Solutions

T. P. Dirkse*

Calvin College, Grand Rapids, Michigan 49506

ABSTRACT

Light scattering, density, and viscosity data are presented for electrolytically prepared supersaturated zincate solutions that were allowed to decay naturally. The results indicate that the solute species in the supersaturated solutions are not completely different from those in saturated or unsaturated zincate solutions. An explanation for the formation and behavior of the supersaturated solutions is given based on various solute species that are formed by the reaction of OH^- ions and H_2O molecules with $\text{Zn}(\text{OH})_2$ and the subsequent formation of polynuclear zincate species. The rate and extent to which these are formed depends on the availability of OH^- ions and unbound H_2O molecules at the electrode surface.

When zinc is treated anodically in KOH solutions, the product of the charge transfer reaction is $\text{Zn}(\text{OH})_2$ (1). This substance then dissolves in the electrolyte, and if the anodic process is continued long enough the electrolyte eventually becomes turbid and solid ZnO begins to precipitate from it. The extent to which the $\text{Zn}(\text{OH})_2$ can dissolve in the electrolyte, however, is far greater than the equilibrium solubility of ZnO in the KOH solutions (2). These solutions have a fair degree of stability but the excess zincate is eventually precipitated as ZnO. While the solutions do not have the characteristics of supersaturated solutions (seeding with a crystal does not produce a rapid precipitation of the ZnO in excess of the equilibrium value) they will be referred to as "supersaturated" solutions. The term zincate will be used to refer to any dissolved zinc species.

A few attempts have been made to characterize the solute species in the "supersaturated" solutions but the matter has not yet been resolved. The suggestion that some of this excess zincate is present as colloidal material (3, 4) has not been conclusively disproved, nor has positive evidence been presented for this conclusion. In fact, some work has indicated the absence of colloidal material (5, 6).

One general approach that can be used to determine whether the "supersaturated" zincate species are the same as those found in unsaturated solutions of ZnO in KOH, i.e., $\text{Zn}(\text{OH})_3^-$ or $\text{Zn}(\text{OH})_4^{2-}$, is to measure some property of these solutions as a function of zincate concentration. If discontinuities are observed in the property studied, then the indications are strong that a new species has replaced the others in the solution. Some work along this line using NMR as the property studied has been reported (5). No discontinuities were observed, suggesting that the zincate species in "supersaturated" solutions were not different from those in unsaturated solutions. However, the "supersaturated" solutions used in that work were synthetically prepared by dilution of a stock "supersaturated" solution that had been prepared electrolytically. This is a matter of expediency because the "supersaturated" zincate solutions precipitate out ZnO very slowly.

The work reported here was carried out in order to obtain more information about these "supersaturated" solutions. Furthermore, the "supersaturated" solutions studied were all prepared by natural decay of an electrolytically prepared "supersaturated" solution rather than being prepared by dilution. Again, the

purpose was to observe whether or not discontinuities appeared in certain properties measured at various zincate concentrations.

Experimental

The solutions of KOH + ZnO were prepared from reagent grade solids and doubly distilled deionized water. The "supersaturated" solutions were prepared by treating zinc electrodes anodically in a solution of KOH that had been saturated with ZnO and then filtered through a Pyrex glass frit to remove undissolved ZnO. To do this, two sheet zinc (99.999%) electrodes were placed on either side of a commercial nickel oxide electrode in the saturated solution and a low current rate was passed through the electrodes until the solution became turbid. At this time the electrolyte was removed, filtered through a Pyrex glass frit, and analyzed for zincate content. The solutions were then set aside and from time to time samples were removed, filtered, and used for analysis or other measurements. All the work was carried out at room temperature, about 20°C.

The zincate content was determined by titration with EDTA using Calmagite as indicator. Densities were measured in a 5 ml pycnometer at $25^\circ \pm 0.1^\circ\text{C}$ and viscosities were measured in an Ostwald viscometer also at $25^\circ \pm 0.1^\circ\text{C}$. Turbidity or light scattering data were obtained with a Coleman Model 14 Spectrophotometer having a nephelometric attachment and using radiation of 560 nm.

Results

Numerous results indicate that there is no one solubility value for the "supersaturated" solutions (2). The zincate content can be varied easily by changing the current rate and the time allowed for the process. For example, in one cell in which the electrolyte was a 40% KOH solution the zincate content was 13.9% when the solution became turbid. The current was continued and 5 hr later the zincate content had risen to 15.1%. Apparently, the concentration at any one time is more like a steady-state value than an equilibrium value (6).

This is illustrated by some preliminary work. Three separate series of "supersaturated" solutions (each series consisted of five different starting KOH concentrations) were prepared and allowed to decay normally. A typical set of data is shown on Fig. 1. The dashed line represents the zincate concentration of that KOH solution saturated with ZnO. The zincate content in each of the three series is different at the beginning of each run (when turbidity first appeared).

* Electrochemical Society Active Member.

Key words: electrolyte, battery, discharge, solvation.

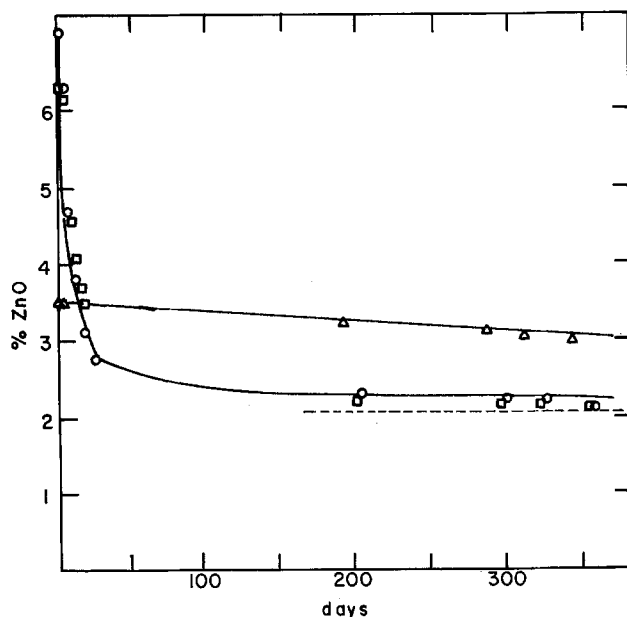


Fig. 1. Decomposition of "supersaturated" zincate solutions in 20% KOH at room temperature. The different symbols refer to separate runs beginning with different extents of supersaturation.

In each instance it required about a year for the zincate content to decrease to that of the equilibrium value. The initial rate of decay depends, in part, on the initial zincate concentration. The greater this is, the faster the rate of decay. Results similar to those on Fig. 1 were obtained for KOH concentrations ranging from 20 to 45 weight percent (w/o) KOH.

Figure 2 illustrates the decay of 6.15M KOH (~30% KOH) solution "supersaturated" with zincate. Figure 3 shows the density and the viscosity of the solutions on Fig. 2. Also included on Fig. 3 are unsaturated solutions that were prepared by diluting with 6.15M KOH a 6.15M KOH solution which had previously been saturated with ZnO.

Some of the solutions represented on Fig. 2 and 3 were also subjected to light scattering measurements to determine whether there was evidence for the presence of colloidal material, especially in the "supersaturated" solutions. The instrument was calibrated by setting the percent light scattering to zero when doubly distilled deionized water was placed in the cuvette. Table I summarizes the results of the physical measurements of these solutions. The results of light

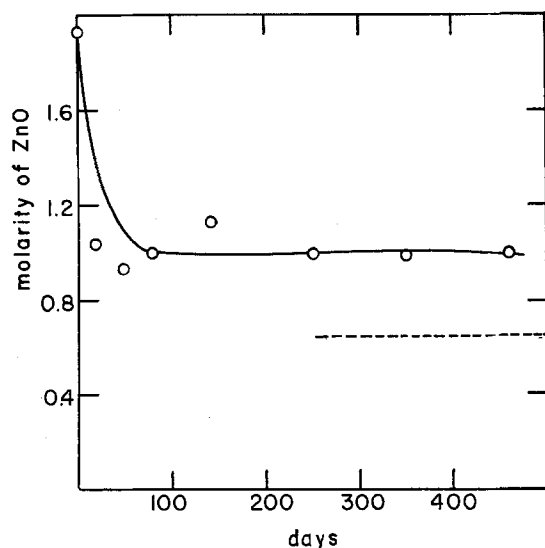


Fig. 2. Decay of "supersaturated" zincate solution in 6.15M KOH at room temperature.

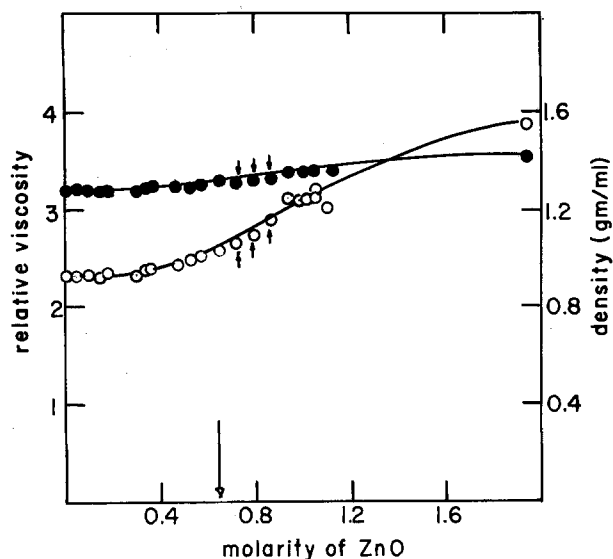


Fig. 3. Density and viscosity of zincate solutions in 6.15M KOH at 25°C. Open circles, relative viscosity, left-hand scale; closed circles, density, right-hand scale. The arrow indicates the composition of a saturated solution of ZnO in 6.15M KOH.

scattering measurements show no indication of the presence of colloidal material. The lines on Fig. 3 show no evidence of discontinuities, suggesting that similar zincate species are present at all concentrations, and are not completely replaced by other species.

The three solutions represented by arrows on Fig. 3 were prepared, about a year after the series was begun, by dilution of the electrolytically "supersaturated" solution. The viscosity and density of these solutions show no significant deviation from the values of "supersaturated" solutions that had decayed during stand. This indicates that the work reported earlier and based on synthetically prepared "supersaturated" solutions (5) does give a fair representation of "supersaturated" zincate solutions, i.e., dilution of these solutions does not alter the properties of the solution compared to solutions which decay on stand.

Discussion

The lack of discontinuities on Fig. 3 argues against the assumption that the zincate species in the "supersaturated" region are completely different from those in saturated or unsaturated zincate solutions. However, there is other evidence that different species are present. Hampson *et al.* (7) found that the emf of a zinc electrode became insensitive to zincate concentration in the "supersaturated" region. They concluded, therefore, that some electroinactive zincate species must be present instead of, or in addition to, the $\text{Zn}(\text{OH})_4^{2-}$ ion. Also Jackovitz and Langer, using Raman spectroscopy, observed that the concentration of $\text{Zn}(\text{OH})_4^{2-}$ did not increase in the "supersaturated" region (8). Later work with Raman spectroscopy (9) was interpreted to indicate the existence of $\text{Zn}(\text{OH})_2(\text{H}_2\text{O})_2$, $\text{Zn}(\text{OH})_3(\text{H}_2\text{O})^-$, and $\text{Zn}(\text{OH})_4^{2-}$ in concentrated zincate solutions but that only small amounts of

Table I. Characteristics of various KOH and zincate solutions

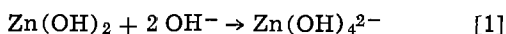
| Solution | Molarity of KOH | Molarity of ZnO | Density, g ml ⁻¹ | Relative viscosity | Percent light scattering |
|----------|-----------------|-----------------|-----------------------------|--------------------|--------------------------|
| A | 6.15 | 0 | 1.2788 | 2.33 | 0 |
| B* | 6.15 | 0.65 | 1.3152 | 2.59 | 0 |
| C# | 6.15 | 1.94 | 1.4178 | 3.88 | 0 |

* 6.15M KOH saturated with ZnO.
6.15M KOH "supersaturated" with zincate.

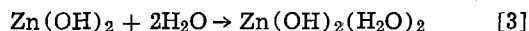
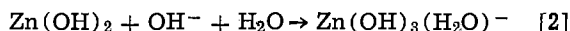
$\text{Zn}(\text{OH})_4^{2-}$ are present in solutions containing 1.5M ZnO in 15M KOH. This is in contrast to earlier reported work where the concentration of $\text{Zn}(\text{OH})_4^{2-}$ was said to increase with increasing KOH concentration while that of $\text{Zn}(\text{OH})_3^-$ decreased (10).

The above results indicate that the "supersaturated" region does not represent the replacement of the zincate species present at concentrations less than that of saturated solutions. Rather, the zincate species present in saturated and unsaturated solutions are also present in the "supersaturated" region but in this region other zincate species also begin to appear. This interpretation is consistent with the absence of discontinuities such as in Fig. 3 and with the work mentioned earlier (7, 8). Thus the problem stated earlier amounts to identifying the other zincate species that appear in the "supersaturated" region as suggested by others (7, 8).

Some attempts have been made to characterize these zincate species by the use of Raman spectra (7, 9). However, there is disagreement as to what the interpretation is. The work of Sharma and Reed (9) does offer a resolution to the problem of interpreting the data for "supersaturated" zincate solutions. They suggest that both OH^- and H_2O serve as ligands for the zinc atom in $\text{Zn}(\text{OH})_2$. Therefore, three solute species are possible if one assumes a coordination number of 4 for the zinc atom: $\text{Zn}(\text{OH})_2(\text{H}_2\text{O})_2$, $\text{Zn}(\text{OH})_3(\text{H}_2\text{O})^-$, and $\text{Zn}(\text{OH})_4^{2-}$. Some have also suggested the presence of $\text{Zn}(\text{OH})(\text{H}_2\text{O})_3^+$ (11). As the $\text{Zn}(\text{OH})_2$ is produced by the charge transfer reaction at the electrode any of these species may form. Which particular one is formed will depend on the availability of the ligands OH^- and H_2O at the electrode surface. If one assumes a hydration number of 4 for the K^+ ion (12) and of 3 for the OH^- ion (13), then the amount of unbound water molecules in the KOH solutions is shown in Table II. In solutions more concentrated than about 33 w/o KOH there is insufficient water to hydrate the K^+ and OH^- ions normally. Thus, in these solutions the initial dissolution of the $\text{Zn}(\text{OH})_2$ is limited to reaction [1]



However, as the OH^- ions combine with the $\text{Zn}(\text{OH})_2$ they release their water of hydration and at the electrode surface the following two reactions may then occur in addition to that of Eq. [1]



For KOH solutions less concentrated than 33 w/o (about 7M), all three reactions may occur immediately following the formation of $\text{Zn}(\text{OH})_2$ at the electrode surface. Thus all three possible zincate species may form at the zinc electrode during anodization, and the amount of OH^- and H_2O at the electrode surface will determine in which manner the $\text{Zn}(\text{OH})_2$ will dissolve in the electrolyte. Of these species only the $\text{Zn}(\text{OH})_4^{2-}$ appears to be the electroactive one for determining the emf of the zinc electrode (14).

Analysis of saturated solutions of ZnO in aqueous KOH indicate that the amount of $\text{Zn}(\text{OH})_4^{2-}$ in these

solutions is limited by equilibrium considerations. The equilibrium constant expression for Eq. [1] is

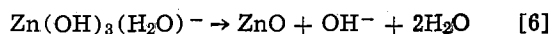
$$K = \frac{a_{\text{Zn}(\text{OH})_4^{2-}}}{a_{\text{Zn}(\text{OH})_2} \cdot (a_{\text{OH}^-})^2} \quad [4]$$

Assuming the $\text{Zn}(\text{OH})_2$ to be a pure solid, the above expression becomes

$$K = a_{\text{Zn}(\text{OH})_4^{2-}} / (a_{\text{OH}^-})^2 \quad [5]$$

The activities of the two species in Eq. [5] are not known for these solutions but if molarities are substituted for them, and if the assumption is made that $\text{Zn}(\text{OH})_4^{2-}$ is the dissolved zincate species, then the experimentally determined ratio shown in Eq. [5] is 0.026 ± 0.002 for saturated solutions of ZnO in aqueous KOH ranging from 20 to 40 w/o KOH.

On the basis of the above information, a possible explanation for the "supersaturated" zincate solutions is the following. As $\text{Zn}(\text{OH})_2$ is formed at the electrode it first dissolves according to Eq. [1] and this continues until the zincate content reaches the equilibrium value for ZnO in aqueous KOH. By this time even a 40 w/o solution will have some unbound water molecules in it because of the water of hydration released by the OH^- ions as they react according to Eq. [1]. If the zinc electrode is to be oxidized beyond this, the $\text{Zn}(\text{OH})_2$ must dissolve some alternate way, Eq. [2] or [3], or else the electrode surface will become covered with solid $\text{Zn}(\text{OH})_2$ and be passivated. Either the $\text{Zn}(\text{OH})_3(\text{H}_2\text{O})^-$ or the $\text{Zn}(\text{OH})_2(\text{H}_2\text{O})_2$ then is unstable with respect to ZnO and the following reactions occur slowly



The ZnO precipitates out of the solution. Reaction [6] can occur only as water becomes available to hydrate the released OH^- ions. This scenario is summarized in Fig. 4.

The scheme outlined on Fig. 4 is consistent with the published information concerning "supersaturated" zincate solutions. It explains the fact that while the dissolved zincate concentration increases in the "supersaturated" solutions, the $\text{Zn}(\text{OH})_4^{2-}$ concentration does not increase (8). It also accounts for the insensitivity of the emf of the zinc electrode to increasing zincate concentrations in the "supersaturated" region (7). The fact that no discontinuities are observed on Fig. 3 nor were observed in earlier NMR work (5) can be explained by noting that the $\text{Zn}(\text{OH})_4^{2-}$ ions are present at all concentrations and do not disappear in the "supersaturated" region. In fact, it is quite likely that several of the zincate species are present at all times with the $\text{Zn}(\text{OH})_4^{2-}$ form being the most abundant up to the equilibrium concentration of ZnO. There is emf evidence for this (3). In that work the emf of the zinc electrode, when plotted to conform to the

Table II. Amount of solute ions and unbound water molecules in 1 liter of aqueous KOH solutions

| w/o KOH | Moles of K^+ | Moles of OH^- | Moles of unbound water |
|---------|-----------------------|------------------------|------------------------|
| 22 | 4.7 | 4.7 | 23 |
| 28 | 6.5 | 6.5 | 12 |
| 33 | 8.0 | 8.0 | 0 |
| 40 | 10.1 | 10.1 | 0 |

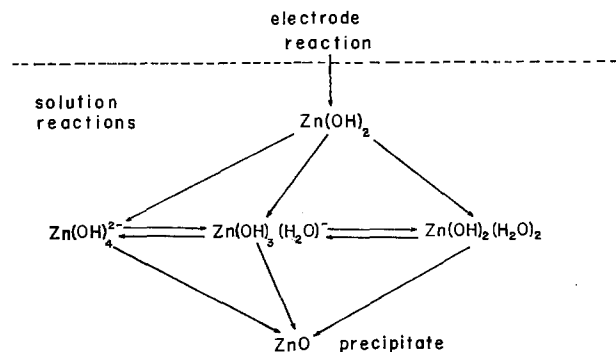


Fig. 4. Summary of reactions to form zincates

Nernst equation, showed discontinuities. The first part corresponded to Eq. [1], the second part to Eq. [2], and the third part to Eq. [3].

A linear potentiodynamic study of the passivation of the zinc electrode in KOH solutions showed the presence of two peaks at a slow scan rate (15). These peaks were at that time interpreted as corresponding to reactions [1] and [2] and referring to the dissolution processes of the charge transfer product. At faster scan rates the charge transfer product is produced faster than it can be dissolved and the electrode then becomes covered with a layer of the reaction product resulting in temporary passivation of the electrode.

Thus, the interpretation presented here for the composition and formation of "supersaturated" zincate solutions is consistent with previously reported data and provides a ready explanation of them. It is basically the interpretation that has been reported earlier (3). Which of the three zincate species is produced at any one time will depend on the availability of OH⁻ and H₂O ligands at the electrode surface. In the more concentrated KOH solutions, reaction [1] is favored up to the saturation concentration of ZnO in KOH while reactions [2] and [3] will not take place until sufficient H₂O has been released by the OH⁻ ions in forming Zn(OH)₄²⁻. In the more dilute KOH solutions, reactions [1], [2], and [3] are equally likely except that reactions [2] and [3] appear to proceed much more slowly than does reaction [1].

However, there is an alternate scheme that should also be considered. This involves the formation of polynuclear zincate species in the "supersaturated" region. This has been suggested in the case of aluminate ions (16). The common zincate ion, Zn(OH)₄²⁻, is considered to have a tetrahedral configuration. The loss of H₂O between zincate ions could give rise to polynuclear species of the type shown on Fig. 5. The bridging elements in these species may be OH groups as well as the O atoms shown on Fig. 5. Polynuclear species of types II and III, Fig. 5, are probably less likely because the bond angles in the cyclic parts of the structures would be under some strain. Thus, if the

polynuclear species do form they would most likely be of the type I variety.

As these polynuclear species form and grow they will eventually become large enough to form colloidal or suspended particles, leading to turbidity and the formation of a precipitate. In order to precipitate ZnO these polynuclear species would first release OH⁻ ions and H₂O molecules.

Conclusion

The solute species in the "supersaturated" zincate solutions may to a large extent be either of those shown on Fig. 4 or the type I shown on Fig. 5. At present there is no direct experimental method readily available to identify any of these species positively. Even the IR and NMR data that are available have been the subject of some disagreement and the interpretation of these data even more so, as noted above. However, the existence of any of these solute species is dependent on the availability of OH⁻ ions and unbound H₂O molecules in the electrolyte. In all likelihood, such solutions consist of a variety of the species indicated.

Acknowledgment

This work was made possible by a research grant from the General Electric Company. Dr. Roger DeKock and Dr. W. VanDoorne gave considerable help in interpreting the data and discussing the nature of the solute species.

Manuscript submitted Nov. 14, 1980; revised manuscript received Feb. 9, 1981. This was Paper 77 presented at the Pittsburgh, Pennsylvania, Meeting of the Society, Oct. 15-20, 1978.

Any discussion of this paper will appear in a Discussion Section to be published in the December 1981 JOURNAL. All discussions for the December 1981 Discussion Section should be submitted by Aug. 1, 1981.

Publication costs of this article were assisted by the Johnson Wax Fund.

REFERENCES

- H. Gerischer, *Z. Phys. Chem.*, **202**, 302 (1953).
- T. P. Dirkse, "Power Sources 3," D. H. Collins, Editor, p. 485, Oriel Press, Newcastle upon Tyne, England (1971).
- A. G. Briggs, N. A. Hampson, and A. Marshall, *J. Chem. Soc. Faraday Trans. 2*, **70**, 1978 (1974).
- V. N. Flerov, *Zh. Fiz. Khim.*, **31**, 49 (1957).
- W. VanDoorne and T. P. Dirkse, *This Journal*, **122**, 1 (1975).
- T. P. Dirkse, *ibid.*, **102**, 497 (1955).
- N. A. Hampson, G. A. Herdman, and R. Taylor, *J. Electroanal. Chem. Interfacial Electrochem.*, **25**, 9 (1970).
- J. F. Jackovitz and A. Langer, "Zinc Silver Oxide Batteries," J. J. Lander and A. Fleischer, Editors, p. 29, John Wiley, New York (1971).
- S. K. Sharma and M. D. Reed, *J. Inorg. Nucl. Chem.*, **38**, 1971 (1976).
- T. P. Dirkse, C. Postmus, Jr., and R. Vandenbosch, *J. Am. Chem. Soc.*, **76**, 6022 (1954).
- K. M. El'kind, M. G. Mikhalenko, and V. N. Flerov, *Zh. Prikl. Khim. (Leningrad)*, **51**, 1225 (1978).
- G. W. Brady and J. T. Krause, *Norelco Rep.*, **5**, 111 (1958).
- G. Yagil and M. Anbar, *J. Am. Chem. Soc.*, **85**, 2376 (1963).
- T. P. Dirkse, *This Journal*, **126**, 1456 (1979).
- T. P. Dirkse and N. A. Hampson, *Electrochim. Acta*, **17**, 387 (1972).
- L. A. Carreira, V. A. Maroni, J. W. Swaine, Jr., and R. C. Plumb, *J. Chem. Phys.*, **45**, 2216 (1966).

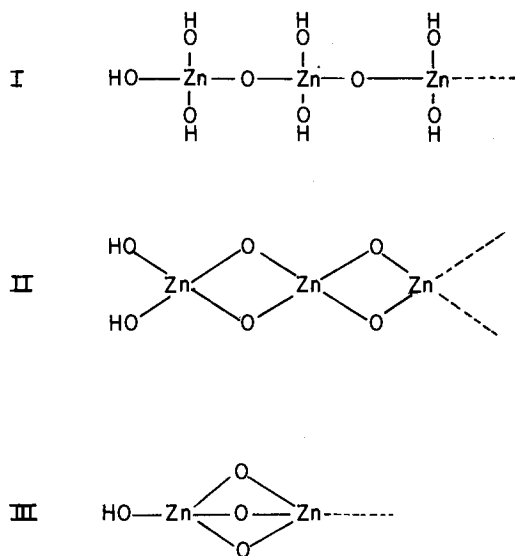


Fig. 5. Polynuclear zincate species

Lead Acid Battery Expander

II. Expander Activity Correlation Between Microelectrode and Pasted Electrode

B. K. Mahato*

Johnson Controls, Incorporated, Electrochemical Research, Milwaukee, Wisconsin 53201

ABSTRACT

The efficacy of the microelectrode cycle life index in predicting the influence of expander on the pasted electrode performance was carried out from the simultaneous testing of four lignosulfonate expanders by the microelectrode and pasted electrode. Expander was included in the test solution for the microelectrode and in the paste for the pasted electrode. The studies of the effect of expander concentration on both the microelectrode cycle life index and 90% DOD cycle life of negative limited 98 A-hr test cells were identical, showing an optimum expander concentration for a maximum cyclic performance. Testing of three expander materials obtained from the process variations of the same source material also showed a correlation between the microelectrode cycle life index and the specific capacity of the pasted electrode. Expander activity on the lead electrode performance was observed to vary with the quality and concentration of expander. The application of the microelectrode technique as a quality control tool of the expander material was established.

The word "expander" is used here to mean the lignin constituent of the conventional lead acid battery expander, which is a composite of a sulfonate derivative of lignin, barium sulfate, and carbon black. Expander present in the test system either in the paste or in the test electrolyte influences the lead electrode performance, particularly its dischargeability and its capacity maintenance behavior during cycling. The determination of expander activity outside the test battery was proposed by Mahato (1) from the relative change in the microelectrode capacity that occurs when a microelectrode is potentiostatically cycled between -1160 and -860 mV (*vs.* $\text{Hg}/\text{Hg}_2\text{SO}_4/\text{mH}_2\text{SO}_4$) at 0.5 mV/sec in 1.250 sp gr sulfuric acid solution with expander for a period of 48 hr. This expander activity was termed as the cycle life index (η) and defined as $\eta = (Q_f - Q_o)/Q_o$ where Q_o and Q_f are initial and final capacity of the electrode, respectively. The major advantages of this technique are the straightforward measurement, the elimination of the complexities of the pasted electrode, and the capability the technique provides for evaluating the expander material outside the test battery, which has to date been the only vehicle in determining the efficacy of the expander material. However, application of this cycle life index in predicting the expander's influence on the pasted electrode performance has remained ambiguous. This is primarily due to the difference in the mode of inclusion of expander in the two systems; it is included in the test solution for the microelectrode system and in the paste for the pasted electrode system. The objective of the present work is to correlate the microelectrode cycle life index and the pasted electrode performance, *i.e.*, the dischargeability of the lead active mass and its capacity maintenance behavior during deep discharge cycling.

Experimental

Materials.—Four lignosulfonate compounds designated A, B, B', and B" were obtained from American Can Company, Rothschild, Wisconsin. The type A compound which is very similar to "Maracell-XC" is a brown color material with 0.8% total sulfur, 0.1% inorganic sulfur, 0.3% Ca, 6.5% Na, 0.2% reducing sugar,

and 13.9% $-\text{OCH}_3$. The B, B', and B" were modified versions of A and their compositions were not known. The ultraviolet absorption spectra of all four samples at pH 7.0 were identical showing a weak peak at 320 nm, moderate peak at 280 nm, and a shoulder at 235 nm. In all cases the differential spectra at pH 11.8 *vs.* 1.7 showed strong peaks at 355 and at 250 nm and a shoulder at 295 nm wavelength. All these materials were completely soluble in water, but their solubility decreased with increasing acid concentration.

The test and counterelectrodes of the microelectrode system were prepared out of 99.999% Pb (Cominco). The test electrode was 2 mm diameter and 2 cm long. The counter was a 1.27 cm diam cast rod.

The current collector grids of the pasted negative and positive electrodes were made out of Pb-0.13Sr-0.04Al-1.00Sn and Pb-4.67Sb-0.20As-0.19Sn alloy, respectively. The conventional ball mill oxide with 33 \pm 5% free lead, barium sulfate, and carbon black, all available at the laboratory, were used for the leady oxide paste preparation. Test solutions were made out of the reagent grade chemicals and laboratory distilled water.

Microelectrode technique.—The microelectrode technique uses a test cell with a 2 cm long, 2 mm diam lead electrode, an oversized lead counterelectrode, and an $\text{Hg}/\text{Hg}_2\text{SO}_4/\text{mH}_2\text{SO}_4$ reference electrode, all immersed in 50 ml sulfuric acid test electrolyte. The preparation of a porous electrode out of the well-defined microelectrode was carried out by linear potential sweep cycling of the microelectrode between -1160 and -860 mV (*vs.* $\text{Hg}/\text{Hg}_2\text{SO}_4$) at 0.5 mV/sec in 1.050 sp gr H_2SO_4 solution for a 2 day period. The experimental details along with the automatic data collection system are described elsewhere (1).

Pasted electrode evaluation.—Two types of pasted negative electrodes were prepared out of experimental paste made from the dry blended mixture of ball mill oxide, barium sulfate, carbon black, lignin compound, and dynel fiber with 110 ml 1.325 sp gr sulfuric acid and 110-130 ml water per kilogram oxide. The concentration of barium sulfate, carbon black, and dynel fiber in the blend were 0.3, 0.15, and 0.06%, respectively, based on the weight of oxide. The pasted electrodes were conventionally cured and dried. The dry paste density was 4.25 ± 0.05 g/cm³.

* Electrochemical Society Active Member.
Key words: lead electrode, voltammetry, additive.

The type I test electrodes had dimensions of $18.92 \times 22.66 \times 0.152$ cm in which the concentration of type A expander varied from 0 to 0.5% based on the weight of oxide. The test electrodes thus prepared were assembled with matching $18.92 \times 22.66 \times 0.203$ cm size positive electrodes and microporous PVC separators to prepare thirteen plate element negative limited test cells. The positive electrodes were overpasted to obtain a theoretical capacity in excess of 3.5 times that of the negatives. The particulars of the negative limited test cell series in terms of dry paste weight and expander concentration in the test negatives are given in Table I. The average theoretical capacity of these test cells based on 0.93g metallic lead per gram of paste and 53% coulombic efficiency at the 3 hr discharge rate was 98 A-hr. These test cells were electroformed in triplicate in 1.100 sp gr H_2SO_4 under 2.50V constant voltage with 40A maximum current for a 40 hr period. This was followed by the adjustment of acid concentration to 1.290 ± 0.010 sp gr, initial capacity testing at 40A, and the continuous deep discharge cycling of the test cells. The deep discharge cycle was arbitrarily selected as a 6 hr cycle with 132 min discharge at 40A followed by 228 min constant voltage (2.50V) charge with 33A current maximum. The 132 min discharge at 40A (88 A-hr) corresponds to 90% depth of discharge of the 98 A-hr test cells. The cycling of the test cells was continued to the point at which they could not sustain 90% DOD. The capacity checks of test cells were carried out at different points of cycling. Following the capacity test the cells were recharged approximately 10% excess of the amount of discharge. At no time was extra charge or boosting allowed outside the test mode described during cycle life test.

The type II electrodes had grid dimensions of $19.30 \times 33.17 \times 0.191$ cm and were prepared using a negative paste identical with type I except for the type of expander included. The expander formulations used in preparing this new series of pastes are given in Table II. The objective of testing this new series of electrodes was to determine the efficacy of type B expander with and without type A expander. The follow-up electrode preparation, i.e., curing and drying of the electrodes, was identical to the type I electrodes. The type II electrode thus prepared was then assembled with two counter preformed positives and micro-

porous PVC separators in between to compose a test cell. This was followed by constant voltage electroformation in 1.100 sp gr H_2SO_4 at $26^\circ \pm 2^\circ C$ at 2.60V with 15A current maximum and subsequent adjustment of electrolyte concentration at 1.300 ± 0.005 sp gr H_2SO_4 . Formation was followed by testing the cells in duplicate for the steady state material utilization of the active mass at 16.6 A/plate, which corresponds to the 3 hr discharge rate. In every case the test electrode was discharged up to $-0.500V$ (vs. Hg/Hg_2SO_4). The steady-state capacity was achieved between the 10th and 15th discharge. At the end of the test, the electrode was washed with water followed by rinsing with acetone and drying under a vacuum at $70^\circ \pm 2^\circ C$. This was followed by active material analysis for specific surface area and microstructure. The specific surface area was determined by BET nitrogen adsorption using a Quantasorb analyzer and the morphology of the freshly fractured cross section was examined by JEOL U3 Scanning Electron Microscope.

Results and Discussion

Evaluation of type A expander.—Figure 1 shows the effect of type A expander concentration in 1.250 sp gr H_2SO_4 on the microelectrode cycle life index (CLI). The presence of an optimum concentration for a maximum cycle life index is evident. It suggests that the cyclic behavior of the lead electrode is sensitive to expander concentration in the test solution. The influence of expander on the discharge as well as charge kinetics of the lead electrode is well known and its possible role on the reaction mechanism and electrode structure have recently been discussed (1). In acidic environment it remains within the electrode matrix as surface adsorbed and/or suspended material. During discharge as the acidity of the reaction interface changes it desorbs from the lead sites, forms a transient Pb-lignin complex, and adsorbs on the freshly precipitated lead sulfate, all of which are responsible in delaying the electrode passivation process. At the end of discharge as the acidity of the reaction product phase approaches that of the bulk concentration the expander stays within the lead sulfate matrix with a strong tendency of being adsorbed on the metallic lead sites. This in turn brings charge inhibition which is mostly due to lack of deposition sites for electrochemically reduced lead adatoms and to a small extent due to retardation in the lead sulfate dissolution process. However, this charge inhibition, if not excessive,

Table I. Active material distribution in 98 A-hr negative limited test cells (6:7 = neg:pos per cell) as function of type A expander concentration in negative paste

| Type A expander concentration in negative based on weight of oxide (w/o) | Dry negative paste per cell (g) | Dry positive paste per cell (g) | Theoretical capacity ratio of positive and negative active mass per cell* |
|--|---------------------------------|---------------------------------|---|
| 0 | 768 | 2902 | 3.66 |
| 0.02 | 764 | 2876 | 3.64 |
| 0.10 | 760 | 2918 | 3.72 |
| 0.30 | 760 | 2910 | 3.58 |
| 0.50 | 765 | 2903 | 3.68 |

* Calculation based on 0.93g lead per gram of negative paste and 1.04g lead dioxide per gram of positive paste.

Table II. Expander formulations in type II electrodes

| Test series | Weight percent based on the weight of oxide | | | |
|-------------|---|--------|---------|----------|
| | Type A | Type B | Type B' | Type B'' |
| 32 | | 0.30 | | |
| 34 | | 0.30 | | |
| LDT-12* | 0.30 | | 0.30 | |
| LDT-34 | 0.30 | | 0.30 | |
| LDT-5 | 0.30 | | | 0.30 |

* No barium sulfate in the paste.

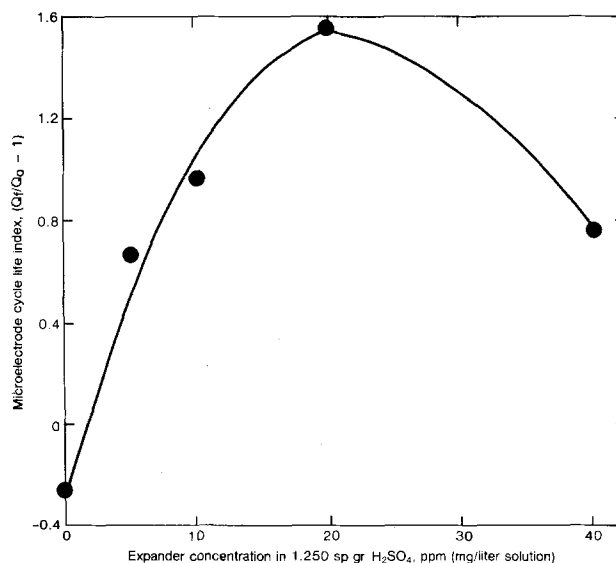


Fig. 1. Effect of type A expander concentration in the test solution on the lead microelectrode cycle life index values.

helps to improve and/or to maintain the surface area of the electrode matrix.

In the absence of expander in the test solution the CLI value of the electrode takes a negative value (Fig. 1). This is indicative of the gradual loss of electrode capacity or the effective surface area on repeated charge-discharge cycling, in agreement with the reported agglomeration of the lead active mass during cycling (2).

Expander in the test solution alters the electrode kinetics by physical adsorption on the electrode surface whether or not it takes part in the cyclic electrode reactions. Presence of an optimum expander concentration for a maximum cycle life index (Fig. 1) suggests that the modifying influence of expander on the cyclic electrode reaction may be controlled by two diverse processes: (i) physical adsorption on the electrode surface and (ii) the sensitivity of the ionic adsorbed material to desorb, to migrate to the high energy surface, to dissolve or reprecipitate in the interfacial electrolyte depending on the pH, and to form a transient compound with the opposite ionic species. At higher expander concentration adsorption continues on the electrode surface until it suppresses the rates of the cyclic electrode reactions. This is partly illustrated in Fig. 2d from the voltammogram of the test electrode taken with 40 ppm expander concentration in the test solution.

Figure 2d also shows a significant charge inhibiting influence of the expander. The expander affects the charge kinetics by blocking coverage of the deposition sites for lead adatom and by restricting the dissolution rate of lead sulfate precipitates. The microcrystalline structure of the lead dendrites observed in the test electrode when cycled in the test electrolyte with 40 ppm expander (Fig. 3d) indicates that the charge kinetics are mostly controlled by the blocking coverage of the deposition site and not by the dissolution behavior of the lead sulfate layer. This is apparent from the low electrode capacity (Fig. 2d) in spite of the extremely fine nature of the electrodeposit (Fig. 3d).

The charge inhibiting influence of the expander may also be related to the physical nature of the expander and its pH dependent adsorption behavior on the electrode surface. The conventional lignosulfonate expander is an anionic polymer with coiled structure (3). During discharge as the pH of the reaction interphase increases the coiled structure of the lignin

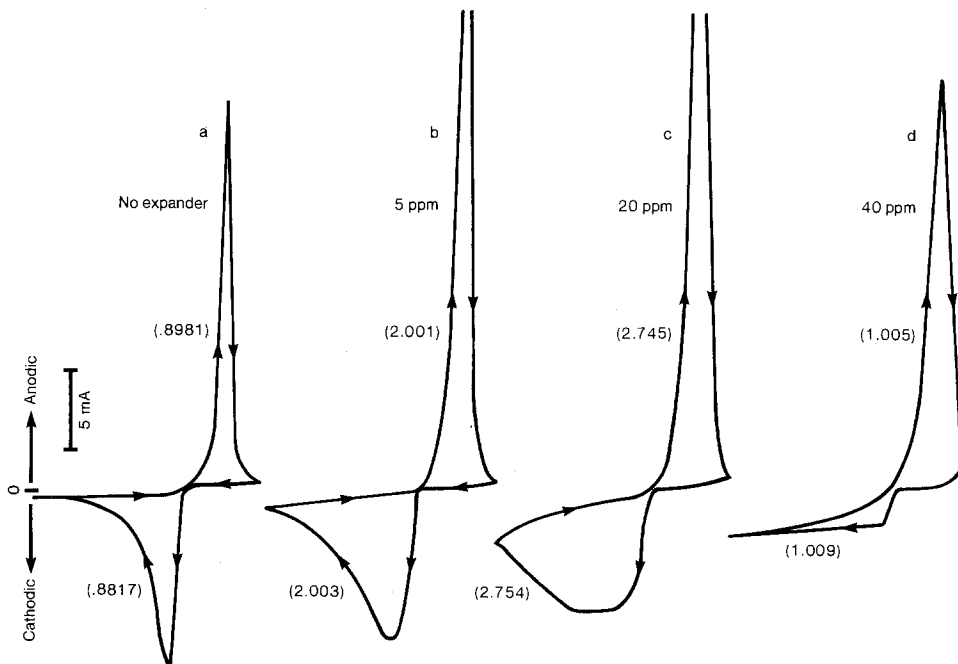
stretches and to some extent dissolves and takes part in the electrode reactions with available Pb^{2+} ions. During discharge as the pH of the reaction interphase increases the coiled structure of the lignin shrinks or moves to high energy sites providing a chance for formation of high surface area electrodeposit. However, at a higher expander concentration, as adsorption continues, the adsorbed molecule may become oriented more and more perpendicular to the surface with its hydrophilic head oriented toward the bulk solution (4), causing the noticeable charge inhibition shown in the voltammogram in Fig. 2d.

At expander concentrations lower than the optimum (Fig. 1), the cyclic electrode reaction is favorably influenced by increasing expander concentration in the test solution as noted by the increasing CLI values (Fig. 1) as well as by the voltammograms (Fig. 2) and the electrode surface morphology as observed by SEM (Fig. 3).

Figure 2 demonstrates the effect of expander concentration in the test solution on the lead electrode voltammograms. The increased charge inhibition of the lead electrode with increasing expander concentration is apparent from these voltammograms. This is noted from the gradual reduction in the cathodic peak current with increasing expander concentration in the test solution. The reduction in the cathodic peak current is accompanied by broadening of the peak area and increased current acceptance at the end of the cathodic sweep. This in turn results in an overall increase in charge input with increasing expander concentration in the test solution up to 20 ppm. The anodic portions of the voltammograms, which show a corresponding increase in electrode capacity up to 20 ppm, indicate that the greater charge input to the system is associated with the electrode quality improvement (i.e., surface area) rather than any secondary electrochemical reaction. At an expander concentration greater than 20 ppm in the test electrolyte, a decline in electrode CLI (Fig. 1) is associated with the excessive charge inhibition apparently caused by multilayer surface adsorption of expander material and/or its orientation on the electrode surface.

The effect of expander concentration on the cycled lead electrode morphology is shown in Fig. 3. An agglomerated nodular mass with large voids was typical for the test electrode cycled in pure sulfuric acid solution. This electrode morphology, however, was altered in presence of expander in the test solution and

Fig. 2. Effect of type A expander concentration (ppm, mg/liter) in 1.250 sp gr H_2SO_4 on the lead microelectrode voltammograms at 145th cycle. Figures within parenthesis are charge in coulombs.



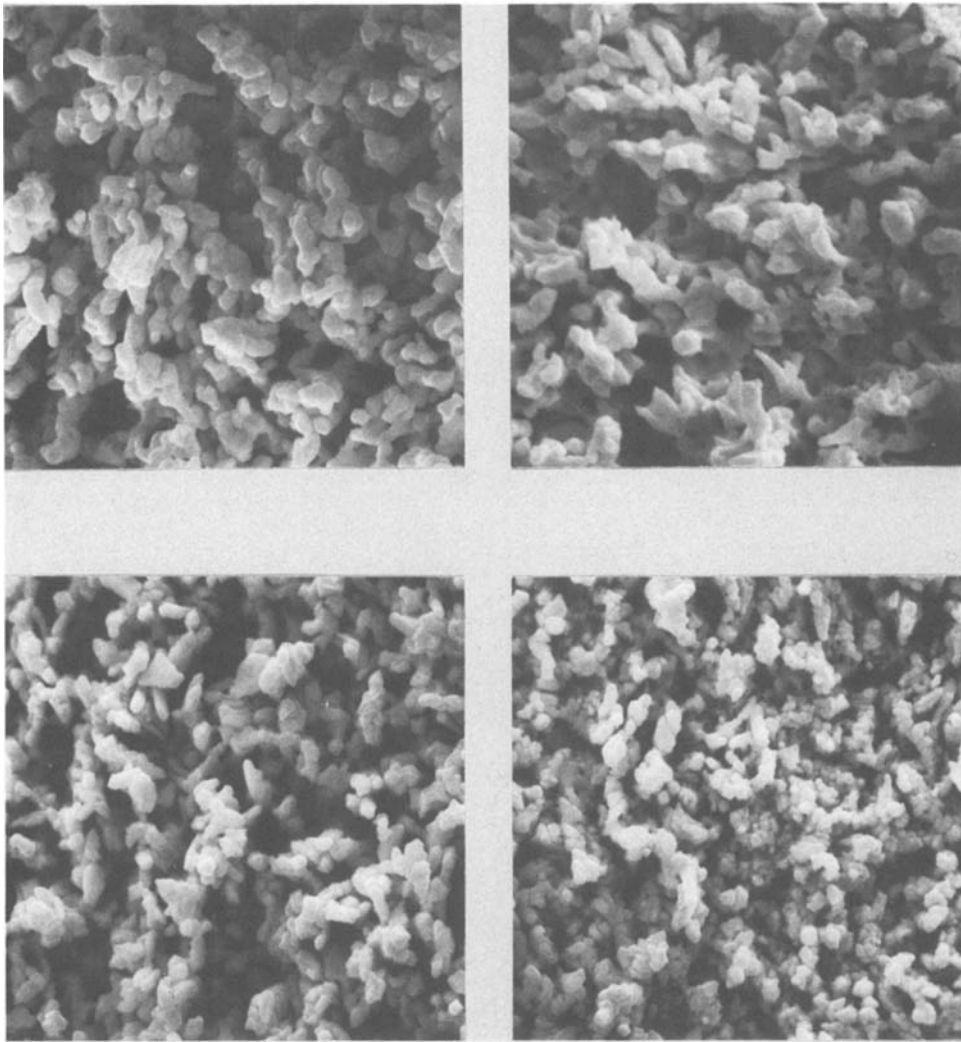


Fig. 3. The influence of expander concentration in the test solution on lead microelectrode surface morphology at 145th cycle; (a, top left) 0 (b, top right) 5 ppm (c, bottom left) 20 ppm and (d, bottom right) 40 ppm. Magnification $3000\times$.

became increasingly finer with increasing expander concentration in the test solution. The morphology of the test electrode cycled in test solution with 40 ppm expander was basically very fine (Fig. 3d) and close to the structure obtained after the development cycle. The retention of this fine structure after 48 hr cycling was caused by the protective coverage of expander as evident by the highly suppressed electrode kinetics (Fig. 2d).

Figure 4 is a plot of 90% DOD cycle life of 98 A-hr negative limited test cell vs. the type A expander concentration in the negative paste. Each test cell had 760g of negative paste in which the concentration of expander was varied from 0 to 0.5 weight percent (w/o) based on the weight of oxide. The average capacity of these test cells based on five identical discharges immediately after electroformation and adjustment of acid concentration to 1.290 ± 0.010 sp gr were 77.0, 91.8, 99.1, 104.5, and 106.7 A-hr for 0, 0.02, 0.10, 0.30, and 0.50 expander concentration in the negative paste, respectively. The nominal capacity of these test cells was considered to be 98 A-hr at the 40A rate. These test cells cycled with 90% DOD per cycle. The cycle mode was arbitrarily selected as 132 min discharge at 40A followed by 228 min charge with 2.50V constant voltage charging with 33A maximum current per cycle. The test cells which had no expander in the negative paste had initial capacities less than that required to sustain 90% DOD cycling and hence were not cycled. In the test the capacity of the negative electrode was always limiting. This was checked by the half-cell potential measurement during test cycling and periodic capacity measurement.

The presence of an optimum expander concentration in the paste for a maximum 90% DOD cycle life of the negative limited test cells is evident from Fig. 4. The optimum concentration of type A expander in the paste was 0.3 w/o. The 90% DOD cycle lives of the test cells with 0.3 w/o expander in the negative paste were 65 and 106% superior to the test cells with 0.1 and 0.5 w/o expander in the negative paste. The effect

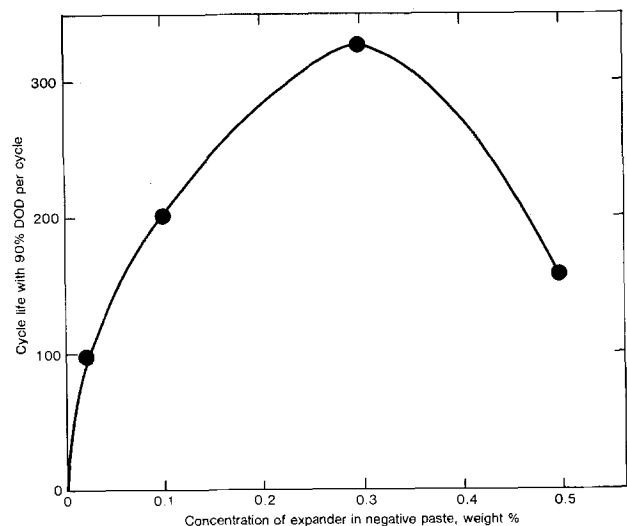


Fig. 4. Effect of type A expander concentration in the negative paste on the cycle life of negative limited test cells with 90% DOD per cycle.

of type A expander concentration on the electrode morphology after formation is shown in Fig. 5. A highly sintered nodular structure lead active mass with large voids was dominant in absence of expander in the paste matrix. This structure was modified in the presence of 0.1 w/o expander in the paste to form a coherent porous active mass consisting of well-distributed acicular dendrites covered with nodular deposits. Upon increasing expander concentration to 0.3 w/o the deposits became finer and well separated from each other to cause a highly microporous matrix (Fig. 5c). At 0.5 w/o expander the deposit structure became extremely fine and dense and the pore size appeared to have reached a submicron size. The physical examination of these micrographs (Fig. 5a, b, c, and d) did indicate the seemingly better structure of Fig. 5c compared to Fig. 5a, b, and d and explains the superior performance of the test cells with 0.3 w/o expander in the negative paste. The specific surface area of the test negatives were 0.37, 0.50, 0.65, and 0.69 m²/g for electrodes with expander concentration 0, 0.1, 0.3, and 0.5 w/o, respectively.

A strong similarity exists between the effect of expander concentration on the microelectrode cycle life index (Fig. 1) and the 90% DOD cycle life of the pasted electrode (Fig. 4). This is true in spite of the fact that the expander is included in the electrolyte for the microelectrode system and in the paste for the pasted electrode system. The almost identical influence of expander concentration on the microelectrode cycle life index and the 90% DOD cycle life of the pasted electrode suggests that the microelectrode cycle life index (CLI) could be used to determine either the optimum expander concentration or the deep discharge

cycle life of the pasted electrode or both. This also reveals that this technique could be economically used for selective evaluation of expander candidate materials for application-oriented lead acid battery test cells. This is highly attractive since the expander selection is usually based on its evaluation in a lead acid battery, which is often time consuming and costly. The analogous behavior of Fig. 1 and 4 points out that the 20 ppm type A expander concentration in the microelectrode system is equivalent to 0.3 w/o in the pasted electrode system based on the weight of the oxide.

A comparison of Fig. 3 and 5 indicates that the expander's influence on the lead electrode morphology is very similar for the microelectrode system in which it is included in the test solution and for the pasted electrode in which it is incorporated in the paste. This similarity of expander action on the electrode morphology suggests that the mechanism of expander action must in the case of the pasted electrode involve dissolution from the paste matrix followed by the adsorption on the electrode surface.

Comparison of type A and B expanders.—The microelectrode test data of type A and B expanders at 60 ppm concentration in 1.250 sp gr H₂SO₄ are given in Table III. Type B material is noted to be significantly different and superior to type A, particularly at 60 ppm concentration. The inferior cycle life index of type A is the result of its excessive charge inhibition as noted in Fig. 6 from the cyclic voltammograms taken at the end of the test. Due to this wide difference in their cycle life index values, the type A and B expanders were chosen to test the efficacy of the microelectrode

Fig. 5. Structure of freshly formed fractured negative as affected by type A expander concentration in the paste: (a, top left) no expander, (b, top right) 0.1 w/o, (c, bottom left) 0.3 w/o and (d, bottom right) 0.5 w/o. Micrographs were taken close to the edge. Magnification 3000 \times .

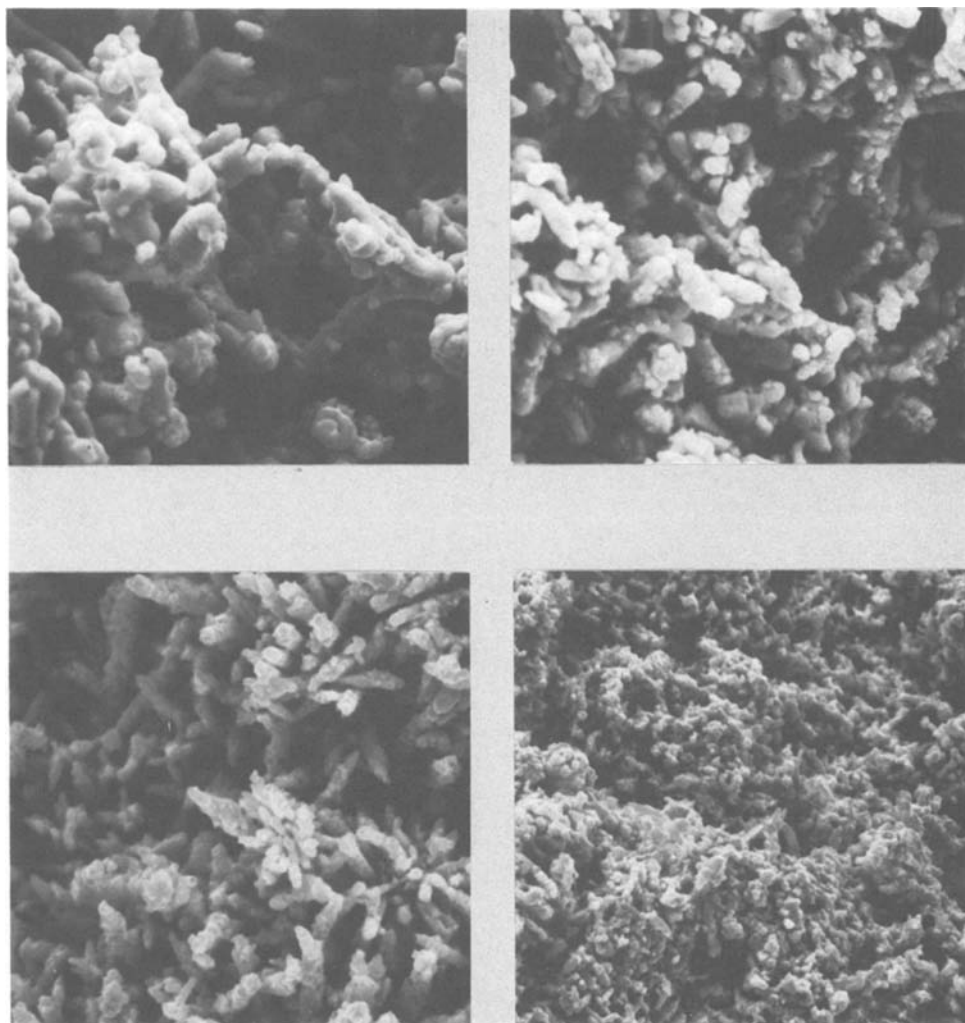


Table III. Microelectrode evaluation of type A and B expanders at 60 ppm (mg/liter) in 1.250 sp gr H₂SO₄

| Expander material | Q _{in} (C) | Q _r (C) | Cycle life index, |
|-------------------|---------------------|--------------------|-------------------------------|
| | | | $\frac{Q_r - Q_{in}}{Q_{in}}$ |
| Type A | 1.354 | 1.131 | -0.17 |
| Type B | 1.293 | 2.463 | 0.91 |

technique in predicting the influence of expander quality on the deep discharge cycle life of the pasted electrode. The 60 ppm concentration in the microelectrode system was assumed to be equivalent to close to 0.5 w/o in the pasted electrode. The test electrodes with 0.5 w/o type A and B were prepared according to the procedures given in the experimental section. These test electrodes were assembled with the heavily pasted counter positives to form 98 A-hr negative limited test cells.

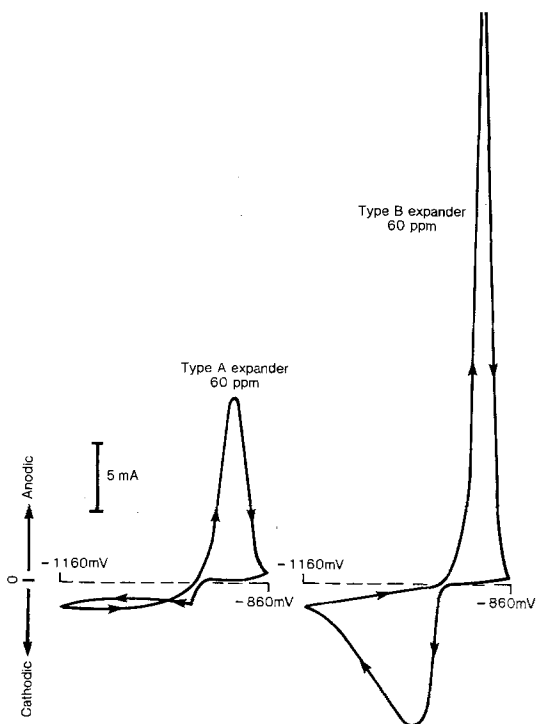


Fig. 6. Lead microelectrode voltammograms taken at 145th cycle demonstrate a strong charge inhibition of type A expander compared to type B in 1.250 sp gr H₂SO₄ solution.

The capacity maintenance behavior of these two test series during cycle life testing with 90% DOD per cycle are given in Fig. 7. Test cells with type B expander had relatively low initial capacity which, however, did gradually build up to an equivalent level to that of the previous series within 30 cycles and showed a 90% DOD cycle life close to 330. This demonstrates that the type B expander is superior to type A in improving the deep discharge cycle life of the pasted electrode system (Fig. 7), in agreement with the microelectrode observation (Fig. 6).

Relation between CLI and electrode capacity.—The expander present in the test solution alters the lead matrix morphology during linear potential sweep cycling of the microelectrode. Thus the cycle life index reflects the expander's influence on the steady-state capacity of the microelectrode. Analogous to this, expander present in the pasted electrode matrix is expected to alter the lead matrix morphology during formation and subsequently to help the electrode attain a steady-state capacity on repeated deep discharge cycling. Thus a correlation between the expander's influence on the microelectrode cycle life index and the dischargeability or the specific capacity of the pasted electrode (A-hr/kg active mass) is anticipated. This was carried out with the simultaneous evaluation of three B-type expanders by the microelectrode and the pasted electrode.

The B, B', and B'' type expanders were experimental lignosulfonate samples prepared by American Can

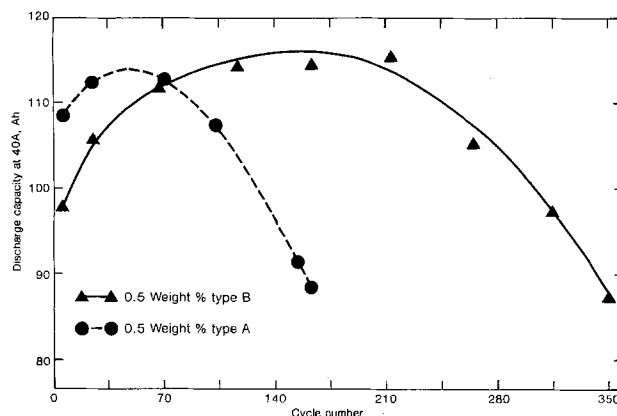


Fig. 7. Effect of expander type in the negative paste on the capacity maintenance behavior of 98 A-hr negative limited test cells.

Specific discharge capacity at 43.5 A/kg, Ah/kg

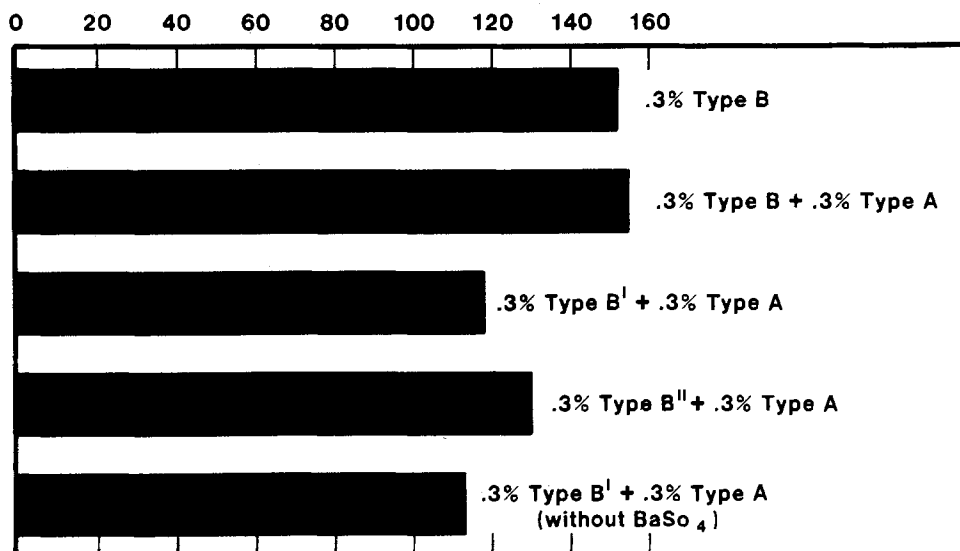


Fig. 8. The effect of three type B expanders on the specific discharge capacity of lead electrode with and without type A expander and BaSO₄ at 52.7 A/kg and 25° ± 1°C in 1.300 ± 0.005 sp gr H₂SO₄ solution.

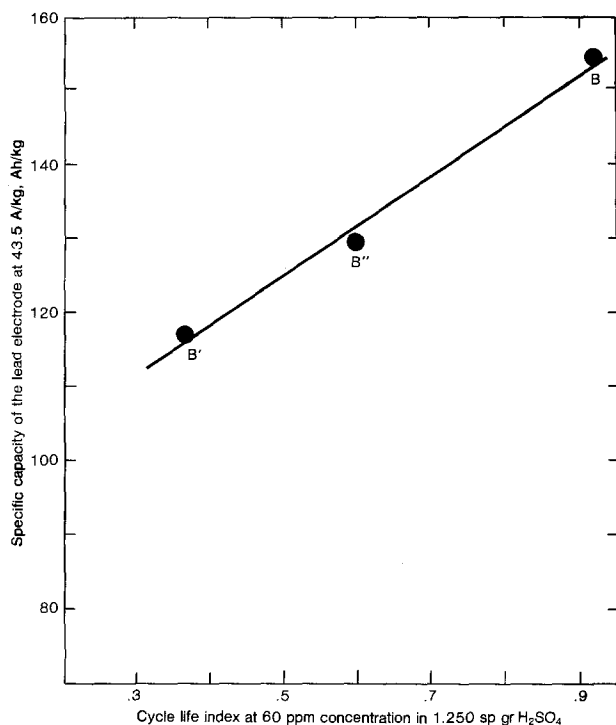


Fig. 9. Correlation between the effect of three B-type expanders on the lead electrode specific capacity and the microelectrode cycle life index.

Company, Rothschild, Wisconsin, for this test. All these materials were prepared from the same source material with some unknown change in processing conditions. The variation of these samples was not detected by u.v. and infrared spectroscopy. However, the microelectrode testing of these materials had shown the CLI values to be 0.91, 0.36, and 0.59 for B, B', and B'', respectively, at 60 ppm concentration in 1.250 sp gr H₂SO₄ solution.

The efficacy of these expanders on the steady-state capacity development was tested on type II electrodes prepared out of conventional paste in which the type B, B', and B'' expanders were included with and without type A expander. The test plates were conventionally formed and tested in duplicate in a three-plate element test cell.

The summary results of the five test series measured in duplicate are shown in Fig. 8 in the form of a bar diagram. This diagram indicates that the material utilization of the lead active mass is not significantly influenced by the 0.3 w/o type A lignin in the presence of 0.3 w/o type B lignin; second, the influence of BaSO₄ in promoting the material utilization of the active mass under this composition range is heavily controlled by the type B lignin. The material utilization shows that the expander activity of B, B'', and B' are in the decreasing order in agreement with the cycle life index value of these materials at 60 ppm mentioned earlier.

Figure 9 is a plot of steady-state capacity of the pasted electrode and the microelectrode cycle life

index for B, B', and B'' expanders. It shows a linear correlation between the cycle life index and the specific capacity of the pasted electrode and further demonstrates the predictability of the microelectrode technique in determining the efficacy of expander on the lead electrode performance.

Conclusions

Microelectrode cycle life index is shown to have an acceptable correlation with the expander's influence on the deep discharge cycle life and the material utilization of the pasted type lead electrode. An optimum concentration of expander exists both in the paste matrix and in the test solution for a maximum deep discharge cycle life. The prediction of this optimum concentration in the pasted electrode is possible from the microelectrode test data. However, it is highly likely that this optimum concentration may vary with the nature of the material. The microelectrode cycle life index has been noted to be sensitive to the quality of expander prepared from the same source material and has proved to be useful as a quality control tool. The fundamental reasons for an optimum expander concentration for a maximum deep discharge cycle life, whether they are related to physical properties or to the chemical structure and associated reactions, are not clear. More work is needed to elaborate the expander activity as function of the chemical structure and the physicochemical properties of the expander. The microelectrode technique as an economic screening technique of candidate expanders appears to be extremely helpful in finding a better material which in turn could improve the energy density and cycle life of the lead electrode or the whole lead acid battery.

Acknowledgments

This work was sponsored by Argonne National Laboratory under Contract No. 31-109-38-4205. The author is grateful to W. Tiedemann for his encouragement and support, K. Bullock and S. Hanna for timely discussion, and J. Strebe for experimental assistance. Expander samples were obtained from the American Can Company, Rothschild, Wisconsin. Pasted electrodes and test cells were prepared by Globe Battery Division.

Manuscript submitted Oct. 15, 1980; revised manuscript received Feb. 4, 1981. This was Paper 101 presented at the Hollywood, Florida, Meeting of the Society, Oct. 5-10, 1980.

Any discussion of this paper will appear in a Discussion Section to be published in the June 1982 JOURNAL. All discussions for the June 1982 Discussion Section should be submitted by Feb. 1, 1982.

Publication costs of this article were assisted by Johnson Controls, Incorporated.

REFERENCES

1. B. K. Mahato, *This Journal*, **127**, 1679 (1980).
2. B. K. Mahato, *ibid.*, **124**, 1663 (1977).
3. J. W. Hollis, Jr., Private communication.
4. M. J. Rosen, "Surfactant and Interfacial Phenomena," p. 48, John Wiley & Sons, Inc., New York (1978).

Composite Cell Testing of Corrosion-Resistant Pasted Lead-Acid Battery Grids

I. Weight Loss and Grid Integrity of Low Antimony and Antimony-Free Grids

E. M. L. Valeriotte*

Cominco Limited, Product Research Centre, Mississauga, Ontario, Canada, L5K 1B4

ABSTRACT

A comprehensive set of long duration corrosion tests was carried out under conditions closely approaching those in a lead-acid battery to compare the corrosion characteristics of twelve different materials, including expanded mesh grids produced from cast strip and rolled strip as well as book-mold cast grids. Seven lead-calcium-tin grids, one lead-calcium grid, one lead-strontium-tin grid, and two lead-antimony grids were included as pasted plates in each composite cell, along with a coupon sample of unexpanded, unpasted, cast lead-calcium-tin strip. Tests were conducted under well-defined conditions of temperature and electrode potential, simulating conditions of SLI service in a vehicle. Weight loss and grid integrity measurements were supplemented by metallographic examinations. Rate laws indicated a change in corrosion mode for lead-calcium-tin alloys as test conditions were made more severe. A semi-quantitative model was developed indicating that this change in corrosion mode was associated with more deeply penetrating corrosion. This behavior contrasted to that for antimonial and strontium-lead alloys and for a low-calcium-lead alloy for which the same form of rate law was observed under all conditions. The corrosion characteristics of two particular expanded grids were outstanding. One of these was an expanded cast strip grid of composition Pb-0.09Ca-0.3Sn; the other was a soft expanded cast-strip grid of composition Pb-0.007Ca.

During the 1970's the lead-acid battery industry experienced a major processing change toward high volume plate manufacturing technology based on the fabrication of continuous strip and conversion to grid mesh. Coincidental with this change was the introduction of battery alloys which reduce water loss, thus allowing batteries to be partially sealed and permitting maintenance-free operation. Certain of the contending alloys have sufficiently narrow freezing ranges to be cast continuously as strip by solidification on a rotating drum caster (1-4).

These, as well as other alloys, may also be rolled into strip form or cast by the conventional book-mold process. The most important commercially are the lead-calcium-tin alloys, which are currently produced both as discrete cast grids and as rolled or cast strip. The strip can be converted into grids by punching or by metal expansion methods.

For several years, sealed cylindrical lead-acid cells have been produced commercially with grids punched from cast strip. On an even larger scale, automotive starting-lighting-ignition (SLI) batteries are produced with book-mold-cast grids or with grids made by expanding heavily rolled (wrought) strip. Book-mold casting involves a batch process which is highly labor intensive and skill demanding. Expansion involves the partial slitting and separation of strip to form a network of diamonds.

Expanded diamonds are formed by three distinct actions: slitting, stretching, and expanding. Slitting creates a pattern of interrupted cuts in the material. Nodes are located in the area where no slitting occurs while the slit sections become the strands. In order to maintain the required node-to-node length the strands are stretched or elongated to prevent the contraction of the diamond during the final expansion step. Either

a rotary or a reciprocating-type action can be applied to metal expansion. The reciprocating method has hitherto been most widely used commercially. Patents for the rotary equipment are pending or granted (5). The Cominco rotary method carries out the three operations in two steps: first a simultaneous slitting and stretching action, followed immediately by the expansion or pulling apart of the diamond components to produce a mesh. The reciprocating method combines all three actions by means of an up-and-down punch press operation whereby the strip material is indexed rapidly through the expander where the tooling slits, stretches, and expands one row of strands and nodes during each stroke.

In spite of rapidly growing industrial acceptance of both cast and wrought ternary lead-calcium-tin grid alloys, very few results of corrosion testing of these alloys have been published (6-13). Even fewer results are available for corrosion of expanded grids (11) and none for rotary-expanded grids. Since the metal deformation which occurs during strip expansion or rolling results in substantial changes of metallurgical structure, and thus to possible changes in electrochemical characteristics, it is desirable to test alloys in their final form, *i.e.* as expanded grids. The results of bare metal corrosion tests may also not be directly relatable to pasted plate/battery grid performance (7). It has been shown that similar rates of corrosion are obtained for pasted and unpasted halves of a grid under float charge conditions (11). However, this might not hold if periodic discharges are experienced (as occurs in battery service) because of the mass transfer characteristics of the porous active mass in a pasted plate in comparison to that of the free electrolyte at the surface of the corrosion film on bare metal. Thus, it is desirable to test pasted plates in a battery environment under well-defined conditions relevant to the intended application.

* Electrochemical Society Active Member.

Key words: alloy, battery, potential, corrosion.

This paper describes corrosion testing of grid materials related to maintenance-free SLI battery applications. Alloys were selected having calcium and tin contents within the range normally used by the SLI battery industry. In addition, a composition typical of cylindrical sealed cells (Pb-0.007Ca) was chosen as well as a strontium alloy and two low-antimony alloys. Cast strip, rolled strip, and book-mold grids were fabricated into test cells as described below.

The tests were carried out under constant potential charging conditions, interrupted periodically by shallow discharges, or under open-circuit stand conditions. Tightly supported pasted grids, contained in composite cells (i.e., each cell contained all of the twelve test materials selected for this investigation), were tested at various temperatures and overpotentials. The cells were constructed so as to be as similar as possible to cells in SLI batteries except for the unusual multi-component positive plate arrangement. Weight loss, grain size, depth of penetration, tensile strength, and various other physical measurements were made for grids before and after the corrosion test. The weight loss and grid integrity results are discussed below.

Experimental

Thirty-seven experimental cells, each containing the twelve test materials were constructed in cell containers made by cutting up group 24 battery cases and covers. Normally sized expanded grids were hand-pasted for negatives with a leady oxide mix having a wet paste density of $4.7 \pm 0.1 \text{ g-cm}^{-3}$. After curing, the negative plates were enveloped and post straps were cast on to produce a normal negative plate group. Expanded mesh for positive mini-grids was made by rotary expansion of 0.9 mm thick strip followed by the punching out of mini-grids 5 cm wide and 10 cm high (excluding tab) from the expanded mesh. The grid materials and fabrication methods are shown in Table I. The cast strip lead-calcium-tin alloys were expanded 8 weeks after casting the strip. Alloys K and R were rolled within one day of casting. Alloy S was expanded the same day as it was cast. Alloy B was well aged (>6 months) after rolling and expanding. Commercial book-mold grids, having wires with cross sections comparable in size to the expanded grids, were cut to the same plate dimensions. One of the positive plate test materials (Lab code A) was unexpanded strip, 2.5 cm wide \times 10 cm high, which was to remain unpasted. The other eleven mini-grids were hand-pasted using a positive mix of wet density $4.27 \pm 0.07 \text{ g-cm}^{-3}$, which was cured in the same manner as the negatives, i.e., 40°C, 100% RH for ~3 days. The elemental compositions of major alloying agents, as determined by AA spectroscopy, are given in Table I. For the first nine alloys, the first digit of the mnemonic code indicates the nominal calcium content in hundredths of a percent, and the next two digits indicate the nominal tin contents in tenths of a percent. The portion of the mnemonic code following

the hyphen indicates fabrication method, as explained by the entries in the final column of Table I.

For each cell two positive mini-groups, containing six plate types each, were assembled by casting on a strap-post to each mini-group. Before pasting, each of the 444 (37×12) grids was individually coded, detailed metallographic and dimensional measurements were made, grid surface area was estimated, and the grids were stripped in an alkaline hydrazine-mannitol stripping solution (14) at 60°-70°C. The stripping solution contained approximately 10% sodium hydroxide, 1% hydrazine dihydrochloride, and 2% mannitol. The ratios of tab/grid weights were determined for similar grids prepared at the same time since it would be necessary to detach the tab (by cutting along the top of the upper grid bar) after exposure to the corrosion test, in order to determine final weights and corresponding weight loss. The standard deviation of this ratio was ~2% for each grid type.

The two positive mini-groups and the negative group were sandwiched together to form assembled elements, as shown schematically in Fig. 1. The two positive posts (shown as one in Fig. 1) were burnt together and appropriate leads were soldered to each of the terminal posts. All cells were given a 24 hr formation in 1.115 sp gr forming acid, initially at 10A (8.4 mA/cm^2) for 16 hr by which time the cell voltage reached the limit set of 2.67 V/cell. This corresponded to a positive plate potential (E_+) of 1.40V with respect to an Hg/Hg₂SO₄/1.30 sp gr H₂SO₄ reference electrode, to which all electrode potentials in this work are referred. Formation continued for another 8 hr at the constant voltage limit of 2.67 V/cell, during which time E_+ decreased to 1.35V, current decreased to a final value of 2.5A (2.1 mA/cm^2), and temperature also decreased. Electrolyte temperature above the plates was 32°-50°C during the entire formation period, reaching a maximum 3 hr after formation began and attaining a lesser maximum at the time when the cell voltage limit was reached. The forming acid was then replaced by 1.30 sp gr sulfuric acid and the cells were further charged overnight at 2.67 V/cell ($E_+ = 1.37\text{V}$). The specific gravity in the test cells was 1.27 ± 0.02 at 25°C. Water was regularly added to a reference mark in the cells undergoing testing.

After formation and charging, one cell was dismantled and, after removal of active material and chemical stripping, weight losses were determined before metallographic examination began. The remaining thirty-six cells were divided into six equal groups. Each group was maintained under the following conditions for the test durations indicated, with periodic cell removals for weight loss and other measurements: (i) 40° \pm 2°C, open-circuit (OC) stand, E_+ decreased from 1.18 to 1.10V during the 18 week duration; (ii) 50° \pm 3°C, OC, E_+ decreased from 1.18 to 1.11V during the 15 week duration; (iii) 50° \pm 3°C,

Table I. Grid alloys and fabrication methods for composite pasted plate cell test

| Lab code | Mnemonic code | % Elemental composition | | | | | Fabrication method |
|----------|---------------|-------------------------|-------------------|------|-----|------------|---------------------|
| | | Sn | Ca | Sr | Sb | Others | |
| A | 606-CS | 0.57 | 0.058 | — | — | — | Cast strip |
| C | 606-CX | 0.56 | 0.058 | — | — | — | Cast, expanded (X) |
| K | 606-C3X | 0.58 | 0.05 _s | — | — | — | Cast, 30% rolled, X |
| R | 606-C6X | 0.57 | 0.058 | — | — | — | Cast, 60% rolled, X |
| B | 606-R9X | 0.6 _s | 0.062 | — | — | — | Rolled >90%, X |
| D | 903-CX | 0.33 | 0.087 | — | — | — | Cast, X |
| P | 906-BM | 0.62 | 0.10 _s | — | — | — | Book mold |
| E | 909-CX | 0.89 | 0.086 | — | — | — | Cast, X |
| L | 100-CX | — | 0.007 | — | — | — | Cast, X |
| S | 2Sr-CX | 0.91 | — | 0.18 | — | 0.003 (Al) | Cast, X |
| V | 1Sb-BM | 0.09 | — | — | 1.4 | 0.03 (Se) | Book mold |
| W | 2Sb-BM | 0.11 | — | — | 2.3 | 0.02 (Se) | Book mold |

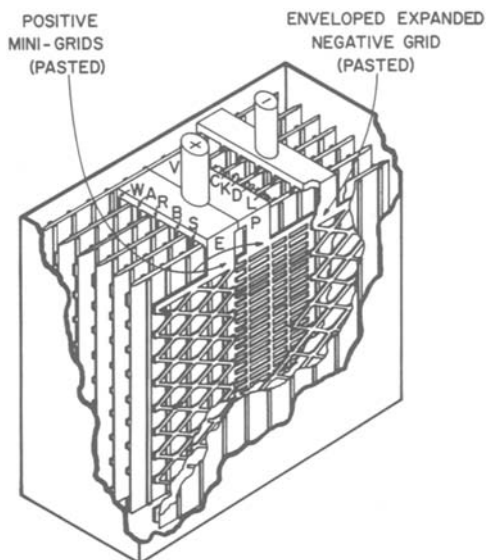


Fig. 1. Artist's schematic illustration of composite pasted plate test cell, indicating positions of test alloys.

$E_+ = 1.280 \pm 0.014V$ ($\eta = 100$ mV), 15 weeks; (iv) $40^\circ \pm 2^\circ C$, $E_+ = 1.382 \pm 0.011V$ ($\eta = 200$ mV), 10 weeks; (v) $50^\circ \pm 3^\circ C$, $E_+ = 1.381 \pm 0.015V$ ($\eta = 200$ mV), 46 days; and (vi) $65^\circ \pm 1^\circ C$, $E_+ = 1.380 \pm 0.014V$ ($\eta = 200$ mV), 27 days.

The electrode potentials were controlled by manual adjustment of cell voltage using power supplies. They remained within the indicated error limits for cells maintained at constant potential except for the approximately 1 hr required for cells controlled at 200 mV overpotential to recover from a discharge of 100 A-min each working day and the approximately 3 hr required for recovery of the 100 mV overpotential cells.

As cells were periodically removed from test, the positive mini-plates were individually stripped, the tab was removed along a line coincident with the top of the upper grid bar, and the grids were weighed. Metal surface areas were calculated from grid wire

and frame dimensions with an accuracy of about 8% for expanded metal grids (48 cm²), 6% for book-mold grids (60 cm²), and 1.5% for the bare coupon sample (55 cm²). Weight losses were expressed per unit area of metal immersed in the electrolyte in the test cell. Measurements were made to determine both vertical and horizontal growth of the grids for each cell on test. However, because of the uncertain effects of handling the expanded grids on their dimensions and the breakage of many grids due to wire severance, these data appeared unreliable and have not been reported. All grids were examined closely and rated with respect to integrity on a scale of 1 (best: no broken wires) to 5 (disintegrated into many fragmented wires) before being mounted for metallographic examination and measurements.

Results

Weight loss results are shown in Fig. 2 for cells tested at 50°C and at an overpotential, η , of 200 mV. Experimental points are indicated using the lab code given in Table I to indicate grid and alloy type and both lab and mnemonic codes are shown on the figure. High correlation coefficients, r , were obtained for a linear least squares fit of the weight loss (w) data with time (t)

$$w = a + bt \quad [1]$$

for alloys V ($r = 0.966$), W (0.996), S (0.997), L (0.984), A (0.983), D (0.983), and C (0.962). The latter four, however, had comparable and usually somewhat higher correlation coefficients, L (0.983), A (0.989), D (0.993), C (0.965), when fitted to an exponential function

$$w = a \exp(bt) \quad [2]$$

For the remaining grids, the exponential function clearly gave the best fit: K (0.9998), B (0.998), P (0.994), R (0.993), and E (0.936). The grids best described by exponential rate laws have been included in Fig. 2 and have been replotted on a semilogarithmic scale in Fig. 3. The standard error of the fit is indicated only for the fit of the data having the highest correlation coefficient in each figure. Power ($w = at^b$) and logarithmic ($w = a + b \log t$) two parameter rate laws were also tested but gave relatively poor correlations

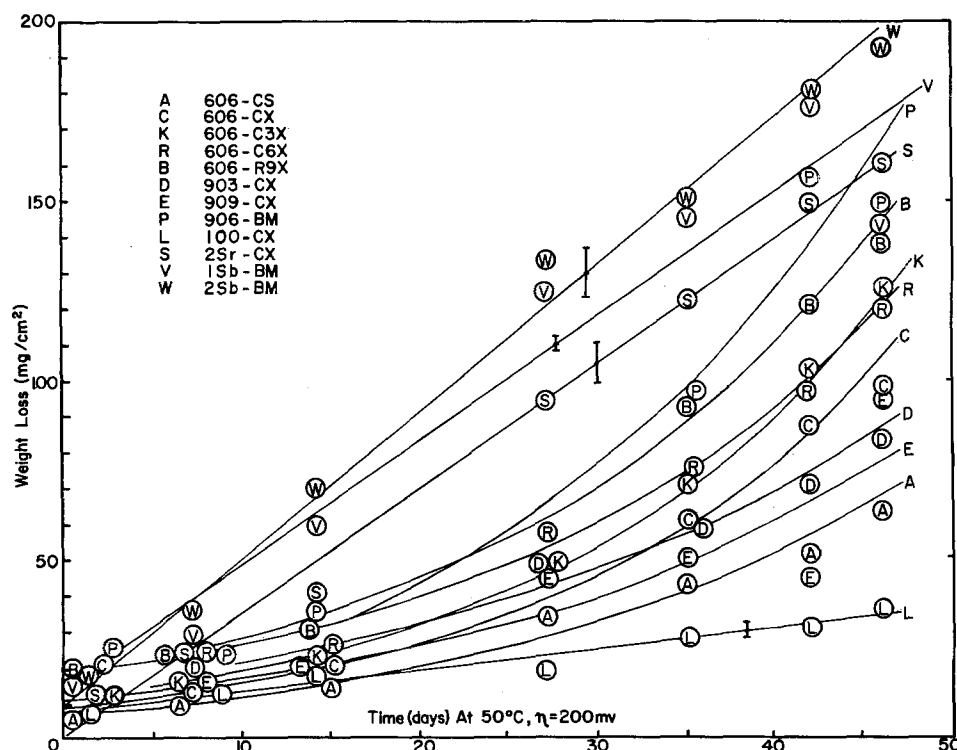


Fig. 2. Weight loss time-dependence for test materials at 50°C and 1.38V. Circled letters are experimental points and refer to the alloys of Table I. Error bars are shown for linear time dependences. Curves are exponential fits. Some points have been offset or omitted for the sake of clarity.

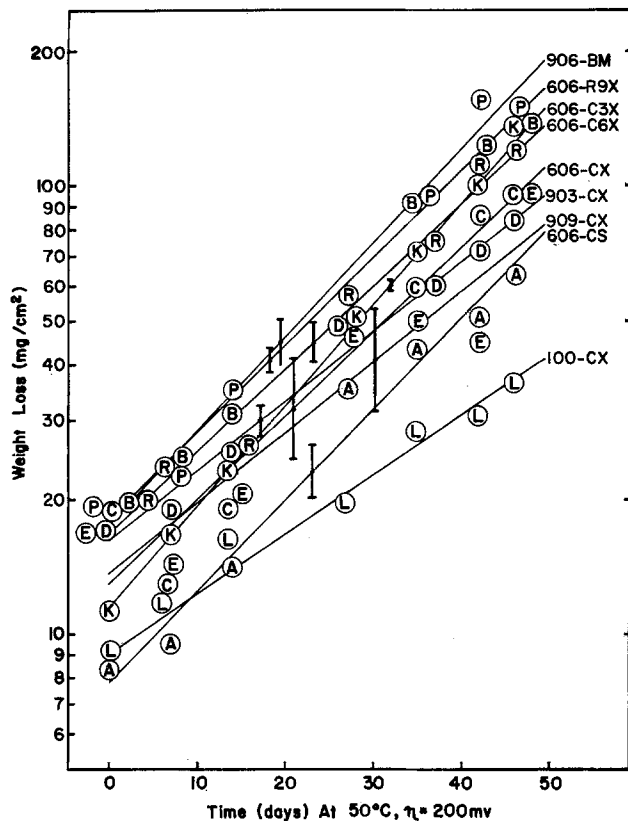


Fig. 3. Data of Fig. 2, for lead-calcium alloys, replotted on a logarithmic scale to indicate exponential dependence on time. Error bars are given for the eight ternary alloys best fitted by an exponential rate law.

in almost all cases for these and the other data described in this paper. In most cases where the exponential fit was best of all the two parameter rate laws tested, a higher correlation could be obtained with a second-order polynomial. However, often a fourth, or even higher, order polynomial was required to match the goodness of fit of the exponential function. "Paired-*t*" statistical analysis of the correlation coefficients for linear and exponential fits indicated, with a high level of confidence (>97.5%), that the exponential function described the data for the lead-calcium grids better than a linear function.

For these eight grids the correlation coefficients were 0.98 ± 0.02 s.d. For the other four grids, it could not be stated at the 90% confidence level that the linear fit was superior, because of the limited data under these conditions. When considered in association with the data obtained under other experimental conditions, it was possible to state, at the 99% confidence level (c.l.) that V, W, and S were best described by the linear function. The apparent preference for the linear fit with alloy L, however, could have occurred by chance with at least 10% probability.

The weight loss results for cells tested at 50°C, $\eta = 100$ mV, are shown in Fig. 4. Under these conditions, all of the grids, with two possible exceptions (B and D), appeared to be best described by a linear rate law. For the alloys containing calcium, however, correlation coefficients for the linear fits were relatively low ($r = 0.86 \pm 0.05$ s.d.). Even though higher values of r were obtained, for the antimony and strontium alloys, comparable to those at 50°C, $\eta = 200$ mV, it was still impossible (using the 50°C, $\eta = 100$ mV data only) to show at the 90% c.l. that the linear function gave a better fit than the exponential for either the calcium or the noncalcium groups.

The cell removed at 28 days had accepted a substantially higher current (2.15 ± 0.26 A for the last 21

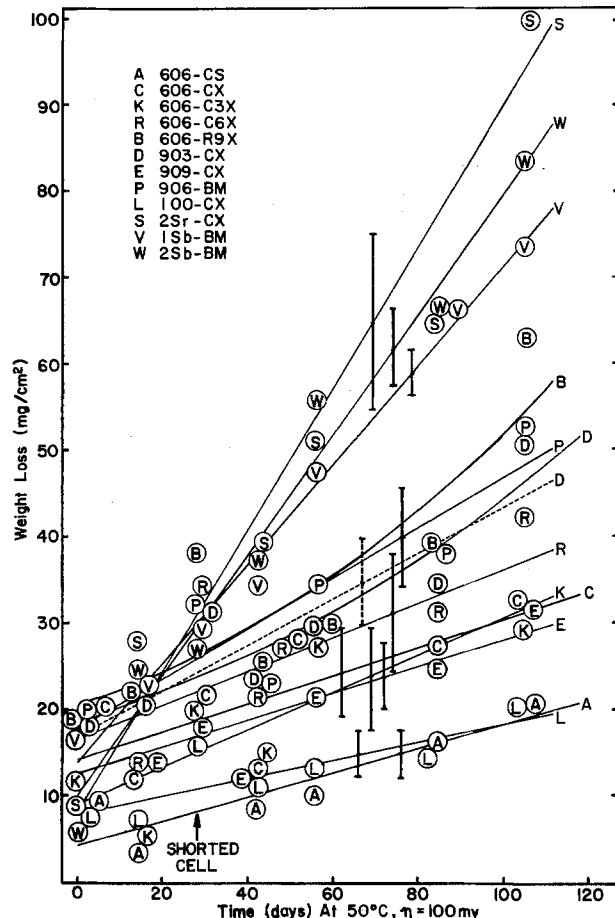


Fig. 4. Dependence of weight loss on time for test materials anodized at 50°C, 1.28V positive potential. Both the marginally better exponential fit (solid curve) and linear fit (broken line) are given for alloy D. Error bars are given only for linear fits.

days) than the other cells (0.32 ± 0.08 A for the same period) during the entire duration of the test, suggesting an internally shorted cell. When dismantled, visual inspection revealed that a short had developed between electrode A and the negative strap. The weight loss for A was very high due to loss of lead through fusion caused by the short. Weight losses for most of the grids from this cell seemed somewhat high, but since the electrode potentials were maintained at acceptable values (1.260 ± 0.015 V) in a potential region where corrosion is relatively insensitive to potential, the results were not discarded (except for one damaged grid, S). Other cells which developed shorts were removed from test as soon as possible after shorts were discovered and confirmed.

Under open-circuit stand conditions at 40° and 50°C (see Fig. 5), all of the alloys were best described by linear rate laws at the 95% c.l. However, the preference for a linear fit was not large. The difference in r values (Δr) between the two functions was 0.05 ± 0.07 s.d. All but two alloys gave r values ≥ 0.92 at 40°C and all but one gave $r \geq 0.95$ at 50°C for the linear fit.

At 200 mV overpotential, the results at 40°C were very similar to those at 50°C (Fig. 3), apart from the time scale, with all eight lead-calcium-tin alloys being well described by exponential rate laws ($r = 0.98 \pm 0.01$ at 40°C and $\bar{r} = 0.98 \pm 0.02$ at 50°C) at the 99% c.l. and the other four alloys being well described by linear rate laws (90% c.l.). The ratio of the b parameter of the exponential law at 50°C (slope in Fig. 3) to that at 40°C was 1.93 ± 0.24 for the eight alloys. The corresponding b parameter ratio for the linear laws was 1.75 ± 0.13 for alloys V, W, and S

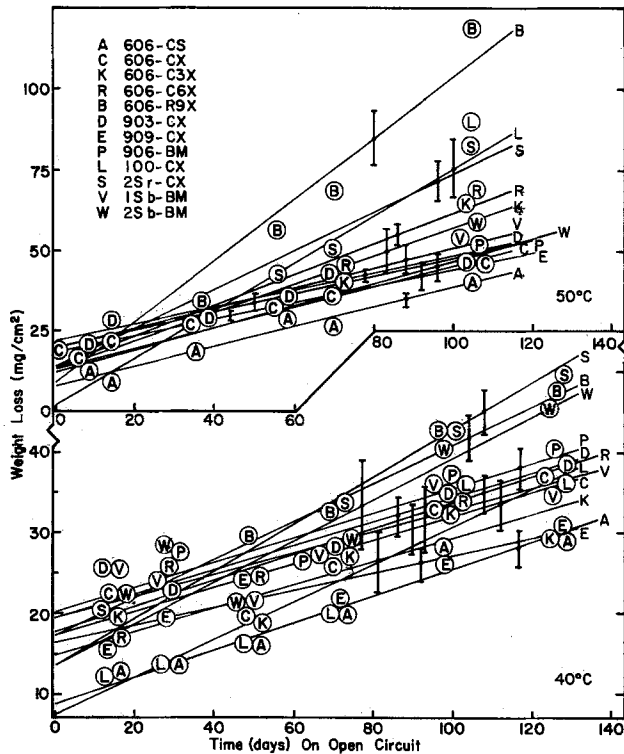


Fig. 5. Dependence of weight loss on time on open circuit at 40°C (lower) and 50°C (upper). Many points have been omitted or offset for clarity.

and 1.30 for alloy L. At 65°C, the pattern was noticeably different. Whether the data were grouped as before or taken all together, it was impossible at the 90% c.l. to show that one function fitted the data better than the other. The weight losses are shown as a linear function of time in Fig. 6. Linear fits for the three alloys (C, D, and L), which gave (insignificantly) higher r values for the exponential law, are shown with broken error bars. Further experiments were carried out with unpasted expanded cast strip coupons of alloys C, D, and two other compositions at 50°C and $\eta = 200$ mV. A potentiostat was used to control the potential much more accurately than was possible for the composite pasted plate cells. The current was observed to increase exponentially with time for as long as 70 days before reaching a constant value.

The data for B, C, and P at 65°C, shown in Fig. 6, have been replotted on a semilogarithmic scale in Fig. 7 for comparison with earlier results obtained in another experiment using unpasted grids from the same lots, B', C', and P'. The data for the unpasted grids appeared to fit exponential rate laws better than linear rate laws, although the preference was not significant, even at the 75% c.l., and data have been plotted on the semilogarithmic scale only for convenience. Weight losses for the expanded heavily rolled strip grids were greater than those for expanded cast strip grids by factors of 1.3-2.2. The results for alloy C were similar for pasted and unpasted expanded grids except that the unpasted grids required 2 weeks more to attain the same weight losses. A somewhat shorter delay was observed for alloy B (approximately 1 week at mid-experiment) and the slopes of the fitted line for B and B' were significantly different. For alloy P, as for alloy C, the same slopes were obtained for pasted grids as for bare grids; however, the weight losses were very much larger for the pasted grids than for the bare grids, corresponding to a 3 week delay in reaching a similar weight loss for unpasted grids. Of even more consequence is the apparent reversal of the order of corrosion rate for alloy P, in com-

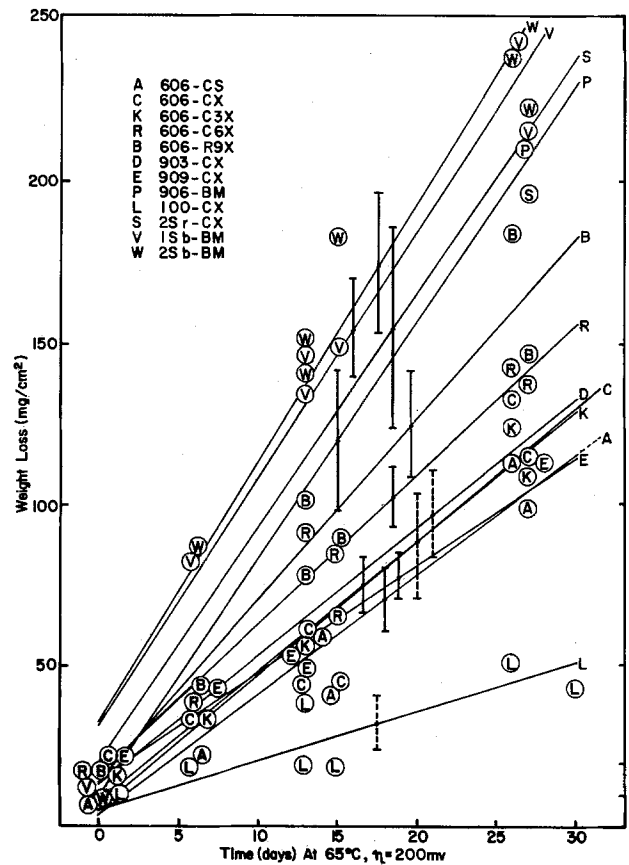


Fig. 6. Linear fit of weight loss data at 65°C, 1.38V positive potential.

parison to B and C, with P being the most corrosion resistant of the three materials for most of the life of the bare grids, but the least corrosion resistant when compared as pasted grids. Alloy P' also had a much higher slope than the other bare grids B' and C', in-

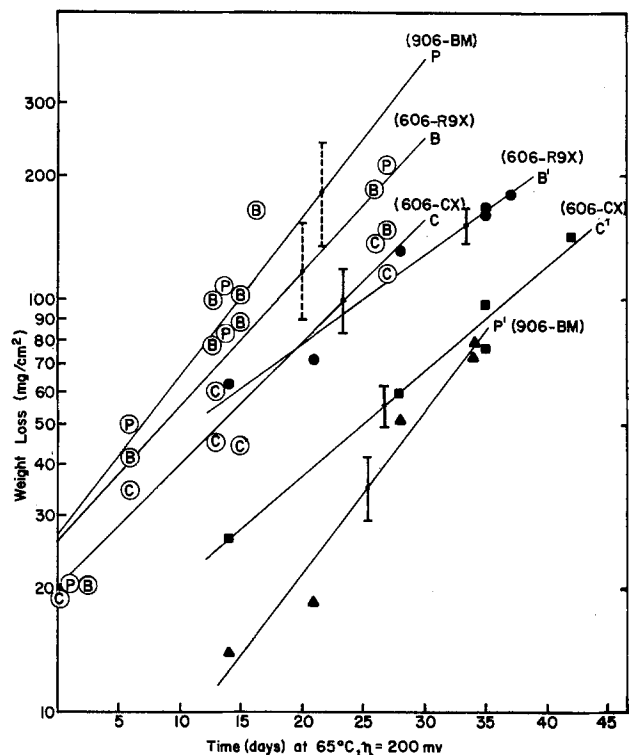


Fig. 7. Dependence of weight loss on time at 65°C and 1.38V potential for unpasted grids (B', C', and P') from same lots as pasted grids B, C, and P.

dicating a possible change of corrosion resistance for the P' grids during the experimental run. In fact, similar tests on other well-aged book-mold grids of somewhat different compositions (Pb-0.03Ca-0.6Sn and Pb-0.09Ca-1.0Sn) from a different source gave a lower slope, similar to those for B', C', and to other expanded grids of similar composition. The expanded mesh was tested as bare grids within a few weeks of expanding from strip. The cast strip was expanded 2 months after casting. The commercial heavily rolled strip was aged at least 6 months after rolling and before expansion. The book-mold grids were cast approximately 1 month before being tested as bare grids. However, these same materials were not tested as pasted plates for an additional 4-6 months. The high slopes for P' and possibly P may have been due to an aging process, taking place at an accelerated rate during the 65°C test, and possibly at room temperature in the interval between bare grid and pasted grid testing. Metallographic results and tensile testing indicated that changes in metallurgical structure and strength, due to elevated temperature of the test, does occur for B grids (15). These results will be discussed in a later publication (16). Such changes may have also caused the increase in slope for B in comparison to B', although this seems less likely since this material was already well aged before either test. No significant difference in slopes was obtained for C in comparison to C'.

The weight loss results, while important, are not sufficient to evaluate the usefulness of these alloys for an intended application. Accordingly, such metallurgical and dimensional parameters as grain size, depth of corrosion penetration, and grid growth were also measured. This work is still in progress and is not presented here. However, a macroscopic assessment of grid integrity has been completed for all cells. Figure 8 shows the stripped (and in some cases, reconstructed) grids of a cell, which had been con-

trolled at 50°C and 200 mV overpotential for 35 days. The weight losses (mg/cm²) are given below each grid, along with the lab and mnemonic codes. In Fig. 9, a similar comparison is presented for grids taken from another cell after 46 days at 50°C and $\eta = 200$ mV. As is apparent, grids having very similar weight losses often suffered markedly different losses of grid integrity as judged by broken wires. Loss of grid integrity was quantified on a scale from 1 to 5, with 1 indicating excellent retention of grid integrity, with no broken wires and little thinning (e.g., grids D and L in Fig. 8 and 9) and 5 indicating complete disintegration (grid S). Intermediate figures of merit were assigned, according to the number of broken wires and degree of grid fragmentation. The results of this assessment are displayed for the data obtained at 200 mV positive overpotential and at 40°, 50°, and 65°C in Fig. 10. Ranking of grid integrity, as based on such assessments, is given in Table II for 0, 100, and 200 mV overpotentials. Grids should only be compared within a column since comparison between columns is dependent on the duration of the tests at each overpotential. Grids in the same row within a column are approximately equal but superior to grids in lower rows. Where more than one test temperature was used, the ranking was averaged over all temperatures. A slight rearrangement of order is possible if ranking at only one temperature is of interest.

Discussion

Examination of the corrosion (weight-loss)-time dependences observed indicated that, with a high degree of confidence (99% c.l.) the antimonial alloy grids (V and W) and the strontium-tin alloy grids (S) had linearly increasing weight losses (i.e., constant corrosion rate) at all the temperatures and potentials investigated. The tin-free, low calcium grids (L) also appeared to show linearly increasing weight losses,

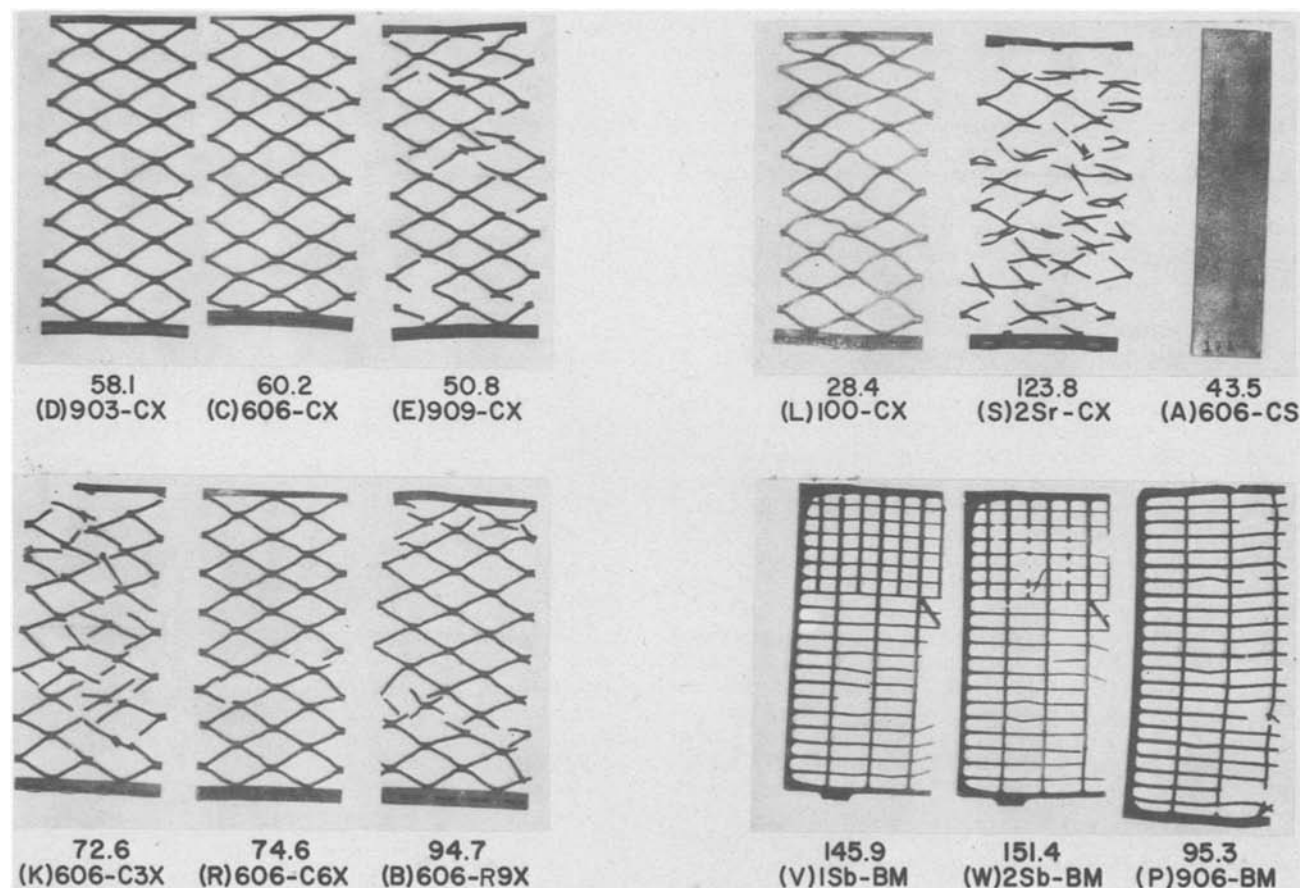


Fig. 8. Stripped grids and coupon from composite cell after anodization at 50°C, 1.38V ($\eta = 200$ mV) potential for 35 days. Codes identifying alloys and weight losses (mg/cm²) are indicated below each grid.

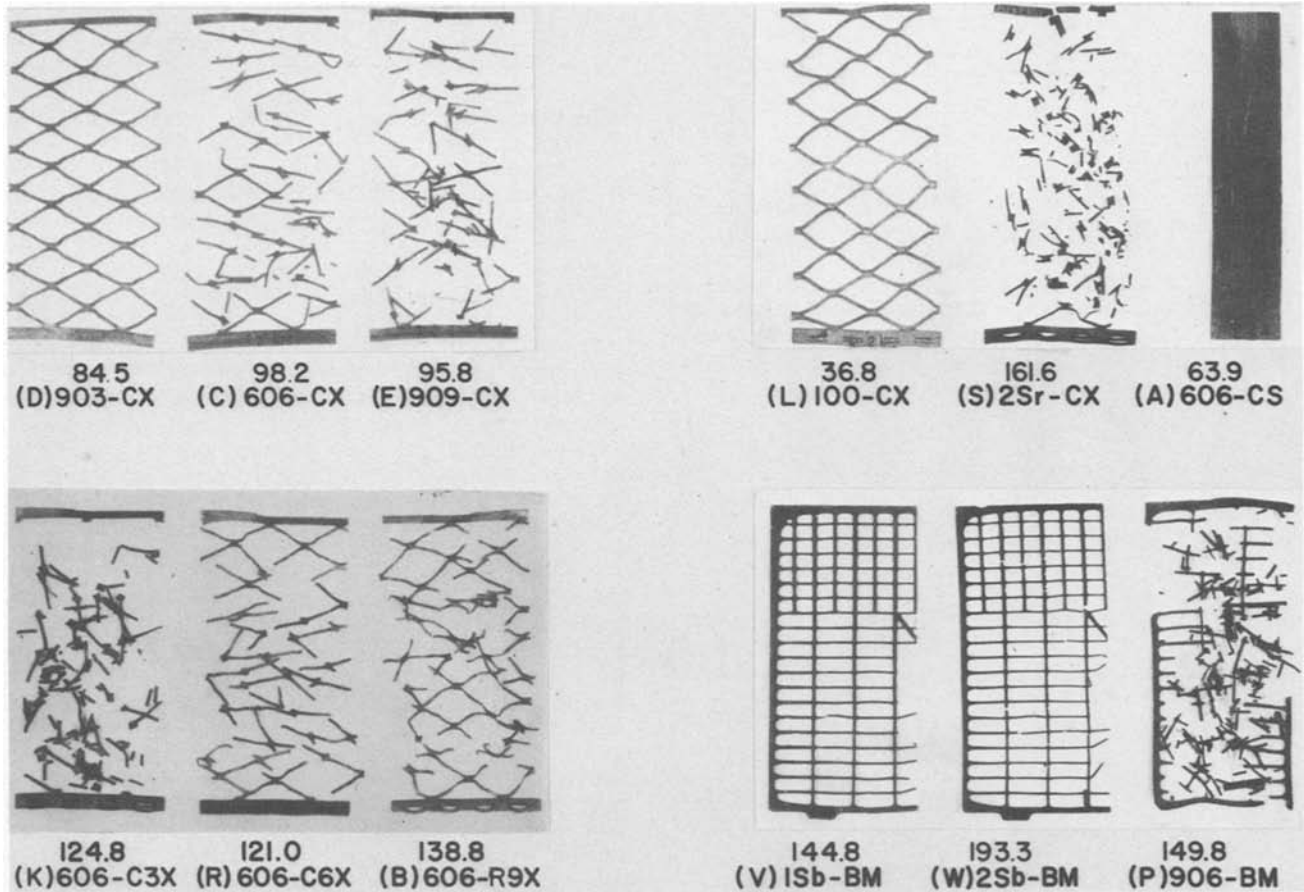


Fig. 9. Stripped grids and coupon from composite cell after anodization at 50°C, 1.38V ($\eta = 200$ mV) potential for 46 days. Identifying codes and weight losses (mg/cm²) are indicated in the figure.

but the slopes and corresponding correlation coefficients were low (due to the high corrosion resistance of this alloy) and there was a probability of over 10% that the preference for the linear fit was only due to chance.

For the lead-calcium-tin grids, however, the pattern was more complicated. At $\eta = 200$ mV a temperature dependence appeared such that all the lead-calcium-tin alloys clearly best fit exponential rate laws at 40° and 50°C. However, the preference for an exponential over a linear time dependence was reduced from the 99.5% c.l. at 40°C to the 97.5% c.l. at 50°C. At 65°C, the lead-calcium-tin grids showed no clear preference for exponential or linear behavior. As the potential was reduced from $\eta = 200$ mV at 50°C, the preference for exponential behavior again disappeared. At $\eta = 100$ mV, it was impossible to support one dependence over the other at the 90% c.l. At $\eta = 0$, the same was true if the lead-calcium-tin alloys were considered alone as a group. However, if all 12 alloys were grouped together at 50°C (or at 40°C) a linear dependence was preferred at the 95% c.l.

Thus, it appears that a change in the mode of corrosion must occur as overpotential is increased from the range of normal SLI operating conditions ($\eta = 0-$

100 mV) to the more severe charging conditions ($\eta = 200$ mV) corresponding to ~ 2.8 V/cell for a battery. In addition, as the temperature of the test is increased, the mode of corrosion either reverts to that under the milder conditions or else a third mode appears, which also follows a linear increase of weight loss. For the grids which did not contain calcium and tin, however, linear behavior was observed under all conditions. In the latter case, the more severe conditions appear to accelerate the relevant corrosion modes but for lead-calcium-tin alloys, it is possible that other corrosion modes irrelevant to the application may be induced if inappropriate choices of temperature and potential are made.

In the case of alloy B, preliminary metallography and tensile measurements (16) indicated that this material was undergoing metallurgical changes under the elevated temperatures of the experiment. For the other alloys, the reason for the complicated behavior was less obvious. However, it is possible to propose a model, consistent with most of the data. At least two obvious modes of corrosion were observed with these alloys. One was an apparently uniform corrosion, which would be expected to result in a constant corrosion current and, therefore, a linear increase of weight loss. The other was an intergranular, more penetrating, corrosion which would be expected to result in an increasing corrosion current, due to the generation of new electroactive area with time. If the current, i , is assumed to increase with time due to an increase of electrochemical area, A , then the rate of current increase can be expressed as

$$\frac{di}{dt} = j \frac{dA}{dt} \quad [3]$$

where j is the real current density. In the case of

Table II. Grid integrity ranking

| η | 0 mV | 100 mV | 200 mV |
|--------|--------------------|----------------------------------|--|
| E_+ | OCV | 1.28 V | 1.38 V |
| Best | L, D, V W, P, C | D, C, V, R E, K, P, B L, W | L D V, W, R P, C B K, E |
| Worst | E K, R B, S | S | S |

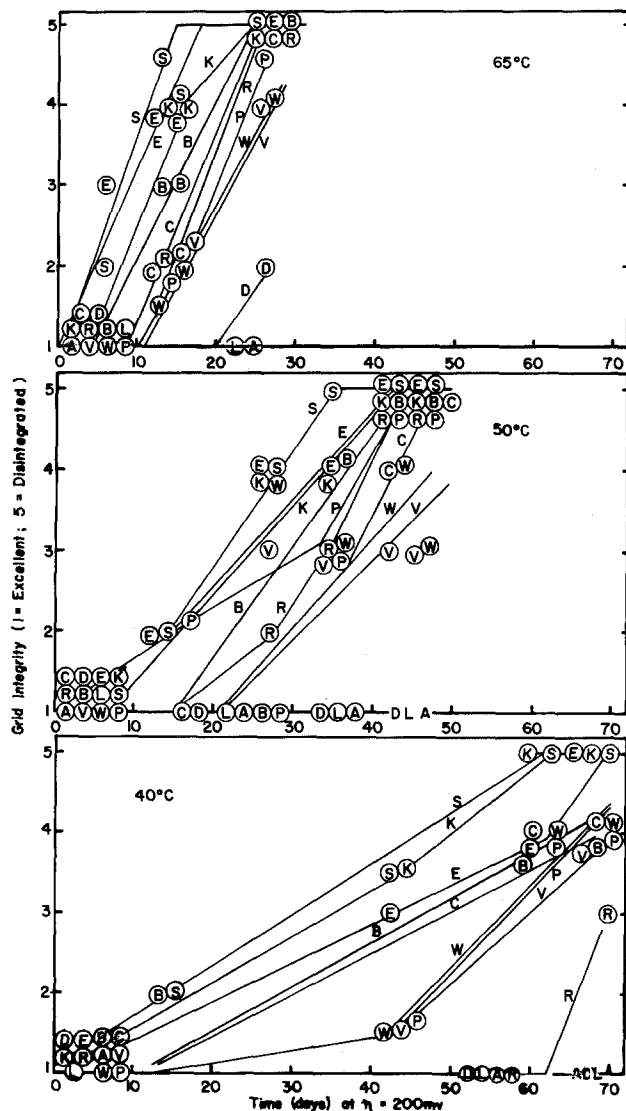


Fig. 10. Variation of grid integrity (see text) with time for grids corroded at 1.38V potential at three temperatures. Uncircled letters identify lines joining circled experimental points. Some points have been offset for clarity.

purely penetrating corrosion, if the increase of electrochemical area is $f_A \text{ cm}^2 \text{ C}^{-1}$, then

$$dA = f_A dq = f_A i dt \quad [4]$$

Upon integration

$$i = i_0 \exp(bt) \quad [5]$$

where $b = (i_0 f_A / A_0) s^{-1}$ and i_0 and A_0 are the initial current and electrochemical area, respectively. To exemplify the meaning of f_A , consider a model representing the lead lattice by an array of cubes having faces of area a_0 . For removal of one cube (atom) from a partially corroded surface layer, no new area is generated and $f_A = 0$; if a cube is removed from a new layer, however, four additional cube faces are exposed and $f_A = 4a_0 N/nF$ where N is Avogadro's constant and nF is the number of equivalents per mole of charge passed.

Integration of Eq. [5] to obtain the weight loss due to pure penetrating corrosion, w_p , gives

$$w_p = \frac{Mi_0}{bnF} [\exp(bt) - 1] \quad [6]$$

where M is the atomic weight of lead. In addition a constant current component, i_u , and a linearly increasing weight loss, w_u , will also occur due to uniform corrosion. The relative contributions of w_p and

w_u to the total weight loss will change with time since the currents in Eq. [3] and [4] are only identical if the current is solely due to one mode of penetrating corrosion. For large enough values of bt , the second term in Eq. [6] can be neglected as an approximation. For very small values of bt , $\exp(bt) - 1 \approx bt$ and Eq. [6] becomes linear in time.

Unfortunately the value of b and the relative contributions of i_p and i_u cannot be obtained *a priori* or treated exactly. Furthermore, using values of b obtained from the fits of Eq. [2], values of bt were found to be $\sim 1-2$ at the end of all experiments. Iteration methods might have been attempted to obtain an improved exponential fit using Eq. [6], rather than the more approximate Eq. [2]. However, this was not considered worthwhile in view of the other approximations involved and since only part of the total weight loss consists of w_p . Thus the degree of exponential behavior can only be taken as an indication of the relative extent of penetrating corrosion. Development and testing of a more detailed or exact model requires additional metallographic or other data.

Comparison of Fig. 2-6 indicates that ranking of the corrosion resistance of the alloys changes according to the applied potential. Thus at $\eta = 200 \text{ mV}$, the lowest corrosion rate at the end of the test was found for L and the highest for V and W, followed by S, P, and B. This ranking was also true at $\eta = 100 \text{ mV}$ except that alloy S suffered relatively more corrosion and P relatively less in comparison to the ranking at 200 mV. Under open-circuit conditions (Fig. 5), L corroded relatively rapidly and antimonial grids (V and W) were relatively much more corrosion resistant. In the absence of an applied potential, a corrosion cell exists between the alloys with this experimental arrangement so that the differences in corrosion rate will be reduced in comparison to the results expected with isolated grids. However, the order of corrosion rates should not be affected. The cast lead-calcium-tin grids remained slow to corrode, with the book-mold grids behaving much more like the expanded grids than they had at the higher overpotentials. The grids made from expanded rolled strip (B, R, and K) corroded relatively rapidly on open circuit, the corrosion rate increasing with degree of rolling at all potentials. However, as is evident from Fig. 8, a light rolling appeared to give rise to more localized attack at $\eta = 200 \text{ mV}$ than either a reduction of at least 60% or no rolling at all. Such an increase in macroscopically observable localized attack (*i.e.*, broken wires) was also seen for the cast grids having higher calcium and tin levels (E and P) at $\eta = 0$ and 200 mV, and for the rolled grids under open-circuit conditions.

The preliminary metallography generally supported these observations and the model discussed above. However, rather than the sharp penetration observed for some of the cast alloys, B (and R) appeared to suffer a broader localized attack with the formation of hemispherical pits of about 200 μm diam (see Fig. 11, top). The merging of these pits generated localized thinning. L also suffered localized thinning, but in this case, the attack at the corroding surface was uniform and the thinned areas extended over macroscopic dimensions, noticeable with the unaided eye. Grids S, E (Fig. 11, center), and K tended to exhibit a very sharply localized penetrating corrosion apparently either intergranular in nature or due to crack propagation. The other cast lead-calcium-tin grids (C, P, and D) show a limited intergranular attack ranging from moderate for C and P to slight for D (Fig. 11, bottom). This was combined with hemispherical pitting for the significantly rolled grids (B and R). The intergranular nature of the attack, even for heavily rolled, fine grained lead-calcium-tin can be seen in the high magnification photomicro-

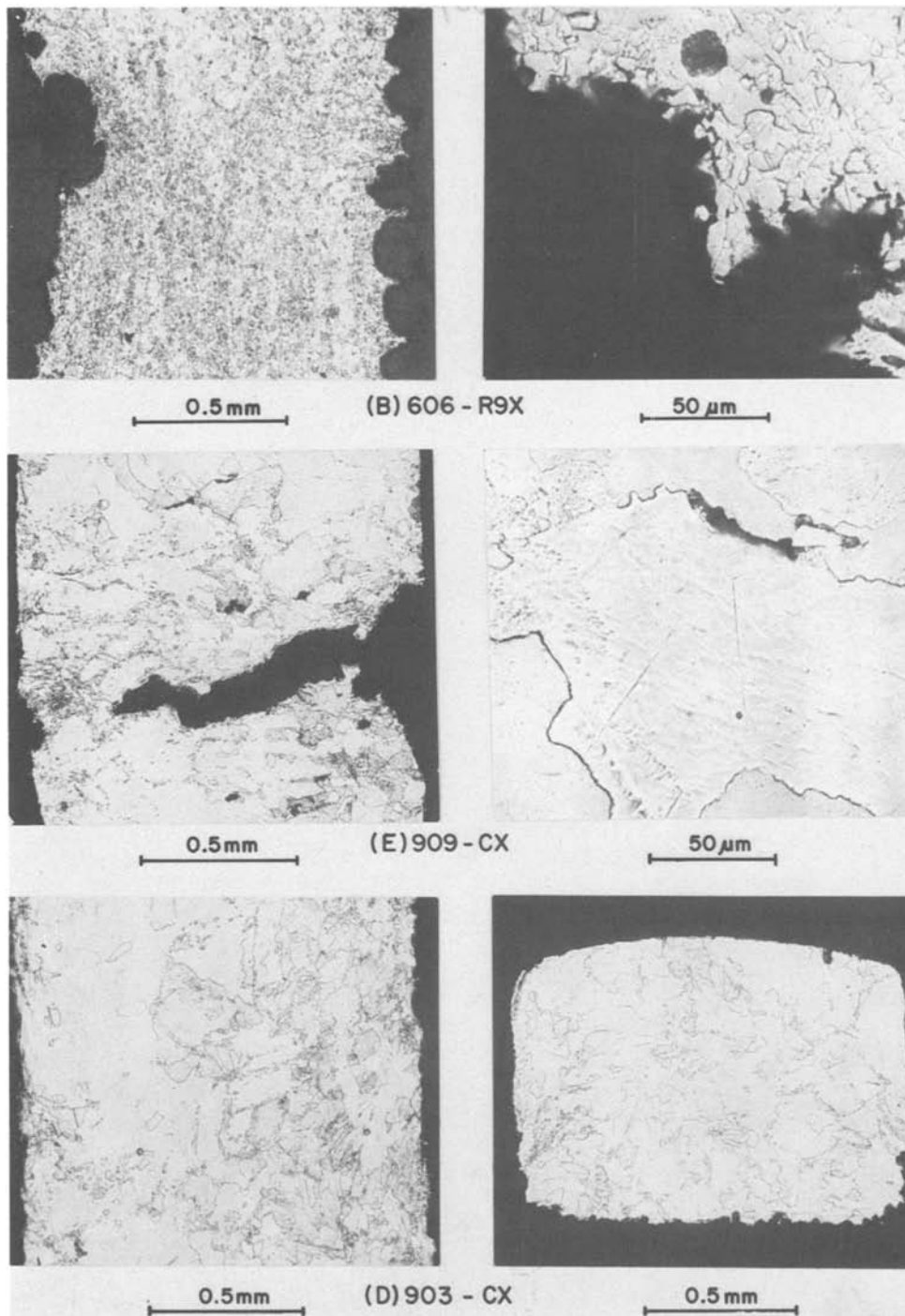


Fig. 11. Photomicrographs of longitudinally sectioned stripped grid samples after an open-circuit stand (following formation) of 105 days at 50°C. A transverse section is also shown for D, which showed the best corrosion characteristics of all the SLI grids tested.

graphs of Fig. 11. The antimonial grids, V and W, corroded very uniformly with minor surface pitting except for a few deep, highly localized penetrations, particularly near the wire intersections, believed to be due to casting defects. The results shown in Fig. 11 are similar to the metallography obtained for two cells at 200 mV overpotential, one at 50°C for 35 days and the other at 65°C for 13 days.

The exponential increase in weight loss with time is attributable to an increase in surface area as discussed above, whereas a linear increase indicates constant corrosion current (and thus area) with time. The increase in the rate constant for the exponential growth law from its initial value can be used to estimate this area increase. For the linear law, the rate constant is equal to the slope of the fitted line by differentiation of equation (1)

$$\frac{dw}{dt} = b \quad [7]$$

For the exponential fit

$$\frac{dw}{dt} = ab \exp(bt) \quad [8]$$

and the rate constant increases with time due to the increasing area available for corrosion. The initial grid area and the rate constant ab , referred to this initial area, were determined; the factor $\exp(bt)$ represents the dependence of electrode area on time during the course of each experiment. This factor ranged from 5 to 8 for the lead-calcium-tin grids which behaved exponentially at $\eta = 200$ mV. Grid B may have obeyed an exponential dependence for the tests at 0 and 100 mV. However, this can be confirmed only at the 75% c.l. and tensile testing and metallography indicated weakening and recrystallization occurring at the elevated temperature of the test (16). Recrystallization results in a thermally induced grain growth which may result in an increase in weight

loss and in depth of penetration (7-10). Such a dependence on grain size has only been shown to exist for grains grown from wrought samples by heat-treatment (10). Thus, the exponential increase in weight loss for the B grids may indicate an increasing susceptibility to corrosion with time as the unstable wrought structure recrystallizes, rather than solely an increase in area, as is probably the case for the cast lead-calcium-tin grids. After moderate lengths of time (2-7 weeks) at 0 and 100 mV, relatively uniform corrosion (not as uniform as for the antimonial grids) with some shallow pitting was observed. This is in agreement with previously reported results under similar conditions (10). However, after longer times or under more severe conditions, pitting effects became increasingly apparent.

In an effort to obtain further information about the corrosion kinetics, activation energies were determined from Arrhenius plots for the data obtained at $\eta = 200$ mV and 40°, 50°, and 65°C. Plots of $\ln b$ vs. $1/T$ and $\ln(ab)$ vs. $1/T$ were constructed for alloys with linear and exponential weight loss characteristics, respectively. For the eight lead-calcium-tin alloy samples obeying an exponential rate law, activation energies of 12.4 ± 1.0 kcal/mol¹ were obtained. For the other four alloys (L, S, V, and W) corroding at constant rate, activation energies were 10.7 ± 0.6 kcal/mol at $\eta = 200$ mV. At $\eta = 0$ (less reliable because only two data points could be used for the Arrhenius plot and because of possible electrochemical interaction between the coupled grids) activation energies were 17.2 ± 8 and 15.6 ± 7 kcal/mol for the eight lead-calcium-tin and four other alloys, respectively. These values are similar to one of two sets of values reported earlier for very low temperatures (i.e., -50°C to 0°C) of approximately 10 kcal/mol (17, 18) and 13 kcal/mol (19) for certain stages of the anodic oxidation, derived from experiments of much briefer duration (~ minutes or hours). Such values suggest that the rate-limiting process is either solid-state diffusion or a surface diffusion process through partially blocked pores. Pavlov reported activation energies of 7-11.5 kcal/mol which he ascribed (20) to solid-state diffusion of O_2^- ions through a PbO layer at potentials below the open-circuit value, and values of 10-17 kcal/mol have been reported (21-23) for open-circuit self-discharge. Regardless of the exact nature of the activation process, it is apparently the same at a given potential for all the alloys tested and so the activation energies give no information relevant to the differences in corrosion modes among the alloys. The activation energies at $\eta = 0$ were not sufficiently accurate to indicate a difference in corrosion mode from that at $\eta \sim 200$ mV, although it is likely that such a difference exists in view of the minimum in the corrosion rate at overpotentials of ~ 100 mV (23-26).

The exponential dependence of the weight loss results obtained for lead-calcium grids appear to be explained by the generation of additional electrochemically accessible surface due to intergranular penetration under the moderately severe (40° and 50°C, $\eta = 200$ mV) test conditions. Under milder conditions, more uniform and time-independent corrosion occurs. Changes of the metallurgical structures with time for heavily worked materials or the emergence of an additional, as yet unknown, factor at higher temperatures introduce new variables, which require further investigation.

This explanation is consistent with the linear weight loss increases observed for alloys V, W, and probably L and the metallographic results which indicate very uniform corrosion modes. It is not consistent with the results for the strontium-tin alloy (S), however,

which also followed a linear weight loss law, but exhibited a very nonuniform, intergranular or interdendritic mode of corrosion, in agreement with observations by Bagshaw (27) under corrosion conditions which were much more severe but of shorter duration than those used in the present work. While the Al content in the melt of the alloy tested here (0.03%) was similar to that of the cast alloys tested elsewhere (26, 27), the aluminum content of our cast expanded grid was much lower (0.003% Al), indicating that most of the aluminum in the melt was not incorporated into the strip during casting. Test conditions comparable to those reported here (but of shorter duration) have also been applied to the study of lead-strontium-tin-aluminum coupons (26) and no evidence was found for interdendritic penetration at the potentials investigated. It is hoped that further metallographic results and additional experimental work currently in progress will resolve the inconsistency of interpretation raised by the results for alloy S.

Notwithstanding this one possible anomaly, the weight loss and preliminary metallography suggest that the corrosion results obtained at higher potentials ($\eta = 200$ mV) are indicative of those which would occur under charging conditions corresponding to normal service (i.e., $\eta = 0$ and 100 mV) for the low antimony alloys tested (V and W) and the binary alloy (L) with very low calcium content. The same conclusion might tentatively be reached based on the weight loss data alone for the lead-strontium-tin alloy. However, for lead-calcium-tin alloys, whether produced as cast grids, or as expanded wrought or cast strip, corrosion modes at $\eta = 200$ mV may be more penetrating than those at lower potentials and further differences may appear at high temperatures. Thus, the predictive value of accelerated corrosion testing has not been clearly established for lead-calcium-tin alloys and will depend on the appropriateness of the accelerating conditions chosen.

In particular, constant current overcharge tests currently prescribed, such as the overcharge life test in SAE J-537j (28), are unsuitable for lead-calcium-tin batteries unless modified to limit the voltage to values that accelerate the normal corrosion modes (or actual failure modes if not corrosion-related) and do not induce or accelerate irrelevant modes. There are also some indications that elevated temperatures must be similarly limited and it is hoped to clarify this by work in progress.

Conclusions

Comparisons of corrosion rates for pasted lead-calcium-tin and lead-strontium-tin rotary expanded grids made from cast and/or rolled strip and book-mold lead-calcium-tin and low antimony grids indicated that all had acceptable weight losses under environmental and electrical conditions corresponding to normal vehicle service. However, there were appreciable differences in weight loss and grid integrity between the alloys. The antimonial and strontium grids gave the highest weight loss under charging conditions. Weight loss of the cast lead-calcium-tin alloys increased with degree of rolling. Results for pasted book-mold grids appeared anomalously high. A tin-free low-calcium soft grid suffered the lowest weight losses under charging conditions but relatively high weight loss after long periods on open circuit. The antimonial grids gave relatively low weight loss on open circuit.

Changes of the rate laws for the lead-calcium-tin grids with increases in potential and temperature suggest changes in corrosion mode with these parameters. This indicates the need for further definition of the conditions which accelerate the relevant corrosion modes without inducing new modes, and

¹ 1 kcal = 4.18 kJ.

reassessment of standard corrosion or failure-accelerating tests in terms of their applicability to non-antimonial batteries. No change in corrosion mode with temperature or potential could be deduced from the weight loss data for the antimonial or the tin-free grids within the limits investigated. This was also true for the strontium-tin alloy, although preliminary metallographic data were in conflict with interpretations of the rate laws observed in this case.

Consideration of macroscopically observable grid integrity indicated wide variations in degrees of susceptibility to a penetrating corrosion attack. The lightly rolled (30%) Pb-0.06Ca-0.6Sn grids, the lead-strontium-tin grids, and the Pb-0.09Ca-0.9Sn grids showed a high vulnerability to such attack, which preliminary metallography indicated was intergranular and/or due to the wedging action of corrosion products on preexisting cracks (29), generated during fabrication. For all of the lead-calcium-tin grids, regardless of whether or not they had been rolled before expansion, the attack appeared to be intergranular. This attack eventually led to nonuniform corrosion or to localized penetration for all SLI compositions (including the uniformly corroding antimonial alloys) except Pb-0.09Ca-0.3Sn. The latter alloy exhibited no broken wires under any of the test conditions, except at the end of the most severe test (65°C, $\eta = 200$ mV). Almost all other SLI compositions showed some wire breakage half-way through the test. For rolled materials in comparison to cast, the localized corrosion tended to appear more as hemispherical pits, as a result of grain undercutting. On the basis of observations of grid integrity, the Pb-0.09Ca-0.3Sn expanded cast strip clearly showed the best corrosion resistance of the SLI compositions; its performance was exceeded only by the soft Pb-0.007Ca binary alloy grid.

Further work is planned or in progress to clarify some of the new questions raised by the results discussed, including quantitative metallography on samples of the grids reported and new corrosion testing of further compositions of interest.

Acknowledgments

Useful discussions with P. C. Coghlan and P. Nielsen, and the metallographic assistance of W. W. Gregory, are particularly acknowledged, as well as technical assistance by D. Kilby, L. D. Groenendyk, and other Cominco employees, and illustrations by C. Garcia. The collaboration of G. H. Laurie and R. T. Sakauye in the preparation of a preliminary presentation of this work (30) and to the introductory section of this paper is duly acknowledged.

Manuscript submitted Oct. 12, 1980; revised manuscript received Feb. 20, 1981. This was Paper 55 presented at the Los Angeles, California, Meeting of the Society, Oct. 14-19, 1979.

Any discussion of this paper will appear in a Discussion Section to be published in the June 1982 JOURNAL. All discussions for the June 1982 Discussion Section should be submitted by Feb. 1, 1982.

Publication costs of this article were assisted by Cominco Limited.

REFERENCES

1. A. M. Vincze, *The Battery Man*, p. 16 (April 1976).
2. G. H. Laurie, T. J. Seymour, T. W. Watson, and J. R. Wellington, Proceedings of 86th Battery Council International Convention, London, May 13-16, 1974, p. 24.
3. K. D. Geiger, S. J. Horvath, V. P. Kallay, T. J. Seymour, T. W. Watson, and J. Zervoudis, U.S. Pat. 3,926,247 (1975); Patent Specification 1,487,142, Patent Office, London, 1977; Canadian Pat. 1,031,533 (1978).
4. L. Battiston, P. Niessen, J. R. Wellington, and T. W. Watson, U.S. Pat. 3,858,642 (1975); Canadian Pat. 978,324 (1975).
5. G. H. Laurie, J. V. Marlow, R. T. Sakauye, and T. J. Seymour, Canadian Pat. Applications 315,190 (1978) and 333,003 (1979); U.S. Pat. Application 970,298 (1978)/granted March 30, 1981.
6. J. J. Lander, *This Journal*, **99**, 467 (1952).
7. J. A. Young and J. B. Barclay, Proceedings of 85th Battery Council International Convention, San Francisco, May 1-3, 1973, p. 37.
8. M. V. Rose and J. A. Young, Proceedings of 5th International Lead Conference, Paris, Nov. 18-22, 1974.
9. J. A. Young and M. V. Rose, Proceedings of 87th Battery Council International Convention, Hollywood-by-the-Sea, Fla., April 8-10, 1975, p. 127.
10. A. T. Balcerzak, J. A. Young, and R. L. Amistadi, Abs. 16, p. 38, The Electrochemical Society Extended Abstracts, Toronto, Ont., Canada, May 11-16, 1975.
11. J. L. Weininger and E. G. Siwek, *This Journal*, **123**, 602 (1976).
12. J. L. Weininger, *J. Power Sources*, **2**, 241 (1977-1978).
13. R. D. Prengaman, Abs. 61, p. 166, The Electrochemical Society Extended Abstracts, Atlanta, Ga., Oct. 9-14, 1977.
14. J. J. Lander, *This Journal*, **103**, 1 (1956).
15. P. C. Coghlan and F. N. Coady, Cominco Product Research Centre, Unpublished data, January 18, 1980.
16. E. M. Valeriote and P. C. Coghlan, Work in progress.
17. E. M. L. Valeriote and L. D. Gallop, Paper No. 5, in "Power Sources 5," Proceedings of 9th International Power Sources Symposium, Brighton, September 1974, D. H. Collins, Editor, Academic Press, New York (1975).
18. E. M. L. Valeriote and L. D. Gallop, *This Journal*, **124**, 380 (1977).
19. T. G. Chang, M. M. Wright, and E. M. L. Valeriote, Paper No. 7, in "Power Sources 6," Proceedings of 10th International Power Sources Symposium, Brighton, September 1976, D. H. Collins, Editor, Academic Press, New York (1977).
20. D. Pavlov, *Electrochim. Acta*, **23**, 845 (1978).
21. K. R. Bullock and D. H. McClelland, *This Journal*, **123**, 327 (1976).
22. P. C. Milner, *Bell Syst. Tech. J.*, **49**, 1321 (1970).
23. P. Ruetschi and R. T. Angstadt, *This Journal*, **111**, 1323 (1964).
24. J. J. Lander, *ibid.*, **98**, 213 (1951).
25. C. E. Weinlein, J. R. Pierson, and D. Marshall, Paper No. 5, in "Power Sources 7," Proceedings of 11th International Power Sources Symposium, Brighton, September 1978, J. Thompson, Editor, Academic Press, New York (1979).
26. K. R. Bullock and W. H. Tiedemann, *This Journal*, **127**, 2112 (1980).
27. N. E. Bagshaw, *J. Power Sources*, **2**, 337 (1977-1978).
28. SAE Handbook, 1979, Part 1, Section 22, Society of Automotive Engineers, Inc., Warrendale, Pa. (1979).
29. D. Kelly, University of Waterloo, Private communication.
30. G. H. Laurie, R. T. Sakauye, and E. M. Valeriote, Abs. 55, p. 139, The Electrochemical Society Extended Abstracts, Los Angeles, Calif., Oct. 14-19, 1979.

Chemical and Morphological Characteristics of Lithium Electrode Surfaces

S. P. S. Yen, D. Shen, R. P. Vasquez,
F. J. Grunthaler, and R. B. Somoano*

Jet Propulsion Laboratory, California Institute of Technology, Pasadena, California 91103

ABSTRACT

In order to elucidate the physical and chemical characteristics of the anode passivating film in secondary lithium batteries, we have conducted ESCA (electron spectroscopy for chemical analysis) and SEM (scanning electron microscopy) studies of lithium electrode surfaces. The samples include lithium metal as-received from the vendor, and lithium electrodes which were cycled in a 1.5M lithium arsenic hexafluoride/two-methyl tetrahydrofuran (LiAsF₆/2-Me-THF) electrolyte. The results of studies of the as-received lithium indicate that the surface is covered by a film containing only carbon, oxygen, and lithium. Binding energy analysis and model compound studies indicate that this "native" film has a probable two-layer structure consisting of Li₂O covered by an outer Li₂O-CO₂ adduct, at a total thickness of 100-200Å. No evidence of Li₃N was found. ESCA/SEM studies of cycled lithium electrodes reveals the presence of a second film formed in the electrochemical environment. This film appears to consist, in some part, of degradation products and impurities associated with the LiAsF₆/2-Me-THF electrolyte, possibly in the form of lithium arsenic oxyfluorides.

The battery system consisting of a lithium anode, a lithium arsenic hexafluoride/two-methyl tetrahydrofuran (LiAsF₆/2-Me-THF) electrolyte, and a titanium disulfide (TiS₂) intercalatable cathode shows promise of yielding high energy density and cycle life (1). However, the organic electrolyte is unstable in the presence of lithium. Cells of this type function only because a reaction occurs at the lithium anode/organic electrolyte interface which results in the formation of a passivating film on the anode surface (2-4). This film, in turn, imparts some degree of kinetic stability to the system. In order to evaluate, and hopefully exploit, the beneficial characteristics of these ambient temperature lithium cells, a fundamental understanding of the basic physical and chemical processes which occur in this film and relate to battery performance is required. Surface spectroscopy studies involving the use of ESCA (electron spectroscopy for chemical analysis) and SEM (scanning electron microscopy) offer the opportunity to directly determine and correlate the chemical and morphological characteristics of the passivating film. We report the results of our ESCA and SEM studies of lithium electrodes both before and after exposure to an electrochemical environment.

Experimental

The ESCA spectrometer used in this work is a modified HP 5950A system (5). Aluminum K_α radiation (1486.6 eV) is used and all data are referenced to the Fermi level of gold. Samples were loaded into dessicators while in an argon glove box. Upon evacuation, the dessicators were transported to the spectrometer where the samples were mounted while in a high purity argon atmosphere maintained in a stainless steel dry box connected to the instrument. Spectra were accumulated at pressures not exceeding 5×10^{-10} Torr and a resolution of 0.4 eV. The spectrometer senses a sample area of 1×5 mm with an observation depth, for these studies, of ~ 100 Å. The ESCA spectra give information on elemental composition, but more importantly, permits assignment of the chemical state of various surface species. The

SEM studies were carried out using in-house facilities. The scanning electron microscope is a Cambridge S4-10 Stereoscan instrument equipped with an energy dispersive spectrometer (EDS) which permits detection of all elements of atomic number greater than nine, within the field of view. The spectrometer utilizes energy dispersive analysis by x-rays (EDAX) for element detection. The lithium samples were studied using a 20 kV beam voltage which yields an observation depth of ~ 20 μm and an element detectivity of approximately 1% by weight.

Two types of lithium samples were examined: (i) lithium metal as-received from the vendor (Foote Mineral Company); and (ii) lithium electrode surfaces which have undergone stripping and plating in a 1.5M LiAsF₆/2-Me-THF electrolyte. For this experiment, a cell containing two lithium electrodes (3 cm² area per electrode) was used. Lithium was stripped and plated at constant voltage (0.8 and 2.1V) corresponding to current densities of ~ 3 and 8 mA/cm², respectively, at room temperature.

The electrolyte salt, LiAsF₆, (from U.S. Steel Corporation) was outgassed at 75°C for 12 hr to remove any volatile impurities (6). The electrolyte solvent, 2-Me-THF, was purified by column distillation (~ 40 theoretical plate number) after being stirred with CaH₂ for three days. The solvent was then vacuum distilled from a sodium-potassium (NaK) naphthalide solution to further remove trace amounts of H₂O and active hydrogen containing compounds, e.g., alcohols. A final vacuum distillation from a lithium naphthalide solution was carried out to remove lithium-sensitive impurities, i.e., THF. The solvent was analyzed by gas chromatography, high pressure liquid chromatography, and gas chromatography/mass spectroscopy (GC/MS). The results of these analyses indicated that commercial 2-Me-THF (as received) is quite impure, containing methyl-furan, higher alcohols, and an inhibitor. Column and vacuum distillation procedures successfully remove most of these impurities, but methyl-furan remains at a significant level ($\sim 0.4\%$ by weight). Thus, the presence and possible contribution of this compound must be considered when investigating electrochemical degradation mechanisms.

* Electrochemical Society Active Member.
Key words: secondary lithium battery, ESCA/SEM studies, passivation, degradation, organic electrolyte.

Two model compounds, Li_2O which was deliberately exposed to air and Li_2CO_3 , were also examined by ESCA in order to assist the interpretation of the ESCA chemical shift data taken on lithium electrode surfaces. These compounds were outgassed at 200°C for 2 hr prior to study. Special techniques were used to transfer all of the samples from the glove box to the ESCA and SEM facilities in order to insure that they were never exposed to any atmosphere other than argon or high vacuum during the duration of this investigation.

Results and Discussion

ESCA/SEM studies of as-received lithium.—A typical ESCA spectra of the surface of as-received lithium metal is shown in Fig. 1. The spectra is a 0-1280 eV binding energy scan of the kinetic energy distribution. The ordinate reflects the number of photoelectrons and the abscissa shows the binding energy (eV) increasing from right to left. Since it is often necessary to take spectra under different conditions, only the relative intensities are important. The important feature to notice is that only carbon, oxygen, and lithium were detected. Figure 2(a), (b), and (c) show expanded (high resolution) views of the spectra associated with each of these elements. Two types of carbon, two types of oxygen, and two types of lithium are observed. Based on binding energy analysis, we find: (a) one type of carbon is associated with hydrocarbons (from the pumping facility and hydraulic press in the dry box) adsorbed on the lithium surface while the other carbon indicates polar bonding, e.g., C-O; (b) one type of oxygen is associated with lithium as Li_2O while the other oxygen appears bonded to carbon and also associated with lithium; and (c) both types of lithium present are ionic. It was initially thought that the second type of oxygen and lithium were combined in the form of Li_2CO_3 . However, measurement of binding energy differences, a measure of charge transfer (5), for the model compounds, Li_2O exposed to air and Li_2CO_3 , indicate that pure Li_2CO_3 is not present on the surface of as-received lithium. Instead, it is an $\text{Li}_2\text{O}/\text{CO}_2$ adduct. This adduct occurs upon exposure of the Li_2O to air which contains moisture and CO_2 . The hydrogen bonding associated with the moisture encourages the adduct formation. Note that lithium metal, Li^0 , was not observed. Thus, it appears that the surface of as-received lithium is covered by a "native" film consisting of Li_2O and an $\text{Li}_2\text{O}/\text{CO}_2$ adduct.

In order to assess the ability to remove this native film, the lithium surface was etched with an argon ion beam (1 mA for as long as 90 min) while in the ESCA facility. Initial etching removes the hydrocarbons. Continued etching results in the increase of

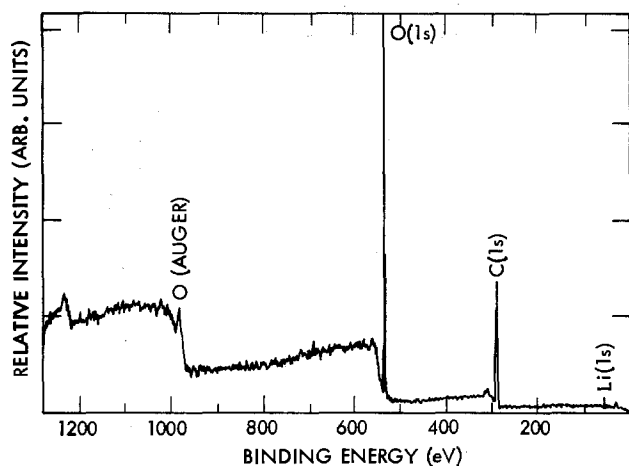


Fig. 1. ESCA spectra (wide scan) of as-received lithium

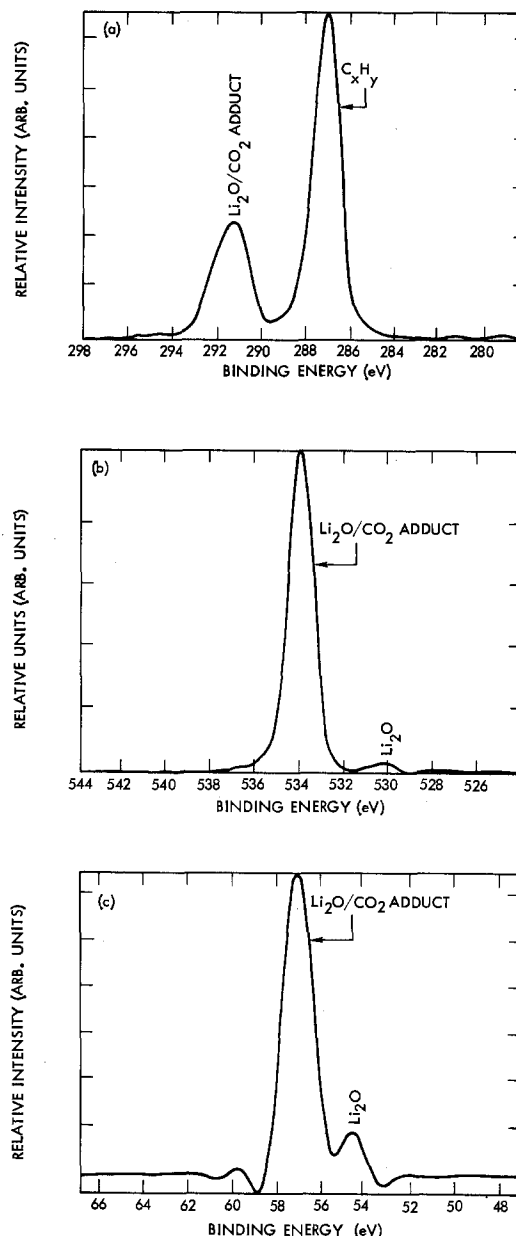


Fig. 2. As-received lithium: (a) smoothed carbon 1s spectrum; (b) smoothed oxygen 1s spectrum; and (c) deconvoluted lithium 1s spectrum.

the oxygen component associated with lithium only (i.e., Li_2O) compared to that associated with the $\text{Li}_2\text{O}/\text{CO}_2$ adduct [compare Fig. 3(a) with Fig. 2(b)]. This could indicate removal of CO_2 from the adduct or removal of the $\text{Li}_2\text{O}/\text{CO}_2$ adduct layer. Prolonged etching reveals the emergence of the underlying bulk lithium metal, Li^0 [compare Fig. 3(b) with Fig. 2(c)]. No evidence of lithium nitride was observed, reflecting the absence of moisture in the environment in which the metal was prepared and handled. The etching experiments also revealed the presence of Si, in the form of lithium silicate [Fig. 3(a) and (b)] as well as fluorine, possibly in the form of LiF . Note that neither silicon nor fluorine were observed by ESCA on the surface of as-received lithium prior to etching. The source of the fluorine is attributed to previous etching experiments using HF in the ESCA facility. The silicate is a bulk impurity in lithium. These results indicate that the surface of as-received lithium is covered by an Li_2O film which is then covered by an outer $\text{Li}_2\text{O}/\text{CO}_2$ adduct film. The thickness of this native film was determined to be between $\sim 100\text{-}200\text{\AA}$ from the etching experiments.

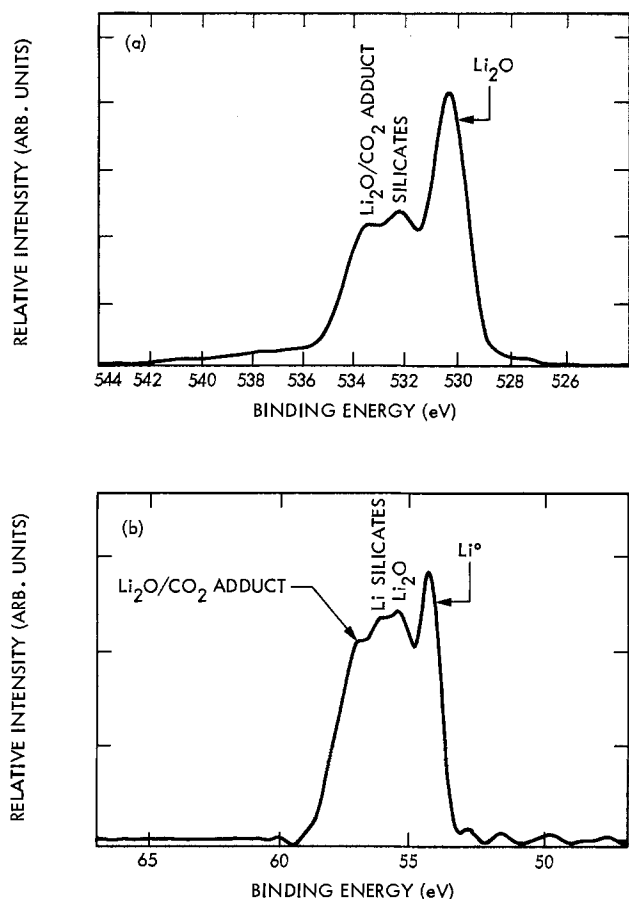


Fig. 3. As-received lithium after etching with an argon ion beam: (a) smoothed oxygen 1s spectrum and (b) smoothed lithium 1s spectrum.

SEM studies of the surface of as-received lithium reveal the presence of sizable defects, pinholes, and ridges on the scale of 1-10 microns. In addition, the surface does not appear dense and flat, but rather exhibits a rippled appearance. Argon etching (to remove the oxide and adduct films) does not appear to further degrade the surface. Energy dispersive spectroscopy (EDS) studies also show Si to be present in the bulk of the sample, in agreement with the ESCA results on etched samples. No black spots were observed on the lithium surface (7).

ESCA/SEM studies of cycled lithium electrode surfaces.—Initial ESCA/SEM studies were carried out on lithium electrode surfaces which had undergone one stripping or plating half-cycle.

Stripped electrode surfaces.—Upon stripping (discharge), examination of the surface by ESCA revealed the presence of As, F, Si, and Mg in addition to the usual Li, O, and C elements, Fig. 4(a) and (b). ESCA studies were also carried out on LiAsF₆. The results of this work confirm that LiAsF₆ is not absorbed on the lithium electrode surface and, thus, indicate that the presence of As and F are the results of electrolyte degradation. Although Si was found in the bulk of as-received lithium by EDS, the Si observed on the surface by ESCA, as well as Mg, are believed to originate from the LiAsF₆ salt where they are present as trace impurities (6). A careful analysis of the binding energies of the observed peaks plus the absence of any high binding energy peak which would be associated with LiF indicates that neither LiF nor arsenic oxides are present. While the actual chemical form of the elements observed by ESCA on the stripped electrode surface is uncertain at present, the most likely candidates appear to be lithium arsenic oxyfluorides and, possibly, lithium

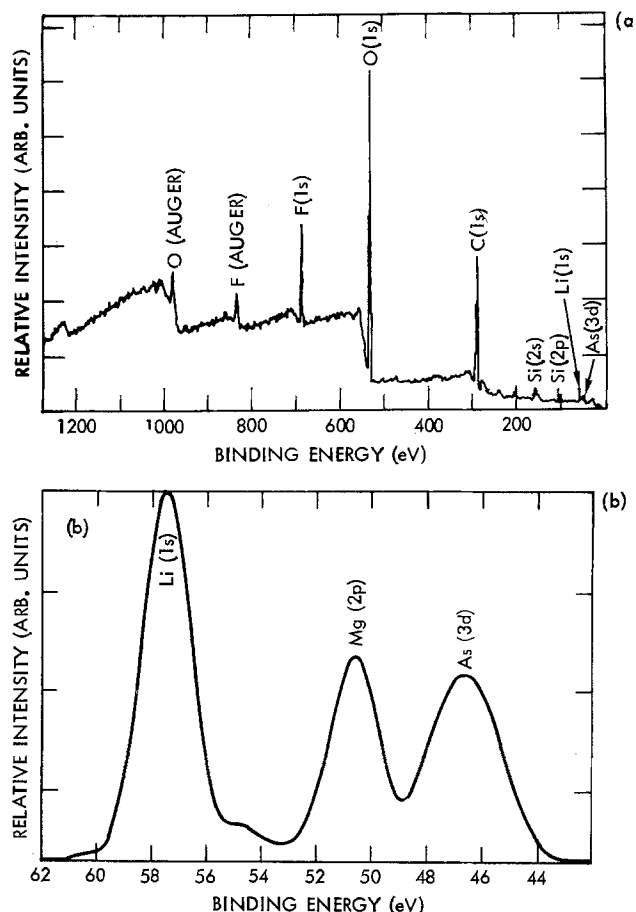


Fig. 4. ESCA spectra of a lithium electrode surface which has undergone one stripping half-cycle: (a) wide scan; and (b) smoothed lithium 1s, magnesium 2p, and arsenic 3d spectra. The arsenic Auger and 3p peaks are also observed. The narrow, well-defined arsenic 3d peak has been singled out for study.

fluorosilicates, e.g., Li₂SiF₆. This suggestion is based on two facts: (i) the binding energy of the fluorine peak is shifted upward relative to that observed in LiAsF₆, indicative of fluorine-oxygen binding; and (ii) the LiAsF₆ salt is unstable in the presence of 2-Me-THF degradation products, in which case lithium arsenic oxyfluorides may be formed (6, 8). In addition, during synthesis, LiAsF₆ may be hydrolyzed, in the presence of silica [e.g., 100 ppm Si impurity in the LiAsF₆ salt (6)], to yield fluorosilicate impurities. Upon cycling, the fluorosilicate anions may react with lithium to form insoluble lithium fluorosilicates on the electrode surface.

SEM studies of the stripped electrode surface reveal the presence of black spots formed randomly on the surface (Fig. 5). As mentioned above, no black spots were observed prior to placing the lithium electrode into the cell. EDS analysis indicates that these spots contain As and Si. It should be stressed that unlike ESCA, EDS cannot detect fluorine or discriminate between Mg and As due to similarities in their binding energies. A "white" fluffy compound is also observed over many of the black spots (Fig. 5). Measurements of the count rate of x-ray emitted during EDS measurements suggests that the white fluffy material may be more electrically conductive than the black spots or the Li₂O/CO₂ adduct substrate. The white material contains As and Si. Studies of the stripped surface which had been exposed to a 2-Me-THF vapor environment revealed the following results: (i) the white compound has limited solubility in this solvent; and (ii) upon prolonged exposure to the solvent vapor and subsequent drying, the white compound dissolves and recrystallizes as small cubic-

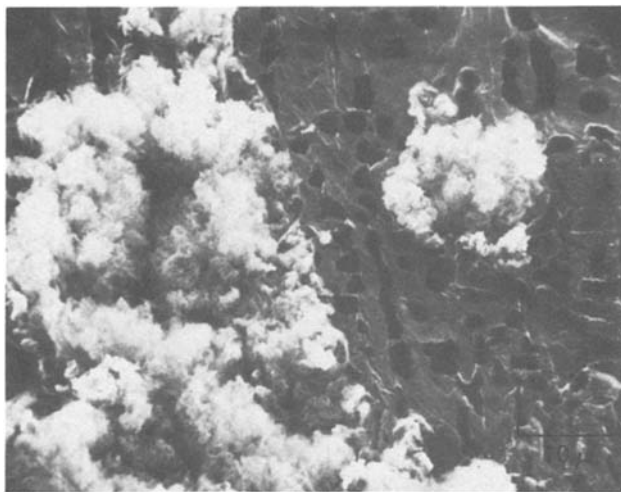


Fig. 5. Scanning electron micrograph of a lithium electrode surface which has undergone one stripping half-cycle.

shaped crystals, thereby revealing the presence of pits in the stripped lithium electrode surface which were formerly covered by the fluffy compound [see Fig. 6(a) and (b)].

Studies of a stripped electrode surface which had previously undergone three complete cycles gave similar results except that the white fluffy compound covered the entire surface uniformly [Fig. 7(a) and (b)] at a thickness of $\sim 8\text{--}10\ \mu\text{m}$ [Fig. 7(b)]. Another exception was the absence of any evidence of lithium fluorosilicates on the stripped lithium surface as indicated by the absence of Si and F (associated with lithium fluorosilicates). As mentioned above, the lithium fluorosilicate formation may be catalyzed by the silicates present as impurities in the LiAsF_6 salt. The absence of these compounds on stripped cycled lith-

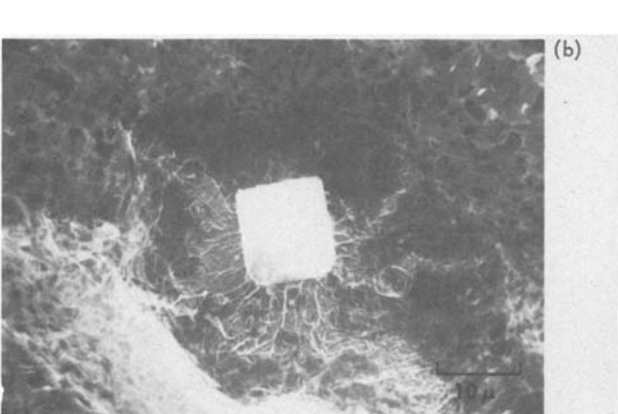
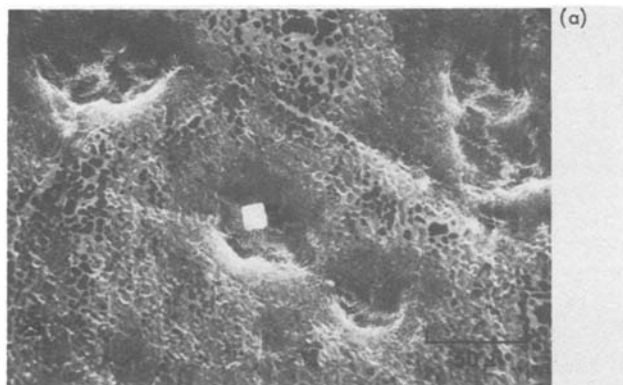


Fig. 6. Scanning electron micrographs of a stripped lithium electrode surface which has been exposed to a 2-Me-THF vapor environment (see text). (a) and (b) are at different magnifications.



Fig. 7. Scanning electron micrographs of a stripped lithium electrode surface which has undergone three complete cycles. In (b), the sample has been tilted $\sim 90^\circ$ with respect to the substrate in order to estimate film thickness.

ium surfaces suggests that the silicate impurities were depleted in the lithium fluorosilicate formation during the initial cycling.

Plated electrode surfaces.—ESCA studies of lithium surfaces which have undergone one plating half-cycle indicate the presence of the same elements as observed on stripped surfaces except that the fluorine content (shown full scale, Fig. 8) increased relative to that observed on stripped surfaces, Fig. 5. This reflects the fact that the newly deposited lithium metal is in a highly exposed, or unprotected, state and can more readily react with the electrolyte. The observation of Si on the plated surface supports the

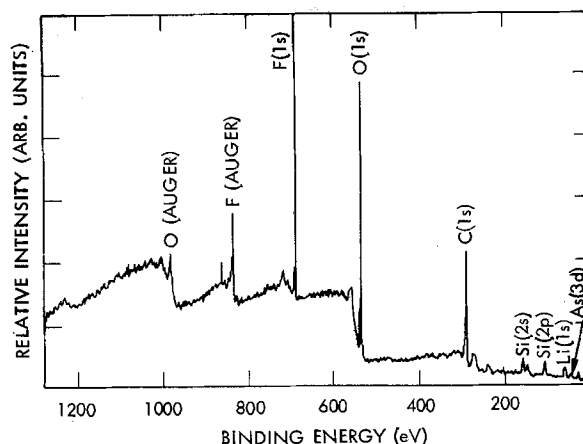


Fig. 8. ESCA spectra (widescan) of a lithium electrode which has undergone one plating half-cycle.

contention that the source of this element is the LiAsF_6 salt and not the bulk lithium metal. High resolution ESCA data clearly indicate a greater concentration of silicon on plated electrodes compared to stripped electrodes. The concentration of silicon on both electrodes decreases with cycling and is below the detection limit of the instrument after three cycles. This suggests that cycling a lithium electrode in an $\text{LiAsF}_6/2\text{-Me-THF}$ electrolyte may be an effective way of purifying the electrolyte of the silicate impurities prior to actual use in a cell. SEM studies show that the white fluffy compound forms preferentially along grain boundaries and surface defects, Fig. 9. In contrast to the stripped electrode surface, no pits or black spots are observed. EDS analysis of the white compound indicates the presence of As and Si in agreement with the ESCA results. In all of the measurements mentioned above, no evidence of Li_3N was found.

The Li^+ transport process through this native film and the channel formation mechanism must be established. The above results suggest the following scenario. Upon stripping (discharge), lithium ions migrate through the native film creating channels, or pathways, through which the electrolyte, electrolyte degradation products, or impurities can react with the bare Li^0 surface. The black spots may reflect the chemical diffusion and associated chemical reactions which can occur in the reducing environment of the anode. The pits in the surface reflect these reaction processes. When these processes give rise to larger channels, and thereby expose the lithium metal to more electrolyte, the white fluffy compound forms, normally in the vicinity of the black spots. Upon charge, the Li^0 substrate is protected and the black spots and pits do not form. The increase in the fluorine content reflects the reaction between the salt/solvent and the newly plated lithium. Another possibility involves the native passivating film initially having small, undetectable channels filled with electrolyte. Then large inhomogeneous electric fields (and, hence, a large local current density) could develop at the lithium metal/electrolyte interface. This could lead to breakdown of the native film and to the growth of larger channels, or pathways, as reflected by the black spots.

Conclusions

The surface of the as-received lithium metal is found to be already covered by a "native" film composed of LiO_2 and an $\text{Li}_2\text{O}/\text{CO}_2$ adduct. This film is between $\sim 100\text{-}200\text{\AA}$ thick, although its actual thickness is unknown. This film can be removed via ion beam etching (*i.e.*, sputtering) but the effectiveness of this procedure remains to be determined. No evi-

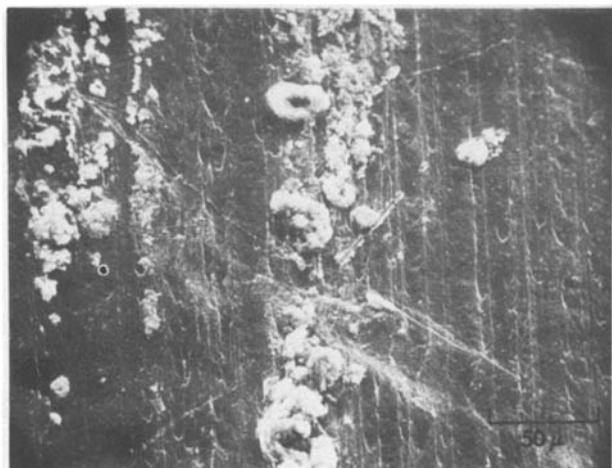


Fig. 9. Scanning electron micrographs of a lithium electrode surface which has undergone one plating half-cycle.

dence of Li_3N was found. Upon exposure of the lithium electrode (covered by the native passivating film) to a $1.5\text{M LiAsF}_6/2\text{-Me-THF}$ electrochemical environment, a second film is observed to form on the surface. This film consists primarily of As, Si, and F, possibly in the form of lithium arsenic oxyfluorides or lithium fluorosilicates. The film does appear to have a slight solubility in 2-Me-THF. There is a question whether this film forms instantly upon exposure to the electrolyte or requires electrochemical action. It does appear that the LiAsF_6 salt degrades to some extent, with its degradation products combining, or reacting, with its impurities to contribute to the film formation. It is likely that electrochemical action encourages this effect. It will be useful to carry out surface studies of lithium electrodes exposed to the electrolyte, but without undergoing the stripping and plating process. It should also be realized that the chemical composition of the film formed upon prolonged cycling (8) may be somewhat different from that reported here, since modest cycling may yield films which represent precursor, or intermediate, compounds.

The results of this work have provided some insight into the nature of the passivating films on lithium electrodes exposed to a $1.5\text{M LiAsF}_6/2\text{-Me-THF}$ electrochemical environment. It has also raised numerous new questions, *e.g.*, what is the actual chemical composition of the second film, which film is most important to the passivating action, how do processes in the two films couple, etc. It is hoped that this work will stimulate further efforts towards answering these and similar questions.

Acknowledgments

It is a pleasure to thank W. Worrell, B. Brummer, V. Koch, and A. Rembaum, for their encouragement and useful discussions. We also wish to acknowledge K. Evans for carrying out the SEM/EDS experiments. This work represents one phase of research performed by the Jet Propulsion Laboratory, California Institute of Technology, sponsored by the National Aeronautics and Space Administration, Contract NAS7-100.

Manuscript submitted Sept. 19, 1980; revised manuscript received Jan. 26, 1981.

Any discussion of this paper will appear in a Discussion Section to be published in the June 1982 JOURNAL. All discussions for the June 1982 Discussion Section should be submitted by Feb. 1, 1982.

Publication costs of this article were assisted by California Institute of Technology.

REFERENCES

1. G. L. Holleck, *NASA Conference Publication*, **2117**, 144 (1979).
2. R. J. Jasinski, "High Energy Batteries," Plenum, New York (1967).
3. V. R. Koch and J. H. Young, *This Journal*, **125**, 1371 (1978).
4. E. Peled, *ibid.*, **126**, 2047 (1979).
4. F. J. Grunthaner, P. J. Grunthaner, R. P. Vasquez, B. F. Lewis, J. Maserjian, and A. Madhukar, *J. Vac. Sci. Technol.*, **16**, 1443 (1979); *Phys. Rev. Lett.*, **43**, 1683 (1979).
6. R. C. Cannon, C. C. Stone, and R. A. Wiesboeck, in "Proceedings of the Symposia on Power Sources for Biomedical Implantable Applications and Ambient Temperature Lithium Batteries," B. B. Owens and N. Margalit, Editors, p. 321, The Electrochemical Society Softbound Proceedings Series, Princeton, N.J. (1980); R. C. Cannon, Private communication.
7. D. J. David, M. H. Fronig, T. N. Wittberg, and W. E. Moddeman, *Appl. Surf. Sci.*, To be published. M. H. Fronig, T. N. Wittberg, and W. E. Moddeman, Abstract No. 14, p. 44, The Electrochemical Society Extended Abstracts, Los Angeles, Calif., Oct. 14-19, 1979.
8. V. R. Koch, *This Journal*, **126**, 181 (1979).

A-C Modulation of a Rotating Zinc Electrode in an Acid Zinc-Chloride Solution

D-T. Chin* and S. Venkatesh*¹

Department of Chemical Engineering, Clarkson College of Technology, Potsdam, New York 13676

ABSTRACT

A study has been made of the effect of alternating current (a.c.) on the behavior of a rotating zinc hemispherical electrode in an acid zinc-chloride solution. It was found that a.c. shifted the rest potential of the zinc electrode toward the negative direction and caused a change in the shape of the cathodic polarization curve. Visual observation under a scanning electron microscope revealed that a.c. initiated pitting corrosion when the electrode was polarized in the anodic direction. For the cathodic deposition reaction, a.c. greatly increased the rate of nucleation and produced a more uniform deposit on the zinc electrode. The result was substantiated with the numerical computation of a three-dimensional nucleation model.

The zinc electrode plays an important role in electrochemical energy conversion systems. The zinc-chlorine cell is one of the systems that has attracted interest recently (1). The zinc electrode in this system dissolves into the circulating zinc chloride electrolyte during discharge and is plated out as a porous deposit from the flowing electrolyte during charge. A state-of-the-art review of the zinc electrode has been given by McBreen and Cairns (2).

Gaiser and Heusler (3) reported that the zinc deposition is a first-order reaction. Hurlen *et al.* (4, 5) examined the kinetics of the Zn, Zn(Hg)/Zn²⁺ in acidified chloride solutions. The effect of alkali cations and halides on the Zn(Hg)/Zn²⁺ reaction was studied by Eriksurd (6). Sierra Alcazar and Harrison (7) proposed a two-electron transfer step for the cathodic reduction of zinc ions in chloride solutions with the Zn²⁺/Zn⁺ step being the rate-controlling step. A complex reaction scheme was suggested by Epelboin and co-workers (8-11). Weber and Tomassi (12) investigated the electrodeposition of zinc in sulfate and chloride solutions. Hurlen and Breivik (13) reported the activities of Zn²⁺ in aqueous sulfate solutions. Kim and Jorne (14) studied the transport properties and the kinetics of zinc electrode in acidic chloride solutions.

One major problem in the development of the zinc electrode is the dendrite growth and the electrode shape changes caused by nonuniform zinc deposition during the charge cycles. In the electroplating industry, superimposed alternating current (a.c.) has been used to increase the rate of electroplating (15). It appears that a.c. gives more compact deposit with better adhesion to the substrate. Carlin (16) demonstrated that superimposed a.c. altered the nature of anodic dissolution of nickel in a nickel plating electrolyte and eliminated sponge formation and undesired residues at certain pH levels. Jeney and Lengyel (17) have studied the effects of superimposed a.c. on nickel deposits produced from a sulfamate solution. They found that the deposits had a highly disoriented texture, high hardness, and low internal stress. Rectangular a.c. (18) has been used to inhibit the polarization of a base metal and to improve the current distribution on the electroplating of cylindrical surfaces. The influence of sinusoidal a.c. on the plating of cadmium, nickel, and tin was considered by Rehim *et al.* (19-21). Kronra-shin *et al.* (22) have examined the kinetics of an oxide coating produced by a.c. Superimposed a.c. has been

found to improve the epitaxy in zinc, cadmium, tin, and lead electrodeposits (23-24). Ahmed *et al.* (25) studied the electrocrystallization of zinc on single copper crystal planes under the influence of a.c. Sheshadri (26) examined the copper deposits under the influence of a.c. and concluded that a.c. reduced grain size and produced more leveled and smoother deposits. Enchev (27) used a.c. in the electrowinning of nonferrous alloys; he obtained higher quality deposit and higher current efficiency. The electrodeposition of zinc on nickel electrodes has been studied by Jovicevic *et al.* (28) with a potential pulse technique. They found that the morphology of the zinc deposit varied with the amplitude of the pulses.

In view of the foregoing background, it seems that superimposed a.c. might help to prevent the dendrite formation and to improve the uniformity of zinc deposits during the charge of the zinc electrode. The method would be useful to the zinc-chlorine battery, where the dendritic zinc deposits during the charge process still pose a problem. This paper describes a study of the effect of a.c. on the behavior of the zinc electrode in an acid ZnCl₂ solution.

Experimental

A rotating zinc hemispherical electrode was used for the study (29). The electrode consisted of a replaceable zinc² hemispherical head mounted on one end of a Teflon cylindrical rod; the other end of the rod was attached to the spindle shaft of a high speed rotator. The zinc hemispherical head was 0.317 cm in diameter and had a surface area of 0.628 cm² exposed to the electrolyte. A Pyrex cell containing a stationary zinc counterelectrode and a saturated calomel reference electrode was used for the experiment. The electrolyte used was 0.5M ZnCl₂ in 1.0M KCl (pH = 4.0).

The method of a-c modulation (30) was used to measure the anodic and the cathodic polarization curves of the zinc electrode. In this method, a constant a.c. superimposed to a given direct current (d.c.) was applied to the zinc electrode, and the resulting potential fluctuations as well as the time averaged (or d-c) electrode potential was measured as a function of d-c densities. The details of the experimental setup and the measuring circuit have been described elsewhere (31-32) and are not repeated here.

The electrode was pretreated by polishing with a 600 grit emery paper and was rinsed in distilled water before being transferred to the cell. The anodic and the cathodic polarization curves were obtained with two separate runs because zinc had a tendency to de-

* Electrochemical Society Active Member.
¹ Present address: The Continental Group, Incorporated, Energy Systems Laboratory, Cupertino, California 95014.
Key words: zinc-chlorine battery, surface morphology, electrodeposition, nucleation.

² The zinc used as 99.99% pure (Alfa zinc).

posit as dendrites during the cathodic polarization run. Scanning electron micrographs of the surface were taken after each cathodic and anodic experiment. The range of a.c. investigated was 0-100 mA/cm² rms (root mean square) at 60 Hz. All the measurements were performed at a constant room temperature of 21° ± 1°C.

Results and Discussion

Figure 1 shows a set of steady-state polarization curves for the zinc electrode in 0.5M ZnCl₂ and 1.0M KCl solution (pH = 4.0). In these runs, the speed of rotation of the zinc electrode was maintained at 2500 rpm. At this speed, no concentration polarization was observed. It is seen that the cathodic curve for the run without superimposed a.c. exhibits two reduction waves. This phenomenon has not been reported in the literature, and at present we do not have suitable explanations. The anodic and the cathodic Tafel slopes were found to be 125 and -140 mV, respectively, in good agreement with the values of 109 and -138 mV reported by Kim and Jorne (14). The exchange current density was found to be 19 mA/cm². This value was one order of magnitude greater than Kim and Jorne's value of 1.36 mA/cm² for a pH 2 solution containing 0.5M ZnCl₂ and 1M KCl. Since a pH 4 solution was used in the present study, the increase in the exchange current density was probably due to the difference in the pH values. A similar pH dependence has also been reported by Sierra Alcazar and Harrison (7) for the zinc electrode in 0.003M ZnSO₄.

The effect of superimposed a.c. was to shift the rest potential toward the negative direction. The reason for the potential shift has been discussed in Ref. (31, 33-35), and is not repeated here. A.C. did not appear to have a significant effect on the anodic polarization curve. For the cathodic polarization curves, a.c. increased the current densities at low overpotentials and eliminated the presence of the first reduction wave. With a 100 mA/cm² rms a.c., the first reduction wave

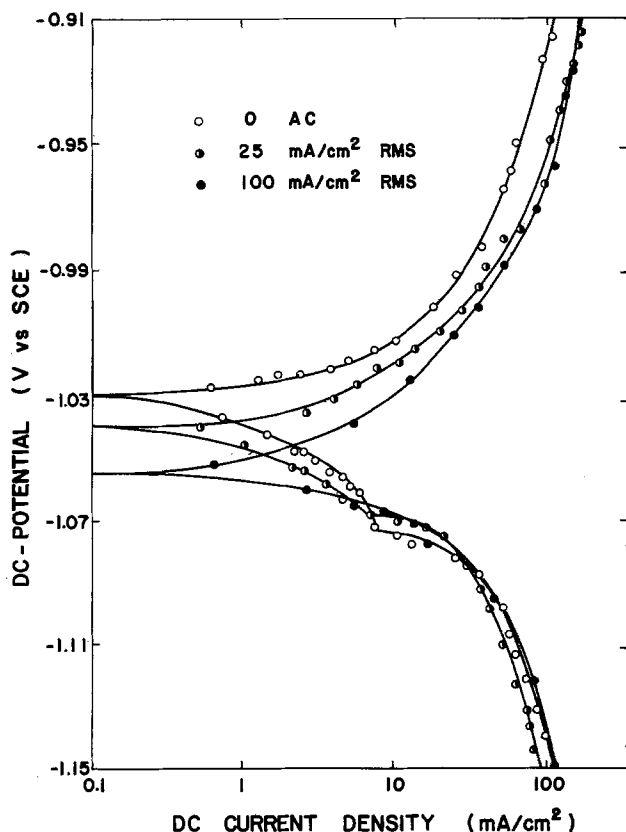


Fig. 1. Effect of a.c. (60 Hz) on the polarization curves of the zinc electrode in 0.5M ZnCl₂ + 1.0M KCl. The speed of rotation was 2500 rpm.

completely disappeared. At high cathodic overpotentials, the effect of a.c. diminished, and the data points for three different superimposed a-c levels seem to merge together into a single curve.

The surface of the zinc electrode was examined under a scanning electron microscope at the end of each polarization run. The photomicrographs are shown in Fig. 2; these pictures were taken at a magnification of 30×. The fine striation lines on the photomicrographs were caused by the mechanical polishing of the zinc hemispherical electrodes before the electrolysis. Figure 2a shows the surface of the zinc electrode after the anodic dissolution with 25 mA/cm² rms a.c. It is seen that pitting corrosion occurred under the superimposed a-c condition. The pits were probably caused by localized breakdown of oxide film by a.c. and the phenomenon was the same as the a-c corrosion of copper and mild steel (30, 36). Figure 2b shows the zinc deposits of the cathodic polarization run without any superimposed a.c. The effect of a.c. on zinc deposits is shown in Fig. 2c-2d. It seems that a.c. greatly increased the nucleation rate. When 25 mA/cm² rms a.c. was superimposed onto the zinc electrode, the grain size of zinc deposits decreased, and the number of grains increased. At 100 mA/cm² rms a.c., the number of zinc grains became so numerous that they clustered together to form a zinc layer. Also the distribution of zinc grains on the electrode surface appeared to be more uniform at high a-c values.

The foregoing phenomenon can be explained with a three-dimensional nucleation theory. For a number of electrode deposition reactions, the relationship between the nucleation rate N , and the overpotential η follows the correlation (37)

$$N = N_{\infty} \exp\left(-\frac{B^2}{\eta^2}\right) \quad [1]$$

where N_{∞} is the nucleation rate at infinitely large overpotentials, and B is a constant whose value depends on the temperature and the nature of the electrode deposition reaction. Equation [1] has been confirmed for the cathodic deposition of silver, lead, and mercury (38, 39), and for the anodic deposition of lead dioxide and manganese dioxide (40, 41). When the electrode is polarized with a d-c overpotential, $\eta_{d.c.}$, plus a superimposed a.c. potential, $\eta_{a.c.}$

$$\eta = \eta_{d.c.} + \eta_{a.c.} \quad [2]$$

the nucleation rate will be fluctuated with time and can be considered to consist of a time-averaged component, $\bar{N}_{a.c.}$, and a fluctuating component, n

$$N = \bar{N}_{a.c.} + n \quad [3]$$

Substituting Eq. [2] and [3] into Eq. [1] and taking the time-average on both sides of the resulting equation, one has

$$\bar{N}_{a.c.} = N_{\infty} \exp\left[-\frac{B^2}{(\eta_{d.c.} + \eta_{a.c.})^2}\right] \quad [4]$$

The overscore in the above equation designates the time-averaging operation. The details of the time-averaging technique have been discussed in previous publications (31, 33) and is not repeated here. Equation [4] can be normalized with the nucleation rate without superimposed a.c.; the result can be rearranged as

$$\frac{\bar{N}_{a.c.}}{N_{d.c.}} = \frac{\exp\left[-\frac{1}{(1 + \eta_{a.c.}/\eta_{d.c.})^2 (\eta_{d.c.}/B)^2}\right]}{\exp\left[-\frac{1}{(\eta_{d.c.}/B)^2}\right]} \quad [5]$$

Here $\bar{N}_{a.c.}/N_{d.c.}$ is the ratio of the time-averaged nucleation rate when the electrode is polarized by a d-c

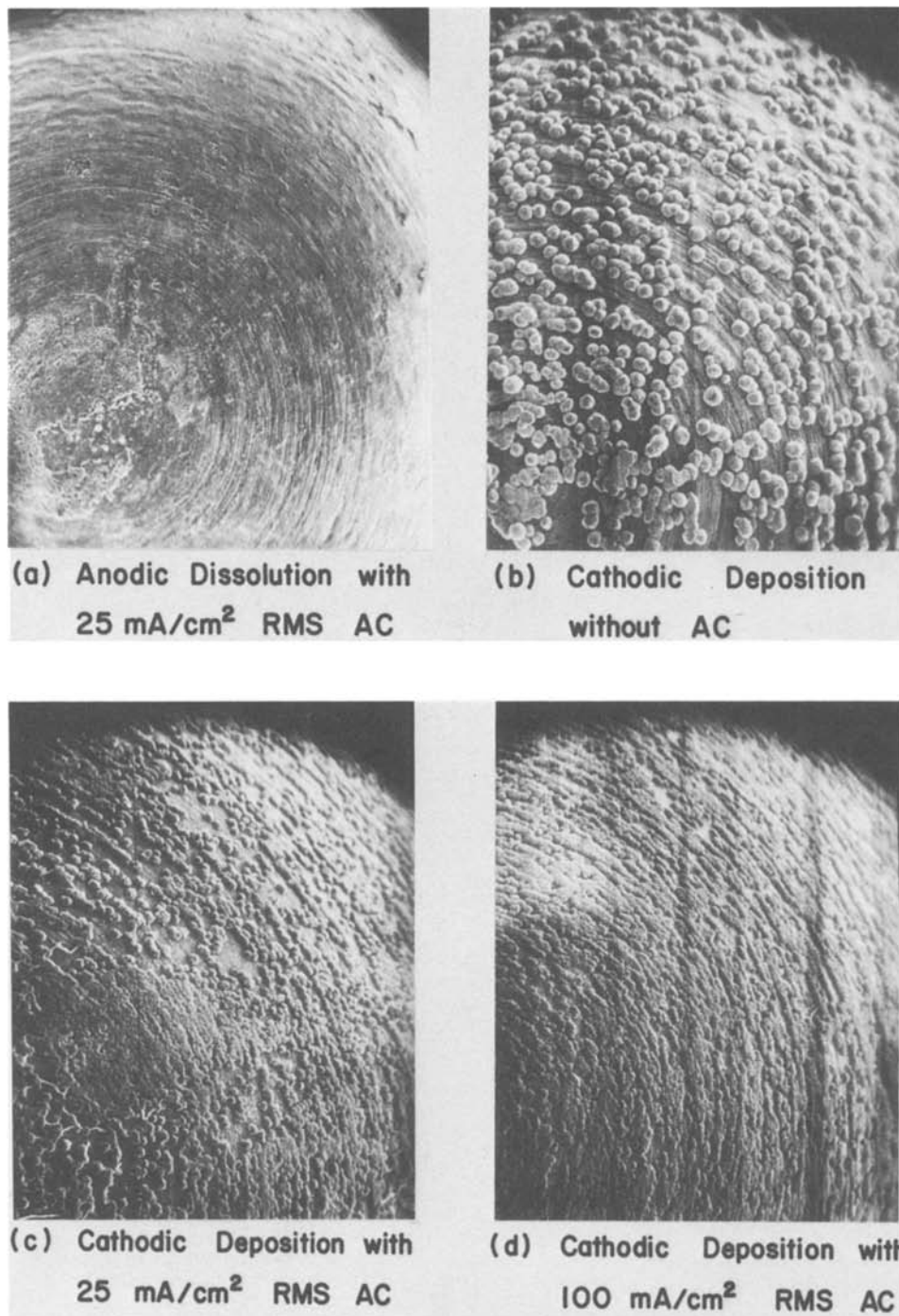


Fig. 2. Photomicrographs of the zinc surface after the polarization measurement. The magnification was $30\times$.

overpotential plus an a-c potential, $\eta_{d.c.} + \eta_{a.c.}$, to the nucleation rate when the electrode is polarized only by a d-c overpotential, $\eta_{d.c.}$. Equation [5] has been numerically evaluated for a square-wave a.c., and the results are plotted in Fig. 3 in the form of $\bar{N}_{a.c.}/N_{d.c.}$ vs. $\eta_{d.c.}/B$. The parameter in the figure is the root mean square of superimposed a-c potential, $\sqrt{\eta_{a.c.}^2}$, normalized by the d-c overpotential. It is seen that at low d-c overpotentials, a.c. can increase the nucleation rate by several orders of magnitude. The result clearly agrees with the experimental observations shown in Fig. 2. Also the effect of a.c. diminishes as the d-c overpotential increases and becomes negligible in the region of $\eta_{d.c.}/B > 1$. It is interesting to note that a large a.c. can slightly reduce the nucleation at large d-c overpotential, as indicated by the $\sqrt{\eta_{a.c.}^2}/\eta_{d.c.} = 1$ curve.

Conclusions

In conclusion, a study has been made of the effect of a.c. on the behavior of the zinc electrode in an acid

zinc-chloride solution. A.C. was found to shift the rest potential of the zinc electrode toward the negative direction and caused pitting corrosion when the electrode was polarized at the anodic potentials. With superimposed a.c., the rate of nucleation was greatly enhanced during the cathodic deposition reaction. This resulted in a more uniform zinc deposit on the electrode. The phenomenon was explained with the time-averaging analysis of a three-dimensional nucleation model.

Acknowledgment

This work was supported by the National Science Foundation Grant ENG77-25153. Acknowledgment is also made to the donors of the Petroleum Research Fund, administered by the American Chemical Society, for partial support of this research.

Manuscript submitted Sept. 30, 1980; revised manuscript received Jan. 23, 1981.

Any discussion of this paper will appear in a Discussion Section to be published in the June 1982 JOURNAL.

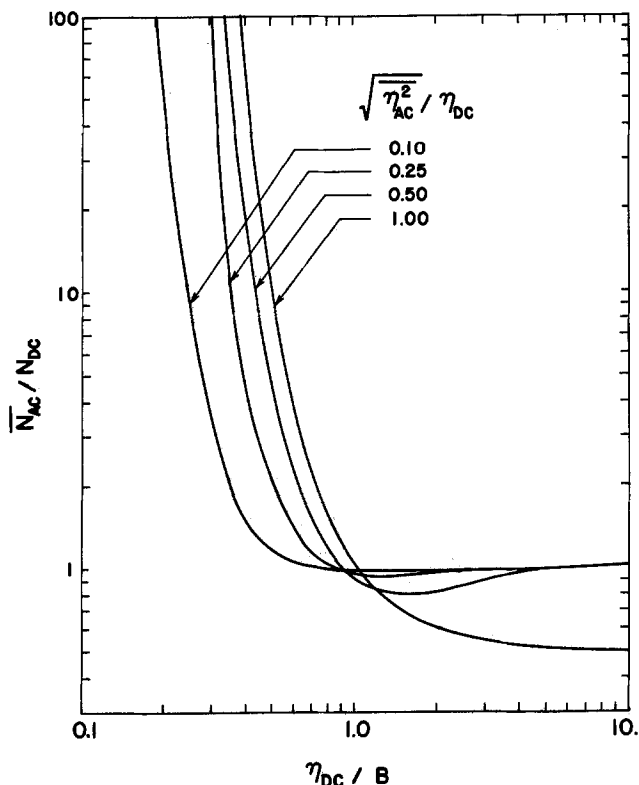


Fig. 3. Calculated results for the effect of a.c. on the rate of nucleation in electrodeposition reactions.

All discussions for the June 1982 Discussion Section should be submitted by Feb. 1, 1982.

Publication costs of this article were assisted by the Petroleum Research Fund.

LIST OF SYMBOLS

| | |
|------------------|---|
| B | a constant defined in Eq. [1], v |
| N | rate of nucleation, number of nuclei/cm ² /sec |
| $\bar{N}_{a.c.}$ | time-averaged nucleation rate when a.c. is superimposed onto the electrode, number/cm ² /sec |
| $N_{d.c.}$ | nucleation rate with only d-c polarization, number/cm ² /sec |
| n | fluctuating nucleation rate, number/cm ² /sec |
| η | overpotential, V |
| $\eta_{d.c.}$ | d-c overpotential, V |
| $\eta_{a.c.}$ | superimposed a-c potential, V |

REFERENCES

- C. J. Warde, P. C. Symons, C. C. Whittlesey, and H. A. Catherine, "Proceedings of the 13th IECEC," Vol. 1, p. 755 (1978).
- J. McBreen and E. J. Cairns, in "Advances in Electrochemistry and Electrochemical Engineering," Vol. 11, H. Gerischer and C. W. Tobias, Editors, p. 273, Interscience, New York (1978).
- L. Gaiser and K. E. Heusler, *Electrochim. Acta*, **15**, 161 (1970).
- T. Hurlen and E. Eriksurd, *J. Electroanal. Chem. Interfacial Electrochem.*, **45**, 205 (1973).
- T. Hurlen and K. P. Fischer, *ibid.*, **61**, 165 (1975).
- E. Eriksurd, *ibid.*, **76**, 27 (1977).
- H. B. Sierra Alcazar and J. A. Harrison, *Electrochim. Acta*, **22**, 627 (1977).
- I. Epelboin, M. Ksouri, E. Lejay, and R. Wiart, *ibid.*, **20**, 603 (1975).
- I. Epelboin, M. Ksouri, and R. Wiart, *This Journal*, **122**, 1206 (1975).
- I. Epelboin, M. Ksouri, and R. Wiart, *J. Electroanal. Chem. Interfacial Electrochem.*, **58**, 433 (1975).
- I. Epelboin, M. Ksouri, and R. Wiart, *ibid.*, **65**, 373 (1975).
- J. A. von Weber and P. Tomassi, *Metalloberfläche*, **31**, 259 (1977).
- T. Hurlen and T. R. Breivik, *Acta Chem. Scand.*, **A32**, 447 (1978).
- J. T. Kim and J. Jorne, *This Journal*, **127**, 8 (1980).
- Chem. Abstr.*, **87**, Abstr. No. 191144d; 208518d (1977).
- F. X. Carlin, *Plating*, **52**, 341 (1965).
- I. Jeney and B. Lengyel, *Trans. Inst. Metal Finish (London)*, **54** (pt. 1), 31 (1976).
- Chem. Abstr.*, **86**, Abstr. No. 150014u (1977).
- S. S. Abd El-Rehim and F. M. Abd El-Halim, *Acta Chim. Acad. Sci. Hung.*, **80**, 65 (1974).
- S. S. Abd El-Rehim and M. H. Fawzy, *ibid.*, **80**, 71 (1974).
- S. S. Abd El-Rehim and M. G. Helmy, *ibid.*, **89**, 215 (1976).
- V. Ya Kondrashin, V. V. Malygin, and A. Yu Shatalov, *Dokl. Akad. Nauk. SSSR.*, **211**, 1386 (1973).
- St. Andurov and N. Stoicher, *Rost. Kristallor. Akad. Nauk. SSSR Inst. Kristallogr.*, **5**, 136 (1965).
- M. F. Ahmed, B. S. Sheshadri, and F. Pushpanaden, *J. Electrodepos. Surf. Treat.*, **3**, 65 (1975).
- M. F. Ahmed, B. S. Sheshadri, and F. Pushpanaden, *J. Mater. Sci.*, **12**, 549 (1977).
- B. S. Sheshadri, *Plat. Surf. Finish.*, **65** (7), 43 (1978).
- I. Enchev, *Hutn. Listy.*, **26**, 820 (1971).
- J. N. Jovicevic, D. M. Drazic, and A. R. Despic, *Electrochim. Acta*, **22**, 589 (1977).
- D-T. Chin, *This Journal*, **120**, 631 (1973).
- S. Venkatesh and D-T. Chin, *Israel J. Chem.*, **18**, 56 (1979).
- D-T. Chin and S. Venkatesh, *This Journal*, **126**, 1908 (1979).
- S. Venkatesh, Ph.D. Dissertation, Clarkson College of Technology, Potsdam, New York (1980).
- D-T. Chin and T-W. Fu, *Corrosion*, **35**, 514 (1979).
- U. Bertocci, *ibid.*, **35**, 211 (1979).
- S. Sathyanarayana, *J. Electroanal. Chem. Interfacial Electrochem.*, **62**, 209 (1975).
- S. R. Pookote and D-T. Chin, *Mater. Perform.*, **17** (3), 9 (1978).
- M. Fleischmann and H. R. Thirsk, in "Advances in Electrochemistry and Electrochemical Engineering," Vol. 3, P. Delahay and C. W. Tobias, Editors, p. 211, Interscience, New York (1963).
- A. Sheludko and G. Bliznakov, *Bull. Inst. Phys. Chem. (Sofia)*, **2**, 227 (1951).
- A. Sheludko and M. Todorova, *ibid.*, **3**, 61 (1952).
- M. Fleischmann and H. R. Thirsk, *Electrochim. Acta*, **1**, 146 (1959).
- M. Fleischmann, H. R. Thirsk, and I. Tordesillas, *Trans. Faraday Soc.*, **58**, 1865 (1962).

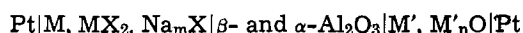
The Stability of $\beta\text{-Al}_2\text{O}_3(\text{Na}_2\text{O} \cdot 11\text{Al}_2\text{O}_3)$ in Oxygen Atmospheres

F. A. Elrefaie and W. W. Smeltzer*

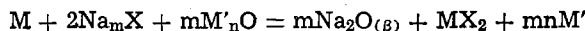
Department of Metallurgy and Materials Science, McMaster University, Hamilton, Ontario, Canada, L8S 4M1

ABSTRACT

The sodium oxide activity in the $\alpha\text{-Al}_2\text{O}_3 + \beta\text{-Al}_2\text{O}_3$ coexistence was determined between 823 and 1198 K by relating measured values of the electromotive force of cells of the type



and the Gibbs energy change of the cell reaction which can be written as



where X refers to halide or sulfide anion. The dependence of activity, $a_{\text{Na}_2\text{O}}$, on temperature, $T(\text{K})$, is

$$\log a_{\text{Na}_2\text{O}} = -\frac{16,400}{T} + 3.60 \quad (823 \leq T \leq 1198 \text{ K})$$

Accordingly, the variation of the sodium vapor pressure of the $\alpha\text{-Al}_2\text{O}_3 + \beta\text{-Al}_2\text{O}_3$ coexistence, p_{Na} (atm), with temperature and oxygen pressure, p_{O_2} (atm), follows the relation

$$\log p_{\text{Na}} = -\frac{24,250}{T} - 0.25 \log p_{\text{O}_2} + 9.94 \quad (823 \leq T \leq 1198 \text{ K})$$

Extrapolation of this relation to higher temperatures demonstrates that p_{Na} attains 1 atm at 1350 K in the environment of the $\text{Al}, \alpha\text{-Al}_2\text{O}_3$ imposed oxygen pressure.

Probes based on $\beta\text{-Al}_2\text{O}_3(\text{Na}_2\text{O} \cdot 11\text{Al}_2\text{O}_3)$ as solid electrolyte have been developed to monitor oxygen pressures as low as those of the $\text{Al}, \alpha\text{-Al}_2\text{O}_3$ coexistence (1) and to sense sodium contents of liquid aluminum in the ppm range (2). The stability of this compound, however, is not well established in such reducing atmospheres. The sodium vapor pressure of the coexistence $\alpha\text{-Al}_2\text{O}_3 + \beta\text{-Al}_2\text{O}_3$ in air has been reported between 1300 and 1900 K (3). From these results, one estimates a value of $-200,832 \text{ J mol}^{-1}$ for the standard Gibbs energy of formation of $\beta\text{-Al}_2\text{O}_3$ from its binary oxides at 1000 K. This value is to be compared to other reported values of $-322,168$ (1), and $-247,199 \text{ J mol}^{-1}$ (2) at the same temperature. The corresponding values of sodium oxide activity in the $\alpha\text{-Al}_2\text{O}_3 + \beta\text{-Al}_2\text{O}_3$ coexistence are 3.2×10^{-11} (3), 1.5×10^{-17} (1), and 1.2×10^{-13} (2). In light of these discrepancies, we initiated this investigation to establish the stability of $\beta\text{-Al}_2\text{O}_3$ using solid-state electrochemical cells with $\beta\text{-}$ and $\alpha\text{-Al}_2\text{O}_3$ as a two-phase electrolyte.

Experimental

Materials used in this investigation are listed in Table I. Wustite powder was prepared by reducing hematite at 1173 K in a flowing $\text{CO-CO}_2\text{-N}_2$ atmosphere.

$\beta\text{-}$ and $\alpha\text{-Al}_2\text{O}_3$ electrolyte tubes were prepared by slip casting an aqueous suspension containing 40g $\alpha\text{-Al}_2\text{O}_3$, 360g $\beta\text{-Al}_2\text{O}_3$, 6 ml HCl, and 3g Darvin C deflocculant in 300 ml distilled water. Before preparing a slip, the $\beta\text{-Al}_2\text{O}_3$ powder (-120 mesh) was ground to less than $8 \mu\text{m}$ in diameter in an isopropyl alcohol medium for 24 hr in a porcelain ball mill using $\alpha\text{-Al}_2\text{O}_3$ balls.

The following procedure was found to be best for preparing a smooth slip: The acidified solution containing the deflocculant was charged to the ball mill

followed by the subsequent addition of the $\beta\text{-Al}_2\text{O}_3$ and $\alpha\text{-Al}_2\text{O}_3$ powders; the mixture was tumbled for 3 hr, its pH being readjusted to 7 each 15 min. The slip was poured into wetted plaster molds, and maintained at the level of the mold top during the casting period of 30 sec. Cracking of a tube was minimal if its upper edge separated from the mold wall using a spatula within 5 min of the casting. A tube was left to dry in its plaster mold for 48 hr which led to a shrinkage of $\sim 10\%$ in its length. The green tubes, ~ 2 mm wall thickness, were dried for a week in air at room temperature; outer surfaces and edges were then polished using 320 grit emery paper. Tubes were fired in a covered Al_2O_3 crucible packed with a coarse powder at 700°C for 14 hr to allow complete drying before sintering at 1800°C for 3 hr in a propane-combustion gas furnace. X-ray diffraction analyses and electron probe tracing of sintered tube cross sections indicated that the $\alpha\text{-Al}_2\text{O}_3$ phase, ~ 3 volume percent (v/o), was homogeneously distributed as discrete particles within the $\beta\text{-Al}_2\text{O}_3$ matrix of the electrolyte tubes, ~ 10 cm in length and 1.5 cm in diameter. Approximately 80% of the sintered tubes exhibited 10^{-8} Torr He-leakage resistance.

Table I. Materials used in this investigation and its sources

| Material | Source and type |
|---|---|
| Nickel, iron, copper, and hematite powders | Ventron, Alfa Products — 99.9% |
| Tungsten powder | Fisher Scientific — purified |
| Nickel oxide powder | Fisher Scientific — 99.8% |
| Cuprous oxide powder | Fisher Scientific — 99.3% |
| Tungsten sulfide and sodium sulfide (anhy.) powders | Ventron, Alfa Products — laboratory grade |
| Nickel sulfide powder (anhy.) | J. T. Baker Chemical — laboratory grade |
| Sodium fluoride powder | J. T. Baker Chemical — 99.5% |
| $\beta\text{-Al}_2\text{O}_3$ powder | ALCOA — superground high quality grade |
| Autostic cement | Carlton Brown & Partners Ltd. |
| Darvin C | R. T. Vanderbilt Company, Inc. |

* Electrochemical Society Active Member.
Key words: electrolyte, solid, stability.

A schematic of the electrochemical cell is shown in Fig. 1. The cell generally consisted of a W, WS_2, Na_2S anode, an Fe, FeO, Ni, NiO , or Cu, Cu_2O cathode, the β - and α - Al_2O_3 solid electrolyte tube, and an α - Al_2O_3 crucible. The M', M'_nO electrodes were tablets, 0.6 cm in diameter and 0.3 cm in thickness, pressed from 1:1 (molar ratio) mixture of the metal and oxide phases using a hydraulic press. The pellets were sintered at $1000^\circ C$ under purified flowing argon for 18 hr and metallographically polished before incorporating into the inner compartment of a solid electrolyte tube. The M', M'_nO electrode and the Pt electrical lead were covered by a protective layer, ~ 2 cm deep, of a powder with the same composition as the tablet. A cathode of one cell was composed of a 3 cm deep compact of Ni, NiF_2, NaF with the molar ratio of 1:1:4; this mixture was dried for 3 hr at $180^\circ C$ in vacuum. The cathode compact was covered by α - and β - Al_2O_3 powder upon its placement in the electrolyte tube. The W, WS_2, Na_2S electrode consisted of a 1:1:4 (molar ratio) mixture of the dried powders (4). Electrode compartments were sealed using Autostic Cement under an argon atmosphere.

A mullite-glass tubular cell assembly was positioned vertically in a tubular electric resistance furnace equipped with a Kanthal noninductively wound heating element (5). The cell was positioned in the constant temperature zone of the furnace, ~ 5 cm in length, which was controlled within $\pm 2^\circ C$ as measured by means of a Chromel-Alumel thermocouple. This assembly was evacuated and flushed with argon several times at room temperature, 200° , 400° , and finally at $925^\circ C$ for cells containing the M', M'_nO electrodes or at $750^\circ C$ for the cell containing the Ni, NiF_2, NaF electrode. During emf measurements a continuous flow of argon was held at a head of 4-6 cm Hg. Argon, containing < 5 ppm impurities, was purified by passage over copper and copper oxide at $180^\circ C$, ascasite, $CaSO_4$, and silica gel. A cell was left overnight before commencing emf measurements for both increasing and decreasing temperature cycles. When the temperature was changed, a new steady emf was reached after 2-3 hr.

Results and Analyses

The emf as a function of temperature of cells I, II, III, and IV are shown in Fig. 2-5

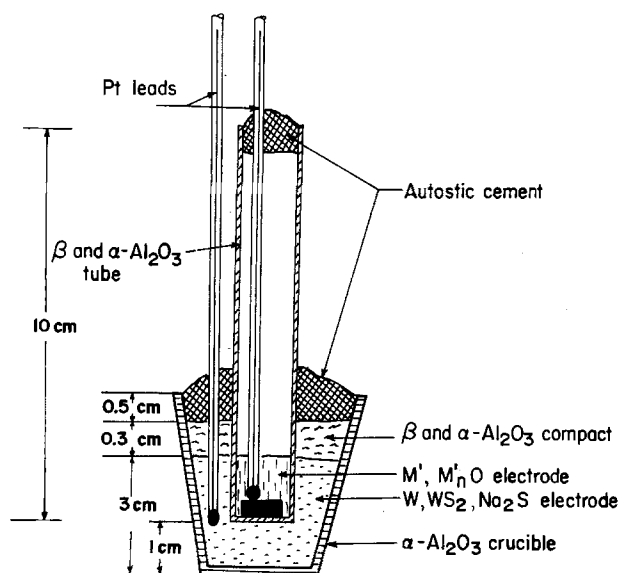
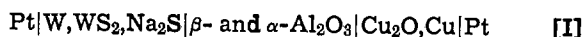


Fig. 1. Schematic of the electrochemical cell utilizing a β - and α - Al_2O_3 two-phase electrolyte.

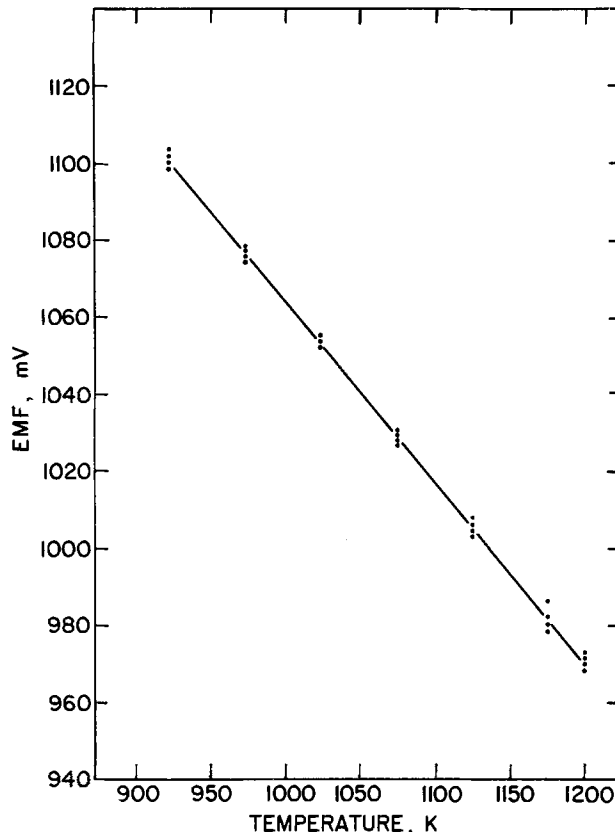
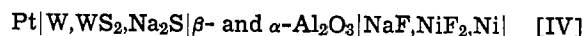
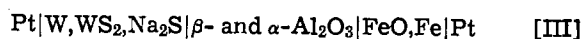
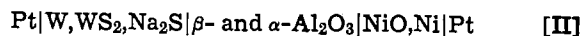


Fig. 2. Variation of emf with temperature for cell [I]



Linear plots were obtained by least-squares analyses and their equations are given in Table II.

Reaction for cells [I], [II], and [III] can be written as

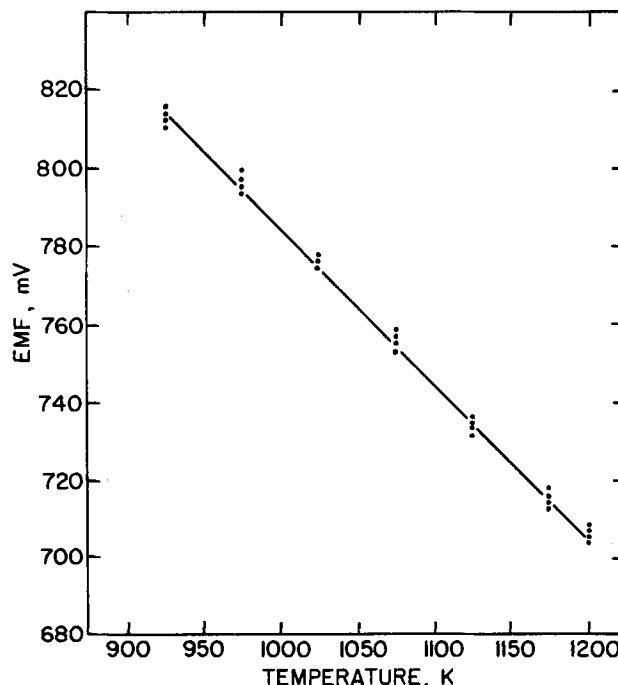


Fig. 3. Variation of emf with temperature for cell [II]

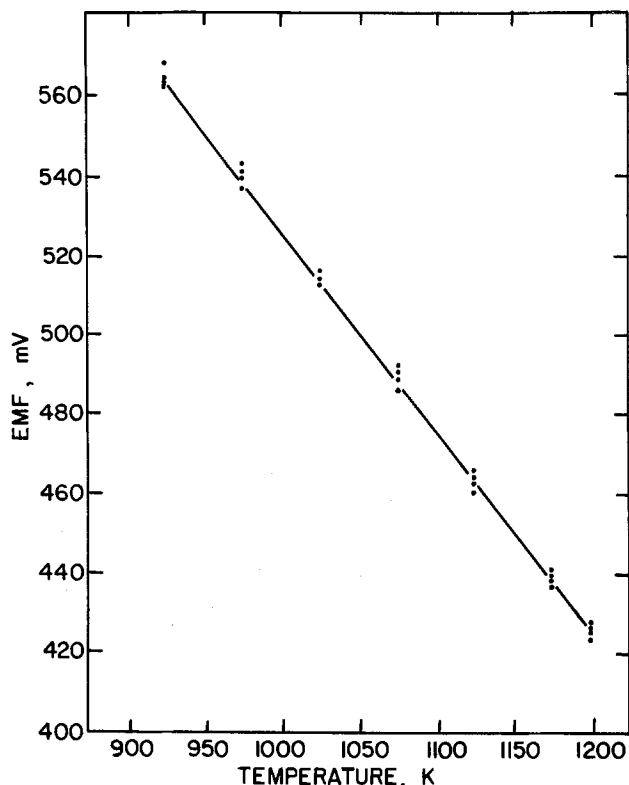


Fig. 4. Variation of emf with temperature for cell [III]

where M'_nO and M' are the oxide and metal phases of the cathode compartment. The Gibbs energy change of reaction [1] is expressed as

$$\Delta G = -4FE = 2RT \ln a_{Na_2O} + \sum \nu_i \Delta G^{\circ}_f(i) \quad [2]$$

where F is the Faraday constant, R is the gas constant, ν_i is the number of moles of compound i , and $\Delta G^{\circ}_f(i)$ is the standard Gibbs energy of formation of compound i . Using relation [2], the values of $\log a_{Na_2O}$ shown in Fig. 6 were calculated between 923 and 1198 K using the emf results for cell [I], [II], and [III] and the required thermodynamic data from Table III.

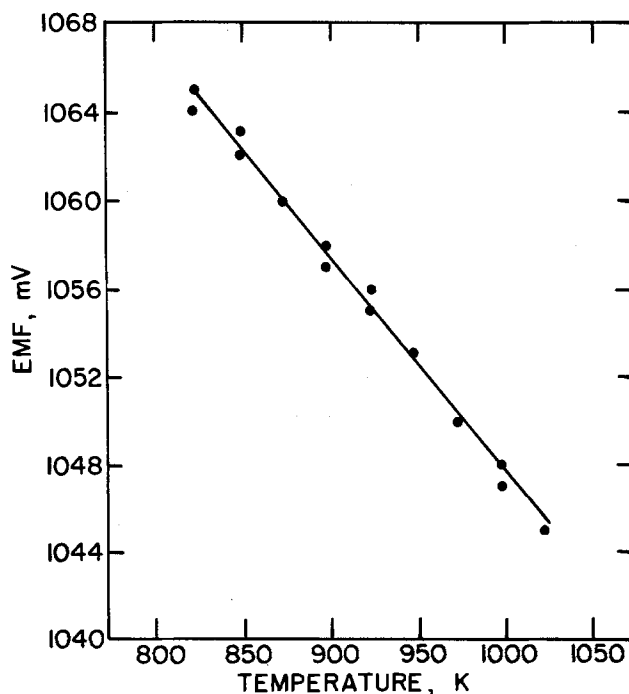


Fig. 5. Variation of emf with temperature for cell [IV]

Table II. Least squares analyses of the emf results of cells [I], [II], [III], and [IV]

| Cell | Temperature range (K) | $E(\text{mV}) = a(\pm S_a) - b(\pm S_b)T$ | | | | Standard deviation (mV) |
|-------|-----------------------|---|-------|-------|--------|-------------------------|
| | | a | S_a | b | S_b | |
| [I] | 923-1198 | 1538 | 4 | 0.474 | 0.004 | ± 2 |
| [II] | 923-1198 | 1180 | 4 | 0.396 | 0.004 | ± 2 |
| [III] | 923-1198 | 1032 | 4 | 0.506 | 0.004 | ± 2 |
| [IV] | 823-1023 | 1146 | 2 | 0.098 | 0.0002 | ± 1 |

Table III. Thermochemical data used in this investigation

| Compound | Temperature range (K) | $\Delta G^{\circ}_f(\text{cal/mol}) = A + BT$ | | Ref. |
|-------------------|-----------------------|---|---------|------|
| | | $-A$ | $+B$ | |
| $Al_2O_3(\alpha)$ | 300-900 | 1,674,977 | 312.963 | (7) |
| | 1000-1900 | 1,685,922 | 325.515 | (7) |
| $NiO(\alpha)$ | 900-1400 | 234,158 | 84.893 | (8) |
| $Cu_2O(\alpha)$ | 900-1300 | 167,046 | 71.463 | (8) |
| $FeO(\alpha)$ | 873-1600 | 264,575 | 65.396 | (8) |
| $Na_2O(\alpha)$ | 400-1100 | 420,015 | 146.022 | (9) |
| $Na_2S(\alpha)$ | 400-1100 | 440,232 | 131.378 | (9) |
| $WS_2(\alpha)$ | 1370-1565 | 336,394 | 156.482 | (10) |
| $NiF_2(\alpha)$ | 298-1300 | 654,796 | 138.072 | (11) |
| $NaF(\alpha)$ | 371-1178 | 571,806 | 104.579 | (11) |

Combination of the emf- T relations obtained for cells [1] and [IV], Table III, yielded Eq. [3] which gives the emf between Ni, NiF_2, NaF and $CuCu_2O$ electrodes

$$E(\text{mV}) = 392 - 0.376T \quad [3]$$

For this cell, the reaction is

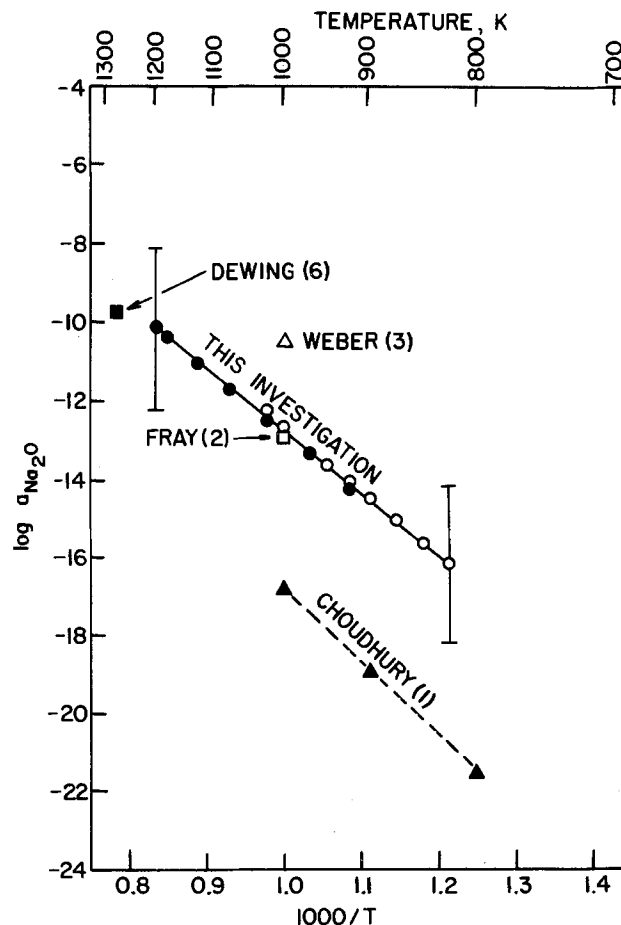


Fig. 6. Dependence of the sodium oxide activity in the $\alpha\text{-Al}_2\text{O}_3 + \beta\text{-Al}_2\text{O}_3$ coexistence on temperature.

Values of $\log a_{\text{Na}_2\text{O}}$ between 823 and 1023 K were calculated using relation [3]; the results are plotted in Fig. 6.

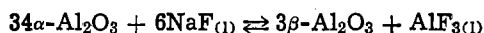
Least-squares analyses of the calculated values for the Na_2O activity in $\beta\text{-Al}_2\text{O}_3$ coexisting with $\alpha\text{-Al}_2\text{O}_3$ from the emf measurements between 823 and 1198 K yielded the relation

$$\log a_{\text{Na}_2\text{O}} = -\frac{16,400}{T} + 3.60 \quad [5]$$

which is shown as a solid line in Fig. 6. The estimated uncertainties in the values of $\log a_{\text{Na}_2\text{O}}$ is ± 2 due to the high uncertainties in the values of ΔG°_f of the halides and sulfides.

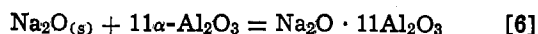
Discussion and Conclusions

The temperature variation of the Na_2O activity in the $\alpha\text{-Al}_2\text{O}_3 + \beta\text{-Al}_2\text{O}_3$ coexistence obtained in this investigation and the previously reported values of $\log a_{\text{Na}_2\text{O}}$ are shown in Fig. 6. The value of Na_2O activity determined in this investigation at 1000 K is 1.6×10^{-13} which is in close agreement with the value calculated from Fray results (2), 1.2×10^{-13} , at the same temperature. Extrapolation of Eq. [5] yields a value of 5.2×10^{-10} for the Na_2O activity at 1273 K which is in good agreement with the value calculated by Dewing (5), 1.5×10^{-10} , for the equilibrium

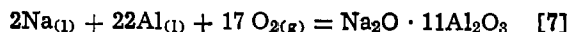


However, the results obtained by Choudhury (1) for $a_{\text{Na}_2\text{O}}$ is 4-5 orders of magnitude more negative than the above results, and the extrapolation to 1000 K of the values based on Weber results (3) at higher temperatures shows positive divergence. The divergence between the $a_{\text{Na}_2\text{O}}$ values determined in this investigation and values extrapolated from Weber's results (3) may be due to the coexistence of sodium aluminate, NaAlO_2 , with a sodium-rich $\beta\text{-Al}_2\text{O}_3$ (12) or $\beta''\text{-Al}_2\text{O}_3$, $\text{Na}_2\text{O} \cdot 5\text{Al}_2\text{O}_3$ (13), rather than its coexistence with $\beta\text{-Al}_2\text{O}_3$ of single composition as assumed by Weber (3). The discrepancy between the values of $a_{\text{Na}_2\text{O}}$ obtained in this investigation, however, with those reported by Choudhury (1) cannot be explained because the same electrochemical reaction (4) has been investigated.

One can calculate from Eq. [5] for the Na_2O activity in $\beta\text{-Al}_2\text{O}_3$ the standard Gibbs energy changes of the following reactions



and



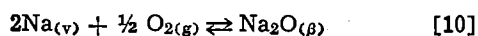
The obtained relations are

$$\Delta G^\circ_f(\beta\text{-Al}_2\text{O}_3) = -314,000 + 68.920 T \quad [8]$$

$$\Delta G^\circ_f(\beta\text{-Al}_2\text{O}_3) = -19,279,200 + 3795.607 T \quad [9]$$

$\Delta G^\circ_f(\beta\text{-Al}_2\text{O}_3)$ is the standard Gibbs energy of formation of $\beta\text{-Al}_2\text{O}_3$ from $\text{Na}_2\text{O}_{(s)}$ and $\alpha\text{-Al}_2\text{O}_3$ in joules and $\Delta G^\circ_f(\beta\text{-Al}_2\text{O}_3)$ is the standard Gibbs energy of formation of $\beta\text{-Al}_2\text{O}_3$ from $\text{Na}_{(l)}$, $\text{Al}_{(l)}$, and $\text{O}_{2(g)}$. The estimated uncertainties in the values of $\Delta G^\circ_f(\beta\text{-Al}_2\text{O}_3)$ and $\Delta G^\circ_f(\beta\text{-Al}_2\text{O}_3)$ are $\pm 42,000$ and $63,000 \text{ J mol}^{-1}$, respectively. The value of $\Delta G^\circ_f(\beta\text{-Al}_2\text{O}_3)$ at 1000 K calculated from Eq. [8] is $-245,080 \text{ J mol}^{-1}$ which is in very good agreement with the value determined by Fray (3), $-247,199 \text{ J mol}^{-1}$, at 1000 K but it is 77,088 J more positive than the value given by Choudhury (1).

The variation of the sodium vapor pressure of the $\alpha\text{-Al}_2\text{O}_3$ and $\beta\text{-Al}_2\text{O}_3$ coexistence can be determined by considering the following reaction



for which

$$\Delta G^\circ_f(\text{Na}_2\text{O}) = -RT \ln \frac{a_{\text{Na}_2\text{O}}}{p_{\text{Na}}^2 \cdot p_{\text{O}_2}^{1/2}} \quad [11]$$

where $\Delta G^\circ_f(\text{Na}_2\text{O})$ is the standard Gibbs energy change of reaction [10]. The standard Gibbs energy of formation of $\text{Na}_2\text{O}_{(s)}$ from $\text{Na}_{(l)}$ and $\text{O}_{2(g)}$ is (9)

$$\Delta G^\circ_f(\text{Na}_2\text{O}) = -420,015 + 146.022 T \quad [12]$$

The phase transformation of Na from the liquid state to monoatomic gas occurs at 1176.9 K with $\Delta H^\circ_v = 97,424 \text{ J mol}^{-1}$ (7). Therefore, for the following reaction



the Gibbs energy change, $\Delta G^\circ_1(\text{Na})$, can be expressed as

$$\Delta G^\circ_1(\text{Na}) = -97,424 + 82.780 T \quad [14]$$

The dependence of $\Delta G^\circ_f(\text{Na}_2\text{O})$ on temperature is obtained by combining Eq. [12] and [14]

$$\Delta G^\circ_f(\text{Na}_2\text{O}) = -614,863 + 311.582 T \quad [15]$$

Equations [5], [11], and [15] yield the following expression

$$\log p_{\text{Na}} = -\frac{24,250}{T} - 0.25 \log p_{\text{O}_2} + 9.94 \quad [16]$$

The estimated error is ± 2 for the values of $\log p_{\text{Na}}$. Equation [16] was used to construct Fig. 7, which shows the variation of $\log p_{\text{Na}}$ with $1/T$ between 823 and 1198 K at oxygen pressures imposed by the ambient atmosphere ($p_{\text{O}_2} = 0.21 \text{ atm}$), Fe, FeO, and Al, $\alpha\text{-Al}_2\text{O}_3$ coexistences. By considering the $\log p_{\text{Na}} - 1/T$ relation for the Al, $\alpha\text{-Al}_2\text{O}_3$ coexistence, one estimates that p_{Na} equals 1 atm at $1350 \pm 100 \text{ K}$. The values of p_{Na} in air between 1300 and 1900 K obtained by Weber and reported by Kummer (3) are also plotted in Fig. 7. These values extrapolate at lower temperature to values larger than those determined in this investigation.

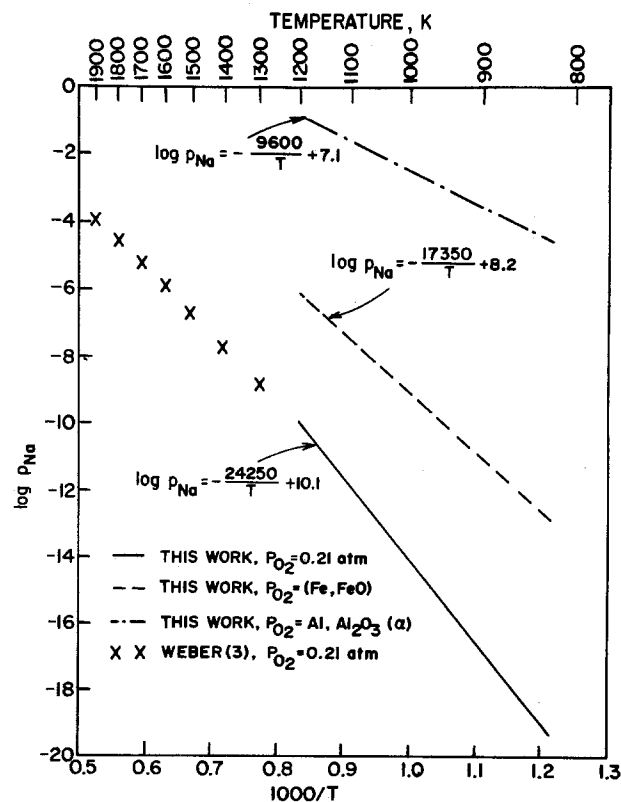


Fig. 7. Variation of the sodium vapor pressure of the $\alpha\text{-Al}_2\text{O}_3 + \beta\text{-Al}_2\text{O}_3$ coexistence with temperature and oxygen pressure.

Acknowledgments

This research is based on the thesis submitted by F. A. Elrefaie to McMaster University, in partial fulfillment of requirements for the Ph.D. degree. He gratefully acknowledges awards of an Aluminum Company of Canada Fellowship in Metallurgy and a National Research Council of Canada Graduate Studentship. The authors were indebted to P. S. Nicholson, D. A. R. Kay, and E. D. Hileman, Jr., for helpful discussions.

Manuscript submitted Oct. 24, 1980; revised manuscript received Feb. 18, 1981.

Any discussion of this paper will appear in a Discussion Section to be published in the June 1982 JOURNAL. All discussions for the June 1982 Discussion Section should be submitted by Feb. 1, 1982.

Publication costs of this article were assisted by McMaster University.

REFERENCES

1. N. S. Choudhury, *This Journal*, **120**, 1663 (1973).
2. D. J. Fray, *Metall. Trans. B*, **8**, 153 (1977).
3. J. T. Kummer, *Prog. Solid State Chem.*, **7**, 141 (1972).
4. W. W. Liang and J. F. Elliott, *This Journal*, **123**, 617 (1976).
5. H. Davis and W. W. Smeltzer, *This Journal*, **119**, 1362 (1972).
6. E. W. Dewing, Private communication.
7. JANAF Thermochemical Tables, Second Edition (1971).
8. B. C. H. Steele, "Electrochemical Measurements in High Temperature Systems," C. B. Alcock, Editor, American Elsevier Publishing Co., New York (1968).
9. J. F. Elliott and M. Gleiser, "Thermochemistry for Steelmaking," Addison-Wesley Publishing Company, Inc., Reading, Mass. (1960).
10. J. P. Hager and J. F. Elliott, *Trans. Met. Soc. AIME*, **329**, 513 (1967).
11. E. Steinmetz and H. Roth, *J. Less Common Metals*, **16**, 295 (1968).
12. Y. Le Cars *et al.*, *Compt. Rend. Acad. Sci., Paris, Ser. C*, **274**, 4 (1972).
13. R. C. DeVries and W. L. Roth, *J. Am. Ceram. Soc.*, **52**, 364 (1969).

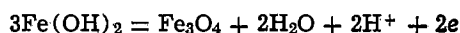
Iron Oxide Film Formed on Platinum During Fe_3O_4 Formation by Air Oxidation of an $\text{Fe}(\text{OH})_2$ Suspension

Yutaka Tamaura, Chika Kameshima, and Takashi Katsura

Department of Chemistry, Tokyo Institute of Technology, Ookayama, Meguro-ku, Tokyo 152, Japan

ABSTRACT

The iron oxide film formed on platinum was studied under conditions where Fe_3O_4 is readily formed by the air oxidation of an $\text{Fe}(\text{OH})_2$ suspension at pH 9.5 and 65°C. Stoichiometric Fe_3O_4 was formed on platinum before the air oxidation, and the potential before the air oxidation was due to the cathodic reaction



The Fe_3O_4 film on platinum became thick during the air oxidation, and it was shown that FeOH^+ is continuously supplied to the surface of the Fe_3O_4 film by the dissolution of the $\text{Fe}(\text{OH})_2$ particles in the reaction suspension and that the Fe_3O_4 -formation reaction takes place on the surface of the Fe_3O_4 layer. The rapid change in the oxidation potential (ORP) at the end of the reaction was due to a change from the electrode potential of Fe_3O_4 (slightly oxidized) to that of $\gamma\text{-Fe}_2\text{O}_3$, which is formed on the surface of the Fe_3O_4 film by the air oxidation at the end of the reaction.

The formation of ferrites by air oxidation of $\text{Fe}(\text{OH})_2$ suspensions containing metal ions has been studied; and Mg-, Cd-, Ti-, Cr-, V-, and Pb-bearing ferrites have been synthesized (1-6). In these studies, the progress of the air oxidation reaction has been measured by following the oxidation potential (ORP) using a platinum electrode (1-9). When an $\text{Fe}(\text{OH})_2$ suspension is oxidized by air at pH 9-10 and at temperatures above 60°C, Fe_3O_4 is formed (10). In this paper, the $\text{Fe}(\text{OH})_2$ suspension is referred to as "the reaction suspension." As the oxidation reaction proceeds, the Fe^{2+} content in the reaction suspension decreases and the ORP value is kept constant. However, at the end of the reaction, the Fe^{2+} content becomes constant and the ORP value changes rapidly from about -800 to 0 mV (*vs.* SCE). During the course of the investigation of the ORP value, we found that some iron oxide film was formed on the

platinum electrode. The ORP value measured during the air oxidation seems to be due to the iron oxide film formed on platinum. The deposition of iron oxide films on platinum from the solution containing ferrous ions has been studied by Cohen *et al.* (11-13) and Formaro (14). Their studies at room temperature have suggested that $\gamma\text{-FeOOH}$ or ferric iron oxide films are formed on platinum (11-14).

In this paper, we studied the ORP value and the iron oxide films formed on platinum during the Fe_3O_4 -formation reaction by air oxidation of $\text{Fe}(\text{OH})_2$ suspensions. The rapid ORP change at the end of the reaction was also studied.

Experimental

Reagents.—Chemical reagents of analytical grade were used. NaOH solutions (0.5 and 3N) were prepared by dissolving NaOH in distilled water free from CO_2 and O_2 . Acetate buffer solution (20 mM, pH 4.1) free

Key words: surfaces, potential, growth.

from O_2 was used for the dissolution of the outer layer of the iron oxide film.

Apparatus.—The reaction vessel for the Fe_3O_4 formation was similar to that used earlier (3-6) (volume 1 liter). Platinum electrodes or plates can be removed from the reaction vessel under a nitrogen atmosphere in the course of the air oxidation. Before every experimental run, the platinum electrodes or plates were treated with concentrated HCl and rinsed with enough water to remove Cl^- as completely as possible. A saturated calomel electrode was used as a reference electrode.

Procedure.—After passing the nitrogen gas into the distilled water (780 ml) at $65^\circ C$ to remove dissolved CO_2 and O_2 , $FeSO_4 \cdot 7H_2O$ (14.4g) was added and dissolved completely. The pH was adjusted with NaOH solution and controlled within ± 0.01 pH using a pH-stat. After standing for 1 hr under a nitrogen atmosphere, the oxidation reaction was initiated by passing air in place of nitrogen gas. During the oxidation, the pH value was kept constant at $pH\ 9.50 \pm 0.01$, and the temperature was controlled at $65^\circ \pm 0.1^\circ C$. The ORP value was measured using a platinum electrode.

For the identification of the phases formed in the reaction suspension during the course of the reaction, an aliquot portion of the reaction suspension was taken out by using a syringe without air contamination, washed with acetone free from oxygen to remove the water as completely as possible, and dried by passing nitrogen gas at room temperature. The sample thus obtained was sealed with Cellophane tape and analyzed by x-ray diffraction measurements.

For the analyses of the Fe^{2+} content of the reaction suspension during the air oxidation, about 20 ml of the suspension was taken out by a syringe. Fe^{2+} and Fe_{total} content in the samples were determined by the titration method using a $K_2Cr_2O_7$ standard solution. Fe_{total} was determined after reducing with zinc amalgam (15).

In the course of the reaction, the platinum plate (cylindrical type, 5.5×10 cm) was taken out under a nitrogen atmosphere, and chemical compositions (Fe^{2+} and Fe_{total}) of the iron oxide film formed on the platinum were determined by spectrophotometric method using 2,2'-bipyridyl (16) after dissolving the film in the acetate buffer solution (pH 4.1) or HCl (1:1) solution. For the measurement of Fe_{total} content, samples were reduced with hydroxylamine. The reflection electron diffraction patterns of the iron oxide films formed on platinum were examined using a smaller platinum plate (1×1 cm). After taking the smaller platinum plate from the reaction suspension, it was rinsed with the acetate buffer solution (pH 4.1) free from oxygen and dried by passing nitrogen gas. Although it seems that reorientation and recrystallization of the iron oxide formed on the platinum plate occurs during the course of the drying, the reflection method would be helpful in identifying iron oxides.

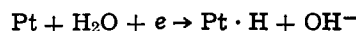
Cathodic reduction.—The cathodic reduction of the iron oxide film formed on the platinum electrode was carried out galvanostatically at a constant current ($10\ \mu A/cm^2$) in a stagnant borate buffer solution (pH 8.4, consisting of equal volumes of 0.15N $Na_2B_4O_7 \cdot 10H_2O$ and 0.15N H_3BO_3 solutions) at $25^\circ C$ under a slow nitrogen gas stream (17). The borate buffer solution was deaerated before the measurement by passing nitrogen gas for several hours. A Beckman Electroscan Model 30 was used for the electrical measurements.

All potential data (ORP) reported in this paper are referred to the saturated calomel electrode.

Results and Discussion

Iron oxide film formed on platinum before the air oxidation at pH 9.5 and $65^\circ C$.—Kiyama (10) has studied the reaction conditions for the formation of Fe_3O_4 with respect to temperature and pH values and has suggested that Fe_3O_4 is most readily obtained in a pH range from 8 to 10 and at temperatures above $60^\circ C$. Here, we investigated the iron oxide film formed on platinum under conditions where Fe_3O_4 is most readily formed. Curve A in Fig. 1 shows a change of ORP value during the Fe_3O_4 -formation reaction at pH 9.5 and $65^\circ C$. Curve B shows the change of the Fe^{2+} content in the reaction suspension. When $FeSO_4 \cdot 7H_2O$ was added at point a (Fig. 1), the ORP value decreased to around 0 mV. At point b, where an alkaline solution was added, the ORP value rapidly decreased to around -800 mV and became constant after standing for 1 hr. At point c, the oxidation reaction was initiated by passing air in place of nitrogen. As seen by curve B, the Fe^{2+} content decreased linearly with the oxidation time and became constant at point d (end point of the oxidation reaction). During the air oxidation reaction (from point c to d), the ORP value was constant, but at the end of the reaction (point d), the ORP value increased rapidly up to nearly 0 mV.

We studied first the iron oxide film formed on the platinum before the air oxidation (point P in Fig. 1). The platinum was taken out from the reaction suspension just before the air oxidation, rinsed with distilled water free from oxygen, and kept in the acetate buffer solution (pH 4.1) free from oxygen for 3 hr to dissolve the ferrous ions on the surface of the iron oxide film. In the reflection electron diffraction patterns of the iron oxide film thus obtained, only the lines due to Fe_3O_4 appeared (Table I). Chemical analyses showed that the amount of the iron in the iron oxide film was 1.45×10^{-4} mmol/cm² and that the Fe^{2+}/Fe_{total} molar ratio of the iron oxide film was 0.334 ± 0.01 . Thus, before the air oxidation at pH 9.5 and $65^\circ C$, stoichiometric Fe_3O_4 is formed on the platinum. Formaro (14) has reported the mechanism of the deposition of an iron oxide film on platinum which is immersed in a solution containing ferrous ion and has suggested that the deposition is caused by a short-circuit galvanic coupling between the (cathodic) reaction of hydrogen adsorption on platinum according to the reaction



and the (anodic) oxidation of Fe^{2+} to Fe^{3+}

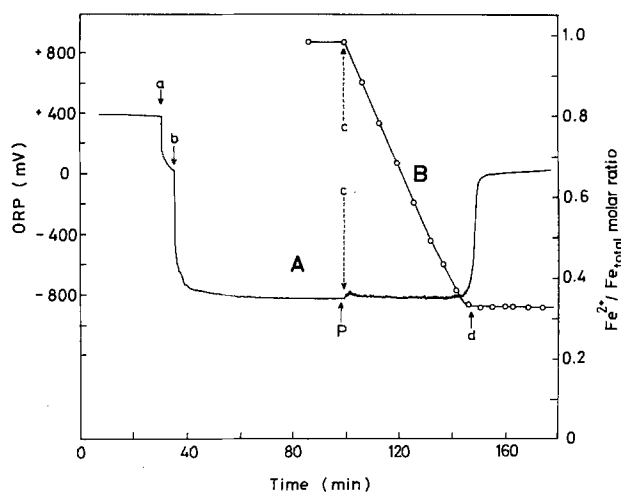


Fig. 1. Changes of ORP value (curve A) and Fe^{2+} content (curve B) in the reaction suspension during the Fe_3O_4 -formation reaction by air oxidation of the $Fe(OH)_2$ suspension at pH 9.5 and $65^\circ C$.

Table I. "d" values of the iron oxide films formed on platinum before and after the air oxidation reaction of the $\text{Fe}(\text{OH})_2$ suspension at pH 9.5 and 65°C

| Before air oxidation | | After air oxidation | |
|----------------------|-----------------------------|---------------------|------------------------------------|
| "d" exp | "d" Fe_3O_4 | "d" exp | "d" $\gamma\text{-Fe}_2\text{O}_3$ |
| | | 2.76 | 2.78 (221) |
| | | 2.51 | 2.52 (311) |
| 2.10 | 2.10 (400) | 2.07 | 2.08 (400) |
| | | 1.69 | 1.70 (422) |
| 1.61 | 1.62 (511) | 1.59 | 1.61 (511,333) |
| 1.48 | 1.49 (440) | 1.47 | 1.48 (440) |
| 1.33 | 1.33 (620) | 1.31 | 1.32 (620) |
| 1.09 | 1.09 (731) | | |



From the mechanism presented by Formaro, it can be seen that Fe^{3+} ion is formed on platinum. Under the conditions where Fe_3O_4 is formed (65°C, pH 9.5) by air oxidation of $\text{Fe}(\text{OH})_2$ suspensions, the Fe^{3+} ion formed on the platinum, by the mechanism suggested by Formaro, seems to react with ferrous ion to form the Fe_3O_4 film. Leibenguth and Cohen (12) and Hashimoto and Cohen (13) have studied the deposition of an iron oxide film on platinum by anodic oxidation. They have reported that a $\gamma\text{-FeOOH}$ film is formed on platinum from the ferrous sulfate or perchlorate solution at 25°C and pH 6.6-8.4. Kiyama (10) has reported that $\gamma\text{-FeOOH}$ (with $\alpha\text{-FeOOH}$) is formed by the air oxidation of $\text{Fe}(\text{OH})_2$ suspensions at lower temperatures (below 40°C) and at a pH below 8. Thus, when the temperature is low (below 40°C), the Fe^{3+} ion, formed by the anodic oxidation or the air oxidation of Fe^{2+} , is hydrolyzed readily to form $\gamma\text{-FeOOH}$. On the other hand, at a higher temperature (65°C), stoichiometric Fe_3O_4 film is formed on the platinum by anodic oxidation, as observed in the present work. There seems to be an agreement in the reaction conditions for the formation of iron oxides by air oxidation of $\text{Fe}(\text{OH})_2$ suspensions and the formation of iron oxide films on platinum by anodic oxidation.

Under the present experimental conditions, there is a possibility that the reaction suspension is contaminated by a small amount of Cl^- from the saturated calomel electrode and that some Cl^- ions remain on the platinum after cleaning with HCl and washing with water. It seems that these Cl^- ions affect the formation of the iron oxide on the platinum electrode. Foley *et al.* (18) reported that when an iron bar is anodically oxidized in the presence of Cl^- , Fe_3O_4 or $\gamma\text{-Fe}_2\text{O}_3$ is not deposited, but $\gamma\text{-FeOOH}$. In the present work, however, this effect of the Cl^- ions, which would exist in the reaction suspension, was not observed.

Potential-pH diagrams for the $\text{Fe-H}_2\text{O}$ system have been established by Pourbaix and his co-workers (19) who considered $\text{Fe}(\text{OH})_3$ and Fe_2O_3 as the favored ferric solid substances. Other diagrams considering $\alpha\text{-}$ and $\gamma\text{-FeOOH}$ have been presented by Misawa (20). According to these diagrams, ferrous hydroxide is thermodynamically stable in alkaline solution and will be oxidized to Fe_3O_4 or $\alpha\text{-FeOOH}$ with an increase of oxidation potential and to $\gamma\text{-FeOOH}$ at a higher oxidation potential. This suggests that Fe_3O_4 can be formed as a stable phase at the pH and electrode potential where the present study was carried out.

Thus, the ORP value measured before the air oxidation can be considered as the potential of the Fe_3O_4 immersed in the reaction suspension. Thuru *et al.* (21) have suggested that Fe_3O_4 immersed in solution is covered with a thin $\text{Fe}(\text{OH})_2$ layer, and that the

electrode potential is determined by a cathodic reaction. If so, the cathodic reaction occurring on the immersed Fe_3O_4 may be given by



In the reaction suspension, there exists many $\text{Fe}(\text{OH})_2$ particles, and the solution is considered to be saturated with ferrous ions. This would facilitate the deposition of the $\text{Fe}(\text{OH})_2$ layer which covers the Fe_3O_4 film formed on the platinum electrode. The pH dependence of the potential derived from Eq. [1] is 67 mV/pH (65°C). Figure 2 shows the relationship between the pH value and the ORP value before the air oxidation. As can be seen, a linear relationship with a slope of 64 mV/pH (65°C), which is nearly equal to that of Eq. [1], was obtained. If the ORP value is the potential due to reaction [1], some ferrous ions of the $\text{Fe}(\text{OH})_2$ layer should be determined on the Fe_3O_4 layer. To dissolve the $\text{Fe}(\text{OH})_2$ layer without dissolving the Fe_3O_4 layer, the electrode was taken out of the reaction suspension and was rinsed with distilled water free from oxygen and kept in the acetate buffer solution (pH 4.1) for 3 hr. The ferrous content determined from the ferrous concentration in the acetate buffer solution was 1.50×10^{-4} mmol/cm². This amount of the $\text{Fe}(\text{OH})_2$ layer is approximately equal to that of the inner Fe_3O_4 layer. These results suggest that the ORP value measured before the air oxidation is the potential due to the cathodic reaction [1]. Here, we call the layer which dissolves in the acetate buffer solution the "outer layer," and that which dissolves in the HCl solution the "inner layer."

Growth of the Fe_3O_4 inner layer formed on the platinum during the air oxidation.—Table II shows the chemical compositions of the inner layer of the iron oxide film formed on the platinum in the course of the air oxidation. As seen in the table, the inner iron oxide layer becomes thick with the oxidation time ($1.45\text{-}6.10 \times 10^{-4}$ Fe mmol/cm²) and the $\text{Fe}^{2+}/\text{Fe}_{\text{total}}$ molar ratios are 0.31-0.32. In the reflection electron diffraction pattern of the inner layer obtained in the course of the air oxidation, lines due to Fe_3O_4 were seen. On the other hand, in the outer layer, iron contents (mostly ferrous ions) determined during the air oxidation were less than 0.02×10^{-4} Fe mmol/cm², which is about $1/10^3\text{-}1/10^4$ of that of the inner layer. Thus, although the amount of fer-

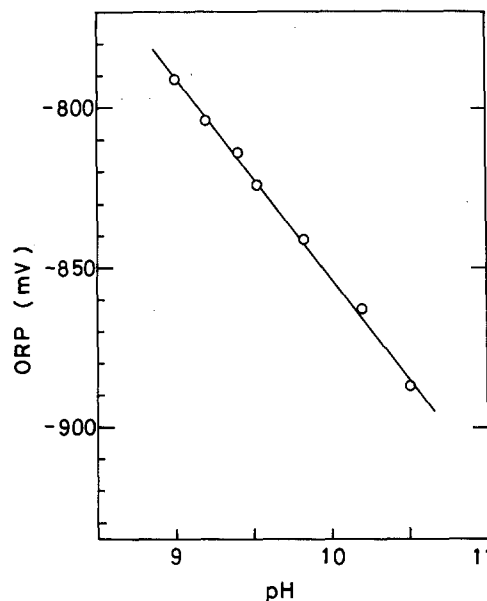


Fig. 2. pH dependency of ORP value before the air oxidation at 65°C.

Table II. Iron content in the inner layer of the iron oxide film formed on platinum during the air oxidation at pH 9.5 and 65°C

| | Fe _{total} ($\times 10^{-4}$ mmol/cm ²) | Fe ²⁺ / Fe _{total} |
|----------------------------------|---|---|
| Just before the air oxidation | 1.45 | 0.334 |
| 10 min oxidation time | 4.10 | 0.312 |
| Just before the rapid ORP change | 6.10 | 0.322 |
| After the rapid ORP change | 6.05 | 0.320 |

rous ions in the outer layer was very small, the inner layer (slightly oxidized Fe₃O₄) became thick during the air oxidation. This shows that some dissolved species such as FeOH⁺ are being supplied continuously to the surface of the Fe₃O₄ layer (slightly oxidized) during the air oxidation and that a reaction takes place on the surface to precede the crystal growth. Figure 3 shows the changes of peak intensities (peak area) of Fe(OH)₂ ($2\theta = 47.5^\circ$, Fe K α) (curve A) and Fe₃O₄ (45.0°) (curve B) in x-ray diffraction patterns of the reaction suspensions during the air oxidation. As seen here, the peak intensities of Fe₃O₄ (curve B) increase with the oxidation time, but those of Fe(OH)₂ (curve A) decrease. Thus, in the reaction suspensions, the growth of Fe₃O₄ particles proceeds with the dissolution of Fe(OH)₂ particles, and the ORP value changes rapidly just at the time when all the Fe(OH)₂ particles are completely dissolved. (The broken line represents the end point of the reaction.) This means that FeOH⁺ is continuously supplied during the air oxidation by the dissolution of the Fe(OH)₂ particles. Kiyama (10) has suggested that Fe₃O₄ will be formed by the precipitation of FeOH⁺ with the ferric oxyhydroxide complex ion which is formed by the oxidation of FeOH⁺. The growth of the Fe₃O₄ layer as seen in the table shows that the reaction as suggested by Kiyama seems to take place on the surface of the Fe₃O₄ layer. The reaction will continue as long as FeOH⁺ is being supplied.

In the outer layer, as mentioned above, a small amount of ferrous ion was determined during the air oxidation. The pH dependence of the ORP value in the course of the air oxidation was 63 mV/pH. These results suggest that the ORP value measured during the air oxidation is due to an electrode potential of the Fe₃O₄ (slightly oxidized) which is covered with a thin Fe(OH)₂ layer. However, as seen by Fig. 4 (the ORP change recorded on an expanded scale), a stable ORP value is measured before the

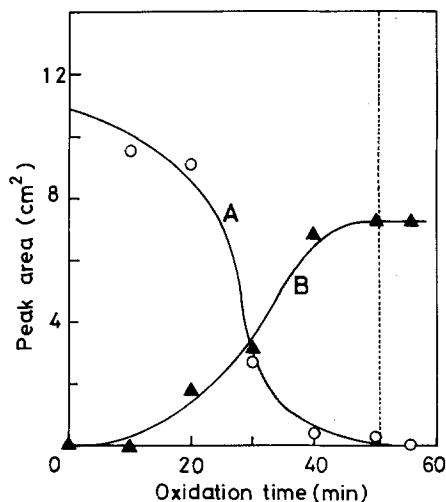


Fig. 3. Changes of peak intensities (peak area) of Fe(OH)₂ ($2\theta = 47.5^\circ$ Fe K α) (curve A) and Fe₃O₄ (45.0°) (curve B) in x-ray diffraction patterns of the reaction suspensions during the air oxidation at pH 9.5 and 65°C.

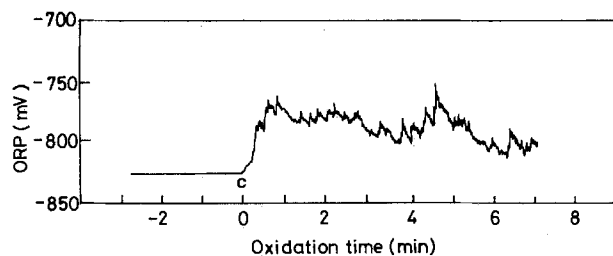


Fig. 4. ORP change recorded on an expanded scale before and after the initiation of the air oxidation.

air oxidation, but when the oxidation was initiated (point c in Fig. 4), the ORP value became unstable and slightly increased by 40-60 mV. This shows that some discharge (e.g., oxidation of FeOH⁺) owing to the Fe₃O₄-formation reaction takes place on the surface of the Fe₃O₄ layer, and the unstable ORP value seems to be due to the reaction occurring on the surface of the layer.

Rapid ORP change at the end of the air oxidation.—Curves A-E in Fig. 5 show the changes of the potential during the cathodic reduction of the iron oxide films formed on the platinum in the course of the air oxidation, and curve F is for the iron oxide film deposited on the iron by the anodic oxidation at 300 mV in the borate buffer solution (pH 8.4) according to the method by Markovac and Cohen (17). As seen in curve F, two arrests appear in the profile of the oxide film formed on the iron, one corresponding to the reduction of γ -Fe₂O₃ (period a-b of curve F) and the other to the reduction of Fe₃O₄ (period b-c) as shown by Nagayama and Cohen (22) and Markovac and Cohen (17). Recently, Haruyama and Thuru (23) and Thuru and Haruyama (24) have reported the results which support the γ -Fe₂O₃ and Fe₃O₄ bilayer model of the iron oxide film on iron. They suggested that when the first wave (period a-b) appears at a much higher potential (-500 mV vs. SCE), it is mainly due to the existence of γ -Fe₂O₃ as the outer layer (17, 22-24). In an interval from before the air oxidation until just before the rapid ORP change (curve A-C in Fig. 5), similar cathodic reduction profiles are obtained, but a marked difference is seen between just before (curve C) and just after (curve D) the rapid ORP changes; i.e., only a single wave appears just before the rapid ORP change, but two waves just after the rapid ORP change. When air is

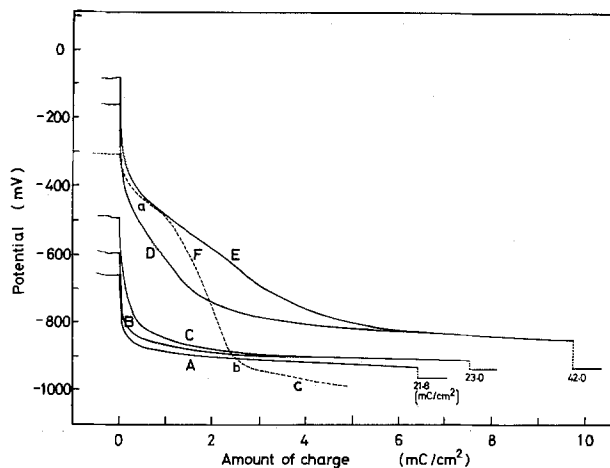


Fig. 5. Cathodic reduction profiles of the iron oxide films formed in the course of the air oxidation ($10 \mu\text{A}/\text{cm}^2$). A, before the air oxidation; B, 30 min oxidation time; C, just before the rapid ORP change; D, just after the rapid ORP change; E, 15 min after the rapid ORP change; F, iron oxide film formed on iron by cathodic oxidation at 300 mV in the borate buffer solution (pH 8.4).

passed further after the rapid ORP change, the first wave becomes large, as seen by curve E. The appearance of the first wave in curves D and E seems to be due to the formation of γ -Fe₂O₃ on the surface of the iron oxide film, and it becomes thick by passing air further after the rapid ORP change. The reflection electron diffraction pattern of the iron oxide film obtained after the rapid ORP change gave lines which differ from those of Fe₃O₄, but are due to γ -Fe₂O₃ ($a = 8.30 \pm 0.03 \text{ \AA}$) (Table I). As seen by curves D and E, a steady potential (-920 mV) (17) corresponding to that of the reduction of Fe₃O₄ is seen after a prolonged cathodic reduction. This shows that Fe₃O₄ is formed inside of the γ -Fe₂O₃ layer just after the rapid ORP change or 15 min after. As seen by curves D and E, higher electrode potentials appear, which are characteristic of the γ -Fe₂O₃ formed on the surface of Fe₃O₄ by air oxidation (25, 26). The high electrode potential has been considered to be due to cation-deficient γ -Fe₂O₃ (25, 26) or to the adsorption of oxygen on γ -Fe₂O₃ (24). The rapid ORP change at the end of the reaction seems to be due to the change of the electrode potential of the Fe₃O₄ (slightly oxidized) to that of the γ -Fe₂O₃ which is formed on the surface of the Fe₃O₄ by the oxidation with oxygen at the end of the reaction.

Conclusions

1. Stoichiometric Fe₃O₄ is formed on platinum which is immersed in the Fe(OH)₂ suspension at pH 9.5 and 65°C.
2. During the course of the air oxidation of the Fe(OH)₂ suspension, growth of the Fe₃O₄ film on the platinum takes place.
3. At the end of the air oxidation of the Fe(OH)₂ suspension, the surface of the Fe₃O₄ film is oxidized to γ -Fe₂O₃, which causes a rapid change in the ORP value.

Acknowledgments

The authors would like to thank Dr. K. Kitayama and Dr. R. Ooki of Tokyo Institute of Technology for preparing magnetite and for taking the reflection electron diffraction patterns

Manuscript submitted Aug. 5, 1980; revised manuscript received Jan. 27, 1981.

Any discussion of this paper will appear in a Discussion Section to be published in the June 1982 JOURNAL.

All discussions for the June 1982 Discussion Section should be submitted by Feb. 1, 1982.

REFERENCES

1. K. Kaneko and T. Katsura, *Bull. Chem. Soc. Jpn.*, **52**, 747 (1979).
2. K. Kaneko, T. Kakei, Y. Tamaura, T. Kanzaki, and T. Katsura, *ibid.*, **52**, 1080 (1979).
3. T. Katsura, Y. Tamara, and G. S. Chyo, *ibid.*, **52**, 96 (1979).
4. Y. Tamaura and T. Katsura, *J. Chem. Soc., Dalton Trans.*, 825 (1980).
5. Y. Tamaura, S. Mechaimonchit, and T. Katsura, *J. Inorg. Nucl. Chem.*, **43**, 671 (1981).
6. Y. Tamaura, U. Rasyid, and T. Katsura, *J. Chem. Soc., Dalton Trans.*, 2125 (1980).
7. T. Katsura, Y. Tamaura, and H. Terada, *Ind. Wat. Jpn.*, **23**, 16 (1977).
8. Y. Tamaura, G. S. Chyo, and T. Katsura, *Water Research*, **13**, 21 (1979).
9. T. Kanzaki, J. Nakajima, Y. Tamaura, and T. Katsura, *Bull. Chem. Soc. Jpn.*, **54**, 135 (1981).
10. M. Kiyama, *ibid.*, **47**, 1646 (1974).
11. V. Markovac and M. Cohen, *This Journal*, **114**, 678 (1967).
12. J.-L. Leibenguth and M. Cohen, *ibid.*, **119**, 987 (1972).
13. K. Hashimoto and M. Cohen, *ibid.*, **121**, 37 (1974).
14. L. Formaro, *Corros. Sci.*, **19**, 631 (1979).
15. T. Katsura, "Zikken Kagaku Koza," Chemical Society of Japan, Maruzen (1958), No. 15, pp. 272-275.
16. I. Iwasaki, T. Katsura, T. Ozawa, M. Mashima, H. Hamamura, and B. Iwasaki, *Bull. Volc. Soc. Jpn.*, *Ser. II*, **5**, 75 (1960).
17. V. Markovac and M. Cohen, *This Journal*, **114**, 674 (1967).
18. C. L. Foley, J. Kruger, and C. J. Bechtoldt, *ibid.*, **114**, 994 (1967).
19. M. Pourbaix, "Atlas of Electrochemical Equilibria in Aqueous Solutions," p. 307, Pergamon, Oxford (1966).
20. T. Misawa, *Corros. Sci.*, **13**, 659 (1973).
21. T. Thuru, T. Zatsumi, K. Masamura, and S. Haruyama, *J. Jpn. Inst. Metals*, **42**, 197 (1978).
22. M. Nagayama and M. Cohen, *This Journal*, **109**, 781 (1962).
23. S. Haruyama and T. Thuru, *Corros. Sci.*, **13**, 275 (1978).
24. T. Thuru and S. Haruyama, *ibid.*, **16**, 623 (1976).
25. C. D. Stockbridge, P. B. Sewell, and M. Cohen, *This Journal*, **108**, 928 (1961).
26. P. B. Sewell, C. D. Stockbridge, and M. Cohen, *ibid.*, **108**, 933 (1961).

Electrochemical Study of an SnO₂-Sb₂O₅ Semiconducting Glaze

P. G. Orsini,* P. Pernice, and L. Egiziano

Faculty of Engineering, University of Naples, Naples, Italy

ABSTRACT

Small electrodes of semiconducting glaze, containing around 30% SnO₂ doped with Sb₂O₅, have been prepared by peeling electrical insulators and have been put in contact with Na₂SO₄ solution or with metallic gold. Alternating or direct current-voltage curves at temperatures between ambient and 60°C, current-time curves, harmonic analysis, and SEM micrographs of the corroded areas are reported. This study was made to simulate the corrosion of high voltage insulators with resistive glazes, operating in salt-contaminated areas and also to obtain a better understanding of conduction in mainly amorphous systems which are heterogeneous on a very small scale.

Resistive glazes, relying on semiconducting properties of doped SnO₂, have been used on high voltage electrical insulators to control flashover caused by

pollution (1, 2). Their use has proved only partially successful as result of a relatively rapid deterioration (3).

A previous study (4) performed on a glaze obtained by the addition of SnO₂, doped with Sb₂O₅, to an alumi-

* Electrochemical Society Active Member.

Key words: coating, cathode, corrosion, reduction.

nosilicate base glaze, pointed out characteristic "pitting" corrosion of the contact glaze/pollutant electrolytic solution when an alternating voltage was applied to the system. An unexpected rectification effect at this contact was also found.

A more detailed knowledge of these phenomena is believed to be fundamental to a deeper understanding not only of the specific problem of the degradation of the glaze in service, but also of the general problem of amorphous semiconducting materials.

Moreover, the distribution of micro-inhomogeneities within the thickness of glaze on porcelain poses various problems of general interest, also in connection with the different nature of air/glaze and glaze/porcelain boundaries.

Characterization of the Glaze

The semiconducting glaze samples were manufactured by a porcelain electric insulator manufacturer. Reagent grade SnO_2 with 2.5 mol percent Sb_2O_5 was calcined for a few hours at 1200°C . The resulted semiconducting powder was mixed, in the proportion 1:2, with a traditional insulating glaze of approximate composition 70% SiO_2 , 9% Al_2O_3 , 4.5% $(\text{Na}, \text{K})_2\text{O}$, 9% CaO , 7.5% ZnO , and sprayed onto unfired electrical porcelain tiles. After firing, a semiconducting glaze coated the porcelain to an average thickness of $150\ \mu\text{m}$. Such glazes have proved (2, 3, 5, 6) to be the best resistive glazes on high voltage insulators of traditional shape.

The scanning electron microscope (SEM) image of a polished section, cut along a plane normal to the glaze surface, is shown in Fig. 1. The semiconducting layer is confined between air/glaze (AG) and glaze/porcelain (GP) boundaries which have been indicated in the figure. The presence, in its thickness, of several gas bubbles having almost spherical shape, indicates that the glaze was a high viscosity liquid at firing tempera-

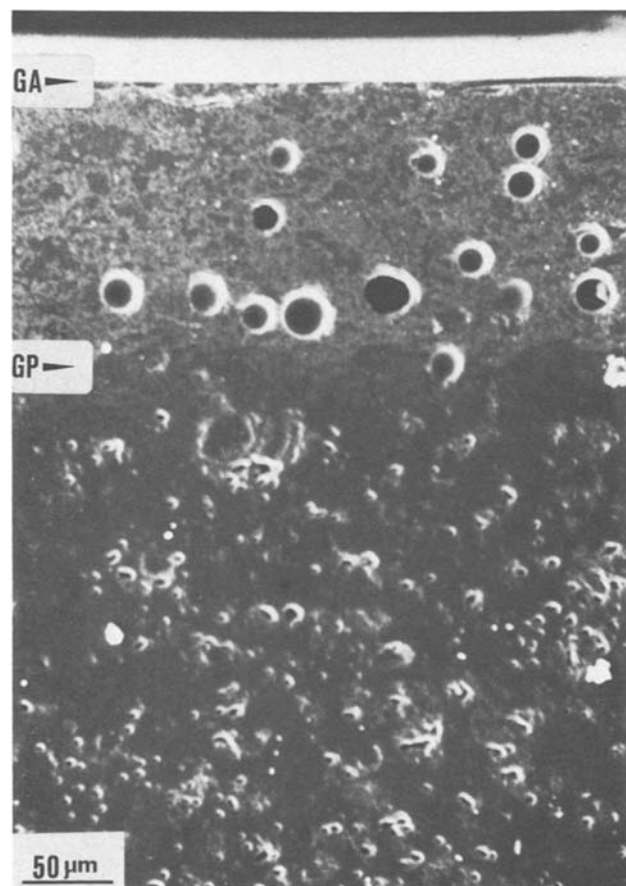


Fig. 1. SEM micrograph of polished transverse section of semiconducting glaze on porcelain. AG and GP: air/glaze and glaze/porcelain boundaries.

ture. While the formation of a liquid has allowed a good "vitrification" of the system, a high viscosity has prevented the escaping of bubbles.

Two distinct phases are present in the glaze: one internal, darker, less abundant; the second external, lighter, continuous. The overall conductivity of this system, measured along a direction parallel to AG and GP boundaries, is $\sigma = 5.5 \times 10^{-6}\ \Omega^{-1}\ \text{cm}^{-1}$ at $T = 31^\circ\text{C}$, under an electrical field $E = 500\ \text{V}\ \text{cm}^{-1}$. Dependence of σ upon T and E has been reported elsewhere (4).

On the basis of previous detailed structural studies (5, 7, 8) by SEM and electron probe microanalysis (EMA), which have revealed the existence and the composition of two different phases in these glazes, considering the relative proportion of the two phases in Fig. 1, and the relative amount of SnO_2 in the glaze, it seems reasonable to conclude that the darker phase corresponds to the SnO_2 -rich, more conductive, phase. According to the x-ray diffraction spectrum of the whole glaze, which shows only the following peaks: $d = 3.36, 2.66, 2.36, 2.31, 1.76, 1.67\ \text{AU}$, all corresponding to SnO_2 (9), the SnO_2 -rich phase seems to be the only crystalline phase in the glaze system.

The Cell with a Glaze Electrode

Thin slabs of semiconducting glaze have been prepared by cutting a tile along the GP boundary (see Fig. 1) with a low speed saw (200 rpm) equipped with a thin (0.25 mm) diamond disk. Approximately square chips, with $50\ \text{mm}^2$ area and 0.15 mm thickness were obtained, one face being the "external" glossy glaze surface (AG, in Fig. 1), the other being the saw-cut surface, finished with grit 600 SiC to remove traces of porcelain.

Each slab was cemented, with the cut surface, to the end of a glass tube (5 mm bore) using a silicone rubber cement. A few drops of Hg in the tube provided the contact with glaze material. This "electrode" was usually dipped in a 25 weight percent Na_2SO_4 solution. Care was taken to minimize current leakage. The counterelectrode in the cell was a Pt wire or net of large area. Such a cell with a glaze electrode was initially prepared to study the effect of a.c. on resistive glazes of insulators in contact with polluting salt solution. The idea was to localize in a definite area any eventual alteration of the glaze surface that can be related to insulator decay, and study it by microscopy. In fact, a glaze electrode, a-c operated for few hours at $10\ \text{mA}\ \text{cm}^{-2}$, presents an appreciable distribution of microscopical corrosion craters. A typical SEM image of corroded glaze surface is shown in Fig. 2. The right lower corner corresponds to an uncorroded area; the rest corresponds to part of a crater on the bottom of which a bubble, like those in Fig. 1, can be seen. Bubbles on the bottom of corrosion craters are a common feature of SnO_2 glaze corrosion morphology.

Besides this surface alteration, the glaze also showed compositional change. During a-c operation, in addition to gas evolution at electrodes corresponding to electrolysis of water, the reduction of SnO_2 to metallic Sn resulted (4). A deposit of metallic tin onto the glaze electrode surface in the central area corresponding to passage of current has been identified by x-ray diffraction. An electrode with metallic deposit showed, in addition to those already reported, the following peaks: $d = 2.92, 2.79, 2.02\ \text{AU}$ which correspond (10) to metallic tin (strongest intensities).

I-V Curves

The unidirectional component of current flowing through the cell powered with a 50 Hz sinusoidal voltage, corresponding to the net reduction of tin, has been systematically measured. The rms value, i_a , and the unidirectional value, i_d , in a cell with a typical glaze electrode and a 25% Na_2SO_4 solution at 20°C are plotted against the rms value V_a of the applied voltage in Fig. 3. This voltage is consistent with the relatively

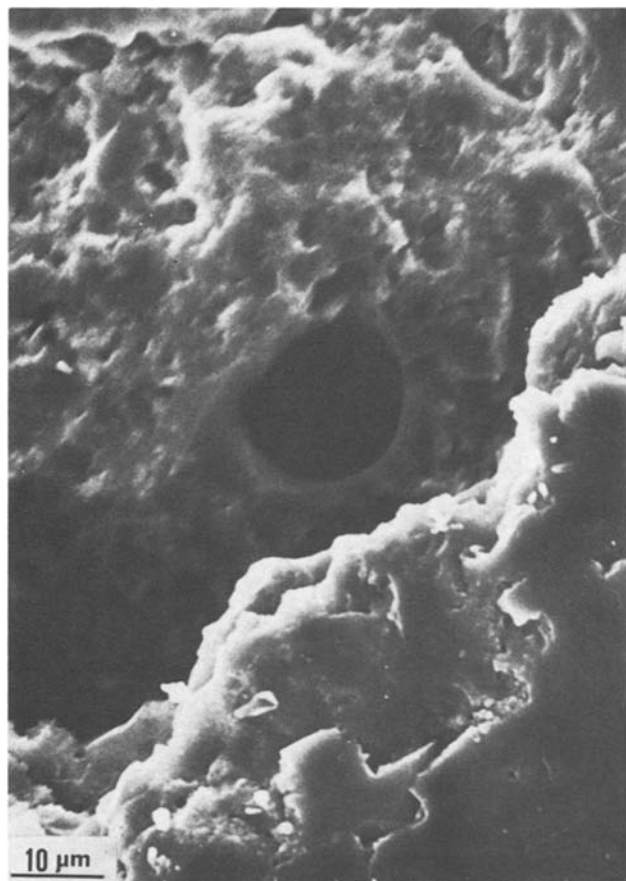


Fig. 2. SEM micrograph of corroded glaze surface

large voltage drop inside the glaze. A variable auto-transformer on the main supply line, an electronic microammeter, and a galvanometer completed the measuring circuit.

Values of current were determined 10 min after each new voltage was set: the system showed a certain delay in reaching a steady value after each voltage change. Stability was reached more rapidly when the voltage was decreased. A really stable current is never obtained because of the progressive chemical change in the glaze. An example gives an idea of the order of magnitude of these variations: an initial alternating current of 350 μA fell to 320 μA in few minutes. Afterward it fell to 300 μA over 40 hr, at a constant rate of 0.5 $\mu\text{A hr}^{-1}$. In fact, limiting the sensitivity of current measurement to 0.5 μA , readings after the initial transient can be considered to be stable within 1 hr.

The rectifying effect raises progressively at $V_a > 10\text{V}$. No threshold value can be given because the i_d curve takes off with zero slope. By increasing the voltage, the ratio i_d/i_a may become as high as 0.4. In any case, different electrodes give slightly different values of i_a and i_d for equal applied voltage, because the natural undulation of the air/glaze surface causes the slab thickness to vary. The dashed curve in Fig. 3 corresponds to i_d values when the gloss on the external surface of the electrode is taken away with an abrasive. The i - V characteristic curve of the same cell when direct voltage is applied gives a better account of the rectification. Measurements are reported in Fig. 4. Again, the voltage reported is the total value applied to the system. This voltage corresponds almost entirely to the drop inside the slab. This is true even when current approaches zero because, as is shown later, glaze resistance increases considerably when the field applied to it is lowered. From this point of view, rather than of an electric cell, one should think of a semiconductor with one electrolytic contact. No values are reported where the current is vanishingly small because a completely steady state is not attained there.

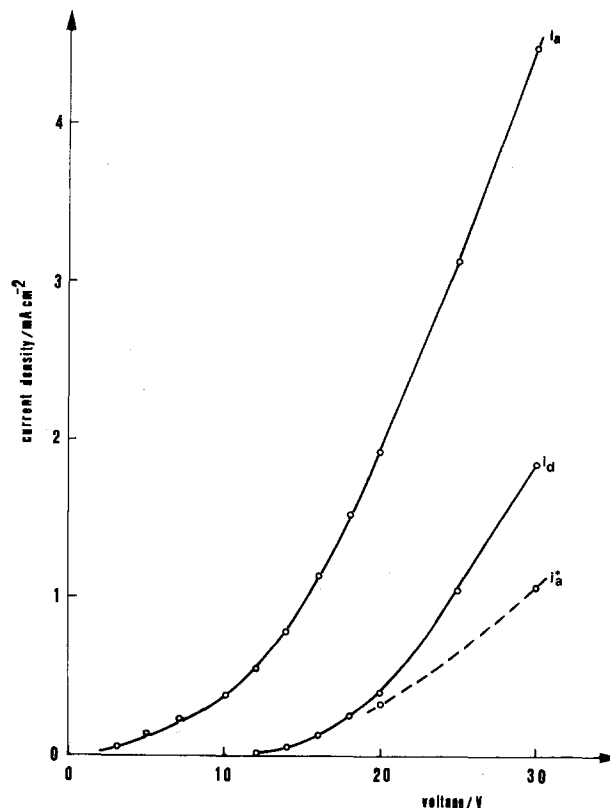


Fig. 3. Current densities vs. 50 Hz sinusoidal voltage (rms) applied to the electrochemical cell. i_a , rms value; i_d , unidirectional component; i_d^* , surface glass taken away.

Figure 4 shows the asymmetric behavior of the cell under investigation when positive or negative voltages are applied. It suggests that in applying to the cell a sinusoidal voltage with high peak-to-peak value the corresponding current will be periodic, not sinusoidal, with an average value within the period differing from zero. Decreasing this voltage, the average value of the current progressively vanishes ($i_d = 0$).

Current Wave Shape

The wave shape of the current through the cell, powered by 50 Hz sinusoidal voltage, has been developed by Fourier analysis with the aid of an HP 2100 calculator.

The voltage drop in a 1 k Ω ohmic resistor in series with the cell ($R = 1\text{M}\Omega$), was passed through a low-pass filter (cut-off frequency 1 kHz) and an analogue-digital converter, ADC, and then into the calculator.

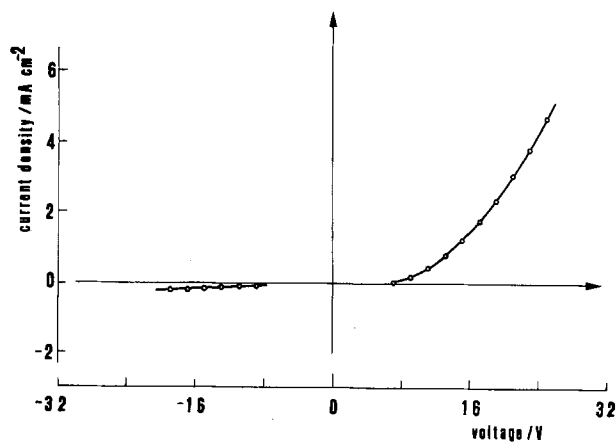


Fig. 4. Current density vs. direct voltage applied to the electrochemical cell.

The noise level of the filter and ADC was to $6 \times 10^{-2} \mu\text{A}$. The sampling frequency was 20 kHz.

In Fig. 5 the amplitude spectrum of the current flowing through the cell at three different voltages is shown. At all voltages lower than 30V the spectra are like Fig. 5a: i_d and even harmonics are negligible. At higher voltages spectra are like those shown in Fig. 5b and c: i_d and even harmonics have progressively higher values.

This behavior is in good agreement with that drawn as a conclusion in describing the "static" characteristic in Fig. 4. On the basis of results like those reported in Fig. 5, at different voltages, we have calculated i - V curves similar to those reported in Fig. 3: the ratio i_d/i_a shows the same trend.

Specimen with Two Metallic Contacts

The role of the contact glaze/electrolytic solution is better understood if the results reported in Fig. 3 and 4 are compared with the i - V curves of a glaze with two metallic contacts.

Thin slabs of semiconducting glaze similar to those used in the electrolytic cell have had gold sputtered onto the central zone of both surfaces (GP and AG, Fig. 1). Contacts between gold deposit and copper leads were secured with Silverdag®.

Values of i_a and i_d , vs. V_a for a temperature of 20°C when a 50 Hz sinusoidal voltage is applied, are reported in Fig. 6; this is the "dry" counterpart of Fig. 3. In the specimen with two gold contacts, the unidirectional current i_d assumes relatively very low values. It vanishes when the external gloss is taken away.

The i - V characteristic curve of the same cell at 31°C when direct voltage is applied is reported in Fig. 7. Positive and negative halves are almost symmetric. This is true at all temperatures between 15° and 60°C. The conductivity of the glaze, calculated at 10V, i.e., at a field of 500 V cm⁻¹, and 31°C, is $\sigma = 2.62 \times 10^{-6} \Omega^{-1} \text{cm}^{-1}$.

Current, as a function of direct voltage can be described by the equation

$$|I| = K |V|^{3/2} \quad [1]$$

The plot of I vs. $V^{3/2}$ reported in Fig. 8 at 31° and 51°C,

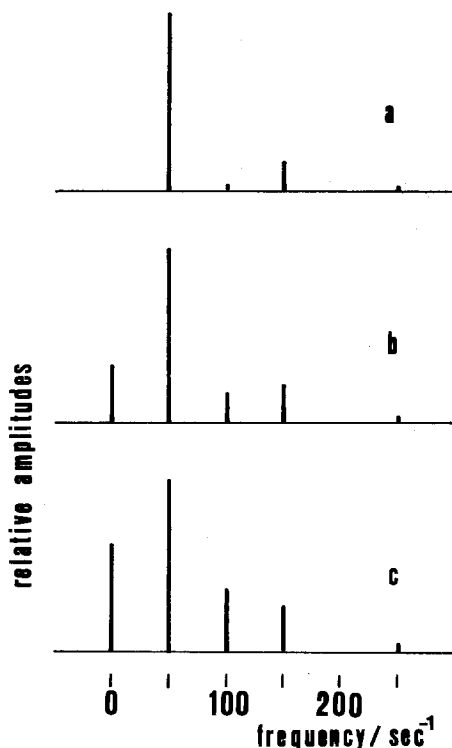


Fig. 5. Amplitude spectra of current through the electrochemical cell. Voltage applied: (a) 25V; (b) 40V; (c) 60V, rms value.

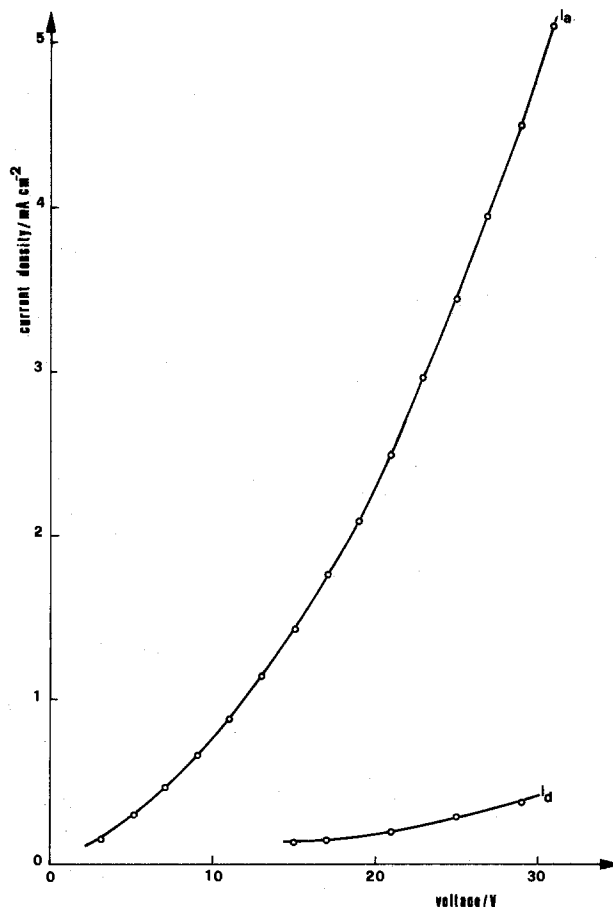


Fig. 6. Current densities vs. 50 Hz sinusoidal voltage, rms, applied to the glaze with two gold contacts. i_a , rms value; i_d , unidirectional component.

is linear to a good approximation in the range of voltages explored at both 31° and 51°C for forward and reverse flow. A positive sign is given when flow of positive charges enters into the glaze through the glossy surface, in accordance with results presented in Fig. 3, 4, 5, 7, and 8.

With the method of least squares the following values for the K parameter have been found at 31° and 51°C:

$$K_{31^+} = 2.98, K_{31^-} = 2.92, K_{51^+} = 3.58, K_{51^-} = 3.48 \mu\text{AV}^{-3/2}$$

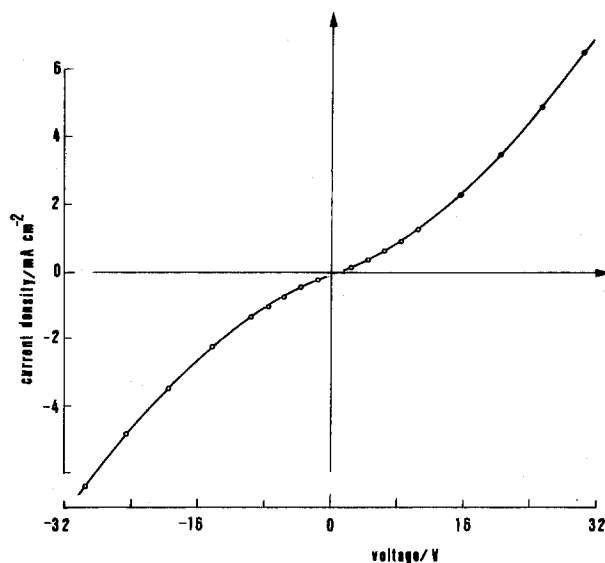


Fig. 7. Current density vs. direct voltage applied to the glaze with two gold contacts, at 31°C.

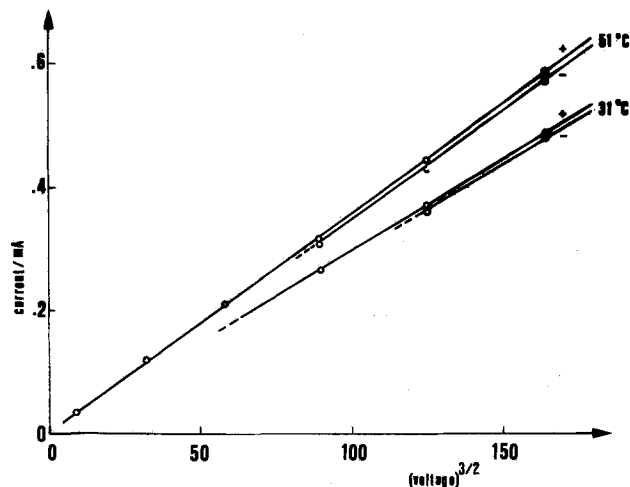


Fig. 8. Test of interpolating function $|V|^{3/2}$. Values measured at 31° and 51°C on the same specimen as in Fig. 7.

The activation energy for the conduction calculated from these values, 0.080 ± 0.001 eV, is independent of the current flow direction, within the limits of error. Experiments have also been performed on a specimen with glaze/silver contacts made with Silverdag directly facing the glaze, instead of glaze/gold/silver. Results are similar to those in Fig. 7 and 8, but steady currents are obtained only after a transient period whose duration depends on experimental conditions. Moreover, current values are very dependent on the sign of voltage applied.

In Fig. 9 a typical transient behavior of current is reported for a specimen with glaze/silver contact at 31°C. Closing the circuit at t_1 , a steady current is attained only after about 1 hr. After changing direction of current at t_2 , a small initial overshoot is followed by a relatively slow rise. A second change of direction at t_3 , produces a larger overshoot which is slowly relaxed. At higher temperatures, e.g., 51°C, the effects are much the same, but the time to attain steady-state results is much shorter.

If the tests reported in Fig. 9 are applied to a specimen with two gold contacts steady current occurs immediately at all temperatures with only slightly differing values of current for either polarity, as already reported in Fig. 7.

The same test, applied to a specimen in which the current flow is parallel to the surface, produces immediately steady values, not dependent either on the polarity or on the material of the two contacts.

Conclusions

A delicate cutting has allowed the separation of glaze from the porcelain and the construction of electrodes, while preserving unaltered the morphology of

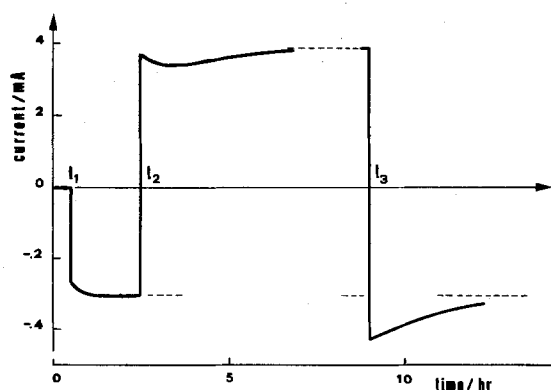


Fig. 9. Plot of current vs. time. Glaze with two silver contacts, at 31°C. Direct voltage applied at t_1 ; sign reversed at t_2 and t_3 .

the coating. Thus besides the characterization of the coating material one can investigate the behavior (chemical, electrical, or mechanical) of the coating layer itself which is responsible for the changes on polluted semiconducting glazed insulators.

A marked rectifying effect originates at the glaze/solution contact. This effect is shown in Fig. 3 and 4 and it seems to be mainly due to the contact between the semiconductor and the electrolytic solution. In fact these curves are influenced only to a very limited extent by changing the concentration of electrolyte solution (e.g., from 25 to 2.5%) or changing electrolyte (e.g., NaCl instead of Na₂SO₄).

On the other hand, at the contact glaze/metal (Au) only a very small rectifying effect exists: the static characteristic curve in Fig. 7 is very nearly symmetric, while in a.c. the ratio i_d/i_a , for equal voltages, assumes much lower values. Even this small residual rectifying effect, whose dependence of intensity on polarity is seen in Fig. 8, can be ascribed to the incomplete symmetry of contacts, because the external glaze surface is relatively SnO₂ poor.

A very thin layer, less than 1 μ m thick, of SnO₂-free glaze has been found by Taylor (4) with ESCA in proximity to the air/glaze surface. In this layer crystallites of SnO₂ are possibly excluded by a surface tension effect, so that the two gold contacts do not face glaze of equal composition. Where the two contacts are made symmetric by polishing away the external SnO₂-poor layer the unidirectional component vanishes as shown in Fig. 6.

In fact, even during electrolysis, when the effect of contact with electrolytic solution is largely prevailing, the influence of external SnO₂-poor layer is still evident. The removal of this layer produces a slight reduction of i_d (dashed line in Fig. 3).

The transient behavior depicted in Fig. 9 is also an indirect proof of the existence of an external layer with different composition. When contacts do not face this layer, as in the case of current flow parallel to the external surface, steady values are immediately obtained. The transient phenomena seem to depend on metal-glass diffusion because: (i) at higher temperature steady state is attained more rapidly; (ii) gold, compared with silver, has a much lower diffusivity in accordance with their ionic diameters; (iii) when one of the Ag contacts faces the SnO₂-poor layer, the rate of diffusion depends on polarity: reversing polarity causes different transient phenomena (t_2 and t_3 , Fig. 9).

Values of conductivity are fairly dependent on direction of current flow. Again, this can be ascribed to the presence of a thin SnO₂-poor layer. Along a direction parallel to the surface, the conductivity is $5.55 \times 10^{-6} \Omega^{-1} \text{cm}^{-1}$ at 31°C and 500 V cm⁻¹. In the same conditions, along the direction normal to the surface, the conductivity was only $2.62 \times 10^{-6} \Omega^{-1} \text{cm}^{-1}$. The difference is well above any uncertainty due to experimental errors.

Manuscript submitted Oct. 21, 1980; revised manuscript received Jan. 19, 1981.

Any discussion of this paper will appear in a Discussion Section to be published in the June 1982 JOURNAL. All discussions for the June 1982 Discussion Section should be submitted by Feb. 1, 1982.

Publication costs of this article were assisted by the University of Naples.

REFERENCES

1. P. J. Lamberth, *Proc. IEE*, **118**, 1107 (1971).
2. D. B. Binns, *Trans. Br. Ceram. Soc.*, **73**, 7 (1974).
3. D. G. Powell, *Amer. Ceram. Soc. Bull.*, **25**, 600 (1973).
4. G. Bagnasco, P. Pernice, and P. G. Orsini, *Cerurgia Intern.*, **5**, 161 (1979).
5. R. H. Taylor, *J. Mater. Sci.*, **12**, 873 (1977).
6. L. Egiziano, G. Lupo, and B. Macchiaroli, "Con-

- siderations on the Design of New Insulators for Contaminated Areas," I. Welc, Moscow (1977).
7. R. H. Taylor, D. L. Allinson, and T. I. Barry, *J. Mater. Sci.*, **13**, 876 (1978).

8. R. M. Morgan, J. Robertson, and R. H. Taylor, *J. Noncryst. Solids.*, **31**, 367 (1979).
9. ASTM Powder Diffraction File, Card No. 21-1250.
10. ASTM Powder Diffraction File, Card No. 4-673.

Mössbauer Spectroscopic Study of the Chemical State of Cobalt in an Electrodeposited Zinc-Cobalt Alloy

H. Leidheiser, Jr.,* A. Vértes,* and M. L. Varsányi*

Center for Surface and Coatings Research, Lehigh University, Bethlehem, Pennsylvania 18015
and Loránd Eötvös University, Budapest, Hungary

ABSTRACT

An electrogalvanized steel containing small amounts of cobalt and chromium is of interest because of its claimed corrosion resistance under service conditions. Zinc-cobalt-chromium alloys were electrodeposited from a sulfate bath at 35° and 60°C and a current density range of 2-10 A/dm². The baths were doped with ⁵⁷Co so that emission Mössbauer spectroscopy could be employed. The cobalt content of the deposits was 0.01-2%. In the case of all deposits the cobalt was present as isolated atoms in the zinc matrix. No evidence was found for aggregates of cobalt atoms. The electrodeposited zinc-cobalt alloys thus represent supersaturated solutions of cobalt in zinc. Cobalt probably functions as a corrosion inhibitor because of its influence on the properties of the surface oxide film which it enters during active corrosion.

Much interest exists in the development of a more corrosion-resistant galvanized steel. Galvanized steel consists of a substrate that provides structural strength and resistance to deformation and a zinc coating that is anodic to steel. The lifetime of the coating, and hence corrosion protection, may be thought of in terms of two stages: (i) the time during which the zinc coating is the only metal exposed to the atmosphere, and (ii) after corrosion has occurred, the time during which the zinc coating and the steel substrate are both exposed. Corrosion of zinc during the second stage generally occurs at a faster rate because the exposed steel serves as cathode and accelerates the anodic reaction of the zinc. The ideal type of zinc coating is one which corrodes at a very low rate and yet provides protection to the steel substrate at those sites where steel becomes exposed. As pointed out previously (1), the development of such a coating appears practical because the rate of corrosion of zinc under mildly corrosive conditions is controlled by the cathodic reaction, $\text{H}_2\text{O} + \frac{1}{2} \text{O}_2 + 2e^- = 2 \text{OH}^-$. If the zinc could be made a very poor cathode, it would corrode at a lower rate, yet would still protect steel at exposed sites because the steel would serve as the cathode when the bimetallic couple was in contact with an aqueous corrosive environment.

Recently, an electrogalvanized steel containing chromium and cobalt that is claimed to have excellent corrosive resistance (2, 3) has appeared on the market. Work by one of us (4) has also shown that pretreatment of zinc in a cobalt-containing solution results in corrosion inhibition in 3% NaCl solution. The present work was undertaken as one phase of a program designed to understand the role of cobalt in enhancing the corrosion resistance of zinc. The specific objective of the present work was to determine the chemical state of cobalt in zinc since Adaniya (3) was unsuccessful in his attempts to

gain information about the chemical state of cobalt from x-ray photoelectron studies. He was, however, able to show that the chromium was present in the form of an oxide. The question of the chemical state of cobalt in zinc is not a trite one since it has been established that a significant amount of cobalt is present in cobalt-hardened gold electrodeposits in the form of an hydroxyoxide and a cyanide complex (5, 6).

Experimental Procedure

All electrodeposits were prepared from a plating solution of the composition

| | |
|--|-----------------|
| ZnSO ₄ · 7H ₂ O | 150 g/liter |
| Na ₂ SO ₄ · 10 H ₂ O | 45 g/liter |
| CoSO ₄ · 7H ₂ O | 10-95.4 g/liter |
| Cr ₂ (SO ₄) ₃ · 18H ₂ O | 0.3 g/liter |
| Sodium acetate · 3H ₂ O | 75 g/liter |
| pH | 4.2 |

The deposits were formed on steel cathodes and a zinc sheet was used as a counterelectrode. The plating bath was doped with ⁵⁷Co such that the plating bath volume, 10 cm³, had an activity equivalent to 2.4×10^8 Bq in the case of the more dilute solutions and 3.7×10^8 Bq for the more concentrated solutions. The ⁵⁷Co was added to the plating bath as a solution of the chloride. The clarity of the plating bath indicated that all the constituents were solvated. It is assumed, and there was no reason to believe otherwise, that the ⁵⁷Co in the plating bath existed in the same chemical state as the natural cobalt. The determinations of the cobalt content of the electrodeposit from the radioactivity measurements are based on this assumption. The current efficiency for all depositions was very close to 100% as determined by gravimetric measurements. Seventeen radioactive deposits were prepared and studied. The conditions under which they were prepared are summarized in Table I. Samples 1-11 yielded deposits which were

* Electrochemical Society Active Member.
Key words: alloy, coatings, electrodeposition, metals.

light in color and typical of a normal zinc deposit and samples 15-17 were darker in color. Samples 12-14 were prepared from a plating bath that was aged for 3 months. The deposits in this case had a blackened appearance. Mössbauer emission spectra were obtained for frozen solutions of an unaged and an aged plating bath but no obvious difference was observed in the two spectra.

Deposition conditions were selected so as to give a very low cobalt content (samples 1-8) and a relatively high cobalt content (samples 9-17). A cobalt content of 0.5% (samples 9-11) represents the high end of the cobalt content of commercial material.

The cobalt content of equivalent nonradioactive deposits was determined by a method outlined by Okác (7). The zinc electrodeposit was dissolved in 0.025M H_2SO_4 and 10 ml of this solution was adjusted to pH 3.5. Approximately 10g of solid NH_4SCN was added to the solution in order to form the blue cobalt thiocyanate complex. The complex was extracted with 10 cm^3 of a diethyl ether-amyl alcohol mixture and the cobalt concentration was determined colorimetrically by comparison with a series of cobalt standards.

All Mössbauer spectra were obtained using $K_4[Fe(CN)_6] \cdot 3H_2O$ as an absorber, but the Mössbauer parameters are given relative to iron.

Experimental Results

Composition of the deposit.—The chemical analyses of the deposits from samples 1-8 yielded cobalt contents ranging from 0.008 to 0.014% with the higher values originating from the deposits formed at 60°. Calculations based on the radioactivity of the sample and the radioactivity of the solution confirmed that the cobalt content of the deposits was of the order of 0.01%. The data shown in Table I, although giving no quantitative information about absolute composition, do indicate that the cobalt content of the deposit from baths containing 10 g/liter of $CoSO_4 \cdot 7H_2O$ is not strongly a function of the current density.

The cobalt content of the radioactive deposits (samples 9-17) was not determined chemically. However, nonradioactive deposits were analyzed and the approximate concentration of the cobalt in the radioactive deposits was calculated from the radioactivity of the deposits, the radioactivity of the solution, and the ratio of radioactive cobalt/nonradioactive cobalt in the solution. The concentration of cobalt in samples 9-11 was thus approximately 0.5%; in samples 15-17 it was approximately 0.75%; and in samples 12-14 it was approximately 2%.

Table II. Correlation between the Co concentration and pH of the plating solution and the Co concentration in the electrodeposit. Plating conditions: 4 A/dm², 35°C

| CoSO ₄ ·7H ₂ O in the plating solution (g/liter) | pH of the plating solution | Measured Co concentration in dissolved Zn-Co electrodeposit, % |
|--|----------------------------|--|
| 75 | 4.2 | 0.68-0.90 |
| 75 | 6 | 0.12-0.24 |
| 10 | 5 | 0.68-0.12 |
| 10 | 6 | 0.03-0.1 |

Although no extensive study was made of the effect of pH on the composition of the deposit, it was observed that the cobalt content of the deposit decreased with increase in pH as shown by the data in Table II.

Chemical nature of the cobalt in the electrodeposit.—Mössbauer spectra of all deposits were obtained in emission geometry. Representative spectra for samples 11 and 14 at room temperature are given in Fig. 1. It will be noted from an inspection of the Mössbauer parameters listed in Table III that the values of the isomer shift and the full width at half maximum are approximately the same for all deposition conditions. Aging samples containing 0.01% cobalt at room temperature for approximately 9 months did not cause any measurable change in the Mössbauer spectrum.

Sample 1 was heated for 6 hr at 300°C in a hydrogen atmosphere, cooled to room temperature in hydrogen, and the Mössbauer spectrum again obtained. Figure 2 shows the Mössbauer spectrum of the heat-treated specimen. It will be noted that the room temperature peak broadened considerably from 0.39 mm/sec to 0.74 mm/sec after heat-treatment.

Discussion

The Mössbauer data conclusively show that the electrodeposited cobalt is present in the metallic form on the basis of a comparison with the work of Dezsi *et al.* (8) and that of Qaim (9), both of which workers studied very dilute solutions of ⁵⁷Co in zinc formed by a diffusion process. Comparative values are listed below

| Isomer shift (mm/sec) | Quadrupole splitting (mm/sec) |
|---------------------------|-------------------------------|
| This work | |
| −0.49 (average value) | 0.30-0.51 (range of values) |
| Qaim not given | 0.52 |
| Dezsi <i>et al.</i> −0.50 | 0.37 |

Table I. Zinc electrodeposits doped with ⁵⁷Co used in Mössbauer study

| Number | CoSO ₄ ·7H ₂ O concn. (g/liter) | Temperature (°C) | pH | Current density (A/dm ²) | Time of deposition (min) | Normalized radioactivity of deposit* |
|--------|---|------------------|-----|--------------------------------------|--------------------------|--------------------------------------|
| 1 | 10 | 35 | 6.2 | 4 | 4.5 | 0.37 |
| 2 | 10 | 35 | 6.2 | 10 | 3 | 0.47 |
| 3 | 10 | 35 | 6.2 | 2 | 6 | 0.17 |
| 4 | 10 | 35 | 6.2 | 4 | 3 | 0.14 |
| 5 | 10 | 60 | 6.2 | 4 | 3 | 0.23 |
| 6 | 10 | 60 | 6.2 | 4 | 4.5 | 1.00 |
| 7 | 10 | 60 | 6.2 | 7 | 3 | 0.64 |
| 8 | 10 | 60 | 6.2 | 3 | 6 | 0.43 |
| 9 | 47.7 | 35 | 4.2 | 4 | 7.5 | 1.3 |
| 10 | 47.7 | 35 | 4.2 | 4 | 7.5 | 1.4 |
| 11 | 47.7 | 35 | 4.2 | 4 | 7.5 | 1.4 |
| 12 | 71.5 | 35 | 4.2 | 4 | 7.5 | 2.4 |
| 13 | 71.5 | 35 | 4.2 | 4 | 7.5 | 2.5 |
| 14 | 71.5 | 35 | 4.2 | 4 | 7.5 | 2.2 |
| 15 | 95.4 | 35 | 4.2 | 4 | 7.5 | 1.0 |
| 16 | 95.4 | 35 | 4.2 | 4 | 7.5 | 1.04 |
| 17 | 95.4 | 35 | 4.2 | 4 | 7.5 | 1.04 |

* Line in table differentiates experiments done at different times. Each set (1-8 and 9-17) are normalized to a different sample (No. 6 in upper set and No. 15 in lower set).

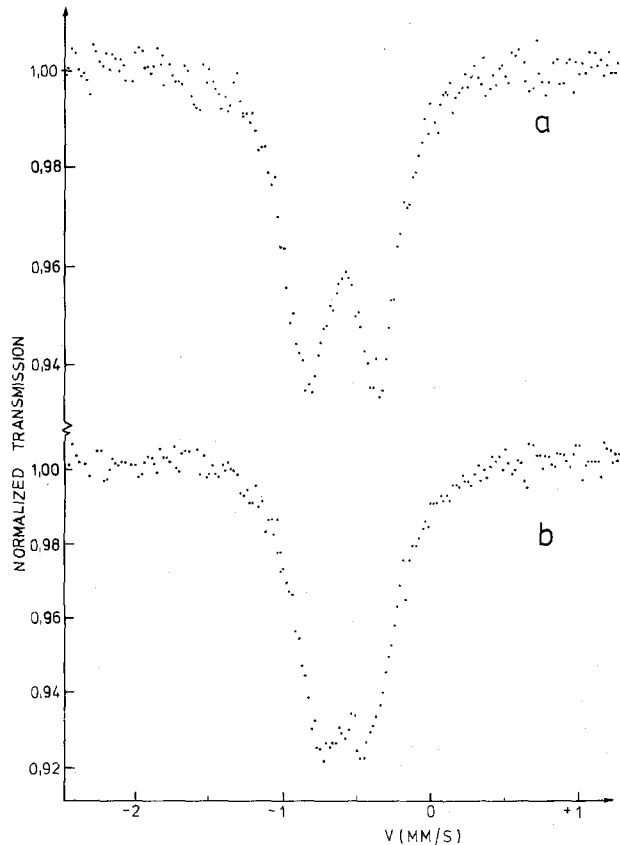


Fig. 1. Mössbauer emission spectra at room temperature of (a) sample No. 11 and (b) sample No. 14.

The narrow linewidth (0.4 mm/sec) in the present work is indicative of the fact that the cobalt atoms occupy substitutional sites in the zinc matrix and that there is no clustering of the cobalt atoms. Comparable values for the linewidth for cobalt codeposited with gold have been observed by Cohen *et al.* (6) where the evidence was that cobalt atoms existed substitutionally at gold atom sites.

The research reported herein on zinc-cobalt alloys and the prior work on gold-cobalt alloys (5) provide excellent support for the concept that electrodeposition is a method for preparing supersaturated solutions in two-component alloy systems. The solubility of cobalt in zinc is less than 0.01% (10) and yet the Mössbauer spectra of the deposits containing 2% cobalt indicated solid solution, as opposed to phase separation.

As is noted from Table III, the values of the quadrupole splitting were different in the case of deposits containing 0.5-2% cobalt than those observed

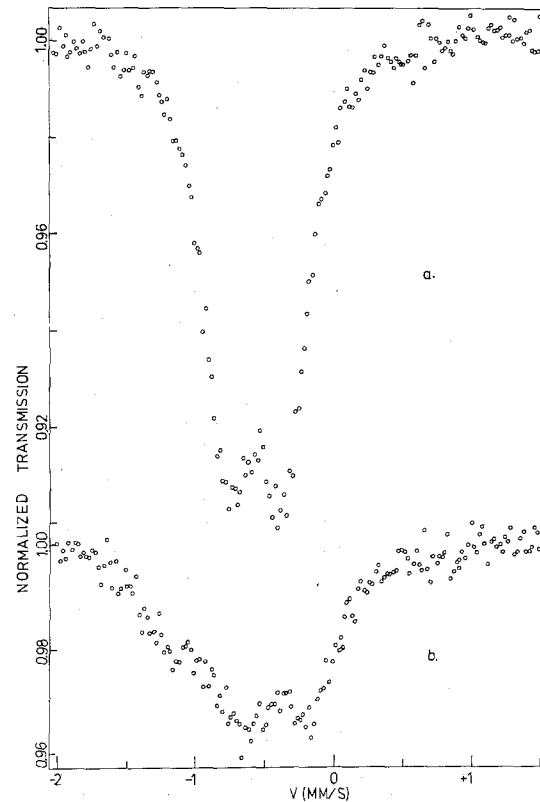


Fig. 2. Mössbauer emission spectra of sample No. 2: (a) before heat-treatment and (b) after heating for 6 hr at 300°C in a hydrogen atmosphere. Spectra were taken at room temperature.

with the dilute alloys. The average values at the different concentrations were

| Concn. of cobalt in zinc-cobalt alloy | Average Quadrupole splitting value |
|---------------------------------------|------------------------------------|
| 0.01% | 0.40 mm/sec |
| 0.5% | 0.47 |
| 0.75% | 0.32 |
| 2% | 0.37 |

The range of values of the quadrupole splitting (0.3-0.5 mm/sec) obtained in the present study encompasses the values obtained by Dezsi *et al.* and by Qaim. It is probable that this range of values is real and is not reflective of imprecision in the experimental measurements. A survey of the data in Table III indicates that similar sets of samples, each prepared in a separate experiment, give approximately the same quadrupole splitting value. For example, samples 1-8 give a range of 0.39-0.42 mm/sec; samples 9-11 give a

Table III. Mössbauer parameters for zinc-cobalt electrodeposits

| Sample number | Temperature | Isomer shift (mm/sec) | Mössbauer parameters quadrupole splitting (mm/sec) | Full width of peak at half maximum (mm/sec) |
|---------------|-------------|-----------------------|--|---|
| 1 | RT | -0.527 ± 0.004 | 0.40 ± 0.006 | 0.40 ± 0.01 |
| 2 | RT | -0.48 ± 0.01 | 0.41 ± 0.02 | 0.39 ± 0.02 |
| 3 | RT | -0.49 ± 0.04 | 0.40 ± 0.03 | 0.41 ± 0.03 |
| 4 | RT | -0.49 ± 0.01 | 0.39 ± 0.01 | 0.42 ± 0.03 |
| 5 | RT | -0.46 ± 0.007 | 0.40 ± 0.01 | 0.38 ± 0.02 |
| 6 | RT | -0.50 ± 0.008 | 0.41 ± 0.01 | 0.39 ± 0.01 |
| 7 | RT | -0.51 ± 0.01 | 0.42 ± 0.02 | 0.47 ± 0.03 |
| 8 | RT | -0.49 ± 0.01 | 0.40 ± 0.02 | 0.42 ± 0.02 |
| 1 | Liq. Na | -0.62 ± 0.01 | 0.43 ± 0.015 | 0.42 ± 0.02 |
| 9 | RT | -0.537 ± 0.005 | 0.509 ± 0.009 | 0.40 ± 0.01 |
| 10 | RT | -0.532 ± 0.003 | 0.443 ± 0.005 | 0.374 ± 0.009 |
| 11 | RT | -0.540 ± 0.002 | 0.460 ± 0.004 | 0.354 ± 0.006 |
| 12 | RT | -0.515 ± 0.003 | 0.297 ± 0.006 | 0.39 ± 0.01 |
| 13 | RT | -0.496 ± 0.002 | 0.332 ± 0.004 | 0.399 ± 0.008 |
| 14 | RT | -0.516 ± 0.002 | 0.326 ± 0.004 | 0.386 ± 0.008 |
| 15 | RT | -0.516 ± 0.004 | 0.360 ± 0.006 | 0.40 ± 0.01 |
| 16 | RT | -0.514 ± 0.003 | 0.377 ± 0.005 | 0.38 ± 0.01 |
| 17 | RT | -0.504 ± 0.004 | 0.381 ± 0.007 | 0.37 ± 0.01 |

range of 0.44-0.51 mm/sec; samples 12-14 give a range of 0.30-0.33 mm/sec; and samples 15-17 give a range of 0.36-0.38 mm/sec. It also should be pointed out that the samples with quadrupole splitting values of 0.39-0.51 were zinc in color; those having values of 0.36-0.38 mm/sec were slightly darkened; and those having values of 0.30-0.33 mm/sec were black in color. In other words, there was a trend to lower values of the quadrupole splitting as the deposit became darker in color. At the present time, we consider it appropriate to point out these facts but insufficient information is available to give an interpretation.

The absence of any magnetic hyperfine splitting (hfs) in the spectrum taken at liquid nitrogen temperature provides additional evidence that the cobalt is not aggregated, at least in sufficient amount, to show magnetic behavior. This absence of hfs at liquid nitrogen temperature is a consequence of the fact that as the size of a ferromagnetic cobalt particle is reduced, the magnetic anisotropy energy becomes comparable in magnitude to the thermal excitation energy. The magnetization direction of the particle fluctuates rapidly and the lifetime approaches or becomes less than the lifetime of the excited state of the ^{57}Fe daughter. The net effect is that the hfs is not detected in the Mössbauer spectrum and only a quadrupole-split line is observed. No data on the effect of particle size on the hfs of cobalt particles in a zinc matrix are available. Krop and Williams (11) showed that hfs only occurred with cobalt particles in a copper matrix when the particle diameter was greater than 2.6 nm. Cohen *et al.* (12) studied cobalt particles in a gold matrix and found a good hfs spectrum when the particle diameter was 9 nm; they did not determine experimentally the minimum particle size at which the hfs spectrum disappeared.

Simmons (13) has carried out an extensive study of the Mössbauer emission spectra of a variety of cobalt oxides, hydroxides, and oxyhydroxides. Since it is reasonable to expect that such materials might be occluded in the deposit as a result of precipitation in the vicinity of the cathode, or migration as a colloid to the cathode, it is important to examine the possibility of their presence in the deposit. The presence of cobalt oxyhydroxide and cobalt cyanide complexes in gold deposits (5, 6) was an additional incentive to explore the likelihood of the occlusion of a cobalt compound in the deposit. Comparison of our Mössbauer parameters with the data of Simmons indicated that none of the oxygen-containing compounds was a reasonable candidate to explain the features of the spectrum.

The broadening of the absorption peak after heating the zinc-0.01%-cobalt deposit at 300°C in hydrogen probably results from a clustering of cobalt atoms. The cluster size should be very small at cobalt concentrations of 0.01% because of the absence of any hyperfine spectrum (Fig. 2b). The larger value of the half-width after heat-treatment is suggestive of a range of cobalt cluster geometries and sizes.

The conclusion reached herein that the cobalt is present in the zinc deposit as isolated atoms in substitutional sites in the zinc suggests that cobalt enters the oxide film on zinc during the corrosion process as an isolated atom or ion. Since it is known that metallic cobalt on the surface of zinc accelerates the corrosion of zinc in 3% NaCl solution (4), the absence of clustered cobalt atoms in the zinc electrodeposit is very favorable for corrosion inhibition.

Manuscript submitted Dec. 8, 1980; revised manuscript received Feb. 6, 1981.

Any discussion of this paper will appear in a Discussion Section to be published in the June 1982 JOURNAL. All discussions for the June 1982 Discussion Section should be submitted by Feb. 1, 1982.

Publication costs of this article were assisted by Lehigh University.

REFERENCES

1. H. Leidheiser, Jr. and I. Suzuki, *Corrosion*, **36**, 701 (1980).
2. T. Adaniya and M. Ohmura, *Metall.*, **31**, 1100 (1977).
3. T. Adaniya, *Sheet Metal Indus. Inter.*, **55**, No. 12, 73 (1978).
4. H. Leidheiser, Jr. and I. Suzuki, *This Journal*, **128**, 242 (1981).
5. H. Leidheiser, Jr., A. Vértes, M. L. Varsányi, and I. Czako-Nagy, *ibid.*, **126**, 391 (1979).
6. R. L. Cohen, F. B. Koch, L. N. Schoenberg, and K. W. West, *ibid.*, **126**, 1608 (1979).
7. A. Okác, "Qualitative Analytical Chemistry," Geest and Portig, 680 pp. (1959).
8. I. Dezsi, A. Balogh, Z. Kajcsos, D. L. Nagy, and E. Zsoldos, *J. Phys. F, Metal Phys.*, **9**, 999 (1979); and Private communications.
9. S. M. Qaim, *J. Phys. C, Solid State Phys.*, **2**, 1434 (1969).
10. F. Pawlek, *Z. Metallk.*, **36**, 105 (1944).
11. K. Krop and J. M. Williams, *J. Phys. F*, **1**, 938 (1971).
12. R. L. Cohen, F. B. Koch, L. N. Schoenberg, and K. K. West, *This Journal*, **127**, 1199 (1980).
13. G. W. Simmons, "Passivity of Metals," R. P. Frankenthal and J. Kruger, Editors, p. 898, The Electrochemical Society, Princeton, N.J. (1978).

Solution Redox Couples for Electrochemical Energy Storage

I. Iron (III)-Iron (II) Complexes with O-Phenanthroline and Related Ligands

Yih-Wen D. Chen, K. S. V. Santhanam,¹ and Allen J. Bard*

Department of Chemistry, The University of Texas at Austin, Austin, Texas 78712

ABSTRACT

Iron (III)-Iron (II) complexes with o-phenanthroline and related ligands have been examined by electrochemical techniques in aqueous H₂SO₄ media with respect to their suitability as redox couples for electrochemical energy storage. The iron (II) complexes undergo a rapid 1 electron oxidation at graphite and platinum electrodes to yield iron (III) complexes; these complexes showed varying stabilities depending on the nature of the substituents on the complexes. The iron (II) complexes examined in this study were formed with (i) monodentate, (ii) bidentate, or (iii) tridentate ligands. The redox couples have a higher E° value which has been a positive consideration in the storage. Although the aquo iron (II)-iron (III) couple has an E° less than the complexes, it certainly has shown greater promise in terms of storage stability. The kinetics of iron (II) complexation has been followed by cyclic voltammetry.

A redox flow cell (or battery) (1-8) is one in which the chemical species which participate in the electrode reactions are soluble. The cell is charged with the input of electrical energy to drive the overall cell reaction in a thermodynamically uphill direction and the oxidized species produced at an inert electrode in one half-cell and the reduced form from the other are stored in external vessels. Electricity is produced in these cells when the stored reactants flow back into the cell and react at the electrodes. Thus these cells are of interest as secondary or rechargeable batteries. The energy densities of these systems (i.e., energy stored per unit weight of battery) suffer in comparison to more conventional secondary batteries which utilize solid reactants, because of the weight of the solvent and electrolyte. However, they offer the possibility of much better cycle life, since the repeated charge and discharge cycles do not involve phase changes and the accompanying changes of electrode morphology. These systems are of interest in stationary applications such as electrical energy storage and in utility load leveling.

Another related area involving soluble redox couples in energy devices is that of photoelectrochemical (PEC) (or liquid junction photovoltaic) cells with semiconductor electrodes (9). These cells, which are based on the light-driven redox processes of solution species at semiconductors, are of two types. In the PEC cell without energy storage, a single redox couple is employed, and the electrode reaction at the counterelectrode is the reverse of the photo-redox process at the semiconductor. In PEC cells with storage [types of photoelectrosynthetic cells (9)], the reactants formed during irradiation are stored and employed to generate electricity, in the same or a separate cell, during dark periods.

The redox couples for these applications, represented by the reaction in [1]



must satisfy a number of requirements: (i) both forms, O and R, must be highly soluble to minimize the storage volume and mass and to allow high mass transfer rates and current densities during charging and discharging; (ii) the formal potential, E° , of one couple must be highly positive, and E° of the other highly negative to maximize the cell voltage and energy density; (iii) the heterogeneous reaction rate for the charging and discharging reactions at the inert electrodes should be rapid (i.e., the standard rate constant, k° , for [1] should be large) so that the electrode reactions occur at their mass transfer controlled rates; (iv) both O and R should be stable during generation and storage, and this stability pertains to reaction with solvent, electrolyte, atmosphere, and electrode materials, and, for metal complexes, stability with respect to ligand loss; (v) the materials should be safe, inexpensive, and abundant; (vi) the couple should not be corrosive and react with cell materials, or the storage vessel, indeed, in PEC cells the redox couple is often called upon to stabilize and protect the semiconductor electrode from photocorrosion (10, 11); and (vii) for PEC cells, the redox species should not absorb light in the wavelength region of semiconductor absorption.

A number of redox couples have been proposed for such systems. These include Fe(III)/Fe(II) (HCl) (5, 6); Cr(III)/Cr(II) (HCl) (4-6); Ti(IV)/Ti(III) (7); Br₂, Br⁻ (12-14); and, for PEC cells, S₂²⁻ and Se²⁻, Se₂²⁻ (15, 16). A difficulty in a storage cell is the possible intermixing of the components of the two half-cells, because of imperfect separators or membranes, which leads not only to loss of capacity and efficiency but more seriously to cross-contamination of the redox solutions. Approaches to minimizing this intermixing problem include the use of a single element system in three oxidation states [e.g., Cr(VI), Cr(III)//Cr(III), Cr(II) (4)] or the use of two oxidation states of the same element with the redox potentials shifted by complexation with different ligands.

The work reported here, as well as other current investigations (1, 2), is concerned with the application of metal ion coordination compounds as redox

* Electrochemical Society Active Member.
¹ Current address: Tata Institute of Fundamental Research, Bombay 400 005, India.

Key words: battery, voltammetry, solubility, chelates.

couples in flow cells. By suitable choice of ligand the formal potential of the couple can be shifted in the desired direction. Moreover such complexes may show improved characteristics with respect to stability and color in comparison to the uncomplexed species. The chemical principles related to the formation and properties of metal complexes are well developed and many new and potentially useful ligands have been reported. We describe here investigations of the Fe(III)/Fe(II) couple with ligands related to o-phenanthroline and bipyridine. Iron species were chosen for this initial investigation because iron is an abundant and inexpensive element with many highly soluble compounds. Such couples may be useful in the positive half-cell of redox flow systems or with n-type semiconductors in PEC cells.

Experimental

Reagents.—1,10-(or o-)phenanthroline (phen), 2,9-dimethylphenanthroline (2,9-dmp), 4,7-dimethylphenanthroline (4,7-dmp), and 4-methylphenanthroline (mp) were obtained from Alfa Chemicals. 2,2'-Bipyridine (bpy) was obtained from Aldrich Chemical Company. Tripyridine triazine (tpt), 4-cyanopyridine (cp), and 2-pyridine carboxaldehyde-2-pyridyl hydrazine (p-cph) were obtained from J. T. Baker Company. $\text{FeSO}_4 \cdot 7\text{H}_2\text{O}$ was reagent grade (Matheson, Coleman and Bell). Surfactants IGEPAL-Co430 (MW = 396) and 530 (MW = 484) were obtained from GAF Corporation (Atlanta, Georgia) and "Texas-1" (MW = 404) was made by Dr. Y. B. Youssef of The University of Texas. The former two surfactants carry ethylene oxide groups and the latter is the sodium salt of 8(p-phenyl sulfanato) hexadecane. All solutions were prepared with doubly distilled water and the solutions were degassed with prepurified gas that was passed through a chromous sulfate solution and then distilled water.

Apparatus.—A Model 173 potentiostat in combination with a Model 179 digital coulometer (Princeton Applied Research Corporation, Princeton, New Jersey) was employed for all electrochemical experiments. The current-voltage curves were recorded on a Houston Instruments Model 2000 X-Y recorder. The current time curves were recorded on a Model 564 storage oscilloscope (Tektronix) during potential-step chronoamperometry and on a National Panasonic strip-chart recorder during coulometric experiments.

Procedure.—The usual supporting electrolyte was aqueous H_2SO_4 prepared by suitable dilution of concentrated H_2SO_4 . All solutions were degassed with nitrogen before the electrochemical experiments. The complexes were usually prepared directly in the electrochemical cell by mixing known concentrations of ferrous sulfate and the ligand. A mole ratio of ligand/Fe(II) of greater than 5 was used. Controlled potential electrolyses were conducted with a large area graphite sheet electrode (area, 6.5 cm^2) (Ultra Carbon, Sherman, Texas) with continuous nitrogen gas bubbling. Some of the electrochemical experiments were carried out in the dark. All of the potentials were measured with respect to an aqueous saturated calomel electrode (SCE). An H-cell with a porous sintered-glass disk separating the two compartments was used in coulometric investigations. For cyclic voltammetric investigations, a single compartment cell with a solution capacity of 5 ml was employed, with either platinum wire ($A = 0.12 \text{ cm}^2$), platinum disk ($A = 0.14 \text{ cm}^2$), or graphite rod (taken from a C-cell battery, area $A = 0.14 \text{ cm}^2$) working electrodes. The platinum electrodes were pretreated by fast pulsing between +1.0 to -1.0V in H_2SO_4 .

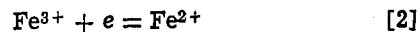
The solubilities of the complexes were estimated by dissolving the specified concentration of $\text{FeSO}_4 \cdot 7\text{H}_2\text{O}$

and an excess of ligand in 0.5M H_2SO_4 . The complex formed would precipitate at this initial ion concentration. The precipitate was then just dissolved in the solution by adding 0.5M H_2SO_4 solution gradually. The concentration and the solubility were then estimated by the degree of the dilution of the solution (Table I). These measurements were done at room temperature.

The stabilities of ferrous and ferric complexes were monitored with a Cary 14 spectrophotometer. The ferric complexes were prepared either by electrochemical oxidation of the ferrous complexes or by Ce(IV) oxidation in H_2SO_4 medium.

Results

To shift the potential of the half-reaction



toward values positive of the E° (+0.77V vs. NHE), ligands which form more stable complexes with Fe(II) are required. Since Fe^{2+} (d^6) is a good π -donor cation, ligands with low-lying vacant π^* orbitals complex strongly with it (17). Fe^{3+} has poorer π -donor properties because of its higher charge. Thus ligands such as bpy and phen (Fig. 1) are known to shift the potential of the redox couple in a positive direction. Further manipulation of the potential is possible by substitution on the rings of these ligands. A number of highly stable complexes of these ligands are known (17). The structure and abbreviations for those ligands used in this study are shown in Fig. 1 and Table II.

Solubilities.—Table I is a list of the solubilities of the complexes in aqueous 0.5M H_2SO_4 . Uncomplexed Fe(II) and Fe(III)-sulfate salts are quite soluble and yield solutions with metal ion concentrations $\sim 1\text{M}$. The solubility of the complexes vary with the nature of the ligand. The ligands themselves are soluble in acidic media to $\sim 2\text{M}$ (e.g., phen, 2,9-dmp). The complexes in 1M concentrations form solutions which are viscous and deeply colored. The uncomplexed Fe(II) and Fe(III) ions in H_2SO_4 are quite transparent in the visible region.

E° values.—The formal potentials of the various Fe(II)/Fe(III) complexes were evaluated from the cyclic voltammetric peak potential values at low scan rates ($E_{pa} = E^\circ + 0.028/n$) (see Table II). The complexes with cp, tpt, 2,9-dmp, and p-cph show more positive peak potentials, but the reversible potential values are difficult to estimate because of the instability of the ferric complex. The E° -values for the other ligands are all more positive than E° for the aquo Fe ($3+/2+$) couple in H_2SO_4 . In the phen-complexes substitution of methyl groups produces less positive peak potentials; while nitro- and chloro-group substitution yields more positive potentials compared to complexes with the unsubstituted ligand. Similar observations have been made by Fan and

Table I. Estimated solubilities of ferrous-ferric couples and ligands*

| Substance | Solubility (g/100 ml) | Concentration (M) |
|--|-----------------------|-------------------|
| $\text{FeSO}_4 \cdot 7\text{H}_2\text{O}$ | 27.8 | 1.0 |
| $\text{Fe}_2(\text{SO}_4)_3 \cdot 9\text{H}_2\text{O}$ | 44.0 | 0.8 |
| $\text{Fe}(\text{phen})_3\text{SO}_4$ | 52.5 | 0.8 |
| $\text{Fe}(\text{bpy})_3\text{SO}_4$ | 43.8 | 0.7 |
| $\text{Fe}(2,9\text{-dmp})_3\text{SO}_4$ | 37.2 | 1.0 |
| $\text{Fe}(\text{tp})_3\text{SO}_4$ | 22.4 | 0.3 |
| Phenanthroline | 40.0 | 2.2 |
| Bipyridyl | 31.6 | 2.0 |
| Terpyridine | 44.0 | 1.8 |
| 4-Cyanopyridine | 10.5 | 1.0 |

* Measured in 0.5M H_2SO_4 . See experimental section for method.

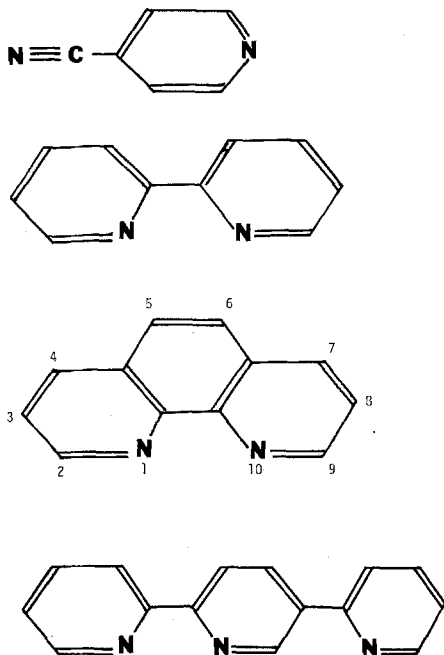


Fig. 1. Structure of ligands used in the study

Faulkner (18) at a phthalocyanine covered metal electrode.

Cyclic Voltammetric Measurements

Electron transfer kinetics.—Cyclic voltammetry (*cv*) was employed to survey a system with respect to heterogeneous electron transfer kinetics and stability of the Fe(III)-L species. Since the heterogeneous electron transfer rate constants, k^0 , are all moderately large ($>10^{-3}$ cm/sec), at low scan rates, v , the electrochemical behavior (in the absence of fast following reactions) is characteristic of a Nernstian reaction and show ΔE_p -values ~ 60 mV ($\Delta E = E_{pa} - E_{pc}$). When v is increased, shifts of E_{pa} and an increase in ΔE_p are observed signaling the onset of effects of the heterogeneous electron transfer rate (in the absence of uncompensated resistance effects) (19-21). Information about k^0 can then be obtained from the variation of E_{pa} or ΔE_p with v using methods developed by Matsuda and Ayabe (19) and Nicholson (20). The approach taken here was to determine the value of ψ from the E_p - v behavior (assuming $\alpha \sim 1/2$), where

$$\psi = \frac{k^0}{\sqrt{\pi a D_{Fe^{2+}}}} \quad [3]$$

where $a = nFv/RT$ and $D_{Fe^{2+}}$ is the diffusion coefficient of the Fe(II) ion in the medium employed. The

diffusion coefficients of Fe(II) and Fe(III) were determined from the peak currents i_{pa} and i_{pc} . For the aquo-species in 0.5M H_2SO_4 , $D_{Fe^{2+}} = D_{Fe^{3+}} = 2.5 \times 10^{-6}$ cm²/sec. Typical D -values for the complexed Fe(II) species determined by *cv* are listed in Table II. With these D -values and the measured ψ -values, k^0 was obtained. These are also listed in Table II. For example, in a typical study with 10 mM Fe(II)-phen complex in 0.5M H_2SO_4 , the *cv* wave showed $E_{pa} = 0.85V$ and, on scan reversal, $E_{pc} = 0.79V$ at $v = 50$ mV/sec. When v increased, ΔE_p increased, and at $v = 50$ V/sec, $\Delta E_p = 0.09V$; $v = 100$ V/sec, $\Delta E_p = 0.10V$; $v = 200$ V/sec, $\Delta E_p = 0.12V$; $v = 500$ V/sec, $\Delta E_p = 0.18V$. These measurements were made with full iR compensation. From these values, an average value of $k^0 = 5.8 \times 10^{-2}$ cm/sec was obtained. With the Fe(II) coordination compounds only values for 0.5M H_2SO_4 are listed in Table II, since in 3M H_2SO_4 protonation of the ligands (with pK_a 's $\sim 4-6$) competes very strongly with complexation with Fe(II) and appreciable complexation does not occur.

Values of k^0 for the Fe(3+/2+) couple in the absence of added ligand were also obtained in 0.5 and 3M H_2SO_4 , yielding values of 1.6×10^{-3} and 1.2×10^{-2} cm/sec, respectively. Typical *cv* curves are shown in Fig. 2. The electrochemical oxidation of Fe(II) in aqueous H_2SO_4 has been previously investigated at platinum and carbon paste electrodes (22, 23). The results are in general agreement with those found here. The rate of the electrode reaction appears to depend on the concentration of the acid as well as the nature of the electrode surface (*e.g.*, the presence of oxide films). However, the coordinated species generally have larger k^0 -values than the aquo-species under similar conditions (0.5M H_2SO_4).

Stability (*cv*).—Stability of the coordination compound and the product of the electrode reaction can also be monitored by *cv*. Consider the oxidation of FeL_x^{2+} . The observed *cv* behavior depends on the ligand, L, and the tendency of FeL_x^{3+} formed during the anodic sweep to decompose (Fig. 3). During the time scale of the *cv* sweep the Fe(III) complexes with phen (or bpy) and tp are stable while that with cp is not. In the latter case oxidation of the stable Fe(II) complex leads to the Fe(III) form which decomposes rapidly, probably by loss of ligand to form a different Fe(III) species. The general reaction sequence is thus

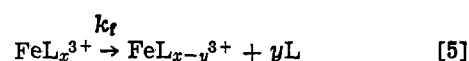
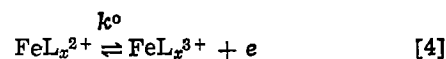


Table II. Thermodynamic and kinetic constants for ferrous-ferric couples*

| Ligands | E^0 (V vs. SCE) | k^0 (cm/sec) | k_1^{**} (sec ⁻¹ × 10 ²) | k_1^{\dagger} (M ⁻¹ sec ⁻¹ × 10 ⁻⁴) | D (cm ² sec ⁻¹ × 10 ⁹) | Abbreviation of ligand |
|-------------------------------|-------------------|---|---|---|--|------------------------|
| Aquo | 0.45 | 1.6×10^{-3} $1.2 \times 10^{-2\dagger}$ | | | 2.5 | H ₂ O |
| Bipyridine | 0.82 | 5.6×10^{-2} | 0.063 | 3.0 | 1.11 | bpy |
| o-Phenanthroline | 0.82 | 5.8×10^{-2} | 0.012 | 3.0 | 1.22 | phen |
| 4-Methyl-o-phenanthroline | 0.73 | 4.9×10^{-2} | 0.005 | — | 1.07 | mp |
| 4,7-Dimethyl-o-phenanthroline | 0.69 | 2.5×10^{-2} | 0.003 | 6.3 | 1.00 | 4,7-dmp |
| 2,9-Dimethyl-o-phenanthroline | 0.82 | | >0.6 | | | 2,9-dmp |
| 5-Chloro-o-phenanthroline | 0.97‡ | | 0.14 | | | CIP |
| 5-Nitro-o-phenanthroline | 1.07‡ | | 0.91 | | | Np |
| Terpyridine | 0.82 | 6.0×10^{-3} | 0.18 | 800 | 1.80 | tp |
| 2-Pyridinecarboxaldehyde | 0.67 | | >0.6 | | | p-cph |
| Tripyridinetriazine | 1.24 | | >0.6 | | | tpt |
| 4-Cyanopyridine | 0.82 | | >0.6 | | | cp |

* Medium 0.5M H_2SO_4 ; electrode material graphite. $T = 23 \pm 2^\circ C$.

** Rate constant value refers to decomposition of ferric complexes determined by spectrophotometry. The value (>0.6) was estimated by *cv*.

† Rate constant for the complexation of ferrous ion determined by *cv* method.

‡ Medium 3M H_2SO_4 .

§ K. Ogura and K. Miyamoto, *Electrochimica Acta*, 22, 1357 (1977).

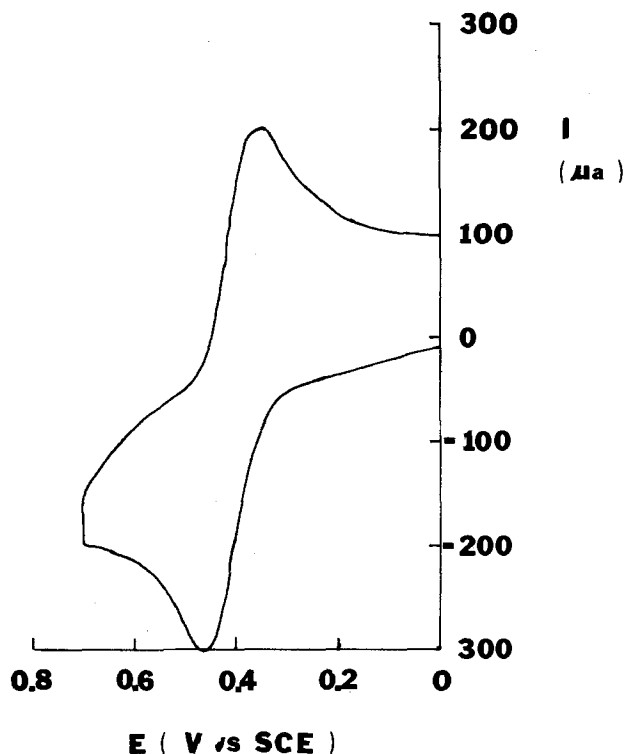


Fig. 2. (a) Cyclic voltammogram curve for the oxidation of 10 mM Fe^{2+} in aqueous 3M H_2SO_4 working electrode: Graphite, reference electrode: aqueous saturated calomel electrode. $v = 0.50$ V/sec.

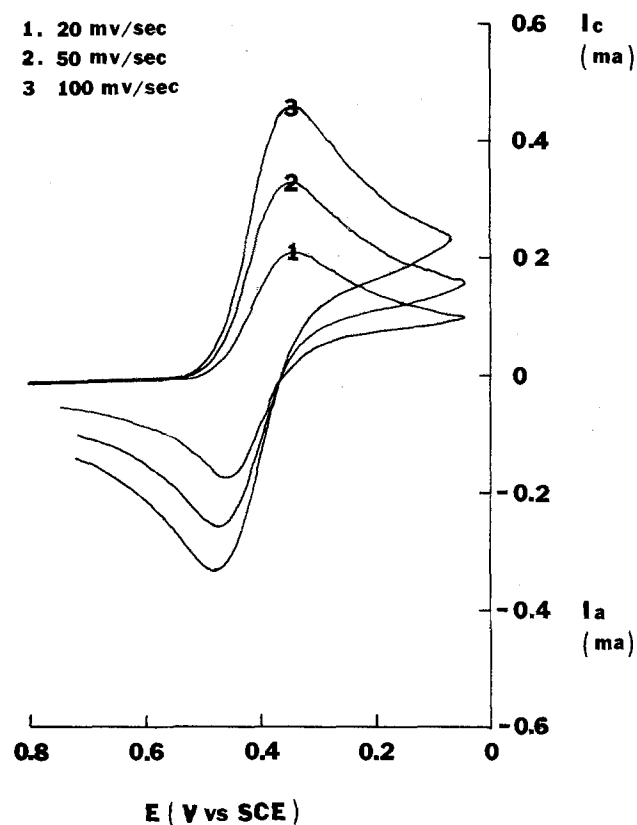


Fig. 2. (b) The current-voltage curve after controlled potential exhaustive electrolysis at $+0.80\text{V}$ in 0.5M H_2SO_4 .

(for simplicity, the state of protonation of the ligand is not indicated in the equations). Instability on the cv time scale for v up to 50 V/sec was also found for 2,9-dmp and several other ligands, as indicated in Table II.

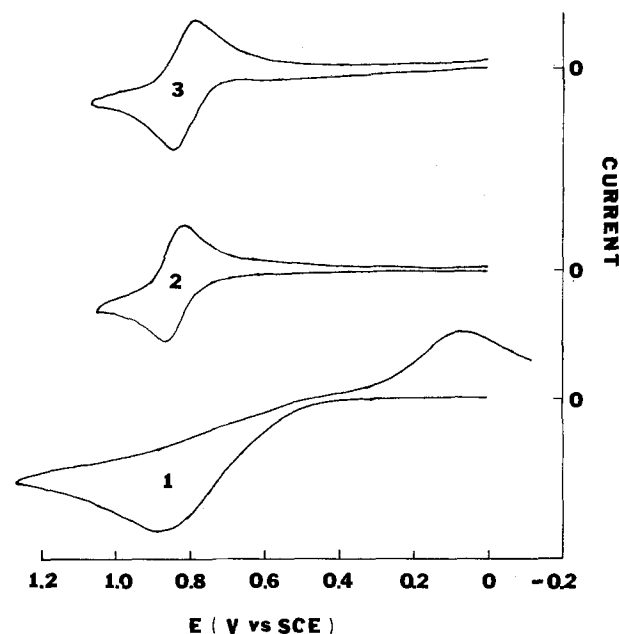
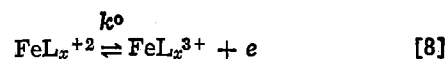
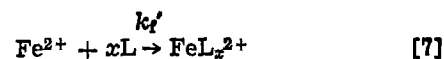
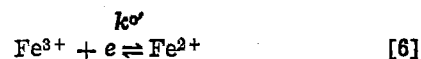


Fig. 3. Cyclic voltammograms for $\text{Fe}(\text{II})$ ion coordinated with: 1, monodentate (cp); 2, bidentate (bpy); 3, tridentate (tp) at graphite electrode. Solution contained 10 mM aquo $\text{Fe}(\text{II})$ ion and at least 50 mM ligand. $v = 0.05$ V/sec.

The rate of formation of the $\text{Fe}(\text{II})$ -ligand complexes was also of interest and this was determined by cv for complexes with bpy, phen, 4,7-dmp, and tp. In all cases the $\text{Fe}(\text{III})$ complex is thermodynamically unstable in 0.5M H_2SO_4 , although it is kinetically inert so that it decomposes to Fe^{3+} and free ligand quite slowly. Thus if one prepares a solution containing a mixture of free Fe^{3+} and L essentially no complexation occurs. Upon reduction of the Fe^{3+} to Fe^{2+} rapid reaction with L takes place so that on scan reversal oxidation of $\text{Fe}(\text{II})$ occurs both as free Fe^{2+} and as FeL_x^{2+} , i.e., the reaction sequence is



Typical results for a solution containing 5 mM Fe^{3+} and 300 mM phen in 0.5M H_2SO_4 at a Pt electrode are shown in Fig. 4. Note that at very slow sweep rates ($v = 20$ mV/sec) the anodic peak for Fe^{2+} oxidation following Fe^{3+} reduction is barely detectable, while the $\text{Fe}(\text{phen})_3^{2+}$ oxidation wave is fully developed. At higher sweep rates i_{pa} for Fe^{2+} oxidation increases and the $\text{Fe}(\text{phen})_3^{2+}$ oxidation wave becomes relatively smaller. At very high sweep rates ($v = 100$ V/sec) only the Fe^{2+} oxidation is observed with the same general characteristics as the uncomplexed Fe^{3+} couple in the absence of phen at this v . The rate constant, k_f' for Fe^{2+} disappearance can be estimated from the ratio of i_{pa}/i_{pc} for the $\text{Fe}^{3+/2+}$ couple. Typical data for the cv of these complexes is shown in Table III along with the rate constants obtained using the treatment of a second-order following (EC) reaction (24). Since the ligand concentrations are high, the EC reaction is essentially pseudo-first order and the treatment of this EC-reaction scheme (25) also applies. The calculated values of k_f' are based on the free ligand concentration, $[\text{L}]$, at the given H_2SO_4 concentration which is in equilibrium with the various protonated forms. The pK_a values employed in calculation of $[\text{L}]$ were:

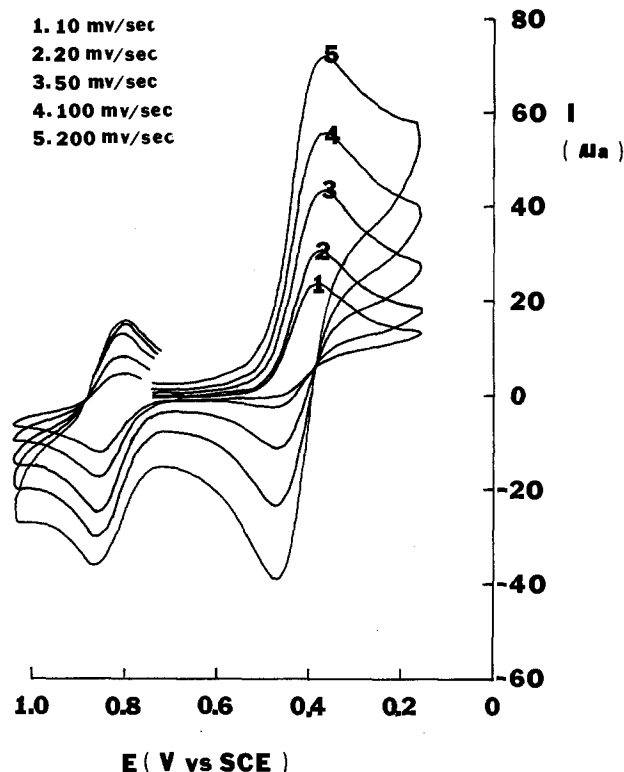


Fig. 4. Cyclic voltammogram for 5 mM Fe(III) reduction in the presence of phenanthroline (300 mM) at a platinum electrode.

bpy, $pK = 4.47$; phen, $pK = 4.98$; tp, $pK_1 = 2.64$, $pK_2 = 4.33$ (26, 27). The k'_i -values obtained by this procedure are listed in Table II.

A digital simulation of current-voltage curves was carried out for the reduction of Fe(III) in the presence of the ligands. In this simulation the following mechanism was assumed. Reaction [6] was followed by

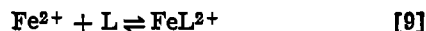


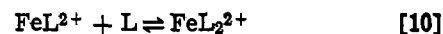
Table III. Electrochemical studies of complexation rate of Fe^{2+} : complexation with bipyridine, o-phenanthroline and terpyridine*

| Sweep rate (V/sec) | t_{pa}/t_{pc} | τ (sec) | $k_{app}\dagger$ ($\text{M}^{-1} \text{sec}^{-1}$) | $k_{ct}\ddagger$ ($\text{M}^{-1} \text{sec}^{-1} \times 10^{-5}$) |
|---|-----------------|--------------|--|---|
| Concentration of bipyridine: 0.3M | | | | |
| 0.05 | 0.230 | 5.00 | 4.00 | 0.27 |
| 0.05 | 0.275 | 4.00 | 3.51 | 0.24 |
| 0.05 | 0.254 | 4.00 | 4.11 | 0.28 |
| 0.10 | 0.307 | 2.50 | 4.52 | 0.31 |
| 0.10 | 0.367 | 2.00 | 3.94 | 0.27 |
| 0.10 | 0.341 | 2.00 | 4.56 | 0.31 |
| 0.20 | 0.435 | 1.25 | 4.49 | 0.30 |
| 0.20 | 0.539 | 1.00 | 3.65 | 0.25 |
| 0.20 | 0.458 | 1.00 | 5.06 | 0.34 |
| 0.50 | 0.619 | 0.50 | 5.54 | 0.38 |
| 0.50 | 0.656 | 0.40 | 6.80 | 0.42 |
| Concentration of o-phenanthroline: 0.3M | | | | |
| 0.02 | 0.256 | 12.50 | 1.30 | 0.29 |
| 0.05 | 0.474 | 5.00 | 0.94 | 0.21 |
| 0.10 | 0.528 | 2.50 | 1.52 | 0.34 |
| 0.20 | 0.747 | 1.25 | 1.82 | 0.34 |
| 0.50 | 0.780 | 0.50 | 2.46 | 0.55 |
| 1.00 | 0.857 | 0.25 | 5.78 | 1.28 |
| Concentration of terpyridine: 0.02M | | | | |
| 0.05 | 0.617 | 11.00 | 3.80 | 82.8 |
| Concentration of terpyridine: 0.04M | | | | |
| 0.05 | 0.416 | 11.20 | 4.11 | 75.8 |

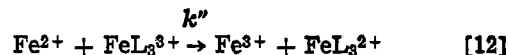
* Medium 0.5M H_2SO_4 . Working electrode platinum. (Area = 0.14 cm^2). Adsorption of the organic on the electrode sometimes produced irreproducibility. Temperature of the solutions $\sim 25^\circ\text{C}$. Concentration of $\text{Fe}^{3+} = 5.0 \text{ mM}$.

† Calculated employing the total concentration of the ligand and assuming formation of the mono-complex is rate determining.

‡ Calculated with the effective ligand concentration using pK_a values reported in text.



and reaction [8], where k^o and k^o' are heterogeneous electron transfer rate constants. If [9] is taken as the rate-determining step and neglecting dissociation rate, the simulated curves are nearly identical to the experimental one as shown in Fig. 5. The small discrepancy for the Fe^{3+} reduction wave might be due to the onset of background reduction. The second oxidation wave (that of FeL_3^{2+}) and its corresponding reversal reduction wave might also be perturbed by the occurrence in homogeneous solution of the reaction



Although the Fe^{2+} concentration in the vicinity of the electrode at the potentials of these waves is small, this reaction is known to be rapid, $k'' = 2.2 \times 10^5 \text{ M}^{-1} \text{ sec}^{-1}$ for $\text{L} = \text{bpy}$ in 0.5M H_2SO_4 (28). The inclusion of this reaction in the simulation did not affect the observed i - E curves for k'' -values up to $10^4 \text{ M}^{-1} \text{ sec}^{-1}$. Within the number of iterations used in the simulation explicit values of k'' higher than this could not be employed. However, even if k'' is assumed to be at the mass transfer controlled limit, so that Fe^{2+} and FeL_3^{3+} cannot coexist in a simulation space element, the effect of the i - E curves, shown as dashed lines in Fig. 5, is small.

It is interesting to compare these results of complexation of Fe^{2+} by bpy with those obtained by stopped flow methods (29), where a second-order

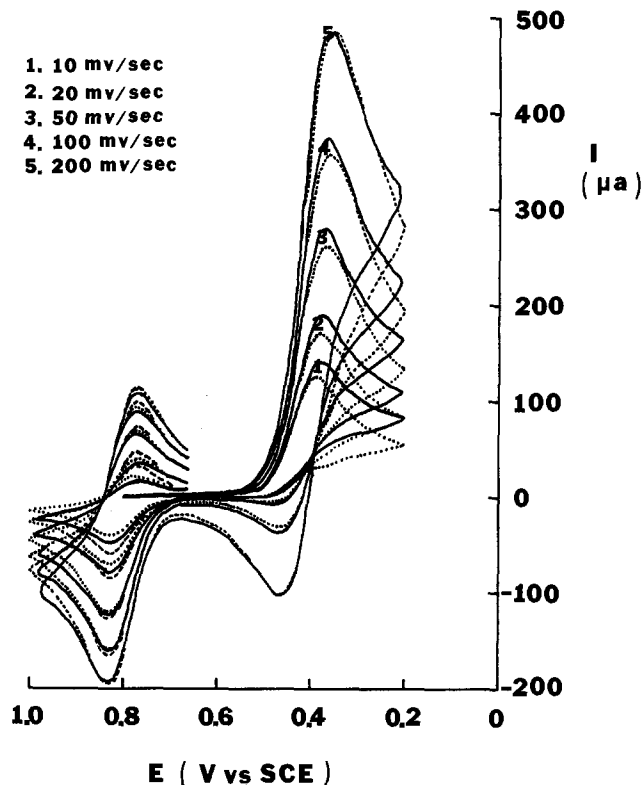


Fig. 5. Digital simulation for the ECE process of the ferric-bipyridine system in 0.5M H_2SO_4 . (—) Experimental curves; digital simulation curves (---) assuming infinite rate of reaction [12] and (···) assuming rate of reaction [12] = 0. $C_{\text{Fe}^{3+}} = 20 \text{ mM}$, $C_{\text{bpy}} = 300 \text{ mM}$, $k_{app} = 2.5 \text{ M}^{-1} \text{ sec}^{-1}$; $D_{\text{Fe}^{3+}} = 2.5 \times 10^{-6} \text{ cm}^2/\text{sec}$, $D_{\text{Fe}(\text{bpy})_3^{3+}} = 2.6 \times 10^{-6} \text{ cm}^2/\text{sec}$. Area of platinum electrode = 0.148 cm^2 .

$E^o(\text{Fe}^{3+,2+}) = 0.41\text{V}$, $E^o(\text{Fe}(\text{bpy})_3^{3+,2+}) = 0.80\text{V}$, $\alpha(\text{Fe}^{3+,2+}) = 0.5$, $\alpha(\text{Fe}(\text{bpy})_3^{3+,2+}) = 0.5$, $k_s(\text{Fe}^{3+,2+}) = 1.61 \times 10^{-3} \text{ cm}^2/\text{sec}$, and $k_s(\text{Fe}(\text{bpy})_3^{3+,2+}) = 5.64 \times 10^{-2} \text{ cm}^2/\text{sec}$.

rate constant of $2.8 \times 10^4 \text{ M}^{-1} \text{ sec}^{-1}$ at 0.2°C was reported. This rate constant was assigned to the first step in the complexation formation of $\text{Fe}(\text{bpy})_2^{2+}$ (reaction [9]). The addition of the second and third bpy ligands is faster; for the third step the rate constant is $1.4 \times 10^5 \text{ M}^{-1} \text{ sec}^{-1}$, while for phen the rate of addition of the third ligand is $1.5 \times 10^6 \text{ M}^{-1} \text{ sec}^{-1}$ (29). The medium and temperature effects on the dissociation rates of the bpy and phen complexes have been investigated by Basolo *et al.* (30).

Controlled Potential Coulometric (cpc) Measurements

The long term stability and current efficiency for the processes on cycling were investigated by controlled potential electrolysis techniques. The oxidation of Fe^{2+} in the uncomplexed form carried out at 0.2V past the anodic *cv* peak showed an n_{app} (faraday/mol) of 0.98-1.00. The current decayed smoothly to the background value and a plot of $\log i$ vs. t yielded a straight line (31) (Fig. 6). Reversal electrolysis, reduction of the electrogenerated Fe^{3+} , carried out at $\sim 0.10\text{V}$, consumed essentially the same number of coulombs as in the forward electrolysis. These experiments were carried out at concentrations up to 1M and electrolysis times of ~ 0.5 hr.

Oxidation of $\text{Fe}(\text{II})$ -complexes with bpy, phen, 2,9-dmp, and tp were carried out at 1.0V vs. SCE at a graphite electrode. In all cases the oxidations consumed 0.95-1.00 faraday/mol (see Table IV) and the current-time curve decayed smoothly to background. For electrolysis times ~ 1.0 hr, reversal electrolysis of the solution at 0.10V consumed about the same number of coulombs as the forward electrolysis. Repetitive electrolysis, cycling between the oxidized and reduced forms four times at 0.5 hr intervals produced similar results.

To examine the lifetime of the complex $\text{Fe}(\text{III})$ species, *cv* experiments were undertaken on solution following cpc oxidation. For ordinary cpc electrolysis of 30 min to 1 hr duration, *cv* showed reduction waves of height and location consistent with the presence of FeL_x^{3+} . However, when these solutions were allowed

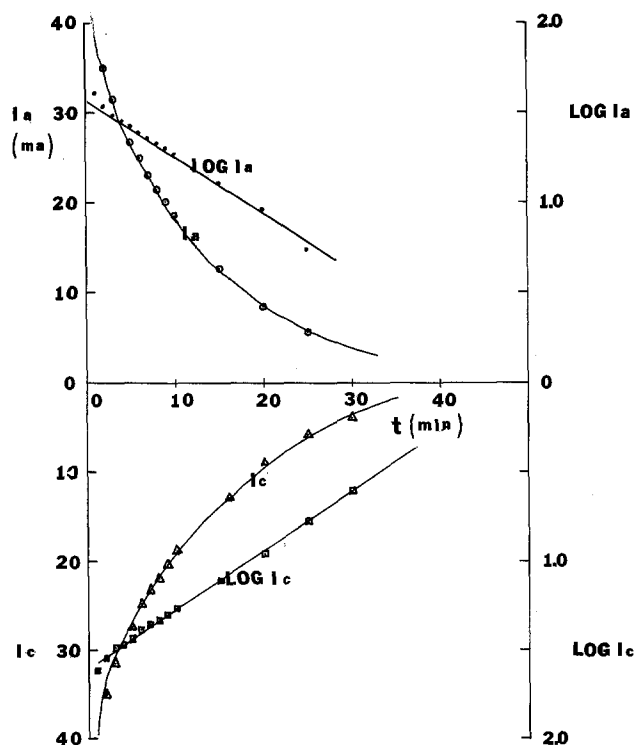


Fig. 6. Current-time curve during exhaustive electrolysis of 10 mM $\text{Fe}(\text{phen})_3^{2+}$ in aqueous H_2SO_4 at a graphite working electrode.

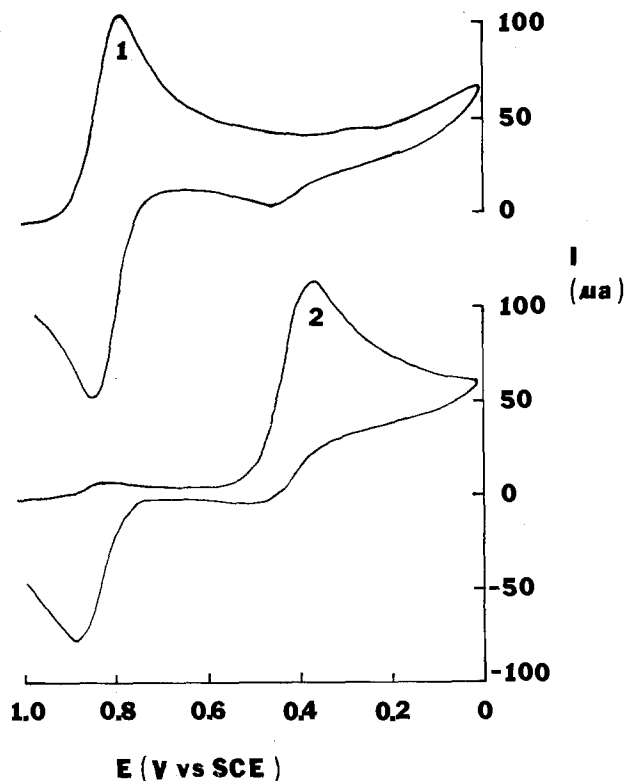


Fig. 7. Stability of $\text{Fe}(\text{phen})_3^{3+}$ in 1N H_2SO_4 . Upper curve: cyclic voltammogram for 10 mM $\text{Fe}(\text{phen})_3^{2+}$ immediately after controlled potential electrolysis at +1.0V at graphite electrode. Lower curve: cyclic voltammogram of the same solution after standing 24 hr in air.

to stand for times of 10-20 hr (Fig. 7), *cv* revealed that i_{pc} for FeL_x^{3+} reduction decreased and a wave for uncomplexed Fe^{3+} appeared. Thus a slow decomposition of the FeL_x^{3+} species ($L = \text{bpy}, \text{phen}, \text{mp}, 4,7\text{-dmp}$) does occur. The rate of decomposition of the FeL_x^{3+} was determined by spectrophotometry, as described below.

Stability of $\text{Fe}(\text{III})$ Species

Since the long duration storage capabilities of these systems appear limited by the stability of FeL_x^{3+} , measurements of the rate of decomposition of the $\text{Fe}(\text{III})$ species and some attempts at stabilization were carried out. The stability of $\text{Fe}(\text{III})$ complexes were examined spectrophotometrically. The $\text{Fe}(\text{III})$ complexes were formed by chemical oxidation by mixing millimolar concentrations of $\text{Fe}(\text{II})$ complexes and excess $\text{Ce}(\text{IV})$ sulfate in 0.5M H_2SO_4 and monitoring the disappearance of the $\text{Fe}(\text{III})$ complex absorption (32). The rate constants for the first-order decay of the FeL_x^{3+} species, k_t , are listed in Table V. Substitution of a methyl group on phen more than doubles the half-life with 4,7-dmp being the most stable of the complexes examined. The 2,9-dmp complex is very unstable, because in this case the placement of the methyl groups produces steric hindrance to bonding between the $\text{Fe}(\text{III})$ and the phenanthroline nitrogens.

The background medium also appears to play a role in the rate of decomposition of $\text{Fe}(\text{III})$ complexes. Thus $\text{Fe}(\text{phen})_3^{3+}$ is reported to be stable in high concentrations of H_2SO_4 (22, 23). We found, in bulk electrolysis experiments with the complexes, that the stability was decreased in H_2SO_4 solutions at a pH of ~ 1 , compared with 0.5M H_2SO_4 . The stability of $\text{Fe}(\text{II})$ and $\text{Fe}(\text{III})$ complexes has been studied previously (33, 34). The general conclusions are that the instability of the complex can be attributed to nucleophilic attack by water, resulting in replacement of the ligands by water molecule. The exact nature of

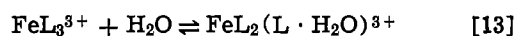
Table IV. Controlled potential electrolysis of ferrous ions*

| Moles taken | Q _r ^o (C) | Moles of Fe ²⁺ (oxdn) | Q _b ^o (C) | Moles of Fe ²⁺ recovered (redn) | n _{app} [†] (faradays mol ⁻¹) |
|---|---------------------------------|----------------------------------|---------------------------------|--|---|
| Free Fe ²⁺ ions | | | | | |
| 0.061 × 10 ⁻³ | 6.39 | 0.066 × 10 ⁻³ | 6.08 | 6.3 × 10 ⁻⁵ | 1.08 |
| 0.061 × 10 ⁻³ | 6.64 | 0.068 × 10 ⁻³ | 6.28 | 6.5 × 10 ⁻⁵ | 1.10 |
| 1.19 × 10 ⁻³ | 114.5 | 1.18 × 10 ⁻³ | 109.1 | 1.13 × 10 ⁻³ | 0.99 |
| 3.00 × 10 ⁻³ | 285.3 | 2.96 × 10 ⁻³ | 265.0 | 2.75 × 10 ⁻³ | 0.98 |
| 3.00 × 10 ⁻³ | 288.6 | 2.99 × 10 ⁻³ | 269.2 | 2.78 × 10 ⁻³ | 0.99 |
| 1.50 × 10 ⁻³ | 1706.9 | 1.70 × 10 ⁻³ | 1470.0 | 1.52 × 10 ⁻² | 1.10 |
| 3.00 × 10 ⁻³ | 2826.8 | 2.93 × 10 ⁻³ | 2830.0 | 2.93 × 10 ⁻³ | 0.98 |
| Fe (phen) ₃ ²⁺ | | | | | |
| 4.67 × 10 ⁻⁴ | 42.77 | 4.43 × 10 ⁻⁴ | 45.20 | 4.68 × 10 ⁻⁴ | 0.95 |
| 4.67 × 10 ⁻⁴ | 43.57 | 4.51 × 10 ⁻⁴ | 41.00 | 4.24 × 10 ⁻⁴ | 0.97 |
| 1.07 × 10 ⁻³ | 104.10 | 1.07 × 10 ⁻³ | 92.00 | 0.95 × 10 ⁻³ | 1.00 |
| Fe (2,9-dmp) ₃ ²⁺ | | | | | |
| 3.10 × 10 ⁻⁴ | 34.05 | 3.52 × 10 ⁻⁴ | 33.00 | 3.4 × 10 ⁻⁴ | 1.10 |
| 3.10 × 10 ⁻⁴ | 33.75 | 3.49 × 10 ⁻⁴ | — | — | 1.10 |
| Fe (tp) ₃ ²⁺ | | | | | |
| 2.00 × 10 ⁻⁴ | 19.55 | 2.02 × 10 ⁻⁴ | 19.80 | 2.0 × 10 ⁻⁴ | 1.02 |
| 4.00 × 10 ⁻⁴ | 44.45 | 4.60 × 10 ⁻⁴ | — | — | 1.10 |

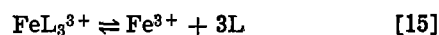
* Working electrode: graphite. Forward electrolysis was carried out at +1.0V and reverse electrolysis at 0.0V.

† Values for oxidation.

the intermediate complex is not clear. Some authors (35) favor the reaction sequence



In our studies we observed the formation of free Fe³⁺ in 0.5M H₂SO₄ from FeL₃³⁺ upon standing for long duration, even in the presence of excess ligand. This demonstrated that total replacement of the ligand by H₂O eventually occurs, i.e.



(where L = phen, bpy). When excess ligand is not present, a cathodic peak at +0.10V appears on standing, which might represent dimeric species such as a bridge complex formed (18) by the following reaction

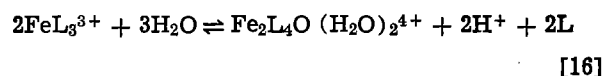


Table V. Cyclic voltammetric data on the bulk electrolysis products*

| Sweep rate (V/sec) | E _{pa} (V) | i _{pa} (mA) | E _{pc} (V) | i _{pc} (mA) | Remarks |
|--|---------------------|----------------------|---------------------|----------------------|-------------------------------------|
| Unbound Fe ²⁺ Conc = 1M | | | | | |
| 0.02 | 0.48 | 3.80 | 0.40 | — | Before bulk electrolysis |
| 0.05 | 0.48 | 5.20 | 0.40 | — | Before bulk electrolysis |
| 0.02 | — | — | 0.40 | 3.90 | After electrolysis at +0.80V |
| 0.05 | — | — | 0.40 | 5.60 | After electrolysis at +0.80V |
| Reversal electrolysis at 0.0V | | | | | |
| 0.02 | 0.48 | 3.80 | 0.40 | — | |
| 0.05 | 0.48 | 5.20 | 0.40 | — | |
| Fe (phen) ₃ ²⁺ Conc = 20.0 mM | | | | | |
| 0.02 | 0.86 | 0.14 | 0.80 | 0.14 | |
| 0.05 | 0.86 | 0.22 | 0.80 | 0.22 | |
| 0.02 | — | — | 0.80 | 0.14 | After bulk electrolysis at +1.0V |
| 0.05 | — | — | 0.80 | 0.22 | After bulk electrolysis at +1.0V |
| 0.02 | 0.86 | 0.15 | 0.80 | 0.15 | Reversal electrolysis at +0.26V |
| 0.05 | 0.86 | 0.23 | 0.80 | 0.23 | Reversal electrolysis at +0.26V |
| Fe (2,9-dmp) ₃ ²⁺ Conc = 20.0 mM | | | | | |
| 0.02 | 0.80 | 0.11 | 0.12 | 0.03 | Before bulk electrolysis |
| 0.05 | 0.87 | 0.17 | 0.08 | 0.08 | Before bulk electrolysis |
| 0.02 | — | — | 0.10 | 0.11 | After oxidation at +1.0V |
| 0.05 | — | — | 0.08 | 0.17 | After oxidation at +1.0V |
| 0.02 | 0.80 | 0.11 | 0.12 | 0.03 | After reversal electrolysis at 0.0V |
| 0.05 | 0.87 | 0.17 | 0.08 | 0.08 | After reversal electrolysis at 0.0V |

* Measurements were made at graphite electrode in the same medium used for controlled potential electrolysis.

Since attack by water causes decomposition of the Fe(III) species, blocking of the central metal ion by a hydrophobic environment or decreasing the water activity in the bulk solution may improve stability. Indeed the improved stability of the 4-mp and 4,7-dmp may partially represent such an effect, although the electron-donating properties of the methyl groups may also play a role. Attempts at providing a more hydrophobic environment were made by introducing various surface active agents and monitoring the concentration of the Fe(III) complex by cv. Results for the Fe(bpy)₃³⁺ complex are shown in Fig. 8 in 0.5M H₂SO₄ solutions containing butanol, heptanol, and the surfactant IGEPAL. Considerable improvement was noticed with 1-butanol in the medium. The abrupt changes in cyclic voltammetric peak current in the presence of a few surfactants (e.g., curve 8) occurs when phase separation takes place.

Electrolysis of Fe(II) complexes was also conducted in the presence of 1M AlCl₃ or 1M MgSO₄ or saturated solutions of Li₂SO₄. The decay of the Fe(III) complex concentration was noticed even in the presence of the above salts. When saturated solutions were used, the solutions became viscous and the

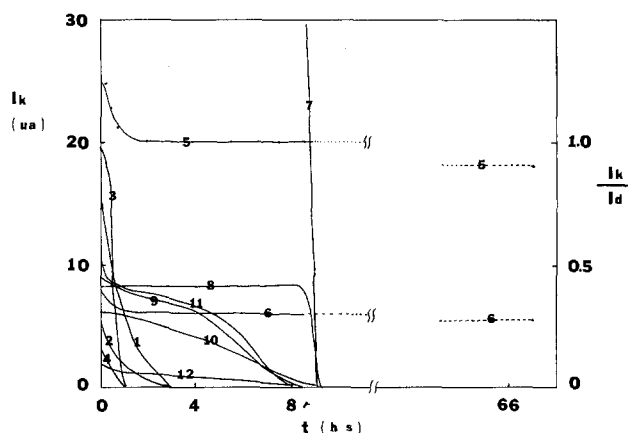


Fig. 8. The decay of Fe(III)-bpy complex in 1N H₂SO₄ in the presence of stabilizing agents. The Fe(III)-bpy complex was obtained by controlled potential electrolysis of Fe(II)-bpy complex. *i_k* is cyclic voltammetric peak current after controlled potential electrolysis (cathodic peak at +0.80V) *i_d* is the diffusional peak current. *i_k* = 1, 3, 5, 7, 9, and 11 and *i_k*/*i_d* = 2, 4, 6, 8, 10, and 12, *i_k* (*t* = 0) = 36 μA for line 7. 1, 2 = No stabilizer; 3, 4 = Texas-1 (excess); 5, 6 = 5 ml 1-butanol; 7, 8 = IGEPAL Co-430; 9, 10 = IGEPAL Co-530; 11, 12 = 1-heptanol.

duration of electrolysis was very long; with Li_2SO_4 saturated solution in 0.5M H_2SO_4 , electrolysis of 12.6 mmols $\text{Fe}(\text{phen})_3^{3+}$ took about 4 hr. At the end of electrolysis, a cathodic peak at 0.31V for free Fe(III) was observed in the cyclic voltammograms.

Discussion

Aquo Fe(II)/Fe(III) couple in 6N H_2SO_4 appears to be well suited as a redox positive couple for an extended period of time and appears to meet the major requirements of stability, solubility, fast electron exchange, and high electrical conductivity in the acid medium. A measurement of electron transfer rate constant in the 2N HCl medium was undertaken to compare it with H_2SO_4 medium. At platinum disk or graphite electrodes, an average of five measurements gave k^0 values of 1.9×10^{-3} and 1.34×10^{-3} cm/sec, respectively. These values are slightly smaller than the value obtained in H_2SO_4 (see Table I). However, a disadvantage of using HCl medium is the somewhat less positive background limiting potential value compared with H_2SO_4 (22). An advantage of H_2SO_4 medium over Cl for PEC cells is the lighter colors of the Fe(II) and Fe(III) species in this medium.

Complexation of Fe(II)/Fe(III) couple can provide higher E^0 -values [e.g., 1.07V for np compared to 0.53V (vs. SCE)] and faster electrode kinetics. The solubility of the complexes is approximately the same as uncomplexed Fe(II) or Fe(III). While the Fe(II) complexes are highly stable over days in the absence of O_2 , Fe(III) complexes decay in the medium employed by loss of ligand (see Fig. 7). This process results in loss of stored energy since the redox couple so produced is at a less positive potential. However, this loss is slightly compensated by the fast complexation of Fe(II) by ligand during a discharge cycle. Note that if the rate of complexation of Fe(II) were rapid enough, the Fe(III) reduction wave would shift to potentials near those for the oxidation of the complexed Fe(II) species.

Conclusions

The results here describe how coordination of the central metal ion can affect the potential and the kinetics of the electrode reaction to produce systems which might be utilizable in redox flow batteries. The aquo iron (3+/2+) system in H_2SO_4 appears to be an alternative to the iron (3+/2+) system in HCl media currently under investigation. Complexation with phenanthroline or bipyridyl-type ligands results in significant positive shifts in the potential of the redox couple. The solubility of these couples appears satisfactory, but instability of the ferric form results in partial loss of capacity upon long-term storage.

Acknowledgment

This work was supported by a grant from Texas Instruments, under TI/DOE cooperative agreement DE-FC01-79ER10.000. We appreciate the comments of a reviewer pointing out the significance of reaction [12] in the interpretation of the *cv* data.

Manuscript submitted Oct. 20, 1980; revised manuscript received Feb. 20, 1981.

Any discussion of this paper will appear in a Discussion Section to be published in the June 1982 JOURNAL. All discussions for the June 1982 Discussion Section should be submitted by Feb. 1, 1982.

Publication costs of this paper were assisted by The University of Texas at Austin.

REFERENCES

- J. Giner, L. Swette, and A. Cahill, "Screening of Redox Couples and Electrode Materials" CR 134705, for NASA-Lewis Research Center, Cleveland, Ohio, September, 1976.
- J. N. Butler, J. Giner, and H. Stark, "Complex Redox Couples for Energy Storage," Project 727-2. Prepared for EPRI, June 1979.
- C. Ciprios, W. Erskine, Jr., and P. G. Grimes, "Redox Bulk Energy Storage System Study," Vol. I and II, CR 135206, Exxon Research Engineering Co., for NASA-Lewis Research Center, Cleveland, Ohio, February 1977.
- K. D. Beccu and G. Crespy, "Large Scale Energy Storage by Means of Dissolved Redox Flow Systems," SPE Meeting, Grenoble, France, April 9, 1976.
- L. H. Thaller, "Redox Flow Energy Storage Systems," NASA-TM 79143, Terrestrial Energy Systems Conference sponsored by the American Institute of Aeronautics and Astronautics, Orlando, Florida, June 4-6, 1979; NASA-TM 79067, January 1979.
- L. H. Thaller, "Redox Flow Development and Demonstration," Symposium on Load-Leveling sponsored by The Electrochemical Society, Atlanta, Georgia, Oct. 10-13, 1977.
- R. F. Savinelli, C. C. Liu, R. T. Galasco, S. H. Chiang, and J. F. Coetzee, *This Journal*, **126**, 357 (1979).
- M. Warshay and L. Wright, *ibid.*, **124**, 173 (1977).
- A. J. Bard, *J. Photochem.*, **10**, 59 (1979).
- A. J. Bard and M. S. Wrighton, *This Journal*, **124**, 1706 (1977).
- H. Gerischer, *J. Electroanal. Chem. Interfacial Electrochem.*, **82**, 133 (1977).
- P. M. Spaziante, G. C. Sioli, R. Trotter, A. Perego, and J. McBreen, "Hydrogen-Halogen Energy Storage System," BNL 25212.
- E. Gileadi, S. Srinivasan, F. J. Salzano, C. Braun, A. Beaufriere, S. Gottsfeld, L. J. Nuttall, and A. B. LaConti, *J. Power Sources*, **2**, 191 (1977).
- R. S. Yeo and J. McBreen, *This Journal*, **126**, 1682 (1979).
- A. B. Ellis, S. W. Kaiser, and M. S. Wrighton, *J. Am. Chem. Soc.*, **98**, 1635 (1976).
- B. Miller and A. Heller, *Nature (London)*, **262**, 680 (1976).
- R. G. Wilkins, "The Study of Kinetics and Mechanism of Reactions of Transition Metal Complexes," Allyn and Bacon, Inc., Boston, Mass. (1974).
- F. R. F. Fan and L. R. Faulkner, *J. Am. Chem. Soc.*, **101**, 4779 (1979).
- H. Matsuda and Y. Ayabe, *Z. Elektrochem.*, **59**, 494 (1955).
- R. S. Nicholson, *Anal. Chem.*, **37**, 1351 (1965).
- A. J. Bard and L. R. Faulkner, "Electrochemical Methods," Chap. 6, John Wiley & Sons, Inc., New York (1980).
- R. N. Adams, "Electrochemistry at Solid Electrodes," p. 145, Marcel Dekker, Inc., New York (1969).
- D. H. Angill and T. Dickinson, *J. Electroanal. Chem. Interfacial Electrochem.*, **35**, 55 (1972) and references therein.
- J. M. Saveant, *Electrochimica Acta*, **12**, 999 (1967).
- R. S. Nicholson and I. Shain, *Anal. Chem.*, **36**, 706 (1964).
- H. Irving and D. H. Mellor, *J. Chem. Soc.*, 5222 (1962).
- R. B. Martin and J. A. Lissfelt, *J. Am. Chem. Soc.*, **78**, 938 (1956).
- M. H. Ford-Smith and N. Sutin, *ibid.*, **83**, 1830 (1961).
- R. H. Holyer, C. D. Hubbard, S. R. A. Kettle, and R. G. Wilkins, *Inorg. Chem.*, **4**, 929 (1965).
- J. E. Dickens, F. Basolo, and H. M. Neumann, *J. Am. Chem. Soc.*, **79**, 1286 (1957).
- K. S. V. Santhanam and A. J. Bard, *Electroanal. Chem.*, **4**, 215 (1970).
- J. Burgess and R. I. Haines, *Inorg. Nucl. Chem.*, **39**, 1705 (1977).
- R. D. Gillard, L. A. P. Kane-Maguire, and P. A. Williams, *J. Chem. Soc. Dalton Trans.*, 1792 (1977).
- R. D. Gillard, *Coordination Chem. Rev.*, **16**, 67 (1975).
- D. L. Ehman and D. T. Sawyer, *Inorg. Chem.*, **8**, 900 (1969).

On Fitting Error Functions to Data

R. Ghez* and M. B. Small*

IBM Thomas J. Watson Research Center, Yorktown Heights, New York 10598

ABSTRACT

Error functions, which offer solutions to a wide variety of diffusion problems, contain unknown physical parameters in a nonlinear way. We propose a simple iterative method that takes advantage of the geometry of these functions. The method rests on simple analytic relations between the parameters and the first two moments of the distribution. The requisite numerical integrations do not add noise to the data as do methods that estimate slopes. Our method is applied to measured profiles in LPE (GaAl)As. It is simple, efficient and accurate.

Statement of the Problem

Fitting a given function to experimental data is difficult when that function is nonlinear in the unknown parameters. The usual method consists in fitting data in asymptotic regions where the function might have a simpler form, presumably linear in these parameters. This is hazardous both because one must choose, somewhat arbitrarily, what data points to retain, and because these points are often subject to larger experimental uncertainties than those which were deleted. Of course, one can use nonlinear least squares procedures (1), but their application is sometimes nothing short of an art.

Contrary to the above methods that seek to pass a "best" curve through the data, we propose a method that takes advantage of the geometric properties of the function to be fitted. In particular, our method computes areas rather than slopes, a procedure that smoothes data rather than enhancing the noise. We develop the method for error functions of the form

$$x(z, t) = x_0 \frac{\operatorname{erfc} [z/2(Dt)^{1/2} - \beta]}{\operatorname{erfc} (-\beta)} \quad [1]$$

and apply it to measured Al profiles in LPE-processed $\text{Ga}_{1-x}\text{Al}_x\text{As}$ wafers (2). Here, z is the distance into the wafer, t is the processing time, x is the mole fraction of AlAs, x_0 is the surface concentration, D is the diffusivity, and β is a constant proportional to the growth rate. The function [1] is linear in x_0 , but it is nonlinear in both D and β . This function is also representative of a large class of similarity solutions of the Stefan Problem.

We note that our method is only applicable when it is otherwise known that the experimental data are correctly described by a given functional form such as Eq. [1]. In the present case, this means that some underlying theory (3, 4) predicts error function behavior, and that the parameters x_0 , D , and β are truly constants. In particular, since we develop no measure of "goodness of fit," it is not as yet possible to discriminate between competing functional forms (*i.e.*, theories) for a given set of data.

Solution of the Problem

When the solid grows ($\beta > 0$), the function [1] has the appearance shown on Fig. 1; it has an inflection point characteristic of sharp junctions. One shows easily that this inflection has the coordinates

$$z_i = 2\beta(Dt)^{1/2} \quad [2a]$$

$$x_i = \frac{x_0}{\operatorname{erfc} (-\beta)} \quad [2b]$$

Moreover, the total area A under the curve is

* Electrochemical Society Active Member.
Key words: data-fitting, error function, diffusion coefficient.

$$A = \int_0^\infty x(z, t) dz = 2x_0(Dt)^{1/2} \frac{i^1 \operatorname{erfc} (-\beta)}{\operatorname{erfc} (-\beta)} \quad [3a]$$

where $i^n \operatorname{erfc} (\bullet)$ is the n^{th} iterated error function (5). Likewise, the area A_i reckoned from the inflection point forward is

$$A_i = \int_{z_i}^\infty x(z, t) dz = \frac{2x_0}{\operatorname{erfc} (-\beta)} (Dt/\pi)^{1/2} \quad [3b]$$

Finally, the centroid \bar{z} of the distribution is

$$\bar{z} = A^{-1} \int_0^\infty z x(z, t) dz = 2(Dt)^{1/2} \frac{i^2 \operatorname{erfc} (-\beta)}{i^1 \operatorname{erfc} (-\beta)} \quad [3c]$$

The idea of the method is now very simple. If one eliminates $(Dt)^{1/2}$ from Eq. [3] by using Eq. [2a], then these are three equations in the three unknowns x_0 , z_i , and β , in terms of the three measurable quantities A , A_i , and \bar{z} . Equation [2a] then yields the diffusivity D . Now the quantities A , A_i , and \bar{z} are reckoned by numerical integration over the experimental data, to which one adjoins the estimated initial and inflection points, $(0, x_0)$ and (z_i, x_i) . The process can then be iterated.

Simplified formulas obtain when the growth constant β is large. In fact, for $\beta \geq 2$, the following asymptotic expansions hold to better than 1%

$$\operatorname{erfc} (-\beta) \sim 2 \quad [4a]$$

$$i^1 \operatorname{erfc} (-\beta) \sim 2\beta \quad [4b]$$

$$i^2 \operatorname{erfc} (-\beta) \sim \beta^2 + \frac{1}{2} \quad [4c]$$

Terms neglected in Eq. [4] are of order $\exp(-\beta^2)$. In

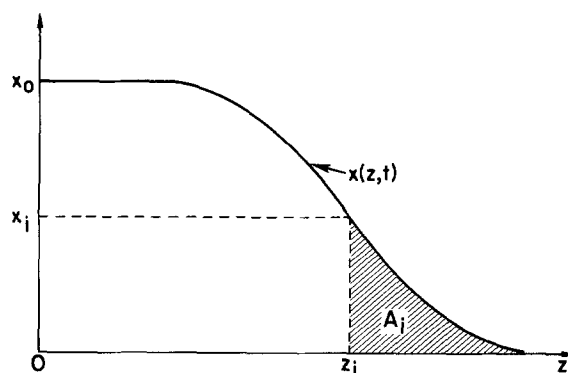


Fig. 1. Schematic of the error function profile, Eq. [1], for positive values of the growth constant β . It displays the relevant geometrical features: inflection point, surface concentration, and area beyond the inflection.

this case, Eq. [3] become simply

$$A = x_0 z_1 \tag{5a}$$

$$A_1 = \frac{x_0 z_1}{2\pi^{1/2}\beta} \tag{5b}$$

$$\bar{z} = \frac{z_1}{2} \left(1 + \frac{1}{2\beta^2} \right) \tag{5c}$$

and these are invertible algebraically to give the unknowns

$$x_0 = A/z_1 \tag{6a}$$

$$\beta = A/2\pi^{1/2} A_1 \tag{6b}$$

$$z_1 = 2\bar{z}/[1 + (2\beta^2)^{-1}] \tag{6c}$$

Our iterative procedure begins with an initial guess of x_0 and z_1 . One then adjoins the estimated initial point $(0, x_0)$ and inflection point $(z_1, x_0/2)$ to the experimental data. Next, one evaluates numerically the areas A and A_1 , and the centroid \bar{z} ; in practice the trapezoidal rule is sufficient. These values are inserted into Eq. [6] to give new values of x_0 and z_1 , and the process can be repeated. At each iteration one can compute the diffusivity D and the growth constant β according to Eq. [6b] and [2a]. This procedure is illustrated in the next section.

Numerical Results

Figure 2 shows three Al profiles obtained by SIMS measurements. The open symbols correspond to the experimental data; the closed ones stand for the computed values of the surface concentrations and inflection points. Because of a longitudinal temperature gradient in the furnace, these profiles correspond to different undercoolings between a single wafer and its solution. The processing time t was 309 sec. The experiment has been fully described and analyzed elsewhere (2), and a review of ternary III-V LPE is also available (6). We note that the data appear to have the shape of Fig. 1, but that data points are quite sparse, particularly in the neighborhood of the inflection point. This experiment provides therefore an ideal test of our method.

We purposely choose a "bad" initial guess: $z_1 = 350, 250,$ and 110 nm for the positions of the inflection points, and $x_0 = 0.9$ for the surface composition of all three profiles. Figures 3 and 4 show how the growth constant β and the diffusivity D converge as a function of the number of iterations. The symbol code on these figures is the same as that of Fig. 2 and Table I. We find that at most 15 iterations are sufficient to ensure a relative error less than 1%. As was also noted else-

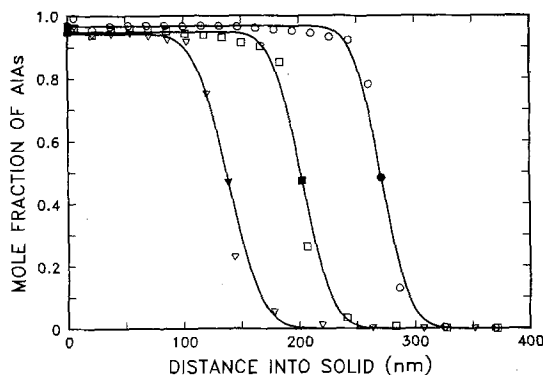


Fig. 2. Three profiles in (GaAl)As obtained by SIMS (2). The open symbols represent the experimental data, the closed symbols are the computed inflection points and surface concentrations, and the solid lines show how Eq. [1] fits the data.

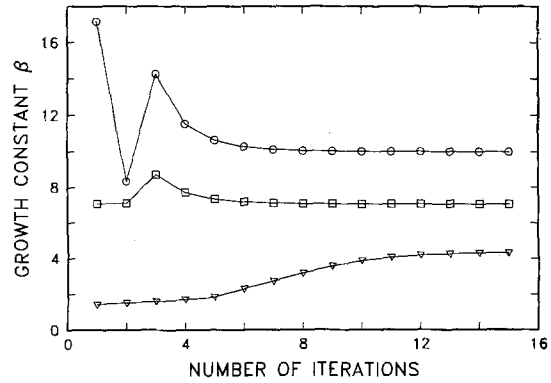


Fig. 3. The growth constants β in Eq. [1] as a function of number of iterations for the three profiles of Fig. 2. The symbol code is the same as in that figure. The deepest profile has the largest β , i.e., the growth rate was largest here.

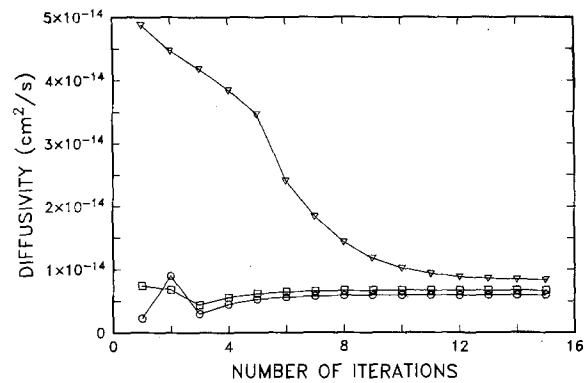


Fig. 4. Same as Fig. 3 for the diffusivity D of Al in (GaAl)As. Comparing Fig. 3 and 4, one sees that D increases as the growth rate decreases.

where (2), the diffusivity D of Al in (GaAl)As increases with decreasing growth constant β . This was even more noticeable (2) for dissolving crystals ($\beta < 0$). Table I shows the final value, after 15 iterations, of all the variables we have been discussing: The measured values $A, A_1,$ and \bar{z} , and the unknown parameters $x_0, \beta,$ and D . We also list the final abscissa z_1 of the inflection point. We emphasize that the estimation of all these quantities never required numerical differentiation of the experimental data. The solid lines on Fig. 2 correspond to the function [1] computed with these values of the parameters. The fit is excellent, particularly in view of the sparseness of the data.

The method we have presented is heuristic in the sense that we attempted no investigation of its convergence. However, it is presumably a one-point iteration method (1) of the form $x_{n+1} = \phi(x_n)$, whose properties are well known. It is also obvious that similar procedures could be devised for other functional forms different from error functions.

Table I. Shows the final computed values, after 15 iterations, of the measured quantities and the unknown parameters. The numbers are accurate to at least two decimal places.

| Symbol | A (nm) | A ₁ (nm) | \bar{z} (nm) | z ₁ (nm) | x ₀ | β | D × 10 ¹⁵ (cm ² /sec) |
|--------|--------|---------------------|----------------|---------------------|----------------|---------|---|
| ○ | 262.60 | 7.39 | 136.35 | 271.34 | 0.97 | 10.02 | 5.93 |
| □ | 192.46 | 7.70 | 102.40 | 202.75 | 0.95 | 7.05 | 6.69 |
| ▽ | 131.02 | 8.49 | 71.31 | 138.95 | 0.94 | 4.35 | 8.25 |

Manuscript submitted July 7, 1980; revised manuscript received Feb. 6, 1981.

Any discussion of this paper will appear in a Discussion Section to be published in the June 1982 JOURNAL. All discussions for the June 1982 Discussion Section should be submitted by Feb. 1, 1982.

Publication costs of this article were assisted by IBM Corporation.

REFERENCES

1. G. Dahlquist and A. Björk, "Numerical Analysis," pp. 438-446, Prentice-Hall, New Jersey (1974).
2. M. B. Small, R. Ghez, W. Reuter, and R. M. Potemski, *J. Appl. Phys.*, **52**, 814 (1981).
3. M. B. Small and R. Ghez, *ibid.*, **50**, 5322 (1979).
4. M. B. Small and R. Ghez, *ibid.*, **51**, 1589 (1980).
5. M. Abramowitz and I. A. Stegun, "Handbook of Mathematical Functions," Chap. 7, Dover Publications, New York (1965).
6. R. Ghez and M. B. Small, *J. Cryst. Growth*, **52**, 699 (1981).

The Cathodic Cleavage of Ethanetetracarboxylate Esters

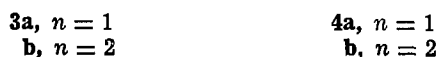
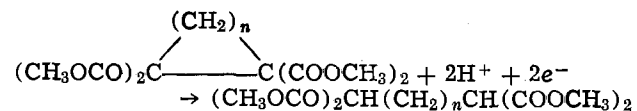
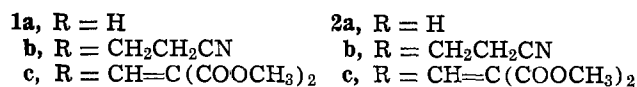
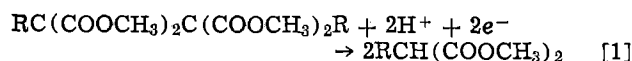
Donald A. White¹ and John H. Wagenknecht*

Monsanto Company, Corporate Research and Development Staff, St. Louis, Missouri 63166

ABSTRACT

The electrochemical reduction of tetramethyl ethane-1,1,2,2-tetracarboxylate to dimethyl propanedioate (dimethyl malonate) and the similar cleavage of some substituted and some cyclic analogs are reported.

The cleavage of carbon-carbon single bonds is an unusual, though not unreported (1-4), phenomenon in cathodic processes. *A priori* facile cleavage might be expected when the carbon atoms bear substituents likely to stabilize carbanionic intermediates. Ethanetetracarboxylate esters (**1**, **3**) are a very favorable case, but their electrochemical reduction has not been reported previously. Furthermore, there is only a single example of a similar chemical reaction, and this uses sodium metal in a mixture of liquid ammonia and tetrahydrofuran as the reducing agent (5). The results reported here provide a more convenient way of carrying out such reactions as well as establishing their generality by the presentation of several examples.



Experimental

Reagents.—Dimethylformamide (DMF) and tetraethylammonium perchlorate were obtained from Fisher Scientific Company, Fairlawn, New Jersey. The former was used as supplied. The latter was recrystallized from water, then from methanol before use. Literature procedures were used for the preparation of **1a**, **1b**, **3** (6), and **1c** (7, 8).

Equipment.—A Varian 3700 gas-liquid chromatograph fitted with a thermal conductivity detector and with a stainless steel column (0.32 × 50 cm) packed with 5% OV101 on Chromosorb G-HP (100/120) was used for the analysis of reaction mixtures. The ¹H-NMR spectra of the products were obtained using a Varian EM-390 spectrometer. The power supply for

preparative electrolyses was a Lambda Model LP-412A-FM. Cyclic voltammetry was carried out using a PAR Model 173 potentiostat, PAR Model 175 Universal Programmer, and Houston Model 2000 X-Y recorder. The cyclic voltammetry cell consisted of a modified beaker with SCE separated by a glass frit, Pt wire secondary electrode, and hanging Hg drop working electrode. Air was excluded from the voltammetry cell by a blanket of flowing dry N₂.

Reduction of ethanetetracarboxylate esters.—The ethanetetracarboxylate ester (0.010 mol) and tetraethylammonium perchlorate (2.30g; 0.010 mol) were dissolved in a mixture of DMF (50 ml) and water (5 ml) at ca. 60°C. A current of 0.25A was passed through the solution for 2.5 hr (0.023 F) for all compounds except **1c**, 3.25 hr (0.030 F), while the electrolyte temperature was kept at 60°-65° by external heating. A mercury pool (ca. 3.5 cm diam) and platinum sheet (ca. 2 cm² area) were the cathode and anode, respectively. The anode was horizontal and ca. 1 cm above the mercury surface. Agitation was provided by a small magnetic stirring bar floating on the mercury.

In the case of **1a** the electrolyte was cooled, dimethyl succinate was added as an internal standard, and unchanged starting material and product (**2a**) were determined by gas-liquid chromatography.

In the case of **1b** the solvent was removed *in vacuo*. The solid/liquid mixture obtained was stirred with chloroform (ca. 20 ml) and filtered to remove the majority of the electrolyte. Evaporation of the filtrate gave a viscous oil (5.70g). Analysis by NMR showed it to consist of **1b** and **2b** (3.67g combined), DMF (0.86g), and hydroxymethyl(methyl)formamide (0.71g). The oil was stirred with ether (100 ml). The solid (1.05g) formed was removed by filtration and was found by NMR to consist of electrolyte (0.46g) and unchanged starting material (**1b**); 0.59g; this value used for computing the data in Table I). This solid was recrystallized from methanol (30 ml) to give pure **1b** [0.51g; mp, 170°-2°; lit. (6), mp 169°-70.5°]. The ether filtrate gave on evaporation a liquid (4.32g) consisting (by NMR analysis) of DMF (0.65g), hydroxymethyl(methyl)formamide (0.66g), and **2b** (3.01g; this value used for computing the data in Table I). The liquid was again taken up in ether. The ether solution was washed six times with water to remove the amides. It was then dried (CaSO₄), filtered, and evaporated. The residue

* Electrochemical Society Active Member.

¹ Present address: Exxon Chemical Company, Allendale, New Jersey 07401.

Key words: C-C bond cleavage, bimalonate, reductions, preparative electrolysis voltammetry.

Table I. Reduction of ethanetetra-carboxylate esters

| Starting material (0.01 mol) | Unchanged starting material ^a (%) | Products ^a (% yield) ^b | E _p ^c vs. SCE (V) |
|------------------------------|--|--|---|
| 1a | 1 | 2a (89) | -2.64 |
| 1b | 16 | 2b (97) | -2.64 |
| 1c | nd | 2c (72), 4a (24) | -1.37 |
| 3a | <1 | 4a (95) | -2.29 |
| 3b | 19 | 4b (100) | -2.56 |

^a After passage of 2.3 F/mole (except for 1c, 3 F/mole); nd = not detected.

^b Yield based on starting material consumed.

^c Potential of the first cathodic peak observed via cyclic voltammetry for the starting material (ca. 1.1 × 10⁻³M) in dry DMF containing [(C₂H₅)₄NClO₄] (0.1M). No reverse peaks at scan rates up to 1000 mV/sec.

was distilled to give pure dimethyl-3-cyanopropane-1,1-dicarboxylate [2b, 2.21g, bp 108°-10° (0.05 mm)]. Found: C, 52.0, 52.1; H, 6.0, 6.0; N, 7.4, 7.6%; M, 173 (by osmometry in chloroform). C₈H₁₁NO₄ requires: C, 51.9; H, 6.0; N, 7.6%; M, 185.

For 1c and 3 procedures similar to those described above for 1b were used to generate the data shown in Table I. Compounds 2c [mp, 49°-51°; lit. (8), mp 49°-50°] and 4a [mp, 46-8°; lit. (9), mp 48°] were obtained as white crystalline solids from ether and 4b [mp, 77°-8°; lit. (10), mp 77.6°-8.4°] in similar form from methanol.

The ¹H-NMR spectral data for the products are shown in Table II.

Oxidation of dimethylformamide.—A current of 0.25A was passed through a solution of tetraethylammonium perchlorate (2.30g; 0.010 mol) in a mixture of DMF (150 ml) and water (5 ml) at 60°-65°C in the cell used for the ester reductions. As soon as the current flow was initiated, the formation of a black solid, assumed to be tetraethylammonium amalgam (12), was noted on the surface of the mercury cathode. It dissolved within a few seconds after a temporary discontinuation of current flow. After 22.5 hr (0.21F), the electrolysis was stopped. The solution was evaporated. The residue was taken up in ether (ca. 100 ml) and the electrolyte was removed by filtration. The filtrate was evaporated to give an oil (4.50g) containing (by NMR analysis) hydroxymethyl(methyl)formamide (3.53g), methylformamide (0.90g), and DMF (0.07g). Distillation gave hydroxymethyl(methyl)formamide containing ca. 10 mole percent (m/o) methylformamide as a water-white liquid [1.03g; bp, 108°-10° (0.2 mm)]. In its ¹H-NMR spectrum hydroxymethyl(methyl)formamide shows, in common with other

Table II. ¹H-NMR spectral data for the cleavage products

| Compound | Chemical shifts ^a | | | | Olefinic CH |
|----------|----------------------------------|-----------------------|--------------------|-----------------------|----------------------|
| | COOCH ₃ | CH ₂ | CH ₂ CN | CH | |
| 2b | 3.74 (6) | 2.27 (2) t, 7 Hz | 2.49 (2) m | 3.53 (1) t, 7.5 Hz | |
| 2c | 3.74 (6) 3.80 (3) 3.78 (3) | | | 4.69 (1) d, 10 Hz | 7.19 (1) d, 10 Hz |
| 4a | 3.72 (12) | 2.46 (2) t, 7.5 Hz | | 3.49 (2) t, 7.5 Hz | |
| 4b | 3.69 (12) | 1.91 (4) m | | 3.34 (2) m | |

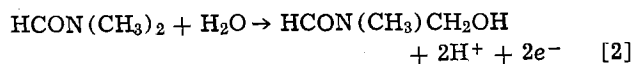
^a Measured in ppm downfield from internal tetramethylsilane reference in CDCl₃ solution at 90 MHz. Relative area is shown in parentheses. The multiplicity (d = doublet, t = triplet, m = multiplet) and coupling constants of nonsinglet resonances are indicated below the chemical shift data.

amides, peaks for two isomers due to restricted rotation about the N-CO bond. The major isomer (80%) showed peaks at 2.91 (CH₃), 4.78 (CH₂), and 8.13 (CHO) ppm downfield from an internal tetramethylsilane reference. The minor isomer showed similar peaks at 3.04, 4.81, and 8.00 ppm. In addition, a common hydroxyl peak was observed at ca. 5.4 ppm which was broad and exchanged with D₂O. Hydroxymethyl(methyl)formamide contaminated with a little methylformamide was also obtained by reaction of methylformamide with paraformaldehyde (12) and its NMR spectrum is identical to that of the anodically formed material.

Results and Discussion

Tetramethyl ethane-1,1,2,2-tetra-carboxylate (1a), some substituted derivatives (1b, c), and cyclic analogs (3a, b) undergo reductive cleavage at a mercury cathode in aqueous DMF. High yields and current efficiencies are obtained at high conversions in an undivided cell using a constant current mode of operation (Table I). In the case of 1c, (CH₃OCO)₂C=CH—C(COOCH₃)₂—C(COOCH₃)₂—CH=C(COOCH₃)₃, electrochemical reduction has been reported previously (7). The formation of a cyclopentane derivative by saturation of one double bond followed by an intramolecular Michael addition to the other has been claimed. While the formation of the cyclopentane on catalytic hydrogenation of 1c (8) has been confirmed, its formation on electrochemical reduction of 1c could not be reproduced. In both aqueous DMF and methanol containing sulfuric acid, cf. (7), the initial product was 2c, (CH₃OCO)₂C=CHCH(COOCH₃)₂, which underwent further reduction to 4a, (CH₃OCO)₂CHCH₂CH(COOCH₃)₂. The reduction potential of 2c in DMF is slightly more negative (E_p = 1.54V) than that of 1c (E_p = -1.3V vs. SCE).

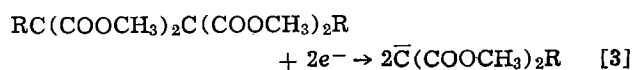
The anode reaction accompanying the cathodic cleavages is the oxidation of DMF to hydroxymethyl(methyl)formamide, Eq. [2]. This is not

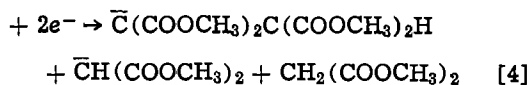
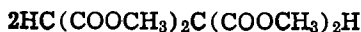


surprising as this compound is an intermediate in the formation of the ether, [CHON(CH₃)CH₂]₂O, which results when a stoichiometric quantity of water is used (13). In the absence of an ethanetetra-carboxylate ester, hydroxymethyl(methyl)formamide is the sole product isolated.

The reductive reactions reported here are a reverse of the anodic oxidation of propanedioate esters, which proceeds via direct oxidation (14) of the carbanion or indirectly via anodically generated halogen, especially iodine (6). Use of neutral conditions, partially aqueous solvent, and a nonhalide electrolyte avoids these anodic reactions and permits the convenience of an undivided cell. The esters 1b and 1c are not very soluble, and the reaction temperature used (60°-5°C) was that required to keep these compounds in solution. In spite of this elevated temperature and the presence of water, hydrolysis of ester groups did not seem to be a problem, perhaps because of the relatively short reaction times (usually 2.5 hr) used.

The first reduction peak (Table I) for the esters 1 and 3 corresponds in all cases to an irreversible process. For 1b, c, and 3 the peak height is comparable to that of tetramethyl ethanetetra-carboxylate which corresponds to a two-electron process. For these compounds the peak height and peak potential are not affected by addition of a proton donor (1 × 10⁻²M phenol) or by carrying out the voltammetry in dry DMF in the presence of a water scavenger (alumina, Woelm grade I). For 1b, c, and 3 the peak appears to correspond to the process shown in Eq. [3]. For 1a

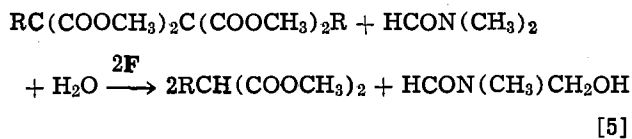




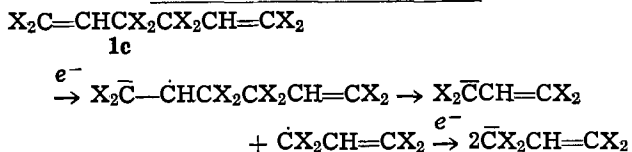
the peak height is approximately half the height observed for the other compounds. This is attributed to **1a** acting as a proton donor (in dry DMF), which should lead to approximately equal quantities of the dimeric and monomeric carbanions because of the comparable acidities of the two carbon acids. This leads to the stoichiometry shown in Eq. [4]. As expected, addition of a proton donor (diethylmalonate) approximately doubles the height of this peak.

The observed reduction potential (-1.37V) for **1c** is clearly remote from those of the other compounds examined but is close to that of **2c** (-1.54V). For the reduction of **1c** it is suggested that initial electron transfer to one of the double bonds occurs and is followed by cleavage and a second electron transfer to the radical species formed (Scheme 1). Similar cleavage following a remote electron transfer has been suggested in the Birch reduction of some strained bibenzyl derivatives (15). For the reduction of **1a**, **1b**, and **3**, remote electron transfer to a carbonyl group (Scheme 3) may occur. Other observed ester reductions may be rationalized in these terms, e.g., the reduction of propanedioate esters to the corresponding carbanions (6, 16) as shown in Scheme 4, or the cleavage of esters of benzyl alcohols (17). Additionally, these mechanisms are similar to that suggested for the cathodic reduction of cyclohexane-1,4-dione to hexane-2,5-dione (18).

In the undivided cell, the carbanions formed in the cathodic processes (Eq. [3], Schemes 1, 2, and 3) are neutralized by anodically generated (Eq. [2]) protons. In the case of **1a**, it is easily seen that this will also result in a net two-electron reaction, even though the cathodic process (Eq. [4]) involves only one electron per mole of substrate. The net cell reaction for compounds **1** is then as shown in Eq. [5] and a similar equation may be written for the cyclic compounds **3**.

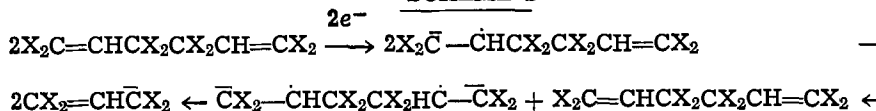


SCHEME 1 (X = COOCH₃)

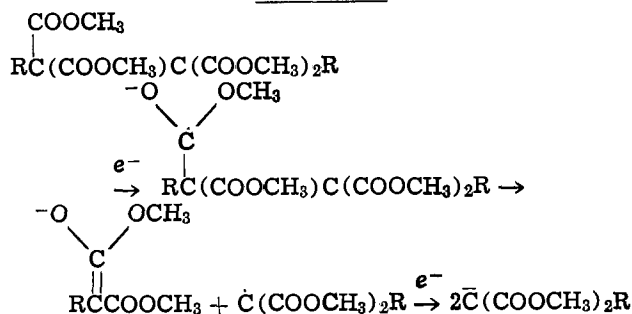


Another possible reaction pathway is the disproportionation (19) of the initially formed anion-radical of **1c** to form the dianion of **1c** which could cleave to give the observed product (Scheme 2). A similar scheme can be written for the reduction of **1a**, **1b**, and **3**.

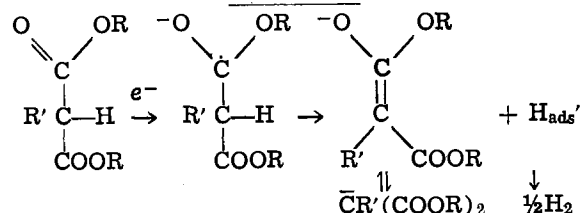
SCHEME 2



SCHEME 3



SCHEME 4



REFERENCES

1. M. Fleischmann, G. Mengoli, and D. Pletcher, *J. Electroanal. Chem. Interfacial Electrochem.*, **43**, 308 (1973).
2. M.-A. Michel, G. Mousset, and J. Simonet, *Electrochim. Acta*, **20**, 143 (1975).
3. B. F. Becker and H. P. Fritz, *Liebigs Ann. Chem.*, 1015 (1976).
4. V. G. Mairanovskii and A. N. Ponomarev, *J. Gen. Chem. USSR*, **47**, 2137 (1976).
5. E. Bertele, H. Boos, J. D. Dunitz, F. Elsinger, A. Eschenmoser, I. Felner, H. P. Gribl, H. G. Schwend, E. F. Meyer, M. Pesaro, and R. Scheffold, *Angew. Chem.*, **76**, 393 (1964).
6. D. A. White, *This Journal*, **124**, 1177 (1977).
7. C. K. Ingold, M. K. Parekh, and C. W. Shoppee, *J. Chem. Soc.*, 142 (1936).
8. C. W. Shoppee and N. W. Hughes, *J. Chem. Soc. (c)*, 3673 (1971).
9. M. Guthzeit and M. Lobeck, *J. Prakt. Chem.*, **185**, 43 (1908).
10. C. S. Marvel and R. D. Vest, *J. Am. Chem. Soc.*, **81**, 984 (1959).
11. J. D. Littlehales and B. J. Woodhall, *Disc. Faraday Soc.*, **45**, 187 (1968).
12. L. Birkhofer and H. Dickopp, *Chem. Ber.*, **101**, 3579 (1968).
13. S. D. Ross, M. Finkelstein, and R. C. Peterson, *J. Am. Chem. Soc.*, **88**, 4657 (1966).
14. H. G. Thomas, M. Streukens, and R. Peek, *Tetrahedron Lett.*, 45 (1978).
15. P. H. Ruehle, T. K. Dobbs, L. L. Ansell, D. van der Helm, and E. J. Eisenbraun, *J. Org. Chem.*, **42**, 1098 (1977).
16. N. Negishi and R. Osa, Japan Kokai, 74,124,011; *Chem. Abstr.*, **83**, 199499 (1975).
17. R. E. Erickson and C. M. Fisher, *J. Org. Chem.*, **35**, 1604 (1970).
18. E. Kariv and B. J. Cohen, *J. Chem. Soc. Perkin II*, 509 (1972).
19. M. Szwark, *Acc. Chem. Res.*, **5**, 169 (1972).

Selective Electrosyntheses on Chemically Modified Electrodes

III. Regio-Selective Anodic Chlorination of Some Benzene Derivatives with a Cyclodextrin Chemically Modified Electrode

Tomokazu Matsue, Masamichi Fujihira, and Tetsuo Osa*

Pharmaceutical Institute, Tohoku University, Aobayama, Sendai 980, Japan

ABSTRACT

The regio-selective anodic chlorination of some benzene derivatives with an α -cyclodextrin (α -CD) chemically modified graphite electrode via "ester bonding" (α -CD-CME) and with an α -CD adsorbed graphite (α -CD-AE) was studied. In the C 1s ESCA spectrum of the α -CD-CME, a small peak which is considered to be based on carbon atoms in α -CD appeared at a higher binding energy side of the main peak, indicating that α -CD can be immobilized on the electrode surface. The immobilized α -CD as well as the adsorbed α -CD had a pronounced effect on the *para*-position selective chlorination of anisole and toluene, but such an effect could not be observed in the chlorination of chlorobenzene. Increasing the conversion of a substrate resulted in a decrease in the ratio of *para*- to *ortho*-chlorination product, *p/o* ratio, since the products have an inhibition effect on the inclusion of the substrate in α -CD's cavity. Although the homogeneous chlorination by NaOCl in the presence of α -CD in solution also showed a relatively high *p/o* ratio, it revealed that the ratio observed in the electrochemical method was slightly higher than that observed in the homogeneous method. The α -CD-CME used repeatedly showed relatively high regio-selectivity even after a month of immersion of the electrode in water, whereas the α -CD-AE showed decrease of the *p/o* ratio with increasing immersion time.

With the progress of chemical modification of adsorbents for chromatography, new means for alteration of electrode surface have been devised. Miller and his co-workers put a chiral field at an electrode surface by immobilizing optically active compounds to use for asymmetric electrolyses (1-3). However, the optical yields in their works were not high. To realize a high selective electrosynthesis with a chemically modified electrode (CME), not only a strong interaction with a substrate but also a sufficient stability toward redox reactions are the requirements for modified species. Among the compounds meeting such requirements are cyclodextrins (CD's). These molecules are cyclic 1,4-linked D-glucopyranose oligomers containing several glucose units and have the shape of hollow truncated cones. One of the most remarkable properties of the compounds is the ability to include a variety of organic compounds of appropriate size in their hydrophobic interiors (4) and, in some cases, to catalyze a reaction of guest molecule with the assistance of secondary hydroxyl group at the rim of the cavities (5). Because of their enzyme-like behaviors, the CD's have received a great deal of attention. Taking advantage of the specific environment of the cavity of α -CD (containing 6 glucose units), we carried out the regio-selective anodic chlorination of anisole with α -CD bound on a graphite electrode surface and present in solution (6, 7). From the results by Breslow *et al.* (8), the anodic chlorination with the α -CD chemically modified graphite electrode (α -CD-CME) would proceed via selective donation of chlorine from one of the C-3 hydroxyl groups of α -CD to *para*-position of an aromatic ring as shown in Scheme 1. In our previous paper (7), a high regio-selectivity was observed in the anodic chlorination of anisole when α -CD was in solution; however, the α -CD-CME via "ether linkage" showed only a slight selectivity. This low regio-selectivity on the α -CD-CME via "ether linkage" might be attributed to the low surface concentration of α -CD at the electrode surface by ESCA analysis. In order to enhance the sur-

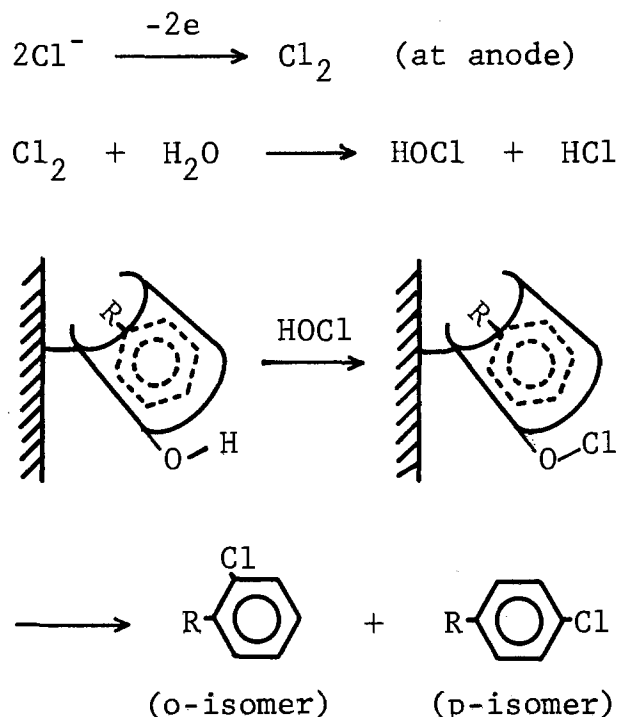
face concentration of α -CD, an alternative method for the modification of a graphite surface with α -CD via "ester linkage" was planned. This paper describes the selective chlorination of anisole, toluene, and chlorobenzene with the α -CD-CME via "ester linkage" including the results in the previous communication (6) in detail together with the stability of the α -CD-CME toward repetition of electrolyses.

Experimental

A polycrystalline graphite plate was obtained from Tokai Carbon Company (G 2080) and cut into $30 \times 20 \times 2$ mm plates for electrolyses and $17 \times 5 \times 2$ mm plates for ESCA measurements. All electrolyses were carried out using a Yanaco VE-8 controlled potential electrolyzer. The electrolysis cell was a divided H-type with a graphite anode ($30 \times 20 \times 2$ mm), a platinum gauze cathode, and a saturated calomel electrode (SCE) as the reference electrode inserted near the anode. The anolyte consisted of 1.0×10^{-3} M substrate (anisole, toluene, and chlorobenzene) and 5.0×10^{-1} M NaCl or HCl as the supporting electrolyte dissolved in 50 ml of distilled water (nonbuffered), and was stirred with a magnetic bar. The cell was kept at a constant temperature by thermostatic control. After the electrolysis, the anolyte was extracted with ether three times. The extracted ethereal solution was dried with Na_2SO_4 and concentrated under a reduced pressure for gas chromatography. Gas chromatographic analyses were carried out by using a Shimadzu gas chromatograph Model GC-6A equipped with a flame ionization detector. Nitrogen was used as the carrier gas. The column used for the analyses of the reaction products in the chlorinations of anisole and chlorobenzene was $2\text{m} \times 3\text{mm}\phi$ SUS packed with 10% Carbowax 20M on Chromosorb W. For the analysis in the toluene chlorination, a $2\text{m} \times 3\text{mm}\phi$ SUS column packed with 10% 4,4'-azoxydianisole on Uniport B was used. Quantitative analyses of the chlorination products formed in the electrolyses were carried out by comparison with a calibration line of authentic samples. The ratio of *p*- to *o*-isomer (*p/o* ratio), the conversion of substrate, and the yield of monochlorides of all products were deter-

* Electrochemical Society Active Member.

Key words: chemically modified electrode, α -cyclodextrin, anodic chlorination, regio-selective.



Scheme 1. A mechanism of the regio-selective anodic chlorination with the α -CD-CME.

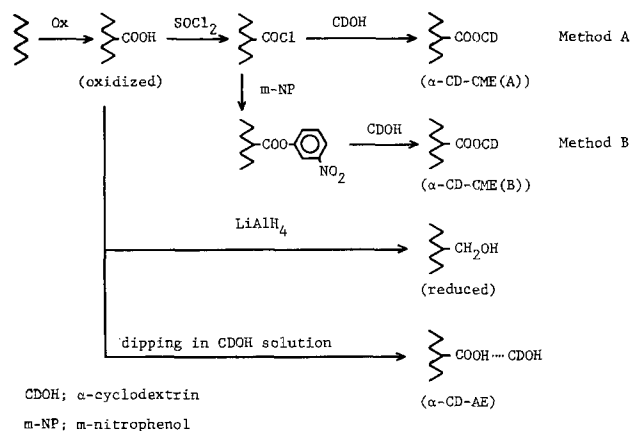
mined by using these gas chromatographic data. The homogeneous chlorination was also carried out. In this reaction, a specific amount of NaOCl was added to aqueous $1.0 \times 10^{-1}\text{M}$ HCl solution containing a substrate ($1.0 \times 10^{-3}\text{M}$), and the solution was stirred with a magnetic bar for 1 min. After the reaction the solution was extracted with ether, and was analyzed with the same gas chromatographic method as described above.

An AEI Model ES-200 was used for ESCA measurements with an Mg anode under a vacuum of 10^{-8} – 10^{-9} Torr. The binding energies were computed and corrected for charging effect by referencing to the 285 eV C 1s peak and the 532 eV O 1s peak (9, 10).

The dissociation constants of α -CD complexes were determined by the spectrophotometric method (11).

Synthetic procedure for α -CD-CME.—The graphite plates were first dipped in water for 2 hr to remove water soluble impurities from the electrode surfaces, treated with a solution of 0.2M $\text{K}_2\text{Cr}_2\text{O}_7$ in concentrated H_2SO_4 for 2 hr to introduce the surface functional groups containing oxygen, and then thoroughly washed with water and dried. The carboxyl groups thus introduced on the oxidized graphite were converted to chlorocarbonyl groups by refluxing in SOCl_2 . After 1 day's treatment, the electrode was removed from the solution and then washed with dry benzene repeatedly. The graphite plate thus obtained was rapidly dipped in an α -CD saturated dry pyridine and dimethylformamide solution. The solution was refluxed 1 day followed by standing at room temperature for a week. After the reaction, the α -CD-CME was taken out of the solution and washed with water (method A in Scheme 2).

In order to compare the regio-selective ability of the α -CD-CME with that of a physically adsorbed α -CD graphite electrode (α -CD-AE), the α -CD-AE was prepared by dipping in aqueous $1.0 \times 10^{-1}\text{M}$ α -CD solution for 1 day. A reduced graphite electrode was prepared by reducing the oxidized graphite with LiAlH_4 (12) in tetrahydrofuran for 2 days. To obtain the ESCA spectrum of α -CD, the α -CD on silicon chip was also prepared by dropping the aqueous α -CD solution on the chip followed by drying.



Scheme 2. Synthetic procedures of various surface derivatizations

The α -CD-CME's were also prepared by the ester-exchange reaction between the *m*-nitrophenol modified graphite and α -CD (method B in Scheme 2), and by the direct condensation between the oxidized graphite and α -CD using dicyclohexylcarbodiimide, but these α -CD-CME's did not show good results. Therefore, the following discussion is concentrated on the α -CD-CME obtained via method A.

Results and Discussion

ESCA results.—Figure 1 shows wide ESCA spectra of the oxidized graphite, the reduced graphite, the α -CD-CME, and α -CD on a silicon chip. There are strong peaks of O 1s at 532 eV and C 1s at 285 eV on the oxidized graphite, which are almost the same as those obtained for glassy carbon baked in air (13). No peak either for Cr or for K from $\text{K}_2\text{Cr}_2\text{O}_7$ appears. In the ESCA spectra of other types of graphites, no peaks, except O 1s and C 1s, were observed. Higher resolution ESCA spectra of O 1s on the above three types of electrodes and the α -CD on silicon chip are shown in Fig. 2. The relative peak height of O 1s on the reduced graphite was lower than that on the oxidized one, indicating that some amount of oxygen atoms on the

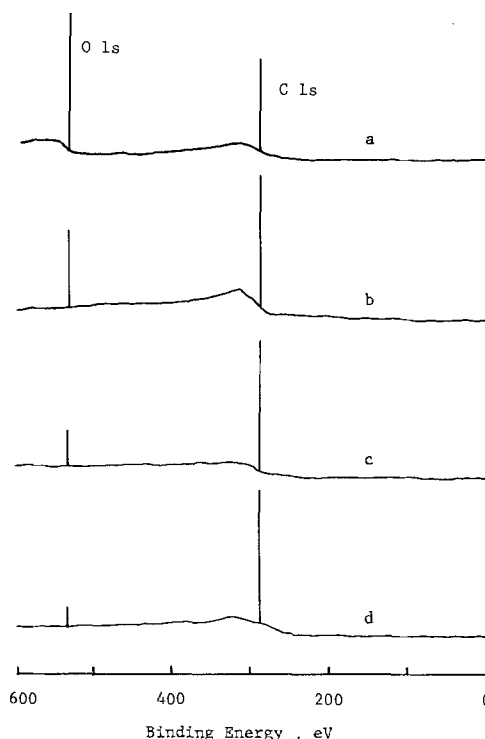


Fig. 1. ESCA spectra of the α -CD on silicon chip (a), the α -CD-CME(A) (b), the oxidized (c), and the reduced (d) graphite electrodes.

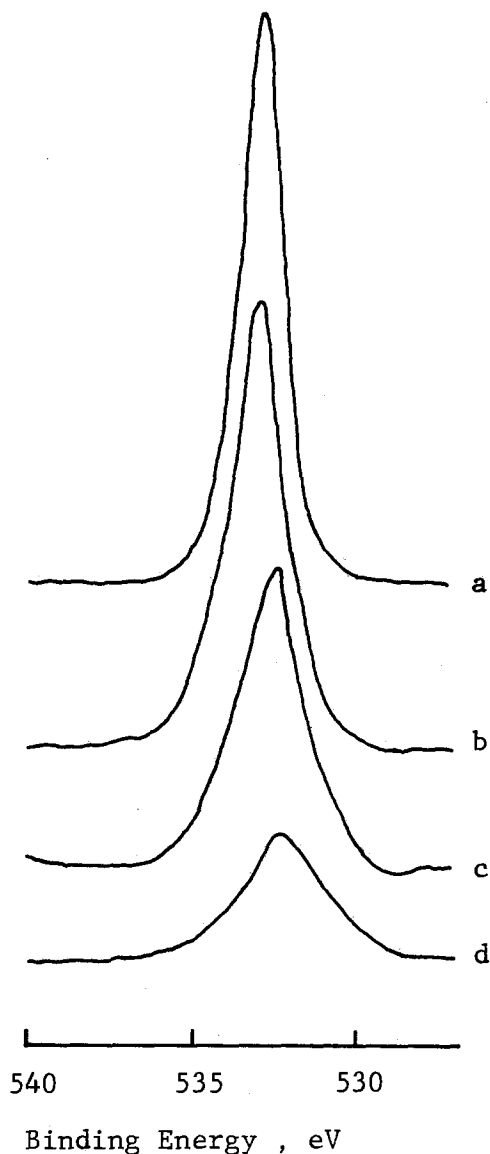


Fig. 2. O 1s ESCA spectra of the α -CD on silicon chip (a), the α -CD-CME(A) (b), the oxidized (c), and the reduced (d) graphite electrodes.

oxidized graphite was removed by the reduction with LiAlH_4 . On the other hand, the intensity of the peak was increased by the chemical modification of the oxidized graphite with α -CD. The enhancement in the peak in the spectrum of the α -CD-CME is attributed to the oxygen atoms in the α -CD molecule immobilized on the electrode surface. This is reinforced by the results of the wide ESCA spectrum of the α -CD on silicon chip as shown in Fig. 1, i.e., the O 1s peak is large compared with the C 1s peak. A slight shift of the O 1s peak on the α -CD-CME toward a higher binding energy side was also observed. It is, however, difficult to assign the chemical shift since the shift was too small; furthermore, various types of oxygen atoms, including contamination, exist on the graphite surfaces. The changes in higher resolution ESCA spectra of C 1s for the same kind of samples used in O 1s ESCA measurements are shown in Fig. 3. By performing chemical modification of α -CD on the oxidized graphite surface via method A, a small peak appeared at a higher binding energy side (ca. 287 eV) of the main peak at 285 eV. The peak at ca. 287 eV could not be observed in the spectra of the oxidized and the reduced graphites. The small peak may be attributed to the carbon atoms in α -CD immobilized on the graphite surface, since, in the C 1s ESCA spectrum of the α -CD on silicon chip, the main peak appeared at the same binding energy. This

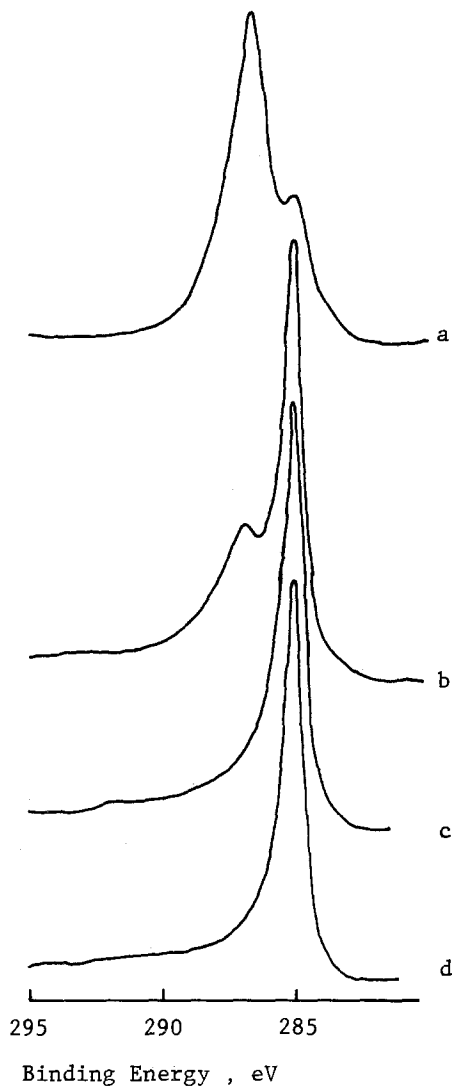


Fig. 3. C 1s ESCA spectra of the α -CD on silicon chip (a), the α -CD-CME(A) (b), the oxidized (c), and the reduced (d) graphite electrodes.

chemical shift in the C 1s peak is accounted for by considering the charge (14) on every carbon atom in α -CD molecule which adjoins oxygen atoms of high electronegativity. In comparison of the present results with the previous one on α -CD-CME (via ether bonding) (7), α -CD can be more easily introduced by the ester linkage than by the ether linkage because the peak at 287 eV was observed as only a small shoulder in the C 1s ESCA spectrum of the α -CD-CME (via ether bonding). The α -CD-CME's prepared by the ester-exchange reaction and by the direct condensation showed no peak at 287 eV in the C 1s ESCA spectra.

Chlorination of anisole.—The anodic chlorination of anisole using various types of electrodes was carried out at a constant potential. Excellent yields of monochloroanisoles were observed for all cases. The current efficiencies of the electrolyses were within a range of 40-60%, and the values were almost independent of the surface derivatizations. Although most of the reaction products at low conversion of anisole were monochloroanisole isomers, the yield of *m*-isomer was only a trace amount. The results in the absence and presence of α -CD in solution are summarized in Table I. The *p/o* ratio on the oxidized graphite in the present study was slightly higher than that observed in the previous one (7). This might be attributed to the difference in the surface properties of the graphite plate used. The electrode potential seemed to have some influence on the *p/o* ratio. The ratio on the reduced graphite electrode was higher than that on the oxidized

Table I. The anodic chlorination of anisole in the absence and presence of α -CD in solution^a

| Run | [α -CD] $\times 10^2$ (M) | Conver- sion (%) | p/o ^b | Yield of monochlo- rides (%) ^c | Re- mark |
|-----|---|---------------------|------------------|---|-------------|
| 1 | 0 | 4.1 | 4.2 | 83 | d |
| 2 | 0 | 0.9 | 3.5 | 84 | e |
| 3 | 0 | 3.4 | 2.8 | | |
| 4 | 1.0 | 4.8 | 27 | 89 | |
| 5 | 1.0 | 13 | 20 | 80 | f |

^a Standard electrolytic condition was the following except as indicated in the column of remarks: electrode, oxidized graphite; electrode potential, 1.20V vs. SCE; electrolyte, 0.5M NaCl; temp., 20°C.

^b Ratio of p- to o-isomer formed in the electrolysis.

^c Yield of monochlorides out of all products.

^d Electrode, reduced graphite; electrode potential, 1.10V vs. SCE.

^e Electrode potential, 1.10V vs. SCE.

^f Electrolyte, 0.5M HCl.

one; however, the ratio decreased with repetition of electrolyses owing to the oxidation of electrode surface. The addition of α -CD to the solution made the p/o ratio become high. This indicates that p-isomer was formed with considerably high selectivity in the presence of α -CD in solution, because the o-position of anisole is blocked by the inner wall of α -CD (6, 7, 15). Nevertheless only 54% of anisole was included in α -CD in bulk solution [as the dissociation constants for α -CD-anisole and α -CD-Cl⁻ complexes are 3.75×10^{-3} M (8) and 3.9×10^{-1} M (16), respectively], high selectivity was observed in the presence of α -CD in solution. This is mainly due to the fact that the chlorination rate of the included substrate is rapid compared with that of the free substrate (8). Another probable cause for this observation is higher concentration of α -CD at the electrode surface due to adsorption compared with that in bulk solution.

The homogeneous chlorination of anisole by NaOCl in an acidic medium proceeded very fast. Table II shows the results. The p/o ratio in this chlorination in the absence of CD showed lower values than those observed in the anodic chlorination. By the addition of α -CD to the reaction solution, the ratio was increased. However, the ratio was not high as that observed in the anodic chlorination in the presence of α -CD in solution. In the anodic chlorination, the concentration of α -CD at the electrode surface may be higher than that in bulk solution, so that p-position chlorination proceeds effectively at the electrode since α -CD can promote the chlorination of the included anisole (8). Increasing the concentration of NaOCl in solution in the homogeneous reaction resulted in a decrease in the yield of monochlorides accompanied by an increase in the yields of di- and trichlorides.

The results of the anodic chlorination of anisole with the α -CD-CME and the α -CD-AE are summarized in Table III. By performing chemical modification and adsorption of α -CD on the oxidized graphite surfaces, the p/o ratio increased. In particular, in the case of the α -CD-AE, the ratio exceeded 25, which indicates that the p-isomer was formed in more than 96%. The α -CD-CME also showed a high p/o ratio of 18 at 1.10V vs.

Table II. The homogeneous chlorination of anisole at room temperature

| Run | [NaOCl] $\times 10^2$ (M) | Conver- sion (%) | p/o | Yield of monochlo- rides (%) | Yield of dichlo- rides (%) | Yield of trichlo- rides (%) |
|----------------|---------------------------------|---------------------|-----|------------------------------------|----------------------------------|-----------------------------------|
| 1 | 0.5 | 28 | 1.7 | 93 | 6 | |
| 2 | 1.0 | 55 | 1.8 | 92 | 7 | |
| 3 ^a | 1.0 | 60 | 6.7 | 93 | 6 | |
| 4 | 5.0 | 99 | 4.7 | 2 | 97 | |
| 5 | 50 | 100 | | | 57 | 31 |

^a Result in the presence of α -CD in solution.

Table III. The anodic chlorination with the α -CD-CME and with the α -CD-AE^a

| Run | Anode | Conver- sion (%) | p/o | Yield of monochlo- rides (%) | Remark |
|-----|------------------|---------------------|-----|------------------------------------|--------|
| 1 | α -CD-AE | 1.0 | 25 | 84 | b |
| 2 | α -CD-CME | 2.1 | 18 | 83 | c |
| 3 | α -CD-CME | 3.2 | 10 | 84 | d |
| 4 | α -CD-CME | 2.9 | 6.3 | 87 | |
| 5 | α -CD-CME | 10 | 5.7 | 86 | |
| 6 | α -CD-CME | 61 | 2.7 | | |
| 7 | α -CD-CME | 1.7 | 10 | | e |
| 8 | α -CD-CME | 5.3 | 5.3 | 86 | f |
| 9 | α -CD-CME | 0.4 | 4.3 | 85 | g |
| 10 | α -CD-AE | 0.5 | 3.7 | 82 | h |

^a Standard electrolytic condition was the following except as indicated in the column of remarks: electrode potential, 1.20V vs. SCE; electrolyte, 0.5M NaCl; temp., 20°C.

^b Electrode potential, 1.10V vs. SCE.

^c Result before thoroughly washing with water; electrode potential, 1.10V vs. SCE.

^d From this result, the turnover number of the immobilized α -CD may be $>10^3$. In order to obtain the turnover number, the surface concentration of immobilized α -CD was determined by the capacitance measurement of the α -CD-CME since the other methods such as cyclic voltammetry and ESCA were not suitable for the α -CD-CME. Although the method is not accurate enough, the surface concentration of α -CD was roughly estimated to be 10^{-10} - 10^{-11} mol/cm². The turnover number was obtained on the assumption that the difference in the p/o ratio on the oxidized graphite and on the α -CD-CME was attributable to the immobilized α -CD on the α -CD-CME.

^e Temp., 5°C.

^f Electrolyte, 0.5M HCl.

^g Results after the treatment by $K_2Cr_2O_7$ for 2 hr.

SCE. However, the ratio seems to contain the contribution of adsorbed α -CD on the α -CD-CME. The p/o ratio on the α -CD-CME became 10 by dipping the electrode in water for several days. Consequently, the difference in the p/o ratio observed before and after the immersion would be due to desorption of the adsorbed α -CD on the α -CD-CME. The electrode potential has an influence on the p/o ratio. The ratio on the α -CD-CME at 1.20V vs. SCE was lower than that observed at 1.10V vs. SCE. At high electrode potential, the relative contribution of the chlorination of free anisole becomes large compared with that of included anisole in α -CD's cavity, since the concentration of HOCl at the electrode surface becomes high. Accordingly, the ratio is considered to be low at high potentials. Increasing the conversion of anisole resulted in a decrease in the p/o ratio. This decrease in the ratio is interpreted as due to the inhibition effect of chloroanisoles on the inclusion of substrate in the cavity of α -CD. The dissociation constants for α -CD-p-chloroanisole and α -CD-o-chloroanisole complexes are 3.3×10^{-4} M and 2.6×10^{-3} M, respectively. These values are sufficiently small compared with that for α -CD-anisole complex (3.75×10^{-3} M).

Inhibition is more pronounced with p-chloroanisole. At the initial stage of the electrolysis, the concentration of the monochlorides in the vicinity of the electrode surface is low, so that the inhibition effect is small. After a long electrolysis, the effect becomes large due to the increase of the concentration of monochlorides at the electrode surface. The temperature during the electrolysis also affected the regio-selectivity. When the electrolysis was carried out at 5°C, the p/o ratio was observed to be 10 which was higher than the 6.3 value observed at 20°C. This phenomenon must be a reflection of the thermodynamic nature of α -CD complex in which CD includes substrate(s) more easily at low temperature (13). The dependence of the ratio on the temperature was also observed in the anodic chlorination of anisole in the presence of β -CD in solution (7). The p/o ratio on the α -CD-CME using HCl as the supporting electrolyte did not show a large discrepancy with that using NaCl. When the α -CD-CME and the α -CD-AE were treated with $K_2Cr_2O_7$ for 2 hr, the ratios decreased to 3.7 and 4.3, respectively, owing to the elimination of α -CD on the electrode surfaces by the oxidative degradation.

Chlorination of toluene.—The anodic chlorination of toluene also resulted in the formation of chlorotoluene isomers. Benzyl chloride formed by the side-chain chlorination could not be detected. The results are summarized in Table IV. In this chlorination, the *p/o* ratio on the oxidized graphite electrode at low conversion showed *ca.* 0.5 which is almost a statistical ratio of *p-* to *o-* positions. This tendency was also observed in the homogeneous chlorination of toluene by NaOCl in an acidic medium. From these results, it seems that there is nearly no difference in the reactivity between *o-* and *p-* positions of toluene toward the chlorination by HOCl. The *p/o* ratio on the oxidized graphite became large with the addition of α -CD to the solution. However, the ratio in this case was not as high as that observed in the anodic chlorination of anisole in the presence of α -CD in solution. As the dissociation constant of α -CD-toluene complex is *ca.* 3×10^{-3} M, there is no significant difference in the values between α -CD-toluene and α -CD-anisole complexes. However, the ability of α -CD to the regio-selectivity was greatly different between both compounds. The difference between *p-* position of toluene and the catalytic site of α -CD, C-3 hydroxyl group, may be long compared with α -CD-anisole complex. The anodic chlorination in the presence of α -CD in solution showed a higher selectivity than the homogeneous one. With the α -CD-CME, the *p/o* ratio became large compared with that observed before the modification, although the ratio was not as high as that observed in the presence of α -CD in solution. The ratio was gradually decreased with increasing the conversion of toluene due to the inhibition effect of chlorotoluenes. High yields of monochlorides were observed in this reaction, and current efficiencies of the electrolyses ranged from 40 to 60%. No significant difference in the yields and the current efficiencies was observed among three conditions, *i.e.*, in the absence of CD, in the presence of α -CD in solution, and in the presence of immobilized α -CD on the electrode surface.

Chlorination of chlorobenzene.—The results of the anodic chlorination of chlorobenzene, together with those of the homogeneous chlorination, are summarized in Table V. The *p/o* ratio observed on the oxidized graphite electrode became large by the addition of α -CD to the solution. However, the increase in the ratio by the addition of α -CD in this case was not large compared with the trends observed in the anodic chlorination of anisole and toluene. This is mainly caused by the low complex formation of chlorobenzene with α -CD since the dissociation constant for α -CD-chlorobenzene complex is *ca.* 1×10^{-2} M which is *ca.* three times larger than those for α -CD-anisole and α -CD-toluene complexes. The current efficiencies in these cases were only 1-2%, and the conversions of chlorobenzene in the homogeneous chlorination were less than 4%, even in the same reaction time as the chlorinations of anisole and toluene. From these results, the chlorination rate for chlorobenzene by HOCl seems to be very slow. This is also considered to be one of the reasons for this low regio-selectivity. The *p/o* ratio on the α -CD-

Table IV. The anodic chlorination of toluene

| Run | Anode | Conversion (%) | <i>p/o</i> | Yield of monochlorides (%) |
|------------------------------|------------------|----------------|------------|----------------------------|
| 1 | Oxidized | 5.2 | 0.53 | |
| 2 | Oxidized | 24 | 0.46 | 90 |
| 3 | Oxidized | 56 | 0.42 | |
| 4 ^a | Oxidized | 4.3 | 2.2 | |
| 5 | α -CD-CME | 4.3 | 0.81 | |
| 6 | α -CD-CME | 18 | 0.55 | 94 |
| 7 | α -CD-CME | 30 | 0.48 | 95 |
| cf. homogeneous chlorination | | | | |
| 8 | — | 58 | 0.47 | 95 |
| 9 ^a | — | 53 | 1.1 | 95 |

^a Results in the presence of 1.0×10^{-2} M α -CD in solution.

Table V. The anodic chlorination of chlorobenzene

| Run | Anode | Conversion (%) | <i>p/o</i> | Yield of monochlorides (%) |
|------------------------------|------------------|----------------|------------|----------------------------|
| 1 | Oxidized | 3.0 | 1.8 | 95 |
| 2 ^a | Oxidized | 2.2 | 2.3 | 90 |
| 3 | α -CD-CME | 3.7 | 1.9 | 95 |
| cf. homogeneous chlorination | | | | |
| 4 | — | 3.7 | 1.8 | 95 |
| 5 ^a | — | 0.8 | 2.3 | 95 |

^a Results in the presence of 1.0×10^{-2} M α -CD in solution.

CME(A) was almost equal to that observed on the oxidized graphite, indicating that immobilized α -CD on the electrode surface had very little contribution to the regio-selectivity. Because of the low chlorination rate, the chlorination would proceed in bulk solution in this case, so that α -CD on the electrode surface could not affect the chlorination position of chlorobenzene.

Stability of the α -CD-CME(A).—Finally, we examined the stability of the α -CD-CME(A) toward repetition of electrolyses. The results of occasional anodic chlorination of anisole with the α -CD-CME and the α -CD-AE, both dipped in distilled water, are shown in Fig. 4. The α -CD-AE showed a high regio-selectivity at the initial stage of the immersion, but the *p/o* ratio gradually fell with increasing immersion time. After 17 days, the ratio on the α -CD-AE reached below 6 because of the desorption of the α -CD from the electrode surface. On the other hand, the adsorbed α -CD on the reduced graphite was removed with ease by washing with water (7). The difference in these phenomena observed on the oxidized and the reduced graphites may imply that there is a specific interaction, although unknown, between the adsorbed α -CD and functional groups on the oxidized graphite surface. The ratio on the α -CD-CME was also decreased within a few days to *ca.* 10, owing to the desorption of the adsorbed α -CD on the electrode surface, but the value, *ca.* 10, was maintained even after a month of immersion in water. These results indicate that the ester linkage on the α -CD-CME was considered to be relatively stable, although the α -CD on the α -CD-CME was removed by treatment with a strong oxidant such as $K_2Cr_2O_7$. The α -CD-CME had an advantage from a viewpoint of stability over the α -CD-AE (although the former was inferior to the latter in the regio-selectivity at the initial stage).

Conclusions

The α -CD-CME (via ester bonding) as well as the α -CD-AE showed regio-selectivities in the anodic chlorinations of anisole and toluene. However, the regio-selectivity observed in the chlorination of toluene with the α -CD-CME was lower than that observed in the chlorination of anisole, although the binding

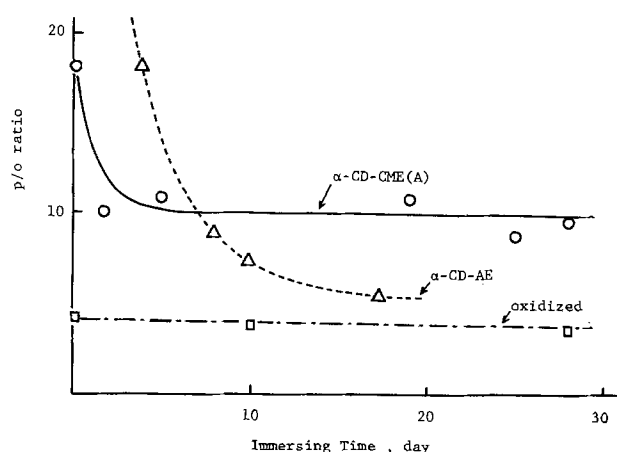


Fig. 4. Time dependence of *p/o* ratios of chloroanisole isomers

abilities of α -CD for both substrates are almost equal. This indicates that the distance between the *p*-position of toluene included in α -CD and the catalytic site of α -CD, C-3 hydroxyl group, may be longer than that in the α -CD-anisole complex. In the chlorination of chlorobenzene the regio-selectivity on the α -CD-CME could not be observed, probably due to the slow chlorination rate. The aromatic substrate substituted by an electron-donating group is necessary to attain a certain regio-selectivity in this reaction. The regio-selectivity in the anodic chlorination with the α -CD-CME may be also affected by the orientation of immobilized α -CD on the electrode surface as well as by the surface concentration of α -CD. It is, however, difficult to determine the number of ester linkage between the oxidized electrode surface and one α -CD molecule and which of the hydroxyl group in α -CD, primary or secondary hydroxyl group, is bound to the electrode surface. The α -CD-CME revealed to have considerable stability toward repetition of the anodic chlorination.

Acknowledgment

This work was partially supported by a Grant-in-Aid for Scientific Research from the Ministry of Education (No. 247072).

Manuscript submitted July 23, 1980; revised manuscript received Oct. 14, 1980.

Any discussion of this paper will appear in a Discussion Section to be published in the June 1982 JOURNAL. All discussions for the June 1982 Discussion Section should be submitted by Feb. 1, 1982.

Publication costs of this article were assisted by Tohoku University.

REFERENCES

1. B. F. Watkins, J. R. Behling, E. Kariv, and L. L. Miller, *J. Am. Chem. Soc.*, **97**, 3549 (1975).
2. B. E. Firth, L. L. Miller, M. Mitani, T. Rogers, J. Lennox, and R. W. Murray, *ibid.*, **98**, 8271 (1976).
3. B. E. Firth and L. L. Miller, *ibid.*, **98**, 8272 (1976).
4. F. Cramer, *Naturwissenschaften*, **38**, 188 (1951); F. Cramer and F. A. Henglein, *Quat. Rev. (London)*, **68**, 649 (1958); F. Cramer and H. Hettle, *Naturwissenschaften*, **54**, 625 (1967).
5. F. Cramer and W. Kampe, *Tetrahedron Lett.*, **1962**, 353; N. Henrich and F. Cramer, *J. Am. Chem. Soc.*, **87**, 1121 (1965); F. Cramer and G. Mackensen, *Angew. Chem.*, **78**, 641 (1966); M. L. Bender, R. L. VanEtten, G. A. Clowes, and J. F. Sebastain, *J. Am. Chem. Soc.*, **88**, 2318 (1966); R. L. VanEtten, J. F. Sebastain, G. A. Clowes, and M. L. Bender, *ibid.*, **89**, 3242, 3253 (1967); D. E. Tutt and M. A. Schwartz, *Chem. Commun.*, **1970**, 113.
6. T. Matsue, M. Fujihira, and T. Osa, *This Journal*, **126**, 500 (1979).
7. T. Matsue, M. Fujihira, and T. Osa, *Bull. Chem. Soc. Jpn.*, **52**, 3692 (1979).
8. R. Breslow and P. Campbell, *J. Am. Chem. Soc.*, **91**, 3085 (1969); *Bioorg. Chem.*, **1**, 140 (1971); R. Breslow, H. Kohn, and B. Siegel, *Tetrahedron Lett.*, **1976**, 1645.
9. M. Fujihira, T. Matsue, and T. Osa, *Chem. Lett.*, **1976**, 875; *Electrochimica Acta*, **13**, 1679 (1977).
10. G. Johansson, J. Hedman, A. Berndtsson, M. Klas-son, and R. Nilsson, *J. Electron Spectrosc.*, **2**, 295 (1973).
11. F. Cramer, W. Saenger, and H.-Ch. Spatz, *J. Am. Chem. Soc.*, **89**, 14 (1967).
12. M. Fujihira and T. Osa, "Progress in Batteries and Solar Cells," Vol. 2, p. 244, JEC Press Inc., Cleveland, Ohio (1979).
13. M. Fujihira, A. Tamura, and T. Osa, *Chem. Lett.*, **1977**, 361.
14. K. Siegbahn *et al.*, "ESCA-Atomic, Molecular and Solid State Structure Studied by Means of Electron Spectroscopy," p. 137, Almquist and Wiksells, Uppsala (1967); K. Siegbahn, "ESCA—Applied to Free Molecule," p. 113, North-Holland Publishing Co., Amsterdam-London (1969).
15. T. Osa, T. Matsue, and M. Fujihira, *Heterocycles*, **6**, 1833 (1977).
16. R. P. Rohrbach, L. J. Rodriguez, E. M. Eyring, and J. F. Wojcik, *J. Phys. Chem.*, **81**, 944 (1977).

Theoretical Approach to the Resistive Behavior of Thin Solid Film Electrodes under Direct Current Polarization

R. I. Tucceri and D. Posadas¹

Instituto de Investigaciones Fisicoquímicas Teóricas y Aplicadas (INIFTA), Sucursal 4, Casilla de Correo 16, 1900 La Plata, Argentina

ABSTRACT

The problem of the potential distribution along a thin metal film electrode under d-c polarization is reconsidered assuming that the electrode process fits a Butler-Volmer current-potential relationship and that the potential within the electrode can be linearized. The solution of the potential distribution along the film is applied to develop the theory of the method of electrode resistivity measurement in the presence of a faradaic electrochemical process. The possibility of coupling between the faradaic and measuring currents within the electrode is taken into account. Under the assumption of not too high electrochemical currents, this coupling effect is found to be negligible. An equation is obtained from which it is possible to evaluate the resistivity of the film.

Thin film electrodes are receiving increasing attention since the advent of transparent electrodes (1)

and their application to the study of different electrochemical reactions (2, 3).

¹Present address: Case Laboratories for Electrochemical Research, Case Western Reserve University, Cleveland, Ohio 44106.
Key words: electrode resistivity, thin metal film electrode, electrode potential distribution.

It is well known that when the thickness of a metal film is smaller than the mean-free path of the conduction electrons inside the metal, its electronic con-

ductivity is diminished (4, 5). This thickness dependence of the conductivity can be accounted for in terms of the Fuchs-Sondheimer model (5). When ions or neutral molecules from a gaseous phase are adsorbed on such a thin film, the decrease in conductivity is enhanced (5). This phenomena has been applied to the study of the adsorptive behavior of molecules from gas phase (5) and, in recent years, it has also been applied to the study of adsorption of ions and molecules, and the electroadsorption of molecules and intermediates of electrochemical reactions (6-15). In this case one is mainly concerned with the conductivity changes produced as the potential difference at the metal solution interface is changed.

Two major phenomena are involved in the potential dependence of the resistivity change of a thin metal film electrode (11, 13). The first is associated with the change of the concentration of the electrical carriers (electrons) at the surface of the metal as the electrical state of the interphase is changed, giving way to the so-called field effects (5). These effects have been first observed experimentally by Anderson and Hansen (10) in an electrochemical system. Thus

$$\frac{\Delta\sigma}{\sigma} = \frac{\Delta q}{q} \quad [1]$$

where σ is the conductivity and q is the total charge per unit surface, of the carriers.

The second is due to the formation of the adsorptive bond that perturbs the electron velocity distribution in the film and thus changes the conductivity (5). It may also be considered, in terms of Sondheimer's-like models, by the formation of dispersion centers at the surface of the metal that changes the specularly parameter of the surface (16). In this case

$$\frac{\Delta\sigma}{\sigma} = \alpha \frac{\Delta n}{n} \quad [2]$$

where n is the coverage by the adsorbed species and α is a proportionality constant.

The change of resistivity can, in principle, provide information about: (i) changes of the electrical state of an ideally polarizable interface; (ii) changes of the amount of adsorbed species and/or changes of the nature of the adsorption bond; and (iii) information complementary to modulated spectroscopy since as is well known the real component of the complex conductivity is directly related to the imaginary part of the complex refractive index (17).

The experimental technique, which has already been applied to different electrochemical systems (6-14), measures the change of resistance along the length of the thin film electrode while applying d-c polarization at the midpoint of the film. For this purpose either a-c or d-c resistance bridges as well as d-c polarization methods have been used (6-10, 13, 14, 16, 18, 19) (see Fig. 1). From the experimental point of view two cases could be distinguished: (i) at the potential of adsorption the electrode behaves as an ideally polarizable interphase and (ii) faradaic current flows during the resistance measurement. The first case poses no special requirements on the resistance measurement. In the latter the faradaic current generates a p.d. at the extremes of the film which adds to that due to the resistance measuring device. Thus, when a faradaic current flows through the thin film-electrolyte interface, a potential drop along the thin film electrode is produced due to the thin film resistance. This causes a potential distribution which depends, in principle, on the current-potential relationship governing the electrochemical process. On the other hand, when the resistivity of the thin film is measured, an additional "measuring"

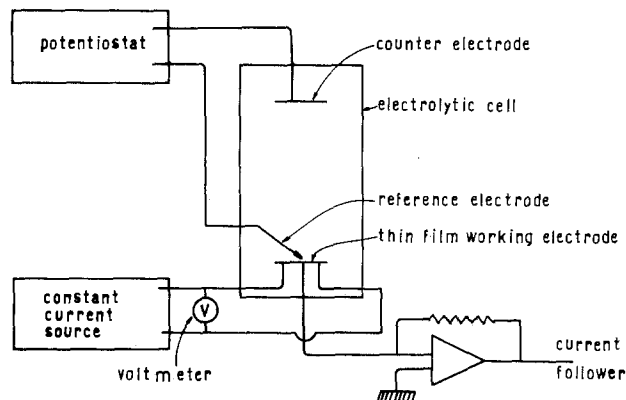


Fig. 1. Circuitry to measure the resistance of an electrode in the presence of faradaic current.

current is fed along the electrode which may couple with the faradaic current. In order to obtain the resistivity of the electrode, the polarization (faradaic) current contribution to the potential difference due to the measuring current must be negligible.

The potential distribution problem of a wire subject to a constant external current assuming a linear current potential relationship for the electrode process was considered by Harvey (20).

Conway *et al.* (21) have treated the potential distribution problem of a wire of length L assuming a Tafel relationship, i.e., high overpotentials, and that the p.d. within the electrode can be linearized. These authors did not consider the value of the current at the end of the wire ($x = L$) thus leaving the potential along the wire (partially) undetermined {see Eq. [10] and [12a] of Ref. (21)}. Further inconsistencies if $L = \infty$ were pointed out by Rangarajan, Dignam, and Conway (22). The latter extended the mentioned treatment to any value of the p.d. within the electrode under the assumption of equal anodic and cathodic Tafel slopes obtaining a formal solution in terms of Jacobi's elliptic functions. Thus, the solution must be calculated numerically for each particular case. Other approaches consider the electrode divided in discrete portions (18, 23). This allows one to handle more general current-potential relationships. Since this treatment leads to numerical solutions they will not be considered in the present work.

On the other hand, the theory of the resistance measurement was considered by Sutton and Dickinson (12) who obtained an equation for the p.d. at the extremes of a thin film electrode in the presence of a measuring current and assuming a linear current-potential relationship. However, their results are not physically sound since the p.d. between the ends of the film does not reduce to the simple Ohm's law in the absence of the faradaic process {see Eq. [1], Ref. (12)}.

This short analysis shows the convenience of re-considering both the potential distribution problem and the theory of electrode resistance measurements. Here we will consider an electrochemical reaction that fits a Butler-Volmer current-potential relationship. Mass transfer complications are assumed negligible. It will also be assumed that the p.d. within the thin film can be linearized, i.e., it is smaller than RT/eF . This assumption, as shown below, is well justified for thin film electrodes. The equations derived from the present treatment can be straightforwardly applied to the interpretation of the thin film electrode resistance measurements under d-c polarization.

The Potential Distribution Problem

Let us first consider a homogeneous and isotropic film on an inert substrate, of thickness h , width D ,

height l , and resistivity ρ . One of the film faces of area $s = Dl$, is exposed to the electrolytic solution. The bottom of the film (see Fig. 2) ($x = l$), which is in contact with the polarization (electrochemical) current, I_p , measuring device, is grounded. I_p results from the integration of i_x , the local current density at the point x over the whole surface area

$$I_p = \int_0^s i_x ds = D \int_0^l i_x dl \quad [3]$$

It is further assumed that the polarization current density is given by a Butler-Volmer relationship

$$i = i_0 \left[\exp \left(\frac{\alpha_a \eta F}{RT} \right) - \exp \left(- \frac{\alpha_c \eta F}{RT} \right) \right] \quad [4]$$

where i_0 is the exchange current density, α_a and α_c are the electrochemical transfer coefficients for the anodic and cathodic currents, respectively, η , is the overvoltage and F , R , and T have their usual meanings. The C.D. is positive for the anodic reaction and negative for the cathodic one.

Inside the film a positive current flows from points of higher to lower potential. However, for a positive current, the overpotential η_x at the point x is smaller by V_x , the potential difference from the point x to the bottom inside the film. V_x ($x = l$) is arbitrarily taken as zero. Thus, the overpotential at the point x can be written as

$$\eta_x = \eta_x(x=l) - V_x \quad [5]$$

Taking into account Eq. [5], the local current density can be written as follows

$$i_x = i_0 \left\{ \exp \left[\frac{\alpha_a (\eta - V_x) F}{RT} \right] - \exp \left[- \frac{\alpha_c (\eta - V_x) F}{RT} \right] \right\} \quad [6]$$

When V_x is sufficiently small, after expanding the corresponding exponential, Eq. [7] results

$$i_x = a - bV_x \quad [7]$$

where a is the current density (Eq. [4]) at $x = l$ ($V_x = 0$) and

$$b = \frac{i_0 F}{RT} \left[\alpha_a \exp \left(\frac{\alpha_a \eta F}{RT} \right) - \alpha_c \exp \left(- \frac{\alpha_c \eta F}{RT} \right) \right] \quad [8]$$

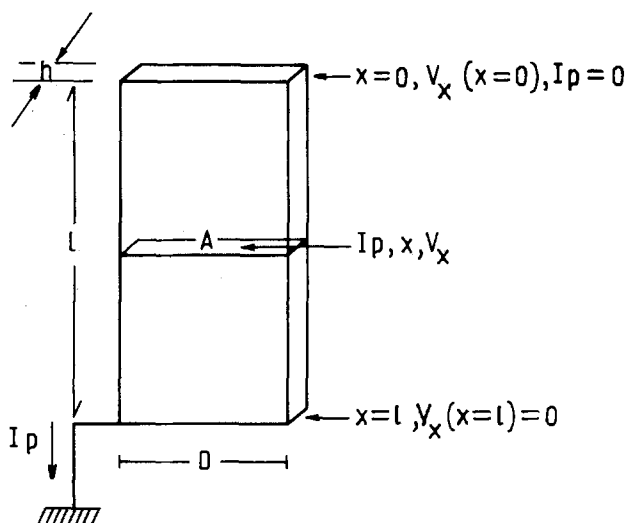


Fig. 2.

In the homogeneous thin film E_x , the field strength is proportional to J_x , the current density across the film

$$E = - \frac{dV_x}{dx} = J_x = \frac{I_{p,x}}{A} \quad [9]$$

where $A = Dh$ is the cross section of the film. $I_{p,x}$, the current at x can be written as

$$I_{p,x} = D \int_0^x i_x dx = D \int_0^x (a - bV_x) dx \quad [10]$$

because $I_p = 0$ at $x = 0$. Thus, after replacing [10] into [9], it follows that

$$\frac{d^2 V_x}{dx^2} = - \frac{\alpha^2 a}{b} + \alpha V_x \quad [11]$$

where

$$\alpha = \left(\frac{\rho D b}{A} \right)^{1/2} \quad [12]$$

The solution of Eq. [11] is of the type (12)

$$V_x = C_1 e^{\alpha x} + C_2 e^{-\alpha x} + \frac{a}{b} \quad [13]$$

The constants C_1 and C_2 can be evaluated with the boundary conditions²

$$\left(\frac{dV_x}{dx} \right)_{x=0} = 0 \quad [14]$$

and

$$V_x(x=l) = 0 \quad [15]$$

or

$$\left(\frac{dV_x}{dx} \right)_{x=l} = - \frac{\rho}{A} I_p \quad [16]$$

Conditions [14]-[16] are equivalent.

From the boundary conditions [14]-[16] it results

$$C_1 = C_2 = - \frac{a}{2b} \frac{1}{\cosh \alpha l} \quad [17]$$

When C_2 is replaced into Eq. [13] one obtains

$$V_x = \frac{a}{b} \left(1 - \frac{\cosh \alpha x}{\cosh \alpha l} \right) \quad [18]$$

and the potential at $x = 0$ is

$$V_x(x=0) = \frac{a}{b} \left(1 - \frac{1}{\cosh \alpha l} \right) \quad [19]$$

A plot of $V_x/V_{(x=0)}$ as a function of x/l is shown in Fig. 3.

I_p is calculated through Eq. [3] and [18] as

$$I_p = \frac{aD}{\alpha} \tanh \alpha l \quad [20]$$

The parameter α corresponds to a reciprocal length and depends, among other things, on the exchange C.D. and the overpotential, that is, on the actual current flowing through the interface. For not too highly conductive materials and relatively low currents is $\alpha l < 1$. In Fig. 4 αl is plotted as function of η for different values of i_0 .

Under the condition $\alpha l < 1$ after expanding in series $\tanh \alpha l$ and neglecting higher order terms, Eq. [17] becomes

$$I_p \approx aDl \quad [21]$$

Thus, if $\alpha l < 1$, the current density at any point along

² Boundary condition [14] implies $I_{p,0} = 0$. This is correct since mathematically $I_{p,x}$ can be considered as a distribution function, the corresponding density function being $i_x = a \cosh \alpha x / \cosh \alpha l$ which is different to zero even at $x = 0$.

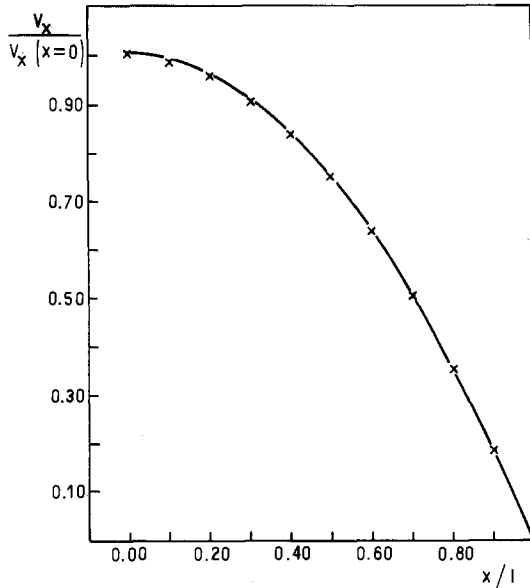


Fig. 3. $V_x/V_x(x=0)$ as a function of x/l , $i_0 = 10^{-6} \text{ A cm}^{-2}$, $\rho = 6.14 \times 10^{-6} \Omega \text{ cm}$; $D = 0.215 \text{ cm}$, $l = 1.65 \text{ cm}$, $h = 25 \text{ nm}$, $\eta = 20 \text{ mV}$, $\alpha_a = \alpha_c = 0.5$.

the film is equal to the current density at $x = l$. Hence, the potential drop along the film has no influence on the current density distribution.

On the other hand, after expanding $\cosh \alpha l$ in Eq. [20], it results in

$$V_x(x=0) = \frac{\alpha D \cdot l^2 \rho}{2A} = \frac{I_p}{2} R \quad [22]$$

where

$$R = \frac{\rho l}{A} \quad [23]$$

It is interesting to note that $I_p/2$ is just the average current, I_p , over the electrode surface of the polarization current I_p as given by Eq. [21].

Equation [20] is plotted as $V_x F/2RT$ against $\eta F/2RT$ for different values of i_0 in Fig. 5. As η increases, $V_x F/2RT$ tends to unity. This upper limit should be considered carefully since it was assumed $V_x < RT/\alpha F$. Figure 5 shows, however, that for reasonable

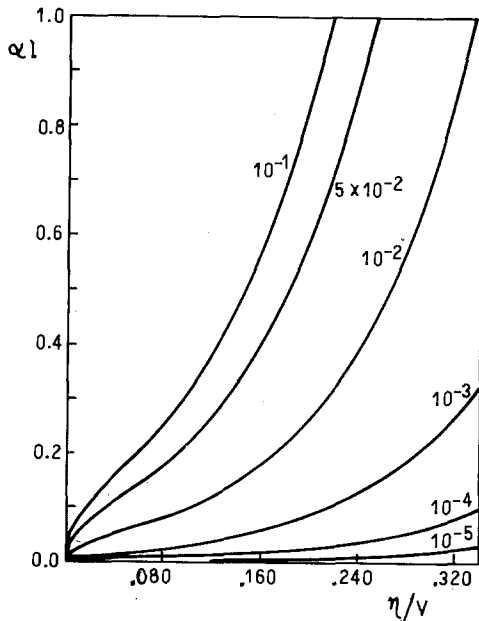


Fig. 4. αl as a function of η for the values of i_0 in A cm^{-2} indicated in the graph. Calculated with the same parameters as those indicated in Fig. 3.

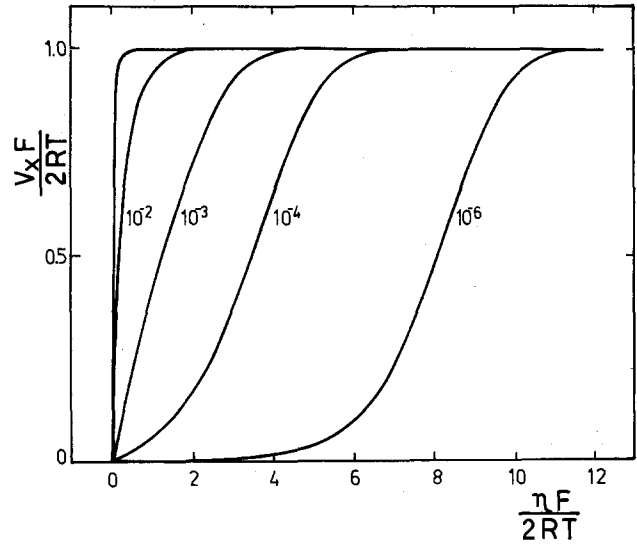


Fig. 5. $V_x F/2RT$ as a function of $\eta F/2RT$ for different values of i_0 in A cm^{-2} . Calculated with the same parameters as those indicated in Fig. 3.

values of i_0 , V_x is small even at relatively high values of η .

Notice that Eq. [19] does not directly relate the potential drop along the film with the polarization current and therefore can not be tested experimentally unless the complete V_x vs. η behavior is measured. Alternatively, at low values of i_0 and η , Eq. [22] relates the two experimentally measurable magnitudes V_p and I_p .

The Measurement of the Resistivity Change

To measure the potential dependence of the resistivity, a three contact method is usually employed. The central contact is at ground and imposes the overvoltage to the interface. At the extremes (see Fig. 1) a constant current I_m is fed along the electrode. The principle of the method is to measure the potential drop produced by I_m which should be proportional to the electrode resistance. However, the faradaic process will produce an additional potential drop that interferes with the measurement. The central problem is to investigate under what conditions the latter can be diminished or completely eliminated. Therefore, we will consider the potential distribution along the resistive electrode in the presence of a superimposed constant current I_m . To start with, we will treat, by simplicity, the two contact problem. The extension to the three contact case is almost immediate.

A constant current I_m is introduced at $x = 0$ (Fig. 1) and as before the ground potential is maintained at $x = l$. It is assumed that effects of co-conduction in the solution can be neglected. It has been shown that this effect contributes in the order of 1% to the total resistivity (6).

For the constant current, I_m , a constant field E_m should contribute to the total field along the film

$$E_m = \frac{\rho I_m}{A} = - \frac{dV_m}{dx} \quad [24]$$

The corresponding potential V_m at different points in the film varies linearly according to

$$V_m = \frac{\rho(l-x)I_m}{A} \quad [25]$$

Obviously, the solution to this problem is, in virtue of the superposition principle

$$V_t = V_m + V_x \quad [26]$$

that is

$$V_t = \frac{a}{b} \left(1 - \frac{\cosh \alpha x}{\cosh \alpha l} \right) + \frac{\rho(l-x)}{A} I_m \quad [27]$$

The result of Eq. [27] should be considered as a first approximation. We may further consider that the overpotential η_x comprises both V_x and V_m . By mathematical convenience, currents flowing opposite to the anodic electrochemical current are taken as positive. According to [24] and [25] a positive (negative) value of I_m will set a V_m value that should increase (diminish) η_x and vice versa. Then

$$\eta_x = \eta(x=0) - (V_x \pm V_{m,x}), \quad \text{for } \mp I_m \quad [28]$$

and the i_x is

$$i_x = i_0 \left[\exp \left\{ \alpha_a [\eta - (V_p \pm V_{m,x})] - \frac{F}{RT} \right\} - \exp \left\{ -\alpha_c [\eta - (V_x \pm V_{m,x})] - \frac{F}{RT} \right\} \right] \quad [29]$$

where the \pm sign is chosen accordingly to $\mp I_m$.

The field along the film in terms of the potential, V , can be written as

$$E = -\frac{dV}{dx} = I_m \frac{\rho}{A} + \frac{D\rho}{A} \int_0^x i_x dx \quad [30]$$

or

$$E = \frac{I_m \rho}{A} + \frac{D\rho}{A} \int_0^x (a - bV_x) dx \mp \frac{\rho D b}{A} \int_0^x V_{m,x} dx \quad [31]$$

According to Eq. [19] and [25], the solution is

$$V = \frac{\rho I_m (l-x)}{A} - \frac{a}{b} \left(1 - \frac{\cosh \alpha x}{\cosh \alpha l} \right) \pm \alpha^2 \left(cl \frac{x^2}{2} - \frac{cx^3}{3} \right) \mp \frac{1}{3} \alpha^2 c l^3 \quad [32]$$

where $c = \rho I_m / A$ and the first term of the rhs is $V_{m,x}$, the second is V_x , and the last two terms represent the coupling of the two current terms. When $x = l$, these terms reduce to $\pm 1/3 \alpha^2 c l^3$, which is of the order of $\alpha^2 l^2$ for $I_m < 1$ A. As in general $\alpha l < 1$, the interaction of the two currents is a second-order correction term and can, therefore, be neglected.

The three contact method provides, in principle, a way to evaluate the resistivity with only one measurement. In this case the polarization current is determined in the middle of the film (Fig. 6). At the experimental middle point, the film comprises one portion of length l , and another of length $l(1+g)$, where $0 < g < 1$. Consequently, I_p is divided into two contributions $I_1 = yI_p$ in the upper half of the film and $(1-y)I_p = I_2$, in the lower half of the film (Fig. 5), where $0 < y < 1$. The factor y can be calculated from [10] and [20]

$$\frac{1}{y} = \frac{I_p}{I_1} = 2 + \frac{\int_l^{(1+g)l} (a - bV_x) dx}{\frac{aD}{\alpha} \tanh \alpha l} \quad [33]$$

After taking into account Eq. [19] into [33], it results

$$\frac{1}{y} = 2 + 2 \frac{\cosh \frac{1}{2} [\alpha l(1+g) + \alpha l] \sinh \frac{1}{2} \alpha g}{\sinh \alpha l} \quad [34]$$

The potential distribution is obtained by applying to each half of the film the result of Eq. [27], V_1 for the upper half; and V_2 for the lower one. Thus

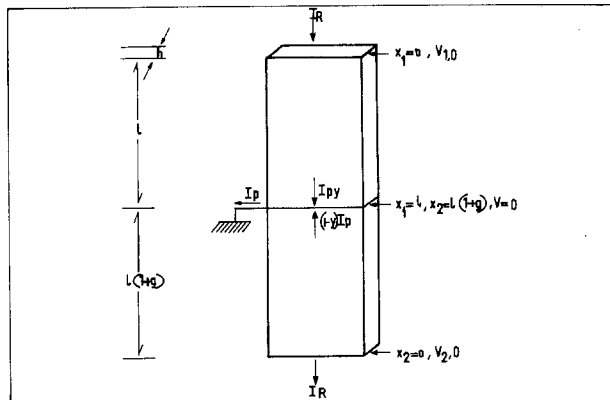


Fig. 6.

$$V_1 = \frac{a}{b} \left(1 - \frac{\cosh \alpha_1 x}{\cosh \alpha_1 l} \right) + \frac{\rho(l-x)}{A} I_m \quad [35]$$

and

$$V_2 = \frac{a}{b} \left(1 - \frac{\cosh \alpha_2 x}{\cosh \alpha_2 l(1+g)} \right) - \frac{\rho[l+g]-x}{A} I_m \quad [36]$$

where

$$\alpha_1 = \alpha y^{1/2}, \quad \alpha_2 = \alpha(1-y)^{1/2} \quad [37]$$

From [35] and [36], the potential difference between the extremes of the film are

$$\begin{aligned} ({}^{1\Delta^2}V)_1 &= V_1(x=0) - V_2(x=0) \\ &= \frac{a}{b} \left[\frac{1}{\cosh \alpha_2 l(1+g)} - \frac{1}{\cosh \alpha_1 l} \right] - \frac{\rho(2l+g)}{A} I_m \end{aligned} \quad [38]$$

If the direction of the current I_m is reversed

$$\begin{aligned} ({}^{1\Delta^2}V)_2 &= \frac{a}{b} \left[\frac{1}{\cosh \alpha_2 l(1+g)} - \frac{1}{\cosh \alpha_1 l} \right] \\ &\quad + \frac{\rho(2l+g)}{A} I_m \end{aligned} \quad [39]$$

then, from [38] and [39] it results

$$\begin{aligned} \frac{({}^{1\Delta^2}V)_1 + ({}^{1\Delta^2}V)_2}{2} &= \frac{a}{b} \left[\frac{1}{\cosh \alpha_2 l(1+g)} - \frac{1}{\cosh \alpha_1 l} \right] \end{aligned} \quad [40]$$

Equation [40] gives only the potential due to the faradaic process. The difference

$$\frac{({}^{1\Delta^2}V)_1 - ({}^{1\Delta^2}V)_2}{2} = \frac{\rho(2l+g)}{A} I_m \quad [41]$$

Thus, the conductivity of the film free from the effect of the faradaic process can be determined through Eq. [41].

Equation [41] differs from that previously obtained (12) in that, besides the sign, it does not depend on the polarization parameters, thus effectively allowing one to determine the resistivity changes in the presence of a faradaic process.

Equation [39] implies, in agreement with previous results (12), that as g tends to zero, the value of V corresponds exclusively to the resistive contribution. This would allow the evaluation of ρ with only one measure of ${}^{1\Delta^2}V$.

Conclusions

Assuming that the p.d. along the electrode can be linearized, a solution to the potential distribution for a resistive electrode, valid for both anodic and cathodic currents, is obtained. This is a generalization of

previous results and free from the inconveniences pointed out in the introduction.

When the applied overpotential is sufficiently small, the C.D. equals the polarization current divided by the electrode area and the p.d. in the film follows a simple Ohm's law relationship which involves the average current in the film.

The theory of the method to obtain the resistivity change of an electrode is developed. For not too high electrochemical and measuring currents, the coupling between them can be ignored. Under these conditions the p.d. between the extremes of the film in the three contact method can be split and the ohmic contribution determined. The latter allows the evaluation of the resistivity of the electrode if the dimensions of the film are known. Alternatively, if the film does not dissolve, the change of resistivity with overpotential can be obtained from the change of resistance. If the film is symmetric with respect to the central contact, one measure of the p.d. at the extremes will suffice to obtain the resistance. Since these points have not been seemingly taken into account before, previous results concerning resistivity changes in the presence of faradaic current should be considered carefully if no other means have been employed to diminish the V_p contribution.

Experimental work is underway in our laboratory to test Eq. [20], [22], and [41] which will be the subject of a future publication.

Acknowledgments

The authors wish to express their sincere appreciation to Prof. A. J. Arvia for valuable discussions and critical reading of the paper. R.I.T. thanks the CONICET for a fellowship during the period in which this work was carried out. INIFTA is sponsored by the Consejo Nacional de Investigaciones Científicas y Técnicas, the Universidad Nacional de La Plata, and the Comisión de Investigaciones Científicas (Provincia de Buenos Aires). This work was partially supported by the Regional Program for the Scientific and Technological Development of the Organization of the American States.

Manuscript submitted May 9, 1980; revised manuscript received Dec. 11, 1980.

Any discussion of this paper will appear in a Discussion Section to be published in the June 1982 JOURNAL. All discussions for the June 1982 Discussion Section should be submitted by Feb. 1, 1982.

Publication costs of this article were assisted by the Instituto de Investigaciones Fisicoquímicas Teóricas y Aplicadas (INIFTA).

LIST OF SYMBOLS

| | |
|------------|--|
| a | current density at a point of the electrode where resistive effects are absent, $A\text{ cm}^{-2}$ |
| A | cross section of the electrode, cm^2 |
| b | auxiliary parameter, $\Omega^{-1}\text{ cm}^{-2}$ (Eq. [8]) |
| C_1, C_2 | constants related to the solution of differential Eq. [11], V |
| c | auxiliary parameter, $V\text{ cm}^{-1}$ |
| D | width of the film electrode, cm |
| E | electric field strength, $V\text{ cm}^{-1}$ |
| F | Faraday constant, coulombs |
| g | dimensionless factor related to the position of central contact |
| h | thickness of the film electrode, cm |
| i | current density, $A\text{ cm}^{-2}$ |
| i_x | current density at the point x , $A\text{ cm}^{-2}$ |
| i_o | exchange current density, $A\text{ cm}^{-2}$ |
| I_p | total current due to the electrochemical process, A |
| $I_{p,x}$ | fraction of the total current between $x = 0$ and x, A |
| I_m | constant measuring current flowing between the extremes of the film electrode, A |
| J | current density flowing across the sectional |

| | |
|----------------------|---|
| | area of the electrode, $A\text{ cm}^{-2}$ |
| l | length of the film electrode, cm |
| n | number of adsorbed or electroadsorbed particles either on a metal or an electrode, molecules cm^{-2} |
| q | surface concentration of carriers, $C\text{ cm}^{-2}$ |
| R | universal gas constant, $J\text{ mol}^{-1}\text{ deg}^{-1}$ |
| R | resistance of the film electrode, Ω |
| s | electrochemical active area of the film electrode, cm^2 |
| T | absolute temperature, K |
| V_x | p.d. within the electrode due to an electrochemical process, V |
| V_m | p.d. within the electrode due to the measuring current, V |
| V_t | total p.d. within the electrode assuming no coupling, V |
| V | total p.d. within the electrode considering coupling between both currents, V |
| V_1, V_2 | p.d. within the upper (lower) part of the film in the three contact method, V |
| $(I\Delta^2V)_1$ | p.d. at the extremes of the film when I_m in forward sense in the three contact method, V |
| $(I\Delta^2V)_2$ | p.d. at the extremes of the film when I_m is reversed in the three contact method, V |
| x | coordinate parallel to the length of the electrode, cm |
| y | dimensionless factor for the current due to the asymmetry of the central contact |
| α | auxiliary parameter defined in Eq. [12], cm^{-1} |
| α_a, α_c | anodic and cathodic electrochemical transfer coefficients |
| η | overpotential |
| η_x | overpotential at the point x , V |
| ρ | resistivity of the metal film electrode, $\Omega\text{ cm}$ |
| σ | conductivity, $\Omega^{-1}\text{ cm}^{-1}$ |

REFERENCES

1. J. F. Goetz, A. M. Yacynych, H. B. Mark, Jr., and W. R. Heineman, *J. Electroanal. Chem. Interfacial Electrochem.*, **103**, 277 (1979).
2. J. Horkans *ibid.*, **106**, 245 (1980).
3. R. C. Kainthla, D. K. Pandya, and K. L. Chopra, *This Journal*, **127**, 277 (1980); D. E. Hall, *ibid.*, **127**, 308 (1980); C. Ho, I. D. Raistrick, and R. A. Huggins, *ibid.*, **127**, 343 (1980).
4. R. G. Chambers, in "The Physics of Metals, 1 Electrons," Chap. 4, J. M. Ziman, Editor, Cambridge Univ. Press, Cambridge (1969).
5. K. L. Chopra, "Thin Film Phenomena," McGraw Hill Co., New York (1969).
6. H. Shimizu, *Electrochim. Acta*, **13**, 27, 45 (1968); **14**, 55 (1969).
7. J. O'M. Bockris, B. D. Cahan, and G. E. Stoner, *Chem. Instr.*, **1**, 273 (1969).
8. K. Niki and T. Shirato, *J. Electroanal. Chem. Interfacial Electrochem.*, **42**, App. 7 (1973).
9. W. N. Hansen, *Surf. Sci.*, **16**, 205 (1969).
10. W. J. Anderson and W. N. Hansen, *J. Electroanal. Chem. Interfacial Electrochem.*, **43**, 329 (1973); **47**, 229 (1973).
11. W. J. Anderson and W. N. Hansen, *This Journal*, **121**, 1570 (1974).
12. T. Dickinson and P. R. Sutton, *Electrochim. Acta*, **19**, 427 (1974).
13. M. Fujiwara and T. Kuwana, *ibid.*, **20**, 565 (1975).
14. L. Müller, G. N. Mansurov, and O. A. Petrii, *J. Electroanal. Chem. Interfacial Electrochem.*, **96**, 159 (1979).
15. J. P. Ganon, C. Nguyen Van Huong, and J. Clavilier, *Surf. Sci.*, **79**, 245 (1979).
16. M. Watanabe and A. Hiratuka, *Surf. Sci.*, **86**, 398 (1979).
17. J. M. Ziman, "Principles of the Theory of Solids," Cambridge Univ. Press, Cambridge (1972).
18. G. M. Schmidt and N. Hackerman, *This Journal*, **107**, 142, 647 (1960).
19. O. B. Denjanovskii, G. N. Mansurov, and O. A. Petrii, *Sov. Electrochem.*, **9**, 1718 (1973).
20. W. W. Harvey, *This Journal*, **109**, 638 (1962).
21. B. E. Conway, E. Gileadi, and H. G. Oswin, *Can. J. Chem.*, **41**, 2447 (1963).
22. S. K. Rangarajan, M. J. Dignam, and B. E. Conway, *Can. J. Chem.*, **45**, 422 (1967).
23. I. V. Tolkashev, *Sov. Electrochem.*, **15**, 130 (1979).

Changes in Surface Crystallinity and Morphology of CdS and CdSe Photoelectrodes upon Use in Polysulfide Electrolyte

David Cahen and Baruch Vainas

Weizmann Institute of Science, Rehovot, Israel 76100

and Joka M. Vandenberg

Bell Laboratories, Murray Hill, New Jersey 07974

ABSTRACT

Surface changes that occur when CdS and CdSe photoelectrodes are used in photoelectrochemical cells containing polysulfide redox couples are investigated using low angle x-ray diffraction, reflection electron diffraction, and scanning electron microscopy. Both single crystal CdS and CdSe, and thin layer polycrystalline CdSe samples are used and in all cases restructuring of the surface, accompanied by some decrease in crystallinity of the surface layer, exposed to the electrolyte, is observed. For CdSe samples, crystallographic evidence for a predominant CdS top layer was seen after deactivation. Impurities in thin film CdSe samples are not affected by deactivation and they themselves do not seem to influence electrode activity or stability. These results support the occurrence of a dynamic restructuring process of the electrode surface in this system, which can cause electrode deactivation, by the formation of a layer that impedes charge transfer, if high current densities are used. Evidence is presented that surface recrystallization can occur in the dark, when such a process occurs probably very slowly.

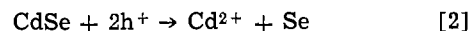
n-CdS and CdSe have attracted much attention as photoelectrodes in photoelectrochemical cells (PEC's) containing polychalcogenide ($S_x^=$, $SSe_x^=$, $Se_x^=$) redox couples because of the possibility to stabilize the photoelectrodes against photocorrosion in such systems, and the use of such PEC's for practical solar energy conversion devices (1-8).

Several explanations have been presented for the stabilizing influence of the chalcogenide redox couples in these systems. They include the common ion effect (for the $CdS/S_x^=$ and $CdSe/Se_x^=$ systems) (9), the relative positions of the $S_x^=$, $SSe_x^=$, and $Se_x^=$ redox potentials with respect to the semiconductor bandedges and decomposition potentials (10, 11), specific adsorption of $S_x^=$ on CdS (and $Se_x^=$ on CdSe) (2, 12), and the favorable kinetic behavior of the chalcogenide redox couples which facilitates proper matching of the rate of the electrochemical reaction to that of the light-induced charge carrier generation, and especially the rate at which these carriers reach the semiconductor/electrolyte interface (13).

It is quite likely that no one of these alone explains the stabilization effect and that a combination of them is responsible. Any explanation, however, should account for the fact that the system's stability is not absolute, i.e., conditions can be defined under which for example the $CdSe/S_x^=$ system is grossly unstable, while under different conditions it may be stable for at least months under normal day/night solar illumination (12). Various factors are involved in determining the behavior of this kind of PEC. They include illumination intensity (actually, real current density across the semiconductor/electrolyte interface), composition of the electrolyte (e.g., ratio of added S to added $S^=$; presence or absence of Se in the solution), temperature, and stirring rate (12, 14, 15).

The exchange of Se by S in CdSe photoanodes was one of the first observations made on the $CdSe/S_x^=$ system (2) and several subsequent studies, by photoelectron and Auger spectroscopy (12, 15-17), electron beam-induced luminescence (15), and by photocurrent

spectroscopy (18) have corroborated the initial observations and defined the degree and rate of exchange. This exchange reaction (which takes place in the dark as well, at least to a small extent) can be explained by: (i) the instability of CdSe in $S_x^=$ solution (with respect to CdS), and (ii) a certain degree of photocorrosion. This last process can be written as



Ideally, reaction [2] should not occur at all and instead



or its polysulfide equivalent should take place. It has been suggested that the extent to which [2] occurs instead of [4] and the (in)ability of the photogenerated holes to reach the surface, through the CdS layer formed by [3] determines the long-term stability of the system (12, 13).

Because reactions [2] and [3] give rise to a reprecipitation of CdS, out of the solution layer immediately adjacent to the surface, onto the electrode, a change in surface morphology and possibly surface crystallinity is expected, especially for a photocorroded electrode. The same holds for the $CdS/S_x^=$ system, where no change in chemical composition should accompany the surface restructuring.

The formation of a polycrystalline layer on a single crystal CdSe photoanode, after use in polysulfide solution was inferred from preliminary ellipsometry experiments (12). Gerischer and Gobrecht made a similar suggestion for CdS and CdSe photoanodes, based on Mott-Schottky plots, which indicate an increase of charge in the semiconductor surface layer after use in a polysulfide PEC (18). Noufi *et al.* deduced from SEM pictures for single crystal CdS photoanodes, after use in polyselenide solution an increase in surface roughness (16).

In this study we report direct experimental evidence for surface restructure in single crystal CdS, and single

Key words: photoelectrochemistry, surface restructure, SEM.

crystal and polycrystalline CdSe photoanodes, after deactivation in polysulfide solutions, as detected by Guinier thin film x-ray diffraction (GXD), reflection electron diffraction (RED), and scanning electron microscopy (SEM). Such a study was deemed important to try to define the surface changes taking place, especially in as far as they influence PEC output stability, and as a basis for comparison with similar studies on surface changes observed for CuInS₂ photoanodes in S_x⁼ solutions (19), where output stability behavior quite different from that of Cd chalcogenides is observed (20).

Experimental

CdS and CdSe crystals were obtained from Cleveland Crystals, Cleveland, Ohio (CdS: 1.1 Ω-cm; CdSe: 1.3 Ω-cm). Unless specified, the (1120) (CdS) or (1010) (CdSe) face was exposed to the electrolyte and contacts were made with an In-Ga alloy and Ag paint. Polycrystalline thin film CdSe photoelectrodes were prepared by electroplating on Ti (21) and also by applying a slurry containing CdSe powder to Ti substrate (22). The electrolyte was 1M each in KOH, Na₂S·9H₂O, and S, prepared and kept under N₂.¹ Except for a small surface area exposed to the solution, the electrodes were covered with tar or an insulating epoxy. After the use, described below, this layer was dissolved in toluene or warm dimethyl sulfide. In case of thin film samples, two pieces, from the same electrode, one, solution-exposed, the other, originally covered by epoxy or tar, were cut out and used for further study.

Single crystals were first polished flat (3 μm alumina). The CdS single crystal samples were etched prior to use in a 3M HCl solution (30 sec), rinsed with H₂O, etched in Br₂/MeOH (30 sec), and rinsed. The CdSe single crystal samples were etched for 30 sec in aqua regia, rinsed with water, put for 30 sec in 10% KCN solution, and rinsed again. The thin film polycrystalline CdSe electrodes were etched for 10 sec in 5% aqua regia solution, and treated further as the single crystals. This etching treatment, which improved output stability, was also used to prepare the samples in a reproducible manner for further experiments. After deactivation all samples were washed with sulfide solution and rinsed with water.

The electrodes were used in a 2-electrode PEC, and run under short-circuit conditions, where a large surface area carbon ring constituted the counterelectrode whose polarization was shown to be minimal at the current densities used (~1-2 mV/mA photocurrent). Oxygen-free N₂ was bubbled through the solution during the experiment. Illumination was provided by a 150W tungsten-halogen lamp (Oriel Corporation) through Pyrex or quartz windows. Light intensities were adjusted to obtain the desired initial photocurrents, and varied between ~100 and ~600 mW/cm². A Schoeffel GM 250 monochromator was inserted for photocurrent spectra (3.3 nm bandpass). The exciting beam was modulated at 100 Hz and the true photocurrent detected by a Brookdeal 9505SC lock-in amplifier.

For the x-ray diffraction (GXD) a Huber-Guinier thin film camera was used with a low angle of incidence (~5°) on the specimen and monochromatic Cu K_{α1} radiation. The penetration depth is at least one micron. For RED a General Electric electron diffraction camera was used. The electron beam energy was adjusted to 50 keV. The information obtained is due to the crystallinity of approximately the first 100Å from the sample surface. Scanning electron microscope pictures were obtained on an ETEC AUTOSCAN or JEOL SEM at 20 or 25 keV, respectively. Information is obtained from within 200 to 300Å of the sample surface.

¹ Experiments with photoelectrodes in solutions containing, in addition, 5 mM Se and Se⁼ gave results similar to those reported here. Generally some improvement in output stability was observed for both CdS and CdSe photoelectrodes, as compared to selenide-free solutions, in agreement with (7) and supporting the thesis forwarded in (14).

Results

Deactivation of photoanodes.—A CdS single crystal electrode, 0.2 cm² of which was exposed to the solution, declined gradually in short-circuit photocurrent over a period of 98 hr from 1.3 to 0.5 mA/cm².² The higher the initial photocurrent the more rapid the deactivation (Fig. 1). A total photocharge of ~460 C/cm² was passed before the electrode was taken out for further study. Figure 2 shows the photocurrent spectra of the electrode before and after deactivation.

The output of ~0.15 cm² CdSe single crystal electrode declined over a period of 2 hr from 50 to 1 mA/cm², with a total passage of 180 C/cm², in a manner similar to that reported previously (12, 15) (Fig. 3).

² The relatively low photocurrents are due to solution absorption. This solution was used as it provides better stabilization than less-absorbing, S-poor, solutions (12, 14).

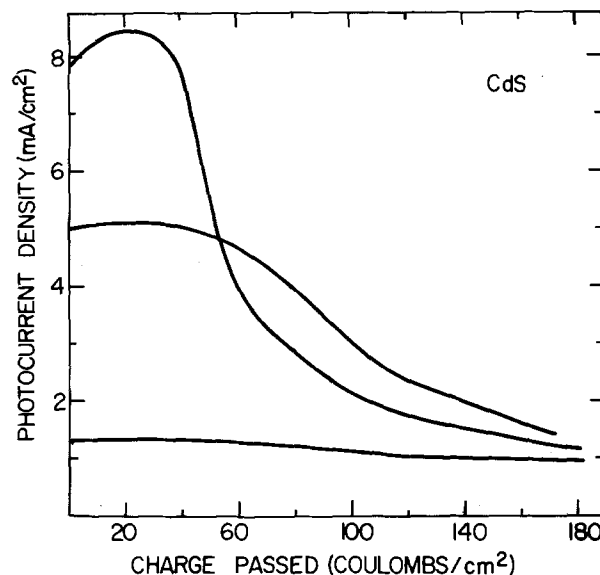


Fig. 1. Output stability of CdS photoanodes for several initial photocurrent densities. The sample with the lower initial photocurrent density, which passed the largest amount of photocharge, was used for further study. Solution temperature: 35° ± 2°C.

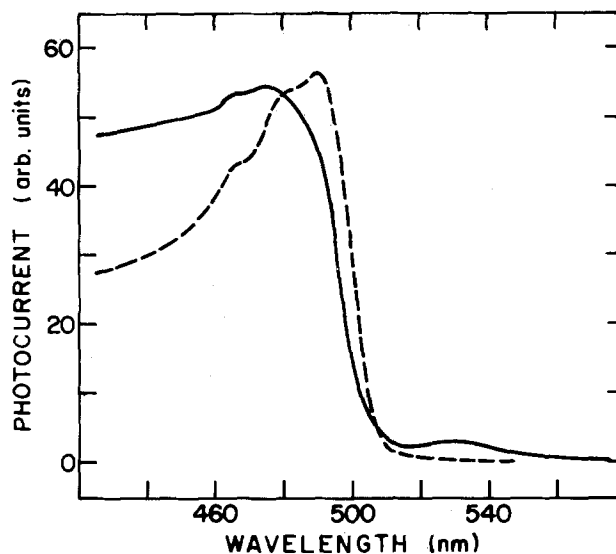


Fig. 2. Wavelength dependence of short-circuit photocurrent of single crystal CdS photoanode before (dashed) and after deactivation. Electrolyte: 1M in OH⁻ and S⁼. Data corrected for wavelength dependence of lamp + monochromator. The photocurrent at 480 nm was used to normalize the spectra. The scale for the deactivated sample is some five times more sensitive than that for the freshly etched one. Re-etching of the deactivated sample very nearly restores the behavior of the original, etched electrode.

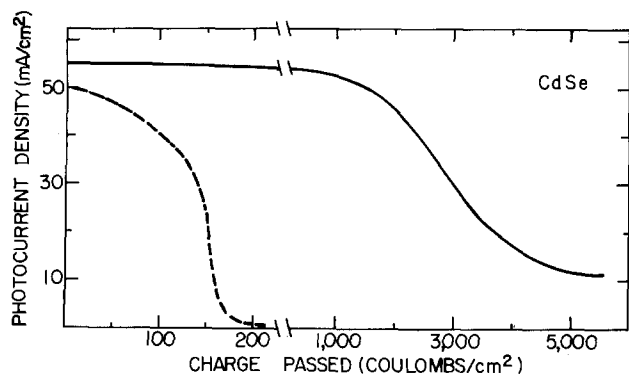


Fig. 3. Output stability of single crystal (dashed line) and painted thin film polycrystalline (solid line) CdSe photoelectrodes. Solution temperature: $35^{\circ} \pm 2^{\circ}\text{C}$.

A 0.2 cm^2 area of a 4 cm^2 polycrystalline electroplated CdSe electrode was exposed, and declined in a near-linear fashion from 37 to 12 mA/cm^2 over a period of 85 hr , passing some 9000 C/cm^2 .

A 0.2 cm^2 area of a 1 cm^2 electrode prepared with CdSe-containing slurry went from 55 to 10 mA/cm^2 over a period of 48 hr , passing a total of 5600 C/cm^2 (Fig. 3).

Approximate initial AM1 conversion efficiencies were $\sim 1\%$ for the CdS single crystal, $\sim 6\%$ for the CdSe single crystal, and $\sim 3\%$ for the polycrystalline samples.

GXD, RED, and SEM results.—In the GXD of CdS crystal the diffraction spots that were obtained from an unused crystal disappeared after deactivation. This indicates that the top layer of the sample becomes either amorphous or polycrystalline with crystallite size less than $\sim 500\text{ \AA}$. The single crystal RED diffraction pattern of unused CdS changes to diffraction rings after deactivation, indicating a polycrystalline top layer. The SEM micrographs (Fig. 4) indicate severe restructuring of the surface upon deactivation [cf. Ref (16)], which can be attributed, when the GXD and RED results are taken into account, to the formation of a polycrystalline surface layer.

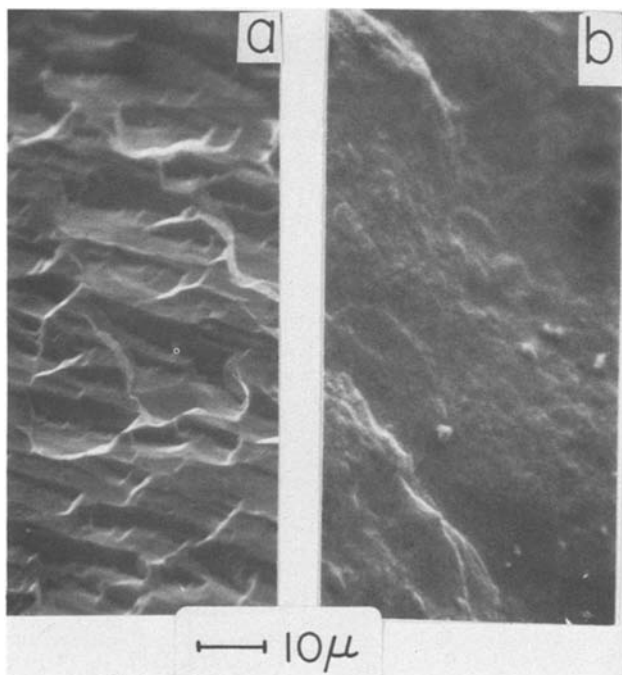


Fig. 4. SEM pictures of CdS crystal: (a) not exposed to solution (after polishing and etching); (b) after deactivation in polysulfide solution. $1000\times$ magnification.

In the GXD of CdSe crystal one very weak single crystal spot is still observed after deactivation, together with very weak lines of hexagonal CdS and CdSe. The superposition of one sharp RED diffraction pattern, and a broad one with a $\sim 3\%$ smaller spacing, shows the presence of both single crystal CdSe and polycrystalline Cd(S, Se). Apparently the single crystal surface is partly maintained. This agrees with the SEM micrograph which shows less of a surface change than is observed for the CdS crystal.

Because of the uneven surface of the thin film polycrystalline CdSe samples, a result of their method of preparation, it was impossible to obtain RED results for them. For comparison sputtered layers were used. These layers (on Ti) gave rather poor photocurrents (a few mA/cm^2 only, under conditions where electroplated samples gave $\sim 35\text{--}45\text{ mA/cm}^2$ short-circuit photocurrents), as their method of preparation was not optimized.

The electroplated layers of CdSe, prepared from reagent-grade materials (21), contain a considerable amount of impurities, which show up in the GXD as strong background intensity, as well as a pattern of broad spotty lines, which can be identified as the high pressure phase of Se (a by-product of the electroplating). These impurities do not seem to influence the photoelectrochemical behavior of these electrodes in an adverse manner. Also, they are not affected by deactivation, while the intensities of the hexagonal CdSe lines drop to about half after deactivation. This decrease is probably due to a decrease in grain size.

The samples that were prepared using the CdSe-containing slurry presented a cleaner and somewhat sharper diffraction pattern. A slight decrease in cell dimensions ($\sim 0.02\%$) is seen upon deactivation indicative of some S/Se exchange as well as a slight decrease in line intensity of the CdSe lines. The RED experiments on sputtered layers showed a clear decrease in line intensity for the deactivated samples. It was not possible to see changes in lattice dimensions here.

The SEM pictures (Fig. 5 and 6) show a restructuring of the surface upon deactivation, and a decrease in average particle size consistent with previous results (16). Figure 5b shows the effect of keeping the electrode in S_x^- solution in the dark, resulting in some surface restructure, while Fig. 5d illustrates the often occurring "charging" on deactivated samples.

Discussion

The results can be summarized as follows. The SEM pictures show in all cases surface changes upon electrode deactivation. The nature of these changes is explained by the results from the diffraction experiments.

In the case of CdS crystal a complete restructuring of the surface through the formation of a finely poly-

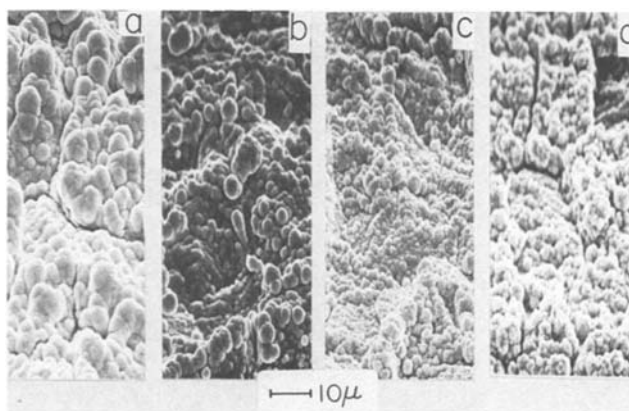


Fig. 5. SEM pictures of electroplated CdSe thin film polycrystalline photoanode. (a) Not exposed to solution (after etching); (b) after standing in the dark in polysulfide solution, overnight; (c) after passing 4 C/cm^2 under illumination; (d) after deactivation. $1000\times$ magnification.

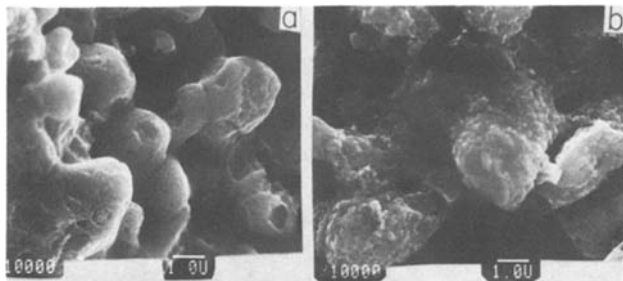


Fig. 6. SEM pictures of painted CdSe thin film polycrystalline photoanode. (a) Not exposed to solution (after etching); (b) after deactivation. 10,000 \times magnification.

crystalline layer is found. This conclusion is supported by the capacitance measurements of Ref. (18) and by the spectral response data from Fig. 2. Those show a photoresponse at energies less than that of the optical bandgap of CdS, for the deactivated sample. This response indicates the presence of defect states within the forbidden gap [also observed for nonetched samples, especially the peak around 540 nm; cf. Ref. (23)]. Such states can be caused by lattice defects and/or impurities within individual grains, or by grain boundaries. In small grain size semiconductor layers, recombinations at grain boundaries will impede the charge transfer of both minority and majority carriers, thus explaining the decrease in absolute photoresponse (quantum efficiency) upon deactivation. The fact that the original photoresponse behavior is restored upon re-etching the deactivated electrode proves that only a (near) surface layer is involved. The rather strong decrease in photoresponse at shorter wavelengths can be due to surface recombination. It is possible that, at the much lower photocurrents obtained with the deactivated sample, this loss mechanism is less important. The sometimes observed initial increase in short-circuit current (cf. Fig. 1) may be a trivial effect, due to a decrease in reflectivity of the electrode surface, which occurs already after passage of a small amount of photocharge [cf. Fig. 5c; Ref. (16), Fig. 8b; earlier mentioned ellipsometry results].

For the CdSe single crystal electrodes a less dramatic surface change is observed by SEM. Here deactivation causes only partial surface degradation. The diffraction data show that while some of the top layer remains single crystalline, some of it is transformed into polycrystalline Cd(Se, S). The mixed composition of the restructured layer fits the earlier Auger and XPS data (15, 16) especially if we realize that in all experiments averaging over some sample depth occurs. Spectral response changes are less than observed for CdS crystal but the same long wavelength response effect is seen [cf. also data on nonetched and etched samples in Ref. (23)]. The polycrystalline nature of the restructured part of the surface is again supported by the data from Ref. (18). Also photoacoustic (PA) measurements on similar CdSe crystal samples show an increase in PA signal after sample deactivation. The fact that this increase is larger ($\sim 2\times$) than the decrease in sample reflectivity can be explained by an increase in real surface area. [In PA measurements the signal is inversely related to the particle size of the probed top layer (24)]. The decreased reflectivity of deactivated samples and the ellipsometry data mentioned in (12) support this conclusion.

In the case of polycrystalline CdSe samples, Fig. 5 and 6 clearly show the surface restructuring upon deactivation. The diffraction experiments indicate that smaller crystallites are present, the composition of which, from the x-ray data, seems to be Cd(Se, S). This agrees with results from XPS for such samples (12, 17). Again, PA experiments show an increase in signal for deactivated samples, as compared to freshly etched ones (24) and the decrease in reflectivity can be observed easily visually.

An interesting additional observation is the occurrence of "charging" in several SEM experiments on deactivated samples (cf. Fig. 5d). This can indicate that the restructured top layer has, effectively, a rather high resistance to current flow, as assumed in the earlier proposed electrolyte-insulator-semiconductor (EIS) model (12). The results from (18) support this explanation.

The thickness of the restructured surface layer is difficult to estimate. It will probably vary between single crystal and polycrystalline samples [cf. Ref. (16) and (12), respectively]; it will depend on the amount of photocharge passed [cf. Ref. (17)], and on the conditions under which the charge is passed (such as real current density, solution composition, and temperature). The surface structure that is present also on etched single crystal surfaces (cf. Fig. 4a) adds another complicating factor. Photoelectron and Auger spectroscopic data suggest thicknesses of ~ 100 - 200\AA for single crystal and polycrystalline CdSe electrodes that passed small to moderate amounts of photocharge, without deactivation (12, 16). However, these values can be considered rough estimates only, because of unavoidable mixing of the top layers upon ion beam sputtering. The results from our RED experiments, which probe the top few hundred angstroms, suggest that these estimates are reasonable ones also for deactivated CdSe single crystals, while thicker layers are probably present on deactivated CdS crystals [cf. also Ref. (16)].

Combining our results with those from Ref. (12, 15-18), it seems probable that a dynamic breaking up and rebuilding of the electrode surface takes place when CdS or CdSe electrodes are used in polysulfide solutions. This process takes place also in the dark [cf. Fig. 5b and Ref. (12)]. It may very well be that such a process, when not going too far, takes care of rejuvenating the electrode surface continuously, so that "bad spots" may not last very long.³ Figure 7 shows strong (accidental) evidence for such a rebuilding of the (0001) surface, for a CdS electrode that was kept in the dark (with very little charge passed) for a prolonged period (26). Although different crystal faces are involved [Fig. 7 can be compared with Fig. 4a [or Fig.

³ The result of deactivation of the slurry-prepared CdSe electrode (Fig. 6b) resembles somewhat the effect of "photoelectrochemical etching" of such electrodes (25), the result of which has been explained, in part, by removal of recombination centers. The often observed improved performance of slightly "aged" (in S_x^{2-}) CdSe electrodes [(12); G. Hodes *et al.*, unpublished results] could possibly be caused by such photoelectrochemical etching in S_x^{2-} solutions, during the passage of an initial, small amount of photocharge.

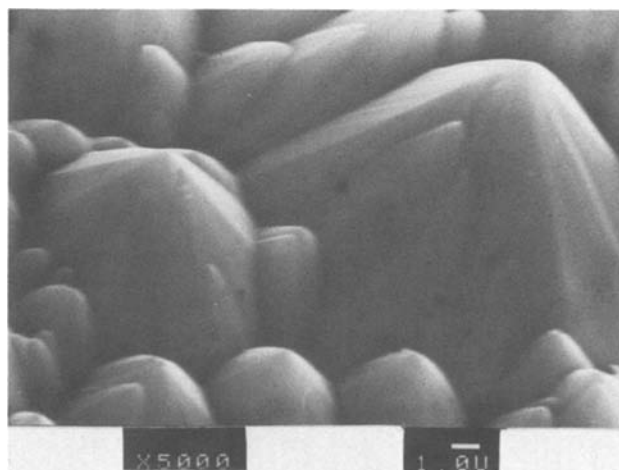


Fig. 7. SEM picture of single crystal CdS electrode [(0001), S-face] after standing in the dark in polysulfide solution, short-circuited to the counterelectrode, for two months. During this period the electrode was used for studies of the temperature dependence (51°C - 0°C) of the current under forward and reverse bias (between 0.22 and -0.22V vs. rest potential, i.e., $S/S^=$ potential) (26).

8a in Ref. 16); here the exposed crystal face is not specified]). No such organized rebuilding occurs, however, when the electrode is pushed too hard, i.e., too high a local current density passes through the electrode/electrolyte interface. Then this dynamic process dooms the electrode, and thus the PEC. This is caused probably by a combination of factors, such as very much decreased grain size (because of too fast a destruction and reprecipitation), too thick a restructured surface layer, which may present too high a resistivity for current to pass because of different dopant concentration of this layer, and/or bad contacts between the newly formed grains. The importance of the illumination intensity here lies in the way it influences the local current density at the surface. While the electrochemical and corrosion reactions (reactions [4] and [2]) seem to take place simultaneously all the time, there exists apparently a limiting current density above which reaction [2] occurs so fast that the surface restructuring becomes destructive in terms of electrode performance {severe rate mismatch between reactions [1] and [4], cf. Ref. (13)}. The results presented here, especially Fig. 7, suggest furthermore that accelerated continuous illumination tests of electrode stability [(12), (15); Hodes, Manassen, Cahen, submitted] may be even more severe ones than previously thought, because of the possible beneficial effect of the dark (night) "breathing" period on the surface restructuring process.

Acknowledgments

D. C. thanks Bell Laboratories for hospitality during the period when part of this work was done, and G. Hodes, A. Heller, and B. Miller for helpful discussions. We thank G. W. Kammlott and R. G. Vadimsky for RED and SEM experiments, respectively.

Manuscript submitted April 16, 1980; revised manuscript received Feb. 23, 1981.

Any discussion of this paper will appear in a Discussion Section to be published in the June 1982 JOURNAL. All discussions for the June 1982 Discussion Section should be submitted by Feb. 1, 1982.

Publication costs of this article were assisted by Bell Laboratories.

REFERENCES

1. D. Cahen, G. Hodes, and J. Manassen, *Bull. Isr. Phys. Soc.*, **22**, 100 (1976).

2. G. Hodes, J. Manassen, and D. Cahen, *Nature (London)*, **261**, 403 (1976).
3. A. B. Ellis, S. W. Kaiser, and M. S. Wrighton, *J. Am. Chem. Soc.*, **98**, 1635 (1976).
4. A. B. Ellis, S. W. Kaiser, J. M. Bolts, and M. S. Wrighton, *ibid.*, **99**, 2839 (1977).
5. B. Miller and A. Heller, *Nature (London)*, **262**, 680 (1976).
6. A. Heller, K. C. Chang, and B. Miller, *This Journal*, **124**, 697 (1977).
7. B. Miller, A. Heller, M. Robbins, S. Menezes, K. C. Chang, and J. Thomson, Jr., *ibid.*, **124**, 1019 (1977).
8. M. A. Russak, J. Reichman, H. Witzke, S. K. Deb, and S. N. Chen, *ibid.*, **127**, 725 (1980).
9. G. C. Barker, *ibid.*, **113**, 1181 (1966).
10. A. J. Bard and M. S. Wrighton, *ibid.*, **124**, 1706 (1977).
11. H. Gerischer, *J. Electroanal. Chem. Interfacial Electrochem.*, **82**, 133 (1977).
12. D. Cahen, G. Hodes, and J. Manassen, *This Journal*, **125**, 1623 (1978).
13. D. Cahen, J. Manassen, and G. Hodes, *Solar Energy Mater.*, **1**, 343 (1979).
14. D. Lando, G. Hodes, J. Manassen, and D. Cahen, *J. Am. Chem. Soc.*, **101**, 3969 (1979).
15. A. Heller, G. P. Schwartz, R. G. Vadimsky, S. Menezes, and B. Miller, *This Journal*, **125**, 1156 (1978).
16. R. N. Noufi, P. A. Kohl, J. W. Rogers, Jr., J. M. White, and A. J. Bard, *ibid.*, **126**, 949 (1979).
17. K. T. L. De Silva and D. Haneman, *ibid.*, **127**, 1554 (1980).
18. H. Gerischer and J. Gobrecht, *Ber. Bunsenges. Phys. Chem.*, **82**, 520 (1978).
19. Y. Mirovsky, D. Cahen, G. Hodes, R. Tenne, and W. Giriat, *Solar Energy Mater.*, **4**, 169 (1981).
20. M. Robbins, K. J. Bachmann, V. G. Lambrecht, F. A. Thiel, J. Thomson, Jr., R. G. Vadimsky, S. Menezes, A. Heller, and B. Miller, *This Journal*, **125**, 831 (1978).
21. J. Manassen, G. Hodes, and D. Cahen, U.S. Pat. 4,064,326 (1977).
22. G. Hodes, J. Manassen, D. Cahen, and M. David, *This Journal*, **127**, 2252 (1980).
23. A. Heller, K.-C. Chang, and B. Miller, *ibid.*, **124**, 697 (1977); *J. Am. Chem. Soc.*, **100**, 684 (1977).
24. D. Cahen and H. Garty, *Anal. Chem.*, **51**, 1865 (1979).
25. R. Tenne and G. Hodes, *Appl. Phys. Lett.*, **37**, 428 (1980).
26. B. Vainas, G. Hodes, J. Manassen, and D. Cahen, *Appl. Phys. Lett.*, **38**, 458 (1981).

High Rate Discharge of Ca/LiClO₄-LiNO₃ Thermal Battery Cells

M. H. Miles* and A. N. Fletcher*

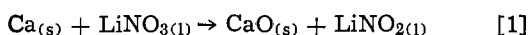
Naval Weapons Center, Chemistry Division, China Lake, California 93555

ABSTRACT

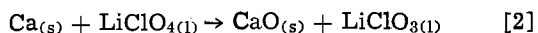
The high rate discharge of the Ca/LiClO₄-LiNO₃/Ni thermal battery cell is limited by the reduction of the oxidizing molten salts on the nickel current collector. With the addition of AgNO₃ to improve the cathodic reaction, this cell can sustain current densities of 100 mA/cm² at 350°C to give cell voltages in excess of 2V for several minutes. In cells containing added AgNO₃, the source of eventual polarization is the anode rather than the cathode. Based upon the weight of the calcium and electrolyte, cell discharge at 100 mA/cm² gives a power density of 740 W/kg and an energy density of 120 W-hr/kg. At a lower rate of discharge (10 mA/cm²), these cells give very stable potentials of about 2.5V for time periods exceeding 60 min. These cells, therefore, show promise for both high and low rate applications of thermal batteries.

Nitrate and perchlorate salts are attractive for use in thermal batteries since these molten salts have relatively low melting points and can function as both the electrolyte and oxidizer. Eutectic mixtures of these oxidizing molten salts generally have much lower melting points than the conventional LiCl-KCl mixtures used in thermal battery cells (1-3). For example, LiNO₃-KNO₃ mixtures melt at temperatures as low as 132°C (4) while an equimolar LiClO₄-LiNO₃ mixture melts at about 150°C (5). For thermal battery cells using molten salt mixtures containing LiClO₄, the operating temperature range is expected to be about 250°-400°C (5). The nature of the molten salt cation plays an important role in the reactions of both nitrates (6, 7) and perchlorates (5). The small lithium ion is more effective than the larger alkali metal cations in catalyzing the electrochemical reduction of molten nitrates.

Thermochemical calculations for the cell reaction



at 350°C indicate a cell potential of about 2.8V and a theoretical energy density of 1380 W-hr/kg. For the Ca/LiClO₄ cell reaction



at 350°C, an even higher cell potential of about 3.2V is calculated that yields a theoretical energy density of 1170 W-hr/kg. Open-circuit cell potentials close to these calculated values have been observed at 350°C in the presence of chloride ions that attack the passivating film on the anode (8, 9).

Previous studies showed that Ca/LiNO₃-LiCl-KCl [50-25-25 mole percent (m/o)] thermal battery cells gave promising results when discharged at 10 mA/cm² over a temperature range of 250°-450°C (9). At current densities above 20-30 mA/cm², however, the cell performance deteriorates due to polarization at the anode. The rate of the calcium anode reaction in molten nitrates is determined largely by the passivating film that hinders the passage of calcium ions across the oxide layer (8). Comparisons of measured and calculated cell resistances suggest that the anodic oxide film makes a sizeable contribution to the total cell resistance (9). This study shows that the presence of LiClO₄ improves the performance of the anode during high rate discharge.

Experimental

The electrochemical cells were fabricated from calcium disks (ROC/RIC, 99%) and fiberglass filter paper disks (Gelman, type A) that contained the electrolyte. The calcium disk was spot-welded to a Ca/Fe bimetallic disk and an aluminum lead wire was spot-welded to the Fe side of the bi-metal. The back side and edges of this disk were masked off by a thin layer of Sauereisen cement (No. 1). All types of disks used were 6.35 mm in diameter (0.32 cm²).

The molten salt mixture was prepared by weighing out equimolar amounts of LiClO₄ (Baker, anhydrous reagent) and LiNO₃ (Baker reagent) that had been dried in a vacuum oven at 130°C. Silver nitrate was added to some of the LiClO₄-LiNO₃ mixtures since this salt had a marked beneficial effect on the cathodic reaction. Dried helium was bubbled through the molten salt mixture at 300°-350°C for several hours to remove the final traces of water. The electrolyte wafers were prepared by simply immersing the fiberglass disks in the molten salt and storing in a desiccator until needed. Cells were assembled and heated as quickly as possible to minimize moisture pick-up. Cell tests with no precautions to minimize moisture gave no unusual results nor did several studies in an argon-filled dry box. The lack of any large effects due to moisture was not unexpected since previous cell studies using LiNO₃ in closed and open systems showed that the presence of air or moisture had little effect on test results (9).

Single cell tests were conducted using an open nickel lid placed on a hot plate (S/P Tek Plate 20) with part of the nickel lid serving as the electrode surface for the cathodic reaction. A slight depression in the center of this lid minimized the spread of excess electrolyte away from the surface in contact with the cell. A metal rod was used with a spring and soapstone spacers to maintain a positive face pressure on the cell (9). An L-shaped reference electrode (0.1M Ag⁺/Ag) was used to monitor the potential of either the anode or the cathode. The temperature of the cell was read to 1°C with a stainless steel-covered thermocouple probe used with a Fluke Model 2165A digital thermometer readout; temperature control during an experiment was generally within 5°C. The electrochemical cells contained about 60 mg of calcium, 40 mg of the electrolyte, and 4 mg of fiberglass filter paper. Constant current cell discharge was maintained by a PAR Model 173 potentiostat/galvanostat and cell and reference potentials were

* Electrochemical Society Active Member.

Key words: current density, films, fused salts, passivity.

plotted using a strip chart recorder (HP 7100B). The cell potential was also read with a Fluke Model 8040A multimeter while the digital readout on the PAR instrument gave the electrode potential *vs.* the reference electrode.

Results and Discussion

Separate studies of cells with LiNO_3 or LiClO_4 electrolytes were made for comparisons with results for the $\text{Ca/LiClO}_4\text{-LiNO}_3/\text{Ni}$ cells. The $\text{Ca/LiClO}_4/\text{Ni}$ cells show a marked improvement in the open-circuit potential as the temperature increases above 250°C . The use of the Ag^+/Ag reference electrode reveals that this change is due to the anodic potential suddenly becoming more negative by as much as 1.3V. Investigations of $\text{Ca/LiNO}_3/\text{Ni}$ cells show much lower cell potentials and no spontaneous improvements as the temperature increases. The addition of about 10 m/o LiCl to the LiNO_3 electrolyte, however, produces a sudden improvement in the open-circuit cell potential that also corresponds to the potential of the calcium anode becoming about 1.3V more negative. Tests in an argon-filled dry box gave almost identical results, suggesting that any moisture retention by the lithium salts is not a major factor in the activation of the anode. Previous studies have shown the beneficial effect of added chloride ions upon the calcium anode and indicate that the chloride ions cause a breakdown of the passivating calcium oxide film (8-10). It is likely, therefore, that the direct reaction of calcium with molten LiClO_4 produces sufficient chloride ions to cause a breakdown of the passivating film.

The open-circuit potential of the $\text{Ca/LiNO}_3/\text{Ni}$ cell at 350°C was generally about 1.5V but increased to about 2.8V in the presence of 10 m/o LiCl while the $\text{Ca/LiClO}_4/\text{Ni}$ cell gave an open-circuit potential of about 3.2V at 350°C . The open-circuit potential of the calcium anode was about -3.1V in LiClO_4 and about -3.0V in LiNO_3 containing LiCl , hence the cathode contributes about 0.3V to the higher open-circuit cell potentials observed in LiClO_4 . Upon drawing current from the cell, the cathode polarizes considerably in both molten LiNO_3 and molten LiClO_4 , while the calcium anode potential remains fairly constant at moderate current densities.

The $\text{Ca/LiClO}_4\text{-LiNO}_3/\text{Ni}$ cell activates similarly to the $\text{Ca/LiClO}_4/\text{Ni}$ cell as the temperature increases above 250°C . Typical open-circuit measurements give potentials of about 2.8V for the cell, -3.0V for the anode potential, and about -0.2V for the cathode potential. Single cell discharge tests of the $\text{Ca/LiClO}_4\text{-LiNO}_3/\text{Ni}$ cell showed that while the anode could sustain current densities as great as 100 mA/cm^2 , the cathode showed considerable polarization and limits the cell performance. The electrochemical reduction of both LiNO_3 and LiClO_4 produces insoluble Li_2O (5, 7) hence the blocking of the electrode surface by this insoluble product is the likely cause of the polarization of the cathode (11).

The use of an $\text{LiClO}_4\text{-LiNO}_3\text{-AgNO}_3$ (40-40-20 m/o) mixture greatly improves the performance of the cathode. The reduction reaction of nickel readily sustains 100 mA/cm^2 with very little polarization in the presence of AgNO_3 . The performance of the calcium anode, however, is poor when placed in direct contact with this mixture. The calcium anode is erratic and slow in attaining its expected large electro-negative potential and cannot sustain high current densities. Problems with the calcium anode in the presence of AgNO_3 is likely related to the removal of chloride ions as insoluble AgCl (12). This removal of the chloride ions that are formed by the reaction of calcium with LiClO_4 would hinder the breakdown of the passivating film on the calcium anode. The preparation of an $\text{LiNO}_3\text{-LiClO}_4\text{-AgNO}_3\text{-KCl}$ (40-40-10-10 m/o) mixture showed that a yellowish solid substance

forms upon melting. Tests on the liquid portion of the melt indicated that very little silver or chloride ions were present; therefore, the Ag^+ and Cl^- ions apparently separate from the molten salt mixture as insoluble AgCl .

The best cell performance was obtained by using an $\text{LiClO}_4\text{-LiNO}_3$ (50-50 m/o) electrolyte wafer next to the calcium anode and an $\text{LiClO}_4\text{-LiNO}_3\text{-AgNO}_3$ (40-40-20 m/o) disk next to the nickel electrode. Results for the discharge of this cell at 100 mA/cm^2 are shown in Fig. 1. In this cell test at 350°C , the cell voltage remained above 2V for 7 min, and the lifetime to 75% of the peak voltage was 9 min. The eventual voltage drop of this cell was due to polarization of the anode rather than the cathode. Figure 1 shows that the potential of the cathode remains quite steady at about -0.4V throughout the cell discharge. Based upon the weights of the calcium, electrolyte, and fiberglass, the energy density for this cell was 120 W-hr/kg while the power density was 740 W/kg . From the weight of calcium consumed, the current efficiency for the anode was 15% in this test. For the conventional $\text{Ca/LiCl-KCl-CaCrO}_4/\text{Ni}$ thermal battery cell operating at about 500°C , typical values are 2.8V for the open-circuit potential, 50 W-hr/kg for the energy density, and about 100 W/kg for the power density (13). Such comparisons, however, suffer from the lack of standard methods for the calculations. Furthermore, experimental power densities for a cell designed for short operating times can be considerably higher than for the same cell designed for long operating times.

Although the emphasis of this study is on high rate discharge, these cells also give very stable potentials for long time periods during low rate discharge. Figure 2 shows the discharge of a $\text{Ca/LiClO}_4\text{-LiNO}_3\text{-AgNO}_3/\text{Ni}$ cell at 10 mA/cm^2 . In this test at 350°C , the cell potential remained above 2.5V for over 70 min and above 2.0V for slightly over 2 hr. The eventual cell voltage drop is again due to polarization of the anode. In another experiment at 350°C on a

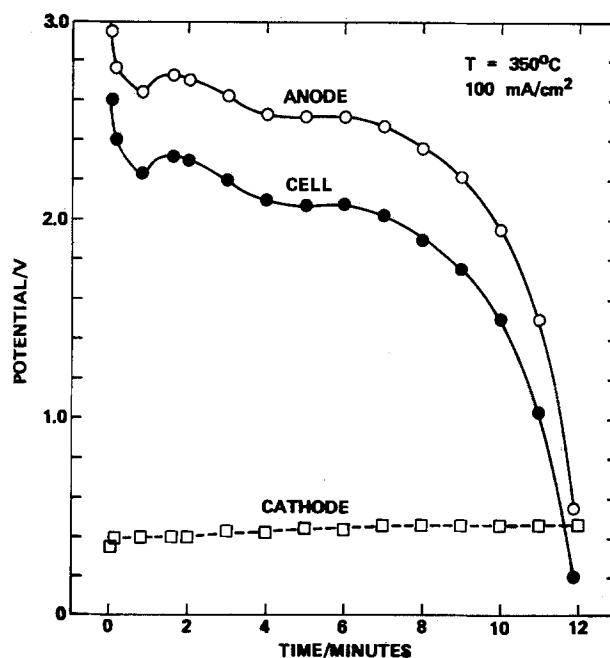


Fig. 1. Cell discharge at 100 mA/cm^2 at 350°C showing anode, cathode, and cell potentials with time. This $\text{Ca/LiClO}_4\text{-LiNO}_3\text{-AgNO}_3/\text{Ni}$ cell consisted of an $\text{LiClO}_4\text{-LiNO}_3$ (50-50 m/o) electrolyte wafer next to the calcium anode and an $\text{LiClO}_4\text{-LiNO}_3\text{-AgNO}_3$ (40-40-20 m/o) wafer next to the nickel electrode. The anode and cathode potentials are both negative in sign as measured against the Ag^+/Ag reference electrode.

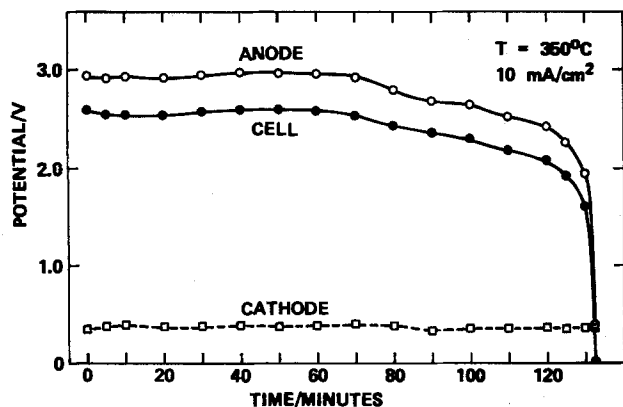


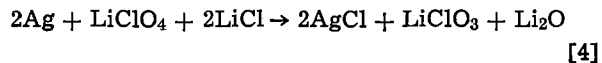
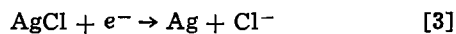
Fig. 2. Discharge of the Ca/LiClO₄-LiNO₃-AgNO₃/Ni cell at 10 mA/cm² at 350°C showing anode, cathode, and cell potential with time. The anode and cathode potentials are both negative in sign as measured against the Ag⁺/Ag reference electrode. This cell was discharged for several minutes at both 100 and 50 mA/cm² prior to this experiment at 10 mA/cm².

cell of this type, discharge at 10 mA/cm² gave a cell voltage that remained above 2.4V for 90 min. In fact, all experiments at low discharge rates gave stable cell potentials for long time periods.

Despite the anode polarization that eventually occurs at 100 mA/cm², the cell is still capable of further discharge and good performance at smaller current densities. For example, in the experiment shown in Fig. 2, the cell was discharged at 100 mA/cm² and again at 50 mA/cm² until cell potentials fell below about 1V due to anode polarization prior to conducting the experiment at 10 mA/cm². The total energy density for this study was about 240 W-hr/kg.

Although the exact role of AgNO₃ has not been determined, it is an obvious possibility that silver ions are being reduced at the cathode. However, the open-circuit and operating cathodic potentials of -0.3 to -0.4V vs. Ag⁺/Ag (Fig. 1 and 2) suggest that the reaction is more complex than this. Another possibility is that AgCl is involved. The use of an AgCl electrode as the cathode in an experiment gave about the same cathodic potentials as the LiClO₄-LiNO₃-AgNO₃/Ni electrode. Chloride ions are a likely final product of various reduction or decomposition reactions involving LiClO₄ (5, 12).

Calculations show that reduction of all the AgNO₃ present would account for only about 30% of the total cathodic current passed in Fig. 1, yet no obvious change in the cathodic potential occurs that indicates a change in the reaction. In the experiment shown in Fig. 2, prior cell discharge at 100 mA/cm² would have theoretically consumed all the AgNO₃ present. These results suggest a recycling of the silver, perhaps by reactions such as



It is also possible that the deposition of silver particles on the nickel surface increases its effective surface area, thereby aiding the reduction of LiClO₄ and LiNO₃.

Any use of an active metal anode with an oxidizing electrolyte presents a possible safety hazard. No problems, however, were observed in any cells using the LiClO₄-LiNO₃ mixtures. In one study of the effect of temperature in molten LiClO₄ during cell discharge at 10 mA/cm², the calcium anode was stable up to about 450°C whereupon it suddenly reacted with a flash of light rather than with an actual explosion. Explosive reactions have been reported following the deposition of lithium metal at the cathode in molten LiClO₄ (14, 15). These results were confirmed by depositing lithium onto the nickel cathode at high rates and then switching to open circuit. Passivating oxide films provide limited stability to the molten lithium metal (mp = 181°C).

Manuscript submitted Aug. 27, 1980; revised manuscript received Nov. 3, 1980.

Any discussion of this paper will appear in a Discussion Section to be published in the June 1982 JOURNAL. All discussions for the June 1982 Discussion Section should be submitted by Feb. 1, 1982.

Publication costs of this article were assisted by the Naval Weapons Center.

REFERENCES

1. F. DeMarco, K. Heitmann, and K. Press, *Batteries Today*, **16**, No. 2/3, 81, February-March (1980).
2. D. A. Nissen, *This Journal*, **126**, 176 (1979).
3. G. C. Bowser, D. Harney, and F. Tepper in "Power Sources, 6. Research and Development in Non-Mechanical Electrical Power Sources," pp. 537-547, Academic Press, New York (1977).
4. D. H. Kerridge in "Inorganic Chemistry: Main Group Elements, Groups V and VI," Series 1, Vol. 2, C. C. Addison and D. B. Sowerby, Editors, pp. 30-60, Butterworths, London (1972).
5. M. H. Miles, Paper 523 presented at the Electrochemical Society Meeting, St. Louis, Missouri, May 11-16, 1980.
6. A. N. Fletcher, M. H. Miles, and M. L. Chan, *This Journal*, **126**, 1512 (1979).
7. M. H. Miles and A. N. Fletcher, *ibid.*, **127**, 1761 (1980).
8. M. H. Miles, D. A. Fine, and A. N. Fletcher, *ibid.*, **125**, 1209 (1978).
9. M. H. Miles and A. N. Fletcher, *J. Appl. Electrochem.*, **10**, 251 (1980).
10. M. H. Miles, Paper 36 presented at The Electrochemical Society Meeting, St. Louis, Missouri, May 11-16, 1980.
11. H. S. Swofford, Jr. and H. A. Laitinen, *This Journal*, **110**, 814 (1963).
12. F. Solymosi, "Structure and Stability of Salts of Halogen Oxyacids in the Solid Phase," pp. 126-140, John Wiley and Sons, New York (1977).
13. C. W. Jennings in "The Primary Battery," Vol. 2, N. C. Cahoon and G. W. Heise, Editors, pp. 263-266, John Wiley and Sons, New York (1976).
14. K. F. Denning and K. E. Johnson, *Electrochim. Acta*, **12**, 1391 (1967).
15. U. Anders and J. A. Plambeck, *This Journal*, **115**, 598 (1968).

The Transport and Kinetics of Minority Carriers in Illuminated Semiconductor Electrodes

W. John Albery and Philip N. Bartlett

Department of Chemistry, Imperial College, London SW7 2AY, England

and Andrew Hamnett and Martin P. Dare-Edwards

Inorganic Chemistry Laboratory, Oxford, England

ABSTRACT

The differential equation describing the transport and kinetics of photo-generated minority carriers in a semiconductor electrode is solved analytically to obtain a solution in terms of confluent hypergeometric functions. Much simpler approximate solutions are also obtained. Comparison of these solutions with results from the full expression show that the approximate solutions hold to within 5%. A simple physical significance can be attached to the different terms in the approximate solutions. The form of the photocurrent voltage curves that arise from the different solutions is discussed.

The recent development of semiconductor electrodes as photocatalysts for solar energy conversion has stimulated several treatments of the kinetics of electron and hole transport and recombination processes within the semiconductor (1-4). Absorption of light of sufficient energy by the semiconductor will generate minority carriers. Electrochemical processes involving these minority carriers at the surface of the electrode will generate a gradient in their electrochemical potential, leading to the transport of further minority carriers to the surface. The observed photocurrent will be equal to the net flow of minority and majority carriers at any point and if we can calculate the net flow at any one point this will be sufficient.

The problem of electrode processes in illuminated semiconductors has been tackled by a number of authors. Gärtner (1) and later Wilson (2) obtained analytical expressions under very limited conditions. Laser and Bard (3) used digital simulation, but because the minority carrier concentration varies over many orders of magnitude in a small region of the space-charge layer they could only obtain results for times very close to the onset of illumination. Reiss (4) made an attempt to include both minority and majority carriers but avoided the field coupling terms, which lead to analytically intractable semilinear equations. Unfortunately the resulting expressions are quite unwieldy and of little value to the experimentalist. Much more rigorous treatments have been proposed, but invariably the resulting equations are too complex to solve analytically.

In this work we follow the approach of Gärtner and Wilson. We make fewer simplifications and in particular our model includes the recombination of holes and electrons in the depletion layer. We show that the results can be described by simple analytical expressions in which each of the terms corresponds to a simple physical process. Furthermore, from the treatment we obtain relatively simple expressions for the concentration profile of the minority carriers.

The Model

The model for the illuminated electrode is illustrated in Fig. 1 where we have chosen to discuss a p-type semiconductor. The semiconductor is divided into two regions. That nearest the surface is the depletion layer and the potential in this region is given by

$$\theta = \theta_0 (1 - x/\sqrt{2\theta_0} L_D)^2 \quad [1]$$

Key words: photoelectrochemistry, energy conversion, current.

where

$$\theta = VF/RT \quad [2]$$

$$\theta_0 > 4$$

L_D , the Debye length, is given by

$$L_D = (\epsilon\epsilon_0 kT/e^2 N_D)^{1/2} \quad [3]$$

where N_D is the doping density of the semiconductor. The light of irradiance I_0 mol cm⁻² sec⁻¹ is normally incident on the surface of the electrode and absorption is assumed to follow the exponential Beer-Lambert law with a characteristic absorption coefficient α cm⁻¹. To avoid inverse units we define the absorption length

$$L_\epsilon = 1/\alpha \quad [4]$$

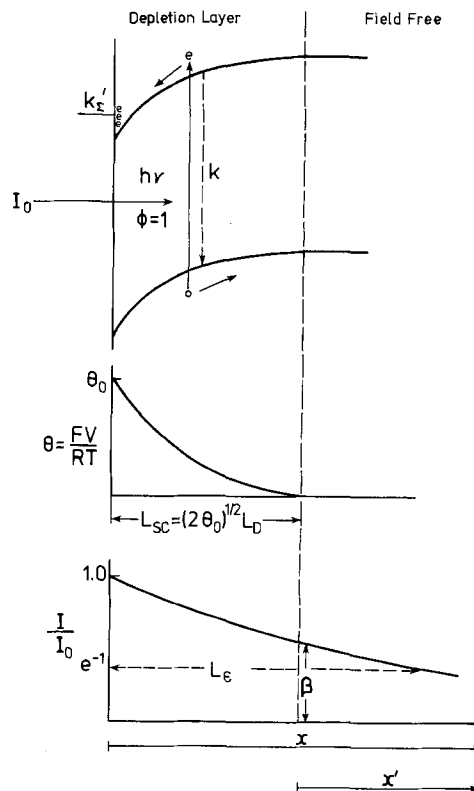


Fig. 1. The model for the semiconductor

In order to avoid cross-coupling terms with the majority carriers, we assume that the buildup of minority carriers at the surface under illumination does not affect the distribution of potential. This important simplification permits us to consider only the equation of motion of the minority carriers. We examine the extent to which this approximation is justified in Appendix A.

The second region $x > \sqrt{2\theta_0 L_D}$ is essentially field free. Minority carriers generated in this region diffuse under a concentration gradient only. To deal with the two regions, Wilson used the principle of superposition of charges to evaluate the flux. We use the alternative procedure of matching the concentration and flux of minority carriers at the boundary of the depletion layer.

The Equation of Motion for Minority Carriers

In a steady state the equation of motion describing the transport and kinetics of the minority carriers (electrons for a p-type semiconductor) is

$$D \frac{\partial}{\partial x} \left(\frac{\partial c}{\partial x} - c \frac{\partial \theta}{\partial x} \right) + \frac{I_0}{L_e} \exp\left(-\frac{x}{L_e}\right) - kc = 0 \quad [5]$$

where we have assumed that the carriers have a sufficiently low mobility for this equation to be applicable. In this expression c is the concentration of electrons with diffusion coefficient D . The field in the depletion layer is described by the dimensionless variable θ defined in Eq. [1]. The first two terms therefore describe transport by diffusion and migration. The next term describes the photogeneration of the carriers by light with a Beer-Lambert profile characterized by L_e . The last term describes the loss by recombination. In this paper we assume that the electrons recombine by first-order kinetics with a rate constant k . This is likely to be true in the field-free region. In the depletion layer traps can be filled or emptied by the field and so the order of kinetics may change. The concentration of majority carriers will be less at the surface because of the band bending. This may decrease the recombination. Reichman (5) has recently considered a particular case using the Sah, Noyce, and Shockley approximation (6). However first-order kinetics will be maintained under conditions of low illumination and if θ_0 is not too large. In this paper we treat this case rigorously. In a subsequent paper we shall extend our treatment to include the other kinetic cases.

Equation [5] must be solved with the two boundary conditions as

$$x \rightarrow \infty \quad c \rightarrow 0 \quad [6]$$

and at $x = 0$

$$NI_0 = D \left[\left(\frac{\partial c}{\partial x} \right)_0 - c_0 \left(\frac{\partial \theta}{\partial x} \right)_0 \right] = k_{\Sigma}' c_0 \quad [7]$$

The boundary condition as $x \rightarrow \infty$ assumes that the thermal population of minority carriers is negligible compared to the population generated by the light. The boundary condition at $x = 0$ relates the flux described by either NI_0 or the transport terms to the kinetics on the surface of the semiconductor described by the overall heterogeneous rate constant k_{Σ}' . The collection efficiency, N , compares the flux of minority carriers lost at the surface by, for instance, recombination and faradaic processes to the flux of incoming photons. When surface recombination ($k_{R'}$) and a faradaic reaction ($k_{F'}$) are the two main processes we define a faradaic collection efficiency, N_F , where

$$N_F = (k_{F'}/k_{\Sigma}') N \quad [8]$$

and

$$k_{\Sigma}' = k_{R'} + k_{F'} \quad [9]$$

To solve Eq. [5] we first solve the equation with boundary condition [6] for the field-free region with

$\theta = 0$ for x greater than W where W is the width of the depletion layer

$$W = (2\theta_0)^{1/2} L_D \quad [10]$$

We thereby obtain a relation between the concentration, c_W , and the flux, c_W' , at $x = W$. Similarly we solve Eq. [5] for the depletion layer with boundary condition [7] and Eq. [1] for θ , to obtain a second relation for the concentration and the flux at $x = W$. Elimination of c_W and c_W' will then lead to an expression for N .

The Field-Free Region

Using Laplace transforms Eq. [5] with boundary condition [6] gives

$$Dc_W' = -\frac{Dc_W}{L_k} + \frac{L_k}{L_k + L_e} \beta I_0 \quad [11]$$

and

$$c = c_W \exp\left(-\frac{x'}{L_k}\right) + \frac{\beta I_0 L_e k^{-1}}{L_k^2 - L_e^2} \left\{ \exp\left(-\frac{x'}{L_k}\right) - \exp\left(-\frac{x'}{L_e}\right) \right\} \quad [12]$$

where

$$x' = x - W$$

$$\beta = \exp(-W/L_e) = \exp[-(2\theta_0)^{1/2} L_D/L_e] \quad [13]$$

and

$$L_k = (D/k)^{1/2} \quad [14]$$

The parameter β describes the fraction of the light that is absorbed in the field-free region, and the length L_k is the diffusion length or reaction layer thickness (7). These results are identical to those obtained for the similar concentration profile for photogeneration in a homogeneous photogalvanic cell (8). Equation [11] shows that the flux at the edge of the depletion layer can be either negative or positive. The first negative term describes the diffusion of electrons out of the space charge layer and their subsequent loss by recombination in a reaction layer of thickness L_k . The second positive term describes the injection of electrons into the depletion layer from photogeneration in the field-free region; the light absorbed is βI_0 and the fraction recovered is $L_k/(L_k + L_e)$. For good recovery L_k must be larger than L_e .

The Depletion Layer

We start by writing

$$c = ue^{\theta} \quad [15]$$

Substitution in Eq. [5] together with Eq. [1] then gives

$$\theta \frac{\partial^2 u}{\partial \theta^2} + (\theta + 1/2) \frac{\partial u}{\partial \theta} - 1/2 \gamma u = -1/2 g e^{-\theta} \quad [16]$$

where

$$\gamma = L_D^2/L_k^2 \quad [17]$$

and

$$g = \frac{\beta I_0 L_D^2}{D L_e} \exp\left[\frac{L_D(2\theta)^{1/2}}{L_e}\right] \quad [18]$$

Equation [16] is an inhomogeneous Kummer equation (9) and is solved below. However, more insight into the physical significance of the mathematics can be obtained from simple analytical expressions found using approximate methods of solution.

The Approximate Method for $L_D < L_k$

In this approach we integrate Eq. [5] using boundary condition [7] to obtain

$$D \left(\frac{\partial c}{\partial x} - c \frac{\partial \theta}{\partial x} \right) = I_0 [N - 1 + \exp(-x/L_e)] + k \int_0^x c dx' \quad [19]$$

Substitution from Eq. [1], [13], [15], and [17] gives

$$\frac{\partial u}{\partial \theta} = -\frac{I_0 L_D}{D} \left\{ N - 1 + \beta \exp \left[\frac{(2\theta)^{1/2} L_D}{L_e} \right] \right\} \frac{\exp(-\theta)}{(2\theta)^{1/2}} - \gamma \frac{\exp(-\theta)}{(2\theta)^{1/2}} \int_{\theta}^{\theta_0} \frac{u \exp(\theta')}{(2\theta')^{1/2}} d\theta' \quad [20]$$

We assume first that $L_D^2 < L_e^2$, which is almost certain to be true for any practical case. Then, when the γ term is negligible, Eq. [20] can be integrated to obtain

$$u_{\gamma=0} = u_0 - \frac{I_0 L_D}{D} \frac{\pi^{1/2}}{2^{1/2}} (1 - \beta - N) [\text{erf } \theta_0^{1/2} - \text{erf } \theta^{1/2}] \quad [21]$$

$$N \approx \frac{1 - \exp \left[\frac{-(2\theta_0)^{1/2} L_D}{L_e} \right] + \frac{L_k}{L_k + L_e} \exp \left[\frac{-(2\theta_0)^{1/2} L_D}{L_e} \right]}{1 + \frac{k}{k_{\Sigma}'} \left[\frac{L_D}{(2\theta_0)^{1/2}} + \frac{L_k}{\exp(\theta_0)} \right]} \quad [29]$$

In this expression the first term on the right-hand side describes the equilibrium distribution of carriers in the field and is dominant near the surface of the semiconductor where θ is close to θ_0 . The second term arises from the transport of carriers in or out of the depletion layer. Its sign depends on $1 - \beta - N$ because the fraction of light absorbed in the depletion layer is $(1 - \beta)$ and the fraction of all the photogenerated carriers that are destroyed at the surface is given by N . When the kinetics in the depletion layer are negligible, then, if $1 - \beta$ is greater than N , carriers are lost to the field-free region and the erf term describes a drop in carrier concentration at the boundary of the depletion layer. Conversely if N is greater than $1 - \beta$ carriers are supplied from the field-free region and the erf term describes a buildup of carriers. In either case the erf term is the dominant term at the boundary of the depletion layer; it arises, because in this region transport by migration is inefficient.

Returning to Eq. [20] we show in Appendix B that for $\gamma < 1$ and $\theta_0 > 6$ the solution for u has the same form as Eq. [21]

$$u \approx u_0 - B [\text{erf } \theta_0^{1/2} - \text{erf } \theta^{1/2}] \quad [22]$$

where B , a constant fixed by the boundary conditions, is

$$B = \frac{\pi^{1/2} \left\{ \frac{I_0 L_D}{D} (1 - \beta - N) - \gamma \frac{c_0}{(2\theta_0)^{1/2}} \right\}}{1 - \gamma \ln(1 + \pi^{1/2} \theta_0^{1/2})} \quad [23]$$

The physical significance of the terms is the same as discussed above. In the numerator of Eq. [23] the γ term allows for the fact that not all the species generated in the depletion layer $(1 - \beta)$ react at the surface (N) or are lost to the field-free region. The term in the denominator means that the solution only holds for

$$\gamma < [\ln(1 + \pi^{1/2} \theta_0^{1/2})]^{-1} \quad [24]$$

From Eq. [15] and [22] we obtain

$$c_w = \exp(-\theta_0) c_0 - B \quad [25]$$

where we have assumed that θ_0 is large enough for $\text{erf } \theta_0^{1/2} \approx 1$. Differentiation of Eq. [25] gives

$$c_w' = -2^{1/2} B / \pi^{1/2} L_D \quad [26]$$

Elimination of c_0 , c_w , c_w' , and B between Eq. [7], [11], [23], [25], and [26] gives

$$N = \frac{1 - \beta + \frac{\beta L_k}{L_k + L_e} f}{1 + \frac{k L_D}{k_{\Sigma}' (2\theta_0)^{1/2}} + \frac{D \exp(-\theta_0) f}{k_{\Sigma}' L_k}} \quad [27]$$

where

$$f = \frac{1 - \gamma \ln(1 + \pi^{1/2} \theta_0^{1/2})}{1 + (\pi\gamma/2)^{1/2}} > 0 \quad [28]$$

and

$$\gamma = L_D^2 / L_k^2$$

Now f will differ significantly from unity only when $L_k \lesssim L_D$. Since we have assumed that $L_D \ll L_e$ the third term in the numerator will be negligible under these conditions. Also under the same conditions the third term of the denominator will be very much smaller than the second. So for most cases we can put $f = 1$ and using Eq. [13] write

In obtaining this result we have made the following approximations and assumptions

$$\theta_0 > 6$$

$$L_D^2 \ll L_e^2$$

$$L_D^2 < L_k^2 / \ln(1 + \pi^{1/2} \theta_0^{1/2})$$

$$f = 1$$

As shown in Fig. 2 each of the terms in Eq. [29] has a simple physical significance. The first two terms in the numerator describe the fraction of light that is

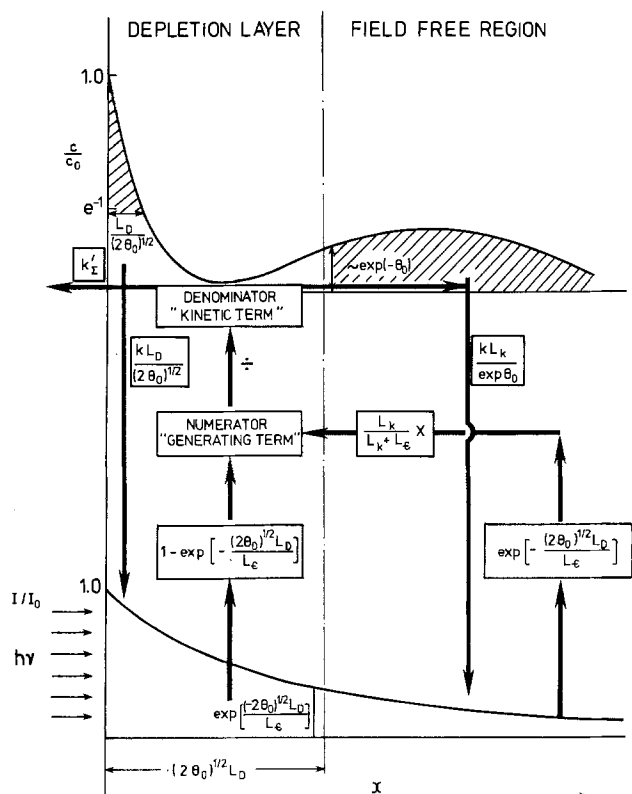


Fig. 2. Diagram illustrating the significance of the various terms in Eq. [29]. The hatching indicates where minority carriers are lost through recombination.

absorbed in the depletion layer; the third term describes the fraction absorbed in the field-free region multiplied by the fraction of those generated that reach the depletion layer boundary. Thus the numerator describes the supply of minority carriers to the surface of the electrode. We call this part of the expression the "generating term." The denominator describes their subsequent fates: the first term reaction at the surface, the second term recombination in the depletion layer, and the third term recombination in the field-free region, where each of the terms is compared to reaction at the surface. We call this group of terms the "kinetic term." Each of the recombination terms contains a characteristic length which describes the volume in which the recombination takes place. In the depletion layer this length is $L_D/(2\theta_0)^{1/2}$. This is because the concentration of minority carriers is largest at the surface of the electrode, and hence for first-order kinetics most recombination takes place close to the surface. At a distance of $L_D/(2\theta_0)^{1/2}$, $c/c_0 \simeq e^{-1}$ and thereafter the concentration continues to fall off as θ drops; this is shown in Fig. 2. For the recombination in the field-free region the characteristic length is L_k . The exponential term describes the difference in concentration between the surface and the boundary of the depletion layer. Therefore the collection efficiency, N , consists of the generating term which describes the supply of minority carriers to the electrode surface divided by the kinetic term which compares the proportion of the carriers which then react at the surface with those which recombine either in the depletion layer or in the field-free region.

From Eq. [7], [15], [22], [23], and [29] we can now write down an expression for the concentration profile of minority carriers in the depletion layer

$$c = \frac{I_0 \exp(\theta)}{k_{\Sigma}' + \frac{kL_D}{(2\theta_0)^{1/2}} + \frac{D \exp(-\theta_0)}{L_k}} \left\{ \left(1 - \beta + \frac{\beta L_k}{L_k + L_{\epsilon}} \right) \exp(-\theta_0) + \frac{(\pi/2)^{1/2} (L_D/D)}{1 + \pi^{1/2} L_D/2^{1/2} L_k} \left[\frac{\beta L_k}{L_k + L_{\epsilon}} \left(k_{\epsilon}' + \frac{kL_D}{(2\theta_0)^{1/2}} \right) - \frac{(1 - \beta) D \exp(-\theta_0)}{L_k} \right] [\operatorname{erf} \theta_0^{1/2} - \operatorname{erf} \theta^{1/2}] \right\} \quad [30]$$

By putting $\theta = 0$ this equation gives the value of c_w to use in Eq. [12] for the field-free region.

Concentration Profiles

Figure 3 shows typical concentration profiles calculated from Eq. [12] and [30]. Note the good join at the boundary of the depletion layer and the way that the depletion layer spreads further into the semiconductor as θ_0 increases. The concentration passes through a minimum in the depletion layer where there need not be many carriers because the transport by migration in the field is efficient. It rises through several orders of magnitude at the surface. This is because there must be sufficient carriers to carry the current into the electrolyte. It is while waiting to react at the surface that the minority carriers are most likely to be destroyed in the depletion layer. It is this feature which, despite the complexities of the differential equation, means that the results are so simple. The profiles are similar to those simulated by Laser and Bard (3), but in our case they are the steady-state profiles.

The Approximate Method for $L_D > L_k$

When $L_D > L_k$ the recombination kinetics are so rapid that, in order to reach the surface, carriers have to be generated in the depletion layer; carriers gen-

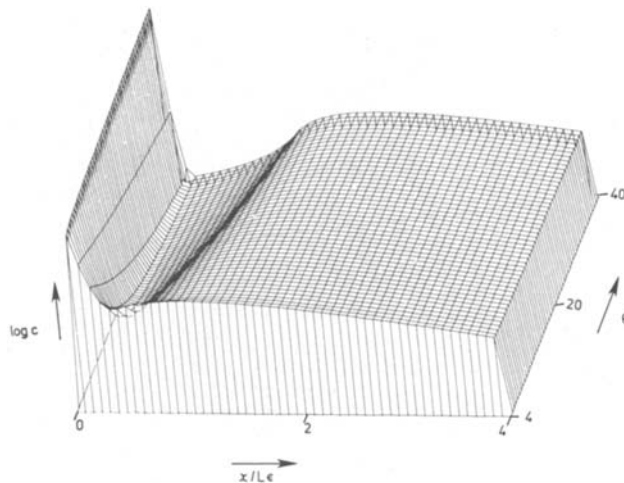


Fig. 3. Typical concentration profiles calculated from Eq. [12] and [30] showing how the concentration varies with distance and the potential across the depletion layer. The following parameters were used: $L_{\epsilon}/L_D = 6.90$, $L_k/L_D = 6.97$, $k_{\Sigma}'L_D/D = 1.45 \times 10^{-2}$.

erated in the field-free region are destroyed before they reach the surface. This means that the important region in determining N is a very thin layer close to the surface of the electrode. Returning to Eq. [5] we can then make a simple approximation; we replace $(\partial\theta/\partial x)$ with its value at the surface

$$(\partial\theta/\partial x) \simeq (2\theta_0)^{1/2}/L_D \quad [31]$$

Equation [5] can then be integrated, using Laplace transforms, to give

$$N = \frac{(1 + L_{\epsilon}/L_A)^{-1}}{(1 + D/k_{\Sigma}'L_A)} \quad [32]$$

$$c = \frac{NI_0}{k_{\Sigma}'} \exp\left(-\frac{x}{L_B}\right) + \frac{I_0 L_{\epsilon}/D}{\left(\frac{L_{\epsilon}}{L_k}\right)^2 + \frac{(2\theta_0)^{1/2} L_{\epsilon}}{L_D} - 1} \times \left[\exp\left(-\frac{x}{L_{\epsilon}}\right) - \exp\left(-\frac{x}{L_B}\right) \right] \quad [33]$$

where

$$L_A = \frac{L_D}{(2\theta_0)^{1/2}} \left[(\frac{1}{4} + \gamma/2\theta_0)^{1/2} - \frac{1}{2} \right]^{-1} \quad [34]$$

and

$$L_B = \frac{L_D}{(2\theta_0)^{1/2}} \left[(\frac{1}{4} + \gamma/2\theta_0)^{1/2} + \frac{1}{2} \right]^{-1} \quad [35]$$

When

$$L_D < (2\theta_0)^{1/2} L_k \quad [36]$$

$$L_A \simeq (2\theta_0)^{1/2} L_k^2/L_D \quad [37]$$

$$L_B \simeq L_D/(2\theta_0)^{1/2} \quad [38]$$

and

$$N \simeq \frac{(1 + L_{\epsilon}L_D/(2\theta_0)^{1/2}L_k^2)^{-1}}{(1 + kL_D/(2\theta_0)^{1/2}k_{\Sigma}')^{-1}} \quad [39]$$

On the other hand, when

$$L_D > (2\theta_0)^{1/2} L_k \quad [40]$$

$$L_A \simeq L_B \simeq L_k \quad [41]$$

and

$$N \simeq \frac{(1 + L_{\epsilon}/L_k)^{-1}}{1 + D/k_{\Sigma}'L_k} \quad [42]$$

Under these extreme conditions the kinetics are so rapid that a simple photostationary state is established inside one Debye length. The field has no effect and we obtain the same result as for a photogalvanic cell (8). In the expression for c the effect of the surface

reactions perturbs the concentration profile over a distance $\sim L_B$. As shown by [38] or [41] this distance is very short and thereby justifies the approximation in [31]. When $x > 5L_B$ the dominant term in [33] is the Beer-Lambert exponential term in (x/L_ϵ) . The expressions for N in [39] and [42] again consist of a generating term, the numerator, and a kinetic term, the denominator. It is satisfactory that the kinetic term of Eq. [32] for N is the same as the kinetic term in the previous result which was derived for the opposite condition that $L_D < L_k$.

The Rigorous Solution

Although the results derived so far are simple and satisfyingly transparent, we can obtain a rigorous solution to the inhomogeneous Kummer equation [16]. The homogeneous equation

$$\theta \frac{\partial^2 u}{\partial \theta^2} + (\theta + 1/2) \frac{\partial u}{\partial \theta} - 1/2 \gamma u = 0$$

has two independent solutions (10)

$$G_1(-\theta) = {}_1F_1(-1/2\gamma; 1/2; -\theta) \quad [43]$$

$$G_2(-\theta) = \theta^{1/2} {}_1F_1(1/2 - 1/2\gamma; 3/2; -\theta) \quad [44]$$

$$N = \frac{\left(\frac{W}{L_\epsilon}\right)^{-\gamma} \exp\left(-\frac{W}{L_\epsilon}\right) \int_0^{W/L_\epsilon} \lambda^\gamma \exp(\lambda) d\lambda + \frac{\beta L_k \theta_0^{-1/2\gamma}}{L_k + L_\epsilon} \cdot \left[\frac{\Gamma(1/2)}{\Gamma(1/2 + 1/2\gamma)} + \frac{\Gamma(1/2)L_D}{2^{1/2}\Gamma(1 + 1/2\gamma)L_k} \right]^{-1}}{1 + kL_D/k_\Sigma'(2\theta_0)^{1/2}} \quad [54]$$

where ${}_1F_1$ is a confluent hypergeometric function (10). The inhomogeneous equation can then be solved by constructing a Green's function and we obtain

$$c \exp(-\theta) = c_W G_1(-\theta) + \frac{G_2(-\theta)}{G_2(-\theta_0)} \left\{ c_0 \exp(-\theta_0) - c_W G_1(-\theta_0) - 2G_1(-\theta_0) \int_0^{\theta_0^{1/2}} g G_2(-\theta') d(\theta')^{1/2} + 2G_1(-\theta) \int_0^{\theta^{1/2}} g G_2(-\theta') d(\theta')^{1/2} + 2G_2(-\theta) \int_{\theta_0^{1/2}}^{\theta^{1/2}} g G_1(-\theta') d(\theta')^{1/2} \right\} \quad [45]$$

When γ is small then (10)

$$G_1(-\theta) \simeq 1 \quad [46]$$

$$G_2(-\theta) \simeq 1/2 \pi^{1/2} \operatorname{erf} \theta^{1/2} \quad [47]$$

If we also assume that $L_D \ll L_\epsilon$ then [45] reduces to the corresponding Eq. [22].

Differentiation of [45] to find c_W' followed by elimination using [7], [11], and [13] gives

$$N = \frac{\beta \left[\frac{L_k}{L_k + L_\epsilon} + \int_0^{\theta_0^{1/2}} g' G_1 d\theta^{1/2} + \frac{2^{1/2} L_D}{L_k} \int_0^{\theta_0^{1/2}} g' G_2 d\theta^{1/2} \right]}{G_1(-\theta_0) + \frac{2^{1/2} L_D G_2(-\theta_0)}{L_k} + \frac{D}{2^{1/2} k_\Sigma' L_D} G_1'(-\theta_0) + \frac{D}{k_\Sigma' L_k} G_2'(-\theta_0)} \quad [48]$$

where

$$g' = \frac{2^{1/2} L_D}{L_\epsilon} \exp\left[-\frac{(2\theta)^{1/2} L_D}{L_\epsilon}\right]$$

$$G_1'(-\theta) = \partial G_1(-\theta) / \partial \theta^{1/2} = 2\gamma \theta^{1/2} {}_1F_1(1 - 1/2\gamma; 3/2; -\theta) \quad [49]$$

$$G_2'(-\theta) = \partial G_2(-\theta) / \partial \theta^{1/2} = {}_1F_1(1/2 - 1/2\gamma; 1/2; -\theta) \quad [50]$$

This general expression for N again consists of a gen-

erating term, the numerator, and a kinetic term, the denominator. For small values of γ the confluent hypergeometric functions may be simplified, as given in Eq. [46] and [47] and

$$G_1'(-\theta_0) \simeq 2\gamma \operatorname{Daw}(\theta_0^{1/2}) \simeq \gamma \theta_0^{-1/2} \quad [51]$$

$$G_2'(-\theta_0) \simeq \exp(-\theta_0) \quad [52]$$

where $\operatorname{Daw}(\lambda)$ is Dawson's integral (11). For values of $\theta_0^{1/2} > 3$ we can make the further approximation in Eq. [51]. Substitution in [48] followed by integration gives

$$N \simeq \frac{1 - \beta + \frac{\beta L_k}{L_k + L_\epsilon} \left(\frac{1}{1 + \pi^{1/2} L_D / 2^{1/2} L_k} \right)}{1 + \frac{kL_D}{k_\Sigma'(2\theta_0)^{1/2}} + \frac{D}{k_\Sigma' L_k} \frac{\exp(-\theta_0)}{(1 + \pi^{1/2} L_D / 2^{1/2} L_k)}} \quad [53]$$

This expression is identical with [27] when, for the same reasons as we could put $f = 1$ in [27], the terms in $\pi^{1/2} L_D / 2^{1/2} L_k$ are ignored. For large values of θ_0 alternative expressions for the confluent hypergeometric functions may be used (10) giving

This result confirms the expression for the kinetic term obtained in the approximate treatments for large values of θ_0 , regardless of whether L_k is greater or smaller than L_D . For the generating term, when γ is small ($L_k^2 > L_D^2$), the numerator reduces to the result in [29]. When γ is ~ 1 and $W < L_\epsilon$, the generating term reduces, after integration, to

$$\text{G.T.} = \frac{W/L_\epsilon}{1 + \gamma} \quad [55]$$

This result may be compared with the two approximate solutions from [29] and [39]

$$\text{G.T.} \simeq W/L_\epsilon \quad \text{for } \gamma \ll 1 \quad [56]$$

and

$$\text{G.T.} \simeq W/L_\epsilon \gamma \quad \text{for } \gamma \gg 1 \quad [57]$$

We can therefore extend the validity of the approximate solution for $\gamma > 1$ by writing, instead of [39]

$$N = \frac{\left[1 + \frac{L_\epsilon}{W} \left(1 + \frac{L_D^2}{L_k^2} \right) \right]^{-1}}{1 + kL_D / (2\theta_0)^{1/2} k_\Sigma'} \quad [58]$$

This expression holds to within 10% for most cases where $2\theta_0^{1/2} > L_D/L_k > 1$. Similarly for $\gamma < 1$ we can modify the complete Eq. [29] using [54] to give

$$N \simeq \frac{1 - \beta}{1 + \beta^{0.3\gamma}} + \frac{\beta L_k}{L_k + L_\epsilon} \frac{\theta_0^{-1/2\gamma}}{1 + (2\gamma)^{1/2} + \gamma}}{1 + \frac{kL_D}{k_\Sigma'(2\theta_0)^{1/2}} + \frac{D}{k_\Sigma' L_k} \exp(-\theta_0)} \quad [59]$$

where the exponent 0.3 has been found to give the best fit to results from the complete equation.

Comparison with Previous Results

Our expression for N may be compared with the previous results obtained by Wilson (2). Using our notation rearrangement of his Eq. [11] and using his Eq. [18] (after correcting a typographical error) we obtain Eq. [29] without the second term in the denominator which describes recombination in the depletion layer. This is because Wilson did not include this effect.

Current Voltage Curves

In dimensionless notation current voltage curves are plots of N_F against θ_0 , where N_F is defined in [8]. While it is always possible that the electrochemical rate constants k_F' and k_R' may depend on potential because, for instance, the reactions may involve surface states, one cannot have a general theory for this effect. We can, however, discuss how N depends on θ_0 and therefore see how far the observed current voltage behavior can be attributed to the transport and kinetics in the semiconductor as opposed to the ubiquitous explanation of surface states (2, 12), remembering always that in this paper we have assumed that the recombination kinetics are first order throughout the depletion layer.

Typical results for N as a function of θ_0 are displayed in Fig. 4, 5, and 6. There is less than 5% difference between those results calculated using the appropriate approximate equations [58] or [59] and those obtained using a computer to evaluate the functions in the complete Eq. [48]. This good agreement justifies the approximations used.

In considering the variation of N with θ_0 it is helpful to depict the various types of behavior that can be found from the generating and kinetic terms; this is done in Fig. 7 for the generating term. The diagram shows different approximate expressions for the generating term and the conditions in terms of θ_0 and L_k/L_D for which the approximations hold. Near the boundary lines between the different approximations the full expression has to be used. We have obtained the expression $(2\theta_0)^{1/2}L_D/L_e$ in the hatched area by following Butler (13) and expanding the exponential terms which is justified in this region. It is interesting that this solution passes smoothly over into the equivalent $\sqrt{\theta_0}$ expression from [39]. In general if there is any variation with potential of the generating term it will vary with $\sqrt{\theta_0}$. The solid lines in the diagram depend only on θ_0 and L_k/L_D , the broken lines depend on L_e . The inset shows how their location varies with L_e/L_D . It can be seen that for $L_e/L_D > 14$ the broken lines do not appear on the diagram at all. Typical

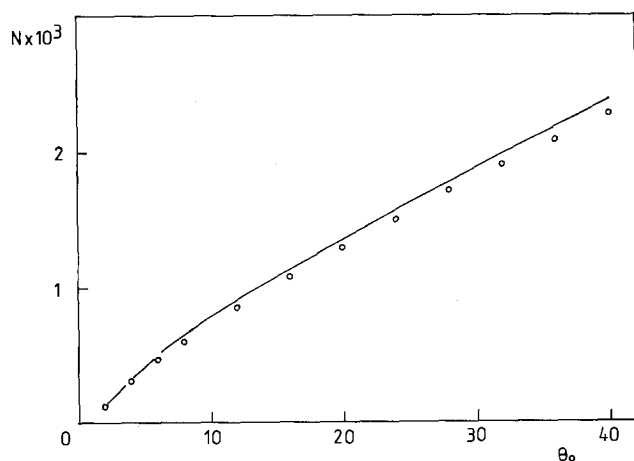


Fig. 4. A current voltage curve for $L_e/L_D = 20$, $L_k/L_D = 4$, $k_{\Sigma}'L_D/D = 4 \times 10^{-5}$. The line is calculated from the approximate Eq. [59] (or Eq. [7]) and the points from the full solution Eq. [48].

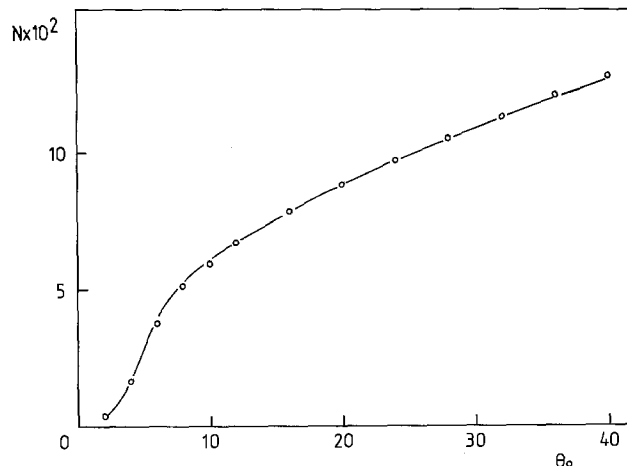


Fig. 5. A current voltage curve for $L_e/L_D = 20$, $L_k/L_D = 25.1$, $k_{\Sigma}'L_D/D = 4 \times 10^{-5}$. The line is calculated from the approximate Eq. [59] and the points from the full solution Eq. [48].

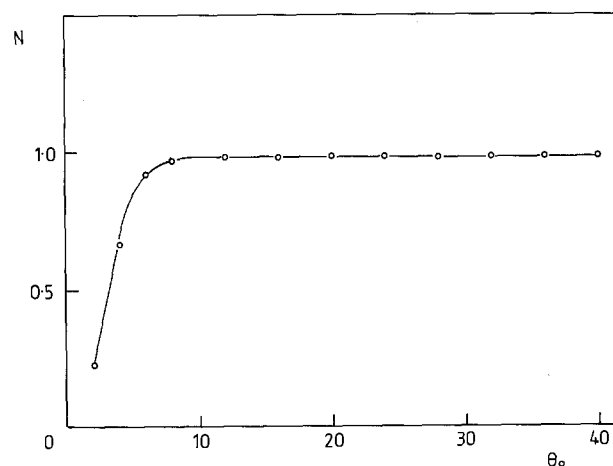


Fig. 6. A current voltage curve for $L_e/L_D = 20$, $L_k/L_D = 1 \times 10^3$, $k_{\Sigma}'L_D/D = 4 \times 10^{-5}$. The line is calculated from the approximate Eq. [59] and the points from the full solution Eq. [48].

values of L_e and L_D are 10^{-4} and 10^{-6} cm, respectively, so for most cases the diagram simplifies to the unhatched area where the field has no effect on the generating term and the hatched region around $L_k = L_D$ where the term depends on $\theta_0^{1/2}$. In Fig. 7 for $L_k > 20L_D$ nearly all the carriers are generated in the field-free region and the supply of these carriers to the surface is determined by the kinetics and transport in that region. On the other hand, when $L_k < L_D/20$ the recombination rate is so rapid that for carriers to reach the surface they have to be generated very close to the surface and the extent of the depletion layer is unimportant. Only when $L_k \approx L_D$ is the width of the depletion layer important in determining how many carriers reach the surface. The more rapid transport by migration in the depletion layer means that carriers generated within the depletion layer have a better chance of reaching the surface than those generated in the field-free region. However we must emphasize that this feature of semiconductor transport and kinetics is only important when L_k is within an order of magnitude of L_D .

Figure 8 is the equivalent diagram for the kinetic term. Again the solid lines depend only on θ_0 and L_k/L_D , while in this case the location of the broken lines depends on the value of $(k_{\Sigma}'L_D/D)$, as shown in Fig. 9. In general Fig. 8 is divided into four regions. For large values of L_k the recombination kinetics are slow and the kinetic term tends to unity. In the extensive hatched area the kinetic term depends on $\theta_0^{1/2}$ and hence the competition is between k_{Σ}' and recom-

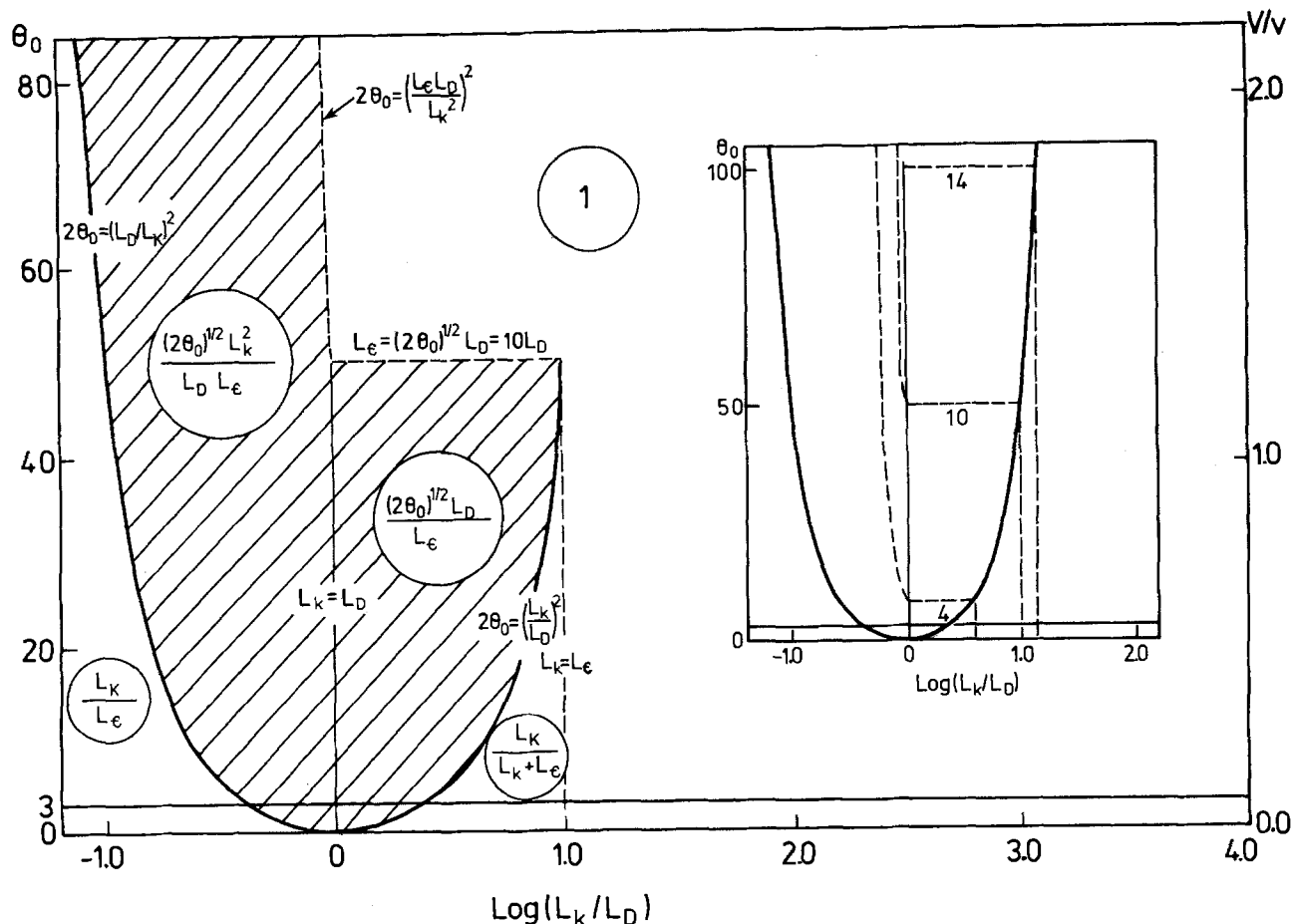


Fig. 7. Approximate solutions for the generating term as a function of L_k/L_D and the applied potential θ_0 . The broken lines also depend on the value of L_e , and the inset shows how their position varies with L_e/L_D . Note that the generating term only varies with θ_0 when $L_k \sim L_D$.

recombination in the depletion layer. In the speckled area the current depends on $\exp(\theta_0)$ and the competition is between $k_{\Sigma'}$ and loss in the field-free region. Finally at low values of L_k , as with the generating term, the recombination kinetics are so rapid that the width of the depletion layer is unimportant. The boundaries between the hatched or the speckled areas and the region where the term is unity represent the half-wave potentials of the current voltage curves (providing that $k_{R'}$ and $k_{F'}$ do not depend on potential). It can be seen that because of the exponential term the speckled area is only found at low values of θ_0 . A potential difference from the flatband of less than 0.3V will usually be sufficient to reach the half-wave potential. By contrast the dependence of current on $\theta_0^{1/2}$ is rather a weak dependence. So in many cases the limiting value for the kinetic term of unity is never reached, and the kinetic term depends on $\theta_0^{1/2}$ over an extensive potential range. Finally in Fig. 10 we combine the results to show how N depends on θ_0 . We have assumed, as discussed above, that $L_k > 20 L_D$. It can be seen that if

$$k_{\Sigma'} < 10^{-4} D/L_D \quad [60]$$

then N depends on $\theta_0^{1/2}$ because of the $\theta_0^{1/2}$ region in the kinetic term rather than the $\theta_0^{1/2}$ region in the generating term. Hence there are two possible explanations of an observed dependence of N on $\theta_0^{1/2}$. The first explanation is that of Butler. This requires that

$$L_k \sim L_D \quad [61]$$

and that

$$k_{\Sigma'} > D/L_D \quad [62]$$

The last condition ensures that the kinetic term is unity and is equivalent to Butler (13) and Gärtner's (1) assumption of rapid interfacial kinetics. With

typical values of D and L_D of $1 \text{ cm}^2 \text{ sec}^{-1}$ and 10^{-5} cm , respectively, we find that

$$k_{\Sigma'} > 10^5 \text{ cm sec}^{-1} \quad [63]$$

This condition is a severe one since a rough estimate suggests that the upper limit for such an electrochemical rate constant is $\sim 10^5$ - 10^6 cm sec^{-1} . In Butler's case $D/\text{cm}^2 \text{ sec}^{-1} = 0.25$ and $L_D/\text{cm} = 3.4 \times 10^{-5}$ so he required $k_{\Sigma'} > 10^4 \text{ cm sec}^{-1}$.

In our view it is more probable that the condition in Eq. [60] will be satisfied and that the explanation of N being linear with $\theta_0^{1/2}$ involves recombination in the depletion layer, always with the assumption that the kinetics are first order throughout. If this explanation is correct, then the gradients of $N/\theta_0^{1/2}$ plots will depend on $k_{\Sigma'}$ and therefore will depend on the medium and the concentrations of electrochemical reactants. This type of behavior has been found, for instance, by Gautron *et al.* (14) for ZnSe. The gradients in HClO_4 , KCl , and KOH are all different. This cannot arise from the Butler explanation because in that case the gradient only depends on the properties of the semiconductor L_e , L_k , and L_D . Hence this is a simple diagnostic test for the two different explanations.

Acknowledgments

We thank Mr. P. Colby for help with the computer graphics. We acknowledge financial support from the SRC and from BP for P.B. This is a contribution from the Oxford Imperial Energy Group.

Manuscript submitted Oct. 27, 1980; revised manuscript received Feb. 4, 1981.

Any discussion of this paper will appear in a Discussion Section to be published in the June 1982 JOURNAL.

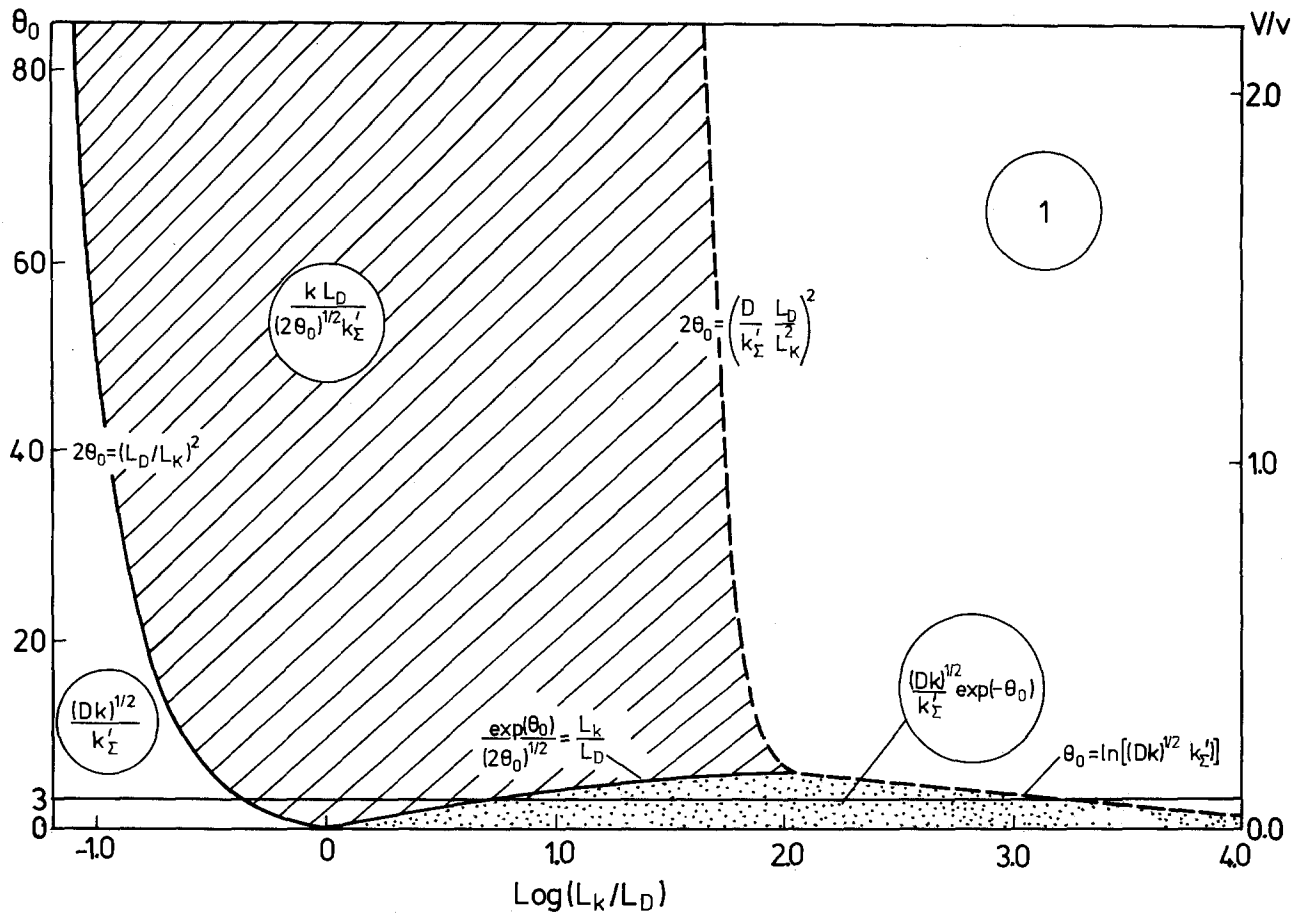


Fig. 8. Approximate solutions for the kinetic term as a function of L_k/L_D and the applied potential θ_0 . The broken lines also depend on the value of $k'_\Sigma L_D/D$ as shown in Fig. 9.

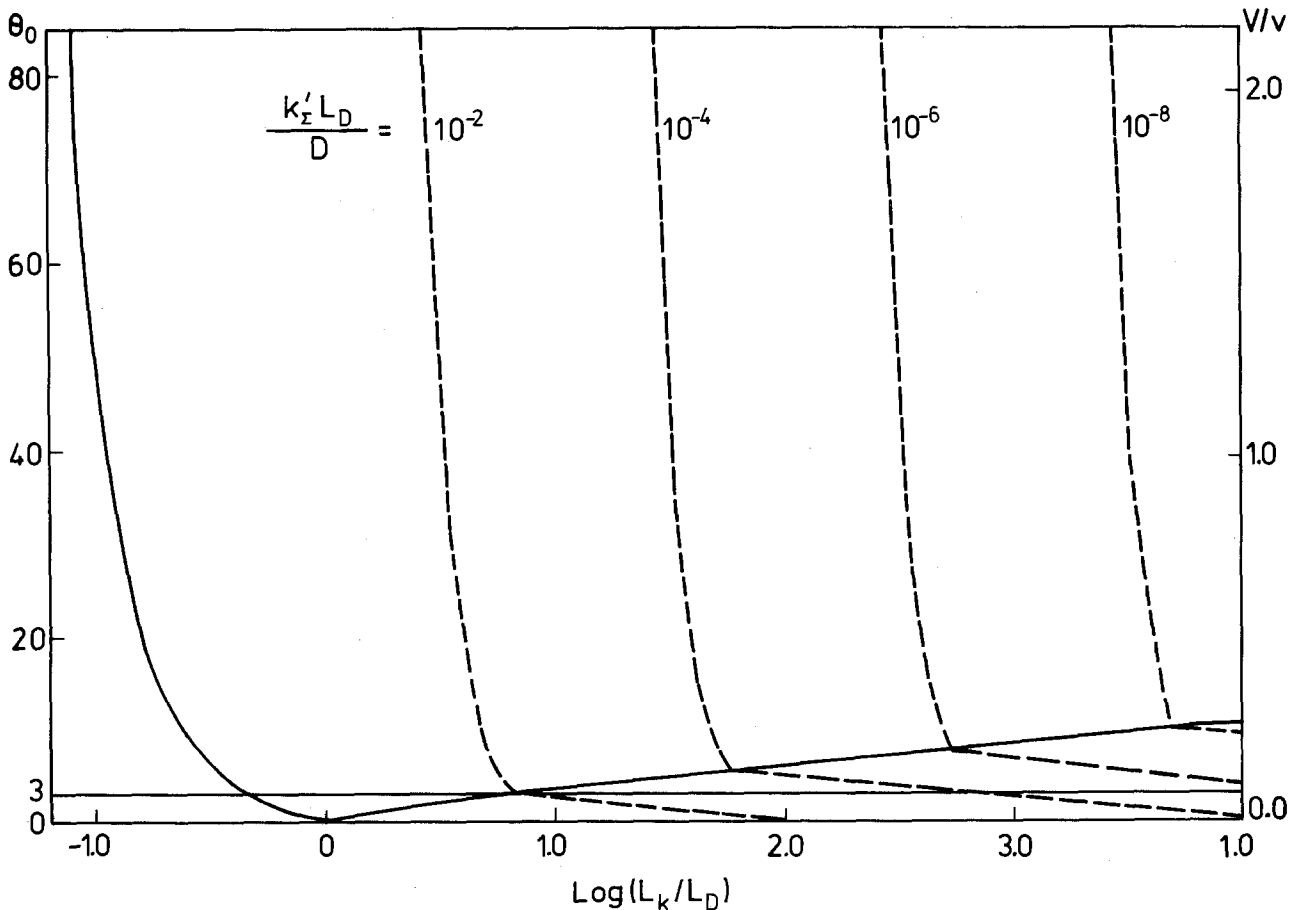


Fig. 9. This figure shows how the broken lines in Fig. 8 vary with $k'_\Sigma L_D/D$

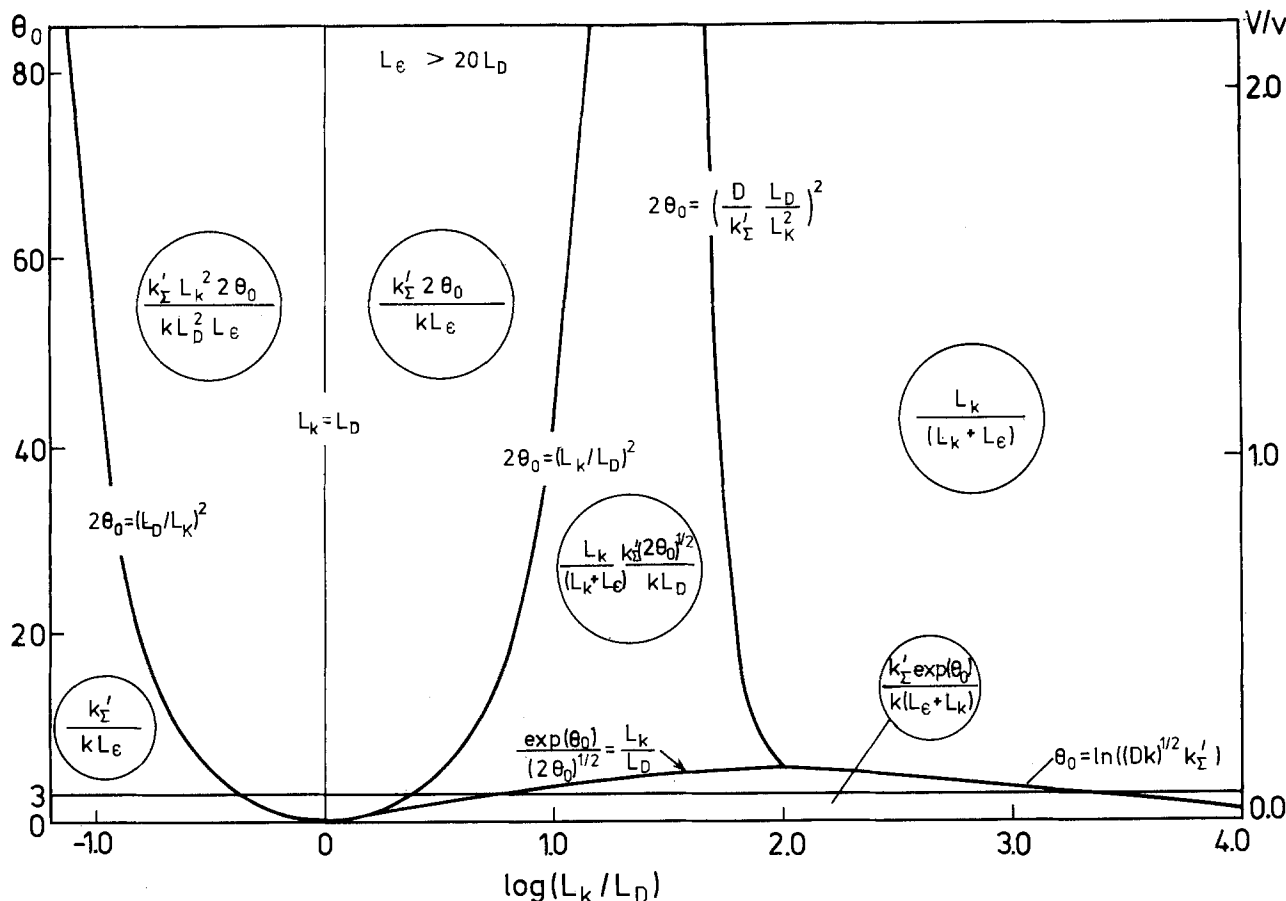


Fig. 10. Approximate solutions for N as a function of L_k/L_D and θ_0 , assuming that $L_e > 20L_D$, for the particular case of $k'_\Sigma L_D/D = 10^{-4}$. Note that the dependence on $\theta_0^{1/2}$ arises from the kinetic term rather than the generating term.

All discussions for the June 1982 Discussion Section should be submitted by Feb. 1, 1982.

APPENDIX A

In our treatment we have assumed that the variation of potential with distance is given by [1]. However, the buildup of minority carriers at the surface of the semiconductor (see Fig. 3) may alter the potential distribution. Close to the surface the concentration of minority carriers is given by

$$c \simeq c_0 \exp(\theta - \theta_0)$$

The Poisson-Boltzmann equation is then

$$\partial^2 \theta / \partial x^2 = 1 + \rho \exp(\theta - \theta_0)$$

where

$$x = x/L_D$$

and

$$\rho = \frac{c_0}{N_D} = \frac{NI_0}{k'_\Sigma N_D} \quad [\text{A-1}]$$

Integration, assuming $\rho \exp(-\theta_0) \ll 1$ gives

$$\partial \theta / \partial x = - [2\theta + 2\rho \exp(\theta - \theta_0)]^{1/2} \quad [\text{A-2}]$$

and

$$2^{1/2} x = \int_{\theta}^{\theta_0} [\theta' + \rho \exp(\theta' - \theta_0)]^{-1/2} d\theta' \quad [\text{A-3}]$$

To evaluate the integral we split it at θ_* where for $\theta < \theta_*$, $\theta \simeq \theta_0 \simeq \theta_*$ and for $\theta > \theta_*$ the term in ρ is negligible.

For $\theta < \theta_*$

$$I_1 = \int_{\theta}^{\theta_*} \theta^{-1/2} d\theta = 2(\theta_*^{1/2} - \theta^{1/2}) \quad [\text{A-4}]$$

For $\theta > \theta_*$

$$I_2 = \int_{\theta_*}^{\theta_0} \frac{d\theta'}{[\theta_* + \rho \exp(\theta' - \theta_0)]^{1/2}} \\ = \theta_*^{-1/2} \ln \left[\frac{P-1}{P+1} \cdot \frac{Q+1}{Q-1} \right] \quad [\text{A-5}]$$

where

$$P = (1 + \rho/\theta_*)^{1/2}$$

and

$$Q = [1 + (\rho/\theta_*) \exp(\theta_* - \theta_0)]^{1/2}$$

Assuming that $\rho/\theta_* < 1$, we use the binomial expansion for P and Q to obtain for I_2

$$I_2 \simeq \theta_*^{-1/2} [\theta_0 - \theta_* - 1/2(\rho/\theta_*) \{1 - \exp(\theta_* - \theta_0)\}]$$

Substitution in [A-3] gives for $\theta < \theta_*$

$$x \simeq (2\theta_0)^{1/2} [1 - \rho/4\theta_0^2] - (2\theta)^{1/2} \quad [\text{A-6}]$$

Hence for most of the depletion layer the parabolic form of [1] still holds and furthermore the effect of the buildup of minority carriers on the actual potential distribution is negligible if

$$\rho = \frac{NI_0}{k'_\Sigma N_D} \ll 4\theta_0^2 \quad [\text{A-7}]$$

With the values $N = 1$, $I_0 = 2 \times 10^{-7}$ mol cm⁻² sec⁻¹, $k'_\Sigma = 1$ cm sec⁻¹, and $N_D = 10^{17}$ cm⁻³, ρ is approximately unity. The effect of the term in ρ is shown in Fig. A-1. It can be seen that the buildup of minority carriers reduces the potential and the width of the layer. From Eq. [A-2] the potential gradient at the surface is steeper

$$(\partial \theta / \partial x)_0 = - [2(\theta_0 + \rho)]^{1/2}$$

This means that, even though [A-7] holds, ρ will have an effect on this gradient when $\rho \sim \theta_0$ and this in turn will affect the loss of minority carriers from recombination in the depletion layer. Hence if ρ is significant compared to θ_0 then in [27], [29], [30], [39], [53], [54], [58], and [59] $(2\theta_0^{1/2})$ should be replaced by $[2(\theta_0 + \rho)]^{1/2}$ in the depletion layer recombination term in the denominator.

APPENDIX B

In this Appendix we integrate Eq. [20] for the conditions $\alpha < 1$ and $\theta_0 > 6$. We start by assuming that the solution has the same form as Eq. [21]

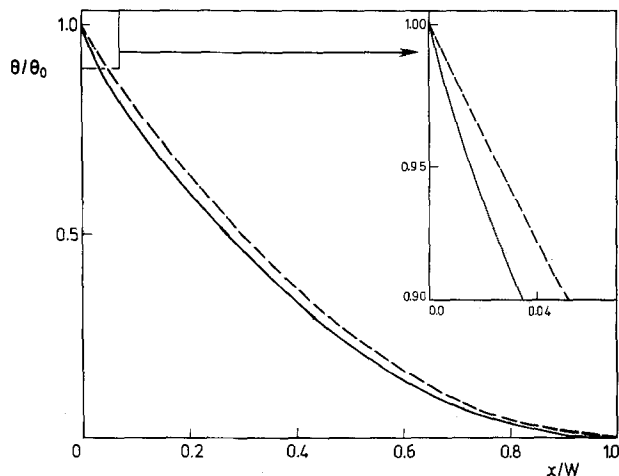


Fig. A-1. The effect of the buildup of minority carriers at the surface on the distribution of potential in the depletion layer, for $\rho = \theta_0 = 10$. The broken line is calculated from Eq. [1] ($\rho = 0$) while the solid line is calculated from Eq. [A-6].

$$u = u_0 - B [\text{erf } \theta_0^{1/2} - \text{erf } \theta^{1/2}] \quad [\text{B-1}]$$

where B is a constant. A simple approximation for the error functions, which is at worst only 18% in error, is

$$\text{erf } \theta_0^{1/2} - \text{erf } \theta^{1/2} \simeq \exp(-\theta) / (1 + \pi^{1/2} \theta^{1/2}) \quad [\text{B-2}]$$

Substitution of [B-1] and [B-2] in [20] followed by integration gives

$$u = u_0 - \frac{I_0 L_D}{D} \frac{\pi^{1/2}}{2^{1/2}} (1 - \beta - N) [\text{erf } \theta_0^{1/2} - \text{erf } \theta^{1/2}] + \gamma \int_0^{\theta_0} \frac{\exp(-\theta')}{(2\theta')^{1/2}} \left[u_0 \int_{\theta'}^{\theta_0} \frac{\exp(\theta'')}{(2\theta'')^{1/2}} d\theta'' - B \int_{\theta'}^{\theta_0} \frac{(2\theta'')^{-1/2}}{1 + (\pi\theta'')^{1/2}} d\theta'' \right] d\theta' \quad [\text{B-3}]$$

The integrals in the γ term are evaluated as follows:
First

$$\int_0^{\theta_0} \frac{\exp(-\theta')}{(2\theta')^{1/2}} \int_{\theta'}^{\theta_0} \frac{\exp(\theta'')}{(2\theta'')^{1/2}} d\theta'' = \int_0^{\theta_0} \frac{\exp(-\theta')}{(\theta')^{1/2}} [\exp(\theta_0) \text{Daw}(\theta_0)^{1/2} - \exp(\theta') \text{Daw}(\theta')^{1/2}] d\theta' \simeq \frac{1}{2} \pi^{1/2} \theta_0^{-1/2} \exp(\theta_0) [\text{erf } \theta_0^{1/2} - \text{erf } \theta^{1/2}] - \frac{1}{2} \ln(\theta_0/\theta) \quad [\text{B-4}]$$

where $\text{Daw}(\lambda)$ is Dawson's integral (11) and for $\lambda > 2$

$$\text{Daw}(\lambda) \simeq \frac{1}{2} \lambda^{-1}$$

In [B-4] the \ln term can be ignored with respect to the first term.

Second

$$\int_0^{\theta_0} \frac{\exp(-\theta')}{(2\theta')^{1/2}} \int_{\theta'}^{\theta_0} \frac{(2\theta'')^{-1/2}}{1 + (\pi\theta'')^{1/2}} d\theta'', d\theta' = \pi^{-1/2} \int_0^{\theta_0} \frac{\exp(-\theta')}{(\theta')^{1/2}} \left[\ln \left\{ \frac{1 + (\pi\theta_0)^{1/2}}{1 + (\pi\theta')^{1/2}} \right\} \right] d\theta' \simeq \ln [1 + (\pi\theta_0)^{1/2}] [\text{erf } \theta_0^{1/2} - \text{erf } \theta^{1/2}] \quad [\text{B-5}]$$

Substitution of [B-4] and [B-5] in [B-3], followed by comparison with [B-1] and using $c_0 = u_0 \exp(\theta_0)$ gives the expression for B in [23]

REFERENCES

1. W. W. Gärtner, *Phys. Rev.*, **116**, 84 (1959).
2. R. H. Wilson, *J. Appl. Phys.*, **48**, 4292 (1977).
3. D. Laser and A. J. Bard, *This Journal*, **123**, 1828 (1976).
4. H. Reiss, *ibid.*, **125**, 937 (1978).
5. J. Reichman, *Appl. Phys. Lett.*, **36**, 574 (1980).
6. C-T Sah, R. N. Noyce, and W. Shockley, *Proc. IRE*, **45**, 1228 (1957).
7. J. J. Koutecky and V. G. Levich, *Zh. Fiz. Khim.*, **32**, 1565 (1958).
8. W. J. Albery and M. D. Archer, *J. Electroanal. Chem. Interfacial Electrochem.*, **86**, 19 (1978).
9. M. Abramowitz and I. A. Stegun, "Handbook of Mathematical Functions," p. 504, Dover Publications, New York (1970).
10. M. Abramowitz and I. A. Stegun, *ibid.*, p. 509.
11. M. Abramowitz and I. A. Stegun, *ibid.*, p. 298.
12. R. H. Wilson, *This Journal*, **126**, 1187 (1979).
13. M. A. Butler, *J. Appl. Phys.*, **48**, 1914 (1977).
14. J. Gautron, P. Lemasson, F. Rabago, and R. Triboulet, *This Journal*, **126**, 1868 (1979).

The Electrochemical Behavior of Synthetic Reformate Fuels on Platinum Electrodes in Trifluoromethanesulfonic Acid Monohydrate

Grayson W. Walker*

U.S. Army Mobility Equipment Research and Development Command, Fort Belvoir, Virginia 22060

and R. T. Foley*

Chemistry Department, The American University, Washington, D.C. 20016

ABSTRACT

Electrode performance of two synthetic reformates, one a 3% CO-12% CH₄-85% H₂ mixture and the other a 2% CO-26% CO₂-72% H₂ mixture, were investigated in trifluoromethanesulfonic acid monohydrate (TFMSA · H₂O). These reformate fuels were found to significantly reduce electrode performance when compared to pure H₂ performance, but the reformate performance in TFMSA · H₂O was superior to pure H₂ performance in 85% H₃PO₄. Comparisons in polarization data and activation energies between the reformates and several CO-H₂ mixtures have shown that CO was the rate-limiting component in the reformate mixtures. Voltammetric techniques were employed as a means of studying CO adsorption in TFMSA · H₂O in more detail.

In the past five years, there has been renewed interest in finding alternative electrolytes for fuel cells which combine the stability of phosphoric acid with the desirable electrochemical properties found in acids such as HF or H₂SO₄. The fluorinated alkanesulfonic acids have been investigated extensively (1-8), and trifluoromethanesulfonic acid monohydrate (TFMSA · H₂O), in particular, has exhibited many desirable properties such as low vapor pressure, high ionic strength, and a noninterfering anion group. Adams *et al.* have shown that, kinetically, hydrogen and propane oxidation reactions proceed at rates 3-10 times faster in TFMSA · H₂O than in H₃PO₄, and the open-circuit potential for oxygen on platinum is approximately 150 mV higher in TFMSA · H₂O (4-6).

If TFMSA · H₂O is to be realistically considered as an alternative to phosphoric acid, it must be characterized under all fuel cell conditions. The need for a synthetic source of hydrogen has been established; therefore, a comprehensive characterization of TFMSA · H₂O should include a study of cell performance with reformate fuels where the effect of the various constituents, particularly carbon monoxide, could be observed. The reformer constitutes a large percentage of total fuel cell cost and the higher the grade of reformate required by the fuel cell, the more complex and costly the system becomes. If it could be shown that any detrimental effects produced by the reformate constituents are reduced in the presence of TFMSA · H₂O, then improved cell performance and cheaper system costs through down-scaling of the reformer should be possible. Such a result would undoubtedly enhance the economic value of the fuel cell.

The purpose of this investigation has been to examine the effect of representative reformate fuel feeds on platinum in TFMSA · H₂O and to attempt to determine if TFMSA · H₂O is a viable alternative to H₃PO₄ for use with reformate fuels.

Experimental

The electrochemical tests were carried out in a three-compartment cell made of Pyrex glass similar

in design to the cell described by Adams *et al.* (1). The center compartment housed the test electrode and was connected to the reference compartment by a Luggin capillary and a fine pore frit and to the counterelectrode compartment by another fine pore frit. The test electrode was made from a piece of 1 cm² platinum gauze which had been electrolytically platinized to give a real surface area of ~30 cm² as measured by the cathodic hydrogen deposition technique (9). The reference electrode was a Giner-type dynamic hydrogen electrode (10) which produced hydrogen *in situ* on a platinized platinum electrode, thereby enabling recorded potentials to be referenced to the hydrogen electrode potential.

A block diagram of the electrochemical test station used in these studies is shown in Fig. 1. With this arrangement, all the necessary electrochemical techniques such as electrode surface area measurement, cyclic voltammetry, and single and multi-step potentiokinetic measurements could be employed. The potentiokinetic technique was used extensively to measure the current-voltage dependence of the anodic reactions on the working electrode at various temperatures. These measurements were made using the potential step-timer circuit coupled to the potentiostat. With this circuit, the working electrode could be cycled through a maximum of 15 independently controlled steps ranging in voltage from 0 to ±2.0V and in time from 30 sec to 15 min. A PAR Series 2000 data acquisition system recorded the data on punched paper tape at the end of each potential step. Upon completion of the voltage cycling, the data were then fed to a Xerox computer which averaged the 15-20 current-voltage readings per step, converted the current to current density, and tabulated the complete cycle into voltage, current, and current density.

The TFMSA · H₂O used in this study was prepared by a modification to the Gramsted-Hazeldine technique (11) in which TFMSA (3M Corporation FC-24) and 50% excess water rather than stoichiometric portions of acid and H₂O, were refluxed together and distilled either by the standard ambient pressure technique or by vacuum distillation. The pure acid monohydrate distilled at 217°-219°C at atmospheric

* Electrochemical Society Active Member.

Key words: fuel cell, electrolyte, reformate, carbon monoxide.

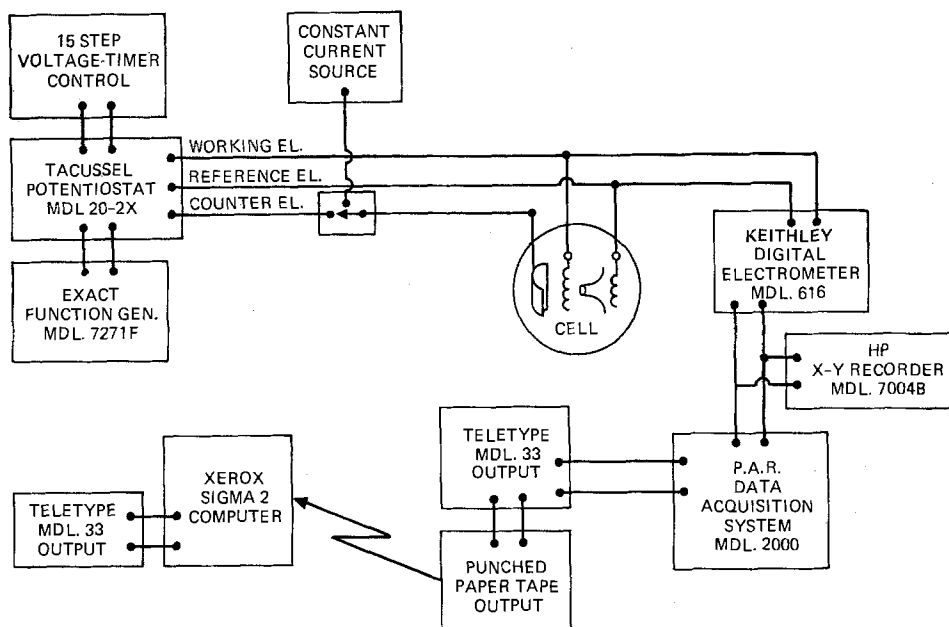


Fig. 1. Schematic diagram of automated electrochemical station.

pressure and at 120°-122°C at 35 mm of pressure. Although both distillation techniques gave the same product, the vacuum technique proved the more desirable because the acid vapor at 120°C was less corrosive to the glass apparatus. The purity of the acid was not determined by separate analysis, but a good qualitative estimation of purity could be made by observing the color, crystallinity of the distillate, and the freezing point of the liquid. Pure TFMSA · H₂O is a white crystalline solid at room temperature, while the refluxed acid-water mixture is a tan, syrupy liquid. With successive distillations, the clarity and ease of crystallization increased to the point that spontaneous crystallization of the product within the condenser became a continual problem. To ensure electrolyte purity, the initial monohydrate product was redistilled at least once, and usually twice, even though little or no change in electrochemical behavior was observed after the first distillation stage.

The commercially purchased reactant gases used in these studies consisted of pure hydrogen (Airco), 3% CO in H₂ (Matheson), 6% CO in H₂ (Matheson), 10% CO in H₂ (Matheson), 3% CO-12% CH₄-85% H₂ (Airco), and 2% CO-26% CO₂-72% H₂ (Matheson). N₂-H₂ and CH₄-H₂ mixtures were also used, but these were blended in the laboratory and their concentrations determined by gas chromatography. During experimentation with the laboratory prepared mixtures, the gas inlet line was monitored continuously to ensure that variation of the component concentrations did not occur. All gas flows were set to the same rotometer setting which for H₂ corresponds to 60 cm³ min⁻¹. This flow rate was selected after a preliminary study of the effect of flow rate on oxidation current. The current rises rapidly with increase in flow rate to a relatively steady value. The measurements were made at rates greater than those at which current was dependent of flow rate.

Results and Discussion

The investigation of reformat performance was begun by first determining baseline performance with pure hydrogen on platinized platinum in the TFMSA · H₂O. The polarization curves for hydrogen oxidation at various temperatures are shown in Fig. 2. All four curves are characterized by a rapid rise in current followed by a relatively broad limiting current region which extends from 70 mV. Normally, one would expect to observe a Tafel region beginning about 25 mV and extending out as far as 300 mV during which the

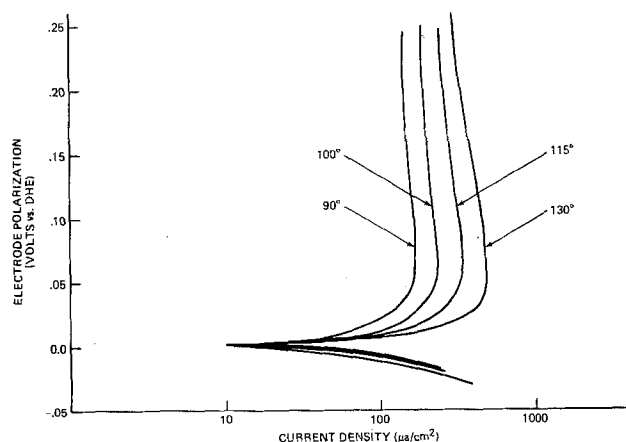


Fig. 2. Hydrogen polarization curves at various temperatures

logarithm of the current would display a linear dependence on potential change (12), but it is obvious from the figure that there is no Tafel region present and that the limiting current region has been attained within only 70 mV of polarization, desirable for an operating fuel cell.

The H₂ oxidation reaction displays a definite positive temperature dependence. Plotting $\ln i$ at 50 mV overpotential vs. $1/T$ yields a straight line (Fig. 3),

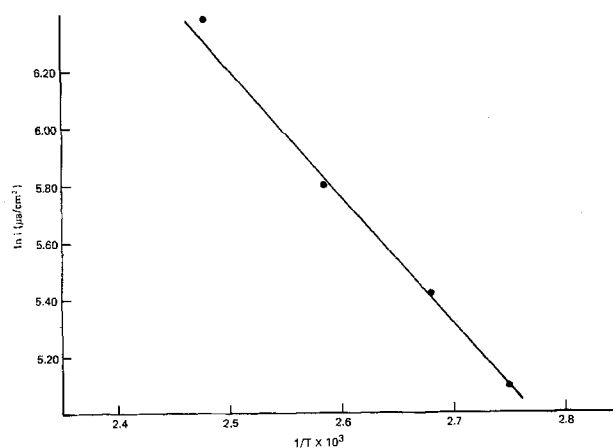


Fig. 3. Temperature dependence of the hydrogen oxidation rate as determined for an electrode held at 50 mV vs. DHE.

corresponding to an activation energy of 9.32 kcal/mol. From similar work published by Adams *et al.* (1), we calculate an activation energy of 7.62 kcal/mol which is in general agreement with our data. Comparing the polarization curves, we observed that the Adams' curves exhibited more gradual increases in current resulting in lower limiting current values. The only obvious difference between the two studies is that we used a platinized platinum electrode ($\sim 30 \text{ cm}^2$) while Adams and co-workers used a smooth platinum wire ($< 0.6 \text{ cm}^2$). While the discrepancy cannot be explained by a simple difference in surface area since all activities have been reported as current/real surface area, the differences in crystallite structure and size might affect the curve shape and ultimately the limiting current and activation energy.

Reformate Performance

Reformate activity with the acid monohydrate was investigated using two synthetic reformate mixtures, one consisting of 2% CO and 26% CO_2 with the balance H_2 and the other containing 3% CO and 12% CH_4 with the balance H_2 . (It should be noted that to simulate exactly the effluent from a methane cracker, the second mixture should have contained CO_2 as well.) Under actual reformer conditions, H_2O would also be a component of the reformate in concentrations as high as 12%, but for these studies, the mixtures were not humidified (13).

Comparisons between pure H_2 and the two reformate mixtures at 100°C are shown in Fig. 4. As expected, both reformate polarization curves indicate decreased kinetics compared to pure H_2 . At an anode polarization of +50 mV, there is a decrease in performance of 89%. In comparing the two reformate mixtures, the CO/CO_2 mixture exhibits a slight improvement in performance over the CO/CH_4 mixture, even though total percentage in diluents is higher in the CO/CO_2 mixture (28% compared to 15%). This would suggest that the electrode performance is controlled by a more complex mechanism than simple dilution of the hydrogen. The temperature dependence of the reformate reaction is shown in Fig. 5. At the higher temperatures, 115° and 130°C , there is no difference in performance between the two mixtures while at the lower temperatures, 90° and 100°C , there is a measurable difference and, in both cases, it is the CO/CO_2 mixture which exhibits the higher activity. Arrhenius plots of the temperature dependence are

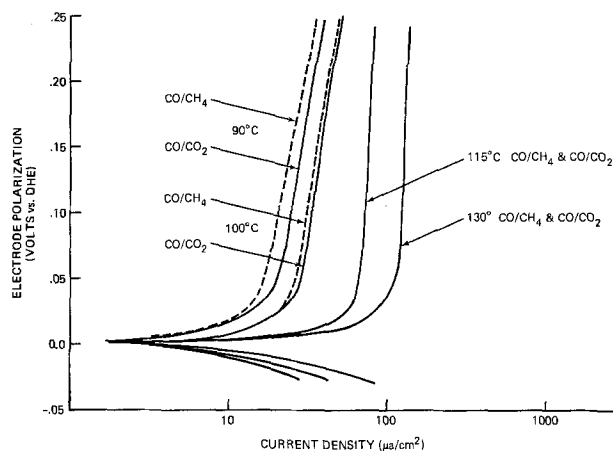


Fig. 5. Comparison of CO/CO_2 and CO/CH_4 reformate polarization curves at various temperatures.

represented in Fig. 6: the two plots represent activation energies of 13.2 and 14.6 kcal/mol corresponding to the CO/CO_2 and the CO/CH_4 mixtures, respectively. The activation energies were obtained by linear regression analysis which yielded correlation coefficients of 0.99 for each calculation. The similarity in activation energy between the two mixtures and the similarity in the kinetics at 115° and 130°C would suggest that not only is the nature of the components a key factor in determining performance, but that there may be a common controlling factor for both of the reformates (14). Carbon monoxide is the only common species in the two reformates other than hydrogen, and to determine if, in fact, CO is the component which most strongly influences the overall reformate performance, mixtures of the individual components with hydrogen were investigated. Hydrogen-carbon monoxide mixtures containing 3%, 6%, and 10% CO were studied at the same temperatures used in the experiments described above. Figure 7 illustrates the performance of these mixtures at 100°C and compares them to pure H_2 and the two reformate mixtures. As expected, the performance decreases with increasing CO concentration. With gas flow rates equal to those used for H_2 , 3% $\text{CO}-\text{H}_2$ causes an 86% decrease in current density at 50 mV polarization. The 6% and 10% CO mixtures further reduce current density by 91% and 93%, respectively. It can be seen

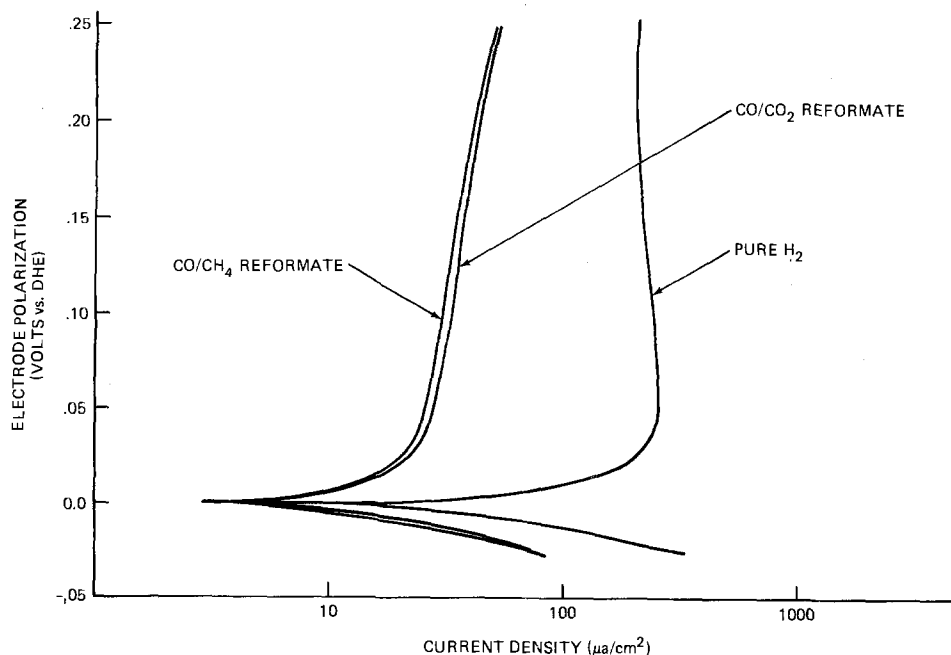


Fig. 4. Comparison of hydrogen and reformate polarization curves at 100°C .

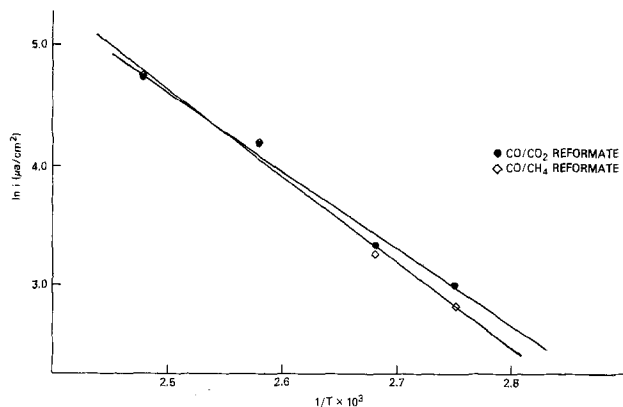


Fig. 6. Comparison of Arrhenius plots for CO/CO₂ and CO/CH₄ reformates as determined for an electrode polarization of 50 mV vs. DHE.

from the plot that both reformat performance curves fall between the 3% CO and 6% CO and correspond to an 89% reduction for CO/CO₂ and a 90% reduction for CO/CH₄ at 50 mV polarization. The sequence of increased performance with decreased CO concentration holds for all temperatures, but the percentage is diminished as the temperature is increased from 90° to 130°C.

An inverse dependence between the current density and temperature ($\ln i$ vs. $1/T$) was also found to exist for the electro-oxidation of the H₂-CO mixtures in the acid monohydrate (Fig. 8). Activation energies of 14.9 and 13.8 kcal/mol were calculated for the 3% and 10% CO mixtures, respectively. The similarity between the two mixtures is to be expected since activation energy is dependent on the specific reacting species involved in the rate-controlling step, but is independent of their concentration. Taking 14.3 kcal/mol as the average activation energy for the CO-H₂ mixture and comparing it with the activation energies for the CO/CO₂ and CO-CH₄ mixtures (13.2 and 14.6 kcal/mol), we observe a close similarity which further suggests that a surface reaction involving carbon monoxide is the rate-controlling step in the reformat oxidation reaction. This does not necessarily mean that the other components do not affect performance, but that in this particular temperature range, their inhibiting effect is small, and they behave more as diluting agents. At the other temperatures (90°, 115°, and 130°C) reformat performance also fell between the 3% CO-H₂ and the 6% CO-H₂ performance curves, and any variation within these limits appeared to be random in nature.

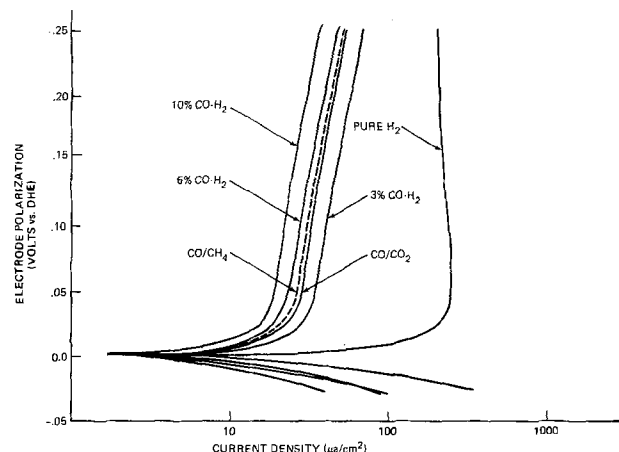


Fig. 7. Performance variation as a function of CO concentration in H₂ at 100°C. Comparisons are made with pure H₂ and the reformat mixtures.

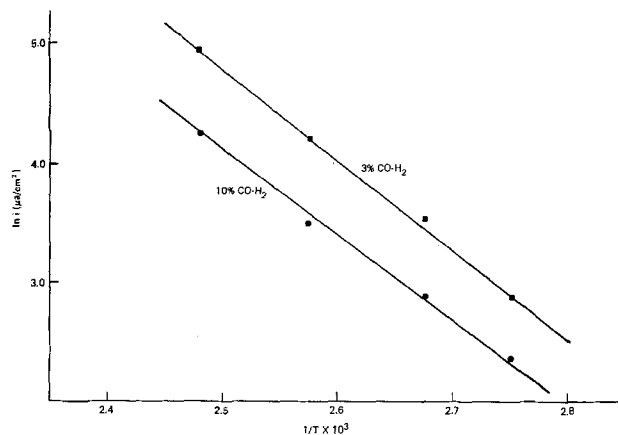


Fig. 8. Arrhenius plots for 3% CO and 10% CO in H₂ as determined for an electrode polarization of 50 mV vs. DHE.

If CH₄ and CO₂ are acting primarily as diluents in the mixtures, their performance, if observed separately, should resemble that of a true diluent. Under these mild reaction conditions, nitrogen would certainly not be expected to interact catalytically with the electrode, and anode performance of N₂-H₂ mixtures would illustrate a diluent's effect on H₂ performance. Figure 9 shows a comparison between pure H₂ and two N₂-H₂ mixtures. Three percent N₂-H₂ and 17% N₂-H₂ mixtures were chosen so that the total diluent content would approximate the nonhydrogen content of the 3% CO-H₂ and the CO/CH₄ reformat mixtures which were 3% and 15%, respectively. The N₂-H₂ performance would demonstrate the manner in which the CO-H₂ and the CO-CH₄ reformat mixtures should perform if the components were only diluents. The figure shows that at 80°C, the N₂-H₂ performance closely approximates the pure H₂ performance, being far superior to that of the CO/CH₄ reformat. At high temperatures the N₂-H₂ performance would probably become indistinguishable from pure H₂. Carrying the diluent test even further, we examined the effect on performance when hydrogen was diluted with 15% CH₄. In Fig. 10, we observe that the 15% CH₄-H₂ has a greater effect on performance than the 17% N₂-H₂ mixture, but the CH₄-H₂ performance is still greater than the CO/CH₄ reformat performance by a factor of 10×. Considerable work has been carried out on the adsorption and oxidation of methane on platinum in various electrolytes, including TFMSA · H₂O. Because methane is electro-oxidizable, it certainly cannot be expected to operate as a diluent, but in this case, its behavior more closely resembles that of a diluent than that

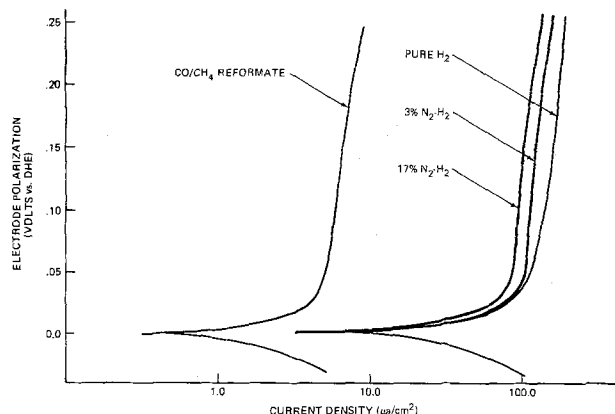


Fig. 9. Electrode performance at 80°C as a function of N₂ concentration in H₂. Comparisons are made with pure H₂ and reformat performance.

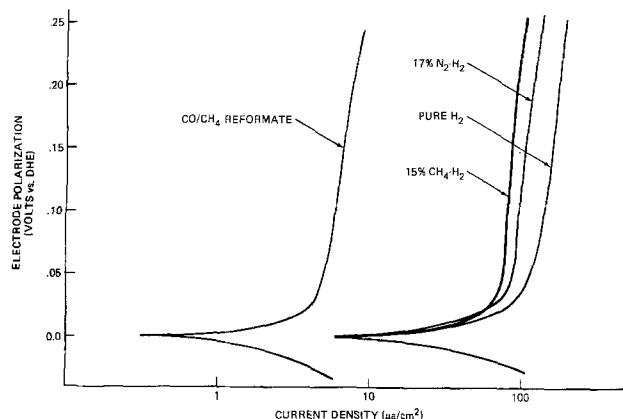


Fig. 10. Electrode performance of 15% CH_4 in H_2 at 80°C compared with pure H_2 , 17% N_2 in H_2 , and reformat performance.

of an inhibitor. When the N_2 - H_2 and the CH_4 - H_2 results are combined with the similarities in limiting currents and activation energies for the CO/CH_4 reformat and the $\text{CO}-\text{H}_2$ mixtures, the data strongly support the supposition that the carbon monoxide concentration is the rate-controlling factor in the observed reformat performance. The similarity in performance between the CO/CH_4 and the CO/CO_2 reformat mixtures suggests that the CO_2 is also a diluent; a truer diluent, in fact, since in every case in which a difference in performance occurred between the two reformates the CO/CO_2 level was always greater.

The cumulative nature of CO inhibition was examined by observing the effect of residual CO on pure H_2 performance. At a temperature of 115°C , the test electrode was cleaned at 1.50V under H_2 , potentiostated to 100 mV , and then the anode reactant was cycled back and forth between 10% $\text{CO}-\text{H}_2$ and pure H_2 . Beginning with a freshly cleaned electrode, Fig. 11 illustrates the decay in pure H_2 performance resulting from exposure to 10% CO . Actually, the figure represents seven complete cycles since the performance loss resulting from the initial exposure to CO repeated exactly for three consecutive cycles; however, to conserve space in Fig. 11 these three cycles were condensed into one cycle. During the first three cycles, electrode exposure to 10% $\text{CO}-\text{H}_2$ lasted 10 min and exposure to pure H_2 lasted 30 min . The pure H_2

performance ($\sim 330\ \mu\text{A}/\text{cm}^2$) was in excellent agreement with the corresponding 100 mV performance in the 115°C polarization experiments. This agreement coupled with the scatter in the H_2 performance observed immediately after the 1.50V treatment would indicate that the initial H_2 performance level in Fig. 11 was artificially high. In our first experiment of this type, we terminated the test after the third cycle and concluded that residual CO , if present, had no effect on pure H_2 performance. A second cycling experiment was conducted and again we observed that through three cycles H_2 performance was unaffected by exposure to CO , but at this point we continued the cycling and at the same time, extended the H_2 exposure time to 60 min . The extended H_2 exposure was instituted in order to determine if the high performance observed immediately after the 1.50V cleaning step could be achieved, but to our surprise, each successive cycle resulted in performance decays 4.3% , 3.7% , 2.5% , and 1.0% , respectively.

According to Breiter (15), the presence of adsorbed CO does not significantly affect hydrogen oxidation until CO coverage has reached about 50% . This would suggest that in these experiments, CO accumulates on the surface during cycling and reaches half-coverage during the fourth cycle. One difficulty presented with this explanation is that the drop-off in electrode activity at half-coverage, as reported in the literature, is truly significant, whereas, in this study the total decrease in oxidation current was only about 11% , and the percent decrease per cycle steadily decreased from 4.8% to 1% from the fourth to the seventh cycle. This question is discussed further below.

In order to explore CO inhibition more fully, surface adsorption techniques such as triangular sweep voltammetry were employed. A background voltammogram for platinum in the acid monohydrate (Fig. 12) was typical of aqueous acid systems exhibiting two reversible hydrogen peaks in the 0.0 - 0.3V region and an irreversible oxide couple in the 0.8 - 1.2V region. Single cathodic sweep voltammograms for CO adsorbed at 0.1V have been included in the figure to illustrate the reduction in hydrogen charge associated with the presence of CO . The greater the amount of adsorbed CO on the electrode, as determined by the area under the CO oxidation peak at 0.80V , the smaller is the charge associated with adsorbed hydrogen. This behavior is quite similar to the observations of Kohlmayr and Stonehart for CO on Pt in

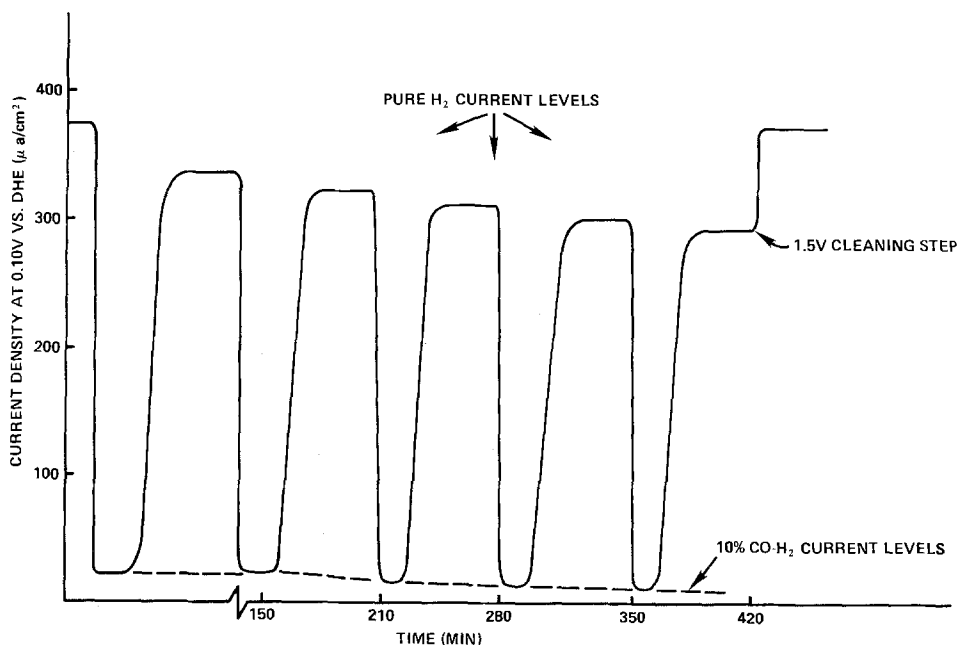


Fig. 11. Comparison of pure H_2 performance after repetitive exposures to 10% $\text{CO}-\text{H}_2$ at 115°C . The first $\text{CO}-\text{H}_2$ /pure H_2 cycle represents three consecutive identical cycles.

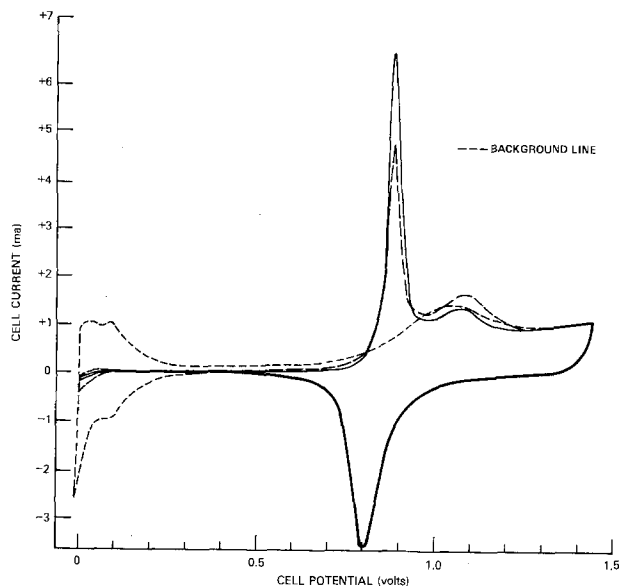


Fig. 12. Voltammogram of N_2 background (---) and two different CO coverages on Pt in TFMSA· H_2O at $115^\circ C$. The two curves with adsorbed CO began at 0.45V in the cathodic direction.

H_3PO_4 (16). The relationship between adsorbed CO and potential of adsorption is shown as a function of temperature in Fig. 13. In determining the charge of adsorbed CO as a function of potential and temperature, the electrode was first cleaned at 1.35V under nitrogen, then stepped to the desired adsorption potential, and the inlet gas switched from N_2 to 10% $CO-H_2$. After exposure to CO for 3 min, the cell was then purged with N_2 to remove all CO and H_2 not adsorbed on the electrode. A linear potential change which went up to 1.5V was applied to the electrode to remove the adsorbed CO. This sequence was run for adsorption potentials ranging from 0.05 to 1.00V and was repeated at five temperatures between 61° and $127^\circ C$. Although the general curve shape is the same at all temperatures (i.e., two maxima and a minimum), a number of features exhibit a dependence on

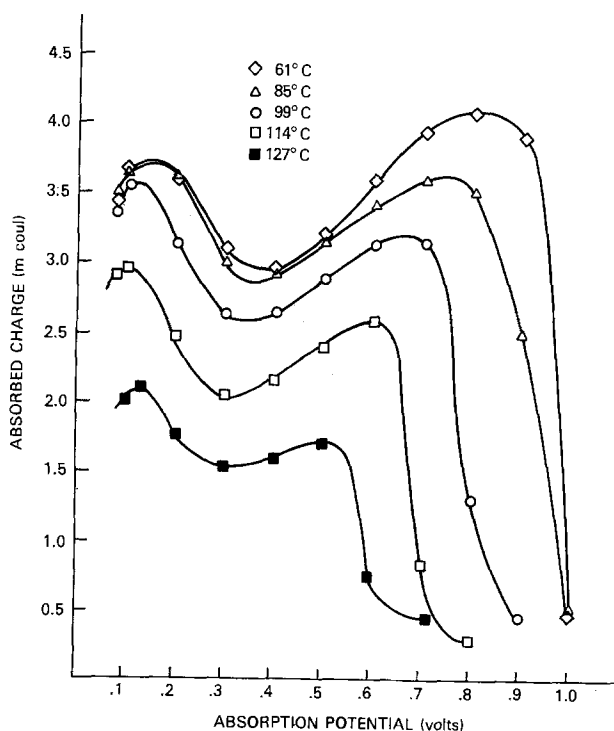
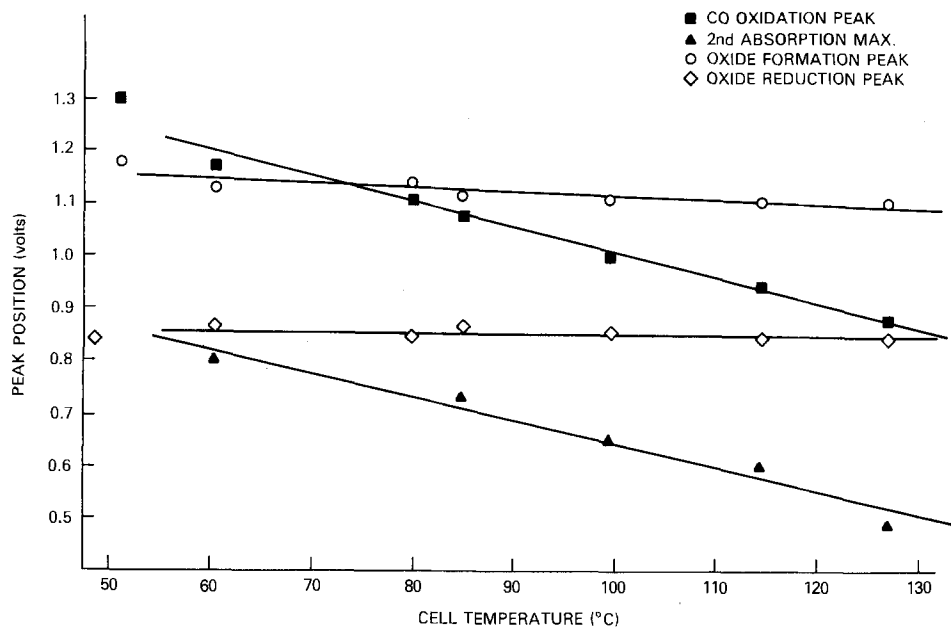


Fig. 13. Variation in adsorbed CO with adsorption potential as a function of temperature.

temperature. The most obvious of these is the total CO adsorption charge which when measured by the area under the curve is seen to decrease with increasing temperature. This trend is consistent with previous studies in both the aqueous and gas phases (17, 18). The position (potential) of the second adsorption maximum, as well as its height relative to the first maximum, also exhibits a dependence on temperature and this is in contrast to the positions of the first maximum and the minimum which exhibit little or no temperature variation. Related closely to the potential variation of the adsorption maximum is the variation in potential of the CO oxidation peak. Figure 14 illustrates this relationship and compares it to the temperature dependence of the oxide formation and the oxide reduction peaks shown in Fig. 12. While oxide formation and reduction are virtually independent of potential, CO oxidation and the second adsorption maximum exhibit identical slopes (5 mV/deg) separated by a constant 350 mV. The similarities in slope for these two features can be used to explain the truncation of the adsorption curve with increasing temperature. CO adsorption appears to be inhibited at low potentials (<50 mV), but as the adsorption potential increases, CO coverage rises rapidly to a maximum at about 100 mV. With continued increase in potential, coverage remains high until the adsorption potential has advanced to within 350 mV of the oxidation potential at which time coverage drops off sharply. Since the CO oxidation potential decreases as the temperature increases, and the 350 mV region of non-adsorption below the oxidation potential remains constant, the adsorption curve must be continually truncated at the high potential end. The data in Fig. 14 were also based on a 3 min adsorption time using 10% $CO-H_2$ followed by a 10 min N_2 sweep; longer sweep periods with N_2 further reduced CO coverage and this desorption process was also found to be sensitive to temperature change. Figure 15 demonstrates the dependence of CO desorption on temperature using an adsorption potential of 100 mV. At $85^\circ C$, desorption appears to cease after 20 min, but at the higher temperatures, desorption continues through the 45 min sweeping period. As the adsorption potential is increased, the desorption rate at a given temperature increases with the result that at $127^\circ C$ and an adsorption potential of 600 mV, complete desorption of CO occurred after only 10 min of N_2 sweeping. Looking more closely at the $114^\circ C$ curve, one observes that 25% of the CO on the surface after 5 min of sweep still remains on the surface after 45 min of sweep. Assuming the dual site adsorption mechanism for H_2 oxidation and the equivalency of sites for CO adsorption and H_2 oxidation, then the adsorbed CO should have affected H_2 performance, but recalling the cycling experiments in Fig. 11, no effect was observed in the first three cycles and the cumulative effect after seven cycles was only an 11% decrease in performance. Although a value for the saturation coverage of CO could not be determined by these measurements, it could be determined that saturation coverage was attained within the first 3 min of electrode exposure to CO. This would mean that a decreased hydrogen oxidation rate should be observed in the first cycle. Another observation from the $114^\circ C$ curve in Fig. 15 is that after 30 min of N_2 sweep only 42% of the CO present on the surface after 5 min of sweep still remains on the platinum and after 60 min of N_2 sweep, only 28% still remains. This argues that if 50% coverage is required to retard the oxidation reaction, then a decrease in H_2 oxidation rate should not have been observed in any of the seven cycles. In any event, the relationship between adsorbed CO and H_2 oxidation appears to be more complicated than one would expect if Q_{CO}/Q_H were unity. This is not surprising since there is equal uncertainty in the literature regarding Q_{CO}/Q_H on plati-

Fig. 14. Dependence of the position of various voltamogram peaks on cell temperature.



num in H_2SO_4 , HClO_4 , and H_3PO_4 . Stonehart *et al.* report a range of 0.83-0.96 depending on the catalyst crystallite size and based on single site adsorption (19). Brummer and Ford (20) and Gilman (21) have proposed a combination of single and bridged (two site) CO adsorption with $Q_{\text{CO}}/Q_{\text{H}}$ values of 0.87 and 0.64, respectively, and Warner and Schuldinger (22) have reported single site coverage ($Q_{\text{CO}}/Q_{\text{H}} = 1.08$) based on a Q_{H} of $453 \mu\text{C}/\text{cm}^2$ at full coverage. We observed in both 5N and 85% H_3PO_4 that the CO oxidation peak is composed of a major peak and a shoulder while the oxidation peak in TFMSA· H_2O is a single peak. This would suggest dual site CO adsorption in the case of

H_3PO_4 and single site adsorption in TFMSA· H_2O , but we would be hesitant to completely rule out multiple site adsorption in TFMSA· H_2O without more data on $Q_{\text{CO}}/Q_{\text{H}}$.

A remaining point to be discussed is the adsorption minimum observed in Fig. 13. This was not expected, and to the best of our knowledge has not been addressed in the literature. The most logical explanation seems to be that some species preferentially adsorb at that potential (350 mV) blocking the adsorption of CO. Although polarization curves developed with pure H_2 and 10% CO-H_2 in this same solution showed no minima, there have been occasions in which minima in the H_2 polarization have been observed in our work. In each case, the decrease in performance was attributed to an acid level imbalance between the cell compartments which resulted in mixing of the solutions in the three compartments. The problem is believed to originate at the counterelectrode where uncontrolled potential excursions could result in decomposition of the acid. In support of this, an odor of sulfide in the counter compartment has also been detected on occasion. These observations agree to some extent with the conclusions of Hughes *et al.* (8), but it should be emphasized that the performance decay has never been observed in the absence of electrolyte mixing between the cell compartments. If the minimum is a result of adsorption from solution, one must then question why, for the same acid sample, a minimum was not observed in the polarization curve, or why the adsorption potential was so specific and why the adsorption potential was not affected by temperature. Further investigation into the nature of the adsorbing species will be necessary in order to adequately answer these questions.

Conclusions

In this investigation, the performance of two synthetic reformates have been compared with that of pure hydrogen and the expected decrease in activity associated with the reformate constituents has been observed. Comparisons of performance between CO-H_2 , $\text{CH}_4\text{-H}_2$, and $\text{N}_2\text{-H}_2$ mixtures and the reformate samples have further shown that CO is the rate-limiting constituent and that CO_2 and CH_4 have very little effect on performance, particularly at the higher temperatures. Finally, the potential sweep studies have shown that the inhibition by CO was due mainly to its resistance to desorption. These experiments and results by themselves cannot yield a complete evaluation of TFMSA· H_2O as an electrolyte since they follow

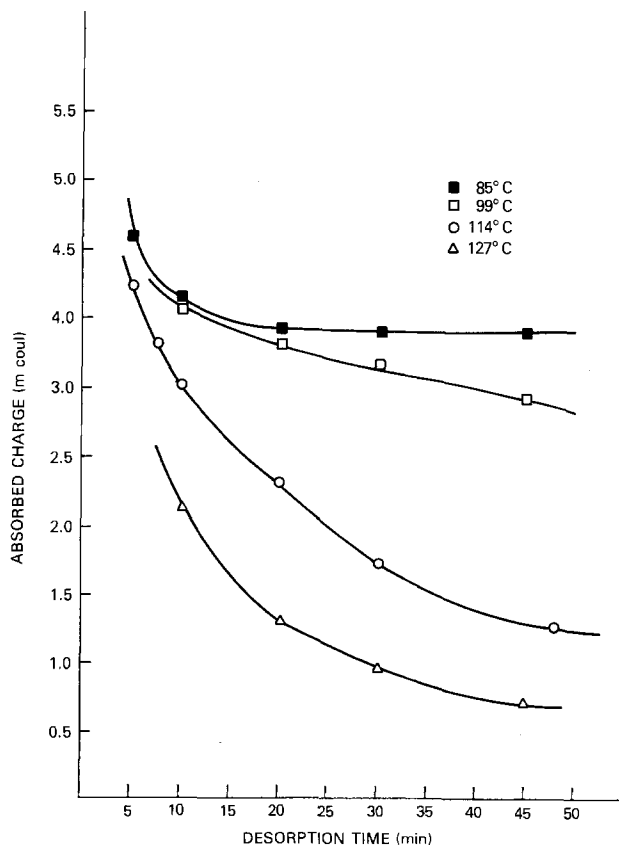


Fig. 15. Variation in CO desorption rate with temperature from an electrode held at 100 mV vs. DHE.

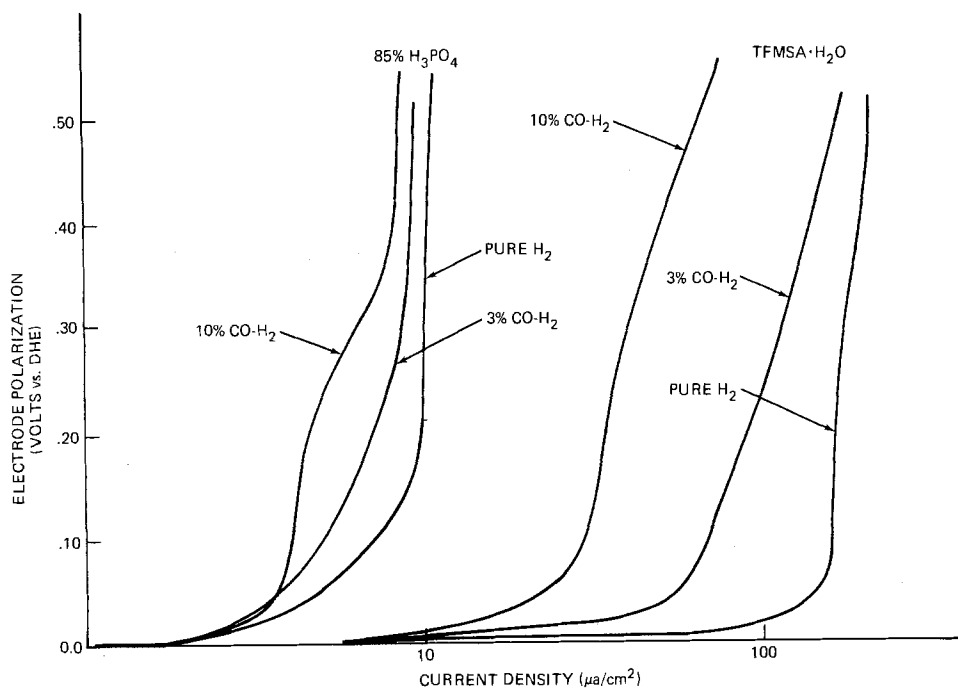


Fig. 16. Electrode performance comparisons in 85% H_3PO_4 and $\text{TFMSA}\cdot\text{H}_2\text{O}$ at 115°C .

in a qualitative way with results reported on the electrochemical behavior of CO in other acids. Therefore, a direct comparison between $\text{TFMSA}\cdot\text{H}_2\text{O}$ and H_3PO_4 is desirable. Figure 16 makes such a comparison utilizing polarization curves for H_2 and $\text{CO}\text{-}\text{H}_2$ mixtures at 115°C (23). On a percentage basis, the activity decrease due to the presence of 3% and 10% CO is less in H_3PO_4 than in the monohydrate, 13% compared to 56% for 3% CO, and 27% compared to 81% for 10% CO. However, more significant is the fact that with 10% CO, a concentration far greater than that produced in a modern reformer, performance in the monohydrate is four times greater than pure H_2 performance in H_3PO_4 . This clearly indicates that at moderate temperatures and with a suitable electrode structure, a $\text{TFMSA}\cdot\text{H}_2\text{O}$ electrolyte fuel cell operating on reformato fuels would yield improved performance over a phosphoric acid cell.

Acknowledgments

This research was sponsored by the U.S. Army Mobility Equipment Research and Development Command, Fort Belvoir, Virginia 22060 under Project No. AOH51P00321. This paper was taken from a dissertation by G.W.W. in partial fulfillment of the requirements for the Ph.D. degree from The American University.

Manuscript submitted April 15, 1980; revised manuscript received Feb. 26, 1981.

Any discussion of this paper will appear in a Discussion Section to be published in the June 1982 JOURNAL. All discussions for the June 1982 Discussion Section should be submitted by Feb. 1, 1982.

Publication costs of this article were assisted by U.S. Army Mobility Equipment Research and Development Command.

REFERENCES

1. A. A. Adams and R. T. Foley, in Final Technical Report No. 2, Contract No. DAAK02-72-C-0084, U.S. Army MERDC, Ft. Belvoir, VA (December 1975).
2. B. Baker, in Final Technical Report, Contract No. DAAK02-73-C-0084, U.S. Army MERDC, Ft. Belvoir, VA (November 1974).
3. S. B. Brummer, J. McHardy, and M. J. Turner, in Annual Report, Contract No. EX-76-C-03-1363, Dept. of Energy (January 1978).
4. A. A. Adams and H. J. Barger, Jr., *This Journal*, **121**, 987 (1974).
5. A. A. Adams, R. T. Foley, and H. J. Barger, Jr., *ibid.*, **124**, 1228 (1977).
6. A. A. Adams and R. T. Foley, *ibid.*, **126**, 775 (1979).
7. T. Sarada, R. D. Granata, and R. T. Foley, *ibid.*, **125**, 1899 (1978).
8. V. B. Hughes, B. D. McNicol, M. R. Andrew, R. B. Jones, and R. T. Short, *J. Appl. Electrochem.*, **7**, 161 (1977).
9. W. T. Grubb and C. J. Michalske, *This Journal*, **111**, 1015 (1964).
10. J. Giner, *ibid.*, **111**, 376 (1964).
11. T. Gramsted and R. N. Hazeldine, *J. Chem. Soc.*, 173 (1956).
12. E. Gileadi, E. Kirowa-Eisner, and J. Penciner, "Interfacial Electrochemistry, An Experimental Approach," pp. 44-46, Addison-Wesley, London (1975).
13. S. S. Kurpit, *IEEE Trans. Aer. El.*, **11**, 945 (1975).
14. E. Gileadi, E. Kirowa-Eisner, and J. Penciner, "Interfacial Electrochemistry, and Electrochemical Engineering," pp. 74-75, Addison-Wesley, London (1975).
15. M. W. Breiter, *J. Electroanal. Chem. Interfacial Electrochem.*, **65**, 623 (1975).
16. G. Kohlmayr and P. Stonehart, *Electrochim. Acta*, **18**, 211 (1973).
17. V. H. Baldwin and J. B. Hudson, *J. Vacuum Sci. Technol.*, **8**, 49 (1971).
18. P. Stonehart and P. N. Ross, Jr., *Electrochim. Acta*, **21**, 441 (1975).
19. J. Bett, K. Kinoshita, K. Routsis, and P. Stonehart, *J. Catal.*, **29**, 160 (1973).
20. S. B. Brummer and J. I. Ford, *J. Phys. Chem.*, **69**, 1355 (1965).
21. S. Gilman, *ibid.*, **66**, 2657 (1962).
22. T. B. Warner and S. Schuldinger, *This Journal*, **111**, 992 (1964).
23. G. W. Walker, A. A. Adams, and H. J. Barger, Abs. 48, p. 102, The Electrochemical Society Extended Abstracts, Toronto, Ont., Canada May 11-16, 1975.

Deposition and Dissolution of Lithium-Aluminum Alloy and Aluminum from Chloride-Saturated LiCl-AlCl₃ and NaCl-AlCl₃ Melts

Ronald A. Carpio and Lowell A. King*

Frank J. Seiler Research Laboratory (Air Force Systems Command),
United States Air Force Academy, Colorado 80840

ABSTRACT

Metal deposition-dissolution studies in the LiCl(satd.)-AlCl₃ melt were conducted primarily on an aluminum substrate, using the techniques of cyclic voltammetry, chronoamperometry, chronocoulometry, and chronopotentiometry. A lithium-aluminum alloy was deposited. The LiAl alloy is formed predominately by a deposition process on the surface of the aluminum substrate rather than by conversion of the aluminum into the alloy by an implantation mechanism, as is the case in other electrolytes. The LiAl electrode would be electrochemically reversible, were it not for a corrosion reaction between the alloy and the melt. For comparison, similar studies were conducted on the behavior of aluminum in the NaCl(satd.)-AlCl₃ melt. The superiority of LiAl in the LiCl(satd.)-AlCl₃ melt to aluminum in the NaCl(satd.)-AlCl₃ melt for battery applications is indicated. A significant finding is that nondendritic, adherent, dense deposits of aluminum or an aluminum alloy, having less than 50 mol percent lithium content, can be electroformed via initial formation of β -LiAl.

A great deal of attention has been focused recently on using the LiAl solid alloy as a negative electrode in secondary batteries employing an LiCl-KCl eutectic melt which is a liquid above 352°C (1-7) or in ambient temperature organic electrolytes (8, 9). However, there has been only one report of the utilization of the LiAl alloy in an AlCl₃-based electrolyte: namely, a patent by Senderoff which claimed a thermal, rechargeable, electrochemical cell having a lithium monoaluminide electrode and lithium tetrachloroaluminate electrolyte (10). Although details are lacking, Senderoff reported that lithium monoaluminide could be deposited from the LiAlCl₄ electrolyte and that this alloy showed less than 0.050V anodic polarization at current densities ranging from 30 to 100 mA/cm². Pure aluminum polarized by more than 0.4V when run anodically at 30 mA/cm². In primary, thermal batteries which are being developed in this laboratory and which employ an NaCl(satd.)-AlCl₃ molten salt electrolyte and a metal chloride cathode such as MoCl₅, we also have found that an LiAl anode is superior in performance to an aluminum anode (11).

We are presently interested in developing a molten salt secondary battery employing an LiAl negative and an LiCl(satd.)-AlCl₃ electrolyte. This particular electrolyte was selected because of its relative ease of preparation, low melting point (ca. 143°C), low volatility (12), good conductivity (13), voltage window greater than 2V, and Li⁺ content. It was necessary to characterize the electrochemical behavior of LiAl. In previous investigations employing other electrolytes, LiAl alloy was formed by the electrochemical incorporation of lithium into an aluminum cathode [e.g., (5, 6, 9)]. In the case of the LiCl(satd.)-AlCl₃ melt, the formation of the alloy directly from the constituents of the melt on a substrate could be possible. When an aluminum substrate is employed, the conversion of the aluminum cathode into LiAl as well as simultaneous or subsequent deposition of LiAl on the substrate surface must be considered. In fact, it is remarkable that LiAl can be electroformed in this melt at potentials so near the Al/Al³⁺ potential. From our potentiometric measurements of molten sodium contained within an Na-

β -alumina tube in the NaCl(satd.)-AlCl₃ melt, we have found that the Na/Na⁺ couple is approximately -1.6V with respect to the Al/Al³⁺ reference. We would expect the Li/Li⁺ to be even more negative relative to Al/Al³⁺ in the LiCl(satd.)-AlCl₃ melt.

Lithium tetrachloroaluminate is used as a solute in organic solvents which are employed as electrolytes in lithium secondary batteries (14, 15). In the thionyl chloride solvent containing LiAlCl₄, the electrodeposition and electrodisolution of lithium are reversible (16). Small amounts of aluminum codeposited with the lithium from some organic solutions such as propylene carbonate containing AlCl₃ and LiCl. The amount depends on the composition of the electrolyte and the current density (17). Also of relevance are recent studies on solutions of the type AlBr₃/MX/ArH, where M⁺ is an alkali metal ion, X⁻ is Cl⁻, Br⁻, or I⁻, and ArH is an aromatic hydrocarbon (18). Cathodic deposition of either aluminum or an alkali metal was observed, depending on the AlBr₃:MX ratio.

For the sake of comparison, the electrochemical behavior of the aluminum electrode in the NaCl(satd.)-AlCl₃ melt was investigated. This comparison is particularly revealing since sodium forms no solid solutions with aluminum.

Experimental

All measurements were performed in an argon-filled glove box with a Model MO-40 DRI-TRAIN (Vacuum/Atmospheres Company), having moisture and oxygen concentrations less than 10 ppm.

The Pyrex electrochemical cell fit snugly into a center well in an insulated, cylindrical block of aluminum. The aluminum furnace block was heated by cartridge heaters, also imbedded symmetrically in the block; the temperature was regulated by a Bayley Model 124 proportional temperature controller. Temperature oscillations did not exceed $\pm 0.1^\circ\text{C}$ during an experiment. Temperature was measured by a Chromel-Alumel thermocouple attached to a DORIC Trendicator 400A, which is precise to $\pm 0.05^\circ\text{C}$. Cylindrical internal cell geometry was employed in the majority of cases to achieve a uniform current distribution on the working electrode and to minimize the IR drop. This geometry is similar to that employed by others (6, 19) with the

* Electrochemical Society Active Member.

Key words: electrode, fused salts, polarization, voltammetry.

exception that in the present study the working electrode was partially clad in shrinkable Teflon (Pope Scientific).

An aluminum reference electrode was always employed and either an aluminum or tungsten counter-electrode was used. Working electrodes were aluminum (Alfa/Ventron, m5n) and tungsten (Alfa/Ventron, m3n) wires or lithium monoaluminide rod (Foote Mineral Company). The aluminum electrode was electrically cycled in the melt until an open-circuit voltage of 0 ± 1 mV was attained with respect to the reference electrode. Tungsten electrodes were cleaned in molten NaNO_2 , then washed, and dried. The exposed portion of the LiAl rod was polished with fine grade emery cloth.

Details of the electrolyte preparation are given elsewhere (20). The $\text{LiCl(satd.)-AlCl}_3$ electrolyte has the composition 49.25 mol percent (m/o) AlCl_3 (20); the $\text{NaCl(satd.)-AlCl}_3$ electrolyte, 49.75 m/o AlCl_3 (21). They were water-clear and free from any impurities which could be detected by cyclic voltammetry.

The majority of potentiostatic and galvanostatic measurements were made with a Princeton Applied Research Model 173 potentiostat/galvanostat, equipped with a Model 179 plug-in coulometer. A few measurements were made with an AMEL Model 551 potentiostat/galvanostat either alone or in conjunction with a Princeton Applied Research Model 379 digital coulometer. The desired electrode perturbations were obtained with a Princeton Applied Research Model 175 programmer. Cell responses were recorded with a Houston Instrument Model 2000 X-Y recorder.

The IR drop, which generally was less than 0.1Ω , was measured using the a-c approach described by Peled and Gileadi (22).

Results and Discussion

Voltammetric measurements.—Cyclic voltammetry.—In the cyclic voltammogram shown in Fig. 1A, an aluminum electrode in the $\text{LiCl(satd.)-AlCl}_3$ melt was swept first in an anodic direction from its rest potential of 0 mV. There was some hint of passivation in this anodic segment. Cathodic current occurred in the reverse scan at potentials positive of the aluminum reference. Another important feature was the appearance of a loop in the cathodic current when the direction of sweep was reversed, which is a normal consequence of crystal growth requiring nucleation (23). The structure on the dissolution segment of the scan is evidence for alloy stripping. Furthermore, it can be seen that the deposit polarized significantly less than the pure aluminum wire, which agrees with Senderoff's observation (10), cited above. The alloying resulted in a shift of the rest potential of the aluminum electrode in the negative direction by approximately 8 mV.

Figure 1B shows the effect of applying the voltage scan initially in a cathodic direction to a pure aluminum electrode in the $\text{LiCl(satd.)-AlCl}_3$ melt. The current-voltage scan was reproducible over multiple scans. The current on the cathodic side rose at a rather slow rate until it reached approximately -0.45V , then it rose much more rapidly with further increase in cathodic overpotential. The cathodic current loop was much more prominent here than in Fig. 1A.

Cyclic voltammograms also were made on a tungsten wire working electrode in the $\text{LiCl(satd.)-AlCl}_3$ melt. No alloy formation involving the tungsten substrate reasonably could be expected. The initial sweep was cathodic. The resemblance to Fig. 1B was striking. The rapid current rise in this case commenced approximately 1V cathodic of the aluminum reference electrode potential. This overpotential was larger than that observed for deposition on the aluminum substrate, and it increased on successive scans. It has been found that the efficiency of the plating-stripping process of lithium on a foreign substrate decreases markedly with cycle (24). The explanation given was that a blockage of portions of the substrate with reaction

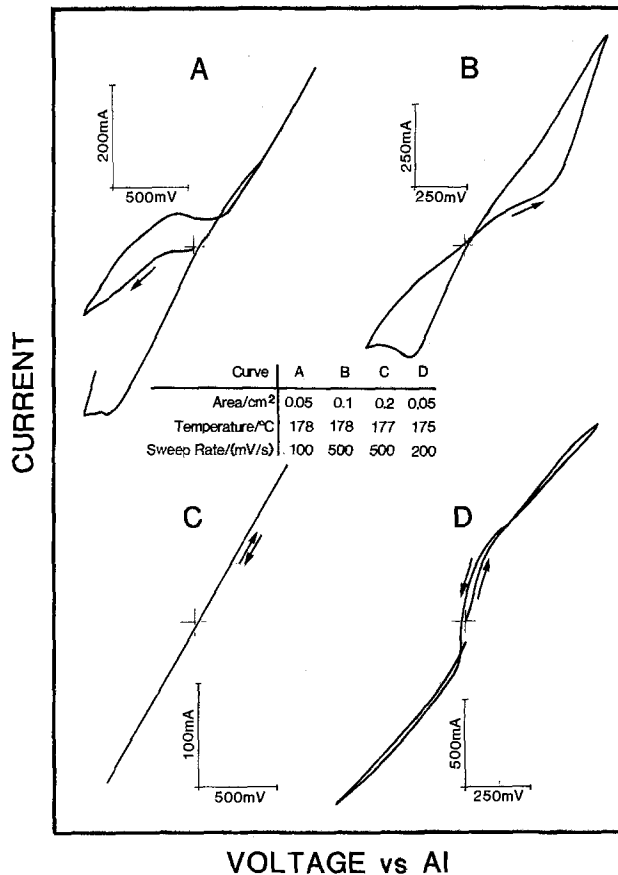


Fig. 1. Cyclic voltammograms: A, on aluminum in $\text{LiCl(satd.)-AlCl}_3$, proceeding first anodically; B, on aluminum in $\text{LiCl(satd.)-AlCl}_3$, proceeding first cathodically; C, on lithium monoaluminide in $\text{LiCl(satd.)-AlCl}_3$; D, on aluminum in $\text{NaCl(satd.)-AlCl}_3$, proceeding first cathodically.

products and an accumulation of insulated lithium occurred. A process resulting in the reduction of active surface area of the substrate with cycling also could be operative here. As has been stated already, a loss of efficiency was not observed on the aluminum substrate. It is interesting to note that the highest efficiencies for lithium cycling have been obtained with metal substrates such as platinum, gold, and aluminum, with which lithium forms alloys (17). Stripping chronopotentiograms following deposition on tungsten from the $\text{LiCl(satd.)-AlCl}_3$ melt showed two transitions. It appears that aluminum was laid down first on the tungsten substrate, and then LiAl was deposited on the layer of aluminum. In view of these results obtained for the tungsten substrate, we decided to restrict further studies to aluminum substrates.

The reversibility of the LiAl electrode in the $\text{LiCl(satd.)-AlCl}_3$ melt is shown clearly in Fig. 1C. The working electrode was a commercial rod of lithium monoaluminide, sealed in a shrinkable Teflon tube, and then ground in the dry box flush with the layer of insulation. Although it is not obvious, multiple cyclic voltammograms are superimposed in this recording.

The cycling behavior of aluminum in $\text{NaCl(satd.)-AlCl}_3$ melts is more difficult to interpret. Surprisingly, an overpotential for aluminum dissolution in this melt has been reported previously (25). In this study no such overpotential was found. The electrode pretreatment consisted of anodizing the aluminum electrode and then allowing it to equilibrate. Measurements were not begun until an open-circuit voltage of 0 mV vs. an aluminum reference electrode was attained. It was then possible to scan either in a cathodic or anodic direction without the appearance of an overpotential for deposition or dissolution, respectively. However, once the cyclic voltammograms were begun, the re-

cordings never again passed through the origin i.e., 0 mV vs. the aluminum electrode. A typical cyclic voltammogram between the limits of -0.5 and $+0.5$ V is shown in Fig. 1D. Current loops were present on both the cathodic and anodic sides, and this cyclic behavior was very reproducible. The cathodic current loop suggests a nucleation process.

In the 60-40 m/o AlCl_3 -NaCl melt, Uhlig also found that the cyclic voltammograms for an aluminum electrode never passed through the null once the scan was started (26). He reported a hysteresis on the cathodic side.

Interpretation of cyclic voltammograms on aluminum in NaCl- AlCl_3 melts is clouded by possible complications introduced by dissolved oxygen species in the melt (26-28). We believe that an in-depth study which is beyond the scope of this paper is warranted in order to clarify the role of oxide formation on the deposition-dissolution behavior of aluminum in the NaCl(satd.)- AlCl_3 melt.

Chronoamperometry.—A typical cathodic chronoamperogram taken of an aluminum working electrode in the LiCl(satd.)- AlCl_3 melt, followed by an anodic chronoamperogram which was obtained using an overpotential of equal height, is shown in Fig. 2. The anodic portion illustrates the larger current initially obtained from the deposited alloy, followed by a smaller current when presumably the pure aluminum substrate was anodized. The first part of the cathodic chronoamperograms was characterized by a sharp drop in current to a minimum (region A). This initial current drop was due in part to the normal decay of the charging current and also was likely due to the penetration of lithium into aluminum. The linearity of plots of current vs. the negative square root of the electrolysis time, $t^{-1/2}$ (Fig. 3A) indicates that this process was diffusion limited, as has been found recently for the penetration of silver into gold (29) and of aluminum into nickel (30).

Fomichev and Chovnyk (31) showed for certain conditions of penetration of one metal into another, the squares of the slopes of curves analogous to those of Fig. 3A should be linearly related to the polarizing potential. This was demonstrated for the penetration of lead into platinum (31) and of aluminum into

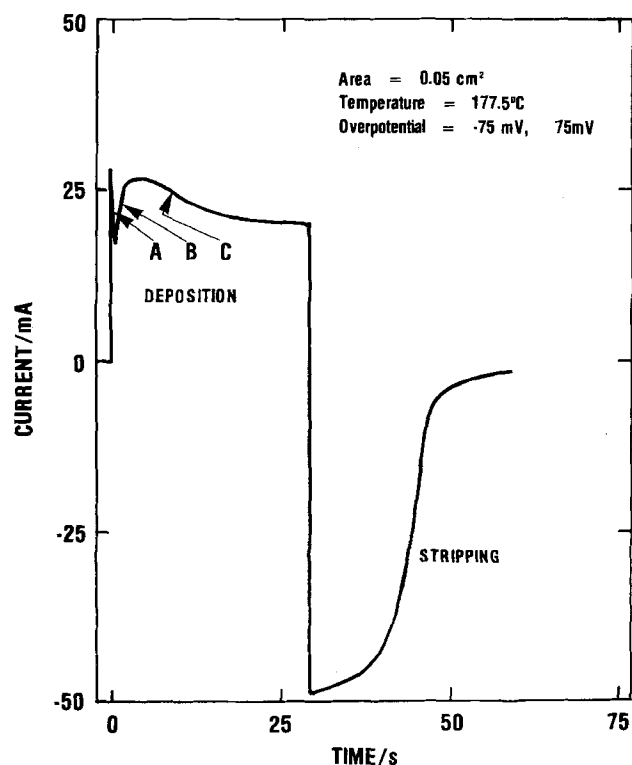


Fig. 2. Deposition and stripping chronoamperograms on aluminum in LiCl(satd.)- AlCl_3 .

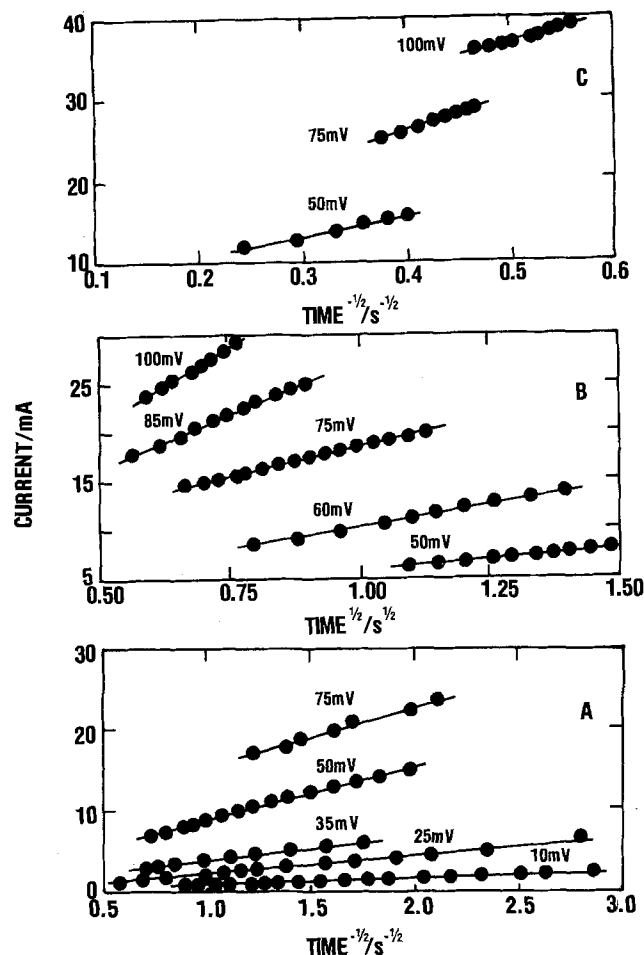


Fig. 3. Portions of cathodic chronoamperograms on aluminum in LiCl(satd.)- AlCl_3 : A, initial current decay region; B, current increase region; C, final current decay region. Imposed overpotentials are given above each curve.

nickel, cited above. The same behavior was observed in the present study for low overpotentials, as shown in Fig. 4. At an overpotential greater than -35 mV there was a departure from linearity. We could not tell if the relationship was again linear at higher overpotentials because the initial descending portion of the cathodic chronoamperogram (corresponding to region A in Fig. 3) became smaller and eventually disappeared at the large overpotentials.

We conclude that for overpotentials smaller than ca. 35 mV the cathodic process was penetration of lithium into an aluminum matrix. At overpotentials greater than ca. 35 mV the deposition mechanism changed probably to alloy formation from the constituents of the melt. This process presumably was necessitated by the small diffusion coefficient of lithium in aluminum. More evidence for this conclusion is presented below.

The cathodic chronoamperograms then showed an increase in current to a maximum, followed by a gradual decay until a plateau was reached (regions B and C on Fig. 2, respectively). The current growth was found to be linear with $t^{1/2}$ and the slope increased with an increase in overpotential as can be seen in 3B. Chronoamperograms displaying such current growth behavior have been reported for other studies of metal deposition processes occurring in molten salts (32-37) and have been considered evidence for three-dimensional nucleation. The current decay observed late in the chronoamperogram was approximately linear with $t^{-1/2}$ (Fig. 3C), again indicative of a diffusion-limited process.

Chronocoulometry.—More insight into the cathodic processes can be attained from an analysis of chronocoulometric curves. A typical set of cathodic and

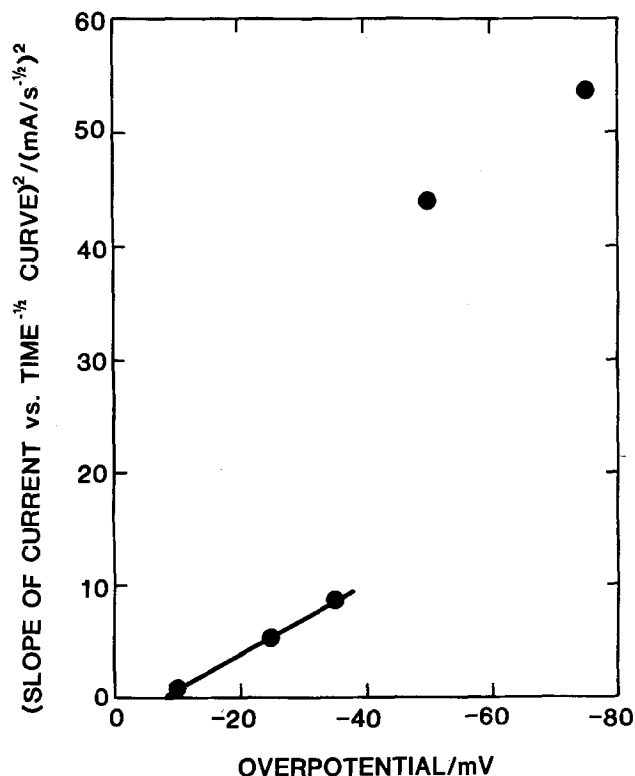


Fig. 4. Linearity test for squares of slopes of current vs. inverse square root of time: initial current decay regions of cathodic chronoamperograms.

anodic chronocoulograms is shown in Fig. 5. In a theoretical examination of electrochemical incorporation of one metal into another, Astakhov (38) postulated that if the incorporation rate were limited by diffusion of one metal into the other, the amount of metal incorporated would be proportioned to $t^{1/2}$. If the rate were limited by a reaction to form an intermetallic com-

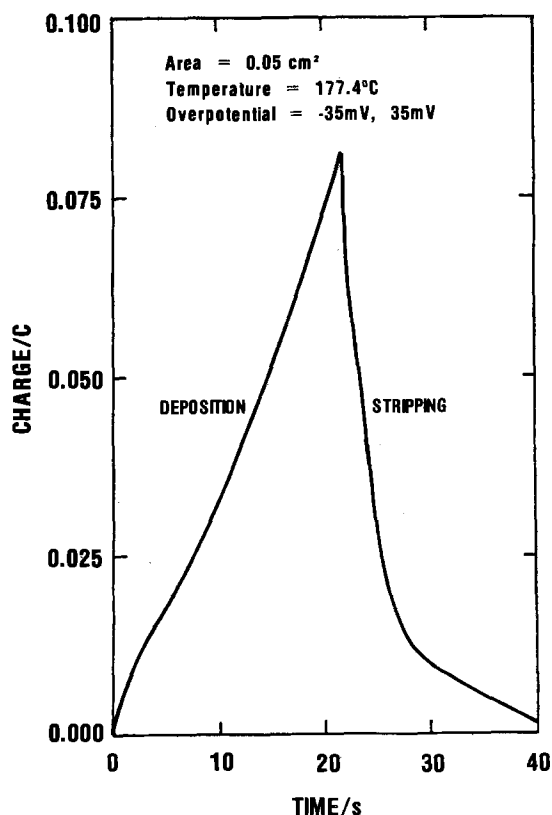


Fig. 5. Cathodic and anodic chronocoulograms on aluminum in LiCl(satd.)-AlCl₃.

pound, the amount of metal incorporated would be directly proportional to t . Melendres (6) observed both types of behavior chronocoulometrically for lithium incorporation into aluminum. At low current densities, lithium penetrated at a diffusion-limited rate into aluminum (or α -LiAl). At higher current densities β -LiAl was formed, followed later by diffusion of lithium into the β phase.

We observed similar behavior in the present study. For a short time after onset of cathodic polarization the number of coulombs passed, Q , was proportional to $t^{1/2}$. The incorporation rate then changed to a linear dependence on t , as seen in Fig. 5. The duration of the diffusion-limited incorporation regime diminished with increased overpotential. This behavior is expected on the basis of the low diffusion coefficient of lithium in aluminum [$D = 4-5 \times 10^{-10}$ cm²/sec at 430°-450°C (5, 6)], which would enhance the formation of a surface layer, and thereby account for the Q vs. t behavior at longer times. At very long times, Q was no longer proportional to either $t^{1/2}$ or t .

Anodic chronocoulograms following the cathodic chronocoulograms were characterized by an approximately linear dependence of Q on t , indicating that the LiAl was being anodized. The recovery of LiAl was always less than 100%. Transition from LiAl anodization to aluminum anodization was signaled by a sharp change in the slope of the Q vs. t curve.

Galvanostatic measurements.—From a battery viewpoint, the charge and discharge processes at constant current are of greatest interest. A typical cathodic chronopotentiogram of aluminum in the LiCl(satd.)-AlCl₃ melt followed by an anodic chronopotentiogram at the same current density is shown in Fig. 6. Notice the superpolarization at the onset of the cathodic chronopotentiogram. This phenomenon has been observed previously in the electrochemical incorporation of lithium into aluminum from the LiCl-KCl melt (6). Melendres attributed the superpolarization in this latter case to the difficulty of initially forming the surface layers of β -LiAl, or stated in different terms, it indicated the onset of electrocrystallization of the intermetallic compound and the large overpotential due to slow nucleation. The superpolarization observed in this study increased with current density.

An example of cyclic chronopotentiograms of an aluminum electrode in the NaCl(satd.)-AlCl₃ melt is shown in Fig. 7. The alternate cathodic and anodic galvanostatic pulses were of equal height and duration. No superpolarization occurred in the cathodic portions. The polarization was almost identical for the cathodic and anodic processes.

In the LiCl(satd.) melt (Fig. 6), it is apparent in the anodic chronopotentiogram that the polarization was very small during discharge of LiAl. As soon as the deposited LiAl had been completely discharged, a transition to the aluminum anodization potential was observed. When deposits were made at lower current densities or allowed to stand before stripping, the transition to the aluminum anodization potential occurred sooner and was more gradual, implying either the diffusion of deposited lithium into the substrate, or corrosion, or both. The discharge region of the LiAl always was shorter than the corresponding cathodic, deposition step. A similar qualitative relationship was observed by James (5) in charge-discharge curves for the LiAl electrode in LiCl-KCl at 430°C.

Figure 8 shows a plot of the ratio r of the transition time for anodic stripping [determined using the procedure described in Ref. (39)], τ_a , and the time of deposition, t_c ; i.e., $r = \tau_a/t_c$. Although there was some scatter in the results, it can be seen that r increased with an increase in the charging current, and then after reaching a maximum, it began to decrease. Some of the scatter could be due to the fact that t_c was varied in the range 30-600 sec. In fact, in a separate study, it was determined that with a constant charging current, the scat-

Fig. 6. Cathodic and anodic chronopotentiograms on aluminum in LiCl(satd.)-AlCl₃.

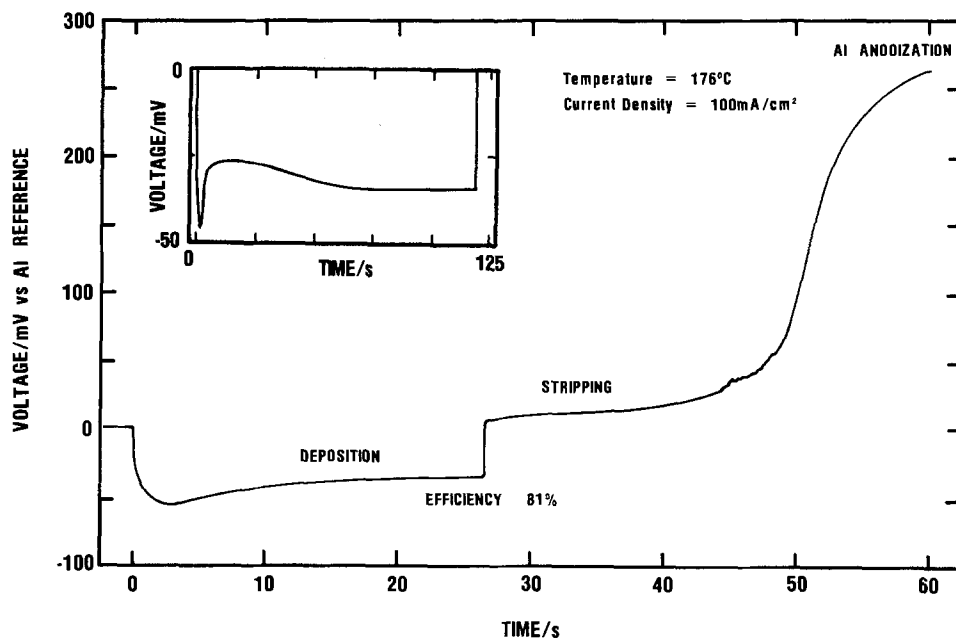
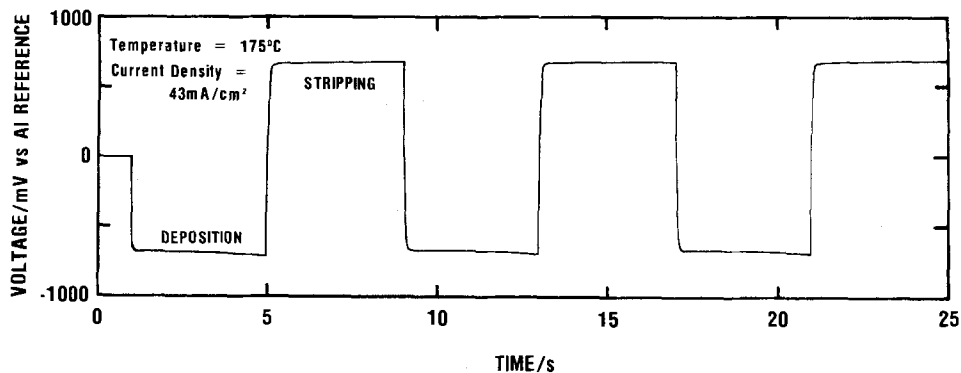


Fig. 7. Cathodic and anodic chronopotentiograms on aluminum in NaCl(satd.)-AlCl₃.



ter in r decreased with an increase in t_c , but the values of r obtained at the different t_c 's did not differ consider-

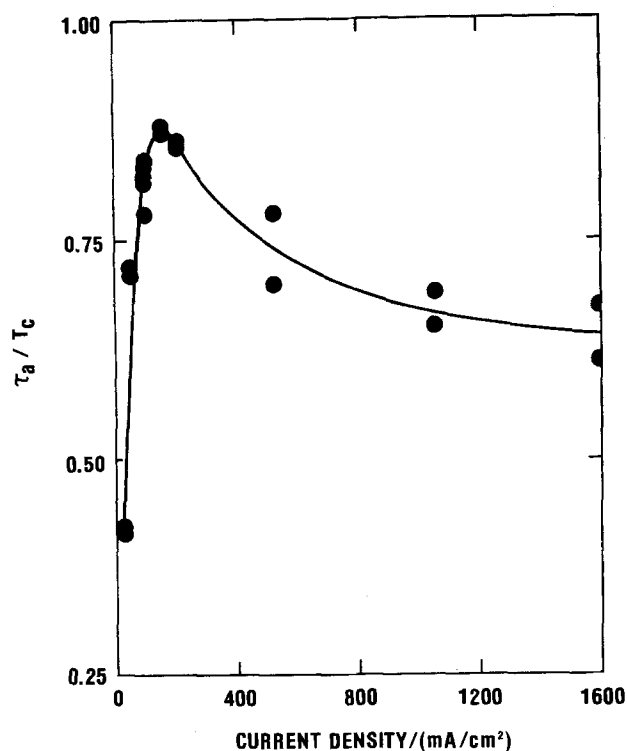


Fig. 8. Cycling efficiency for LiAl retention on aluminum in LiCl(satd.)-AlCl₃.

ably. The lower values of r at the lower current densities would suggest that the solid solution phase was formed by the implantation of lithium into the aluminum electrode. The lithium could not all be extracted in the transition time of the anodic process. As the current density increased, more of the intermetallic LiAl was formed on the surface of the aluminum and was readily accessible for dissolution. Finally, at still higher current densities, a solid solution of lithium with the β phase probably began to form. A portion of this lithium probably reacted with the melt.

In contrast to the work of Besenhard (9), the cycling efficiencies did not improve after repeated cycling. Besenhard explained the improvement he observed on the basis of retention of lithium in the aluminum substrate. The picture which emerges from our work is that the predominant process is the deposition of LiAl on the surface of the aluminum electrode; the incorporation of lithium into aluminum plays only a minor role at the outset of charging. Support for this conclusion comes in part from an experiment in which the charging process was extended to a point where the aluminum working electrode could have been converted totally into lithium monoaluminide. No transition was observed, in contrast to the case for the charging of lithium into aluminum in molten LiCl-KCl (5). The important implication is that the cycling process will not lead to electrode disintegration in AlCl₃ melt as rapidly as it will in the LiCl-KCl melts or the Li⁺-containing organic melts in which cycling results in major structural expansions during the charging process.

Anodic chronopotentiograms observed during the LiAl discharge were very smooth in the plateau region. However, when the voltage rise commenced, noise traces often were observed (see Fig. 6). This suggests

that precipitation of LiCl was occurring on the electrode surface, which is not at all surprising considering that the melt was saturated with respect to LiCl. The LiCl which precipitated on the electrode surface insulated the surface, giving rise to the noisy overvoltage. No noise was observed in the discharge of LiAl in LiCl-KCl (5).

When cathodic chronopotentiograms such as illustrated in Fig. 6 were continued for much longer times, the overpotential decay region following the initial superpolarization was in turn followed by a region of again increasing overpotential. The latter rate of increase was very gradual, and eventually a constant cathodic overpotential was reached. This behavior is illustrated in the inset of Fig. 6, where both cathodic chronopotentiograms were conducted at the same temperature and current density.

In the region of increasing overpotential, overpotential was linear in the square root of time, as shown in Fig. 9. Melendres (6) found similar behavior, which he interpreted as the diffusion of lithium through β -LiAl. He calculated a diffusion constant from the slopes of overpotential vs. $t^{1/2}$ plots, viz., $2RTi/\sqrt{\pi}n^2F^2C_0\sqrt{D}$. Here the symbols have their usual electrochemical significance. C_0 is the lithium concentration in β -LiAl, 0.045 mol/cm³, and i is current density, A/cm².

We obtained $D = 6 \times 10^{-7}$, 2×10^{-7} , and 7×10^{-7} cm²/sec at $i = 0.1$, 0.15, and 1.0 A/cm², respectively. We can find no other studies of lithium diffusion into LiAl or aluminum conducted in the temperature region in which we worked. Several higher temperature studies have been made (5, 6, 40, 41) and report widely divergent values of D , ranging from 5×10^{-5} (5) to 10^{-8} cm²/sec (6) at 430°-450°C.

Stability of the deposit.—The measured open-circuit voltage of a newly electroformed deposit in the LiCl(satd.)-AlCl₃ melt was approximately -7 mV vs. the aluminum reference electrode. After allowing the deposit to stand in the melt, the open-circuit voltage decayed to near 0 mV. This, of course, suggests that the deposit was unstable. In fact, stability tests conducted by deposition on an aluminum cathode followed by anodic stripping after increasing time intervals revealed that the deposit was indeed unstable. This is not unexpected, since at 500 K for the reaction

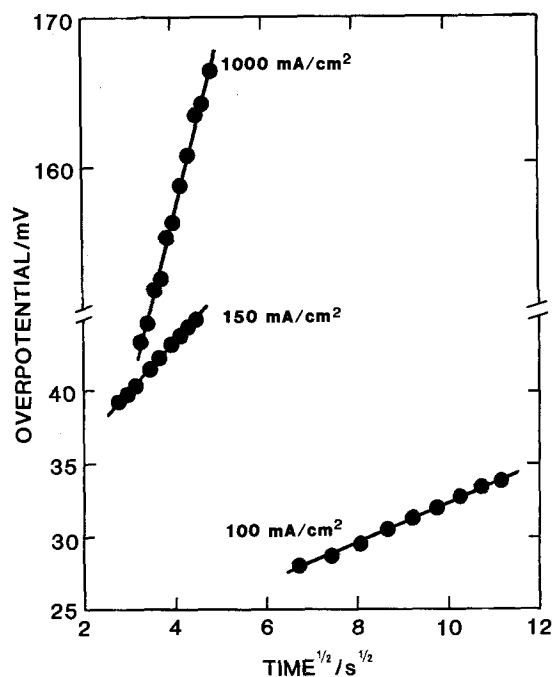
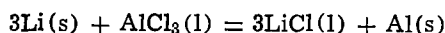


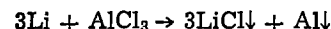
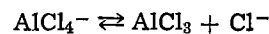
Fig. 9. Slowly increasing overpotential region of cathodic chronopotentiograms on aluminum in LiCl(satd.)-AlCl₃.

$K = 10^{-54.5}$ (42). The activity of LiCl is unity in an LiCl(satd.)-AlCl₃ melt. The activity of AlCl₃ is undeniably lower than unity, but it is far from $10^{-54.5}$, which would be the needed activity for the above reaction to be reversed. This differs from Senderoff's contention that LiAl is stable in the LiAlCl₄ melt (10). On the other hand, we did find that a 1/2 in. diam LiAl (1:1 alloy) rod, prepared by metallurgical procedures, did not show any visible changes after remaining in the melt at approximately 175°C for several weeks.

Cyclic chronopotentiometric experiments provide insight into the nature of the deposit that is formed on the surface of the substrate, provided that the deposition step is followed immediately by stripping. If the substrate is aluminum, allowing the deposit to stand at open circuit could result in a chemical reaction between the deposit and the electrolyte at the interface, diffusional penetration of the lithium from the deposit into the aluminum substrate to produce a homogeneous phase, or both. Thus stripping a thin deposit after a time interval should reveal the effect of any processes potentially contributing to the instability of the deposit. In experiments in which a deposit was laid down on an aluminum substrate and various stand times were allowed before stripping, the low polarization plateau became progressively smaller as the stand times were increased. In addition, the rising portion of the chronopotentiogram between this low polarization plateau and anodization of pure aluminum had a decreasing slope (i.e., the transition to aluminum anodization became less sharp), suggesting the presence of an increasing amount of the α solid solution phase. Thus, this re-establishment of a homogeneous phase cannot be discounted.

To exclude the formation of α -LiAl as the major contributor to the instability of the deposit, a tungsten substrate was used in place of the aluminum. The results obtained were even worse from the standpoint of recovery of total deposited metal than those obtained using an aluminum substrate. Thus we can conclude that a chemical reaction between the LiAl deposit and the melt plays a prominent role in the stability of the alloy. This type of behavior is not unprecedented, for reactivity has been demonstrated between the lithium contained in lithium alloys other than lithium-aluminum alloys, and other solvents (43, 44).

The most plausible chemical reaction is that between the lithium which diffuses out of the intermetallic and the melt, whose primary species is AlCl₄⁻ (45, 46). The following reactions are expected



Any LiCl which is formed should precipitate, since the melt is saturated with LiCl. However, of great significance is that the reaction will also lead to additional aluminum being laid down on the aluminum matrix remaining from the LiAl deposit.

To explore further this stability problem from a macroanalytical approach, a massive amount of the deposit was laid down on a 1 mm diam aluminum wire in an LiCl-AlCl₃ solution to which an excess of solid LiCl was added. An aluminum wire of about the same dimensions as the cathode was employed. Electrolysis was conducted at roughly 50 mA/cm². After electrolysis was terminated, the deposit remained in the melt for less than 1 hr. Quite surprising is that even though the deposition was conducted at a current density which was not symmetrically uniform about the wire, the deposit itself was almost perfectly uniform, as shown in Fig. 10. The deposit had a thickness of 0.75 mm and adhered tenaciously to the aluminum wire substrate. Scanning electron photomicrographs show clearly the lack of dendrites. A photomicrograph obtained under higher magnification is shown in Fig. 11. Features of

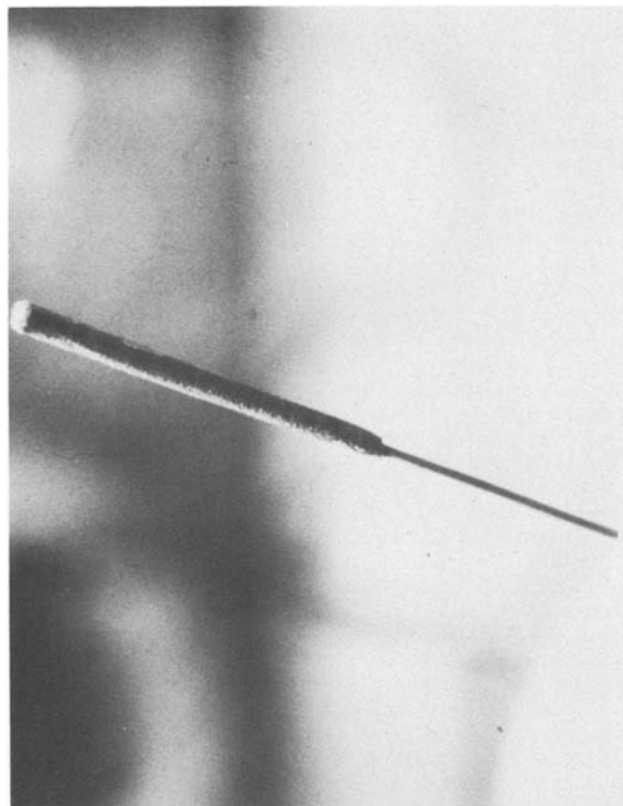


Fig. 10. Electrodeposited LiAl on aluminum in LiCl(satd.)-AlCl₃

note are the presence of cracks and differences in optical reflectivity over the surface. Melendres and Sy (7) found both characteristics in their study of β -LiAl formed in LiCl-KCl. They established that areas of different reflectivity varied in aluminum content, with light areas being richer in aluminum (lower lithium) than darker areas.

The x-ray powder diffraction lines for this deposit along with the ϕ values for lithium, aluminum, and LiAl are listed in Table I. Although there is not a perfect match, it appears that lithium, aluminum, and LiAl lines all were present. A better identification was possible by running a sample of the deposit in a gold pan in a Perkin-Elmer DSC-2 differential scanning calorimeter. A high intensity temperature peak commencing at 605°C and a second, well resolved, lower intensity peak terminating at approximately 665°C were identified. According to the Li-Al phase diagram (48)

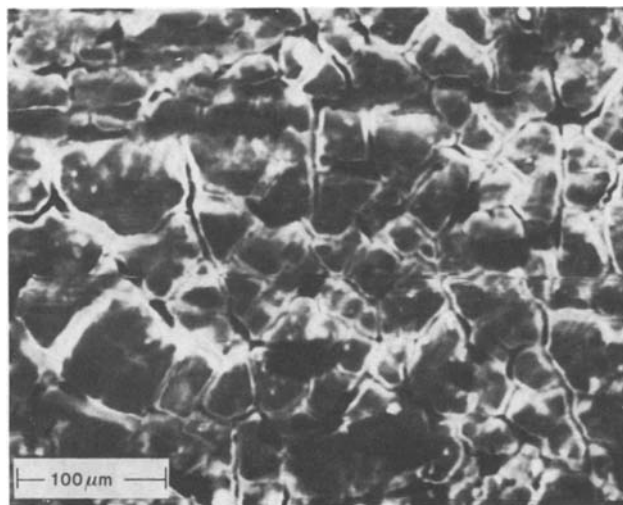


Fig. 11. Scanning electron photomicrograph of the LiAl deposit shown in Fig. 10.

Table I. X-ray powder diffraction lines

| Li ^a (d/Å) | Al ^b (d/Å) | Deposit (d/Å) | LiAl ^c (d/Å) |
|-------------------------|-----------------------|---------------|-------------------------|
| | | 2.935 | 3.65 (75) |
| | | 2.549 | |
| 2.48 (100) ^d | 2.338 (100) | 2.322 | 2.26 (100) |
| | 2.024 (47) | 2.008 | 1.92 (75) |
| 1.758 (30) | | 1.805 | 1.58 (60) |
| | | 1.542 | 1.46 (60) |
| 1.434 (40) | 1.431 (22) | 1.477 | |
| | | 1.425 | |
| 1.242 (20) | | 1.280 | 1.30 (100) |
| | 1.221 (24) | 1.217 | 1.22 (75) |
| | 1.169 (7) | 1.175 | |
| 1.110 (20) | | 1.146 | 1.12 (75) |
| 1.013 (3) | 1.0124 (2) | 1.047 | 1.07 (75) |
| | | 0.987 | 1.01 (85) |
| 0.938 (20) | | | 0.969 (50) |
| | 0.9289 (8) | 0.928 | 0.918 (50) |
| | 0.9055 (8) | 0.907 | 0.889 (75) |
| | | 0.868 | |
| | | 0.856 | |
| | 0.8266 (8) | 0.826 | 0.849 (25) |
| | | 0.813 | 0.827 (100) |
| | | 0.787 | 0.796 (60) |
| | | 0.779 | 0.778 (50) |

^a ASTM X-Ray Index Card 15-40; Ref. (47).

^b ASTM X-Ray Index Card 4-0787; Ref. (47).

^c ASTM X-Ray Index Card 3-125; Ref. (47).

^d Relative intensities shown in parentheses.

this corresponds to a composition of approximately 35 m/o lithium and consists of a mixture of the α and β phases.

Our results appear to support the ideas that lithium is being removed from the electroformed β -LiAl and that the chief driving force for this extraction is the chemical reaction between lithium and the melt. This reaction probably does not proceed to the point where all the lithium has been removed; rather a protective barrier of aluminum and LiCl appeared to be formed at the electrolyte interface. This is analogous to the film which protects lithium in organic electrolytes. Quite significant is the fact that nondendritic, adherent, dense deposits of aluminum or an aluminum alloy having less than a 50 m/o lithium content can be electroformed via the route of initial formation of β -LiAl. Even though the stabilized deposit has inferior properties to pure β -LiAl from a battery standpoint, we have at last the ability to use an aluminum electrode. When compared to other anode candidates, aluminum is highly desirable in the areas of cost, equivalent weight, and electromotive potential. To highlight this discovery is the fact that the deposition of aluminum from the 2AlCl₃-NaCl melt is accompanied by dendritic deposits when coatings over 20 μ m thick are deposited.

Studies are now underway to explore in greater detail the effect of current density, temperature, cycling, etc. on the morphology of the deposit. Cross-sectional elemental profiling and anodic polarization properties of the electroformed alloy after long-term equilibration in the melt are being investigated. In addition, more insight into the reaction mechanisms is being sought using a-c impedance measurements.

Manuscript submitted March 11, 1980; revised manuscript received Feb. 3, 1981.

Any discussion of this paper will appear in a Discussion Section to be published in the June 1982 JOURNAL. All discussions for the June 1982 Discussion Section should be submitted by Feb. 1, 1982.

Publication costs of this article were assisted by the USAF Academy.

REFERENCES

1. H. A. Adams, U.S. Pat. 3,428,493 (1969).
2. E. S. Buzzeli, U.S. Pat. 3,445,288 (1969).
3. J. L. Benak, U.S. Pat. 3,501,349 (1970).
4. E. C. Gay, D. R. Vissers, F. J. Martino, and K. E. Anderson, *This Journal*, **123**, 1591 (1976).
5. S. D. James, *Electrochim. Acta*, **21**, 157 (1976).
6. C. A. Melendres, *This Journal*, **124**, 650 (1977).
7. C. A. Melendres and C. C. Sy, *ibid.*, **125**, 727 (1978).
8. B. M. L. Rao, R. W. Francis, and H. A. Christopher, *ibid.*, **124**, 1490 (1977).
9. J. O. Besenhard, *J. Electroanal. Chem. Interfacial Electrochem.*, **94**, 77 (1978).
10. S. Senderoff, U.S. Pat. 3,751,298 (1973).
11. J. C. Nardi, J. K. Erbacher, C. L. Hussey, and L. A. King, *J. Power Sources*, **3**, 81 (1978).
12. R. K. Bunting, R. A. Carpio, A. A. Fannin, Jr., L. A. King and H. A. Øye, Unpublished data.
13. R. A. Carpio, L. A. King, F. C. Kibler, Jr., and A. A. Fannin, Jr., *This Journal*, **126**, 1650 (1979).
14. J. O. Besenhard and G. Eichinger, *J. Electroanal. Chem. Interfacial Electrochem.*, **68**, 1 (1976).
15. M. Eisenberg, K. Wong, and K-C Tsai, *This Journal*, **120**, 1686 (1973).
16. Y. Avigal and E. Peled, *J. Electroanal. Chem. Interfacial Electrochem.*, **76**, 135 (1977).
17. K. H. M. Braeuer and J. A. Harvey, Status Report on Organic Electrolyte High Energy Density Batteries, Power Sources Division Electronic Components Laboratory, May 1967, AD 654813.
18. E. Peled, A. Mitavski, A. Reger, and E. Gileadi, *J. Electroanal. Chem. Interfacial Electrochem.*, **75**, 677 (1977).
19. S. Ziegel, E. Peled, and E. Gileadi, *Electrochim. Acta*, **23**, 363 (1978).
20. R. A. Carpio, L. A. King, and A. A. Fannin, Jr., *J. Chem. Eng. Data*, **24**, 22 (1979).
21. G. Torsi and G. Mamantov, *Inorg. Chem.*, **10**, 1900 (1971).
22. E. Peled and E. Gileadi, *This Journal*, **125**, 15 (1976).
23. J. N. Jovićević, A. R. Despić, and D. M. Dražić, *Electrochim. Acta*, **22**, 577 (1977).
24. R. D. Rauh, T. F. Reise, and S. B. Brummer, *This Journal*, **125**, 186 (1978).
25. C. L. Hussey, J. C. Nardi, L. A. King, and J. K. Erbacher, *ibid.*, **124**, 1451 (1977).
26. G. F. Uhlig, Ph.D. Dissertation, University of Utah (1973).
27. B. Tremillon, A. Bermond, and R. Molina, *J. Electroanal. Chem. Interfacial Electrochem.*, **74**, 53 (1976).
28. B. Gilbert and R. A. Osteryoung, *J. Am. Chem. Soc.*, **100**, 2725 (1978).
29. D. O. Raleigh and H. R. Crowe, *This Journal*, **116**, 40 (1969).
30. M. E. Niyazimbetov, I. I. Astakhov, and B. N. Kabanov, *Sov. Electrochem.*, **14**, 799 (1978); *Elektrokhimiya*, **14**, 930 (1978).
31. A. M. Fomichev and N. G. Chovnyk, *Sov. Electrochem.*, **10**, 267 (1974); *Elektrokhimiya*, **10**, 284 (1974).
32. G. A. Gunawardena, G. J. Hills, and I. Montenegro, *Electrochim. Acta*, **23**, 693 (1978).
33. P. Rolland and G. Mamantov, *This Journal*, **123**, 1299 (1976).
34. N. P. Bansal and J. A. Plambeck, *ibid.*, **124**, 1036 (1977).
35. C. L. Hussey, L. A. King, and R. A. Carpio, *ibid.*, **126**, 1029 (1979).
36. F. Palmisano, E. Desimoni, L. Sabbatini, and G. Torsi, *J. Appl. Electrochem.*, **9**, 517 (1979).
37. J. Robinson and R. A. Osteryoung, *This Journal*, **127**, 122 (1980).
38. I. I. Astakhov, *Sov. Electrochem.*, **9**, 501 (1973); *Elektrokhimiya*, **9**, 521 (1973).
39. W. H. Reinmuth, *Anal. Chem.*, **33**, 485 (1961).
40. A. L. L'vov, A. A. Gnilomedov, A. P. Selemenev, and E. N. Protasov, *Sov. Electrochem.*, **11**, 1232 (1975); *Elektrokhimiya*, **11**, 1322 (1975).
41. C. J. Wen, B. A. Boukamp, R. A. Huggins, and W. Weppner, *This Journal*, **126**, 2258 (1979).
42. JANAF Thermochemical Tables, 2nd Ed., NSRDS-NBS37, National Bureau of Standards, Washington, D.C. (1971).
43. I. A. Avrutskaya, I. G. Kiseleva, A. V. Chekavtsev, V. S. Shinkarev, M. Ya. Fiochin, and B. N. Kabanov, *Sov. Electrochem.*, **13**, 1297 (1977); *Elektrokhimiya*, **13**, 1516 (1977).
44. A. V. Chekavtsev, I. G. Kiseleva, and B. N. Kabanov, *Sov. Electrochem.*, **14**, 949 (1978); *Elektrokhimiya*, **14**, 1092 (1978).
45. E. Rytter, H. A. Øye, S. J. Cyvin, B. N. Cyvin, and P. Klæboe, *J. Inorg. Nucl. Chem.*, **35**, 1185 (1973).
46. E. Rytter, H. A. Øye, and P. Klæboe, in "Advances in Raman Spectroscopy," Vol. I, J. P. Mathieu, Editor, p. 550, Heyden, London (1973).
47. ASTM Powder Diffraction File 1968, American Society for Testing and Materials, Philadelphia, PA (1968).
48. M. Hansen, "Constitution of Binary Alloys," 2nd ed., p. 104, McGraw-Hill Book Co., New York (1958).
49. Y. K. Delimarsky and N. K. Tumanova, *Electrochim. Acta*, **24**, 19 (1979).

Electrochemical Behavior of Methylene Blue and Its Leucoform at the Mercury Electrode

G. Papeschi, M. Costa, and S. Bordi*

Istituto di Chimica Fisica, Università di Firenze, I-50121, Firenze, Italy

ABSTRACT

The electrochemical behavior of methylene blue (MB) and its leucoform (LMB) in aqueous solutions at pH 7.9 was investigated with a mercury electrode. The polarographic results showed that at very low concentrations (4×10^{-6} M/liter) and $E_{1/2}$ of "Brdička's prewave" is the same as the standard potential of the MB/LMB couple and moves from about -0.290 to -0.180 V (NCE) as the concentration increases. The electrocapillary curves indicate the following: (i) at low concentrations the LMB is less adsorbed than the MB; (ii) γ decidedly decreases when the surface concentration of LMB reaches a value high enough to form a solid deposit on the mercury surface. We suggest that: (a) "Brdička's prewave" which occurs at the lowest concentrations is actually the normal wave of the MB/LMB couple; (b) "Brdička's normal wave" is a step that develops at the standard potential, but on an electrode covered by an insoluble film of LMB.

The electroreduction of methylene blue (MB) to leucomethylene blue (LMB) on a mercury electrode takes place with an anomalous behavior. This system was studied polarographically by Brdička (1, 2) and it is the classical example of reduction product adsorption cited in every textbook of polarography (3-5).

Brdička shows that at pH = 7.96 at concentrations of MB below 6×10^{-5} M a single step ("prewave") is observed, while at higher concentrations a second step ("normal wave") appears at more negative potentials.

In the interpretation of Brdička the "prewave" corresponds to reduction of unadsorbed MB to adsorbed LMB; the height of this step is limited, not by the rate of diffusion of MB, but by the surface available for adsorption of the reduced molecules. He states that the product of MB reduction is adsorbed at the electrode surface as soon as it is formed and this facilitates, from an energy point of view, the reduction itself by allowing it to take place at a potential less negative than the standard potential of the MB/LMB couple. According to Brdička, the "normal wave" is observed when the surface is fully occupied by LMB and requires a more negative potential since the reduced form finds itself in a higher energy state (unadsorbed as opposed to adsorbed). Under these conditions there is no process aiding the reduction and therefore the normal wave should develop in the neighborhood of the standard potential.

After Brdička much work was done (6-14) using different techniques in order to provide the MB/LMB redox couple with new information. Although the majority of these investigations have retained substantially unchanged Brdička's point of view, experimental evidence exists and points out that the MB/LMB system is actually more complicated than Brdička's scheme assumes it to be.

Recently Baumgartner *et al.* (15) have shown by using multiple specular reflection spectroscopy applied to a thin layer electrochemical cell, that, in the first 0.5 sec of the (1×10^{-5} M) MB reduction process, the LMB formed precipitates on the gold electrode surface.

We are presenting here experimental evidence pertaining to the MB/LMB redox system drawn from studies of electrocapillary curves, normal polarographic curves, and anodic voltammetry.

* Electrochemical Society Active Member.
Key words: adsorption, voltammetry.

Experimental

The capillaries used either for drop-time measurements or for polarographic investigations were drawn from 2×10 mm Pyrex tubes and dewetted with dimethyldichlorosilane vapors. Finally by trial those capillaries were chosen which gave a drop time of about 20 sec.

The concentration range 1×10^{-5} - 1×10^{-4} M/liter of MB was explored with 16 electrocapillary curves (Fig. 1) obtained with the drop-time method. The range of potentials $+0.1$ to -1.3 V (NCE) was traversed at 25 mV intervals between $+0.1$ and -0.6 V and at 50 mV intervals between -0.6 and -1.3 V. The

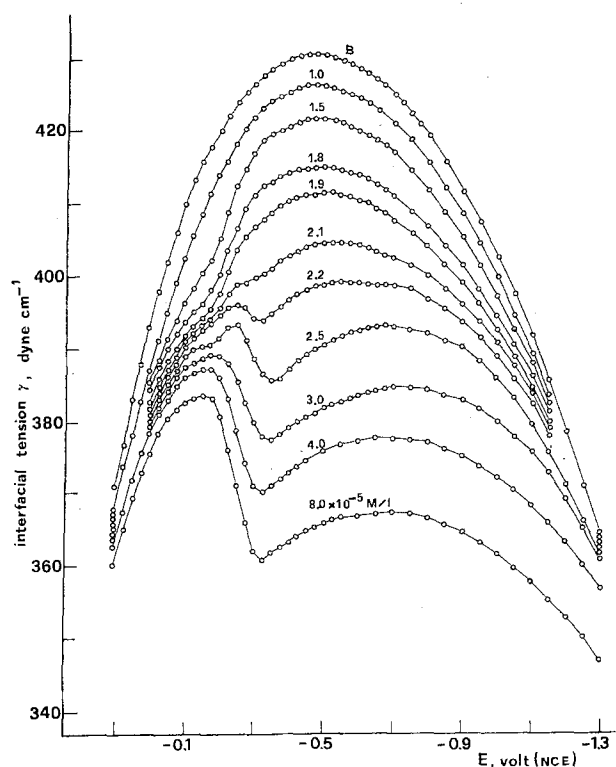


Fig. 1. Electrocapillary curves due to buffered solutions (pH = 7.9) of methylene blue at the given concentrations (the curves of concentrations 0.20, 0.23, 0.35, 0.60, 1.0×10^{-4} M/liter are not shown).

apparatus and other experimental details were as described previously (16).

With an E261 Metrohm polarograph, 20 polarograms were recorded over the concentration range 4×10^{-6} – 5×10^{-4} M/liter. With the same apparatus the remaining polarographic investigation was conducted.

All the potentials were referred to 1N KCl calomel electrode. Both the reference half-cell as well as the working solutions were kept at a constant temperature of $25.0 \pm 0.1^\circ\text{C}$.

A phosphoric buffer solution at pH 7.9 (0.05M KH_2PO_4 and 0.046M NaOH) was used as base electrolyte.

All the chemicals, except the dye, were of Analar Grade, and the water was distilled three times in an all-Pyrex-glass still (17). Merk reagent methylene blue was used without further purification.

Air was bubbled for a long time through the mercury in contact with 5% HNO_3 . After washing and drying it was distilled twice under vacuum.

Results

Excellent agreement is observed between Brdička's and our polarographic results in the field of analytical MB concentration greater than 5×10^{-5} M/liter, where the dye undergoes electroreduction with two different waves, the former with half-wave potential approximately the same as the standard potential, the latter with half-wave potential shifted by about 100 mV toward more positive values.

Our polarographic investigation was extended to MB concentrations below 5×10^{-5} M in order to observe the development of the prewave up to the lower limit of 4×10^{-6} M/liter. This enabled us to verify that the $E_{1/2}$ of the prewave at the lowest concentrations to be the same as the standard potential calculated by Clark, Cohen, and Gibbs (18) at concentrations $< 5 \times 10^{-5}$ M in neutral or alkaline solutions, pH > 6 , with the Nernst equation

$$E = E_0 + \frac{RT}{2F} \ln \frac{[\text{MB}] \cdot [\text{H}^+]}{[\text{LMB}]} \quad [1]$$

where

$$E_0 = +0.226\text{V (NCE)}$$

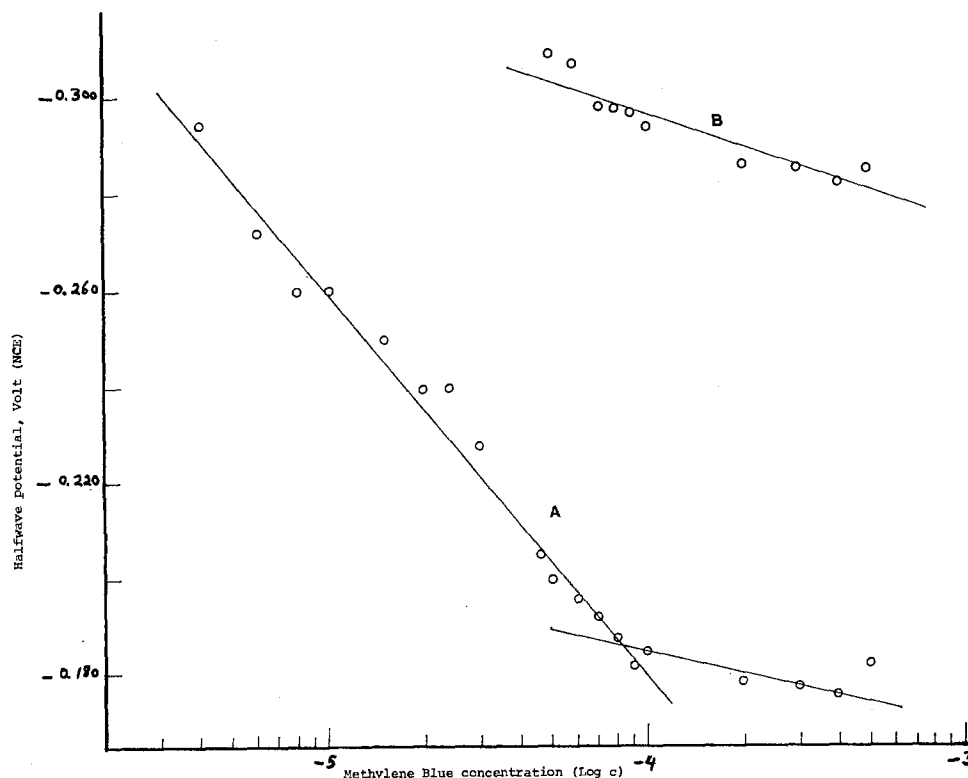


Fig. 2. Half-wave potential of "Brdička's prewave" (curve A) and of "Brdička's normal wave" (curve B), plotted against the MB concentration, as obtained from the polarograms at pH = 7.9.

Moreover as the concentration of MB was increased, the $E_{1/2}$ of the prewave was observed to move from about -0.290V up to -0.180V (NCE). The shift takes place essentially while the concentration is increased from the lowest values to that one at which the second step appears ($c = 5 \times 10^{-5}$ M/liter). In Fig. 2 the half-wave potential of the two reduction steps are plotted against the concentration of MB.

At pH = 7.9 the LMB is slightly soluble and when, for instance, an 8×10^{-5} M MB solution is electroreduced at a constant potential of -0.5V vs. NCE, i.e., at a potential corresponding to the diffusion current of the normal wave, a turbid colorless suspension is obtained. The height of the anodic wave developing in the LMB saturated solution is equal to the height of the cathodic step given by a 1×10^{-5} M solution of MB. It is of interest to note that the half-step potential of both polarograms is the same $E_{1/2} = -0.270 \pm 0.015\text{V}$ (NCE) and in good agreement with the equilibrium potential as calculated by Eq. [1]. If air is bubbled through the solution the LMB is quickly oxidized to MB; consequently the precipitate dissolves while the deep blue color reappears.

Experiments with a stationary mercury electrode have emphasized the consequences of the low solubility of the LMB in aqueous solution buffered at pH = 7.9. When the hanging mercury drop electrode was held for a few minutes under polarization in an 8×10^{-5} M solution of MB at the potential of -0.5V vs. NCE, the formation of a white insoluble film on the mercury surface was observed. Upon shifting the applied potential to a value corresponding to the foot of the prewave, the white precipitate was oxidized back to the soluble form of MB and the mercury drop became clean and bright again.

The formation of an insoluble LMB film was also detected for shorter polarization times. The hanging mercury drop electrode was held at -0.5V for 60 sec in the same 8×10^{-5} M MB solution, and then the potential was shifted at a sweep rate of 4.7 mV/sec toward more positive values. The current flowing through the electrode, as recorded against the potential, exhibits an anodic peak (Fig. 3) at -0.200V . For the $E_{1/2}$ of the prewave at this concentration we read

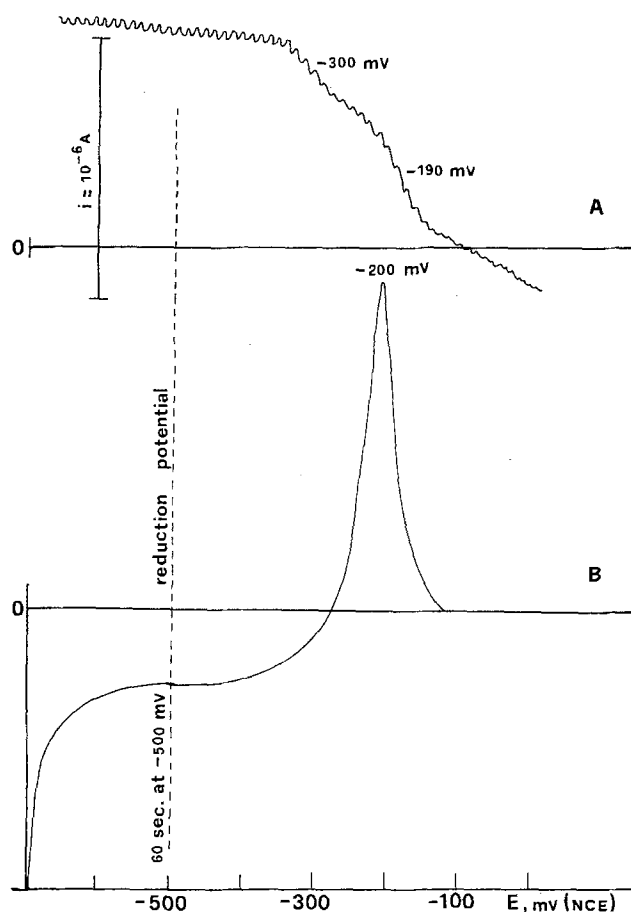


Fig. 3. Curve A: polarogram for MB 8×10^{-5} M/liter at pH = 7.9; curve B: anodic peak due to oxidation of the LMB accumulated on the mercury electrode during 60 sec of electrolysis, in the 8×10^{-5} M/liter MB solution, at -0.5 V (NCE). The potential was shifted at a sweep rate of 4.7 mV/sec toward the anodic values. (Drop surface 4.57 mm 2 ; coulombs 31.0×10^{-6} ; molecules/drop 96.6×10^{12} ; number of layers 21).

-0.190 V. The area under the peak indicates the presence of about 20 monolayers of LMB on the electrode surface, provided we attribute a value of 100 \AA^2 to the area of one molecule of LMB. An anodic peak is also recorded for polarization times of the order of tens of seconds.

One of the most convincing proofs of the strong adsorption of the LMB, was considered by Brdička the change of the shape of the electrocapillary curves obtained in buffered solution of MB. For this reason our investigation was extended to the study of the electrocapillary curves of this dye in phosphoric buffer at pH = 7.9.

In the region of the electrocapillary curves where the adsorption at the interphase is not accompanied by a faradaic process, the lowering of the interfacial tension is simply due to the adsorption of MB on mercury. By using the Gibbs equation

$$\Gamma = -\frac{1}{RT} \left(\frac{\partial \gamma}{\gamma \ln c} \right)_{E,T} \quad [2]$$

where γ is the interfacial tension, c the MB analytic bulk concentration (in place of the activity), Γ the surface excess, R the gas constant, T the absolute temperature, and E the potential, we have calculated Γ and then the area S taken up by one molecule of the dye

$$\Gamma = 1.3 \times 10^{-10} \text{ mol cm}^{-2}$$

$$S = 125 \text{ \AA}^2 \text{ molecule}^{-1}$$

The S value agrees satisfactorily with that attributed

to MB molecule when it is placed flat on the electrode surface.

For concentrations below 2.7×10^{-5} M at a potential value of approximately -0.175 V corresponding to the beginning of the MB reduction, the interfacial tension steps up rapidly as if the product were less adsorbed than the reactant.

For concentrations above 2.0×10^{-5} M in correspondence to a potential of about -0.250 V the interfacial tension decreases ever so rapidly with the increasing concentration and then increases again at about -0.325 V.

Discussion

Let us bear in mind the following main facts arising from our experimental work:

1. The half-wave potential of the prewave shifts toward more positive values with increasing concentration and becomes nearly constant when the second wave appears (Fig. 2).

2. The half-wave potentials of the anodic step for a solution saturated in LMB as well as the half-wave potential of the cathodic wave of equal height for a MB solution, agree within ± 15 mV with the standard potential of the MB/LMB couple as determined by Clark and co-workers at concentrations below 10^{-5} mol/liter and pH greater than 6.

3. An insoluble film of LMB is formed on a stationary mercury electrode after a few of tens of seconds of electrolysis at a potential of -0.500 V (NCE) in an 8×10^{-5} M MB solution.

4. The white precipitate of LMB dissolves with an anodic peak at a value of about -0.200 V; very close to the half-step potential of the prewave recorded at the same MB concentration (Fig. 3).

5. From the electrocapillary curves we can observe the following: (i) at concentrations below 2.7×10^{-5} M and at a potential of about -0.175 V, corresponding to the beginning of the MB reduction, the interfacial tension steps up rapidly (Fig. 1 and 4); (ii) at concentrations above 2.0×10^{-5} M, and at a potential of about -0.250 V the interfacial tension falls down ever so rapidly as the concentration increases, and then rises again at about -0.325 V to reach the electrocapillary maximum (Fig. 1).

Our findings show that the product of reduction is less adsorbed than the oxidized form, as we can observe in the electrocapillary curves, when at the point corresponding to the beginning of the reduction of MB, the interfacial tension decidedly steps up (Fig. 1, and better visible in Fig. 4, points m). When the concentration of LMB produced in the reduction process reaches the saturation limit on the electrode surface, a precipitate of LMB is deposited on the mercury. The interfacial tension at this point is lowered and the greater the amount of LMB deposited, the greater the lowering of γ (Fig. 4, points n).

On this account Brdička's prewave displacement will stop when the amount of MB undergoing reduction is large enough to produce a film of LMB shielding the mercury drop entirely.

Any further reduction of MB to LMB on the electrode covered by the precipitate will proceed in a separate wave.

Many theories have been proposed in the attempt to explain the reduction process of a substance on an electrode covered by an insoluble film of the product: (i) the film of the reduction product is further reduced; (ii) the film undergoes a severe change in its structure at a definite potential; and (iii) a progressive migration of the depolarizer takes place through the film.

In our case one important fact is to be noted: the slope of the normal wave is approximately 20–25 mV. This critical dependence of the penetration current on the applied potential seems to suggest that the charge

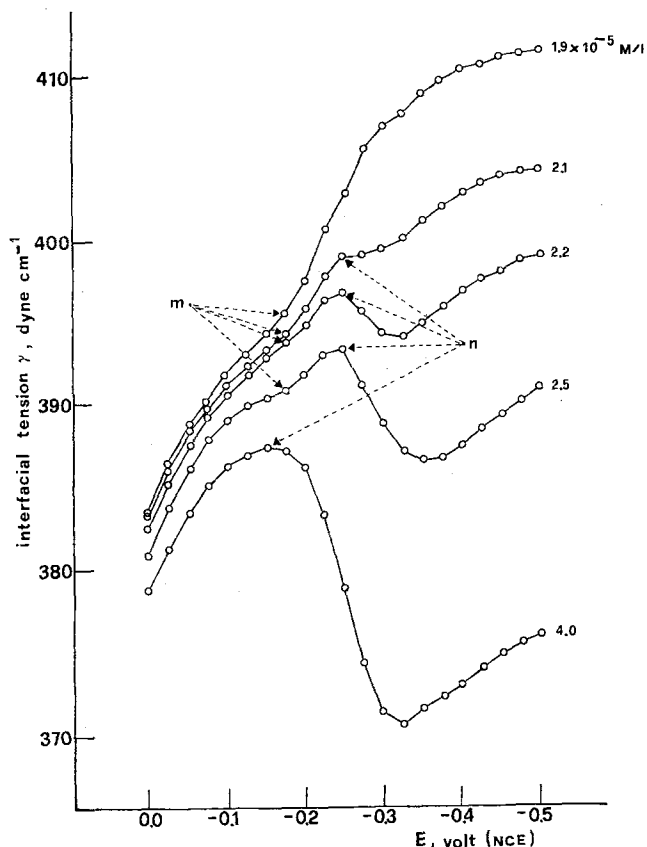


Fig. 4. Detail of the electrocapillary curves in the region where the MB undergoes electroreduction.

carrier through the insoluble film is not the depolarizer but rather the electron. It is known that the probability for an electron to tunnel through a rectangular energy barrier depends exponentially on the product of the thickness of the barrier by the square root of the difference between the energy corresponding to the peak of the barrier and the Fermi level energy in the metal. A shift of the applied potential toward more negative values causes a linear increase in the Fermi level energy and the barrier is rendered more penetrable to electrons. The consequent increase in the cathodic current leads to an increase in the barrier thickness due to the continuous deposition of the reduction product. Both at a dropping and at a hanging drop electrode, however, the thickness of the insoluble film may reach, at the most, a certain maximum value, which is obtained at the end of the electrolysis period, under diffusion control conditions. A sufficiently negative po-

tential may, therefore, be reached at which the electron tunneling through the barrier is so fast that the current is controlled exclusively by the depolarizer diffusion toward the insoluble film surface.

This preliminary examination of the experimental data seems to suggest that the polarographic step which occurs at the lowest concentrations (Brdička's pre-wave) is actually the normal wave, and that Brdička's normal wave is a step that develops at the standard potential of the MB/LMB couple, but on an electrode covered by an insoluble film of LMB.

Manuscript submitted July 25, 1980; revised manuscript received Jan. 16, 1981.

Any discussion of this paper will appear in a Discussion Section to be published in the June 1982 JOURNAL. All discussions for the June 1982 Discussion Section should be submitted by Feb. 1, 1982.

Publication costs of this article were assisted by the Università di Firenze.

REFERENCES

1. R. Brdička, *Z. Electrochem.*, **48**, 278 (1942).
2. R. Brdička, *Collect. Czech. Chem. Commun.*, **12**, 522 (1947).
3. I. M. Kolthoff and J. J. Lingane, "Polarography," Vol. I, p. 256, Interscience Publishers, New York (1965).
4. R. Pointeau and J. Bonastre, "Éléments de Polarographie," p. 112, Masson et C., Paris (1970).
5. H. H. Bauer, "Electrodics," p. 96, Georg Thieme Publishers, Stuttgart (1972).
6. A. M. Mirri and P. Favero, *Ric. Sci.*, **28**, 2307 (1958).
7. W. Kemula, Z. Kublik, and A. Axt, *Rocz. Chem.*, **35**, 1009 (1961).
8. J. M. Los and C. K. Tompkins, *Can. J. Chem.*, **37**, 315 (1959).
9. J. M. Los and C. K. Tompkins, *J. Chem. Phys.*, **24**, 630 (1956).
10. R. H. Wopschall and I. Shain, *Anal. Chem.*, **39**, 1527 (1967).
11. P. J. Hillson and R. B. McKay, *Trans. Faraday Soc.*, **61**, 374 (1965).
12. K. J. Vetter and J. Bardeleben, *Z. Electrochem.*, **61**, 135 (1957).
13. E. Yu. Khmel'nitskaya, G. A. Tedoradze, and Ya. M. Zolotovitskii, *Izv. Akad. Nauk SSSR, Ser. Khim.*, **3**, 496 (1971).
14. G. A. Tedoradze and E. Yu. Khmel'nitskaya, *Soviet Electrochem.*, **3** (2), 166 (1967).
15. C. E. Baumgartner, G. T. Marks, D. A. Alkens, and H. H. Richtol, *Anal. Chem.*, **52**, 267 (1980).
16. G. Papeschi, M. Costa, and S. Bordi, *Electrochim. Acta*, **15**, 2015 (1970).
17. A. Faviani, M. Costa, and S. Bordi, *J. Electroanal. Chem. Interfacial Electrochem.*, **47**, 147 (1973).
18. W. M. Clark, B. Cohen, and H. D. Gibbs, *Public Health Rept. (U.S.)*, **40**, 1131 (1925).

Alloy-Anodes in Fluoride Solid-State Batteries

J. Schoonman* and A. Wolfert

Solid State Department, Physics Laboratory, State University, 3508 TA Utrecht, The Netherlands

Solid-state batteries with a metal anode, a fluoride ion conducting solid electrolyte, and a metal fluoride as cathode are known (1-5). Much attention has been directed toward optimizing the ionic conductivity of promising solid electrolytes. Particularly suitable are concentrated anion-excess solid solutions based on fluorites (6). They have been utilized successfully as solid electrolytes in batteries with pure metals as anode (3-5). However, in such batteries anode passivation will limit the current as fluoride ions react to form pure low-conducting metal fluorides at the anode/solid electrolyte interface (5).

It is the purpose of this note to show that the use of $\text{Ca}_{1-x}\text{Yb}_x$ alloy-anodes in $\text{Ca}_{1-x}\text{Yb}_x/\text{BiO}_{0.1}\text{F}_{2.8}$ solid-state batteries considerably reduces anode passivation. This is ascribed to the formation of anion-excess solid solutions upon discharge.

Small disks of $\text{Ca}_{1-x}\text{Yb}_x$ ($0 \leq x \leq 0.25$) with a diameter of $8 \times 10^{-3}\text{m}$ and a thickness of about $5 \times 10^{-3}\text{m}$ were prepared by melting appropriate mixtures of the metals in graphite crucibles under argon at about 1000°C . The surfaces of the disks were polished under nitrogen in a glove box. They were examined for their composition with a Cambridge Stereoscan 150 electron microscope, equipped with an energy dispersive elementary analysis apparatus.

Solid-state batteries $\text{Ca}_{1-x}\text{Yb}_x/\text{BiO}_{0.1}\text{F}_{2.8}$ with $\text{Ca}_{0.68}\text{U}_{0.02}\text{Ce}_{0.30}\text{F}_{2.34}$ as solid electrolyte were fabricated using a technique which has been reported before (4, 5). The present $5.03 \times 10^{-5}\text{m}^2$ area cells contain $\sim 1.5 \times 10^{-5}\text{kg}$ solid electrolyte, and $\sim 1 \times 10^{-5}\text{kg}$ cathode: capacity $\sim 10\text{C}$. Open-circuit voltages (OCV) and load-circuit voltages (LCV) were measured with a Keithley Model 616 digital electrometer. Load currents i_l were measured with a Keithley Model 445 digital picoammeter and a Solartron data transfer unit, which transferred time and current data to a Facit 4070 tape punch.

Elemental analysis of the surfaces of the anodes revealed complete solid solubility to exist in the system $\text{Ca}_{1-x}\text{Yb}_x$ ($0 \leq x \leq 0.25$). Normalized load-circuit voltages LCV/OCV vs. load-current densities were linear, indicating the absence of polarization. In this respect batteries with alloy-anodes do not differ from batteries with pure metal anodes (4, 5). The d-c resistance of the batteries, having OCV's of 2.6-3.0V in the temperature region $25^\circ\text{-}180^\circ\text{C}$, was calculated using the expression

$$\frac{\text{LCV}}{\text{OCV}} = -\frac{R_{dc}}{\text{OCV}} i_l + 1$$

In these batteries the thickness of the solid electrolyte layer is about $75\ \mu\text{m}$ and of the cathode layer about $30\ \mu\text{m}$. At 227°C these layers have resistances of $4.93 \times 10^4\ \Omega$, and $23.2\ \Omega$ (7, 8) thus indicating that for fresh batteries the solid electrolyte limits the current. Upon

discharge R_{dc} increases. As R_{dc} for fresh batteries is governed by the resistance of the solid electrolyte, the R_{dc} data for partly discharged cells yield the resistance R_{ap} of the anode passivation layers by subtracting R_{dc} of the fresh cells. Plots of $\log(R_{ap}^{-1}T)$ vs. T^{-1} are linear in the temperature region $25^\circ\text{-}200^\circ\text{C}$. They reveal activation enthalpies in the range 0.90-0.95 eV for ϕ , the number of coulombs expended, up to 3C. In the analysis of the d-c resistance data it is assumed that the discharge product is present as a layer between the anode and the solid electrolyte. Plots of $\log R_{ap}$ vs. $\log \phi$ are linear, as is shown in Fig. 1. The curves reveal slopes of 1.16 (a and b), 1.0 (c), and 1.5 (d), indicating a tendency for R_{ap} to be directly proportional to the number of coulombs expended, which is in accordance with the assumed layer geometry.

Figure 2 presents $\log R_{ap}$ vs. x in $\text{Ca}_{1-x}\text{Yb}_x$ alloy anodes for different numbers of ϕ . After passage of 0.2C the conductivity of the passivation layer on the Ca-anode is $7.2 \times 10^{-7}\text{S}$ at 127°C . Literature data of nominally pure CaF_2 (9) lead to the value of $5 \times$

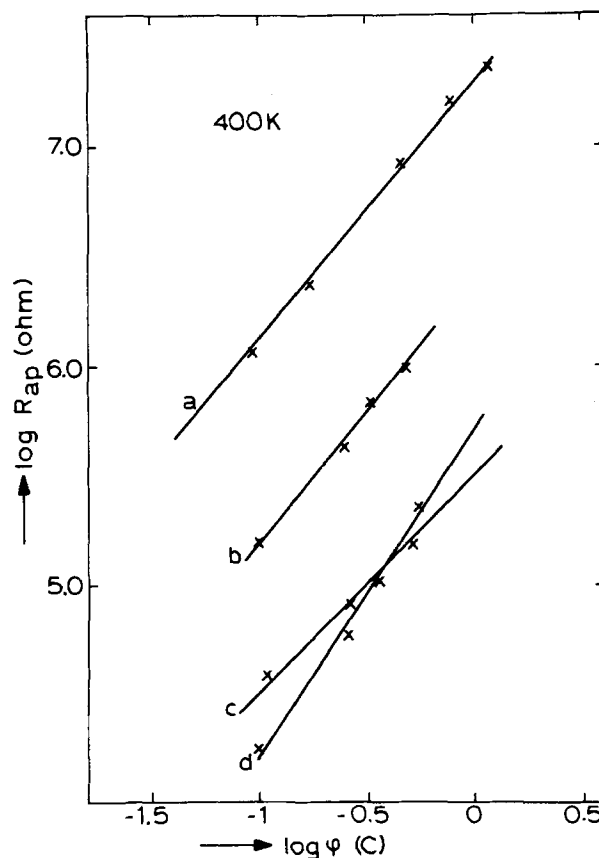


Fig. 1. The resistance R_{ap} vs. the number ϕ of coulombs expended presented as $\log R_{ap}$ vs. $\log \phi$. Curve a, Ca; curve b, $\text{Ca}_{0.915}\text{Yb}_{0.085}$; curve c, $\text{Ca}_{0.75}\text{Yb}_{0.25}$; curve d, $\text{Ca}_{0.865}\text{Yb}_{0.135}$.

* Electrochemical Society Active Member.
Key words: battery, anode, passivation.

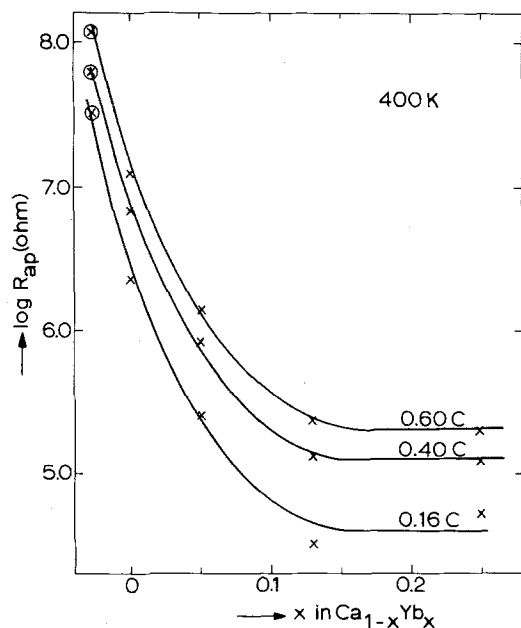
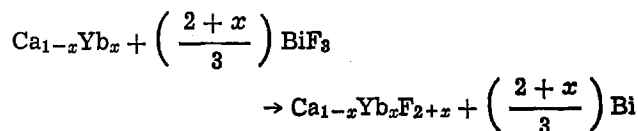


Fig. 2. The dependence of R_{ap} on the composition of $Ca_{1-x}Yb_x$ alloy-anodes at 127°C for several values of ϕ . Included are data (\otimes) calculated from the conductivity of normally pure CaF_2 (10). See text.

$10^{-8}S$ for this passivation layer. Atomic absorption analysis of the employed Ca revealed the presence of 0.9% Al and 0.9% Si as the predominant impurities. This impurity content is equivalent to $x = 0.027$. The calculated R_{ap} values based on the literature data for CaF_2 (9) have been included in Fig. 2 (\otimes) at $x = -0.027$. These data indicate that for the Ca-anodes employed in this study, doped anode passivation layers result. The data in Fig. 2 clearly show that anode passivation is reduced substantially if $Ca_{1-x}Yb_x$ alloy-anodes are employed. A decrease in R_{ap} by a factor of 10^2 - 10^3 is obtained for x up to about 0.13. For larger values of x saturation occurs. As tysonite related $BiO_{0.1}F_{2.8}$ behaves as oxide-doped BiF_3 (8), it is proposed that the alloy-anodes are in principle involved in the following cell reaction



which describes the formation of anion-excess solid solutions as discharge products, in which Yb^{3+} ions are electrically compensated for by F^- interstitials. The enthalpy for migration of fluoride interstitials in doped CaF_2 is found to be 0.92 eV (10). The enthalpy values obtained from the temperature dependence of R_{ap}^{-1} agree very well with this migration enthalpy, thus sustaining the proposed cell reaction.

The present study clearly reveals that alloying Ca with metals M that lead to anion-excess solid solutions $Ca_{1-x}M_xF_{2+x}$ or $Ca_{1-x}M_xF_{2+2x}$ provides a means of reducing anode passivation in this type of solid-state batteries.

Manuscript submitted Oct. 12, 1980; revised manuscript received Jan. 22, 1981.

Any discussion of this paper will appear in a Discussion Section to be published in the June 1982 JOURNAL. All discussions for the June 1982 Discussion Section should be submitted by Feb. 1, 1982.

Publication costs of this article were assisted by State University.

REFERENCES

1. J. H. Kennedy and J. C. Hunter, *This Journal*, **123**, 10 (1976).
2. J. H. Kennedy and R. C. Miles, *ibid.*, **123**, 47 (1976).
3. W. Borger, U. Eullmeine, and E. Voss, U.S. Pat. 3,973,990 (1976).
4. J. Schoonman, *This Journal*, **123**, 1772 (1976).
5. J. Schoonman, K. E. D. Wapenaar, G. Oversluizen, and G. J. Dirksen, *ibid.*, **126**, 709 (1979).
6. J. Schoonman, in "Fast Ion Transport in Solids," P. Vashista, J. N. Mundy, and G. K. Shenoy, Editors, p. 631, North-Holland, New York, Amsterdam, Oxford (1979).
7. K. E. D. Wapenaar, *J. Phys.*, **41**, C6-220 (1980).
8. J. Schoonman, G. J. Dirksen, and R. W. Bonne, *Solid State Commun.*, **19**, 783 (1976).
9. P. W. M. Jacobs and S. H. Ong, *J. Phys.*, **37**, C-311 (1976).
10. W. Bollmann and H. Reimann, *Phys. Status Solidi A*, **16**, 187 (1973).

Cathodic Behavior of Impure Aluminum in Aqueous Media

Kemal Nişancioğlu,* Knut Yngve Davanger, and Øystein Strandmyr¹
SINTEF, Division of Metallurgy, N-7034 Trondheim-NTH, Norway

and Hans Holtan

Laboratories of Industrial Electrochemistry, Norwegian Institute of Technology, N-7034 Trondheim-NTH, Norway

It is well known that the electrochemical and corrosion behavior of impure aluminum is significantly effected by the presence of Fe-rich, insoluble particles on the metal surface (1-3). When the metal is immersed in an unbuffered aqueous medium of neutral pH, pit growth initiates first at these sites (4). The solution inside the pits appears to be alkaline at the outset (5,6) owing to high rates of H_2 evolution on

the particles. In the presence of an aggressive species like Cl^- in the surrounding medium, a few of these pits may become acidic, while many of the original alkaline pits repassivate (7). However, the Fe-rich particles already exposed continue to function as ideal sites for the cathodic reaction (4). The depolarization of the H_2 evolution reaction is also undesirable due to an increased danger of "cathodic corrosion" (8-10) in various practical applications of the metal (8, 11, 12). Corrosion properties and cathodic behavior of impure aluminum can thus be improved if the surface can be cleaned of these particles.

* Electrochemical Society Active Member.

¹ Present address: Mobil Exploration Norway Incorporated, Stavanger, Norway.

Key words: particles, passivity, corrosion.

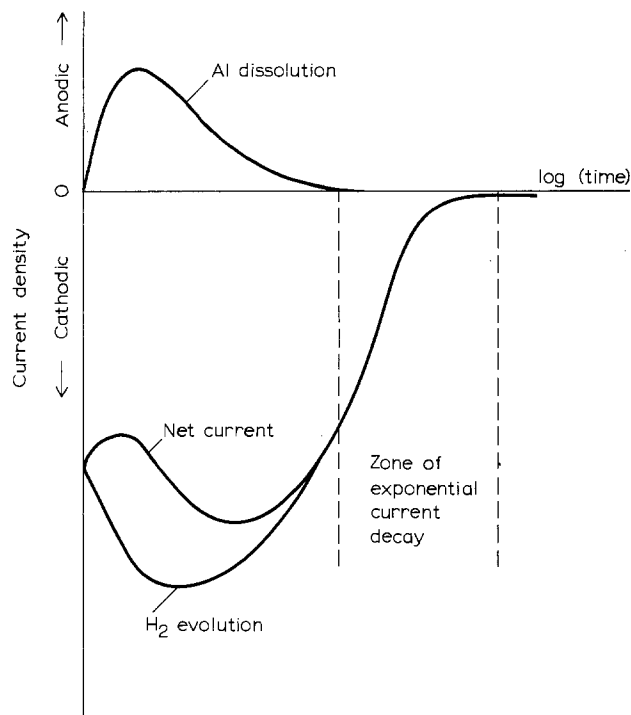


Fig. 1. A schematic representation of net current measured as a function of time under potentiostatic conditions. Postulated trends in the anodic and cathodic current densities are also indicated.

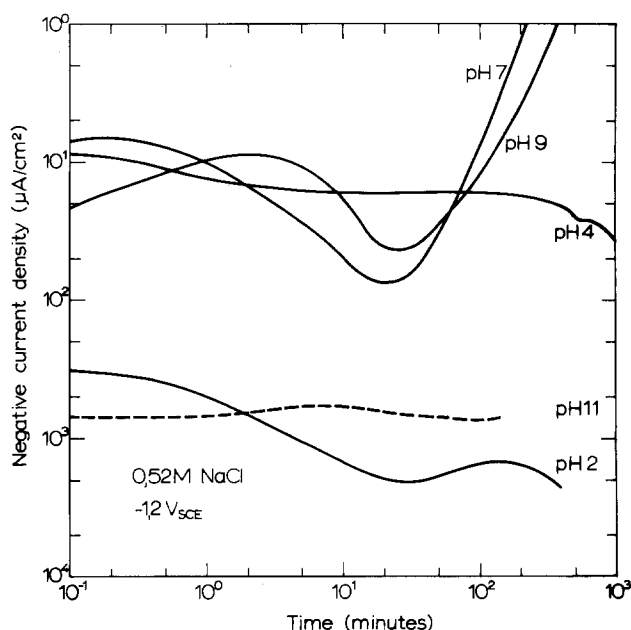


Fig. 2. Typical potentiostatic current-time behavior as a function of bulk pH in unbuffered NaCl solution. The dashed curve is anodic.

In recent papers (7, 10, 13, 14), we investigated the electrochemical behavior of impure aluminum in 3% (0.52M) NaCl solutions. When a constant potential within the passive range is applied to the metal, the net current typically exhibits the trend shown schematically in Fig. 1. In a mathematical sense, the current increases slightly at the outset, then decreases to a minimum, and finally decays to a steady-state level close to zero. This behavior is attributed to the following sequence of events. Immediately after the potential is applied, the film breaks at sites where Fe-rich particles are found, leading to H_2 evolution as well as Al dissolution. The local alkalization of the solution at these sites makes possible a growth of pits as long as the alkalinity is sustained. The pits repassivate once the

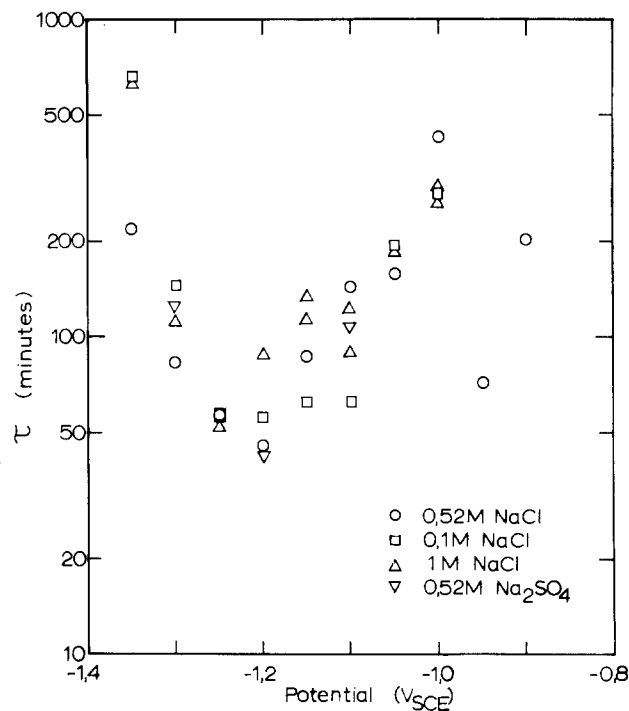


Fig. 3. The time constant for repassivation as a function of applied potential in unbuffered solutions of nearly neutral pH in the bulk (pH range 6-8).

cathodic particles either dissolve or repassivate, as the solubility of the oxide film is exceeded locally due to Al dissolution (10). The present work provides additional electrochemical and metallographic data to support the suggested mechanism.

Experimental

The aluminum contains approximately 0.3% Fe and 0.1% Si and corresponds to the specification AA1050A.² The specimens were machined from extruded rods, covered with "Sevriton" acrylic resin (tooth enamel) on the cylindrical surface, and cast in epoxy to expose a circular area 1 cm in diameter. The resin forms a tight, crevice-free seal around the edge (13). The specimens were polished through 1 μ m alumina. The electrolytic solutions consisted of different concentrations of NaCl and Na_2SO_4 in distilled water maintained at 25°C. The solution pH was adjusted to the desired value and maintained at that value during a polarization test by adding HCl, H_2SO_4 , or NaOH depending

² Supplied by Nordisk Aluminium A/S, Holmestrand, Norway.

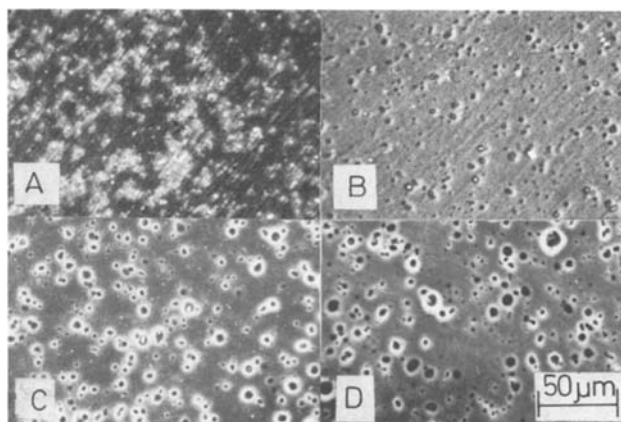


Fig. 4. Pit morphology as a function of polarization time at $-1.2 V_{SCE}$ in 0.52M NaCl solutions. (A) A few minutes after the potential is applied. (B) 15 min.; corresponds roughly to the current minimum. (C) 40 min. (D) 10 hr.

on the pH desired and test solution employed. Additional experimental details for the electrochemical studies were reported earlier (10). The specimen surfaces were analyzed by SEM and EDAX.

Results and Discussion

The discussion is based mainly on experimental data obtained in NaCl solutions. A few runs carried out in Na₂SO₄ solutions, even if not shown in detail, gave similar results in terms of polarization behavior and surface morphology. Thus, the anion (Cl⁻ or SO₄⁼ in this case) does not have an appreciable effect on the observed phenomena. The present results confirm the earlier finding (10) that the repassivation of active areas under potentiostatic conditions results in an exponential decay of net current as indicated in Fig. 1. This behavior was observed also in other work investigating repassivation of active aluminum during either anodic or cathodic polarization (3, 15, 16). The current-time trend shown in Fig. 1 is typical for polarization of impure aluminum in unbuffered aqueous solutions of neutral pH. In acidic or basic solutions, the oxide film cannot stifle cathodic or anodic reactions at the metal surface. The current is therefore controlled by H₂ evolution or Al dissolution kinetics (Fig. 2). In buffered solutions of nearly neutral pH, the initiation of alkaline pits within the passive potential range can largely be eliminated (14).

The exponential part of these current-decay data can be utilized to obtain repassivation rates. A plot of $\ln(i_{\infty} - i)$ vs. time yields straight lines, where i_{∞} is a steady-state current density recorded at long times (after an exposure period of the order of 10³ min depending on the applied potential) (10). The reciprocal slopes of the lines give a "time constant for repassivation," τ . These τ values are fairly reproducible at a given applied potential regardless of stirring conditions and anion concentration. A plot of τ as a function of applied potential, as measured in different aqueous media, is given in Fig. 3. Regardless of the type of solution used, the time constant exhibits a minimum at about $-1.2 V_{SCE}$ for the present batch of specimens, indicating that the active sites on the metal repassivate most rapidly at this potential.

Micrographs of specimen surfaces polarized at $-1.2 V_{SCE}$ for various lengths of time are shown in Fig. 4. The pits initiate at Fe-rich sites as indicated earlier; the particles can be observed as bright spots (Fig. 4A and B) during the earlier stages of polarization. After about 40 min (Fig. 4C), only a few pits still retain particles. After the current decays to a steady-state value, virtually none of the pits retain any particles (Fig. 4D). Figure 5 demonstrates at a higher magnification typical pits during earlier and later stages of polarization. Absence of particles in the pits at later stages was also confirmed by EDAX analyses of interiors of pits. A few exceptions were, however, observed; large occluded pits sometimes trap particles on the bottom even after lengthy periods of polarization (Fig. 5C).

Micrographs of pits grown by polarization for 24 hr at potentials different than $-1.2 V_{SCE}$ are shown in Fig. 6. At more positive potentials, e.g., -0.8 and $-0.9 V_{SCE}$, the particles are not always removed from the surface. Passivation also occurs by film formation on the particles. Most particles fall out or dissolve at potentials less than or equal to about $-1.0 V_{SCE}$. This occurs superficially and without exposing fresh particles from the substrate at potentials more positive than $-1.3 V_{SCE}$. At $-1.3 V_{SCE}$ and below, the alkaline pits become quite large, thereby exposing new particles as they grow. These particles can again be observed as white flecks inside pits (Fig. 6E-G). These large, occluded pits give way to closely packed, shallow hemispherical pits at $-1.38 V_{SCE}$ and below. This type of morphology is characteristic of an aluminum surface

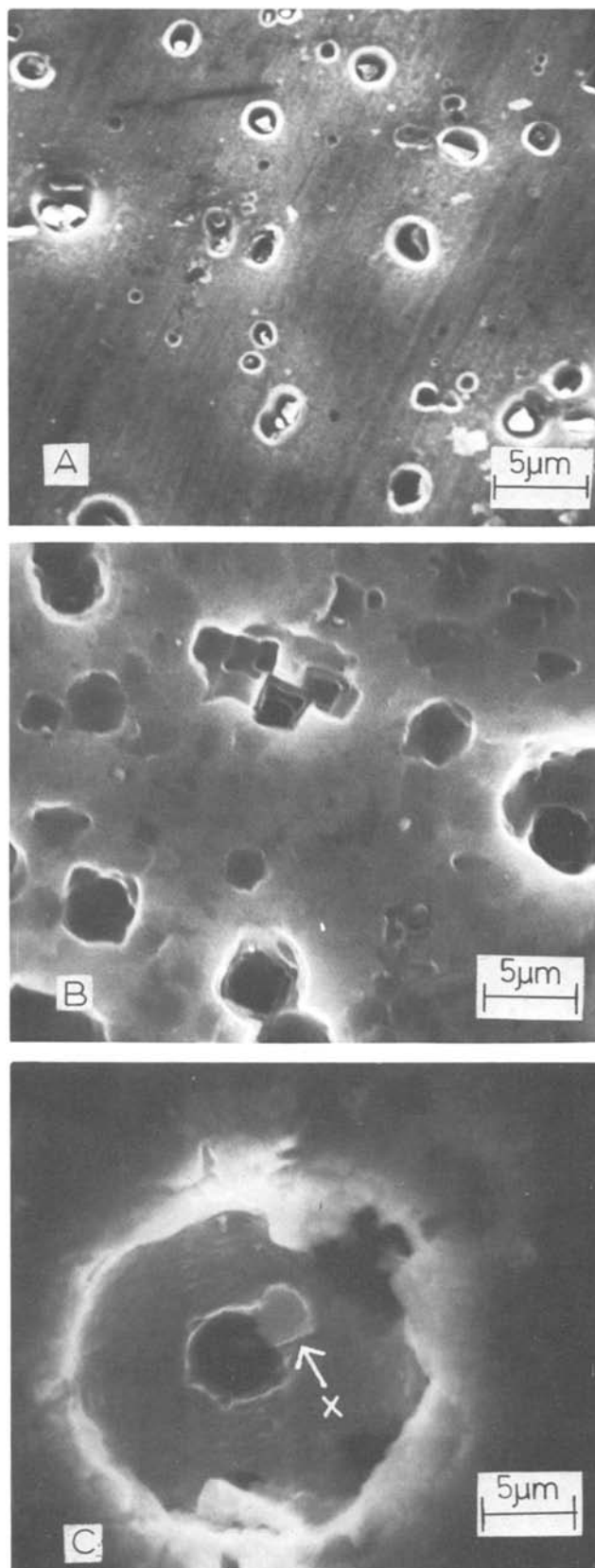


Fig. 5. Examples of pits observed at $-1.2 V_{SCE}$ in 0.52M NaCl corresponding to (A) early stages of polarization when particles can still be observed as bright areas inside the pits and (B) later stage of polarization when pits are free of particles. (C) A large pit with an Fe-rich particle entrained at its bottom (marked X). The dark circular area in the middle is a smaller diameter pit grown inside the larger one.

uniformly etched in alkaline media. Fe-rich particles are also visible on an etched surface (Fig. 6H). These

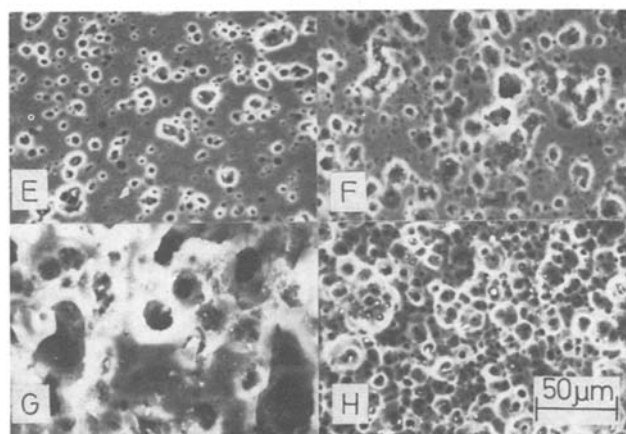
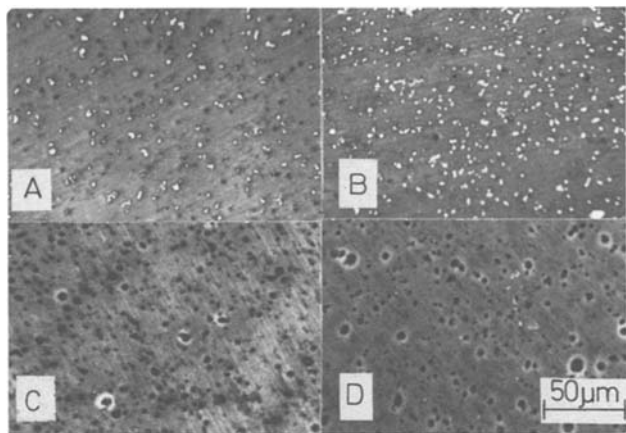


Fig. 6. Pit morphology on specimens polarized for 24 hr in 0.52M NaCl solutions. (A) $-0.8V$, (B) $-0.9V$, (C) $-1.0V$, (D) $-1.1V$, (E) $-1.3V$, (F) $-1.35V$, (G) $-1.37V$, (H) $-1.38V$. All potentials are with respect to SCE.

results explain the cause of slower repassivation rates at the more negative and more positive extremes of the passive potential range. For the present specimens, $-1.2 V_{SCE}$ happens to be the potential where the particles are removed most rapidly without exposing new ones from underneath.

Qualitative analyses of the particles by EDAX and Auger electron spectroscopy indicate that they contain mainly Al and Fe; Si was detected in some of the particles by EDAX. It is well known that the secondary phases existing in commercial-purity aluminum are predominantly Al_3Fe and $\alpha-AlFeSi$ (1). These phases are reported to behave in a similar way electrochemically (17). They are known to be much better cathodes than the Al matrix. In addition, Al_3Fe exhibits active-passive dissolution kinetics in alkaline media (18, 19). The potential range for active dissolution corresponds roughly to the range of present interest, where the particles are efficiently removed from the metal surface. Thus, the present results throw more light

on the cathodic behavior of impure aluminum reported earlier (10) and suggest a possible, low current-density method of cleaning the metal surface of Fe-rich particles. A more common method, which effectively removes the secondary-phase particles and which, in addition, improves the esthetic looks of the surface, is electropolishing in ethanol- $HClO_4$ solutions (20).

Acknowledgment

This work was supported in part by the Royal Norwegian Council for Scientific and Industrial Research and Nordisk Aluminium A/S. Otto Lunder assisted in SEM/EDAX studies.

Manuscript submitted Nov. 3, 1980; revised manuscript received Feb. 24, 1981. This was Paper 38 presented at the St. Louis, Missouri, Meeting of the Society, May 11-16, 1980.

Any discussion of this paper will appear in a Discussion Section to be published in the June 1982 JOURNAL. All discussions for the June 1982 Discussion Section should be submitted by Feb. 1, 1982.

Publication costs of this article were assisted by SINTEF.

REFERENCES

1. L. F. Mondolfo, "Aluminum Alloys: Structure and Properties," Butterworths, London (1976).
2. P. M. Aziz and H. P. Godard, *Corrosion*, **10**, 269 (1954).
3. W. Hübner and G. Wranglén, "Scandinavian Corrosion Congress," Bulletin No. 35, Helsinki (1964).
4. A. P. Bond, G. F. Bolling, H. A. Domian, and H. Biloni, *This Journal*, **113**, 773 (1966).
5. S. Mori, R. E. Loess, and J. E. Draley, *Corrosion*, **19**, 165t (1963).
6. E. I. Storchai and A. V. Turkovskaya, *Zashch. Met.*, **6**, 690 (1970).
7. K. Nişancioğlu and H. Holtan, *Werkst. Korros.*, **30**, 105 (1979).
8. E. P. G. T. van de Ven and H. Koelmans, *This Journal*, **123**, 143 (1976).
9. J. Kunze, *Corros. Sci.*, **7**, 273 (1967).
10. K. Nişancioğlu and H. Holtan, *ibid.*, **19**, 537 (1979).
11. B. E. Miller and H. P. Hack, AIAA Paper No. 72-593 presented at AIAA/SNAME/USN Advanced Marine Vehicles Meeting, Annapolis, Maryland, July 17-19, 1972.
12. G. L. Schnable, R. B. Comizolli, W. Kern, and L. K. White, *RCA Rev.*, **40**, 416 (1979).
13. K. Nişancioğlu and H. Holtan, *Corros. Sci.*, **18**, 835 (1978); *ibid.*, **18**, 1011 (1978).
14. K. Nişancioğlu and H. Holtan, *Electrochim. Acta*, **24**, 1229 (1979).
15. T. P. Hoar and F. P. Ford, *This Journal*, **120**, 1013 (1973).
16. W. J. Rudd and J. C. Scully, *Corros. Sci.*, **20**, 611 (1980).
17. E. Mattsson, L. O. Gullman, L. Knutsson, R. Sundberg, and B. Thundal, *Br. Corros. J.*, **6**, 73 (1971).
18. A. I. Golubev and M. N. Ronzhin, in "Corrosion of Metals and Alloys," N. D. Tomashov and E. N. Mirolyubev, Editors, Oldbourne Press, London (1966).
19. R. Grauer and E. Wiedmer, *Werkst. Korros.*, **31**, 550 (1980).
20. J. Zahavi, A. Zangvil, and M. Metzger, *This Journal*, **125**, 438 (1978).



Investigation of Photoelectrochemical Corrosion of Semiconductors

II. Kinetic Analysis of Corrosion-Competition Reactions on n-GaAs

K. W. Frese, Jr.,* M. J. Madou, and S. R. Morrison

SRI International, Menlo Park, California 94025

ABSTRACT

The model of photoelectrochemical corrosion-stabilization of semiconductors has been extended. Detailed expressions for rate constants are given including capture cross sections and energy levels for hole capture. It is concluded from analysis of experimental data that the first hole in the rate-limiting step is captured at an energy level slightly above the valence band-edge. Analysis of stabilization efficiency *vs.* pH gave a value of 0.72 eV for the rearrangement energy of [Fe(II) EDTA]⁻.

In this paper we further develop our corrosion-stabilization model (1) for semiconductors in contact with electrolytes. The theory attempts to describe the competition between photocorrosion and the photoinduced redox reactions of the stabilizing agent. Without loss of generality we discuss the case of an n-type material such as n-GaAs in contact with an aqueous electrolyte.

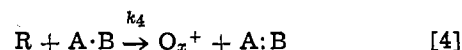
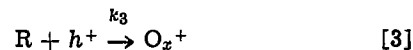
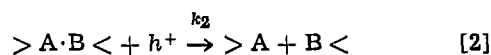
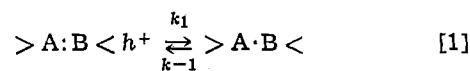
In the earlier study (1) of the simple stabilization/light intensity relationship, developed independently by Gomes *et al.* (2) and ourselves, we were able to identify the most probable reaction mechanism. However, from this simple experiment, important details such as the energy levels involved could not be determined. Thus we have obtained new experimental data, showing the dependence of stabilization on the energy level of the ion in solution and on the pH of the solution for systems selected for their simple behavior. These data are analyzed with the help of a more detailed development of the theory.

The more detailed development given here, such as expressions for corrosion rate constants including activation energy for hole capture and use of the fluctuating energy level model for the redox electrolyte, has provided new insights into the corrosion-competition process. We have been able to determine the characteristic rearrangement energy, λ , of the reducing agent and estimate energy levels for hole capture at surface on back bonds. The use of Eq. [19] below allows a nearly complete separation of the kinetics of corrosion from that of the stabilization process.

Theory

In a previous paper (1) we presented a general kinetic model of semiconductor corrosion and used it to describe the photoelectrochemical corrosion of the A-B type semiconductor GaAs. The model included the competitive reaction of the stabilizing agent, *e.g.*,

Fe(II) EDTA. The following steps were postulated in the corrosion-competition mechanism



In the corrosion mechanism attention is focused on a single electron pair bond, A:B. A hole generated behind the surface row of atoms migrates to the surface and is captured by the surface bond. The surface bonds are between surface Ga or As atoms and the underlying lattice. This surface ($2e^-$) bond, SB, or back-bond, is considered to be a surface state designated E_{SB} . When the first electron is removed or equivalently the first hole captured we have the radical-like ($1e^-$) surface state A·B which we designate E_{SR} (3). We emphasize that E_{SB} and E_{SR} are the surface state energies of the hole when captured. These active surface bonds are between atoms that certainly have bonds to other foreign atoms such as oxygen, hydrogen, or possibly to metal atoms such as gold or ruthenium (4). Therefore the energy levels E_{SB} and E_{SR} will be influenced by other ligands attached to the surface atoms.

Figure 1 shows a diagram of the energy levels in the corrosion model along with the different current paths. The currents j_1 and j_{-1} are the rate of capture and emission of holes between the valence band and the surface bond, E_{SB} . The energy levels of the surface bonds or back-bonds on the clean, relaxed (110) GaAs surface are known (5) to be below the valence band edge. For this reason in Fig. 1, we tentatively place the energy level, E_{SB} , several hundred meV below the valence band edge to include the case when the

* Electrochemical Society Active Member.
 Key words: photoelectrochemical corrosion, corrosion-competition reactions, rearrangement energies, n-GaAs.

1527

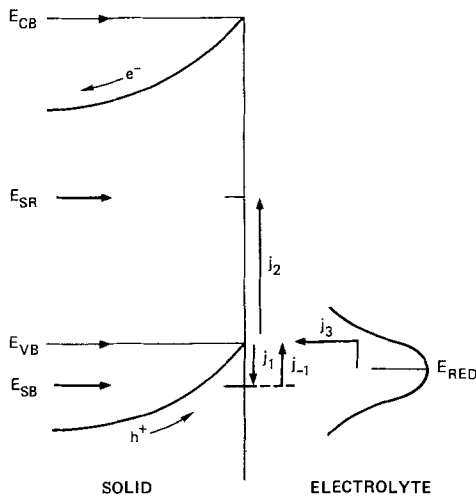


Fig. 1. Energy level diagram of an illuminated n-type wide gap semiconductor under depletion layer conditions. The energy levels and currents associated with each step in the corrosion-stabilization mechanism (Eq. [1]-[3]) are shown. For simplicity the reducing agent captures holes in the energy range E_{VB} to $E_{VB} - 2kT$. E_{SB} and E_{SR} denote surface state energy levels for holes.

first hole capture is activated. Later in the discussion we will estimate $(E_{VB} - E_{SB})$ from experiment. The current, j_2 , represents the irreversible hole capture by the surface state E_{SR} which is represented by the one-electron species, A·B. We assume this hole capture is irreversible because the energy of the unpaired electron is expected to be much higher (weaker bond) than the energy of a paired valence electron, and so the expected energy level, E_{SR} , can be expected to be in the midgap region.

We ignore hole capture by excitation of an electron from E_{SR} to E_{CB} . While the process may be important for Ge (6) the results of Ref. (1) (where corrosion is shown to be second order in hole concentration) suggest it is a minor effect for wide gap materials such as GaAs.

Finally j_3 and j_4 represent the rate of competitive hole capture by the stabilizing (reducing) agent in solution. We believe (1, 2) step [3] in the mechanism (hole capture from the valence bandedge) dominates (1) the stabilization of n-GaAs. This conclusion was discussed in Ref. (1) We therefore have not included the partial current j_4 from E_{red} to E_{SR} in Fig. 1.

Derivation of equations.—The explicit equations for the rate constants in steps [1]-[3] will now be discussed. For step [1] the current j_1 is given by

$$j_1 = k_1 h^+ \quad [5]$$

with

$$k_1 = \langle q\sigma_1 v d \rangle (A \cdot B) e^{-(E_{VB} - E_{SB})/kT} \quad [6]$$

The quantities q , σ , v , and d are the electronic charge, hole capture cross section, hole thermal velocity, and reaction length, respectively. The term $(A \cdot B)$ represents the volume density of bonding electrons susceptible to corrosion (filled states). These electrons may be in bonds on the plane surface, at steps or kink sites, or at the ends of dislocation pipes. If these centers are uncharged, then it is not unreasonable to assume σ , the order to the atomic area, *viz.* 10^{-15} cm^2 .

For j_{-1} we have

$$j_{-1} = k_{-1} (A \cdot B) \quad [7]$$

with

$$k_{-1} = \langle q\sigma_1 v d \rangle N_v \quad [8]$$

where N_v is the density of states at the valence bandedge. The current j_2 is given by

$$j_2 = k_2 h^+ (A \cdot B) \quad [9]$$

where

$$k_2 = \langle q\sigma_2 v d \rangle \quad [10]$$

The cross section σ_2 for capture of the second hole will depend strongly on charge associated with A·B. If a ligand such as OH^- neutralizes the positive charge due to the first hole capture, then σ_2 will probably not differ much from σ_1 (7), *i.e.*, $\sim 10^{-15} \text{ cm}^2$. If, however, OH^- concentration can be made very low as in a non-aqueous solvent, j_2 may be much lower due to coulombic repulsive effects on the cross section, *i.e.*, $\sigma_2 \approx 10^{-21} \text{ cm}^2$. This effect could significantly lower the corrosion rate in nonaqueous solvents.

Finally, j_3 , the rate of hole capture by the reducing agent, is given by

$$j_3 = k_3 C_R h^+ \quad [11]$$

where C_R is the concentration of reducing agent. For the rate constant, k_3 , we write (8, 9)

$$k_3 = \langle q\sigma_3 v_3 d \rangle \left(\frac{kT}{\pi\lambda} \right)^{1/2} e^{-(E_{VB} - E_{red})/4\lambda kT} \quad [12]$$

where σ_3 is the capture cross section of an ion or molecule in solution, v_3 is the mean relative thermal velocity of the hole, d is a reaction length (5-10Å), E_{VB} is the energy of the valence bandedge, E_{red} is the most probable energy level of the electron on the reducing agent, and λ is the rearrangement energy. This form of the rate constant is based on the approximation that only holes within $2kT$ below the valence bandedge react with the stabilizing agent.

A detailed expression was previously derived (1) for the stabilization efficiency, S . Briefly, this quantity is the ratio of the current j_3 to the total hole current j_p . It was shown earlier (1) that

$$j_2 = \frac{k_1 k_2 h^2}{k_{-1} + k_2 h} \quad [13]$$

and if $k_2 h \ll k_{-1}$ or equivalently $h^+ \ll N_v$, the second term in the denominator may be neglected. With aid of this approximation, and after solving Eq. [11] for h^+ and inserting the result into Eq. [13] we obtain

$$j_2 = \frac{k_1 k_2 j_3^2}{k_{-1} k_3^2 C_R^2} \quad [14]$$

Since $j_p = j_2 + j_3$ and $S = j_3/j_p$ we find

$$\frac{1}{S} = 1 + \frac{\alpha j_3}{C_R^2} \quad [15]$$

where α is $k_1 k_2 / k_{-1} k_3^2$. Equation [15] may be used to obtain the parameter α from plots of $1/S$ vs. j_3 . The quantities S and j_3 are readily available from rotating-disk electrode (RRDE) corrosion studies (1, 10). Equation [15] will be applied to experimental stabilization data below.

Some further theoretical development is needed to show how λ_{red} , the rearrangement energy of the reducing agent, may be determined from photoelectrochemical corrosion studies using the above theory. Three different approaches may be made to the problem. All three are based on determining the value of α for the same electrode material under two or more different experimental conditions. Using Eq. [12] and α it is easily shown that

$$\frac{1}{\alpha} = \frac{k_{-1}}{k_1 k_2} \langle q\sigma_3 v_3 d \rangle^2 \frac{kT}{\pi\lambda} e^{-\frac{(E_{VB} - E_{red})^2}{2\lambda kT}} \quad [16]$$

The term E_{VB} is the energy of the valence bandedge and can be determined from capacitance/voltage measurements. The most probable electronic level of the reducing agent, E_{red} , is related to the redox Fermi level according to

$$E_{red} = E_F^{redox} - \lambda_{red} \quad [17]$$

If α is determined for two different reducing agents with different E_{red} and λ , the λ for one reducing agent may be determined if λ is known for the other. For such a case we have from Eq. [16] and [17]

$$\ln \frac{\alpha_1}{\alpha_2} = \ln \left(\frac{\lambda_1}{\lambda_2} \right) - \left[\frac{(E_{\text{VB}} - E_{\text{F}_2}^{\text{redox}} + \lambda_2)^2}{2\lambda_2 kT} - \frac{(E_{\text{VB}} - E_{\text{F}_1}^{\text{redox}} + \lambda_1)^2}{2\lambda_1 kT} \right] \quad [18]$$

All variables in Eq. [18] are known for experiment except the one λ value to be determined. Equation [18] assumes that $\sigma_3 d$ in Eq. [16] is the same for each of the two reducing agents.

A slight variation of Eq. [18] has been used in the present work. If α values for two redox couples with different $E_{\text{F}}^{\text{redox}}$ but same λ are used, a single λ valid for either reducing agent may be determined. Conditions for this application arise, for example, in the case of various Fe(II)-ethylene-amino-polyacetic acid chelates such as EDTA and DTPA. Since the inner coordination structure and overall size of these complex ions are approximately the same, we expect λ to be similar for each ferrous chelate. In the two methods just described Eq. [18] must be solved numerically.

A final approach to obtain λ is to vary the energy level of the solid while holding the solution levels constant (11). Since E_{VB} usually depends on pH in a regular way $dE_{\text{VB}}/dpH \approx 60 \text{ mV}/pH$, variations in electrolyte pH will cause small shifts in the exponent of Eq. [16] leading to large changes in α and S . By taking the \ln of Eq. [16], Eq. [19] is obtained

$$\ln 1/\alpha = \ln \left[\frac{k_1}{k_1 k_2} \langle q \sigma_3 v_3 d \rangle^2 \frac{kT}{\pi \lambda} \right] - \frac{(E_{\text{VB}} - E_{\text{red}})^2}{2\lambda kT} \quad [19]$$

It can be seen that a lot of $\ln 1/\alpha$ vs. $(E_{\text{VB}} - E_{\text{red}})^2$ yields λ from the slope and the intercept contains the ratio of the corrosion rate constants and the preexponential of k_3 . Success of this method depends on the pH invariance of the corrosion process and constant solution redox chemistry. It is advisable to choose a pH range where the $E_{\text{redox}}^{\text{F}}$ is constant, because only then can one hope to have a single solvated form (a single energy level) dominate. This limits the useful pH range in some cases to 2-3 pH units. In the corrosion model the rate constants are for solid-state processes so that Eq. [19] would be applicable. Data below for Fe(II) EDTA/GaAs system are consistent with the pH independence of the corrosion process and the pH dependence of the stabilization process.

Experimental

The rotating ring disk electrode apparatus and technique have been described before (1, 10). All measurements were made on the 100 face of n-GaAs single crystals. The surfaces were chemomechanically polished and etched with an aqueous (1% V/V) solution of chlorox (5.25% sodium hypochlorite). Tellurium donor densities were $2 \times 10^{18} \text{ cm}^{-3}$.

Ferrous EDTA was prepared by dissolving ferrous perchlorate in 0.1M disodium salt of ethylene diamine tetraacetic acid (EDTA). Ferrous DTPA was made similarly from a 0.1M solution of diethylenetriamine-pentaacetic acid and NaOH.

Formal electrode potentials were measured using a bright Pt foil, an SCE electrode, and a Keithley 616 electrometer. The pH of all electrolytes was adjusted with either NH_4OH or HClO_4 .

Experimental Results and Analysis

Figure 2 shows typical plots of reciprocal stabilization efficiency vs. redox stabilizing current for well-etched (100) n-GaAs. The data were plotted according

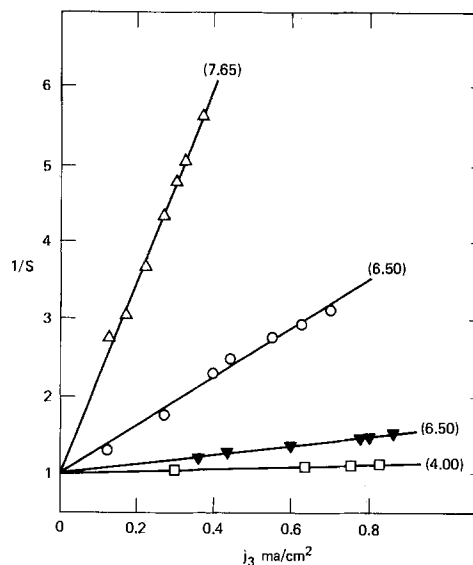


Fig. 2. Reciprocal stabilization efficiency vs. redox stabilization current for well-etched n-(100) GaAs at various pH values. Stabilizing agents: 0.02M Fe(II) EDTA (0.1M EDTA), open symbols; 0.02M Fe(II), DTPA (0.1M DTPA), closed symbols. Electrolyte pH is shown.

to Eq. [15]. The open symbols refer to the case with 0.02M Fe(II) EDTA as the stabilizing agent while the closed symbols refer to the case with 0.02M Fe(II) DTPA. The current density, j_3 , is the observed current on the ring divided by the collection efficiency (0.344) and the disk electrode area (0.195 cm^2). These low concentrations were chosen in order to observe large changes in S . The plots were fairly linear with unit intercepts as required by the theory (Eq. [15]). For the Fe(II) EDTA data it can be seen that the stabilization increases as the pH is lowered. This trend is expected if E_{red} lies below E_{VB} . The plot for Fe(II) DTPA is also very reasonable. The electrode potential of Fe(III-II) DTPA, -0.22 V vs. SCE (12), is $\sim 100 \text{ mV}$ more negative than Fe(III-II) EDTA, -0.12 V vs. SCE (13).

A pH shift of about 2 units with Fe(II) EDTA ($\Delta E_{\text{VB}} \sim 110 \text{ mV}$) produces the same effect on S as using the two different ferrous chelates ($\Delta E_{\text{F}}^{\text{redox}} \sim 100 \text{ mV}$) indicating a similar λ for each ferrous chelate in Fig. 2.

The rate constant ratio α for the n-GaAs/Fe(II) EDTA system was calculated from the slopes of the plots in Fig. 2 (Eq. [15]). Table I summarizes the data for $\alpha = k_1 k_2 / k_1 k_3^2$ when C_{R} is expressed as moles/liter along with the position of the valence bandedge on the SCE potential scale. A value of $+0.20 \text{ V vs. SCE}$ at $pH = 6.5$ was assigned for the valence bandedge and a value of $0.055 \text{ V}/pH$ was used to correct for changes in pH. Capacitance-voltage data (not shown) on n-type GaAs samples in EDTA solutions were used to obtain the electrode potential corresponding to E_{VB} .

Table I. Corrosion-competition data for (100) n-GaAs

| Fe(II) EDTA $E^\circ = -0.125 \text{ V vs. SCE}$ 0.02M | | |
|--|---|------------------------------------|
| pH | $\alpha (\text{M}^2 \text{ cm}^2) / \text{A}$ | $E_{\text{VB}} (\text{V vs. SCE})$ |
| 4.00 | 0.117 | +0.34 |
| 5.50 | 0.429 | +0.25 |
| 6.00 | 0.920 | +0.23 |
| 6.50 | 1.25 | +0.20 |
| 6.70 | 1.50 | +0.190 |
| 7.65 | 5.10 | +0.137 |
| 8.20 | 6.47 | +0.106 |
| Fe(II) DTPA $E^\circ = -0.215 \text{ V vs. SCE}$ 0.02M | | |
| 6.5 | 0.25 | +0.20 |

Figure 3 shows a log plot of $1/\alpha$ vs. $(E_{VB} - E_{red})^2$ according to Eq. [19]. The quantity $(E_{VB} - E_{red})^2$ was calculated using the data of Table I and Eq. [17]. Note that λ must be assumed to calculate the abscissa in Fig. 3. In an iterative calculation the data for pH (4-6.7) were analyzed by least squares until the assumed λ was found in the calculated slope (Eq. [19]). The solid line in Fig. 3 shows the results of such calculation. The assumed λ was 0.72 eV and the calculated value was identical. The correlation coefficient was 0.992. This value of λ applies to the $[\text{Fe(II) EDTA}] =$ ion which is the dominant species of the reduced form in the pH range 4.0-6.7. Deviations occur at pH > 6.7 as shown by the dotted portions in Fig. 3.

Inspection of the insert in Fig. 3 reveals that the measured formal electrode potential of the iron EDTA couple is independent of the pH in the same range where the solid line in Fig. 3 applies. It can also be seen that the deviations in the $\ln 1/\alpha$ plot occur at very nearly the same pH at which the formal electrode potential begins to become more negative. This behavior signals a change in solution chemistry which could lead to a different λ or capture cross section. No attempt was made to analyze this effect.

The value of λ may be calculated another way using Eq. [18]. The assumption is that λ for Fe(II) DTPA and Fe(II) EDTA are equal (as discussed above). From the α and electrode potential data in Table I, pH = 6.5, for these two reducing agents, a λ of 0.69 eV was calculated. This result at constant pH, and variable E_{red} agrees well with the constant E_{red} and variable pH calculation of Fig. 3. These two results for λ may be compared with λ calculated from kinetic data on homogeneous redox reactions. A Marcus-type analysis (14) of the rate constant for electron transfer between Fe(II) EDTA and Fe(III) CyDTA ($\Delta G^\circ \cong 0$) leads to $\lambda_{ox} + \lambda_{red} = 1.4$ eV. If it is assumed that $\lambda_{ox} = \lambda_{red}$ then a value of $\lambda = 0.7$ eV is indicated for Fe(II) EDTA. Again the agreement with the two values derived from corrosion studies and this homogeneous reaction is good. It appears that the functional form of

the rate constant k_3 , Eq. [12], is essentially correct at least in the case when E_{red} lies below E_{VB} .

We turn now to an analysis of the solid-state aspect of the corrosion mechanism. From the intercept in Eq. [19] and Fig. 3 we have

$$\left(\frac{1000}{N_A}\right)^2 \frac{1}{\alpha_0} = \frac{k_{-1}}{k_1 k_2} (q\sigma_3 v d)^2 \frac{kT}{\pi\lambda} \quad [20]$$

where we have introduced the Avogadro term ($1000/N_A$) to convert from molarity M , to particle density (cm^{-3}). The value of $1/\alpha_0$ from Fig. 3 was found to be $53.6 \text{ A/M}^2 \text{ cm}^2$.

We would like to evaluate the term $k_1 k_2 / k_{-1}$ in Eq. [20] and eventually the activation energy for k_1 , $(E_{VB} - E_{SB})$ in Fig. 1. In order to do this we must have estimates for the capture cross sections σ , thermal velocities, v , and reaction length d . The following values were used [σ , $2 \times 10^{-15} \text{ cm}^2$; v , 10^7 cm/sec for holes; d , $10 \times 10^{-8} \text{ cm}$ and $2.5 \times 10^{-8} \text{ cm}$ (GaAs bond length) for the solution and solid-state reaction, respectively]. Using Eq. [6], [7], and [10] with $N_v = 7 \times 10^{18} \text{ cm}^{-3}$ (15) and assuming σ in k_{-1} and k_1 are equal, we obtain

$$(\text{A:B}) e^{-(E_{VB} - E_{SB})/kT} = 6.9 \times 10^{23} \text{ cm}^{-3} \quad [21]$$

To proceed further we must estimate (A:B), the concentration of filled surface states (3). Several cases will be considered. We can determine an upper limit to $(E_{VB} - E_{SB})$ if we assume (A:B) equals the total surface valence electron concentration in back-bonds, $\sim 1/2 (1.8 \times 10^{23} \text{ cm}^{-3})$ for the (100) face. Using this value, $(E_{VB} - E_{SB}) = -0.052 \text{ eV}$ which places the back-level, E_{SB} , slightly above the valence bandedge. Experimental errors could still allow E_{SB} to be slightly below E_{VB} .

If the rate-limiting step involves the concentration of filled states at dislocations, then (A:B) will be $\sim 4 \times 10^{14} \text{ cm}^{-3}$, yielding $(E_{VB} - E_{SB})$ equals -0.55 eV . (The etch pit density of our crystals is $\sim 10^7 \text{ cm}^{-2}$ as reported by the supplier.) We note the surface bond level at a dislocation by this estimate would lie 0.55 eV above the valence bandedge. We can rule out this rate-limiting step since the first hole capture would be irreversible and S would be independent of j_p (1) which is inconsistent with experiment.

Finally, if (A:B) represents the concentration of filled states at steps, we estimate (A:B) = $4.5 \times 10^{20} \text{ cm}^{-3}$. This gives $(E_{VB} - E_{SB})$ equals -0.19 and places E_{SB} 0.19 eV above the valence bandedge. This calculation assumes steps form a line across the whole surface at 1000Å intervals. We conclude the first hole is captured on a level in the energy range approximately $E_{VB} \pm 0.2 \text{ eV}$. The reversible hole exchange that must be invoked is consistent with this energy range. The values of E_{SB} below E_{VB} are not inconsistent with surface back-bond tight-binding calculations of Chadi (4) who found for various relaxation models of the (110) GaAs surface, back-bond levels at ~ 1.0 - 1.9 eV below E_{VB} . These energy levels are for the clean defect-free relaxed (110) surfaces. In the case of corrosion in the presence of ligands such as OH^- which can be attached to GaAs surface atoms, the surface structure will more closely represent the tetrahedral bonding as in the GaAs bulk. This different bonding arrangement will tend to move the surface bond level back toward the valence bandedge. However, the higher electronegativity of oxygen could exert a small stabilizing effect (compared to bulk GaAs bonds) on the GaAs surface bonds and thus we might expect the surface bond level, E_{SB} , to be close to the valence bandedge.

In the near future we will make a similar study on CVD GaAs films. We expect to learn more about the role of defects in the corrosion process. We will also try to measure the corrosion activation energy by studying the temperature dependence of the stabilization efficiency, S.

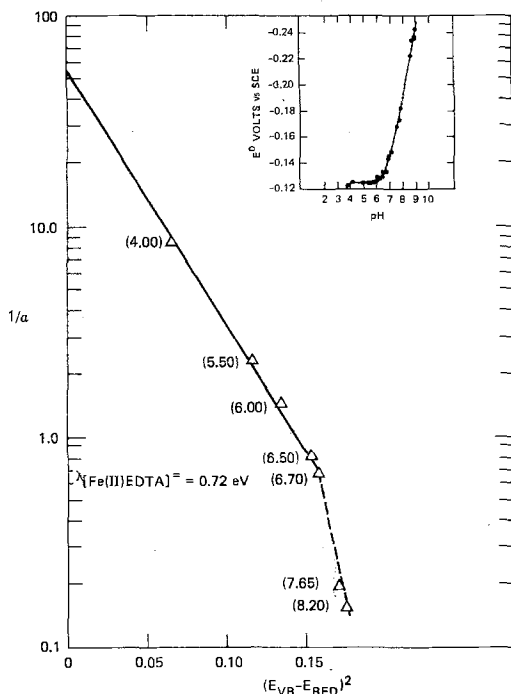


Fig. 3. Plot of logarithm of reciprocal rate constant ratio, $1/\alpha$, vs. energy level difference, $(E_{VB} - E_{red})^2$ for (100)-n-GaAs. Stabilizing agent is 0.02M Fe(II) in 0.1M Na_2 EDTA. The independent experimental variable is the electrolyte pH as indicated. The pH dependence of the formal electrode potential of 0.02M Fe(II)/Fe(III) perchlorate couple in 0.1M Na_2 EDTA is also shown in the figure. pH adjusted with NH_3 or HClO_4 .

Acknowledgment

This work was supported by the Solar Energy Research Institute.

Manuscript submitted July 8, 1980; revised manuscript received Feb. 23, 1981.

Any discussion of this paper will appear in a Discussion Section to be published in the June 1982 JOURNAL. All discussions for the June 1982 Discussion Section should be submitted by Feb. 1, 1982.

Publication costs of this article were assisted by SRI International.

REFERENCES

1. K. W. Frese, Jr., M. J. Madou, and S. R. Morrison, *J. Phys. Chem.*, **84**, 3172 (1980).
2. W. Gomes, Paper presented at the ACS Meeting, Houston, Texas, March 1980.
3. H. Gerischer and W. Mindt, *Electrochim. Acta*, **13**, 1329 (1968).
4. K. W. Frese, Jr., M. J. Madou, and S. R. Morrison, *This Journal*, Accepted for publication.
5. D. J. Chadi, *Phys. Rev. B*, **18**, 1800 (1978).
6. W. H. Brattain and C. G. B. Garrett, *Bell System Tech. J.*, **34**, 129 (1955).
7. M. Lax, *Phys. Rev.*, **119**, 1502 (1960).
8. H. Gerischer, *Surf. Sci.*, **18**, 97 (1969).
9. S. R. Morrison, "The Chemical Physics of Surfaces," Chap. 2, Plenum, New York (1977).
10. M. J. Madou, K. W. Frese, Jr., and S. R. Morrison, *This Journal*, **127**, 987 (1980).
11. R. A. L. Vanden Berghe, F. Cardon, and W. P. Gomes, *Surf. Sci.*, **39**, 368 (1973).
12. J. Vandegaer, S. Chabarek, and A. E. Frost, *J. Inorg. Nucl. Chem.*, **11**, 210 (1959).
13. G. Swarzenbach and J. Heller, *Helv. Chim. Acta*, **37**, 937 (1954).
14. K. W. Frese, Jr., In preparation.
15. "Physics of Semiconductor Devices," S. M. Sze, John Wiley, New York (1969).

Anodic Film Growth on Titanium at Temperatures from 200° to 257°C

A. L. Bacarella,* H. S. Gadiyar,¹ and A. L. Sutton²

Chemistry Division, Oak Ridge National Laboratory, Oak Ridge, Tennessee 37830

ABSTRACT

An electrochemical study of anodic film growth on titanium in oxygenated 0.05M K₂SO₄ at temperatures from 200° to 257°C and at constant potential, below the O₂ evolution potential is presented. At constant applied potential, it is assumed that the voltage drop (V) across the oxide is constant and the field $E = V/X$, where X is the film thickness. The results are interpreted in terms of a rate expression derived by Dignam (20-22) and assume the effective field, E_e , assisting the ionic conduction process is the local field, $E_e = \delta KE$ for $K \gg 1$, where K is the dielectric constant of the oxide and δ is a geometric factor having a value the order of unity.

Much of the work related to anodic film growth on valve metals consists of room temperature studies at high field strength (1-9), where applied voltages greater than 100V are often encountered. The current efficiencies for film growth in such studies are often less than 100% (due to O₂ evolution) and require physical methods (ellipsometry) to determine film thickness. When the temperature is increased above 200°C, sufficient thermal energy becomes available to grow significant film at potentials below the O₂ evolution potential with 100% current efficiency.

Here, the results of a study of anodic film growth on titanium in oxygenated 0.05M K₂SO₄ at 200°-257°C and at potentials below the O₂ evolution potential are presented. This work was begun to test the applicability of the equations developed for high field strength studies to film growth at "low" field strength but high temperatures (above 200°C) and, further, to test the applicability of local field concepts to the kinetic data.

The classical theory (10) of ionic conduction in valve metals predicts an exponential relation between the ionic current and field strength

$$i = i_0 \exp \{-[\phi - qaE]/kT\} \quad [1]$$

* Electrochemical Society Active Member.

¹ Present address: Metallurgy Division, Bhabha Atomic Research Centre, Trombay, Bombay, 400 085 India.

² Chemical Technology Division, Oak Ridge National Laboratory. Key words: anodic film growth, Ti, dielectric constant, high temperature.

where qa is the apparent activation dipole, ϕ is the apparent activation energy, and E the applied macroscopic field. In 1966 Bacarella and Sutton (11) showed that the application of local field concepts to anodic film growth on zirconium provided a more satisfactory interpretation of the kinetic results. At potentials below the O₂ evolution potential, the anodic film growth current on zirconium was shown to be a hyperbolic sine function of the effective field strength, E_e

$$i = 2i_0 \exp(-\phi/kT) \sinh(qaE_e/kT) \quad [2]$$

They also showed that the unusually large values obtained for the apparent activation of dipole, qa , could be rationalized if the Mosotti-Lorentz (M-L) field $E_e = E(K+2)/3$ (12, 13), was the assumed effective field assisting ion transport during film growth. Here, K is the dielectric constant of the oxide.

Glasstone, Laidler, and Eyring (14) and even earlier, Hückel (15) used the M-L field to explain the abnormal mobility of protons in aqueous electrolyte. In 1941, Maurer (16) used the M-L field to explain the temperature dependence of the ionic conductivity of Na⁺ ions in soda-lime glass. Subsequently, Young (17, 18) suggested the applicability of local field concepts to anodic film growth on valve metals.

Prior to these observations typical valve metal behavior was not expected for zirconium. There was evidence (17, 19) that the electric field in the oxide was thickness dependent, increasing with thickness for

constant applied current. More recent measurements by Hopper, Wright, and DeSmet (8) have provided additional evidence of typical valve metal behavior for Zr.

Measurements made by Young (1) and Young and Zobel (2) on Ta and Nb showed that the classical field-dependent rate expression, Eq. [1], did not fit the data. The relation between $\ln(i)$ and E was slightly nonlinear. A better fit was obtained if the activation distance was made a linear function of the field strength (17), ($a = \alpha - \beta E$) and the resulting rate expression

$$i = i_0 \exp \{-[\phi - q\alpha E(1 - \beta E/\alpha)]/kT\} \quad [3]$$

was used. Estimates of ϕ , $q\alpha$, and β/α were obtained from measurements of the thickness as a function of time by *in situ* ellipsometry during anodization at constant potential. Later, Young (19) suggested the condenser pressure as a possible explanation for the quadratic term in E .

Dignam (20-22) arrived at the quadratic term from a detailed analysis of ionic transfer across three potential energy barriers, a clipped parabola potential, a cosine potential, or a Morse potential. From a consideration of the unusually large values for the activation dipole, it was assumed that the effective field assisting the ion transfer process would depend on the polarization of the oxide, P

$$E_e = E + \delta P/\epsilon_0 \quad [4]$$

and since

$$P = (K - 1)\epsilon_0 E \quad [5]$$

for $K \gg 1$

$$E_e = \delta KE \quad [6]$$

Here, E is the applied field, ϵ_0 is the permittivity of free space, and δ is a geometric factor having a value the order of unity. If the geometry for the M-L field is assumed (dielectric isotropy), $\delta = 1/3$. From such considerations, and assuming the M-L field, Dignam's equation becomes, using the symbols in this study

$$i = i_0 \exp \{-[\phi - qa\delta KE(1 - qa\delta KE/c\phi)]/kT\} \quad [7]$$

Here, K is the zero field strength dielectric constant and c assumes values dependent on the shape of the assumed potential function. For the clipped parabola potential $c = 4$, for the cosine potential $c = \pi^2/2$ (~ 4.9), and for the Morse potential c is a function of the mean field strength \bar{E} , $c = f(qa\bar{E}/\phi)$. From the available data for Ta, Nb, and Al, Dignam concluded that the Morse potential provided the best fit, and all three systems, $c \sim 3.4 \pm 0.2$.

If the activation distance in the classical rate expression, Eq. [1], is made a linear function of the effective field, E_e , ($a = \alpha - \beta E_e$), a rate expression empirically equivalent to Eq. [7] is obtained, and for $K \gg 1$

$$i = i_0 \exp \{-[\phi - q\alpha\delta KE(1 - \beta\delta KE/\alpha)]/kT\} \quad [8]$$

This expression differs from the one originally proposed by Young in that the activation distance is made a linear function of the effective field E_e , rather than the applied average macroscopic field E .

Ord, Hopper, and Wang (3), (O, H, & W) showed the nonlinear $\ln(i)$ vs. E behavior follows quite naturally from local field concepts and the experimental observation that at high field strength the dielectric constant is a linear function of the field strength, $K = K_0(1 - \gamma E)$. Combining this relation with the local field $E_e = \delta KE$, they showed

$$i = i_0 \exp \{-[\phi - qa\delta KE(1 - \gamma E)]/kT\} \quad [9]$$

Corrosion engineers interpret corrosion data in terms of rate laws relating film growth (or rate) to time. In 1953 Charlesby (6) showed that these rate laws could be derived from the classical field-dependent rate expression, Eq. [1], and depend only on the parameter

$Z (= qaE/kT)$. For values of $Z > 3$ the growth should be approximately a logarithmic function of time and the slope of the $\log(\text{rate})$ - $\log(\text{time})$ plot is close to -1 ; for $Z \sim 1$ the growth should be approximately cubic and the slope, $(d \log(i)/d \log(t))$, is close to $-2/3$, and for $Z < 1$ the growth approaches the familiar parabolic rate law. For zirconium it was shown (23) that the cubic rate law applied and the slope, $d \log(i)/d \log(t)$, was close to $-2/3$.

If the effective field assisting the ionic conduction process is the local field E_e , then the parameter Z is a function of the dielectric constant K , since the local field is proportional to the dielectric constant for large K , Eq. [6]. If the structure of the oxide grown at temperatures from 200° to 257°C is rutile, a value of $Z > 3$ is expected for titanium since the reported value for the dielectric constant of TiO_2 (rutile) at 25°C is much greater than the dielectric constant of ZrO_2 . The dielectric constant for ZrO_2 at 25°C is 28 (6). TiO_2 (rutile) is anisotropic (24), the dielectric constant perpendicular to the optical axis is 86 and parallel to the optical axis, the dielectric constant is 200. On this basis, for $Z > 3$, the slope of the $\log(\text{rate})$ - $\log(\text{time})$ plot would be closer to -1 .

Experimental

Measurements were made of the anodic film growth current at constant anodic potential at temperatures from 200° to 257°C on rod-type iodide bar titanium. The electrolyte solution was 0.05M K_2SO_4 saturated with 250 psig O_2 at 25°C. The potential of the electrode was held constant with an electronic potentiostat, and the anodic currents were measured by recording the voltage drop across precision resistors in the polarizing circuit. The design and installation of the reference electrodes (Pt or calomel) into the titanium reaction cell was previously (23) described. The apparatus and procedure for the rapid attainment of temperature were also previously (25) described. Cylindrical specimens approximately 5.7 cm long and 0.3 cm diam were used. The area of the specimens ranged from 4.80 to 6.00 cm^2 . The electrodes were first polished in a freshly prepared solution containing 2:2:1 volume of lactic, nitric, and HF (48%) acids. They were rinsed thoroughly with tap distilled water and then triply distilled before being introduced into the cell. It was estimated that the ambient temperature of the cell was about 35°C.

In order to test the applicability of local field concepts to these data, the dielectric constant of the oxide was measured at each experimental temperature. The dielectric constants were obtained from measurements of the capacitance of the oxide as a function of thickness using a galvanostatic pulse technique. Current densities of about 2×10^{-3} A/ cm^2 were pulsed through the electrode for about 3 msec, and the slope of the voltage-time trace during the first 20-50 μsec was obtained with the capacitance $C = i/(dV/dt)$. A roughness factor of unity was assumed. The validity of this assumption is discussed later.

A direct determination of the structure of the oxide was not made. References to the structure being "rutile" is assumed and is based on the large values obtained for the dielectric constant. Similarly to accommodate the design features for the electrochemical measurements at temperatures to 300°C and pressures to 2000 psi, and for the rapid attainment of temperature, the electrode design was such to preclude a direct determination of film thickness.

Results and Discussion

The results assume the potentials at the metal/metal oxide and metal oxide/solution interfaces are constant and independent of the anodic film growth current. Therefore, for constant applied potential, the voltage drop, V , across the oxide is constant.

The primary data obtained are measurements of the anodic film growth current as a function of time at constant potential. In Fig. 1 are shown $\log(i)/\log(t)$ plots for three temperatures 473, 513, and 530 K. The actual experimental data points are shown for a typical run at 513 K, demonstrating the linearity in the $\log(i)/\log(t)$ relationship. The slopes $d(\log i)/d(\log t)$ are -0.92 , -0.91 , and -0.94 for the three runs shown here and average about -0.92 .

The polarization data at various times of exposure (film thickness) are shown in Fig. 2-4. It is seen that the O_2 evolution and O_2 reduction reactions are negligible at the constant potentials employed, and the anodic current is entirely TiO_2 film growth. The film

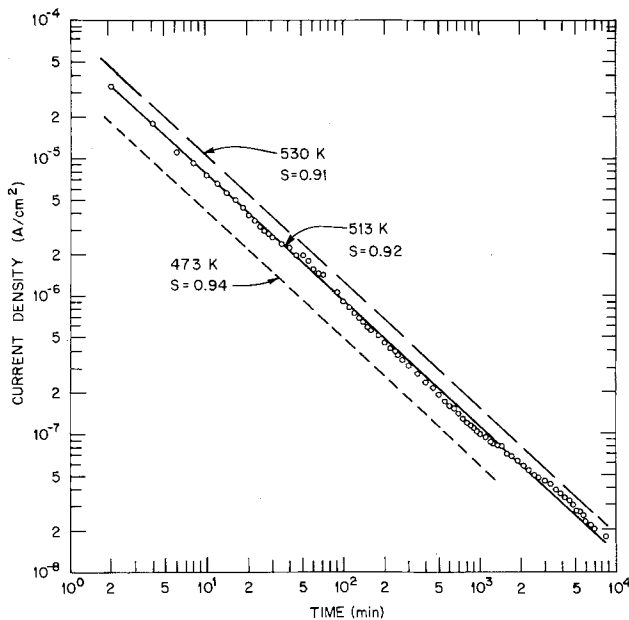


Fig. 1. The anodic film growth current on titanium as a function of time, in oxygenated 0.05M K_2SO_4 and at constant potential below the O_2 evolution potential. $\log(i) - \log(t)$ plots.

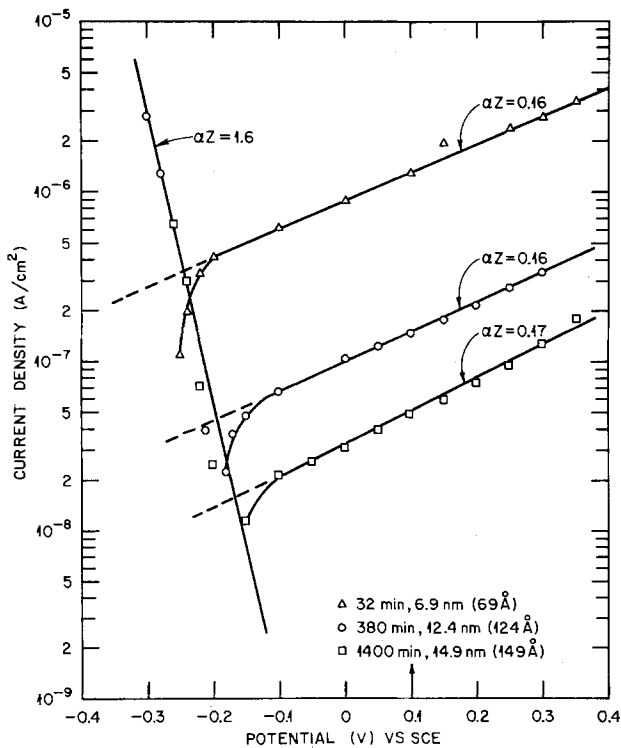


Fig. 2. The polarization of titanium in oxygenated 0.05M K_2SO_4 at 200°C (473 K) at several film thicknesses.

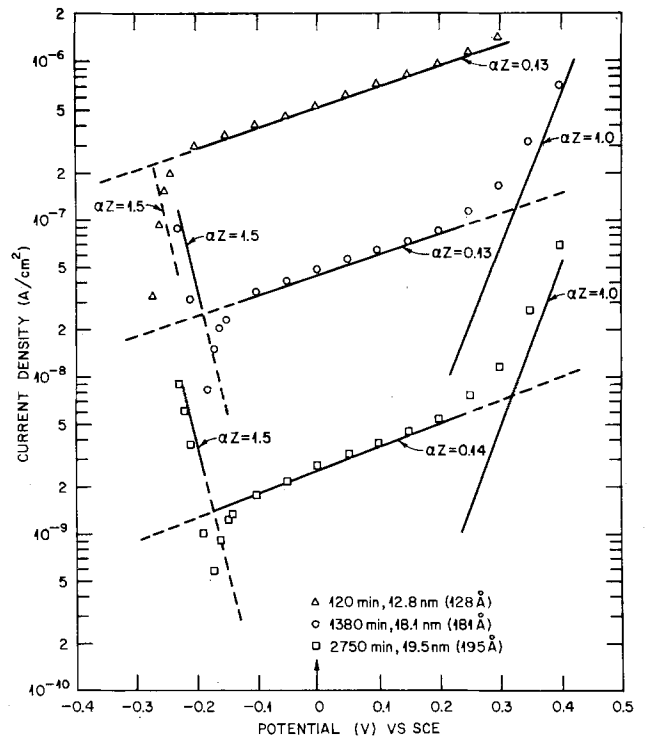


Fig. 3. The polarization of titanium in oxygenated 0.05M K_2SO_4 at 240°C (513 K) at several film thicknesses.

thicknesses were calculated as a function of time based on an estimate of $2.916 \times 10^{-3} \text{ cm/min}/(\text{A/cm}^2)$, and assumed the density for TiO_2 (rutile) at 4.26 g/cm^3 . The electrode was in the solution at ambient temperature (*ca.* 35°C) for a period ranging from 1000-2000 min. An initial film is therefore present on the electrode prior to exposure to the experimental temperature. How this initial film affects the subsequent film growth kinetics at temperature cannot be evaluated. It is assumed that this initial (pre-exposure) film thickness is between 0 and 4 nm (40Å), and most likely about 2 ± 1 nm. An estimate of an initial film thickness of 3 nm on chemically polished Ta and Nb in 0.2N H_2SO_4 at 23°C was obtained by O, H, & W (3) from ellipsometric measurements during constant current anodic film growth.

The results in Fig. 1 show there is negligible film dissolution. If the film dissolution rate was significant

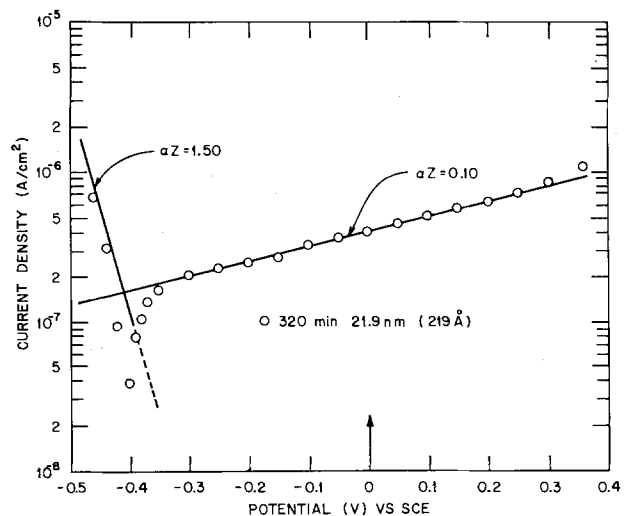


Fig. 4. The polarization of titanium in oxygenated 0.05M K_2SO_4 at 257°C (530 K).

the film growth current would begin to level off after prolonged exposure.

After a sufficient exposure period the solution was cooled and the anodic current, at constant potential, was recorded as a function of the decreasing temperature. A plot of these data is shown in Fig. 5. An average apparent activation energy of 1.22 eV (28.2 kcal/mol) is estimated from the slope, $d(\log i)/d(1/T)$. This estimate of activation energy assumes the potential drop across the oxide is constant during the temperature change.

Charlesby's (6) analysis of the field-dependent rate expression showed that for $10 < Z < 40$ the slope, $S(= \Delta \log(i)/\Delta \log(t))$, ranged from -0.87 to -0.95 . Plotting these values for $Z(= qaE_e/kT)$ vs. S it is found for the value of $S = -0.92$, Fig. 1, that $Z = 22$. Our earlier studies on zirconium (11) have shown that the "true" activation dipole moment (qa) equals 0.15 e nm (1.5×10^{-8} e cm). Dignam (20) has presented arguments that oxygen ions are the ones involved in the ion transport process for all the valve metal systems and the activation dipole moment would not be expected to vary much from system to system. With this assumed value for $qa = 0.15$ e nm, and $Z = 22$, the effective field $E_e = ZkT/qa = 6.5 \times 10^7$ V/cm for the results at 513 K. After 8400 min exposure at 513 K the film thickness (assuming an initial film of 2 nm) is 30 nm (300Å). Choosing an intermediate film thickness of 15 nm, the voltage drop V across the oxide is estimated at ~ 97 V if the average macroscopic field, V/X , is the assumed effective field E_e . Since the film was grown at a potential below the O_2 evolution potential, Fig. 2-4, i.e., at 0.00V vs. Pt/ O_2 , it is unlikely that V could be 97V; more likely V is of the order of magnitude of 1 volt. If, however, the effective field is the local M-L field, $E_e = (K + 2)V/3X$, then for $V \sim 1$ volt and $E_e = 6.5 \times 10^7$ V/cm, it is estimated that the dielectric constant $K \sim 300$. Such a high value for the dielectric constant at 513 K may not be unexpected, considering that the dielectric constant at 298 K is 200 when measured parallel to the optical axis (24). In Fig. 6 the reciprocal of the measured capacitance, $1/C_M$, at 513 and 530 K is plotted as a function of X . Using the parallel plate formula for a condenser, $C_M = (8.85 \times 10^{-8} K)/X$, the dielectric constant of the oxide film can be calculated from the slope, $d(1/C_M)/dX$. Since the dielectric constant of the oxide is large, the solution double layer capacitance, C_{dl} , in series with the oxide film capacitance, C_{ox} , is of comparable magnitude, and the measured capacitance, include a significant contribution from the solution double layer capacitance, ($1/C_{ox} = 1/C_M - 1/C_{dl}$). The double layer capacitance is obtained from an extrapolation of the measured capacitance, C_M , to $X = 0$. At $X = 0$, $1/C_{ox}$

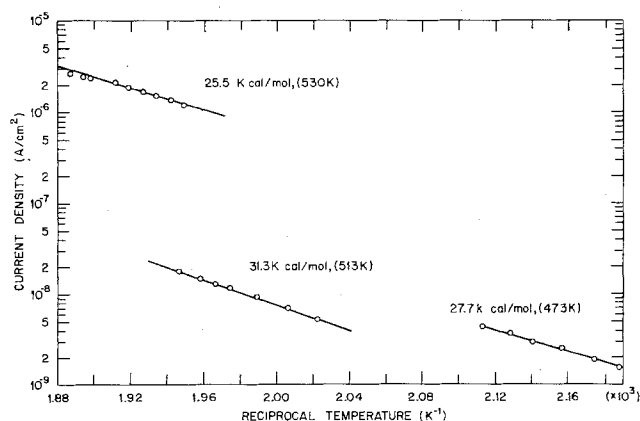


Fig. 5. The temperature dependence of the anodic film growth current at constant potential for titanium in oxygenated 0.05M K_2SO_4 .

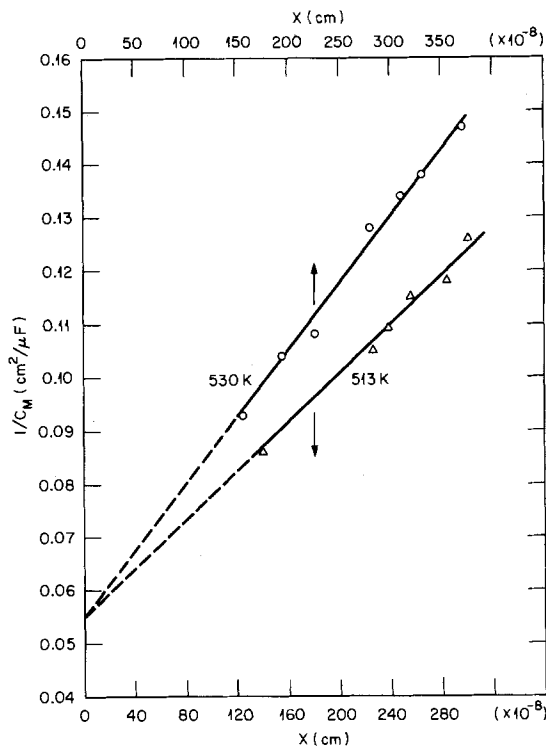


Fig. 6. The reciprocal of the measured capacitance, $1/C_M$, as a function of film thickness, for titanium in oxygenated 0.05M K_2SO_4 at 513° and 530 K and at 0.00V vs. Pt/ O_2 (318 K).

$= 0$ and $C_M = C_{dl} = 18 \mu F/cm^2$ for the measurements at both temperatures. Correcting the measured capacitances for the double layer, the dielectric constant K equals 452 ± 25 at both temperatures. Using this value for K and the M-L effective field, the voltage drop across the oxide is estimated at ~ 0.65 V. This is a more reasonable value than the 97V estimated using the average macroscopic field, V/X , as the effective field. The dielectric constant was not determined at 473 K, but an estimate can be obtained from capacitance measurements at 513 and 530 K. Here, after a sufficient exposure period the solution was cooled and capacitance measurements were made at several temperatures during cooling to room temperature, Fig. 7. If the same double layer correction ($C_{dl} = 18 \mu F/cm^2$) is assumed, independent of temperature, the oxide film capacitances are proportional to the dielectric constants, and $K = 411$ at 473 K.

The classical field-dependent rate expression, Eq. [1], does not provide a fit to the data obtained in this study. A plot of $\log(i)$ vs. $1/X$ was not linear. A better fit is obtained by Eq. [7], [8], or [9]. These equations are empirically equivalent, and $\log(i)$ is a quadratic function of the field strength. In this study, the voltage drop across the oxide is constant, and therefore $\log(i)$ is a quadratic function of the reciprocal film thickness, $1/X$. Equation [9] includes local field concepts in its derivation (3) and meaningful estimates are obtained for the activation dipole moment, but the quadratic parameter, γ , does not include the dielectric constant and its usefulness is limited, particularly relating to the temperature dependence of γ . Equation [8] does include the dielectric constant in the quadratic parameter and the temperature dependence of this parameter is obtained if the ratio β/α is assumed constant. Equation [7] developed by Dignam (21) is the most general. Local field concepts are used, all the parameters are defined, and the temperature dependencies of the parameters can be obtained.

For the purposes of discussing the results obtained here, Eq. [7]-[9] are written in the empirically equivalent form

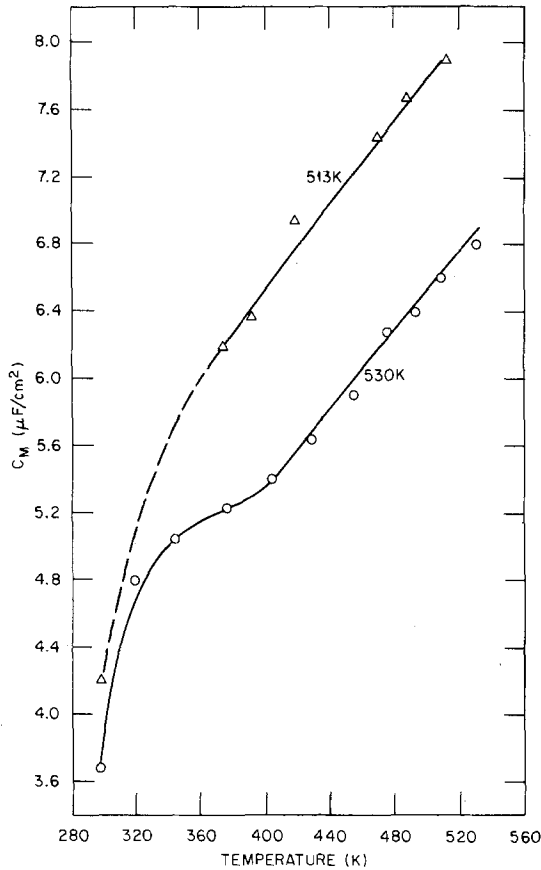


Fig. 7. The measured capacitance, C_M , as a function of temperature for titanium in oxygenated 0.05M K_2SO_4 .

$$i = i_0' \exp \{ [\mu^*V(1 - \gamma V/X)/X]/kT \} \quad [11]$$

where $i_0' = i_0 \exp(-\phi/kT)$, $\mu^* = qa\delta K$, and $\gamma = qa\delta K/c\phi = \beta\delta K/\alpha$. A plot of $\log(i)$ vs. $(1 - 45 \times 10^{-8}/X)/X$ is shown in Fig. 8 for the data at 513 K. The value $\gamma V = 45 \times 10^{-8}$ cm was obtained from a linear least squares fit of $\log(i)$ vs. $(1 - \gamma V/X)/X$ for assumed values of γV . The determination of best fit

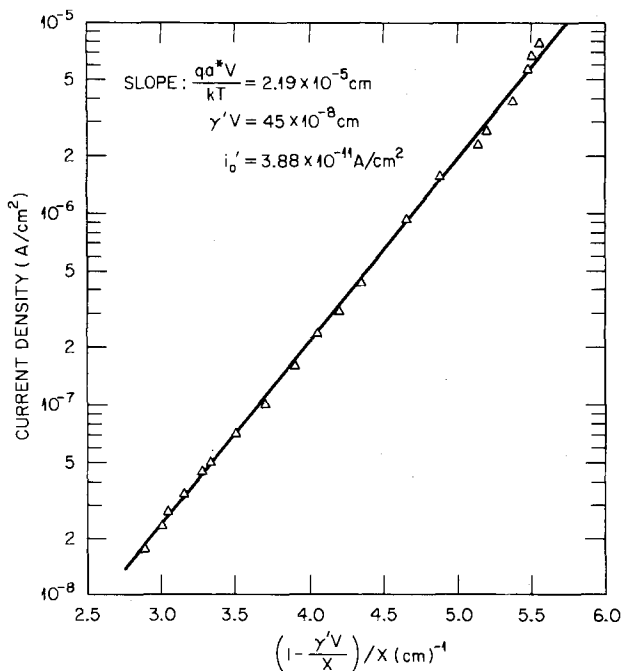


Fig. 8. The log of the anodic film growth current as a function of $(1 - \gamma V/X)/X$, for titanium in oxygenated 0.05M K_2SO_4 at 513 K and 0.00V vs. Pt/ O_2 (318 K): $\gamma V = 45 \times 10^{-8}$ cm.

(best choice for γV) was made when the correlation coefficient (r^2) achieved maximal value. The slope and intercept provide values for $\mu^*V/kT (= 2.19 \times 10^{-5} \text{ cm})$ and $i_0' (= 3.88 \times 10^{-11} \text{ A/cm}^2)$. Here, the calculation of the total film thickness X assumes an initial film thickness $X_0 = 20 \times 10^{-8}$ cm, at $t = 0$, and the first calculated value of the total film thickness commences at $t = 10$ min for all temperatures. These calculations were made with a Texas Instrument SR52 programmable calculator using the linear regression program ST 1-08 from the statistics library. A more sophisticated treatment of the data was obtained using the Runge-Kutta technique in the Marquardt nonlinear least squares program (26-28). Estimates of the parameters (i_0' , μ^*V/kT , γV), were obtained for data at 473, 513, and 530 K assuming values for $X_0 = 0, 10, 20, 30,$ and 40 \AA . Table I shows these estimates for $X_0 = 20 \text{ \AA}$. From estimates of the parameters obtained for $X_0 = 10$ and 30 \AA , the uncertainties in μ^*V/kT , γV , and i_0' are estimated at $\pm 12\%$, $\pm 7\%$, and $\pm 50\%$, respectively, for $X_0 = 20 \pm 10 \text{ \AA}$. The values for qaV were obtained using the M-L field, whereby $qaV = 3\mu^*V/K$.

The film thicknesses used in the least squares treatment of the data were calculated using a roughness factor of unity for the chemically polished Ti surface. In our previous work on chemically polished Zr (11) a roughness factor (σ) of unity was also assumed and the calculated film thicknesses agreed with a visual comparison of the thicknesses on a standard color gauge. Young (29) showed from a combination of Faraday's law, capacity, and spectrophotometric methods that the ratio of the effective to apparent area for chemically polished Ta was 0.99. Ord, Hopper, and Wang (3) assumed σ of unity for chemically polished Ta and Nb, and their measurements of the dielectric constant agreed with previously published values (17). Finally, the experimental errors of measurement are probably greater than any expected deviation of σ from unity.

An interesting analysis of the results can be made on the basis of Dignam's equation, Eq. [7]. Since $\mu^*V = qa\delta KV$ and $\gamma V = qa\delta KV/\phi$

$$c = (\mu^*V/\gamma V\phi) \quad [10]$$

and from the values for μ^*V and γV in Table I and $\phi = 1.22 \text{ eV}$, $c = 1.90 \pm 0.16$ for the three temperatures. This value for c again suggests the form of the potential energy barrier is the Morse potential since $c = 4.0$ for the clipped parabola potential and $c = 4.9$ for the cosine potential. Alternatively if a simple average film thickness, \bar{X} , is obtained at each temperature, the value of the parameter y can be estimated, where $y = \mu^*E/\phi = \mu^*V/\phi\bar{X}$, with $E = V/X$, the mean field strength. From Eq. [26] in Dignam's (21) paper, c can then be determined

$$y = [(1 + 2y^2/c)^{1/2} - 1]$$

$$\{2 + \ln 2 - \ln [(1 + 2y^2/c)^{1/2} - 1]\} \quad [11]$$

Using the value for μ^*V in Table I, $c = 2.0 \pm 0.1$. The value of ϕ used in the above analysis requires further discussion. First, as already stated, the measurement assumes the voltage drop across the oxide is constant as the temperature changes. However, the effective field assisting the ion transfer process depends on the dielectric polarization of the oxide, and it has been shown that the dielectric constant K is temperature dependent. Therefore, although the applied potential is constant, the local field strength is not; the field strength decreases with decreasing temperature. Over the temperature range for which the activation energy was measured, Fig. 5, the dielectric constant K as estimated from the temperature dependence of C_M , changed by $\sim 2-3\%$, Fig. 7. This results in only a 10% error in the estimate of ϕ , and the value of c is therefore in-

Table I. Parameters in the rate equation for anodic film growth on titanium

$$i = i_0' \exp \frac{\mu^*V}{kT} (1 - \gamma V/X)/X$$

$$\mu^*V = (qaVK)/3$$

| Temp (K) | i_0' (A/cm ² × 10 ⁻⁴) | μ^*V/kT (cm × 10 ⁶) | $\frac{\mu^*V}{[(e \cdot \text{cm} \cdot V) \times 10^6]}$ | K | $\frac{qaV}{[(e \cdot \text{cm} \cdot V) \times 10^6]}$ | γV (cm × 10 ⁶) | V (V) | γ [(cm/V) × 10 ⁶] |
|-------------|---|--|--|-----|---|---------------------------------------|-------|---|
| 473 | 2.23 | 1.44 | 58.8 | 411 | 0.43 | 23 | 0.25 | 92 |
| 513 | 3.94 | 2.13 | 93.9 | 452 | 0.62 | 44 | 0.36 | 122 |
| 530 | 7.28 | 2.61 | 118.9 | 452 | 0.79 | 54 | 0.46 | 117 |

creased by 10%, which does not significantly affect any of the conclusions made.

The following speculative discussion is an attempt to obtain the value for the activation dipole moment, qa , from the experimental data. In this study, the voltage, V , across the oxide is not known, and qa is obtained as a product with V , qaV . Ord, Hopper, and Wang (3) and Dignam (20, 21) report values for γ , the quadratic parameter, and K , for Ta, Nb, W, and Al at 298 K. From these values, the ratio γ/K is calculated: for W, $\gamma/K = 8.4 \text{ \AA}/V/31 = 0.27 \text{ \AA}/V$; for Ta, $4.8 \text{ \AA}/V/24 = 0.20 \text{ \AA}/V$; for Nb, $\gamma/K = 8.61 \text{ \AA}/V/38.5 = 0.22 \text{ \AA}/V$; and for Al, $\gamma/K = (\mu^*/\phi)/K = (23.5 \text{ e\AA})/7.83 \text{ eV}/8.85 = 0.33 \text{ \AA}/V$. The average of these values is $0.25 \pm 0.05 \text{ \AA}/V$. Here γV and $\mu^*V (= qa\delta KV)$ are determined experimentally. Since $V = \mu^*V/\mu^*$, and $\gamma = \gamma V/V$, then $\gamma = (\gamma V/\mu^*) \cdot qa\delta K$, and $\gamma/K = (\gamma V/\mu^*V) \cdot qa\delta$. Now, if the value for $\gamma/K = 0.25 \text{ \AA}/V$ is independent of temperature on valve metal systems, then from the values for γV and μ^*V in Table I, $qa\delta = 0.58 \text{ e\AA}$. If the geometry of the M-L field is assumed, $\delta = 1/3$ and $qa = 1.73 \text{ e\AA}$. This is a very reasonable value and compares with the estimate $qa = 1.56 \text{ e\AA}$ for Zr (11). If oxygen ions are involved in the ion transfer process for all the valve metal systems (20), then $qa\delta$ is not expected to differ greatly from one system to the next. Since the oxide is partially ionically bonded, a value of q between 1e and 2e is reasonable, and the activation distance $a \sim 1 \text{ \AA}$ is approximately one-half the interatomic lattice spacing (30). The much larger apparent activation dipole $\mu^* (= qa^*)$ obtained experimentally is due to the dielectric polarization of the oxide, and the dielectric constant K is a measure of the polarization. If the temperature dependence of the dielectric polarization is accounted for by measurement of the dielectric constant, it is not unreasonable to expect γ/K to be independent of temperature.

Having obtained the value for $qa (= 1.73 \times 10^{-8} \text{ e} \cdot \text{cm})$, the voltage drop across the oxide can be calculated, $V (= qaV/qa)$. These values are shown in col. 8 of Table I. Having the values for V , col. 9 gives the values calculated for $\gamma (= \gamma V/V)$.

The value obtained for the activation dipole moment may be compared with those obtained by other investigators (31, 4, 5, 9). These results were obtained from constant current measurements at temperatures below 100°C. The structure of the oxide reported by each investigator was anatase. If the effective field is the M-L local field ($E_e = (K + 2)E/3$), and the dielectric constant $K = 7$ as reported by Allard, Ahrens, and Heusler, (A, A, & H) (9), then the activation-dipole moment, qa , can be obtained from the reported B values, where $B = qa(K + 2)/3kT$. From measurements made by (A, A, and H) (9) in sodium citrate buffered solution, pH = 5 at 25°C, $qa = 2.1 \text{ e} \cdot \text{Å}$. Ammar and Kamal (4, 5) made measurements at 30°C in acid, neutral, and basic solutions and assuming the roughness factor $\sigma = 1$ and $K = 7$, $qa = 1.8 \text{ e} \cdot \text{Å}$. Mizushima (31) used a 10% ammonium borate solution in ethylene glycol solvent (this solution probably contained some water). The measurements were made at several temperatures, ranging from 12° to 85°C. At 31°C, again as-

suming $K = 7$, $qa = 2.0 \text{ e} \cdot \text{Å}$. These values agree very well with the value $qa = 1.7 \text{ e\AA}$ reported here. However, if local field concepts were not used, an apparent activation dipole moment $qa^* = 6 \text{ e\AA}$ would be obtained from the measurements at 30°C, and for the measurements reported here, at 257°C, $qa^* \sim 261 \text{ e\AA}$. Such an unreasonably large value can only be rationalized if the local field is the effective field assisting the ion transport process and from such considerations the dielectric constant plays an important role. Therefore, from a measurement of the dielectric constant of the oxide, $K \sim 7$ at 30°C for TiO₂ (anatase) and $K \sim 452$ at 240°C for TiO₂ (rutile), an estimate for $qa = 2.0 \text{ e\AA}$ is obtained independent of temperature and oxide structure.

Mizushima (31) and Ammar and Ismail (32) obtained B as a function of temperature. The results obtained by Mizushima show B decreasing more rapidly than $1/T$ with increasing temperature. This implies the effective field, and therefore the dielectric constant K decreases with increasing temperature. Ammar and Ismail however show B constant with increasing temperature and therefore, conversely, K increases with temperature. Without a knowledge of the temperature dependence of K it is not possible to determine whose results are correct. A good test of the model postulating the local field as the effective field causing ion transport in TiO₂ (anatase) would be to measure the dielectric constant in addition to determining the kinetic parameters as a function of temperature.

Summary and Conclusions

Titanium was exposed to oxygenated 0.05M K₂SO₄ at temperatures from 200° to 257°C at constant applied potential below the oxygen evolution potential. The apparent activation energy, ϕ , for anodic film growth was measured, and the dielectric constant of the oxide film, at experimental temperature, was determined from measurements of the capacitance of the oxide as a function of film thickness. It was shown that the logarithm of the anodic film growth current was a quadratic function of the field strength.

In terms of a rate expression developed by Dignam, it was shown that the form of the potential energy barrier for the ionic conduction process was the Morse potential function, and if the M-L field is the effective field assisting the ionic transfer process, it was shown that the activation dipole moment $qa = 1.73 \text{ e\AA}$. It was also shown that using the M-L field to calculate qa for TiO₂ (anatase) from the results of other investigators, excellent agreement is obtained, and $qa = 2.0 \text{ e\AA}$.

Acknowledgment

The authors wish to express their appreciation to Dr. Wally Davis, Jr., of the Chemical Technology Division, for his very extensive analysis of the results using the Marquardt nonlinear least squares program. This analysis provided some estimates of the uncertainties in the values of the parameters in the rate expression. The authors also wish to express their appreciation to Dr. R. E. Meyer, of the Chemistry Division, for his critical review of the paper. This research was sponsored by

the Division of Materials Sciences, U. S. Department of Energy under Contract W-7405-eng-26 with the Union Carbide Corporation.

Manuscript submitted Sept. 8, 1980; revised manuscript received ca. Jan. 26, 1981. This was Paper 10 presented at the St. Louis, Missouri, Meeting of the Society, May 11-16, 1980.

Any discussion of this paper will appear in a Discussion Section to be published in the June 1982 JOURNAL. All discussions for the June 1982 Discussion Section should be submitted by Feb. 1, 1982.

Publication costs of this article were assisted by Oak Ridge National Laboratory.

LIST OF SYMBOLS

| | |
|-------------|--|
| a | activation distance |
| C_{ox} | capacitance of the oxide film |
| C_{dl} | capacitance of the double layer |
| c | quadratic constant in Dignam's rate expression |
| e | charge on an electron |
| E | macroscopic field strength |
| \bar{E}_e | the effective field strength |
| \bar{E} | the mean field strength |
| i | the ionic film growth current |
| K | dielectric constant |
| q | charge on mobile ion |
| qa | activation dipole moment |
| V | voltage drop across oxide film |
| X | oxide film thickness (\AA or nm) |
| X_0 | pre-exposure film thickness (\AA or nm) |
| δ | geometric factor related to dielectric polarization of the oxide (= 1/3 for dielectric isotropy) |
| ϕ | apparent activation energy |

REFERENCES

1. L. Young, *Proc. Roy. Soc., Ser. A*, **258**, 496 (1960).
2. L. Young and F. G. R. Zobel, *This Journal*, **113**, 277 (1966).
3. J. L. Ord, M. A. Hopper, and W. P. Wang, *ibid.*, **119**, 439 (1972).
4. I. A. Ammar and I. Kamal, *Electrochim. Acta*, **16**, 1539 (1971).
5. I. A. Ammar and I. Kamal, *ibid.*, **16**, 1555 (1971).
6. A. Charlesby, *Proc. Phys. Soc. London*, **B66**, 317 (1953).

7. J. J. Polling and A. Charlesby, *ibid.*, **B67**, 201 (1954).
8. M. A. Hopper, J. A. Wright, and D. J. DeSmet, *This Journal*, **124**, 44 (1977).
9. K. D. Allard, M. Ahrens, and K. E. Heusler, *Werkst. Korros.*, **26**, 694 (1975).
10. A. Gunterschulze and H. Betz, *Z. Phys.*, **92**, 367 (1934).
11. A. L. Bacarella and A. L. Sutton, *J. Electrochem. Technol.*, **4**, 117 (1966).
12. A. R. von Hippel, Editor, "Dielectrics and Waves," John Wiley & Sons, Inc., New York (1954).
13. L. V. Azaroff and J. J. Brophy, "Electronic Processes in Materials," p. 341, McGraw-Hill Book Co., New York (1963).
14. S. Glasstone, K. J. Laidler, and H. Eyring, "The Theory of Rate Processes," p. 565, McGraw-Hill Book Co., New York (1941).
15. E. Hückel, *Z. Elektrochem.*, **34**, 546 (1928).
16. R. J. Maurer, *J. Chem. Phys.*, **9**, 579 (1941).
17. L. Young, *Trans. Faraday Soc.*, **55**, 632 (1959).
18. L. Young, "Anodic Oxide Films," p. 17, Academic Press, London and New York (1961).
19. L. Young, *This Journal*, **110**, 589 (1963).
20. M. J. Dignam, *ibid.*, **112**, 729 (1965).
21. M. J. Dignam, *Can. J. Chem.*, **42**, 1155 (1964).
22. M. J. Dignam, *This Journal*, **112**, 722 (1965).
23. A. L. Bacarella and A. L. Sutton, *ibid.*, **112**, 546 (1965).
24. A. R. von Hippel, "Dielectric Materials and Applications," p. 302, The Technology Press of M.I.T. and John Wiley, New York (1954).
25. A. L. Bacarella, *This Journal*, **108**, 331 (1961).
26. D. W. Marquardt, *J. Soc. Ind. Appl. Math.*, **11**, 431 (1963).
27. F. D. Hammerling, in "The Computing Technology Center Numerical Analysis Library," G. W. Westley and J. A. Watts, Editors, CTC-39, Oct. 6, 1970.
28. G. N. Lance, "Numerical Methods for High Speed Computers," pp. 54-57, Iliffe and Sons, London (1960).
29. L. Young, "Anodic Oxide Films," pp. 78-83, Academic Press, London and New York (1961).
30. A. F. Trotman-Dickenson, "Comprehensive Inorganic Chemistry," p. 376, Pergamon Press, Compendium Publishers, Elmsford, N.Y. (1973).
31. W. Mizushima, *This Journal*, **108**, 825 (1961).
32. I. A. Ammar and I. K. Ismail, *Werkst. Korros.*, **23**, 25 (1972).

Oxidation of Ti Thin Films Deposited on Vitreous Carbon

R. Müller, M. Wittmer,* and S. Stucki

Brown, Boveri & Company, Research Center, CH-5405 Baden, Switzerland

ABSTRACT

Anodic oxidation of bulk Ti and Ti thin films deposited on vitreous carbon is studied by electrochemical methods, scanning electron microscopy, and Rutherford backscattering analysis. The results show that the resistance to oxidation of the Ti thin film is considerably inferior to that of bulk Ti. The carbon-titanium interface composition plays a major role in the resistance to oxidation of the Ti film. The formation of a thin TiC layer enhances its stability. The thickness of the Ti film plays only a minor role.

The mechanical, chemical, and electrochemical properties of Ti contribute a great deal to the success of this metal in industrial applications (1). There is undoubtedly a renewal of interest in the surface properties of Ti and its oxides. Research in this field is stimulated by the need for large surfaces of Ti with well-defined electrical and electrochemical properties

for industrial applications such as electrolysis (2), and oxygen sensing (3). This work describes an attempt to prevent sacrificial oxidation of carbon anode current collectors for use in a membrane-type water electrolyzer (2) by evaporated films. A good resistance to oxidation and a perfect bond or adherence of the Ti film to the carbon substrate were our main interests. The electrochemical measurements were made in 1N sulfuric acid to produce conditions similar to those used in

* Electrochemical Society Active Member.

Key words: electrolyzers, oxide thin films, titanium.

electrolysis cells. These measurements, however, provide only phenomenological information on the oxidation and passivation process of the Ti thin film. Rutherford backscattering (RBS) analysis (4) was therefore used to study the oxygen distribution at the interface, in the film itself, and on the surface after evaporation, subsequent heat-treatment, and anodic oxidation. This information is very important for the use of Ti-covered anodes in electrolyzers. RBS also gives some information on the composition of the titanium-carbon interface following a heat-treatment. Finally, scanning electron microscopy of the surface of the film was used to analyze the surface morphology of the deposited and annealed Ti films.

Experimental

Ti films 300-3000 Å thick were deposited at room temperature with an E-gun on vitreous carbon substrates at a rate of 10-15 Å/sec and in a vacuum of 10^{-7} Torr. The vitreous carbon substrate, supplied by Le Carbone (France), was cleaned prior to use by heating it for 2 hr at 1050°C in a 10^{-6} Torr vacuum. Some deposited Ti films were heat-treated in a vacuum of 10^{-6} Torr. A pure bulk Ti foil (99.9999%) from Ventron Corporation (USA), and Ar-arc melted Ti pellets, were also used for comparison measurements. The bulk samples were cleaned in hot oxalic acid of 10 weight percent concentration and rinsed in double distilled water prior to use.

Potentiodynamic measurements were made on the Ti samples in an electrochemical Pyrex cell using a PAR 173 potentiostat and a PAR 175 universal programmer. The cell had a standard calomel electrode (SCE) as reference and a carbon counterelectrode. In the following, all voltages indicated are vs. the SCE unless otherwise specified. Current was plotted vs. applied voltage on an X-Y recorder. The electrolyte was an aqueous solution of 1N H_2SO_4 . The sweep rate of the potentiostat was generally 5 mV/sec. Rutherford backscattering analysis was performed to investigate the metallurgical composition of the deposited Ti films and their reaction with the oxygen and the carbon substrate after heat-treatments and after anodic oxidation.

Results and Discussion

It is well known that Ti builds up a thin passivating oxide film on its surface during exposure to oxygen. This oxide film protects the metal from further oxidation. For bulk Ti the thickness of this film in an aqueous solution has been found to increase linearly with anode potential at a rate of approximately 25 Å/V (5, 6). For evaporated thin films the situation is different. The oxidation behavior depends on the substrate, on the interface between substrate and Ti film, and on subsequent heat-treatments. The oxidation behavior of Ti thin films evaporated or sputtered onto hot (450°C) quartz substrates was studied by Armstrong and Quinn (7). This paper presents results on the differences in oxidation behavior between bulk Ti sheets, as evaporated and heat-treated Ti films on vitreous carbon substrates.

The anodic oxidation of bulk Ti has been measured by several research groups (6, 7). In order to have a fair comparison between bulk and thin film specimens, electrochemical properties of Ti were measured under the same experimental conditions. Figure 1 shows the anodic oxidation of Ti in 1N H_2SO_4 solution in the voltage range of 0-9V. A large increase in anodic current is observed above 3V during the first anodic polarization. This indicates the formation of an irreversible oxide layer. After 8-10 cycles between 0 and 9V the current vs. voltage (I/V) curve is fairly stable. The small current flowing above 3V is attributed to oxygen evolution. This result is in agreement with that of Paleolog *et al.* (8).

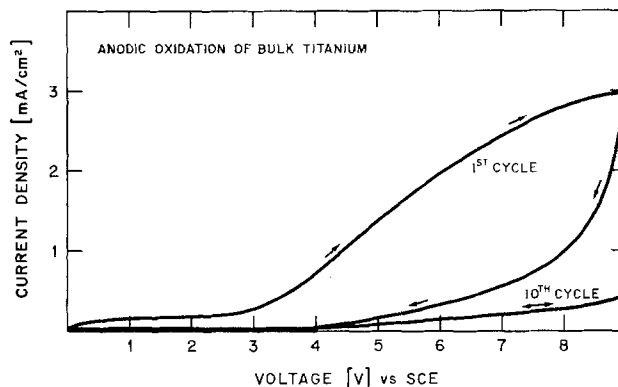


Fig. 1. Anodic polarization of bulk Ti in 1N H_2SO_4 electrolyte, 1st cycle and reversible behavior after 10th cycle. Sweep rate was 5 mV/sec.

The oxide grown on evaporated Ti thin films is less effective in preventing further oxidation than the one grown on bulk Ti. This phenomenon is seen in Fig. 2a, which shows the anodic oxidation of Ti thin films of different thicknesses. The I/V curves show that the oxidation process is characterized by passivation beginning above 0.8V, where the current decreases, or stays constant, followed by a rapid reincrease in current above ca. 1.25V. A further increase in potential leads to cracking of the Ti layer and subsequent peeling off. This might be due to the large Pilling-Bedworth ratio of 1.95 (the volume of oxide formed is almost twice the volume of metal), which results in a high internal stress leading to cracking of the layer. Similar arguments were put forward by Di Quarto *et al.* (9) for peeling of a surface layer on bulk Ti.

RBS analysis of the as-evaporated Ti film, before and after anodic oxidation, is shown in Fig. 3. The vertical arrows indicate the energy of $^4He^+$ particles scattered from surface positions of the corresponding

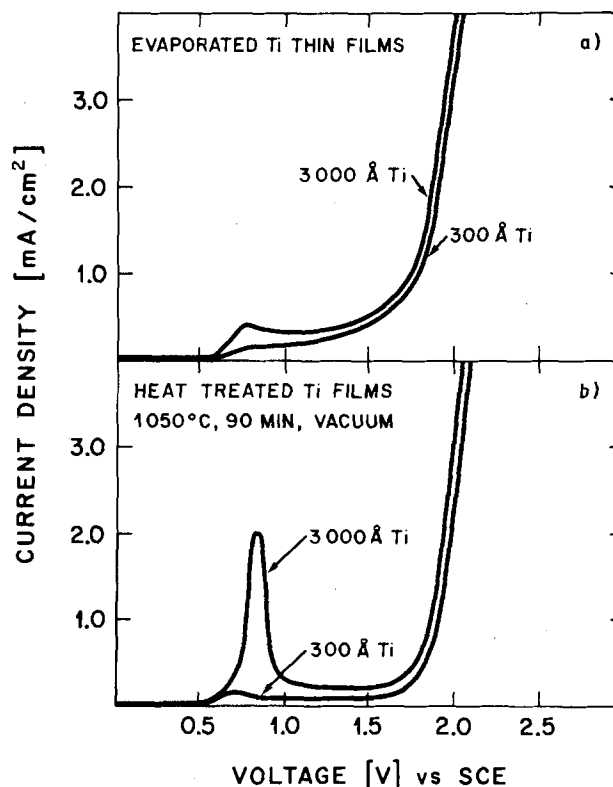


Fig. 2. a. Anodic polarization in 1N H_2SO_4 electrolyte of evaporated Ti thin films of different thicknesses. Sweep rate was 5 mV/sec. b. Anodic polarization in 1N H_2SO_4 of Ti thin films heat-treated during 90 min at 1050°C in a vacuum of 10^{-6} Torr.

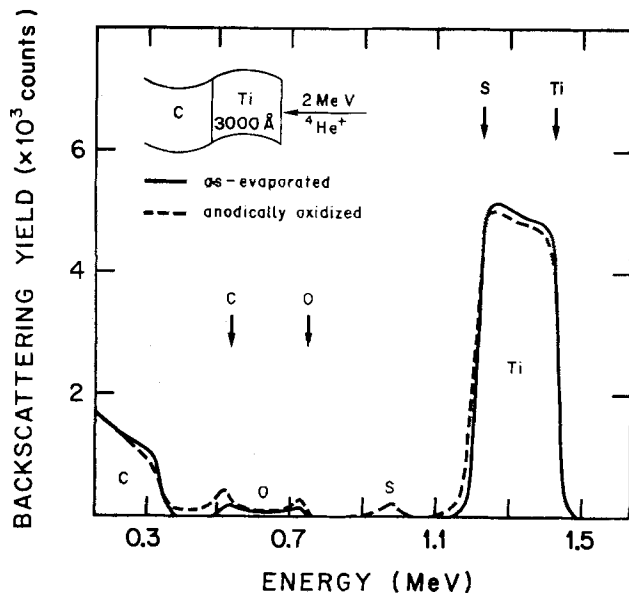


Fig. 3. 2 MeV-RBS spectra of 3000 Å thick Ti film on a vitreous carbon substrate after evaporation (solid line) and after anodic oxidation (dotted line). The vertical arrows indicate the energy of the He ions scattered from surface atoms of the corresponding element.

atoms. The low mass of the carbon allows the analysis of the oxygen distribution in the Ti film. The RBS spectrum of the as-evaporated sample, before anodic oxidation, is given by the solid line. From this spectrum it is seen that a small amount of oxygen is present in the surface region of the Ti film, at 0.75 MeV, and near the carbon-titanium interface, at 0.55 MeV. The oxygen content in the Ti film is lower and amounts to about 8 atomic percent (a/o). The RBS spectrum of the Ti film after anodic oxidation is given by the broken line in Fig. 3. It shows a marked increase of the oxygen content in the surface and interface region of the film. The pronounced peak at about 1.0 MeV marked by "S" and the tail of the oxygen signal at energies below 0.5 MeV arise from sulfuric acid which has reached the carbon-titanium interface via cracks in the Ti film and which has diffused somewhat into the pores of the vitreous carbon substrate.

In most cases the evaporated Ti films peeled off the carbon substrates during the electrochemical measurements. In order to improve the adherence of the films, some samples were heat-treated for 90 min at 1050°C in a vacuum of 10^{-6} Torr following evaporation of the Ti film. The solid line in Fig. 4 shows a RBS analysis of a sample coated with a 1000 Å Ti film before heat-treatment. Again, oxygen can be found in the surface and interface region of the film. The oxygen content in the film is about 6 a/o. This value is lower than the one found in the film whose RBS analysis is shown in Fig. 3. The amount of oxygen contained in the film depends on the evaporation process of the films, because Ti reacts strongly with residual oxygen contaminations of the vacuum system. The RBS spectrum of the annealed Ti film is given by the broken line in Fig. 4. From the oxygen signal it is found that the Ti film is uniformly oxidized. The plateau in the carbon signal at 0.5 MeV, extending almost to the surface position of carbon, indicates that a reaction of about $\frac{1}{2}$ of the Ti film with carbon has taken place. The actual composition of the interface layer is difficult to identify, but is assumed to be some form of titanium-oxy-carbonate. For annealed Ti films 3000 Å thick the interface layer was about one-fifth of the total film thickness.

For evaporated Ti thin films the breakdown voltage is low under anodic oxidation conditions, as shown in Fig. 2a. Annealed thin films are characterized by a

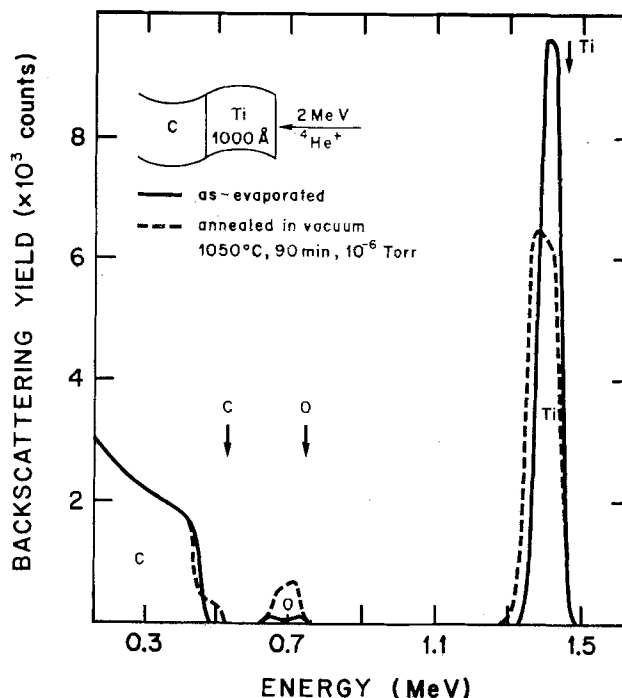


Fig. 4. 2 MeV-RBS spectra of a 1000 Å thick Ti film on a vitreous carbon substrate after evaporation (solid line) and after annealing in a vacuum of 10^{-6} Torr for 90 min at 1050°C (dotted line). The vertical arrows indicate the energy of He ions scattered from surface atoms of the corresponding element.

small shift of the breakdown voltage by approximately 0.4V toward higher voltages (Fig. 2b). Many samples were investigated and the difference in breakdown voltage was found to be consistently reproducible. This shift results in an increased stability of Ti films, which is, however, still insufficient compared to the resistance to cracking of Ti oxide films grown on bulk Ti. RBS analysis, however, shows a clear metallurgical difference between evaporated and annealed Ti thin films.

The 3000 Å thick annealed Ti films show a large peak in corrosion current around 0.75V. The height of this peak varies from sample to sample by approximately $\pm 20\%$, but is always present. It is possible that the heat-treatment causes the development of microcracks in the film due to the large difference in thermal expansion between vitreous carbon and Ti at 1050°C. The passivation of the crack surface results then in the observed current peak.

The uniform oxygen distribution in the sample and the titanium-carbide formed at the interface during heat-treatments did not prevent the destruction of a 3000 Å thick Ti layer under severe anodic oxidation conditions. At voltages over 2V large flakes of titanium oxide form and peel off. A scanning electron micrograph of this phenomenon is shown in Fig. 5. The upper right of the micrograph shows a large flake of titanium oxide which is peeling off. Growing flakes of titanium oxide can be distinguished very clearly underneath. They are specially marked at their edges by ridges due to the volume expansion of the oxide relative to the metal. This "undermining process" has been observed in bulk Ti at voltages around 50V (9). Though the destruction of thick Ti films under severe anodic oxidation conditions is not eliminated by the heat-treatment, the adherence of the film was much improved compared to as-deposited thick Ti films.

Conclusions

Anodic oxidation of bulk Ti and Ti thin films was studied by electrochemical methods, scanning electron microscopy, and RBS analysis. The results show that

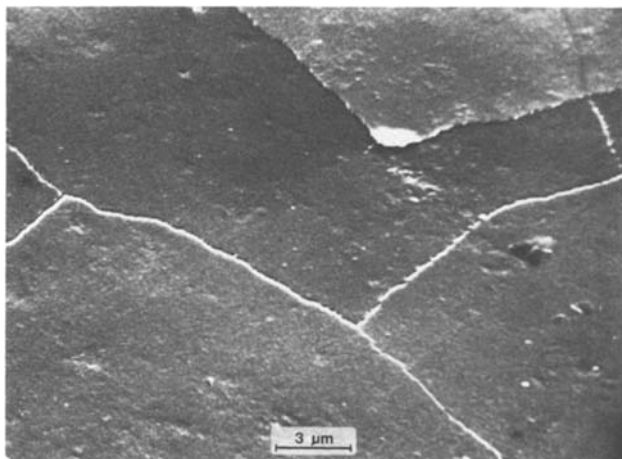


Fig. 5. Scanning electron micrograph of 3000 Å thick film of Ti, heat-treated during 90 min at 1050°C in a vacuum of 10^{-6} Torr and anodically oxidized in 1N H_2SO_4 during 30 min at 1.75V vs. SCE.

the mechanical stability and resistance to oxidation of the Ti thin films is much inferior to that of bulk Ti. The stability of the Ti thin films depends primarily on the adherence to the substrate, because high internal stresses have to be overcome in the Ti film during oxidation. Though good adherence of the Ti films to the substrate is achieved by a heat-treatment at 1050°C, the resistance to oxidation of the films is improved only marginally. The thickness of the Ti film plays only a minor role.

A perfect protection of the graphite substrate cannot be obtained by an evaporated thin film of pure Ti because the formation of a protective oxide leads to mechanical failure. The importance of the oxide peeling effect for the breakdown of the coherent Ti film can be demonstrated by evaporating a layer of noble metal on top of the annealed Ti film. The noble metal layer, catalyzing the O_2 evolution, prevents the formation of the TiO_2 layer and thus the failure of the Ti film under anodic oxidation conditions. This was experimentally shown using a 500 Å layer of Ru as noble metal. The lifetime of such electrodes is ruled by the

lifetime of the Ru layer, Ru being known to corrode at potentials above 1.45V (10). Since one of the objectives of the present investigation was to find a protection for carbon without the use of noble metals, this route was abandoned.

Acknowledgments

The preparation of the samples by H. Keser, the performance of the electrochemical measurements by R. Loitzl, and the SEM analysis by R. Baumann are gratefully acknowledged. We thank the University of Zürich for providing us the opportunity of using their Van de Graff accelerator and R. Pixley for his technical assistance.

Manuscript submitted Sept. 3, 1980; revised manuscript received Jan. 30, 1981. This was Paper 395 presented at the Los Angeles, California, Meeting of the Society, Oct. 14-19, 1979.

Any discussion of this paper will appear in a Discussion Section to be published in the June 1982 JOURNAL. All discussions for the June 1982 Discussion Section should be submitted by Feb. 1, 1982.

Publication costs of this article were assisted by Brown, Boveri & Company.

REFERENCES

1. R. J. Dowsing, *Metals and Materials*, p. 27, July-August 1979.
2. S. Stucki and R. E. Müller, Paper presented in Tokyo, 3rd World Hydrogen Energy Conf., June 23-28, 1980.
3. T. Y. Tien, H. L. Stalder, E. F. Gibbons, and P. J. Zacmanidis, *Am. Ceram. Soc. Bull.*, **54**, 280 (1975).
4. W.-K. Chu, J. W. Mayer, and M.-A. Nicolet, "Backscattering Spectrometry," Academic Press, New York (1978).
5. L. Arsov, M. Froelicher, M. Froment, and A. Hugot-Le-Goff, *J. Chim. Phys.*, **72**, 3 (1975).
6. F. Darland, G. Montelly, and J. C. Sohm, *Surf. Technol.*, **4**, 367 (1976).
7. N. R. Armstrong and R. K. Quinn, *Surf. Sci.*, **67**, 451 (1977).
8. E. N. Paleolog, A. Z. Fedotova, O. G. Derjagina, and N. D. Tomashov, *This Journal*, **125**, 1410 (1978).
9. F. Di Quarto, K. Doblhofer, and H. Gerischer, *Electrochim. Acta*, **23**, 195 (1978).
10. S. Trasatti and G. Buzzanca, *J. Electroanal. Chem. Interfacial Electrochem.*, **29**, 1 (1971).

The Reaction of Phosgene with Copper

A. Goussis, A. Galerie, M. Caillet, and J. Besson*

Laboratoire d'Adsorption et Réactions de Gaz sur Solides,
Ecole Nationale Supérieure d'Electrochimie et d'Electrometallurgie,
Domaine Universitaire, Saint-Martin-D'Herès, France

ABSTRACT

The reaction of phosgene with copper between 260° and 400°C leads to the formation of cuprous chloride $CuCl$. The rate law is of the parabolic type with a pressure influence especially during the parabolic stage. It was shown that, with our experimental conditions, the gaseous phase is always far from equilibrium. A mechanism accounting for the observed rate law is proposed. It involves simultaneously three rate-determining steps: the adsorption of phosgene, the adsorption of carbon monoxide, and the outer interfacial reaction.

Phosgene is an industrial product used today on a growing scale. The purpose of this paper is to present our results concerning its reaction with copper. The

* Electrochemical Society Active Member.

Key words: phosgene, copper, high temperature corrosion.

practical interest of this investigation is clear, but we shall also consider this corrosion from a theoretical point of view and propose a model describing the elementary steps of the reaction accounting for our observations.

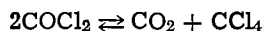
Very little has been published up to now about the reaction of phosgene with metals. Some rather old and always fragmentary results (1, 2, 3) deal, respectively, with the behavior of zinc, mercury, and tin. The paper of Tolley (4) on the reaction of phosgene with nickel-based alloys appears more complete. Nothing is known about the reaction with copper. On the contrary, the corrosion of copper by chlorine has been extensively studied by Tseitlin (5-7) and by Dagoury (8). According to Tseitlin this corrosion can be observed from 150°C up and is rapid enough above 290°C to produce important overtemperatures leading to the melting of the cuprous chloride formed. According to Dagoury, cuprous chloride CuCl forms in contact with the metal while CuCl_2 exists in the outer part of the scale. Under 140°C the rate law is logarithmic whereas at higher temperatures the importance of overtemperatures and the consequent partial sublimation of the reaction products deprive the rate laws experimentally found of any signification.

Thermodynamic Study of the Systems Involved

The system C-O-Cl.—It is well known that phosgene is a metastable compound at room temperature. Its thermal stability and its decomposition have been considered in numerous papers (9-12). We have undertaken a reinvestigation of the problem, taking into account 26 different species, all gaseous, with the exception of carbon. These species are the following: C_1 , C_2 , C_3 , C_4 , C_5 , O , O_2 , Cl , Cl_2 , CCl , CCl_2 , CCl_3 , CCl_4 , CO , CO_2 , C_2O , C_3O_2 , ClO , ClO_2 , Cl_2O , C_2Cl_2 , C_2Cl_4 , C_2Cl_6 , COCl , COCl_2 , $\langle\text{C}\rangle$.

The equilibrium pressures of these species were calculated in the system C-O-Cl by minimizing the total Helmholtz free energy (and not the Gibbs free enthalpy, as our experiments were realized at constant volume). For this minimization Goldfarb's method was used. Generally known as "conjugate gradient projection method" (13, 14), it gives the minimum of a non-linear function (here the free energy) subject to linear constraints [in the present case the equation of mass conservation, cf. (15, 16)]. The values of the Gibbs free enthalpies of formation were taken from the JANAF tables (17).

Figure 1 shows the results obtained for an initial phosgene pressure of 100 Torr. Especially important is the fact that, at low temperatures (<400 K), the gaseous phase consists essentially of CO_2 and CCl_4 according to the reaction



whereas at higher temperatures (> 1100 K) the predominant species are CO and Cl_2 according to

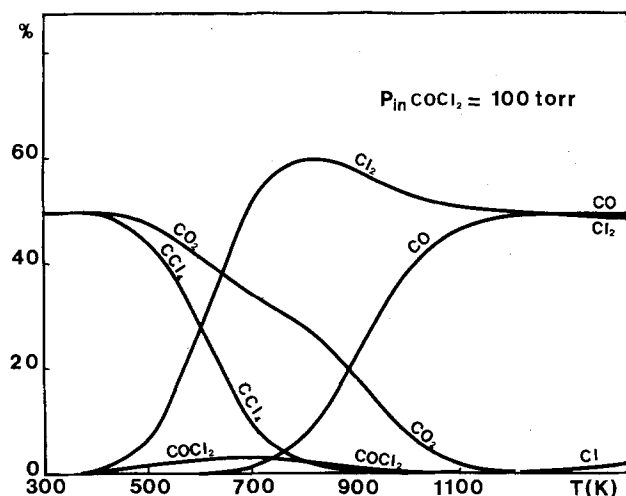
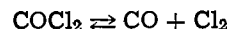


Fig. 1. Composition of the gaseous phase resulting from the decomposition of phosgene.



Between 230° and 900°C solid carbon is present. Table I gives some values of the equilibrium partial pressures of Cl_2 as a function of temperature.

The system C-O-Cl-Cu.—A similar calculation was made for the system C-O-Cl-Cu. The equilibrium composition of the gaseous and solid phases was computed, taking here into account 37 species, namely, the same as in the preceding case plus $[\text{Cu}]$, $[\text{Cu}_2]$, $[\text{CuO}]$, $[\text{CuCl}]$, $[\text{Cu}_3\text{Cl}_3]$, (CuCl) , $\langle\text{CuCl}\rangle$, $\langle\text{CuCl}_2\rangle$, $\langle\text{CuO}\rangle$, $\langle\text{Cu}_2\text{O}\rangle$, $\langle\text{Cu}\rangle$. For these new species, the values of the Gibbs free enthalpy were taken from an INCRA publication (18). Two cases are to be distinguished:

1. If phosgene is in excess, that is if all copper is chlorinated, the reaction product is, most naturally, cupric chloride CuCl_2 while the composition of the gaseous phase remains the same as in the absence of copper (Fig. 1).

2. In the other case (copper in excess), the reaction product is cuprous chloride CuCl , and the equilibrium composition of the gaseous phase is different (Fig. 2). At 600 K, the only species present in nonnegligible amounts at equilibrium are CO_2 , CuCl (solid), C (solid), and Cu (solid). Table II gives the corresponding mol numbers.

Figure 3 (curve a) gives the dissociation pressure of cupric chloride; curve b on the same figure gives the equilibrium chlorine pressure resulting from the decomposition of phosgene (initial pressure 100 Torr). It can be seen that, if equilibrium is reached, the chlorine pressure is sufficient to allow the formation of CuCl_2 up to 550°C.

Experimental Procedure

All experiments were conducted between 260° and 400°C using initial pressures of phosgene between 5 and 400 Torr. Phosgene (purity 99%) was supplied by the company PRODAIR and the copper foils (about $50 \times 10 \times 0.1$ mm) by Metals Research Company; the metal has a purity of 99.9%.

Kinetic curves were obtained in static atmospheres using a quartz spring thermobalance. The experimental procedure has been described in a previous paper (19). Qualitative analysis of the gaseous phase was performed with an infrared Wilks spectrophotometer.

Experimental Results

Reaction products.—The copper compound formed in most of our experiments was cuprous chloride CuCl . The chemical reaction can therefore be written

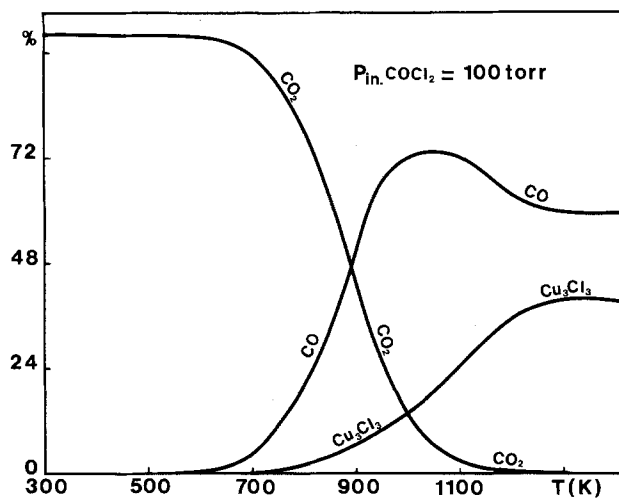
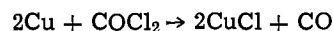


Fig. 2. Composition of the gaseous phase in equilibrium with an excess of copper.

Table I. Chlorine pressure at equilibrium for an initial phosgene pressure of 100 Torr (at room temperature)

| T (K) | 300 | 350 | 400 | 450 | 500 | 550 | 600 | 650 | 700 | 750 | 800 |
|-------------------------|-------|------|------|-----|-------|------|-----|-----|-----|-----|-------|
| PCl ₂ (Torr) | 0.004 | 0.34 | 0.60 | 2.5 | 11.25 | 36.5 | 70 | 112 | 168 | 211 | 242.5 |

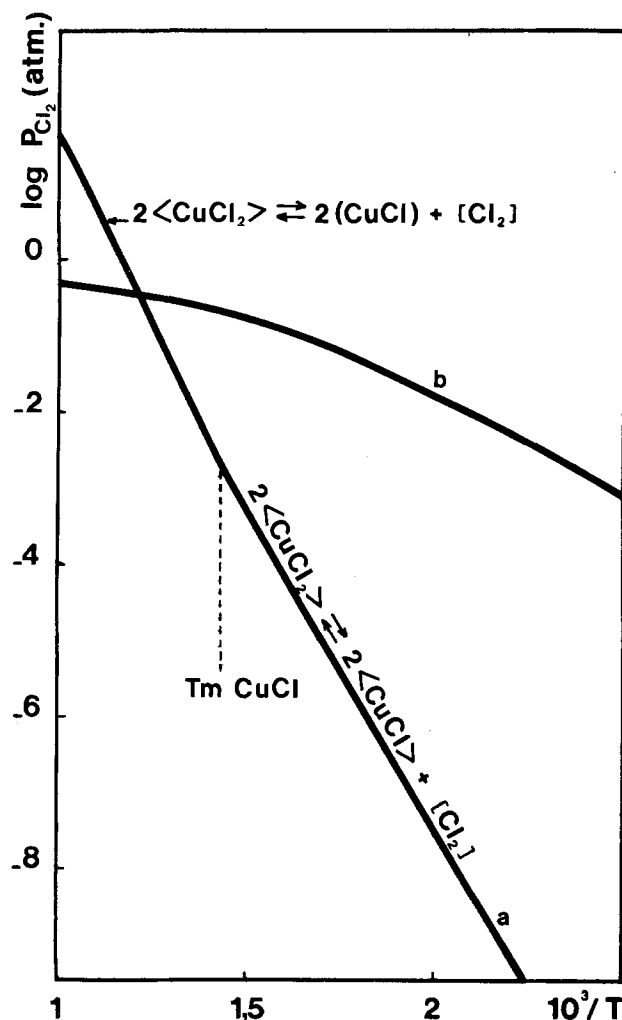
Table II. Mol numbers of every species in equilibrium with an excess of copper

| Initial mol number of <Cu> = 1 | Initial mol number of COCl ₂ = 1.344 · 10 ⁻² | P initial (100 Torr, 600 K) | | |
|--------------------------------|--|-----------------------------|-------------------------|------------------------|
| Species | CO ₂ | Cu Cl (S) | C (S) | Cu (S) |
| Mol number | 0.67 · 10 ⁻² | 2.69 · 10 ⁻² | 0.67 · 10 ⁻² | 9.7 · 10 ⁻¹ |

Only at high temperature and when the reaction has been followed during a sufficiently long time, the formation of a little quantity of cupric chloride CuCl₂ could be observed. In this case, as CuCl₂ is readily hydrated in air, x-ray diffraction patterns showed the presence of CuCl and CuCl₂ · 2H₂O.

Infrared analysis of the gaseous phase never showed another species than phosgene, the quantity of CO formed by the reaction being always well under the detection limit of our apparatus.

The influence of temperature on the rate law.—In the temperature range 260°–380°C and for an initial COCl₂ pressure of 100 Torr, kinetic curves show an initial deceleration followed by a linear stage (Fig. 4 and 5). The linear rate constant obeys the Arrhenius' law with an activation energy of about 100 kJ · mol⁻¹.

Fig. 3. Chlorine pressures resulting from the decomposition of COCl₂ and copper chlorides.

Above 380°C the experimental results become meaningless as already observed by Dagoury (8) because of the sublimation of CuCl.

Influence of the gas pressure.—This influence was studied at 282°C for initial pressures of COCl₂ varying from 5 to 400 Torr (Fig. 6). At low pressures (under 20 Torr, the sublimation of CuCl is noticeable) the experimental results are not significant. For higher pressures an important effect of pressure on the initial stage of the reaction can be observed whereas the linear part of the curves is much less sensible to its influence.

Morphological observations.—Figure 7 shows a typical aspect of the surface of the CuCl layer formed at 282°C, under an initial phosgene pressure of 100 Torr. For lower pressures (10–15 Torr) some larger single crystals appear scattered on the sample (Fig. 8).

Additional experiments.—As chlorine is an important component of the gaseous phase at equilibrium, a comparative investigation of the reaction of pure chlorine and of chlorine-containing gas mixtures was performed.

At 282°C under 10 Torr (that is at a pressure much smaller than the equilibrium pressure resulting from COCl₂ decomposition) pure chlorine reacts so rapidly with copper that it is impossible to follow the kinetics

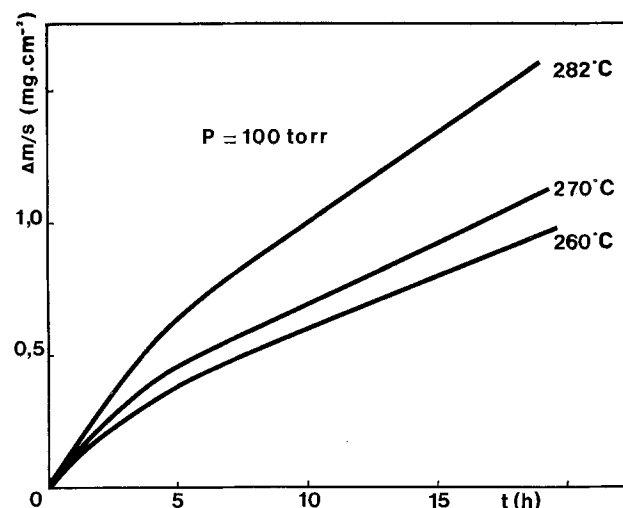


Fig. 4. Rate law: influence of temperature

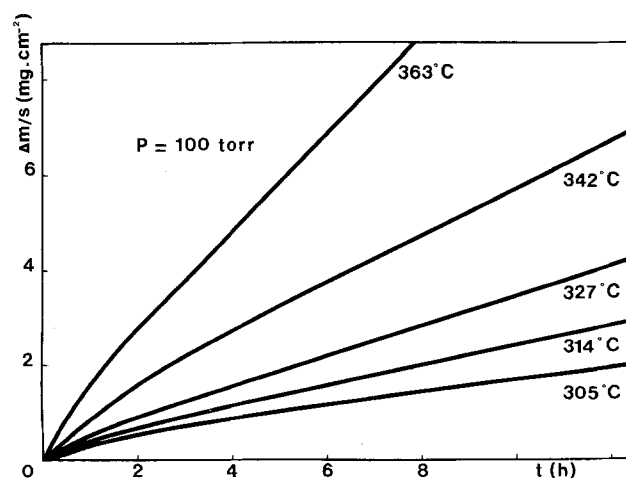


Fig. 5. Rate law: influence of temperature

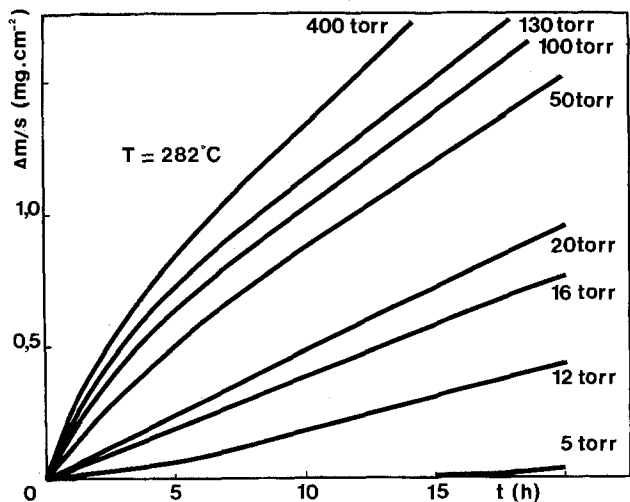
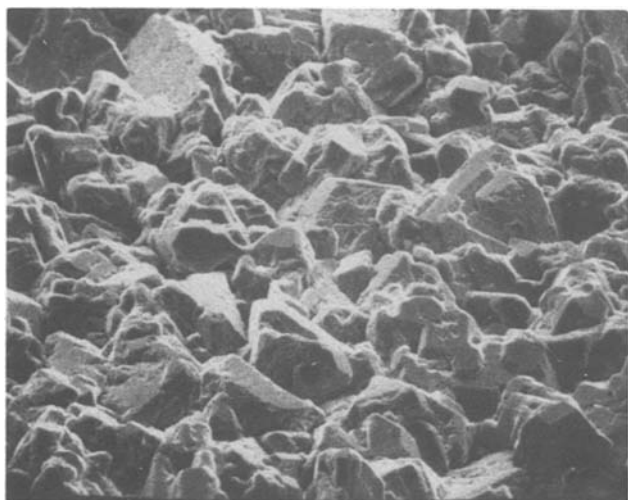
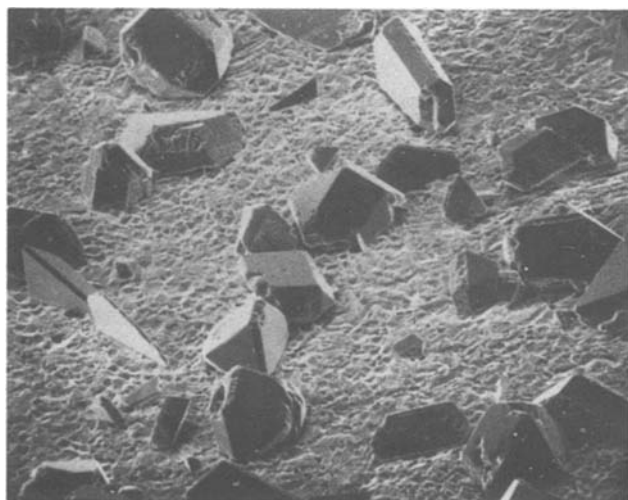


Fig. 6. Rate law: influence of pressure

Fig. 7. Superficial aspect of CuCl formed at higher pressures. 1000 \times .Fig. 8. Superficial aspect of CuCl formed at lower pressures. 400 \times .

of the reaction and that the cupric chloride formed sublimes. With mixtures of Cl_2 and CO (Fig. 9, curve 5) the reaction is always slower than with pure chlorine, but faster than with pure COCl_2 (Fig. 9, curve 1), at least during the first 5 or 10 hr of reaction. After

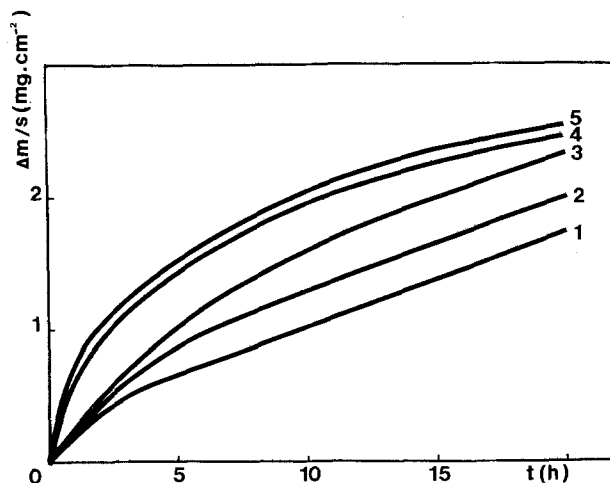


Fig. 9. Reaction of copper with the following gaseous mixtures: 1, COCl_2 (100T); 2, CO (4T) + Cl_2 (4T) + COCl_2 (92T); 3, CO (10T) + Cl_2 (10T) + COCl_2 (80T); 4, CO (10T) + Cl_2 (10T) + A (80T); 5, CO (10T) + Cl_2 (10T).

that time the reaction of $\text{CO} + \text{Cl}_2$ slows down and its rate becomes smaller than that of COCl_2 .

On the other hand, addition of equal quantities of CO and Cl_2 to COCl_2 accelerates the initial stage of the reaction, but has little influence on the reaction rate of the linear part of the curves (Fig. 9, curves 2 and 3). Argon has practically no influence (Fig. 9, curve 4).

The prevailing defects in cuprous chloride (20) are known to be of Frenkel's type (interstitial cations and cationic vacancies). This was easily verified by completely reacting a copper wire with phosgene; on a cross section of the sample (Fig. 10) a hole is clearly visible in the axis of the wire, showing that the reaction proceeds essentially through cationic diffusion.

Discussion

The decomposition and adsorption of phosgene.—As no other species than phosgene is found in measurable quantity in the gaseous phase, it can be concluded that the decomposition equilibrium of COCl_2 is far from being reached. This assumption is supported by the fact that $\text{CO}-\text{Cl}_2$ mixtures react more rapidly with copper than pure phosgene.

On the other hand, their reaction is slower than that of pure chlorine at the same pressure as in the mixture. As in the case of phosgene, the only reaction product is cuprous chloride even when the partial



Fig. 10. Cross section of a copper wire completely reacted with COCl_2 . 100 \times .

pressure of chlorine in the gaseous phase is larger than the thermodynamic value corresponding to the formation of cupric compound. All these facts imply that the chlorine activity in the adsorbed phase is low due to the occupancy of adsorption sites by CO.

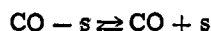
A model accounting for the observed rate law.—In agreement with the preceding remarks we shall assume that the adsorption of phosgene on the CuCl layer formed by the reaction occurs with dissociation and that the adsorption sites occupied by CO and Cl are identical.

The different steps of the reaction can then be written as follows:

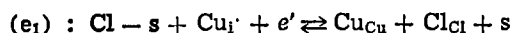
Dissociative adsorption of COCl_2 on CuCl:



Desorption of CO:

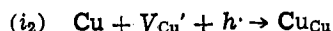
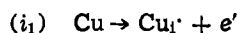


Outer interfacial reactions (Kröger's notation):



Diffusion of copper through vacancies and interstitial sites simultaneously.

Inner interfacial reactions:



As the rate law found experimentally is not parabolic, a diffusion-controlled reaction is excluded. On the other hand, the inner interfacial reaction is exactly the same with phosgene and with pure chlorine. As the two gases behave with copper very differently from one another the inner reaction can also be discarded as the rate-determining step.

Let us therefore assume that the overall reaction obeys a complex rate law controlled simultaneously by the adsorption of COCl_2 , the desorption of CO, and the outer reaction. The following symbols will be used:

θ_1, θ_2 : coverage ratios for the adsorption of CO and Cl respectively.

P : phosgene pressure

k_1, k_2, k_{e1}, k_{e2} : rate constants for the adsorption of COCl_2 , the desorption of CO and the outer reactions.

v_e : velocity of the outer reaction, equal to the sum of the rates of reactions e_1 and e_2 .

a_i : activities of the interstitial cations.

Neglecting then the opposite reaction (an assumption certainly valid far from equilibrium), one can write

$$\frac{d\theta_1}{dt} = k_1 P (1 - \theta_1 - \theta_2)^3 - k_2 \theta_1 \quad [1]$$

$$\frac{d\theta_2}{dt} = 2k_1 P (1 - \theta_1 - \theta_2)^3 - k_{e1} \theta_2 a_i - k_{e2} \theta_2 \quad [2]$$

$$v_e = k_{e1} \theta_2 a_i + k_{e2} \theta_2 \quad (v_e \text{ in mols/surface unit/time unit})$$

The activity of interstitial cations (and of cationic vacancies) is kept constant by the inner reactions which, according to our assumption, are equilibrated.

The reaction rate experimentally measured by the mass increase of the sample

$$v_r = \frac{d\Delta m}{dt}$$

is given by

$$v_r = 35.5 \left[\frac{d\theta_2}{dt} + v_e \right] + 28 \frac{d\theta_1}{dt}$$

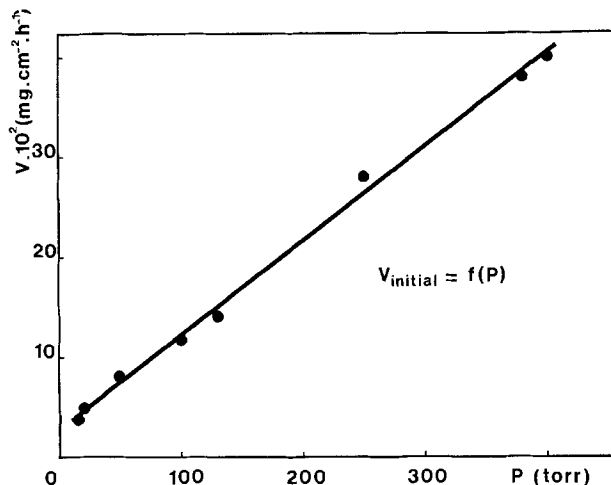


Fig. 11. Influence of pressure on the initial rate

or

$$v_r = 99k_1 P (1 - \theta_1 - \theta_2)^3 - 28k_2 \theta_1$$

$$(V_r \text{ in g/surface unit/time unit})$$

At the beginning of the reaction θ_1 and θ_2 increase and v_r decreases to a limiting value corresponding to a quasi stationary state (θ_1 and θ_2 constant). The rate law becomes then linear. The initial rate ($\theta_1 = \theta_2 = 0$) is proportional to the phosgene pressure (see Fig. 11).

The nonlinear differential system (1) cannot be solved analytically. We shall therefore consider only the quasi stationary (linear) state. The corresponding condition

$$\frac{d\theta_1}{dt} = \frac{d\theta_2}{dt} = 0$$

gives the following equations determining the limiting values θ_{11} and θ_{21} of θ_1 and θ_2

$$k_1 P (1 - \theta_{11} - \theta_{21})^3 = k_2 \theta_{11}$$

$$2k_1 P (1 - \theta_{11} - \theta_{21})^3 = (k_{e1} a_i + k_{e2}) \theta_{21}$$

showing that θ_{11} and θ_{21} are proportional. The reaction rate is then given by

$$v_r = 71k_2 \theta_{11} = 71k_1 P (1 - \theta_{11} - \theta_{21})^3$$

As θ_{11} and θ_{21} depend on P , it is not possible to derive explicitly the $v = f(P)$ relation. But, from the ratio between the reaction rate at $t = 0$ and in the linear part of the curves it is possible to estimate the sum $\theta_{11} + \theta_{21}$. This ratio is equal to $99/71(1 - \theta_{11} - \theta_{21})^3$.

Table III gives the results obtained for different pressures. These values which are always smaller than unity seem acceptable.

Manuscript submitted Oct. 2, 1980; revised manuscript received Jan. 22, 1981.

Any discussion of this paper will appear in a Discussion Section to be published in the June 1982 JOURNAL. All discussions for the June 1982 Discussion Section should be submitted by Feb. 1, 1982.

Publication costs of this article were assisted by A.D.R. Grenoble.

Table III. Limiting values of the coverage ratios as a function of phosgene pressure

| P (Torr) | 100 | 130 | 250 | 380 | 400 |
|-----------------------------|------|------|------|------|------|
| $\theta_{11} + \theta_{21}$ | 0.05 | 0.09 | 0.25 | 0.30 | 0.32 |

REFERENCES

1. A. E. Kretov, *Zh. Prikl. Khim.*, **2**, 483 (1929).
2. R. H. Atkinson, C. T. Heycock, and W. J. Pole, *J. Chem. Soc.*, **117**, 1410 (1920).
3. Yu. P. Kuznetsov, E. S. Petrov, and A. I. Vakh-ruseva, *Izv. Sib. Otd. Akad. Nauk*, **5**, 30 (1968).
4. W. B. Tolley, U.S. Atomic Energy Commission Report HW-30121 (1953).
5. K. L. Tseitlin, *J. Appl. Chem. USSR*, **27**, 889 (1954).
6. K. L. Tseitlin, *ibid.*, **28**, 467 (1955).
7. K. L. Tseitlin and V. A. Strunkin, *ibid.*, **31**, 1832 (1958).
8. G. Dagoury, L. M. Vincent, and J. Oudar, *Métal-lurgie VI*, (4), 173 (1966).
9. M. Bodenstein and G. Dunant, *Z. Phys. Chem.*, **61**, 437 (1908).
10. M. Bodenstein and H. Plaut, *Z. Phys. Chem.*, **110**, 399 (1924).
11. J. A. Christiansen, *Z. Phys. Chem.*, **103**, 99 (1923).
12. A. Lord and H. O. Pritchard, *J. Chem. Thermody-nam.*, **2**, 187 (1970).
13. D. Goldfarb, *SIAM J. Appl. Math.*, **17**, 739 (1969).
14. A. Buckley, *Math. Programming*, **8**, 207 (1973).
15. F. Van Zeggeren and S. H. Storey, "The Computa-tion of Chemical Equilibria," Cambridge Uni-versity Press (1970).
16. R. Holub and P. Vonka, "The Chemical Equilib-rium of Gaseous Systems," Reidel Publishing Co., Holland (1976).
17. JANAF Thermochemical Tables, U.S. Dept. of Commerce, 2nd ed., (1971), Supplements (1974), (1975), (1978).
18. E. G. King, A. D. Mah, and L. B. Pankratz, "Ther-modynamic Properties of Copper and its Com-pounds," INCRA series on "The Metallurgy of Copper," Vol. II, (1973).
19. P. Hadjisavas, M. Caillet, A. Galerie, and J. Besson, *This Journal*, **127**, 569 (1980).
20. T. Matsui and J. B. Wagner, Jr., *ibid.*, **124**, 610 (1977).

Characterization of Plasma-Deposited Silicon Dioxide

A. C. Adams,* F. B. Alexander, C. D. Capio, and T. E. Smith

Bell Laboratories, Murray Hill, New Jersey 07974

ABSTRACT

Silicon dioxide films have been deposited by reacting silane and nitrous oxide in a parallel-plate, radial flow, plasma reactor. Deposition parameters (temperature, power, and gas composition) have been systematically varied, and the films characterized by measuring the infrared spectra, deposition rate, density, etch rate, stress, refractive index, step coverage, breakdown voltage, and annealing behavior. The films, deposited at 100°-340°C and at rates of 200-360 Å/min, contain 2-9 a/o H bonded as H₂O, SiOH, and SiH. The films have densities of about 2.3 g/cm³, refractive indexes of about 1.47, a compressive stress usually less than 1 × 10⁹ dynes/cm², and etch rates about twelve times faster than thermally grown silicon dioxide. Films deposited below 200°C or at high power etch nonuniformly with part of the film etching very fast, possibly indicating a two-phase mixture. The step coverage is not conformal and the films are thin along vertical step walls. The films breakdown at fields of 4-10 MV/cm. During annealing in air at temperatures up to 400°C, the films lose hydrogen and become less dense, but do not crack. The properties of the plasma-deposited silicon dioxide are strongly dependent on the specific deposition conditions. In addition, simple correlations between the properties do not exist. Thus in characterizing plasma deposited silicon dioxide, the exact deposition conditions must be specified and all the film properties of interest must be measured.

There is considerable interest in the deposition at low temperature of silicon dioxide films using a glow discharge to supply the energy for the reaction. Previous depositions have used the oxidation of tetraethoxysilane (1-3), or the reaction of silane with oxygen (4), or with nitrous oxide (5-7). The deposition systems have been small, inductively coupled reactors (1-6); however, recent data have been reported using a large, capacitively coupled, radial flow reactor (7). The plasma-deposited silicon dioxide films are known to contain hydrogen (3, 6), to have a high etch rate (6), a high refractive index (1, 4-7), a low stress (7), and to be oxygen deficient (4, 6, 7). However, a systematic investigation of the effects of deposition conditions on the film properties has not been reported. We have deposited silicon dioxide films in a large, capacitively coupled, radial flow reactor by reacting silane and nitrous oxide in an argon carrier gas and have systematically varied the deposition parameters (substrate temperature, rf power, and gas composition). The effects on the film properties have been measured and are reported in this paper.

Experimental

The plasma deposition reactor is similar to other radial flow reactors that have been described (7-9). The reaction chamber consists of a Pyrex cylinder approximately 15 cm high and 61 cm in diameter sealed with aluminum plates on the top and the base. The aluminum sample holder, 56 cm in diameter, has an area of 2440 cm² and can accommodate twenty-five 75 mm samples. The temperature is maintained by two resistance heaters embedded in the sample table. The gases, individually metered with flowmeters calibrated by volume displacement, are introduced at the outer edge of the sample table and are pumped through a 5 cm diam central port. The pressure is measured at the exit port with a capacitance manometer. The system is pumped by a Roots blower (164 CFM) backed by a 65 CFM mechanical pump. The rf power (13.56 MHz) is supplied through a 58 cm diam aluminum electrode. The spacing between the rf electrode and the grounded sample table is 2.5 cm. The gas mixture consists of argon, 3% silane in argon, and nitrous oxide. The usual conditions for deposition of silicon dioxide in this reactor are: electrode spacing, 2.5 cm; rf power, 24W; temperature, 200°C; pressure, 133 Pa (1 Torr); total gas

* Electrochemical Society Active Member.
Key words: deposition, films, stress.

flow, 3 liters/min; and gas composition, 0.8% SiH₄, 52.0% N₂O, and 47.2% Ar. These conditions give a uniform deposition (within $\pm 5\%$) over the entire sample table with a deposition rate of about 270 Å/min. The substrates are B-doped silicon wafers, 75 mm in diameter. Four samples are used for each deposition and the film properties are averages of at least three of these samples.

The deposition variables that have been investigated are: the sample temperature; the N₂O/SiH₄ ratio keeping the concentration of silane (0.8%) and the total gas flow (3.0 liters/min) constant; the concentration of silane at constant total gas flow and constant N₂O/SiH₄ ratio; and the rf power. These parameters are varied individually keeping all other variables constant.

The film thickness is measured optically with a prism coupler (10), or mechanically with a Taylor-Hobson Talystep. The film refractive index is measured at a wavelength of 0.6328 μm with a prism coupler (10). The film stress is measured by substrate bending using an optically levered laser beam to measure the radius of curvature. Infrared spectra are measured with a Perkin-Elmer Model 580 spectrophotometer using a clean silicon wafer in the reference beam. Etch rates are measured in dilute hydrofluoric acid (100:1 H₂O:49% HF) at 25°C. The film density is calculated from the film thickness, the weight loss after etching the film, and the area of the sample (calculated from the weight and thickness of the substrate using 2.33 g/cm³ for the density of single crystal silicon). Edge effects are avoided by using samples with areas of approximately 6 cm² cleaved from the central part of the silicon wafer. Breakdown voltages are measured using 0.076 cm diam (30 mil) aluminum dots formed by standard photolithography and etching techniques. The measurements are made with the aluminum dot biased negatively so the p-type silicon substrates are in accumulation.

Film Characterization

Infrared.—The infrared spectra of the plasma-deposited films are similar to the spectra reported for silicon dioxide chemically deposited at low temperatures (11, 12). The major absorptions observed in the plasma-deposited films are listed in Table I along with possible assignments suggested from published papers. The absorptions at 1070, 805, and 450 cm⁻¹ are characteristic of silicon dioxide. The two absorptions at high frequencies, 3620 and 3380 cm⁻¹, are O-H stretching modes, with the band at the higher frequency resulting from SiOH and the 3380 cm⁻¹ peak caused by loosely bonded SiOH or adsorbed H₂O. The 2270 cm⁻¹ absorption is an Si-H stretch and has been observed by several authors. The two absorptions at 940 and 885 cm⁻¹ are more difficult to identify. The 885 cm⁻¹ band is frequently observed in deposited silicon dioxide films (11, 12). This absorption has been assigned to: Si-OH (13, 15), Si-H (12), nonbridging oxygen (17), the SiO₂ network (14), and Si₂O₃ (6, 11, 16). The absorption at 940 cm⁻¹, which is less often observed, may be caused by an Si-OH vibration. There are strong correlations between the intensities of the 940 and 885 cm⁻¹ bands and the Si-OH and Si-H stretching modes

Table I. Infrared absorptions for plasma-deposited silicon dioxide

| Frequency, cm ⁻¹ | | Assignment | Ref. |
|-----------------------------|-----------|---|--------------------|
| Median | Range | | |
| 3620 | 3605-3650 | Si-OH | (11-13, 18, 19) |
| 3380 | 3340-3390 | H ₂ O, Si-OH | (11-13, 19) |
| 2270 | 2260-2280 | Si-H | (6, 11-14, 17, 18) |
| 1070 | 1040-1080 | SiO ₂ | (3, 11-17) |
| 940 | 930-950 | Si-OH | (3, 11, 16) |
| 885 | 880-886 | Si-H, Si-OH, Si-O | (6, 11-17) |
| 805 | 800-815 | SiO ₂ , Si ₂ O ₃ | (3, 11-13, 15, 16) |
| 450 | 445-450 | SiO ₂ | (11-13) |

as shown in Fig. 1. These correlations tend to support the Si-OH assignment for the 940 cm⁻¹ peak and the Si-H assignment for the 885 cm⁻¹ absorption, but several of the other proposed assignments are still possible.

In addition to the major absorption bands, less intense absorptions have been observed in some films. Absorptions, which have not been identified, occur at 3500 and 1500 cm⁻¹ for N₂O/SiH₄ ratios less than 15. These may be caused by NH or NH₂ impurities. Absorptions are also observed at 1630 cm⁻¹ (H₂O) (15) and 1460 cm⁻¹ for films deposited at temperatures less than 175°C. Absorptions usually observed in silicon nitride, Si-N at 850 cm⁻¹, Si-H at 2160 cm⁻¹, and N-H at 3350 cm⁻¹, are not observed. However, the SiN and NH bands, if present, would be obscured by the absorption bands in the oxide.

An estimate of the hydrogen concentration at the various bonding sites can be obtained from the peak intensities of the Si-H absorption at 2270 cm⁻¹ and the two OH bands at 3620 and 3380 cm⁻¹. The concentration of Si-H groups is expressed as

$$N = K\alpha H$$

where N is the number of bonds per cm³, K is related to the absorption cross section, α is the apparent absorption coefficient (2.303 A/d , where A is the absorbance and d is the film thickness), and H is the full width at half absorbance. Values for K determined from other films are: 5.9×10^{16} cm⁻¹ for plasma-deposited SiN (19); 10×10^{16} cm⁻¹ for thermally grown SiO₂ (18); and 10×10^{16} cm⁻¹ for oxygen-doped Si (17). Using an average of these three values and the measured half-width for the Si-H peak in the plasma oxide, 60 cm⁻¹, gives

$$N = 5 \times 10^{18} \alpha$$

The concentrations of OH as SiOH and as H₂O or weakly bonded SiOH are calculated using the method given for chemically deposited silicon dioxide assuming that the plasma-deposited films are stoichiometric SiO₂ with a density of 2.3 g/cm³ (11). The results of these calculations are given in Fig. 2 which shows the concentration of hydrogen bonded as SiH, SiOH, and H₂O (or weakly bonded SiOH) as a function of the deposition conditions. Also given is the atom percent hydrogen obtained by summing the hydrogen in the three bonding sites. Hydrogen bonded to other sites and adsorbed hydrogen are not included in the sum. The total hydrogen concentration varies between 2 and 9 a/o with most of the samples containing about 5 a/o H.

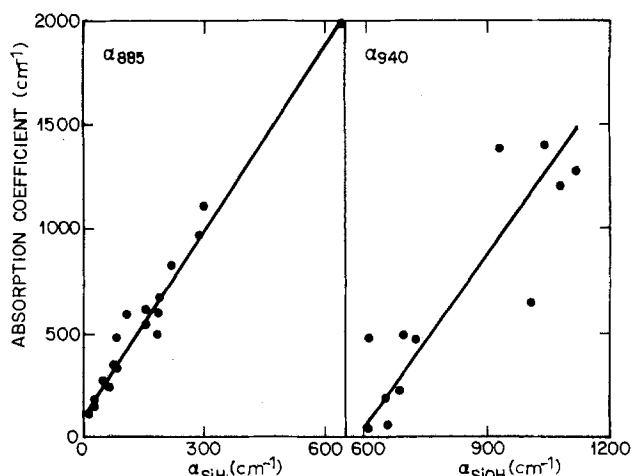


Fig. 1. The correlation between the absorption coefficient at 885 cm⁻¹ and the Si-H stretch at 2270 cm⁻¹; and the absorption coefficient at 940 cm⁻¹ and the Si-OH stretch at 3620 cm⁻¹.

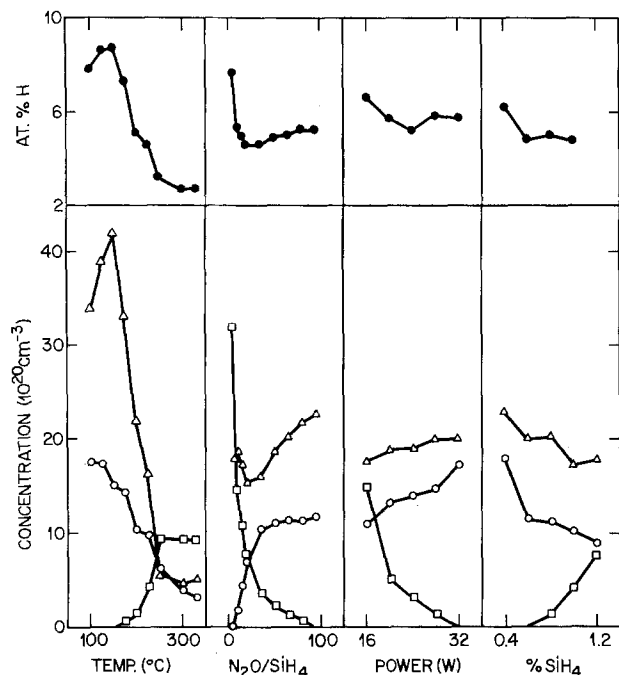


Fig. 2. The concentration of hydrogen groups and the total at percent H for different deposition conditions: triangles, H_2O ; circles, SiOH ; squares, SiH ; closed circles, total hydrogen.

The relative concentration of hydrogen in the three bonding sites depends strongly on the deposition conditions. For instance, the Si-H is favored at high temperature, low $\text{N}_2\text{O}/\text{SiH}_4$ ratio, low power, and high percent SiH_4 . The concentration of water or weakly bonded SiOH is a strong function of the deposition temperature, with very high concentrations observed for films deposited at low temperatures. The concentration of strongly bonded SiOH decreases with increasing temperature, increases with increasing $\text{N}_2\text{O}/\text{SiH}_4$ ratio until it saturates at about $11 \times 10^{20} \text{ cm}^{-3}$ for $\text{N}_2\text{O}/\text{SiH}_4$ greater than 50, and is weakly dependent on the power and the percent SiH_4 . As these data show, the chemical composition of the film depends strongly on the specific deposition conditions.

Deposition rate.—Data showing the deposition rate, density, etch rate, stress, and refractive index are given in Fig. 3-6. The deposition rate increases linearly with temperature (Fig. 3). The apparent activation energy, calculated from an Arrhenius plot, is 0.85 kcal/mole (0.037 eV) and is much lower than for the thermally activated reaction, 32 kcal/mole (20). The low activation energy probably indicates that the deposition is limited by desorption of reaction products; however, other interpretations are also possible. The deposition rate is nearly independent of the $\text{N}_2\text{O}/\text{SiH}_4$ ratio, appears to increase with the square root of the silane concentration, and is proportional to the square root of the power. This last result contrasts to the more nearly linear power dependence observed at much higher powers and for a lower $\text{N}_2\text{O}/\text{SiH}_4$ ratio and a lower frequency (7).

Density.—The average film density for all depositions is 2.29 g/cm^3 ; half of the samples are within $2.26\text{--}2.35 \text{ g/cm}^3$. The density is nearly independent of all deposition variables except power, where high film densities are observed for low powers (Fig. 6). Often the density and the refraction index of silicon dioxide are related (the Lorentz-Lorenz equation or the Gladstone-Dale formula) (11). Neither relationship holds for these plasma-deposited films, probably because the film composition varies. The densities observed for these films are similar to other values reported for plasma oxides, $2.18\text{--}2.44 \text{ g/cm}^3$ (7); and are higher than the values for

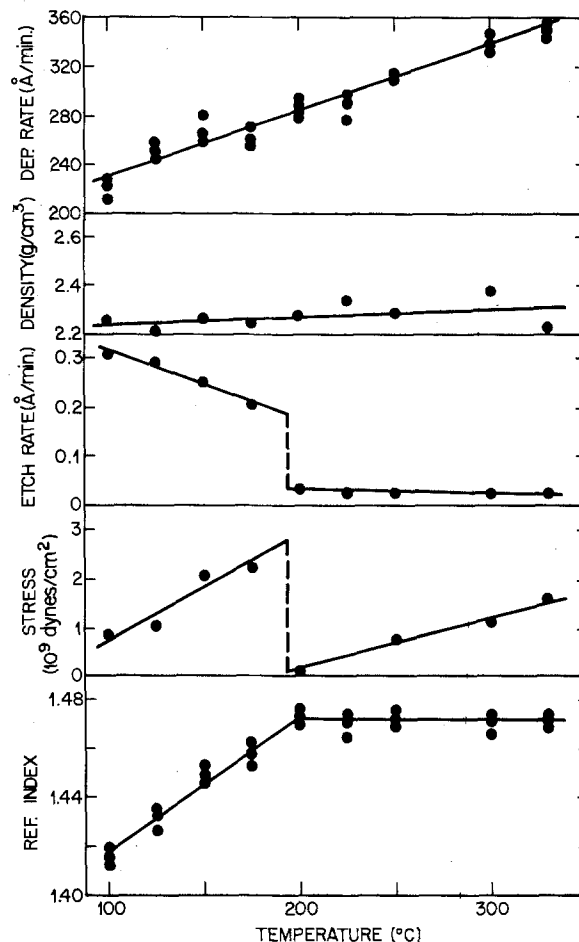


Fig. 3. Film properties vs. deposition temperature for $\text{N}_2\text{O}/\text{SiH}_4 = 65$, $0.8\% \text{ SiH}_4$, and 24W .

fused silica, 2.20 g/cm^3 (11), or for chemically deposited silicon dioxide, $2.07\text{--}2.27 \text{ g/cm}^3$ (16, 21).

Etch rate.—Etch rates have been measured in a dilute hydrofluoric acid (100:1 H_2O :49% HF) which etches thermally grown silicon dioxide at about 25 Å/min (22). The plasma oxide deposited at temperatures above 200°C and at powers less than 28W have etch rates of about $200\text{--}600 \text{ Å/min}$, much faster than for a thermal oxide. The etch rate decreases as the $\text{N}_2\text{O}/\text{SiH}_4$ ratio increases or as the percent SiH_4 increases. The films etch much faster, up to 3000 Å/min , when deposited at low temperature or at high power. The etch rate data in Fig. 3 indicate a sharp transition occurring at about 200°C .

The fast etching films deposited at low temperature or high power do not etch uniformly. The initial etch rates, which are shown in Fig. 3 and 6, are much faster than the final rate. Etch rate data for a film deposited at 125°C are given in Fig. 7 which shows the film thickness, weight, refractive index, and density as functions of etch time. This film etches at a uniform rate of about 3000 Å/min for the first 1.75 min. Etching for additional time occurs at a much slower rate, less than 1000 Å/min . A similar change is shown in the plot of film weight vs. etch time. Surprisingly, the refractive index decreases from 1.43 to 1.08 during the first 1.75 min of etching and then remains nearly constant. The film density follows a similar pattern. These data indicate that the films deposited at low temperature or high power contain fast etching components or regions. As this material etches, a slower etching, porous film remains. The high porosity causes the low refractive index and low density. This etching behavior is confirmed by SEM cross sections which show a porous material remaining after partial etching of the film. The nonuniform etch-

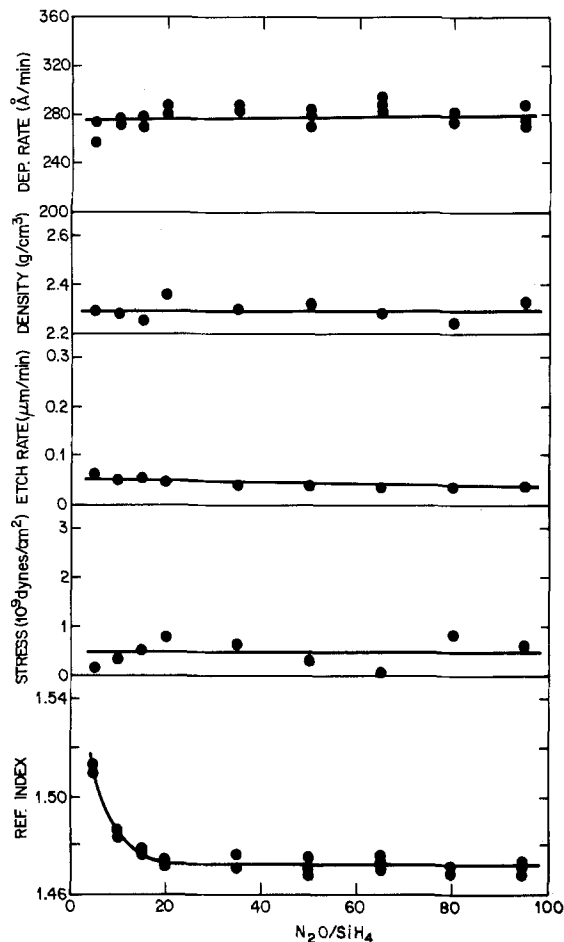


Fig. 4. Film properties vs. N_2O/SiH_4 ratio for $200^\circ C$, $0.8\% SiH_4$, and $24W$.

ing behavior, which appears to be similar to the anomalous etching observed for rf sputtered silicon dioxide (23), is not observed for films deposited at temperatures greater than $200^\circ C$.

The etch rates in different chemical solutions are given in Table II for films deposited at $200^\circ C$. The plasma-deposited films etch about twelve times faster than the thermal oxides in the four etchants investigated.

Stress.—All the plasma-deposited oxides have a small, compressive stress which is nearly independent of the N_2O/SiH_4 ratio and the rf power (Fig. 4 and 6). The average stress for the depositions shown in Fig. 4 and 6 is 0.57×10^9 dynes/cm² with the values ranging between 0.07 and 0.97×10^9 dynes/cm². The film stress increases to 2.4×10^9 dynes/cm² for depositions at low percent SiH_4 (Fig. 5). The film stress increases with increasing temperature with a discontinuity between 175° and $200^\circ C$ (Fig. 3). The film stress has not been correlated with other film properties; although, the dis-

Table II. Etch rates of silicon dioxide films deposited at $200^\circ C$, $N_2O/SiH_4 = 65$, $24W$, and $0.8\% SiH_4$

| Etchant | Etch rate, Å/min. | |
|----------------------------|-------------------|-----------------|
| | Plasma SiO_2 | Thermal SiO_2 |
| 100:1 ^a | 315 | 25 |
| P-etch ^b | 1635 | 130 |
| Dilute P-etch ^c | 125 | 10 |
| BHF ^d | 7010 | 580 |

^a 100:1 H_2O : 49% HF.

^b 3:2:60 49% HF: 70% HNO_3 : H_2O .

^c 3:2:710 49% HF: 70% HNO_3 : H_2O .

^d 10:1 40% NH_4F : 49% HF.

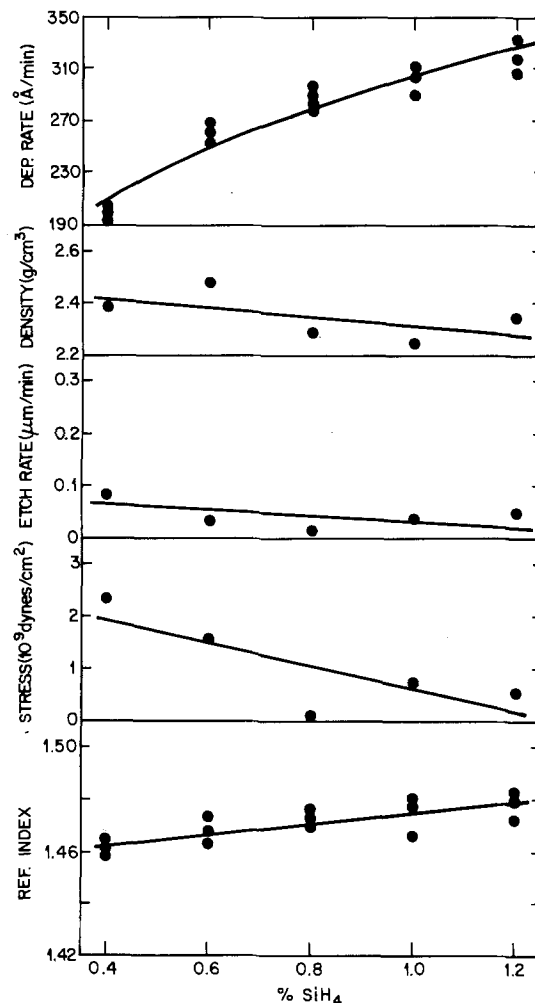


Fig. 5. Film properties vs. percent SiH_4 for $200^\circ C$, $N_2O/SiH_4 = 65$, and $24W$.

continuity between 175° and $200^\circ C$ is also observed in the etch rate, refractive index, and infrared spectra. For comparison, plasma-deposited silicon dioxide has been reported with a compressive stress between 0.1 and 4.0×10^9 dynes/cm² (7), silicon dioxide chemically deposited at about 400° – $450^\circ C$ generally has a tensile stress of $1-4 \times 10^9$ dynes/cm² (24, 25), films chemically deposited at higher temperatures have a low compressive stress, 0.6×10^9 dynes/cm² (21), and thermally grown silicon dioxide films have a compressive stress of $3-4 \times 10^9$ dynes/cm² (26).

Refractive index.—The refractive index of the plasma-deposited silicon dioxide is about 1.47 except for films deposited at low temperatures or high power, where the refractive index is lower, and for films deposited at low N_2O/SiH_4 ratios, where the index is much higher. The average index is slightly higher than the values reported for chemically deposited silicon dioxide, 1.44–1.46 (11, 12, 16, 21), but within the range of values reported for plasma-deposited oxides, 1.4–1.9 (2, 5–7). The slightly high values probably result from an oxygen deficiency (7). The refractive index is not correlated with other film properties except that the fast etching films all have a low refractive index.

Step coverage.—Films deposited over very deep steps are thin along the vertical walls (Fig. 8). This contrasts to the completely conformal coverage observed for silicon dioxide films chemically deposited at reduced pressure and higher temperature (21). The cusps and crevices observed at the top and bottom of steps for chemically deposited phosphorus-doped silicon dioxide are not present in the plasma-deposited films

(27). The step coverage appears to be determined by line-of-sight arrival of species from the plasma with no evidence for surface migration.

Dielectric breakdown.—Breakdown voltages have been measured for samples approximately 1200 Å thick. Distribution plots for samples deposited at two temperatures are given in Fig. 9. The sample deposited at 150°C has a maximum at 4.5–5.0 MV/cm with all the breakdowns occurring between 2.5 and 6.5 MV/cm. The distribution is nearly Gaussian. The distribution for the sample deposited at 250°C is no longer Gaussian, but appears to have two maxima centered at 7.0–7.5 and 9–10 MV/cm. This distribution is characteristic of samples deposited above 200°C. The high temperature samples all start to breakdown at 2–3 MV/cm and have a maximum in the distribution at 5–8 MV/cm but with a significant fraction of the capacitors breaking down at high fields, 9–10 MV/cm. Similar measurements on samples of chemically deposited silicon dioxide show more than 90% of the breakdowns occurring at 8–10 MV/cm, while very thin thermally grown silicon dioxide breaks down at 10–13 MV/cm (22).

Annealing.—In contrast to silicon dioxide films chemically deposited at low temperatures, the plasma-deposited films appear to be stable at room temperature (12). No change is observed in the infrared spectra of films exposed to laboratory air for six months. However, the films do change when annealed in air at temperatures of 150°–400°C. Data showing the annealing characteristics of two films are given in Fig. 10. In general, the film thickness remains nearly constant, and the film weight, the refractive index, and infrared ab-

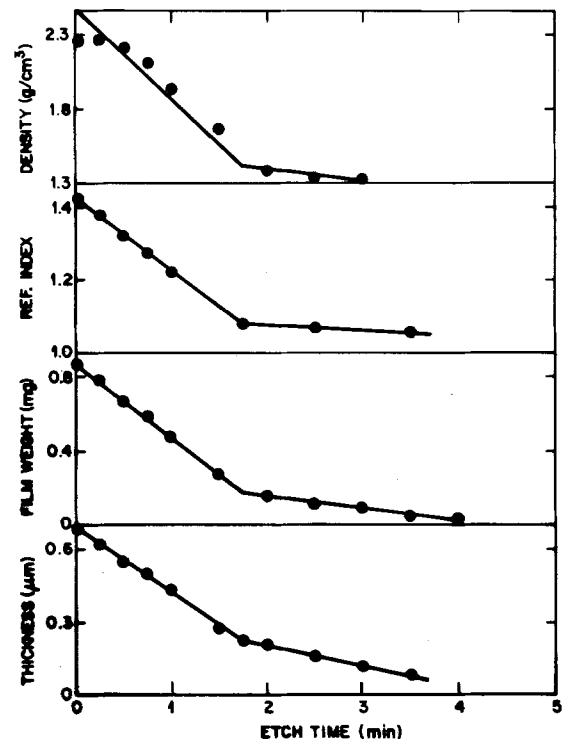


Fig. 7. Etching behavior for a film deposited at 125°C, $N_2O/SiH_4 = 65$, 0.8% SiH_4 , and 24W.

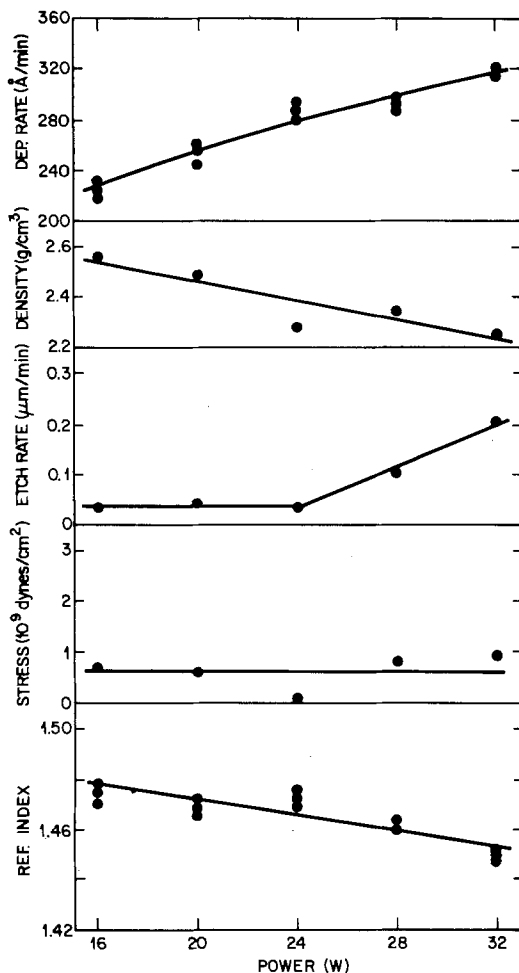


Fig. 6. Film properties vs. rf power for 200°C, $N_2O/SiH_4 = 65$, and 0.8% SiH_4 .

sorptions at 3380 and 940 cm^{-1} (H_2O or $SiOH$) and at 2270 and 885 cm^{-1} (SiH) decrease during annealing. The infrared spectra show that the H_2O and SiH groups are lost during annealing (the $SiOH$ groups absorbing at 3620 cm^{-1} are not affected by annealing); however, the loss in weight is somewhat larger than expected from the composition given in Fig. 2. Either the infrared spectra underestimate the concentrations of these groups or other groups are also removed during annealing. The film densities decrease during annealing to values of about 2.0–2.2 g/cm^3 , similar to the values observed for silicon dioxide chemically deposited at low temperatures (16, 21). The etch rates in dilute hydrofluoric acid are not affected by annealing at temperatures up to 400°C. Films deposited at low temperatures still etch nonuniformly with initial rates of about 3000 Å/min after annealing in air at 400°C. The film properties tend to stabilize after annealing at a given temperature for 1 hr or longer (Fig. 10). However, continued annealing at higher temperatures produces additional decreases in the weight, refractive index, and infrared intensities. The films do not crack

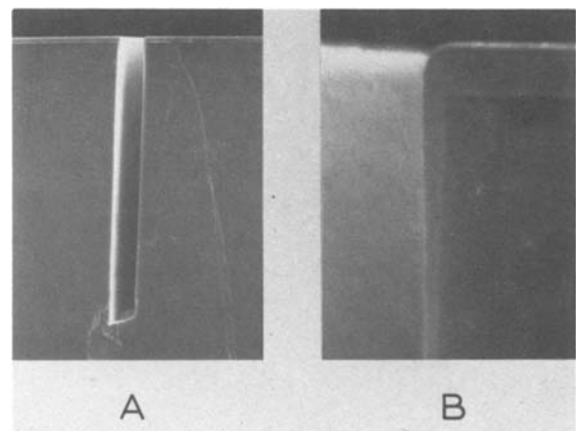


Fig. 8. SEM cross sections showing deposition of silicon dioxide over deep grooves anisotropically etched in Si: (a) 2 KX; (b) 17 KX.

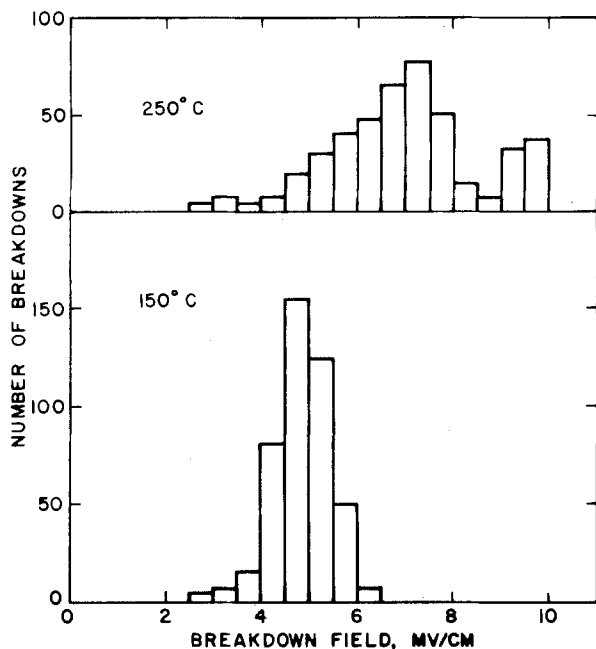


Fig. 9. Distribution plots of the breakdown field for samples deposited at 150° and 250°C, $N_2O/SiH_4 = 65$, 0.8% SiH_4 , and 24W.

after annealing at temperatures up to 400°C (the highest temperature investigated).

Discussion

The plasma deposition system has many variables (for instance, temperature, pressure, power density, rf frequency, electrode spacing, gas composition, gas flow, pumping speed, and reactor geometry) several of which are interrelated (28). In the present work, four of these parameters have been systematically varied. Many properties of the deposited films are strong functions of these variables; consequently, the exact deposition conditions must be given when the properties of plasma-deposited films are described. The strong dependence on deposition conditions makes it very diffi-

cult to compare films from different reactors; in addition, the strong dependence on deposition conditions may also explain many of the discrepancies which have been reported, such as the differences in refractive index, etch rate, composition, and stress.

Because of the variations in composition and in film properties, the name silicon dioxide may not be appropriate for these plasma-deposited films. Other possible names which emphasize the variable nature of the material are plasma silicon oxide, plasma oxide, or polysiloxane. However, the term plasma silicon dioxide has certain advantages. For instance, the composition and properties of the plasma-deposited films are similar to chemically deposited films which are often referred to as silicon dioxide. In addition, the technological uses and applications of the plasma-deposited films are similar to the uses of chemically deposited and thermally grown silicon dioxide films. For these reasons the name plasma silicon dioxide seems preferable. However, the name should not imply an exact chemical composition but rather a class of materials with compositions and properties close to those indicated by the name.

The initial deposition conditions give thickness variations of less than 10% over the deposition zone (twenty-five 75 mm wafers). However, changes in the conditions cause a deterioration in uniformity. The depositions at high power, high temperature, or low percent silane may have thickness variations as large as 40%. The other film properties also vary across the deposition zone but usually much less than the thickness. An exception is the concentration of hydrogen which may vary over the deposition zone by 50% for films deposited at high power or at low N_2O/SiH_4 ratios.

The plasma-deposited silicon dioxide contains hydrogen bonded as H_2O , $SiOH$, and SiH . The total hydrogen concentration varies between 2 and 9 a/o H, in good agreement with a previously reported value of 5.7 a/o H (19). The concentrations of the hydrogen containing groups (H_2O , $SiOH$, and SiH) are strongly dependent on the deposition conditions. Contrary to previous work, the present films contain SiH and OH groups even when deposited above 300°C (6). This difference may be caused by the different reactor geometries. There is no clear indication in the infrared spectra for chemically bonded nitrogen (as N-H or Si-N).

The deposition rate increases slowly with temperature, the apparent activation energy is only 0.85 kcal/mole, and appears to increase with the square roots of the rf power and the silane concentration. The deposition rate is independent of the N_2O/SiH_4 ratio. Previous reports using small, inductively coupled reactors have shown a decrease in deposition rate with increasing temperature, and a temperature dependence that is not Arrhenius (2, 3). These observations again show the strong dependence on geometry and on the specific deposition conditions, implying that the rate is governed by mass transport, reactive species lifetime, or gas phase diffusion rather than on chemical reaction rates.

Most of the films etch about twelve times faster than thermally grown silicon dioxide, and the etch rate is only slightly dependent on the deposition conditions. However, plasma oxide films prepared at low temperature or at high power etch nonuniformly with part of the film etching very fast. Infrared spectra of the material remaining after removing the fast etching portion of the film are nearly identical to the spectra of the original film, indicating that the fast and slow etching regions have similar compositions. This may indicate that films deposited at low temperature or high power are mixtures of two phases. A similar etching behavior has been reported for rf sputtered silicon dioxide (23). Analysis of the etch rate data assuming that the films

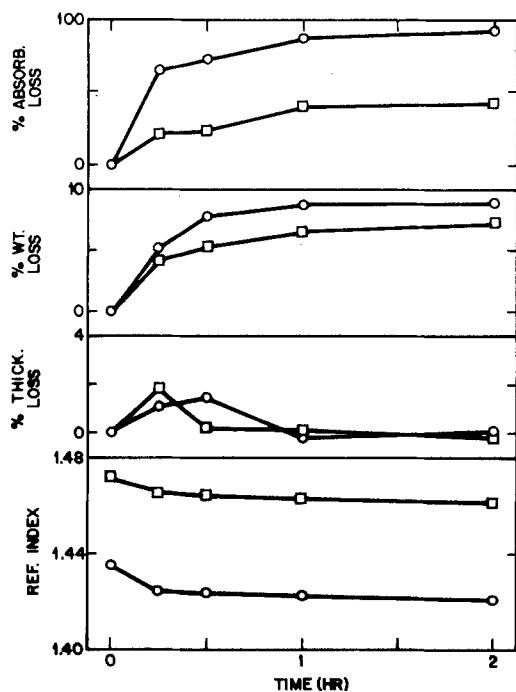


Fig. 10. Changes during annealing in air at 300°C for films deposited at $N_2O/SiH_4 = 65$, 0.8% SiH_4 , and 24W: circles, deposited at 125°C; squares, 250°C.

are two component mixtures shows that the amount of the fast etching component decreases from 80% for films deposited at 100°C to less than 1% for films deposited at 200°C.

The density of the plasma-deposited silicon dioxide is usually 2.26-2.35 g/cm³ and is not strongly affected by the deposition variables. The density decreases to 2.0-2.2 g/cm³ after annealing at temperatures up to 400°C. The film refractive index is about 1.47 except for low deposition temperatures and high power where the index is lower, and for low N₂O/SiH₄ ratios where the index is high. A high index at low N₂O/SiH₄ ratios has been reported before and may result from a silicon-rich stoichiometry (6, 7). The low refractive index correlates with the amount of fast etching component in the film. The deposited films have a compressive stress, often less than 1×10^9 dynes/cm². Correlations between stress and other film properties have not been found. Contrary to previous work, the step coverage is not conformal (7). It appears that deposition occurs by adsorption of species from the plasma with no surface mobility of the adsorbed species. Consequently, films deposited over steps are thin along the vertical walls. Dielectric breakdown occurs at fields of 4-10 MV/cm, significantly lower than the breakdown fields for chemically deposited or thermally grown silicon dioxide. The low breakdown field makes these films unsuitable as an insulator in many applications. The films lose hydrogen during annealing and become more porous, as shown by the lower refractive index and lower density, but cracking does not occur.

Many of the film properties change abruptly at deposition temperatures of 175°-200°C. For instance, discontinuities are observed in the stress, etch rate, refractive index, and infrared spectra. Depositions near this transition temperature should be avoided to insure reproducible and homogeneous film properties.

Summary

The properties of the films formed from silane and nitrous oxide in a large parallel-plate, radial flow reactor at 100°-340°C have been measured. The film properties are strongly dependent on the deposition conditions. This strong deposition dependence probably explains the large range in values previously reported for plasma-deposited silicon dioxide. In general the plasma-deposited films contain 2-9 a/o hydrogen, have a density of about 2.3 g/cm³, have a refractive index near 1.47, have a low compressive stress, and breakdown at fields of 4-10 MV/cm.

Acknowledgment

The authors would like to thank H. J. Levinstein for many discussions.

Manuscript submitted Nov. 3, 1980; revised manuscript received ca. Jan. 28, 1981.

Any discussion of this paper will appear in a Discussion Section to be published in the June 1982 JOURNAL. All discussions for the June 1982 Discussion Section should be submitted by Feb. 1, 1982.

Publication costs of this article were assisted by Bell Laboratories.

REFERENCES

1. S. W. Ing, Jr. and W. Davern, *This Journal*, **112**, 284 (1965).
2. D. R. Secrist and J. D. Mackenzie, *ibid.*, **113**, 914 (1966).
3. S. P. Mukherjee and P. E. Evans, *Thin Solid Films*, **14**, 105 (1972).
4. R. P. Kalnynya, I. A. Felty, L. A. Freiberga, I. E. Eglitis, and I. A. Eimanis, *Inorg. Mater.*, **11**, 511 (1975).
5. H. F. Sterling and R. C. G. Swann, *Solid-State Electron.*, **8**, 653 (1965).
6. R. J. Joyce, H. F. Sterling, and J. H. Alexander, *Thin Solid Films*, **1**, 481 (1967/68).
7. J. R. Hollahan, *This Journal*, **126**, 930 (1979).
8. A. R. Reinberg, Abstract 6, p. 19, The Electrochemical Society Extended Abstracts, San Francisco, California, May 12-17, 1974.
9. A. K. Sinha, H. J. Levinstein, T. E. Smith, G. Guintana, and S. E. Haszko, *This Journal*, **125**, 601 (1978).
10. A. C. Adams, D. P. Schinke, and C. D. Capio, *ibid.*, **126**, 1539 (1979).
11. W. A. Pliskin, *J. Vac. Sci. Technol.*, **14**, 1064 (1977).
12. E. A. Taft, *This Journal*, **126**, 1728 (1979).
13. K. H. Beckmann, *Surf. Sci.*, **3**, 314 (1965).
14. J. C. Knights, R. A. Street, and G. Lucovsky, *J. Non-Cryst. Sol.*, **35-36**, 279 (1980).
15. H. A. Benesi and A. C. Jones, *J. Phys. Chem.*, **63**, 179 (1959).
16. W. A. Pliskin and H. S. Lehman, *This Journal*, **112**, 1013 (1965).
17. W. R. Knolle, H. R. Maxwell, Jr., and R. E. Benson, *J. Appl. Phys.*, **51**, 4385 (1980).
18. K. H. Beckmann and N. J. Harrick, *This Journal*, **118**, 614 (1971).
19. W. A. Lanford and M. J. Rand, *J. Appl. Phys.*, **49**, 2473 (1978).
20. K. Strater, *RCA Rev.*, **29**, 618 (1968).
21. A. C. Adams and C. D. Capio, *This Journal*, **126**, 1042 (1979).
22. A. C. Adams, T. E. Smith, and C. C. Chang, *ibid.*, **127**, 1787 (1980).
23. K. Hara, Y. Suzuki, and Y. Taga, *Jpn. J. Appl. Phys.*, **18**, 2027 (1979).
24. R. Lathlaen and D. A. Diehl, *This Journal*, **116**, 620 (1969).
25. W. Kern, G. L. Schnable, and A. W. Fisher, *RCA Rev.*, **37**, 3 (1976).
26. R. J. Jaccodine and W. A. Schlegel, *J. Appl. Phys.*, **37**, 2429 (1966).
27. A. C. Adams and C. D. Capio, *This Journal*, **128**, 423 (1981).
28. M. J. Rand, *J. Vac. Sci. Technol.*, **16**, 420 (1979).

Electrical Transport Properties of Hydrogenated p-Type InSb Films

A. L. Dawar,¹ O. P. Taneja,² B. K. Sachar,¹ K. V. Krishna, H. K. Sahajwani, and P. C. Mathur

Department of Physics and Astrophysics, University of Delhi, Delhi-110007, India

ABSTRACT

Hall coefficient and d-c conductivity measurements were made on p-type polycrystalline InSb films exposed to hydrogen gas at different pressures. It has been found that the effect of hydrogen in the films is to reduce the concentration of the extrinsic carriers and to decrease their mobility.

The relative importance of various scattering mechanisms limiting the charge carrier mobility in films depends on the conditions under which the films are grown. The inhomogeneities, incorporated or introduced during growth of the film of a compound semiconductor, materially affect the transport properties (1-3). The inhomogeneities in the film can be affected by a number of methods, e.g., doping of foreign elements by co-evaporation (4-6), diffusion (7, 8), annealing in the atmosphere of gases (9, 10), adsorption of gases under pressure (11-13) etc. The effect of adsorption of gases, by exposing the films to gases under various pressures, on the transport properties of the films of semiconductors has recently drawn the attention of many workers (10-13). Most of these workers have, however, studied the effect of adsorption of gases by introducing the gases at low pressures ($\sim 10^{-5}$ Torr to 10^{-2} Torr) for different durations.

In the present work, the effect of hydrogen on the electrical transport properties of p-InSb polycrystalline thin films has been studied by exposing the films to the gas at high pressures (300 and 500 psi). The concentration of the extrinsic charge carriers and their mobility is found to decrease with the increase of pressure of the gas. The motivation for exposing the films at high pressures was that the films exposed to lower pressures were found to have significant desorption effect and the conductivity, which rose due to exposure to the gas, decayed toward its initial value in time periods depending on the exposure parameters. On the other hand, the films exposed at higher pressures and longer durations were found to absorb hydrogen which remained indiffused in the films up to a time period of 30 days.

Experimental Details

Using tantalum masks, films of size 20×4 mm and thickness $0.8 \mu\text{m}$ were grown by evaporating p-type InSb on thin glass cover slips as substrate under a vacuum $\sim 5 \times 10^{-6}$ Torr. The substrate was cleaned chemomechanically by acetone, detergent, and deionized water using an ultrasonic agitator. The substrate was kept at 300°C during growth to maintain the stoichiometry of the film and was then cooled to room temperature in 6 hr in order to fix the structure of the films. A more abrupt cooling was found to result in poor nucleation. Using transmission electron diffraction studies, Dale and Senecal (14) have shown that InSb films grown at a substrate temperature of 300°C , showed characteristic patterns of InSb. Thickness of the film was measured with the help of a quartz crystal thickness monitor (15), which measures frequency

differences up to 10 Hz. Considering the errors introduced due to differences in the density of bulk and thin films, the error in the thickness measurements is estimated to be $\sim 3\%$. The polycrystalline nature of the films was confirmed by electron diffraction studies and the average grain size was found to be $\sim 500\text{\AA}$. The films grown in the same batch were exposed to hydrogen gas of 99.995% purity at room temperature (at 300 and 500 psi) for 2 hr in a specially designed stainless steel cell of cylindrical shape, having a diameter of 2.5 cm and length 7 cm and provided with a pressure gauge.

Ohmic contacts were obtained by evaporating high purity silver under a high vacuum using tantalum masks. The contacts used to pass the current through the sample were spread over the entire width at the two edges while the Hall probe contacts were 0.5 mm in diameter. The ohmic nature of the contacts was confirmed by the linearity of the I - V characteristics, measured throughout the temperature range. The five probe technique, as described by Putley (16), was used to measure d-c conductivity and the Hall coefficient. The sample was mounted on a copper block (with electrical insulation) which was kept in a Dewar flask containing liquid nitrogen. The temperature was measured using a copper constantan thermocouple soldered to the copper block. Errors due to the thermomagnetic effects were eliminated by reversing the current and magnetic field directions. Since the length to width ratio of the film is $l/w = 5.0$, the geometrical errors in the Hall coefficient are negligible. Hall measurements as a function of temperature were taken over 2-3 runs and were found to be reproducible. The observed Hall coefficient was found to be independent of the sample current and the magnetic field applied. The error in R_H , taking into account the errors involved in measuring sample current, magnetic field, and thickness of the film was estimated to be about 3%. The overall error in Hall mobility is about 5%.

Measurements were made on a number of samples of the same thickness (within 5%) which was achieved with the help of electronic shutters, and the results were found to be reproducible within the experimental errors. There was no noticeable aging effect on the transport properties of the exposed films even after storing at room temperature for 30 days in a dessicator.

Results and Discussion

The variation of Hall coefficient R_H with temperature ($\log R_H$ vs. $1/T$) of the unexposed as well as the hydrogenated films (at pressures 300 and 500 psi) is shown in Fig. 1 for magnetic field $B = 5$ kG (no variation of R_H with B was found up to this limit). It is found that the value of R_H at any given temperature increases with the increase of pressure of the gas. The variation of R_H in the low temperature region is char-

¹ Present address Defence Science Laboratory, Metcalfe House, Delhi-110054, India.

² Present address: Government College Gurgaon, Haryana, Gurgaon-122001, India.

Key words: conductivity, charge carrier mobility, films.

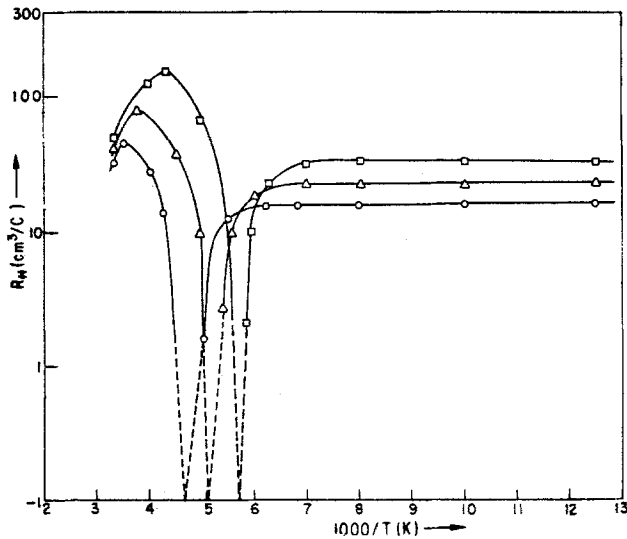


Fig. 1. Variation of Hall coefficient R_H with temperature ($\log R_H$ vs. $1/T$) for all the films: I, $-\circ-$; II, $-\Delta-$; III, $-\square-$.

acteristic of a degenerate extrinsic semiconductor. As the temperature increases, the value of R_H decreases and passes through zero at a temperature known as inversion temperature, at which $p = nb^2$, where p and n are the concentrations of holes and electrons, respectively, and b is the ratio of electrons to hole mobility. Above the temperature of inversion, R_H changes sign and increases algebraically with the increase of temperature. This is because of the increasing contribution of electrons to the conduction phenomenon due to their higher mobility. The value of R_H at any temperature is given by

$$R_H = \frac{1 - xb^2}{ep(1 + xb)^2} \quad [1]$$

where x is the ratio of the concentration of electrons n to that of holes p and e is the electronic charge.

It is also found from Fig. 1 that the Hall coefficient reaches a peak value of R_{H1} (algebraically maximum) and decreases again with further increase of temperature, indicating the onset of intrinsic behavior. At the temperature corresponding to the peak value of the Hall coefficient, the contribution of electrons and holes to the conduction process is equal, i.e., $p = nb$. The values of b can be calculated with the help of the expression

$$\frac{R_{H1}}{R_{H2}} = \frac{(b - 1)^2}{4b} \quad [2]$$

where R_{H2} corresponds to the extrinsic value of the Hall coefficient. The values of b thus calculated for all the films are shown in Table I. It is found that the value of b increases with the increase of pressure of hydrogen gas. The inversion temperature is found to shift towards lower temperatures with the increase of pressure of hydrogen gas. The onset of intrinsic conduction is also found to shift towards lower temperatures with the increase of pressure. There are two possible explanations for the observed results: (i) hydrogen provides surface states which trap the holes, or (ii) hydrogen in InSb acts as donor. The observed Hall coefficient data and the shift in the inversion

Table I.

| Film No. | Figure Caption | Pressure of hydrogen gas in psi | $b = \mu_n/\mu_p$ |
|----------|----------------|---------------------------------|-------------------|
| I | \circ | 0 | 14 |
| II | Δ | 300 | 15 |
| III | \square | 500 | 18 |

temperature can be explained by both (i) and (ii). However, the observed decrease in the mobility of the extrinsic holes in the films exposed to hydrogen suggest that (ii) is more probable.

The value of the intrinsic electron density n_i at the temperature corresponding to peak Hall coefficient is given by

$$n_i = \frac{N_a - N_d}{b - 1} \quad [3]$$

where $N_a - N_d$ is determined from the extrinsic Hall coefficient R_{H2} (N_a and N_d being the concentrations of acceptors and donors, respectively). Assuming that the value b is independent of temperature, the value of n_i at a temperature at which $R_H \rightarrow 0$ can be calculated from Eq. [1]

$$n_i = \frac{N_a - N_d}{b^2 - 1} \quad [4]$$

The values of n_i at other temperatures can also be found by solving Eq. [1] for x . The calculated values of n_i for different films at various temperatures are plotted in Fig. 2 to calculate the bandgap activation energy. The value of the activation energy is found to be 0.28 eV, which is in agreement with the reported value (17).

The variation of the observed mobility μ_H as a function of temperature ($\log \mu_H$ vs. $\log T$) is shown in Fig. 3. The solid line represents the experimental bulk mobility data for a degenerate ($p = 5 \times 10^{17}/\text{sec}$) bulk single crystal. It is observed from the figure that the value of μ_H increases with the increase of temperature, indicating the contribution of some scattering mechanism in which the mobility increases with temperature. The observed Hall mobility μ_H can be expressed as

$$\frac{1}{\mu_H} = \frac{1}{\mu_d} + \frac{1}{\mu_R} \quad [5]$$

where

$$\frac{1}{\mu_R} = \frac{1}{\mu_B} + \frac{1}{\mu_{IIS}} \quad [6]$$

where μ_B is the grain barrier limited mobility, μ_{IIS} the mobility limited by the ionized impurity scattering, and μ_d is the average carrier lattice mobility. Corrected for diffuse scattering it is given by (18)

$$\mu_d = \frac{\mu_1}{1 + \frac{3}{8\gamma}} \quad [7]$$

where μ_1 is the bulk lattice mobility and γ is the ratio

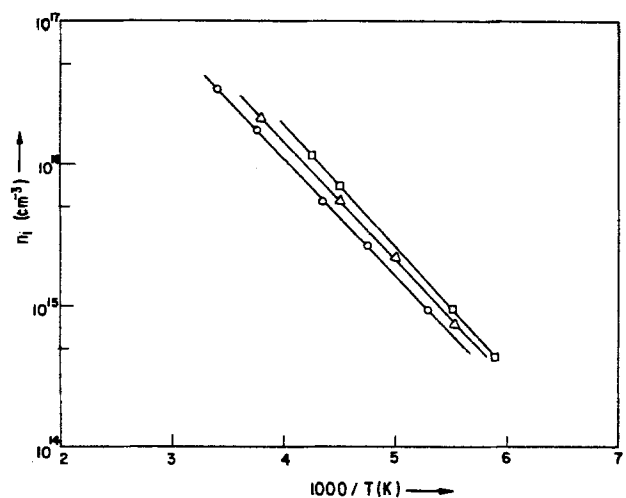


Fig. 2. Electron density n_i as a function of temperature ($\log n_i$ vs. $1/T$): I, $-\circ-$; II, $-\Delta-$; III, $-\square-$.

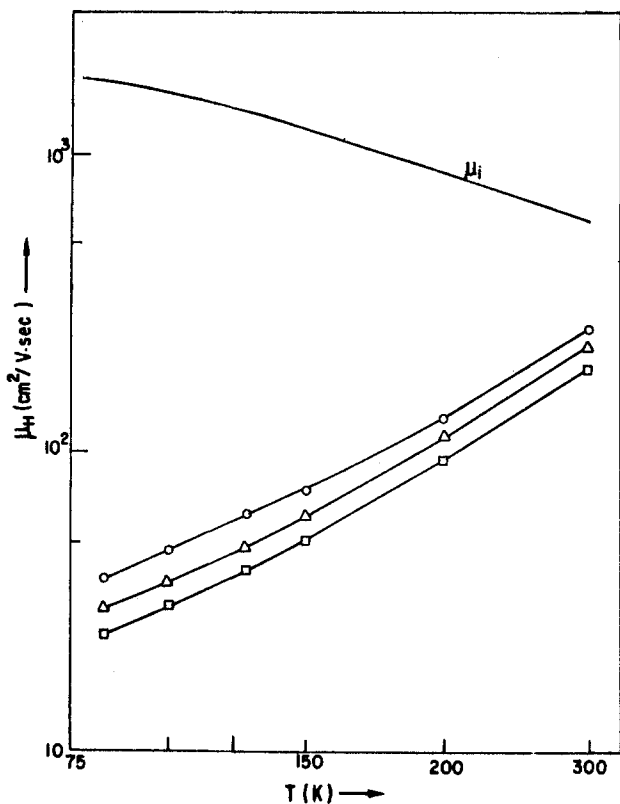


Fig. 3. Variation of Hall mobility μ_H as a function of temperature ($\log \mu_H$ vs. $\log T$): I, \circ —; II, \triangle —; III, \square —. Solid line represents the bulk mobility μ_b .

of film thickness to the mean free path. The contribution of μ_{IIS} to the unexposed film is found to be negligible because, as shown in Fig. 4, the value of μ_R for this film is found to increase exponentially with temperature in accordance with the relation (19)

$$\mu_B = \frac{ev_{th}}{4NKT} \exp\left(\frac{-e\phi}{KT}\right) \quad [8]$$

where v_{th} is the average thermal velocity, N is the number of crystallites per unit length, and ϕ is the magnitude of the grain boundary barrier potential height. The value of ϕ as calculated from Eq. [8] is

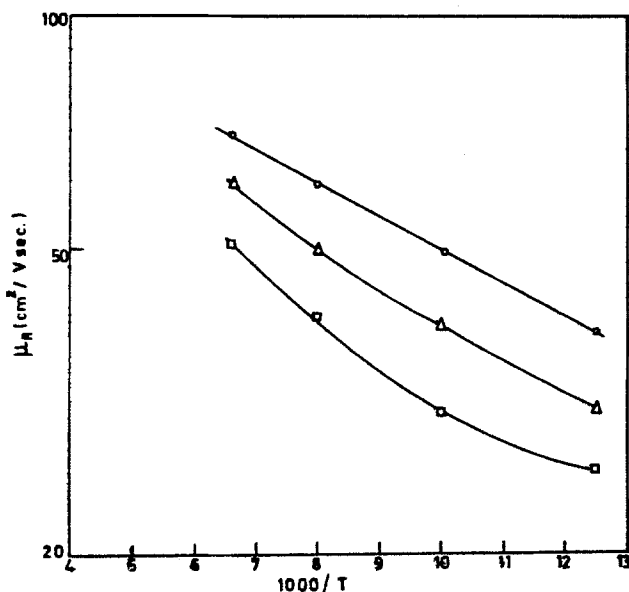


Fig. 4. Variation of remainder mobility μ_R with temperature ($\log \mu_R$ vs. $1/T$): I, \circ —; II, \triangle —; III, \square —.

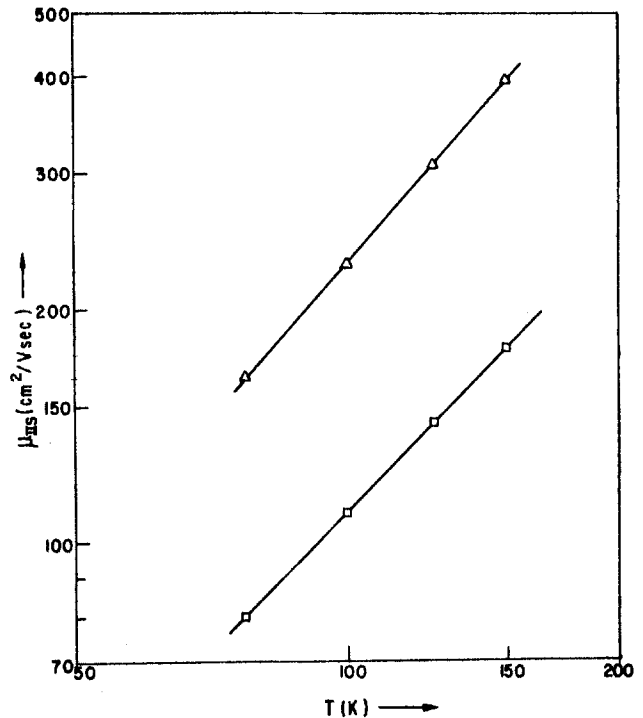


Fig. 5. Mobility limited by ionized impurity scattering μ_{IIS} as a function of temperature ($\log \mu_{IIS}$ vs. $\log T$): II, \triangle —; III, \square —.

found to be ~ 9 meV. On the other hand, for both the exposed films, μ_R shows deviations from exponential behavior which can be due to contribution of the ionized impurity scattering. At any temperature the value of μ_H is found to decrease with the increase of pressure of hydrogen. This explains the increase in the estimated value of b shown in Table I. Assuming the value of μ_B for all the films to be the same (average grain size for all the films is same), the value of μ_{IIS} is estimated as a function of temperature for both the exposed films, and the values are shown in Fig. 5. The values of μ_{IIS} and the slope of $\log \mu_{IIS}$ vs. $\log T$ are found to be smaller for the film exposed to hydrogen gas at higher pressure showing the increase of compensating effects in the films with the increase of pressure of the gas.

It may be mentioned that the observed difference between the temperature variation of μ_R for the unexposed and exposed film can also be due to effect of hydrogen on the grain boundary barrier potential. However, since the $\log \mu_{IIS}$ vs. $\log T$ plots for the exposed films, shown in Fig. 5, are linear (20) with slopes ~ 1.5 , the analysis of the mobility data assuming ϕ to be same for all the films is justified.

Manuscript submitted March 20, 1980; revised manuscript received June 25, 1980.

Any discussion of this paper will appear in a Discussion Section to be published in the June 1982 JOURNAL. All discussions for the June 1982 Discussion Section should be submitted by Feb. 1, 1982.

REFERENCES

1. A. Muller and M. Wilhelm, *Z. Naturforsch. Teil A*, **19**, 254 (1964).
2. H. H. Weider and J. A. Corrol, *J. Appl. Phys.*, **36**, 2321 (1965).
3. N. G. Yaremenko, V. T. Potapov, and V. S. Ivleva, *Sov. Phys. Semicond.*, **6**, 1084 (1974).
4. B. K. Gupta and O. P. Agnihotri, *Philos. Mag. B*, **37**(a), 631 (1978).
5. P. C. Mathur, O. P. Taneja, K. V. Krishna, and A. L. Dawar, *Phys. Status Solidi*, **54**, 391 (1979).
6. A. L. Dawar, O. P. Taneja, K. V. Krishna, and P. C. Mathur, *Thin Solid Films*, **60**, 249 (1979).

7. L. A. Borina, V. P. Masheryakova, V. I. Stafeev, and E. S. Banin, *Sov. Phys. Semicond.*, **7**, 26 (1973).
8. T. Fleisch and R. Abermann, *Thin Solid Films*, **46**, 167 (1977).
9. J. J. Hanser, *Solid State Commun.*, **19**, 1049 (1976).
10. J. P. Hobson and P. A. Redhead, in "Proc. 4th Intern. Vacuum Congr.," **1**, 3 (1968).
11. V. G. Bhide, S. Jatar, and A. C. Rastogi, *Parmana*, **9**, 399 (1977).
12. E. W. Krutz, E. Rieus, and N. Sotnik, *Thin Solid Films*, **42**, 175 (1977).
13. M. Green, Editor, "Solid State Surface Science," Vol. 1, p. 2, Marcel Dekker, New York (1969).
14. B. Dale and G. Scnescse, *J. Appl. Phys.*, **33**, 2526 (1962).
15. J. I. Lue, *J. Phys. E*, **10**, 161 (1977).
16. E. H. Putley, "Hall Effect and Related Phenomena," p. 42, Butterworths, London (1960).
17. E. H. Sondheimer, *Adv. Phys.*, **1**, 1 (1952).
18. O. Madelung and M. Weiss, *Z. Naturforsch. Teil A*, **9**, 527 (1954).
19. M. S. Tyagi, *Phys. Status Solidi A*, **30**, 609 (1975).
20. M. Brooks, *Adv. Electron. Electron. Phys.*, **7**, 156 (1955).

Mechanisms of Plasma-Enhanced Silicon Nitride Deposition Using SiH_4/N_2 Mixture

Haiping Dun, Paihung Pan, Francis R. White, and Richard W. Douse

IBM General Technology Division, Essex Junction, Vermont 05452

ABSTRACT

The mechanism of plasma-enhanced vapor deposition of silicon nitride is studied by varying process parameters, such as substrate temperature, rf power, reactant gas ratio, and total pressure. The film composition (Si, N, O, and H) is determined by electron microprobe and infrared analysis. From these analyses, it is established that the film composition is determined not only by the reactant gas ratio, but also by a combined function of the rf power (W) and total pressure (P) in terms of W^x/P , with x a system-dependent factor. The dependence of film composition on W^x/P can be related to the radical generation processes. The substrate temperature is found to affect the film composition as well. Greater substrate temperature produces films with less hydrogen and more nitrogen, and hence, higher density. The film dielectric property and plasma etching rate are both studied and found to be dependent on the film composition. Finally, a three-step deposition mechanism, namely, radical generation, radical adsorption, and adatom rearrangement, is proposed to explain the reaction scheme, and an ion incorporation mechanism is proposed to explain the change of film physical properties.

Plasma-enhanced chemical vapor deposited (PECVD) silicon nitride film has been widely used as a passivation film in integrated circuit fabrication. The advantages of PECVD silicon nitride are low processing temperatures ($\lesssim 400^\circ\text{C}$), good step coverage, and good passivation for both moisture and sodium ions. Several investigations of PECVD silicon nitride film processing have been reported (1-4). The majority of them use the SiH_4/NH_3 mixture as the reactive gas, since it was found that the SiH_4/N_2 process was less controllable (3). However, the SiH_4/N_2 process has less hydrogen incorporation (5) and a purer source gas. A comprehensive discussion on the deposition of the PECVD silicon-oxygen-nitride films was reported elsewhere (6).

Unlike the conventional chemical vapor deposition (CVD) technique, the PECVD technique should be classified as a highly nonequilibrium reaction process. Gas molecules are mainly dissociated by electron impact to produce very reactive radicals, atoms, and ions in the plasma. These reactive species then condense on the substrate surface to form an amorphous film. As a consequence of the large temperature difference between the impact electron ($\sim 10^5\text{ K}$) and the substrate surface ($\sim 600\text{ K}$) the deposition can be regarded as a quenching process. The incorporated silane radicals are unable to give away their hydrogen due to the low substrate temperature and a hydrogen-containing film results. In addition, since the surface diffusion of adatoms is much retarded, the film normally contains more defects and has a smaller density compared to a

high temperature processed film. A stoichiometric compound is not easily obtained due to this inhomogeneous deposition nature. A better understanding of the plasma state is required to control the film properties. In contrast to the CVD technique, which is controlled by the flow pattern and substrate temperature, a third set of variables dominates the PECVD process. This set of variables, which basically determines the "electron temperature" of the plasma, is rf power and frequency, electrode spacing, gas collision mean free path, and ion diffusivity. In principle, the PECVD process may be related to both the CVD and rf sputtering techniques. The radical generation rate, which is determined by the electron temperature, governs the film stoichiometry. The role played by the ions is still unclear; however, it is believed to be a key factor influencing the film conformity, adhesion, and stress. In this sense, the surface self-biased voltage appears to govern the film properties in terms of physical behavior. Since these parameters are interrelated, the process is difficult to model. A study of each variable, while keeping the rest constant, was performed in order to understand the plasma reaction.

In this paper, we present the results of a study for PECVD silicon nitride deposition using an SiH_4/N_2 gas mixture. The change of film properties is related to variations of process parameters. A better understanding of the reaction kinetics is derived from this investigation.

Experimental

Two LFE Incorporated Model PND-301 reactors were used to deposit all the silicon nitride films. The two reactors, although of the same model, did not give

identical results due to differences in the pumping speed, the rf impedance, and differences in calibration of the flow and pressure monitors. The reaction chamber and the equivalent circuit of the system are sketched in Fig. 1, where a combined LC circuit is used to generate the plasma. For the low power, or high pressure cases, the glow is generated between the gas injecting shower head (G) and the wafer holder (H). At high power, or low pressure, the glow starts to jump above the shower head (G) and eventually occupies most of the quartz bell jar region. The power density (W/cm^3) is drastically changed on the transition between these two modes. During the experiment, we maintained a plasma such that both L and C were excited to avoid any discontinuity in the process.

Reactant gases of SiH_4 (1.5% diluted in Ar) and N_2 were premixed in the flow line and injected through a perforated aluminum shower head to give a uniform flow pattern. When the system vacuum reached 50 mTorr or less, the silane gas was fed into the system and the pressure was recorded. Subsequently, the nitrogen gas was allowed to flow into the system and the total pressure was recorded again. The pressure difference was assigned to be the nitrogen partial pressure. The flow rates were monitored by a Tylan mass flow controller for the silane and a rotameter for the nitrogen. Due to a tendency of the silane flow controller to be clogged, the pressure ratio, instead of the flow ratio, was used for process control methods. This would give a significant error if the pumping speed varied strongly with the pressure. However, since both the silane and total pressures were detected in the same range, the systematic error was expected to be small. This is verified by simultaneously monitoring the gas flows.

Four process parameters, the substrate temperature (T), the rf power (W), the SiH_4/N_2 reactant gas ratio (R), and the total pressure (P), were systematically changed while the rest were held constant. Each experimental condition is listed in Table I. Films of two thicknesses were deposited. Thin films of about 100 nm were deposited over bare silicon wafer for the measurements of refractive index (n), deposition rate (G), and electronic properties.

Thick films of about $1 \mu m$ were deposited over bare silicon or aluminum-coated wafers for the measurements of film composition (% of Si, N, O), hydrogen bonds (Si-H, N-H), and the etch rate (E_r).

The deposition rate and refractive index were simultaneously obtained using an automatic ellipsometer ($\lambda = 632.8 \text{ nm}$). The results for silicon-rich films were not corrected for the absorption component. It was expected that the errors due to absorption for thin films would be small.

The concentrations of Si, H, and O for all samples were measured by the electron microprobe analysis (Applied Research Laboratory Model SEMQ). The CVD silicon nitride ($n = 2.01$) and thermally grown silicon dioxide were used as the standards. The voltage of the incident electron beam was maintained at 5 kV and the beam current was held at $\sim 3 \mu A$. A thin layer

Table I. Deposition process conditions

| Machine No. | T ($^{\circ}C$) ^a | W (W) | R | P (Torr) | Figure |
|-------------|----------------------------------|------------|---------|-------------|-----------------|
| A | 100 ~ 400 | 125 | 0.33 | 1.8 | 2, 3a, b, 7b, 8 |
| A | 300 | 37.5 ~ 325 | 0.33 | 1.8 | 4a, b, 8 |
| B | 300 | 100 | 1 ~ 2.5 | 0.65 | 5a, b |
| B | 300 | 100 | 1 | 0.55 ~ 0.75 | 6a, b |
| B | 300 | 100 | 1 ~ 2.5 | 1.0 | 7a |
| B | 350 | 100 | 1 ~ 2.5 | 0.65 | 9 |

^a Where T is the substrate temperature; W is the rf power; R is the gas ratio between SiH_4 (1.5% diluted in Ar) and N_2 ; and P is the system pressure.

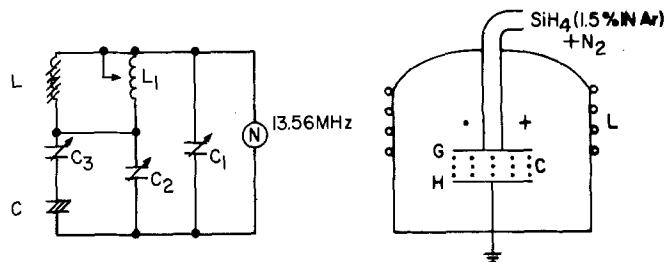


Fig. 1. Schematic of the deposition system and rf circuits

of carbon was evaporated on the film surface to reduce charge effects. The weight percentages of the elements were obtained using the MAGIC IV computer program (7). In this study, the total atomic concentration of Si, N, and O, was not adjusted to achieve 100%. The Si/N ratio, which is usually used as an indication of the film stoichiometry, is refined here to take into account the effect of oxygen, and is written as

$$\frac{Si}{N} \equiv \frac{[Si \text{ atomic } \%]}{[N \text{ atomic } \%] + \frac{2}{3} [O \text{ atomic } \%]}$$

where the factor of 2/3 for the oxygen is used to correct for the bond number. The effect of hydrogen is not included here, however, the Si/N value is used to indicate the amount of "excess silicon" in the film for comparison purpose.

Two infrared techniques were used for hydrogen analysis: the multiple reflection infrared (MRIR) technique (8), and the transmission Fourier transform infrared (FTIR) technique. For the former technique, films deposited over the aluminum-coated substrate were used, while for the latter, films deposited over bare silicon substrates were used. A typical infrared (MRIR) absorption spectra, ranging from 2000 to 3500 cm^{-1} for films deposited at different substrate temperatures, is displayed in Fig. 2, where the absorption peaks are due to N-H stretching bond (3350 cm^{-1}) and Si-H stretching bond (2160 cm^{-1}). For a semiquantitative analysis of the film hydrogen content, the unit areas (UA) of the absorption peaks at 3350 and 2160 cm^{-1} are calculated to represent the content of N-H and Si-H bonds, and the sum of them is used to relate to the total hydrogen content. They are defined as

$$[UA]_{N-H} \equiv 1.4 \times \left[\frac{N-H \text{ bond area}}{\text{film thickness}} \right] \times 100$$

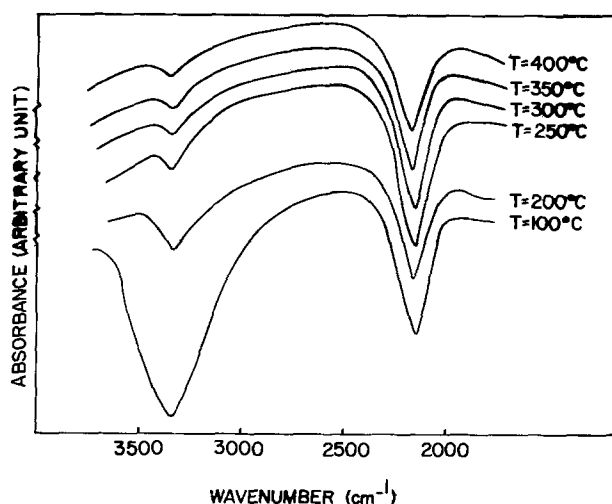


Fig. 2. Multiple reflection infrared absorption spectra ranging from 2000 to 3500 cm^{-1} for samples deposited at different temperatures.

$$[UA]_{Si-H} \equiv \left[\frac{\text{Si-H bond area}}{\text{film thickness}} \right] \times 100$$

$$[UA]_{\text{total H}} \equiv [UA]_{N-H} + [UA]_{Si-H}$$

where the correction factor of 1.4 assigned for the N-H bond was suggested by Lanford and Rand (9). The UA values are normalized to the film thickness instead of the Si-N bond area. This is because the Si-N bond area changes with both the film composition and thickness. The infrared absorption is directly proportional

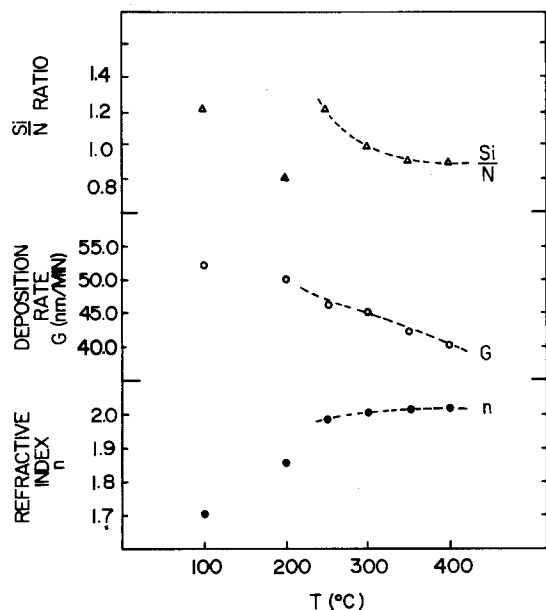


Fig. 3a. Film parameters plotted as a function of substrate temperature. Δ = Silicon nitrogen ratio; \circ = deposition rate; \bullet = refractive index.

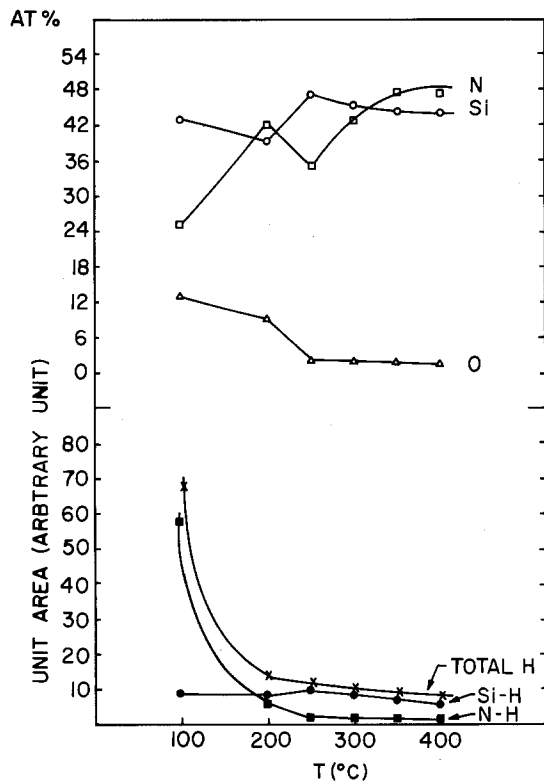


Fig. 3b. Film parameters plotted as a function of substrate temperature. \square = Nitrogen atomic percentage; \circ = silicon atomic percentage; Δ = oxygen atomic percentage; \times = total unit area of hydrogen; \blacksquare = unit area of N-H bond; \bullet = unit area of Si-H bond.

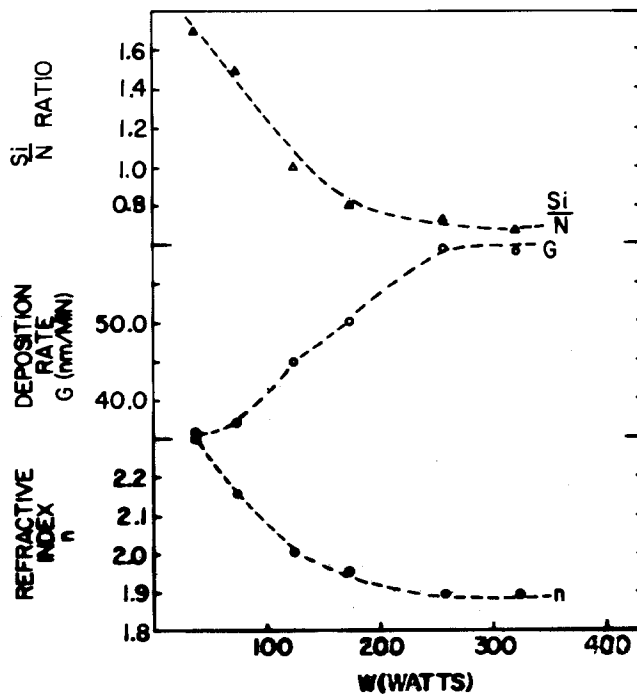


Fig. 4a. Film parameters plotted as a function of rf power. Δ = Silicon-nitrogen ratio; \circ = deposition rate; \bullet = refractive index.

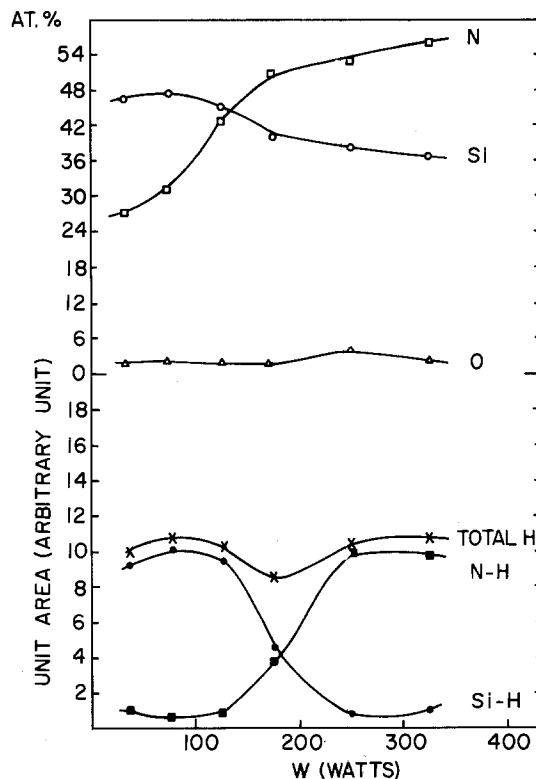


Fig. 4b. Film parameters plotted as a function of rf power. \square = Nitrogen atomic percentage; \circ = silicon atomic percentage; Δ = oxygen atomic percentage; \times = total unit area of hydrogen; \blacksquare = unit area of N-H bond; \bullet = unit area of Si-H bond.

to, and hence, only normalized to, film thickness for the infrared measurement if the detection sensitivity remained unchanged. Since there was no independent calibration for each infrared technique (MRIR and FTIR) that direct comparison between data for the sets of temperature and rf power (Fig. 3b, 4b; MRIR)

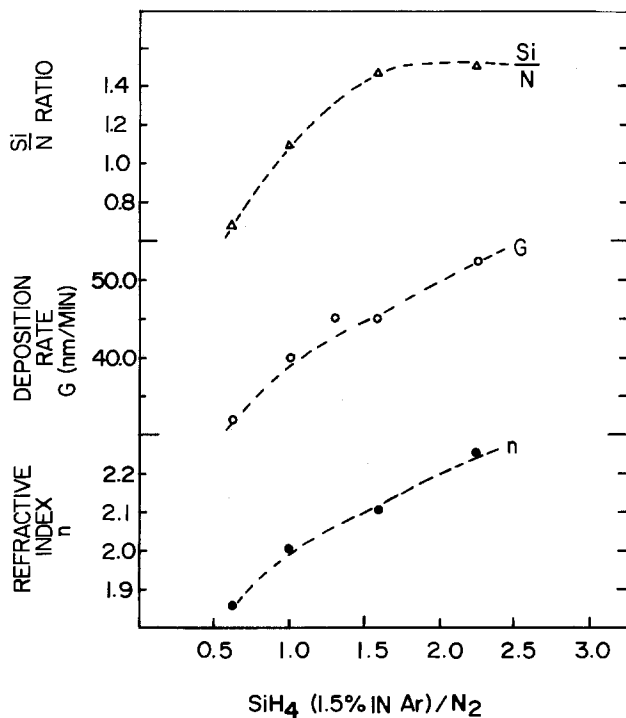


Fig. 5a. Film parameters plotted as a function of reactant gas ratio. Δ = Silicon-nitrogen ratio; \circ = deposition rate; \bullet = refractive index.

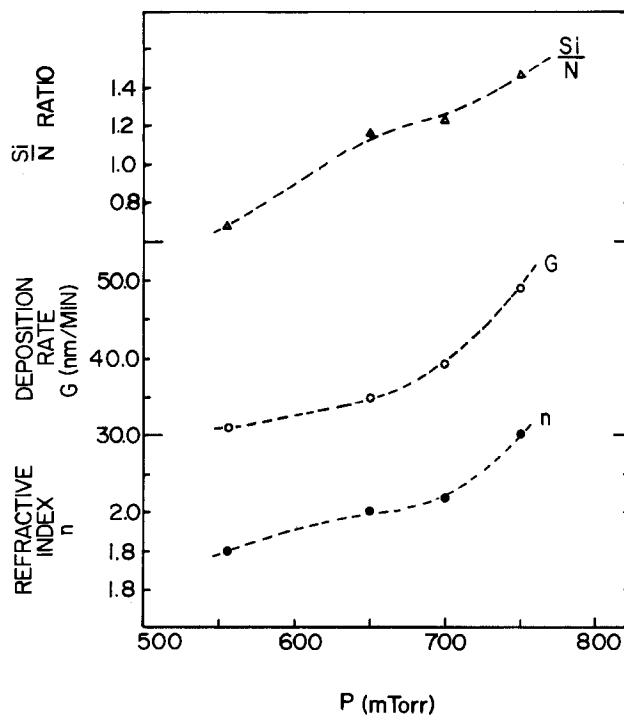


Fig. 6a. Film parameters plotted as a function of total pressure. Δ = Silicon-nitrogen ratio; \circ = deposition rate; \bullet = refractive index.

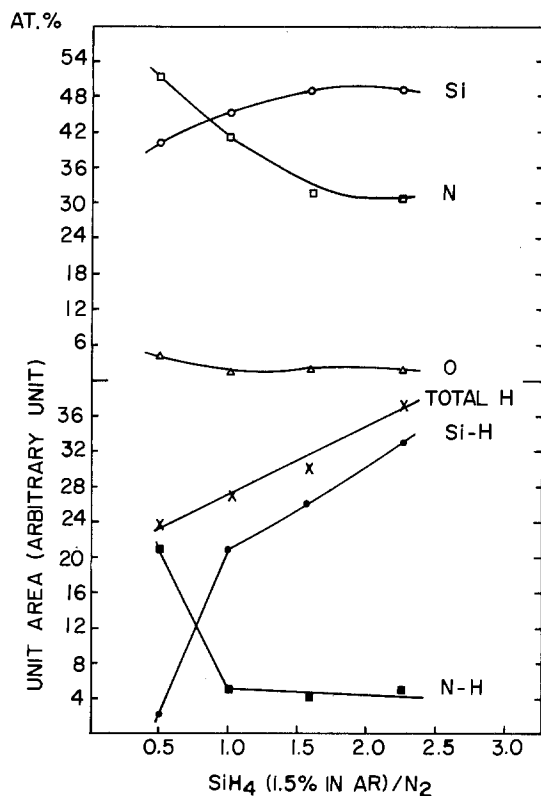


Fig. 5b. Film parameters plotted as a function of the reactant gas ratio. \square = Nitrogen atomic percentage; \circ = silicon atomic percentage; Δ = oxygen atomic percentage; \times = total unit area of hydrogen; \blacksquare = unit area of N-H bond; \bullet = unit area of Si-H bond.

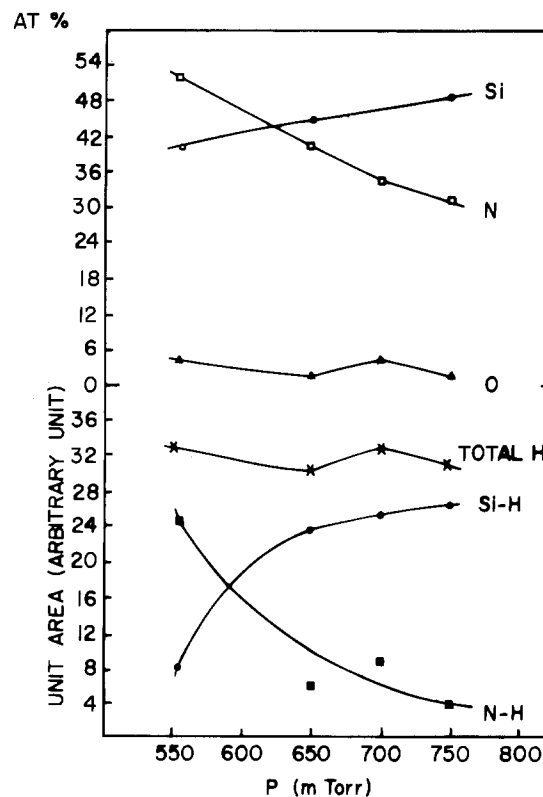


Fig. 6b. Film parameters plotted as a function of total pressure. \square = Nitrogen atomic percentage; \circ = silicon atomic percentage; Δ = oxygen atomic percentage; \times = total unit area of hydrogen; \blacksquare = unit area of N-H bond; \bullet = unit area of Si-H bond.

and the sets of gas ratio and total pressure (Fig. 5b, 6b; FTIR) was not made.

The system used to etch the PECVD silicon nitride samples was a capacitively coupled, barrel plasma reactor with etch tunnel and quartz preheaters.

The etch conditions used were: 86 SCCM total flow, 75°C start temperature, 0.55 Torr, 100W. The gases used

were DE100 and pure CF₄, and the samples were etched one at a time with laser end-point detector.

The film's electrical properties were measured using I-V and breakdown techniques. Aluminum metal dots, 30 mils in diameter, were evaporated over PECVD silicon nitride of thickness ~ 100 nm to form a contact. In order to retain as-deposited film properties, there

is no post contact 400°C forming gas anneal. The film resistivity was obtained from the I-V data measured at a field of 2 MV/cm and room temperature. The film breakdown strength was defined at the field where the current passing through the test dot reached 10 μ A. A computerized automatic breakdown test system was used to find the film average breakdown strength and its statistical mean deviation over a test sample of 50 dots for each film.

Results

The change of film properties as a function of substrate temperature, rf power, reactant gas ratio, and total pressure are expressed in terms of deposition rate (G), refractive index (n), and Si/N value (Fig. 3a, 4a, 5a, 6a), together with the atomic percentages of Si, N, O, and the relative unit area (UA) of Si-H, N-H, and the sum of them (Fig. 3b, 4b, 5b, 6b). A summary of these experimental results is given below.

Substrate temperature (T) effect.—As the substrate temperature is increased from 250° to 400°C, the following results are observed: the deposition rate decreases with a slight increase of the refractive index, the silicon concentration decreases, the nitrogen concentration increases, the amount of oxygen remains unchanged to give a decrease of Si/N ratio (Fig. 3a); the total hydrogen, as well as the Si-H and N-H unit areas, decrease slightly (Fig. 3b). For temperature below 250°C, however, large amounts of oxygen are incorporated, i.e., the oxygen concentration increases from 2 atomic percent (a/o) at $T = 250^\circ\text{C}$ up to 13 a/o at $T = 100^\circ\text{C}$.

The amount of hydrogen, also, increases significantly in this temperature range. Further, it was noticed that the N-H bond UA at $T = 100^\circ\text{C}$ was about 29 times larger than that at $T = 250^\circ\text{C}$, while the Si-H bond UA was nearly unchanged.

The large amount of oxygen incorporated at low temperature is believed to be due to moisture released from the inner wall of the reactor by the plasma. At high substrate temperature, the moisture would be desorbed from the wall as a result of heating prior to deposition.

RF power (W) effect.—As the rf power is increased, the deposition rate is increased and the refractive index is decreased. The silicon concentration decreased and the nitrogen concentration increased to give a decrease in the Si/N value (Fig. 4a). The hydrogen UA is relatively constant with the change of rf power, except for a minimum at 175W. The relative UA of Si-H and N-H, however, switches from the low power case to high power case (Fig. 4b). The oxygen concentration stays constant. The O-H bond peak at 3650 cm^{-1} , as detected from infrared analysis, was observed for the lowest power case (37.5W). All evidence indicates the increase of nitrogen radicals with rf power.

Reactive gas ratio (R) effect.—As the SiH_4 (1.5% diluted in Ar) flow is increased to give a high value of $R (= \text{SiH}_4 [\text{in Ar}]/\text{N}_2)$, the deposition rate, refractive index, and Si/N ratio increased as expected. The silicon atomic percent increased, the nitrogen atomic percent decreased, while the oxygen remained nearly constant (Fig. 5a). The infrared data showed an increase of the Si-H bonds. The cause for the abrupt change in Si-H, N-H, and oxygen atomic percent for sample with $R = 0.76$ is not clear (Fig. 5b).

Total pressure (P) effect.—As total pressure increased, the deposition rate, refractive index, and the silicon atomic percent increased, while the nitrogen atomic percent decreased to give an increase of Si/N value (Fig. 6a). The Si-H bonds increased, the N-H bonds decreased, and the total UA of hydrogen remained nearly constant (Fig. 6b). At $P = 0.7$ Torr, the oxygen atomic percent showed a "bump" with a cor-

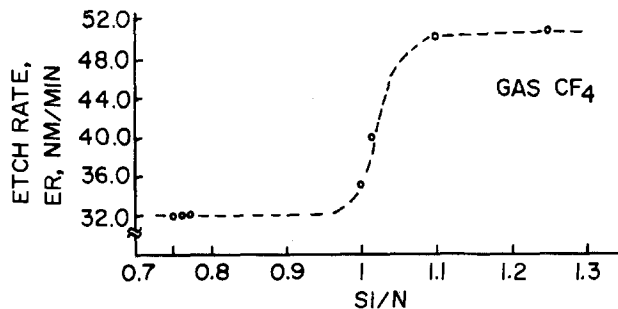


Fig. 7a. Etch rate plotted as a function of silicon-nitrogen ratio using pure CF_4 etching gas.

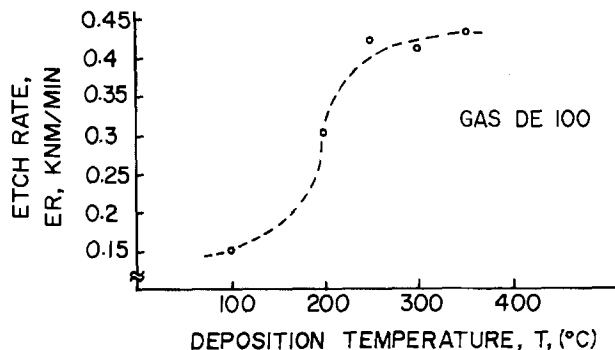


Fig. 7b. Etch rate plotted as a function of deposition substrate temperature using $\text{CF}_4 + 8\% \text{O}_2$ etching gases.

responding "bump" in the N-H bonds. This associated increase of the N-H bonds with the amount of oxygen was also observed for the previous figures (Fig. 3b, 4b, 5b). It appeared to be due to an oxygen-enhanced dissociation of the nitrogen molecules in the plasma.

The plasma etching study results are plotted in Fig. 7a and b. It was found that N_2 purge prior to deposition had no appreciable effect on either the etch rate (E_r), or the amount of oxygen incorporated into the films. However, when oxygen was purposely incorporated into the film by adding O_2 gas into the plasma during deposition, the etch rate decreased. The Si/N ratio of the films affects the etch rate with the silicon-rich films etching faster as seen in Fig. 7a. The break point occurs at an Si/N ratio between 1.0 and 1.1. Figure 7b shows etch rate for films deposited at different substrate temperatures. At temperatures above 250°C, little change in E_r is observed. For temperatures below 250°C, the etch rate decreases with decreasing temperature, which corresponds to an increase of the oxygen concentration in the films as previously discussed. Films processed at different rf powers were also studied as a function of etch rate, however, no conclusions could be drawn.

A sample processed at high pressure (>2 Torr) was etched and showed a radially dependent etch rate. The center of the wafer etched about 4 times faster than the edges indicating that the center had a higher silicon concentration. This can be explained from the following point of view. For the high pressure case, the center of the plasma was close to an arcing condition such that a low voltage, high current plasma was established. Meanwhile, the edge was still in the uniform glow condition such that a higher voltage plasma was maintained. This would result in a film more silicon rich at the center relative to the edge.

In this study, the resistivity (ρ), and the average breakdown strength (E_B) were measured. As shown in Fig. 8, the resistivity, which was measured at room temperature with an applied field of 2 MV/cm, increases from $10^7 \Omega\text{-cm}$ up to $10^{14} \Omega\text{-cm}$ as the Si/N ratio decreases from 1.6 down to 0.8. These samples

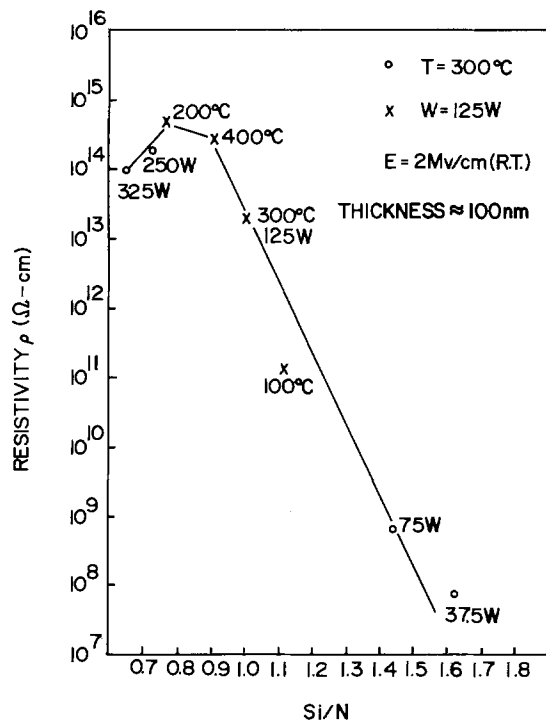


Fig. 8. The film resistivity measured at room temperature with a field of 2 mV/cm plotted as a function of Si/N ratio. \circ = Changing the rf power and fixing the substrate temperature at 300°C; \times = changing the substrate temperature and fixing the rf power at 125W.

were either processed at different substrate temperature or rf power. The exponential decrease of the resistivity vs. Si/N ratio is consistent with the earlier observation of Sinha and Smith (10), although, in their case, SiH_4 and NH_3 were used as the reactants. By changing the gas ratio only, another set of films of different index were deposited to test for breakdown strength. Figure 9 shows the average breakdown strength as a function of the refractive index. The error bar for each data point represents the statistical mean deviation of breakdown strength of 50 tested data across the wafer. The deviation expresses the degree of inhomogeneity of the film. Based on the results of Fig. 8 and 9, it is concluded that the near-stoichiometric film has the best dielectric properties, i.e., minimum leakage and largest breakdown strength.

The resistivity of the best PECVD silicon nitride film obtained, however, is still much lower than the conventional CVD silicon nitride film. Figure 10 illustrates a comparison of the log I - $V^{1/2}$ behavior of one of the PECVD films ($n = 1.95$, Si/N \approx 0.8) with the CVD silicon nitride films reported in the literature (11, 12). The PECVD film, resembling the conventional CVD films, follows the Poole-Frenkel conduction behavior. The slope gives a dielectric constant of 5.7 which is close to that of CVD films. The intercept of the slope, which corresponds to the pre-exponential term, however, is orders of magnitude larger than that obtained for CVD films. This indicates the PECVD film has either a greater amount of traps and/or a shallower trapping level. The result is conceivable since a larger defect concentration is expected to exist in the PECVD silicon nitride film due to the low processing temperature and the great amount of hydrogen in the film.

Discussion

In order to explain the experimental observations, we divided the deposition into three kinetic steps, namely, radical and ion generation in the plasma; radical adsorption and ion incorporation onto the film surface; and surface adatom rearrangement.

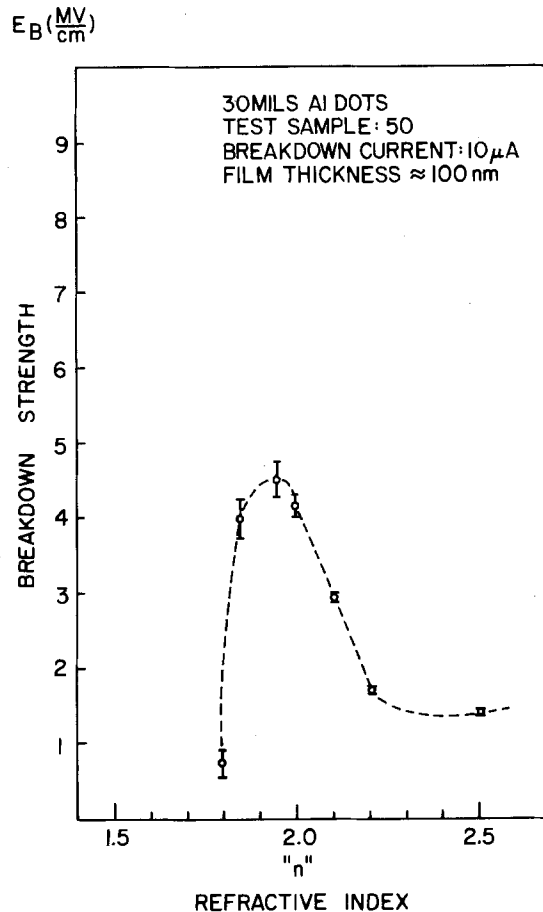


Fig. 9. The average breakdown strength plotted as a function of film refractive index. The error bar represents the statistical mean deviation of the measurements over 50 test dots.

Radical and ion generation.—The dissociation and ionization of gas molecules in a glow discharge are mainly produced by electron impact. Since the dissociation energy is lower than the ionization energy for many gas molecules, the generation rate for radicals is generally greater than that for ions. Positive ions will drift toward the negatively biased surface and recombine with electrons in the vicinity of, or at the wall surface, while neutral radicals may still stay in the plasma and have a longer lifetime. These two effects make the radical concentration higher than that of its ion form. Hence we believe neutral radicals form the major deposition agents.

In order to describe the gas dissociation mechanism, the concept of "electron temperature" is applied. The treatment is similar to that used by Reinberg (6) in the deposition of silicon-oxygen-nitride. The probability of molecules to be dissociated by electron impact can be calculated from the molecular dissociation energy, the electron energy distribution function, and the effective collision cross section (13, 14). With a very crude approximation it is proportional to $e^{-\Delta E/kT_e}$, where ΔE is the dissociation energy, T_e is the electron temperature, and k is the Boltzmann constant. Here the electron is assumed to be a Maxwellian gas. Since the molecular dissociation energy is closely related to its bond energy, the latter can be used to estimate the probability of dissociation without going into detailed calculations.

On increasing the electron temperature, gas species with a greater dissociation energy will undergo a greater change in radical concentration than species with lower dissociation energy. This change of radical ratio will result in a change of film composition. For the case of nitrogen and silane, the former has a bond energy of 9.9 eV and the latter has a bond energy of 3.1 eV (15), increasing the electron temperature will

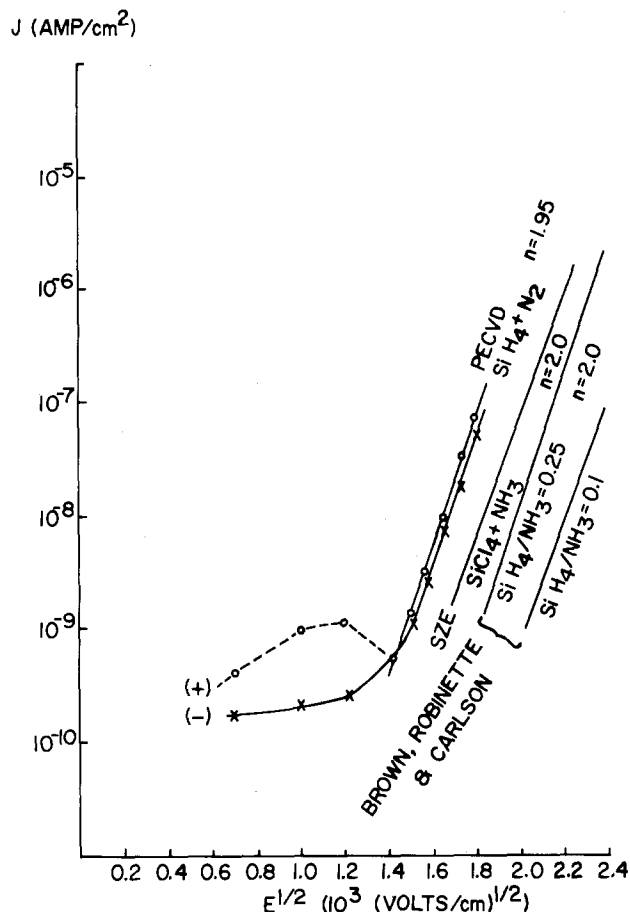


Fig. 10. The comparison of leakage current vs. field strength between PECVD silicide nitride and conventional CVD silicon nitride.

increase the radical ratio between nitrogen and silane, i.e., N/SiH_3 , to give a film of greater N/Si ratio. This explains the experimental observations in Fig. 4a and 6a, i.e., the Si/N ratio is decreased by either increasing the rf power or decreasing the total pressure. Both will increase the electron temperature, a fact which is discussed later. For the case of ammonia and silane, the difference of dissociation energies is small. Hence, one would expect SiH_4/NH_3 process to be more controllable than SiH_4/N_2 process.

As mentioned in the beginning of this paper, the change of electron temperature in a high frequency plasma is a combination of many variables. It is well documented in the literature (16) that the plasma state could be defined in terms of three sets of parameters, i.e., E/P , P/ω , P/d , where E is the rf field strength, P is the pressure, ω is the rf frequency, and d is the electrode spacing. The first set of variables determines the ionization coefficient and the electron temperature. The second set of variables determines the frequency effect. The last set of variables is the high frequency Paschen's law which specifies the geometric effect. When the rf frequency and electrode spacing are fixed, the electron temperature for a specific gas will be solely determined by E/P . The value of E/P can be transformed into the form of W^x/P , where W is the rf power, and x is a system dependent factor which relates rf power to the peak-to-peak rf field strength. In our system, the rf frequency is 13.56 MHz, which falls in between the ion collision frequency and electron collision frequency, it is found that the rf field increases with rf power (i.e., $x > 0$). Hence it is clear that increasing the rf power or decreasing the total pressure will result in the increasing of electron temperature. Other evidences for the increase in electron temperature with W^x/P are that a brighter glow color is observed and an increased NH bond is found in the film

(Fig. 4b, 6b). The increase of NH bond in the film suggests more nitrogen radicals are generated in the plasma. A subsequent radical reaction in the plasma ($N + H \rightarrow NH + \text{light}$) or more likely a surface recombination of adsorbed nitrogen and hydrogen adatoms yields more NH incorporation. The generation of ammonia radicals at high rf power was predicted by Reinberg (6) and should be avoided to minimize hydrogen incorporation.

Radical adsorption and ion incorporation.—This kinetic step deals with the plasma-surface interaction. The deposition surface, which is under electron and ion bombardment and u.v. irradiation, can provide many active sites for radical adsorption. Since radicals are highly reactive, they tend to be adsorbed on a colder surface readily. By maintaining a constant plasma state and only changing the substrate temperature, a change of Si/N ratio in the film was observed (Fig. 3). This indicates there is a possible preference of radical adsorption in favor of nitrogen radical and disfavor of silane radical at higher surface temperature. Moreover, a huge increase of NH bond at low substrate temperature may also reflect some preference of the NH radical adsorption at this temperature range. This latter observation, however, is complicated by the existence of large amounts of oxygen in the film.

The ion-surface interaction is strongly influenced by the surface d-c field and probably weakly dependent on surface temperature. The substrate can be self-biased in an rf plasma due to the difference of electron and ion mobility (17). The self-biased voltage across the substrate is determined by the rf peak-to-peak voltage, the area ratio of the counterelectrode geometry surrounding the plasma, and the external circuit connection (18-20). A direct measurement of the d-c voltage between the plasma and the substrate is not performed in our system. However, we believe large biased voltage can be developed during deposition because the rf power density is high and the substrate is surrounded by a confined geometry.

An independent study of the film stress vs. the rf power (21) showed that films produced in our system became more compressive at a greater power level. The measured stress almost changed linearly with rf power from 1×10^9 dyne/cm² tensile at 50W to 5.5×10^9 dyne/cm² compressive at 300W with the rest of the process variables kept constant ($T = 350^\circ\text{C}$, $R = 1$, $P = 0.65$ Torr). This is in agreement with that of Sinha *et al.* (2), although we use SiH_4/N_2 mixture and our films generally tend to be more compressive. It was also found that the scratching resistance of the deposited film increased with rf power. Ion-surface interaction is believed to play a major role here in determining the film physical properties.

The influence of substrate bias upon the quality of sputtered film has been studied (22). The increase of density and decrease of resistivity with substrate bias were observed for the sputtering of metal films (23, 24). It was also reported that an improvement in film quality and better edge coverage could be obtained by applying a substrate bias for rf sputtered quartz (25). The explanation is based on the substrate resputtering mechanism. Contaminants and poorly adherent spots of the film are resputtered during deposition to give a denser film. The resputtered material will deposit on the side wall to provide a better edge coverage. This mechanism can be extended to some degree to explain the change of density with rf power (2), a better adhesion, and a better edge coverage (26) observed for the PECVD films.

The change of film stress is, however, more likely caused by positive ion incorporation. The phenomenon of ion incorporation into the sputtered film such as Ar and N_2 were reported (27, 28). For the PECVD process, the operating pressure is much higher than for the

rf sputtering process and the substrate bias voltage is normally low ($\lesssim 50\text{V}$). Hence, the resputtering and ion bombardment effect is expected to be reduced. It is, therefore, unlikely for those nonbonding ions such as Ar^+ or N_2^+ to be implanted into the film to change its stress. However, the incorporation of some bonding ions such as H^+ or N^+ , which are the building block of the film, can be promoted by a low surface field since these ions will probably have a large sticking coefficient.

This argument helps to explain the observed switch of Si-H and N-H bond concentrations at great rf power and low pressure. At a greater electron temperature, the silane would give up more hydrogen to produce more H^+ in the plasma and less Si-H bond in the film. The generation of N^+ ion was increased and a more negatively biased surface field was induced as a consequence of greater electron energy and density. Thus, there were more H^+ and N^+ ions incorporated into the film to produce more N-H bond. Although the production of N-H bond in the plasma was also possible, the chance was smaller compared to the surface recombination since a three body collision process was required. Similar observation for the field-promoted ion incorporation was also reported for the glow discharge produced amorphous silicon (29), where the incorporation of hydrogen was found to be enhanced or depleted depending on whether a negative or a positive d-c field was applied to the system.

This "field-promoted deposition," which is similar to the ion-assisted etching (30) case, results in a vertical incoming mass flux toward the substrate. Due to this additional ion flux, the film will relax in a lateral fashion to change the stress toward more compressive. This appears to explain the observed stress change with rf power even though the Si/N ratio remains relatively unchanged. A low frequency ($\sim 50\text{ kHz}$) tool was reported to produce film of compressive stress (31). At this low frequency range, which is lower than the ion collision frequency ($\sim 100\text{ kHz}$), the rf plasma resembles the d-c case. A much higher plate voltage is required to generate a plasma to overcome the ion shielding due to space charge around the plates. As a consequence of external circuit arrangement, a high substrate bias voltage is produced (20). This explains why the films produced in the tool were always in compressive stress.

Adatom rearrangement.—The last step of deposition is for adatoms bonded to each other to form a continuous film. The adsorbed radical has to diffuse into a stable site to become part of the growing film. This film stabilization mechanism is strongly influenced by substrate temperature. As the substrate temperature is increased, the surface adatom gains more energy to diffuse to a stable site faster. The film, thus obtained, will have better quality. The release of hydrogen from the incorporated SiH and NH bonds will also be promoted by substrate heating (Fig. 3b). Therefore, the film density increases with substrate temperature. Since a porous film gives a low refractive index (32) the increase of refractive index with substrate temperature agrees with the density trend (Fig. 3a). This observation is, however, inconsistent with the chemical analysis which shows a decreased Si/N value with temperature. Normally a large Si/N value (>0.8) will give a large refractive index (>2.0) due to more absorptive Si-Si bonds in the film such as shown in Fig. 4a, 5a, and 6a. In Fig. 3a, however, the large Si/N value for low temperature processed film gives an unexpected low refractive index. This indicates that the excess silicon exists mainly in the form of Si-H bond instead of the Si-Si. Thus, the density effect overshadows the Si/N effect, and gives a low refractive index at low substrate temperature.

Conclusions

PECVD silicon nitride deposition, using the SiH_4/N_2 gas mixture has been investigated. Film composition, i.e., percent of Si, N, O, and H, has been found to be sensitively dependent on the process parameters such as substrate temperature, rf power, total pressure, and reactive gas ratio. The plasma etch rate and dielectric properties are studied and found to be influenced by the film composition as well.

The complex deposition process is divided into three kinetic steps, i.e., radical generation, radical adsorption, and adatom rearrangement, to explain the observed change of film chemical and physical properties. The concentration change of silicon and nitrogen with rf power and total pressure is believed to be due to a change in the electron temperature. A combined function of rf power and total pressure, to be expressed as (W^x/P) , influences the electron temperature, and hence the film composition. In both the high power and low pressure cases, the film tends to be less "silicon rich."

The change of hydrogen total content is affected by substrate temperature. However, the change of rf power and total pressure influences the hydrogen incorporation in the form of SiH or NH bond.

Acknowledgments

We acknowledge the constant encouragement and support of E. E. Gardner and P. C. Velasquez during the course of this study. Discussions and suggestions of the film stress phenomenon from G. Schwartz are highly appreciated. Thanks are also given to H. Geipel and N. Hsieh for help in measurements and interpretation of electrical properties, to B. Gleason and W. Natter for the infrared measurements, and to C. Kroll and R. Mohler for technical assistance. Finally, the critical review of the manuscript by R. Silverman is deeply appreciated.

Manuscript submitted Oct. 12, 1980; revised manuscript received Feb. 18, 1981.

Any discussion of this paper will appear in a Discussion Section to be published in the June 1982 JOURNAL. All discussions for the June 1982 Discussion Section should be submitted by Feb. 1, 1982.

Publication costs of this article were assisted by IBM Corporation.

REFERENCES

1. R. Gereth and W. Scherber, *This Journal*, **119**, 1248 (1972).
2. A. K. Sinha, H. J. Levinstein, T. E. Smith, G. Santana, and S. E. Haszko, *ibid.*, **125**, 601 (1978).
3. R. S. Rosler, W. C. Benzing, and J. Baldo, *Solid State Technol.*, **19**, (6), 45 (1976).
4. H. J. Stein, V. A. Wells, and R. E. Hampy, *This Journal*, **126**, 1750 (1979).
5. P. S. Burggraaf, *Semiconductor Int.*, **3**, 23 (March 1980).
6. A. R. Reinberg, *J. Electron. Mater.*, **8**, 345 (1979).
7. J. W. Colby, in Proc. of 6th National Conference on Electron Probe Analysis, Paper 17, Pittsburgh, PA (1971).
8. See for example, H. J. Stein and H. A. R. Wegner, *This Journal*, **124**, 908 (1977).
9. W. A. Lanford and M. J. Rand, *J. Appl. Phys.*, **49**, 2473 (1978).
10. A. K. Sinha and T. E. Smith, *ibid.*, **49**, 2756 (1978).
11. G. A. Brown, W. C. Robineete, Jr., and H. G. Carlson, *This Journal*, **115**, 948 (1968).
12. S. M. Sze, *J. Appl. Phys.*, **38**, 2951 (1967).
13. F. Kaufman, in "Chemical Reactions in Electrical Discharges," R. F. Gould, Editor, Chap. 3, p. 29, "Advances in Chemistry Series 80," American Chemical Society (1969).
14. A. T. Bell, in "Techniques and Applications of Plasma Chemistry," J. R. Hollahan and A. T. Bell, Editors, Chap. 1, p. 1, John Wiley & Sons, New York (1974).
15. R. C. Weast, Editor, "Handbook of Chemistry and

- Physics," p. F-223, 57th ed., CRC Press, Cleveland, Ohio (1977).
16. S. C. Brown, "Introduction to Electrical Discharges," Chap. 10, p. 169, John Wiley & Sons, Inc., New York (1966).
 17. G. S. Anderson, W. N. Mayer, and G. K. Wehner, *J. Appl. Phys.*, **33**, 2991 (1962).
 18. J. W. Coburn and E. Kay, *ibid.*, **43**, 4965 (1972).
 19. H. R. Koenig and L. I. Maissel, *IBM J. Res. Dev.*, **14**, 276 (1970).
 20. J. L. Vossen, *This Journal*, **126**, 319 (1979).
 21. G. Schwartz, Private communication.
 22. J. L. Vossen, *J. Vac. Sci. Technol.*, **8**, 512 (1971).
 23. J. J. Cuomo, R. J. Gambino, and R. Rosenberg, *ibid.*, **11**, 34 (1974).
 24. H. C. Cook, *ibid.*, **4**, 80 (1967).
 25. J. S. Logan, F. S. Maddocks, and P. D. Davidge, *IBM J. Res. Dev.*, **14**, 182 (1970).
 26. B. Mattson, *Solid State Technol.*, **23** (1), 60 (1980).
 27. G. C. Schwargz and R. E. Jones, *IBM J. Res. Dev.*, **14**, 52 (1970).
 28. E. Kay and H. F. Winters, in *Trans. Int. Vac. Congr. 3rd, Stuttgart*, 2 pt. 2, 3, and 1 (1967).
 29. H. Okamoto, T. Yamaguchi, Y. Nitta, and Y. Hamakawa, *J. Non-Crystalline Solids*, **35** and **36**, 201 (1980).
 30. J. Coburn and H. Winter, *J. Appl. Phys.*, **50**, 3189 (1979).
 31. J. R. Hollahan, M. T. Wauk, and R. S. Rosler, in "Chemical Vapor Deposition," L. F. Donaghey, P. Rai-Choudhury, and R. N. Tauber, Editors, p. 224, The Electrochemical Society Softbound Proceedings Series, Princeton, N.J. (1977).
 32. W. A. Pliskin, *J. Vac. Sci. Technol.*, **14**, 1064 (1977).

Vapor Phase Epitaxial Growth of ZnSiAs₂ on Ge and GaAs Substrates

J. E. Andrews*

Research Triangle Institute, Research Triangle Park, North Carolina 27709

H. H. Stadelmaier and M. A. Littlejohn

North Carolina State University, Raleigh, North Carolina 27650

and J. Comas

Naval Research Laboratories, Washington, D.C. 20375

ABSTRACT

The growth conditions required to epitaxially synthesize the tetragonal chalcopyrite semiconductor ZnSiAs₂ on cubic Ge and GaAs substrates are described. Some structural and electrical properties of the resulting epitaxial layers are reported. The routine unique epitaxial growth of (001) ZnSiAs₂ on (100) substrates of Ge and GaAs, in preference to the (100) or (010) ZnSiAs₂ orientations, has been demonstrated. Growth conditions have also been identified that have led to mixtures of the (010) and (001) orientations of ZnSiAs₂ on these (100) cubic substrates. The use of GaAs substrates has led to an autodoping problem similar to that observed for GaAs grown on Ge.

In a previous publication (1), the first successful synthesis of the tetragonal chalcopyrite ZnSiAs₂ by the open-tube chemical vapor deposition (CVD) process was reported. The II-IV-V₂ chalcopyrites are considered to be ternary analogs of the III-V compounds (2), and thus have several potential device applications. This work with ZnSiAs₂ has been primarily oriented toward the investigation of the chalcopyrite semiconductors for solar cells.

In the previous work the as-grown layers were either completely polycrystalline or were polycrystal with preferred orientations, exhibited p-type conductivity, and could be grown in this form on a variety of substrates. Other previous work on the open-tube vapor phase growth of the chalcopyrite ZnSiP₂ also resulted in nonepitaxial growth (3). In this paper the growth conditions which have led to the unique epitaxial deposition of ZnSiAs₂ on the cubic semiconductors Ge and GaAs by CVD are described. These substrate materials provide a good lattice match to ZnSiAs₂. By using CVD in an open-flow system the routine deposition of (001) ZnSiAs₂ with good surface morphology on (100) substrates of both Ge and GaAs has been achieved. This particular growth occurs in preference to the nuclea-

tion of either the (100) or (010) orientations of ZnSiAs₂ for a well-defined range of growth conditions in the growth system used in this work. Furthermore, the reactor growth conditions which result in crystallographic mixtures of the (010) and (001) orientations of ZnSiAs₂ on (100) Ge and GaAs have been identified. Such conditions of "mixed epitaxy," which can occur in deference to "unique epitaxy," require careful evaluation and understanding for the epitaxial growth of the tetragonal chalcopyrite semiconductors.

In the course of study of the reactor growth conditions an n-type phase of the ZnSiAs₂ chalcopyrite was observed. Previous work has indicated that bulk ZnSiAs₂ is inherently a p-type semiconductor (2, 4), although conversion to n-type conductivity has been reported using an arsenic annealing process following bulk crystal growth (5, 6). The interest in characterizing the electrical properties of both the p- and n-type ZnSiAs₂ led to the use of chromium-doped semi-insulating GaAs substrates for electrical isolation of the epitaxial layer from the substrate. The use of GaAs (Cr) has resulted in the identification of what appears to be an autodoping effect involving the outdiffusion of Ga from the substrate into the epitaxial layer. This problem was studied by secondary ion mass spectrometry (SIMS).

* Electrochemical Society Active Member.

Key words: chalcopyrites, II-IV-V₂ semiconductors, SIMS, autodoping.

Materials Synthesis

The details of the horizontal reactor and the reactant distribution system used for the CVD of ZnSiAs_2 have been previously described (1). The growth system employs elemental Zn, SiH_4 , and AsH_3 as reactants with H_2 as the carrier gas. The Zn is transported into the deposition region through physical evaporation from a Zn melt maintained at 610°C into a flowing H_2 carrier gas stream. The SiH_4 and AsH_3 reactants enter the reactor downstream from the Zn source, and the overall reaction is controlled primarily through the pyrolysis of SiH_4 which is apparently catalyzed by the presence of the Zn vapor. The film growth rate is linearly dependent on the SiH_4 flow rate for a range of growth conditions required for epitaxial growth, and these conditions will be subsequently discussed.

The Ge substrates were obtained from the vendor¹ chemically polished and ready for use. The GaAs substrates were purchased² either polished or as-sawn, depending on the availability of polished substrates. The unpolished GaAs was polished chemically, using an $\text{Na}_2\text{CO}_3/\text{NaOCl}/\text{H}_2\text{O}$ solution which was followed by an $\text{NaOCl}/\text{H}_2\text{O}$ solution. The results to be described here were obtained primarily on Ge and GaAs substrates with (100) orientations. These Ge substrates were n-type arsenic-doped crystals having a room temperature electron concentration of nominally 10^{18} cm^{-3} . The GaAs substrates were n-type undoped crystals with a nominal electron concentration of $7 \times 10^{16} \text{ cm}^{-3}$. In addition, work has been conducted using Cr-doped semi-insulating GaAs substrates to facilitate Hall effect measurements on both the p-type and n-type ZnSiAs_2 deposits. Some experiments have been carried out using p-type Ge and GaAs substrates, and other substrate orientations have also been investigated. Preliminary work using (111)-oriented substrates has been carried out for both Ge and GaAs, and results were obtained for GaAs substrates which have been misoriented between 2° to 3° from the (100) to the (110) orientation.

In the standard growth sequence, the substrates are brought to the growth temperature and the reactant flows are initiated and terminated simultaneously. Following deposition at the growth temperature of approximately 650°C , the substrates are then cooled to near room temperature at a rate of $50^\circ\text{C}/\text{min}$ and removed from the reactor. Epitaxial growth was achieved on clean prepolished substrates without *in situ* HCl vapor etching prior to deposition.

General Results

The growth temperature for the synthesis of ZnSiAs_2 by CVD was found to be above approximately 600°C in order to prevent the formation of second-phase structures of Zn_3As_2 and ZnAs_2 , and to be below about 700°C to prevent the thermal decomposition of ZnSiAs_2 which generally led to an Si-rich phase (1). Through careful systematic study of the growth conditions, we have consistently and routinely achieved unique epitaxial growth of ZnSiAs_2 in the temperature range of 650°C - 670°C . The range of these growth conditions for the reactor described in Ref. (1) are stated in Table I.

These conditions result in epitaxial growth of (001) ZnSiAs_2 on (100) substrates of both Ge and GaAs. While less extensive experimentation has been carried out on (111) substrates, the general conditions in Table I have also led to epitaxial growth on this substrate orientation. Surface morphology on (100) Ge and GaAs substrates has varied from a dull gray to a metallic-mirrorlike finish. However, it has been more difficult to routinely achieve the mirrorlike morphology. Figure 1a illustrates the surface morphology, and for comparison Fig. 1b shows a micrograph of a polycrystalline

Table I. Epitaxial growth conditions for ZnSiAs_2

| |
|---|
| 650°-670°C growth temperature |
| 3.8-5.0 sccm Zn |
| 6.5-8.0 sccm SiH_4 |
| 6.5-10 sccm AsH_3 |
| Total flow rate — 4400 sccm |
| (Balance of gas flow was H_2) |

deposit obtained at different growth conditions. The layers crystallized in the chalcopyrite structure with lattice constants measured by x-ray diffraction of $a = 5.60\text{Å}$ and $c = 10.88\text{Å}$, in agreement with other published values (2).

In experiments using high SiH_4 -to-Zn vapor ratios (greater than 4/1 SiH_4/Zn flow rates) n-type deposits were identified by thermal probing of layers grown on Ge substrates. These n-type layers were initially identified in experiments which were intended to study and extend the deposition region in the reactor.

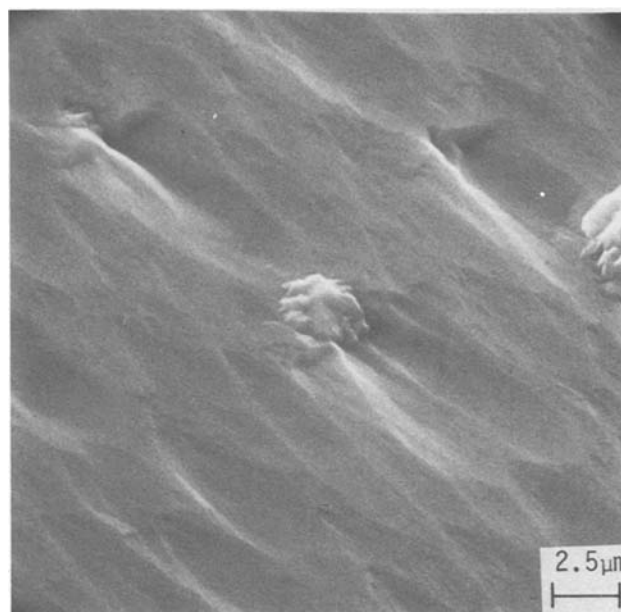


Fig. 1a. Morphology of epitaxial deposits with mirrorlike appearance.

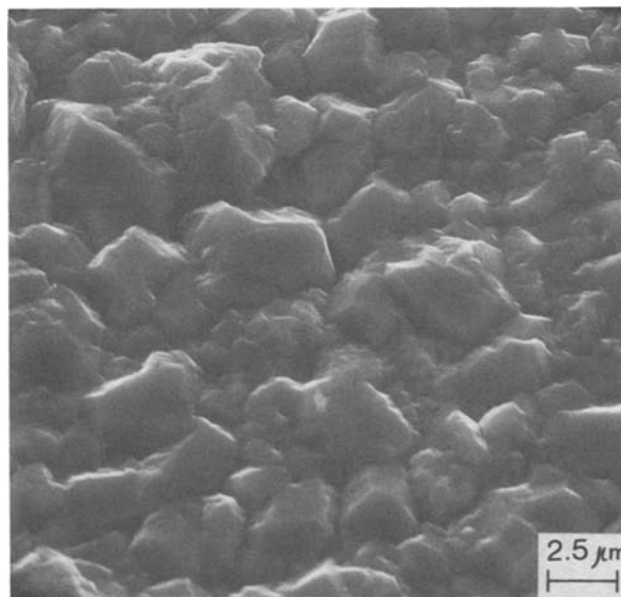


Fig. 1b. Morphology of polycrystalline deposits which give dull light-gray appearance.

¹ General Diode Corporation, Framingham, Massachusetts 01701.

² Laser Diode Corporation, Metuchen, New Jersey 08840.

The deposits were subsequently found to be a unique characteristic of the growth conditions in the reactor, which were not influenced by the type of substrate used. These n-type layers have been observed on Ge, GaAs, Si, and quartz substrates. The deposits are polycrystalline and have the correct constituent compositions, as determined from electron microprobe measurements compared to the same measurements on p-type deposits. The composition of the n-type deposits are relatively sensitive to the vapor phase reactant ratios. In-depth studies of the formation and properties of these n-type deposits will be the subject of future work.

Growth of Tetragonal ZnSiAs₂

ZnSiAs₂ crystallizes in the chalcopyrite³ structure which has tetragonal symmetry. It can be viewed as two stacked zincblende unit cells as illustrated in Fig. 2. The (100) and (010) chalcopyrite orientations are not equivalent to the (001) orientation. In particular, the (001) axis is the only crystallographic direction with fourfold symmetry for the chalcopyrite structure, while both the (100) and (010) axes exhibit twofold symmetry. This is due to the ordered arrangement of Zn and Si atoms on the "A" sublattice.⁴ The "B" lattice is occupied solely by the As atoms. It should be noted that the twofold symmetry axes exist because of the ordered arrangement of the two different atoms that occupy the "A" lattice and not as a result of the slight difference in the pseudocubic lattice dimension, *a'*, along the c-axis direction (i.e., *a'* = *c*/2 vs. *a*; see Fig. 2). In fact, for several of the chalcopyrites such as CdGeAs₂ *a'* = *a* and *c/a* = 2.00. However, because of the ordered arrangement of Cd and Ge, the structure is still tetragonal. The significance of this fact is that the epitaxial growth of either the (100), (010), or

³ Same crystal structure as the mineral chalcopyrite, CuFeS₂, which is a tetragonal structure [Ref. (2), p. 31].

⁴ We use the terminology that is commonly used for the III-V compounds in which the Group III atoms are viewed as occupying one of two interpenetrating fcc lattices denoted as the "A" lattice.

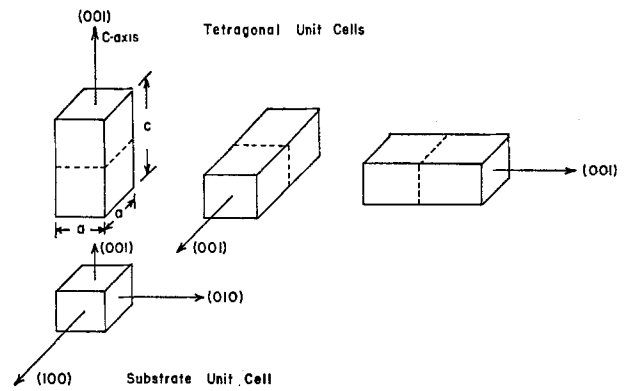


Fig. 3. Illustrations of the three possible epitaxial chalcopyrite orientations on a (100) cubic substrate.

(001) chalcopyrite orientations on a cubic (100) substrate is possible, but not equivalent.

The three possible chalcopyrite epitaxial unit cell orientations on a (100) cubic substrate are illustrated in Fig. 3. A similar situation also exists for the epitaxial growth of a (112)-oriented chalcopyrite on a (111) cubic substrate. For convenience, the definition "mixed epitaxy" will be used to describe a growth consisting of epitaxially deposited domains in which the c-axes of the various domains are not all parallel. A second definition termed "unique epitaxy" denotes the desired situation in which a true single crystal orientation with a unique c-axis direction is achieved throughout the grown layer.

The results of our investigation to date show that ZnSiAs₂ has been deposited with the chalcopyrite structure. This is clearly seen from the x-ray diffraction pattern shown in Fig. 4. This figure, taken for convenience on a polycrystalline sample, shows the splitting of the (100) and (110) reflections into the (020), (004) and (220), (024) doublets, respectively,

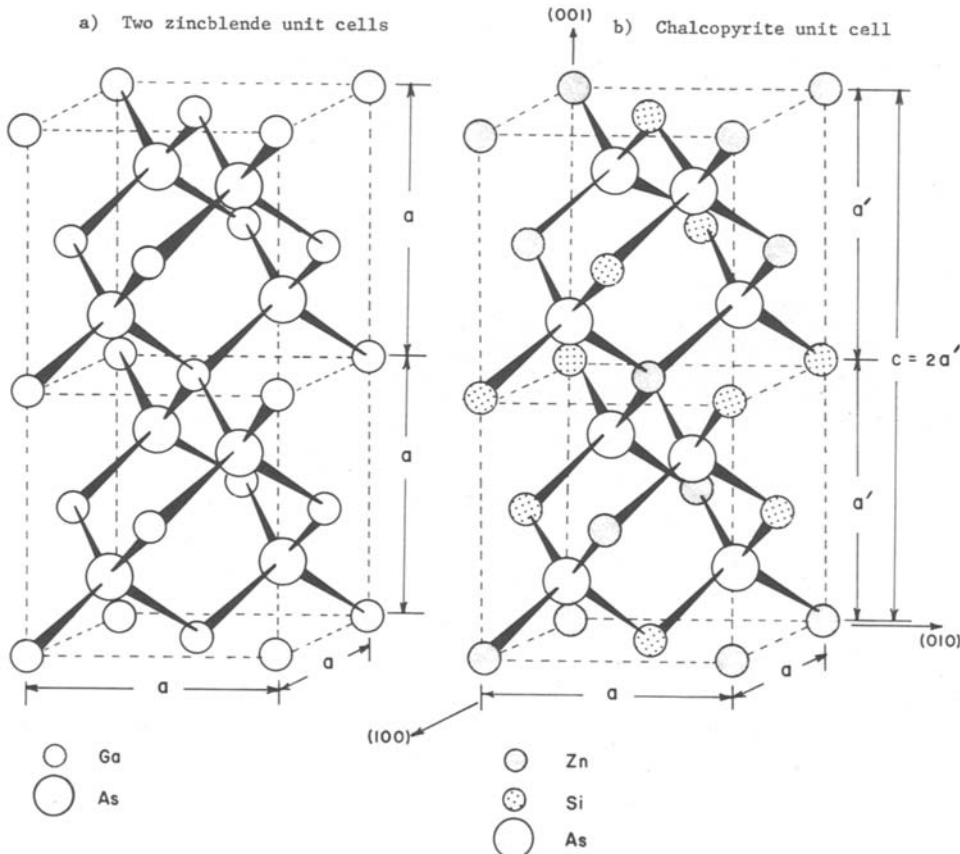


Fig. 2. Comparison of zinc blende and tetragonal chalcopyrite structures.

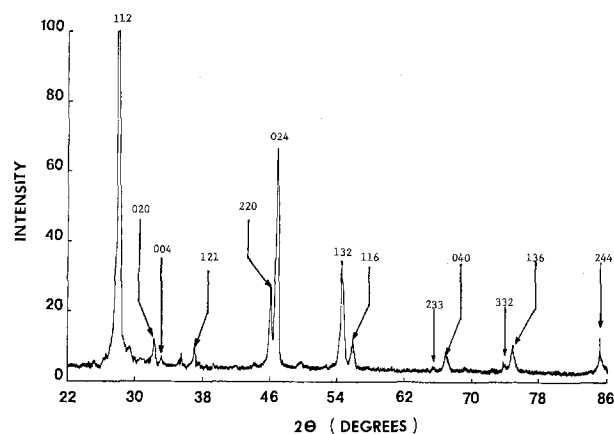


Fig. 4. X-ray diffraction pattern for a polycrystalline layer of ZnSiAs_2 having the tetragonal chalcopyrite structure. The Miller indexes for the various reflections are shown in the figure ($\text{CuK}\alpha$ radiation).

which is characteristic of the tetragonal chalcopyrite structure. In this work, both mixed and unique epitaxial growth have been observed with either (100) or (111) orientations of Ge and GaAs substrates. Table II compares the conditions that have led to the growth of the mixed epitaxy and unique epitaxy deposits.

As one would expect, the preferred orientation was (001) for unique epitaxial growth of ZnSiAs_2 on (100) Ge and GaAs substrates. However, of the three possible c-axis orientations available for the growth of (112) ZnSiAs_2 on (111) Ge and GaAs the one which is preferred appears to be the one that gives the c-axis oriented closest to the surface normal. Thus the (111) substrates apparently should be intentionally mis-oriented toward a (110) direction by several degrees.⁵ This is a tentative conclusion at this time and needs to be investigated in greater depth.

Figure 5 is an x-ray diffraction pattern which shows the desired (001) ZnSiAs_2 orientation on (100) Ge or GaAs which is the unique epitaxial deposit obtained from the conditions listed in Table II. Figure 6 shows the pattern for the mixed epitaxial case. It was found that conditions of high AsH_3 flow rate caused the (010) ZnSiAs_2 to grow in preference to the (001) orientation, although the presence of the (001) orientation was still evident. The growth conditions were not optimized to enhance this growth habit. This case is illustrated through the x-ray diffraction pattern shown in Fig. 7. From these figures, it is seen that the (001) orientation can be deposited essentially to the exclusion of the (010) or (100) orientation and the reverse is also apparently possible. Sample 120B (see x-ray diffraction pattern in Fig. 7) was very close to this condition. The quality of this layer was somewhat poorer as evidenced by the broad, poorly defined peak. It is believed that the structural quality of the (010)-oriented material can be improved due to the existence of the reasonably well-resolved (040) peak seen in Fig. 6. However, this orientation has two possible and nearly equally prob-

⁵ The cases observed to date were on (111) Ge substrates with about 5° misorientation.

Table II. Table of growth conditions that have led to mixed epitaxial growth and unique epitaxial growth on Ge and GaAs substrates

| | Mixed epitaxy | Unique epitaxy |
|---------------------------------|---------------|----------------|
| Growth temperature (°C) | 630-640 | 650-675 |
| Zn flow rate (sccm) | 3.8-5.0 | 3.8-5.0 |
| SiH_4 flow rate (sccm) | 12-15 | 6.5-8.0 |
| AsH_3 flow rate (sccm) | 12-30 | 6.5-10.0 |
| Total flow rate (sccm) | 4400 | 4400 |
| (H_2 balance) | | |

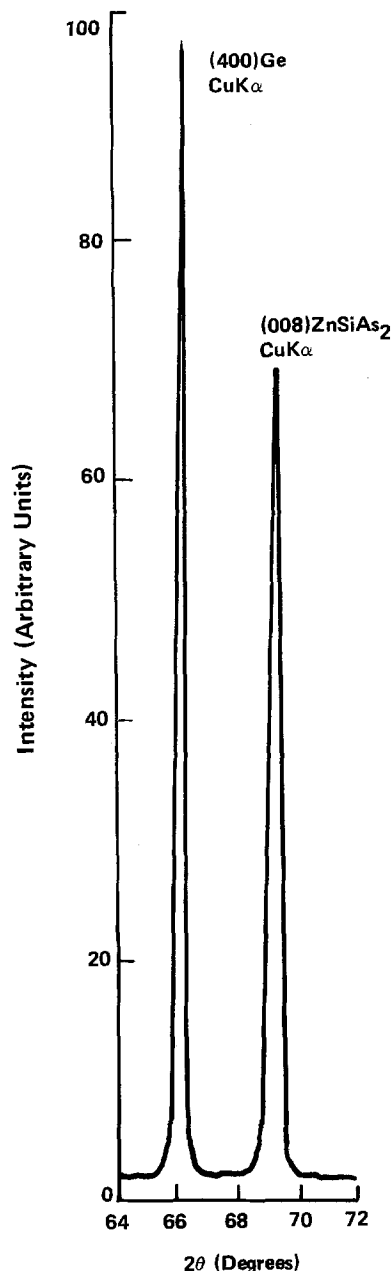


Fig. 5. X-ray diffraction pattern showing unique epitaxy deposition as evidenced by appearance of (008) ZnSiAs_2 reflection only.

able c-axis orientations at right angles to each other and in the plane of the layer. It is expected that by tilting the substrate normal toward one of the (100) directions, a single c-axis orientation will be favored. This hypothesis has not been verified at the present time.

Electrical Properties and Autodoping

The Ge and GaAs substrates used in this work have had some influence on the evaluation of the electrical properties of the ZnSiAs_2 layers. For example, the p-type epitaxial layers grown on n-type Ge were tested with a thermal probe and studied by Hall effect measurements. However, the electrical isolation between the Ge substrates and the epitaxial layers was generally poor. Thus, the interpretation of the Hall effect measurements is difficult and the influence of the substrate on these measurements is hard to ascertain. For these reasons Cr-doped semi-insulating GaAs substrates were the appropriate choice for growing layers suitable for Hall effect measurements. The use of these substrates resulted in good electrical isolation with the epitaxial layer.

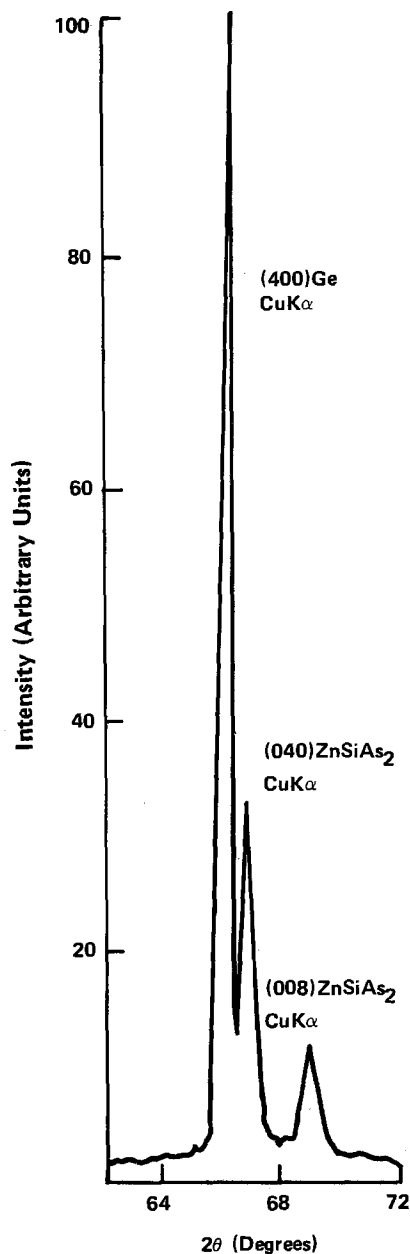


Fig. 6. X-ray diffraction of ZnSiAs_2 showing mixed epitaxy deposition as evidenced by appearance of both the (008) and (040) ZnSiAs_2 reflections.

The deposits on GaAs(Cr) substrates for the growth conditions listed in Table I are p-type with hole concentrations ranging from $5 \times 10^{18} \text{ cm}^{-3}$ to $5 \times 10^{19} \text{ cm}^{-3}$, with $2 \times 10^{19} \text{ cm}^{-3}$ typically observed. These concentrations are relatively insensitive to the variation in growth conditions listed in Table I. Hole mobilities of 40-50 cm^2/Vsec are typical of these p-type layers. The insensitivity of the hole concentration to growth conditions suggested the possibility of an impurity problem arising from the substrate. For this reason secondary ion mass spectrometry (SIMS) was employed to analyze the layers and the interfacial region between the layer and substrate. These studies were conducted on ZnSiAs_2 layers grown on both Ge and GaAs.

Figures 8 and 9 show SIMS profiles of ZnSiAs_2 grown on a Ge and GaAs substrate, respectively. The ZnSiAs_2 grown on (100) Ge appears to be relatively uniform and exhibits a reasonably abrupt interface. However, the ZnSiAs_2 grown on (100) GaAs substrates shows a significant amount of Ga outdiffusion from the substrate into the ZnSiAs_2 layer. Since Ga has been re-

ported to be an acceptor-like impurity for ZnSiAs_2 (4), these results suggest that an autodoping effect is present which could explain why the layers grown on semi-insulating GaAs substrates consistently resulted in heavily doped p-type ZnSiAs_2 layers, for which the background hole concentration was relatively insensitive to growth conditions. Finally, it is apparent that this choice of substrate is not an appropriate vehicle for Hall effect measurements unless steps can be taken to eliminate the autodoping mechanism. This type of problem has been prevalent in the growth of GaAs on Ge substrates, and in the GaAs/Ge system could be circumvented by capping the back side of the substrate with an encapsulant such as SiO_2 (7).

Summary and Conclusions

The open tube vapor phase epitaxial growth technique has been used to synthesize epitaxial layers of ZnSiAs_2 . Of particular significance is the fact that the noncubic (tetragonal) structure admits well-defined growth conditions that result in truly epitaxial growth.

While ZnSiAs_2 does exhibit some degree of tetragonal distortion (c-axis compression gives a c/a ratio of 1.92), it is not known whether this is necessary in order to favor the growth of the (001) orientation over the (100) orientation. It would be necessary to study the deposition of a material such as ZnSnP_2 which has a c/a ratio of exactly 2.0 in order to determine whether some degree of c-axis compression is necessary to demonstrate the preference of the (001) over the (100) orientation. It is suggested here that it is the nature of the bonding rather than the lattice spacing that is crucial to the growth of one of these orientations over the other.

At this point, the high carrier concentrations encountered in these films remain a serious problem. Since an autodoping mechanism appears to be present, the high concentrations are not believed to be indicative of the inherent properties of ZnSiAs_2 , but are more dependent on the choice of substrate and/or growth conditions. In fact, recent work using an organometallic Zn source has resulted in hole concentrations near 10^{18} cm^{-3} , which further supports this conclusion. Additional studies are underway to determine conditions for achieving much lower carrier concentrations.

The formation of n-type ZnSiAs_2 has been particularly encouraging in view of the earlier evidence that the chalcopyrites may have type-conversion problems similar to the II-IV compounds. Our results suggest the possibility of ZnSiAs_2 p-n junction formation, which is essential if this is to be a useful device material.

Acknowledgments

The authors thank the U.S. Department of Energy for financial support of this work under contract No. E(49-18)-2458 and DE-AC04-79ET23001. The support of the Naval Research Laboratories in the study of this material is also appreciated. Also, the technical assistance of Ray Pickett, Gill Fountain, and Steve Edwards in the materials growth and characterization effort is gratefully acknowledged.

Manuscript submitted June 9, 1980; revised manuscript received Jan. 30, 1981.

Any discussion of this paper will appear in a Discussion Section to be published in the June 1982 JOURNAL. All discussions for the June 1982 Discussion Section should be submitted by Feb. 1, 1982.

Publication costs of this article were assisted by North Carolina State University.

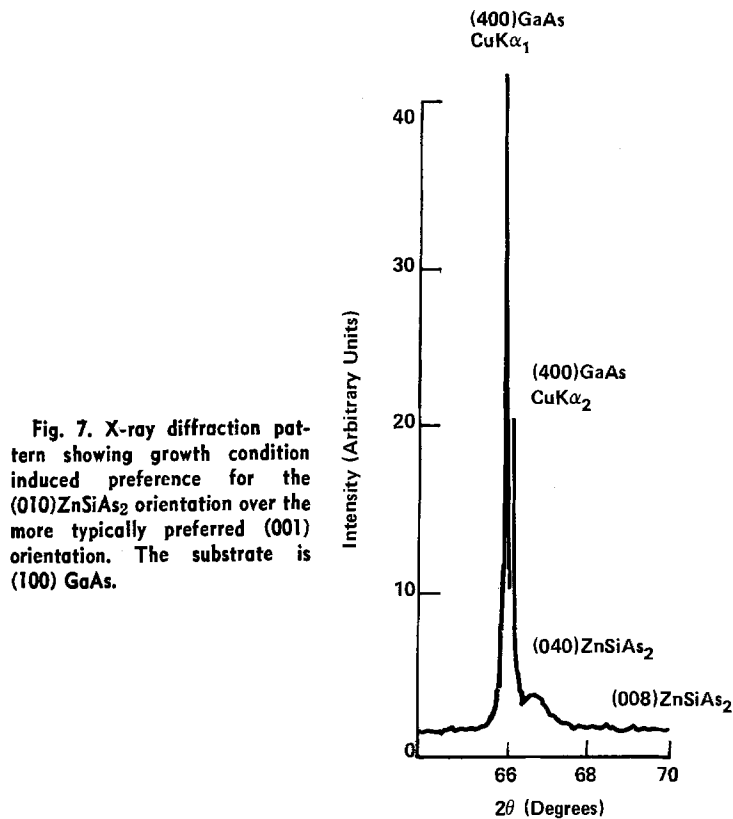
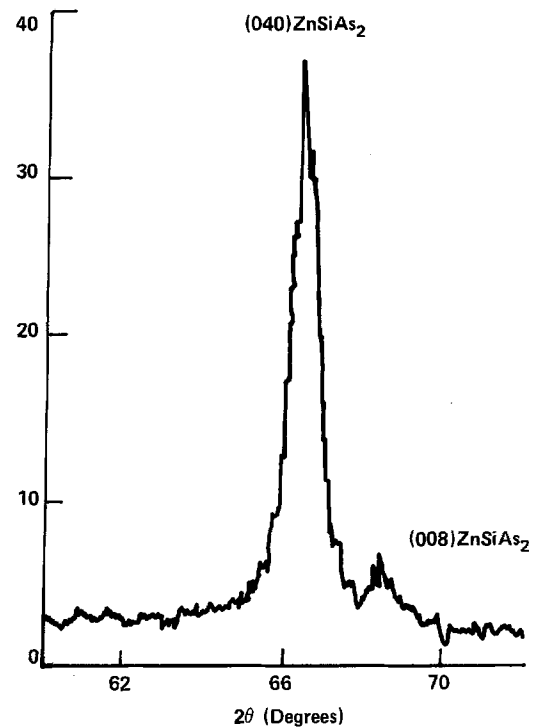


Fig. 7. X-ray diffraction pattern showing growth condition induced preference for the (010)ZnSiAs $_2$ orientation over the more typically preferred (001) orientation. The substrate is (100) GaAs.



a) Sample aligned to show substrate reflection.

b) Sample misaligned to eliminate substrate reflections.
Note: There is little evidence for (008) ZnSiAs $_2$ reflection. Thus c-axis is in plane of substrate.

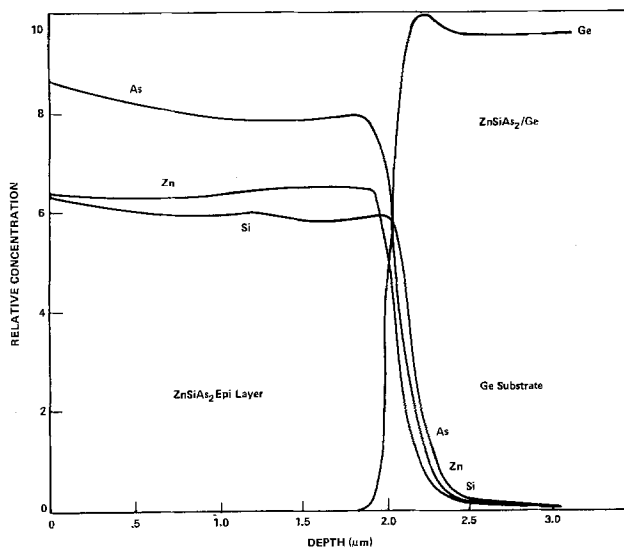


Fig. 8. SIMS concentration profiles obtained for ZnSiAs $_2$ grown on (100) Ge substrates.

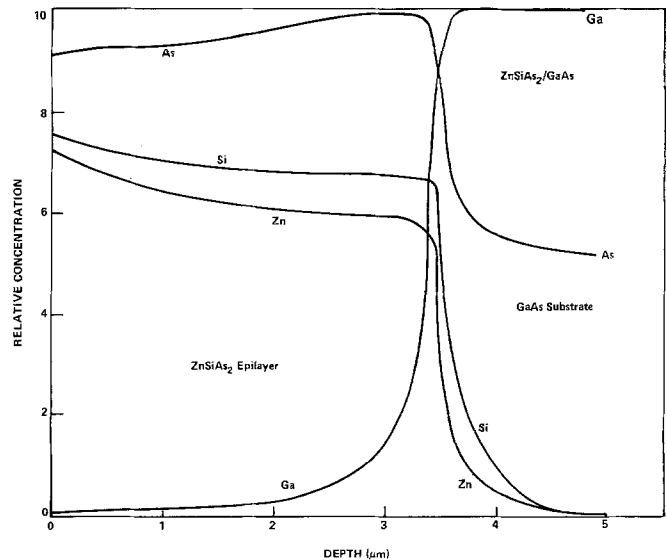


Fig. 9. SIMS concentration profiles obtained for ZnSiAs $_2$ grown on (100) GaAs substrates.

REFERENCES

1. J. E. Andrews *et al.*, *Mater. Res. Bull.*, **12**, 961 (1978).
2. J. L. Shay and J. H. Wernick, "Ternary Chalcopyrite Semiconductors: Growth, Electronic Properties, and Applications," Pergamon Press, Oxford, England (1975).
3. B. J. Curtiss and P. Wild, *Mater. Res. Bull.*, **5**, 69 (1970).
4. G. K. Averkieva, V. D. Prochukhan, and M. Tashtanova, *Inorg. Mater.*, **9**, 435 (1973).
5. G. K. Averkieva, A. H. Imenkov, V. D. Prochukhan, Yu. V. Rud, and M. Tashtanova, *Dokl. Akad. Nauk. SSSR*, **216**, 56 (1974).
6. Yu. V. Rud and K. Ovezov, *Sov. Phys. Semicond.*, **10**, 561 (1976).
7. G. O. Ladd, Jr. and D. L. Feucht, *Metal Trans.*, **1**, 609 (1970).

Implantation Gettering of Gold in Silicon

M. J. T. Lo,^{*1} J. G. Skalnik,* and P. F. Ordnung

Department of Electrical and Computer Engineering, University of California, Santa Barbara, California 93106

ABSTRACT

Neutron activation techniques were used to study the efficiency of ion-implantation gettering of gold in gold-equilibrated silicon samples. The implantation species was 150 keV argon ions. An ion dose of 1×10^{16} Ar/cm² was found to be optimum. Within the range of ion current density investigated, the gettering efficiency increased with the ion current density. Implantation performed at a high temperature provided less gettering than that performed at a lower temperature. A postannealing temperature of either 900° or 1000°C could be superior to 1100°C in gettering gold, provided enough gettering time was allowed.

The optimum conditions for ion-implantation gettering were applied to a typical MOS processing cycle on as-received silicon samples. For an ion dose of 1×10^{16} Ar/cm², a total gettering time of 8 hr at 1000°C increased the MOS generation lifetime significantly compared with that for a control sample. The data from the MOS generation lifetime study are consistent with the results of the neutron activation analysis.

Ion-implantation gettering basically consists of two processing steps; namely, creation of an ion-damaged layer followed by gettering at an elevated temperature. Parameters of each step might influence the efficiency of the gettering. Buck *et al.* (1) found that increasing the gettering time increases the amount of gold gettered. The amount of gold gettered was also found to increase with gettering temperatures between 850° and 1150°C (2). Thus, the residual disorder after annealing seemed to be jointly dependent upon the temperature and time of the annealing (1-5).

Seidel, Meek, and Cullis (2) found that the efficiency of gettering gold by an ion-damaged layer was related to the amount and type of disorder after annealing, and that argon-damaged layers gettered gold more efficiently than layers damaged by other ions. The residual disorder after annealing was found to be dose dependent for various ion species (3, 6, 7). In the absence of good thermal contact between the sample and the sample holder, a high-current high-dose implantation may cause *in situ* sample heating and affect both the as-implanted disorder and the final disorder after annealing (3, 8). Using ion-implantation gettering, Nassibian *et al.* (9) were able to increase the MOS generation lifetime, but the increase was not reproducible.

The present study investigates the effect of several parameters of ion implantation and postannealing on the efficiency of gold gettering in gold-equilibrated silicon. Neutron activation techniques are used as the main investigative tools. The optimum conditions of ion-implantation gettering are applied to as-received silicon samples to study the effect on MOS generation lifetime. This work was not intended to investigate the detailed nature of the damage created by the ion implantation.

The following sections outline the experimental procedures used and include the results of a neutron activation analysis. The effect of ion-implantation gettering on the MOS generation lifetime is described. Finally, a general discussion of the results is given.

Experimental Procedures

For the study of gold gettering in silicon, (100) p-type 10-20 Ω -cm silicon wafers were scribed and cleaned. About 1000Å of Au was evaporated onto both sides of the sample. The sample was then equilibrated

with Au at a temperature of 1080°C in a nitrogen ambient for about 6 hr. The gold-diffused samples were first dipped in buffer HF with ultrasonic agitation to remove the silicon oxide at the surface. A DI water rinse followed. The samples were then immersed in aqua regia for a few minutes and the samples were again rinsed in DI water.

A silicon etching technique was used to remove the surface pile-up of gold in silicon. The solution was composed of HF, HNO₃, H₂O, and HC₂H₃O₂. Based on our neutron activation analysis, the removal of 1.5 mils from each side of the sample was more than sufficient to remove the excess Au at the surface. One side of the sample was polished with Lustrox solution. The unpolished side was covered with 1 μ m of CVD SiO₂, which was deposited at 380°C.

The unpolished side of the sample was attached to the sample holder with indium, which served as a good thermal contact during the implantation. Throughout all the implantation runs, Ar ions of 150 keV were selected and implanted into the polished side of each sample. Parameters such as ion dose, ion current density, and substrate temperature were separately varied from sample to sample. For each sample, all these parameters were carefully monitored.

After implantation, the indium was removed with hydrochloric acid and the CVD SiO₂ was removed with buffer HF. After cleaning, the samples were coated with CVD SiO₂ of about 1 μ m on both sides to prevent possible outdiffusion of gold during the annealing. The samples were then annealed at temperatures between 900° and 1100°C for various time periods between one-quarter hr and 5 hr. After the gettering, the samples were packed with plastic and inserted into a plastic vial. The vial was then ready for neutron activation.

The technique of neutron activation analysis was used to determine the amount of gold contained in each silicon sample. The removal of a silicon layer by etching with a solution of HF, HNO₃, H₂O, and HC₂H₃O₂ was performed alternately with counting of gamma rays from the sample. The amount of gold contained in the damaged layer was determined as the difference in the amounts of gold contained in the sample before and after the removal of the damaged layer. The ratio of the amount of gold gettered in the damaged layer to the amount of gold contained in the whole sample was defined as the percentage of gold gettered by the damaged layer, or the gettering efficiency.

* Electrochemical Society Active Member.

¹ Present address: Xerox Corporation, El Segundo, California 90245.

Key words: gettering, neutron activation, gold, lifetime.

The neutron activation was carried out either with the L-77 reactor at UCSB or the R-1 reactor at UCLA. For the L-77 reactor, the activation was performed at a flux density of 3×10^8 neutrons/(cm²)(sec) for 3 hr. For the R-1 reactor, the activation was performed at a flux density of 1.5×10^{12} neutrons/(cm²)(sec) for a half hour.

A thallium activated NaI detector was used to detect the gamma rays generated from the isotope ¹⁹⁸Au. The energy of the gamma ray is 0.412 MeV. The half-life of ¹⁹⁸Au is 2.7 days.

Results of Neutron Activation Analysis

The gettering was performed at 1100°C for 5 hr. Four substrate temperatures were chosen to study the dependence of gettering efficiency on the substrate temperature during the implantation. To achieve a high substrate temperature, a heater was installed directly under an aluminum substrate holder to heat the substrate to either 212° or 400°C. The heater was under vacuum during the implantation and the temperature was maintained constant by a temperature controller. For low temperature implantation, a hollow aluminum substrate holder was filled with water or liquid nitrogen for 35° or -196°C. All temperatures were monitored by a digital meter throughout the entire implantation process.

As shown in Fig. 1, the gettering efficiency increased with decreasing substrate temperature. This is believed to indicate increased disorder for ion implantation at decreased substrate temperatures. At each substrate temperature, the gettering efficiency is found to be higher for a dose of 1×10^{16} Ar/cm² than for 6×10^{15} Ar/cm².

The amount of gold detected before and after the removal of the CVD layer on the implanted side was always the same for each sample. This indicates that gold does not diffuse into the SiO₂ from the damaged silicon layer at 1100°C.

The projected range of 150 keV Ar ions in silicon at an incident angle of about 7° is known to be less than 1 μm (3, 9). The layer of silicon which getters gold is thus expected to be not more than 1 μm in depth. However, all samples which received a gettering cycle at 1100°C for 5 hr appeared to contain, to a depth of as much as 10 μm, a gold concentration higher than the equilibrated level.

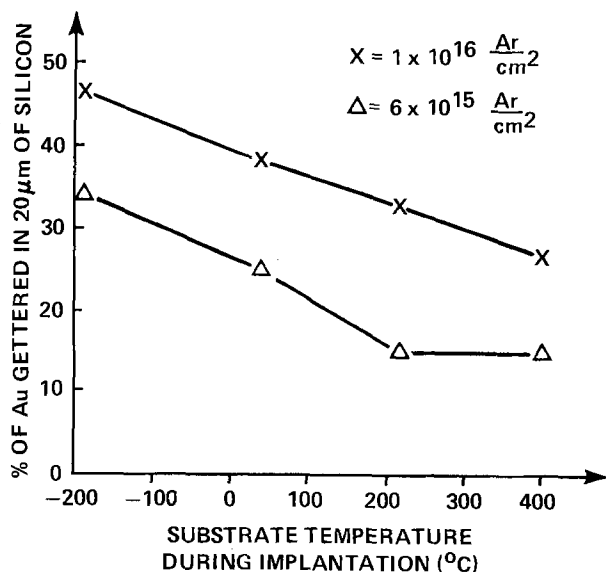


Fig. 1. Gettering efficiency vs. substrate temperature during implantation. The common conditions for all samples are Ar⁺, 150 keV, 7° incident angle, 1.68 μA/cm², 5-hr postannealing at 1100°C. Samples are 406 μm thick.

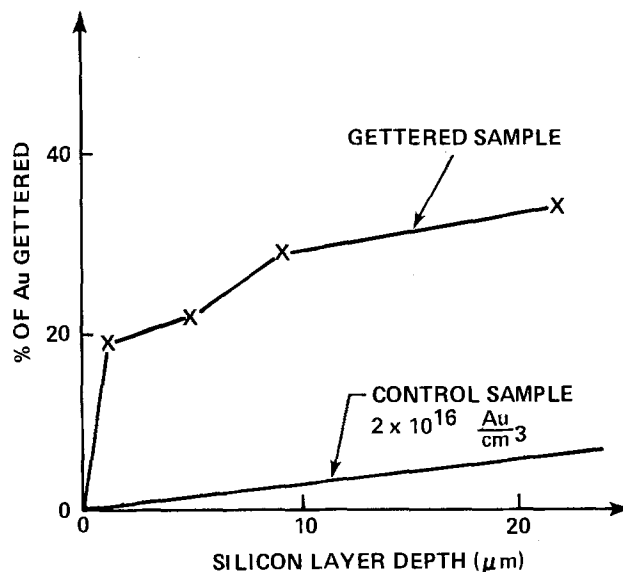


Fig. 2. A plot of percentage of gold gettering vs. the associated total layer depth of silicon in μm. Gettered sample is implanted with 1×10^{16} Ar⁺/cm², 150 keV, 7° incident angle, 1.68 μA/cm², 212°C; postannealing at 1100°C for 5 hr was applied to both gettered and control samples; 396 μm thick.

Figure 2 gives an example of the distribution of gold impurities in layers up to about 20 μm. The percentage of gold gettering is plotted as a function of the total layer depth of silicon measured from the surface of the damaged side of the sample. The slope of each line connecting adjacent data points is proportional to the concentration of gold in that region. The straight line at the bottom of the figure shows an experimental result for a control sample which was uniformly equilibrated with gold to a concentration of 2×10^{16} Au/cm³. Since the control sample also received a 5 hr gettering anneal at 1100°C, the gold distribution in this control sample indicates that the Si-SiO₂ interface does not getter Au during the gettering anneal. Figure 2 also shows that the gold concentration at depths up to 10 μm is higher than that for the control sample. Back-diffusion of gold from the gettering region to the bulk silicon is thought to be the cause.

To confirm the back-diffusion of gold from the gettering region after a 5 hr annealing cycle at 1100°C, samples receiving implantation under a fixed set of conditions were annealed at 1100°C for various time periods ranging from one-quarter hr to 5 hr. The result is shown in Fig. 3. Each number on the various curves represents an experimental point. The number indicates the number of hours of annealing at 1100°C. As the annealing proceeds, gold gradually moves toward the damaged region which is within 1 μm of the silicon surface. The amount of gold gettering in 1 μm depth of silicon increases with annealing time up to about 1 hr. For the curves with an annealing period of 1 hr or less, the gold concentration is higher than the equilibrating level only within a depth of 2 μm. A significant observation is that gold starts to be released by the damage and diffuses back to the bulk silicon after annealing at 1100°C for about 1 hr. This fact is evidenced by comparing curves numbered "3" and "5" with that numbered "1." In the curves numbered "3" and "5," the gold concentration in the region between 6 and 12 μm is higher than the equilibrating level as indicated by the slope of the lines being larger than that for the control sample.

It is believed that after about 1 hr of annealing the damage created by the ion implantation, which has the set of conditions described in Fig. 3, starts to be annealed (3). The driving force for the gold gettering is

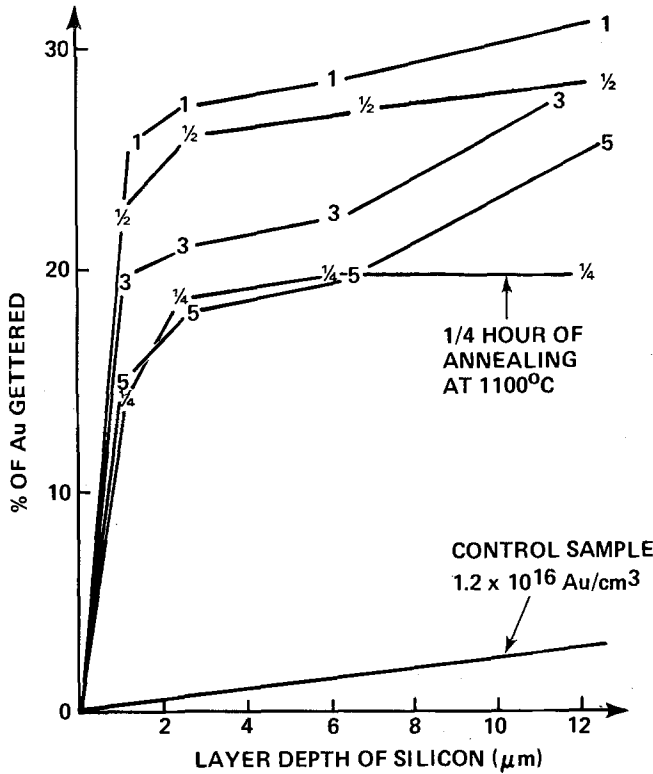


Fig. 3. Percentage of gold gettered vs. total layer depth of silicon on the implanted side. The parameter is number of hours of annealing at 1100°C. The common conditions of implantation for all samples are: $1 \times 10^{15} \text{ Ar}^+/\text{cm}^2$, 150 keV, 7° incident angle, $1.68 \mu\text{A}/\text{cm}^2$, 35°C. Samples are 406 μm thick.

thereby decreased and gold atoms are released in the damaged region. The gold concentration gradient causes gold atoms to diffuse back to the bulk silicon.

Three temperatures, 900°, 1000°, and 1100°C were selected to study the annealing-temperature dependence of gettering. The gettering efficiency is plotted as a function of annealing time for each temperature in Fig. 4. Each experimental point on a given curve in Fig. 4 was obtained from a given individual sample. Although the curve associated with 1100°C retrogrades after a 1 hr annealing cycle, the curves for 900° and 1000°C indicate a gettering efficiency that increases monotonically with annealing time to 5 hr. The curve for 1000°C is higher than that for 1100°C after about 1.75 hr. Also, the curve for 900°C exceeds that for 1100°C after about 2.5 hr.

In the first half-hour of annealing, the gettering efficiency is higher for a higher temperature. Basically the diffusivity of gold in silicon dominates the gettering process in the initial period of annealing. According to the result shown in Fig. 4, it is clear that the gettering temperature and time must be carefully chosen to achieve a desired gettering efficiency.

The dependence of the gettering efficiency on the ion dose and ion current density is illustrated in Fig. 5. The ion dose ranging from $6 \times 10^{14} \text{ cm}^{-2}$ to $2.5 \times 10^{16} \text{ cm}^{-2}$ is indicated on a log scale. Three ion current densities with a ratio of 1:2:4 are also specified.

At each ion current density, the gettering efficiency increases with ion dose to a value of about $1 \times 10^{16} \text{ cm}^{-2}$, which is believed to be an optimum dose for efficient ion-implantation gettering. The relatively high value of $3.36 \mu\text{A}/\text{cm}^2$ ion current density appears to getter gold more efficiently than the two lower ion current densities. It should be noted that the substrate temperature was held constant at 45°C during the implantations.

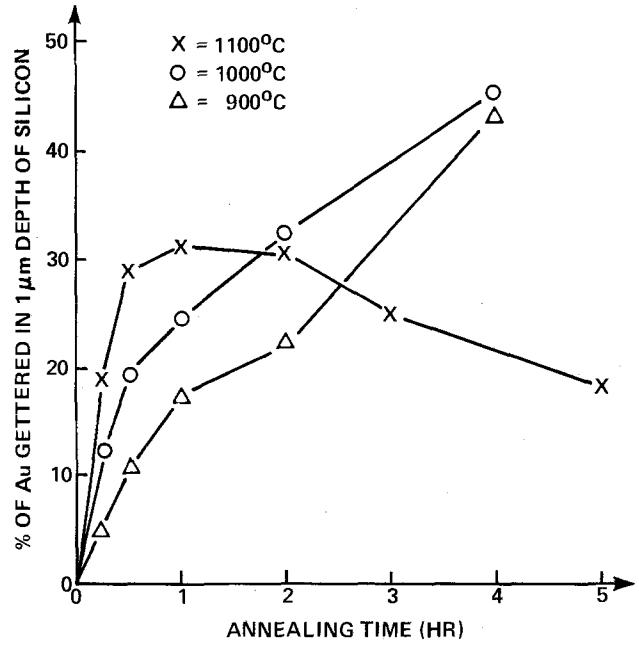


Fig. 4. Gettering efficiency vs. annealing time at various annealing temperatures. The common conditions of implantation for all samples are: $1 \times 10^{15} \text{ Ar}^+/\text{cm}^2$, 150 keV, 7° incident angle, $1.68 \mu\text{A}/\text{cm}^2$, 45°C. Samples are 280 μm thick.

MOS Generation Lifetime

The generation lifetime of an MOS capacitor is a parameter which heavily depends on the quality of the bulk silicon. The generation lifetime is inversely proportional to the density of generation centers for electron hole pairs. Therefore, it is appropriate to monitor the effect of ion-implantation gettering on the generation lifetime of an MOS capacitor.

To simulate standard MOS processing, MOS capacitors were built on as-received silicon samples in which no gold impurity was intentionally added. In addition, during the ion-implantation step, there was no indium between the sample and the sample holder. The beam heating effect in this case may be different from that in which indium serves as a thermal contact to the sample during the implantation. However, it was felt that the absence of indium corresponds more nearly to industrial practice.

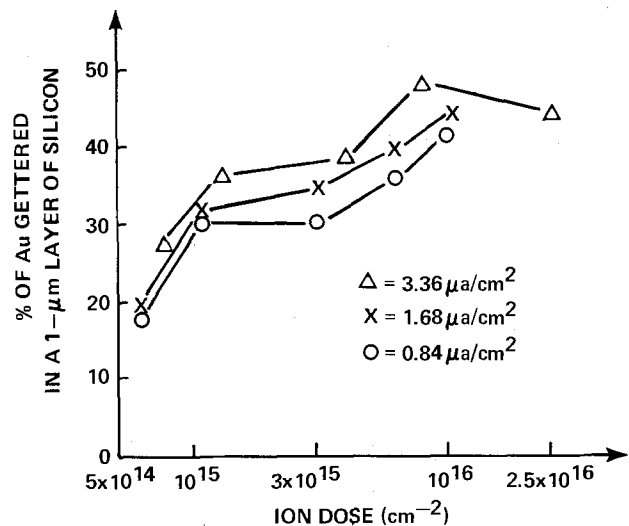


Fig. 5. Gettering efficiency vs. ion dose on a log scale. The parameter is ion current density. The common conditions of implantation for all samples are Ar^+ , 150 keV, 7° incident angle, 1.1 hr postannealing at 1100°C. Samples are 280 μm thick.

Two Czochralski-grown p-type, 16 Ω -cm silicon wafers with a diameter of 2 in. and a thickness of 16 mils were scribed so that the comparison of generation lifetime could be made on pieces from the same wafer. The samples received an RCA cleaning (10). After the cleaning process, one sample from each wafer was not implanted and served as a control sample. The rest of the samples received back-side Ar implantation with a dose of either 1×10^{15} or 1×10^{16} cm $^{-2}$, at 150 keV and 2.2 μ A/cm 2 .

A temperature of 1000°C was used for the gettering and the oxidation. The implanted samples received various gettering periods in nitrogen before the oxidation cycle. The oxidation was performed in dry oxygen for 2.5 hr to grow 1100Å of SiO $_2$. Finally, the ambient was switched to nitrogen for a half hour to reduce the fixed-charge and surface-state densities.

A layer of 5000Å of aluminum was evaporated onto the front side of each sample. A mask which contains an array of circular dots surrounded by guard rings was used to define a pattern for the aluminum layer. To form an ohmic contact, the oxide on the back side of the samples was removed and 5000Å of aluminum was evaporated onto the back side of the samples.

Finally, an anneal was carried out at 450°C in forming gas for 20 min. The samples were then ready for C-t measurement.

A pulsed technique was used for the measurement of the minority carrier generation lifetime in the bulk silicon of an MOS capacitor. Conceptually, the pulsed technique measures the generation lifetime in silicon by observing the rate at which the inversion layer forms in an MOS capacitor after being pulsed to a deep-depletion condition (11). The transient response of the pulsed MOS capacitor was recorded as a plot of the capacitance of the MOS capacitor as a function of time.

Schroder and Guldberg (12) developed a simple approximate theory in which the C-t curve is fitted by a straight line. If t_F is the time required to form the inversion layer, an approximate equation for the extraction of the generation lifetime, τ_g , from the C-t plot was derived as follows

$$\tau_g = \frac{n_i}{8N_A} \frac{C_F}{C_{ox}} t_F \left(1 + \frac{C_o}{C_F} \right)^2$$

where n_i = intrinsic carrier concentration, N_A = doping density of the substrate, C_o = initial capacitance of pulsed MOS capacitor, C_F = final capacitance of pulsed MOS capacitor, and C_{ox} = oxide capacitance. This equation is convenient for a rapid evaluation of the generation lifetime of carriers in a large number of devices.

Table I. Comparison of the generation lifetime of the implanted samples with that for the control sample

| Sample | | Average generation lifetime (μ sec) |
|------------------------|---------------------------|--|
| Control sample | | 555 |
| Ion dose (cm $^{-2}$) | Gettering cycle at 1000°C | |
| 1×10^{16} | O $_2$ 2.5 hr | 600 |
| | N $_2$ 0.5 hr | |
| 1×10^{16} | N $_2$ 5.0 hr | 918 |
| | O $_2$ 2.5 hr | |
| | N $_2$ 0.5 hr | |
| 1×10^{15} | O $_2$ 2.5 hr | Same as control sample |
| | N $_2$ 0.5 hr | |
| 1×10^{15} | N $_2$ 5.0 hr | Shorter than control sample |
| | O $_2$ 2.5 hr | |
| | N $_2$ 0.5 hr | |

Since the silicon surface was observed not to be inverted at zero bias, the guard ring was left floating. A C-t plot was performed and the generation lifetime determined for each MOS capacitor. The generation lifetime for each implanted sample was compared with that of the control sample, as shown in Table I. The average generation lifetime of the control sample is 555 μ sec. When the total annealing time is only 3 hr, the improvement of the generation lifetime is insignificant for both dose levels. As the total annealing time is increased to 8 hr, the sample receiving a dose of 1×10^{16} cm $^{-2}$ had an average generation lifetime of 918 μ sec. The generation lifetime mapping of this sample is shown in Fig. 6. On the other hand, the sample receiving a dose of 1×10^{15} cm $^{-2}$ and 8 hr of annealing had an average generation lifetime slightly shorter than that of the control sample. The slight reduction of the average generation lifetime could be due to local defects. It may also be due to the capture of the reduced damage by the oxidized front side of the silicon sample (4).

Discussion and Conclusion

Thirty minutes of annealing was found to be insufficient for efficient gettering, especially for 900° and 1000°C. On the other hand, ion damage is more permanent when the annealing is carried out at a lower temperature. High temperature annealing for a long time tends to anneal out the damage and reduce the gettering capability.

In the present work, the maximum gettering efficiency of gold is 50%. This corresponds to a few times 10^{18} Au/cm 3 in the gettered region. It is suspected that, at such a high gold concentration, the gettering capability is probably saturated. In the as-received wafer in which no gold is intentionally added, the gold concentration is expected to be 10^{14} Au/cm 3 or less (13). Thus, saturation should not occur and the gettering efficiency is expected to be higher than 50%.

The implantation process performed during normal device fabrication may not include a good thermal contact between the wafer and the wafer holder. In the absence of a good thermal contact, the wafer may be appreciably heated by the high energy ions. For instance, at an ion energy of 150 keV, an ion current density of 1.68 μ A/cm 2 may heat the wafer to 204°C.

The gettering efficiency of gold increases with increasing ion current density and decreases with increasing substrate temperature. In general, the gettering efficiency may be expected to increase with the ion current density until the associated substrate temperature effect is large enough to dominate. For higher current densities, the gettering efficiency will decrease.

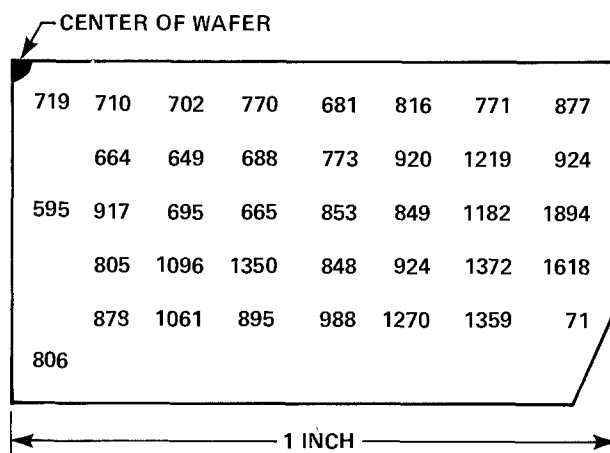


Fig. 6. Generation lifetime mapping of a gettered sample, in μ sec. The conditions of implantation are 1×10^{16} Ar $^+$ /cm 2 , 150 keV, and 2.2 μ A/cm 2 . The average generation lifetime is 918 μ sec. The 8 hr annealing cycle is listed in Table I.

Acknowledgments

The authors thank D. L. Heald, R. C. Neville, and T. E. Seidel for fruitful discussions and D. Zak for his technical assistance. The support for neutron activation given by A. E. Profio, and the facility provided by the Department of Chemical and Nuclear Engineering at UCSB and the Nuclear Energy Laboratory at UCLA is appreciated.

Manuscript submitted June 16, 1980; revised manuscript received Oct. 22, 1980.

Any discussion of this paper will appear in a Discussion Section to be published in the June 1982 JOURNAL. All discussions for the June 1982 Discussion Section should be submitted by Feb. 1, 1982.

Publication costs of this article were assisted by the University of California.

REFERENCES

1. T. M. Buck, J. M. Poate, and K. A. Pickar, *Surf. Sci.*, **35**, 362 (1973).

2. T. E. Seidel, R. L. Meek, and A. G. Cullis, *J. Appl. Phys.*, **46**, 600 (1975).
3. A. G. Cullis, T. E. Seidel, and R. L. Meek, *ibid.*, **49**, 5188 (1978).
4. K. Murase and H. Harada, *ibid.*, **48**, 4404 (1977).
5. P. Revesz, M. Wittmer, J. Roth, and J. W. Mayer, *ibid.*, **49**, 5199 (1978).
6. C. E. Christodoulides, W. A. Grant, and J. S. Williams, *Appl. Phys. Lett.*, **30**, 322 (1977).
7. H. J. Geipel and W. K. Tice, *ibid.*, **30**, 325 (1977).
8. T. E. Seidel, G. A. Pasteur, and J. C. C. Tsai, *ibid.*, **29**, 648 (1976).
9. A. G. Nassibian, V. G. Browne, and K. D. Perkins, *J. Appl. Phys.*, **47**, 992 (1976).
10. J. A. Amick, *Solid State Technol.*, November, 47 (1976).
11. F. P. Heiman, *IEEE Trans. Electron Devices*, **ed-14**, 781 (1967).
12. D. K. Schroder and J. Guldberg, *Solid-State Electron.*, **14**, 1285 (1971).
13. S. P. Murarka, *This Journal*, **123**, 765 (1976).

Stacking Faults and Substructure in GaAs/(Ga,Al)As Heteroepitaxial Layers

I. Origin and Elimination

B. V. Dutt,* S. Mahajan,* R. J. Roedel, G. P. Schwartz,* D. C. Miller, and L. Derick

Bell Laboratories, Murray Hill, New Jersey 07974

ABSTRACT

The origin of stacking faults and substructure observed in (Ga,Al)As layers grown by liquid phase epitaxy on Syton polished GaAs substrates has been studied. The stacking faults primarily originate at the substrate-epilayer interface. These faults presumably occur to accommodate misfit between coalescing islands observed in the early growth studies of heteroepitaxy of (Ga,Al)As on these substrates. The island-like growth appears to correlate with calcium contamination associated with the Syton polished substrates. In addition, dislocation substructure has been observed in (Ga,Al)As and GaAs epi-layers grown on Syton polished substrates. In the case of isoepitaxial layers, no stacking faults are seen. Thus growth of a buffer layer of GaAs eliminates the stacking faults but not the substructure. It is therefore suggested that the dislocation substructure arises from the replication of dislocations present in deformed surface regions of Syton polished substrates. On the other hand, heteroepitaxial layers of (Ga,Al)As grown on Br-methanol polished substrates are largely free from these structural defects.

Stacking faults (SF's), faulted loops, and dislocation tangles in (Ga, Al)As epi-layers, grown on GaAs substrates either by liquid phase epitaxy (LPE) or by vapor phase epitaxy (VPE), have been observed by several investigators (1-3). It is generally recognized that SF's originate at the substrate-epi interface. Since these substructural features are known to have deleterious effects on device performance and reliability, it is of fundamental as well as of technological importance to understand their origin and to devise procedures to eliminate them in device wafers.

In the present paper, the origin of SF's and substructure in ternary (Ga,Al)As layers grown by LPE has been studied by optical microscopy, etching, x-ray topography, transmission electron microscopy (TEM), x-ray photoemission, and Auger spectroscopy. As a result of these investigations, it has been possible to develop substrate preparation procedures using Br-

methanol solution polishing which yield high quality device wafers.

Experimental

The n-type GaAs single crystals used in the present work were obtained from the Sumitomo Corporation, Japan. The average dislocation density is typically $2 \times 10^3/\text{cm}^2$. Prior to the LPE growth, (001) oriented substrates were either Syton¹ polished to a mirror finish or chemically polished in a 1% Br-methanol solution. The polished slices were degreased, followed by a 2-3 min dip in a solution consisting of 1 part HCl and 2 parts H₂O. The cleaned substrates were immediately rinsed in deionized water, dried, and loaded in a graphite slider boat for LPE. The boat containing Ga melts with GaAs and Te or Ge as a dopant was placed in a quartz epitaxial reactor tube at room temperature and flushed overnight with Pd-purified hydrogen flowing at the rate of 500 ml/min. In order to reduce the oxides that may be present, the melts were pre-

* Electrochemical Society Active Member.

Key words: defects, substrate preparation, damage, imperfections.

¹ A Monsanto trademark.

baked at 550°-600°C for about 90 min. After the pre-bake, Al was added to the melts. The temperature was then raised to ~850°C and maintained for 2-3 hr to homogenize the melts. In order to ensure against an inadvertent melt-back of the substrate or the dissolution of one layer in the subsequent melt, the compositions chosen were such that there was always excess GaAs in the melts. The following growth procedure was used to deposit different layers. The furnace was programmed to cool down at a rate of 0.2°C/min. After a drop of 1°C, the substrate was positioned under the Ga-Al-As melt and deposition was carried out for a 50°C drop. This procedure resulted in an approximately 40-50 μm thick, compositionally graded n:Ga_{1-x}Al_xAs layer in which x varied from 0.35 to 0.24. For double heterostructure (DH) device wafers, a 0.5-1 μm active layer of p:Ga_{0.9}Al_{0.1}As was grown next, followed by a 1-2 μm confining layer of p:Ga_{0.75}Al_{0.25}As.

Samples for TEM work consisted of disks, 3 mm in diameter, chemically thinned from the substrate side in a 1.5% Br-methanol solution. Thinned specimens were examined in a JEM 200 microscope operating at 200 keV.

To locate the initiation point of SF's, (110) cleaved sections were etched using H₃PO₄:H₂SO₄:H₂O₂ (100:100:1) solution. Etching was carried out at room temperature for 1-2 min under intense illumination. The etched specimens were examined either optically using Nomarski phase contrast or in a scanning electron microscope (SEM).

The stress and radius of curvature of some wafers were determined using a classical x-ray topography setup. The method is in principle equivalent to the ABAC (automatic Bragg-angle control) technique described by Rozgonyi and Ciesielka (4). The sample was moved manually with an accuracy of 10 μm and the K α_1 peak position measured using the half-width at half maximum method. The curvature was assessed using 220 reflections and Mo K α_1 radiation.

X-ray photoemission (Al K α) and Auger spectra were obtained on Syton and Br-methanol polished surfaces utilizing a Physical Electronics Model 548 spectrometer. The instrumental resolution was 1.3 eV FWHM (full width at half maximum) for photoemission spectra; derivative Auger spectra involved 2 keV electron excitation and 3V peak-to-peak modulation.

Results and Analysis

Shown in Fig. 1 are linear features, approximately 30-50 μm in length, observed on the as-grown surface of a full device wafer by Nomarski contrast. The three DH layers were grown on a Syton polished substrate, and their respective thicknesses were ~50, ~1, and ~2 μm . These features have traces along the <110> directions lying in the (001) plane. This observation is consistent with these features being SF's or SF clusters having {111} habit.

Figure 2 illustrates a substructural feature seen in the top layer of a DH device wafer. In order to assess its crystallography, the feature was examined under different operating reflections. It was thus established that Fig. 2(a) shows two overlapping SF's lying on the (111) planes. The lower fault is intrinsic in nature and the top one is extrinsic. The two faults are interconnected via an intrinsic SF having the (111) habit. The interconnecting fault is out of contrast in Fig. 2(a), but is visible in Fig. 2(b).

Another distinctive characteristic of the micrograph shown in Fig. 1 is shadows formed as a result of the interaction of growth terraces with the linear traces. This effect is not observed when terraces are nearly normal to the traces. Nonomura *et al.* (3) have recently reported similar observations on VPE grown GaAs layers. Since the step produced by an isolated SF on the (001) plane is extremely small, its interaction with

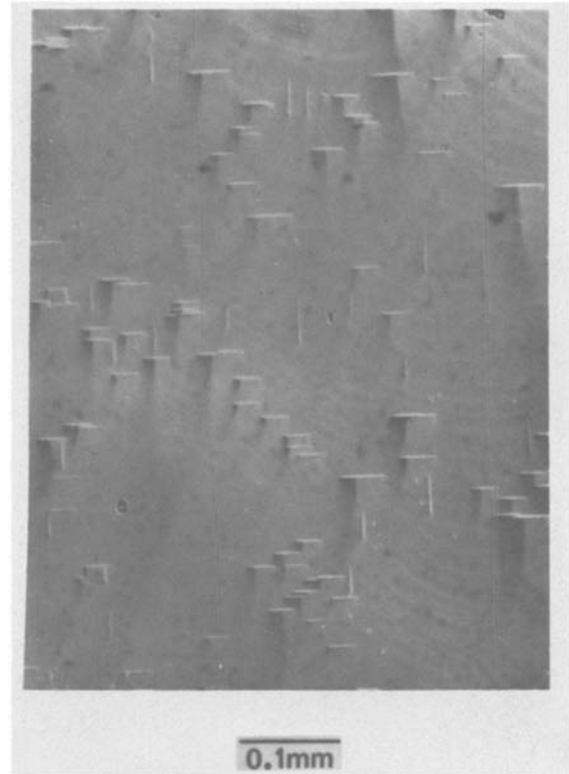


Fig. 1. An optical micrograph showing linear features on the top surface of a device wafer. Note the formation of shadows when growth terraces are nearly parallel to these linear features.

a growth lamella would not be discernible. Therefore to rationalize the observations of Fig. 1, it is suggested that the linear features are stacking fault clusters.

SEM micrographs of etching results on the (110) sections are shown in Fig. 3. Figure 3(a) depicts an SF that appears to originate very close to the substrate-epi interface. Nearly all the SF's examined had a similar origin. Occasionally SF's were observed to start from an inclusion embedded in the first layer. A typical example of this situation is shown in Fig. 3(b).

To assess the quality of the first (Ga,Al)As epi, a ~30 μm thick layer was grown on a Syton polished

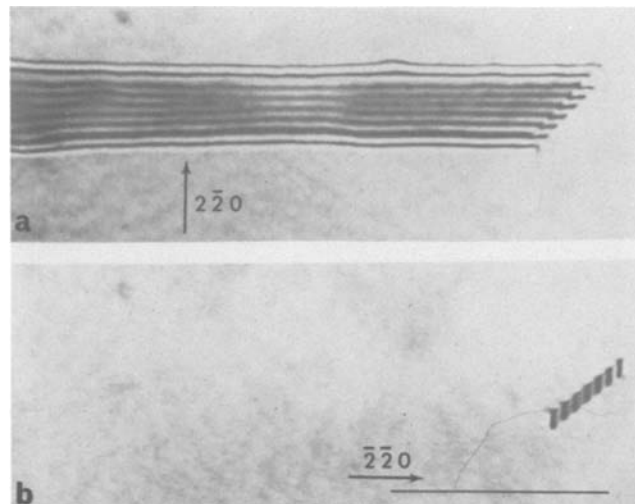


Fig. 2. Transmission electron micrographs showing two overlapping SF's observed in the top layer of a device wafer: (a) overlapping faults are in contrast; (b) a fault connecting the overlapping faults is in contrast. Plane of the micrograph in each case is ~{001}. Marker represents 1 μm .

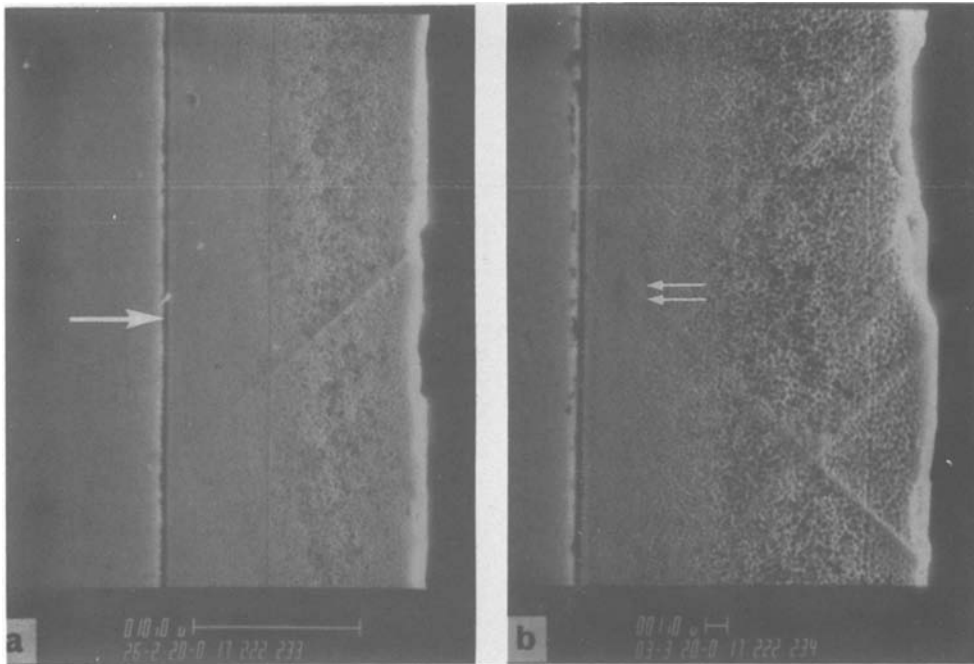


Fig. 3. SEM micrographs showing SF's on the cleaved and etched (110) sections of a device wafer. (a) SF starts at the substrate-(Ga,Al)As epi interface, and this represents a typical situation. (b) SF's start from an inclusion. In both cases, substrates were Syton polished. The substrate-epi interface in (a) and the inclusion in (b) are delineated by single and double arrows, respectively.

wafer. Long SF's similar to those observed on the top layer of the full DH device structure were observed by optical microscopy. Figure 4 depicts the typical situation seen by TEM. Dense dislocation tangles aligned along the [110] direction are the most noticeable microstructural features. Some weakly developed dislocation clusters can also be seen. In addition, microcracks running along the [110] and [110] directions were observed in samples thinned for TEM. This implies the existence of an internal stress. The magnitude of the stress in the layer σ_e was estimated to be 1.7×10^9 dynes/cm² from radius of curvature measurements using an approximation which assumes that the layer thickness t_e is negligible with respect to that of the substrate, t_s , where (4, 5)

$$\sigma_e = -\frac{E}{1-\nu} \cdot \frac{1}{6R} \cdot \frac{t_s^2}{t_e}$$

Here $E/(1-\nu)$ is 1.23×10^{12} dynes/cm² calculated from recent data reported by Jordan (6), and R is



Fig. 4. A transmission electron micrograph substructure observed in a thick (Ga,Al)As layer grown on a Syton polished GaAs substrate. Plane of the micrograph is $\sim(001)$. Marker represents 1 μ m.

the radius of curvature determined to be 0.65m using x-ray transmission measurements. The calculated stress value is a factor of 1.5 to 2 times higher than that reported previously (7, 8). However, in this case the ratio $t_e/t_s = 0.07$, which makes the negligible film thickness approximation questionable. Furthermore, contribution of the damage caused by the Syton polishing is not known and could be a factor in increasing the measured stress above that normally observed for layers in this composition range.

Substrate surface contamination was examined using x-ray photoemission and Auger spectroscopy. Both techniques indicated that the major contaminants were carbon and oxygen. Photoemission spectra of the As 2p_{3/2} core levels (Fig. 5) show comparable amounts of oxide present as As₂O₃ on both Syton and Br-methanol polished surfaces. The areas and binding energy positions of the Ga 2p_{3/2} core level spectra are also comparable, although in this case the resolution of our instrument is insufficient to separate the 1.1-1.2 eV (9, 10) chemical shift between substrate (GaAs) and oxide (Ga₂O₃) signals.

Derivative Auger spectra taken from Syton (slice No. 9) and Br-methanol (slice No. 84) polished wafers from the same boule (9104-2) are shown in the bottom two panels of Fig. 6. Carbon and oxygen are the pre-

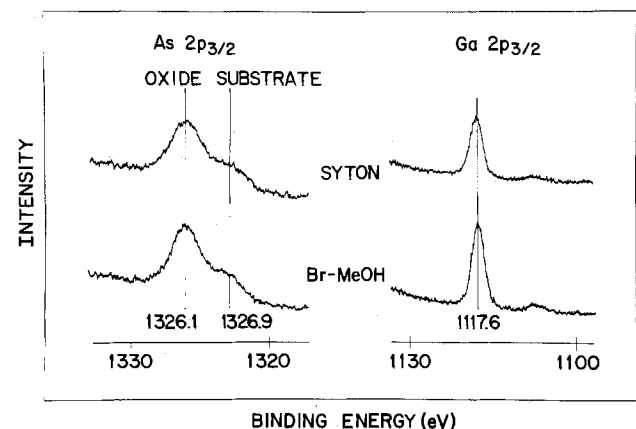


Fig. 5. X-ray photoemission spectra of the As and Ga 2p_{3/2} core levels observed on Syton (top) and Br-methanol (bottom) polished surfaces of GaAs.

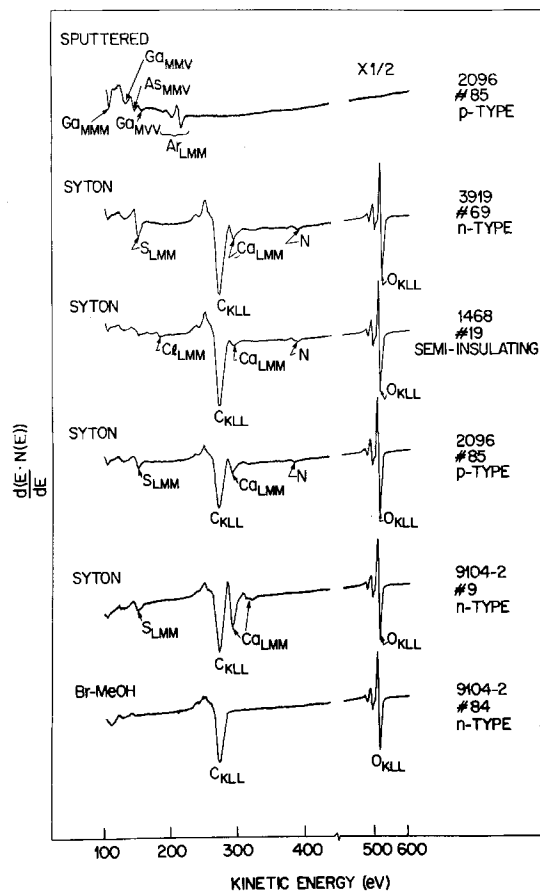


Fig. 6. Electron stimulated derivative Auger spectra for four Syton polished and one Br-methanol surface of GaAs.

dominant contaminants on both wafers, but appreciable calcium is also detected on the Syton polished surface along with traces of sulfur. The calcium signal decreases with time presumably due to electron stimu-

lated desorption. Syton polished samples from three different boules with differing carrier types were also examined. Calcium was systematically detected on all Syton polished surfaces as a major contaminant in addition to carbon and oxygen. Traces of sulfur and nitrogen appear sporadically as minor contaminants. The chlorine signal observed on wafer No. 1468-19 probably originates from inadvertent handling since chlorine was not detected on any other wafer.

The p-type sample from boule No. 2096 was mounted on a hot stage and sputter cleaned with argon ions at 500 eV. Calcium was not observed to segregate to the surface after heating the sample to 350°C for 2 hr; the calcium detected on the surface of Syton polished wafers appears to be strictly a surface contaminant which was not removed by organic cleaning agents such as acetone and chloroform but should be removed by substrate etchants such as $\text{H}_2\text{SO}_4:\text{H}_2\text{O}_2:\text{H}_2\text{O}$ (4:1:1).

To evaluate the influence of surface contamination on growth morphology, $\text{Ga}_{1-x}\text{Al}_x\text{As}$ ($x = 0.35$) layers were deposited simultaneously from the same melt on GaAs wafers that were prepared in three different ways. These were Syton polished, Syton polished and etched in a 4:1:1 solution of $\text{H}_2\text{SO}_4:\text{H}_2\text{O}_2:\text{H}_2\text{O}$, and Br-methanol polished wafers. A third of the wafers with these surface preparations and the normal organic solvent cleaning filled the substrate recess in the slider boat for this experiment. For investigating the early stages of growth morphology, deposition was carried out only for 2 sec, and these results are reproduced in Fig. 7. It is evident that growth on a Syton polished substrate [Fig. 7(a)] occurs in an island-like fashion, whereas layers grown on Syton + chemically etched [Fig. 7(b)] and Br-methanol polished [Fig. 7(c)] substrates are more or less continuous. These morphological differences are indeed reflected in the structural characteristics of thicker layers, $\sim 50 \mu\text{m}$, shown in Fig. 8. Large SF's are observed in the layer grown on a Syton polished wafer [Fig. 8(a)], while these features are absent in Syton polished and chemically etched [Fig. 8(b)] and Br-methanol polished [Fig. 8(c)] substrates.

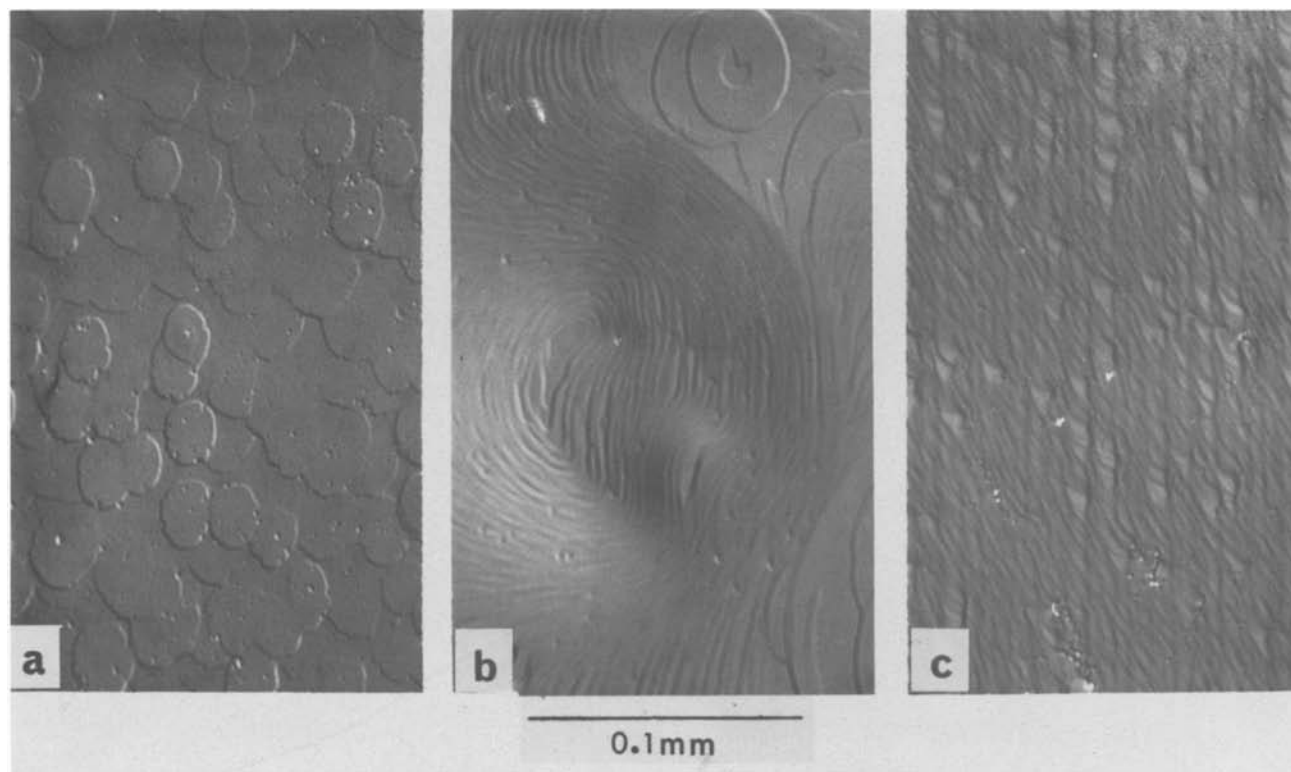


Fig. 7. Optical micrographs showing results of a 2 sec $(\text{Ga,Al})\text{As}$ epi growth on (a) Syton, (b) Syton polished and chemically etched, and (c) Br-methanol polished GaAs substrates. Note island-like growth morphology in (a).

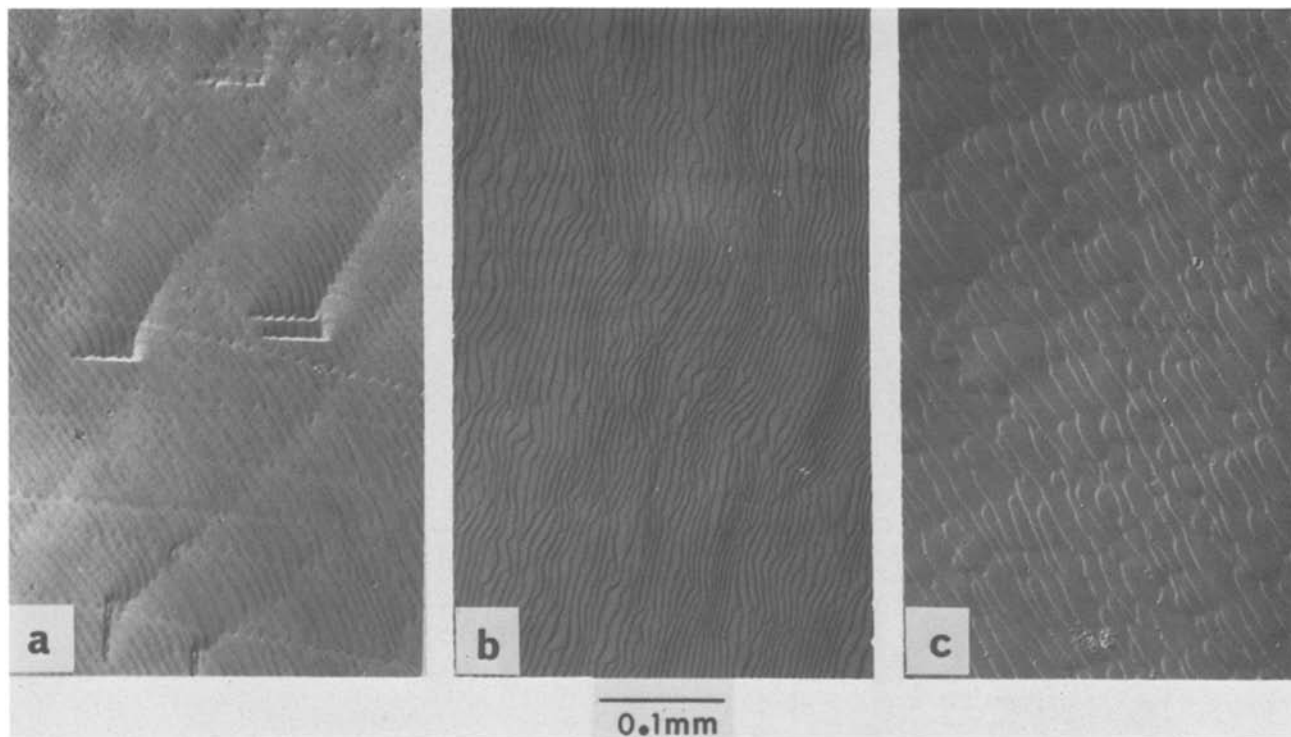


Fig. 8. Optical micrographs showing results of a 30 μm thick (Ga,Al)As epi growth on (a) Syton, (b) Syton and chemically etched, and (c) Br-methanol polished GaAs substrates. Note that SF's are only observed in (a).

In order to understand the origin of the defects, iso-epitaxial layers grown on Syton polished substrates were also studied. In this case the stacking faults were not observed, but the dislocation substructure was similar to that observed in Fig. 4 for the (Ga,Al)As/GaAs heteroepitaxy.

The above investigations suggest that the presence of calcium on the surface is a possible source for the origin of stacking faults. Two additional experiments were performed to ascertain the role of Ca, and consisted of simultaneous deposition of a 50 μm thick (Ga,Al)As layer on two substrates placed adjacent to each other. In the first case, the two substrates were cleaved from the same Syton polished wafer, but one of them was subsequently Ar-sputtered to remove Ca from the surface. The sputtering is estimated to remove 30-50Å of GaAs from the surface, essentially leaving the polishing damage unaffected. The ternary layer grown on the unsputtered wafer contained a large density of SF's while that on the sputtered sample showed virtually no faults. In the second experiment, the two substrates were cleaved from the same bromine-methanol polished wafer, but one was soaked in an aqueous solution of calcium nitrate to intentionally contaminate the surface with Ca. Prior to growth these two substrates were cleaned in chloroform and isopropanol. SF's were observed only in the ternary layer grown on the calcium contaminated substrate.

Discussion

The important observations which emerge from the preceding study are the following. (i) (Ga,Al)As epi-layers grown on (001) oriented Syton polished substrates contain fairly long SF's or SF clusters and fairly well-developed slip bands aligned along the [110] and $[\bar{1}\bar{1}0]$ directions. (ii) These layers are internally stressed and have a small radius of curvature. (iii) In the early stages of LPE of (Ga,Al)As, island-like morphology is observed on Syton polished substrates whose surfaces are contaminated with Ca. (iv) (Ga,Al)As layers grown on Syton polished and chemically etched as well as on Br-methanol polished substrates are essentially free of SF's (v) Iso-epitaxy of

GaAs on Syton polished GaAs is free from SF's but dislocation substructure is essentially similar to that observed in the case of (Ga,Al)As on GaAs. (vi) Calcium contamination appears to be necessary for the formation of stacking faults in the present situation.

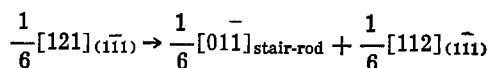
The mode of nucleation and initial growth of epi-layers is governed to a large extent by the bonding between deposit and substrate. A qualitative description of different situations which may evolve during LPE can be developed using the expression, $\sigma_{\text{SL}} = \sigma_{\text{SD}} + \sigma_{\text{DL}} \cos \theta$, where θ_{SL} , σ_{SD} , and σ_{DL} are the surface free-energies of the substrate-liquid, substrate-deposit, and deposit-liquid interfaces and θ is the contact angle between the substrate and deposit which is assumed to be in the form of a hemispherical cap. Following Bauer (8), three distinct cases could arise during initial film formation. When a deposit wets the substrate, i.e., $\theta = 0$, $\sigma_{\text{SL}} = \sigma_{\text{SD}} + \sigma_{\text{DL}}$ and growth would occur in a layer-by-layer manner as discussed by Frank and van der Merve (9). If $\sigma_{\text{SL}} < \sigma_{\text{SD}} + \sigma_{\text{DL}} \cos \theta$ and θ is finite, the layer nucleates by the formation of discrete three-dimensional islands which subsequently agglomerate to form a continuous layer. On the other hand, if $\sigma_{\text{SL}} > \sigma_{\text{SD}} + \sigma_{\text{DL}} \cos \theta$, continuous layers may form initially and at a later stage, discrete nuclei may form on top of these layers. It appears from the present observations that, due to the presence of Ca on Syton polished surfaces, (Ga,Al)As layer growth falls into the second category. Furthermore, since it was feasible to grow SF-free GaAs LPE layers on Syton polished substrates, it is inferred that contamination-free surfaces are more crucial in the growth of (Ga,Al)As layers.

Based on the work that was mainly carried out by Matthews (13), Bassett *et al.* (14), Pashley (15), Bassett and Pashley (16), Phillips (17), and Bassett (18), Pashley (19) has discussed various possibilities for the introduction of dislocations during epitaxial growth, and these are: (i) the replication of substrate dislocations; (ii) the aggregation of point defects leading to the formation of dislocation loops; (iii) the accommodation of translational and rotational displacements between coalescing islands that are close to epitaxial

orientation; (iv) plastic deformation of the layer, both during growth and subsequent cooling. If dislocations are homogeneously distributed in the substrate and the density is low, source (i) is expected to be of primary significance under ideal growth conditions, i.e., iso-epitaxy of thin layers on noncontaminated substrates (20). However, in the case of (Ga,Al)As epi growth on Syton polished GaAs substrates, the situation is more complex. Syton polishing is observed to introduce extensive dislocation damage in the surface regions of InP crystals (21), and it is very likely that a similar situation exists in the case of GaAs. This polishing-induced damage would certainly be replicated in epi-layers. In addition, the difference in the coefficients of expansion of (Ga,Al)As and GaAs may result in stresses during the cool down and this may promote deformation. The presence of high internal stress, small radius of curvature, and substructure observed in Fig. 5 are consistent with this suggestion. Furthermore, island-growth is certainly observed as shown in Fig. 8, but from the present experiments it is difficult to assess its contribution to the evolution of total substructures. It appears from the preceding discussion that probably all of the four sources listed above could be contributing to the observed dislocation structures.

The central question that remains to be resolved in the present study concerns the evolution of SF's in epi-layers. A plausible explanation may pertain to the accommodation of misfit between coalescing islands as discussed by Matthews (22). If the translational misfit between two agglomerating islands is equal to or close to an allowed shear vector for an SF, it is possible that a portion of the misfit is accommodated by the formation of an SF, whereas the remainder is taken up elastically. Similar arguments can be evoked to rationalize more complex situations involving the agglomeration of more than two islands. It appears that in the presence of a contaminant on the surface, the probability for the misfit to develop between two coalescing islands increases. It is however not clear why this probability is higher in the case of (Ga,Al)As epi-layers. This could be due to some complex interaction between Ca and Al.

The formation of the SF configuration observed in Fig. 2 can be rationalized if it is assumed that the Shockley partial bounding the lower fault dissociates into a stair-rod dislocation and another Shockley partial that can glide on the $(1\bar{1}1)$ plane. For example, if the lower fault is bound by the $\frac{1}{6}[121]$ partial, dissociation could occur according to the following reaction



The $\frac{1}{6}[112]$ dislocation could glide to form the connecting fault. This partial may subsequently dissociate resulting in the $\frac{1}{6}[121]$ and $\frac{1}{6}[0\bar{1}1]$ dislocations. The glide of the former partial on the $(1\bar{1}1)$ plane could produce the top fault.

Conclusion

The stacking faults observed in the LPE of (Ga,Al)As on Syton polished substrates are attributed to surface

contamination associated with calcium. On the other hand, the observed dislocation substructure could result from the replication of mechanical damage associated with the surface regions. Further, the layer are internally stressed, have a small radius of curvature and contain deformation-induced dislocation substructure. However, these problems can be obviated by chemical polishing with Br-methanol solutions which yields nearly defect-free layers.

Acknowledgments

The authors thank F. Ermanis for his help with the scanning electron microscope. We also acknowledge fruitful discussions with A. K. Chin, V. G. Keramidas, and R. H. Saul and appreciate the comments of O. G. Lorimor, G. Y. Chin, and J. H. Wernick on the manuscript.

Manuscript submitted Oct. 27, 1980; revised manuscript received Feb. 17, 1981. This was Paper 458 presented at the Hollywood, Florida, Meeting of the Society, Oct. 5-10, 1980.

Any discussion of this paper will appear in a Discussion Section to be published in the June 1982 JOURNAL. All discussions for the June 1982 Discussion Section should be submitted by Feb. 1, 1982.

Publication costs of this article were assisted by Bell Laboratories.

REFERENCES

1. T. Kotani, O. Ueda, K. Akita, Y. Nishitani, T. Kusunoki, and O. Ryuzan, *J. Cryst. Growth*, **38**, 85 (1977).
2. S. Komiya and T. Kotani, *This Journal*, **125**, 2019 (1978).
3. Y. Nonomura, Y. Okuno, and J. Nishizawa, *J. Cryst. Growth*, **46**, 795 (1979).
4. G. A. Rozgonyi and T. J. Ciesielka, *Rev. Sci. Instrum.*, **44**, 1053 (1973).
5. A. Brenner and S. Sonderoff, *Nat. Bur. Stand. J. Res.*, **42**, 105 (1949).
6. A. S. Jordan, *J. Cryst. Growth*, **49**, 631 (1980).
7. G. A. Rozgonyi, P. M. Petroff, and M. B. Panish, *ibid.*, **27**, 106 (1974).
8. E. Estpo, A. Izrael, and M. Savage, *Acta. Crystallogr. Sect. A*, **32**, 627 (1976).
9. Y. Mizokawa, H. Iwaski, R. Nishitani, and S. Nakamura, *J. Electron Spectrosc. Relat. Phenom.*, **14**, 129 (1978).
10. G. P. Schwartz, G. J. Gualtieri, G. W. Kammlott, and B. Schwartz, *This Journal*, **126**, 1737 (1979).
11. E. Bauer, *Z. Kristallogr.*, **110**, 395 (1958).
12. F. C. Frank and J. H. van der Merve, *Proc. Roy. Soc., A*, **198**, 216 (1949).
13. J. W. Matthews, *Philos. Mag.*, **4**, 1017 (1959).
14. G. A. Bassett, J. W. Menter, and D. W. Pashley, in "Structure and Properties of Thin Films," C. A. Neugebauer, J. B. Newkirk, and D. A. Vermilyea, Editors, p. 11, John Wiley, New York (1959).
15. D. W. Pashley, *Philos. Mag.*, **4**, 324 (1959).
16. G. A. Bassett and D. W. Pashley, *J. Inst. Metals*, **87**, 449 (1959).
17. V. A. Phillips, *Philos. Mag.*, **5**, 571 (1960).
18. G. A. Bassett, in "Proc. European Regional Conf. Electron Microscopy," Delft, A. L. Houwink and B. J. Spits, Editors, Vol. 1, p. 270, De Nederlandse Vereniging voor Electron mikrosco., Delft (1960).
19. D. W. Pashley, *Adv. Phys.*, **14**, 327 (1965).
20. S. Mahajan, V. G. Keramidas, A. K. Chin, W. A. Bonner, and A. A. Ballman, Submitted to *This Journal*.
21. S. Mahajan, V. G. Keramidas, and W. A. Bonner, Unpublished work (1980).
22. J. W. Matthews, *Philos. Mag.*, **7**, 915 (1962).

Thermally Induced Defect Behavior and Effective Intrinsic Gettering Sink in Silicon Wafers

Fumio Shimura, Hideki Tsuya, and Tsutomu Kawamura

Nippon Electric Company, Limited, Fundamental Research Laboratory,
Basic Technology Research Laboratories, Miyazaki, Takatsu, Kawasaki, Japan

ABSTRACT

Dislocation-free Czochralski silicon wafers have been subjected to a two-step annealing procedure to explore the intrinsic gettering (IG) phenomenon and the behavior of thermally induced microdefects using infrared absorption, preferential etching, and transmission electron microscopy (TEM). As a result, it is found that plastic lattice deformation introduced by dislocation and/or stacking faults is necessary for effective IG sinks. In spite of their extremely high density, microprecipitates with elastic strain but no plastic deformation do not result in effective IG. TEM observations clarify the change in density and/or structure of inner defects by precipitate dissolving after the second annealing at high temperature.

Czochralski-grown (CZ) silicon crystals are the main wafer source for the semiconductor devices such as bipolar and MOS. However, as a result of the precipitation of supersaturated oxygen, a variety of defects are produced when CZ silicon crystals are heat-treated because of their high concentration of oxygen.

These microdefects caused by oxygen precipitation are beneficial as is the case with intrinsic gettering (IG). Although IG has been regarded as an effective gettering technique for IC or LSI processing (1-7), effective sinks for IG and the behavior of inner defects during high temperature heat-treatments have not been examined closely yet.

The studies using infrared absorption, preferential etching, and transmission electron microscopy (TEM) analysis reported in this paper involve the IG phenomenon and the behavior of microdefects generated in two-step-annealed silicon wafers. As a result, the *sine qua non* of inner defects for IG effectiveness is shown. Furthermore, the TEM observation result of inner-defect conversion during the second annealing at high temperature (1230°C) suggests that inner defects should be freshly introduced during the following IC device processes.

Experimental

Samples used in this study were taken from the seed end of a 76 mm diam boron-doped $\langle 111 \rangle$ CZ crystal with regular diam overall length of approximately 30 cm and resistivity of 10-20 $\Omega \cdot \text{cm}$. Wafers 2 mm thick were etched to remove the damaged layer and then mirror polished on both sides in the usual fashion. Oxygen content of the as-grown specimen was $17.5-18.6 \times 10^{17} \text{ cm}^{-3}$ by the ASTM procedure F-121 (8). The radial distribution of oxygen content measured with a $0.4 \times 10 \text{ mm}$ infrared beam was observed to be uniform overall except at the rim of 5 mm in the wafers. In addition, the carbon content was less than $3 \times 10^{15} \text{ cm}^{-3}$ (detection limit). During the first annealing, specimens were subjected to heat-treatment at each temperature (600°, 750°, 950°, and 1100°C) for 16 hr in a dry O_2 atmosphere while the second annealing was at 1230°C for 2 hr in the same atmosphere. The heat-treated specimens were quenched by means of rapid withdrawal from a furnace and then were examined by infrared absorption, modified-Dash etching, and TEM with an accelerating voltage of 200 kV.

Results and Discussion

The infrared measurements, plotted as the concentration of interstitial oxygen before and after heat-

Key words: plastic deformation, transmission electron microscopy, high temperature annealing, defect structure conversion, Si-O precipitate dissolving.

treatments vs. the first annealing temperature, are shown in Fig. 1. A drastic change in the oxygen concentration occurred after the first annealing is mainly due to the precipitation of Si-O complex and the change after the second annealing is due to the synergism of Si-O precipitate dissolving (3) and the oxygen outdiffusion (9).

Surface- and inner-microdefect (about 100 μm from the surface) distribution in the annealed specimen is shown in Fig. 2. The first annealing temperature of the first quadrant in all specimens was 600°C, of the second quadrant in all specimens 750°C, etc., as shown in Fig. 2. After the first annealing no surface microdefects can be seen; however, swirl-like inner defect distribution can be observed in each quadrant except 600°C-annealed. On the other hand, surface microdefects were very apparent only in the 600°C-annealed quadrant after the second annealing.

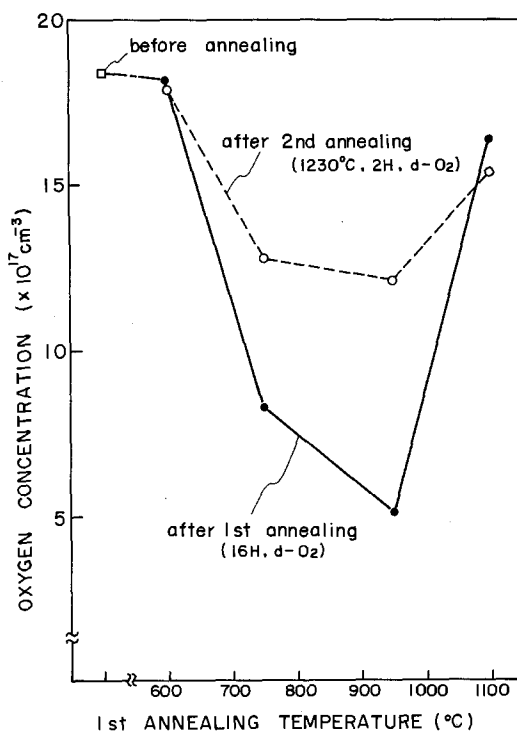


Fig. 1. Interstitial oxygen concentration change before and after first and second annealing.

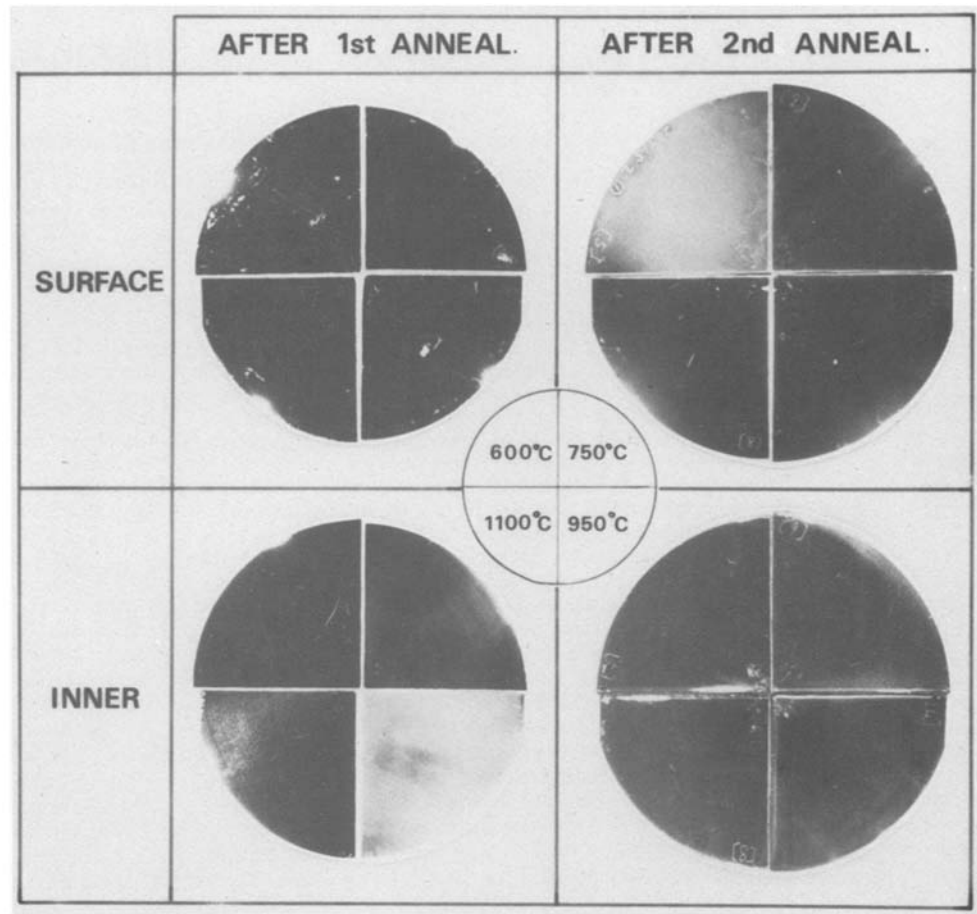


Fig. 2. Surface and inner defect distribution in annealed silicon wafer.

As previously reported (10), surface microdefects are apt to be generated in ungettered wafers annealed above 1100°C in a wet O₂ or above 1200°C in a dry O₂ atmosphere.

Optical micrographs of surface microdefects, revealed by modified-Dash etching, in each quadrant after the second annealing are shown in Fig. 3. Surface microdefects with the density of $4 \times 10^6 \text{ cm}^{-2}$ were generated only in the quadrant preannealed at 600°C. However, there are almost no surface defects in other

quadrants. TEM observation revealed that most of surface microdefects were impurity clusters (11) and some of them were small stacking faults with precipitates at the center. The small stacking fault figure agrees with the TEM image previously reported (10) and quite different from inner microdefects being presented below. A slight peak suggestive of the existence of copper was obtained by STEM-XMA examination for the precipitates located at the center of the small stacking faults (10). This suggests that impurity

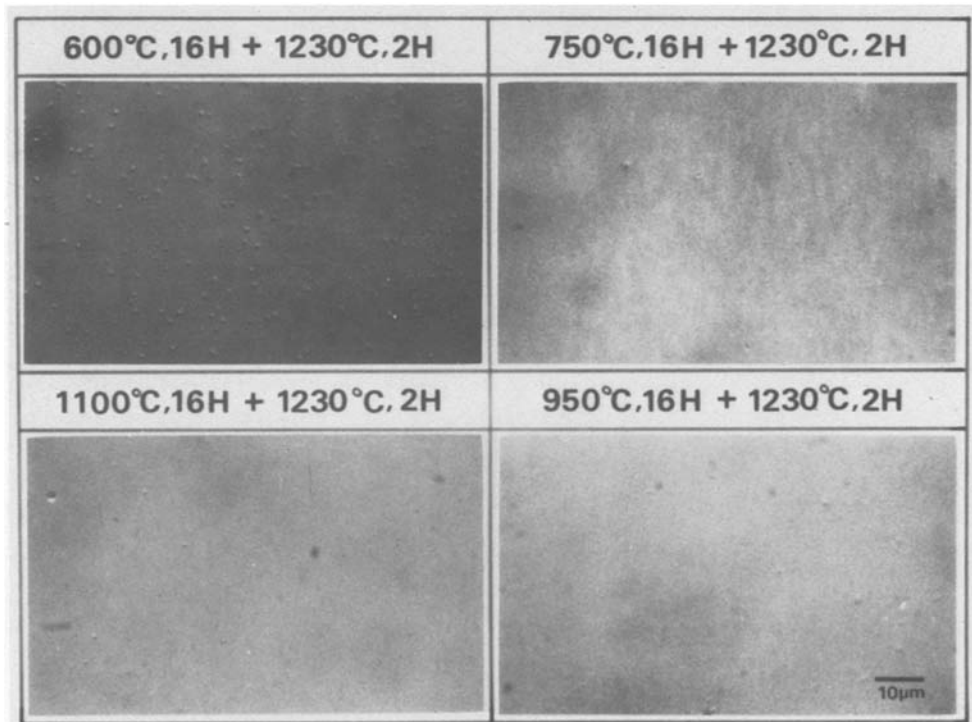


Fig. 3. Surface microdefects after second annealing revealed by modified-Dash etching.

clusters mentioned above originate small stacking faults under certain conditions.

Recently, Kishino *et al.* (12) verified the ability of IG using inner microdefects on copper-diffused wafers with the help of a neutron activation analysis (NAA). The result showed that the copper concentration was enhanced in the bulk region where a high density of microdefects were induced and the concentration in the denuded zone near the surface was proved to be below the detection limit of the NAA technique.

Consequently, Fig. 2 and 3 distinctly illustrate the IG phenomenon since surface microdefects are possibly caused by process-induced "heavy metal contamination" such as copper while inner microdefects act as gettering sinks for IG.

Inner microdefect etched shapes in the quadrants after the first and second annealing are shown in Fig. 4. In specimens after the first annealing, defect generation depends on the annealing temperatures, resulting in the decrease in oxygen concentration shown in Fig. 1.

Oxygen precipitation occurs by heterogeneous nucleation with grown-in precipitates and/or lattice defects (13). The precipitated oxygen $\Delta[\text{O}i]_T$ at the temperature T may be qualitatively described by the simplified function

$$\Delta[\text{O}i]_T = f(D_T, S_T, N_T, F, t) \quad [1]$$

where D_T is the diffusion constant of oxygen in silicon at T , S_T the supersaturated ratio of oxygen at T , N_T the number of "precipitate-nuclei" larger than critical radius at T , F the number and type of lattice defects introduced at the early stage of heat-treatment, and t the annealing time.

Although the oxygen precipitation depends on many factors as mentioned above, the most remarkable oxygen precipitation occurred in the specimen annealed at 950°C in this experiment. It is considered that the

largest oxygen precipitation in the 950°C-annealed specimen may be mainly due to more faults F introduced during the heat-treatment. That is, lattice defects induced by oxygen precipitates can be secondary heterogeneous nuclei for following oxygen precipitation during heat-treatment. Detailed discussion on oxygen precipitation using Eq. [1] will be presented in another paper.

The main defects in the 1100°C-annealed quadrant are large stacking faults. There are also microdefects with a low density. This shows that the swirl-like pattern in the 1100°C-annealed quadrant shown in Fig. 2 is mainly due to large (several tens micron) stacking faults, not to Si-O complex precipitates.

A distinct decrease in the density of inner microdefects is observed after the second annealing. This decrease is strongly correlated with the redissolving of Si-O complex precipitates. Differential infrared (DIR) and TEM studies have revealed that SiO_2 precipitates are obvious in an as-grown silicon crystal and the grown-in precipitates grow or shrink depending on annealing conditions (13).

Although modified-Dash etching cannot reveal inner microdefects in the 600°C-annealed specimen, the TEM weak-beam image indicates precipitate particles with a density of $\sim 1 \times 10^{14} \text{ cm}^{-3}$, as shown in Fig. 5. Dominant particles are around or under 60Å in size but are easily recognized by the strong compressive stress field in the surrounding matrix (14). The distribution of particle size in the annealed specimen may also depend on the grown-in precipitate size distribution in an as-grown crystal. The largest precipitate in the 600°C-annealed specimen is about 350Å and shows platelike morphology with a thickness of about 50Å. The result shows that the surface defects in the 600°C-annealed quadrant are not intrinsically gettering in spite of the high density of precipitates.

Figure 6 shows inner microdefects generated in the 750°C-annealed quadrant. Several hundred micron precipitates are dominant; in addition, dislocation dipoles and long-shaped dislocation loops are also observed.

Various kinds of microdefects such as precipitates, perfect dislocation loops (PL), and stacking faults (SF) with precipitate colonies at the center were observed in the 950°C-annealed quadrant as shown in Fig. 7. In Fig. 7(a) SF's (A, B, C, and D), that are extrinsic in nature and bounded by $a/3$ [111] Frank partials, are observable. From the observations under different conditions (g, z) as shown in Fig. 7(a), (b), (c), analysis of the SF faulted planes reveals A, B, C, and D to be $(11\bar{1})$, $(\bar{1}11)$, (111) , and (111) . Despite repeated observations and analyses of SF's, the frequency of the faults in any of the $\{111\}$ planes did not exhibit any particular tendency. Consequently, any $\{111\}$ plane could be the possible faulted plane. This homogeneous

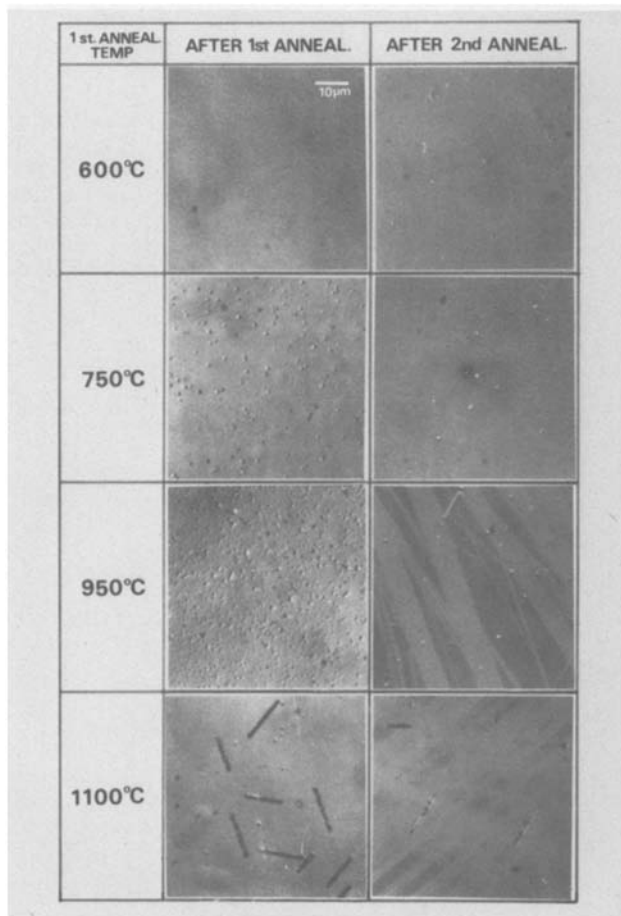


Fig. 4. Inner defects after first and second annealing revealed by modified-Dash etching.

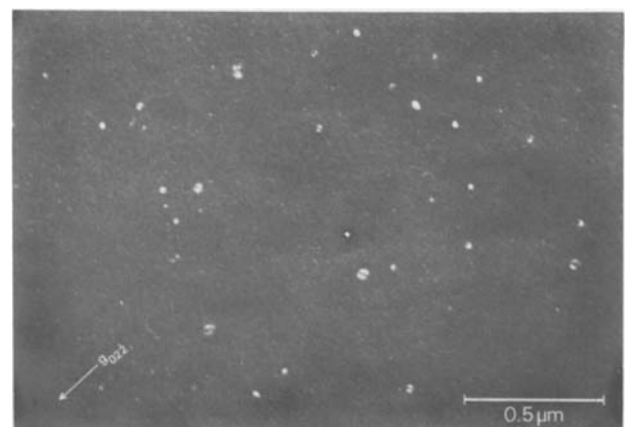


Fig. 5. TEM weak beam image of microprecipitates in 600°C-annealed specimen. $g = [022]$, $z \sim [433]$, $3g = 0$.

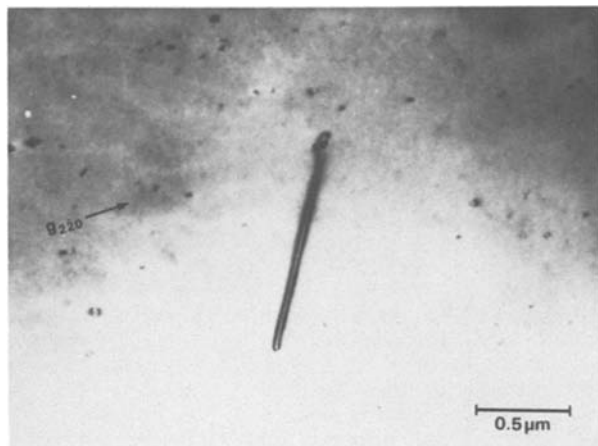


Fig. 6. Inner defects in 750°C-annealed specimen. $g = [\bar{2}20]$, $z \sim [332]$.

faulted plane distribution is explained by having prepared TEM samples at a 100 μm depth from the surface when SF size is only 0.6–0.8 μm . As a result, the influence of surface direction $\langle 111 \rangle$ is negligible. With extrinsic-type SF's the SF size increases nearer the wafer surface (Si-SiO₂ interface) because large vacancy undersaturation is generated by the oxidation process near the crystal surface (15). In fact, the SF size observed at a depth of 20 μm from the wafer surface is around 1.4 μm , or twice the size of SF's in the deeper region, as shown in Fig. 7.

In the 1100°C-annealed quadrant, regular octahedral precipitates, punched-out dislocations (POD), climbing dislocations (CD), and several ten micron SF's generated by the above precipitate (16) are observed. POD and CD from octahedral precipitate are shown in Fig. 8. Although the density of inner defects generated in the 1100°C-annealed quadrant is not large, as shown in

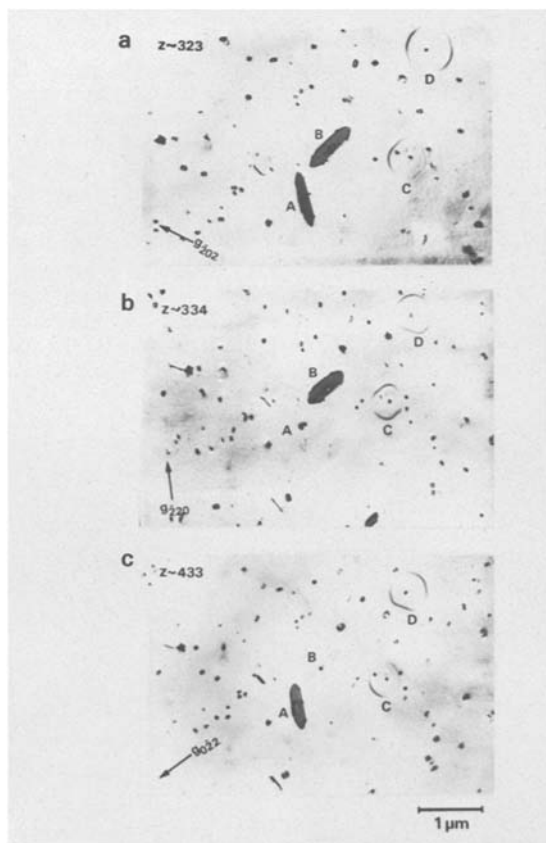


Fig. 7. Variety of inner microdefects in 950°C-annealed specimen: (a) $g = [\bar{2}02]$, $z \sim [323]$, (b) $g = [\bar{2}02]$, $z \sim [334]$, (c) $g = [022]$, $z \sim [433]$.

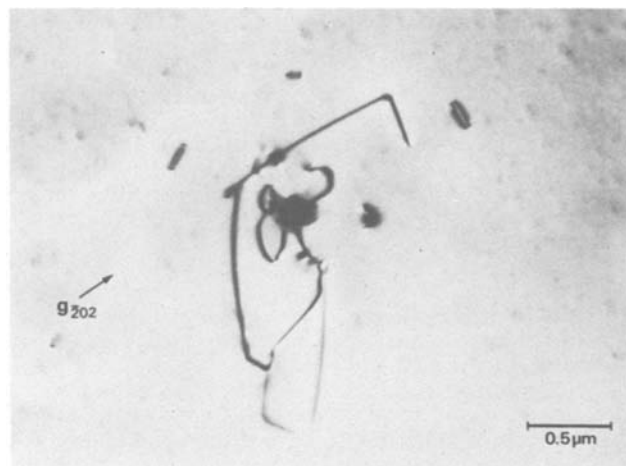


Fig. 8. Punched-out and climbing dislocations from octahedral precipitate in 1100°C-annealed specimen. $g = [\bar{2}02]$, $z \sim [111]$.

Fig. 4, distinct IG phenomenon is observed in the 1100°C-annealed quadrant as shown in Fig. 2 and 3.

The observations mentioned above support the conclusion that IG is determined more by the lattice defect and/or a precipitate being larger than a critical size than by the defect density. However, large precipitates which elastically compress the surrounding must repulse interstitial atoms rather than attract them. Consequently, the plastic deformation or dangling sites introduced by POD, CD, and SF may be necessary for IG when the IG mechanism and origin of surface microdefects is taken into consideration.

As mentioned previously, Si-O complex precipitates redissolve during the second annealing at 1230°C. Microprecipitates observed in 600°C- and 750°C-annealed specimens were not observed after the second annealing by TEM. They must have shrunk to an undetectable size as a result of redissolving (13). Although large SF's still existed, octahedral precipitates had become deformed in the 1100°C-annealed specimen after the second annealing, as shown in Fig. 9. The corners and edges of the octahedral precipitate are unclear because the unstable parts of corners and edges where dangling bonds exist redissolved preferentially. In addition, few POD and CD as shown in Fig. 8 were observable after the second annealing.

The most remarkable change in the inner defects before and after the second annealing occurred in the 950°C-annealed specimen. As shown in Fig. 7, many

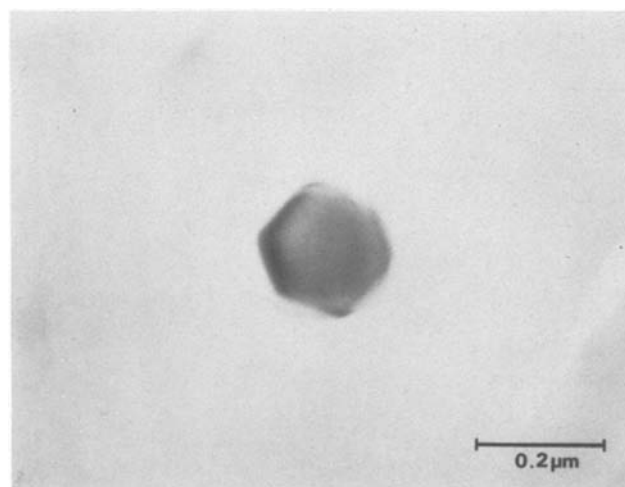


Fig. 9. Deformed-octahedral precipitate in specimen annealed at 1100°C for 16 hr and 1230°C for 2 hr. $g = [\bar{2}02]$, $z \sim [111]$.

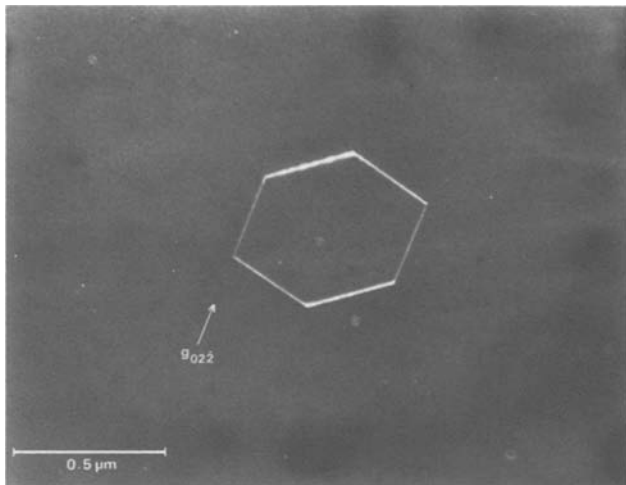


Fig. 10. TEM weak beam image of hexagonal perfect dislocation loop in specimen annealed at 950°C for 16 hr and 1230°C for 2 hr. $g = [022]$, $z \sim [433]$, $3g = 0$.

small precipitates and SF's with precipitate colonies at their center were observed in the 950°C-annealed specimen; however, few precipitates were observed after the second annealing. Instead, hexagonal-shaped perfect dislocation loops (PL) appeared, as shown in Fig. 10. This suggests that the conversion of the SF to PL occurred during the second annealing at high temperature. In the process oxygen atoms diffuse out of Si-O precipitates toward the bulk and silicon interstitials flow back to the precipitate location. Consequently, the vacancy-interstitial balance will be modified and the associated SF and dislocation are expected to change in shape and location. The mechanism for the conversion of SF to PL may be complicated, however, it is clear that the driving force for the change is oxygen redissolving and redistribution.

Conclusion

Intrinsic gettering (IG) phenomenon has been examined during two-step annealing and inner defects correlated with IG effectiveness analyzed using infrared absorption, preferential etching, and TEM techniques. As a result, it was found that plastic lattice deformation or dangling sites introduced by dislocation and/or stacking faults are necessary for effective IG sinks. Highly dense microprecipitates with elastic strain but no plastic deformation do not result in IG.

In addition, TEM observation clarified the conversion of a stacking fault to a perfect dislocation loop and the precipitate dissolving during high temperature heat-treatment. The behavior of inner defects suggests that the effectiveness of introduced inner defects for IG probably decreases after annealing at high temperatures such as 1230°C and that inner defects should be freshly introduced during the following IC device processes.

Acknowledgment

The authors wish to acknowledge Dr. T. Okada for his continued interest and encouragement in this work. They also wish to express their thanks to M. Mito for his technical assistance.

Manuscript submitted Nov. 18, 1980; revised manuscript received Feb. 2, 1981.

Any discussion of this paper will appear in a Discussion Section to be published in the June 1982 JOURNAL. All discussions for the June 1982 Discussion Section should be submitted by Feb. 1, 1982.

Publication costs of this article were assisted by Nippon Electric Company, Limited.

REFERENCES

1. T. Y. Tan, E. E. Gardner, and W. K. Tice, *Appl. Phys. Lett.*, **30**, 175 (1977).
2. G. A. Rozgonyi and C. W. Pearce, *ibid.*, **31**, 343 (1978).
3. G. A. Rozgonyi and C. W. Pearce, *ibid.*, **32**, 747 (1978).
4. L. E. Katz and O. W. Hill, *This Journal*, **125**, 1151 (1978).
5. K. H. Yang, H. F. Kappert, and G. H. Schwuttke, *Phys. Status Solidi A*, **50**, 221 (1978).
6. H. Tsuya, K. Tanno, and F. Shimura, *Appl. Phys. Lett.*, **36**, 658 (1980).
7. H. Tsuya, K. Ogawa, and F. Shimura, *Jpn. J. Appl. Phys.*, **20**, L31 (1981).
8. Annual Book of ASTM Standards, American Society for Testing Materials, Philadelphia (1977).
9. J. T. Yue and H. J. Ruiz, in "Semiconductor Silicon 1977," H. R. Huff and E. Sirtl, Editors, p. 596, The Electrochemical Society Softbound Proceedings Series, Princeton, N.J. (1977).
10. F. Shimura, H. Tsuya, and T. Kawamura, *J. Appl. Phys.*, **51**, 269 (1980).
11. F. Shimura, H. Tsuya, and K. Ogawa, Unpublished.
12. S. Kishino, K. Nagasawa, and T. Iizuka, *Jpn. J. Appl. Phys.*, **19**, L466 (1980).
13. F. Shimura, H. Tsuya, and T. Kawamura, *Appl. Phys. Lett.*, **37**, 467 (1980).
14. W. Patric, E. Hearn, W. Westdorp, and A. Bohg, *J. Appl. Phys.*, **50**, 7176 (1979).
15. K. V. Ravi, *Philos. Mag.*, **30**, 1081 (1974).
16. F. Shimura, *This Journal*, **127**, 910 (1980).

Thermodynamic Approach to the Deposition of Nonstoichiometric Solids from the Gas Phase: Example of Titanium Carbide at High Temperature

L. Vandenbulcke*

CRCCHT (CNRS) and Université d'Orléans, 45045 Orléans Cédex, France

ABSTRACT

A thermodynamic approach based on the minimization of the Gibbs free energy is used to calculate the pressure-temperature-composition ranges of stability of various solid phases in multicomponent gas-solid systems including nonstoichiometric solid phases. The conditions for the chemical vapor deposition of nonstoichiometric titanium carbide from $\text{TiCl}_4\text{-CH}_4\text{-H}_2$ at high temperature are given. The influence of nonstoichiometry and uncertainties of the thermodynamic data on the deposition domains of the various solids are pointed out. The relationships between the composition of the gaseous phase and the composition of the solid are also discussed.

The computation of chemical equilibrium appears as the first step of a fundamental study in chemical transport and chemical vapor deposition of a polycomponent system.

In chemical transport, suitable solvent components and temperature gradient can be chosen on a theoretical basis. Thus feasibility of the transport can be derived from calculations of two equilibria, at the source and sink end of the tube, by minimization of the Helmholtz free energy (1). Indications about the transport rate by diffusion and convection are obtained by a diffusion/laminar flow model using thermodynamic results of the Gibbs free energy minimization technique; this model takes into account all gaseous species and does not require specifying individual chemical reaction (1-3).

Chemical vapor deposition is also a very complex dynamic process, where chemical kinetics combined with mass transport often control the deposition rate. But at high enough deposition temperature and low mass flow rate, the deposition rate is limited only by mass transport since the temperature dependence of chemical rate-limiting steps is much greater than the temperature dependence of gaseous diffusion; thus, the heterogeneous chemical kinetics is sufficiently fast to allow equilibrium conditions at the gas-solid interface to be approached. In all cases, a model of mass transfer combined with a dynamic equilibrium at the gas-solid interface permits the calculation of maximum limits for the conversion of reactants into products at the interface, and of the deposition rate when homogeneous nucleation is avoided. It is the rate that would be achieved in the absence of significant surface resistances to the deposition (4, 5).

Therefore, of special interest is the increasing use of the thermodynamic approach to calculate the gas phase composition in equilibrium with the solid and the theoretical efficiencies of the deposition at equilibrium, to ascertain the chemical compatibility of the substrate with the gas phase in the first stages of the deposition, to define the pressure-temperature-composition ranges of stability of various solid phases in multicomponent gas-solid systems [reviewed in (6)]. All these calculations apply to the deposition of stoichiometric solids. But many solid solutions can be deposited, the compositions of which vary with temperature, pressure, and composition of the gas phase; moreover, good control of these compositions is necessary to obtain satisfactory results and optimize the properties of the materials.

The calculations would be therefore extended to the deposition of nonstoichiometric solids.

In this paper, a thermodynamic approach to the chemical vapor deposition of nonstoichiometric titanium carbide from $\text{TiCl}_4\text{-CH}_4\text{-H}_2$ mixtures is presented. The Ti-C-H-Cl system has been extensively studied but stoichiometric TiC was generally considered (7-9). Only one paper was devoted to the deposition of nonstoichiometric TiC_x , but the method employed is not general as it imposes the composition of the TiC_x phase; thus, only the limits of the deposition domains of $\text{Ti} + \text{TiC}_{0.52}$ and $\text{TiC} + \text{C}$ with the titanium carbide phase can be easily determined (9).

Generalities of the Calculation Procedure

The chemical equilibrium calculations involve the minimization of the total Gibbs free energy of the system, taking into account several constraints. In CVD systems, these constraints are the mass balance of each element, constant temperature, and constant total pressure. Several programs have been reported for such computation (10-12). A slightly modified version of SOLGASMIX program written by Eriksson (12) has been employed to perform the calculations of this paper. In this program, nonstoichiometric solids can be considered.

The calculation requires specifying the species which can be formed at equilibrium and the corresponding thermodynamic data.

Species in the Ti-C-H-Cl system.—The attack of the substrate during the initial stages of deposition (13), or of the CVD reactor wall, or of the tube in transport processes sometimes introduces new species in the system. Here, all of these solids are considered as inert toward the gaseous phase.

The following species have been considered: H_2 , CH_4 , C_2H_2 , CCl_4 , Cl_2 , HCl , TiCl_4 , TiCl_3 , TiCl_2 , and TiCl as constituents of the gas phase (other species like H , Cl ... were eliminated as their equilibrium concentrations were negligible); pure Ti, pure C and TiC_x as solids [pure Ti was considered, as the solubility of C in Ti is low (14)].

Thermodynamic data.—To calculate the total free energy of the system, values of the Gibbs free energy of formation of the species from the elements in their chosen reference states have to be specified. For all species in the gaseous phase, values were taken from the JANAF thermochemical tables (15). However, data from other sources must be used in the case of nonstoichiometric titanium carbide.

* Electrochemical Society Active Member.
Key words: solids, thermodynamics, CVD.

The extent of the homogeneity range of the TiC_x is fairly well known. At $T = 1900$ K, the limits of the atomic ratio C/Ti are about 0.51 and 0.98 (14). At this temperature, Storms has measured the Ti pressure over various composition of TiC_x using a mass spectrometer. His results (14) are reported in Fig. 1 with, in addition, the value of the Ti pressure over pure solid Ti given by Nesmeyanov ($p_{\text{Ti}}^{\circ}(1900 \text{ K}) = 3 \times 10^{-6}$ atm) (16). In order to utilize these data, a relationship giving the activity or activity coefficient as a function of the composition must be known. In general, a polynomial expression is used which fits the curve to the set of data points by the method of least squares. For $0.51 < C/\text{Ti} < 0.98$, the curve of Fig. 1 is inferred from the following relation

$$\ln \gamma_{\text{Ti}} = -1702.72 + 10865.97 X_{\text{Ti}} - 26354.96 X_{\text{Ti}}^2 + 28651.25 X_{\text{Ti}}^3 - 11728.11 X_{\text{Ti}}^4 \quad [1]$$

where γ_{Ti} is the activity coefficient for Ti and X_{Ti} is the molar fraction of Ti in TiC_x .

When $C/\text{Ti} \geq 0.98$ (in the two-phases domain $\text{TiC}_{0.98} + \text{C}$), the activity of C equals 1 and the activity of titanium is constant and equal to its value in $\text{TiC}_{0.98}$, that is

$$a_{\text{Ti}} = p_{\text{Ti}}(\text{in TiC}_{0.98})/p_{\text{Ti}}^{\circ}(\text{pure}) \\ \gamma_{\text{Ti}} = 4 \times 10^{-5}/X_{\text{Ti}}$$

To define completely the thermodynamic properties of the TiC_x phase, one must know the values of the activity of carbon as a function of the composition. The activity coefficient of carbon can be obtained from the values of γ_{Ti} by integration of the Gibbs-Duhem equation. The following relation was obtained

$$\ln \gamma_{\text{C}} = -34.74 + 44.50 X_{\text{C}} + 111.97 X_{\text{C}}^2 - 46.89 X_{\text{C}}^3 - 366.19 X_{\text{C}}^4 - 162.03 X_{\text{C}}^5 + 1256.05 X_{\text{C}}^6 \quad [2]$$

which applies in the range $0.51 < C/\text{Ti} < 0.98$.

When $C/\text{Ti} \leq 0.51$ (in the two-phases domain $\text{Ti} + \text{TiC}_{0.51}$), the activity of titanium is supposedly equal to 1 and the activity of carbon is constant and equal to its value in $\text{TiC}_{0.51}$, that is $a_{\text{C}} = 1.448 \times 10^{-6}$.

Initial parameters.—The calculations of the complex equilibrium in the Ti-C-H-Cl system were carried

out as a function of the initial composition in $\text{TiCl}_4\text{-CH}_4\text{-H}_2$. The temperature and total pressure were constant and equal to 1900 K and 1 atm, respectively.

Results and Discussion

Thermodynamic calculations are often used to specify the ranges of initial composition which will produce the desired solids at equilibrium. The location of the limits between the different domains of solid deposition can be influenced by taking into account the nonstoichiometry of the solids and by the accuracy of the thermodynamic data used.

Influence of nonstoichiometry and uncertainties of the thermodynamic data on the deposition domains of the solid phases.—Figure 2 shows how the phase boundaries change as a function of TiCl_4 and CH_4 partial pressures. Hydrogen makes up the difference between 1 atm and the sum of the titanium tetrachloride and methane partial pressures. The full lines give the boundaries obtained for nonstoichiometric titanium carbide (TiC_x); the dotted lines present, for comparison, the results obtained if deposition of stoichiometric TiC is assumed. The boundary shift is not very important, particularly for the limit between the TiC_x and $\text{TiC}_{0.98} + \text{C}$ domains of deposition. As expected, the TiC_x domain is enlarged relative to the stoichiometric TiC domain, in the Ti-rich region.

The accuracy with which an equilibrium composition can be computed lies in the uncertainties of the thermodynamic data used. Table I gives, as an example, the values of the free energy of formation of TiCl_2 , TiCl , and CCl_4 from JANAF 1971 and JANAF 1966 (17). All the other values remain constant in the second edition.

Figure 3 shows the influence of these values on the amount of solid phases deposited at equilibrium for $p_{\text{TiCl}_4}^{\circ} = 10^{-4}$ atm and different values of $p_{\text{CH}_4}^{\circ}$. The calculations were carried out for stoichiometric TiC. Variations of the data used do not produce sensitive differences in the amounts of TiC and C which are represented as full lines. The amount of Ti is more influenced; it is reported, respectively, as a full line and a dotted line when data of JANAF 1971 and JANAF 1966 are used. For constant $p_{\text{CH}_4}^{\circ}$, the amount of Ti decreases when the stability of the titanium dichloride increases.

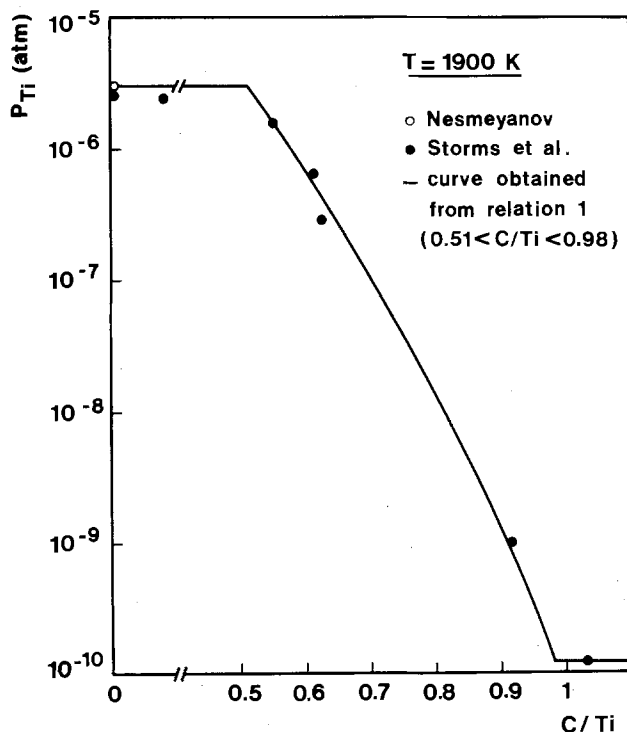


Fig. 1. Pressure of Ti over Ti-C solids

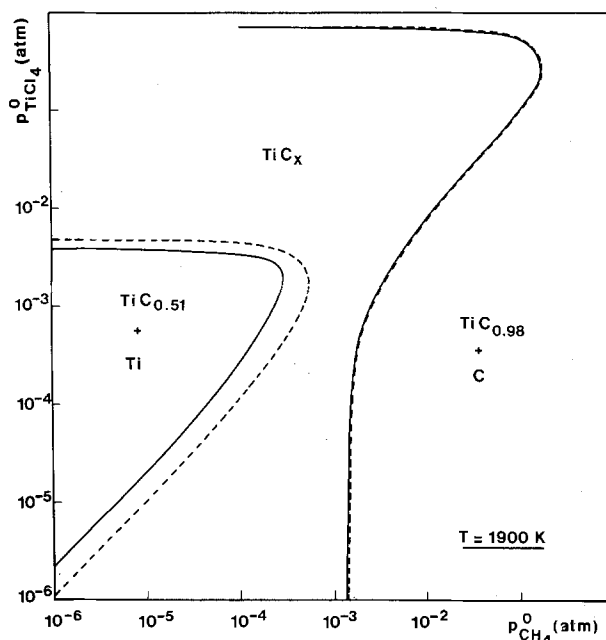


Fig. 2. Phase fields for solid species deposited at equilibrium. The full and dotted lines represent, respectively, the single phase limits of nonstoichiometric and stoichiometric titanium carbide. The hydrogen partial pressure brings the total pressure to 1 atm.

Table I. ΔG_f° values given by JANAF 1971 and JANAF 1965-1966 (cal/mol)

| | JANAF 1971 | JANAF 1965-1966 |
|-------------------------------|------------|-----------------|
| H ₂ | 0 | |
| CH ₄ | 28,522 | |
| TiCl ₄ | -127,453 | |
| TiCl ₃ | -105,714 | |
| TiCl ₂ | -65,341 | -76,145 |
| TiCl | -8720 | -8528 |
| Cl ₂ | 0 | |
| HCl | -25,353 | |
| C ₂ H ₂ | 29,199 | |
| CCl ₄ | 37,488 | -34,553 |
| C | 0 | |
| Ti | 0 | |
| TiC | -38,291 | |

For comparison, the arrows give the deposition limits of the nonstoichiometric TiC_x single phase, which show that the influence of nonstoichiometry is lower than the influence of uncertainties in the thermodynamic data of the titanium subchlorides.

The primary interest in the present calculations, which take into account nonstoichiometric condensed species, lies principally in the determination of the variation of the TiC_x composition in the single phase domain.

Deposition of nonstoichiometric titanium carbide.—

As shown on Fig. 2, titanium carbide is deposited at equilibrium as a single phase under a wide variety of initial composition. TiC_x is codeposited with C at high initial partial pressure of CH₄; it is codeposited with Ti at low $p_{\text{CH}_4}^\circ$ except for high initial partial pressure of TiCl₄. This is a result of the high stabilities of TiC_x and titanium chlorides as compared to Ti.

The production of the different solids is bound to the composition of the gaseous phase, as can be seen in Fig. 4 which gives for $p_{\text{TiCl}_4}^\circ = 10^{-4}$ atm and $p_{\text{CH}_4}^\circ$ varying from 10^{-5} to 10^{-2} atm, the equilibrium yields (η) of the different gaseous and solid species. η are defined with respect to $n_{\text{TiCl}_4}^\circ$ for titanium-containing species (curves in full lines) and $n_{\text{CH}_4}^\circ$ for carbon-containing species (curves in dotted lines)

$$\eta = n_i (\text{Ti}_y\text{X}_z) / n_{\text{TiCl}_4}^\circ \quad \text{and} \quad \eta = n_i (\text{C}_y\text{X}_z) / n_{\text{CH}_4}^\circ$$

where n_i represents the number of Ti and C atoms in species i at equilibrium and $n_{\text{TiCl}_4}^\circ$ and $n_{\text{CH}_4}^\circ$ the initial number of TiCl₄ and CH₄ moles ($n_i^\circ = p_i^\circ$ as $\sum n_i^\circ = 1$ mole and $P = 1$ atm). The equilibrium yields of the following species TiCl₄, Cl₂, and CCl₄ are not reported as n_i is lower than 10^{-10} atoms. On the other hand the concentrations of H₂ and HCl are always important. Several facts can be noted from this figure.

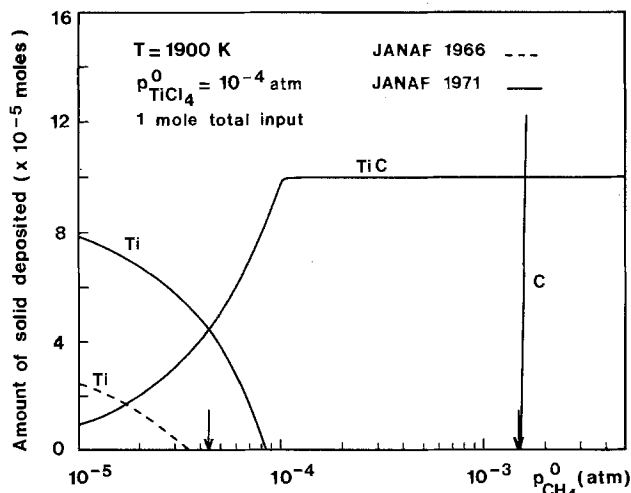


Fig. 3. Influence of the thermodynamic data on the single phase limits of stoichiometric TiC. The TiC/TiC + C limit is unchanged; the Ti + TiC/TiC limit varies. Arrows represent the limit for nonstoichiometric TiC_x ($0.51 \leq x \leq 0.98$).

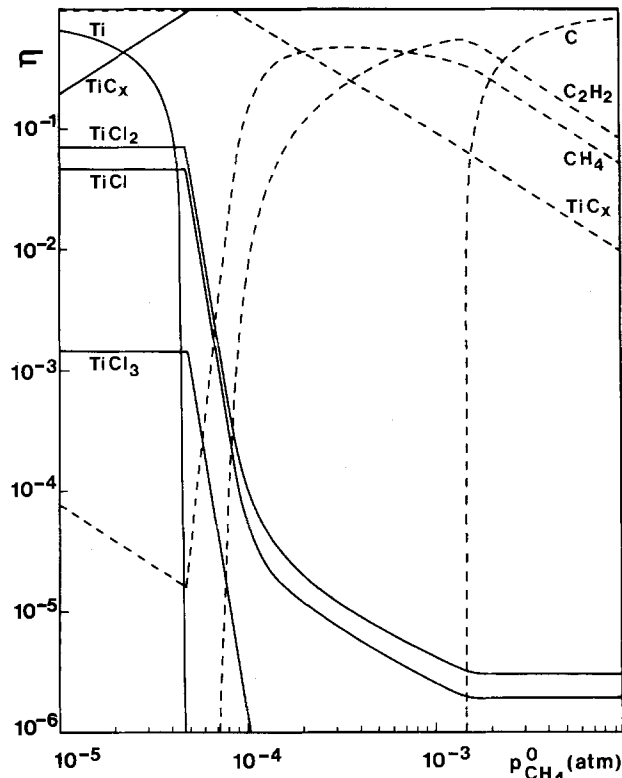


Fig. 4. Variations of the equilibrium yield of the principal species as function of $p_{\text{CH}_4}^\circ$. (The value of $p_{\text{TiCl}_4}^\circ$ is constant and equal to 10^{-4} atm, $T = 1900$ K).

1. The concentrations of the titanium subchlorides are high in the (Ti + TiC_{0.51}) two-phase domain and decreases in the TiC_x single phase domain as $p_{\text{CH}_4}^\circ$ increases. Conversely, the concentrations of CH₄ and C₂H₂ which are negligible in the (Ti + TiC_{0.51}) deposition domain become preponderant in the (TiC_{0.98} + C) one.

2. Accordingly, almost all titanium is engaged in the titanium carbide when $p_{\text{CH}_4}^\circ / p_{\text{TiCl}_4}^\circ > 1$ and all carbon is incorporated in the titanium carbide when $p_{\text{CH}_4}^\circ / p_{\text{TiCl}_4}^\circ < 1$. The amount of titanium carbide increases when $p_{\text{CH}_4}^\circ$ increases, up to $p_{\text{CH}_4}^\circ / p_{\text{TiCl}_4}^\circ = 1$ where it reaches nearly the maximum possible value. The amounts of pure Ti and C are clearly strong functions of the excess in TiCl₄ and CH₄ input species.

The corresponding variation of the atomic ratio C/Ti in the titanium carbide phase is shown in Fig. 5 to-

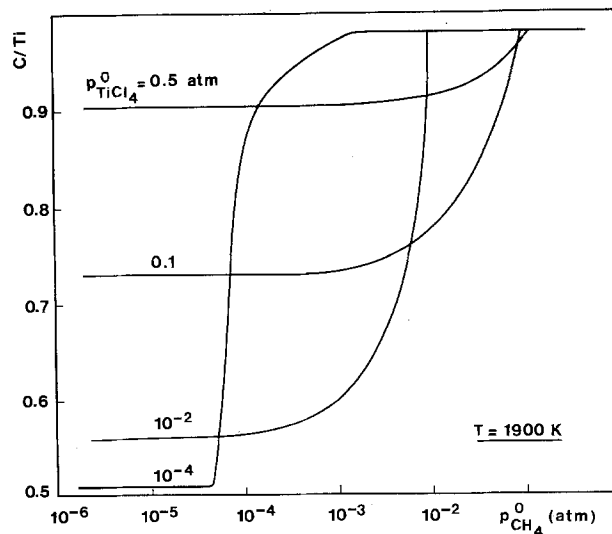


Fig. 5. Variations of the C/Ti ratio in the nonstoichiometric titanium carbide phase as function of $p_{\text{CH}_4}^\circ$.

gether with the curves obtained for other values of $p_{\text{TiCl}_4}^0$, equal to 10^{-2} , 10^{-1} , and 0.5 atm. One can note that the minimum possible value of C/Ti increases when $p_{\text{TiCl}_4}^0$ increases. This fact can also be observed in Fig. 6 which represents the complete "CVD phase diagram" for Ti-C solids deposited from $\text{TiCl}_4\text{-CH}_4\text{-H}_2$. Titanium carbide can be deposited as a single phase from a wide variety of input gaseous compositions, but this diagram shows, the sensitivity to the experimental conditions for depositing this phase with the desired composition.

Comparison between this thermodynamic approach and some experimental results at high temperature cannot now be done. Only the experimental work of Nadal and Ducarroir was carried out at high temperature (1800 K); the limit between the titanium carbide and titanium carbide plus free carbon was experimentally found, but the compositions in the single phase domain were not determined (18). Their work on this is in progress (19).

Conclusions

The chemical transport and chemical vapor deposition in multicomponent gas-solid systems are complex processes in which many factors can affect the deposition mechanisms and the final composition and structure of the materials. In a first attempt, a thermodynamic approach gives information about the optimum conditions for the synthesis of specified solid phases, keeping in mind that the accuracy of the conclusions can be limited (i) by the uncertainties of the thermodynamic data; for many species, accurate values are not available; (ii) because significant departure from equilibrium can be produced, especially in open flow reactors; (iii) because important departure from equilibrium is necessary to produce specific solid structures, for example amorphous materials.

Another limitation is avoided by considering nonstoichiometric phases. For example, titanium carbide of all compositions within the homogeneity range can be deposited at equilibrium as a function of the initial parameters: temperature, total pressure, and principally the input composition of the gaseous phase. In-

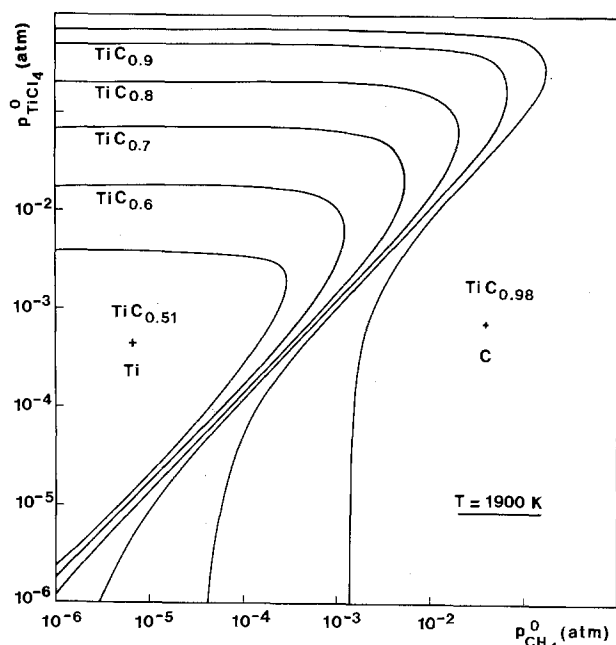


Fig. 6. Phase fields for solid species deposited at equilibrium in the Ti-C-H-Cl system, showing the iso-concentration curves in the titanium carbide single phase domain.

formation is also obtained about the composition of the gaseous phase in equilibrium with the different solids, which permits one to deduce the preponderant species and thus derive the principal chemical reactions.

The thermodynamic approach to the deposition of nonstoichiometric titanium carbide will be extended to lower temperatures. More experimental results on the CVD of titanium carbide are indeed available at lower temperature and pressure, and the fundamental interest of such calculations lies also in determining the influence of some departure from equilibrium on the solid composition which often arises at low temperature [this factor was shown to be very important in the CVD of boron carbide at relatively low temperatures (5)]. Moreover, industrial applications have shown that control of the deposit's composition must be improved, for example, to optimize the wear resistance of coatings such as titanium carbide.

Manuscript submitted Nov. 19, 1980; revised manuscript received March 3, 1981.

Any discussion of this paper will appear in a Discussion Section to be published in the June 1982 JOURNAL. All discussions for the June 1982 Discussion Section should be submitted by Feb. 1, 1982.

Publication costs of this article were assisted by the Centre National de la Recherche Scientifique.

REFERENCES

1. C. Bernard, G. Constant, and R. Feurer, in "Seventh International Conference on CVD," T. O. Sedgwick and H. Lydtin, Editors, p. 368, The Electrochemical Society Softbound Proceedings Series, Princeton, N.J. (1979).
2. B. I. Nölång and M. W. Richardson, *J. Cryst. Growth*, **34**, 198 (1976).
3. B. I. Nölång and M. W. Richardson, *ibid.*, **34**, 205 (1976).
4. L. Vandenbulcke and G. Vuillard, *This Journal*, **124**, 1931 (1977).
5. L. Vandenbulcke in "Seventh International Conference on CVD," T. O. Sedgwick and H. Lydtin, Editors, p. 315, The Electrochemical Society Softbound Proceedings Series, Princeton, N.J. (1979).
6. K. E. Spear in "Seventh International Conference on CVD," T. O. Sedgwick and H. Lydtin, Editors, p. 1, The Electrochemical Society Softbound Proceedings Series, Princeton, N.J. (1979).
7. M. Ducarroir, M. Jaymes, C. Bernard, Y. Deniel, and A. Jacquot, *J. Cryst. Growth*, **23**, 299 (1974).
8. M. Ducarroir, M. Jaymes, C. Bernard, and Y. Deniel, *J. Less Common Metals*, **40**, 173 (1975).
9. F. Teyssandier, M. Ducarroir, and C. Bernard, *Industrial Use of Thermochemical Data*, Gilford-England, Sept. 11-13, 1979.
10. S. Gordon and B. J. McBride, NASA SP-273 (1971).
11. C. Bernard, Y. Deniel, A. Jacquot, P. Vay, and M. Ducarroir, *J. Less Common Metals*, **40**, 165 (1975).
12. G. Eriksson, *Chem. Scr.*, **8**, 100 (1975).
13. J. Thébault, R. Naslain, and C. Bernard, *J. Less Common Metals*, **57**, 1 (1978).
14. E. K. Storms, in "The Refractory Carbides," J. L. Margrave, Editor, Academic Press, New York, London (1967).
15. JANAF Thermochemical Tables, 2nd ed., National Standard Reference Data Series, National Bureau of Standards, NSRDS-NBS 37, U.S. Government Printing Office, Washington, D.C. 20402.
16. A. N. Nesmeyanov in "Vapor Pressure of Chemical Elements," R. Gary, Editor, N.B.S., Elsevier Publishing Company (1963).
17. JANAF Thermochemical Tables, 1st edition and Third addendum, Dow Chemical Co., Midland, MI (1965 and 1966).
18. M. Nadal and M. Ducarroir, 9th Int. Symp. on the Reactivity of Solids, Cracovie-Poland, Sept. 1-6, 1980.
19. M. Ducarroir, Personal communication.

Preparation of AlN Coatings on Mo by RF-Reactive Ion Plating: The Deposition Mechanism

Masahiro Kitajima, Masao Fukutomi, Masatoshi Okada, and Ryoji Watanabe

National Research Institute for Metals, Tsukuba Laboratories,
1-2-1, Sengen, Sakura-Mura, Niihari-Gun, Ibaraki-Ken, Japan

ABSTRACT

Aluminum nitride films were deposited at 0.15-0.33 $\mu\text{m}/\text{min}$ on Mo by rf-reactive ion plating as an application of a low-Z material or a refractory coating. The structure, chemical state, and composition of the deposits were analyzed by scanning electron microscopy, x-ray diffraction, infrared and AES spectra, and x-ray microanalyzer; the deposits were confirmed to be aluminum nitride. Any nitride films improved the oxidation resistance of Mo up to 1100°-1200°C, and the adhesion and thermal cycle stability of the coatings were good. The composition of the deposit effectively depended on the partial pressures of reactant gases. The free Al of the nonstoichiometric deposits may lead to local film failure under high temperature vacuum. The relation between degree of nitridation and mean free path of the gas suggests that the reaction between Al and NH_3 occurs on the substrate surface. The morphology is discussed in terms of the mean free path, and the nitridation rate is also described.

Aluminum nitride has been regarded as a useful ceramic, because of its excellent mechanical properties and chemical stability at high temperature, and is applied as an insulator of electronic materials and as a material corrosion resistant to molten metals or salts. Recently, low atomic number (low-Z) materials are receiving increased attention for fusion devices. The release of plasma contaminants with large atomic number Z from first wall components in plasma devices causes significant increases in plasma resistivity and in plasma losses due to electromagnetic radiation. This can prevent the ignition of fusion reactions. The effect may be minimized by use of low-Z materials (1, 2). In our laboratory, a series of studies of ceramic coatings such as SiC (3) and Si_3N_4 (4,5) on Mo have been carried out from the standpoint of low-Z coating and the oxidation-resistant coating. This report describes the preparation of the coatings of AlN on Mo by reactive ion plating. Recent work of Komiya *et al.* (6) points out that AlN deposited by physical vapor deposition is attractive also as a clean vacuum deposit on conventional substrate materials because of its low outgassing rate; nitride films such as TiN, Si_3N_4 , and AlN form no hygroscopic oxide layer on the surface.

Bulk AlN has been synthesized by many methods; the direct nitridation of solid Al (7), chemical vapor reaction (CVR) with disproportionation of aluminum halide (8), d-c arc discharge (8), and the ammonolysis of $\text{AlCl}_3 \cdot x\text{NH}_3$ (9). Several authors have presented studies on the preparation of AlN films by reactive sputtering (10-13). Little work, however, has been done on the preparation of AlN by ion plating. Furthermore, there is no report on the AlN coating of Mo. The ion-plating technique consists of making the substrate (Mo) to be coated a part of a cathode of a d-c high voltage circuit, thermally evaporating the metal (Al) by electron beam power, and establishing a gas (NH_3 + evaporated Al) glow discharge by rf coil. One of the principal advantages of this method is that the reactive coatings can be formed without heating the substrate; the reaction is accelerated by the glow discharge. The standard Gibbs energies of formation ΔG° , which indicate the driving force of reaction for several low-Z nitrides, are shown in Fig. 1. The order of the driving forces is $B > \text{Ti}, \text{Al} > \text{Si}$. BN is the most stable and TiN and AlN rank next. The reaction rate of reactive

ion plating is accelerated by activation and/or ionization of the gas. The ionization energy gives a measure of this effect; the small ionization energy can be advantageous for the acceleration of the reaction. Furthermore, the molecules in the gas phase attract each other near the substrate surface to form the compound. The molecular association may depend on the difference in electronegativity, a large difference stimulating the association. Table I gives the ionization energy and electronegativity for each low-Z element. Al has the most advantageous values in both factors of ionization energy and electronegativity difference from N; Ti comes after it. Thus, the preparation of aluminum nitride ceramic proves to be advantageous by rf-reactive ion plating at low temperature.

| | B | Al | Si | Ti |
|---|---------------|-----|----|-----|
| ΔG° at 650°K (Kcal/mol) | -86 | -36 | -5 | -38 |
| order of driving force | B) Ti, Al) Si | | | |

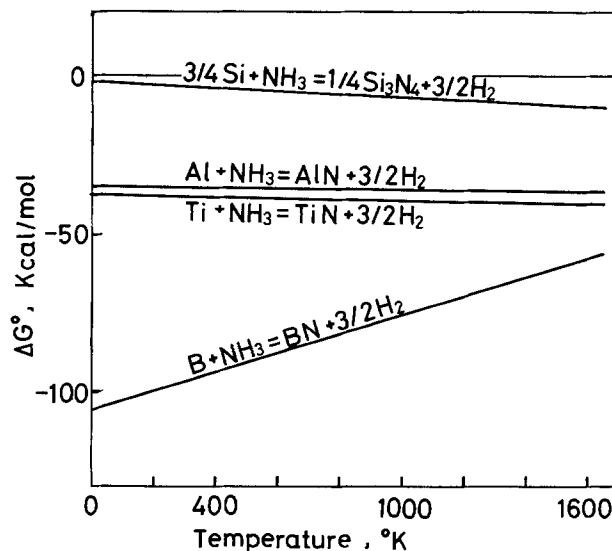


Fig. 1. Standard Gibbs energies of formation for low-Z nitrides

Key words: coatings, ion plating, oxidation.

Table I. Ionization energies and electronegativities of elements

| | B | Al | Si | Ti |
|---|-----------------|-------|-------|------|
| First ionization energy I_1 (kcal/mol) | 191.2 | 137.9 | 187.9 | 157 |
| Order of ionization | Al > Ti > Si, B | | | |
| Electronegativity, χ_e | 2.0 | 1.5 | 1.8 | 1.5 |
| Difference of χ_e from nitrogen, $\Delta\chi_e$ | -1.0 | -1.5 | -1.2 | -1.5 |
| Order of $-\Delta\chi_e$ | Al, Ti > Si > B | | | |

The structures, compositions, and chemical states of the deposits were analyzed by the scanning electron microscope (SEM), x-ray microanalyzer (XMA), x-ray diffractometer, infrared and AES spectra. The oxidation and the thermal cyclic testing of the AlN-coated Mo were examined by using thermogravimetry and an infrared-image furnace. In this paper the relation of the nitridation with the mean free path in the gas is described and the deposition mechanism is discussed.

Experimental

The rf-reactive ion-plating apparatus has been described elsewhere (4). Some gas molecules were ionized and/or activated in the glow-discharged region by rf power (13.56 MHz) and were accelerated to substrate by applying a negative d-c bias. The substrate was subjected to inert (Ar) ion bombardment and cleaned by sputtering. Since the ion bombardment was continued up to and during deposition, the surface was maintained clean. The ion bombardment confines the energy flux to the substrate surface giving high surface temperature without the need for bulk heating; the temperature rose to about 350°C in this work. This surface temperature enhances chemical reaction and diffusion. AlN was formed by the reaction of Al vapor and NH₃ gas. Al with a purity of 99.99% was used as the evaporation source, and the purity of ammonia used as a source of nitrogen was also 99.99% (Matheson Gas Products). The substrate was prepared from sintered and electrochemically polished molybdenum sheet. Al was evaporated by an electron beam from a water-cooled copper hearth which was covered with tantalum sheet in order to avoid heat loss. An NH₃ gas was introduced into a chamber through a leak valve. The Al was weighed before and after deposition. The coating conditions are given in Table II: the rf power was 200-230W, d-c bias -0.4 to -0.6 kV, the electron beam power 2.0-3.5 kW, the pressure of NH₃ gas $1-7 \times 10^{-3}$ Torr with residual pressure of 2.0×10^{-6} Torr; \dot{m}_{Al} denotes the evaporation rate of Al. The evaporation was difficult to control by electron beam power; \dot{m}_{Al} did not have similar values even for the same electron beam power. This may have resulted from differences in the rate of thermal loss from aluminum to the hearth and in different NH₃ gas pressure. The distance between the substrate and the hearth was about 10 cm and the coating time was 10 min.

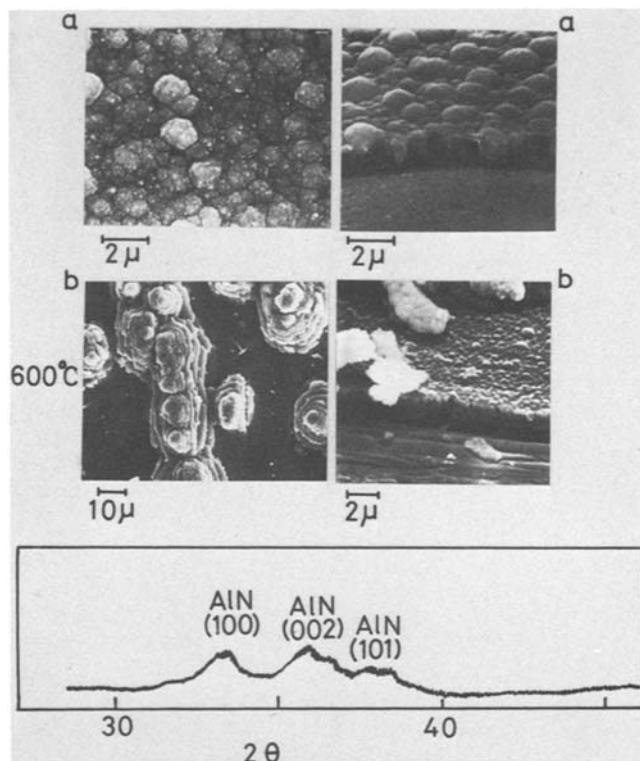


Fig. 2. Scanning electron micrographs and an x-ray diffraction pattern (run 22) of the deposits. a, Substrate was not heated (run 22); b, substrate was heated to 600°C (run 29).

Most of the coatings were carried out without heating the substrate, but for some coatings the substrate was heated by electroresistance heating. The substrate temperature was measured by Chromel-Alumel thermocouple placed in contact with its back side.

Results

Characterization of deposits.—The morphology, chemical composition, and structure of the deposits depended on the experimental conditions, especially on the partial pressures of NH₃ gas and Al vapor. Figure 2 shows SEM micrographs and an x-ray diffraction pattern of the deposits. The deposits with round growth features have x-ray diffraction peaks which indicate AlN. Deposit colors were dark green or brown, but some were blue. Contamination with impurities such as carbon and/or oxygen causes color changes for the deposits, as discussed by several authors (14, 15). The round growth features were also observed in the deposits of CVD-SiC (3) and ion-plated Si₃N₄ (4). The deposits prepared on the substrate heated to 600°C have also peaks indicating AlN in the x-ray diffraction pattern, but the coatings show comparatively large nodules on the surface (Fig. 2b); the deposits indicated gray color. The deposits with rugged features indicated the presence of free Al (x-ray diffraction) as shown in

Table II. Experimental conditions and chemical compositions of the deposited films*

| Run | P_{NH_3} (10^{-3} Torr) | \dot{m}_{Al} (g/min) | Temp (°C) | EB (kW) | Bias (-kV) | Composition (wt %) | | | (N)/ (Al) | R_d ($\mu\text{m}/$ min) |
|-----|------------------------------------|---------------------------|--------------|------------|---------------|--------------------|------|-----|--------------|-----------------------------------|
| | | | | | | Al | N | O | | |
| 11 | 1.0 | 0.17 | — | 2.2 | 0.6 | 74.9 | 21.0 | 4.1 | 0.54 | 0.41 |
| 15 | 3.0 | 0.1 | — | 2.2 | 0.6 | 63.4 | 35.0 | 1.6 | 1.1 | 0.30 |
| 17 | 3.0 | 0.075 | — | 2.4 | 0.6 | 61.4 | 36.4 | 2.1 | 1.1 | 0.17 |
| 20 | 2.5 | 0.11 | — | 2.1 | 0.4 | 67.2 | 28.5 | 4.3 | 0.82 | 0.33 |
| 22 | 2.5 | 0.06 | — | 2.2 | 0.4 | 63.5 | 31.5 | 5.0 | 0.96 | 0.22 |
| 23 | 3.0 | 0.07 | — | 2.4 | 0.4 | 61.0 | 34.0 | 5.0 | 1.1 | 0.15 |
| 25 | 3.0 | 0.2 | — | 2.9 | 0.4 | 77.0 | 22.1 | 0.9 | 0.55 | 0.28 |
| 29 | 7.0 | 0.15 | 600 | 3.2 | 0 | 64.4 | 31.6 | 1.0 | 1.0 | 0.15 |

* —: not heated. Temperature rises to about 350°C. \dot{m}_{Al} : evaporation rate of Al; R_d : deposition rate.

Fig. 3. Such deposits have spherical fine particles on the surface, colored gray or black. The deposits with free Al were formed at high evaporation rate of Al. The chemical states of AlN were analyzed by infrared spectra (double-beam spectrometer) (Fig. 4). The deposits were mechanically removed from the substrate, ground to microsize with KBr, and the mixture was pressed into a pellet. A strong broad band with its center at 750 cm^{-1} indicated the Al-N bond. The peak location is close to that for hexagonal AlN crystal (16) and midway between those of sputtered deposited AlN by Itoh *et al.* (11) and Duchene *et al.* (12). The absorption intensity is weakened in AlN deposits with free Al. The Auger electron spectrum of a deposit sputter-cleaned by Ar ions, together with those of metal Al, Al_2O_3 , and hot-pressed AlN, is shown in Fig. 5. The AES spectrum of ion-plated AlN indicates that carbon and oxygen are contained in the deposits as impurities. Peak locations and shapes of two Al peaks of the AES spectra at 50 and 1400 eV from the ion-plated AlN are in good agreement with those from hot-pressed AlN. X-ray diffraction, infrared and AES spectra confirmed that Al was present as AlN.

The chemical compositions of AlN deposits determined by XMA and their coating conditions are sum-

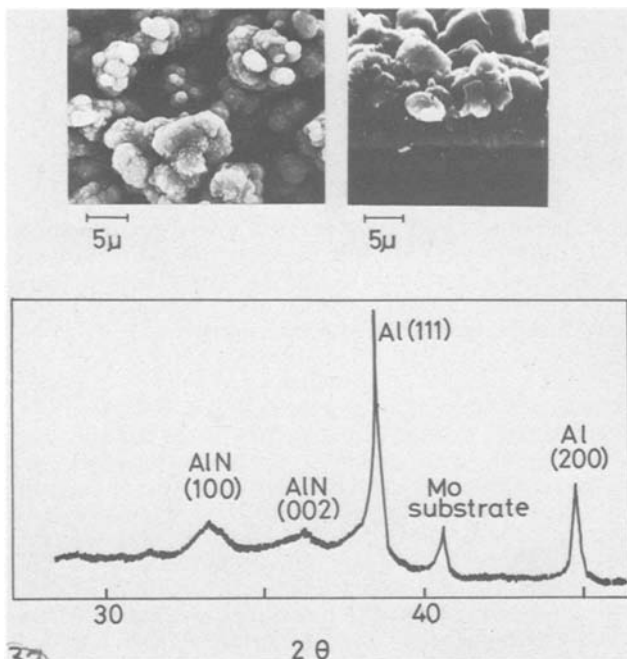


Fig. 3. Scanning electron micrographs and an x-ray diffraction pattern of the deposit (run 11).

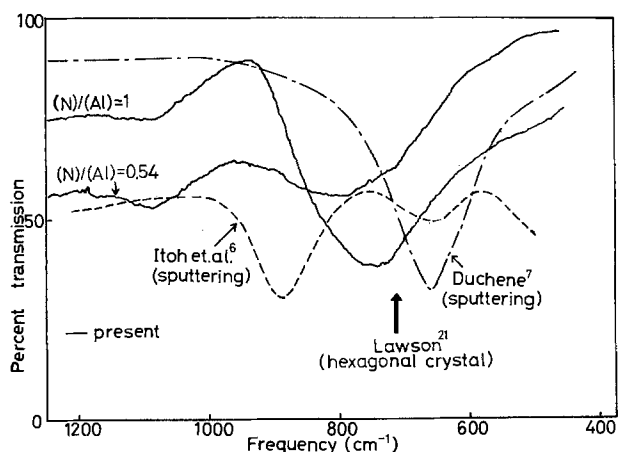


Fig. 4. Infrared absorption spectra of AlN

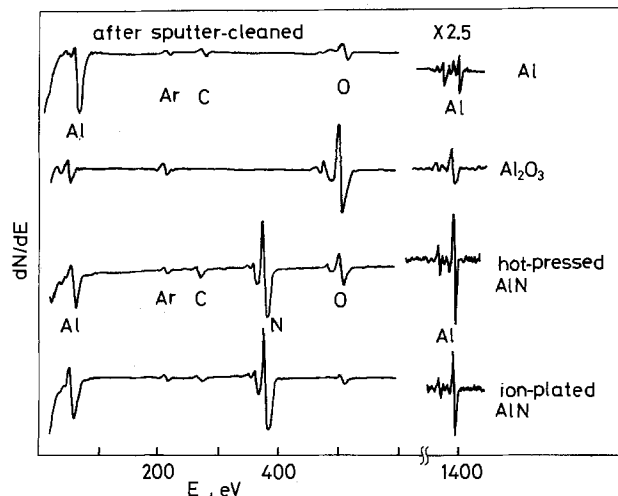


Fig. 5. Auger electron spectra of the ion-plated AlN deposit, pure Al, Al_2O_3 , and hot-pressed AlN.

marized in Table II. Single crystals of AlN and Al_2O_3 were used as the standard samples for Al, N, and O. R_d denotes the deposition rate of AlN. The degree of nitridation was good without substrate heating. The ratio $(\text{N})/(\text{Al})$ exceeds unity for some deposits; the trend was severe in thinner films, perhaps because of error in the quantitative analytical method for nitrogen in the thin films. The peak-to-peak profiles from AES for deposits exposed to ambient air after preparation are shown in Fig. 6, in which Ar^+ was used as the sputtering ion. Oxygen is remarkably enriched on the surface; this may result from surface decomposition of AlN by the attack of H_2O contained in air (8). Heating of the substrate caused no apparent change in composition (run 29). The nitridation characteristics were governed mainly by the pressure of ammonia, P_{NH_3} , and the evaporation rate of Al. When m_{Al} was large (over $\sim 0.1\text{ g/min}$) a film of rugged morphology with free Al was deposited, as mentioned previously. Now, consider the dependence of the degree of nitridation of the deposits on the partial pressures of NH_3 and Al vapor. In the dynamic situation it is difficult to estimate P_{Al} . In this work, the equation of Langmuir (17, 18) was used for calculation of P_{Al} . Figure 7a and b show the dependence on the ratio of partial pressures $P_{\text{NH}_3}/P_{\text{Al}}$ of the deposition rate R_d and the atomic concentration ratio $(\text{N})/(\text{Al})$ of deposits. Values for m_{Al} calculated from the vapor pressure of Al (19) by the Langmuir equation (for $T = 1.5T_{\text{Melt}}$, T is the Al-source temperature) generally agreed with the experimental m_{Al} in this work. The deposition rate drastically

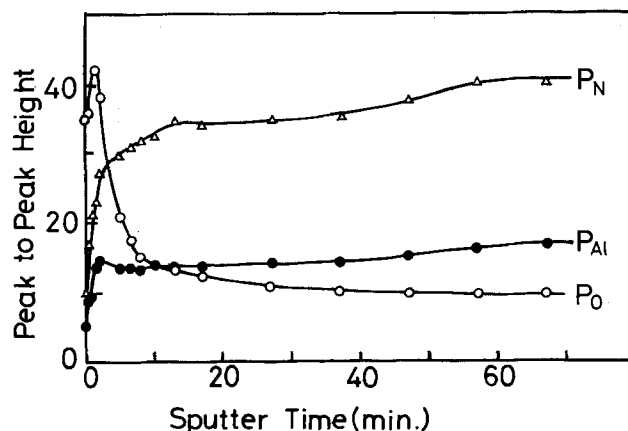


Fig. 6. AES-depth profiles of Al, N, and O of the deposits. Sputter etching was carried out by argon ion bombardment.

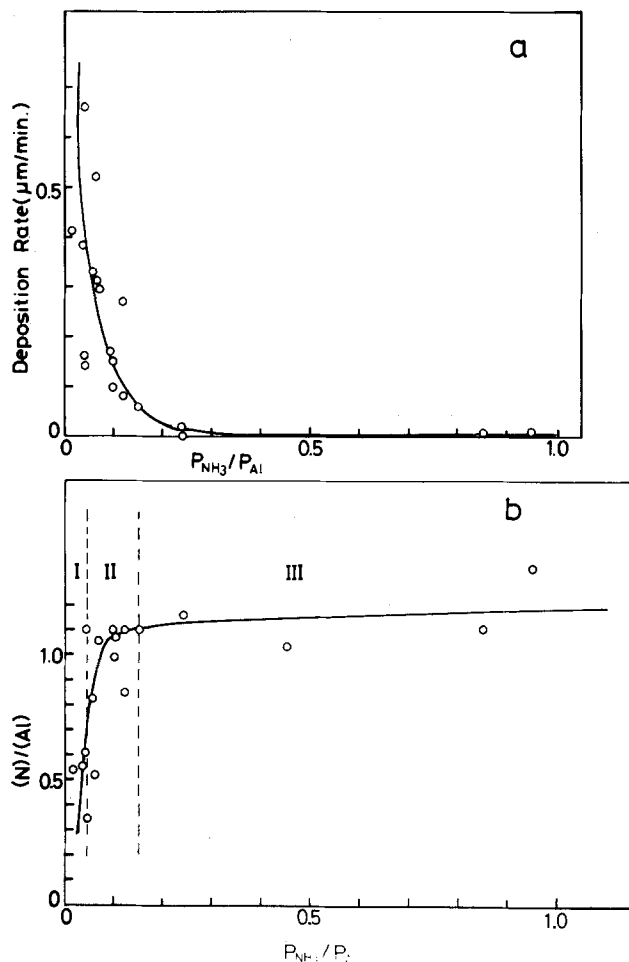


Fig. 7. Deposition rate and nitridation degree (N)/(Al) as a function of $P_{\text{NH}_3}/P_{\text{Al}}$. a, Deposition rate; b, nitridation degree.

decreases with an increase of $P_{\text{NH}_3}/P_{\text{Al}}$ (Fig. 7a). A similar relation was found between the deposition rate and P_{N_2} in sputtered-deposited AlN (11). The ratio (N)/(Al) increases almost linearly with $P_{\text{NH}_3}/P_{\text{Al}}$ when $P_{\text{NH}_3}/P_{\text{Al}}$ is small; such films indicated the morphology with rugged features (Fig. 3). The regime denoted as I in Fig. 7b is low in nitridation degree and that denoted as III is too low in deposition rate. Therefore, the area II shows the optimum condition for the preparation of AlN deposits by the ion plating ($0.15\text{--}0.33 \mu\text{m}/\text{min.}$); these deposits correspond to those shown in Fig. 2.

Oxidation test and thermal cyclic stability test of the coatings.—The oxidation resistance was examined by thermogravimetry. Coated specimens of $0.5 \text{ cm} \times 0.5 \text{ cm} \times 0.07 \text{ mm}$ were heated at a rate of $20^\circ\text{C}/\text{min}$ in Ar-1% O_2 gas mixture with a flow rate of $\sim 200 \text{ ml}/\text{min}$. Figure 8 shows the results of the oxidation test for typical coated specimens. Uncoated Mo specimen experienced a drastic weight decrease at about 790°C because of the evolution of MoO_3 which has a high vapor pressure. But AlN films protect the Mo substrate from oxidation in the high temperature environment up to $1100\text{--}1200^\circ\text{C}$. Little difference in oxidation resistance between the stoichiometric and the nonstoichiometric coatings was observed. SEM micrographs and an AES spectrum of typical specimens after the oxidation test are given in Fig. 9. Figure 9a denotes the morphology of the coating surface at oxidation temperature where the drastic weight loss has not begun (arrow a in Fig. 8). No morphological change is found in the specimen of Fig. 9a. Figure 9b shows the specimen after the drastic weight decrease (arrow b in Fig. 8). The AlN films disappeared, and needle-like

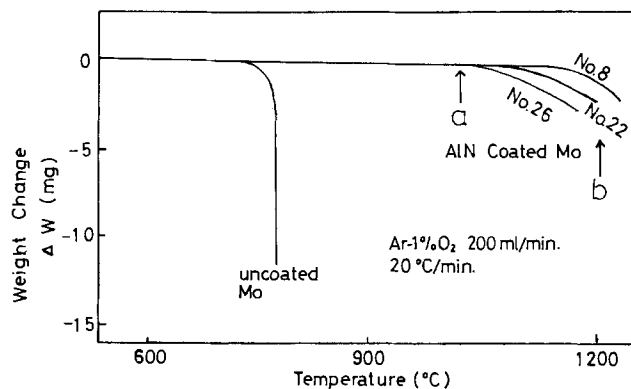


Fig. 8. Relation of weight change of the AlN-coated Mo with oxidation temperature.

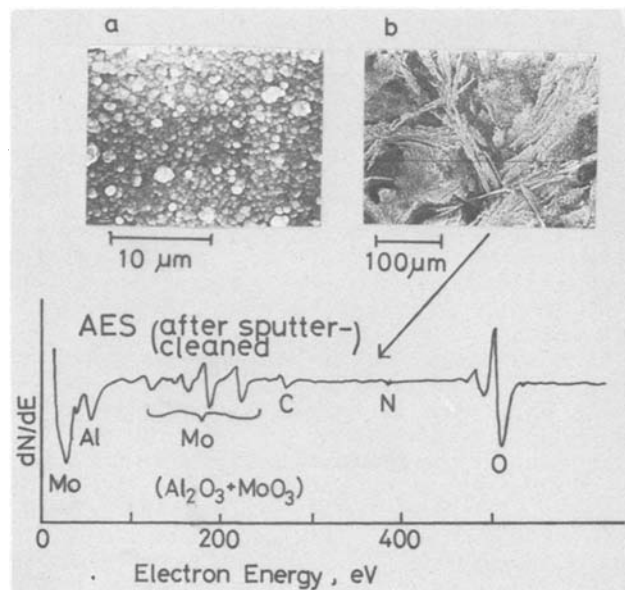


Fig. 9. Scanning electron micrographs and an Auger electron spectrum of the specimen after the oxidation test (run 20).

products covered the substrate surface (b). From the AES spectrum, the peak of nitrogen disappears and the product consists of Al_2O_3 and MoO_3 .

In order to evaluate the stability of a coated specimen, a thermal cycle test was carried out in vacuum by use of an infrared-image furnace. The thermal cycle was set between 900° and 1200°C with a rate of temperature rise $130^\circ\text{C}/\text{min}$ and a fall rate of $-180^\circ\text{C}/\text{min}$. This thermal cycle condition simulates that of the JAERI Experimental Fusion Reactor (20). No weight loss was observed in any AlN coated specimens (Fig. 10). Figure 11 shows SEM micrographs after 10 thermal cycles. Cracks were observed in the stoichiometric films prepared on the unheated substrate, but spalling never occurred. On the other hand, no crack was observed for a nonstoichiometric coating containing free Al (Fig. 11) or for a stoichiometric coating on a heated substrate (not shown).

Discussion

The AlN coating improved the oxidation resistance up to about 1200°C , which is similar to the result of Si_3N_4 coatings (4). Pinholes present in the Si_3N_4 films ion plated on Mo cause the pitting corrosion of Mo under a high temperature oxidizing environment (5). A more severe problem occurred for the AlN coatings: no pitting corrosion was observed, but the AlN decomposed. AlN is unstable in water vapor (21), and ion-plated AlN may be decomposed by H_2O attack contained in the oxidizing gas.

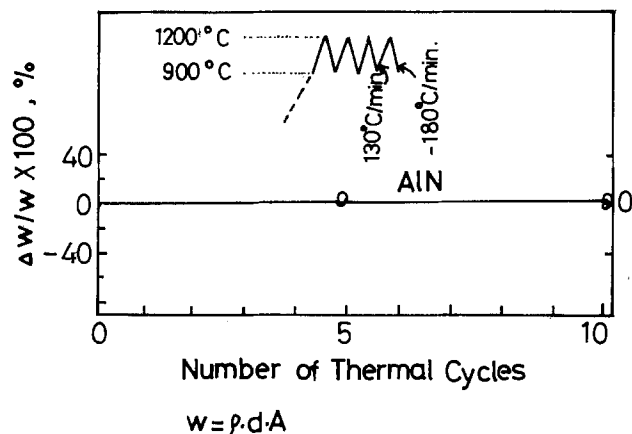


Fig. 10. Percentage of weight change of the deposits by thermal cycles under vacuum. ρ , d , and A are density, thickness, and surface area of the deposits.

Generally, the adherence of ceramic coatings on metals is poor. Si_3N_4 films coated on Mo by the ion plating showed poor adherence to the substrate (4, 5) upon bending the specimens. In the case of AlN coatings, only a small part of surface peeled off by bending through 90° , though cracks were observed (not shown). Furthermore, no spalling was observed for specimens after the thermal cyclic tests in vacuum at high temperature, as described in the previous section. Thus, the AlN coatings on Mo are comparatively good in adhesion.

Little difference between the stoichiometric and the nonstoichiometric (with free Al) coatings was observed in the oxidation test and the thermal cycle stability test. The test described below was carried out in order to make the difference clear. The coated specimens were kept in vacuum ($\sim 10^{-6}$ Torr) at 1400°C for 10 min. After this test, no change of the morphology and the thickness of the stoichiometric AlN film was observed (Fig. 12a). The weight of deposited AlN films was about 1.1×10^{-3} g/cm 2 ($3.3 \mu\text{m}$). The evaporation rate of high purity massive sintered AlN in vacuum in a temperature range of 1180°C - 1600°C is about 3.8×10^{-5} g/cm 2 sec (22). If the vaporized weight is calculated directly from this evaporation datum, such thin films should disappear after 30 sec. Actually, little evaporation of the stoichiometric deposits prepared by the ion plating (present work) was observed. The contamination of oxygen and carbon (Table II) may cause strengthening of the chemical bond of the AlN and lowering of the Al vapor pressure.

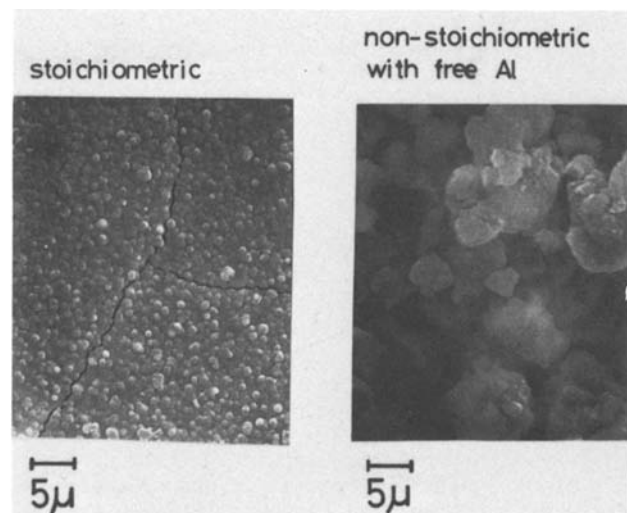


Fig. 11. Scanning electron micrographs of the deposits after the thermal cycle test.

A hole-like flaw is observed in the nonstoichiometric AlN film with free Al (Fig. 12b). The vaporization of free Al contained in the nonstoichiometric film is responsible for this local failure of film surface. Thus, nonstoichiometric AlN is not always suitable for high temperature use in vacuum, though the coated Mo specimens have good oxidation resistance and thermal cycle stability.

The nitridation degree correlated with the local vaporization of the deposits in a high temperature vacuum. The degree of nitridation and the deposition rate of films by ion plating depend on experimental factors such as partial pressures of reactants, electron beam power, bias voltage, and temperature. In the ion-plating deposition of Si_3N_4 (4), the most important factors were an electron beam power into the Si evaporation source and the rf-discharge power, which are effective for the ionization and/or activation of reactants. For the ion plating of AlN, however, the partial pressures of reactant gases strongly influence the nitridation rate of Al. With an increase of pressure, the mean free path of reactants becomes small and the number of molecular collisions in the gas phase increases. The mean free path of species i , λ_i , and the partial pressure P_i are related by (23)

$$\lambda_i = \left(\sum_j \pi (d_i + d_j)^2 n_j (1 + M_i/M_j)^{1/2} \right)^{-1}, \quad (i, j = \text{Al}, \text{NH}_3) \quad [1]$$

where d_i is the diameter of i , M_i is the atomic or molecular weight, and the number density of i , n_i , can be given by $n_i = P_i/k_B T$. The diameters used for the cal-

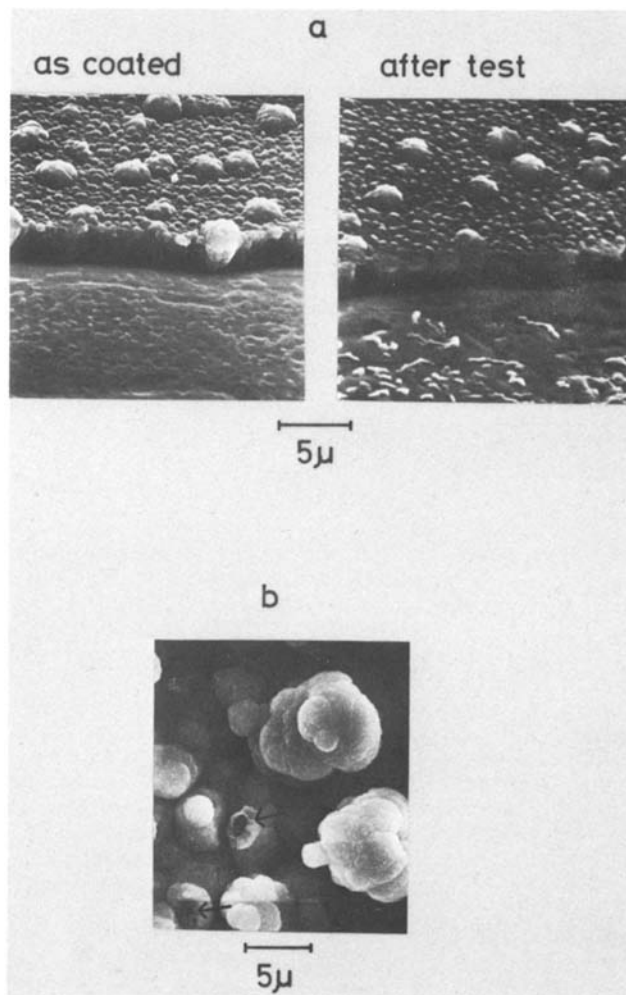


Fig. 12. Scanning electron micrographs of the coated specimens after keeping them in vacuum at 1400°C for 10 min. a, Stoichiometric film; b, nonstoichiometric film.

ulation were 1.4Å for d_{NH_3} and 2.4Å for d_{Al} . In Fig. 13a and 13b, the nitridation degree, i.e., atomic ratio (N)/(Al), is shown as a function of the mean free path. There is a similar trend between Al and NH_3 . The ratio (N)/(Al) decreases drastically on the low side of the mean free path; the decrease is almost linear, and (N)/(Al) approaches zero when the mean free path is zero. When the mean free paths are very small, the number of the intermolecular collisions in the gas phase becomes very large. In the physical vapor deposition of metals, a combination of the evaporated atoms upon collision in the gas phase results in formation of clusters when the pressures are large (24). These clusters grow gradually because of the successive collisions, and large spherical particles are developed. For the ion plating of AlN, a similar process is expected, namely, evaporated Al atoms (and/or ions) collide with one another to grow to large particles in the gas phase when the mean free path is small (high pressure). Thus, such large particles are considered to cause the rugged morphology and the presence of the free Al in the AlN deposits. For a mean free path of over about 0.6 cm for λ_{Al} and 1 cm for λ_{NH_3} , the deposits have nearly stoichiometric concentration, independent of film thickness. Since the distance between the substrate and the hearth is 10 cm, the collision number of an Al atom with others in the gas phase is very small, 0-3 times for large λ_{Al} over 3 cm during the deposition. Nevertheless, the nitridation is sufficient. Furthermore, the (N)/(Al) ratio of the deposits becomes almost zero when the mean free paths approach zero. If collisions in the gas phase make some contri-

bution to the reaction between Al and NH_3 , (N)/(Al) should be comparatively large for small mean free path. Hence, the reaction is deduced to occur mainly on the substrate surface, not in the gas phase. Thus, the rate of reactant supply to the surface can be an important factor.

The nitridation rate of Al, r_{N} , which is defined as the number of gram-atoms of nitrogen incorporated in deposits per unit area per unit time, can be given by

$$r_{\text{N}} = R_{\text{d}} \rho x_{\text{N}} \quad [2]$$

where x_{N} is the atomic fraction of N and ρ is atomic density of deposits. The averaged values of AlN and Al were used for ρ . The values of r_{N} , together with those of AlN prepared by other methods, are shown in Table III. The r_{N} value of the present work is smaller than those for CVR with disproportionation of aluminum halide and d-c discharge which are synthetic methods at high temperature. However, the present ion plating gives a large nitridation rate of Al without heating the substrate up to high temperature. The r_{N} value is larger by an order of magnitude than those of sputtering methods and corresponds to the reaction of AlCl_3 and NH_3 at 1000°C.

The reaction between Al and NH_3 was found to occur on the surface, and the reaction rate depends on concentrations of the reactants near the surface. There are three types of molecules (or atoms) in the glow discharge region: ionized (ions), activated, and unactivated neutral molecules. The neutral unactivated molecules have little contribution to the reaction because the ion plating was performed at rather low temperature. The rate of reactant supply to the surface J_i can be expressed by

$$J_i = n_i^+ v_i^{\text{ac}} + \frac{1}{4} n_i^* v_i^{\text{T}} \quad [3]$$

where n_i^+ and n_i^* are the densities of ionized and activated molecules of i , and v_i^{ac} and v_i^{T} are the velocity of ions accelerated by the bias and the thermal velocity, respectively. n_i^+ and n_i^* are proportional to the total number of i , n_i , i.e., $n_i^+ = x_i^+ n_i$ where x_i^+ is the fraction of ionized molecules. Therefore, J_i is proportional to the pressure P_i ($P_i = n_i/k_{\text{B}}T$). The total surface concentration of these species is proportional to P_i , since it should be proportional to J_i . Hence, P_i indicates a measure of the surface concentration of i . Now, the nitridation rate will be analyzed by a typical method of chemical kinetics (25). Figure 14 gives the relation of the nitridation rate, r_{N} , with the product of partial pressures of reactants, $P_{\text{Al}}P_{\text{NH}_3}$. A linear relation is found between $\log r_{\text{N}}$ and $\log (P_{\text{Al}}P_{\text{NH}_3})$, and its slope is about unity (0.9): the nitridation rate is almost proportional to the product of partial pressures. The result indicates that the nitridation mechanism is unchanged, independent of the partial pres-

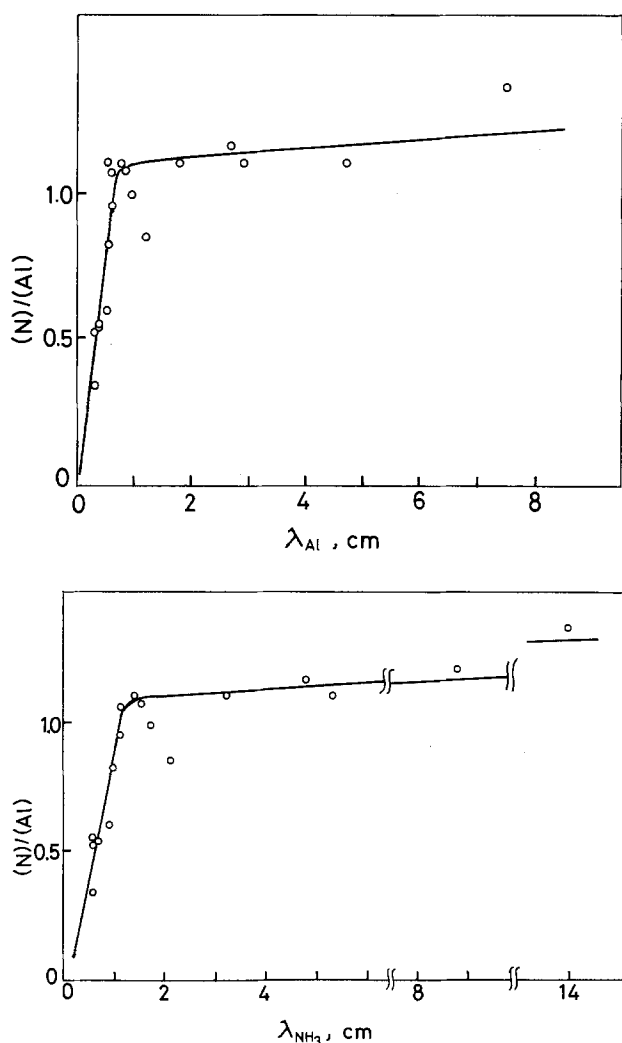


Fig. 13. Relation between (N)/(Al) and mean free path calculated from Eq. [1]. a (top), Al; b (bottom), NH_3 .

Table III. Nitridation rates of AlN

| Method | r_{N} (g-atom/ cm ² sec) | Temp (°C) |
|--|---|--------------|
| Direct N_2 -nitridation of solid Al (7) | 1.6×10^{-11} | 530 |
| CVR with disproportionation of aluminum halide (8) | 8.1×10^{-7} | 970 |
| D-C-arc discharge (Al + N_2) (8) | 3.4×10^{-9} | >1000 |
| AlCl_3 (gas) + $\text{NH}_3 \rightarrow \text{AlN} + 3\text{HCl}$ (9) | 2.7×10^{-8} | 1000 |
| RF-sputter (Al + N_2) (12) | 1.3×10^{-9} | — |
| RF-sputter (Al + N_2) (11) | 3.2×10^{-9} | — |
| RF-ion-plating (Al + NH_3)* (present work) | 3.4×10^{-8} | — |

* The value of the stoichiometric deposit with the deposition rate of 0.33 $\mu\text{m}/\text{min}$ is tabulated.

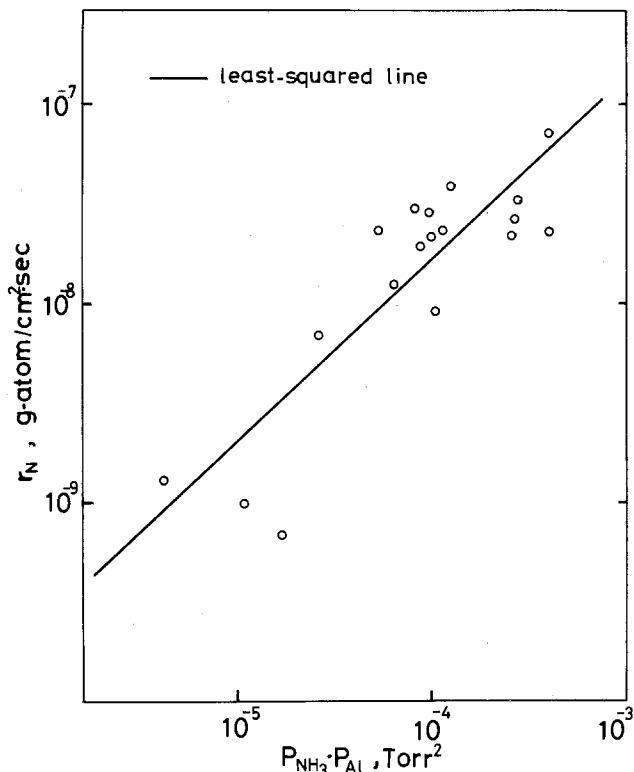


Fig. 14. Relation between nitridation rate r_N and $(P_{NH_3} P_{Al})$

sures (mean free path) and that activated and/or ionized aluminum and ammonia react on the substrate surface with second order. Thus, the reaction process is considered not to be affected by many intermolecular collisions in the gas phase. The gas-phase collision never affects the nitridation reaction on the surface, though at high evaporation rate of Al it causes the development of free Al.

The discharge effect will be briefly described. The ionization energies of Al and NH_3 are 138 and 241 cal/mol. The ionization of Al is much easier than that of NH_3 ; α_{Al^+} becomes large. In addition to the ionization, the NH_3 molecule decomposes in the glow-discharge region. The major decomposed state at 800°C is an active NH_2 , confirmed by mass spectrometry (26). The decomposition energy of N-H bond is 93.4 cal/mol, which is small compared with that for the ionization of Al. This suggests that the decomposition of NH_3 is easier than the ionization of Al. NH_3 forms active states more easily than Al; the second term of Eq. [3] is rather important for NH_3 . Hence, good nitridation can occur for low NH_3 pressures compared with that of Al vapor ($P_{NH_3}/P_{Al} \geq 0.1$), as indicated in Fig. 7b. Direct evidence by using analytical methods such as infrared, Raman, photoemission, and mass spectra are needed for understanding the reaction mechanism.

Conclusions

Coatings of AlN on Mo were performed by rf-reactive ion plating with the intention to form a low-Z coating for the fusion reactor and a refractory coating. For most of the coatings, the Mo substrate was not heated during the deposition. The following conclusions are offered:

1. Analyses of the structure, composition, and chemical state of the deposits showed that Al was present as AlN. Nearly stoichiometric nitride deposits were formed, but nonstoichiometric films with free Al also were obtained when P_{NH_3}/P_{Al} was small. Contamination with C and O was observed.

2. The oxidation resistance up to 1100°-1200°C of Mo improved by AlN layers is similar to the results

for Si_3N_4 coatings. No pitting corrosion was observed in the specimens after the test, but the AlN film disappeared; the needle-like products developed were found to consist of Al_2O_3 and MoO_3 .

3. Ten thermal cycles from 900° to 1200°C in vacuum resulted in no weight loss for any AlN coated specimens; cracks were observed in the stoichiometric films, but no spalling was observed. The nonstoichiometric films had no cracks. Thus, the AlN coatings on Mo are good in adhesion.

4. Little difference in oxidation resistance and thermal cycle stability was found between the stoichiometric and nonstoichiometric coatings. However, the free Al contained in the nonstoichiometric film caused the local failure of films in vacuum at high temperature.

5. The surface reaction of Al and NH_3 (on the substrate surface) was suggested from the relation between the nitridation degree and the mean free path of gas. Furthermore, the relation of nitridation rate with the product of reactant pressures indicated that the surface reaction could be described by the second-order reaction.

6. The large particles developed by the successive collisions of Al in the gas phase are deduced to be responsible for the rugged morphology when P_{NH_3}/P_{Al} is small.

Acknowledgments

The authors would like to express their gratitude to Mr. T. Kimura and Mr. H. Araki for the measurement of XMA. The standard single crystal of AlN was prepared by Dr. M. Iwata, Dr. T. Sakai, and Dr. T. Sato of National Institute for Research in Inorganic Materials, and hot-pressed AlN was by Dr. H. Inomata and Dr. H. Tanaka of the same institute. Thanks are also due to them.

Manuscript submitted Sept. 10, 1980; revised manuscript received Jan. 28, 1981.

Any discussion of this paper will appear in a Discussion Section to be published in the June 1982 JOURNAL. All discussions for the June 1982 Discussion Section should be submitted by Feb. 1, 1982.

Publication costs of this article were assisted by the National Research Institute for Metals.

REFERENCES

1. D. M. Mattox, *Thin Solid Films*, **63**, 213 (1979).
2. L. H. Rovner and G. R. Hopkins, *Nucl. Technol.*, **29**, 274 (1976).
3. M. Fukutomi, M. Kitajima, M. Okada, and R. Watanabe, *J. Nucl. Mater.*, **87** (1), 101 (1979).
4. M. Fukutomi, M. Kitajima, M. Okada, and R. Watanabe, *This Journal*, **124**, 1420 (1977).
5. M. Kitajima, M. Fukutomi, M. Okada, and R. Watanabe, *J. Electrochem. Soc. Jpn.*, **47**, 21 (1979).
6. S. Komiya, N. Umezu, and C. Hayashi, *Thin Solid Films*, **63**, 341 (1979).
7. P. Stapitanonda and J. L. Margrave, *J. Phys. Chem.*, **60**, 1628 (1956).
8. T. Sato and M. Iwata, "Report of the Study on Aluminum Nitride," National Institute for Research in Inorganic Materials, p. 5 (1973); T. Sato and M. Iwata, *J. Chem. Soc. Jpn.*, No. 10, 1869 (1973).
9. A. J. Noreika and D. W. Ing., *J. Appl. Phys.*, **39**, 5578 (1968).
10. A. J. Noreika, N. H. Francombe, and S. A. Zeitman, *J. Vac. Sci. Technol.*, **6**, 194 (1969).
11. A. Itoh and S. M. Misawa, *J. Vac. Soc. Jpn.*, **15**, 214 (1972).
12. J. Duchene, *Thin Solid Films*, **8**, 69 (1971).
13. Y. Hirohata, T. Abe, and T. Yamashina, *Jpn. J. Appl. Phys.*, **45**, 402 (1973).
14. K. M. Taylor and C. Lenie, *This Journal*, **107**, 308 (1960).
15. G. Long and L. M. Foster, *J. Am. Ceram. Soc.*, **42** (2), 53 (1959).
16. K. E. Lawson, "Infrared Absorption of Inorganic

- Substances," Part II, Reinhold Publishing Corp., New York (1961).
17. T. Sata, in "Reactivity of Solids, Chemical Review 9," M. Taniguchi, Editor, p. 127, (1975); Chem. Soc. Jpn., Tokyo.
 18. J. F. Detorre, T. G. Knorr, and E. H. Hall, in "Vapor Deposition," C. F. Powell, J. H. Oxley, and J. M. Blocher, Jr., Editors, p. 62, John Wiley & Sons, Inc., New York (1966).
 19. R. Hultgren, P. D. Desai, D. T. Hawkins, M. Gleiser, K. K. Kelly, and D. D. Wagman, "Selected Values of the Thermodynamic Properties of the Elements," American Society for Metals (1973).
 20. Report from Japan Atomic Energy Research Institute, JAERI-M7300, p. 165 (1977).
 21. T. B. Shaffer, "High Temperature Materials 1, Materials Index," p. 259, Plenum Press, New York (1964).
 22. G. Long and L. M. Foster, *This Journal*, **109**, 1176 (1962).
 23. H. Kumagai, G. Tominaga, Y. Tuzi, and G. Hori-koshi, "Vacuum Science and Engineering," Chap. 2, Shokabo Press, Tokyo (1970).
 24. H. Tamura, *Jpn. J. Appl. Phys.*, **38**, 1122 (1969).
 25. K. J. Laidler, "Chemical Kinetics," McGraw-Hill Publishing Co., New York (1973).
 26. Sin-Shong Lin, *This Journal*, **124**, 1945 (1977).

Thermodynamic Equations for the Liquidus of (A_{1-u}B_u)_{2-y}C_y(s) with y Near One and with Congruently Melting End Members

R. F. Brebrick,* Tse Tung, Ching-Hua Su, and Pok-Kai Liao

*Materials Science and Metallurgy Program, College of Engineering,
Marquette University, Milwaukee, Wisconsin 53233*

ABSTRACT

A number of equivalent exact and useful approximate equations for the liquidus of (A_{1-u}B_u)_{2-y}C_y(s) with y near unity and with congruently melting end members ($u = 0, 1$) are obtained. These are general in so far as the liquid phase is concerned, except that the forms written for associated solution models of the liquid depend upon the species assumed. The congruent melting of the end members leads to important, usually ignored, links between the thermodynamic properties of the liquid and those of the binary compounds. It is shown that the common assumption that the heat capacity of a binary, end member, compound equals that of its supercooled liquid is generally incorrect and is unnecessary. The results are applied to a number of recent analyses of liquidus surfaces and lines.

The thermodynamic equation for the liquidus of a congruently melting, narrow homogeneity range compound has been derived in a number of papers (1-6). That given by Vieland (6) has been widely used, extended to ternary systems, and used with an associated solution model for the liquid (7-10) following Jordan's development of a simplified version of this model (11, 12). The derivation given by Vieland has been re-examined for the case of the liquidus of a pseudobinary solid (13). Although the derivation and liquidus equation given by Vieland are correct and simple, they have suffered in usage. First of all, one step of the thermodynamic cycle used in the derivation recognizes the equality of the Gibbs free enthalpy of the compound and its melt at the congruent melting point. However, equations that directly follow from this equality, and which provide an important link between the thermodynamic properties of the compound and the liquid, were not emphasized and are almost universally ignored. Secondly, the liquidus equation contains as one term the integral over temperature of the difference between the heat capacity of the compound and its supercooled liquid. This difference is almost always set to zero. In fact, such a step is unnecessary, is in principle usually incorrect, and in practice is often seriously incorrect when associated solution models are used for the liquid. Finally, there are other equivalent liquidus equations that are more convenient

to use in certain cases. The purpose here is to demonstrate these points and to apply the results to a number of recent analyses.

We consider the liquid in equilibrium with a ternary solid solution, (A_{1-u}B_u)_{2-y}C_y(s), with congruently melting end members ($u = 0, 1$). It is assumed that the C atoms occupy sites in their own sublattice and, because y is always near unity, that the site-fraction of atom point defects is small. The chemical potentials of AC and BC in the solid are then independent of y to a good approximation (14). Consequently, as we shall show, the thermodynamic equations for the liquidus surface of the solid solution depend upon u but not y . Thus the liquidus equations are formally identical with those for a pseudobinary solid. The liquidus equations for the binary compounds, AC(s) and BC(s) are of course obtained as special cases.

Liquidus Equations

We consider the equilibrium between (A_{1-u}B_u)_{2-y}C_y(s) and a liquid phase in the solid-liquid-vapor system. The system has two degrees of freedom. We first seek equations that are general in so far as the liquid phase is concerned, and which are therefore applicable with any thermodynamically valid model of the liquid phase. At equilibrium the chemical potential of each component must be the same in the solid and liquid. This gives three equations

$$\mu_A^L = \mu_A^S \quad [1]$$

$$\mu_B^L = \mu_B^S \quad [2]$$

* Electrochemical Society Active Member.
Key words: liquidus equations, Vieland equation, thermodynamics.

$$\mu_C^L = \mu_C^S \quad [3]$$

By adding pairs of equations from Eq. [1]-[3], one obtains

$$\mu_A^L + \mu_C^L = \mu_A^S + \mu_C^S \quad [4]$$

$$\mu_B^L + \mu_C^L = \mu_B^S + \mu_C^S \quad [5]$$

Now we suppose the solid phase is a solution, $(A_{1-u}B_u)_{2-y}C_y(s)$, in which A and B are distributed among the sites of one sublattice and C occupies a second sublattice. If the range of y about the value 1 is less than about 0.01, then the right-hand members of Eq. [4] and [5] are independent of y to a good approximation (14) and can be written as

$$\mu_{AC}^S(u, T) = \mu_A^S + \mu_C^S \quad [6]$$

$$\mu_{BC}^S(u, T) = \mu_B^S + \mu_C^S \quad [7]$$

In writing the variables determining the chemical potentials of AC and BC in the solid, we omit the total pressure and rely upon the relative insensitivity of the thermodynamic properties of condensed phases to hydrostatic pressure. For the liquid phase the chemical potentials are of the general form

$$\mu_j^L = h_j - Ts_j + RT \ln(x_j) + \mu_j^{o,L}(T) \quad j = A, B, C \quad [8]$$

where $\mu_j^{o,L}(T)$ is the chemical potential of pure j liquid, h_j is the relative partial molar enthalpy of j , and s_j is the relative excess partial molar entropy of j . (To avoid excessive superscripts we do not follow the convention here that the excess quantities are marked by a superscript x or xs .) Both of these partial molar quantities are zero for pure j liquid, i.e., when $x_j = 1$. Our basic equations are now Eq. [4] and [5]. The thermodynamic problem has thus been conveniently broken into two parts. That part retained in Eq. [4] and [5] relates the composition of the liquid phase to the solid composition variable u . Since y does not appear, the equations are identical to those for a pseudo-binary solid solution. The second part would relate both y and u for the solid to the liquid composition and is not pursued here.

The chemical potentials of the components AC and BC in the solid solution can also be written formally in terms of relative partial molar enthalpies and excess entropies as

$$\mu_{AC}^S = h_{AC}^S - Ts_{AC}^S + RT \ln(1-u) + \mu_{AC}^{o,S}(T) \quad [9]$$

$$\mu_{BC}^S = h_{BC}^S - Ts_{BC}^S + RT \ln(u) + \mu_{BC}^{o,S}(T) \quad [10]$$

where $\mu_{AC}^{o,S}(T)$ and $\mu_{BC}^{o,S}(T)$ are the chemical potentials of pure AC(s) and pure BC(s), respectively. When $u = 0$, $h_{AC}^S = s_{AC}^S = 0$. When $u = 1$, $h_{BC}^S = s_{BC}^S = 0$.

The Gibbs free enthalpy of formation per mol of each binary compound from its liquid elements can be written as

$$\Delta G_{o_f}(AC) = \Delta H_{o_f}(AC) - T\Delta S_{o_f}(AC) \\ = \mu_{AC}^{o,S} - \mu_A^{o,L} - \mu_C^{o,L} \quad [11]$$

$$\Delta G_{o_f}(BC) = \Delta H_{o_f}(BC) - T\Delta S_{o_f}(BC) \\ = \mu_{BC}^{o,S} - \mu_B^{o,L} - \mu_C^{o,L} \quad [12]$$

The last equality in each equation follows from the fact that the chemical potentials of the pure compounds are independent of the deviation from stoichiometry for small deviations (15, 16). Using Eq. [6]-[12] in Eq. [4] and [5] gives the enthalpy-entropy of formation liquidus equations

$$h_A + h_C - T(s_A + s_C) + RT \ln(x_A x_C) = h_{AC}^S$$

$$- Ts_{AC}^S + RT \ln(1-u) + \Delta H_{o_f}(AC) - T\Delta S_{o_f}(AC) \quad [13]$$

$$h_B + h_C - T(s_B + s_C) + RT \ln(x_B x_C) = h_{BC}^S$$

$$- Ts_{BC}^S + RT \ln(u) + \Delta H_{o_f}(BC) - T\Delta S_{o_f}(BC) \quad [14]$$

These are sometimes convenient. Their usage guarantees that the sums of the chemical potentials in the binary melts AC(l) and BC(l) equal the Gibbs free enthalpies of formation of, respectively, AC(s) and BC(s). However, the melting points of the binary compounds calculated from these equations do not necessarily agree with the observed values unless two constraining equations are imposed. These are obtained from Eq. [13] and [14] by requiring the former be satisfied for $x_A = x_C = \frac{1}{2}$ and $T = T_{AC}$, the melting point of AC(s), and the latter be satisfied for $x_B = x_C = \frac{1}{2}$ and $T = T_{BC}$, the melting point of BC(s). As a result, not all of the parameters of the liquid phase model can be independent. The liquidus equations can be recast into a form that depends upon the enthalpy and entropy of melting of each binary compound by first expressing the temperature dependence of the enthalpy and entropy of formation for each binary compound. For AC(s) one can write in general that

$$\Delta H_{o_f}(AC) = \Delta H_{o_f}(AC, T_{AC}) + \int_{T_{AC}}^T \Delta C_{AC}^S dT \quad [15]$$

$$\Delta S_{o_f}(AC) = \Delta S_{o_f}(AC, T_{AC}) + \int_{T_{AC}}^T \Delta C_{AC}^S d \ln T \quad [16]$$

where the standard, relative, constant pressure, heat capacity per mol of AC(s), ΔC_{AC}^S , is given by

$$\Delta C_{AC}^S = C_{AC}^S - C_A^{o,L} - C_C^{o,L} \quad [17]$$

and $C_A^{o,L}$ and $C_C^{o,L}$ are the constant pressure heat capacities per g-atom of, respectively, pure A(l) and pure C(l) and C_{AC}^S is that of AC(s) per mol. Completely analogous equations hold for BC(s). Then, because the Gibbs free enthalpy of melting for AC(s) is zero at $T = T_{AC}$, one has two equations

$$\Delta H_{o_f}(AC, T_{AC}) = h_A^* + h_C^* - H_{AC}^m \quad [18]$$

$$\Delta S_{o_f}(AC, T_{AC}) = s_A^* + s_C^* + R \ln 4 - H_{AC}^m/T_{AC} \quad [19]$$

where H_{AC}^m is the enthalpy of melting per mol of AC(s) and the asterisk superscript indicates that the partial molar quantities are evaluated at $x_A = x_C = \frac{1}{2}$ and $T = T_{AC}$. The analogs for BC(s) are

$$\Delta H_{o_f}(BC, T_{BC}) = h_B^{**} + h_C^{**} - H_{BC}^m \quad [20]$$

$$\Delta S_{o_f}(BC, T_{BC}) = s_B^{**} + s_C^{**} + R \ln 4 - H_{BC}^m/T_{BC} \quad [21]$$

where T_{BC} is the melting point of BC(s), H_{BC}^m is its enthalpy of melting, and the double asterisk indicates a quantity is evaluated at $x_B = x_C = \frac{1}{2}$ and $T = T_{BC}$. The desired liquidus equations can now be obtained by using Eq. [15]-[16] and [18]-[21] to eliminate the enthalpy and entropy of formation quantities in Eq. [13] and [14]. Upon rearrangement the result is

$$T = \frac{h_A - h_A^* + h_C - h_C^* + H_{AC}^m + \int_T^{T_{AC}} (1 - T/r) \Delta C_{AC}^s dr - h_{AC}^s}{s_A - s_A^* + s_C - s_C^* + H_{AC}^m/T_{AC} + R \ln [(1 - u)/4x_A x_C] - s_{AC}^s} \quad [22]$$

$$T = \frac{h_B - h_B^{**} + h_C - h_C^{**} + H_{BC}^m + \int_T^{T_{BC}} (1 - T/r) \Delta C_{BC}^s dr - h_{BC}^s}{s_B - s_B^{**} + s_C - s_C^{**} + H_{BC}^m/T_{BC} + R \ln [u/4x_B x_C] - s_{BC}^s} \quad [23]$$

where, it is emphasized, the partial molar entropies are excess quantities. Equations [22] and [23] are general in so far as the liquid phase model is concerned, and are exact except that the effect of hydrostatic pressure on the properties of the liquid and solid phases is neglected. The equations are not in general explicit equations for T unless ΔC_{AC}^s and ΔC_{BC}^s are zero and all the partial molar quantities are independent of T . They are consistent with a melting temperature of T_{AC} for AC(s) and T_{BC} for BC(s). Finally, r in the integrals is obviously a dummy integration variable.

The "exact" liquidus equations can be put in a form resembling Vieland's equation for a binary liquidus by using the thermodynamic definitions

$$RT \ln (\gamma_i) = h_i - Ts_i \quad i = A, B, C \quad [24]$$

$$RT \ln (\Gamma_{jk}) = h_{jk}^s - Ts_{jk}^s \quad jk = AC \text{ or } BC \quad [25]$$

and the equality below for A-C and an analogous one for B-C

$$\begin{aligned} h_A^* + h_C^* - T(s_A^* + s_C^*) &= h_A^\dagger + h_C^\dagger \\ &- T(s_A^\dagger + s_C^\dagger) + \int_T^{T_{AC}} (1 - T/r) \Delta C_{AC}^L dr \\ &= RT \ln (\gamma_A^\dagger \gamma_C^\dagger) + \int_T^{T_{AC}} (1 - T/r) \Delta C_{AC}^L dr \quad [26] \end{aligned}$$

where $\Delta C_{AC}^L = C_{AC}^L - C_{A^0}^L - C_{C^0}^L$ is the constant pressure heat capacity of the 50 atomic percent (a/o) liquid, and hence ΔC_{AC}^L is the relative heat capacity of two g-atoms of the 50 a/o liquid, AC(l). (See Eq. [17].) The dagger superscript indicates evaluation at $x_A = x_C = 1/2$ and an arbitrary T . Upon rearrangement the result is

$$\begin{aligned} RT \ln \left[\frac{4\gamma_A \gamma_C x_A x_C}{\gamma_A^\dagger \gamma_C^\dagger (1 - u) \Gamma_{AC}} \right] &= H_{AC}^m (T/T_{AC} - 1) \\ &- \int_T^{T_{AC}} (1 - T/r) (\Delta C_{AC}^s - \Delta C_{AC}^L) dr \quad [27] \end{aligned}$$

$$\begin{aligned} RT \ln \left[\frac{4\gamma_B \gamma_C x_B x_C}{\gamma_B^\dagger \gamma_C^\dagger u \Gamma_{BC}} \right] &= H_{BC}^m (T/T_{BC} - 1) \\ &- \int_T^{T_{BC}} (1 - T/r) (\Delta C_{BC}^s - \Delta C_{BC}^L) dr \quad [28] \end{aligned}$$

The differences $\Delta C_{AC}^s - \Delta C_{AC}^L$ and $\Delta C_{BC}^s - \Delta C_{BC}^L$ are the ΔC_p that appear in Vieland's equation and which have been indiscriminantly set equal to zero. Equations [27] and [28] are equivalent to Eq. [22] and [23]. For either binary system, A-C or B-C, they reduce to a generalization of the Vieland equation previously obtained by Jordan and Weiner. However, neither Vieland nor Jordan and Weiner explicitly stated the dependence of these equations upon the validity of the auxiliary conditions, Eq. [18]-[21], which

is emphasized here. In Vieland's derivation, the Gibbs free enthalpy of formation of the binary solid compound is eliminated in favor of the enthalpy and entropy of fusion and other quantities using the results of a thermodynamic cycle. One step of this cycle involves the congruent melting of the binary compound and so could have been used to introduce Eq. [18] and [19]. Knowing the thermodynamic properties of the binary compounds, the auxiliary conditions impose two constraints upon the parameters of the liquid phase model in each of the A-C and B-C binaries. If the parameters of the liquid phase model are determined by a fit to phase diagram data without prior use of the auxiliary conditions, then their subsequent use allows a calculation of the enthalpy and entropy of formation of each binary compound (from its liquid elements and at its melting point) for check against the experimental values.

The standard relative heat capacities of the stoichiometric binary liquids appearing in Eq. [27] and [28] are determined by the liquid phase model used. Those of the binary compounds are to be obtained from experiment.

Approximate Equations when ΔG_f° for AC(s) and BC(s) are Linear Functions of T

The heat capacities are known for some compounds up to their melting points, but often they are not. On the other hand, the Gibbs free enthalpy of formation of compounds is frequently known at high temperatures and often is accurately given as a linear function of T . When this is the case, a useful approximate form of the exact equations given by Eq. [22] and [23] or Eq. [27] and [28] can be obtained. Assume the Gibbs free enthalpy of formation of AC(s) from the pure liquid elements is given in terms of a constant effective enthalpy of formation, $\overline{\Delta H}_f$, and a constant effective entropy of formation, $\overline{\Delta S}_f$ by

$$\Delta G_f^\circ(\text{AC}) = \overline{\Delta H}_f - T\overline{\Delta S}_f + \delta(T) \quad [29]$$

where $\delta(T)$ is a small correction that depends upon T . A parameter, Δ_{AC} , is defined as the difference between the effective enthalpy of formation and its actual value at the melting point by

$$\Delta_{AC} = \overline{\Delta H}_f - \Delta H_f^\circ(\text{AC}, T_{AC}) \quad [30]$$

From Eq. [29] and the thermodynamic equation for $\Delta G_f^\circ(\text{AC})$, it follows that

$$\overline{\Delta S}_f = \Delta S_f^\circ(\text{AC}, T_{AC}) + \Delta_{AC}/T_{AC} + \delta(T_{AC})/T_{AC} \quad [31]$$

With Eq. [30] and [31], the integral in the numerator of Eq. [22] can be written as

$$\begin{aligned} \int_T^{T_{AC}} (1 - T/r) \Delta C_{AC}^s dr &= \Delta_{AC} (T/T_{AC} - 1) \\ &+ T \delta(T_{AC})/T_{AC} - \delta(T) \quad [32] \end{aligned}$$

Substituting this equation into Eq. [22], and its analog for BC(s) into Eq. [23] and rearranging gives

$$T = \frac{(h_A - h_A^*) + (h_C - h_C^*) - h_{AC}^s + (H_{AC}^m - \Delta_{AC}) - \delta_{AC}(T)}{(s_A - s_A^*) + (s_C - s_C^*) - s_{AC}^s + (H_{AC}^m - \Delta_{AC} - \delta(T_{AC}))/T_{AC} + R \ln [(1-u)/4x_A x_C]} \quad [33]$$

$$T = \frac{(h_B - h_B^{**}) + (h_C - h_C^{**}) - h_{BC}^s + (H_{BC}^m - \Delta_{BC}) - \delta_{BC}(T)}{(s_B - s_B^{**}) + (s_C - s_C^{**}) - s_{BC}^s + (H_{BC}^m - \Delta_{BC} - \delta(T_{BC}))/T_{BC} + R \ln [u/4x_B x_C]} \quad [34]$$

These are still exact equations. The approximation consists of neglecting the $\delta_i(T)$ terms. In particular cases it is possible that the effective enthalpies and entropies of formation can be chosen so that $\delta_{AC}(T_{AC})$ and $\delta_{BC}(T_{BC})$ are zero. The error in neglecting $\delta_{AC}(T)$ and $\delta_{BC}(T)$ in the numerators can then be easily calculated. Equations [33] and [34] in their approximate form are particularly convenient for they are explicit equations for T whenever all the partial molar quantities are independent of T .

Using Eq. [32] and its analog for B-C, the generalized Vieland equations given by Eq. [27] and [28] can be written as

$$RT \ln \left[\frac{4\gamma_A \gamma_C x_A x_C}{\gamma_A^\dagger \gamma_C^\dagger (1-u)\Gamma_{AC}} \right] = (H_{AC}^m - \Delta_{AC}) \\ (T/T_{AC} - 1) - T\delta_{AC}(T_{AC})/T_{AC} + \delta_{AC}(T) \\ + \int_T^{T_{AC}} (1 - T/r) \Delta C_{AC}^L dr \quad [35]$$

$$RT \ln \left[\frac{4\gamma_B \gamma_C x_B x_C}{\gamma_B^\dagger \gamma_C^\dagger u\Gamma_{BC}} \right] = (H_{BC}^m - \Delta_{BC}) \\ (T/T_{BC} - 1) - T\delta_{BC}(T_{BC})/T_{BC} + \delta_{BC}(T) \\ + \int_T^{T_{BC}} (1 - T/r) \Delta C_{BC}^L dr \quad [36]$$

With the use of thermodynamic definitions, the integrals above can be written as

$$\int_T^{T_{AC}} (1 - T/r) \Delta C_{AC}^L dr = h_A^* + h_C^* \\ - h_A^\dagger - h_C^\dagger - T(s_A^* + s_C^* - s_A^\dagger - s_C^\dagger) \quad [37]$$

$$\int_T^{T_{BC}} (1 - T/r) \Delta C_{BC}^L dr = h_B^{**} + h_C^{**} \\ - h_B^\dagger - h_C^\dagger - T(s_B^{**} + s_C^{**} - s_B^\dagger - s_C^\dagger) \quad [38]$$

Again the approximate liquidus equations result by neglecting the $\delta_i(T)$ terms in Eq. [35] and [36]. For both sets of equivalent approximate equations, those derived from Eq. [33] and [34] and those derived from Eq. [35] and [36], the effect of linearly temperature-dependent Gibbs free enthalpies of formation for AC(s) and BC(s) is to replace the integrals involving ΔC_{AC}^s and ΔC_{BC}^s by terms Δ_{AC} and Δ_{BC} , respectively, which modify the corresponding enthalpies of fusion. On the other hand, the integrals of Eq. [37] and [38] are in general both zero only if the partial molar quantities for the liquid phase components are independent of T , for then $h_A^* = h_A^\dagger$ etc. Otherwise, Eq. [37] and [38] contribute temperature-dependent corrections to the right-hand members of Eq. [35] and [36], whose magnitudes depend upon the model of the liquid phase.

Liquidus Equations for Associated Solution Models of the Liquid Phase

If the liquid phase is described by an associated solution model, three of the species will correspond to the uncombined components and their mol fractions are written as y_a , y_b , and y_c . Quantities associated with solution species will all be denoted by lower case subscripts. For internal equilibrium within the liquid, the chemical potential of each component must equal that of its corresponding uncombined species, i.e.

$$\mu_A - \mu_A^0 = RT \ln (\gamma_A x_A) = RT \ln (\gamma_a y_a) = \mu_a - \mu_a^0 \quad [39]$$

$$\mu_B - \mu_B^0 = RT \ln (\gamma_B x_B) = RT \ln (\gamma_b y_b) = \mu_b - \mu_b^0 \quad [40]$$

$$\mu_C - \mu_C^0 = RT \ln (\gamma_C x_C) = RT \ln (\gamma_c y_c) = \mu_c - \mu_c^0 \quad [41]$$

The exact enthalpy-entropy of formation liquidus equations given by Eq. [13] and [14] can be rewritten in terms of properties of the species using Eq. [39]-[41] as

$$RT \ln [\gamma_a \gamma_c y_a y_c / (1-u)\Gamma_{AC}] = \Delta H_f^0(AC) \\ - T\Delta S_f^0(AC) \quad [42]$$

$$RT \ln [\gamma_b \gamma_c y_b y_c / u\Gamma_{BC}] = \Delta H_f^0(BC) - T\Delta S_f^0(BC) \quad [43]$$

These of course must be augmented by equations describing the equilibrium between each molecular species and the corresponding uncombined species.

The left-hand members of the approximate, generalized Vieland equations, given by Eq. [35] and [36] with the $\delta_i(T)$ quantities all set to zero, can immediately be written in terms of quantities referring to uncombined species with Eq. [39]-[41]. It is now desired to express Eq. [37] and [38] in terms of quantities referring to the species. In order to do so it is necessary to identify the species in the A-C and B-C binaries. We take them to be a, c, and ac, a molecule consisting of one A atom and one C atom, and b, c, and bc, a similar molecule composed of one B atom and one C atom. The necessary arguments are given here only for the A-C binary, those for the B-C binary being completely analogous. When $x_A = x_C = 1/2$, let $y_{ac} = y_{ac}^\dagger = z$. When in addition $T = T_{AC}$, let $y_{ac} = z^*$. Then $y_a^\dagger = y_c^\dagger = (1/2)(1-z)$ and the number of g-atoms of components per mol of species is $1+z$. Therefore, the enthalpy and entropy of mixing of the stoichiometric liquid from the pure liquid elements can be written both in terms of the partial molar quantities for the components and those for the species as

$$h_A^\dagger + h_C^\dagger = \{2/(1+z)\} \{1/2(1-z)(h_a^\dagger + h_c^\dagger) \\ + zh_{ac}^\dagger - z\Delta H_D\} \quad [44]$$

$$s_A^\dagger + s_C^\dagger = -R \ln 4 + \{2/(1+z)\} \{1/2(1-z) \\ (s_a^\dagger + s_c^\dagger) + zs_{ac}^\dagger - z\Delta S_D - R(1-z) \\ \ln [(1-z)/2] - Rz \ln z\} \quad [45]$$

where ΔH_D and ΔS_D are, respectively, the standard enthalpy and entropy of dissociation of pure ac molecule into its liquid elements. The corresponding asterisk quantities are obtained by replacing the dagger superscripts in Eq. [44] and [45] by asterisks, denoting the quantities evaluated at $x_A = x_C = 1/2$ are now also evaluated at $T = T_{AC}$, and by replacing z by z^* . Using Eq. [44] and [45] in Eq. [37] and the B-C analogs of Eq. [44] and [45] in Eq. [38], the integral terms involving the relative heat capacity of the binary stoichiometric liquids can be evaluated for the particular associated solution model used, both in the exact liquidus equations given by Eq. [27] and [28], and in the approximate equations given by Eq. [35] and [36] with the δ_i quantities all set to zero.

The pertinent equations for an associated solution model of the liquid can then be summarized as

(a) Liquidus equations

$$RT \ln \left[\frac{\gamma_a \gamma_c y_a y_c}{\gamma_a^\dagger \gamma_c^\dagger y_a^\dagger y_c^\dagger (1-u) \Gamma_{AC}} \right] = H_{AC}^m (T/T_{AC} - 1) - \int_T^{T_{AC}} (1 - T/r) \Delta C_{AC}^s dr + \int_T^{T_{AO}} (1 - T/r) \Delta C_{AC}^L dr \quad [46]$$

$$RT \ln \left[\frac{\gamma_b \gamma_c y_b y_c}{\gamma_b^\dagger \gamma_c^\dagger y_b^\dagger y_c^\dagger u \Gamma_{BC}} \right] = H_{BC}^m (T/T_{BC} - 1) - \int_T^{T_{BC}} (1 - T/r) \Delta C_{BC}^s dr + \int_T^{T_{BO}} (1 - T/r) \Delta C_{BC}^L dr \quad [47]$$

(b) Approximations for the case that the Gibbs free enthalpies of formation of the binary compounds, AC(s) and BC(s), are taken as linear functions of T

$$\int_T^{T_{AO}} (1 - T/r) \Delta C_{AC}^s dr = \Delta_{AC} (T/T_{AC} - 1) \quad [48]$$

$$\int_T^{T_{BO}} (1 - T/r) \Delta C_{BC}^s dr = \Delta_{BC} (T/T_{BC} - 1) \quad [49]$$

where ΔC_{AC}^s is defined by Eq. [17], Δ_{AC} by Eq. [30], and the corresponding quantities for BC are obvious by analogy.

(c) The last integral in the liquidus equations given by Eq. [46] and [47], involving the relative heat capacity of a stoichiometric binary liquid, is given in terms of the partial molar excess quantities of the components by, respectively, Eq. [37] and [38]. These forms are particularly convenient in those versions of the associated solution model (8, 9, 11) in which the excess chemical potentials of the solution species are written in terms of the atom fractions of the components. In more general versions of the associated solution model, these excess chemical potentials are written in terms of the mol fractions of the species. Then one can use Eq. [44] and [45] in Eq. [37], if the species in the A-C liquid are a, c, and ac, or obvious generalizations of Eq. [44] and [45] for some other choice of solution species. The equations for the B-C liquid for use in Eq. [38] and then Eq. [47] are entirely analogous.

The liquidus equations must of course be augmented by two equations describing the equilibrium between the associated complex, ac and its uncombined species and a similar equilibrium for bc. These equations follow from the fact that the chemical potential of ac must equal the sum of those for a and c, while that for bc must equal the sum of those for b and c. One uses Eq. [39]-[41] for the chemical potentials of the uncombined species, and the equations below for those of the associated complexes

$$\begin{aligned} \mu_{ac} - \mu^{\circ A} - \mu^{\circ C} &= RT \ln (\gamma_{ac} y_{ac}) + \mu^{\circ ac} - \mu^{\circ A} - \mu^{\circ C} \\ &= RT \ln (\gamma_{ac} y_{ac}) - \Delta H_D(ac) \\ &\quad + T \Delta S_D(ac) \\ &= h_{ac} - T s_{ac} + RT \ln y_{ac} \\ &\quad - \Delta H_D(ac) + T \Delta S_D(ac) \quad [50] \end{aligned}$$

$$\begin{aligned} \mu_{bc} - \mu^{\circ B} - \mu^{\circ C} &= RT \ln (\gamma_{bc} y_{bc}) + \mu^{\circ bc} - \mu^{\circ B} - \mu^{\circ C} \\ &= RT \ln (\gamma_{bc} y_{bc}) - \Delta H_D(bc) \\ &\quad + T \Delta S_D(bc) \quad [51] \end{aligned}$$

Discussion

In a number of published analyses, a starting liquidus equation has been obtained by setting $\Delta C_p = 0$ in Vieland's equation, i.e., setting $\Delta C_{AC}^L = \Delta C_{AC}^s$ in Eq. [27], and the liquidus fit using some model for the liquid phase. One immediate application of the results

obtained here is to assess the error incurred thereby in each specific analysis. This we shall do. However, it should be noted that another important potential use of the liquidus equations is to test the thermodynamic self-consistency of sets of experimental data, which would include liquidus point data and partial molar quantity data for the liquid among others. The liquidus equations given by Eq. [13] and [14] or by [22] and [23] would seem to be the ones most useful for this purpose since they involve only quantities for stable states and do not involve the relative heat capacities of the stoichiometric, supercooled binary liquids.

The liquidus lines (17) in III-V binaries and liquidus surfaces in related ternaries have been fit using simple solution models. Within the framework of our derivation these analyses justifiably use the approximate form of the generalized Vieland equations (Eq. [35] and [36] with $\delta_{AC} = \delta_{BC} = 0$) with $\Delta C_{AC}^L = \Delta C_{BC}^L = 0$ and $\Delta_{AC} = \Delta_{BC} = 0$. The relative heat capacities of the stoichiometric binary liquids are exactly zero since the partial molar enthalpies and excess entropies of the liquid model used are independent of T . Moreover, for a number of III-V compounds, ΔG_f° is accurately a linear function of T and Δ_{AC} and Δ_{BC} (see Eq. [30]) are small relative to, and comparable to the accuracy of, the corresponding enthalpies of melting (18). However, the auxiliary conditions of Eq. [18]-[21], not being explicit in Vieland's derivation, were not applied so that the thermodynamic properties of the liquid phase established by the fit are inconsistent with the known properties of the binary compounds. A more extensive fit to four III-V binaries using a subregular model of the liquid does satisfy the auxiliary conditions (18). A recent fit (19) to the Ga-As-Sb ternary, including a fit to the tie lines, justifiably uses the same approximation of the generalized Vieland equations for the same reasons as cited above, but also ignores the auxiliary conditions. Again, the values of ΔH_f° and ΔS_f° of the binary compounds calculated from the parameters of the best fit liquidus are in significant disagreement with experiment.

We now discuss the specific form taken by Eq. [46] for two widely used versions of the associated solution model and the errors incurred for some specific binary systems by using the common form of the Vieland equation instead. This common form is of course Eq. [46] with both integrals set equal to zero. For the specific systems considered, the Gibbs free enthalpy of formation of the solid compound is a linear function of T to within present experimental error. Therefore, in obtaining numerical values for the errors the relative heat capacity of the solid compound is taken as zero. The error is then that introduced by indiscriminately taking the integral over the relative heat capacity of the stoichiometric binary liquid—a quantity determined by the liquid model and the values taken for its parameters—as zero.

In a separate study (20), we have used an extension of Jordan's model (11) to analyze the HgTe-CdTe-Te system. In the appendix to that work, Eq. [46] is evaluated for this model. It is found that the integral over ΔC_{AC}^L is zero only if the liquid is completely associated or completely dissociated. The error incurred in using the Vieland equation for the Cd-Te and Zn-Te systems (8) was found to be less than 1°C because the degree of dissociation taken was zero or near zero. (However, as a result the values predicted for the enthalpy and entropy of formation of the solid compounds through Eq. [18] and [19] are far from the experimental values.) The errors incurred (21) for the Ga-Sb and In-Sb systems were not calculated but, since the degree of dissociation is intermediate, are most likely not negligible.

Osamura *et al.* (9, 10) have developed another simplified version of the associated solution model for cases in which the degree of association is small. In the

earlier work (9), the chemical potentials given do not satisfy the Gibbs-Duhem relation and so this original model is not discussed further. The relative chemical potentials of components 1 and 2 are given by Eq. [3a, 3b] of Ref. (10). The relative partial molar enthalpies and entropies can be readily evaluated and the integral over the relative heat capacity of the stoichiometric binary liquid defined by Eq. [37] obtained. Changing their notation to consider the liquidus of a binary compound AC(s), rather than AB(s), the result is

$$\int_T^{T_{AC}} (1 - T/r) \Delta C_{AC}^L dr = (1/4) (\omega_{A,AC} + \omega_{C,AC} - \omega_{AC}) F \quad [52]$$

where the ω 's are constant interaction coefficients and

$$F = k^* [1 + \Omega(T_{AC} - T)/RT_{AC}^2] - k \quad [53]$$

Here k is the dissociation constant of the liquid phase molecule, ac, and is given in terms of two constants, k^0 and Ω , by

$$k = k^0 \exp(\Omega/RT) \quad [54]$$

The asterisk superscript on the first k in Eq. [53] means that it is evaluated at T_{AC} . Thus, the integral given by Eq. [52] is zero, and Eq. [46] reduces to the Vieland equation, only under the very special circumstances that $\omega_{A,AC} + \omega_{C,AC} - \omega_{AC} = 0$, or $k = k^0 = 0$, or $\Omega = 0$, or $T = T_{AC}$. The liquid model parameters identified as giving the best fit to the liquidus lines of AlSb and GaSb are listed in Table III of Ref. (10). The quantities given there as κ_{AlSb} and κ_{GaSb} should be read (22) as, respectively, $1/k^0_{AlSb}$ and $1/k^0_{GaSb}$. Liquidus temperatures were calculated for each binary using Eq. [46] with both integrals set equal to zero. These are denoted at T_v . They were also calculated using Eq. [46] and Eq. [52] with the ΔC_{AC}^L in Eq. [46] set equal to zero. These are considered the "exact" temperatures. For GaSb, T_v is high by about 4°C at atom fractions of Sb near 0.1 and 0.9. This is comparable to the standard deviation of 4.6°C between observed and calculated liquidus temperatures [using the observed liquidus points tabulated in Ref. (18)] and is therefore not acceptable. For AlSb the error is even greater, T_v being high by 15° at $x_{sb} = 0.2$ and high by 150°C at $x_{sb} = 0.90$. As a result, the quantitative aspects of the analysis given in Ref. (10) are unfortunately of doubtful value. Because the excess Gibbs free enthalpy of mixing for Osamura's model depends upon the atom fractions of the components, Eq. [22]-[23] or [33]-[34] are more convenient for calculation purposes than the generalized Vieland form given by Eq. [46]-[47]. For more general versions of the associated solution model, the mol fraction of the species appears

in the free enthalpy of mixing. Then the enthalpy-entropy of formation liquidus equations given by Eq. [42]-[43] are most likely the easiest to use.

Acknowledgment

The authors wish to express their gratitude for support by the Air Force Office of Scientific Research, Air Force Systems Command under Grant No. AFOSR-78-3611.

Manuscript submitted April 15, 1980; revised manuscript received Feb. 6, 1981.

Any discussion of this paper will appear in a Discussion Section to be published in the June 1982 JOURNAL. All discussions for the June 1982 Discussion Section should be submitted by Feb. 1, 1982.

Publication costs of this article were assisted by Marquette University.

REFERENCES

1. C. Wagner, *Acta Metall.*, **6**, 309 (1958).
2. A. Steiner, E. Miller, and K. Komarek, *Trans. Metall. Soc., AIME*, **230**, 1361 (1964).
3. R. F. Brebrick, *Metall. Trans.*, **2**, 1657 (1971).
4. A. S. Jordan and M. E. Weiner, *J. Phys. Chem. Solids*, **36**, 1335 (1975).
5. R. F. Brebrick, *Metall. Trans. A*, **7**, 1609 (1976).
6. L. J. Vieland, *Acta Metall.*, **11**, 137 (1963).
7. A. Laugier, *Rev. Phys. Appl., Suppl. J. Phys.*, **8**, 259 (1973).
8. S. Szapiro, *J. Electron. Mater.*, **5**, 223 (1976).
9. K. Osamura and Y. Murakami, *J. Phys. Chem. Solids*, **36**, 931 (1975).
10. K. Osamura, K. Nakijima, and Y. Murakami, *This Journal*, **126**, 1992 (1979).
11. A. S. Jordan, *Metall. Trans.*, **1**, 239 (1970).
12. A. S. Jordan, in "Calculation of Phase Diagrams and Thermochemistry of Alloy Phases," Y. A. Chang and J. F. Smith, Editors, p. 100, The Metallurgical Society of AIME, Warrendale, Pa. (1979).
13. A. S. Jordan, *Metall. Trans.*, **2**, 1959 (1971).
14. R. F. Brebrick, *J. Phys. Chem. Solids*, **40**, 177 (1979).
15. G. G. Libowitz and J. B. Lightstone, *J. Phys. Chem. Solids*, **28**, 1145 (1967).
16. R. F. Brebrick, *J. Solid State Chem.*, **1**, 88 (1969).
17. M. B. Panish and M. Ilegems, "Progress in Solid State Chemistry," Vol. 7, Chap. 2, H. Reiss and J. O. McCaldin, Editors, Pergamon Press, Oxford (1972).
18. R. F. Brebrick, *Metall. Trans. A*, **8**, 403 (1977).
19. M. F. Graton and J. C. Wooley, *This Journal*, **127**, 55 (1980).
20. T. Tung, L. Golonka, and R. F. Brebrick, *ibid.*, **128**, 1601 (1981).
21. S. Szapiro, *J. Phys. Chem. Solids*, **41**, 279 (1980).
22. K. Osamura, Private communication.

Thermodynamic Analysis of the HgTe-CdTe-Te System Using the Simplified RAS Model

Tse Tung, Leszek Golonka,¹ and R. F. Brebrick*

*Materials Science and Metallurgy Program, College of Engineering,
Marquette University, Milwaukee, Wisconsin 53233*

ABSTRACT

A quantitatively good overall fit is obtained to the phase diagram and thermodynamic data in the HgTe-CdTe-Te system. In the binaries the partial pressures along the three-phase curves are fit in addition to the liquidus points. Moreover, the liquid phase parameters are constrained so that the enthalpy and entropy of mixing of the stoichiometric binary melts are properly related to the enthalpy and entropy of formation of the binary compounds. Also included in the fit are the HgTe-CdTe pseudobinary liquidus and solidus points, the partial pressure of Hg in the pseudobinary melt, and the partial pressures of Hg, Cd, and Te₂ for the Te-saturated pseudobinary solid, Hg_{1-u}Cd_uTe. Finally, a choice is made for the most reliable ternary liquidus points and these are included. Portions of the phase diagram, as yet unmeasured, are then calculated and presented. The liquid phase is described by a simple extension of the regular associated solution model of Jordan and Szapiro in which the interaction coefficients and dissociation constants are allowed to depend upon temperature. The partial molar quantities for the liquid phase components are derived and used in liquidus equations that are more exact than the commonly used version of the Vialand equation. Errors in some previous studies are discussed in the appendix. It is concluded that the model cannot provide a satisfactory fit to the entire Hg-Cd-Te system. Neither can it fit analogous systems in which the liquidus lines of the binary compounds are asymmetric.

In this paper we gather the experimental data and report quantitatively good overall fits to all the phase diagram and thermodynamic data for the HgTe-CdTe-Te system. Recently derived liquidus equations (1), more generally valid than the commonly used Vialand equation (2), are used and the liquid phase is described by the simplified version of the associated solution model (3, 4). In the process this model is tested more extensively than previously. The liquid phase parameters leading to an overall optimum fit are used to generate calculated curves that are hopefully useful in smoothing, interpolating, and extrapolating the experimental data and guiding further experimentation.

The associated solution model offers a relatively simple way of obtaining a strong composition dependence in the properties of a liquid phase. Such a dependence has been observed in a number of cases, various properties showing an extremum at or near compositions at which solid phases appear at lower temperatures (5, 6). The model has become very popular recently, and has been applied to a number of systems including HgTe-CdTe-Te (7), Zn-Cd-Te (4), a number of III-V binaries (8, 9), and to Al-Ga-Sb (10). Unfortunately, the analyses cited are flawed to an unknown extent in that they take as their starting point liquidus equations arrived at by assuming the partial molar enthalpies and excess entropies of the liquid components are independent of T , an assumption that is generally invalid for associated solution models (1). Moreover, they ignore the fact that the enthalpy of formation of a congruently melting, narrow homogeneity range compound, AC(s), plus the enthalpy of fusion equals the enthalpy of mixing of the liquid of the same composition, as well as the corresponding entropy relationship (1, 11, 12).

In the simplified version of the associated solution model developed by Jordan (3), mole fractions of species occurring in terms representing the interaction among these species are in effect replaced by atom fractions of the components and two interaction coefficients are assumed equal. As used here, the model is extended in a simple and obvious manner by allowing the interaction coefficients and dissociation constants to depend upon T . Thus, by setting certain parameters to zero the original model is regained. The simplified model is used here because it is reported to give good fits in systems with a high degree of ionic binding (3, 4, 7, 13). Moreover, it possesses the attractive feature that its central results are expressible in analytical form for binary systems. Here, not only are liquidus points fit, but also partial pressures; and this is done under constraints (Eq. [6]-[9]) that insure the satisfaction of the relations referred to above between the thermodynamic quantities of the binary compounds HgTe(s) and CdTe(s) and those of the stoichiometric binary liquids. Jordan has previously fit the liquidus points (3) and the partial pressures on the Te-rich side of the Zn-Te (13) and CdTe (14) systems. However, more recent and extensive partial pressure measurements are now available. Moreover, although he showed that the value calculated for the Gibbs free enthalpy of compound formation from the best fit liquid model was close to experiment, he did not check the enthalpy and entropy of formation individually.

Liquidus Equations

We use recently derived (1) equations for the liquidus in equilibrium with a pseudobinary solid, A_{1-u}B_uC(s), with narrow homogeneity range, congruently melting end members, AC(s) and BC(s). In terms of symbols listed at the end of this paper, these equations are

* Electrochemical Society Active Member.

¹ Department of Electrical Engineering, The Technical Institute of Wrocław, Wrocław, Poland.

Key words: liquidus, binary compounds, thermodynamics.

$$T = \frac{h_A - h_A^* + h_C - h_C^* - h_{AC}^s + H_{AC} - \Delta_{AC}}{s_A - s_A^* + s_C - s_C^* - s_{AC}^s + (H_{AC} - \Delta_{AC})/T_{AC} + R \ln(1-u)/4x_A x_C} \quad [1]$$

$$T = \frac{h_B - h_B^{**} + h_C - h_C^{**} - h_{BC}^s + H_{BC} - \Delta_{BC}}{s_B - s_B^{**} + s_C - s_C^{**} - s_{BC}^s + (H_{BC} - \Delta_{BC})/T_{BC} + R \ln u/4x_B x_C} \quad [2]$$

The above equations follow from more fundamental ones (1) if the Gibbs free enthalpy of formation from the pure liquid elements of both AC(s) and BC(s) are linear functions of T , e.g.

$$\Delta G^{\circ}_f(AC) = \overline{\Delta H}_f(AC) - T\overline{\Delta S}_f(AC) \quad [3]$$

with $\overline{\Delta H}_f(AC)$ and $\overline{\Delta S}_f$ constants. Then, if $\Delta H^{\circ}_f(AC, T_{AC})$ is the actual enthalpy of formation of AC(s) at its melting point

$$\Delta_{AC} = \overline{\Delta H}_f(AC) - \Delta H^{\circ}_f(AC, T_{AC}) \quad [4]$$

Analogously we have

$$\Delta_{BC} = \overline{\Delta H}_f(BC) - \Delta H^{\circ}_f(BC, T_{BC}) \quad [5]$$

The liquidus equations are dependent upon the validity of relations based upon the zero change of the Gibbs free enthalpy upon congruent melting of both AC(s) and BC(s). These are

$$\Delta H^{\circ}_f(AC, T_{AC}) = h_A^* + h_C^* - H_{AC} \quad [6]$$

$$\Delta S^{\circ}_f(AC, T_{AC}) = s_A^* + s_C^* + R \ln 4 - H_{AC}/T_{AC} \quad [7]$$

$$\Delta H^{\circ}_f(BC, T_{BC}) = h_B^{**} + h_C^{**} - H_{BC} \quad [8]$$

$$\Delta S^{\circ}_f(BC, T_{BC}) = s_B^{**} + s_C^{**} + R \ln 4 - H_{BC}/T_{BC} \quad [9]$$

These auxiliary relations can be used to fix two liquid phase model parameters in each of the A-C and B-C binaries or, alternatively, to calculate values for the enthalpy and entropy of formation of the binary compounds.

Equations [1] and [2] reduce to equations that are the same as the commonly used Vieland equation (2) with his $\Delta C_p = 0$, except that $H_{AC} - \Delta_{AC}$ and $H_{BC} - \Delta_{BC}$ appear in place of the heats of fusion, only if the partial molar enthalpies and excess entropies of the liquid components are independent of T . This is not the case for the liquid model used here.

Liquid Model

Jordan (3) used a model of the liquid phase in the Zn-Te and Cd-Te systems that assumed the presence of binary molecules which interacted with one another and with the uncombined atoms like a regular solution. The interaction terms were simplified to depend upon the atom fractions of the components, rather than the mol fractions of the species, in order to obtain analytical expressions. This approach was generalized to a ternary system by Szapiro (4) and we adopt his equations defining this simplified regular associated solution model with two obvious extensions noted below. The pertinent equations are summarized below. Then, since it is desired to use the liquidus equations given by Eq. [1] and [2] and the auxiliary conditions given by Eq. [6]-[9], the equations for the partial molar quantities of the liquid phase components are given. This requires some algebra to obtain the partial molar quantities of the components. However, this effort is compensated by the more rapid computer calculations possible with Eq. [1] and [2] than with equivalent equations (1) depending upon the partial molar quantities of the solution species.

Consider a ternary A-B-C system. The mol fractions of the species are written as y_i and are related to the atom fractions of the components by the equations

$$y_a = x_A(1 + y_{ac} + y_{bc}) - y_{ac} \quad [10]$$

$$y_b = x_B(1 + y_{ac} + y_{bc}) - y_{bc} \quad [11]$$

$$y_c = x_C(1 + y_{ac} + y_{bc}) - y_{ac} - y_{bc} \quad [12]$$

The chemical potentials of the species are assumed to be given by the equations

$$\mu_a = \omega x_B^2 + \alpha_1 x_C^2 + (\omega + \alpha_1 - \alpha_2) x_B x_C + RT \ln(y_a) + \mu^{\circ}_A \quad [13]$$

$$\mu_b = \omega x_A^2 + \alpha_2 x_C^2 + (\omega - \alpha_1 + \alpha_2) x_A x_C + RT \ln(y_b) + \mu^{\circ}_B \quad [14]$$

$$\mu_c = \alpha_1 x_A^2 + \alpha_2 x_B^2 + (\alpha_1 + \alpha_2 - \omega) x_A x_B + RT \ln(y_c) + \mu^{\circ}_C \quad [15]$$

$$\mu_{ac} = \omega x_B(1 - 2x_A) + (\alpha_1 x_A + \alpha_2 x_B - 0.5\alpha_1)(1 - 2x_C) + RT \ln(y_{ac}) + \mu^{\circ}_{ac} \quad [16]$$

$$\mu_{bc} = \omega x_A(1 - 2x_B) + (\alpha_1 x_A + \alpha_2 x_B - 0.5\alpha_2)(1 - 2x_C) + RT \ln(y_{bc}) + \mu^{\circ}_{bc} \quad [17]$$

The form of Eq. [16] and [17] was chosen (4) so that the Gibbs-Duhem relation is obeyed for the ternary system. The standard chemical potentials define an enthalpy and entropy of dissociation and an equilibrium constant for each molecule through the equations

$$\mu^{\circ}_A + \mu^{\circ}_C - \mu^{\circ}_{ac} = \Delta H_D(ac) - T\Delta S_D(ac) = -RT \ln K_1 \quad [18]$$

$$\mu^{\circ}_B + \mu^{\circ}_C - \mu^{\circ}_{bc} = \Delta H_D(bc) - T\Delta S_D(bc) = -RT \ln K_2 \quad [19]$$

For internal equilibrium within the liquid, the chemical potential of ac must equal the sum of those for a and c and that of bc must equal the sum of those for b and c. Using Eq. [13]-[17] and Eq. [18] and [19], the equilibrium equations are

$$y_a y_c / y_{ac} = K_1 \exp(-\alpha_1/2RT) = \kappa_1 \quad [20]$$

$$y_b y_c / y_{bc} = K_2 \exp(-\alpha_2/2RT) = \kappa_2 \quad [21]$$

Using these last two equations and Eq. [10]-[12], the mole fractions of the species can be written as

$$y_c = x_C - y_c(1 - y_c) \{ x_A / (y_c + \kappa_1) + x_B / (y_c + \kappa_2) \} \quad [22]$$

$$y_{ac} = x_A y_c (1 - y_c) / (1 - x_C) (y_c + \kappa_1) \quad [23]$$

$$y_{bc} = x_B y_c (1 - y_c) / (1 - x_C) (y_c + \kappa_2) \quad [24]$$

Thus, for given T , composition of the liquid in atom fractions of the components, interaction coefficients α_1 and α_2 , and dissociation constants K_1 and K_2 , Eq. [22] is a cubic equation in y_c and can be solved by various means. Equations [23] and [24] can then be solved for y_{ac} and y_{bc} , respectively, and Eq. [10] and [11] solved for y_a and y_b , respectively.

The model used by Jordan and Szapiro is extended for use here in two straightforward ways. The interaction coefficients appearing in Eq. [13]-[17] are assumed to depend linearly upon T

$$\omega = W + VT \quad [25]$$

$$\alpha_1 = \gamma_1 + \delta_1 T \quad [26]$$

$$\alpha_2 = \gamma_2 + \delta_2 T \quad [27]$$

and the dissociation constants defined by Eq. [18] and

[19] are allowed to be temperature dependent. Thus, the enthalpies of dissociation are allowed to be nonzero. For brevity of notation we take the κ -quantities defined in Eq. [20] and [21] as

$$\kappa_1 = a_1 \exp(-b_1/T) \quad [28]$$

$$\kappa_2 = a_2 \exp(-b_2/T) \quad [29]$$

For internal equilibrium within the liquid, the chemical potential of component A must equal that of species a and similarly for the chemical potentials of B and b and those of C and c. On this basis, the relative partial molar quantities for the components can be obtained using thermodynamic definitions and Eq. [13]-[15] and Eq. [25]-[27] as

$$s_C^t = -\partial(\mu_C - \mu^{\circ}C)/\partial T = -\delta_1 x_A^2 - \delta_2 x_B^2 + (V - \delta_1 - \delta_2)x_A x_B - R \ln y_C - RT \partial \ln y_C / \partial T \quad [30]$$

$$h_C = \mu_C + T s_C = \gamma_1 x_A^2 + \gamma_2 x_B^2 + (\gamma_1 + \gamma_2 - W)x_A x_B - RT^2 \partial \ln y_C / \partial T \quad [31]$$

$$s_A^t = -V x_B^2 - \delta_1 x_C^2 + (\delta_2 - \delta_1 - V)x_B x_C - R \ln y_A - RT \partial \ln y_A / \partial T \quad [32]$$

$$h_A = W x_B^2 + \gamma_1 x_C^2 + (W + \gamma_1 - \gamma_2)x_B x_C - RT^2 \partial \ln y_A / \partial T \quad [33]$$

$$s_B^t = -V x_A^2 - \delta_2 x_C^2 + (\delta_1 - \delta_2 - V)x_A x_C - R \ln y_B - RT \partial \ln y_B / \partial T \quad [34]$$

$$h_B = W x_A^2 + \gamma_2 x_C^2 + (W + \gamma_2 - \gamma_1)x_A x_C - RT^2 \partial \ln y_B / \partial T \quad [35]$$

where the partial derivatives are taken at constant x_A , x_B , and x_C and where the superscript t indicates that the relative partial molar entropies are not excess quantities. Evaluation of the above equations depends upon the partial temperature derivative of y_C since those of y_A and y_B can be expressed in terms of y_{ac} and y_{bc} using Eq. [10] and [11] and these in turn can be expressed in terms of y_C using Eq. [23] and [24], respectively. The result for y_C is given by

$$\partial y_C / \partial T = N/D \quad [36]$$

where

$$N = \{y_C(1 - y_C)/T\}^2 \{x_A b_1 \kappa_1 (y_C + \kappa_2)^2 + x_B b_2 \kappa_2 (y_C + \kappa_1)^2\}$$

and

$$D = -y_C^2(1 - y_C)^2 \{x_A (y_C + \kappa_2)^2 + x_B (y_C + \kappa_1)^2\} + (y_C + \kappa_1)^2 (y_C + \kappa_2)^2 (y_C^2 + x_C - 2x_C y_C)$$

The partial molar quantities of the components can be obtained in analytical form for the A-C and B-C binary systems. The equations for the former are given below, those for the B-C binary being completely analogous. The partial molar entropies given are again the excess quantities

$$h_A = \gamma_1 x_C^2 - x_C Q_1 / (P_1 + 1 - 2x_C) \quad [37]$$

$$h_C = \gamma_1 x_A^2 - x_A Q_1 / (P_1 - 1 + 2x_C) \quad [38]$$

$$s_A = -\delta_1 x_C^2 - x_C Q_1 / (P_1 + 1 - 2x_C) T - R \ln [(P_1 + 1 - 2x_C) / (P_1 + 1)] + R \ln x_A \quad [39]$$

$$s_C = -\delta_1 x_A^2 - x_A Q_1 / (P_1 - 1 + 2x_C) T - R \ln [(P_1 - 1 + 2x_C) / (P_1 + 1)] + R \ln x_C \quad [40]$$

where

$$Q_1 = R b_1 \{ \kappa_1 / (\kappa_1 + 1) \} \{ (1 - P_1) / P_1 \} \quad [41]$$

and

$$P_1 = [1 - 4x_A x_C / (1 + \kappa_1)]^{1/2} \quad [42]$$

Using the above equations, the constants appearing in the liquidus equations given by Eq. [1] and [2] can be written as

$$h_A^* + h_C^* = \frac{1}{2} \gamma_1 - R b_1 (1 - P_1^*) \quad [43]$$

$$s_A^* + s_C^* = -\frac{1}{2} \delta_1 - 2R \ln [P_1^* / (1 + P_1^*)] - R b_1 (1 - P_1^*) / T_{AC} - R \ln 4 \quad [44]$$

$$h_B^{**} + h_C^{**} = \frac{1}{2} \gamma_2 - R b_2 (1 - P_2^{**}) \quad [45]$$

$$s_B^{**} + s_C^{**} = -\frac{1}{2} \delta_2 - 2R \ln [P_2^{**} / (1 + P_2^{**})] - R b_2 (1 - P_2^{**}) / T_{BC} - R \ln 4 \quad [46]$$

We note that P_1^* and P_2^{**} are the degree of dissociation of ac and bc, respectively, at the melting points of the solid compounds. Equations [43]-[46] are used also in the auxiliary conditions given by Eq. [6]-[9]. Thus, by using Eq. [43] in Eq. [6], γ_1 can be eliminated in favor of a_1 and b_1 , etc. Thus, the A-C binary parameters γ_1 and δ_1 can be eliminated in favor of a_1 and b_1 of Eq. [28] and the B-C binary parameters γ_2 and δ_2 can be eliminated in favor of a_2 and b_2 of Eq. [29].

It can be seen from Eq. [37]-[42] that the partial molar quantities of the components in the A-C binary (and in the B-C binary) are functions of T because of the temperature dependence of κ_1 defined by Eq. [20] and [28]. If the parameter b_1 in Eq. [28] is zero, then κ_1 is a constant, Q_1 of Eq. [41] is zero, and all the partial molar quantities for the components are independent of T . The parameter b_1 is given by the equation

$$b_1 = [\frac{1}{2} \gamma_1 + \Delta H_D(ac)] / R \quad [47]$$

Therefore, the parameter b_1 is zero if either both γ_1 and $\Delta H_D(ac)$ are zero or if $\frac{1}{2} \gamma_1 + \Delta H_D(ac) = 0$. In either case, the mol fraction of ac is strictly independent of T at all compositions. Neither case would appear to describe physically realistic situations.

Finally, even for the version of the simplified, regular associated solution model used here, in which the interaction coefficients and dissociation constant depend upon T , the quantities $h_A + h_C$ and $s_A + s_C$ in the A-C binary can be seen from Eq. [37]-[42] to be symmetric about $x_A = x_C = \frac{1}{2}$. Therefore, from Eq. [1] with $u = 0$, the liquidus line in equilibrium with the compound AC(s) is also symmetric about $\frac{1}{2}$. This liquid model therefore suffers an inherent weakness.

Solid Solution Model

For a narrow homogeneity range solid solution, the thermodynamic analysis of the phase diagram can be broken into two steps (1). We are concerned with the first step which involves the liquidus in equilibrium with what can be treated as a pseudobinary solid solution (15). It therefore is necessary only to express the composition dependence of the chemical potentials of HgTe and CdTe in the solid, $(\text{Hg}_{1-u}\text{Cd}_u)\text{Te}(s)$. We assume the solid solution is quasiregular so that the chemical potentials are given by

$$\mu_{\text{HgTe}} = (W_s - V_s T) u^2 + RT \ln(1 - u) + \mu^{\circ}_{\text{HgTe}}(s) \quad [48]$$

$$\mu_{\text{CdTe}} = (W_s - V_s T) (1 - u)^2 + RT \ln u + \mu^{\circ}_{\text{CdTe}}(s) \quad [49]$$

where W_s and V_s are constants independent of T and u . Measurements of the optical absorbance between 220 and 700 nm of the vapor coexisting with solid solutions containing 0, 10, 20, 41.6, and 58.1 mole percent CdTe have been made (16, 17). These establish the partial pressures along the three-phase curves for each composition and, in principle, the above chemical potentials. However, although the partial pressure measurements are fairly precise, the relative chemical po-

tentials, especially that of HgTe, are relatively small differences of two large numbers. Consequently, the validity of the model incorporated in Eq. [48] and [49] and a precise determination of the model parameters, W_s and V_s , are not possible. The data do indicate (17) that the solid solutions depart from ideal, but only slightly with a value of $W_s - V_s T$ of about 600 cal at 880 K. Consistent with this, we adopt values of -333 cal for W_s and -1.0129 eu for V_s .

Experimental Data

HgTe.—For $X_{Te} > 1/2$ there are 12 liquidus points from thermal analysis (18) and 2 from optical absorbance measurements (19). The eutectic temperature determined from cooling curve halts for 7 compositions between 65 and 87.5 atomic percent (a/o) Te seems to be well defined as $413.3^\circ \pm 0.2^\circ\text{C}$ and the eutectic composition is 83.5 ± 0.5 a/o Te. These points are shown in Fig. 1. Optical absorbance measurements (19) of the coexisting vapor give P_{Hg} and P_2 along the Te-rich leg of the three-phase curve for HgTe(s), agree with the maximum melting point of 670°C , and determine the standard Gibbs free enthalpy of formation of HgTe(s) from Hg(g) and Te₂(g). They give no indication of the liquid miscibility gap reported by Delves (20).

The vapor pressure of mercury is given to within 1% of selected values (21) between 0.5 and 10 atm by the equation

$$\log_{10} P^\circ_{Hg}(\text{atm}) = -3099/T + 4.920 \quad [50]$$

(In this paper \log_{10} is the logarithm to base 10 while \ln is the natural logarithm.) This equation also agrees to within 1% with measured values to 30 atm (22), with optical absorbance measurements of the vapor over pure Hg to 20 atm (19), and with one point near 30 atm obtained by detecting the complete vaporization of a known weight of Hg in a known volume by optical absorbance of the vapor (16). Between 10^{-3} and 10^{-1} atm, the selected values (21) are given to within 1% by the equation

$$\log_{10} P^\circ_{Hg} = -3157/T + 5.028 \quad [51]$$

At high pressures Hg(g) is nonideal. From the equation of state given by Sugawara and Sato (22), which is based in part on their vapor pressure measurements to 30 atm, the chemical potential is given by

$$\mu_{Hg(g)} = RT \ln f = RT \ln P_{Hg} + 4857.6 P_{Hg} (-1.793/T + 251/T^2 + 0.001071) \quad [52]$$

where P_{Hg} is in atm and f is the fugacity. For the data considered here, the fugacity differs significantly from P_{Hg} only for the pseudobinary melt.

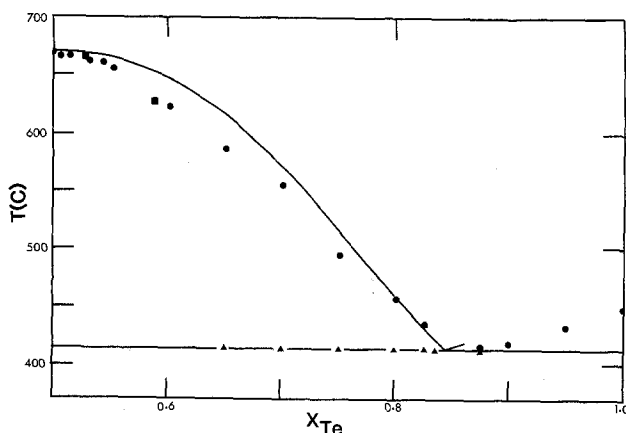


Fig. 1. HgTe-Te liquidus. Circles and triangles are from Ref. (18), two squares are from Ref. (19). Solid line is calculated using parameters in row 6 of Table I.

The saturated vapor over Te(1) is all Te₂(g) and the vapor pressure is taken as

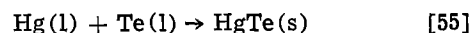
$$\log_{10} P^\circ_2(\text{atm}) = -5960.2/T + 4.7191 \quad [53]$$

This equation does not agree with the selected values of Hultgren *et al.*, being about 20% higher at the 449.5°C melting point of Te but agreeing at about 600°C and higher. It does agree with the results of optical absorbance measurements (23) as low as 449°C and with a number of determinations (24-26) between 10^{-3} and 1 atm. Contrary to the choice made here, Hultgren *et al.* chose the silica Bourdon gauge data of Machol and Westrum (27), which show a pronounced curvature on a $\log P_2$ vs. $1/T$ plot and fall increasingly below the values given by Eq. [53] as T is decreased from 600°C .

Using Eq. [50] and [53] and the data of Ref. (19), one obtains

$$\Delta G^\circ_f(\text{cal}) = -13933 + 9.5377T \quad [54]$$

for the reaction



Lacking any high temperature heat capacity or enthalpy data for HgTe(s), the effective quantities, ΔH°_f and ΔS°_f of Eq. [3] are taken from Eq. [54] and Δ of Eq. [4] taken as zero. These quantities, along with the corresponding ones for CdTe(s) discussed below, are collected in Table I.

To the best of our knowledge, there is only one reliable estimate for the enthalpy of fusion of HgTe(s) and its determination is unpublished. The value, given in Table I, was quoted by Steininger (28) and used subsequently by Laugier (7). It follows from a thermodynamic analysis of the combined liquidus point data and partial pressures along the HgTe(s) three-phase curve made by the last author of this paper. A value of 8.5 kcal/mol from total vapor pressure measurements (29) over the liquid and solid is obtained by a questionable thermodynamic argument, although it is close to the value in Table I. A value of 13.39 kcal/mol follows from requiring a quasichemical model of the liquid to fit the experimental Hg-rich liquidus points and therefore has no strong basis (30).

CdTe.—The liquidus points for Te-rich compositions are shown in Fig. 2. Steininger (31) and Lorenz (32) used thermal analysis. For three compositions, optical absorbance of the coexisting vapor (an essentially static technique), was used (33). Data from Kulwicki (34), as much as $40^\circ\text{--}50^\circ\text{C}$ higher, and from de Nobel (35), as much as 20°C higher, are rejected.

The optical absorbance measurements (33) also give P_2 along the Te-rich leg of the CdTe(s) three-phase curve, give a few values of P_{Cd} near the melting point, agree with a melting point of 1092°C , and establish the standard Gibbs free enthalpy of CdTe(s) relative to Cd(g) and Te₂(g). Partial pressures from two other sources are in poor agreement with the above and are rejected (32, 35).

Selected values (21) for the vapor pressure of Cd between 10^{-8} and 1 atm are reproduced to within 2.5% by the equations

Table I.

| | mp (K) | Heat-of-fusion (cal/mol) | $-\overline{\Delta H^\circ_f}$ (cal/mol) | $-\overline{\Delta S^\circ_f}$ (eu) | Δ (cal/mol) |
|------|--------|--------------------------|--|-------------------------------------|--------------------|
| CdTe | 1365.1 | 12,000 | 30,024 | 10.346 | -144 |
| HgTe | 943.1 | 8,680 | 13,933 | 9.5377 | 0 |

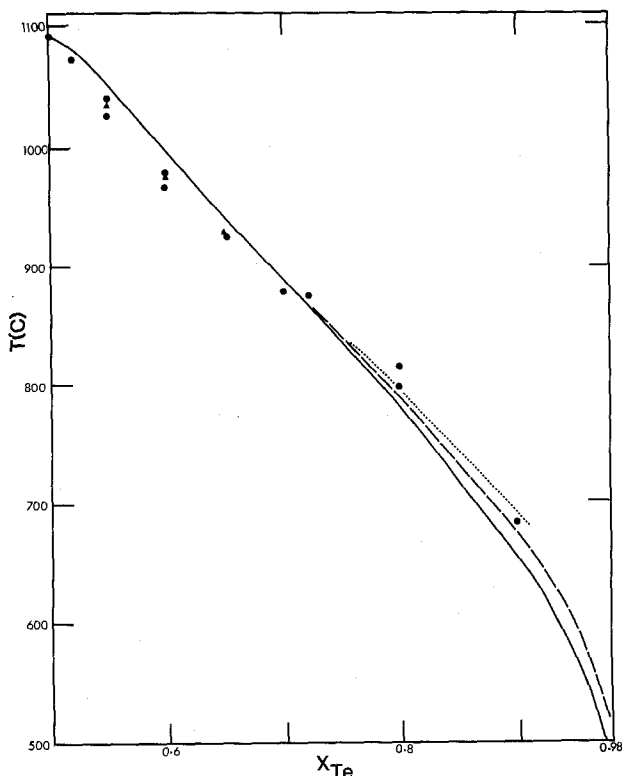
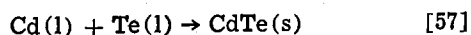


Fig. 2. CdTe-Te liquidus. Experimental points shown as circles are from Ref. (31)-(32). Solid line calculated with $a_2 = 5$, dashed line with $a_2 = 10$, dotted line with $a_2 = 20$. Values of other model parameters are given in Table IV in each case. Triangles are from Ref. (33).

$$\log_{10} P^{\circ}_{\text{Cd}} = -5808/T + 5.956 \quad T < 594 \text{ K} \quad [56]$$

$$\log_{10} P^{\circ}_{\text{Cd}} = -5317/T + 5.119 \quad T > 594 \text{ K}$$

The tabulated, selected values (37) for the standard Gibbs free enthalpy for the reaction



are accurately represented by

$$\Delta G^{\circ}_f = -30,024 + 10.346T \quad [58]$$

Optical absorbance measurements (33, 36) agree to within 200 cal/mol with the above equation for temperatures above 900°C.

The effective enthalpy and entropy of formation given in Table I are taken directly from Eq. [58]. The tabulated selected values (37) for ΔH°_f and ΔS°_f show an abrupt curvature at 1100 K, the highest temperature of the tabulation. Here we draw a straight line through the ΔH°_f points plotted against T , neglecting the 1100 K point. Extrapolation to the melting point leads to a relatively small value of -144 cal for Δ_{CdTe} .

There is only one experimental value for the enthalpy of fusion from Kulwicki which is given in Table I. The eutectic point from Kulwicki is nearly degenerate with the melting point of Te and the eutectic temperature is $449 \pm 2^{\circ}\text{C}$. Partial pressures of Te_2 have also been determined for 55, 60, and 65 a/o Te liquids (33). The temperature ranges are too narrow to accurately establish the partial molar enthalpy and entropy of Te, but do fix the chemical potential of Te.

HgTe-CdTe pseudobinary.—Experimental liquidus (38, 39) and solidus points (40) have been scaled from graphs and are shown in Fig. 6. Most of the solidus points were obtained by chemical analysis of the first crystal to grow from a large volume of melt of known composition, the temperature being taken from a smoothed liquidus line separately determined by

thermal analysis. Three of the solidus points come from optical absorbance measurements (17) and fit in well with the others cited. One set of solidus points scatters about those shown in Fig. 6 and are rejected (41).

The optical absorbance measurements (16, 17) also give P_{Hg} , P_2 , and P_{Cd} over coexisting, Te-saturated solid solution and Te-rich liquid for known compositions of the solid of about 10, 20, 41.6, and 58.1 m/o CdTe. The relation between these partial pressures and the thermodynamics of the solid solution has been discussed in the "Solid Solution Model" section.

Steininger (39) has determined P_{Hg} for pseudobinary melts by a reflux technique for compositions between 0 and 60 m/o CdTe. The results for HgTe are in fair to good agreement with those from optical absorbance measurements. He finds the striking result that, for all the compositions, P_{Hg} is given by a single equation

$$\ln P_{\text{Hg}}(\text{atm}) = -7.149/T + 10.206 \quad [59]$$

Ternary.—Liquidus temperatures in the Te-rich portion of the ternary have been obtained by thermal analysis for 5, 10, 15, and 20 m/o CdTe liquids, but are reported briefly with almost no experimental details (42). Using differential thermal analysis, Bower *et al.* (43) and Harman (44), as given in a preliminary report, obtain liquidus temperatures 30° - 60°C lower. Schmit has also obtained liquidus temperatures and tie lines near 500°C in the growth of epitaxial films on CdTe substrates (45). The liquidus points are in fair agreement with the latter two studies and therefore in poor agreement with the first.

Analysis

The simplified regular associated solution model of the liquid phase contains 10 adjustable parameters: γ_1 , δ_1 , a_1 , and b_1 for the Hg-Te binary; γ_2 , δ_2 , a_2 , and b_2 for the Cd-Te binary, and W and V for the Hg-Cd binary. It proved impossible to obtain simultaneous, satisfactory fits to the liquidus points, partial pressures, and auxiliary conditions of Eq. [6]-[9] for the complete Cd-Te and Hg-Te binaries. This of course might have been anticipated, since the liquid phase model predicts the liquidus of AC(s) is symmetric about 50 a/o. The HgTe-CdTe-Te portion of the phase diagram, for which there are some ternary liquidus points, was therefore fit. Then the parameters W and V , along with the other eight, determine the properties of the pseudobinary and ternary liquid. The parameters for the pseudobinary solid, W_s and V_s , are fixed at, respectively, -333 cal and -1.0129 eu, as discussed in the "Solid Solution Model" section.

A measure of fit σ was defined by the equation

$$\sigma^2 = \left(\frac{\sigma_T}{w_T} \right)^2 + (\sigma_{\text{Hg}}/w_{\text{Hg}})^2 + (\sigma_{\text{Cd}}/w_{\text{Cd}})^2 + (\sigma_2/w_2)^2 \quad [60]$$

where

$$\sigma_T^2 = \sum_{j=1}^M (T_{j,\text{cal}} - T_{j,\text{obs}})^2/M \quad [61]$$

and

$$\sigma_j^2 = \sum_{j=1}^N [(P_{j,\text{cal}} - P_{j,\text{obs}})/P_{j,\text{obs}}]^2/N; \quad j = \text{Hg, Cd, or 2 for Te}_2 \quad [62]$$

The w 's in Eq. [60] are estimated accuracies of the experimental values and were typically taken as 10°C, 0.1, 0.1, and 0.1 for, respectively, w_T , w_{Hg} , w_{Cd} , and w_2 .

When data were missing or inappropriate, *e.g.*, σ_{Cd} in the HgTe-Te binary, the corresponding term was omitted in Eq. [60].

Best fit parameters were established by a trial and error search subroutine which varied the model parameters in an attempt to minimize σ . As an option, any

subset of the model parameters from none to all could be held fixed at the values initially entered for them. The simultaneous solution of the liquidus equations given by Eq. [1] and [2] was considered accomplished when the right-hand members (RHM) of these equations agreed to within 0.001. Since the equations are not explicit equations for T , the RHM depending implicitly upon T , an iteration scheme was used to solve them when it was necessary to obtain a calculated value for T . This is not necessary, of course, when a partial pressure had to be calculated or when it was desired to calculate a liquidus isotherm for some set of the model parameters. As an illustrative example of the calculations, consider a fit to a set of ternary liquidus points. The experimental data input consists of sets of values for the observed values of T , x_{Hg} , and x_{Cd} and it is desired to obtain calculated values of T and u for each of these. For each liquidus composition, the value of u is varied by an interval-halving subroutine seeking to find a value that will make the RHM of Eq. [1] and [2] agree to better than 0.001°C. The interval-halving subroutine is contained within a do-loop defining an iteration scheme. The values of the RHM of Eq. [1] and [2] in the n th iteration, $T_{1,n}$ and $T_{2,n}$, respectively, are evaluated using $T_{1,n-1}$. For the first iteration, the experimental value of T is used. In the n th iteration, the interval-halving varies u until $T_{1,n}$ and $T_{2,n}$ differ by less than 0.001°C. Then, if $T_{1,n}$ and $T_{1,n-1}$ differ by 0.001°C or more, another iteration is performed. If not, then $T_{1,n}$ is taken as the calculated value for T . Usually five iterations or less were required. At each iteration, T and the liquid and solid compositions are specified. Therefore, the mol fraction of species c, y_c , can be calculated from Eq. [22]. This cubic equation in y_c was solved using Cardan's method to within the 16 significant figure accuracy of the computer.

The temperature derivative of y_c can then be calculated using Eq. [36] and the partial molar quantities for the components obtained from Eq. [30]-[35].

Results and Discussion

HgTe-Te binary.—Table II summarizes the fit to this binary. Rows 1-3 illustrate fits in which the auxiliary conditions given by Eq. [6] and [7] are used after the fit to obtain calculated values for ΔH°_f , ΔS°_f , and ΔG°_f at 670°C for the formation of the compound from its liquid elements. For rows 4-7, the auxiliary conditions are applied prior to the fit, and so these calculated quantities match our selected experimental values given in Table I. Row 1 corresponds to the parameters used by Laugier, in which the dissociation constant for the HgTe molecule is temperature independent and small and in which the Hg, Te, and HgTe species in the liquid form an ideal solution. Although the fit to the liquidus points is good, that to the partial pressures is not, the calculated values of P_{Hg} being much too small. Moreover, the calculated thermodynamic properties of the compound are in poor agreement with experiment. Row 2 corresponds to the best fit with a tempera-

ture-independent interaction energy and dissociation constant. The fit to the partial pressures has improved while that to the liquidus has deteriorated. The calculated thermodynamic properties of HgTe(s) are in better agreement with experiment. Row 3 gives the best fit to the liquidus alone with all four parameters free. The fit to the liquidus of 5°C is very good but at the expense of much too negative values for ΔH°_f and ΔS°_f . The fit to the Hg pressures is poor. Row 4 represents the best fit with the auxiliary conditions of Eq. [6] and [7] met and is satisfactory. However, the calculated eutectic temperature is too far from the experimental value of $413.3^\circ \pm 0.2^\circ\text{C}$. The best-fit values of a_1 and b_1 shown in row 4 lie on a "best-fit curve" in the a_1 - b_1 plane. As the values of a_1 and b_1 are changed from their best-fit values, the quality of the fit changes only slowly if the best-fit curve is followed, but rapidly otherwise. A similar best-fit curve is found for the CdTe-Te binary and is a common phenomenon in least squares fits. Rows 5-7 show values of a_1 and b_1 from along the best-fit curve that give a eutectic temperature $+1^\circ$, 0° , and -1°C from the experimental value. We choose the parameters of row 6 as giving the best overall fit. It should be noted that the fits of rows 4-7 are not much different, even though the predicted eutectic temperatures differ.

Figure 1 shows the experimental liquidus points with the calculated liquidus line from the parameters of entry 6. The calculated line is about 20°C too high between 60 and 66 a/o Te. This discrepancy is present for all of the rows 4-7 and can be removed only by ignoring the auxiliary conditions of Eq. [6] and [7].

CdTe-Te binary.—Table III summarizes some preliminary fits. Although the model parameters from the literature shown in rows 1 and 2 give the very best fits to the liquidus, they also give poor fits to the partial pressures and unacceptable values for the thermodynamic functions of CdTe(s). The parameters in row 3 from the literature were obtained using different partial pressures than are selected here. Row 4 shows the best fit obtainable with the same simplified version of the model as in Row 3 using the partial pressures selected here. The fit to the partial pressures is good, but that to the liquidus has deteriorated somewhat. Moreover, although the calculated value for ΔG°_f is close to experiment, those for ΔH°_f and ΔS°_f are too far removed to be acceptable. Row 5 shows the best simultaneous fit attainable to the liquidus and partial pressures with all 4 liquid parameters adjustable.

Further discussion of the CdTe-Te binary involves the first eight rows of Table IV. For all of the entries, Eq. [8] and [9] were applied prior to the fits so that the calculated values of ΔH°_f , ΔS°_f , and ΔG°_f at 1092°C agree exactly with our selected experimental values in Table I. The values of row 6, titled liq. σ_2 , refer to the fit to the partial pressure of Te_2 for melts containing 55, 60, and 65 a/o Te (33). Although the parameters cover a wide range, there is no great change in the fits to the various quantities of the CdTe system. Values less

Table II. Fits to Te-rich side of Hg-Te binary, calculated thermodynamic functions for HgTe(s) at 670°C, eutectic temperature in °C, and composition in atom-fraction Te. Fit 14 liquidus points, 10 partial pressures of Hg, and 10 of Te_2 along HgTe(s) three-phase curve.

| No. | γ_1 | δ_1 | a_1 | b_1 | σ_T (°C) | σ_2 | σ_{Hg} | $-\Delta H^\circ_f$ (kcal/mol) | $-\Delta S^\circ_f$ (cal/K-mol) | $-\Delta G^\circ_f$ (kcal/mol) | T_{eu} (°C) | x_{eu} | Comment |
|-----|------------|------------|--------------------------|----------|--------------------|------------|----------------------|-----------------------------------|------------------------------------|-----------------------------------|-------------------------|-----------------|---|
| 1 | 0 | 0 | 1.60 (10 ⁻³) | 0 | 11.2 | 0.65 | 0.95 | 8.68 | -3.74 | 12.21 | — | — | Parameters from Ref. (7) |
| 2 | -5247 | 0 | 1680 | 0 | 23.8 | 0.14 | 0.18 | 11.30 | 6.45 | 5.22 | — | — | |
| 3 | 4119 | -2.349 | 3619.9 | 11,089.9 | 5.1 | 0.25 | 0.67 | 25.00 | 19.77 | 6.36 | — | — | Best fit to liquidus alone |
| 4 | 14,881 | -15.840 | 7388.5 | 10,138.0 | 12.1 | 0.06 | 0.126 | 13.93 | 9.54 | 4.94 | 417.7 | 0.845 | Best fit to liquidus pts. and pressures |
| 5 | 11,919 | -12.854 | 2615.3 | 9100 | 12.9 | 0.056 | 0.124 | 13.93 | 9.54 | 4.94 | 414.2 | 0.844 | |
| 6 | 11,981 | -12.00765 | 1936.01 | 8800 | 13.2 | 0.056 | 0.123 | 13.93 | 9.54 | 4.94 | 413.3 | 0.844 | Best overall fit |
| 7 | 10,249 | -11.168 | 1433.2 | 8500 | 13.5 | 0.056 | 0.123 | 13.93 | 9.54 | 4.94 | 412.4 | 0.844 | |

Table III. Fits to the CdTe-Te binary and calculated thermodynamic functions for CdTe(s) at 1092°C. Experimental input consists of 15 liquidus pts., 19 partial pressures of Te₂, and only 4 of Cd

| No. | γ_2 | δ_2 | a_2 | b_2 | σ_T (°C) | σ_2 | σ_{Cd} | $-\Delta H^\circ_f$ (kcal/mol) | $-\Delta S^\circ_f$ (cal/K-mol) | $-\Delta G^\circ_f$ (kcal/mol) | Comment |
|-----|------------|------------|-------------------|-------|--------------------|------------|---------------|-----------------------------------|------------------------------------|-----------------------------------|-----------------------------------|
| 1 | 1675.6 | 0 | 0 | 0 | 8.3 | 0.43 | 1.00 | 11.16 | ∞ | ∞ | Parameters from Szapiro; Ref. (4) |
| 2 | 1700 | 0 | 0 | 0 | 8.3 | 0.43 | 1.00 | 11.15 | ∞ | ∞ | Parameters from Laugier; Ref. (7) |
| 3 | 3100 | 0 | $3.03 (10^{-3})$ | 0 | 31.9 | 0.70 | 0.50 | 10.45 | -2.95 | 14.48 | Parameters from Jordan; Ref. (3) |
| 4 | 470.8 | 0 | $2.242 (10^{-3})$ | 0 | 19.4 | 0.16 | 0.13 | 11.76 | -3.52 | 16.57 | All four parameters free |
| 5 | 8344 | -6.691 | $7.955 (10^{-3})$ | 1375 | 19.2 | 0.14 | 0.10 | 10.41 | -4.48 | 16.53 | |

Table IV. Fits obtained with various values of the liquid parameters for the CdTe-Te system. For all but the fits in rows 3-8, the liquid parameters for the Hg-Te system are required and are taken from row 6 in Table II and the values, $W_s = -333$ cal, $V_s = -1.01292$ eu are used

| | a_2 | 5 | 10 | 20 | 50 | 80 |
|----|-----------------|----------------------------|-----------|-----------|-----------|-----------|
| 2 | b_2 | 10,152.9 | 11,043.7 | 11,922.6 | 13,091.8 | 13,697.5 |
| 3 | σ_T (°C) | 20.0 | 17.5 | 16.6 | 17.3 | 18.3 |
| 4 | CdTe-Te | σ_2 | 0.203 | 0.189 | 0.176 | 0.162 |
| 5 | | σ_{Cd} | 0.158 | 0.158 | 0.158 | 0.159 |
| 6 | | liq. σ_2 | 0.313 | 0.315 | 0.32 | 0.325 |
| 7 | T (°C, eut.) | 445.9 | 447.2 | 448.0 | 448.7 | 448.9 |
| 8 | X_{Te} (eut.) | 0.985 | 0.990 | 0.994 | 0.997 | 0.998 |
| 9 | W | -15,159.7 | -15,095.2 | -14,986.2 | -14,895.1 | -14,857.5 |
| 10 | V | 16.4972 | 16.4943 | 16.4548 | 16.4533 | 16.4663 |
| 11 | Pseudobinary | σ_T (°C, liq.) | 8.1 | 8.1 | 8.1 | 8.1 |
| 12 | | σ_T (°C, solid) | 5.3 | 5.3 | 5.3 | 5.3 |
| 13 | | σ_{Hg} | 0.213 | 0.22 | 0.226 | 0.234 |
| 14 | Te-saturated | σ_{Hg} | 0.09 | 0.092 | 0.093 | 0.095 |
| 15 | | σ_{Cd} | 0.33 | 0.331 | 0.332 | 0.333 |
| 16 | | σ_2 | 0.134 | 0.137 | 0.141 | 0.146 |
| 17 | Ternary liquid | σ_T [°C, Ref. (42)] | 47.36 | 34.5 | 22.7 | 10.57 |

than 5 for a_2 give too low a eutectic temperature and so might be ruled out. The calculated liquidus curves for all the sets of parameters shown are essentially the same between 50 and 60 a/o Te and are all high by about 25°C at 60 a/o Te. As shown in Fig. 2, the calculated curves for various values of a_2 do tend to diverge between 80 and 90 a/o Te, values between 10 and 20 giving the closest fits. For all values of a_2 in Table IV, the mol fraction of CdTe molecules in the melt at 1092°C and 50 a/o Te is between 0.89 and 0.90.

Pseudobinary and ternary.—For each pair of values for a_2 and b_2 in Table IV, and the HgTe liquid parameters given in row 6 of Table II, the best fit to the pseudobinary liquidus and solidus points was used to fix W and V shown in rows 9 and 10. The fits are good and almost identical, as can be seen from rows 11 and 12. With all of the liquid and solid model parameters determined, fits to the remaining data were calculated and, except for those to the ternary liquid in row 17, are almost identical. In row 13, σ_{Hg} is the fit to 28 Hg pressures for the pseudobinary liquid (39). Rows 14-16 give the fits to the partial pressures over Te-saturated HgTe-CdTe solid solutions containing 9.4, 19.6, 41.6, and 58.1 m/o CdTe (16, 17). In row 17, it can be seen that 20 ternary liquidus points from Ref. (42) can be fit to an average of 10.6°C with $a_2 = 50$ but that values of 10 and 20 for a_2 give fits of, respectively, 34.5° and 23°C.

The wide range of ternary liquidus surfaces that can be generated while still maintaining almost equally good fits to the binaries, pseudobinary, and partial pressures is illustrated by Fig. 3, which shows the liquidus isotherm at 500°C for various values of the CdTe parameter, a_2 . The ternary liquid surface for various fixed values of $x_{Cd}/(x_{Cd} + x_{Hg}) = u$ in the melt between 0 and 0.2 is shown in Fig. 4 for $a_2 = 5$ along with the experimental points. The experimental points from Ref. (42) for a $u = 0.2$ liquid are shown as the upper set of three circles, which are 30°-60°C higher than the calculated curve, while those for a

$u = 0.1$ liquid are shown as the lower set of four circles which cross the calculated line for 0.2, but again are 30°-70°C higher than the calculated curve for 0.1. The experimental points for $u = 0.05$ and 0.15 liquids are omitted for clarity but are also high. The experimental points from Ref. (43) are shown as error bars along dashed lines. The upper set is for a $u = 0.10$ liquid while the lower set is for 0.067. The former fall 10°-15°C below the calculated line for $u = 0.1$ while the latter cross the calculated curve for $u = 0.05$. The two triangles are from Ref. (45), and the experimental data from this reference are summarized in

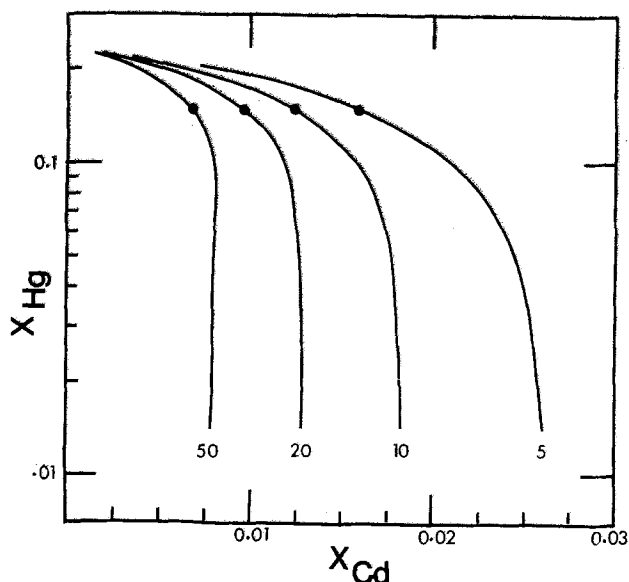


Fig. 3. Ternary liquid isotherms for 500°C calculated for labeled values of a_2 . Circles mark liquid composition in equilibrium with a 40 m/o CdTe solid solution.

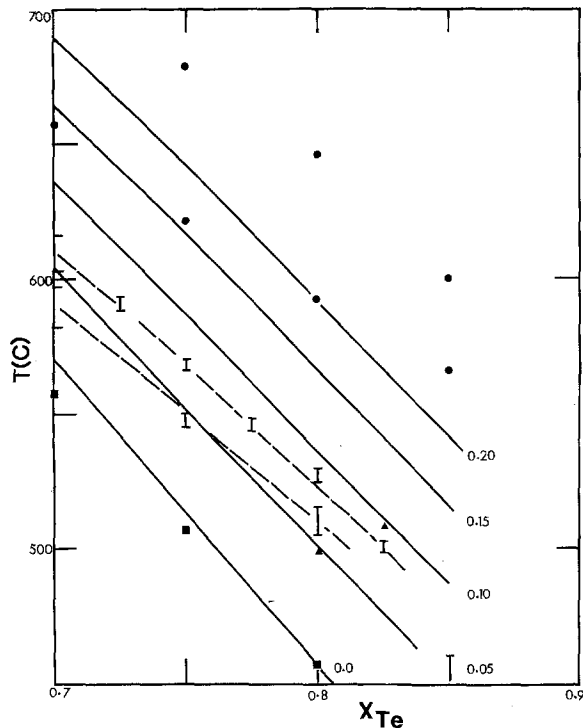


Fig. 4. Solid lines give temperature vs. atom fraction of Te for liquids with fixed, labeled, values of $u^L \equiv X_{Cd}/(X_{Hg} + X_{Cd})$ in the liquid as calculated with $a_2 = 5$ and other overall optimum parameters given in Table VI. Circles are from Ref. (42), the upper 3 are for $u^L = 0.20$, the lower 4 are for $u^L = 0.10$. Points with error bars and connected by dashed lines are from Ref. (43), the upper set corresponding to $u^L = 0.10$, the lower to $u^L = 0.067$. Two triangles are from Ref. (45) as summarized in Table V. The squares are from Ref. (18).

Table V. These latter experimental points are shown again in Fig. 5, which shows calculated liquidus isotherms and solid isoconcentration lines in the low temperature range for $a_2 = 5$. The left-most experimental point falls on the 500°C isotherm where it should be, but is slightly displaced from the calculated solid isoconcentration line for $u = 0.20$, falling closer to that for $u = 0.22$. The three clustered experimental points fall closer to the 515°C isotherm by interpolation than to that for 508°C. By interpolation they fall on isoconcentration lines for $u = 0.33, 0.37, \text{ and } 0.39$ compared to the experimental values of, respectively, 0.29, 0.37, and 0.40. Although not perfect, the agreement is close.

Optimum fit to the HgTe-CdTe-Te ternary.—Here we take the data of Schmit in Table V as the most nearly correct ternary data and consequently take a_2 as equal to 5.0. The complete set of parameters is then fixed and is collected in Table VI. These lead to the optimum overall fit to all of the data considered, and we shall refer to the calculated data obtained with this set of parameters as the optimum fit. The optimum HgTe-Te liquidus line is, then, that shown in Fig. 1; that for CdTe-Te is that shown in Fig. 2 for $a_2 = 5$; and the optimum calculated ternary liquidus is shown in Fig. 4 and 5 for the low temperature range.

Table V. Composition of liquid given by the atomic fractions of Hg and Cd and that of the coexisting solid solution, $Hg_{1-u}Cd_uTe(s)$, from Ref. (45)

| T (°C) | X_{Hg} | X_{Cd} | u |
|--------|----------|----------|------|
| 499 | 0.19 | 0.01 | 0.20 |
| 507 | 0.175 | 0.0156 | 0.29 |
| 508 | 0.163 | 0.017 | 0.37 |
| 508 | 0.162 | 0.018 | 0.40 |

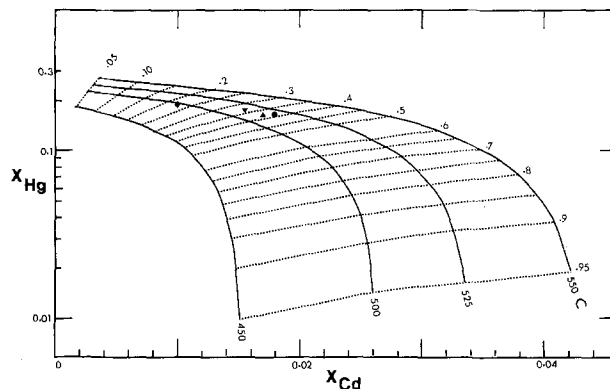


Fig. 5. Liquid isotherms (solid lines) and solid solution isoconcentration lines (dashed lines) as calculated with $a_2 = 5$ and other overall optimum parameters of Table VI. The symbols are from Ref. (45) as tabulated in Table V. Numbers along the upper curve give the mol fraction of CdTe in the HgTe-CdTe solid solution.

The optimum calculated pseudobinary liquidus and solidus is shown in Fig. 6. Although the fits are good numerically, as can be seen from rows 11 and 12 in Table IV, the calculated solidus is slightly below all the experimental points but one.

The optimum calculated fit to P_{Hg} for the pseudobinary liquid ($X_{Te} = 0.5$) is shown in Fig. 7 along with the experimental points for various mol fractions of CdTe. For clarity only segments of the calculated lines are shown, each segment falling just below the associated experimental points for each mol fraction of CdTe. The calculated results are low by 21.3% as indicated in row 13, column 1 of Table IV. The correction for the nonideality of Hg(g) results in the calculated values for P_{Hg} being about 4% lower than if the correction were omitted. As can be seen, the calculated values of P_{Hg} for 10.8-60 m/o CdTe fall along slightly different lines, P_{Hg} being lower at a given T the larger the m/o CdTe. In contrast, the experimental points of Steininger (39) are tightly clustered and were represented as a single straight line by him.

Figure 8 shows calculated values of P_{Hg} for Te-saturated solid solutions of fixed mol percent CdTe and the experimental points. The fit to the experimental points between 10 and 58 m/o CdTe solid is about 9% and is good. The calculated values of P_{Hg} at the calculated solidus temperatures fall close to a straight line up to 70 m/o CdTe, the effect of increasing solidus temperature dominating the effect of decreasing Hg content. Between 95.2 and 95.3 m/o CdTe, P_{Hg} at the solidus temperature reaches a maximum value of 52.3 atm between 993.5° and 994.9°C and then decreases for larger Cd content. This calculated result is off-scale in Fig. 8.

Figure 9 shows the experimental points and the optimum calculated curves for P_2 over Te-saturated solid solutions of various mol percent CdTe. For comparison, the vapor pressure of Te(1) is shown as the upper-

Table VI. Values of the model parameters giving the best overall fit to the HgTe-CdTe-Te system. The degree of dissociation, β , of the liquid phase molecule, HgTe, at the melting point of HgTe(s) and that of the liquid phase molecule, CdTe, at the melting point of CdTe(s) as calculated from these parameters is also given

| i | γ_i (cal) | δ_i (eu) | a_i | b_i (K) | β_i |
|---------------------|------------------|-----------------------|---------|--------------------------------|-----------|
| 1, i.e., HgTe | 11,081 | -12.0076 | 1936.01 | 8800 | 0.3827 |
| 2, i.e., CdTe | 2401.5 | -1.4647 | 5.0 | 10,153 | 0.054 |
| W (cal) = -15,160 | | V (eu) = 16.497 | | Pure ternary liquid parameters | |
| W_s (cal) = -333 | | V_s (eu) = -1.01292 | | Solid solution parameters | |

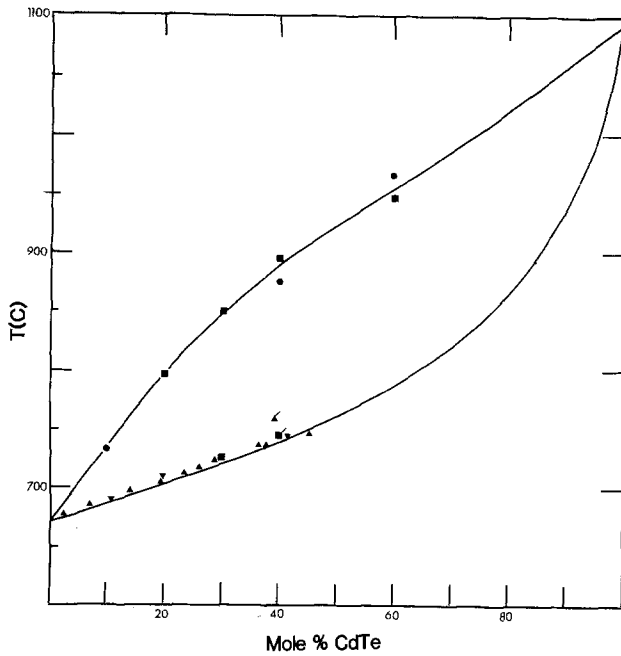


Fig. 6. Solid lines show the liquidus and solidus in the $Hg_{1-u}Cd_uTe$ pseudobinary as calculated using the overall optimum parameters of Table VI. Circles: Ref. (38), squares: Ref. (39), triangles: Ref. (40), inverted triangles: Ref. (16) and (17). Triangle and square with attached line segment were omitted from the fits.

most straight line. The fits are good as seen in row 16, $a_2 = 5$ column of Table IV. The experimental values for 9.4 and 19.6 m/o CdTe fall below the calculated curves near their maxima. In addition, the experimental points for different CdTe content tend to merge together at the lowest temperature to a greater degree than shown by the calculated curves. However, the measured values of P_2 are near the limit of detectability from the optical absorbance of $Te_2(g)$ in the visible. Moreover, at these low temperatures, internal equilibrium of the solid solution phase and equilibrium be-

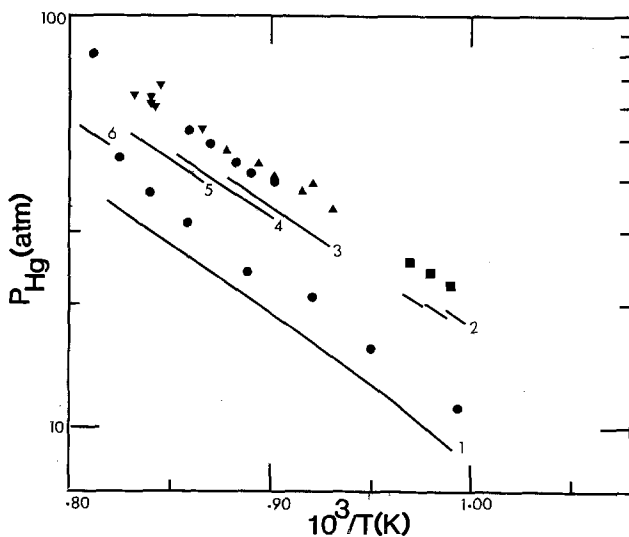


Fig. 7. The partial pressure of $Hg(g)$ for various pseudobinary melts as a function of $10^3/T$ and for line 1, for a 60 a/o Te, 12 a/o Cd melt. Line segments are calculated using the parameters of Table VI and cover the same temperature range as the corresponding experimental points from Ref. (39) and, for the squares, from Ref. (17). Line 2, squares: 10.8 m/o CdTe pseudobinary liquid; line 3, triangles: 20 m/o CdTe; line 4, circles: 30 m/o CdTe; line 5, inverted triangles: 40 m/o CdTe; line 6; single circle: 60 m/o CdTe.

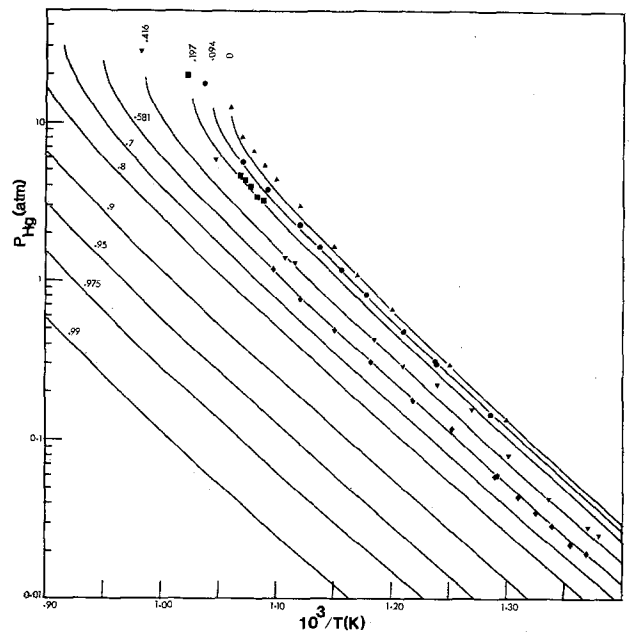


Fig. 8. The mercury partial pressure over Te-saturated $Hg_{1-u}Cd_uTe(s)$ as a function of $10^3/T$. Solid curves with labeled values of u are calculated using parameters of Table VI. Experimental points are from Ref. (16) and (17) and, for $HgTe(s)$, from Ref. (19).

tween it and the vapor phase is possibly not always achieved.

Figure 10 shows the experimental points and calculated curves for P_{Cd} over solid solutions of various mol percent CdTe. The experimental points are generally higher than the corresponding curves, particularly for 9.4 m/o Cd although the overall fit is to within 33% as seen in column 1, row 15 of Table IV. The calculated curves cross at high temperatures. The experimental data (17), which are available for both metal-saturated and Te-saturated solid solutions, do the same thing. At low temperatures, P_{Cd} is higher, the larger the mole percent CdTe, for both metal and Te-saturated solid solution.

General Discussion

A quantitative simultaneous fit to the phase diagram and thermodynamic data in the $HgTe-CdTe-Te$ system

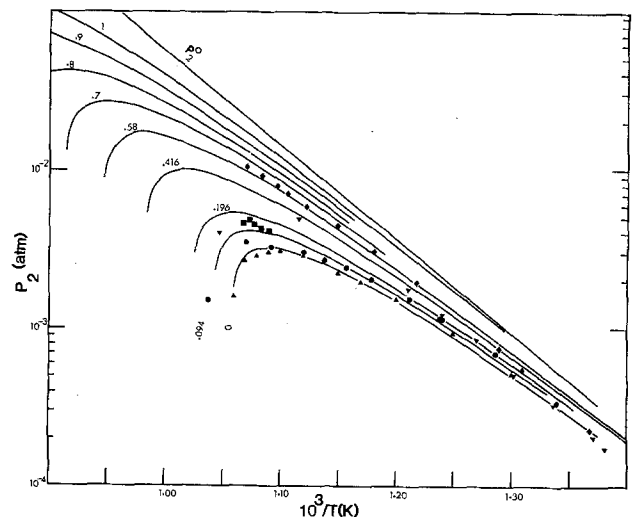


Fig. 9. The vapor pressure of Te shown as the uppermost line and the partial pressure of Te_2 over Te-saturated $Hg_{1-u}Cd_uTe(s)$ vs. $10^3/T$. Solid curves with labeled values of u are calculated using the parameters of Table VI. Experimental points are from Ref. (16) and (17). Those for CdTe from Ref. (33) are off-scale at higher temperatures.

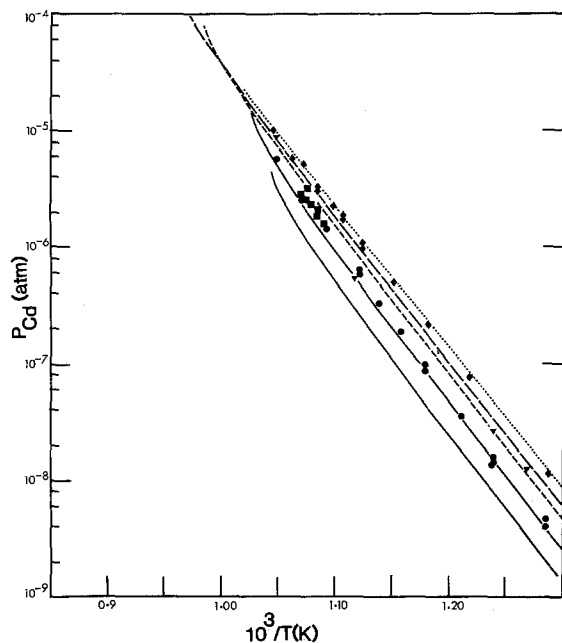


Fig. 10. The partial pressure of Cd over Te-saturated $\text{Hg}_{1-u}\text{Cd}_u\text{Te}(s)$ vs. $10^3/T$. Experimental points are from Ref. (16) and (17). Lines are calculated using the parameters of Table VI. Except for $u = 0.58$ and 1, they terminate at the solidus temperature. Uppermost, dot line: $u = 1.0$; 2nd, long-dash line, diamonds: $u = 0.581$; 3rd, short-dash line, inverted triangles: $u = 0.416$; solid line, squares: $u = 0.197$; bottom solid line, circles: $u = 0.094$.

has been obtained using an extension of the simplified, regular associated solution model of Jordan (3) and Szapiro (4) for the liquid phase. The analysis differs from previous ones based upon this model in a number of respects. First, the model is extended to allow the interaction coefficients and dissociation constants of the species to depend upon T . It is shown that this is necessary to obtain satisfactory fits. Second, more exact liquidus equations are used that are thermodynamically consistent with the temperature dependence of the partial molar quantities for the components in this liquid phase model. Third, the fits are much more extensive than any previously attempted with this model. As an example, not only are the liquidus points in the HgTe-Te and CdTe-Te binaries fit, but also the partial pressures along the three-phase curves for the binary compounds. Moreover, and most importantly, this is done with constraints applied to the liquid phase model parameters that insure that the thermodynamic properties of the stoichiometric liquids, $\text{HgTe}(l)$ and $\text{CdTe}(l)$, are consistent with the known enthalpies and entropies of formation of $\text{HgTe}(s)$ and $\text{CdTe}(s)$.

The quantitative fits obtained should prove useful for interpolating and extrapolating the experimental data and in guiding further experiments. In addition to this practical result, the present analysis provides the most extensive test of this liquid phase model to date. There are signs the model may not be flexible enough even in the HgTe-CdTe-Te system. There are portions of the data, such as parts of the HgTe-Te and CdTe-Te liquidus curves, and P_{Hg} over the pseudobinary melts, in which the calculated results seem to differ significantly from experiments. No firm conclusion can be drawn here, however, since these discrepancies may be due in large part to errors in the experimental input data including the enthalpies of fusion. A surer indication of an inherent weakness in the model lies in the theoretical demonstration here that it can only predict symmetric liquidus lines for a 50 a/o compound. Thus, it is found inadequate to fit well either the entire Cd-Te binary or the Hg-Te binary. Dividing such a binary

Table VII. A listing for various compounds of the melting point, the enthalpy of compound formation from the pure liquid elements at the melting point, the enthalpy of fusion, and the enthalpy of formation of the stoichiometric liquid at the melting point. All enthalpies are in kcal/mol

| Compound | T_m ($^{\circ}\text{C}$) | $-\Delta H^{\circ}_f$ | ΔH_m | $-\Delta H_{M^L}$ ($X = 1/2$) |
|----------|------------------------------|-----------------------|--------------|------------------------------------|
| InSb | 525 | 13.27 | 11.41 | 1.86 |
| GaAs | 709.2 | 16.30 | 15.80 | 0.50 |
| InAs | 942 | 21.30 | 18.40 | 2.90 |
| GaS | 1240 | 28.25 | 25.18 | 3.07 |
| HgTe | 670 | 13.93 | 8.68 | 5.25 |
| PbTe | 924 | 22.2 | 13.7 | 8.5 |
| PbSe | 1081 | 26.6 | 11.8 | 14.8 |
| CdTe | 1092 | 29.88 | 12.0 | 17.9 |

phase diagram in half, and fitting each half with different values of the parameters, has been done (3). However, this introduces discontinuities in the thermodynamic properties of the liquid phase and is unacceptable once one wishes to go beyond a fit to the liquidus line alone. (If both sets of parameters are required to satisfy the auxiliary conditions given by Eq. [6]-[7], the discontinuities at the melting point disappear. Then the partial pressures along the three-phase curve as well as the liquidus line are continuous at $x = 1/2$. Above the melting point the discontinuities in the liquid phase properties still exist.) Thus, although the model is attractive in view of its relative simplicity, and should prove useful in fitting significant portions of phase diagram data, a more powerful model is desirable. This might be found in the more general forms of the associated solution model in which the interaction terms are more properly written in terms of the mol fractions of the species, and not in terms of the atom fractions of the components. In studies of the Cu-S and similar systems (46, 47) the interaction terms among the solution species are assumed to depend upon cubic as well as quadratic terms in the mol fractions of the species, i.e., subregular interactions.

We believe that those systems, which are difficult to fit and which probably will require complicated, many-parameter, liquid phase models, rather than simple solution or subregular models, can be anticipated. Generally they are liquids in which the ionic component of binding is significant. Specifically, they are liquids whose heat-of-mixing at the composition of a solid compound is a substantial fraction of the heat-of-formation of the compound itself, i.e., systems in which the cohesive energy is not greatly altered by the loss of long-range order accompanying melting. This is illustrated in Table VII. For the III-V systems listed [data sources identified in Ref. (48)] the heat of fusion is comparable to the enthalpy of formation of the solid compound from its pure liquid elements at the melting point. Consequently, the heat-of-mixing of the liquid phase at the melting point is relatively small and a subregular liquid phase model can do well in fitting the phase diagram and thermodynamic data (48). The contrast with the other systems listed is marked.

Acknowledgment

This work was supported by the Air Force Office of Scientific Research, Air Force Systems Command under Grant No. AFOSR-78-3611. The authors wish to express their gratitude to Dr. A. J. Strauss for sending us his tabulated HgTe liquidus points and to Mr. J. L. Schmit for sharing his results before publication.

Manuscript submitted April 23, 1980; revised manuscript received Nov. 18, 1980.

Any discussion of this paper will appear in a Discussion Section to be published in the June 1982 JOURNAL. All discussions for the June 1982 Discussion Section should be submitted by Feb. 1, 1982.

Publication costs of this article were assisted by Marquette University.

APPENDIX

Previous applications (3, 4, 7) of the simplified RAS model have started with a version of the Vieland liquidus equation in which the heat capacity of the binary compound and that of the liquid of the same composition were taken as equal. Here we obtain the liquidus equation in a form similar to the Vieland form and written explicitly for the RAS liquid model, so that the above assumption can be critically judged. We consider only one of the two equations necessary to describe the ternary liquid in equilibrium with the pseudobinary solid, $A_{1-u}B_uC$, since the other is completely analogous. In terms of the activity coefficients, γ_i , and mol fractions of species, y_i , $i = a, c$, an "exact" liquidus equation is given by Eq. [46] of Ref. (1) and is

$$RT \ln \left[\frac{\gamma_a \gamma_c y_a y_c}{\gamma_a^\dagger \gamma_c^\dagger y_a^\dagger y_c^\dagger (1-u) \Gamma_{AC}} \right] = H_{AC}(T/T_{AC} - 1) - \int_T^{T_{AO}} (1 - T/r) (\Delta C_{AC}^s - \Delta C_{AC}^L) dr \quad [A-1]$$

Most of the quantities have been defined in the text in connection with Eq [1] and [2]. The dagger superscript indicates a quantity is evaluated at $x_A = x_C = 1/2$ and arbitrary T . (In the B-C analog of Eq. [A-1], the dagger superscript would mean evaluation at $x_B = x_C = 1/2$.) The heat capacities appearing on the right side of Eq. [A-1] are those for AC(s) and the liquid of the same composition. Both are relative to the pure liquid elements, A(l) and C(l). For the A-C binary, $u = 0$, $\Gamma_{AC} = 1$.

The first point to be made in connection with Eq. [A-1] is that the temperature integrals of the heat capacities ought to be considered separately; that for the solid is experimentally accessible, if not yet determined; and that for the liquid is set by the liquid model and its parameter values in the type of application ordinarily made. In many cases, the Gibbs free enthalpy of formation of AC(s) from its pure liquid elements is very nearly a linear function of T . Then the integral over the relative heat capacity of AC(s) is given by Eq. [32] of Ref. (1) as

$$\int_T^{T_{AO}} (1 - T/r) \Delta C_{AC}^s dr = \Delta_{AC}(T/T_{AC} - 1) + T\delta(T_{AC})/T_{AC} - \delta(T) \quad [A-2]$$

where Δ_{AC} is defined by Eq. [4] and $\delta(T_{AC})$ and $\delta(T)$ are small terms that can often be neglected, as discussed in Ref. (1). Indeed, the quantity Δ_{AC} often turns out to be small and of the order of the accuracy in the heat of fusion, H_{AC} , [(48), "Experimental Section" of text here].

The integral over the relative heat capacity of the liquid, AC(l), is given by Eq. [37] of Ref. (1) in terms of the partial molar excess quantities of the liquid phase components and is

$$\int_T^{T_{AO}} (1 - T/r) \Delta C_{AC}^L dr = h_A^* + h_C^* - h_A^\dagger - h_C^\dagger - T(s_A^* + s_C^* - s_A^\dagger - s_C^\dagger) \quad [A-3]$$

where the asterisk superscript indicates the quantity is evaluated as $x_A = x_C = 1/2$ and $T = T_{AC}$. For assumed liquid species a, b, c, ac, and bc, the chemical potentials defining the simplified RAS liquid model are given by Eq. [13]-[17]. The partial molar excess quantities for the components are given by Eq. [37]-[42] for the A-C binary. Substituting these into Eq. [A-3] and rearranging gives

$$\int_T^{T_{AO}} (1 - T/r) \Delta C_{AC}^L dr = (\Delta H_D + 1/2 \gamma_1) (1 - T/T_{AC}) (\kappa^*)^{1/2} / (1 + \kappa^*)^{1/2} + 2 RT \ln \left[\frac{(1 + \kappa)^{1/2} + \kappa^{1/2}}{(1 + \kappa^*)^{1/2} + \kappa^{*1/2}} \right] \quad [A-4]$$

The interaction coefficients appearing in the defining Eq. [13]-[17] are assumed to depend linearly upon T as given by Eq. [26] and κ , the product of the dissociation equilibrium constant and the activity coefficient

ratio for the liquid phase molecule, ac, is defined by Eq. [20]. Using Eq. [A-2] and [A-4], the liquidus equation given by Eq. [A-1] can be written as

$$RT \ln \left[\frac{\gamma_a \gamma_c y_a y_c}{\gamma_a^\dagger \gamma_c^\dagger y_a^\dagger y_c^\dagger (1-u) \Gamma_{AC}} \right] = [H_{AC} - \Delta_{AC} - (\Delta H_D + \gamma_1/2) \kappa^{*1/2} / (1 + \kappa^*)^{1/2}] [T/T_{AC} - 1] + 2 RT \ln \left[\frac{(1 + \kappa)^{1/2} + \kappa^{1/2}}{(1 + \kappa^*)^{1/2} + \kappa^{*1/2}} \right] \quad [A-5]$$

This equation differs from that previously used by the presence of the Δ_{AC} term and the two terms containing κ and κ^* . The importance of these terms increases as T departs from T_{AC} . As mentioned above, neglect of Δ_{AC} is often justified. However, the magnitude of the other two terms depends upon the parameters of the liquid model and their neglect is not justified in general. When the degree of association becomes very strong, κ goes to zero and so do these additional terms. In the special case that $\Delta H_D + \gamma_1/2$ is zero, κ is independent of T , ΔC_{AC}^L is zero, and both terms involving κ disappear. Finally, when the degree of association becomes vanishingly small and κ becomes indefinitely large, the two κ terms in Eq. [A-5] cancel one another and the integral over the relative heat capacity of AC(l) given by Eq. [A-4] goes to zero. The resulting liquidus equation is then what one expects for a liquid model in which the relative partial molar quantities are independent of T .

In fitting the Cd-Te and Zn-Te binaries, Szapiro (4) assumed the dissociation constant of the liquid molecules was independent of T , or in effect that $\Delta H_D = 0$. For the Te-rich side of each binary, he used $\kappa = 0$, thus incurring no error through his starting liquidus equation. For the metal-rich sides, he used values of 0.044 and 0.111 for κ . We have checked indirectly whether these are small enough to neglect the κ -terms in Eq. [A-5]. First, Szapiro's parameters were used in Eq. [1] for the A-C binary ($u = h_{AC}^s = s_{AC}^s = 0$) and with $\Delta_{AC} = 0$ to obtain "exact" liquidus temperatures. Secondly, the calculations were repeated to give approximate liquidus temperatures using Eq. [1] for the A-C binary and with $\Delta_{AC} = 0$, but with the asterisk superscript replaced by the dagger superscript. Such a replacement is valid if the relative heat capacity of AC(l), as given by Eq. [37] of Ref. (1), is set equal to zero. The exact and approximate liquidus temperatures agreed to within a few tenths of a degree centigrade for both Cd-CdTe and Zn-ZnTe. For Cd-CdTe our calculated temperatures also agree with those in Szapiro's Table 1 to within a few tenths of a degree, with the exception of $X_{Te} = 0.45$, for which he lists 1084.9°C and we get 1069.1°C. For Zn-ZnTe, our calculated temperatures differ by as much as 2-3°C from Szapiro's. However, in view of the above, this is probably due to calculation errors rather than to the liquidus equation used. We have not carried out a similar check for the entire Cd-Zn-Te ternary. Neither have we checked Jordan's calculations (3), since as Szapiro has pointed out (4), Jordan's assumption that κ is independent of T is erroneous.

In a more recent analysis of the Ga-In-Sb ternary, Szapiro [*J. Phys. Chem. Solids*, **41**, 279 (1980)] has used the same liquidus equations as before, obtaining values of κ^* of 0.0104 and 0.303 for, respectively, GaSb and InSb. The latter value is most likely large enough that significant error is made in not using Eq. [A-5].

LIST OF SYMBOLS

| | |
|-----------------------|---|
| A, B, C | components of ternary system corresponding to, respectively Hg, Cd, and Te |
| a, b, c, ac, bc | assumed species in ternary liquid; ac and bc are diatomic molecules containing one atom of A and one of C, and one atom each of B and C, respectively |
| x_i , $i = A, B, C$ | atom fraction of component i in the liquid |
| y_j , $j = a, b, c$ | ac, bc mol fraction of species j in the liquid |
| u | mol fraction of BC in solid solutions, $A_{1-u}B_uC(s)$ |
| T_{AC}, T_{BC} | maximum melting points in K of AC(s) and BC(s) |
| H_{AC}, H_{BC} | enthalpies of fusion in cal/mol of AC(s) and BC(s) |

| | |
|--|--|
| $h_i, s_i, i = A, B, C$ | relative partial molar excess enthalpy and entropy of component i in the liquid. The pure elemental liquids are taken as the standard state for each component |
| $s_i^t, i = A, B, C$ | relative partial molar entropy (not excess) for component i in the liquid |
| * | asterisk superscript indicates a quantity is evaluated at $x_A = x_C = \frac{1}{2}$ and $T = T_{AC}$ |
| ** | double asterisk superscript indicates a quantity is evaluated at $x_B = x_C = \frac{1}{2}$ and $T = T_{BC}$ |
| $\Delta H_f^{\circ}(AC, T), \Delta S_f^{\circ}(AC, T)$ | enthalpy and entropy of formation of AC(s) from its pure liquid elements in cal/mol and cal/K-mol, respectively |
| $\Delta H_f^{\circ}(BC, T), \Delta S_f^{\circ}(BC, T)$ | similar quantities for BC(s) |
| $\Delta \bar{H}_f(AC), \Delta \bar{S}_f(AC)$ | effective or average enthalpy and entropy of formation of AC(s) as defined in Eq. [3] |
| $\Delta \bar{H}_f(BC), \Delta \bar{S}_f(BC)$ | similar average quantities for BC(s) |
| Δ_{AC}, Δ_{BC} | difference between the average enthalpy of formation and its actual value at the melting point for the compounds AC(s) and BC(s). Defined in Eq. [4] and [5] |
| h_{AC}^s, s_{AC}^s | excess partial molar enthalpy and entropy of species AC in the solid solution, $A_{1-x}B_xC(s)$, relative to AC(s) |
| h_{BC}^s, s_{BC}^s | similar quantities for species BC and relative to BC(s) |
| $\mu^{\circ}_i, i = A, B, C$ | chemical potentials of the pure liquid elements |
| $\mu^{\circ}_{ac}, \mu^{\circ}_{bc}$ | chemical potential of a hypothetical liquid consisting entirely of, respectively, ac and bc molecules |
| $\Delta H_D(ac), \Delta S_D(ac), K_1$ | enthalpy and entropy of dissociation to the pure liquid elements and dissociation equilibrium constant for the liquid phase molecule, ac |
| $\Delta H_D(bc), \Delta S_D(bc), K_2$ | similar quantities for the liquid phase molecule, bc |
| ω | interaction coefficient between the liquid phase species a and b in cal/g-atom |
| α_1 | interaction coefficient between the liquid phase species a, c, and ac, i.e., Hg, Te, and HgTe |
| α_2 | interaction coefficient between the liquid phase species, b, c, and bc, i.e., Cd, Te, and CdTe |
| κ_1, κ_2 | product of dissociation constant and activity coefficient ratio for ac and bc. Definitions given by Eq. [20] and [21] |
| $W, V, \gamma_1, \delta_1, \gamma_2, \delta_2$ | temperature and composition independent parameters describing the linear temperature dependence of the interaction coefficients for the liquid phase species. Definitions given in Eq. [25]-[27] |
| W_s, V_s | constant parameters describing the relative chemical potentials of the quasiregular solid solution. See Eq. [48]-[49] |
| $\mu^{\circ}_{HgTe}(s)$ | chemical potential (or Gibbs free enthalpy of formation) of HgTe(s) |
| $\mu^{\circ}_{CdTe}(s)$ | similar quantity for CdTe(s) |

REFERENCES

- R. F. Brebrick, T. Tung, C.-H. Su, and P.-K. Liao, *This Journal*, **128**, 1595 (1981).
- L. J. Vieland, *Acta Metall.*, **11**, 137 (1963).
- A. S. Jordan, *Metall. Trans.*, **1**, 239 (1970).
- S. Szapiro, *J. Electron. Mater.*, **5**, 223 (1976).
- B. Predel, in "Calculation of Phase Diagrams and Thermochemistry of Alloy Phases," Y. A. Chang and J. F. Smith, Editors, p. 72, The Metallurgical Society of AIME, Warrendale, Pa. (1979).
- A. S. Jordan, in "Calculation of Phase Diagrams and Thermochemistry of Alloy Phases," Y. A. Chang and J. F. Smith, Editors, p. 100, The Metallurgical Society of AIME, Warrendale, Pa. (1979).
- A. Laugier, *Rev. Phys. Appl., Suppl. J. Phys.*, **8**, 259 (1973).
- K. Osamura and Y. Murakami, *J. Phys. Chem. Solids*, **36**, 931 (1975).
- K. Osamura and B. Predel, *Trans. Jpn. Inst. Met.*, **18**, 765 (1977).
- K. Osamura, K. Nakajima, and Y. Murakami, *This Journal*, **126**, 1992 (1979).
- R. F. Brebrick, *Metall. Trans. AIME*, **2**, 1657 (1971).
- R. F. Brebrick, *Metall. Trans. A*, **7**, 1609 (1976).
- A. S. Jordan and R. R. Zupp, *This Journal*, **116**, 1264 (1969).
- A. S. Jordan and R. R. Zupp, *ibid.*, **116**, 1285 (1969).
- R. F. Brebrick, *J. Phys. Chem. Solids*, **40**, 177 (1979).
- J. P. Schwartz, T. Tung, and R. F. Brebrick, *This Journal*, **128**, 438 (1981).
- T. Tung, L. Golonka, and R. F. Brebrick, *ibid.*, **128**, 451 (1981).
- A. J. Strauss, Private communication. Dr. Strauss has kindly supplied his tabulated data which appear in graphical form in Ref. (40).
- R. F. Brebrick and A. J. Strauss, *J. Phys. Chem. Solids*, **26**, 989 (1965).
- R. T. Delves and B. Lewis, *Br. J. Appl. Phys.*, **16**, 343 (1965).
- R. Hultgren, P. Desai, D. Hawkins, M. Gleiser, and K. K. Kelley, "Selected Values of the Thermodynamic Properties of the Elements," American Soc. for Metals, Metals Park, Ohio (1973).
- S. Sugawara and T. Sato, *Bull. Jpn. Soc. Mech. Engrs.*, **5**, 711 (1962).
- R. F. Brebrick, *J. Phys. Chem.*, **72**, 1032 (1968).
- L. S. Brooks, *J. Am. Chem. Soc.*, **74**, 227 (1952).
- A. A. Kudryavtsev and G. P. Ustygov, *Russ. J. Inorg. Chem.*, **6**, 1227 (1961).
- E. H. Baker, *J. Chem. Soc. A*, 1558 (1967).
- R. E. Machol and E. F. Westrum, *J. Am. Chem. Soc.*, **80**, 2950 (1958).
- J. Steininger, *J. Appl. Phys.*, **41**, 2713 (1970).
- T. D. Levitskaya, A. V. Vanyukov, A. N. Krestovnikov, and V. P. Byistrov, *Izv. Akad. Nauk. Neorgan. Mater.*, **6**, 559 (1970).
- A. Pajaczowska and E. Z. Dziuba, *J. Cryst. Growth*, **11**, 21 (1971).
- J. Steininger, A. J. Strauss, and R. F. Brebrick, *This Journal*, **117**, 1305 (1970).
- M. R. Lorenz, *J. Phys. Chem. Solids*, **23**, 939 (1962).
- R. F. Brebrick, *This Journal*, **118**, 2014 (1971).
- B. M. Kulwicki, Ph.D. Dissertation, University of Michigan (1963).
- D. de Nobel, *Philips Res. Rep.*, **14**, 361 (1959).
- R. F. Brebrick and A. J. Strauss, *J. Phys. Chem. Solids*, **25**, 1441 (1964).
- R. Hultgren, P. Desai, D. Hawkins, M. Gleiser, and K. K. Kelley, "Selected Properties of the Thermodynamic Properties of Binary Alloys," American Soc. for Metals, Metals Park, Ohio (1973).
- J. Blair and R. Newnham, "Metallurgy of Elemental and Compound Semiconductors," p. 393, Interscience Publications, New York (1961).
- J. Steininger, *J. Electron. Mater.*, **5**, 299 (1976).
- T. C. Harman, "Physics and Chemistry of II-VI Compounds," Chap. 15, M. Aven and J. S. Prener, Editors, North-Holland Pub. Co., Amsterdam (1967).
- J. L. Schmit and C. J. Speersneider, *Infrared Phys.*, **8**, 247 (1968).
- R. Ueda, O. Ohtsuki, K. Shinohara, and Y. Ueda, *J. Cryst. Growth*, **13/14**, 668 (1972).
- J. E. Bowers, J. L. Schmit, and J. A. Mroczkowski, To be published in IRIS.
- T. C. Harman, Paper presented at the 21st Electronic Materials Conference, AIME, Boulder, Colorado, June 27-29, 1979.
- J. L. Schmit, Private communication.
- J. M. Larrain and H. H. Kellogg, in "Calculations of Phase Diagrams and Thermochemistry of Alloy Phases," Y. A. Chang and J. F. Smith, Editors, p. 130, The Metallurgical Society of AIME, Warrendale, Pa. (1979).
- Y. A. Chang and R. C. Sharma, in "Calculations of Phase Diagrams and Thermochemistry of Alloy Phases," Y. A. Chang and J. F. Smith, Editors, p. 145, The Metallurgical Society of AIME, Warrendale, Pa. (1979).
- R. F. Brebrick, *Metall. Trans. A*, **8**, 403 (1977).



The Effect of Heat-Treatments on the Chemical State of Phosphorus in SiO₂

Koichiro Hoh

Electrotechnical Laboratory, 1-1-4 Umezono, Sakura-mura, Niihari-gun, Ibaraki 305, Japan

and Manzoh Saitoh¹ and Yoshio Miura¹

*Cooperative Laboratories, VLSI Technology Research Association,
4-1-1 Miyazaki, Takatsu-ku, Kawasaki 213, Japan*

Charge trapping centers in thermal SiO₂ cause deteriorating effects of the threshold voltage shift in short channel MOS transistors. Among the experiments for the reduction of the trapping centers, it has been reported that the implantation of phosphorus ions into SiO₂ followed by the annealing in oxygen is effective for trap reduction while annealing in nitrogen after the implantation has no effect (1).

To clarify the difference in the behavior of P atoms after O₂- and N₂-annealing, we made XPS (x-ray photoelectron spectroscopy) measurements of the chemical state of P atoms in SiO₂. So far, the structure of P-implanted SiO₂ has been investigated using infrared absorption spectra by Fritzsche and Rothenmund (2), and Ahn, Gordon, and Pliskin (3). The latter authors observed the absorption due to P-O bonds (P=O) after the annealing. The XPS measurement has been reported for P-doped CVD SiO₂ and P-implanted thermal SiO₂ by Saxena and Powell (4). However, the change of XPS spectra due to heat-treatments has not been studied.

Experimental Procedure

SiO₂ films were grown thermally in pyrogenic steam at 950°C on the (100) surface of single crystal 1 μ m p-type (boron-doped) silicon wafers. Phosphorus ions were implanted into SiO₂ with the energy of 40 kV and the flux of 1×10^{16} ions/cm². After the implantation, samples were annealed in either dry N₂ or dry O₂ at 950°C for 20 min. SIMS measurement showed that the distribution of P atoms had its peak at 36-40 nm from the SiO₂ surface and the maximum concentration of P was 2.6×10^{21} cm⁻³ (6.9 weight percent). The distribution was changed little by the annealing.

The XPS spectra were obtained by using an ES-200 spectrometer (Kokusai Electric Company Limited) together with the data processing system DS-300. Samples were excited by Al K α (1487 eV) radiation in a vacuum of 6×10^{-9} Torr at a temperature 25°C. The binding energy, E_B , of an electronic level with respect to the Fermi level is determined from the relationship $E_B = h\nu - E_k - \phi$ where $h\nu$ is the energy of the x-ray source (1487 eV), E_k is the measured kinetic energy of the photoelectron, and ϕ is the spectrometer work function. The value $h\nu - \phi$ has been determined as 1486.5 eV for the present measurement because the carbon 1s line ($E_B = 284.5$ eV) appeared at $E_k = 1202.2$ eV. The measurement was made after the oxide was sputter-etched with an Ar⁺ ion beam (1.25 kV, 20 μ A/

cm²) until the peak in the P distribution was reached. The thickness of the removed oxide layer was determined from the etching time, assuming an etching rate for SiO₂ of 1.4 nm/min which was estimated from the rate of the decrease of the Si 2p signal in SiO₂.

Results and Discussions

Figure 1(a) shows the P 2p signals observed in as-implanted SiO₂ samples. The signal consists of four peaks, P1-P4, among which P3 and P4 are overlapped. Similar spectra for the N₂-annealed and O₂-annealed

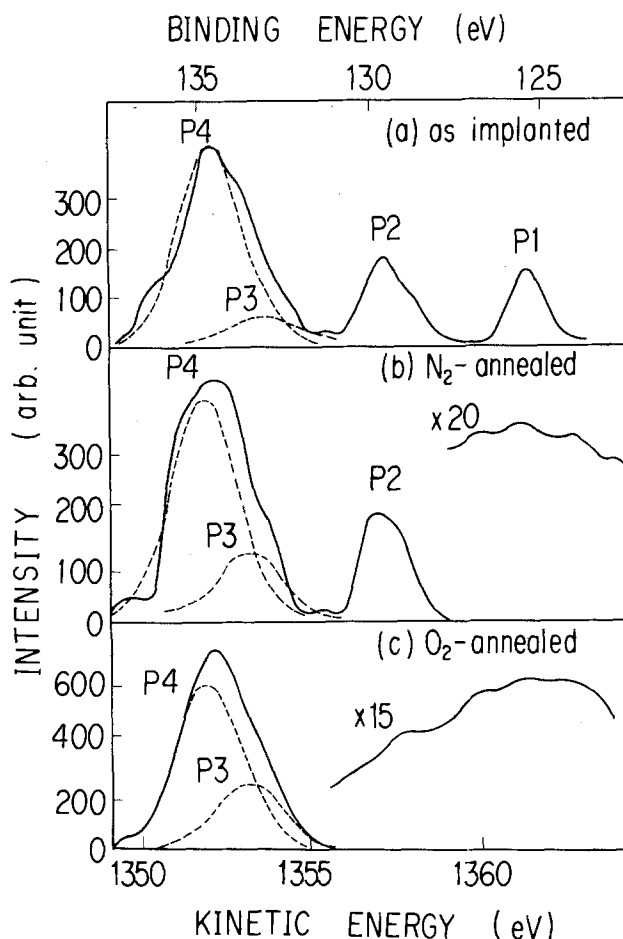


Fig. 1. P 2p peaks in (a) as-implanted, (b) N₂-annealed, and (c) O₂-annealed thermal SiO₂.

¹ Present address: Nippon Electric Company Limited, Kawasaki, Japan.

Key words: SiO₂, P-implantation, XPS spectra, annealing, trapping centers.

Table I. Binding energies of P 2p levels in SiO₂ (first two columns) and in several compounds (third column) (in eV).

| This work | Saxena and Powell (4) | Pelavin <i>et al.</i> (5) |
|-----------|-----------------------|----------------------------|
| P1 125.6 | | |
| P2 129.7 | E1 129.1 (implanted) | 129.5 (BP) |
| P3 133.5 | E2 133.3 (implanted) | |
| | 133.5 (CVD) | |
| P4 134.7 | | 134.4 (POBr ₃) |

samples are shown in Fig. 1(b) and (c). It is seen in these figures that the peak P1 appears only in the as-implanted samples and the peak P2 vanishes in the O₂-annealed samples. The peak shift due to the annealing is not observed clearly. The binding energies, E_B , of these peaks are listed in Table I together with those reported by other workers (4, 5).

From Table I it can be seen that the E_B value of our peak P2 is near to that of the E1 peak of Saxena and Powell, which they attribute to the interstitial P atoms in the network of SiO₄ tetrahedra, and it is also similar to that of phosphorus in its intermetallic compounds [for example, BP in Ref. (5)]. The P2 peak can therefore be attributed to P—Si bonds of P atoms in the interstitial site in the SiO₂ network. Our P3 peak nearly corresponds to the E3 peak of Saxena and Powell, which they attribute to P atoms substituting Si sites in SiO₄ tetrahedra, *i.e.*, PO₄³⁻. Though P4 has no counterparts in Saxena and Powell's spectra, it has the E_B value in the range of those of P atoms with the oxidation number 5 [for example, POBr₃ in Ref. (5)]. Therefore, P4 can also be interpreted as the signal from P—O bonds in the SiO₂ network. The origin of P1 is presently unknown.

The integrated intensities of the peaks P2, P3, and P4, normalized by the summation of all the integrated intensities of P 2p peaks, are plotted in Fig. 2 for the as-implanted, N₂-annealed, and O₂-annealed samples. This figure shows that by O₂ annealing the P2 peak disappears and the P3 and P4 peaks simultaneously increase in intensity. Taking the assignment of the peaks into consideration, these results can be interpreted as evidence that O₂ annealing at 950°C has the effect of converting P—Si bonds to P—O bonds in the SiO₂ network while N₂ annealing has no such effect. These results coincide with those of the infrared absorption study by Ahn *et al.* (3) which showed the increase of P—O bonds after the annealing in an oxidizing ambient. The present study proves that the XPS measurement is useful in evaluating the effects of heat-treatments of P-implanted SiO₂.

Acknowledgment

The authors are indebted to A. Ishitani and F. Soeda of Toray Research Center Incorporated for the XPS measurement.

Manuscript submitted Aug. 13, 1980; revised manuscript received Dec. 1, 1980.

Observation of Growth Striations in Undoped GaSb Single Crystals

Shun-ichi Tohno and Akinori Katsui

Nippon Telegraph and Telephone Public Corporation,
Ibaraki Electrical Communication Laboratory, Tokai, Ibaraki, 319-11, Japan

Observation of growth striations appearing in crystals grown from the melt is useful for the study of op-

Key words: GaSb, growth striations, native defect, x-ray topography, chemical etching.

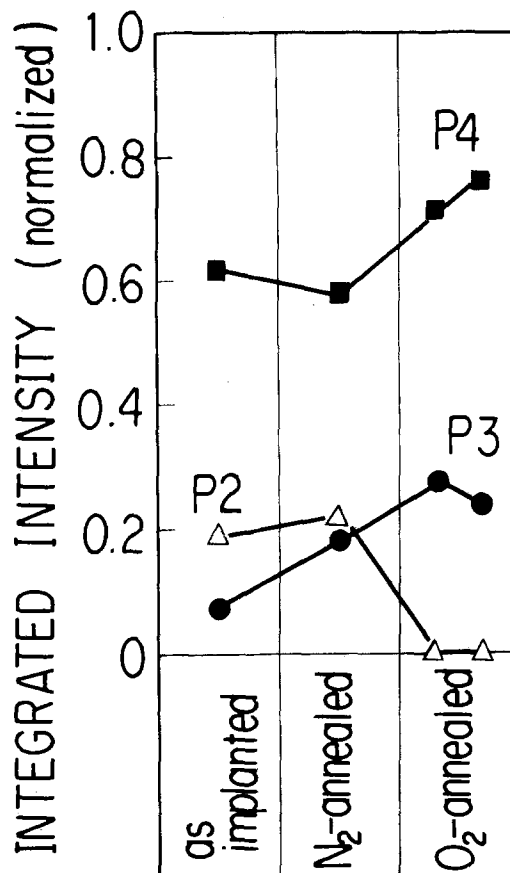


Fig. 2. Integrated intensity of P 2p peak normalized by the summation of all the integrated intensities of P 2p peaks.

Any discussion of this paper will appear in a Discussion Section to be published in the June 1982 JOURNAL. All discussions for the June 1982 Discussion Section should be submitted by Feb. 1, 1982.

Publication costs of this article were assisted by the Electrotechnical Laboratory.

REFERENCES

1. S. Iwamatsu and Y. Tarui, *This Journal*, **126**, 1387 (1979).
2. C. R. Fritzsche and W. Rothmund, *ibid.*, **119**, 1243 (1972).
3. J. Ahn, B. M. Gordon, and W. A. Pliskin, *IBM Tech. Discl. Bull.*, **13**, 1798 (1970); W. A. Pliskin, *J. Vac. Sci. Technol.*, **14**, 1064 (1977). [The authors are grateful to the referee for informing them of Ref. (2) and (3).]
4. A. N. Saxena and R. A. Powell, "The Physics of SiO₂ and Its Interfaces," S. T. Pantelides, Editor, p. 195, Pergamon Press, New York (1978).
5. M. Pelavin, D. N. Hendrickson, J. M. Hollander, and W. L. Jolly, *J. Phys. Chem.*, **74**, 1116 (1970).

timum conditions to grow high quality crystals. The growth striations are usually formed by doping impurities of high concentration. This note reports that the growth striations were observed in undoped GaSb

Table I. Binding energies of P 2p levels in SiO₂ (first two columns) and in several compounds (third column) (in eV).

| This work | Saxena and Powell (4) | Pelavin <i>et al.</i> (5) |
|-----------|-----------------------|----------------------------|
| P1 125.6 | | |
| P2 129.7 | E1 129.1 (implanted) | 129.5 (BP) |
| P3 133.5 | E2 133.3 (implanted) | |
| | 133.5 (CVD) | |
| P4 134.7 | | 134.4 (POBr ₃) |

samples are shown in Fig. 1(b) and (c). It is seen in these figures that the peak P1 appears only in the as-implanted samples and the peak P2 vanishes in the O₂-annealed samples. The peak shift due to the annealing is not observed clearly. The binding energies, E_B , of these peaks are listed in Table I together with those reported by other workers (4, 5).

From Table I it can be seen that the E_B value of our peak P2 is near to that of the E1 peak of Saxena and Powell, which they attribute to the interstitial P atoms in the network of SiO₄ tetrahedra, and it is also similar to that of phosphorus in its intermetallic compounds [for example, BP in Ref. (5)]. The P2 peak can therefore be attributed to P—Si bonds of P atoms in the interstitial site in the SiO₂ network. Our P3 peak nearly corresponds to the E3 peak of Saxena and Powell, which they attribute to P atoms substituting Si sites in SiO₄ tetrahedra, *i.e.*, PO₄³⁻. Though P4 has no counterparts in Saxena and Powell's spectra, it has the E_B value in the range of those of P atoms with the oxidation number 5 [for example, POBr₃ in Ref. (5)]. Therefore, P4 can also be interpreted as the signal from P—O bonds in the SiO₂ network. The origin of P1 is presently unknown.

The integrated intensities of the peaks P2, P3, and P4, normalized by the summation of all the integrated intensities of P 2p peaks, are plotted in Fig. 2 for the as-implanted, N₂-annealed, and O₂-annealed samples. This figure shows that by O₂ annealing the P2 peak disappears and the P3 and P4 peaks simultaneously increase in intensity. Taking the assignment of the peaks into consideration, these results can be interpreted as evidence that O₂ annealing at 950°C has the effect of converting P—Si bonds to P—O bonds in the SiO₂ network while N₂ annealing has no such effect. These results coincide with those of the infrared absorption study by Ahn *et al.* (3) which showed the increase of P—O bonds after the annealing in an oxidizing ambient. The present study proves that the XPS measurement is useful in evaluating the effects of heat-treatments of P-implanted SiO₂.

Acknowledgment

The authors are indebted to A. Ishitani and F. Soeda of Toray Research Center Incorporated for the XPS measurement.

Manuscript submitted Aug. 13, 1980; revised manuscript received Dec. 1, 1980.

Observation of Growth Striations in Undoped GaSb Single Crystals

Shun-ichi Tohno and Akinori Katsui

Nippon Telegraph and Telephone Public Corporation,
Ibaraki Electrical Communication Laboratory, Tokai, Ibaraki, 319-11, Japan

Observation of growth striations appearing in crystals grown from the melt is useful for the study of op-

Key words: GaSb, growth striations, native defect, x-ray topography, chemical etching.

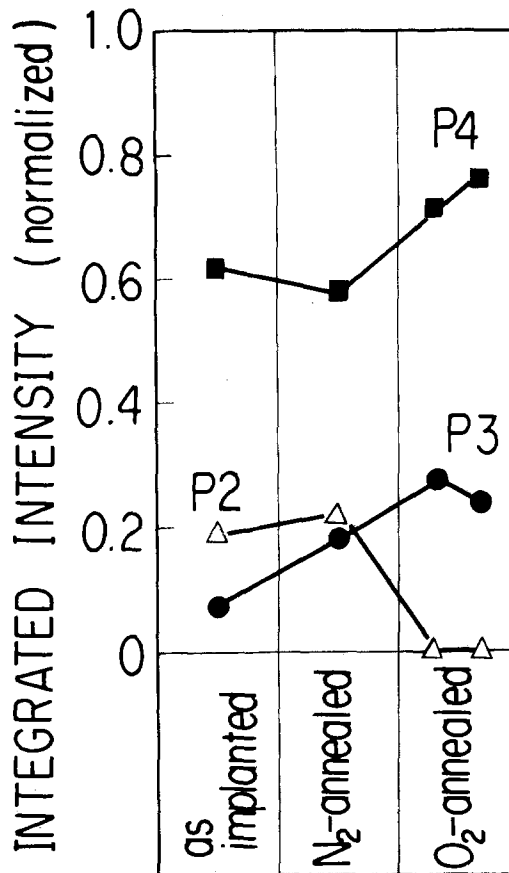


Fig. 2. Integrated intensity of P 2p peak normalized by the summation of all the integrated intensities of P 2p peaks.

Any discussion of this paper will appear in a Discussion Section to be published in the June 1982 JOURNAL. All discussions for the June 1982 Discussion Section should be submitted by Feb. 1, 1982.

Publication costs of this article were assisted by the Electrotechnical Laboratory.

REFERENCES

1. S. Iwamatsu and Y. Tarui, *This Journal*, **126**, 1387 (1979).
2. C. R. Fritzsche and W. Rothemund, *ibid.*, **119**, 1243 (1972).
3. J. Ahn, B. M. Gordon, and W. A. Pliskin, *IBM Tech. Discl. Bull.*, **13**, 1798 (1970); W. A. Pliskin, *J. Vac. Sci. Technol.*, **14**, 1064 (1977). [The authors are grateful to the referee for informing them of Ref. (2) and (3).]
4. A. N. Saxena and R. A. Powell, "The Physics of SiO₂ and Its Interfaces," S. T. Pantelides, Editor, p. 195, Pergamon Press, New York (1978).
5. M. Pelavin, D. N. Hendrickson, J. M. Hollander, and W. L. Jolly, *J. Phys. Chem.*, **74**, 1116 (1970).

timum conditions to grow high quality crystals. The growth striations are usually formed by doping impurities of high concentration. This note reports that the growth striations were observed in undoped GaSb

single crystals with low concentration of residual impurities.

GaSb crystals mentioned in this study were grown by the liquid encapsulated Czochralski (LEC) technique using B_2O_3 -3.2 mole percent (m/o) Na_3AlF_6 as the encapsulant (1). The apparatus used consisted of a conventional RF-heating Czochralski puller. The growth conditions of single crystals were almost the same as those described in the previous paper (1). The major conditions are summarized in Table I. Contamination by impurities contained in the B_2O_3 -3.2 m/o Na_3AlF_6 was negligibly small (1) and did not have direct influence on the results of this work.

Table II shows the levels of residual impurities in the grown crystals measured by spark source mass spectrometric analysis. It is confirmed that the total concentration of residual impurities in the crystal is less than 3 ppma ($5 \times 10^{16} \text{ cm}^{-3}$).

The growth striations were observed by x-ray diffraction topography (Mo $K\alpha_1$ radiation) and chemical etching technique, using specimens cut along the growth axis of the pulled crystals.

Figure 1 shows an x-ray transmission topograph of the initial diverging part of a crystal grown in the $[111]$ direction at the rotation rate of 10 rpm. The growth direction is downward (arrow sign in the figure). Specimens were etched for 1 min at room temperature with a mixture of 9 HNO_3 , 1 HF , and 20 CH_3COOH after mechanically polishing to about 200 μm thickness. The diffraction plane was (111). The growth striations are visible as many fine lines. The contrast of these striations reversed in the $(\bar{1}\bar{1}\bar{1})$ diffraction topograph. It is concluded, from this result, that the observed striations are formed by impurities segregation (2), not by their precipitation. As shown in Fig. 1, two regions can be distinguished in the crystal, although the resolution of the topograph is not so high that detailed structure of the striations is revealed. One is the off-facet region consisting of striations curved toward the growth direction at the periphery of the crystal. The other is the facet region, which locates in the central part of the crystal and consists of straight striations perpendicular to the growth direction. Observation of the striations using x-ray topography has been carried out on the $\langle 111 \rangle$ grown crystals by the LEC technique with the $KCl + NaCl$ encapsulant (3).

Figure 2 shows a topograph diffracted from the (400) plane of a $[100]$ pulled crystal. The striations are also encountered in the $[100]$ pulled crystals. However, no central facet is visible.

Figure 3 shows an optical micrograph of the chemically etched $\{211\}$ surface of a crystal grown in the $[\bar{1}\bar{1}\bar{1}]$ direction. In order to reveal growth striations, a mixture of 1 $KMnO_4$, 0.05M, 1 HF , and 1 CH_3COOH , which was developed for InSb (4), was employed. The mechanically polished specimen was etched with the mixture for 1-2 min at room temperature. The growth

Table I. LEC growth conditions of GaSb single crystals

| | |
|-----------------------------------|---|
| Growth direction | $\langle 111 \rangle$, $\langle 100 \rangle$ |
| Pulling rate | 10-12 mm/hr |
| Crystal rotation | 6.0-11.0 rpm |
| Charge weight for GaSb | 100g |
| Melt composition | Ga/Sb = 50/50 a/o |
| Continuous flow rate of N_2 gas | 3 liters/min |

Table II. Mass spectrometric analysis of residual impurities in the grown undoped GaSb crystal in atomic ppm (ND < 0.1 ppm)

| Crystal number | Element | | | | | | | | |
|----------------|---------|----|-----|----|-----|----|-----|-----|-----|
| | Zn | Hg | S | Te | Si | Sn | Cr | Fe | Al |
| LEC 45-1 | 0.1 | ND | 1.0 | ND | 0.3 | ND | 0.1 | 0.3 | 0.3 |
| LEC 63-3 | 0.1 | ND | 1.0 | ND | 1.0 | ND | 0.1 | 0.3 | 0.3 |

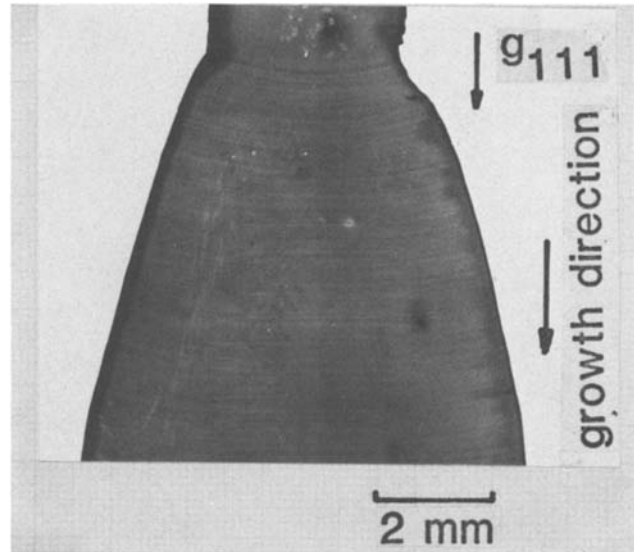


Fig. 1. X-ray transmission topograph of undoped GaSb wafer cut parallel to $[111]$ pulling direction.

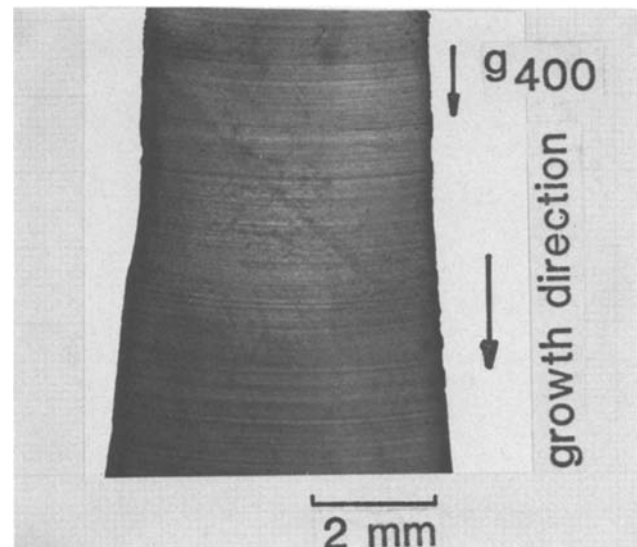


Fig. 2. X-ray topograph of undoped GaSb wafer cut parallel to $[100]$ pulling direction.

striations in the facet and off-facet regions on the etched surface are observed with high resolution suitable for the study of the striations.

As described above, the growth striations are encountered in the undoped GaSb crystals in which the residual impurities concentration is low. The total impurities concentration is less than $5 \times 10^{16} \text{ cm}^{-3}$, as shown in Table II. However, electrically active impurities concentration of approximately $1.1 \times 10^{17} \text{ cm}^{-3}$ was contained in the grown crystals, which was estimated by measurement of Hall coefficient. Excess impurities are attributed to native defects (5) caused by smaller atomic volume of Ga than that of Sb. Therefore, it is thought that the native defects arising from the deviation in stoichiometry lead to the formation of the growth striations in the undoped crystals.

Variations in sharpness, intensity, and periodicity of growth striations strongly reflect the growth conditions of the crystals. Figure 4 shows a micrograph of the etched $\{211\}$ surface in the constant diameter part of $[\bar{1}\bar{1}\bar{1}]$ pulled crystal. This crystal was grown at two different rates of seed rotation. The upper and lower parts of the figure were pulled at rates of 10.5 and 6.2 rpm, respectively. Rotational striations with regular spacings appear in both regions which were grown at

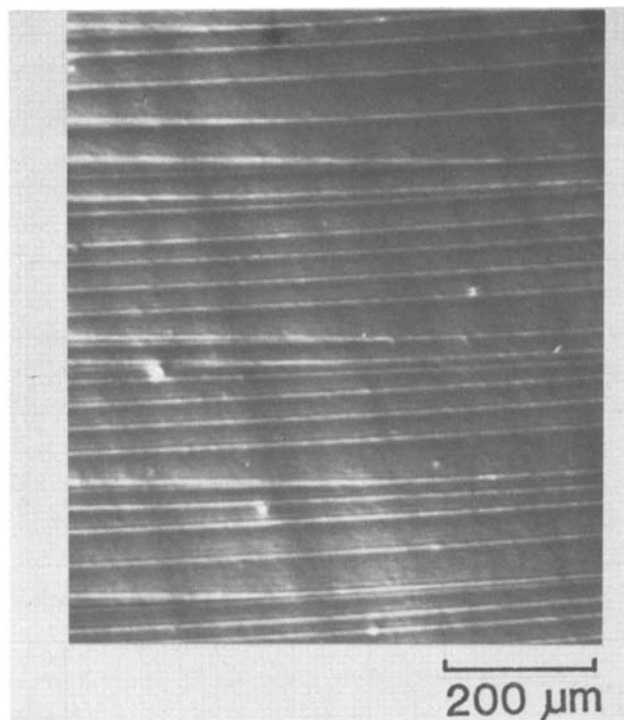


Fig. 3. Micrograph of etched $\{211\}$ surface of $[\bar{1}\bar{1}\bar{1}]$ pulling crystal. Striations appearing in the boundary region between facet (straight lines in the left side of the figure) and off-facet are shown.

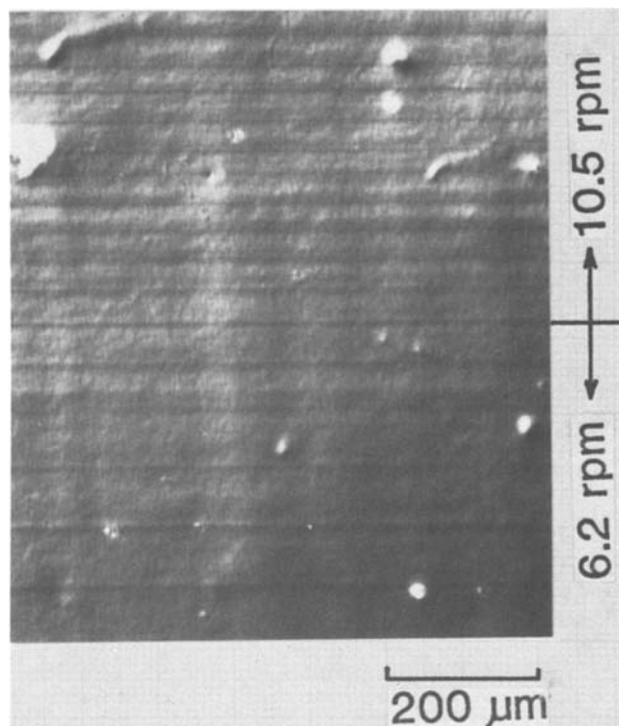


Fig. 4. Micrograph of etched surface of $[\bar{1}\bar{1}\bar{1}]$ pulling crystal grown at different rates of seed rotation. Upper part is grown at 10.5 rpm and lower part is grown at 6.2 rpm.

different rotation rates. As can be seen in Fig. 4, variation in the rate of the seed rotation had an apparent effect on the spacing of the rotational striations. Their periodic spacings agreed with values calculated from the pulling and rotation rates after correcting for the continuous decrease in the melt. On the other hand, in Fig. 1-3 which show the striations in the crystal diameter enlarging process, nonrotational striations are dominant and the striation spacings are irregular. This may be due to intense temperature fluctuations caused by such factors as rf power variation and irregular thermal convection in the melt.

Acknowledgments

The authors express their sincere thanks to Dr. N. Niizeki, Dr. H. Takata, and Dr. K. Kudo for their encouragement throughout this work, and to Mr. C. Uemura and Mr. S. Shinoyama for their valuable suggestions. We are much indebted to Mr. C. Honma for performing mass spectrometric analysis.

Manuscript submitted Sept. 22, 1980; revised manuscript received Feb. 20, 1981.

Any discussion of this paper will appear in a Discussion Section to be published in the June 1982 JOURNAL. All discussions for the June 1982 Discussion Section should be submitted by Feb. 1, 1982.

Publication costs of this article were assisted by Nippon Telegraph and Telephone Public Corporation.

REFERENCES

1. A. Katsui and C. Uemura, *Jpn. J. Appl. Phys.*, **19**, L318 (1980).
2. G. H. Schwuttke and V. Slis, *J. Appl. Phys.*, **34**, 3127 (1963).
3. S. Kondo and S. Miyazawa, Private communication.
4. A. F. Witt, *This Journal*, **114**, 298 (1967).
5. Y. J. Van Der Meulen, *J. Phys. Chem. Solids*, **28**, 25 (1967).

On the Removal of Insulator Process Induced Radiation Damage from Insulated Gate Field Effect Transistors at Elevated Pressure

A. Reisman,* J. M. Aitken,* A. K. Ray,* M. Berkenblit,* C. J. Merz,* and R. P. Havreluk*

IBM Thomas J. Watson Research Center, Yorktown Heights, New York 10598

When subjected to radiative processes during fabrication, high levels of fixed positive charge and neutral traps are generated in the insulators of insulated gate

* Electrochemical Society Active Member.

Key words: radiation damage, insulator annealing, high pressure insulator annealing, process induced radiation damage annealing, fixed positive charge annealing

field effect transistors (1), IGFET's. In the case of positive charge, the effect can be manifested by a drastic reduction in threshold voltage in n-channel IGFET's (2). In process sequences prior to metallization, such traps are readily annealed at 550°-600°C. Following metallization, however, when annealing temperatures

may, of necessity, be restricted to brief time periods at 400°C or thereabouts in forming gas or hydrogen, particularly in shallow junction devices, it is difficult to remove this damage to desirable device and circuit design levels. This represents both a time zero and more important, a reliability exposure. For example, when metal interconnection levels are delineated using E-beam lithographic techniques in the dose range from 5 to 30 $\mu\text{C}/\text{cm}^2$, or the metal itself is deposited using E-beam metal evaporation techniques, up to a few hundred mV of residual equivalent positive charge is detected in the gate insulator via hot electron injection techniques after conventional annealing treatments have been applied (1, 3). Such residual levels pose a design problem, because during normal device operation hot electrons penetrating the silicon-oxide interface are trapped by positively charged and neutral trap sites causing threshold shifts as a function of time.

Experimental Results and Discussion

Using an elevated pressure reactor of IBM design, to be described at a later date, the effects of 10% hydrogen-90% argon forming gas annealing at 400°C and 50 atm on radiation damaged metal gated capacitors, polysilicon gated capacitors, and insulated gate field effect transistors were studied. These results were compared with control samples annealed in either forming gas or pure hydrogen at 400°C and atmospheric pressure.

Both the metal and polysilicon gated capacitors were fabricated on p-type, 2 $\Omega\text{-cm}$, 57 mm diam 0.38 mm (15 mil) thick silicon wafers. The insulators were grown in dry oxygen to a thickness of 35 nm. In the case of the metal gated capacitors, 0.81 mm (32 mil) diam aluminum dot patterns, 500 nm thick, were deposited through a physical mask using an rf heated aluminum source which causes no radiation damage. In the case of the polysilicon gated capacitors, a blanket layer of polysilicon 250 nm thick was chemically vapor deposited on the insulator. The polysilicon was then doped with phosphorous using POCl_3 . A 500 nm thick aluminum dot pattern was then deposited on the doped polysilicon using the same physical mask as for the metal gated capacitors. This deposited aluminum dot pattern, in turn, was then used as a plasma etching mask for delineating the polysilicon gates. The aluminum dots were left in place after the polysilicon delineation to serve as probe contacts.

The insulated gate field effect transistors were fabricated in p-type, 0.5 $\Omega\text{-cm}$ silicon using a simplified polysilicon gate process. Junctions were phosphorous diffused to a depth of 0.5 μm and gate insulators were 35 nm thick. Isolation was planar (no recessed oxide) and was 350 nm thick. Junction contact metallurgy was $\text{Pd}_2\text{Si-Al}$. While the vertical characteristics of these devices, prepared via optical lithography techniques simulated 1 μm device design technology (4), horizontal dimensions covered a wide range of channel lengths and channel width to length ratios. For hot electron injection studies 2:1 width:length ratio devices with 100 μm (4 mil) channel lengths were the most appropriate for us to examine (1). Additionally, some measurements were made on special test devices of all E-beam lithography fabricated polysilicon gate, recessed oxide IGFET's.

Radiation damage was introduced into the finished polysilicon gated capacitors and the planar polysilicon gated transistors by first overcoating the wafers with 0.4 μm of photoresist, then blanket evaporating 500 nm of aluminum on top of the photoresist in an E-gun system which we have found causes significant insulator damage. The photoresist-aluminum composite was then lifted off leaving the radiation damaged wafers ready for measurement. E-beam lithography and E-beam metal evaporation doses were estimated to be in the 10^7 rad SiO_2 range.

The metal gated capacitors were employed solely as controls to insure that the high pressure annealing system created no problems in terms of contamination. Following fabrication, the metal gated capacitors were post metal annealed at 400°C for 20 min in either 10% hydrogen-90% nitrogen (forming gas, F.G.) at 1 atm or at 400°C for 20 min in pure hydrogen at 1 atm. These samples were then compared with capacitors annealed at 400°C for 20 min in 10% hydrogen-90% argon at 50 atm.

The 1 atm annealed capacitors exhibited flatband voltages ranging between -0.82 and -0.83V . The 50 atm annealed capacitors exhibited flatband voltages ranging between -0.80 and -0.81V . Interface trap density, D_{it} (5) was approximately $1 \times 10^{10}/\text{cm}^2$ eV at mid bandgap for the three types of annealed capacitors. These results provided confidence in the cleanliness of the high pressure system, at least for time zero measurements.

The results obtained with polysilicon gated capacitors are shown in Table I at different stages of processing. The different annealing treatments prior to irradiation included forming gas at either 1 or 50 atm. Following irradiation, annealing treatments were either in forming gas or hydrogen at 1 atm or in forming gas at 50 atm, as noted. As can be seen from Table I, wafers 1-8, conventional annealing in forming gas yielded flatbands ranging from -1.10 to 1.14V , while the elevated pressure annealed capacitors, wafers 9 and 10, exhibited values around -0.97V . Wafers which had initially received the forming gas 1 atm type of post metal annealing treatment, wafers 1 and 2, exhibited flatband voltages of approximately -2.6V following irradiation. After 1 atm annealing in forming gas or hydrogen for 20 min at 400°C, wafers 1-6, the flatbands recovered to values ranging from -1.25 to -1.28V . On the radiation damaged wafers subjected to 50 atm forming gas annealing at 400°C for 20 min, wafers 7-10, the flatbands recovered to values of -1.01 to -1.06V . These results indicate that on the large capacitor structures some 250 mV or equivalent unannealed positive charge remained following conventional annealing, while some 60 mV of charge remained following high pressure annealing. Because of the very large diameter of the capacitor structures, it was anticipated that fixed time annealing cycles might be less effective than they would be with transistor structures, since diffusion paths from the edges of the gate region into the insulator are many times greater in the capacitors than they would be in IGFET's, even in the large channel length structures discussed below. The cited results with elevated pressure capacitor annealing indicated that such a treatment is considerably more effective than 1 atm anneals. This was confirmed with IGFET annealing studies.

Following irradiation, IGFET device thresholds shifted negatively some 1.2-1.5V. After conventional annealing in pure hydrogen, these devices were subjected to hot electron injection (5×10^{13} electrons/ cm^2) to assess residual positive charge levels. At this injection level, the radiation induced positive charges have been found to be annihilated completely by injected electrons (1). These large devices have been found to behave similarly to 1 μm channel length IGFET's in terms of damage susceptibility and annealing characteristics. The results are shown in Fig. 1 which is a plot of drain current, I_{SD} , vs. gate voltage, V_G of these radiation damaged devices. Trace 1 shows the I - V characteristic following radiation damage and subsequent 1 atm hydrogen annealing at 400°C for 30 min. The state of the device is here representative of an as yet unknown level of residual radiation damage after conventional annealing. Trace 2 shows the I - V characteristic after injecting 5×10^{13} electrons/ cm^2 to neutralize such residual unannealed positive charge, and indicates that the residual positive charge follow-

Table I. Annealing studies of poly gated capacitors

| Wafer No. | Post Metal* Annealing Conditions | Flat-band** (Volts) | Std. Dev. (Volts) | Irradiate-Flatband (Volts) | Std. Dev. (Volts) | Reannealing Conditions | Flat-band (Volts) | Std. Dev. (Volts) | Avg. Flat-band (Volts) | Std. Dev. (Volts) |
|-----------|-------------------------------------|------------------------|----------------------|-------------------------------|----------------------|---|----------------------|----------------------|---------------------------|----------------------|
| 1 | 400°C;FG;1atm; 20 min; SF | -1.087 | 0.018 | -2.581 | 0.246 | N.A. | -2.581 | 0.246 | -2.604 | 0.250 |
| 2 | " | -1.100 | 0.023 | -2.627 | 0.263 | N.A. | -2.627 | 0.263 | | |
| 3 | " | -1.132 | 0.007 | - | - | 400°C;H ₂ ;1atm; 20 min; SF | -1.264 | 0.011 | -1.273 | 0.013 |
| 4 | " | -1.115 | 0.015 | - | - | " | -1.282 | 0.008 | | |
| 5 | " | -1.101 | 0.009 | - | - | 400°C;FG;1atm; 20 min; SF | -1.278 | 0.013 | -1.263 | 0.024 |
| 6 | " | -1.099 | 0.010 | - | - | " | -1.248 | 0.024 | | |
| 7 | " | -1.142 | 0.023 | - | - | 400°C;FG';50atm; 20 min; HPS | -1.066 | 0.013 | -1.040 | 0.032 |
| 8 | " | -1.128 | 0.008 | - | - | " | -1.053 | 0.014 | | |
| 9 | 400°C;FG';50atm; 20 min; HPS | -0.965 | 0.003 | - | - | " | -1.007 | 0.011 | | |
| 10 | " | -0.974 | 0.024 | - | - | " | -1.032 | 0.040 | | |

*FG = Forming Gas; 10% H₂ - 90% N₂

FG' = Forming Gas; 10% H₂ - 90% Ar

SF = Silicon Facility

HPS = High Pressure System

**12 capacitors measured on each wafer

ing conventional annealing was equivalent to approximately 115 mV, based on the magnitude of the observed threshold shift between traces 1 and 2. The range observed on such devices was 90-136 mV. Trace 3 shows the *I-V* characteristic after injecting an additional 1×10^{16} electrons/cm² to partially fill neutral traps. The neutral traps that are filled at this injection level, based on the earlier cited work (1), have cross sections greater than 10^{-15} cm². The observed shift between traces 2 and 3 indicates some 200 mV of residual neutral trap equivalent have been filled.

A companion wafer was given the same radiation damage treatment, followed this time by a 400°C, 30

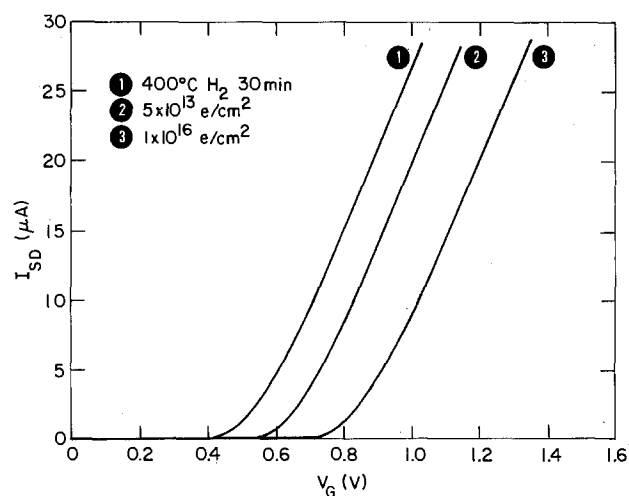


Fig. 1. Drain current vs. gate voltage following hot electron injection in a 1 atm hydrogen annealed device.

min, 50 atm forming gas anneal. The results obtained with identical electron injection procedures are shown in Fig. 2. It is seen that <20 mV of residual positive charge equivalent, and some 80 mV of residual neutral trap equivalent have been filled, traces 2 and 3, respectively. The range of the positive charge equivalent was from approximately 12 to 18 mV, and that of the neutral traps from 80 to 100 mV. Both of these levels are quite acceptable from a device design point of view. In the absence of radiation damage, similar devices show <5 mV of positive charge equivalent and some 50 mV of neutral traps with cross section $>10^{-15}$ cm².¹

The small threshold differences on injected samples seen between Fig. 1 and 2 are due to normal oxide thickness variations, and normal wafer resistivity variations obtained by us on these devices.

Finally, one additional piece of pertinent information was obtained to support further the capacitor and IGFET results cited above. On 1 μ m E-beam lithographically delineated device wafers, two identical radiation damage test device structures were incorporated. Their channel lengths, 10 μ m, were identical, but the metal contact locations to them were different. In one of them, device A, the source drain contacts were close to the gate region, <2 μ m, while in the other, device B, they were farther away, 12.5 μ m. Consequently, in metal interconnection delineation E-beam lithography, the scattered E-beam dose seen by the device A gate insulator was considerably greater. Following hydrogen anneal, device A showed a threshold, V_T , of 0.700V, while device B showed a V_T of 0.735V.

¹ It should be noted that from a design point of view the positively charged traps, because of their large cross section, pose by far the most serious long-term device stability problem. The much smaller neutral traps only fill after these positive traps are neutralized, since the probability of trapping is proportionate to the cross-sectional area of the trap.

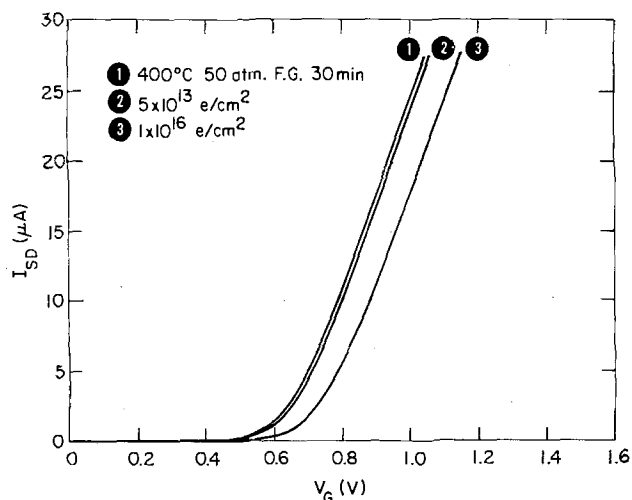


Fig. 2. Drain current vs. gate voltage following hot electron injection in a 50 atm forming gas annealed device.

This indicated greater residual unannealed radiation damage in the device A structure. However, after a 50 atm anneal in forming gas for 20 min, the device A threshold shifted 50 mV to 0.750V, while the less damaged device B threshold shifted 15 mV to 0.750V, our design value for such a device.

The high pressure annealing technique appears to provide a practical solution for process induced radiation damage removal, and is being investigated further as a function of annealing pressure, time, and temperature

Acknowledgments

The authors wish to thank B. L. Crowder and C. M. Osburn for their helpful discussions, as well as S. K. Lai and F. L. Pesavento for providing interface state measurements.

Manuscript submitted Oct. 27, 1980; revised manuscript received Jan. 13, 1981.

Any discussion of this paper will appear in a Discussion Section to be published in the June 1982 JOURNAL. All discussions for the June 1982 Discussion Section should be submitted by Feb. 1, 1982.

Publication costs of this article were assisted by IBM Corporation.

REFERENCES

1. J. M. Aitken, *IEEE J. Solid State Circuits*, **sc-14**, 294 (1979).
2. H. N. Yu, A. Reisman, C. M. Osburn, and D. L. Critchlow, *ibid.*, **sc-14**, 240 (1979).
3. T. H. Ning, *J. Appl. Phys.*, **49**, 4077 (1978).
4. R. H. Dennard and F. H. Gaensslen, *IEEE J. Solid State Circuits*, **sc-14**, 247 (1979)
5. B. E. Deal, *IEEE Trans. Electron Devices*, **ed-27**, 606 (1980).

Salt Water Vapor Interactions Using the Piezoelectric Effect

D. W. Rice* and P. Peterson

IBM Corporation, General Products Division, San Jose, California 95193

The chemistry and physics of salt and water vapor interactions play an important role in many practical problems. Water soluble salts on metal surfaces can significantly accelerate the metal's corrosion rate (1). Salt particles form the nucleation sites for raindrop formation (2) and are used in cloud seeding experiments (3). Fertilizer stability in humid environments is a subject of some concern (4). Electronic device failure is often associated with the interaction of water vapor and surface salt residues (5).

The interaction of water vapor with salt particles can be described by three water vapor pressure (P_{H_2O}) regimes. At low P_{H_2O} , the H_2O molecule physically adsorbs on the salt surface sometimes in clusters (6), but does not form stable bulk hydrates. At intermediate P_{H_2O} , for salts with multiple hydrates, solid-solid hydration reactions will be observed in addition to physical adsorption. Finally, at high P_{H_2O} , a salt solution will be in equilibrium with water vapor. Application of the phase rule teaches us that P_{H_2O} is invariant when three phases are present at a fixed temperature for a two component system. This will be the case when two solid hydrates and water vapor are present or when a solid, saturated solution and water vapor are present.

This note discusses the use of a piezoelectric quartz oscillator to measure water vapor and salt interactions for small quantities of water-soluble salts on gold surfaces. The majority of results focus on the equilibrium P_{H_2O} when a saturated salt solution and solid salt (or hydrate) are present. The relative humidity at this equilibrium is often referred to as the critical relative

humidity (CRH). Large quantities of water are absorbed at this relative humidity and the salt dissolves.

The advantage of the piezoelectric microbalance, in addition to its comparative ease and simplicity, is its 10^{-8} g/cm² sensitivity (7). Furthermore, because of the small amount of material required for a mass measurement, the response time is very fast (<10 sec) compared to powder beds (0.5 → 4 hr) (8). The piezoelectric technique has proven itself as a valuable tool in pressure, molecular weight, and mass measurements as demonstrated by Stockbridge (9). Important improvements in quartz cutting and piezoelectric theory (10) have broadened the potential of the method. Adsorption isotherms (11), oxidation kinetics (12), evaporation rates, and deposition rates (13) are among the more common gas-solid interactions examined by the technique. The latter is the most commercially exploited.

Experiment

Two AT-cut quartz crystals with gold surface electrodes were mounted in a 100 cm³ Pyrex glass chamber with the associated frequency sensing and driver electronics. Commercially available evaporation rate monitoring equipment was used for these measurements. The partial pressure of water vapor was increased or decreased in the chamber at a rate of 0.15 Torr/min (0.75% RH/min) at 23.0°C. High purity nitrogen was used as the reference carrier gas and the partial pressure of water was measured by the dew point method (14). The total pressure was 740 ± 20 Torr. Figure 1 is a schematic of the experimental setup.

The experimental procedure involved, first, establishing a reference resonant frequency of the gold-

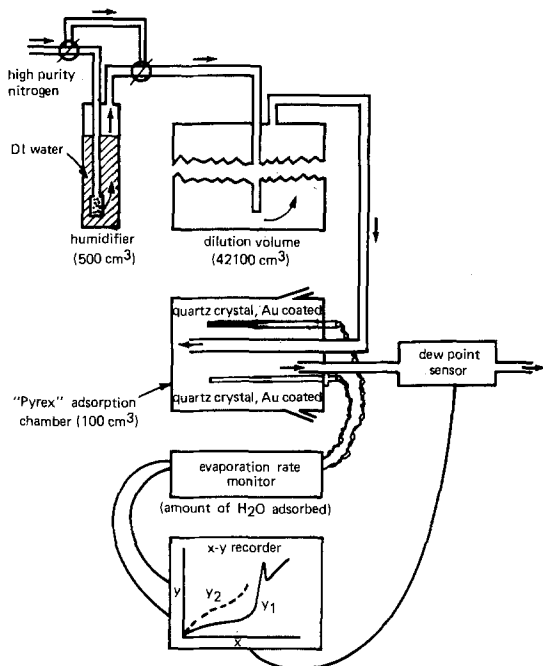


Fig. 1. Experimental setup of salt-H₂O adsorption

coated quartz oscillator at a $P_{H_2O} < 0.4$ Torr ($< 2\%$ RH) in high purity nitrogen. A solution of water-soluble reagent grade salt was then added to the gold surface from a micropipette which contained a known concentration of salt. Both the amount and area could be easily varied by this method. The solution was then dehydrated to less than 2% RH and the new resonant frequency established. The weight/cm² actually added was used to determine the sensitivity factor, K , for the quartz crystal in the equation: M/A (weight/cm²) = $K \cdot \Delta f$ (thickness in angstroms on the digital read-out). The sensitivity factor was $0.021 \pm 0.005 \mu\text{g}/\text{cm}^2 \text{ \AA}$ for the salts in this study. The next step in the procedure was to increase the P_{H_2O} slowly (0.15 Torr/min) and measure both the weight of water added, either adsorbed or absorbed, and the rate of H₂O addition. The P_{H_2O} was then decreased slowly.

In separate experiments, the time necessary to achieve an equilibrium mass when the P_{H_2O} was instantly stepped from 0.4 Torr to 10.5 Torr or 21 Torr was determined to be 1 and 7 sec, respectively, for 10 μg of NaCl on the Au surface. These are very rapid response times in comparison to both the P_{H_2O} scan rate (0.15 Torr/min) and powder bed response times which are the order of hours.

Results and Discussion

Figure 2 shows a typical adsorption isotherm for NaCl (26 $\mu\text{g}/\text{cm}^2$) on the gold-coated quartz piezoelectric crystal. The region of physical adsorption shows

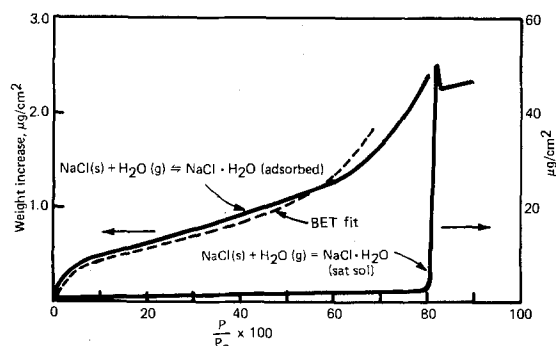


Fig. 2. Water adsorption/absorption ($\mu\text{g}/\text{cm}^2$) vs. percentage relative humidity ($P/P_0 \times 100$), $t = 23^\circ\text{C}$, HP nitrogen.

comparatively small quantities of adsorbed water. The data was fit to a Brunauer, Emmett, and Teller (BET) isotherm over the P/P_0 (RH) range 0.02-0.5. The calculated heat of adsorption is 12.5 kcal/mol based on a heat of vaporization of 10.6 kcal/mol for water. Monolayer coverage occurs at 17% RH and the true surface area, Σ , of the adsorbing surface is 6.8 cm² based on a water molecule area on the surface of 10.5×10^{16} cm². The true area is therefore 6.8 times greater than the projected area of 1 cm². Kanazawa *et al.* have estimated monolayer coverage to occur at 7-9% RH from surface conductivity measurements (15). This value is less than our work, but demonstrates that in either case monolayer coverage occurs at comparatively low relative humidities. Hall and Tompkins have shown that heats of H₂O adsorption on both soluble (16) and insoluble (17) salts is 11-13 kcal/mol for a coverage, θ , greater than 0.1 (10%). This is in good agreement with the above value for NaCl. Papee and Laidler have measured the heat of adsorption by calorimetric methods (18). They calculate $\Delta H_{ad} = 36$ kcal/mol, but state that this is too high for physical adsorption. Surface area changes are speculated to result in these high heats by the authors.

The P_{H_2O} will reach a value that represents the equilibrium partial pressure above saturated NaCl. At this pressure, shown at the right of Fig. 2, large quantities of H₂O are absorbed until saturated NaCl is achieved. Note the sharp increase in mass.

A similar analysis of the physical adsorption isotherm was performed on LiCl, KCl, and RbCl. The summary is given in Table I.

Figure 3 shows some typical H₂O mass increase vs. P_{H_2O} curves for simple salts that do not form solid hydrates. Optical observation of the surface indicated that the peak in the curve is identical with the onset of solution formation. Also, the rate of H₂O pickup drops precipitously at the peak. The reason for a peak instead of a more subtle change in slope is not clear. One would expect that the amount of water should continue to increase above the solid-liquid vapor invariant pressure. The pressure would control the salt concentration and hence more water should deposit to decrease the salt concentration as P_{H_2O} increases. The peak most likely results from a local area increase around each surface solution nucleation site that results in a decrease in the mass per unit area. Data beyond the peak cannot be used until one understands the cause for apparent reduction in mass. The peak helps identify more precisely the equilibrium P_{H_2O} in the 3-phase system. Sodium iodide is the most complex of these salts. Significant quantities of H₂O were adsorbed before actual solution of the salt was observed.

Table II lists the equilibrium P_{H_2O} above saturated salt solutions (3-phase region) measured for the alkali halides in this study, the critical relative humidity, and other literature values.

The transition metal chlorides generally have many hydrated forms. The weight-pressure curves in this study were more complex than the alkali metal halides. Figure 4 shows some representative plots of weight increase vs. P_{H_2O} . For Fe, Co, and Ni chlorides, two pressure arrest points were observed. For NiCl₂

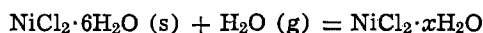
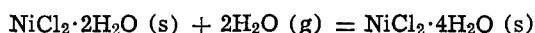
Table I. Summary of heats of H₂O adsorption, RH (P/P_0) at monolayer coverage, and true surface area, Σ , for 1 cm² projected geometric area of alkali metal chlorides

| Salt | ΔH_{ad} (kcal/mol) | P/P_0 at monolayer coverage | Σ (cm ²) (H ₂ O adsorption area) |
|------|-------------------------------|-------------------------------------|--|
| LiCl | 11.2 | 0.36 | 11.9 |
| NaCl | 12.8 | 0.17 | 6.8 |
| KCl | 12.2 | 0.20 | 10.1 |
| RbCl | 12.1 | 0.19 | 6.5 |

Table II. Summary of water vapor pressure (P_{H_2O}) in equilibrium with saturated salt solutions (23°C) and associated critical relative humidity (% RH crit)

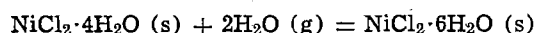
| Salt | P_{H_2O} (23°C) | % RH crit (This study) | % RH crit (Literature) | Salt | P_{H_2O} (23°C) | % RH crit (This study) | % RH crit (Literature) |
|--------------------|-------------------|------------------------|------------------------|---|---------------------|------------------------|------------------------|
| LiCl | 1.9 | 9 | 15 (18) | Li ₂ SO ₄ | 19 | 90 | — |
| NaF | 21 | 100 | 97 (18) | Na ₂ SO ₄ | 19 | 90 | 95 |
| NaCl | 17.1 | 81 | 75 (15) | CoSO ₄ | 20.4 | 97 | — |
| NaBr | 10.7 | 51 | 56 (19) | NiSO ₄ | 18.9 | 90 | — |
| NaI | 8.1 | 39 | 50.4 (18) | CuSO ₄ | (No break in curve) | — | 98 (18) |
| KCl | 19.2 | 92 | 86 (20) | (NH ₄) ₂ SO ₄ | 17.5 | 83 | 81 |
| KBr | 18.6 | 89 | 82 (15) | | | | |
| KI | 15.5 | 74 | 68 (15) | | | | |
| RbCl | 17.3 | 83 | — | | | | |
| NH ₄ Cl | 16.5 | 79 | 78-80 (18) | | | | |
| MgCl ₂ | 6.5 | 30 | — | | | | |
| MnCl ₂ | 9.5 | 46 | — | | | | |
| FeCl ₃ | 11.9 | 57 | 40 | | | | |
| CoCl ₂ | 12.8 | 61 | — | | | | |
| NiCl ₂ | 9.8 | 46 | — | | | | |
| CuCl ₂ | 15.7 | 75 | 69 | | | | |

the pressures are similar to those measured for the reactions



(saturated solution)

The intermediate solid-solid hydrate reactions were not observed, which is indeed a puzzle. For example, we should have seen



Zinc, ferric, and calcium chloride showed no pressure breaks but very large adsorption of water. ZnCl₂ and

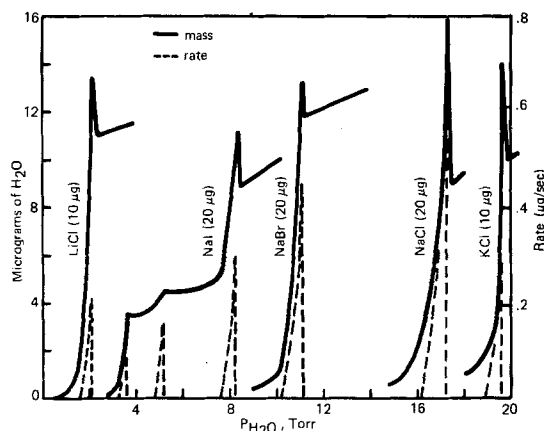


Fig. 3. Water weight increase vs. P_{H_2O} for simple salts. $t = 23^\circ\text{C}$, HP nitrogen.

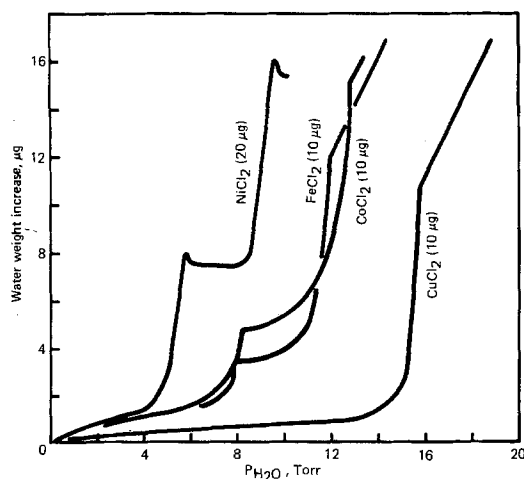


Fig. 4. Water weight increase of NiCl₂, FeCl₂, CoCl₂, and CuCl₂ salts vs. P_{H_2O} , Torr, $t = 23^\circ$, HP nitrogen.

FeCl₃ are not stable in the presence of water vapor and will yield HCl and complex metal oxyhydroxides. These products showed no distinct pressure break.

The sulfates showed one pressure arrest for the reaction of the highest solid hydrate with gaseous water vapor to form a saturated sulfate solution. These are summarized in Table II. We could not detect solid-solid hydrate transformations for the sulfates even though they are known to exist.

Summary

The piezoelectric effect can be used to measure critical relative humidities for soluble salts as well as physical adsorption isotherms. The heats of adsorption of LiCl, NaCl, KCl, and RbCl were calculated from the BET isotherm to range between 11 and 13 kcal/mol. The technique could not generally measure solid-solid hydrate reactions except for the nickel, ferrous, and cobalt chlorides.

Manuscript submitted Oct. 3, 1980; revised manuscript received Feb. 2, 1981.

Any discussion of this paper will appear in a Discussion Section to be published in the June 1982 JOURNAL. All discussions for the June 1982 Discussion Section should be submitted by Feb. 1, 1982.

Publication costs of this article were assisted by IBM Corporation.

REFERENCES

- (a) W. H. J. Vernon, *Trans. Faraday Soc.*, **27**, 265 (1931).
- (b) F. Mansfeld and J. V. Kenkel, *Corrosion*, **33**, 13 (1977).
- B. Kraus, in "The Encyclopedia of Atm. Science and Astrogeology," R. W. Fairbridge, Editor, Reinhold Pub. Corp., New York (1967).
- P. V. Hobbs and M. K. Politovich, *T. Appl. Meteorol.*, **644** (1966).
- Y. A. Vakhrusher and Y. B. Gradiner, *Appl. Chem. USSR*, **47**, 627 (1974).
- J. D. Sinclair, *This Journal*, **125**, 734 (1974).
- A. C. Zettlemoyer, K. Tcheurekdjian, and C. H. Chessick, *Nature*, **192**, 623 (1961).
- C. S. Lu and O. Lewis, *J. Appl. Phys.*, **43**, 4385 (1972).
- T. Kanazawa, M. Chikazawa, M. Kaiho, and T. Fujimaki, *Nippon Kagaku Kaishi*, **9**, 1669 (1973).
- C. Stockbridge, "Vacuum Micro Balance Techniques," Vol. 5, Plenum Press, Inc., New York (1966).
- J. G. Miller and D. I. Bolef, *J. Appl. Phys.*, **39**, 4589 (1968).
- D. W. Rice, P. B. P. Phipps, and R. Tremoureux, *This Journal*, **126**, 1459 (1979).
- W. Lee and J. Eldridge, *ibid.*, **124**, 1747 (1977).
- G. Sauerbrey, *Z. Phys.*, **155**, 206 (1959).
- R. G. Wylie, D. K. Davies, and W. A. Caw, in "Humidity and Moisture," Vol. 1, A. Wexler, Editor-in-chief, R. E. Ruskin, Editor, pp. 125-134, Reinhold Publishing Corp., New York (1965).
- T. Kanazawa, M. Chikazawa, M. Kaiho, and T. Fu-

- jimaki, *Nippon Kagaku Kaishi*, **9**, 1673 (1973).
16. P. G. Hall and F. C. Tompkins, *Trans. Faraday Society*, **58**, 1734 (1962).
 17. P. G. Hall and F. C. Tompkin, *J. Phys. Chem.*, **66**, 2260 (1962).
 18. H. M. Papee and K. J. Laidler, *Can. J. Chem.*, (1958).
 19. "Handbook of Chemistry and Physics," 60th ed., R. C. Weast, Editor, CRC Press, Boca Raton, Florida (1980).
 20. M. Chikazawa, M. Kaiho, and T. Kanazawa, *Nippon Kagaku Kaishi*, **3**, 410 (1976).
 21. M. Chikazawa, M. Kaiho, and T. Kanazawa, *ibid.*, **5**, 874, E46 (1972).



A Note on the Ability of CVD Polysilicon to Deposit Nearly Inaccessible Areas of IC Topology

W. E. Ham,* M. S. Abrahams,* and C. J. Buiocchi

RCA Laboratories, David Sarnoff Research Center, Princeton, New Jersey 08540

Abstract.--Cross sectional transmission electron microscopy (XTEM) samples having a cavity behind a thin microcrevice show sub-crystalline deposits of chemically vapor deposited (CVD) polycrystalline silicon in the cavity. The ability of CVD poly silicon to migrate to extremely isolated areas of IC topology is thereby established. This data suggests the use of CVD poly silicon for different types of electrical and mechanical sealing applications.

We have recently had the opportunity to observe - quite by accident - the phenomenal ability possessed by CVD silicon to deposit in remote, nearly inaccessible areas of IC topology in the initial phases of its deposition. In order to understand the TEM micrograph which shows the observation, it is necessary to first describe the rather unusual conditions which lead to fabrication of the sample.

The sample was made in an attempt to observe the similarity between thermal oxidation of poly silicon layers on bulk silicon and similar oxidations of silicon-on-sapphire structures. The silicon-on-sapphire observations have been published elsewhere (1). The basic idea was to deposit a thin layer of poly silicon (5000 Å) (poly silicon I) (Fig. 1) on a bulk silicon wafer which had been oxidized (thermal oxide I), and to subsequently oxidize the poly silicon (thermal oxide II). It was recognized that the silicon substrate would also oxidize during the poly oxidation if an oxidation barrier were not used under the poly silicon. Therefore, the structure shown in Fig. 1 was used; the silicon nitride was intended to provide the oxidation barrier.

The deposited oxide layer (see Fig. 1) was defined using standard photolithographic methods and chemical etching. After stripping the photoresist, the poly silicon was etched in a KOH solution in a manner typically used for silicon-on-sapphire epi

layers. At this point the usual procedure is to strip the deposited oxide in a strong HF solution and this was done. It was later found that this oxide stripping process also etched the Si_3N_4 layer and the thermal oxide under the Si_3N_4 . This left the sample in a condition similar to that shown in Fig. 2. Fig. 2 is a reasonable guess only.

The thermal oxidation of the poly silicon (thermal oxide II) was done at 900°C in HCl/steam for 50 minutes. This oxidation also oxidized the exposed bulk silicon (see Fig. 2). After this oxidation, a very thick ($\approx 5 \mu\text{m}$) layer of poly silicon (poly silicon II) was deposited in order to outline the oxide. Both poly silicon layers were deposited at atmospheric pressure by silane decomposition in H_2 at $\approx 700^\circ\text{C}$. The result of this procedure is shown in Fig. 3, which is a cross sectional transmission electron micrograph of the final structure (2). It is clear from Fig. 3 that the thermal oxidation II has caused the silicon nitride ledge to become bent and depressed at its outer edge to the point where it is essentially resting on the thermal oxide II growing from the bulk substrate. The basic causes for this downward bending are not clearly understood but are not critical to the phenomenon being addressed in this note. This structure leaves a microcrevice between the outer edge of the silicon nitride layer and the thermal oxide II grown from the bulk substrate. A space exists immediately below the silicon nitride ledge which is partially filled with poly silicon from the deposition of the thick poly layer (poly silicon II).

The important point in this note is that the poly silicon in this space had to be transported through the microcrevice during the initial phase of the poly deposition before complete coverage was achieved. It is, of course, possible that the microcrevice was slightly wider at points along the edge other than shown in Fig. 3 and that some lateral transport along the edge occurred. Regardless of this possibility, a phenomenal amount of silicon was deposited in this

*Electrochemical Society Active Member.

nearly inaccessible region. CVD poly depositions in areas having severe retrograde slopes have been previously shown to occur at the edges of SOS islands and silicon epitaxy has been observed at the bottom of deep grooves but the present observation is even more indicative of the penetrating ability of CVD poly silicon (1)(3). Low pressure depositions would probably enhance the effect.

This data suggests that perhaps CVD poly silicon can be used as a very effective sealant for many types of structural defects. This sealant could be of a mechanical or electrical nature depending on the application.

As a point of further note, the upper part of the poly silicon edge exhibits a sharp point and thinned oxide after oxidation in much the same way as the silicon-on-sapphire (1). Another point of interest is the small-grained poly silicon adjacent to the silicon nitride layer. The consequences of such a layer were discussed previously (1).

The authors thank E. M. Strouse for her expert sample fabrication and A. S. Buchholtz for his expert polishing and thinning of the samples.

Manuscript received April 13, 1981.

Publication costs of this article were assisted by RCA Laboratories.

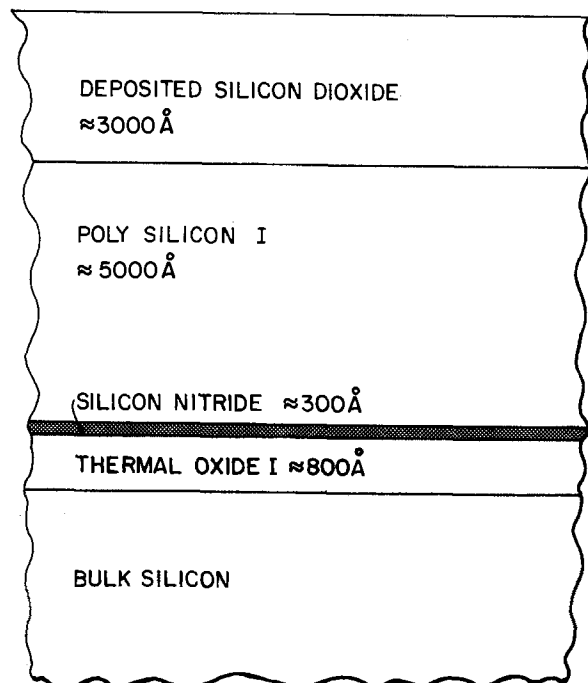


FIGURE 1 INITIAL STRUCTURE

REFERENCES

- (1) W. E. Ham, M. S. Abrahams, J. Blanc and C. J. Buiocchi, "The Study of Microcircuits by Transmission Electron Microscopy", RCA Review 38, 351 (1977).
- (2) M. S. Abrahams and C. J. Buiocchi, "Cross-Sectional Specimens for Transmission Electron Microscopy", J. Appl. Phys. 45, 3315 (1974).
- (3) R. K. Smeltzer, "Epitaxial Deposition of Silicon in Deep Grooves", J. Electrochem. Soc. 122, 1666 (1975).

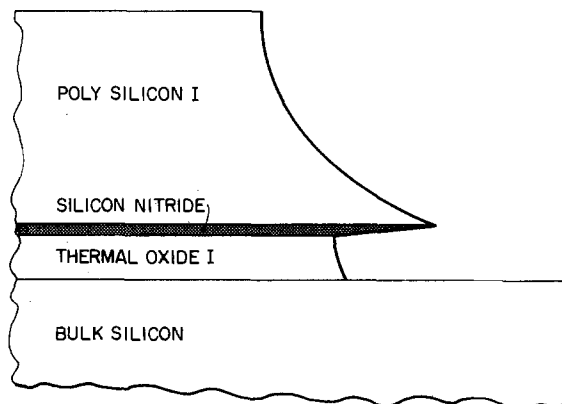


FIGURE 2 PROBABLE STRUCTURE AFTER STRIPPING DEPOSITED SiO_2 IN HF.

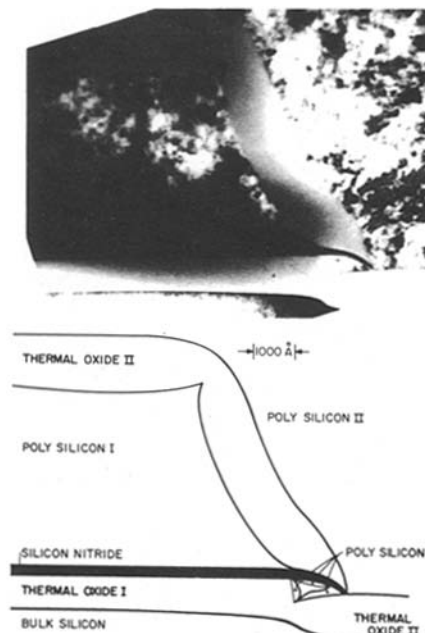


FIGURE 3 BRIGHTFIELD XTEM SHOWING POLY SILICON DEPOSIT IN THE MICRO CAVITY. SEE TEXT.

Stabilization of n-Si Photoanodes to Surface Corrosion in Aqueous Electrolyte with a Thin Film of Polypyrrole

Terje Skotheim, Ingemar Lundström,* and Jiri Prejza

Laboratory of Applied Physics, Linköping Institute of Technology, 581 83 Linköping Sweden

All n-type narrow band gap semiconductor materials are susceptible to photoanodic decomposition in aqueous media. This has been the main impediment to the exploitation of the potential of electrochemical solar cells. Attempts at controlling the interfacial charge transfer processes at semiconductor-liquid junctions by derivatization of the semiconductor (1) or electrochemically growing thin polymer films on the semiconductor surface (2) and thereby preventing photoanodic corrosion/oxidation have yielded encouraging results. Photoelectrochemical generation of conductive polypyrrole films on n-GaAs electrodes has been reported to result in substantial stability in organic based solvents (2). However, film peeling in aqueous media remains a problem. We have studied the attachment of polypyrrole films to semiconductor surfaces and in this communication we describe a method for improving the adherence on n-Si by modifying the semiconductor surface with a 5Å Pt film before the electrodeposition of polypyrrole.

Electrodeposition of polypyrrole films on Au and Pt electrodes has been reported to yield film conductivities up to $100 (\text{ohmcm})^{-1}$ (3-5). Deposition of polypyrrole on Pt electrodes results in extremely good adherence to the substrate and the films are difficult to remove by chemical means. This observation prompted us to study the adherence of polypyrrole films to n-Si surfaces modified with a thin Pt film.

The semiconductor electrodes were 0.5 mm thick single crystal wafers of n-Si (1,0,0) purchased from Wacker Chemie. They had a resistivity of 2.0 ohmcm and had been polished to 0.25 μm. The electrodes were etched in 10% HF before use. Ohmic contacts were made with an In-Ga eutectic and the crystals were mounted with an epoxy on glass slides. The 5Å Pt film was deposited by a vacuum evapora-

tion source at a rate of $1\text{Å}\cdot\text{sec}^{-1}$ at 10^{-7} torr on the semiconductor substrates (at room temperature). Pt films of that thickness tend to form disconnected islands rather than continuous films.

The photoelectrochemical generation of thin polypyrrole films on the Si surface was performed with a tungsten-halogen lamp (140 mW/cm^2). The electrode potential was held constant at 1.0V vs. SCE (saturated calomel electrode). The monomer solution contained 0.1M pyrrole and 0.1 M Et_4NBF_4 in acetonitrile with 1% water. Deposition of polypyrrole on n-Si begins at 0.65V (SCE) vs. 0.8V on Pt electrodes. At lower voltages rapid oxide formation electrically passivates the n-Si anode. The thickness of the film was calculated on the basis of the amount of charge passed assuming the same value ($50 \mu\text{C cm}^{-2}$ per monolayer) as on Au electrodes. For the photoelectrochemical measurements the counter electrode was Pt ($\sim 5 \text{ cm}^2$).

In order to determine the stability of the n-Si/Pt/polypyrrole electrodes against photo-oxidation the short circuit photocurrent was monitored as a function of time. The thickness of the polypyrrole layer was generally 100-250 monolayers. The medium was I_3/I^- redox couple in aqueous KCl solution. Data are shown in Fig. 1. The cell showed no decay running continuously for 6 days at $\sim 9 \text{ mA cm}^{-2}$. The experiment was then interrupted and the cell irreversibly damaged at a current density of 35 mA/cm^2 . For comparison a n-Si/Pt cell without polypyrrole decays in about 4 hours with an initial current density 7% higher. The somewhat lower current density for the n-Si/Pt polypyrrole cell is probably due to absorption in the slightly brown polypyrrole film. A n-Si/polypyrrole cell without Pt surface modification decays in a few minutes in this medium and with an initial photocurrent 36% of the value for n-Si/Pt/polypyrrole. A bare n-Si photoanode decays in ~ 1 min in this medium and the initial transient photo current is only 25% of n-Si/Pt/polypyrrole value. This is surprising as the cell without polypyrrole coating would be ex-

*Electrochemical Society Active Member.

Key words: silicon, stabilization, electrode-deposition, polypyrrole.

pected to have contributions from the photo-oxidation current as well. This difference indicates efficient electron transfer across the interface and decreased rate of carrier recombination for polypyrrole coated electrodes.

The open circuit voltage was measured for a range of redox couples and was found to vary only slowly with the redox potential.

For the $\text{Fe}(\text{CN})_6^{4-/3-}$ couple (0.08V vs. SCE) V_{oc} was 345 mV and for $\text{Ce}^{3+/4+}$ (1.33V vs. SCE) it was 425 mV with 140 mW/cm^2 illumination. This slow variation of V_{oc} with the redox potential indicates substantial fermi level pinning.

Fig. 2 shows a current voltage curve for a n-Si/Pt/polypyrrole cell in an aqueous solution of 0.4 M KI , 0.02 M I_2 and 0.5 M KCl under illumination of 60 mW/cm^2 . The values are uncorrected for reflection and absorption in the electrolyte. Due to the cell construction the light passed through 3.5 mm of the solution which absorbed most of the light of wavelengths below 600 nm. The output characteristics are stable.

These results show that one may be able to control the semiconductor - liquid interface with electroactive polymer films and substantially suppress photodissolution/oxidation. The present work indicates that it may be possible to modify the polymer/semiconduc-

tor interaction to produce a sufficiently rugged interface for a practical electrochemical solar cell. The conversion efficiencies observed in our rather crude test cell are also encouraging.

ACKNOWLEDGEMENT

The authors thank ms. A Spetz for preparation of the electrodes and mr. O Inganäs for helpful discussions.

REFERENCES

- (1). A.B. Bocarsly, E.G. Walton, and M.S. Wrighton, *J. Am. Chem. Soc.* **102**, 3390 (1980).
- (2). R. Noufi, D. Tench, and L.F. Warren, *J. Electrochem. Soc.* **127**, 2310 (1980).
- (3). A.F. Diaz, K.K. Kanazawa, and G.P. Gardini, *J.C.S. Chem. Comm.*, 635 (1979).
- (4). K.K. Kanazawa, A.F. Diaz, R.H. Geiss, W.D. Gill, J.F. Kwak, J.A. Logan, J. Rabolt, and G.B. Street, *J.C.S. Chem. Comm.*, 854 (1979).
- (5). A.F. Diaz and J.I. Castillo, *J.C.S. Chem. Comm.*, 397 (1980).

Manuscript received March 30, 1981.

Publication costs of this article were assisted by Linköping Institute of Technology.

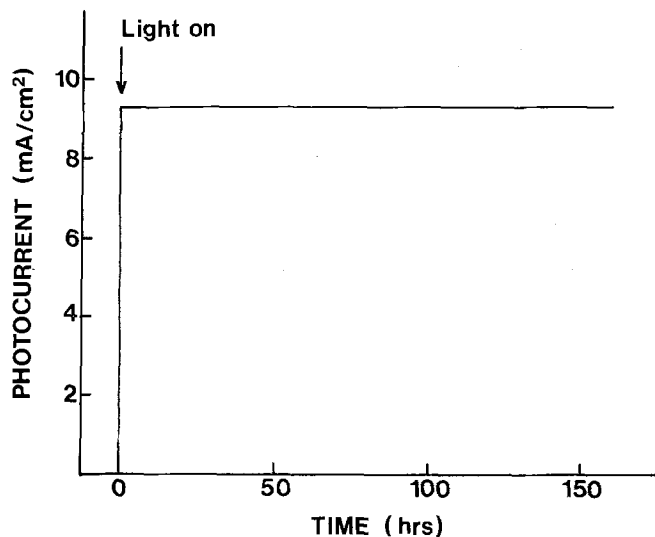


Fig. 1. Short circuit photocurrent for n-Si/Pt/polypyrrole in aqueous 0.1 M KI , 0.01 M I_2 and 0.1 M KCl . The polypyrrole layer was 250 monolayers thick. Illumination was by a tungsten halogen lamp at 75 mW/cm^2 .

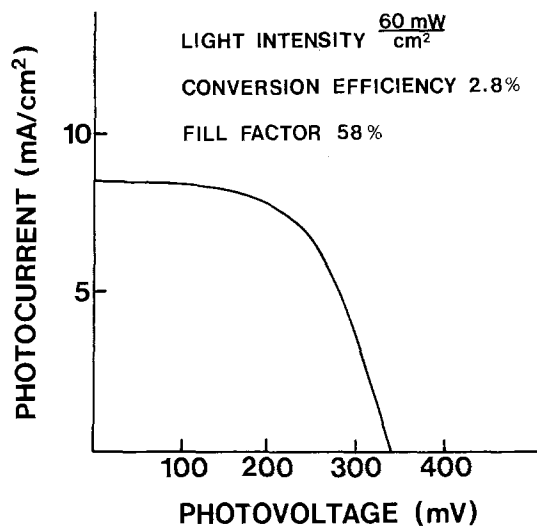


Fig. 2. Photocurrent-voltage characteristics for a n-Si/Pt/polypyrrole cell in aqueous 0.4 M KI , 0.02 M I_2 and 0.5 M KCl under illumination at 60 mW/cm^2 with tungsten-halogen light.

Chemically Deposited CdSe Thin Films for Photoelectrochemical Cells

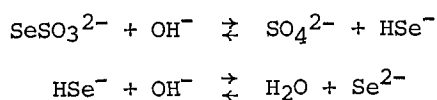
Dexter R. Pratt, Margaret E. Langmuir,* Robert A. Boudreau, and R. David Rauh*

EIC Laboratories, Incorporated, Newton, Massachusetts 02158

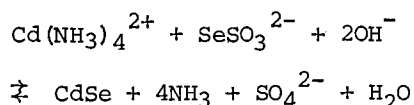
The chemical deposition of thin films of CdSe on glass, copper, Si, and Ge substrates has been studied in detail by Kainthla, Pandya, and Chopra (1). We have applied this method to the preparation of thin CdSe films on titanium foil substrates for use in photoelectrochemical cells. The method does not require expensive capital equipment and can be scaled up to large electrode areas without problems of edge effects that one encounters in electro-deposition methods.

The principle of the deposition process is to provide a slow generation of Cd(II) and Se²⁻ ions such that the solubility product of CdSe is just exceeded. Growth of CdSe films then occurs preferentially on surfaces with a similar crystal structure where the free energy change of nucleation is small, thereby facilitating nucleation on the substrate as opposed to nucleation in the bulk solution.

The selenide ion concentration is controlled by the following equilibria:



Cd(II) ion is complexed with ammonia, present in large enough concentration to prevent its precipitation as Cd(OH)₂. The overall reaction is therefore:



The equilibria for both ions are temperature dependent and therefore the growth rate may be controlled by the bath temperature. The reaction of Se²⁻ with dissolved oxygen to give Se and the precipitation of CdSe in the bulk

solution are competing processes which must be minimized.

Titanium wire was spot-welded to one side of 1 cm² titanium foil substrates, and the assembly subsequently degreased in chromic acid and rinsed in distilled water. The substrates were dipped in a nitrogen or argon purged bath containing 0.05M Cd(Ac)₂, 0.05M Na₂SeSO₃, and 2.1M NH₄OH and maintained at 77°C for 60 to 90 minutes. After plating, the films were rinsed with distilled water, dried, and annealed. The annealed films appeared uniform, adherent, and specularly reflecting. The photoelectrochemical activity of the electrodes was evaluated in a three-electrode cell containing aqueous polysulfide electrolyte (1M Na₂S, 1M S, 1M NaOH).

The effect of annealing temperature was studied by maintaining the substrates at the given temperature for four hours in argon atmosphere. Figure 1 shows the results from temperatures from 350°C to 600°C. The similar symbols indicate substrates coated in the same batch. At 600°C, the films evaporate exposing the substrate, as evidenced by metallic behavior and no photoresponse when tested by current-voltage measurements under dark and light conditions. For films annealed 4 hours in argon, ~500°C produces the optimum photoresponse. Air annealing has been shown to be beneficial for CVD prepared CdSe films on titanium (2). Therefore we have annealed some of our films in air. Those air annealed at 600°C for 7 minutes perform as well as those annealed 4 hours in argon at 500°C.

Surface treatment of the chemically deposited films increases their photoresponse much as one observes with single crystal n-CdSe (3) and painted CdSe films (4). The following etch and ion treatments have been used:

A - Dip in 10M HCl for 2 to 3 sec followed by distilled water rinse and air dry.

*Electrochemical Society Active Member

Key words: photoelectrochemical cell, solar cell, chemical deposition.

B - Treatment A followed by 10 sec dip in 2M $ZnCl_2$, partial rinse in distilled water, and air dry.

C - Treatment A followed by 10 sec dip in 2M $Na_2Cr_2O_7$ and rinse in polysulfide electrolyte.

D - Dip in 6M HCl saturated with sulfur for 2-3 sec followed by distilled water, rinse and air dry.

Figure 2 shows half cell photocurrent-voltage curves for electrodes given various surface treatments and tested in aqueous polysulfide.

Based on weight gain of the substrates, we calculate a terminal film thickness of about 0.4 micron for most substrates, although some substrates have been coated 1 micron thick. Optimization of deposition conditions may produce even thicker coatings. We have demonstrated that it is possible to add successive coatings to increase thickness. Figure 3 demonstrates the effect of increasing thickness of the deposit by two successive coatings. The short circuit photocurrent is increased significantly, probably due to increased absorbance of the incident light by the thicker film. The dashed line, B, is for an electrode with two coatings given successive etch treatments D and B. For the latter electrode, a light to power conversion efficiency of 2.7% at 67 mW/cm^2 Xe arc excitation has been achieved. Since Xe arc excitation is rich in sub-bandgap radiation compared to solar excitation for CdSe, we expect the performance of this electrode to be even better under AM2 conditions.

We are very encouraged by our initial results with chemical deposition of CdSe films on titanium substrates for use in photoelectrochemical cells. Additional experiments to relate process variables to cell efficiencies are now in progress.

ACKNOWLEDGMENT

The authors gratefully acknowledge the support of this work by the Department of Energy through Subcontract No. XP-9-8002-7 from the Solar Energy Research Institute.

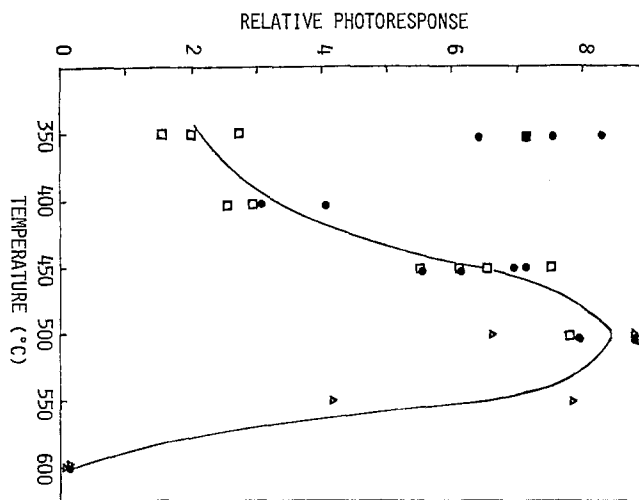


Fig. 1. Effect of annealing temperature on chemically deposited CdSe electrode performance. Electrodes annealed 4 hours in argon atmosphere. Symbols indicate electrodes chemically deposited in the same batch. Photoresponse was measured in aqueous polysulfide.

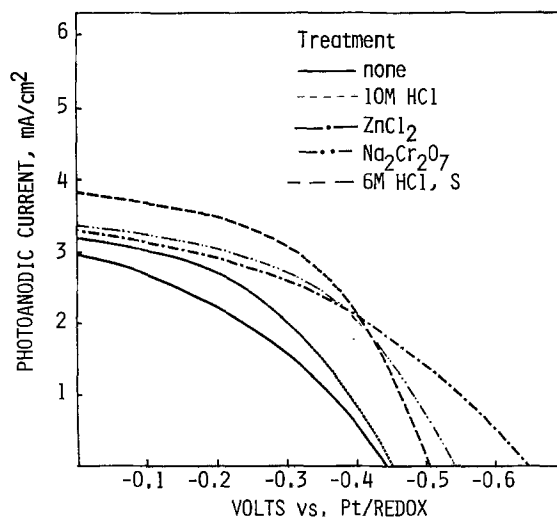


Fig. 2. Effect of various etch treatments on chemically deposited CdSe films on Ti. Single deposition annealed 4 hours at 500°C in argon. Half cell measurement in aqueous polysulfide at 67 mW/cm^2 Xe.

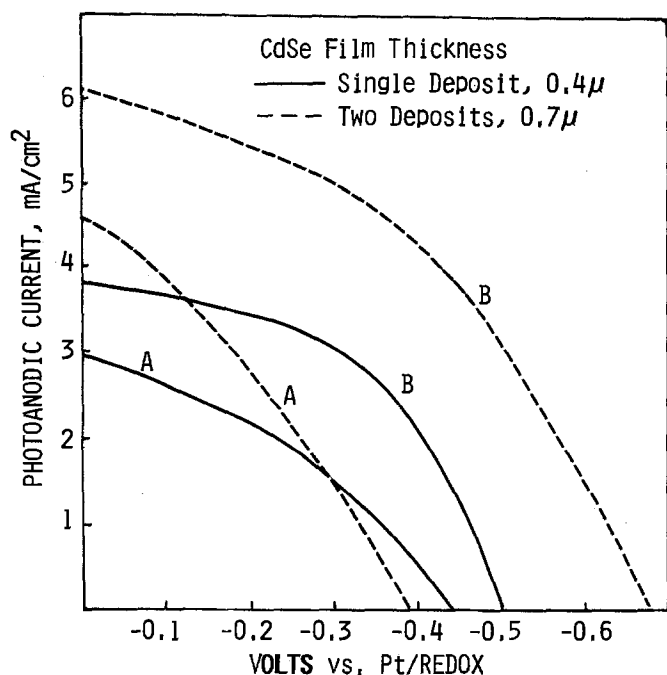


Fig. 3. Effect of number of chemical depositions on film thickness and photoresponse. CdSe films on Ti substrates annealed 4 hours at 500°C in argon. Curves: A, before etch treatment; B, after HCl, S etch. Half cell measurement in 1M Na₂S, 1M S, 1M NaOH at 67 mW/cm².

REFERENCES

1. R. C. Kainthla, D. K. Pandya, and K. L. Chopra, This Journal, 127, 277 (1980).
2. M. A. Russak, J. Reichman, H. Witzke, S. K. Deb, and S. N. Chen, This Journal, 127, 725 (1980)
3. A. Heller, K. C. Chang, and B. Miller, This Journal, 124, 697 (1977).
4. G. Hodes, D. Cahen, J. Manassen, and M. David, This Journal, 127, 2252 (1980).

Manuscript received Jan. 13, 1981.



Information Sources for Superconductors

Charles W. Moulton*

Chemical Abstracts Service, Columbus, Ohio 43210

The overall subject of superconductivity and superconducting devices—rather like all Gaul—can be divided into three more or less distinct areas of interest: (i) *superconductivity* as a fundamental physical phenomenon—the domain of the physicist; (ii) *superconductors* as materials—the domain of the chemist and the metallurgist; and (iii) *applications* of superconductivity and superconductors—the domain of the electrical engineer.

Information sources for superconductors are discussed here primarily from the standpoint of material scientists, chemists and chemical engineers, metallurgists, electrical engineers, and chemical and engineering physicists. Several abstracting organizations, as well as a number of specialized information centers, are described. *Chemical Abstracts* and its related services are also used as examples of secondary literature sources.

Information Services

The brief discussion that follows on organizations that furnish information on superconductors cannot be in any way exhaustive, but is intended to represent the major types of the various services that are available to the scientist searching for information about superconductors (1).

1. The American Institute of Physics began in January 1979 an association with the Deutsche Physikalische Gesellschaft and the Fachinformationszentrum Energie, Physik, Mathematik to publish *Physics Briefs* (PB) as a successor to the long-established *Physikalische Berichte*. PB, which is published in English in the Federal Republic of Germany, emphasizes the literature of physics.

2. The American Society for Metals (ASM) and the Metals Society of London cooperate to produce *Metals Abstracts* in the specialized area of metallurgy and the physics, chemistry, and engineering of metals and alloys. Related ASM services include *Metal Abstracts Index*, *Alloys Index*, and the *ASM Digest Series*. There are also the tape services *Metalert* for current awareness, and *Metadex*, which is *Metals Abstracts Index* on tape. ASM also cooperates with other societies throughout the world to produce *World Aluminum Abstracts*.

3. Cambridge Scientific Abstracts, Incorporated, publishes *Electronics and Communications Abstracts Journal*, *Science Research Abstracts Journal*, and *Solid State Abstracts Journal*, all of which contain information on the physics and engineering of superconductors.

4. The Chemical Abstracts Service division of the American Chemical Society produces a wide range of services, including *Chemical Abstracts*, that direct the scientist to sources of information about superconductors in the primary literature. These services will be discussed in greater detail below.

5. *Engineering Index* emphasizes engineering and engineering physics. In addition to the principal EI

abstract and index publications, there are available *Energy Abstracts* and the computer-readable file, *Compendex*.

6. The *INIS Atomindex* of the International Atomic Energy Agency emphasizes nuclear science and technology. A tape file is available.

7. The Institute of Science Information has a wide-ranging array of services. These include, in the *Current Contents* series, *Physical and Chemical Sciences* and *Engineering, Technology and Applied Sciences*. Also available are *Science Citation Index*, *Index to Scientific and Technical Proceedings*, and the tape files *Scisearch* and *Ascotopics*.

8. The Institution of Electrical Engineers of London, through its Information Service in Physics, Electro-Technology and Control (INSPEC), produces *Electrical and Electronics Abstracts* and *Physics Abstracts*, as well as current-awareness journals based on titles alone. The INSPEC data base is available on magnetic tape.

In addition to these particular items that have been mentioned, these services generally provide various other types of publications, tape files, and microform copies.

Information and Data Centers and Online Services

Another type of information source, the information and data centers, will now be briefly discussed. Four that compile information on superconductors from many other sources include:

- Alloy Data Center. U.S. National Bureau of Standards in Washington, DC.
- Cryogenic Data Center. US National Bureau of Standards in Boulder, Colorado.
- Metals and Ceramics Information Center. Battelle Memorial Institute in Columbus, Ohio.
- Superconductive Materials Data Center. General Electric Company in Schenectady, New York.

Of these, only the GE Center specializes in superconductors *per se*. The others process information on superconductivity as an alloy property or as an aspect of the technology of cryogenics.

Centers of this type may include in their holdings not only material selected from the standard primary technical literature, but also reports of limited availability. Some publish periodic current-awareness journals in their specialized areas, as well as bibliographies, monographs, and compilations of numerical data. They can provide computerized retrieval and microform copies of documents in their fields.

And lastly, there are the online services. Most of the abstract-index files that have been described are available to the online searcher through the domestic vendors such as the following:

- Bibliographic Retrieval Services, Scotia, New York (BRS).

* Electrochemical Society Active Member.

Key words: superconductors, secondary literature sources, abstracting.

b. Lockheed Information Systems, Palo Alto, California (DIALOG).

c. SDC Search Service, System Development Corporation, Santa Monica, California (ORBIT).

d. US Department of Energy, Technical Information Center, Oak Ridge, Tennessee (DOE/RECON).

Online services are also becoming established throughout many other parts of the world, including the following:

a. Canada Institute for Science and Technology, National Research Council, Ottawa, Canada (CISTI).

b. European Space Agency, Space Documentation Institute, Frascati, Italy (ESA/RECON).

c. Japanese Information Center of Science and Technology, Tokyo, Japan (JICST).

While these listings are far from complete, they are representative of the wide range of services available. For those with online access, these services can provide extremely rapid, efficient, and thorough searches of the technical literature by means of series of interrelated queries (known as search profiles in the jargon of the trade), framed by the individuals who request the search.

Familiarity with the relatively simple mechanics of making online searches is so readily mastered that anyone can have the satisfaction of obtaining his or her own information without relying on a library staff or spending long periods of time poring through volumes of printed publications. The online technique will, without a doubt, become the normal mode by which comprehensive searches of the scientific and technical literature are carried out.

Superconductors in Chemical Abstracts

The function of a comprehensive abstracting service such as Chemical Abstracts Service (CAS) is to furnish easy access to the primary technical literature by providing both abstracts and the indexes to them. CAS directs the searcher, both for current awareness and retrospectively, through its Collective Indexes, to the research papers, conference proceedings, books, and patents that report and discuss the chemical work carried out in the laboratories and industrial sites throughout the world. It does not provide either archival or critically evaluated compilations of data, nor does it judge the intrinsic validity or merit of the work that is reported; such judgments remain the responsibilities of the users of the information.

Abstracts.—Information on superconductors has appeared in Chemical Abstracts (CA) since shortly after its inception seventy-two years ago. The first Decennial Index to CA, covering the years 1907-1916, carries four references to superconductors, the first abstract having appeared in 1914. This was just three years after Kamerlingh Onnes' epochal papers on the discovery of superconductivity were published. In contrast, in Issue 2 of Volume 90, dated Jan. 8, 1979, and covering just one 2-week period, the researcher will find 28 abstracts concerned with superconductors and superconductor devices.

At CAS documents selected from some 14,000 journals and conference proceedings are routinely abstracted. These are, of course, predominately chemical in nature, that is, material-oriented. But large numbers of these documents overlap with certain areas of physics and engineering. For superconducting materials in particular, many of the journals most frequently cited would normally be regarded as devoted primarily to physics and engineering.

Most of the abstracts of papers and patents that deal with superconductors can be found in a section of CA entitled "Electric Phenomena" (Section 76). This is the section that is concerned most directly with materials of interest from the electrical standpoint. An entire

subsection (8) is devoted to superconductors and to superconductivity as a material property.

However, various applications of superconductors can fall into several other sections, depending on the emphases of the studies; e.g., metallurgical aspects in CA Section 56; magnets in CA Section 77, or, when intended for particle accelerators or fusion reactors, in CA Section 71; plant and laboratory apparatus in CA Section 47; certain aspects related to power generation and transmission in CA Section 52 (2).

Figure 1 illustrates an abstract of a paper that deals with a superconducting material. Included are the CA access number (volume and sequence numbers), the title, author names and work location, bibliographic data, language, and finally the abstract text, which provides a precis of the content of the document.

Indexes.—The usefulness of a secondary publication depends to a considerable extent on the adequacy of its indexing. The content of CA is indexed and cross-indexed in a variety of ways.

The *Keyword Index* printed in each of the Abstract Issues serves a current-awareness purpose, directing to those abstracts that appear in the various sections throughout that particular issue of CA dealing with a particular subject. An example of entries from this index is shown in Fig. 2. This is an alphabetically arranged, permuted keyword-in-context (KWIC) index, characterized by an uncontrolled vocabulary and an essentially unarticulated word string of restricted length, seldom more than four or five words. It is based mainly on the titles and abstracts, and so is not an "in-depth" index to the entire contents of the documents abstracted.

The *Subject Index* that is associated with each of the semiannual volumes of CA has, on the other hand, a controlled vocabulary insofar as the subject headings and certain subordinate details are concerned. It also represents a considerably greater depth of indexing. Figure 3 presents some of the principal subject headings that are concerned with superconductors. For the indexing of materials in CA, we have found that there is little point in trying to distinguish between superconductivity as a phenomenon and those materials that display it as a property; the main index heading in the

90: 65300a Superconductivity in the barium lead bismuth oxide ($\text{BaPb}_{1-x}\text{Bi}_x\text{O}_3$) system. Protasov, E. A.; Zaitsev-Zotov, S. V.; Venevtsev, Yu. N.; Bogatko, V. V. (Mosk. Inzh.-Fiz. Inst., Moscow, USSR). *Fiz. Tverd. Tela (Leningrad)* 1978, 20(11), 3503-5 (Russ). The superconducting transition temp. and crit. magnetic fields of polycryst $\text{BaPb}_{0.7}\text{Bi}_{0.3}\text{O}_3$ were detd. as functions of compn. ($x = 0.2-0.5$). The magnetic field dependence of the resistivity of $\text{BaPb}_{0.7}\text{Bi}_{0.3}\text{O}_3$ showed hysteresis at $\leq 5-10$ kOe and neg. magnetoresistance at higher fields.

Fig. 1. Example Abstract

Keyword Index

Supercond
alkali tungsten bronze 65324m
ferromagnetism layered system 65595a
niobium germanium ion irradi 65312f
tunneling spectroscopy 65289d
vanadium silicide transition 64699a

Ferromagnetism
supercond layered system 65595a

Niobium
germanium supercond ion irradi 65312f

Fig. 2. Keyword Index

Subject Index Headings

| | |
|---------------------------------------|-----------------|
| Superconductors | Magnets |
| Superconductor devices | superconducting |
| Cryotrons | Electric cables |
| | superconducting |
| Indium alloy | |
| Niobium, compounds | |
| compd. with tin (3:1) | |
| Vanadium silicide (V ₃ Si) | |

Fig. 3. Subject Index Headings

conceptual sense is thus Superconductors. But those documents that deal with devices are indexed under several other related headings. Superconductor devices is the major heading of this type, while certain types of devices that receive substantial numbers of index citations are provided their own headings (e.g., Cryotrons, Magnets, Electric cables; note under the latter two headings the alerting phrase "superconducting").

Also illustrated in Fig. 3 are several examples of entries for superconductive substances. To facilitate organization of the index material for effective searching, the *CA Subject Index* is divided into two parts:

1. The *General Subject Index*—for those index entries that are concerned with scientific concepts, properties, processes, types of apparatus, and classes and poorly defined substances; and

2. the *Chemical Substance Index*—for those entries that are devoted to specific substances (elements, compounds, alloys).

An example from the Subject Index is shown in Fig. 4. Brief phrases appearing under the heading state the contexts of the studies, and are followed by the CA abstract numbers. The code letter R identifies a review paper; similarly, books are coded with a B and patents with a P.

Indexing policies that relate to the *Subject Index* are documented in an adjunct publication, the *Index Guide*, in the form of extensive general introductory descriptive material and by scope notes and cross-references. Figure 5 presents the note and cross-references that pertain to the heading "Superconductors."

In addition to the *Keyword* and *Subject Indexes*, there is a family of more specialized indexes:

(a) *Author*—an alphabetical index to the authors of documents and to the inventors and patent assignees in the patent literature;

(b) *Formula*—an alphanumeric index to molecular formulas;

Subject Index

| |
|---|
| Superconductor devices |
| R 162101c |
| bolometers, bismuth, 92283x |
| bridges, Josephson, from metal wires, 57449z |
| junctions |
| Josephson, indium-cadmium sulfide-lead, 201793b |
| niobium, nitrogen implantation for, 181112y |
| quantum interference |
| from niobium-tin compd. films, 114118s |
| from metal-oxide film structures, 181114a |

Fig. 4. Subject Index

Index Guide

Superconductors

Superconductivity is also indexed at this heading devices

see such heading as

Cryotrons

Electric cables

superconducting

Magnets

superconducting

Superconductor devices

Fig. 5. Index Guide

(c) *Ring Systems*—an alphanumeric index to the component rings of cyclic compounds, based on the numbers, sizes, and elemental compositions of the rings. (This and the Formula Index will take on increasing significance with the burgeoning interest in potential organic superconductors.);

(d) *Patent*—a numerical index of patent abstracts, arranged by issuing nation;

(e) *Patent Concordance*—a numerical index that interlinks those patents that have been applied for or granted in various nations for a particular invention; cross-references relate to the CA abstract numbers for those citations that had first appeared in CA.

These several indexes allow access to the content of CA by various complementary means, providing searchers with considerable flexibility in carrying out literature searches. All of these indexes are compiled for the semiannual volumes of CA, and are then incorporated into the five-year, ten-volume *Collective Indexes*. These indexes provide the means for retrospective searching, as distinct from the current-awareness purpose of the *Keyword Index*.

Specialized services.—The heart of the CAS services remains *Chemical Abstracts* itself, the printed *Abstract Issues* with their attendant indexes. But in addition, there is an array of special services made available in various formats for specialized purposes.

Among the services available in print, *Chemical Titles* is intended to alert the reader by document title to papers in some 700 of the most important journals of chemistry. Bibliographic data and author and keyword indexes are included. *Chemical Titles* is also available on magnetic tape; the file content is the same as that of the printed version.

The *Section Groupings* provide the total content of the CA *Abstract Issues* in five packages: the biochemical, organic, macromolecular, applied and engineering, and physical and analytical groupings. Complete bibliographic information is included, as well as the *Keyword Index* entries for the entire issue from which a particular grouping is extracted.

"Energy Reviews and Books" is a representative of a relatively new family of services, *CA Selects*. This is a printed current-awareness service, with the bibliographic information and abstracts for those review papers and book titles that appear throughout CA dealing with the general topic of energy. This publication, along with more than 100 others in specialized subject areas, was introduced to provide an inexpensive current-awareness service for those who either desire a conveniently scanned, brief abstract journal or are unable to rely on computerized information retrieval. The information provided for these various topics is extracted from the CAS data base by computerized retrieval based on customized search profiles.

The *Abstract Issues* and their indexes are also available on microform, both as microfilm and microfiche.

CA Search is a computer-readable tape service, issued biweekly, that the user can access through certain online services. It contains a compilation of the bibliographic information, Section and Subsection numbers, keywords, Registry Numbers for specific substances, and the index entries that are subsequently compiled for the semiannual *Subject and Formula Indexes*. Abstracts are not included, but are associated with the file content through the abstract numbers that appear in the printed *Abstracts Issues*. CA Search is a merger of what had been provided by the previously available tape files CA Condensates (CACon) and CA Subject Index Alert (CASIA) (3).

Summary

A wide array of secondary information sources is available to those scientists and engineers who are concerned with superconductors. These sources range from the traditional printed services—abstracts, indexes, and various types of current-awareness publications, through the information and data centers which can provide batch-mode retrievals, to the expanding online services that provide access to a group of information files. These various types of services cover the

gamut in content from the highly specialized (those data centers, for example, that deal exclusively with superconductors) to those that encompass nearly all of the scientific literature. The workers in the fields of superconductivity and of superconducting materials and devices thus have many valuable sources to rely on for their information needs.

Manuscript received March 12, 1980. This was Paper 405 presented at the Boston, Massachusetts, Meeting of the Society, May 6-11, 1979.

Any discussion of this paper will appear in a Discussion Section to be published in the June 1982 JOURNAL. All discussions for the June 1982 Discussion Section should be submitted by Feb. 1, 1982.

REFERENCES

1. For more detail on these and other information systems, see A. T. Kruzas, Editor, "Encyclopedia of Information Systems and Services," 3rd ed., Gail Research Co., Detroit, Michigan.
2. "Subject Coverage and Arrangement of Abstracts by Sections in *Chemical Abstracts*," 1975 ed., Chemical Abstracts Service, Columbus, Ohio.
3. The CAS database concept is described by R. E. O'Dette, *J. Chem. Inf. Comput. Sci.*, **15**, 165 (1975); *Pure Appl. Chem.*, **49**, 1781 (1977).

Report of the Electrolytic Industries for the Year 1980¹

E. J. Rudd*

Diamond Shamrock Corporation, T. R. Evans Research Center, Painesville, Ohio 44077

W. Bruce Darlington*

*PPG Industries, Incorporated, Industrial Chemical Division,
Corpus Christi Technical Center, Corpus Christi, Texas 78408*

Chlorine-Caustic Soda

Production and capacity—After an 11% increase in chlorine production in 1979 to 12 million tons per year, U.S. production increased only 4% in 1980 to 12.5 million tons (1). Production capacity increased 1.3% from 14.4 million tons per year to 14.6 million tons (2).

An estimate of the capacity of various U.S. producers is shown in Table I (3).

Allied Chemical sold their last chlor-alkali plant to Linden Chemicals and Plastics (4).

PPG Industries completed a \$150 million expansion of its chlorine and caustic production at Lake Charles, Louisiana. The 350 ton per day increase in chlorine capacity raises total capacity of the plant to 3000 tons per day, while the caustic increase of 400 tons per day raises its capacity to 3400 tons per day (5-7).

FMC announced that contrary to rumors, it has no plans to shut down its chlor-alkali facility at Charleston, West Virginia (8).

Hooker Chemical brought on line at Niagara Falls

* Electrochemical Society Active Member.

¹ This report is sponsored by the Industrial Electrolytic Division of The Electrochemical Society. It represents a summary of the published information on production, plant capacities, consumption, markets and trends, prices, raw materials, new developments, health and environmental aspects in the electrolytic and related industries.

The material presented herein has been obtained from many sources, as noted in the list of references, and does not necessarily represent the opinions of the authors.

The Industrial Electrolytic Division is grateful for the support received from the Vittorio de Nora-Diamond Shamrock Fund in assisting with the publication costs of this report.

an energy from waste plant that produces 20% of the power required for its adjacent chlor-alkali plant (9).

Chloro de Tehuantepec began production of chlorine and caustic in a plant at Pajaritos, Mexico. This plant's capacity of 236,000 metric tons per year of chlorine more than doubled the existing Mexican capacity of 176,000 tons per year (10).

Canadian Industries, Limited completed a \$100 million expansion of its chlor-alkali facility at Beacanour, Quebec, which doubled the capacity to 255,000 metric tons per year of chlorine. The new plant

Table I. Capacity of U.S. chlorine producers
tons per day

| | |
|------------------|--------|
| BASF | 906 |
| Convent | 300 |
| Diamond Shamrock | 3,380 |
| Dow | 11,800 |
| du Pont | 2,220 |
| Ethyl | 300 |
| FMC | 800 |
| Georgia-Pacific | 1,400 |
| Hooker | 3,200 |
| ICI | 471 |
| IMC | 330 |
| Kaiser | 590 |
| Linden | 1,355 |
| Mobay | 300 |
| Olin | 2,600 |
| Pennwalt | 1,285 |
| PPG | 4,300 |
| Shell | 288 |
| Stauffer | 1,065 |
| Vulcan | 1,335 |
| Weyerhaeuser | 385 |
| Others | 870 |
| Total | 39,480 |

uses ICI-Solvay diaphragm cell technology. The DMT-43 cells are said to be more compact than the older cells because stabilized diaphragms allow for closer spacing of electrodes (11).

Diamond Shamrock announced it will increase its dry caustic soda capacity by 20% at Deer Park, Texas, by the fourth quarter of 1980 (12, 13).

Markets and prices.—The chlorine and caustic markets remained unbalanced during 1980 because of lack of demand for chlorine. As a result, caustic soda supplies were in short supply (14). In April, Gulf Coast prices for chlorine were \$145 per ton and for caustic soda, \$160-170 per ton (15). After that, however, steady price increases produced a December price of caustic soda of \$220-260 per ton.

Early in the year U.S. chlorine demand was predicted to grow 3.1% per year through 1984 (16, 18). Later in the year, however, this growth rate was reduced to 2% per year, reaching 13.5 million tons per year by 1984 (21). World capacity increase should be somewhat greater at 4% per year reaching 45 million tons per year by January, 1984 (17).

Some of chlorine's markets, such as fluorocarbons and trichloroethylene, have been hurt by government regulations. Also, new technology, such as Arco's MDI route and du Pont's direct cyanation process for nylon production, may hurt future chlor-alkali markets. End uses of chlorine are as follows: plastics, 20%; pulp and paper, 13%; chlorinated methanes, 13%; inorganic chemicals, 11%; propylene oxide, 10%; other organic chemicals, 21%; water treatment, 6%; miscellaneous, 6% (16).

Early in the year, caustic soda demand in the U.S. was expected to grow at a somewhat higher rate than that for chlorine at 4.4% per year (20). Later in the year, however, the projected increase was reduced to 2.7% per year, reaching 14.5 million tons per year in 1984 (21). End uses of caustic soda are estimated to be: organic chemicals, 41%; pulp and paper, 17%; inorganic chemicals, 11%; aluminum processing, 6%; textiles, 6%; petroleum, 4%; soaps and detergents, 4%; miscellaneous, 11% (20, 21). Due to environmental pressures, such as neutralization of waste acids, caustic soda use will grow faster than that of chlorine, and thus it will remain in short supply.

Membrane cells.—Activity in the commercialization of chlor-alkali cell plants based on membrane cell technology remained at a high level in 1980.

Du Pont started up its first commercial facility to produce Nafion perfluorinated ion exchange membranes at its Fayetteville, North Carolina, works (22).

Olin Corporation and du Pont announced a cooperative program where Olin will evaluate high performance Nafion membranes from du Pont at its Charleston, Tennessee, facility (23, 24).

Diamond-Shamrock announced plans to spend \$50 million to increase chlor-alkali capacity by 40% at its Laport, Texas, plant. The increase, estimated at between 600-1000 tons per day of chlorine, will use Diamond-Shamrock's proprietary membrane-cell technology (25-27).

ROT Quimica of Monterrey announced plans to install Diamond-Shamrock membrane cells to produce 14 tons per day of potassium hydroxide and 10 tons per day of chlorine. The caustic potash will be used to produce potassium carbonate for the Monterrey glass industry (28, 29).

Paik Kwang Pharmaceutical Company, Limited (South Korea) will build a 30 m tons per day chlorine-caustic soda plant using Diamond-Shamrock membrane cell technology by 1981 (42). Another chlor-alkali plant using Diamond-Shamrock membrane cell technology will be built by Taiwan Pulp

Company. The 8000 m tons per year caustic soda plant is due on-stream in 1982 (43).

Akzo Zout Chemie has awarded a contract to Comprimo (Netherlands) to construct its 250,000 metric tons per year chlorine plant at Bottek. The plant using Asahi Chemical's membrane cell technology is scheduled for start-up in 1982 (30-33).

Asahi Chemical is planning to replace its mercury cells at Nobeoka with membrane cells by 1982. It is working to extend membrane life beyond the current 1-2 years (34). They also announced a licensing agreement with Tasman Pulp and Paper, Limited of Auckland, New Zealand. This company is the sixth licensee of their permionic membrane process. This plant will replace existing capacity of 5000 metric tons per year of chlorine by mid-1982 (35).

Kanagafuchi Chemical has developed an ion-exchange membrane process using monopolar cells which reportedly use less titanium than diaphragm cells. They will convert an existing 120,000 tons per year (Cl_2) diaphragm cell plant to the new process by the end of 1981. In addition, another two 60,000 metric tons per year mercury cell plants will be converted to membrane cells by 1985 (34).

Toyo Soda will test a new ion exchange membrane chlor-alkali process in a 5000 metric tons per year pilot plant. If successful, they will convert 132,000 metric tons per year mercury cell capacity to the new technology. They have already converted 59% of their capacity to diaphragm cells (36).

Tofte Cellulosfabrikk (Norway) will use Hooker MX membrane cells in a 14,000 metric tons per year chlor-alkali plant to be completed in 1981 (37).

Asahi Glass will build a 150,000-200,000 metric tons per year chlor-alkali plant at Kashima, Japan, by 1984 using its own membrane cell technology (38). They have also developed a membrane cell process to produce caustic potash and will build a plant using the technology at Amagasaki (34). Asahi Glass licensed its membrane cell technology to three West German firms, Uhde, Hoechst, and Bayer. Uhde plans to first evaluate the membranes in pilot cells and later to evaluate them in full scale cells (39). Asahi Glass announced a new chlor-alkali membrane cell process using a new Flemion membrane. The AZEC process requires 1950-2140 kW-hr/mT NaOH, which is 28-35% less than for mercury cells and 14.4-22% less than required for existing ion exchange membrane processes (41).

Ionics, Incorporated sold a 5 tons per day Chloromat membrane cell system to Trinidad to produce chlorine and caustic soda. This is the first chlor-alkali production facility on the island (40).

Health and environment.—The Supreme Court allowed OSHA to impose the NIOSH criterion limiting worker chlorine exposure to a 0.5 ppm ceiling limit. Chlorine producers must now install equipment necessary to meet this standard (44).

The Consumer Product Safety Commission ordered manufacturers and importers of certain types of consumer products to supply them with information regarding the use of asbestos. In particular, data concerning the purpose of asbestos in the products, the end use patterns of the products, testing of the products for asbestos fiber emissions, and possible substitutes for asbestos were requested. This information, which is due by February 20, 1981, is to be used to determine if any regulatory action is required to protect consumers from any risk of injury from asbestos in these products (45).

Unreleased studies by the U.S. Council on Environmental Quality found a link between heavily chlorinated drinking water and malignant tumors. These studies were made in North Carolina, Illinois, Wisconsin, and Louisiana (46). Because chlorine has

been found to be capable of producing over 200 toxic chemicals in drinking water, ozone and filtration are proposed as alternatives to achieve water purification. The possibility of fermentation of trihalomethanes and trichloroethylene and other such chlorinated compounds to more toxic compounds when soft drinks made from chlorinated water are left on the shelves too long was discussed. Ozone dissolved in water is claimed to destroy bacteria and viruses that can cause deterioration of bottled water products (47).

A continuous wastewater treatment process for removing mercury down to 0.01 ppm was developed by Energie and Industrias Argonesas and Quimica Industrial (Spain). The process utilizes an organic solvent to extract mercury chloride and permits the recovery of 99.9% (48).

Other Alkali or Chlorine Compounds

Caustic potash.—Domestic production of potash for the 1980 crop year was 2.2 million metric tons, or about the same as in 1979. Sales, however, declined 6% (49).

Prices rose steadily during the year to \$36-40/100 lb for flake caustic potash by year's end (50).

Diamond-Shamrock and Oriental Chemical Industry set up a 50-50 joint venture to produce 10,000 m tons per year caustic potash and 10,000 m tons per year potassium carbonate in South Korea. The plant, scheduled for operation in 1981, will utilize Diamond-Shamrock's monopolar chlor-alkali membrane cells for the caustic potash production and also their technology for potassium carbonate (51-54).

Soda ash.—U.S. producers of naturally occurring soda ash continued to have an edge on world markets because of abundant supplies and ready access to shipping facilities. U.S. consumption of all types of soda ash in 1980 declined to 6,976,000 tons (67). U.S. consumption has grown only 2% per year, but exports have grown 12.5% per year since 1975. U.S. natural ash capacity is currently 8.9 million tons per year with actual production in 1980 of about 7.5 million tons per year (55). Total U.S. production of soda ash, including Solvay process material, was estimated at 8.2 million tons in 1980, or about the same as in 1979 (56, 67). The distribution of U.S. soda ash production by producer is shown in Table II (57).

Exports of soda ash increased to a record 1.2 million tons per year (67).

End use distribution of soda ash was 55% for glass production, 25% in chemical production, 5% in pulp and paper, 5% in soaps and detergents, and 10% in other uses (58).

Exports of soda ash were estimated to be 1 million tons per year (58). This has caused producers in other countries to cut back production. Imperial Chemical Industries said it will cut its work force by 18% at 3 soda ash plants within 2 years. This will eliminate 500 jobs and allow them to compete more favorably with producers in the U.S. who have a 10% advantage in production costs (59-61).

Kerr-McGee began supplying soda ash to East Coast markets in September from its California production

facilities. The initial 25,000 ton shipment was made by ship (62).

FMC announced the development of a solution mining process for soda ash in Green River Basin, Wyoming. Commercialization of this technique will increase their capacity by 1 million tons per year (63).

Texasgulf announced plans for a \$63 million expansion of its Granger, Wyoming, plant to increase capacity to 2 million tons of soda ash per year by 1987 (64).

Multi Mineral Corporation said they will construct a plant at Piceance Creek Basin, Colorado, to produce 3.7 million tons per year of soda ash, and 400,000 tons per year of alumina, if pilot plant tests are successful. Plant completion is scheduled by 1986 (65).

Kerr-McGee is spending \$200 million to double the capacity of its Trona, California, soda ash plant. Future expansions in southern and central California may be severely restricted, however, by new Interior Department air pollution guidelines. These guidelines have redesignated 2 million acres of land near the Death Valley Monument as a Class 1 air pollution control area, and may add an additional 4 million acres (66).

Sodium chlorate.—Sodium chlorate prices rose throughout the year, reaching \$405 per ton (68, 75). Potassium chlorate prices were also increased in November by 5 cents per pound to a range of 38-41.75 cents per pound (69, 70).

U.S. sodium chlorate capacity decreased by 40,000 tons per year when IMC sold its sodium chlorate plant at Orrington, Maine, to PPG Industries which plans to move it to Beauharnois, Quebec (Canada) (71-74). U.S. capacity now stands at 392,000 tons per year. Production, however, remains at about 250,000 tons per year. Total demand has grown less than 4% per year since 1980. The distribution of the U.S. production capacity is shown in Table III (75, 76).

About 80% of sodium chlorate production goes into paper bleaching. This has been a growing market over the past several years as environmental regulations have favored the use of sodium chlorate over other chemicals used for bleaching (77).

The only new sodium chlorate capacity announced in 1980 for the U.S. was for a \$25 million expansion by Pennwalt at its Tacoma, Washington, facility (78). The engineering, procurement, and construction contract for the plant, to be completed in 1982, was awarded to Catalytic (79).

Activity in sodium chlorate production was much greater in Canada, with several sizeable new facilities being announced. Canadian Occidental Petroleum, Limited will build an \$8.4 million, 8300 tons per year sodium chlorate solution plant at Nanaimo, British Columbia. Chemetics International has the design and construction contract (80). Another plant to be built in British Columbia was announced by Erco Industries. It will expand its facilities in North Vancouver, British Columbia, by 12,000 tons per year to a total of 70,000 tons per year by 1982. Erco also plans a 20,000 ton per year expansion at Thunder Bay (81). Also in British Columbia, B. C. Chemicals will increase sodium chlorate capacity by 6000 tons per year to 31,000 metric tons per year at Prince George. The \$8.2 million plant using

Table II. U.S. Soda ash production capacity

| Producer/Location | 1000 Tons/Year |
|---------------------------|----------------|
| Allied/Green River, WY | 1900 |
| Syracuse, NY | 920 |
| FMC/Green River, WY | 2550 |
| Kerr-McGee/Trona, CA | 500 |
| West End, CA | 150 |
| Stauffer/Green River, WY | 1520 |
| Texasgulf/Green River, WY | 1000 |
| Tenneco/Green River, WY | 1000 |
| Total | 9540 |

Table III. U.S. Sodium chlorate production capacity
(Thousands of short tons)

| | |
|---------------------|------------|
| Brunswick Chemical | 25 |
| Erco | 25 |
| Georgia-Pacific | 27 |
| Hooker Chemical | 131 |
| Huron | 11 |
| Kerr-McGee | 67 |
| Olin | 20 |
| Pacific Engineering | 6 |
| Pennwalt | 80 |
| Total | 392 |

Krebs technology should be completed by the second quarter of 1982 (82, 83).

PPG Industries, Stanchem Division, is moving IMC's Orrington, Maine, plant to Beauharnois, Quebec. The 40,000 tons per year expansion will raise total capacity at this site to 70,000 tons per year (84). The \$20 million expansion will be completed in 1981 (85).

Metals

The Federal Emergency Management Agency finally released its proposed modernization plans for the \$18.5 billion national defense stockpile of minerals and metals (86). After more than two years of work interrupted by administrative reorganization and by wild swings in commodity prices, the Agency is beginning its program cautiously, with only \$152 MM in purchases in the fiscal year beginning October 1, 1980. Purchase of significantly more aluminum, lead, platinum, tin, and titanium sponge is planned due to concerns about availability of supplies or shortages in the U.S. defense requirements. The Agency has also assured mineral producers that any divestitures would be gradual to avoid upset of market conditions.

The U.S. is not alone in the renewed concern about building stockpiles of critical minerals. Of nine Common Market countries, however, only France and West Germany have taken definite steps to ensure emergency supplies, France actually beginning in 1975.

U.S. strategic and critical stockpile goals for those metals reviewed in this report of the electrolytic industries are shown as Table IV.

Aluminum.—Primary aluminum production in the U.S. during 1980 was estimated at 10.2 billion pounds (94). Aluminum shipments in 1980 were estimated at 13.7 billion pounds, but were expected to rise to 14.1-15.2 billion pounds in 1981 (87, 88). World aluminum consumption was predicted to decrease by 5% in 1980, but demand was expected to rise slightly more in 1981, and be up by 10% in 1982 (89). World primary aluminum production rose 3.1% in 1979 to 11,785 million metric tons (95). While U.S. domestic aluminum sales were down in 1980, particularly in the first half, world demand was brisk (91).

Shipments of recycled aluminum ingot dropped to the lowest level in four years at 1,651,395 pounds (96). Alcoa, however, increased its collection of metal cans for recycling by 118%, to 2.5 billion cans or 109 million pounds (97).

Growth in aluminum consumption during the 1980's will be held back by tight supplies, high energy costs, and inadequate plant capacity (90, 93). Producers

will just about be able to keep up with the 5% rise in demand in an increasingly tight seller's market. This tightness will allow producers to pass along production cost increases and significantly increase company profits (92, 98, 100). Aluminum is predicted to be the only nonferrous base metal to be used in larger quantities in North American automobiles in the 1980's, but the amount to be used will be one-half of what was previously predicted (101).

A review of the economic aspects of the bauxite/aluminum industry cited an increasing decentralization trend. More capacity is being installed in nontraditional areas closer to bauxite sources (99).

Distribution of annual aluminum consumption to various markets in 1980 was as follows: transportation, 1.36 million tons; container/packaging, 1.695 million tons; building/construction, 1.34 million tons (103).

Noncommunist world primary aluminum production is shown in Table V (102).

Mitsui and Company's two joint ventures may make it the world's leading aluminum trader. It receives 25% of the 180,000 metric tons per year produced at Mt. Holly, South Carolina, and will receive 20% of the 238,000 metric tons per year to be produced in New South Wales, Australia, beginning in 1984.

Primary aluminum ingot was priced at 66¢ per lb at the beginning of 1980, but rose steadily throughout the year reaching 76¢ per lb in early October (105, 106).

The primary aluminum industry began 1980 with about 165,000 tons of annual capacity shut down in the Pacific Northwest (PNW) because of a power shortage. An additional 48,000 tons was shut down in March. Advance power and interruptible power were made available temporarily in April and May, and 190,000 tons of capacity was reactivated. However, curtailment of interruptible power in July and advance power at the end of September resulted in a shutdown of nearly 100,000 tons of capacity in the PNW in October. In other parts of the country, annual primary aluminum capacity in operation was reduced by a net total of over 200,000 tons during the year because of market conditions (94). By December some production was resumed in the Pacific Northwest. Alcoa restarted 78,000 short tons per year capacity idled since July 26 (107). Alcoa also announced it was bringing its 325,000 tons per year Rockdale, Texas, smelter to full capacity (108).

Apex International Alloys, Incorporated shut down its Mt. Holly, North Carolina, secondary aluminum smelter because of uneconomical costs to install EPA required pollution controls (109). A primary aluminum production plant was started up in Mt. Holly, North Carolina, by Alumax. This plant is the first grass-roots facility built in the U.S. since 1973. The \$350-million plant will produce 197,000 tons per year. The company is owned 50% by Amax, 45% by Mitsui, and 5% by Nippon Steel (110, 111).

Coastal and Offshore Plant Systems, Incorporated announced plans to build a \$400 million, 200,000 tons per year aluminum smelter near Tabor City, North Carolina (112). It received a state permit in November (114).

Table IV. U.S. Strategic and critical stockpile goals

| | New stockpile objective 5/1/80 | Old stockpile objective 10/1/76 | Stockpile inventory 9/30/79 |
|--------------------------|-----------------------------------|------------------------------------|--------------------------------|
| Aluminum | 700,000 st | 0 | 1,733 st |
| Beryllium metal group | | | |
| Beryl ore 11% BeO | 18,000 st | 0 | 17,986 st |
| BeCu master alloy | 7,900 st | 16,710 st | 7,387 st |
| Be metal | 400 st | 895 st | 229 st |
| Chromium metal group | | | |
| Cr, ferro, high carbon | 185,000 st | 236,000 st | 402,695 st |
| Cr, ferro, low carbon | 75,000 st | 124,000 st | 318,891 st |
| Cr, ferro, silicon | 90,000 st | 69,000 st | 58,356 st |
| Cr, metal | 20,000 st | 10,000 st | 3,763 st |
| Copper | 1,000,000 st | 1,299,000 st | 29,049 st |
| Manganese metal group | | | |
| Mn, ferro, high carbon | 439,000 st | 439,000 st | 599,764 st |
| Mn, ferro, low carbon | 0 | 0 | 0 |
| Mn, ferro, medium carbon | 0 | 99,000 st | 28,291 st |
| Mn, ferro, silicon | 0 | 81,000 st | 23,574 st |
| Mn, metal, electrolytic | 0 | 15,000 st | 14,171 st |
| Nickel | 200,000 st | 204,335 st | 0 |
| Titanium sponge | 195,000 st | 131,503 st | 32,331 st |
| Zinc | 1,425,000 st | 1,313,000 st | 375,947 st |

Figures compiled by *Metals Week*.
st = short ton.

Table V. Noncommunist world primary aluminum production
(000 Metric Tons)

| Region | 1978 | 1979 | 1980 |
|---------------|--------|--------|--------|
| N. America | 5,409 | 5,400 | 5,752 |
| Latin America | 413 | 664 | 836 |
| W. Europe | 3,543 | 3,620 | 3,817 |
| Africa | 336 | 400 | 452 |
| S. Asia | 385 | 368 | 520 |
| E. Asia | 1,126 | 1,074 | 1,138 |
| Oceania | 414 | 422 | 432 |
| Total | 11,626 | 11,948 | 12,947 |

Source: S. Spector of Oppenheimer & Co.

Alcoa announced plans to increase its U.S. production by 450,000 tons per year by 1985 to meet expected market requirements in aircraft and automobiles (113). Alcoa will add a 55,000 tons per year potline to its Badin, North Carolina, smelter by 1983 (115, 116).

Martin Marietta will expand its Goldendale, Washington, aluminum reduction plant by 65,000 tons per year at a cost of \$125 million (117, 118).

A \$100-million aluminum smelting plant was commissioned at Point Henry, Victoria (Australia) by Alcoa of Australia, Limited. The 65,000 metric tons per year expansion raises capacity to 165,000 metric tons per year making it Australia's largest (119).

Alcan Aluminum, Limited and Conalum SA will build a 45,000 tons per year primary aluminum smelter in Tampico, Mexico (120).

Southwire and National Steel plan to build a 180,000 metric tons per year primary aluminum smelter in Trinidad and Tobago using Jamaican bauxite (121).

Pechiney Ugine Kuhlmann plans to construct a 200,000-300,000 tons per year aluminum plant at Becancour, Quebec (Canada) for \$800 million (122).

Alcoa Alumino SA (Brazil) is building a 500,000 metric tons per year bauxite-100,000 metric tons per year aluminum smelter complex near San Luis, Brazil; at a cost of \$900 million (123).

Alcoa's new process for producing aluminum by electrolysis of aluminum chloride has proven successful, but the plant producing the aluminum chloride has had trouble. The \$25 million, 15,000 tons per year smelter in Palestine, Texas, has been cut back to 7500 tons per year. The process uses 30% less energy and produces less pollution than the conventional process (124).

An air-aluminum power cell, fueled by water, has been developed at the Lawrence Livermore Laboratory. It is claimed to increase the range of electric cars and could be commercialized by 1990 (125).

Environmental Research and Technology Incorporated has developed a mathematical model to forecast dispersion patterns of air emissions from aluminum smelters under sponsorship of the Aluminum Association (126, 127).

The U.S. Justice Department has dropped an antitrust investigation into the U.S. aluminum industry. The probe focused on whether or not a shared monopoly existed in the industry, and if price signaling had taken place. Firms involved in the investigation included Kaiser Aluminum & Chemical Corporation, Aluminum Company of America, Reynolds Metals Company, Alcan Aluminum Limited, Anaconda Company, and Phelps Dodge Corporation (128).

Beryllium.—In 1980 the domestic production of beryllium minerals increased significantly relative to 1979. The United States, a major producer of beryllium ore in the world, almost exclusively mines the ore, bertrandite, and is in fact the only nation commercially exploiting deposits of this ore (129).

Approximately 1400 short tons of beryl, the second major beryllium ore, were imported into the United States in 1980 (130). It is interesting that from 1976 until 1979 Brazil had supplied 46% of the imported ore, with India and Argentina providing a further 25%. However, in 1980, the Peoples Republic of China became a major source of this ore.

Complete data for the consumption of beryllium is not yet available but total shipments of beryllium metal, beryllium alloys, and beryllium oxide in 1980 showed a distinct improvement over 1979. Primary uses of this metal are: (i) in the aerospace industry and in nuclear reactors (38%); (ii) as an alloy in electrical equipment (37%); and (iii) in electronic components (16%) (131).

As of November 1980, the government stockpile inventories were as follows:

| | |
|-------------------------------|----------------|
| Beryl ore (11% BeO) | 720 short tons |
| Beryllium/copper master alloy | 295 short tons |
| Beryllium metal | 229 short tons |

Brush Wellman, Incorporated (Cleveland, Ohio), has announced plans to expand its facilities at Delta, Utah, at an estimated cost of \$6 MM. Completion late in 1981 will increase the plant's capacity to extract beryllium approximately 25%. A further \$5 MM is also to be invested in expansions to the mines in Juab and Millard Counties in Utah (132, 133).

In 1980 Brush Wellman, Incorporated opened a new pilot plant in Tucson, Arizona, for the fabrication and metallization of beryllium oxide parts (130).

A consortium headed by J. Abeles has acquired Consolidated Beryllium (U.K.) from Cabot (U.S.) Consolidated Beryllium is the only manufacturer of beryllium ceramics in Europe (134).

It has been shown that beryllium is an excellent substrate material for optical mirrors, according to Kawecki Berylco Industries (135). The metal resists aging, recrystallization, and phase transformation up to temperatures as high as 800°C, providing long-term dimensional stability.

A new technique to remove impurities from the surface of beryllium-containing materials has been developed by Vacuumschmelze GMBH (West Germany) (136). The company has applied the process to the production of strip-mill Beryvac (copper/beryllium and nickel/beryllium alloys) to give good surface properties, which facilitates subsequent processing.

The new limits for exposure to beryllium proposed by OSHA in 1975 have yet to be imposed upon the industry and it appears unlikely to happen in the near future (130).

Chromium.—The slow U.S. economy took its toll on chromium demand in 1980, when it reached its lowest level since 1976. The reduced demand stemmed primarily from decreased stainless steel production. Consumption of chromite was 1,040,000 tons or 14% less than in 1979. Imports of chromite were about 990,000 tons, and the balance of that consumed came from industry stockpiles (137).

Chromium alloys, on the other hand, were imported in record amounts, reaching an expected 350,000 tons. South Africa accounted for 78% of these imports. Supplies of alloys were adequate and prices rose only slightly. At year end, domestic charge chrome containing 66-70% chromium sold for 48.5¢ per lb of contained chromium and low carbon ferrochrome sold for \$1 per lb on the same basis (137). Union Carbide raised the price of electrolytic chromium metal by 9% in December (138). South African charge chrome containing 50-55% chromium was increased from 45-47¢ per lb of contained chromium to 50-51¢ per lb in December (143).

The U.S. Bureau of Mines estimates that 73,000 tons of chromium is lost in scrap every year. They are promoting a program to develop new chromium recovery methods and to determine domestic chromium supplies to avoid problems in supply if foreign sources are disrupted (139).

Zimbabwe's largest chromium mining and smelting group, Rhodesian Alloys (Pty), Limited, has gone public and is expanding its operations (140).

Toyo Soda Industries (Japan) announced an increase in chrome metal production capacity due to rising demand from high-grade alloy makers. It will increase the capacity of its Vamagata plant by 50 mtpm to 350 mtpm and add another 50 mtpm at a later date (141).

Outokumpu Oy (Finland) and Eikem Spigewerket (Norway) have signed an agreement with Turkish Etibank Company to provide equipment and engineer-

ing services to build a ferrochromium plant in central Turkey. The 100,000 metric ton addition will expand existing capacity (142).

Copper.—Production, U.S. and free world.—The strikes in the United States copper industry, which began in July and carried into late November before all companies had settled, unquestionably had an impact upon the world copper market. Obviously costly to the U.S. mining companies, the strikes did, however, offset a potentially large surplus of copper (~200,000 metric tons) and, in fact, the year end saw a deficit. It is estimated (144) that the loss of production, attributed to the 1980 strikes, amounted to approximately 350,000 metric tons of copper.

The unions struck over demands for a new three-year contract similar to the settlement negotiated by the steel industry in April. This pact provided a cost-of-living escalator that was equivalent to 30-37% wage increases over three years and the copper workers union bargained for similar considerations (145, 146). The labor strike was the longest in the history of the U.S. copper industry and at its peak immobilized most operations of ten major companies that normally account for 85% of domestic mine production and ~90% of refinery production (147).

Surprisingly, the mine production of copper in the free world declined only marginally in 1980 (144) due to significant increases in production in Canada, Zaire, the Philippines, and Mexico, and to new capacity coming on-stream in Yugoslavia. Domestic mine production decreased approximately 270,000 metric tons in 1980 according to the U.S. Bureau of Mines (147).

It was announced that Noranda (Canada) may close the 275,000 tons per year copper smelter at Rouyn in Quebec due to governmental requirements to improve collection of solid waste and install a sulfur dioxide recovery system (148). Noranda Mines Limited also suspended development of a copper mining project at Andacollo, Chile (149), a deposit estimated at 230 MM tons of ore averaging 0.56% copper.

Anaconda Copper Company will permanently close the copper smelter at Anaconda (Montana) because the 78 year-old facility cannot comply with state and federal clean air standards (150-152). Studies showed that the plant could not be "retrofitted" to satisfy the environmental standards and yet be cost-competitive with large-scale modern smelters. Similar considerations led to the closing of a refinery at Great Falls, Montana (Anaconda Copper Company) (147).

Construction began in late June on a 15,000 short tons per day open-pit copper mine and concentrating mill near Hillsboro, Sierra County, New Mexico (155). The \$98 MM development, expected to be on-stream early in 1982, is a project of the Copper Flat Partnership, comprising Quintana Minerals Corporation (Tucson, Arizona) and Phibro Mineral Enterprises, Incorporated (New York). It is anticipated that the facilities will yield 20,000 tons of copper per year when fully operational.

Noranda Mines Limited has announced its intent to develop a copper-zinc mine in Gold Stream Valley, British Columbia, Canada. Scheduled for late 1982 at an estimated cost of \$62 MM, the mine will produce 75,000 tons per year of copper concentrates (156).

Asarco, Incorporated has also announced plans to permanently close the refinery at Tacoma, Washington, which has been idle for approximately two years (147). Louisiana Land and Exploration Company plans to replace its copper smelting plant with an electrolytic facility at White Pine, Michigan (153). The 60,000 tons per year facility will be completed in 1982.

Noranda Lakeshore Mines, Incorporated has resurrected the copper mine and metallurgical complex on the Papago Indian Reservation near Casa Grande, Arizona. Currently, the company is block-caving oxide ore

at a rate of 4000 short tons per day, vat leaching 2000 short tons per day for an electrowinning plant, and stockpiling the remainder of the ore (154). Although presently working at reduced capacity, it is expected that full capacity (~6000 short tons per day) would be achieved by the end of 1980.

Consumption, U.S. and free world.—Consumption of refined copper in the United States declined 13% to an estimated total of 1.87 MM tons (147), but imports nearly tripled to a total of 0.37 MM tons for 1980.

New capacity, new facilities.—Kennecott Corporation will invest an estimated \$270 MM to modernize its facilities in Chino, New Mexico (158-160), which will increase the output to 110,000 tons per year. Under a preliminary agreement, Mitsubishi Corporation (Japan) will share the costs and receive part of the copper produced. The project also includes construction of a new concentrator and modifications to the smelting plant. The facilities are scheduled to be operational in 1984.

Copper Range Company (Denver, Colorado) has awarded a contract for \$78,000 to Fluor Mining and Metals for the construction of an electrolytic refinery in White Pine, Michigan (161). Texasgulf, Incorporated (Stamford, Connecticut) announced plans to further expand its copper smelting facility in Kidd Creek, Ontario, to approximately 112,000 metric tons per year by 1985 (162, 163). The expansion also includes new oxygen and sulfuric acid plants and will cost an estimated \$250,000.

Kennecott Corporation has started a new copper plant near Hayden, Arizona, based upon solvent extraction (SX) technology (164). The plant is expected to produce a more concentrated, high-purity copper electrolyte for the electrowinning process. Improvements in cathode quality are also anticipated. Production at the SX plant, designed by Jacobs Engineering Group for a maximum capacity of 108 short tons per

Table VI. Mine production of copper in the free world, 1978-1980 (144)
(MM metric tons)

| | 1978 | 1979 | 1980 |
|-------------------|-------|-------|-------|
| Australia | 0.22 | 0.24 | 0.25 |
| Canada | 0.66 | 0.64 | 0.73 |
| Chile | 1.03 | 1.06 | 1.07 |
| Mexico | 0.087 | 0.11 | 0.16 |
| Papua, New Guinea | 0.2 | 0.17 | 0.14 |
| Peru | 0.37 | 0.4 | 0.355 |
| Philippines | 0.26 | 0.3 | 0.32 |
| South Africa | 0.21 | 0.20 | 0.21 |
| United States | 1.36 | 1.44 | 1.17 |
| Yugoslavia | 0.12 | 0.096 | 0.13 |
| Zambia | 0.64 | 0.59 | 0.6 |
| Zaire | 0.42 | 0.4 | 0.44 |
| Other | 0.51 | 0.48 | 0.47 |
| Totals | 6.1 | 6.12 | 6.05 |

Table VII. Production and consumption of refined copper in the free world (1978-1980) (144)
(MM metric tons)

| | Production | | | Consumption | | |
|----------------|------------|-------|-------|-------------|-------|-------|
| | 1978 | 1979 | 1980 | 1978 | 1979 | 1980 |
| Australia | 0.175 | 0.174 | 0.17 | — | — | — |
| Belgium | 0.396 | 0.369 | 0.4 | 0.29 | 0.303 | 0.302 |
| Canada | 0.446 | 0.397 | 0.5 | 0.25 | 0.243 | 0.216 |
| Chile | 0.749 | 0.779 | 0.79 | — | — | — |
| France | — | — | — | 0.319 | 0.358 | 0.39 |
| Italy | — | — | — | 0.344 | 0.352 | 0.41 |
| Japan | 0.959 | 0.983 | 1.005 | 1.24 | 1.33 | 1.3 |
| Spain | 0.147 | 0.145 | 0.155 | — | — | — |
| United Kingdom | 0.126 | 0.122 | 0.150 | 0.502 | 0.499 | 0.41 |
| United States | 1.832 | 1.96 | 1.56 | 2.193 | 2.168 | 1.833 |
| West Germany | 0.405 | 0.383 | 0.38 | 0.78 | 0.794 | 0.748 |
| Yugoslavia | 0.151 | 0.138 | 0.135 | — | — | — |
| Zambia | 0.627 | 0.564 | 0.615 | — | — | — |
| Others | 0.905 | 1.06 | 1.11 | 1.298 | 1.462 | 1.511 |
| Totals | 6.918 | 7.094 | 6.972 | 7.217 | 7.509 | 7.179 |

Table VIII. Consumption of refined copper in the United States (157)
(MM metric tons)

| | Wire rod mills | | Brass mills | | Secondary copper smelters | | Totals | |
|-----------------------|----------------|------|-------------|-------|---------------------------|-------|--------|------|
| | 1979 | 1980 | 1979 | 1980 | 1979 | 1980 | 1979 | 1980 |
| Cathodes | 0.81 | 0.71 | 0.27 | 0.23 | 0.002 | 0.001 | 1.09 | 0.95 |
| Wire bars | 0.67 | 0.56 | 0.028 | 0.022 | — | — | 0.7 | 0.58 |
| Ingots and ingot bars | — | — | 0.074 | 0.05 | 0.004 | — | 0.08 | 0.05 |
| Cakes and slabs | — | — | 0.11 | 0.08 | — | — | 0.1 | 0.08 |
| Billets | — | — | 0.13 | 0.12 | — | — | 0.13 | 0.12 |
| Other | 0.013 | 0.34 | — | — | — | 0.001 | 0.01 | 0.03 |
| Totals | 1.5 | 1.31 | 0.61 | 0.51 | 0.006 | 0.002 | 2.16 | 1.85 |

day, is presently approximately 90 short tons per day. The process was developed at Kennecott's Research Center in Salt Lake City and involved selection of a proprietary reagent P-5100 produced by Acorga Limited. The final extractant is the P-5100 diluted by a high purity kerosene (164).

Cities Service Company began construction of a second solvent extraction/electrowinning plant in mid-July, the site being at the new Pinto Valley operation west of Miami, Arizona. The facility is expected to produce 99.99% copper cathode from leach solutions recovered from waste dumps at Pinto Valley, waste dumps that have accumulated for several years (165). The company's first SX-EW plant was completed in 1976 and recovers copper from leach solutions circulated in underground workings of the old Miami mine, closed in the 1950's.

Future outlook for the copper industry.—According to T. D. Barrows (Kennecott Corporation), the copper industry may be in its strongest position in several years (166) due to the present shortages in the world supplies. Although a growth rate of only 2.8% per year has been realized through the last decade, it is believed that consumption will again reach the 4-5% per year growth rate by the mid-1980's (167).

A less rapid growth is predicted by R. G. Adams (Chase Econometrics, Bala Cynwyd), but with overall optimism regarding the copper industry. Although the market may remain "tight," Mr. Adams projects that the demand for refined copper in the free world will increase to 10.4 MM metric tons per year in 1990 (168).

The U.S. Bureau of Mines believes the copper industry to be in a competitive position for the future decades (169). Production in the United States should increase to 3 MM metric tons per year by the year 2000. The financial standing of the industry will be strengthened by diversification and merger, by joint venture to defray the risks of mining projects and by an increased reliance upon the financial community. G. B. Munroe (Phelps Dodge) was similarly optimistic concerning the U.S. copper industry through the 1980's (170).

Activity in various parts of the world would support the overall optimism, with expansions, new refinery mining developments in Albania (171), Poland (172), Yugoslavia (173), China (174), Bulgaria (175), Iran (176), Peru (177), Pakistan (178), and Chile (179).

New processes, new markets.—A Montana state research agency is seeking Department of Energy (and other) funding for a pilot copper smelter to evaluate a dead roast-segregation process developed by Amax Base Metals Research and Development (New Jersey). It is claimed that the new system reduces energy consumption 33% and is significantly less expensive to construct (180).

Scientists are developing a new extraction method for copper, called electro-slurry of finely ground ore, in a cooperative program between the University of Utah, Envirotech Research Center (Salt Lake City) and the R & D Laboratories of Martin Marietta Company

(Baltimore). The technique avoids emission of sulfur dioxide and is expected to consume 25% less energy (181, 182). The University of Utah has developed a method of grinding the ore to particles of 2-3 microns and Envirotech developed the high current density electrolyzer.

Inco (Canada) is to undertake a feasibility study for a commercial-scale operation to reduce sulfur dioxide emissions from its smelting facility in Copper Cliff (183, 184). The new technology involves removal of the sulfur-rich pyrrhotite from the concentration prior to smelting.

Amax Incorporated is experimenting with a smelter process to allow production of copper-nickel at the Minnamax facility on a smaller scale than originally estimated (185). The process removes sulfur by roasting to leave a low-sulfur copper-nickel matte.

A process that converts existing copper reverberatory furnaces into oxygen flash smelters has been developed (186). While it is recognized that "oxygen sprinkle smelting" is costly to implement, it is claimed to greatly enhance plant metallurgy and economy and is an effective and cheaper way of modernizing outmoded plants.

Copper-based alloys with heat-triggered "memory" will be available on the European market in 1981. It is claimed that the memory range is from -100°C to $+100^{\circ}\text{C}$ depending upon the particular alloy (187). NV Bekaert and Metallurgie Hoboken-Overspelt (both Belgian companies) are developing the materials under the name "proteus." In the U.K. Delta Metal has formed Delta Memory Metal to manufacture approximately 600 new alloy products.

The use of copper-nickel alloys for antifouling of ships has been claimed to offer several advantages (188, 189). The cost of marine biofouling is significant and it has been shown that appreciable fuel savings can be realized by using the alloys in construction of the ships.

A new series of fine-grained, precipitation hardenable copper alloys shows an excellent combination of high strength, ductility, and good resistance to atmospheric and tap-water corrosion (190).

A. McCarthy, a physicist with General Dynamics Incorporated has developed an inexpensive method to produce Copper-65, a metal that could substitute for gold in electronics and other applications (191). The copper isotope is described as malleable, electrically conductive and more resistant to oxidation and corrosion.

Lithium.—Consumption of lithium in the U.S. during 1980 remained at about 3200 short tons. Exports of lithium products were about the same in 1980 at 2400 short tons of contained lithium (192, 193).

The U.S. continued to be the leading producer of lithium concentrates and compounds. The largest use, consuming one-third of the U.S. production, is in aluminum potlines where it is used to improve aluminum metal production. Other major applications are in glass, ceramic, and lubrication industries (192).

Year-end prices of lithium compounds were up 12% (192).

The lifting of economic sanctions against Zimbabwe has made some Li ores available which will be imported and distributed by Lithium Corporation of America (194).

Foote Mineral Company and Society Chilena de Litio Ltda (Chile) will jointly invest \$26 million by 1984 to produce 12 million pounds per year of lithium chemicals (195).

The U.S. Bureau of Mines continued bench-scale experiments to develop methods of recovering lithium from clays (192).

Further information on the role of lithium in the treatment of psychiatric disorders was discovered at the National Institute of Mental Health. Lithium helps block the shift from depression to manic phase by interfering with receptors for the neurotransmitter (196).

Magnesium.—According to the estimates of the International Magnesium Association, the worldwide production of magnesium metal in 1980 was approximately 240,000 metric tons, representing 91% utilization of the industry capacity. This is also the highest recorded production of magnesium since 1945 (197, 198).

In the United States, the production of magnesium remained strong throughout the year, although a slight decline was observed in the fourth quarter (199). According to data published by the Bureau of Mines (199), 51,000 metric tons of magnesium and magnesium alloys were exported in 1980. Imports of the metal, in all forms, totalled only 3300 metric tons.

The price of magnesium increased during 1980 to \$1.25 per lb of primary metal and \$1.21 per lb for the die-casting alloy (199).

Strong growth was observed in both the sales and production of magnesium die-castings in the U.S. in 1980. The increase, estimated to be 21% (197), was achieved without substantial contributions from the U.S. auto industry. Nevertheless, sustained growth is anticipated because of the demand for light-weight, fuel-efficient cars. In this regard, the price ratio between primary magnesium and primary aluminum, long considered to be important, is beginning to approach the 1.5:1 equal-volume price ratio.

Further growth in the total consumption of magnesium is attributed to its increased use in ferrous desulfurization products. Again, the slowdown experienced in the U.S. steel industry in 1980 has not delayed the installation of desulfurization stations in the steel mills (197).

It was announced that Amax will acquire the magnesium plant at Rowley, Utah, offered for sale by N. L. Industries. The purchase price was stated to be \$60 MM. Amax has indicated early expansions in the facility to meet the anticipated demands for magnesium, particularly by the U.S. auto industry (197, 209-212).

In South America two Brazilian plants are planned to come on-stream by the mid-1980s. The total production capability will be approximately 30,000 metric tons per year, sufficient to provide the majority of the magnesium required by Brazilian aluminum producers and steel makers and the Brazilian auto industry (197).

Norsk Hydro with an annual production of 50,000 metric tons of primary magnesium per year and the

Table IX. Production of primary magnesium, 1977-1985

| Year | Production of primary magnesium (MT)* | |
|-----------|---------------------------------------|----------|
| | World | USA |
| 1977 | 185,000 | — |
| 1978 | 209,000 | 135,000 |
| 1979 | 226,000 | 145,000 |
| 1980 | ~240,000 | ~151,000 |
| Est. 1985 | 288,000 | — |

* From References (200-202).

largest exporter of the metal in the world, has announced improvements and expansions to their facilities based on in-house R&D programs (205). The company is completing improvements in (i) the production of water-free magnesium chloride, (ii) new electrolysis technology, and (iii) new molding techniques.

Magnohrom Oour Bela Stena (Yugoslavia) has opened a 5000 metric tons per year plant at Baljevac Na Ibru, Serbia, based on magnetherm technology developed by So-Frem (213, 214). Production in 1980 was expected to reach 80% of capacity, one-half of which would be exported.

Dow Chemical (USA) will spend \$20 MM to increase the production at Freeport (Texas) to approximately 125,000 metric tons magnesium per year. A new low-energy process will be incorporated into the facility and startup is scheduled for late 1982 (215, 216).

Short-term economic concerns have delayed plans for construction of a new 24,000 MT per year plant, outlined by Chromasco Limited and expected to begin during 1980 (197). The Canadian company has continued to upgrade capacity and improve operations at its plant in Haley, Ontario, thereby increasing capacity 100% since 1975.

Near the end of the fourth quarter of 1980, the American Magnesium Company closed its primary magnesium production facility at Snyder, Texas, due primarily to the lack of brine feed (199).

Fomb/Agusta SPA (Italy), a manufacturer of helicopters, has awarded a contract to produce high performance magnesium casting alloys to Magnesium Elektron (UK). MEL has developed a range of magnesium/zirconium alloys designed specifically for the aircraft industry (218).

The levels of magnesium in "soft" drinking water have been linked to sudden death, inchemic heart disease in studies at the Down State Medical Center (Brooklyn) of the State University of New York (219). The findings indicate that a deficiency of magnesium in the water may be a factor in the disease sequence of progressive vasoconstriction, coronary artery spasm, and sudden death.

Manganese.—There was no domestic production of manganese ore containing 35% or more manganese again in 1980. Low grade ores were produced and shipped from mines in Minnesota, New Mexico, and South Carolina. More manganese was imported as ferro-alloys than as ore, although consumption of both

Table X. Consumption of primary magnesium, 1977-1985
World consumption of primary magnesium (MT)*

| Use | 1977 | 1978 | 1979 | Est. 1980 | Proj. 1985 | % Growth |
|--------------------------|--------|---------|---------|-----------|------------|----------|
| Aluminum alloys | 93,000 | 100,000 | 109,000 | 113,000 | 125,000 | 3.2 |
| Chemical synthesis | 29,000 | 31,000 | — | 32,000 | 38,000 | 3.0 |
| Die-casting | 36,000 | 32,000 | 33,000 | 38,000 | 58,000 | 8.4 |
| Nodular iron | 19,000 | 20,000 | — | 20,000 | 26,000 | 3.8 |
| Desulfurization of steel | 4,000 | 5,000 | 7,000 | 9,000 | 23,000 | 14.4 |
| Structural | 15,000 | 13,000 | — | 15,000 | 18,000 | 4.7 |

* From References (197, 203, 204, 208).

Table XI. Magnesium extraction plants in the western world (217)

| Plant | Country | Process | Capacity (MT/Y) |
|---------------------|---------|--------------|-----------------|
| Chromasco | Canada | Thermal | 12,000 |
| Sofrem | France | Thermal | 11,000 |
| Saim | Italy | Thermal | 12,000 |
| Furu Kawa | Japan | Thermal | 7,000 |
| Ube | Japan | Thermal | 55,000 |
| Showa Denko | Japan | Thermal | 250 |
| Norsk Hydro | Norway | Electrolytic | 44,000 |
| Amer. Magnesium | USA | Electrolytic | 10,000 |
| Dow Chemical | USA | Electrolytic | 120,000 |
| NL Ind. (Amax) | USA | Electrolytic | 45,000 |
| Northwestern Alloys | USA | Thermal | 24,000 |

was down. Ferromanganese imports were 20% lower than in 1979 (220).

Prices for high-carbon ferromanganese containing more than 78% manganese were from \$490 to \$530 per metric ton of alloy from domestic producers. Imported alloy of the same grade decreased from \$430-\$440 per metric ton at the beginning of the year to \$350 per metric ton by mid-summer (220). Electrolytic manganese metal increased to 70¢ per lb in December (221-223).

Some companies have complained that current ferromanganese prices are too low to attract new investment (224). Others say expansion will be limited due to lack of mineral reserves and expensive energy (225).

It has been reported that offshore deposits of manganese could supply the U.S. with all its needs (226). South Africa has 12.14 billion tons of recoverable land-based manganese ore, while Russia has 2.6 billion tons (227).

About 95% of manganese ore produced worldwide ends up in steel, while the other 5% goes into many markets, including chemicals and batteries (228).

Following an increase in demand by the uranium processing industry, Rand London Manganese Mines opened a new mine in the Transvaal which will increase production by 3000-4000 mt per month (229). Delta Manganese (South Africa) will increase manganese metal production from 20,500 to 26,000 tons per year with a \$17 million expansion (230).

Nickel.—The Bureau of Mines reported domestic mine production of nickel was 16,000 tons in 1980. Consumption of primary nickel in the U.S. decreased 15% to 165,000 tons in 1980. Total nickel consumption, including secondary nickel, was estimated at 197,000 tons (231).

Domestic production from ore mined in Oregon and nickel recovered from primary copper smelters in 1980 was about 12,500 tons. The Amax Nickel Refinery in Louisiana produced about the same amount of primary nickel in 1980 as in 1979 from imported matte (231). Low demand caused Amax to idle 15% of its 80 million lb per year capacity in September.

Weak demand for nickel resulted in Falconbridge Nickel Mines, Incorporated (Canada) shipping 54,159,000 lb in 1980 compared to 86,454,000 lb in 1979. Nickel inventories in Canada reached 155 million pounds by the end of 1980, up from 89 million pounds in 1979 (233).

Noncommunist world production and consumption of nickel were about in balance in 1980 at 1,200,000 million pounds (234).

Nickel prices were increased 25¢ per lb. This resulted in major nickel buyers holding off purchase (235). In order to stimulate purchases, major producers offered a 6% discount on nickel products in November (236). In August, mills were operating at 60% of capacity and buying 20% of the usual amount of nickel (237).

U.S. nickel consumption is expected to rise 4-4.5% per year in the 1980's and become tighter after 1985 (238). Domestic consumption in 1981 is predicted to equal that in 1980 (240). Current world nickel smelting

and refining capacity is expected to increase from the current 700,000 mtpy to 715,000-760,000 mtpy by 1985 (239-244). New applications in the defense and energy related industries should contribute to the expanding demand in the 1980's.

Inco (Canada) will spend \$15 million on process improvements to its Indonesian nickel project to try to reach its capacity of 100 million pounds. Corrosion problems severely limited production, which is expected to reach 60-65 million pounds in 1981 (245).

Nickel-SLN (France) has developed a process to produce super-refined nickel of 99.98% purity for the nuclear and aerospace industries. A 16,000 tons per year plant will be constructed to produce the material (246).

A new process for electrolytic nickel has been commercialized by Falconbridge Nikkelwerk (Norway) in a 38,000 mtpy plant. Nickel concentration in the air is kept below 0.2 mg/m² (247).

Inco (Canada) started up a 10 million lb per year expansion of its Clydach, S. Wales, smelter, raising its capacity to 120 million lb per year. The new process utilizes a fluid-bed roaster with the SO₂ being converted to sulfuric acid (248).

Cuba's plan to produce 100,000 tons per year of nickel by 1985 has been set back to 1990. Only \$26 million of a planned \$275 million have been spent and the second stage expansion will not be completed before 1984 (249).

Sumitomo Metal Mining (Japan) will partially re-equip its nickel smelter in 1982 with a resulting decrease in capacity from 23,400 to 21,360-21,600 tons per year (250).

Inco Limited is reducing sulfur dioxide emissions at its Sudbury, Ontario, nickel smelter by 25% through the installation of a \$40 million pyrrhotite flotation process. This installation will allow it to meet governmental standards by 1983. The plant capacity will remain at 280 million lb per year nickel (251). The same firm will limit SO₂ emissions at its Thompson, Manitoba plant by producing high strength SO₂ to make sulfuric acid (252).

Although lung cancers and nasal sinus cancers among nickel smelter workers may result from the carcinogenicity of the metal, they may also be caused by the presence of chrysotile asbestos in the ores. Regardless of the cause, adequate hygiene measures must be taken to prevent inhalation of dusts arising during ore processing (253).

A process for recovering nickel from low-grade domestic laterite ores has been demonstrated by the Bureau of Mines in a 5 tons per day pilot plant. The process may lead to a reduction in U.S. dependence on imported nickel, currently 93% of consumption (254).

Sodium.—Data regarding the annual production of metallic sodium for 1980 have not appeared in the usual sources. However, it has been stated (255) that the current industry capacity of 190,000 short tons is expected to meet the demand for metallic sodium over the next several years.

It is expected that due to legislative controls on automobile emissions, the use of metallic sodium in the manufacture of tetramethyl and tetraethyl lead will continue to decline. This use accounted for approximately 80% of the metallic sodium produced.

Some growth may be expected in the use of sodium to produce metallic titanium. Other uses include the manufacture of herbicides, pesticides, dye stuffs, pharmaceutical chemicals, sodium hydride, and sodium borohydride, but little growth is anticipated.

Potential new uses for metallic sodium include sodium-sulfur batteries and as a heat transfer medium in nuclear reactors (255).

Titanium.—Although the predicted decrease in orders for commercial aircraft did occur in 1980, the de-

mand for titanium metal in other areas remained strong both in the United States and in Europe. Record customer orders were placed during essentially the first three quarters of 1980 so that the increased sponge and melting capacity in the industry led to record shipments. By the end of the year, however, the decline in the aircraft industry did have an effect and lead times for titanium products were noticeably reduced (256).

The U.S. strategic stockpile goal for titanium sponge was increased to 195,000 tons because of increased requirements and limited domestic capacity. Current inventories show approximately 32,000 tons of sponge metal (258).

The published price of domestic titanium sponge was increased from \$3.98 per lb to \$7.02 per lb in July 1980. Sponge metal imported from Japan also suffered a significant price change in April 1980, increasing from \$3.60 to approximately \$8 per lb (258).

RMI Company (Niles, Ohio), jointly owned by the National Distillers and Chemical Company and U.S. Steel, has completed an expansion to the facilities in Ashtabula, Ohio, at an estimated cost of \$3.5 MM. The expansion effectively increases the company's capability to produce titanium sponge from 15 MM to 19 MM pounds annually (259).

D-H Titanium Company, a joint venture of Dow Chemical and Howmet (a subsidiary of Pêchiney-Ugine-Kuhlmann of France), began operation of a new semicommercial titanium plant this year. The plant, located in Freeport, Texas, utilizes nonconventional electrolysis technology. It has been reported that further expansion is being considered to allow production of approximately 5 MM pounds of titanium annually by 1982 (260).

IMI Titanium (Witton, U.K.) plans to double the company's present capacity to produce titanium alloy, i.e., approximately 5000 MT/year, over the next five years. The initial stage involves expenditure of \$18 MM to install vacuum-arc melting furnaces, plasma-welding units, rolling and finishing equipment (261).

Sumitomo Metal Industries, Osaka Titanium, and other members of the Sumitomo group, are considering expansion of metal titanium production. According to the announcement, an attractive site for a new titanium plant is Australia, with cheap power and an abundant supply of rutile (262). Plans are to increase titanium sponge capacity to approximately 18,000 tons per year. Osaka Titanium expects to increase its capacity to 5000 tons per year.

Billiton International, the metals subsidiary of the Royal Dutch/Shell group, is considering investment in a titanium plant in the United Kingdom. The total cost of the project is estimated to be \$75 MM with Billiton providing 60-70% (263). The other partners in this project are Rolls Royce and IMI, the former being the priority customer of the 5000 tons per year plant, to ensure supplies of the metal for aero-engine production. Courtaulds Engineering has been awarded the construction contract and the plant is expected to come "on-stream" in 1982.

Osaka Titanium has also announced plans to install a new titanium ingot furnace at its plant in Amagasaki, capable of producing ingots of approximately eight tons and capacity of 200 ton per year. The furnace

will be able to utilize scrap titanium as 10% of its feed (264).

A feasibility study has been undertaken for the construction of a \$100,000 titanium metal plant in New South Wales, Australia. General Dynamics (U.S.) is involved in this study under a 30% offset deal, since the company has recently submitted a proposal to build F-16 fighter planes for the Australian Air Force (265).

Howmet Turbine Components Corporation purchased the Whittaker titanium ingot facility in Reno, Nevada, which has been idle since 1976. This plant will supplement the melting operations in Whitehall, Michigan, and add a further 4 MM lb per year of ingot capacity (256).

Westinghouse Electric Corporation, Pittsburgh, Pennsylvania, was awarded a \$1 MM contract by the Electric Power Research Institute to compare the performance of titanium and steel blades in steam turbines (266). Preliminary studies in the 100,000 kilowatt steam turbine in Georgia have yielded encouraging results in that the titanium blade is significantly more resistant to pitting.

NL Industries, Inc has developed a new modification of its sulfate pigment process which the company calls liquid phase digestion (267). The new procedure reportedly reduces air and water emissions, lowers manufacturing costs, and will effectively expand plant capacity. The agreement to install this new production system before September 1981 was part of a settlement with state and federal authorities in regard to alleged violations of environmental regulations at the pigment plant in Sayreville, New Jersey.

In March 1980 the Department of Commerce proposed a set-aside program for titanium products, to facilitate equitable handling of defense-rated orders under the Defense Materials System and the Defense Priorities System (266). A strong negative response to the program from the titanium industry prompted its withdrawal in May.

In a civil antitrust suit, arising from a criminal case in 1979 involving a price-fixing conspiracy, four titanium companies agreed to an injunction barring price fixing, bid rigging, or the trading of price information (266). The companies involved were RMI Company, Crucible, Incorporated, Lawrence Aviation Industries, Incorporated, and Titanium Metals Corporation of America. The suit against the fifth defendant, Martin Marietta Aluminum, Incorporated, is continuing.

Focusing on new materials, automotive designers are studying improved coil springs for suspension systems. Ford has indicated that titanium springs offer a 53% savings in weight (168).

Mine production of ilmenite decreased 14% in 1980, totalling 550,000 tons (estimated) in contrast to approximately 640,000 mined during 1979 (256, 258). The only U.S. plant producing synthetic rutile, located in Alabama, was reopened during 1980, but was operating at only 70% of capacity (258).

Imports of ilmenite, predominantly from Australia, were significantly higher than in 1979 and were estimated at 320,000 tons (258). One hundred sixty-one thousand tons of natural rutile, primarily from Australia, were imported in 1980, being essentially unchanged from 1979, whereas 37% less synthetic rutile was imported.

Associated Minerals Consolidated Limited (AMC), a subsidiary of the Consolidated Gold Fields, Australia, Limited, exercised its option to purchase the assets and mining rights of the Titanium Enterprises mineral sands operation at Green Cove Springs in Florida (266). AMC expects to produce 25,000 MT of rutile, 25,000 MT of zircon, and 50,000 MT of ilmenite annually over the next 15-20 years. The purchase price was reported to be \$11.7 MM.

Table XII. U.S. titanium metal supply and demand (257)
(short tons)

| | | 1979 | 1980 |
|-----------------|----------|--------|--------|
| Titanium sponge | Imported | 2,488 | 4,777 |
| | Exported | 180 | 113 |
| Titanium ingots | Consumed | 23,937 | 26,937 |
| | Produced | 37,414 | 41,786 |
| Titanium scrap | Consumed | 35,987 | 42,477 |
| | Exported | 4,967 | 3,300 |
| | Imported | 6,140 | 4,138 |
| | | 13,986 | 15,412 |

In the light of anticipated growth in the demand for titanium chemicals, Gulf and Western Natural Resources has announced plans to expand its facilities in Ashtabula, Ohio. The cost of construction is estimated to be \$3.7 MM, completion expected in early 1982 (269).

Zinc.—Although the zinc industry in the United States experienced a severe mid-year slump, demand through the third and fourth quarters and an improved pricing forecast led to a better year than anticipated and a more optimistic outlook (270). However, uncertainty continues to surround both the automotive industry and the construction industry, particularly in light of 1980's high interest rates, and these industries are primary markets for zinc metal.

According to W. G. Weeks (Noranda Sales Corporation Limited) product research, market development and supply security must be successfully integrated for the zinc industry to move into the 1980's. The industry must recognize that it is essential to create zinc end-products that meet a need, which demands product research and market development, leading to a sound market and hence the investment to assure dependable supply (271).

Zinc demand is predicted to rise 1.5% per year through the 1980's in the free world, but this requires reduction in capacity to return the industry to profitability, according to the Commodities Research Unit (U.K.). Growth in Western Europe, U.S.A. and Japan will be less than 1.5% per year (272). World capacity for the production of zinc is shown as Table XIII.

The zinc industry in Western Europe may be required to increase exports or alternatively to reduce capacity (274) in order to maintain profitable operations. Although consumption of zinc in the developing countries has increased at approximately 8% per year for several years, these markets are dominated by Canada. Furthermore, the developing countries are themselves expanding smelter capacity. Ironically, the smelters in Western Europe are highly modernized and among the best and most economic producers of zinc in the world.

The opening of a new mine and the absence of strikes in 1980 appear to be factors that contributed to an estimated annual mine production of 310,000 metric tons, an increase of approximately 20% over 1979 (275). In contrast the primary production of zinc metal declined to 350,000 metric tons, decreasing 25% from 1979 production levels. World-wide shortages of

the zinc concentrates may have been a major factor in the curtailment of production (275) although several plant closings also occurred.

Consumption of zinc decreased 15% in 1980, probably due to the reduced activity in the automotive and construction industries (275). The major uses for slab zinc and estimated consumption in 1979 and 1980 are shown as Table XIV.

New Jersey Zinc Company, a unit of Gulf and Western Industries, announced that it will close its zinc smelting operation in Palmerton, Pennsylvania, including the zinc ore roasting, sulfuric acid and vertical retort facilities. Production of zinc oxide will be maintained however (275,277). Reasons cited for this decision were the decreased demand for zinc and rapidly rising production costs (278).

St. Joe Zinc (Pittsburgh), a division of St. Joe Minerals Corporation, closed the 250,000 tons per year electrothermic zinc smelter in Monaca, Pennsylvania, at the end of 1979 (279,280). The primary reason cited was the failure of the domestic zinc industry to gain relief from excessive imports of slab zinc. After preliminary studies of designs for a new 120,000 tons per year electrolytic zinc refinery, St. Joe decided not to replace the Monaca smelter (281,282). It was also announced (283) that negotiations for long-term purchases of 20,000 tons per year of zinc ingots were ongoing between St. Joe Minerals and several Japanese companies.

Citing poor market conditions, Jersey Miniere is planning to reduce production at the 90,000 short tons per year zinc refinery in Clarkesville, Tennessee, to approximately 40% of its capacity (284). Development work at the company's zinc mine at Gordonsville, Tennessee, will also be curtailed.

Japanese zinc smelters have efficiently reduced their energy consumption by (i) use of nighttime electrical power, (ii) recycling of hot gases, and (iii) introduction of new technology (285). However, it is expected that production will be reduced approximately 5% (i.e., 40,000 tons per year) due to escalating power costs which already account for 60% of smelter revenues (286).

Preussag AG (Hanover, West Germany) announced plans to reduce capacity at the 100,000 tons per year zinc plant at Harz to allow the necessary modifications to be made to the facility to meet the stricter regulations governing air pollution (287).

STE Industrielle de Prayon (Belgium) announced that production of zinc ingots at the Ehein Electrolytic plant will be stopped due to the high cost of zinc concentrates and depressed prices in the zinc market (288). The plant had an annual capacity of 35,000 tons.

St. Joe Minerals expects to develop a recently discovered ore-body at Pierrepont, New York (275,289). It is estimated that approximately 2.5 million tons of zinc ore (15% metal) may be realized from this deposit.

Bechtel (Canada) announced that it has been commissioned by Cominco Limited to design and construct a mine on Little Cornwallis Island (Northwest Territories) to produce ore containing 14.1% zinc and 43% lead. The size of the reserve will make the mine at least the 11th largest producer in the world (290).

The historic Broken Hill mining district in western New South Wales (Australia) is the scene of an exploration program estimated to cost \$11 MM over the next five years (291). Australian Mining and Smelting Limited, a wholly owned subsidiary of Conzinc Riotinto of Australia, decided to intensify its efforts to establish sufficient reserves to supply smelters in South Australia and New South Wales into the 21st century.

Allied Metal Company (Chicago, Illinois) has begun operation of a new zinc smelter to increase plant capacity to approximately 20 MM tons per year. The ex-

Table XIII. World zinc capacity (273)
(metric tons)

| | Nominal capacity 1980 | Production capacity 1980 | Nominal capacity 1985 |
|---------------|-----------------------|--------------------------|-----------------------|
| Europe | 2,325,000 | 2,000,000 | |
| Africa | 275,000 | 235,000 | 275,000 |
| Canada | 633,000 | 605,000 | 663,000 |
| U.S.A. | 613,000 | 557,000 | 240,000 |
| Mexico | 200,000 | 180,000 | 345,000 |
| South America | 193,000 | 160,000 | 325,000 |
| Australia | 325,000 | 310,000 | 295,000 |
| Asia | 205,000 | 158,000 | 295,000 |
| Japan | 1,000,000 | 900,000 | 1,000,000 |
| Totals | 5,769,000 | 5,106,000 | 6,301,000 |

Table XIV. Consumption of slab zinc in the United States (276)

| End use | 1979 Consumption (metric tons) | 1980 Consumption (metric tons) |
|------------------|--------------------------------|--------------------------------|
| Galvanizing | 411,200 | 345,100 |
| Brass and bronze | 139,000 | 96,400 |
| Zinc-base alloys | 282,400 | 208,300 |
| Rolled zinc | 22,000 | 22,000 |
| Zinc oxide | 35,500 | 29,860 |
| Other | 28,900 | 25,000 |
| Totals | 919,000 | 826,660 |

pansion is estimated to have cost \$200,000 and included installation of electronic controllers to monitor smelting operations (292).

Pacific Smelting Company has announced plans to construct a 10,000 tons per year zinc refinery in Memphis, Tennessee, based on muffle furnace technology. Completion of the project is expected to be late in 1981 (293).

A zinc plant owned by Cia Mineira de Metars (Brazil) became operational during the fourth quarter of 1979 (294). The plant has the capability to treat 500 tons per day of dry zinc ore in a large rotary furnace.

Hindustan Zinc Limited has undertaken a \$13 MM improvement program at its smelting facilities at Debari. When completed early in 1983, zinc output capacity will be approximately 48,000 tons per year (295).

In September 1980, St. Joe Minerals reopened part of the smelter at Monaca, Pennsylvania, to produce French-process zinc oxide and prime western zinc, with a combined capacity reported to be 50,000 short tons per year (270).

The zinc output in Peru is expected to be increased to 130,000 tons per year in 1981 when operations at the new refinery at Cajarnaquilla begin (296).

Bunker Hill Company (Kellogg, Idaho) became the first domestic primary zinc producer to market zinc foundry alloys and is presently posting prices for three alloys (297). The emerging market for zinc as a foundry alloy affords the industry an opportunity to market aggressively. Bunker Hill has announced its intention to work closely with customers to develop applications. Texasgulf has announced its entry into this market (298) predicting that it could reach 385,000 tons within the next decade.

The zincex process for recovery of zinc from leach liquors has been incorporated into Metalquimica Del Nervio SA's plant at Bilboa, Spain, and into a new 11,000 metric tons per year plant in Lisbon, Portugal (299).

The Electrical Industry

The energy future.—A five-year overview and strategy summary recently published by the Electric Power Research Institute (EPRI) strikes a somber note regarding the energy future in the United States (300):

"The issue is not a choice of conservation or coal or nuclear or renewable resources: rather it is our willingness to use conservation and coal and nuclear and renewable resources. We do not enjoy the luxury of selecting from these alternatives, we must utilize all of them."

The document is a summary of a more detailed study and the present focus of the Institute is clearly upon technological developments with anticipated pay-off within the next decade. It is pointed out that without expansion of the supply of electricity some areas of the nation may experience severe shortages of power over the next twenty years.

The report predicts the development of a "coal economy," demanding a two or threefold increase in the production of coal in less than twenty years. The electric utilities will consume approximately 70% of that coal by the year 2000. But even with this objective being realized, EPRI regards nuclear power generation as a matter of necessity (300).

A similar viewpoint was expressed by D. Schauster of the Bonneville Power Administration (301), who stated that there will be limited supplies of electrical energy during the 1980's at significantly increased cost to the consumer. In his opinion, it is unlikely that alternative sources of energy will be capable of relieving this situation until the end of this century. With particular references to the Pacific Northwest,

Mr. Schauster cited mounting costs and regulatory obstacles as the major hurdles confronting the utilities in their efforts to establish new power stations. Additional generating capacity could cost 3-5 times as much as it did in the 1970's. Similar concerns were expressed by the aluminum makers, chemical companies, and forest-product companies (302).

The situation is further aggravated by the fact that construction of nuclear power plants may not occur without speedier licensing and higher power prices (301). Presently, it is estimated that approximately 33% of the cost of the new nuclear plants stems from construction delays. The uncertain growth of nuclear power generation and the concerns of the general public with respect to the environment and safety, may be reflected in the federal energy budget for the fiscal year 1981 (303). Here funding for the development of nuclear fusion technology has been reduced 22%.

Marshall McDonald (Chairman of the Board and Chief Executive Officer, Florida Power Light Company) believes that a major problem facing the electric utilities today is to convince the general public that there is an energy crisis (304) and that the solution will not be cheap.

A somewhat more optimistic outlook was expressed in a report produced by the American Petroleum Institute (API), which stated that the United States ought to be "in good shape" by 1990, if appropriate decisions are made now (305). The opportunities available, according to the API report, include the development of coal and nuclear programs, effective changes in the current environmental laws, and deriving more energy from federal lands.

The World Coal Study, an international project involving over eighty people from sixteen major coal-using and coal-producing countries, concluded that,

"A massive effort to expand facilities for the production, transport, and use of coal is urgently required to provide for even moderate growth economically in the world between now and the year 2000. Without such increases in coal, the outlook is bleak." (306).

Power generation in the United States.—The economy, the weather, and conservation were three forces that impacted upon usage of electrical power in the United States in 1980. The predicted recession for the year became a serious depression, significantly worse than the downturn experienced in 1974-1975. On the positive side for the utilities a long, hot summer with record-breaking temperatures led to high demands for electricity. Through all of this, the consumer, facing high rates of inflation, was forced to "conserve" wherever possible in order to match income and expenses.

Sales of electricity in 1980 totaled 2097 billion kW-hr, which represents an increase of only 1% (307) but higher than forecast (308). A 2.7% decrease in sales to industry was offset by the increased sales to residential customers, 4% vs. 2.1% in 1979 (Table XV).

Revenues accumulated by the electric utilities increased approximately 18% to \$91.7 billion in 1980 with increases of 16, 18, and 20% being realized from sales to industrial, residential, and commercial customers,

Table XV. Electric utility sales, 1978-1980 (307)
(Billions kW-hr)

| | Residential | Industrial | Commercial | Other | Total |
|-----------|-------------|------------|------------|-------|--------|
| 1978 | 679.2 | 782.1 | 480.7 | 75.8 | 2017.8 |
| 1979 | 693.8 | 813.6 | 494.4 | 75.9 | 2077.8 |
| 1980 | 721.1 | 791.6 | 509.8 | 74.4 | 2097 |
| % Change | | | | | |
| 1978-1979 | +2.1 | +3.8 | +2.7 | — | +2.85 |
| % Change | | | | | |
| 1979-1980 | +3.9 | -2.7 | +3.0 | — | +1.0 |

Table XVI. Average annual use, electric rate, and utility bill 1978-1980 (307)

| Year | Residential | | | Industrial | | | Commercial | | |
|------|------------------|---------------------|-----------------------|------------------|---------------------|----------------------|------------------|---------------------|-----------------------|
| | Avg. use (kW-hr) | Avg. bill (¢/kW-hr) | Avg. annual bill (\$) | Avg. use (kW-hr) | Avg. bill (¢/kW-hr) | Avg. annual bill (%) | Avg. use (kW-hr) | Avg. bill (¢/kW-hr) | Avg. annual bill (\$) |
| 1978 | 8,849 | 4.03 | 356.7 | 1,702,939 | 2.59 | 44,156 | 53,085 | 4.1 | 2,177 |
| 1979 | 8,828 | 4.33 | 382.1 | 1,709,997 | 2.85 | 48,812 | 53,249 | 4.39 | 2,337 |
| 1980 | 8,973 | 4.93 | 442.3 | 1,657,317 | 3.41 | 56,464 | 53,640 | 5.1 | 2,733 |

respectively (307). The sharp rise in the revenues is attributed primarily to the increased power rates granted to the investor-owned facilities.

The conservation of energy by the residential customer seen in 1979 was not maintained in 1980, due probably to the long, hot summer. As is seen in Table XVI the average power usage increased 1.6% to 8973 kW-hr and the cost jumped 0.6¢ to set a new post-World War II high of 4.93¢ per kW-hr (308). In all, then, the average residential bill increased almost \$60 over that of 1979.

In the five-year period since the end of 1975, the average residential usage has increased only 10%, but the rate has increased 50% and the average bill approximately 70% (307).

Repeated pleas for increases in the power rates appeared to be the utilities' defense against inflation, according to the *Wall Street Journal* (309). Hit hard by soaring costs of construction, fuel, and capital, the first half of 1980 saw approximately 86 utilities file requests for rate increases. From figures released by Ebasco Business Consulting Company (307), 97 utilities were granted \$5.67 billion in rate hikes in 1980, an increase of 24% from 1979. A further 70 applications are pending (Table XVII).

Similarly, Edison Electric Institute reports \$5.93 billion in rate increases in 1980 as an "improvement in the attitudes of state commissions towards the utilities" (307).

Generation capability for the electrical utilities increased 2.7% during 1980 and, based on data from DOE's Energy Information Administration, the year-end capability of all U.S. utilities was 613,582 MW compared with 597,523 MW as of December 1979. The consumption of the various fuels (Table XIX) shows approximately an 8% increase in the use of coal to generate electricity and as in 1979, there was a significant decrease in the amount of oil used.

Table XX, energy generated by fuel type, illustrates the marked, and accelerating, trend towards fossil fuels and the dominance of coal in this category.

Projected capability beyond 1981 is presented as Table XXI.

Capital expenditures primarily for generation, transmission, and distribution of electricity in the United States were \$35.9 billion, which, compared with 1979, was essentially without growth, contrary to a projected increase of approximately 8.6% (307). A sluggish economy, reduced forecasts for load growth, and a poor financial picture were thought to have held down utility spending. The biggest change in capital expenditures between 1980 forecast and actual 1980 figures occurred in the area of municipal, state, and public-power-district system. Actual spending for this segment of the industry was off 60% from the estimated figures. It is added, however (307)

Table XVII. Electric rate increases 1978-1980 (307)

| Year | Granted | | Pending 12/1980 | |
|------|---------------|---------|-----------------|---------|
| | No. companies | \$ MM | Applications | \$ MM |
| 1978 | 73 | 2,362.7 | 59 | 3,458.9 |
| 1979 | 80 | 4,567.0 | 70 | 4,715.4 |
| 1980 | 97 | 5,677.0 | 70 | 7,381.0 |

that the forecast was highly uncertain due to limited information.

Energy from fossil fuels.—Over the last four to five years, approximately 70% of the power generated in the United States has utilized fossil fuels (see Table XVIII), and as stated earlier, a substantial decrease in the consumption of oil by the electrical utilities was maintained through 1980.

With respect to capability beyond 1980, planned addition would utilize fossil fuels to generate 46.7% of the electrical power (see Table XX).

Coal gasification.—The Department of Energy has given conditional approval for a \$250 MM loan guarantee to partly finance construction of the Great Plains coal-gasification plant to be built near Beulah, North Dakota (310, 311). A consortium of five gas-pipeline companies, led by American Natural Resources Company of Detroit, expects to begin construction by the end of the year with the complex becoming operational in 1984. The plant is designed to produce 125 MM cubic feet of high-Btu gas per day, which is equivalent to 20,000 barrels per day of fuel oil.

Table XVIII. Energy generated and source 1978-1980 (307) (Billions kw-hr)

| | Coal | Oil | Gas | Nuclear | Total |
|--------------------|--------|-------|-------|---------|--------|
| 1978 | 976.6 | 364.2 | 305.4 | 276.4 | 1922.6 |
| 1979 | 1075.6 | 303 | 329.5 | 255.2 | 1967.6 |
| 1980 | 1161.2 | 245.8 | 345.9 | 251.1 | 2009.6 |
| % Change 1978-1979 | +10.1 | -17 | +7.9 | -7.6 | +2.1 |
| % Change 1979-1980 | +8 | -19 | +5 | -1.6 | +2.2 |

Table XIX. Fuel consumption by the electrical industry (307)

| | Coal | Oil | Gas |
|--------------------|------------|------------|---------------|
| | MM of tons | MM barrels | MM cubic feet |
| 1978 | 481.6 | 635.8 | 3188.4 |
| 1979 | 527.3 | 523.3 | 3490.5 |
| 1980 | 569.4 | 421.3 | 3679.7 |
| % Change 1978-1979 | +7.3 | -17.6 | +9.4 |
| % Change 1979-1980 | +8.0 | -19.5 | +5.4 |

Table XX. Electric power industry capability, MW (307)

| Fuel type | Total capability Dec. 31, 1980 | | Capability additions 1981 & beyond | | Totals | |
|---------------------|--------------------------------|------|------------------------------------|------|---------|------|
| | MW | % | MW | % | MW | % |
| Hydro* | 76,351 | 12.4 | 16,324 | 8.0 | 92,675 | 11.3 |
| Fossil fuel | 424,524 | 69.2 | 95,480 | 46.7 | 520,004 | 63.6 |
| Nuclear | 56,526 | 9.2 | 89,400 | 43.7 | 145,926 | 17.8 |
| Internal combustion | 5,540 | 0.9 | 117 | 0.1 | 5,657 | 1.0 |
| Combustion turbine | 50,642 | 8.3 | 3,186 | 1.5 | 53,828 | 6.4 |
| Total industry | 613,582 | | 204,507 | | 818,089 | |

* Includes Pumped Storage.

Table XXI. Commercial applications of solar energy

| Company | Application | Energy savings Btu/year |
|--------------------------------------|--------------------------|----------------------------|
| Campbell Soup (Sacramento) | Can washing | 1.8 Billion |
| Johnson & Johnson (Sherman, TX) | Bleaching, sterilization | 1.5 Billion |
| Lamanuzzi Foods (Fresno, CA) | Food drying | 1.0 Billion |
| Reedy Creek Utility (Florida) | Air conditioning | 800 Million |
| Gold Kist (Decatur, AL) | Soy bean drying | 800 Million |
| Anheuser-Busch (Jacksonville, FL) | Pasteurization | 500 Million |
| Riegel Textile (La France, SC) | Dyeing | 400 Million |

Northern Resources are considering the construction of a coal gasification plant in Billings, Montana, to produce approximately 19 MM cubic feet of medium-Btu gas per day. The Department of Energy may oppose the company's request for a grant to conduct a feasibility study, forcing Northern Resources to seek private financing (312).

The initial results from the underground coal gasification studies conducted in northeast Wyoming during 1979 are considered to successfully demonstrate the feasibility of *in situ* coal conversion (313). The project is sponsored by the Department of Energy and the Gas Research Institute. The final experiments in the so-called Deep-1 series will begin in the third or fourth quarter of the year and will be a study of the Uniwell gasification method, designed specifically for the coal common to western U.S.A.

Two U.S. energy companies will undertake a one-year feasibility study of an underground lignite gasification project in Texas. Following the award of a grant from the Department of Energy, Mitchell Energy and Development and Republic of Texas Coal will investigate controlled *in situ* gasification of lignite too deep to be mined economically (314).

Panhandle Eastern Pipe Line Company has a preliminary agreement to become partners with Pacific Gas and Electric Company, San Francisco, and Ruhr-gas Aktiengesellschaft, Essen, West Germany, in its Wyoming coal gasification project (315).

A 15-month study has been initiated that may result in the first commercially sized coal gasification power plant (316). Central Maine Power Company, under a \$3.5 MM grant from the Department of Energy, will examine the feasibility of integration of a large coal gasification plant with combined cycle (gas turbines and steam turbines) power generation. Located at Sears Island, Maine, the proposed plant would combine Texaco's coal gasification technology and General Electric's combined cycle technology. Two other studies for the design of integrated coal gasification/combined cycle power plants that could be in operation in 1981 have also been funded (317).

During the third quarter, the Tennessee Valley Authority began trial operations of a fully integrated coal gasification plant (318, 319). Located at Muscle Shoals, Alabama, the plant has utilized Texaco's partial oxidation technology, and the cost of the unit is estimated to be \$43 MM with an additional expenditure of \$20 MM for further trials over the next three years.

In Europe, Esso Nederland has revealed details of the Exxon technology to be utilized in a coal gasification complex planned for construction at its Rosenberg site (320). It is claimed that the catalytic process shows significant cost advantages. The National Coal Board (U.K.) is considering designs of a plant estimated to cost approximately \$2 billion, which is expected to process 2000 tons of coal per day (321).

Coal liquefaction.—The Energy Department and Occidental Research have jointly developed a process to liquefy coal at pressures significantly lower than those employed by several advanced liquefaction processes (322). The method is based on flash pyrolysis to rapidly heat the coal at atmospheric pressures in a chamber filled with an inert gas. Under a new \$4.5 MM contract, Occidental Research Laboratories in Irvine, California, will begin bench-scale trials of the process.

Exxon has successfully started up its coal liquefaction pilot plant at Baytown, Texas. The plant, estimated to have cost \$118 MM, is currently using approximately 100 tons of coal per day. Operations over the next two to three years is expected to provide data on plant and equipment design, product quality, and engineering scale-up (323).

A comparison of several leading liquefaction processes indicates that the lowest cost energy, \$3.13 per million Btu, is produced by the Dow process. By way of comparison, the energy cost stated for imported oil (at \$25 per barrel and 5.8 MM Btu per barrel) is \$4.51 per million Btu (324).

Preliminary results from continuing work by C-E Lummus, under contract with the U.S. Department of Energy, indicate that the company's advanced two-stage process can deliver higher liquid fuel yields, with lower hydrogen consumption and good catalyst performance (325, 326). The process development unit is being operated at the company's engineering development center in New Brunswick, New Jersey.

The initial coal processing phase of a large experimental coal liquefaction plant has been initiated according to Ashland Synthetic Fuels, Incorporated, a unit of Ashland Oil, Incorporated (327). A formal experimental program is expected to continue through 1981 using various types of coal. When operating at peak capacity, the plant is designed to process approximately 600 tons of coal per day to produce 1800 barrels of synthetic product.

Four companies of the Mitsubishi group in Japan claim to have improved their coal liquefaction process, recycling liquefied coal rather than using asphalt or other residual oils as the hydrogen donor (328). A pilot plant is already in operation and a second unit is under construction at the Mitsubishi Heavy Industries research center in Hiroshima.

The National Coal Board in the U.K. has completed designs for a coal liquefaction plant to be built at the Point of Ayr colliery in North Wales. The plant, the only coal liquefaction project that would be operating in the U.K., will use a process developed by the Coal Board in cooperation with British Petroleum (329).

Two major coal liquefaction plants are planned for construction in Victoria, Australia (330). Both plants will be joint ventures, one with Japanese companies and the other with West German interests. Both plants will utilize the brown coal mined in Victoria.

With both coal gasification and coal liquefaction processes advancing rapidly, the need for materials and equipment able to withstand particularly severe operating conditions becomes more urgent (331). The new technologies operate at higher temperatures and pressures than commercial, first-generation processes such as the modified Fischer-Tropsch synthesis used in South Africa by Sasol. Process designers have expressed concern about the lack of suitable equipment, but remain optimistic about early solutions to the problems.

Shale oil.—According to Exxon officials, the OPEC price increases in 1980 make shale oil competitive with imported oil (332, 333). Furthermore, the U.S. synthetic fuels potential is significantly larger than the domestic proven and undiscovered oil and gas reserves. It was claimed that there are 1.4 trillion barrels of

shale oil in the ground that an estimated 580 billion barrels could be recovered by surface mining. The U.S. shale oil and coal reserves were estimated to be capable of yielding 15 MM barrels of oil per day by the year 2010.

This optimistic view was not shared by D. Roger Loper, president of Chevron Shale Oil Company. Depending on rates of inflation, the cost of bringing a large facility "on-stream" may cost approximately \$7 billion. However, forty companies have invested in the development of shale oil (333), ultimately providing a combined capacity of approximately 715,000 barrels per day within the next decade. The present pace of development is gradual, but with recent indications of an acceleration.

A study made by the Office of Technology Assessment is believed to lend credence to fears in the western United States that rapid development of the shale oil industry would create severe social and economic problems (334). However, the conclusion drawn from this study is that the capability to produce 400,000 barrels per day by 1990 can be achieved, allowing substantial technical, environmental, and economic information to be generated and reducing the socioeconomic impact.

Under the sponsorship of the Department of Energy, ten companies will work jointly on design and demonstration of a commercial-size facility to produce oil from Utah shale oil (335). The group, the Paraho Development Corporation, will require approximately eighteen months to plan and design a single, above-ground retort and the support facilities.

According to preliminary statistics developed by the Department of Energy, approximately 1000 billion barrels of oil could be found in the predominantly coal-rich fields of Kentucky, West Virginia, and Ohio (336). However, leading analysts have stated that because of low oil yields, the cost of extracting the oil would approach \$40-50 per barrel, significantly higher than western shale oil.

A dispute over endangered fish appears to have delayed development of the White River oil shale project in Utah (337). The project is a joint venture of Phillips Petroleum, Sun Oil, and Standard Oil of Ohio. The Bureau of Land Management requires a decision from the Fish and Wildlife Service on the possible dangers to three species of fish caused by construction of a dam on the White River.

Energy from nuclear fuels.—For several years, advocates of nuclear power have had little to become excited about. Since 1975 only thirteen new nuclear power plants have been ordered in the United States, while plans for fifty plants have been canceled (338). Executives of utilities and companies that supply the nuclear power plants are presently optimistic that the new Reagan administration will be more helpful than its predecessor. It is believed (338) that the utility industry will press for changes in the Nuclear Regulatory Commission, particularly to ease "red tape" with respect to licensing. Delays have increased construction costs excessively.

The industry's most difficult obstacle may be the financial aspects (338). Cost overruns engulf almost every nuclear project. For example, a plant in Michigan is projected to cost \$3.1 billion to construct, almost ten times the original estimate. With the slower growth in the demand for electricity, the utilities today have less capability to generate cash internally and outside investors are reluctant to provide the vast sums of capital required.

It was recently reported (339) that over the last three decades the federal government has subsidized the growth of commercial nuclear power to a level of \$37 billion. This included support for initial research on nuclear reactors, supply of uranium fuel, produc-

tion incentives for uranium miners, assistance to equipment manufacturers, and nuclear waste-disposal techniques.

Extensive analysis of the plant at Three Mile Island and of the accident which occurred there revealed the importance of several chemical processes and operations used at nuclear power plants (340). The initiating event, the unfavorable thermodynamic conditions for the reactor coolant during the accident, the zirconium-water reaction (which proved to be the most damaging occurrence), and the misunderstanding surrounding the "hydrogen bubble" could have been avoided or mitigated. However, the chemical industry and the utilities may benefit from the information now available to improve safety standards, operator training, emergency procedures, instrumentation and control philosophies in the design and operation of plants (340, 341).

The Nuclear Regulatory Commission concluded that existing methods are adequate for the decontamination and clean-up of Unit 2 at the Three Mile Island nuclear power plant. It is anticipated that only very small releases of radioactivity will result (342).

General Public Utilities Corporation, owners of the utility that operates Three Mile Island power plant, has estimated that the cost of clean-up will be \$855 MM with restoration of full service not likely before 1985 (343). GPU is asking other utilities and the federal government for assistance.

After a series of false starts, venting of krypton-85, trapped inside the crippled reactor at Three Mile Island since March 28, 1979, began June 30, 1980. Traces of radioactivity were detected by monitors on an observation platform overlooking the facility and on a nearby island in the Susquehanna River. However, federal officials stated that there was no danger to public health (344).

The Nuclear Regulatory Commission has allowed the Virginia Power Company to bring its nuclear power plant at Mineral, Virginia, to full power (345). The action came after the Commission had reviewed the results of an emergency drill conducted by the company and the Federal Emergency Management Agency. Since the moratorium against new licenses, the Agency has allowed two other facilities to begin low-power tests.

Electrical failure in a nonnuclear instrument panel closed down Unit 3 of Florida Power Corporation's nuclear power plant at Crystal River (346). All safety systems worked as specified and no leakage of radioactivity occurred.

The Tennessee Valley Authority decided against further deferrals of nuclear units and four projects, totaling 5200 MW, will be undertaken (347). TVA has three nuclear units on-line at Brown's Ferry and has plans for fourteen other plants into the 1990's. A major reason for the action is the latest estimates of the growth in demand through the year 2000 and the likelihood of "brown-outs" in the near future.

The Department of Energy's original plan for disposing of high-level nuclear waste by sealing it in underground repositories, has foundered on the fact that geology is not a predictive science. This inability to guarantee the stability of such repositories for at least a thousand years has forced a major shift in the approach to the problem of nuclear waste. Presently, the DOE is stressing the concept of multiple "engineered" barriers. The world's most advanced program of research on engineered barriers is the Swedish project KBS (348).

A new technique that disposes of low-level radioactive liquid wastes from nuclear power plants has successfully passed pilot plant tests. The Inert Carrier Radiowaste process, developed jointly by Norden Systems' Chemical Systems Division (Coyote, California)

and General Electric, reduces the volume of wastes approximately 90%. The wastes are then encapsulated in an impermeable plastic (349).

Nuclear waste disposal experts at Tennessee Valley Authority will spend \$750,000 in 1981 to study several dry disposal methods that involve above- and below-ground safekeeping (350).

Energy from other sources.—Batteries, fuel cells.—A Management Review Task Force established by the Department of Energy has recommended increased spending on fuel cell technology for commercial use in 1986-1987 (351, 352). Present programs, having a five-year accumulated cost of approximately \$130 MM, consist of field tests at fifty sites with natural gas companies (40 kW units), a 4-8 MW demonstration plant at Con Edison in New York City, and the research and development in molten carbonate systems with General Electric and United Technologies.

Hitachi (Tokyo) has developed a prototype methanol fuel cell that is expected to become commercial in 3-5 years. Recent developments incorporating a platinum-ruthenium catalyst have enabled the cell voltage to be increased to 12V, using 50% methanol solutions and air as the feed streams. Estimated cost of power produced by the unit is \$47.60 per watt (353).

Gulf and Western Industries announced the development of a zinc-chlorine energy storage system designed to meet peak electricity demand in electric utilities and to make electric vehicles a reality (354, 355). Under development since 1972, testing has shown that the system now has lower cost, longer life and superior performance as compared to the lead-acid or nickel-zinc systems. By mid-1981, Gulf and Western will deliver the first one hundred units to a test facility near Hillsboro, New Jersey.

NASA has announced that a redox fluid battery system is ready for large-scale development (356). Industry has been requested to submit proposals for a multi-kilowatt prototype, scheduled for field tests in 1983. Recent improvements have enhanced the performance of the redox battery so that it is compatible with solar photovoltaic and wind energy storage applications.

Recent discoveries at the General Motors Research Laboratories have encouraged efforts to utilize the lithium electrode in the development of low-cost, long-life rechargeable batteries (357).

A promising battery system for vehicle propulsion has been successfully tested at Lawrence Livermore Laboratory (358-360). Based on aluminum-air electrodes, it is claimed that eventually the battery will be capable of operating in automobiles at a cost comparable to gasoline. A 300 mile range could be achieved by a 60 cell battery, weighing approximately 1000 lb, whereas the same weight of lead-acid cells could power a car for only 30 miles (360).

Construction of the world's largest storage battery, a lead-acid unit to be used as a load-leveling device, has been undertaken by the Wolverine and Northern Michigan Utilities (361). Made up of 2280 cells, the unit will weigh 5.25 MM lb and be able to supply 10 MM watts of power for three hours. The estimated cost of this unit is \$8.5 MM.

The Environmental Protection Agency has proposed standards for control of air pollution to limit levels of lead emitted by lead-acid battery manufacturers in the U.S. (362). The new standards will affect approximately 200 plants.

General Motors Corporation, the only major U.S. automaker currently developing electric cars, has postponed the introduction of its battery-powered commuter car until 1985, a one-year delay from the original target date (363). A company spokesman indicated that it had been determined that the new technology required additional development time.

Thermonuclear fusion.—Thermonuclear fusion occurs when a mixture of hydrogen isotopes (deuterium and tritium), heated to extremely high temperatures and pressures, form heavier helium atoms with the release of large amounts of energy. It presently is believed that fusion may be achieved either by inertial confinement or by magnetic confinement (364). Opinion is that commercialization of thermonuclear fusion will occur through use of magnetic confinement techniques.

A 20 year, \$20 billion research and development program to establish a magnetic fusion test facility by 1987 and a demonstration plant in the year 2000, was overwhelmingly approved by the House (365). The bill now moves to the Senate, presently considering its own significantly more modest bill to fund development of this technology.

Studies at Oak Ridge National Laboratories have identified beams of higher power that can be an integral part of the heating systems in magnetic confinement fusion devices (366).

The Elmo Bumpy Torus fusion concept, combining some of the best features of the Tokamak and magnetic mirror machines, will be tested at Oak Ridge, Tennessee, according to the Department of Energy (367). The new experimental facility will be built and operated by McDonnell Douglas Astronautics Company (St. Louis). The contract was reported to be approximately \$100 MM (368).

Geothermal.—According to the U.S. Geological Survey, (369) the western United States and Canadian Cascade Mountain range could produce thermal energy as well as volcanoes. Under favorable conditions, it is possible to drill and tap energy in subterranean reservations and produce steam to drive a turbine. A special Congressional appropriation is helping to support research to determine the area's geothermal potential.

Presently, "The Geysers," approximately forty miles north of San Francisco, is the only site in the U.S. where electricity is being generated commercially from geothermal energy (369). The generating capacity installed at The Geysers is 663 MW, sufficient electricity to support a city of about 700,000 people.

Construction of the largest U.S. geothermal power plant has been approved by the Department of Energy (370). The agency is funding half the cost of the \$143 MM, 50 MW demonstration project to be built by Bechtel Corporation in Sandoval County, New Mexico. The project should be completed in 1982.

A method to remove hydrogen sulfide from geothermal steam has been developed through the R&D programs at the Department of Energy's Pacific Northwest Laboratories (Richland, Washington). Geothermal steam is passed through a reactor packed with activated carbon in the presence of oxygen or air (371).

Ocean thermal energy conversion (OTEC).—This technology received attention and increased sponsorship from U.S. federal and state authorities during 1980. In the U. S. Congress, Representative Don Fuqua, chairman of the House Committee on Science and Technology, put into motion a bill to accelerate commercialization of the technology (372). The Department of Energy presently supports \$40 MM per year of research in OTEC and is preparing a proposal to build a \$500 MM, 40 MW plant in 1985 (373).

Three alternative concepts are being considered under DOE's guidance, all variations on the floating platform/closed cycle system (374): (i) "grazing" plantships that sail the world's oceans seeking the best thermal gradients; (ii) open-cycle systems which could produce fresh water as well as electricity; and (iii) mist- or foam-based lifting cycles that use pressure differentials caused by the thermal gradients to

force water across a power turbine. Most of the research studies are being conducted by the U.S. Solar Energy Research Institute (Golden, Colorado).

Photovoltaic.—Southern California Edison Company and Pacific Gas and Electric Company are to fund a development program for an automated solar cell production technique. The photovoltaic cells were developed by Westinghouse Electric Corporation and consist of ribbons, named dendritic webs, produced from molten silicon (375, 376).

A new process for producing wafer-thin silicon ribbon has been developed by A. D. Little (Cambridge, Massachusetts) and may accelerate the production of low-cost solar cells used for direct conversion of sunlight into electricity (377, 378).

Describing it as a breakthrough in thin-film, solar cell technology, research efforts at Boeing Aerospace Company have led to the development of a copper indium selenide/cadmium sulfide cell with an efficiency of 9.4% (379).

An organic solar cell that is claimed to essentially duplicate plant photosynthesis has been developed at the University of Western Ontario in Canada. It is estimated that for as little as \$1000, the organic solar cells could provide sufficient energy for an average home (380).

The Department of Energy's Solar Energy Research Institute in Golden, Colorado, has awarded a \$16.5 MM contract to Martin-Marietta for the design, construction, and operation of a 350 kW photovoltaic power system in Saudi Arabia (381).

Goals set by the Department of Energy for photovoltaic conversion have been a conversion efficiency of 10% with materials costs at 70¢ per watt. Results of research programs at the University of Delaware indicate that both goals may be achieved (382). Emphasis in their studies has been on the cadmium sulfide/copper sulfide cell and it is now believed that efficiencies of 12-16% will be realized. Furthermore, process development studies with respect to the materials suggest an overall cost of approximately 50¢ per watt (382).

A \$14 MM plant in its final stages of construction in El Paso, Texas, may provide a "giant step towards commercialization" for photovoltaic devices (383). Photon Power, a joint venture of Compagnie Francaise des Petroles (55.5%), Libby-Owens-Ford (42.5%), and the cell's inventor, J. F. Jordan of El Paso (2%), will operate the plant to produce 5-7 MW per year of solar-powered units. The unit cell is a layer of tin oxide and cadmium sulfide sprayed onto float glass and part of the CdS is then converted to copper sulfide.

Solar energy.—The Department of Energy has selected seven proposals totaling \$3 MM for new process applications to exploit sunlight (384, 385). Included for consideration for contracts are solar hot water and steam for electricity generation, solar-heated air for copper smelting, solar steam for enhanced oil recovery, solar steam for natural gas processing and superheated solar steam for a sugar mill process.

A large scale solar industrial process heat system contract was awarded to Stauffer Chemical Company (386) to furnish 25 billion Btu per year.

Typical commercial applications of solar energy presently in operation are shown in Table XXI (387).

REFERENCES

1. *Chemical and Engineering News*, p. 11, April 7, 1980.
2. *Chemical Week*, p. 29, July 23, 1980.
3. *Chemical Marketing Reporter*, pp. 1-2, Oct. 1, 1980.
4. *Chemical Week*, p. 24, April 16, 1980.
5. *Chemical and Engineering News*, p. 21, Aug. 25, 1980.
6. *Chemical Engineering*, p. 32, Sept. 8, 1980.
7. *Chemical Purchasing*, p. 16, Sept. 1980.
8. *Journal of Commerce*, p. 7, Nov. 5, 1980.
9. *Chemical Engineering*, p. 79, Sept. 22, 1980.
10. *Chemical and Engineering News*, p. 14, Nov. 24, 1980.
11. *Canadian Control*, pp. 28-30, Feb. 1980.
12. *Chemical Marketing Reporter*, p. 7, Sept. 8, 1980.
13. *Chemical Purchasing*, p. 13, Oct. 1980.
14. *Chemical Week*, pp. 29-30, July 23, 1980.
15. *Ibid.*, p. 24, April 16, 1980.
16. *Chemical Marketing Reporter*, p. 9, April 14, 1980.
17. *Infochemie*, pp. 89-106, July 1980.
18. *Chemical Purchasing*, p. 36, July 1980.
19. *Journal of Commerce*, p. 7, Dec. 29, 1980.
20. *Chemical Marketing Reporter*, April 21, 1980.
21. *Ibid.*, p. 1, Oct. 1, 1980.
22. *Ibid.*, Part 1, p. 7, Oct. 20, 1980.
23. *Chemical Week*, July 23, 1980.
24. *Daily News*, p. 13, July 21, 1980.
25. *Chemical Week*, p. 13, May 14, 1980.
26. *Chemical Marketing Reporter*, p. 3, May 12, 1980.
27. *Chemical Week*, p. 30, July 23, 1980.
28. *European Chemical News*, p. 26, Sept. 15, 1980.
29. *Chemical Week*, p. 26, Sept. 10, 1980.
30. *Chemie Act.*, p. 9, Sept. 26, 1980.
31. *European Chemical News*, p. 23, Aug. 11, 1980.
32. *Chemical Engineering*, p. 29, Sept. 8, 1980.
33. *European Chemical News*, p. 28, Jan. 1, 1980.
34. *European Chemical News*, p. 23, Sept. 1, 1980.
35. *Japan Economic Journal*, p. 9, Oct. 28, 1980.
36. *European Chemical News*, p. 26, July 14, 1980.
37. *Kjemi*, p. 13, Feb. 1980.
38. *Japan Economic Journal*, p. 9, May 13, 1980.
39. *European Chemical News*, p. 28, Feb. 11, 1980.
40. *Chemical Marketing Reporter*, p. 5, Nov. 24, 1980.
41. *Japan Economic Journal*, p. 16, Nov. 25, 1980.
42. *Chemical Purchasing*, p. 71, June 1980.
43. *Japan Chemicals*, p. 7, July 31, 1980.
44. *Journal of Commerce*, Section 1, p. 12, Oct. 8, 1980.
45. *Federal Register*, p. 84384, Dec. 22, 1980.
46. *Chemical Marketing Reporter*, Fact 1, p. 7, Oct. 20, 1980.
47. *Beverage World*, p. 208, Nov. 1980.
48. *European Chemical News*, p. 21, Feb. 18, 1980.
49. *Journal of Commerce*, Section 1, p. 5, Oct. 10, 1980.
50. *Chemical Marketing Reporter*, p. 36, Dec. 8, 1980.
51. *Journal of Commerce*, p. 5, April 9, 1980.
52. *Japan Chemicals*, p. 8, July 3, 1980.
53. *Chemische*, p. 424, June 1980.
54. *European Chemical News*, p. 31, April 21, 1980.
55. *Chemical Week*, pp. 35-36, Nov. 26, 1980.
56. *Chemical Purchasing*, p. 60, April 1980.
57. *Chemical Marketing Reporter*, *Chemical Business*, p. 13, May 5, 1980.
58. *Chemical and Engineering News*, p. 13, April 7, 1980.
59. *Chemical Week*, p. 62, Sept. 10, 1980.
60. *Chemical Marketing Reporter*, p. 5, Sept. 8, 1980.
61. *European Chemical News*, p. 8, Sept. 1, 1980.
62. *Journal of Commerce*, p. 8, Oct. 9, 1980.
63. *Beverage World*, p. 8, Feb. 1980.
64. *Chemical Week*, p. 9, Nov. 5, 1980.
65. *Minerals and Materials*, p. 5-6, July 1980.
66. *Chemical Week*, pp. 16-17, Sept. 3, 1980.
67. *Mineral Industry Surveys*, Sodium Compounds in 1980, U.S. Dept. of the Interior, Bureau of Mines, Dec. 31, 1980.
68. *Journal of Commerce*, p. 5, Nov. 21, 1980.
69. *Chemical Week*, p. 47, Dec. 3, 1980.
70. *Chemical Marketing Reporter*, Part 1, p. 32, Nov. 17, 1980.
71. *Paper Journal*, p. 3, Oct. 15, 1980.
72. *Chemical Purchasing*, p. 14, July 1980.
73. *Chemical and Engineering News*, p. 15, Aug. 18, 1980.
74. *Chemical Week*, June 25, 1980.
75. *Chemical Marketing Reporter*, Part 1, p. 33, Sept. 22, 1980.
76. *Chemical Purchasing*, p. 47, July 1980.
77. *Journal of Commerce*, p. 7, Sept. 22, 1980.
78. *Chemical Marketing Reporter*, Part 1, p. 33, Sept. 22, 1980.
79. *Chemical Week*, p. 22, Dec. 3, 1980.
80. *Chemical Engineering*, p. 25, Nov. 3, 1980.
81. *Ibid.*, p. 52, Aug. 11, 1980.
82. *CPI Management*, p. 1, Aug. 18, 1980.
83. *European Chemicals*, p. 397, Nov. 23, 1980.

84. *CPI Management*, p. 3, June 23, 1980.
85. *Wall Street Journal*, Eastern ed., p. 20, Dec. 15, 1980.
86. *Engineering and Mining Journal*, p. 47, June 1980.
87. *American Metal Market*, p. 1, Dec. 3, 1980.
88. *Ibid.*, p. 6, Nov. 18, 1980.
89. *Metals Bulletin*, p. 19, July 29, 1980.
90. *Chemical Marketing Reporter*, p. 5, 25, Nov. 24, 1980.
91. *Financial Times*, pp. 35-38, Oct. 8, 1980.
92. *American Metal Market*, p. 7, Dec. 5, 1980.
93. *Metal Bulletin*, p. 23, April 1, 1980.
94. Mineral Industry Survey, Aluminum and Bauxite in 1980, U.S. Department of the Interior, Bureau of Mines, Annual Preliminary, Dec. 31, 1980.
95. *InfoChemie*, p. 84, 86, June 1980.
96. *American Metal Market*, p. 12, Feb. 13, 1981.
97. *Solid Waste Management*, p. 18, Sept. 1980.
98. *Financial Times*, pp. 35-38, Oct. 8, 1980.
99. *Journal of Metals*, pp. 12-16, Aug. 1980.
100. *Metals Bulletin*, p. 23, April 1, 1980.
101. *American Metal Market*, p. 1, 20, Oct. 15, 1980.
102. *Metals Bulletin*, p. 77, May 1980.
103. *Iron Age*, p. 37, Oct. 15, 1980.
104. *Japan Chemicals*, p. 1, Nov. 11, 1980.
105. *American Metal Market*, p. 1, 12, Oct. 1, 1980.
106. *Ibid.*, p. 9, Oct. 2, 1980.
107. *New York Times*, p. D3, Dec. 12, 1980.
108. *Chemical Week*, p. 24, Sept. 9, 1980.
109. *American Metal Market*, p. 31, Nov. 3, 1980.
110. *Chemical Week*, p. 26, Nov. 12, 1980.
111. *Minerals and Materials*, p. 12, Aug. 1980.
112. *American Metal Market*, p. 6, April 10, 1980.
113. *Chemical Marketing Reporter*, p. 4, 36, March 10, 1980.
114. *American Metal Market*, p. 7, Nov. 26, 1980.
115. *Ibid.*, p. 1, 21, July 15, 1980.
116. *Chemical Marketing Reporter*, p. 26, July 21, 1980.
117. *Chemical Engineering*, p. 88, March 10, 1980.
118. *Chemical and Engineering News*, p. 13, April 28, 1980.
119. *American Metal Market*, p. 2, Dec. 10, 1980.
120. *Chemical Engineering*, p. 21, July 28, 1980.
121. *American Metal Market*, p. 1, Dec. 30, 1980.
122. *Chemical Engineering*, p. 27, Sept. 8, 1980.
123. *Metal Bulletin*, p. 20, Aug. 1, 1980.
124. *New York Times*, p. D2, Jan. 1, 1980.
125. *Journal of Commerce*, p. 3, Oct. 9, 1980.
126. *Journal of Light Metals*, p. 34, Aug. 1980.
127. *American Metal Market*, p. 7, July 23, 1980.
128. *Chemical Marketing Reporter*, p. 3, 28, Nov. 24, 1980.
129. *Mineral Trade Notes*, p. 10, June 1979.
130. *Engineering and Mining Journal*, pp. 130-131, March 1981.
131. Mineral Commodity Summaries, p. 18, Published by the U.S. Bureau of Mines, 1981.
132. *Minerals and Materials*, p. 1, 43, Nov. 1979.
133. *Chemical Engineering*, p. 32, Dec. 31, 1979.
134. *Metal Bulletin*, p. 24, June 13, 1980.
135. *Optical Spectra*, pp. 50-51, Aug. 1979.
136. *Metall*, p. 8, Jan. 1980.
137. Chromium in 1980, Mineral Industry Surveys, Annual Preliminary, U.S. Department of the Interior, Bureau of Mines, Dec. 31, 1980.
138. *American Metal Market*, p. 10, Nov. 13, 1980.
139. *Ibid.*, p. 7, Dec. 18, 1980.
140. *World Minerals*, p. 87, Sept. 1980.
141. *Metal Bulletin* (London), p. 25, Nov. 28, 1980.
142. *American Metal Market*, p. 2, Nov. 11, 1980.
143. *Ibid.*, p. 1, Dec. 3, 1980.
144. *Engineering and Mining Journal*, pp. 82-88, March 1981.
145. *Ibid.*, p. 11, Aug. 1980.
146. *Wall Street Journal*, p. 26, Aug. 20, 1980.
147. Copper in 1980, Mineral Industry Surveys, Annual Preliminary, U.S. Department of the Interior, Bureau of Mines, Dec. 31, 1980.
148. *Metal Bulletin*, p. 21, Feb. 15, 1980.
149. *Electrochemical Progress*, p. 5, Dec. 1980.
150. *American Metal Market*, p. 1, 12, Oct. 1, 1980.
151. *Chemical and Engineering News*, p. 13, Oct. 13, 1980.
152. *Chemical Week*, p. 11, Oct. 8, 1980.
153. *Electrochemical Progress*, p. 4, Dec. 1980.
154. *Engineering and Mining Journal*, p. 43, Oct. 1980.
155. *Ibid.*, p. 47, Aug. 1980.
156. *Electrochemical Progress*, p. 6, April 1980.
157. Copper in 1980, Copper Industry, Annual Supplement, U.S. Department of the Interior, Bureau of Mines, April 20, 1981.
158. *Minerals and Materials*, p. 3, July 1980.
159. *Wall Street Journal* (SPR), p. 19, June 10, 1980.
160. *Metal Bulletin*, p. 20, June 13, 1980.
161. *American Metal Market*, p. 9, Dec. 5, 1980.
162. *Ibid.*, p. 26, Sept. 30, 1980.
163. *CPI Management*, p. 2, Oct. 6, 1980.
164. *Engineering and Mining Journal*, p. 35, June 1980.
165. *Ibid.*, p. 65, 237, Sept. 1980.
166. *Chemical Marketing Reporter*, p. 4, 19, Oct. 29, 1979.
167. *Metal Bulletin*, p. 21, Feb. 1, 1980.
168. *Journal of Metals*, p. 7, May 1980.
169. *American Metal Market*, p. 11, Dec. 12, 1980.
170. *Engineering and Mining Journal*, p. 35, 37, Dec. 1980.
171. *Metal Bulletin*, p. 21, Feb. 15, 1980.
172. *Ibid.*, p. 20, Feb. 15, 1980.
173. *Metal Bulletin Monthly*, pp. 30-36, Dec. 1979.
174. *Japan Chemicals*, p. 1, Jan. 24, 1980.
175. *Metal Bulletin*, p. 21, Nov. 13, 1979.
176. *Ibid.*, p. 20, Jan. 11, 1980.
177. *Ibid.*, p. 21, March 28, 1980.
178. *Engineering and Mining Journal*, p. 49, July 1980.
179. *Metall*, p. 102, Feb. 1980.
180. *Engineering and Mining Journal*, p. 13, Dec. 1980.
181. *Electrochemical Progress*, p. 7, Sept. 1980.
182. *Chemical and Engineering News*, p. 7, June 9, 1980.
183. *Metal Bulletin*, p. 26, March 11, 1980.
184. *Journal of Metals*, p. 8, May 1980.
185. *Minerals and Materials*, p. 8, Jan. 1980.
186. *Journal of Metals*, pp. 12-15, Jan. 1980.
187. *Usine Nouveau*, pp. 142-143, Sept. 20, 1979.
188. *Metal Bulletin Monthly*, p. 27, 29, April 1980.
189. *Wall Street Journal*, p. 25, Dec. 5, 1980.
190. *Journal of Metals*, pp. 53-59, March 1980.
191. *Wall Street Journal* (SPR), p. 37, June 10, 1980.
192. Mineral Industry Surveys, Lithium in 1980, Annual Preliminary, U.S. Department of the Interior, Bureau of Mines, Dec. 31, 1980.
193. *Journal of Commerce*, p. 5, Feb. 3, 1981.
194. *Ceramic Industries*, pp. 14-15, July 1980.
195. *Chemical Engineering*, p. 58, Sept. 22, 1980.
196. *Chemical and Engineering News*, p. 48, Nov. 11, 1980.
197. *Engineering and Mining Journal*, pp. 113-116, March 1981.
198. *Journal of Metals*, p. 4, Nov. 1980.
199. Mineral Industry Survey, Magnesium, Quarterly Survey, U.S. Department of the Interior, Bureau of Mines, March 13, 1981.
200. *Light Metals*, p. 31, April 1980.
201. *Chemical Week*, p. 37, Sept. 17, 1980.
202. *American Metal Market*, p. 7, April 8, 1980.
203. *Chemische*, p. 784, Nov. 1979.
204. *Metal Bulletin Monthly*, p. 66, Sept. 1979.
205. *Kjemi*, p. 12, Aug. 16, 1979.
206. *Chemical Engineering*, p. 69, June 16, 1980.
207. *Engineering and Mining Journal*, p. 13, Sept. 1980.
208. *American Metal Market*, p. 2, June 13, 1980; p. 6A, Sept. 17, 1980.
209. *Chemical and Engineering News*, p. 11, Aug. 18, 1980.
210. *Chemical Engineering*, p. 58, Sept. 22, 1980.
211. *Chemical Marketing Reporter*, p. 3, 26, Aug. 18, 1980.
212. *Chemical Week*, p. 22, Aug. 20, 1980.
213. *Metal Bulletin*, p. 23, Jan. 22, 1980; p. 21, May 2, 1980.
214. *Light Metals*, p. 21, April 1980.
215. *American Metal Market*, p. 1, 12, June 3, 1980.
216. *Chemical and Engineering News*, p. 21, Aug. 25, 1980.
217. *Metal Bulletin Monthly*, p. 15, Aug. 1980.
218. *Metal Bulletin*, p. 24, Oct. 21, 1980.
219. *Science News*, p. 263, April 26, 1980.
220. Mineral Industry Surveys, Annual Preliminary, Manganese in 1980, U.S. Department of the Interior, Bureau of Mines, Dec. 31, 1980.
221. *American Metal Market*, p. 2, Nov. 19, 1980.
222. *Ibid.*, p. 32, Dec. 22, 1980.

223. *Chemical Marketing Reporter*, Part 1, p. 31, Dec. 15, 1980.
224. *American Metal Market*, p. 1, Aug. 14, 1980.
225. *Metal Bulletin*, pp. 24-25, Oct. 17, 1980.
226. *American Metal Market*, p. 11, Feb. 25, 1980.
227. *Metal Bulletin*, pp. 31-33, June 1980.
228. *Industrial Minerals* (London), pp. 21-23, 25, 27, 29 Aug. 1980.
229. *Ibid.*, p. 15.
230. *Metals Bulletin*, p. 24, March 7, 1980.
231. Mineral Industry Surveys, Nickel in 1980, Annual Preliminary, U.S. Department of the Interior, Bureau of Mines, Dec. 31, 1980.
232. *American Metal Market*, p. 10, Feb. 5, 1981.
233. *Ibid.*, p. 1, 20, Sept. 11, 1980.
234. *Metals Bulletin*, p. 23, May 1980.
235. *American Metal Market*, p. 2, March 13, 1980.
236. *Ibid.*, p. 1, Nov. 10, 1980.
237. *Ibid.*, p. 1, Aug. 1, 1980.
238. *Chemical Marketing Reporter*, p. 7, 61, Sept. 15, 1980.
239. *Metall*, pp. 82-83, Jan. 1980.
240. *American Metal Market*, p. 1, 24, Oct. 14, 1980.
241. *Ibid.*, p. 8, Oct. 7, 1980.
242. *Metals Bulletin*, p. 22, April 18, 1980.
243. *Ibid.*, p. 20, Nov. 11, 1980.
244. *Chemical Marketing Reporter*, p. 7, 61, Sept. 15, 1980.
245. *Metals Bulletin*, pp. 21-22, April 3, 1980.
246. *Usine Nouveau*, pp. 68-69, Feb. 21, 1980.
247. *Kjemi*, pp. 8-10, Sept. 1980.
248. *Metals Bulletin*, pp. 543-547, Oct. 1980.
249. *Ibid.*, p. 22, Oct. 21, 1980.
250. *Ibid.*, p. 19, Oct. 1, 1980.
251. *American Metal Market*, p. 12, Sept. 3, 1980.
252. *Chemical Week*, p. 45, Feb. 20, 1980.
253. *Science*, pp. 420-423, July 18, 1980.
254. *Chemical Engineering*, pp. 43-45, Nov. 3, 1980.
255. Mineral Commodity Profiles, "Soda Ash (Sodium Carbonate), Sodium Sulfate, and Sodium," Bureau of Mines, United States Department of the Interior, Dec. 1979.
256. *Engineering and Mining Journal*, pp. 116-117, March 1981.
257. Mineral Industry Surveys, Titanium Quarterly, U.S. Department of the Interior, Bureau of Mines, March 19, 1981.
258. Mineral Industry Surveys, "Titanium in 1980," Annual Preliminary, U.S. Department of the Interior, Bureau of Mines, Dec. 31, 1980.
259. *Chemical Purchasing*, p. 13, Aug. 1980.
260. *Chemical and Engineering News*, p. 8, Jan. 5, 1981.
261. *Chemical Engineering*, p. 56, Oct. 6, 1980.
262. *Chemical Economy and Engineering Review*, p. 48, June/July 1980.
263. *European Chemical News*, p. 34, Sept. 1, 1980.
264. *Metal Bulletin*, p. 25, Nov. 21, 1980.
265. *Ibid.*, p. 23, Oct. 21, 1980; p. 23, Nov. 4, 1980.
266. Mineral Industry Surveys, Titanium Quarterly, U.S. Department of the Interior Bureau of Mines, June 20, 1980.
267. Mineral Industry Surveys, Titanium Quarterly, U.S. Department of the Interior, Bureau of Mines, Sept. 18, 1980.
268. *Design Engineering*, pp. 40-41, Aug. 1980.
269. *Chemical Purchasing*, p. 11, Dec. 1980.
270. *Engineering and Mining Journal*, pp. 76-77, March 1981.
271. *American Metal Market*, p. 1, 20, April 10, 1980.
272. *Metal Bulletin*, p. 25, March 11, 1980.
273. *Metal Bulletin Monthly*, p. 75, July 1979.
274. *Ibid.*, pp. 23-29, Feb. 1980.
275. Zinc in 1980, Mineral Industry Surveys, Annual Preliminary, U.S. Department of the Interior, Bureau of Mines, May 15, 1980.
276. Zinc Industry, Monthly, Mineral Industry Surveys, U.S. Department of the Interior, Bureau of Mines, May 15, 1980, and April 9, 1981.
277. *Electrochemical Progress*, pp. 4-5, Sept. 1980.
278. *American Paint*, p. 28, Sept. 8, 1980.
279. *Wall Street Journal*, p. 10, Nov. 19, 1980.
280. *American Metal Market*, p. 1, 11, Nov. 29, 1979.
281. *Chemical and Engineering News*, p. 10, April 21, 1980.
282. *Chemical Marketing Reporter*, p. 3, April 21, 1980.
283. *Japan Chemicals*, p. 14, Jan. 3, 1980.
284. *Engineering and Mining Journal*, p. 15, Aug. 1980.
285. *Metal Bulletin*, p. 22, Oct. 7, 1980.
286. *Ibid.*, p. 22, April 1, 1980; p. 21, April 11, 1980.
287. *American Metal Market*, p. 11, Sept. 16, 1980.
288. *Metal Bulletin*, p. 21, Nov. 4, 1980.
289. *Chemical Week*, p. 13, Aug. 27, 1980.
290. *Journal of Metals*, p. 8, Sept. 1980.
291. *Engineering and Mining Journal*, p. 31, June 1980.
292. *American Metal Market*, p. 5, July 18, 1980.
293. *R & P News*, p. 1, Dec. 22, 1980.
294. *Infchimie*, p. 109, Dec. 1979.
295. *American Metal Market*, p. 6, Feb. 8, 1960.
296. *Metal Bulletin*, p. 22, Oct. 10, 1980.
297. *American Metal Market*, p. 7, Nov. 13, 1980.
298. *Journal of Metals*, p. 14, June 1980.
299. *Chem. Ind.*, pp. 63-67, Jan. 19, 1980.
300. *Chemical and Engineering News*, p. 6, Jan. 5, 1981.
301. *Chemical Week*, p. 20, 41, Aug. 27, 1980.
302. *Ibid.*, p. 17, Nov. 5, 1980.
303. *Electrochemical Progress*, p. 4, June 1980.
304. *Electrical World*, pp. 30-34, July 1, 1980.
305. *Chemical and Engineering News*, p. 10, Aug. 25, 1980.
306. *Chemical Engineering Progress*, p. 29, July 1980.
307. *Electrical World*, pp. 73-104, April 1981.
308. *Ibid.*, pp. 55-70, Sept. 15, 1980.
309. *Wall Street Journal*, p. 17, Aug. 28, 1980.
310. *Chemical Week*, p. 14, July 30, 1980.
311. *European Chemical News*, p. 24, July 28, 1980.
312. *Chemical Week*, p. 11, Sept. 3, 1980.
313. *Chemical and Engineering News*, p. 37, July 21, 1980.
314. *European Chemical News*, p. 22, Aug. 4, 1980.
315. *Wall Street Journal*, p. 2, Dec. 5, 1980.
316. *Chemical and Engineering News*, p. 33, Nov. 3, 1980.
317. *Chemical Week*, p. 14, Nov. 12, 1980.
318. *Chemical Engineering*, p. 105, Nov. 17, 1980.
319. *Chemical Week*, p. 20, Oct. 22, 1980.
320. *European Chemical News*, p. 46, June 16, 1980.
321. *Ibid.*, p. 32, Nov. 10, 1980.
322. *Chemical Week*, p. 10, Oct. 29, 1980.
323. *Chemical and Engineering News*, p. 7, July 7, 1980.
324. *Ibid.*, p. 32, July 7, 1980.
325. *European Chemical News*, p. 36, Sept. 15, 1980.
326. *Chemical Week*, p. 44, Aug. 13, 1980.
327. *Chemical Purchasing*, p. 13, July 1980.
328. *European Chemical News*, p. 33, Nov. 17, 1980.
329. *Ibid.*, p. 40, June 30, 1980.
330. *Ibid.*, p. 40, July 7, 1980.
331. *Chemical Engineering*, p. 35, June 2, 1980.
332. *Engineering and Mining Journal*, p. 35, 39, Oct. 1980.
333. *Chemical Week*, pp. 11-12, July 2, 1980.
334. *Chemical and Engineering News*, p. 5, June 30, 1980.
335. *Ibid.*, p. 19, July 7, 1980.
336. *Chemical Engineering*, p. 42, June 2, 1980.
337. *Chemical Week*, p. 21, Dec. 10, 1980.
338. *Wall Street Journal*, p. 21, Dec. 15, 1980.
339. *Ibid.*, p. 11, Dec. 15, 1980.
340. *Chemical Engineering Processes*, pp. 13-20, Sept. 1980.
341. *Chemical Week*, p. 60, July 16, 1980.
342. *Chemical and Engineering News*, p. 22, Aug. 25, 1980.
343. *Ibid.*, p. 16, Aug. 18, 1980.
344. *Ibid.*, p. 14, July 7, 1980.
345. *Wall Street Journal*, p. 7, Aug. 21, 1980.
346. *Electrical World*, p. 13, March 15, 1980.
347. *Ibid.*, p. 17, Sept. 1, 1980.
348. *Chemical and Engineering News*, p. 41, Sept. 8, 1980.
349. *Chemical Week*, p. 43, Nov. 19, 1980.
350. *Chemical Engineering*, p. 107, Nov. 17, 1980.
351. *Electrochemical Progress*, p. 7, May 1980.
352. *Chemical Engineering*, p. 68, April 21, 1980.
353. *Chemical Week*, p. 53, Nov. 12, 1980.
354. *Engineering and Mining Journal*, p. 11, July 1980.
355. *Chemical and Engineering News*, p. 5, June 16, 1980.
356. *Ibid.*, p. 28, Dec. 1, 1980.
357. *Ibid.*, p. 6, 7, July 21, 1980.
358. *Ibid.*, p. 32, Oct. 20, 1980.
359. *Ibid.*, p. 36, 37, Nov. 3, 1980.
360. *Chemical Week*, p. 57, Oct. 15, 1980.
361. *Ibid.*, p. 57, Oct. 15, 1980.
362. *Electrochemical Progress*, p. 4, Feb. 1980.

363. *Wall Street Journal*, p. 3, Oct. 16, 1980.
364. *Chemical Engineering*, p. 35, Sept. 22, 1980.
365. *Chemical and Engineering News*, p. 17, Sept. 1, 1980.
366. *Chemical Week*, p. 54, July 16, 1980.
367. *Chemical and Engineering News*, p. 17, Sept. 22, 1980.
368. *Wall Street Journal*, p. 3, Sept. 12, 1980.
369. *Chemical Purchasing*, p. 21, Sept. 1980.
370. *Chemical Engineering*, p. 67, June 16, 1980.
371. *Chemical Week*, p. 52, Oct. 22, 1980.
372. *Chemical Engineering*, p. 68, June 16, 1980.
373. *Chemical Week*, p. 14, June 25, 1980.
374. *Chemical Engineering*, pp. 66-68, Aug. 11, 1980.
375. *Electrochemical Progress*, p. 6, Nov. 1980.
376. *Chemical Engineering*, p. 19, Aug. 11, 1980.
377. *Ibid.*, p. 43, Dec. 1, 1980.
378. *Chemical Week*, p. 79, Oct. 29, 1980.
379. *Chemical and Engineering News*, p. 34, Aug. 25, 1980.
380. *Chemical Week*, p. 59, June 18, 1980.
381. *Electrochemical Progress*, p. 6, Feb. 1980.
382. *Chemical and Engineering News*, p. 37, Oct. 6, 1980.
383. *Chemical Week*, p. 46, Nov. 19, 1980.
384. *Chemical Engineering*, p. 20, Aug. 11, 1980.
385. *Chemical Week*, p. 48, Aug. 6, 1980.
386. *Chemical Processing*, p. 18, Nov. 1980.
387. *Chemical Week*, p. 33, Dec. 3, 1980.



The Li/Cl₂ in SO₂Cl₂ Inorganic Battery System

II. D Cell Discharge Characteristics

C. C. Liang,* M. E. Bolster, and R. M. Murphy*

Electrochem Industries (E-I) Incorporated, A Greatbatch Enterprises Company, Clarence, New York 14031

ABSTRACT

Investigations were conducted on the discharge and safety characteristics of the spirally wound D cells of the Li/Cl₂ in SO₂Cl₂ (Li/CSC) system. The realized capacities obtained for these cells further emphasized the effect of Cl₂ addition to SO₂Cl₂ on cell discharge behavior. Further, discharge tests showed that practical D cells of the Li/CSC system at ambient temperature yield energy densities of 0.8-1.1 W-hr cm⁻³ dependent on discharge rates (e.g., 1.0-20.0Ω loads respectively). Cells were discharged at various temperatures from -30° to +93°C. Additionally, no significant loss in capacity has been observed for cells discharged at ambient temperatures after storage at 74°C for periods up to 30 days. The results of preliminary safety testing which included incineration, short circuiting, and the sequence of force discharge/charge further indicate that the Li/CSC system does indeed possess those characteristics necessary for a variety of high rate applications.

Although investigations of the lithium-thionyl chloride inorganic electrolyte system have been conducted in many laboratories (1), only a few studies have been undertaken for lithium-sulfuryl chloride. The discharge characteristics of the Li/SO₂Cl₂ system have been reported by Auburn *et al.* (2, 3) and Gilman (4, 5), while results of cyclic voltammetric studies have been given by Behl (6) and Blomgren *et al.* (7). Investigations were conducted in this laboratory to study the characteristics of the Li/SO₂Cl₂ inorganic electrolyte system, particularly relative to the effects of Cl₂ addition to SO₂Cl₂. Results using AA cells as the test vehicle for the Li/Cl₂ in SO₂Cl₂ (Li/CSC) system have been recently reported (8). In the present investigation, spirally wound D cells were used as the test vehicle in order to study both the discharge and the safety characteristics for this system. The realized capacities for spirally wound D cells further emphasized the effect of Cl₂ addition to SO₂Cl₂ on the cell discharge characteristics at ambient temperatures, especially at high drain rates. Furthermore, cells have been discharged at various temperatures from -32° to +93°C. Cells exhibited no loss in realized capacity when discharged at ambient temperature after storage at 74°C for extended periods up to 30 days. Spirally wound D cells with no vent structure were subjected to incineration, short circuiting, and the sequence of forced discharge/charge. In no instance did the cells vent with flame, explode, or in any way create a hazard to personnel.

Experimental

Lithium tetrachloroaluminate was prepared by the fusion of LiCl (Fisher Scientific Company) and AlCl₃ (Fluka) after an initial heating period of 20 hr at 100°C under dynamic vacuum. Sulfuryl chloride (Alfa-Ventron) was distilled after refluxing over lithium foil

for 20 hr. The resultant liquid was colorless to pale yellow in color. The electrolyte solution was obtained by first preparing the desired solution of LiAlCl₄ in SO₂Cl₂ (a slight excess of the salt was necessary to compensate for a very small volume expansion upon chlorine addition). Chlorine was obtained by first condensing the Cl₂ (Matheson) gas in a liquid nitrogen/ethanol trap. The resultant liquid Cl₂ was then added to the solution with care. In contrast to the filling methods previously described (8), the D cells in the study were vacuum filled immediately upon solution preparation. The final concentrations of Cl₂ and LiAlCl₄ were determined by both weight gain and final volume measurements.

Practical, hermetically sealed D cells constructed from 304 stainless steel (Hudson Tool and Die Incorporated) were used throughout these experiments. The current collectors for both the anode and cathode consisted of an expanded nickel screen (Exmet Corporation) which extended the entire length of the respective electrodes. The separator material was Mead glass (6% binder, 0.013 cm thick). The lithium anode (Foote Mineral Company) was fabricated from 0.055 cm thick foil. An overlay of lithium foil was used to cover the area of the nickel screen exposed to that portion of the carbon electrode in the inner windings of the spirally wound cell components.

Two types of spirally wound D cells were fabricated for use in these studies: the first having a carbon electrode (Shawinigan black, 50% compressed) geometric surface area of 147 cm² (4.9 cm width × 15 cm length × 2 sides), the second having a carbon electrode geometric surface area of 294 cm² (4.9 cm width × 30 cm length × 2 sides). The average carbon electrode thickness for the two types were 0.30 and 0.15 cm, respectively. Cell filling was accomplished using vacuum filling techniques with especial care taken to avoid moisture contamination during filling. The typi-

* Electrochemical Society Active Member.

Key words: electrode, cathode, capacity, discharge.



cal electrolyte fill volume was 27 cm³ for both types of D cells. All manipulations involved with cell fabrication and filling were performed in a dry atmosphere (less than 0.5% humidity, -50°C dew point). Cells were discharged at -22° ± 2°C, -32° ± 2°C, ambient temperature (+25° ± 2°C), +76° ± 2°C, and +93° ± 2°C under constant loads. For those cells tested at the lower and higher temperatures, the loads were positioned in the ambient environment, externally to the temperature chamber. The load voltage was measured through use of a timed sequential electrometer and displayed on a recorder. D cells were stored at a constant temperature of 74° ± 2°C for periods up to 30 days. In addition, all realized capacities cited in this article were obtained to a 2V cutoff.

Three types of safety tests were performed on D cells: incineration, short circuiting, and the sequence of force discharge/charge. Cells of both the 147 and 294 cm² carbon electrodes were fitted with thermocouples to measure skin temperature and suspended approximately 10 cm above the surface of a naphtha reservoir. The results of the tests were monitored by either film or videotape. Cells were short circuited through a cable having a total resistance of 0.023Ω. The short-circuit current was measured using a Current Gun (F. W. Bell Incorporated, Model CG-100A) while the cell voltage and skin temperature were recorded throughout the short-circuit test. The sequence of force discharge/charge was accomplished through use of a Keithley 227 current source. Both the cell voltage and the skin temperature were measured throughout the entire test sequence.

Results and Discussion

Spirally wound D cells having carbon cathodes with a geometric surface area and thickness of 147 cm² and 0.30 cm, respectively, were fabricated and filled with 1M LiAlCl₄ in SO₂Cl₂ and 1M LiAlCl₄ in 0.3M Cl₂ in SO₂Cl₂. The ambient temperature discharge curves for both sets of D cells are presented in Fig. 1. Constant loads of 1.0 and 1.5Ω were employed. The realized capacities for the 1.0Ω discharge (approximately 3A) were 6.4 and 12.3 A-hr for the Li/SO₂Cl₂ and Li/0.3M Cl₂ in SO₂Cl₂ cells, respectively. At a load of 1.5Ω (approximately 2A), the realized capacities increased to 8.4 and 13.6 A-hr, for Li/SO₂Cl₂ and Li/0.3M Cl₂ in SO₂Cl₂, respectively. The corresponding average current densities for the 1.0 and 1.5Ω loads were 20.4 and 13.6 mA cm⁻², respectively, for the Li/0.3M Cl₂ in SO₂Cl₂ cells. It was noted that the initial load voltage for the Li/0.3M Cl₂ in SO₂Cl₂ cell discharged under a 1.0Ω load was 1.60V. The cell load voltages were measured by a sequential electrometer in conjunction with a recorder. The dwell time for any one measurement was 6 sec. The load voltage for the Li/0.3M Cl₂ in SO₂Cl₂ cell discharged under a 1.0Ω load was measured initially in this series of cells. It would be reasonable to assume that the second cell in the series (Li/0.3M Cl₂ in SO₂Cl₂ discharged under the 1.5Ω load) would also exhibit similar initial polarization. However, the recorded initial voltage for the Li/0.3M Cl₂ in the SO₂Cl₂ cell measured 6 sec after load application was 3.06V. Similar initial low load voltage levels are apparent for the Li/SO₂Cl₂ cells.

It is further evident from Fig. 1 that the effect of chlorine addition to SO₂Cl₂ increases not only the realized capacity but also the rate capability. The complete set of ambient temperature discharge curves for the Li/0.3M Cl₂ in SO₂Cl₂ D cells is presented in Fig. 2. The realized capacities for the set differ very little whether the discharge load is 1.0Ω (12.3 A-hr) or 150Ω (14.0 A-hr). A plot of realized capacity vs. log I (9) for this particular set of discharge data is presented in Fig. 3. The realized capacity is also nearly independent of the discharge load between 5.0 and

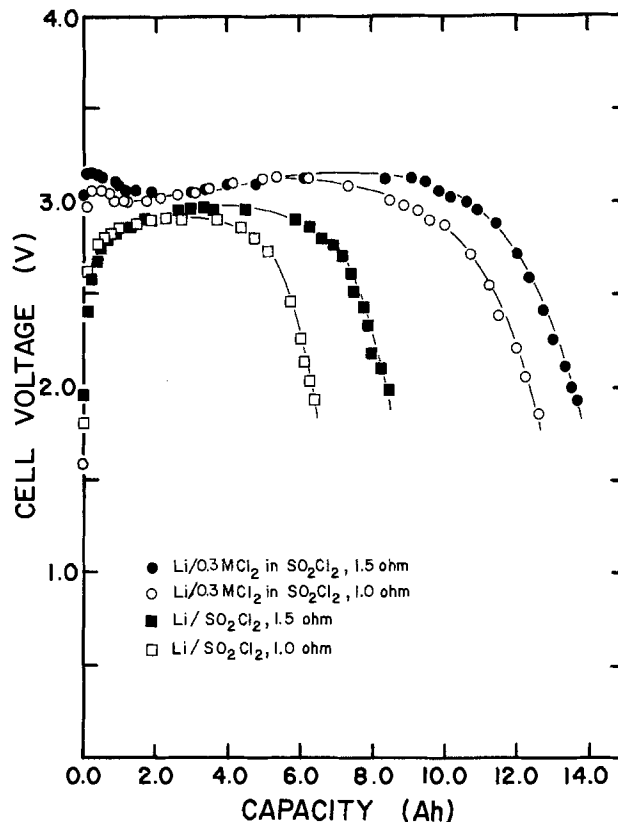


Fig. 1. Ambient temperature discharge curves of Li/SO₂Cl₂ and Li/CSC spirally wound D cells (geometric surface area: 147 cm²).

150Ω. There is, however, a slight decrease in realized capacity for the moderately high drain rates at 1.0, 1.5, and 3.0Ω.

The realized capacities obtained for Li/SO₂Cl₂ D cells discharged under 1.0, 1.5, and 3.0Ω loads were,

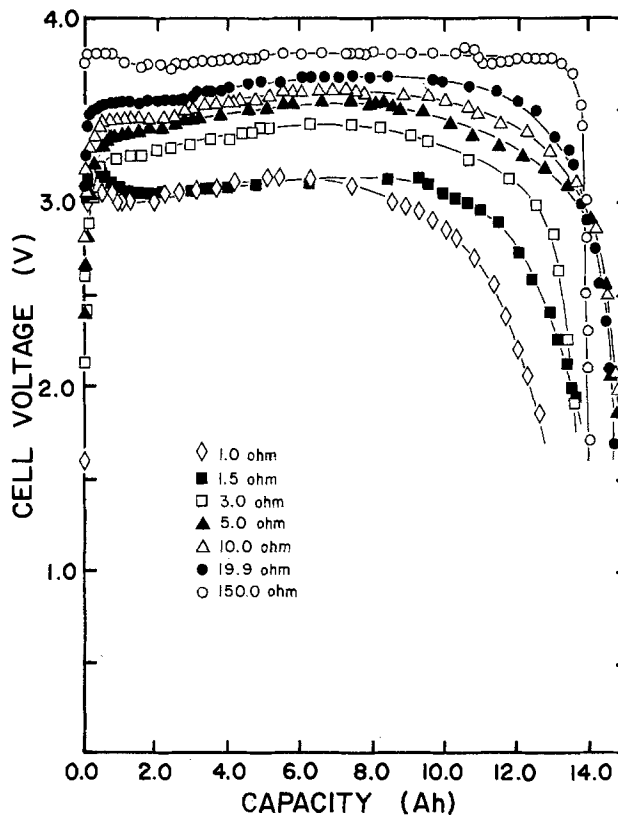


Fig. 2. Ambient temperature discharge curves of Li/0.3M CSC D cells (geometric surface area: 147 cm²).

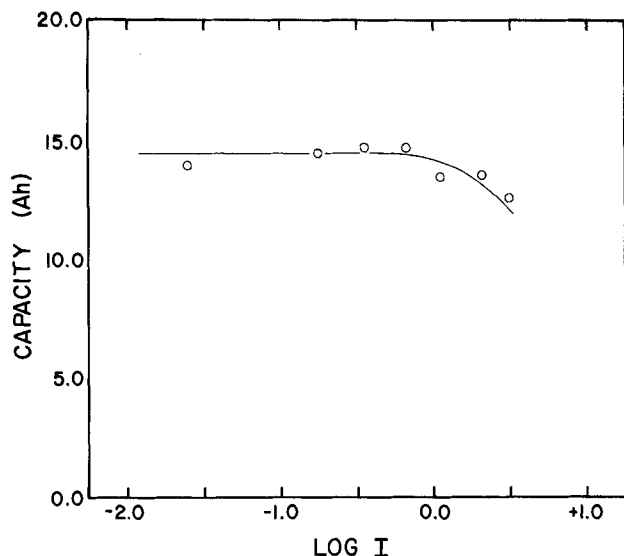


Fig. 3. Capacity vs. log I for Li/0.3M CSC D cells discharged at $25 \pm 2^\circ\text{C}$.

respectively, 6.4, 8.4, and 8.9 A-hr. The capacities obtained for this system increase with decreasing discharge rates at a faster rate than those for the Li/Cl₂ in SO₂Cl₂ system. However, even at relatively low current densities of less than 1 mA cm⁻² (8), the realized capacity was more than 15% higher for cells of the Li/CSC system than for cells of the Li/SO₂Cl₂ system. Further, the realized capacity of 12.3 A-hr for a Li/CSC D cell discharged under a 1.0Ω load represents a yield of approximately 80%, based on initial amounts of both SO₂Cl₂ and Cl₂ contained in the cell.

Investigations in our laboratory have also been concerned with studies of the effects of Cl₂ and LiAlCl₄ concentrations on the discharge characteristics of the Li/CSC system. Cells containing Cl₂ concentrations from 0.10 to 1.02M and salt concentrations from 1.0 to 1.5M were fabricated and discharged. It is evident that the discharge characteristics are enhanced by the addition of Cl₂ to SO₂Cl₂. However, the optimum performance is obtained from those cells which contain 0.25-0.60M Cl₂ in SO₂Cl₂. The discharge characteristics for cells with Cl₂ concentrations in this range are virtually identical. Table I shows typical discharge results for spirally wound cells containing various Cl₂ and LiAlCl₄ concentrations. It is apparent, especially in consideration of the data for those Cl₂ concentrations of 0.1 and 1.02M, that the results for the cell performance are less than optimal at these Cl₂ concentration extremes. It is also apparent from Table I, however, that the addition of Cl₂ at any concentration level enhances the discharge characteristics. The results for cells containing Cl₂ concentrations from 0.3 to 0.6M indicate that the Cl₂ concentration dependence is not critical, i.e., the realized capacities for cells discharged at the

relatively high drain rates of 1.0, 1.5, and 3.0Ω are within the experimental error of the measurement system.

The high temperature discharge characteristics for D cells have also been studied. Figures 4 and 5 show the results obtained for the Li/CSC system at 76° and 93°C, respectively. The realized capacities for these cells discharged at the elevated temperatures are only slightly less than those for cells discharged at ambient temperatures (e.g., 3.0Ω constant load at 25°, 76°, and 93°C: 14.0, 12.8, and 10.7 A-hr, respectively). The load voltages, however, are higher than those at ambient temperature.

The low temperature discharge tests for cells constructed with carbon electrodes having a geometric surface area of 147 cm² showed a voltage delay as well as a low load voltage. For example, a load of 3.0Ω was applied to one such cell thermally equilibrated at -22°C. The voltage delay to reach a 2.5V level was about 20 min and the highest load voltage attained during the course of discharge was approximately 2.9V. In an attempt to alleviate the low load voltage and delay problems, a series of D cells were constructed with carbon electrodes having twice the geometric surface area (4.9 cm width × 30 cm length × 2 sides = 294 cm²) and one-half the electrode thickness (0.15 cm) than those cells previously discussed. The low temperature discharge curves for these cells are presented in Fig. 6 and 7 for temperatures of -22° ± 2° and -32° ± 2°C, respectively. The realized capacities for cells discharged under a 3.0Ω load were 12.8 and 10.0 A-hr for -22° and -32°C, respectively. The corresponding load voltages, however, were 3.0 and 2.9V, respectively.

Cells comprising carbon electrodes of the greater geometric surface area were discharged at ambient temperature. The results are presented in Fig. 8. The realized capacities for these cells were between 11.8 and 13.3 A-hr when discharged under loads of 1.0 to 20.0Ω. These results represent a narrower capacity range than the realized capacity range for D cells having a carbon electrode geometric surface area of 147 cm² (Fig. 2). The load voltages for the cells, however, average approximately 0.2V higher than those in Fig. 2. The current densities for those cells with the larger geometric surface area are one-half that for the cells with carbon electrodes of 147 cm² geometric surface area, presumably the reason for the higher load voltage levels. Thus, the low temperature results for carbon electrodes of 294 cm² geometric surface area compare favorably to the ambient temperature results obtained for similarly constructed cells (13.2 A-hr).

Ambient temperature discharge curves for spirally wound D cells having the 147 cm² carbon electrodes and which were stored at 74° ± 2°C for periods as long as 30 days are shown in Fig. 9. The realized capacities obtained for the cells discharged under a 3.0Ω load were 14.4 and 13.5 A-hr for cells stored 11 and 30 days, respectively. These results compared favorably with

Table I. Realized capacities (A-hr) to a 2V cutoff for D cells having carbon electrodes of 147 cm² geometric surface area and containing various concentrations of Cl₂ and LiAlCl₄

| Load (Ω) | Molar concentrations of Cl ₂ and (LiAlCl ₄) | | | | | | | |
|----------|--|--------------|--------------|--------------|--------------|--------------|---------------|----------------|
| | 0.0 (1.0) | 0.1 (1.0) | 0.3 (1.0) | 0.4 (1.3) | 0.4 (1.5) | 0.5 (1.5) | 0.55 (1.1) | 1.02* (1.0) |
| 1.0 | 6.4 | 6.6 | 12.3 | 11.7 | 12.0 | 11.2 | 10.2 | 11.6 |
| 1.5 | 8.4 | 10.9 | 13.6 | 12.5 | | 13.8 | | 11.7 |
| 3.0 | 8.9 | 13.1 | 13.5 | 14.4 | 14.2 | 14.7 | 14.4 | 12.9 |
| 5.0 | | 14.2 | 14.7 | 14.6 | 14.6 | 14.4 | 14.5 | 13.8 |
| 10.0 | | 14.2 | 14.8 | 15.0 | 14.4 | | 15.0 | 14.3 |
| 20.0 | | 14.3 | 14.6 | 14.0 | | 14.6 | 14.0 | 13.5 |

* 1.02M Cl₂ represents a saturated solution of Cl₂ in SO₂Cl₂.

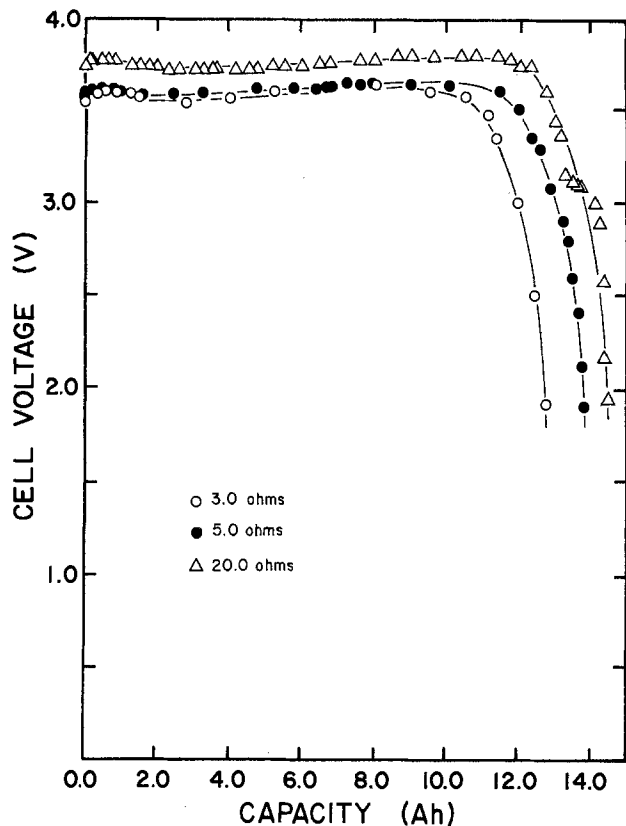


Fig. 4. High temperature ($76^{\circ} \pm 2^{\circ}\text{C}$) discharge curves for D cells (geometric surface area: 147 cm^2 , 0.45M Cl_2).

the capacity obtained for a newly fabricated cell discharged at ambient temperature (14 A-hr). The capacity results for the stored cells were well within the experimental limits for the measuring system. The load voltages of approximately 3.0V, however, were lower than the corresponding load voltages for newly

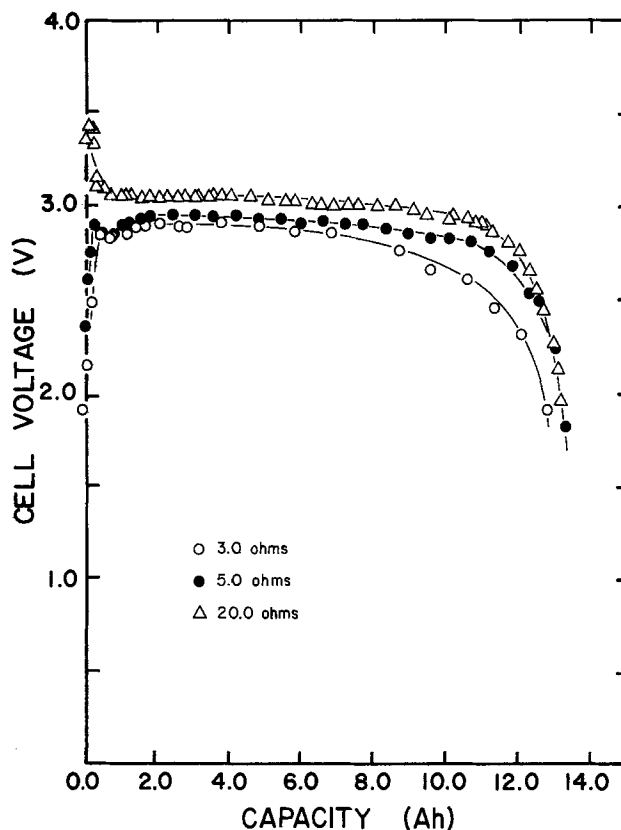


Fig. 6. Low temperature ($-22^{\circ} \pm 2^{\circ}\text{C}$) discharge curves for D cells (geometric surface area: 294 cm^2 , 0.44M Cl_2).

fabricated cells (3.4V). Thus, storage of cells of the Li/CSC system at either ambient temperature or elevated temperatures results in decreased rate capability, but no decrease in realized capacity.

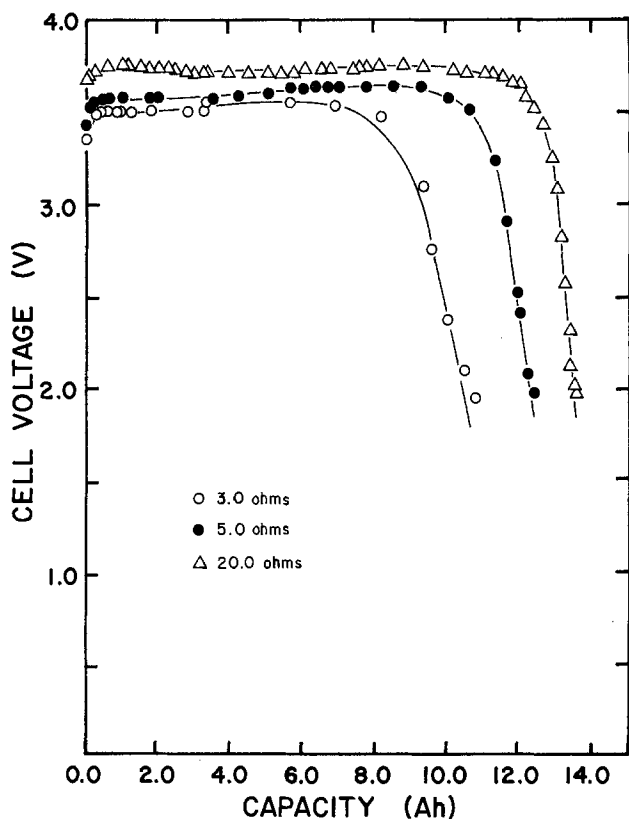


Fig. 5. High temperature ($93^{\circ} \pm 2^{\circ}\text{C}$) discharge curves for D cells (geometric surface area: 147 cm^2 , 0.35M Cl_2).

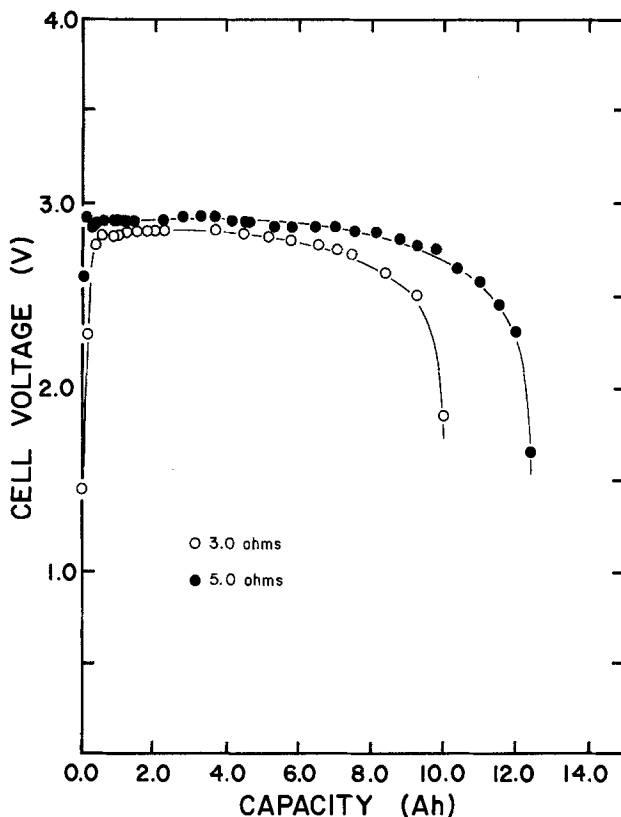


Fig. 7. Low temperature ($-32^{\circ} \pm 2^{\circ}\text{C}$) discharge curves for D cells (geometric surface area: 294 cm^2 , 0.45M Cl_2).

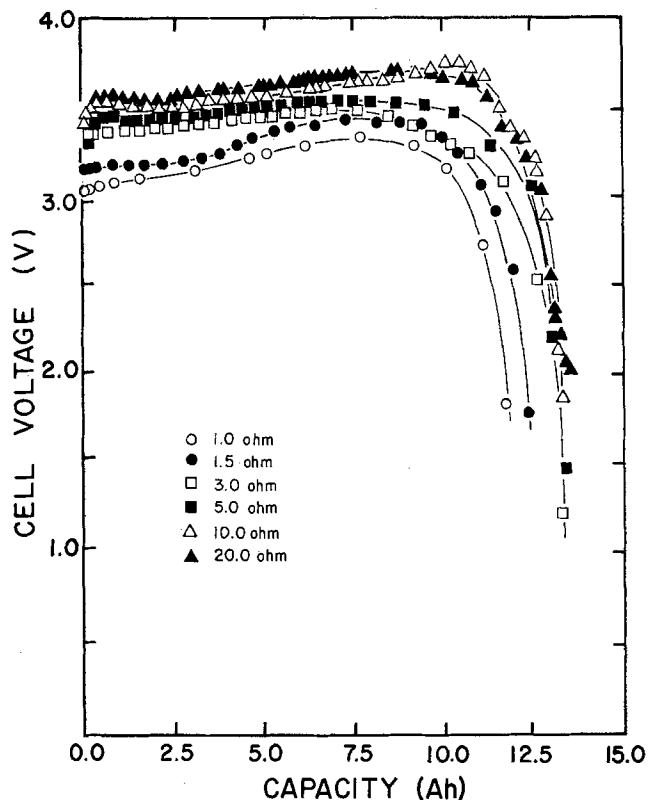


Fig. 8. Ambient temperature discharge curves of Li/0.45M CSC D cells (geometric surface area: 294 cm^2).

Preliminary safety tests of D cells of the Li/CSC system indicate that the battery system in its present configurations exhibits exceptionally safe features under both normal and abusive conditions. Although containing no vent structure, Li/CSC D cells having both

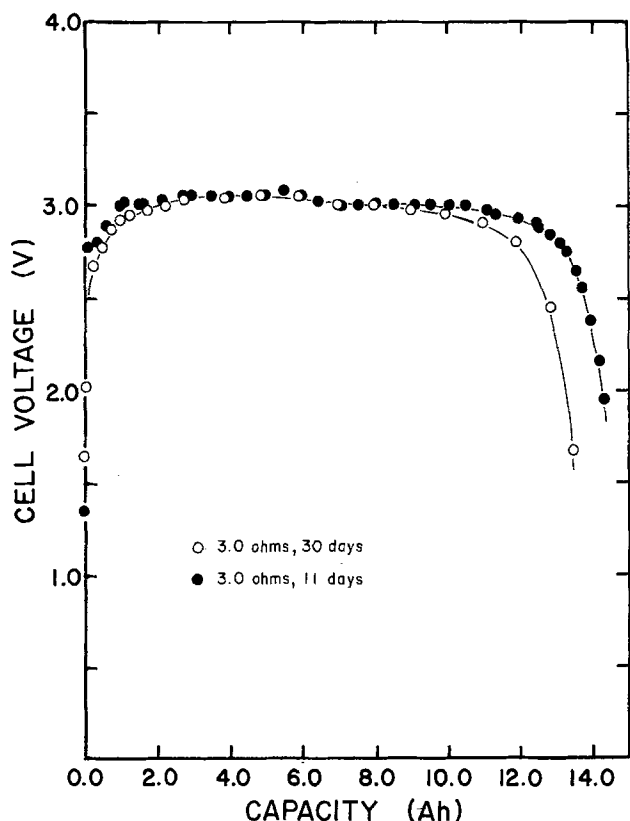


Fig. 9. Ambient temperature discharge curves for D cells after storage at $74^\circ \pm 2^\circ \text{C}$ (geometric surface area: 147 cm^2 , 0.3M Cl_2).

carbon electrodes were incinerated at 800°C in a naphtha flame for extended periods of time. The cells exhibited only mild venting through a rupture in the glass to metal seal. Indeed, depending on cell orientation above the flame, the venting gases/vapors often extinguished the flame.

Short-circuit tests were also performed on spirally wound D cells having both the low and high geometric area carbon electrodes (i.e. 147 and 294 cm^2) at ambient temperatures. No explosion hazard was ever encountered during these tests. D cells have been force discharged and subsequently charged at a constant current of 1A . Figure 10 shows the results of one such test sequence. After a 16 hr force discharge period, the cell was charged at the 1A rate. Initially, the cell voltage remained slightly above the zero volt level. This was then followed by a rapid voltage increase to slightly greater than 4.0V . After a period of approximately 1 hr , the voltage reverted to a constant 3.85V and remained at that level for a period of approximately 20 hr . The charging mode was then interrupted, resulting in a decrease in cell voltage to approximately 3.0V . The cell was subsequently charged at a rate of 10A . After a period of 5 min in this latter mode, the cell vented mildly through the glass to metal seal. The cell skin temperature profile is analogous to the charging mode for the cell, i.e., an abrupt increase in temperature immediately after onset of the 1A charging mode followed by a constant temperature plateau of 45°C for a period of 20 hr . After the 1A charging mode ceased, the temperature decreased to approximately 25°C . An abrupt rise in temperature was noted after the onset of the 10A charge. The temperature rapidly rose to 58°C whereupon the cell vented through the glass to metal seal.

At no time during any of the safety testing for spirally wound D cells did any cell explode, vent with flame, or create a hazard to personnel.

Conclusions

The Li/CSC system has a high current delivering capability even when spirally wound D cells comprising carbon electrodes of limited geometric surface area are discharged from ambient temperature to approximately 93°C . Furthermore, cells containing carbon electrodes of twice the geometric surface area deliver high currents at temperatures as low as -32°C . An increase in the discharge rate from less than 1 mA cm^{-2} to 21 mA cm^{-2} does not significantly affect the realized capacity. The shelf-life characteristics of the Li/CSC system indicate that little realized capacity is lost whether the cell has been stored at elevated temperatures or ambient temperature for extended periods

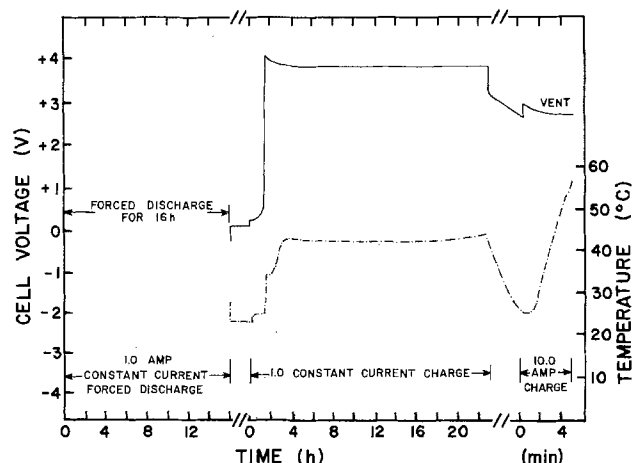


Fig. 10. Safety characterization of a D cell force discharged at 1A , charged at 1A , and finally charged at 10A (geometric surface area: 147 cm^2 ; solid line, cell voltage; broken line, temperature).

of time. However, the load voltages and, therefore, the current capabilities are less than those for newly fabricated cells.

The safety features exhibited by the Li/CSC cells show them to represent no danger to personnel during use under both normal and abusive conditions. The mild venting observed for incineration tested cells often extinguished the naphtha flame.

These features indicate that the Li/CSC system represents a particularly safe battery for use under various high rate applications.

Acknowledgment

The authors wish to thank Mr. Paul W. Krehl and Mr. David A. Danner for their technical assistance during these studies.

Manuscript submitted Oct. 17, 1980; revised manuscript received Feb. 23, 1981. This was Paper 66 presented at the Hollywood, Florida, Meeting of the Society, Oct. 5-10, 1980.

Any discussion of this paper will appear in a Discussion Section to be published in the June 1982 JOURNAL.

All discussions for the June 1982 Discussion Section should be submitted by Feb. 1, 1982.

Publication costs of this article were assisted by Electrochem Industries, Incorporated.

REFERENCES

1. A. N. Dey, *Thin Solid Films*, **43**, 131 (1977).
2. J. J. Auborn and N. Marincic, in "Power Sources 5," D. H. Collins, Editor, p. 683, Academic Press, London (1975).
3. J. J. Auborn, R. D. Bezman, K. W. French, A. Heller, and S. I. Lieberman, in Proc. 26th Power Sources Symposium, p. 45 (1974).
4. S. Gilman, in *ibid.*, p. 29.
5. S. Gilman and W. Wade, Jr., *This Journal*, **127**, 1427 (1980).
6. W. K. Behl, *ibid.*, **127**, 1444 (1980).
7. G. E. Blomgren, V. Z. Leger, T. Kalnoki-Kis, M. L. Kronenberg, and R. J. Brodd, in "Power Sources 7," J. Thompson, Editor, p. 583, Academic Press, London (1979).
8. C. C. Liang, M. E. Bolster, and R. M. Murphy, in Proc. 29th Power Sources Symposium, To be published (1981).
9. R. Selim and P. Bro, *This Journal*, **118**, 829 (1971).

Electrochemical Investigation of the Lithium-Gallium System

C. John Wen^{*1} and Robert A. Huggins*

Department of Materials Science and Engineering, Stanford University, Stanford, California 94305

ABSTRACT

The thermodynamic properties of the lithium-gallium binary system have been investigated by the use of electrochemical methods, with special attention being given to the phase "LiGa." Measurements have also been made of the mass transport parameters in "LiGa," including the determination of the composition dependence of the chemical diffusion coefficient, the self-diffusion coefficient, and the enhancement factor. The data on emf vs. composition, obtained by use of the coulometric titration technique at 415°C, show that all three intermediate phases, whose nominal compositions are LiGa, Li₂Ga₂, and Li₃Ga, have appreciable ranges of stoichiometry. The existence of these three phases was further substantiated by x-ray diffraction analysis. At 415°C, the constant emf values in the two-phase regions are 565, 122, 91, and 20 mV with respect to pure liquid lithium, in the order of increasing lithium concentration. Measurements are reported on the temperature dependence of the most gallium-rich plateau, leading to values of the partial molar entropy and enthalpy of lithium in that two-phase region. The lithium activity has been found to follow Henry's law in liquid lithium-gallium alloys and electrochemical measurements of the temperature dependence of the solubility of lithium in liquid gallium confirmed earlier results. The activity of lithium in the vario-stoichiometric phase "LiGa" lies between 7.26×10^{-5} and 0.126 at 415°C over a composition range from 44.8 to 56.0 a/o Li. The Gibbs free energy of mixing was determined as a function of composition across the phase "LiGa," and found to have a minimum value of -25.8 kJ/mol at 47.6 a/o Li. The standard Gibbs free energy of formation of all three intermediate phases was evaluated at their nominal stoichiometric compositions; the values are -51, -115, and -62 kJ/mol, respectively. The chemical diffusion coefficient within the phase "LiGa" varies from 1.6×10^{-8} to 6.8×10^{-5} cm²/sec. On the lithium-rich side of LiGa, the chemical diffusion coefficient increases slightly with increasing lithium concentration. On the lithium-deficient side of the ideal stoichiometry, the chemical diffusion coefficient increases rapidly as lithium is deleted. After reaching a maximum value at 47.6 a/o Li, it gradually decreases again with further decrease in lithium content. The enhancement factor, which relates the chemical and self-diffusion coefficients, is also composition dependent. It reaches a maximum value of 56 at the same composition as the peak in the chemical diffusion coefficient and the minimum in the Gibbs free energy of mixing.

There is great current interest in lithium-based battery systems with molten salt electrolytes. These batteries are generally operated at temperatures of

400°-450°C. Present versions employ either lithium-aluminum (1, 2) or lithium-silicon (3-5) alloys as active constituents in their negative electrodes.

The work reported here is part of a series of investigations of the thermodynamic and kinetic properties of a number of lithium alloy systems which might be

* Electrochemical Society Active Member.

¹ Current address: Shell Development Company, Houston, Texas 77001.

Key words: thermodynamics, x-ray diffraction analysis, emf.

considered for use as either reactants or mixed-conducting matrices in lithium-based battery electrodes. The lithium chemical potential, and its compositional dependence, determine the potential and the capacity of electrode reactants. The fundamental parameter related to their kinetic behavior is the chemical diffusion coefficient, which controls the rate of compositional equilibration within the solid constituents of the electrode structure.

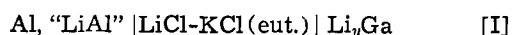
The phase designated as "LiGa," which is analogous to the important phase "LiAl" in the lithium-aluminum system, was first reported by Zintl and Brauer (6) to have the cubic NaTl (B32) type structure with a lattice parameter $a = 6.207\text{\AA}$. Thummel and Klemm investigated the binary system of lithium-gallium by thermal analysis (7). They found the phase "LiGa" to exist over a wide composition range from 46 to 54 atomic percent (a/o) Li. The lattice parameter was shown to have a linear dependence upon the mol fraction of lithium in this phase. The phases Li_3Ga_2 and Li_2Ga (or Li_3Ga_4) have been reported to form by peritectic reactions. Yatsenko and co-workers (8) proposed a phase diagram for the lithium-gallium system which contains five intermediate phases, with LiGa melting congruently at 740°C . LiGa_4 , LiGa_2 , and Li_2Ga were indicated to decompose peritectically at the respective temperatures 290° , 365° , and 510°C , and Li_3Ga_2 to decompose peritectoidally at 480°C . The crystal structures of the phases Li_3Ga_2 and Li_2Ga have been determined by Muller and Stohr (9).

Yatsenko *et al.* (10) determined the thermodynamic properties of molten lithium-gallium alloys from emf measurements at 750°C . The partial and excess partial molar Gibbs free energies and enthalpies of mixing are negative. The integral molar Gibbs free energies, enthalpies, and entropies of mixing are also negative. Their maximum values occur close to the equiatomic composition. Schneider and Hilmer (11) used drop calorimetry to determine the enthalpy and entropy of fusion for nominal stoichiometric LiGa, with melting apparently occurring over a range of temperature, being complete at 760°C . The data indicate that the heat capacity at constant pressure is 12.9 cal/deg-mol for the solid in the temperature range $550^\circ\text{--}700^\circ\text{C}$ and 9.1 cal/deg-mol for the liquid in the temperature range $760^\circ\text{--}820^\circ\text{C}$.

No data appear in the literature on the thermodynamic properties of the intermediate phases in the lithium-gallium system. An NMR study (12) on LiGa at or near the stoichiometric composition showed indications that the diffusive motion of lithium in that phase is extremely fast, and the activation energy was estimated to be 0.15 eV . However, the value of the self-diffusion coefficient of lithium in LiGa was not given.

Experimental Procedures

The coulometric titrations, emf, and chemical diffusion measurements were all made using the following three-electrode galvanic cell



In the above cell, Li_yGa is the lithium-gallium alloy under investigation. The LiCl-KCl eutectic molten salt was used as electrolyte. The reference and counter-electrodes, Al/"LiAl," were made of two-phase mixtures of lithium-aluminum with an overall composition of 40 a/o Li. A similar experimental setup has been described in more detail elsewhere (13-18). The emf *vs.* composition data were obtained by direct coulometric titration of lithium into pure liquid gallium, which was held in a molybdenum bucket within the salt. The electrochemical measurements were made by using either a PAR 173 potentiostat/galvanostat with a plug-in coulometer or an Aardvark PEC-1 potentiostat with a free-standing PAR 379 digital coulometer.

The temperature was measured by Chromel-Alumel thermocouples sheathed with 304 stainless steel, and maintained constant within one or two degrees.

Cold-pressed and sintered pellets were used in diffusion measurements. The single-phase stoichiometric LiGa alloys were prepared by melting the lithium (99.9%, Foote Mineral) and gallium (99.9999%, United Mineral and Chemicals) metals together in the stoichiometric proportion in an Mo cup at a temperature about 750°C for approximately 10 min. The alloys were then annealed at 450°C for 66 hr in order to promote homogenization. After annealing, the cast alloy was cooled to room temperature in several hours. The solid alloys were powdered and sieved to 150 mesh. The alloy powder was pressed into pellets at a pressure about $9.0 \times 10^4\text{ psi}$. Because the "LiGa" phase is very hard and brittle, pressed pellets often partially collapsed when they were removed from a $\frac{3}{8}$ in. stainless steel die. However, if extreme care was taken to handle the pellets properly, it was possible to obtain one or two intact pellets on about 20% of the trials. The surviving pellets were sintered at 705°C for about 5 min, after which they showed much better mechanical strength and physical integrity.

A ring of thin molybdenum sheet was tightened around the circumference of the thin pellets, and used as both sample holder and electrical lead. This shielded the edge, but permitted diffusion into the pellet from both flat sides. The LiGa pellet was first slowly preheated to drive off any residual gas before it was inserted into the molten salt electrolyte for diffusion measurements. After the sample electrode reached a steady state, the open-circuit voltage was measured with respect to the Al, "LiAl" reference electrode, a small voltage step of 4-8 mV was then imposed between the sample electrode and the reference electrode. The transient current, $I(t)$, was monitored as a function of time, t , until it became negligibly small. Another voltage step was then imposed to repeat the diffusion measurements. After each voltage step the

chemical diffusion coefficient, \tilde{D} , was evaluated from the long-time expression for a potentiostatic experiment as follows (13)

$$I(t) = \frac{2Q\tilde{D}}{L^2} \exp\left(-\frac{\pi^2\tilde{D}t}{4L^2}\right) \quad \text{if } t \gg L^2/\tilde{D} \quad [11]$$

where L and Q were the half-thickness of the sample pellet and the total charge accumulated after a given voltage step. Since the current was controlled by the diffusion of lithium into the solid (from both flat sides), rather than transport through the liquid electrolyte, the current distribution within the electrolyte was of no consequence. While the samples may have not achieved 100% density during the sintering step, this question has relatively little influence upon the results obtained from this long-time solution to the diffusion equations.

The single-phase alloys used for x-ray diffraction analysis were made electrochemically by applying constant voltages determined from the coulometric titration curve to ensure that they were at the desired single-phase compositions. Upon removal from the cell, the alloys were allowed to rapidly cool to room temperature. They were then crushed and sieved to fine powder (150 mesh). The resulting powder was uniformly spread over double-stick Scotch tape (3M) using a glass slide as a support. A thin Kapton film was used to protect the powder from the ambient atmosphere. The x-ray diffraction analysis was accomplished using a Norelco diffractometer employing $\text{Cu K}\alpha$ radiation and an Ni filter. LiCl and KCl salts were used as internal standards. The integrated intensity for each peak was estimated from the area under the diffraction curve above the background.

Results

The coulometric titration curve for the lithium-gallium system at 415°C, starting with pure molten gallium, is shown in Fig. 1. The emf with respect to pure lithium, E , at a given temperature, T (K), was calculated according to the expression (1, 13, 17)

$$E = E_{\text{meas}} + (451 - 0.220 T(\text{K})) \text{mV} \quad [2]$$

where E_{meas} represented the directly measured cell emf with respect to the two-phase Al, "LiAl" reference electrode. Figure 1 shows three intermediate phases and four two-phase voltage plateaus from pure Ga to a composition of 75 a/o Li. The nominal compositions of the three intermediate phases are LiGa, Li_3Ga_2 , and Li_2Ga , respectively. The constant emf values in the two-phase regions are 565, 122, 91, and 20 mV relative to pure lithium at 415°C, in order of increasing lithium concentration. The corresponding lithium activities are 7.26×10^{-5} , 0.126, 0.215, and 0.967, respectively.

As shown in Fig. 1, all three intermediate phases have appreciable ranges of stoichiometry. The x-ray powder diffraction pattern of the phase LiGa was found to possess the NaTl (B32) structure, as reported by Zintl and Brauer (6). The lattice parameter was found to be 6.213Å at the ideal stoichiometric composition by a least square fit to the Nelson-Riley extrapolation function.

In 1977, Muller and Stohr (9) determined the crystal structures for the phases Li_3Ga_2 and Li_2Ga , but they gave no detailed information about their x-ray diffraction patterns. The x-ray powder diffraction patterns obtained in this work for these phases are given in Tables I and II. The phase Li_3Ga_2 , which is isotypic with the phase Li_3Al_2 in the lithium-aluminum system (19), crystallizes with a rhombohedral unit cell, space group $R\bar{3}m-D_{3d}^5$, $a = 4.367\text{Å}$, $c = 13.896\text{Å}$, $Z = 3$ formula units (hexagonal setting), with the Ga atoms forming layers of puckered six-membered rings (9). In Table I, the x-ray powder diffraction pattern of the phase Li_3Ga_2 was indexed on the basis of both rhombohedral ($a = 5.274\text{Å}$ and $\alpha = 48.916^\circ$) and hexagonal axes. Two extraneous lines with interplanar spacings (d values) of 3.576 and 2.718Å having relatively low intensities were found which could not be indexed with the others. Li_2Ga crystallizes orthorhombically, space group $\text{Cmcm}-D_{2h}^{17}$, $a = 4.562\text{Å}$, $b = 9.542\text{Å}$, $c = 4.364\text{Å}$, and $Z = 4$ formula units. In this structure, the Ga sublattice consists of zigzag chains (9). The x-ray powder diffraction pattern for this phase, given in Table II, produced interplanar spacings in excellent agreement with those calculated using the lattice parameters given above and the assigned Miller indexes.

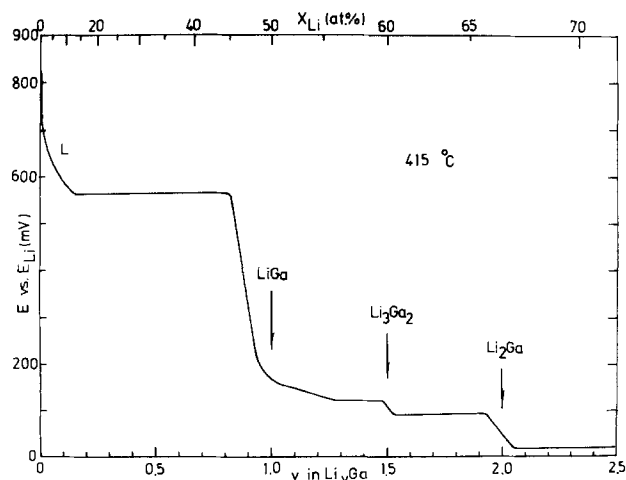


Fig. 1. Coulometric titration curve for the lithium-gallium system at 415°C.

Table I. X-ray powder diffraction pattern of the phase Li_3Ga_2

| h | k | l | d -calc (Å) | H | K | L | d -calc (Å) | d -obs (Å) | I/I_0 (%) |
|-----|-----|-----|---------------|-----|-----|-----|---------------|--------------|-------------|
| 1 | 1 | 1 | 4.632 | 0 | 0 | 3 | 4.632 | 4.634 | 74 |
| 1 | 0 | 0 | 3.649 | 1 | 0 | 1 | 3.649 | 3.670 | 9 |
| — | — | — | — | — | — | — | — | 3.576 | 6 |
| 1 | 1 | 0 | 3.322 | 0 | 1 | 2 | 3.322 | 3.345 | 100 |
| — | — | — | — | — | — | — | — | 2.718 | 10 |
| 2 | 2 | 1 | 2.240 | 0 | 1 | 5 | 2.240 | 2.243 | 54 |
| 1 | 0 | —1 | 2.184 | 1 | 1 | 0 | 2.184 | 2.092 | 90 |
| 2 | 1 | 0 | 1.975 | 1 | 1 | 3 | 1.975 | 1.976 | 28 |
| 2 | 0 | 0 | 1.825 | 2 | 0 | 2 | 1.825 | 1.829 | 32 |
| 3 | 2 | 2 | 1.758 | 1 | 0 | 7 | 1.758 | 1.771 | 13 |
| 3 | 1 | 1 | 1.563 | 2 | 0 | 5 | 1.563 | 1.567 | 22 |
| 2 | 1 | —1 | 1.400 | 1 | 2 | 2 | 1.400 | 1.404 | 12 |
| 4 | 3 | 3 | 1.304 | 1 | 0 | 10 | 1.304 | 1.308 | 14 |
| 4 | 2 | 2 | 1.279 | 2 | 0 | 8 | 1.279 | 1.277 | 21 |
| 3 | 2 | 0 | 1.271 | 1 | 2 | 5 | 1.721 | 1.274 | 12 |

Table II. X-ray powder diffraction pattern for Li_2Ga

| h | k | l | d -calc (Å) | d -obs (Å) | I/I_0 (%) |
|-----|-----|-----|---------------|--------------|-------------|
| 0 | 2 | 0 | 4.771 | 4.770 | 17 |
| 1 | 1 | 0 | 4.116 | 4.118 | 89 |
| 0 | 2 | 1 | 3.220 | 3.227 | 43 |
| 1 | 1 | 1 | 2.994 | 2.998 | 19 |
| 2 | 0 | 0 | 2.281 | 2.281 | 14 |
| 1 | 3 | 1 | 2.240 | 2.240 | 100 |
| 0 | 0 | 2 | 2.182 | 2.183 | 22 |
| 0 | 4 | 1 | 2.093 | 2.095 | 11 |
| 1 | 1 | 2 | 1.928 | 1.930 | 16 |
| 2 | 2 | 1 | 1.861 | 1.863 | 14 |
| 1 | 5 | 1 | 1.633 | 1.634 | 5 |
| 0 | 6 | 0 | 1.590 | 1.593 | 5 |
| 2 | 6 | 0 | 1.305 | 1.305 | 10 |

For compositions less than about 8.3 a/o Li, the lithium activity in liquid lithium-gallium alloys was found to obey Henry's law, i.e.

$$-FE = RT \ln a_{\text{Li}} = RT \ln \gamma_{\text{Li}} X_{\text{Li}} \quad [3]$$

where F , R , γ_{Li} , and X_{Li} are the Faraday constant, the gas constant, the activity coefficient of lithium, and the mol fraction of lithium, respectively. As shown in Fig. 2, the emf with respect to pure lithium, E , is a linear function of $\ln X_{\text{Li}}$. The slope $dE/d \ln X_{\text{Li}}$ is $-5.93 \times 10^{-2}\text{V}$, which is identical to the value of $(-RT/F)$ at the temperature of 688 K. The activity coefficient of lithium in molten lithium-gallium at that temperature is thus 4.49×10^{-4} . The lithium activities in liquid alloys of lithium-cadmium (20),

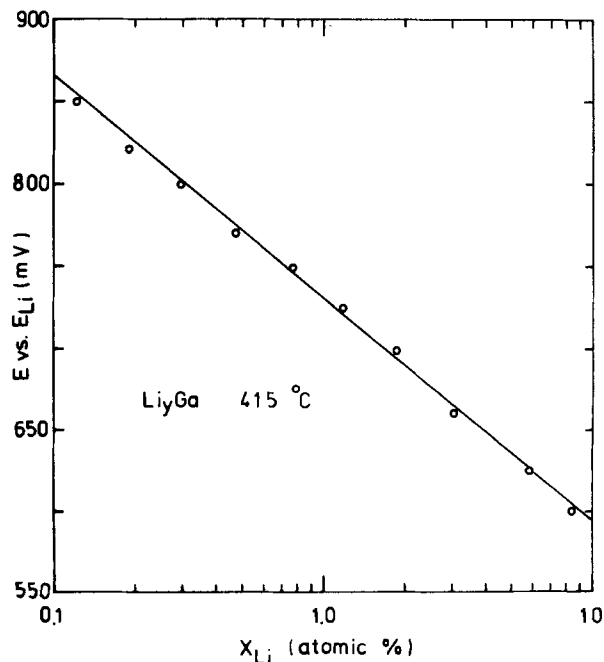


Fig. 2. Semi-logarithmic plot of the emf vs. mol fraction of lithium at 415°C.

lithium-indium (21), lithium-tin (22), lithium-lead (23), and lithium-bismuth (24) systems have also been found to obey Henry's law at low lithium concentrations.

Figure 3 presents the temperature variation of the emf of the two-phase system consisting of the saturated liquid alloy of lithium in gallium and the vario-stoichiometric intermediate phase "LiGa" at an overall composition of 40 a/o Li. Over the temperature range from 380° to 575°C, the emf of this liquid-solid mixture shows a linear dependence upon temperature, which can be expressed as

$$E = 929 - 0.532 T(\text{K}) \text{ mV} \quad [4]$$

The corresponding partial molar entropy and enthalpy of lithium in this two-phase region are -51.3 J/deg-mol and -89.6 kJ/mol , respectively.

The temperature dependences of these two-phase boundaries were investigated by use of the coulometric titration technique. The solubility of lithium in liquid gallium was found to be 10.0, 12.6, 18.2, and 26.1 a/o Li at 390°, 415°, 500°, and 585°C, respectively. These results are in close agreement with those reported in the literature (7). The gallium-rich phase boundary of the phase "LiGa" was observed to be essentially constant (44.8 a/o Li) over the temperature range of 390°-585°C. No effort was made to determine the lithium-rich phase boundary of "LiGa" because of a slow voltage drift with time at high lithium activities, due to electronic conduction in the electrolyte.

Figure 4 shows the detailed results obtained on the coulometric titration curve of the phase "LiGa." The emf vs. composition data can be approximated by two straight lines with different slopes. However, the change in slope does not occur at the ideal stoichiometry. The experimental data showed excellent agreement and reproducibility. This is illustrated by the correspondence of the data from three runs, as denoted by the different symbols in Fig. 4. At 415°C, the emf of the phase "LiGa" lies between 565 and 122 mV with respect to pure lithium and the lithium activity varies by more than three orders of magnitude over the composition range from 44.8 to 56.0 a/o Li.

The Gibbs free energy of mixing, ΔG_m , was calculated across this phase by graphical integration of the coulometric titration curve given in Fig. 1 using the expression (17, 18)

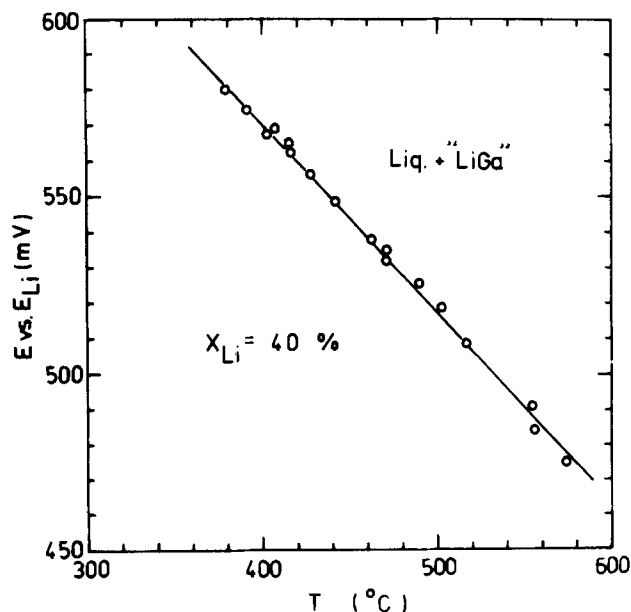


Fig. 3. Temperature dependence of the emf of two-phase lithium-gallium alloy with overall composition of 40 a/o Li.

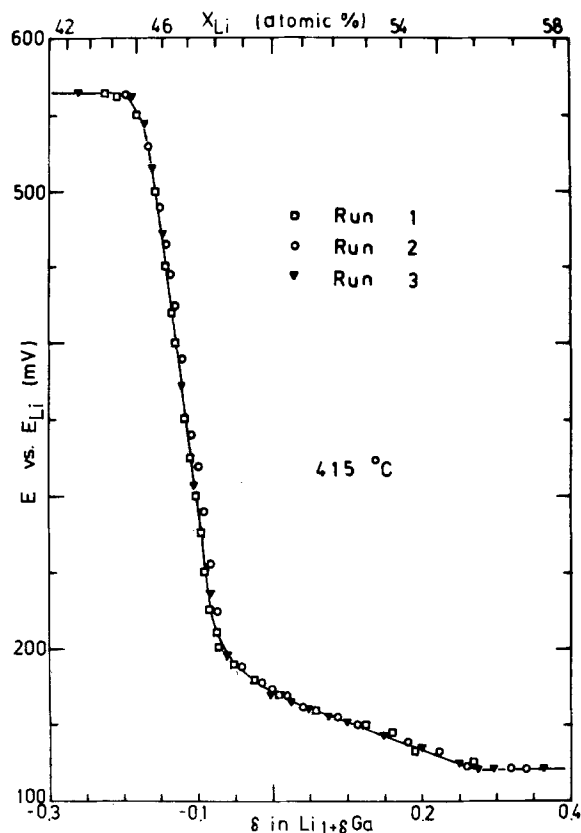


Fig. 4. Coulometric titration curve of the phase "LiGa;" three runs at 415°C.

$$\Delta G_m = - \frac{F}{1+y} \int_0^y E dy \quad [5]$$

where y is the atomic ratio of lithium to gallium. The results are presented in Fig. 5, where it is seen that the Gibbs free energy of mixing shows a minimum of -25.8 kJ/mol at 47.6 a/o Li.

The standard Gibbs free energy of formation, ΔG_f , was evaluated according to the following expression

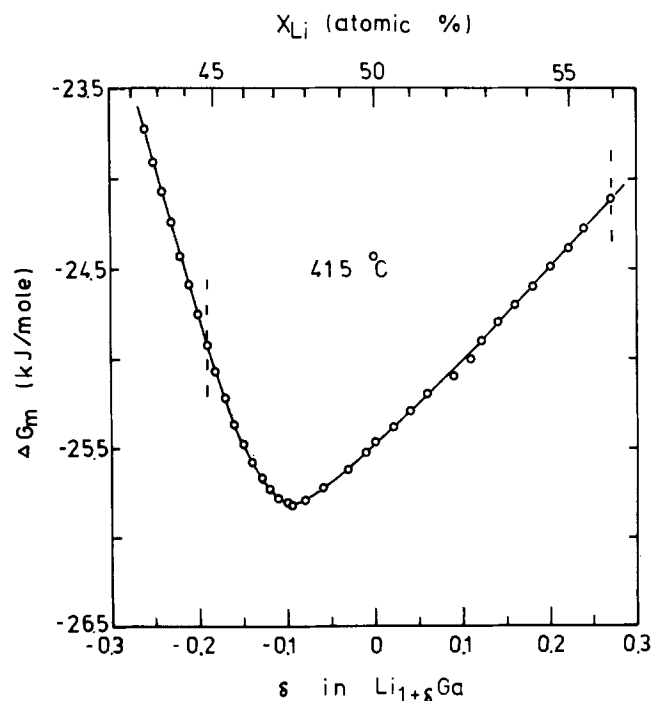


Fig. 5. Compositional dependence of Gibbs free energy of mixing over the compositional range of the phase "LiGa" at 415°C.

(17, 18)

$$\Delta G_f(\text{Li}_a\text{Ga}_b) = -bF \int_0^y E dy \quad [6]$$

where $y = a/b$. The values for the stoichiometric compositions within the phases LiGa , Li_3Ga_2 , and Li_2Ga at 415°C are -51 , -115 , and -62 kJ/mol, respectively. The corresponding formation reaction can be described as



The chemical diffusion coefficient was determined as a function of composition within the phase "LiGa." The results are plotted in Fig. 6. It can be seen to vary from 1.6×10^{-6} to 6.8×10^{-5} cm²/sec, with a maximum value at the composition 47.6 a/o Li. On the lithium excess side of LiGa, the chemical diffusion coefficient increases only slightly with increasing lithium concentration. On the lithium deficit side of LiGa, however, it is very composition dependent, increasing rapidly with a small lithium deficiency, but again decreasing in value at greater lithium deficits after a maximum at 47.6 a/o Li.

The chemical diffusion coefficient, \tilde{D} , which concerns mass transport under the influence of a chemical potential gradient, is related to the lithium self-diffusion coefficient, D_{Li} , which describes the random motion of the lithium atoms or ions in the absence of a chemical concentration gradient, by the following expression (15, 25)

$$\tilde{D} = D_{\text{Li}} \left(\frac{d \ln a_{\text{Li}}}{d \ln (1 + \delta)} \right) \quad [8]$$

where δ represents the deviation from the ideal stoichiometry of the phase "LiGa." The above expression is valid only for the case that the gallium atoms (or ions) do not move appreciably compared with the lithium atoms (or ions). An NMR study of LiGa supports this approximation (12)

The quantity in the bracket on the right-hand side of Eq. [8], the enhancement factor, often assumes values greater than unity for alloy phases exhibiting non-ideal thermodynamic behavior. Its magnitude was calculated as a function of composition by using the emf vs. composition data as follows

$$\frac{d \ln a_{\text{Li}}}{d \ln (1 + \delta)} = - \frac{F}{RT} (1 + \delta) \frac{dE}{d\delta} \quad [9]$$

where $dE/d\delta$ denotes the local slope of the coulometric

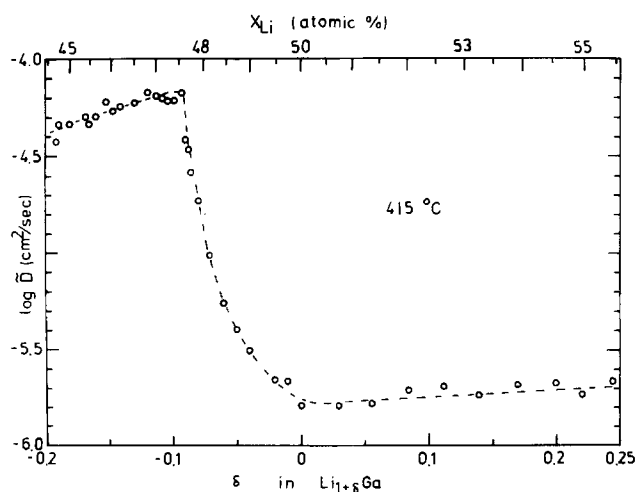


Fig. 6. Compositional dependence of the chemical diffusion coefficient within the phase "LiGa" at 415°C .

titration curve at a given composition. The calculated results are shown in Fig. 7. On the lithium excess side of LiGa, the enhancement factor increases slightly with lithium concentration. However, it increases rapidly with decreasing lithium concentration on the lithium-deficient side, reaching a maximum value of 56 at 47.6 a/o Li. It then decreases again as the composition moves toward the gallium-rich phase boundary. As shown in Fig. 6 and 7, the compositional dependence of the chemical diffusion coefficient within the phase "LiGa" is quite similar to that of the enhancement factor, and they both peak at the composition corresponding to the minimum Gibbs free energy of mixing, i.e., 47.6 a/o Li.

Figure 8 shows the compositional variation of the lithium self-diffusion coefficient at 415°C . For compositions greater than 48.0 a/o Li or less than about 47.6 a/o Li, this parameter was found to be independent of composition. The constant values are 1.1×10^{-6} and 5.0×10^{-7} cm²/sec on the lithium deficit and excess sides of LiGa, respectively.

Discussion

The work reported here is an example of the great power of electrochemical techniques for the quantitative determination of a host of both thermodynamic and kinetic data in alloy systems. Of special value is the ability to readily evaluate fundamental param-

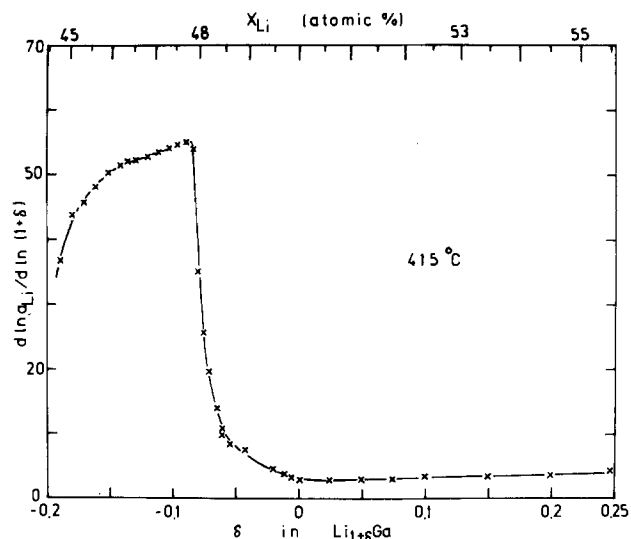


Fig. 7. Compositional dependence of the enhancement factor within the phase "LiGa" at 415°C .

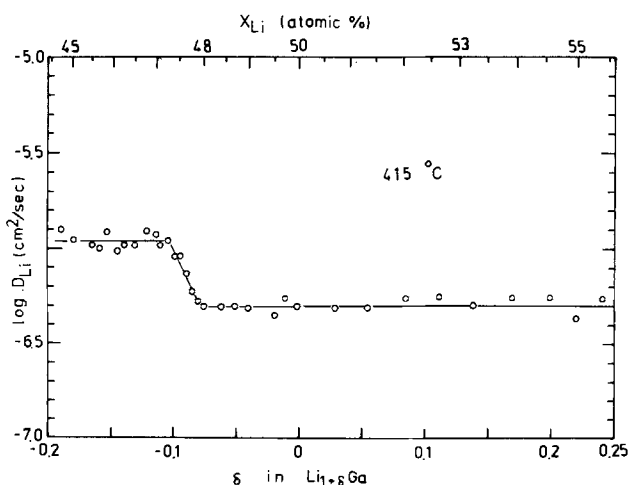


Fig. 8. Compositional dependence of the lithium self-diffusion coefficient within the phase "LiGa" at 415°C .

eters which would be of importance in the application of such materials in electrochemical systems, such as primary or secondary batteries.

Questions such as the ranges of electrochemical stability of intermediate phases and the potentials and capacities of two-phase equilibria that might be used as ion reservoirs will play a critical role in the design of new electrode systems. While not specifically employing the results of this study of the lithium-gallium system, this approach has recently been used to design novel all-solid electrodes with composite microstructures containing a finely dispersed reactant imbedded in a stable mixed-conducting matrix with a high chemical diffusion coefficient for the electroactive species (26). Although they are fully solid, such electrodes can have the kinetic properties of conventional finely divided powders.

Acknowledgment

This work was sponsored by the U.S. Department of Energy under Contract No. EC-77-S-02-4506 and LBL Subcontract No. 4503110.

Manuscript submitted May 5, 1980; revised manuscript received Dec. 23, 1980.

Any discussion of this paper will appear in a Discussion Section to be published in the June 1982 JOURNAL. All discussions for the June 1982 Discussion Section should be submitted by Feb. 1, 1982.

Publication costs of this article were assisted by Stanford University.

REFERENCES

1. N. P. Yao, L. A. Heredy, and R. C. Saunders, *This Journal*, **118**, 1039 (1971).
2. E. C. Gay, D. R. Vissers, F. J. Martino, and K. E. Anderson, *ibid.*, **123**, 1591 (1976).
3. S. C. Lai, *ibid.*, **123**, 1196 (1976).
4. R. A. Sharma and R. N. Seefurth, *ibid.*, **123**, 1763 (1976).
5. R. N. Seefurth and R. A. Sharma, *ibid.*, **124**, 1207 (1977).
6. E. Zintl and G. Brauer, *Z. Phys. Chem.*, **B20**, 245 (1933).
7. R. Thummel and W. Klemm, *Z. Anorg. Allg. Chem.*, **376**, 44 (1970).
8. S. P. Yatsenko, K. A. Chuntunov, S. J. Alyamovskii, and E. N. Dieva, *Izvest. Akad. Nauk SSSR, Metal* No. 1, 185 (1973).
9. W. Muller and J. Stohr, *Z. Naturforsch. Teil B*, **32**, 631 (1977).
10. S. P. Yatsenko, E. A. Saltykova, E. N. Dieva, and L. N. Rykova, *Z. Fiz. Khim.*, **47**, 2417 (1973) and *Russ. J. Phys. Chem.*, **47**, 1365 (1973).
11. A. Schneider and O. Hilmer, *Z. Anorg. Allg. Chem.*, **286**, 97 (1956).
12. H. E. Schone and W. D. Knight, *Acta Metall.*, **11**, 179 (1963).
13. C. J. Wen, W. Weppner, B. A. Boukamp, and R. A. Huggins, *This Journal*, **126**, 2258 (1979).
14. C. J. Wen, W. Weppner, B. A. Boukamp, and R. A. Huggins, *Metall. Trans.*, **11B**, 131 (1980).
15. W. Weppner and R. A. Huggins, *This Journal*, **124**, 1569 (1977).
16. W. Weppner and R. A. Huggins, *J. Solid State Chem.*, **22**, 297 (1977).
17. W. Weppner and R. A. Huggins, *This Journal*, **125**, 7 (1978).
18. B. E. Liebert, Ph.D. Dissertation, Stanford University (1977).
19. K. F. Tebbe, H. G. v. Schnering, B. Ruter, and G. Rabeneck, *Z. Naturforsch. Teil B*, **28**, 600 (1973).
20. C. J. Wen, Ph.D. Dissertation, Stanford University (1980).
21. C. J. Wen and R. A. Huggins, *Mater. Res. Bull.*, **15**, 1225 (1980).
22. C. J. Wen and R. A. Huggins, *This Journal*, **128**, 1181 (1981).
23. A. I. Demidov, A. G. Morachevskii, and L. N. Gerasimenko, *Elektrokhimiya*, **9**, 848 (1973) and *Sov. Electrochem.*, **9**, 813 (1973).
24. A. I. Demidov and A. G. Morachevskii, *Elektrokhimiya*, **9**, 1393 (1973) and *Sov. Electrochem.*, **9**, 1321 (1973).
25. L. S. Darken, *Trans. AIME*, **175**, 184 (1948).
26. B. A. Boukamp, G. C. Lesh, and R. A. Huggins, Paper 85 presented at The Electrochemical Society Meeting, Hollywood, Florida, Oct. 5-10, 1980.

Deep Discharge Cycle Life of Cells Constructed with Wrought Antimonial Lead Grids

J. L. Devitt*

Consulting Engineer, Denver, Colorado 80222

and M. Myers

ASARCO Incorporated, Central Research Department, South Plainfield, New Jersey 07080

ABSTRACT

Three antimonial lead alloys have been continuously cast followed by rolling and expansion to standard battery grid designs. Cells were constructed and cycled to failure in a deep discharge regime. Cells of cast grids were similarly tested for comparison. In these tests the wrought grid cells failed prior to the cast due to excessive grid growth. Possible means to overcome the grid growth are discussed.

In recent years there have been many papers published concerned with the metallurgy and electrochemistry of cast low antimony lead alloys for use in low maintenance auto batteries (1-4). Similarly there has been much work published on the metallurgy,

electrochemistry, and manufacture of calcium lead alloy battery grids for the same market. These latter papers encompass a good deal of work on the continuous production of wrought calcium-lead grids (5, 6). There has not as yet been work published combining the advantages of deep discharge behavior of antimonial lead alloys, with the economic advantage

* Electrochemical Society Active Member.
Key words: cast grids, grid growth, cell failure.

of continuous wrought grid manufacture for the mass production of grids for electric vehicle or load leveling batteries.

Many characteristics of batteries constructed of wrought grids are yet to be determined. While it is well known (7) that in battery service cast antimonial lead has the disadvantage of low hydrogen overvoltage as compared to calcium lead, electrochemical characteristics of wrought vs. cast antimonial leads have not been reported upon. Further, the creep resistance of wrought antimonial lead is known to be significantly less than that of the cast alloys. The effect this may have on battery life is unknown. Another factor of importance which may be affected by the metal structure is the corrosion rate under deep discharge cycling. Grid growth is another area which could affect battery life and which very likely depends on the metallurgical condition of the grid metal.

In order to test the feasibility of wrought grid, deep discharge, antimonial lead batteries, test cells were constructed using wrought grids of antimonial lead at three concentrations. These cells were cycled to failure in a severe deep discharge (75%) regime along with a set of cast grid cells as controls. The results proved the cast grid cells to be clearly superior to any of the wrought grid cells. There were, however, indications that wrought grids can be made to perform by adjustments to the design and metallurgical structure of the grids.

Materials and Fabrication

Wrought grids.—As a first step it was necessary to determine whether or not antimonial leads could be continuously cast. Casting was carried out at the Hazelett Strip Casting Corporation, Malletts Bay, Vermont, on a Model 21 machine. Four compositions were chosen all of which cast without mishap. The actual compositions are shown in Table I. Nominal arsenic and tin levels were supposed to be 0.5% as in some common cast grid alloys.

The alloys were cast continuously into strips 3.3 in. wide \times 0.75 in. thick at a rate of about 20 ft/min. The melt temperature was held within the range 340°–370°C, and the casting emerged from the machine at about 180°C.

For each alloy starting with alloy A (1% Sb) about 1960# of metal was charged to the melting pot. Of that 1960# about 60% was cast producing a strip roughly 90 ft long. The middle 30 ft was retained for the project and the two remaining sections were returned to the pot for the following castings. Antimony, arsenic, and tin additions were made as hardener alloys. Unfortunately, the presence of high As and Sn in the addition ingots caused excesses of these elements in the product alloys.

The surfaces of the cast strips were generally smooth and uniform. Grain size of the castings decreased as alloy content increased. Some centerline shrinkage was apparent in each alloy, especially alloy D, see Fig. 1.

Rolling of the alloys was done on a 2-high laboratory mill using 4 in. diam rolls, 6 in. wide. The cast strip was cut to 6 in. lengths and rolled in a direction parallel to the casting direction. Each pass reduced the thickness by 0.08 in. to a thickness 0.1 in. From 0.1 in. to the final size 0.045 in. reductions were limited to

0.020 in. per pass. Alloys A and B rolled to final size without problems. Alloy D could not be rolled more than 3 passes, about 33% reduction in thickness, without separating through the wide centerline, a phenomenon known as "alligatoring." Alloy C required an intermediate anneal (150°C–1 hr–air cool) at about 60% reduction to prevent alligatoring. Strip of alloy D was finally produced by hot rolling at 150°C. Some edge cracking was noted on alloys C and D. Tensile strength of the strips measured one day after rolling are recorded in Table II.

Coils of strip (alloys A–D) rolled to 0.045 in. were shipped for expansion to a battery manufacturer presently producing expanded metal grids. This expander was unable to treat the metal supplied efficiently due to excessive camber in the coils. Insufficient high quality material was returned to allow a valid series of tests. It was made clear, however, that of the alloys supplied, alloy D was the most difficult to expand, excessive cracking being encountered.

Rolling technique was improved and fresh coils shipped to two other grid metal expanders. Expander I was shipped alloys A, B, C, and D while Expander II was shipped only alloys A, B, and C. Difficulty was reported by Expander I in expanding alloys C and D due to edge cracks in the rolled strip. Expander II could not expand alloy A due to excessive limpness (low strength).

Expander I provided grids of alloys A and B cut to shape ready for pasting. Expander II supplied strips of expanded alloys B and C about a yard long from which grids had to be cut by hand.

Cast grids.—Control cells were to be constructed of grids of moderate to low antimony content with weights and size similar to those of the wrought grids. Analyses of the cast grids obtained are included in Table I. A photograph of the cast and wrought grids is shown in Fig. 2.

Cell fabrication.—In all, five different grid types were tested: the cast, Expander I alloys A and B, and Expander II alloys B and C. Three cells were constructed of each grid type totaling 15 cells. Variations in the grid physical dimensions were dictated by the manufacturing equipment and were thus unavoidable. Overall dimensions of the grids prior to pasting are summarized in Table III. Note in column five of Table III, Approximate metal thickness, that the variation represents variation in setting on the expander rather than in the metal supplied which was 0.043 ± 0.002 in. Also note in column six of the same table that the overall thickness of the wrought grids reflects a degree of corrugation not present in cast grids.

Pasting of the grids was done using a conventional high density formula. Efforts were made to keep the paste weight per unit area of positive plate constant regardless of grid type. As the grids were inescapably of different sizes it was desired to keep the paste thickness the same in all 15 cells in order to make comparison more meaningful. Since the positive plate capacity was intentionally limiting in all cells, care was taken to obtain the same total weight of positive active material in each of the three cells of a test group. This was done by weighing all of the pasted

Table I. Alloy composition

| | Sb (w/o) | As (w/o) | Sn (w/o) |
|------------|----------|----------|----------|
| A | 1.07 | 0.78 | 0.48 |
| B | 2.02 | 0.85 | 0.56 |
| C | 3.62 | 0.93 | 0.69 |
| D | 5.12 | 1.1 | 0.82 |
| Cast grids | 2.75 | 0.13 | 0.13 |

Table II. Tensile data,* wrought antimonial grid alloys

| Alloy | UTS (psi) | E (%) |
|-------|-----------|-------|
| A | 4160 | 44 |
| B | 4810 | 38 |
| C | 4590** | 27 |
| D | 5990† | 37 |

* All data average of three tests. Strain rate, 0.2 min⁻¹.

** Annealed at 60% reduction in thickness.

† Hot rolled 150°C.

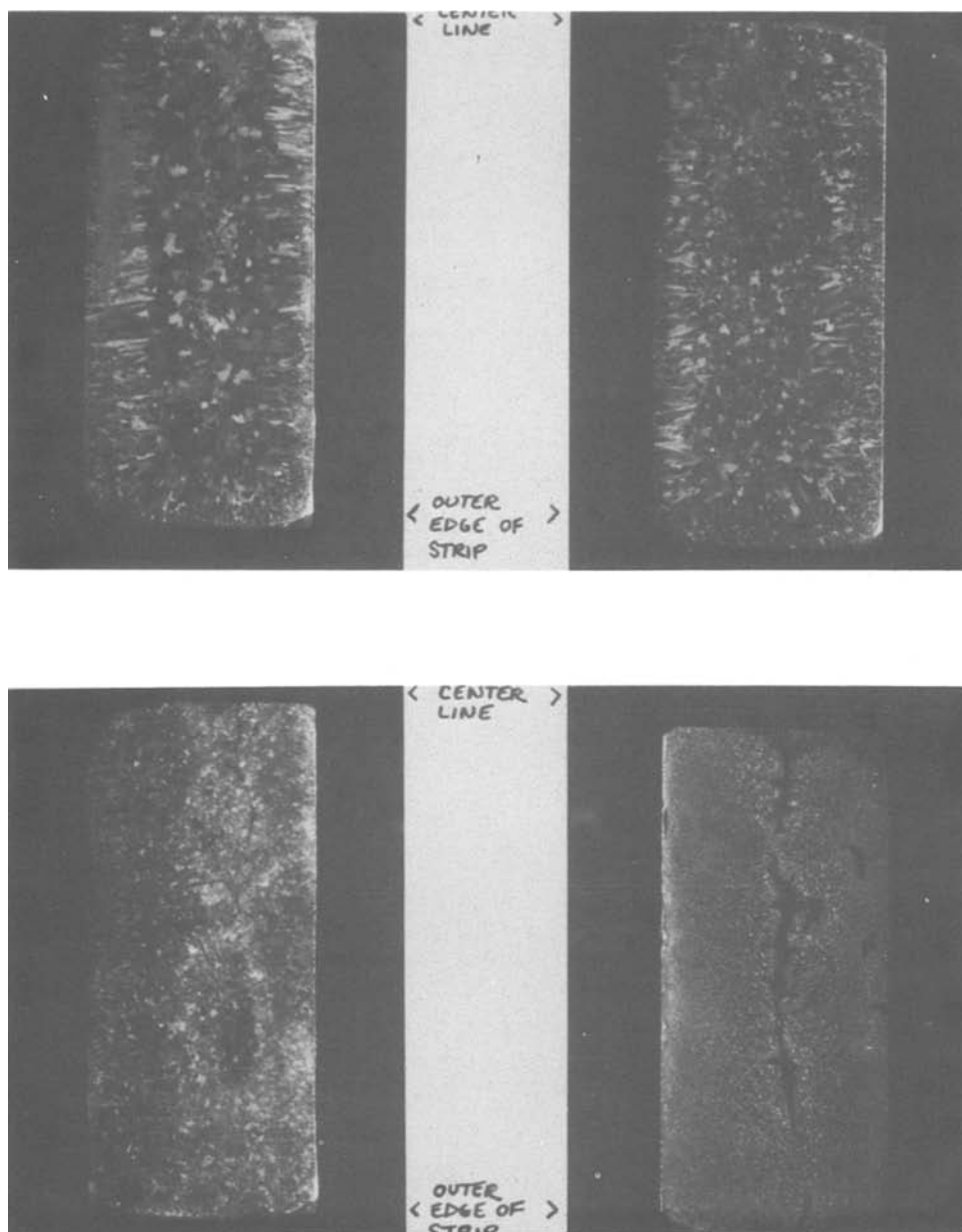


Fig. 1. Macro-etched cross sections of Hazelett-cast alloys. Alloy A (upper left), Pb-1.07Sb-0.78As-0.48Sn. Alloy B (upper right), Pb-2.02Sb-0.85As-0.56Sn. Alloy C (lower left), Pb-3.62Sb-0.93As-0.69Sn. Alloy D (lower right), Pb-5.12Sb-1.1As-0.82Sn.

plates and then sorting them into groups of similar aggregate weight. There were no side frames on the expanded metal grids, thus extreme care to avoid losing paste pellets along the side of the pasted plates was required. Such losses could account for a significant proportion of the total active material. Table IV contains data on the weight of active material in the cells.

The cells were constructed using, as far as was possible, methods and procedures similar to those employed in commercial battery fabrication.

Commercially available golf cart separators (Grace Armor-rib with 0.020 glass mat) were used. The cells were formed conventionally using constant current

formation and an electrolyte of 1.110 sp gr. After formation the cells were dumped and refilled with 1.320 sp gr acid, adjusting them individually to a final range of 1.265-1.275.

Cell testing.—Prior to the beginning of the automatic cycling manual cycles were run on each cell to determine initial cell capacities. Discharges were run at rates of 1.5, 8, 10, and 14A. The results agreed well with one another and with the theoretical capacity of the cells. Averaged data for the 1.5 and 10A tests are presented in Table V.

Using the capacity information obtained from the manual cycling, the automatic cycle apparatus was set to provide a 2 hr discharge followed by a 9.5 hr

Table III. Grid parameters

| Alloy | Nominal % Sb | Grid rectangle size (in.) | Active area** (sq-in.) | Approx. metal thickness (in.) | Approx. overall thickness (in.) | Average grid weight (g) |
|----------------|--------------|---------------------------|------------------------|-------------------------------|---------------------------------|-------------------------|
| Cast (control) | 2.75 | 5.69w × 3.91h | 21 | — | 0.043 | 42.2 |
| I-A | 1.0 | 5.69 × 4.12 | 21 | 0.045 | 0.11 | 51.0 |
| I-B | 2.0 | 5.69 × 4.12 | 21 | 0.051 | 0.11 | 54.5 |
| II-B | 2.0 | 5.69 × ~5.0* | ~27 | 0.040 | 0.075 | 46.2 |
| II-C | 3.6 | 5.69 × ~5.0* | ~27 | 0.040 | 0.075 | 45.9 |

* The Expander I grids varied in height from 4.8 to 5.2 in.

** The active area includes only the portion of the grid containing paste openings, omitting the solid strip at the top.

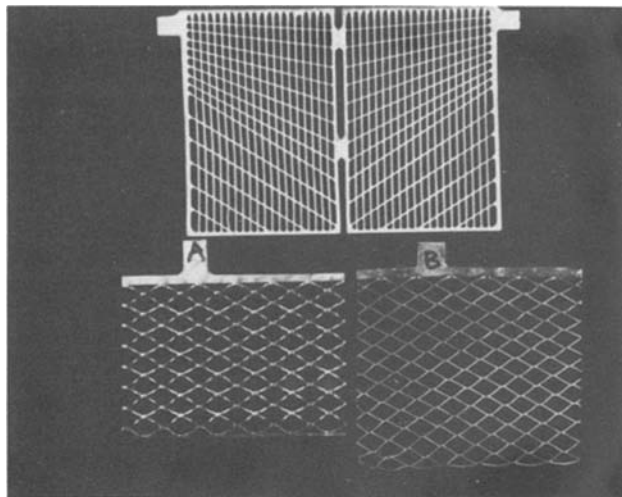


Fig. 2. Test grids as received. Top, cast. Bottom left, alloy I-A. Bottom right, alloy II-B.

charge twice each day. As the discharge time was the same for each cell but capacity varied (mainly due to plate size), it was necessary to vary discharge current load to yield the desired 75% depth of discharge for every cell.

The cells were charged for 9.5 hr through current limiting resistors from a regulated 2.6V bus. The current was limited to the 2 hr rate at the beginning of charge. Following charge there was a one-half hour rest.

Discharge was carried out so as to yield 75% depth after 2 hr. As the cells progressed toward the end of life the voltage dropped below 1.75V before the end of the 2 hr discharge period. In that case an automatic cell cut-off circuit terminated the discharge at 1.75V in order to avoid an unrealistically deep

Table IV. Cell parameters

| Cell No. | Grid alloy type | Total cured positive paste per cell (g) | Same for negative | Positive weight (g/sq in.) | Average neg/pos capacity ratio |
|----------|-----------------|---|-------------------|----------------------------|--------------------------------|
| 1 | Cast | 319 | 399 | 15.2 | |
| 2 | Cast | 323 | 394 | 15.4 | 1.2 |
| 3 | Cast | 320 | 397 | 15.2 | |
| 4 | I-A | 330 | 569 | 15.7 | |
| 5 | I-A | 329 | 569 | 15.7 | 1.7 |
| 6 | I-A | 327 | 566 | 15.6 | |
| 7 | I-B | 332 | 656 | 15.8 | |
| 8 | I-B | 334 | 660 | 15.9 | 2.0 |
| 9 | I-B | 332 | 665 | 15.8 | |
| 10 | II-B | 436 | 565 | 16.1 | |
| 11 | II-B | 430 | 595 | 15.9 | 1.3 |
| 12 | II-B | 437 | 564 | 16.2 | |
| 13 | II-C | 423 | 591 | 15.7 | |
| | II-C | 422 | 593 | 15.6 | 1.4 |
| | II-C | 423 | 605 | 15.7 | |

Table V. Average capacities of cell groups

| Grid alloy | Actual A-hr capacity | | Theoretical positive A-hr capacity* | Positive utilization in % of theoretical | |
|------------|----------------------|----------|-------------------------------------|--|----------|
| | 1.5A rate | 10A rate | | 1.5A rate | 10A rate |
| Cast | 39 | 26 | 58 | 67 | 46 |
| I-A | 40 | 29 | 59 | 67 | 49 |
| I-B | 41 | 26 | 60 | 68 | 44 |
| II-B | 50 | 29 | 78 | 64 | 37 |
| II-C | 48 | 30 | 76 | 64 | 40 |

* Theoretical capacities are based on total positive active material in cell. Paste formula yields 179.7 A-hr/kg of cured paste.

cycle. Failure was defined to have occurred when cell capacity fell below 50% of the capacity of the 10th cycle. Base capacity was defined as the 10th cycle value in order to avoid initial transients. The cells were individually taken off test after failure.

Cells were cycled at room temperature, separated from each other so as to minimize heating effects.

Cell dismantling.—After failure by the 50% capacity criterion the cells were fully charged and then carefully dismantled.

The positive plates were washed thoroughly in water and dried at room temperature. During handling some loss of active material pellets was experienced in the expanded metal plates. Tabs were removed from all plates after which they were weighed and measured. All weights reported in the tables are without tabs.

A representative set of positive plates from each of the five test groupings was chemically treated to remove all of the lead dioxide from the grids. The bare grids were then re-weighed.

Sections of the corroded grids were examined metallographically and compared. Photographs of samples taken from the center of typical plates are shown in Fig. 3-5.

Results

Cycles to failure, water required over life, active material loss, grid weight loss, and percent grid growth for each cell are presented in Table VI. The data are averaged per 100 cycles of life for each alloy

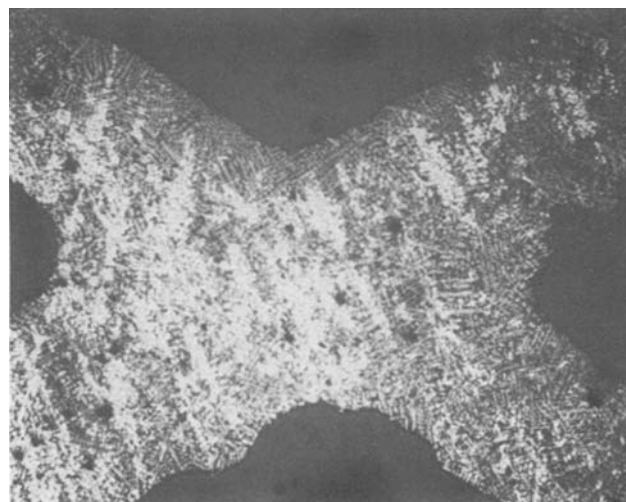


Fig. 3a. Positive grid section from cell No. 2. Etched, 50X

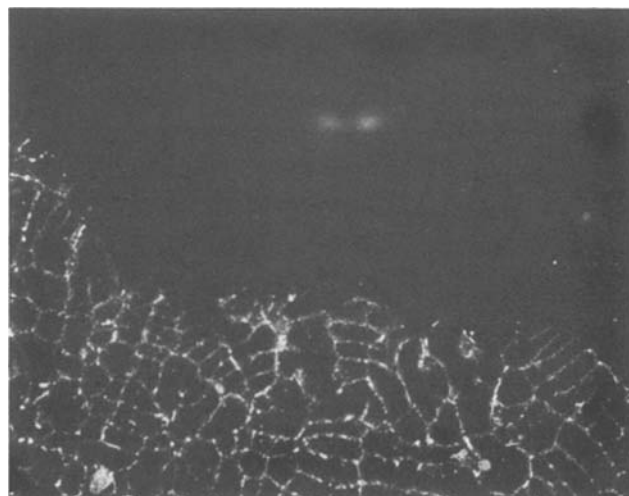


Fig. 3b. Positive grid section from cell No. 2. Etched, 400X

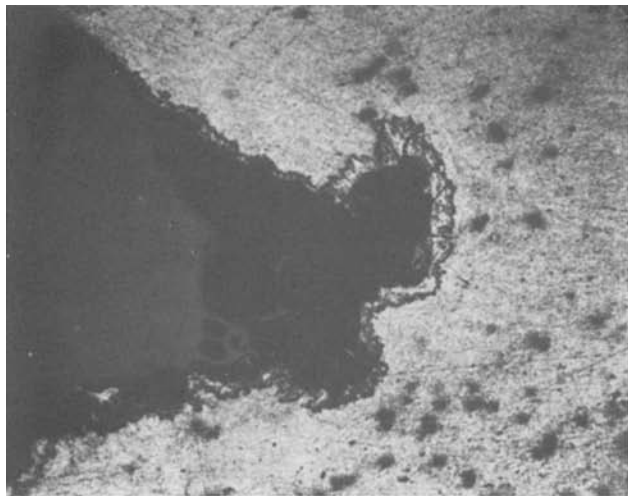


Fig. 4a. Positive grid section from cell No. 8. Etched, 50×

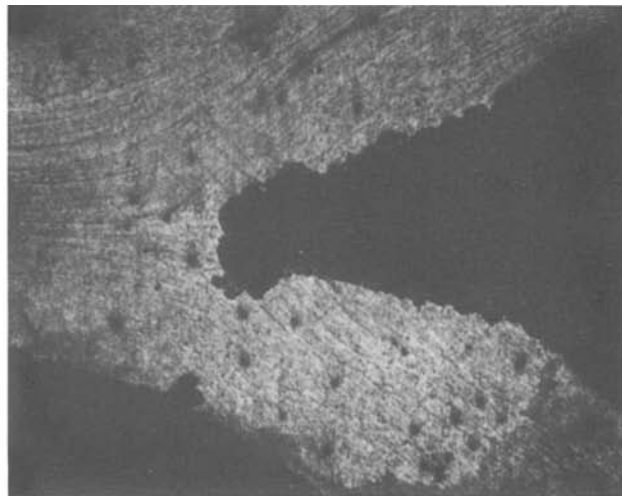


Fig. 5a. Positive grid section from cell No. 10. Etched, 50×

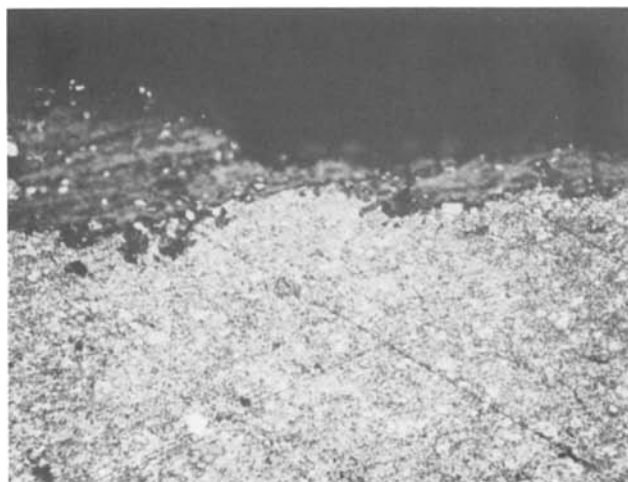


Fig. 4b. Positive grid section from cell No. 8. Etched, 400×

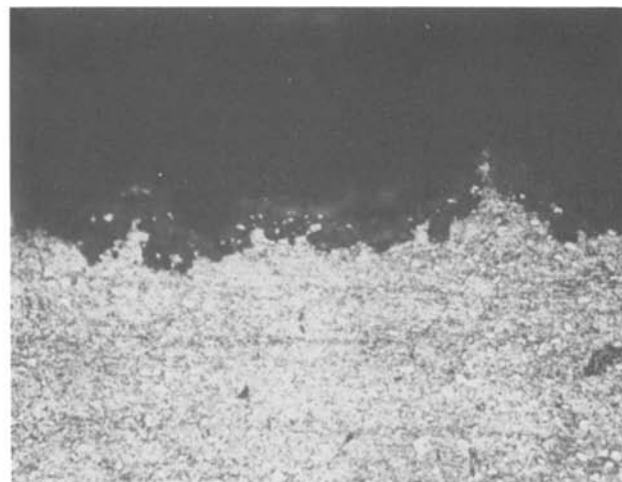


Fig. 5b. Positive grid section from cell No. 10. Etched, 400×

group in Table VII in order to obtain values directly related to rate of deterioration.

Discussion

From the data of Tables VI and VII it is clear that under the test conditions reported the cells made of cast grids out-performed the wrought grid cells. However, some interesting lessons can be learned by examining the data which may make future wrought low antimony lead grids more competitive.

First, the cycle life data of Table VI show that the greatest disparity in behavior lies between the wrought grids taken as a group and the cast grids rather than between alloy content groups or expander groups. Within the wrought grid groupings design variation seems overriding. For example, cells of group II-B performed significantly better than those in group I-B although the alloys were identical and the test conditions, other than cell size, similar. It seems unlikely that size difference could account for the variation in cycle life, considering the controls on each cell described above.

Water loss, although varying considerably cell to cell was on average (Table VII) consistently in the range 58-68 ml/100 cycles. The only exceptions were the cells made of the lowest antimony content grids (1% Sb), group I-A. These cells used water at the rate of only 16 ml/100 cycles. Clearly there is an advantage in reduced maintenance to the very low antimony level. This reduction in water loss is unexpected considering the paper of Ruetschi and Cahan

(8) who reported a less than expected rate of decline in hydrogen overvoltage with increasing antimony (1-5%) in cast antimonial leads.

Active material loss was much greater in the wrought grid cells than in the cast even though the cast grid cells experienced a substantially greater number of cycles. Two possible reasons are proposed. First, it is possible that for some reason the well documented (9) paste adhesion of cast antimonial lead grids does not operate for wrought grids

Table VI. Results of cycling

| Cell No. | Cycles to failure | Water added over life (ml) | Positive active material loss (%) | Grid weight loss (%) | % Grid growth width | % Grid growth height |
|----------|-------------------|----------------------------|-----------------------------------|----------------------|---------------------|----------------------|
| 1 | 305 | 275 | 39 | 41 | 0 | 1.0 |
| 2 | 245 | 153 | 27 | 22 | 0 | 0.5 |
| 3 | 242 | 120 | 37 | 20 | 0 | 0.5 |
| 4 | 185 | 20 | 48 | 14 | 1.7 | 5.0 |
| 5 | 185 | 28 | 36 | 14 | 1.7 | 4.8 |
| 6 | 196 | 44 | 29 | 19 | 2.4 | 4.1 |
| 7 | 165 | 120 | 50 | 29 | 2.3 | 8.3 |
| 8 | 175 | 120 | 54 | 25 | 2.2 | 6.1 |
| 9 | 186 | 110 | 54 | 25 | 2.3 | 6.1 |
| 10 | 240 | 205 | 58 | 24 | 3.2 | 6.4 |
| 11 | 190 | 56 | 44 | 27 | 3.3 | 4.0 |
| 12 | 215 | 124 | 58 | 25 | 2.5 | 6.3 |
| 13 | 195 | 131 | 23 | 31 | 2.6 | 7.6 |
| 14 | 190 | 123 | 38 | 36 | 3.3 | 5.6 |
| 15 | 175 | 82 | 49 | 25 | 3.7 | 5.8 |

Table VII. Averaged cycling results per 100 cycles of life

| Alloy group | Avg. cycle life | Water use (ml) | Positive active material loss (%) | Grid weight loss (%) | Grid growth (%) | |
|-------------|-----------------|----------------|-----------------------------------|----------------------|-----------------|--------|
| | | | | | Width | Height |
| Cast | 264 | 67 | 13 | 10 | 0 | 0.2 |
| I-A | 187 | 16 | 20 | 9 | 1.0 | 2.5 |
| I-B | 175 | 67 | 30 | 15 | 1.3 | 4.1 |
| II-B | 215 | 58 | 25 | 12 | 1.4 | 2.5 |
| II-C | 187 | 60 | 20 | 16 | 1.7 | 3.4 |

of essentially the same composition. Second, it is possible that the larger pellet sizes of the wrought grids (Fig. 2) leads to reduced grid-active material interfacial area which together with increased grid growth brings on decohesion and loss of active material. While it is not possible in this work to tell which possibility is correct it seems likely that the wrought condition of the grids would not substantially change the mechanism by which antimony promotes adherence. Thus active material loss through reduced surface contact and increased grid growth seems more probable. The relationship between grid growth and active material loss has been confirmed in the literature (10,11). Also scanning electron microscope examination of the active material from failed plates shows the structure of the oxides to be quite similar in the cast and wrought cells, see Fig. 6a and b. The

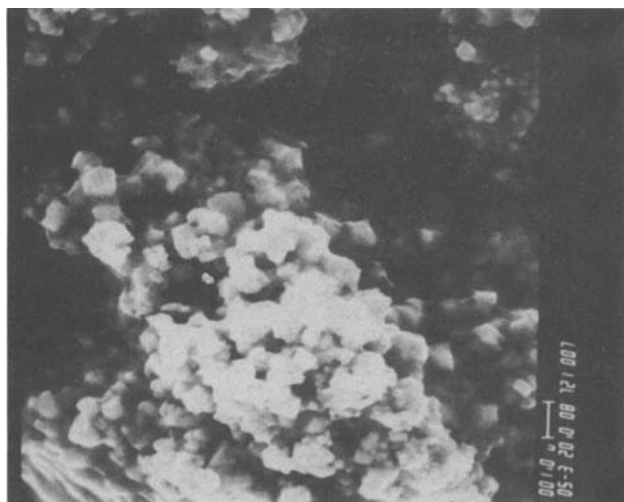


Fig. 6a. SEM image of active material from cell No. 2 after failure. 5000X.

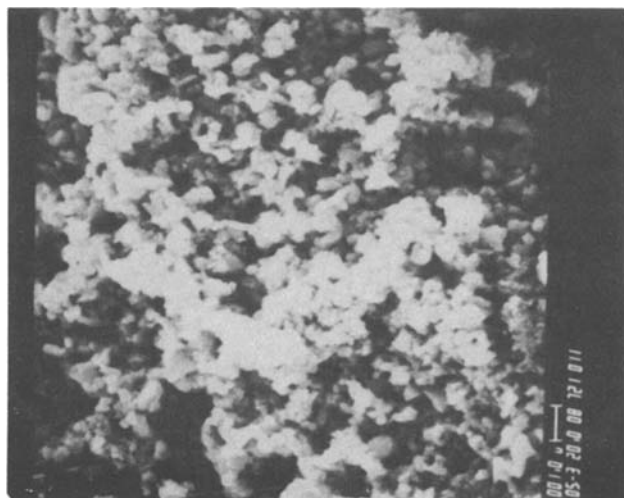


Fig. 6b. SEM image of active material from cell No. 14 after failure. 5000X.

relation between grid composition, oxide morphology, and paste adherence has been discussed by Burbank (9).

Grid corrosion as measured by grid weight loss overall and per 100 cycles generally was higher in the wrought grids than in the cast grids. Again the exceptions were the very low antimony cells (I-A) emphasizing the importance of alloy content in these alloys. Without having the experimental data, one would expect the cast alloy grids to corrode more rapidly than the wrought grids of the same antimony content. This is because the continuous interdendritic eutectic phases found in castings have been shown (10) to be preferred regions of corrosive attack in battery grids. This continuous structure is broken up by the rolling process making deep penetration of corrosion more difficult. The photomicrograph in Fig. 3b confirms that interdendritic attack did occur in the castings while general dissolution seems to have been the mode of corrosion for the wrought alloys (Fig. 4b and 5b). The only excessive corrosion in the wrought grids as compared to the castings was in the vertices of the cruciate locations (Fig. 4a and 5a). Here the corrosion may have been enhanced by the presence of residual stress caused by the expansion process. It is also possible that the excessive Sn_4As_3 in the wrought alloy enhanced the corrosion rate. In any case corrosion was not observed to play a significant role in the failure of these cells with the possible exception of cell No. 1 which lasted far longer than any other.

The most striking variation in behavior between cast and wrought grids was in grid growth. This is believed to have been a major factor in causing cell failure as mentioned earlier. Growth in the cast grid cells was 1% or less overall and less than 0.2% per 100 cycles of life over a relatively long lifetime. Wrought grid expansion ranged up to 8.3% increase in height (cell 7) and ranged from 1 to 4% per 100 cycles over relatively shorter lives. The relation of cycle life to grid growth is shown graphically in Fig. 7. Antimonial lead standby batteries on constant charge are known to suffer gross grid growth by interdendritic corrosion causing the volume of the grid to effectively increase because of the corrosion product (10). Examination of the photographs in Fig. 3-5 shows this mechanism not to be operating in either the cast or wrought grids as there is virtually no sign of interdendritic attack below the immediate surface of the metal. The means by which grid growth occurs, then, must be mechanical. It is proposed that mechanical deformation of the grids occurred through repeated expansion and contraction of the active material during charge and discharge. A

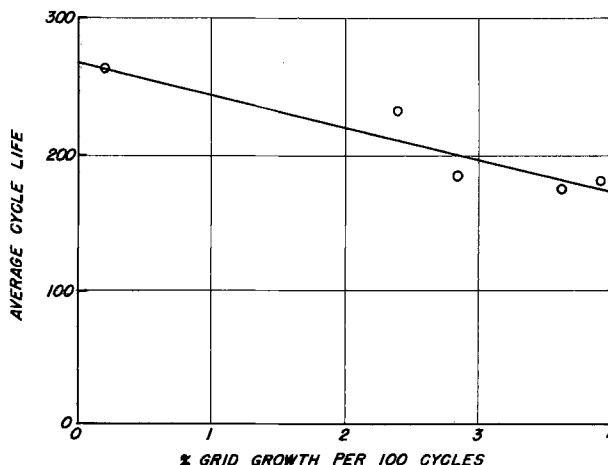


Fig. 7. Cycle life vs. grid growth

similar mechanical explanation of grid growth has been proposed by Lander (11) on unpasted lead. The cast grids, while subject to similar forces of expansion and contraction, are expected to possess tensile strength well in excess of the 4000-5000 psi determined for the wrought alloys as rolled. Further the cast grid design has been optimized over the years to reduce active material loss and growth. As may be seen the cast grids have substantial supporting members on each side and continuous supports running horizontally and at varying inclines to the vertical. The wrought grids in both designs were unsupported at the ends and tend to yield to stress not unlike an accordion. It is this structural instability which we believe allows excessive grid growth which in turn causes active material loss and shorting, the prevalent mode of failure.

Work underway at ASARCO has indicated that wrought low antimony grids can be hardened to tensile strengths in excess of 6000 psi with very short term heat-treatments. Further, recently reported potentiodynamic studies (12) show a relation between cold work and low H_2 overvoltage. A short anneal thus may improve the gassing rate of wrought grids. Also it now seems likely that the levels of arsenic and tin chosen for this test were high and that corrosion resistance and ease of working may be improved by smaller additions of those elements.

Conclusions

1. Continuous casting of low antimony grid alloys has been demonstrated.
2. Difficulty in cold working the continuous cast material increased with increasing alloy content. These problems would be significantly diminished in a commercial rolling situation.
3. Expansion of low antimonial lead alloy sheet for battery grids has been demonstrated.
4. In deep discharge cycling the expanded low antimony grids did not perform as well as did cells

constructed with cast low antimony grids, although some of the wrought grid cells achieved more than 200 cycles to failure.

5. Failure of the wrought grid cells resulted from the effects of excessive grid growth not related to corrosion.

6. It is suggested that wrought grid cell life may be extended by (i) employing an alloy of 1-2% Sb with small addition of As and Sn; (ii) heat-treating the metal to achieve greater resistance to stress, and higher gassing voltage; and (iii) design wrought grids to provide more structural support.

Manuscript received Feb. 9, 1981.

Any discussion of this paper will appear in a Discussion Section to be published in the June 1982 JOURNAL. All discussions for the June 1982 Discussion Section should be submitted by Feb. 1, 1982.

Publication costs of this article were assisted by ASARCO Incorporated.

REFERENCES

1. H. Borchers, S. C. Nijhawan, and W. Scharfenberger, *Metallwissenschaft Technik*, 863 (1974).
2. T. Rogatchev, St. Ruvski, and D. Pavlov, *J. App. Electrochem.*, 6, 33 (1976).
3. D. Berndt and S. C. Nijhawan, *J. Power Sources* 1, 3 (1976-1977).
4. U. Heubner and A. Uebenechaer, *Metall.*, 963 (1977).
5. W. B. Wylam, Paper presented at BCI 89th Annual Convention, April 27, 1977, Washington, D.C.
6. British Pat. 1338823 (1973).
7. D. D. Hakarine, SAE Paper 770326, International Automotive Engineers Congress, Feb. 28-March 4, 1977, Detroit.
8. P. Ruetschi and B. D. Cahan, *This Journal*, 94, 406 (1957).
9. J. Burbank, *ibid.*, 111, 1112 (1964).
10. N. L. Parr, A. Muscott, and A. J. Crocker, *J. Inst. Metals*, 87, 321 (1958-1959).
11. J. J. Lander, *This Journal* 98, 220 (1951).
12. E. G. Haney, ASARCO Research Report 4977.

The Behavior of Na-TiS₂ and Na-TiS₃ as Solid Solution Electrodes

Margherita Zanini, J. L. Shaw, and G. J. Tennenhouse

Ford Motor Company, Research Staff, Dearborn, Michigan 48121

ABSTRACT

We have investigated the behavior of TiS₂ and TiS₃ electrodes in a sodium cell at temperatures between 230° and 280°C using the solid electrolyte β'' -alumina. The electrochemical reaction of TiS₂ with sodium was found to be reversible, while TiS₃ was found to decompose.

Several transition metal chalcogenides (TMC) can be intercalated with high concentrations of alkali metals (1). Although the sodium-TMC compounds are expected to have a large free energy of formation, high electrical conductivity, and high sodium diffusivity (2), their behavior as solid solution electrodes has not been so widely studied as that of the lithium-TMC compounds (1). Energy density considerations and difficulties associated with the electrolyte instability and the high sodium reactivity have made the lithium compounds more attractive for applications (3, 4). However, the compatibility of TMC's with sodium makes it possible to use and study

Key words: electrolyte, decomposition, metals.

these electrode materials in conjunction with the solid electrolyte β'' -alumina (5). The stability of this electrolyte, its low resistivity, and the reliability of the Na/ β'' -alumina half cell (5) open very interesting possibilities of utilizing TMC's in rechargeable batteries with both high energy and power densities. In this paper we report studies of the behavior of TiS₂ and TiS₃ electrodes at temperatures between 230° and 280°C in a sodium cell using β'' -alumina as an electrolyte. We discuss the reversibility and the energy density of Na-TiS₂ and Na-TiS₃ solid solution electrodes at high temperatures. We also discuss the advantages of using β'' -alumina as an electrolyte both for studies and for applications.

Experimental

Small crystallites of TiS_2 (platelets) and TiS_3 (fibers) were prepared by direct reaction of titanium wire (10 mils, 99.9% pure from MRC) and sulfur (99.999% pure from ASARCO). The elements were reacted in stoichiometric amounts in quartz ampuls at 650°C for TiS_2 (6) and at 560°C for TiS_3 (7). The Debye-Scherrer patterns obtained for these materials indicated the presence of a single phase. Analysis of the compounds by complete oxidation to TiO_2 showed that the compounds were stoichiometric within our experimental error of ± 0.005 . Microprobe, ESCA, and X-ray fluorescence tests were also made on the electrodes to verify their composition and to test that only trace impurities were present. Powders of TiS_2 from CERAC were also used in the experiments.

The TMC electrodes were made by isostatically pressing finely divided material with no binder into pellets about 3 mm in diameter and 50-100 microns thick. Thinner electrodes of TiS_2 (5-10m) used for the cyclic voltammetry experiments were pressed on aluminum foil as a support. The pressed TiS_2 pellets had very smooth surfaces, and did not crumble on handling, while the TiS_3 pellets had rougher surfaces. The pellets retained their structural integrity throughout the electrochemical tests.

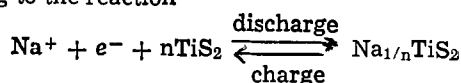
The density of some pellets was measured by a gravimetric technique. First a sample was weighed (weight W_1). Then it was immersed in a liquid (either alcohol or ethylene glycol) for several hours and kept under a low pressure to favor degassing. As soon as a sample was removed from the bath, its surface was gently wiped and the sample immediately weighed (weight W_2). From the known densities of the bulk material (d_b) and of the liquid (d_1), the density of the pellet (d) was derived according to

$$d = \frac{W_1 \cdot d_1 \cdot d_b}{W_2 \cdot d_b - W_1 \cdot (d_b - d_1)}$$

and found to be 80-90% of the bulk density. Samples 200 microns thick gave more reproducible results and less scattering in the data than 50 microns thick pellets, because of the more favorable volume to surface ratio.

Cells were made by sealing a β'' -alumina disk (8) (12 mm in diameter, 1 mm thick) to the end of a ceramic container into which sodium was vacuum transferred. A spring loaded cell holder pressed the TMC pellet against the solid electrolyte. The whole unit was heated in a furnace. The temperature of the cell, monitored by a shielded thermocouple in the sodium bath, was controlled within 1°C . The measurements were made in a dry box. At the end of the measurements small fractions of the cathodes were removed and sealed in glass capillaries for x-ray diffraction tests.

The cells were automatically cycled in galvanostatic mode between preset voltage limits and their voltage recorded on a strip chart recorder. In some tests, the cell operation was automatically switched from galvanostatic to potentiostatic mode as soon as a voltage limit was reached. A coulometer measured the charge flowing during a cycle. Thus the concentration of sodium in the electrode was derived according to the reaction



Quasi-equilibrium open-circuit voltage data were obtained by discharging a cell with a fresh electrode in steps at constant current. After each step, the cell voltage was measured every hour. When the voltage was observed to change in one hour less than

2% of the amount it changed during the first hour, the cell was considered in quasi-equilibrium.

Cyclic voltammetry was also used to characterize the TMC electrodes. Since the geometry of our cells did not allow the addition of a reference electrode, the sodium electrode was used both as counter and reference. This configuration did not introduce a large error since the polarization of the sodium electrode was low. This was verified by measuring the voltage across an $\text{Na}/\beta''\text{-alumina}/\text{Na}$ cell, through which a constant current was flowing.

The IR drop of the $\text{Na}/\beta''\text{-alumina}/\text{TMC}$ cells was measured by abruptly interrupting the current and measuring the sudden voltage change between positive and negative electrodes.

Results

Typical charge/discharge curves for TiS_2 electrodes are shown in Fig. 1 and 2. The data were obtained cycling the cells galvanostatically between voltage limits of 2.9 and 1.1V at current densities ranging from 0.2 to 2 mA/cm^2 and at temperatures of 230° and 280°C .

The curves show two regions, at molar concentrations of sodium of approximately $x < 0.4$ and $x > 0.7$, in which the voltage is relatively independent of x . These two plateaus occur around 2.1 and 1.5V in discharge and are also observed in equilibrium open-circuit voltage measurements. In between, the voltage changes almost linearly. These features can be detected in all the curves taken at increasingly higher currents, although the length of the plateaus decreases faster than that of the intermediate region. The total depth of the charge and discharge increases with the temperature and decreases with the current, suggesting that the full utilization of the electrode is kinetically hindered because of the slow diffusion of sodium into the bulk of the electrode. Typically, the electrodes were cycled about 5-7 times for each different current level and temperature. No appreciable loss in capacity (less than 1%) was observed between cycles done at the same current and temperature,

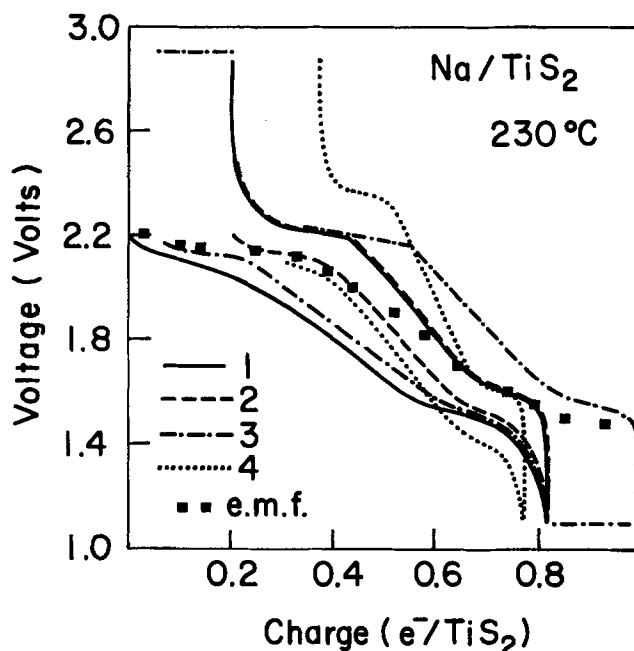


Fig. 1. Galvanostatic discharge and charge curves for a TiS_2 electrode of 2.3 mg. Curve No. 1 is the first cycle performed at $0.2 \text{ mA}/\text{cm}^2$; No. 2 is the second at $0.2 \text{ mA}/\text{cm}^2$; No. 3 the eighth cycle at $0.2 \text{ mA}/\text{cm}^2$ which was, however, prolonged in potentiostatic mode; No. 4 is the twelfth cycle which was performed at $0.5 \text{ mA}/\text{cm}^2$. The squares are quasi-equilibrium open-circuit values for a fresh electrode.

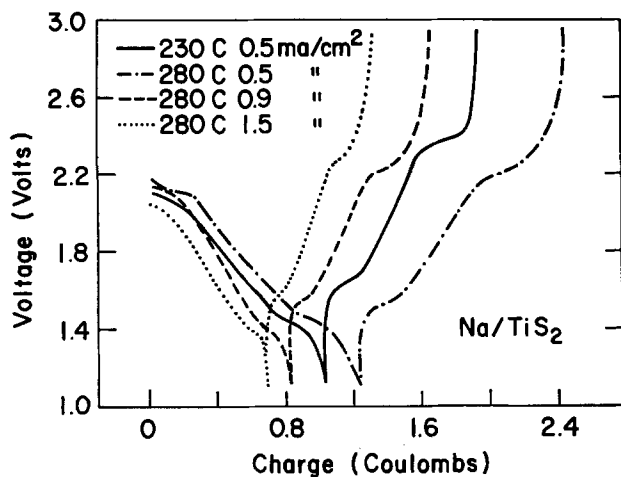


Fig. 2. Galvanostatic discharge and charge curves for TiS_2 at different current densities and temperatures. For this electrode a charge of $2.2C$ corresponds to a sodium molar concentration of 1.

indicating that the electrochemical process was reversible.

In some experiments (curve 4 in Fig. 1 for example), both the charge and the discharge tests, were continued in potentiostatic mode when the cell voltage reached, respectively, 2.9 and 1.1V. In this way, a rechargeable capacity as high as $0.96 e^-/\text{TiS}_2$ (equivalents/mole) was measured. Furthermore, electrodes were cycled so that a fixed charge was obtained in each cycle, demonstrating that the loss of capacity in tests at higher currents is not due to irreversible phenomena.

The reversibility of the intercalation process is also demonstrated by slow scan rate cyclic voltammetry. In Fig. 3 we show a cyclic voltammogram obtained for an electrode less than 10 microns thick at a scan rate of 0.1 mV/sec . Three reduction peaks occur at 2.18, 2.12, and 1.46V and the corresponding oxidation peaks at 2.26, 2.18, and 1.54V. At higher scan rate (0.5 mV/sec) the two peaks at higher voltage become broader and are no longer resolved. The peaks observed in the voltammogram indicate that the intercalation process occurs in different steps according to the concentration range of the electrode. The presence of symmetrical reduction and oxidation peaks is an indication that each step is reversible. The potentials at which peaks appear in the voltammogram compare closely with the voltages at which plateaus are seen in the galvanostatic sweeps.

The voltage difference between the charge and discharge curves of Fig. 1 and 2 is essentially due to concentration polarization in the positive electrode, since IR drop contribution was found to be small.

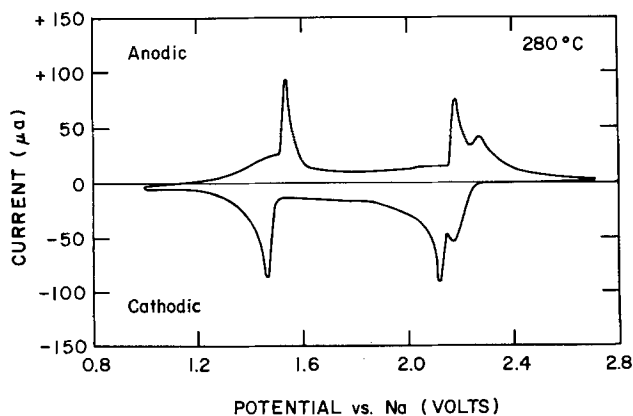


Fig. 3. A voltage scan for a thin TiS_2 electrode of 0.38 mg and 0.2 cm^2 . The scan rate was 0.1 mV/sec .

The observed high polarization does not seem to be related to poor stoichiometry of our electrode materials which can decrease the sodium diffusivity. This effect was previously observed in metal-rich TiS_2 (2, 9). However, chemical analysis of our compounds showed that the excess metal was less than 0.1%. In addition, our materials had been carefully annealed to remove defects. Both commercial material and our compounds showed similar behavior in our tests.

We found that at temperatures below $140^\circ\text{--}160^\circ\text{C}$, the cell polarization was quite large. Since the resistivity of the electrolyte (5) decreases exponentially as the temperature increases (10), and the wettability of sodium to β'' -alumina increases, we performed our tests above 180°C . Although we did not make tests above 300°C , the temperature of utilization of the cell should be only limited by the thermal stability of the chalcogenide electrode.

In Fig. 4 we show data obtained for a TiS_3 electrode. Although the first discharge for this material could be carried up to $2.4 e^-/\text{TiS}_3$ at 0.1 mA/cm^2 , subsequent cycles show a much smaller capacity (less than $1 e^-/\text{TiS}_3$) and completely different features. Two breaks in the voltage vs. concentration curves are observed at about 2.1 and 1.5V, similar to what was observed for TiS_2 . This is evidence that TiS_3 transforms into TiS_2 during the electrochemical reaction as confirmed by x-ray diffraction analysis. In fact, the Debye-Scherrer patterns of samples taken from the cycled electrodes showed the characteristic lines of TiS_2 , although very broad, but no TiS_3 lines or other lines. Successive cycles are similar to the second discharge/charge, although the capacity progressively decreases.

Discussion

Our data show that at high temperatures TiS_2 can be used in a sodium cell as a reversible solid solution electrode in the concentration range $0 < x < 1$. Our results are in good agreement with the emf values reported by Winn *et al.* (2) for stoichiometric single crystals studied at room temperature. Instead, our findings disagree with the poor reversibility observed by Newman *et al.* (4) in their experiments with a room temperature cell using a liquid electrolyte. Also, the voltage vs. concentration data of our Na/TiS_2 cells are 200-300 mV higher than the values reported in Ref. (4). Such a difference cannot be attributed to the temperature because the cell voltage decreases, increasing the temperature.

The use of a solid electrolyte has the advantage of preventing side reactions with the electrodes and of avoiding electrolyte cointercalation in the electrode. It is therefore possible to study the intrinsic behavior of TMC electrodes free of other background reactions. In addition, the sodium electrode is free of contamination and polarization effects. On the other hand, we

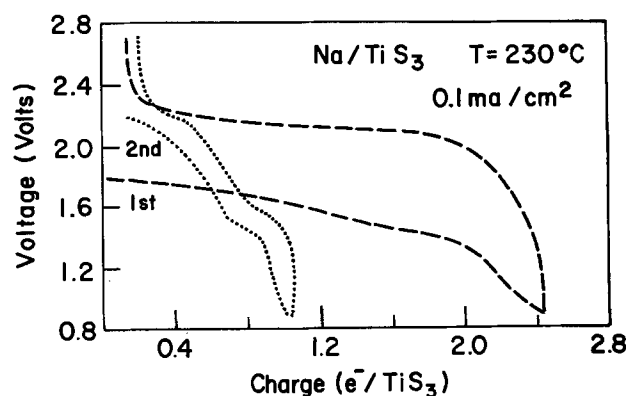


Fig. 4. Galvanostatic discharge/charge curves for a TiS_3 electrode of 2.2 mg .

probably do not achieve intimate contact between the TMC electrode and the electrolyte in our present configuration. The high polarization that we observed in our cells is likely due to poor contact and not to intrinsic low sodium diffusivity in the electrode material. The interfacial problem could be overcome by adding a suitable molten salt to the cathode or by sintering TMC's to β'' -alumina.

In our nonoptimized cells with cathodes approximately 50 microns thick, we obtained a rechargeable capacity of about $0.8 e^-/\text{TiS}_2$ at $0.2 \text{ mA}/\text{cm}^2$ and 230°C , as shown in Fig. 1, and a corresponding energy density of $290 \text{ W-hr}/\text{kg}$ for the Na_xTiS_2 cathode. At lower discharge rates and/or at higher temperatures, this value increases. The maximum energy density (theoretical) for NaTiS_2 was derived from the emf data of Fig. 1 and found to be $360 \text{ W-hr}/\text{kg}$. This value is about 25% less than the theoretical energy density of LiTiS_2 electrodes, which is $480 \text{ W-hr}/\text{kg}$ at room temperature (1).

The plateaus observed in the curves of Fig. 1 and 2, and the peaks seen in the voltammogram of Fig. 3, can be related to the phases of the Na-TiS_2 system. Previous x-ray diffraction studies (11) have found three structurally different phases. The first phase, observed for sodium concentration $0.17 < x < 0.33$, was described as a second stage compound with sodium occupying trigonal prismatic sites. The second, extending for $0.38 < x < 0.72$, was determined to be a first stage with sodium in trigonal prismatic sites. The third, for concentrations $x > 0.79$, was found to be a first stage with sodium in a trigonal antiprismatic (distorted octahedral) site. We associate the lower voltage plateau with the onset of the "octahedral" phase and the higher voltage plateau with the onset of the "trigonal prismatic" phase. The two peaks which appear in the cyclic voltammogram of Fig. 3 around 2.1V can be associated with the trigonal prismatic first and second stage phases. Detailed x-ray work on ternary compounds obtained electrochemically needs to be done to better understand the structural transformations of the Na-TiS_2 system and the concentration values for the phase boundaries.

The sodium diffusivity in TiS_2 could be substantially different for each phase (1). Our preliminary measurements of the diffusion coefficient of sodium in TiS_2 obtained with the voltage-relaxation method (2, 12), seem to show that diffusion is at least one order of magnitude slower for sodium concentrations approximately $x < 0.4$ and $x > 0.7$, although the change does not seem to occur abruptly. This correlates with the results of the galvanostatic sweeps which show that the length of the plateaus decrease at higher currents. Because of the uncertainty of the actual contact area in our cells, we cannot derive the absolute value of the sodium diffusivity, but we can compare values obtained for the same electrode.

As observed in the case of lithium (13, 14), TiS_3 transforms during the electrochemical intercalation of sodium and the high capacity of the first discharge is not recovered on subsequent cycles. This material does not therefore look attractive for practical purposes.

Conclusion

We have reported the feasibility of using TiS_2 electrodes coupled with β'' -alumina electrolyte to build a high temperature rechargeable battery. The voltage range of our $\text{Na}/\beta''\text{-alumina}/\text{TiS}_2$ cell is about 15% lower on average than for Li/TiS_2 room temperature cells. However, the availability and the cost of sodium compared to lithium may make the sodium compounds more attractive for practical applications, especially if they are used with the stable β'' -alumina electrolyte with a good interfacial contact. The diffusion rate in TMC's may be slower for sodium than for the smaller lithium ions, therefore reducing the power achievable in these cells. However, the use of a solid electrolyte allows the operation of this kind of cell at high temperatures where diffusion processes are faster. The diffusion mechanisms in solid solution electrode materials need to be studied further to prove the feasibility of a practical high power device.

Acknowledgments

We wish to thank H. Wroblowa, E. M. Logothetis, and C. A. Kukkonen for many helpful discussions and F. D. Runkle and A. D. Colvin for technical assistance.

Manuscript submitted Nov. 10, 1980; revised manuscript received Feb. 23, 1981.

Any discussion of this paper will appear in a Discussion Section to be published in the June 1982 JOURNAL. All discussions for the June 1982 Discussion Section should be submitted by Feb. 1, 1982.

Publication costs of this article were assisted by Ford Motor Company.

REFERENCES

1. M. S. Whittingham, *Prog. Solid State Chem.*, **12**, 1 (1978).
2. D. A. Winn, J. M. Shemilt, and B. C. H. Steele, *Mater. Res. Bull.*, **11**, 559 (1976).
3. K. M. Abraham, R. Schiff, and S. B. Brummer, Abstract 154, p. 399, The Electrochemical Society Extended Abstracts, Los Angeles, California, October 5-10, 1979.
4. G. H. Newman and L. P. Klemann, *This Journal*, **127**, 2097 (1980).
5. J. T. Kummer, *Prog. Solid State Chem.*, **7**, 141 (1972).
6. A. H. Thompson, C. R. Symon, and F. R. Gamble, *Mater. Res. Bull.*, **10**, 915 (1975).
7. F. K. McTaggart and A. D. Wadsley, *Aust. J. Chem.*, **11**, 445 (1958).
8. S. A. Weiner and R. P. Tischer, Research on Electrodes and Electrolyte for the Ford Sodium-Sulfur Cell, Ford Motor Co., Ann. Rep., July 1976, Contract NSF-C805.
9. M. S. Whittingham, U.S. Pat. 4,007,055 (1975).
10. J. L. Sudworth, M. D. Hames, M. A. Storey, M. F. Azim, and A. R. Tilley, *Power Sources*, **4**, 1 (1973).
11. J. Rouxel, M. Danot, and J. Bichon, *Bull. Soc. Chim. Fr.*, **11**, 3930 (1971); A. Leblanc-Soreau, M. Danot, L. Trichet, and J. Rouxel, *Mater. Res. Bull.*, **9**, 191 (1974).
12. W. Weppner and R. A. Huggins, *Ann. Rev. Mater. Sci.*, **8**, 269 (1978).
13. M. S. Whittingham, *This Journal*, **123**, 315 (1976).
14. G. L. Holleck and J. R. Driscoll, *Electrochim. Acta*, **22**, 647 (1977).

Lightweight Rechargeable Storage Batteries Using Polyacetylene, $(\text{CH})_x$ as the Cathode-Active Material

Paul J. Nigrey, David MacInnes, Jr., David P. Nairns, and Alan G. MacDiarmid*

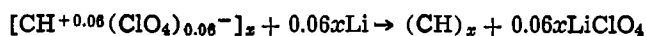
Department of Chemistry, University of Pennsylvania, Philadelphia, Pennsylvania 19104

and Alan J. Heeger

Department of Physics, University of Pennsylvania, Philadelphia, Pennsylvania 19104

ABSTRACT

Polyacetylene, $(\text{CH})_x$ can be controllably doped electrochemically through the semiconducting to the metallic regime using a solution of LiClO_4 in propylene carbonate and a lithium cathode. Flexible, golden, free-standing films of $[\text{CH}^{+\nu}(\text{ClO}_4)_y^-]_x$ ($y = 0$ to 0.06) having conductivities up to $\sim 10^3 \Omega^{-1} \text{cm}^{-1}$ are readily obtained. Electrochemical "undoping" of the $[\text{CH}^{+\nu}(\text{ClO}_4)_y^-]_x$ allows this doped film to be used as the cathode-active material in lightweight rechargeable storage batteries. The overall complete discharge reaction is

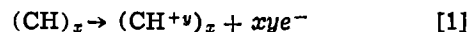


A 0.5 cm^2 piece of the 6% doped film ($1.0 \times 0.5 \times 0.01 \text{ cm}$; $\sim 3 \text{ mg}$) exhibited an open-circuit voltage of 3.7 V and an initial short-circuit current of 25 mA . No change in the open-circuit voltage characteristics of a battery could be detected even after 326 successive constant current partial charge/discharge cycles. No degradation of the polyacetylene electrode was observed. Experimental energy densities of $\sim 176 \text{ W-hr/Kg}$ were obtained based on the weight of the $[\text{CH}^{+0.06}(\text{ClO}_4)_{0.06}^-]_x$ initially employed and the weight of Li consumed (exclusive of weights of electrolyte, solvent, and packaging material) during partial discharge when $[\text{CH}^{+0.06}(\text{ClO}_4)_{0.06}^-]_x$ was converted to $[\text{CH}^{+0.024}(\text{ClO}_4)_{0.024}^-]_x$.

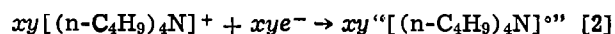
Polyacetylene, $(\text{CH})_x$ is the first example of a covalent organic polymer which may be chemically doped either p- or n-type to give a series of semiconductors and ultimately "organic metals" (1). The electrical conductivity can be varied over twelve orders of magnitude depending on the dopant concentration (1). Detailed studies have shown that a semiconductor-metal transition occurs at dopant concentrations near 1 mole percent (m/o). In the metallic range, (1-10 m/o) the conductivity increases at a relatively slow rate as a function of dopant concentration up to a value of $\sim 10^3 \Omega^{-1} \text{cm}^{-1}$ at room temperature. We have shown previously that $\sim 0.1 \text{ mm}$ thick films of $(\text{CH})_x$ may also be controllably doped electrochemically in a very simple, rapid procedure, either in aqueous or nonaqueous solution, through the semiconducting to the metallic regime (2). Thus, the use of aqueous KI solutions or CH_2Cl_2 solutions of, e.g., $[(n\text{-C}_4\text{H}_9)_4\text{N}]^+[\text{ClO}_4]^-$, $[(n\text{-C}_4\text{H}_9)_4\text{N}]^+[\text{AsF}_6]^-$, etc. yield flexible, golden-silvery films of $[\text{CH}]_{0.07}^+$ ($\sigma_{25^\circ\text{C}} = 9.7 \Omega^{-1} \text{cm}^{-1}$), $[\text{CH}(\text{ClO}_4)_{0.0645}]_x$ ($\sigma_{25^\circ\text{C}} = 970 \Omega^{-1} \text{cm}^{-1}$), and $[\text{CH}(\text{AsF}_6)_{0.059}]_x^+$ ($\sigma_{25^\circ\text{C}} = 260 \Omega^{-1} \text{cm}^{-1}$), respectively. When doping is carried out using approximately 0.1 mm thick cis-rich $(\text{CH})_x$ film as the anode and a platinum cathode with an applied potential difference of approximately 9 V between the electrodes, the metallic-doped state is generally reached in 30-60 min (2). This relatively rapid doping is undoubtedly assisted by the fact that the film consists of an interwoven network of ca. 200 \AA $(\text{CH})_x$ fibrils which fill only about one-third of the volume of the film (1). The surface area of the $(\text{CH})_x$

fibrils in the film is $40\text{-}60 \text{ m}^2/\text{g}^2$ (1). A 1 cm^2 piece of film 0.1 mm in thickness therefore has an effective surface area of approximately $2.5 \times 10^3 \text{ cm}^2$. In the doped state, the polyacetylene is believed to exist as the stabilized polycarbonium ion, $(\text{CH}^{+\nu})_x$, with the corresponding number of monovalent counter anions such that the overall composition is $[(\text{CH}^{+\nu})\text{A}_y^-]_x$ (1). In the case of iodine doping, it has been shown that at least a large amount of the iodine exists as the I_3^- ion (3).

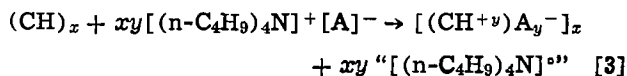
The anode reaction occurring upon doping, using $[(n\text{-C}_4\text{H}_9)_4\text{N}]^+\text{A}^-$ as an electrolyte, involves oxidation of $(\text{CH})_x$, viz.



The corresponding cathode reaction, at an inert electrode such as platinum, is



The $[(n\text{-C}_4\text{H}_9)_4\text{N}]^+$ upon reduction may be regarded as producing $[(n\text{-C}_4\text{H}_9)_4\text{N}]^{\circ}$ momentarily. This will then break down in a complex manner to give amines and hydrocarbons. The overall electrochemical doping reaction may therefore be summarized as



It will be noted that the A^- ion is not oxidized or reduced during the electrochemical reaction. It serves only as a negative counterion to preserve electrical neutrality in the system.

An important extension of the electrochemical doping study is the attempted electrochemical "undoping" of $[(\text{CH}^{+\nu})\text{A}_y^-]_x$ to reform the original $(\text{CH})_x$. This also has now been accomplished. The doping reaction given by Eq. [1], involving partial oxidation of the $(\text{CH})_x$, may also be regarded as a possible battery

* Electrochemical Society Active Member.

Key words: polyacetylene, battery, doping, lithium, perchlorate. ¹Elemental analyses (Schwarzkopf Microanalytical Laboratory, Woodside, New York, 11377) show that the material has the composition $[\text{CH}(\text{AsF}_6)_{0.0592}]_x$. Found: C = 54.71; H = 4.74; As = 20.19; F = 20.81% (Total = 100.45%). Calc.: C = 54.79; H = 4.60; As = 20.16; F = 20.45%. An unknown side reaction apparently occurs to reduce $(\text{AsF}_6)^-$ to $(\text{AsF}_4)^-$.

"charging reaction" to produce a doped polymer which could be utilized as a cathode-active battery material. The discharge reactions are the reverse of those given above.

A number of different dopant ions, solvents, electrolytes, electrolyte concentrations, and battery configurations have been investigated, only one of which is described below in order to illustrate the potential application of $(\text{CH})_x$ in batteries. This system is not necessarily the most preferred one nor are its parameters necessarily optimized to give the best output characteristics.

Experimental

Materials and reagents.—Cis-rich $(\text{CH})_x$ film (ca. 80% cis isomer; ca. 0.1 mm thickness; density ca. 0.4 g/cm³) was prepared as previously described (4).² Propylene carbonate (Aldrich Reagent grade) was stirred over lithium chips for 14 days. This was used to make a 0.3M solution of LiClO_4 which was passed through Woelm activated basic alumina to yield a colorless solution. Anhydrous LiClO_4 (Alfa-Ventron) was dried by melting *in vacuo* before use. Lithium metal (Alfa-Ventron Company) was scraped under an LiClO_4 solution in propylene carbonate with a knife immediately before use.

Doping experiments.—Doping experiments were carried out in a dry, inert atmosphere using a glass vessel containing the LiClO_4 /propylene carbonate solution. A strip of $(\text{CH})_x$ film ($3 \times 1.5 \times 0.01$ cm), to the top of which a platinum wire had been attached by mechanical pressed contact, was placed in the solution so that the film and wire were completely immersed. A platinum counterelectrode (3 cm^2) was placed in the solution at a distance of ~ 12 cm from the $(\text{CH})_x$ working electrode. An Ag/Ag^+ (0.1M AgNO_3 in CH_3CN) reference electrode was then placed in the container ~ 1 cm from the $(\text{CH})_x$ working electrode. The three electrodes were attached to a Princeton Applied Research (PAR) Model 173 potentiostat/galvanostat equipped with a PAR Model 179 digital coulometer.

Electrochemical doping of the $(\text{CH})_x$ with $(\text{ClO}_4)^-$ was accomplished by having it serve as the anode. It was held at a potential of +1.0V with respect to the Ag/Ag^+ reference electrode. After 10 sec, the film was withdrawn so that the top of the platinum wire was ~ 3 mm above the surface of the solution. The 10 sec doping period increased the conductivity of the $(\text{CH})_x$ film around the platinum wire contact. Although it is not really necessary to withdraw the platinum wire from the electrolyte since one is operating at a potential where no oxidation of the electrolyte or solvent occurs, this technique was found in certain cases to control the rate of doping. As doping proceeded and the conductivity of the film increased, the current also increased. The extent of doping was followed by observing the value of the current. At the very beginning, the current was 40 μA and after 43 min it had increased to 4 mA. It stayed constant at this value for an additional 4 min and then began to decrease. Doping was discontinued at this stage, the film was washed several times with propylene carbonate, then with CH_2Cl_2 , and dried *in vacuo* with constant pumping overnight. The flexible, golden film had a 4-probe conductivity of 700 $\Omega^{-1} \text{ cm}^{-1}$ at room temperature. Its composition from the number of coulombs passed was $[\text{CH}(\text{ClO}_4)_{0.043}]_x$. This composition is not necessarily expected to agree exactly with that obtained from elemental analysis since there is uncertainty in the extent of doping of that 3 mm portion of the film above the solution. A portion of that part of the film which had been completely immersed in the solution was analyzed com-

mercially.³ Its composition was $[\text{CH}(\text{ClO}_4)_{0.058}]_x$. Found: C = 63.23% H = 5.71%; Cl = 10.21%; O (by difference) = 20.85%. Calc. for $\text{CHCl}_{0.058}\text{O}_{0.232}$: C = 63.96%; H = 5.37%; Cl = 10.95%; O = 19.77%.

Battery experiments.—A strip of $(\text{CH})_x$ film ($0.5 \times 1 \times 0.01$ cm), either undoped or previously doped, was placed in the 0.3M solution of LiClO_4 in propylene carbonate as described previously. Platinum wire was attached to the top of the film as in the doping experiments. The lithium counterelectrode ($0.5 \times 2 \times 0.1$ cm) was placed ~ 0.5 cm from the (working) $(\text{CH})_x$ electrode. A similar strip of lithium metal was placed approximately equidistantly from the working and counterelectrodes and was used as the reference electrode. In one experiment, a 0.5 cm² piece of $(\text{CH})_x$ film, on one side of which 600Å of gold had been evaporated, was employed. Platinum wire was attached to one end by pressed mechanical contact and the electrode was then placed in 0.5M LiClO_4 in propylene carbonate.

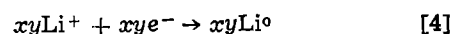
In some experiments, $(\text{CH})_x$ film previously doped with perchlorate was used initially. This was because the composition of that 3 mm portion of the film above the surface of the solution would then be the same as that below the surface. When undoped $(\text{CH})_x$ film was used initially, it could not necessarily be assumed that the composition of that portion of the film above the surface of the solution was fully doped or whether it might become more doped on each charging cycle during a series of charge/discharge cycles. When undoped $(\text{CH})_x$ film was employed, it was first electrochemically doped *in situ* at a constant current of 1 mA for ca. 26 min for a 0.5 cm² piece of film, to give a film of composition $[\text{CH}(\text{ClO}_4)_{0.06}]_x$ (6% doping) as calculated from the weight of the film employed and the number of coulombs passed. In some instances, film doped only to 5% was employed.

Discharge/charge studies were carried out using two different methods: (i) Constant current investigations employed a Model 173 galvanostat where the change in voltage *vs.* a lithium reference electrode during a discharge or charge cycle was monitored by means of a Keithley Model 177 digital multimeter connected to a Houston Omnigraphics 2000 XY recorder. Voltage *vs.* time measurements were recorded at a number of different discharge currents (0.1-4 mA); (ii) short-circuit studies involved discharge through a Keithley Model 177 digital multimeter, where current and voltage were measured until the cell was completely discharged. The battery was recharged to its original level after each discharge cycle by means of a d-c power supply set at 4V or by a constant current method using the PAR 173 galvanostat at 1 mA.

Results and Discussion

Doping of $(\text{CH})_x$ with $(\text{ClO}_4)^-$.—We have shown previously that $(\text{CH})_x$ film can be doped readily to composition $[\text{CH}(\text{ClO}_4)_{0.0645}]_x$ from a 0.5M solution of $[(n\text{-C}_4\text{H}_9)_4\text{N}]^+[\text{ClO}_4]^-$ in CH_2Cl_2 when it is used as the anode with an applied potential difference between the anode and cathode of approximately 9V. In the present study, we have shown that doping may also be carried out conveniently to ca. 6% using a 0.3M solution of LiClO_4 in propylene carbonate at an applied potential of +1.0V (*vs.* Ag/Ag^+) during 47 min at room temperature.

When LiClO_4 is used instead of $[(n\text{-C}_4\text{H}_9)_4\text{N}]^+\text{A}^-$, and Li metal is used instead of Pt at the cathode, then the reaction corresponding to Eq. [2] is

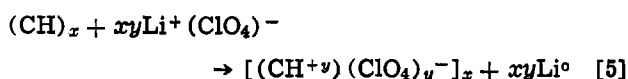


The overall doping reaction corresponding to Eq. [3]

² Similar results were obtained with $(\text{CH})_x$ film kindly supplied by Rohm and Haas Company, Bristol, Pennsylvania.

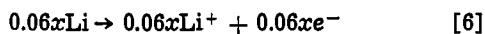
³ Galbraith Laboratories, Incorporated, Knoxville, Tennessee 37921.

is then

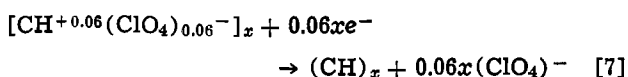


Battery experiments.—The simplest battery configuration is shown diagrammatically in Fig. 1. It consists basically of a piece of $(\text{CH})_x$ film, nearly all of which was immersed in a propylene carbonate solution of LiClO_4 . The top of the film was attached by means of a wire to the positive terminal of a galvanostat. The negative terminal was attached to a lithium metal electrode immersed in the solution. The battery was charged at 1 mA for ca. 30 min to give a film of approximate composition $[\text{CH}(\text{ClO}_4)_{0.06}]_x$. The overall charge reaction is given by Eq. [5] ($y = 0.06$).

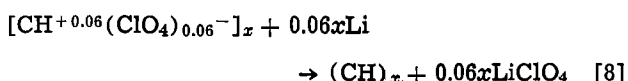
The anode discharge reaction, assuming complete discharge is



and the corresponding cathode reaction is



The net discharge reaction, is, therefore



Short-circuit discharge characteristics.—The open-circuit voltage, (V_{oc}), of a 6% predoped film, i.e., $[\text{CH}(\text{ClO}_4)_{0.06}]_x$, prepared by passing 1.7C was 3.7V and the short-circuit current (I_{sc}), was 23 mA for a 0.5 cm² (~3 mg) piece of film. This varied from ~15 to 35 mA depending on the sample of $(\text{CH})_x$ film employed and the extent of doping, etc. The high current density may be related to the large effective surface area of the $(\text{CH})_x$ fibrils in the film. Because of the small mass of the film used in these experiments, the short-circuit current falls rapidly as the battery discharges. For example, after ~30 sec of short-circuit discharge, the voltage was essentially unchanged and I_{sc} was 17 mA. More than half of the total coulombs evolved were given off during this period. After 1 min, the voltage was 3.2V and I_{sc} was 3.2 mA. After a total of 3.0 min, the voltage began to fall rapidly and I_{sc} decreased to 0.1 mA. At this stage, a total of 1.0C, (59% recovery) had been released and the dopant concentration was reduced to 2.4%, a concentration approaching that defining the metal-semiconductor transition where the conductivity of p-doped $(\text{CH})_x$ films begins to fall rapidly. The discharge reaction involved in this particular experiment is given by Eq. [9]

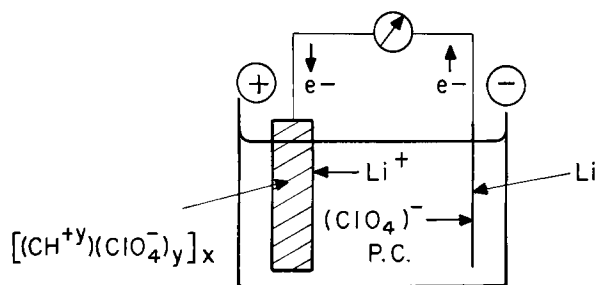
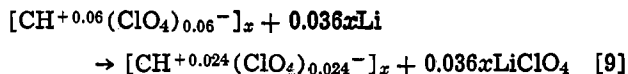


Fig. 1. Schematic representation of the discharge process in a $(\text{CH})_x/\text{LiClO}_4/\text{Li}$ rechargeable storage battery. Electrons flow in the external circuit from the Li to the $[\text{CH}^{+y}(\text{ClO}_4)_y]_x$ while at the same time Li^+ ions and $(\text{ClO}_4)^-$ ions migrate towards the $[\text{CH}^{+y}(\text{ClO}_4)_y]_x$ and the Li electrodes, respectively. (See eq. [6]-[9]).



Successive short-circuit discharging to 3% dopant concentration ($V_{oc} = 2.7\text{V}$; $I_{sc} = 1.0\text{ mA}$) and recharging to 6% dopant concentration showed that the number of coulombs involved in the charging and discharging process were identical to within experimental error.

The I_{sc} values and the average V_{oc} value during the above partial discharge give an energy density of 176 W-hr/kg based on the weight of the $[\text{CH}^{+0.06}(\text{ClO}_4)_{0.06}]_x$ initially employed and the weight of lithium consumed according to the reaction given by Eq. [9]. Since the weight of lithium consumed is extremely small compared to the weight of the $[\text{CH}^{+0.06}(\text{ClO}_4)_{0.06}]_x$, an essentially identical energy density value is obtained even if the weight of lithium used is that obtained from the reaction given by Eq. [8]. The theoretical energy density for the reaction given by Eq. [8], assuming complete discharge, is 307 W-hr/kg. Empirical rules may be applied to obtain a rough estimate of the expected energy density of a packaged battery, including the weight of electrolyte, solvent, and casing, from the experimental energy density of 176 W-hr/kg. A reduction factor of seven gives a reasonably conservative estimate and results in a value of 25 W-hr/kg for the completely packaged battery. This is approximately the same value as that found for the average lead/acid automobile battery. Although these energy densities are interestingly large even with 6% doped film, they are not necessarily the maximum obtainable since as shown in the following section it is possible to dope $(\text{CH})_x$ to values greater than 6% with $(\text{ClO}_4)^-$; furthermore, other dopants such as Br_3^- , I_3^- , AsF_4^- , etc. are known (1, 2) where higher doping levels might possibly be achieved.

It is more difficult to obtain meaningful estimates of the power density of the $[\text{CH}(\text{ClO}_4)_{0.06}]_x/\text{Li}$ battery in the final packaged state. The product of the initial V_{oc} (3.7V) and I_{sc} (23 mA) obtained above for 4.5 mg of $[\text{CH}(\text{ClO}_4)_{0.06}]_x$ film and the weight of lithium consumed in the reaction given by Eq. [8] yields a value of 19,000 W/kg. On dividing by a factor of four to obtain an approximate value of the useful power available (when the resistance of the external load and of the battery are equal), and then by a factor of seven for weight of electrolyte, solvent, and packaging, a value of 680 W/kg is obtained. This is considerably in excess of common power densities and is presumably related to the open fibrillar morphology of the $(\text{CH})_x$ film but it should be regarded with the utmost caution in view of the large approximations made in arriving at this value.

In a real battery operation, the weight of the cathode current collector electrode must also be added to the weight of the cathode-active material. In the $(\text{CH})_x$ cathode configuration, because the $(\text{CH})_x$ is a free-standing metal itself, it serves both as the current collector and as the cathode-active material, thus saving significantly in total weight. Furthermore, as mentioned earlier, the (metallic) conductivity of $[\text{CH}(\text{ClO}_4)_y]_x$ changes relatively little for values of $y \approx 0.02-0.06$. Hence, a large fraction of the material can be gainfully used electrochemically without significant change of those current-collecting properties related to its conductivity.

Constant current discharge characteristics.—A number of experiments were carried out at constant charge and discharge currents, with the charge and discharge currents having the same value. The change in voltage was recorded throughout each experiment. An example of such an experiment is summarized in Fig. 2. This involved three complete

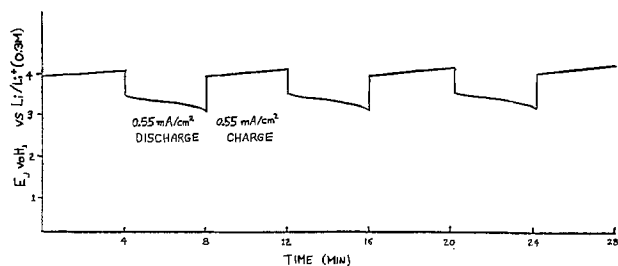


Fig. 2. Three complete charge/discharge cycles of a $(\text{CH})_x/\text{LiClO}_4/\text{Li}$ (0.3M LiClO_4 in PC) rechargeable storage battery at a controlled constant current of 0.55 mA for a 0.5 cm^2 piece of $(\text{CH})_x$ film.

charge/discharge cycles using currents of 0.55 mA and a 0.5 cm^2 piece of cis-rich $(\text{CH})_x$ film (total surface area of both sides, 1.0 cm^2). There is no particular significance in the choice of this current value; it is simply of a convenient magnitude. The charging voltage at the end of a charge cycle was 4.1V. This fell instantly to 3.7V at the very beginning of a discharge cycle. At the end of a discharge cycle it was 3.2V. Each charge and discharge cycle involved 120 mC and took 4 min for the charge cycle and 4 min for the discharge cycle.² The composition at the beginning of each of the charge cycles at 0.55 mA (shown in Fig. 2) was $[\text{CH}(\text{ClO}_4)_{0.045}]_x$, and at the end of each charge cycle it was $[\text{CH}(\text{ClO}_4)_{0.050}]_x$ (10% discharge). The difference in composition [involving 0.005 mol of $(\text{ClO}_4)^-$] was obtained from the coulombs passed.

Studies involving longer discharge periods at lower controlled constant current conditions were also carried out. For example, a single, constant current discharge at 0.55 mA resulted in a drop in voltage to 2.7V after 25 min (0.83C liberated) and a 2 mA discharge gave a voltage of 2.7V after 7 min (0.84C liberated). Voltage recovery was noted under certain conditions when a period of discharge was followed by a rest period during which no current was drawn from the cell. Thus, after the last discharge cycle shown in Fig. 2, (when $V_{oc} = 3.2$) the cell was permitted to stand for ~ 3 min. It then again displayed a voltage of 3.7V and a further discharge cycle at 0.55 mA had similar characteristics to those given in Fig. 2. To the accuracy of the measurements, the $(\text{CH})_x$ electrode was found to be reversible with no observable degradation. It should also be noted that the cell does not spontaneously lose its charge. Thus a

charged cell after standing for 48 hr still showed the same initial open-circuit voltage (3.7V) and discharged at 0.55 mA exactly as before.

An extension of these studies involved an 0.5 cm^2 piece of $(\text{CH})_x$ film to which electrical contact was made by means of a 600\AA coating of gold on one side. It was initially oxidized to composition $[\text{CH}(\text{ClO}_4)_{0.097}]_x$ by means of the passage of 2.73C and was then discharged and recharged for 326 cycles, each cycle consisting of a 100 sec discharge at 2.0 mA (0.20C; 7.3% discharge) and a 100 sec charge at 2.0 mA. Before the first discharge, the open-circuit voltage was 4.13V; at the end of the 320th discharge cycle, it was 4.16V.

The results of the present studies on the use of doped polyacetylene as the cathode-active material in batteries are most encouraging. They suggest the possibility of relatively inexpensive lightweight rechargeable batteries made with polyacetylene which may have a variety of potential technological applications.

Acknowledgment

The authors wish to thank Dr. G. C. Farrington for helpful discussions and the Office of Naval Research for support of this research.

Manuscript submitted Oct. 27, 1980; revised manuscript received March 16, 1981.

Any discussion of this paper will appear in a Discussion Section to be published in the June 1982 JOURNAL. All discussions for the June 1982 Discussion Section should be submitted by Feb. 1, 1982.

Publication costs of this article were assisted by the University of Pennsylvania.

REFERENCES

1. A. G. MacDiarmid and A. J. Heeger, *Synth. Met.*, **1**, 101 (1979/80); A. J. Heeger and A. G. MacDiarmid, in "The Physics and Chemistry of Low Dimensional Solids," L. Alcácer, Editor, p. 353, D. Reidel Publishing Co., Dordrecht, Holland, (1979); A. G. MacDiarmid and A. J. Heeger, in "The Physics and Chemistry of Low Dimensional Solids," L. Alcácer, Editor, p. 393, Reidel Publishing Co., Dordrecht, Holland (1979).
2. P. J. Nigrey, A. G. MacDiarmid, and A. J. Heeger, *J. Chem. Soc. Chem. Commun.*, 594 (1979); D. MacInnes, Jr., M. A. Druy, P. J. Nigrey, D. P. Nairns, A. G. MacDiarmid, and A. J. Heeger, *ibid.*, 317 (1981).
3. S. L. Hsu, A. J. Signorelli, G. P. Pez, and R. H. Baughman, *J. Chem. Phys.*, **69**, 106 (1978).
4. H. Shirakawa and S. Ikeda, *Synth. Met.*, **1**, 175 (1979/80).

Current Distributions in Soluble Battery Electrodes

I. Theoretical

Y. Yamazaki¹ and N. P. Yao*

Argonne National Laboratory, Chemical Engineering Division, Argonne, Illinois 60439

ABSTRACT

The current or reaction distribution in a soluble porous electrode has been formulated using a migration model. The mathematical equations were numerically solved for Zn/zincate electrode in alkaline solution. The result of the calculation revealed different reaction distributions during charge and discharge processes, even in a relatively small electrode current region where no passivation exists. The origin of the difference was discussed in terms of the resistivity variation of pore electrolyte and the interfacial reaction resistance at the electrolyte and the pore wall in the electrode.

The basic processes which limit the cycle life of the porous electrodes used in rechargeable batteries are: (i) irreversible side reactions, (ii) mechanical failure, and (iii) mismatching of the reaction distributions in the porous electrode between charge and discharge processes. The irreversible side reaction refers to gradual changes of active materials to inactive form during the cycle, such as in the lead/lead dioxide electrodes (1-3). The mechanical failure refers to a break off or a shedding of active material from the electrode plates caused by the agitation of gas evolution or by the concentration of thermal stresses or crystallographic stresses generated during the electrode reaction. The mismatching of the reaction distributions in a porous electrode between charge and discharge processes causes dimensional changes in pore structure and in electrode shape (4, 5), consequently, the process sometimes brings serious troubles in a soluble electrode such as the Zn/zincate electrode. An accurate description of these dimensional changes is important in engineering studies to improve the performance of battery electrodes.

It has been shown by Choi, Bennion, and Newman (6) that the mismatching will occur in an alkaline zinc electrode if the electrolyte flows in the porous electrode by the electro-osmotic pressure across the battery separator. The reaction distribution in sparingly soluble systems was studied by Dunning, Gu, and Newman (7, 8), and intensive discussions were made on the relationship between the current profile and the change of reaction surface area caused by a precipitation of reaction products on the pore wall. The concentration variation in the pore electrolyte is a fundamental parameter for current distribution analysis. Normally the effect was discussed through the polarization equation (9-11), however, it is difficult to handle the equation without the knowledge of the electrode reaction steps which will give the appropriate values of the reactant concentration during the ion discharge step. Actually, for Zn/zincate electrode, it was reported that the exchange current density does not depend on the zinc concentration in the electrolyte (12, 13). In this study the reaction rate of the electrochemical step on the pore wall is assumed independent of electrolyte concentration and to be a linear function of the overpotential.

Mathematical Treatment

The electrode is assumed one dimensional as shown

* Electrochemical Society Active Member.

¹ Present address: Department of Electrochemistry, The Graduate School at Nagatsuta, Tokyo Institute of Technology, 4259 Nagatsuta, Midori-ku, Yokohama 227, Japan.

Key words: battery, current distribution, porous electrode, zinc electrode.

in Fig. 1. The potential gradient along the electrode thickness is given by Ohm's law (14)

$$-\frac{d\phi}{dx} = Ri_m \quad [1]$$

where ϕ is the potential in the pore solution, x is the distance measured from the front of the electrode, R is the longitudinal resistance of pore electrolyte for a unit area of electrode, and i_m is the migration current in the pore solution for a unit area of electrode. The potential in the pore solution is also related to the current toward the pore wall as

$$-\left(R^* \frac{di_m}{dx} + R_s \frac{di}{dx}\right) = \phi \quad [2]$$

where R^* is the transverse resistance of the pore electrolyte, R_s is the resistance related to the electrode reaction at the pore wall, and i is the total current in the pore solution for a unit area of electrode, i.e., the sum of the migration and the diffusion currents

$$i = i_m + i_d \quad [3]$$

Resistances of R , R^* , and R_s are related to electrode parameters as

$$R = \frac{\rho}{e} \quad [4]$$

$$R^* = \frac{\delta\rho}{e} \quad [5]$$

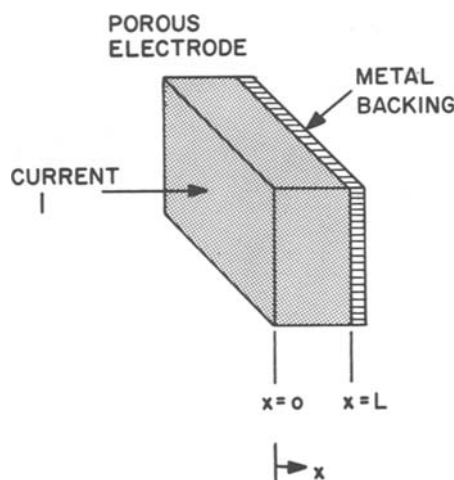


Fig. 1. One-dimensional porous electrode

$$R_s = \frac{R_d}{\gamma} \quad [6]$$

where ρ is the resistivity of pore electrolyte, ϵ is porosity, δ is pore radius, γ is pore wall area per unit volume of electrode, and R_d is the resistance for a unit area of pore wall and is caused by the electrode reaction involving the charge transfer process at the pore wall. The diffusion current i_d is related to the concentration gradient of the reactant in the pore electrolyte as

$$-\frac{dc}{dx} = \frac{i_d}{zFD} \quad [7]$$

where c is concentration, D is diffusion coefficient, ϵ is porosity, z is ionic charge, and F is Faraday's constant.

The resistivity in pore solution is a function of the concentrations of ion species, then

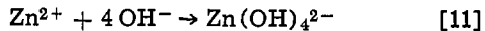
$$\rho = \frac{1}{\kappa} \quad [8]$$

$$\kappa = \sum_r z_r \lambda_r c_r \quad [9]$$

$$\sum_r z_r c_r = 0 \quad [10]$$

where ρ is the resistivity, κ is the conductivity of electrolyte, and z_i , λ_i , and c_i are equivalence, equivalent conductivity, and the concentration of species i , respectively. The ion species which play a role in the conduction process must include those species generated by the chemical reaction between the electrolyte and the ionized species at the pore wall.

Calculation for alkaline zinc electrode.—In the case of alkaline zinc electrode, zinc cation reacts with hydroxyl ion and forms zincate ion (15) as



For simplicity we discuss the case where the charge compensation for the zinc ion concentration change is achieved by OH^- concentration change, i.e.

$$\Delta c_{\text{OH}^-} = 2\Delta c_{\text{Zn}^{2+}} \quad [12]$$

where Δc_{OH^-} and $\Delta c_{\text{Zn}^{2+}}$ are the concentration changes of hydroxyl and zinc ions measured from the bulk electrolyte. The formation of zincate ion in the pore electrolyte consumes the free hydroxyl ions, consequently it reduces the conductivity of the pore electrolyte. The conductivity of the pore electrolyte κ is

$$\kappa = \kappa_0 + \Delta\kappa \quad [13]$$

$$\Delta\kappa = \lambda_{\text{OH}^-} (\Delta c_{\text{OH}^-} - 4\Delta c_{\text{Zn}^{2+}}) + 2\lambda_{\text{Zn}(\text{OH})_4^{2-}} \Delta c_{\text{Zn}^{2+}} \quad [14]$$

Substituting Eq. [12] gives

$$\kappa = \kappa_0 + 2(\lambda_{\text{Zn}(\text{OH})_4^{2-}} - \lambda_{\text{OH}^-}) \Delta c_{\text{Zn}^{2+}} \quad [15]$$

where κ_0 is the conductivity of bulk electrolyte.

Numerical calculation.—The reaction current densities $-(di/dx)$ were calculated for several values of R_d by solving Eq. [1]–[8] and [15] with the additional condition

$$i_d = \xi i \quad [16]$$

where ξ is constant. The boundary conditions are

$$i = I \text{ at } x = 0 \quad [17]$$

$$i = 0 \text{ at } x = L \quad [18]$$

$$c = c_0 \text{ at } x = 0 \quad [19]$$

where I is electrode current, L is electrode thickness, and c_0 is the reactant concentration in the bulk electrolyte. The constants employed for the calculation are $\epsilon = 0.5$, $\delta = 1.0 \times 10^{-3}$ cm, $\gamma = 1.0 \times 10^3$ cm⁻¹, $D = 6.8 \times 10^{-6}$ cm²/sec, $\xi = 0.15$, $z = 2$, $L = 0.1$ cm, $c_0 =$

1.2×10^{-3} mol/cm³, $\kappa_0 = 0.45$ Ω^{-1} /cm, $\lambda_{\text{OH}^-} = 33.0$ Ω^{-1} cm²/equiv., and $\lambda_{\text{Zn}(\text{OH})_4^{2-}} = 15.0$ Ω^{-1} cm²/equiv.

Results

The calculated reaction rate and the zincate concentration change for $I = \pm 120$ mA/cm² and $R_d = 10$ Ω cm² are shown in Fig. 2. From the graphs we see that the charging reaction rate is less than the discharging one at the entrance of the pore, but the relation is reversed at the end of the pore. Generally the differences between the charging reaction rates and the discharging ones are large for large values of $|I|$ and R_d . The penetration of the current in solution phase and the thickness of the reaction zone are large for large values of R_d .

The results of the calculations for the different values of I and R_d are summarized in Table I. The variation of the concentration in pore electrolyte is large at large values of $|I|$ and R_d . From Table I we see more than 25% of concentration change in pore electrolyte at the end of the pore for $|I| = 100$ mA/cm² and $R_d = 1.0$ and 10.0 Ω cm². The penetration depth of the solution-phase current i , and that of the reaction current density $-(di/dx)$ depend strongly on R_d , especially when the value of R_d is greater than 0.01 Ω cm². We see about 2.2% of difference in reaction rate at the pore entrance between charge and discharge process for $|I| = 100$ mA/cm² and $R_d = 10$ Ω cm², and about 1% of difference was calculated for $|I| = 100$ mA/cm² and $R_d = 1.0$ Ω cm².

Discussion

Reaction distribution.—From the calculated results shown in Table I, we see two origins for the mismatching between charging current profile and discharging current profile. First, the profile changes by the electrolyte resistivity change which is caused by the concentration variation in the pore solution. Second, the current profile depends on the reaction resistance R_d which exists between the pore solution and the electrode matrix. A difference in R_d between charge and discharge may arise because of a dependence of R_d on the concentration of reactant in the solution phase. Generally the reaction rate may be written for the charging process as

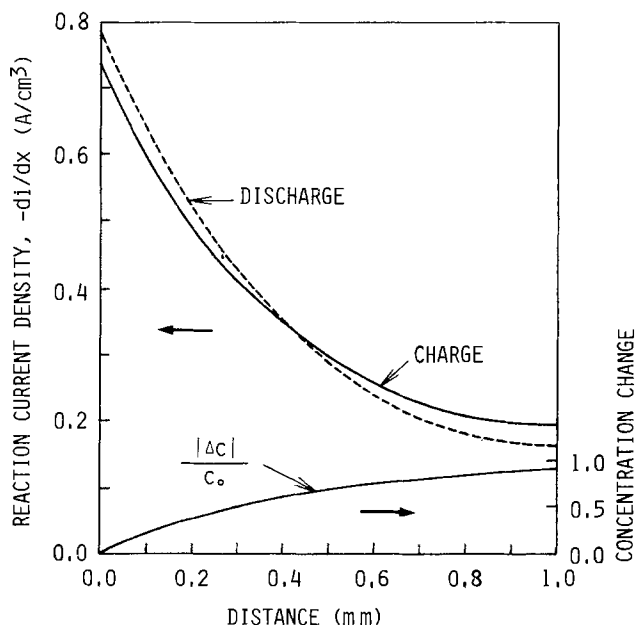


Fig. 2. Calculated distributions of the reaction current density and the zinc ion concentration change in Zn/zincate porous electrode for the electrode current of ± 120 mA/cm², $R_d = 10$ Ω cm².

Table I. Calculated reaction current densities at $x = 0$, the penetration depth of the reaction zone, and the zinc ion concentration deviation at the end of the pore

| Electrode current (mA/cm ²) | Reaction current density at $x = 0$ (A/cm ²) | Penetration depth of reaction zone* (mm) | Concentration change at $x = L$ (%) |
|---|--|--|-------------------------------------|
| $R_d = 0.1 \Omega \text{ cm}^2$ | | | |
| 10 Charge | 1.708 | 0.05320 | -0.9167 |
| 10 Discharge | -1.708 | 0.05318 | 0.9083 |
| 100 Charge | 17.05 | 0.05329 | -9.167 |
| 100 Discharge | -17.11 | 0.05308 | 9.083 |
| $R_d = 1.0 \Omega \text{ cm}^2$ | | | |
| 10 Charge | 0.5907 | 0.1645 | -3.000 |
| 10 Discharge | -0.5912 | 0.1643 | 3.000 |
| 100 Charge | 5.880 | 0.1649 | -30.28 |
| 100 Discharge | -5.939 | 0.1639 | 29.75 |
| $R_d = 10.0 \Omega \text{ cm}^2$ | | | |
| 10 Charge | 0.1999 | 0.6097 | -7.250 |
| 10 Discharge | -0.2004 | 0.6059 | 7.250 |
| 100 Charge | 1.980 | 0.6267 | -72.98 |
| 100 Discharge | -2.024 | 0.5909 | 71.58 |

* Penetration depth refers to the point where the reaction current density $- (di/dx)$ reduces to $1/e$.

$$\frac{di}{dx} = ai_0 \frac{c_1}{c_1^0} \exp [-\beta(\Phi_1 - \Phi_2)] \quad [20]$$

where i_0 is exchange current density in Tafel polarization, c_1^0 is the reference concentration of the reactant, $\beta = \alpha zF/RT$, Φ_1 and Φ_2 are potentials in the matrix and in the solution phase, respectively. On the other hand, the discharging reaction rate is

$$\frac{di}{dx} = ai_0 \exp [\beta'(\Phi_1 - \Phi_2)] \quad [21]$$

where $\beta' = (1 - \alpha)zF/RT$. However, it is reported that the exchange current density measured with an alkaline zinc electrode does not depend on the concentration of zinc in the electrolyte (12, 13) for a wide range of 0.016-0.64 mol/liter in 7N KOH electrolyte. The origin of the experimental result is believed to be that dislocation and diffusion of adsorbed zinc atoms is the rate-determining step. Using this result, we see that a change of rate-determining step may also change the reaction current distribution through the change of R_d . The charge transfer resistance ($R_D = RT/zFi_0$) calculated from the reported exchange current densities (12) ranges from 0.2 to 0.9 $\Omega \text{ cm}^2$. These values give the lower limit for the estimation of the real value of R_d .

Overpotential.—The overpotential of the porous electrode is obtained by substituting the calculated value of di/dx at $x = 0$ to Eq. [2]. Table II shows the calculated values of the potential ϕ_0 for $I = 10 \text{ mA/cm}^2$ and different values of R_d . It is noted that the overpotential ϕ_0 is not proportional to R_d but to $\sqrt{R_d}$ because the increase of the penetration depth of i with

Table II. Calculated overpotential on the Zn/zincate porous electrode for different reaction resistances and for the electrode current of 10 mA/cm²

| R_d ($\Omega \text{ cm}^2$) | Overpotential ϕ_0 (mV) | Penetration depth of solution potential (mm) |
|---------------------------------|-----------------------------|--|
| 0.1 Charge | 0.2212 | 0.04313 |
| 0.1 Discharge | -0.2213 | 0.04313 |
| 1 Charge | 0.6390 | 0.1505 |
| 1 Discharge | -0.6396 | 0.1504 |
| 10 Charge | 2.047 | 0.5909 |
| 10 Discharge | -2.051 | 0.5878 |

R_d brings an increase in the reaction area in the electrode, consequently it reduces the electrode impedance.

Effect of pore size.—The effects of the pore size on the charging characteristics of the electrode can also be discussed using the same model. A decrease in pore size with a constant porosity brings an increase in surface area of the porous electrode. Table III compares the calculated results of the working characteristics of the electrodes for a porosity of 0.5 and for pore sizes of 1, 10, and 100 μ . The surface area γ was calculated using a straight-pore model, i.e., $\gamma = 2\epsilon/\delta$. From the result we see that an increase in the penetration of the reaction zone is accompanied by an increase in electrode overpotential as the pore size increases. Thus the desire to reduce electrode impedance with the fine pore structure must be carefully balanced with the undesirable reduction of the utilizable area in the electrode caused by the limited penetration of reaction zone into the electrode.

Diffusion rate.—The ratio of the diffusion current to the total solution-phase current, introduced as ξ in Eq. [16], is an important parameter. However, the estimation or the formulation of the value as a function of x is difficult. The value of ξ depends on the potential gradient in the solution phase and on the dissociation rate of zincate ion to zinc cation under the local electric field. Equation [1] is useful for the estimation of the potential gradient.

Convective flow.—Another point which we have to mention is the convective flow which may change the concentration profile in the pore solution. Actually considerable amount of down flow of electrolyte near the surface of a flat and vertical zinc electrode is experimentally observed in a discharging process. This convective flow may reduce the concentration variation in pore electrolyte. The calculation of the reaction rate distribution under a gravity convection flow is not impossible, however, we need actual geometric data of the front face of the electrode and the facing separator, and also we need the flow resistivity which may depend on the pore size distribution on the electrode.

Conclusions

A mathematical model on the reaction profile in soluble porous electrodes has been developed and the reaction profiles in a zinc/zincate electrode have been calculated for a set of typical electrode parameters. The calculated results showed that considerable differences in current distribution exist during charge and discharge processes. The physical origins for the differences could be traced to a resistivity change in pore electrolyte and to a change in interfacial reaction resistance at the electrolyte and pore matrix surface. The electrolyte resistivity change is caused by a chemical reaction between the pore electrolyte and the product species of the electrochemical reaction on the pore wall. The calculation suggests that the pore structure of an alkaline zinc electrode will change

Table III. Calculated reaction properties of Zn/zincate porous electrode for different pore diameter, $\epsilon = 0.5$, $|I| = 10 \text{ mA/cm}^2$, and $R_d = 1.0 \Omega \text{ cm}^2$

| Pore diameter (μ) | Reaction rate at $x = 0$ (A/cm ²) | Penetration depth of reaction zone (mm) | Concentration change at $x = L$ (%) | Electrode overpotential (mV) |
|-------------------------|---|---|-------------------------------------|------------------------------|
| 1 Charge | 1.721 | 0.05244 | -0.7000 | 0.2194 |
| 1 Discharge | -1.722 | 0.05238 | 0.7000 | -0.2194 |
| 10 Charge | 0.5907 | 0.1645 | -3.000 | 0.6390 |
| 10 Discharge | -0.5912 | 0.1643 | 3.000 | -0.6396 |
| 100 Charge | 0.1984 | 0.6207 | -7.250 | 2.069 |
| 100 Discharge | -0.1988 | 0.6168 | 7.250 | -2.073 |

during discharge and charge cycles even in a relatively small current region where no passivation film is formed. The effect of pore size on the current distribution and on the overpotential of the electrode was also numerically discussed using the model.

Acknowledgment

This work was supported by the Department of Energy, Division of Electrochemical Energy Systems and Division of Electric and Hybrid Vehicle Program.

Manuscript submitted Jan. 25, 1980; revised manuscript received March 10, 1981. This was Paper 545 presented at the Seattle, Washington, Meeting of the Society, May 21-26, 1978.

Any discussion of this paper will appear in a Discussion Section to be published in the June 1982 JOURNAL. All discussions for the June 1982 Discussion Section should be submitted by Feb. 1, 1982.

Publication costs of this article were assisted by Argonne National Laboratory.

LIST OF SYMBOLS

| | |
|--------------|---|
| c_i | concentration of species i (mol/cm ³) |
| Δc_i | concentration change of species i (mol/cm ³) |
| D | diffusion coefficient (cm ² /sec) |
| F | Faraday's constant |
| i | current in pore electrolyte for a unit area of electrode (A/cm ²) |
| i_m | migration current in pore electrolyte (A/cm ²) |
| i_d | diffusion current in pore electrolyte (A/cm ²) |
| I | electrode current (A/cm ²) |
| L | electrode thickness (cm) |
| R | solution resistance along x direction (Ω cm) |
| R^* | transversal resistance of pore solution (Ω cm ³) |
| R_s | reaction resistance (Ω cm ³) |
| R_d | reaction resistance for a unit area of pore wall (Ω cm ²) |
| x | distance through the one-dimensional porous electrode (cm) |
| z | ionic charge |
| γ | pore wall area per unit volume of electrode (cm ⁻¹) |

| | |
|-------------|---|
| δ | pore radius (cm) |
| ϵ | porosity |
| ξ | ratio of diffusion current to total solution-phase current |
| ρ | resistivity of pore electrolyte (Ω cm) |
| ϕ | potential of pore electrolyte (V) |
| λ_i | ionic equivalent conductivity of species i (Ω^{-1} cm ² /equiv.) |
| κ | conductivity of pore electrolyte (Ω^{-1} /cm) |
| κ_0 | conductivity of bulk electrolyte (Ω^{-1} /cm) |

REFERENCES

1. J. Burbank, A. C. Simon, and E. Willihnganz, in "Advances in Electrochemistry and Electrochemical Engineering," Vol. 8, pp. 157-251 (1971).
2. A. C. Simon, S. M. Caulder, and J. T. Stemmler, *This Journal*, **122**, 461 (1975).
3. V. H. Dodson, *ibid.*, **108**, 406 (1961).
4. J. McBreen, *ibid.*, **119**, 1620 (1972).
5. J. J. Lander, "Zinc-Silver Oxide Batteries," pp. 457-470, John Wiley & Sons, Inc., New York (1971).
6. K. W. Choi, D. N. Bennion, and J. Newman, *This Journal*, **123**, 1616 (1971).
7. J. S. Dunning, D. N. Bennion, and J. Newman, *ibid.*, **118**, 1251 (1971).
8. H. Gu and D. N. Bennion, *ibid.*, **123**, 1364 (1976).
9. J. S. Newman and C. W. Tobias, *ibid.*, **109**, 1183 (1962).
10. I. G. Gurevich and V. S. Bagotskii, "Fuel Cells," Institute of Electrochemistry Academy of Sciences of the USSR, Authorized translation from the Russian, Consultants Bureau New York, pp. 47-63 (1966).
11. J. Newman and W. Tiedemann, *AIChE J.*, **21**, 25 (1975).
12. J. P. G. Farr and N. A. Hampson, *J. Electroanal. Chem. Interfacial Electrochem.*, **113**, 433 (1967).
13. T. P. Dirkse, *This Journal*, **126**, 541 (1979).
14. R. DeLevie, in "Advances in Electrochemistry and Electrochemical Engineering," Vol. 6, pp. 329-397, P. Delahay, Editor, Interscience Publishers, New York (1967).
15. T. P. Dirkse, *This Journal*, **101**, 328 (1954).

Current Distributions in Soluble Battery Electrodes

II. Experimental

Y. Yamazaki¹ and N. P. Yao*

Argonne National Laboratory, Chemical Engineering Division, Argonne, Illinois 60439

ABSTRACT

A simulated, sectioned porous electrode was developed using the photolithography technique. The current distributions in Zn/zincate and Cu/CuSO₄ porous electrodes were measured using the simulated electrodes for the study of charge and discharge processes. The result showed different current distributions for charge and discharge processes; the charging reaction current in the Zn/zincate system penetrated more deeply into the electrode than the discharging current did. The discharging reaction current in the Cu/CuSO₄ system penetrated more than the charging current. These observed characteristics of the current distributions were analyzed using the theoretical results which were mathematically derived based on a migration model. Other applications of the simulated porous electrodes were also demonstrated for study of electrode passivation phenomena and for transient current distribution measurements.

As has been theoretically derived (1), there are considerable differences in the current distributions in a porous zinc electrode during charge and dis-

charge processes even in the relatively low current density regions where no passivation occurs. In this paper the reaction distributions in soluble porous electrodes are experimentally demonstrated. For this purpose, a novel sectioned porous electrode was designed for the *in situ* measurement of the reaction current distribution within the electrode.

* Electrochemical Society Active Member.

¹ Present address: Department of Electrochemistry, the Graduate School of Nagatsuta, Tokyo Institute of Technology, 4259 Nagatsuta, Midori-ku, Yokohama 227, Japan.

Key words: battery, current distribution, porous electrode, zinc electrode.

Normally, current distribution within a porous electrode has been determined indirectly through a chemical analytical method (2, 3) or directly by a sectioned electrode method (4-7). The former method can be adapted to a variety of electrodes and the measurements can be made using commercial electrodes. However, the measurements are limited to the operating range where the electrode reaction causes sufficient precipitation of reaction products to be observed. On the other hand, the sectioned electrode method has an advantage of the continuous *in situ* measurements of the reaction current distribution. Unfortunately, very few results have been reported about the sectioned electrode method because of the difficulty of the electrode fabrication and experimentation. The accuracy of the current distribution measurement with a sectioned electrode largely depends on the electrode design. Particularly it is important to design the experimental electrode so that the real electrode system is well simulated and that the reaction profile is not disturbed by connecting measuring circuits.

Recently the sectioned electrode method was improved when thin film technology was introduced by Szpak and Katan (4) for the fabrication of the electrode segments. By using this technique, they succeeded in reducing the pore size and the thickness of the electrode segments. However, the small interface area at the electrolyte and the matrix of their single pore electrode may generate an error in the measurement. Another deficiency in their design was the large spaces between the segments. Experimentally it is very difficult to reduce the segment distance without the risk of breaking the electric insulation between the segments.

This paper discusses a novel method of fabricating a sectioned porous electrode based on the photolithography technique. The method remedies the deficiencies of conventional experimental sectioned electrodes. Porous sectioned electrodes based on this method have been effectively applied to the study of current distributions within porous zinc/zincate and copper/copper sulfate electrodes.

Experimental

Measurement circuit.—The concept of the sectioned electrode designed for the current distribution measurements is shown in Fig. 1. The measurement circuit connected to the electrode is shown in Fig. 2. The currents passing through each segment of the electrode were measured by the voltage drops across shunt resistors (0.33Ω). A low voltage scanning switch (Keithley Instruments, Incorporated, Model 702/7029) and a strip chart recorder with a high sensitivity plug-in

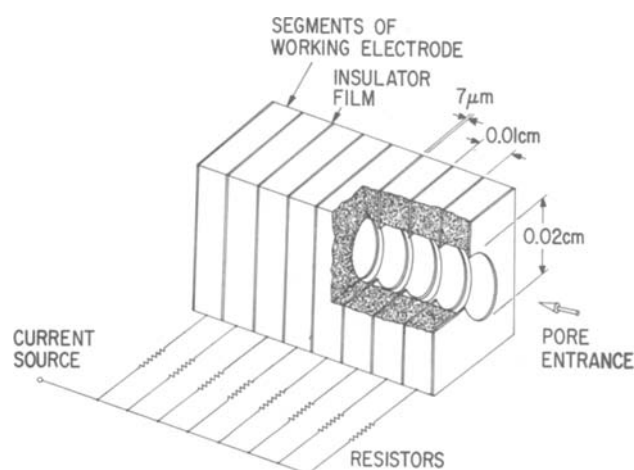


Fig. 1. Schematic representation of the segmented porous electrode.

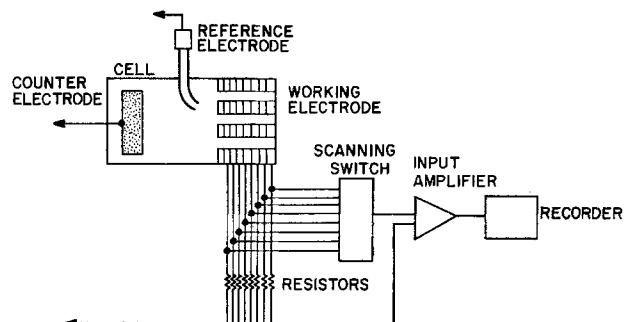


Fig. 2. Schematic diagram of the equipment for current distribution measurement.

module (Hewlett Packard, Model 17505A) were used for the measurement of the voltages across the shunt resistors. A precision power supply (Hewlett Packard, Model 6114A) was used as a potential source, and the total amount of charge passed through the electrode was monitored with a digital coulometer (Princeton Applied Research, Model 379).

Preparation of sectioned electrode.—The perforated metal sheets representing the segments in Fig. 1 were fabricated by conventional photolithography techniques. First, the pore pattern of the electrode was designed and the drawing was photographed with a high contrast film (Kodak High Contrast Copy Film) to make a photolithography mask. The metal sheets were then coated by photoresist resin and the pore pattern was printed using the prepared mask and a mercury-xenon arc lamp. The process was carried out on both sides of the metal sheets. In order to obtain a close fitting of the pore patterns between both sides of the metal sheets, the mask positions were carefully adjusted. The exposed photoresist films were developed by the spray developing method. The metal sheets covered with the developed resist films were dried at 121°C for 10 min and then etched in the solution shown in Table I. The photoresist films on both sides of the metal sheets act as insulators in the fully assembled electrode. The conditions for the photofabrication of the porous segments are shown in Table I. The prepared metal sheets coated with insulator films were stacked to align the holes and then fixed with a lucite frame. Figure 3 shows the stacked segments after wiring, and Fig. 4 shows the mounted electrode stack. The elements were pressed from both sides with a lucite frame (shown as F in Fig. 4) to facilitate close stacking. The electrode parameters are listed in Table II.

Electrolyte preparation.—Electrolytes used for the experiment were prepared as follows: (i) KOH [40 weight percent (w/o)] aqueous solution which had been prepared by dissolving AR grade KOH into distilled and oxygen purged water and then stirred overnight in a nitrogen atmosphere; and (ii) CuSO_4 aqueous solution (1 mol/liter) was prepared by dissolving AR grade CuSO_4 in distilled water.

Experimental procedure.—A fresh electrolyte was placed in the cell for 2 hr before the potential was applied to the electrode. The electrode was first dis-

Table I. Photofabrication condition

| | |
|------------------------|---|
| Photoresist | KPR |
| Dye material | Kodak Photo Resist Dye Blue |
| Coating method | Spin coating |
| Developing method | Spray development |
| Prebaking temperature | 5 min at 80°C |
| Postbaking temperature | 10 min at 121°C |
| Exposing source | Mercury-xenon arc lamp |
| Masking material | Kodak high contrast copy film |
| Etching solutions: | |
| For copper sheets | FeCl_3 aqueous solution (20 w/o) |
| For zinc sheets | HNO_3 aqueous solution (10 w/o) |

Table II. Electrode characteristics

| Parameter | Cell I | Cell II |
|--------------------------------------|--|---|
| Electrolyte | CuSO ₄ (1 mol/liter) aqueous solution | KOH (40 w/o) ZnO saturated aqueous solution |
| Electrode matrix | Cu | Zn |
| Pore diameter (μm) | 200 | 200 |
| Number of pores | 396 | 396 |
| Distance between adjacent pores (μm) | 400 | 400 |
| Porosity | 0.2 | 0.2 |
| Thickness of one segment (μm) | 127 | 100 |
| Thickness of insulator film (μm) | 10 | 7 |
| Number of segments | 8 | 15 |
| Reference electrode | Calomel | Hg-HgO |
| Counterelectrode | Cu | Zn |

charged at constant cell voltage and the currents passing through each segment were recorded using the scanning switch. The scanning rate was 0.5 sec/segment for the first 1 min of the measurement, then it was changed to 2 sec/segment. The current profile usually varied for a period which was dependent on the total electrode current, then it became steady. The measurement was usually continued for 2 hr. After the discharge measurement, the cell was disconnected from the power source and was permitted to stand for 2 hr before a charging potential was applied. The charging current measurement was made with the same conditions as the discharge case and was terminated after the same quantity of charge had passed through the cell.

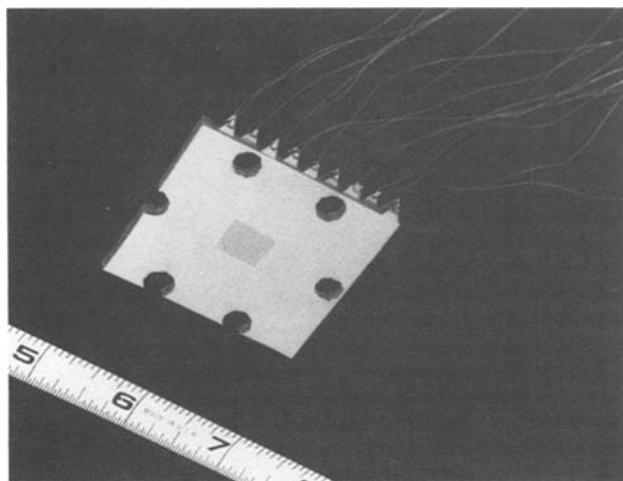


Fig. 3. Stacked zinc electrode segments

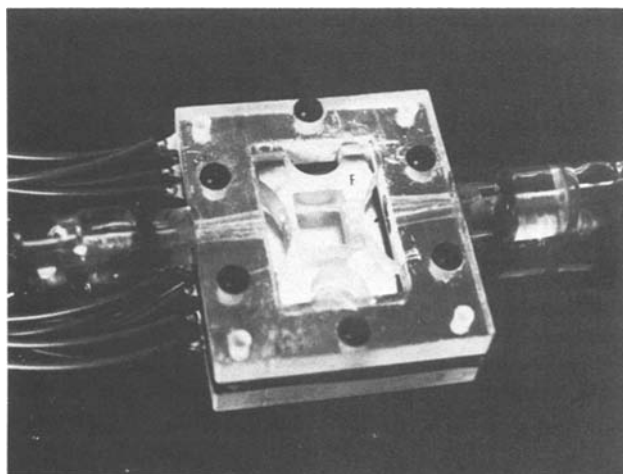


Fig. 4. Mounted electrode stack

The reaction current density was calculated from the measured current through the segments by using the relation

$$i_{\text{reac}} = \frac{i_n}{Sd} \quad [1]$$

where S is the electrode surface area, d is the thickness of an electrode segment, and i_n is the current passing through segment n . The reaction current density i_{reac} is equivalent to $-(di/dx)$, where i is the current in the solution phase for a unit area of electrode and x is the distance measured from the front of the electrode.

Results and Discussion

Reaction distributions in the Zn/zincate electrode.—The reaction current distributions measured with the Zn/zincate electrode are shown in Fig. 5 and 6 for electrode currents of 15.8 and 78.9 mA/cm², respectively. The unit of the vertical axes of the figures indicates the transfer current from solution to matrix phase for a unit volume of the electrode. Generally the reaction currents for the charging process penetrated more deeply into the electrode than that of the discharging process. The difference is in good agreement with the theoretical result obtained based on a migration model (1). The calculated curves for charging and discharging processes, in solid and dotted lines, are also shown in the figures. The calculation

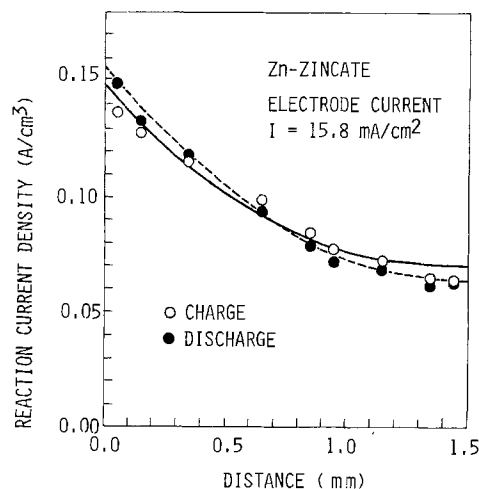


Fig. 5. Reaction distribution in porous zinc/zincate electrode. The curves are theoretical values for $R_d = 4.7 \Omega \text{ cm}^2$ and $\xi = 0.25$.

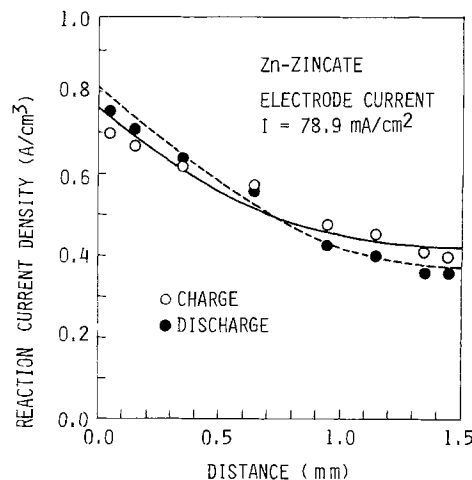


Fig. 6. Reaction distribution in porous zinc/zincate electrode. The curves are theoretical values for $R_d = 6 \Omega \text{ cm}^2$ and $\xi = 0.07$.

was made using the experimental conditions of pore size, porosity, and electrode thickness shown in Table II. The agreement between the calculated curves for the current density of $I = 15.8 \text{ mA/cm}^2$, $R_d = 4.7 \Omega \text{ cm}^2$, $\xi = 0.25$, and the experimental data is good. However, the agreement deteriorates somewhat at the higher current density of $I = 78.9 \text{ mA/cm}^2$. The values of R_d , which were determined by comparing the theoretical curves to the experimental data, are reasonable since the charge transfer resistance (8)

$$R_D = \left(-\frac{\partial \eta}{\partial i} \right)_{\eta=0} \quad [2]$$

measured with an alkaline zinc electrode using the double pulse method was $0.2\text{--}1.0 \Omega \text{ cm}^2$ at room temperature and R_d is the sum of R_D and the additional resistance based on the concentration polarization at the vicinity of the pore wall.

Table III compares the measured potential of the bulk electrolyte and the theoretical overpotential which is calculated for the pore electrolyte at the front end of the electrode (1). The agreement is reasonably good. The difference in the calculated potential between charge and discharge processes is originated by the resistivity change of pore solution caused by the concentration change.

Reaction distribution in Cu/CuSO₄ electrode.—The reaction distribution was also measured with the Cu/CuSO₄ electrode. The theoretical calculation was conducted in the same manner as for the Zn/zincate electrode. However, we must change Eq. [15] shown in the theoretical part of this study (1), to

$$\kappa = \kappa_0 + 2\Delta c_{\text{CuSO}_4} \Delta c_{\text{CuSO}_4} \quad [3]$$

$$\Delta c_{\text{CuSO}_4} = c_{\text{CuSO}_4} - c_{\text{CuSO}_4,b} \quad [4]$$

where Δc_{CuSO_4} is the equivalent conductivity of CuSO₄, c_{CuSO_4} and $c_{\text{CuSO}_4,b}$ are the concentrations of CuSO₄ in the pore and in the bulk solution, respectively, and κ_0 is the conductivity of the bulk electrolyte.

Figure 7 shows the measured reaction distributions in the Cu/CuSO₄ electrode for a small electrode current of 0.79 mA/cm^2 . The charging current concentrates at the front part of the electrode. The theoretical curve for the charging reaction, the solid line, is shown in the figure. The calculation was based on $\Delta c_{\text{CuSO}_4} = 27.0 \Omega^{-1} \text{ cm}^2/\text{equiv.}$, $\kappa_0 = 0.053 \Omega^{-1}/\text{cm}$, $D = 1.0 \times 10^{-5} \text{ cm}^2/\text{sec}$, $R_d = 3.0 \Omega \text{ cm}^2$, and $\xi = 0.1$. The measured reaction distribution for the discharging process shows a deeper penetration into the electrode. The theoretical curve for $R_d = 20.0 \Omega \text{ cm}^2$ is also shown in the figure as the dotted line. The large value of R_d for the discharge curve is probably due to a formation of Cu₂O film on the pore wall. The film will decompose during the charging process. The concentration variations in pore solution discussed in previous paper (1) was very small because of the low (0.79 mA/cm^2) electrode current imposed. The calculated reaction rate differences at the pore entrance gives the differences of 1.0% for $R_d = 3.0 \Omega \text{ cm}^2$ and 1.2% for $R_d = 20.0 \Omega \text{ cm}^2$.

The calculated electrode overpotential for the charging curve ($R_d = 3.0 \Omega \text{ cm}^2$) was 21.8 mV. This agreed well with the measured overpotential of 18.9 mV. The calculation for the discharging process gave

Table III. Polarization data for the Zn/zincate porous electrode

| Electrode current (mA/cm ²) | Experimental value (mV) | Theoretical value (mV) |
|---|-------------------------|------------------------|
| 15.8 Charge | 24.2 | 19.7 |
| 15.8 Discharge | 26.0 | 20.7 |
| 78.9 Charge | 93.0 | 115.0 |
| 78.9 Discharge | 95.0 | 123.0 |

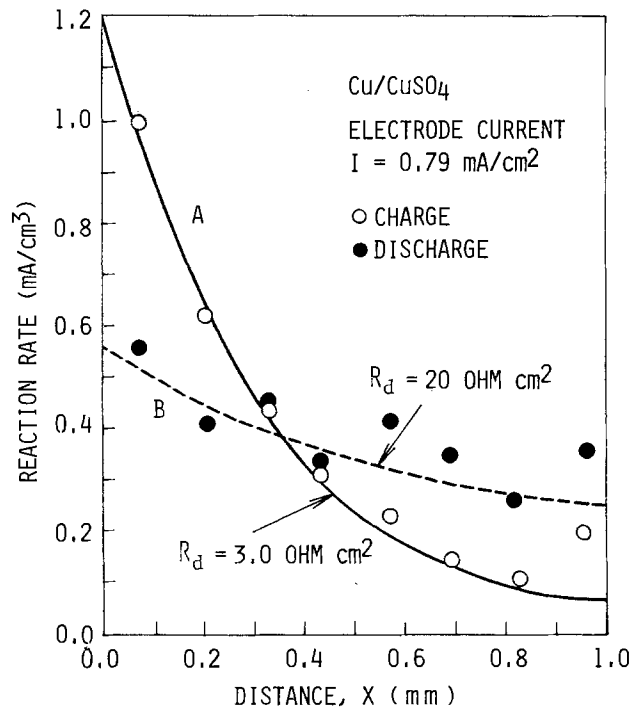


Fig. 7. Reaction distribution in porous copper/copper sulfate electrode. Curves A and B are theoretical values for $R_d = 3.0$ and $20 \Omega \text{ cm}^2$, respectively, and $\xi = 0.1$.

a relatively large value of 61.7 mV compared to the measured overpotential of 24.3 mV.

Passivation in Zn/zincate electrode.—When a relatively large (649 mA/cm^2) discharge current was passed through the Zn/zincate electrode for 3 min, an abrupt current reduction was observed. From the change in the current profile shown in Fig. 8, we see a masking of active area on the pore wall by the formation of a passivation film (9, 10). The observed result that the passivation starts from the entrance of the pore is consistent with the result of the microscopic examination reported by Katan (11) on a formation of passivation films in a single pore zinc electrode.

Transient measurement.—By using this type of sectioned electrode, the time progression of the reaction profile could be detected. Figure 9 shows the result of a transient measurement during the discharging process in the Zn/zincate electrode. The measurement was made for 35 min from the beginning of the electrolysis. As seen from the figure, the reaction currents decreased initially and then gradually increased to constant values. These changes in the reaction currents

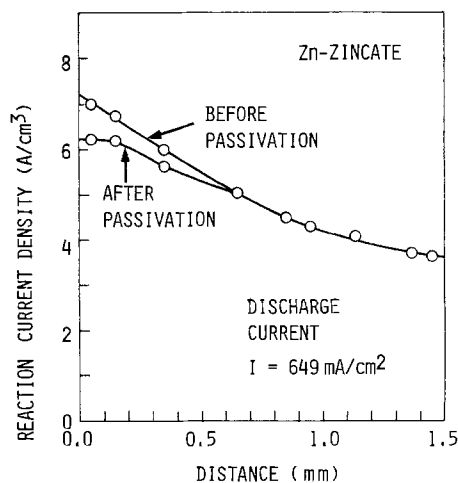


Fig. 8. Reaction distribution in partially passivated porous zinc/zincate electrode.

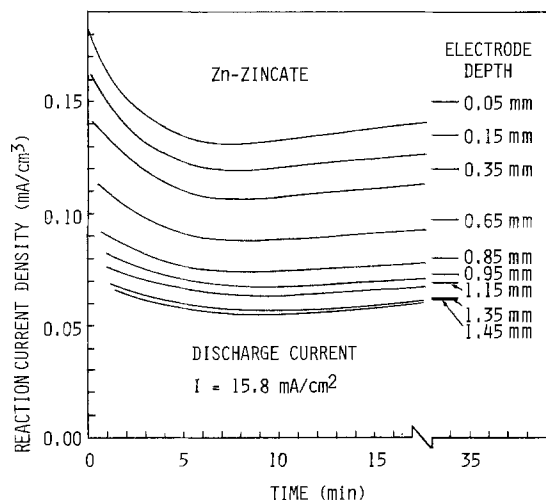


Fig. 9. Time progression of reaction current in porous zinc/zincate electrode at various electrode depth.

are particularly large at the front part of the electrode.

Summary and Conclusions

Novel sectioned porous electrodes based on the photolithography technique have been developed and applied to the measurement of reaction distributions within the porous electrodes. The measured reaction profile in the Zn/zincate porous electrode showed a difference in penetration depth of reaction zone between charge and discharge processes. The amount of the difference agreed well with the theoretical value calculated based on a migration model. The reaction resistance at pore electrolyte and pore matrix, determined by comparing the measured reaction profile and the calculated one, showed reasonable values. The effectiveness of this experimental method was also demonstrated, capable of determining the resistance of the thin film formed on the anode surface of the Cu/CuSO₄ electrode.

Acknowledgment

This work was supported by the Department of Energy, Division of Electrochemical Energy Systems and Division of Electric and Hybrid Vehicle Program.

Manuscript submitted Jan. 25, 1980; revised manuscript received March 10, 1981. This was Paper 545 presented at the Seattle, Washington, Meeting of the Society, May 21-26, 1978.

Any discussion of this paper will appear in a Discussion Section to be published in the June 1982 JOURNAL. All discussions for the June 1982 Discussion Section should be submitted by Feb. 1, 1982.

Publication costs of this article were assisted by Argonne National Laboratory.

LIST OF SYMBOLS

| | |
|--------------------|--|
| c_i | concentration of species i (mol/cm ³) |
| Δc_i | concentration change of species i (mol/cm ³) |
| d | thickness of an electrode segment (cm) |
| D | diffusion coefficient (cm ² /sec) |
| i | current in pore electrolyte for a unit area of electrode (A/cm ²) |
| i_n | current passing through electrode segment n (A) |
| i_{react} | reaction current for a unit volume of electrode (A/cm ³) |
| I | electrode current (A/cm ²) |
| R_d | reaction resistance for a unit area of pore wall (Ω cm ²) |
| R_D | charge transfer resistance for a unit area of pore wall (Ω cm ²) |
| S | electrode surface area (cm ²) |
| ξ | ratio of diffusion current to total solution-phase current |
| η | electrode overpotential (V) |
| Λ_i | equivalent conductivity of species i (Ω^{-1} cm ² /equiv.) |
| κ | conductivity of pore electrolyte (Ω^{-1} /cm) |
| κ_0 | conductivity of bulk electrolyte (Ω^{-1} /cm) |

REFERENCES

- Y. Yamazaki and N. P. Yao, *This Journal*, **128**, 1655 (1981).
- Z. Nagy and J. O'M. Bockris, *ibid.*, **119**, 1129 (1972).
- K. W. Choi, D. Hamby, and D. N. Bennion, *ibid.*, **123**, 1628 (1976).
- S. Szpak and T. Katan, *ibid.*, **122**, 1063 (1975).
- J. McBreen, *ibid.*, **119**, 1620 (1972).
- J. J. Coleman, *ibid.*, **98**, 26 (1951).
- V. A. Panov, V. S. Borovkov, and P. D. Lukovtsev, *Soviet Electrochem.*, **5**, 164 (1969).
- J. P. G. Farr and N. A. Hampson, *J. Electroanal. Chem. Interfacial Electrochem.*, **13**, 433 (1967).
- M. Eisenberg, H. F. Bauman, and D. M. Brettner, *This Journal*, **108**, 909 (1961).
- N. A. Hampson, M. J. Tarbox, and J. T. Lilley, *Electrochem. Technol.*, **2**, 309 (1964).
- T. Katan, Paper 44, p. 120, The Electrochemical Society Extended Abstracts, Atlanta, Georgia Oct. 9-14, 1977.

Passivation of Zinc Anodes in KOH Electrolytes

Ming-Biann Liu,* G. M. Cook,* and N. P. Yao*

Argonne National Laboratory, Chemical Engineering Division, Argonne, Illinois 60439

ABSTRACT

Passivation times of horizontally upward-facing and downward-facing zinc microanodes in KOH electrolytes of five concentrations are reported. These measurements extend passivation data into a low current-density region for evaluating conflicting interpretations of published work. To interpret our data, a new mechanism for anodic passivation is proposed. In high current-density regions, passivation occurs when compact ZnO covers the electrode surface; in low current-density regions, passivation occurs when the mass transfer of hydroxide ions across a porous ZnO layer is less than that required for anodization. This work also discusses passivation in porous zinc battery electrodes.

Alkaline batteries employing zinc electrodes are under development for use in electric vehicles. Knowledge of the passivation behavior of a zinc electrode in KOH electrolyte is required for optimizing the electrode design.

The utilization of a zinc electrode in alkaline batteries depends on the ability of the electrode to remain active during the anodic dissolution process. At anodic potentials near the equilibrium value, the soluble oxidation product of zinc in concentrated alkaline solutions is $Zn(OH)_4^{2-}$, as evidenced by nuclear magnetic resonance (NMR), and Raman and infrared reflection spectroscopic studies (1-3). Many workers (4-25) have made galvanostatic studies using planar zinc electrodes in alkaline solution. These studies describe derivations of the zinc passivation mechanism, morphological observation of the passivation film, and the relation of passivation time to the current density. Several techniques were used to study the passive films. Microscopic observation provided morphological data (15, 16, 23, 24). An ellipsometer measured the relative changes of amplitude and phase of light specularly reflected by the passivation film (14, 25). X-ray analysis identified ZnO as the passivation film (21); however, this analytic method requires the removal and subsequent drying of the passivation film, which could result in the conversion of all the zinc-containing species to ZnO. *In situ* identification of the chemical nature of the passivation film is not available.

The mechanism of passivation and the relationship between current density and passivation time for zinc anodes in alkaline solution has been reviewed by the authors (26) and will be discussed later. In the literature, there are conflicts in the treatment of passivation data and in the interpretation of the process for determining passivation time. In the former, for a given electrolyte, Dirkse and Hampson (13) indicated that a single modified Sand equation could cover the current-density region from 0 to 10 A/cm². Bartelt and Landsberg (7) found that two equations were required: one for high current-density regions (>0.32 A/cm²) and one for lower current-density regions. In the latter, Hampson and his co-workers (11, 13) postulated that the electrode passivates instantly when ZnO is precipitated from supersaturated zincate at the electrode surface. Other investigations (14, 16, 25) indicated the passivation is not likely to happen at the moment ZnO is produced. These conflicts were not resolved since the measurements in the literature were usually complicated by free convection. Therefore, we have used electrodes designed to minimize free convection to carry out passivation measure-

ments in five concentrations of KOH electrolytes over a wide range of current densities (0.06-1.53 A/cm²). Based on our results, we propose a new scheme that describes the passivation time in terms of sequential reaction steps. We have extended measurements to the current-density region of interest in battery design (below 0.1 A/cm² at 7M KOH). These data were then used to estimate the effect of passivation on the utilization of a porous zinc battery electrode.

Experimental

The standard experimental cell and other apparatus used is described elsewhere (26). Rectangular zinc electrodes, 0.05 × 0.13 cm, were cut from a zinc sheet of 99.99% purity purchased from United Mineral and Chemical Corporation (New York). The impurities were specified to be as follows: Cd, 5 ppm; Pb, 5 ppm; Fe, 3 ppm; Cu, 2 ppm; Au, 1 ppm; Sn, 1 ppm; Fe, 0.5 ppm; and In, 0.5 ppm. The electrodes, set in acrylic plastic (purchased from Fulton Products Corporation, Saxonburg, Pennsylvania), were mounted horizontally in either the upward- or downward-facing position. The upward-facing microanode has the following special features: (i) It provides conditions required for a stable stratification of fluid near the electrode surface since the electrochemically formed zincate is denser than the bulk electrolyte, (ii) the acrylic plastic surrounding the anode provides the means to maintain a high zincate concentration at the edge of the electrode, i.e., there is no sharp change in the diffusion boundary layer at the edge, and (iii) the small size of the electrode (0.05 × 0.13 cm) compared to its distance from the counterelectrode (1.5 cm) provides a relatively uniform electric field over its surface. The electrolyte was reagent-grade KOH at concentrations of 0.784, 2.92, 4.98, 7.24M KOH or 7.24M KOH saturated with analytical reagent-quality zinc oxide. The solutions were prepared with doubly distilled water and de-aerated by bubbling purified nitrogen through them. The experiments were performed at room temperature (approximately 20°C).

Before each experiment, the zinc electrode was anodically etched at 10 μ A for 5 sec and then allowed to stand for at least 10 min to ensure a quiescent state in the electrolyte and to establish electrode/electrolyte equilibrium conditions. Before an electrode was reused, it was repolished and its surface finish was measured with a calibrated optical microscope. Periodically, experiments were repeated to determine experimental reproducibility; average reproducibility of the experimental data was found to be 8.4% about the mean value.

Results

The relationship between current density, i , and passivation time, t , is usually expressed by the modi-

* Electrochemical Society Active Member.

Key words: battery, mass transfer, porous electrode, oxide.

fied Sand equation (26)

$$i = kt^{-1/2} + i_e \quad [1]$$

where k and i_e are constants. Therefore, least squares fitted passivation data are plotted in the form of i vs. $t^{-1/2}$ in Fig. 1-3. Plotted in Fig. 1 are the data for upward- and downward-facing zinc microelectrodes which were anodized in 7.24M KOH electrolyte at current densities ranging from 61 to 1620 mA/cm² and for upward-facing electrodes anodized in 7.24M KOH saturated with ZnO at 122-1530 mA/cm². For passivation times less than 7 sec, the data for upward- and downward-facing anodes in 7.24M KOH electrolyte are in agreement within experimental uncertainty. However, for longer times, a downward-facing anode has a longer passivation time at a given current density. The data also show that the presence of zincate in the electrolyte shortens the passivation time.

Figure 2 presents the passivation data for the upward-facing anode in four concentrations of KOH (0.784, 2.92, 4.98, and 7.24M). The data show that for passivation times less than 100 sec ($t^{-1/2} = 0.1 \text{ sec}^{-1/2}$), higher concentrations of KOH result in longer passivation times at any given current density. For passivation times longer than 100 sec, these data are plotted on the expanded scale of Fig. 3. It is clear that the KOH concentration effect is the same for the longer passivation times. (Current densities below 100 mA/cm² are of interest to battery applications.)

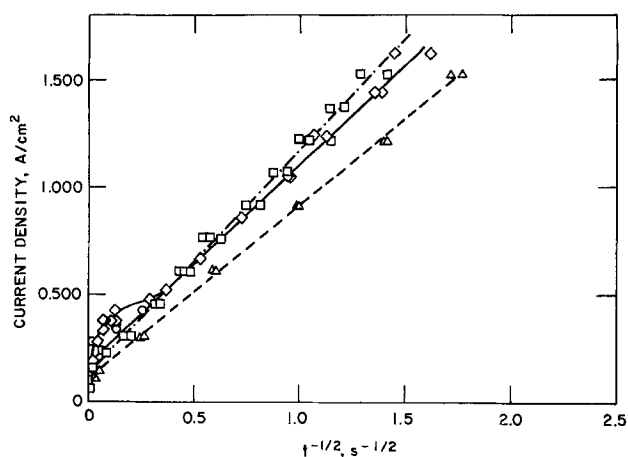


Fig. 1. Effect of orientation and bulk zincate on current density vs. passivation time, t , of zinc anodes in 7.24M KOH (squares, upward anode; diamonds, downward anode; circles, downward anode with 1 mm plastic channel; triangles, upward anode using electrolyte saturated with zincate).

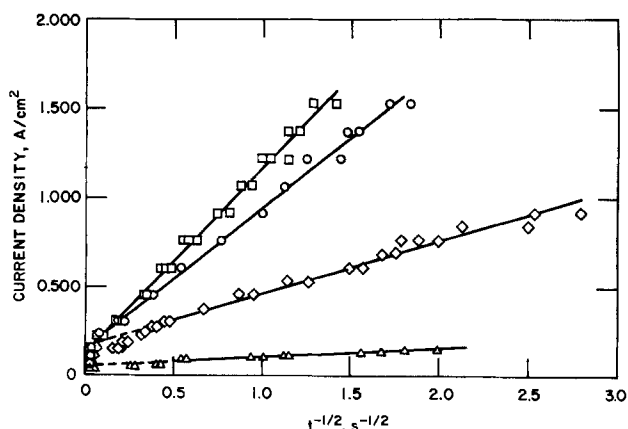


Fig. 2. Current density vs. passivation time for upward-facing zinc anodes in 7.24M (squares), 4.98M (circles), 2.92M (diamonds), and 0.784M (triangles) KOH electrolyte.

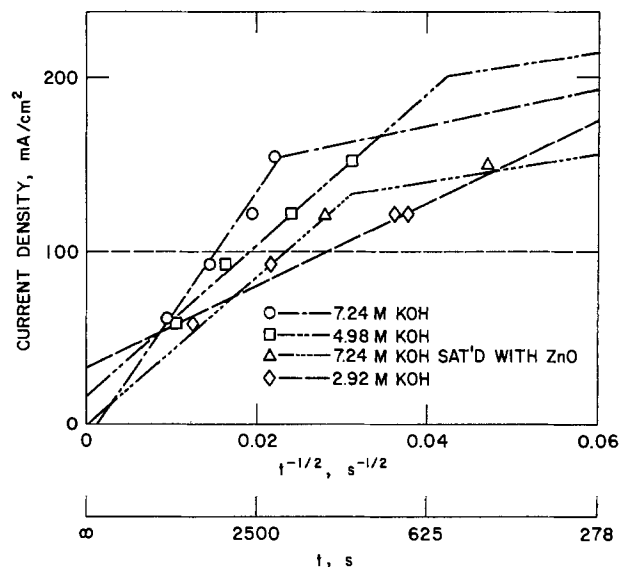


Fig. 3. Current density vs. passivation time for upward-facing anodes (low current-density region).

The constants of Eq. [1] (k , i_e) for zinc microelectrodes in the KOH electrolytes are tabulated in Table I. Since, for the upward-facing anode, the passivation times are substantially longer at low current densities than at high values, the constants are given for two current-density regions. From Table I, in the low current-density region, the intercept (i_e) for 7.2M KOH is near zero. On this basis, a zero intercept of the i vs. $t^{-1/2}$ curve was assumed in order to calculate k for the low current region of series 3 from the single datum at 122 mA/cm².

Discussion

Potential-time curve.—Our potential vs. time curves were similar to those observed by Dirkse and Hampson (13), except that we observed a short-life transition just prior to the onset of passivation, as also observed by Bartelt and Landsberg (7) and Elder (12). Since the electrode potential at the transition is in the vicinity of the Zn/ZnO standard potential, the transition may be associated with the direct formation of the passivating type II ZnO film observed by Powers and Breiter (15).

Relationship between current density and passivation time.—It is generally agreed that a zinc oxide film is responsible for the passivation of zinc anodes in alkaline electrolytes (26). The disagreement relates to the nature of the rate-determining steps in the processes associated with passivation. Table II summarizes the rate-determining steps and the relationships between current density and passivation time proposed in the literature.

Table I. The constants of Eq. [1] for the zinc anodes ($i = kt^{-1/2} + i_e$)

| Expt. series* | Electrolyte (M) | Current density (mA/cm ²) | $k \times 10^{-2}$ (mA/sec ^{1/2} /cm ²) | $i_e \times 10^{-2}$ (mA/cm ²) |
|---------------|----------------------|---------------------------------------|--|--|
| 1 | 7.24 | 200-1530 | 10 ± 0.2 | 1.3 ± 0.2 |
| | | 60-153 | 69 ± 7 | -0.08 ± 0.12 |
| 2 | 7.24 | 525-1620 | 9.2 ± 0.5 | 1.9 ± 0.6 |
| | | 200-1530 | 8.1 ± 0.1 | 1.1 ± 0.1 |
| 3 | (Saturated with ZnO) | 0-122 | 44 | 0 |
| | | 200-1530 | 7.8 ± 0.2 | 1.7 ± 0.2 |
| 4 | 4.98 | 60-153 | 43 ± 2 | 0.18 ± 0.05 |
| | | 300-916 | 2.9 ± 0.1 | 1.8 ± 0.1 |
| 5 | 2.92 | 60-122 | 23 ± 3 | 0.36 ± 0.09 |
| | | 60-153 | 0.54 ± 0.04 | 0.52 ± 0.04 |
| 6 | 0.784 | 60-153 | 0.54 ± 0.04 | 0.52 ± 0.04 |

* The electrode orientation was horizontally facing-upward except in series 2 where it was horizontally facing-downward.

Table II. Comparison of proposed rate-determining steps given in the literature for the passivation of zinc anodes in alkaline electrolytes

| Authors | Rate-determining steps | Relationship between current density and passivation time ^c |
|------------------------------|--|--|
| Dirkse <i>et al.</i> (13) | Diffusion of zincate ^a | $i(t^{1/2}) = (C_{crit} - C_b)nF\sqrt{\pi D/4}$ |
| Eisenberg <i>et al.</i> (6) | Diffusional and convective mass transfer of zincate ^b | $(i - i_e)t^{1/2} = k$ |
| Elder (12) | Chemical reaction of discharged product to zincate and diffusion of zincate ^a | $i(t^{1/2}) = k_0 - k_{12}t$ |
| Yamashita <i>et al.</i> (14) | Diffusion of zincate and growth of ZnO film ^a | $(i - i_e)t^{1/2} = k$ |

^a No convection.

^b Free convection.

^c C_{crit} — the critical concentration of zincate ions for the precipitation of ZnO. C_b — the concentration of zincate ions in the bulk electrolyte.

Dirkse and Hampson (13) postulated that passivation occurs when a critical concentration of zincate ion is established in the layer of electrolyte in contact with the electrode surface. According to their hypothesis, the slope of i vs. $t^{-1/2}$ can be estimated using the equation shown in Table II. In comparison with the k values predicted by the equation of Dirkse and Hampson with our experimental values in Table I, our calculated k values are about the same (0.86–1.5 times) in the high current-density region and about one order of magnitude lower in the lower current-density region. The i_e value predicted by this equation is zero (independent of current-density region); however, our experimental data are not zero in the high current-density region. These results indicate that their mechanism is not useful for describing our experimental data.

Eisenberg *et al.* (6) introduced a concept of free convection to interpret their passivation data. An estimated diffusion-excluded convective current density, i_e , is used to modify the Sand equation to the form given in Table II. The magnitude of i_e corresponds to the rate of mass transfer of zincate ions away from the electrode surface by free convection. If the applied anodic current density is below i_e , a critical concentration of zincate ions is never established at the electrode surface and no passivation occurs.

Free convection at a horizontal electrode occurs when (i) the passivation time is sufficiently long and (ii) heavier fluid overlies a lighter one (unstable stratification) (27). The formation of zincate ions during the discharge of a zinc anode increases the density of electrolyte at the electrode surface. Under this circumstance, condition (ii) is met by a downward-facing electrode. Free convection could develop if condition (i) is also met. For the upward-facing anode condition, (ii) is not met; therefore, free convection is not expected to occur. We may use our data to determine the existence of condition (i) for the downward-facing electrode. When the passivation time is shorter than 7 sec, at a caustic concentration of 7.24M KOH, electrodes with either upward-facing or downward-facing orientation behave in the same way within experimental uncertainty (Fig. 1). When the passivation time of the downward-facing electrode is longer than 7 sec, for any current density < 525 mA/cm², the passivation time is longer than that of the upward-facing electrode. Therefore, condition (i) is met only at times longer than about 7 sec. Accordingly, Eisenberg *et al.* (6), would predict $i_e = 0$ for passivation times shorter than 7 sec. Since our data show that $i_e = 186$ mA/cm² in the high current-density region, the diffusion-excluded convective current concept does not explain our results.

Elder (12) proposed that either chemical dissolution of zinc or complex formation of dissolved zinc species is a rate-controlling step in the passivation process of zinc anodes in alkaline media. Thus, he used the equa-

tion given in Table II to correlate his data. According to his hypothesis, i is not linearly related to $t^{-1/2}$ in any region of current density. Since our data show linear relationships, his approach does not provide an acceptable description of our results.

Yamashita *et al.* (14) discovered two distinct discontinuities in the optical phase shift vs. time curve for light reflected by the zinc electrode during an anodic discharge. They proposed that the first discontinuity, t_1 , occurred when the type I zinc oxide film began to form and grow on the anode. The second discontinuity, t_2 , occurred when the passivation compact type II zinc oxide was forming. Yamashita *et al.* (14) demonstrated that t_1 varied with current density according to the expression given by Dirkse and Hampson (Table II). Their equation in Table II is of the same form as that of Eisenberg *et al.* (6), the term i_e is not diffusion-excluded convective current density. Therefore it also does not predict the two regions found in our work.

In summary, none of the mechanisms given in Table II can satisfactorily explain our data.

Proposed passivation mechanism.—In order to explain our experimental data, we propose the scheme shown in Fig. 4 for all processes associated with the anodic passivation of zinc in alkaline solutions. In the first step, the anodic reaction proceeds for a time, t_a , producing zincate ions which accumulate near the electrode surface because diffusion is too slow to dissipate them. Finally zincate ions accumulate to a concentration, C_{crit} , at which point type I ZnO begins to precipitate. The value of C_{crit} is believed to be a factor of three to four times the solubility of ZnO in KOH solution (11, 13, 14, 29, 30) and is independent of the initial zincate concentration (C_b). The term $(C_{crit} - C_b)$ (Table II) implies that the presence of zincate in the electrolyte shortens the passivation time; our results confirm this conjecture (Fig. 1). However, it is difficult to detect the time at which C_{crit} is attained on

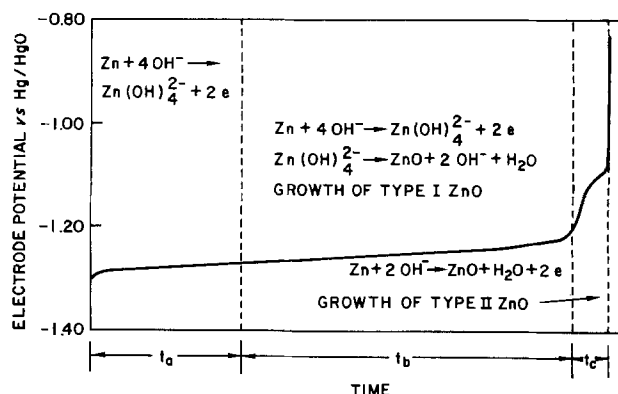


Fig. 4. Proposed scheme for the processes associated with the anodic passivation of zinc in alkaline solutions.

chronopotentiograms. The partial transformation of zincate to zinc oxide (type I) and the mass transport of OH⁻ ions through this porous zinc oxide (15) permit the continuation of the electrode reaction. After a time, t_b , the rate of mass transfer of hydroxide ions through the ZnO falls below that required for the zincate formation reaction. Thus the formation of type II zinc oxide is initiated on the electrode surface. After an additional time, t_c , the electrode surface is covered by compact type II ZnO, thereby limiting the transport of OH⁻ ions and passivating the electrode. This proposed mechanism of anodic film growth is in agreement with observations by Smith using ellipsometry and scanning electron microscopy (25).

The total time to passivation is expressed by

$$t = t_a + t_b + t_c \quad [2]$$

As concluded by Yamashita *et al.* (14), one may use ellipsometry to determine t_a or use the expression of Dirkse and Hampson (13) to estimate it from C_{crit} and D (Table II). The example in Fig. 5 illustrates how to obtain $t_b + t_c$ from the passivation data for the upward-facing anodes in 7.24M KOH. Line a is predicted by the Sand equation (13) with the assumption that the passivation is caused by the exhaustion of OH⁻ species at the electrode surface without any precipitates. Line b represents t_a calculated by substituting the solubility data for electrochemically generated ZnO (29) and the diffusion coefficient of zincate (28) into the equation of Dirkse *et al.* (13) (Table II). Curve c shows our passivation time data. Curve d was derived from curve c and line b, *i.e.*, $(t - t_a)$. At the intersection of line b and curve d, $t_a = t_b + t_c$. To the left of this intersection, $t_b + t_c > t_a$ and to the right, $t_a > t_b + t_c$.

According to our proposed mechanism, the following can be derived:

1. If $t_a \gg t_b + t_c$, then $t = t_a$. This is the case proposed by Dirkse and Hampson (13) in which the electrode is instantaneously passivated by the formation of compact ZnO once a given level of zincate is achieved.
2. If $t_b \gg t_a + t_c$, then $t = t_b$. Here the passivation is caused by limitation of mass transfer by a thick porous ZnO layer.
3. If $t_c \gg t_a + t_b$, then $t = t_c$. In this case, passivation is caused by mass transfer, limited by immediate formation of compact ZnO layers.
4. If t_c is negligible, then $t = t_a + t_b$. This is the case proposed by Yamashita *et al.* (14).
5. If t_b is negligible, then $t = t_a + t_c$. Here, formation of compact ZnO follows immediately after a critical zincate concentration is established at the electrode surface.
6. If t_a is negligible, then $t = t_b + t_c$. In this case, passivation is caused by mass transfer, limited by the

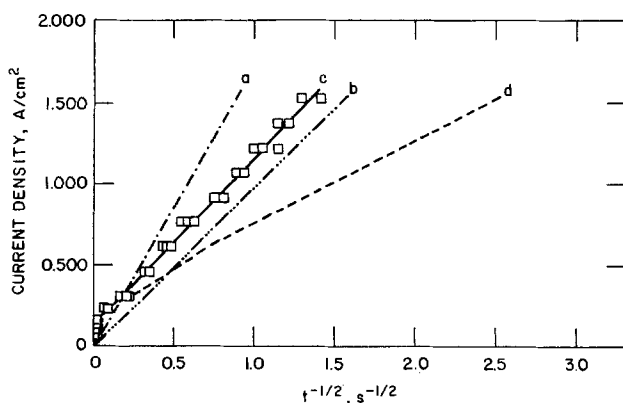


Fig. 5. Analysis of passivation data for upward-facing Zn anodes in 7.24M KOH (significance of the various lines is explained in the text).

immediate formation of porous ZnO followed by the formation of compact ZnO.

7. If t_a , t_b , and t_c are of the same order of magnitude, then $t = t_a + t_b + t_c$.

In Fig. 1 and 2 we obtained nonzero intercepts when correlating our high current-density data, because, as shown in Fig. 5, our high current-density data probably belong to example 7 in which the intercepts are not diffusion-excluded convective current densities.

The values of i_e for the low current-density data are nearly zero (Table I and Fig. 3). Figure 5 shows that the slope of the low current-density data is greater than the slope of line a. Therefore, it is likely that the passivation of the zinc anodes was not caused by the limited rate of diffusion of OH⁻ ions across a boundary layer. The calculation using the equation of Dirkse and Hampson (13) (Table II) shows that t_a is only 1.5–8.4% of the passivation time shown in Fig. 3 for the low current-density region. The time, t_c , is probably only a small fraction of t since it takes only a short time to grow a thin layer of type II ZnO (porosity 0.003) (25). Therefore, it is likely that the low current-density data belong to case 2 in which $t_b \gg t_a + t_c$. The electrode finally passivates because the anodic reaction rates are limited by the transport of OH⁻ ions through this zinc oxide film (25). In our experiments, in which the electrodes were set in acrylic plastic, the anodic dissolution of Zn erodes the solid zinc, leaving space surrounded by the plastic wall for the growth of the type I ZnO film, which has pores of about 7500Å on the average (24) and an average porosity of 0.056 in 0.5M KOH and 0.28 in 6M KOH (25); this film, consequently, presents some resistance to mass transfer. To obtain a quantitative description of the mass transfer resistance of the type I ZnO film, we assumed that, at the electrode surface, the rate of supply of OH⁻ ions is equal to the rate of consumption of OH⁻ ions by the electrode reaction. Therefore, if there is no convective mass transfer, the equation describing the consumption of OH⁻ ions can be written as

$$\frac{4i}{nF} = \frac{\epsilon^{1+\xi} D_3}{\delta} (C_{3b} - C_{3s}) + \frac{-it_3}{z_3 F} + \frac{2yi}{nF} \quad [3]$$

where the term on the left-hand side is the consumption rate of OH⁻ ions by the anodic process; the terms on the right-hand side represent the supply of OH⁻ ions by diffusion, migration, and precipitation of ZnO (Fig. 4), respectively. In Eq. [3], ϵ and ξ are the porosity and the tortuosity factor of the ZnO film, respectively; D_3 is the diffusion coefficient of OH⁻ ions; C_{3b} and C_{3s} are the concentrations of OH⁻ ions in the bulk and at the electrode surface, respectively; y is the ratio of the rate of precipitation of ZnO to that of the electrochemical formation of zincate, and δ is the thickness of the mass-transfer boundary layer (assumed to be equal to the thickness of the ZnO film); z_3 and t_3 are the charge number and the transference number of OH⁻ ions, respectively. The thickness of the ZnO increases with time and therefore affects the OH⁻ supply. The rate of increase in the thickness of the ZnO film can be written as

$$\frac{d\delta}{dt} = \frac{\bar{V}_{ZnO}}{(1-\epsilon)} \frac{yi}{nF} \quad [4]$$

where \bar{V}_{ZnO} is the partial molar volume of ZnO. Since, in the low current-density region, the time required to establish C_{crit} is negligible in comparison to the passivation time, $\delta = 0$ at $t = 0$. Therefore, from Eq. [4] we obtain

$$\delta = \frac{\bar{V}_{ZnO}}{(1-\epsilon)} \frac{yi}{nF} t \quad [5]$$

Combining Eq. [3] and [5]

$$\frac{\bar{V}_{\text{ZnO}}}{(1-\epsilon)} \frac{y}{nF} \left[\frac{(4-2y)}{nF} + \frac{t_3}{z_3 F} \right] i^2 t = e^{1+\epsilon D_3} (C_{3b} - C_{3s}) \quad [6]$$

At the time when C_{3s} is equal to zero, the electrode passivates. Thus

$$i(t_{1/2}) = \left\{ \frac{e^{1+\epsilon D_3} C_{3b}}{\frac{\bar{V}_{\text{ZnO}}}{(1-\epsilon)} \frac{y}{nF} \left[\frac{(4-2y)}{nF} + \frac{t_3^0}{z_3 F} \right]} \right\}^{1/2} \quad [7]$$

By comparing Eq. [7] with Eq. [1], we obtain

$$i_a = 0$$

and

$$k = \left\{ \frac{e^{1+\epsilon D_3} C_{3b}}{\frac{\bar{V}_{\text{ZnO}}}{(1-\epsilon)} \frac{y}{nF} \left[\frac{(4-2y)}{nF} + \frac{t_3^0}{z_3 F} \right]} \right\}^{1/2} \quad [8]$$

k can be estimated from Eq. [8] for the low current-density region. The value of y is probably close to unity since the rate of mass transfer of zincate ions from the electrode surface through the ZnO film to the bulk electrolyte is small in comparison to the rate of $\text{Zn}(\text{OH})_4^{2-}$ formation of Fig. 4. By using the data: $y = 1$, $D_3 = 3 \times 10^{-5}$ cm²/sec (28); $\epsilon = 0.5$, $\bar{V}_{\text{ZnO}} = 14.51$ cm³/mol, and $t_3 = 0.72$ (31); $z_3 = -1$, and $\epsilon = 0.056$ and 0.28 , k was calculated and is compared with the experimental results (Table I) in Table III. The calculated values of k are of the same order of magnitude as the experimental values. Therefore, we conclude that in the low current-density region, passivation may be caused by a limited mass transfer rate of OH^- ions across the thick porous ZnO layer.

Application to Battery Technology

In Ni/Zn alkaline batteries under development for vehicle propulsion, the electrolyte is typically 30% KOH (7M) saturated with ZnO with the zinc anode formed *in situ* by electrodeposition. Anode passivation should be avoided to achieve maximum utilization. From our data, we estimate the conditions necessary for passivation, noting the following differences between our zinc electrodes and those of Ni/Zn batteries

| Electrodes used in this study | Ni/Zn battery electrodes |
|-------------------------------|---|
| Solid zinc electrode | A porous zinc electrode (in most cases) |
| Excess electrolyte | Limited electrolyte |
| Uniform current density | Current densities dependent upon location on and in the electrode |

Table III. Comparison of the calculated values of k (Eq. [8]) and experimental results for the low current density region of upward-facing electrodes

| Expt. series ^a | Experimental | Calculated | |
|---------------------------|--------------|--------------------|-------------------|
| | | $\epsilon = 0.056$ | $\epsilon = 0.28$ |
| 1 | 6.9 ± 0.7 | 3.5 | 10 |
| 3 ^b | 4.3 | 3.2 | 9.4 |
| 4 | 4.3 ± 0.2 | 2.9 | 8.6 |
| 5 | 2.3 ± 0.3 | 2.2 | 6.6 |

^a The experimental series was defined in Table I.

^b OH^- concentration = 5.96M.

The basic assumption is that an electrodeposited-zinc porous battery electrode cycled at the 2 hr rate has an apparent current density of 20 mA/cm². To compare planar electrodes with porous electrodes, it is necessary to assess the effective interfacial surface area per unit macroscopic area and then to calculate the corresponding current density in the porous electrode.

The assessment of the effective interfacial surface area requires a knowledge of the structure of zinc electrodeposits. Naybour (32) observed that the deposits were dendritic at 100 mA/cm², consisted of layered growths with some granular growths at 20 mA/cm², and were mossy or spongy at 4 mA/cm². The zinc electrode in a typical Ni/Zn battery cycled at a 2 hr rate (*i.e.*, 20 mA/cm²) consists of metallic sponge zinc (33) with a charge density of 144 C/cm². From the charge density data and the size and density of the spongy deposits described by Naybour (32), the porosity of the expected deposit is 0.6. Using these data and the molar volume of solid zinc [9.15 cm³/mol (31)], it is calculated that, during a single charge, zinc deposits to a thickness of 114 μm or slightly more than the characteristic reaction penetration depth, 90 μm (34). Therefore, the characteristic reaction depth is used to estimate the effective interfacial surface area.

Since the specific surface area is about 300 cm²/cm² [Ref. (31)], an effective interfacial surface area of 2.7 cm²/cm² of electrode area is calculated. This yields an effective current density of 7.4 mA/cm². The equation in this current density range (Table I) is

$$i = (4.3 \times 10^3) t^{-1/2} \quad [9]$$

Using Eq. [9], a passivation time of 9 hr is calculated. This is much longer than the 2 hr discharge time.

Assuming that the effective interfacial surface area remains constant the maximum current density for 100% utilization of the zinc electrode can be calculated from Eq. [9] and the equation of utilization

$$Q = 10^{-3} i t \quad [10]$$

where Q is the capacity of the electrode, in C/cm², t is the passivation time, in seconds, and the constant 10^{-3} is used to convert the current density from mA/cm² to A/cm². Since Q equals 144 C/cm², a maximum current density of 125 mA/cm² is calculated. This corresponds to a current density of 338 mA/cm² for the porous zinc electrode and is 17 times the designed current density, which is not expected to occur even under severe driving conditions. Therefore, simple surface passivation is not expected to limit the utilization of a newly formed porous zinc electrode.

Conclusions

The passivation time of zinc anodes in KOH electrolytes can be expressed by the equation, $t = t_a + t_b + t_c$; where t_a is the time at which a critical concentration of zincate is established, and t_b and t_c are the times during which the respective porous and compact ZnO films are formed. At high current-density levels, passivation occurs when compact ZnO covers electrode surface. In low current-density regions, passivation occurs when mass transfer of hydroxide ions across a porous ZnO layer is less than that required for anodization. Finally it can be concluded that simple surface passivation does not limit the utilization of a newly formed porous zinc battery electrode.

Acknowledgments

This work was supported by the U.S. Department of Energy, Division of Energy Storage Systems and Office of Transportation Programs. We thank Z. Nagy for his valuable comments.

Manuscript submitted Oct. 24, 1980; revised manuscript received Feb. 23, 1981. This was Paper 517 pre-

sented at the St. Louis, Missouri, Meeting of the Society, May 11-16, 1980.

Any discussion of this paper will appear in a Discussion Section to be published in the June 1982 JOURNAL. All discussions for the June 1982 Discussion Section should be submitted by Feb. 1, 1982.

Publication costs of this article were assisted by Argonne National Laboratory.

REFERENCES

1. W. Van Doorne and T. P. Dirkse, *This Journal*, **122**, 1 (1975).
2. G. H. Newman and G. E. Blomgren, *J. Chem. Phys.*, **43**, 2744 (1965).
3. J. S. Fordyce and R. L. Baum, *ibid.*, **43**, 843 (1965).
4. R. Landsberg, *Z. Phys. Chem.*, **206**, 291 (1957).
5. R. Landsberg and H. Bartelt, *Z. Electrochem.*, **61**, 162 (1957).
6. M. Eisenberg, H. F. Bauman, and D. M. Brettner, *This Journal*, **108**, 909 (1961).
7. H. Bartelt and R. Landsberg, *Z. Phys. Chem.*, **222**, 217 (1963).
8. N. A. Hampson and M. J. Tarbox, *This Journal*, **110**, 95 (1963).
9. N. A. Hampson, M. J. Tarbox, L. T. Lilley, and J. P. G. Farr, *Electrochem. Technol.*, **2**, 309 (1964).
10. T. P. Dirkse, D. DeWit, and R. Shoemaker, *This Journal*, **115**, 442 (1968).
11. N. A. Hampson, P. E. Shaw, and R. Taylor, *Br. Corros. J.*, **4**, 207 (1969).
12. J. P. Elder, *This Journal*, **116**, 757 (1969).
13. T. P. Dirkse and N. A. Hampson, *Electrochim. Acta*, **16**, 2049 (1971).
14. M. Yamashita, T. Yoshimura, Y. Imanaka, and H. Furuta, *Doshisha Daigaku Rikogaku Kenkyu Hokoku*, **18**, 58 (1977).
15. R. W. Powers and M. W. Breiter, *This Journal*, **116**, 719 (1969).
16. S. Szpak and C. J. Gabriel, *ibid.*, **126**, 1914 (1979).
17. E. A. Ivanov, T. I. Popova, and B. N. Kabanov, *Sov. Electrochem.*, **5**, 643 (1969).
18. M. N. Hull and J. E. Toni, *Trans. Faraday Soc.*, **67**, 1128 (1971).
19. R. D. Armstrong, G. M. Bulman, and H. R. Thirsk, *J. Electroanal. Chem. Interfacial Electrochem.*, **22**, 55 (1969).
20. H. Kaesche, *Electrochim. Acta*, **9**, 383 (1964).
21. R. W. Powers, *This Journal*, **116**, 1652 (1969).
22. R. W. Powers, *ibid.*, **118**, 687 (1971).
23. Z. Nagy and J. O'M. Bockris, *ibid.*, **119**, 285 (1972).
24. T. Katan, J. R. Savory, and J. Perkins, *ibid.*, **126**, 1835 (1979).
25. C. G. Smith, "Ellipsometry of Anodic Film Growth," LBL-8082 (1978).
26. M.-B. Liu, G. M. Cook, and N. P. Yao, "Galvanostatic Polarization of Zinc Microanodes in KOH Electrolytes," ANL/OEPM-80-1 (1980).
27. J. R. Selman and J. Tavakoli-Attar, *This Journal*, **127**, 1049 (1980).
28. J. McBreen and E. J. Cairns, *Adv. Electrochem. Electrochem. Eng.*, **11**, 273 (1978).
29. A. G. Briggs, N. A. Hampson, and A. Marshall, *Trans. Faraday Soc.*, **70**, 1978 (1974).
30. A. Langer and E. A. Pantier, *This Journal*, **115**, 990 (1968).
31. W. G. Sunu, Ph.D. Thesis, Univ. of California, Los Angeles (1978).
32. R. D. Naybour, *Electrochim. Acta*, **13**, 763 (1968).
33. M. Klein and D. Dube, ANL-K76-3541-1 (1976).
34. M.-B. Liu, Y. Yamazaki, G. M. Cook, and N. P. Yao, ANL/OEPM-80-6 (1981).

Photoelectrochemical Characterization of the Passive Films on Iron and Nickel

S. Mark Wilhelm* and Norman Hackerman**

Department of Chemistry, Rice University, Houston, Texas 77001

ABSTRACT

Increases in surface reaction rates caused by periodic illumination of iron and nickel passive films with polychromatic and monochromatic light have been measured. The electrode photoresponse is caused by excitation of a surface film which is the product of anodic oxidation. The dependence of the photocurrent magnitude on electrode potential and excitation energy suggests that the passive layers possess semiconductor characteristics. Capacitance and kinetic measurements are reported which support a proposed model.

The phenomenon of metal passivity has been actively investigated for almost two centuries (1). Although any metal which resists corrosion in spite of a thermodynamic tendency to react may be described as passive, the traditional definition of passivity is limited to metals in which the active and passive surfaces cannot be distinguished visually. Fe, Cr, and Ni are the best examples and it is with these metals that the phenomenon of passivity is most commonly associated. Iron is unique among metals which passivate in that the process is seemingly reversible. Under certain conditions, iron can oscillate between an active and passive condition with a period on the order of several seconds (2).

The exact chemical and structural compositions of the passive films on iron and nickel are still unresolved. Several oxides and hydroxides have been postulated.

* Electrochemical Society Active Member.

** Electrochemical Society Honorary Member.

Key words: semiconductor, photoconductivity, capacitance, kinetics.

Although passive surfaces have been subjected to rigorous analysis, most techniques suffer from the inability to scrutinize films *in situ*. The most widely accepted model in the case of Fe is a duplex film of Fe₂O₃ and Fe₃O₄ (3). For Ni, a NiO film has been suggested (4). There is general agreement that such films are inhomogeneous and hydrated.

It has been suggested (5-10) that the passive films which form on iron and nickel are semiconductors and that their electrochemical behavior is due, at least in part, to their solid-state electronic properties. This postulate is supported by observations of the semiconducting properties of thick anodic oxides on other metals (11) and those of polycrystalline iron and nickel oxides (12-14).

One method of determining the electronic structure of semiconducting electrode materials quantitatively is to observe the effect of illumination on electrochemical reaction rates. The influence of light on the iron passive

surface was first noted by Oshe and Rosenfeld *et al.* (15-18). They detected changes in electrode potential caused by irradiation with u.v. light. The effect of light on semiconductor electrodes is to produce electrons and holes in the conduction band and valence band, respectively. In an electrochemical cell this translates into photovoltages and photocurrents which arise from the separation of charge. Recently, the present authors reported measurements of photocurrents generated by illumination of the iron passive film (13). This investigation has been expanded to include the nickel passive film and the process of anodic oxidation in near neutral pH solutions.

We have chosen to interpret the photocurrent data presented here in terms of the theory of semiconductor electrodes. It is customary in discussing the electrochemistry of semiconducting materials to simplify the band structure, *i.e.*, to assume well-defined parallel energy bands of infinite width. This is a reasonable conceptual simplification for single crystal semiconductors (19). Although the same simplification will be adopted here, it should be pointed out that the interaction of electronic energy levels in transition metal oxides does not necessarily give bands in a traditional sense. In fact some studies (20) suggest that the conductivity of Fe_2O_3 and NiO differ fundamentally from that of broad band semiconductors. Additional difficulties in defining the electronic structure of thin passive films are introduced by their polycrystalline and possibly amorphous nature. It has been demonstrated, however, that explanations of the electrochemistry of metal oxides based on a simplified energy level diagram are useful and accurate within proper limits.

Experimental

All solutions were made with triply distilled water ($R > 10^6$). Chemicals were reagent grade or better. The solutions were degassed with purified nitrogen (99.95% N_2) which had passed through a heated (350°C) column of copper turnings to remove traces of oxygen. The temperature of all experiments was 297 ± 2 K.

The aqueous solutions were 1N in Na_2SO_4 unless noted. Sodium borate and H_3BO_3 were added in ratios which buffered the solutions to a pH between 6 and 9. The standard buffer solution of pH 8.4 was 0.0375M in $\text{Na}_2\text{B}_4\text{O}_7$ and 0.10M in H_3BO_3 . Solutions containing the redox couple were 1N in Na_2SO_4 and buffered to pH 8.4. The hexacyanoferrate redox couple was 0.10N in $\text{K}_3\text{Fe}(\text{CN})_6$ and 0.10N in $\text{K}_4\text{Fe}(\text{CN})_6$.

A standard three-compartment electrochemical cell was used. The main compartment incorporated a working electrode, a gas inlet, and an optical quartz window through which light could be focused on the working electrode surface. The counterelectrode was platinum gauze and the reference electrode was a saturated calomel electrode (SCE). All electrode potentials are reported vs. SCE.

Electrodes were prepared from 1 cm \times 1 cm \times 2 mm pieces of zone-refined iron (99.99% Fe) or high purity nickel (99.99% Ni). One side of each electrode was abraded with successively finer grades of silicon carbide paper, 4/0 emery paper, and finally polished to a mirror finish with 0.05μ aluminum oxide. Electrodes used in photocurrent experiments were not polished with aluminum oxide, rather their surfaces were left abraded in order to increase the surface area. After polishing, a microscopic examination revealed no impurity particles (SiC , Al_2O_3) on the electrode surface. Roughness factors of 1.3 and 2 for the polished and abraded surfaces were estimated by comparison of capacitance values. Electrical contact was made to the unpolished side of the electrode by silver epoxy to a nickel wire enclosed in a glass tube. The sides and back of the electrode were covered by silicone adhesive (Dow Corning) leaving only a flat 1 cm^2 surface exposed to solution.

In photoelectrochemical experiments the working electrode was positioned 1 cm from an optical quartz window through which polychromatic or monochromatic (15 nm bandwidth) light was focused on the electrode surface. A phase sensitive amplification system (13) was employed to measured photocurrents. The light beam was periodically chopped ($F = 34$ Hz) and the corresponding periodic component of the electrode current was selectively amplified. In some experiments the photoresponse was of sufficient magnitude to record it directly without phase sensitive amplification. A 150W xenon light source was used. The absolute photon flux at each wavelength (Φ_λ) was measured with a calibrated Oriel Model 7090 pyroelectric detector. The monochromatic irradiance was between 1 and 200 $\mu\text{W}/\text{cm}^2$ and the polychromatic irradiance was about 2 mW/cm^2 . Spectral data are reported as absolute efficiencies ($\alpha = i^*/\Phi_\lambda$) and are not corrected for reflection at the film solution interface. In polychromatic light experiments, the incident beam was filtered to remove wavelengths greater than 900 nm.

Iron electrodes were cathodically treated (20 $\mu\text{A}/\text{cm}^2$) for 1 hr and the solution replaced under nitrogen prior to all experiments unless noted. Similarly the Ni electrodes were held at a cathodic potential of -1.0V for 30 min and the solution changed prior to any measurements. Typical polarization curves for freshly prepared electrodes are shown in Fig. 1. The potentials were scanned in the anodic direction at $+0.5$ mV/sec. The results shown in Fig. 1 are for electrodes in which the final surface preparation was with emery paper (4/0). In all cases, the electrochemical behavior of unpolished electrodes was identical to that of electrodes polished to a mirror finish.

Tafel plots were obtained for planar Ni and Pt electrodes prepassivated for 1 hr in pH 8.4 solutions. The electrodes were transferred under nitrogen to a cell containing the redox couple (0.10M $\text{K}_3\text{Fe}(\text{CN})_6$, 0.10M $\text{K}_4\text{Fe}(\text{CN})_6$) and scanned potentiodynamically at 0.2 mV/sec in the anodic direction. Exchange current densities were calculated using the linear polarization method.

Results and Discussion

When illuminated with light of energy greater than their bandgaps, the passive films on iron and nickel generate photocurrents which have a sizable magnitude considering the thicknesses of the films. The appearance of a photoresponse demonstrates not only conductivity but also implies a degree of crystallinity. Although an amorphous or loosely coordinated lattice might absorb visible light, it is doubtful that this would result in a measurable photoresponse unless there exists at least some short range order. The photoresponse also implies that the lattice anion is oxide rather than hydroxide, at least in that portion of the film which gives rise to the photoresponse. The light sensitive semiconductor properties of iron and nickel oxides are

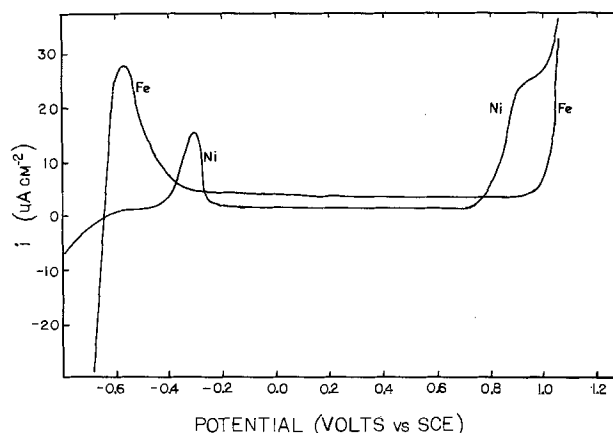


Fig. 1. Current vs. potential; pH 8.4; scan rate $+0.5$ mV/sec

well documented while photoconductivity, or even conductivity for that matter, has not been observed on iron or nickel hydroxides.

Periodic illumination of semiconductor electrodes under potentiostatic control has two separate effects on electrochemical reaction rates. First, the creation of electron-hole pairs by sufficiently energetic radiation alters the concentration of minority carriers at the surface and thereby can accelerate kinetic reactions which are minority carrier limited if the relative position of solution and solid energy levels are appropriate. Second, alteration of the electrode charge distribution by sudden illumination is manifested by capacitance charging currents and charge flow to reverse the tendency of the bands to move toward the flatband condition under illumination (21). The latter phenomenon does not require the direct participation of minority carriers in the charge transfer process and accounts for the observation of photocurrents of opposite sign to those expected from conductivity type (13).

The magnitude of the photoresponse is a function of several parameters (22) including the absorptivity (α) of the absorbing molecules, the photon flux (Φ), the amount of band bending ($V - V_{FB}$), the thickness of the absorbing layer (ρ), the electrode capacitance (C), and the concentration of electron donors or acceptors in solution. The amount of band bending affects both recombination and charge transfer rates and hence strongly influences photogenerated carrier lifetime. For thin ($<50\text{\AA}$) films the Debye length, the carrier diffusion length, and light penetration depth are limited by the film thickness and therefore the film thickness can be the dominant factor in determining the photocurrent magnitude.

In Fig. 2 and 3 the total current (i) and photocurrent (i^*) were measured when an electrode was suddenly (<1 msec) polarized to a potential in the passive region ($+0.70\text{V}$ for Fe, $+0.60\text{V}$ for Ni). Prior to each measurement the electrodes were cathodically reduced as described previously. The exponential decrease in the total current with time is characteristic of oxide growth (3, 4). The increase in the photoresponse corresponds to the increasing amount of metal oxide on the electrode surface. At $t = 60$ sec the magnitude of i^* is assumed to be 90% of the value after 1 hr of polarization. For Ni the 90% point was reached in approximately 30 sec. This behavior suggests that the semiconducting nature of the films is not a slowly developing process and that the film is inherently photoconductive. The increase in i^* as the total current is decreasing offers strong evidence that the observed photoresponse is not derived from excitation of any solution species. Photocurrents were not affected in any way by solution agitation.

The thickness of the films were calculated by integration of the anodic charging curves of Fig. 2 and 3 after 1 hr growth period. Oxidation of Fe and Ni was

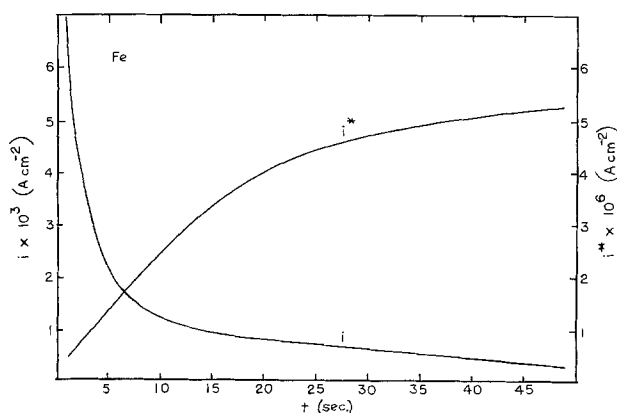


Fig. 2. Current (i) and photocurrent (i^*) vs. time for sudden anodic polarization, Fe, $+0.70\text{V}$, pH 8.4, polychromatic light; $200 < \lambda < 900$ nm.

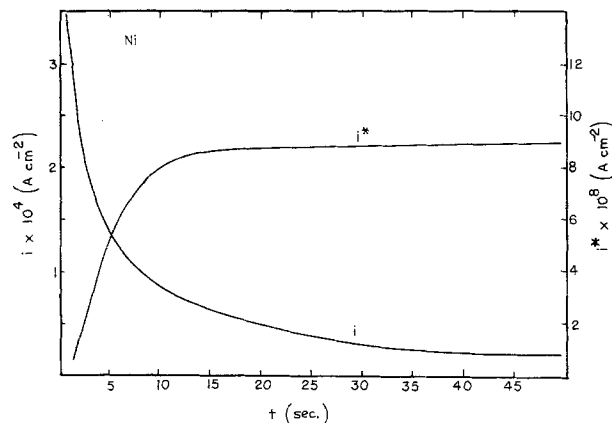


Fig. 3. Current (i) and photocurrent (i^*) vs. time for sudden anodic polarization, Ni, $+0.60\text{V}$, pH 8.4, polychromatic light, $200 < \lambda < 900$ nm.

assumed to form Fe_2O_3 and NiO of densities of 5.1 and 6.8 g/cm^3 , respectively. The solutions were analyzed (atomic absorption) and the charge corresponding to dissolved Fe^{2+} or Ni^{2+} cations was subtracted from the total charge passed during the experiment. Films grown on iron after 1 hr $+0.70\text{V}$ in pH 8.4 solution are approximately 30\AA thick and on nickel are approximately 10\AA thick. The total amount of charge passed for the abraded electrodes was approximately twice that of polished electrodes of the same apparent surface area. The larger magnitude of the photoresponse of Fe films grown at constant potential as opposed to Ni films grown in the same manner is due in part to the fact that the Fe films are thicker.

The magnitude of the photoresponse as a function of electrode potential was measured with polychromatic light and is shown in Fig. 4 and 5. In order to maintain a constant film thickness and/or stoichiometry, a potential pulse technique was used. The electrode was held at its growth potential ($+0.70\text{V}$ for Fe, $+0.60\text{V}$ for Ni) prior to each measurement. The electrode was then suddenly polarized (<1 msec) to the desired potential, the photoresponse measured (<1 sec), and the potential returned (<1 msec) to its original value. The reason for this procedure was the observation in steady-state measurements of i^* that when the electrode potential was altered, the magnitude of i^* equilibrated rapidly at the new potential and then decayed (for negative shifts in V) or increased (for positive shifts in V) slowly with time, reaching a new steady-state value in approximately 30-60 min. We presume that either the amount of absorbing material changed slowly with time or more likely that the magnitude of i^* is sensitive to the defect concentration which is

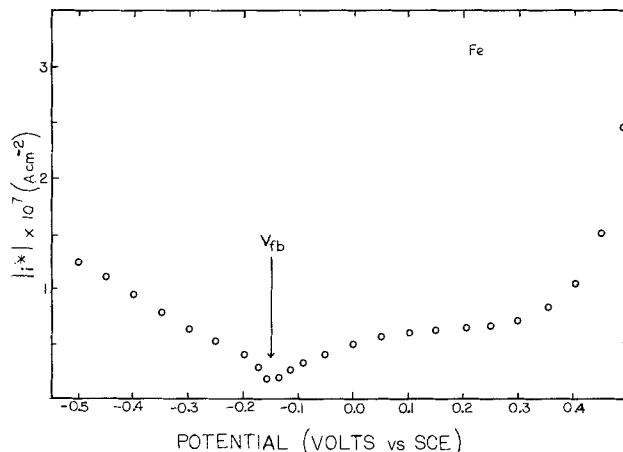


Fig. 4. Photocurrent vs. potential, Fe, pH 8.4, polychromatic light, $200 < \lambda < 900$ nm.

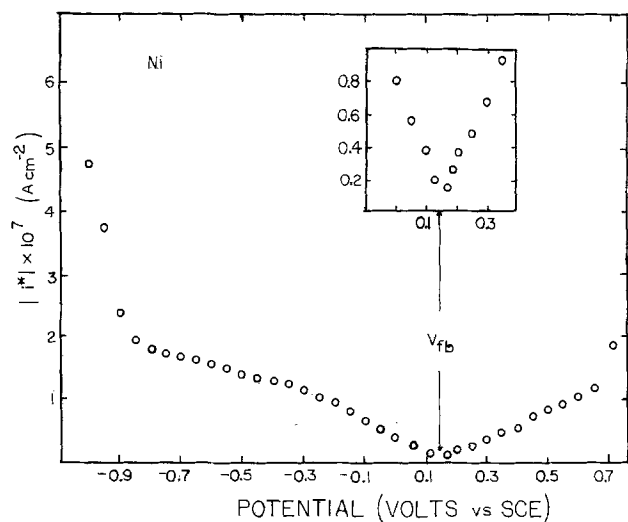
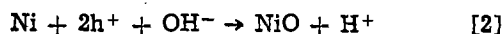
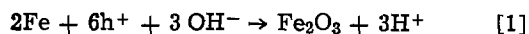


Fig. 5. Photocurrent vs. potential, Ni, pH 8.4, polychromatic light, $200 < \lambda < 900$ nm.

affected by changes in electrode potential. The time constant for the process is on the order of that expected for an ionic transport process (23).

The instantaneous measurement of i^* describes the electronic distribution of the film prior to any defect rearrangement and is proportional to the amount of band bending. In Fig. 4 and 5 the photoresponse vanished at a characteristic potential which in the semiconductor model would be V_{FB} . The absence of a net photocurrent response indicates that potential where the rate of photoassisted oxidative charge transfer is equal to the rate of photoassisted cathodic charge transfer and defines the situation where the bands are flat. The sign of i^* also inflected at V_{FB} . The change in sign was detected with a storage oscilloscope and with the lock-in amplifier at a 180° phase shift in the quadrature component. Anodic of V_{FB} , i^* was anodic while at potentials negative to V_{FB} , the increase in current due to illumination was cathodic.

Although both positive and negative photocurrents could be detected near V_{FB} , at larger displacements in potential the photocurrents were in accord with those expected from conductivity type. The passive film on Fe (n-type) showed larger photocurrents at potentials anodic to V_{FB} and the film on Ni (p-type) showed larger photocurrents cathodic of V_{FB} . Cathodic photocurrents were attributed to either film reduction or hydrogen evolution. At intermediate anodic potentials, photogenerated holes (h^+) may participate directly in further oxidation of the metal surface



or indirectly via surface states. Equations [1] and [2] serve only as examples of innumerable pathways. At more anodic potentials oxygen evolution becomes the principal photoassisted reaction.

The position of V_{FB} from photocurrent measurements was compared to that obtained from Mott-Schottky plots. Parameters derived from capacitance data at different values of solution pH are given in Table I with a comparison of V_{FB} from photocurrent and capacitance data given in Table II. The analysis of capacitance data was performed in the manner described previously (24). Although it is generally agreed that Mott-Schottky plots should not be relied on for an accurate determination of V_{FB} and to some extent donor/acceptor densities, two aspects of the capacitance data are applicable and support the assumed semiconductor character of the passive films. First, the sign of the slope of the C^{-2} vs. V plot is an indicator of conductivity type. As expected the sign of the Mott-Schottky

Table I. Semiconductor parameters from Mott-Schottky plots

| Material | Type | pH | N_D (cm^{-3}) | N_A (cm^{-3}) | V_{FB} (V) |
|-------------------------------|------|-----|----------------------------|----------------------------|--------------|
| $\gamma\text{Fe}_2\text{O}_3$ | n | 6.9 | 10^{20} | — | -0.173 |
| $\gamma\text{Fe}_2\text{O}_3$ | n | 7.8 | 10^{20} | — | -0.225 |
| $\gamma\text{Fe}_2\text{O}_3$ | n | 8.4 | 10^{20} | — | -0.268 |
| $\gamma\text{Fe}_2\text{O}_3$ | n | 9.0 | 10^{20} | — | -0.317 |
| NiO | p | 7.8 | — | 10^{20} | +0.070 |
| NiO | p | 8.4 | — | 10^{20} | +0.037 |
| NiO | p | 9.0 | — | 10^{20} | +0.016 |

Table II. V_{FB} from capacitance and photocurrent measurements

| pH | Fe | | Ni | |
|-------------------|----------|------------|----------|------------|
| | V_{FB} | V_{FB}^* | V_{FB} | V_{FB}^* |
| 6.9 | -0.173 | -0.030 | | +0.260 |
| 7.8 | -0.225 | -0.105 | +0.070 | +0.205 |
| 8.4 | -0.268 | -0.150 | +0.037 | +0.150 |
| 9.0 | -0.317 | -0.180 | +0.016 | +0.120 |
| δV_{FB} | 68 | 58 | 45 | 46 |
| δpH | | | | |

V_{FB} = flatband potential from capacitance measurements.
 V_{FB}^* = flatband potential from photocurrent measurements.

slopes determined for the passive films indicated p-type conductivity for the Ni film and n-type conductivity for the Fe film. Second, the change in V_{FB} is in the anodic direction with decreasing pH for both photocurrent and capacitance data and the slopes are close to the theoretical 59 mV/unit pH. Donor and acceptor identity is inferred from semiconductor data on bulk Fe and Ni oxides. Ferric oxides tend to be oxygen deficient and Fe^{2+} donors give rise to n-type conductivity. Nickel oxides tend to be cation deficient with p-type conductivity arising from Ni^{+3} acceptors.

The separation of energy levels which give rise to photoassisted charge transfer was determined from the dependence of i^* on light energy for films grown for 1 hr at constant potential. The spectral response curves (Fig. 6 and 7) were identical except for magnitude regardless of solution composition (pH, K^+ , Na^+ , Fe^{2+} , Cl^- , NO_3^- , SO_4^{2-} , $\text{B}_4\text{O}_7^{2-}$) or electrode potential. This suggests that the chemical environment of oxidized metal ions does not change significantly with varying electrolyte conditions or electrode potential.

The approximate bandgap can be obtained from the extrapolation of the linear portion of the normalized spectral response curve. The values obtained (2.5 eV for Fe, 3.1 eV for Ni) compare favorably with bandgap measurements on bulk $\alpha\text{Fe}_2\text{O}_3$ [2.0 eV (25)] and NiO [3.7 eV (26)] and with a photoconductivity edge at 3.7

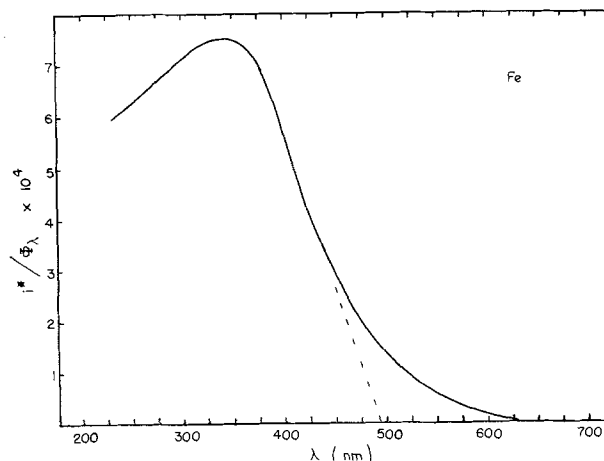


Fig. 6. Photocurrent efficiency (α) vs. wavelength (λ), Fe, pH 8.4, constant potential $V = +0.70V$.

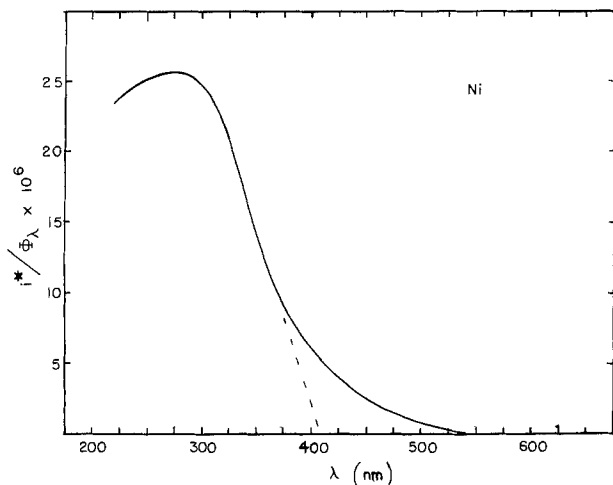
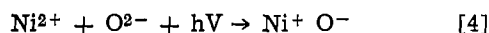
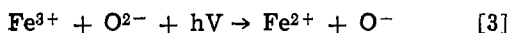


Fig. 7. Photocurrent efficiency (α) vs. wavelength (λ), Ni, pH 8.4, constant potential $V = +0.60V$.

eV that has been reported for NiO (27). This infers that the separation of energy levels for Fe^{3+} or Ni^{2+} in the octahedral oxygen lattice of the passive films is roughly equivalent to that of more stoichiometric materials.

The dominant feature of the optical absorption spectra of both NiO (28) and αFe_2O_3 (29) is a characteristic absorption edge which is several orders of magnitude more intense than crystal field transitions. The photocurrent spectra presented here show a dependence on wavelength which appears to coincide with this optical absorption edge. There is considerable disagreement as to the exact nature of the electronic excitation which gives rise to this absorption. Some authors (29, 30) state that the principal absorbances in the visible-near u.v. region are charge transfer related



Photoconductivity is likely to be of the Verway type (31) in this case. Alternatively more recent interpretations which take into account electronic correlation and electron-phonon coupling describe the excitation as allowed transitions of the ground-state metal ions ($3d^8 \rightarrow 4d^7 4s$ NiO, $3d^5 \rightarrow 3d^4 4p$ Fe). Conductivity in this case can be described in terms of a narrow band model. At present there is no clear resolution to this question.

The long wavelength "tail" in the photocurrent spectra indicates deviation from a fixed stoichiometry in the absorbing oxide. This is to be expected for thin films in that cations near the metal or at the surface (surface states) will have a perturbed distribution of energy levels. Photocurrents due to a smaller separation of energy states will be superimposed on the normal spectrum at longer wavelengths. The same phenomenon may account for the displacement of the absorption edge to longer wavelengths over that of bulk materials.

From the semiconductor parameters determined herein, models of the band structure of the passive films on iron and nickel can be constructed. One reason for this exercise is that band models are predictive to some extent in explaining rates of electron transfer reactions (ETR) at film covered electrodes. Some knowledge of the electronic distribution in the solid phase is prerequisite to successful calculations of ETR rates. Details of the procedures involved in such calculations and in constructing models have recently been discussed (32). Pictorial representations of the band diagrams for Fe and Ni passive films at the redox potential of $Fe(CN)_6^{-3}/Fe(CN)_6^{-4}$ are shown in Fig. 8.

As depicted in the diagrams, V_{FB} gives the position of the conduction or valence band edge if we assume

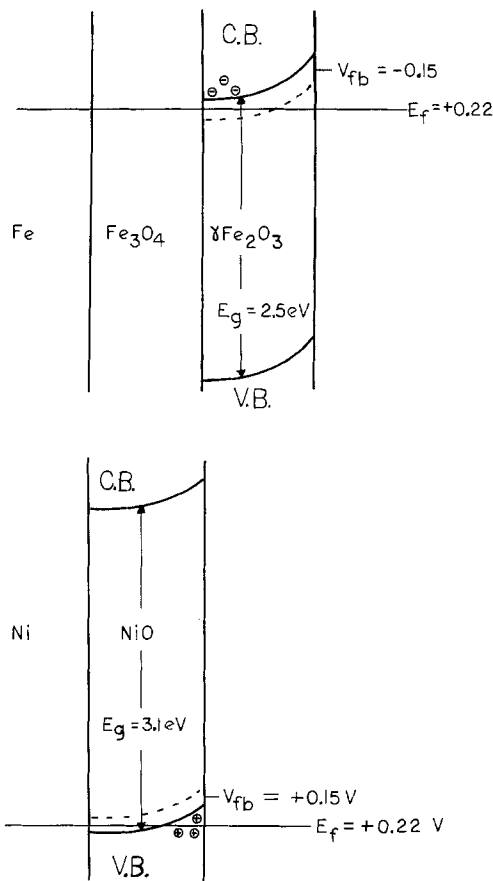


Fig. 8. Energy level diagram for the Fe and Ni passive films at 0.22V, pH 8.4.

that the Fermi energy (E_f) lies between the donor level and conduction band for n-type conductors and between the valence band and acceptor level for p-type and that the separation of donor or acceptor levels from their respective bands is small (100% ionization). At the redox potential the bands are bent "up" at the surface giving rise to a depletion of majority carriers in the case of Fe and an accumulation of majority carriers in the case of Ni.

One aspect of the mechanism of ETR is of interest in connection with the present study of semiconductor properties of iron and nickel films. It has been postulated that charge transfer at passivated metals occurs not only between metal and solution but also between film and solution. In the former case the film is considered to act as a barrier to electron tunneling between the metal and solution and hence film thickness is rate controlling. In the latter case, the excess surface charge density resides in the film itself and the rate of charge transfer will depend on the electronic distribution in the film, band bending, and the partition of the potential drop between oxide and solution. There is substantial evidence to support the postulate that the conductivity and electronic distribution of the passive film has a sizable influence on ETR rates even for very thin films.

For comparative purposes, exchange current densities (i_0) were measured for Fe and Ni anodic oxide electrodes in the hexacyanoferrate redox couple. The difference in i_0 at Fe (10^{-7} A cm^{-2}) and Ni (10^{-4} A cm^{-2}) anodic oxides is significantly greater than can be accounted for by the difference in film thickness. In fact, if one accepts a duplex layer model for the film on Fe, the thickness of the semiconducting layer (γFe_2O_3) might be roughly equal to that on Ni. Also, i_0 at a thermal Fe oxide is essentially equal to i_0 on the anodic oxide (10^{-7} A cm^{-2}). The thickness of the semiconducting layer on the thermal oxide (αFe_2O_3) is at least 100 times that of the anodic oxide (13).

Additional evidence for film conductivity and for the direct participation of the film in ETR comes from analysis of the structure of the Tafel plots (Fig. 9). The rate of ETR on semiconductor electrodes is usually larger for transfer corresponding to conductivity type, i.e., p-type materials show a greater oxidative capability and n-type materials a greater reductive capability. This results in Tafel plots which are asymmetrical. At single crystal semiconductor electrodes, ET opposite to conductivity type can be completely blocked except under illumination when minority carriers are generated. At semiconducting film covered electrodes, Tafel asymmetry is mitigated by alternative ET mechanisms, such as direct elastic tunneling between the metal and solution, which do not depend strongly on the semiconducting characteristics of the film.

In Fig. 9, asymmetrical Tafel behavior is exhibited by the Ni anodic oxide. The larger diffusion limited current for the anodic branch of the Tafel plot is in accord with the p-type conductivity of Ni electrodes. At Fe electrodes, the cathodic reaction is favored in accord with n-type conductivity (32).

From the band models derived herein, some qualitative explanations of the above-described behavior can be advanced. First, at the redox potential of $\text{Fe}(\text{CN})_6^{-3}/\text{Fe}(\text{CN})_6^{-4}$ (+0.22V vs. SCE) a depletion layer exists in the Fe film, i.e., the band bending is such that the concentration of majority carriers is greatest near the metal rather than at the surface. This requires charge transfer to occur by tunneling either from the conduction band or the metal and therefore lower exchange currents are to be expected. A similarity in kinetic behavior between anodic and thermal Fe oxides (13) infers that tunneling involves participation of the conduction band in the case of Fe (33).

At nickel oxide electrodes the situation is reversed. At the redox potential, majority carriers (holes in the valence band) are accumulated and exchange currents should be large as observed. Asymmetry in the redox kinetics results from the fact that accumulated valence band holes have a higher probability for oxidative ET because of the shorter tunnel distance involved. An accumulation of majority carriers at potentials anodic to V_{FB} as opposed to a depletion layer is manifested, therefore, by higher exchange current densities and rates of ET that approach those of Pt. The higher conductivity inherent in this situation also results in a larger portion of the potential drop across the interface to be in the Helmholtz layer. Since the potential drop in the film strongly affects film thickness, this may account for the fact that Fe films grow to a greater thickness at constant potential than do Ni films and more generally that p-type films (Ni, Cr, Cu) have smaller thicknesses than do n-type films (Fe, Ti, Sn, Nb).

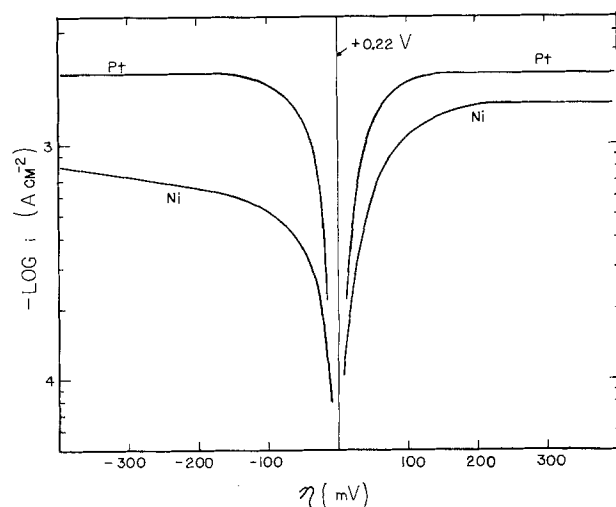


Fig. 9. Tafel plots for Ni and Pt electrodes, 0.10N $\text{K}_3\text{Fe}(\text{CN})_6$, 0.10N $\text{K}_4\text{Fe}(\text{CN})_6$, pH 8.4.

Conclusions

Semiconductor characteristics of Fe and Ni passive films are manifested by the following experimental observations:

1. When directly illuminated with sufficiently energetic radiation, a photoresponse is observed at Fe and Ni films that is proportional to the surface thickness of their respective anodic oxidation products.
2. The sign of the photoresponse in each case inverts at a characteristic potential where the rates of oxidative and reductive charge transfer are equal. This potential changes with pH in a manner consistent with its identification as V_{FB} .
3. The dependence of the photoresponse on light energy shows a characteristic absorption edge that is comparable to that observed on Fe and Ni oxides.
4. Charge transfer via Fe and Ni films is favored in the direction indicated by conductivity type.

Acknowledgments

The authors wish to thank the Robert A. Welch Foundation of Houston, Texas, for financial support of this research. They also wish to thank Dr. Sergio Kapusta, Dr. K. S. Yun, and Alfred Viehbeck for helpful discussions and suggestions concerning this investigation.

Manuscript submitted Jan. 4, 1980; revised manuscript received March 4, 1981.

Any discussion of this paper will appear in a Discussion Section to be published in the June 1982 JOURNAL. All discussions for the June 1982 Discussion Section should be submitted by Feb. 1, 1982.

Publication costs of this article were assisted by Rice University.

REFERENCES

1. J. Keir, *Philos. Trans.*, **80**, 359 (1790).
2. J. Podesta, R. Piatti, and A. J. Arvia, *This Journal*, **126**, 1363 (1979).
3. M. Nagayama and M. Cohen, *ibid.*, **109**, 781 (1962).
4. B. MacDougall and M. Cohen, *ibid.*, **121**, 1152 (1974).
5. A. C. Makrides, *ibid.*, **111**, 392 (1964).
6. A. C. Makrides, *ibid.*, **113**, 1158 (1966).
7. R. V. Moshtev, *Ber. Bunsenges. Phys. Chem.*, **71**, 1097 (1967).
8. R. V. Moshtev, *ibid.*, **72**, 452 (1968).
9. R. V. Moshtev, *Electrochim. Acta*, **16**, 2039 (1971).
10. M. Stimming and J. W. Schultz, *Ber. Bunsenges. Phys. Chem.*, **80**, 1297 (1976).
11. A. K. Vijh, in "Oxides and Oxide Films," Vol. 2, J. W. Riggle, Editor, Marcel Dekker, New York (1972).
12. L. S. R. Yeh and N. Hackerman, *This Journal*, **124**, 833 (1977).
13. S. M. Wilhelm, K. S. Yun, L. Ballenger, and N. Hackerman, *ibid.*, **126**, 419 (1979).
14. J. H. Kennedy and K. W. Frese, *ibid.*, **125**, 723 (1978).
15. E. K. Oshe and I. L. Rosenfeld, *Elektrokhimiya*, **4**, 1200 (1968).
16. E. K. Oshe, I. L. Rosenfeld, and V. G. Doroshenko, *Dokl. Akad. Nauk SSSR*, **194**, 614 (1970).
17. E. K. Oshe, I. L. Rosenfeld, and V. G. Doroshenko, *Zasch. Met.*, **7**, 38 (1971).
18. E. K. Oshe, I. L. Rosenfeld, and V. G. Doroshenko, *ibid.*, **13**, 410 (1977).
19. R. Memming and G. Schwandt, *Argem. Chem. Internat. Ed.*, **6**, 851 (1967).
20. A. J. Bosman and H. J. Van Daal, *Adv. Phys.*, **19**, 1 (1970).
21. H. Gerischer, *J. Electroanal. Chem. Interfacial Electrochem.*, **58**, 263 (1975).
22. H. Reiss, *This Journal*, **125**, 937 (1978).
23. A. T. Fromhold, in "Passivity of Metals," R. P. Frankenthal and J. Kruger, Editors, p. 59, The Electrochemical Society, Princeton, N.J. (1978).
24. K. S. Yun, S. M. Wilhelm, S. Kapusta, and N. Hackerman, *This Journal*, **127**, 85 (1980).
25. F. J. Morin, *Phys. Rev.*, **93**, 1195 (1954).
26. J. L. McNatt, *Phys. Rev. Lett.*, **23**, 915 (1969).
27. Y. M. Ksendzov and I. A. Drabkin, *Sov. Phys.-Solid*

- State*, **9**, 512 (1967).
28. D. Adler and J. Feinleib, *Phys. Rev. B*, **2**, 3112 (1970).
29. K. A. Wickersheim and R. A. Lefever, *J. Chem. Phys.*, **36**, 844 (1962).
30. R. Newman and R. M. Chrenko, *Phys. Rev.*, **114**, 1507 (1959).
31. E. J. W. Verway, P. W. Haaijman, and F. C. Romeyn, *J. Chem. Phys.*, **15**, 181 (1947).
32. U. Stimming and J. W. Schultze, *Electrochim. Acta*, **24**, 859 (1979).
33. J. W. Schultze, in "Passivity of Metals," R. P. Frankenthal and J. Kruger, Editors, p. 82, The Electrochemical Society, Princeton, N. J. (1978).

Effects of Substitution of Iron by Molybdenum in the Naphthalocyanine Structures upon Their Electrocatalytic Properties for O₂ Reduction and Evolution in Alkaline Media

G. Magner, M. Savy,* and G. Scarbeck

Laboratoire d'Electrochimie Interfaciale du C.N.R.S., 92190 Meudon-Bellevue, France

and J. Riga and J. J. Verbist

Laboratoire de Spectroscopie Electronique, Faculté N. D. de la Paix, B 5000 Namur, Belgium

ABSTRACT

Mixed Fe-Mo and Mo naphthalocyanine samples have been synthesized and investigated by XPS and electrochemically using cyclic voltammetry and rotating disk techniques. As loadings on carbon black supports for industrial-type electrode structures, they present higher activities than the corresponding iron samples, for both anodic and cathodic polarizations. Data are interpreted with the aid of electron transfer theories in terms of bridged-type mechanisms which reveal reversible conditions for both adsorption and transfer steps.

The interest of Fe naphthalocyanine films as loadings on carbon black supports for air cathode catalysis has been stressed recently (1). Under both anodic and cathodic recycling, the life expectancy increased with the dilution of the loadings. The generation of H₂O₂ occurs only after a time equal to the life expectancy of the support. In addition, using the ultrathin electrode technique, it has been shown that the introduction of molybdenum ions into the structure corresponds to an extension of the Tafel zone of polarization over that of iron by more than one decade. This enhancement was interpreted as being due to a drop of the resistance of the solid phase. Therefore, one may seek to synthesize Mo naphthalocyanine (NP_c) samples and to undertake similar investigations as for Fe(NP_c).

The gas-solid activity of mixed iron molybdenum phthalocyanines for fast oxygen uptake and desorption has been reported by Inoue (2). For the 3d metal transition series the effect of the central ion on the electroreduction of oxygen on the phthalocyanine compounds has been investigated (3). A linear relationship between the potentials at a constant current density and the redox potential of the central ion has been emphasized (4). More generally a linear relationship between the redox potential of the central ion in porphyrin or phthalocyanine structure and corresponding redox potentials in various solvents can be established (5a, b). For solutions in aqueous media, Mg, H₂, and Pd lie at the bottom of the scale with a redox potential close to the H₂/H⁺ couple. Sn and Mn are at the top corresponding to oxygen evolution, Fe and Mo couples being located near the O₂/H₂O couple.

The aim of the present work is first to synthesize Mo (with or without iron) naphthalocyanine structures

and to prove their efficacy as catalyst materials for cathodic reduction or anodic evolution of oxygen in alkaline media. As XPS¹ results (6) were useful in the case of iron polyphthalocyanine compounds for showing correlations between their structure and their electrochemical properties, this technique is employed in the present study, mainly for the identification of the oxygen species present on the surface.

In addition, as the interpretation of the data obtained on industrial types of porous electrode structures are very often difficult, cyclic voltammetry is also performed on the same materials on a rotating disk (1).

Experimental

Synthesis and elementary analysis.—The mode of synthesis is similar to that performed for iron naphthalocyanine (1). The molybdenum donor compound consists of ammonium paramolybdate in the ratio of 1 mol per 4 mols of dicyanonaphthalene. The samples have been prepared by heating the reactant mixture at 300°C for 20 hr. After preparation the samples were thoroughly washed with benzene, ethanol, 10% HCl, distilled water, and ethanol. In addition some of them have undergone a washing treatment with 5M KOH for 12 hr in order to eliminate the remaining oxide.

By varying the amount of ammonium paramolybdate with respect to the amount of iron dipivaloylmethane it has been possible to vary the ratio Mo/Fe in the overall structure. Three sorts of samples have been prepared: samples (I, Fe) consisting of Fe naphthalocyanine as in Ref. (1), samples (II, Fe-Mo) where the ratio Mo/Fe is about 1, and samples (III, Mo) containing only Mo.

* Electrochemical Society Active Member.
Key words: battery, catalysis, chelates.

¹ X-ray photoelectron spectroscopy.

A typical elementary analysis for samples (II, Fe-Mo) is given in Table I. The ratios found for the various components in C and H agree with the theoretical composition. Fe appears to be 30% below the theoretical value. However, a systematic deficiency in nitrogen content can be noted. In order to rule out a distortion due to the technique of analysis, Fe and Mo contents have also been measured by x-ray fluorescence.² In comparison with the theoretical value, an excess of molybdenum for samples (III, Mo) has been determined while the iron content value previously obtained can be confirmed for (I, Fe) and (II, Mo-Fe).

XPS analysis.—The XPS investigations have been performed using the HP 5950 A spectrometer described in Ref. (6). In addition a glove box has been set up to allow the introduction of samples under deaerated conditions.

The samples prepared under argon atmosphere as indicated in Ref. (1) were examined after different times of exposure to air. Before introduction into the apparatus, some samples have been treated with ethanol and deionized water to speed up the wetting process and to reveal any effect associated with the adsorption of water. In order to discriminate between the effects associated with iron from those with molybdenum, these experiments have been carried out with Mo samples (III, Mo) and Fe (I, Fe).

While on samples (III, Mo) the intensity of the O_{1s} peak is higher in approximately the ratio 1.5/1 on unwetted samples than on the wetted, a reverse effect is observed on samples (I, Fe).

On these compounds (I, Fe), however, for longer times of exposure at air, no appreciable differences between wetted and unwetted can be detected. In addition, if the samples are kept under vacuum in the apparatus, the O_{1s} signal of the wetted samples drops and after 2 hr becomes nearly equal to that of the unwetted samples.

At the introduction into the apparatus, the O_{1s} signal, initially split into two components on samples (I, Fe), yields a single peak under flood gun (electron bombardment) conditions, an effect which is characteristic of a mixture rather than a well-defined compound. These phenomena are not observed with samples (III, Mo).

As a function of the time of exposure at air the O_{1s} signal grows continuously on both samples (I, Fe) and (III, Mo). After 1 min, however, the intensity of O_{1s} on (III, Mo) samples is about 2-4 fold higher than on (I, Fe). On these latter samples (I, Fe), the saturation signal is not observed after less than 2 months, while it is attained within 2 weeks with (III, Mo) samples. In this case, the intensity remains 3-4 fold higher with (III, Mo) than with (I, Fe) samples. This occurs mainly by an enhancement of the component located at 532.3 eV.

The iron samples (I, Fe) prepared and introduced under deaerated conditions present only slight traces

²The authors acknowledge Prof. G. Deconninck and Dr. F. Bodart for x-ray fluorescence measurements.

Table I.

| | Elementary | | Analysis | | | | |
|--------------------------------|------------|---|----------|-----|------|-----------|-----------|
| | | | C | H | N | Fe | |
| I $\overline{\text{FeNpC}}$ | Found | % | 75.5 | 3.1 | 13.3 | 5.3 | |
| | Expected | % | 75 | 3.1 | 14.6 | 7.3 | |
| II $\overline{\text{FeMoNpC}}$ | | | C | H | N | Fe* | Mo* |
| | Found | % | 75 | 3.4 | 13.2 | 4.7 ± 0.2 | 5.5 ± 0.2 |
| | Expected | % | 75 | 3.1 | 14.6 | | |

*Determination by x ray Fluorescence caused by Proton Bombardment

of oxygen with a high binding energy of about 534 eV. Under air exposure times shorter than a few minutes an oxygen form with $E_B = 533.0$ eV readily develops. For longer times of exposure Fe^{III} becomes apparent and an oxygen form with $E_B = 531.0$ eV is more and more apparent.

In the case of sample (III, Mo) analysis, after short exposure times (about 1 min) at air, two distinct forms of oxygen are visible at $E_B = 531$ and $E_B = 532.2$ eV. This latter form becomes predominant for the samples which have been thoroughly washed with concentrated KOH to eliminate the oxide component.

For samples (III, Mo) the relative intensities of the Mo^{3d} 3/2-3d 5/2 signals are given vs. the times of exposure at air in Table II. While the Mo^V signal remains relatively stable and below 5%, the growth of the Mo^{VI} signal occurs simultaneously with the drop of the Mo^{IV} component.

On samples (I, Fe) and (III, Mo) the different oxygen species are given in Table III in accord with the possibilities of coordination of the central ion in the naphthalocyanine structure or perhaps in the oxide in the case of samples (III, Mo). It should be pointed out in this last case that for short exposure times in air (less than 1 min) the O₂^{δ-} species is predominant, while in the case of (I, Fe) samples the predominant form turns out to be O₂ with a covalent character. This effect corresponds to a stronger bond than in the case of samples (I, Fe).

Electrochemical investigations.—Two techniques of investigation have been worked out as described in Ref. (1). An investigation on a porous electrode structure (A) (industrial type) and a porous electrode structure (B) confined in the hollow cavity of a rotating ring disk equipment. In order to allow comparisons with data obtained on the iron samples investigated as in Ref. (1) the same ex CO carbon black support has been chosen for impregnation at the loading 2.5%.

Electrode structure A.—Tests have been carried out in 8M KOH solutions at 22°C with air. The samples were cycled between + 10 mA/cm² during 1.5 hr and - 100 mA/cm² during 0.5 hr to test the effect of oxidation of the support and the stability of the electrode texture or for cathodic polarizations the effect of O₂ depletion. Data at a scan rate of 1.5 mV/sec are presented in Fig. 1 for iron (Fe) and (Fe-Mo) samples, solid and dashed lines, respectively. At 100 mA/cm² the working potential lies at approximately 900 mV above the potential of the hydrogen electrode, about 200 mV more positive than the value obtained with pure Fe samples. For anodic polarizations on (II, Fe-Mo) samples, oxygen evolution takes place at about + 400 mV Hg/HgO on the anodic scan. From previous work (1) the peak near O can be identified with H₂O₂ formation.

Data for both samples after a 150 cycle treatment for samples (II, Fe-Mo) and a 350 cycle treatment for samples (I, Fe), under the same scanning conditions, are represented in Fig. 2. For cathodic polarizations the activities are now almost identical while for anodic polarizations samples (II, Fe-Mo) remain slightly more active. However, the main difference with the

Table II. Relative intensities, %, for Mo^{3d} 3/2-3d 5/2 peak for samples (III, Mo)

| Exposure times in air | Mo ^{VI} | Mo ^{V*} | Mo ^{IV} |
|-----------------------|------------------|------------------|------------------|
| 1 mn | 15 | Traces | 80 |
| 3 days | 45-50 | id | 45-50 |
| 2 weeks | 70-75 | id | 20-25 |

* The Mo^V signal is relatively low and widely spread.

Table III. Oxygen species vs. their binding energies

| a | E_B (eV) | 534.0 | 533.0 | 531.0 |
|-------------------|------------|--|--|---|
| Samples (I, Fe) | Species | O_2 Physisorbed traces | O_2 Covalent | O_2^{2-} Strong ionic bond (initially weak) stronger intensity after exposure |
| b | E_B (eV) | 532.2 | 531.1 | |
| Samples (III, Mo) | Species | O_2^{2-} Ionic bond between O_2 and Mo in the naphthalocyanine structure, strong | O_2^{2-} Strong ionic bond oxide structure. Weaker intensity after extended KOH intensity washing | |

preceding experiment concerns the H_2O_2 generation. As with the ex CO carbon black support a high peak is apparent with mixed Fe-Mo samples (II, Fe-Mo) while the H_2O_2 formation remains below the detection threshold in the case of pure Fe samples (I, Fe).

Electrode structure B.—In order to provide an interpretation of these data obtained with structure A [mainly the observed initial high activity followed by its decline after anodic and cathodic scans on samples (II, Fe-Mo) and (III, Mo)], fundamental studies have been performed using the rotating disk equipment and the preparations described in Ref. (1). The same scan rate has been used as in the case of structure A.

With the rotating disk technique, the cathodic performances obtained on samples (I, Fe), (II, Fe-Mo), and (III, Mo) are represented in Fig. 3, in the Tafel region, vs. an Hg/HgO reference electrode. It should be pointed out that differences in activity are relatively small. The limiting currents, which are not plotted here, are identical for all these samples within the limits of reproducibility. These data substantiate those obtained on the ultrathin electrodes (1).

The activities of the same samples under anodic polarizations are shown in Fig. 4. In contrast to the preceding experiments, samples (II, Fe-Mo) and (III, Mo) are notably more active with respect to samples (I, Fe), at constant current density the potentials being about 120 mV more negative. These curves were obtained after several cycles and remain stable under further anodic scanning conditions. They are closely similar to those obtained recently on $La_{0.5}Ba_{0.5}CoO_3$ (7).

For the studies of the activities vs. temperature a small Hg/HgO reference electrode has been employed and arranged inside the electrochemical cell in order to minimize the temperature gradient between the working and the reference electrode.

The effect of temperature on the activities of samples (I, Fe), (II, Fe-Mo), and (III, Mo) for reduction is given in Fig. 5. The curves have also been obtained in the Tafel region as in Fig. 3. No appreciable differences are visible between the different samples. It should be pointed out that after correction for the shift of the reference electrode vs. temperature given in Ref. (8) the current potential plots are almost superposable: the measured shift calibrated with H_2 is 0.37 mV/K vs. 0.29 mV/K given for the reference electrode.

For anodic polarizations, the effect of temperature variation is given in Fig. 6. In the case of samples (II, Fe-Mo) and (III, Mo) a lack of stability of these

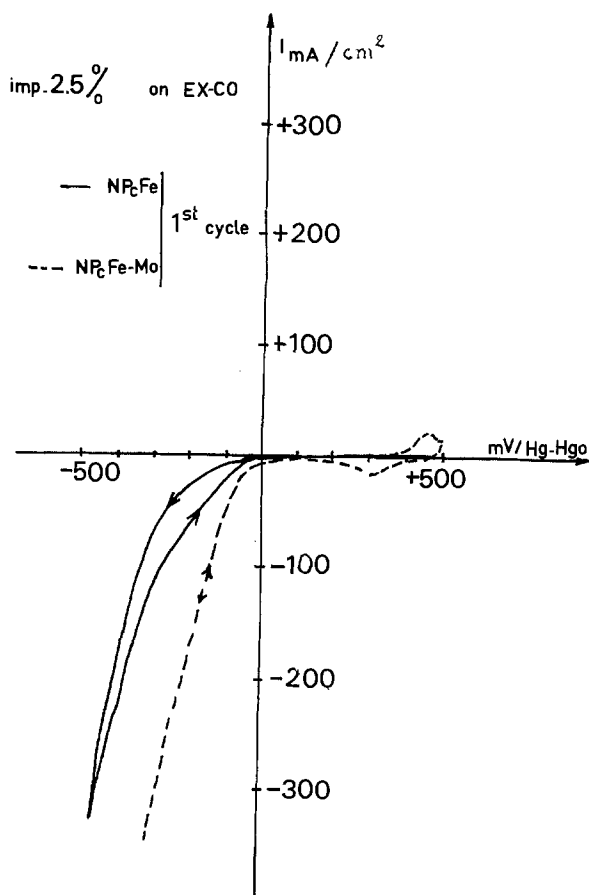


Fig. 1. Cyclic voltammety curves on industrial-type porous electrodes. Solid line: samples (I, Fe) on ex CO carbon black support. Dashed line: samples (II, Fe-Mo) supported as (I, Fe) 2.5% loading.

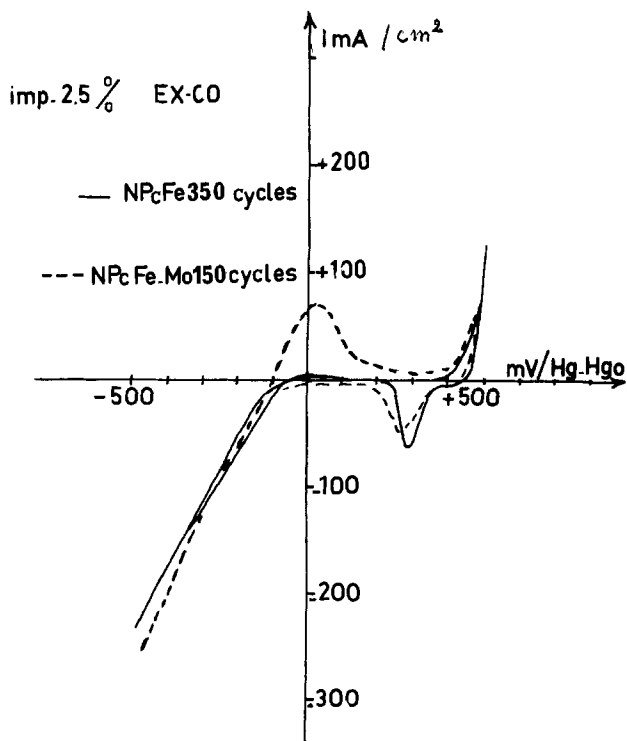


Fig. 2. As in Fig. 1 after 150 cycles, samples (II, Fe-Mo) and 350 cycles, samples (I, Fe).

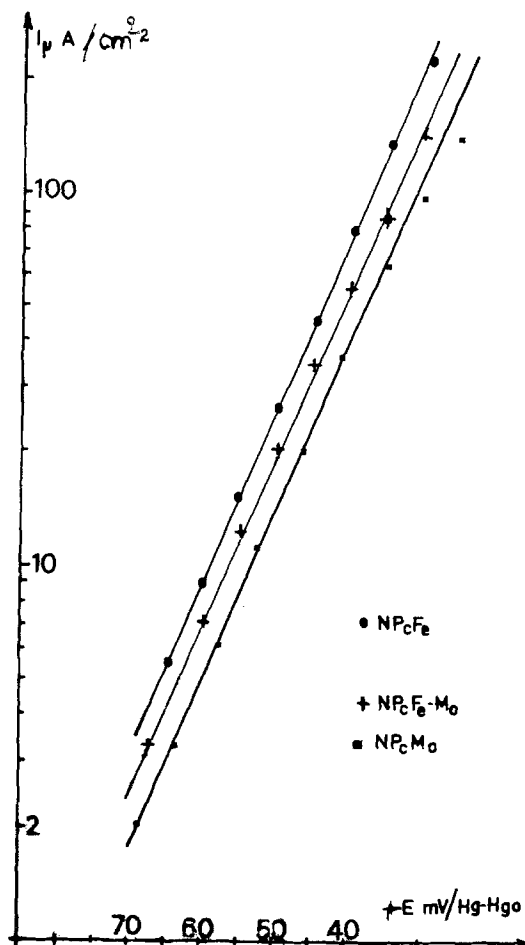


Fig. 3. Cyclic voltammery on rotating disk electrode in the cathodic Tafel region. Samples supported as in Fig. 1. ●, NPcFe (I, Fe); +, NPcFe-Mo (II, Fe-Mo) ■, NPcMo (III, Mo). $N = 80$ rps, $v = 0.2$ mV/sec.

plots at the lowest applied potentials can be noticed. However, after several cycles, the activity becomes reproducible in the region where oxygen evolution is taking place. In this region the same conclusions about temperature variations can be drawn as for cathodic polarizations: the observed differences in activity are almost negligible after correction of the shift of the reference electrode (0.48 mV/K) at $i = 300$ $\mu\text{A}/\text{cm}^2$. They drop at 0.33 mV/K at $i = 500$ $\mu\text{A}/\text{cm}^2$.

Discussion

It should be pointed out first that the similar plots (with the absence of H_2O_2) obtained on the different samples with the rotating ring disk technique involve the $4 e \text{O}_2$ reduction reported (9) on porphyrin- and phthalocyanine-type compounds. As shown previously the rds is a coupled chemical and electrochemical reaction between radicals (10).

In contrast in the case of structure A electrodes no Tafel region is observed and the differences in potentials for the Fe and Mo samples at constant C.D. are much higher than in this preceding case, therefore a different rds must be assumed. In view of the high current densities observed, the rate-limiting process can be assumed to be due to the low conductivity into the solid phase as shown in Ref. (11, 12). The application of the same charge transfer complex models developed in Ref. (13) requires that the conductivity is higher in the solid phase with Mo-containing samples than with (I, Fe) samples. This can be easily explained on the basis of XPS experiments involving a faster $\text{Mo}^{\text{IV}}/\text{Mo}^{\text{VI}}$ couple compared to $\text{Fe}^{\text{II}}/\text{Fe}^{\text{III}}$.

Before entering into a sophisticated analysis of the relationship between the binding energies of molyb-

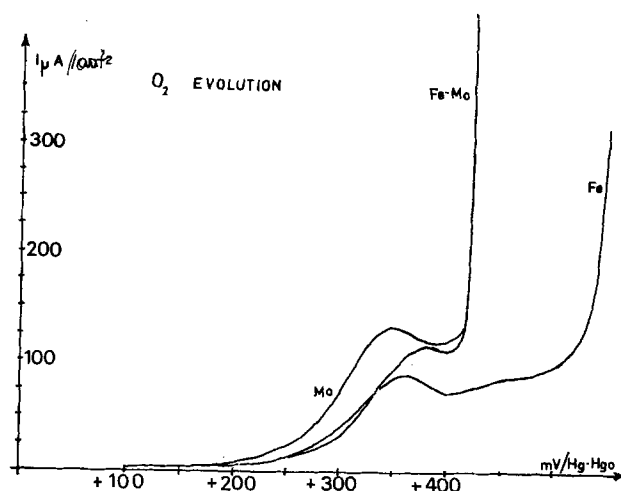


Fig. 4. Same labels as Fig. 3 anodic scans. $N = 80$ rps, $v = 0.2$ mV/sec.

denum electronic levels and their structure of coordination with the oxide or the naphthalocyanine lattices, it must be pointed out that a difference in the state of the active couples in the electrochemical reaction must be detectable between experiments in an inert atmosphere and those at short exposure times to air. This time of 1 min required for the XPS experiment appears exceedingly large compared with the time in which the electrochemical reaction occurs. As the oxygen penetration is found to be a slow process in both cases of samples (I, Fe) and (III, Mo) the difference in favor of samples (III, Mo) may play a role just for the life expectancy.

If this model is valid (13), the decline in the (III, Mo) performances can perhaps be correlated with the variations in the stoichiometry of the oxide or the naphthalocyanine structure due to a depletion in the more labile oxygen content and the subsequent sta-

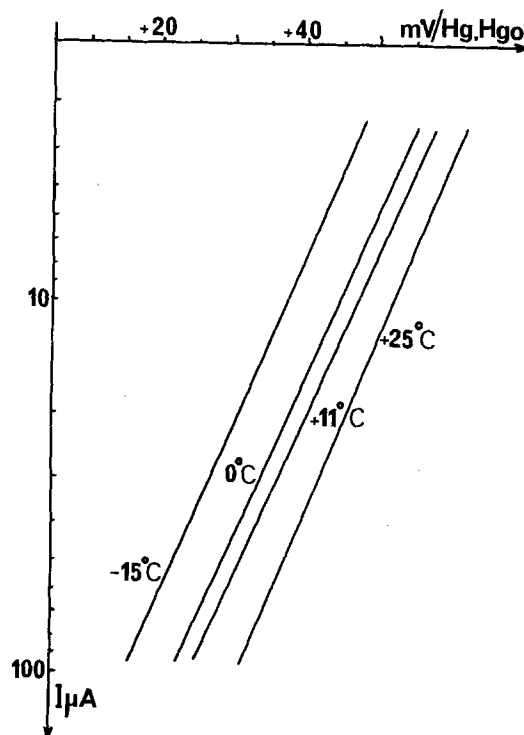


Fig. 5. Influence of temperature: cyclic voltammery as in Fig. 3. Numbers in parenthesis are temperature (Celsius $^{\circ}$). Variations among samples (I, Fe), (II, Fe-Mo), and (III, Mo) are not significant. The corrections are not made here for the shift of the reference electrode.

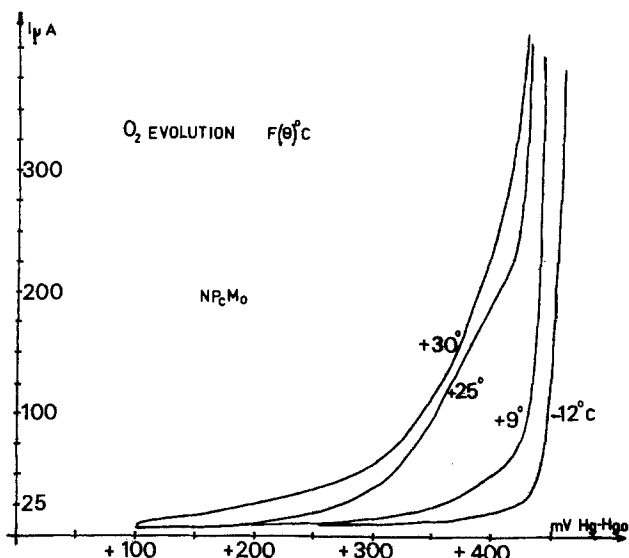
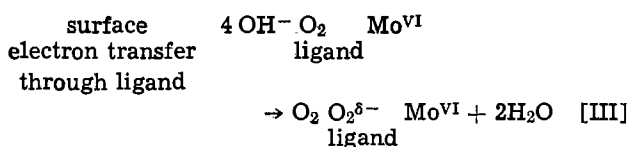
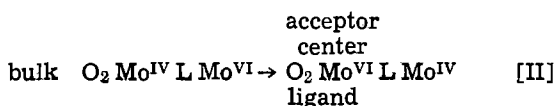
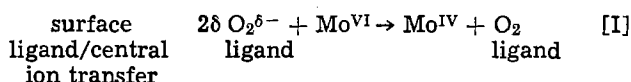


Fig. 6. Same labels as Fig. 5 for anodic scans. Samples (III, Mo). Corrections not made for the shift of the reference electrode.

bilization of one valency of the metal instead of the initial mixing of two valence states.

In the case of anodic polarizations, where a catalytic effect is observed as molybdenum ions are introduced into the structure, an interpretation of the data can be sought through the differences in nature of the adsorbed oxygen species. In this respect, the main difference between molybdenum and iron is concerned (as seen by XPS) by the development of the $O_2^{\delta-}$ species with molybdenum instead of the covalent form of oxygen observed with iron. These radicals may act as bridges (14) between free oxygen molecules and OH^- ions, the donor character of the intermediate (readily regenerated during the reaction) being enhanced with a destabilizing effect resulting from the filling of the antibonding orbitals of the oxygen molecule. Therefore, one can assume coupled electron transfer reactions are taking place among the oscillations of the Mo^{IV}/Mo^{VI} valencies, metal/oxygen ligand exchange, and OH^- oxygen ligand exchange. They may involve OH or HO_2 radical formation as already explained in Ref. (9). The reaction sequence can be written as³



One may hope to gain some information from theories (15, 16) concerning the effects of intermediate species on the rate process and the Marcus (17) and Levich (18) theories for electron transfer in redox systems in order to achieve an optimization of the catalyst structure.

In the case of adsorption of intermediate species (15, 16) the rate expression must contain a factor f which can be written as

$$f = \exp - \beta \frac{(\Delta G_{ads})}{RT} \quad \text{[1]}$$

³ The coordination structure of Mo ions will be presented in a future work.

where ΔG_{ads} represents the standard free adsorption energy of the intermediate species and β a factor generally equal to one-half.

In the domain of transfer control the current density i can be expressed as (18)

$$i = nF \frac{kT}{h} KN_s \theta \exp - \frac{\Delta F^+}{RT} \quad \text{[2]}$$

where n is the number of exchange electrons, K is the transmission coefficient generally independent of the temperature, θ the coverage of the active site N_s per unit area, and ΔF^+ the free energy of activation which includes an entropy factor of activation ΔS^+ . In Eq. [2] ΔF^+ is expressed in the same units as RT , ΔS^+ as R (standard state 1 atm).

$$\Delta F^+ = \Delta H^+ - T\Delta S^+ \quad \text{[3]}$$

which can be also written as

$$\Delta H^+ = \Delta F^+ - Td \frac{\Delta F^+}{dT} \quad \text{[4]}$$

ΔF^+ is a function of the applied potential and can be expressed as

$$\Delta F^+ = \Delta F_o^+ - n' \alpha F (E - E_R) \quad \text{[5]}$$

where n' is the number of electrons in the activation state and ΔF_o^+ represents the free energy of activation of the exchange current at $E = E_R$ either for cathodic ΔF_o^{+c} or for anodic polarizations ΔF_o^{+a} .

In the present work the domain of polarizations corresponding to the transfer control appears to be too narrow compared to the domain of overvoltage $E - E_R$ to allow from the data a direct determination of ΔF_o^{+c} or ΔF_o^{+a} which hence must be obtained from a calculation. However, from the studies *vs.* temperature one obtains (correction being made for the shift of the reference electrode)

$$\Delta F^{+c} = 0.8RT \quad \text{[6]}$$

$$\Delta F^{+a} = 1.2RT \quad i = 300 \mu A/cm^2 \quad \text{[7]}$$

$$\Delta F^{+a} = 0.8RT \quad i = 500 \mu A/cm^2$$

These relationships mean that for $E \neq E_{1/2}$ for cathodic polarizations ($E_{1/2}$ being approximately the potential where $i = I_{L/2}$, I_L being the diffusion limiting current)

$$\Delta F^{+c} < RT \quad (E \neq E_{1/2}) \quad \text{[8]}$$

For anodic polarizations, the same expression is valid when $E = E_w$, E_w being the potential corresponding to rapid oxygen evolution, e.g., $500 \mu A/cm^2$ or above

$$\Delta F^{+a} < RT \quad E \neq E_w \quad \text{[9]}$$

Hence from Eq. [5]

$$\Delta F_o^{+c} \neq n_c' \alpha F |E_{1/2} - E_R| \quad \text{[10]}$$

$$\Delta F_o^{+a} \neq n_a' \alpha F |E_w - E_R| \quad \text{[11]}$$

where $n_{a,c}'$ is the number of electrons in the activation state, anodic and cathodic.

Writing Eq. [4] in the case of the 4 electron process one obtains with $\alpha = 0.5$, $n_c' = 4$

$$\Delta H_o^{+c} = 2F(E_R - E_{1/2}) - 2FT \frac{d\eta}{dT} \quad \text{[12]}$$

and for the anodic process $n_a' = 1$

$$\Delta H_o^{+a} = 0.5F(E_w - E_R) + -0.5FT \frac{d\eta}{dT} + \Delta F^{+a} \quad \text{[13]}$$

Substituting $E_{1/2}$, E_w , and $d\eta/dT$ by their experimental value: $|E_{1/2} - E_R| = 270 \text{ mV}$, $d\eta/dT = -0.08 \text{ mV/K}$ for cathodic polarizations, $E_w - E_R = 150 \text{ mV}$

$d\eta/dT = -0.33$ mV/K for anodic polarizations, and $t = 30^\circ\text{C}$ (neglecting dE_R/dT)

$$\Delta H_o^{+c} = 56.7 \text{ kJ mol}^{-1} \quad [14]$$

$$\Delta H_o^{+a} = 12.7 \text{ kJ mol}^{-1} \quad [15]$$

The value obtained ΔH_o^{+c} for cathodic polarizations fits remarkably with the $T\Delta S$ value of 56 kJ mol^{-1} (19) corresponding to only the loss of the degrees of freedom of the oxygen molecule (standard state 1 atm) hence ΔG (Gibbs free energy) = 0 for O_2 . The adsorption and the transfer steps obey reversible conditions as also reported (20) for the transfer on similar compounds.

For the anodic process the $T\Delta S$ corresponding to the solvation of OH^- ions reference hydrogen is from the table (21) 3.16 kJ mol^{-1} . As the evolution reaction involves 4 mols of OH^- , one finds the same conclusions as previously for the O_2 adsorption case. Therefore, for both anodic and cathodic polarizations in the case of NP_6Mo samples the irreversibility of the process appears to coincide with the enthalpy equal in this case to the entropy change due to the fixation of one molecule of O_2 or 4 OH^- ions from the liquid phase to the surface.

As the rate processes are equivalent for cathodic polarizations between (I, Fe) and (III, Mo) samples, one can assume that electronic factors such as the work function or electron energy densities on Fe and Mo sites are similar under the control of the ligand structure. For improving our knowledge of the structure of the solvent at the interface, XPS data concerning the interaction of the surface with water may throw some light.

Experiments comparing wetted and unwetted samples display a very weak type of interaction. These data substantiate findings of Ref. (22) where from infrared techniques, no adsorption of water takes place on phthalocyanine materials. They conflict with other references (23), but in this latter case it should be pointed out that adsorption of water on the iron sites obeys slow kinetics. Therefore, on both theoretical and experimental supports one can assume that the rate of electron transfer is limited because of the too distant approach of the water molecule from the active sites.

Conclusion

From a practical view point of applications in the problem of generators or electrolyzers, the substitution of iron by molybdenum into the naphthalocyanine structure seems to be rather promising under the double condition of fast oxygen transfer and ohmic drop limitations in the solid phase. On both cathodic and anodic polarization the rate appears to obey reversible conditions for the adsorption and transfer steps.

It might also be considered first that in the synthesis a common material is used for the central metal introduction instead of a more elaborate compound.

Second, the improvements of the performances for both anodic and cathodic polarizations on industrial types of electrode have to be emphasized. At constant current densities, compared to iron samples the drop in the overvoltage reaches about 100 mV for cathodic and 130 mV for anodic polarizations.

XPS and cyclic voltammetry techniques on a rotating disk equipment have substantiated an interpretation of the data and of the decline of the cathodic performances observed after more than 100, 2 hr cycles of both cathodic and anodic polarizations.

The enhancement of the activity with Mo ions can be related to a redox process in the solid phase which occurs simultaneously with a better oxygen penetration in the Mo-containing samples. In the case of cathodic polarizations data can be explained by an increase of the conductivity of the naphthalocyanine films. For anodic polarizations the presence of negatively charged

oxygen ligands acts as bridges for the electron transfer processes.

The decline in the cathodic performances appears to be mainly due to changes in the solid phase stoichiometry, presumably in the oxide which is less stable, remaining present with the naphthalocyanine structure.

For both anodic and cathodic polarizations, the investigations vs. temperature reveal a nonactivated process which can be interpreted with the aid of the Marcus and Levich theories as a quantum mechanical tunneling. The rate appears, therefore, to be limited by a too distant approach of the solvent molecules from the active sites (central ion and oxygen ligands). The entropy factor and the tunneling term of probability in the rate expression are both dependent on the closest distance of approach, the latter being much more sensitive to this than the former.

Acknowledgments

The authors acknowledge M. Dupeyrré and Dr. G. Feuillade of the C.G.E. Research Laboratories (Marcoussis) for the realization of experiments on industrial-type electrodes, Dr. Parsons for a critical reading of the manuscript, and the Direction d'Études et de Recherches Techniques and the Franco-Belgium Cultural Exchanges for their financial support.

Manuscript submitted Oct. 15, 1980; revised manuscript received Jan. 22, 1981. This was Paper 506 presented at the St. Louis, Missouri, Meeting of the Society, May 11-16, 1980.

Any discussion of this paper will appear in a Discussion Section to be published in the June 1982 JOURNAL. All discussions for the June 1982 Discussion Section should be submitted by Feb. 1, 1982.

Publication costs of this article were assisted by the Laboratoire d'Electrochimie Interfaciale du C.N.R.S.

REFERENCES

1. G. Magner, M. Savy, and G. Scarbeck, *This Journal*, **127**, 1076 (1980).
2. H. Inoue, Y. Kida, and E. Imoto, *Bull. Chem. Soc. Jpn.*, **38**, 2214 (1965).
3. P. Andro, C. Bernard, and M. Savy, *Croat. Chem. Acta*, **107**, 688 (1972).
4. J. P. Randin, *Electrochim. Acta*, **19**, 83 (1974).
5. (a) J. H. Fuhrop, K. M. Kadish, and D. G. Davis, *J. Am. Chem. Soc.*, **95**, 5140 (1973). (b) K. M. Kadish, L. A. Bottomley, and R. D. Rhodes, *Abstracts*, p. 1148, The Electrochemical Society Extended Abstracts, St. Louis, Missouri, May 11-16, 1980.
6. S. Maroie, M. Savy, and J. Verbist, *Inorg. Chem.*, **18**, 2560 (1979).
7. A. G. Kobussen and C. M. Mesters, *J. Electroanal. Chem. Interfacial Electrochem.*, **115**, 131 (1980).
8. D. G. Ives and G. J. Janz, "Reference Electrodes," p. 336, Academic Press, New York (1961).
9. P. Jones and I. Wilson, "Metal Ions in Biological Systems," Vol. 7, H. Sigel, Editor, p. 195, Marcel Dekker (1978).
10. A. J. Appleby, J. Fleisch, and M. Savy, *J. Catal.*, **44**, 281 (1976).
11. A. J. Appleby and M. Savy, *Electrochim. Acta*, **21**, 567 (1976).
12. A. J. Appleby and M. Savy, *ibid.*, **22**, 1315 (1977).
13. A. J. Appleby and M. Savy, in "Electrode Materials and Processes for Energy Conversion and Storage," J. D. E. McIntyre, S. Srinivasan, and F. G. Will, Editors, p. 321, The Electrochemical Society Softbound Proceedings Series, Princeton, N.J. (1977).
14. Y. Kharkats and J. Ulstrup, Publication 455, National Bureau of Standards (1976).
15. R. Parsons, *Trans. Faraday Soc.*, **54**, 1053 (1958).
16. H. Gerischer, *Bull. Chim. Soc. Belge*, **67**, 506 (1958).
17. R. A. Marcus, *J. Chem. Phys.*, **38**, 1858 (1963).
18. V. G. Levich, in "Advances in Electrochemistry and Electrochemical Engineering," Vol. 4, P. Delahay, Editor, p. 249, Interscience (1966).

19. J. P. Collman, *J. Am. Chem. Soc.*, **97**, 7185 (1975).
 20. H. Tachikawa and L. R. Faulkner, *ibid.*, **100**, 4379 (1978).
 21. "Handbook of Chemistry and Physics," 50th Ed., R. C. Weast, Editor, D68, The Chemical Rubber Co. (1970).
 22. B. Stymme, F. Sauvage, and G. Wettermark, *Spectrochim. Acta*, **35A**, 1195 (1979).
 23. A. Mongilardi, P. Ehrburger, and J. Lahayes, *C.R. Acad. Sci. Paris*, t 289 C (1979).

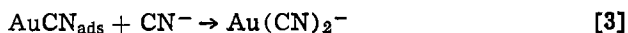
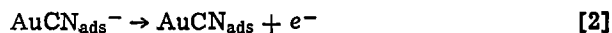
Activation Energies of Anodic Gold Reactions in Aqueous Alkaline Cyanide

C. P. Thurgood,* D. W. Kirk,** F. R. Foulkes,** and W. F. Graydon

Department of Chemical Engineering and Applied Chemistry,
 University of Toronto, Toronto, Ontario, Canada M5S 1A4

ABSTRACT

The kinetics of the anodic reactions of gold in aqueous alkaline cyanide in the potential range -0.81 to $+0.64$ V were studied by means of potentiostatic and potentiodynamic measurements for the temperature range 0° - 50° C. The effects of mass transfer were also investigated. As in earlier works, three distinct regions of anodic activity (*i.e.*, regions of anodic reactions) were found in potentiostatic measurements. The kinetic behavior of the gold reaction in each of these regions was found to behave in the manner predicted by the single reaction mechanism



The dissolution reaction in the most cathodic of the three regions (-0.56 to -0.26 V) was characterized by a high apparent activation energy (93 ± 8 kJ/mol) and a lack of dependence on mass transfer. The second step in the reaction mechanism was identified as the rate-determining step. The gold dissolution reaction in the intermediate potential region -0.26 to $+0.39$ V was found to have a relatively high apparent activation energy (47 - 55 kJ/mol) and a small dependence on the mass transfer. The second step in the reaction mechanism was identified as the rate-determining step. In the most anodic of the three regions (-0.39 to $+0.64$ V), the gold dissolution reaction was found to be under diffusion control with an apparent activation energy of 16 - 18 kJ/mol. The third step in the reaction mechanism was identified as the rate-determining step. A fourth region (-0.81 to -0.56 V) observed in potentiodynamic measurements was found to have an apparent activation energy of 62 ± 2 kJ/mol with little dependence on mass transfer. The reaction was identified as an adsorption reaction.

An understanding of the electrochemical behavior of gold in alkaline cyanide media is required for the development of efficient methods of electrochemical gold recovery from industrial liquors, electroplating wastes, and scrap metal (1).

Although the anodic behavior of gold in aqueous alkaline cyanide has been the subject of a number of studies (2-8), the nature of some of the complex behavior has only recently been identified (9-11). In slow potential sweep measurements or steady-state measurements, three potential regions are found which display an anodic current peak. Between these regions passivation of the gold surface is evident (11). The cause of the anodic reactions was uncertain until gold weight loss measurements were conducted in each of the regions (6, 9) and were interpreted as indicating the same overall dissolution reaction for all regions (6, 9)



The dissolution process has been shown to follow the sequence (5, 6) given in the Abstract.

This reaction sequence, unlike some of the other mechanisms found in the literature (2, 3), provided an

explanation for the gold dissolution behavior at each of the anodic peak regions. Although the same overall reaction was found for the three regions, the rate-determining step was not the same for the three regions. The gold dissolution reaction rates in the two most cathodic regions (-0.81 to -0.26 V and -0.26 to $+0.39$ V¹ vs. SHE) were reported to be controlled by step [2] of the reaction sequence while the dissolution rate in the most anodic region (-0.39 to $+0.64$ V) was reported to be controlled by step [3].

In addition to this steady-state behavior, the potentiodynamic measurements of Kirk and Foulkes (10) revealed an additional anodic potential peak in the region -0.81 to -0.56 V for sweep rates greater than 2 mV \cdot sec⁻¹. Cyclic potential sweep measurements carried out by MacArthur (4) at elevated temperatures revealed only two prominent anodic regions. It is not clear whether the change in temperature or the repetitive potential cycling is responsible for the disappearance of two of the anodic regions found at room temperature.

As a result of the complexity of the anodic behavior of gold in aqueous alkaline cyanide and of the fact that many industrial processes are carried out at elevated temperatures (1), a study of the variation of the

* Electrochemical Society Student Member.
 ** Electrochemical Society Active Member.
 Key words: metal, activation, voltammetry.

¹ All potentials are reported vs. SHE.

anodic reactions with temperature was carried out. The determination of activation energies for each of the anodic reactions provided an independent method of identifying the rate-controlling steps involved. The influence of mass transport was also studied.

Experimental

The equipment consisted of a Wenking potentiostat (Model 70TS1), Wenking voltage scan generator (Model VSG 72), and a Wenking Integrator (Model SS170). The potential sweep measurements were recorded on a Princeton Applied Research X-Y recorder (Model 9002-A).

The cell consisted of a Pyrex container with a Teflon top. Two glass fitted tubes set either side of the working electrode housed the counterelectrodes. A Luggin capillary was used to hold the saturated calomel reference electrode and the capillary tip was drawn to a diameter of 0.1 cm and set 0.2 cm from the surface of the working electrode. This configuration has been found to reduce IR drop to a negligible value. Other details of the cell have been described previously (6).

The cell was operated in a Plexiglas water bath that was connected to an external reservoir of water. A Tecam (Model TE-7) combination heater/pump controlled temperatures to within $\pm 0.2^\circ\text{C}$. Pure gold (99.99%) was used for both the working and counterelectrode. Solutions were prepared from analytical grade reagents and doubly distilled water. All runs used 1.0M KOH + 0.1M KCN as the electrolyte.

Purified nitrogen was obtained by passing the gas through an oxygen scrubber containing an aqueous solution of vanadous chloride. The electrolyte was then deoxygenated by bubbling the purified gas through it for at least 30 min. The rate of mass transfer at the gold solution interface was controlled by altering the rate of gas bubbling through the cell, and hence altering the boundary layer thickness.

A standard pretreatment was necessary to achieve reproducible measurements. The electrode was first immersed in aqua regia for 5 sec, washed in doubly distilled water, and then heated gently above a natural gas flame. Finally, the electrode was given a 5 min reduction interval in the electrolyte at -0.96V .

For the temperature measurement in the potential region of peak 1, the pretreatment procedure was modified in order to improve the resolution of the peak 1 complex. After immersion in the aqua regia for 5 sec, and washing in doubly distilled water, the electrode was held at $+0.39\text{V}$ for 2 min in a 0.1M KOH + 0.1M KCN solution. The brown film that formed on the surface as a result of this procedure was eliminated by gently heating the electrode over a natural gas flame. The reduction period in the electrolyte at -0.96V was increased to a minimum of 10 min.

Slow potential sweep measurements (2 mV/sec) were used in the peak 1 region so that peak 1 and peak 1a could be distinguished. For peaks 2 and 3, a fast potential sweep (500 mV/sec) was used to set the potential of the electrode at the working value after cathodic reduction at -0.96V . This was to ensure that the surface was not perturbed due to dissolution at the preceding peaks. A minor manual adjustment in the potential was made to set the current at its maximum value. The maximum current was recorded after reaching steady state. This usually occurred within 3-5 min for peak 2 and within 1 min for peak 3.

The surface area of the electrode was determined from potential scan measurements using the linear relation between the current peak height and the square root of the voltage scan rate for the reversible oxidation of $\text{Fe}(\text{CN})_6^{4-}$. The relation given by Nicholson and Shain (12) is

$$\frac{i_p}{nFAC_0 \left[\frac{D_0 n F V}{RT} \right]^{1/2}} = 0.4463$$

where C_0 is the concentration of $\text{Fe}(\text{CN})_6^{4-}$ ($\text{mol} \cdot \text{cm}^{-3}$), D_0 is the diffusion coefficient of $\text{Fe}(\text{CN})_6^{4-}$ ($\text{cm}^2 \cdot \text{sec}^{-1}$), i_p is the peak current (A), A is the area (cm^2), n is the number of electrons transferred in the oxidation, V is the scan rate ($\text{V} \cdot \text{sec}^{-1}$), and F , R , and T have their usual meanings. For a 4 mM solution of $\text{Fe}(\text{CN})_6^{4-}$ in 1M KCl, $D_0 = 6.32 \times 10^{-6} \text{cm}^2 \cdot \text{sec}^{-1}$ at 25°C (13).

In order to reduce the effect of changing surface area, a correction was applied to the measured surface area for each run. This was calculated by assuming a linear variation of the area with the number of coulombs passed through the electrode between successive surface area determinations. This correction was small as the area changed only by about 5% between successive determinations.

Results and Discussion

In Fig. 1 a typical potential scan of gold in aqueous alkaline cyanide is presented. The temperature and sweep rate were 29.6°C and $2 \text{mV} \cdot \text{sec}^{-1}$, respectively. The three dominant anodic regions seen in the figure are identified as peak 1, 2, and 3. The small peak cathodic of peak 1 is identified as peak 1a. This small peak is an anodic reaction which is only observed in potentiodynamic measurements.

Before the variation of the rate of reaction with temperature was studied, it was necessary to determine the effect of temperature on the peak potentials. Since the reference electrode (a saturated calomel electrode) was within the cell and therefore at the same temperature as the solution, a temperature-dependent potential correction was required to convert the potential measurements to the SHE scale. The temperature coefficient of the SCE electrode is $-0.67 \text{mV}/^\circ\text{C}$ (14). Figures 2 and 3 show the variation of the peak potentials with temperature from slow potential sweep measurements ($2 \text{mV} \cdot \text{sec}^{-1}$). The three peaks (1, 2, and 3) found in steady-state measurement all have a peak potential which becomes more negative (cathodic) with increasing temperature. The rate of cathodic shift for peaks 1, 2, and 3 are 2.0 ± 0.5 , 1.7 ± 0.8 , and $2.5 \pm 0.8 \text{mV}/^\circ\text{C}$, respectively. These temperature coefficients are greater than that predicted for the

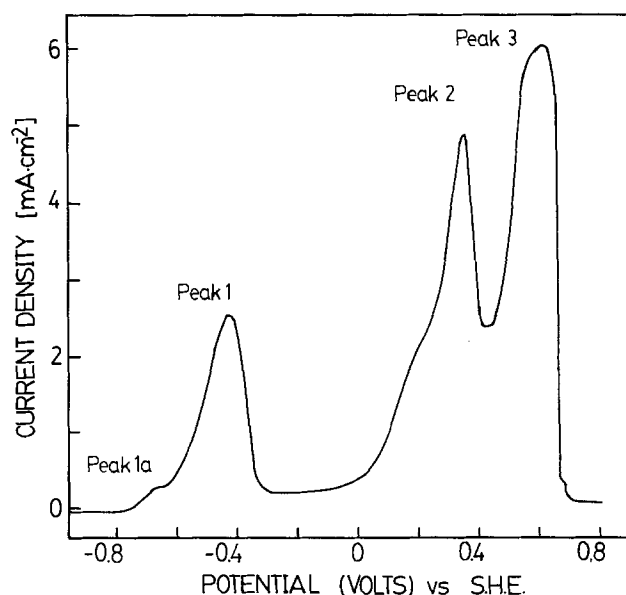


Fig. 1. A typical voltage scan in a 0.1M KOH + 0.1M KCN electrolyte; sweep rate = 2 mV/sec; temperature = 29.6°C ; quiescent solution.

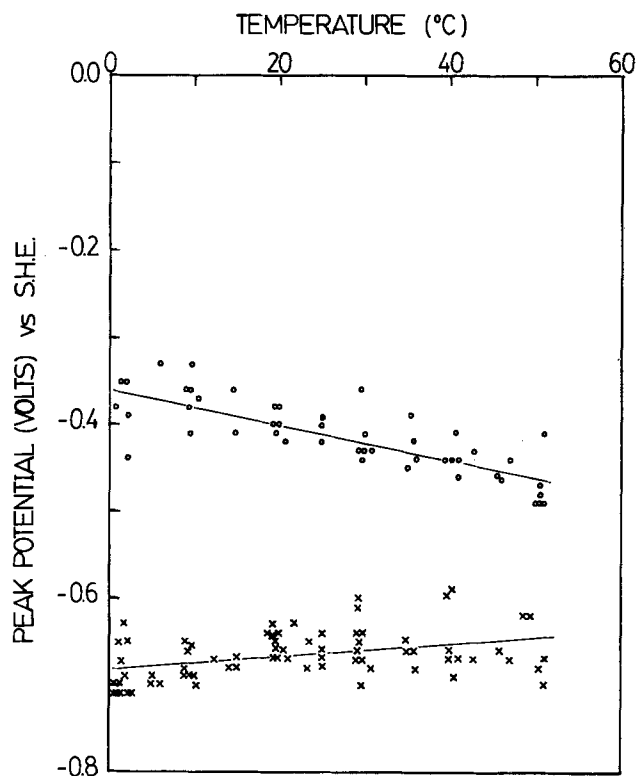


Fig. 2. Peak potential vs. temperature; \times , peak 1(a); \circ , peak 1

variation of the reversible potential ($0.176 \text{ mV}/^\circ\text{C}$) of the gold dissolution reaction. (See Appendix for details.) Some of this difference may be attributed to the change of the effective concentration of $[\text{CN}^-]$ and $[\text{Au}(\text{CN})_2^-]$ with temperature. In addition, the peak formation has been shown to be the result of competing passivating reactions (11) and would therefore also be affected by the temperature dependence of these reactions. Peak 1a does not show the same

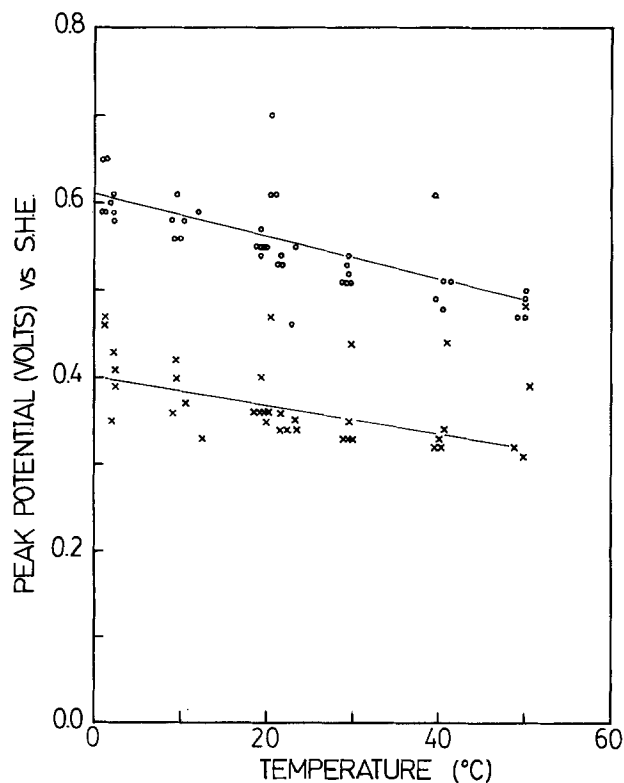


Fig. 3. Peak potential vs. temperature; \times , peak 2; \circ , peak 3

peak potential variation as the other peaks, and shifts in the positive (anodic) direction with increasing temperature. This contrast in behavior of peak 1a relative to peaks 1, 2, and 3 suggests that the reaction causing peak 1a may be fundamentally different from that of the other peaks.

As a result of the cathodic shift of peak 1 and the anodic shift of peak 1a, the two peaks overlap at higher temperatures and result in peak 1a appearing as a small shoulder on peak 1 at elevated temperatures. From the potential scan in Fig. 1 a small shoulder can be observed at the base of peak 2. This shoulder becomes more prominent at higher temperatures but was not studied because the narrow temperature range over which it could be distinguished, was insufficient to allow the determination of the apparent activation energy.

The results of the activation analysis for peak 1a are presented in Fig. 4 (a discussion of the use of peak potentials for activation analysis is given in the Appendix). The current density changes by about two orders of magnitude over the temperature range $0^\circ\text{--}50^\circ\text{C}$. A regression analysis carried out using the 44 experimental measurements presented in Fig. 4 yields the relationship

$$\log i_p = (9.70 \pm 0.20) - \left(\frac{3248 \pm 177}{T} \right)$$

with a linearity coefficient $r^2 = 0.98$ (15). The apparent activation energy is $62 \pm 3 \text{ kJ/mol}$. The activation energy is unchanged when the sweep rate is increased from $2 \text{ mV} \cdot \text{sec}^{-1}$ to $10 \text{ mV} \cdot \text{sec}^{-1}$ indicating that pseudo-equilibrium is achieved during the potential sweep. The high activation energy indicates that the peak 1a reaction is activation rather than diffusion controlled over the temperature range $0^\circ\text{--}50^\circ\text{C}$. This, combined with the fact that peak 1a is not observed

^a $r = 1$ indicates perfect linearity of the data.

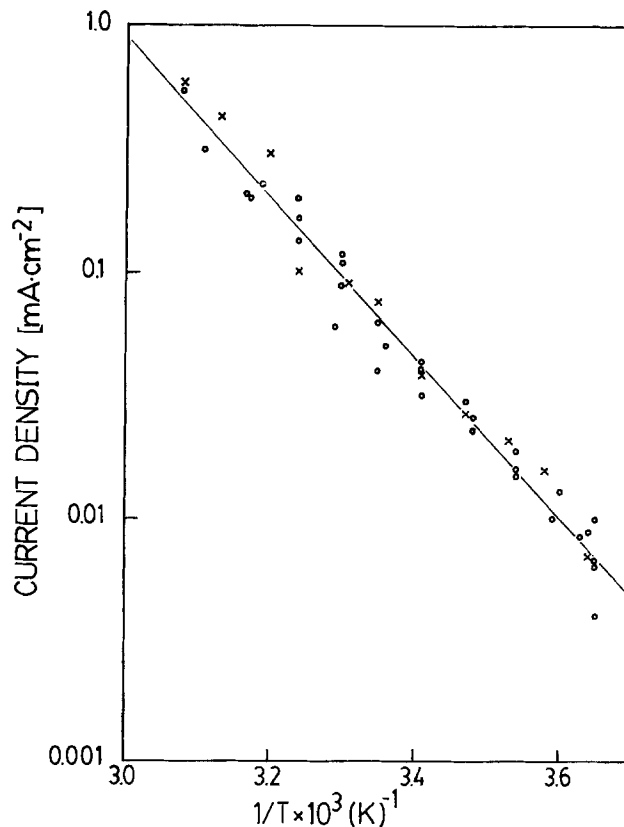


Fig. 4. Peak current density vs. reciprocal temperature for peak 1(a); \circ , sweep rate = 2 mV/sec ; \times , sweep rate = 10 mV/sec ; $0.1\text{M KOH} + 0.1\text{M KCN}$; quiescent solution.

in steady-state measurements and therefore does not directly result in gold dissolution, indicates that the reaction is an adsorption reaction.

The results of the activation analysis for peak 1 are presented in Fig. 5. The peak current density increases by three orders of magnitude over the temperature range 0°-50°C. A regression analysis for the 46 experimental points presented in Fig. 5 yields the relationship

$$\log i_p = (15.69 \pm 0.51) - \left(\frac{4876 \pm 418}{T} \right)$$

with a linearity coefficient of $r = 0.96$. The apparent activation energy is 93 ± 8 kJ/mol. The activation energy is unchanged when the sweep rate is increased from $2 \text{ mV} \cdot \text{sec}^{-1}$ to $10 \text{ mV} \cdot \text{sec}^{-1}$ indicating that pseudo-equilibrium is achieved during the potential sweep. The magnitude of the activation energy clearly indicates activation rather than diffusion control. From the reaction sequence [1], [2], and [3], steps [1] and [3] should show some diffusion control and therefore step [2] of the reaction mechanism is indicated as the rate-determining step. This is in agreement with earlier work (10).

The results of the activation analysis for peak 2 are presented in Fig. 6. These data, obtained from steady-state measurements, show that the current density for peak 2 changes by approximately two orders of magnitude from 0° to 50°C. Above 30°C however, some measurements show a much reduced current density (see Fig. 6). These data suggest that the dissolution reaction is being passivated by other reactions occurring on the gold surface. The cause of the premature passivation is not known. A regression analysis for the 34 experimental measurements from 0° to 30°C presented in Fig. 6 yields the relationship

$$\log i_p = (8.87 \pm 0.23) - \left(\frac{2474 \pm 235}{T} \right)$$

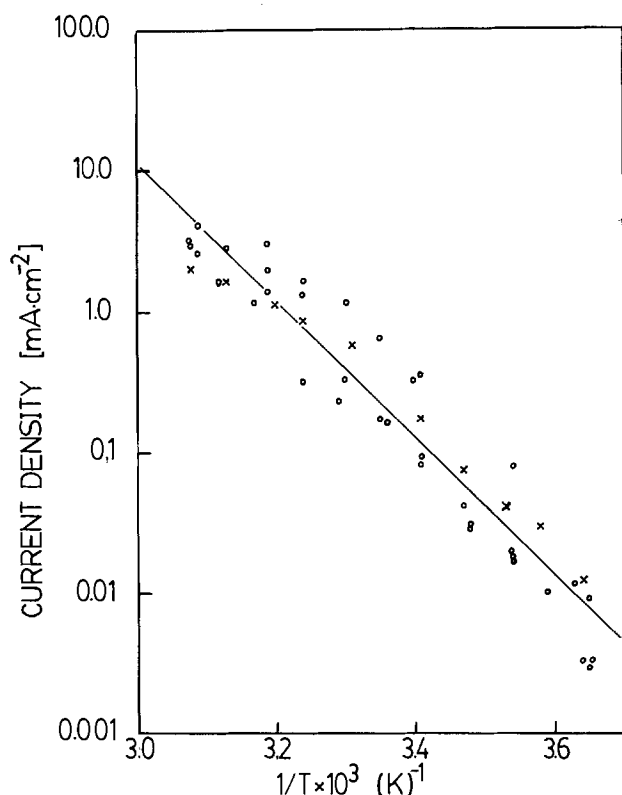


Fig. 5. Peak current density vs. reciprocal temperature for peak 1; \circ , sweep rate = 2 mV/sec ; \times , sweep rate = 10 mV/sec ; $0.1\text{M KOH} + 0.1\text{M KCN}$; quiescent solution.

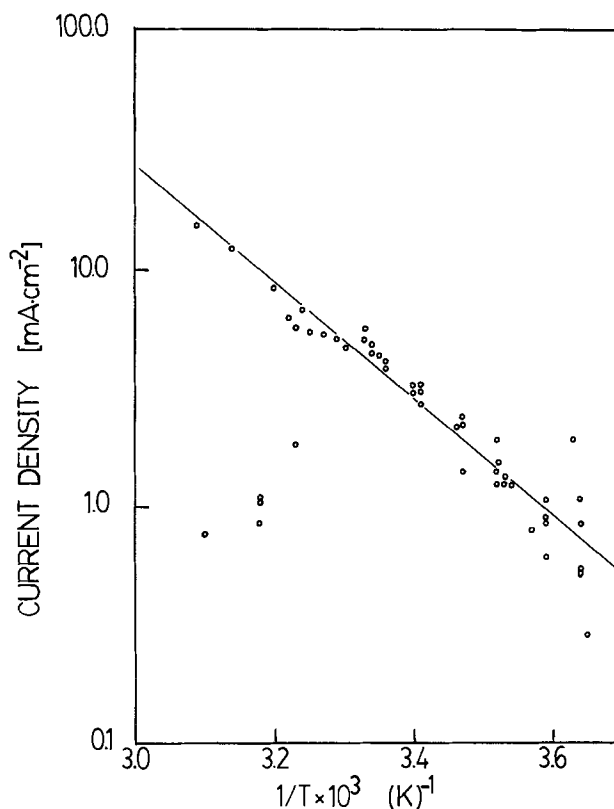


Fig. 6. Peak current density vs. reciprocal temperature for peak 2; $0.1\text{M KOH} + 0.1\text{M KCN}$; quiescent solution.

with a linearity coefficient of $r = 0.95$. The data above 30°C that do not show the passivation phenomena fit the correlation. The apparent activation energy is 47 ± 5 kJ/mol. Although the activation energy is much smaller than either peak 1 or peak 1a, the magnitude is sufficient to predict a rate-determining step which is activation rather than diffusion controlled. To confirm this prediction the experiments were repeated with nitrogen gas vigorously bubbling through the solutions to promote an increased mass transfer rate. The results are presented in Fig. 7. The dissolution current does increase at a slightly greater rate with temperature than in the unstirred case. The apparent activation energy for the data 0°-30°C is 55 ± 6 kJ/mol. Although the values for the stirred and unstirred cases are very close, a statistical test (11) shows that the hypothesis that the activation energies are the same can be rejected at the 95% confidence level. Therefore, although the process is predominantly activation controlled, there is also some influence from mass transfer. Since activation control is found, step [2] of the reaction mechanism is predicted to be the rate-determining step. This is the same rate-controlling step as predicted for peak 1. Since the rate of reaction at peak 2 is approximately 20 times the rate at peak 1, the partial influence of mass transfer on the reaction rate at peak 2 is reasonable. The identification of step [2] as the rate-determining step is in agreement with earlier work (6).

The results of the activation analysis for peak 3 are presented in Fig. 8. These data, obtained from steady-state measurements, show that the current density for peak 3 changes by approximately threefold from 0° to 50°C. A regression analysis for the 19 experimental points presented in Fig. 8 yields the relationship

$$\log i_p = (3.91 \pm 0.02) - \left(\frac{957 \pm 30}{T} \right)$$

with a linearity coefficient of $r = 0.998$. The reduced scatter in the measurements allowed fewer points to

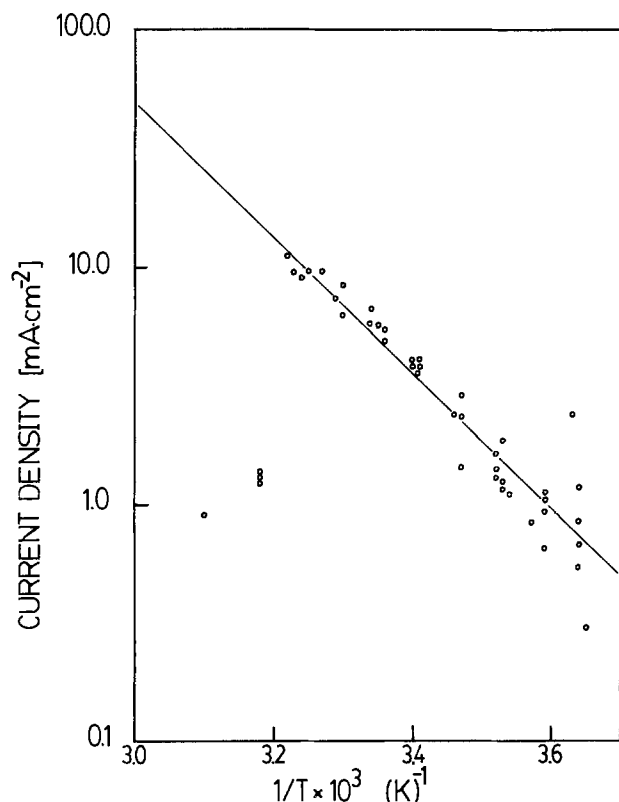


Fig. 7. Peak current density vs. reciprocal temperature for peak 2; 0.1M KOH + 0.1M KCN; stirred solution.

be taken than in the other peak regions and still achieve a good correlation. The apparent activation energy is 18.3 ± 0.6 kJ/mol. This value is much smaller than those for the previous peaks and predicts a diffusion-controlled reaction. To confirm this prediction the measurements were repeated with vigorous gas bubbling through the solutions to promote an in-

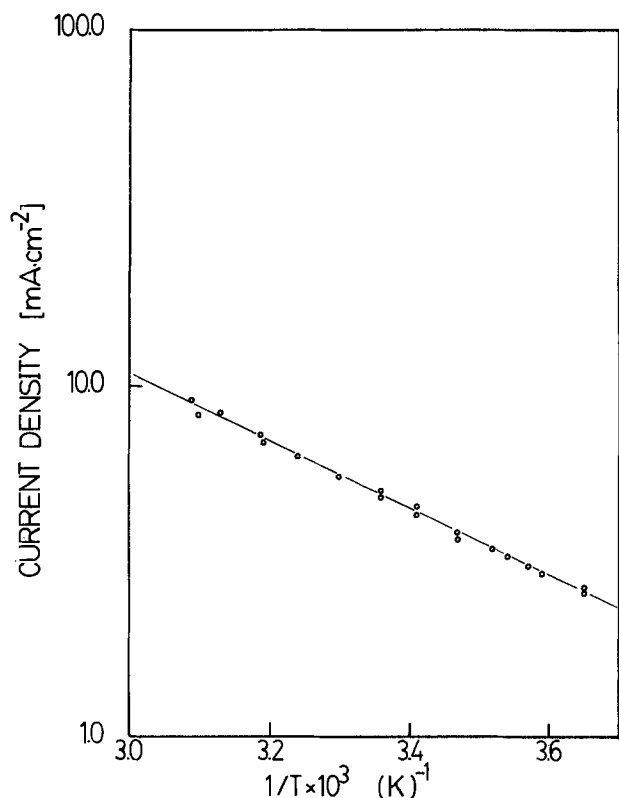


Fig. 8. Peak current density vs. reciprocal temperature for peak 3; 0.1M KOH + 0.1M KCN; quiescent solution.

creased mass transfer rate. The results are shown in Fig. 9. The increase in the mass transfer rate from the gas bubbling causes an increase in the current density of approximately 80% compared to the unstirred case. These results are characteristic of a diffusion-controlled reaction in which stirring reduces the diffusion layer and causes a greater current density. The apparent activation energy with stirring is 16 ± 4 kJ/mol. A statistical test (15) shows that the two activation energies are not significantly different. The reaction rate at peak 3 is greater than that of peak 2 and it would appear that the mass transfer rate has become the rate-controlling mechanism. Thus, step [3] is predicted to be the rate-controlling step in agreement with earlier work (6).

The effect of mass transfer has been shown to be negligible at small dissolution rates (peak 1), to exert some influence at moderate reaction rates (peak 2), and to dominate the dissolution process at the greatest reaction rates (peak 3).

Summary

1. The persistence of the four peaks over the temperature range 0-50°C indicates that the reaction mechanism remains unchanged over the same temperature range.

2. Peak 1a, with an apparent activation energy of 62 ± 3 kJ/mol, is an activation-controlled reaction, most likely an adsorption reaction.

3. Peak 1 is an activation-controlled dissolution reaction with an apparent activation energy of (93 ± 8) kJ/mol.

4. Peak 2 is a dissolution reaction predominantly controlled by activation with an apparent activation energy of 47-55 kJ/mol.

5. Peak 3 is a diffusion-controlled dissolution reaction with an apparent activation energy of 16-18 kJ/mol.

6. The reaction mechanism [1], [2], and [3] is consistent with the activation energies for each peak and with the effects of mass transfer.

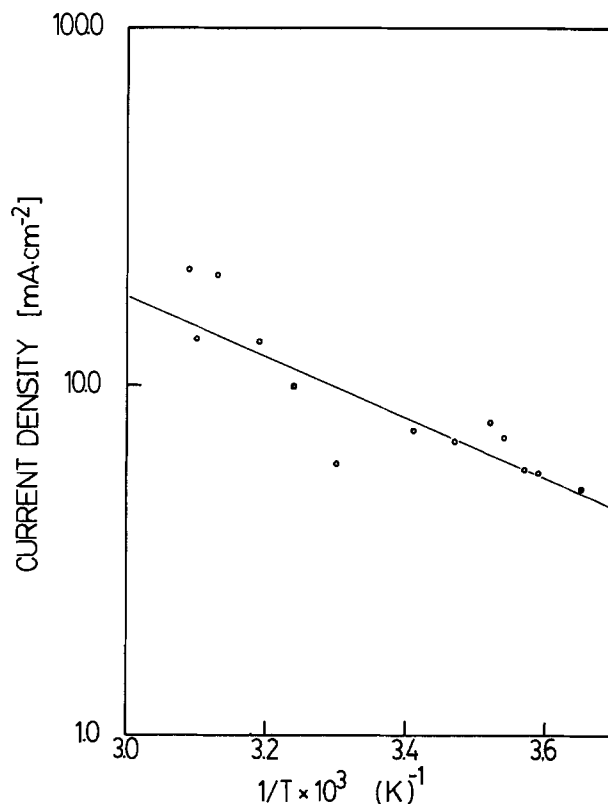


Fig. 9. Peak current density vs. reciprocal temperature for peak 3; 0.1M KOH + 0.1M KCN; stirred solution.

Acknowledgment

The financial assistance from the Natural Sciences and Engineering Council of Canada is gratefully acknowledged.

Manuscript submitted July 15, 1980; revised manuscript received Jan. 26, 1981.

Any discussion of this paper will appear in a Discussion Section to be published in the June 1982 JOURNAL. All discussions for the June 1982 Discussion Section should be submitted by Feb. 1, 1982.

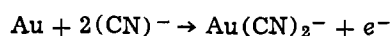
Publication costs of this article were assisted by the University of Toronto.

APPENDIX

Use of Peak Potentials for Activation Analysis

For the conditions of constant overpotential and composition, the required applied potential can be calculated knowing the variation of the thermodynamic reversible potentials of the half-cell reaction and the reference electrode reaction.

For the reaction



$$\Delta G \text{ at } 25^\circ\text{C}^3 = -5.899 \times 10^4 \text{ J}$$

$$\Delta G \text{ at } 50^\circ\text{C}^4 = -5.941 \times 10^4 \text{ J}$$

converting the data to thermodynamic potentials ($\Delta G^\circ = -nF\epsilon^\circ$)

$$\Delta\epsilon \text{ reversible} = +0.176 \text{ mV}/^\circ\text{C}$$

The saturated calomel electrode potential decreases by 0.67 mV/°C (14). This value was used to convert the potential scales to the SHE scale. Thus, the condition of constant overpotential would require that the applied potential be increased by 0.176 mV/°C after correcting for the change in the potential of the reference electrode. This assumes that the peak potential is not exceeded (resulting in passivation of the reaction) and that the electrolyte composition remains fixed. The measurement of peak potentials (*vs.* SHE) in Fig. 2 and 3 shows that the potential shifts by about 2 mV/°C. Thus, the difference between the conditions of constant overpotential and peak potential is apparently ~1.8 mV/°C. However, the condition of constant composition must be carefully examined.

The Nernst relationship is

$$\epsilon = \epsilon^\circ - \frac{RT}{F} \ln \frac{a_{\text{CN}^-}^2 - a_{\text{Au}}}{a_{\text{Au}(\text{CN})_2^-}}$$

If it is assumed that the activity change due to temperature change is small, then a_{CN^-} is approximately constant since the concentration of $[\text{CN}^-] \approx 0.1\text{M}$ and the dissolution of gold will not significantly alter the $[\text{CN}^-]$ bulk concentration during the course of the experiment. However, the activity of the $\text{Au}(\text{CN})_2^-$ species will depend on the rate of formation and the

rate of removal from the surface. The rate of formation is directly proportional to the current while the rate of removal depends on diffusion and conduction forces. Indeed, conduction will only aid $\text{Au}(\text{CN})_2^-$ removal negative of the pzc (*i.e.*, at potentials $< -0.08\text{V}$ in 0.1M KOH) (18). It is therefore likely that the surface concentration of $\text{Au}(\text{CN})_2^-$ will rise with increasing current and this will shift the reversible potential to more positive values. Thus the difference between the potential required for constant overpotential and that of the peak potential will be less than 1.8 mV/°C calculated above, and because of the uncertainty of surface concentrations, the peak potentials are probably the most appropriate values to use in this situation.

The determination of the difference between activation analysis carried out under constant overpotential and peak potential for peak 1a is very difficult since the application of the reaction sequence [1], [2], and [3] may not be appropriate. The behavior of the reaction causing peak 1a is quite different from that of the other peaks. (The temperature coefficient of the peak potential is positive and the reaction is only detected under nonsteady-state conditions.)

REFERENCES

1. F. H. Reid and W. Goldie, Editors, "Gold Plating Technology," Electrochemical Publications Ltd., Glasgow (1974).
2. K. J. Cathro and D. F. A. Koch, *This Journal*, **111**, 1416 (1964).
3. D. M. MacArthur, *ibid.*, **119**, 672 (1972).
4. J. D. E. McIntyre and W. F. Peck, *ibid.*, **123**, 1800 (1976).
5. E. T. Eisenmann, *ibid.*, **125**, 717 (1978).
6. D. W. Kirk, F. R. Foulkes, and W. F. Graydon, *ibid.*, **125**, 1436 (1978).
7. T. P. Pan and C. C. Wan, *J. Appl. Electrochem.*, **9**, 653 (1979).
8. T. P. Pan and C. C. Wan, *J. Chem. Tech. Biotechnol.*, **29**, 427 (1979).
9. D. W. Kirk, F. R. Foulkes, and W. F. Graydon, *This Journal*, **126**, 2287 (1979).
10. D. W. Kirk and F. R. Foulkes, *ibid.*, **127**, 1994 (1980).
11. D. W. Kirk, F. R. Foulkes, and W. F. Graydon, *ibid.*, **127**, 1962 (1980).
12. R. S. Nicholson and I. Shain, *Anal. Chem.*, **36**, 706 (1964).
13. M. von Stackelberg, M. Pilgram, and W. Toome, *Z. Electrochem.*, **57**, 342 (1953).
14. M. Lavaliee, O. F. Schanne, and N. C. Hebert, Editors, "Glass Microelectrodes," p. 7, John Wiley and Sons, Inc., New York (1976).
15. A. Hughes and D. Grawoig, "Statistics: A Foundation for Analysis," p. 247, Addison-Wesley Publishing Co., Reading, Mass. (1971).
16. H. E. Barner and R. V. Scheuerman, "Handbook of Thermochemical Data for Compounds and Aqueous Species," John Wiley and Sons, New York (1978).
17. C. M. Criss and J. W. Cobble, *J. Am. Chem. Soc.*, **86**, 5390 (1964).
18. D. D. Bode, Jr., T. N. Andersen, and H. Eyring, *J. Phys. Chem.*, **71**, 792 (1967).

³ Data from Ref. (16).

⁴ Data from Ref. (16) using Criss and Cobble extrapolation (17).

Effects of Activation and Acceleration on Magnetic Properties of Chemically Deposited Co-P Thin Films

Tetsuya Osaka* and Hideaki Nagasaka

Department of Applied Chemistry, Waseda University, Okubo Shinjuku-ku, Tokyo 160, Japan

and Fumio Goto

Memory Research Laboratory, Basic Technology Research Laboratories,
Nippon Electric Company Limited, Miyazaki, Takatsu-ku, Kawasaki 213, Japan

ABSTRACT

The effects of pretreatment (*i.e.*, activation and acceleration) and substrate species on the magnetic properties of Co-P electrolessly plated thin films for high density storage medium were investigated with various PdCl₂/SnCl₂ catalysts and accelerators. The activity of surfaces to be plated controlled the magnetic properties of Co-P thin films, and the coercivity became lower with increase in the catalytic activity of surfaces. The magnetic properties of Co-P films were also affected by the substrate species and were controlled by grain size of substrate surfaces, but the larger surface roughness which was produced by emery papers did not affect the magnetic properties. The Co-P thin film on acetylcellulose whose coercivity was the highest in the experiments was investigated with transmission electron diffraction analysis. The pretreatment for electroless plating was observed to influence not only the distribution of crystallite grain sizes but also the orientation of the c-axis of the hexagonal α -cobalt lattice plated onto acetylcellulose.

For high density storage applications, thin recording media are in demand, and since Fischer's paper (1) a number of workers have studied metallic thin-film layers of electrolessly or chemically deposited Co-P (or Co-Ni-P) as one of the thin-film formation techniques for high density storage media. The magnetic properties are strongly dependent on the preparation conditions and are affected by many factors such as phosphorus content, film thickness, crystallite grain size, crystallite orientation, substrate materials, and so on. Among those factors, the phosphorus content is considered to play the most important role in determining the magnetic properties of the thin film, and the relationship between phosphorus content and crystallite grain size has been discussed by many workers (2-5). The maximum value of the coercivity was reported to be around 600Å thickness for Co-P and Co-Ni-P by Bate *et al.* (4, 6, 7). The effect of substrate material on magnetic properties was extensively studied by Tago *et al.* (8), and the high coercivity and high squareness of thin films were obtained by using a proper substrate. We have examined mixed PdCl₂/SnCl₂ catalysts for electroless metal deposition and have reported that the activated surface conditions are largely dependent on catalyst and accelerator species (9, 10). Since the surface conditions of the substrate are considered to critically affect the magnetic properties of electroless Co-P plating film, in this paper we investigate and discuss the effects of activation and acceleration on electroless Co-P plating film formation and its magnetic properties.

Experimental

Four samples of mixed PdCl₂/SnCl₂ catalysts, which were used in the previous study (9, 10), were employed in the experiments. The samples "A" (low catalytic activity) and "D" (high catalytic activity) were prepared in our laboratory with reference to

some patents, and the samples "E" and "F" were the commercial ones of Hitachi Kasei Company HS-101B and Shipley Company Cataposit No. 44 where the latter is one of the salty catalysts using NaCl instead of HCl. The details of preparation and composition were previously shown in Ref. (9 and 10). Five accelerators, 1M NaOH, 6M HCl, 1.12M H₂SO₄, 1M NH₄OH, and 1M NH₄BF₄ were used in accordance with several papers (11). The ammoniacal alkaline cobalt tartrate plating bath was adopted as the electroless Co-P plating bath [CoSO₄ 0.05M, Na₂C₄H₄O₆ 0.5M, (NH₄)₂SO₄ 0.50M, NaH₂PO₂ 0.20M, pH 9.2 adjusted with NH₄OH, bath temperature 80°C]. The process of electroless plating was as follows: polished with MgO powder (only in the case of Cu sheet), degreased in ethanol or acetone, immersed in 10% HCl, activated in mixed PdCl₂/SnCl₂ catalyst solution (3 min), immersed in accelerator solution (3 min), and electroless plating was started (plating time *ca.* 30 sec). A water rinse was used after each of the steps. The deposition rate and the film thickness of the deposits were calculated from weight change, which was measured by a Mettler microbalance (the density of deposits was assumed to be 8.6 g·cm⁻³). Copper sheet was used as substrate and the mixed potential measurement for monitoring the initial time of plating was performed with copper wires. Electrolessly plated Ni-P (Blue Sumer, Japan Kanigen Company Limited), Ni-Cu-P (Niculoy 22, Shipley Far East Limited), Cu (Cuposit Copper Mix 328L, Shipley Far East Limited), Au (Noncyanide electroless gold, Nippon Engerhard Company Limited), and acetylcellulose were also used for the tests of substrate species. Acetylcellulose sheet was rendered hydrophilic by immersing in 0.1M NaOH solution before activating its surface. The surface roughness was varied with several emery papers and measured with a stylus technique (Rank-Taylor-Hobson Talystep 1). The compositional analysis of cobalt and phosphorus in the electroless Co-P plated films was done by atomic absorption spectroscopy for cobalt, and by spectrophotometry using the molybdenum blue

* Electrochemical Society Active Member.
Key words: electroless, films, magnetism.

method for phosphorus. The electrochemical measurement technique was previously shown in Ref. (9 and 10). A gold wire or disk was used as the test electrode. Silver/silver chloride (Ag/AgCl) and mercury/mercuric oxide (Hg/HgO) were used as reference electrodes and all potentials are referred to a saturated calomel electrode (SCE). The coercivity and squareness of the films were measured with a sensitive vibrating sample magnetometer (VSM-3 Type, Toei Kogyo Company Limited) and a digital BH curve tracer (DG-1, Sakata Works Limited). Electron microscopy measurements were made using a JEOL JEM-7A instrument with a 100 kV electron source. Electron diffraction patterns were analyzed with reference to the instrumental factor determined by a standard sample of evaporated gold. Samples for transmission electron microscopy and transmission electron diffraction analyses were prepared with the Co-P plating on acetylcellulose sheet. Samples for reflection electron diffraction analysis were the Co-P films electrolessly plated on copper sheet.

Results and Discussion

Acceleration effect on catalyst activity for electroless cobalt plating.—The catalyst activity can be determined from the mixed potential measurements, as previously shown in Ref. (9). The induction time from immersion to initiation of plating can be obtained from the dramatic potential change, and the reciprocal order of the induction time corresponds to the order of catalyst activity. Typical mixed potential variations in the electroless cobalt plating bath are shown in Fig. 1, and the induction times with various conditions of activators and accelerators are also demonstrated in Table I. The arrows in the figure show the starting point of plating. The variation of the induction time in this case became smaller than that in the previous case of nickel deposition [cf., Ref. (9)], and sometimes no cobalt deposition was observed in the case of nonacceleration. The catalytic activity order can be identified as follows: $E \approx D > F > A$, and after acceleration, the order of activity is poorly characterized because of the induction time being almost the same. The activity in the case of NaOH, however, may be the highest in these five cases. Since the films initially deposited, in the case of nonacceleration, are patched and uneven, even though the induction time is generally shorter than that in the case of nickel deposition, the acceleration in the case of cobalt deposition is considered to be a very significant process as well as in the case of nickel deposition. The variation of the immersion time in the accelerator solution on the induction time was observed to become constant after ca. 5 min for sample A, and after several tens of seconds for sample D; except for the case of NaOH, the

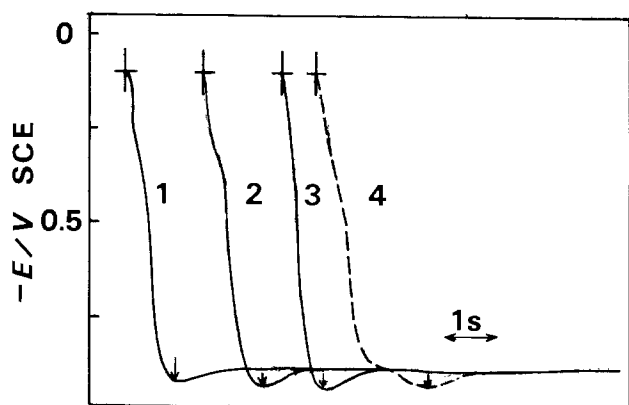


Fig. 1. Time variation of mixed potential in the Co-P electroless plating bath on copper wire after activation (3 min) and acceleration (3 min) with several accelerator solutions. 1, D-NaOH; 2, D-NH₄BF₄; 3, D-HCl; 4, D only.

Table I. Effects of activation and acceleration on induction time in the Co-P electroless plating bath (sec)

| Act. | Acc. | | | | | |
|------|------|-----|--------------------------------|---------------------|-----------------------------------|-----------|
| | NaOH | HCl | H ₂ SO ₄ | NH ₄ OH* | NH ₄ BF ₄ * | No acc.** |
| A | 2.2 | 1.7 | No dep. | No dep. | No dep. | No dep. |
| D | 0.9 | 1.0 | 1.2 | 0.9 | 1.0 | 2.3 |
| E | 0.9 | 0.9 | 0.8 | 0.8 | 0.8 | 1.0 |
| F | 0.8 | 0.8 | 0.9 | 0.9 | 0.8 | 1.0 |

* The condition of films initially deposited in the cases of NH₄OH and NH₄BF₄ was worse than those in the cases of NaOH, HCl, and H₂SO₄.

** The induction time in the case of no acceleration did not show good reproducibility, and sometimes no cobalt deposition was observed. The initially deposited films in the case of no acceleration were patched and uneven.

induction time gave the minimum value around 1 min immersion time and gradually increased with the increase in immersion time. The catalytic activity in all cases except for NaOH is considered to be constant after initial immersion; however, in the case of NaOH accelerator, the catalytic activity gradually becomes lower after long immersion time, which may be caused by the removal of active nuclei.

Though the effects of dissolved oxygen in the mixed catalyst solution were of importance in the preparation process as pointed out in Ref. (9), the effects of dissolved oxygen in the electroless plating solution on the induction time were scarcely observed.

Determination of plating time.—Figure 2 shows the relationship between plating time and film thickness for several accelerations after activation with catalyst D. The film thickness increases linearly with the increase in the plating time up to ca. 1000Å for each case. The highest and lowest deposition rates were observed in the cases of NaOH and NH₄OH accelerators. The 500Å thickness of the electrolessly plated cobalt film is obtained by plating ca. 30 sec. The variation of coercivity of the film plated for ca. 30 sec indicated that the coercivity is almost the same value in the region around 30 sec (i.e., around 500Å thickness). Therefore, we adopted 30 sec for all cases because the

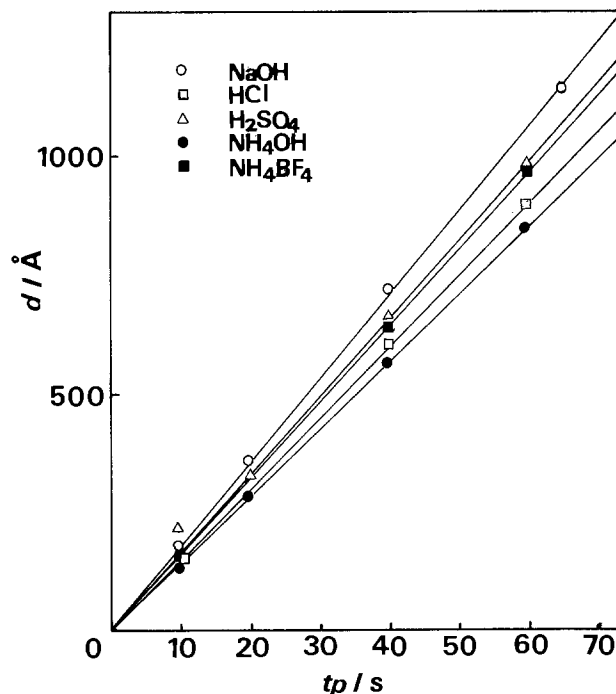


Fig. 2. Effect of acceleration on deposition rate in the Co-P electroless plating bath. Activation and acceleration were performed with sample D for 3 min and with various accelerators for 3 min. t_p designates the plating time.

coercivity of the film was scarcely affected by the variation of film thickness around 500Å.

Electrochemical approach using gold electrode.—Figure 3 shows single anodic voltammograms on a gold electrode in 1M HCl after activation with D and acceleration with several accelerators. It has been confirmed in the previous paper (9) that the three anodic peaks at ca. -0.10, ca. 0.20, and ca. 0.45V correspond to the desorption of adsorbed Sn(O), the oxidation of Sn(II) to Sn(IV), and the dissolution of Pd(O), respectively. The residual amount of Sn on the substrate surface after acceleration can be qualitatively compared with the two anodic peaks at ca. -0.10 and ca. 0.20V. In the cases of NaOH and HCl accelerators, the anodic peaks due to the desorption of Sn(O)_{ad} and the oxidation of Sn(II) were not observed, and only the anodic peak due to the dissolution of Pd(O) was observed. The order of the residual amount of Sn can be H₂SO₄ > NH₄BF₄ ≈ NH₄OH > NaOH ≈ HCl. Since the two anodic peaks due to Sn desorption and oxidation were not observed in the single anodic voltammograms after activation with E and acceleration with HCl and NH₄BF₄, which were previously shown Ref. (9), the residual amount of Sn on the surface is considered to depend also on the activator species. In view of the fact that the order of the Sn residual amount corresponds nearly to that of the induction time, catalytic activity is affected by the residual amount of Sn which is controlled not only by activators but also by accelerator species.

Effects of activation and acceleration on magnetic properties.—The variation of magnetic properties of

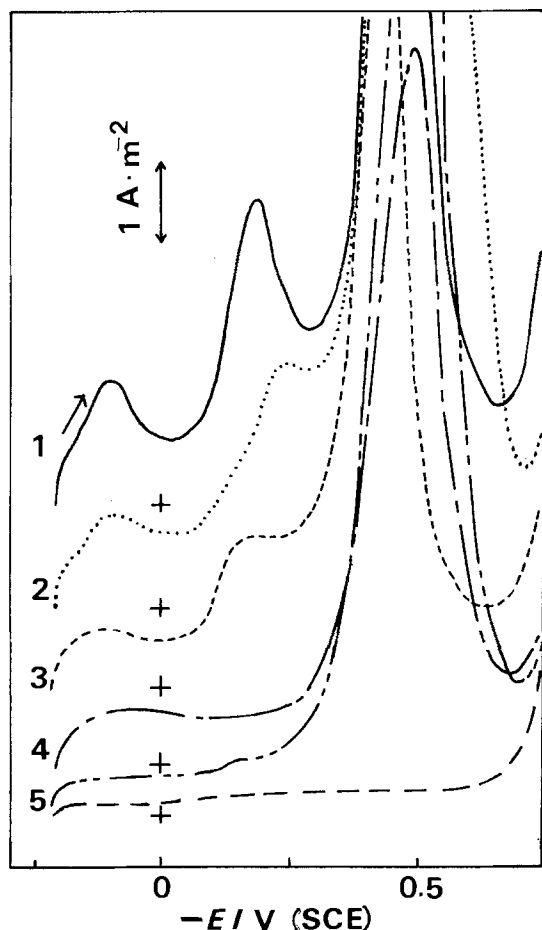


Fig. 3. Single anodic voltammograms on Au electrode in 1M HCl after activation with sample D (1 min) and acceleration with various accelerators (15 sec) at 25°C. Scan rate, 0.10 V sec⁻¹; dashed line: anodic scan without activation and acceleration. 1, D-H₂SO₄; 2, D-NH₄BF₄; 3, D-NH₄OH; 4, D-NaOH; 5, D-HCl.

Table II. Effects of activation and acceleration on magnetic properties

| Act. | Acc. | NaOH | HCl | H ₂ SO ₄ | NH ₄ OH | NH ₄ BF ₄ |
|------|--|------|------|--------------------------------|--------------------|---------------------------------|
| A | H _c (oe) | 630 | 610 | No dep. | No dep. | No dep. |
| | B _r ·B _m ⁻¹ | 0.67 | 0.53 | | | |
| D | H _c (oe) | 510 | 640 | 600 | 700 | 760 |
| | B _r ·B _m ⁻¹ | 0.75 | 0.67 | 0.56 | 0.55 | 0.56 |
| E | H _c (oe) | 420 | 650 | 680 | 690 | 685 |
| | B _r ·B _m ⁻¹ | 0.70 | 0.66 | 0.63 | 0.57 | 0.53 |
| F | H _c (oe) | 480 | 630 | 570 | 580 | 630 |
| | B _r ·B _m ⁻¹ | 0.77 | 0.59 | 0.70 | 0.57 | 0.55 |

Co-P films, where various activators and accelerators are used for the pretreatment of copper substrate, is demonstrated in Table II. The cobalt-phosphorus film was not deposited in the case of activator A using accelerators of H₂SO₄, NH₄OH, and NH₄BF₄. There is an approximate tendency for the accelerators NaOH and HCl to give relatively lower coercivity and higher squareness compared to the accelerator group of NH₄OH and NH₄BF₄. In these systems, the squareness tends to increase with the decrease in the coercivity. The coercivity of the film plated with galvanic initiation, which is shown in Table IV, becomes lower than that of the film plated with activation and acceleration. It is very interesting that the magnetic properties of thin film can be varied widely by changing the activation and acceleration processes. It is clearly attributed to the difference of catalytic activity of surface conditions which are controlled by the pretreatment process.

The relationship between the phosphorus content and the coercivity of Co-P film is shown in Table III. It is shown that the pretreatment giving the higher catalytic activity tends to produce the higher phosphorus content of the film. Tasaka *et al.* (12) reported that palladium is useful as a catalyst for the oxidation of hypophosphite ion in alkaline solution. The XPS results (9) showed that the Pd-Sn active sites on surfaces consist of a system in which the ratio of Pd/Sn depends on the catalytic activity and that the Pd/Sn ratio of the active sites increases with increasing catalyst activity. Since the oxidation of hypophosphite ion which is accelerated by the active sites of catalysts enhances not only the reduction of cobalt but also the phosphorus deposition which may be caused by the side oxidation reaction of hypophosphite ion, the pretreatment giving the higher catalytic activity is considered to result in the higher phosphorus content in the film. One of the authors (13) and Speltios *et al.* (6) reported that the coercivity shows a maximum with the increase in the phosphorus content up to 5-7 w/o for these very thin Co-P storage films and that the above correlation is mainly attributed to the grain size, which is determined by the phosphorus content in these systems. Therefore, the tendency for the thin film having the higher phosphorus content to have lower coercivity might also be explained by the above assumption.

Effects of substrate species and surface roughness on magnetic properties.—Magnetic properties of the Co-P films in the cases of six kinds of substrate materials are tabulated in Table IV, where the Co-P films de-

Table III. Relationship between phosphorus content and coercivity of the thin films

| Act.-Acc. | P (w/o) | H _c (oe) |
|-----------------------------------|---------|---------------------|
| D-NaOH | 2.2 | 510 |
| D-HCl | 2.2 | 640 |
| D-H ₂ SO ₄ | 2.5 | 600 |
| D-NH ₄ OH | 1.6 | 700 |
| D-NH ₄ BF ₄ | 1.9 | 760 |
| A-NaOH | 1.8 | 630 |

Table IV. Effect of substrate species on magnetic properties

| Substrate | Magnetic properties | | |
|----------------------|--|-------------|------|
| | GI* | Act.-Acc.** | |
| Cu | H _c (oe) | 480 | 510 |
| | B _r ·B _m ⁻¹ | 0.72 | 0.75 |
| Au† | H _c (oe) | 340 | 670 |
| | B _r ·B _m ⁻¹ | 0.91 | 0.76 |
| Ni-P† | H _c (oe) | 615 | 825 |
| | B _r ·B _m ⁻¹ | 0.78 | 0.78 |
| Ni-Cu-P† | H _c (oe) | 650 | 690 |
| | B _r ·B _m ⁻¹ | 0.78 | 0.80 |
| Cu† | H _c (oe) | 405 | — |
| | B _r ·B _m ⁻¹ | 0.74 | — |
| Acetylcel- lulose | H _c (oe) | — | 900 |
| | B _r ·B _m ⁻¹ | — | — |

* GI means the Co-P plating whose electroless plating is initiated with iron wire contact (galvanic initiation)

** The Co-P plating film was plated with the conditions of Act. (D) and Acc. (NaOH).

† These films were electrolessly plated.

posited with galvanic initiation are also shown for discussion. In the case of electrolessly deposited copper, the magnetic properties were not obtained because of the dissolution of copper in the activator solution. The deposition on acetylcellulose by galvanic initiation also did not occur because the substrate was not a conductor. The coercivity on acetylcellulose is the highest, and among the metal substrate species, the order of coercivity becomes as follows: electrolessly plated Ni-P > electrolessly plated Ni-Cu-P > electrolessly plated Au > Cu. The coercivity and squareness of the film initiated with activation and acceleration processes tend to become higher than those in the case of galvanic initiation. Tago *et al.* (8) reported that the materials of Ni-P, Rh, and Au are useful as the substrate of cobalt film for storage medium and concluded that the variation of magnetic properties with various substrates may be attributed to the difference of grain size of the substrate surfaces.

The effect of surface roughness of copper sheet on magnetic properties is shown in Table V, where the film is deposited with activation (D) and acceleration (NaOH). The coercivity and squareness of the film do not vary with various roughness of R_{max} (maximum value of roughness). Therefore, it is concluded that the larger variation of surface roughness obtained by such

Table V. Effect of substrate roughness on magnetic properties

| Number of emery paper | R_{max} (μm) | H _c (oe) | B _r ·B _m ⁻¹ |
|-----------------------|-----------------------------|---------------------|--|
| 1500 | 0.17 | 510 | 0.68 |
| 800 | 0.50 | 515 | 0.68 |
| 400 | 2.30 | 510 | 0.68 |
| 240 | 3.70 | 500 | 0.66 |

Table VI. Electron diffraction profiles of Co-P film on acetylcellulose with several conditions of activation and acceleration

| D-NaOH | | | | D-HCl | | | | D-H ₂ SO ₄ | | | |
|--------|---------------------|---------------------|----|-------|---------------------|---------------------|----|----------------------------------|---------------------|---------------------|----|
| hkl | d _{ob} (Å) | d _{c1} (Å) | I | hkl | d _{ob} (Å) | d _{c1} (Å) | I | hkl | d _{ob} (Å) | d _{c1} (Å) | I |
| (100) | 2.19 | 2.22 | vs | (100) | 2.28 | 2.23 | vs | (002) | 2.07 | 2.15 | vs |
| (101) | 1.92 | 1.96 | vs | (101) | 1.95 | 1.96 | s | (102) | 1.56 | 1.56 | w |
| (102) | 1.53 | 1.53 | w | (110) | 1.55 | 1.29 | w | (110) | 1.29 | 1.31 | w |
| (110) | 1.27 | 1.28 | s | (103) | 1.17 | 1.17 | m | (201) | 1.09 | 1.09 | s |
| (112) | 1.06 | 1.09 | s | (203) | 0.87 | 0.87 | m | (114) | 0.83 | 0.83 | m |
| (202) | 0.97 | 0.98 | w | | | | | | | | |
| (211) | 0.81 | 0.82 | m | | | | | | | | |

| | | | | | |
|----------------------------------|--|----------------------------------|--|----------------------------------|--|
| H _c = 900 (oe) | | H _c = 1220 (oe) | | H _c = 590 (oe) | |
| Hexagonal { a = 2.56 c = 4.21 | | Hexagonal { a = 2.58 c = 4.12 | | Hexagonal { a = 2.58 c = 4.23 | |

d_{ob} and d_{c1} mean the lattice constants observed and calculated, respectively. I means relative intensity of diffraction ring (vs: very strong, s: strong, m: medium, w: weak).

as emery paper is too rough to affect the magnetic properties and that the smaller variation of surface roughness produced by the difference of crystallite grain size influences largely the magnetic properties. It is natural that the finest surface condition of acetylcellulose produces the highest coercivity in these experiments.

Effects of activation and acceleration on magnetic properties using acetylcellulose substrate.—Figure 4 shows the typical transmission electron micrographs of Co-P films plated on acetylcellulose with various pretreatment conditions of D accelerators. The grain size of Co-P films on acetylcellulose increases with the increase in coercivity such as 200 ~ 500Å for H₂SO₄ accelerator (590 oe), 500 ~ 800Å for NaOH (900 oe), and 1000 ~ 2000Å for HCl (1220 oe). In the case of ammonia-containing systems (D-NH₄BF₄ and D-NH₄OH), the grain sizes are uneven and there is no correlation between grain size and coercivity. As we pointed out in a previous paper (10), the active surface conditions after acceleration with the ammonia-containing solution group was quite different from those of the former three cases. Ammonia-containing group accelerators coagulate the small particles after activation to produce high density particles and it may result from some ammoniate compounds such as Pd-ammonia complexes. The above different surface conditions in the case of ammonia-containing accelerators result in the uneven grain size conditions of Co-P film which give no correlation between coercivity and grain size. Therefore, it can be concluded that the surface conditions activated with various catalysts and accelerators affect largely the magnetic properties of electrolessly plated Co-P films and that grain size of the film may be one of the important factors to control the magnetic properties of Co-P films.

Since the three cases of H₂SO₄, NaOH, and HCl show the clear correlation between coercivity and grain size, the typical results of transmission electron diffraction profiles of Co-P films on acetylcellulose are demonstrated in Table VI. The d values directly observed from the diffraction radii and the intensity of diffraction rings are given as d_{ob} and I. The calculated d values named as d_{c1} are calculated by using the hexagonal lattice parameters of a and c shown in Table VI, which are determined from the lattice constant becoming nearly constant when the Miller indexes h, k, l are allotted to d_{ob} values. It is shown by the good agreement of d_{ob} with d_{c1} that the Miller index allotment is fairly proper in these cases. Since β-cobalt with fcc lattice and cobalt phosphide alloy such as Co₂P with orthorhombic lattice are not observed in the case of electrolessly plated Co-P films, the electrolessly plated cobalt film is considered to be α-cobalt with the hexagonal lattice as reported by

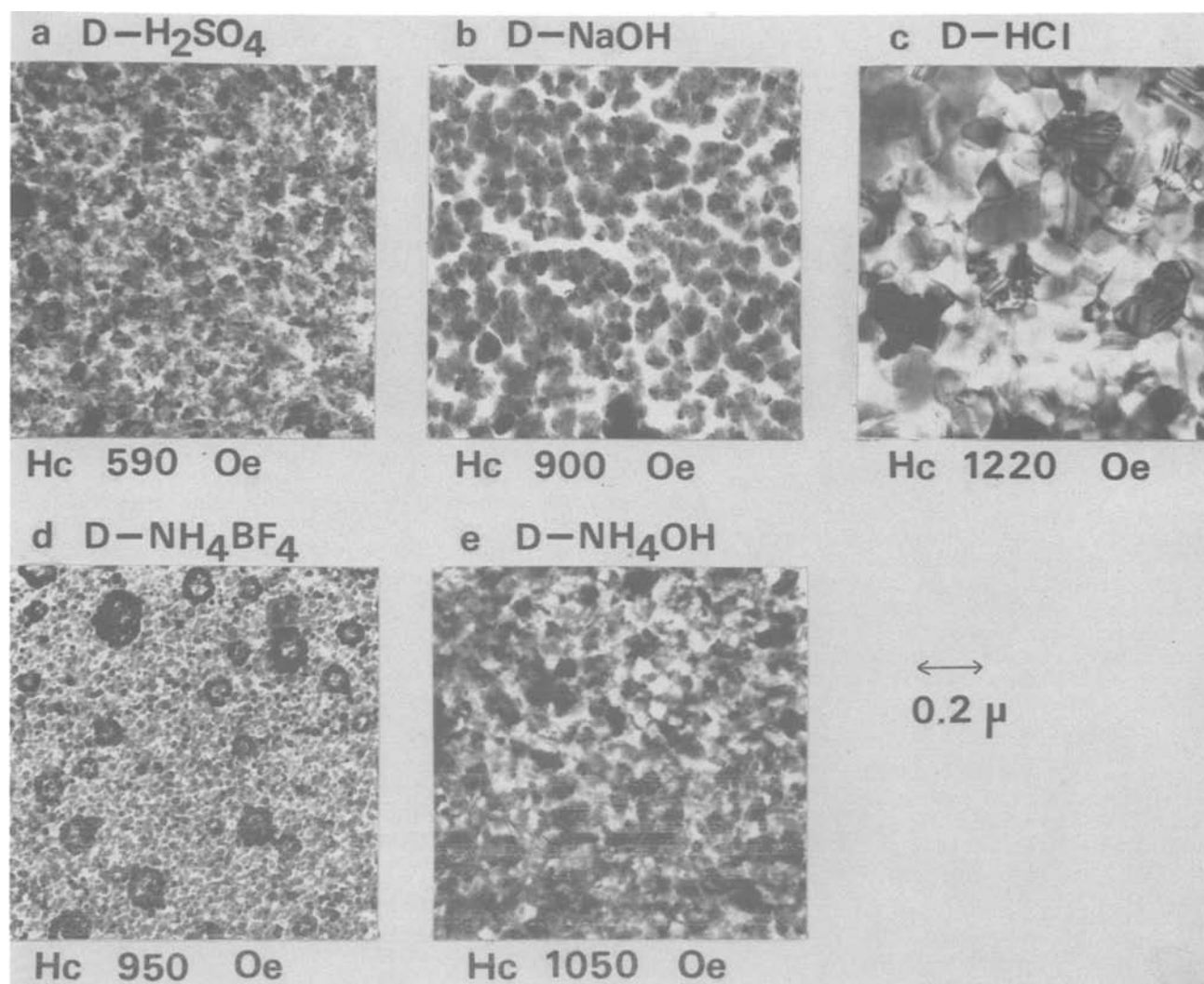


Fig. 4. Transmission electron micrographs of Co-P film on acetylcellulose with various surface conditions produced by using several accelerators. a, D-H₂SO₄; b, D-NaOH; c, D-HCl; d, D-NH₄BF₄; e, D-NH₄OH.

Aoki *et al.* (2). The lattice parameters in these cases are a little larger than those in the case of α -Co ($a = 2.502\text{\AA}$ and $c = 4.061\text{\AA}$), and it might be attributed to the addition of phosphorus in the α -cobalt lattice. It is very interesting that the c -axis of Co films in the cases of D-NaOH and D-HCl orients preferentially normal to the film because of the presence of (100) plane with no appearance of (002) plane, and that the c axis in the case of D-H₂SO₄ orients preferentially parallel to the film because of the presence of a strong diffraction ring of the (002) plane. Therefore, the orientation of the c axis of α -cobalt of electrolessly plated thin-film Co-P can be controlled by the pretreatment combination. In the cases of ammonia-containing accelerators (which are omitted in Table VI), the polycrystallite α -cobalt thin film was observed because of strong diffraction rings of both (100) and (002) planes being observed and it might be attributed to the uneven surface conditions after acceleration. The Co-P films plated on copper sheet with various pretreatments showed only the case of the c axis being parallel to the substrate plane, which was confirmed by the results of reflection electron diffraction profiles. Therefore, it can also be concluded that the pretreatment and substrate affect not only the grain size contribution but also the orientation of the c -axis of the α -cobalt hexagonal lattice of electrolessly plated Co-P films.

Acknowledgments

The authors would like to thank Professor Dr. Tadashi Yoshida, Waseda University, Dr. Takashi Furuoya and Mr. Yoji Suganuma, Basic Technology Laboratories, Nippon Electric Company, for their encouragement of this research, and also Mr. Fumio Sugawara for his experimental assistance. They are greatly indebted to the Kurata Research Grant from the Kurata Foundation and the Research Fund of Waseda University for financial support.

Manuscript submitted Aug. 11, 1980; revised manuscript received Feb. 18, 1981.

Any discussion of this paper will appear in a Discussion Section to be published in the June 1982 JOURNAL. All discussions for the June 1982 Discussion Section should be submitted by Feb. 1, 1982.

Publication costs of this article were assisted by Nippon Electric Company Limited.

REFERENCES

1. R. D. Fischer and W. H. Chilton, *This Journal*, **109**, 485 (1962).
2. K. Aoki, S. Iseki, O. Takano, and S. Ishibashi, *J. Metal Finishing Soc. Jpn.*, **19**, 301 (1968); O. Takano, *ibid.*, **23**, 406 (1972).
3. M. G. Miksic, R. Travieso, A. Arcus, and R. H. Wright, *This Journal*, **113**, 360 (1966).
4. D. E. Spiliotis, J. S. Judge, and J. R. Morrison, *J. Appl. Phys.*, **37**, 1158 (1966).
5. M. Hirose, K. Shinjo, K. Yokoyama, K. Ito, H.

- Hayashida, F. Soeda, and R. Tsunoi, IECE Tech. Group Meeting at Magn. Rec. Jpn., MR75-22 (1975); F. Soeda, K. Yoshimura, H. Hayashida, D. Sekiya, K. Yokoyama, K. Ito, and R. Kadoi, *ibid.*, MR75-23 (1975).
6. J. S. Judge, J. R. Morrison, D. E. Speliotis, and G. Bate, *This Journal*, **112**, 681 (1965).
 7. G. Bate and D. E. Speliotis, *J. Appl. Phys.*, **34**, 1073 (1963).
 8. A. Tago and A. Ishibashi, IECE Tech. Group Meeting at Magn. Rec. Jpn., MR72-18 (1972); A. Tago, T. Masuda, and Y. Ando, *ECL Tech. J. (Jpn.)*, **26**, 471 (1977).
 9. T. Osaka, H. Takematsu, and K. Nihei, *This Journal*, **127**, 1021 (1980).
 10. T. Osaka, H. Nagasaka, and F. Goto, *ibid.*, **127**, 2343 (1980).
 11. A. Rantell and A. Holtzman, *Plating*, **61**, 326 (1974); *Trans. Inst. Metal Finishing*, **51**, 62 (1973); *ibid.*, **52**, 31 (1974).
 12. A. Tasaka, T. Fujita, M. Yamashita, and M. Kubokawa, *Denki Kagaku (J. Electrochem. Soc. Jpn.)*, **42**, 626 (1974); M. Tasaka, T. Fujita, and M. Kubokawa, *ibid.*, **44**, 103 (1976).
 13. F. Goto and Y. Suganuma, Ext. Abst. the 6th Annual Conf. on Magnetics in Jpn., 1974, p. 170; Y. Suganuma and M. Nagao, Ext. Abst. Conf. Phys. Soc. Jpn., 1971, p. II-46.

Adsorption and Alloy Formation of Zinc Layers on Silver

G. Adzic,^{*1} J. McBreen,* and M. G. Chu*

Brookhaven National Laboratory, Department of Energy and Environment, Upton, New York 11973

ABSTRACT

The deposition of zinc on silver from alkaline zincate solutions has been investigated using cyclic voltammetry, potential pulse methods, x-ray diffraction, and scanning electron microscopy. Approximately one monolayer of zinc is formed in the underpotential deposition region prior to bulk deposition. The underpotential shift (ΔE_p) is 0.15V. Zinc forms at least two alloys with the substrate. One was identified as AgZn_3 and the other as the β' phase of AgZn . The bulk zinc deposit consists of hexagonal platelets that are oriented both parallel and perpendicular to the basal plane.

The deposition of zinc on silver is of technological importance because of the use of silver current collectors in zinc-silver oxide and zinc-nickel oxide batteries (1). When zinc electrode formulations contain either zinc sheet or zinc powder in contact with the silver, the current collector turns to a gray zinc-like color on the addition of KOH electrolyte (2). This was investigated by Dirkse and Vrieland (3) and they found that the phenomenon did not depend on amalgamation of the electrode. Thermodynamically, the only satisfactory explanation is that a surface alloy of zinc is formed.

Straumanis and Fang (4) found that when silver was electrochemically displaced by zinc that the zinc deposited as a very thin layer on the surface of the silver grains. Raub and Wullhorst (5) studied deposition of silver-zinc alloys from cyanide solutions. All phases present in the phase diagram were found except the ζ phase.

The underpotential deposition of Tl (6), Pb (7), Bi (8), and Cd (9) on silver has been investigated in some detail. Kolb, in his review (10), refers to unpublished results for underpotential deposition of Zn on silver from sulfate solutions.

The present study was part of an investigation of substrate effects on zinc deposition on several metals from zincate solutions. The techniques used were cyclic voltammetry potential pulse methods, scanning electron microscopy, and x-ray diffraction.

Experimental

Cell.—The electrochemical measurements were made in a simple PTFE beaker cell with a machined PTFE cover that had a Viton O-ring seal and PTFE pipe fittings for gas feed, electrical connections, and a reference electrode Luggin capillary. An Hg/HgO reference electrode and a nickel screen counterelectrode were used.

* Electrochemical Society Active Member.

¹ Present address: Institute of Chemical Power Sources, ICTM, Beograd, Yugoslavia.

Key words: amalgam, battery, electrodeposition.

Working electrodes.—Two types of working electrodes were used. One was a simple "flag" type sheet electrode (1×1 cm), the other a machined disk electrode (0.686 cm^2). The silver electrodes were polycrystalline and were at least 99.998% pure.

The silver sheet electrodes were degreased in acetone and washed with triply distilled water prior to incorporation in the cell. The silver disk electrodes were mounted in a PTFE holder with a Kel-F collar compression seal. The disks were polished successively with 600 grit SiC paper, Microcut Sheets (Buehler Limited), 5 and 0.5μ alumina. The electrodes were finally washed with triply distilled water prior to incorporation into the cell.

Amalgamated "flag" electrodes were also used. These were prepared by deposition of mercury from a 2% solution of HgO in a 1:1 mixture of distilled water and glacial acetic acid, at a current density of 9 mA/cm², using platinum counterelectrodes. Various deposition times from 5 to 60 min were used.

Electrolytes.—The electrolytes were prepared from triply distilled water, reagent grade KOH and ZnO (New Jersey Zinc USP-19).

Electrochemical studies.—After cell assembly, the solutions were deaerated by bubbling nitrogen through the solution for 15 min prior to the start of measurements. The nitrogen was purified by passage through molecular sieves.

All the cyclic voltammetry studies were made in voltage envelopes that were more negative to +0.020V.² At no time did the voltage scan go into a potential region where the substrate could oxidize.

The potential step experiments consisted of zinc deposition at various potentials between -1.11 and -1.46V followed by an anodic pulse at -1.25V and a second anodic step to -1.0V. One of the problems with using the cathodic potential pulse methods in zinc deposition is interference by coevolution of hydrogen

² All potentials are with respect to an Hg/HgO reference electrode in the same electrolyte.

to an unknown extent. Despic has proposed the use of an anodic pulse following the cathodic pulse as a solution to the problem (11). In this work, a two step anodic pulse was used in an attempt to separate the contributions of underpotential deposition, bulk deposition, and alloy formation.

Scanning electron microscopy and x-ray diffraction.—Sample preparation for the scanning electron microscopy and the x-ray diffraction studies was as follows. The zinc was deposited on the "flag" sheet electrodes at a fixed potential until a required number of coulombs were deposited. The electrode was immediately removed from the electrolyte, washed repeatedly in distilled water, rinsed in acetone, air dried, and stored in a desiccator until mounted in either the scanning electron microscope or the x-ray goniometer. The diffraction pattern was determined using Cu-K α radiation. The samples prepared for the morphology and deposit orientation studies were deposited from 8.4M KOH + 0.74 ZnO. Three samples on each substrate were prepared. The deposition conditions were 0.5 C/cm² at -1.40V, 2 C/cm² at -1.42V, and 5 C/cm² at -1.44V.

Results

Cyclic voltammetry.—Figure 1 is a cyclic voltammogram on a silver sheet electrode in the potential envelope +0.020 to -1.345V in 1M KOH + 0.08M ZnO. A cyclic voltammogram in 1M KOH is shown for comparison. Underpotential deposition of zinc starts at about -1.08V. In this case there were well-defined current peaks in the underpotential deposition region. With some electrode samples, particularly by the disk electrodes, there were no sharp peaks. Samples that yielded two peaks in the underpotential deposition region could be prepared by the peroxide-cyanide etch method, described by Bewick and Thomas (6). Figure 2 is a cyclic voltammogram for silver sheet in 1M KOH + 0.08M ZnO in the voltage envelope +0.020 to -1.4V. When the electrode is continuously swept, the pattern for underpotential deposition and zinc deposition and dissolution can be clearly discerned. However, if the electrode is held at a potential of -1.4V for 4 sec two other dissolution peaks, one at -1.05V and the other at -0.2V, become apparent. When the cyclic voltammetry is carried out in the voltage envelope +0.020 to -1.5V the two extra dissolution peaks are also apparent.

Several attempts were made to further elucidate the nature of these dissolution peaks by cyclic voltammetry. Figure 3 shows what happens when the sweep is arrested for 5 sec at -1.4V and the potential swept

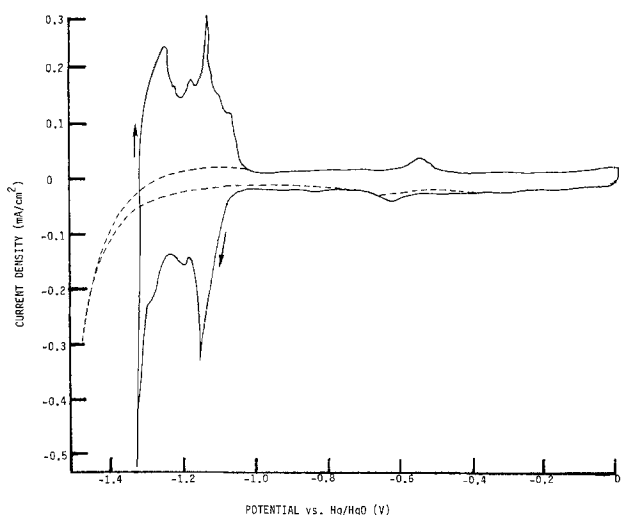


Fig. 1. Cyclic voltammograms on sheet Ag electrode (2 cm²); solid line 1M KOH + 0.08M ZnO; broken line 1M KOH, sweep rate 100 mV/sec.

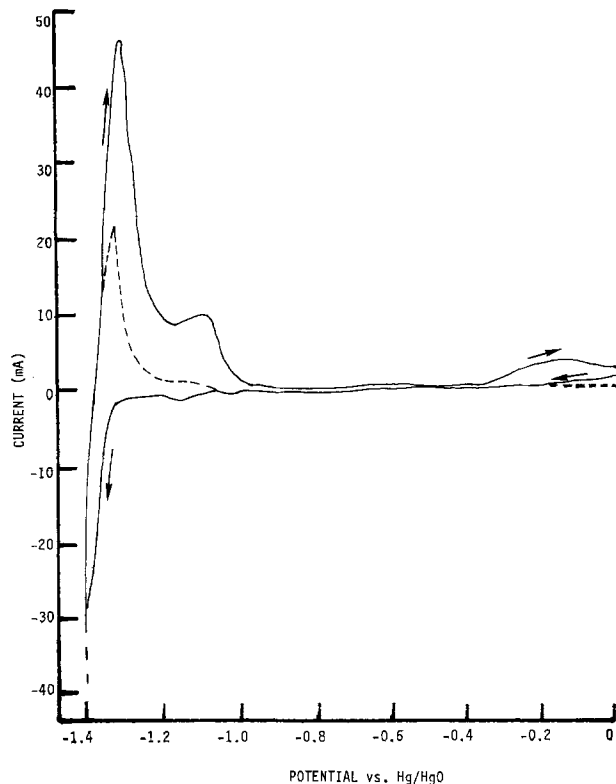


Fig. 2. Cyclic voltammogram for Ag sheet electrode (2 cm²) in 1M KOH + 0.08M ZnO; broken line is a continuous sweep; solid line is for electrode held at -1.4V for 4 sec, sweep rate 100 mV/sec.

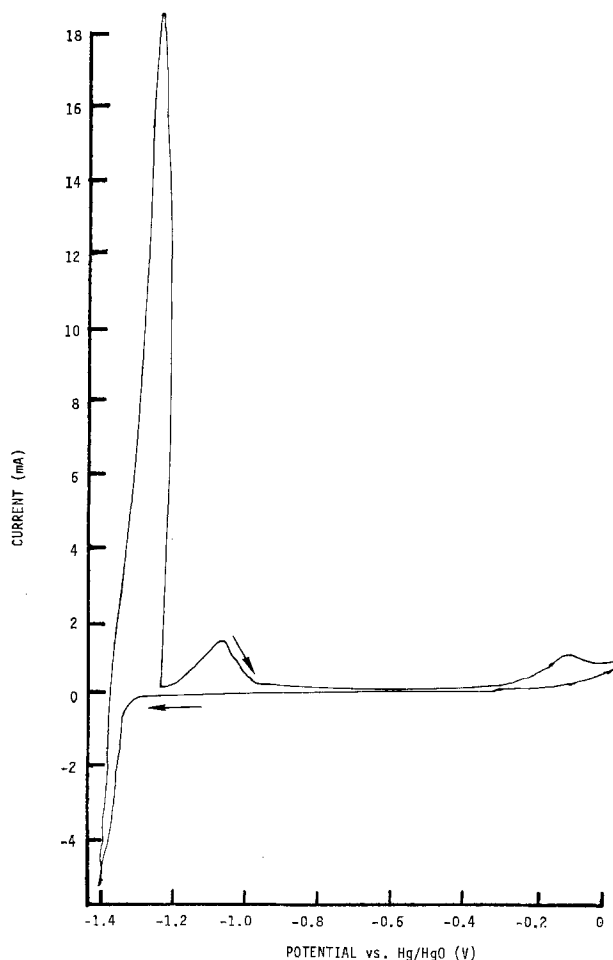


Fig. 3. Cyclic voltammogram on Ag disk (0.686 cm²) in 1M KOH + 0.08M ZnO. Potential was held at -1.4V for 5 sec and arrested on the anodic sweep at -1.24V for 5 min, sweep rate 100 mV/sec.

anodically to -1.24V where it is again arrested until the current reached zero (5 min). Upon resumption of the anodic sweep, the two dissolution peaks are clearly discernable. When the anodic arrest is increased to -1.17V (Fig. 4), the first peak is decreased whereas the peak at -0.2V remains unaffected. Figure 5 is a plot of the total anodic charge under the peak at -0.2V vs. the reciprocal of the square root of the sweep rate when the voltage envelope is between $+0.020$ and -1.5V . The dependence is linear. Figure 6 shows cyclic voltammograms in the voltage envelopes

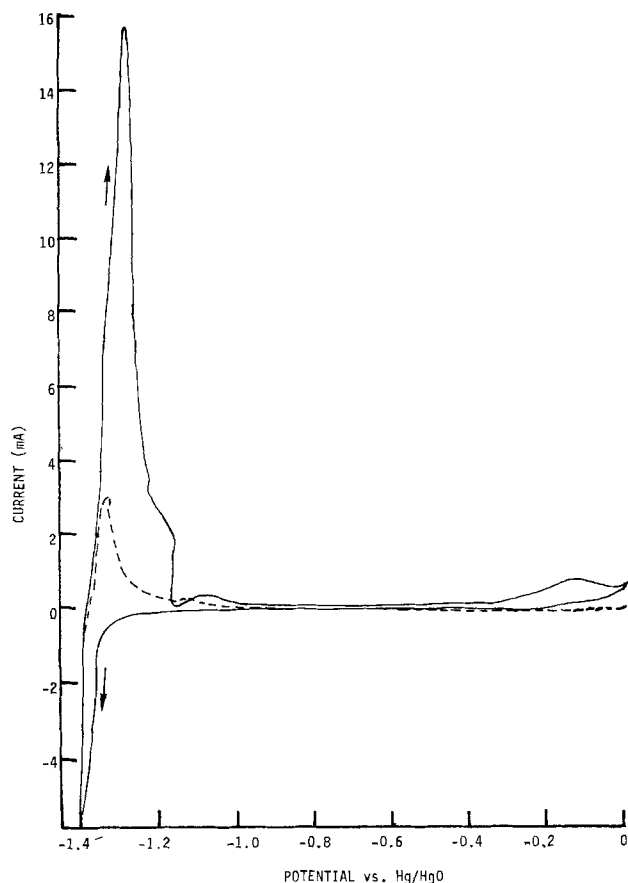


Fig. 4. Cyclic voltammogram on Ag disk (0.686 cm^2) in $1\text{M KOH} + 0.08\text{M ZnO}$; potential was held at -1.4V for 5 sec and arrested at -1.17V on the anodic sweep for 5 min, sweep rate 100 mV/sec ; broken line is a continuous sweep.

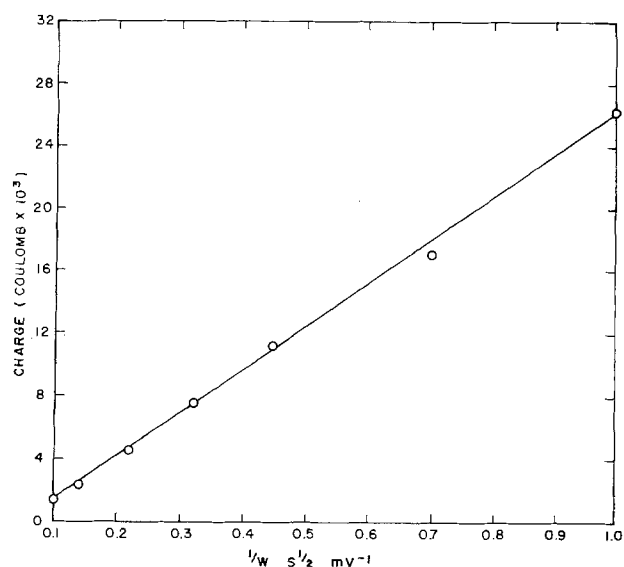


Fig. 5. Anodic charge under peak at -0.2V vs. reciprocal square root of the sweep rate; for Ag disk (0.686 cm^2) in $1\text{M KOH} + 0.08\text{M ZnO}$. Cyclic voltammetry voltage envelope $+0.020$ to -1.5V .

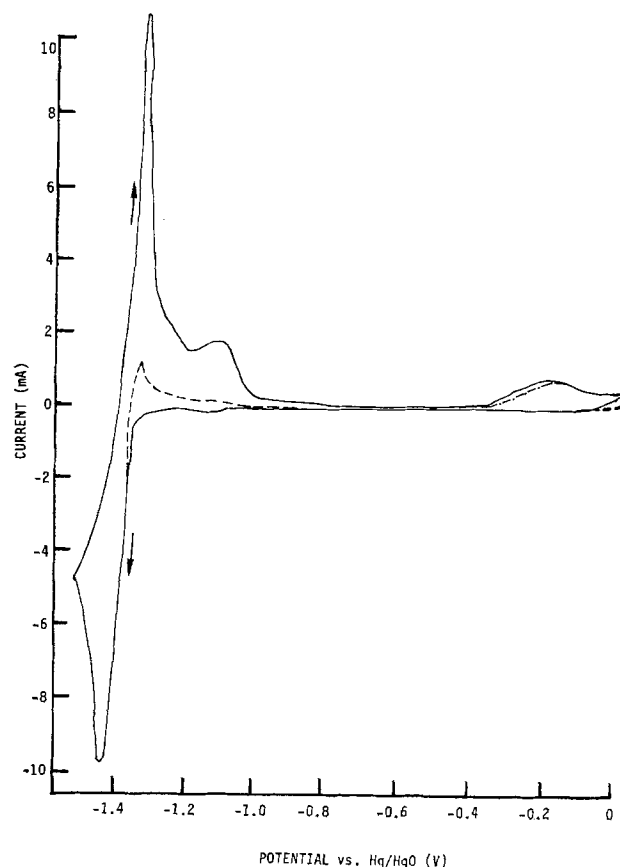


Fig. 6. Cyclic voltammogram on Ag disk electrode (0.686 cm^2) in $1\text{M KOH} + 0.08\text{M ZnO}$; solid line for a voltage envelope between 0.02 and -1.5V ; broken line for a voltage envelope between 0.02 and -1.35V ; lines with dashes and dots show anodic peak after 5 min arrest at -0.65V , sweep rate 50 mV/sec .

$+0.02$ and -1.35 and $+0.02$ and -1.5V . When the cyclic voltammogram between $+0.020$ and -1.5V is arrested in the anodic sweep at -0.65V for 5 min the anodic peak at -0.2V is only minimally affected. Figure 7 shows a cyclic voltammogram in the voltage envelope $+0.020$ to -1.5V followed by a number of cyclic voltammograms in the voltage envelope -0.9 to -1.5V and finally by another cyclic voltammogram between $+0.20$ and -1.5V . When the electrode is swept in the voltage envelope -0.9 to -1.5V the cathodic peak at -1.42V decreases, the anodic peak at -1.3V increases, and the anodic peak at -1.14V decreases. On extending the sweep to $+0.20\text{V}$ after three sweeps between -0.9 and -1.5V there is an increase in the anodic peak at -0.2V .

Cyclic voltammetry studies were also carried out in 6M KOH 0.8M ZnO and in $7.85\text{M KOH} + 0.74\text{M ZnO}$. No features were found in the other electrolytes that did not exist in 1M KOH . Thus, only the results in 1M KOH are presented in detail here.

The investigations on amalgamated silver were preliminary in nature. Typical results are shown in Fig. 8. Amalgamation completely suppresses underpotential deposition and reduces the cathodic current at -1.4V .

Potentiostatic pulse studies.—Figure 9 shows the current-time behavior for zinc deposition at various potentials for 100 sec. The anodic stripping profile at -1.25V is also shown. The anodic peak current increases with deposit thickness. Figure 10 shows the anodic stripping charge for two potentiostatic pulse profiles in $8.40\text{M KOH} + 0.74\text{M ZnO}$. The results indicate that about one monolayer of zinc is deposited before the bulk zinc deposition. When the bulk deposit is stripped in two stages (-1.25 and -1.0V) most of the dissolution occurs at -1.25V . The remainder of the deposit (up to 30 monolayers) is stripped at -1.0V .

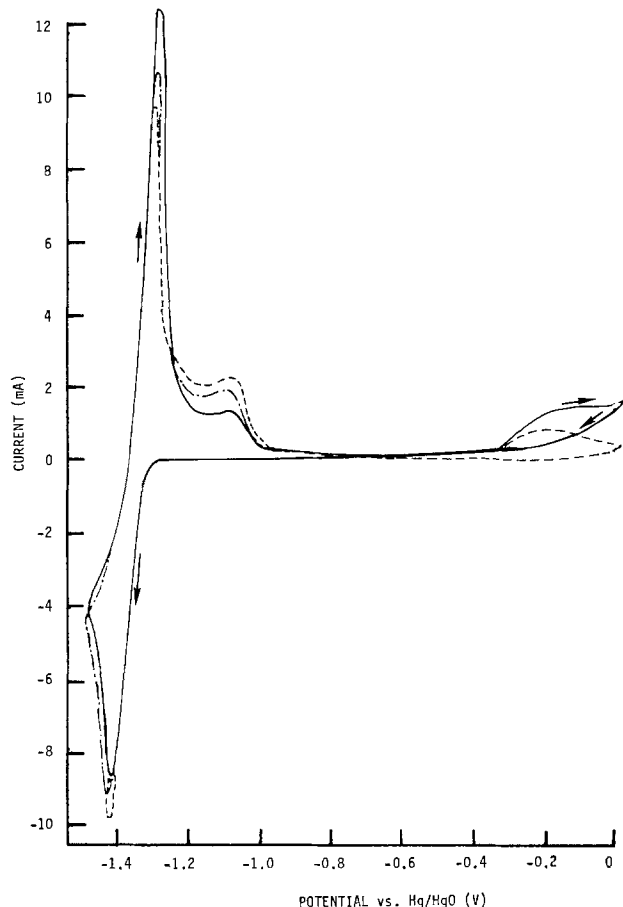


Fig. 7. Cyclic voltammogram on Ag disk (0.686 cm^2) in $1\text{M KOH} + 0.08\text{M ZnO}$; broken line is first sweep between 0.02 and -1.5V . This was followed by three sweeps between -0.9 and -1.5V ; solid line is final sweep between -1.5 and 0.02V , sweep rate 50 mV/sec .

Figure 11 shows the results when all of the deposit is stripped at -1.0V . The anodic current-time profile is indicative of a fast dissolution process followed by a slow dissolution process.

X-ray diffraction studies.—Table I summarizes some of the x-ray diffraction results for the silver-zinc system. The cycling regime on the three samples were as follows:

Sample I: Sample I was swept in the cathodic direction in $1\text{M KOH} + 0.08\text{M ZnO}$ at a sweep rate of 50 mV/sec to a potential of -1.45V and held there for 1 hr prior to removal and washing.

Sample II: Sample II was treated in a similar fashion, held at a potential of -1.44V , and then swept to a potential of -1.1V at 1 mV/sec before removal from the cell.

The treatment of sample III was similar to sample II except that the anodic sweep was to a potential of -0.7V . The d values for Zn, Ag, AgZn_3 , and the ζ phases of AgZn are shown in Table I for comparison. There was no evidence of a ZnO pattern in any of the samples.

The x-ray diffraction results may be summarized as follows. In sample I there was a clear pattern for Zn, Ag, and AgZn_3 . In sample II there was no pattern for Zn. However, there was a strong AgZn_3 pattern. In sample III there was no evidence of zinc and the AgZn_3 pattern was weaker than in sample II. There was slight evidence of an AgZn pattern in samples I and III. However, its presence could not be unequivocally determined in these samples. However, in the samples prepared for morphology and deposit orientation studies, strong diffraction peaks at $2\theta = 28.4^\circ$, 50.05° , and 58.65° occurred. These could be attributed to either the β' or ζ form of AgZn .

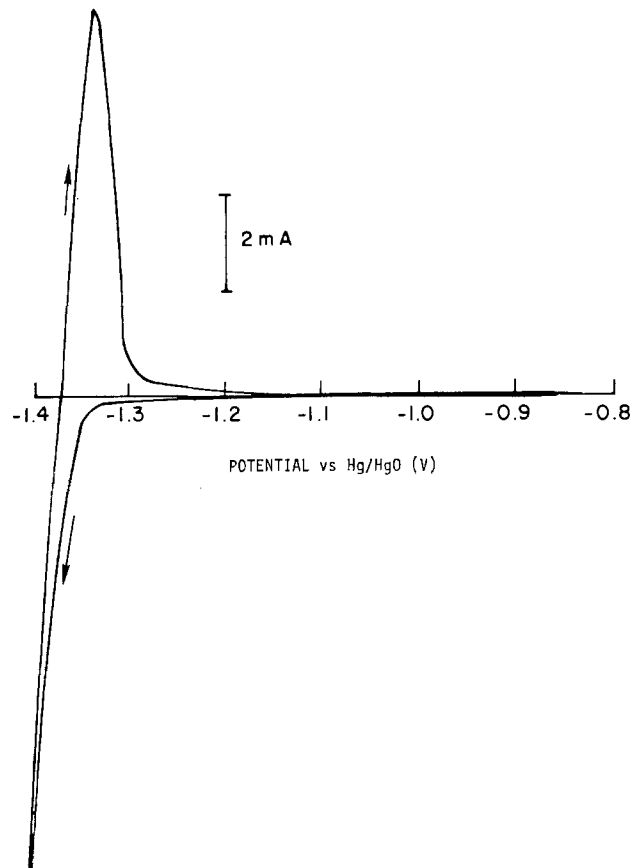


Fig. 8. Cyclic voltammogram on amalgamated Ag sheet (2 cm^2) in $1\text{M KOH} + 0.08\text{M ZnO}$, sweep rate 100 mV/sec .

Deposit morphology and orientation.—Figure 12 is a scanning electron micrograph of a zinc deposit on silver. The deposit consisted of hexagonal platelets. The x-ray diffraction results indicated that the deposit consisted of a combination of layers parallel to the basal plane and perpendicular to the basal plane. There were no significant morphology changes in the thickness range of $1\text{--}5 \text{ C/cm}^2$.

Discussion

The cyclic voltammetry, potential pulse, and x-ray diffraction studies indicate that the deposition of zinc on silver is a rather complex process consisting of

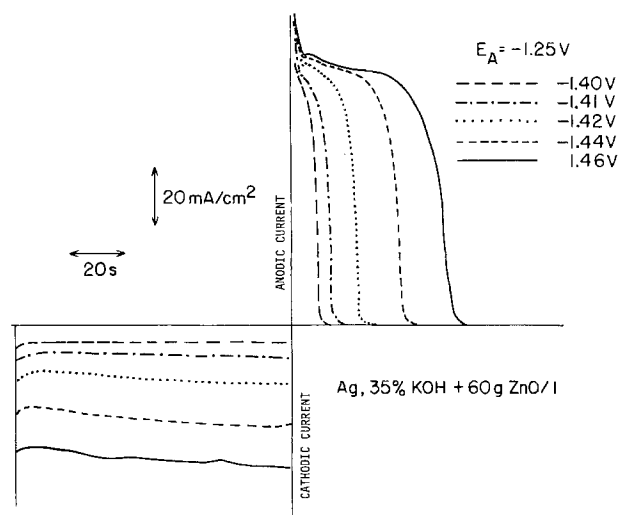


Fig. 9. Current transients for zinc deposition on Ag sheet electrode in $8.4\text{M KOH} + 0.74\text{M ZnO}$ at various potentials. Current transients for anodic stripping at -1.25V also shown.

Table I. d-Spacings and relative intensities for Ag substrate samples. All samples held at $-1.45V$ in $1M$ KOH + $0.08M$ ZnO for 1 hr. Samples II and III anodically polarized at 1 mV/sec to -1.1 and $-0.7V$, respectively. d-Values and relative intensities given for Ag, Zn, AgZn₃, and two forms of AgZn

| Sample I | | Sample II | | Sample III | | Ag | | Zn | | AgZn ₃ | | AgZn (ζ) | | AgZn (cubic) | |
|----------|------------------|-----------|------------------|------------|------------------|------|------------------|------|------------------|-------------------|------------------|----------|------------------|--------------|------------------|
| d | I/I ₀ | d | I/I ₀ | d | I/I ₀ | d | I/I ₀ | d | I/I ₀ | d | I/I ₀ | d | I/I ₀ | d | I/I ₀ |
| 2.79 | 15 | | | | | | | | | | | 2.60 | 10 | | |
| 2.59 | 10 | | | | | | | | | | | 2.49 | 10 | | |
| 2.46 | 20 | | | | | | | 2.47 | 53 | 2.43 | 12 | 2.27 | 40 | | |
| 2.43 | 100 | 2.43 | 15 | 2.43 | 100 | | | 2.30 | 40 | | | 2.27 | 40 | | |
| 2.34 | 80 | 2.43 | 100 | 3.34 | 100 | 2.35 | 100 | | | 2.21 | 35 | | | 2.23 | 100 |
| 2.23 | 30 | 2.21 | 15 | | | | | | | | | 2.20 | 100 | | |
| 2.19 | 25 | 2.18 | 15 | | | | | | | 2.13 | 100 | 2.15 | 100 | | |
| 2.13 | 100 | 2.11 | 50 | 2.13 | 100 | | | | | | | 1.87 | 60 | | |
| 2.08 | 50 | 2.03 | 15 | | | | | 2.09 | 100 | | | 1.83 | 50 | | |
| 1.64 | 10 | | | 1.63 | 40 | 2.04 | 40 | 1.68 | 28 | 1.64 | 35 | 1.58 | 50 | 1.57 | 50 |
| 1.629 | 20 | | | | | | | | | | | 1.51 | 80 | | |
| 1.44 | 100 | 1.43 | 100 | 1.44 | 100 | 1.47 | 25 | | | | | 1.41 | 10 | 1.41 | 30 |
| 1.41 | 50 | | | 1.41 | 30 | | | | | 1.41 | 50 | 1.33 | 70 | | |
| | | | | | | | | 1.34 | 25 | | | 1.28 | 80 | 1.28 | 100 |
| | | | | | | | | | | | | 1.27 | 90 | | |
| | | | | | | | | | | | | 1.25 | 80 | | |
| 1.25 | 10 | | | 1.25 | 30 | | | 1.33 | 21 | 1.26 | 40 | 1.23 | 60 | | |
| 1.23 | 15 | | | 1.23 | 20 | 1.23 | 26 | | | | | 1.19 | 70 | | |
| 1.18 | 20 | | | 1.18 | 30 | | | | | 1.19 | 25 | 1.17 | 70 | | |
| 1.17 | 25 | | | 1.17 | 20 | 1.17 | 12 | 1.17 | 23 | 1.17 | 5 | 1.18 | 90 | | |
| 0.937 | 50 | | | 0.937 | 15 | 1.12 | 17 | | | | | 1.10 | 70 | 1.11 | 50 |
| | | | | | | | | | | | | 1.09 | 60 | 0.998 | 100 |
| | | | | | | | | | | | | | | 0.911 | 100 |

underpotential deposition, alloy formation, and growth of bulk zinc.

Underpotential deposition.—Approximately a monolayer of underpotential deposited zinc is formed prior to bulk deposition and alloy formation. The underpotential shift (ΔE_p) is $\sim 0.15V$. This is in good agreement with the results of Kolb (10) and correlates well with the differences in work function between silver and zinc. On this basis, the suppression of underpotential deposition by amalgamation is to be expected (Fig. 8).

The degree of structure in the current peaks in the underpotential deposition region varied from sample to sample and depended on electrode pretreatment. This is presumably due to differences in the adsorption behavior on various crystal faces, as was observed by Bewick and Thomas for the case of Tl on silver (6,

12). They found good qualitative agreement between the underpotential deposition pattern for Tl on chemically polished polycrystalline silver and the chemical polished 110 face of single crystal silver. In the present work, well-defined peaks were only obtained on silver sheet electrodes. These were fabricated from rolled silver sheet that had a preferred 110 orientation. The ill-defined peaks, particularly on the disk electrodes are presumably due to deviations from this orientation.

Bulk deposition and alloy formation.—Quantitative treatment of the cyclic voltammograms and cathodic current transients is essentially impossible because of the unknown contribution of the hydrogen evolution reaction. However, the anodic dissolution behavior in the cyclic voltammograms and the anodic current transients in the potential step experiments yield valuable information which complements the results of the x-ray diffraction analysis. The results of the cyclic voltammetry studies (Fig. 2-7) indicate the formation of at least two alloys by diffusion of zinc into metal. On holding the electrode at $-1.4V$ for 4 sec (Fig. 2) two additional current dissolution peaks appear at -1.05 and $-0.2V$. Potential arrests on the anodic

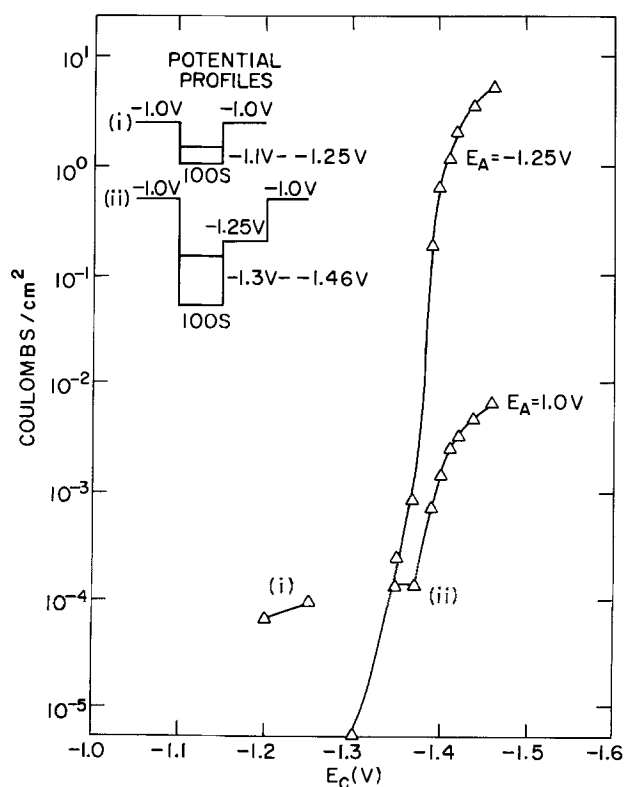


Fig. 10. Anodic stripping charge for zinc deposits on Ag sheet in $8.4M$ KOH + $0.74M$ ZnO. Inset shows the deposition and stripping potential profiles. Deposition time 100 sec.

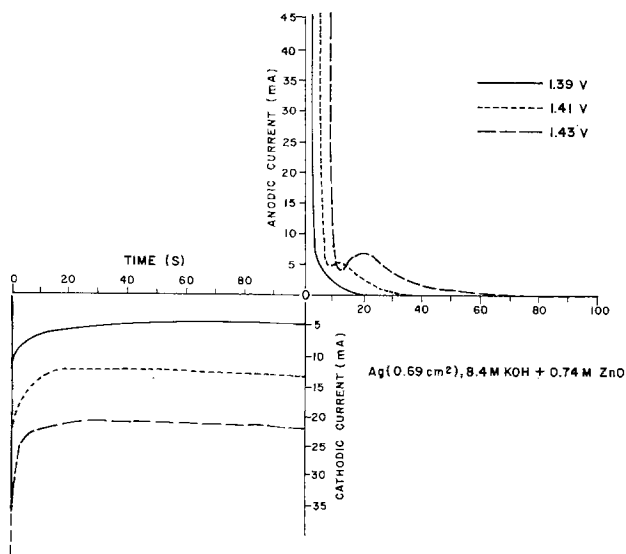


Fig. 11. Current transients for double cathodic/anodic pulse experiments on Ag disk (0.686 cm²) in $8.4M$ KOH + $0.74M$ ZnO. Potential profile was $-0.6V$ for 10 sec, followed by a cathodic step to the potentials indicated on the figure for 100 sec, and an anodic step to $-1.0V$ for 100 sec.

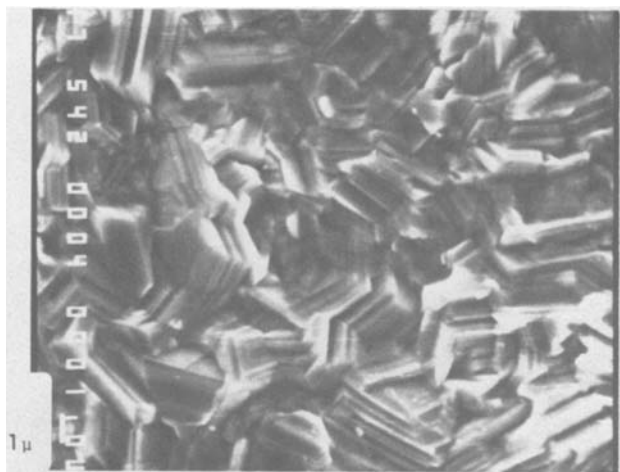


Fig. 12. Scanning electron micrograph of zinc deposit on Ag sheet. Electrolyte 8.4M KOH + 0.74M ZnO; 5 Zn C/cm² at -1.44V. 5400 \times .

sweep do not affect these dissolution peaks (Fig. 3-4) so therefore they are not due to dissolution of bulk zinc.

In the x-ray diffraction analysis (Table I), at least two silver-zinc alloys could be identified. One was AgZn₃ with a hexagonal ϵ -brass structure. The other was an alloy with a lower zinc composition. The x-ray results indicate that this may be β' -phase of AgZn. The work of King and Massalski (13) indicated that the ordered body-centered cubic β' -phase was the equilibrium structure at room temperature, for alloys with close to 50% Zn. This alloy is very stable and dissolution does not occur until -0.2V. The sweep dependence of the amount of alloy formed (Fig. 5) indicates that it is formed by diffusion into the bulk metal. For simple diffusion with a zinc concentration of C_0 at the surface the dependence of the dissolution charge (Q) on reciprocal square root of the sweep rate $(1/\omega)^{1/2}$ should be

$$dQ/d(1/\omega)^{1/2} = 4FAC_0(D/\pi)^{1/2}$$

where F is the Faraday constant, A the electrode area, and D the diffusion coefficient of zinc in silver. If one assumes a value of $C_0 = 10^{-1}$ M/cm³ then $D = 3.35 \times 10^{-12}$ cm² sec⁻¹. This value is high, but it is reasonable when compared with an estimated value of $D < 10^{-14}$ cm² sec⁻¹ for cadmium in silver at room temperature (9). The β' -AgZn phase is very stable as indicated by its high dissolution potential (-0.2V) and by the fact that a 5 min arrest of the anodic sweep at -0.65V only minimally affects the dissolution peak (Fig. 6).

The results of the cyclic voltammograms in Fig. 7 indicate that AgZn₃ is initially formed and is transformed into β' -AgZn. On cycling in the voltage envelope -0.9 to -1.5V, the dissolution peak for AgZn₃ at -1.05V decreases. However, on extending the sweep to -0.02V there is a considerable increase in the dissolution peak at -0.2V, indicating a transformation of the AgZn₃ to AgZn.

The results of the potential pulse measurements essentially confirm the results of the cyclic voltammetry. Because of the small underpotential shift it is difficult to quantitatively separate the charge associated with the underpotential deposited layer. However, it approximates to a monolayer. When dissolution is carried out in two steps, at -1.25 and -1.0V, the anodic dissolution of AgZn₃ can be separated from bulk zinc dissolution. The results in Fig. 10 indicate the formation of up to 50 monolayers of AgZn₃. The amount of alloy formation increases with potential. This has been observed for other systems and has been attributed to an increase in surface vacancies due to a decrease in

surface energy at more negative potentials (14). If all the dissolution is carried out at -1.0V the current transient for the dissolution of AgZn₃ can clearly be seen (Fig. 11).

The cyclic voltammetry results (Fig. 2-7) and the potential pulse measurements indicate that the apparent nucleation overvoltage for zinc deposition on silver is low. Similar results were found by Despic (11) for zinc deposition on copper and gold from sulfate solutions and these were correlated with the presence of underpotential deposited layers. In an investigation of lead deposition on silver in perchlorate solutions, Lorenz and his co-workers (15) found that the rate of three dimensional nucleation decreased with increase in the coverage by the underpotential deposited layer. Unfortunately, the present results are of little help in resolving this controversy since the results can either be due to the absence of a nucleation overvoltage or to alloy formation in the potential region between the reversible deposition potential and the underpotential deposition region.

Deposit morphology and orientation.—The hexagonal growth habit of the deposit is typical for growth parallel to the basal plane (16). This is in agreement with the x-ray results. It has been found that the surface area of zinc deposits, oriented parallel to the basal plane, increases with deposit thickness (17). The anodic current transients in Fig. 9 indicate an increase in dissolution activity with deposit thickness. This is probably due to an increase in the amount of steps and edges that act as active dissolution sites.

Summary

1. Approximately a monolayer of zinc is formed on polycrystalline silver prior to bulk deposition. The underpotential shift (ΔE_p) of ~ 0.15 V is in good agreement with the differences in work function. Amalgamation suppresses underpotential deposition.
2. At least two alloys of silver and zinc are formed. One was identified as AgZn₃ the other as β' -phase of AgZn.
3. Bulk deposition proceeds without any detectable nucleation overvoltage. This may be due to alloy formation. The deposit consists of hexagonal platelets that are oriented either parallel or perpendicular to the basal plane.

Acknowledgments

This work was supported by the Naval Ship Engineering Center (NAVSEC) and the U.S. Department of Energy. The authors acknowledge helpful discussions with A. Himy of NAVSEC, O. C. Wagner of the U.S. Army Electronics Research and Development Command (ERADCOM), Professor B. E. Conway of the University of Ottawa, and W. E. O'Grady, R. R. Adzic, W. Visscher, and S. Srinivasan of Brookhaven National Laboratory (BNL). The authors wish to thank O. Kammerer (BNL) for the x-ray analysis and R. L. Sabatini (BNL) for the scanning electron microscopy. One of the authors (G.A.) had financial support from the Research Fund of Serbia, Yugoslavia, during the course of this work.

Manuscript submitted Oct. 29, 1980; revised manuscript received ca. Feb. 12, 1981. This was Paper 15 presented at the St. Louis, Missouri, Meeting of the Society, May 6-11, 1980.

Any discussion of this paper will appear in a Discussion Section to be published in the June 1982 JOURNAL. All discussions for the June 1982 Discussion Section should be submitted by Feb. 1, 1982.

Publication costs of this article were assisted by Brookhaven National Laboratory.

REFERENCES

1. S. U. Falk and A. J. Salkind, "Alkaline Storage Batteries," pp. 163-167, John Wiley & Sons, Inc., New York (1969).

2. J. M. Booe, *This Journal*, **91**, 197C (1952).
3. T. P. Dirkse and E. G. Vrieland, *ibid.*, **106**, 997 (1959).
4. M. E. Straumanis and C. C. Fang, *ibid.*, **98**, 9 (1951).
5. E. Raub and B. Wullhorst, *Metallforsch.*, **2**, 41 (1947).
6. A. Bewick and B. Thomas, *J. Electroanal. Chem. Interfacial Electrochem.*, **65**, 911 (1975).
7. D. M. Kolb, M. Przasnyski, and H. Gerischer, *ibid.*, **54**, 25 (1974).
8. E. Schmidt and H. R. Gygax, *ibid.*, **12**, 300 (1966).
9. E. Schmidt, M. Christen and P. Beyelar, *ibid.*, **42**, 275 (1973).
10. D. M. Kolb, in "Advances in Electrochemistry and Electrochemical Engineering," Vol. 11, H. Gerischer and C. W. Tobias, Editors, John Wiley & Sons, Inc., New York (1958).
11. A. R. Despic, in "Electrode Processes," S. Bruckenstein, J. D. E. McIntyre, B. Miller, and E. Yeager, Editors, p. 235, The Electrochemical Society Soft-bound Proceedings Series, Princeton, N.J. (1979).
12. A. Bewick and B. Thomas, *J. Electroanal. Chem. Interfacial Electrochem.*, **70**, 239 (1976).
13. H. W. King and T. B. Massalski, *Trans. AIME*, **221**, 1063 (1961).
14. B. N. Kabanov, I. G. Kiseleva, and I. I. Astakhov, *Elektrokhimiya*, **8**, 955 (1972).
15. W. J. Lorenz, E. Schmidt, G. Staikov, and H. Bork, *Faraday Symp. Chem. Soc.*, **12**, 14 (1978).
16. I. Sunagawa, in "Crystal Growth Characterization," R. Ueda and J. B. Mallin, Editors, pp. 347-359, North Holland Publishing Co., Amsterdam (1975).
17. J. McBreen, M. G. Chu, and G. Adzic, Unpublished results.

Measurement of the Viscosity and Specific Conductivity of an Aluminum Plating Bath— The Non-Stokesian Mechanism of Electrolytic Conductivity

E. Peled,* M. Brand, and E. Gileadi

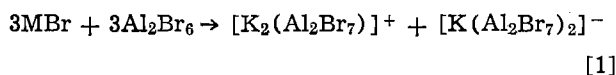
Department of Chemistry, Tel-Aviv University, Ramat Aviv, Israel

ABSTRACT

The viscosity, conductivity, and density of solutions of Al_2Br_6 and KBr (or LiBr) in several aromatic hydrocarbons were determined, as the function of the composition of the bath and of temperature. The alkali bromide has a major role in increasing both the viscosity and the conductivity, while its effect on the density of the solution is relatively minor. The results observed lend further support to the non-Stokesian relay-type mechanism of conductivity proposed earlier for this system. The data presented can be useful in the design and routine operation of aluminum plating baths.

In a previous study, the mechanism of high conductivity in a medium of low dielectric constant consisting of Al_2Br_6 and MBr in toluene was discussed (1). The specific conductivity and the viscosity of solutions were measured over a wide range of concentrations of Al_2Br_6 and MBr , where M stands for Li, K, and in a few experiments also Rb. At low concentrations (below 10^{-2}M) the molar conductivity was found to decrease with increasing concentration in a manner consistent with the theory of Fuoss and Kraus (2-4) for strong electrolytes in a medium of low dielectric constant. At higher concentrations, however, the molar conductivity was found to increase rapidly with increasing concentration reaching values as high as $5\text{-}6\text{ cm}^2\ \Omega^{-1}\text{mol}^{-1}$.

Measurement of the transference numbers in the concentrated solutions led to the conclusion (1) that the predominant ionic species were complex ions formed in the following reaction



Accordingly, the equivalent conductivity is three times the molar conductivity, i.e., $15\text{-}18\text{ cm}^2\ \Omega^{-1}\text{equiv}^{-1}$. This should be compared to a value of ca. $90\text{ cm}^2\ \Omega^{-1}\text{equiv}^{-1}$ for a 1M aqueous solution of KBr , bearing in mind that the viscosity of the concentrated nonaqueous solution is more than twice that of water at the same temperature.

The high value of the equivalent conductivity along with several other experimental observations (1) led

to the conclusion that electrolytic conductivity cannot occur by way of the regular hydrodynamic movement of ions through the viscous medium. It was assumed that aggregates were formed in the solution, consisting of the various ionic species and probably also the neutral molecules of Al_2Br_6 . An ion could reach an aggregate on one side and another ion would emerge at the other end almost simultaneously, in a relay-type mechanism. The virtual movement of the ion through the aggregate leads in this way to an enhanced apparent mobility and explains the high conductivity observed.

The formation of aggregates is expected to lead to an increase of the viscosity of the solution. It was indeed observed that an increase of conductivity was associated with an increase of viscosity. This is in sharp contrast to the behavior of simple ions in aqueous solutions, where the conductivity is inversely proportional to the viscosity.

In the present study, the measurements of viscosity and conductivity were extended over a temperature range of $0^\circ\text{-}80^\circ\text{C}$ in an attempt to gain further experimental information which could verify the relay-type mechanism of conductivity discussed above (1).

The system of Al_2Br_6 and MBr dissolved in an aromatic hydrocarbon can serve as a plating bath for the electrodeposition of aluminum (5-10). Therefore, the results derived below are of practical as well as theoretical value.

Experimental

General procedure.—Solutions were prepared in a glove box (VAC, Model DL001-D-G) filled with highly purified argon, which was continuously passed through a catalytic purifier (VAC Model HE-493 DRI-TRAIN).

* Electrochemical Society Active Member.

Key words: mechanism of conductivity, non-Stokesian conductivity, electroplating of aluminum, nonaqueous electrochemistry, aluminum bromide.

Details of purification of materials and preparation of solutions were given elsewhere (11-13). The viscosity and conductivity were measured in the cells shown in Fig. 1a and b, respectively. The cells were filled with solutions of a given composition inside the glove box, closed to the atmosphere with Rotaflo valves, and removed from the glove box to a thermostat, where the temperature was controlled to $\pm 0.3^\circ\text{C}$. The concentrations of aluminum and potassium or lithium were determined at the end of a series of experiments by atomic absorption spectroscopy, as described earlier (5, 6). In a given series of experiments, the ratio of concentrations of Al_2Br_6 to MBr was maintained strictly constant, since all solutions were prepared by

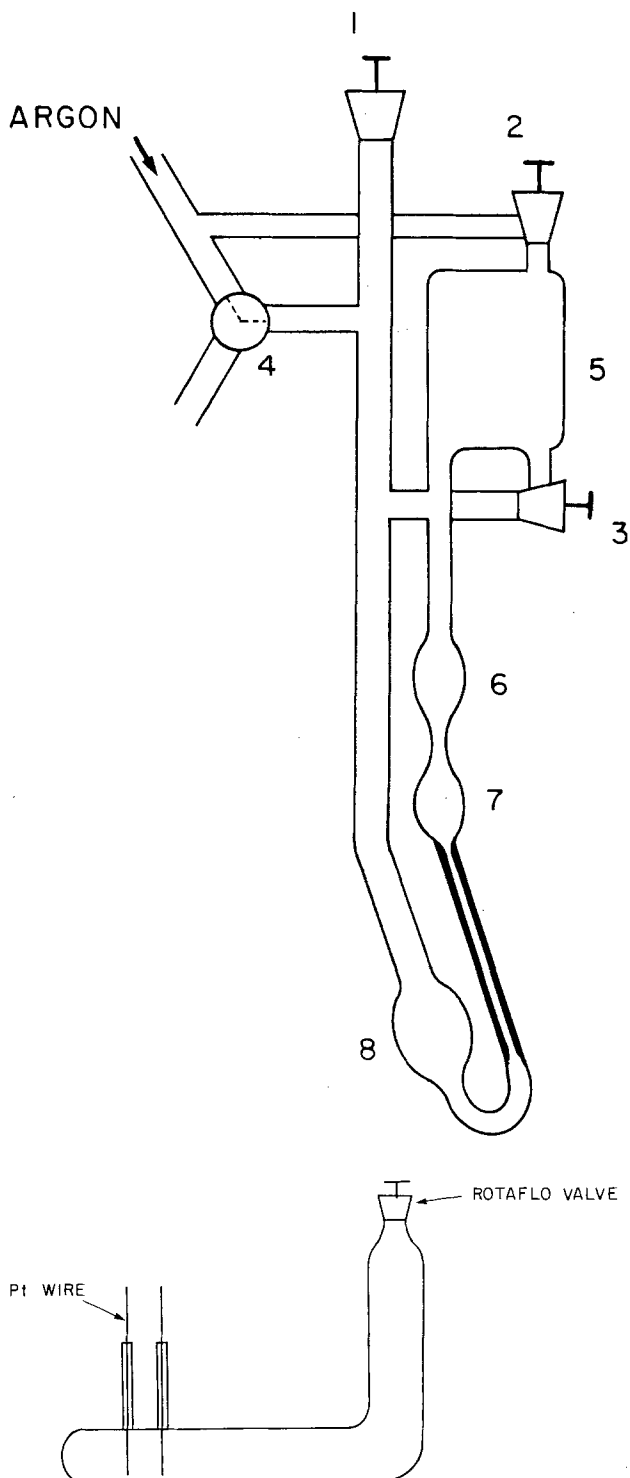


Fig. 1. a (top) Modified Ostwald viscosimeter for measurement of the viscosity under a controlled atmosphere. b (bottom) Cell for conductivity measurements.

diluting the most concentrated solution with the solvent.

Measurement of viscosity.—The viscosity was measured with a modified Ostwald viscosimeter shown in Fig. 1a. The viscosimeter was loaded with a fixed volume (13 cm^3) of solution inside the glove box, through stopcock 1. All stopcocks were then closed and the viscosimeter was transferred to the thermostat and connected to the line of pure argon. Stopcock 4 was turned to allow the argon into the viscosimeter. This pushed the solution from bulb 8 through the capillary into bulb 7 and part of bulb 6. Stopcock 4 was then turned to let the argon out through the other branch. Stopcock 2 was opened next for a few seconds to release the pressure on the other side of the viscosimeter. (By releasing pressure through this stopcock, oxygen and humidity cannot come in contact with the solution.) Stopcock 3 is opened next for equalization of the pressure on the two branches of the viscosimeter and left open throughout the rest of the experiment. The time taken for the liquid to flow through the capillary was measured in the usual manner (1), after the pressures in the two tubes have been equalized. Bulb 5 has a large volume, relative to bulbs 6 and 7, to minimize pressure changes when the liquid is transferred from one side to the other in the viscosimeter.

The viscosity was measured several times at each temperature and some of the measurements were repeated at ascending and descending temperatures. The color of the solution did not change during measurement, indicating that the amount of air entering the viscosimeter during the pressure-equalizing step was negligible.

The viscosimeter was calibrated with distilled water over the temperature range of measurement ($10^\circ\text{--}80^\circ\text{C}$).

Conductivity.—The cell used for conductivity measurements is shown in Fig. 1b. Two platinized platinum wires ($\phi = 0.5\text{ mm}$; $l = 13\text{ mm}$) were sealed into the glass at a distance of 13 mm . The cell constant was determined with 0.1M KCl as 1.30 . Conductivity was measured with a four digit autoranging conductometer (Opal) at a frequency of 1000 Hz . The accuracy varied from 0.1 to 1.0% in different ranges of measurement.

Density.—The density was determined with a regular picnometer, which was fitted with a graduated capillary closed at the top. It was filled with distilled water to a certain level near the bottom of the graduated capillary and weighed accurately. Subsequently it was placed in the thermostat at various temperatures and the height of the water in the capillary was noted. The volume of the picnometer and capillary were determined from the known dependence of the density of water on temperature.

The picnometer was next filled with the test solution inside the glove box, sealed with a tapered glass joint which had the graduated capillary, and transferred to the thermostat. The volume was determined at each temperature from the height of the liquid in the graduated capillary, which has been calibrated with water. Weighing the picnometer before and after filling then yielded the density as a function of temperature.

Results and Discussion

Density.—The density of solutions of Al_2Br_6 and MBr ($\text{M} = \text{K}$ or Li) in toluene and mesitylene was measured over a range of temperatures from 10° to 80°C as a function of concentration. The data in Fig. 2 are for two temperatures and two solvents, employing a fixed ratio of concentrations $R = c(\text{Al}_2\text{Br}_6)/c(\text{KBr})$ of 1.1 in the case of toluene and 1.2 in the case of mesitylene. While the variation of density with concentration is very significant (ca. 60% increase in $1\text{M Al}_2\text{Br}_6$, 0.9M KBr compared to the pure solvent) it is relatively independent of the solvent (only 2% difference) and the

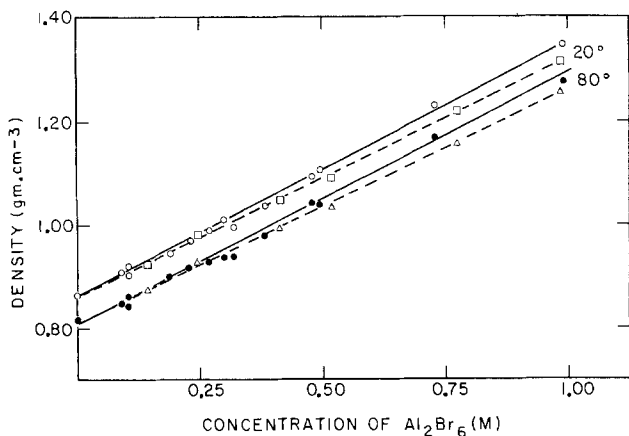


Fig. 2. Density vs. concentration of Al_2Br_6 . Solid line: toluene ($R = 1.1$); broken line: mesitylene ($R = 1.2$).

decrease of density with increasing temperature amounts to about 4.2% between 20° and 80°C.

Replacing KBr by LiBr results in somewhat lower densities, and removal of MBr altogether reduces the density even further, as seen in Fig. 3. However, the density is much more sensitive to the concentration of Al_2Br_6 than to that of KBr. Thus, of the 60% increase from the pure solvent to the most concentrated solution tested, only ca. 10% can be attributed to the presence of KBr while ca. 50% is due to Al_2Br_6 , as evidenced by the lowest line in Fig. 3.¹

In view of the possible application of this solvent system for the electroplating of aluminum, it may be noted that the marginal dependence of the density on the type of solvent, the temperature, and the concentration of MBr, combined with its rather large dependence on the concentration of Al_2Br_6 , may allow a rapid estimation of the concentration of the latter in industrial plating operations for routine quality control purposes.

Viscosity.—The viscosity of the solutions studied was found to be a sensitive function of the concentration, as shown in Fig. 4 for mesitylene as the solvent, at a constant ratio of concentration of the inorganic salts ($R = 1.2$). In 1.0M Al_2Br_6 (and 0.83M KBr) the viscosity at 20°C is 5.7 times that of the pure solvent, while at 80°C the ratio is decreased to 3.3. A comparison of toluene and mesitylene as the solvent is shown in Fig. 5. Unlike the density, the viscosity changes significantly with the solvent and its variation may serve as an indication for changes in the composition of the solvents in industrial plating baths during extended periods of time. Ethyl benzene was also used as a solvent. The resulting viscosity was found to be intermediate between that of toluene and mesitylene but closer to the former.

Replacing KBr by LiBr decreases the viscosity significantly, as seen in Fig. 6. Rather surprisingly, this is

¹This is the reverse of the effect on conductivity, as will be seen later.

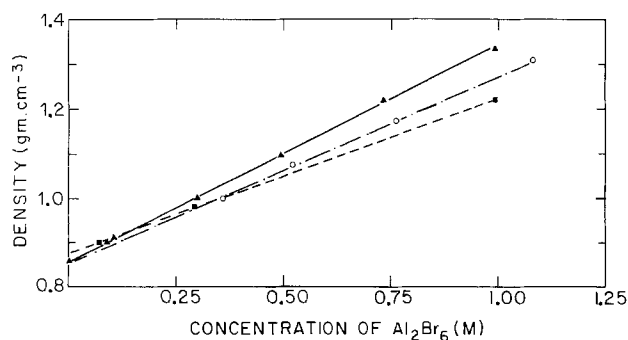


Fig. 3. Density vs. concentration of Al_2Br_6 in toluene at 30°C. $\blacktriangle\blacktriangle\blacktriangle$ KBr ($R = 1.1$); $\circ\circ\circ$ LiBr ($R = 1.21$); $\blacksquare\blacksquare\blacksquare$ no MBr.

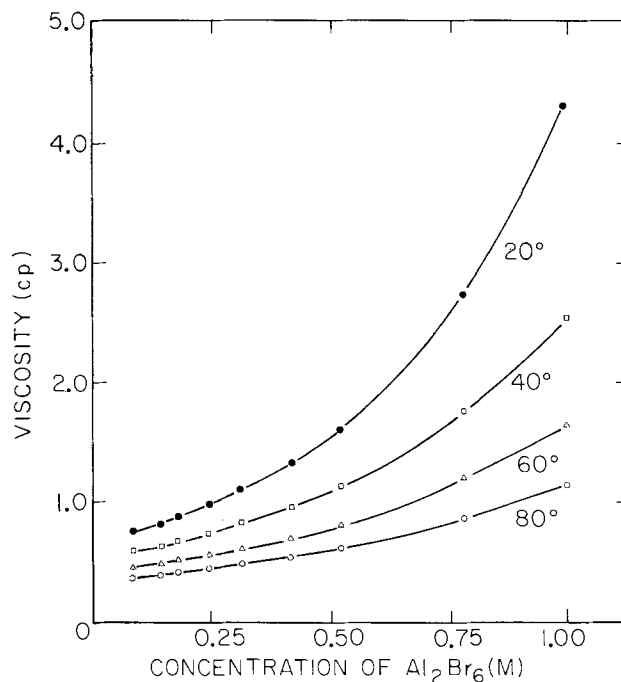


Fig. 4. Viscosity vs. concentration of Al_2Br_6 in mesitylene ($R = 1.2$).

accompanied by a decrease in specific conductivity, as will be shown below.

The viscosity as a function of temperature in solutions of toluene is shown in Fig. 7 at a number of concentrations of Al_2Br_6 and a fixed ratio of concentrations ($R = 1.1$). It is clearly seen in this figure that both the value of the viscosity and its temperature dependence increase significantly with increasing concentration of the solutes. This result is important for the understanding of the structure of these solutions as will be discussed below.

In Fig. 8 the variation of viscosity with temperature is compared for a few systems, all at high concentration of Al_2Br_6 . Mesitylene is compared to toluene and KBr is compared to LiBr in the same solvent (toluene). The two lowest curves refer to concentrated solutions of Al_2Br_6 in mesitylene and in toluene with no MBr

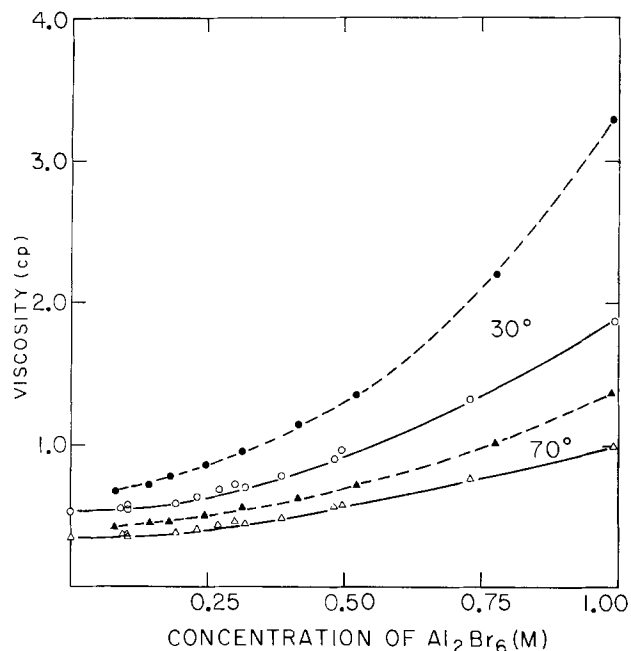


Fig. 5. Viscosity vs. concentration of Al_2Br_6 . solid line: toluene ($R = 1.1$); broken line: mesitylene ($R = 1.2$).

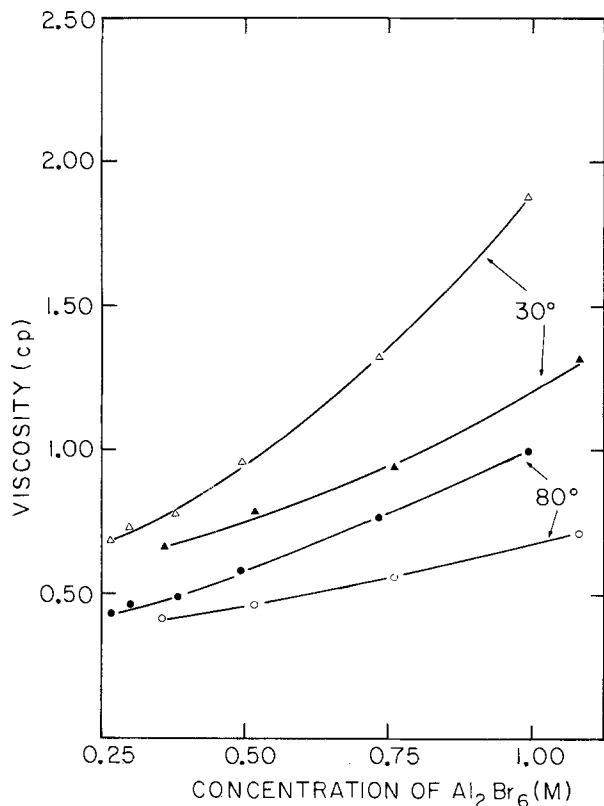


Fig. 6. Viscosity vs. concentration of Al_2Br_6 . $\triangle\triangle\triangle$ and $\bullet\bullet\bullet$ KBr ($R = 1.1$); $\blacktriangle\blacktriangle\blacktriangle$ and $\circ\circ\circ$ LiBr ($R = 1.25$).

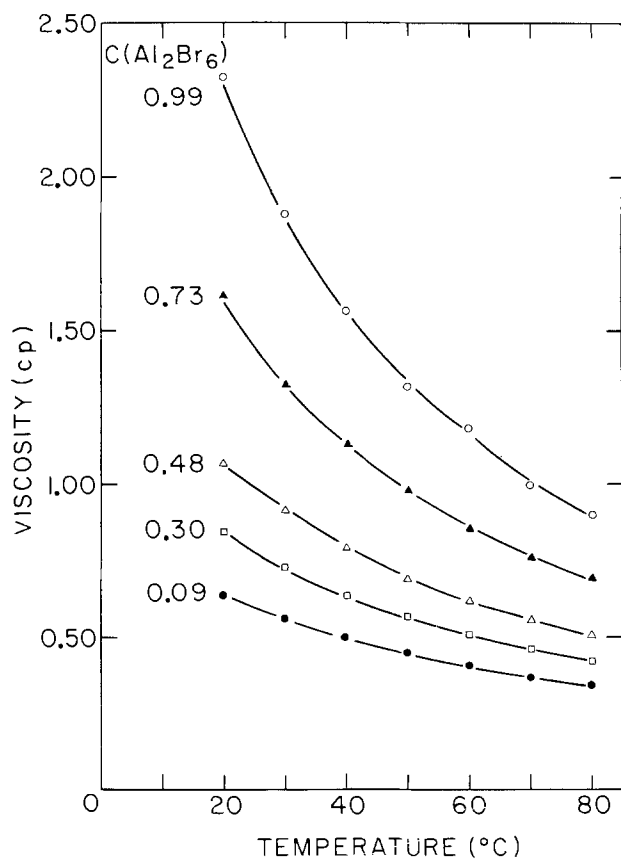


Fig. 7. Viscosity vs. temperature for different solution compositions in toluene ($R = 1.1$).

added. Removal of the monovalent salt results in a very substantial decrease in viscosity (from 4.32 to 1.48 cp in mesitylene at 20°C and by a similar factor in toluene). Thus, unlike the density, the viscosity is very

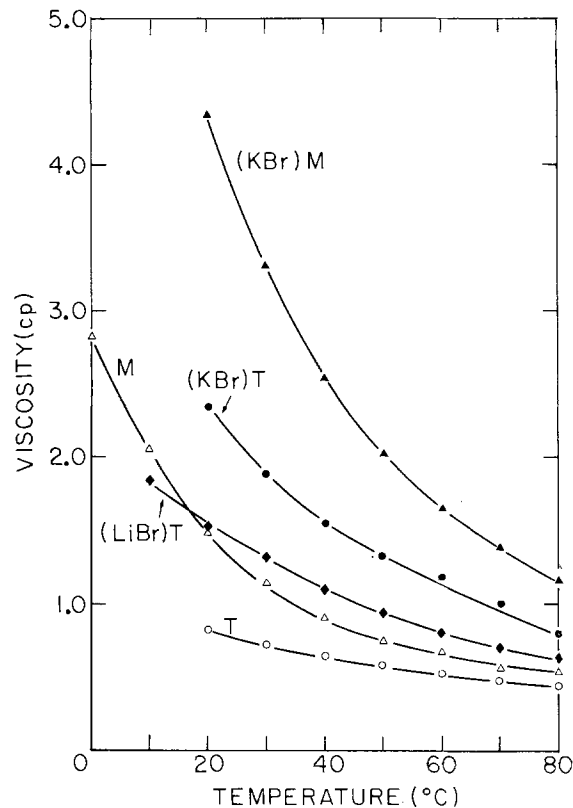


Fig. 8. Viscosity vs. temperature. Comparison of LiBr to KBr and of mesitylene to toluene. $\circ\circ\circ$ toluene, 1.0M Al_2Br_6 no MBr; $\triangle\triangle\triangle$ mesitylene 0.86M Al_2Br_6 no MBr; $\blacklozenge\blacklozenge\blacklozenge$ toluene 1.08M Al_2Br_6 0.86M LiBr; $\bullet\bullet\bullet$ toluene 1.0M Al_2Br_6 0.91M KBr; $\blacktriangle\blacktriangle\blacktriangle$ mesitylene 1.0M Al_2Br_6 0.83M KBr.

sensitive to the concentration of MBr and is significantly affected by the nature of M.

Apparent energies of activation E^\ddagger for the viscosity were calculated from plots of $\log \eta$ vs. reciprocal temperature, and are shown in Fig. 9 as a function of concentration. The steady increase of E^\ddagger with increasing concentration in both solvents clearly indicates a change in the structure of the solution and the fundamental hydrodynamic processes occurring in it, as will be discussed below.

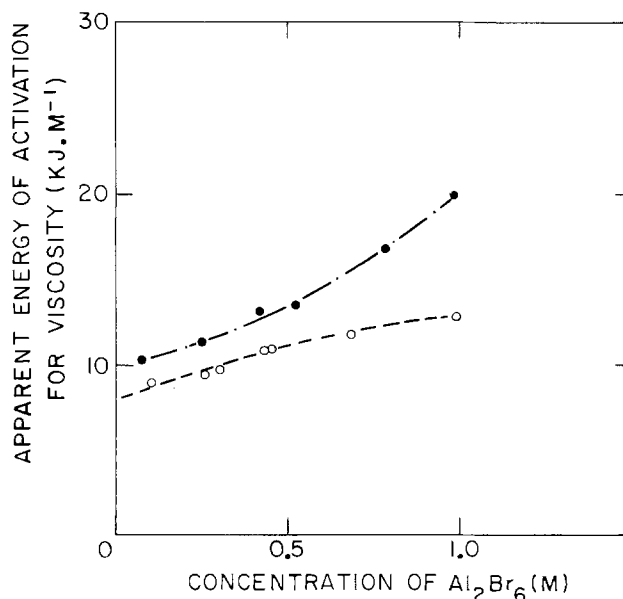


Fig. 9. Apparent energy of activation for viscosity vs. concentration of Al_2Br_6 . $\bullet\bullet\bullet$ mesitylene ($R = 1.2$); $\circ\circ\circ$ toluene ($R = 1.1$).

The kinematic viscosity.—The kinematic viscosity ν , defined as the ratio of viscosity to density (η/d) is shown in Fig. 10 for toluene as the solvent at two temperatures, as a function of the concentration of Al_2Br_6 . It is very interesting to note that in the presence of KBr (constant ratio $R = 1.1$) the kinematic viscosity grows rapidly with concentration of Al_2Br_6 , while in its absence, ν is essentially independent of the concentration of Al_2Br_6 . Similar results were observed when ethyl benzene or mesitylene were used as the solvent. In mesitylene, the kinematic viscosity increased to some extent with concentration of Al_2Br_6 in the absence of KBr at 20°C, but at 80°C it was found to be entirely independent of concentration, as observed for toluene and ethyl benzene.

The viscosity and the kinematic viscosity depend on the structure of the liquid in a complex manner and a detailed molecular theory has not yet been developed. The difficulty of theoretical interpretation is even further compounded when a multicomponent solution is considered. It is well known, however, that the formation of small particles or large molecular aggregates will increase the viscosity significantly. This can be qualitatively seen by considering the kinematic viscosity as a function of concentration for a number of inorganic salts and acids shown in Fig. 11. The value of ν changes relatively little in all cases, except in solutions of sulfuric and phosphoric acids, which are known to be highly associated.

Thus the large change of the kinematic viscosity with concentration of Al_2Br_6 at a constant ratio of concentration of Al_2Br_6 to KBr ($R = 1.1$) shown in Fig. 10, is consistent with a model assuming the formation of aggregates, which has been suggested previously (1). These aggregates form only in the presence of MBr, as seen by the lack of dependence of ν on the concentration of Al_2Br_6 when KBr is not present.

The effect of KBr on the kinematic viscosity is shown in a different way in Fig. 12 where ν/ν (solvent) is plotted as a function of the concentration of KBr at a constant concentration of Al_2Br_6 (1.0M). It is important to note that the relative increase of ν (compared to the value in the pure solvent at the same temperature) decreases as the temperature is increased. This is also consistent with the notion of formation of aggregate, which may be expected to dissociate partially as the temperature is raised, leading to a smaller effect on the kinematic viscosity at higher temperatures.

The specific conductivity.—The specific conductivity σ is shown in Fig. 13a and b for toluene and mesitylene as the solvents, respectively, as a function of temperature. The value of σ is about 4.5-5.0 times higher in toluene than in mesitylene at 20°C and about 3.0-4.0

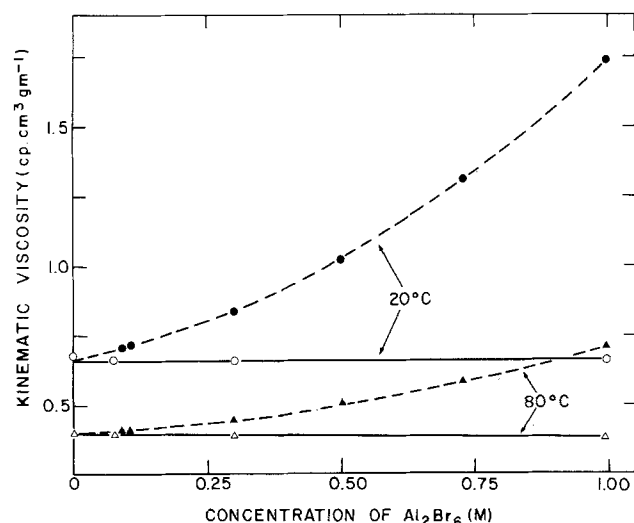


Fig. 10. Kinematic viscosity vs. concentration of Al_2Br_6 in toluene. ●●● and ▲▲▲ $R = 1.1$; ○○○ and △△△ no MBr.

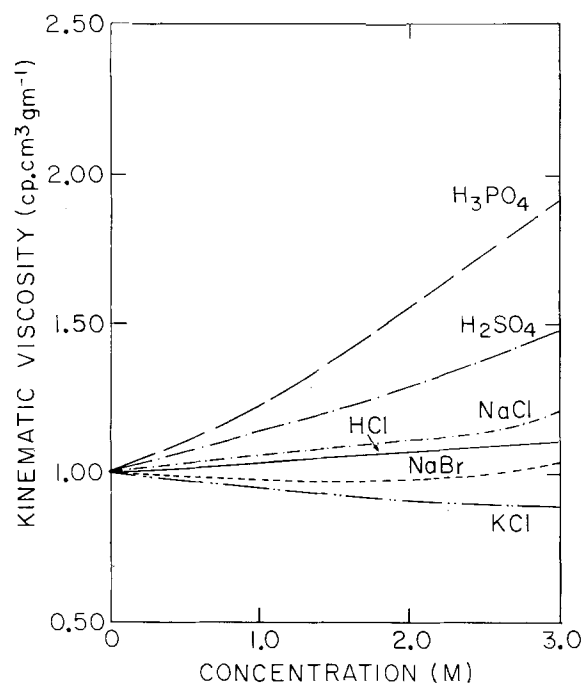


Fig. 11. Kinematic viscosity vs. concentration for some aqueous electrolytes.

times higher at 80°C, depending on the concentration of the solutes. The variation of the specific conductivity with concentration of Al_2Br_6 (at a fixed ratio of concentrations $R = 1.1$ for toluene and 1.2 for mesitylene) is shown in Fig. 14 at two temperatures. It should be noted that the scale for mesitylene is 2.5 times that for toluene in the last two figures. When ethyl benzene is used as the solvent, the specific conductivity is found to be about halfway between that of toluene and mesitylene at comparable concentrations of the solvents.

The molar conductivity.—It was shown earlier (1) that the conductivity of very pure solutions of Al_2Br_6 in toluene is extremely low, increasing by several orders of magnitude upon the addition of KBr or LiBr. It was therefore considered appropriate to calculate the

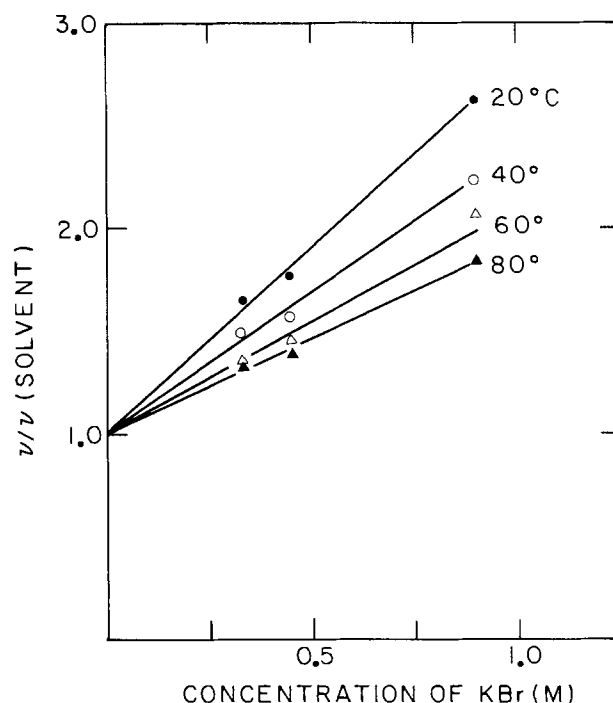


Fig. 12. Relative value of the kinematic viscosity vs. $C(\text{KBr})$ at constant $C(\text{Al}_2\text{Br}_6) = 1.0\text{M}$ in toluene.

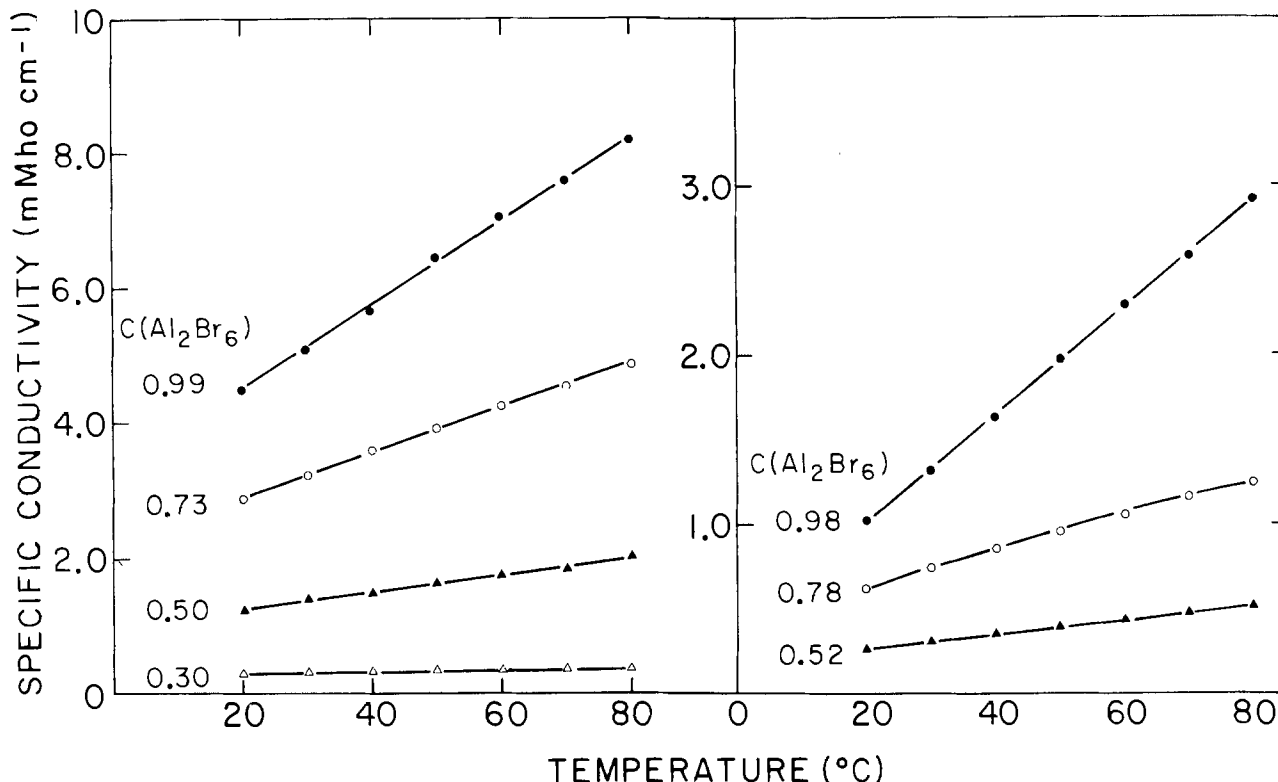


Fig. 13. Specific conductivity vs. temperature: (a) toluene ($R = 1.1$), (b) mesitylene ($R = 1.2$)

molar conductivity Λ on the basis of the concentration of MBr rather than that of Al_2Br_6 . In Fig. 15 the molar conductivity calculated in this manner is plotted as a function of concentration of Al_2Br_6 for toluene and mesitylene at two temperatures. As in Fig. 13 and 14, the scale for mesitylene is 2.5 times that for toluene.

The molar conductivity is seen to increase with increasing concentration, contrary to the behavior observed in aqueous solutions of simple salts, pointing to the possibility that new ionic species are formed in solution as the concentration is increased and that the mechanism of conduction may be radically different in concentrated solutions than that in dilute solution or in aqueous media.

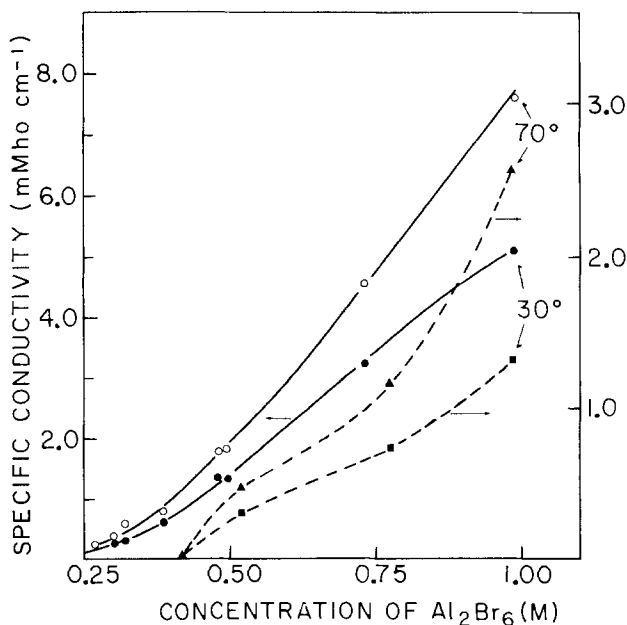


Fig. 14. Specific conductivity vs. concentration at two temperatures. Solid lines: toluene ($R = 1.1$); broken lines: mesitylene ($R = 1.2$).

The Walden product.—For an ion moving through a viscous fluid under the influence of an external electric field, Stokes law yields

$$\lambda\eta = K\tau \quad [2]$$

where λ is the molar conductivity of the ion and τ is its solvated radius. Thus the Walden product $\lambda\eta$ should be independent of temperature, to the extent that the radius of solvation is constant over the range of temperature considered. Such behavior is observed for most ions in aqueous solutions except for H_3O^+ and OH^- as shown in Fig. 16. It is well known (14) that proton conduction in acid and alkaline media occurs by a non-Stokesian hopping mechanism [the Grothuss mechanism (15)] which is not associated with movement of the whole ion through the viscous medium. As a result, the decrease of viscosity with increasing temperature does not lead to a corresponding increase of molar conductivity. On the other hand, the hopping mechanism is believed to depend on the existence of

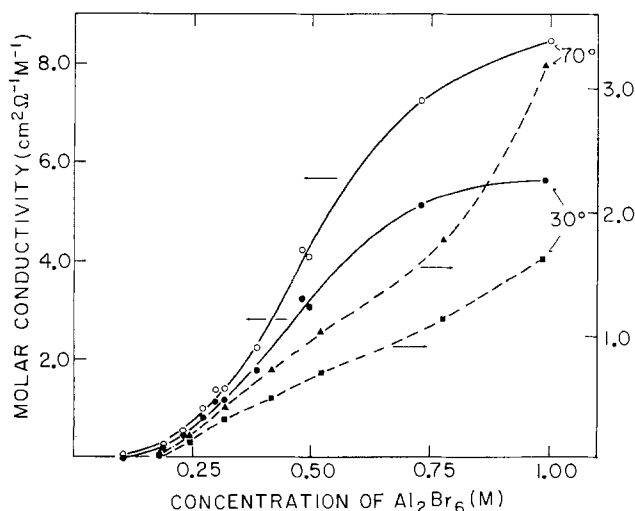


Fig. 15. Molar conductivity vs. concentration at two temperatures. Solid lines: toluene ($R = 1.1$); broken lines: mesitylene ($R = 1.2$).

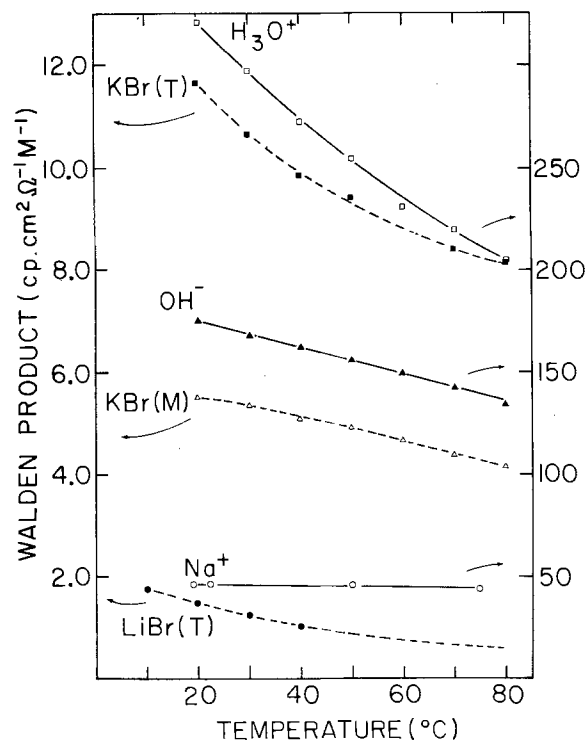


Fig. 16. Walden product in concentrated solutions of Al_2Br_6 and MBr in toluene and mesitylene. Comparison to ions in aqueous solutions.

aggregates of solvent molecules and/or a certain degree of long range order, both of which are gradually eliminated as the temperature is increased. Thus a significant decrease in the Walden product $\lambda\eta$ with increasing temperature is indicative of an unusual mechanism of conduction, probably associated with the hopping of a relatively light charge carrier between larger aggregates or a relay-type transfer of charge along a chain. The latter behavior was indicated recently in measurements of the conductivities of Br^- and I^- ions in liquid bromine and iodine, respectively (16-18). In these systems the specific conductivity was found either to be independent of temperature or to decrease somewhat with increasing temperature. Thus, a substantial decrease of the Walden product with increasing temperature was again associated with a non-Stokesian mechanism of conduction.

In Fig. 16 the dependence of $\lambda\eta$ on temperature for three ions in aqueous solutions is compared to that of concentrated solutions of KBr (or LiBr) and Al_2Br_6 in toluene or mesitylene. While the data had to be plotted on a different scale for the aqueous and the nonaqueous solvents to accommodate them on the same diagram, it can be clearly seen that the present system behaves very much like the H_3O^+ and the OH^- ions and unlike Na^+ and most other ions in aqueous solution. It could be argued that the molar conductivity Λ , which is given for a one-one electrolyte by

$$\Lambda = \alpha(\lambda_+ + \lambda_-) \quad [3]$$

may depend on temperature, due to the variation of the degree of dissociation, α , with temperature. This, however, would lead to an effect opposite to that observed experimentally, since α will most likely increase with increasing temperature.

In Fig. 17 the ratio of the Walden product at two temperatures is plotted as a function of the concentration of Al_2Br_6 in mesitylene. The data points for H_3O^+ , OH^- , and Na^+ in aqueous solutions are shown for comparison. Similar results were observed when toluene was used as the solvent or when KBr was replaced by LiBr . Down to about 0.30M Al_2Br_6 , a non-Stokesian mechanism of conductivity is seen to be

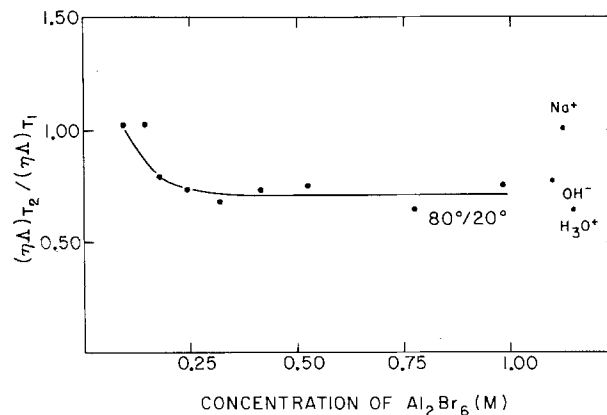


Fig. 17. Ratio of Walden products at two temperatures $80^\circ/20^\circ\text{C}$ as a function of concentration of Al_2Br_6 and KBr in mesitylene ($R = 1.2$). Values for three ions in aqueous solution are given for comparison.

predominant, leading to a value of $(\lambda\eta)_{80^\circ}/(\lambda\eta)_{20^\circ}$ significantly lower than unity, somewhere between the values reported for H_3O^+ and OH^- . As the concentration is further decreased, the above ratio approached unity gradually, indicating a change in the mechanism of conduction to regular hydrodynamic movement of the ions in the viscous medium.

Conclusions

Mechanisms of conductivity.—The results presented above lend further support for the non-Stokesian relay-type mechanism of conductivity proposed earlier (1). The values of the molar conductivity observed are unexpectedly high in view of the low dielectric constant and the high viscosity of the electrolyte. The Walden product is found to decrease with increasing temperature in a manner similar to that found for H_3O^+ and OH^- in aqueous solution and for Br^- and I^- in liquid bromine and iodine, respectively.

In solutions of Al_2Br_6 alone in toluene, the kinematic viscosity is independent of concentration (while the density increases by over 50% from the pure solvent to a 1M solution of Al_2Br_6). In mesitylene a slight increase is observed at 20°C which disappears completely as the temperature is raised to 80°C . When KBr or LiBr are added, the kinematic viscosity increases very significantly. These observations are consistent with the assumption that large molecular aggregates are formed in concentrated solution containing both solutes. It may reasonably be expected that aggregates would tend to dissociate with increasing temperature. It is indeed observed (cf. Fig. 12) that the relative increase of kinematic viscosity upon the addition of KBr to a solution having a fixed concentration of Al_2Br_6 is lowered as the temperature is increased.

Determination of the Walden product as a function of temperature in solutions of different composition indicates that a transition from the relay-type mechanism of conductivity proposed here to a more conventional Stokesian mechanism starts below a concentration of ca. 0.25M Al_2Br_6 and 0.22 KBr in toluene, although the rapid increase in molar conductivity with concentration has been observed in our previous study (1) at concentrations about an order of magnitude below this value.

Operation of plating bath.—The data presented above can be useful in the design and routine operation of aluminum plating baths.

First it is noted that both the viscosity and the specific conductivity depend on the nature of the cation in MBr . The use of KBr is preferred to LiBr in most cases because of the significantly enhanced specific conductivity, in spite of a moderate increase in viscosity. RbBr was found (1) to behave much like KBr . Other

salts, particularly of the NR_4Br type, may be found to yield even higher values of the specific conductivity.

Increasing the temperature would be desirable, since it increases the specific conductivity and decreases the viscosity. This should, however, be weighed against a possible decrease in the lifetime of the bath, due to higher rates of evaporation of the solvents, faster rates of undesirable side-reactions (particularly if the bath is not kept under rigorously dry conditions), and enhanced corrosion of all the components in the system.

Rapid analysis for quality control is of major importance in any industrial plating bath operation. Careful analysis of the data given above indicates that a combination of measurements of density, viscosity, and conductivity could serve to obtain the desired information. It was noted above that the density was mainly a function of the concentration of Al_2Br_6 , and varied very little with solvent. The viscosity, on the other hand, depends very much on the concentration of MBr and on the nature of the solvent. One mode of deterioration of a wet bath is the formation of higher molecular weight solvent molecules. This could probably be detected by a significant increase in viscosity. Since the concentration of MBr is the least likely to change during operation of the bath, a decrease of conductivity associated with increasing viscosity would also be an indication for a change in the composition of the solvent. On the other hand, a significant increase in the specific conductivity can be due to the contamination of the bath with water, which leads to the formation of HBr. This will cause a decrease in the cathodic efficiency and shorten the lifetime of the bath (5, 6).

Manuscript received Sept. 12, 1980.

Any discussion of this paper will appear in a Discussion Section to be published in the June 1982 JOURNAL.

All discussions for the June 1982 Discussion Section should be submitted by Feb. 1, 1982.

REFERENCES

1. A. Reger, E. Peled, and E. Gileadi, *J. Phys. Chem.*, **83**, 869, 873 (1979).
2. R. M. Fuoss and C. A. Kraus, *J. Am. Chem. Soc.*, **55**, 21, 2387, 3614 (1933).
3. C. A. Kraus, *J. Chem. Educ.*, **35**, 324 (1958).
4. R. M. Fuoss and F. Accascina, "Electrolytic Conductance," Interscience, New York (1959).
5. E. Peled and E. Gileadi, *Plating*, **62**, 342 (1975).
6. E. Peled and E. Gileadi, *This Journal*, **123**, 15 (1976).
7. V. A. Plotnikov and S. L. Yakubson, *Z. Phys. Chem.*, **138**, 251 (1928).
8. V. A. Plotnikov and S. L. Yakubson, *ibid.*, **147**, 227 (1930).
9. G. A. Capuano and W. G. Davenport, *This Journal*, **118**, 1688 (1971).
10. G. A. Capuano and W. G. Davenport, *Plating*, **60**, 251 (1973).
11. A. Reger, E. Peled, and E. Gileadi, *This Journal*, **123**, 638 (1976).
12. E. Peled, A. Mitavski, A. Reger, and E. Gileadi, *J. Electroanal. Chem. Interfacial Electrochem.*, **75**, 677 (1977).
13. S. Ziegel, E. Peled, and E. Gileadi, *Electrochim. Acta*, **23**, 363 (1978).
14. T. Erdey-Gruz and S. Lengyel, in "Modern Aspects of Electrochemistry," Vol. 12, Chap. 1, J. O'M. Bockris and B. E. Conway, Editors, Plenum Press, New York (1977).
15. R. A. Robinson and R. H. Stokes, "Electrolytic Solutions," Butterworth, London (1955).
16. I. Rubinstein and E. Gileadi, *This Journal*, **126**, 1368 (1979).
17. I. Rubinstein, M. Bixon, and E. Gileadi, *J. Phys. Chem.*, **84**, 715 (1980).
18. I. Rubinstein and E. Gileadi, *J. Electroanal. Chem. Interfacial Electrochem.*, **108**, 191 (1980).

Electrodeposited Chromium-Graphite Composite Coatings

Raj Narayan and B. H. Narayana¹

Department of Metallurgical Engineering, Indian Institute of Technology, Kanpur 208016 India

ABSTRACT

Electrodeposited chromium-graphite composite coatings have been produced by suspending graphite particles, using mechanical stirring, in a conventional chromium plating bath. The effect of various plating variables on the graphite content of the coating has been studied. It has been concluded that under the plating conditions studied, the second adsorption step of the two-step adsorption mechanism proposed by Guglielmi controls the deposition kinetics in this system.

A variety of particles like borides, e.g., TiB_2 (1), ZrB_2 (2, 3); carbides, e.g., B_4C (1, 4), B_6C (1, 4), Cr_3C_2 (5), TiC (1); sulfides, e.g., MoS_2 (1); and oxides, e.g., Al_2O_3 (1, 6), SiO_2 (5, 6), ZrO_2 (6) have been codeposited with chromium. Very little work has been reported on codeposition of graphite particles with chromium. Young (1) showed that codeposition of graphite with chromium was possible in the presence of Li^+ ions. However, the effect of various bath parameters on the amount of codeposited graphite was not studied.

The present investigation was undertaken to study the effect of various plating bath variables on the

amount of graphite codeposited with chromium. The applicability of Guglielmi's model in the chromium-graphite composite coating system was also studied.

Experimental

Graphite powder particles were added to the chromium plating bath of the following composition at the indicated conditions: chromic acid, 250 g/liter; sulfuric acid, 2.5 g/liter; temperature, 50°C; current density, 50 A/dm² unless otherwise stated; and plating time, 10 hr.

The solution containing the graphite powder was blended for about 3-4 hr to ensure good wetting and uniform distribution of the powder particles in the bath. Water was added to make up evaporation loss during plating.

¹ Present address: R and D Centre, Hindustan Brown Boveri Limited, Baroda, India.

Key words: codeposition, adsorption, Guglielmi's model.

Graphite content of the coatings was determined gravimetrically by dissolving it in concentrated sulfuric acid containing a few drops of formaldehyde, diluting the acid approximately 4:1 to prevent it from attacking the filter paper, filtering through a previously weighed Whatman filter paper No. 40, drying, and reweighing.

The microhardness of the coating was measured on a Tukon microhardness tester with 156° apex angle diamond pyramid indentor at 1 kg load.

Results

Increasing the graphite powder content in the plating bath increases its content in the coating at 50 A/dm² at different temperatures (Fig. 1). This behavior is in agreement with the results of other investigators in other plating systems.

Variation of current density from 20 to 55 A/dm² has practically no effect on the graphite content of the coating (Table I). This behavior is observed at all graphite contents in the plating bath.

In a conventional plating bath the concentration of chromic acid in the plating bath is about 250 g/liter. Decreasing this concentration, at a fixed ratio 1:100 between sulfuric acid and chromic acid, to 150 g/liter results in practically no codeposition of graphite, whereas increasing its concentration to 400 g/liter has practically no effect on the amount of codeposited graphite (Table I). The chromic acid concentration of the conventional plating bath, therefore, appears to be adequate for codeposition of graphite with chromium.

Increasing the solution blending time, to ensure adequate wetting and distribution of graphite in the plating bath, increases the graphite content of the coating up to 3 hr of blending (Table I). Blending beyond 3 hr does not have much effect. This trend is observed at two different bath loads of graphite, and it is expected that the trend will follow at other bath loads also.

To see the effect of aging of the plating bath on the amount of codeposited graphite, the plating baths containing different graphite contents were allowed to

Table I. Effect of current density, CrO₃ concentration, blending time, and bath aging on the amount of graphite codeposited with chromium

| Variable | Graphite content, wt, in the coating at a bath load (g/liter) | | | | | | |
|---|---|-------|-------|-------|----|----|-----|
| | 20 | 40 | 50 | 70 | 80 | 90 | 100 |
| Current density (A/dm²) | | | | | | | |
| 20 | 8.90 | 14.20 | 16.20 | 18.10 | | | |
| 30 | 9.20 | 14.00 | 15.90 | 17.60 | | | |
| 40 | 9.10 | 14.20 | 15.80 | 18.00 | | | |
| 50 | 8.80 | 13.80 | 16.20 | 17.80 | | | |
| 55 | 9.10 | 14.10 | 15.90 | 18.00 | | | |
| 60 | — | 13.90 | 15.50 | — | | | |
| CrO₃ concentration in the bath, g/liter | | | | | | | |
| 150 | 0.00 | 0.00 | 0.26 | 0.50 | | | |
| 250 | 12.10 | 12.90 | 15.00 | 17.10 | | | |
| 400 | 12.60 | 13.70 | 15.40 | 16.90 | | | |
| Blending time, hr | | | | | | | |
| 0.5 | | | 13.50 | 15.64 | | | |
| 1.0 | | | 13.63 | 15.58 | | | |
| 1.5 | | | 14.14 | 16.55 | | | |
| 2.5 | | | 14.80 | 17.30 | | | |
| 3.0 | | | — | 17.50 | | | |
| 3.5 | | | 14.95 | 17.48 | | | |
| 4.0 | | | 14.96 | 17.52 | | | |
| Bath aging time, days | | | | | | | |
| 0 | | | 15.00 | 17.20 | | | |
| 3 | | | 14.80 | 17.40 | | | |
| 8 | | | 15.10 | 17.00 | | | |

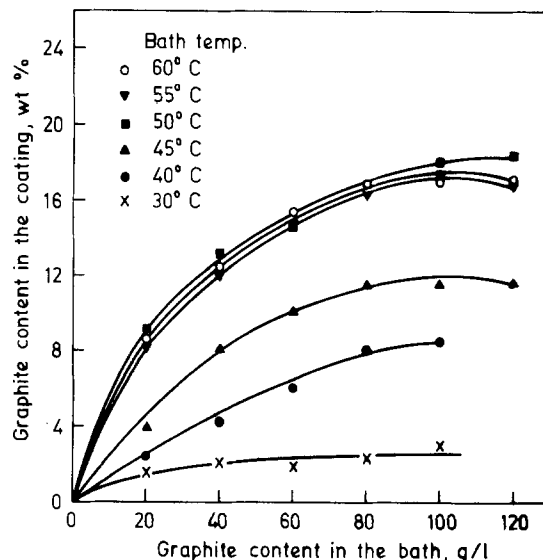


Fig. 1. Effect of graphite content in the plating bath on its content in the coating at 50 A/dm² and different temperatures.

age at room temperature. Aging up to 8 days has practically no effect (Table I).

Increasing the temperature of the plating bath from 30° to 50°C increases the amount of codeposited graphite. Beyond 50°C increasing temperature has practically no effect (Fig. 2).

Coating thickness at the center and at the edge of the specimen at two current densities and two bath loads was uniform for all practical purposes.

The microhardness of composite coatings increases with increasing graphite content, the effect becoming less pronounced with increasing annealing temperature (Fig. 3). Increasing the annealing temperature decreases the microhardness of all coatings. The beneficial effect of graphite appears to be practically lost as the annealing temperature increases (Fig. 4).

The cathode current efficiency increases with increasing current density up to about 50 A/dm² beyond which there appears to be practically no effect (Fig. 5). Variation of graphite content in the bath at a given current density does not appear to have any effect on cathode current efficiency.

Discussion

In order to explain the mechanism of codeposition Guglielmi (7) proposed a mechanism based on two successive adsorption steps. In the first step, loosely adsorbed particles are in equilibrium with particles

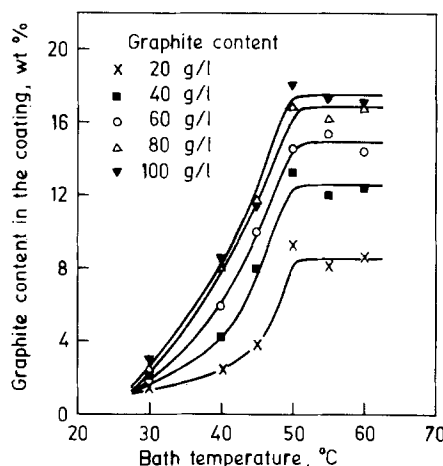


Fig. 2. Effect of plating bath temperature on the graphite content in chromium coating at 50 A/dm² and different graphite contents in the bath.

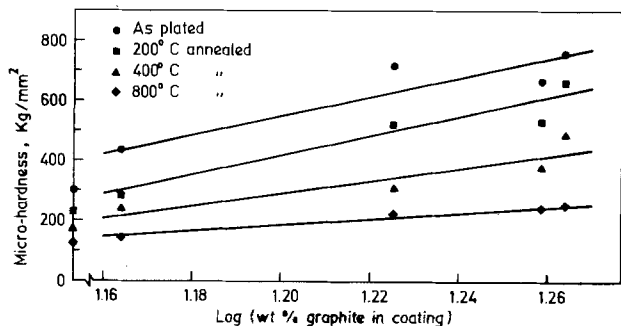


Fig. 3. Variation of the microhardness of the coating with the graphite content in the coating after annealing at different temperatures for 4 hr. (Similar effect is observed after annealing for 2 hr.)

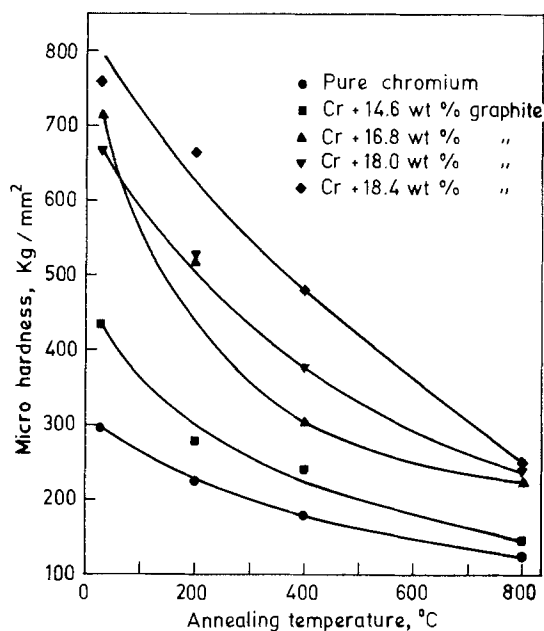


Fig. 4. Effect of annealing for 4 hr at different temperatures on the microhardness of Cr and Cr-graphite composite coatings. (Similar effect is observed after annealing for 2 hr.)

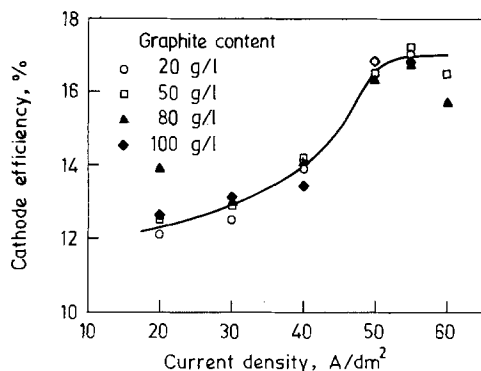


Fig. 5. Variation of cathode efficiency with current density at 50°C and different graphite contents in the bath.

in suspension and are surrounded by adsorbed ions and solvent molecules. In the second step, these adsorbed ions and solvent molecules break away from the particles so that a strong irreversible electrochemical adsorption of particles on the cathode takes place. Then these invisibly adsorbed particles are engulfed in the depositing metal. By a mathematical treatment the following expression, relating the concentration of co-deposited particles to the suspension concentration and the electrode potential, was deduced

$$\frac{C}{\alpha} = \frac{W i_0 e^{(A-B)\eta}}{n F d v_0} \cdot \left(\frac{1}{K} + C \right) \quad [1]$$

where C = concentration of particles in the bath expressed as volume percent, α = volume fraction of particles in the deposit, W = atomic weight of the deposited metal, n = valence of the metal, d = density of the metal, F = Faraday's constant, η = overpotential, K = adsorption constant, i_0 , A = constants related to metal deposition, and v_0 , B = constants related to particle deposition.

According to this model, if C/α is plotted against C at different overpotentials, a set of straight lines converging at the point where $C = 1/K$ is obtained. It has been shown that this model is valid in Ni-TiO₂, Ni-SiC, and Cu-Al₂O₃ systems. The significance of the rate-determining adsorption step and relative values of A and B in terms of the amount of co-deposited particles at different current densities has been discussed in an earlier publication (8). On the other hand, the Tafel relationship gives

$$\eta = \frac{2.303RT}{\alpha n F} \log (i_0/i)$$

Therefore, if the above model is applicable to any composite plating system, plotting C/α against C for different values of i or T should give a set of straight lines converging at a point where $C = 1/K$.

On plotting C/α against C at different temperatures, for the present investigation we obtain a set of straight lines converging at a point where $1/K = -0.95$ (Fig. 6). Although there is some scatter in the results, especially at low temperatures, it seems reasonable to conclude that the two-step mechanism proposed by Guglielmi is also applicable in the present chromium-graphite system.

After establishing the validity of the two-step adsorption mechanism in the system, attempts have been made to determine the rate-controlling adsorption step in the system by studying the effect of different

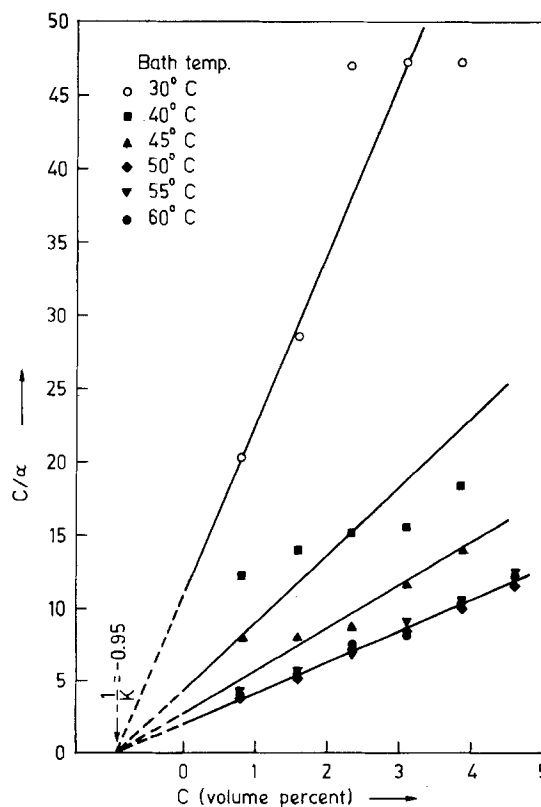


Fig. 6. Variation of the parameter C/α with C at different temperatures and 50 A/dm² in Cr-graphite system.

plating variables on the amount of codeposited particles at 50°C. The volume fraction of the codeposited particles in the coating, α , was plotted against the volume percent of particles in the bath, C , at different current densities. The resulting curve had the characteristic asymptotic shape (Fig. 7), indicating that at all current densities studied at 50°C the deposition kinetics were under the control of the same adsorption step. On plotting $\alpha i/C$ against current density, i , we observe that the term $\alpha i/C$ does not tend to become constant but keeps on increasing at all current densities at different volume percents of particles in the bath (Fig. 8). This, as discussed earlier (8), indicates that the deposition kinetics is controlled by the second adsorption step.

Plotting C/α vs. C at different current densities at 50°C yields a straight line (Fig. 9). This indicates that the two-step adsorption mechanism is also valid under these conditions. However, a single straight line is obtained instead of a set of straight lines. This would mean that under these conditions $B = A$. It was discussed earlier that when the second step controls the deposition kinetics and $B = A$, then the amount of particle codeposited, α , would be independent of current density. Our experimental results confirm this conclusion (Fig. 10).

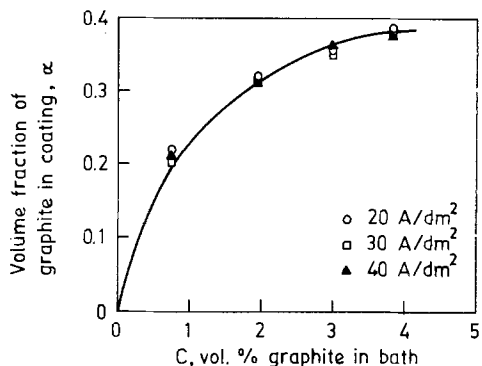


Fig. 7. Variation of the parameter α with C at different current densities at 50°C. (Data at 50, 55, and 60 A/dm² are not shown in the plot due to overlapping.)

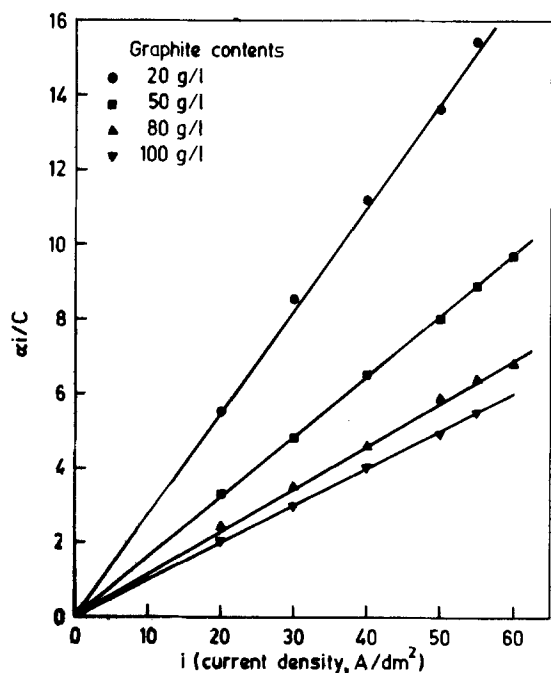


Fig. 8. Variation of the parameter $\alpha i/C$ with i at different graphite contents in the bath at 50°C in Cr-graphite system.

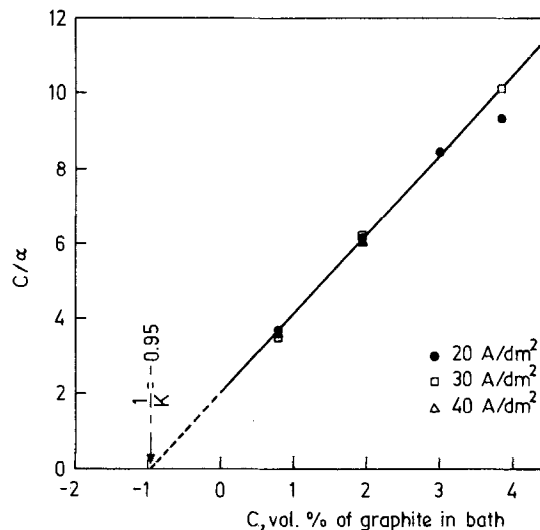


Fig. 9. Variation of the parameter C/α with C at different current densities at 50°C. (Data at 50, 55, and 60 A/dm² are not shown in the plot due to overlapping.)

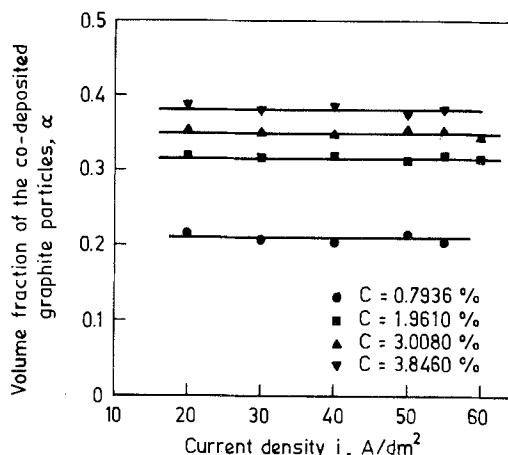


Fig. 10. Effect of current density on the volume fraction of the codeposited graphite particles at 50°C and different graphite contents in the bath in Cr-graphite system.

From Fig. 2 it can be seen that the amount of graphite codeposited with chromium increases with increasing temperature up to about 50°C, and thereafter it was practically independent of temperature. The Tafel relationship shows that both temperature and current density affect overpotential and, therefore, the amount of codeposited particles in the coating in the same way. Thus these results would indicate that up to 50°C, $B > A$ and beyond this temperature $B = A$.

At low concentrations of chromic acid, e.g., 150 g/liter, practically no codeposition of graphite particles takes place (Table I) and C/α becomes infinity. Assuming Guglielmi's two-step adsorption mechanism to be valid in this case, it follows that in Eq. [1] C/α can become infinity only if either i_0 or η is equal to infinity or the parameter v_0 or K is equal to zero. The parameters i_0 and η are related to the metal deposition, and since the cathode efficiency of the plating bath remains practically constant with the decrease in chromic acid concentration in the bath (Table I), it would appear that the parameters i_0 and η do not become infinity on decreasing the concentration of chromic acid in the plating bath. Decreasing the chromic acid concentration in the bath decreases the amount of chromium ions available to be adsorbed on the graphite particle and their subsequent reduction. The parameter v_0 , which is related to the rate of re-

duction of these adsorbed ions, can become zero if no adsorption of chromium ions takes place on the graphite particle. On the other hand, if adsorption of these ions takes place, but is not sufficient to bring about any interaction of these particles with the cathode, then K may become equal to zero. It can, therefore, be concluded that by decreasing the chromic acid concentration in the bath either the parameter v_0 or K becomes equal to zero.

Conclusions

1. It is possible to codeposit graphite from commercial hexavalent chromium plating baths without the addition of Li^+ ions.

2. The amount of graphite in the coating increases with its content in the bath at all temperatures.

3. The amount of graphite in the coating increases with increasing temperature up to about 50°C beyond which it remains constant.

4. Current density and aging time of the bath have practically no effect on the amount of graphite in the coating.

5. Codeposition of graphite with chromium does not occur if the chromic acid concentration in the plating bath is reduced to 150 g/liter.

6. Sufficient blending time is essential to obtain optimum codeposition at any bath load of graphite.

7. For all practical purposes the thickness of the coating was uniform.

8. Microhardness of the coating increases with increase in graphite content of the coating in both as-received and annealed conditions. The effect becomes less pronounced with increasing annealing temperatures.

9. Cathode current efficiency increases with increasing current density up to 50 A/dm^2 , beyond which it practically remains constant at about 16.5%. Temperature and chromic acid concentration have practically no effect.

10. Guglielmi's two-step adsorption mechanism is valid in this system.

11. The second adsorption step controls the deposition kinetics under the plating conditions studied.

12. On decreasing chromic acid concentration to 150 g/liter the amount of chromium ions adsorbed on the graphite particles either become equal to zero resulting in $v_0 = 0$ or insufficient to cause any interaction between the graphite particles and the cathode, resulting in $K = 0$.

Acknowledgments

Thanks are due to the Head, Department of Metallurgical Engineering and the Director, Indian Institute of Technology, Kanpur, India, for providing the experimental facilities.

Manuscript submitted Feb. 6, 1980; revised manuscript received Feb. 26, 1981.

Any discussion of this paper will appear in a Discussion Section to be published in the June 1982 JOURNAL. All discussions for the June 1982 Discussion Section should be submitted by Feb. 1, 1982.

REFERENCES

1. J. P. Young, Research Directorate, Weapons Laboratory, Rock Island Arsenal, Illinois, Report No. NB SIR 74-615 (Nov. 1974).
2. E. C. Kedward, K. W. Wright, and A. A. B. Tennett, *Tribol. Inst.*, 7 (5), 221 (1974).
3. E. C. Kedward, B. Kieman, and R. A. Duffin, *Brit. Pat.* 1,220,331 (1971).
4. J. P. Young, *Plating Surf. Finish*, 62 (4), 348 (1975).
5. C. A. Addison and E. C. Kedwards, *Trans. Inst. Metal Finish.*, 55 (Pt. 2), 41 (1977).
6. V. Skominas, E. Manibiene, and J. Matulis, *Liet. TSR Mokslu Akad. Drab. Ser B(1)*, 101 (1971); C. A. 75-14103W.
7. N. J. Guglielmi, *This Journal*, 119, 1009 (1972).
8. R. Narayan and B. H. Narayana, To be published in "Reviews on Coatings and Corrosion," Vol. 3, No. 4, Freund Publishing House, Israel.

Electrodeposition of Silicon onto Graphite

Gopalakrishna M. Rao,* Dennis Elwell,* and Robert S. Feigelson

Center for Materials Research, Stanford University, Stanford, California 94305

ABSTRACT

Dense, well-adherent silicon was successfully deposited at $-0.75 \pm 0.05\text{V}$ vs. Pt or Ag onto an inexpensive graphite substrate from the $\text{K}_2\text{SiF}_6/\text{LiK-KF}$ molten salt system at $745 \pm 5^\circ\text{C}$. The solute concentration was in the range of 8-14 m/o. Cross-sectional views through the deposits indicate a nodular or dendritic growth up to several millimeters on top of an underlying coherent layer of 0.2-0.5 mm thick silicon. The polycrystalline silicon has a columnar structure with normal grain size of $250 \mu\text{m}$. The impurities detected were Cu, Fe, and Ni at levels less than 0.005%. The room temperature resistivity has been found to be greater than $1\Omega \text{ cm}$. The dependence of the electrodeposition parameters on the morphology and the possibility of direct use of electrodeposited polycrystalline silicon in solar cells are discussed.

Crystalline silicon is one of the most promising materials for terrestrial solar cells and extensive research has been directed toward cost reduction.

The production of low cost solar cell grade silicon by electrodeposition from a solution of K_2SiF_6 in a fluoride melt is very attractive because 99% pure K_2SiF_6 can be produced cheaply as a fertilizer by-product. Well-adherent, inclusion-free, and relatively pure (impurities less than 10 ppm) silicon electrodeposited

onto silver from such solutions at 750°C was reported recently (1). Silver is clearly a very expensive material for use on a large scale and, although the substrates could be reused if bulk silicon were stripped from the cathode after deposition, a less expensive substrate material would be preferable.

The deposition of silicon layers on electrically conducting low cost substrates such as steel, brass, nickel, tungsten, or graphite would be a very promising approach to reduce the material processing cost of solar cells. Unfortunately, the majority of these substrates are not suitable for silicon electrodeposition since

* Electrochemical Society Active Member.

Key words: polycrystalline silicon, electrocrystallization, semiconductor, solar cell, graphite.

they form silicides at the operating temperature of 750°C. Because of its availability in the United States, graphite appears to be a good candidate as an inexpensive substrate, especially since its reactivity with silicon at 750°C is low.

A carbon cathode was first used for electrodeposition of silicon in 1854 (2). Several workers (3-6) have since then employed graphite cathodes in their studies. Although the work of Monnier *et al.* (4) yielded up to 99.99% pure silicon, the electrodeposits on graphite were, in general, powdery and incoherent and required a subsequent separation process to remove entrapped solvent.

The objective of the present study was to electrodeposit high purity silicon onto a low cost graphite substrate, in bulk form or as films with large grain size, from an inexpensive source. The morphology of the polycrystalline films produced and its dependence on the electrodeposition conditions are discussed.

Experimental

The apparatus, chemicals, and most experimental conditions used were similar to those reported by Rao *et al.* (1). An "ultracarbon" rod cathode with vitreous carbon, pyrolytic graphite or 0.73 g cm⁻³ density graphite crucible anodes, and silver or platinum flag reference electrodes were used in this study.

Because higher solute concentrations were previously found to give improved deposits (1), 8-14 mole percent (m/o) of K₂SiF₆ was mixed with the KF/LiF binary eutectic (mp 492°C), which was prepared earlier and melted to form a solution. This melt was later purified by pre-electrolysis and the purified solution was used for two or three deposition experiments.

The electrodeposition was performed at 745° ± 5°C in a three-electrode configuration with the melt contained in a vitreous carbon crucible except when the crucible was used as anode.

The morphology of the deposits was investigated by scanning electron microscopy and optical microscopy. The samples were analyzed for impurities by x-ray diffraction and by energy dispersive x-ray, electron microprobe, and emission spectroscopic analysis. Four-probe resistivity and spreading resistance measurements were made on representative samples.

Results

Electrochemical.—Dense, coherent, and well-adherent silicon was successfully electrodeposited onto graphite at constant potentials from the K₂SiF₆ system.

In our previous publication (1) it had been shown that high K₂SiF₆ concentrations were essential to obtain continuous inclusion-free silicon films. The solute concentration was, therefore, maintained in the

range of 8-14 m/o. Because the same melt was used in two or three experiments, and solute volatility was appreciable at this working temperature, the values of solute concentration given in column 2 of Table I are estimates which are corrected for volatilization by weighing the melt before and after deposition and assuming all the evaporation to be of K₂SiF₆.

Both Pt and Ag quasi-reference electrodes behaved similarly. Since Pt foil anodes were attacked and tended to fracture at the metal-vapor interface during prolonged electrolysis, graphite anodes of various types (although they are prone to fluoride attack) were used in this study. Of the graphite anodes studied, the relative rate of anode consumption was greatest for the low density graphite (0.73 g cm⁻³) and least for pyrolytic graphite.

The deposition potential was calculated from current-potential plots for each experiment. Reproducibility was rather poor between experiments, and these values varied by ±50 mV between runs in each experiment. Such variations are anticipated when uncertainties in the solute concentration and the shift in reference potential are considered (1). In contrast to experiments using a silver cathode, a nucleation overpotential of 30-100 mV was required to initiate the electrodeposition of silicon onto graphite. Although Table I shows a few extreme values, the applied potential was generally -0.75 ± 0.05V.

Current fluctuations were very common but the observed current densities were normally in the range of 10-100 mA cm⁻². Regular oscillations from 10 to 15 mA in amplitude were frequently noted during the deposition of uniform, dense, silicon electrodeposits. The cathodic current efficiencies were low at low charge densities. Higher efficiencies of up to 80% were, however, achieved during electrolysis for large charge densities.

Morphology.—Silicon electrodeposits up to 1 mm thick at the side wall and up to 2 mm thick at the edge of the graphite rod were obtained during electrolysis for several days; this wedge shape was similar to the deposits on small silver electrodes (1). It is interesting to note that electrodeposited silicon could be stripped as a sheet from the graphite substrates with little applied force. The fairly smooth surface at the silicon-graphite interface suggested uniform adhesion between the deposit and the graphite. A typical micrograph of a silicon-graphite interface is shown in Fig. 1 and provides evidence for the absence of voids, inclusions, or other discontinuities at the interface.

Cross-sectional views through the deposits, as in the example of Fig. 2, indicate nodular or dendritic growth up to several millimeters on top of an underlying coherent layer of 0.2-0.5 mm thick silicon. The upper

Table I. Experimental parameters and results

| Experiment No. | Concentration of K ₂ SiF ₆ (m/o) | Cathode potential | Approximate current density (mA cm ⁻²) | Total charge (C cm ⁻²) | Efficiency (%) |
|----------------|--|-------------------|--|------------------------------------|-----------------------|
| 1 | 11 | -0.75V vs. Pt | 160 to 100 | 5894 | Not calculated |
| 2 | 9* | -0.70V vs. Pt | 140 | 12,320 | Not calculated |
| 3 | 8* | -0.40V vs. Pt | 208 to 15 | 6570 | 60 |
| 4† | 6* | -0.60V vs. Pt | 50 to 583 | 16,067 | 7.4 |
| 5 | 13.7 | -0.55V vs. Pt | 9 | 880 | No observable deposit |
| 6 | 12* | -0.80V vs. Ag | 13 to 70 | 9017 | 69 |
| 7 | 10* | -0.78V vs. Ag | 27 | 5890 | 81.3 |
| 8 | 9* | -0.82V vs. Pt | 6.6 | 1166 | 15.3 |
| 9 | 10.5* | -0.75V vs. Pt | 10 | 8962 | 58 |
| 10 | 9* | -0.80V vs. Pt | 13 | 10,469 | 33 |
| 11 | 11.8 | -0.82V vs. Ag | 15 to 29 | 1452 | 16.8 |
| 12 | 10* | -0.85V vs. Ag | 9 to 20 | 1192 | 12.5 |
| 13 | 8* | -0.80V vs. Ag | 15 to >1000 | 121,800 | 79.3 |

* Estimated values.

† No electrolysis for about 20 hr while the furnace was accidentally shut off and during remelting.

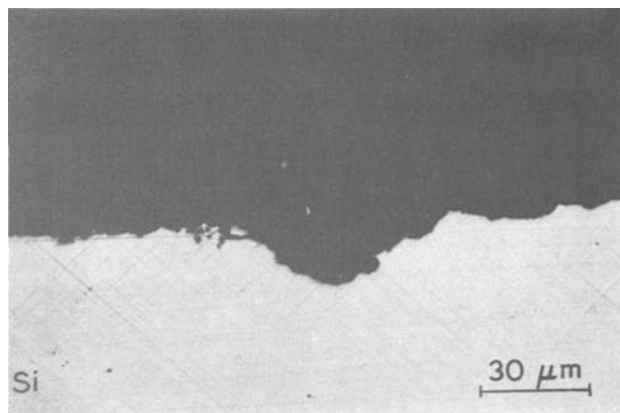


Fig. 1. Micrograph of silicon-graphite interface for experiment 10.

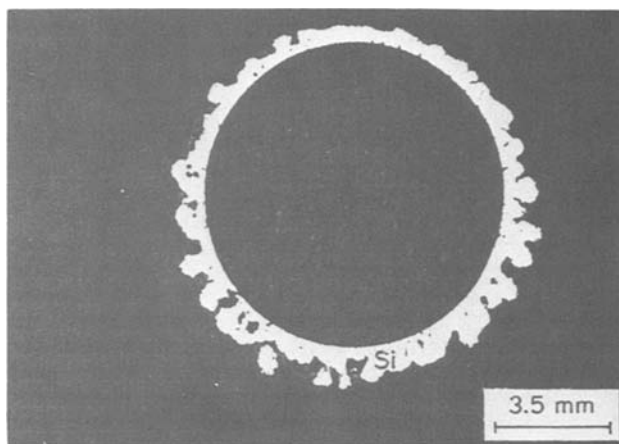


Fig. 2. Cross-sectional view of silicon deposit for experiment 10

layers of thick deposits are, in general, porous. Layers produced during electrolysis for short periods were often spongy and less crystalline (Fig. 3a), but prolonged electrolysis, however, led to densification (Fig. 3b). A grain size of $250\ \mu\text{m}$ (Fig. 4) was normal, but larger grains up to $750\ \mu\text{m}$ in diameter were observed in a few deposits. Large grains were common in the deposits produced over several days or in electrolysis involving large charge densities. The increase in grain size with increasing film thickness as shown for silicon electrodeposits on silver (1) is characteristic of samples presently produced by this method.

Figure 5 shows the grain structure of a typical deposit as revealed by an HNO_3/HF etch. Growth is columnar with a large grain size as required for the material to be used directly for solar cell fabrication.

Purity.—X-ray analysis showed only polycrystalline silicon. Moreover, electron microprobe and energy dispersive x-ray analysis did not show any impurities. Although impurity levels in the order $\text{Li} > \text{Cr} > \text{Ni} > \text{Fe} > \text{Cu} > \text{Ag} > \text{Mn} > \text{Pb} > \text{Al}$ up to 0.02% were detected in emission spectroscopic analysis for a few samples, the most common impurities were Cu, Fe, Ni, and Ag of total concentration less than 0.005%. Among the latter impurities, Cu, Fe, and Ni at this concentration level would not seriously degrade the solar cell performance (7). The fluoride attack on the furnace and the electrode materials could contaminate the melt (1) and these easily reducible metal ion contaminants are likely to co-deposit with silicon as major impurities. The source of Li could be from the entrapped melt since LiF , a major component of the melt, is highly insoluble in water or acids, and is therefore not easily removed from the deposit during cleaning.

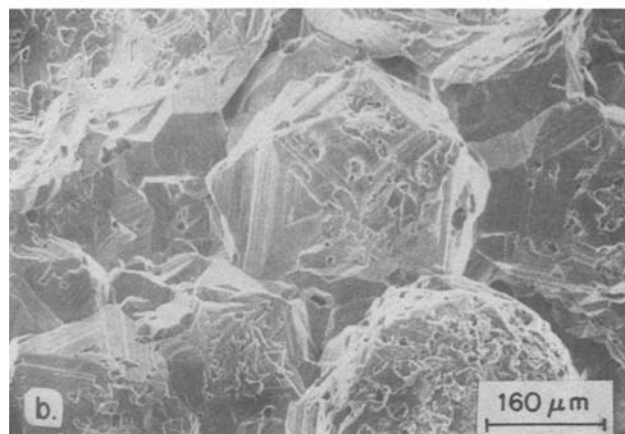
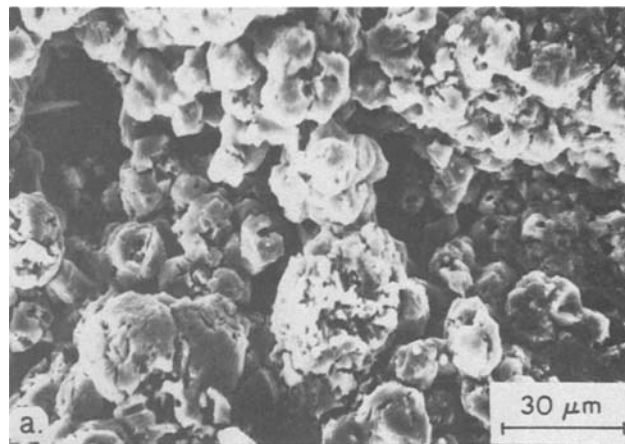


Fig. 3. Scanning electron micrograph of silicon deposits for (a) experiment 11 and (b) experiment 6.

The purity of electrodeposits, greater than 99.99%, must be compared with a purity of only 99% for the starting materials employed in the melt preparation. Thorough pre-electrolysis of the melt and an alternative furnace design as suggested in our previous report (1) would certainly yield silicon of greater purity and better quality.

Resistivity.—Preliminary measurements by a four-probe method on selected samples gave encouraging results. The measured resistivities were different in different locations of the electrodeposited silicon. Spreading resistance measurements confirmed that the major variations were due to surface roughness, but the room temperature resistivity of electrodeposited

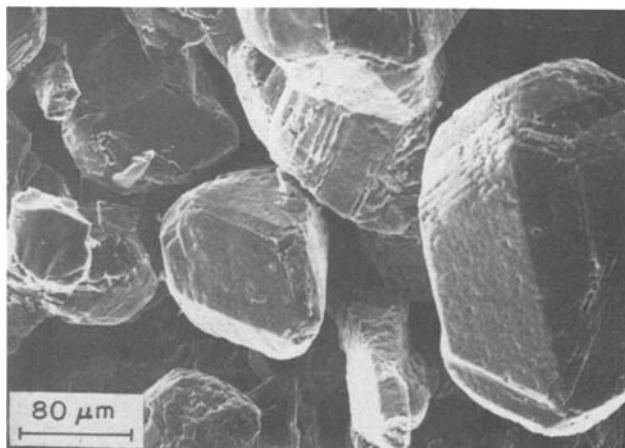


Fig. 4. Scanning electron micrograph of a silicon deposit for experiment 3.

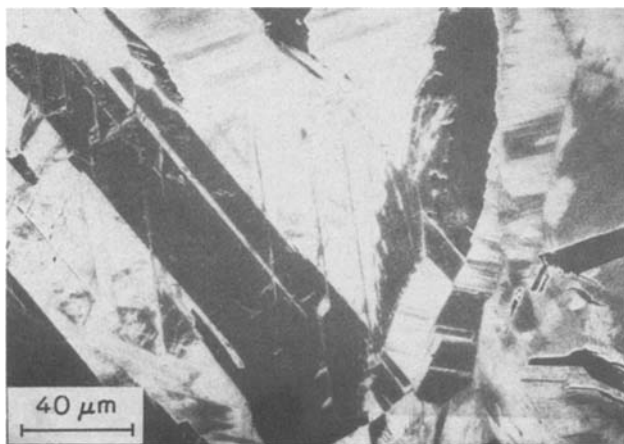


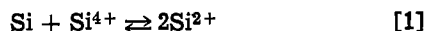
Fig. 5. Scanning electron micrograph of etched silicon surface for experiment 13.

silicon from this system has been found to be always greater than $1 \Omega \text{ cm}$.

Discussion and Conclusions

The mechanism for the transformation of silicon in the fluorosilicate into a crystalline form under the influence of an electric field is very complicated. It was suggested (1) that polynuclear silicon complexes are present in the fluoride melt and their slow dissociation, a preceding step to the charge-transfer reaction, favors the deposition of coherent films.

To explain powdery and dendritic or spongy deposits on silver during deposition at the higher cell potentials (-2V vs. Pt) used and on prolonged electrolysis of dilute K_2SiF_6 solutions at the deposition potential, respectively, we have proposed a reaction between the deposited silicon and the melt (1)



Deposition of silicon and subsequent dissolution due to reaction [1] may be a plausible explanation for the 10-15 mA current oscillations under constant potential electrocrystallization. Initially deposited silicon is assumed to be partially redissolved because of its interaction with tetravalent silicon ions in the solution according to reaction [1] to give divalent silicon ions. In consequence of this secondary reaction, the deposits for short periods of electrolysis were spongy (Fig. 3a) and of low current efficiency (Table I). When the divalent silicon ions concentration exceeded the equilibrium value (that is, upon continued electrolysis for longer periods), reaction [1] should shift to the left. This condition results in a coherent, dense, and crystalline deposit (Fig. 3b). It is interesting to note that the growth process appeared to correct the initial spongy appearance of the deposit during electrolysis for several days (Fig. 3a and b).

The porous outer surfaces of some deposits (e.g., Fig. 3b) are believed to be due to vapor phase attack of the sample while it was left above the melt in the furnace during cooling. In an independent experiment, a silicon wafer held for 6 hr above the KF-LiF melt lost nearly 0.05g and showed a brittle, black top layer. Furthermore, Cohen has also reported the vapor phase attack of electrodeposited silicon (8).

The characteristics required of a polycrystalline silicon layer for use in photovoltaic cells are as follows: (i) 100-200 μm thick to capture an acceptable fraction of the incident sunlight; (ii) individual grains of at least 100 μm to yield an efficiency of photovoltaic energy conversion greater than 10%; and (iii) relative absence of impurities that would give rise to deep-level recombination centers.

The electrodeposited silicon onto graphite from K_2SiF_6 solutions has the following properties: (i) coherent layers of 0.2-0.5 mm thick; (ii) a grain size of 250 μm ; (iii) impurity level of 0.005% of Cu, Fe, Ni, and (iv) resistivity greater than $1 \Omega \text{ cm}$.

Since crystals doped with Cu, Fe, and Ni have no observable discrete levels (7), these electrodeposited silicon samples with columnar structure show considerable promise toward meeting the requirements of solar-grade material.

Taking into consideration the cost of slicing bulk deposits into thin wafers, the electrodeposition of thick layers does not appear to be economically viable even if nodular or dendritic growth could be avoided. Deposition of thin layers of adequate grain size is the most effective way to minimize material costs. Increasing the grain size and the purity of the deposits would be highly advantageous to improve the solar cell performance. Ongoing studies will include attempts to increase the grain size by laser annealing and to reduce the impurities by the use of an alternative furnace design with internal graphite element and water-cooled stainless steel jacket.

Electrogrown silicon surfaces, in general, are not microscopically smooth. An irregular surface could have a beneficial effect in solar cells because of an increased surface area of light absorption.

Silicon costs probably represent the major economic barrier to meeting the Department of Energy cost goals for nonconcentrating arrays in the early 1980's. It was mentioned earlier (1) that electrodeposition has the potential to yield solar grade silicon at about \$1-\$2 per kg. Although deposition on silver leads to easier silicon nucleation and better morphology of the deposits, graphite has the great advantage of low cost and the greater cathodic current efficiencies. Thus, graphite appears highly promising as an inexpensive substrate for the deposition of solar-grade silicon.

Acknowledgments

This work was supported by the Department of Energy (Basic Energy Studies Division) under contract No. DE-A503-76SF-0326 PA67. Some use was also made of facilities made available to the Center for Materials Research by the National Science Foundation through its MRL Program.

Manuscript submitted Nov. 3, 1980; revised manuscript received March 9, 1981. This was Paper 378 presented at the Hollywood, Florida, Meeting of the Society, Oct. 5-10, 1980.

Any discussion of this paper will appear in a Discussion Section to be published in the June 1982 JOURNAL. All discussions for the June 1982 Discussion Section should be submitted by Feb. 1, 1982.

Publication costs of this article were assisted by Stanford University.

REFERENCES

- G. M. Rao, D. Elwell, and R. S. Feigelson, *This Journal*, **127**, 1940 (1980).
- H. St. C. Deville, *Ann. Chim. Phys.*, **43**, 31 (1854); **49**, 69 (1857).
- R. Monnier, D. Barakat, and J. C. Giacometti, U.S. Pat. 3,254,010 (1966).
- R. Monnier and D. Barakat, U.S. Pat. 3,219,561 (1965).
- G. Boe, K. Grjotheim, K. Matiašovský, and P. Fellner, *Can. Metall. Q.*, **10**, 179 (1971).
- J. M. Olson, Abstract 28, p. 74, The Electrochemical Society Extended Abstracts, St. Louis, Missouri, May 11-16, 1980.
- L. J. Cheng and D. C. Leung, Abstract 303, p. 762, The Electrochemical Society Extended Abstracts, St. Louis, Missouri, May 11-16, 1980.
- U. Cohen, *J. Electron. Mater.*, **6**, 607 (1977).

Electrodeposition of Silicon at Temperatures above Its Melting Point

Robert C. De Mattei, Dennis Elwell,* and Robert S. Feigelson

Center for Materials Research, Stanford University, Stanford, California 94305

ABSTRACT

The electrowinning of molten silicon has been achieved for the first time using a BaO/SiO₂/BaF₂ melt. The silicon formed roughly spherical or ellipsoidal droplets up to 15 mm in diameter in the small experimental system used, and these solidified with a grain size of up to 1 mm. Material of 99.97% purity can be produced from 99.5% pure starting material without additional purification or pre-electrolysis.

The electrodeposition of silicon was first achieved in 1854 (1), and it was recently (2) shown that material of 99.999% purity can be produced by this method. A major limitation in electrodeposition of solids is that a growing solid-liquid interface becomes unstable at a critical current density of approximately 40 mA/cm² (3), which for silicon would correspond to a linear growth rate of about 45 μm/hr. This limitation does not apply to electrodeposition of liquids, and the Hall process for production of aluminum is commercially viable because deposition occurs at temperatures above the melting point of aluminum. An industrial unit for Al electrodeposition operates at a current of 100-200 kA which has the additional advantage that the deposition temperature can be maintained by Joule heating by the deposition current.

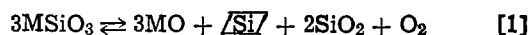
The aim of this investigation has been to develop an analogous process which can be used for electrodeposition of molten silicon. Although the energy cost of electrodeposition at temperatures above 1415°C is high, this disadvantage can be more than offset by the much higher deposition rate which is possible when the cathodic product is in the liquid state.

The furnace which was developed for electrodeposition at temperatures in the range from 1420° to 1500°C used an internal, resistance-heated graphite element with two graphite heat shields and an outer silica shield (4). The melt used for electrolysis was contained in a graphite crucible 6 cm in diameter and in height, supported on an alumina pedestal. The stainless steel jacket and brass flanges were water cooled, arrangements being provided for evacuating the chamber and for the introduction of a flowing argon atmosphere. The upper flange had fittings for the insertion into the melt of a central cathode through a vacuum feedthrough with rotation and translation capability, and for an anode which was inclined to the vertical at an angle of 6°. Both electrode fittings were insulated from the flange by machinable glass inserts which were individually cooled and attached to the flange by epoxy cement. The upper flange also had a 5 cm sapphire viewpoint which was normally protected by a movable shutter. The furnace temperature was controlled by a Eurotherm controller with step-down transformer, the controlling element being a sheathed Pt-6% Rh/Pt-30% Rh thermocouple.

The most suitable source material for silicon electrodeposition at ~ 1450°C is SiO₂. Microcrystalline silica deposits of 99.5% purity are found in large quantities near Cairo, Illinois.¹ This material was formed from the skeletal remains of marine creatures of the Devonian period and has been purified by the action of ground water. The major impurities are 0.15 weight

percent (w/o) CaO and 0.025 w/o Fe₂O₃, with 50-100 ppm each of Al₂O₃, MgO, and TiO₂.

In view of the high melting point of SiO₂, a binary or ternary system must be used to permit electrolysis at 1450°C. The simplest choice of melt is an alkali metal or alkaline earth silicate obtained by reacting the SiO₂ with the appropriate carbonate. There are three competing reactions in an electrolytic cell, which give rise, respectively, to silicon, silicon monoxide, or the alkali or alkaline earth metal as the cathodic product



Thermodynamic data for calculation of the free energy changes are not available in all cases of practical interest. However, estimates of the range of free energies over which the favorable reaction [2] will occur can be made (5) following the method of Johnson (6). These estimates indicate that potassium and sodium silicates are unfavorable for silicon electrodeposition, while aluminum, calcium, lithium, and magnesium silicates are much more favorable.

An additional consideration is that the metal oxide/SiO₂ system chosen should have one or more eutectic points below 1415°C. Most alkali metal and alkaline earth silicate systems meet this requirement, and attempts to deposit silicon at temperatures around 1450°C have been made on a range of compositions. Silicon was not produced from Rb₂O/SiO₂ or CaO/SiO₂ melts, and it was found that potassium was the primary product of electrolysis of several K₂O/SiO₂ compositions. Electrolysis of lithium silicate melts has given silicon, but not at temperatures above 1415°C. Best results were obtained using BaO/SiO₂ melts, with BaF₂ added to facilitate melting and lower the viscosity of the melt. Silicon has also been electrodeposited from melts in the system SrO/SiO₂/SrF₂.

The BaO/SiO₂ system has a single eutectic point (7) around 1370°C and composition 53 w/o SiO₂; 47 w/o BaO. A mixture of barium carbonate and silica of the corresponding molar concentration reacts and melts very slowly at 1500°C but the addition of a few percent of BaF₂ greatly facilitates melting through its fluxing action.

Figure 1 shows a current vs. voltage plot for a melt of original composition 63.2 mole percent (m/o) SiO₂; 22.2 m/o BaCO₃; 14.5 m/o BaF₂ at temperatures above and below the melting point of silicon, using graphite electrodes. The minimum deposition potential in both cases is in the region of 0.25V and the difference in the slopes is about 60%.

Deposition normally proceeds at a constant potential in the range 0.8-16V, with a corresponding current

* Electrochemical Society Active Member.

Key words: silicon, electrodeposition, solar cell, semiconductor.

¹ Illinois Mineral Corporation.

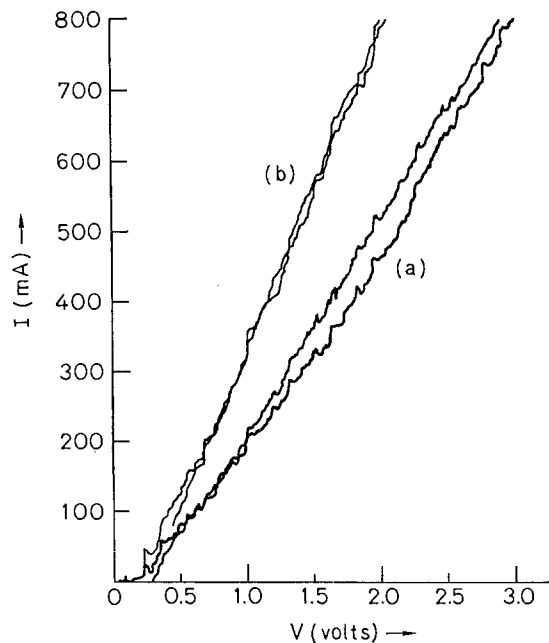


Fig. 1. Plot of current vs. potential difference between graphite electrodes for $\text{BaO/SiO}_2/\text{BaF}_2$ melt at (a) 1393°C , (b) 1465°C .

between 120 mA and 2.0A on a cathode area of about 2 cm^2 . The deposit is in the form of small lumps roughly spherical in shape and up to several mm in diameter. A typical deposit is shown in Fig. 2. The silicon normally gathers in a horizontal layer close to the end of the cathode rod. The density of the silicon appears to be very similar to that of the melt and it does not show a marked tendency to rise or sink, the rate of movement being very slow because of the high melt viscosity. In order to remove the silicon efficiently from the melt it is desirable to collect the deposit into larger pieces. This coagulation may occur during prolonged electrolysis, and Fig. 3 shows an example of a single lump of silicon weighing over 1.6g, produced from a 125g melt. This lump contained a little over 1/3 of the total silicon deposited.

The faradaic efficiency (weight deposited divided by weight calculated by Faraday's law) of deposition is typically 15-22%, but 40% has been achieved during electrolysis for about two days. The origin of the departure from 100% efficiency has not been fully established, but the simultaneous liberation of silicon monoxide is a competing process and ohmic conduction in the melt may occur via electronic conductivity or via carbon particles which become detached from the anode and float on the melt surface. Variations in

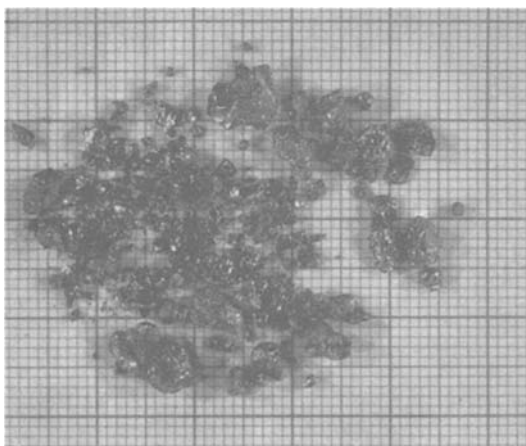


Fig. 2. Silicon produced in a typical electrodeposition experiment from $\text{BaO/SiO}_2/\text{BaF}_2$ melt at temperature above its melting point.

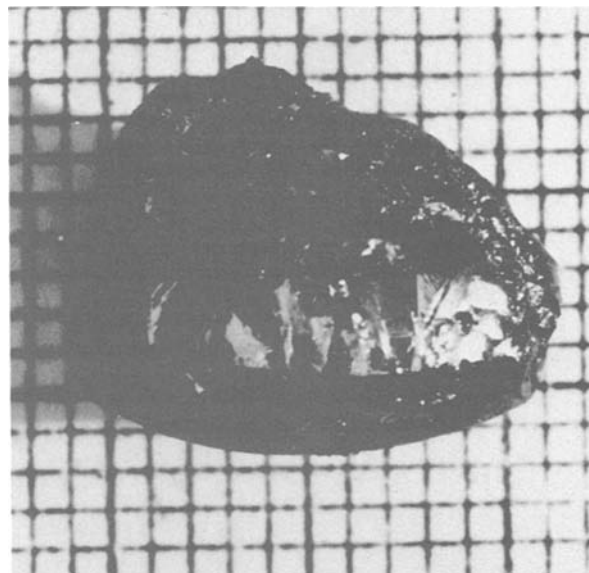


Fig. 3. Lump of electrodeposited silicon weighing 1.6g, produced during an experiment of 50 hr duration.

cathodic efficiency cannot be correlated with the concentration of fluoride in the melt, which has been varied from 8 to 20 m/o. It appears likely that the efficiency is reduced by the back-reaction between anodic and cathodic products, since it depends on the geometry of the electrode arrangement.

The purity of material produced to date is 99.97 w/o, the major impurities being 0.02 w/o iron, 0.003 w/o calcium, 0.002 w/o manganese, 0.001 w/o strontium, and 0.001 w/o titanium. This level of impurities is, of course, much too high for solar cell applications, but experience has shown that the impurity level can be reduced by pre-electrolysis using a sacrificial cathode (2, 8) or other techniques. Reduction of the impurity level by an order of magnitude or more should be possible without significant increase in the complexity or cost of the process.

The room temperature resistivity of the silicon is about $0.2\ \Omega\text{-cm}$. If allowance is made for grain boundary effects, this value corresponds (9) to an active impurity concentration of $\sim 10^{18}$ carriers cm^{-3} . This level is considered promising in view of the fact that a pre-electrolysis stage was not used.

Purification will be a major aspect to be studied in future work, as will improving the deposition efficiency and developing a technique for removing the silicon from the melt.

Acknowledgments

The authors would like to thank the Department of Energy for support of this work under contract No. DE-A503-76SF00326 PA67, and Susan M. Cain for technical assistance during part of the program. Some use was made of facilities provided to the Stanford Center for Materials Research through the NSF/MRL Program.

Manuscript submitted Nov. 3, 1980; revised manuscript received March 9, 1981. This was Paper 377 presented at the Hollywood, Florida, Meeting of the Society, Oct. 5-10, 1980.

Any discussion of this paper will appear in a Discussion Section to be published in the June 1982 JOURNAL. All discussions for the June 1982 Discussion Section should be submitted by Feb. 1, 1982.

Publication costs of this article were assisted by Stanford University.

REFERENCES

1. H. St. C. Deville, *Compt. Rend. Acad. Sci. Paris*, **39**, 323 (1854).

2. G. M. Rao, D. Elwell, R. S. Feigelson, *This Journal*, **127**, 1940 (1980).
3. R. C. DeMattei and R. S. Feigelson, *J. Cryst. Growth*, **44**, 115 (1978).
4. R. C. DeMattei and D. Elwell, Unpublished.
5. J. A. Poris and R. A. Huggins, Private communication.
6. K. E. Johnson, "High Temperature Technology," pp. 493-98, Butterworths, London (1967).
7. "Phase Diagram for Ceramists," E. M. Levin, C. R. Robbins, and H. F. McMurdie, Editors, Amer. Ceram. Soc., Columbus, OH (1964).
8. U. Cohen, *J. Electron. Mater.*, **6**, 607 (1977).
9. M. Newberger and S. J. Welles, Silicon, Rept. AD 698342, (October 1969).

Mass Transport Characterization of Donnan Dialysis: The Nickel Sulfate System

Patrick K. Ng* and Dexter D. Snyder*

General Motors Research Laboratories, Electrochemistry Department, Warren, Michigan 48090

ABSTRACT

There is a need for reliable models of the mass transfer characteristics of hollow tube Donnan dialyzers, to guide application to industrially significant problems such as recovery from electroplating waste water. This work is focused on determining mass transport correlations in a shell-and-tube dialyzer, fabricated from ion-selective membranes, used to extract nickel from dilute nickel sulfate solution with sulfuric acid as the stripping agent. Correlations between mass transport coefficient and Reynolds number are reported for both laminar and turbulent flow regimes.

Donnan dialysis concentration of ions, using selective membranes and a chemical potential gradient, has only recently been considered seriously as an industrial separation and purification technique. Wallace, an early advocate, used the approach to concentrate uranyl, strontium, lanthanum, silver, and copper salts (1, 2). Until very recently, Donnan dialysis has been judged too slow to be practical. Since separation is diffusion controlled, one typically needs extremely thin membranes which are effective ion-selective barriers. Membranes available in the late 1960's and early 1970's were relatively thick and lacked chemical durability. Better membranes are available today, but there is a lack of data and models by which to design practical systems.

Elements of Donnan dialysis concentration of nickel ions are illustrated in Fig. 1. The cation-selective membrane ideally excludes the anions, but permits cations to exchange as the system approaches the equilibrium dictated by the Donnan relation, in this case

$$\frac{(a_{\text{Ni}^{\text{I}}})}{(a_{\text{Ni}^{\text{II}}})} = \frac{(a_{\text{H}^{\text{I}}})^2}{(a_{\text{H}^{\text{II}}})^2} \quad [1]$$

in which a is the activity of the ions on either side of the membrane. If the gradient of the stripping chemical, sulfuric acid in this case, is kept high, the nickel ions can actually be transported against their activity gradient. In the present case where 0.5M sulfuric acid is used to strip nickel from 0.0017M nickel sulfate (100 ppm Ni), the nickel ions can be transferred almost quantitatively. The rate at which this ion exchange occurs depends both on the membrane properties and on the boundary-layer film at the membrane-solution interfaces.

Wallace and other workers (1, 3) dealt with relatively slow flows of both feed and stripping streams. However, the hydrodynamic environment of the membrane often controls the performance. Lake and Mel-sheimer (4) approached this issue by examining the exchange of sodium, potassium, and hydrogen ions across a cation-selective membrane, using a plate-and-

frame dialyzer. Their approach involved determining the membrane resistance at high agitation, and determining the boundary-layer mass transport coefficients using a computer iteration scheme. For Reynolds numbers up to 500, they observed a dependence of ion transport rate on the 0.65 power of the Reynolds number.

Eisenmann and Smith (5) carried out an extensive evaluation of Donnan dialysis softening as a possible adjunct to distillation desalting of brackish water. With limited success, they introduced the affinity driving force and built an analytical model of the process which they used for economic projections. They found a dependence of the sodium-calcium exchange rate on a power of the Reynolds number in the range 0.33-0.67 for a tortuous path spacer. Eisenmann (6) recently reported on the use of Donnan dialysis to recover nickel sulfate concentrate from dilute plating rinse

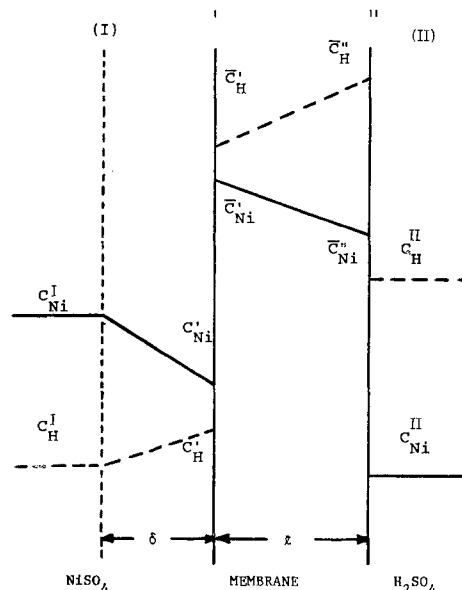


Fig. 1. Donnan dialysis

* Electrochemical Society Active Member.

Key words: membrane, interfaces, connection, ion exchange.

water. Using perfluorosulfonic acid membranes, in hollow tube form, he measured nickel fluxes in the range $0.3\text{--}3 \times 10^{-9}$ mol/(cm² · sec) for a feed in the range 25–100 ppm nickel ion. His experiments spanned the Reynolds number range 50–300.

The present work was focused on determining mass transfer correlations for the boundary layer, and on estimating the interdiffusion coefficient of nickel in the membrane. The two-cation system offers results which can be interpreted and compared with previous results, and the nickel waste is also a significant industrial problem worthy of better solutions than now exist commercially. Tubular cation-selective membranes were selected for their suitability in designing recovery and recycle modules with high surface-to-volume ratios, giving potentially higher volumetric nickel separation rates. Both sulfuric acid and nickel waste streams were circulated continuously through the dialyzer.

Experimental

Membrane dimension measurements.—Table I shows the dimensions of the membranes used in this study. Dimensions were determined by first soaking a piece of the tubing in a mixture of nickel sulfate (100 ppm in nickel) and 1N sulfuric acid. The tubing was then cut open and its thickness measured with a micrometer. Its outside diameter was measured using a microscope and the inside diameter was subsequently calculated.

Apparatus.—The dialyzer is pictured in Fig. 2, and a schematic diagram of the experimental setup is shown in Fig. 3. Membranes used were commercial perfluorosulfonic acid type. The shell-and-tube module was 17.15 cm long and the inside diameter of the shell was 0.48 cm. For membrane 810, only a single membrane tube was used. In the case of the smaller membrane 811, three membrane tubes were used to guarantee an appreciable change in nickel concentration over the experiment period. Nickel sulfate solution (100 ppm in nickel) was circulated through the tube side, while sulfuric acid (1, 2, or 4N) was pumped continuously through the shell side. Each stream contained initially 250 ml solution, and its flow rate was controlled by a tubing pump and monitored with a flowmeter.

Preliminary results suggested that the boundary-layer resistance on the feed solution side (nickel sulfate) was dominant. In practice, the process does not depend on which side of the membrane each solution contacts. However, with the feed solution being the principal target of this study, one could achieve higher linear velocities when this feed was passed through the tube, and this extended the range of the correlation which was ultimately established.

Procedures.—The dialyzer was first flushed with distilled water to remove any nickel sulfate and sulfuric acid left in the system. This water was then drained and both streams of electrolyte were pumped through their respective loops to start the experiment. Samples were taken from each reservoir at time intervals, and the nickel concentration of each was determined by atomic absorption analysis. To minimize the error of changing volume, the total amount taken for sampling over the experiment was limited to less than 10% of the initial reservoir volume (250 ml). At the end of the experiment (3–4 hr), the volume of each stream was measured by draining the solution. In addition, both temperature and pH of the solutions were measured. Results indicate that pH of the tube-side

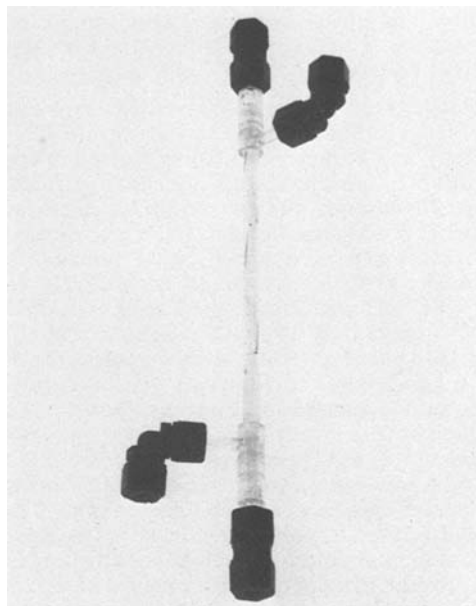


Fig. 2. Dialyzer

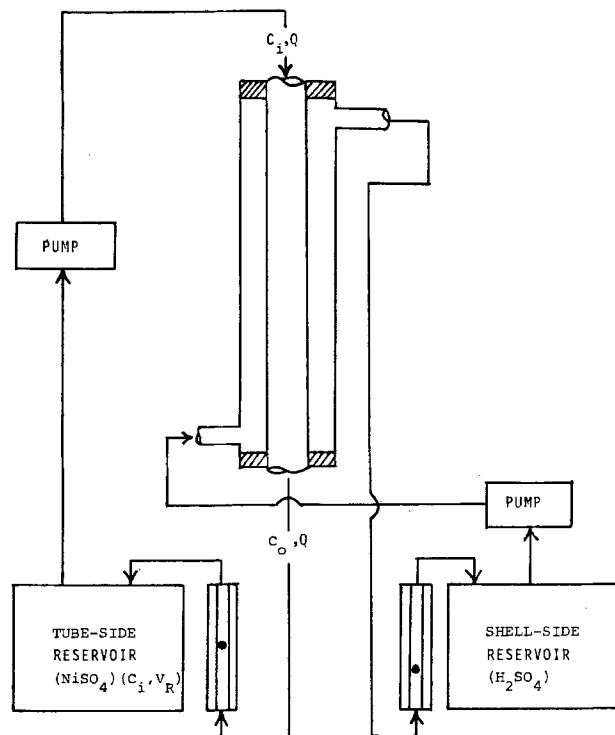


Fig. 3. Schematic diagram of the experiment

reservoir changed typically from about 5.5 to 2.2. The shell-side pH remained relatively constant, with a maximum increase of about 0.1 pH unit. Due to heat generated by the tubing pumps, temperature increases from 2°C (low flow rates) to 7°C (high flow rates) were found. All experiments indicated a volume decrease for the tube-side reservoir of 5–6 ml. This can be explained by a combination of evaporation, osmotic transport, and the migration of hydration water with the ions.

Results and Discussion

This work was focused on separating the membrane and boundary-layer effects in the Donnan dialysis concentration of nickel sulfate from an extremely dilute starting solution. This has been approached by studying the nickel transport rate as a function of the hydrodynamic condition of the membrane dialyzer.

Table I. Membrane dimensions

| Membrane | Thickness (cm) | Inside diam (cm) | Outside diam (cm) |
|----------|----------------|------------------|-------------------|
| 810 | 0.0368 | 0.2383 | 0.3119 |
| 811 | 0.0127 | 0.0637 | 0.0891 |

Specifically, the nickel concentration-time relation is determined for a membrane tube dialyzer operated under preset flow conditions.

Rate constant of the tube-side reservoir.—Figure 4 shows typical results for the 810 membrane. The mass of nickel in the reservoir is here plotted instead of concentration to eliminate any discrepancy introduced by change in volume due to sampling. Qualitatively, higher nickel feed rates favor faster removal of nickel from the reservoir. The nickel mass increase in the sulfuric acid reservoir was found consistently to be a mirror of the decrease in the feed reservoir. Thus, the membrane appears to be neither source nor sink for nickel in this process. These nickel mass-time results (Fig. 5) suggest that the reservoir can be regarded as a reactor with a first-order rate constant (m) equaling the slope of the best fit line.

Experiments were also conducted to study the effects of shell-side flow rate and sulfuric acid concentration on the transfer rate, and the results are shown in Fig. 6a and b. From examination of Fig. 6a, it is clear that both acid-side flow rate and acid concentration (1-4N) are unimportant in affecting the nickel transport rate. These findings agree with the work of Lake and Mel-sheimer (4), where they find that the boundary-layer resistance on the acid side is small. The independence from sulfuric acid concentration is reasonable because the acid gradient remains high in this 1-4N range. Temperature effects can be considered to be small because the maximum change at high flow rate was only 7°C.

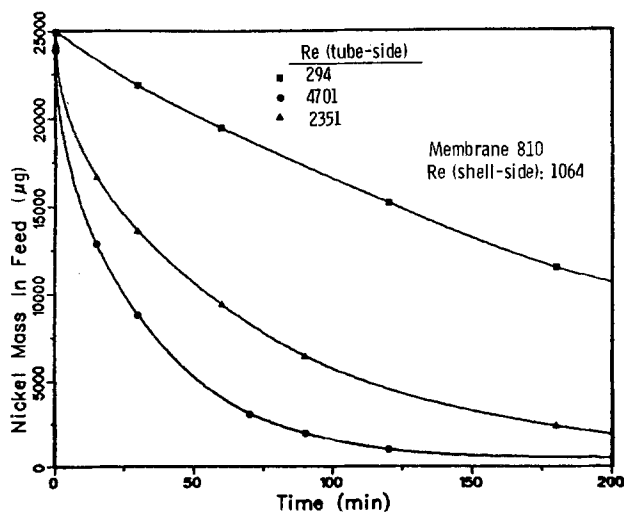


Fig. 4. Transient variation of nickel mass in the reservoir

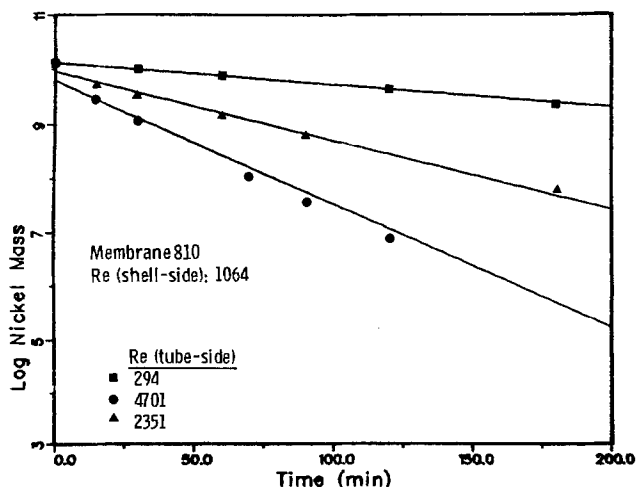


Fig. 5. Transient variation of log nickel mass in the reservoir

Boundary layer and membrane resistances.—Results in Fig. 6 indicate that the tube-side boundary-layer resistance and the membrane resistance are the controlling factors for the nickel transport. The relative values of these two resistances can be estimated with a series model used by Helfferich (7), Gregor (8), and others. For the case of nickel and hydrogen, we will assume complete coion exclusion and define diffusion coefficients by the following flux equations

$$J_{Ni} = \frac{\bar{D}_{Ni-H}}{l} (\bar{C}'_{Ni} - \bar{C}''_{Ni}) = \frac{D_{Ni}}{\delta} (C_{Ni}^I - C'_{Ni}) \quad [2]$$

$$J_H = \frac{\bar{D}_{Ni-H}}{l} (\bar{C}'_H - \bar{C}''_H) = \frac{D_H}{\delta} (C_H^I - C'_H) \quad [3]$$

\bar{D}_{Ni-H} , and D_{Ni} and D_H are the diffusion coefficients in the membrane and the boundary layer, respectively. Figure 1 gives meaning to the other symbols. An effective mass transfer coefficient (K_m) can also be defined for the membrane as

$$K_m = \frac{\bar{D}_{Ni-H}}{l} \quad [4]$$

At each interface, the ions are assumed to be distributed according to the Donnan equilibrium, ignoring activity effects

$$\frac{C'_{Ni}}{C'_{Ni}} = \frac{(C'_H)^2}{(C'_H)^2} \quad [5]$$

on feed side and

$$\frac{C_{Ni}^{II}}{C''_{Ni}} = \frac{(C_H^{II})^2}{(C'_H)^2} \quad [6]$$

on acid side.

Electroneutrality within the membrane is expressed by

$$\sum z_i \bar{C}_i - \bar{X} = 0 \quad [7]$$

where \bar{X} is the concentration of fixed negative charges in the wetted membrane. With zero net current, the fluxes are related by

$$\sum z_i J_i = 0 \quad [8]$$

The interfacial concentrations can be written as follows by rearrangement of Eq. [2] and [3], and by use of Eq. [8]

$$C'_{Ni} = -\frac{\delta J_{Ni}}{D_{Ni}} + C_{Ni}^I \quad [9]$$

$$C'_H = \frac{2\delta J_{Ni}}{D_H} + C_H^I \quad [10]$$

Equations [2], [5]-[7], [9], and [10] can now be solved for fluxes and interfacial concentrations as functions of bulk concentrations, diffusivities, and membrane and boundary-layer thicknesses. Figures 7a and b show the result of such a calculation using parameter values close to those expected in the experiments. For bulk nickel concentration less than 10^{-5} mol/ml, the boundary layer is the major controlling factor for the nickel transfer. The membrane resistance is negligible until the bulk nickel concentration reaches 10^{-4} mol/ml. Helfferich (7) gives a detailed description of these resistances.

Figure 7 suggests that the tube-side boundary-layer resistance is the dominant limitation for nickel transfer in the concentration range studied in this work. This resistance depends on the hydrodynamic conditions and is best characterized by a mass transfer coefficient, K_{BL} . K_{BL} can be calculated from the rate constant of the reservoir based on a model with the following assumptions: (i) Nickel concentration at the membrane surface is negligible compared to the bulk concentration; (ii) the tube-side solution is well mixed and its concentration is thus uniform and equal to the

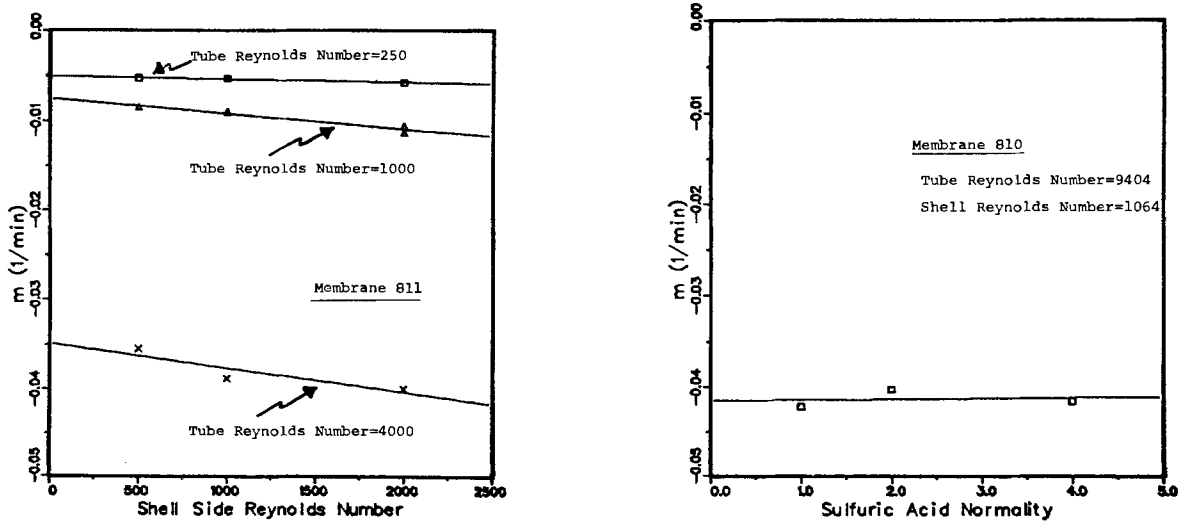


Fig. 6. Dependence of mass transfer on secondary factors. (a) Shell side (1N H₂SO₄) Reynolds number; (b) sulfuric acid concentration

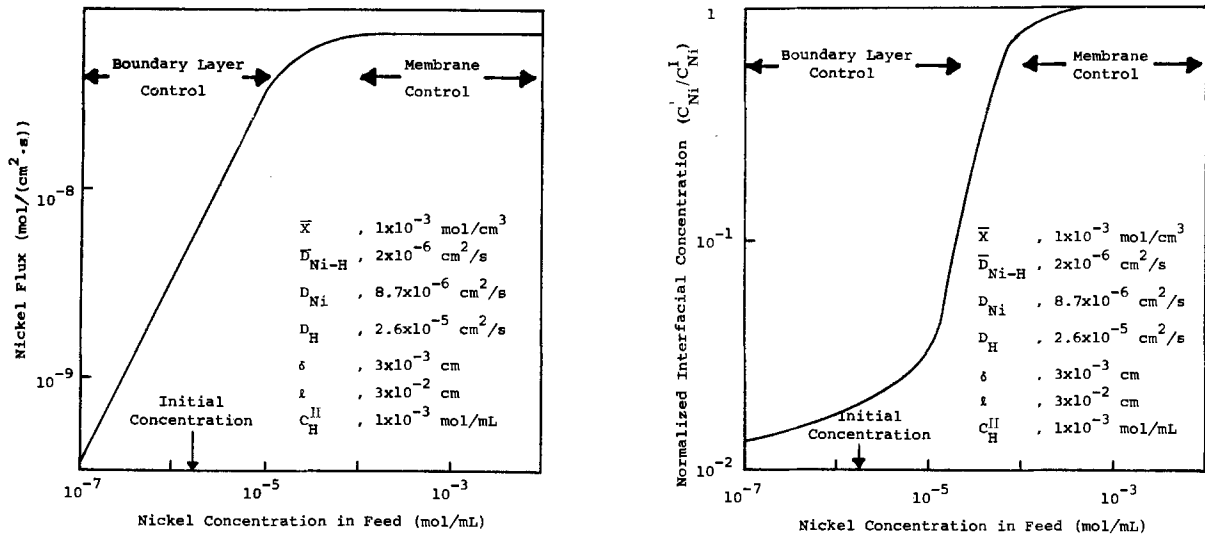


Fig. 7. (a, left) Dependence of flux on bulk nickel concentration; (b, right) dependence of interfacial nickel concentration on bulk nickel concentration.

outlet concentration; (iii) at each time, the dialyzer operates at steady state.

The first assumption implies that any nickel transferred to the membrane surface will be transported immediately through the membrane, and its validity is illustrated in Fig. 7b. Assumptions (ii) and (iii) are reasonable if the flow rates are relatively high. Referring to the schematic diagram in Fig. 3, one can obtain a mass balance equation for nickel in the tube side of the dialyzer, as follows

$$Q(C_i - C_o) = K_{BL}AC_o \quad [11]$$

where A is the membrane area based on the inside diameter and Q is the volumetric flow rate. C_i and C_o represent the bulk concentration of Ni in the tube side and are understood to be the same as C_{Ni}^I in Fig. 1. Similarly, a mass balance of the reservoir gives

$$V_R \frac{dC_i}{dt} = Q(C_o - C_i) \quad [12]$$

where V_R is the reservoir volume. The results in Fig. 5 also imply that

$$C_i = C_i^o \exp(mt) \quad [13]$$

where C_i^o is the initial nickel concentration in the reservoir, and m is the rate constant. Combining Eq. [11]-[13], one obtains the relationship between K_{BL} and m , that is

$$K_{BL} = \frac{-mV_R}{A \left(1 + \frac{mV_R}{Q}\right)} \quad [14]$$

The flux J can also be calculated by

$$J_{Ni} = \frac{Q}{A} (C_i - C_o) = \frac{-mV_R}{A} C_i \quad [15]$$

With the K_{BL} values calculated by Eq. [14], mass transfer correlations were subsequently obtained and are shown in Fig. 8. The exponent on the Schmidt number (Sc) was taken as 1/3 according to convective mass transfer in the pipe. Kinematic viscosity of water and diffusion coefficient of NiSO₄ at infinite dilution ($D_{NiSO_4} = 8.674 \times 10^{-6}$ cm²/sec) were used to estimate Sc . The transition from laminar flow to turbulent flow occurs at Reynolds numbers in the range 1000-2000. The generally accepted Reynolds number transition value for smooth tubes is about 2100, but vibration of this membrane tubing could well introduce turbulence at lower Reynolds number. Least square fits to the two regions give the following correlations

$$\begin{aligned} Sh &= 0.00272 Re^{1.024} Sc^{1/3} & 10^3 < Re < 10^4 \\ Sh &= 0.1663 Re^{0.475} Sc^{1/3} & Re < 10^3 \end{aligned} \quad [16]$$

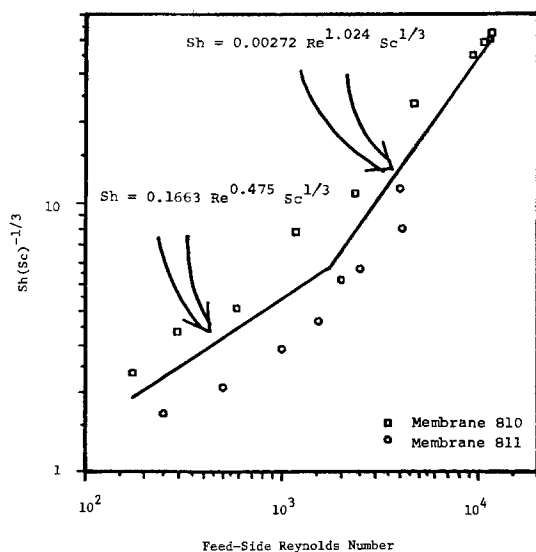


Fig. 8. Mass transfer correlations

An important property of the membrane is the interdiffusion coefficient of nickel and hydrogen ions ($\bar{D}_{\text{Ni-H}}$). Although experiments were performed where boundary-layer resistance is controlling, $\bar{D}_{\text{Ni-H}}$ can be estimated by extrapolating results at high flow rates. As the flow rate increases, the membrane becomes more dominant and the interfacial concentrations can be approximated by bulk concentrations. Equations [2], [5], [6], and [7] can then be used to calculate K_m at any flow rate and bulk nickel concentration. By extrapolating the data in a plot of $1/\text{Re}$ vs. $1/K_m$, one can obtain the value of K_m at infinite flow rate where membrane is the only resistance. Figure 9 shows the result of this exercise for membranes 810 and 811 at bulk nickel concentrations of 100 and 55 ppm. Interdiffusion coefficients ($\bar{D}_{\text{Ni-H}}$) thus calculated are summarized in Table II and their magnitude agrees with the range reported in literature. The dependence of $\bar{D}_{\text{Ni-H}}$ on bulk concentration needs further investigation.

Conclusions

Donnan dialysis, even with its low transfer rate, is now a promising separation technique with the availability of hollow fiber membranes from which modules can be built to give high surface area-to-volume ratio. The transfer rate depends, in general, on both membrane properties and hydrodynamic conditions outside

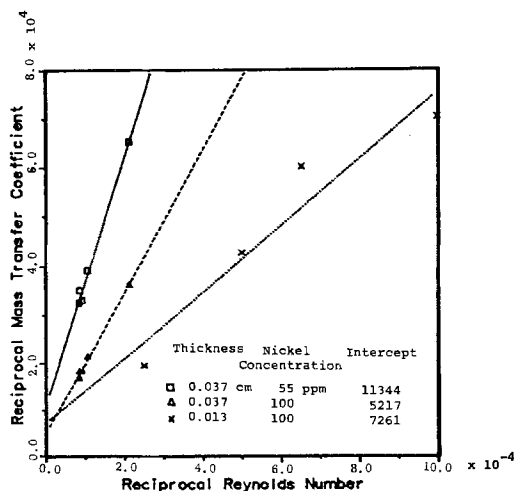


Fig. 9. Extrapolation of membrane resistance

Table II. Membrane interdiffusion coefficient

| Membrane | Bulk Ni concentration mol/ml ($\times 10^6$) | $\bar{D}_{\text{Ni-H}}$ cm ² /sec ($\times 10^6$) |
|----------|--|--|
| 810 | 1.7 | 7.053 |
| 810 | 0.935 | 3.244 |
| 811 | 1.7 | 1.75 |

the membrane. For removal of nickel from dilute sulfate solution, this work characterized these two dependencies, particularly that for hydrodynamic conditions and generated correlations for design purposes.

Within the 0-0.0017M range of nickel concentration studied, the results indicate that the boundary layer is the major resistance to nickel transport. Membrane resistance is important only at high flow rates and high concentrations. A series model was employed to estimate the relative importance of these two resistances under different experimental conditions.

The boundary-layer effect is characterized by mass transfer correlations based on a mass balance for the dialyzer. In dimensionless quantities, these correlations are given by

$$\text{Sh} = 0.00272 \text{Re}^{1.024} \text{Sc}^{1/3} \quad 10^3 < \text{Re} < 10^4$$

$$\text{Sh} = 0.1663 \text{Re}^{0.475} \text{Sc}^{1/3} \quad \text{Re} < 10^3$$

and the exponents are in reasonable agreement with values in the literature.

The membrane interdiffusion coefficient ($\bar{D}_{\text{Ni-H}}$) can be estimated by extrapolation, using data at high flow rates. Its magnitude (10^{-6} cm²/sec) agrees with the range reported in literature for other metal ions. As Lake and Melsheimer (4) have indicated in their work, the extrapolation technique gives more reliable results at high concentrations. However, at high concentrations, the membrane and the acid-side boundary layer may contribute significantly to the nickel transfer rate, and study of this more complex system is beyond the scope of this work.

Manuscript submitted Nov. 18, 1980; revised manuscript received ca. March 9, 1981. This was Paper 619 presented at the Hollywood, Florida, Meeting of the Society, Oct. 5-10, 1980.

Any discussion of this paper will appear in a Discussion Section to be published in the June 1982 JOURNAL. All discussions for the June 1982 Discussion Section should be submitted by Feb. 1, 1982.

Publication costs of this article were assisted by General Motors Research Laboratories.

LIST OF SYMBOLS

- a activity of ions, mol/ml
- A membrane surface area, cm²
- C_I nickel concentration in reservoir, mol/ml
- C_o tube-side nickel concentration, mol/ml
- C_{I^o} initial nickel concentration, mol/ml
- \bar{C} concentration in the membrane, mol/ml
- C^I, C^{II} bulk concentration, mol/ml
- C^I surface concentration on side I, mol/ml
- C^{II} surface concentration on side II, mol/ml
- d membrane diameter, cm
- D diffusion coefficient in bulk solution, cm²/sec
- \bar{D} diffusion coefficient in membrane, cm²/sec
- J flux, mol/(cm² · sec)
- K_{BL} boundary-layer mass transfer coefficient, cm/sec
- K_m membrane transfer coefficient, cm/sec
- l membrane thickness, cm
- m reservoir rate constant, sec⁻¹
- Q volumetric flow rate, ml/sec
- Re Reynolds number = vd/ν , dimensionless
- Sc Schmidt number = ν/D , dimensionless
- Sh Sherwood number = $K_{BL}d/D$, dimensionless
- t time, sec
- v solution velocity, cm/sec
- V_R reservoir volume, cm³
- \bar{X} fixed charge concentration in membrane, eq/ml

z_i charge of ions

Greek Characters

ν kinematic viscosity, cm^2/sec
 δ boundary layer thickness, cm

REFERENCES

1. R. M. Wallace, *IEC Proc. Des. Dev.*, **6**, 423 (1967).
2. R. M. Wallace, U.S. Pat. 3,454,490 (1969).
3. W. E. Rush, M.S. Thesis, University of South Carolina (1973).
4. M. A. Lake and S. S. Melsheimer, *AIChE J.*, **24**, 130 (1978).
5. J. L. Eisenmann and J. D. Smith, "Donnan Softening as a Pretreatment to Desalination Processes," OSW R&D Progress Report No. 506 (1970).
6. J. L. Eisenmann, Second Annual EPA-AES Conference on Advanced Pollution Control, Kissimmee, Florida (1979).
7. F. Helfferich, "Ion Exchange," Chap. 8, McGraw-Hill, New York (1962).
8. M. A. Peterson and H. P. Gregor, *This Journal*, **106**, 1051 (1959).

Photoelectrochemical Properties of n-Type In_2O_3

J. F. McCann¹

Chemistry Discipline, School of Physical Sciences, Flinders University, Bedford Park 5042, South Australia

and J. O'M. Bockris

Chemistry Department, Texas A & M University, College Station, Texas 77843

ABSTRACT

The electrochemical and photoelectrochemical properties of single crystal n-type In_2O_3 were examined in 1M NaOH and 1N H_2SO_4 . The photocurrent-wavelength response indicated the absorption edge is an indirect transition of about 2.3-2.5 eV. The flatband potentials were determined from Mott-Schottky plots to be -0.72 and 0.22V (vs. SCE) in 1M NaOH and 1N H_2SO_4 , respectively. The photocurrent from the n- In_2O_3 electrode was steady during 13 hr while illuminating the sample in 1M NaOH at 0.3V (vs. SCE).

A wide range of semiconductors have been investigated to assess their performance as photoelectrodes in solar photoelectrolysis cells (1). In this work we have applied standard electrochemical and photoelectrochemical techniques to examine single crystal n-type In_2O_3 electrodes. To the authors' knowledge the photoelectrochemical properties of n-type In_2O_3 have not been previously reported, although a study of the dark current-voltage characteristics has been published (2).

Experimental

Single crystals of In_2O_3 which had been grown by two different techniques were donated by Dr. J. H. W. De Wit of the Inorganic Chemistry Department, University of Utrecht, Utrecht, The Netherlands. The first sample was grown in a $\text{PbO-B}_2\text{O}_3$ flux as described elsewhere (3). Two electrical contacts were made by soldering indium onto the back of the crystal. The i - V relation was linear indicating that the In contacts were ohmic. The resistivity of this sample was determined as $0.004 \Omega \cdot \text{cm}$. The color of pure In_2O_3 powder is light yellow, whereas this crystal was black. This observation suggests that the crystal had occluded impurities from the flux medium during its growth. In subsequent photoelectrochemical studies of this sample using medium intensity xenon irradiation ($\sim 26 \text{ mW cm}^{-2}$), the photocurrent was negligible as a function of applied voltage.

The second sample was an In_2O_3 single crystal grown from the vapor phase as described in Ref. (3). The crystal was green and was transparent. An indium contact was soldered onto the back of the crystal. The sample was then fabricated into an electrode by soldering a tin-coated copper wire to the indium contact and fixing the sample in a Teflon holder with

epoxy. The resistivity of the sample was measured from a high frequency impedance plot and calculated as $\sim 1200 \Omega \text{ cm}$ which was much higher than that of the flux grown In_2O_3 crystal. However, since the photoelectrochemical response of the electrode fabricated from the vapor grown crystal was substantial, the results reported in this study were derived from this sample.

A Wenking potential stepping motor control Model SMP 69 and a PAR Model 173 potentiostat fitted with a PAR Model 176 current-to-voltage converter were used to control the electrode potential and also to perform current-voltage scans. A 900W xenon lamp was used as the light source. An infrared absorbing filter (Oriol G-776-7100) was placed between the lamp and the cell to reduce heating effects. The illumination intensity was measured with a Hewlett-Packard Radiant Flux Detector Model 8334A. Monochromatic light was obtained by passing xenon light through a high intensity Bausch and Lomb scanning monochromator. Monochromatic light intensities were measured with a Carl Zeiss calibrated thermopile Model VT Q3/A. Capacitance measurements were made with the use of a General Radio impedance bridge Model 1608-A fitted with a General Radio tuned amplifier Model 1232A. The reference electrode was saturated calomel (SCE) and the counterelectrode was Pt. Rectified alternating photocurrent voltammograms were performed using the technique and apparatus to be reported elsewhere (4).

Results and Discussion

A flux grown n- In_2O_3 single crystal electrode examined in this study exhibited negligible photoelectrochemical activity. Other flux grown semiconductor electrodes including Fe_2TiO_5 , CoTiO_3 , and PbTiO_3 which were examined by the authors, but have not been reported here, have also lacked photoelectrochemical activity. It is probable that the absence of

¹ Electrochemical Society Active Member.

² Present address: School of Physics, University of New South Wales, Kensington, N.S.W. 2033, Australia.

Key words: indium oxide, photoelectrolysis, oxide electrochemistry, energy conversion.

significant photoelectrochemical responses for all of the above-mentioned flux grown single crystals is a direct consequence of the occlusion of flux impurities in the samples during the crystallization stages. The impurities act as recombination centers for photo-generated carriers according to the relation

$$\tau_p = (\sigma_p^{imp} V_p \rho_p^{imp})^{-1} \quad [1]$$

where τ_p is the hole lifetime, σ_p^{imp} is the capture cross section of holes by the impurity recombination center, V_p is the thermal velocity of holes, and ρ_p^{imp} is the density of impurity recombination centers. Clearly the larger the magnitude of ρ_p^{imp} the smaller the hole lifetime and subsequently the smaller the photocurrent. It is conceivable that for very large ρ_p^{imp} , as might be the case in the flux grown samples, that τ_p could become so short as to render the sample photo-inactive.

Cyclic voltammograms of the vapor phase prepared n-In₂O₃ electrode were recorded using a voltage scan rate of 20 mV/sec both in the dark and under illumination from a 900W xenon lamp (26 mW cm⁻²) in 1M NaOH and 1N H₂SO₄ and are shown in Fig. 1(a) and (b). The dark current was small in both electrolytes (< 1.5 × 10⁻⁵ A cm⁻²) up to a critical positive applied voltage after which a steep increase in the anodic current was observed (presumably due to either dark H₂O₂ formation or O₂ evolution and/or dissolution). The d-c photocurrent commenced at about -0.2 and 0.6V (vs. SCE) in 1M NaOH and 1N H₂SO₄, respectively, and steadily increased as the applied voltage was increased in both instances. The

hystereses of the dark curves and the illuminated curves were small.

The rectified alternating photocurrent-voltage (RAP-V) curves recorded using a voltage scan rate of 20 mV/sec in the forward direction in 1M NaOH and 1N H₂SO₄ are shown in Fig. 2(a) and (b), respectively. According to these relations, the photocurrent commences at -0.57 and 0.11V (vs. SCE) in 1M NaOH and in 1N H₂SO₄, respectively.

The shape of an RAP-voltammogram can be divided into two regions—the onset region and the plateau region. The plateau region represents the saturation of the tuned amplifier and does not refer to the saturation of the photocurrent at the semiconductor electrode. The onset region ideally represents the photocurrent near to the flatband potential of the semiconductor electrode. The differences between the onset of the photocurrent in the d-c photovoltammograms and the RAP-V curves (~0.37V in 1M NaOH and ~0.49V in 1N H₂SO₄) can be attributed to the fact that RAP voltammetry tends to be much less sensitive to the depression of the photocurrent due to surface recombination that occurs in d-c voltammetry. This arises because in RAP-voltammetry the illumination is modulated and the resulting modulated photocurrent is amplified by a large factor. Hence in RAP-voltammetry the onset of the photocurrent occurs at either the real flatband potential of the semiconductor, V_{FB} or at the potential close to V_{FB}.

The difference between the potential onsets of both the d-c photocurrent and RAP potential curves in 1M NaOH and 1N H₂SO₄ were 62 and 53 mV/pH unit,

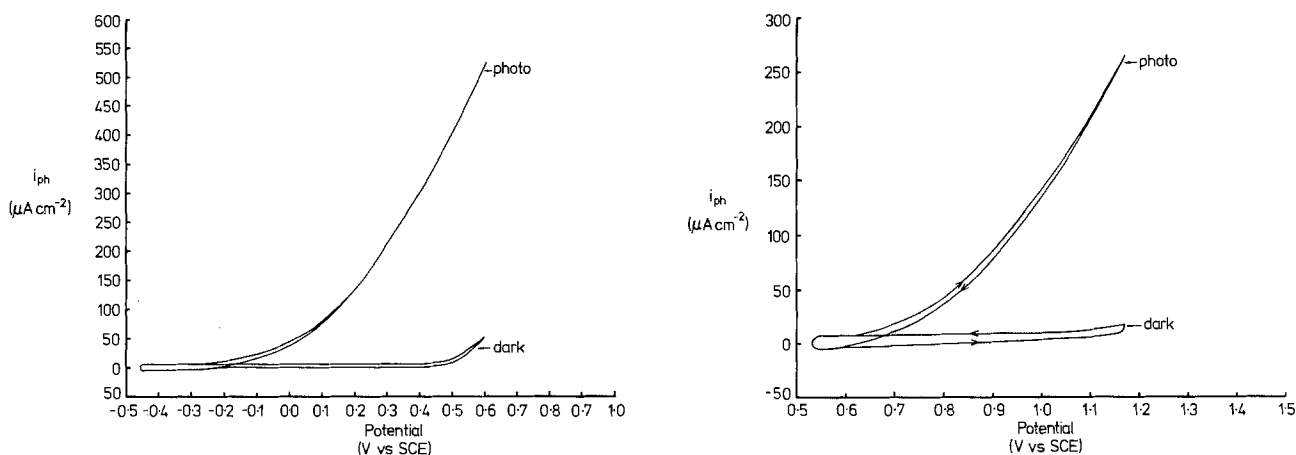


Fig. 1. Dark and photocurrent vs. voltage curves for n-In₂O₃ (a, left) in 1M NaOH and (b, right) in 1N H₂SO₄. Illumination intensity of xenon light 26 mW cm⁻².

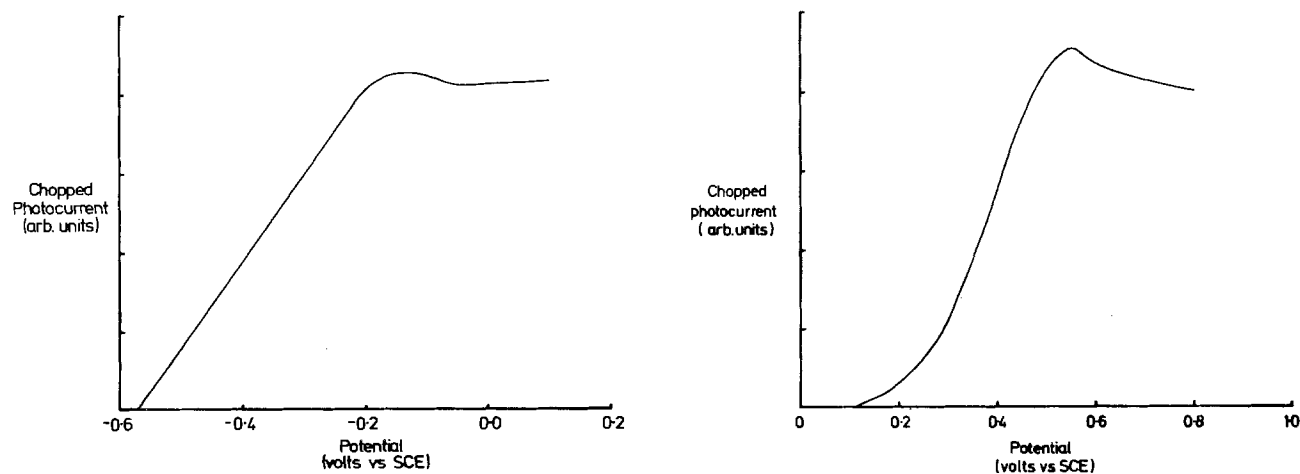
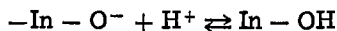


Fig. 2. Rectified alternating photocurrent voltammograms for n-In₂O₃ (a, left) in 1M NaOH and (b, right) in 1N H₂SO₄. Chopping frequency 70 Hz. Xenon light illumination intensity, 26 mW cm⁻².

respectively. These observations are consistent with a (pH dependent) Nernstian equilibrium of the following type occurring at the In_2O_3 /electrolyte interface (5)



The differences between the Nernstian predicted 59 mV/pH unit difference and the measured differences of 62 mV/pH unit and 69 mV/pH unit are attributed to experimental error. Typically the dark and \bar{d} -c photocurrent-voltage curves of a stable conductor are reproducible and any hysteresis is slight. The hystereses of the dark and photocurrent vs. voltage curves for the In_2O_3 electrode were small over the potential ranges measured in both electrolytes [see Fig. 1(a) and (b)]. In addition, the curves were reproducible. These observations suggest that n-type In_2O_3 is a stable electrode in 1M NaOH and 1N H_2SO_4 within the limits of the potential ranges studied.

Spectral response curves were measured from 3000 to 5200Å for applied potentials of 0.45, 0.30, 0.10, and 0.0V (vs. SCE) in 1M NaOH. Quantum efficiencies were calculated as a function of wavelength using the relation (6)

$$\eta = \frac{i_{\text{ph}} - i_{\text{dark}}}{N_{\text{ph}}(0)} = \frac{\text{Number of photoelectrons}}{\text{Number of incident photons}} \quad [2]$$

where η is the quantum efficiency, i_{ph} and i_{dark} are the electrode current densities with and without irradiation, and $N_{\text{ph}}(0)$ is the incident photon intensity. The calculated quantum efficiency vs. wavelength curves are shown in Fig. 3. It is clear from these plots that for a specified wavelength less than the absorption edge the quantum efficiency is larger the greater the applied anodic potential. This is expected since the semiconductor depletion layer width widens as the anodic potential is increased resulting in a large number of photoholes reaching the semiconductor surface which raises the quantum yield. In the wavelength range 4000-5200Å, the photoconversion efficiency was always less than 2%. Below 4000Å, the quantum efficiency increased steadily and reached a maximum value at about 3100Å for all potentials. A significant proportion of the energy of the visible solar spectrum lies between 5200 and 4000Å (~33%). If n-type In_2O_3 was an efficient photoconverter in this wavelength range, then it could be considered as a serious prospect as a photoelectrode in a heterotype n-p photoelectrolysis cell. It is therefore appropriate to consider the most likely factors which may have caused the low conversion efficiencies observed in the visible wave-

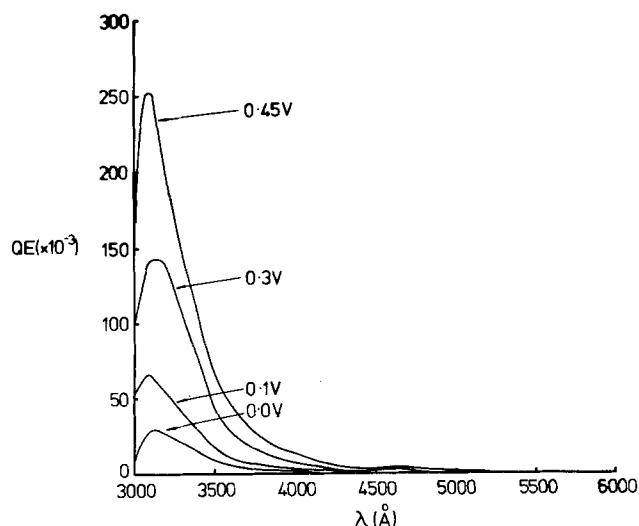


Fig. 3. Quantum efficiency vs. wavelength curves for n- In_2O_3 at 0.45, 0.30, 0.10, and 0.00V in 1M NaOH.

length range for the n-type In_2O_3 electrode examined in this study.

Normal incidence photons are absorbed in semiconductors according to the Bouguer-Lambert-Beer law

$$N_{\text{ph}}(x) = N_{\text{ph}}(0) e^{-\alpha(\lambda)x} \quad [3]$$

where $N_{\text{ph}}(x)$ is the photon flux after passing through x cm of semiconductor, and $\alpha(\lambda)$ is the absorption coefficient for a designated wavelength λ . The magnitude of $\alpha(\lambda)$ is an intrinsic property of a given material determined by the effective photon absorption cross section, $\sigma(\lambda)$, and by the concentration of the absorption centers, N , according to the relation (7)

$$\alpha(\lambda) = \sigma(\lambda)N \quad [4]$$

For indirect bandgap semiconductors, such as In_2O_3 , the magnitudes of the $\alpha(\lambda)$'s are typically small in the wavelength region just less than the semiconductor absorption edge. It follows from Eq. [3] that for visible wavelength illumination, the majority of the holes photogenerated in an In_2O_3 electrode will be created deep inside the semiconductor. The smaller the value of $\alpha(\lambda)$, the greater the distance inside the semiconductor that an average photohole is formed and the higher the probability that it will recombine before it can reach the surface and react. The recombination rate in an illumination n-type semiconductor is mainly dependent on the values of the hole lifetime and the hole mobility. The values of the hole mobility and hole lifetime in a given semiconductor are affected by the densities of stacking faults, dislocations, and defects and by the concentration of impurities. Therefore, their values vary from sample to sample and they are determined to a significant extent by the method used to prepare the semiconductor electrode. Since the spectral response of only one sample of n- In_2O_3 has been measured, it follows that further experiments need to be performed on other samples of n- In_2O_3 prepared by various methods, to ascertain whether the mobility and lifetime and hence whether the quantum efficiencies of this semiconductor can be increased significantly for the wavelength range between 4000 and 5200Å.

For a wide bandgap semiconductor/electrolyte junction the quantum efficiency is related to the photon energy by (8)

$$\eta \propto \frac{(h\nu - E_g)^{n/2}}{h\nu} \quad [5]$$

where $h\nu$ is the photon energy, E_g is the energy gap, and n is a parameter whose value depends on the nature of the optical transition ($n = 1$ for a direct transition and $n = 4$ for an indirect transition).

A plot of $(\eta h\nu)^{1/2}$ vs. $h\nu$ at an applied potential of 0.45V vs. SCE in 1M NaOH is shown in Fig. 4. The relationship is linear which confirms that the band transition for n- In_2O_3 is indirect, close to the absorption edge. The magnitude of the energy gap was determined as 2.27 eV from the $h\nu$ intercept of the plot. The values of the bandgap determined from similar plots to the one shown in Fig. 4 for applied potentials of 0.3, 0.1, and 0.0V (vs. SCE) were 2.32, 2.36, and 2.46 eV, respectively. A similar dependence of the value of the energy gap on the applied potential has been reported previously for WO_3 (14). The effect was attributed to potential induced crystallographic distortions. It is the latter phenomenon that may also be responsible for slight discrepancies between the values determined for the energy gap by the photoelectrochemical method and those determined by solid-state absorption or reflection techniques in which there is no applied potential. For example, in this instance the value reported for the energy gap of In_2O_3 , which was determined by solid-state techniques, of 2.6 eV (11) differs slightly from the values of 2.27-2.246 eV deter-

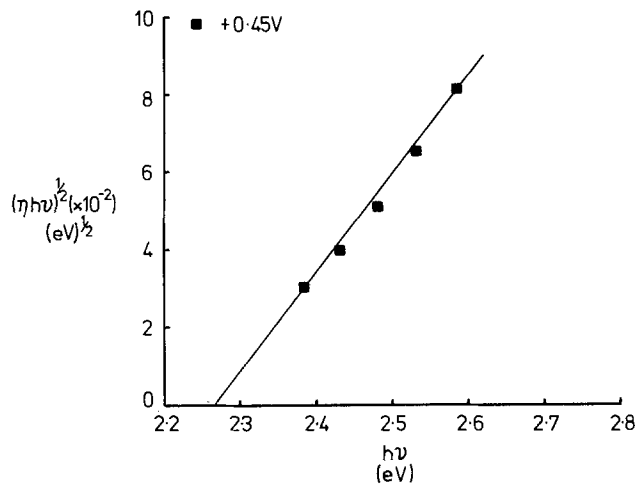


Fig. 4. $(\eta h\nu)^{1/2}$ vs. $h\nu$ relationships for n-In₂O₃ at 0.45V in 1M NaOH.

mined in the present study by the photoelectrochemical method.

The photocurrent for n-In₂O₃ in 1M NaOH was monitored over 13 hr for an applied potential of 0.3V (*vs.* SCE) in 1M NaOH and a xenon light illumination intensity of 26 mW cm⁻² in 1M NaOH. The photocurrent density (275 μ A cm⁻²) did not deteriorate during the experiment [see Fig. 5(a)]. In addition, there was no apparent visible change in the electrode surface at the completion of the experiment. In another i_{ph} vs. t experiment under similar conditions (0.3V, xenon irradiation intensity of 26 mW cm⁻², 1M NaOH) over 20 hr, the photocurrent density did not deteriorate and the weight of the electrode remained constant.

The photocurrent was also monitored for n-In₂O₃ in 1N H₂SO₄ over 10.5 hr at an applied potential of 0.6V and a xenon illumination intensity of 26 mW cm⁻² [see Fig. 5(b)]. In this experiment, the photocurrent density dropped from about 6 μ A cm⁻² to 5 μ A cm⁻² after 2 hr and then remained steady for 3.5 hr. There was no visible change in the electrode surface at the end of the experiment.

The stability of the photocurrent as a function of time as well as the reproducibility and slight hysteresis of the dark and photocyclic voltammograms suggest that n-In₂O₃ is a stable photoelectrode in 1M NaOH. In 1N H₂SO₄, the n-In₂O₃ electrode examined in this study was semistable at low photocurrent densities. However, since In₂O₃ is slightly soluble in solutions of low pH, it would be impractical to consider it as a possible photoelectrode in acidic electrolytes.

The capacitance of the system n-In₂O₃/electrolyte/platinized Pt was determined as a function of electrode potential in 1M NaOH and 1N H₂SO₄ at both 10 and 20 kHz. The flatband potentials were determined from the linear plots of $1/C^2$ vs. V shown in Fig. 6(a) and (b) as -0.72 and 0.22V (*vs.* SCE) in 1M NaOH and 1N H₂SO₄, respectively, a difference of 72 mV/pH unit. The capacitance in both electrolytes was dependent on frequency [see Fig. 6(a) and (b)]. According to Dutoit *et al.* (9) this behavior originates from dielectric relaxation phenomena in the semiconductor. The flatband potential for an n-type semiconductor is given by

$$V_{FB} \approx EA + \Delta E_{fc} - E_0 + \Delta_{pH} \quad [5]$$

where EA is the electron affinity of the semiconductor, E_0 is the potential of the reference electrode relative to vacuum level, ΔE_{fc} is the difference between the doped Fermi level and the bottom of the conduction band,

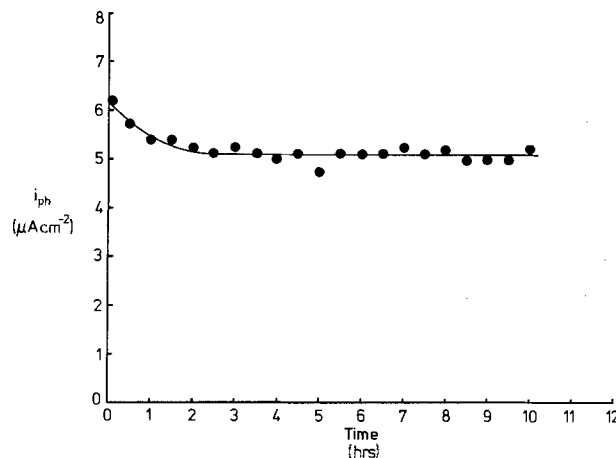
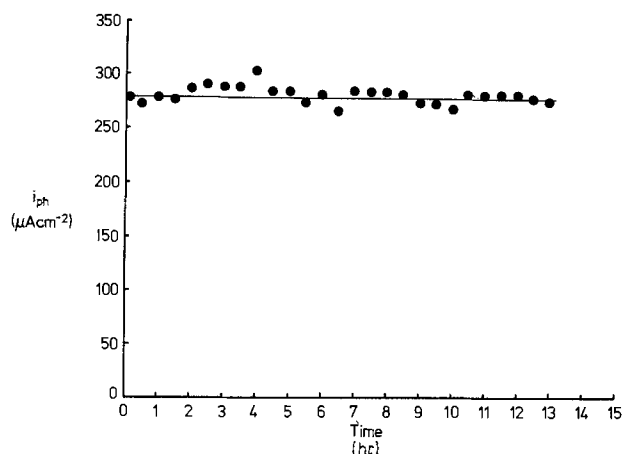


Fig. 5. Photocurrent-time relationships for n-In₂O₃ (a, left) in 1M NaOH (0.3V *vs.* SCE) and (b, right) in 1N H₂SO₄ (0.6V *vs.* SCE). Illumination intensity of xenon light 26 mW cm⁻².

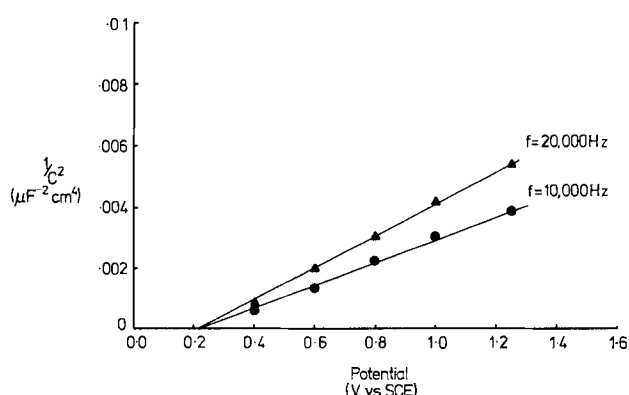
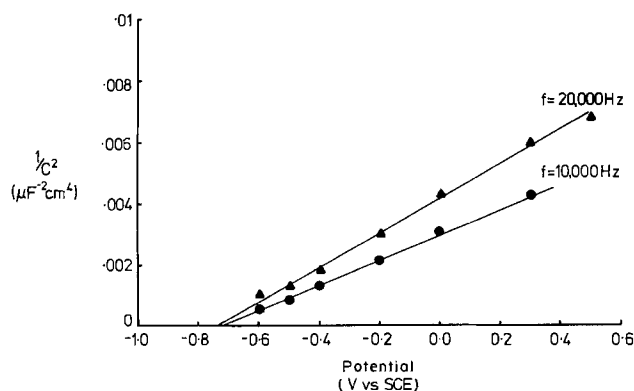


Fig. 6. Mott-Schottky plots for n-In₂O₃ (a, left) in 1M NaOH and (b, right) in 1N H₂SO₄.

and Δ_{pH} is the correction term due to the net surface charge of the adsorbed species on the electrode surface (this term may be neglected at the zeta potential of zero charge).

The electron affinity was calculated with the usual relation (8)

$$EA = \chi(\text{In}_2\text{O}_3) - \frac{1}{2} E_g \quad [6]$$

where $\chi(\text{In}_2\text{O}_3)$ refers to the electronegativity of In_2O_3 determined from

$$\chi(\text{In}_2\text{O}_3) = [\chi^2(\text{In})\chi^3(\text{O})]^{1/5} \quad [7]$$

The pH where the zeta potential is zero (pzzp) was estimated to be 12.5 from a correlation between the electronegativity and pH that has been reported by Butler and Ginley (10). The calculated V_{FB} and the value of V_{FB} at pzzp determined by interpolating the experimental values obtained for V_{FB} in 1M NaOH and 1N H_2SO_4 together with the value of each parameter used in the calculation are listed in Table I. The calculated value of -0.61V (vs. SCE) agrees satisfactorily with the experimentally interpolated value of -0.66V .

The minimum bias required for photo-oxygen evolution on an n-type semiconductor in a Schottky-type photoelectrolysis cell, $V_{n-\text{min}}$, when the flatband potential, $V_{n-\text{FB}}$, is more positive than the $2\text{H}^+/\text{H}_2$ redox potential, $V_{2\text{H}^+/\text{H}_2}$ is

$$V_{n-\text{min}} = V_{n-\text{FB}} - V_{2\text{H}^+/\text{H}_2} \quad [8]$$

Substituting either -0.72V (from Mott Schottky plots) or -0.57V (from RAP voltammetry) for the $V_{n-\text{FB}}$ of In_2O_3 and -1.03V for $V_{2\text{H}^+/\text{H}_2}$ in 1M NaOH, into Eq. [8] values of 0.31 and 0.46V, respectively, are obtained. Hence the minimum bias required for an n- In_2O_3 /1M NaOH/Pt cell to decompose water is in the range 0.31-0.46V. On the other hand, it may be possible to use n- In_2O_3 in an n-p photoelectrolysis cell without applying a bias provided a stable p-type semiconductor is used whose onset potential for H_2 evolution is more positive than -0.72V in 1M NaOH.

Summary and Conclusions

The electrochemical and photoelectrochemical properties of an n-type In_2O_3 single crystal electrode have

Table I. Values of the parameters used to calculate the flatband potential of n-type In_2O_3 at the potential of zero zeta potential (pzzp) as well as the calculated and estimated V_{FB} 's

| Parameter | Literature or calculated value | Estimated value from present experiments |
|-------------------------------|--------------------------------|--|
| $\chi(\text{In}_2\text{O}_3)$ | 5.24 eV | — |
| E_g | 2.6 eV (11) | 2.27-2.46 eV |
| EA | 3.94 eV | — |
| E_o (vs. SCE) | 4.55V (12, 13) | — |
| Δ_{fc} * | — | — |
| Δ_{pH} | — | — |
| pH _(pzzp) | 12.5 | — |
| V_{FB} (pzzp) (vs. SCE) | -0.61V | -0.66V |

* The energy level difference between the conduction band and the Fermi level was neglected.

been studied. The spectral response and photocurrent-time curves obtained in this work suggest that In_2O_3 may be potentially useful as a photoelectrode in a solar photoelectrolysis cell. The flatband potentials have been determined in 1M NaOH and 1N H_2SO_4 from Mott-Schottky plots. The flatband potential (V_{FB}) determined from the calculated electronegativity of n- In_2O_3 agreed satisfactorily with V_{FB} at pzzp estimated by interpolating the experimentally determined V_{FB} 's.

Acknowledgments

The authors thank Dr. J. H. W. De Wit for donating the single crystals of In_2O_3 . J. McCann is grateful for the support of an Australian Commonwealth Postgraduate Scholarship.

Manuscript submitted July 28, 1980; revised manuscript received ca. Dec. 1, 1980. This was Paper 634 presented at the Los Angeles, California, Meeting of the Society, Oct. 14-19, 1979.

Any discussion of this paper will appear in a Discussion Section to be published in the June 1982 JOURNAL. All discussions for the June 1982 Discussion Section should be submitted by Feb. 1, 1982.

Publication costs of this article were assisted by the University of New South Wales.

REFERENCES

- (a) H. H. Kung, H. S. Jarrett, A. W. Sleight, and A. Ferretti, *J. Appl. Phys.*, **48**, 2463 (1977); (b) A. Fujishima and K. Honda, *Nature*, **238**, 37 (1972); (c) M. Wrighton, A. Ellis, P. Wolczanski, D. Morse, H. H. Abrahamson, and D. Ginley, *J. Am. Chem. Soc.*, **98**, 44 (1976); (d) R. Quinn, R. Nasby, and R. Baughman, *Mater. Res. Bull.*, **11**, 1011 (1976); (e) A. Ellis, S. Kaiser, and M. Wrighton, *J. Phys. Chem.*, **80**, 1325 (1976); (f) K. Hardee and A. Bard, *This Journal*, **123**, 1024 (1976); (g) P. Clechet, J. Martin, R. Oliver, and C. Vallouy, *C.R. Acad. Sci. C*, **282**, 887 (1976).
- N. R. Armstrong, W. C. A. Lin, M. Fujihara, and T. Kuwana, *Anal. Chem.*, **48**, 741 (1976).
- J. H. W. De Wit, *J. Cryst. Growth*, **12**, 183 (1972).
- J. F. McCann and J. Pezy, *This Journal*, **128**, 1735 (1981).
- H. Gerischer, in "Physical Chemistry," Vol. IX, A. H. Eyring, D. Henderson, and W. Jost, Editors, Chap. 5, Academic Press, New York (1970).
- K. Ohashi, J. McCann, and J. O'M. Bockris, *Energy Res.*, **1**, 259 (1977).
- P. S. Kireev, "Semiconductor Physics," Mir Publishers, Moscow (1975) (Engl. translation).
- M. A. Butler and D. S. Ginley, in "Semiconductor Liquid Junction Solar Cells," A. Heller, Editor, p. 290, The Electrochemical Society Softbound Proceedings Series, Princeton, N.J. (1977).
- E. C. Dutoit, R. L. Van Meirhaeghe, F. Cardon, and W. Gomes, *Ber. Bunsenges. Phys. Chem.*, **79**, 1206 (1975).
- M. A. Butler and D. S. Ginley, *This Journal*, **125**, 228 (1978).
- R. L. Weiher and R. P. Ley, *J. Appl. Phys.*, **37**, 299 (1966).
- J. O'M. Bockris and S. Argade, *J. Chem. Phys.*, **49**, 5133 (1968).
- S. Trasatti, *J. Electroanal. Chem. Interfacial Electrochem.*, **52**, 313 (1974).
- M. A. Butler, *J. Appl. Phys.*, **48**, 1914 (1977).

Mechanisms of Charge Transfer at the n-GaAs/Room Temperature Molten Salt Electrolyte Interface

P. Singh*[†] and K. Rajeshwar

Department of Electrical Engineering, Colorado State University, Fort Collins, Colorado 80523

ABSTRACT

Photoelectrochemical (PEC) characterization was carried out on n-GaAs electrodes in contact with a room temperature molten salt electrolyte comprising mixtures of AlCl_3 and n-butyl pyridinium chloride (BPC) in varying molar ratios. The ferrocene/ferricenium ion couple was used as the redox system in these studies. The barrier height for charge transfer, which determines the ultimate efficiency of any photovoltaic system, was determined from dark current-voltage measurements. These data were in good agreement with previously determined values from capacitance measurements. The residual barrier heights in the illuminated PEC system were determined from open-circuit voltage and short-circuit current densities using Schottky barrier theory. A simple method for estimating the reorganization energy (λ) of a redox system from dark current-voltage measurements is presented. A value of $\lambda = 0.23$ eV was thus deduced for the ferrocene/ferricenium ion couple in the AlCl_3 -BPC electrolyte. The acidic AlCl_3 -BPC electrolyte showed larger dark currents and inferior photoresponse relative to the case of n-GaAs electrodes in contact with basic electrolytes. Using the measured values of λ and the semiconductor bandedges, energy band diagrams were developed for the present PEC system as a function of electrolyte composition. The direct correlation which was seen between PEC performance and electrolyte composition is rationalized on the basis of these diagrams. The larger dark currents in the acid electrolytes were shown to result from greater overlap of the empty redox levels with the conduction bandedge in n-GaAs. On the other hand, in basic electrolyte systems, the filled redox levels overlap better with the n-GaAs valence bandedge leading to more efficient charge transfer on illumination. The role of surface states in mediating charge transfer and degrading PEC performance is discussed in this regard. A key finding of the present work is that the electrical behavior of semiconductor/electrolyte junctions is well described by Schottky barrier theory once the differences in the energy distribution in metals vis-à-vis electrolytes, are rationalized.

Photoelectrochemical (PEC) methods of solar energy conversion have been the topic of much discussion in recent years (1, 2). A major obstacle to practical applications of PEC devices is the photodissolution undergone by the semiconductor photoanode. Most small bandgap semiconductors are prone to photoanodic dissolution in contact with aqueous electrolytes (1). Attempts have been made, therefore, in recent years to construct PEC devices based on non-aqueous electrolytes (3-5). A promising class of solvents in this regard are the room temperature molten salts; these electrolytes offer the combined advantage of good electrical conductivity coupled with aprotic chemical characteristics (6). The feasibility of solar energy conversion in PEC devices, based on molten salt electrolytes, was demonstrated in this laboratory using a model system comprising the n-GaAs/ AlCl_3 -n-butyl pyridinium chloride (BPC) interface¹ (7). An attractive feature of the AlCl_3 -BPC system is the possibility of varying the Lewis acid-base characteristics of the electrolyte over a wide range by suitable adjustment of the relative molar ratios of the two components. This immediately points toward strategies of modifying the potential and charge distribution across the electrode/electrolyte interface and thereby tailoring a particular system to optimum requirements for

PEC applications. For example, in a PEC device, the barrier height which determines the ultimate photovoltaic efficiency is given by $V_{\text{FB}} - V_{\text{redox}}$, where V_{FB} is the flatband potential of the semiconductor and V_{redox} is the equilibrium redox potential. The more negative the V_{FB} value is with respect to V_{redox} for a given semiconductor/electrolyte junction, the greater will be the ultimate solar conversion efficiency. The V_{FB} values in the n-GaAs/ AlCl_3 -BPC system were found to shift in the negative direction at the rate of 120 mV/pCl² when the electrolyte was made more basic by the addition of BPC (8), while the redox potential of the ferrocene/ferricenium ion ($\text{Fe}(\text{Cp})_2/\text{Fe}(\text{Cp})_2^+$) couple was insensitive to electrolyte composition (7). From the above, this would imply a higher photovoltaic efficiency for devices based on basic electrolytes relative to the case of acidic AlCl_3 -BPC mixtures. This was indeed found to be the case for the n-GaAs/ AlCl_3 -BPC, $\text{Fe}(\text{Cp})_2/\text{Fe}(\text{Cp})_2^+/\text{C}$ PEC system (7). In this paper, we present more detailed correlations of the PEC behavior with electrolyte composition for the above model system. A variety of PEC characterizations including dark current-voltage measurements were utilized to establish the degree of overlap of electrolyte energy levels with the corresponding electronic states in the semiconductor. A simple method of estimating the reorganization energy, λ , of a redox couple from dark current-voltage measurements is also presented.

² The magnitude of the shift in V_{FB} with pCl was found to be sensitive to the crystallographic orientation of the electrode surface exposed to the electrolyte. Thus the $\langle 111 \rangle$ -orientation showed a shift of 120 mV/pCl as compared to 60 mV/pCl for $\langle 100 \rangle$ orientations (9).

* Electrochemical Society Student Member.

[†] Present address: Arco Enterprises, Incorporated, Troy, Michigan 48064.

Key words: photoelectrochemistry, Schottky barrier theory, Lewis acid-base equilibria.

¹ It is perhaps more correct to use the term "interphase" in place of "interface" because the semiconductor/electrolyte junction is not sharp and the region between the two is several angstroms thick. The two terms, however, are used synonymously in the following discussion bearing this distinction in mind.

A secondary objective of this work was to examine the efficacy of the Schottky barrier model for semiconductor/electrolyte junctions (10), in which the electrolyte replaces the metal in a Schottky barrier. Two major differences exist in the electrical properties of a metal vis-à-vis an electrolyte: (i) charge transfer in a metal occurs via electronic conduction (i.e., conduction by electrons or holes) whereas in an electrolyte, the conduction is ionic, and (ii) there is a continuum of electronic energy states below the Fermi level in a metal whereas the energy levels are more localized in an electrolyte [cf. Ref. (11)]. In this work, the dark current-voltage characteristics of the model system comprising the n-GaAs/AlCl₃-BPC interface were analyzed by equations conventionally adopted in the treatment of metal/semiconductor contacts (12). The selected variables were temperature and electrolyte composition. A key finding of the present work was that semiconductor/electrolyte junctions are reasonably well explained by Schottky barrier theory once the differences noted above are taken into account.

Experimental

Wafers of single crystal n-GaAs (Te-doped, As-terminated <111> orientation, donor density: $2.17 \times 10^{17} \text{ cm}^{-3}$) were obtained from commercial sources (Laser Diode Laboratories Incorporated, New Jersey). They were degreased with xylene, rinsed with methanol, and dried under nitrogen. They were then given a chemomechanical polish with 1% solution of bromine in methanol. Individual electrodes were scribed from these wafers after providing them with ohmic contacts consisting of thermally evaporated Ge-Au alloy on the back surface which was subsequently annealed in nitrogen at 450°C for 15 min. A Teflon-coated copper wire was attached to the contacts using conducting silver epoxy. The entire back surface and the edges of the electrodes were covered with nonconducting epoxy resin. The electrodes were etched in 10% HCl for 15 min to remove any native oxide and the damaged surface layers. This was followed by etching in H₂SO₄:H₂O₂:H₂O (3:1:1) for 15 sec. The electrodes were rinsed with deionized water and etched for 30 sec in 6M HCl. After rinsing with deionized water and ethyl alcohol the electrodes were dried under vacuum and then transferred into the dry box. The geometric area of the electrodes was nominally 0.10-0.25 cm². A vitreous carbon plate (nominal dimensions: 1.5 × 15 × 30 mm) was used as the counterelectrode in the PEC devices.

Molten salt electrolytes consisting of AlCl₃ and BPC in the 1:1 molar ratio were prepared according to procedures described elsewhere (7). Ferrocene was obtained from commercial sources and purified by extraction with petroleum ether and subsequent recrystallization. Ferricinium chloride was prepared using standard procedures (13). Nominal concentrations of Fe(Cp)₂ and Fe(Cp)₂Cl in the electrolyte were 0.2M and 20 mmols, respectively. All manipulations with the electrolytes and redox chemicals were carried out in a dry box.

A 300W tungsten halogen lamp was used to illuminate the n-GaAs electrodes. The intensity of the light source was calibrated using a radiometer/photometer. The light intensities reported herein are not corrected for reflection and absorption losses in the cell and in the electrolyte.

Dark current-voltage measurements were performed using a PAR 173 potentiostat (Princeton Applied Research Corporation, Princeton, New Jersey) equipped with PAR 179 coulometer accessory. Three-electrode geometry was employed for these measurements. An aluminum wire immersed in the AlCl₃-BPC electrolyte (2:1 molar ratio) and separated from the main cell compartment by a fine-porosity glass frit was

employed as the quasi-reference electrode. Photocurrent *vs.* potential data were obtained by using a Hewlett-Packard 721 A power supply in series with the PEC cell. The cell current was monitored by measuring the potential drop across a 10 kΩ resistor in series with the cell.

Results and Discussion

Barrier height from photocurrent-voltage measurements.—At the semiconductor/electrolyte interface, the net photocurrent generated in the semiconductor can be split into two components: current due to minority carriers generated within the depletion layer and that arising from carriers photogenerated in the bulk which diffuse into the depletion region (14). Based on arguments presented by previous authors, the net hole current density for an n-type semiconductor is given by the expression (14, 15)

$$J_p = -q\phi_0 [\exp(-\alpha W) - 1] + q\phi_0 \frac{\alpha L_p}{1 + \alpha L_p} \exp(-\alpha W) + qp_0 \frac{D_p}{L_p} \quad [1]$$

where ϕ_0 is the photon flux, L_p is the hole diffusion length, D_p is the hole diffusion coefficient, W is the depletion layer width, α is the optical absorption coefficient, and p_0 is the equilibrium hole concentration in the dark. The depletion layer width is given by the expression (15)

$$W = W_0(V - V_{FB})^{1/2} \quad [2]$$

where V is the applied potential relative to a reference electrode and W_0 is a constant for a particular semiconductor given by the equation

$$W_0 = \left(\frac{2\epsilon_s \epsilon_0}{qN_D} \right)^{1/2} \quad [3]$$

Here N_D is the semiconductor doping density, ϵ_s is the low frequency dielectric constant of the semiconductor, and ϵ_0 is the dielectric permittivity of free space.

If the last term in Eq. [1], is neglected, rearrangement of Eq. [1], after substitution of Eq. [2] yields the following equation

$$J_p \approx q\phi_0 \left(1 - \frac{\exp[-\alpha W_0(V - V_{FB})^{1/2}]}{1 + \alpha L_p} \right) \quad [4]$$

If the additional assumptions are made that $\alpha L_p \ll 1$ and $\alpha W_0(V - V_{FB})^{1/2} \ll 1$, the exponential term in Eq. [4] can be expanded to yield the following relation between photocurrent and applied potential (15)

$$V - V_{FB} \approx \left(\frac{J_p}{q\phi_0 \alpha W_0} \right)^2 \quad [5]$$

According to Eq. [5], a plot of J^2 *vs.* V should be a straight line with an intercept on the potential axis given by V_{FB} . Figure 1 illustrates such plots for the n-GaAs|AlCl₃-BPC, Fe(Cp)₂/Fe(Cp)₂⁺|C system at two different light intensities. The electrolyte in this case was adjusted to be slightly on the basic side of the neutral (1:1 molar ratio, AlCl₃:BPC) composition. Although the straight line relationship is obeyed in apparent agreement with Eq. [5], two points are worthy of note: (i) the intercept shifts to more negative potentials with increasing light intensity and (ii) the value for V_{FB} obtained from the intercept is significantly positive of that obtained ($-0.90 \pm 0.05V$ *vs.* Al/Al³⁺) from capacitance voltage measurements for the same electrolyte composition (7).

The above discrepancies can be rationalized on a reexamination of the assumptions underlying Eq. [5]. Assuming the following typical values for n-GaAs: $\alpha = 5 \times 10^4 \text{ cm}^{-1}$, $D_p = 100 \text{ cm}^2/\text{sec}$, $L_p = 10^{-3} \text{ cm}$ (16), we obtain the ratio, $D_p/L_p = 10^5 \text{ cm}/\text{sec}$. How-

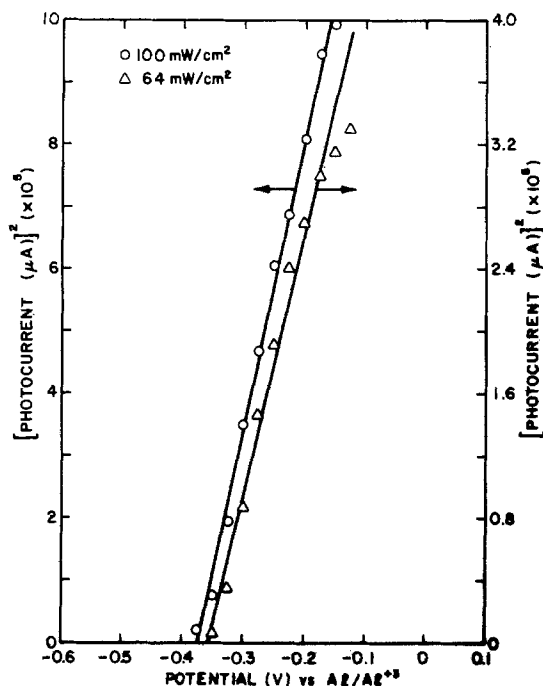


Fig. 1. Plot of square of the photocurrent vs. applied potential (cf. Eq. [5] in text) for n-GaAs|AlCl₃-BPC, Fe(Cp)₂/Fe(Cp)₂⁺|C system. The electrolyte was adjusted to be slightly on the basic side of the neutral 1:1 composition.

ever, the equilibrium hole concentration p_0 is negligibly small so that the above assumption that the term $qp_0 D_p/L_p$ may be neglected in comparison with the first term in Eq. [1] is valid under normal operating conditions. On the other hand, $\alpha L_p = 50$ so that the assumption that $\alpha L_p \ll 1$ is clearly invalid in this case. Again taking $\epsilon_s = 10.9$ (16), $N_D = 2.2 \times 10^{17}/\text{cm}^3$, and $V - V_{FB} = 1\text{V}$, we obtain $\alpha W_0 (V - V_{FB})^{1/2} \approx 0.37$ so that the assumption that $\alpha W_0 (V - V_{FB})^{1/2} \ll 1$ is reasonably valid. It is easily shown that Eq. [4] would yield a straight line relationship even if αL_p is not $\ll 1$, but now the intercept is no longer V_{FB} and is shifted from the "true" V_{FB} by a constant term.

The shift in intercept potentials toward more negative values with increasing light intensity (Fig. 1) suggests that the true V_{FB} will be attained only at very high light intensities ($\gg 100 \text{ mW/cm}^2$) when the energy bands in the semiconductor are completely flattened at the surface. The residual barrier height or the barrier height remaining under illumination (10) may be estimated in the following manner.

Consider the energy band diagram shown in Fig. 2. At equilibrium equal and opposite exchange currents, J_0 , flow through the device such that the magnitude of J_0 may be related to the barrier height, ϕ_B by the expression (12)

$$J_0 = A^* T^2 \exp(-\phi_B/kT) \quad [6]$$

where T is the absolute temperature and A^* is the Richardson's constant given by the expression

$$A^* = \frac{4\pi m_e^* q k^2 T^2}{h^3} \quad [7]$$

Here m_e^* is the effective mass of an electron, and the other terms have their usual significance.

Under illumination, electron-hole pairs are generated in the semiconductor by bandgap excitation (Fig. 2). The field across the barrier separates these pairs so that electrons move into the semiconductor bulk and the holes are drawn to the surface. A current density equal to J_{sc} and directly proportional to the

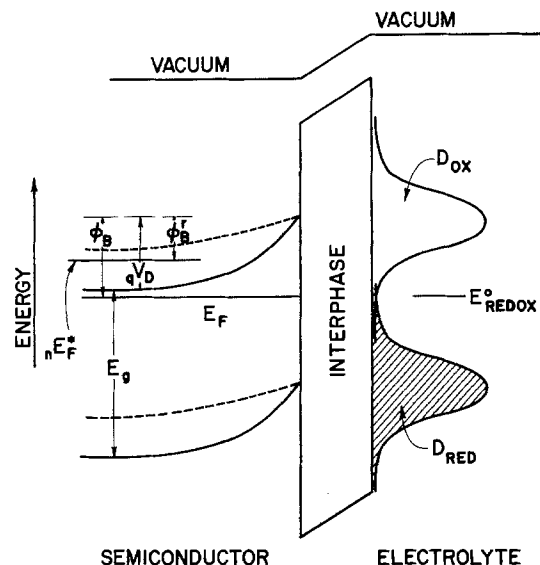


Fig. 2. Energy-band diagram for a semiconductor/electrolyte interface. The solid lines represent the dark (equilibrium) case and the dotted lines denote the interface under illumination. E_F = Fermi level in the dark, nE_F^* = quasi-Fermi level for majority carriers, E_g = energy bandgap. Other symbols are defined in the text.

incident light intensity, I_L is obtained under short-circuit conditions. We assume for the following analyses (*vide infra*) a current collection efficiency of unity such that there is no rate limitation for the discharge step at the interface. The approximation may then be made that $J_{sc} \approx J_L$ where J_L is the light-generated current density. Under open circuit, an equilibrium is established such that (10)

$$J_e = J_{sc} \quad [8]$$

where J_e is the current density for electron flow from the semiconductor into the electrolyte. Comparison of Eq. [6] and [8] yields the following relation between the short-circuit current density, J_{sc} , and the residual barrier height, ϕ_B^r

$$J_{sc} = A^* T^2 \exp(-\phi_B^r/kT) \quad [9]$$

Values of ϕ_B^r computed from Eq. [9] are assembled in Table I for the n-GaAs|AlCl₃-BPC, Fe(Cp)₂/Fe(Cp)₂⁺|C system. A^* was taken to be $8.6 \text{ A cm}^{-2} \text{ K}^{-2}$ for these computations (12). Data are shown at three different light intensities and electrolyte compositions. The ϕ_B^r values show the expected decrease with increasing light intensity. Furthermore, even at an I_L value of 155 mW/cm^2 , ϕ_B^r shows a nontrivial magnitude supporting the above interpretation of the data in Fig. 1.

The barrier height, ϕ_B , under equilibrium is given by $\phi_B^r + qV_{oc}$, where V_{oc} is the open-circuit voltage. Values for ϕ_B computed from calculated values of ϕ_B^r (Eq. [9]) and measured V_{oc} are also shown in Table I. A check for the internal consistency for these results is provided by a comparison of ϕ_B values in Table I with data obtained previously from capacitance measurements (7). As noted above the barrier height for a semiconductor/electrolyte interface in equilibrium is given by $q(V_{FB} - V_{redox})$. Using measured values for V_{FB} and V_{redox} of -0.90 and 0.30V (vs. Al/Al³⁺), respectively, (7), we obtain a value for ϕ_B of 1.2 eV which is in good agreement with that shown in Table I for the slightly basic electrolyte.

The systematic increase in $\phi_B (= qV_{oc} + \phi_B^r)$ values in Table I with increasing light intensity is to be noted. The barrier height, ϕ_B , should be ideally independent of the value of I_L . We attribute this to the error involved in the computation of ϕ_B^r at high values

Table I. Residual barrier heights in the n-GaAs/AlCl₃-BPC, Fe(Cp)₂/Fe(Cp)₂⁺/C system as a function of light intensity and composition

| Parameter | Composition | | | | | | | | |
|---|-----------------|-------|-------|---------|-------|-------|----------------|-------|-------|
| | Slightly acidic | | | Neutral | | | Slightly basic | | |
| I _L , mW/cm ² | 14 | 50 | 155 | 14 | 50 | 155 | 14 | 50 | 155 |
| J _{sc} , 10 ⁹ A/cm ² | 193 | 675 | 1550 | 308 | 1083 | 2710 | 340 | 1268 | 3350 |
| V _{oc} , V | 0.366 | 0.412 | 0.457 | 0.490 | 0.591 | 0.651 | 0.625 | 0.693 | 0.746 |
| φ _B ^r , eV | 0.55 | 0.52 | 0.50 | 0.54 | 0.51 | 0.49 | 0.54 | 0.51 | 0.48 |
| qV _{oc} + φ _B ^r , eV | 0.92 | 0.93 | 0.96 | 1.03 | 1.10 | 1.14 | 1.17 | 1.20 | 1.23 |

of I_L when the above assumption that J_{sc} ∝ I_L breaks down. Charge transfer limitations at the n-GaAs/AlCl₃-BPC interface lead to departure from the linear dependence of J_{sc} on I_L so that the J_{sc} values that are actually measured are lower than they should be under conditions of infinite rate of charge transfer (i.e., no carrier recombination). This behavior was observed in a previous study at I_L values above ~100 mW/cm² (17). The lowering of φ_B^r with increasing I_L is thereby reduced (cf. Eq. [9]) resulting in an artifactual increase in φ_B with increasing I_L (Table I).

Barrier height from dark current-voltage measurements.—The current-voltage characteristics of a semiconductor/electrolyte junction may be represented in terms of Schottky barrier theory by the equation (12)

$$J_e = J_o[\exp(qV/nkT) - 1] \quad [10]$$

Here J_e is the measured dark current density, J_o is the reverse saturation current density (Eq. [6]), and n is the junction identity factor. For bias voltages in excess of 3kT/q, the last term in the bracket in Eq. [10] may be neglected so that J_o is given by the zero bias intercept of a linear plot of ln J_e vs. V whose slope is given by 1/n. Such plots are shown in Fig. 3 for the n-GaAs|AlCl₃-BPC, Fe(Cp)₂/Fe(Cp)₂⁺|C system with temperature as a parameter.

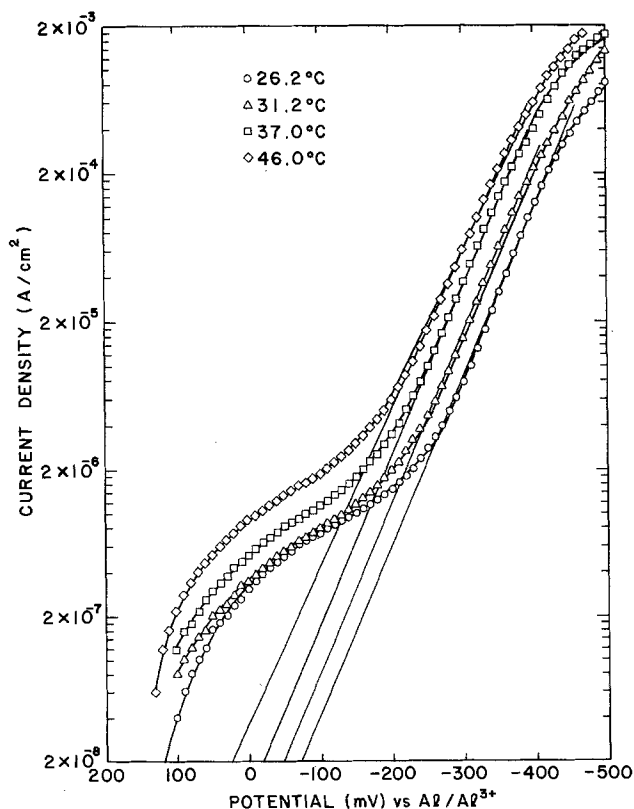


Fig. 3. Dark current-voltage characteristics of the n-GaAs/AlCl₃-BPC, Fe(Cp)₂/Fe(Cp)₂⁺/C system with temperature as a parameter. Electrolyte composition same as in Fig. 1. The cell potential zero lies at +170 mV (vs. Al/Al³⁺).

The effect of the identity factor, n, on the current-voltage characteristics is clearly seen in the data in Fig. 3. An ideal device (n = 1) would show linear ln J vs. V characteristics. At low values of reverse bias, the voltage dependence of J_e is seen to slow down appreciably in Fig. 3. At large forward bias, on the other hand, the ln J-V characteristics depart from linear behavior because of series resistance effects (12). The intermediate voltage region yields a straight line region with an n value of ~1.5. Values of n greater than 1 are attributed to current-voltage behavior dominated by carrier recombination and generation effects either at the surface or in the semiconductor bulk (18). The above value of n is in good agreement with that deduced from previous measurements on the n-GaAs/AlCl₃-BPC system at varying light intensity (17).

Rearranging Eq. [6] and taking logarithms, we obtain

$$\ln(J_o/T^2) = \ln A^* - q\phi_B/kT \quad [11]$$

so that a plot of ln(J_o/T²) vs. 1/T yields the barrier height and A* from the slope and intercept, respectively. Figure 4 illustrates a typical plot for the n-GaAs|AlCl₃-BPC, Fe(Cp)₂/Fe(Cp)₂⁺|C system. The electrolyte was again adjusted to be slightly basic of the neutral 1:1 composition. Values of J_o at various temperatures were obtained from extrapolation of the straight-line region in Fig. 3 to zero cell potential. The barrier height, φ_B, obtained from the slope is 1.0 ± 0.1 eV which is in agreement with that obtained from photovoltage and capacitance measurements (vide supra) within limits of experimental error. The inter-

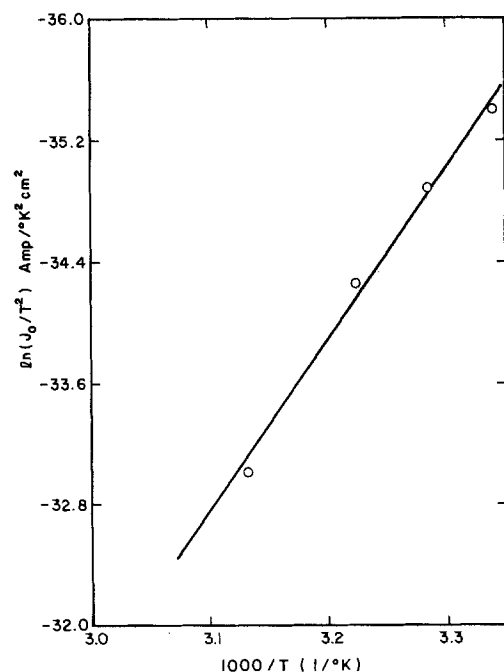


Fig. 4. Plot of ln(J_o/T²) vs. 1/T (cf. Eq. [11] in text) for the n-GaAs|AlCl₃-BPC, Fe(Cp)₂/Fe(Cp)₂⁺|C system. Electrolyte composition same as in Fig. 1.

cept in Fig. 4 yields a value of $A^* = 9.6 \pm 0.2 \text{ A cm}^{-2} \text{ K}^{-2}$. This may be compared with $A^* = 8.6 \text{ A cm}^{-2} \text{ K}^{-2}$ reported for n-GaAs-based Schottky barrier diodes (12).

It is noted here that the barrier heights obtained from capacitance measurements do not take into account image-force lowering (12), since the differential capacitance is determined by the width of the depletion region which depends only on the diffusion voltage, V_D , (cf., Fig. 2) and the donor density. On the other hand, barrier-height lowering by image forces is implicit in the analysis of current-voltage data and the quantity that is measured (cf., Eq. [9] and [11]) is actually $\phi_B^1 = \phi_B - \Delta\phi_{bi}$ (where $\Delta\phi_{bi}$ is the amount of barrier-height lowering). However, $\Delta\phi_{bi}$ is usually small ($\sim 0.1 \text{ eV}$) so that the accuracy of the present analyses does not warrant a distinction between ϕ_B and ϕ_B^1 .

Reorganization energy of $\text{Fe}(\text{Cp})_2/\text{Fe}(\text{Cp})_2^+$ redox couple in the $\text{AlCl}_3\text{-BPC}$ electrolyte.—An important parameter underlying the performance of PEC devices is the reorganization energy of the redox couple, λ , which determines the extent of separation of empty, D_{ox} , and filled energy levels, D_{red} , in the electrolyte (19). Ideally, λ should have a small value so that the degree of overlap of D_{ox} with the conduction band in the n-type semiconductor and, thereby, the extent of the deleterious back reaction is minimized. In order to assess the effect of variations in electrolyte composition (*vide infra*) on PEC performance, it is necessary to map the relative disposition of the electrolyte and semiconductor energy levels on a common energy scale. Since values of λ for the $\text{Fe}(\text{Cp})_2/\text{Fe}(\text{Cp})_2^+$ couple in the $\text{AlCl}_3\text{-BPC}$ electrolyte were not available in the literature, a method was devised to estimate λ from dark current-voltage data.

The current flow associated with charge transfer between the semiconductor conduction band and D_{ox} is given by (20)

$$J_e = J_o \left[\exp\left(\frac{qV}{kT}\right) - 1 \right] \quad [12]$$

where the exchange current density, J_o , is given by the expression

$$J_o = q\bar{K}(E_c) \left(\frac{kT}{\pi\lambda}\right)^{1/2} \exp\left[-\frac{(E_c + qV_{redox} - \lambda)^2}{4\lambda kT}\right] \cdot c_{ox}n_{so} \quad [13]$$

Here, $\bar{K}(E_c)$ is the average transfer coefficient at the conduction bandedge (16), E_c is the conduction bandedge, c_{ox} is the concentration of oxidized redox species, and n_{so} is the surface concentration of electrons at equilibrium. Equation [13] may be rewritten as

$$J_o = AT^{1/2} \exp\left[-\frac{(E_c + qV_{redox} - \lambda)^2}{4\lambda kT}\right] \quad [14]$$

where the constant A is assumed to be temperature independent³ and is given by

$$A = q\bar{K}(E_c) \left(\frac{k}{\pi\lambda}\right)^{1/2} c_{ox}n_{so} \quad [15]$$

Taking logarithms and rearranging Eq. [14], we have

$$\ln(J_o/T^{1/2}) = \ln A - \frac{(E_c + qV_{redox} - \lambda)^2}{4\lambda kT} \quad [16]$$

According to Eq. [16] a plot of $\ln(J_o/T^{1/2})$ vs. $1/T$ should be a straight line and λ may be estimated from the slope if E_c and V_{redox} are known. Figure 5 illustrates a typical plot for the n-GaAs| $\text{AlCl}_3\text{-BPC}$,

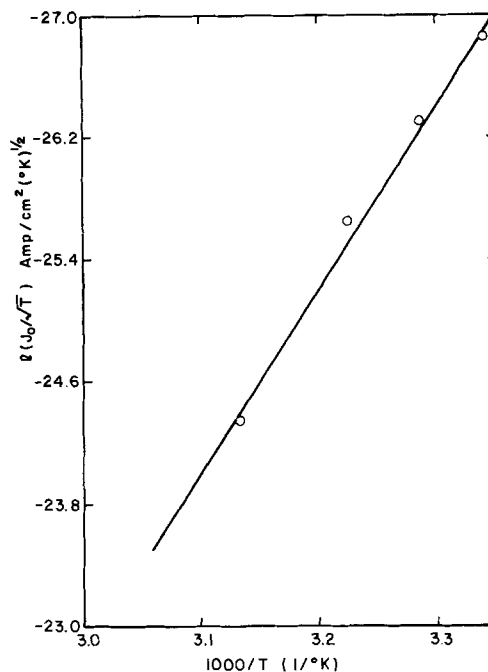


Fig. 5. Plot of $\ln(J_o/T^{1/2})$ vs. $1/T$ (cf Eq. [16] in text) for the n-GaAs| $\text{AlCl}_3\text{-BPC}$, $\text{Fe}(\text{Cp})_2/\text{Fe}(\text{Cp})_2^+$ |C system. Electrolyte composition same as in Fig. 1.

$\text{Fe}(\text{Cp})_2/\text{Fe}(\text{Cp})_2^+$ |C system. Values for J_o were obtained from Fig. 3. From previously measured values, $V_{redox} = 0.3 \text{ V}$ (vs. Al/Al^{3+}) and $E_c \approx qV_{FB} \approx -0.9 \text{ eV}$ (vs. Al/Al^{3+}) (7) and solving for the quadratic in the slope of Eq. [16], a value for $\lambda = 0.23 \text{ eV}$ was deduced. [The second root of the quadratic was too large (6.3 eV) to be of physical significance.]

Two points are worth noting here: (i) the above value of λ for the $\text{Fe}(\text{Cp})/\text{Fe}(\text{Cp})_2^+$ couple in the $\text{AlCl}_3\text{-BPC}$ electrolyte is significantly lower than values observed in aqueous solutions [e.g., $\lambda \approx 1 \text{ eV}$ for $\text{Fe}(\text{CN})_6^{3-/4-}$] (12). A value of 0.45 eV has also been recently reported for $\text{Fe}(\text{Cp})/\text{Fe}(\text{Cp})_2^+$ in ethanol (21), and (ii) the weak interaction and the relative insensitivity of V_{redox} for the $\text{Fe}(\text{Cp})/\text{Fe}(\text{Cp})_2^+$ couple in the $\text{AlCl}_3\text{-BPC}$ electrolyte (7) to electrolyte composition suggest that λ does not vary significantly with the relative molar ratios of AlCl_3 and BPC. The lower values of λ for redox couples in aprotic solvents relative to aqueous solutions offer a significant advantage in the use of these electrolytes in PEC systems (*vide supra*) and is a consequence of the reduced degree of solvation in nonaqueous media in general.

Effect of electrolyte composition on current-voltage behavior.—In previous studies in this laboratory (7, 8), the location of the bandedges of n-GaAs electrodes was found to show a systematic variation with electrolyte composition in the $\text{AlCl}_3\text{-BPC}$ system. The consequences of the observed negative shift in V_{FB} values for more basic electrolytes are threefold: (i) since V_{redox} is fixed, basic electrolytes are expected to show a higher photovoltaic output relative to acidic systems (*vide supra*), (ii) there is a critical electrolyte composition in the basic range beyond which photocurrent suppression (2) would result because of unfavorable matching of D_{red} of the $\text{Fe}(\text{Cp})_2/\text{Fe}(\text{Cp})_2^+$ couple with the valence bandedge in n-GaAs, and (iii) the degree of overlap of D_{ox} levels with the conduction bandedge in n-GaAs would be greater for the acidic electrolyte so that increased dark currents and consequent deterioration in photovoltaic output ensue.

Typical results illustrating the effects of (i) and (iii) above are shown in Fig. 6 and 7, respectively.

³ The charge-transfer coefficient $\bar{K}(E_c)$ is a function of temperature. The temperature range in the present study, however, is small enough that this dependence may be ignored.

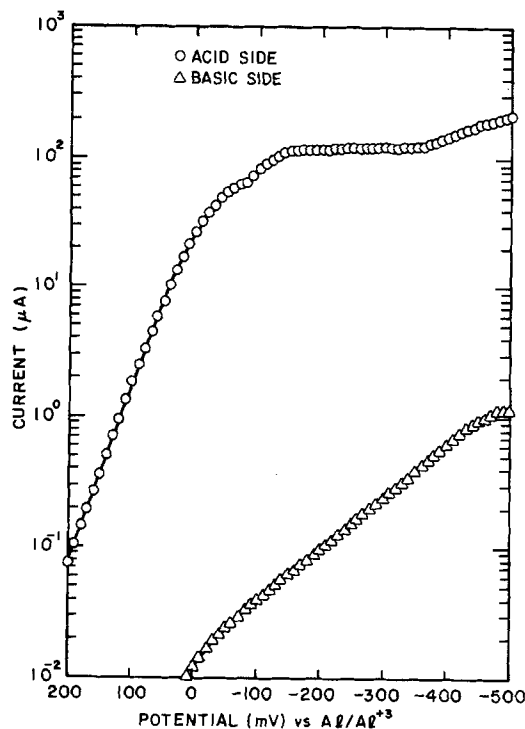


Fig. 6. Dark current voltage behavior of n-GaAs as a function of electrolyte composition. The electrolyte and redox couple were $\text{AlCl}_3\text{-BPC}$ and $\text{Fe}(\text{Cp})_2/\text{Fe}(\text{Cp})_2^+$, respectively.

The same n-GaAs electrode was used in both the electrolytes for ease of comparison. The two electrolytes were adjusted to be slightly acidic and basic of the 1:1 composition by addition of small amounts of AlCl_3 and BPC, respectively. Further illustration of the direct correlation between electrolyte composition and photovoltaic performance is provided by the results shown in the last column in Table I. The barrier height increases in the order: slightly acidic < neutral < slightly basic. More basic electrolytes ($\text{AlCl}_3\text{:BPC}$ molar ratio < 0.75:1) showed a deterioration in photovoltaic output consistent with (ii) above.

The above trends may be understood with the help of energy band diagrams shown in Fig. 8 where the relative positions of the semiconductor energy levels and the redox energy distribution in the $\text{AlCl}_3\text{-BPC}$ electrolyte are compared on a common potential scale for the basic electrolyte (Fig. 8a) and acidic case (Fig. 8b). The interphase layer is not shown in these diagrams for the sake of clarity. It is, however, pertinent to note that alterations in the potential distribution

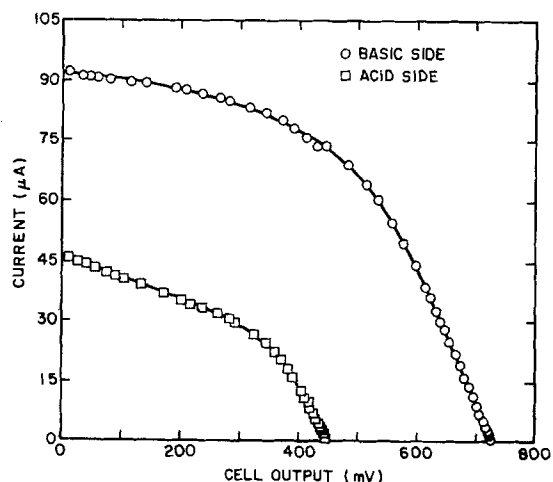
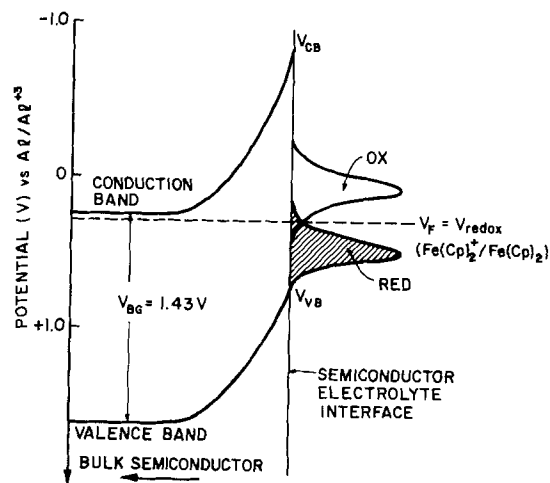
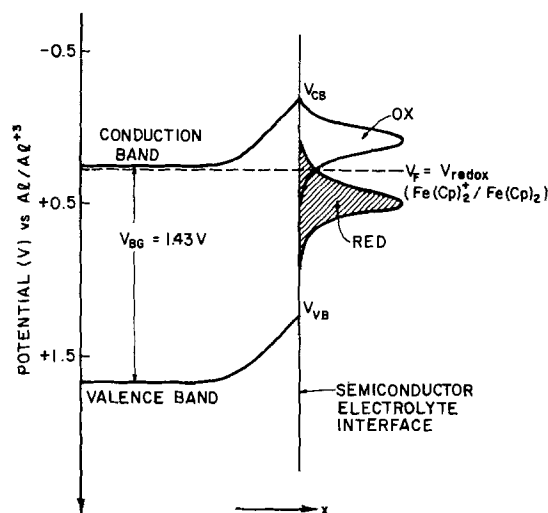


Fig. 7. Effect of electrolyte composition on the PEC behavior of the n-GaAs| $\text{AlCl}_3\text{-BPC}$, $\text{Fe}(\text{Cp})_2/\text{Fe}(\text{Cp})_2^+$ |C system (8).



(a)



(b)

Fig. 8. Comparison of the relative position of the n-GaAs band-edges and the $\text{Fe}(\text{Cp})_2/\text{Fe}(\text{Cp})_2^+$ redox levels in (a) basic $\text{AlCl}_3\text{-BPC}$ and (b) acidic $\text{AlCl}_3\text{-BPC}$ electrolytes. The interphase is not shown for clarity.

across this layer brought about by specific ion adsorption (8) and other chemical interactions (e.g., dissociation equilibria involving surface species) are undoubtedly an important factor in the observed shift in energy levels in the two cases (Fig. 8a and b).

Mechanisms of charge transfer at the n-GaAs/ $\text{AlCl}_3\text{-BPC}$ interface.—Based on the data presented above, the various charge transport mechanisms in the n-GaAs| $\text{AlCl}_3\text{-BPC}$, $\text{Fe}(\text{Cp})_2/\text{Fe}(\text{Cp})_2^+$ |C system are schematized in Fig. 9. The filled circles represent processes taking place in the dark and the open circles denote light-assisted processes. It is emphasized that the two sets of charge-flow paths act in opposite directions and the greater the extent to which the filled circles are minimized in the device, the better will be its ultimate light conversion efficiency. This is accomplished to a greater degree in the basic $\text{AlCl}_3\text{-BPC}$ electrolyte case relative to the acidic system for reasons discussed in the preceding section. The dark current processes labeled a, b, c, and d represent, respectively, thermionic emission of electrons from the semiconductor over the top of the barrier into the electrolyte, quantum-mechanical tunneling through the barrier, space-charge recombination-generation and recombination generation in the neutral region (12). The process labeled e denotes isoenergetic charge

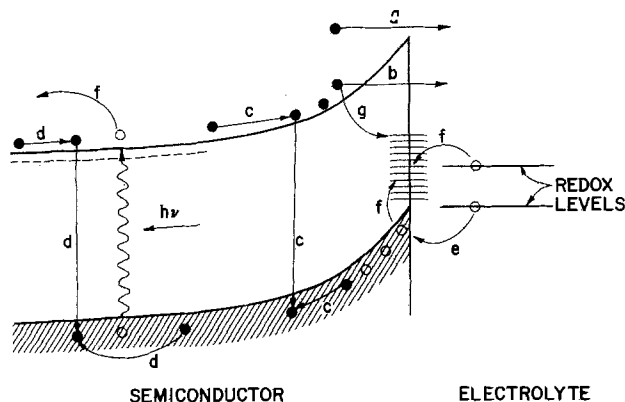
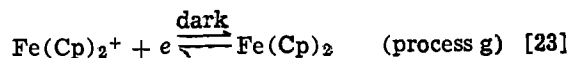
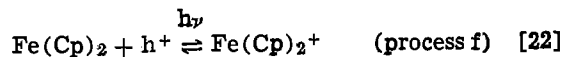
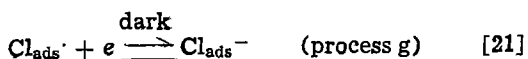
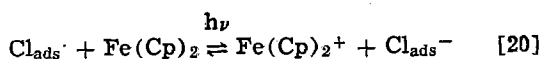
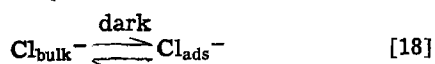
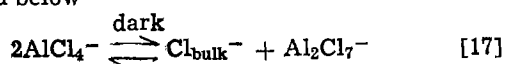


Fig. 9. Charge transport mechanisms at the illuminated n-GaAs/ AlCl_3 -BPC interface. The interphase and the distribution of energies in the redox system are not shown for the sake of clarity.

transfer between D_{red} and the valence band edge in n-GaAs. This process is expected to be more predominant in the basic electrolyte case relative to the acidic electrolyte because of the relative positions of V_{redox} and V_{VB} (compare Fig. 8a and b). Additional processes in the illuminated n-GaAs/ AlCl_3 -BPC, $\text{Fe}(\text{Cp})_2/\text{Fe}(\text{Cp})_2^+|\text{C}$ system are the charge transfer paths f and g involving electronic states in the bandgap of the semiconductor. Evidence for mediation of surface states in the charge-transfer process was presented in a previous study where it was shown that dark reduction of the $\text{Fe}(\text{Cp})_2^+$ ion occurred at potentials well positive of V_{FB} (7). Process f represents surface-state assisted photooxidation of solution species (D_{red}) by photogenerated holes in the semiconductor. Process g involves inelastic tunneling of an electron to the surface state where it reduces back the oxidized species. Alternatively, this process may be viewed as a recombination current involving photogenerated electron-hole pairs. Examination of Fig. 8 again suggests that processes f and g play a more dominant role in the charge-transfer dynamics in the acidic electrolyte relative to the basic AlCl_3 -BPC system. All the processes described above with the exception of e and f have a deleterious influence on the photovoltaic output of the system. The propensity of processes a-d and g at the n-GaAs/ AlCl_3 -BPC interface was indicated by data from a previous study (17) and is also suggested by the current-voltage behavior shown in Fig. 3. Kinetics undoubtedly plays a major role and the more facile process f is, the greater will be the degree to which processes g, c, and d can be suppressed. Processes a, b, and g will play a dominant role at high values of forward bias. Process b is dependent to a large degree on the depletion layer width and on doping density (22).

The precise chemical nature of the surface states at the n-GaAs/ AlCl_3 -BPC system is not clear although we speculate that adsorbed Cl species induce electronic states in the n-GaAs bandgap [cf., Ref. (23)]. A tentative scheme for the sequence of photoprocesses in the n-GaAs/ AlCl_3 -BPC, $\text{Fe}(\text{Cp})_2/\text{Fe}(\text{Cp})_2^+|\text{C}$ system offered below



The above scheme is consistent with several experimental observations: (i) equilibrium [17] lies far to the right in basic AlCl_3 -BPC electrolytes (24) which explains the negative shift in V_{FB} for more basic electrolytes, (ii) the charge transfer under illumination is quite sluggish at the n-GaAs/ AlCl_3 -BPC, $\text{Fe}(\text{Cp})_2/\text{Fe}(\text{Cp})_2^+$ interface (17). This is surprising because of the rapid kinetics typical of the $\text{Fe}(\text{Cp})_2/\text{Fe}(\text{Cp})_2^+$ couple in other electrolytes and suggests that electron transfer may be mediated via surface adsorbed Cl^- species (Eq. [20]), and (iii) cathodic current spikes are observed with chopped light indicating the back reaction of either $\text{Cl}_{\text{ads}}^\cdot$ or $\text{Fe}(\text{Cp})_2^+$ via reactions [21] and [23]. Experiments are in progress in this laboratory to distinguish between reactions [19] and [20] representing the photoanodic processes and between [21] and [23] comprising the cathodic dark current flow.

Comparison of metal/semiconductor and electrolyte/semiconductor junctions.—The similarity of the current-voltage expressions in Schottky barrier theory (Eq. [10]) and the fluctuating energy level model (Eq. [12]) is worthy of note. The former has been conventionally applied to metal/semiconductor contacts (12) whereas the latter pertains to semiconductor/electrolyte junctions (19, 20). The major difference lies in the formal expressions for the exchange current densities (compare Eq. [6] and [13]) and underlines the aspects where the two approaches start to diverge from each other.⁴ The thermionic-emission theory represented by Eq. [6] considers the control exercised on the current by the number of Bloch states in the metal which can communicate with corresponding energy levels in the semiconductor (12). On the other hand, the fluctuating level mechanism (Eq. [12]) explicitly takes into account the discreteness in the distribution of energy levels in the electrolyte in contrast to the metal case. The key question which the present study has attempted to address is whether it is valid to employ the two approaches in an interchangeable fashion in the treatment of semiconductor/electrolyte junctions once the above differences are rationalized. The present data show that it is. The following observations support this argument: (i) the forward-bias current-voltage behavior of semiconductor/electrolyte junctions show good adherence to Eq. [6] (Fig. 4), (ii) the V_{oc} values show the logarithmic dependence on I_L as predicted by Schottky diode equations (25), and (iii) values of A^* obtained from Eq. [6] for the n-GaAs/ AlCl_3 -BPC interface (*vide supra*) are in good agreement with those measured on GaAs/Au Schottky diodes (12).

Further analogies may be drawn on the effect of the interface layer on the electrical behavior of metal/semiconductor and electrolyte/semiconductor junctions. The role of this layer in modifying barrier heights in Schottky diodes is well recognized (26). This has led to the development of a class of devices based on metal-insulator-semiconductor (MIS) junctions wherein an interfacial layer is intentionally incorporated to improve the photovoltaic performance (27). The present data have clearly shown how changes in the interface layer can affect the PEC behavior of electrolyte/semiconductor junctions. This layer comprises the inner Helmholtz region and any

⁴ It must be noted that the use of both Eq. [6] and [13] involves the implicit assumption that the processes of diffusion and drift of the electronic carriers within the semiconductor are not limiting the current flow at the semiconductor/electrolyte interface. Charge-transfer processes at the interface are assumed to be the major impediment to current flow.

surface layer on the electrode surface formed by prior treatment (e.g., etching).

Acknowledgment

This research program was supported by the Solar Energy Research Institute and the U.S. Department of Energy under Grant XP-9-8002-9. Dr. J. DuBow provided many helpful suggestions during the course of this work.

Manuscript submitted Nov. 3, 1980; revised manuscript received Feb. 23, 1981.

Any discussion of this paper will appear in a Discussion Section to be published in the June 1982 JOURNAL. All discussions for the June 1982 Discussion Section should be submitted by Feb. 1, 1982.

Publication costs of this article were assisted by Colorado State University.

REFERENCES

1. K. Rajeshwar, P. Singh, and J. DuBow, *Electrochim. Acta*, **23**, 1117 (1978).
2. S. Kar, K. Rajeshwar, P. Singh, and J. DuBow, *Solar Energy*, **23**, 129 (1979).
3. P. A. Kohl and A. J. Bard, *This Journal*, **126**, 598 (1979); see also references therein.
4. K. D. Legg, A. B. Ellis, J. M. Bolts, and M. S. Wrighton, *Proc. Natl. Acad. Sci. U.S.A.*, **74**, 4116 (1977).
5. H. Tsubomura, M. Matsumura, K. Nakatani, K. Yamamoto, and K. Maeda, *Sol. Energy*, **21**, 93 (1978).
6. R. A. Carpio, L. A. King, R. E. Lindstrom, J. C. Nardi, and C. L. Hussey, *This Journal*, **126**, 1644 (1979).
7. P. Singh, K. Rajeshwar, J. DuBow, and R. Job, *J. Am. Chem. Soc.*, **102**, 4676 (1980).
8. P. Singh, R. Singh, R. Gale, K. Rajeshwar, and J. DuBow, *J. Appl. Phys.*, **51**, 6286 (1980).
9. R. Gale, P. Smith, P. Singh, K. Rajeshwar, and J. DuBow, *Adv. Chem. Ser.*, **146**, Chap. 22, p. 343, American Chemical Society (1981).
10. R. Williams, *This Journal*, **114**, 1173 (1980).
11. S. R. Morrison, *J. Vac. Sci. Technol.*, **15**, 1417 (1978).
12. E. H. Rhoderick, "Metal-Semiconductor Contacts," Chap. 1-3, Clarendon Press, Oxford (1978).
13. D. N. Hendrickson, Y. S. Sohn, and H. B. Gray, *Inorg. Chem.*, **10**, 1559 (1971).
14. W. W. Gärtner, *Phys. Rev.*, **116**, 84 (1959).
15. M. A. Butler and D. S. Ginley, *J. Mater. Sci.*, **15**, 1 (1980).
16. S. M. Sze, "Physics of Semiconductor Devices," p. 20, Wiley-Interscience, New York (1969).
17. P. Singh, R. Singh, K. Rajeshwar, and J. DuBow, *This Journal*, **128**, 1145 (1981).
18. A. S. Grove, "Physics and Technology of Semiconductor Devices," p. 189, John Wiley & Sons, Inc., New York (1967).
19. S. R. Morrison, "The Chemical Physics of Surfaces," p. 50, Plenum Press, New York (1977).
20. H. Gerischer, in "Physical Chemistry, An Advanced Treatise," Vol. IX A, H. Eyring, Editor, Chap. 5, p. 492, Academic Press, New York (1970).
21. S. R. Morrison, M. J. Madou, and K. W. Frese, Jr., *Adv. Chem. Ser.*, **146**, Chap. 11, p. 179, American Chemical Society (1981).
22. e.g., R. Memming, F. Schröppel, and V. Bringmann, *J. Electroanal. Chem. Interfacial Electrochem.*, **100**, 307 (1979).
23. S. R. Morrison, "The Chemical Physics of Surfaces," Chap. 5, p. 151, Plenum Press, New York (1977).
24. R. J. Gale and R. A. Osteryoung, *Inorg. Chem.*, **18**, 1603 (1979).
25. H. J. Hovel, "Semiconductors and Semimetals," Vol. 11, p. 176, Academic Press, New York (1975).
26. H. C. Card and E. H. Rhoderick, *J. Phys. D.*, **4**, 1589 (1971); D. R. Lillington and W. G. Townsend, *Appl. Phys. Lett.*, **28**, 97 (1976).
27. S. M. Sze, "Physics of Semiconductor Devices," Chap. 9, p. 425, Wiley-Interscience, New York (1969).

The Investigation of Current Doubling Reactions on Semiconductor Photoelectrodes by Temperature Change Measurements

Yasuhisa Maeda, Akira Fujishima,* and Kenichi Honda

Department of Synthetic Chemistry, Faculty of Engineering, The University of Tokyo, Hongo, Tokyo 113, Japan

ABSTRACT

Current doubling effects in the photoanodic reactions of HCOOH or HCOONa on n-type semiconductor electrodes (ZnO, CdS, and TiO₂) and the photocathodic reaction of (NH₄)₂S₂O₈ on a p-type semiconductor (GaP) were studied by the measurement of the temperature change of a semiconductor electrode surface. The results of the temperature change measurements show that these photoelectrode reactions proceed with quantum efficiencies greater than 1 but less than 2. The temperature changes are interpreted in terms of the current doubling process.

Morrison *et al.* (1-4) proposed that the photoelectrochemical oxidation of the formic ion on a ZnO photoanode occurs by the current doubling mechanism, a two-step oxidation process. According to this mechanism, in the case of an n-type semiconductor electrode such as ZnO, a current doubling reagent R is first oxidized to R⁺ by a hole photogenerated in the valence band, and then an electron from R⁺ is injected into

the conduction band and R⁺ is converted to R²⁺. In this case, the maximum value of the quantum efficiency for the photoelectrode reaction will be 2.0.

We have studied photoelectrochemical reactions at semiconductor electrodes by the temperature change technique and determined the quantum efficiencies and the energy efficiencies of the reactions (5-7).

In this paper, the current doubling phenomenon was studied by the direct measurement of the temperature change of the surface of a semiconductor electrode [n-type (ZnO, CdS, and TiO₂) and p-type (GaP)]

* Electrochemical Society Active Member.

Key words: photoelectrochemistry, semiconductor electrode, quantum efficiency.

obtain the intrinsic quantum efficiency of the current doubling reaction and to elucidate the reaction mechanism.

When a semiconductor electrode is illuminated with a pulse of monochromatic light having an energy E (eV/photon) with an average absorbed intensity I (photons/sec) for a time t (sec), the relationship between temperature change and potential is represented by Eq. [1] which applies in a limited photocurrent region (5)

$$E \frac{\Delta T}{\Delta T^\circ} = \frac{Q_{s.c.} + T\Delta S}{It} + \eta e(V - V_{FB}) \quad [1]$$

where ΔT = temperature change of the semiconductor surface, ΔT° = temperature change of the semiconductor surface in the open circuit, ΔS = entropy change of the semiconductor electrode reaction, $Q_{s.c.}$ = heat evolved in the semiconductor via recombination and radiationless processes, η = quantum efficiency of the photoelectrode reaction, V = applied potential (V vs. reference electrode), V_{FB} = flatband potential (V vs. reference electrode).

Under conditions of constant illumination, i.e., EIt = constant, a plot of $E(\Delta T/\Delta T^\circ)$ vs. $(V - V_{FB})$ yields the quantum efficiency, η , from the slope of the straight line, and information related to the electrode reaction heat is obtained from the intercept (the value of $E(\Delta T/\Delta T^\circ)$ at $V = V_{FB}$).

As reported in previous papers (5-7), the evaluation of the slope from the measurement of the temperature change for various photoreactions at semiconductor electrodes in the absence of a current doubling reagent yielded a maximum quantum efficiency of 1.0. However, in case of a photoelectrode reaction occurring by the current doubling mechanism, the temperature measurement is expected to yield a maximum quantum efficiency of 2.0.

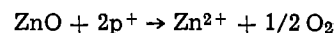
Experimental

The experimental method was described in previous papers (5-8). The photothermal responses were obtained for the photoelectrodes during polarization and under open-circuit conditions in the electrolyte solutions. The temperature changes and the photocurrent were plotted as a function of the potential vs. flatband potential or the applied potential. The light source was a 500W high pressure mercury lamp (Ushio Electric). An interference filter was used to provide monochromatic light (340 nm), and a shutter was employed to fix the irradiation period precisely. The current-potential and current-time curves were measured under potentiostatic conditions using a potentiostat and a potential programmer (Nikko Keisoku). The semiconductors used were n-type polycrystalline ZnO, single crystal CdS [Teikoku Tsushin, (0001)], single crystal TiO₂ [Nakazumi Crystal, (001)], and p-type single crystal GaP [Sumitomo Metal Mining, (100)]. A platinum electrode was used as the counterelectrode and a saturated calomel electrode as the reference electrode. All chemicals were of reagent grade and were used without further purification.

To measure the temperature changes, we used a matched pair of thermistors (Shibaura Electronics, BSB4-41A). The thermistors were used in a differential arrangement with one held against the front surface of the semiconductor electrode and the other positioned behind the electrode but not touching it. The cell was carefully positioned so that the monochromatic light beam struck only the electrode and not the thermistors. The temperature change caused by irradiating the electrode resulted in a resistive change in the thermistors and a voltage imbalance in the d-c bridge. This small voltage was amplified and then displayed on a recorder.

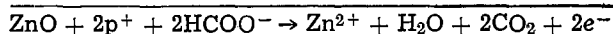
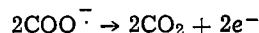
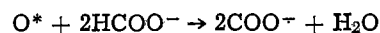
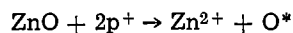
Results and Discussion

ZnO-HCOOH.—In Fig. 1, a plot of $E\Delta T/\Delta T^\circ$ vs. applied anodic polarization potential is shown for the ZnO polycrystalline photoanode with and without formic acid. In the supporting Na₂SO₄ electrolyte solution, the photoelectrode reaction at the electrode/electrolyte interface is the dissolution of ZnO (9)



$E\Delta T/\Delta T^\circ$ increased linearly with anodic polarization, and from the slope of the line, the quantum efficiency of the ZnO photoanode was found to be 0.90, which was in close agreement with the value obtained by chemical actinometry (6, 7). Like this, quantum efficiencies of one-step oxidations can be obtained from the temperature method (5-7).

When sufficient quantity of formic acid was added, current doubling was observed. The quantum efficiency was found to be 1.8, which was twice as large as the value obtained in the supporting electrolyte. We propose the following current doubling mechanism



because we have observed that with HCOONa present in solution the current efficiencies of the products of Zn²⁺, O₂, and CO₂ are 0.5, 0.0, and 0.5, respectively, in accordance with the stoichiometry of the above equation (10). In these reactions, we have proposed O* as an intermediate chemical species, which we have not proved directly. This mechanism is different from that proposed by other workers (1-4).

CdS-HCOONa.—In Fig. 2, plots of photocurrent and $E\Delta T/\Delta T^\circ$ vs. V applied to the CdS photoanode are

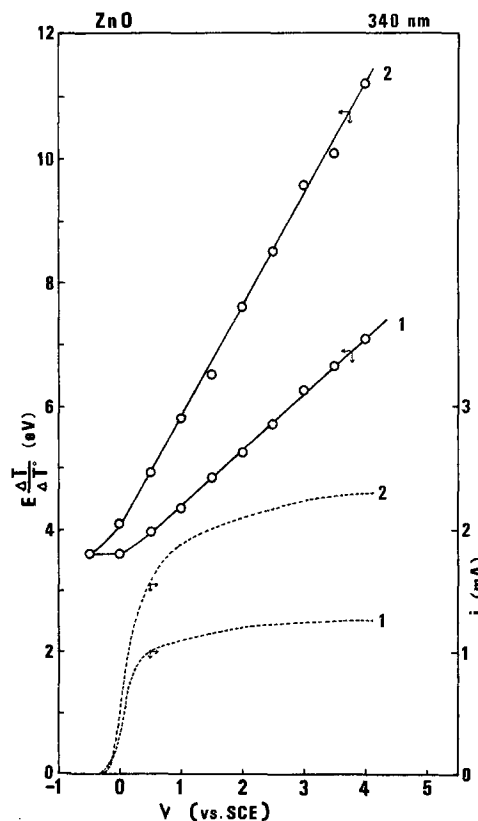


Fig. 1. Normalized temperature change vs. potential and photocurrent vs. potential of a ZnO polycrystalline electrode. Curve 1, 0.2M Na₂SO₄; curve 2, 0.3M HCOOH in 0.2M Na₂SO₄.

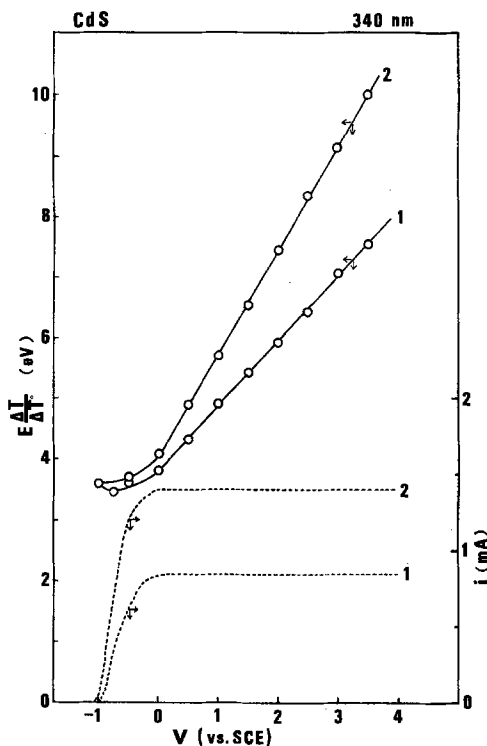
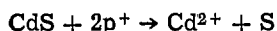
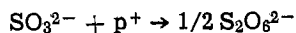


Fig. 2. Normalized temperature change vs. potential and photocurrent vs. potential of a CdS single crystal electrode. Curve 1, 0.1M Na_2SO_3 in 0.2M Na_2SO_4 ; curve 2, 0.5M HCOONa in 0.2M Na_2SO_4 .

shown for the sulfate solutions containing either sulfite or HCOONa . In the supporting electrolyte we account for the photocurrent by a photoelectrode reaction of the dissolution of CdS

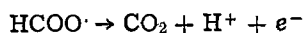
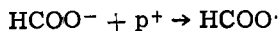


In the case of Na_2SO_3 (curve 1), the photoelectrode reaction is the oxidation of SO_3^{2-} which occurs only by a hole transfer reaction, but not the photodissolution reaction of CdS (11)



The quantum efficiency of the one-step reaction of SO_3^{2-} was found to be 1.0 from the slope of the linear plot.

In the case of HCOONa (curve 2), the observed photocurrent was probably due to the oxidation of HCOO^-



because the current efficiencies of Cd^{2+} and CO_2 formed were approximately 0.0 and 0.5, respectively. The quantum efficiency was found to be 1.7. The quantum efficiency was not 2.0, *i.e.*, double the value for Na_2SO_3 alone, probably because part of the intermediate species (HCOO^\cdot) (12) formed in the first hole transfer reaction could not inject electrons into the conduction band.

TiO₂-HCOONa.—In Fig. 3, plots of photocurrent and $E\Delta T/\Delta T^\circ$ vs. V for the TiO_2 photoanode are shown for electrolytes containing Na_2SO_4 , with or without HCOONa . In the absence of HCOONa (curve 1), the photoelectrode reaction results in oxygen evolution. The quantum efficiency of the oxygen evolution reaction was found to be 0.53. [The quantum efficiency of the TiO_2 electrode was found to be dependent on the degree of reduction of the TiO_2 crystal resulting from a pretreatment to increase its conductivity (5).] An increase in the photocurrent was observed when HCOONa was added to the electrolyte. However, the amount of increased photocurrent was smaller than

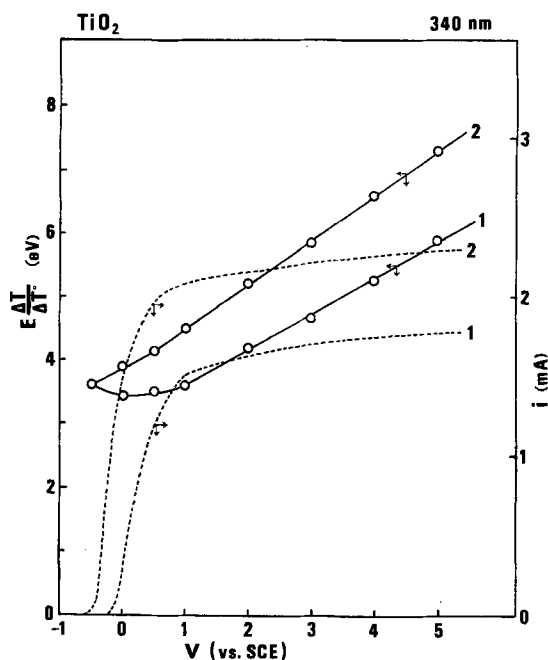
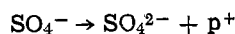
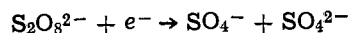


Fig. 3. Normalized temperature change vs. potential and photocurrent vs. potential of a TiO_2 single crystal electrode. Curve 1, 0.2M Na_2SO_4 ; curve 2, 1M HCOONa in 0.2M Na_2SO_4 .

that in the case of ZnO or CdS, even when a large quantity of HCOONa was added. The observed photocurrent was also believed to be due to the oxidation of HCOO^- as in the case of CdS, because oxygen formation measured by an oxygen meter could not be observed, but CO_2 was generated. However, we do not understand why the current doubling effect for TiO_2 is considerably smaller than that observed for ZnO and CdS. The quantum efficiency was found to be only 0.70.

GaP-(NH₄)₂S₂O₈.—As shown in Fig. 4, irradiation of the p-type GaP semiconductor electrode resulted in a cathodic current and $E\Delta T/\Delta T^\circ$ increased linearly with the cathodic polarization in the sulfuric acid solution. The cathodic photoelectrode reaction was due to hydrogen evolution, and the intrinsic quantum efficiency was 0.75 as obtained from the slope of the linear relationship between $E\Delta T/\Delta T^\circ$ and V .

When $(\text{NH}_4)_2\text{S}_2\text{O}_8$ was added to the sulfuric acid solution, the cathodic photocurrent increased. According to Memming (13), the photoelectrode reaction is due to the reduction of the persulfate ion through a two-step mechanism. The first step occurs by an electron transfer from the conduction band, and the second step by hole injection into the valence band



In this case, the slope of the $E\Delta T/\Delta T^\circ$ vs. V plot was 1.5, a value twice as large as that obtained with only sulfuric acid. It was ascertained by the temperature measurement that the photoelectrode reaction of $(\text{NH}_4)_2\text{S}_2\text{O}_8$ on the p-type GaP electrode proceeded with high quantum efficiency.

Interpretation of the temperature changes from the current doubling mechanism.—The behavior of the temperature changes observed during the current doubling reactions can be explained by charge transfer in the space charge layer, as shown in Fig. 5. In the case of an n-type semiconductor, when the photogenerated electrons in the conduction band move from the surface of the electrode through the potential gradient of the space charge region to the bulk of the semiconductor, heat is produced in an amount depending on the polarizing potential and the electron current. Con-

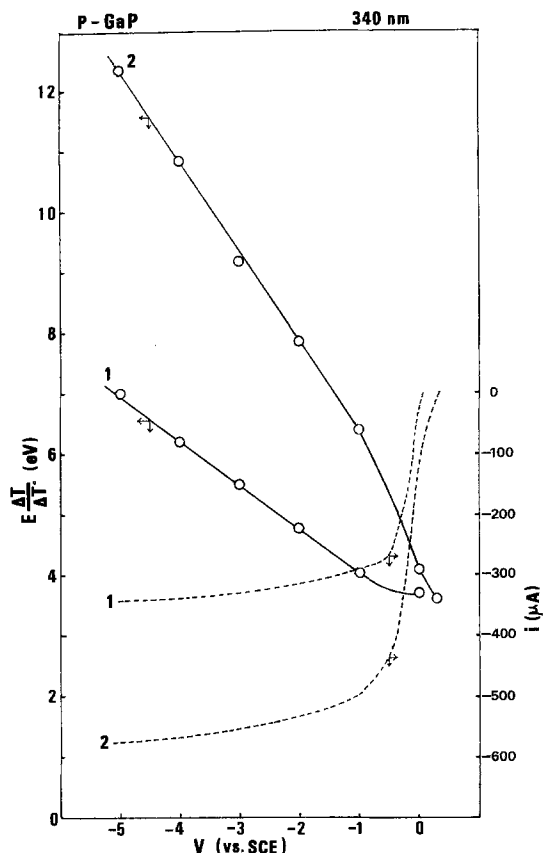


Fig. 4. Normalized temperature change vs. potential and photo-current vs. potential of a p-type GaP single crystal electrode. Curve 1, 0.5M H_2SO_4 ; curve 2, 0.1M $(\text{NH}_4)_2\text{S}_2\text{O}_8$ in 0.5M H_2SO_4 .

sequently plots of $E\Delta T/\Delta T^\circ$ vs. $(V - V_{\text{FB}})$ (or V) increase linearly and their slopes are equal to the quantum efficiencies, as already mentioned.

Addition of a current doubling reagent, such as HCOO^- , caused the slope to nearly double except in the case of TiO_2 . This fact can be interpreted by a mechanism in which heat is produced not only by the photoexcited electron flow, but also by the flow of the electrons injected from the intermediate chemical species. Namely, the increase in the slope is due to the increase in the number of electrons flowing within the conduction band.

In the case of a p-type semiconductor, the heat is produced by the photogenerated hole in the valence band flowing from the surface of the electrode to the semiconductor bulk. This heat becomes larger with the polarizing potential. Then, the plot of $E\Delta T/\Delta T^\circ$ vs. $(V - V_{\text{FB}})$ is a linear relationship similar to that of an n-type semiconductor. By the addition of $(\text{NH}_4)_2\text{S}_2\text{O}_8$ into the sulfuric acid supporting electrolyte, the slope nearly doubled, which shows that the second hole was injected from the intermediate chemical species formed as a result of the first electron transfer into the valence band.

These observations suggest that an increase in the slope results from electron injection into the conduction band for an n-type semiconductor electrode, and hole injection into the valence band for a p-type one.

The value obtained by extrapolation of the linear portion of $E\Delta T/\Delta T^\circ$ vs. $(V - V_{\text{FB}})$ plots to 0V (i.e., $V = V_{\text{FB}}$) corresponds to $(Q_{\text{s.c.}} + T\Delta S)/It$. The heat of the electrode reaction thus obtainable may give information about the current doubling mechanism. This subject is currently under investigation.

In conclusion, the temperature measurement method proved to be useful for obtaining information about the current doubling effect.

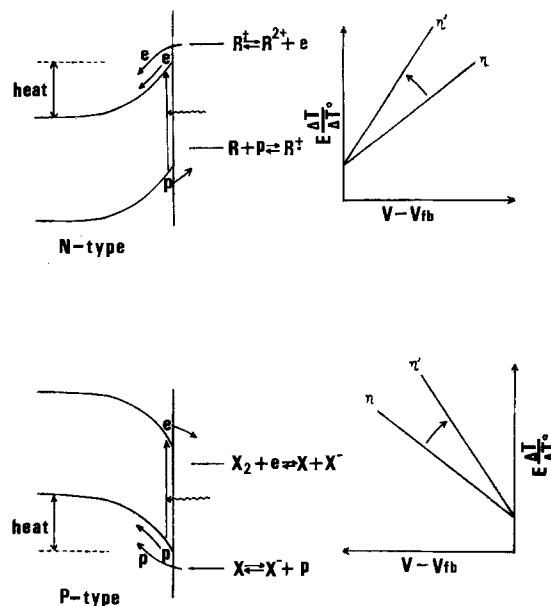


Fig. 5. The mechanism of current doubling, and the relation between the behavior of the temperature change and applied potential. (Upper left) For an n-type semiconductor, a current doubling reagent R is first oxidized by a photogenerated hole in the valence band to R^+ which then injects an electron to the conduction band. (Lower left) For a p-type semiconductor, a current doubling reagent X_2 is first reduced by a photogenerated electron in the conduction band to X and X^- , X then injects a hole to the valence band. η and η' are quantum efficiencies obtained from the plots of $E\Delta T/\Delta T^\circ$ vs. $(V - V_{\text{FB}})$ for both the n-type (upper right) and the p-type (lower right) semiconductors in the absence and the presence of a current doubling reagent, respectively.

Acknowledgment

The authors would like to thank Dr. Kenneth M. Sancier and Dr. Boon H. Loo at SRI International for their valuable suggestions. The support of this research by The Toyota Foundation is gratefully acknowledged.

Manuscript submitted Oct. 27, 1980; revised manuscript received March 10, 1981.

Any discussion of this paper will appear in a Discussion Section to be published in the June 1982 JOURNAL. All discussions for the June 1982 Discussion Section should be submitted by Feb. 1, 1982.

Publication costs of this article were assisted by The University of Tokyo.

REFERENCES

- W. P. Gomes, T. Freund, and S. R. Morrison, *This Journal*, **115**, 818 (1968).
- S. R. Morrison and T. Freund, *J. Chem. Phys.*, **47**, 1543 (1967).
- S. R. Morrison and T. Freund, *Electrochim. Acta*, **13**, 1343 (1968).
- W. P. Gomes, T. Freund, and S. R. Morrison, *Surf. Sci.*, **13**, 201 (1968).
- A. Fujishima, Y. Maeda, K. Honda, G. H. Brilmyer, and A. J. Bard, *This Journal*, **127**, 840 (1980).
- Y. Maeda, A. Fujishima, and K. Honda, *Chem. Lett.*, 271 (1980).
- A. Fujishima, Y. Maeda, and K. Honda, *Bull. Chem. Soc. Jpn.*, **53**, 2735 (1980).
- G. H. Brilmyer, A. Fujishima, K. S. V. Santhanam, and A. J. Bard, *Anal. Chem.*, **49**, 2057 (1977).
- H. Gerischer, *This Journal*, **113**, 1174 (1966).
- A. Fujishima, T. Kato, E. Maekawa, and K. Honda, *Bull. Chem. Soc. Jpn.*, **54**, 1671 (1981).
- T. Inoue, T. Watanabe, A. Fujishima, K. Honda, and K. Kohayakawa, *This Journal*, **124**, 719 (1977).
- J. R. Harbour and M. L. Hair, *J. Phys. Chem.*, **83**, 652 (1979).
- R. Memming, *This Journal*, **116**, 785 (1969).

The Measurement of the Flatband Potentials of n-Type and p-Type Semiconductors by Rectified Alternating Photocurrent Voltammetry

J. F. McCann¹ and J. Pezy

Chemistry Discipline, School of Physical Sciences, Flinders University, Bedford Park, 5042, South Australia

ABSTRACT

The flatband potentials (FBP's) of a number of n-type and p-type semiconductors have been measured by rectified alternating photocurrent voltammetry (RAPV). The values of the FBP's obtained by this technique have been compared with those obtained from capacitance-potential (C-V) measurements. A correlation was observed between the values of the respective FBP's obtained from RAPV and C-V measurements. The advantages of using RAPV to determine the FBP of a semiconductor are described.

The value of the flatband potential, V_{FB} , of an n-type or p-type semiconductor predetermines the maximum open-circuit photovoltage, $V_{oc}(\max)$ of a given semiconductor/electrolyte/counterelectrode cell according to the relation (1)

$$V_{oc}(\max) = V(\text{redox}) - V_{FB} \quad [1]$$

where $V(\text{redox})$ is the redox potential of the electrolyte.

Therefore, in order to determine the $V_{oc}(\max)$ of a liquid junction photocell it is necessary to measure the V_{FB} of the semiconductor in the particular electrolyte used in the cell. In this report we describe how rectified alternating photocurrent voltammetry can be used to determine V_{FB} for an n-type or p-type semiconductor. Firstly, however, the limitations of some other methods that can be used to determine V_{FB} will be briefly discussed. The discussion is in terms of n-type semiconductor/electrolyte systems but the arguments are equally applicable to p-type semiconductor/electrolyte systems.

The capacitance of an n-type semiconductor with no surface states in an electrolyte is related to V_{FB} by the Mott-Schottky relation (2)

$$\frac{1}{C_{sc}^2} = \frac{2}{qD\epsilon_0 N_D} (V - V_{FB}) \quad [2]$$

where C_{sc} is the capacitance of the semiconductor space charge layer, q is the electronic charge, D_ϵ is the dielectric constant of the semiconductor, ϵ_0 is the permittivity of a vacuum, N_D is the donor density, and V is the semiconductor potential. Strictly a kT/q term should also be included in the $(V - V_{FB})$ term but it is frequently neglected.

In practice the measured capacitance does not necessarily correspond to the exact value of C_{sc} due to the addition of other capacitances such as that of the Helmholtz layer, the Gouy layer, surface states, deep donor levels, and dielectric relaxation. Therefore, it would be advantageous to use an alternative method to check the value of V_{FB} derived from capacitance-potential studies.

An alternative method for measuring V_{FB} is from photocurrent-potential plots. Consider a typical n-type semiconductor/electrolyte/counterelectrode cell. Such a cell is depicted schematically in Fig. 1. Neglecting depletion layer recombination, the hole current reacting at an irradiated n-type semiconductor surface

from the interior of the semiconductor, $i_p^{CT}(o)$ is

$$i_p^{CT}(o) = i_p^{DL} + i_p^B - i_p^{SR} \quad [3]$$

where i_p^{DL} is the hole current generated in the depletion layer, i_p^B is the hole current at the depletion layer/bulk layer boundary, and i_p^{SR} is the surface recombination current. The following expression can be derived for $i_p^{CT}(o)$ [see Ref. (3) and (4)]

$$i_p^{CT}(o) = -P_{CT}qI_0 \left(1 - \frac{e^{-\alpha W_0(V-V_{FB})^{1/2}}}{1 + \alpha L_p} \right) \quad [4]$$

where I_0 is the effective photon intensity, W_0 is the depletion layer width for a potential drop of 1V across the depletion layer, α is the absorption coefficient, L_p is the hole diffusion length, and P_{CT} is the charge transfer probability given by (4)

$$P_{CT} = \frac{v_{CT}}{v_{CT} + v_{SR}} \quad [5]$$

Equation [5] represents a form of Gartner's relation, Ref. (3), which has been modified to take surface recombination into account. For a more detailed treatment of charge transfer at semiconductor/electrolyte interfaces and the effect of the surface recombination velocity, the reader is referred to Ref. (5).

In cases where thermodynamic factors can be neglected, the potential onset of the d-c photocurrent, V_{onset} , will differ from V_{FB} when $v_{SR} \gg v_{CT}$. The value of v_{SR} partially depends on the potential difference $(V - V_{FB})$. However, the way in which v_{SR} varies with $(V - V_{FB})$ is complex and not readily

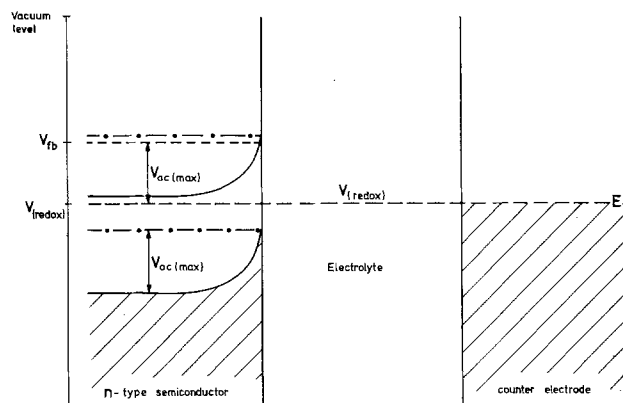


Fig. 1. Schematic diagram of an n-type semiconductor/electrolyte/counterelectrode cell.

¹Present address: Physics Department, University of New South Wales, Kensington, N.S.W. Australia 2033.

Key words: photoelectrochemical, solar energy, semiconductor electrode, capacitance.

calculable without simplifying assumptions. Despite the problems associated with calculating the exact value of v_{SR} , it is known that v_{SR} usually decreases as $(V - V_{FB})$ increases [see, e.g., Ref. (5)]. Hence it can be seen in a qualitative way from Eq. [4] that the magnitude of the difference $(V_{onset} - V_{FB})$ will depend on the initial magnitude of v_{SR} and how the value of the latter parameter changes with potential. These effects vary from sample to sample for a particular semiconductor material and also from semiconductor to semiconductor, since the number of surface recombination centers and their energy distribution are partially dependent on intrinsic factors such as crystal orientation and partially on surface preparation (5). Schematic quantum efficiency-potential relations with and without surface recombination effects which are shown in Fig. 2 qualitatively illustrate the effect of v_{SR} on the photocurrent-potential curve [see Ref. (5)].

It is apparent from Eq. [4] and Fig. 2 that it should be possible to determine V_{FB} from the V_{onset} of a photocurrent-potential plot even when P_{CT} is small if very small photocurrents are detected and monitored. Below a method is described for detecting V_{onset} using a simple but sensitive photocurrent detection circuit.

Experimental

The method employed for measuring low photocurrents consisted of detecting a modulated photocurrent with a tuned amplifier, amplifying the signal, and plotting the rectified amplified photocurrent as a function of potential on an X-Y recorder. A schematic diagram of the experimental setup used for measuring rectified alternating photocurrent voltammograms (RAPV's) is shown in Fig. 3. The potential of the semiconductor electrode was controlled and the cur-

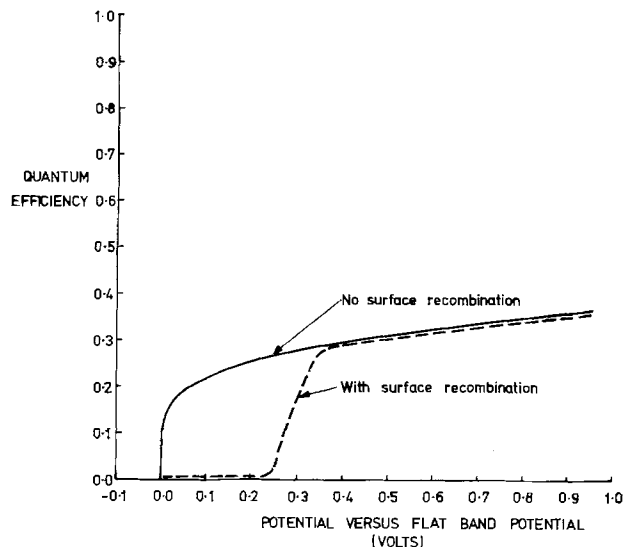


Fig. 2. Schematic diagram of the quantum efficiency-potential relations of an n-type semiconductor electrode with and without surface recombination.

rent measured with a PAR potentiostat (Model 173) fitted with a PAR current to voltage converter (Model 176). The potential was swept at the desired rate with respect to SCE by connecting the output of a Wenking SMP 69 potential stepping motor control to the external potential signal input of the potentiostat. An IR filter (Oriel Model G-776-7100) and a PAR mechanical light chopper (Model 175) operating at 70 Hz were interposed between the xenon light source (900W xenon lamp powered by a Canrad Hanovia

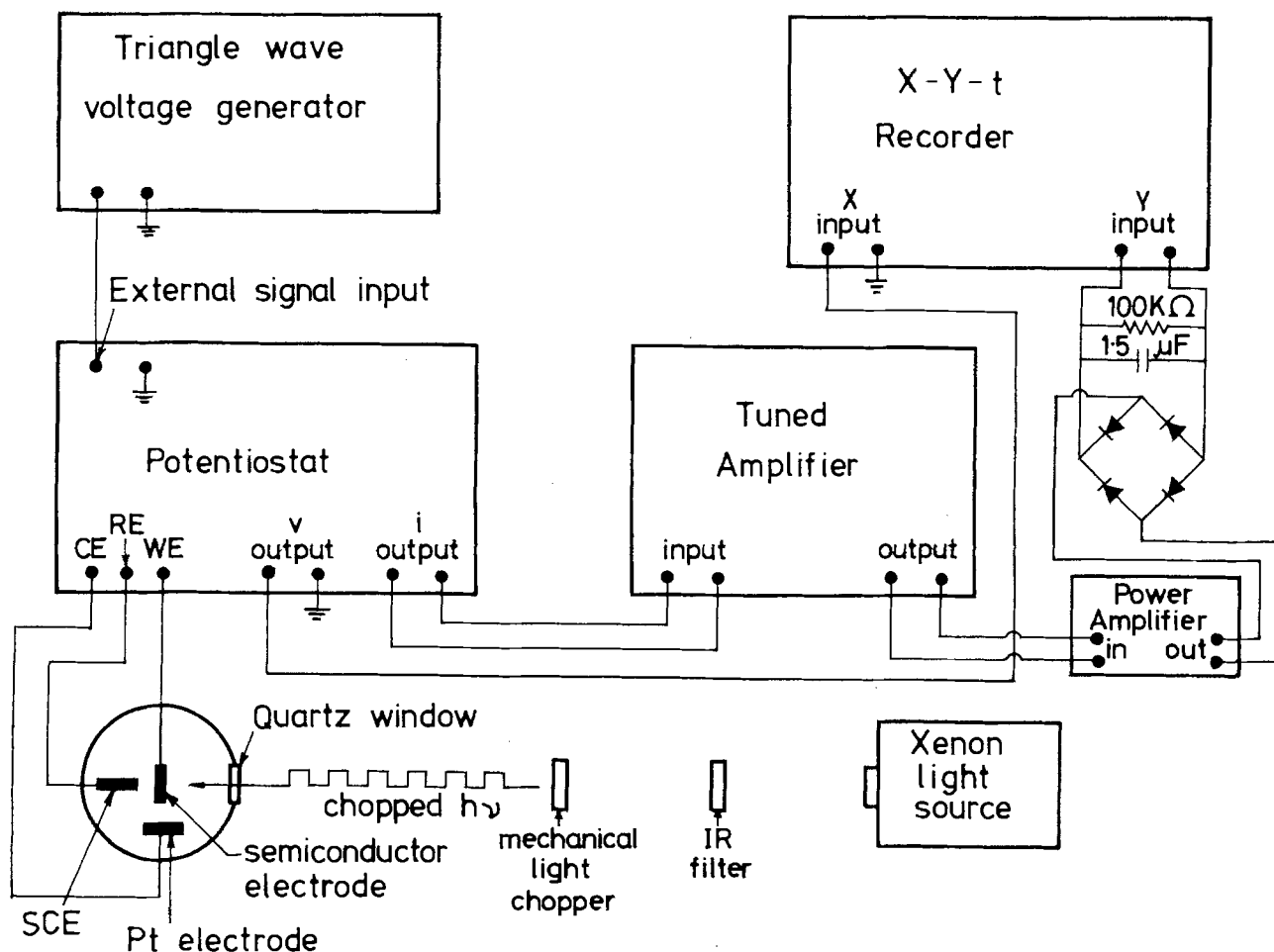


Fig. 3. Schematic diagram of the experimental setup for rectified alternating photocurrent-potential measurements

1000W power supply) and the semiconductor electrode in the electrochemical cell. The modulated photocurrent from the current to voltage converter was detected and amplified with a General Radio tuned amplifier (Model 1232-A), amplified with a power amplifier (Mini-Lab Model bwd 603A), rectified, filtered, and finally recorded on a X-Y recorder (Hewlett-Packard Model 7004B) as a function of potential. Measurements of d-c dark and photovoltammograms were made by using the appropriate instruments described above and the usual techniques. A conventional circuit described elsewhere (6) was used to measure the semiconductor electrode capacitance as a function of potential. A General Radio impedance bridge (Model 1608-A) was used in this circuit. Electrodes were fabricated by epoxying single crystals of InSe and p-type GaSe into Teflon holders which fitted into an electrochemical cell. Both electrodes were abraded and etched in conc. HNO_3 for 1 min and then rinsed in 10% W/V KCN to dissolve any excess selenium from the surfaces of the electrodes. A calcium titanate single crystal doped with 0.5 weight percent (w/o) NiO and 0.2 w/o Co_2O_3 was reduced in H_2 at 1000°C for 8 hr to make it electrically conducting before fabricating it into an electrode. Ohmic contacts were made to the three crystals using a 50:50 Ga:In amalgam. A wide variety of other n-type and p-type semiconductors have also been examined.

Results and Discussion

The values obtained for the flatband potentials of n,p-InSe, p-GaSe, and n- CaTiO_3 as determined by d-c photovoltammetry, capacitance voltage measurements, and RAPV are discussed below in detail to illustrate some features of RAPV.

In the case of the n,p-InSe electrode used in this study, the d-c photocurrent in 1M NaOH passed

through an anodic-cathodic photocurrent transition at -1.02V [see Fig. 4(a)]. Since the modulated photocurrent in RAPV is rectified, the RAP voltammogram should pass through a minimum at the voltage of the anodic-cathodic photocurrent transition. A minimum photocurrent was in fact observed in the RAP voltammogram of this electrode at -1.0V as expected [see Fig. 4(b)]. This potential also corresponded to the value of the flatband potential (-1.0V) determined from a Mott-Schottky plot [see Fig. 4(c)]. Hence for this particular indium selenide electrode the values of the flatband potential determined by the three methods under consideration were the same within the experimental error.

The d-c dark and photovoltammograms for a p-GaSe electrode in 1N NaOH are shown in Fig. 5(a). The onset of the d-c photocurrent occurred at about -0.51V . Mott-Schottky plots and an RAP voltammogram for the p-GaSe electrode in 1M NaOH are shown in Fig. 5(c) and (b), respectively. A value of -0.2V for the flatband potential was determined from these latter plots. This electrode represents a case where there is a significant discrepancy between the d-c photocurrent onset and the flatband potential. The discrepancy can be readily explained as being due to a surface recombination controlled $i_p^{\text{CT}}(o) - V$ relation. That is, between -0.51 and -0.2V the effective surface recombination velocity v_{SR} is large enough to cause the d-c photocurrent to be negligible in this potential range for the particular p-GaSe electrode which was examined. On the other hand, it proved possible with RAPV not only to detect the photocurrent between -0.51 and -0.2V but also to observe a cathodic-anodic photocurrent transition at -0.2V [see Fig. 5(b)]. The observed potential at which the cathodic-anodic photocurrent transition occurs represents the potential at which the conduction and val-

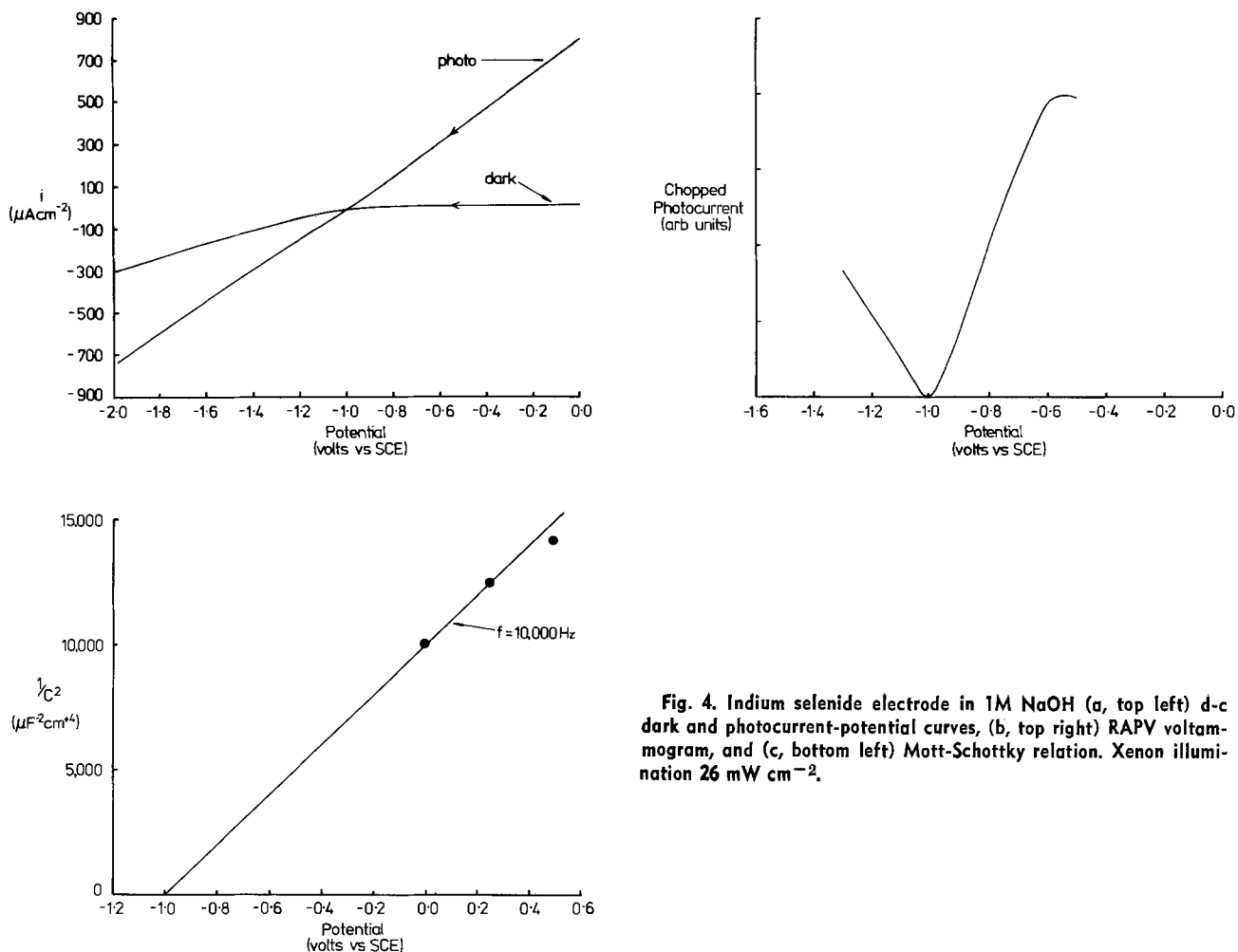


Fig. 4. Indium selenide electrode in 1M NaOH (a, top left) d-c dark and photocurrent-potential curves, (b, top right) RAPV voltammogram, and (c, bottom left) Mott-Schottky relation. Xenon illumination 26 mW cm^{-2} .

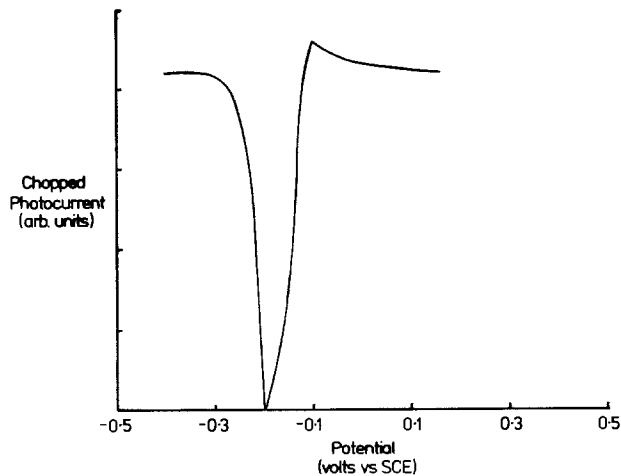
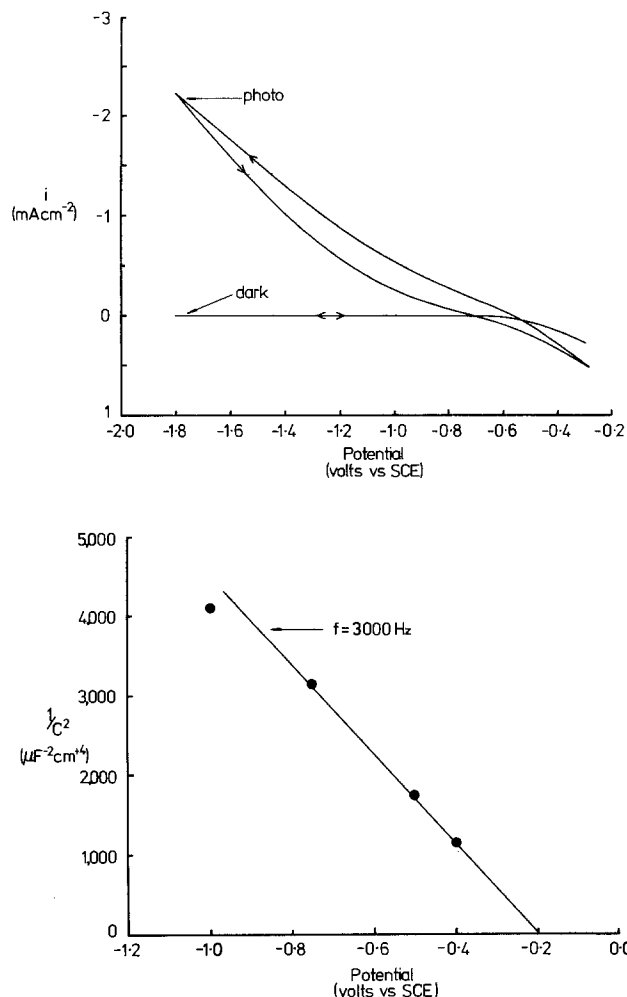


Fig. 5. Gallium selenide electrode in 1M NaOH (a, top left) d-c dark and photocurrent-potential curves, (b, top right) RAP voltammogram, and (c, bottom left) Mott-Schottky relation. Xenon illumination 26 mW cm^{-2} .

ence bands are flat, since for p-GaSe for potentials negative of -0.2V the bands are bent up (i.e., GaSe behaves as a p-doped photocathode) and for potentials positive of -0.2V the bands are bent down (i.e., GaSe behaves as a photoanode). Hence we have classified the potential of the cathodic-anodic photocurrent transition for p-GaSe, that is -0.2V , as the V_{FB} of this particular sample of the semiconductor in 1M NaOH. This conclusion is supported by the experimental finding that the values of V_{FB} determined from Mott-Schottky plots (-0.2V in 1M NaOH) coincided with the potential observed for the cathodic-anodic photocurrent transition. It is noted that Gerischer *et al.* (6) have reported the V_{FB} for p-GaSe as being about 0.5V and pH independent. The differences between the latter results and the present results which show a pH dependence are attributed to intrinsic differences and different surface pretreatments. In the present study the p-GaSe was not oriented but abraded and etched whereas in the previous study (6) the face exposed to the electrolyte was specifically chosen as either $\parallel\text{C}$ or $\perp\text{C}$ axis. Similarly, the V_{FB} 's reported for InSe in this study refer to an abraded and etched electrode and not to an oriented sample.

Attention is drawn to the fact that although anodic-cathodic photocurrent transitions were observed for both InSe and GaSe electrodes, a distinction has been drawn between the doping concentrations of the two electrodes. Indium selenide has been classified as a highly doped both n-type and p-type semiconductor on the basis that the photocurrents were of such magnitudes at potentials both anodic and cathodic of the transition that they can be easily seen on the d-c photovoltammograms of this electrode [see Fig. 4(a)]. That is, n-type and p-type areas of the InSe electrode were in contact with the electrolyte giving rise to the

observed behavior. However, for GaSe only a cathodic photocurrent was observable on the d-c photovoltammogram as would be expected for a p-doped semiconductor photocathode. The anodic photocurrent for this electrode was only detectable as a highly amplified modulated photocurrent [see Fig. 5(b)]. The latter observation is consistent with a low n-type character in the GaSe electrode. Therefore, for the GaSe electrode the potential of the cathodic-anodic photocurrent transition has been classified as the V_{FB} of a p-doped sample.

The d-c dark and photovoltammograms for an n-CaTiO₃ electrode in 1M NaOH are shown in Fig. 6(a). The potential onset of the d-c photocurrent occurred at about -1.16V . Mott-Schottky plots and an RAP voltammogram for the n-CaTiO₃ electrode in 1M NaOH are shown in Fig. 6(c) and (b), respectively. The values for the flatband potential determined from these plots were -2.09 and -1.2V , respectively. In this case the potential onset of the d-c photocurrent (-1.16V) agreed with that of the RAPV (-1.2V) indicating that for this sample of n-CaTiO₃, the v_{SR} was small in comparison to the v_{CT} or in other words the onset of the photocurrent was not appreciably controlled by surface recombination. The striking observations for this particular n-CaTiO₃ electrode were the large discrepancies between the value of V_{FB} determined by d-c and RAP voltammetry (-1.16 and -1.2V , respectively) and that determined from the Mott-Schottky plots ($\sim -2.09\text{V}$) of -0.93 and -0.89V , respectively. It appears in this instance that the intercepts of the Mott-Schottky plots for this particular n-CaTiO₃ electrode do not correspond to the real flatband potential of n-CaTiO₃.

On the other hand it seems that the values for V_{FB} determined by d-c and RAPV approximate to the

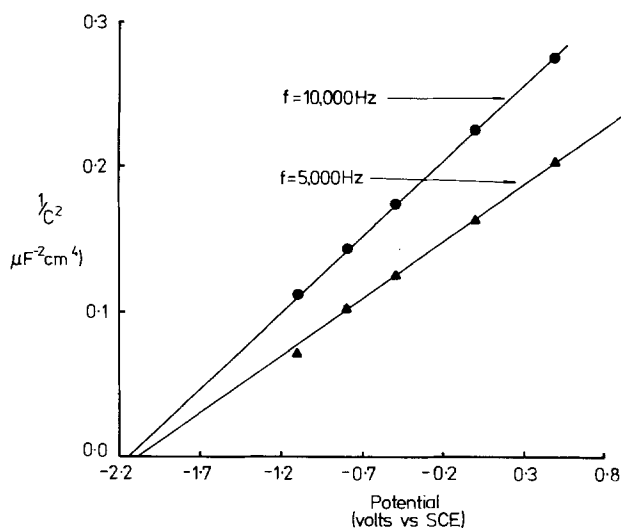
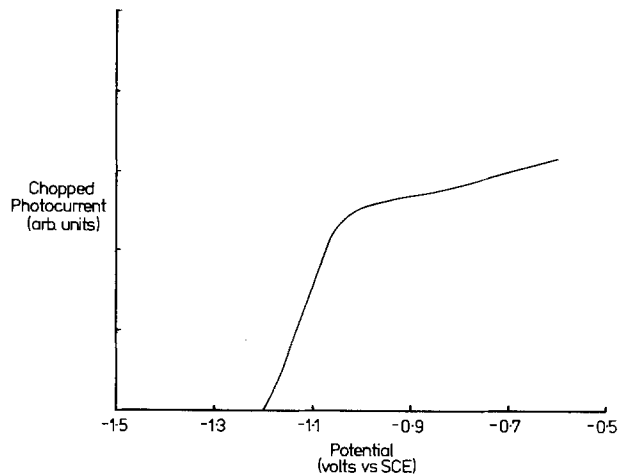
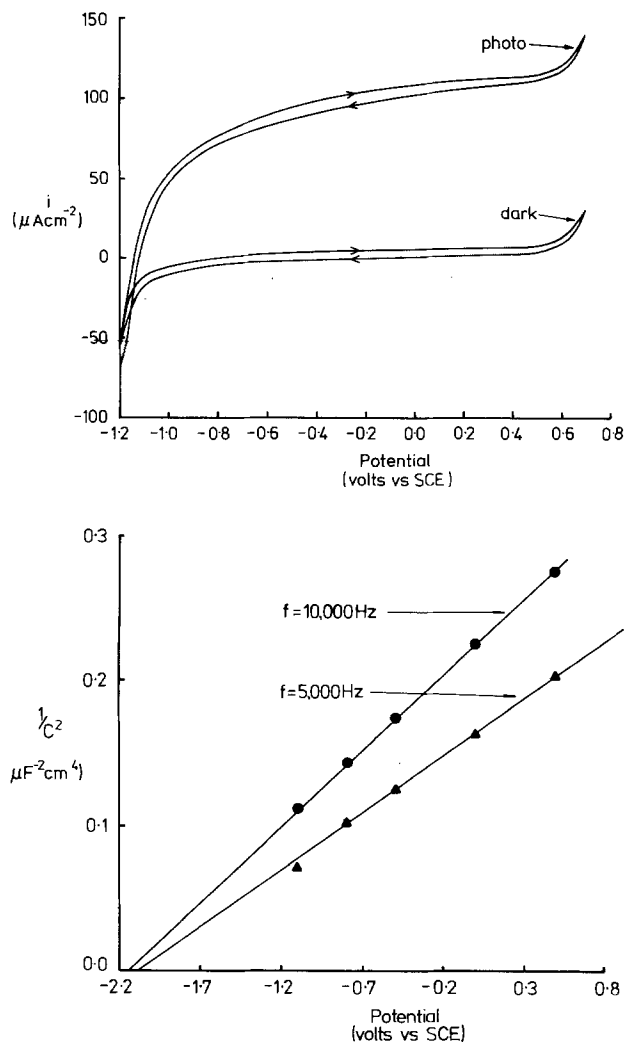


Fig. 6. Calcium titanate electrode in 1M NaOH (a, top left) d-c dark and photocurrent-potential curves, (b, top right) RAP voltammogram, and (c, bottom left) Mott-Schottky relations. Xenon illumination 26 mW cm^{-2} .

correct value within the experimental error. The evidence for this is that the value of V_{FB} for n- CaTiO_3 in 1N H_2SO_4 reported by Tchernev (7) of -0.50V is in agreement with the values obtained by d-c and RAPV in this work when the -0.59 V/pH shift is taken into account. Secondly, V_{FB} at the zeta potential of zero change ($\text{pH} \sim 14$) has been calculated as -1.172V (8) which is also in agreement with the value obtained by RAPV in this study. One possible reason for the highly negative V_{FB} 's determined from capacitance measurements for the CaTiO_3 sample examined might be due to the presence of NiCO_2O_4 which may have formed during the H_2 reduction of the doped CaTiO_3 crystal.

The flatband potentials for a wide range of n-type and p-type semiconductors which have been determined from Mott-Schottky plots and RAPV are listed in Table I. It can be seen from these results that with the exception of the n- CaTiO_3 electrode used in this study the values obtained from the Mott-Schottky plots and RAPV agree within experimental error. This suggests that RAPV can be used as a method for determining the V_{FB} of a semiconductor. Difficulties may arise in using RAPV to measure V_{FB} when the semiconductor photocorrodes and deposits the products on the electrode surface. In such a case the measured V_{FB} may be significantly different from the real V_{FB} due to the change in surface composition. In such instances it would be more appropriate to measure V_{FB} in the dark using the capacitance method.

Anodic-cathodic photocurrent transitions were observed for all the p-type semiconductors examined in this study whereas no such transitions were observed for the n-type semiconductors. The origin of the n-type behavior for p-type materials could have

been due to the larger intrinsic electron concentrations in the p-type semiconductors which had significantly smaller bandgaps than the n-type semiconductors examined. Alternatively the p-type materials may have been inadvertently doped with some n-type impurities during their crystal growth.

It is noted that a typical RAPV has a similar appearance to a d-c photovoltammogram. This is a sharp

Table I. Comparison of the flatband potentials of a number of n-type and p-type semiconductors determined from capacitance measurements and rectified alternating photocurrent voltammetry

| Semi-conductor | Elec-trolyte | Flatband potential (V vs. SCE) | | |
|-------------------------|----------------------------|--------------------------------|------------|--|
| | | Capacitance measurements | | Rectified alternating photocurrent voltammetry |
| | | This work | Other work | |
| n-type | | | | |
| TiO_2 | 1M NaOH | -1.11 | -1.05 (9) | -1.08 |
| SrTiO_3 | 1M NaOH | -1.27 | -1.22 (10) | -1.25 |
| CaTiO_3 | 1M NaOH | -2.09 | — | -1.2 |
| | 1N H_2SO_4 | -1.0 | -0.50 (7) | -0.51 |
| NaNbO_3 | 1M NaOH | -1.38 | — | -1.28 |
| | 1N H_2SO_4 | -0.52 | — | -0.34 |
| In_2O_3 | 1M NaOH | -0.72 | — | -0.57 |
| | 1N H_2SO_4 | -0.22 | — | 0.11 |
| Fe_2O_3 | 1M NaOH | -0.75 | — | -0.67 |
| | 2M NaOH | — | -0.73 (11) | — |
| p-type | | | | |
| CdTe | 1M NaOH | -0.03 | 0.21 (12) | -0.08 |
| GaP | 1M NaOH | -0.05 | 0.18 (12) | 0.07 |
| GaSe | 1M NaOH | -0.2 | 0.5 (6) | -0.2 |
| | 1N H_2SO_4 | -0.65 | 0.5 (6) | 0.68 |
| CuInS_2 | 1M NaOH | — | — | 0.06 |
| | 1N H_2SO_4 | — | — | 0.59 |
| n,p-type | | | | |
| InSe | 1M NaOH | -1.0 | — | -1.02 |
| | 1N H_2SO_4 | — | — | -0.48 |

rise in the photocurrent followed by a saturation region. It should be pointed out that this saturation is not due to the saturation of the photocurrent but is in fact due to the saturation of the tuned amplifier. Further, the accuracy of the value of V_{FB} determined by RAPV of semiconductors which do not have a detectable anodic-cathodic photocurrent transition will depend on sensitivity of the tuned amplifier. The General Radio tuned amplifier used in the present study was found to be satisfactory but this may not necessarily apply to other brands of tuned amplifiers.

The small photocurrents measured near the flatband potential have been interpreted in this study as being due to photoelectrochemical effects. However the observations might also originate from modulation effects such as photoconductivity or photocapacitive behavior. It is noted however, that even if either of the latter interpretations is more correct the method presented here for determining V_{FB} is not invalidated.

Summary

In the present study the use of rectified alternating photocurrent voltammetry as a method to determine the flatband potentials of n-type and p-type semiconductors has been presented. The values of the V_{FB} 's for the p-type semiconductors examined in this study coincided with potentials which clearly represented anodic-cathodic photocurrent transitions. For the n-type semiconductors examined no such transitions were observed and the values of the V_{FB} 's for these electrodes were taken as the potential onsets of the rectified amplified alternating photocurrents. The technique of RAPV has the advantage over capacitance-potential measurements of being easy to set up and run in the laboratory on a routine basis.

Acknowledgments

The authors thank Dr. K. Imai and Dr. Yu. Abe of the Department of Nuclear Engineering, Hokkaido investigations of anodic processes in lutetium diphthalocyanine films (1-4). Generally, these are 2-Jersey for the n-CaTiO₃ crystal, and Dr. A. M. Mancini

of the Instituto di Fisica Università di Bari, Bari, Italy for the GaSe crystal. J. McCann thanks Prof. D. Haneman for some helpful discussions and the Australian Government for a Commonwealth Postgraduate Scholarship.

Manuscript submitted Aug. 4, 1980; revised manuscript received Jan. 20, 1981.

Any discussion of this paper will appear in a Discussion Section to be published in the June 1982 JOURNAL. All discussions for the June 1982 Discussion Section should be submitted by Feb. 1, 1982.

Publication costs of this article were assisted by the University of New South Wales.

REFERENCES

- H. Gerischer, *J. Electroanal. Chem. Interfacial Electrochem.*, **58**, 263 (1975).
- V. A. Myamin and Y. V. Pleskov, "Electrochemistry of Semiconductors," Nauka, Moscow (1976), Plenum Press, New York (1967).
- W. W. Gartner, *Phys. Rev.*, **116**, 84 (1959).
- Z. A. Rotenberg, T. V. Dzhavrishvilli, Y. V. Pleskov, and A. L. Asatiani, *Sov. Electrochem.*, **14**, 1555 (1978).
- R. H. Wilson, *J. Appl. Phys.*, **48**, 4292 (1977).
- H. Gerischer, J. Gobrecht, and J. Turner, *Ber. Bunsenges. Phys. Chem.*, **84**, 596 (1980).
- D. I. Tchernev, Abstract C3 presented at the Internat. Conf. on Photochem. Conv. and Storage of Solar Energy, London, Ontario (1976).
- J. F. McCann, Ph.D. Dissertation, Flinders University of South Australia (1980).
- T. Watanabe, A. Fujishima, O. Tatsuoki, and K. Honde, *Bull. Chem. Soc. Jpn.*, **49**, 8 (1976).
- H. H. Kung, H. S. Jarrett, A. W. Sleight, and A. Ferretti, *J. Appl. Phys.*, **48**, 2463 (1977).
- J. H. Kennedy and K. W. Frese, in "Electrode Materials and Processes for Energy Conversion and Storage," J. D. E. McIntyre, S. Srinivasan, and F. G. Will, Editors, p. 77, The Electrochem. Society Softbound Proceedings Series, Princeton, N.J. (1979).
- J. O'M. Bockris and K. Uosaki, *This Journal*, **124**, 1348 (1977).

Cathodic Electrochromism of Lutetium Diphthalocyanine Films

M. M. Nicholson* and F. A. Pizzarello

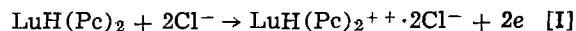
Rockwell International, Autonetics Strategic Systems Division, Anaheim, California 92803

ABSTRACT

Cathodic electrochromism of lutetium diphthalocyanine films on insulating substrates was investigated by a moving-boundary technique. Reduction occurred by injection of electrons from a gold contact and cations from a liquid electrolyte. Light blue products formed with aqueous or organic solutions of alkali metal salts, while a dark violet product formed with aqueous hydrochloric acid. The dark material had a charge-carrier mobility of 8×10^{-7} cm²/Vsec and an estimated bulk resistivity of 1800 Ω -cm. Reduced forms of the dye appear to be solid cation conductors.

Previous papers from this laboratory have reported investigations of anodic processes in lutetium diphthalocyanine films (1-4). Generally, these are 2-electron oxidations in which the color of the dye changes from green to red. The electrochromic reaction was shown to occur with migration of anions from the

aqueous electrolyte into the organic solid. With a chloride solution, it is represented¹ by



A solid-state moving-boundary technique was used to determine the faradaic n values, ionic mobilities, and

* Electrochemical Society Active Member.

Key words: diphthalocyanines, electrochromism, cathodic reduction, cations.

¹ H₂Pc is the usual abbreviation for metal-free phthalocyanine; Pc⁻ is the anion C₂₈H₁₆N₈, and LuH(Pc)₂ is commonly called lutetium diphthalocyanine.

approximate bulk resistivities in the red phases formed with chloride and sulfate ions (1). The anion mechanism was confirmed in a subsequent tracer study (2), and its dependences on ambient water vapor and oxygen were reported recently (4).

Lutetium diphthalocyanine also undergoes cathodic reactions. As a result, it is a multicolor electrochromic material of considerable interest for display applications (5-7). Colors of the reduced films can range from blue-green through blue, dark blue, and violet. Reference (5) gives absorption spectra recorded at 0.1V intervals on a tin-oxide supported film under essentially open-circuit conditions in both anodic and cathodic ranges. Spectral characteristics as well as Munsell and CIE color coordinates are summarized in Ref. (5) and (6).

This paper describes the results of cathodic moving-boundary experiments on lutetium diphthalocyanine films supported by insulating substrates. The electrolytes were aqueous HCl, aqueous KCl, KI in acetonitrile (AN), and LiCl in dimethyl sulfoxide (DMSO). Again, the solid reaction products appeared to be ionic conductors. The propagated color was light blue with the metal salt solutions and violet with HCl.

Experimental

Lutetium diphthalocyanine films were prepared by vacuum sublimation of the dye onto sapphire or Mylar strips 1.25 cm wide and approximately 5 cm long. The weight of dye per cm² was determined from the optical density (OD) of the green film at the 670 nm absorption maximum. The geometric film thickness was estimated from this weight and the approximate crystal density. It ranged from 530 to 1060Å. Details of the dye synthesis and specimen preparation were given previously (1). The other materials were reagent-grade chemicals. The organic solvents were dried by allowing them to stand over a molecular sieve.

A sputtered gold contact was applied at the upper end of the dye film, and the lower end was immersed in the liquid electrolyte. The counterelectrode was silver foil. A drawing of the moving-boundary cell is given in Ref. (1). The cell was assembled in a helium-atmosphere glove box, where the oxygen level did not exceed a few ppm. Constant cathodic currents of 0.2-2 μ A were applied with a PAR 173 galvanostat, and the total applied voltage was monitored with a Keithley 610C electrometer and a strip-chart recorder. The boundary-propagation distance was measured by viewing the film against a back-lighted screen of millimeter graph paper under $\sim 2\times$ magnification. The electric field in the color-converted film could be determined by raising the electrolyte level in successive increments and observing the corresponding voltage decreases. In several cases, the specimens were examined after propagation by energy-dispersive x-ray spectroscopy (EDS), using an ETEC Autoscan scanning electron microscope. Comparisons of lutetium, potassium, and chlorine levels in different regions of the films were made in this way.

Results and Discussion

Visual observations.—The color change always began at the dye/electrolyte interface and traveled upward toward the electronic contact. This behavior is consistent with an ion-injection mechanism. It differs from that of Yamana's qualitative experiments, wherein the blue coloration of erbium diphthalocyanine films on glass began at the metal contact (8). In our experience, color-converted diphthalocyanine films are prone to crack and peel away from glass. If this occurred in Yamana's cell, the dye could have become wet with electrolyte by capillary action. Cathodic reaction then would have occurred in the upper part of the film.

The adhesion problem was mitigated, though not fully avoided, in the present work by using a sapphire

or Mylar substrate.² With aqueous electrolytes, the cathodic boundary propagation tended not to proceed as uniformly as it did for the anodic green-to-red process (1), but the boundary velocity and field were measurable in a number of experiments, as shown by Fig. 1-3. Occasionally, the boundary was too irregular for quantitative use.

An additional difficulty arose with the organic electrolytes. Although the initial green form of the dye was insoluble in several organic liquids, including AN and DMSO, the blue reduced form was soluble. This led to poor electrical contact during the boundary propagation and prevented determination of the field by changing the electrolyte level.

The propagated color depended on the electrolyte cation. With HCl, the product was dark violet. With KCl, KI, and LiCl, only a light blue appeared. In contrast, we have observed that anodic boundary propagation with different anions yields a single red color (4).

² The dye film adheres well to tin oxide, but that substrate cannot be used in moving-boundary studies because it is electronically conductive.

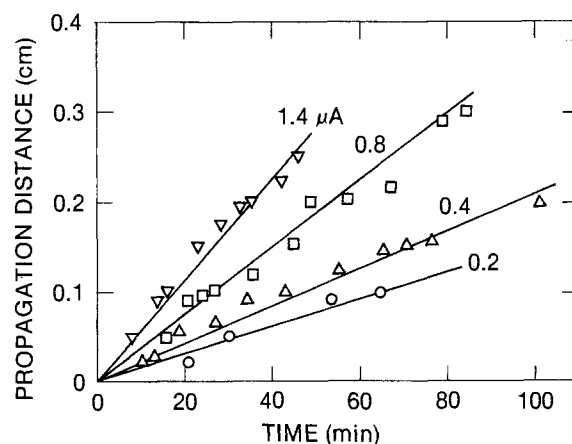


Fig. 1. Dependence of boundary propagation distance on time with aqueous 1.2M HCl electrolyte. Specimen 1.

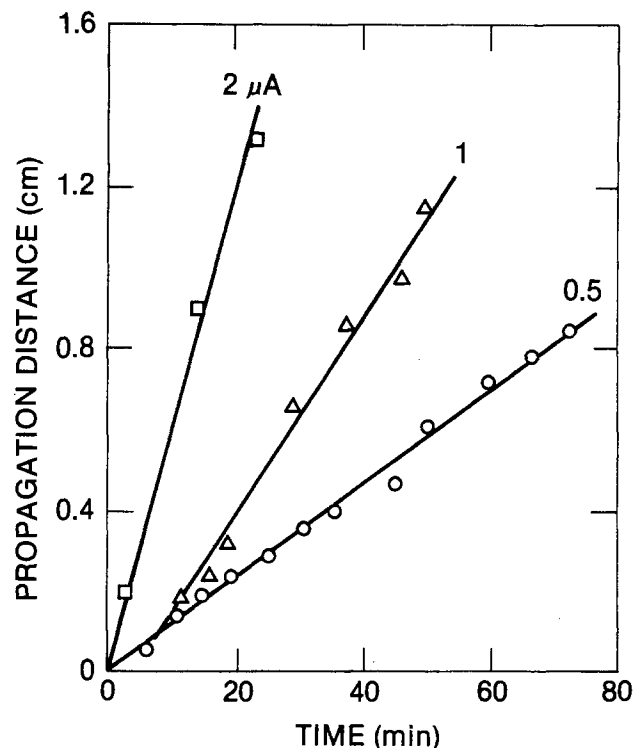


Fig. 2. Dependence of boundary propagation distance on time with aqueous 1M KCl electrolyte. Specimens 3, 4, and 5.

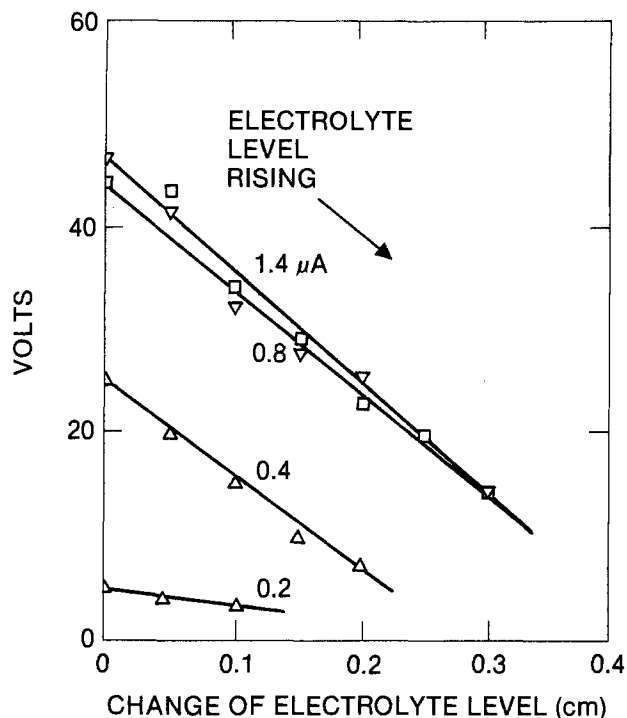


Fig. 3. Plots for determination of electric field in the blue film with aqueous 1.2M HCl electrolyte. Specimen 1.

Electrical parameters.—The results for aqueous and nonaqueous solutions are summarized in Table I. Although the total applied currents were in the micro-ampere range, the estimated current densities through the cross sections of the films were 15–200 mA/cm². This range includes current densities that would be used in potentiostatic switching of a diphthalocyanine electrochromic display (7).

The apparent number n of electrons transferred per molecule of dye was calculated from the current, the area converted per unit time, and the optical density of the green film. Plots for evaluating the boundary velocity are shown in Fig. 1 and 2. With aqueous KCl, n was 1.9 ± 0.2 . With HCl, the apparent n was considerably larger, and on specimen 1, it was shown to increase systematically with the applied current. The large apparent n 's in the acid solution probably were caused by a side reaction forming elemental hydrogen. The apparent n at $0.4 \mu\text{A}$ was 5.2 for specimen 1 and 12 for specimen 2. One could surmise from this comparison that the sapphire substrate was more conductive than Mylar to proton transport beneath the dye film, but further investigation would be needed to verify such a mechanism. Extrapolation of the apparent n to zero current yielded a value of 3.5 for the Mylar-supported film contacted by 1.2M HCl. Fewer data were recorded for nonaqueous electrolytes because of the blue-solubility problem, but an n value of 1.1 was ob-

tained with both Mylar- and sapphire-supported films contacted by LiCl-DMSO.

A carrier mobility μ in the converted film was found from the relationship

$$\mu = v/\mathcal{E} \quad [1]$$

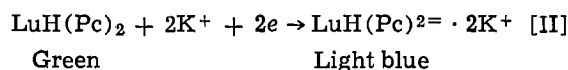
where v is the boundary velocity and \mathcal{E} is the electric field determined by raising the electrolyte level (1). Figure 3 shows plots for the evaluation of \mathcal{E} in the Mylar-supported film propagated from aqueous HCl. The average mobility was $8 \times 10^{-7} \text{ cm}^2/\text{Vsec}$. Since the current and the approximate film thickness were known, the bulk resistivity ρ_b of the blue phase could be estimated from Eq. [2], where I is the current density

$$\rho_b = \mathcal{E}/I \quad [2]$$

The average resistivity for specimen 1 was 1800 $\Omega\text{-cm}$. This is similar to the resistivities of 1300 and 2000 $\Omega\text{-cm}$ for the red oxidation products containing chloride and sulfate ions (1).

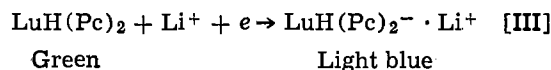
Interpretations.—The violet phase propagated from an aqueous HCl interface appears to be an ionic conductor. This is suggested by the magnitude of the carrier mobility, which is compared in Table II with those of related solid electrolytes. Dependence of the reduction-product color on the electrolyte cation also is consistent with a cation-injection mechanism. Moreover, EDS analysis confirmed the presence of potassium, and the absence of chlorine, in blue areas propagated from KCl, while neither of these elements was found in green areas of the same plates.

The reaction for aqueous KCl may be written



This process is analogous to the anodic oxidation utilizing two chloride ions and forming the divalent organic cation.

The measurements with LiCl in DMSO indicated a 1-electron reduction, which might be represented by



With dissolved lutetium diphthalocyanine, Corker, Grant, and Clecak also reported cathodic formation of a radical anion (11). The electrolyte was tetrabutylammonium fluoborate in dimethylformamide, and the working electrode was platinum. Reduction beyond the 1-electron stage with LiCl in the moving-boundary cell might have been prevented by separation of the two phthalocyanine rings to form LiHPc and LuPc. Such a process could account for the higher solubility in organic solvents.

Further work is needed to characterize the reduction products. It is significant, however, that dark blue or violet colors never were obtained with metal cations in the moving-boundary experiments, even at a current density as high as 200 mA/cm². An acidic electrolyte is

Table I. Results of cathodic boundary propagation in lutetium diphthalocyanine films

| Specimen | Initial OD at 670 nm | Substrate | Solvent | Electrolyte | Current (μA) | Color formed | Apparent n | μ (cm^2/Vsec) $\times 10^7$ |
|----------|----------------------|-----------|---------|-------------|---------------------------|--------------|--------------|---|
| 1 | 1.15 | Mylar | Water | 1.2M HCl | 0 | Violet | 3.5* | — |
| | | | | | 0.2 | | 4.7 | 13 |
| | | | | | 0.4 | | 5.2 | 4.1 |
| | | | | | 0.8 | | 7.6 | 6.2 |
| | | | | | 1.4 | | 8.8 | 8.4 |
| 2 | 1.02 | Sapphire | Water | 1M HCl | 0.4 | Violet | 12 | — |
| 3 | 0.82 | Sapphire | Water | 1M KCl | 0.5 | Light blue | 1.7 | — |
| 4 | 0.85 | Sapphire | Water | 1M KCl | 1 | Light blue | 2.1 | — |
| 5 | 0.85 | Sapphire | Water | 1M KCl | 2 | Light blue | 1.8 | — |
| 6 | 0.69 | Sapphire | AN | 0.1M KI | 0.5 | Light blue | ~3 | — |
| 7 | 0.58 | Mylar | DMSO | ~2M LiCl | 0.5 | Light blue | 1.1 | — |
| 8 | 1.02 | Sapphire | DMSO | ~2M LiCl | 0.5 | Light blue | 1.1 | — |

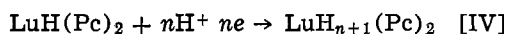
* By extrapolation of n vs. i to $i = 0$.

Table II. Solid-state ionic mobilities near 25°

| Material | Form | Mobile ion | Mobility (cm ² /Vsec) × 10 ⁶ | Ref. |
|---|-----------------|------------------------------|--|--------------------|
| Anodic oxidation product of LuH(Pc) ₂ | Thin film | Cl ⁻ | 4 | (1) |
| | | SO ₄ ⁼ | 4 | (1) |
| Cathodic reduction product of LuH(Pc) ₂ | Thin film | H ⁺ | 0.8 | This investigation |
| H ₂ WO ₃ | Thin film | H ⁺ | 0.8 | (9) |
| HUO ₂ PO ₄ ·4H ₂ O | Polycrystalline | H ⁺ | 8 | (10) |

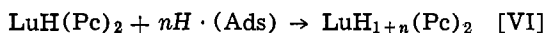
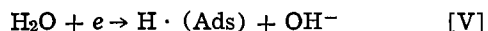
required to form the dark product in insulator-supported films. Yet dark blue and violet are readily obtained with aqueous KCl when the dye is on semi-conductive tin oxide (5,6). We propose the following mechanisms to account for this difference in the electrochromic behavior.

With an adequate supply of protons, reduction of the dye can proceed by a double-injection mechanism similar to that of reaction [II]



Green Dark blue or violet

All or part of the $n+1$ hydrogen atoms may be ionized in the solid state. When the supply of protons is insufficient, the dye may be converted at a tin oxide electrode by a coupled chemical reaction rather than direct electron transfer



Green Dark blue or violet

The reactive intermediate is represented as an adsorbed hydrogen atom because a species with such characteristics is known to form on tin oxide at cathodic potentials (12, 13). Furthermore, a pH increase accompanies cathodic formation of a blue product on tin oxide in aqueous KCl, and hydrogen ions are released to the solution on its anodic oxidation (14).

The dark blue and violet forms cannot yet be distinguished on the basis of the n values. One of our previous investigations provides evidence, from correlation of absorption spectra with approximate open-circuit potentials of the reduced films, that the dark blue and violet colors may involve two discrete oxidation states of the dye (5). We now estimate that n is 2 or 3 for the dark blue state, and 3 or 4 for the violet.

Moskalev and Kirin originally proposed field-induced ionization to H⁺ and Lu(Pc)₂⁻ to account for the cathodic electrochromism of lutetium diphthalocyanine films (15). The present study has shown that these color changes are due, instead, to faradaic processes. Although the acidic hydrogen may not be firmly bound to the organic structure in rare-earth diphthalocyanines (16), it is the electrolyte cation that plays a vital role in the electrochromism at cathodic potentials.

Acknowledgment

This work was supported in part by the Office of Naval Research.

Manuscript submitted Nov. 10, 1980; revised manuscript received March 3, 1981.

Any discussion of this paper will appear in a Discussion Section to be published in the June 1982 JOURNAL. All discussions for the June 1982 Discussion Section should be submitted by Feb. 1, 1982.

Publication costs of this article were assisted by Rockwell International.

REFERENCES

1. M. M. Nicholson and F. A. Pizzarello, *This Journal*, **126**, 1490 (1979).
2. F. A. Pizzarello and M. M. Nicholson, *J. Electron. Mater.*, **9**, 231 (1980).
3. M. M. Nicholson and F. A. Pizzarello, *This Journal*, **127**, 821 (1980).
4. F. A. Pizzarello and M. M. Nicholson, *ibid.*, **127**, 2617 (1980).
5. M. M. Nicholson and R. V. Galiardi, Final Report, Contract N62269-76-C-0574, AD-A039596, May 1977.
6. M. M. Nicholson and R. V. Galiardi, *SID Int. Symp. Dig.*, **IX**, 24 (1978).
7. M. M. Nicholson, F. A. Pizzarello, and T. J. La Chappelle, Final Report, Contract N00014-79-C-0434, ONR-CR399-005-1F, June 1980.
8. M. Yamana, *Oyo Butsuri*, **48**, 441 (1979).
9. B. W. Faughnan, R. S. Crandall, and M. A. Lampert, *Appl. Phys. Lett.*, **27**, 275 (1975).
10. P. E. Childs and T. K. Halstead, *Mater. Res. Bull.*, **13**, 609 (1978).
11. G. A. Corker, B. Grant, and M. J. Clecak, *This Journal*, **126**, 1339 (1979).
12. H. A. Laitinen, C. A. Vincent, and T. M. Bednarski, *ibid.*, **115**, 1024 (1968).
13. M. M. Nicholson and R. V. Galiardi, Unpublished work.
14. M. M. Nicholson, F. A. Pizzarello, R. V. Galiardi, and G. A. Layman, Final Report, Contracts F49620-77-C-0074 and F49620-77-C-0104, June 1980.
15. P. N. Moskalev and I. S. Kirin, *Russ. J. Phys. Chem.*, **46**, 1019 (1972).
16. K. Kasuga, M. Tsutsui, R. C. Pettersen, K. Tatsumi, N. Van Opdenbosch, G. Pepe, and E. F. Meyer, Jr., *J. Am. Chem. Soc.*, **102**, 4835 (1980).

Photoelectrochemical Characterization of CdSe Thin Film Anodes

K. Rajeshwar, L. Thompson, and P. Singh*¹

Department of Electrical Engineering, Colorado State University, Fort Collins, Colorado 80523

and R. C. Kainthla and K. L. Chopra

Department of Physics, Indian Institute of Technology, New Delhi 110029, India

ABSTRACT

Photoelectrochemical characterization of CdSe thin films prepared by a chemical solution growth technique was carried out by linear-sweep voltammetry, current-voltage measurements under forward and reverse bias, photocurrent-wavelength measurements, and electrical impedance measurement techniques. The quality of the present CdSe/electrolyte junctions for photovoltaic applications was assessed by examining the effect of varying light intensity on current-voltage behavior. The ideality factors (n) were determined for these junctions by modeling the CdSe/electrolyte junction in terms of a Schottky barrier. Values of n close to 2 were obtained and were attributed to the dominating influence of recombination-generation currents (either at the surface or in the depletion region) on the overall photovoltaic characteristics. The presence of a thin, tunnelable CdS layer on the CdSe electrode surface was postulated as causing the nonideal current-voltage behavior particularly in the reverse-bias regime. Equivalent circuits for the CdSe/electrolyte interface were developed using a novel technique for measuring the equivalent parallel conductance and capacitance as a function of signal frequency and applied bias. A method of extracting flatband potentials based on conductance measurements is demonstrated using the CdSe thin film/electrolyte interface.

Cadmium selenide has shown considerable potential for applications related to photoelectrochemical (PEC) methods of solar energy conversion. Stable and efficient CdSe-based PEC devices have been reported recently (1, 2). Photoanodes have been fabricated from n-type CdSe in the form of single crystal (3, 4), sintered aggregates (1, 4), pastes (2), and thin films (4, 5-7). Both aqueous (1-6) and nonaqueous electrolytes (7, 8) have been employed in these PEC devices.

In this work, we describe the photoelectrochemical characterization of CdSe thin films prepared by a chemical solution growth technique (9). This technique is relatively inexpensive, simple, and amenable to routine manufacture on a large scale. A variety of electrical and electrochemical techniques was employed to assess the quality of photoresponse of these films. These included linear-sweep voltammetry, current-voltage measurements under forward and reverse bias, photocurrent-wavelength measurements, and electrical impedance characterization as a function of signal frequency and applied bias. The sensitivity of the photoresponse to light intensity was also studied as an effective measure of the junction quality for applications related to solar energy conversion.

Equivalent circuits were developed for the n-CdSe/electrolyte interface from conductance and capacitance data as a function of frequency and applied bias. A novel technique for extracting semiconductor flatband potentials from electrical impedance measurements is presented. Frequency dispersion in the measured space-charge capacitance values is often a problem in the determination of flatband potentials (10). This difficulty is circumvented in the present approach by utilizing conductance data and exploiting the relationship of equivalent parallel conductance to the space-charge capacitance in the semiconductor (11).

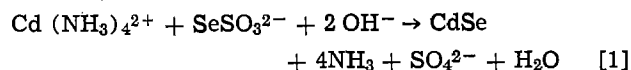
* Electrochemical Society Active Member.

¹ Present address: Arco Enterprises, Incorporated, Troy, Michigan 48064.

Key words: chemical solution growth, electrical impedance characterization, Schottky barrier theory.

Experimental

Thin films of CdSe on titanium foil substrates were prepared at the Indian Institute of Technology, New Delhi, by the overall chemical reaction



Relevant details on the growth of these films are given elsewhere (9, 12). The films labeled Film 1, 2, and 3, were prepared at 85°C with 2.1, 2.8, and 3.5M NH₃ concentrations and had thicknesses ~0.7, 0.85, and 0.9 μm, respectively. The as-grown films were n-type with resistivity ~10⁷-10⁸ Ω-cm. On annealing at 280°C for 30 min in vacuum (10⁻⁵ Torr), the resistivity was brought down to the range 1-10 Ω-cm. The annealed films had carrier concentrations in the range 5 × 10¹⁷-5 × 10¹⁸ cm⁻³ and carrier mobilities in the range 1-10 cm²/V-sec.

Electrode fabrication consisted of cutting the 3 × 4 cm² as-prepared sheets of thin films into small wafers of area in the range 0.15-0.5 cm². The CdSe film was scraped off from one side of the wafer and a back contact was made to the exposed titanium by application of conductive silver epoxy. A Teflon-coated copper wire was attached to the back contact by using the same epoxy. The entire back surface and edges of the electrodes were then covered with nonconducting epoxy resin.

A mixture of solutions of 1M Na₂S, 1M S, and 1M NaOH in deionized water was used as the electrolyte in the PEC cells. The cells were continually purged with a slow stream of prepurified argon gas. Both two-electrode and three-electrode PEC configurations were employed. A vitreous carbon plate (1.5 × 15 × 30 mm, Atomergic Chemetals Corporation, New York) was used as the counterelectrode in both cases. A saturated calomel electrode (SCE) was used as the reference electrode for potentiostatic measurements.

Two types of etching were employed for the CdSe thin film photoanodes prior to their use in the PEC cells: a chemical etch consisting of successive non-

convective dips in 6, 1, and 0.1M HCl for 3-5 sec followed by a rinse in deionized water, and a photoetch according to the procedure described by a previous author (2), wherein the photoelectrode is illuminated under short-circuit conditions in a dilute aqueous acid solution, for example 0.1M HCl.

Current-voltage measurements were carried out on a Princeton Applied Research (PAR) Model 175 universal programmer and PAR 173 potentiostat/galvanostat in the case of three-electrode PEC cells or on a custom-built variable load current-to-voltage converter for studies on two-terminal devices.

A 150-W ELH tungsten-halogen lamp was used to illuminate the CdSe photoanodes. The intensity of the light source was calibrated by using neutral density filters and an Ealing Corporation Model LIMS 920 radiometer/photometer. The light intensities quoted below are not corrected for reflection and absorption losses in the cell and in the electrolyte.

A Bausch and Lomb light source and a high-intensity monochromator in conjunction with a series of narrow bandpass filters were used for the photocurrent-wavelength measurements. The working electrode was potentiostated against the SCE reference electrode and the photocurrents were measured on the PAR electrochemistry system.

Electrical impedance measurements were carried out on the n-CdSe/electrolyte interface by an automated technique developed in this laboratory (13). This technique utilizes measurements of the changes in the amplitude and phase characteristics of a small amplitude a-c signal to generate values of the parallel conductance and capacitance as a function of a-c signal frequency and applied bias. These values are then used to derive equivalent circuit elements for the semiconductor electrode/electrolyte interface. A Hewlett-Packard (HP) frequency synthesizer (Model HP-3320B), an HP Model 3570A network analyzer, and an HP Model 9825A desk-top computer were used for these measurements. Further details may be found elsewhere (13).

Results and Discussion

Current-voltage measurements.—Figures 1-3 illustrate the current-voltage behavior of PEC cells based on solution-grown CdSe thin films. These data were obtained on two-terminal devices although no significant differences in behavior were observed in the potentiostatic mode with three-electrode PEC cells. Polarization effects at the counterelectrode (*vide supra*) can be therefore ignored in the following discussion. Open-circuit potentials (V_{oc}) in the range 0.20-0.26V, short-circuit current densities (J_{sc}) ranging from 0.1 to 2 mA/cm², and fill-factors spanning the range 0.20-0.35 were observed for the various devices depending on the prior thermal treatment of the film and surface preparation. Table I summarizes the performance parameters for the various PEC devices tested in the

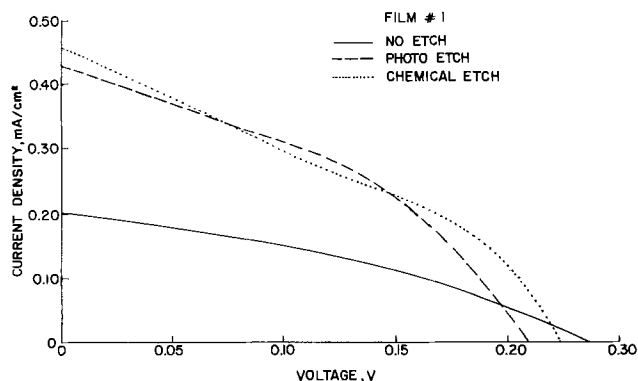


Fig. 1. Photocurrent-voltage curves for solution-grown CdSe photoanodes (film No. 1). Light source, tungsten-halogen lamp; light intensity, 100 mW/cm².

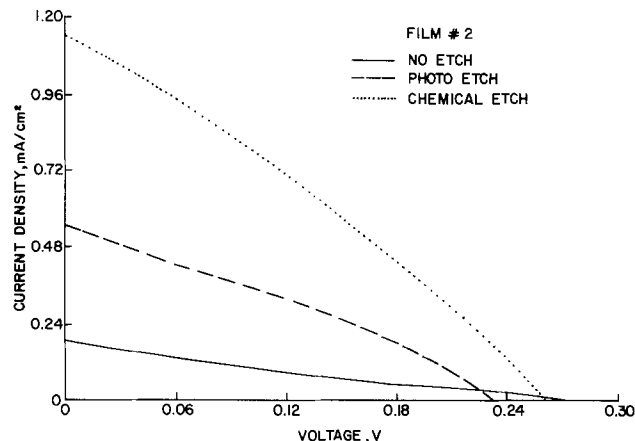


Fig. 2. Photocurrent-voltage curves for solution-grown CdSe photoanodes (film No. 2). Light source and intensity same as in Fig. 1.

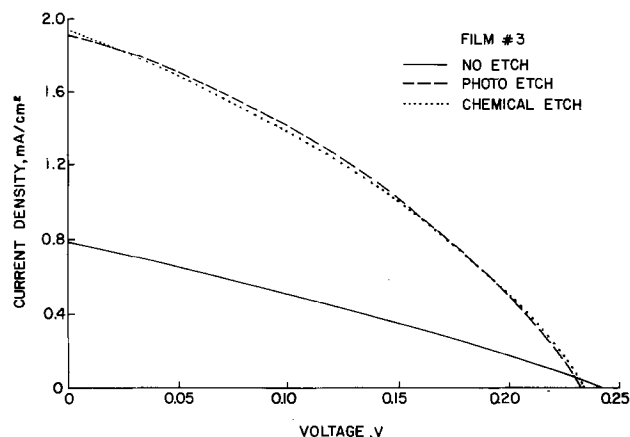


Fig. 3. Photocurrent-voltage curves for solution-grown CdSe photoanodes (film No. 3). Light source and intensity same as in Fig. 1.

present study. In general, photo and chemical etching tends to improve the J_{sc} values and therefore the energy conversion efficiency of the device. Film No. 3 was found to yield better quality electrodes than films No. 1 and No. 2 (Table I) as expected from thickness considerations (*vide supra*). No attempt was made in these experiments to optimize cell geometry, redox concentration, etc. since the main objective of this work was to characterize the overall photoelectrochemical behavior of solution-grown CdSe thin films. However, by using suitably recrystallized and etched CdSe film deposited on SnO₂:F coated glass substrates, V_{oc} values in the range 0.40-0.62V, J_{sc} up to 6 mA/cm² (50 mW/cm² light intensity), and fill-factors as high as 0.50 have been obtained. The details of these prior treatments and the performance of the corresponding PEC cells are reported elsewhere (14).

Table I. Performance parameters of PEC devices based on solution-grown CdSe thin films

(Light intensity, 100 mW/cm²; electrolyte, 1M S, 1M Na₂S, 1M NaOH)

| Film No. | Prior treatment | V_{oc} (V) | J_{sc} (mA/cm ²) | FF | Conversion efficiency (%) |
|----------|-----------------|--------------|--------------------------------|------|---------------------------|
| 1 | None | 0.28 | 0.21 | 0.35 | 0.021 |
| | Chemical etch | 0.25 | 0.47 | 0.33 | 0.039 |
| | Photoetch | 0.22 | 0.44 | 0.38 | 0.037 |
| 2 | None | 0.28 | 0.20 | 0.20 | 0.011 |
| | Chemical etch | 0.25 | 0.56 | 0.23 | 0.032 |
| | Photoetch | 0.23 | 1.17 | 0.29 | 0.078 |
| 3 | None | 0.24 | 0.78 | 0.27 | 0.051 |
| | Chemical etch | 0.23 | 1.92 | 0.34 | 0.150 |
| | Photoetch | 0.23 | 1.90 | 0.34 | 0.149 |

Figure 4 compares the current-voltage behavior in the dark and under illumination for film No. 3. These data were obtained under potentiostatic conditions. Similar behavior was observed for films No. 1 and 2. The usual rectification behavior expected in the reverse bias regime for semiconductor/electrolyte junctions in the dark is observed here. From Fig. 4 and similar data for the other films, the flatband potential (V_{FB}) is seen to be more negative than ca. $-1.0V$ (vs. SCE) in the polysulfide solution. A more precise location of the V_{FB} value is obtained from the electrical impedance measurements described below.

A feature worthy of note in the data shown in Fig. 4 is the gradual increase in current with increasing reverse bias in the dark. This increase is particularly pronounced on illumination of the device. At voltages significantly anodic of ca. $0.5V$ (vs. SCE), a very rapid increase in current (not shown in Fig. 4) was noted for all the films examined in the present study. This behavior is commonly encountered in solid-state devices and is attributed to dielectric breakdown (15). The gradual increase in current prior to this abrupt change, however, is of more relevance to this study. There are three possible explanations for this "anomalous" behavior: (i) in the reverse bias direction, the presence of an interfacial layer causes the effective barrier height to decrease with increasing bias, so that the reverse current does not saturate (15), (ii) hole-electron pairs are thermally generated in the depletion region under conditions of large reverse bias (i.e., large band bending in the semiconductor), and (iii) the current increases due to the onset of electron injection from the electrolyte because the barrier becomes thin enough for tunneling to take place.

Of the above possibilities, we prefer the explanations based on (i) and (iii) above. Support for (i) derives from observations (5, 16, 17) on the formation of a thin CdS layer on the surface of the CdSe electrodes by S/Se substitution. On the other hand, the more pronounced increase in the currents in the reverse bias direction on illumination relative to the dark case (Fig. 4), suggests that the tunneling process (i.e., electron injection from the electrolyte) might be enhanced because of the slight increase in the majority carrier density at the interface. Under potentiostatic conditions such as those employed for the measurements in Fig. 4, this is equivalent to heavier doping of the semiconductor and hence a thinner surface barrier.

A more detailed discussion of the current-voltage characteristics and the effect of interfacial layers is postponed to a later section.

Effect of light intensity.—If we model the semiconductor/electrolyte interface as a Schottky barrier, it is possible to represent the current-voltage characteristic by the following expression (18)

$$J = J_{ph} - J_d = J_{ph} - J_o [\exp(qV/nkT) - 1] \quad [2]$$

Here J is the net current density (current per unit area), J_{ph} and J_d are the photocurrent density and

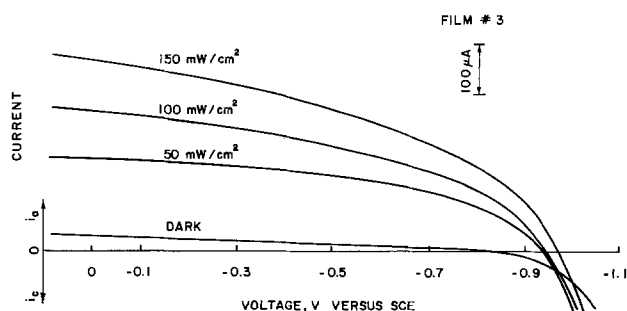


Fig. 4. Potentiostatic current-voltage curves in the dark and under illumination for solution-grown CdSe photoanodes (film No. 3).

dark current density, respectively, J_o is the reverse saturation current density, V is the voltage, n is the "junction-ideality" factor, and other terms have their usual significance. For bias voltages exceeding $3kT/q$, we can neglect the last term in the bracket in Eq. [2]. Also at equilibrium (open-circuit conditions), $J_{ph} = J_d$ and $V = V_{oc}$ so that rearrangement of Eq. [2] yields

$$V_{oc} \cong \frac{nkT}{q} \ln \frac{J_{sc}}{J_o} \quad [3]$$

where V_{oc} is the open-circuit voltage and J_{sc} is the short-circuit current density. If we further assume that $J_{sc} \propto I_L$ (= incident light intensity) and $J_{sc} \gg J_o$, Eq. [3] reduces to the following expression

$$V_{oc} \propto \frac{nkT}{q} \ln I_L \quad [4]$$

A plot of V_{oc} against $\ln I_L$ should yield a straight line from which values of n may be determined for the particular device. An ideal device should have an n value of unity so that the slope of a straight line plot of V_{oc} vs. $\log I_L$ should be ca. 60 mV. Figure 5 illustrates such plots for CdSe films No. 1, 2, and 3. An alternative method involves plotting V_{oc} vs. $\log J_{sc}$ (cf. Eq. [3]). The slopes determined by these analyses are assembled in Table II. The magnitudes of these slopes can be rationalized only if $n \approx 2$.

The above assumption that J_{sc} is directly proportional to the light intensity is borne out by the data shown in Fig. 6. The linear dependence also demonstrates that transport of electroactive S^{2-} species to the CdSe/electrolyte interface is not limiting the rate of the overall charge-transfer reaction over the range of light intensities employed in this study.

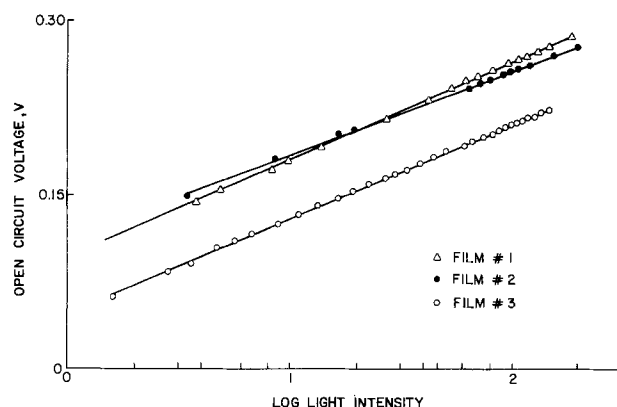


Fig. 5. Plots of open-circuit voltage vs. log light intensity for solution-grown CdSe photoanodes.

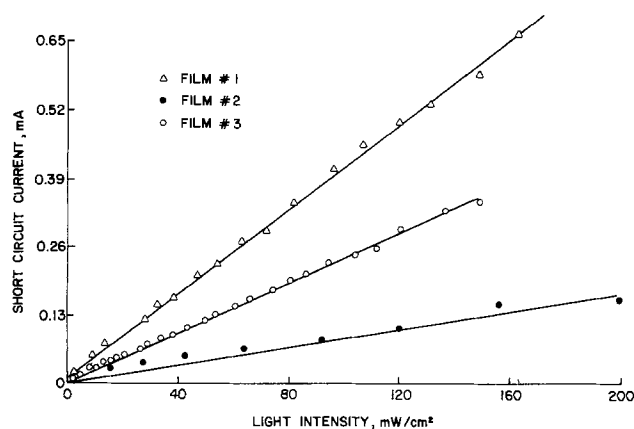


Fig. 6. Dependence of short-circuit current density on light intensity for solution-grown CdSe photoanodes.

Table II. Junction ideality factors for the illuminated CdSe/electrolyte interface

| Method of determination | Slope (V) | | | n | | |
|---|------------|------------|------------|------------|------------|------------|
| | Film No. 1 | Film No. 2 | Film No. 3 | Film No. 1 | Film No. 2 | Film No. 3 |
| V_{oc} vs. $\log J_{sc}$ | 0.120 | 0.108 | 0.107 | 2.03 | 1.83 | 1.81 |
| V_{oc} vs. $\log I_L$ (cf. Eq. (41)) | 0.108 | 0.130 | 0.115 | 1.83 | 2.20 | 1.95 |

The functional dependence of J_{sc} and V_{oc} on light intensity for CdSe-based PEC cells was noted by previous authors in studies on single crystals (3) and on thin films prepared by vacuum evaporation (6).

Photocurrent-wavelength measurements.—Figure 7 illustrates the spectral response of solution-grown CdSe thin film electrodes in polysulfide solution. The sharp decrease in response below ~ 520 nm is consistent with the increased absorption of polysulfide solutions below these wavelengths (1, 3). The long wavelength cutoff is less sharp relative to the behavior of single crystal electrodes (6) and reflects the nonoptimized thickness of the present CdSe films leading to a consequent deterioration in long wavelength response. The gradual decrease in photoresponse into the short-wavelength region is indicative of surface recombination of photogenerated minority carriers presumably mediated by electronic states in the bandgap [cf. Ref. (19, 20)]. Application of reverse bias to the electrode results in the expected increase in photocurrents arising from better field separation of photogenerated carriers although the surface recombination component is not significantly reduced (Fig. 7).

Equivalent circuit representation.—Equivalent circuit representation of the semiconductor/electrolyte interface (21, 22) enables identification of specific components of the overall electrical network that are responsive to potential and current perturbations. Figures 8a, b, c, and d illustrate successive reductions of the equivalent circuit for a model semiconductor/electrolyte interface leading to the highly idealized system shown in Fig. 8d. Here C_{sc} is the space-charge capacitance, C_H is the Helmholtz layer capacitance, C_G is the Gouy layer capacitance, R_B is the internal series resistance comprising the contributions from the electrolyte, bulk semiconductor, and the back ohmic contact, R_F is the resistance associated with Faradaic charge-transfer processes at the interface, and C_{ss} and R_{ss} are the capacitance and resistance terms arising from surface states or traps at the interface. For an ideal device, C_G and C_H should be large relative to

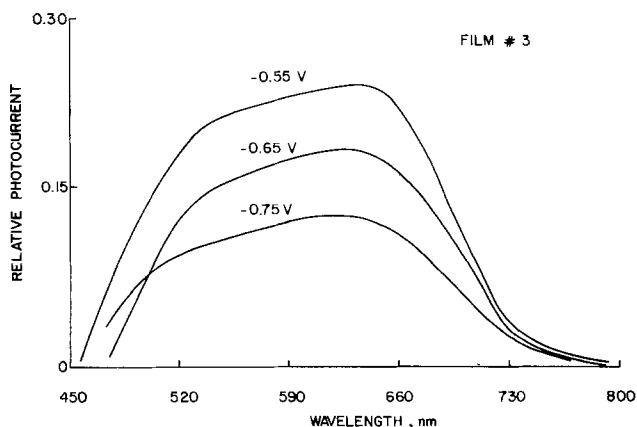


Fig. 7. Photocurrent-wavelength characteristics for solution-grown CdSe photoanodes (film No. 3) at various values of reverse bias. The voltages refer to SCE reference electrode. The photoresponse was normalized to take into account variations in intensity and quantum flux with wavelength.

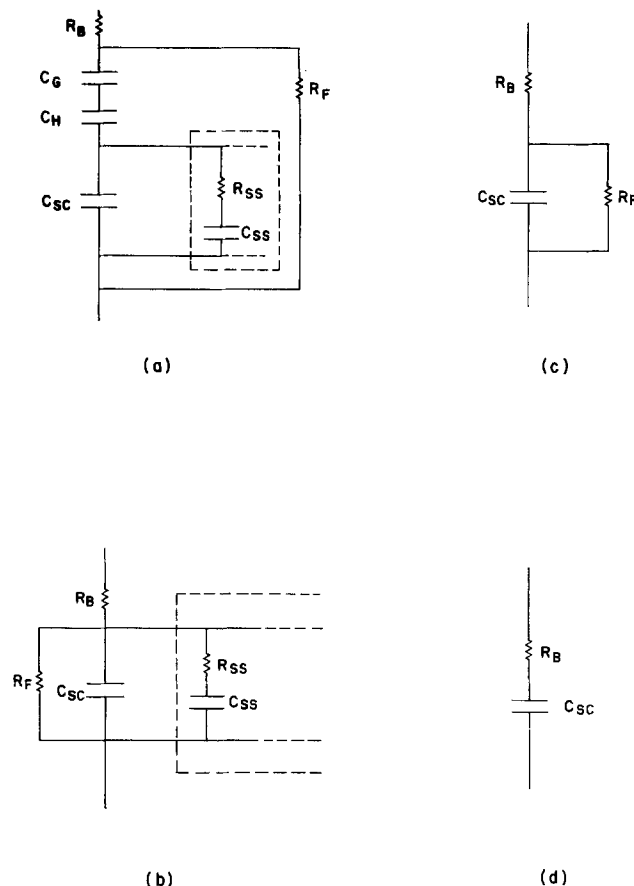


Fig. 8. Equivalent circuit representations of the semiconductor/electrolyte interface. Figures 10a, b, c, and d show successive reductions in the complexity of the electrical network. See text for description of symbols.

C_{sc} , R_B should be small, R_F should be large, and surface-state effects should be absent or at least minimal. In concentrated electrolytes such as those employed in the present study, the C_G term may be ignored and since usually $C_H \gg C_{sc}$, an expression for the parallel admittance may be derived (13) (cf. Fig. 8c)

$$\omega C_p = \frac{(G_B + G_F)(\omega G_B C_{sc}) - \omega G_B G_F C_{sc}}{(G_B + G_F)^2 + (\omega C_{sc})^2} \quad [5]$$

and

$$G_{p/\omega} = \frac{(G_B G_F / \omega)(G_B + G_F) + G_B \omega C_{sc}^2}{(G_B + G_F)^2 + (\omega C_{sc})^2} \quad [6]$$

It is noted that in the above, effects from surface states have not been taken into account *per se*. The conductance terms G ($= 1/R$) have been employed in the above expressions in place of resistances, since the measured quantity here is the parallel conductance.

Each C-G combination above causes a peak in $G_{p/\omega}$ vs. ω curves. Unless the G_F term becomes very large, it will not overlap the peak that is caused by the C_{sc} - G_B combination. The more ideally polarized the interface, the smaller is the G_B term and hence the lower the frequency range at which it will have an appreciable effect. For very low frequencies ($\omega \rightarrow 0$) and for $G_B \gg G_F$, $G_p \approx G_F$. Typical $G_{p/\omega}$ vs. ω curves are shown in Fig. 9 and 10 for films No. 1 and 3, respectively. Values for C_{sc} and R_B can be determined from these data from the expressions (11, 13)

$$C_{sc} = 2[G_{p/\omega}]_{\max} \quad [7]$$

$$R_B = 1/G_B = 1/(2\omega[G_{p/\omega}]_{\max}) \quad [8]$$

G_F (or R_F) is given by the extrapolated value of the low-frequency data to the $G_{p/\omega}$ axis (cf. Fig. 9 and 10). Values of C_{sc} , R_B , and R_F thus determined and the

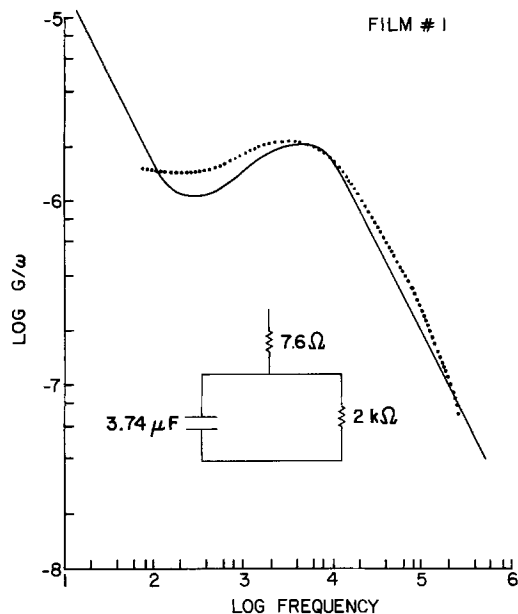


Fig. 9. Impedance spectra of solution-grown CdSe photoanodes (film No. 1). Solid circles, experimental points; line, theoretical curve based on the circuit elements shown in inset of the figure. Electrode potential, -0.75V (vs. SCE).

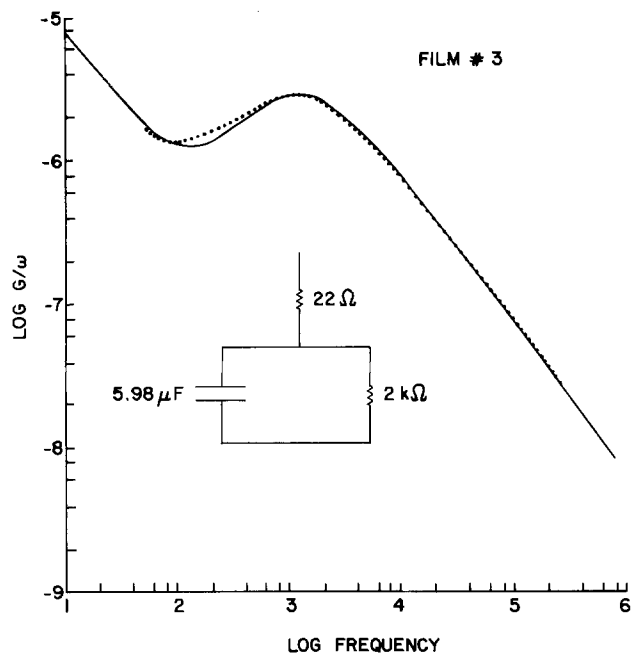


Fig. 10. Impedance spectra of solution-grown CdSe photoanodes (film No. 3). Description same as in Fig. 11. Electrode potential, -0.80V (vs. SCE).

overall circuit for the CdSe/electrolyte interface are shown in the inset of Fig. 9 and 10. The solid circles in Fig. 9 and 10 represent experimental data; the lines are "theoretical" curves based on calculated values of the circuit elements. Computational procedures for data fitting and other relevant details may be found elsewhere (13).

It is again noted that the circuit representations in Fig. 9 and 10 for the CdSe/electrolyte interface are somewhat idealized since surface-state effects have been ignored. Based on previous measurements in this laboratory on the n-GaAs/molten-salt electrolyte interface, the discrepancy between the theoretical curves and the experimental data in the intermediate frequency regime in Fig. 9 and 10 may be attributed to the influence of surface states. Attempts to include this

effect in computation of the theoretical G_p/ω curves were not entirely successful because adequate resolution of peaks arising from $C_{ss}-G_{ss}$ and $C_{sc}-G_B$ combinations, was impeded by the shift of the $C_{sc}-G_B$ peak toward lower frequencies relative to the GaAs case (23). Either a decrease in G_B (with constant C_{sc}) or an increase in C_{sc} (with constant G_B) can cause this shift (13).

The C_{sc} values computed from Eq. [7] under conditions of varying bias may be utilized to determine V_{FB} values by the Mott-Schottky relationship (24)

$$1/C_{sc}^2 = \frac{2}{q\epsilon_s N_D A^2} (V - V_{FB} - kT/q) \quad [9]$$

Here ϵ_s is the permittivity of the semiconductor, N_D is the semiconductor doping density, and A is the electrode area. Figure 11 illustrates Mott-Schottky plots for films No. 1 and 3. A V_{FB} value of $-1.56 \pm 0.06\text{V}$ (vs. SCE) was deduced from plots such as those shown in Fig. 11 for the CdSe films examined in this study. This value pertains to that obtained in the polysulfide electrolyte and may be compared with values of -1.45 , -1.34 , and -1.30V (vs. SCE) reported by previous authors for single crystal, vacuum-deposited thin films and for sintered pellets, respectively (3, 4).

General Discussion

In a broad sense, the present data may be regarded as representative of the manner in which many analogous features in the electrical characteristics of the semiconductor/electrolyte junction and a Schottky barrier (25) may be utilized to assess the quality of the photoactive junction in a PEC electrode/electrolyte interface. For example, n values close to 2 have been observed for the present CdSe thin film electrodes (cf. Table II). Values of $n = 2$ are characteristic of the propensity of recombination processes involving photogenerated electron-hole pairs either at the semiconductor surface or in the depletion region (18). This causes a deviation from the ideal current/voltage characteristic especially at low values of applied bias. We postulate that a significant factor in this nonideal behavior is the presence of an ultrathin, tunnelable layer consisting of CdS on the CdSe surface (cf. Fig. 12). This layer is believed to be electrically insulating because of compensation of excess Cd and/or Se vacancies (16). The effect of this insulating layer on the photovoltaic characteristics of the CdSe/electrolyte junction is twofold: (i) because of the potential drop across this layer, the zero-bias barrier height, ϕ_b^0 , is lower than it would be in the absence of this layer (cf. Fig. 12) and (ii) when a bias is applied, part of the bias voltage is dropped across the CdS layer so that the barrier height, ϕ_b , will be a function of bias voltage. The effect of this bias dependence of ϕ_b is to

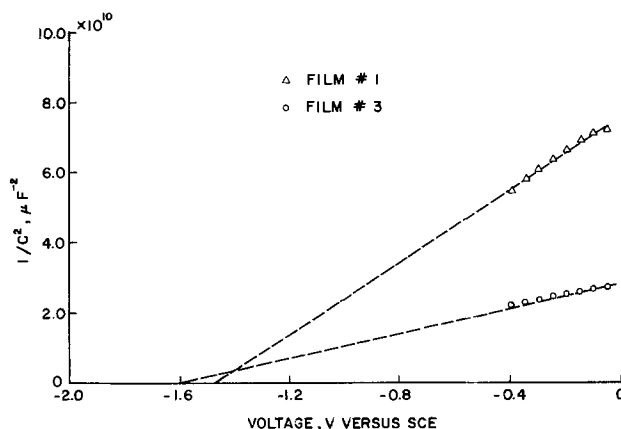


Fig. 11. Mott-Schottky plots for CdSe thin-film photoanodes (films No. 1 and 3).

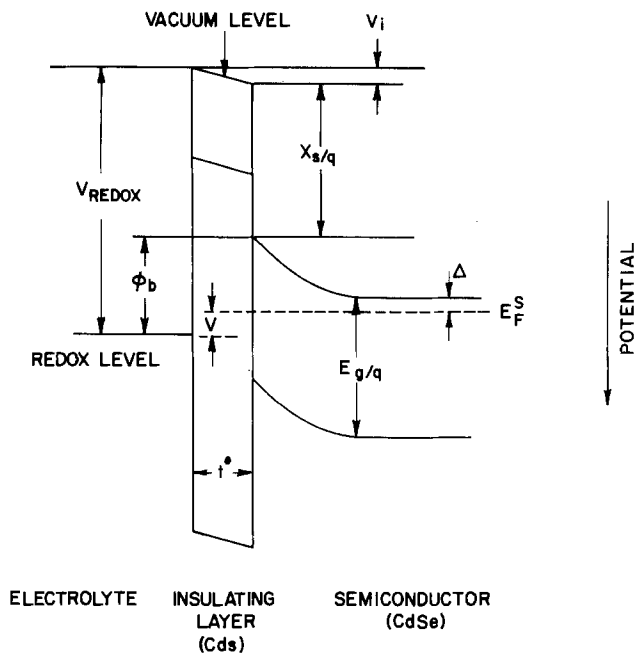


Fig. 12. Energy band diagram for the CdSe/electrolyte interface under any arbitrary forward bias. V_{redox} is the redox potential, χ_s is the semiconductor electron affinity, E_F^S is the Fermi level in the semiconductor, and E_g is the energy bandgap in the semiconductor. Other symbols are defined in the text.

change the shape of the current/voltage characteristic in a manner represented by the inclusion of an ideality factor, n (cf. Eq. [1]).

The above effects may be represented by the expression (26)

$$\phi_b = \phi_b^0 - \alpha (2qN_D/\epsilon_s)^{1/2} \left(\phi_b - V - \Delta - \frac{kT}{q} \right)^{1/2} \quad [10]$$

Here $\alpha = t\epsilon_s/(\epsilon_1 + qtD_{ss})$, ϵ_1 is the permittivity of the insulating layer, t is its thickness, D_{ss} is the surface state density, and Δ is the difference between the conduction bandedge and the Fermi level.

Figure 12 illustrates the electrostatic aspects of the semiconductor/electrolyte interface in the presence of an ultrathin insulating layer. An estimate of the barrier-height lowering may be obtained from Eq. [10], assuming $t = 20\text{ \AA}$, $D_{ss} = 10^{17} \text{ eV}^{-1} \text{ m}^{-2}$, $\epsilon_s = \epsilon_1 \approx 9\epsilon_0$ (27), and $(\phi_b - V - \Delta + kT/q) \approx 1\text{ V}$; a value $\phi_b^0 - \phi_b = 0.02\text{ V}$ is obtained. This effect will be enhanced by a larger doping level in the semiconductor and a thicker insulating CdS layer. [Depth profiles reported by previous authors for CdSe photoelectrodes indicate a layer thickness of the order of 80\AA, Ref. (16). The above value therefore is to be taken as a conservative estimate.] The barrier-height lowering would also be more pronounced under reverse bias because of the increase in the $(\phi_b - V - \Delta - kT/q)^{1/2}$ term in Eq. [10].

The electrical impedance measurements illustrate the manner in which difficulties encountered in "conventional" capacitance measurements with frequency dispersion of C_{sc} values (10) may be avoided. Meaningful V_{FB} values may be extracted by utilizing the relationship of $G_{p/\omega}$ peak maxima with C_{sc} (cf. Eq. [7]). Indeed, capacitance measurements using the standard lock-in technique (28) at discrete signal frequencies failed to yield reproducible Mott-Schottky plots for the present CdSe thin films. An additional advantage with the present approach is that changes in electrical conductance with voltage are much greater than corresponding variations in the capacitance (11), thereby enhancing the sensitivity of the technique. Further details of this new technique for

measuring V_{FB} values are being published in companion papers (29).

Work is continuing in these laboratories toward improvement of the surface quality of solution-grown CdSe thin films and thereby optimizing their performance in regenerative PEC devices for conversion of solar energy into electricity.

Acknowledgment

This research project was funded by the U.S. Department of Energy and the Solar Energy Research Institute under Grant XP-9-8002-9. The authors thank Gary Hodes, of the Weizmann Institute, Israel, for many stimulating discussions and Peter Smith for invaluable assistance in the electrical impedance measurements.

Manuscript submitted Dec. 16, 1980; revised manuscript received Feb. 23, 1981.

Any discussion of this paper will appear in a Discussion Section to be published in the June 1982 JOURNAL. All discussions for the June 1982 Discussion Section should be submitted by Feb. 1, 1982.

Publication costs for this article were assisted by Colorado State University.

REFERENCES

1. B. Miller, A. Heller, M. Robbins, S. Menezes, K. C. Chang, and J. Thomson, Jr., *This Journal*, **124**, 1019 (1977); A. Heller, G. P. Schwartz, R. G. Vadimsky, S. Menezes, and B. Miller, *ibid.*, **125**, 1156 (1978).
2. G. Hodes, *Nature*, **285**, 29 (1980).
3. A. B. Ellis, S. W. Kaiser, J. M. Bolts, and M. S. Wrighton, *J. Am. Chem. Soc.*, **99**, 2839 (1977).
4. R. N. Noufi, P. A. Kohl, and A. J. Bard, *This Journal*, **125**, 375 (1978).
5. K. T. L. DeSilva and D. Haneman, *ibid.*, **127**, 1554 (1980).
6. M. A. Russak, J. Reichman, H. Witzke, S. K. Deb, and S. N. Chen, Paper 240 presented at The Electrochemical Society Meeting, Boston, Massachusetts, May 6-11, 1979.
7. W. D. K. Clark and D. E. Hall, Paper 639 presented at The Electrochemical Society Meeting, Los Angeles, California, Oct. 14-19, 1979.
8. S. N. Chen and M. McDonough, Paper 640 presented at The Electrochemical Society Meeting, Los Angeles, California, Oct. 14-19, 1979.
9. R. C. Kainthla, D. K. Pandya, and K. L. Chopra, *This Journal*, **127**, 277 (1980).
10. F. Cardon and W. P. Gomes, *J. Phys. D*, **11**, L63 (1978).
11. E. H. Nicollian and A. Goetzberger, *Bell Syst. Tech. J.*, **46**, 1055 (1967).
12. I. J. Kaur, D. K. Pandya, and K. L. Chopra, *This Journal*, **127**, 943 (1980).
13. P. Smith, M.S. Thesis, Colorado State University, Fort Collins, Colorado (1980), Unpublished.
14. R. C. Kainthla, D. K. Pandya, and K. L. Chopra, *Appl. Phys. Lett.*, Submitted.
15. E. H. Rhoderick, "Metal-Semiconductor Contacts," p. 9, Clarendon Press, Oxford (1978).
16. D. Cahen, G. Hodes, and J. Manassen, *This Journal*, **125**, 1623 (1978).
17. R. N. Noufi, P. A. Kohl, J. W. Rogers, Jr., J. M. White, and A. J. Bard, *ibid.*, **126**, 949 (1979).
18. E. H. Rhoderick, "Metal-Semiconductor Contacts," p. 7, Clarendon Press, Oxford (1978).
19. S. N. Frank and A. J. Bard, *J. Am. Chem. Soc.*, **97**, 7427 (1975).
20. R. N. Noufi, P. A. Kohl, S. N. Frank, and A. J. Bard, *This Journal*, **125**, 246 (1978).
21. V. A. Myamlin and Yu. V. Pleskov, "Electrochemistry of Semiconductors," Plenum Press, New York (1967).
22. S. Kar, K. Rajeshwar, P. Singh, and J. DuBow, *Solar Energy*, **23**, 129 (1979).
23. H. Gerischer, in "Physical Chemistry—An Advanced Treatise," Vol. IX A, H. Eyring, Editor, p. 475, Academic Press, New York (1970).
24. R. Gale, P. Smith, P. Singh, K. Rajeshwar, and J.

- DuBow, *Adv. Chem. Series*, **146**, Chap. 22, American Chemical Society (1981).
25. R. Williams, *This Journal*, **114**, 1173 (1967).
26. E. H. Rhoderick, "Metal-Semiconductor Contacts," p. 36, Clarendon Press, Oxford (1978).
27. A. Manabe, A. Mitsuishi, and H. Yoshinaga, *Jpn. J. Appl. Phys.*, **6**, 593 (1967).
28. P. Singh, K. Rajeshwar, J. DuBow, and R. Job, *J. Am. Chem. Soc.*, **102**, 9676 (1980).
29. P. Smith, K. Rajeshwar, J. DuBow, R. Gale, J. Cooper, and A. Nozik, To be published; P. Smith, T. Mraz, K. Rajeshwar, and J. DuBow, *J. Electroanal. Chem. Interfacial Electrochem.*, In press.

Effect of Temperature on the Operation of a Photoelectrochemical Device: Studies on the n-GaAs/Room Temperature Molten Salt Electrolyte Interface

K. Rajeshwar, P. Singh,^{*1} and R. Thapar*

Department of Electrical Engineering, Colorado State University, Fort Collins, Colorado 80523

ABSTRACT

The effect of temperature on the photovoltaic performance of a photoelectrochemical (PEC) system was evaluated by measurements on a model system comprising the n-GaAs|AlCl₃-butyl pyridinium chloride (BPC)|carbon cell containing the ferrocene/ferricenium ion (Fe(Cp)₂/Fe(Cp)₂⁺) couple. Changes in the solar cell parameters for this system with temperature were monitored for the range from ambient to 85°C. The short-circuit current densities (J_{sc}) showed a systematic increase over the temperature range while the open-circuit voltage (V_{oc}) and fill-factor (FF) showed a linear decrease at the rate of 3.6 mV/°C and 0.001/°C, respectively. The energy conversion efficiency (η) of the device showed a maximum at an intermediate temperature (~50°C) beyond which the decline in V_{oc} and FF outweighed the beneficial effect of temperature on J_{sc} , leading to a rapid fall-off in η at temperatures above ~60°C. The linear decrease of V_{oc} with increasing temperature was seen to be directly related to the increased dark current density at elevated temperatures. Analysis of the dark current vs. voltage data by Schottky diode theory revealed the expected exponential dependence of the reverse saturation current density on temperature for the model PEC system. Measurement of the semiconductor flatband potential (V_{FB}) for the n-GaAs/AlCl₃-BPC interface at varying temperatures revealed a further origin for the increase in dark currents with temperature. The shift in V_{FB} to positive potentials with increasing temperature reduced the effective activation energy (or barrier height) for electron injection from the electrolyte into the semiconductor in the dark. These results are discussed in terms of two mechanisms: (i) direct charge transfer between the semiconductor and the occupied redox levels in the electrolyte and (ii) electron injection into the semiconductor mediated by trap levels in the energy bandgap of the semiconductor. Finally, the effect of temperature on the Schottky diode parameters of the n-GaAs/AlCl₃-BPC, Fe(Cp)₂/Fe(Cp)₂⁺|carbon cell is discussed in terms of enhanced surface and bulk carrier recombination effects at elevated temperatures. These lead to the observed deterioration in the fill-factor because of the increased series resistance associated with recombination-generation current flow paths.

There has been much discussion in recent years on photoelectrochemical (PEC) methods of solar energy conversion (1, 2). A key element of PEC devices is the semiconductor/electrolyte interface. The degree of effectiveness of minority-carrier charge transfer across this interface will have a direct bearing on the ultimate energy conversion efficiency of the system. The strategy of enhancing this charge exchange by elevating the temperature (3) has the added advantage of utilizing the near IR region of the solar spectrum, which otherwise would be wasted. Temperature also has beneficial effects on the optical properties of the semiconductor. Thus, recent studies have shown a red shift in the wavelength response of SnO₂-based PEC cells (4). Although semiconductor bandgap narrowing is a favorable mechanism contributing to im-

proved solar efficiency, analogous studies on solid-state devices have revealed a simultaneous deterioration in the blue response because of carrier recombination at the surface (5). The objective of the present study was to critically evaluate the effect of temperature on the photovoltaic performance of a model semiconductor/electrolyte interface. Of particular relevance to this work was the finding that temperature-induced changes in the charge and potential distribution at the interface have substantial effects on the overall PEC behavior. The main conclusion from this study is that there is an optimum temperature beyond which the beneficial effects of temperature on the electronic and optical properties of the semiconductor/electrolyte interface are nullified by unfavorable shifts in the flatband potential (V_{FB}) to positive potentials leading to a reduced barrier height (or band bending) in equilibrium. The consequence is a lowered open-circuit voltage (V_{oc}) and increased dark

* Electrochemical Society Student Member.

¹ Present address: Arco Enterprises, Incorporated, Troy, Michigan 48064.

Key words: flatband potential shift, diode quality factor, Schottky barrier theory.

currents and carrier recombination with a concomitant deterioration in the overall energy conversion efficiency of the PEC system.

Experiments were carried out on a model PEC cell comprising the n-GaAs|AlCl₃-n-butyl pyridium chloride (BPC), ferrocene/ferricenium ion couple|carbon system (6-8).

Experimental

PEC devices were fabricated from single crystal n-GaAs (Te-doped, <111> orientation with As exposed to the electrolyte) electrodes. These electrodes had doping densities of $2.17 \times 10^{17} \text{ cm}^{-3}$ as quoted by the manufacturer (*vide infra*). Electrode fabrication, etching, and other surface treatment procedures followed those outlined previously (7). The surface area (uncorrected for surface roughness) of these electrodes was nominally 0.23 cm².

Molten salt electrolytes consisting of mixtures of AlCl₃ and BPC in varying molar ratios were prepared according to procedures described elsewhere (6). Redox chemicals were obtained from commercial sources and purified further by recrystallization. Nominal concentrations of ferrocene (Fe(Cp)₂) and ferricenium chloride (Fe(Cp)₂Cl) were 0.2M and 20 mmols, respectively. All manipulations with the electrolytes and redox chemicals were carried out in a dry box.

A 300W tungsten halogen lamp was used to illuminate the n-GaAs electrodes. A nominal light intensity of 100 mW/cm² (AM1 solar simulation) was used for these experiments. The solar cell parameters reported herein are not corrected for light reflection and absorption losses in the cell and in the electrolyte.

Dark current-voltage measurements were performed as outlined previously (7, 8). Three-electrode geometry was employed for these measurements as well as for the capacitance voltage measurements using the lock-in technique (6). An aluminum wire immersed in the AlCl₃-BPC electrolyte (2:1 molar ratio) and separated from the main cell compartment by a fine-porosity glass frit, was employed as the quasi-reference electrode. Solar cell measurements were carried out on two-electrode PEC cells using vitreous carbon as the counterelectrode.

Measurements at elevated temperatures were carried out in a thermostated cell assembly. The temperatures reported below are accurate to $\pm 1^\circ\text{C}$.

Results and Discussion

Figure 1 illustrates current-voltage census for the n-GaAs|AlCl₃-BPC, Fe(Cp)₂/Fe(Cp)₂⁺|carbon PEC cell with temperature shown as the parameter. The AlCl₃-BPC electrolyte in this case was adjusted to be slightly basic of the 1:1 (AlCl₃:BPC) molar ratio composition since previous studies had shown this composition to be most suitable in combination with n-GaAs electrodes for photovoltaic applications (6-8). An increase in the short-circuit current density (J_{sc}) and a decrease in the open-circuit voltage (V_{oc}) are observed with increasing temperature. These trends are better illustrated by the data shown in Fig. 2 on the variation of J_{sc} , V_{oc} , fill-factor (FF), and solar conversion efficiency (η) with temperature. The V_{oc} values decrease at the rate of $\sim 3.6 \text{ mV}/^\circ\text{C}$ whereas the FF shows a corresponding decline of $\sim 0.001/^\circ\text{C}$. We note here that similar decreases in V_{oc} with temperature (2.3-2.6 mV/ $^\circ\text{C}$) have been noted by previous authors for solid-state p-n junction and Schottky barrier devices based on silicon (9, 10).

The observed increase in the J_{sc} values for the present cells has its origin both on temperature-induced changes in the optical and electrical properties of the semiconductor as well as on corresponding variations in the potential and charge distribution across the semiconductor/electrolyte interface (*vide infra*). For the purposes of the present study, we will concentrate

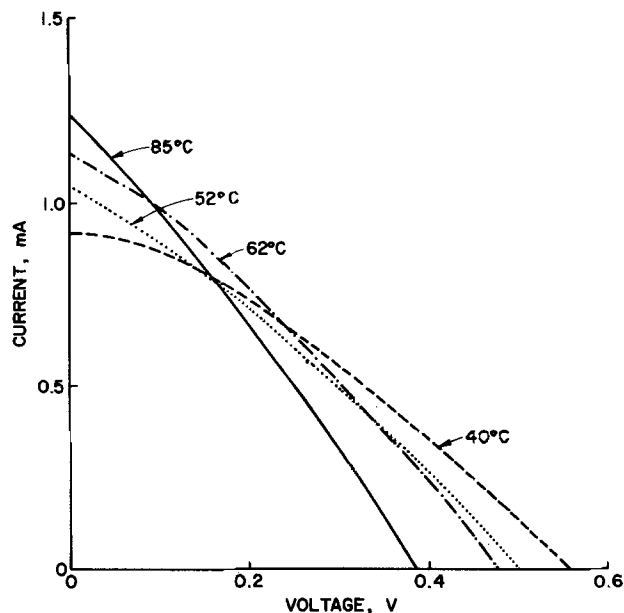


Fig. 1. Current-voltage curves for two-electrode n-GaAs 1:1 AlCl₃-BPC, Fe(Cp)₂/Fe(Cp)₂⁺|carbon PEC cell at different temperatures. Illumination with tungsten-halogen lamp at $\sim 100 \text{ mW}/\text{cm}^2$ incident light intensity (uncorrected, see text).

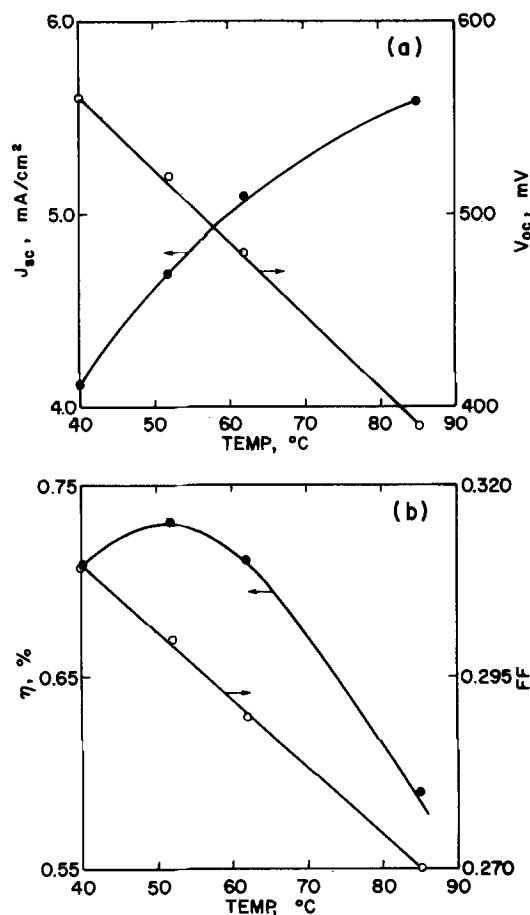


Fig. 2. (a) Variation of short-circuit current density (J_{sc}) and open-circuit voltage (V_{oc}) with temperature for model PEC device. (b) Variation of energy conversion efficiency (η) and fill-factor (FF) with temperature for model PEC device.

on the latter aspect since previous studies on solid-state cells (5) have clearly shown how temperature affects the electronic and optical behavior of the semiconductor. We briefly note, however, that these studies

have revealed the following: (i) the wavelength response shifts toward the red with increasing temperature because of bandgap narrowing, (ii) the diffusion length of photogenerated carriers increases with increasing temperature, and (iii) the absorption coefficient at longer wavelengths increases with increasing temperature because of (i) above. All of the above contribute to the observed increase in J_{sc} values with increasing temperature (Fig. 1 and 2).

In order to understand the temperature dependence of V_{oc} (Fig. 2), we consider the Schottky diode equation for the semiconductor/electrolyte interface (11)

$$J = J_{ph} - J_d = J_{ph} - J_o [\exp(qV/nkT) - 1] \quad [1]$$

where J is the total current density, J_{ph} is the photocurrent density, J_d is the dark current density, J_o is the reverse saturation current density, V is the bias voltage, and n is the diode quality factor [$n = 1$ for an ideal device; $n > 1$ for a nonideal device, cf. Ref. (6)]. For bias voltages exceeding $3kT/q$, we can neglect the last term in the bracket in Eq. [1]. Moreover at equilibrium (open-circuit conditions), $J_{ph} = J_d$ and $V = V_{oc}$ so that rearrangement of Eq. [1] yields

$$V_{oc} \approx \frac{nkT}{q} \ln \frac{J_{ph}}{J_o} \quad [2]$$

Equation [2] shows that the larger the value of J_o the smaller will be the V_{oc} value generated by the device for same value of J_{ph} . Figure 3 is a plot of J_o as a function of temperature for the n-GaAs|AlCl₃-BPC, Fe(Cp)₂/Fe(Cp)₂⁺|carbon PEC cell. Values of J_o were obtained from the intercept with the current axis of the extrapolated linear portion of $\ln J_d$ vs. V curves at zero cell potential. The exponential increase in J_o with temperature is consistent with the equation (11)

$$J_o = A^* T^2 \exp(-\phi_b/kT) \quad [3]$$

where A^* is the Richardson's constant [$\sim 9 \text{ A cm}^{-2} \text{ K}^{-2}$ for the present PEC system, Ref. (11)] and ϕ_b is the barrier height at equilibrium. Equation [3] clearly shows that J_o is thermally activated. In PEC systems, ϕ_b is given by the difference between E_{CB} and E_{redox} , where E_{CB} is the energy corresponding to the semiconductor conduction bandedge and E_{redox} is the equilibrium redox potential (cf. Fig. 4).

Since recent studies have shown that charge transfer in PEC systems is largely mediated via surface-states (6, 7, 12), an alternative picture of the situation at the semiconductor/electrolyte interface is also shown in Fig. 4 where E_t denotes a discrete trap level at the interface introduced by defects, specifically adsorbed

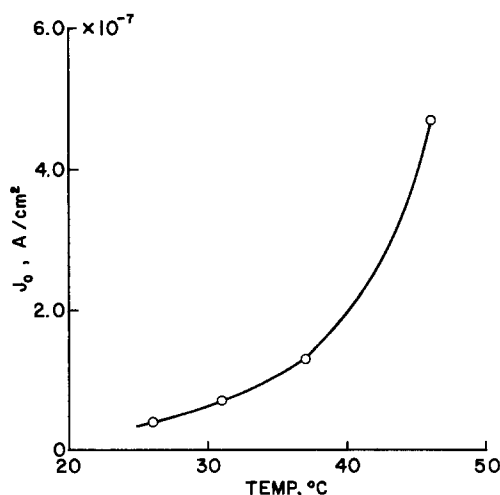


Fig. 3. Variation of reverse saturation current density (J_o) with temperature for model PEC device.

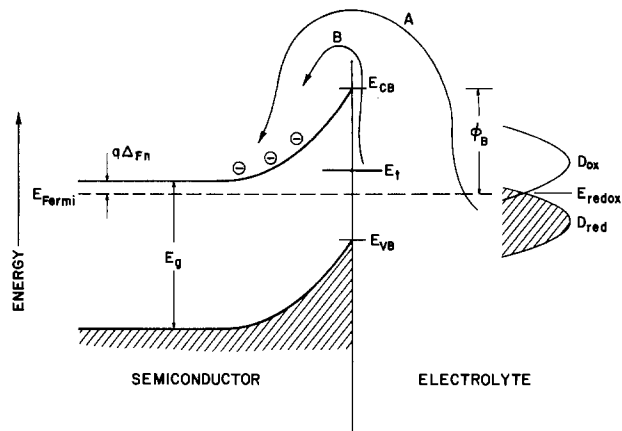


Fig. 4. Energy-band diagram for a PEC device at equilibrium. E_g is the semiconductor energy bandgap, D_{red} is the reduced redox levels, and D_{ox} denotes the oxidized (empty) levels in the electrolyte. See text for description of other symbols. The interphase between the semiconductor and the electrolyte is not shown for the sake of clarity.

electrolyte ions, etc. Evidence for the mediation of surface states in charge transfer in the n-GaAs|AlCl₃-BPC, Fe(Cp)₂/Fe(Cp)₂⁺|carbon system was presented in previous work (6). It was also speculated that specific adsorption of Cl⁻ ions on the n-GaAs surface was the origin of these bandgap states (8). Under condition of relatively large reverse bias such that there is high band bending and consequently majority carrier depletion at the interface, we can neglect the forward current flow of electrons from the semiconductor into the electrolyte. We then have the following equation for the rate of electron transfer from the trap level into the semiconductor conduction band (13)

$$J_o \approx q \frac{dn_t}{dt} = -qK_n n_t N_c \exp\left(-\frac{E_{CB} - E_t}{kT}\right) \quad [4]$$

where K_n is the rate constant given by $\bar{c}\sigma$ (\bar{c} = thermal velocity of electrons and σ = capture cross section of trap level), n_t is the density of occupied trap states, and N_c is the density of available states in the conduction band. Equation [4] shows that electron injection is thermally activated with an activation energy $E_{CB} - E_t$. We also see from Eq. [3] and [4] that the relative position of the semiconductor energy levels with respect to either the trap or redox levels is an important parameter in determining the magnitude of this activation energy. For the following discussion, we assume that $qV_{FB} \approx E_{CB}$ which is a reasonable approximation for relatively heavily doped semiconductors since the difference $|E_{CB} - qV_{FB}| \leq \sim 0.1 \text{ eV}$.

Figure 5 illustrates the dependence of V_{FB} on temperature for the n-GaAs|AlCl₃-BPC, Fe(Cp)₂/Fe(Cp)₂⁺|carbon system. The data are displayed in the form of conventional Mott-Schottky plots (14). The AlCl₃-BPC electrolyte in this case was adjusted to be basic ($pCl = \sim 7$) by addition of appropriate amounts of BPC to the neutral 1:1 composition. A systematic shift in V_{FB} to positive potentials is evident in the data in Fig. 5. This shift has important consequences on the magnitude of J_o and therefore J_d (cf. Eq. [1]). Considering the direct charge exchange between the reduced redox species in the electrolyte and the conduction band in the semiconductor (represented by scheme A in Fig. 4 and Eq. [3]), we now estimate the corresponding temperature-induced changes on E_{redox} . We have the following Nernst equations

$$E_t = E^0 + \frac{kT_1}{n_e q} \ln \frac{[ox]}{[red]} \quad [5]$$

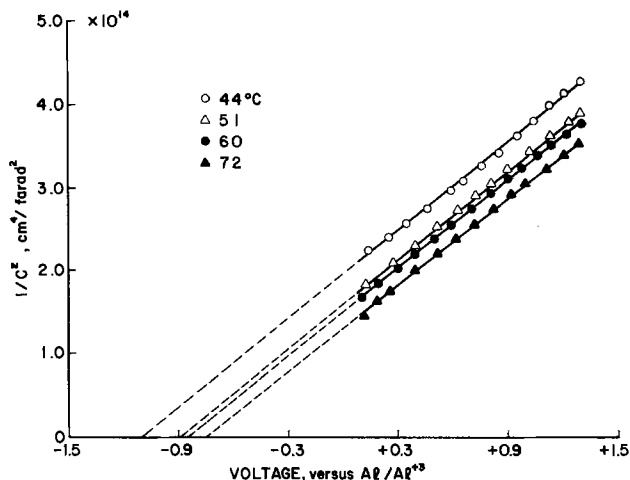


Fig. 5. Mott-Schottky plots for the n-GaAs|AlCl₃-BPC interface at different temperatures. The a-c signal frequency was 10 kHz for these measurements.

$$E_2 = E^0 + \frac{kT_2}{n_e q} \ln \frac{[\text{ox}]}{[\text{red}]} \quad [6]$$

where E^0 is the standard redox potential, [ox] and [red] denote bulk concentrations of oxidized and reduced redox species, respectively, n_e is the number of electrons involved in the redox reaction, and the subscripts 1 and 2 denote two different temperatures. To a first approximation we can neglect temperature-induced changes in the redox concentrations and the reference electrode potential, so that subtraction of Eq. [6] from Eq. [5] yields

$$\Delta E_{\text{redox}} = E_2 - E_1 = \frac{k(T_2 - T_1)}{q} \ln(0.1) \quad [7]$$

where the molar concentrations of Fe(Cp)₂⁺ and Fe(Cp)₂ have been inserted. An estimate of ΔE_{redox} from Eq. [7] and corresponding changes in V_{FB} as a function of temperature are shown in Table I. The data clearly show that changes in V_{FB} (and therefore E_{CB}) far outweigh the effect of temperature on E_{redox} . For all practical purposes, therefore, the direction of the shift in V_{FB} with temperature will immediately indicate the magnitude of the dark current density at elevated temperatures. Again the implicit assumption is involved that E_{CB} does not shift with applied bias or illumination. In the presence of high surface-state densities and consequent dependence of the potential distribution across the semiconductor/electrolyte interphase on the bias voltage, the simple model described above will be no longer applicable. The present data on the n-GaAs|AlCl₃-BPC, Fe(Cp)₂/Fe(Cp)₂⁺|carbon cell as well as previous work (6, 7), however, suggest a behavior consistent with this simplified model. The barrier-height reduction with temperature is shown in Table II for this PEC system.

By arguments analogous to those described above, we see that the barrier height $E_{\text{CB}} - E_t$ is also modi-

Table I. Comparison of the magnitude of the temperature shift of V_{FB} and E_{redox} for the n-GaAs|AlCl₃-BPC, Fe(Cp)₂/Fe(Cp)₂⁺|C system

| Temperature (°C) | V_{FB} (V vs. Al/Al ³⁺) | ΔV_{FB} (V) | ΔE_{redox} (V)* | E_{redox} (V vs. Al/Al ³⁺) |
|------------------|--|----------------------------|--------------------------------|---|
| 44 | -1.12 | 0 | 0 | 0.3000 |
| 51 | -0.86 | 0.26 | 0.0014 | 0.2986 |
| 60 | -0.83 | 0.03 | 0.0018 | 0.2968 |
| 72 | -0.75 | 0.08 | 0.0024 | 0.2944 |

* Cf. Eq. [7].

Table II. Variation of the zero-bias barrier-height (ϕ_B)^{*} with temperature for the n-GaAs|AlCl₃-BPC, Fe(Cp)₂/Fe(Cp)₂⁺|carbon PEC system

| Temperature (°C) | ϕ_B (eV) |
|------------------|---------------|
| 44 | 1.42 |
| 51 | 1.16 |
| 60 | 1.13 |
| 72 | 1.05 |

* Taken as the difference between V_{FB} and the redox potential [0.30V vs. Al/Al³⁺, Ref. (6)].

fied at elevated temperatures (cf. scheme B in Fig. 4 and Eq. [4]). The location of E_t is not expected to vary appreciably with temperature so that the magnitude of the activation energy, $E_{\text{CB}} - E_t$, is largely determined by the shift in E_{CB} . Contrary to the direct charge transfer case (cf. scheme A in Fig. 4), however, experimental evidence is less conclusive in support of the trap-mediated electron injection mechanism in the present PEC system. For example, barrier-height data obtained from the slopes of J_0/T^2 vs. $1/T$ plots [cf. Eq. [3], see Ref. (8)] are in excellent agreement with the results of capacitance measurements on the n-GaAs|AlCl₃-BPC, Fe(Cp)/Fe(Cp)₂⁺|carbon PEC system. On the other hand, if we place the location of E_t/q as $-0.1V$ (vs. Al/Al³⁺) based on the observed position of reduction waves on n-GaAs (6), we obtain $E_{\text{CB}} - E_t = 0.65$ eV for the slightly basic AlCl₃-BPC electrolyte [$V_{\text{FB}} = -0.75V$, Ref. (6)] which is considerably less than the value (~ 1 eV) obtained from dark current-voltage data (8). The above alternative model was considered as a general case since its occurrence in other PEC systems is supported by previous studies in the literature (12).

The temperature dependence of V_{FB} has been discussed by previous authors (15) in terms of the following expression

$$qV_{\text{FB}} = EA - E_0 - q\Delta_{\text{fn}} - q\Delta V_{\text{H}} \quad [8]$$

Here EA is the electron affinity of the semiconductor, E_0 is the position of the reference electrode relative to the vacuum level, Δ_{fn} is the potential difference between the Fermi level and the bottom of the conduction band (cf. Fig. 4), and ΔV_{H} is the potential across the Helmholtz layer due to adsorbed ions. We speculate that the origin of the positive potential shift in V_{FB} with temperature (Fig. 5) in the n-GaAs|AlCl₃-BPC system lies in temperature-induced desorption of Cl⁻ ions from the n-GaAs electrode surface. The surface thereby acquires an increasing positive charge with increasing temperature leading to the observed shift in V_{FB} .

We note that the slopes of the Mott-Schottky plots in Fig. 5 yield semiconductor doping densities of $0.74 \times 10^{17} \text{ cm}^{-3}$ at 44°C, $0.71 \times 10^{17} \text{ cm}^{-3}$ at 51°C, $0.71 \times 10^{17} \text{ cm}^{-3}$ at 60°C, and $0.74 \times 10^{17} \text{ cm}^{-3}$ at 72°C, respectively. The constancy of these values at different temperatures provides a further check on the reliability of the Mott-Schottky analyses in Fig. 5.

Table III shows the effect of temperature on Schottky diode parameters for the n-GaAs|AlCl₃-BPC, Fe(Cp)₂/Fe(Cp)₂⁺|C system. The parameter V_0 is determined by the change in the voltage, ΔV , for a decade change in the current density (16) and was computed from the dark-current vs. voltage data in Ref. (8). For nonideal Schottky diodes, V_0 is given by (16)

$$V_0 = nkT/q \quad [9]$$

The diode quality factor is therefore given by the equation

$$n = V_0/kT/q \quad [10]$$

Values of n computed from Eq. [10] as a function of

Table III. Schottky diode parameters for the n-GaAs|AlCl₃-BPC, Fe(Cp)₂/Fe(Cp)₂⁺|C system

| Temperature (°C) | kT/q (mV) | V_0 (mV)* | n |
|------------------|-------------|-------------|------|
| 26 | 25.8 | 38.0 | 1.47 |
| 31 | 26.2 | 39.6 | 1.51 |
| 37 | 26.8 | 41.6 | 1.55 |
| 46 | 27.5 | 50.7 | 1.84 |

* Computed from experimental data in Ref. (8).

temperature are assembled in Table III. By analogy with the behavior of p-n junction solid-state devices, values of $n > 1$ may be interpreted in terms of the dominating influence of recombination-generation currents on the current-voltage behavior of the device (7, 8). The systematic increase in n with temperature is indicative of the propensity of such processes either in the semiconductor bulk or at the interface at elevated temperatures. The deterioration in the fill-factor as seen in Fig. 2b may be therefore attributed to the series resistance associated with recombination-generation current flow paths. Precedence for such effects is found in previous work on solid-state p-n junction devices where the blue wavelength response is seen to degrade at elevated temperatures, presumably because of carrier recombination effects at the surface (5).

Summary and Conclusions

Although temperature has beneficial effects on the short-circuit current densities of a PEC device, there is an optimum temperature beyond which the deleterious effect of high dark current densities begins to degrade the overall energy conversion efficiency of the system. Apart from the thermal activation of the reverse saturation current density at elevated temperatures, which is analogous to the case of a solid-state Schottky barrier device, temperature brings about unfavorable modifications in the potential and charge distribution across the semiconductor/electrolyte interface. The consequence of positive potential shifts in V_{FB} at elevated temperatures is a net reduction in the barrier height at equilibrium and a concomitant increase in the reverse saturation current density. It must be noted, however, that the direction of the shift in V_{FB} and V_{CB} is determined largely by temperature-induced changes in the chemistry of the semiconductor/

electrolyte interface and as such must be specific to each semiconductor/electrolyte combination.

Acknowledgments

This research program was funded by Solar Energy Research Institute and the U.S. Department of Energy under Grant XP-9-8002-9.

Manuscript submitted Dec. 16, 1980; revised manuscript received Feb. 23, 1981.

Any discussion of this paper will appear in a Discussion Section to be published in the June 1982 JOURNAL. All discussions for the June 1982 Discussion Section should be submitted by Feb. 1, 1982.

Publication costs of this article were assisted by Colorado State University.

REFERENCES

1. K. Rajeshwar, P. Singh, and J. DuBow, *Electrochim. Acta*, **23**, 117 (1978).
2. S. Kar, K. Rajeshwar, P. Singh, and J. DuBow, *Solar Energy*, **23**, 129 (1979).
3. P. V. Kamat, M. D. Karkhanavala, and P. N. Moorthy, *J. Appl. Phys.*, **50**, 4228 (1979).
4. M. S. Wrighton, D. L. Morse, A. B. Ellis, D. S. Ginley, and H. B. Abrahamson, *J. Am. Chem. Soc.*, **98**, 44 (1976).
5. A. Agarwala, V. K. Tiwary, S. K. Agarwal, and S. A. Jain, *Solid State Electron.*, **23**, 1021 (1980).
6. P. Singh, K. Rajeshwar, J. DuBow, and R. Job, *J. Am. Chem. Soc.*, **102**, 4676 (1980).
7. P. Singh, R. Singh, K. Rajeshwar, and J. DuBow, *This Journal*, **128**, 1145 (1981).
8. P. Singh and K. Rajeshwar, *This Journal*, **128**, 1724 (1981).
9. S. M. Vernon and W. A. Anderson, *Appl. Phys. Lett.*, **26**, 707 (1975).
10. J. Wysocki and P. Rappaport, *J. Appl. Phys.*, **31**, 571 (1960).
11. E. H. Rhoderick, "Metal-Semiconductor Contacts," Chap. 2 and 3, Clarendon Press, Oxford (1978).
12. S. N. Frank and A. J. Bard, *J. Am. Chem. Soc.*, **97**, 7427 (1975).
13. S. R. Morrison, "The Chemical Physics of Surfaces," Chap. 2, p. 42, Plenum Press, New York (1977).
14. H. Gerischer, in "Physical Chemistry—An Advanced Treatise," Vol. IX A, H. Eyring, Editor, Chap. 5, p. 473, Academic Press, New York (1970).
15. M. A. Butler and D. S. Ginley, *Nature*, **273**, 524 (1978).
16. A. N. Saxena, *Surf. Sci.*, **13**, 151 (1969).



Enhancing Performance of the Ti(III)/Ti(IV) Couple for Redox Battery Applications

C. C. Liu*¹ and R. T. Galasco

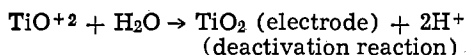
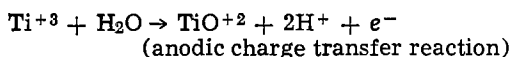
Department of Chemical and Petroleum Engineering, University of Pittsburgh, Pittsburgh, Pennsylvania 15261

and R. F. Savinell*

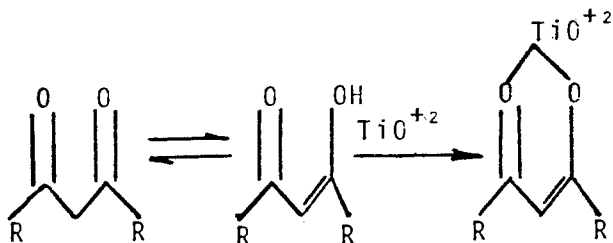
Department of Chemical Engineering, The University of Akron, Akron, Ohio 44325

Redox battery systems in recent years have generated interest as a means for large-scale energy storage. Of the redox couples, Fe-Cr ($E^\circ = 1.18V$) (1, 2) and Fe-Ti ($E^\circ = 0.67V$) (3-7) are considered promising. However, the Fe-Ti system was less attractive due to a combination of unfavorable pH and kinetic effects. Recent analysis of the Fe-Ti system indicates that the titanium half-cell reaction during discharge is the rate-limiting one (5, 6). Improvement in the performance of this half-cell is needed for the Fe-Ti system in order to make it into an attractive energy storage device.

In our earlier studies, it was suspected that the kinetic activation limitations in the titanium half-cell might be caused by partial blockage of active anodic surface area by TiO_2 precipitation. This TiO_2 precipitation is most likely the result of a reaction between the titanium (IV) oxide with water in the bulk electrolyte. Schematically, this reaction sequence can be represented as



If TiO_2 precipitation does occur, this precipitation can be hindered by adding a soluble chelating agent to the anolyte. Consequently, this may lead to the enhancement of the performance of the titanium half-cell as well as the redox battery system. Due to the strong affinity of titanium for oxygen, thus, theoretically, oxygen chelating agents in acid solution can be expressed as

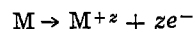


Additionally, the chelating agent may enhance the stability of the titanium (IV) oxide, resulting in more favorable kinetics for the cathodic reaction. Of course, in order for a chelating agent to be effective in an actual battery system, the chelation reaction must al-

low for the reduction of the stabilized TiO^{+2} species when the battery is undergoing charge.

Another possible method of minimizing the formation of TiO_2 in the titanium half-cell would be the addition of a reducing agent to the anolyte. The reducing agent can react with the titanium (IV) oxide producing titanium (III) ions in the bulk anolyte. It is possible that this reaction will occur preferentially to the TiO_2 formation reaction both during battery charge and discharge modes of operation.

In addition to the possible minimization of TiO_2 formation, the reducing agent itself may be a primary participator in the electrode reaction, *i.e.*



This reaction may either replace or supplement the anodic charge transfer from the titanous ion. In either case, the role of the reducing agent must be reversible so that the agent can be regenerated upon charging the battery. Otherwise, consumption of the agent will result eventually in a change of electrolyte characteristics and in excessive costs.

Experimental

The chelating agents used in this study should be highly soluble and physically stable in the concentrated HCl- $TiCl_3$ anolyte and good chelates for titanium (IV) oxide in the acid solution. Acetylacetone, disodium EDTA, oxalic acid, and glycerol were selected as possible chelating agents.

The reducing agent used in the system should be able to reduce titanium (IV) oxide ions to titanium (III) ions at a reasonable rate. Also, solid reducing agents should have a high H_2 overpotential and should be relatively stable in the concentrated HCl- $TiCl_3$ anolyte.

Reducing agents used for the reduction of titanium (IV) ions to titanium (III) ions have been reported and are generally in the form of granular metal or amalgams, metal or amalgam foils, or liquid amalgams with excess mercury. For the system studied, liquid amalgam would be impractical, hence granular metals and solid amalgams were chosen in this investigation.

Granular lead particles (Fisher Scientific) and porous lead structure (10 pores per linear inch, Energy Research and Generation, Incorporated, Oakland, California) were evaluated as well as granular tin and amalgams of zinc and cadmium. Since the reducing agent must be stable in the electrolyte, a qualitative visual examination was used to determine those agents which do not, at least apparently, generate hydrogen gas when in contact with solution. The test solutions are given in Table II. In the electrolyte having sodium

* Electrochemical Society Active Member.

¹ Present address: Chemical Engineering Department, Case Western Reserve University, Cleveland, Ohio 44106.

Key words: redox, battery, titanium.

chloride salt, the salt replaced the acid to a certain extent with the intention of reducing protons available for hydrogen production while maintaining sufficient supporting electrolyte for adequate charge transfer in solution.

The redox prototype used in this study was a stationary cell which is shown schematically in Fig. 1. The membrane separator employed was the MA-3475 commercial membrane produced by Ionac Chemical Sybron Corporation (Birmingham, New Jersey). Graphite foil of 0.0254 cm thickness (Grade GTA, Union Carbide Corporation) was used at the cathode and as the anode current collector. The electrodes and the membrane had an exposed area of 19.6 cm². In the earlier experiments the chelating agent was added to the anolyte only. In all cases the molar ratio of chelating agent to TiCl₃ was greater than one. For example, in the case of acetylacetone, 12.5 cm³ of acetylacetone was added to 50 cm³ of anolyte (1M TiCl₃/3N HCl) giving a molar ratio of chelating agent to reactant of 2.4 to 1.

In the later experiments the reducing agent was added to the anode compartment as solid granules. For example, when lead was studied as the reducing agent, 35g of lead granules were added to 16.6 cm³ of anolyte. The result was a mixture having a lead to TiCl₃ molar ratio of 10.2.

Results and Discussion

Table I summarizes the experimental results of using chelating agents in the anolyte of the Fe-Ti redox system.

Of the chelating agents studied, only oxalic acid and acetylacetone showed evidence of possible chelation through color change. However, the discharge performance of cells having these agents present in the electrolyte were unchanged or inferior when compared to the standard Fe-Ti cell.

The experimental results of the system using acetylacetone indicated a decrease of approximately 70 mV in anodic overpotential at a discharge current density of 8.5 mA/cm². The amount of acetylacetone addition in this work was the same as reported by Reid and Gahn (3). However, they report a lowering of anodic overpotential by 300 mV. Furthermore, they observed a corresponding increase in cell discharge potential of 300 mV (presumably, with constant load discharge, the operating cell current density of their cell appears to be ~10 mA/cm²). In our study with acetylacetone, the enhanced anodic performance was not accompanied by a corresponding increase in overall cell potential. Consequently, we observed no net gain in cell discharge performance.

In our studies with reducing agents, the qualitative test for determining metal stability in electrolyte shows that only lead was apparently stable. Some reaction

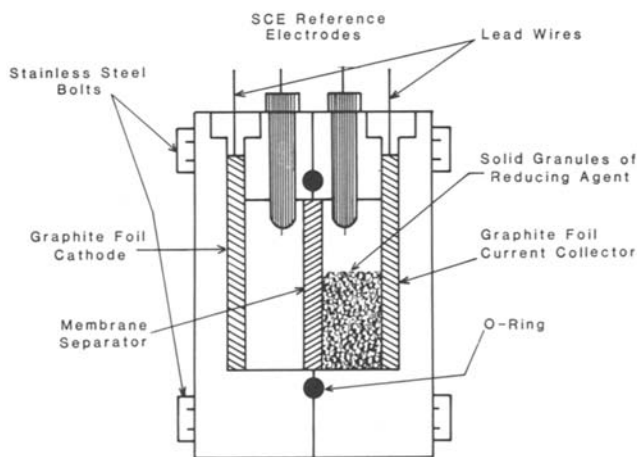


Fig. 1. Schematic of the stationary test cell

Table I. Results of chelating agent experiments

| Chelating agent | Molar ratio chelating TiCl ₃ agent | Vis- ible chela- tion | Performance |
|-------------------------------------|---|--------------------------------|--|
| 2-4 pentanedione (acetylacetone) | 2.4:1 | Yes | Discharge perform- ance similar to standard cell |
| Disodium EDTA | 1.05:1 | — | Precipitates rapidly from solution |
| Oxalic acid | 1:1 | Yes | Poor discharge per- formance |
| Glycerol | 2:1 | No | Discharge perform- ance similar to standard cell |

was obviously occurring at the surface of tin while copious amounts of hydrogen were produced at the surfaces of the zinc amalgam and the cadmium amalgam.

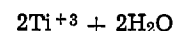
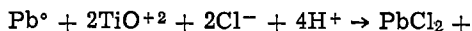
The open-circuit potentials for Fe-Ti systems containing lead or tin reducing agents are listed in Table II. The open-circuit potential of the Fe-Ti cell without any reducing agent is shown for comparison. With a reducing agent present, the open-circuit potential increased between 350-400 mV depending upon electrolyte composition. At this time we are unsure of the cause of this increase in observed potential but we suspect that it may be due to Nernstian effects and/or electrochemical oxidation of the reducing agent. The basis for this suspicion is the fact that a lead chloride deposit was found on the lead particles following a cell discharge. Further studies were restricted to using lead as the reducing agent.

Although the lead chloride found on the granules may be formed by the reaction



we do not believe this reaction to be of significance in this case. The chemical oxidation of lead in acid chloride medium has been reported as being of less importance as compared to electrochemical oxidation (8). In our qualitative stability test for the reducing agents in electrolyte, we observed no hydrogen generation from lead. Furthermore, the lead chloride deposit only was found after cell discharge.

One reaction which may account for the lead chloride formation and the enhanced cell potential is



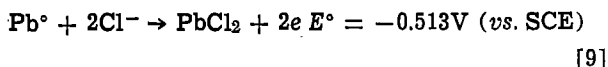
In order to account for the magnitude of increase observed in the open-circuit potential, the activity ratio of Ti⁺³/TiO⁺² must be ca. 10⁶. The above mechanism also would create a favorable effect on reaction rates. That is, since this reaction occurs at the lead surface, it would increase the reactant concentration at the surface and diminish the product concentration. Consequently, with first-order forward and backward kinetics, the rate of Ti⁺³ oxidation should be enhanced.

Another possible explanation for phenomena in the anode compartment of a Fe-Ti redox cell can be given

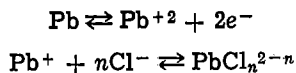
Table II. Battery open-circuit potentials for Fe-Ti systems containing reducing agents (mole reducing agent/moles TiCl₃ = 10.2)

| Type of reducing agent | Electrolyte concentration | Open circuit potential (V) | Anode potential vs. SHE (V) | Cathode potential vs. SCE (V) |
|------------------------|--|----------------------------|-----------------------------|-------------------------------|
| None | 3.0N HCl in catholyte 3.5N HCl in anolyte | 0.782 | 0.071 | 0.853 |
| Pb | 3.0N HCl in catholyte 3.5N HCl in anolyte | 1.193 | -0.366 | 0.825 |
| Pb | 0.53N HCl, 2.5M NaCl | 1.17 | — | — |
| Sn | 3.0N HCl in catholyte 3.5N HCl in anolyte | 1.17 | — | — |
| Sn | 0.53N HCl, 2.5M NaCl | 1.14 | — | — |

as the following reaction



In this case, enhanced performance may be directly attributed to the electrochemical characteristics of this reaction. The oxidation of lead in chloride medium has been recently reviewed by Kuhn (9). Although PbCl_2 will often passivate the electrode, with some forms of PbCl_2 deposits and under certain operating conditions this will not occur (8, 10-13). Barradas (13) has shown that a lead electrode in HCl solution undergoes the 2-electron oxidation reaction of



where $4 > n > 0$. In this mechanism the high chloride concentration favors the complex ion formation of the second reaction which in turn diffuses to the bulk electrolyte. Under these conditions, the oxidation of lead occurs with considerable reversibility. In our studies we have found the presence of titanium chloride to be necessary for maintaining the enhanced performance of a lead electrode in an acid chloride medium.

A comparison of constant load short-term discharge between a standard Fe-Ti cell and an Fe-Pb(Ti) cell is shown in Fig. 2. The Fe-Ti cell shows a useful cell discharge potential approaching only 20% of the initial ($t = 0$) cell open-circuit potential after a short discharge time. Moreover, battery performance is limited by the anodic overpotential which is greater than 40% of the initial cell open-circuit potential. By comparison, the Fe-Pb(Ti) cell has a useful cell discharge potential

near 40% of the initial cell open-circuit potential. The anodic overpotential is less than 14% of this open-circuit potential. However, the cathodic overpotential now represents a more significant contribution to cell polarization at 27% of open-circuit potential. The increase in cathodic overpotential and membrane IR loss are a direct result of the greater discharge current (constant load discharge) obtained with the Fe-Pb(Ti) cell.

We have examined the role of lead and titanium chloride in an Fe-Pb(Ti) cell. The results of this investigation along with charge/discharge operating characteristics of this cell will be reported in a separate communication.

Conclusions

In summary, the results of this study showed that the approach of using a chelating agent in the anolyte for an Fe-Ti redox system only shows marginal improvement in cell discharge performance. However, the application of a solid reducing agent in the anolyte, particularly lead, showed enhancement in the performance of the redox system. This effect has been investigated and will be reported in detail separately.

Acknowledgments

Technical advice provided by Professors J. F. Coetzee and S. H. Chiang of the University of Pittsburgh is gratefully appreciated. A graduate fellowship provided by Shell Co. (R.T.G.) and partial support of this research by Alcoa Foundation are also acknowledged.

Manuscript submitted Nov. 14, 1980; revised manuscript received Feb. 18, 1981.

Any discussion of this paper will appear in a Discussion Section to be published in the June 1982 JOURNAL. All discussions for the June 1982 Discussion Section should be submitted by Feb. 1, 1982.

Publication costs of this article were assisted by the University of Pittsburgh.

REFERENCES

1. L. H. Thaller, NASA TM-79143, Terrestrial Energy Systems Conference Sponsored by the American Institute of Aeronautics and Astronautics, Orlando, Florida, June 4-6, 1979.
2. L. H. Thaller, NASA TM-79186, Fourteenth Intersociety Energy Conversion Engineering Conference, Boston, Massachusetts, Aug. 5-10, 1979.
3. M. A. Reid and R. F. Gahn, "Factors Affecting the Open-Circuit Voltage and Electrode Kinetics of Some Iron/Titanium Redox Flow Cells," NASA TMX-73669 (1977).
4. L. H. Thaller, Abstract 85, p. 229, The Electrochemical Society Extended Abstracts, Atlanta, Georgia, Oct. 9-14, 1977.
5. R. F. Savinell, C. C. Liu, R. T. Galasco, S. H. Chiang, and J. F. Coetzee, *This Journal*, **126**, 357 (1979).
6. R. F. Savinell, Ph.D. Dissertation, University of Pittsburgh, Pittsburgh, Pa. (1977).
7. R. T. Galasco, Ph.D. Dissertation, University of Pittsburgh, Pittsburgh, Pa. (1979).
8. J. Ambrose, R. G. Barradas, K. Belinko, and D. W. Shoemith, *J. Colloid. Interface Sci.*, **47**, 441 (1974).
9. A. T. Kuhn, Editor, "The Electrochemistry of Lead," pp. 383-397, Academic Press, New York (1979).
10. R. G. Barradas, K. Belinko, and J. Ambrose, *Can. J. Chem.*, **53**, 389 (1975).
11. R. G. Barradas, K. Belinko, and E. Ghibaudi, *ibid.*, **53**, 407 (1975).
12. R. G. Barradas, K. Belinko, and W. Shoemith, *Electrochim. Acta*, **21**, 357 (1976).
13. R. G. Barradas and S. Fletcher, *ibid.*, **22**, 237 (1977).

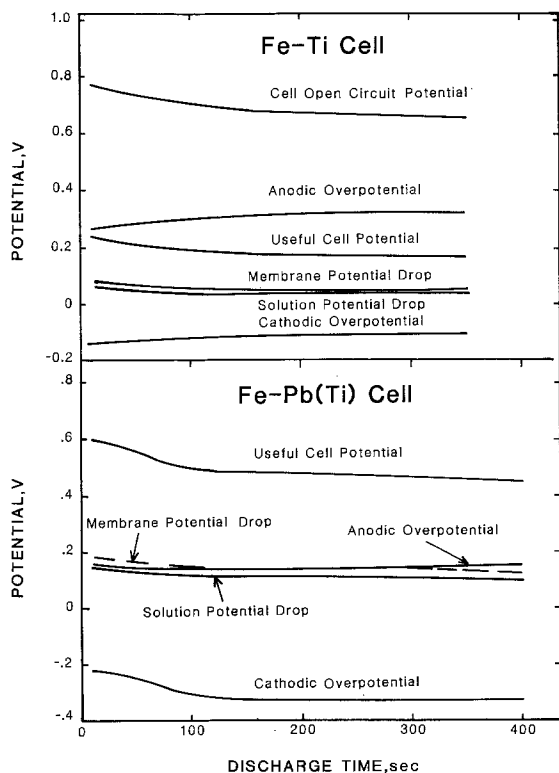


Fig. 2. A comparison of short-term constant load (1Ω) discharge performance of the standard Fe-Ti cell [reported in Ref. (5)] with the Fe-Pb(Ti) cell.



Synthesis, Radiation Degradation, and Electron Beam Resist Behavior of Fluorine-Containing Vinyl Polymers

C. U. Pittman, Jr., M. Ueda,¹ and C. Y. Chen²

Department of Chemistry, University of Alabama, University, Alabama 35486

J. H. Kwiatkowski and C. F. Cook, Jr.

US Army Electronics Technology and Devices Laboratory, Fort Monmouth, New Jersey 07703

and J. N. Helbert*

Motorola SG/SRD, Phoenix, Arizona 85008

ABSTRACT

Novel vinyl monomers containing the α -CF₃ group are shown to increase the propensity toward chain scission during radiation degradation and increase the electron beam sensitivity in copolymers with methyl methacrylate and methacrylonitrile. The incorporation of 32 m/o of α -trifluoromethacrylonitrile (TFMAN) into poly(methyl methacrylate) increases sensitivity from 20×10^{-5} to 3×10^{-5} C/cm² (at 2 keV), increases G_s from 1.3 to 3.1, and decreases the etch rate from 100 to 79 Å/min. Similar beneficial results come from incorporating TFMAN into methacrylonitrile (MCN) copolymers. Poly(trifluoroethyl methacrylate) is a highly sensitive resist ($Q = 2$ to 3×10^{-5} C/cm²) but it exhibits a high etch rate (230 Å/min). Incorporation of 31 m/o MCN into this polymer decreases the etch rate to 93 Å/min while preserving a high sensitivity ($3\text{--}4 \times 10^{-5}$ C/cm²). The G_s and G_x values of these homo- and copolymer systems as well as the copolymer of methacrylonitrile with methyl α -fluoroacrylate (MFA) were obtained. The homopolymer of MFA cross-links on irradiation but its MCN copolymers tend to be positive resists with G_x values lower than that expected if G_x were a linear function of the MFA mole fraction.

The incorporation of fluorine and chlorine into vinyl polymers for use as electron-beam (1) or x-ray (2) resists is a topic of increasing interest. Fluorine and chlorine each have high x-ray absorption coefficients. The atomic absorption coefficient at 4.15Å for chlorine is 1614 (21 times that of carbon) while that for fluorine at 8.3Å is 1898 (3.4 times that of carbon). Also, the incorporation of halogens might modify the radiation degradation chemistry (3) by providing favored pathways for chain scission. Indeed, we have shown that poly(methyl α -chloroacrylate) exhibits a very high chain scission propensity ($G_s > 6$) (4). Recently, we reported that fluorine incorporation at the α -position of an acrylate (*i.e.*, [CH₂C(F)(CO₂CH₃)]_n) dramatically reversed the degradation behavior found for other α -substituents (*e.g.*, CN, CH₃, Cl, CH₂CO₂CH₃), to that of a predominantly cross-linking negative resist (5, 6).

In contrast, fluorine incorporation into the ester group of methacrylate polymers (*e.g.*, [CH₂C(CH₃)(CO₂CH(CF₃)₂)]_n) was found to enhance the chain scission susceptibility over that of the classical system, poly(methyl methacrylate) (5).

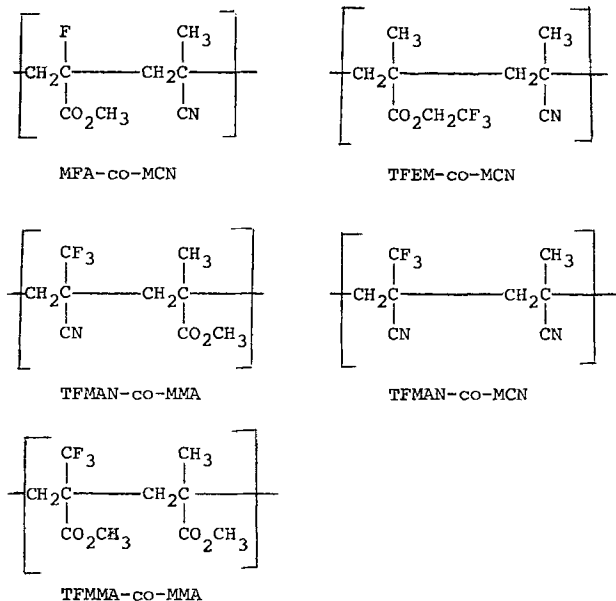
Such studies provide the fundamentally important radiation G -values and allow successful prediction of radiation resist behavior for integrated circuit fabrication applications. We now report further novel fluorine-containing polymers including those where the α -substituent is -F or -CF₃, as well as copolymers of 2,2,2-trifluoroethyl methacrylate (TFEM) with methacrylonitrile (MCN). The monomer α -trifluoromethylacrylonitrile (TFMAN) was copolymerized with methacrylonitrile and methyl methacrylate (MMA), while methyl α -trifluoromethylacrylate (TFMMA) was copolymerized with methyl methacrylate. The radiation degradation susceptibilities, electron beam sensitivities, and plasma etch rates for these systems have been obtained. The structural formulas and designated abbreviations used throughout the paper are shown on the following page.

* Electrochemical Society Active Member.

¹ Present address: Yamagata University, Yamagata, Japan.

² Present address: Union Carbide, Chemicals and Plastics, South Charlestown, WV.

Key words: electron beam lithography, positive resists, plasma etching.



These polymer structures are of particular interest in view of Kakuchi's report (7) that the electron beam sensitivity of poly(hexafluorobutyl methacrylate) was 4×10^{-7} C/cm² and its x-ray sensitivity was 46 times more sensitive than poly(methyl methacrylate), e.g., PMMA. They represent new structures in a larger program in our laboratories to ascertain the radiation degradation susceptibilities, electron beam behavior, and plasma etch rates of potential resist polymers as a function of polymer structure (8-16).

Experimental

Polymer molecular weights were determined by gel permeation chromatography (GPC) or membrane osmometry (MOSM). GPC was performed using a Water Associates Model 201 chromatograph equipped with four microstyrigel columns (exclusion sizes: 10^6 , 10^5 , 10^4 , and 10^3). GPC measurements were made at a flow rate of 1.0 cm³/min of CHCl₃, THF, or DMF; the solvent used was dictated by the copolymer solubility. The "Universal Calibration" method was used to analyze the GPC data, and the PMMA calibration curve was used for CHCl₃ and THF data. A polystyrene calibration curve was used for DMF GPC data. MOSM was performed with a WESCAN Model 230 Osmometer at 30° using acetonitrile or MEK as solvent. Molecular weight data for the polymers synthesized and fractionated in this study, prior to irradiation, are found in Table I. γ -Irradiations and data analysis to obtain G (scission), G_s , and G (cross-link), G_x , were carried out as described previously (8-13).

The synthesis of methyl α -fluoroacrylate, MFA, has been described elsewhere (14) and the preparation of trifluoromethacrylonitrile and methyl α -trifluoromethylacrylate will be described subsequently (15). The MFA/MCN copolymers were prepared by emulsion polymerization at 50° using K₂S₂O₈ as the initiator and sodium lauryl sulfate as the surfactant. The emulsions were deoxygenated by nitrogen purging and stirred magnetically. The copolymer lattices were coagulated by pouring into stirred methanol, filtered, and dried overnight *in vacuo* at 40-50°C. MFA/MCN copolymers were fractionated by dissolving 25g of polymer into 650 ml of acetonitrile and adding methanol dropwise in the usual fashion. The copolymer compositions were determined by elemental analysis for fluorine and for carbon. The synthetic details are given in Table II.

2,2,2-Trifluoroethyl methacrylate was prepared in good yield from methacrylyl chloride and 2,2,2-trifluoroethanol in the presence of triethylamine using standard methods. It was copolymerized with MCN using the emulsion method described above for MFA/MCN copolymerizations and the conditions and results are in Table II.

Trifluoromethacrylonitrile was copolymerized with MMA or MCN by bulk polymerization using azobisisobutyronitrile (e.g., AIBN) as the initiator. The monomers and AIBN were weighed into an ampul and the solution was degassed by three alternate vacuum freeze thaw cycles. The ampul was sealed, immersed in an oil bath for the reaction period, cooled, broken, and the resulting block of polymer was dissolved in acetone. The copolymers were purified by reprecipitations from acetone into methanol followed by drying *in vacuo*. Methyl α -trifluoromethylacrylate was copolymerized with MMA in the same manner. Table II lists conditions and results.

The electron beam resist sensitivities, in Table IV, were obtained at 20 keV using an ETEC LEBES E-beam microfabricator. The values are for a 6800A original resist thickness with no loss in unexposed resist thickness during development. Resist film thicknesses were measured with a Tencor Alpha-step profilometer.

Plasma etch rates were obtained with either an IPC 4005 or Tegal 421 reactor. The rf power during etching was 100 and 150W for the IPC 4005 and the Tegal 421, respectively. The pressures were 0.7 and 0.5 Torr of CF₄/4% O₂ and CF₄/8% O₂ gas mixtures, respectively. The reported values are reproducible to $\pm 15\%$.

Results and Discussion

The MFA/MCN copolymers, when γ -irradiated *in vacuo*, predominantly degrade, as shown in Table III. The MCN homopolymer exhibits a large (3.3) value of

Table I. Molecular weights and compositions of fluorine-containing vinyl polymers and copolymers

| Polymer or copolymer | Mole percent F-containing monomer | T_g (°C) | $\bar{M}_n \times 10^{-5}$ (MOSM) ^a | $\bar{M}_n \times 10^{-5}$ (GPC) ^b | $\bar{M}_w \times 10^{-5}$ (GPC) | \bar{M}_w/\bar{M}_n (GPC) |
|----------------------|-----------------------------------|------------------|--|---|----------------------------------|-----------------------------|
| PMFA | 100 | 131 ^c | 0.54 | 0.88 | 4.5 | 5.1 |
| P(MFA-co-MCN) | —A | 49 | 124 ^c | 3.8 | 3.6 | 7.8 |
| | —B | 20 | — | 6.5 | 2.9 | 8.3 |
| | —C | 16 | — | 3.4 | 3.5 | 8.3 |
| PMCN | — | 120 | 2.1 | 0.93 | 3.4 | 3.4 |
| P(TFEM-co-MCN) | —A | 30 | 0.97 | 0.46 | 1.1 | 2.5 |
| | —B | 69 | 86 ^c | 2.0 | 2.1 | 4.4 |
| PTFEM | — | 69 ^c | 14.9 | 6.8 | 9.25 | 1.35 |
| P(TFMAN-co-MCN) | —A | 4 | 1.13 | 1.0 | 8.0 | 8.0 |
| | —B | 12 | 0.77 | 6.8 | 16.8 | 2.5 |
| P(TFMAN-co-MMA) | —A | 9 | 7.1 | 7.2 | 15.9 | 2.2 |
| | —B | 32 | 98 ^c | 1.5 | 3.1 | 2.0 |
| P(TFMMA-co-MMA) | —A | 5 | 1.3 | 1.6 | 5.2 | 3.2 |
| | —B | 11 | 1.8 | 1.3 | 3.7 | 2.8 |
| PMMA | — | 105 | 1.5 | 1.6 | 4.1 | 2.5 |

^a MOSM is membrane osmometry.

^b GPC is gel permeation chromatography.

^c Measured by DSC using a du Pont Model 990 Thermal analyzer by Honeywell CMSC under contract DAAB07078-C-2975.

Table II. Summary of the experimental conditions and results in the synthesis of MFA, TFEM, TFMAN, and TFMMA copolymers

| Monomer | | Initiator K ₂ S ₂ O ₈ or AIBN ^d (g) | Surfactant SLS ^c (g) | Temp. (°C) | Time (hr) | Yield (%) | η (dl/g) | Polymer (m ₁ /m ₂) |
|--------------------|--------------------|---|------------------------------------|------------|-----------|-----------|-------------------|--|
| M ₁ (g) | M ₂ (g) | | | | | | | |
| MFA (10) | MCN (30) | 0.05 | 0.4 | 50 | 24 | 98 | 5.8 ^a | 16/84 |
| MFA (17) | MCN (23) | 0.06 | 0.4 | 50 | 28 | 50 | 3.0 ^a | 20/80 |
| MFA (27) | MCN (13) | 0.06 | 0.4 | 50 | 26 | 89 | 6.0 ^a | 57/43 |
| TFEM (1) | MCN (9) | 0.04 | 0.3 | 60 | 48 | 90 | — | 15/85 |
| TFEM (5) | MCN (5) | 0.04 | 0.3 | 60 | 48 | 82 | 0.78 ^b | 30/70 |
| TFEM (8) | MCN (2) | 0.03 | 0.3 | 60 | 42 | 81 | 1.62 ^b | 69/31 |
| TFMAN (1) | MMA (9) | 0.02 ^d | — | 60 | 24 | 90 | 2.91 ^b | 9/91 |
| TFMAN (5) | MMA (5) | 0.02 ^d | — | 65 | 48 | 80 | 0.98 ^b | 32/68 |
| TFMAN (1) | MCN (9) | 0.02 ^d | — | 80 | 504 | 90 | 2.6 ^b | 4/96 |
| TFMAN (5) | MCN (5) | 0.02 ^d | — | 80 | 504 | 50 | 2.0 ^b | 12/88 |
| TFMMA (0.9) | MMA (8.1) | 0.02 ^d | — | 65 | 48 | 92 | 0.86 ^b | 5/95 |
| TFMMA (1.9) | MMA (6) | 0.02 ^d | — | — | — | 89 | 0.98 ^b | 11/89 |

^a Measured in acetonitrile at 30°.

^b Measured in acetone at 30°.

^c SLS = sodium lauryl sulfate.

^d These reactions employed AIBN as the initiator.

Table III. Radiation degradation susceptibilities of fluorine-containing homo- and copolymers^a

| Polymer or copolymer | Mole percent F-containing monomer | G _s - G _x (MOSM) | G _s - G _x (GPC) | G _s (MOSM) | G _x (GPC) |
|----------------------|-----------------------------------|--|---------------------------------------|-----------------------|----------------------|
| PMFA ^b | 100 | -1.1 | 0.53 | 0-0.05 | 1.0 |
| P(MFA-co-MCN) | —A | 49 | 1.9; 1.8 | 1.9 | 0.04 |
| | —B | 20 | 2.0 | 2.0 | 0 |
| | —C | 16 | 2.1; 2.3 | 2.3 | 0 |
| PMCN | 0 | 0 | 3.3 | 3.3 | 0 |
| P(TFEM-co-MCN) | —A | 30 | 3.0 | 4.7 | 0 |
| | —B | 69 | 2.2 | 1.6; 1.5 | 2.2 |
| PTFEM ^b | 100 | 2.3 | 3.7 | 2.3 | 0 |
| P(TFMAN-co-MCN) | —A | 4 | 2.8 | 2.6; 2.5 | 2.8 |
| | —B | 12 | 3.3 | 3.6 | 3.3 |
| P(TFMAN-co-MMA) | —A | 9 | 3.0 | 2.6; 2.3 | 3.0 |
| | —B | 32 | 3.1 | 2.3 | 3.1 |
| P(TFMMA-co-MMA) | —A | 5 | 1.8 | 1.8 | 1.8 |
| | —B | 11 | 2.4 | 2.0 | 2.4 |
| PMMA | 0 | 1.3 | 1.4 | 1.3 | 0 |

^a See Table I for compositions and initial molecular weights of these polymers.

^b See Ref. (1).

G_s and G_x is zero, whereas the MFA homopolymer is a negative resist (G_s - G_x = -1.1). As one increases the MFA content of MFA/MCN copolymers from 16 to 20 to 49 mole percent (m/o), the values of G_s fall from 2.3 to 2.0 to 1.9, respectively. It is remarkable that the G_x value is zero for both the 16 and 20 MFA m/o copolymers and that of the 49% copolymer is almost zero (i.e., 0.04) when the G_x value for the MFA homopolymer is about +1. Apparently, the cross-linking is a second-order process which is largely "diluted out" in the copolymer samples. These results are graphically displayed in Fig. 1. As we recently found for other copolymers, G_s is approximately linearly related to the M₁/M₂ composition and G_x varies as a power dependence. This was previously shown for several copolymer systems including: methyl α-chloroacrylate/methacrylonitrile (4), methyl α-fluoroacrylate/methyl methacrylate (6), α-chloroacrylonitrile/methyl methacrylate (16), and vinylidene chloride/methyl methacrylate (16). The G_x experimental values all fall below those predicted by a straight line drawn between the homopolymer values.

The homopolymer of 2,2,2-trifluoroethyl methacrylate, TFEM, and its methyl methacrylate, MMA, copolymers were shown to be positive resists. The homopolymer exhibits G_s = 2.3 and G_x = 0. Similarly, TFEM/MCN copolymers degrade efficiently over the entire M₁/M₂ composition range and no evidence for cross-linking was found (e.g., G_x = 0, see Table III). Since G_x = 0 for both the homopolymers of TFEM and MCN, this was expected for the copolymers. As the MCN content increases, G_s increases.

All these copolymers have a greater propensity toward scission than MMA. The MCN component dominates because PMCN has the larger homopolymer G_s value.

The goal of examining the effect of α-trifluoromethyl substitution was achieved by (i) preparing α-trifluoromethylacrylonitrile and methyl α-trifluoromethylacrylate, (ii) copolymerizing the former with MMA and MCN, and (iii) copolymerizing the latter with MMA. Radical initiated homopolymerizations of these new monomers were sluggish and their homopolymers were not examined. Since the C-F bond is stronger than the C-H bond and F is much more electronegative than H, the effect of replacing -CH₃ by -CF₃ on chain scission was of interest. As shown in Table III, the incorporation of 9 or 32 m/o of TFMAN into TFMAN/MMA copolymers causes a large increase in G_s (e.g., to 3.1 in the latter case vs. G_s = 1.3 for PMMA). No tendency to cross-link was found for TFMAN/MMA, TFMAN/MCN, or TFMMA/MMA copolymers (e.g., G_x = 0). The TFMAN/MCN copolymers degrade with approximately the same propensity as PMCN. Furthermore, when only 11% TFMMA is incorporated into the TFMMA/MMA copolymer, G_s increases to 2.4 from its value of 1.3 for PMMA. Taken together, these results show that an α-CF₃ group at a quaternary position leads to ready radiation degradation.

These systems were next studied as electron beam resists. Lithographic images can be developed with poly(methacrylonitrile), PMCN, but toxic nitrile developers need to be used. However, PMCN does have a high glass transition temperature (T_g = 120°) and good plasma etch resistance. Thus, its copolymers, which are soluble in a variety of solvents, are logical resist candidates. Poly(2,2,2-trifluoroethyl methacrylate), PTFEM, exhibits an electron beam sensitivity of 2-3 × 10⁻⁵ C/cm² which is 1.6× more sensitive than PMCN, but PTFEM has a lower T_g (69°) and a poorer CF₄/O₂ etch resistance than PMCN (i.e., 230 Å/min for PTFEM vs. 36 Å/min for PMCN). The TFEM/MCN

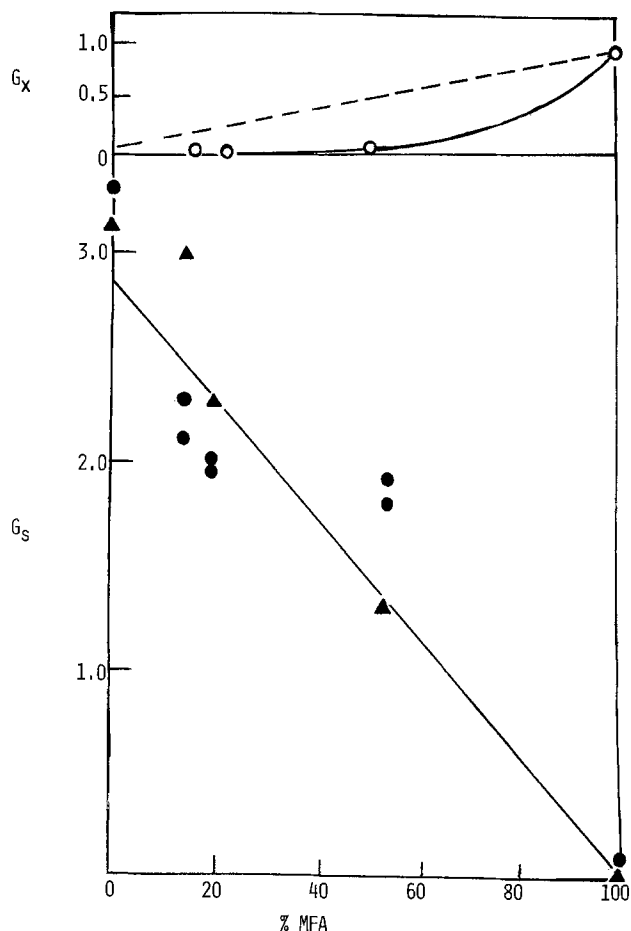


Fig. 1. G_s and G_x vs. m/o MFA for irradiated MFA/MCN copolymers. The solid line (lower) is a least squares fit of all G_s data. The triangles are GPC data, the closed circles MOSM data, and the open circles GPC data. The upper solid line is a power curve fit of the G_x data, $G_x = 9.44 \times 10^{-10} [\text{MFA}]^{4.5}$. The dash line is a straight line connecting the homopolymer G_x values.

copolymer system should blend the better characteristics of both homopolymers. Indeed, the 69/31 TFEM/MCN copolymer ($G_s = 2.2$, $G_x = 0$) was found to have an intermediate glass transition temperature of 86° and an intermediate CF_4/O_2 etch rate of 93 Å/min while maintaining a sensitivity 5-6 times higher than that of PMMA (i.e., $Q = 3-4 \times 10^{-5} \text{ C/cm}^2$ for this copolymer vs. $Q = 20 \times 10^{-5}$ for PMMA, $5-7 \times 10^{-5} \text{ C/cm}^2$ for PMCN, and $2-3 \times 10^{-5} \text{ C/cm}^2$ for PTFEM).

The observed E-beam resist sensitivity of the 70/30 TFEM/MMA copolymer ($2-3 \times 10^{-5} \text{ C/cm}^2$) is very close to that of the PTFEM homopolymer value. Since this copolymer, like the 69/31 TFEM/MCN copolymer, contains about 70% TFEM, these sensitivities are not surprising. Approximately half of the increase in sensitivities vs. PMMA can be accounted for on the basis of the larger copolymer G_s values. The remainder must be attributed to dissolution rate effects caused by the buildup of deesterification radiation products (e.g., CO , CO_2 , CH_3CF_3 , etc.) in the polymer.

The MFA/MCN copolymers behave as positive resists. When the MFA concentration is $\geq 50\%$, however, the resist dose working range gets prohibitively small and swelling of the resist becomes unacceptably poor, as is observed for the negative behaving PFMA homopolymer. At 20/80 MFA/MCN, however, the copolymer performs well and swelling is minimal. The sensitivity of the 20/80 MFA/MCN copolymer is very close to that of PMCN, and its T_g is higher. The etch rates for all the MFA/MCN copolymers are low as expected, based on the low etch rates of PMFA and PMCN (see Table IV).

Table IV. Plasma etching rates and electron beam sensitivities of fluorine-containing homo- and copolymers

| Polymer or copolymer | F-containing monomer (m/o) | Plasma etch rate ^a (Å/min) | Sensitivity (at 20 keV) $Q \times 10^5$ C/cm ² |
|-----------------------------|----------------------------|---------------------------------------|---|
| PFMA | 100 | 40 | $>> 1^b$ |
| P(MFA-co-MCN)—A | 49 | 46 | 6 |
| P(MFA-co-MCN)—B | 20 | 30 | — |
| P(MFA-co-MCN)—C | 16 | 38 | — |
| PMCN | 0 | 36 | 5-7 |
| P(TFEM-co-MCN)—B | 69 | 93 | 3-4 |
| PTFEM | 100 | 230 | 2-3 |
| P(TFEM-co-MMA) | 70 | — | 2-3 |
| P(TFMAN-co-MCN)—B | 12 | 33 | 5 |
| P(TFMAN-co-MMA)—B | 32 | 79 | 3 |
| P(TFMMA-co-MMA)—B | 11 | 100 | 15 |
| PMMA | 0 | 100 | 20 |
| P(TFEM-co-MMA) ^d | | | |

^a Using CF_4/O_2 plasmas (see Experimental section).

^b A negative resist at 10 keV.

^c Resist swells badly (see text).

^d This polymer exhibits a T_g of 75° which is between that of PMMA (105°) and PTFEM (69°).

The effect on lithographic properties of incorporating an α -trifluoromethyl group can be illustrated by the 32/68 TFMAN/MMA copolymer (Table IV). Its electron beam sensitivity was $3 \times 10^{-5} \text{ C/cm}^2$ which is about the same as that exhibited by P(TFEM) and 6-7 times that of PMMA. This is consistent with its high observed G_s value of 3.1 and undetectable (i.e., $G_x = 0$) cross-linking propensity. Another benefit is this copolymer's relatively high T_g value (98°C). Finally, the incorporation of 32 m/o TFMAN reduced the CF_4/O_2 plasma etch rate from 100 Å/min for PMMA to 79 Å/min. Clearly, the incorporation of $-\text{CF}_3$ at the alpha position leads to improved resists.

The same beneficial properties were observed for the 12/88 TFMAN/MCN copolymer. Its etch rate (33 Å/min) was slightly lower than that of PMCN (36 Å/min) and its sensitivity ($5 \times 10^{-5} \text{ C/cm}^2$) was slightly better than that of PMCN (see Table IV). Even the incorporation of only 11 m/o of TFMMA into an MMA copolymer increased the electron beam sensitivity from 20×10^{-5} to $15 \times 10^{-5} \text{ C/cm}^2$. This correlates with this copolymer's high G_s value of 2.4 and $G_x = 0$. Thus, the α - CF_3 group appears to be a very promising structural feature to incorporate into electron beam lithographic resists. Synthetic work to prepare copolymers with higher TFMAN and TFMMA contents are now underway.

Acknowledgments

This work is part of a program to develop high sensitivity polymer resists for integrated circuits supported at the University of Alabama by Army Research Office Grant No. DAAG-29-79-C-0128.

Manuscript submitted Oct. 21, 1980; revised manuscript received March 2, 1981. This was Paper 322 presented at the Hollywood, Florida, Meeting of the Society, Oct. 5-10, 1980.

Any discussion of this paper will appear in a Discussion Section to be published in the June 1982 JOURNAL. All discussions for the June 1982 Discussion Section should be submitted by Feb. 1, 1982.

Publication costs of this article were assisted by the University of Alabama.

REFERENCES

- L. F. Thompson and R. E. Kerwin, *Ann. Rev. Mater. Sci.*, **6**, 267 (1976).
- E. Spiller and R. Feder, *Top. Appl. Phys.*, **22**, 35 (1978).
- M. Dole, "The Radiation Chemistry of Macromolecules," Vol. I, Academic Press, New York (1973).
- C. Y. Chen, C. U. Pittman, Jr., and J. N. Helbert, *J. Polym. Sci. Polym. Chem. Ed.*, **18**, 169 (1980).
- C. U. Pittman, Jr., C. Y. Chen, M. Ueda, and J. N. Helbert, *Polymer Preprints*, **20**, 602 (1979).
- C. U. Pittman, Jr., C. Y. Chen, M. Ueda, J. N. Hel-

- bert, and J. H. Kwiatkowski, *J. Polym. Sci. Polym. Chem. Ed.*, In press (1980).
7. M. Kakuchi, S. Sugawara, K. Murase, and K. Matsuyama, *This Journal*, **124**, 1648 (1977).
 8. C. U. Pittman, Jr., M. Iqbal, C. Y. Chen, and J. N. Helbert, *J. Polym. Sci. Polym. Chem. Ed.*, **16**, 2721 (1978).
 9. C. Y. Chen, M. Iqbal, C. U. Pittman, Jr., and J. N. Helbert, *Makromol. Chem.*, **179**, 2109 (1978).
 10. J. N. Helbert, E. H. Poindexter, G. A. Stahl, C. Y. Chen, and C. U. Pittman, Jr., *J. Polym. Sci. Polym. Chem. Ed.*, **17**, 49 (1979).
 11. J. N. Helbert, C. Y. Chen, C. U. Pittman, Jr., and G. L. Hagnauer, *Macromolecules*, **11**, 1104 (1978).
 12. J. N. Helbert, C. F. Cook, Jr., C. Y. Chen, and C. U. Pittman, Jr., *This Journal*, **126**, 694 (1979).
 13. J. H. Lai, J. N. Helbert, C. F. Cook, Jr., C. U. Pittman, Jr., *J. Vac. Sci. Technol.*, **16**, 1992 (1979).
 14. C. U. Pittman, Jr., M. Ueda, K. Iri, and Y. Imai, *Macromolecules*, **13**, 1031 (1980).
 15. C. U. Pittman, Jr., M. Ueda, and E. Wallace, Unpublished studies.
 16. J. N. Helbert, E. H. Poindexter, C. U. Pittman, Jr., and C. Y. Chen, *Polym. Eng. Sci.*, **9**, 630 (1980).

Nonstoichiometry in SrTiO₃

N.-H. Chan,* R. K. Sharma,* and D. M. Smyth*

Materials Research Center, Lehigh University, Bethlehem, Pennsylvania 18015

ABSTRACT

The defect chemistry of polycrystalline SrTiO₃ has been studied by means of the equilibrium electrical conductivity as a function of temperature, oxygen activity, Sr/Ti ratio, and impurity additions. Reduction, excess TiO₂, and acceptor impurities all contribute to the oxygen vacancy content and their effects are therefore highly interdependent. The effect of added donor-impurities, e.g., 500 ppm Nb, is highly dependent on the presence and amount of excess TiO₂.

While the equilibrium defect chemistry of BaTiO₃ has been studied in considerable detail as a result of its application as a ferroelectric and piezoelectric material (1-9), SrTiO₃ has received comparatively little attention. Walters and Grace measured the electrical conductivity in the temperature range 900°-1300°C in H₂O-H₂ mixtures (10), and Yamada and Miller used the Hall effect to measure the electron concentration at room temperature for samples quenched from 1200°-1400°C after equilibration with oxygen pressures in the range 10⁻¹² < P_{O₂} < 10⁻⁷ atm (11). Both of these studies on single crystalline SrTiO₃ are in good agreement with a model in which the major defects are doubly ionized oxygen vacancies and electrons created by loss of oxygen from the crystals at low P_{O₂}. Yamada and Miller also found good agreement between measured density changes and those calculated from the doubly ionized vacancy model. There was no indication of the precise Sr/Ti ratio of the crystals used in either of these studies. The existing phase information for SrTiO₃ gives no indication of any solubility for excess TiO₂ (12), while the phase diagram of Rase and Roy for the BaO-TiO₂ system implies a single phase region from the ideal composition of BaTiO₃ up to about 51 mole percent (m/o) TiO₂ at 1400°C (13) [a value which we now feel to be much too high (14)]. Since excess TiO₂ can be accommodated by the formation of relatively favorable point defects such as strontium vacancies and oxygen vacancies, V_{Sr}^{''} and V_O^{••}, some solubility is to be expected. The incorporation of excess SrO by a simple point defect model, on the other hand, requires the formation of either interstitial strontium and oxygen, Sr_I^{••} and O_I^{••}, or titanium and oxygen vacancies, V_{Ti}^{'''} and V_O^{••}. The difficulty of fitting large ions into interstitial sites in the close-packed perovskite structure, and the high formal charge on the titanium vacancy, makes simple solution of excess SrO in significant amounts quite unlikely. It is known, however, that excess SrO can be accommodated in layers separated by n perovskite layers in a homologous series SrO·

nSrTiO₃ (15, 16). This may account for the region of apparent excess SrO shown in the phase diagram of Cocco and Massazza [included in Ref. (12)].

SrTiO₃ which has been equilibrated with air is a light colored, insulating material at room temperature. By analogy with BaTiO₃, one would expect this to represent an oxygen-excess composition, with p-type conduction, since n-type material is dark colored and semiconducting. The equilibrium conductivity has not previously been investigated for the region of high P_{O₂}, and a conductivity minimum reflecting a transition from n-type conduction at low P_{O₂} to p-type conduction at high P_{O₂} has not been reported. This paper presents equilibrium conductivity measurements made on sintered, polycrystalline samples over the range 10⁻²⁰ < P_{O₂} < 1 atm, at temperatures from 750° to 1000°C, and includes results obtained from donor-doped and acceptor-doped samples and from samples having different Sr/Ti ratios.

Experimental

The SrTiO₃ was prepared by a modification of a technique developed by Pechini (17). Several liters of titanium stock solution were prepared by combining batches made in the following way: 200 ml of tetraiso-propyl orthotitanate, obtained from E. I. du Pont de Nemours as Tyzor "TPT," was added with stirring to 2 liters of Fisher Certified ethylene glycol; 350g of Fisher Certified ACS Anhydrous citric acid was added and the mixture was stirred until complete solution was achieved and then heated until the strong odor of isopropyl alcohol disappeared. Presumably during this procedure the isopropoxy groups attached to the titanium are replaced by the multifunctional ethylene glycol, which can thermally polymerize with the multifunctional citric acid by an esterification reaction. After the combined batches had been allowed to homogenize for 2 weeks in a polyethylene container, weighed samples were thermally polymerized and ignited to TiO₂ to determine the Ti content of the solution, which was 0.054504g TiO₂/g solution. Donor- and acceptor-dopant solutions were prepared by solution of niobium oxalate, obtained as a 10% solution from Kawecki-Berylco, and Eastman practical grade tri-

* Electrochemical Society Active Member.

Key words: defect chemistry, ternary oxides, perovskites, conductivity, impurity effects.

iso-propyl aluminate, respectively, in ethylene glycol. Both solutions were assayed by the ignition of weighed portions to the corresponding oxide.

The source of Sr was Johnson-Matthey Specpure SrCO₃, reported to contain 5 ppm Ba, 2 ppm Fe, 1 ppm Ag, and <1 ppm Ca, Cu, and Mg, all on a weight basis. Approximately 7g samples of SrTiO₃ were prepared by dissolution of weighed amounts of the SrCO₃, dried by ignition in CO₂, in weighed portions of the Ti stock solution, containing weighed amounts of dopant solution where appropriate. Dissolution of the carbonate, by reaction with the citric acid content, was achieved by heating over a period of several hours. The viscosity was kept low by additions of water until solution was complete. The mixture was then allowed to polymerize thermally to a glassy solid, without phase separation, to transform the homogeneity of the liquid solution to the solid glass which was then calcined at 900°C to yield a fine SrTiO₃ powder. All chemical preparations were performed in clear fused SiO₂ or Pt, and stock solutions were stored in polyethylene or polypropylene containers.

The sample compositions are expressed in terms of Sr/Ti ratios where it should be understood that the Ti includes any added Al or Nb content, since these dopants are assumed to occupy only Ti sites, based on their similarity in size. These ratios are thus actually site occupation ratios. Accordingly, for each gram atom of dopant added, one mol of TiO₂ was left out, i.e., Al₂O₃ and Nb₂O₅ were substituted for 2TiO₂. The dopant and impurity contents are expressed in ppm atomic based on Ti sites, e.g., (No. of added Al atoms × 10⁶)/(No. of Ti and added Al atoms).

Samples of 0.6g of the powder, with 7% by weight water to improve pressability, were pressed into rectangular bars at 100,000 psi. All faces and edges were scraped with the edge of a silica slide to remove contamination from the steel die. The samples were typically sintered at 1420°C for 16 hr in a fore-pump vacuum and furnace-cooled. Final dimensions were about 1.5 × 5.5 × 13 mm. Voltage leads of 10 mil Pt wire were sintered into the samples by insertion through two holes drilled through the largest face prior to sintering. Unfluxed Pt paste, Engelhard 6926, was fired onto the ends to serve as current leads. The conductivity was measured by four-point d-c technique, using both polarities with applied currents in the range 10⁻⁷-10⁻²A to maintain a voltage drop of about 0.1V.

Figure 1 shows an SEM view of the microstructure of a fracture surface of a typical sample, demonstrating the large grain size and low porosity. While most fracture is transgranular and does not show the grain size clearly, there are occasional small areas such as that shown in Fig. 1 where intergranular fracture occurs.

The major impurity in titanates prepared by this technique is silicon. Extensive investigation of the starting materials and the process steps by emission spectroscopy indicate that the major sources are the tetra-iso-propyl orthotitanate and the container used during the calcination of the polymeric glass. When fused silica or conventional glazed porcelain crucibles were used for the latter step, silicon contents of 1800-2600 ppm have been observed. The TiO₂ residue obtained by ignition of the orthotitanate in a Pt crucible contains about 400 ppm Si. During the latter part of this study, all samples have been prepared in Pt crucibles and typical Si contents are in the 500-1000 ppm range. The Pt content is 30-40 ppm. Similar impurity levels have been found in a much more extensive study of BaTiO₃, during which similar samples have been studied and no effect of variable Si content on the equilibrium conductivity has been discerned. It is our opinion that the conductivity is not affected.

The Si contents observed in this work are similar to those reported in a number of studies of polycrystalline

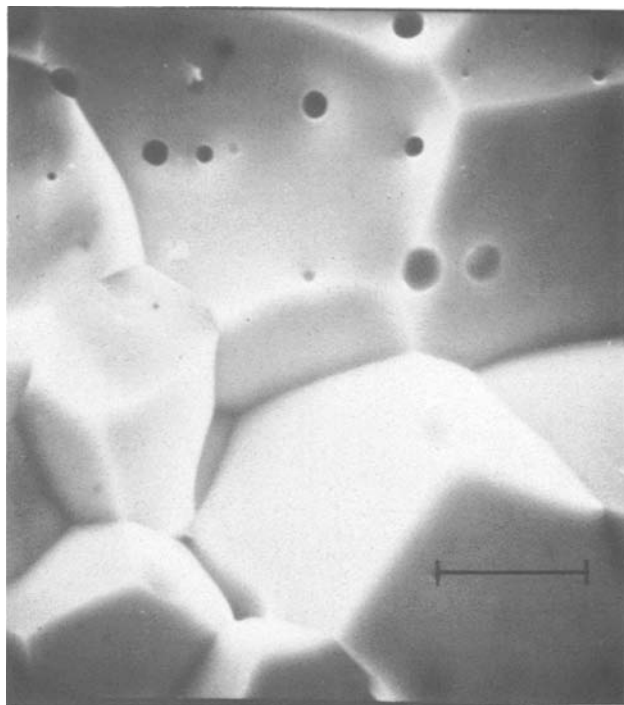


Fig. 1. Scanning electron micrograph of a fracture surface of undoped, polycrystalline SrTiO₃ with Sr/Ti = 1.0000. Scale mark = 5 μm.

BaTiO₃, prepared by a variety of ways. The potential chemical significance is distorted, however, by the common practice of reporting impurity contents in ppm or percent by weight, particularly in this case of a light element like Si in a heavy matrix like SrTiO₃ or BaTiO₃. The multiplying factor needed to transform a weight basis of Si to a formula unit basis is 6.53 for SrTiO₃ and 8.30 for BaTiO₃. Thus a level of 0.01% by weight, commonly reported for BaTiO₃, corresponds to 830 ppm based on atoms of Si per formula unit of BaTiO₃.

Additional impurities found by spark-source mass spectrographic analysis are listed in Table I. These results were obtained from Micro-Trace Analytical Services, Santa Barbara, California 93103, while the emission spectroscopy was done by the Burgess Analytical Laboratory, North Adams, Massachusetts 01247.

The regions of high and low P_{O2} were obtained by precisely metered mixtures of Ar-O₂ and CO-CO₂. For the intermediate pressure range, a CaO-stabilized ZrO₂ closed-end tube, with inner and outer platinized electrodes, was inserted into the sample area to serve as an electrochemical oxygen leak or pump. The inside of the ZrO₂ tube was exposed to air, and the resulting oxygen concentration cell was allowed to discharge through a variable resistance, or was operated as an electrochemical pump by means of an applied voltage, to obtain the desired P_{O2}. The resulting oxygen activity was determined by measurement of the emf of a separate closed-end tube of stabilized ZrO₂, platinized inside and outside only at the tip, and continuously flushed with oxygen, which was located adjacent to the conductivity samples.

The sample holder accommodates three samples. One end of each was connected to a common lead while the other leads passed through separate alumina tubes which were supported by a metal spacer well outside of the hot zone.

Results and Discussion

Typical experimental results are shown in Fig. 2. The similarity to results presented previously for BaTiO₃ (3, 4, 5, 9) is quite striking. Results obtained in this laboratory for both compounds are compared

Table I. Impurity content of sintered SrTiO₃ by spark-source mass spectrographic analysis (Micro-Trace Analytical Service). * Includes only those impurities present in amounts >0.1 ppm by weight.

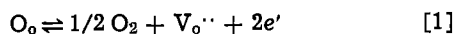
| | Atoms of impurity per 10 ⁶ formula units of SrTiO ₃ | ppm by weight |
|------------|---|---------------|
| Carbon | 33 | 0.4 |
| Nitrogen | 9 | 0.1 |
| Fluorine | 4 | 0.1 |
| Magnesium | 62 | 1.7 |
| Aluminum | 8 | 0.2 |
| Phosphorus | 22 | 0.7 |
| Chlorine | 63 | 2.4 |
| Calcium | 42 | 1.8 |
| Chromium | 26 | 1.5 |
| Iron | 87 | 5.3 |
| Nickel | 11 | 0.7 |
| Cobalt | 21 | 1.3 |
| Gallium | 14 | 1.1 |
| Germanium | 22 | 1.7 |
| Arsenic | 33 | 2.7 |
| Yttrium | 11 | 1.1 |
| Antimony | 20 | 2.7 |

* (Silicon, sodium, sulfur, copper, zinc, selenium, and bromine could not be determined because of interference. Sodium, copper, and zinc were not detected by emission spectroscopy, which indicates levels of <10 ppm by weight. Silicon is discussed in the text).

directly in Fig. 3. The coincidence of results in the oxygen-deficient, n-type region, where the conductivity increases with decreasing P_{O₂}, suggests that the properties in this region are almost wholly determined by the Ti-O sublattice. The results differ somewhat more in the p-type region, particularly in the case of the temperature dependence near P_{O₂} = 1 atm. Some experimental results from Walters and Grace for single crystalline SrTiO₃ are also shown (10). Their data cover a much lower range of P_{O₂} and barely overlap with ours, but appear to be quite comparable. Comparison of conductivity data obtained for polycrystalline and single crystalline BaTiO₃ has shown similar agreement (9), which indicates that the conductivity is determined by bulk properties in these large grained, polycrystalline samples.

The experimental results can be correlated by means of a model in which doubly ionized oxygen vacancies, V_O^{••}, are the key defect and for which three major sources are postulated. The defect notation is that developed by Kröger and Vink (18)

Reduction or loss of oxygen



Cation nonstoichiometry in the sense of excess TiO₂

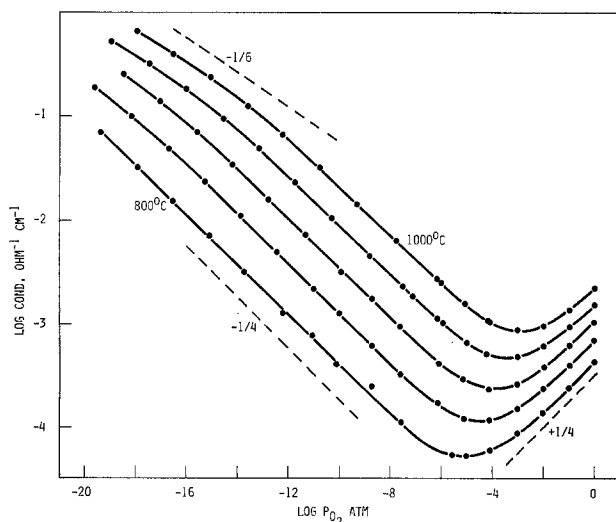


Fig. 2. Equilibrium conductivity profiles of polycrystalline SrTiO₃, undoped, Sr/Ti = 1.0000. Temperatures at 50°C intervals. Dashed lines indicate ideal log-log slopes.

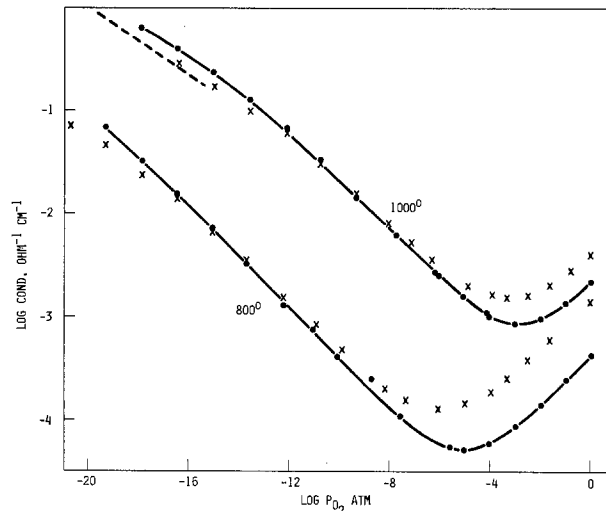
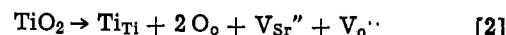


Fig. 3. Equilibrium conductivity profiles of polycrystalline SrTiO₃ ●, and BaTiO₃ × (5), at 1000° and 800°C. Both materials undoped and Sr/Ti = Ba/Ti = 1.0000. ---, SrTiO₃ single crystal at 1000°C (10).



The incorporation of acceptor-type impurities such as substitution of Al₂O₃ for 2TiO₂



The reduction reaction is indicated as an equilibrium reaction because it is reversible in reasonable time spans at both the sintering temperature and at the temperatures used for conductivity measurements. The lack of saturation of electrical properties with additions of up to 1080 ppm Al indicates that the solubility limit has not been exceeded and the acceptor impurities are thus assumed to be completely and irreversibly incorporated during the sintering step. The irreversibility is supported by indications of extremely low cation diffusion on the Ti-sublattice of the perovskite structure, even at the sintering temperature (19). Excess TiO₂ will dissolve up to its solubility limit during the sintering process, and it will be assumed that the excess TiO₂ content is frozen at 1000°C and below, where the conductivity measurements were made. At the time of final equilibration of the sample with excess TiO₂, we can assume local equilibrium. From the mass-action expression for this process

$$[\text{V}_{\text{Sr}}''] [\text{V}_o^{\bullet\bullet}] = K_2 a_{\text{TiO}_2} \quad [4]$$

where a_{TiO_2} is the activity of TiO₂ in the SrTiO₃, we can see that the solubility limit for TiO₂ will depend on the number of V_O^{••} present due to acceptor impurities and the reduction reaction. For cases where sufficient excess TiO₂ is available, therefore, its solubility will be a function of the oxygen partial pressure, the impurity content, and the final equilibration temperature.

For undoped and acceptor-doped SrTiO₃, the complete expression for the condition of charge neutrality is

$$2[\text{V}_o^{\bullet\bullet}] + p = 2[\text{V}_{\text{Sr}}''] + [\text{A}'] + n \quad [5]$$

where [A'] represents the net acceptor content, both accidental and added, expressed as the equivalent concentration of single-level acceptor centers, $n \equiv [e']$, and $p \equiv [h\cdot]$. The conductivity plots, e.g., Fig. 2, can be divided into three characteristic regions depending on whether the SrTiO₃ has a stoichiometric deficiency or excess of oxygen, and depending on which terms in Eq. [5] are most important. The following analysis is very similar to that previously proposed for BaTiO₃ (5, 9, 20), and a schematic representation of the defect model is shown in Fig. 4.

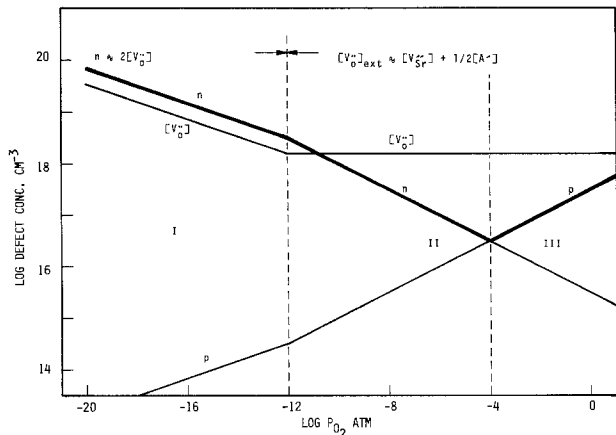


Fig. 4. Schematic representation of equilibrium defect model for undoped and acceptor-doped SrTiO₃. Defect concentrations calculated from conductivities at 1000°C with $\mu_n = 0.2 \text{ cm}^2/\text{V}\cdot\text{sec}$ and $\mu_p = 0.1 \text{ cm}^2/\text{V}\cdot\text{sec}$. Regions I, II, and III defined in text.

Region I.—In the region of lowest P_{O_2} , the material is oxygen deficient and the reduction reaction, Eq. [1], is the major source of defects and the approximate condition of charge neutrality is thus

$$2[V_o''] \approx n \quad [6]$$

The mass-action expression for the reduction reaction is

$$[V_o''] n^2 = K_1 P_{O_2}^{-1/2} \quad [7]$$

Combination of Eq. [6] and [7] leads to

$$n \approx (2K_1)^{1/3} P_{O_2}^{-1/6} \quad [8]$$

which agrees with the P_{O_2} dependence of conductivity found by Walters and Grace (10) and of the electron concentration found by Yamada and Miller (11). The agreement between the P_{O_2} dependence of the conductivity and the electron concentration found by these two groups indicates that the electron mobility is not composition dependent under these conditions. Our own results barely reach into Region I at the lowest P_{O_2} and highest temperature and exhibit this P_{O_2} dependence in a very limited region.

Region II.—This region is bounded on the low P_{O_2} side by Region I and on the high P_{O_2} side by the conductivity minima. The pressure dependence of the conductivity is approximately $P_{O_2}^{-1/4}$ which indicates oxygen-deficient, n-type behavior. This P_{O_2} dependence for the electron concentration can be obtained from the mass-action expression for the reduction reaction, Eq. [7], if $[V_o'']$ is independent of P_{O_2} , i.e., if there is an extrinsic source of V_o'' , such that the reduction reaction is no longer the major source of V_o'' . This could be due to either excess TiO_2 or to acceptor impurities, Eq. [2] and [3]. It is proposed that even in undoped material with $Sr/Ti = 1.000$, there is sufficient accidental net excess of acceptor impurities to control $[V_o'']$ in this region (5). Only in the region of lowest P_{O_2} and highest temperatures does the reduction reaction, Eq. [1], become the major source of V_o'' . The preponderance of acceptor impurities is related to the relative natural abundances of such impurity elements as compared to donor impurity elements and is supported by the analytical results reported in Table I. The approximate condition of charge neutrality is then

$$[V_o''] \approx [V_{sr}'''] + 1/2 [A'] \quad [9]$$

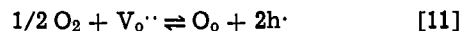
where $[V_{sr}''']$ represents the contribution to $[V_o'']$ made by excess TiO_2 , while $1/2 [A']$ is the contribution made by the net excess acceptor content. The sum of these two contributions will be referred to as the ex-

trinsic V_o'' content. Combination of Eq. [7] and [9] gives

$$n \approx \left\{ \frac{K_1}{[V_{sr}'''] + 1/2 [A']} \right\}^{1/2} P_{O_2}^{-1/4} \quad [10]$$

This P_{O_2} dependence is characteristic of a wide region of our experimental results.

Region III.—This is the oxygen excess, p-type region lying between the conductivity minima and $P_{O_2} = 1$ atm. As suggested previously (5), it is proposed that the stoichiometric excess of oxygen is accommodated by the extrinsic V_o'' present because of a net excess of acceptor impurities or an excess of TiO_2



Thus there is no crystallographic excess of oxygen and no need to propose such unfavorable defects as O_i'' or V_{Ti}''' . This is in accord with the very modest enthalpy of oxygen addition as indicated by the small temperature dependence of conductivity in this region. The approximate condition of charge neutrality is the same as in Region II, Eq. [9], as long as a negligible fraction of the extrinsic V_o'' is consumed by the oxygen excess. Combination of the mass-action expression for Eq. [11]

$$\frac{p^2}{[V_o'']} = K_{11} P_{O_2}^{1/2} \quad [12]$$

with Eq. [9] gives

$$p \approx K_{11}^{1/2} \{ [V_{sr}'''] + 1/2 [A'] \}^{1/2} P_{O_2}^{1/4} \quad [13]$$

This is a good representation of the P_{O_2} dependence of conductivity observed in this region.

Figure 5 shows an Arrhenius plot of the conductivity at $P_{O_2} = 1$ atm for several samples. The plots are not linear, tending to be concave downward. The slopes indicate activation enthalpies between 0.7 and 1.2 eV,

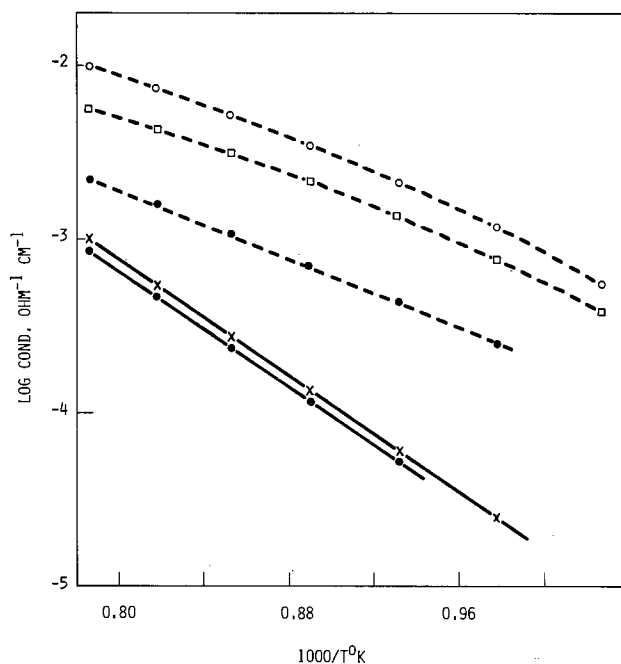


Fig. 5. Arrhenius plots of equilibrium conductivity data for polycrystalline SrTiO₃. Dashed lines, in equilibrium with 1 atm O₂. Solid lines, at the conductivity minima.

| | ppm added Al | Sr/Ti |
|---|--------------|--------|
| ● | None | 1.0000 |
| □ | None | 0.9950 |
| ○ | 1080 | 0.9950 |
| × | 1080 | 0.9950 |

with the most linear result, that for the undoped sample with Sr/Ti = 1.000, giving 0.98 eV. These are all considerably higher than the value of 0.4 eV found for the same region in BaTiO₃ (9).

The conductivity minima.—The conductivity minima correspond to the p-n transitions where the electron and hole contributions to the conductivity are equal

$$n\mu_n = p\mu_p \quad [14]$$

where μ_n and μ_p are the electron and hole mobilities. At the point of exact compensation, which is offset from the conductivity minimum by the mobility ratio, the only source of carriers is by ionization across the bandgap

$$nil \rightleftharpoons e' + h \cdot \quad [15]$$

$$np = K_{15} = K_{15}' e^{-E_g^\circ/kT} \quad [16]$$

where nil refers to the standard state with all electrons in the lowest available energy states, and E_g° is the bandgap at 0 K or the enthalpy of the ionization reaction, Eq. [15]. At the point of compensation

$$n = p = (K_{15}')^{1/2} e^{-E_g^\circ/2kT} \quad [17]$$

The temperature dependence of the minima is primarily determined by E_g° ; the small contribution of the temperature dependence of the mobility and density of state terms has been discussed elsewhere (9). Arrhenius plots of the minima are also shown in Fig. 5, and the slopes indicate $E_g^\circ = 3.30$ eV, very close to the values of 3.1 and 3.27 eV found for BaTiO₃ (4, 9) and in good agreement with the optically determined value of 3.2 eV for single crystalline SrTiO₃ (21, 22).

The effects of excess TiO₂ and acceptor impurities.—By combination of Eq. [10] and [13], the P_{O_2} at the minimum, $P_{O_2}(\text{min.})$, can be expressed as

$$\begin{aligned} P_{O_2}(\text{min.}) &= \left(\frac{\mu_n}{\mu_p}\right)^2 \frac{K_1}{K_{11}} \frac{1}{\{[V_{Sr}'] + 1/2 [A']\}^2} \\ &= \left(\frac{\mu_n}{\mu_p}\right)^2 \frac{K_1}{K_{11}} \frac{1}{[V_{O'}']^2_{\text{ext}}} \end{aligned} \quad [18]$$

Where $[V_{O'}']_{\text{ext}}$ is the extrinsic $V_{O'}'$ concentration. The shift of $P_{O_2}(\text{min.})$ with $[V_{O'}']_{\text{ext}}$ is independent of the mobilities

$$\frac{d \log P_{O_2}(\text{min.})}{d \log [V_{O'}']_{\text{ext}}} = -2 \quad [19]$$

Thus at a given temperature, the minimum moves to lower P_{O_2} by two orders of magnitude for each order of magnitude increase in $[V_{O'}']_{\text{ext}}$, and this shift serves as a measure of the relative extrinsic $V_{O'}'$ contents of various samples. This parameter is independent of the absolute values of the conductivity and thus of the sample geometry and density.

Figure 6 shows conductivity profiles at 1000°C for three samples of undoped SrTiO₃ prepared so as to have Sr/Ti ratios of 1.000, 0.999, and 0.995, which correspond to 50.000, 50.025, and 50.125 m/o TiO₂, respectively. The conductivity minima occur at lower P_{O_2} for Sr/Ti < 1, indicating an increase in extrinsic $V_{O'}'$ content with excess TiO₂, as expected from Eq. [2]. Since the positions of the P_{O_2} minima are similar for Sr/Ti = 0.999 and 0.995, it would appear that for the conditions under which these samples were sintered, the SrTiO₃ saturates with TiO₂ at less than 50.1 m/o.

Figure 7 shows conductivity profiles at 1000°C for some acceptor-doped samples, as well as for the undoped sample having Sr/Ti = 1.000. For a sample containing 281 ppm Al and Sr/Ti = 0.995 the minimum occurs at significantly lower P_{O_2} , while the addition of 1080 ppm Al moves the minimum to even lower P_{O_2} , representing the expected effect on the concentration of extrinsic $V_{O'}'$.

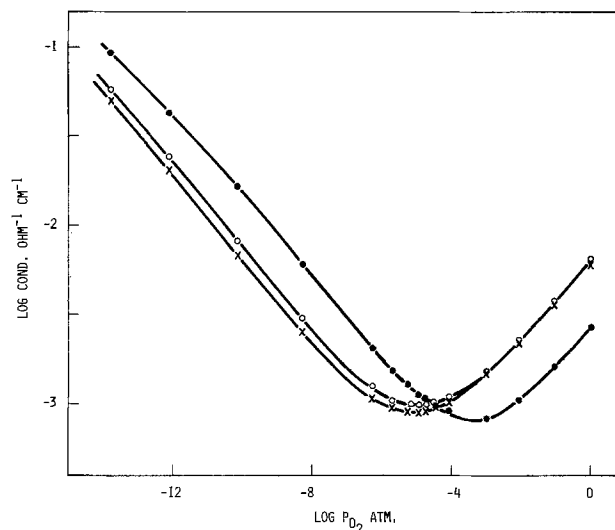


Fig. 6. Equilibrium conductivity profiles of undoped, polycrystalline SrTiO₃ at 1000°C. ● Sr/Ti = 1.0000, × Sr/Ti = 0.9990, ○ Sr/Ti = 0.9950.

Takahashi has reported large ionic contributions to the conductivity of perovskite-structure oxides containing large amounts of acceptor impurities (23). For SrTiO₃ with 10% of the Ti replaced by Al, for example, he reports ionic transport numbers between 0.6 and 0.9 in the temperature range 650°–1000°C. This material has a relatively P_{O_2} -independent conductivity at 800°C for $10^{-6} > P_{O_2} > 10^{-16}$ atm, presumably due to the P_{O_2} -independent concentration of extrinsic $V_{O'}'$. In our data, an ionic contribution would be most apparent at the conductivity minima. Figure 8 shows several conductivity minima compared with the ideal shape. The experimental curves have been placed such that they blend asymptotically into the ideal curve on either side of the minimum. At 1000°C, the undoped sample with Sr/Ti = 1.000 has an almost ideal minimum, while at 800°C it is somewhat raised and flattened. At the latter temperature, the minima become higher as the extrinsic $V_{O'}'$ content is enhanced by additions of TiO₂ and Al₂O₃. The shapes of the minima in these cases are in good agreement with an ideal minimum with an additive, P_{O_2} -independent contribution which could represent oxygen vacancy conduction.

Wernicke found a value of 1×10^{-4} cm²/sec for the effective diffusion constant of $V_{O'}'$ at 1000°C in single

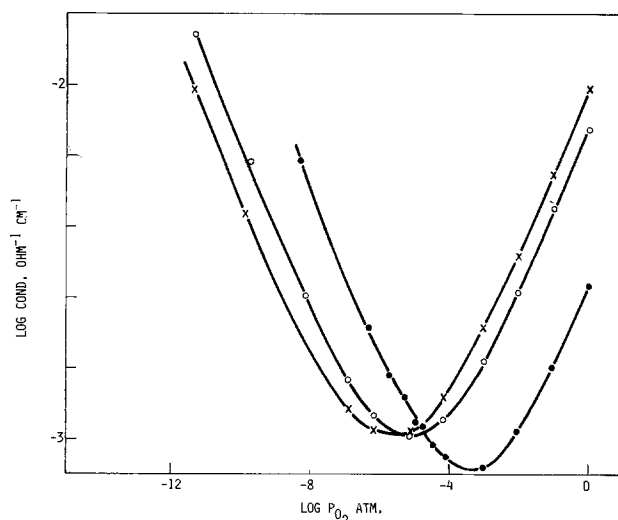


Fig. 7. Equilibrium conductivity profiles of acceptor-doped, polycrystalline SrTiO₃ at 1000°C. ● undoped, Sr/Ti = 1.0000; ○ 281 ppm Al, Sr/Ti = 0.9950, × 1080 ppm Al, Sr/Ti = 0.9950.

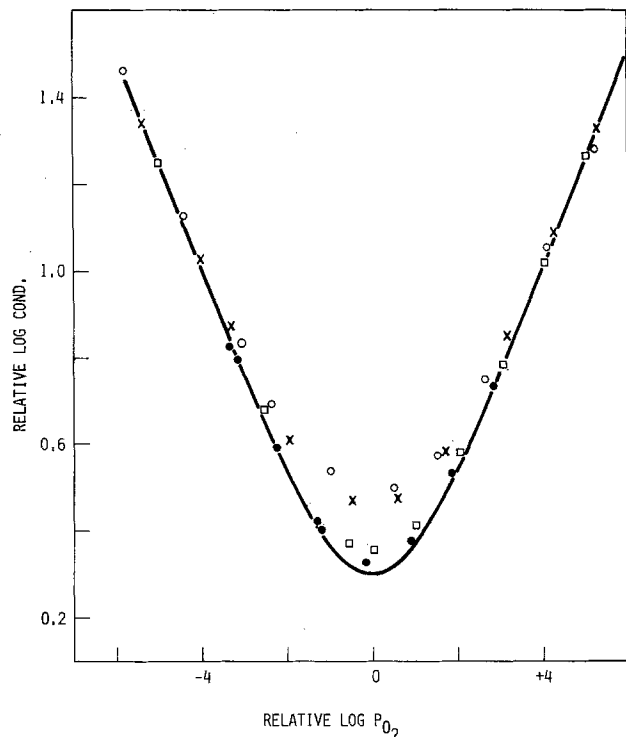


Fig. 8. Conductivity minima compared with ideal construction from log-log slopes of $\pm 1/4$ (solid line).

| | Temp (°C) | ppm added Al | Sr/Ti |
|---|-----------|--------------|--------|
| ● | 1000 | None | 1.0000 |
| □ | 800 | None | 1.0000 |
| × | 800 | None | 0.9950 |
| ○ | 800 | 1080 | 0.9950 |

crystal SrTiO₃ (24). This was derived from the time dependence of the conductivity following step changes in the oxygen partial pressure. If it is assumed that the diffusion experiment involved ambipolar diffusion of V_o^{••} and electrons, the true vacancy diffusion constant is 1/3 of the effective value. From the Nernst-Einstein relationship, this corresponds to a V_o^{••} mobility of 6×10^{-4} cm²/sec at 1000°C. For the most highly doped sample in Fig. 8 (1080 ppm Al) this gives an ionic conductivity of 1.5×10^{-3} Ω⁻¹ cm⁻¹. The conductivity minimum for this sample lies about 25% above the value of 9×10^{-4} Ω⁻¹ cm⁻¹ for the undoped sample with Sr/Ti = 1.000, suggesting an ionic contribution of 2.2×10^{-4} Ω⁻¹ cm⁻¹, somewhat less than predicted by the diffusion data. If the effectiveness of Al for producing apparent V_o^{••} concentrations is similar in SrTiO₃ to the values found recently in BaTiO₃ (25), the predicted contribution is 4×10^{-4} Ω⁻¹ cm⁻¹, which is within a factor of two of the observed effect. Since the conductivities were measured with a d-c current, the effect of the ionic conduction may have been reduced by polarization. Some slight polarization effects were observed in the vicinity of the conductivity minima.

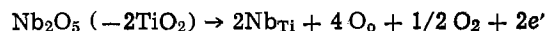
Paladino determined the chemical diffusion constant for oxygen in SrTiO₃ from the rate of weight change following step changes in P_{O₂} (26). His value at 1000°C is about half that reported by Wernicke. The data of Takahashi yield a mobility which predicts a smaller contribution than is indicated by our results. If the 10% Al content used by Takahashi is beyond the solubility limit, and the resulting extrinsic V_o^{••} content is thus less than 5%, his results are in closer agreement with ours.

Wernicke reported an activation energy for oxygen diffusion in SrTiO₃ of 1.1 eV (24), while Paladino found values of 0.98, 1.13, and 1.27 eV (26, 27). The

first of these was obtained from the oxidation kinetics of reduced SrTiO₃ while the last two were obtained from the isotopic exchange rate. If the total oxygen vacancy contents of these samples were extrinsic, as postulated in the model described here, these energies should represent the enthalpy of motion of V_o^{••}. These enthalpies are less than 1/2 E_g^o which we found to be 1.65 eV. Thus the minima have a greater temperature dependence than does the mobility of V_o^{••}, and ionic conductivity should make larger fractional contributions with decreasing temperature. This agrees with our observation that the minima become flatter with decreasing temperature as demonstrated in Fig. 8.

In any case, the level of vacancy conduction needed to account for the observed shapes of the conductivity minima is not unreasonable. A similar deviation from the ideal shape of the conductivity minimum has been observed in BaTiO₃ (28). The conductivity levels at the minima in Fig. 6 and 7 differ probably by a combination of the effect shown in Fig. 8 and because of small geometric differences between samples.

Donor-doped samples.—The effect of the Sr/Ti site occupation ratio is particularly striking in the case of donor-doped samples. Figure 9 shows conductivity profiles at 1000°C for three samples having identical amounts of added Nb, but Sr/Ti ratios of 1.000, 0.999, and 0.995. It is doubtful that the former two samples were completely equilibrated for P_{O₂} > 10⁻¹⁰ atm. The V_o^{••} content in these cases should vary as P_{O₂}^{-1/2} over this range, and the resulting low V_o^{••} concentration leads to very slow equilibration. The sample with Sr/Ti = 1.000 behaves very much like donor-doped BaTiO₃ (5). The replacement of 2TiO₂ by Nb₂O₅ can be written



[20]

The expulsion of the fifth oxygen from the filled lattice leaves free electrons which compensate the charged donor centers. This leads to a region of impurity-controlled, P_{O₂}-independent electron concentration and conductivity. In the case of Sr/Ti = 0.999, the conductivity is significantly reduced in the impurity-controlled region, and for Sr/Ti = 0.995, the donor-doped behavior is lost completely and the conductivity plot looks very much like that of an undoped sample. Apparently, as the V_o^{••} content increases with the amount of excess TiO₂, increasing amounts of the extra oxygen carried by the Nb₂O₅ can be accommodated in the lattice until finally it is all retained and the characteristic donor-type behavior is no longer

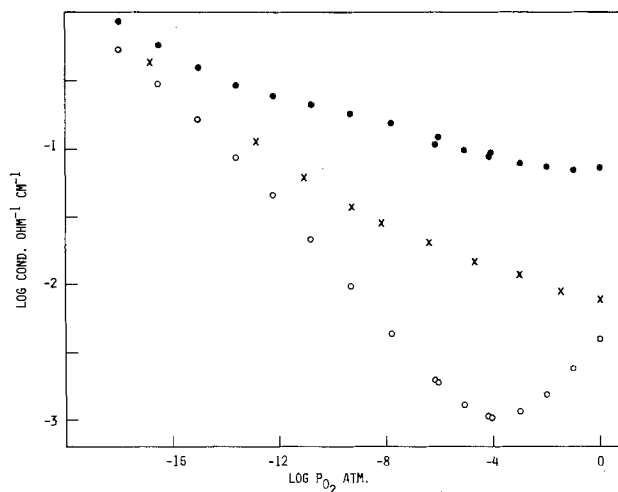
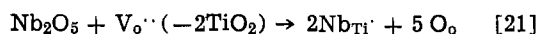


Fig. 9. Conductivity profiles of donor-doped, polycrystalline SrTiO₃ at 1000°C. ● 498 ppm Nb, Sr/Ti = 1.0000; × 498 ppm Nb, Sr/Ti = 0.9990; ○ 498 ppm Nb, Sr/Ti = 0.9950.

observed.



Since the Nb content corresponds to only 249 ppm extra oxygen, and there is a large change in properties as the TiO_2 excess is increased from 1000 to 5000 ppm, there must be an equilibrium between O_2 , $\text{V}_o^{\cdot\cdot}$, e' , and h' , essentially as represented by Eq. [7] and [16], rather than a complete accommodation where every $\text{V}_o^{\cdot\cdot}$ can be filled. In contrast to undoped and acceptor-doped samples, donor-doped SrTiO_3 shows a dramatic change in properties as Sr/Ti is reduced from 0.999 to 0.995. This suggests that the solubility of TiO_2 may be enhanced by the tendency of the Nb_2O_5 content to reduce the $\text{V}_o^{\cdot\cdot}$ content. This phenomenon results in a dramatic change in room temperature properties for SrTiO_3 containing modest amounts of donor impurities. After equilibration in air or oxygen, the material can be either a dark colored semiconductor if Sr/Ti = 1.000, or a light colored insulator if Sr/Ti < 1.000. The conductivity can be changed several orders of magnitude by very modest changes in the Sr/Ti ratio.

Conclusions

In the temperature range included in this report, 800°-1000°C, SrTiO_3 maintains equilibrium with the oxygen activity in the ambient. It behaves as a degenerate semiconductor with all donor levels introduced by reduction giving mobile electrons, and each oxygen in excess of stoichiometry contributing two mobile holes. Carrier mobilities have not been measured in this temperature range, but since the conductivity is almost identical with that of BaTiO_3 in the reduction region, and the enthalpies of the reduction reaction and intrinsic ionization are also almost identical, similar mobilities should be anticipated.

Perluzzo and Destry have measured Hall mobilities in SrTiO_3 from room temperature to 650 K (29). Their result of about 6 $\text{cm}^2/\text{V} \cdot \text{sec}$ for single crystalline material at room temperature agrees well with a value of 5.8 $\text{cm}^2/\text{V} \cdot \text{sec}$ obtained by Gerthsen, Härdtl, and Csillag for both single crystalline and polycrystalline SrTiO_3 (30). If the mobility results of Perluzzo and Destry are fit to a $T^{-3/2}$ temperature dependence, which is a good approximation to the electron mobilities measured for BaTiO_3 up to 1000°C by Seuter (4, 31), extrapolation to 800° and 1000°C gives electron mobilities of 0.5 and 0.4 $\text{cm}^2/\text{V} \cdot \text{sec}$, respectively, for SrTiO_3 . These are somewhat higher than the values obtained from the expression used by Ihrig (31) to describe the results obtained by Seuter (4) for BaTiO_3 , 0.19 and 0.15 $\text{cm}^2/\text{V} \cdot \text{sec}$ at 800° and 1000°C. There is no quantitative information on hole mobilities in either compound, although the results of Seuter indicate that $\mu_p < \mu_n$. These extrapolated values seem a little high when compared with the results obtained from donor-doped samples where n is determined by the net excess donor content. Although the data shown in Fig. 9 for a sample with 498 ppm Nb and Sr/Ti = 1.000 are poorly equilibrated at high P_{O_2} , the trend near $P_{\text{O}_2} = 10^{-12}$ atm suggests a leveling off at a conductivity of about 0.2 $\Omega^{-1} \text{cm}^{-1}$. Assuming a net donor excess of 400 ppm, this gives $\mu_n \sim 0.2 \text{ cm}^2/\text{V} \cdot \text{sec}$. In the schematic plot of defect concentrations in Fig. 4, this value has been used for μ_n , and μ_p has been arbitrarily set at 0.1 $\text{cm}^2/\text{V} \cdot \text{sec}$, in order to derive carrier concentrations from the measured conductivities.

The additive effect of reduction, excess TiO_2 , and acceptor impurities is a strong indication that all three lead to a common defect, the doubly ionized oxygen vacancy. This implies little or no defect association under the conditions of conductivity measurement. The dielectric constants of SrTiO_3 and BaTiO_3 remain high even at elevated temperatures. The high frequency dielectric constants at 500°C, far into the paraelectric region, have been reported to be 150 and

450 for SrTiO_3 and BaTiO_3 , respectively, (32), and the static values must be even higher. This parameter is a measure of the polarizability of the lattice, which reduces the electrostatic attraction between charged defects accordingly. Thus for "normal" compounds like MgO and NiO, which have dielectric constants similar to those of the alkali halides, high temperature association between multiple charged defects should be a major effect, but this is drastically reduced in SrTiO_3 and BaTiO_3 because of their extreme polarizabilities.

The results and defect model discussed here suggest that the sintering conditions can play an important role in determining the properties of polycrystalline SrTiO_3 when excess TiO_2 is available. The solubility of TiO_2 should depend on the total $\text{V}_o^{\cdot\cdot}$ content which can be enhanced by the presence of acceptor impurities and reduced P_{O_2} . Of course, the solubility should also be temperature dependent. The effect of variations in sintering conditions are currently under investigation.

Acknowledgment

The authors appreciate the support of this work by NSF Grant DMR74-21095.

Manuscript submitted Aug. 14, 1980; revised manuscript received Feb. 23, 1981.

Any discussion of this paper will appear in a Discussion Section to be published in the June 1982 JOURNAL. All discussions for the June 1982 Discussion Section should be submitted by Feb. 1, 1982.

Publication costs of this article were assisted by Lehigh University.

REFERENCES

- H. Veith, *Z. Angew. Phys.*, **20**, 16 (1965).
- F. Kosek and H. Arend, *Phys. Status Solidi*, **24**, K69 (1967).
- S. A. Long and R. N. Blumenthal, *J. Am. Ceram. Soc.*, **54**, 515 (1971).
- A. M. J. H. Seuter, *Philips Res. Rep.*, Suppl. 3 (1974).
- N.-H. Chan and D. M. Smyth, *This Journal*, **123**, 1584 (1976).
- J. Daniels and K. H. Härdtl, *Philips Res. Rep.*, **31**, 489 (1976).
- J. Daniels, *ibid.*, **31**, 489 (1976).
- D. Hennings, *ibid.*, **31**, 516 (1976).
- N. G. Eror and D. M. Smyth, *J. Solid State Chem.*, **24**, 235 (1978).
- L. C. Walters and R. E. Grace, *J. Phys. Chem. Solids*, **28**, 239 (1967).
- H. Yamada and G. R. Miller, *J. Solid State Chem.*, **6**, 169 (1973).
- E. M. Levin, C. R. Robbins, and H. F. McMurdie, "Phase Diagrams for Ceramists," American Ceramic Society, Columbus (1964), Fig. 297, 298. 1969 Supplement, Fig. 2334.
- D. E. Rase and R. Roy, *J. Am. Ceram. Soc.*, **38**, 102 (1955).
- R. K. Sharma, N.-H. Chan, and D. M. Smyth, Submitted to *J. Am. Ceram. Soc.*
- S. N. Ruddlesden and P. Popper, *Acta Crystallogr.*, **11**, 54 (1958).
- R. J. D. Tilley, *J. Solid State Chem.*, **21**, 293 (1977).
- M. Pechini, U.S. Pat. 3,330,697 (1967).
- F. A. Kröger and H. J. Vink, in "Solid State Physics," Vol. 3, F. Seitz and D. Turnbull, Editors, Academic Press, New York (1956).
- M. Kahn, *J. Am. Ceram. Soc.*, **54**, 455 (1971).
- S. A. Long and R. N. Blumenthal, *ibid.*, **54**, 577 (1971).
- H. W. Gandy, *Phys. Rev.*, **113**, 795 (1959).
- M. Cardona, *Phys. Rev. A*, **140**, 651 (1965).
- T. Takahashi, in "Physics of Electrolytes," Vol. 2, J. Hladik, Editor, Chap. 24, Academic Press, New York (1972).
- R. Wernicke, Thesis, Rheinische-Westfälischen Technischen Hochschule, Aachen (1975).
- N.-H. Chan, R. K. Sharma, and D. M. Smyth, Submitted to *J. Am. Ceram. Soc.*
- A. E. Paladino, *J. Am. Ceram. Soc.*, **48**, 476 (1965).
- A. E. Paladino, L. G. Rubin, and J. S. Waugh, *J. Phys. Chem. Solids*, **26**, 391 (1965).

28. N.-H. Chan, R. K. Sharma, and D. M. Smyth, Submitted to *J. Am. Ceram. Soc.*,
 29. G. Perluzzo and J. Destry, *Can. J. Phys.*, **54**, 1482 (1976).
 30. P. Gerthsen, K. H. Hårdtl, and A. Csillag, *Phys. Status Solidi A*, **13**, 127 (1972).
 31. H. Ihrig, *J. Phys. C*, **9**, 3469 (1976).
 32. A. von Hippel *et al.*, Technical Report 191, Laboratory for Insulation Research, M.I.T., ML-TDR-64-219, pp. 62-65, Cambridge (1964).

Compositional Studies Related to Sputtered Cd-Si-As Films

A. F. Carroll,^{*1} C. F. Smith,² L. C. Burton, and L. H. Slack²

Departments of Materials and Electrical Engineering,
 Virginia Polytechnic Institute and State University, Blacksburg, Virginia 24061

ABSTRACT

Thin films containing Cd, Si, and As were rf sputtered from a CdSiAs_2 target and Si/CdAs_2 composite targets. The compositions of the films were found to be a function of the sputtering power, substrate temperature, post-deposition heat-treatment in a Cd and As_4 atmosphere, and in the case of the composite targets, the Si/CdAs_2 area ratio. These results are related to differences in sputtering yield and the different resputtering tendencies of the elements. The films were amorphous as deposited, but became polycrystalline with the chalcopyrite structure during the postdeposition heat-treatments.

CdSiAs_2 is a semiconducting compound having the chalcopyrite crystal structure (1, 2). It is a II-IV-V analog of the III-V compounds, and as such, it has many potential electronic applications, one of which is photovoltaic energy conversion. The CdSiAs_2 , which is p-type and has a bandgap of 1.55 eV (3), could potentially be used in homojunction and heterojunction configuration. Of special interest is its good lattice and electron affinity match with n-type CdS. A close lattice match between the absorber (CdSiAs_2) and window (CdS) layers would tend to minimize the recombination rate at the heterojunction. CdS has a (110) spacing of 5.851Å, compared with the (100) lattice parameter for CdSiAs_2 of 5.885Å, providing a lattice mismatch of less than 0.6%.

The purpose of this work is to achieve a workable method of preparing CdSiAs_2 thin films, but evaluation of their photovoltaic characteristics is beyond the scope of this paper. In order to enhance the compositional homogeneity, radio frequency sputtering from large (3 in. diam) targets was used. This technique provides the necessary compositional versatility (4, 5) and good film adherence (6) to substrates. The good adhesion results from the plasma interaction with the substrate which results in substrate cleaning before and during the initial stages of deposition and/or aids in the formation of interfacial compounds.

Procedure

Target fabrication.—Two target designs were used, one being a macroscopically homogeneous CdSiAs_2 plate and the other being an Si plate containing inserts of CdAs_2 . The first target was prepared by direct fusion of CdSiAs_2 that had previously been synthesized by direct fusion from the pure elements. Crushed pieces of CdSiAs_2 (containing small amounts of CdAs_2 , Cd_3As_2 , and SiAs) were placed in a fused silica cylindrical container which contained a 3 in. graphite disk

on which the CdSiAs_2 rested. The container, 3¼ in. in diameter and 2 in. high, was evacuated and sealed. It was then heated according to the thermal schedule shown in Fig. 1. When the container was rapidly cooled, the sides and top were kept hot with insulating material so that the more volatile components would not condense on the vessel, but onto the target. This target had an irregular shape approximately 2 in. in diameter and ¼ in. thick. It was bonded to an aluminum backing plate with conducting epoxy.

The composite targets, one shown in Fig. 2, were prepared by core drilling 23/64 in. holes in a 3 in. diam polycrystalline silicon plate and inserting 11/32 in. CdAs_2 disks into those holes. The silicon and inserts were bonded to a 3-1/4 in. diam copper backing plate, again with thermosetting epoxy.

The CdAs_2 inserts were synthesized by weighing stoichiometric quantities of pure (5N) cadmium and arsenic into hollow graphite cylinders, which were in turn sealed into evacuated heavy-wall silica tubing. The graphite liners kept the final ingot from fracturing on cooling. The thermal schedule used for melting and

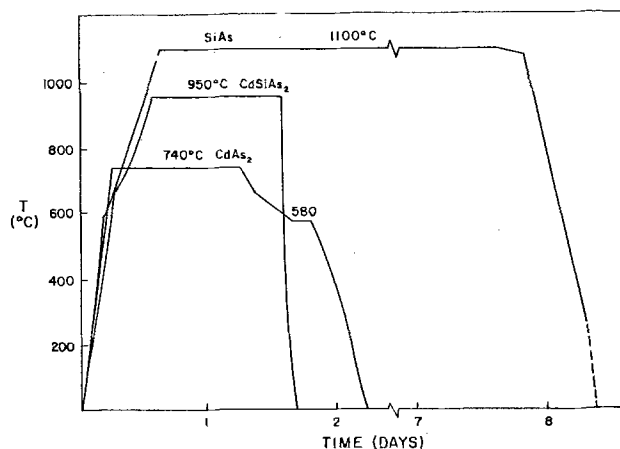


Fig. 1. Thermal schedules for materials used in targets and as EMPA standard.

* Electrochemical Society Active Member.

¹ Present address: The Carborundum Company, Refractories Division, Niagara Falls, New York 14302.

² Present address: E. I. du Pont de Nemours & Company, Incorporated, Electronic Materials Division, Niagara Falls, New York 14302.

Key words: CdSiAs_2 , heat-treatment, rf sputtering, chalcopyrite.

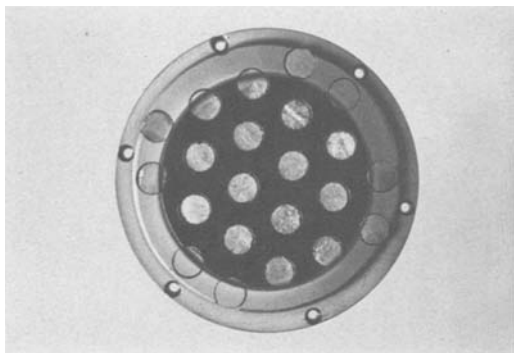


Fig. 2. Photograph of composite target HEX C

solidification of this compound is also shown in Fig. 1.

The resulting CdAs_2 ingots were found to be single phase and crystalline by electron microprobe and x-ray diffraction analyses, respectively. The relative ease of CdAs_2 synthesis is associated with its congruent melting and solidification behavior. The ingots were sectioned into disks and ultrasonically cleaned in acetone and methanol.

Four composite targets have been fabricated. The first was a silicon disk with a single CdAs_2 disk bonded at its center (bullseye-BE). It was used to characterize the geometry of sputtering from a single insert as a test of possible imaging effects (7) between the two-phase target and the substrate plane.

The other three composite targets (HEX A, HEX B, and HEX C) consisted of an Si plate with CdAs_2 disks inserted in a hexagonal array. The number and spacing of the inserts were chosen to yield Si/ CdAs_2 area ratios of 1.00, 1.47, and 2.27 (HEX A, HEX B, and HEX C).

Sputtering.—The radio frequency sputtering system used to deposit Cd-Si-As thin films consisted of a commercial sputtering module³ mounted on a vacuum system utilizing a turbomolecular pump.⁴ The sputtering parameters used are listed in Table I.

The film thicknesses were determined by weighing the substrates before and after deposition, and assuming a composition of CdSiAs_2 of near theoretical density, 5.0 g/cm³. These thicknesses were within $\pm 5\%$ agreement of those obtained by optical interferometry.⁵

The rate of material removal from the target was also monitored by determining the geometrical profile of the target surface with a sheet metal micrometer.

Heat treatments of films.—Some of the films were heated either during the sputtering process or afterwards. In the first case, the stage supporting the substrates was heated to a controlled temperature during

³ R. D. Mathis, Model SP310.

⁴ Welch, Model No. 3102.

⁵ Varian Associates, Angstrom Scope.

Table I. Sputtering parameters

| Sputtering target | RF power (W) | Argon pressure (mTorr) | Substrate + heating (°C) | D-C voltage (kV) | Duration (hr) |
|---------------------------------------|--------------|------------------------|--------------------------|------------------|---------------|
| CdSiAs_2 | 40-220 | 5-32 | RT to 535 | 1.5-4.0 | 3.0-7.5 |
| Bullseye (BE) | 80-190 | 7-16 | — | 0.7-1.8 | 2.5-6.0 |
| HEX A (Si/ CdAs_2 = 1.00) | 100-200 | 9-32 | — | 0.4-1.6 | 1.5-3.5 |
| HEX B (Si/ CdAs_2 = 1.47) | 100-200 | 9-12 | — | 2.0-3.0 | 3.0-6.0 |
| HEX C (Si/ CdAs_2 = 2.27) | 100-200 | 7-15 | — | 2.1-3.3 | 3.5-4.0 |

the deposition. The rf plasma heated the top surface of the substrates to a temperature higher than the control temperature by $150^\circ \pm 10^\circ\text{C}$, as determined by a platinum thin film surface temperature measuring device.⁶

In the second case, the coated substrate and a small fragment (approx. $\frac{1}{2}$ g) of CdAs_2 were sealed in an evacuated Vycor ampul. The ampul was heated to 600°C for one day. The CdAs_2 provided an overpressure of Cd and As_4 vapor.

Film characterization.—Elemental compositions of the films were determined by electron microprobe analysis⁷ (EMPA) and their structures by x-ray diffraction analysis (XRD). The films were thick enough ($\sim 1 \mu\text{m}$) to intercept all of the radiation in the EMPA experiments so that the analysis was not affected by the substrates.

Two sets of standards have been used for the microprobe analyses. The first was Cd, GaAs, and Si. A fresh surface of Cd was exposed for microprobe analyses on a daily basis. Because the Si and As x-ray emission peaks overlap, some error was found to exist using these initial standards. The overlapping of these peaks in the Cd-Si-As films, but not in the standards, was responsible for this error. The second set consisted of SiAs crystals (a mica-like cleavable material synthesized here in ingot form by melting the pure elements in evacuated sealed silica ampuls using the thermal schedule shown in Fig. 1) and Cd metal. The second set of standards provides analyses on bulk CdSiAs_2 that agreed with careful chemical analyses. All of the microprobe results reported here were made using the second set, or were corrected using appropriate correction factors.

Results and Discussion

Films from ternary target.—The films formed by sputtering from the polycrystalline CdSiAs_2 target were cadmium deficient. Attempts to induce crystallinity by heating the substrates were not successful. The effect of substrate heating on film composition is seen in Fig. 3. The first substrate support temperature shown in Fig. 3 is that obtained without applying power to the substrate heater. The temperature was measured inside the substrate support. When the substrates were heated to only 270°C , the cadmium content had dropped to less than 2%, and became even lower as higher substrate support temperatures were used. At very high temperatures (above 400°C), the As content also dropped from 53 to 30%.

The re-emission of Cd and As_4 from the thin film is probably a result of the combined effects of thermal and particle impact induced decomposition mechanisms. These two mechanisms occur simultaneously during the sputter deposition process in an interdependent manner.

A study (8) of the thermal decomposition of bulk CdSiAs_2 in vacuum determined the temperature range for Cd and As_4 sublimation to be $570^\circ\text{--}710^\circ\text{C}$. Both species were sublimed in an approximate ratio of 4 to 1, respectively, leaving a residue of SiAs. At temperatures exceeding 710°C , As_4 was sublimed from the SiAs leaving a residue of Si. The two steps of this decomposition process were separated by a temperature difference of 140°C . The temperature difference between the two same steps occurring in the presence of a high energy plasma is greater than 130°C shown in Fig. 3. The relatively constant difference in temperature indicates that the same bonds are broken in the thermal decomposition of the previous study and the thermo-physical decomposition of this study.

⁶ Omega Engineering, Model TFD Thin Film Detector, Stamford, Connecticut.

⁷ Applied Research Lab., Model 131,000-46. SEMQ, Automated Electron Microprobe.

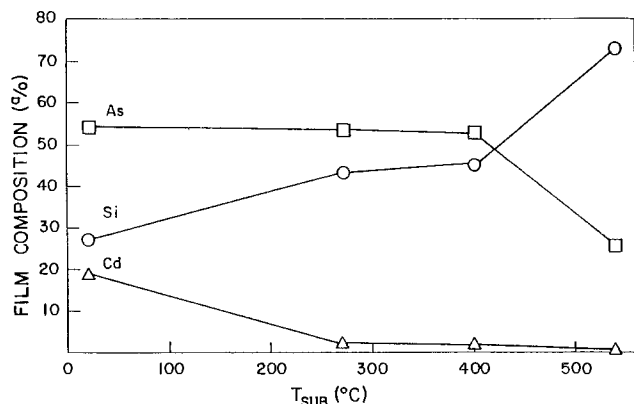


Fig. 3. Effect of substrate support temperature on film composition.

The difference in temperature is related to the different bond strengths of the Cd-As and Si-As bonds in the CdSiAs₂ crystal. Another indication of the different bond strengths is the difference in melting temperature of CdAs₂ and decomposition temperature of SiAs₂, 621° and 944°C, respectively.

The cadmium content was also found to be a function of the previous service of the polycrystalline CdSiAs₂ target. This is evident in data reported in Table II where the Cd content dropped from 21 to 17%, and to 11% in three 200W runs. This table is a chronological summary of the progressive depletion of Cd from the films sputtered at 200W and the effect of substrate temperature on this depletion. It is evident that the target surface was becoming Cd deficient with continued use and this depletion was hastened when the chamber was heated by turning on the substrate heater. Deliberate substrate heating was discontinued and the substrate holder was cooled with circulating room temperature water in the subsequent research.

The composite Si/CdAs₂ targets were adopted because of their greater ease of fabrication and the flexibility gained by the variable Si/CdAs₂ ratio.

Films from bullseye target.—Sputtering from the first composite target (BE), consisting of a single CdAs₂ disk at the center of a silicon plate, established that the transport of sputtered particles was a multi-collision process between the target and substrates. The Cd and As atoms were evenly distributed over the entire substrate holder area, even though they originated from a small spot. This is shown by the microprobe elemental analyses of Cd, As, and Si shown as a function of substrate location in Fig. 4. If the atoms had not experienced the mixing effects of numerous collisions with argon atoms (and each other), then the Cd and As concentrations would have followed a cosine law (6) with distance from the center of the substrate holder. This experiment con-

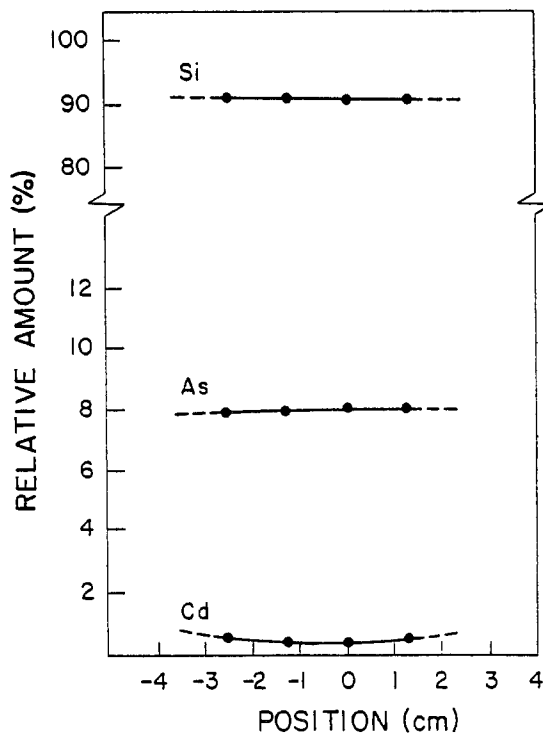


Fig. 4. Bullseye target film compositions as a function of substrate position.

firmed that there would be no imaging effects between the two-phase target and the substrates.

Films from hexagonal targets.—In these experiments, the films' compositions are controlled by varying the Si/CdAs₂ area ratio of the target, by heat-treatment, and by varying the power level used during sputtering.

The effect of the target's Si/CdAs₂ area ratio on film composition is shown in Table III. The films here were all sputtered at 100W. As the target's Si area increases, the silicon content increases and the Cd and As contents decrease. If the Cd, Si, and As atoms sputtered in proportion to their concentrations in the target surface, then the HEX A target would have provided stoichiometric CdSiAs₂, but the Si content was too low by a factor of approximately two. It is apparent that Si sputters more slowly than the CdAs₂ inserts. This was confirmed by monitoring the surface profile of the target, where it was found that the CdAs₂ inserts sputter about 5-8 times faster than the silicon.

The As/Si atomic ratio approached the stoichiometric ratio of 2 when the Si/CdAs₂ target area ratio was increased to 2.27, but the film was Cd deficient. When this film was heat-treated at 600°C for one day in an overpressure of Cd and As₄ vapor, the film was replenished in Cd and the composition was Cd_{0.97}Si_{1.05}As_{1.98}. This is close to the ideal CdSiAs₂, but slightly deficient in Cd and As.

The x-ray diffraction pattern obtained from this film indicated that the film had crystallized in the chalcopyrite structure (2). The pattern was undistorted, further indicating that the film was near to stoichiometry. No other crystalline phases were detected.

The rf power level used during sputtering also controls the composition. The HEX C target is used here as an example and is representative of the trends seen with the other hexagonal targets. The effect of power on film composition (center of substrate stage) is shown in Fig. 5 for the HEX C target. The Cd content decreases from 17 to 12 atomic percent (a/o) as the power is increased from 100 to 200W. The other components increase correspondingly.

Table II. Chronological listing of unheated sputter depositions using the ternary CdSiAs₂ Target

| RF power (W) | Argon pressure (mTorr) | Composition | | |
|--------------|------------------------|-------------|------|------|
| | | Cd | Si | As |
| 200 | 18 | 21.1 | 27.5 | 51.4 |
| 190 | 7 | 18 | 27.4 | 54.6 |
| 200 | 7 | 17 | 27.4 | 55.6 |
| 80 | 32 | 14.3 | 35.7 | 50.0 |
| 200 | 14 | 11.2 | 35.6 | 53.2 |

* The substrates were heated as high as 300°C.

** The substrates were heated as high as 535°C.

Table III. Film composition for films sputtered in position 3 at 100W

| Target | Si/CdAs ₂ ratio | Cd | Composition (%) | | Elemental ratios | | |
|--|-------------------------------|------|-----------------|------|------------------|-------|-------|
| | | | Si | As | As/Si | Cd/Si | As/Cd |
| Stoichiometric CdSiAs ₂ | | 25.0 | 25.0 | 50.0 | 2.00 | 1.00 | 2.00 |
| HEX A | 1.0 | 25.4 | 14.8 | 59.9 | 4.05 | 1.72 | 2.35 |
| HEX B | 1.47 | 25.7 | 17.6 | 56.7 | 3.22 | 1.46 | 2.21 |
| HEX C | 2.27 | 17.2 | 28.7 | 54.1 | 1.89 | 0.60 | 3.15 |
| HEX C (Heat-treat at 600°C in Cd, As ₄ ambient) | 2.27 | 24.2 | 26.3 | 49.5 | 1.88 | 0.92 | 2.04 |

The additional effect of substrate location on the substrate cooling plate is shown in Fig. 6. The cadmium content is consistently less in the center of the substrate holder, and this effect is more pronounced at the higher power levels. The Cd contents of the films varied about 1% over the central 2 cm when power levels of 100 and 150W were used. At 200W the variation was 9.5%.

These cadmium deficiencies at and near the center of the stage are associated with elevated temperatures in the films. The thin film temperature sensor detected a center temperature of 540°C when the power level was 200W, and only 325°C when it was 100W. In the latter case, the temperature was 319°C at 2 cm from the center and 179°C at 4 cm. These strong temperature profiles are due to the greater plasma densities near the center and cause more pronounced Cd re-emission. These findings indicate that large targets and lower power levels are needed to provide films with uniform Cd contents.

Increasing the rf power alters the rf plasma-substrate interaction. There are several effects that occur at the substrate in the gas discharge environment (3): (i) condensation of sputtered material; (ii) bombardment by energetic ions and neutral particles; and (iii) heating (due in major part to electron bombardment). All three of these effects are interactive and operate simultaneously in the sputter deposition process.

The film that forms during cosputtering of Si/CdAs₂ targets is a result of the different sputtering yield (emission), condensation, and re-emission (resputtering, sublimation) behavior of each elemental con-

stituent. The CdAs₂ disks sputtered 5-8 times more rapidly than the Si, as measured by a micrometer, but the films had Cd/Si and As/Cd ratios nearer to the desired values of 1 and 2. This results from the fact that Si has a higher condensation rate and a lower re-emission rate than does either Cd or As.

Conclusions

1. All of the sputtered Cd-Si-As films were amorphous as deposited, even though many of the compositions were far from the bulk glass-forming region.

2. All of the films from the ternary target were Cd deficient with respect to CdSiAs₂ because Cd tended to re-emit from the substrates. This effect became more pronounced as the substrates were deliberately heated. Cadmium's tendency to be resputtered is associated with its low bond strength with the other atoms and high vapor pressure at 298 K.

3. The Si/CdAs₂ composite targets maintained a constant surface composition during several runs, and consequently the compositions of the films remained constant. This was not the case with the polycrystalline CdSiAs₂ target, probably due to target heating during substrate heating experiments.

4. The features of the composite Si/CdAs₂ target are not imaged in the compositions of the films. Evidently, the sputtered atoms experience multiple collisions with argon atoms (and perhaps each other) on their way to the substrates.

5. The Si/As ratio can be controllably adjusted in large steps by changing the Si/CdAs₂ area ratio in the target. It can be fine-adjusted by varying the sputtering power.

6. The Cd content of the films can be adjusted by adjusting the target's Si/CdAs₂ ratio, sputtering power, substrate temperature, and by heating the films in a Cd atmosphere.

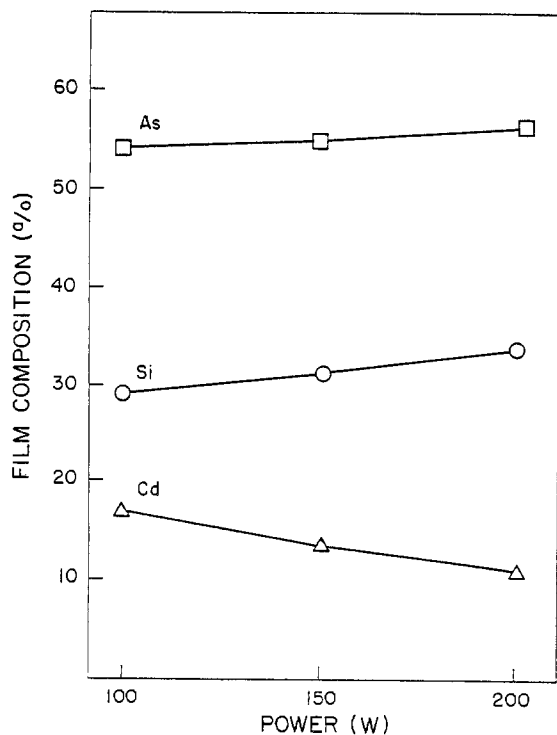


Fig. 5. Effect of rf power on film composition in position 3 using target HEX C.

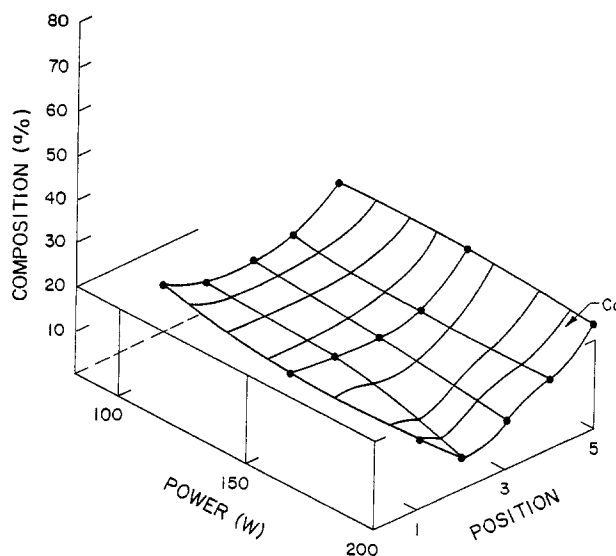


Fig. 6. Film cadmium content as a function of rf power and substrate position along the diameter of the substrate holder with position 3 at the center.

Acknowledgments

The authors wish to express sincere thanks to Mr. Wayne Koegel, Mr. Todd Solberg, and Mr. Rick Keith for their technical assistance. This work was supported by the U.S. Department of Energy and was monitored by the Solar Energy Research Institute.

Manuscript submitted Dec. 14, 1979; revised manuscript received Dec. 8, 1980.

Any discussion of this paper will appear in a Discussion Section to be published in the June 1982 JOURNAL. All discussions for the June 1982 Discussion Section should be submitted by Feb. 1, 1982.

Publication costs of this article were assisted by Virginia Polytechnic Institute and State University.

REFERENCES

1. J. L. Shay and J. H. Wernick, "Ternary Chalcopyrite Semiconductors: Growth, Electronic Properties and Applications, The Science of the Solid State," Vol. 7, B. R. Pamplin, Editor, Pergamon Press, New York (1975).
2. A. F. Carroll, Ph.D. Dissertation, Virginia Polytechnic Institute and State University (1980).
3. J. Houserova and A. Hruby, *Czech. J. Phys. B*, **22**, 861 (1972).
4. J. L. Vossen, *J. Vac. Sci. Technol.*, **8**, 512 (1971).
5. L. I. Maissel, "Handbook of Thin Film Technology," L. I. Maissel and R. Glang, Editors, Chap. 4, McGraw-Hill, New York (1970).
6. W. D. Westwood, "Progress in Surface Science," Vol. 7, S. G. Davison, Editor, p. 71, Pergamon Press, New York (1977).
7. J. J. Hanak, H. W. Lehmann, and R. K. Wehner, *J. Appl. Phys.*, **43**, 1666 (1972).
8. C. F. Smith, L. C. Burton, A. F. Carroll, and L. H. Slack, *Thermochim. Acta*, **40**, 235 (1980).

Annealing Behavior of Molybdenum Films Containing Rhenium

Keiichiro Uda,¹ Yoshiaki Matsushita,² and Shin-ichiro Takasu²

Cooperative Laboratories, VLSI Technology Research Association, 4-1-1, Miyazaki, Takatsuku, Kawasaki, Japan

ABSTRACT

The annealing behavior of molybdenum (Mo) films containing from 3 to 30 w/o rhenium (Re) is investigated with high resolution scanning electron microscopy. The grain size of the alloy films decreases with the increase of Re content. The electrical resistivity of Mo films with 10% Re is approximately twice that of pure Mo films, and the activation energy for the grain growth is higher than the pure Mo films one. The interdiffusion of Mo, Re, and Si atoms across the metal-SiO₂ interface is also observed after 1000°C annealing.

The study of gates and interconnection materials with low resistivity has become essential to the rapid progress of LSI technology (1). Intense study of refractory metals such as molybdenum (2) and tungsten has produced fine-patterned and high speed device fabrication technologies. These metals, which are fine grained, produce high quality devices and can withstand high temperature heat-treatments. However, the corrosion properties of these materials make them troublesome to deal with in device fabrication processes. Conversely, refractory metal silicides are easy to handle, and exhibit a higher resistance to oxidation than the refractory metals (3).

In the present study, the refractory metal Re, which is resistant to corrosion (4), is added to Mo films for possible use as a new gate material. The annealing behavior of the alloy films is examined with a high resolution scanning electron microscope (SEM), and the electrical characteristics of the alloy are also explored.

Experimental Procedure

p-Type 1-2 Ω·cm (100) oriented silicon wafers were used as the substrate, and 3000Å Mo films containing Re were deposited by electron gun co-evaporation on 1500Å thermally grown silicon dioxide films. The Re content in the Mo films was varied from 3 to 30%. The deposition rate of Mo and Re was 15-20 Å/

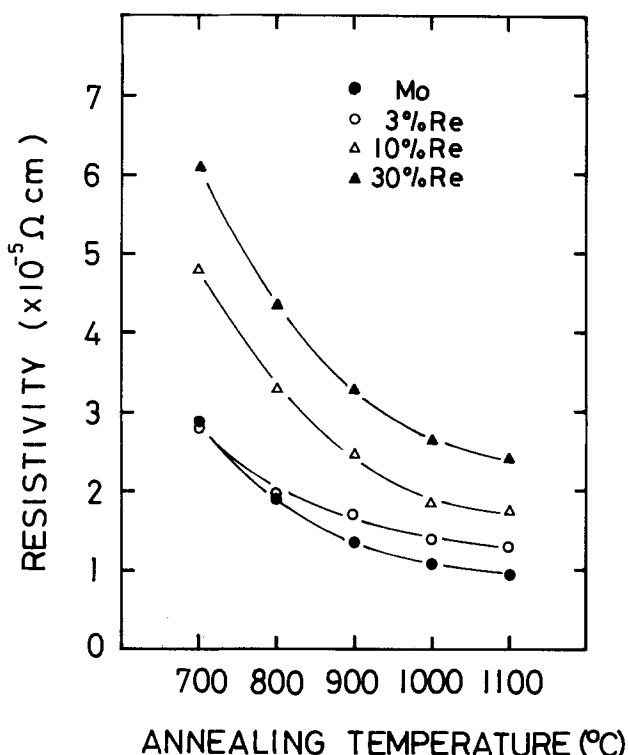


Fig. 1. Relation between resistivity and annealing temperature for Mo films containing various amounts of Re.

¹ Present address: Nippon Electric Company Limited, 1120 Shimokuzawa, Sagami-hara, Japan.

² Present address: Toshiba Corporation, Kawasaki, Japan.

Key words: molybdenum, rhenium, grain size, electrical resistivity, interdiffusion.

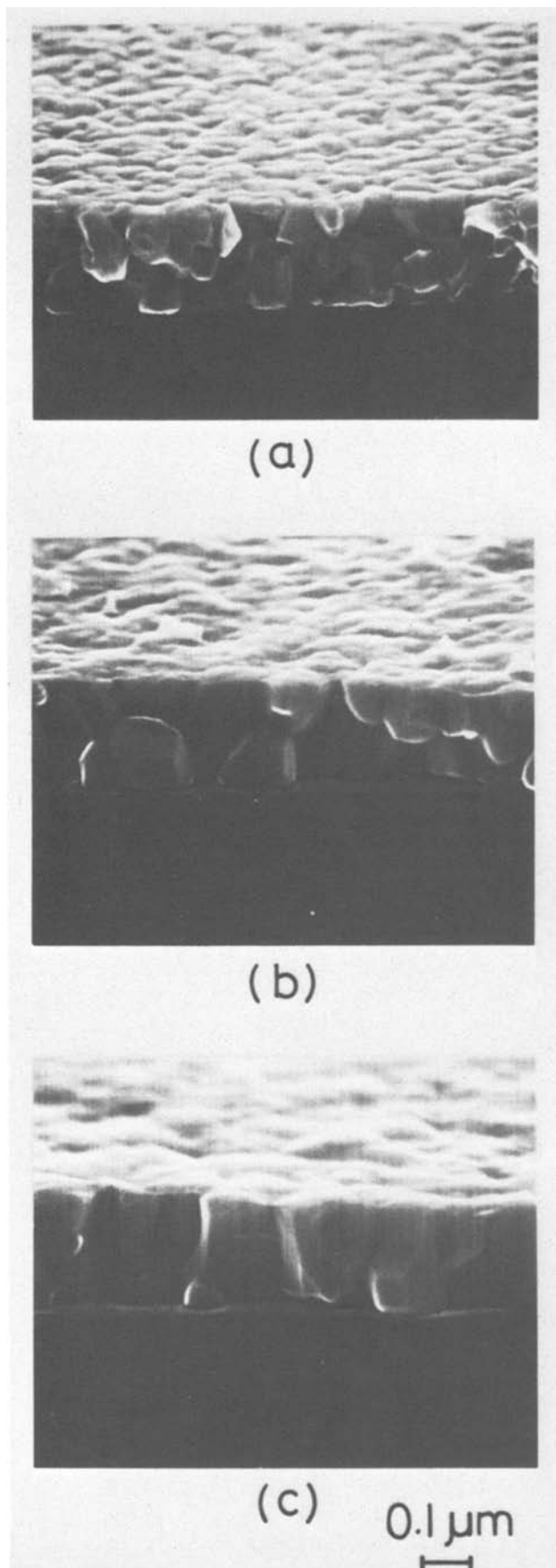


Fig. 2. SEM images of cleaved 3000 Å Mo films annealed at (a) 900°C, (b) 1000°C, and (c) 1100°C.

sec and 0.4–4 Å/sec, respectively, and each film thickness was also monitored. During evaporation, substrates were held at 150°C and vacuum pressure was

below $3 \cdot 10^{-6}$ Torr. Samples were carefully annealed at 700–1100°C in a dry N_2 atmosphere for 3–100 min. A JEOL Model JEM-100C high resolution scanning electron microscope was used to directly observe the microstructure and grain size at cleaved surfaces of the samples. The electrical resistivity of the samples was measured with a four-point probe, and in-depth profiles of Mo, Re, and Si atoms were made before and after heat-treatment with an ion microanalyzer (CAMECA, IMS-300), where O_2 leak was used.

Results and Discussion

Figure 1 shows the relation between electrical resistivity and annealing temperature as a function of Re content. Pure Mo films show the lowest resistivity, and the resistivity decreases as the annealing temperature increases. However, the resistivity of the films containing Re increases with the increase of the Re content. The resistivity of the film with 30% Re is two to three times higher than that of the pure Mo film, both before and after annealing.

Figure 2 shows SEM images of three cleaved 3000 Å Mo films (2) which were annealed at 900°, 1000°, and 1100°C. The microstructure of the sample annealed at 900°C is faceted, with grain size less than 1000 Å. Annealing at 1100°C induces significant grain growth, and the microstructure of the films shows an almost columnar structure. Figure 3 shows the SEM images of Mo films annealed at 1000°C which contain from 3 to 30% Re. The more Re that is present, the smaller the grain size becomes. The grain size of Mo films with 30% Re is several hundred angstroms in diameter, even after the 1000°C annealing. However, when an excess of Re is added to the Mo films, the film demonstrates some undesirable characteristics. In the case of 30% Re, film adhesion to the substrate is drastically weakened. Such effects will be the subject of a future report.

Figure 4 shows three SEM images of cleaved 10% Re films, where samples were annealed at 900°, 1000°, and 1100°C. The grain size of these films is smaller

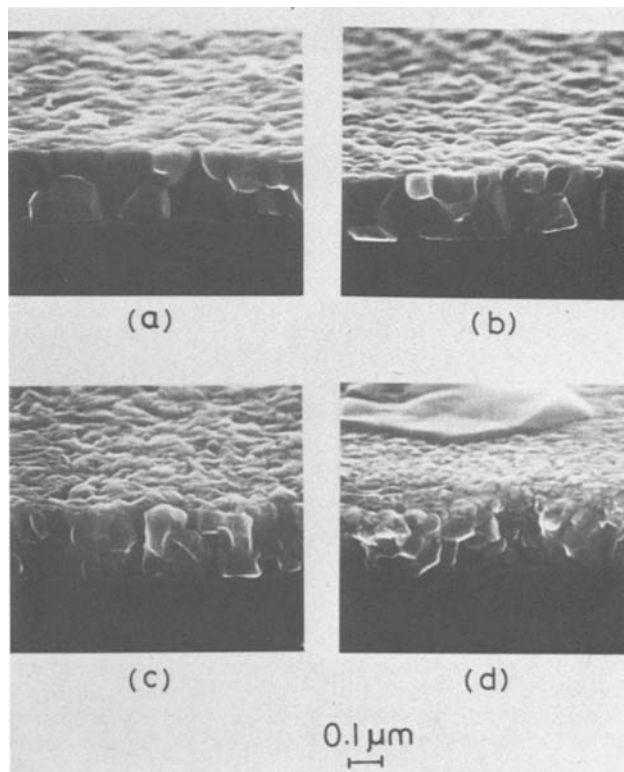


Fig. 3. SEM images of cleaved Mo films containing various amounts of Re, (a) pure Mo, (b) 3% Re, (c), 10% Re, and (d) 30% Re after 1000°C annealing.

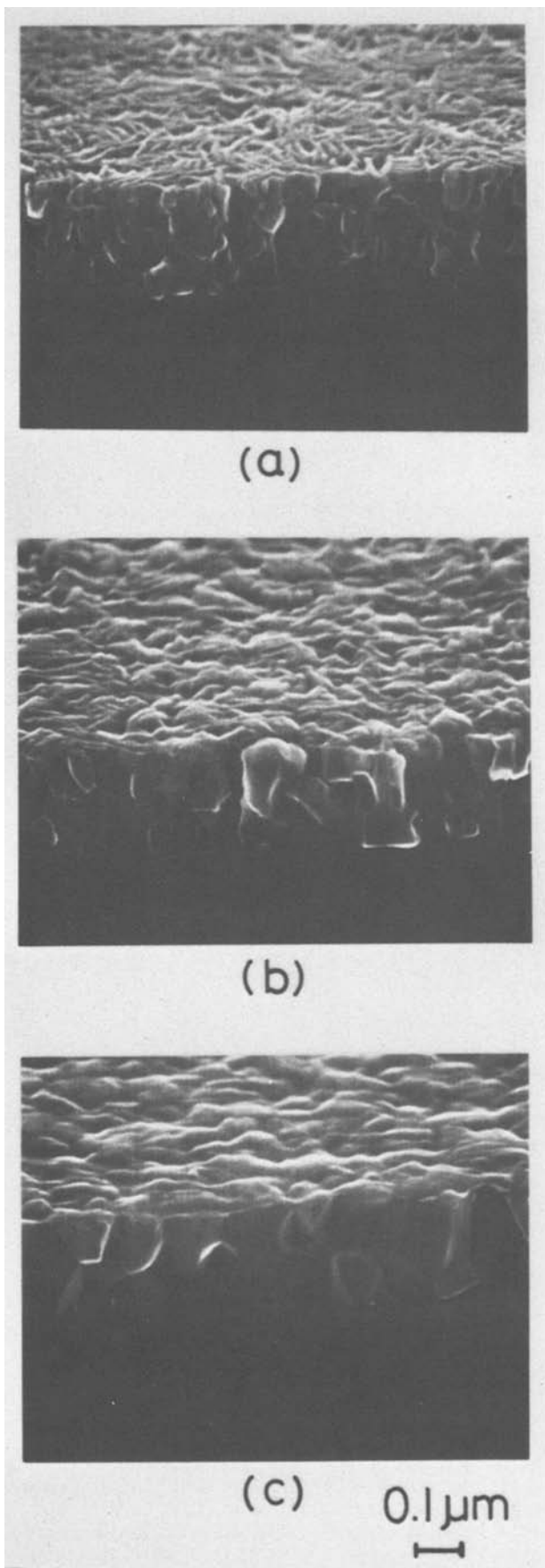


Fig. 4. SEM images of cleaved Mo films with 10% Re annealed at (a) 900°C, (b) 1000°C, and (c) 1100°C.

than pure Mo films (Fig. 2). In our investigation, Mo films containing 10% Re exhibited the most favorable characteristics for LSI technology. In the Arrhenius

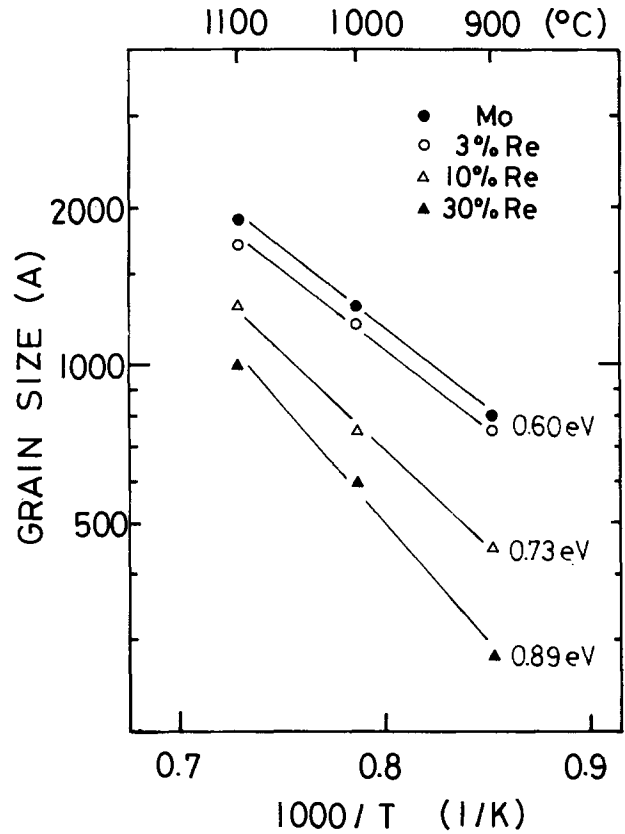


Fig. 5. Arrhenius plot of grain size for Mo films with various amounts of Re.

plot shown in Fig. 5, the mean grain size is shown as a function of Re content. In this work, the grain size of the films was directly and statistically measured using scanning electron microscopy, where surfaces and cleaved faces of the films were carefully observed. As observed in Fig. 2-4, the mean grain size of the pure Mo film shows the largest value, about 2000Å after 1100°C annealing. The activation energy of this sample is 0.6 eV. On the other hand, Mo films containing Re had smaller grain size, and the greater the Re content, the higher the activation energy. The 10 and 30% Re samples had activation energies of 0.73 and 0.8 eV, respectively. These phenomena may be due to a blocking effect by Re during the grain growth.

Figure 6 shows in-depth profiles obtained with the ion microanalyzer for Mo⁺, Re⁺, and Si⁺ ions with a

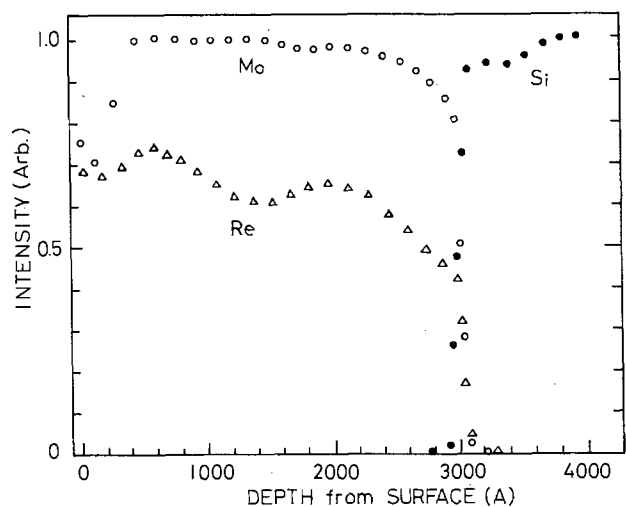


Fig. 6. In-depth profiles for Mo, Re, and Si atoms of Mo films with 30% Re before annealing.

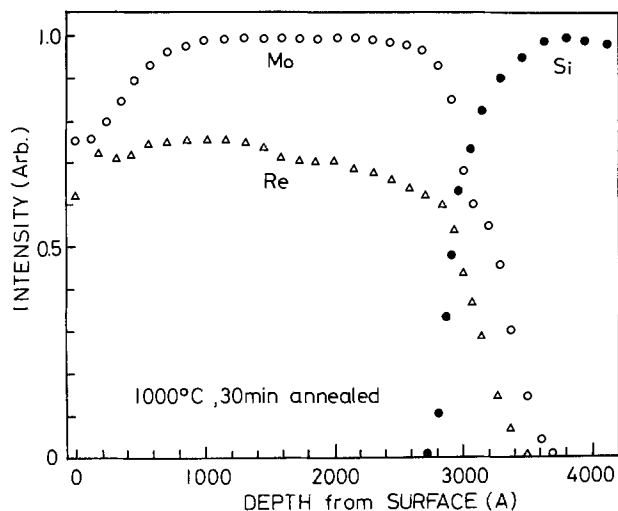


Fig. 7. In-depth profiles for Mo, Re, and Si atoms of Mo films with 30% Re after 1000°C annealing.

3000Å sample with 30% Re before annealing. Mo and Re atoms show a fairly uniform distribution in the film, and are not segregated at any locale. In this sample, the intensity of each ion shows drastic decrease at the metal-SiO₂ interface. However, as shown in Fig. 7, interdiffusion of Mo, Re, and Si atoms across the interface was observed after 1000°C annealing. The Mo atom penetrates deeper into the SiO₂ film than the Re atom. In our measurement, O₂ leak technique was used to reduce matrix effect. Therefore, this phenomenon can be considered a result of the diffusion coefficient difference between Mo and Re atoms.

Summary

Annealing behavior of 3000Å Mo films containing Re has been investigated. The electrical resistivity of the alloy films increases with the increase of Re content. The microstructure of Mo films with Re exhibits a similar structure as that of pure Mo film. However, the grain size of the alloy films decreases with the increase of Re content. The activation energy for the grain growth of alloy films is higher than that of the pure Mo films. The interdiffusion of Mo, Re, and Si atoms across the metal-SiO₂ interface is also observed after 1000°C annealing.

Acknowledgment

The authors would like to thank T. Iizuka for his invaluable discussions and continuous encouragement.

Manuscript submitted July 15, 1980; revised manuscript received Jan. 20, 1981.

Any discussion of this paper will appear in a Discussion Section to be published in the June 1982 JOURNAL. All discussions for the June 1982 Discussion Section should be submitted by Feb. 1, 1982.

Publication costs of this article were assisted by VLSI Technology Research Association.

REFERENCES

1. See, for example, M. Kondo *et al.*, *IEEE J. Solid-State Circuits*, **sc-13**, 611 (1978).
2. K. Uda, Y. Matsushita, and S. Takasu, *J. Appl. Phys.*, **51**, 1039 (1980).
3. S. P. Murarka, *J. Vac. Sci. Technol.*, **17**, 775 (1980).
4. I. Machlin, R. T. Begley, and E. D. Weisert, "Refractory Metal Alloys," Plenum Press, New York (1968).

Thin Film Growth of InP LPE for MESFET Applications

T. Ishibashi, Y. Imai, and M. Ida

Musashino Electrical Communication Laboratory,

Nippon Telegraph and Telephone Public Corporation, 3-9-11, Midori-Cho, Musashino-Shi, Tokyo 180, Japan

ABSTRACT

InP epitaxial layers with submicron thickness were grown employing a phosphorus ambient LPE technique without In melt etching. The grown layer surfaces were smooth and there was no wave-like morphology, which showed good melt wetting on the substrates. The measured electron Hall mobility in the epilayer was maintained large near the interface with the substrate, and the electron saturated velocity in the FET channel was estimated at $v_s = 2.8 \times 10^7$ cm/sec. InP MESFET's with $0.8 \times 200 \mu\text{m}$ gate dimensions were fabricated in the grown layers. A d-c maximum transconductance of 22 ms and a current gain cutoff frequency of about 40 GHz have been obtained.

InP field effect transistor (FET) has been expected to have better microwave and switching performances than GaAs FET, due to the higher electron peak drift velocity. About 50% higher current gain cutoff frequency of InP MESFET's than that of GaAs MESFET's was reported (1). Since the active layer for a MESFET is very thin, its electrical properties are greatly affected by substrate and growth conditions in the initial stage of epitaxy. Morkoc *et al.* pointed out the substrate dependence of InP MESFET performances, for their VPE layers (2, 3). The reported electron velocity in the FET channel, for a current saturation region, was 1.7×10^7 cm/sec for a Cr-doped substrate and 1.3×10^7 cm/sec for an Fe-doped substrate. These

Key words: films, transistors, growth.

values are smaller than the desirable electron peak drift velocity of about 2.5×10^7 cm/sec (4). If the drift velocity is further improved by better crystal quality, higher FET performance can be achieved.

Liquid phase epitaxy (LPE) is expected to provide better interface than VPE as the LPE growth proceeds from quasi-equilibrium solution. InP LEP growth is not so commonly applied for MESFET fabrication because of somewhat poorer morphological uniformity of the epitaxial layers and the problem of substrate surface degradation in the growth procedure. Interface characteristics of LPE InP have not been studied from a MESFET performance viewpoint.

InP surface degradation is a serious problem as the phosphorus partial pressure in InP is relatively high

compared with GaAs. In order to remove the surface damage, melt etching by In has usually been employed in the InP LPE process. However, surface flatness becomes worse for relatively deep etching, making sub-micron photolithography for MESFET's fabrication difficult.

Clawson *et al.* reported the elimination of thermal damage by introducing PH_3 in H_2 ambient (5). They showed that the threshold PH_3 partial pressure for InP decomposition corresponds to that in In-P liquidus. The phosphorus ambient technique will provide useful means of preventing the InP surface degradation, especially for the thin film LPE growth.

In this paper, the LPE InP preparation for MESFET's using PH_3 introduction is described. Growth conditions for submicron thick InP layers, such as the growth temperature, substrate misorientation, and PH_3 flow rate in the reactor were studied. The In melt etching was not made. In order to ensure melt wetting of the substrate, fresh melt pushed just prior to the growth was used, and the surface morphology of the grown layer was investigated. The electron mobility had a relatively high value near the interface with substrate.

A Ge-doped, submicron-thick InP epilayer grown on Fe-doped substrate was used for MESFET's fabrication. The electron saturation velocity in the FET channel under the gate was measured in order to verify the crystal quality, which is the most important electrical property for MESFET.

S-parameter measurements were carried out for the MESFET's with $0.8 \times 1.2 \mu\text{m}$ gate dimension, and current gain and power gain were calculated. It was demonstrated, from the electrical evaluation and the microwave performance on InP MESFET's, that the LPE growth of InP under the PH_3 ambient has high quality epitaxial layer feasibility with submicron thicknesses.

Experimental Procedure

Prior to the LPE growth experiment, the conditions for PH_3 partial pressure in the H_2 gas, which prevent the substrate thermal degradation, were studied under the same situation as that for LPE growth. The apparatus consisted of a graphite slider boat centered at a uniform temperature zone ($\pm 0.2^\circ\text{C}$) about 25 cm long, in a 55 mm diam quartz tube. The flow of dilute PH_3 (0.1 volume percent in H_2) was controlled by a mass flow controller and mixed with Pd-diffused H_2 . The total flow rate in the reactor was 1000 cm^3/min . Residual O_2 content and dew point in H_2 were below 0.02 ppm and about -70°C , respectively. Fe-doped semi-insulating substrates, with a 10^7 - $10^8 \Omega \cdot \text{cm}$ resistivity, were mechanochemically polished and deep-etched about 10 μm by 5% Br-methanol solution. About 10 μm deep-etch was sufficient for suppressing the enhanced thermal damage, such as scratches, which would make the characterization of surface difficult. The specimens were annealed for 80 min in various PH_3 contents at temperatures of 600° , 650° , and 700°C . The surface observation was made by a Nomarski optical microscope, and thermal pits were investigated. Leakage current of substrate surface was measured in order to check the electrical conversion produced by thermal degradation.

LPE growth experiments were carried out as follows. Epitaxial layers were grown at the PH_3 flow rate which provided no morphological defects on the substrate surface. About twice as high PH_3 flow rate than that of threshold for an elimination of the thermal degradation was chosen for each growth temperature. The substrate was held exposed to the ambient on the graphite boat until the growth started. The dew point of ambient in the exhaust was typically -65°C when the growth started, after the quartz tube had been set in the furnace for about 1.5 hr. Six-nines In (Johnson-Matthey; AIA) of 1.5g was etched in HCl-ethanol

solution and rinsed by water, then loaded in the melt well. In purification by long time baking in H_2 was not intentionally made. Step-cooling growth was used to grow LPE layers at the precise supercooling temperature and to minimize temperature nonuniformity of In melts. Growth temperatures were 593° , 615° , and 638°C , and the supercooling temperatures at the starting point of the growth was 10°C for each case. The phosphorus saturation of In melt was achieved by contacting an undoped InP wafer with In melt for 60 min. Two kinds of graphite boats were used. One was a conventional slider boat. The other had a two-well structure, as shown in Fig. 1, in which the fresh melt was pushed just prior to the growth and contacted with the substrate. The grown epilayers were electrically evaluated by van der Pauw-Hall measurements. The carrier concentration and mobility depth profile were then determined. InP MESFET's were fabricated in a 0.3 μm thick epilayer doped with Ge. The electron saturation velocity under the FET gate was evaluated from d-c characteristics and FET S-parameters were measured by means of an automatic-network analyzer.

Results and Discussions

Annealing of Fe-doped InP substrates.— InP surfaces annealed at 650°C for 80 min, with the PH_3 introduction of 50, 100, and 200 ppm, are shown in Fig. 2. With 50 ppm PH_3 concentration, the surface was heavily thermal etched and rectangular pits, which lie in the $\langle 110 \rangle$ direction, were observed. The In drops are seen in the pits whose depths range from several tenths of a micron to a few microns. When the PH_3 concentration is increased to 100 ppm, the rectangular pit disappears; however, the shallow pits spread on the surface. Here, the shallow pit pattern does not depend on crystallographic orientation, and In drops are not observed. No morphological surface variation from the one that was not thermally treated was observed for the surface annealed with 200 ppm PH_3 . At another annealing temperature, similar thermal pits to the 650°C case were observed, below the threshold PH_3 density. Beyond the threshold, thermal pits were completely eliminated from the surface, up to 700°C . For characterization of the thermally degraded surface, they are classified into three types: (i) deeply etched surface with In drops, (ii) weakly degraded surface with shallow pits and without In drops, and (iii) surface with no morphological change. In Fig. 3, the surface degradation dependence on temperature and PH_3 concentration is shown. The two solid lines indicate the reported P_2 and P_4 partial pressures in the equilibrium with the liquidus in the In-P system (6). The PH_3 partial pressure is considerably higher than P_2 and P_4 partial pressures. As the PH_3 decomposes thermally by the following reaction

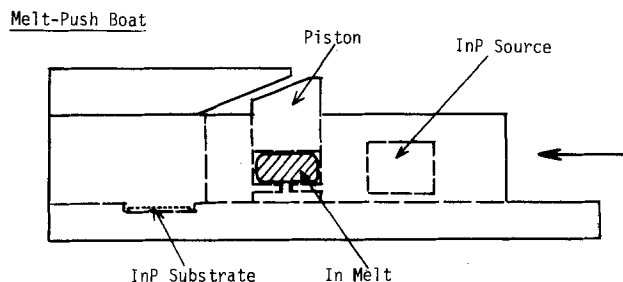
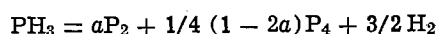


Fig. 1. Carbon boat for InP LPE. The In melt saturation by P is made by contacting the InP source wafer to the side wall of the melt. Fresh melt is pushed to the neighboring area from the upper well.

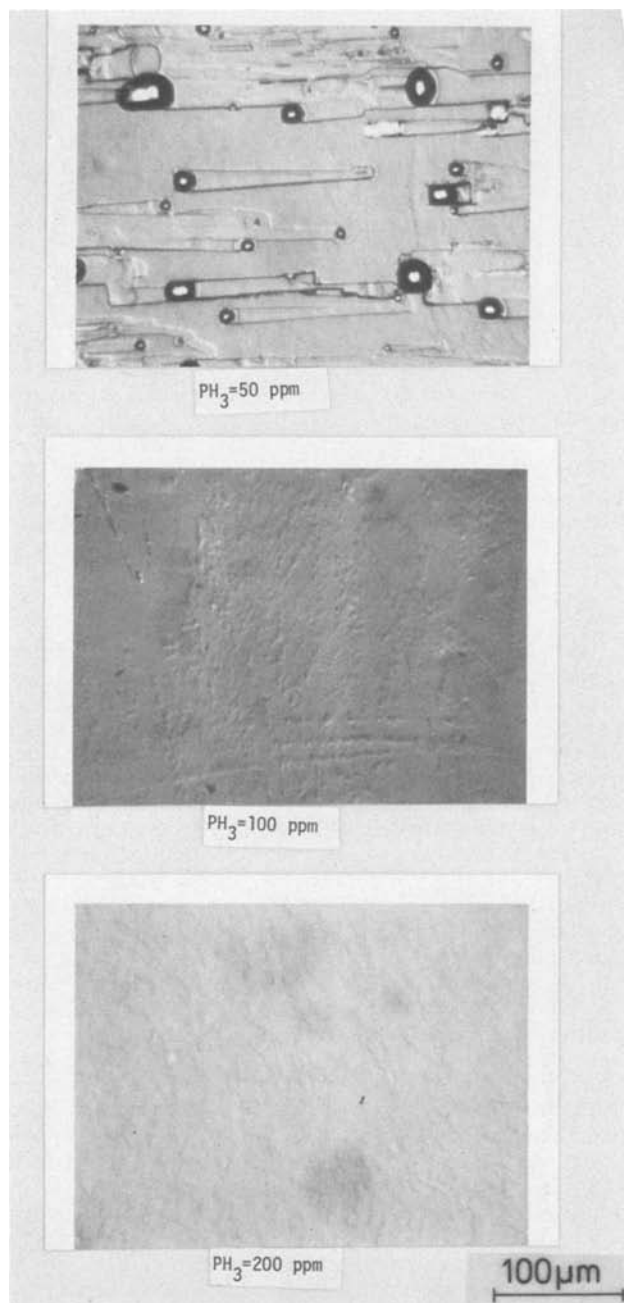


Fig. 2. Fe-doped (100) surface annealed at 650°C for 80 min. In various PH_3 concentrations, the total flow rate was maintained at 1000 cm^3/min .

the phosphorus pressure is reduced from the PH_3 value by a factor of 2-4. Considering these factors, the PH_3 required for thermal damage elimination is about five times for 700°C and about 100 times for 600°C larger than the phosphorus pressure in equilibrium. As described by Clawson *et al.*, the thermal degradation occurs at a lower phosphorus pressure than the equilibrium. Our results show that the effective phosphorus partial pressure depends strongly on the temperature and the apparatus. Ban *et al.* (7) reported the PH_3 decomposition rate in their VPE system as 40% at 700°C and 25% at 600°C. Therefore, the difference in 700°C data may be explained mainly by inadequate PH_3 decomposition. The larger excess PH_3 , at a temperature lower than 700°C, reveals the phosphorus vapor loss absorbed by the carbon boat and quartz tube.

Surface leakage current for 650°C annealed samples was measured in the dark and under a W lamp illumination. Figure 4 shows leakage currents between

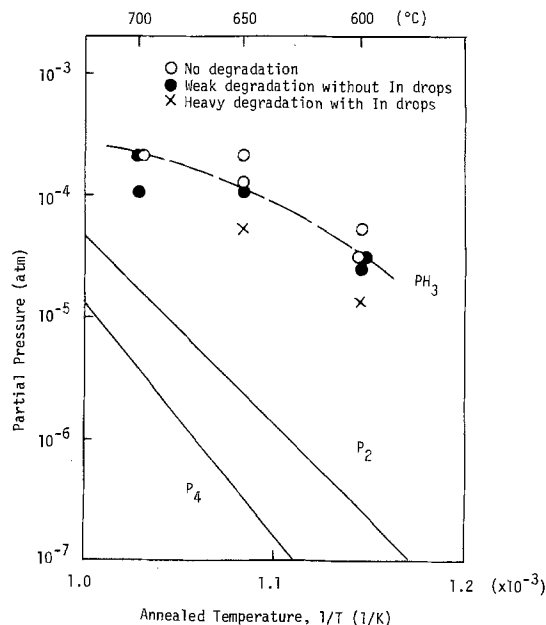


Fig. 3. (100) surface thermal degradation dependence on temperature and introduced PH_3 partial pressure. P_2 and P_4 show reported phosphorus partial pressures in equilibrium with the liquidus in the In-P system (6).

two 3 mm spaced Sn alloyed electrodes, applying 10V. In the dark, the leakage currents for 50 and 100 ppm treated samples show about twice the value for untreated sample. However, the 200 ppm treated sample shows no change from an untreated one. Excess current under the illumination is proportional to light intensity for each case. The 50 ppm treated sample, which is deeply degraded, has the largest photocurrent. This large photocurrent implies an increase in carrier lifetime near the InP surface. It was shown that the electrical conversion on the surface can also be eliminated by phosphorus ambient.

LPE growth.—Undoped InP epitaxial layers were grown under the step-cooling condition with a 10°C supersaturation temperature, flowing 60 ppm PH_3 at

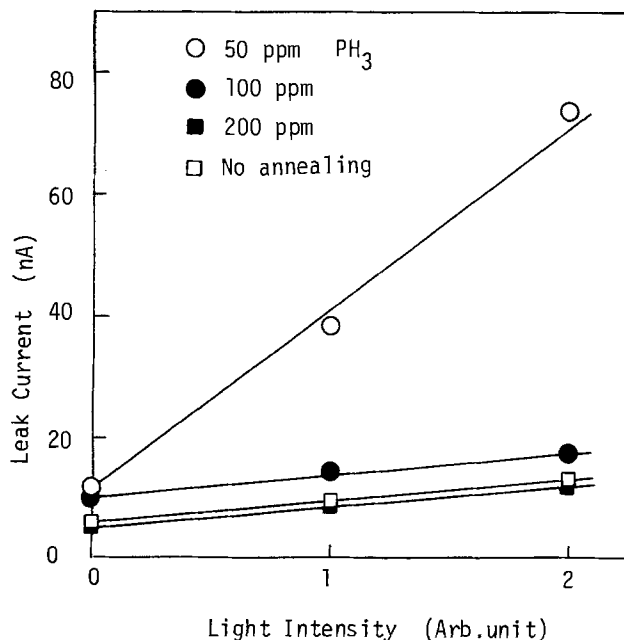


Fig. 4. Surface leakage current of annealed and nonannealed Fe-doped substrates. 10V was applied between two electrodes with 3 mm spacing.

593° and 615°C, and 120 ppm at 638°C growth temperatures. Figure 5 shows epitaxial layer thickness vs. growth time, where the melt-push type boat with a 1 mm melt thickness was used. The grown layer thickness was determined by an optical microscope on the cleaved and stain-etched layer and/or by sheet carrier variation with step-etching. The calculated saturated grown thickness was deduced from the 10°C supersaturation, indicated by ●, ○, and □. Published data by Hsieh (8) are also included in Fig. 5. Up to about 200 sec, the layer thickness varies with the \sqrt{t} law. After that time, it shows a saturation tendency. The difference between 638°C growth and Hsieh's data is reasonable in the \sqrt{t} law region. It was shown that, at relatively low growth temperature around 600°C, the InP epitaxial layer thickness was controlled to sub-micron thickness.

The morphology dependence on substrate misorientation and the effect on pushed fresh melt were also investigated. Figure 6 shows the surface of LPE layers about 0.5 μm thick, grown at 593°C. The slider boat was used for (A), (B), and (C) and the melt-push boat was used for (D). On the grown layer with (100)

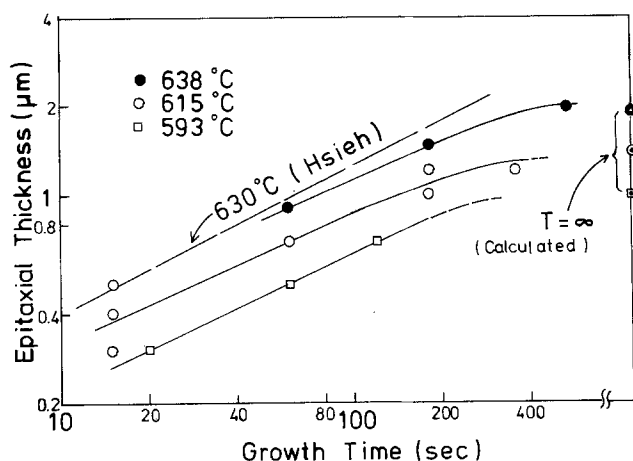


Fig. 5. Grown thickness of InP epilayers. Supercooling temperature was 10°C for each case.

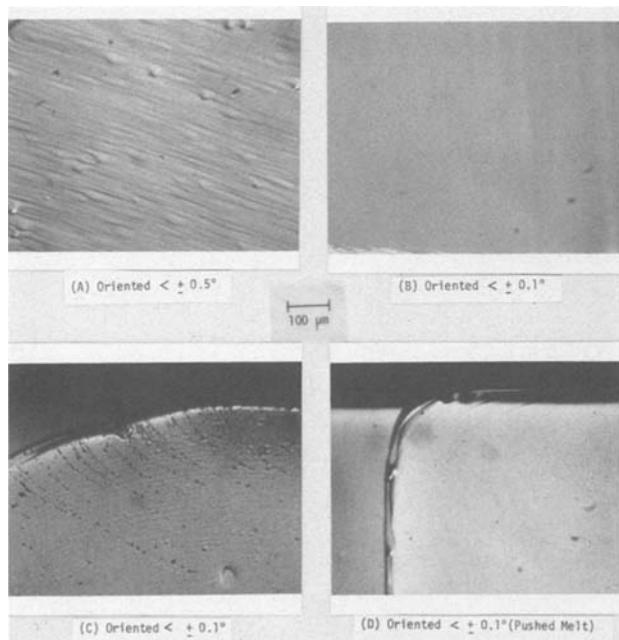


Fig. 6. Surface morphology of grown layer under the Nomarski micrograph. A conventional slider boat was used for (A), (B), and (C), and a melt-push boat was used for (D).

$\pm 0.5^\circ$ oriented substrate in Fig. 6(A), a wave-like morphology is observed. The wave direction does not depend on the wipe direction of melt. With an exactly oriented substrate (100) $\pm 0.1^\circ$ in Fig. 6(B), the "wave" is almost not seen on the surface where the growth melt wets the substrate properly. However, poor wetting sometimes occurred around the growth edge in the case of the slider boat, as shown in Fig. 6(C). Shallow voids on the epilayer were observed. Dark spots were also seen, which were considered to be slag left by growth melt when it was wiped off. When the melt-push boat was used, better and more reproducible wetting was obtained, as shown in Fig. 6(D). There is no feature in the morphology. These results indicated that adequate melt wetting with the substrate can be provided by the contact with fresh melt in PH_3 ambient growth, in spite of no melt-etching. It was made clear that the wave-like morphology arises from substrate misorientation.

The electron concentration and Hall mobility of grown layers were measured for undoped and Ge-doped InP. For undoped samples, carrier concentration of $7 \times 10^{15}/\text{cm}^3$ with 77 K mobility of 27,000 cm^2/Vsec was obtained. The Ge distribution coefficient was $K_{\text{Ge}} = 0.006$ in atomic fraction, which was in good agreement with published data (9).

The electrical properties near the interface between epilayer and substrate are important, especially for MESFET's applications, since the channel is formed there. Figure 7 shows the carrier concentration and mobility profiles in depth for Ge-doped n-InP epilayer, grown at 615°C, for 15 sec. The profiles were determined by repeated Hall measurement after every 500Å etching step. The etchant used was $\text{H}_2\text{SO}_4:\text{H}_2\text{O}_2:\text{H}_2\text{O} = 4:1:1$, which gave good uniformity for InP. The measured area was 1 mm square in the cloverleaf pattern. As shown in Fig. 7, electron mobility at the surface is 3800 cm^2/Vsec which is as large as that in the thick epilayers. The mobility decreases gradually toward the interface. Its drop near the interface is only about 20% from the surface value. The dashed line in the carrier profile shows the extrapolated slope obtained from C-V measurement. The arrow indicates the interface determined by sheet carrier variation in Hall measurement. These results imply that the thin InP epilayer grown without melt-etching has considerably good electrical characteristics and carrier profile suitable for MESFET's applications. The electron saturated velocity determined by FET's d-c characteristics is described in the next section.

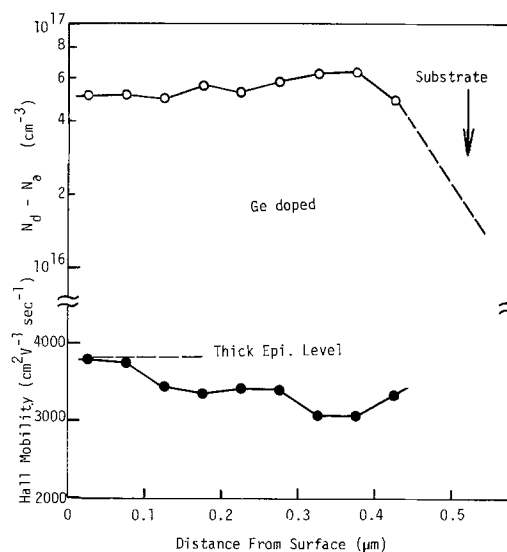


Fig. 7. Carrier concentration and Hall mobility profiles for InP epilayer grown at 615°C for 15 sec.

MESFET performances.—InP MESFET's with $0.8 \mu\text{m}$ gate length were fabricated in Ge-doped epilayer grown at 593°C . The carrier concentration and thickness of the active layer determined by Hall measurements were $n = 6 \times 10^{16}/\text{cm}^3$ and $0.3 \mu\text{m}$, respectively. The sheet mobility was $3400 \text{ cm}^2/\text{Vsec}$ and the mobility at the surface was $3600 \text{ cm}^2/\text{Vsec}$. After the device area was isolated in mesa structure by ion-milling, Au · Ge/Ni source and drain contacts were defined by the lift-off process, and were alloyed at 450°C for 15 sec. The evaporated Au · Ge/Ni thickness was 1500\AA and the source-drain spacing was $3.6 \mu\text{m}$. The recess structure was made, and then a Schottky barrier gate was formed by lifting off the vacuum evaporated Ti(1000\AA), Al(5000\AA), and Pt(100\AA). Two kinds of MESFET's with gate width of 200 and $20 \mu\text{m}$ were fabricated on the same wafer.

Drain I - V characteristics for a MESFET with a $0.8 \times 200 \mu\text{m}$ gate dimension are shown in Fig. 8. Maximum transconductance (g_m) is 22 msec and pinch-off voltage (V_p) is -2.2V . In order to evaluate the electron saturated velocity under the FET gate, the drain current v_s vs. effective gate bias V_{eff} is plotted in Fig. 9. Here, the smaller MESFET with a $0.8 \times 20 \mu\text{m}$ gate

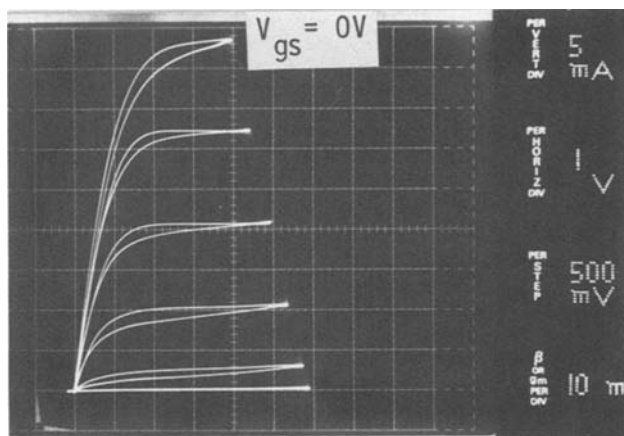


Fig. 8. Drain I - V characteristics for InP MESFET with $0.8 \times 200 \mu\text{m}$ gate dimension.

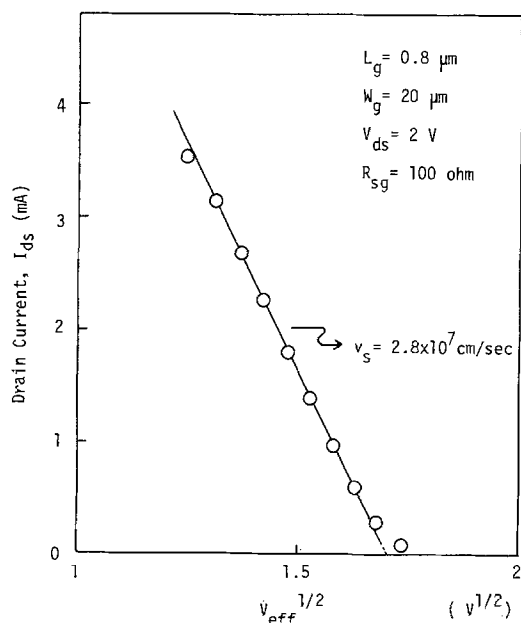


Fig. 9. Drain current vs. effective gate bias voltage $V_{\text{eff}} = V_{\text{bi}} + I_d R_{\text{sg}} + E_m \cdot L_g - V_{\text{gs}}$. The threshold field E_m of 10 kV/cm was assumed.

dimension was used for the evaluation in order to obtain the better uniformity for the pinch-off. The built-in voltage of $V_{\text{bi}} = 0.41 \text{ eV}$, measured for a large area diode, was used in the estimation. The saturated velocity was calculated as $v_s = 2.8 \times 10^7 \text{ cm/sec}$, from drain current slope (10). The slope holds its linearity up to the vicinity of the pinch-off voltage. This fact indicates the good uniformity of carrier concentration and saturated velocity. The obtained value of $v_s = 2.8 \times 10^7 \text{ cm/sec}$ is larger than that in the device fabricated by VPE grown InP layer, reported by Morkoc *et al.* (3). They estimated $v_s = 1.3 \times 10^7 \text{ cm/sec}$ for Cr-doped substrate. The evaluated velocity in the present LPE layer is as high as the peak velocity in bulk InP. Our results show that the LPE layer has good interface characteristics concerning the electron drift velocity.

The S-parameter measurement was made for the FET with $0.8 \times 200 \mu\text{m}$ gate dimension, and current gain and power gain were calculated. $|H_{21}|^2$ and $|S_{21}|^2$ are shown in Fig. 10. The current gain cutoff frequency f_T of about 40 GHz has been obtained. The maximum oscillating frequency was about $f_{\text{max}} = 46 \text{ GHz}$. The $f_T = 40 \text{ GHz}$ is about twice that in GaAs MESFET in the same dimensions, although f_{max} is smaller. The improved current gain is consistent with the high electron saturated velocity in the LPE InP active layer.

Conclusion

Thermal degradation of the Fe-doped InP surface was investigated under various PH_3 partial pressures, in order to find the condition for the eliminating of thermal pits. The InP LPE layer grown on the accurately oriented substrate had a smooth surface and showed no wave-like morphology. Fresh melt pushed just prior to the growth provided adequate wetting on the substrate without melt etching. The mobility in the epilayer was maintained large near the interface and the electron saturated velocity in the FET channel was $v_s = 2.8 \times 10^7 \text{ cm/sec}$, which almost agreed with that in bulk InP. The MESFET with 0.8

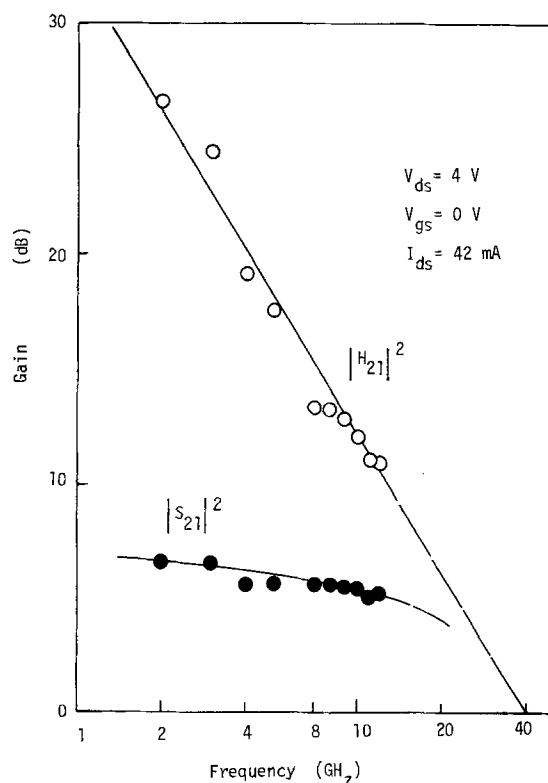


Fig. 10. Frequency dependences of $|H_{21}|^2$ and $|S_{21}|^2$ of InP MESFET with $200 \mu\text{m}$ gate width.

μm gate length showed a transconductance of 22 ms for 200 μm gate width and a current gain cutoff frequency of about 40 GHz was obtained. The results in electrical properties and rf performance indicate the capability of InP LPE growth, under the PH_3 ambient without In melt etching, for MESFET applications.

Acknowledgment

The authors are extremely grateful to Y. Ishii for supplying the photomasks designed for GaAs MESFET, and to Y. Uchida for helpful discussions in device fabrication. Also the authors would like to thank Dr. M. Ohmori, Mr. M. Fujimoto, and Dr. M. Watanabe for their encouragement and suggestions.

Manuscript submitted Dec. 12, 1980; revised manuscript received Feb. 20, 1981.

Any discussion of this paper will appear in a Discussion Section to be published in the June 1982 JOURNAL. All discussions for the June 1982 Discussion Section should be submitted by Feb. 1, 1982.

Publication costs of this article were assisted by Nippon Telegraph and Telephone Public Corporation.

REFERENCES

1. J. S. Barrera and R. J. Archer, *IEEE Trans. Electron. Dev.*, ed-22, 1023 (1975).
2. H. Morkoc, J. Andrews, S. B. Hyder, and S. G. Bandy, in "Proc. 7th Int. Symp. on GaAs and Related Compounds," Int. Phys. Conf. Ser. No. 45, pp. 295-304 (1978).
3. H. Morkoc, J. T. Andrews, and S. B. Hyder, *Electron. Lett.*, 14, 715 (1978).
4. W. Fawcett and D. C. Herbert, *ibid.*, 9, 308 (1973).
5. A. R. Clawson, W. Y. Lum, and G. E. McWilliams, *J. Crystal Growth*, 46, 300 (1979).
6. M. B. Panish and J. R. Arther, *J. Chem. Thermodyn.*, 2, 299 (1970).
7. V. S. Ban and M. Ettenberg, *J. Chem. Solid.*, 34, 1119 (1973).
8. J. J. Hsieh, in "Proc. 6th Int. Conf. on GaAs and Related Compounds," Int. Phys. Conf. Ser. No. 336, pp. 74-80 (1976).
9. M. G. Astles, F. G. H. Smith, and E. W. Williams, *This Journal*, 120, 1750 (1973).
10. H. Morkoc, S. G. Bandy, R. Sankaran, G. A. Antypas, and R. L. Bell, *IEEE Trans. Electron Dev.*, ed-25, 619 (1978).

Interfacial Structure Studies of Gold-Tin-Aluminum Metallizations on GaAlAs

S. Nakahara* and R. J. McCoy

Bell Laboratories, Murray Hill, New Jersey 07974

ABSTRACT

A transmission electron microscope (TEM) was used to study the cause for an erratic adhesion problem which occurred between Au-Sn-Al metallizations and GaAlAs during the fabrication of light emitting diodes (LED's). A cross-section study revealed that the metallization layer was actually separated from much of the GaAlAs surface by a complex void structure. The presence of such an interfacial void is thus a potential source for poor adhesion. Previous TEM studies have shown that the void structure in fact consists of two prominent features: isolated hemispherical pores and an almost continuous interfacial crack. In this work, Sn-Au interdiffusion mechanisms are proposed to explain the origin and nature of the complex void structure. Rapid grain boundary diffusion of Sn into Au and rapid bulk diffusion of Au into Sn are used to describe the origin of the observed pores. On the other hand, the occurrence of the interfacial crack is attributed to interdiffusion-induced high tensile stresses which cause the separation of the metallization layer from the GaAlAs substrate. The microstructure of the Sn and Au layers is shown to be important in determining the possible formation of such a void.

Gold-tin-aluminum metallizations are employed in the large-scale production of GaAlAs LED's for various opto-electronic devices. The processing using this metallization scheme, the details of which have been described elsewhere (1), results in ohmic contacts with excellent electrical properties. More recently, however, difficulties in achieving uniformly good adhesion between the metallization and GaAlAs were encountered with this particular procedure. This problem was solved by a simple modification of the original metallization (2).

Previous analyses of both as-deposited and post-annealed Au-Sn-Al/GaAlAs¹ interfaces have revealed the presence of voids which are seen to separate the

metallization layer from much of the semiconductor surface (2, 3). From these results it was concluded that the presence of such interfacial voids could explain the erratic adhesion obtained with the original metallization scheme. Although these analyses also showed room temperature interdiffusion of Sn and Au to be responsible for the void formation, the exact diffusion mechanisms remained unresolved.

In order to understand further how the voids are formed, we have made additional TEM studies on the original Au-Sn-Al metallization. It will be shown that the voids generally observed in previous TEM work (3) arise from rapid grain boundary diffusion of Sn into Au coupled with rapid bulk diffusion of Au into Sn. Furthermore, it is proposed that the Sn-Al interdiffusion at room temperature prior to post-annealing induces high tensile stresses in the metallization. A model using such stresses is presented as an explanation for the observed interfacial cracking.

* Electrochemical Society Active Member.

Key words: TEM, LED's, metallizations.

¹ We are here adopting a notational convention that follows successive metal layers into a substrate. For example, Au-Sn-Al/GaAlAs means that Al is the layer in contact with the substrate (GaAlAs), Sn is on top of Al, etc.

Experimental

All samples discussed in this work were metallized by conventional electron beam deposition in a vacuum of $\leq 1 \times 10^{-6}$ Torr. Some metallized GaAlAs samples were post-annealed at 420°C for 10 min in a reducing gas environment. This particular annealing treatment is employed in order to obtain ohmic contacts (1). All other samples were stored at room temperature after metallization.

Metallizations were performed on two types of substrates in this study: GaAlAs and NaCl. Samples were prepared from metallizations deposited on the n-side of (001) GaAlAs wafers. In this case, the production scheme (1) used in the fabrication of LED devices was employed. A schematic cross-sectional view of this metallization is shown in Fig. 1. Metal layer thicknesses are 35Å (Al), 500Å (Sn), and 30,000Å (Au) (1).

Air-cleaved (001) NaCl substrates were also used in this work. Here, various combinations (and thicknesses) of Al, Sn, and Au were employed as shown in Fig. 2. The use of this substrate was justified on the basis of the observation (2) that void formation essentially results from Sn-Au interdiffusion at room temperature, with the underlying substrate playing no important role in the diffusion. The use of an inert substrate such as a NaCl crystal permitted simple sample fabrication for the TEM. Metallized layers were directly examined after dissolving away the NaCl in distilled water. Cross sections of metallized GaAlAs for TEM examination were prepared by the following procedure. Metallized GaAlAs wafers were first cut into small ($0.5 \times 2.5 \text{ mm}^2$) pieces using a diamond saw. The sliced pieces were then sandwiched with their metallized faces together and glued with epoxy cement. About seven pieces could be glued as a laminate within the 3 mm diam area which is the maximum al-

lowable size for a TEM specimen stage. The wide plane, in which the metallized cross section lies, was then mechanically polished to a thickness of $\sim 25 \mu\text{m}$. The laminated samples were finally ion-milled using a Technics MIM IV ion-milling machine.

Transmission electron microscopy was carried out using a JEM 200 electron microscope operated at 200 kV. For the observation of small ($\sim 10\text{Å}$) voids, the defocus contrast technique (4) was used.

Results

Metallizations on GaAlAs.—Metallizations deposited on the GaAlAs were often found to be readily peeled off the substrate (2). The peeled face of the metal films contained a high density ($\sim 6 \times 10^6 \text{ cm}^{-2}$) of large (1000 \sim 3000Å diam) pores. A typical example of this pore structure observed on the back side of an as-deposited metallization layer is shown in Fig. 3. It was found that the pore size and shape in the as-deposited film was not significantly altered after the post-annealing treatment. This result indicates that the void formation is nearly completed during the film deposition and/or subsequent room temperature aging period prior to post-annealing. Furthermore, an examination of the peeled GaAlAs surface before annealing revealed essentially no indication of interfacial reactions with the metallization layer. This further confirms that the void formation primarily takes place during the room temperature interdiffusion of Au and Sn.

A similar void structure was also observed from cross-sectional studies of as-deposited metallizations. Figure 4 is an SEM micrograph, showing the presence of the large pores at the Au-Sn-Al/GaAlAs interface. Figure 4(b) is taken at slightly higher magnification from the regions of Fig. 4(a) in order to bring up more details of the interfacial structure. The use of the high-resolution defocusing technique in the TEM (4) permitted the detection of a hidden important structural feature in addition to the isolated pores. As seen in Fig. 5, a slit-like crack running along the exact interfacial plane is revealed. This crack apparently separates the metallization layer from most of the GaAlAs substrate surface and provides an explanation for the origin of the erratic adhesion problem in this metallization. In Fig. 5, we also note the details of a large pore, the size of which was found to be about 500Å high and 2000Å wide. In addition to the pores, there are some islands left within a thickness of 500Å from the inter-

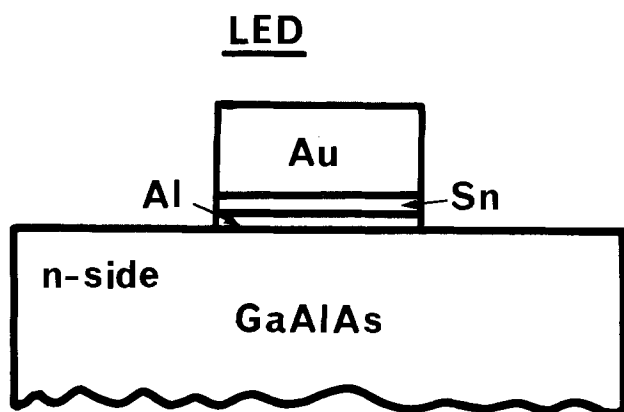


Fig. 1. A schematic view showing the cross section of the metallized n-side in GaAlAs LED's. Metal film thicknesses are 35Å (Al), 500Å (Sn), and 30,000Å (Au) (1).

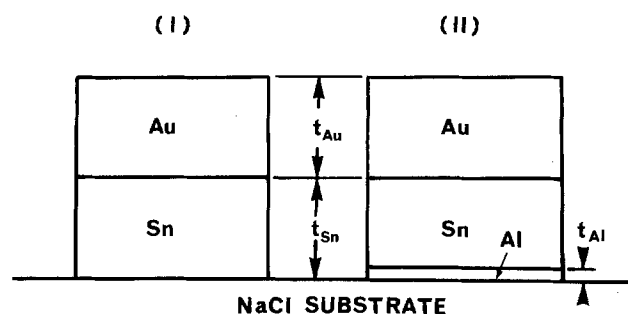


Fig. 2. A schematic view of metallization on air-cleaved (001) NaCl substrates. Two metallizations are shown: (I) Au-Sn and (II) Au-Sn-Al. Symbols, t_{Au} , t_{Sn} , and t_{Al} denote the thickness of Au, Sn, and Al films, respectively.

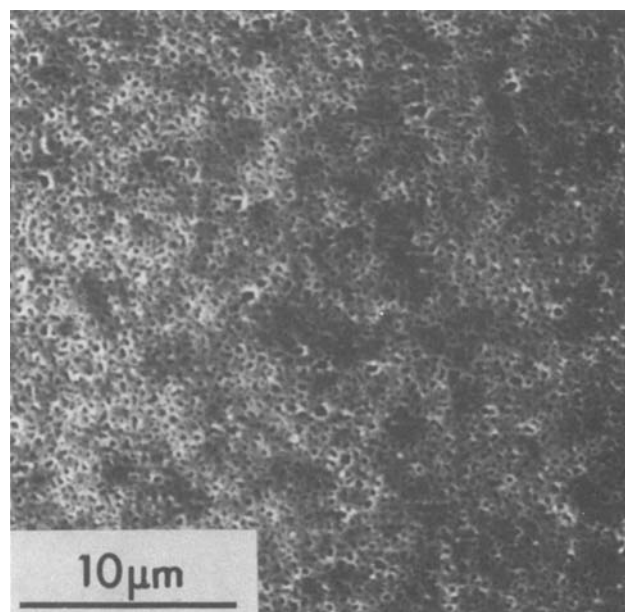


Fig. 3. SEM micrograph of the back side of an Au-Sn-Al metallization layer peeled from a GaAlAs substrate, showing a high density of large isolated pores.

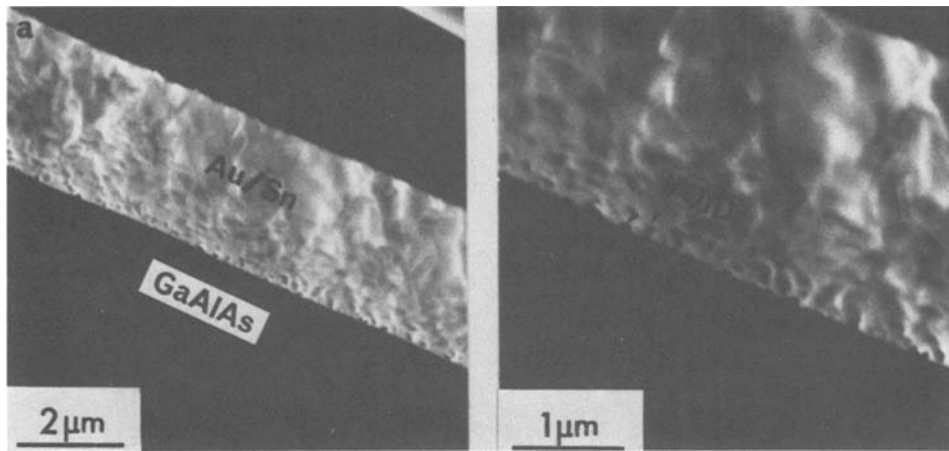


Fig. 4. SEM micrograph showing the cross-sectional view of as-deposited, metallized GaAlAs. The presence of interfacial pores is indicated with arrows in (b) which is taken at a slightly higher magnification from the region shown in (a).

face. An electron diffraction analysis has shown that these islands consist of intermetallic compound AuSn. From these observations, three prominent structural features, *i.e.*, pores, interfacial crack, and AuSn compound formation, are seen to evolve during the room temperature interdiffusion of Au and Sn.

As already mentioned, the basic void structure is not significantly altered by the post-annealing treatment. In Fig. 6, pores and interfacial crack similar to those observed in the as-deposited sample are also visible after post-annealing. An additional feature in the cross section after that treatment is the appearance of an acicular reaction product between Au and GaAlAs (see arrows in Fig. 6). Some aspects of the reaction product have previously been discussed elsewhere (3).

Metallizations on NaCl.—Figure 7 compares the structure of 500Å Sn with 500Å Sn-35Å Al films. Both films grow as islands in this thickness range, but the latter structure appears to be a little finer and more uniform than the former. The thin Al deposition seems to increase the subsequent Sn nucleation density, thus resulting in the somewhat more uniform structure. As will be seen below, this minor structural modification is not significant for the void formation.

With the use of an offset configuration (5) in the deposition pattern, it is demonstrated in Fig. 8 how the metallization structure evolves after Au is deposited on Sn. In the offset configuration, three regions, *i.e.*, pure Au, Au-Sn (or Au-Sn-Al) overlap, and pure Sn (or Sn-Al) can be fabricated simultaneously on one substrate by masking a portion of the substrate for an

Sn (or Sn-Al) deposition, and offsetting the mask before Au is deposited. Figures 8(a), (b), and (c) represent the structure of 500Å Au, 500Å Au-500Å Sn-35Å Al, and 500Å Sn-35Å Al films obtained from the offset configuration. Comparing Fig. 8(a) and (c) with (b), we find that the overlap region (b) appears to be effectively the superposition of the structures (a) and (c). In detail, however, the overlap region is not exactly the superposition of the two. It is noted in Fig. 8(b) that voids are formed around the perimeter of each Sn island. An electron diffraction analysis has shown that the islands surrounded by the voids consist of AuSn, whereas the fine-grained film outside the islands is pure Au. The presence of Al could not be detected. It is interesting to note that the overlap region is characterized as a duplex structure, in which reacted AuSn islands and unreacted pure Au exist. Finally, in Fig. 9, the overlap region of 500Å Au-500Å Sn also shows a similar duplex structure to that of 500Å Au-500Å Sn-35Å Al [compare with Fig. 8 (b)]. This demonstrates that the Al deposition plays a minor role in the Au-Sn interdiffusion.

Discussion

It has been previously shown that the void formation primarily takes place during room temperature inter-

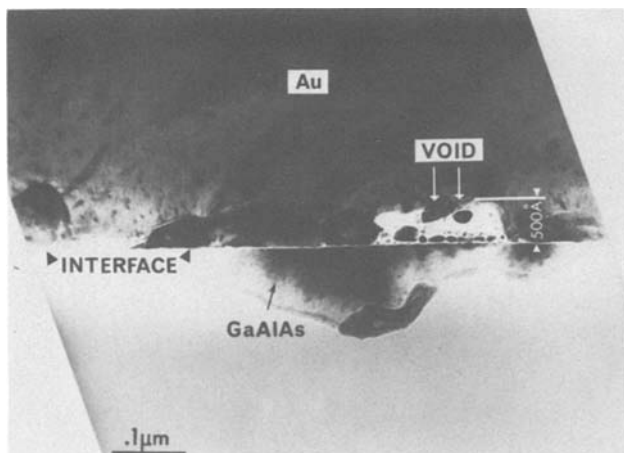


Fig. 5. TEM micrograph of the cross section of metallized, as-deposited GaAlAs, taken using the high-resolution defocusing technique (4). In addition to an interfacial void, the presence of a slit-like crack is now revealed along the exact interfacial plane. Due to a preferential etching effect by ion-milling, only a small piece of GaAlAs is seen to remain.

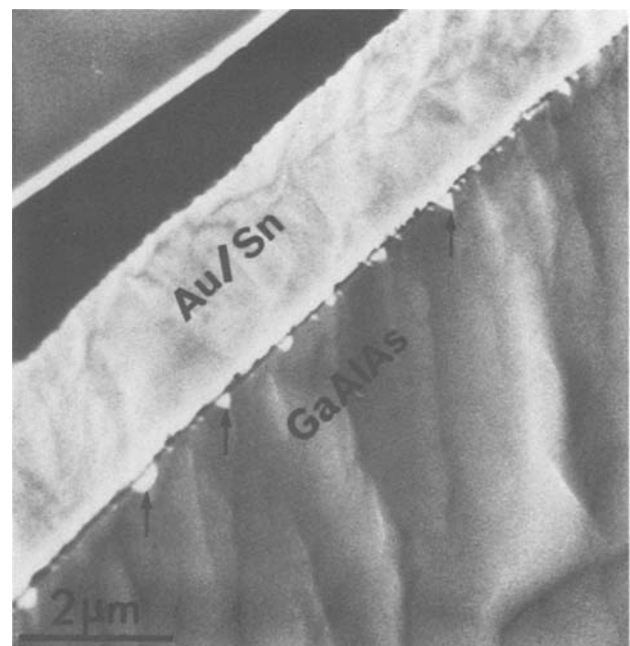


Fig. 6. Cross-sectional view of metallized GaAlAs after post-annealing. In addition to the presence of voids and interfacial crack, acicular reaction products (such as denoted by the arrows) are seen to have grown into the GaAlAs.

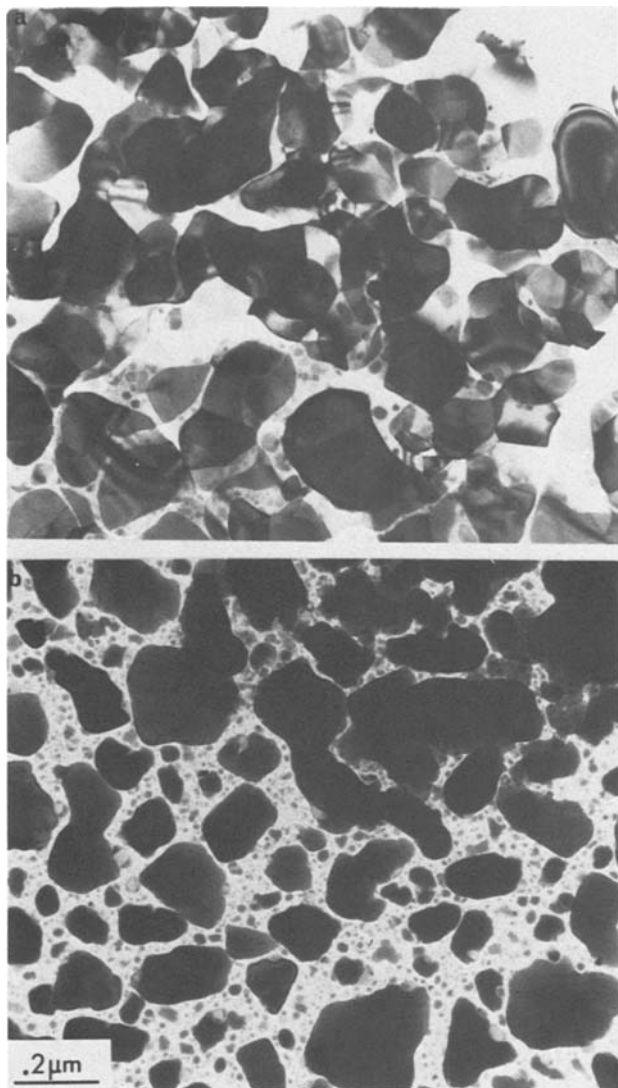


Fig. 7. Structure of (a) 500 Å Sn and (b) 500 Å Sn-35 Å Al films deposited on NaCl. Both films are seen to grow in the form of islands but (b) appears to produce somewhat smaller and more uniform islands than (a).

diffusion of Sn and Au (2). The obvious conclusion from the analysis of the metallized GaAlAs samples is that Sn is the faster diffusing species in an Sn-Au diffusion couple, as Sn is found to diffuse into Au completely, leaving apparently large Kirkendall voids (pores). This conclusion is, however, not consistent with past work (6) where it was found that Au is the faster diffusing species in Sn-rich Sn-Au alloys. On the other hand, the void structure in the Au-Sn and Au-Sn-Al films prepared on NaCl clearly demonstrates that Au is the faster diffusing species, in agreement with Ref. (6). In this case, the rapid diffusion of Au into Sn islands transforms the islands into intermetallic compound AuSn and at the same time produces void regions around the perimeter. The formation of these voids effectively prevents the surrounding Au from further reaction. This in fact explains why the duplex structure (e.g., Fig. 8b) of reacted and unreacted regions is produced.

Thus, Sn-Au interdiffusion observations on metallized GaAlAs and NaCl give apparently opposite identities for the fast diffusing species. Moreover, the shape of the voids produced in these two systems is different. For the case of Au-Sn-Al films on NaCl, one sees voids delineating the perimeters of AuSn islands. On the other hand, pores are observed at Au-Sn-Al/GaAlAs interfaces and these possess an empty, roughly hemispherical shape. It is clear that an understanding of the exact diffusion mechanism (or mechanisms) is needed to interpret these results.

One obvious difference between the NaCl and GaAlAs samples is the film thicknesses employed. The metallizations on GaAlAs have a thickness ratio t_{Au}/t_{Sn} which is extremely large (~ 60) and corresponds to $\sim 99\%$ Au-rich alloy if complete intermixing is assumed. Diffusivities for both Au and Sn in Au-rich alloys have been previously determined (7, 8). When extrapolated to room temperature (25°C), these diffusivities amount to $10^{-32} \sim 10^{-29} \text{ cm}^2/\text{sec}$ for Au and $10^{-27} \sim 10^{-26} \text{ cm}^2/\text{sec}$ for Sn in Au-Sn alloys for which $C_{Sn} = 0 \sim 1.5$ atomic percent (a/o). Such bulk diffusivities are extremely small and cannot account for the Au-Sn-Al/GaAlAs observations. On the other hand, the metallizations performed on NaCl have a thickness ratio $t_{Au}/t_{Sn} \sim 1$, corresponding to $C_{Sn} \sim 40$ a/o. In this range, the room temperature diffusivity of Au can be estimated from AuSn phase growth rates (9) to be $\sim 10^{-14} \text{ cm}^2/\text{sec}$. This high value can indeed account for the perimeter void growth observed in Fig. 8 and 9. Thus, the concentration dependence of the bulk diffusivity of Au in Au-Sn alloys explains why

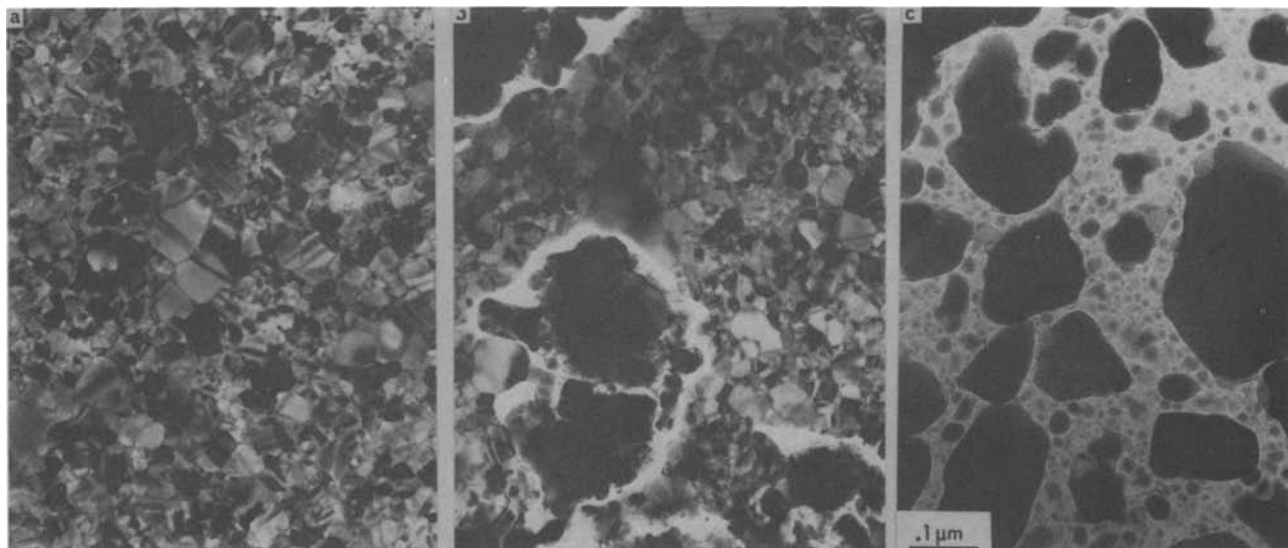


Fig. 8. TEM micrographs showing the structure of (a) 500 Å Au, (b) 500 Å Au-500 Å Sn-35 Å Al, and (c) 500 Å Sn-35 Å Al films deposited on NaCl in an offset (5) configuration. Note that voids around the perimeter of the original Sn islands delineate the islands and leave pure fine-grained Au unreacted.

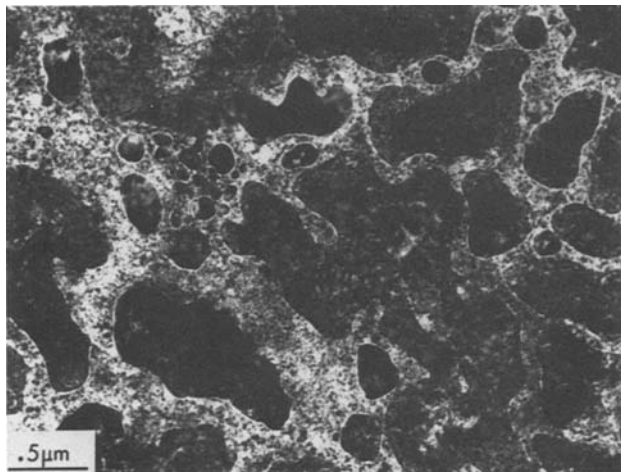


Fig. 9. Structure of 500Å Au-500Å Sn film deposited on NaCl. The film exhibits a well-defined duplex structure, in which the original Sn islands are seen to be delineated by the formation of voids around their perimeter. Unreacted pure Au surrounds the islands.

rapid Au diffusion is not observed in the case of the GaAlAs samples.

The above discussion shows that the observed rapid diffusion of Sn into Au seen for Au-Sn-Al/GaAlAs cannot be accounted for by a bulk diffusion mechanism. The only other possible mode of Sn diffusion is through Au grain boundaries. Indirect evidence supporting this diffusion mechanism can be found in an Auger electron spectroscopy (AES) analysis of similar metallized GaAlAs specimens (10). Depth profiling has shown that an as-deposited Au-Sn-Al film contains an essentially constant amount of Sn throughout the Au thickness and $\sim 25\text{\AA}$ Sn on top of the Au surface. We interpret these results as follows. The constant Sn concentration throughout the Au thickness suggests that the high diffusing paths along Au grain boundaries homogenize the Sn concentration, as opposed to the usual bulk diffusion in which a gradual concentration decay of Sn from the interface is expected. The presence of 25\AA Sn on the top surface of Au is probably due to the formation of SnO_2 (10). If the rapid diffusion of Sn into Au is due to a grain-boundary mechanism, most of the diffused Sn atoms are expected to lie in Au grain boundaries unless an infinite Sn consumption occurs at the Au surface by the formation of, for example, SnO_2 . As already seen by AES (10), the Au top surface is not an infinite sink for Sn atoms. The possibility that all diffused atoms can be accommodated in Au grain boundaries is readily justified. If it is assumed that the average grain size in the $30,000\text{\AA}$ thick Au film is 250\AA (5), a simple calculation shows that the available grain boundary area greatly exceeds the space which would be required by monolayer coverage of all the Sn atoms in the 500\AA thick Sn layer. Therefore, most of the Sn atoms can diffuse out from the Sn layer and leave the observed pores at the interface. It should be noted that the Sn atoms lying at Au grain boundaries do not diffuse into Au grains, as this diffusion process involves the extremely small bulk diffusivity of Sn in Au-rich alloys (7, 8). The grain boundary diffusion mechanism postulated here has been directly verified in other work (5).

It has been shown that the deposition of the thin (35\AA) Al film plays a minor role in the void formation. The Al layer appears only to increase the nucleation sites for the subsequent Sn deposition (Fig. 7). Examination of thicker (500\AA Sn- 500\AA Al) films has shown that the Al film and the subsequent Sn layer maintain their original structure without detectable interdiffusion. Furthermore, the depth profile obtained by AES also shows (10) that the Al layer is retained

at the interface without appreciable diffusion. From these observations, it is reasonable that the room temperature interdiffusion takes place between only Au and Sn without significant influence from the thin Al deposition.

The above observations now permit the construction of a model of how the pore formation observed at the Au-Sn-Al/GaAlAs interface comes about. It is clear that rapid grain boundary diffusion of Sn into Au is operating. Furthermore, the presence of AuSn compound formation indicates that rapid bulk diffusion of Au into Sn is simultaneously present. The observed large pore sizes, however, indicate that Sn grain boundary diffusion is dominant. The fact that AuSn formation proceeds at a diffusivity of $\sim 10^{-14}$ cm²/sec at room temperature (9) then sets this value as a lower bound for the grain boundary diffusivity of Sn into Au.

It is interesting to note from these observations that the Au-Sn system possesses rapid, room temperature diffusion mechanisms for both species which can operate at the same time and in opposite directions. Additionally, it is seen that variation of $t_{\text{Au}}/t_{\text{Sn}}$ can identify and separate these mechanisms (5).

It is well known (11) that rapid interdiffusion generates high stresses and can induce a local plastic deformation. For example, the formation of dislocations has been observed during interdiffusion (12, 13) as has the formation of cracks (14). During the Au-Sn interdiffusion, high tensile stresses are therefore expected to be developed near and/or at the Au-Sn-Al/GaAlAs interface. If grain-boundary diffusion is assumed to be the dominant interdiffusion mechanism, it is possible to estimate the magnitude of this interdiffusion-induced tensile stress. Using the formula given by Schlipf (15), we obtain $\sim 1.5 \times 10^8$ g/cm² (1.1×10^{10} psi) for the stress. This value is a few orders of magnitude larger than the yield stress of any solid, and thus a plastic deformation is inevitable during interdiffusion.

Since, for the case of Au-Sn-Al/GaAlAs, the metal layers are known to be weakly bonded to the substrate (2), the induced tensile stress will act primarily to break the bonding, resulting in the observed interfacial cracking. The way the interfacial cracking proceeds is shown schematically in Fig. 10. Here, Sn atoms diffuse out of the islands and travel along a network of Au grain boundaries. During this diffusion, a high tensile stress develops in such a way that the interfacial bonding is broken. The Sn outdiffusion also leaves voids similar in shape to the original Sn islands.

The details of the stress development, of course, depend on the Sn morphology. Since the Au-Sn interface follows the profile of the Sn islands, a more complex stress pattern is to be expected than for the case of a planar interface (14). The initially high stresses become gradually smaller as void nucleation and growth proceeds at the sites of the Sn islands. The tendency of stress relaxation has been discussed theoretically by Schlipf (15) and observed experimentally by Geguzin *et al.* (14).

The occurrence of interdiffusion-induced stress cracking has also recently been noted by Buene (16) in a similar thin film couple. According to his observation, during the deposition of Au onto a previously In-coated bell jar wall, a violent reaction between Au and In takes place, resulting in the film cracking and flaking off the bell jar wall. This observation suggests that an interdiffusion-induced high stress develops during the Au deposition leading to cracking at the weakly-bonded interface between the metal film and the glass.

The erratic adhesion problem associated with the Au-Sn-Al metallization on GaAlAs has been recently solved (2) by an alternative metallization in the sequence Au-Sn-Au-Al (28 kÅ Au, 500Å Sn, 2 kÅ Au, 35Å Al). Cross-section studies of this metallization have indicated the absence of both pores and interfacial crack (2, 3). From our proposed model of interdiffusion-induced tensile stress, it is now clear that the deposition of 2000\AA Au prior to the Sn layer is essential in

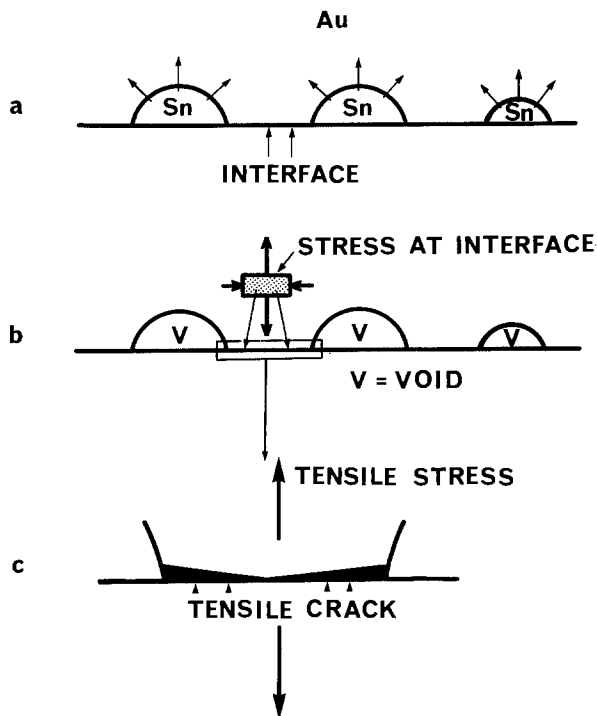


Fig. 10. A schematic view illustrating how interfacial cracking may take place during the Au-Sn interdiffusion. The illustration shows that Sn diffuses rapidly along Au grain boundaries in (a). This interdiffusion induces a tensile stress which acts to separate the film from the substrate and at the same time form voids at the sites of Sn islands as shown in (b). The action of the tensile stress results in the interfacial cracking shown in (c).

order to avoid the generation of stress at the GaAlAs interface. Furthermore, the absence of pores strongly indicates that both bulk and grain boundary diffusions are taking place uniformly. With respect to the GaAlAs interface, the essential change in the new metallization scheme is from Au-Sn to Sn-Au. We also deposited Sn-Au films on NaCl in order to see how the structure might change from that of Au-Sn. Figure 11 compares the microstructures of (a) 500Å Au-500Å Sn with (b) 500Å Sn-500Å Au. It is seen that the new scheme provides a considerable improvement in homogeneity. This observation is consistent with that of Buene *et al.* (17). Homogeneity in the Sn-Au metallization indicates that Sn nucleates uniformly on Au. This suggests an absence of void formation within the LED metallization for the sequence Au-Sn-Au-Al.

Conclusion

A transmission electron microscope was used to determine the cause for an erratic adhesion problem which occurred between Au-Sn-Al metallization layers and GaAlAs substrates. A cross-section study of the Au-Sn-Al/GaAlAs interface revealed the presence of large isolated pores and a slit-like interfacial crack. The formation of the pores and interfacial crack were found to result primarily from the room temperature interdiffusion of Sn and Au. It is proposed that the rapid diffusion of Sn into Au via a grain-boundary mechanism induces high tensile stresses which cause the separation of the metallization layer from much of the GaAlAs substrate. This interdiffusion-induced high stress can be partially relieved by the formation and growth of pores at the sites of original Sn islands. Structural comparison with metallizations on NaCl substrates provided additional information on the nature of Au-Sn interdiffusion mechanisms, in which both bulk and grain boundary diffusions are found to be operative. A model for the interfacial cracking is proposed to explain the origin of the erratic adhesion problem in Au-Sn-Al metallization scheme.

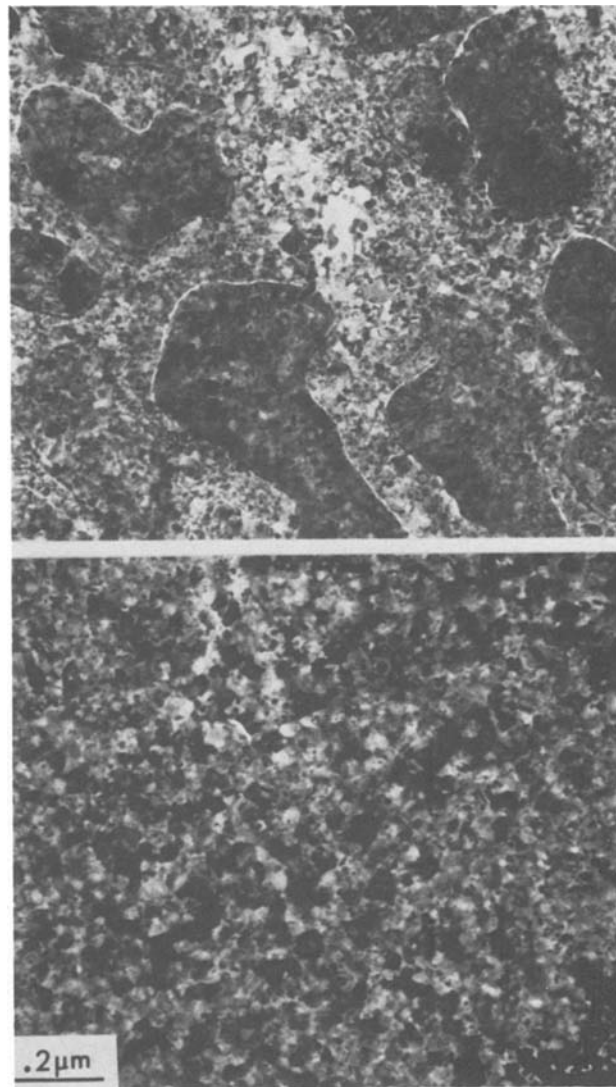


Fig. 11. Structural comparison of (a) 500Å Au-500Å Sn with (b) 500Å Sn-500Å Au films grown on NaCl. Note the significant difference in structural homogeneity between the two.

Acknowledgment

The authors wish to thank Dr. L. Buene for useful discussions and for showing his results prior to publication. We are also grateful to L. B. Hooker for his careful sample preparation.

Manuscript submitted Nov. 26, 1980; revised manuscript received March 2, 1981.

Any discussion of this paper will appear in a Discussion Section to be published in the June 1982 JOURNAL. All discussions for the June 1982 Discussion Section should be submitted by Feb. 1, 1982.

Publication costs of this article were assisted by Bell Laboratories.

REFERENCES

1. V. G. Keramidas, in "Proceedings of the Int. Symp. on GaAs and Related Compounds," St. Louis, 1978, Institute of Physics Conf. Series No. 45, p. 396, London.
2. R. J. McCoy and F. Ermanis, Paper presented at the Third IEEE Specialist Conf. on the Technology of Electroluminescent Diodes, San Francisco, 1978 (Unpublished).
3. C. C. Chang, T. T. Sheng, R. J. McCoy, S. Nakahara, V. G. Keramidas, and F. Ermanis, *J. Appl. Phys.*, **50**, 7030 (1979).
4. S. Nakahara and Y. Okinaka, in "Properties of Electrodeposits—Their Measurement and Significance," Chap. 3, R. Sard, H. Leidheiser, Jr., and F. Ogburn, Editors, The Electrochemical Society

- Softbound Proceedings Series, Princeton, N.J. (1975).
5. S. Nakahara and R. J. McCoy, *Appl. Phys. Lett.*, **37**, 42 (1980).
 6. B. F. Dyson, *J. Appl. Phys.*, **37**, 2375 (1966).
 7. C. Herzig and T. Heumann, *Z. Naturforsch. Teil A*, **27**, 1109 (1972).
 8. C. Herzig and W. Wiemann, *Phys. Status Solidi A*, **26**, 459 (1974).
 9. L. Buene, *Thin Solid Films*, **47**, 159 (1977).
 10. C. C. Chang, V. G. Keramidas, and R. J. McCoy, Unpublished results (1980).
 11. J. A. Brinkman, *Acta Metall.*, **3**, 140 (1955).
 12. P. S. Ayres and P. G. Winchell, *J. Appl. Phys.*, **39**, 4820 (1968).
 13. P. S. Ayres and P. G. Winchell, *ibid.*, **43**, 816 (1972).
 14. Y. Y. Geguzin, A. M. Kudin, and L. N. Paritskaya, *Phys. Met. Metall.*, **45**, 142 (1979).
 15. J. Schlipf, *Acta Metall.*, **21**, 435 (1973).
 16. L. Buene, Private communication.
 17. L. Buene, H. Falkenberg-Arell, and J. Taftø, *Thin Solid Films*, **65**, 247 (1980).

An Analysis of Color-Changing Penetration-Type Cathodoluminescent Phosphor Screens

Willi Lehmann*

Westinghouse R&D Center, Pittsburgh, Pennsylvania 15235

ABSTRACT

Electron penetration through solid barrier layers into polycrystalline cathodoluminescent phosphors can be described by a relatively simple mathematical equation which, in turn, permits the computation of color changes available from phosphor blends containing such coated particles. An extension of the analysis covers also multilayer cathodoluminescent films. The calculations permit predetermination of the efficiencies and color characteristics of such screens and design of screens to meet given specifications.

The principle most frequently used in voltage-sensitive color-changing cathodoluminescent phosphor screens involves a simple blend of two individual phosphor powders of different colors and of different brightness-voltage dependences. For instance, the blend may consist of a red and a green component. The red phosphor may be a normal material showing essentially linear voltage dependence of the emission intensity while the particles of the green phosphor are overcoated with nonluminescent surface layers which the electrons have to penetrate to reach the luminescent core. The emission intensity, B , of such "onion-skin" phosphor" increases strongly superlinearly with low voltage, V , but approaches roughly linear dependence above a somewhat diffuse threshold, the "dead voltage," V_0 .¹ An example is shown in Fig. 1. It is clear that the emission color of such blend varies with the voltage; it is more red at low and more green at high voltage.

Several variations of color-changing phosphors have been described in the literature (1-10) but at least some of them appear to be obtained only by trial and error and are far from optimized. The technically most important aspects are the efficiency which, naturally, is desired to be as high as possible, the voltage range where the color change occurs, and the rate of color change within this voltage range. The following analysis offers a way to calculate these properties in advance for any given phosphor combination and permits (within limits) tailoring the phosphor blends to given specifications. The analysis is first limited only to phosphor powders but later is extended to cover phosphor films. For simplicity, only color changes between red and green will be considered but the analysis also is applicable to phosphor systems changing between any two given end colors.

* Electrochemical Society Active Member.

Key words: phosphors, luminescence, cathodoluminescence, color, electron penetration.

¹The expression "dead voltage" is somewhat of a misnomer since some weak emission appears even below V_0 . Nevertheless, it is so much in common use that it may be maintained here.

Phosphor Powders

Most of our experimental work on color-changing phosphor powders was restricted to blends of green $\text{Zn}_2\text{SiO}_4:\text{Mn}^{2+}$ (ZS) and red $\text{YVO}_4:\text{Eu}^{3+}$ (YVOE). The particles of the latter were left uncoated while those of the ZS were coated with layers of Al_2O_3 by precipitation of $\text{Al}(\text{OH})_3$ out of aqueous solution of $\text{AlNH}_4(\text{SO}_4)_2$ and subsequent dehydration of the hydroxide. An example of such coated particles is shown in Fig. 2. The phosphors were tested in a demountable cathode ray tube with E-beams of low current density ($\sim 1 \mu\text{A}/\text{cm}^2$). The emission intensities were compared to that of uncoated ZS whose brightness-voltage dependence was ascertained to be essentially linear over the voltage range of interest (~ 5 -25 kV) except an insignificant dead voltage ($\sim 60\text{V}$) possibly due to surface contaminations on the particles.

The emission intensity of the uncoated YVOE varies essentially linearly with voltage so that the efficiency is approximately constant. The external efficiency of

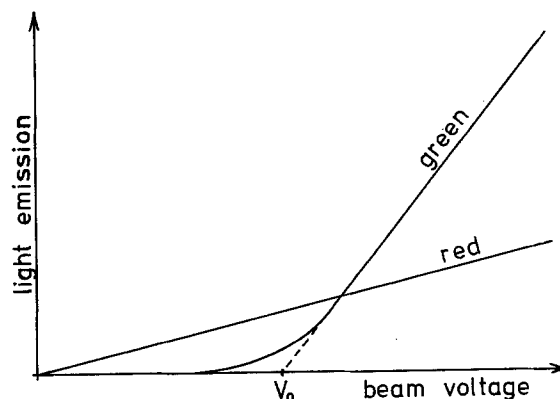


Fig. 1. Emission contributions from two phosphor components in a color-changing penetration-type cathodoluminescent screen (schema).

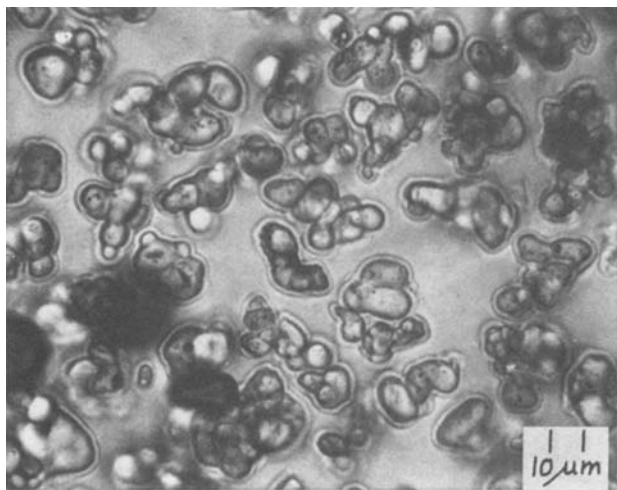


Fig. 2. ZS phosphor particles coated with aluminum oxide. $V_0 = 13$ kV.

the coated ZS, however, varies strongly with the voltage, and this variation depends on the thickness and on the uniformity of the dead coat. Defective and nonuniform coats can visually be identified by optical microscopy; they cause the efficiency to vary relatively slowly with the voltage. Conversely, the more uniform the coat is the steeper does the efficiency, η , increase with the voltage, V . In best samples where microscopic inspection reveals nearly defect-free coats of uniform thickness, we observe a good fit of the experimental data to the equation

$$\eta = A \exp(-2V_0^2/V^2) \quad [1]$$

where V_0 is the dead voltage. The constant A contains the internal efficiency of cathodoluminescence of the uncoated material and the current density of the exciting E-beam. This equation has been tested on many samples in diagrams where $\log \eta$ is plotted as function of $1/V^2$. Some examples are shown in Fig. 3. The coating on sample C in Fig. 3 is slightly imperfect, causing a deviation from the straight line at low voltage. Included in Fig. 3 are also points (curve E) taken from a diagram published by Kingsley and Prener (5) on coated ($0.381 \mu\text{m}$) ZnS phosphor claimed to be very uniform in coat thickness. The good fit to straight lines is evident. We believe it to indicate that Eq. [1] very closely describes the voltage dependence of cathodoluminescence of coated phosphors under best conditions.

It is somewhat surprising that an equation as simple as [1] can describe the situation so closely. Neverthe-

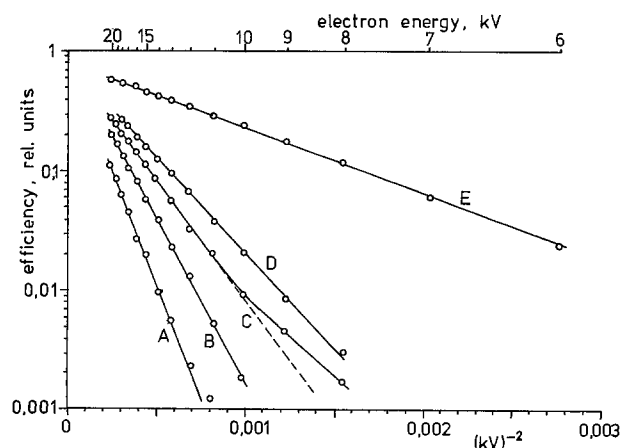


Fig. 3. Efficiencies of some coated phosphors showing validity of Eq. [1].

less, we do not believe Eq. [1] to have a simple physical interpretation. Electron penetration through thin layers is a very complicated effect, particularly if these thin layers cover irregularly shaped and oriented phosphor particles. Equation [1] probably is nothing more but a good approximation describing a much more complicated reality.

Since the emission intensity, B , is proportional to $\eta \times V$, the $B(V)$ dependence of a coated phosphor follows

$$B = AV \exp(-2V_0^2/V^2) \quad [2]$$

This equation is graphically shown in Fig. 4 for several different values of V_0 . Although the approximation to straight lines at $V > V_0$ is quite good, the $B(V)$ dependence in that range is not linear but is S-shaped and contains a point of inflection which, by differentiation, is determined to be at $V_1 = 2V_0$. The slope of the curve at that point is $dB/dV = 2A \exp(-1/2) \approx 1.213A$ and the tangent through it intersects the abscissa at V_0 . For an uncoated phosphor, of course, $V_0 = 0$ and $B = AV$.

The opposite of a phosphor particle coated with a dead layer is a dead particle coated with a phosphor layer (11). Its $B(V)$ dependence must be the difference between that of an uncoated phosphor ($V_0 = 0$) and Eq. [2] i.e.

$$B = AV [1 - \exp(-2V_0^2/V^2)] \quad [3]$$

This function is graphically shown in Fig. 5. It may especially be noted that the curves go through a maximum and approach zero (although very slowly) with increasingly high values of V .

In either case, the quantity V_0 measures the layer thickness. The relationship between V_0 and the physical thickness, S , of the surface layer is not linear. It has been determined by Kingsley and Prener (5) to be approximately $S = CV_0^{5/3}$ which is very close to

$$S = CV_0^{5/3} \quad [4]$$

In this instance, C is a constant essentially describing the stopping power of the material for electrons. For Al_2O_3 and for ZnS, $C \approx 0.0115$ if the thickness is measured in μm and the dead voltage in kV. For other coatings, the stopping power can reasonably be expected to be proportional to the densities of the coating materials.

The above equations can be used to calculate the characteristics of color-changing phosphor blends as

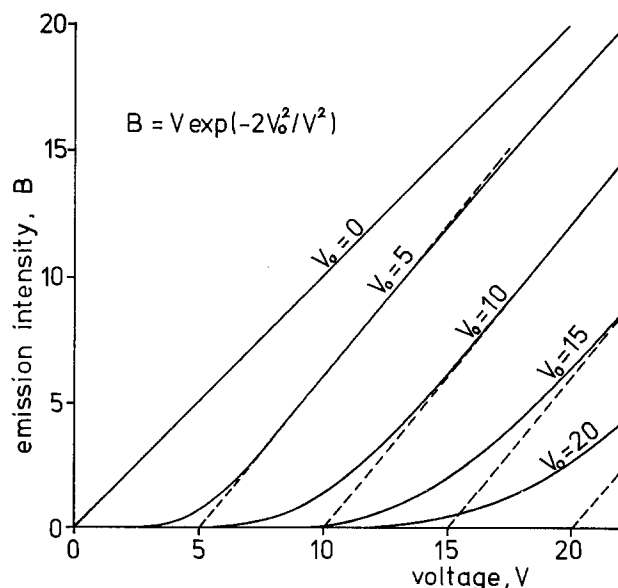


Fig. 4. $B(V)$ functions of phosphor particles surrounded by dead layers.

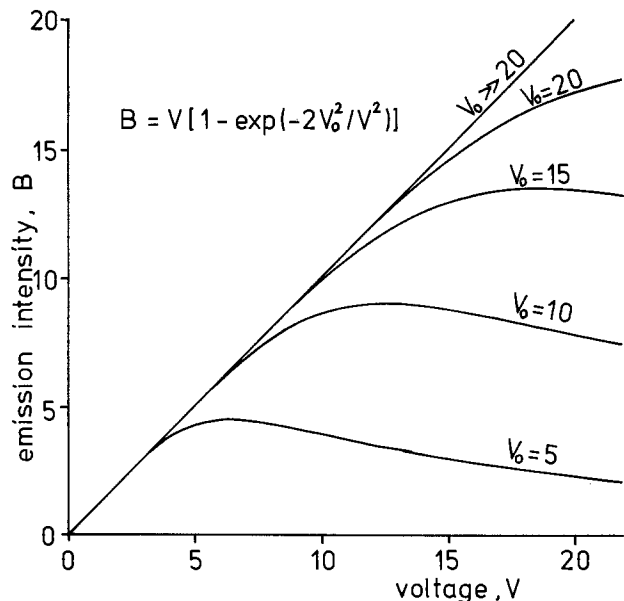


Fig. 5. $B(V)$ functions of dead particles surrounded by phosphor layers.

function of the electron beam voltage. An example is shown in Fig. 6 for the assumed case of a blend consisting of 8% (by volume) of red YVOE and 92% green ZS. The particles of the latter are coated with a dead layer corresponding to $V_0 = 16$ kV which, for Al_2O_3 , translates to a physical thickness of about 1.2 μm . Figure 6 indicates the red-green color shift to occur between about 12-20 kV.

Phosphor Films

Cathodoluminescent film screens consisting of several phosphor and other layers deposited on top of each other have been reported by Feldman (12-14).

For an analysis, consider a thin nonluminescent film covering a thick phosphor film (Fig. 7, top) The exciting electrons have to penetrate the dead film to reach and excite the phosphor. The situation is qualitatively identical to the case of a coated phosphor powder but it is quantitatively different because of the different geometry. Certainly, Eq. [1] cannot be used to describe the $B(V)$ dependence. An approach is possible by a generalization of Eq. [1]

$$B_1 = AV \exp [-a(V_{01}/V)^n] \quad [5]$$

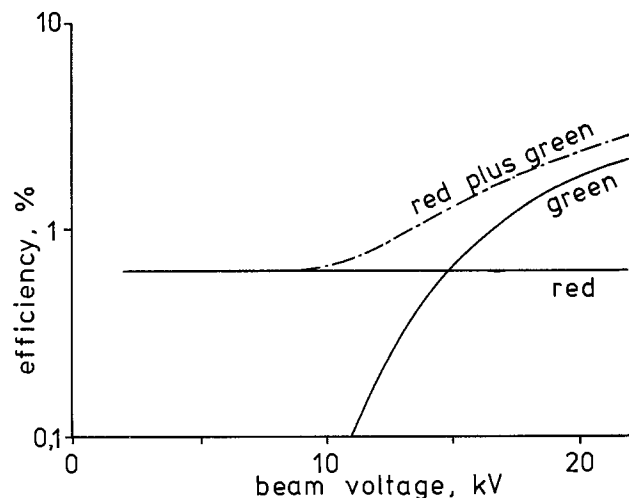


Fig. 6. Characteristic of a powder screen containing a blend of 8% red YVOE (uncoated) and 92% green ZS (coated, $V_0 = 16$ kV). The efficiencies of uncoated YVOE and ZS are assumed to be each 7%.

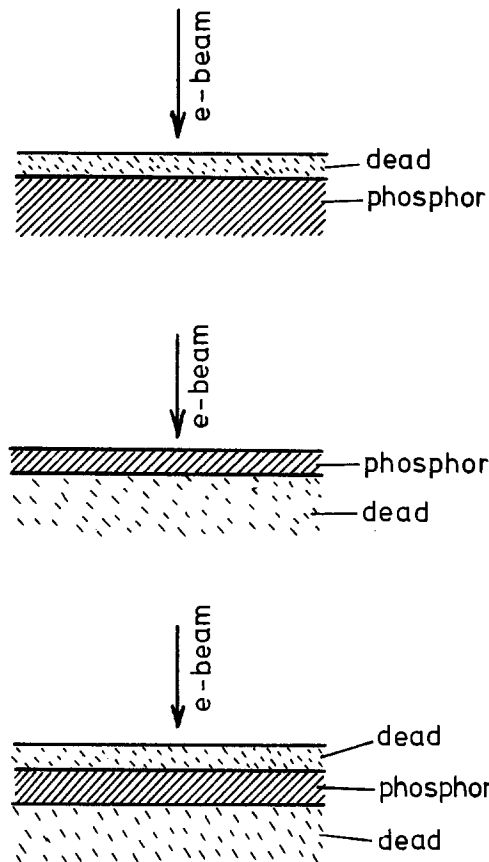


Fig. 7. Some combinations of phosphor and dead films

where the values of the constants a and n still have to be determined. As in case of Eq. [1], the dead voltage, V_{01} , may be defined by the intersection of the tangent through the point of inflection of the S-shaped curve with the abscissa. Differentiation yields the relationship

$$a = [n/(n - 1)]^{n-1} \quad [6]$$

As in case of powders, $V_{01} = 0$ means a plain phosphor without dead material, responding linearly to the voltage: $B = AV$. The difference between this and Eq. [5]

$$B_2 = AV \{1 - \exp [-a(V_{02}/V)^n]\} \quad [7]$$

must be the $B(V)$ dependence of a thin phosphor film covering a dead substrate (Fig. 7, center). One might also visualize a phosphor film on a dead substrate and covered by a dead film (Fig. 7, bottom). The $B(V)$ dependence of such structure follows a combination of [5] and [7] to be

$$B_3 = AV \{\exp [-a(V_{01}/V)^n] - \exp [-a(V_{02}/V)^n]\} \quad [8]$$

where V_{01} represents the thickness of the top dead layer and V_{02} the combined thickness of the top dead layer and the phosphor layer. An approximate conversion to physical thickness is again possible with the help of Eq. [4].

Equation [7] has been checked against a $B(V)$ curve on Gd_2O_3 (0.35 μm thick) published by Prener (15). A very good fit is obtained for $n = 8/3$ (Fig. 8). Accepting this value, the constant a becomes

$$a = (8/5)^{5/3} \approx 2.189$$

and above equations change to

$$B_1 = AV \exp [-2.189(V_{01}/V)^{8/3}] \quad [5a]$$

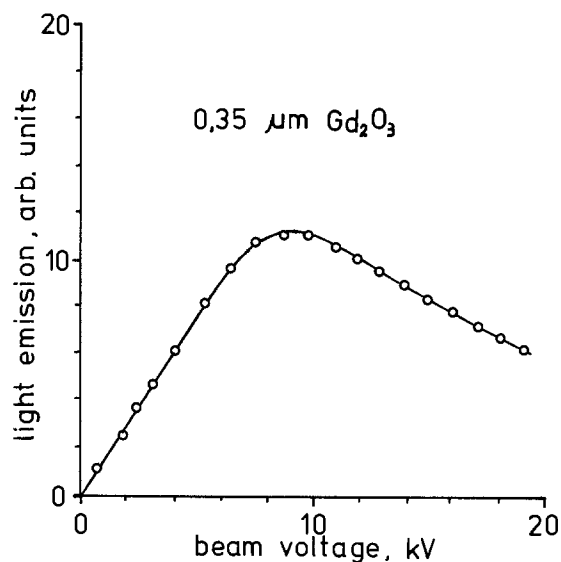


Fig. 8. Fit of Eq. [7] for $n = 8/3$ and $V_{o2} = 7.6$ kV (solid curve) to experimental points by Prener.

$$B_2 = AV\{1 - \exp[-2.189(V_{o2}/V)^{8/3}]\} \quad [7a]$$

$$B_3 = AV\{\exp[-2.189(V_{o1}/V)^{8/3}] - \exp[-2.189(V_{o2}/V)^{8/3}]\} \quad [8a]$$

The two Eq. [5a] and [7a] describe a somewhat steeper variation of the emission intensity with voltage of films compared to powders. An example is shown in Fig. 9.

The above equations can be used to calculate the color variation of a screen consisting of several thin films deposited on top of each other. An example is shown in Fig. 10 where two ZnS-CdS:Ag films, red and green, are each assumed to possess internal efficiencies of cathodoluminescence of 10%. That is just about possible with these materials if the films are translucent or otherwise slightly light scattering (16). Figure 10 indicates a range of red-green color variation between 12-18 kV.

Discussion

The present analysis of color-changing penetration-type phosphor screens is mainly application oriented.

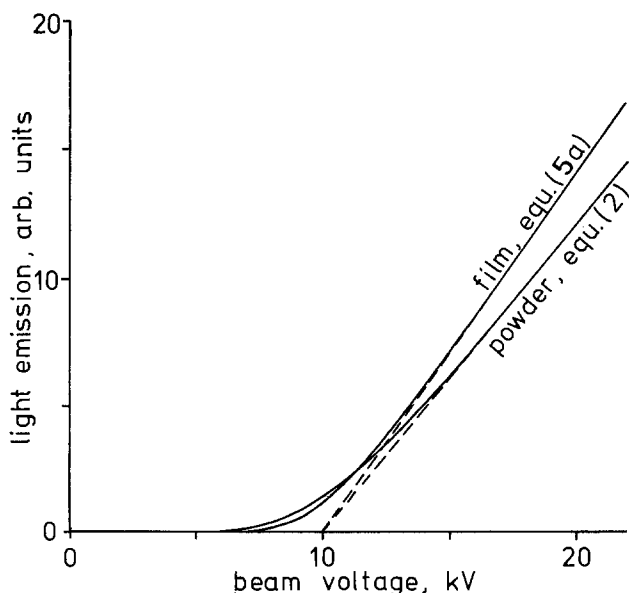


Fig. 9. $B(V)$ dependence of a phosphor coated with a thin dead layer, comparison of powder and film. $V_o = 10$ kV in both cases.

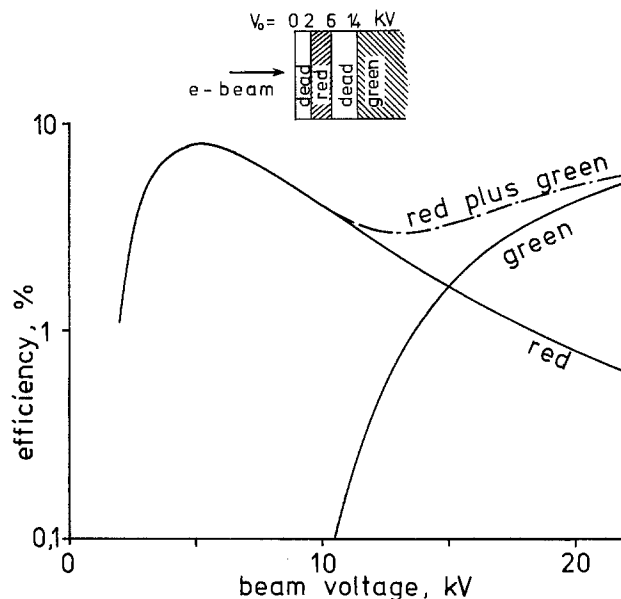


Fig. 10. Calculated characteristic of a multiple film screen (insert) containing two translucent ZnS-CdS:Ag films each assumed to show 10% internal cathodoluminescent efficiency. Physical thicknesses of the individual films: first dead film: ~ 0.045 μm ; red film: ~ 0.19 μm ; second dead film: ~ 0.61 μm ; green film: > 2 μm .

It permits the "design" of powder blends or film structures to meet given requirements. The obtainable color range, the color resolution (*i.e.*, the rate of color change), the voltage range where the color change occurs, and the external efficiency can be calculated.

A weak point of the analysis is the necessary knowledge of the internal cathodoluminescent efficiencies of the individual phosphor components since these affect the color balance of the final screen. The color variation can be predetermined only to that degree of accuracy as the internal efficiencies of the components are known. Fortunately, these internal efficiencies are relatively well under preparational control for powder phosphors so that the color characteristic of a powder screen can fairly reliably be predicted. The situation is not as well defined with film screens since our present state of technology does not yet permit a close control of the internal efficiencies of cathodoluminescent phosphor films. That will probably improve, however.

The external efficiency of a color-changing screen containing any dead material must necessarily be lower than the internal efficiencies of the phosphor components. It is possible to construct screens without any dead material, their external efficiencies are comparable to those of the phosphor components, but such screens show very poor color resolution. Conversely, the higher the required color resolution, the more dead material must be incorporated into the screen, and the lower external efficiency of the entire screen. High external efficiency and high color resolution are mutually exclusive.

Manuscript submitted Jan. 19, 1981; revised manuscript received March 18, 1981. This was Paper 156 presented at the Minneapolis, Minnesota, Meeting of the Society, May 10-15, 1981.

Any discussion of this paper will appear in a Discussion Section to be published in the June 1982 JOURNAL. All discussions for the June 1982 Discussion Section should be submitted by Feb. 1, 1982.

Publication costs of this article were assisted by Westinghouse Electric Corporation.

REFERENCES

1. D. H. Pritchard, U.S. Pat. 3,204,143 (1961).
2. R. Carvell, U.S. Pat. 3,523,905 (1970).
3. S. R. Shortes, U.S. Pat. 3,560,398 (1971).
4. J. S. Prener and J. D. Kingsley, *This Journal*, **119**, 1254 (1972).
5. J. D. Kingsley and J. S. Prener, *J. Appl. Phys.*, **43**, 3073 (1972).
6. M. Tecotzky and J. J. Mattis, U.S. Pat. 3,791,844 (1974).
7. J. P. Galves, Paper 124 presented at The Electrochemical Society Meeting, San Francisco, California, May 12-17, 1974.
8. V. V. Prikhodko, G. A. Kitaev, N. P. Soshchin, and V. S. Chaisov, *Izv. Akad. Nauk SSSR Ser. Fizi.*, **38**, 1178 (1974).
9. W. H. Byler and J. J. Mattis, U.S. Pat. 3,875,449 (1975).
10. S. F. Ignasiak, U.S. Pat. 3,939,377 (1976).
11. S. A. Lipp, Paper 87 presented at The Electrochemical Society Meeting, San Francisco, California, May 12-17, 1974.
12. C. Feldman and M. O'Hara, *J. Opt. Soc. Am.*, **47**, 300 (1957).
13. C. Feldman, *ibid.*, **47**, 790 (1957).
14. C. Feldman, U.S. Pat. 3,046,154 (1962) and 3,225,238 (1965).
15. J. S. Prener, *This Journal*, **122**, 1561 (1975).
16. A. Vecht, "Physics of Thin Films," Vol. 3, G. Hass and R. E. Thun, Editors, p. 201, Academic Press, New York (1960).

Molecular Orbital Studies of Positive Electron Resists

Tsukasa Tada¹

VLSI Technology Research Association, Cooperative Laboratories, Takatsu, Kawasaki, 213, Japan

ABSTRACT

The overlap population (F) in the HOMO (highest occupied molecular orbital) is calculated by the extended Hückel method, assuming that the HOMO plays an important role in radiation chemistry. For representative samples, calculated results are closely associated with the experimental $G(S)$ values. Based on this result, F values are calculated for the model compounds of various positive electron resists in order to elucidate the electronic structure and scission efficiency. Several predictions are made in cases where experimental results are not available. Thermal stability of positive electron resists is also discussed based on the population analysis.

Up to now many investigations on electron or x-ray resists seem to have been focused mainly on the following two items. The first concerns the studies on resist processing, such as problems on resist profiles, baking conditions, developing conditions, etch resistance, and so forth. The second concerns the studies of energy dissipation in the resist film when exposed to x-ray or electron beam radiation. The analysis of this problem is essential, particularly in correcting for proximity effects, and is carried out using the depth-dose function or the Monte Carlo method from a macroscopic viewpoint.

On the other hand, there exists relatively little literature on the molecular structure of resist materials. Moreover, studies on this subject have been carried out only from a macroscopic viewpoint and are highly qualitative. For example, it is often pointed out that the incorporation of a phenyl ring makes the polymer less sensitive to ionizing radiation. However, it is not well understood why a phenyl ring causes the polymers to react defensively to ionizing radiation.

Considering a positive electron resist, its sensitivity is closely associated with the following two factors: Scission efficiency and solubility characteristics. Therefore, study on these factors is important for the analysis and development of positive electron resists. Of these two factors, scission efficiency is conclusively determined by the molecular electronic structure, regardless of the other factors, such as the developing process. In this paper, argument is focused mainly on scission efficiency.

In treating scission efficiency, it is essential to take a quantum mechanical approach, since the chemical reactions caused by ionizing radiation are essentially quantum mechanical phenomena. Here, the LCAO-MO

theory has been employed since it is the most successful theory which treats many-electron systems in molecules.

The purpose of this paper is to characterize the electronic structures of resist materials by employing the LCAO-MO theory in order to elucidate and predict scission efficiency and to provide a basic foundation for the design of positive electron resists. In the first half of this paper, a basic theory of scission efficiency is presented and is confirmed by being applied to existing positive resists. In the latter half, based on the results of the first half, we present some applications of this theory to various positive electron resists including some theoretical resists. Several predictions are also made in cases where experimental results are not available.

The Role of the HOMO in Radiation Chemistry

Radiation chemistry, especially that of organic molecules, is highly complicated in terms of predicting specific mechanisms. Furthermore, mechanisms differ from molecule to molecule. However, as far as the primary process is concerned, it is generally considered that all molecules pass through the same process.

Figure 1 is a diagram of the primary process in radiation chemistry. In the first stage of radiation chemistry, as shown in Fig. 1, ionizing radiation causes high energy electrons, positive holes, and in some cases, atomic displacements. In the case of an electron beam of 10-30 keV or soft x-ray, atomic displacements can be neglected. Ejected high energy electrons also cause electronic excitations, positive holes, and secondary electrons. The electronic excitations may lead to luminescence or decomposition of molecules. The positive holes created by high energy electrons also may lead to decomposition. On the other hand, remaining positive holes after ejection of high energy electrons may lead to decomposition or recombine with ejected electrons.

¹ Present address: Toshiba Research and Development Center, Saiwai, Kawasaki, 210, Japan.

Key words: electron beam, positive resist, HOMO, extended Hückel, population analysis.

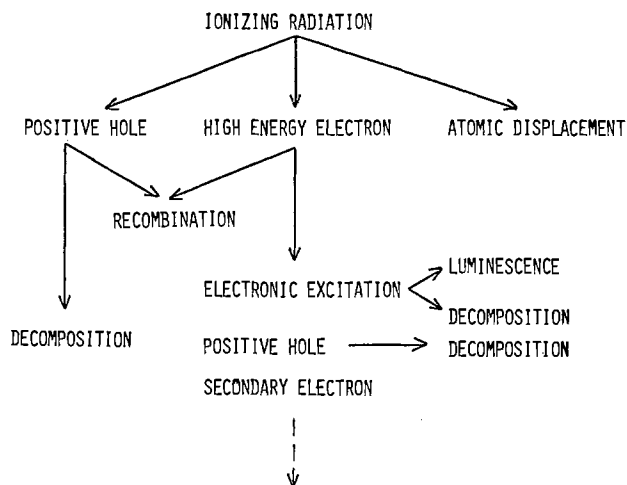


Fig. 1. Diagram of primary process in radiation chemistry

Therefore, there are two decomposition patterns, as follows: (i) Ionization leads to decomposition; and (ii) electronic excitation of a neutral molecule leads to decomposition. In analyzing these two cases in terms of energy levels, two or three processes can be expected in each case, as shown in Fig. 2.

In the case of ionization, ionizing radiation ejects an electron from one of the various occupied levels. Ejection of an electron from the HOMO directly causes a positive ion in its ground state. When an electron is ejected from the inner level, its electronic state is immediately converted to the ground state through a rearrangement of remaining electrons. In another case, ionizing radiation may cause a super excited state (1), which is immediately converted to the ground state of the positive ion. As mentioned above, by ionizing radiation, a neutral molecule is immediately converted to a positive ion in its ground state. Chemical reactions are considered to begin after these processes.

In the case of excitation, an electron is excited from the HOMO or the inner levels, and the remaining electrons are immediately converted to the state where

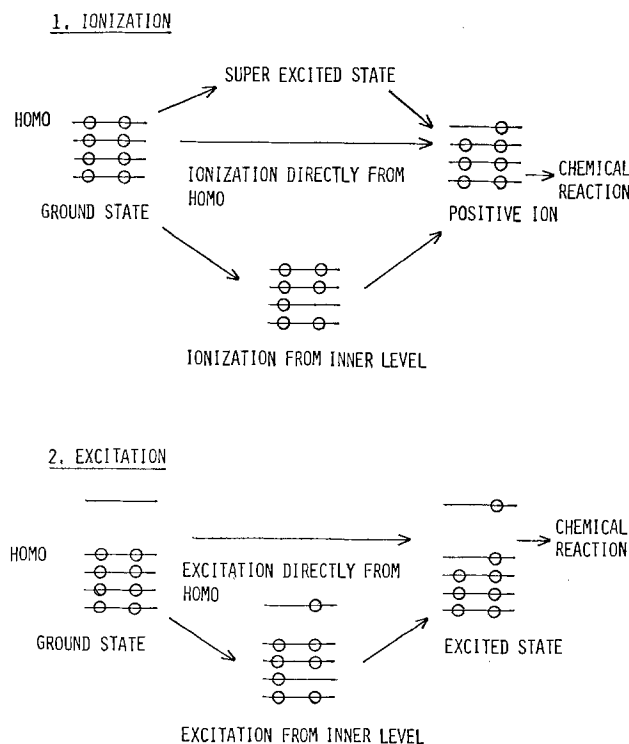


Fig. 2. Energy level diagram in radiation chemistry

the previous HOMO is occupied with an unpaired electron. It is considered that the chemical reactions begin after this state.

In both cases, ionization and excitation, it should be noticed that the HOMO is always perturbed by ionizing radiation. From this point of view, it can be easily expected that the HOMO makes an important contribution to the chemical reaction caused by ionizing radiation. Consequently, it is also expected that the region of the largest HOMO density is the most reactive one in a molecule. In other words, the extent of the HOMO localization can be regarded as a measure of chemical reactivity by ionizing radiation.

Therefore, from this standpoint, one can predict the reactivity of a molecule when exposed to ionizing radiation by analyzing its molecular wave functions. In the case of polymer materials, the HOMO localization can be visualized by taking the case of two different models, specifically polymer A and polymer B, as shown in Fig. 3. In the case of polymer A, whose HOMO is largely localized on the main chain bond region, its reactive site corresponds to the main chain bond region. Accordingly, it is expected that polymer A is easily degraded by ionizing radiation. On the other hand, polymer B, whose HOMO is largely delocalized or shifted toward its side chain, is not expected to be as easily degraded by ionizing radiation as is polymer A.

As a measure of the HOMO localization in the bond region, overlap populations in the HOMO are employed in this paper. This is because, as analyzed by Mulliken (2), they can be used firstly as a measure of charge density between two different nuclei X and Y, and secondly as a measure of bonding and antibonding strength of X-Y covalent bond. In the present calculations, the overlap population of X-Y bond in the HOMO is defined as follows

$$F(X Y) = 2 \sum_{\mu} \sum_{\nu} c_{\mu} c_{\nu} S_{\mu\nu}$$

where c_{μ} and c_{ν} are coefficients of atomic orbitals ϕ_{μ} and ϕ_{ν} in the HOMO, and $S_{\mu\nu}$ is the overlap integral between the atomic orbitals ϕ_{μ} and ϕ_{ν} .

Calculation

Calculations were performed by the extended Hückel method (3), the simplest all-valence electron procedure. In spite of the well-known shortcomings of this method, particularly in the quantitative prediction of observables, it faithfully models the shape of the molecular wave functions of any molecule compared with even more sophisticated methods. In addition, it has the advantage of short computing time.

Consequently, in most cases, the extended Hückel method gives a reasonable qualitative or semi-quantitative picture of the electronic structures of mole-

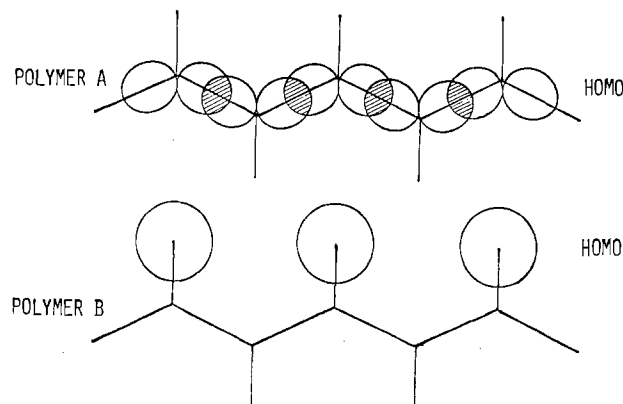


Fig. 3. Shape of HOMO for two different polymers

cules with comparatively short computing time. Therefore, extended Hückel calculation is sufficient for gross estimation of the shape of molecular wave functions and is suitable for treating large molecules because of its short computing time.

In the extended Hückel secular Eq. [1]

$$\det|H_{\mu\nu} - \epsilon S_{\mu\nu}| = 0 \quad [1]$$

the diagonal element is approximated by the ionization potential, and the off diagonal element is approximated by the Wolsberg-Helmholtz formula (4) as [2] and [3]

$$H_{\mu\mu} = -I_{\mu} \quad [2]$$

$$H_{\mu\nu} = \frac{K}{2} (H_{\mu\mu} + H_{\nu\nu}) S_{\mu\nu} \quad (\mu \neq \nu) \quad [3]$$

where I_{μ} is the ionization potential of the atomic orbital ϕ_{μ} , $S_{\mu\nu}$ is the overlap integral between the atomic orbital ϕ_{μ} and ϕ_{ν} , and K is a constant.

In treating resist materials, calculations were carried out on the model compounds of resist materials as shown in Fig. 4. We restrict our considerations to the region within the frame of the dotted line, which corresponds to a polymer unit. The estimations of overlap population F and total overlap populations (2) P were made on bonds 1, 2, and 3. The gross atomic populations (2) Q were calculated on α -carbon.

The geometries of the model compounds were based on the data shown in Table I. For other geometries, Pople's standard geometrical models (5) were employed. For the ionization potential, Pritchard's data (6) were employed. Constant K was taken to be 1.75.

Polymer Materials Containing Quaternary Carbon in Their Main Chains

In most cases, polymer materials containing quaternary carbon in their main chains are employed as positive electron resists, because this kind of polymer is usually degraded by ionizing radiation, for example, by a soft x-ray or a high energy electron beam. In this section, using the following four samples that have representative structures in this kind of polymer, we have calculated their molecular wave functions, F values, and total overlap populations, P . Representative samples are, poly(isobutylene) PIB, poly(methacrylonitrile) PMN, poly(methyl methacrylate) PMMA, and poly(α -methylstyrene) P α MS. Of these polymers, PIB is in the simplest structure and has the highest $G(S)$ value. On the other hand, P α MS is known to be considerably insensitive to ionizing radiation and has excellent resistance to reactive ion etching. PMMA is a typical and widely used positive electron resist, and most of the reported positive electron resists consist of PMMA family. PMN is also reported to be a sensitive positive electron resist (7).

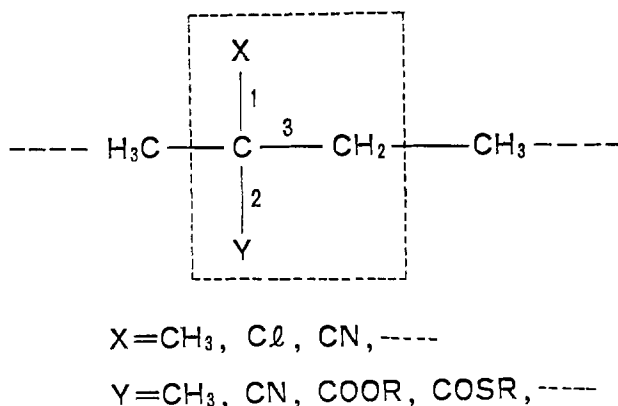


Fig. 4. Molecular structure of polymer model compound

Table I. Geometries of substituents in model compounds

| Substituents | Bond distance (Å) | | Bond angle (degree) | | |
|--------------|-------------------|------|---------------------|-------|---------------------|
| | r | C=O | 1.22 | <CCO | 120 ^a |
| | r | C—O | 1.36 | <OCO | 125 |
| | r | O—C | 1.46 | <COC | 115 |
| | r | C—S | 1.714 | <CCS | 115 ^b |
| | r | S—C | 1.813 | <OCS | 125 |
| | r | C—Cl | 1.7712 | <CCCl | 109.55 ^b |
| | r | C—Cl | 1.775 ^b | | |
| | r | Si—H | 1.465 | <HSiH | 109.5 ^b |

^a T. Ukaji, *Bull. Chem. Soc. Jpn.*, 32, 1275 (1959).

^b R. W. G. Wyckoff, "Crystal Structures," Interscience Pub., New York (1971).

Calculated F values are summarized in Table II, together with the experimental data on $G(S)$ and electron beam sensitivity, where $F(1)$ and $F(2)$ represent the F value of side chain bonds 1 and 2, respectively (in this case, bond 1 corresponds to the C—CH₃ side chain bond), and $F(3)$ represents that of the main chain bond 3, as shown in Fig. 4. Table II indicates the following interesting results.

Firstly, $F(3)$ have exceedingly high values, compared with $F(1)$ and $F(2)$ values. In the case of PIB, for example, $F(3)$ has a value of 0.188. On the other hand, $F(1)$ and $F(2)$ have a value of -0.014 . This result might give one of the reasons for the fact that the polymer materials containing quaternary carbon in their main chains are usually degraded by ionizing radiation, instead of crosslinking.

Secondly, it should be noticed that the $F(3)$ values, which indicate the reactivity of the main chain bond by ionizing radiation, are closely associated with the experimental $G(S)$ values. For example, $F(3)$ of PIB has a value of 0.188, and $F(3)$ of P α MS has a much smaller value of 0.067, which indicates that PIB is easily degraded by ionizing radiation and P α MS is not as easily affected by ionizing radiation as PIB is. For experimental $G(S)$ values, PIB has a value of 4.0 and P α MS has a smallest value of 0.3. Therefore, calculated results in Table II are closely associated with the experimental results. In other words, these results confirm the assumption that the HOMO makes an important contribution to the chemical reactions caused by ionizing radiation. Consequently, it can be said that this expedient method of calculating F values provides a reliable prediction of scission efficiency, at least as far as C—C σ bonds are concerned. The reported sensitivities in Table II are also generally associated with the $F(3)$ and $G(S)$ values.

Table II. Calculated F and experimental data for representative polymers containing quaternary carbon

| Poly-mers | $F(1)$ | $F(2)$ | $F(3)$ | $G(S)$ | Sensi-tivity ($\mu\text{C}/\text{cm}^2$) |
|---------------|--------|--------|--------|------------------|--|
| PIB | -0.014 | -0.014 | 0.188 | 4.0 ^a | 20 ^a |
| PMN | -0.027 | 0.018 | 0.139 | 2.1 ^b | 15 ^c |
| PMMA | -0.022 | 0.029 | 0.123 | 1.7 ^a | 50 ^a |
| P α MS | 0.021 | -0.020 | 0.067 | 0.3 ^a | 100 ^a |

^a L. F. Thompson and M. J. Bowden, *This Journal*, 120, 1723 (1973).

^b J. N. Helbert, E. H. Poindexter, G. A. Stahl, C. Y. Chen, and C. U. Pittman, *J. Polym. Sci., Chem. Ed.*, 17, 49 (1979).

The differences among calculated $F(3)$ values can be rationalized in terms of the perturbation theory or, in other words, from the standpoint of substituent effects. In the case of PIB, the HOMO is mainly localized on the main chain bond. In cases where another substituent group is incorporated into PIB, some interactions between the unperturbed HOMO and the orbitals of the substituent group more or less take place. If orbitals of the substituent group strongly interact with the HOMO, the HOMO is very much perturbed by this interaction and the $F(3)$ value is drastically changed. For example, the orbitals of a phenyl ring strongly interact with the HOMO. Therefore, if a phenyl ring is incorporated, the HOMO is perturbed and is largely delocalized into the π orbitals of the phenyl ring. The fairly small $F(3)$ value of P α MS is a consequence of this orbital interaction.

Since $F(3)$ represents not only HOMO density but also the HOMO's contribution to the bonding strength, another explanation for the differences among the $G(S)$ values can be put forward by analyzing the total overlap populations of the main chain bond, in other words, from the standpoint of bond energies. Table III shows the calculated total overlap populations of the C—C main chain bond of four representative samples, where $P(3)$ and $P^+(3)$ represent the total overlap populations in the preionized neutral molecule and ionized positive ion, respectively.

As analyzed by Mulliken, the total overlap populations give a measure of the non-Coulombic parts of bond energies. Therefore, as far as C—C covalent bonds are concerned, the total overlap populations can be roughly regarded as a measure of the covalent bond energy or the covalent bonding strength. One may expect that the bond energy or bonding strength have a close correlation with the $G(S)$ value. From this point of view, $G(S)$ values are expected to be increased with a decrease in $P(3)$ values. However, Table III indicates the opposite result. For example, PIB has the highest $P(3)$ value with the highest $F(3)$ and $G(S)$ values. This result implies that the bonding strength in the preionized state does not always have a close correlation with scission efficiency caused by ionizing radiation.

On the contrary, it is rather the $P^+(3)$ value that is generally associated with the $G(S)$ value. For example, PIB has the lowest $P^+(3)$ value and P α MS has the highest $P^+(3)$ value, indicating that the main chain bonding strength of ionized PIB is weaker than that of ionized P α MS. These results imply that, while the main chain bonding strength of PIB is fairly decreased by being ionized, that of P α MS is affected very little by being ionized. Consequently, it can be said that the bonding strength in the ionized state is generally associated with the $G(S)$ value, at least as far as C—C covalent bonds are concerned. These results also confirm that the ionized state plays an important role in radiation chemistry.

As mentioned above, the differences among the $G(S)$ values can also be explained in terms of bonding strength or bond energy. However, since the $F(3)$ value corresponds to the difference between the $P(3)$ and $P^+(3)$ values, the above explanation is, in a sense, equivalent to the explanation in terms of HOMO density.

Table III. Calculated $P(3)$ values in neutral and ionized states

| Poly- mers | $P(3)$ | $P^+(3)$ | $F(3)$ | $G(S)$ |
|---------------|--------|----------|--------|--------|
| PIB | 0.779 | 0.591 | 0.188 | 4.0 |
| PMN | 0.731 | 0.592 | 0.139 | 2.1 |
| PMMA | 0.754 | 0.631 | 0.123 | 1.7 |
| P α MS | 0.762 | 0.695 | 0.067 | 0.3 |

Although the excited levels have been neglected so far, they are also worthy of being analyzed because, in some cases, the excited state is expected to contribute to polymer degradation. In order to rigorously calculate the excited levels and their wave functions, it is necessary to use the CI or other sophisticated methods based on the SCF MO theory. Nevertheless, even within the extended Hückel framework, one can get some insights into the excited states on the basis of the virtual orbitals. Analysis of the virtual orbitals provides the following interesting results.

Concerning PIB, the LUMO (lowest unoccupied molecular orbital) level is found to be of a considerably high energy level (1.05 eV). Although certain LUMO density is observed in the main chain bond region, the LUMO has a bonding character in this bond region. Slightly antibonding character is observed in the C—H bond region.

On the other hand, relatively low excited levels are found in the rest of the samples, and their excited levels are mostly localized or delocalized to their side chains. In the case of PMMA, the C=O π^* level (−8.71 eV) is found as the LUMO. This π^* level corresponds to the excited level caused by deep-u.v. radiation. PMMA is known to be a positive working resist for deep-u.v. radiation (8), as are other poly(methacrylate) series positive electron resists. Furthermore, it is reported that even poly(glycidyl methacrylate) negative electron resist acts as a positive working resist for deep-u.v. radiation (9). These experimental results suggest that the C=O π^* state contributes to the degradation of poly(methacrylate) series polymer materials. However, since little LUMO density is observed in the main chain bond region, it is considered that the C=O π^* state contributes to the main chain bond dissociation through the secondary process. In the case of PMN, the C≡N π^* level (−7.90 eV) is found as the LUMO. The vacant π^* levels (−8.35 ~ −4.76 eV) of the phenyl ring are found in the case of P α MS, indicating that the relatively low excited levels of P α MS are mostly concentrated on the phenyl π -system. These π^* states, being relatively stable ones, may contribute little to the polymer degradation.

Poly(methacrylate) Series Positive Resists

Most of the reported positive electron resists consist of poly(methacrylate) series polymer materials. However, their reported sensitivities are considerably different according to their ester side chains. In this section, we focus our attention primarily on the following questions: (i) To what extent does the substitution of an ester side chain affect the electronic state of the C—C main chain bond region? (ii) Which factor plays an important role in determining the sensitivities of these resists? In order to study these problems, we have calculated F values for a series of poly(methacrylate) resists and compared them with the experimental values of electron beam sensitivity. Calculated results are listed in Table IV together with the experimental results, where $F(1)$, $F(2)$, and $F(3)$ represent the F values for the same position as in the previous section.

For poly(methacrylic acid) and poly(alkyl methacrylate) resists, although one can observe a trend whereby $F(3)$ value is slightly decreased with an increase in the size of the alkyl group, their $F(3)$ values amount to almost the same value, namely around a 0.12 value. These results indicate that the electronic state of the C—C main chain bond region is little affected by the size of alkyl ester side chain. In other words, it is indicated that poly(alkyl methacrylate) resists have generally the same scission efficiency when exposed to ionizing radiation. Reported $G(S)$ values of PMMA, PEMA, and PnBMA are 1.7, 1.3 (10), and 0.7 (10), respectively. Therefore, these $G(S)$ values

Table IV. F values and electron beam sensitivity for poly(methacrylate) series polymers

| Polymers | $F(1)$ | $F(2)$ | $F(3)$ | Sensitivity ($\mu\text{C}/\text{cm}^2$) |
|----------|--------|--------|--------|---|
| PMA | -0.022 | 0.029 | 0.122 | — |
| PMMA | -0.022 | 0.029 | 0.123 | 50 |
| PEMA | -0.021 | 0.030 | 0.121 | 75 |
| PnBMA | -0.020 | 0.031 | 0.118 | 0.5 |
| PTFEMA | -0.022 | 0.029 | 0.122 | 4.5 |
| PTCEMA | -0.024 | 0.029 | 0.125 | 1.25 |
| PPhMA | 0.000 | 0.004 | 0.003 | 155 |
| PMTMA | -0.005 | 0.116 | 0.049 | 7.5 |

PMA: poly(methacrylic acid), PMMA: poly(methyl methacrylate), PEMA: poly(ethyl methacrylate), PnBMA: poly(*n*-butyl methacrylate), PTFEMA: poly(trifluoroethyl methacrylate), PTCEMA: poly(trichloroethyl methacrylate), PPhMA: poly(phenyl methacrylate), PMTMA: poly(methyl thiomethacrylate).

confirm above indication. However, electron beam sensitivity is drastically enhanced by butyl substitution into the ester side chain. This discrepancy between the value of $F(3)$ and electron beam sensitivity indicates that the high PnBMA sensitivity is mainly due to solubility characteristics, rather than scission efficiency. In the case of PnBMA, considerable decrease in T_g (glass transition temperature) is also observed at the same time. There might be some relationship between T_g and solubility characteristics.

The same trend is also observed for poly(haloalkyl methacrylate) resists. For example, PTFEMA and PTCEMA (EBR-1) (11) have almost the same $F(3)$ value as that of PEMA, indicating that halogen substitution into the ester side chain has no significant effect on the electronic state of the C—C main chain bond region. On the other hand, their electron beam sensitivities are drastically enhanced compared with that of PEMA. These results suggest that halogen substitution into the ester side chain mainly improves solubility characteristics.

Contrary to alkyl or halogenated alkyl substitution, phenyl substitution into the ester side chain or sulfur substitution of oxygen atom in an ester group have significant effects on the electronic state of the C—C main chain bond region. As is evident from the $F(3)$ values of PPhMA and PMTMA, phenyl substitution drastically reduces the $F(3)$ value, and sulfur substitution reduces the $F(3)$ value and enhances the $F(2)$ value. Therefore, the relatively high PMTMA sensitivity can be attributed to its good solubility characteristics. On the other hand, the considerably low $F(3)$ value for PPhMA suggests low scission efficiency and low sensitivity. The reported $G(S)$ value (0.44) (12) and sensitivity are consistent with the calculated result. This result also predicts that the same trend is also observed in the case of other aryl substitution into the ester side chain.

Substituent Effects on the α -Position of Acrylate Polymer Materials

In the previous section we discussed substituent effects into the ester side chain of poly(methacrylate) resists. Another feasible modification is a substitution on the α -position. In this section, concern is on substituent effects on the α -position. In order to estimate these substituent effects on the electronic state of the C—C main chain bond region and scission efficiency, we have specifically calculated F values for poly(trifluoroethyl acrylate) series polymer materials including theoretical ones, regardless of the polymer synthesis possibility. Calculated results are listed in Table V with experimental data on electron beam sensitivity, where $F(1)$, $F(2)$, and $F(3)$ values represent the F values of the C-substituent, C—COOCH₂CF₃, and C—C main chain bonds, respectively.

Table V. F values and electron beam sensitivity for α -substituted poly(trifluoroethyl acrylate) series polymers

| α -substituents | $F(1)$ | $F(2)$ | $F(3)$ | Sensitivity ($\mu\text{C}/\text{cm}^2$) |
|------------------------|--------|--------|--------|---|
| Cl | -0.042 | 0.032 | 0.165 | 0.75 |
| OCH ₃ | -0.029 | 0.038 | 0.136 | — |
| CH ₃ | -0.022 | 0.029 | 0.122 | 4.5 |
| CF ₃ | 0.007 | 0.038 | 0.119 | — |
| NH ₂ | -0.062 | 0.106 | 0.118 | — |
| CN | 0.017 | 0.030 | 0.109 | 20 |
| SiH ₃ | 0.166 | 0.084 | -0.045 | — |
| COOH | 0.063 | 0.061 | -0.049 | — |

In Table V, it should be noted that Cl and OCH₃ substituents enhance the $F(3)$ value compared with the case of poly(methacrylate), suggesting that these substituents enhance scission efficiency when exposed to ionizing radiation. Accordingly, enhancement of the sensitivity can be expected by chlorine or methoxy substitution on the α -position.

On the other hand, an opposite trend is observed in the case of other substituents. The $F(3)$ value is somewhat decreased by CF₃, NH₂, and CN substituents, and is drastically decreased by SiH₃ and COOH substituents. Among them, NH₂ and SiH₃ substituents enhance the $F(2)$ and $F(1)$ values, respectively, indicating that the HOMO is shifted toward the side chain bond region in these cases. Therefore, the enhancement of the sensitivity cannot be expected by these substitutions, provided that solubility characteristics are not so much changed. Table V also indicates that there is no simple relationship between the $F(3)$ value and the electron-withdrawing nature of α -substituents. Detailed discussion on this problem is given in the next section.

For experimental data, electron beam sensitivity is enhanced by chlorine substitution and is rather deteriorated by cyano substitution compared with that of poly(methacrylate). These experimental results are consistent with the calculated results. Therefore, the higher sensitivity of poly(trifluoroethyl α -chloroacrylate) EBR-9 (13), compared with poly(trifluoroethyl methacrylate), can be attributed to the enhancement of the $F(3)$ value. Helbert *et al.* (14) reported the $G(S)$ value of poly(methyl α -chloroacrylate) to be 5.1. This experimental result is also consistent with the present calculated results. However, they also reported the $G(S)$ value of poly(methyl α -cyanoacrylate) to be 11 (15),² which is comparable to that of PBS (16). Even if the large fluctuations among the reported $G(S)$ values are considered, this $G(S)$ value seems to be too high, and is inconsistent with the present calculated and experimental results. If this $G(S)$ value is sufficiently reproducible, this discrepancy means that the author's theory is not a good approximation to poly(α -cyanoacrylate).

As mentioned above, substitutions on the α -position fairly affect the $F(3)$ value in comparison with substitution into the ester side chain. However, it should be noted that no substituents in Table VI enhance the $F(3)$ value more than that of PIB. Therefore, although the enhancement of $G(S)$ values can be expected to some extent by α -substituents, drastically high $G(S)$ values are not generally expected from the calculated results.

Substituents Electron-Withdrawing Effect on Scission Efficiency

It is often suggested that polar side chains weaken the main chain bond and lead to enhancement of scission efficiency (15, 17). However, there is no theoretic

² Such a high $G(S)$ value means that poly(methyl α -cyanoacrylate) can be a highly sensitive positive electron resist comparable to PBS. However, its electron beam sensitivity is not reported.

Table VI. $F(3)$ and $Q(\alpha)$ values for 1, 1-substituted vinyl polymer materials

| Substituents | $F(3)$ | $Q(\alpha)$ |
|--------------------|--------|-------------|
| Cl | 0.133 | 3.30 |
| CN | 0.103 | 3.71 |
| CH ₃ | 0.188 | 3.88 |
| COOCH ₃ | -0.049 | 3.94 |

cal justification on this suggestion. In this section, arguments are focused on the problem as to whether some relationship exists or not between the electron-withdrawing nature of side chains and scission efficiency. As a measure of electron-withdrawing or electron-donating nature of side chains, we have employed the gross atomic populations (2) Q of the α -carbon atom in the main chain.

Table VI shows the calculated $F(3)$ and $Q(\alpha)$ value of 1, 1-substituted vinyl polymer materials, where $F(3)$ and $Q(\alpha)$ represent the F value of the main chain bond and the Q value of α -carbon, respectively. As shown in Table VI, polymers with CH₃ and COOCH₃ substituents have relatively large $Q(\alpha)$ values. On the other hand, Cl and CN substituents reduce the $Q(\alpha)$ value. This result indicates that Cl and CN substituents have an electron-withdrawing effect compared with CH₃ and COOCH₃ substituents. However, the $F(3)$ value is rather decreased by the electron-withdrawing substituents such as Cl and CN groups. Table VI also indicates that the $F(3)$ value is drastically decreased by COOCH₃ substituents. Therefore, the $F(3)$ values have no simple correlation with the electron-withdrawing effect of substituents, and scission efficiency is not expected to be enhanced by the electron-withdrawing substituents in this kind of polymer.

Table VII shows the calculated $F(3)$ and $Q(\alpha)$ values of α -substituted poly(trifluoroethyl acrylate) polymer materials, where $F(3)$ and $Q(\alpha)$ represent the F value of the main chain bond and the Q value of α -carbon, respectively. In Table VII, calculated polymers are the same samples discussed in the previous section and are rearranged according to their $Q(\alpha)$ values. In this case, polymers with relatively high $F(3)$ values can be found in those with electron-withdrawing substituents such as Cl or OCH₃ group. However, the $F(3)$ value does not always have a correlation with the $Q(\alpha)$ value. For example, poly(α -chloroacrylate) has a higher $F(3)$ value than poly(α -methoxyacrylate) does.

As mentioned above, the $F(3)$ value does not always correlate with the electron-withdrawing nature of the substituents. Therefore, these calculated results indicate that there is no simple relationship between scission efficiency (by ionizing radiation) and electron-withdrawing nature of substituents. Secondly, it should be noticed that substituent effects differ according to the kinds of polymers. In the case of 1, 1-substituted vinyl polymers, for example, Cl substituent reduces the $F(3)$ value compared with the case of CH₃ substituent. On the other hand, an opposite result is obtained in the case of poly(trifluoroethyl acrylate) polymers. From the standpoint of the perturbation theory, the change in $F(3)$ value is con-

Table VII. $F(3)$ and $Q(\alpha)$ values for α -substituted poly(trifluoroethyl acrylate) series polymers

| Substituents | $F(3)$ | $Q(\alpha)$ |
|------------------|--------|-------------|
| OCH ₃ | 0.136 | 3.37 |
| NH ₂ | 0.118 | 3.62 |
| Cl | 0.165 | 3.64 |
| CN | 0.109 | 3.63 |
| CH ₃ | 0.122 | 3.91 |
| COOH | -0.049 | 3.94 |
| CF ₃ | 0.119 | 4.00 |
| SiH ₃ | -0.045 | 4.26 |

sidered to be a result of complicated orbital interactions between the unperturbed orbitals on the main chain and the substituent orbitals. The above results indicate that the orbital interactions are too complicated to be rationalized in terms of electron-withdrawing or donating nature of substituents.

Thermal Stability of Positive Electron Resists

Since thermal stability is an important factor for positive electron resists, it is worthy of being analyzed in terms of the molecular orbital theory. As previously mentioned, total overlap populations P give a measure of the covalent bonding strength. Therefore, they are expected to provide some insights into the thermal stability of positive electron resists.

Thermal stability is considered to be a function of bonding strengths of all chemical bonds constituting a polymer material. However, it is also considered that thermal stability mainly depends upon the main chain bonding strength, provided that the bonding strengths in side chains do not seriously differ. Therefore, the P value of the C—C main chain bond can be roughly regarded as a measure of the thermal stability. In this sense, poly(trifluoroethyl acrylate) series polymer materials provide a context in which to check this assumption.

Table VIII shows calculated P values for poly(trifluoroethyl acrylate) series polymer materials, where $P(3)$ and $P(1)$ represent the P values of the main chain and C-substituent bond, respectively. The experimental data on the initial thermal degradation point $T_d(i)$ are also presented in Table VIII. As can be seen in Table VIII, $P(3)$ have generally the same value among polymers with Cl, CH₃, and CH₂F substituents. This result suggests that poly(α -chloroacrylate) has the same thermal stability as poly(methacrylate) does. On the other hand, the $P(3)$ value is fairly decreased by CN substituent, suggesting that the thermal stability of poly(α -cyanoacrylate) is deteriorated compared with that of poly(methacrylate).

As to the experimental data, measured $T_d(i)$ are generally consistent with the calculated results. In particular, $T_d(i)$ is considerably decreased by CN substituent, as suggested by the calculated results. Therefore, in spite of a crude approximation, this method of calculating P values can provide a prediction of thermal stability to some extent.

As is evident from Table VII and VIII, there also exists no simple relationship between the $P(3)$ value and the electron-withdrawing nature of substituents. The $P(3)$ value is rather associated with the $P(1)$ value. This result means that the s character of the main chain bond is decreased with an increase in the s character of the C-substituent bond, in this kind of polymer. Therefore, the relatively poor thermal stability of poly(α -cyanoacrylate) can be attributed to the relatively high s character of C—CN side chain bond rather than the electron-withdrawing effect of the CN group.

Conclusions

The following principal conclusions derive from the present work and are worthy of special mention.

1. In chemical reactions caused by ionizing radiation, the HOMO plays an important role. In four typical

Table VIII. P values and $T_d(i)$ for α -substituted poly(trifluoroethyl acrylate) series polymers

| Substituents | $P(3)$ | $P(1)$ | $T_d(i)$ (°C) |
|-------------------|--------|--------|------------------|
| Cl | 0.757 | 0.606 | 230 |
| CH ₃ | 0.754 | 0.714 | 240 |
| CH ₂ F | 0.750 | 0.737 | 230 |
| CF ₃ | 0.733 | 0.800 | — |
| CN | 0.700 | 0.913 | 180 |

polymers containing quaternary carbon in their main chains, for example, their different $G(S)$ values can be explained in terms of the HOMO density on their main chain bonds.

2. Since the overlap population F in the HOMO can be employed as a measure of the HOMO density on a covalent bond, the method of calculating the F value provides a reliable prediction of the C-C bond's scission efficiency when exposed to ionizing radiation, to some extent.

3. Concerning poly(methacrylate) series polymer materials, the F values of their main chains are not so much affected by substitutions into the ester side chain, with the exception of phenyl-including substituents. Their sensitivities are determined mainly by solubility characteristics rather than by scission efficiency.

On the other hand, α -substituents fairly affect the F value. However, drastically high scission efficiency is not generally expected by the substitution on the α -position.

4. Scission efficiency by ionizing radiation is not always associated with that by heating. The former is associated with F values and the latter is associated with total overlap populations P , at least as far as C-C covalent bonds are concerned. Therefore, P values give some information about the thermal stability of positive electron resists. As a practical positive electron resist, it is desirable that the main chain bond have a high F value and a high P value.

5. No simple relationship exists between scission efficiency and the electron-withdrawing nature of side chains. Moreover, the substituent effects differ according to the kinds of polymers. Scission efficiency by heating is rather associated with the s -character of the C-substituent bond, at least in the case of α -substituted poly(acrylate) series polymers.

Acknowledgment

The author is grateful to Dr. T. Kawamura of Kyoto University for his helpful comments and discussions. The author also wishes to thank Dr. Y. Tarui,

Dr. Y. Takeishi, and Dr. K. Yada for their encouragement throughout this work.

Manuscript submitted Oct. 17, 1980; revised manuscript received Jan. 15, 1981. This was Paper 177 presented at the Pittsburgh, Pennsylvania, Meeting of the Society, Oct. 15-20, 1978.

Any discussion of this paper will appear in a Discussion Section to be published in the June 1982 JOURNAL. All discussions for the June 1982 Discussion Section should be submitted by Feb. 1, 1982.

Publication costs of this article were assisted by VLSI Technology Research Association.

REFERENCES

1. R. L. Platzman, *Radiat. Res.*, **17**, 419 (1962).
2. R. S. Mulliken, *J. Chem. Phys.*, **23**, 1833 (1955); R. S. Mulliken, *ibid.*, **23**, 1841 (1955).
3. R. Hoffmann, *ibid.*, **39**, 1397 (1963).
4. M. Wolfsberg and L. Helmholz, *ibid.*, **20**, 837 (1952).
5. J. A. Pople and M. S. Gordon, *J. Am. Chem. Soc.*, **89**, 4253 (1967).
6. H. O. Pritchard and H. A. Skinner, *Trans. Faraday Soc.*, **49**, 1254 (1953).
7. J. N. Helbert, C. F. Cook, C. Y. Chen, and C. V. Pittman, *This Journal*, **126**, 694 (1979).
8. B. J. Lin, *J. Vac. Sci. Technol.*, **12**, 1317 (1975).
9. Y. Mimura, T. Ohkubo, T. Takeuchi, and K. Sekigawa, "Proc. of 14th Symp. on Semicond. and IC Tech.," Tokyo, p. 54 (1978).
10. H. R. Schultz, *J. Polym. Sci.*, **35**, 369 (1959).
11. T. Tada, *This Journal*, **126**, 1635 (1979).
12. R. K. Graham, *J. Polym. Sci.*, **37**, 441 (1959).
13. T. Tada, *This Journal*, **126**, 1829 (1979).
14. J. N. Helbert, C. V. Pittman, and J. H. Lai, "Proc. of 5th International Conf. on Photopolymer," p. 137, Ellenville (1979).
15. J. N. Helbert, P. J. Caplan, and E. H. Poindexter, *J. Appl. Polym. Sci.*, **21**, 797 (1977).
16. L. F. Thompson and M. J. Bowden, *This Journal*, **120**, 1722 (1973).
17. K. Murase, M. Kakuchi, and S. Sugawara, "Proc. of the International Conf. on Microlithography," p. 261, Paris (1977).

A Computer Model for Pulsed Laser Heating of Device Structures

D. J. Godfrey,¹ A. C. Hill, and C. Hill

Plessey Research (Caswell) Limited, Allen Clark Research Centre, Caswell, Towcester, Northants., England

ABSTRACT

A rigorous, two-region implicit Crank-Nicolson finite difference solution of the heat diffusion equation for pulsed laser heating has been developed. The computer model includes the temperature, phase, and material dependences of the major optical and thermal properties. Melting is modeled by separating the heat equation into three distinct regions. The first corresponds to the solid phase, the third to the liquid phase, and the second to the situation where latent heat is being stored. The run time required for the most complex model situation is approximately 40 min c.p.u. time. The model is applied to a typical device structure which includes photoengraved thermally grown silicon dioxide with unimplanted and implanted windows. Good agreement is obtained in situations where experimentally measurable effects can be compared with model predictions, and the application of the model to laser annealing of oxide covered silicon is discussed with reference to parallel experimental studies.

The use of pulsed laser annealing to remove ion implantation damage has been reported by many authors (1). Much of this work has concentrated on the materials aspects of laser annealing and there has been less effort directed toward practical device structures. A typical structure to which laser annealing might be applied is shown in Fig. 1. Here a thermal oxide layer is used to define the regions for implantation and to passivate the silicon surface. For successful laser annealing it must be possible to anneal the implantation damage in the windows without deleteriously affecting the SiO₂/Si interface. Experimental studies of such structures show that the SiO₂/Si interface is disturbed at the incident energy densities required for annealing the implant (2). Figure 2 shows an optical micrograph of such a structure where an implant of 40 keV 1 × 10¹⁶ ions cm⁻² As and a 1.9 J cm⁻² 25 nsec ruby laser pulse has been used. Ripple is visible in the surface over large areas of the annealed region. A model has been proposed for this rippling (2) which requires the oxide to move with respect to the underlying silicon; where this movement is constrained rippling may take place. In order to obtain a clear understanding of such effects it is necessary to be able to predict the temperature cycling of both the oxide and the underlying silicon during laser annealing. For this reason the computer model described in the next section has been developed.

Computer Model of Laser Heating

The light energy from the laser is absorbed by excitation of electrons which transfer their excess energy to heating the lattice in very short times ($\sim 10^{-12}$ sec) (3). Thus for pulse lengths greater than a few nanoseconds, the spatial distribution of the absorbed light is a good indication of the initial distribution of the heat energy. This local heating can then diffuse in the usual manner by thermal conduction. Hence, the thermal effects induced can be described by using the heat equation with a source term to include light absorption. If we ignore sideways diffusion the following form of the equation describes the temperature variation with depth and time.

$$c\rho \frac{\delta T}{\delta t} = \alpha I(z,t) + \frac{\delta}{\delta z} K(T) \frac{\delta T}{\delta z}$$

¹Present address: General Electric Company, Hirst Research Centre, Wembley, Middlesex, England.

Key words: pulsed laser annealing, numerical analysis, thermal cycling, silicon device structures.

where c is the heat capacity, ρ is the mass density, α is the absorption coefficient, K is the thermal conductivity, I is the laser power density, t is the time, and z is the depth.

Several analytical and numerical solutions of this equation are available in the literature (4). The major limitations of the analytical solutions are their inability to include the temperature and material dependences of the optical and thermal parameters and the change of phase. The numerical solutions available have been nonrigorous in their treatment of layered structures and have required a large amount of computer time to model realistic time and depth scales. However, the present numerical solution has been developed to give a more general and rigorous

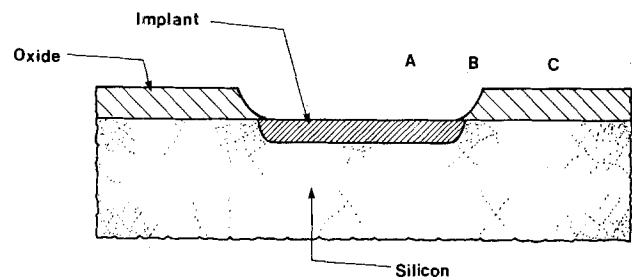


Fig. 1.

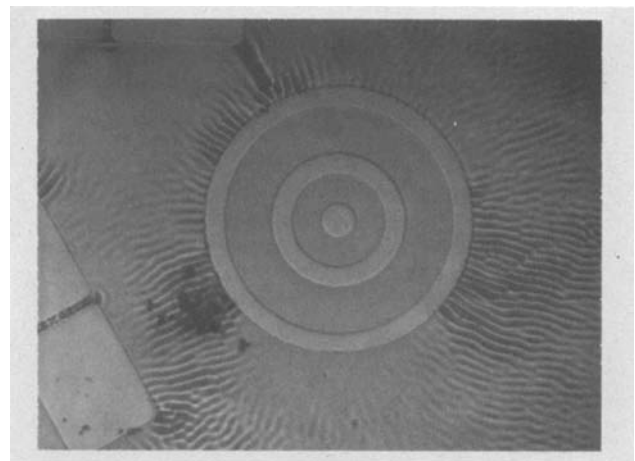


Fig. 2. Micrograph of photoengraved structure

approach while requiring less computer time. There are two major reasons for this improvement. First, the modeling of layered structures (such as oxide on silicon) has been treated as two separate regions with two separate heat equations joined at the interfaces by boundary conditions. Previous numerical solutions have assumed that layered structures can be modeled by allowing the optical and thermal parameters to vary discontinuously across the boundary while solving one diffusion equation for the complete structure. However, as will be shown in a further publication (5), this approach is mathematically inconsistent. Second, previous numerical solutions have used an explicit mathematical formulation of the problem. This approach leads to a severe constraint on the depth and time increments which will allow the solution to converge. The approach adopted here is an implicit solution using the Crank-Nicolson (6) method, which enables larger increments in depth and time while achieving sufficient accuracy in the solution. This allows practical time scales (up to 1 μ sec) and depth scales (up to 10 μ m) to be modeled with reasonable speed and accuracy (typical run time for nonmelting version of the program \sim 2 min with accuracy \sim 0.5%). The accuracy of the numerical solution has been tested against a number of analytical solutions to the diffusion equation. For example, Fig. 3 shows the variation of surface temperature with time for a "top hat" laser pulse. The numerical solution is indistinguishable from the exact analytical solution. The numerical solution has been compared with a solution of the heat equation where the thermal conductivity varied with temperature. Again, the error introduced by the numerical solution was of the order of 0.5%. The computer program which has been developed allows the parameters α and K in the diffusion equation to be temperature and material dependent and c and ρ to be material dependent. Also, the effect of multiple reflections at the material interface is included. Further details of the mathematical formulation and the validation of the computer model will be given in a future publication (5).

Modeling the Phase Change

For short pulse lengths (less than 10^{-7} sec) melting is required for appreciable distances of crystal growth (1). Thus a fundamental requirement of any model is the incorporation of the phase change. This is particularly difficult in analytical solutions due to the discontinuity at the solid liquid interface. However, numerical models are more able to deal with the phase change. For example, the model developed by Baeri *et al.* (4) treats melting in the following manner. When the temperature of a particular numerical slice reaches the melting point, any further heat received,

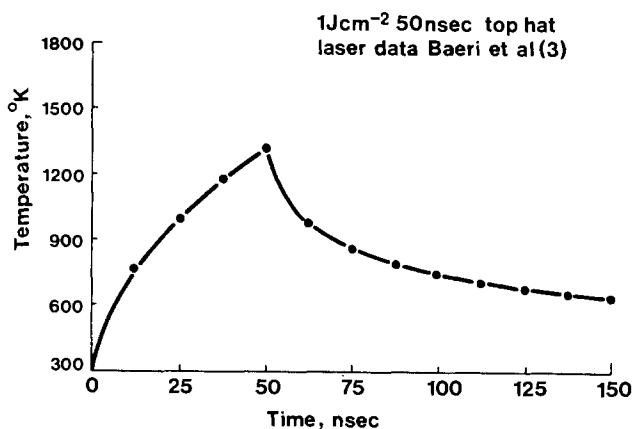


Fig. 3. Comparison of numerical solution with analytical solution

either by absorption or conduction, is stored as latent heat. Once the amount of latent heat required for melting has been received the layer melts and the temperature begins to rise again. This change of phase requires that a moving boundary, equivalent to the melt front, be included in the mathematical modeling.

The inclusion of such a boundary within an implicit numerical solution is technically more difficult. The effect of the phase change in the present model has been incorporated in the following manner. The diffusion equation has been rewritten as below (7)

$$\frac{\delta H(T)}{\delta t} = \alpha I(z,t) + \frac{\delta}{\delta z} K(T) \frac{\delta T}{\delta z}$$

The function $H(T)$ is shown in Fig. 4. In the first region $H = c\rho T$ to give the normal diffusion equation. The second region approximates the storage of latent heat at a constant temperature by a region of finite width (typically 10° - 100° C wide). For many experimental situations using a range of temperature of which melting occurs is physically more reasonable than the approach outlined above. The third region of the $H(T)$ junction again reduces to the normal diffusion equation with the possibility of using different values for c and ρ . This transformation of variable has the effect that the $H(T)$ function is single valued for all temperatures. Again, two layer structures (e.g., oxide on silicon) have been modeled by solving two separate diffusion equations with different $H(T)$ functions.

Summary of Parameter Values Used in the Model

A major difficulty in applying the computer model has been the limited number of experimental measurements available for the optical (8) and thermal (9) parameters under the conditions found in pulsed laser annealing. Table I gives the basic materials constants used in the program. Figure 5 summarizes the values taken for the temperature-dependent thermal conductivity in this present work and Fig. 6 and 7 give the values taken for the absorption coefficient for the ruby and Nd:YAG wavelengths. It can be seen that the strongest temperature dependences for both the thermal conductivity and the absorption coefficient are found for single crystal silicon, emphasizing the need to take such temperature effects into account if reliable modeling is to be achieved. At present there is some difficulty in obtaining convergence in the

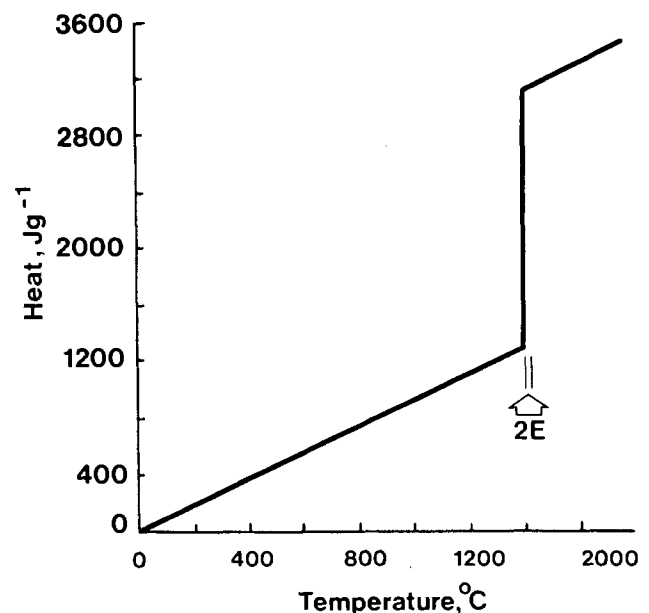


Fig. 4. H vs T graph for crystal silicon

Table I. Material constants used in model

| | Silicon | Amorphous Silicon | Silicon Dioxide |
|--|---------|-------------------|-----------------|
| Mass Density (g cm^{-3}) | 2.33 | 2.33 | 2.22 |
| Specific Heat ($\text{J g}^{-1}\text{K}^{-1}$) | 0.95 | 0.95 | 0.75 |
| Melting Point ($^{\circ}\text{C}$) | 1385 | 1200 | 1800 |
| Latent Heat (J g^{-1}) | 1809 | 1220 | 1200 |
| Refractive Index (Ruby) | 3.865 | 4.0 | 1.47 |
| Refractive Index (Nd:YAG) | 3.37 | 3.37 | 1.47 |

model when liquid thermal conductivities are included. This is due to the rapid change in thermal conductivity [typically a factor of ~ 20 over a small temperature range ($\sim 100^{\circ}\text{C}$)]. Thus, unless explicitly stated, the temperature profiles given in this paper do not include the effect of the high value of the liquid thermal conductivity. In conclusion, it should be noted that as the absorption coefficient and thermal conductivity are not well known, they constitute a major source of uncertainty in the computed profiles.

Modeling of Pulsed Laser Heating of Single Crystal Silicon

In this section the heating of single crystal silicon by a pulsed ruby laser has been modeled. Figure 8 shows the time for which the surface is molten as a function of the energy density (25 nsec FWHM Gaussian pulse). It can be seen that once a threshold energy density is reached, the length of time of the melt increases linearly with energy density. It is also possible to calculate the penetration of the melt depth as a function of time for given energy densities (see Fig. 9). From this figure it is possible to find the maximum melt depth which can then be drawn as a function of energy density (see Fig. 10). Again, once a threshold energy is reached the maximum melt depth increases approximately in a linear fashion with energy density. The slope of this line is $2.2 \text{ J cm}^{-2}/\mu\text{m}$ compared with a value of $2.5 \text{ J cm}^{-2}/\mu\text{m}$ obtained by

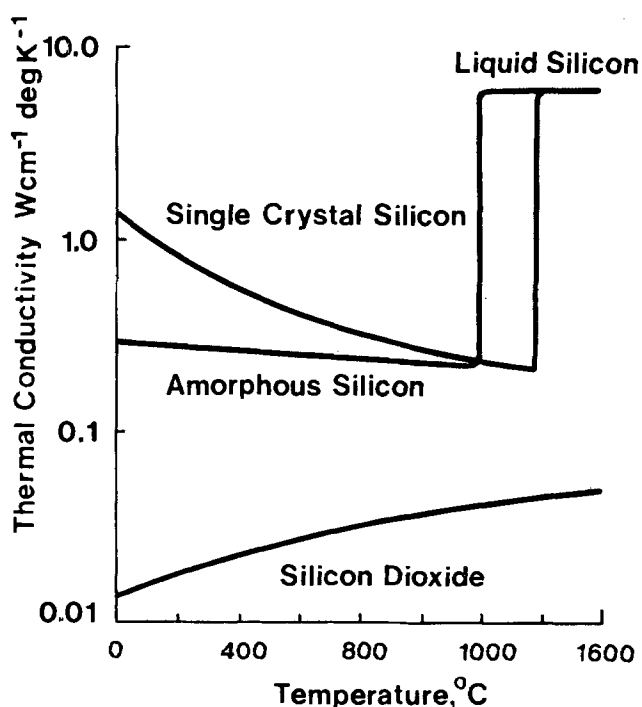
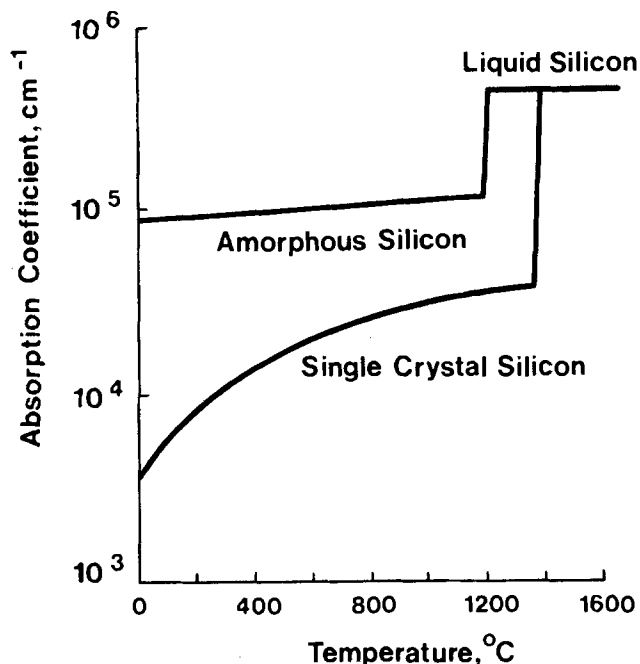
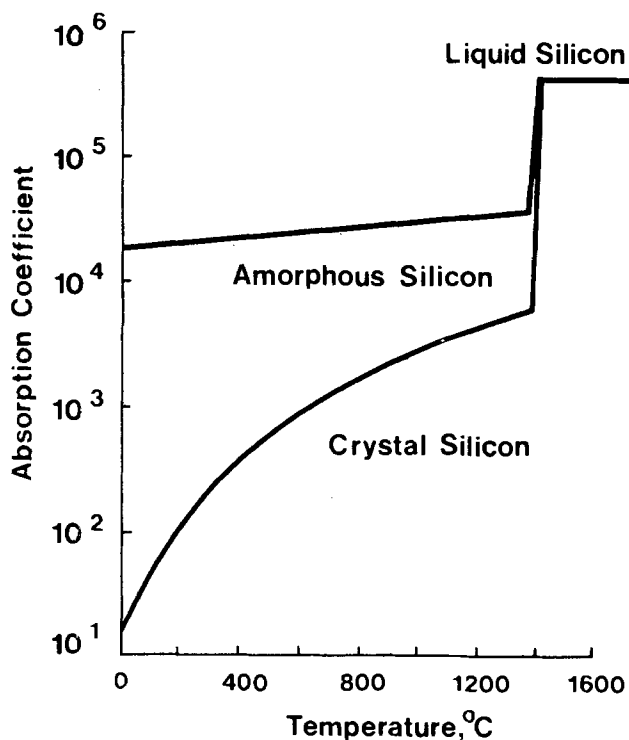


Fig. 5. Temperature dependence of thermal conductivity

Fig. 6. Temperature dependence of absorption coefficient for ruby wavelength, $0.693 \mu\text{m}$.

Baeri *et al.* (3) for a 50 nsec Gaussian pulse. The major reason for this is that parameter values used in the two programs are not identical.

The results detailed above were obtained with the temperature dependence of the solid thermal conductivity taken throughout. Figure 11 illustrates the difference obtained for the surface temperature when the liquid thermal conductivity is included. The major effects are to greatly reduce the peak surface temperature and lessen the length of time for which the surface is molten. Both these effects are due to the increased diffusion of heat away from the surface into the bulk.

Fig. 7. Temperature dependence of absorption coefficient for neodymium, $1.06 \mu\text{m}$.

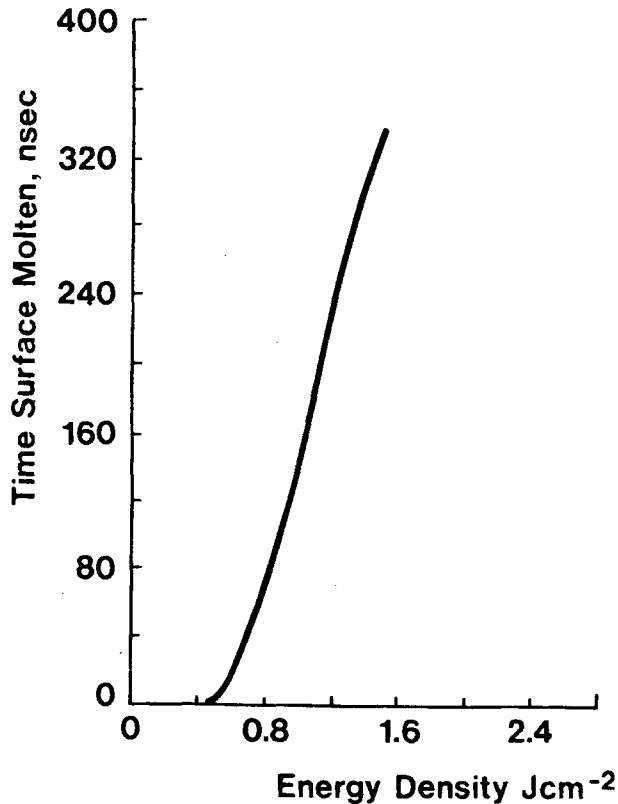


Fig. 8. Ruby laser of crystal. Time surface molten. No liquid reflectivity.

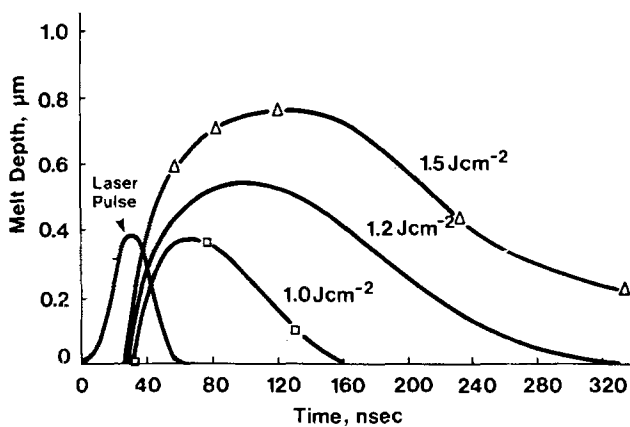


Fig. 9. Ruby laser on single crystal silicon—duration of melt. No liquid reflectivity.

Temperature Profiles Obtained for Device Structure

A major application of the computer model described in this paper is studying the thermal cycling of device structures such as shown in Fig. 1. This structure can be approximated by three separate regions: (i) Single crystal silicon (corresponding to unimplanted or low dose implanted windows), (ii) thin amorphous layer on a single crystal substrate (corresponding to a high dose implant such as 1×10^{16} ions cm^{-2} 40 keV As emitter), and (iii) oxide layer on silicon substrate (corresponding to the defining oxide shown in Fig. 1). It has been shown that the thermal and optical parameters of these three regions are very different (see Fig. 5, 6, and 7.) A further difference which must be considered is the reflectivity of these layered structures. It is known (10) that a surface oxide can act as an antireflection coating in laser annealing. Thus, the reflectivity found in region (iii) will be dependent upon the oxide thickness for coherent light. However, in parallel experimental studies

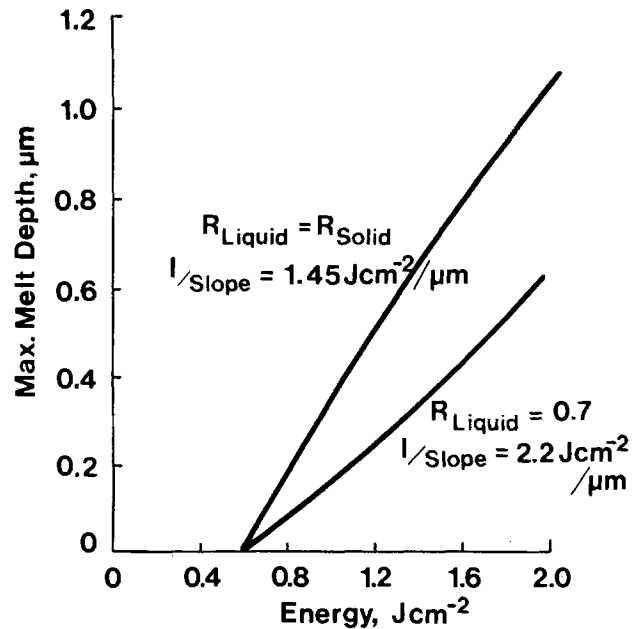


Fig. 10. Ruby laser on crystal silicon melt depth vs. energy density

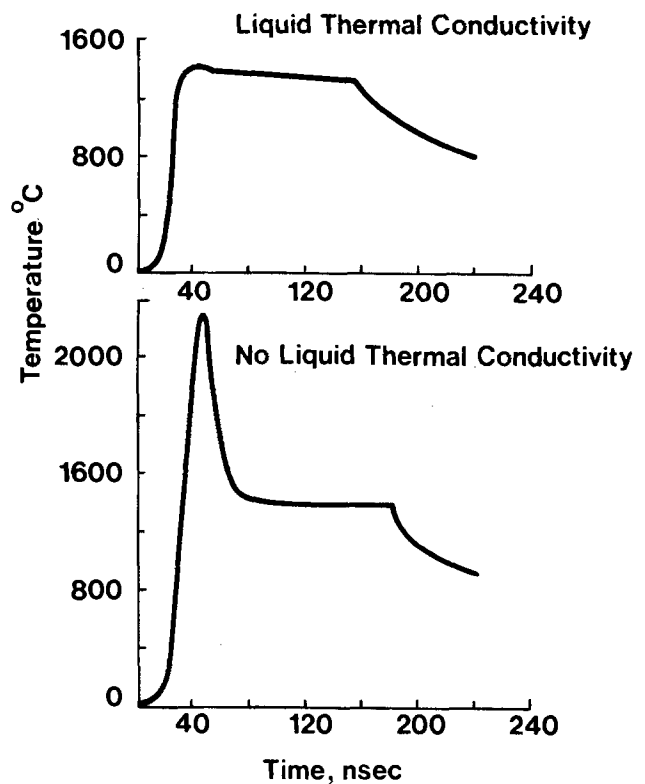


Fig. 11. Ruby laser on single crystal silicon. 1.0 J cm^{-2} surface temperature with time.

a waveguide has been used in order to obtain a more uniform energy density for the laser. This causes the laser light to be highly divergent, such that the conditions for constructive and destructive interference are met over a wide range of angles. This effectively reduces the amplitude of the interference effect. However, the mean reflectivity will still be higher than for bare silicon. In the computer model this average reflectivity is calculated from the following equation

$$R = \frac{(n_1 - n_2)^2 + (K_1 - K_2)^2}{(n_1 + n_2)^2 + (K_1 + K_2)^2}$$

where $n_1' = n_1 - iK_1$ and $n_2' = n_2 - iK_2$ and n_1' and

n_2' are the complex refractive indexes of the two materials involved. This approach has been adopted for the thin amorphous region and for the liquid reflectivity once the melt depth is greater than the skin depth.

Figure 12 shows the temperature profiles present at the peak of a 0.5 J cm^{-2} 25 nsec FWHM Gaussian pulse for the device structure. In this figure and in Fig. 13 the values for the liquid thermal conductivity

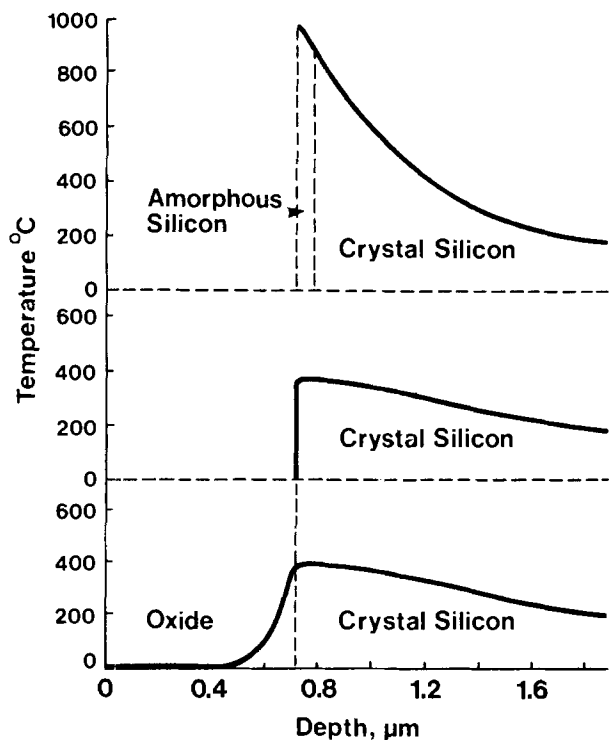


Fig. 12. Temperature profiles for photoengraved structure. 0.5 J cm^{-2} 25 nsec pulse profiles taken at peak of pulse.

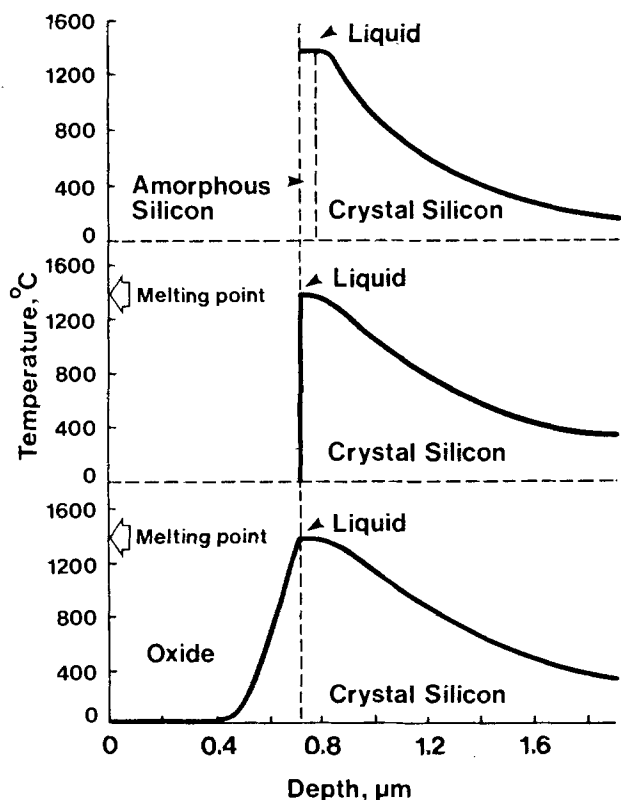


Fig. 13. Temperature profiles for photoengraved structure. 1.0 J cm^{-2} 25 nsec pulse (taken at peak of pulse).

and liquid absorption coefficients have been included. It can be seen that the reduced reflectivity of the oxide-covered silicon causes the interface temperature to be greater than for the bare silicon case. This is in spite of some heat loss from the silicon due to conduction into the oxide. For 0.5 J cm^{-2} no melting is obtained for the photoengraved structure at the peak of the pulse whereas for 1.0 J cm^{-2} (see Fig. 13) melting occurs in all three cases. It can be seen that the largest melt depth at the peak of the pulse is obtained for the ion-implanted region and that the silicon dioxide layer is only heated to above 400°C to a thickness of $0.15 \mu\text{m}$. It is also useful to be able to determine the heating of the oxide as a function of time. Figure 14 shows temperature profiles for oxide on silicon at 25 nsec intervals after the peak of the pulse. It can be seen that the whole oxide is heated quite slowly and a temperature of above 800°C is only reached 100 nsec after the peak of the pulse when the underlying silicon has almost resolidified.

A model previously proposed (2) to explain ripple in oxide overlayers on silicon after pulsed laser anneal required both melting of the silicon and simultaneous compressive stress in the oxide. The stress was attributed to thermal expansion, requiring temperatures in excess of 1500°C to account for the observed ripple. The present computation shows that melting does indeed occur under commonly used experimental conditions but that oxide temperatures are much lower than were assumed. More recent experimental evidence (11) suggests that the compressive stress is in-built in the oxide and that the ripple is due to elastic strain which can occur at the low oxide temperature computed here.

Melting for $1 \times 10^{16} \text{ ions cm}^{-2}$ 40 keV As Implanted Silicon

A further area where the present model can be applied is the calculation of the melt depth achieved for high dose As implants. Laser annealing is a particularly promising technique for such implants as good single crystal material with levels of dopant above the solid solubility limit can be produced. Much experimental effort has been focused in this laboratory on the annealing of $1 \times 10^{16} \text{ ions cm}^{-2}$ 40 keV As emitter

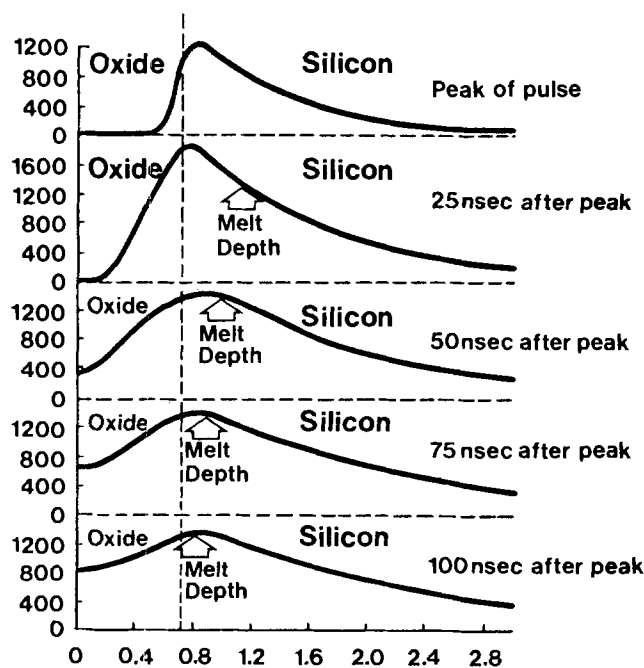


Fig. 14. Development of oxide heating with time. 1.0 J cm^{-2} 25 nsec ruby pulse on oxide covered silicon.

implants. A process technology has been developed (10) which allows the oxide to be protected during laser anneal, Figure 15 shows the junction depth obtained from such an implant after varying energies of pulsed ruby laser heating. Also shown in this figure is the calculated maximum melt depth from the computer program. It can be seen that the threshold for melting is approximately 0.75 J cm^{-2} and that the slope of the graph is $3.5 \text{ J cm}^{-2}/\mu\text{m}$. Using the computer model, it is possible to calculate the melt depth as a function of time and energy density. The expected junction depth can then be found using $x = N\sqrt{Dt}$. The result of such calculations is shown in Fig. 15. It can be seen that the agreement between the theoretical and experimental junction depth is good.

Figure 16 shows the calculated melt depth for an Nd:YAG laser pulse of the implanted silicon. Due to the lower absorption coefficient for this wavelength in both the amorphous and single crystal regions, the threshold for melting is much higher than for the ruby wavelength. However, once melting occurs the differences in the optical parameters for the solid are less important. Thus the slopes of the two lines for the ruby and Nd:YAG laser pulses are similar.

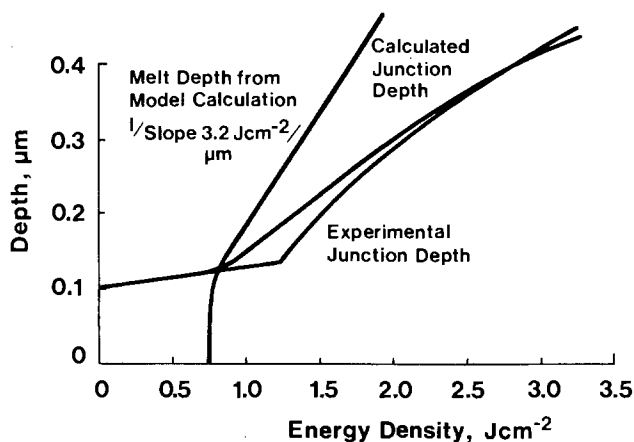


Fig. 15. Ruby laser. Includes liquid reflectivity

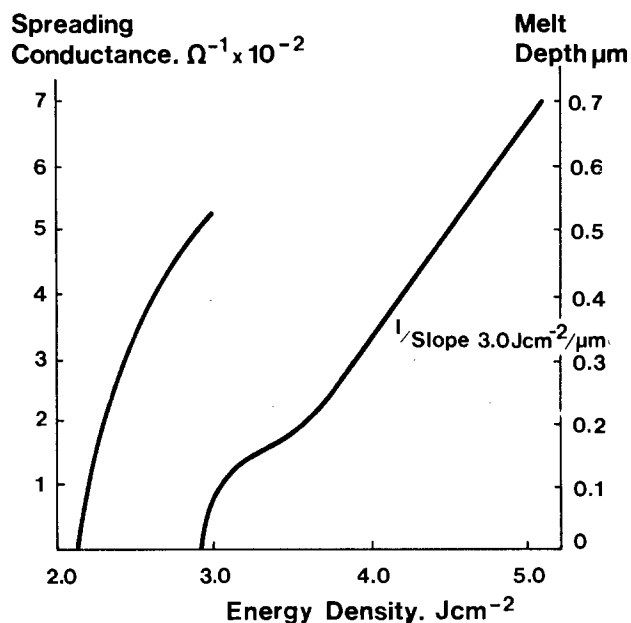


Fig. 16. $1 \times 10^{16} \text{ ions cm}^{-2}$ 40 keV As implant in silicon melt depth for Nd:YAG.

Summary of Computer Model

A fast implicit Crank-Nicolson numerical solution to the heat diffusion equation has been produced. The model treats rigorously the temperature dependences of the optical and thermal parameters, the change of phase, and two layer structures. A computing time of approximately 1 hr is required for runs involving the most complex situations for which the model has been developed. If melting is not required a faster program (run time 2 min) can be used.

The results obtained from the model agree reasonably well with experimental values, where direct comparison is possible. A major difficulty in applying the program is the lack of reliable experimental data available for the optical and thermal parameters. A major application of the model is for situations where experimental measurements are not possible (for example, the transient heating of oxide layers). The reliability of such predicted temperature profiles is dependent upon the level of known physical effects which are included in the model. It is for this reason that such a large amount of effort has been expended in producing this first rigorous solution of the heat diffusion equation for laser heating.

Further developments of the program will include improvements in the range of values which may be taken for the thermal and optical parameters. At present there are difficulties with convergence when liquid thermal conductivity is taken into account. It is also hoped that the effect of carrier diffusion may be included in the source term of the equation. However, this effect can only be fully included by the solution of two coupled diffusion equations. Finally, the present model could be used to calculate the diffusion of dopants during pulsed laser annealing.

Acknowledgments

We would like to thank R. Allen for his help with problems associated with S.O.R. techniques. This work is funded by the British M.O.D. and thanks are due to them and to the Plessey Company Limited for permission to publish.

Manuscript submitted Jan. 4, 1981; revised manuscript received Feb. 10, 1981.

Any discussion of this paper will appear in a Discussion Section to be published in the June 1982 JOURNAL. All discussions for the June 1982 Discussion Section should be submitted by Feb. 1, 1982.

Publication costs of this article were assisted by Plessey Research (Caswell) Limited.

REFERENCES

1. e.g., C. W. White and P. S. Peercy, "Laser and Electron Beam Processing of Materials," MRS Meeting, November 1979, Cambridge, Massachusetts.
2. C. Hill and D. J. Godfrey, *J. Phys. Coll. C4 Suppl.*, No. 5, C4-79 (May 1980).
3. e.g., E. J. Yoffa, *Appl. Phys. Lett.*, **36**, 37 (1980).
4. Analytical Solution: J. R. Meyer, F. J. Bartoli, and M. R. Kruer, *Phys. Rev. B*, **21**, 1559 (1980); Numerical Solution: P. Baeri, S. U. Campisano, G. Foti, and E. Rimini, *J. Appl. Phys.*, **50**, 788 (1979).
5. A. C. Hill and D. J. Godfrey, To be published.
6. G. D. Smith, "Numerical Solution of Partial Differential Equations: Finite Difference Methods," Clarendon Press, Oxford (1978).
7. G. H. Meyer, *SIAM J. Numer. Anal.*, **10**, 522 (1973).
8. e.g., A. G. Reversz, *J. Non-Crystal. Solids*, **11**, 309 (1973) and references quoted in Ref. (3) and C. Hill and D. J. Godfrey, Unpublished data.
9. A. E. Bell, *RCA Rev.*, **40**, 296 (1979) and references quoted in Ref. (3).
10. C. Hill, *AIP Conf. Proc.*, **50**, 419 (1978).
11. C. Hill and D. J. Godfrey, To be published.

Antimony Diffusion from Spin-On Doped Oxide

Schy-yi Wu*

Motorola, Semiconductor Group, Phoenix, Arizona 85008

ABSTRACT

A new antimony diffusion process using spin-on doped oxide source was characterized and developed. Diffusion is enhanced in dilute oxidizing ambient due to increased surface concentration while diffusivity remains essentially the same in both nitrogen and dilute oxidizing ambient. Wright etch reveals no diffusion induced dislocation when surface concentration is less than $2.4 \times 10^{19} \text{ cm}^{-3}$. The thinner and less concentrated glass diffused in lower oxygen concentration ambient is less prone to glass devitrification. This process was proven to be suitable for buried layer formation in the fabrication of bipolar integrated circuits.

In the fabrication of silicon bipolar integrated circuits, the first diffusion step is the buried layer diffusion, which is followed by epitaxial growth. The bases and emitters are fabricated on epitaxial layers. The device performance is related to the epitaxial quality which in turn is related to the buried layer quality. Buried layers can be fabricated by arsenic diffusion or antimony diffusion. Two advantages associated with arsenic are (i) its nearly perfect match in silicon lattice; and (ii) high solid solubility in silicon, both of which are required for very low resistivity buried layers.

Antimony is larger than silicon in atomic size and has lower solid solubility than arsenic. However, antimony has lower diffusivity and lower vapor pressure and thus would exhibit less out-diffusion than arsenic in subsequent high temperature processes. Less lateral out-diffusion is desired for increased device packing density. Less autodoping into epitaxial layers is desired for thin and low resistivity epi which is required for high speed circuitry.

A new antimony diffusion process using proprietary spin-on doped oxides (1), suitable for buried layer formation is described. The thickness of glass can be easily controlled by spin speed and viscosity of the antimony glass solution. This spin-on method of source application offers higher throughput with better uniformity than the conventional atmospheric chemical vapor deposition process, better processing simplicity than the low pressure CVD process, and lower capital requirement than the ion implantation process. The spin-on antimony diffusion process results in improved yield compared to the spin-on arsenic process and device speeds comparable to that obtained by antimony ion implantation for low power Schottky T²L devices.

Experimental

Antimony source.—The antimony concentration in the glass is controlled by the weight ratio of an antimony compound to TEOS (tetraethylorthosilicate). The viscosity of the antimony glass solution, and thus the thickness of the spun film, are controlled by the weight ratio of TEOS to solvent.

Silicon wafers.—Wafers were CZ grown, boron-doped 3 in. diam. Three types of wafers were used: (i) <100> crystal orientation, 0.8-1.2 $\Omega \text{ cm}$; (ii) <100> crystal orientation, 7-17 $\Omega \text{ cm}$; and (iii) <111> crystal orientation, 7-17 $\Omega \text{ cm}$.

Wafer clean.—Wafers were cleaned by 1 min 10 H₂O:1 HF (49%) and/or 10 min 7 H₂SO₄:3 H₂O₂ at 110° ± 10°C, with UPDI H₂O rinse between the two steps. Wafers were spin-rinsed and spin-dried in hot N₂.

Source application.—The wafer was placed on a Headway EC101 spinner, and the antimony glass solu-

tion was applied to the surface. The wafers were spun at various speeds for 10 sec to achieve the desired thickness and baked at 150° or 400°C in N₂ ambient for 30 min.

Diffusion.—Temperatures inside the polysilicon diffusion tube were measured by calibrated thermocouples and temperature indicators. Temperature was uniform within 2°C across the "flat zone" without a wafer load. The actual temperature uniformity with a wafer load can vary by more than 2°C (2). Wafers were placed in a quartz boat and pushed at 4 in./min into the diffusion tube at 800°C (except where noted) to prevent thermal stress induced dislocations and warpage. The temperature was ramped to 1250°C, kept at 1250°C for various times, then ramped down to the starting temperature. Wafers were pulled at 4 in./min. Nitrogen and oxygen of various flow rates (10-11 liters/m total, measured by rotameters) were passed through the diffusion tube.

Evaluations.—Thickness of oxides (antimony glass after source bake, and antimony glass-thermal oxide composite after diffusion) was measured by an IBM 7840 film thickness analyzer using the refractive index for thermal oxide. Wafers were etched in HF solution to remove all oxides. Sheet resistance was measured by four point probe. Five points were measured on each wafer: center and four equi-spaced peripheral points, one-third of an inch from the wafer edge. Junction depth was measured by grooving, staining, and fringe counting with an interferometer. Spreading resistance probe measurements were used to determine the dopant profile.

Results and Discussions

Diffusion ambient.—Pertinent data for the 3 hr diffusions at 1250°C in two diffusion ambients (0% O₂ and 10% O₂) are shown in Tables I and II. Source concentration was $2.77 \times 10^{21} \text{ cm}^{-3}$, source thickness was variable, and source bake temperature was 400°C. The above data show that the 10% O₂ ambient resulted in lower sheet resistance, deeper junction, higher sheet conductivity, and thus higher surface concentration as well as higher doping level than the 100% N₂ ambient. This kind of effect is also observed in arsenic diffusion from doped oxide sources including CVD oxide (3) and spin-on oxide (2). Sakurai *et al.* (3)

Table I. Diffusion data for $C_0 = 2.77 \times 10^{21} \text{ cm}^{-3}$ in N₂ ambient; $T_b = 400^\circ\text{C}$, $T = 1250^\circ\text{C}$, $t = 3 \text{ hr}$

| | | | | | |
|--|--------|--------|---------|---------|---------|
| $X_s, \mu\text{m}$ | 0.0275 | 0.0560 | 0.1264 | 0.1552 | 0.1910 |
| $X_o, \mu\text{m}$ | 0.0430 | 0.0632 | 0.0643 | 0.1024 | 0.1516 |
| $\Delta th, \mu\text{m}$ | 0.0155 | 0.0072 | -0.0621 | -0.0528 | -0.0394 |
| $R_s, \Omega/\square$ | 96.32 | 94.34 | 82.8 | 74.38 | 64.24 |
| $X_j, \mu\text{m}$ | — | 4.59 | 4.59 | — | — |
| $\sigma_j (\Omega \cdot \text{cm})^{-1}$ | — | 23.1 | 26.3 | — | — |
| $C_s, \text{cm}^{-3} \times 10^{18}$ | — | 1.5 | 1.8 | — | — |
| $\bar{D}_m, \mu\text{m}^2/\text{hr}$ | — | 0.250 | 0.244 | — | — |

* Electrochemical Society Active Member.

Key words: doping, junction, diode, semiconductor.

Table II. Diffusion data for $C_0 = 2.77 \times 10^{21} \text{ cm}^{-3}$ in 10% O_2 ambient: $T = 1250^\circ\text{C}$, $t = 3 \text{ hr}$, $T_b = 400^\circ\text{C}$

| | | | |
|---|--------|--------|---------|
| $X_s, \mu\text{m}$ | 0.0863 | 0.1226 | 0.2683 |
| $X_o, \mu\text{m}$ | 0.1560 | 0.1742 | 0.2448 |
| $\Delta t/h, \mu\text{m}$ | 0.0697 | 0.0516 | -0.0235 |
| $R_s, \Omega/\square$ | 24.4 | 19.7 | 14.0 |
| $X_j, \mu\text{m}$ | 5.27 | 5.0 | — |
| $\sigma, (\Omega \cdot \text{cm})^{-1}$ | 77.8 | 101.5 | — |
| $C_s, \text{cm}^{-3} \times 10^{19}$ | 1.55 | 2.3 | — |
| $D_m, \mu\text{m}^2/\text{hr}$ | 0.247 | 0.214 | — |

attributed this effect to the difference in properties of the interface between doped oxide and silicon. For diffusion in N_2 , arsenic is reduced by silicon and accumulated at the interface and the surface concentration in silicon is not so high. On the other hand, for diffusion in an oxidizing ambient, the accumulation phenomenon is not observed and the surface concentration is higher than that obtained by diffusion in N_2 . When N_2 was used in antimony diffusion from spin-on doped oxide ($\geq 0.1 \mu\text{m}$) a hydrophobic surface with brown stain was obtained after the oxide was etched off in HF solution following the diffusion. The brown stain may be an indication of antimony accumulation at the interface. No brown stain was observed for $0.056 \mu\text{m}$ source since oxidation occurred due to residual oxidant in N_2 ambient (Table I). Listed in Tables I and II are also some estimated diffusivity data assuming Gaussian distribution of dopant and substrate concentration equal to $1.34 \times 10^{15} \text{ cm}^{-3}$. The latter value is the average substrate concentration of the wafers used in these experiments. These estimated diffusivity data were calculated by using $t = 3 \text{ hr}$. The effective diffusion time at 1250°C is greater than 3 hr since wafers were loaded and unloaded at 800°C . It can be shown later that the Gaussian distribution is valid for the calculations of diffusivities reported in Tables I and II. The diffusivity is essentially the same for both 100% N_2 and 10% O_2 ambients. Hence the enhanced diffusion reported herein is due to increased surface concentration in oxidizing ambient. This is not to be confused with "oxidation-enhanced diffusion" reported by Francis and Dobson (4). In the latter case diffusivity is increased due to growth of stacking faults by oxidation.

Figure 1 shows sheet resistance vs. oxygen concentration for $C_0 = 9.01 \times 10^{21} \text{ cm}^{-3}$ for various source thicknesses diffused for 3 hr at 1250°C . These data were obtained by using 150°C source bake. In general, higher oxygen concentration is required for thicker source to achieve minimum sheet resistance. For $C_0 = 9.01 \times 10^{21} \text{ cm}^{-3}$, 5% O_2 resulted in the lowest sheet resistance for $0.1211 \mu\text{m}$ source, whereas 10% O_2 resulted in lowest sheet resistance for $0.1690 \mu\text{m}$ source. This indicates that enhanced diffusion is a function of oxide growth. The rate of oxidation is increased as oxygen concentration is increased, and the source thickness is required for thicker source than for thinner source to grow the same amount of oxide. When oxygen concentration is too high, the oxidation process competes with the diffusion process and higher sheet resistance is obtained. Among the diffusion ambients studied, lowest sheet resistance and highest surface concentration were obtained in 1% O_2 for $C_0 = 2.77 \times 10^{21} \text{ cm}^{-3}$ and $X_s = 0.0762 \mu\text{m}$; in 5% O_2 for $C_0 = 9.01 \times 10^{21} \text{ cm}^{-3}$ and $X_s = 0.0900 \mu\text{m}$. Again diffusivity is essentially the same for all sources. Sheet resistance and junction depths obtained for the 3 hr diffusion at 1050°C in 0.75, 10, and 100% O_2 are shown in Table III for three sources. These data show that the effects of diffusion ambients are also true at 1050°C .

Source bake temperature and wafer clean.—The effects of these two variables on sheet resistance were determined in a 3 hr diffusion at 1250°C in 3% O_2 ambient. Wafers were cleaned by 10 H_2O :1 HF (49%) or 7 H_2SO_4 :3 H_2O_2 (piranha). The source with $C_0 = 9.01 \times$

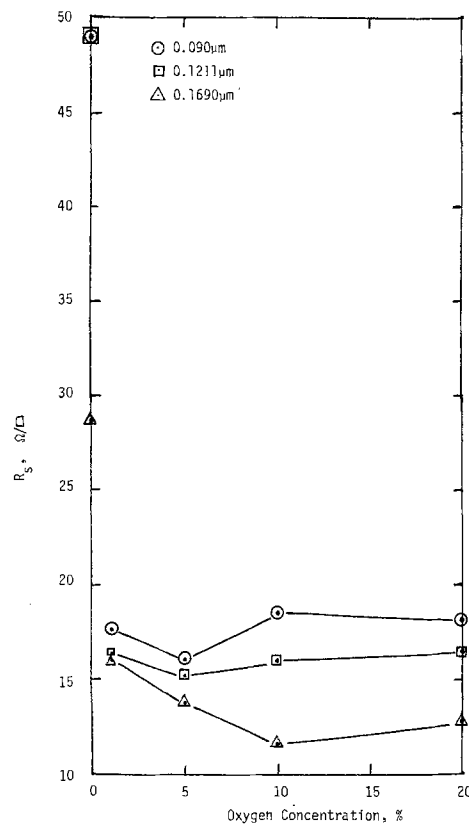


Fig. 1. Sheet resistance as a function of oxygen concentration in diffusion ambient: $C_0 = 9.01 \times 10^{21} \text{ cm}^{-3}$, $T_b = 150^\circ\text{C}$, $T = 1250^\circ\text{C}$, $t = 3 \text{ hr}$.

10^{21} cm^{-3} was spun at 4 Krpm. The spun wafers were baked at 150° or 400°C . Source thicknesses are 0.0800 and $0.0670 \mu\text{m}$, respectively. Sheet resistances and final oxide thicknesses measured after diffusion are listed in Table IV. The 400°C source bake resulted in higher sheet resistance than the 150°C source bake. This may be in part caused by more dopant loss at the higher bake temperature. Atomic absorption analysis showed that antimony concentration was decreased from 34.8 to 31.1% when bake temperature was increased from 150° to 400°C for the source of same concentration ($X_s = 0.1211 \mu\text{m}$ if baked at 150°C). More reduction in antimony concentration is expected for the thinner source. Note that the melting point of Sb_2O_3 is 650°C . The difference in sheet resistance also appears to be related to oxide growth, which in turn is related to

Table III. Sheet resistance and junction depth as functions of oxygen concentrations for the 3 hr diffusion at 1050°C

| Source | Diffusion ambient, % O_2 | | | | | | | |
|--------|--------------------------------------|--------------------|-----------------------|--------------------|-----------------------|--------------------|-----------------------|--------------------|
| | $C_0, \text{cm}^{-3} \times 10^{21}$ | $X_s, \mu\text{m}$ | 0.75 | | 10 | | 100 | |
| | | | $R_s, \Omega/\square$ | $X_j, \mu\text{m}$ | $R_s, \Omega/\square$ | $X_j, \mu\text{m}$ | $R_s, \Omega/\square$ | $X_j, \mu\text{m}$ |
| 2.77 | 0.1250 | 828.3 | — | 416.0 | 0.27 | 3811 | 0 | |
| 4.88 | 0.1350 | 587.8 | 0.27 | 364.0 | — | 461.4 | 0.18 | |
| 16.4 | 0.7500 | — | — | 359.4 | 0.27 | 158.8 | 0.27 | |

Table IV. Effect of source bake temperature and wafer clean on sheet resistance and oxide growth

| Bake temp., $^\circ\text{C}$ Clean | 150 | | 400 | |
|---------------------------------------|-----------------------|--------------------|-----------------------|--------------------|
| | $R_s, \Omega/\square$ | $X_o, \mu\text{m}$ | $R_s, \Omega/\square$ | $X_o, \mu\text{m}$ |
| H_2O/HF | 15.24 | 0.1091 | 17.36 | 0.1018 |
| Piranha | 15.56 | 0.1071 | 20.44 | 0.0986 |

sheet resistance as discussed earlier. Specifically, Fig. 1 shows that for $C_0 = 9.01 \times 10^{21} \text{ cm}^{-3}$, sheet resistance is increased as the oxide growth is decreased from that amount produced by 3% O_2 ambient. The sheet resistance was lower and the final oxide was thicker when source was baked at 150°C than at 400°C . This indicates that the more densified glass has a greater resistance to silicon oxidation in diffusion ambients of $\leq 3\%$ O_2 . When the source was baked at 400°C , piranha clean resulted in higher sheet resistance and thinner final oxide than the $\text{H}_2\text{O}/\text{HF}$ clean. The very small amount of oxide produced by piranha appears to be a significant resistance to oxidation in $\leq 3\%$ O_2 ambient.

Dopant profile and diffusivity.—Typical R_s vs. X_s data are represented by Fig. 2 for diffusion at 1250°C for 1 hr in 10% O_2 ambient for substrate resistivity ranging from 7 to $17 \Omega \text{ cm}$. Junction depth vs. time data are presented in Fig. 3 for two substrate resistivity ranges 7–17 and 0.8 – $1.2 \Omega \text{ cm}$. The average substrate concentrations, \bar{C}_B , are 1.34×10^{15} and $1.72 \times 10^{16} \text{ cm}^{-3}$ for the two resistivity ranges. The junction depth data are applicable to surface concentration range from $1.5 \times 10^{19} \text{ cm}^{-3}$ to $3.0 \times 10^{19} \text{ cm}^{-3}$. This range corresponds to $80 \Omega \mu\text{m} \leq R_s X_j \leq 137 \Omega \mu\text{m}$ for $\bar{C}_B = 1.34 \times 10^{15} \text{ cm}^{-3}$ and $71.5 \Omega \mu\text{m} \leq R_s X_j \leq 116 \Omega \mu\text{m}$ for $\bar{C}_B = 1.72 \times 10^{16} \text{ cm}^{-3}$. Deeper junctions were obtained for the lower substrate concentration. If dopant profiles follow Gaussian distributions (5), then

$$X_j = 2\sqrt{D(\Delta t + t)} [\ln(C_s/C_B)]^{1/2} \quad [1]$$

where t is the diffusion time at 1250°C and Δt accounts for diffusion during the ramp up and the ramp down cycles. Equation [1] indicates that junction depth is decreased as substrate concentration is increased or surface concentration is decreased. For surface concentrations between 1.5×10^{19} and $3.0 \times 10^{19} \text{ cm}^{-3}$, the junction depth should vary within 3.6% for $\bar{C}_B = 1.34 \times 10^{15} \text{ cm}^{-3}$ and 5.1% for $\bar{C}_B = 1.72 \times 10^{16} \text{ cm}^{-3}$. These variations are within measurement errors. The error in junction depth measurement is ± 0.135 or $0.27 \mu\text{m}$. For data presented in Fig. 3, the minimum error in junction depth measurement is 5% for $C_B = 1.34 \times 10^{19} \text{ cm}^{-3}$ ($0.27 \mu\text{m} \div 5.4 \mu\text{m}$), and 5.6% for $C_B = 1.72 \times 10^{16} \text{ cm}^{-3}$ ($0.27 \mu\text{m} \div 4.86 \mu\text{m}$). The mea-

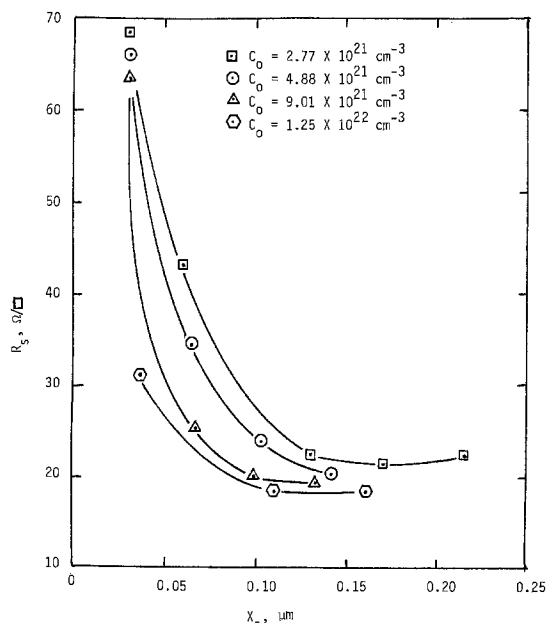


Fig. 2. Sheet resistance data for 1 hr diffusion at 1250°C in 10% O_2 ambient: $T_b = 400^\circ\text{C}$.

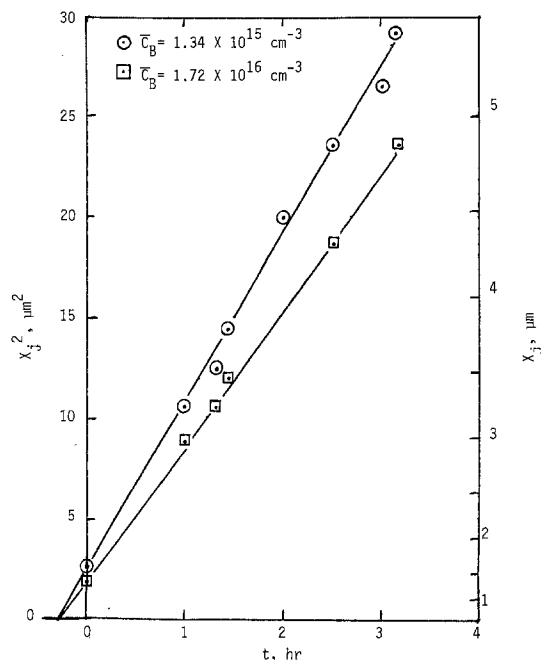


Fig. 3. Junction depth data for various diffusion time: $T = 1250^\circ\text{C}$, diffusion ambient = 10% O_2 .

surement errors are greater for shallower junctions. Thus, within experimental error, junction depth can be considered to be independent of surface concentration in the range 1.5×10^{19} to $3.0 \times 10^{19} \text{ cm}^{-3}$. Equation [1] can be written as

$$X_j^2 = 4D \Delta t \ln \frac{C_s}{C_B} + 4Dt \ln \frac{C_s}{C_B} \quad [2]$$

and $t = -\Delta t$ when $X_j = 0$.

Thus, a plot of X_j^2 vs. t should be straight line [when $\ln(C_s/C_B) = \text{constant}$], and the intercept at $X_j = 0$ is an estimate of Δt . Figure 3 shows that the plots of X_j^2 vs. t are straight lines and $\Delta t = 0.3$ hr which is the equivalent diffusion time at 1250°C for the combined ramp up and the ramp down cycles.

The dopant profile obtained by spreading resistance probe measurements for the 2 hr diffusion at 1250°C in 1% O_2 ambient using $C_0 = 9.01 \times 10^{21} \text{ cm}^{-3}$ and $X_s = 0.1160 \mu\text{m}$ is shown in Fig. 4. The solid curve represents the theoretical Gaussian distribution with $C_s = 2.5 \times 10^{19} \text{ cm}^{-3}$ and $4D(\Delta t + t) = 1.95 \mu\text{m}^2$. It can be seen that the dopant profile follows a Gaussian distribution very well. The junction depths obtained, $4.32 \mu\text{m}$ for $\bar{C}_B = 1.34 \times 10^{15} \text{ cm}^{-3}$ and $3.78 \mu\text{m}$ for $\bar{C}_B = 1.72 \times 10^{16} \text{ cm}^{-3}$, also agree very well with the Gaussian distribution. Since Δt was estimated to be 0.3 hr, diffusivity, D , can be calculated to be $0.212 \mu\text{m}^2/\text{hr}$. This is to be compared with $0.173 \mu\text{m}^2/\text{hr}$ reported by Fuller and Ditzenberger (6).

Surface quality.—Diffusion-induced dislocations and glass damage are related to buried layer quality and epitaxial layer quality. No dislocations were revealed by 1 min Wright etch when surface concentration was lower than $2.4 \times 10^{19} \text{ cm}^{-3}$. When surface concentration was greater than $2.4 \times 10^{19} \text{ cm}^{-3}$, shallow etch pits were observed. Rao, *et al.* (7) observed dislocations for surface concentrations greater than $2.4 \times 10^{19} \text{ cm}^{-3}$ using the same sources. The major glass damage is caused by devitrification. Glass devitrification causes raised steps on the silicon surface. The raised steps appear like rosettes (Fig. 5) or irregular in shape (Fig. 6). Thinner and less concentrated glasses used in lower oxygen ambient are less prone to devitrification. Surface conditions, such as particulates, residual photoresist, and impurities, are thought

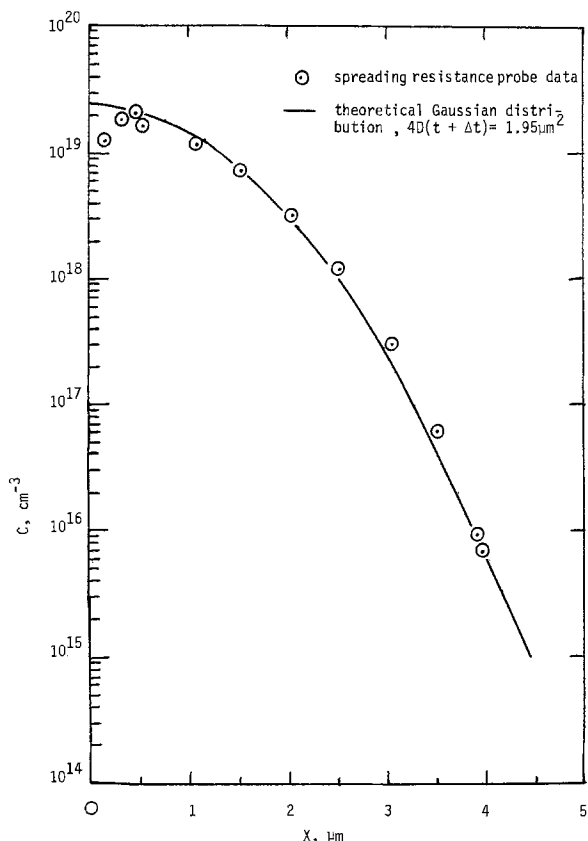


Fig. 4. Carrier concentration profile after 2 hr diffusion at 1250°C in 1% O₂ ambient: $C_0 = 9.01 \times 10^{21} \text{ cm}^{-3}$, $X_s = 0.116 \text{ } \mu\text{m}$ ($T_b = 150^\circ\text{C}$).

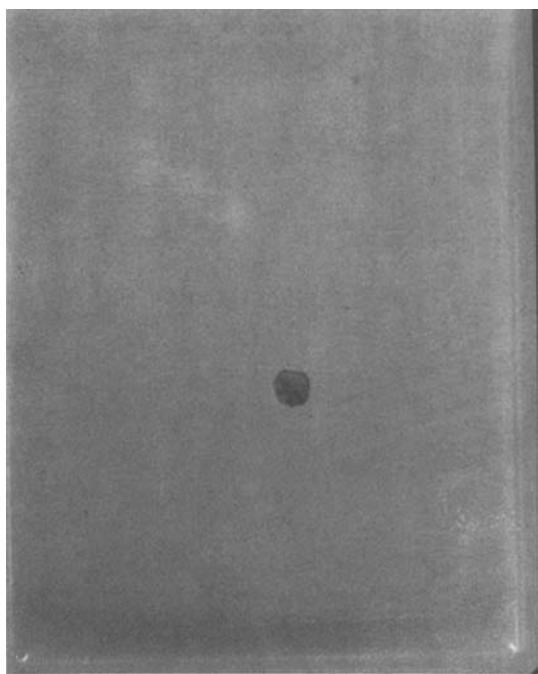


Fig. 5. Glass devitrification called rosetts (700X)

to be related to glass devitrification. Another type of surface damage is surface roughness caused by reaction between glass and moisture in air during source application. With proper source formulation, the spun glass film is insensitive to humidity up to at least 50% RH.

Uniformity and repeatability.—Typical sheet resistance uniformity defined by the coefficient of variability ($2 \times$ standard deviation \div mean), is $\leq 5\%$ over a wafer, and 6% over an 80 wafer load. Even though

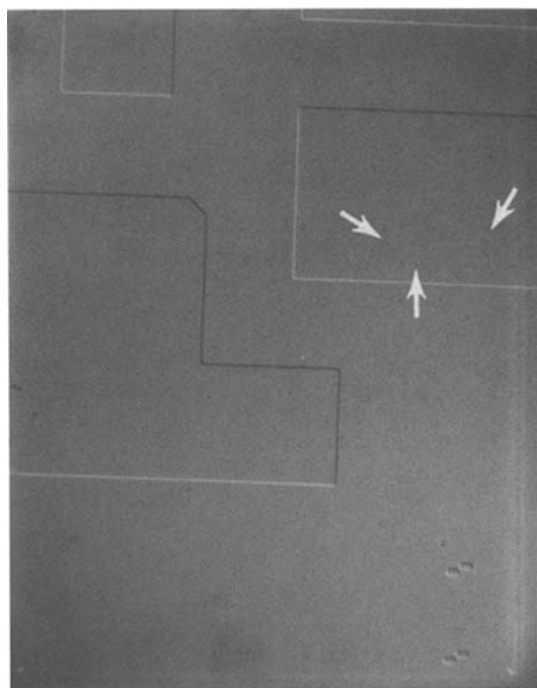


Fig. 6. Raised steps, irregular in shape, caused by glass devitrification. (130X)

the temperature of the empty diffusion tube is uniform within 2°C across the "flat zone," the actual temperature nonuniformity with a wafer load may be greater than 2°C (2). The load size and the load uniformity are essentially limited by temperature uniformity and length of the diffusion tube. Sheet resistance repeatability, such as $22.83 \pm 2.62 \text{ } \Omega/\square$, was obtained for six runs, diffused over 50 days.

Summary and Conclusions

A new antimony diffusion process using spin-on doped oxide was developed and characterized. The major points are listed below.

1. Diffusion is enhanced by some oxide growth which results in lower sheet resistance, higher surface concentration, and higher doping density while diffusivity remains essentially the same. As oxygen concentration in the diffusion ambient is increased from 0%, sheet resistance is decreased to a minimum. As oxygen concentration is further increased, sheet resistance is increased. Higher oxygen concentration is required for thicker source to achieve minimum sheet resistance. The 400°C source bake results in less oxide growth and higher sheet resistance than the 150°C source bake in a 3 hr diffusion at 1250°C in 3% O₂ ambient. Under the same diffusion conditions, piranha clean results in less oxide growth and higher sheet resistance when source is baked at 400°C. These two results indicate that the more densified glass and the very small amount of oxide produced by piranha appear to be significantly resistant to oxidation in 3% O₂ ambient.

2. The electrically active dopant concentration profile follows a Gaussian distribution for practical application in buried layer fabrications.

3. Wright etch reveals no diffusion-induced dislocations when surface concentration is lower than $2.4 \times 10^{19} \text{ cm}^{-3}$.

4. The thinner and less concentrated glass diffused in lower oxygen concentration ambient is less prone to glass devitrification. A properly formulated source is not sensitive to humidity up to 50% RH.

5. Typical sheet resistance uniformity is $\leq 5\%$ for individual wafers, and 6% for an 80 wafer load. The size of the wafer load is diffusion tube length limited.

6. Run to run repeatability, such as $22.83 \pm 2.62 \Omega/\square$, was achieved.

Linear devices have been fabricated with spin-on antimony buried layers (13-50 Ω/\square and 9 μm) and the device yields are comparable to those obtained with spin-on arsenic buried layers (13-30 Ω/\square and 5 μm). Evaluation on low power Schottky T²L devices showed that spin-on antimony buried layers resulted in improved device yields over the spin-on arsenic buried layers and gave comparable switching speeds to ion implanted buried layers.

Acknowledgments

The author wishes to acknowledge A. Chavez for the preparation of antimony glass solutions, M. Mills and R. Peterson for diffusion processing, P. Fejes for spreading resistance probe measurements, H. Hughes for reading the manuscript, and B. Saltzman for typing.

Manuscript submitted Dec. 12, 1980; revised manuscript received March 6, 1981. This was Paper 497 presented at the Hollywood, Florida, Meeting of the Society, Oct. 5-10, 1980.

Any discussion of this paper will appear in a Discussion Section to be published in the June 1982 JOURNAL. All discussions for the June 1982 Discussion Section should be submitted by Feb. 1, 1982.

Publication costs of this article were assisted by Motorola.

LIST OF SYMBOLS

C diffused carrier concentration in silicon, cm^{-3}
 C_B substrate concentration, cm^{-3}

\bar{C}_B average substrate concentration, cm^{-3}
 C_o source concentration assuming complete densification to thermal oxide, cm^{-3}
 C_s silicon surface concentration, cm^{-3}
 D diffusivity, $\mu\text{m}^2/\text{hr}$
 \bar{D}_m maximum diffusivity assuming $\Delta t = 0$ and $C_B = \bar{C}_B$
 R_s sheet resistance, Ω/\square
 t diffusion time, hr
 Δt equivalent diffusion time at T to account for the combined ramp up and ramp down cycles, hr
 Δth $X_o - X_s$, μm
 T diffusion temperature, $^\circ\text{C}$
 T_b source bake temperature, $^\circ\text{C}$
 X depth below silicon surface, μm
 X_j junction depth, μm
 X_o final oxide thickness measured after diffusion, μm
 X_s source thickness after bake, μm
 σ sheet conductivity, $(\Omega \text{ cm})^{-1}$

REFERENCES

1. K. Ritchie, U.S. Pat. 3,789,023.
2. S. Wu and D. L. Flowers, Abstract 156, p. 416, The Electrochemical Society Extended Abstracts, Boston, Massachusetts, May 6-11, 1979.
3. T. Sakurai, H. Nishi, T. Furuya, H. Hashimoto, and H. Shibayama, *Appl. Phys. Lett.*, **22**, 219 (1973).
4. R. Francis and P. S. Dobson, *J. Appl. Phys.*, **50**, 280 (1979).
5. A. S. Grove, "Physics and Technology of Semiconductor Devices," p. 50, Wiley, New York (1967).
6. C. S. Fuller and J. A. Ditzenberger, *J. Appl. Phys.*, **27**, 544 (1956).
7. K. S. Rao, L. J. Demer, and K. M. Mar, Abstract 231, p. 572, The Electrochemical Society Extended Abstracts, May 21-26, 1978.

Effects of Material Properties and Overlay Processing Variations on Magnetic Bubble Device Performance

W. A. Johnson,* F. B. Hagedorn,* R. Wolfe, G. P. Vella-Coleiro, J. L. Smith,
and R. S. Wagner

Bell Laboratories, Murray Hill, New Jersey 07974

ABSTRACT

The effects of the uniaxial anisotropy field, high processing temperatures ($\cong 300^\circ\text{C}$), film spacings, pattern misalignments, and film stresses on device operation are described. It is found that accurate process control, particularly with respect to processing temperatures, and a specification for the uniaxial anisotropy field are required for consistent device performance. The best device operation is obtained with high H_k epitaxial garnet material, low stressed overlay films, and geometric spacings that minimize the bubble-stress field interaction.

The Bell System is now using magnetic bubble devices in the 13A Voice Announcement System (1). This system uses the 29A (2) magnetic bubble package which contains four "matched" 68,121 bit reentrant shift register chips. Details of the design of this chip and its operating parameters have been reported elsewhere (3). Major-minor loop chips such as those described by Bonyhard *et al.* (4) have also been used in a similar four-chip package. As the production of these

devices has increased, so has the need to obtain more consistent chip to chip device operation. The latter is essential to improve circuit and package yields and for reduced testing times.

This investigation was undertaken to determine the extent to which various film overlay processing parameters and epitaxial material properties affect device performance. Particular attention was devoted to those parameters that affect the minimum current required to nucleate a bubble or that limit bias field operating margins. These included: (i) the effects due to the initial uniaxial anisotropy field of the epitaxial

* Electrochemical Society Active Member.

Key words: uniaxial anisotropy field, epitaxial film, process control.

garnet film, (ii) the effects due to exposure of the wafers and their overlay circuit structure to temperatures $\geq 300^\circ\text{C}$ during processing, (iii) the effects due to different geometric film spacings and/or pattern misalignments, and (iv) the effects due to overlay film stresses.

Circuit Fabrication and Testing

For this study, standard 16 μm period field access circuit structures consisting of 4000Å SiO_2 prespacer/5000Å 4.5 weight percent (w/o) Cu-Al conductor/4000Å SiO_2 insulator/4500Å Permalloy propagator and detector/10,000Å SiO_2 passivation/levels were fabricated on nominal 3 μm $\text{Y}_{1.2}\text{Lu}_{0.5}\text{Sm}_{0.4}\text{Ca}_{0.9}\text{Ge}_{0.9}\text{Fe}_{4.1}\text{O}_{12}$ epitaxial films (5). Either rf sputtering or plasma-assisted CVD processes were used to deposit the SiO_2 films. The 4.5 w/o Cu-Al alloy films used for the conductor metallization were deposited by single source e-beam or by S-gun techniques. The Permalloy films were deposited by either single source e-beam or by rf sputtering techniques. The nominal deposition temperatures that were used in these processes and the typical stresses that were measured for the deposited films are listed in Table I.

No operational differences were measured when device structures were fabricated by different deposition techniques so long as comparable film deposition temperatures were used and comparable film stresses were achieved. Thus, no differences were observed in the operational behavior between devices fabricated with S-gun or e-beam deposited Al-Cu alloy metallizations. The effects of film stresses on measured bias field operating margins are discussed.

The material specifications for the garnet epitaxial films are listed in Table II. Note that a specification for the uniaxial anisotropy field of the epitaxial film has been included. The need for such a specification is one of the primary subjects of this paper and is discussed in detail. For hard bubble suppression (6) the epitaxial films were implanted with 100 kV Ne^+ ions at a dose of $2 \times 10^{14}/\text{cm}^2$.

Full function bias field operating margins, ΔH , and the current required to nucleate a bubble, $I_g(\text{min.})$, were measured either by a visual quasi-static technique (7) or electronically at 100 kHz with a computer-controlled test station (8), both of which have been described previously. For determining the

$I_g(\text{min.})$ values, a 0.3 μsec current pulse was used and the bias field margins were typically measured at a nominal 40 oe rotating field drive. The initial uniaxial anisotropy field of the epitaxial film, H_k , was measured either directly by a microwave resonance technique (9) on the as-grown garnet films or calculated from other epitaxial film properties (strip width, collapse field, film thickness) which were measured by standard techniques (10).

Minimum Generator Current Measurements

The geometric configuration of the nucleate generator that was characterized in this study is outlined in Fig. 1. The dependences at 25°C of the minimum current required to generate a bubble, $I_g(\text{min.})$, on the effective anisotropy field, $H_k - 4\pi M_s$, for as-processed wafers (250°C maximum processing temperature) and after these same wafers were successively annealed at 310° , 380° , and 440°C , are shown in Fig. 2. The linear dependences of $I_g(\text{min.})$ on the initial H_k of the epitaxial garnet film for the different maximum processing temperatures are clearly demonstrated. Although the latter results conflict with early data re-

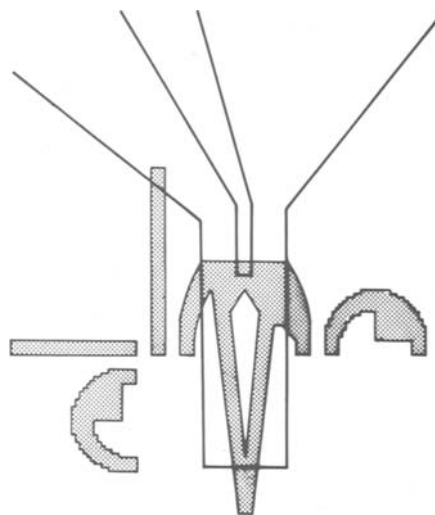


Fig. 1. The nucleate generator design

Table I. Nominal film deposition temperatures and film stresses for various deposition processes

| Process | Nominal deposition temperature ($^\circ\text{C}$) | Nominal film stress ($\times 10^9$ dynes/cm 2) |
|-----------------------------|---|---|
| RF sputtered SiO_2 | 200-225* | -1.5 |
| Plasma SiO_2 | 150-270 | -2.5 |
| E-beam Al-Cu | 25 | $\sim 0.1^{**}$ |
| S-gun Al-Cu | 25 | $\sim 0.1^{**}$ |
| E-beam Permalloy | 300-350 | +5.0 |
| RF sputtered Permalloy | $\leq 200^*$ | NM |

* Heat sinking by wafer clamping is required to maintain these temperatures.

** Stress of Al-Cu will increase with increasing temperatures, typical stresses are $+4 \times 10^9$ dynes/cm 2 .

Table II. Nominal epitaxial material specifications for 3 μm diameter bubbles

| | |
|---|--|
| Strip width | $3.0 \pm 0.3 \mu\text{m}$ |
| Thickness, h | $3.0 \pm 0.3 \mu\text{m}$ |
| Collapse field, H_c | $170 \pm 4 \text{ oe}$ |
| Quality factor, q | ≥ 4 |
| Mobility, μ | $\geq 250 \text{ cm sec}^{-1} \text{ oe}^{-1}$ |
| Coercivity, H_{coer} | $\leq 0.5 \text{ oe}$ |
| Defect density | $\leq 3 \text{ cm}^{-2}$ |
| Temperature dependence at 50°C of $\{\Delta H_0/\Delta T/H_0\}$ | $-0.20\text{-}0.24\% \text{ } ^\circ\text{C}^{-1}$ |
| Uniaxial anisotropy field, H_k | $1900 \pm 200 \text{ oe}$ |

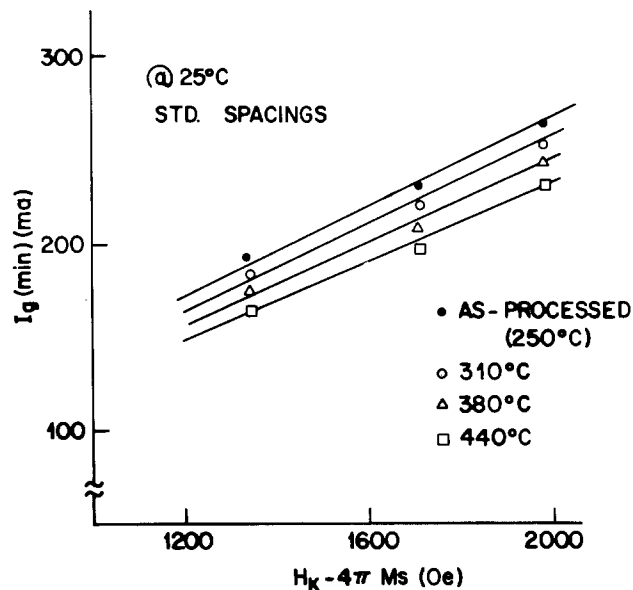


Fig. 2. Plots of the minimum generator currents measured for fully processed wafers vs. the effective uniaxial anisotropy field of the epitaxial garnet films and the maximum temperature to which the wafer was exposed during processing or subsequent annealing.

ported by Nelson *et al.* (11), the annealing results are consistent with observations previously reported by Wolfe and Johnson (12). In that work, the reduction in the $I_g(\text{min.})$ values with increasing annealing temperatures was correlated with stress buildups in the overlying Al-Cu conductor metallization.

The linear dependence of $I_g(\text{min.})$ values on H_k was not observed in early processing days because the H_k value for each wafer was not accurately known, and at times wafers were exposed nonuniformly to high processing temperatures. Processes in which the high temperatures can still be a problem are the deposition of Permalloy by either e-beam or rf sputtering techniques, and the rf sputter deposition of SiO_2 . Wafer temperatures in excess of 500°C have been observed when wafers are not properly clamped and heat sunk during rf sputter deposition of SiO_2 . Similarly, temperature spikes of $60^\circ\text{--}80^\circ\text{C}$ that are superimposed on the standard 300°C predeposition temperature soak have been measured during e-beam deposition of Permalloy (13).

To check the possibility that any annealing of the implant layer affects the $I_g(\text{min.})$ values measured, wafers with known H_k values were annealed at 440°C for 2 hr under flowing N_2 prior to the fabrication of the overlying circuit structure. The $I_g(\text{min.})$ values that were measured were found to correspond closely to the values obtained for 250°C as-processed wafers. Reductions of $I_g(\text{min.})$ were measured only when these wafers were given subsequent anneals at temperatures $\geq 300^\circ\text{C}$ with the conductor metallization in place. Therefore, annealing of the implant layer is not a factor in the $I_g(\text{min.})$ shifts that are measured.

Measurements of $I_g(\text{min.})$ and H_k at temperatures other than 25°C show that $I_g(\text{min.})$ and H_k have identical temperature dependences over the normal device operating temperature range 0° to $+70^\circ\text{C}$. Measured values for the temperature coefficient of $I_g(\text{min.})$ range from -0.6 to -1.0 mA/ $^\circ\text{C}$ depending upon the 25°C H_k value of the epitaxial garnet material. Similar temperature dependences have been reported by Danylchuk and Bobeck (14).

As a consequence of these combined effects, a wide range of $I_g(\text{min.})$ values will be obtained unless tight controls are specified for both the H_k of the epitaxial material and the wafer temperatures during processing. In production it has been found practical to control the H_k values at 25°C to 1900 ± 200 oe (15). This range of H_k values ensures $I_g(\text{min.})$ values that are high enough to prevent unwanted nucleations of bubbles at other current-controlled functions such as the replicator, particularly at high device operating temperatures, yet low enough to ensure bubble nucleation at low device operating temperatures for the specified minimum generator current.

The geometric factors associated with the overlay circuit structures that affect $I_g(\text{min.})$ values are: (i) the spacing between the hairpin conductor and the garnet surface, SiO_2I ; (ii) the spacing between the Permalloy film and the hairpin conductor, SiO_2II ; and (iii) any misalignment of the overlying Permalloy pattern with respect to the hairpin conductor. The geometric complexity of the nucleate generator structure precludes any quantitative predictions of the spacing dependences from magnetostatic theory. However, qualitative considerations would indicate that higher $I_g(\text{min.})$ values should be measured if either the conductor to garnet spacing (SiO_2I) or the conductor to Permalloy spacing (SiO_2II) is increased. In the latter case, the interaction of the Permalloy with the current conductor fields which causes the fields in the garnet to be "intensified" is reduced with increased conductor to Permalloy spacing. The data that were obtained in this investigation for variable SiO_2I and SiO_2II spacings are shown in Fig. 3-5.

The expected trends where higher $I_g(\text{min.})$ values are measured for wafers with thicker SiO_2I or SiO_2II

layers are seen in Fig. 3 and 4, respectively. The sensitivity of $I_g(\text{min.})$ to SiO_2I variations ($\Delta I_g/\Delta \text{SiO}_2 \sim 30$ mA/1000Å of SiO_2) is higher than that determined for SiO_2II variations ($\Delta I_g/\Delta \text{SiO}_2 \sim 20$ mA/1000Å of SiO_2) since both the conductor field and the Permalloy-conductor field interaction in the garnet are reduced with increased SiO_2I spacing. For increased SiO_2II spacing, only the Permalloy-conductor field interaction is reduced.

The data that were obtained with variable SiO_2I spacings but constant SiO_2II spacing is shown

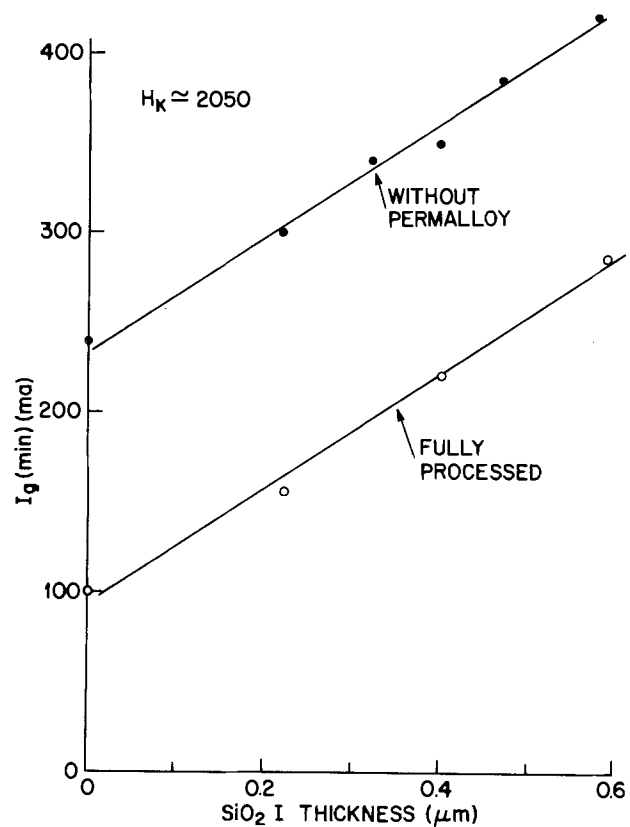


Fig. 3. Plots of the minimum generator current measured on fully processed wafers (and the same wafers after the Permalloy had been etched off) vs. the plasma deposited SiO_2I (Prespacer) thickness.

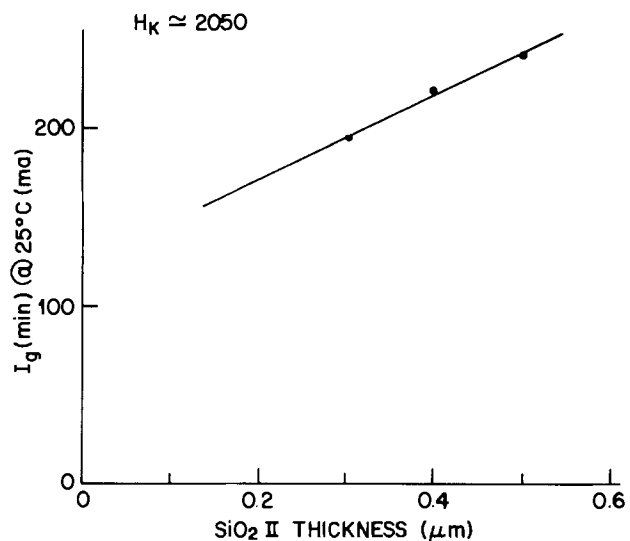


Fig. 4. A plot of the minimum generator current measured for fully processed wafers vs. the plasma deposited SiO_2II (Insulator) thickness.

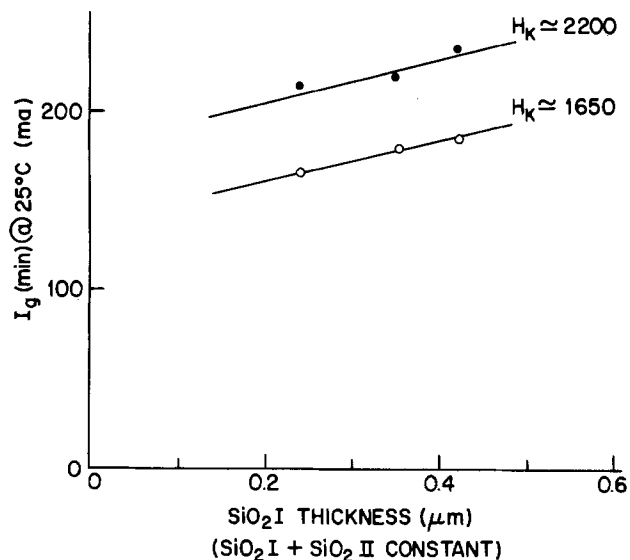


Fig. 5. Plots of the minimum generator current measured for fully processed wafers vs. variable conductor spacing but constant Permalloy to garnet spacing.

in Fig. 5. In this case, the spacing sensitivity that is measured ($\Delta I_g / \Delta \text{SiO}_2 \text{I} \sim 10 \text{ mA}/1000\text{\AA}$ of SiO_2) is small, because the Permalloy-conductor field interaction increases and offsets the effects due to the increased conductor to garnet spacing ($\text{SiO}_2 \text{I}$). This result can be useful in device production since it gives a means to make real time compensations in $\text{SiO}_2 \text{II}$ thicknesses to correct for erroneous $\text{SiO}_2 \text{I}$ deposition thicknesses. However, it is preferred that both $\text{SiO}_2 \text{I}$ and $\text{SiO}_2 \text{II}$ be controlled independently since other device functions also depend on the thicknesses of the insulating layers.

To measure the magnitude of the Permalloy-conductor field interaction, the Permalloy elements were etched off the wafers in which the thicknesses of the $\text{SiO}_2 \text{I}$ were varied. The results of the conductor-only $I_g(\text{min.})$ measurements are shown in Fig. 3. It is seen that at all $\text{SiO}_2 \text{I}$ thicknesses that the conductor-only $I_g(\text{min.})$ values are substantially higher ($\sim 130 \text{ mA}$) than those measured for the standard structure. Thus, the Permalloy-conductor interaction that acts to "intensify" the magnetic fields generated in the garnet is significant and should be considered for all current-controlled functions.

To test the sensitivity of the Permalloy pattern placement with respect to the hairpin conductor loop, a wafer was rotationally misaligned. Photographs of the various misalignments that were obtained and the $I_g(\text{min.})$ values that were measured are shown in Fig. 6. Inspection of the data shows that the values of $I_g(\text{min.})$ do not vary significantly unless the overlay Permalloy element is pulled back from the end of the hairpin loop such that the Permalloy to garnet spacing is increased by the conductor thickness (5000\AA). At this point, the measured values of $I_g(\text{min.})$ increase abruptly by approximately 75 mA. Thus, the placement of the Permalloy pattern over the hairpin loop can be critical. In production it has been found that a coded $2 \mu\text{m}$ overlap is sufficient to cover the $\pm 1 \mu\text{m}$ misalignments that are encountered.

Bias Field Operating Margin Measurements

The same variables that affect the values of the minimum generator current can also affect the strength of the interaction between magnetic domains and the stress field gradients associated with the overlaying circuit structure. The results of bias field margin measurements, in which the high ends of the margins are limited by stress field interactions, are discussed in this section.

To determine the effects of the uniaxial anisotropy field, H_k , on bias margins, a number of device batches with low and high H_k wafers were processed with major-minor loop circuit structures such as those described by Bonyhard *et al.* (16). The geometric configuration of the gate regions for the read and the write lines are shown in Fig. 7 and 8, respectively. The full function bias margins that were measured at 70°C for both 35 and 45 oe rotating drive fields at 100 kHz are listed in Table III. For a given wafer batch, it is seen that higher bias field margins are consistently measured for the wafers with the higher H_k values. These results are consistent with the work reported by Dishman *et al.* (17) in that the strength of the interaction between bubbles and the stress field gradients associated with the overlay circuit structure is predicted to decrease with increasing H_k values.

The different bias field margins that were measured for a given H_k material between different device lots were interpreted to be due in part to exposure of the different wafer batches to different maximum processing temperatures. As described in the previous section, higher processing temperatures lead to larger stress-field interactions due to the increased stress of the Al-Cu metallization. This effect is more clearly demonstrated with the data presented in Fig. 9. For this experiment, the bias field operating margins of the replicator function (Fig. 7) were measured at 70°C on an as-processed wafer, and after it had been given subsequent anneals at 400° and 450°C . While it appears that the annealing causes a low end margin loss, this is not the case. Post-process annealing affects the ion implanted layer as well as the stress of the Al-Cu metallization.

Independent annealing experiments on various implanted wafers have shown that annealing causes the stability range of the bubbles to shift uniformly with the increase in the free bubble collapse field. The magnitudes of these shifts are determined by the implant conditions and the time and the temperatures of the anneals (18). Thus, the apparent low end bias margin losses seen in Fig. 9 are in reality due to the combined effects of: (i) a shift of the bubble stability range to higher bias fields (implant anneal) and (ii) an increased stress field interaction that costs high end margin losses that are proportional to the stress field interaction.

The dielectric levels overlaying the conductor metallization will also contribute to the stress field gradients found at conductor edges. From elementary line edge stress theory (19), it can be shown that compressively stressed dielectric films will enhance the stress fields associated with a tensile-stressed conductor level whereas tensile-stressed dielectrics will reduce or "balance-out" these stress fields. To determine the magnitudes of these effects in this investigation, bias field margins were measured before and after various dielectric passivations and for various combinations of stressed insulator and prespacer levels with the standard tensile-stressed Al-Cu metallization.

Table III. Average measured minimum generator currents and bias field margins for various processed wafer batches

| Batch | No. of wafers | H_k (oe) | $\langle I_g(\text{min.}) \rangle$ (mA) | $\langle \Delta H \rangle$ (oe) |
|-------|---------------|------------|---|---------------------------------|
| 1 | 4 | 2600 | 186 | 13.1 |
| 1 | 3 | 1900 | 148 | 10.1 |
| 2 | 3 | 1920 | 153 | 17.5 |
| 2 | 3 | 1600 | 132 | 14.4 |
| 3 | 3 | 2000 | 163 | 13.9 |
| 3 | 3 | 1770 | 142 | 11.0 |
| 4 | 3 | 2200 | 166 | 15.2 |
| 4 | 2 | 1780 | 136 | 13.5 |
| 5 | 2 | 1900 | 149 | 14.5 |
| 5 | 3 | 1500 | 126 | 10.8 |
| 6 | 2 | 2300 | 171 | 15.3 |
| 6 | 3 | 1900 | 152 | 14.8 |

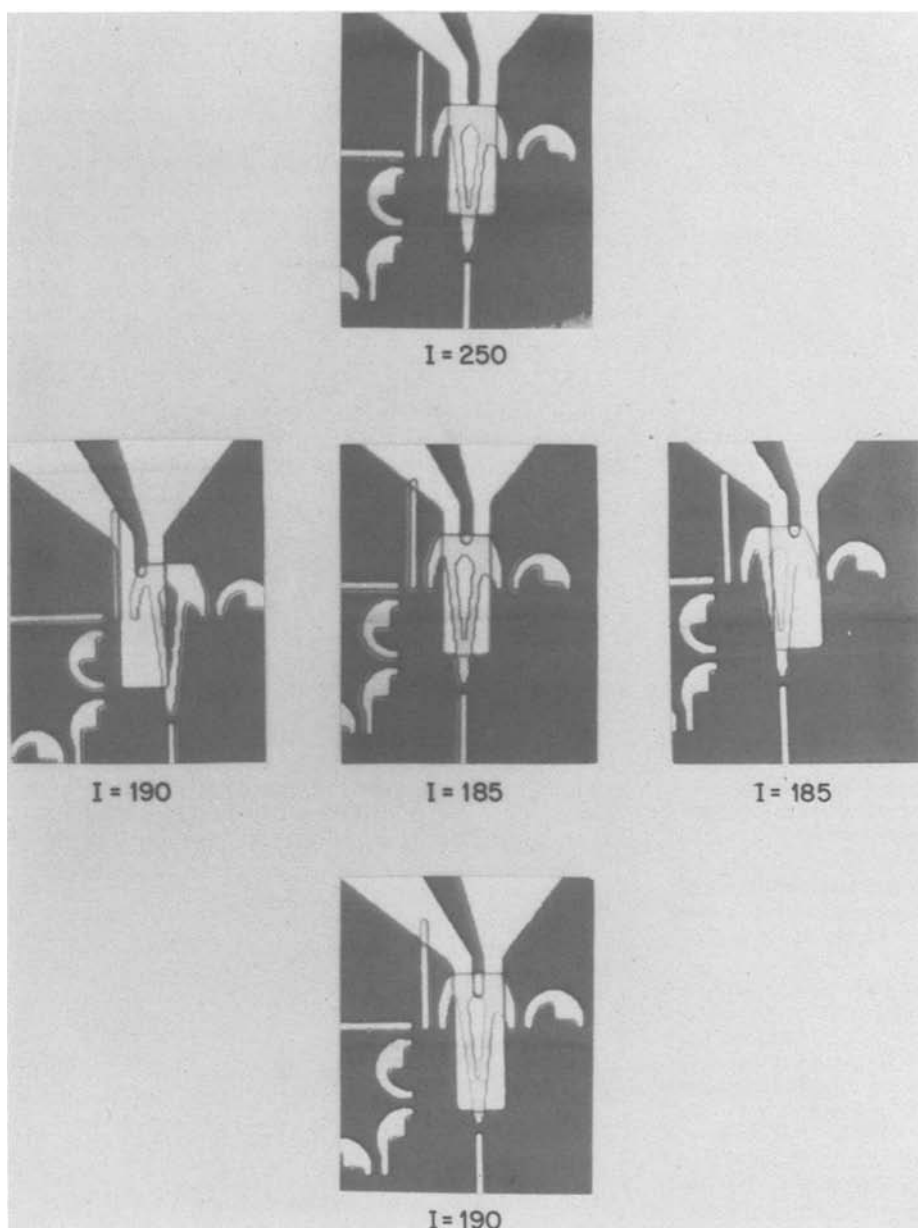


Fig. 6. Photomicrographs of different Permalloy to conductor pattern misalignments and the corresponding minimum generator currents that were measured.

The results that were obtained when highly compressive plasma-deposited SiN films (-7×10^9 dynes/cm²)

were used to passivate circuits using write gates such as those shown in Fig. 8, are shown in Table IV. It is seen that the stress interaction roughly scales

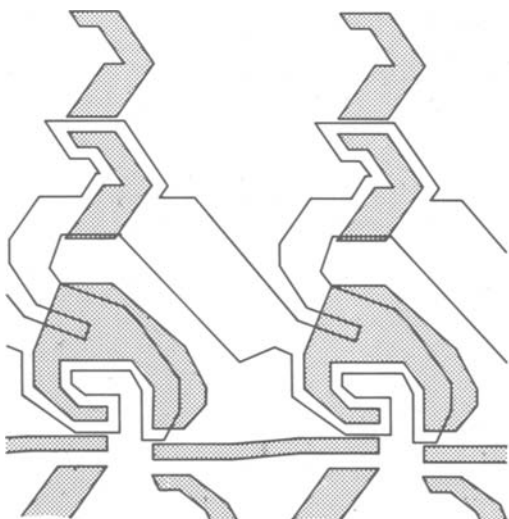


Fig. 7. The replicator gate design

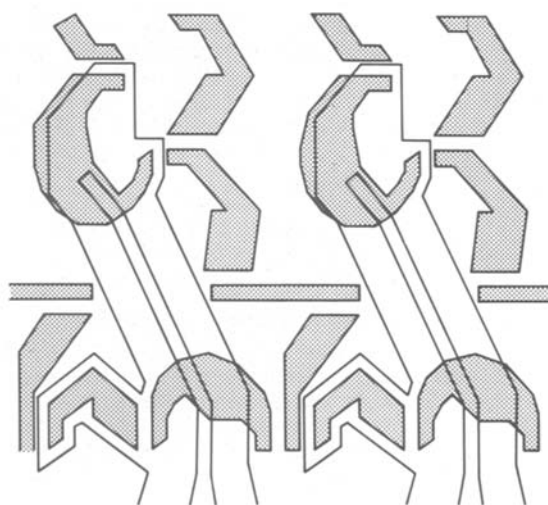


Fig. 8. The write line (swap gate) design

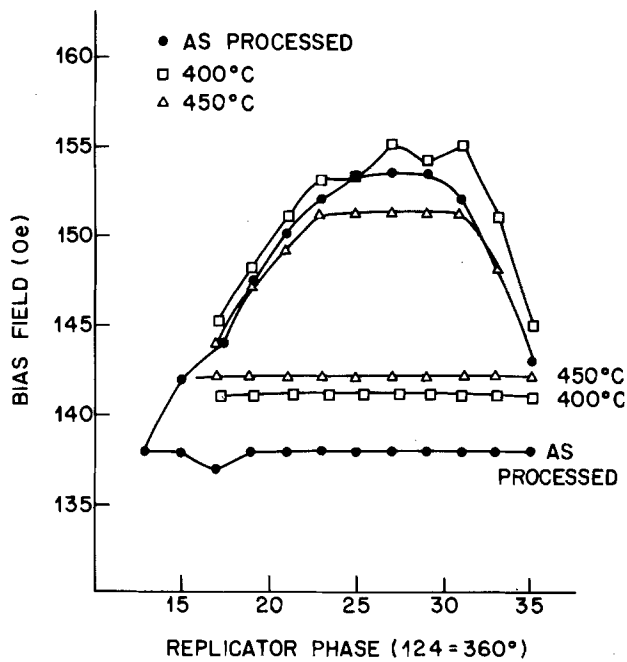


Fig. 9. Plots of the bias field margins measured for fully processed wafers vs. the phase of the replicator pulse and the maximum temperature to which the wafers were exposed during processing or subsequent annealing.

with the thickness of the stressed SiN film and that the full bias field margins are recovered when the SiN is stripped off. The failure mechanism that is observed is bubble hang-up on the leading conductor edge until the rotating field causes the minor loop pickup element to become attractive. Then the bubble is spontaneously transferred into the minor loop. (No blocking current was applied to the conductor.)

The bias field margins that were measured when different stress levels were used for the insulator level (SiO₂II) are listed in Table V. Analysis of the data shows that the best operating bias margins were obtained when the stress of the dielectric level was ten-

Table IV. Average bias field margins measured for different device structures (with and without passivation)

| Device structure | Average bias margins | |
|---|----------------------|------------------|
| | At $H_D = 45$ oe | At $H_D = 35$ oe |
| SiO ₂ I/Al-Cu/SiO ₂ II/Permalloy (no passivation) | 21.8 | 13.8 |
| Above with 1200Å of SiN(C) | 21.5 | 13.4 |
| Above with another 1.2 μm of SiN(C) | 16.4 | 7.1 |
| SiO ₂ I/Al-Cu/SiO ₂ II/Permalloy (SiN stripped off) | 22.4 | 13.4 |

Table V. Average bias field margins measured for device structures with different plasma deposited SiO₂II (Insulator) stress levels

| Wafer* | Structure** | Plasma deposited SiO ₂ II (Insulator) stress ($\times 10^9$ dynes/cm ²) | Average bias field margins (oe) | |
|--------|---|---|---------------------------------|------------------|
| | | | At $H_D = 35$ oe | At $H_D = 45$ oe |
| 3409B2 | SiO ₂ (C)/SiN(T) | +2.0 | 13.5 | 20.9 |
| 3346B2 | SiO ₂ (C)/SiN(T) | +0.2 | 12.1 | 18.4 |
| 3703C2 | SiO ₂ (C)/SiO ₂ (C) | -2.0 | 12.2 | 18.9 |
| 4310D1 | SiO ₂ (C)/SiN(C) | -5.0 | 10.8 | 16.1 |

* Note: These are not "matched" H_K wafers.
 ** (T) Tensile stress. (C) Compressive stress.

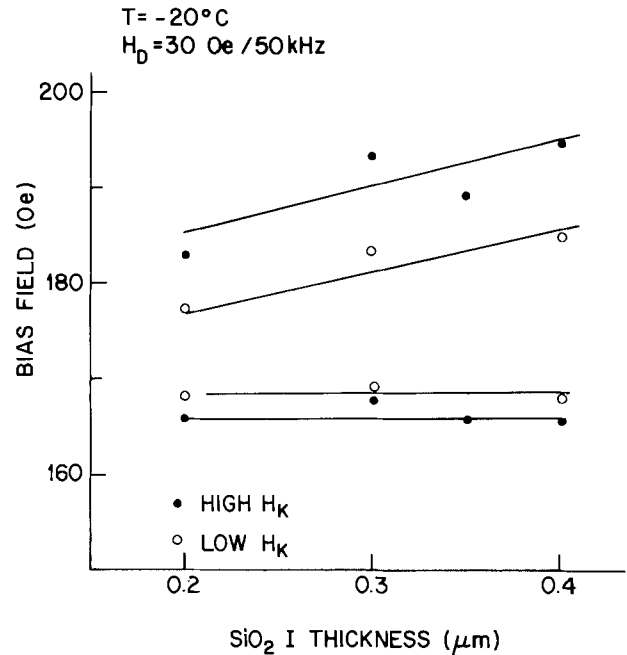


Fig. 10. Plots of the bias field margins measured for fully processed wafers vs. the rf sputtered SiO₂I (Prespacer) thickness. The data for two different values for the uniaxial anisotropy of the epitaxial garnet films are shown.

file and tended to "balance" the tensile stress of the Al-Cu metallization. Similar results have been reported by Roman *et al.* (20). However, since a routine process for obtaining tensile-stressed dielectric films has not been developed, the general procedure to date has been to utilize low stressed SiO₂ films, to minimize Al-Cu metallization stress buildups by using low temperature processes and to minimize stress field gradients by taper-etching the conductor metallization.

To determine the effects of increasing the spacing between the Al-Cu conductor metallization and the garnet film, two sets of matched H_K wafers in which pairs of low H_K and high H_K wafers were processed with different SiO₂I thicknesses but constant garnet to Permalloy spacings. The bias field margins that were measured at -20°C (where the stress interaction is strongest) are shown in Fig. 10. It is seen that improved bias margins are measured both for increased SiO₂I thicknesses and for wafers with higher H_K values.

Conclusions

The results reported in this paper show the importance of accurate process control, particularly with respect to temperature, and the need to include a specification for the uniaxial anisotropy field in a list of the epitaxial film property requirements. These considerations are important not only in manufacture for obtaining more consistent device operation but also when any new device designs or processing techniques are developed. In the latter cases, the maximum use of batch processing at all fabrication steps (except the one being tested) and the use of "matched" H_K wafers (preferably from the same growth dip) minimize any possible erroneous conclusions that could be obtained when test results are compared.

Acknowledgments

The authors wish to thank A. H. Bobeck, P. I. Bonyhard, S. L. Blank, R. D. Pierce, and T. J. Nelson for many helpful discussions and suggestions. We also thank B. J. Roman, R. O. Miller, A. J. Perneski, R. W. Garrett, L. J. Pietruszynski, and T. W. Mendel for their help in fabricating the various test structures.

Manuscript submitted Sept. 21, 1980; revised manuscript received ca. March 2, 1981.

Any discussion of this paper will appear in a Discussion Section to be published in the June 1982 JOURNAL. All discussions for the June 1982 Discussion Section should be submitted by Feb. 1, 1982.

Publication costs of this article were assisted by Bell Laboratories.

REFERENCES

1. R. J. Radner and J. H. Wuorinen, IEEE International Solid-State Circuits Conf., p. 178 (1976).
2. A. H. Bobeck, P. I. Bonyhard, and J. E. Geusic, Proc. IEEE, **63**, 1176 (1976).
3. A. H. Bobeck and I. Danylchuk, IEEE Trans. Magn., **mag-13**, 1370 (1977).
4. P. I. Bonyhard and J. L. Smith, *ibid.*, **mag-12**, 614 (1976).
5. S. L. Blank, P. Wolfe, L. C. Luther, R. C. LeCraw, T. J. Nelson, and W. A. Biolsi, J. Appl. Phys., **50**, 2155 (1979).
6. R. Wolfe, J. C. North, and Y. P. Lai, Appl. Phys. Lett., **22**, 603 (1973).
7. R. Wolfe and W. A. Johnson, IEEE Trans. Magn., **mag-13**, 1595 (1977).
8. F. B. Hagedorn, L. F. Rago, D. E. Kish, Y. S. Chen, W. E. Hess, H. R. Beurrier, and W. D. P. Wagner, *ibid.*, **mag-13**, 1364 (1977).
9. G. P. Vella-Coleiro, Rev. Sci. Instrum., **46**, 1188 (1975).
10. R. D. Pierce, J. Cryst. Growth, **27**, 295 (1974).
11. T. J. Nelson, Y. S. Chen, and J. E. Geusic, IEEE Trans. Magn., **mag-9**, 289 (1973).
12. R. Wolfe and W. A. Johnson, AIP Conf. Proc., **29**, 117 (1975).
13. A. D. Butherus, Private communication.
14. I. Danylchuk and A. H. Bobeck, AIP Conf. Proc., **29**, 41 (1975).
15. S. L. Blank, R. C. LeCraw, R. D. Pierce, and W. A. Biolsi, Unpublished.
16. P. I. Bonyhard, IEEE Trans. Magn., **mag-13**, 1785 (1977).
17. J. M. Dishman, R. D. Pierce, and B. J. Roman, J. Appl. Phys., **45**, 4076 (1974).
18. J. E. Davies, IBM J. Res. Dev., **21**, 522 (1977).
19. S. M. Hu, J. Appl. Phys., **50**, 4661 (1979).
20. B. J. Roman, T. J. Nelson, and J. L. Smith, IEEE Trans. Magn., **mag-16**, 489 (1980).

Iron and Chromium Redistribution in Semi-Insulating InP

J. D. Oberstar* and B. G. Streetman*

Department of Electrical Engineering and Coordinated Science Laboratory,
University of Illinois at Urbana-Champaign, Urbana, Illinois 61801

and J. E. Baker and Peter Williams

Materials Research Laboratory, University of Illinois at Urbana-Champaign, Urbana, Illinois 61801

ABSTRACT

The redistribution of the compensating dopants, iron or chromium, in semi-insulating indium phosphide has been studied using secondary ion mass spectrometry. Annealing with silicon nitride encapsulation results in impurity accumulation within the first 1000Å of the surface followed by depletion extending to a depth of $\sim 1 \mu\text{m}$. Profiles resulting from the implantation of "neutral" elements (He, B) exhibit accumulation at the surface and also accumulation at the projected range peak. The profiles are explained in terms of gettering of the compensating dopant to defect-rich regions.

InP and its related alloys are attracting considerable attention due to their applications in microwave and optoelectronic devices. Semi-insulating InP is extremely important in the fabrication of such devices because it can serve as a substrate for the subsequent growth of an epitaxial device layer, and it can provide the necessary device isolation when implantation directly into the material itself is employed. Whereas presently almost all semi-insulating GaAs is undoped or chromium-doped, semi-insulating InP can be obtained by doping either with chromium or iron. Cr has a much lower solid solubility in InP than in GaAs, which necessitates the use of high purity starting material to achieve high resistivity (1). Since such purity in InP is still not routinely obtained, Fe, which has a higher solid solubility in InP than does Cr, is being used as an alternative in the growth of semi-insulating InP (2, 3). Recently, a number of studies have shown the redistribution of Cr in annealed GaAs (4-6) and in implanted GaAs (7, 8). We report here the redistribution of the bulk compensating dopants, Fe or Cr, in annealed and implanted semi-insulating InP.

Experimental Methods

The (100) semi-insulating InP used in this work was grown by the liquid-encapsulation Czochralski (LEC) method at the Naval Research Laboratory (9). The Fe-doped material had a resistivity $\rho \sim 1 \times 10^7 \Omega \text{ cm}$, and the Cr-doped material had $\rho \sim 5 \times 10^8 \Omega \text{ cm}$. Implantations were performed at room temperature with the sample normal inclined 7° from the incident beam to minimize channeling effects. The encapsulant employed to suppress thermal degradation during annealing was an essentially oxygen-free Si_3N_4 (10), rf plasma-deposited at 350°C to a thickness of $\sim 2300\text{Å}$ on both sides of the sample. All samples were annealed in a silica furnace tube with a flow of $200 \text{ cm}^3/\text{min}$ of desiccated forming gas (4% H_2 in N_2). Following the anneals, the Si_3N_4 encapsulant was removed in electronic grade HF and the samples were rinsed in deionized water and standard solvents.

Impurity profiles were measured by secondary ion mass spectrometry (SIMS) using the CAMECA IMS-3f ion microscope. The O_2^+ primary beam (7.7 keV impact energy) was rastered over areas of $\sim 250 \mu\text{m}^2$ and standard precautions were taken to reject spurious signals arising from the crater walls. A Sloan Dektak

* Electrochemical Society Active Member.

Key words: SIMS, anneal, gettering.

stylus instrument was used to measure the resultant crater depths. These measurements together with the assumption of a constant sputtering rate were used to convert the time scale to a depth scale. Our experience and that of others (8) show the uncertainty in such measurements to be $\pm 5-6\%$. The concentration scales for Fe and Cr were obtained from a standard prepared by implanting Fe and Cr into semi-insulating InP. The conversion factor relating ion intensity to concentration was corrected for background effects in the standard. In this manner we determined the background concentrations in these samples to be: Cr, $6.5 \times 10^{16} \text{ cm}^{-3}$; Fe, $8.1 \times 10^{16} \text{ cm}^{-3}$.

Redistribution Resulting from Annealing

Figures 1 and 2 exhibit the profiles of Fe and Cr resulting from annealing the substrates with an Si_3N_4 cap. With the exception of a large Fe accumulation within the first 1200Å of the surface, the Fe profile in the 550°C, 30 min anneal is otherwise indistinguishable from the unannealed profile. This is not true of the profile resulting after a 800°C, 30 min anneal. Again, an Fe accumulation region with a maximum concentration of $\sim 4 \times 10^{17} \text{ cm}^{-3}$ extends from the surface to a depth of $\sim 1000\text{Å}$. However, following this zone is an Fe depletion region. This broad, flat-bottomed region originates within 1000Å of the surface and returns to the normal background level at a depth of $\sim 1.2 \mu\text{m}$. The minimum Fe concentration within this region is $\sim 1.4 \times 10^{16} \text{ cm}^{-3}$.

The redistribution of Cr resulting from annealing differs significantly from that of Fe. As with Fe there is no evidence of major redistribution resulting from a 550°C, 30 min anneal. Qualitatively, the Cr profile after a 800°C, 30 min anneal is similar to that of Fe, in that

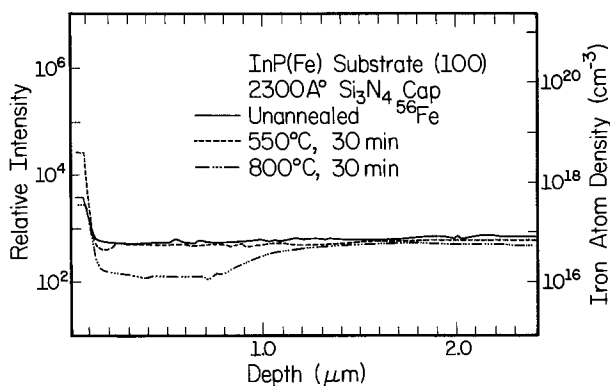


Fig. 1. SIMS profiles of Fe in a semi-insulating InP substrate following 30 min anneals at 550° and 800°C with an Si_3N_4 encapsulant.

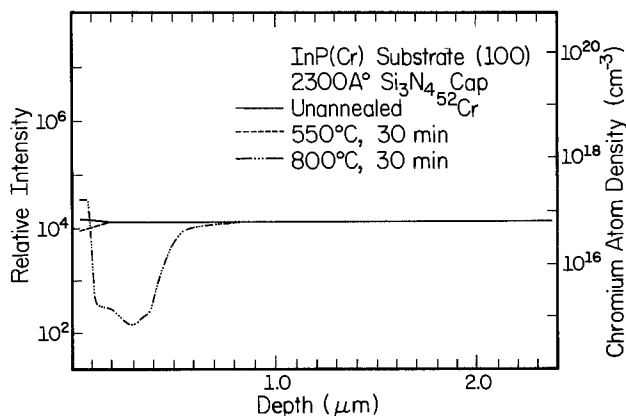


Fig. 2. SIMS profiles of Cr in a semi-insulating InP substrate following 30 min anneals at 550° and 800°C with an Si_3N_4 encapsulant.

a surface accumulation region and a depletion zone appear. The surface accumulation zone ends at a depth of $\sim 1000\text{Å}$, while the Cr depletion region extends to a depth of $\sim 8000\text{Å}$. The minimum Cr concentration within this region is $\sim 9.2 \times 10^{14} \text{ cm}^{-3}$. Although redistribution of Cr occurs over a region of $\sim 8000\text{Å}$ vs. $\sim 12,000\text{Å}$ for Fe, Cr redistribution is more severe in the sense that the concentration of the compensating dopant is an order of magnitude lower in the depletion zone than in Fe-doped substrates.

The depletion regions observed in the Fe- and Cr-doped substrates are in keeping with reports of conductive surface layers following thermal annealing of InP substrates (11, 12). Additionally, the redistribution is very similar to recent reports of Cr migration in annealed GaAs substrates (4-6, 8). Originally, the accumulation and subsequent depletion regions of Cr in GaAs were speculated to be due to a strain-induced effect caused by the thermal mismatch between the encapsulant and the GaAs (7). However, recent work by Vasudev *et al.* (8), indicates the Cr redistribution in GaAs is not significantly influenced by the encapsulant and is in fact larger under capless anneal conditions. Moreover, Kasahara and Watanabe (6) reported that Cr redistribution in GaAs is controlled by the partial pressure of arsenic during the anneal, which confirms an early observation by Tuck *et al.* (4) concerning the role of As overpressure with relation to Cr redistribution. At present, therefore, it appears that the best explanation of Cr redistribution in GaAs is the gettering of Cr to surface regions which have high concentrations of defects introduced either by annealing or by mechanical damage (13). There is reason to believe that the same relationship between defects and compensating dopant also explains our results in InP. It is unclear at present what importance should be attached to the quantitative differences observed between Fe and Cr redistribution profiles in InP. Possibly the differences can be explained in terms of the surface solubility and original background density of the compensating dopant, as suggested by Vasudev *et al.* (8). Furthermore, differences between Cr and Fe outdiffusion into the Si_3N_4 cap must be considered. Obviously further work is needed to determine if important differences do indeed exist between Fe and Cr redistribution in InP as our results suggest.

Redistribution Resulting from the Implantation of Neutral Dopants

Impurity gettering to damaged (*i.e.*, vacancy-rich) regions produced by ion implantation is often observed in Si (14, 15) and in GaAs (7, 8, 16, 17). In this section we report the gettering of Fe and Cr to damaged regions produced by the implantation of electrically neutral species in semi-insulating InP. Helium was chosen as one such species because it should remain electrically and chemically inactive in the crystal, thereby having no effect on the compensating dopants except for the damage it creates. It is possible for "gas bubbles" or voids to form by the diffusion of insoluble gas atoms to nucleation sites (18, 19). To rule out redistribution due to the possible presence of such voids, we implanted a nongaseous element, boron. We assume that boron fills column III sites, and is therefore electrically inactive in the crystal (although the possibility of chemical activity cannot be completely ruled out).

An He fluence of $1.06 \times 10^{15} \text{ cm}^{-2}$ was implanted into the samples at 51 keV and 0.5 μA scanned current. Under these conditions the LSS projected range is 3640Å with the profile of energy deposited into nuclear collisions peaking at $\sim 3200\text{Å}$ (20). Figures 3 and 4 show the Fe and Cr profiles, respectively, resulting from 30 min anneals of He-implanted InP. As in the previously discussed unimplanted samples, a surface accumulation zone exists within the first 1000Å for both types of compensating dopants. Surface accumulation of Fe is much more pronounced than that of Cr,

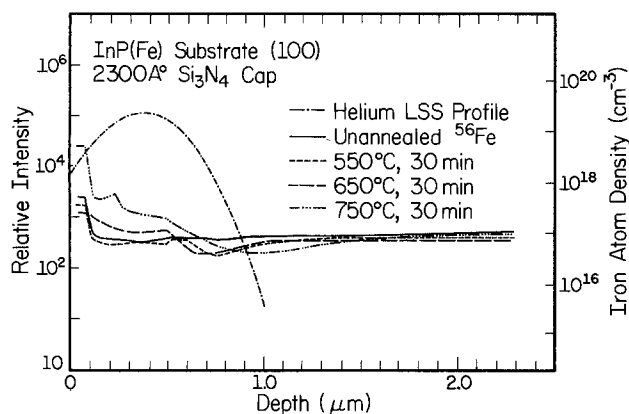


Fig. 3. SIMS profiles of Fe in a semi-insulating InP substrate implanted with He ($1.06 \times 10^{15} \text{ cm}^{-2}$, 51 keV) and annealed for 30 min at the indicated temperatures with an Si_3N_4 encapsulant.

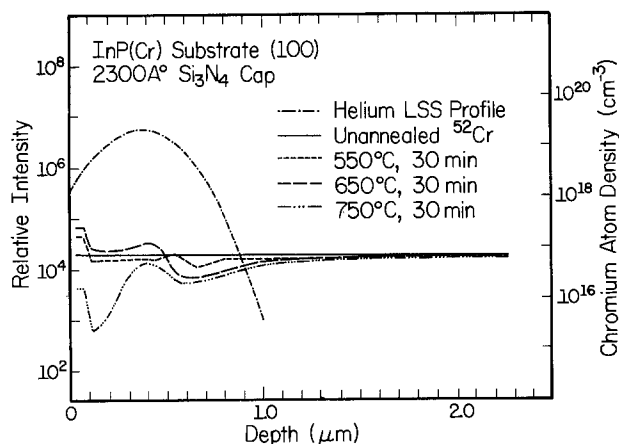


Fig. 4. SIMS profiles of Cr in a semi-insulating InP substrate implanted with He ($1.06 \times 10^{15} \text{ cm}^{-2}$, 51 keV) and annealed for 30 min at the indicated temperatures with an Si_3N_4 encapsulant.

which is also consistent with our previous results. However, unlike the profiles in the unimplanted samples, we find in the He-implanted samples an accumulation region followed by a depletion region rather than broad depletion regions extending to $\sim 1 \mu\text{m}$. It is clear that both Fe and Cr accumulate in a region about the projected range of He. The 550°C , 30 min anneal profiles show little restructuring except for small depletion regions on the bulk side of the projected range peak. The 750°C , 30 min annealed Fe-doped sample has an accumulation zone with a concentration of $\sim 2.6 \times 10^{17} \text{ cm}^{-3}$ and a depletion zone with a concentration of $\sim 3.4 \times 10^{16} \text{ cm}^{-3}$. The Cr-doped sample annealed under identical conditions shows even larger variations of concentration in the various regions.

Boron was implanted at 126 keV and $0.5 \mu\text{A}$ to a fluence of $6.8 \times 10^{14} \text{ cm}^{-2}$ in Fe-doped InP substrates. The LSS projected range is 3640 \AA and the damage profile peaks at $\sim 2890 \text{ \AA}$ (20). The as-implanted boron profile obtained by SIMS is shown in Fig. 5. As in the 550°C profiles of He-implanted Fe-doped InP, an Fe depletion zone is formed on the bulk side of the projected range peak with a minimum Fe concentration of $\sim 1.6 \times 10^{16} \text{ cm}^{-3}$. Accumulation of Fe into the implant region and toward the surface is evident in the 650° and 750°C anneals. The qualitative similarities between the redistribution of Fe in the He- and B-implanted samples appears to indicate that we are observing the gettering of the compensating dopant by implant related defects rather than diffusion due to gas voids or chemical effects.

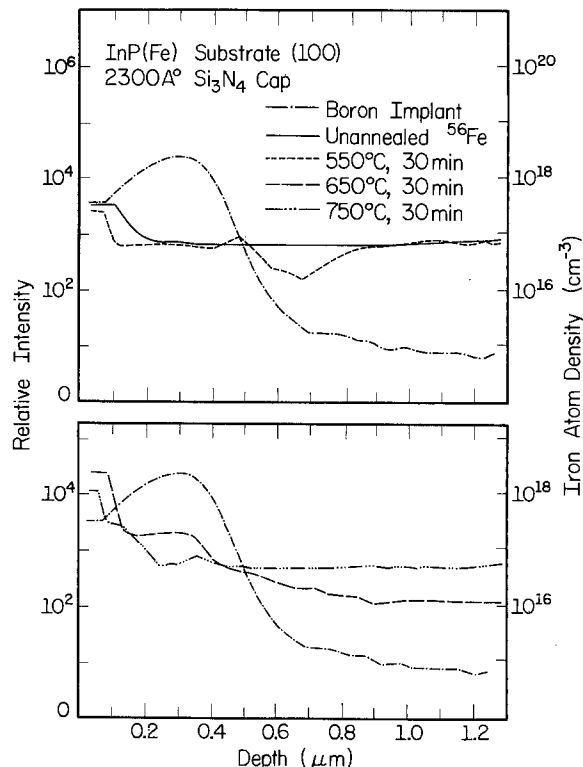


Fig. 5. SIMS profiles of Fe in a semi-insulating InP substrate implanted with B ($6.8 \times 10^{14} \text{ cm}^{-2}$, 126 keV) and annealed for 30 min at the indicated temperatures with an Si_3N_4 encapsulant.

Conclusions

We have studied the redistribution of the compensating dopants Fe or Cr in semi-insulating InP, resulting from annealing only and from the implantation of electrically inactive elements. Annealing with an Si_3N_4 cap forms an accumulation region within the first 1000 \AA of the surface followed by a depletion region extending to a depth of $\sim 1 \mu\text{m}$. Cr profiles exhibit larger concentration gradients under these conditions than do Fe profiles. Profiles resulting from the implantation of "neutral" dopants exhibit surface accumulation regions followed by accumulation regions under the projected range peak.

We believe these results can be explained by the gettering of the compensating dopant to defect-rich regions. In the case of simple anneals, a defect-rich region is produced at the interface which getters Fe or Cr, leading to the accumulation and depletion zones observed. This same mechanism is probably responsible for the surface accumulation regions observed in the implanted profiles. However, where the annealed-only profiles exhibit depletion regions, implant profiles show accumulation regions. Since this accumulation occurs in the implanted region, we presume this effect to be due to gettering of the compensating dopant to defect regions produced by the implantation. By implanting electrically and chemically inactive impurities, we believe we have excluded the possibility of redistribution arising from effects other than those related to implant damage.

Acknowledgments

This work was supported in part by the Office of Naval Research under Contract N00014-76-C-0806, the Joint Services Electronics Program (U.S. Army, U.S. Navy, and U.S. Air Force) under Contract N00014-79-C-0424, and by NSF MRL Grant DMR-77-23999. The authors wish to express their sincere thanks to E. M. Swiggard and R. L. Henry of the Naval Research Laboratory for providing us with the InP substrates. We also wish to thank J. Hiatt and E. Sammann for tech-

nical support. One of us (J. D. Oberstar) also wishes to acknowledge the support provided by an IBM predoctoral fellowship during this time period.

Manuscript received Nov. 24, 1980.

Any discussion of this paper will appear in a Discussion Section to be published in the June 1982 JOURNAL. All discussions for the June 1982 Discussion Section should be submitted by Feb. 1, 1982.

Publication costs of this article were assisted by the University of Illinois.

REFERENCES

1. J. B. Mullin, A. Royle, and B. W. Straughan, *Int. Symp. on GaAs and Related Compounds*, 1970, Inst. Phys. Conf. Ser. 9, p. 41, London (1971).
2. O. Nizuno and H. Watanabe, *Electron. Lett.*, **11**, 118 (1975).
3. H. Morkoc, J. T. Andrews, and S. B. Hyder, *ibid.*, **14**, 715 (1978).
4. B. Tuck, G. A. Adegboyega, P. R. Jay, and M. J. Cardwell, *Int. Symp. on GaAs and Related Compounds*, 1978, Inst. Phys. Conf. Ser. 45, p. 114, London (1979).
5. A. M. Huber, G. Morillot, N. T. Linh, P. N. Favennec, B. Deveaud, and B. Toulouse, *Appl. Phys. Lett.*, **34**, 858 (1979).
6. J. Kasahara and N. Watanabe, *Jpn. J. Appl. Phys.*, **19**, L151 (1980).
7. C. A. Evans, Jr., V. R. Deline, T. W. Sigmon, and A. Lidow, *Appl. Phys. Lett.*, **35**, 291 (1979).
8. P. K. Vasudev, R. G. Wilson, and C. A. Evans, Jr., *ibid.*, **36**, 837 (1980).
9. R. L. Henry and E. M. Swiggard, *Int. Symp. on GaAs and Related Compounds*, 1976, Inst. Phys. Conf. Ser. 33b, p. 28, London (1977).
10. M. J. Helix, K. V. Vaidyanathan, B. G. Streetman, H. B. Dietrich, and P. K. Chatterjee, *Thin Solid Films*, **55**, 143 (1978).
11. J. P. Donnelly and C. E. Hurwitz, *Appl. Phys. Lett.*, **31**, 418 (1977).
12. D. Eirug Davies, J. P. Lorenzo, and T. G. Ryan, *Solid-State Electron.*, **21**, 981 (1978).
13. T. J. Magee, J. Peng, J. D. Hong, C. A. Evans, Jr., V. R. Deline, and R. M. Malbon, *Appl. Phys. Lett.*, **35**, 277 (1979).
14. T. E. Seidel, R. L. Meek, and A. G. Cullis, *J. Appl. Phys.*, **46**, 600 (1975).
15. W. Akutagawa, H. L. Dunlap, R. Hart, and O. J. Marsh, *ibid.*, **50**, 777 (1979).
16. H. B. Dietrich and J. Comas, "Ion Implantation in Semiconductors, 1976," p. 735, Plenum, New York (1977).
17. C. O. Bozler, J. P. Donnelly, W. T. Lindley, and R. A. Reynolds, *Appl. Phys. Lett.*, **29**, 698 (1976).
18. P. D. Townsend, J. C. Kelly, and N. E. W. Hartley, "Ion Implantation, Sputtering, and Their Applications," p. 84, Academic Press, London (1976).
19. A. G. Cullis, T. E. Seidel, and R. L. Meek, *J. Appl. Phys.*, **49**, 5188 (1978).
20. K. Bruce Winterbon, "Ion Implantation Range and Energy Deposition Distributions," Vol. 2, IFI/Plenum, New York (1975).

Two-Phase Annealing of Single Crystal CdS

J. W. Sherohman

Lawrence Livermore National Laboratory, University of California, Livermore, California 94550

ABSTRACT

Single CdS crystals of low resistivity have been converted to high resistivity material by annealing them in the presence of a two-phase system consisting of a CdS solid and a liquid rich in sulfur. Ambient temperature measurements of dark d-c resistivity indicated that resistivity values greater than $10^{13} \Omega \text{ cm}$ were obtained.

The possibility of applying electro-optics to the design of tunable filters has resulted in an interest in producing CdS crystals in the form of a thin plate of high resistivity ($>10^{12} \Omega \text{ cm}$). Crystals of CdS having high resistivity have been grown by the vapor transport technique (1-6). However, due to the sensitivity of the electrical conductivity to the partial pressures of Cd and S during growth of CdS crystals (7, 8), it is often difficult to consistently produce material having very high resistivity. A study has shown that annealing can be used to convert single crystal CdS material of low resistivity ($<10^2 \Omega \text{ cm}$) to that of high resistivity ($>10^{13} \Omega \text{ cm}$). The method developed uses a controlled vapor-phase heat-treatment to produce thin CdS plates with high resistivity by annealing them in the presence of a two-phase system of solid CdS and a sulfur-rich liquid.

Annealing in the presence of a multi-phase system is a method to control the stoichiometry of a compound having a single phase width (9-11). However, in the case of influencing the electrical conductivity, and hence resistivity, the purpose of a controlled atmosphere of Cd and S surrounding the CdS crystalline material is to insure that the neutral vacancy concentrations of both Cd and S remain essentially unchanged (i.e., there is no self-diffusion) while, at the same time,

existing charged defects proceed to an equilibrium state through chemical diffusion.

Experimental

A two-phase compound was prepared by arbitrarily mixing 140g of CdS powder with 40g of sulfur in a quartz ampul. The mixture was then heated with a hot-air gun until the sulfur liquefied and reacted with the CdS. The ampul was vacuum sealed and heat-treated for 2 hr at 300°C. The furnace temperature was then raised at 200°C/hr to a temperature of 900°C and held there for 24 hr. The ampul was cooled in the furnace and the resulting compound was used as the two-phase material for the annealing of as-grown single crystals of CdS.

Single crystals of CdS grown by the vapor phase transport technique were oriented and sawed in the direction of the c-axis of the crystal. The sawed plates were lapped, polished, cleaned in perchloroethylene and HCl, and then given a deionized water and an acetone rinse. At ambient temperature, measurements of the dark d-c resistivity of the prepared sample were taken in a guard-ring configuration using ohmic contacts provided by an In-Ga alloy. Data are included in Table I.

The two-phase material (CdS + S) and single crystal CdS samples were placed in separate quartz tubes

Key words: resistivity, chemical diffusion, stoichiometry.

Table I. Resistivities of single crystals of CdS before and after two-phase annealing

| Sample | Resistivity before annealing (Ω cm) | Heat treatment | Resistivity after annealing (Ω cm) |
|---------|---|------------------|--|
| 5-30-6 | 2.5 | 900°C for 5 min | 3.0×10^{15} |
| 5-30-6 | 2.5 | 900°C for 5 min | 2.8×10^{15} |
| 3-2-18 | 9.8 | 900°C for 35 min | 6.9×10^{15} |
| 3-23-19 | 15.9 | 900°C for 2 hr | 6.7×10^{15} |
| 6-15-18 | 2.5 | 900°C for 112 hr | 7.8×10^{15} |
| 11-29-7 | 0.82 | 900°C for 115 hr | 5.3×10^{15} |

designed to fit together by ground points (see Fig. 1). The ground joints permitted the quartz tubes to be reused. The tubes, after being connected, were inserted inside a quartz ampul 4 cm in diameter by 23 cm long. Ampuls were subsequently sealed in vacuum and annealed at 900°C for various periods of time. After furnace cooling to ambient temperature, the inner tubes were removed from each ampul. The single crystal samples were again cleaned and their d-c resistivity in a dark environment was measured.

Results and Discussion

The dark d-c resistivities of the samples, measured at ambient temperatures, before and after annealing are given in Table I. All samples showed marked increases in resistivity, to values greater than 10^{13} Ω cm. Figure 2 shows the variation of resistivity with time in a dark environment for two samples of different thickness. Both samples had been heat-treated at 900°C for 5 min. The resistivity curves of the samples are essentially identical. Other samples annealed for longer times at 900°C had resistivities that were also very high, but not as high as samples annealed for 5 min.

A two-phase annealed sample that was heat-treated at 900°C for 5 min is compared in Fig. 3 with that of a high resistivity CdS crystal obtained from Cleveland Crystal Company, Cleveland, Ohio. The two-phase an-

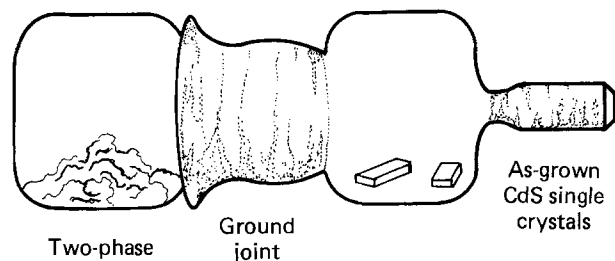


Fig. 1. Quartz apparatus for the two-phase annealing of CdS single crystals.

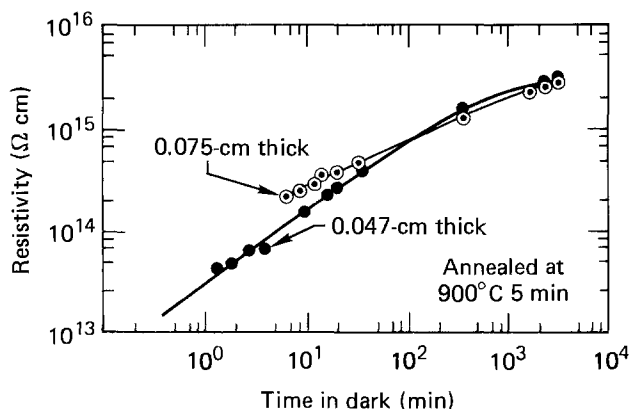


Fig. 2. A comparison of the d-c dark resistivity of two samples of different thickness that had been two-phased annealed for 5 min at 900°C.

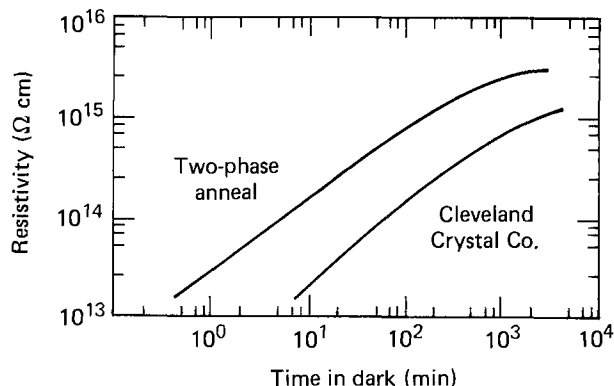


Fig. 3. A comparison of the d-c dark resistivity of a two-phase annealed sample with that of a high resistivity sample obtained from Cleveland Crystal Company, Cleveland, Ohio.

nealed sample had the same resistivity behavior as the Cleveland crystal sample, but reached a higher maximum resistivity.

The atmosphere in which the single crystal samples of CdS were heat-treated is fixed by the two-phase mixture. As long as the two phases are present, the mixture provides a constant partial pressure of both Cd and S. These fixed partial pressures, if given enough time, will force the stoichiometry of a CdS crystal to the sulfur-rich side of its single-phase width. At that point the partial pressure of Cd and S above the crystal equals the partial pressure of Cd and S generated by the two-phase mixture. The crystal remains single phase with its stoichiometry fixed by the sulfur-rich side of the single phase width. However, this occurs by a slow self-diffusion process. The purpose of the two-phase mixture is to insure that the neutral vacancy concentrations of both Cd and S in the CdS crystals remain essentially unchanged for various time period anneals.

The electrical conductivity of CdS can be affected by chemical diffusion of existing charged defects (12-14). Chemical diffusion, which does not depend on the product of the diffusivity and concentration of the defect, is a rapid diffusion process as compared to self-diffusion (15). It has been suggested that in the presence of high activity of sulfur (low P_{Cd} condition), the diffusion of S is controlled by neutral interstitials, while the diffusion of Cd is controlled by ionized cadmium vacancies, V_{Cd}'' (13). If it is assumed that the chemical diffusion process is controlled by V_{Cd}'' , the chemical diffusion coefficient would be on the order of $D_{V_{Cd}''}$, where $D_{V_{Cd}''} = D_{Cd}^*/(V_{Cd}'')$. D_{Cd}^* , the tracer diffusivity of Cd, has been observed at 900°C under a low P_{Cd} condition to have a value of approximately 10^{-11} $\text{cm}^2 \text{sec}^{-1}$ (12, 13). The (V_{Cd}'') at this temperature, as given in Ref. (13), is on the order of 10^{-8} site fr. for $P_{Cd} = 10^{-5}$ atm. This indicates that D_{chem} is in the range of 10^{-4} - 10^{-3} $\text{cm}^2 \text{sec}^{-1}$ and that chemical diffusion of existing defects would occur in less than a minute within a 1 mm thick sample at 900°C. The very high resistivity of the samples after a heat-treatment of 5 min suggests the presence of a fast chemical diffusion process.

The major finding of this study is that by annealing as-grown, single crystal CdS material in an atmosphere fixed by a two-phase mixture consisting of solid CdS and a sulfur-rich liquid, resistivity of the material can be raised by more than ten orders of magnitude.

Acknowledgments

The author would like to thank B. Corson for making the d-c resistivity measurements, C. Seeger for growing the CdS single crystals, and C. Wiersma and J. Stevens for preparing the samples. This work was performed at Hughes Aircraft Company, Industrial

Products Division, Carlsbad, California.

Manuscript submitted Oct. 24, 1980; revised manuscript received ca. Jan. 22, 1981.

Any discussion of this paper will appear in a Discussion Section to be published in the June 1982 JOURNAL. All discussions for the June 1982 Discussion Section should be submitted by Feb. 1, 1982.

Publication costs of this article were assisted by Lawrence Livermore Laboratory.

LIST OF SYMBOLS

| | |
|----------------|--|
| P_{Cd} | partial pressure of Cd |
| V_{Cd}'' | ionized Cd vacancies |
| (V_{Cd}''') | concentration of ionized Cd vacancies |
| $D_{V_{Cd}''}$ | diffusion coefficient for ionized Cd vacancies |
| D_{Cd}^* | tracer diffusivity of Cd |
| D_{chem} | chemical diffusion coefficient |

REFERENCES

- R. H. Fahrig, *Electrochem. Tech.*, **1**, 362 (1963).
- L. Clark and J. Woods, *Br. J. Appl. Phys.*, **17**, 319 (1966).
- E. V. Markov and A. A. Davydov, *Izv. Akad. Nauk SSSR Neorgan. Mat.*, **7**, 575 (1971).
- L. C. Greene, D. C. Reynolds, S. J. Czyak, and W. M. Baker, *J. Chem. Phys.*, **29**, 1375 (1958).
- L. R. Shiozawa and J. M. Jost, "Research on Improved II-VI Crystals," ARL 71-0054, Contract F 33615-68-C-1601-P003 (1971).
- E. V. Markov and A. A. Davydov, *Izv. Akad. Nauk SSSR Neorgan. Mat.*, **11**, 1755 (1975).
- M. A. Subhan, M. N. Islam, and J. Woods, *J. Phys. Chem. Solids*, **33**, 229 (1972).
- L. Clark and J. Woods, *J. Cryst. Growth*, **3**, 127 (1968).
- W. Albers and H. J. Vink, *Chemisch Weekblad*, **61**, 61 (1965).
- R. L. Holman and R. M. Fulrath, *J. Am. Ceram. Soc.*, **55**, 192 (1972).
- R. L. Holman and R. M. Fulrath, *J. Appl. Phys.*, **44**, 5227 (1973).
- D. Shaw and R. C. Whelan, *Phys. Status Solidi*, **36**, 705 (1969).
- V. Kumar and F. A. Kroger, *J. Solid State Chem.*, **3**, 387 (1971).
- V. Kumar and F. A. Kroger, *ibid.*, **3**, 406 (1971).
- P. G. Shewmon, "Diffusion in Solids," Chap. 5, McGraw-Hill, New York (1963).

Desalination by Photoelectrodialysis. II.

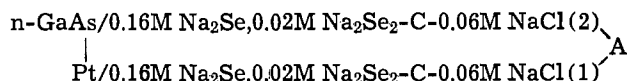
George W. Murphy*¹

Solar Energy Research Institute, Golden, Colorado 80401

ABSTRACT

Continuing experiments on photoelectrodialytic desalination now include the addition of a cell buffer compartment to keep unwanted ions leaking through imperfect membranes from contaminating the product water, different membranes, and thin film polycrystalline n-CdSe electrodes in sulfide/polysulfide electrolyte. Both the rate and extent of desalination have been markedly improved. Economic feasibility projections are updated.

A laboratory demonstration of photoelectrodialytic desalination was recently announced (1); the symbolic representation of the 4-compartment cell employed is



where C is a cation and A an anion selective membrane. Irradiation of the n-GaAs leads to desalination of compartment 1 and salt enrichment in 2. In this communication we furnish additional experimental details, extend the experimental investigation in several ways, and assess the economic potential. Photoelectrodialytic desalination is one of several model systems which couple a photoelectrochemical driving unit through ion selective membranes to cell components containing raw materials and deliver a useful product (2).

Experimental

Construction features for all experimental cells are illustrated by the 4-compartment cell drawing in Fig. 1, other details of which are given in Ref. (1). In this cell product water is subject to selenide ion contamination because of imperfect selectivity of the membrane separating the two solutions. One remedy for

this problem is the introduction of a fifth "buffer" compartment as illustrated schematically in Fig. 2. Contamination of this compartment can occur, but the reject salt solution contained is swept out at a rate sufficient to keep the product water contamination free.

Another problem encountered in early work was makeup of the selenide solution. Colorless alkali metal selenides are extremely air sensitive, forming orange-

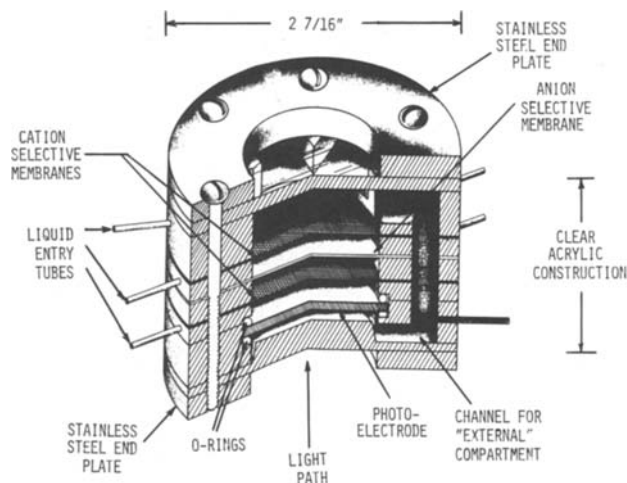


Fig. 1. Cutaway drawing of 4-compartment experimental cell

* Electrochemical Society Active Member.

¹ On sabbatical leave from the University of Oklahoma, Norman, Oklahoma 73019.

Key words: photoelectrochemistry, solar energy conversion, semiconductor electrodes, membrane processes.

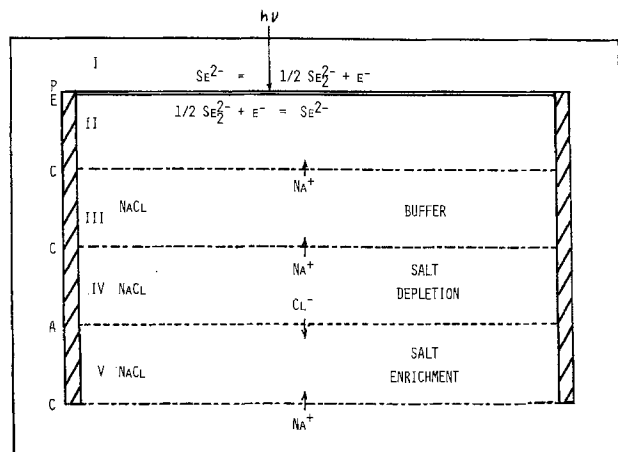


Fig. 2. Schematic of 5-compartment cell, illustrating principle of operation.

brown polyselenide. Cerac Chemical Company 99.9% Na_2Se packed under argon formed an optically dense aqueous solution even with nitrogen atmosphere glove box technique. Consequently the solution employed in the first desalination experiment (1) contained an unknown but considerably larger amount of diselenide than the "made-up" 0.02M. The principal effect is to decrease the amount of light reaching the electrode, therefore decreasing the desalination performance. Selenide solutions employed subsequently were made by bubbling H_2Se (Scientific Gas Products) through alkali metal hydroxide solutions (3). The amber color of the resulting solution was caused by traces of air during transfer operations. No elemental selenium was added. The solution employed in subsequent desalination experiments is designated 0.18M Na_2Se , (Na_2Se_2), instead of 0.16M Na_2Se , 0.02M Na_2Se_2 .

Two sets of membranes were employed: Nafion 417 9G-3009 cation (du Pont) and Raipore 5035 anion-selective [RAI Research Corporation 5035 has essentially the same properties as 5025 employed in Ref. (1)]; and Ben Gurion University of the Negev Applied Research Institute (BGARI) cation- and anion-selective, obtained through the courtesy of Prof. Chaim Forgacs. Preparation of the latter membranes has been described by de Körösy and Schorr (4).

In addition to the single crystal n-GaAs electrode described previously (1), a thin film polycrystalline n-CdSe disk electrode was received from Weizmann Institute of Science, Israel (5) for testing. This electrode had been deposited on a titanium disk substrate, to which we cemented with silver epoxy a brass counterelectrode. The Hodes etching procedure (5) was followed prior to photodesalination experiments. This electrode was coupled first with the 0.18M Na_2Se (Na_2Se_2) and later with 0.1M Na_2S , 0.1M Na_2S_2 redox electrolyte solutions.

In desalination experiments fresh 0.06M NaCl solution from an overhead reservoir was run sequentially through the "buffer" and the salt-enriched compartments at a rate of about 1 ml/min. A peristaltic pump (Scientific Industries Model 700) circulated solution via a closed loop between the two selenide (or sulfide) ion compartments at a rate of about 1 ml/min.

Results

The results of several desalination experiments are graphed in Fig. 3. Curve A is from Ref. (1). The improvement shown in curve B is due both to the elimination of product water contamination and the reduction of solution light absorption. The further improvement shown in curve C is due to the higher conductivity of BGARI membranes. Curves D and E are impressively still better, due probably to the lower overall resistance of the electrode assembly. The excellent perform-

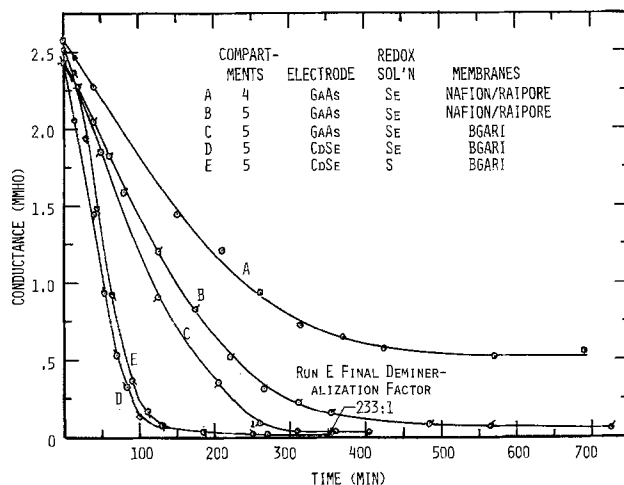


Fig. 3. Results of five desalination experiments

ance shown in curve E is particularly important, because it proves that selenide can be replaced by a cheaper and less obnoxious solution.

The economic potential of photoelectrodialytic desalination has been examined briefly (2); it was concluded that about $\$35 \text{ m}^{-2}$ could be afforded for cell construction as a generally applicable method for desalting brackish water, based on assumed 7% light to electric energy conversion, 10 year lifetime, and $\$0.28 \text{ m}^{-3}$ product water. Adjusted for inflation, this figure would now be about $\$50 \text{ m}^{-2}$. However, there are potential remote installations that could justify an expenditure several times higher, and the first developmental stage could focus on this limited market. The thin film polycrystalline n-CdSe (and CdSe-CdTe alloys) coupled with BGARI membranes appear capable of satisfying these cost requirements, if lifetime conditions can be met. The cost of CdSe for a 0.02 mm film would be less than $\$10 \text{ m}^{-2}$. The membranes, not presently in mass production, are estimated at $\$5 \text{ m}^{-2}$, with four required per square meter of cell area.

Electrodialytic desalination driven by solid-state solar cells is now being considered seriously (6, 7), first in sunny regions remote from conventional power sources, but later extended to more general usage as the cost of solar cells comes down and conventional power costs continue their inexorable rise.

What theoretical advantage does photoelectrodialysis have over electrodesalination driven by solid-state or electrochemical solar cells? The answer is less barrier area, i.e., the sum of membrane and electrode area. Other things being equal, barrier area determines total process cost. In the latter case both the driving and driven units must have separate electrode sets, whereas in the former they are shared. Less electrode overpotential loss would also be a factor favoring photoelectrodialysis.

What advantage does solar driven electrodesalination have over solar distillation? The answer is a much lower energy requirement. Consider the minimum energy requirement for electrodesalination, obtained through the Nernst equation in the concentration approximation. Per differential equivalent of salt removed at the reversible concentration potential

$$E = \frac{2RT}{F} \ln \frac{C_2}{C_1} = 0.1183 \log \frac{C_2}{C_1} \quad (25^\circ\text{C})$$

it is the product FE , where F is the Faraday constant, and C_1 and C_2 are the depleted and enriched salt stream concentrations. Suppose $C_1/C_2 = 100$. The potential difference is then $2 \times 0.1183 = 0.2366\text{V}$, and the minimum energy requirement to desalt is $0.2366 \times 96,500/100 = 22.8 \text{ kJ}$. If the source water is 0.06M, a

typical brackish concentration, the amount of desalted water produced is $1 \text{ mol}/0.06 \text{ mol liter}^{-1} = 16.67$ liters. To distill the same amount of water would require $16,667 \text{ g} \times 2.32 \text{ kJ/g} = 38,732 \text{ kJ}$, a factor of 1697 greater. If the power for electrodialysis is to be furnished photoelectrically, one must enter an efficiency factor of about 10%. Still, solar driven electrodialysis has at least a 170-fold advantage over single stage solar distillation, no allowance having been taken in the latter case for imperfect collection efficiency.

Manuscript submitted Aug. 15, 1980; revised manuscript received ca. March 2, 1981.

Any discussion of this paper will appear in a Discussion Section to be published in the June 1982 JOURNAL.

All discussions for the June 1982 Discussion Section should be submitted by Feb. 1, 1982.

Publication costs of this article were assisted by the Solar Energy Research Institute.

REFERENCES

1. G. W. Murphy, *This Journal*, **127**, 2088 (1980).
2. G. W. Murphy, *Solar Energy*, **21**, 403 (1978).
3. B. Miller, A. Heller, M. Robbins, S. Menezes, K. C. Chang, and J. Thomson, Jr., *This Journal*, **124**, 1019 (1977).
4. F. de Körösy and J. Schorr, *Bull. Res. Council. Isr.*, **11A**, 40 (1962).
5. G. Hodes, *Nature*, **285**, 29 (1980).
6. J. E. Lundstrom, *Desalination*, **31**, 469 (1979).
7. I. Savchenko, B. V. Tarnizhevskii, T. M. Kotina, and B. I. Lemasov, *Appl. Solar Energy*, **14**, 32 (1978).



Variation of the Conductivity of MnO_2 with Lithium Insertion

M. Voinov*¹

Leclanché S.A., 48 route de Grandson, 1401 Yverdon, Switzerland

The variations of the electrode potential of Li_xMnO_2 with x has been reported (1,2) and attributed to a modification of the band structure of MnO_2 when Lithium enters its lattice. It was proposed that this modification is such that Li_xMnO_2 turns from a small bandgap into a wide bandgap n-type semi-conductor at 0.5 Li inserted per mole. Consequently at this amount of Li inserted the conductivity of Li_xMnO_2 should decrease.

In fact it is already known that the electronic conductivity of a similar compound, namely H_xMnO_2 decreases during reduction (3) but its variation with x has not been published. On the other hand, increases of the total internal impedance of Zn- MnO_2 (4) and Li- MnO_2 (1) cells with depth of discharge have been reported but the contribution of the depolariser electronic conductivity variation to the total change was not isolated. The purpose of the present investigation was precisely to determine such a contribution in the case of Li_xMnO_2 and to check the predictions made about its band structure modification at $x=0.5$.

Short of a full frequency response analysis, it is not conceptually possible in an electrochemical cell to separate the electrolyte and depolariser ohmic drops from the various interface and Warburg impedances. With the further complication introduced by porous electrodes, even the utility of such a frequency response analysis is doubtful except in a few simple cases (5). One must use approximate methods.

*Electrochemical Society Active Member
Keywords: Lithium, Manganese dioxide
button cells

¹Present address: 74 route de Saint Julien,
1212 Grand Lancy, Geneva, Switzerland

In the present approach, Li- MnO_2 cells were partially discharged by known amounts. They were then left in open-circuit to smooth out diffusion gradients. Subsequently the cells were addressed with small (1 μC) discharge pulses. It is assumed that, during these pulses, no diffusion gradients are established in the depolariser or in the electrolyte to contribute a Warburg impedance. It is also assumed that the interface impedance between Lithium and the electrolyte remains the same during discharge of the cells. Therefore the variations with depth of discharge of the total cell tension drop at the end of a pulse should reflect mainly the variations of the ohmic drop in Li_xMnO_2 with a possible contribution of the interface impedance between Li_xMnO_2 and the electrolyte.

Cathode limited Li- MnO_2 button cells (\emptyset 11.6 h 2 mm) were assembled in a glove box (< 1 ppv H_2O , 20 ppv O_2). The MnO_2 was heat-treated at 350°C for 24 hours then mixed with 10% by weight of carbon and 5% by weight of a fluorinated hydrocarbon binder. The mixture was then pressed in the shape of 50% porous pellets. The solvent was Propylene Carbonate distilled at 90°C under vacuum. The electrolyte was LiClO_4 (1 M) dried under vacuum.

The cells were discharged at room temperature to various degrees. They were then left in open-circuit until their tensions did not vary by more than 10 mV/24 h. As the electrolyte is invariant during discharge, the open-circuit tensions of the cells represented the electrode potential of Li_xMnO_2 versus Lithium in the same solution (fig. 1). Short (1 ms, 2 μs rise time) low intensity (1 mA)

constant current discharge pulses corresponding roughly to the demand of a miniature step motor, were applied to the cells and their responses recorded with a Digital Storage Oscilloscope (Gould OS 4000).

It is observed that the internal impedance variation (potential drop after 1 ms divided by 1 mA, minus the corresponding value for the undischarged cell) increases sharply at 0.5 Li inserted per MnO_2 (Fig. 1). As the carbon used has about the same conductivity as undischarged MnO_2 , this increase cannot be due to the volume increase of Li_xMnO_2 during discharge. Furthermore the value of 0.5 Li/mole corresponds precisely to the prediction made about the increase of resistivity of Li_xMnO_2 . This band model modification proposed (1,2) is therefore to that extent verified. Furthermore, between 50°C and -20°C the impedance variation decreases with increasing temperature. The approximate activation energy is 0.25 eV for $x = 0.75$ and a pulse current of 1 mA.

However, it was also predicted (1,2) that above 0.5 Li/ MnO_2 , the resistivity should again decrease slightly. This is not what is observed, and the matter needs more experimental results rather than ad hoc assumptions about the Li_xMnO_2 - electrolyte interface impedance.

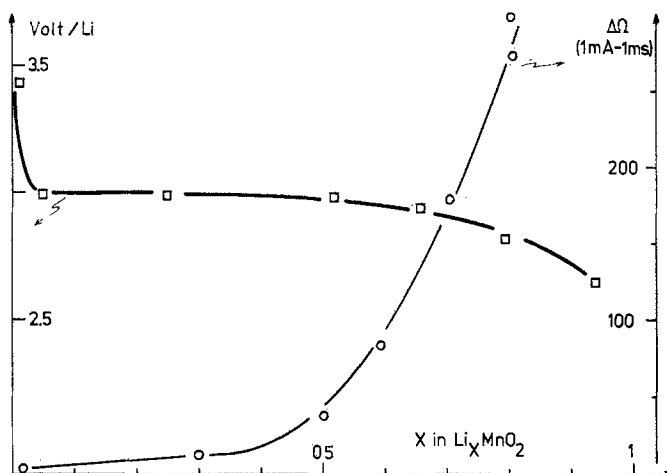


Figure 1. Electrode potential of Li_xMnO_2 (\square) and internal impedance increase (\circ) of partly discharged and open-circuited Li- MnO_2 cells.

REFERENCES

- (1) M.Voinov, Proc. Lithium Battery Symp., Electrochem. Soc. meeting (October 1980)
- (2) M.Voinov, to be published in *Electrochimica Acta*
- (3) M.L.Kronenberg, this Journal, Vol 121, 3 p.375 (1974)
- (4) D.Boden et al., *ibid.* Vol 114, p. 415 (1967)
- (5) R.de Levie, *Advances in Electrochemistry and Electrochemical Engineering*, Vol 6, p.329, Interscience (1967)

Manuscript submitted Jan. 26, 1981;
revised manuscript received ca. May 8, 1981.

Publication costs of this article were assisted by Leclanche S.A.

Surface Stabilization of Polycrystalline-Silicon Films during Laser Recrystallization

T. I. Kamins*

Hewlett-Packard Laboratories, Palo Alto, California 94304

In the past several years numerous attempts have been made to recrystallize thin films of fine-grain CVD polycrystalline silicon into large-grain material in order to reduce the influence of the grain boundaries. Recrystallization with a scanned CW laser has been found to increase the average grain size to several microns (1). The consequent reduction in defect concentration makes possible the fabrication of active devices, such as MOSFETs with their active channels within the layer of laser-recrystallized polysilicon (2,3). Such devices can be used in monolithic silicon integrated circuits to improve packing density or performance or can be constructed in silicon films deposited on inexpensive substrates for applications such as flat-panel displays.

In the initial work, recrystallization was found to occur more satisfactorily when the polysilicon was deposited on silicon-nitride-coated silicon wafers, rather than on oxidized wafers. In the latter case, at the high laser powers needed to melt the entire thickness of the polysilicon, the silicon tends to agglomerate or delaminate, leaving regions of the underlying oxide exposed. Although the recrystallization proceeds more controllably on silicon nitride, the electrical properties of an underlying polysilicon/silicon-dioxide interface are far superior to those of a polysilicon/silicon-nitride interface (4). Consequently, attempts were made to improve the controllability of the recrystallization process on silicon dioxide.

* Electrochemical Society Active Member

Keywords: Polycrystalline silicon, laser recrystallization, silicon nitride

Initial work by the Stanford group (5) utilized an 1100°C furnace anneal in a nitrogen atmosphere for one hour to prevent agglomeration during the subsequent laser recrystallization, thus broadening the useful range of laser powers. This high temperature anneal, however, is not compatible with the future direction of IC technology, which restricts processing to lower temperatures to avoid wafer deformation. In addition, the high temperature nitrogen anneal often degrades the unprotected silicon surface. Consequently, a better method of stabilization is needed. This note will show that the stabilization is an effect occurring at the exposed top surface of the polysilicon, rather than being predominately related to a change in the bonding at the underlying polysilicon/silicon-dioxide interface. It will also demonstrate that a thin layer of silicon nitride deposited on top of the polysilicon provides an optimum surface stabilization layer.

Auger analyses were performed to study the depth profiles of the surface layers formed by the thermal or laser processing. While the Auger depth profile after nitrogen annealing did not indicate any significant nitrogen-containing layer, the thickness of the native oxide layer on the surface of the polysilicon increased from approximately 15 Å to about 50 Å during the nitrogen anneal. This layer did not change significantly during the subsequent laser recrystallization. We believe that the 50 Å thick oxide layer stabilizes the surface during laser melting by changing the surface-tension forces which tend to pull the molten layer of silicon apart. Although no oxygen is purposely introduced into the furnace during the nitrogen anneal, the hot wafer surface

could be exposed to oxygen from back-streaming of oxygen into the furnace or during removal from the furnace tube, as well as by trace quantities of oxygen in the nitrogen supplied to the furnace.

The presence of a surface layer which stabilizes the film during laser recrystallization is consistent with other observations: (1) The beneficial effect of the 1100°C nitrogen anneal is removed by etching the surface in a standard buffered oxide etch for a short time (~ 1 min) before laser recrystallization. (2) Although no difference is seen before laser recrystallization, the surfaces of films with and without the thermal anneal appear markedly different under an optical microscope after laser recrystallization. Films which have been thermally annealed retain the appearance of the fine-grain polysilicon films (a fine-scale surface roughness) even though the grain size has increased. Films which have not been thermally annealed before laser recrystallization exhibit greatly different surface features, corresponding to large-grain material.

Once it was shown that the high-temperature anneal formed a thin, protective layer on the polysilicon surface, experiments were performed to develop a surface stabilization process more compatible with advanced IC fabrication technology.

In all cases to be discussed below, the polysilicon films were 0.5 μm thick and were deposited by low-pressure CVD at 625°C from SiH_4 onto silicon wafers covered with 1.4 μm of thermally grown SiO_2 . A CW argon laser (Coherent, Inc. Model 5000 laser annealer) was used to recrystallize the polysilicon, although the results are expected to be applicable to any scanned laser (or possibly electron beam). The laser beam was scanned across the wafer surface with galvanometer-controlled mirrors at a velocity of 25 cm/sec. The spot size was approximately 80 μm , and the beam was stepped about 40 μm between successive scans. The substrate temperature was 500°C during recrystallization.

Films of silicon oxide (from N_2O and SiH_2Cl_2) approximately 50 Å thick and of silicon nitride (from NH_3 and

SiH_2Cl_2) approximately 90 Å thick were deposited in the LPCVD reactor. While the oxide layer was somewhat effective in stabilizing the surface, the nitride layer provided marked surface stabilization. In the latter case, after laser recrystallization the surface was smoother than observed in any previous experiment, and a wide range of laser powers produced satisfactory recrystallization. At the higher powers, however, isolated irregularities (protrusions or pits) formed, their density increasing with increasing laser power.

In a more detailed experiment three different thicknesses of LPCVD nitride (approximately 60, 90, and 140 Å) were deposited on polysilicon. In addition, a 100 Å-thick layer of nitride was deposited from NH_3 and SiH_4 in a hydrogen carrier gas at atmospheric pressure in order to avoid the presence of any chlorine species. Each sample was recrystallized with a series of different laser powers with one watt increments from 8 W until significant agglomeration occurred or the upper limit of the laser power (17W) was reached. After recrystallization, the microstructure was observed in an optical microscope, and the power necessary for the formation of the large-grained structure was noted along with the power which caused agglomeration. The difference indicated the range of satisfactory laser powers which could be used, with the largest possible allowable range being desired for process flexibility. In the case of the nitride layers, an upper limit was set by the formation of the isolated irregularities since the films did not agglomerate even at the highest laser power. As can be seen from Table I the largest allowable range was obtained with the thinnest LPCVD nitride layer. No isolated irregularities were seen at even the highest laser power. By contrast, irregularities were seen in the nitride film deposited from SiH_4 , indicating that these irregularities are not caused by chlorine inclusion.

Other stabilization treatments investigated provided additional insight into the process. Heat treatments at 900°C in 1% O_2 with the balance either argon or nitrogen formed about 35Å of oxide in each case.

These thin oxide layers appeared to provide a small increase in the allowable range of laser powers (Table I). An anneal at 1000°C in 1% O₂ with the balance nitrogen formed about 60 Å of oxide. While this oxide layer increased the allowable range, the change was much less than caused by a layer of CVD nitride of similar thickness. This result, coupled with the previous observation of only a slight increase in the allowable range from a deposited oxide layer, indicates a fundamental difference between the effects of oxide and nitride layers. This difference may possibly be related to the stiffer silicon nitride film better resisting the surface-tension forces which tend to pull the molten silicon film apart. A thermal oxynitride film formed in a 1% O₂ - 49% NH₃ - 50% N₂ ambient at 1000°C (target thickness 30-50 Å) increased the allowable range noticeably but not as significantly as did the deposited nitride layer.

The surface topology seen after laser recrystallization is quite different for films with the various stabilization layers. In particular, the silicon nitride stabilization layer leads to a markedly smoother surface, as has been reported in Ref. 6. Sirtl etching after recrystallization to reveal the grain boundaries and other defects, however, shows that the grain structure of all films is qualitatively similar (as also reported in Ref. 6 for silicon nitride). The elongated grains characteristic of laser-recrystallized polysilicon (1) are clearly visible in all cases, indicating that the basic nature of the recrystallization process is not greatly altered by the presence of the different stabilization layers.

In summary, the formation of a foreign surface film on the top surface of a polysilicon layer can markedly widen the allowable range of laser powers which can be used to recrystallize polysilicon films deposited on silicon dioxide. Of the layers investigated, a 50-100 Å-thick, CVD silicon nitride layer has been found to provide the best control over the successful recrystallization of polysilicon to form a large-grain structure.

ACKNOWLEDGEMENT

The author would like to thank Drs. C.J. Dell'Oca, A. Gat, and D. Illic for encouragement during this investigation and S. Eglash, M. Guerin-Brown, and Y. Strausser for the Auger analyses.

REFERENCES

1. A. Gat, L. Gerzberg, J.F. Gibbons, T.J. Magee, J. Peng, and J.D. Hong, *Appl. Phys. Lett.* **33**, 775 (15 Oct. 1978).
2. K.F. Lee, J.F. Gibbons, K.C. Saraswat, and T.I. Kamins, *Appl. Phys. Lett.* **35**, 173 (15 July 1979).
3. T.I. Kamins, K.F. Lee, J.F. Gibbons, and K.C. Saraswat, *IEEE Trans. Electron Devices* **ED-27**, 290 (Jan. 1980).
4. T.I. Kamins, K.F. Lee, and J.F. Gibbons, *IEEE Electron Device Lett.* **EDL-1**, 5 (Jan. 1980).
5. A.F. Tasch, Jr., T.C. Holloway, K.F. Lee, and J.F. Gibbons, *Electronics Lett.* **15**, 435 (5 July 1979).
6. N.M. Johnson, D.K. Biegelsen, and M.D. Moyer, *Proceedings of Symposium on Laser and Electron Beam Solid Interactions and Materials Processing*, November 1980 (Boston), in press.

TABLE 1

Effect of Surface Stabilization Treatments

| Treatment | Minimum Power For Large-Grain Structure (W) | Agglomeration Above (W) | Pits or Protrusions Above (W) | Allowable Power Range (W) |
|---|---|----------------------------|-------------------------------------|---------------------------------|
| ~60Å LPCVD Si ₃ N ₄ | 11 | >17 | None Seen | >6 |
| ~90Å LPCVD Si ₃ N ₄ | 8 | >17 | 10 | 2 |
| ~140Å LPCVD Si ₃ N ₄ | <8 | >17 | 9 | ≥1 |
| ~100Å APCVD Si ₃ N ₄ | 9 | >17 | 8 | 0 |
| 1100° N ₂ | 11 | 12 | | 1 |
| 1100° N ₂ + Oxide Etch | 11 | 10 | | 0 |
| 900° Ar/O ₂ (~34Å) | 11-12 | 11-13 | | 1 |
| 900° N ₂ /O ₂ (~38Å) | 11-12 | 11-12 | | ½ |
| 1000° N ₂ /O ₂ (~60Å) | 10-11 | 12 | | 1½ |
| 1000° Oxynitride | 11 | 13 | | 2 |

Manuscript submitted March 6, 1981;
revised manuscript received March 31, 1981.

Publication costs of this article were
assisted by Hewlett-Packard Laboratories.



Electrochemistry of Dimethyl Sulfite

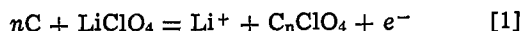
Su-Chee Simon Wang^{*,1} and Douglas N. Bennion^{*,2}

Chemical, Nuclear, and Thermal Engineering Department, University of California, Los Angeles, California 90024

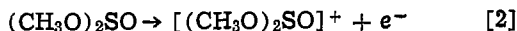
ABSTRACT

The reactions occurring in cells of the type $\text{Li}/\text{LiClO}_4, (\text{CH}_3\text{O})_2\text{SO}/\text{C}$ have been investigated. One charge plateau at 5.1V and two discharge plateaus, one about 4.2V and the other about 3V, were observed. The possible involvement of solvent, $(\text{CH}_3\text{O})_2\text{SO}$, in the cell reactions was studied by using nuclear magnetic resonance (NMR) to test the electrolytic solution in the cell compartments. Based on these experimental results, it is shown that the solvent is the primary reactant. It is also found that the solvent is degraded at a potential above 4.6V relative to a lithium wire reference electrode.

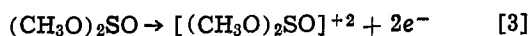
A battery system using a lithium negative electrode, an electrolytic solution of LiClO_4 and dimethylsulfite (DMSU), and a graphite positive electrode has been reported (1-4). It was proposed (2) that a lamellar compound of graphite formed at the positive electrode



Later results (4, 5) suggest that other reactions also occur during anodic operation of the graphite electrode and that DMSU is involved directly in the reaction. Deshpande and Bennion (5) proposed that DMSU oxidized during charging, forming radical cations



or



In this paper, the involvement of DMSU in electrochemical reactions and its suitability as a solvent for electrochemical systems is investigated.

Experimental

DMSU was vacuum distilled in the apparatus described by Tiedemann (6). Water content was reduced to less than 100 ppm. No reaction was observed between purified DMSU and lithium over two weeks of observation. Test solutions were 2.0M LiClO_4 in DMSU. The biggest source of impurity was H_2O with the LiClO_4 , even though the powdered LiClO_4 had been vacuum dried at 150°C for several weeks. The DMSU- LiClO_4 solution was stirred with lithium chips for more than one day to reduce active impurities further.

Natural graphite powder, 99.95% pure, 0.8 μm in size, originating from Madagascar was used for the test electrodes. Teflon molding powder and Union Carbide National C-34 glue were used as binders for the graphite powder and to hold it to either carbon cloth or titanium sheet backing plates.

Three views of the glass test cell are shown in Fig. 1. The test electrode and the lithium counterelectrode are held on the bottom of their respective compart-

ments by glass sleeves, 2 cm inside diameter, 1.25 cm high. Each compartment contained about 10 cm^3 of electrolytic solution. The reference electrode was a lithium wire. All experiments were run inside an argon atmosphere glove box. The electrical circuit is shown in Ref. (7). A Varian T-60 NMR Spectrometer and a Varian CFT-20 C13-NMR Spectrometer were used to analyze the electrolytic solution before and after cell operation. Further details are given elsewhere (7).

Three basic types of electrodes were tested. Types A and B are shown in Fig. 2.

(A) Titanium backing plate, titanium side walls forming a cavity of 0.38 mm thick and 1 cm^2 area. The cavity was filled with 0.0419g graphite powder with enough C-34 glue to make a thick paste. The electrode was cooked for 1.5 hr at 1000°C under vacuum. After cooling, a piece of nonwoven polypropylene cloth was placed over the cavity and held in place with a ring of 0.001 in. thick sheet Ti spot welded in place.

(B) Same as (A) except an extra sheet of 0.38 mm thick Ti was spot welded in place to allow a gap be-

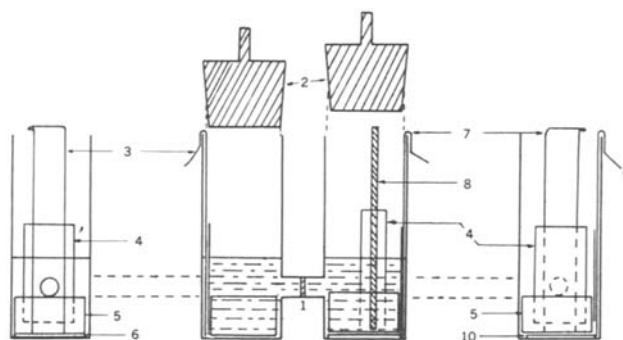


Fig. 1. The H-cell used in all experiments. 1. Glass frit; 2. polyethylene stoppers; 3. negative lead; 4. polypropylene masks for the three electrode leads; 5. glass sleeve; 6. negative electrodes; 7. positive lead; 8. reference electrode; 9. reference lead; 10. positive electrode.

* Electrochemical Society Active Member.

¹ Present address: General Motors Research Laboratory, Warren, Michigan 48090.

² Present address: Department of Chemical Engineering, Brigham Young University, Provo, Utah 84602.

Key words: discharge, solvents, electrode.

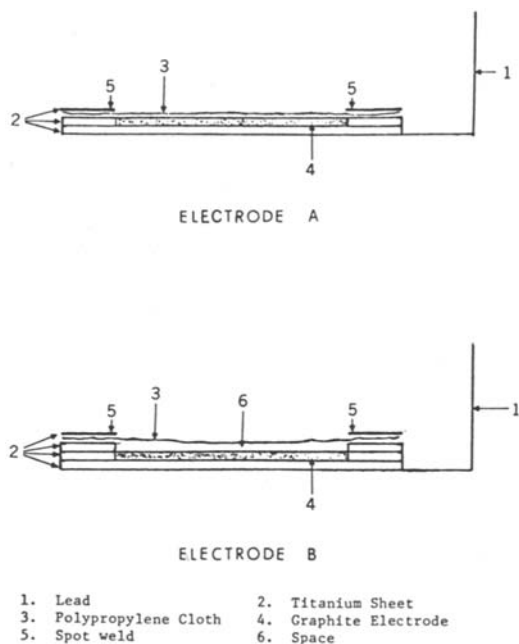


Fig. 2. The cross sections of electrode A and B

tween the sintered graphite and covering polypropylene cloth as shown in Fig. 2.

(C) This electrode was prepared by spreading 0.07g of graphite powder and C-34 glue over a 2 cm² area and cooking for 0.5 hr under vacuum.

All three electrode types had porous structures which adhered well to the backing materials. The resistance across the electrodes as measured with probe contacts was about 10Ω. Electrodes were soaked in DMSU-LiClO₄ solution for 4 hr before use.

The potential between the positive electrode and the lithium wire reference electrode was measured as a function of time at constant current.

Results and Discussion

There were two major, cathodic discharge plateaus, one beginning at 4.2V, the other at 3.0V. Current was 1.0 mA/cm². The upper plateau varied between a small shoulder up to one-third of the total discharge capacity. The lower plateau varied between 3.0 and 2.0V. Charging took place at a constant potential of 5.1V. A typical cycle is shown in Fig. 3.

Examining the upper plateau, the charge out is shown in Fig. 4 as a function of the charge in. Type A and B electrodes show fixed capacities of about 0.02

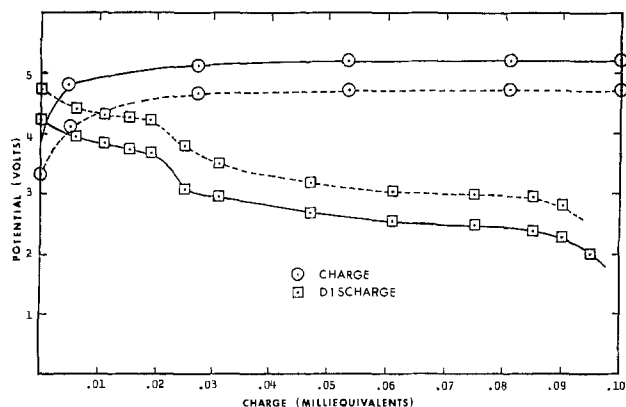


Fig. 3. Galvanostatic charge and discharge curves for the cell Li/LiClO₄, DMSU/C (electrode A), cycle 7, *i* = 1 mA/cm². — Galvanostatic potential; - - - - open-circuit potential.

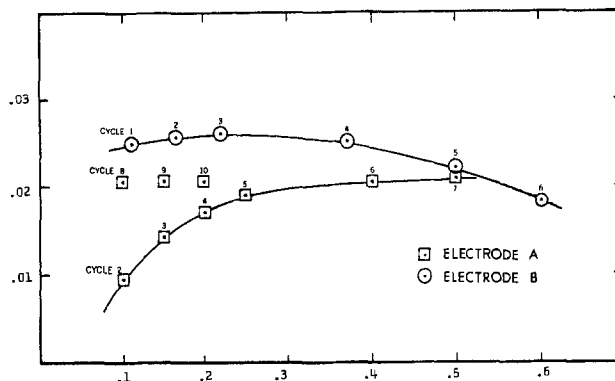


Fig. 4. Galvanostatic charge in vs. charge out curves for the cell Li/LiClO₄, DMSU/C (electrode A or B), *i* = 1 mA/cm². Upper discharge plateau only.

milliequivalents, independent of the quantity of charge put in. Electrode A increased in volume roughly proportional to the charge put in until the covering separator was stretched and restrained further expansion. Electrode B could expand more freely, and showed higher initial capacity. The swelling is believed to be an indication of increasing internal surface area. The primary anodic reaction product is believed to be an oxidized form of DMSU which adsorbs or possibly intercalates into the swelling graphite. On subsequent cathodic discharge, the adsorbed reaction product is hypothesized to react at near 4.2V to reform DMSU. No direct experimental evidence has yet been realized which allows direct confirmation of the primary anodic reaction product (PARP). It appears that the PARP desorbs and further reacts to form secondary products as discussed below. After 10 hr wet stand, the upper cathodic discharge plateau disappears.

Electrode type C was used to create reaction products in high enough concentration to detect. Anodic operation was begun at 2 mA/cm² after a short forming cycle of 0.1-0.05 milliequivalents. Much larger charge input was used compared to the earlier runs. The 4.2V cathodic discharge plateau was very small compared to the anodic charge plateau or the subsequent discharge at the 3.0V plateau. Samples were taken from positive and negative compartments at 5.4 and 13.49 milliequivalents, for example, during charging. The electrolytic solution volume was 10 cm³ in each compartment. Samples were sealed into nuclear magnetic resonance (NMR) tubes inside the argon filled glove box. Solution level in each compartment was kept constant by adding fresh solution to each compartment to replace the 1.0 cm³ removed as a sample. Results of the NMR spectra for the positive compartment are shown in Fig. 5. Four new peaks appeared and became larger as charging continued. Figure 6 shows an NMR spectra for the negative compartment. One new peak formed. Initially, the only hydrogen in the system is in the DMSU molecule. New peaks are due to altered structure of the basic DMSU molecule causing shifts in the resonance frequency for the hydrogen atoms. Thus, four reaction products have been identified for the anodic charging reaction. The NMR peaks which appear and grow with continued discharge are conclusive evidence that DMSU reacts anodically above 4.6V forming soluble reaction products.

A cathodic discharge half cycle at 2 mA/cm² was begun immediately after the 13.49 milliequivalents anodic cycle. Samples were taken, for example, after 4.9 and 6.9 milliequivalents of cathodic operation. The NMR spectra are shown in Fig. 5. Peaks 1, 3, and 4 diminish or disappear during cathodic operation and

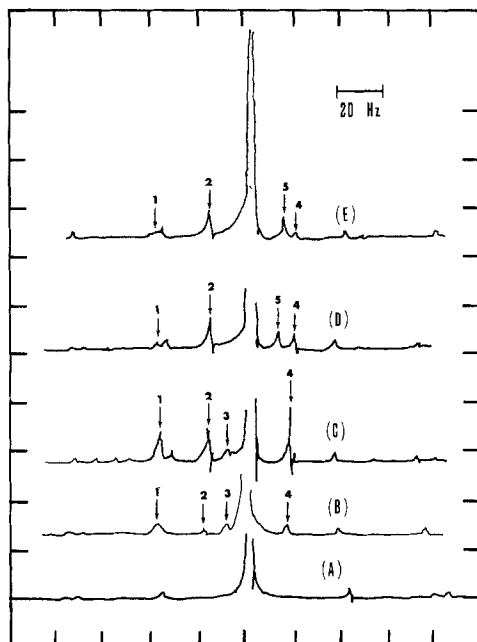


Fig. 5. NMR spectra of the electrolytic solutions: (A) before charging; (B) after 5.4 milliequivalents charged in; (C) after 13.49 milliequivalents charged in; (D) after 4.9 milliequivalents discharged following charging; (E) after 6.9 milliequivalents discharged following charging. Data for second cycle of a cell Li/LiClO₄, DMSU/C.

a new peak, labeled peak 5, appears. These observations indicate that at least one of the anodic products, peak 2, is not cathodically active. In addition, all or some of the products of the subsequent cathodic or discharging reaction are a material named peak 5 which is not DMSU. A complete, reversible charge-discharge cycle does not exist under the conditions tested. However, at least limited cyclic operation does occur.

To further examine cyclic operation of the DMSU reaction, multiple cycles were run consecutively. A

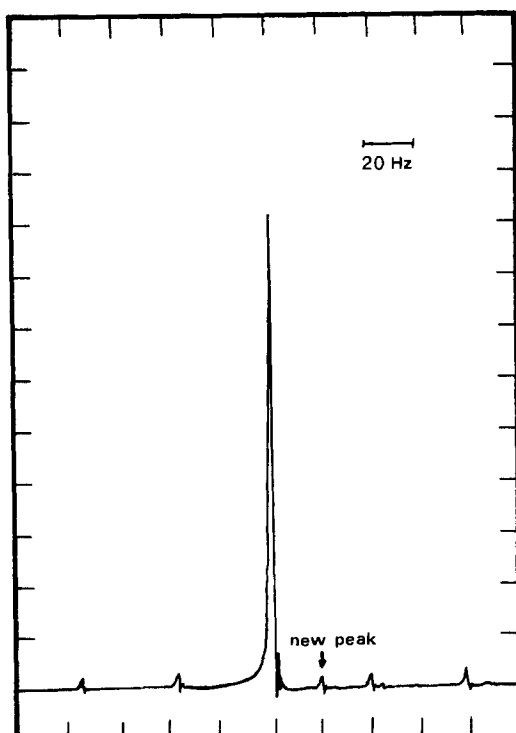


Fig. 6. NMR spectrum after 6.9 milliequivalents was charged out, cycle 2 of the cell Li/LiClO₄, DMSU/C (electrode C).

Table I. The positions and intensities of peaks in the C¹³ NMR spectrum after 9.44 milliequivalents were charged in, cycle 4 of the cell Li/LiClO₄, DMSU C (electrode C)

| Peak No. | Relative intensities | Positions (Hz) |
|----------|----------------------|----------------|
| 1 | 18 | 1998.8 |
| 2 | 14 | 1858.4 |
| 3 | 13 | 1826.2 |
| 4 | 14 | 1793.7 |
| 5 | 18 | 1482.2 |
| 6 | 14 | 1287.7 |
| 7 | 27 | 1282.0 |
| 8 | 19 | 1278.0 |
| 9 | 18 | 1272.9 |
| 10 | 300 | 1259.0 |
| 11 | 12 | 1151.2 |
| 12 | 13 | 271.4 |

type C electrode was operated anodically at 2.5 mA/cm² for 10.84 milliequivalents and then discharged cathodically to a 2.0V cutoff potential which allowed 6.3 milliequivalents of cathodic current to be passed. Samples were taken following the 3rd complete cycle and after 9.44 milliequivalents charged in at 2 mA/cm² on the anodic or first half of the 4th cycle. Peak 5 appears to persist following cathodic discharge, indicating that the species corresponding to peak 5 represents a species not or at most partially electrochemically active.

As a double check on DMSU involvement in the electrochemical reactions, a C¹³ NMR spectrum was run on the sample taken in the 4th cycle. Positions and intensities of peaks are shown in Table I. Peaks 2, 3, and 4 are for deuterium chloroform used to lock the spectrum during accumulation of signals. Peak 12 is for tetramethyl silane (TMS), used as the standard. Peak 10 is for DMSU. The remaining seven peaks are derivatives of DMSU which accumulate as cycling proceeds.

The accumulation of DMSU reaction products in the positive compartment and the appearance of a DMSU reaction product in the negative compartment indicates that at the extreme potentials investigated DMSU is degraded.

Conclusions

1. Lamellar compound of graphite formation is not an effective charge storage mechanism in competition with dimethylsulfite reactions at a positive electrode.
2. An upper cathodic plateau at 4.2V vs. Li/Li⁺ reference electrode is an electrochemically reversible reaction involving an adsorbed or intercalated primary reaction product formed by anodic oxidation of dimethylsulfite.
3. The primary reaction product of anodic oxidation of dimethylsulfite desorbs and forms secondary oxidation products, of which at least some are electrochemically reactive in subsequent cathodic, electrochemical reactions.
4. Some of the reaction products of cathodic and anodic reactions are not electrochemically active. Thus, a simply closed, complete secondary battery cycle does not appear to exist although numerous charge-discharge cycles are possible in an excess of dimethylsulfite.

Acknowledgment

Financial support by the Office of Naval Research is gratefully acknowledged.

Manuscript submitted Aug. 20, 1979; revised manuscript received March 31, 1981.

Any discussion of this paper will appear in a Discussion Section to be published in the June 1982 JOURNAL. All discussions for the June 1982 Discussion Section should be submitted by Feb. 1, 1982.

Publication costs of this article were assisted by the Office of Naval Research.

REFERENCES

1. J. Bessenhard and H. P. Fritz, *This Journal*, **119**, 1697 (1972).
2. J. S. Dunning, W. H. Tiedemann, L. Hsueh, and D. N. Bennion, *ibid.*, **118**, 1886 (1971).
3. Z. I. Mirza, M.S. Thesis, University of California, Los Angeles, California (1971).
4. R. K. Hebbar, M.S. Thesis, University of California, Los Angeles, California (1974).
5. S. L. Deshpande and D. N. Bennion, *This Journal*, **125**, 687 (1978).
6. W. H. Tiedemann, Ph.D. Dissertation, University of California, Los Angeles, California (1971).
7. S. S. Wang, M.S. Thesis, University of California, Los Angeles, California (1977).

Ionic Conductivity in Lithium and Lithium-Sodium Beta Alumina

J. L. Briant* and G. C. Farrington*,¹

General Electric Corporate Research and Development, Schenectady, New York 12301

ABSTRACT

This paper presents measurements of ionic conductivity in single crystals of Li⁺ and mixed Li⁺/Na⁺ beta alumina. The crystals were prepared by ion exchange of Na⁺ beta alumina crystals in LiCl, LiNO₃, or LiNO₃ with NaNO₃ added. The measured room temperature conductivity of Li⁺ beta alumina, about $3 \times 10^{-3} \Omega^{-1} \text{cm}^{-1}$, is higher than earlier values. The activation energy was found to be 0.24 eV from -80° to 400°C . Room temperature conductivities of Li⁺/Na⁺ beta alumina crystals pass through a minimum as the composition is varied from pure Na⁺ to pure Li⁺ beta alumina. The activation energy achieves a maximum at the same composition. The theory of Hendrickson and Bray for mixed-alkali conduction in glasses is adapted to explain this effect. The deleterious effect of water on lithium transport in beta alumina is also examined.

Many research efforts over the past 15 years have searched for a solid electrolyte with high room temperature Li⁺ conductivity. Although beta alumina was one of the first Li⁺ solid electrolytes investigated, earlier measurements of its conductivity were inconclusive. Reported room temperature conductivities varied from $1.3 \times 10^{-4} \Omega^{-1} \text{cm}^{-1}$ (d-c measurements) (1) to $8.3 \times 10^{-4} \Omega^{-1} \text{cm}^{-1}$ (dielectric loss) (2). In addition, Whittingham and Huggins (1) found an increase in the slope of the Arrhenius plot for the conductivity of lithium beta alumina around 180°C , the only such observation for a beta alumina isomorph. Table I summarizes the pre-exponential factors and activation energies found for Li⁺ beta alumina by dielectric loss, d-c conductivity, and tracer diffusion measurements. Figure 1 illustrates the discrepancies among these data.

Many other Li⁺ solid electrolytes have also been investigated. Shannon *et al.* (3) explored ionic conductivity in a variety of structures consisting of isolated polyhedra. Of the compounds they described, one of the best conductors is polycrystalline $\text{Li}_{0.8}\text{Zr}_{1.8}\text{Ta}_{0.2}\text{P}_3\text{O}_{12}$, which has a conductivity of $4.1 \times 10^{-6} \Omega^{-1} \text{cm}^{-1}$ at 25°C (extrapolated) and $9.1 \times 10^{-3} \Omega^{-1} \text{cm}^{-1}$ at 300°C (see Fig. 1). Hong (4) synthesized a new compound, $\text{Li}_{14}\text{Zn}(\text{GeO}_4)_4$ (LISICON), and reported it to have a conductivity of $1.2 \times 10^{-1} \Omega^{-1} \text{cm}^{-1}$ at 300°C . von Alpen (5) estimated the single crystal conductivity of LISICON by complex admittance analysis of polycrystalline LISICON samples. He found a much lower conductivity, $2 \times 10^{-6} \Omega^{-1} \text{cm}^{-1}$ at 50°C and $1.2 \times 10^{-2} \Omega^{-1} \text{cm}^{-1}$ at 200°C . Ionic conductivity in single crystals of Li_3N was measured by von Alpen *et al.* (6) and found to be 5.4×10^{-4} at 25°C . However, conductivity measurements on this material are complicated

by hydrogen doping (which enhances conductivity) and surface layers of LiOH and Li_2CO_3 (which degrade conductivity) (7). While Li_3N is the only lithium ion conductor shown to be stable in contact with molten lithium, it is unstable in contact with the atmosphere.

In 1977 Roth and Farrington (8) observed that certain mixed Li⁺/Na⁺ beta alumina polycrystalline ceramics (Li:Na about 1:1) have very high room temperature conductivities. They estimated the equivalent single crystal conductivity of mixed Li⁺/Na⁺ beta alumina (1:1) to be about $1 \times 10^{-3} \Omega^{-1} \text{cm}^{-1}$. Because this value was higher than the values of 1×10^{-4} to $8 \times 10^{-4} \Omega^{-1} \text{cm}^{-1}$ previously reported for pure Li⁺ beta alumina, they postulated that the increased conductivity of the mixed Li⁺/Na⁺ composition was due to a co-ionic effect. The initial goal of the present research effort was to confirm the earlier measurements of mixed Li⁺/Na⁺ beta alumina conductivity on single crystal instead of polycrystalline specimens. These values were indeed confirmed, but a much more interesting observation was also made, namely, that earlier measurements significantly underestimated the conductivity of pure Li⁺ beta alumina. We have found that the conductivity of pure Li⁺ beta alumina is about $3 \times 10^{-3} \Omega^{-1} \text{cm}^{-1}$ at 25°C . Li⁺ beta alumina is therefore the most conductive Li⁺ solid electrolyte yet reported. We have also found that the conductivities of mixed Li⁺/Na⁺ beta alumina compositions do not

Table I. Conductivity data reported for Li⁺ beta alumina

| Method | σ_0 ($\Omega^{-1} \text{cm}^{-1} \text{K}$) | E_A (eV) | Temperature range ($^\circ\text{C}$) | Ref. |
|---------------------|--|------------|--|------|
| A. D-C conductivity | 5.4×10^4 | 0.187 | -100 to 180 | (1) |
| B. D-C conductivity | 9.7×10^8 | 0.372 | 180 to 800 | (1) |
| C. Tracer diffusion | 3.0×10^4 | 0.379 | 200 to 400 | (19) |
| D. Dielectric loss | 5.9×10^6 | 0.376 | 7 to 67 | (2) |
| E. This work | 1.75×10^4 | 0.265 | -73 to 400 | |

* Electrochemical Society Active Member.

¹ Present address: Department of Materials Science and Engineering, University of Pennsylvania, Philadelphia, Pennsylvania 19104.

Key words: crystals, conduction, activation energy.

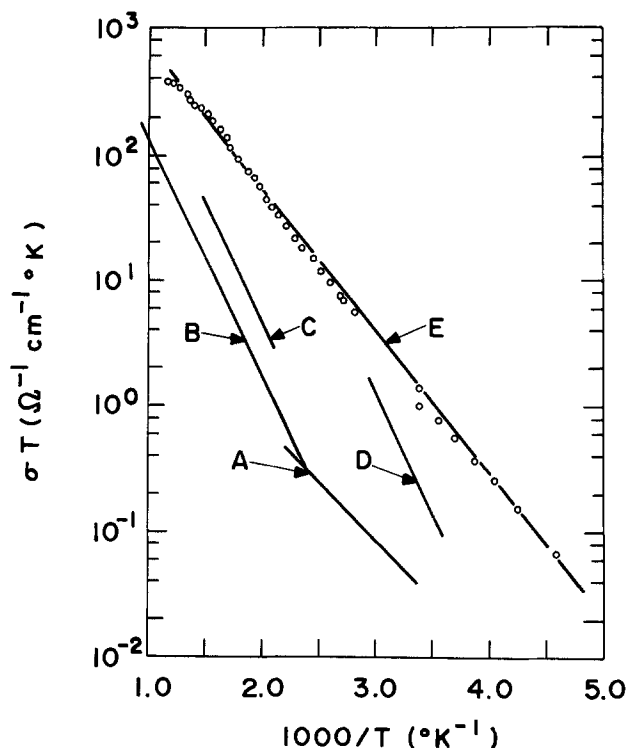


Fig. 1. Conductivity of lithium beta alumina: A and B; d-c measurements (1); C: tracer diffusion (19); D: dielectric loss (2); E: this work.

vary linearly between pure Na^+ and Li^+ beta alumina conductivities, but instead go through a minimum. This effect is analogous to mixed alkali conduction in glasses and consistent with the properties of mixed Na^+/K^+ beta aluminas (2, 9) and Na^+/K^+ beta and beta" gallates (9), analogous structures to the beta and beta" aluminas.

In this paper we present our results on three topics: (i) The conductivity of pure lithium beta alumina; (ii) the conductivity of mixed Li^+/Na^+ beta alumina; and (iii) the influence of water on ionic conductivity of all of these materials. Discussions of each topic follow the results in each section. We also offer a likely explanation for the confusion of earlier measurements. No review of the beta alumina structure is included. We refer readers interested in detailed discussions of the structure of sodium beta alumina to several other papers (10, 11, 12).

Experimental

Single crystal samples (typically $1 \times 2 \times 4$ mm) of sodium beta alumina were cut from a single crystal boule grown by the Union Carbide Corporation. The weight changes observed for samples of this type upon ion exchange of sodium by potassium or silver indicate that their compositions vary from about $1.13 \text{ Na}_2\text{O} \cdot 11 \text{ Al}_2\text{O}_3$ to $1.24 \text{ Na}_2\text{O} \cdot 11 \text{ Al}_2\text{O}_3$. Other investigators (13, 14) have observed that samples cut from the outside of Union Carbide sodium beta alumina boules have lower Na_2O contents than samples cut from the center. Lithium beta alumina samples were prepared by ion exchange in highly pure LiCl at 675°C . Mixed Li^+/Na^+ beta alumina samples were prepared by ion exchange in molten LiNO_3 with 0-1% NaNO_3 added. The extent of ion exchange for each sample was determined by measuring its weight before and after exchange.

Single crystals were mounted on alpha Al_2O_3 substrates for complex impedance measurements. Conductivity was measured using blocking Au electrodes and a-c complex impedance analysis. Samples were dried at 350°C in a dry He atmosphere in the measurement cell before measurement and maintained in this

He atmosphere during measurement. Details of these techniques have been described elsewhere (15).

Results and Discussion

Ionic conductivity in lithium beta alumina.—Our results indicate that lithium beta has the highest ionic conductivity at 25°C of all lithium ion solid electrolytes yet reported. The conductivities of five crystals measured at 25°C varied from $2.1 \times 10^{-3} \Omega^{-1} \text{ cm}^{-1}$ to $3.7 \times 10^{-3} \Omega^{-1} \text{ cm}^{-1}$ (see Table II). Since all of the samples were prepared by ion exchange, they could have contained variable amounts of residual sodium (1-2%) or slight concentrations of secondary alkali or divalent ions. Such small variations in composition or in stoichiometry might reasonably have produced the range of conductivities we observed. We will demonstrate that the variation is not due to thermal aging effects.

The conductivities of three samples were measured as a function of temperature from 25° to 400°C , and two others were measured from -80° to 400°C . The temperature dependence of conductivity for each sample followed a simple Arrhenius relationship (Eq. [1]). Activation energies (E_A) ranged from 0.23 to 0.25 eV with an average value of 0.24 eV. The straight-line Arrhenius behavior observed here contrasts with the two-line behavior reported by Whittingham and Huggins (1), who found a change in activation energy around 180°C (see Fig. 1)

$$\sigma T = \sigma_0 \exp(-E_A/kT) \quad [1]$$

We have also briefly examined the influence of heating to 675°C upon ionic conductivity in Li^+ beta alumina. These experiments were suggested by the work of Whittingham and Huggins (1), who found that annealing Li-exchanged beta alumina above 800° produced a marked decrease in conductivity, and of Dubin *et al.* (16), who found that heating Li^+/Na^+ beta alumina at 900°C for 4 hr results in the trapping of a fraction of lithium ions in immobile sites presumably located in the spinel block. In our experiments heating to 675°C had no significant influence upon conductivity. Two experiments were carried out. Although most samples were exchanged in LiCl at 675°C for about 1 hr, two samples were exchanged for about 16 hr. Their conductivities at 25°C and activation energies are comparable to values observed for crystals exchanged for only 1 hr. Another crystal was exchanged for 30 min, heated in air at 675°C for six days, and then re-exchanged for 30 min. Its conductivity and activation energy are also comparable. If trapping does occur at 675°C , it influences conductivity very slowly.

The high conductivity of lithium beta alumina focuses attention on several aspects of the microscopic mechanism of Li^+ migration in the beta alumina structure. Previous investigators have explained the apparently low conductivity of lithium beta alumina by noting that Li ions are too small to occupy sites on the conducting plane and bond simultaneously to both close-packed oxygen layers. Therefore, Li^+ should be displaced toward one or the other close-packed layers. Because of their high charge to radius ratio, lithium

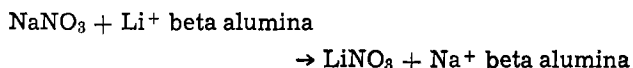
Table II. Conductivity of Li^+ beta alumina

| Sample | Exchange conditions ^a | $\sigma_{25^\circ\text{C}}$ ($\Omega^{-1} \text{ cm}^{-1}$) | σ_0 ($\Omega^{-1} \text{ cm}^{-1} \text{ K}$) | E_A (eV) |
|---------|----------------------------------|--|--|---------------|
| 1 | 18 | 3.7×10^{-3} | 7.9×10^3 | 0.23 |
| 2 | 2 | 2.3×10^{-3} | 7.2×10^3 | 0.24 |
| 3 | 16 | 2.1×10^{-3} | 9.7×10^3 | 0.25 |
| 4 | 1 | 2.2×10^{-3} | 6.9×10^3 | 0.24 |
| 5 | 2 | 3.3×10^{-3} | 10.4×10^3 | 0.24 |
| Average | | 2.7×10^{-3} | 8.4×10^3 | 0.24 |

^a Hours in LiCl at 675°C .

ions are more polarizing than other alkali ions. Li ions therefore can form stronger covalent bonds with the oxygen atoms in the conducting plane of beta alumina. Covalent bonding increases the activation energy for conductivity and decreases the conductivity at 25°C. The only study (17) of the structure of beta alumina containing lithium ions, which was carried out on a mixed (1:1) Li⁺/Na⁺ composition, has indeed located Li ions off the conduction plane above the mid-oxygen sites bonded to either of the two close-packed oxygen layers. The Li⁺ diffusion pathway probably then involves ionic hopping along the close-packed oxygen layers or the movement of Li⁺ from one close-packed oxygen layer to the other across the conduction plane. If Li⁺ ions hop between positions above and below the conduction plane, this motion should give rise to a dielectric dispersion in the c direction of the crystal. Anderson (18) has reported observing the effect of Li⁺ ion hopping parallel to the "c" axis in the low energy excitation spectrum of Li⁺ beta alumina. Off-plane bonding can explain why the activation energy for conductivity in Li⁺ beta alumina (0.24 eV) which we observed is considerably larger than that of Na⁺ beta alumina (0.16 eV).

Ionic conductivity in mixed Li⁺/Na⁺ beta alumina.—In 1967 Yao and Kummer (19) published classic data on the ion-exchange properties of Na⁺ beta alumina in mixed NaNO₃-XNO₃ melts (X = Ag, Li, K, Tl, Rb, Cs). They demonstrated that thermodynamic equilibrium at 300°-350°C favors the reaction



Because of the trace quantity of sodium in nominally pure LiNO₃, Na⁺ beta alumina crystals immersed in LiNO₃ become only 60-80% exchanged to Li⁺ beta alumina. Addition of 1% NaNO₃ to nominally pure LiNO₃ lowers the extent of exchange to about 35%. Small variations in such data from melt to melt are presumably due to variations in the amount of sodium impurity.

The results of our conductivity measurements on Li⁺/Na⁺ beta alumina are summarized in Table III. Activation energy and room temperature resistivity as functions of composition are shown in Fig. 2 and 3. Both the activation energies and room temperature resistivities pass through maxima at compositions of about 70% Li, 30% Na.

All of the Arrhenius plots which we measured are straight lines except one (sample D, Fig. 4). This sample was exchanged in LiNO₃ and had a composition of 75% Li, 25% Na. Its Arrhenius plot is very similar to that described by Whittingham and Huggins for Li⁺ beta alumina. The room temperature conductivities are comparable and both plots have a change in activation energy from 0.18 eV below 180°C to 0.38 eV above 180°C. Such unusual behavior could be the effect of either this particular mixed composition or of hydration. We suggest that the discrepancies in earlier data are due to measurement of samples with uncertain Li⁺/Na⁺ compositions and uncertain states of hydration.

Table III. Conductivity of Li⁺/Na⁺ beta alumina

| Sample | Compo- sition (% Li) | $\sigma_{25^\circ\text{C}}$ ($\Omega^{-1}\text{cm}^{-1}$) | σ_0 ($\Omega^{-1}\text{cm}^{-1}$) | E_A (eV) |
|---------|----------------------------|--|---|------------------------------------|
| | 0 | 2.5×10^{-2} | 3.6×10^3 | 0.16 |
| A | 12 | 6.7×10^{-3} | 2.5×10^3 | 0.18 |
| B | 39 | 1.5×10^{-3} | 9.5×10^2 | 0.26 |
| C | 50 | 4.9×10^{-4} | 4.9×10^2 | 0.27 |
| D | 75 | 2.1×10^{-4} | 6.8×10^1 | 0.18 below 180° 0.38 above 180° |
| E | 84 | 4.2×10^{-4} | 6.1×10^2 | 0.28 |
| Average | 100 | 2.7×10^{-3} | 8.4×10^3 | 0.24 |

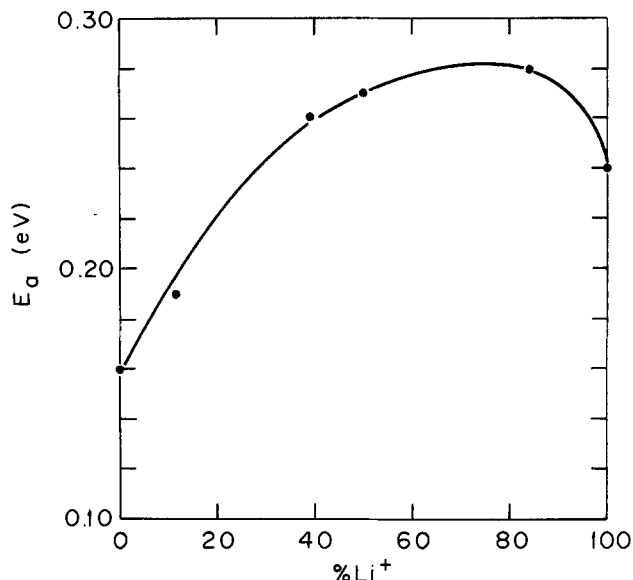


Fig. 2. Activation energy for conduction as a function of Li-Na beta alumina composition.

The only other investigation of the ionic conductivity of mixed Li⁺/Na⁺ beta alumina was described by Kaneda *et al.* (20). They measured the conductivity of a single crystal of 18% Li⁺, 82% Na⁺ beta alumina prepared by ion exchange of Union Carbide sodium beta alumina, the same starting material which we used. They found a room temperature resistivity of about 160 $\Omega\text{-cm}$ and a straight-line Arrhenius plot with an activation energy of 0.23 eV. The resistivity is consistent with ours but their activation energy is somewhat higher.

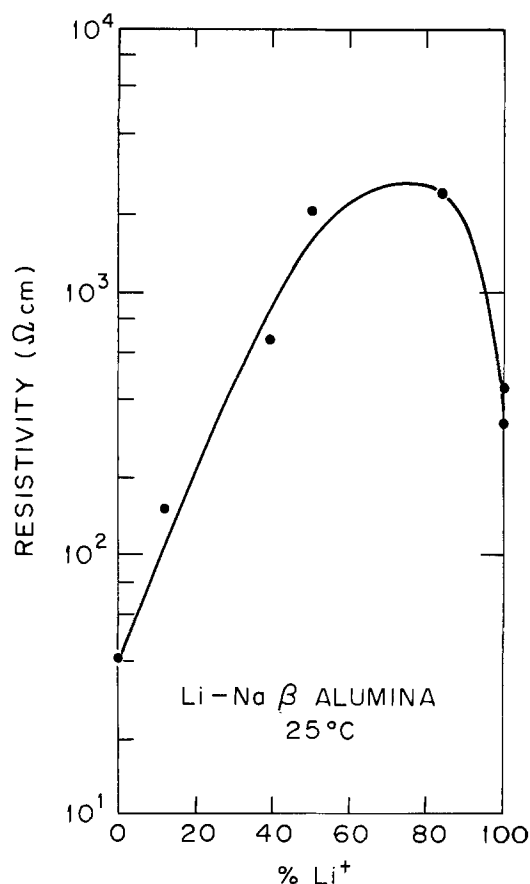


Fig. 3. Resistivity at 25°C as a function of Li-Na beta alumina composition.

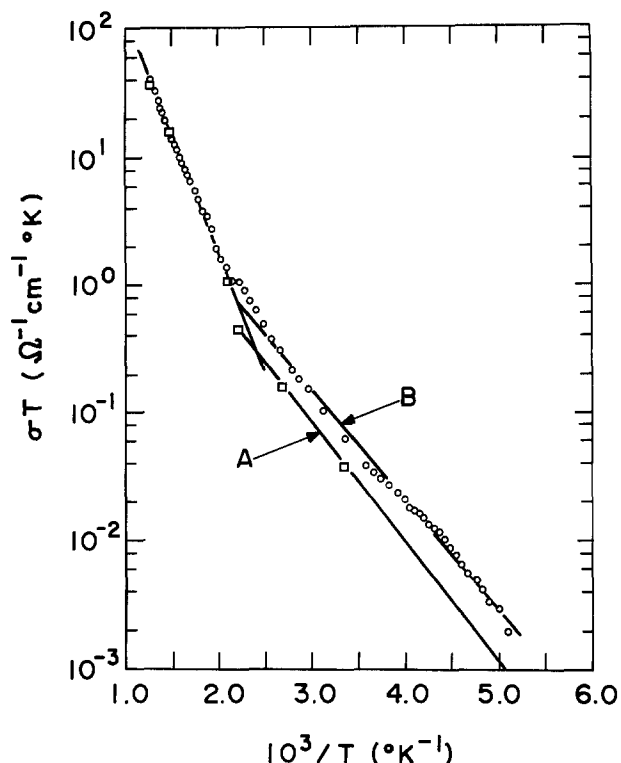


Fig. 4. Examples of nonlinear Arrhenius plots. A: sample composition reported to be pure lithium beta alumina (1); B: sample composition was 75% Li, 25% Na (this work).

The conduction properties of mixed Li^+/Na^+ beta alumina are consistent with those of Na^+/K^+ beta and beta" gallates (9), Na^+/K^+ beta alumina (2, 9), and mixed alkali conduction in glasses. In all these materials the resistivities and activation energies for conduction pass through maxima at some intermediate composition.

Although the mixed-alkali effect in glasses is best known as it applies to conductivity, it also can be seen in many other properties including viscosity, density, transformation temperature, softening temperature, chemical durability, and mechanical properties. The magnitude of the effect depends on the difference between the masses of the alkalis. Many theories have been proposed which can account for the mixed alkali influence on certain, but not all properties. However, Hendrickson and Bray (21) have proposed an attractive theory which explains the mass dependence of the effect and has the potential of accounting for the non-linearity in all these properties. Their idea is simple and can be applied easily to Li^+/Na^+ beta alumina.

Hendrickson and Bray consider two types of alkali ions residing in sites in a glass network. These ions oscillate about the energy minima of their sites in thermal equilibrium with their environment. Since each positively charged ion in its negatively charged site forms an electric dipole, the vibration of each ion produces an oscillating dipole field in its neighborhood. Other nearby ions respond to this field. Each of these oscillating dipoles has a natural resonant frequency determined by the ion mass, temperature, and the curvature of the energy minimum. Different alkali ions (and even different isotopes) will clearly have different frequencies. While like neighboring ions will drive each other at resonant frequency, unlike ions will drive each other at off-resonant frequencies. Hendrickson and Bray have derived both classical and quantum mechanical expressions for the interaction energy and have shown that it is in general negative for unlike ions. (It is zero for identical ions.) Therefore the potential energy wells of mixed ion pairs are deeper and

the activation energy for ion motion should be larger.

This theory can provide an explanation of the mixed-alkali effect in beta alumina. The mobile alkali ions in beta alumina reside in sites in the layered conduction planes. While the sites form an ordered crystalline array, occupancy of the sites is believed to be considerably disordered. Furthermore, beta alumina contains excess alkali (in this case 13-24% excess) over the composition of one alkali ion per unit cell in the conduction plane. Therefore, while three-quarters of the cells will be singly occupied, one-quarter will be doubly occupied. A widely accepted calculation by Wang *et al.* (22) has shown that the activation energy for motion of an ion in a singly occupied cell of Na^+ beta alumina is very high, about 2 eV. However, the activation energy calculated for motion of the interstitial pairs in doubly occupied cells is much lower (0.14 eV) and agrees well with experimental data (0.15-0.16 eV). It is therefore likely that such interstitial pairs provide most of the ion motion in beta alumina. In Li^+/Na^+ beta alumina many such pairs can be expected to consist of unlike ions, which will interact as off-resonant oscillating dipoles as in glasses. Indeed the problem of small variations in the curvature of the energy minima in glasses has been eliminated in beta alumina, because the sites are identical crystallographically. Therefore the activation energies and resistivities of Li^+/Na^+ beta alumina compositions should pass through maxima.

This theory also predicts an interesting effect which has already been observed in the mixed Na^+/K^+ beta and beta" gallate system. It predicts that the mixed ion effect should be substantially reduced in the beta" structure from the beta structure. Since there are two low energy ion sites in each plane unit cell of the beta" structure while there is only one in the beta structure, all excess alkali ions can be accommodated in these low energy sites in the beta" structure and interstitial pairs are less likely to form. The predominant conduction mechanism is expected to be individual ion hopping. Ion-pair interactions and consequently the mixed alkali effect are expected to be considerably reduced. Chandrashekar and Foster have indeed observed that Na^+/K^+ beta gallate shows a more pronounced mixed alkali effect than Na^+/K^+ beta" gallate in both conductivity and activation energy (9).

Influence of H_2O on conductivity in lithium beta alumina.—Kline *et al.* (23) have previously reported that exposure of sodium beta alumina powder to water vapor results in a broadening of the NMR line associated with sodium ion motion. Heating the hydrated sample above about 200°C restores a normal sodium ion spectrum. Yao and Kummer (19) have also indicated, on the basis of infrared absorption measurements, that water appears to reversibly intercalate into the conduction planes of lithium and sodium beta alumina.

We have found that the conductivities of lithium beta alumina crystals at 25°C decrease steadily when exposed to atmospheric humidity. Heating to 350°-400°C results in a constant high conductivity. In separate thermogravimetric analysis experiments we found that powdered samples of lithium beta alumina reversibly absorb and desorb about 3 weight percent water when exposed to 10 Torr water vapor partial pressure at 25°C. The water is reversibly lost in a single dehydration step around 250°C. Our data show that high conductivity is only observed for carefully dried samples of lithium beta alumina.

Furthermore, the hydration of Li^+ beta alumina crystals distorts the shapes of their complex impedance and admittance plots and can even render them uninterpretable. Well-dried specimens exhibit classically shaped and easily interpreted complex impedance and admittance plots.

Conclusions

When small single crystals of sodium beta alumina are immersed in very pure molten LiCl at 675°C, essentially complete ion exchange takes place. The product, lithium beta alumina, has a lithium ion conductivity at 25°C of about 3×10^{-3} (Ω cm)⁻¹. The variation of the conductivity of lithium beta alumina with temperature follows a straight line Arrhenius plot from -80° to 400°C with an activation energy of 0.24 eV. Lithium beta alumina hydrates rapidly upon exposure to water vapor at 25°C. Hydration dramatically decreases its conductivity. High conductivity is regained by heating at 350°C. It is possible that incomplete ion exchange or incomplete dehydration contributed to the higher resistivities reported earlier for Li⁺ beta alumina (1, 2, 19).

The conductivity of mixed Li⁺/Na⁺ beta alumina displays the classic mixed alkali effect. At 25°C it goes through a minimum of 2×10^{-4} (Ω cm)⁻¹ at an approximate composition of Li_{0.93}Na_{0.37}Al₁₁O_{17.12}. The conductivities of the mixed compositions also follow straight line Arrhenius plots over the range of our measurements (-80°-400°C). Hendrickson and Bray's theory of the mixed alkali effect can be adapted to explain the resistivity maximum of Li⁺/Na⁺ beta alumina.

Although lithium beta alumina is an exceptionally good lithium ion conductor, it cannot be used in direct contact with molten lithium metal. As are essentially all Li⁺ solid electrolytes, lithium beta alumina is rapidly reduced by molten lithium. At elevated temperatures, lithium beta alumina could not be used in the presence of low lithium activity, perhaps buffered from direct contact with lithium by a molten salt. At lower temperatures, lithium beta alumina could function well as a separator in lithium nonaqueous electrolyte cells. Solid-state cells with direct contact between lithium and lithium beta alumina should also be stable, since slow kinetics should preclude significant lithium/electrolyte reactions.

Finally, in considering applications of lithium beta alumina, we should emphasize that the conductivities reported in this paper are single crystal values. Because single crystals of beta alumina conduct in only two dimensions and cleave readily, polycrystalline membranes must be used in practical applications. Polycrystalline ceramics contain grain boundaries which introduce additional impedance to ion transport. Conductivities attained in actual solid electrolyte devices are therefore typically lower (2-10³ times) than those observed for single crystals.

Manuscript submitted Oct. 6, 1980; revised manuscript received March 18, 1981.

Any discussion of this paper will appear in a Discussion Section to be published in the June 1982 JOURNAL. All discussions for the June 1982 Discussion Section should be submitted by Feb. 1, 1982.

Publication costs of this article were assisted by General Electric Company.

REFERENCES

1. M. S. Whittingham and R. A. Huggins, in "Solid State Chemistry," R. S. Roth and S. J. Schneider, Jr., Editors, p. 148, Spec. Publ. 364, National Bureau of Standards, Washington, D.C. (1972).
2. R. H. Radzilowski, Y. F. Yao, and J. T. Kummer, *J. Appl. Phys.*, **40**, 4716 (1969).
3. R. D. Shannon, B. E. Taylor, A. D. English, and T. Berzins, *Electrochim. Acta*, **22**, 783 (1977).
4. H. Y-P. Hong, *Mater. Res. Bull.*, **13**, 117 (1978).
5. U. von Alpen, M. F. Bell, and W. Wichelhaus, *Electrochim. Acta*, **23**, 1395 (1978).
6. U. von Alpen and G. Muller, Abstract 19, p. 55, The Electrochemical Society Extended Abstracts, Atlanta, Georgia, Oct. 9-14, 1977.
7. A. Hooper, T. Lapp, and S. Skaarup, *Mater. Res. Bull.*, **14**, 1617 (1979).
8. W. L. Roth and G. C. Farrington, *Science*, **196**, 1332 (1977).
9. G. V. Chandrashekhara and L. M. Foster, *Solid State Commun.*, **27**, 269 (1978).
10. C. R. Peters, M. Bettman, J. W. Moore, and M. D. Glick, *Acta Crystallogr. B*, **27**, 1826 (1971).
11. C. A. Beevers and M. A. Ross, *Z. Kristallogr.*, **97**, 59 (1937).
12. W. L. Roth, F. Reidinger, and S. LaPlaca, in "Superionic Conductors," G. D. Mahan and W. L. Roth, Editors, p. 223, Plenum, New York (1976).
13. L. M. Foster, in "Fast Ion Transport in Solids," P. Vashishta, J. N. Mundy, and G. K. Shenoy, Editors, p. 249, North-Holland, New York (1979).
14. K. K. Kim, J. N. Mundy, and W. K. Chen, *J. Phys. Chem. Solids*, **40**, 743 (1979).
15. J. L. Briant and G. C. Farrington, *J. Solid State Chem.*, **33**, 385 (1980).
16. R. R. Dubin, J. S. Kasper, J. B. Bates, and T. Kaneda, in "Fast Ion Transport in Solids," P. Vashishta, J. N. Mundy, and G. K. Shenoy, Editors, p. 361, North-Holland, New York (1979).
17. B. C. Tofield and G. C. Farrington, *Nature*, **278**, 438 (1979).
18. A. C. Anderson, in "Fast Ion Transport in Solids," P. Vashishta, J. N. Mundy, and G. K. Shenoy, Editors, p. 255, North-Holland, New York (1979).
19. Y-F. Y. Yao and J. T. Kummer, *J. Inorg. Nucl. Chem.*, **29**, 2453 (1967).
20. T. Kaneda, J. B. Bates, J. C. Wang, and H. Engstrom, in "Fast Ion Transport in Solids," P. Vashishta, J. N. Mundy, and G. K. Shenoy, Editors, p. 371, North-Holland, New York (1979).
21. J. R. Hendrickson and P. J. Bray, *Phys. Chem. Glasses*, **13**, 107 (1972).
22. J. C. Wang, M. Gaffari, and S.-i. Choi, *J. Chem. Phys.*, **63**, 772 (1975).
23. D. Kline, H. S. Story, and W. L. Roth, *J. Chem. Phys.*, **57**, 5180 (1972).

On the Stability of Boron Nitride with Lithium Alloy Electrodes in Molten Salt Cells

Ram A. Sharma* and Thompson G. Bradley*

General Motors Research Laboratories, Electrochemistry Department, Warren, Michigan 48090

ABSTRACT

Experiments were carried out to determine the stability of boron nitride separator material in molten salt cells using lithium chloride-potassium chloride (LiCl-KCl) eutectic electrolyte and two stainless steel screen electrodes. The potentials of these electrodes were set by two separate electrical circuits and a lithium-silicon (Li-Si) reservoir electrode. The boron nitride separator was found stable at potentials above -136 mV with respect to a lithium-aluminum reference electrode at 700 K. The separator reacted with lithium and became conductive at potentials more reducing than ~ -200 mV. Formation of a boride and Li_3N led to the conductivity.

Compact cells comprising lithium-aluminum or lithium-silicon negative electrodes, iron disulfide positive electrodes, lithium chloride-potassium chloride electrolyte, and boron nitride separators are undergoing development for batteries of high specific energy and high specific power (1-3). In the case of the lithium-aluminum electrode, the cell operates at 700 K in the α - β region of the lithium-aluminum phase diagram (4) at a negative electrode potential of 290 mV with respect to pure lithium (5). Some of the cells lasted more than 10,000 hr (1) and post-test analysis showed that failure was not due to chemical attack of the boron nitride separator by the lithium-aluminum electrode (6).

In the case of the lithium-silicon electrode, the cell operates at 700 K in the composition regions, $\text{Si-Li}_2\text{Si}$, $\text{Li}_2\text{Si-Li}_{21}\text{Si}_3$, and $\text{Li}_{21}\text{Si}_3\text{-Li}_{15}\text{Si}_4$. The respective plateaus of potential corresponding to these composition regions occur at 330, 281, and 154 mV with respect to pure lithium (5). During charging of the cell, high self-discharge is observed in the region where $\text{Li}_{15}\text{Si}_4$ is formed. Boron nitride has been observed to react with pure lithium at ~ 700 K (6). It may also react with $\text{Li}_{15}\text{Si}_4$ to form a conductive boride permitting self-discharge.

This investigation was carried out to develop a technique suitable for evaluating separator materials for lithium-alloy/iron disulfide cells in general and to determine the stability of boron nitride in particular, at the potential of the $\text{Li}_{21}\text{Si}_3\text{-Li}_{15}\text{Si}_4$ plateau and, further, to determine the range of potentials at which boron nitride is stable. These data will help select compositions of the negative electrode which will allow cell operation with minimal self-discharge.

Experimental

All of the experimental work was done in a helium atmosphere glove box. The data were obtained by a cell (Fig. 1) in which two stainless steel screen electrodes and lithium chloride-potassium chloride electrolyte were used. The electrodes sandwiched the boron nitride separator, and the potentials were set by two separate electrical circuits and a lithium-silicon reservoir (counter) electrode in the cell. The electrical circuit is shown in Fig. 2. This arrangement allowed us to subject the boron nitride to various potentials (i.e., various lithium activities) and to monitor the lithium consumed in the reaction with boron nitride.

For preparing the reservoir (counter) electrode, a nickel current collector (98% porous) was placed in a circular stainless steel chamber one face of which was already closed by spot-welding a double layer of

stainless steel screens (400 mesh followed by 150 mesh). The chamber was vibration-loaded with 60/100 mesh particles of Li_2Si and its open face was closed by spot-welding a double layer of the screens. Complete details of the electrode and Li_2Si preparation are described in Ref. (7). The electrode was 3.5 cm in diameter and of 2.6 A · hr capacity.

Each screen electrode was made by spot-welding a stainless steel screen (150 mesh) onto a stainless steel ring (2.5 cm diam). They were cleaned by acetone and deionized water rinses in an ultrasonic cleaner.

A lithium-aluminum reference electrode whose composition was always maintained in the α - β phase region (4) was used. Preparation of the reference electrode is given in the Appendix and the potential with respect to pure lithium is given (5) by the equation

$$V(\text{mV}) = 464.438 - 0.2488T \quad [1]$$

The boron nitride cloth was 2 mm thick, had twill weave, and was purified by vacuum treatment as described in Ref. (6). The cloth was impregnated with electrolyte at ~ 725 K under vacuum.

The LiCl-KCl eutectic electrolyte mixture was prepared using 99.6% pure lithium chloride and 99.9% pure potassium chloride. The mixture was purified by bubbling chlorine through the melt at ~ 725 K for about 14.5 msec and subsequently scavenging the chlorine by bubbling helium for about 3.6 msec (5).

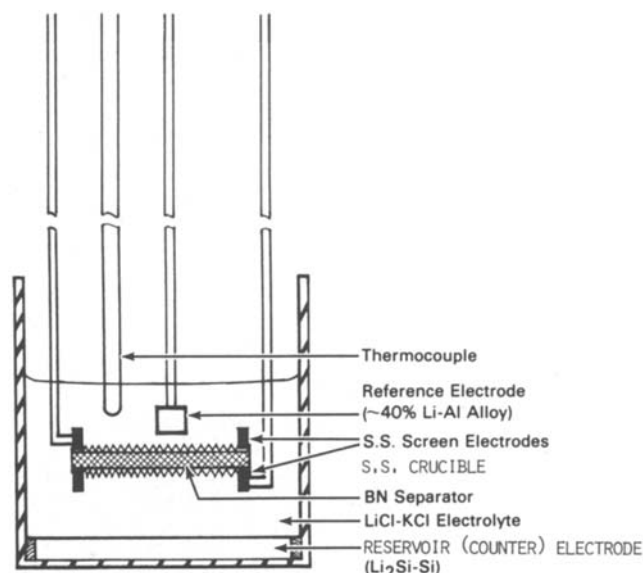
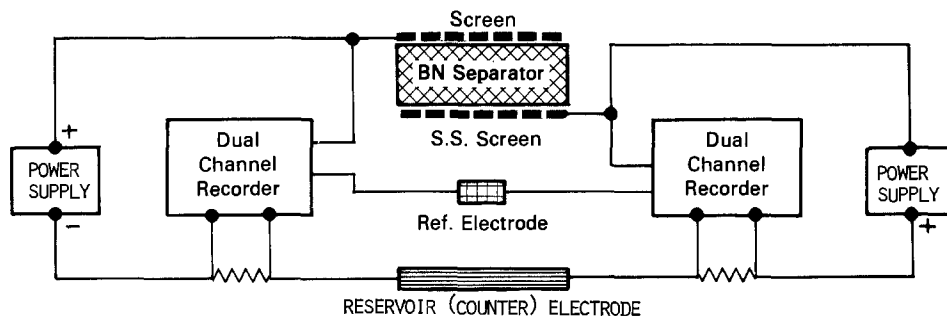


Fig. 1. Schematic diagram of the cell

* Electrochemical Society Active Member.

Key words: BN, separator, fused salt, corrosion.

Fig. 2. Schematic diagram of the circuitry.



A tubular furnace (150 mm high, 75 mm diam) was used in conjunction with a variable transformer to heat the cell. Chromel-Alumel thermocouples and a millivolt potentiometer were used for temperature measurements. The other electrical instruments included two d-c power supplies and two dual-channel recorders for measuring current and potentials. In addition, two digital meters were used to check the voltages and currents recorded by the dual-channel recorders.

Procedure

About 250g of the electrolyte was placed in the stainless steel container with the reservoir (counter) electrode attached. The container was inserted into a quartz enclosure in the furnace. The electrolyte was heated to the operating temperature. The screen electrodes with the boron nitride separator, reference electrode, and thermocouple were positioned in the melt. After thermal equilibrium, the top screen electrode (anode) was set as 0.5V or 1.5V with respect to the lithium-aluminum reference electrode,¹ and the bottom screen electrode (cathode) was held at the desired potential. Steady-state currents to maintain the potentials at the screen electrodes were measured. In the absence of electronic conductivity in the separator the cathodic current in the bottom screen supports two electrochemical phenomena. These are the scavenging of impurities and the production of lithium which either is transported by diffusion and convection processes to the bulk electrolyte or reacts with the boron nitride separator. The reaction with boron nitride is distinguished from the other phenomena by comparison of currents measured under two types of experiments. In the first type, base level currents were measured with the boron nitride contacting only the anode. This was done to preclude the reaction of the boron nitride with lithium while maintaining the same potentials and hydrodynamic conditions as for the subsequent measurements. In the second type of experiments carried out to study the boron nitride reaction with lithium, the boron nitride was in contact with both the cathode and anode or only with the cathode.

Results and Discussion

Base-level current data are given in Table I and Fig. 3a. In order to obtain these data, the bottom screen was set at 1.5V and the top screen was set at potentials between -75 and -280 mV. The values are averaged from three sets of readings taken over a period of 1350 ksec. Cathodic current to deposit lithium on a screen is positive in the table and anodic current to remove lithium from a screen is negative.

Steady-state current data for various imposed potentials of the bottom screen electrode (cathode) at 725 K when both screens were in contact with the boron nitride cloth are also given in Table I and presented graphically in Fig. 3b. The top screen (anode) was held at 500 mV. Upon setting the bottom screen (cathode) potential, the current surged and then characteristically tapered off. But at lower potentials (~ -267

¹ Henceforth all of the potentials will be given with respect to the lithium-aluminum reference electrode.

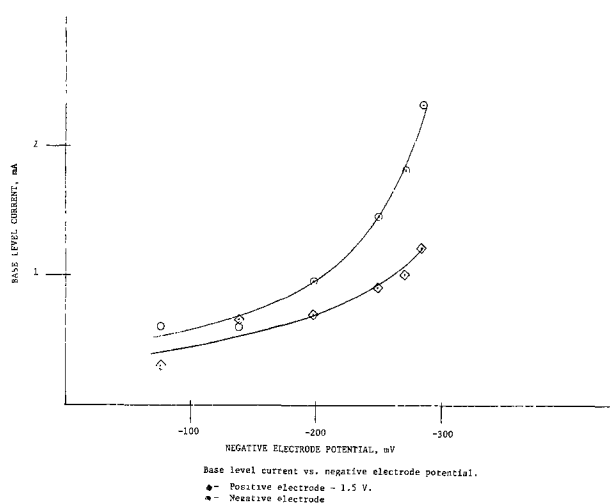


Fig. 3a. Base level current vs. negative electrode potential. \diamond Positive electrode, 1.5V; \odot negative electrode.

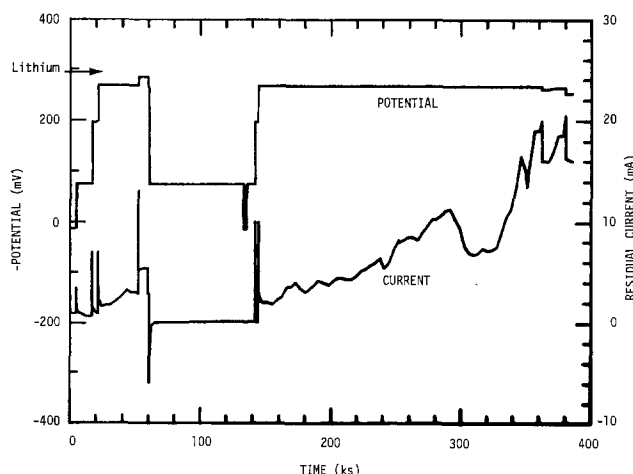


Fig. 3b. Residual current at various bottom screen cathode potentials. Top screen anode at ~ 500 mV.

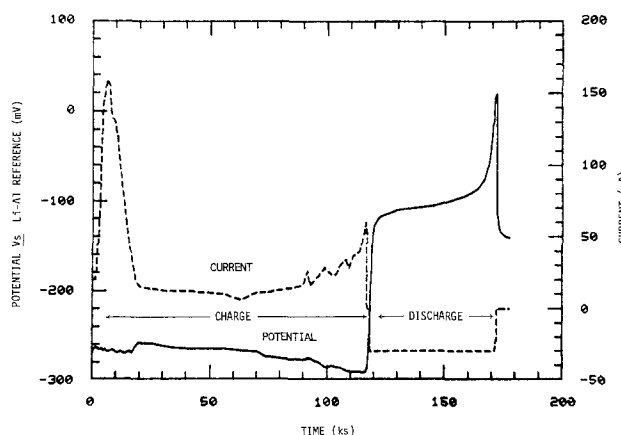


Fig. 3c. Current and potential of the bottom screen as a function of time during the third cycle.

Table I. Potential and current data of the two screen electrodes.
Temperature = 725 K.

| Top screen | | Bottom screen | | Hold time (ksec) | Comment |
|---|--------------|---------------|--------------|---------------------|--|
| Potential | Current (mA) | Potential | Current (mA) | | |
| Only the bottom screen electrode was in contact with the boron nitride cloth* | | | | | |
| -75 mV | 0.6 | 1.5V | -0.3 | 260 | |
| -136 to -138 | 0.6 | 1.5 | -0.65 | 270 | |
| -195 to -196 | 0.95 | 1.5 | -0.70 | 151 | |
| -243 to -247 | 1.45 | 1.5 | -0.90 | 173 | |
| -266 to -268 | 1.8 | 1.5 | -1.0 | 173 | |
| -280 | 2.3 | 1.5 | -1.2 | 86 | |
| Both screen electrodes were in contact with the boron nitride cloth | | | | | |
| 0.500V | — | +12.8 mV | 0.9 | 4.5 | |
| 0.500 | -1.4 | -76 | 0.9 → 0.6 | 12.0 | The first reading was taken 1.8 ksec after the initial surge |
| 0.500 | -1.3 | -197 | 1.2 → 0.9 | 4.5 | The first reading was taken 1.8 ksec after the initial surge |
| 0.500 | -1.7 | -268 | 1.7 → 2.9 | 30 | Decreased after the surge to 1.7 mA in 3 ksec, then gradually increased to 2.9 mA in 30 ksec |
| 0.500 | -2.1 | -286 | 5.2 → 5.4 | 5.0 | 1.04 was attained in 0.3 ksec |
| 0.500 | -2.0 | -269 | 2.9 | 1.0 | Attained within 0.12 ksec |
| 0.500 | -2.0 → -0.8 | -75 | -0.3 → 0.2 | 63 | After discharging for 1.5 ksec at 1.5 mA (averaged) |
| 0.500 | -0.6 | +15 | 0.1 | 2.4 | |
| 0.500 | -0.6 | -75 | 0.2 | 5.4 | |
| 0.500 | -0.5 | -196 | 0.6 | 6.0 | |
| 0.500 | -0.7 → -1.0 | -267 | 2.0 → 20 | 234 | Reached limiting current of 20 mA |
| 0.500 | -1.0 | -253 | 15 | 5.4 | |
| 0.500 | 0 | -195 | 0.2 | 3.6 | Current dropped from 15 to 0.2 mA in 0.36 ksec |

* Base level current data.

mV), the current again increased irregularly, at far greater than the base level currents, indicating the reaction of boron nitride with lithium at these potentials. After ~700 ksec the separator became electronically conductive. The top screen potential could not be maintained at 500 mV by passing even 10 mA anodically in its circuit. Rather, it fell to the potential of the bottom screen. A large quantity of charge was necessary to attain this shorted condition. This charge was removable. Lithium equivalent to ~0.9 A · hr could be discharged from 1g of the separator using both the top and bottom screens with a total anodic current of 77 mA. Subsequently, the top screen anodic current diminished to 2 mA and its potential increased to 500 mV. This indicated that the separator lost its electronic conduction after the discharge. Henceforth, lithium could be repeatedly cycled between the separator and the reservoir (counter) electrode. The third cycle is shown in Fig. 3c. The discharge of this cycle was carried out using the circuit of the bottom screen only. A voltage plateau indicative of a well-established compound decomposition, possibly Li_7B_6 was observed. At the end of the plateau, the open-circuit potential was -142 mV. Later, the open-circuit potential of the reacted separator was -147 mV over a period of 55 ksec at the end of the fifth discharge.

At the end of the test, the fibers of the boron nitride separator were observed to be destroyed. Only a solid mass in the shape of the separator cloth remained. This mass reacted with water, evolving a gas. This reaction was presumably due to lithium contained in a reaction product boride.

In another test, vitreous carbon was used for the top electrode (anode) which contacted the boron nitride separator and was held at 1.5V. The bottom electrode (cathode) also in contact with boron nitride was a stainless steel screen held at -136 mV. The currents (0.7 mA in the top circuit and 1 mA in the bottom circuit) obtained during 3600 ksec of operation at 700°C were essentially the same as the base-level currents (Table I).

Steady-state current data were also obtained with only the cathodic electrode contacting the boron nitride cloth. The current in the circuit of the bottom screen (cathode) was indicative of the lithium consumed in

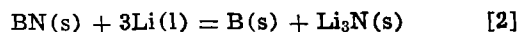
the reaction with the boron nitride cloth. The top electrode (anode) was set at 1.5V and the bottom electrode (cathode) in contact with cloth was held at -135, -195, and -244 mV at 700 K. The magnitude of the current in both circuits increased above the base level indicating the reaction of boron nitride when the potential of the bottom screen (cathode) was less than -200 mV.

After maintaining a potential of -210 mV for 280 ksec, chromatographic analysis of the helium above the electrolyte indicated 216 ppm by volume of nitrogen as compared with 22 ppm nitrogen in the helium atmosphere of the glove box. The source of this nitrogen was lithium nitride dissolved in the electrolyte. The imposed potential, 1.5V between the top screen (anode) and the reservoir (counter) electrode, decomposed the dissolved nitride evolving nitrogen at the (anode) screen and depositing lithium at the counter-electrode. The nitrogen from the (anode) screen escaped into the space above the electrolyte.

The boron nitride separator was freed from lithium by discharging it at ~25 mA for 8 hr. Again it was observed that the separator reacted with lithium at potentials lower than ~-200 mV to hold ~0.2 A · hr. Any remaining lithium in the separator was removed by holding both screens at 1.5V for a few days. During this time, the magnitudes of the currents in both circuits dropped to practically zero. The separator was removed from the cell and cleaned by washing with water.

Microscopic examination indicated that the cloth, which was in contact with the screen wires, was compressed and dented by the wires. Photographs by scanning electron microscope (SEM) of some representative sections of the separator indicated a crusty reaction product and some fine fibers formed from the original boron nitride fibers (Fig. 4). The crusty reaction product, some of which was sticking to the original fibers of boron nitride, is shown at higher magnification in Fig. 5. The fine fibers of the reaction product are also shown in Fig. 6.

The standard free energy change, $\Delta G^\circ_{\text{reaction}}$, for the reaction



is 100 kJ at 700 K (8). This reaction is not thermodynamically favored. Boron nitride has been observed to



Fig. 4. SEM photograph showing boron nitride fibers, crusty reaction product, and fine fibers of the reaction product. Magnification 300 \times .

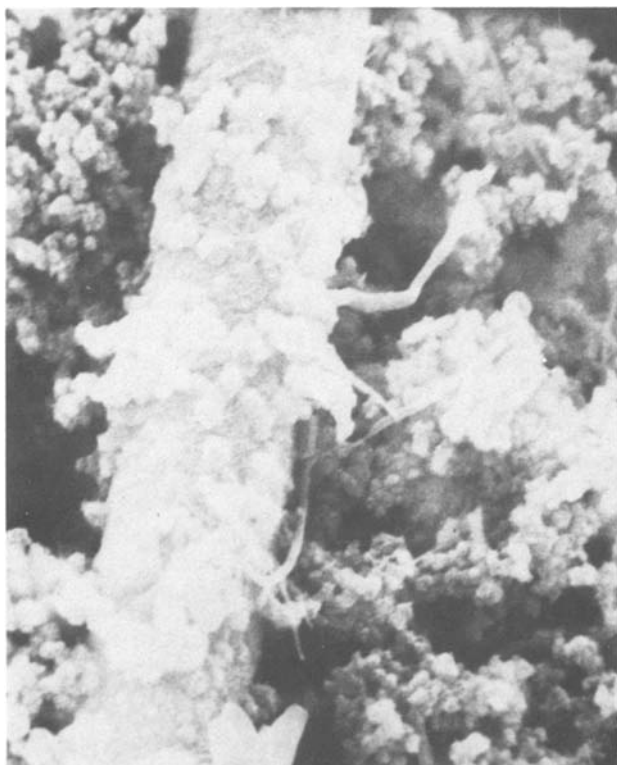
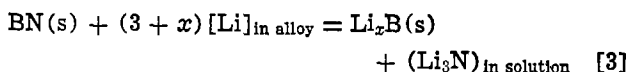


Fig. 5. SEM photograph showing one slightly reacted boron nitride fiber; mostly crusty reaction product and a few fine fibers of the reaction product. The surface of the original fiber indicates the formation of the crust and fibers in the product. Magnification 6000 \times .

react with lithium at 700 K forming Li_3N and a boride (6). The possibility of forming Li_7B_6 and LiB_3 has also been reported (9). Lithium nitride has been reported to be soluble to the extent of 10.1 mol percent (m/o) in lithium chloride at 923 K (10).

A small amount of Li_3N was added to a lithium chloride-potassium chloride eutectic melt in a stainless steel cup at 700 K. A potential of $\sim 1.8\text{V}$ was imposed between the cup and a carbon rod which was placed at its center. The lithium nitride was observed to decompose evolving nitrogen at the rod. The decomposition potential decreased with further addition of Li_3N to the melt and ultimately reached $\sim 0.4\text{V}$ which is very near to the literature value, 0.31V (8). The carbon electrode polarized possibly due to nitrogen evolution when a layer of zirconia fabric was wrapped around it. Thus, Li_3N is appreciably soluble in lithium chloride-potassium chloride eutectic melt. It decomposes by any imposed potential in the range of 0.3-1.8V forming nitrogen and lithium.

In the case of boron nitride which is subjected to the lower potentials of lithium, the following reaction should be considered



The boron nitride is at unit activity; the lithium activity will be governed by the imposed potential. The boron activity will be the same in the boride and the boron nitride; it will be unity when the boride is in equilibrium with boron. In this case

$$-\Delta G^\circ_{\text{reaction}} = RT \ln a_{\text{Li}_3\text{N}} - 3RT \ln a_{\text{Li}} \quad [4]$$

where a is the activity of the designated component, R is the gas constant, and T is the temperature degree Kelvin.

Activities of Li_3N with respect to pure solid Li_3N can be calculated at the different imposed potentials (corresponding to various lithium activities) from the equation. The mol fractions can be calculated using the

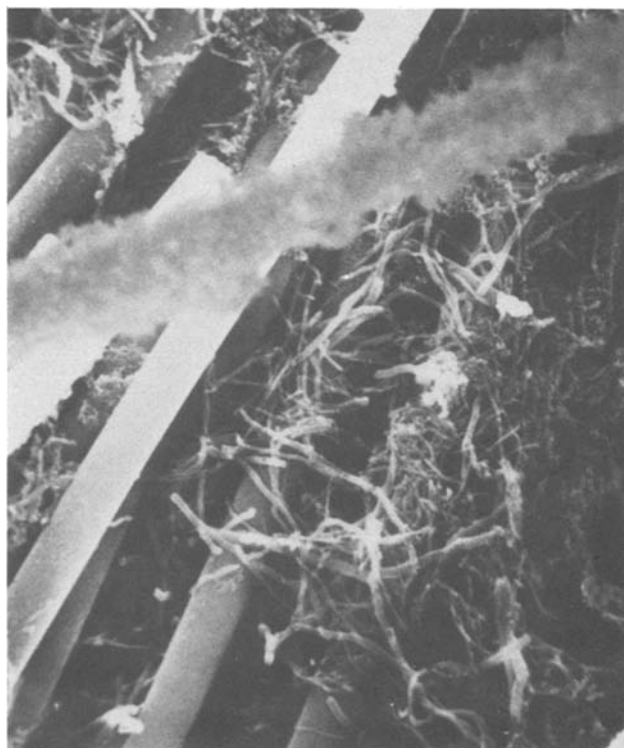


Fig. 6. SEM photograph showing the original boron nitride fibers and the fibers of the reaction product. Magnification 2000 \times .

activity coefficient of Li_3N , 6.1×10^{-4} , the same as reported in pure lithium chloride at 923 K (10). The activity coefficient remains constant below the mol fraction of Li_3N of 0.005. The equilibrium formation potential, E , of lithium nitride can be calculated from the relation

$$E = E^\circ - RT/nF \ln a_{\text{Li}_3\text{N}}$$

where E° is the standard formation potential, n is the number of electrons, and F is the Faraday constant. The calculated data are given in Table II.

The measured current corresponding to the imposed potential of the bottom screen electrode (cathode) are shown against time in Fig. 7. These data were taken after the bottom screen electrode (cathode) had been in the cell for 234 ksec at -267 mV (Table I). As observed from the curves, the residual current dropped to zero and remained so for ~ 3.5 ksec when the potential increased from -253 to -195 mV. During this time the top screen electrode (anode) was at 500 mV and the current in its circuit was practically zero (Table I). In another case, the potential of the bottom screen electrode (cathode) was allowed to float while its circuit was used in charging the reference electrode for ~ 7 ksec. During this time, the top screen (anode) was at 500 mV with no current flowing in its circuit. When the bottom screen electrode (cathode) was put in the circuit, its potential at zero current was observed to be -190 mV. These two observations indicate the decomposition potential of Li_3N to be 500 mV when the bottom screen electrode (cathode) was held between -190 and -195 mV. This is in good agreement with the calculated value of 460 mV (i.e., 750 mV with respect to lithium) as given in Table II.

The activities and potentials of Li_3N in Table II indicate that boron nitride will react with lithium even at its very low activities. The reaction will continue and go to completion if a potential between any two electrodes in the electrolyte greater than the potential of Li_3N formation at its activity is imposed. This is true in the case of lithium alloy/iron disulfide cells, where the potential between the negative and the positive electrodes varies from 1.325 to 1.9V (1-3).

On the other hand, lithium nitride can also be scavenged by the silicon in the negative electrode, particularly, in the region of Li_2Si and silicon.

Table II shows that an electronically conductive boride, possibly Li_7B_6 (9), may form at potentials more reducing than ~ -147 mV. The formation of this boride will make boron nitride an unsuitable material for a separator in lithium-alloy/iron sulfide cells which have negative electrodes with potentials smaller than -147 mV. A nonconductive boride (LiB_3) or boron may form at potentials greater than -147 mV. In the case of the formation of boron which is practically an insulator [resistivity, $1.8 \times 10^6 \Omega \cdot \text{cm}$ (11)], boron nitride will not become conductive. Boron density, 2.5 g/cm³, is not much different from that of boron nitride,

Table II. Activities and potentials of lithium and lithium nitride at equilibrium of the reaction $\text{BN}(s) + (3 + x)[\text{Li}]_{\text{in alloy}} = \text{Li}_x\text{B}(s) + (\text{Li}_3\text{N})_{\text{in solution}}$
Temperature = 700 K

| Lithium potential w.r.t. Li-Al (V) | Lithium activity w.r.t. lithium | Potential of formation of Li_3N (V) | Li_3N | |
|------------------------------------|---------------------------------|---|-----------------------|-----------------------|
| | | | Activity | Mole fraction |
| -0.290 | 1 | 0.65 | 3.3×10^{-8} | 5.5×10^{-5} |
| -0.195 | 0.21 | 0.75 | 3.0×10^{-10} | 4.8×10^{-7} |
| -0.170 | 0.14 | 0.77 | 1.0×10^{-10} | 1.4×10^{-7} |
| -0.147 | 0.093 | 0.80 | 2.7×10^{-11} | 4.4×10^{-8} |
| -0.136 | 0.078 | 0.81 | 1.6×10^{-11} | 2.5×10^{-8} |
| -0.010 | 0.0097 | 0.93 | 3.0×10^{-14} | 4.9×10^{-11} |
| 0 | 0.0082 | 0.94 | 1.8×10^{-14} | 3.0×10^{-11} |
| +0.39 | 0.0043 | 0.98 | 2.5×10^{-15} | 4.3×10^{-12} |

* Conductor.
** Nonconductor.

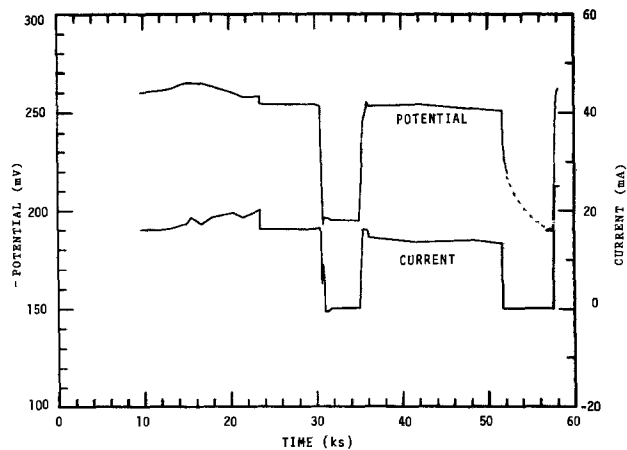


Fig. 7. Variation of the current with bottom screen potential (cathode). Top screen (anode) at ~ 500 mV.

2.27 g/cm³ (11). Therefore, formation of boron should not destroy the structural integrity of boron nitride. A boron coating on the surface of boron nitride may form and inhibit further reaction. The compound, LiB_3 , may also behave just like boron. This may be the reason that boron nitride separators have lasted for thousands of hours in lithium-aluminum/iron sulfide cells which have negative electrodes of lithium potentials higher than -147 mV.

In static immersion tests of boron nitride in lithium, negligible amounts of lithium nitride at its equilibrium concentration will form, so boron nitride can appear stable in these tests. In tests of two lithium electrodes with a boron nitride separator in LiCl-KCl electrolyte, the boron nitride will react with lithium. The reaction will continue to form lithium nitride only up to its equilibrium concentration and then will stop. Because the potential between the two lithium electrodes is smaller than the potential of lithium nitride decomposition at its equilibrium concentration, boron nitride tested in such cells reacted only slightly (6).

Conclusion

Boron nitride is chemically stable with lithium at potentials greater than -136 mV with respect to a lithium-aluminum reference electrode at 700 K. That means boron nitride is stable with $\text{Li}_{15}\text{Si}_4$ which displays the above lithium potential and which is used as the negative electrode reactant of the Li-Si/FeS₂ cells.

Boron nitride reacts with lithium at potentials below -200 mV with respect to the reference electrode forming a boride and lithium nitride.

Acknowledgment

The authors would like to thank Dr. J. S. Dunning of the Electrochemistry Department for useful suggestions and discussions. We also thank Dr. R. A. Murie of the Electrochemistry Department for his assistance in performing the gas chromatographic analysis and Mr. Walter H. Lange of the Analytical Chemistry Department for the SEM photographs.

Manuscript submitted July 11, 1980; revised manuscript received Oct. 7, 1980.

Any discussion of this paper will appear in a Discussion Section to be published in the June 1982 JOURNAL. All discussions for the June 1982 Discussion Section should be submitted by Feb. 1, 1982.

Publication costs of this article were assisted by General Motors Research Laboratories.

APPENDIX

Reference Electrode

A clean aluminum wire (15 cm long, 0.08 cm diam, 0.083g) was coiled around one end of a 0.3 cm diam

rod of stainless steel. A cover of stainless steel screen was formed over the coil by spot-welding. The coil was first charged at 30 mA to have its composition in the β -phase of the lithium-aluminum phase diagram (4) in a cell with lithium-chloride-potassium chloride electrolyte and lithium-silicon counterelectrode at ~ 700 K. The composition of the coil at the end of the charge was the β -phase. The coil was then discharged to have its composition in the α - β two-phase region. The final composition of the reference electrode was frequently checked and maintained at the above composition.

REFERENCES

1. J. S. Dunning, T. G. Bradley, and E. J. Zeitner, in "Proc. 11th IECEC," Vol. I, p. 491, State Line, Nev., September 1976.
2. E. J. Zeitner, Jr., and J. S. Dunning, in "Proc. 13th IECEC," Vol. 1, p. 697, Soc. of Auto. Engrs., Warrendale, Penn., August 1978.
3. P. A. Nelson *et al.*, "Progress Report for the Period

- January-March 1978," Report No. ANL-78-45, Argonne National Laboratory, Argonne, Illinois, July 1978.
4. K. M. Myles *et al.*, U.S. ERDA Report ANL-76-8, p. B-80 (1976).
 5. R. A. Sharma and R. N. Seefurth, *This Journal*, **123**, 1763 (1976).
 6. R. A. Sharma, *Am. Ceram. Soc. Bull.*, **57**, 1103 (1978).
 7. R. N. Seefurth and R. A. Sharma, *This Journal*, **124**, 1207 (1977).
 8. JANAF Thermochemical Tables, 2nd ed., NSRDS-NBS-37 (1971).
 9. S. Dallek, D. W. Ernst, and B. F. Larrick, *This Journal*, **126**, 866 (1979).
 10. A. Bonomi, M. Hadate, and F. Breda, *ibid.*, **126**, 248 (1979).
 11. N. A. Lange, "Handbook of Chemistry," 12 ed., pp. 3-2, 4-30, 4-31, McGraw-Hill Book Co., New York (1979).

Caustic Leaching of Al-Cu-Zn Alloys to Produce Raney Catalysts

I. Morphological Development

J. B. Friedrich, D. J. Young,* and M. S. Wainwright

School of Chemical Engineering and Industrial Chemistry,
The University of New South Wales, Kensington, N.S.W. 2033, Australia

ABSTRACT

The leaching behavior in aqueous NaOH of Al-Cu-Zn alloys containing 50 weight percent (w/o) Al has been examined and interpreted in terms of alloy phase constitution. Alloys containing approximately 0, 5, 10, 17, 26, 33, and 50 w/o Zn having quenched structures consistent with the ternary phase diagram were partially leached and the product material examined metallographically. In all cases a sharply defined interface developed between the as yet unaffected alloy and the reaction product layer. This layer was of uniform thickness. The principal reaction product was porous copper (containing small amounts of zinc and aluminum) which resulted from leaching of the alloy $\text{Cu}(\text{Zn})\text{Al}_2$ phase. The microstructure of the alloy was reproduced in the reaction product, suggesting that the mechanism is one of selective dissolution.

A recent study (1) has shown that zinc-promoted Raney copper catalysts can be used for the production of methanol from carbon monoxide and hydrogen. This novel range of catalysts is produced from aluminum-copper-zinc alloys by extraction of aluminum and zinc with aqueous sodium hydroxide to leave porous reaction product zones which act as the catalysts. In that study the inclusion of zinc in the Cu-Al alloy was found to increase the activity of the catalyst for the production of methanol. The effect of Raney copper-zinc catalysts on some other reactions has been reported.

Sultanov and Maslennikova (2) reported the use of a Raney copper-zinc catalyst for the reduction of furfural to sylvan and recommended as the most effective catalysts one which had an initial alloy composition of 33 weight percent (w/o) copper, 50 w/o aluminum, and 17 w/o zinc. Standfield and Robbins (3) presented a kinetic study of the hydrogenation of various functional groups of organic molecules using Raney copper-type catalysts and reported that the addition of zinc to replace aluminum in the alloy failed to yield a more active catalyst. In none of the above studies on Raney copper-zinc was any attempt made to examine the

leaching behavior of the various phases in the Al-Cu-Zn system. A recent paper by Young *et al.* (4) contains information on the leachability of the phases present in a Cu-50 w/o Al alloy. This alloy had a quenched structure, containing CuAl_2 as primary precipitate, and material of the composition of the binary Al-CuAl₂ eutectic. The CuAl_2 leached to form Raney copper whereas the eutectic mixture leached completely, leaving no solid residue. Since the leaching process will in a large part determine the physicochemical properties of the resultant catalyst, the reaction is of some interest.

The dissolution of a component from an alloy to leave behind a spongy material is a familiar, albeit poorly understood, phenomenon. Dezincification of brass is possibly the best known example (5-7), but others have also been studied (8, 9). Two mechanisms have been suggested for the process in binary alloys. In the first, it is supposed that simultaneous dissolution of both constituents is followed by reprecipitation of the less reactive metal. The difficulty with this mechanism is that mass transfer is required from a source of low activity, the alloy, to a region of high activity, the pure metal. Alternatively, it is suggested that the more reactive constituent is selectively removed leaving an accumulation of the less reactive metal at the

* Electrochemical Society Active Member.

Key words: metals, catalysis, dissolution, corrosion.

alloy surface. For this mechanism to be available, diffusion within the alloy must be sufficiently fast to support the leaching process. Although solid-state diffusion coefficients are low at ambient temperatures, the highly porous nature of the leached alloys indicates a reaction morphology which requires only short diffusion distances. The production of a Raney catalyst is a reaction of the type under discussion. In the absence of leaching studies, however, it is not possible to say which of the above mechanisms is operative.

The present work is divided into two parts. The first part provides new information on leaching of the various phases in the Al-Cu-Zn system by a systematic study using metallographic, x-ray diffraction, and electron microprobe methods of analysis. In the second part, the kinetics of aqueous sodium hydroxide attack on the various aluminum-copper-zinc alloys are investigated.

Experimental

Alloy and catalyst preparation.—Alloy melts were prepared by induction melting the required proportions of copper (99.5% pure), aluminum (99.9% pure), and zinc (99.8% pure) as described by Marsden *et al.* (1). The homogeneous melts were cast onto a chilled copper mold to form a plate from which rectangular prisms ($6 \times 6 \times 9$ mm) were machined. The actual compositions of the alloys are listed in Table I and are shown plotted on the Al-Cu-Zn liquidus projection diagram in Fig. 1. The samples machined from the castings were used in leaching experiments without further heat-treatment.

Leaching experiments were carried out by reacting the rectangular prisms isothermally at 50°C with 20 w/o aqueous NaOH, the amount of solution provided being equivalent to three times the stoichiometric amount of aluminum present in the alloy. No means of stirring was provided. After various times of reaction the partially extracted alloy pieces were thoroughly washed with distilled water until the pH of the wash water was 7. The samples were then mounted in cold setting resin, cross sectioned at right angles to an original face of the specimen, and metallographically polished to a 1 μ m finish. The reaction-affected rim of the alloy piece was then clearly visible under an optical microscope.

Alloy pieces of 500-700 μ m diam were leached to provide material for x-ray diffraction studies and atomic absorption analysis. In these runs 20g of the alloy was placed in 111g of distilled water at 50°C. After the apparatus had been thoroughly flushed with hydrogen, 40 w/o caustic solution was added over a time period of 0.75 hr so that the reaction temperature was kept to $50 \pm 2.5^\circ\text{C}$. No means of stirring was provided. After complete extraction had taken place (as determined by the hydrogen evolved from the reaction) the catalyst pieces were thoroughly washed with distilled water until the pH of the wash water was 7.

Phase identification.—Phases present in the unaffected alloy and in the reacted rim were analyzed with an electron probe microanalyzer. Point counts obtained

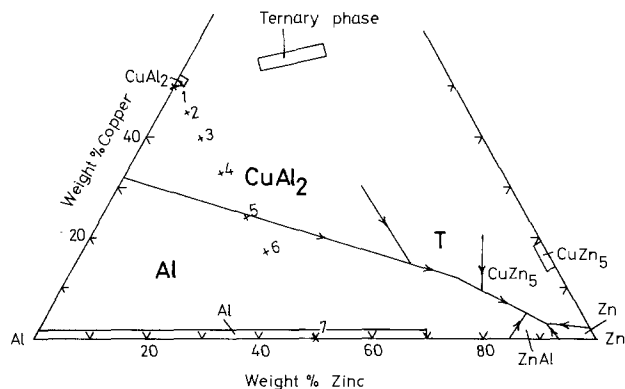


Fig. 1. Liquidus projection (12) for the system Al-Cu-Zn showing the compositions of the initial alloys (x) and the phase compositions of CuAl_2 , Al, the ternary phase, and CuZn_5 at 650 K.

from the probe were analyzed with respect to CuAl_2 , Al, and Zn standards. Systematic corrections were applied to the data for atomic number, mass absorption, and fluorescence effects.

Microprobe results were supplemented by powder x-ray diffraction studies. Samples of powdered alloys were examined with a diffractometer in the usual way. Powdered catalyst samples were prepared from 500 to 700 μ m alloy pieces leached under the conditions described above. The powdered catalysts were pyrophoric and were therefore coated with collodion prior to examination.

The crystallite size in the reaction product was determined from the broadening of the Cu(200) diffraction line using the Scherrer equation. Corrections for instrumental broadening were obtained from the silicon (220) diffraction line. In both cases $\text{CuK}\alpha$ radiation was used and phase identification was accomplished by comparing diffraction patterns with those in the ASTM files. The ternary phase T was identified from the diffraction pattern reported by Köster and Moeller (10). The CuZn_5 phase was identified from the pattern reported by Owen and Preston (11).

The composition of the alloys and the completely extracted 500-700 μ m catalyst pieces were determined by atomic absorption spectroscopy of acid digested samples. Copper and zinc analyses were determined by the standard addition technique, while aluminum was determined by comparing the unknown with matched standards.

Results

Micrographs in Fig. 2 show the interface, or reaction front, between the unaffected alloy and the reaction product zone which had developed after 4 hr of reaction. In all cases a clearly defined boundary was found to exist. At all reaction times investigated for all samples this boundary was found to be parallel to the original alloy surface. The cast alloy structures showed no preferential orientation except in the case of samples 2, 3, and 4 where some evidence of directional solidification was observed. In the cases where some directional solidification was evident in the alloy, the thickness of the reacted zone appeared not to vary with the angle between the directions of solidification and leach reactions (Fig. 3). Microprobe analyses for each of the phases seen in the micrographs are listed in Table II. No results are reported for alloys 5 and 6 in which the microstructure could not be resolved with the microprobe. Phases identified by x-ray diffraction for the alloys and their reaction products are shown in Table III.

Microprobe scans showed that no concentration gradient existed in any of the phases within the alloys. At the interface a discontinuous change in concentration for all three metals was observed. Analyses of

Table I. Atomic absorption analysis of alloys and their product Raney catalysts, 500-700 μ m particles

| Sample | Alloy (w/o) | | | $\text{Cu}(\text{Zn})\text{Al}_2$ (v/o) | Catalyst (w/o) | | |
|--------|-------------|------|------|--|----------------|------|------|
| | Al | Cu | Zn | | Al | Cu | Zn |
| 1 | 50.2 | 50.6 | 0 | 99.5 | 1.6 | 98.7 | 0 |
| 2 | 50.7 | 44.6 | 5.3 | 99.0 | 1.1 | 98.0 | 0.8 |
| 3 | 50.3 | 39.3 | 9.8 | 97.5 | 1.3 | 97.5 | 1.5 |
| 4 | 49.7 | 33.5 | 17.1 | 92.5 | 1.6 | 97.1 | 2.8 |
| 5 | 49.8 | 24.6 | 26.0 | — | 2.0 | 90.0 | 8.7 |
| 6 | 48.5 | 17.2 | 33.0 | — | 3.9 | 64.4 | 33.0 |
| 7 | 48.8 | 0 | 52.0 | — | 0.8 | 0 | 99.8 |

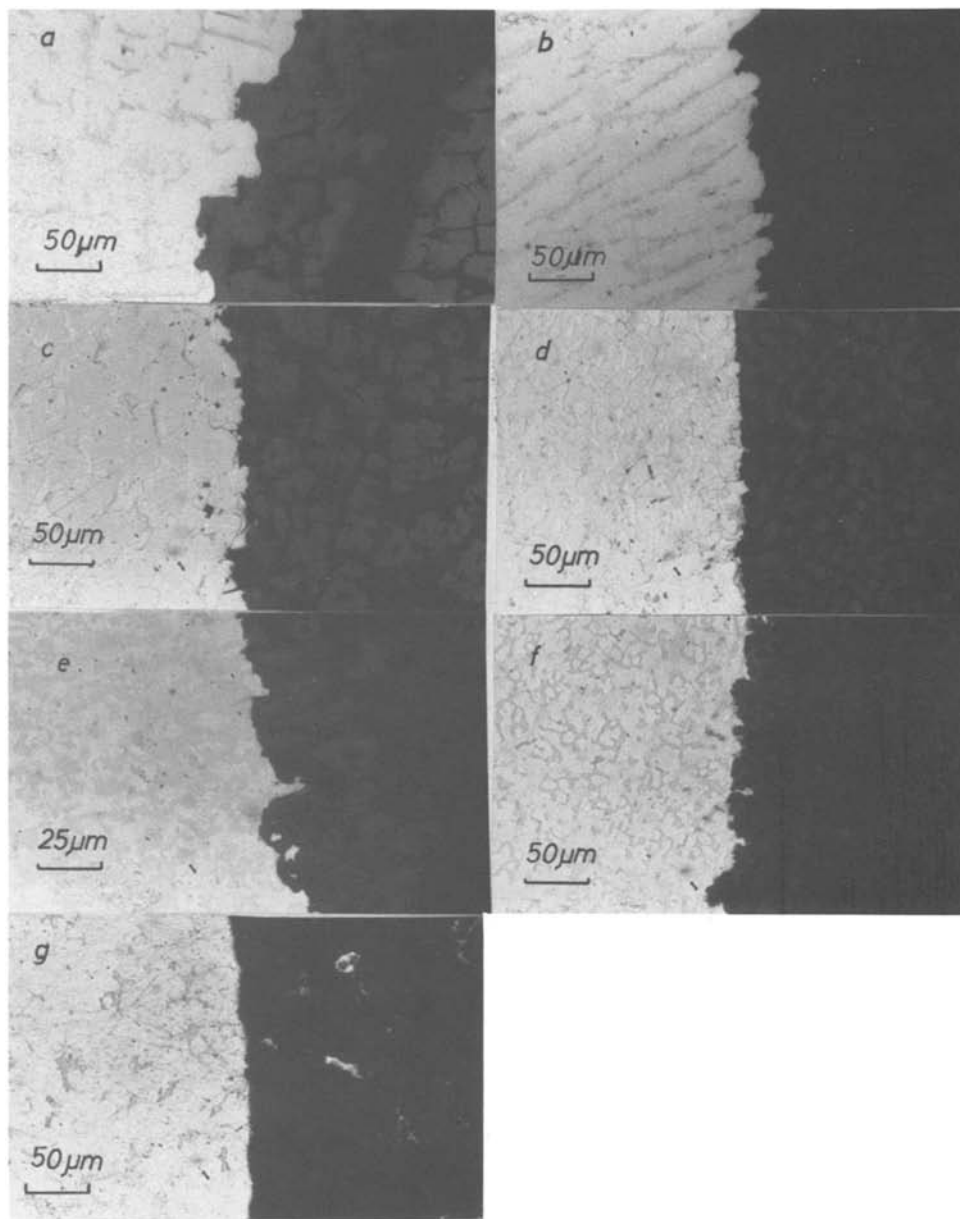


Fig. 2. Micrographs of sections through partially leached alloys (a) Al-50Cu; (b) Al-44Cu-5Zn; (c) Al-40Cu-10Zn; (d) Al-33Cu-17Zn; (e) Al-24Cu-26Zn; (f) Al-17Cu-33Zn; (g) Al-5Zn.

the phases in the reaction product zone were found to total substantially less than 100% indicating either that oxide is present or that the analysis of these porous materials is unreliable. Atomic absorption analysis of the catalyst particles (Table I) showed that there was no oxide present. Microprobe scans of the copper phase in the reaction product zone for alloys 1-4 showed that in each case an aluminum concentration gradient was

present and in the case of alloys 2-4 a zinc concentration gradient was present. In each case the zinc and

Table II. Microprobe analyses of alloys and their product Raney catalysts

| Sample | Alloy | Catalyst (analysis near original alloy face) |
|--------|---|--|
| 1 | Light precipitate— $\text{Cu}_{32}\text{Al}_{68}$ liquid— $\text{Cu}_{10}\text{Al}_{90}$ | *Gray phase— $\text{Cu}_{67}\text{Al}_3$ Black region—void |
| 2 | Light precipitate— $\text{Cu}_{31.1}\text{Al}_{68.3}\text{Zn}_{0.6}$ liquid—Al based solution variable composition | *Gray phase— $\text{Cu}_{68}\text{Al}_{1.7}\text{Zn}_{0.9}$ Black region—void |
| 3 | Light precipitate— $\text{Cu}_{30.4}\text{Al}_{68}\text{Zn}_{1.7}$ liquid—Al based solution variable composition | *Gray phase— $\text{Cu}_{62.7}\text{Al}_{3.3}\text{Zn}_{2.0}$ Black region—void |
| 4 | Light precipitate— $\text{Cu}_{30.3}\text{Al}_{67.8}\text{Zn}_{1.8}$ liquid—Al based solution variable composition | *Gray phase— $\text{Cu}_{60.2}\text{Al}_{6.6}\text{Zn}_{3.2}$ Black region—void |

* Analyses total less than 100% and have been normalized.

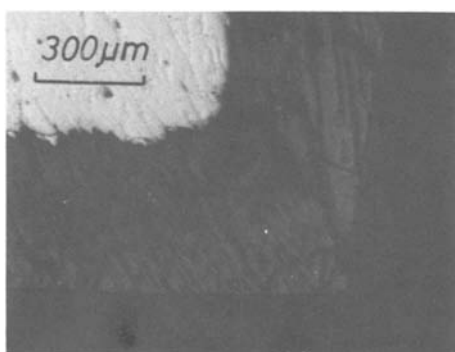


Fig. 3. Micrograph of section through partially leached Al-44Cu-5Zn alloy showing directional solidification.

Table III. X-ray diffraction analyses of alloys and their product Raney catalysts*

| Sample | Alloy | Catalyst |
|--------|--|-----------------------|
| 1 | CuAl ₂ , Al | Cu, Cu ₂ O |
| 2 | CuAl ₂ , Al, T (tr) | Cu, Cu ₂ O |
| 3 | CuAl ₂ , Al, T (tr) | Cu, Cu ₂ O |
| 4 | CuAl ₂ , Al, T (tr) | Cu, Cu ₂ O |
| 5 | Al, CuAl ₂ , T (tr) | Cu, Cu ₂ O |
| 6 | Al, CuAl ₂ , T (tr), CuZn ₅ (tr) | Cu, Cu ₂ O |

* Phases listed in approximate order of abundance; (tr) indicates trace.

aluminum were in greater concentration near the reaction interface.

The grain size of the primary precipitate in alloys 1-4 decreased as the copper content of the base alloy decreased. As expected from the phase diagram, the volume percent of Cu(Zn)Al₂ primary precipitate also decreased with increasing alloy zinc content. Results are reported in Table I. In alloys containing higher concentrations of zinc, the Cu(Zn)Al₂ phase could not be satisfactorily resolved with the microscope. The x-ray diffraction estimates of the copper crystallite size in the extracted catalyst pieces are shown in Table IV.

The reaction products of alloys 1, 2, and 3 showed the same morphologies at all stages of reaction. However, alloys 4, 5, and 6 exhibited a different reaction morphology in the initial stages of leaching. Micrographs in Fig. 4 show the development of this morphology for alloy 4. They show that for reaction times of up to 2 hr the reaction product zone consists of two layers, the outer layer containing dark colored grains and the inner layer light colored grains. Microprobe analysis showed that the grains in the outer layer were essentially copper while those in the inner layer were unreacted Cu(Zn)Al₂. The intergranular material had leached completely to leave void space in both layers.

Discussion

Alloy structures.—X-ray diffraction and microprobe results for the alloys confirmed one another except for the cases of the ternary phase, T, and the CuZn₅ phase. These two phases, which are minority phases when present in the alloy, could be detected by XRD but could not be distinguished with the microprobe. The ternary phase T has a field of existence of 56-58% Cu, 10-30% Zn (12).

The alloy microstructures are consistent with predictions for quenched alloys made from the liquidus projection diagram (Fig. 1). Alloys 1-4 have as their primary precipitate the phase Cu(Zn)Al₂ with the Zn content in this phase increasing with the alloy Zn level. This is consistent with the fact that the CuAl₂ phase can dissolve up to 2-3 w/o Zn with little change in lattice parameters (12). The primary precipitate for alloys 5, 6, and 7 is the aluminum-based solution.

The identity of the secondary precipitate is determined by the alloy Zn level. Alloy 1 produces as its secondary solidification product material of the composition of the binary Al-CuAl₂ eutectic. Alloys 2-4 precipitate the aluminum-based solution as their secondary product. Alloys 5 and 6 precipitate Cu(Zn)Al₂

Table IV. Copper crystallite diameters and pore diameters (500-700 μm particles) for fully extracted Raney catalysts

| Sample | Copper crystallite diameter (Å) | Pore diameter (Å) | Calculated interpore distance (Å) |
|--------|---------------------------------|-------------------|-----------------------------------|
| 1 | 112 | 460 | 194 |
| 2 | 112 | 354 | 182 |
| 3 | 104 | 332 | 171 |
| 4 | 104 | 284 | 138 |
| 5 | 70 | 230 | 119 |
| 6 | 62 | 101 | 69 |

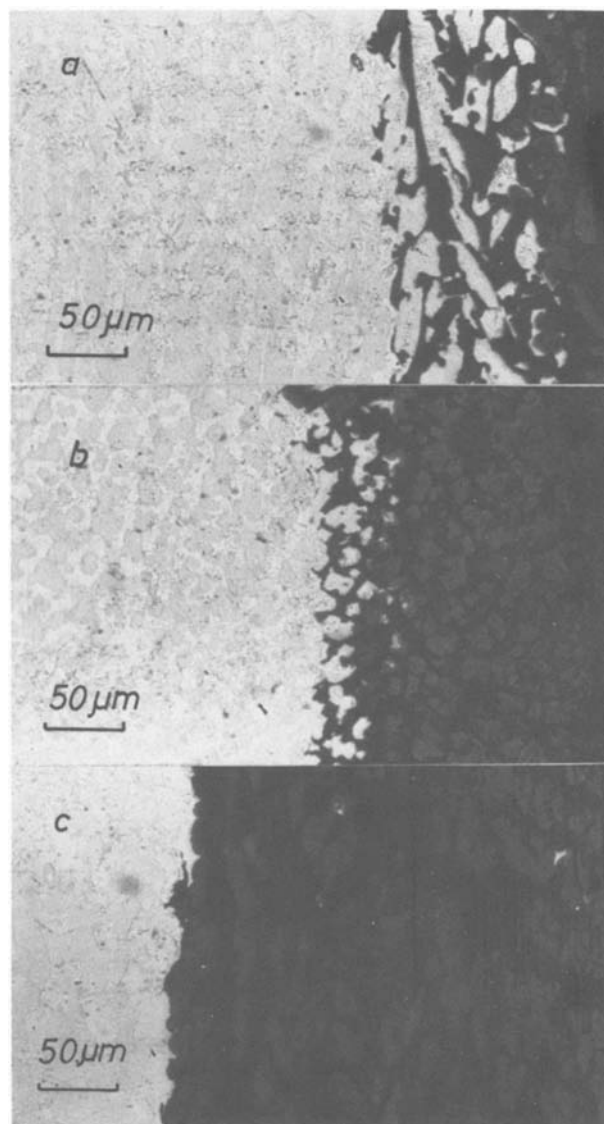


Fig. 4. Micrographs of sections through partially leached Al-33Cu-17Zn alloy showing morphological development: (a) 0.5 hr; (b) 1.0 hr; (c) 2.0 hr.

as their secondary product. On further cooling the ternary phase T is the final solidification product for alloys 2-5. Alloy 6 also contains the ternary phase T as well as having CuZn₅ as its final solidification product. The reactions forming the ternary phase T and the CuZn₅ phase are peritectic reactions. These peritectic reactions have been arrested by quenching to leave a very fine structure that could not be resolved by the microprobe. The intergranular material in sample 7 is zinc-rich frozen liquid.

Catalyst structure.—Examination of Fig. 2 together with Tables II and III reveals the morphology of the reaction product catalysts. Leaching of the CuAl₂ phase from alloy 1 leads to the formation of copper containing low levels of aluminum. Similarly the leaching of the Cu(Zn)Al₂ phase from alloys 2-4 leads to the formation of copper containing low levels of both aluminum and zinc.

In a subsequent paper (13), we show that the completely extracted catalyst pieces are highly porous, with a BET surface area of approximately 20 m²/g, with pore radii ranging from 50-230 Å.

The microstructure of the alloy, in samples 1-4, has been reproduced in the reaction product catalysts. Examination of the interface between alloy and catalyst

shows that the size of the Cu(Zn)Al₂ grain has been preserved when leached to leave porous copper. Copper crystallite sizes given in Table IV show that for catalysts 1-4 there are no major differences in diameter. There is a marked decrease in the copper crystallite size for catalysts 5 and 6 which derive from alloys in which Cu(Zn)Al₂ is a secondary precipitate.

Pore volume and pore diameter measurements (13) were used to calculate average interpore distances on the assumption of parallel, straight, cylindrical pores the cross sections of which are hexagonally arrayed. The results of this calculation are compared with measured crystallite sizes in Table IV, and agreement is seen to be good. It is concluded that the microstructural rearrangement accompanying leaching takes place on an exceedingly small scale and that pore size and crystallite size are interdependent.

The leaching of the intergranular material from alloys 1-4 leads to void space in the reaction product zone. However, examination of the reacted rim near the reaction front for alloy 4 suggests that some of the intergranular material is still visible, but has disappeared at the outer surface where time of exposure has been greatest. The reason for the decrease in reactivity of the intergranular material with increased Zn levels could not be determined. Microprobe analysis of the intergranular material in the reaction product zone proved to be extremely unreliable, a fact which may be attributed to the porosity of the reaction product zone and to the fine scale of the microstructure in the intergranular material. X-ray diffraction did not constitute a satisfactory analysis technique for the intergranular material in the reacted catalyst pieces since the diffraction lines for the ternary phase T were either masked by elemental copper or were not visible. There was no diffraction attributable to the aluminum solid solution in the reaction product catalysts. Evidently the addition of zinc to the base alloy resulted in the intergranular material being more resistant to caustic attack than the Al-CuAl₂ eutectic. The present results do not show whether this is due to decreased reactivity of the Al-Zn solid solution or to increasing amounts of the ternary phase, T, which might be of low reactivity.

The leaching of the zinc-rich alloys 5 and 6 leads to void space from the aluminum solid solution and to pockets of porous copper from the intergranular material. The problems encountered with the microprobe and x-ray diffraction results for the copper-rich samples were again evident in the analysis of the reaction product zone. The leaching of alloy 7 leads to void space from the aluminum-rich primary precipitate while the zinc-rich frozen liquid appears to be unreacted at this stage.

Reaction morphology development.—In all samples studied there was a sharply defined alloy catalyst interface. As the reaction proceeds this interface appears to cut across the phases present. Thus apart from rare localized variations both the primary precipitate and the intergranular solidification product leach at the same rate. This observation is consistent with a diffusion-controlled reaction rate. The stability of the interface together with the speed of the reaction indicates that it is liquid phase diffusion which supports the reaction. This conclusion is supported by the observation that in the case of directionally solidified alloys (Fig. 3) the reaction rate is not a function of the orientation of the alloy grains with respect to the reaction front.

This description does not hold true for alloys containing 17 w/o Zn or more at short time periods. Examination of Fig. 4 shows that the intergranular solidification product leaches at a faster rate than the Cu(Zn)Al₂ phase at short time periods. However at longer leaching periods, 4 hr or greater, both the primary precipitate and the intergranular solidification

product leach at the same rate. Thus it appears that the high zinc alloys leach according to a more complex mechanism in the early stages of the reaction but subsequently via a liquid phase diffusion-controlled process.

In the case of the low zinc alloys, the preservation of the alloy microstructure in the leached product suggests strongly that the reaction of the Cu(Zn)Al₂ grains proceeds via a selective dissolution process rather than a dissolution-reprecipitation process. The latter mechanism has been suggested to be operative under some circumstances in the dezincification of brass (5). This difference is readily explicable in view of the extremely low solubility of Cu in the caustic solutions used in the present work (14). The microstructure of the higher zinc alloys appears also to be preserved in their leach products, but the failure to obtain useful microanalysis results prevents a similar conclusion being reached.

It has been shown that the nature of Raney Cu-Zn catalysts is determined by the phase constitution of their precursor alloys. The principal leach reaction product is porous copper containing small amounts of zinc and aluminum. This product derives from the leaching of the alloy Cu(Zn)Al₂ phase. The other major alloy phase is an Al-Zn solid solution which usually leaches completely, leaving void space. At very high zinc levels, however, this phase becomes resistant to leaching. In all cases, the alloy microstructure is preserved in the reaction product and a sharp interface develops between the product and the as yet unaffected alloy. These observations are consistent with a selective dissolution reaction whose rate is controlled by diffusion through the product layer. The kinetics of this reaction are reported in the following paper (15).

Acknowledgments

Support was provided under the National Energy Research, Development and Demonstration Program administered by the Commonwealth Department of National Development.

Manuscript received Nov. 13, 1980.

Any discussion of this paper will appear in a Discussion Section to be published in the June 1982 JOURNAL. All discussions for the June 1982 Discussion Section should be submitted by Feb. 1, 1982.

Publication costs of this article were assisted by The University of New South Wales.

REFERENCES

1. W. L. Marsden, M. S. Wainwright, and J. B. Friedrich, *Ind. Eng. Chem. Prod. Res. Dev.*, **19**, 551 (1980).
2. A. S. Sultanov and V. A. Maslennikova, *Zh. Prikl. Khim.*, **32**, 595 (1959).
3. J. A. Stanfield and P. E. Robbins, *Actes Congr. Int. Cat. (2nd)*, Paris, **2**, 2579 (1960).
4. D. J. Young, M. S. Wainwright, and R. B. Anderson, *J. Catal.*, **64**, 116 (1980).
5. H. W. Pickering and C. Wagner, *This Journal*, **114**, 698 (1967).
6. H. G. Feller, *Corros. Sci.*, **8**, 259 (1968).
7. H. Sugawara and H. Ebiko, *ibid.*, **7**, 513 (1967).
8. J. D. Harrison and C. Wagner, *Acta Metall.*, **7**, 722 (1959).
9. J. I. Gardiazabal and J. R. Galvele, *This Journal*, **127**, 255 (1980).
10. W. Köster and K. Moeller, *Z. Metallkd.*, **34**, 206 (1942).
11. E. A. Owen and G. D. Preston, *Proc. Phys. Soc. London*, **36**, 49 (1923).
12. L. F. Mondolfo, "Aluminium Alloys: Structures and Properties," Butterworths, London (1976).
13. J. B. Friedrich, M. S. Wainwright, and D. J. Young, To be published.
14. M. Pourbaix, "Atlas of Electrochemical Equilibria in Aqueous Solutions," Pergamon Press, London (1966).
15. J. B. Friedrich, D. J. Young, and M. S. Wainwright, *This Journal*, **128**, 1845 (1981).

Caustic Leaching of Al-Cu-Zn Alloys to Produce Raney Catalysts

II. Leaching Kinetics

J. B. Friedrich, D. J. Young,* and M. S. Wainwright

*School of Chemical Engineering and Industrial Chemistry,
The University of New South Wales, Kensington, N.S.W. 2033, Australia*

ABSTRACT

The leaching kinetics of Al-Cu-Zn alloys containing 50 weight percent (w/o) Al in aqueous NaOH have been examined by measuring the depth of attack on the alloy pieces as a function of time and also by measuring the evolution of hydrogen as a function of time. Alloys containing approximately 0, 5, 10, 17, 26, and 33 w/o Zn were found to have parabolic leaching kinetics, the reaction mechanism being one of selective dissolution controlled by liquid phase diffusion through the product layer. The product layer was porous copper which resulted from leaching of the alloy $\text{Cu}(\text{Zn})\text{Al}_2$ phase. This porous copper was found to contain a zinc and an aluminum concentration profile throughout the reacted zone. The shape of these profiles was consistent with liquid phase diffusion control except for a narrow region near the alloy surface where a degree of chemical reaction control was found. This observation is consistent with the experimental activation energy of $41 \pm 5 \text{ kJ mol}^{-1}$.

It has been shown (1) that Al-Cu-Zn alloys containing 50 weight percent (w/o) Al leach in strong caustic solution at 50°C to produce a product layer of porous Cu containing small amounts of Al and Zn. This product layer is of uniform thickness and a sharply defined interface is established between it and the underlying, as yet unaffected alloy. The alloys contained as principal phases $\text{Cu}(\text{Zn})\text{Al}_2$ and Al-Zn solid solution, the former of which leached to leave the porous copper whereas the latter reacted completely, leaving void space. The alloy microstructure was preserved in the product layers. These observations were interpreted as implying a reaction mechanism of selective dissolution whose rate was controlled by diffusion through the product layer.

Preferential removal of an alloy constituent by a chemical reaction which leaves unaffected a more noble alloy constituent is a common phenomenon and has been widely studied in connection with the dezincification of brass (2-4). Reaction rates are high when a porous product and a convoluted alloy-product layer interface are formed. This situation has been analyzed theoretically by Wagner (5) and the analysis applied to the kinetics of liquid metal and molten salt attack on binary alloys containing one component which was noble with respect to the environment (6). The observation of parabolic kinetics was attributed to rate control by diffusion in the liquid phase, rapid alloy diffusion being facilitated by the short diffusion distances associated with porous reaction product. More recently, the chlorination of Co-Pt and Fe-Pt alloys has been studied by Pickering (7) who showed that the formation of a volatile base metal chloride left a porous Pt layer which thickened at a rate independent of time. Since the chloride vaporization rate is independent of product layer thickness and since the reaction must be supported by microsegregation of Pt and base metal at the reaction front, it is apparent that the rate of this latter process is time independent.

It is apparent that a knowledge of the kinetics of the process whereby a solid leach residue accumulates is a valuable aid in the dissection of the reaction mechanism. This paper reports the results of an investiga-

tion of the leaching kinetics of a series of Cu-Al-Zn alloys and an account of the probable reaction mechanism.

Experimental

Several Cu-Al-Zn alloys were leached in 20 w/o aqueous NaOH solution. Alloy compositions, sample shape, and leaching procedures used for the kinetic investigation were fully described in the previous paper (1). The extent of reaction was determined by measuring the depth of attack on the alloy pieces as a function of time. The depth of chemical attack was measured at right angles to an original alloy face under an optical microscope with a graduated eyepiece. Measurements were taken after various periods of reaction up to a maximum of 24 hr.

The extent of reaction was also measured by monitoring the evolution of hydrogen as a function of time using a wet test gas meter. An amount of NaOH solution, equivalent to three times the stoichiometric amount of aluminum present in the alloy, was added to six alloy pieces at 50°C, after first purging the system with hydrogen. No means of stirring was provided. Readings were taken at the same time intervals used for the distance measurements.

Elemental concentration profiles were measured in the reaction product layer formed on alloys 1-4 by point counting on an electron probe microanalyzer. Temperature dependence experiments were carried out on an alloy of composition Al-36 w/o Cu-14 w/o Zn to determine an activation energy for the leaching reaction. The leaching experiments were carried out at temperatures of 6°, 27°, 54°, and 82°C and on roughly spherical alloy pieces of 2.4-4.0 mm diam. A 20g sample of alloy was placed in 111g of distilled water at the required temperature. 111g of 40 w/o aqueous sodium hydroxide solution was added after first purging the system with hydrogen. No means of stirring was provided. The extent of reaction was monitored by the evolution of hydrogen. Temperature control in these experiments was to within $\pm 2.5^\circ\text{C}$.

Results

The thickness of the reaction-affected rim around the partially extracted alloy pieces as a function of leaching time is shown in Fig. 1. Data at 0.5 and 1 hr

* Electrochemical Society Active Member.

Key words: metals, catalysis, dissolution, corrosion.

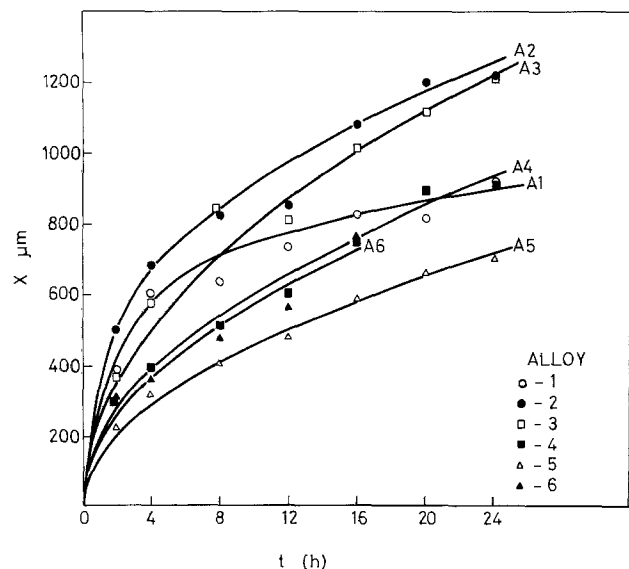


Fig. 1. Average thickness of reaction-affected rim as a function of leaching time.

have not been included in Fig. 1. The shape of the curves indicates parabolic leaching kinetics. Accordingly, the data have been replotted in Fig. 2 where the straight lines are the results of regression on the equation

$$X^2 = k_p t \quad [1]$$

where X is the thickness of the reaction-affected rim formed in time t and k_p is a parabolic rate constant. The 0.5 and 1 hr leaching data have been included in the regression calculation. Values of k_p are presented in Table I. Alloy 6, the high zinc alloy, showed irregular kinetics due to the product layer's inability to hold its structure around the alloy. Therefore data

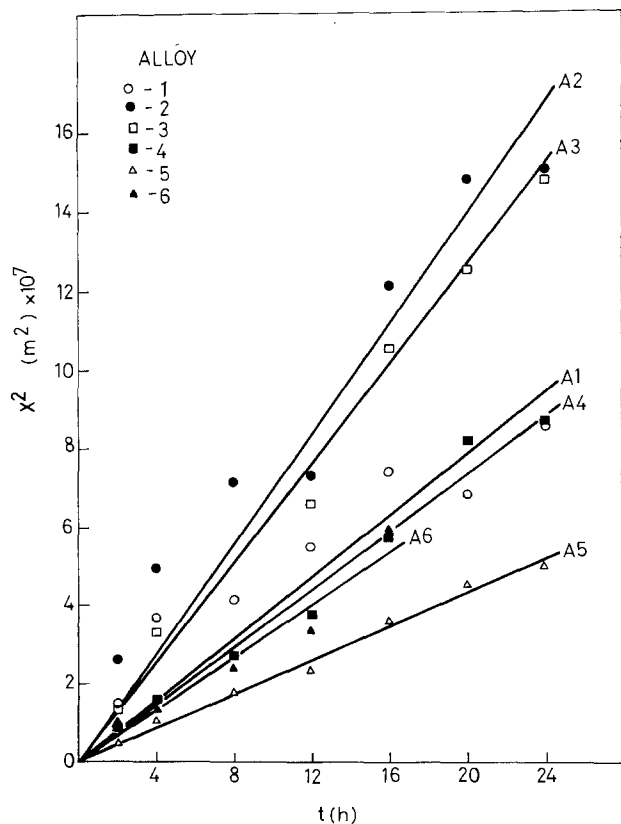


Fig. 2. Parabolic plots from Fig. 1 where the straight lines are the results of regression on Eq. [1].

Table I. Alloy composition and leaching rate constant for Al-Cu-Zn alloys

| Alloy number | Alloy composition (w/o) | | | k_p (cm ² /sec) × 10 ⁷ |
|--------------|-------------------------|------|------|--|
| | Al | Cu | Zn | |
| 1 | 50.2 | 50.6 | 0 | 1.09 ± 0.27 |
| 2 | 50.7 | 44.6 | 5.3 | 1.94 ± 0.32 |
| 3 | 50.3 | 39.3 | 9.8 | 1.76 ± 0.22 |
| 4 | 49.7 | 33.5 | 17.1 | 1.02 ± 0.10 |
| 5 | 49.8 | 24.6 | 26.0 | 0.60 ± 0.04 |
| 6 | 48.5 | 17.2 | 33.0 | 0.92 ± 0.18 |

after leaching times of 16 hr on alloy 6 were not considered.

The extent of reaction as measured by hydrogen evolution as a function of leaching time is shown in Fig. 3. The volume of hydrogen produced, V_H measured at 25°C, 1 atm, is related to the volume of alloy reacted, ΔV , by a stoichiometric constant

$$V_H = k_H \Delta V \quad [2]$$

If corner effects are ignored, it may be shown that the volume reacted of a rectangular prism of original dimensions $L \times L \times W$ is related to the reaction zone depth by

$$\Delta V = 8X^3 - aX^2 + bX \quad [3]$$

where $a = 8L + 4W$, $b = 2L^2 + 4LW$. Combination of Eq. [1], [2], and [3] leads to the result

$$V_H = k_H [8(k_p t)^{3/2} - a k_p t + b (k_p t)^{1/2}] \quad [4]$$

Regression on this equation was carried out for the hydrogen evolution data for one alloy piece and the resulting estimates of k_H are shown in Table II along with values for the 95% confidence interval on the regression coefficient. The small values obtained for this latter quantity indicate that Eq. [4] fits the data well.

Temperature effects on leaching rates were determined from hydrogen evolution measurements. Since the relationship between hydrogen evolution and reaction product layer thickness is shape dependent, measurements were restricted to the early stages of reaction where such effects are small. The rate constant was determined from the expression

$$V_H^2 = k_a t \quad [5]$$

where an Arrhenius plot for k_a is shown in Fig. 4. The

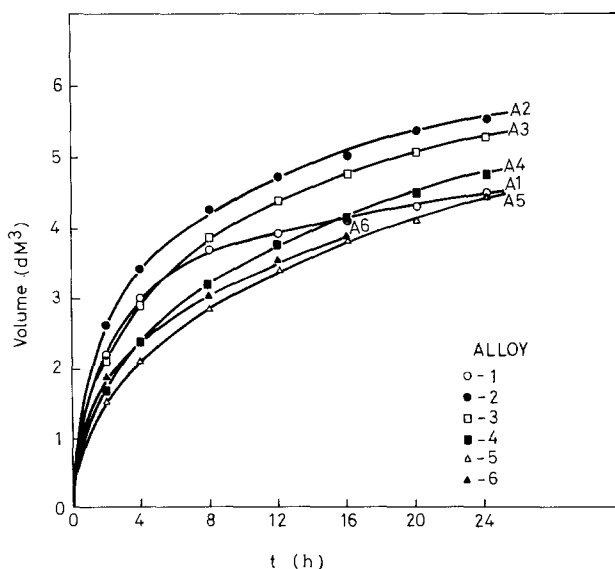


Fig. 3. Hydrogen evolution (corrected to 25°C, 1 atm) from the reaction-affected rim as a function of leaching time.

Table II. Stoichiometric constants for the leaching of the Al-Cu-Zn alloys

| Alloy number | Regression coefficient k_H (Eq. [4]) $\times 10^{-3}$ | Stoichiometric coefficient k_H (Eq. [2]) $\times 10^{-3}$ |
|--------------|---|---|
| 1 | 3.66 ± 0.57 | 3.37 ± 0.17 |
| 2 | 3.62 ± 0.38 | 3.40 ± 0.17 |
| 3 | 3.33 ± 0.19 | 3.36 ± 0.17 |
| 4 | 3.85 ± 0.15 | 3.37 ± 0.17 |
| 5 | 4.20 ± 0.10 | 3.52 ± 0.17 |
| 6 | 3.75 ± 0.35 | 3.54 ± 0.18 |

activation energy was determined to be 41 ± 5 kJ mol⁻¹.

Concentration profiles for aluminum and zinc in the copper phase of the reacted rim as determined by microprobe analysis for alloys 1-4 are shown in Fig. 5 and 6 where the position coordinate has been nor-

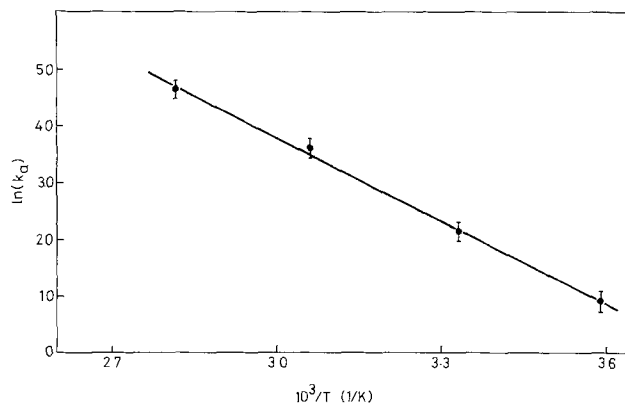


Fig. 4. Arrhenius plot for the leaching of Al-36Cu-14Zn alloy according to Eq. [5].

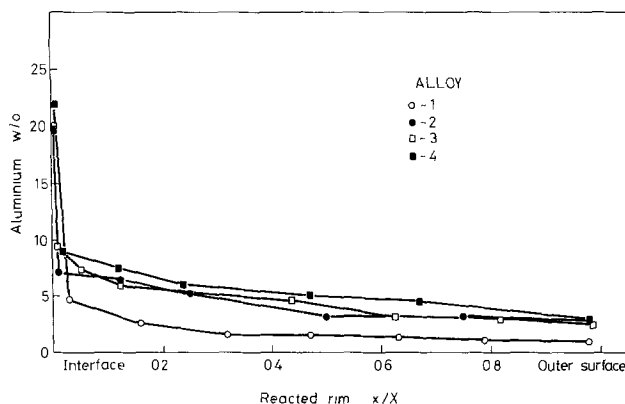


Fig. 5. Aluminum concentration profile in the porous copper grains of the reaction product zone.

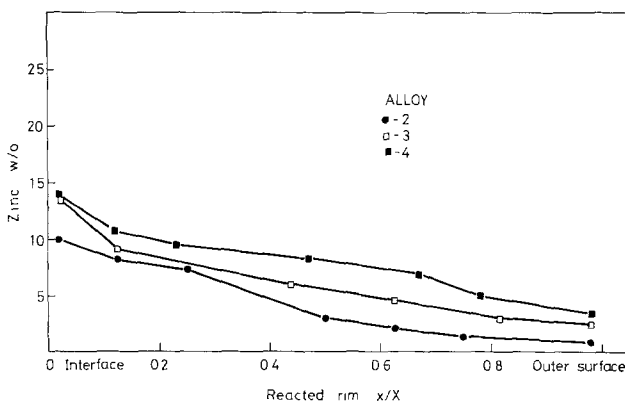
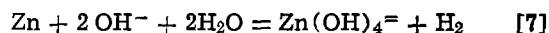
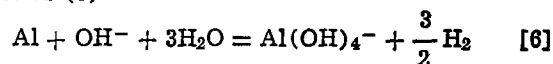


Fig. 6. Zinc concentration profile in the porous copper grains of the reaction product zone.

malized with respect to layer thickness. The microprobe analyses of the copper phase in the reaction product zone were found to total substantially less than 100%, and these analyses have been normalized. Figure 7 shows the plot of zinc concentration as a function of position in the copper phase near the interface. The concentration of zinc in the copper phase is greater than would be expected from that zinc originally present in the Cu(Zn)Al₂ phase. Microprobe scans parallel to the interface through the copper grain near the interface showed no variation in zinc and aluminum concentration. Microprobe scans parallel and at right angles to the interface through a copper grain midway in the reaction product zone again showed no variation in zinc and aluminum concentration.

Discussion

The chemical reactions involved in the leaching of the Al-Cu-Zn alloy with caustic solution may be represented as (8)



These reaction stoichiometries, combined with the values of alloy densities and Al and Zn concentrations, yield a value for the stoichiometric coefficient k_H appearing in Eq. [2] and [4]. Values of k_H calculated in this way are compared with the experimentally determined quantity in Table II. The experimental values are close to the values calculated from reaction stoichiometries, indicating that leaching is close to complete.

The parabolic kinetics of the leaching reaction suggest that the process is diffusion controlled. This diffusion control could arise from three mechanisms: (i) solid-state diffusion in the product layer, (ii) diffusion within the alloy where the noble metal remains as a continuous film at the alloy surface and selective dissolution proceeds by volume diffusion of the active metal through the noble metal layer, and (iii) liquid phase diffusion within the product layer. Mechanism (i) is extremely unlikely since solid-state diffusion in the product layer would be too slow to support the leaching rates experimentally determined.

To determine whether mechanism (ii) could support the observed leaching rate a calculation based on the mechanism proposed by Pickering and Wagner (2) is performed. According to these authors, the flux $J_{\text{Al,Zn}}$ of aluminum or zinc atoms toward the surface is given for high concentrations of Al or Zn by

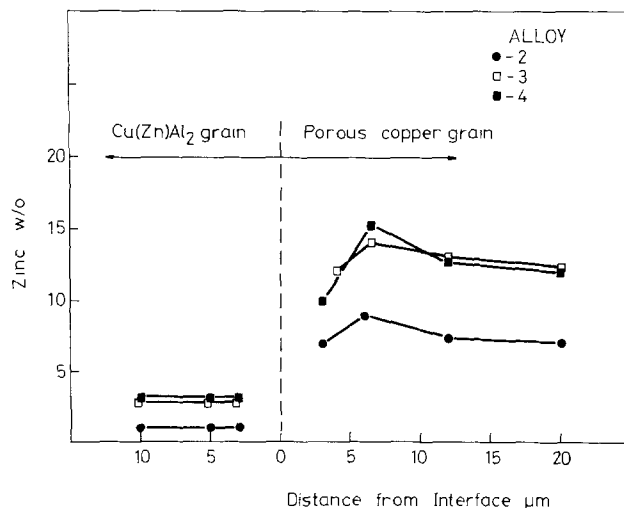


Fig. 7. Zinc concentration profile through a Cu(Zn)Al₂-Cu grain at the alloy-reaction product zone interface.

$$J_{Al,Zn} = \frac{N_{Al,Zn}^0}{V_m} \left[\frac{D_{Al,Zn}}{2(1 - N_{Al,Zn}^0)t} \right]^{1/2} \quad [8]$$

where $N_{Al,Zn}^0$ is the bulk mol fraction of aluminum or zinc in the alloy, V_m is the molar volume which is approximated as a constant, and $D_{Al,Zn}$ is the alloy diffusion coefficient of aluminum or zinc. From the parabolic leaching kinetics, Eq. [1], it follows that

$$dX/dt = 1/2 (k_p/t)^{1/2} = k_p/2X \quad [9]$$

and the combined flux of aluminum and zinc arriving at the surface is

$$dX/dt = V_m (J_{Al} + J_{Zn}) \quad [10]$$

Combining Eq. [8], [9], and [10] and making use of the approximation $D_{Al} \simeq D_{Zn} = D_A$, one has

$$2D_A = k_p \left/ \left[\frac{N_{Al}^0}{(1 - N_{Al}^0)^{1/2}} + \frac{N_{Zn}^0}{(1 - N_{Zn}^0)^{1/2}} \right] \right. \quad [11]$$

which can be used to estimate approximate values for alloy diffusion coefficients.

The average value of D_A from Eq. [11] for the range of alloys studied was found to be 3×10^{-8} cm²/sec. This value is far too high for the accepted values for alloy diffusion at the low temperatures studied and so mechanism (ii) is rejected as the rate-controlling step for the leaching reaction.

If liquid phase diffusion within the product layer is the rate-determining step then alloy diffusion, more specifically diffusion within the Cu(Zn)Al₂ phase, must be fast enough to support it. Alloy diffusion for a planar alloy-product layer interface would be impossible since diffusion distances would be quite large. However, the alloy-product interface is not planar but highly convoluted as is indicated by surface area and pore size measurements (9). A schematic representation is shown in Fig. 8. A similar situation can arise during the oxidation of alloys involving noble metals as has been discussed by Wagner (5) and explored experimentally (6). In the situation shown in Fig. 3

$$J_{Al,Zn} \simeq -D_{Al,Zn} \frac{\partial C_{Al,Zn}}{\partial y} \quad [12]$$

and

$$\frac{\partial C_{Al,Zn}}{\partial y} \simeq \frac{C_{Al,Zn}^0}{\delta} \quad [13]$$

where y is the position coordinate within the alloy, $C_{Al,Zn}^0$ is the bulk molar concentration of aluminum or zinc in the Cu(Zn)Al₂ phase, and δ is the effective thickness of the alloy interdiffusion zone. It follows immediately that



Fig. 8. Schematic representation of a Cu(Zn)Al₂-Cu grain at the alloy-reaction product zone interface.

$$J_{Al,Zn} = D_A \frac{C_{Al,Zn}^0}{\delta} \quad [14]$$

where use has again been made of the approximation $D_{Al} \simeq D_{Zn} = D_A$. Combining Eq. [9], [10], and [14] one obtains

$$D_A = \frac{\delta k_p}{2X(N_{Al}^0 + N_{Zn}^0)} \quad [15]$$

This result was used to estimate D_A on the assumption that δ approximately equals half the interpore separation distance. This distance has been estimated from pore volume and pore diameter measurements (9).

The average value of D_A calculated from Eq. [15] for the range of alloys studied was found to be 2×10^{-12} cm²/sec. Values of diffusion in solidified Cu-Al eutectic mixtures at high temperatures are reported by Smithells (10). A value of 3×10^{-25} cm²/sec was calculated at 50°C by extrapolation of this high temperature data. However, a value of 1.3×10^{-12} cm²/sec has been deduced by Pickering and Wagner (2) for the diffusion of copper atoms by divacancies at 25°C in a copper-gold alloy. This latter value compares favorably with the value calculated from Eq. [15]. It seems, therefore, that liquid phase diffusion within the product layer is the most likely mechanism, since alloy diffusion at the convoluted interface is probably fast enough to support it.

If the leaching reaction is controlled by diffusion in the liquid phase within the product layer then the reaction rate should reflect the mobilities of the solute species responsible for mass transport. The transport of hydroxyl ions from the bulk liquid to the alloy-product layer interface, where reaction occurs, is now considered. Since the product layer is composed largely of copper, no electrostatic potential gradient can be sustained and the appropriate transport equation is simply

$$J_{OH^-} = -D_{OH^-} \frac{\partial C_{OH^-}}{\partial x} \quad [16]$$

where x is the position coordinate. To a first approximation then

$$J_{OH^-} = D_{OH^-} C_{OH^-}^{(o)}/X \quad [17]$$

where $C_{OH^-}^{(o)}$ is the hydroxyl ion concentration at the outer surface of the product layer. In the steady state, the rate of arrival of hydroxyl ions at the alloy surface must be stoichiometrically equivalent to the rate of leaching

$$|J_{OH^-}| = J_{Al} + 2J_{Zn} \quad [18]$$

Since leaching is close to quantitative, the metal fluxes are related according to the bulk alloy composition

$$J_{Al}/J_{Zn} = N_{Al}^0/N_{Zn}^0 \quad [19]$$

Thus the mass balance at the alloy-product layer interface is described by Eq. [18] and [19] which, together with Eq. [9] and [10] yield

$$k_p = 2V_m D_{OH^-} C_{OH^-}^{(o)} \left(\frac{1 + N_{Zn}^0/N_{Al}^0}{1 + 2N_{Zn}^0/N_{Al}^0} \right) \quad [20]$$

The application of this equation to present results, using the molar volume of Al, yields an estimate of $D_{OH^-} = 1 \times 10^{-6}$ cm² sec⁻¹, equivalent to a mobility of 3.6×10^{-5} cm² sec⁻¹ V⁻¹. This is significantly less than the reported value for hydroxyl ions of 2×10^{-3} cm² sec⁻¹ V⁻¹ at 25°C (11). In view of the fact that solution viscosity and pore tortuosity effects have not been taken into account, the agreement is reasonable. The appropriate data for Al(OH)₄⁻ and Zn(OH)₄²⁻ appears to be unavailable and no conclusion can be reached as to the nature of the rate-determining species in the solution.

The leaching of alloy 1, as seen in Fig. 1 and 3, displays a different trend to the alloys which contain zinc. This is possibly due to the higher copper content in the eutectic material. The effect of alloy composition on the leaching rate is shown in Fig. 9. Introduction of a small amount of zinc to the alloy substantially increases the leaching rate, but addition of more zinc results in a decrease in the leaching rate. If, as has been argued above, the leaching process is controlled by liquid phase diffusion, then these effects of alloy composition on the rate must indicate changes in the boundary values for the activities of the diffusing species. Since the hydroxyl ion activity is controlled at one boundary by the bulk solution and since its activity at the other boundary is probably very low, the hydroxyl ion diffusion rate is not expected to be sensitive to variation in alloy composition. However, the outward diffusion rates of $\text{Al}(\text{OH})_4^-$ and $\text{Zn}(\text{OH})_4^{2-}$ ions will depend on the boundary values of their activities at the product-layer alloy interface where they are created. These values are in turn expected to depend on alloy composition.

As zinc is added to the alloy its activity must rise and, if equilibrium at the alloy-product interface obtains, so too must the activity of $\text{Zn}(\text{OH})_4^{2-}$ ion at this boundary. The effect on alloy aluminum activity may be seen by modeling the alloys as belonging to a simple two-phase system: $\text{Cu}(\text{Zn})\text{Al}_2$ plus Al-Zn solid solution. It has been shown (1) that addition of zinc to the former phase is at the expense of the copper, the total effect being small. In the series of alloys under discussion, zinc has been incorporated at the expense of the copper, the aluminum concentration remaining constant. Most of this zinc is taken up in the Al-Zn solid solution, the volume fraction of which increases accordingly. The consequent decrease in $\text{Cu}(\text{Zn})\text{Al}_2$ volume fraction is shown as a function of alloy zinc content in Fig. 9. As a result, the aluminum activity in the Al-Zn solid solution is expected to decrease with increasing alloy zinc content. If equilibrium exists within the alloy, the aluminum activity in $\text{Cu}(\text{Zn})\text{Al}_2$ also decreases. If equilibrium obtains at the alloy-product layer interface, the decrease in alloy aluminum activity will lead to a decrease in the activity of $\text{Al}(\text{OH})_4^-$ ion at this boundary. Consequently the rate of outward diffusion of this species will be lessened. Since the rates of leaching of aluminum and zinc are related by the mass balance, the overall leaching reaction is therefore decreased in rate. Such a model could explain the decrease in leaching rate observed as the alloy zinc content is increased from 5 to 26 w/o, but does not explain the increase in rate observed as the zinc level is increased from zero to 5 w/o. It is quite possible that at this low level of zinc,

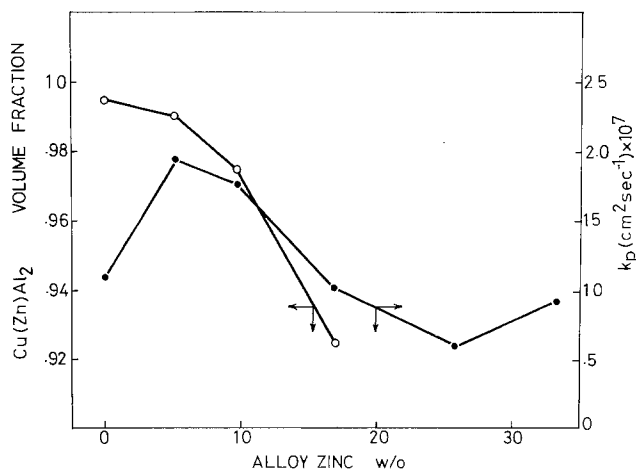


Fig. 9. Leaching rate constant and alloy volume fraction of $\text{Cu}(\text{Zn})\text{Al}_2$ as a function of alloy zinc content.

interactions within the ternary system are such as to increase the aluminum activity and hence accelerate the leaching process. Although qualitatively successful, this description is incomplete as it fails to take into account kinetic effects arising from a contribution to rate control due to the interfacial reaction. The importance of this chemical reaction control is now considered.

The activation energy deduced from Fig. 4 was $41 \pm 5 \text{ kJ mol}^{-1}$. This value is higher than for a strictly liquid phase diffusion process where values of 8-25 kJ mol^{-1} have been reported (12). However, the activation energy is not quite in the chemical reaction region where values of 100-175 kJ mol^{-1} have been reported (12). Thus the value obtained for the activation energy suggests that there may be some element of chemical reaction control in the leaching process. Further support for this conclusion is provided by the shape of the concentration profiles in the product layers (Fig. 5 and 6).

The form of the transport equation appropriate to solute Al and Zn species in the liquid phase within the reaction product layer is given by Eq. [16]. For a divergence-free flux it follows, therefore, that the concentration gradient is constant. If local equilibrium exists between the copper and the adjacent liquid, it follows that the concentration gradients of Al and Zn within the solid must also be constants. The linear concentration profiles predicted from this model for alloy 3 are seen in Fig. 10 and 11 to be a reasonable approximation to experimental observation for both Al and Zn over most of the product layer thickness. It is apparent, however, that the model is inapplicable in the region adjacent to the alloy-product layer interface.

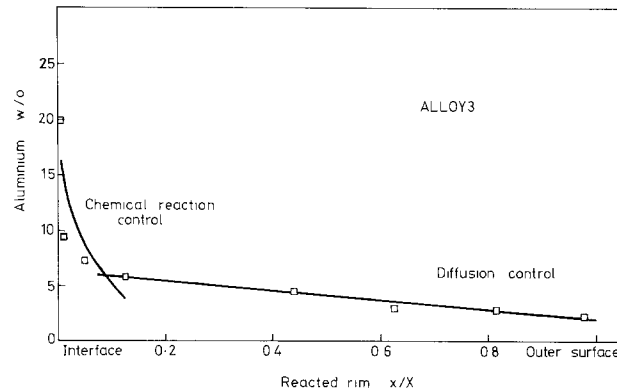


Fig. 10. Aluminum concentration profile in the porous copper grain of the reaction product zone for alloy 3 showing lines resulting from regression for diffusion control and for chemical reaction control, Eq. [23].

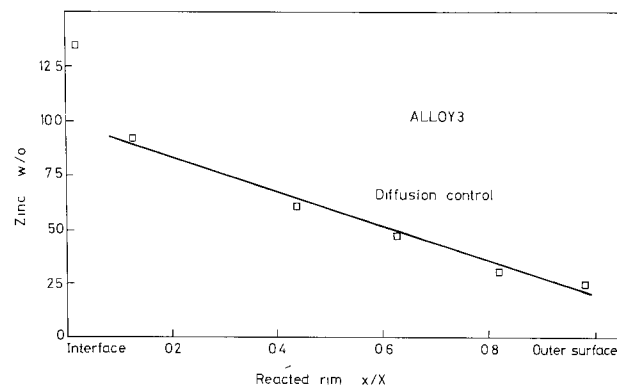


Fig. 11. Zinc concentration profile in the porous copper grain of the reaction product zone for alloy 3 showing the line resulting from regression for diffusion control.

If, instead of equilibrium, chemical reaction control prevails over the solid-liquid partition of Al and Zn within the product layer then the remnant concentrations of Al and Zn within the Cu phase are, to a first approximation, independent of liquid phase concentrations. Instead, the concentration of leachable elements will be determined by the rate law governing the reaction and by the time for which the portion of solid being considered has been exposed to the liquid phase. In this case, the reaction might well be pseudo-first order with respect to metal concentration

$$C_{\text{Al,Zn}} = C^{\circ}_{\text{Al,Zn}} \exp(-k_c t_e) \quad [21]$$

where t_e is the time of exposure and k_c is the reaction rate constant. If x is the position coordinate within the layer with $x = 0$ at the interface then, from Eq. [1]

$$t_e = \frac{2xX - x^2}{k_p} \quad [22]$$

Which, upon substitution in Eq. [21], yields

$$\ln(c/c^{\circ})_{\text{Al,Zn}} = (x^2 - 2xX)k_c/k_p \quad [23]$$

Regression on this equation of the aluminum concentration data near the alloy-product layer interface revealed a better fit than the linear concentration profiles. An example is shown in Fig. 10. It is concluded that the leaching of aluminum proceeds under liquid phase diffusion control except when the concentration of Al is high, where chemical reaction control obtains. This latter regime is restricted to a narrow region of the product layer near the alloy surface. No such conclusion is possible in the case of Zn, where the concentration profile shows a maximum near the alloy-product layer interface (Fig. 7).

Values of the zinc concentration at the maximum points in the profiles are listed in Table III. Also shown in this table are the maximum concentrations of Zn predicted from the composition of the precursor Cu(Zn)Al₂ phase on the assumption that initially only Al is leached. Clearly the observed Zn levels cannot be accounted for on this basis and movement of Zn into the leached Cu(Zn)Al₂ grain from elsewhere must be occurring. The ultimate source of the excess Zn is, of course, the alloy Al-Zn solid solution phase. This phase leaches readily, leading to a high liquid phase activity of Zn. When such a liquid reacts with Cu(Zn)Al₂ to dissolve Al the hydroxyl ion activity is depleted. The solubilities of Al and Zn in caustic solutions are widely different (13): assuming that the precipitation product of Al is hydrargillite Al₂O₃ · 3H₂O and that of Zn is Zn(OH)₂ then the ratio of Al solubility to Zn solubility is 16/1. Clearly then, the dissolution of Al from Cu(Zn)Al₂ can deplete the OH⁻ activity to the point where Zn is precipitated. It is suggested that this is the reason for the observed accumulation of Zn in the solid phase near the reaction front. As that front recedes, the OH⁻ activity rises and Zn commences to redissolve. Simultaneously, fur-

ther precipitation occurs near the receding reaction front where the OH⁻ activity is depleted. The location of the Zn concentration maximum in the solid phase is determined by the OH⁻ activity gradient in the liquid and is therefore found to follow the alloy-product layer interface.

Conclusions

It has been shown that the leaching kinetics of aluminum-copper-zinc alloys with aqueous sodium hydroxide are parabolic in nature. The reaction mechanism is one of selective dissolution where the rate is controlled by liquid phase diffusion through the product layer. The product layer consists of porous copper, derived from leaching the alloy Cu(Zn)Al₂ phase, containing a zinc and an aluminum concentration profile. The aluminum and zinc profiles in the porous copper were shown to be consistent with reaction control by liquid phase diffusion over most of the product layer. Chemical reaction control was shown to prevail near the alloy-product layer interface for aluminum leaching. No such conclusion is possible for zinc where the concentration profile shows a maximum near the alloy-product interface. A small component of chemical reaction control is consistent with minor deviations from parabolic leaching kinetics and an activation energy that does not quite fit into the diffusion control regime. An explanation for the unexpectedly high zinc content in the porous copper near the alloy-product layer interface has been proposed.

Acknowledgments

Support was provided under the National Energy Research, Development and Demonstration Program administered by the Commonwealth Department of National Development.

Manuscript received Nov. 13, 1980.

Any discussion of this paper will appear in a Discussion Section to be published in the June 1982 JOURNAL. All discussions for the June 1982 Discussion Section should be submitted by Feb. 1, 1982.

Publication costs of this article were assisted by The University of New South Wales.

REFERENCES

1. J. B. Friedrich, D. J. Young, and M. S. Wainwright, *This Journal*, **128**, 1840 (1981).
2. H. W. Pickering and C. Wagner, *ibid.*, **114**, 698 (1967).
3. H. G. Feller, *Corros. Sci.*, **8**, 259 (1968).
4. R. H. Heidersbach and E. D. Verink, *Corrosion*, **28**, 397 (1972).
5. C. Wagner, *This Journal*, **103**, 571 (1956).
6. J. H. Harrison and C. Wagner, *Acta Metall.*, **7**, 722 (1959).
7. H. W. Pickering, in "Corrosion Problems in Energy Conversion and Generation," C. S. Tedman, Editor, p. 151, The Electrochemical Society Soft-bound Proceedings Series, Princeton, N.J. (1974).
8. A. I. Vogel, "Macro and Semimicro Qualitative Inorganic Analysis," 4th ed., Longman (1974).
9. J. B. Friedrich, M. S. Wainwright, and D. J. Young, To be published.
10. C. J. Smithells, "Metals Reference Book," Vol. II, Butterworths, London (1955).
11. S. Glasstone, "An Introduction to Electrochemistry," D. Van Nostrand, New York (1942).
12. S. Glasstone, K. J. Laidler, and H. Eyring, "The Theory of Rate Processes," McGraw-Hill, New York (1941).
13. M. Pourbaix, "Atlas of Electrochemical Equilibria in Aqueous Solutions," Pergamon Press, London (1966).

Table III. Zinc concentration in the porous copper grains of the reaction product zone

| Alloy number | Maximum zinc measured (w/o) | Maximum zinc expected from Cu(Zn)Al ₂ grain (w/o) |
|--------------|-----------------------------|--|
| 2 | 9.6 | 2.1 |
| 3 | 14.1 | 5.3 |
| 4 | 16.0 | 5.8 |

The Primary Passive Film on Li in SOCl₂ Electrolyte Solutions

R. V. Moshtev, Y. Geronov, and B. Puresheva

Central Laboratory of Electrochemical Power Sources, Bulgarian Academy of Sciences, Sofia 1040, Bulgaria

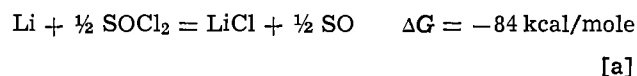
ABSTRACT

The primary passive film on Li in SOCl₂ electrolyte solutions is studied by galvanostatic pulse technique. The evolution of the resistance and capacitance of the Li electrode in SOCl₂ solutions of LiAlCl₄ under open-circuit conditions is interpreted in terms of a two-stage process involving the formation of a continuous dense LiCl film and its growth by ion migration and/or diffusion across the solid film. The film resistivity, its activation energy, the Tafel current-field relation, and the high field transients give evidence for an ion conducting solid film. The film growth is limited by its chemical dissolution. The rate of the latter controls the self-discharge rate of the Li anode as well as the growth of the secondary porous film, which is responsible for the voltage delay effects in Li/SOCl₂ primary cells.

In all nonaqueous electrolyte solutions used for practical Li cells, the Li anode is passivated by the formation of a protective film (1). In electrolyte solutions with organic solvents, e.g., propylene carbonate, tetrahydrofuran, and acetonitrile with SO₂, the film is comparatively thin and of no great consequence to the cell performance. In SOCl₂ electrolyte solutions, however, the film grows almost throughout the whole useful life of the cell and causes the severe voltage delay problems. It is evident that the film which is capable of inhibiting completely one of the most vigorous chemical reactions between the most negative metal and one of the most powerful oxidants should possess exceptionally good insulating properties. One could hardly assume, however, that the coarse crystalline, porous film exhibited in the SEM pictures in the papers of Dey (1, 2) could have the barrier properties necessary for the complete passivation of Li. The full suppression of the corrosion of Li in SOCl₂ electrolyte solutions as revealed by the long storage life of practical Li/SOCl₂ cells used in pacemakers (3, 4) strongly suggests that beneath the porous film observed under the microscope there exists a thinner nonporous film, serving as an efficient barrier between the metal and the oxidant.

In two preliminary communications (5, 6) it was reported that the primary passive film on Li in SOCl₂ solutions has a high specific resistance and conducts according to the law of field-assisted ionic migration. Later Peled *et al.* (7) developed similar ideas on the properties of the passive film on lithium in SOCl₂ electrolyte solutions.

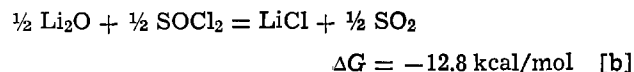
Chua *et al.* (8) have studied the composition of the secondary passive film on Li obtained in SOCl₂ solutions using energy dispersion spectrometry and x-ray diffractometry. They have shown that the film consists essentially of LiCl with minor amounts of S. The SEM pictures of Dey (1), showing the cubic crystallites of LiCl forming the film, confirm these findings. It is usually assumed that the reaction leading to the initial formation of the LiCl film is



However, as shown by the recent Auger electron spectroscopic (AES) measurements of David *et al.* (9), even at extremely low oxygen exposures (66 Langmuirs) the freshly cut Li surface is immediately covered by an Li₂O film. Under practical conditions in Ar

flushed dry boxes the exposure time and oxygen concentration are much higher and one should always take into account the thin oxide film on the Li surface which could modify the mechanism and kinetics of growth of the primary passive film in SOCl₂ solutions.

Using AES technique Keil *et al.* (10) have demonstrated under stringently controlled environmental conditions that the reaction of the oxide-covered Li surface with SOCl₂ vapors produces a thin LiCl film (~100Å) as a primary reaction product. The free energy change of this reaction



is much lower than that of reaction [a]. This explains the absence of a strong exothermal effect upon the immersion of Li in SOCl₂.

Experimental

Three-compartment cells were used housing the test, the counter, and the reference electrode, all made of Li metal (Merck). The free surface area of the test electrodes was 0.1-0.3 cm². The reference was an Li wire with 1 mm OD plugged in Teflon. The test electrode was polished by pressing a freshly cut disk to a polyester foil, whereby the Li surface acquired a mirror-like appearance. The electrodes and the cells were prepared and assembled in an Ar flushed dry box (H₂O less than 20 ppm). A second dry box was used for the electrolyte preparation and for the filling of the cell with the solution in order to eliminate the tarnishing of the Li surface by SOCl₂ vapors.

Thionyl chloride (Merck) was distilled after refluxing for several hours with Li wire. Reagent grade LiCl was recrystallized and dried under vacuum at 160°C for 24 hr. P.a. grade AlCl₃ was resublimated 3 times before use. The LiAlCl₄ solutions were prepared by the successive dissolution method. A 10% excess of LiCl over the stoichiometric ratio was added in some cases to neutralize completely the free AlCl₃. Water content in the solvent and in the solutions was determined by IR spectroscopy (11, 12) and did not exceed 50 ppm.

The changes occurring at the surface of the Li test electrode after its immersion in the SOCl₂ electrolyte solution were followed by measuring periodically the electrode resistance and capacitance by means of the galvanostatic pulse technique. The capacitance and the IR drop in the solution were determined by applying short galvanostatic pulses (5-20 μsec) with an ampli-

Key words: batteries, passivity, film formation.

tude not exceeding 2 mA/cm^2 . The initial slope of the potential-time transients recorded by a Textronix 5541 storage oscilloscope (Fig. 1a) was used to estimate the electrode capacitance. The electrode resistance was assessed from longer cathodic galvanostatic pulses ($0.5\text{--}5 \text{ msec}$) but with a lower amplitude ($<0.5 \text{ mA/cm}^2$) whereby the steady-state overvoltage in the transient (Fig. 1b) did not exceed $10\text{--}20 \text{ mV}$ (*i.e.*, in the linear polarization range). In both measurements the charge associated with the pulses was less than $2 \mu\text{C/cm}^2$ corresponding to a film thickness less than 0.4 \AA . Thus any changes in the film thickness due to the measuring pulses were much smaller than the thickening of the film during the polarization-free interaction between the Li surface and the SOCl_2 solution. The temperature of the cell was maintained at 25°C with the aid of a small air thermostated dry box.

Results and Discussion

Evidence for a nonporous film.—One of the first questions arising when studying a thin passive film is whether it is porous or compact. In order to answer this question an Li electrode was kept for 24 hr in a 1 M LiAlCl_4 solution whereby the resistance and the capacitance attained steady-state values: $R = 247 \Omega \cdot \text{cm}^2$ and $C = 0.267 \mu\text{F/cm}^2$, implying that the growth of the primary passive film has ceased. After that the electrolyte solution in the cell was substituted by a 0.1 M LiAlCl_4 solution and the values of R and C were determined again and after 2, 6, and 16 hr. In all the measurements R remained exactly the same ($247 \Omega \cdot \text{cm}^2$), while C showed a slightly lower value of $0.216 \mu\text{F/cm}^2$. After that the electrolyte solution was changed once more to the initial 1 M concentration. The measurements immediately after the change revealed that the initial values of R and C were restored ($247 \Omega \cdot \text{cm}^2$ and $0.267 \mu\text{F/cm}^2$).

The constancy of the film resistance R when the electrolyte solution resistance was lowered by one order of magnitude (\times of 1 M LiAlCl_4 in SOCl_2 is $1.5 \times 10^{-2} \Omega^{-1} \cdot \text{cm}^{-1}$ and that of 0.1 M LiAlCl_4 , $1 \times 10^{-3} \Omega^{-1} \cdot \text{cm}^{-1}$) lends a strong evidence for a dense, pore-free passive film. The decrease of the electrode capacitance, on the other hand, with the lowering of the electrolyte concentration suggests that the electrode impedance comprises a series capacitance reflecting the diffuse double layer (d_l) in the electrolyte solution.

Ionic conduction of the primary passive film.—Figure 2 presents a typical set of experimental plots reflecting the increase of the electrode resistance R and the reciprocal capacitance $1/C$ with time of an Li electrode immersed in a 0.5 M LiAlCl_4 solution in SOCl_2 . Figure 3 gives the same experimental data in the form of a $1/C$ vs. R plot, each point (full symbols) pertaining to one and the same moment. It was found in more than 50 separate experiments, carried out in solutions with various electrolyte concentrations, that in all cases the $1/C$ - R plots reveal two distinct rectilinear regions

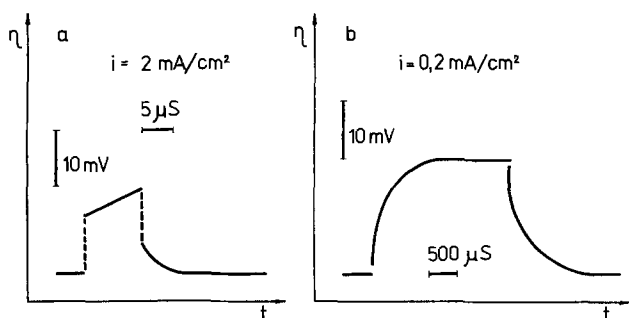


Fig. 1. Typical potential-time transients: a, short transient for the measurement of the electrode capacitance; b, long transients for the measurement of the electrode polarization resistance.

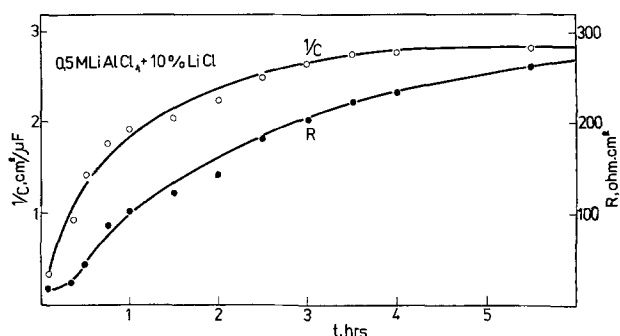


Fig. 2. Increase with time of the electrode reciprocal capacitance $1/C$ and the electrode resistance R .

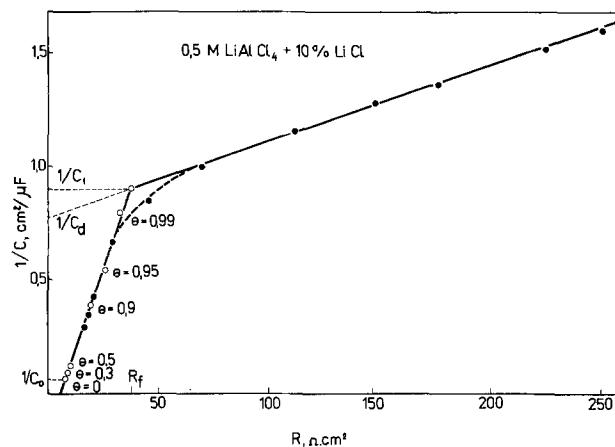


Fig. 3. Typical $1/C$ vs. R plot

with different slopes, as illustrated by Fig. 3. Depending on the electrolyte composition and the thickness of the initial oxide film, the ratio of the slopes in the two regions may vary from 3:1 to 10:1 and the transition from the first to the second straight line is in most cases abrupt.

The slope in the first region $k_1 = (d(1/C)/dR)$ varied in the separate experiments from 0.02 to $0.05 \mu\text{F}^{-1} \cdot \Omega^{-1}$. No relation was found between k_1 and the electrolyte composition. The extrapolated value of $R = R'$ at $1/C = 0$ is from 0 to $6 \Omega \cdot \text{cm}^2$.

Special experiments were carried out to assess the initial (in time) values of R and C as soon as possible after the contact of Li with the solution, *i.e.*, when the surface of the metal is essentially free of an LiCl film ($\theta = 0$). The limiting values of R and C were $C_0 = 14\text{--}18 \mu\text{F/cm}^2$ and $R_0 = 2\text{--}6 \Omega \cdot \text{cm}^2$ for times not exceeding 3-4 min.

The present findings could be interpreted in terms of a two-stage growth of the primary passive film on Li. The first stage is assumed to involve the formation of LiCl crystal nuclei and the increase of their number with time. The increase of $1/C$ and R with time at this stage is assigned to the increase of the electrode coverage θ by LiCl grains. In the second stage the increase of $1/C$ and R is determined only by the increase of the LiCl film thickness which eventually grows by ionic migration across the solid phase.

For a more comprehensive discussion of the present experimental results the following simplified equivalent circuit is assumed (Fig. 4). Here R' denotes the small intercept of the $1/C$ - R plot at $1/C = 0$, presumably due to incorrectly compensated IR drop in the solution. C_0 and R_0 represent the capacitance and resistance of the initial thin oxide film. C_f and R_f pertain to the completed layer of the primary LiCl film with an initial thickness y_1 at the moment when the coverage θ has reached unity.

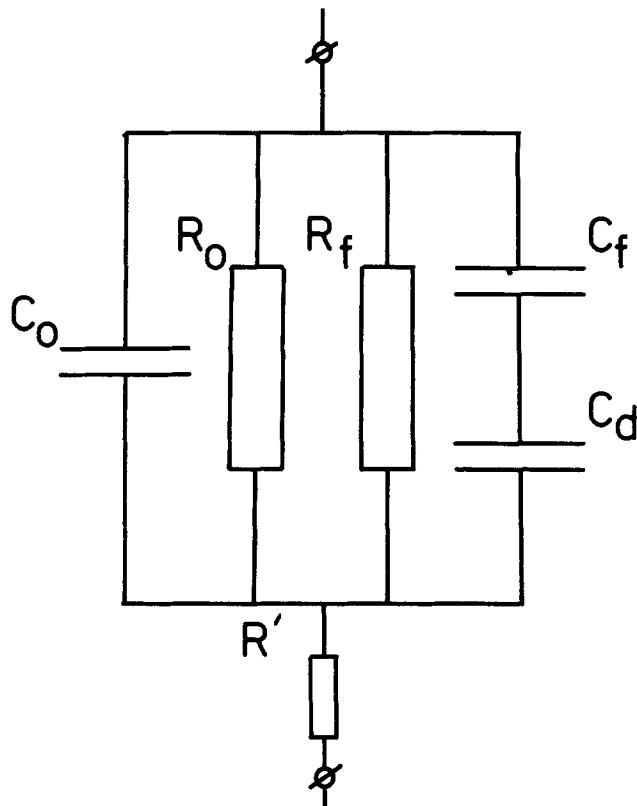


Fig. 4. Simplified equivalent circuit of the Li electrode during the formation and growth of the primary passive film (see text).

It is difficult to assess directly the physical meaning of the capacitance C_d in series with the film capacitance C_f . The results in the previous section, showing that the electrode capacitance decreases with the lowering of the electrolyte concentration, suggest that C_d might reflect the dl capacitance in the diffuse layer of the liquid electrolyte solution.

During the first stage of the film formation both C and R are functions of θ according to

$$C = (1 - \theta)C_0 + \theta C_f \cdot C_d / (C_f + C_d) \quad [1]$$

$$R = R_0 \cdot R_f / [\theta R_0 + (1 - \theta)R_f] + R' \quad [2]$$

where C_0 , R_0 , C_f , R_f , R' , and C_d are assumed to be independent of θ . This implies that the oxide film thickness and the average size of the LiCl nuclei remain practically constant during the formation of the film in the first stage.

It is reasonable to suppose that the intersection point of the two rectilinear portions of the $1/C$ - R plot (Fig. 3) corresponds to the conditions $\theta = 1$ and hence from the values of $C = C_1$ and $R = R_1$ at this point one can obtain $R_f = R_1 - R'$ and $1/C_f = 1/C_1 - 1/C_d$ pertaining to the first completed layer of the LiCl primary film.

By way of an example, Eq. [1] and [2] were exploited with the experimental data shown in Fig. 3: $1/C_0 = 0.063 \text{ cm}^2/\mu\text{F}$, $1/C_d = 0.72 \text{ cm}^2/\mu\text{F}$, $1/C_1 = 0.84 \text{ cm}^2/\mu\text{F}$, $R_1 = 32 \Omega \cdot \text{cm}^2$, $R_0 = 2 \Omega \cdot \text{cm}^2$, $R' = 1 \Omega \cdot \text{cm}^2$ at several values of θ . The calculated points (open symbols) fall closely on the experimental line (full symbols) and give an idea of the effect of θ on R and $1/C$ during the first stage of the film formation. This result implies that the slope

$$k_1 = \frac{\partial(1/C)/\partial\theta}{\partial R/\partial\theta} \approx 1/R_0 C_0 \quad [3]$$

is independent of θ and is a function only of the properties of the initial oxide film residing on the Li surface prior to its contact with the SOCl_2 solution. It should

be noted that Eq. [3] is valid only in cases like the present where $R_f \gg R_0$, $1/C_f \gg 1/C_0$, and $1/C_d \gg 1/C_f$.

The thickness of the primary LiCl film y can be calculated by the formula of the parallel plate capacitors connected in series

$$y = 8.85 \times 10^{-8} \epsilon \sigma (1/C - 1/C_d), \text{ cm} \quad [4]$$

where the capacitances are in $\mu\text{F}/\text{cm}^2$ and σ is the roughness coefficient. The thickness of the film can be estimated also from the film resistance by

$$y = xR \cdot \sigma, \text{ cm} \quad [5]$$

with R in $\Omega \cdot \text{cm}^2$ and x in $\Omega^{-1} \cdot \text{cm}^{-1}$. By equating [4] and [5] and differentiating, one can obtain the slope of the $1/C$ - R plot in the second region

$$k_2 = \frac{\partial(1/C)/\partial y}{\partial R/\partial y} = [\partial(1/C)/R] = \frac{x}{\epsilon \cdot 8.85 \times 10^{-8}}, \quad \mu\text{F}^{-1} \cdot \Omega^{-1} \quad [6]$$

It was established that the slope k_2 is strongly dependent on the concentration of the free Lewis acid AlCl_3 in the 1M LiAlCl_4 solution as shown in Fig. 5. On the other hand, it is known that LiAlCl_4 solutions in SOCl_2 prepared by the successive dissolution method (as in the present investigation) always contain some free AlCl_3 since the neutralizations of the last portions of AlCl_3 by LiCl proceed rather slowly. This fact explains the results in Fig. 6 where the slope k_2 is plotted vs. the time of neutralization of the free AlCl_3 in a 0.5M LiAlCl_4 solution containing 10% excess of LiCl above the stoichiometric amount. Each point in Fig. 6 reflects the value of k_2 obtained with a new Li electrode immersed in the solution after the latter has been kept for neutralization for the time shown on the abscissa. It can be seen that with the progress of the neutralization, k_2 diminishes to reach a steady-state value of $2.8 \times 10^{-8} \mu\text{F}^{-1} \cdot \Omega^{-1}$ after 20 days.

The application of Eq. [4] and [5] for the determination of the film thickness requires the knowledge of x and ϵ . Data of x and ϵ for thin LiCl films are not available so one is compelled to use values reported for bulk samples. Hence we shall use here $\epsilon = 10.62$ reported for pure LiCl bulk samples (13).

The specific conductivity of bulk samples of pure and Mn^{2+} -doped LiCl crystals has been studied in detail by Haven (14). In the impurity region ($130^\circ < t^\circ < 400^\circ\text{C}$) the temperature dependence of x is described by

$$\log x = \log N - W/2.3kT \quad [7]$$

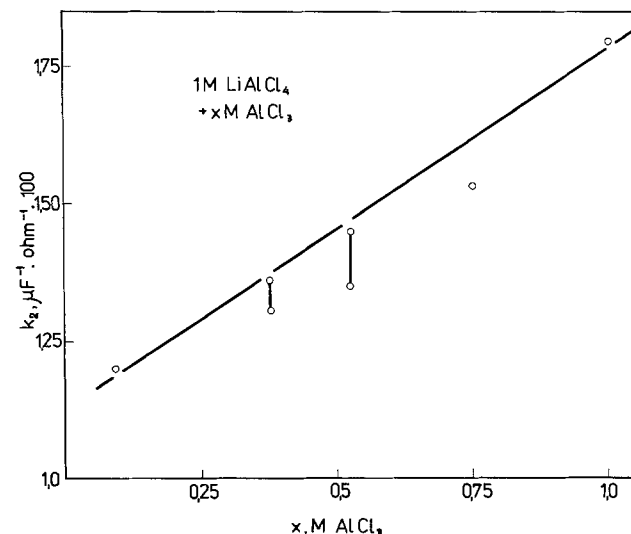


Fig. 5. Effect of the concentration of free AlCl_3 in a 1M LiAlCl_4 solution on the slope k_2 (Eq. [6]) of the $1/C$ - R plots.

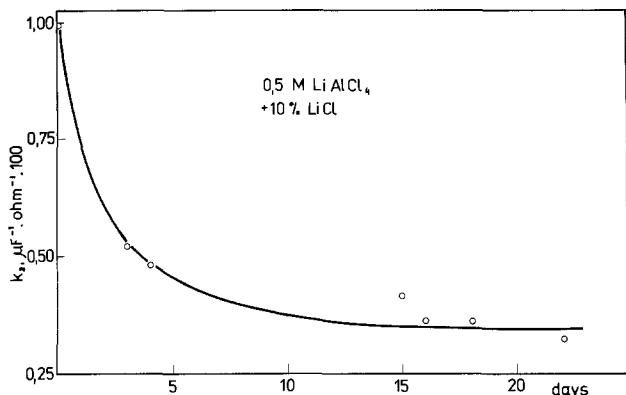


Fig. 6. Effect of neutralization of a 1M LiAlCl₄ solution with 10% excess of LiCl on the slope k_2 (Eq. [6]).

where N is proportional to the impurity concentration and $W = 0.41$ eV. The value of α at 298 K calculated by Eq. [7] with $N = 0.03$ pertaining to undoped LiCl samples with the lowest impurity level (14), was found to be $3.7 \times 10^{-9} \Omega^{-1} \cdot \text{cm}^{-1}$. Introducing the above values of α and ϵ in Eq. [6] for the slope k_2 we obtain $3.9 \times 10^{-3} \mu\text{F}^{-1} \cdot \Omega^{-1}$. This is fairly close to the present experimental value $k_2 = 2.8 \times 10^{-3} \mu\text{F}^{-1} \cdot \Omega^{-1}$, observed for an Li electrode immersed in a 0.5M LiAlCl₄ solution, which has been kept prior to the experiment for 20 days with a 10% excess of LiCl (Fig. 6). Since the dielectric constant of ionic crystals is not very sensitive to aliovalent impurities it is reasonable to assign the effect of AlCl₃ on k_2 (Eq. [6]), demonstrated in Fig. 5 and 6, to the increase of α only. This effect is supposedly associated with the inclusion of Al³⁺ in the crystal lattice of LiCl leading to a respective increase in the cation vacancy concentration. A substitution of Li⁺ by Al³⁺ appears feasible in view of the ionic radii of these ions: 0.68Å for Li⁺ and 0.57Å for Al³⁺.

The agreement (within 30%) between the experimental and calculated values of k_2 offers a certain reliability in the estimation of the film thickness by Eq. [4] or [5] using the experimental values of R and C . It should be noted that the film thicknesses thus evaluated ought to be regarded as relative values, until experimental data acquired by direct optical or physical methods become available.

It was found that the thickness of the first complete layer of the primary LiCl film y_1 at $\theta = 1$ varies from 11 to 60Å in the separate experiments. The mean value of $y_1 = 32 \pm 5$ Å corresponds to 5 ± 1 monolayers of LiCl (lattice parameter 5.13Å).

The apparent activation energy $W = 0.37$ eV of the ionic conductivity was assessed by the temperature dependence of α of a primary film with a constant thickness ($y = 400$ Å) in the temperature range -38° to $+7^\circ\text{C}$. This is close to the value $W \pm 0.41$ eV reported by Haven (14) for LiCl bulk samples in the temperature range 130° - 400°C .

Unfortunately, there is no literature data for W in the lower temperature range for a more complete comparison.

Kinetics of the film growth.—The kinetics of the primary film growth was studied by y - t plots using y values estimated by Eq. [4] or [5] with data of α and $1/C_d$ calculated from the respective $1/C$ - R plot assuming $\epsilon = 10.62$ and $\sigma = 1$. Figure 7 presents a series of y - t plots of films with various specific conductivities. It is seen that the rate of growth at one and the same thickness increases as the specific conductivity grows. The inspection of numerous kinetic curves showed that they all have an initial parabolic region, followed by an asymptotic one. These results as well as the high field behavior of the film suggest that the

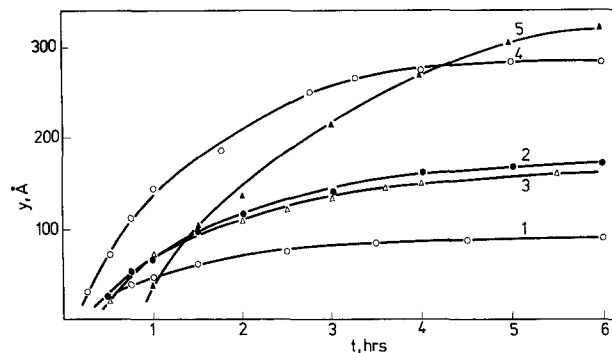


Fig. 7. Kinetic curves for the growth of primary passive films on Li with various specific conductivities ($\Omega^{-1} \text{cm}^{-1} \times 10^{-8}$): curve 1, 0.39; curve 2, 0.74; curve 3, 0.94; curve 4, 1.03; curve 5, 1.27.

primary film grows through ionic migration and/or ionic diffusion in the solid phase and is at the same time subjected to a slow chemical corrosion.

As a first approximation the instantaneous net rate of the film growth v can be expressed by the general differential equation

$$\left[\frac{\partial v}{\partial t} \right] = v = v_g + v_d - v_c, \quad \text{cm/sec} \quad [8]$$

The first term v_g reflects the rate of the film growth by ionic migration due to a small constant potential difference $\Delta\phi$, set up by the redox couple in the solution $\text{SOCl}_2/\text{Cl}^-$.

The second term v_d accounts for the film growth by ionic diffusion due to the eventual concentration difference ΔC at the two interfaces (metal/film and film/solution) of the diffusing species, e.g., the cation vacancies.

The third term v_c expresses the rate of the film corrosion v_c due to its chemical dissolution, which is assumed to be constant under isothermal conditions.

Assuming the validity of Ohm's law at the prevailing low electric field, we may write

$$v_g = \left(\frac{1}{y} \right) \left[\frac{\Delta\phi \cdot V_m \cdot \alpha}{F} \right], \quad \text{cm/sec} \quad [9]$$

with $V_m = 20.6 \text{ cm}^3/\text{mol}$ the molar volume of LiCl.

Assuming further the validity of the Nernst-Einstein relation, the second term of [8] can be given by

$$v_d = \left(\frac{1}{y} \right) [\Delta C \cdot D \cdot V_m] = \left(\frac{1}{y} \right) \left[\frac{\Delta C}{C} \cdot \frac{\alpha \cdot V_m RT}{F^2} \right] \quad \text{cm/sec} \quad [10]$$

with D the diffusion coefficient of the diffusing species.

Introduction of [9] and [10] into [8] and rearrangement yields

$$v = \left(\frac{1}{y} \right) \left[\frac{\alpha \cdot V_m}{F} \right] \left[\Delta\phi - \frac{\Delta C}{C} \cdot \frac{RT}{F} \right] - v_c, \quad \text{cm/sec} \quad [11]$$

or

$$v = A/y - v_c, \quad \text{cm/sec} \quad [12]$$

with

$$A = \left[\frac{\alpha \cdot V_m}{F} \right] \left[\Delta\phi - \frac{\Delta C}{C} \cdot \frac{RT}{F} \right], \quad \text{cm}^2/\text{sec} \quad [13]$$

Figure 8 illustrates the experimental check of Eq. [12] where the net rate of the film growth v , obtained by graphical differentiation of the y - t curves in Fig. 7, is plotted vs. the reciprocal film thickness $1/y$. The slope of the v - $1/y$ relations gives the value of the kinetic constant A , Eq. [12], while its intercept on the abscissa yields the steady-state thickness y_{∞} , which is

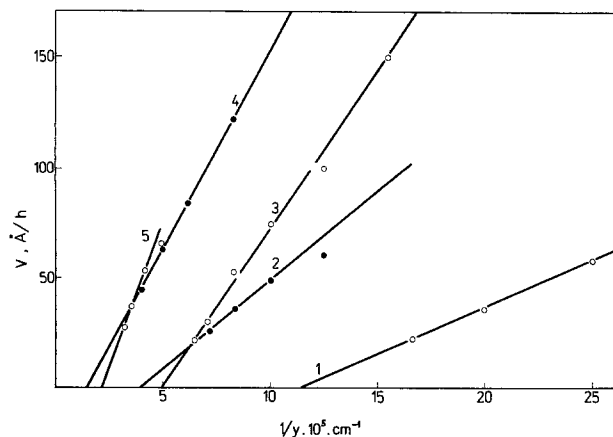


Fig. 8. Dependence of the net rate of the film growth v on the reciprocal film thickness $1/y$ for films with various conductivities as shown in Fig. 7.

attained at a zero rate v . Under this condition Eq. [12] can be used to determine the corrosion rate of the film

$$v_c = A/y_{\infty} \quad \text{cm/sec} \quad [14]$$

Figure 9 illustrates the effect of the specific conductivity χ of the films, as presented by their kinetic curves in Fig. 7, on the kinetic constant A . The latter is estimated from the slope of the respective $v-1/y$ plot in Fig. 8. As expected from Eq. [14], A is proportional to χ . The slope of the plot in Fig. 9, according to Eq. [13], yields the value of $(\Delta\phi - C/C \cdot RT/F) = 0.2$ mV.

Assuming the maximum range of $\Delta C/C$ from 0 to +1 the value of $\Delta\phi$ should vary from 0.2 to 26 mV.

Table I presents the kinetic data obtained from the plots in Fig. 7 and 8.

It is seen from Table I that while A grows with χ , v_c is not dependent on χ . The steady-state thickness y_{∞} increases with A according to Eq. [12].

The integration of Eq. [12] from y_1 to y and from 0 to t yields

$$t = [(y_1 - y)/v_c] - (y_{\infty}/v_c) \ln [(y_{\infty} - y)/(y_{\infty} - y_1)], \quad \text{sec} \quad [15]$$

Since $y_1 \ll y_{\infty}$ Eq. [15] becomes

$$t = [(y_1 - y)/v_c] - (y_{\infty}/v_c) \ln (1 - y/y_{\infty}), \quad \text{sec} \quad [16]$$

It can be shown that at low film thicknesses when $y/y_{\infty} < 0.3$ the first parabolic term prevails, while at larger thicknesses the second asymptotic term is determining. A good correlation between the experimental $y-t$ curves and those calculated by Eq. [16] was found when using the values of y_{∞} and v_c determined from the respective differential plots.

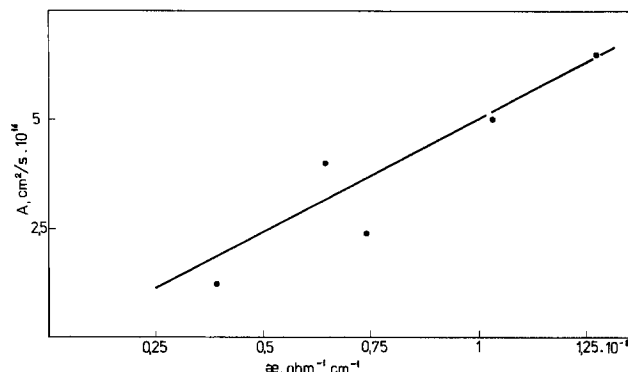


Fig. 9. Dependence of the kinetic constant A (Eq. [12]) on the specific conductivity of the film.

Table I.

| Curve No. | $\chi, \Omega^{-1} \cdot \text{cm}^{-1} \times 10^8$ | $A, \text{cm}^2 \cdot \text{sec}^{-1} \times 10^{10}$ | $v_c, \text{cm} \cdot \text{sec}^{-1} \times 10^{10}$ | $y_{\infty}, \text{Å}$ |
|-----------|--|---|---|------------------------|
| 1 | 0.39 | 1.2 | 1.4 | 85 |
| 2 | 0.64 | 4.0 | 2.0 | 200 |
| 3 | 0.74 | 2.4 | 0.96 | 250 |
| 4 | 1.03 | 5.0 | 0.75 | 660 |
| 5 | 1.27 | 6.5 | 1.4 | 460 |

Despite the fact that the present kinetic data cannot claim a high accuracy, they nevertheless give qualitatively the effect of the factors governing the kinetics of the primary film growth.

The film corrosion and self-discharge.—The corrosion rate of the primary LiCl film, i.e., the dissolution rate of the LiCl crystals in a heterogeneous chemical process, is governed by the diffusion conditions. Being essentially a solvation process it can be also limited by the solvation rate of Li^+ and Cl^- by SOCl_2 which appears to be rather low. As seen from Table I the value of v_c varies from 0.8 to 2.0×10^{-10} cm/sec or 30–72 Å/hr. The mean value 1.3×10^{-10} cm/sec expressed in current units amounts to $0.60 \mu\text{A}/\text{cm}^2$, which approximates the rate of self-discharge of Li in Li/ SOCl_2 cells for cardiac stimulators, $0.07 \mu\text{A}/\text{cm}^2$, for a period of 4–5 years as reported by Babai and Gal (4).

On the other hand, the results of Dey (1, Fig. 45) reveal that the rate of growth of the secondary porous film, observed by SEM, remains constant over a period of 160 days. The rate of growth in a 0.5M LiAlCl_4 solution at 25°C determined from the slope of his $y-t$ plot, 1.4×10^{-10} cm/sec is almost equal to the average corrosion rate of the primary passive film found here. The constancy in the rate of the secondary film growth clearly demonstrates that this film does not possess any protective properties. Likewise, Babai and Gal (4) have established that the self-discharge rate of Li in SOCl_2 is practically independent of the storage time, despite that the secondary film grows continuously during the entire test period (~ 4 years).

The agreement between the rate of the primary film corrosion and the rate of the secondary film growth clearly shows that the secondary film grows at the expense of the dissolution of the primary one. The dissolved Li^+ ions accumulate at the primary film surface and LiCl crystals are precipitated when the necessary supersaturation is attained.

High field transients.—It was established that the primary passive film on Li can withstand short galvanostatic cathodic pulses with very high amplitudes without any appreciable damage (breakdown, dissolution). Figure 10a illustrates an overvoltage transient recorded with an Li electrode covered by a primary film 250Å thick upon the application of a cathodic pulse of $133 \text{ mA}/\text{cm}^2$ for 1.5 msec. The peak overvoltage corrected for ohmic drop in the solution is 2.9V which corresponds to an electric field of 1.2×10^9 V/cm. Similar high field transients have been observed

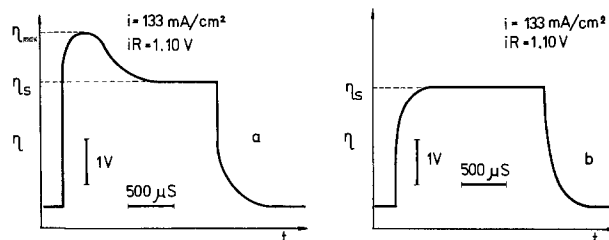


Fig. 10. Overvoltage transients at high electric field of a film-covered Li electrode: a, the first pulse transient; b, the transient at the 5th pulse in a series applied at a frequency 3 pulses per sec.

by Dewald (15), who studied the transient behavior of anodic oxide films on Ta. The overvoltage maxima are attributed by Dewald to high-field generation of carriers which are subsequently annihilated during their migration across the film through capturing by vacancies. It is assumed that in the case of oxide films the excess carriers are most probably interstitial cations, but the model developed by Dewald is claimed as valid regardless of the nature of the excess carriers.

The transient behavior of the primary film on Li was qualitatively studied by repetitive pulse application. It was found that when the high-field pulses are applied at an interval of 10 sec or more the transients are completely reproduced with the shape of the first one, as shown in Fig. 10a. This implies that a rest period of 10 sec is sufficient for the capturing of all the excess carriers generated during the preceding pulse and that the high cathodic pulse cannot change appreciably the resistance and hence the thickness of the film.

When, however, the interval between the pulses was 0.3 sec or less the peak on the overvoltage transients was leveled off after 4-5 pulses so that the initial overvoltage became equal to the steady-state overvoltage η_s as shown in Fig. 10b. Evidently a rest interval of 0.3 sec is not sufficient for the annihilation of the excess carriers. If the pulse interval is again increased to 10 sec the initial transient as that in Fig. 10a is reproduced. The recovery of the initial transient after such a short pause (10 sec) cannot be associated with the build-up of the film after its eventual damage during the preceding pulses, since the growth of the film is incomparably slower.

Tafel plots.—The current-voltage characteristics of the primary passive film on Li at higher electric fields is illustrated by the Tafel plot in Fig. 11. A constant film thickness of 500Å was obtained by keeping an Li electrode for 16 hr in a 0.5 LiAlCl₄ solution at 25°C. The dependence is plotted with the peak overvoltage values recorded on oscilloscopic traces similar to that shown in Fig. 10a. According to the high field ionic migration theory (16) at fields higher than 10⁶ V/cm the ionic current should obey the expression

$$i = 2Fan \nu \exp(-W/kT) \exp(qaE/kT) = i_0 \exp(BE), \quad \text{A/cm}^2 \quad [17]$$

where a is the half-jump distance of the migrating species with a concentration n , q is its charge, ν the jump frequency, and W the apparent activation energy.

As seen in Fig. 11, the Tafel slope becomes linear at fields somewhat lower than 10⁶ V/cm. Despite this discrepancy the slope of the Tafel dependence 1.1×10^{-6} cm/V yields according to Eq. [17] the half-jump distance $a = 2.8\text{\AA}$ in close agreement with the inter-ionic distance Li-Cl in the crystal lattice of LiCl, 2.75Å. From the pre-exponent $\log i_0 = 0.95$ (mA/cm²) one can estimate the ionic conductivity of the film by the low-field approximation formula $\kappa = i_0 \cdot B$, which gives $1.0 \times 10^{-8} \Omega^{-1} \cdot \text{cm}^{-1}$. This is close to the value of $\kappa = 1.3 \times 10^{-8} \Omega^{-1} \cdot \text{cm}^{-1}$ calculated by Eq. [4] from the slope of the respective 1/C-R plot of the same Li electrode measured during the growth of the film.

Mechanism of the film growth.—In the lower temperature region ($T < 670$ K) the conductance of LiCl is determined by the migration of cation vacancies. The latter are usually due to the inclusion of aliovalent cations (e.g., Mn²⁺, Al³⁺) in the crystal lattice of LiCl (14). Being a typical ionic crystal with a large forbidden gap LiCl is an electronic insulator, which makes it difficult to explain the film growth at electric fields as low as several thousand volts per cm. According to Mehl and Hale (17) however, when an insulator is put in contact with an oxidant, electrons are transported from the solid to the insulator/solution interface, where they are consumed by the cathodic reaction. Simultaneously the excess carriers (in the present case holes) are injected into the valence band and enhance the electronic conductivity of the film.

Another possibility for enhanced electron transport in ionic crystals is pointed out by Kleitz *et al.* (18). It is assumed that the Fermi level is located very close to the relevant surface state. As a result alkali metals generally induce large electronic conductivities in the alkali metal halides with which they are in equilibrium (18).

The above considerations are corroborated by the recent finding of Povarov *et al.* (19), that the Li electrode in 1M LiAlCl₄ solutions of SOCl₂ exhibits photoelectrochemical properties, which are usually associated with the formation of colored centers.

Conclusions

1. The passivity of Li in SOCl₂ electrolyte solutions is due to a thin (150-500Å) dense insulating film of LiCl and not to the thicker (1-2 μm) porous film.
2. The passive film grows by ionic migration and diffusion in the solid phase, while the secondary porous film grows by a dissolution-precipitation mechanism.
3. The values of the specific conductivity and the field coefficient, the Tafel dependence, and the high field transient behavior of the passive film describe the latter as a typical ionic crystal insulating film.
4. The passive film is dissolved at a constant rate which controls the limiting film thickness and determines the rate of self-discharge of the Li electrode in SOCl₂ electrolyte solutions.
5. The specific conductivity of the primary passive film is dependent on the concentration of aliovalent cations in the electrolyte solution.
6. The value of the specific ionic conductivity of the passive film and its activation energy are practically equal to those of bulk samples of LiCl.

Acknowledgment

The authors are much indebted to Dr. I. Iliev for the stimulating discussions and the helpful suggestions during the preparation of this paper.

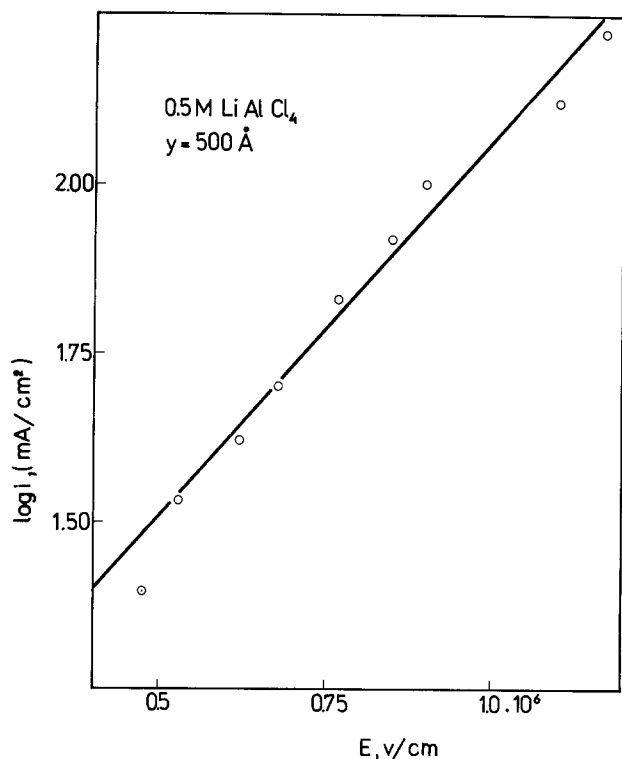


Fig. 11. Tafel plot obtained from the peaks in the overvoltage transients on a film 500Å thick in a 0.5M LiAlCl₄ solution.

Manuscript submitted Oct. 12, 1980; revised manuscript received March 20, 1981.

Any discussion of this paper will appear in a Discussion Section to be published in the June 1982 JOURNAL. All discussions for the June 1982 Discussion Section should be submitted by Feb. 1, 1982.

REFERENCES

1. A. N. Dey, *Thin Solid Films*, **43**, 131 (1977).
2. A. N. Dey, *Electrochim. Acta*, **21**, 21 (1976).
3. M. J. Harney and S. Brown, Paper 72 presented at The Electrochemical Society Meeting, Los Angeles, California, Oct. 14-19, 1979.
4. M. Babai and Y. Gal, Paper 39 presented at The Electrochemical Society Meeting, Los Angeles, California, Oct. 14-19, 1979.
5. R. Moshtev, Y. Geronov, B. Puresheva, and A. Nas-salevska, Proc. 28th ISE Meeting, Varna, Sept. 1977, Vol. 2, Abstr. No. 153.
6. R. Moshtev, Y. Geronov, and B. Puresheva, Proc. 29th ISE Meeting, Budapest, Sept. 1978, Vol. 2, p. 818.
7. E. Peled, *This Journal*, **126**, 2047 (1979).
8. D. Chua, W. Merz, and W. Bishop, in "Proc. 27th Power Sources Symp.," Atlantic City, N.J. (1977).
9. D. J. David, M. H. Froning, T. N. Wittberg, and W. E. Modeman, Paper 14 presented at The Electrochemical Society Meeting, Los Angeles, California, Oct. 14-19, 1979.
10. R. Keil, J. Hoenigman, W. Modeman, T. Wittberg, and J. Peters, Interim Techn. Report, Oct. 1979, AFWAL-TR-80-2018, Univ. of Dayton Research Inst., Dayton, OH.
11. K. French, P. Cukor, C. Persiani, and J. Auburn, *ibid.*, **121**, 1015 (1974).
12. Y. Geronov, B. Puresheva, R. Moshtev, and B. Yordanov, *J. Appl. Electrochem.*, **9**, 641 (1979).
13. Landolt-Börnstein, Tabellen, II Band, 6 Teile.
14. Y. Haven, *Rec. Trav. Chim. Pays Bas*, **69**, 1476 (1950).
15. J. E. Dewald, *J. Phys. Chem. Solids*, **2**, 55 (1957).
16. L. Young, "Anodic Oxide Films," Academic Press, London (1961).
17. W. Mehl and J. M. Hale, *Advances in Electrochem. Electrochem. Eng.*, **6**, 399 (1967).
18. M. Kleitz, P. Fabry, and E. Schouder, in "Electrode Processes in Solid State Ionics," M. Kleitz, Editor, p. 1, D. Reidel Publ. Co. (1975).
19. Y. M. Povarov and L. A. Beketaeva, *Elektrokhimiya*, **16**, 1252 (1980).

Kinetics of GaAs Plasma Anodization

P. Friedel, S. Gourrier, and P. Dimitriou

Laboratoires d'Electronique et de Physique Appliquée, 94450 Limeil-Brévannes, France

ABSTRACT

The kinetics of GaAs plasma anodization at constant total current have been studied. The plasma source is a multipole (hot cathode associated with a magnetic confinement). The results show a decrease of the growth rate as the oxide thickness increases, in contrast with wet anodization at constant total current. The presence of unoxidized arsenic in the bulk and at the oxide semiconductor interface, which is characteristic of plasma grown GaAs oxides, does not seem to have a significant influence on the kinetics. An ion space charge which can modify the ratio of the electronic and ionic currents during the growth can account for the observed kinetics. Satisfactory agreement is obtained by using a very simplified space charge model. The calculations give order of magnitude of phenomenological ion "migration" (i.e., field aided diffusion, etc.) coefficients which are much larger than usual diffusion coefficients.

Field-assisted transport processes which occur during wet (1) or plasma (2) anodization are still poorly understood. In fact, motions of charged species under high electric fields may be very specific phenomena. Complex reactions at both interfaces (oxidizing medium/oxide and oxide/substrate) also play a determinant role in the oxide growth process. In addition to these general features plasma anodization is characterized by a large electron flow through the oxide and by electron-induced reactions at the oxide surface which most probably (2) create the majority of the oxygen ions involved in the growth. These complex factors control the oxide growth kinetics. In particular, significant differences exist between the kinetics of wet and plasma anodization. As an example we study and discuss in this paper the kinetics of constant current GaAs plasma anodization.

Experimental

Description of the system.—The plasma source is a multipole and has been described in detail elsewhere (3). A hot cathode associated with a magnetic confinement creates an homogeneous plasma of density 10^{10} – 10^{11} cm⁻³ at low oxygen pressures (10^{-2} – 10^{-1}

Pa). The sample (n-type GaAs with an impurity concentration of 2×10^{18} cm⁻³) is placed on a copper sample holder which can be biased with respect to the plasma. The area exposed to the plasma is defined by an alumina cap with a circular opening of 10 mm in diameter. In order to control the actual current flowing through the exposed area of the sample, care has been taken in insulating any other biased surface (metallic parts of the sample holder, connections). The back side of the sample is thermoregulated with an accuracy of $\pm 5^\circ\text{C}$. A liquid nitrogen trap is mounted near the sample, and the base pressure of the system is in the high 10^{-5} Pa range. The thickness of the oxide can be continuously measured by *in situ* real time ellipsometry at 632.8 nm. Anodizations can be carried out either at constant anodization voltage V_a (potential of the copper sample holder) or at constant total current density J_{tot} .

The voltage drop between the surface of the oxide and the back side of the sample was calculated by estimating the potential of the surface V_s . In the first experiments V_s was deduced by measuring the total current flowing through the sample and using a predetermined *I-V* characteristic obtained under the same plasma conditions with a gilded plate mounted in

place of the sample. This method proved to be critically dependent on the discharge conditions (especially the ion and electron temperatures). Therefore we replicated the sample holder with a flat, gilded probe, surrounded by an alumina cap, and placed it on the axis of the multipole chamber. Simultaneous *I-V* characteristics of this probe and of a gold plate mounted in place of the sample differed by less than 1V under typical discharge and anodization conditions (surface potential lower than the plasma potential V_p). The potential of this probe was taken to be the surface potential of the sample. This method, as well as the previous one, neglected the work functions difference between gold and the oxide (2). We assumed this difference to be small (1-2V).

Results.—Figure 1 shows typical oxide growth kinetics at constant current (density 7.7 mA/cm²) at temperatures ranging from 50° to 200°C. The inset shows V_a vs. time. The initial growth rates vary from 24 to 90 nm/m and large thicknesses can be obtained in a reasonable time (450 nm in 10m at 200°C). Note the decrease of the oxidation rate as the thickness increases. This has been frequently reported (2, 3) in constant current plasma anodization experiments. In contrast, no saturation is observed in anodization of GaAs in an aqueous electrolyte (4); the rate of growth is constant during the experiment.

In the next section we analyze this different behavior and deduce information concerning the transport mechanisms during GaAs plasma anodization.

Discussion

Exposed conducting surfaces.—Since the plasma expands around the sample holder, a "leakage current" flows through any exposed surface. This surface is at the anodization potential and the "leakage" current should increase with time, thus reducing the current flowing through the sample. However, in our system, this "leakage" current is found to be very small. An anodization voltage of 100V applied to the sample holder under typical plasma conditions with a glass plate mounted in place of the sample corresponds to "leakage" currents of the order of 10 μ A, three orders of magnitude lower than the total anodization current (in the mA range).

Charge effects on the alumina cap result in unoxidized edges around the anodized area. These edges are exposed to the plasma and may modify the current distribution around the sample and the kinetics. Their influence was ruled out by the following experiment: After anodization up to a certain depth, the protecting cap was replaced by a smaller one covering the edges of the previously anodized area. The sample was then

further anodized using the same current density. The initial growth rate was equal to the final rate at the end of the first anodization, indicating that the presence of unoxidized edges has no significant influence on the kinetics.

Role of the nature of the oxides.—Spectroscopic ellipsometry (5) on plasma-grown GaAs oxides indicates the presence of an optically absorbing material (above 3.5 eV) in the bulk and of a highly absorbing interface layer between the oxide and the semiconductor (6). According to thermodynamics (higher stability of gallium oxide), the absorbing material is probably unoxidized arsenic. Auger spectroscopy (7), TEM observations (8), and Raman scattering (9) also confirm the presence of an amorphous elemental As layer at the oxide/semiconductor interface. The thickness of this layer increases with the oxide thickness. In contrast, wet anodic oxides (and their interfaces with GaAs) are almost nonabsorbing below 4.5 eV (10). In order to estimate the influence of this striking difference in composition between wet and plasma-grown oxides, an oxide was grown in an H₃PO₄ solution up to ~150 nm and further oxidized in the plasma. The kinetics were then exactly the same as in the case of an oxide entirely grown in the plasma, indicating that the presence of unoxidized As has no influence on the kinetics. In another experiment, an oxide was formed in the plasma up to 200 nm and was ion sputtered down to 75 nm to produce a film with an artificially thick As interfacial layer. A further anodization of this oxide using the same current density yielded the same growth rate as during the first anodization (before erosion) at 75 nm; therefore, the As interfacial layer does not control the kinetics. It may, however, have an influence on the early stage of oxidation on clean surfaces of GaAs (below 1-5 nm). In summary, those two experiments show that the nature of the oxide (either wet anodic or plasma grown with an abnormally thick As interface layer) does not strongly influence the growth.

Diffusion-limited kinetics.—Another possibility would be a limitation due to the diffusion of the oxidizing species through the oxide. Such a process is known to lead to a parabolic ($t^{1/2}$) law of kinetics (11). This dependence was not found on our experimental curves above 20 mA whereas power laws in t^q exist for 6 mA. The exponent q is an increasing function of temperature and varies from 0.55 at 50°C to 0.8 at 200°C. Thus, pure diffusion transport cannot account for the observed kinetics. This is expected because ions are the mobile species during anodic oxidation, and therefore their transport is controlled by the high field in the oxide.

Space charge layer.—During plasma anodization, a very large electron flux is supplied to the sample (2). This is one of the most striking differences between wet and plasma anodization. Some of these electrons have relatively large energies; for instance, in the multipole plasma source, primary electrons of typical energy 50 eV are emitted by the filament and can reach the sample. Energetic electrons can be injected in the conduction band of the oxide, resulting in a large electronic current in the oxide. The current efficiency (ratio of the ion current to the total current) is very low (a few percent). In contrast, in most cases (Si is an exception) current efficiencies above 90% are reported in wet anodization experiments (1). During plasma anodization at constant total current, a small change in the field through the oxide can create a small relative change in the electronic current, resulting in a large relative change in ionic current and in the kinetics. Variations of the field can originate from a gradient of uncompensated ionic charges in the bulk of the oxide. This will be studied in more detail using a space charge model developed by Fromhold

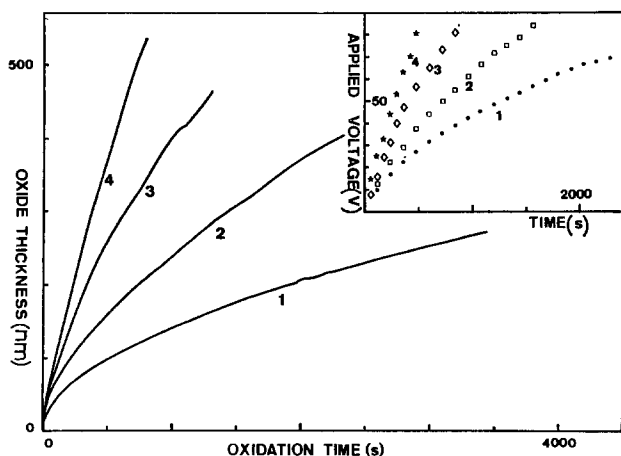


Fig. 1. Experimental kinetics at 4 different temperatures (curve 1, 50°C; curve 2, 100°C; curve 3, 150°C; curve 4, 200°C). The insert represents anodization voltage vs. time.

(12) for wet anodization and applied by Labunov *et al.* for Al plasma anodization (13).

The model relies on several basic assumptions.

1. The boundary concentrations of mobile ions are time independent and fixed by interfacial reactions and not by the field in the oxide. Interfacial reactions are fast enough to compensate the loss of ions due to the migration in the oxide. This seems plausible, at least for oxygen ions, which are to a large extent only created by plasma electron assisted surface reactions. Other space charge models are based upon the oxide field created by trapped charges in the oxide (2). Our assumptions only take into account the ion concentration gradient imposed by the interfacial reactions.

2. There is only one ionic species movement during the growth. This allows a rather simple mathematical treatment of the problem. However, it is not generally true. In most cases, wet or plasma anodization proceeds by simultaneous transport of negative oxygen ions toward the substrate and positive substrate cations toward the surface [Zr is an exception (14)]. As an example, plasma anodization of Al/GaAs (15) or Si/GaAs (3) structures have demonstrated that both As and Ga positive ions and oxygen negative ions are mobile during GaAs anodization. Calculations taking into account two kinds of ionic mobile species have been carried out. However, they lead to a system of equations which is analytically tractable only in a few very limiting cases. Therefore, we restrict ourselves to one kind of mobile species model assuming either oxygen movement or cations movement. The migration coefficients and activation energies for both processes can then be calculated. We assume that they give the correct order of magnitude of the actual values. Such a procedure seems plausible, because anodization of Al/GaAs structures have shown that the contributions to the oxide thickness of oxygen transport and cations transport are comparable (3, 15).

3. The only mobile species are ions.

4. The migration of ions in the oxide can be described using a periodic potential barrier W , which is lowered in the presence of the field.

5. A quasi-steady state is met at every oxide thickness (interface reactions are fast compared to bulk migration).

The expression of the ion current density J_1 can be written

$$J_1(x) = Z \times e \left(\frac{D C(x)}{a} \sinh \frac{Z \times e a E(x)}{kT} - D \frac{dC(x)}{dx} \cosh \frac{Z \times e a E(x)}{kT} \right)$$

where $E(x)$ is the electric field at depth x in the oxide (the origin is at the surface or at the oxide/GaAs interface for oxygen and cations movement, respectively); $Z \cdot e$ is the net charge of the migrating species; $2a$ is the distance between two minima of the potential energy (typically, distance between two oxygen atoms in the oxide); $C(x)$ is the concentration of migrating ionic species; and D is the "migration" coefficient corresponding to the motion of ionic species under a high field. We use the term "migration" since it can be different from the diffusion coefficient, as will be discussed later.

The field in the oxide is of the order of a few 10^6 V/cm. We are in the high field limit ($E(x) \gg kT/Z \cdot e a$). Therefore, neglecting the effect of the concentration gradient (dC/dx should be of the order of C/a for this term to be appreciable), we obtain

$$J_1(x) = Z \times e \frac{D C(x)}{2a} \exp \left(\frac{E(x) Z \times e a}{kT} \right) \quad [1]$$

The steady-state assumption $J_1(0) = J_1(x) = J_1(L)$ where L is the oxide thickness, and the integration of

Poisson's equation¹ yields

$$J_1 = Z \cdot e \frac{D C_0}{2a} g(L) \exp \left(-\frac{u}{L E'} + 1 \right) \quad [2]$$

$$g(L) = \left(1 + \frac{L}{L'} \right)^{-(1+L'/L)} \quad L' = \frac{\epsilon \epsilon_0 kT}{(Z e)^2 a C_0}$$

where C_0 is the boundary concentration of ions; ϵ is the dielectric constant of the oxide; u is the voltage drop through the oxide; L' is the typical width of the space charge layer (to a first approximation, it corresponds to the depth at which the concentration of mobile ions is one-half of the boundary concentration); and $g(L)$ represents the reduction of the ionic current due to the space charge (as compared to the homogeneous field case). Typical values are several orders of magnitude lower than unity.

A complete theoretical treatment requires the knowledge of the electronic current density J_e as a function of the field in the oxide. In agreement with Labunov *et al.* (13) we assume that this current is a function of the mean field \bar{E} in the oxide.

The determination of the electronic current density is made using constant voltage anodization and recording simultaneously the current and the oxide thickness. The ionic current estimated from the growth rate (see below) was subtracted from the total current to yield the electronic current. The voltage drop through the oxide is calculated by estimating the surface potential as a function of the current. Since GaAs anodization requires holes (4), an additional voltage drop appears in the semiconductor at the oxide interface to generate electron-hole pairs. Neglecting any radiation-induced generation process, we assume that the holes are created by avalanche breakdown, which corresponds in our case (GaAs n-type impurity concentrations $2 \times 10^{18} \text{ cm}^{-3}$) to a voltage drop of 3V (16). Figure 2 shows the electronic current as a function of the field in the oxide for temperatures of 20°, 40°, and 100°C.

The lower part of the curves (steep slope) is sample temperature dependent, and therefore seems to be due to an oxide limited conduction. The mechanism of this conduction is not clear; most probably insulator conduction processes [such as Frenkel Poole conduction (13, 16)] are superimposed on the transport of energetic electrons injected directly from the plasma to the conduction band of the oxide.

¹ Poisson's equation was written $\frac{\partial E}{\partial x} = \frac{Z \cdot e C(x)}{\epsilon \epsilon_0}$ neglecting the electronic density $C_e(x)$. We shall see later on that most of the electronic current is very likely due to hot ballistic electrons, with high velocities of the order of 10^6 m/sec. With typical values of electronic current, C_e is of the order of 10^{10} cm^{-3} , which is much lower than the ion concentration, as will be seen later.

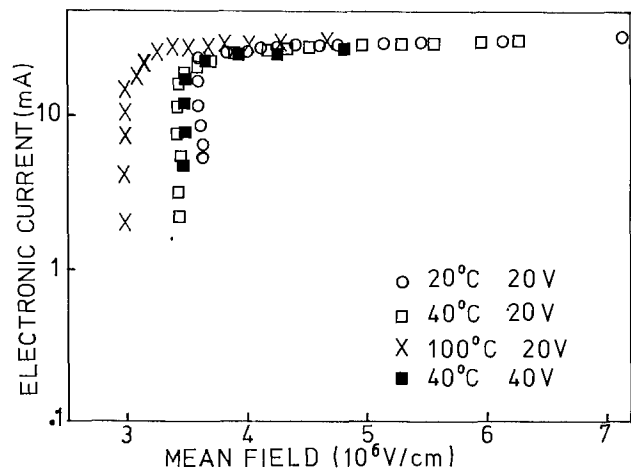


Fig. 2. Electronic current vs. mean field at 20°, 40°, and 100°C measured during constant voltage anodizations at 20 and 40V.

The upper part of the curves is sample temperature independent, and therefore is most likely due to a plasma-limited charge supply. The sample probably behaves like a flat probe for which a large increase of the surface potential above the plasma potential results in a small current increase (because of the small relative extension of the sheath around the sample).

At this point, three equations

$$J_1 = \frac{D C_0}{2a} \exp\left(\frac{\bar{E}}{E'} + 1\right) g(L)$$

$$J_1 + J_e = J_{tot}$$

$$J_e = f(\bar{E})$$

can be resolved for given D , and C_0 to give $J_1 = f(L)$. J_1 is directly related to dL/dt by assuming that each ion reaching the boundary corresponds to an increase v in oxide volume. The volume v is estimated using the atomic density of Ga and As in the semiconductor ($2.2 \times 10^{22} \text{ cm}^{-3}$); the volume increase of GaAs after oxidation (~ 1.6) (3); and the assumption of composition $\text{Ga}_2\text{O}_3 + \text{As}_2\text{O}_3$. We then obtain

$$J_1 = \frac{Z \cdot e}{v} \frac{dL}{dt} \quad \text{with} \quad \frac{1}{v} = 4.14 \times 10^{22} \text{ cm}^{-3}$$

The relation $J_1 = Z \cdot e/v \cdot dL/dt = f(L)$ can be numerically integrated to give the kinetics $L = f(t) \cdot D$ and C_0 are adjusted to fit the experimental curves. The results of this method (assuming only oxygen transport) are given in Table I and Fig. 3 for an anodization at $J_{tot} = 25.6 \text{ mA/cm}^2$ at 50°C . The fit is satisfactory up to 250 nm.

This technique is rather tedious and depends on the reproducibility of the plasma conditions between the experiments used to calculate $J_e = f(\bar{E})$ and the anodizations. Small errors in the calculation of \bar{E} due to surface potential variations can result in order of magnitude changes in D and C_0 .

A simplified procedure which does not use the electronic current was then applied. It can be noted that the mean field \bar{E} calculated from Eq. [2] as a function of thickness is almost constant except for small thicknesses ($L \leq L'$) where variations remain small (at 50°C in a typical anodization \bar{E} varies from 3.1 to $3.4 \times 10^6 \text{ V/cm}$ from $L = 0$ to $L = L'$). This is consistent with the experimental curves of voltage drop vs. thickness shown in Fig. 4. A constant value of \bar{E} is therefore determined from the experimental data and injected in Eq. [2]. As in the previous technique, a numerical integration gives the kinetics curve which is fitted to the experimental ones by adjusting D and C_0 .

Fits of the kinetics assuming only oxygen movements are presented in Fig. 5. Figure 6 shows D and C_0 deduced from the fits as a function of $1/T$ for oxygen anions movement and cations movement. The activation energies of D are 0.6 and 0.8 eV for oxygen and cation movement, respectively. These activation energies are relatively low and correspond to very large values of D ($10^{-10} \text{ cm}^2/\text{sec}$), several orders of magnitude higher than usual diffusion coefficients. In fact, assuming such large values for the diffusion coefficient after anodization would lead to a fast flattening of any concentration gradient in the oxide. This is contradicted by Yamasaki and Sugano's results (17),

Table I.

| | |
|------------|--|
| C_0 | $= 3.49 \times 10^{18} \text{ cm}^{-3}$ |
| D | $= 4.07 \times 10^{-14} \text{ cm}^2\text{sec}^{-1}$ |
| L' | $= 3.15 \text{ nm}$ |
| T | $= 300 \text{ K}$ |
| $2a$ | $= 0.5 \text{ nm}$ |
| Z | $= -2$ |
| ϵ | $= 8$ |

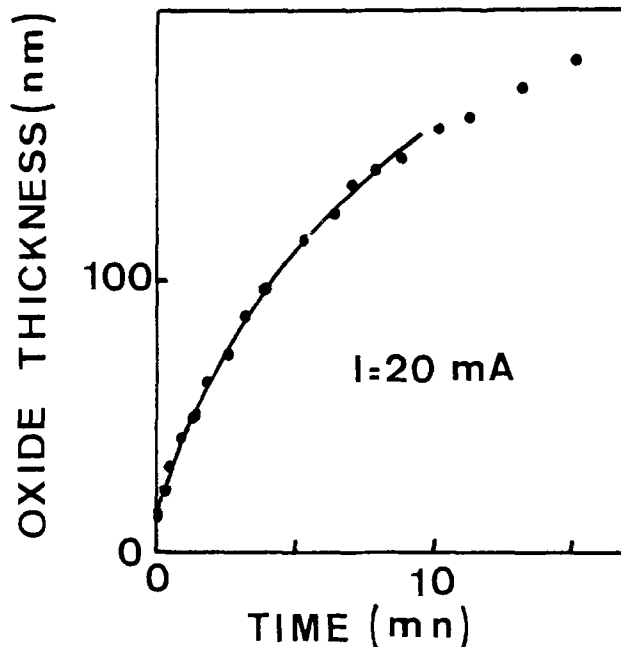


Fig. 3. Fit of constant current (20 mA) kinetics at 40°C by the first method. Dotted curve is experimental, full line theoretical.

who were able to measure ^{18}O and ^{16}O concentration gradients after sequential anodizations. We must then assume that the values of D deduced from the kinetics do not correspond to diffusion but rather to "migration," defined as the transport of charged species under a very high field.

C_0 decreases with increasing temperature. This could indicate that ion desorption is much more thermally activated than surface ionization. The order of magnitude of C_0 (assuming only oxygen transport) shows that the ratio of ionized oxygen to neutral oxygen on the oxide surface varies from 10^{-4} to 10^{-6} between 50° and 200°C .

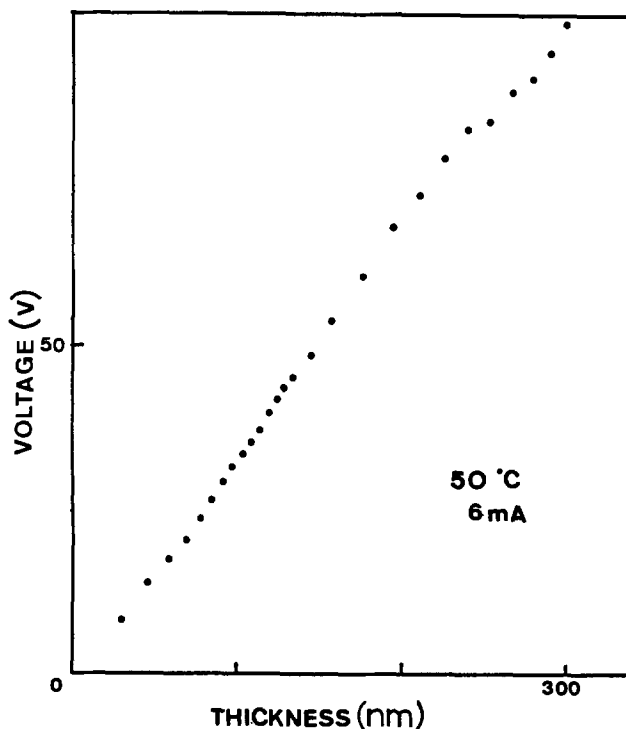


Fig. 4. Anodization voltage at 6 mA total current vs. oxide thickness at 50°C .

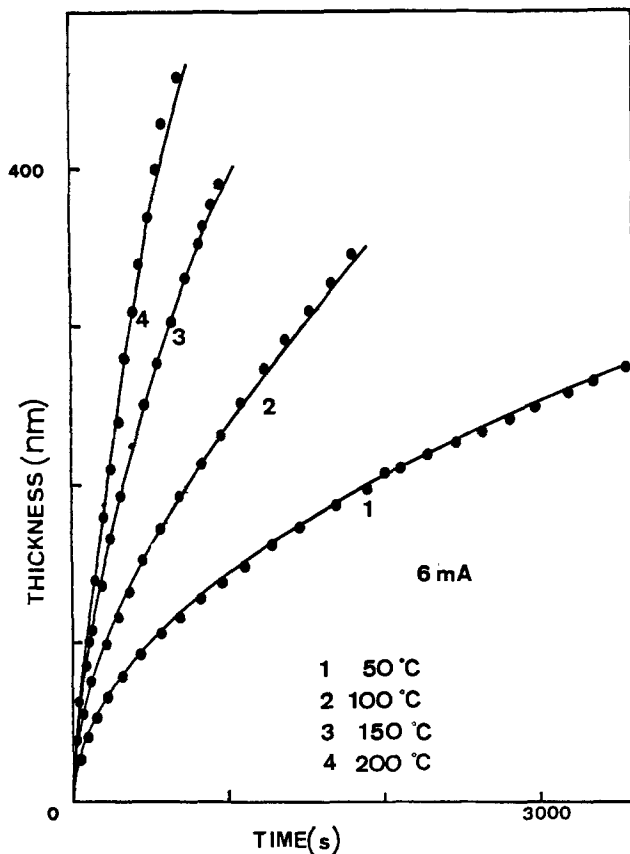


Fig. 5. Fit of constant current (6 mA) kinetics at 4 different temperatures (curve 1, 50°C; curve 2, 100°C; curve 3, 150°C; curve 4, 200°C) supposing only oxygen ions movement.

Conclusion

The kinetics of GaAs plasma anodization in a multipole at a constant total current show a decrease of the oxide growth rate as the thickness increases. The presence of unoxidized As in the bulk and at the oxide/semiconductor interface (which is a characteristic of GaAs plasma grown oxides) has no significant influence on the kinetics at least for thicknesses larger than a few nanometers. Satisfactory agreement was obtained by using a very schematic space charge model assuming one type of mobile ionic species. Using the model, values of "migration" coefficients are deduced which are much larger than usual diffusion coefficients in the absence of a field. They can be considered as characteristic of a field-enhanced transport mechanism.

Acknowledgments

The authors are grateful to Sir Nevill Mott for useful discussions and Dr. J. Siejka and J. Perriere for helpful advice. They also wish to thank Mr. C. Blanjot for technical assistance. This work has been partly supported under contract by DIELI.

Manuscript submitted Nov. 20, 1980; revised manuscript received March 27, 1981.

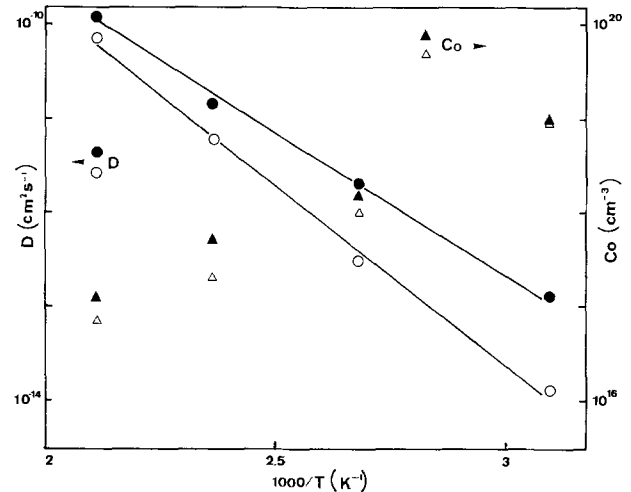


Fig. 6. D and C_0 vs. inverse of temperature assuming movement of oxygen (\bullet for D , \blacktriangle for C_0); cations from the substrate (\circ for D , \triangle for C_0).

Any discussion of this paper will appear in a Discussion Section to be published in the June 1982 JOURNAL. All discussions for the June 1982 Discussion Section should be submitted by Feb. 1, 1982.

REFERENCES

1. C. J. Dell'Oca, D. L. Pulfrey, and L. Young, *Phys. Thin Films*, **6**, 1 (1971).
2. J. F. O'Hanlon, in "Oxides and Oxide Films," Vol. 5, A. K. Vijh, Editor, p. 105, Marcel Dekker Inc., New York and Basel (1977).
3. S. Gourrier, A. Mircea, and M. Bacal, *Thin Solid Films*, **65**, 315 (1980).
4. H. Hasegawa and H. L. Hartnagel, *This Journal*, **123**, 713 (1976).
5. J. B. Theeten, R. P. H. Chang, D. E. Aspnes, and T. E. Adams, *ibid.*, **127**, 378 (1980).
6. S. Gourrier, A. Mircea, J. B. Theeten, and M. Bacal, in "Proceedings of the 4th ISPC," p. 181, Zurich (1979).
7. C. C. Chang, R. P. H. Chang, and S. P. Murarka, *This Journal*, **125**, 482 (1978).
8. R. P. H. Chang, T. T. Sheng, C. C. Chang, and J. J. Coleman, *Appl. Phys. Lett.*, **33**, 341 (1978).
9. R. P. H. Chang, in "Proceedings of the 11th Conf. on Solid State Devices," Tokyo (1979); *Jpn. J. Appl. Phys.*, **19**, supplement 19-1, 483 (1979).
10. D. E. Aspnes, G. P. Schwartz, G. J. Gualtieri, A. A. Studna, and B. Schwartz, *This Journal*, **128**, 590 (1981).
11. K. Hauffe, in "Treatise in Solid State Chem.," Vol. 4, N. B. Hannay, Editor, Plenum Press, New York (1976).
12. A. T. Fromhold, Jr., *This Journal*, **124**, 538 (1977).
13. V. Labunov, V. Parkhutik, and E. Tkharev, *J. Cryst. Growth*, **45**, 399 (1978).
14. C. Ortega, Private communication.
15. R. P. H. Chang, *Thin Solid Films*, **56**, 89 (1979).
16. S. M. Sze, "Physics of Semiconductor Devices," J. Wiley and Sons, New York (1969).
17. K. Yamasaki and T. Sugano, *J. Vac. Sci. Technol.*, **17**, 959 (1980).

The Effect of Fe(II) Ions on Kinetics and Mechanism of Anodic Dissolution and Cathodic Deposition of Copper

Z. D. Stanković*

The University of Belgrade, Faculty of Engineering Bor, 19210 Bor, J.N.A., 12 Yugoslavia

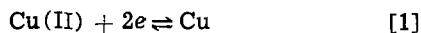
ABSTRACT

The influence of the presence of Fe(II) ions on kinetics and mechanism of anodic dissolution and cathodic deposition of copper in acidic sulfate system has been investigated. The galvanostatic single-pulse method has been used. Results indicate that the presence of Fe(II) ions decreases the exchange current density determined from the Tafel analysis of the cathodic reaction.

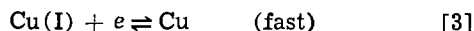
The influence of foreign cations on the kinetics and mechanism of anodic dissolution and cathodic deposition of copper has been scarcely investigated in spite of the great importance of this topic both for theoretical implications and for practical industrial consequences. Some evidence of effects of small amounts of foreign metal ions in solution on metal deposition kinetics and morphology as well as on corrosion behavior of metals can be found, particularly in the plating literature.

In the present work an attempt was made to obtain insight into the effect of Fe(II) ion on kinetics and mechanism of anodic dissolution and cathodic deposition of copper, since the solutions used in electrolytic plants for the production of copper usually contain some Fe(II) ions. The concentrations of Fe(II) ions in the acidic sulfate solutions investigated were chosen to be close to those in the commercial plants for the production of copper.

For the electrochemical dissolution and deposition of copper



it has been found by Mattson and Bockris (1) and verified by numerous authors (2-7) that in the acid sulfate system the reaction proceeds in two steps



The assumption of Butler-Volmer kinetics with a symmetry factor $\beta = \alpha_c = 0.5$ for the slow reaction [2] and of equilibrium for the fast reaction [3] yields

$$j = j_0 (\exp(\alpha_a F\eta/RT) - \exp(-\alpha_c F\eta/RT)) \quad [4]$$

where j is the net current density, j_0 is the exchange current density, α_a and α_c are the anodic and cathodic transfer coefficients, whose theoretical values are 1.5 and 0.5, respectively.

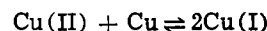
Experimental

Solutions were made from copper sulfate (p.a. Merck), ferrous sulfate (p.a. Merck), sulfuric acid (suprapure Merck), and bidistilled water. The concentrations of copper sulfate and sulfuric acid were 0.7M and 1.5M, respectively. The concentrations of ferrous sulfate were 0.005, 0.05, 0.15, and 0.3M. The solutions were deaerated by bubbling nitrogen of high purity for 1 hr. Stirring was effected by employing a magnetic stirrer. During measurements stirring was stopped while nitrogen was slowly bubbled through the solution.

* Electrochemical Society Active Member.

Key words: inhibition, Tafel slope, transients.

The cell was a commercial product (AMEL Model 494/GC + 494/TJ). The working electrode, a platinum sphere 0.55 mm diam (with an exposed surface area approximately 0.013 cm²), was formed by melting an end of a platinum wire 0.3 mm diam in an oxy-coal gas flame. The counterelectrode was spiral-shaped Pt wire 0.5 mm diam and 20 cm length. A spectroscopically pure copper wire of the same quality, 4 cm in length, was used to equilibrate solutions (9), according to



Before measurements copper deposit was freshly grown on the counter and working electrodes for 30 min at 15 mA · cm⁻² from the solutions employed in the subsequent experiments (1, 2). The potential difference between the electroplated and reference copper electrodes was always less than 5 mV in the absence of current.

The single pulse method was carried out using a potentiostat-galvanostat (AMEL Model 551) programmed with a function generator (AMEL Model 565). The pulse was made long enough for the activation overvoltage to reach a constant value. A series of transients was recorded covering the current density range 7.4×10^{-2} - 7.4×10^2 mA · cm⁻². All anodic transients were taken first followed by cathodic ones, in the order from low to high current densities. The overvoltage-time transients were recorded on a storage oscilloscope (Tektronix Type 549 B). Temperature was maintained at 303 ± 0.1 K.

Results and Discussion

The rest potential of the working copper electrode in all solutions investigated was 0.316V vs. NHE. Quasi-steady-state overvoltage values at different current densities were found from the plateaus of the galvanostatic transients, and Tafel plots were established. This has been done for both the anodic and the cathodic directions of the process and for each of the solutions. The Tafel plots were made with the potential expressed against SCE, and a summary of the results is given in Fig. 1 and in Table I. All cathodic Tafel slopes were 115 mV, and anodic slopes between 40 and 50 mV. The corresponding transfer coefficients are $\alpha_c = 0.52$ and $\alpha_a = 1.35 \pm 0.15$. The sum of α_c and α_a is 1.87 ± 0.15 , close to the theoretical value of 2.

The agreement between j_0 's obtained by extrapolation of the cathodic and anodic Tafel lines at high potentials to $\eta = 0$ is fair, but it should be noted that there is a slight but definite tendency for the values from the anodic Tafel lines to be smaller, as can be seen in Fig. 1 and in Table I. The transfer coefficients and exchange current density obtained in this study agree closely with results obtained by Bockris and

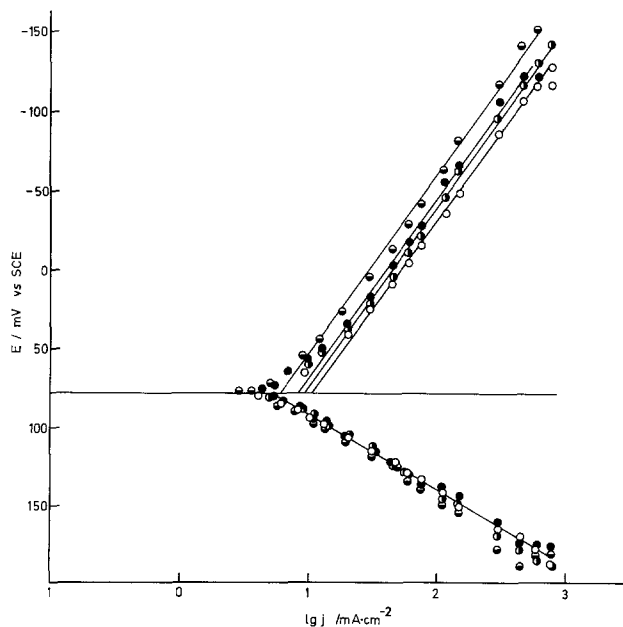


Fig. 1. Anodic and cathodic Tafel plots at different concentrations of Fe(II) ions: ○, 0.005M Fe(II); ◐, 0.05M Fe(II); ●, 0.15M Fe(II); ◑, 0.3M Fe(II).

Enyo (2), Bockris and Mattson (1), and Albaya and Lorenz (8) as can be seen in Table I.

The exchange current densities obtained from the cathodic Tafel lines for solutions with different concentrations of Fe(II) ions were found to decrease with increasing concentration of Fe(II) ions, as can be seen in Fig. 1-3.

Figure 2 shows that the decrease in the cathodic exchange current density with the increase in the concentration of Fe(II) ions can be expressed by the empirical relation

$$(j_0)_c = 9.45 \exp(-1.36 C_{\text{Fe(II)}})$$

where 9.45 is the value for the exchange current density in the absence of Fe(II) ions, and $C_{\text{Fe(II)}}$ is the molar concentration of Fe(II) ions.

Figure 3 shows that the concentration dependence of the cathodic current density at any constant value of the potential in the cathodic region of 50-150 mV vs. SCE on the Fe(II) ion is

$$(\partial \log j_c / \partial \log C_{\text{Fe(II)}})_{E, C_{\text{Cu(II)}}, T} = -0.14$$

A value of -0.14 indicates an inhibitive effect of Fe(II) ions on the Cu(II) discharge.

Dražić and co-workers (10) found a similar inhibitive effect of a foreign cation on the cathodic hydrogen evolution rate. Namely, they showed that the addition of Cd(II) ions at relatively small concentrations (10^{-2} - 10^{-1} M) decreases the cathodic hydrogen evolution rate on iron and other non-noble metals. In a recently published paper by Jüttner (11) it was shown that Pb and Tl not only decrease the hydrogen

Table I. Comparison of kinetic parameters for electrodeposition and dissolution of Cu

| | Cu(II) M | Fe(II) M | $(j_0)_a$ mA·cm ⁻² | $(j_0)_c$ mA·cm ⁻² | α_a | α_c |
|---------------------|-------------|-------------|----------------------------------|----------------------------------|-----------------|------------|
| This work | 0.7 | — | 5.0 | 9.45 | 1.35 ± 0.15 | 0.52 |
| | 0.7 | 0.005 | 5.6 | 9.4 | | |
| | 0.7 | 0.05 | 5.6 | 9.2 | | |
| | 0.7 | 0.15 | 5.6 | 8.1 | | |
| | 0.7 | 0.3 | 5.6 | 6.0 | | |
| Bockris and Mattson | 0.5 | — | 5.1 | 8.3 | 1.64 ± 0.25 | 0.49 |
| Bockris and Enyo | 0.46 | — | 5.2 | 8.3 | 1.51 ± 0.04 | 0.42 |
| Albaya and Lorenz | 0.51 | — | 3.6 | 3.6 | 1.50 ± 0.11 | 0.57 |

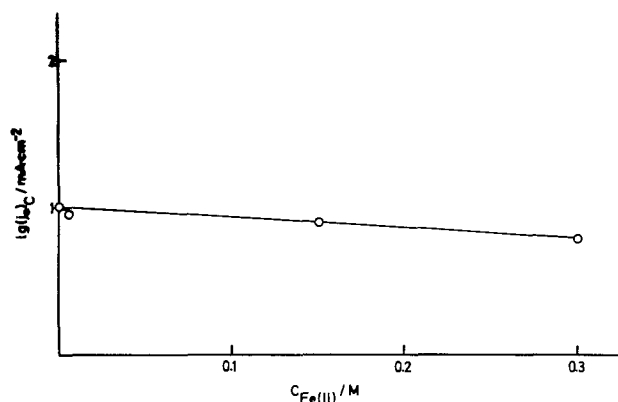


Fig. 2. Dependence of the cathodic exchange current density on the concentration of Fe(II) ions.

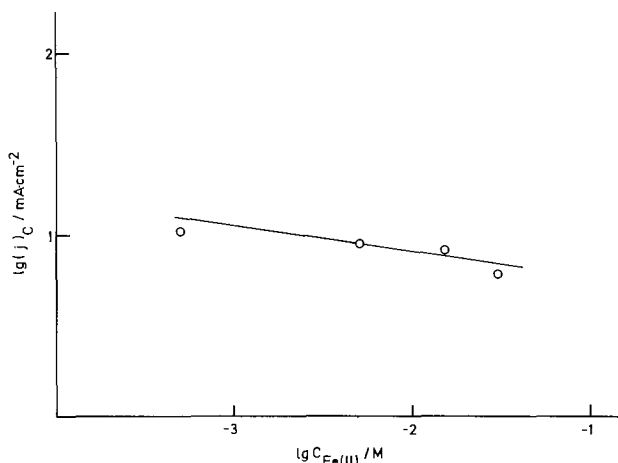


Fig. 3. Dependence of the cathodic current density at any constant value of the potential in the cathodic region of 50-150 mV vs. SCE on the concentration of Fe(II) ions.

evolution rate but also inhibit the dissolution of iron. The explanations given by the authors mentioned above for this phenomenon are in connection with the so-called "underpotential deposition" and the re-distribution effect of cation adsorption. Nevertheless, it seems that an exact model for these effects is not known at present. The same could be said with respect to the inhibitive effect of Fe(II) ions on the electrodeposition of copper obtained in the present work. Any further interpretation of this phenomenon cannot be offered on the basis of the experimental results presented here. Nevertheless, the most likely explanation appears to be that given by Schmickler (12), which is based on electrostatic cation adsorption effects, in which the presence of an adsorbate alters the double layer structure and decreases the rate of an electrochemical reaction. On the other hand, Conway and co-workers (13) presented a so-called co-sphere/co-plane overlap model for interaction of hydrated ions in the double layer with each other and with the oriented water layer at the electrode. Based on these two theories, it may be assumed that the inhibitive effect of Fe(II) ions on the electrodeposition of copper is due to the electrostatic contact adsorption of Fe(II) ions, which decreases the free and active surface of the electrode, resulting in an increase of the overvoltage and the corresponding displacement of cathodic Tafel lines to the region of higher overvoltages.

Conclusion

The inhibitive effect of Fe(II) ions on the kinetics of the cathodic deposition of copper in the acid sulfate system has been demonstrated. The electrostatic cation adsorption and the co-sphere/co-plane overlap

model for interaction of hydrated ions in the double layer as well as the decrease of the active surface of the electrode, have been suggested for the explanation of this phenomenon. However, further systematic investigation is needed before a more definite interpretation can be offered.

Acknowledgment

The author wishes to acknowledge helpful discussion with A. R. Despić.

Manuscript submitted Oct. 31, 1979; revised manuscript received April 6, 1981. This was Paper 456 presented at the Los Angeles, California, Meeting of the Society, Oct. 14-19, 1979.

Any discussion of this paper will appear in a Discussion Section to be published in the June 1982 JOURNAL. All discussions for the June 1982 Discussion Section should be submitted by Feb. 1, 1982.

REFERENCES

1. E. Mattson and J. O'M. Bockris, *Trans. Faraday Soc.*, **58**, 1586 (1962).
2. J. O'M. Bockris and M. Enyo, *ibid.*, **58**, 1187 (1962).
3. O. R. Brown and H. R. Thirsk, *Electrochim. Acta*, **10**, 383 (1965).
4. D. R. Turner and G. R. Johnson, *This Journal*, **109**, 798 (1962).
5. I. M. Pearson and G. F. Shradler, *Electrochim. Acta*, **13**, 2021 (1968).
6. R. Caban and T. W. Chapman, *This Journal*, **124**, 1371 (1977).
7. T. Hurlen, G. Ottesen, and A. Staurset, *Electrochim. Acta*, **23**, 23 (1978).
8. H. G. Albaya and W. J. Lorenz, *Phys. Chem. N.F.*, **81**, 294 (1972).
9. A. Damjanović, M. Paunović, and J. O'M. Bockris, *J. Electroanal. Chem.*, **9**, 93 (1965).
10. D. M. Dražić and L. Z. Vorkapić, *Corros. Sci.*, **18**, 907 (1978).
11. K. Jüttner, *Werkst. Korros.*, **31**, 358 (1980).
12. W. Schmickler, in "Electrode Processes," S. Bruckenstein, J. D. E. McIntyre, B. Miller, and E. Yeager, Editors, p. 65, The Electrochemical Society Softbound Proceedings Series, Princeton, N.J. (1979).
13. B. E. Conway, H. Angerstein-Kozłowska, D. M. Novak, and M. de Smet, in "Electrode Processes," S. Bruckenstein, J. D. E. McIntyre, B. Miller, and E. Yeager, Editors, p. 271, The Electrochemical Society Softbound Proceedings Series, Princeton, N.J. (1979).

Concentration Profiles in Electrowinning Circuits

I. Current Efficiency

F. M. Kimmerle

Departement de Chimie, Université de Sherbrooke, Sherbrooke, Québec, Canada, J1K 2R1

R. L. LeRoy*

Centre de Recherche Noranda, Pointe Claire, Québec, Canada H9R 1G5

and O. Vittori

Université Lyon 1, Claude Bernard, Villeurbanne, France

ABSTRACT

Factors affecting the current efficiency of electrowinning processes are investigated theoretically, and the resulting expressions are tested experimentally for the electrodeposition of copper. The results derived predict the dependence of current efficiency on metal-ion concentration and on total current, for different thermodynamic and kinetic parameters of the electrowinning system. It is found that in rotating disk experiments, where transport parameters are independent of current density, the current efficiency can be approximated by the relationship $\epsilon = \epsilon_{\infty} [1 - \exp(-BC/\Sigma i)]$. This result is further simplified in a model electrowinning circuit having gas-evolving electrodes where transport processes depend on current density and current efficiency can be represented with surprising accuracy by $\epsilon = \epsilon_{\infty} [1 - \exp(B'C)]$, where ϵ_{∞} and B' are constants which depend on cell geometry and electrolyte composition.

In industrial electrowinning or electrorefining processes, concentration gradients of the metal ions are found within the electrolyte layer near the cathode. If current density is increased beyond a limiting value at which the metal ion concentration at the electrode reaches zero, competing processes take place and the quality of the deposit deteriorates. At the same time, the current efficiency of the desired process drops considerably below the limiting value which is observed at low current densities or high metal-ion concentrations.

In a typical electrorefining process, such as zinc electrodeposition from sulfuric acid electrolyte, a

high current efficiency is maintained for the desired process, by using chemical replenishment to maintain metal ion concentration at a high level (typically 60 g/liter for Zn^{2+}) and by use of current densities below the limiting value (1.5 kA/m² for zinc) (1). In electrorefining processes such as the purification of blister copper, metal ion concentration is maintained fairly constant by electrochemical dissolution of the anode.

There are many industrial electrodeposition applications, however, in which metal-ion concentration varies sharply with time. Examples are the purification circuit of a copper electrorefinery (2) and circuits used for recovery and treatment of pickling and plating solutions (3-5). Also, although theoretical and experimental characterization of flow-through porous

* Electrochemical Society Active Member.
Key words: current efficiency, metal electrowinning, copper deposition.

electrodes is reaching an advanced state (6-8), it is likely that a large number of ill-defined reaction sequences will be encountered using these electrodes in plant-scale operations.

It is, therefore, pertinent to examine the current efficiency for metal-ion deposition as a function of concentration and current density. The ultimate objective is to use the resulting function for prediction of concentration profiles in dynamic electropurification and electrowinning circuits. This is the subject of part II of this series (9). The present paper deals with the current-efficiency function itself. Because of its practical importance, and because the more fundamental aspects have been thoroughly established (10-12), copper deposition has been chosen as the subject of experiments illustrating the theoretical development.

Theory

Most electrode processes are irreversible, and current is controlled not only by mass transport to the electrodes, but also by heterogeneous rate constants which account for the slow electron transfer or slow nucleation steps. The Tafel relationship is often used to describe such systems. However, when currents may approach their limiting values or when a reverse reaction such as dissolution of the electrode deposit may not be excluded, the behavior is better approximated by a more general expression

$$E = E_{1/2} + \frac{RT}{\alpha n F} \ln \left(\frac{i - i_1^c}{i_1^a - i} \right) \quad [1]$$

The transfer coefficient α depends on the nature of the electrode reaction, while the half-wave potential $E_{1/2}$ is a function of the rate constant, the diffusion coefficient, and the standard reduction potential. Both α and $E_{1/2}$ may be readily determined from laboratory polarization experiments using expression [1]. This expression is valid for electrochemical reactions in which the transport process is the same for all reacting species.

While ohmic-resistance effects and deviations from uniform current distribution will affect measured potentials in practical systems, Eq. [1] is useful as a first approximation. It can serve to illustrate sensitivity to the three key parameters which determine electrodeposition current efficiency when two (or more) processes are possible, the desired process 1 and the undesired process 2. These are the difference in half-wave potentials $\Delta E_{1/2}$, the ratio of the limiting current densities i_1^c/i_2^c , and the degree of reversibility of the two competing reactions as measured by $(\alpha n)_1$ and $(\alpha n)_2$.

Since current densities and not electrode potentials are normally controlled, it is instructive to plot current efficiency as a function of the ratio of the limiting current density for deposition of the desired metal to the total current density, $(i_1/\Sigma i)$. Figure 1 records typical results calculated from Eq. [1] for two closely-

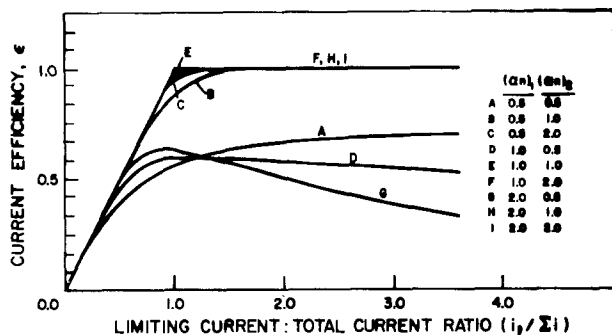


Fig. 1. Current efficiency as a function of current density for $i_{12} = 100 i_1$ and $\Delta E_{1/2} = 5 \times 0.059V$.

spaced ($\Delta E_{1/2} = 5 \times 0.059V$) cathodic processes. It is clear that when the two cathodic reactions are sufficiently separated in potential (curves f, h, and i), the result consists essentially of two straight-line sections. For current densities less than i_1 the desired process 1 can furnish all of the current, while for current densities exceeding i_1 the current efficiency decreases linearly as process 2 becomes increasingly important.

If the two waves are not sufficiently separated, the region around $i_1/\Sigma i = 1$ becomes rounded (curves e, c, and b in Fig. 1), while for a highly irreversible competitive process [curve a, $(\alpha n)_2 = 0.5$] the limiting current efficiency is significantly less than unity.

Figure 2 examines the sensitivity of current efficiency to limiting current density and $\Delta E_{1/2}$ for kinetic parameters characteristic of metal deposition in competition with hydrogen evolution, $(\alpha n)_1 = 2.0$ and $(\alpha n)_2 = 0.5$.

As the limiting current density for the competing process increases with respect to that for metal deposition (curves a, b, c, and e), the current efficiency decreases and the maximum becomes more pronounced. As $\Delta E_{1/2}$ decreases (curves f, e, and d) the desired process becomes increasingly inefficient.

In the example of zinc electrowinning from acid electrolyte, where $\Delta E_{1/2}$ is less than zero, the current efficiency approaches a maximum less than 1.0 as $i_1/\Sigma i$ increases, and decreases to zero at high values. In the case of copper deposition from acid electrolyte, of particular interest in this paper, $\Delta E_{1/2}$ is greater than zero, and three regions can be identified from examination of Fig. 1 and 2:

1. When current density greatly exceeds the limiting current density, efficiency will approach the asymptotic value $\epsilon_\infty = 1$ when the transfer coefficient for the metal deposition reaction is less than that for the competing reaction. In the more likely event that the competing reaction is the less reversible, the efficiency passes through a broad maximum and eventually approaches zero.

2. When current density greatly exceeds the limiting current density, then only the fraction $i_1/\Sigma i$ can be usefully employed even under ideal conditions. Since the limiting current density depends on the local concentration C and transport parameter k through the relationship $i_1 = nFkC$, the current efficiency will approach

$$\epsilon = \frac{i_1}{\Sigma i} = \frac{nFkC}{\Sigma i} \quad [2]$$

Although the current efficiency always approaches this limiting behavior, for unresolved processes the limit may be reached at such high current densities, and at such low values of ϵ , that it is of little practical interest.

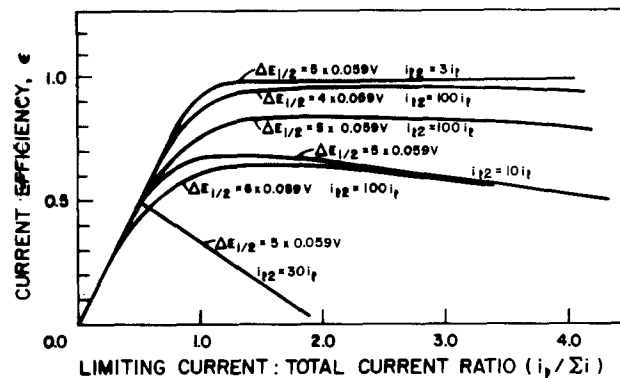


Fig. 2. Current efficiency variation for kinetic parameters characteristic of metal deposition in competition with hydrogen evolution, $(\alpha n)_1 = 2.0$ and $(\alpha n)_2 = 0.5$.

3. For the case of greatest practical interest, where the current density approaches the limiting current density, it is necessary to consider the respective equilibrium potentials and kinetic parameters of the two or more alternative current paths in order to arrive at a satisfactory description of the phenomena. A clear requirement for a descriptive function is that ϵ vary in a monotonic fashion from case 1 to case 2, and that $\lim \epsilon = \epsilon_\infty$ and $\lim \epsilon = 0$

$$C \rightarrow \infty \quad C \rightarrow 0$$

One convenient expression meeting these requirements for two closely spaced electrode processes is

$$\epsilon = \epsilon_\infty [1 - \exp(-B''i_1/\Sigma i)] \quad [3]$$

Figure 3 illustrates how Eq. [3] can approximate the limiting behavior of the current efficiency quite closely, for representative values of the parameters ϵ_∞ and B'' . The intermediate behavior for overlapping waves can be fitted quite satisfactorily, as exemplified by the agreement of curves d and e. Curve b overestimates the current efficiency somewhat at low $i_1/\Sigma i$ ratios, approaching 1.0 less quickly than calculated for the limiting case. Equation [3] cannot reproduce the maximum which appears under extreme conditions, for example for $i_{12} = 100 i_1$ and $\Delta E_{1/2}$ less than $6 \times 0.059V$ (cf. Fig. 2). Thus, numerical interpolation from experimental efficiency data may be necessary in some applications, for highest accuracy.

In summary, Eq. [3] can be considered a useful mathematical function which permits analytical treatment of a wide variety of electrode processes. A useful extension of this expression which is more directly applicable to experimental data is obtained by substituting for the limiting current density

$$\epsilon = \epsilon_\infty [1 - \exp(-BC/\Sigma i)] \quad [4]$$

Experimental

Preliminary deposition experiments were carried out using a Tacussel E5 rotating disk electrode. The surface was prepared by mechanically polishing the end of 2 mm copper wire which was embedded in a 1 cm Teflon disk followed by electrodeposition of copper at $-0.35V$ vs. the standard calomel electrode (SCE) for 7 min from a 0.01M $CuSO_4$, 0.5M H_2SO_4 solution. Identical results were obtained for copper deposited in the same way on a platinum surface. The electrode pretreatment was repeated if the electrode was exposed to the atmosphere, or if its potential was moved outside the range -0.7 to $+0.1V$ vs. SCE.

The electrolysis experiments were carried out in a Plexiglas purification cell fitted for 11 lead anodes and 10 copper cathodes, each having dimensions 9×9 cm. The electrodes could be mounted alternatively

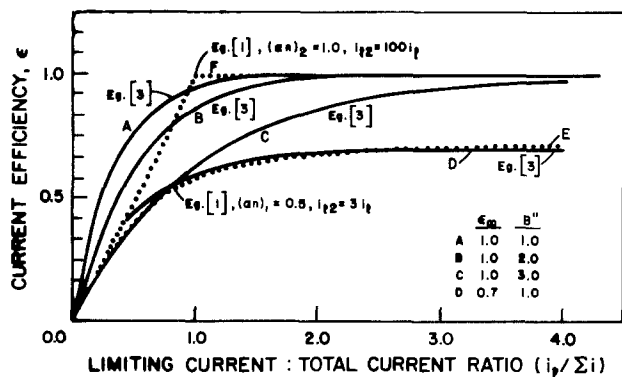


Fig. 3. Use of Eq. [3] for prediction of the current-density dependence of current efficiency, for cathodic processes having $\Delta E_{1/2} = 5 \times 0.059V$ while $(an)_1 = 2.0$.

with a 1 cm spacing so that 20 individual compartments were formed, each of them holding about 160 cm^3 of electrolyte. This arrangement is illustrated schematically in Fig. 4. Solution could be passed as indicated at flow rates from 0 to 0.5 cm^3 sec^{-1} , cascading from one compartment to the next. Direct current was applied either at fixed potential or at fixed current by a McKee Pederson MP 1026 or a Lambda Model LP 522 FM power supply. Acidified copper sulfate solutions for the electrowinning experiments (0.1M $CuSO_4$ and 2M H_2SO_4) were prepared in 20 liter batches from Analar reagent grade $CuSO_4$ and H_2SO_4 . Copper concentrations were monitored, after dilution, by atomic absorption (Varian Spectrophotometer) and pulse polarography (Princeton Applied Research Model 174).

Current efficiencies were calculated by two methods. When a relatively small volume was circulated through a part of the test cell, or when the complete cell was used, calculations were based on the measured decrease in copper concentration. When a large volume of fixed concentration was quickly passed through the cell, efficiencies were determined by measuring the weight of copper deposited onto the cathodes. Electrolyte circulation within individual cells was assured by the gas evolution on the anodic and, in varying degrees, cathodic surfaces. The bulk flow rates in a direction perpendicular to the electrodes were not found to influence the limiting current significantly, and no other agitation was provided.

The mechanically polished cathode surfaces aged significantly during the course of a run. Both the appearance and adherence of electrodeposited copper varied greatly with the electrolysis conditions, but no effort was made to determine the exact physical nature of the deposits.

Results and Discussion

Rotating disk electrode experiments.—Voltammograms recorded with rotating copper disk electrodes in acidified copper sulfate solution were used to estimate the current efficiency as a function of electrode potential and copper concentration. The potential was scanned from 0.0V vs. SCE in the cathodic direction, and the scan was reversed when obvious hydrogen evolution occurred. Anodic and cathodic scans did not show a hysteresis unless an anodic current was inadvertently passed and the surface reoxidized. Current efficiencies were estimated by comparison of currents measured in the $CuSO_4/H_2SO_4$ electrolytes with currents measured in identical experiments using 0.5M H_2SO_4 electrolytes.

Results are recorded in Fig. 5. Current efficiency was found to decrease with increasing cathodic cur-

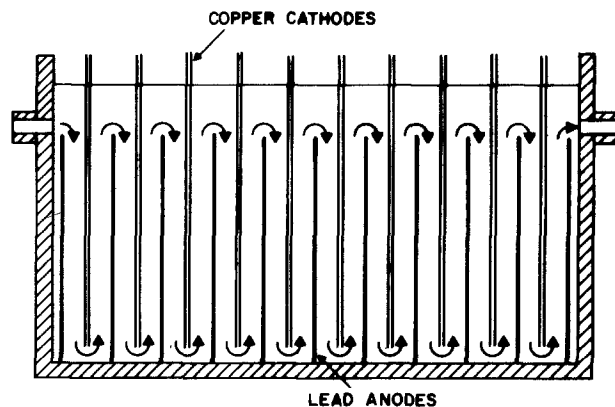


Fig. 4. Plexiglas electrolysis cell having provision for 11 lead anodes and 10 copper cathodes. Electrodes having dimensions 9×9 cm were spaced 1 cm apart, forming 20 cell compartments each having a volume of 80 cm^3 .

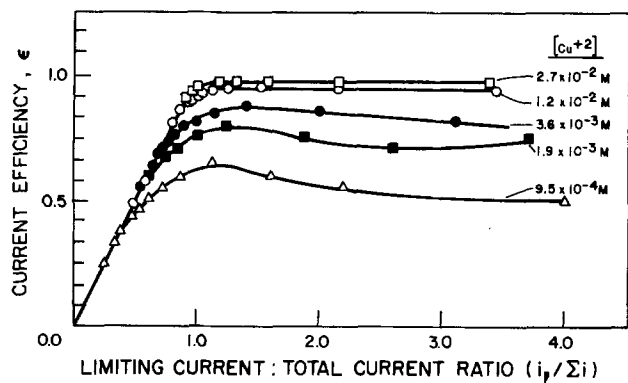


Fig. 5. Cathodic current efficiency for electrodeposition of copper on a rotating disk electrode, for different copper ion concentrations.

rent density and with decreasing copper concentration. When plotted as a function of $i_l/\Sigma i$, the current efficiency could be approximated by two straight-line portions at concentrations below 0.01M. In these cases, current efficiency exceeded 95% for current densities below the limiting value. At lower copper-ion concentrations, however, the current efficiency decreased to about 60% even under the most favorable current conditions. Detailed results showed the limiting current density, i_l , to be a linear function of copper concentration from 10^{-3} to 1.0M, and to vary with the square root of the rotational velocity of the disk down to 50 rpm, as expected from the Levich expression and reported earlier by Caban and Chapman (12). Plots of current efficiency vs. $i_l/\Sigma i$ at different rotational speeds (not shown) coincided at concentrations greater than 10^{-2} M Cu^{2+} .

Figure 6 records results obtained for current efficiency as a function of copper concentration. The data obtained at different current densities fell on a single curve, in good agreement with the prediction of Eq. [4]. The parameter B in this case reflects the transport characteristics of the system and can be expected to vary with the rotational velocity.

Isolated-cathode experiments.—A copper cathode was installed at one end of the electro-winning cell of Fig. 4 and was separated from a lead anode at the other end of the cell by a porous polypropylene diaphragm. The 1.6 liter volume of the cell assured relatively fixed copper concentration during electrolysis, and the cathode was effectively shielded from the gas evolution at the anode. The deposits obtained for copper ion concentrations greater than 3 g liter⁻¹ were uniformly dense, bright, and pale colored, while those obtained at lower concentrations were generally fragile, porous, nonadherent, and subject to air oxidation

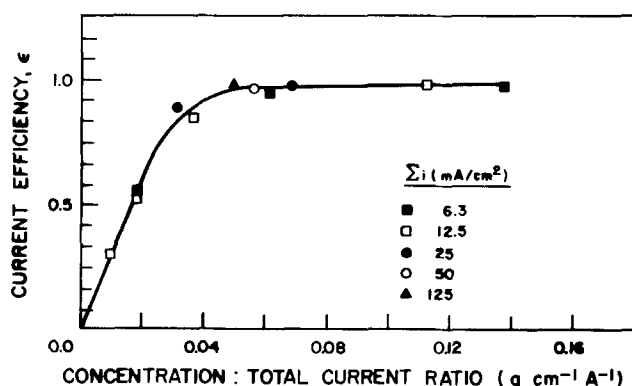


Fig. 6. Cathodic current efficiency for electrodeposition of copper on a rotating disk electrode. Rotation speed was 500 rpm, electrode area was 2 mm², and copper-ion concentration varied from 0.001 to 0.1M.

which tended to form a dark copper-oxide film. Current efficiencies calculated from the weight gain of the copper sheet (100-300 mg) at fixed current densities (2-15 mA/cm²) are recorded in Fig. 7. Copper concentrations ranged from 0.02 to 0.1M. The current efficiencies tended to a limiting value of $\epsilon_{\infty} = 0.98 \pm 0.02$ at the higher concentrations and lower current densities. Unlike the results obtained using the rotating disk electrode (Fig. 6), the efficiencies measured at different concentrations did not coincide.

This apparent discrepancy can be rationalized based on the relatively low electrolyte circulation at the isolated cathode. The total current density can be expressed as

$$\Sigma i = i_{\text{H}_2} + 2Fk[\text{Cu}^{2+}] \quad [5]$$

The dotted line in Fig. 7 was calculated assuming a fixed k value estimated from the current at the onset of hydrogen evolution as 1.6×10^{-5} cm sec⁻¹. For a diffusion coefficient of 5×10^{-6} cm² sec⁻¹ this would correspond to an effective diffusion-layer thickness $\delta \sim 0.033$ cm. The experimental current efficiencies of Fig. 7 are all higher than those predicted from the simple model.

The enhancement of the transport rate at gas-evolving electrodes has been studied extensively (13-16) and is described by the empirical relationship

$$\ln \delta = -m \ln i_{\text{H}_2}^2 + C \quad [6]$$

Idl *et al.* (14) cite m values ranging from 0.25 to 0.59 for hydrogen evolution in acid media. More recently, Janssen (16) has reported values as high as $m = 0.9$ for horizontal electrodes. A close fit to the data of Fig. 7 is obtained using the parameters $m = 0.38$ and $C = -6.8$. Although this fit is relatively insensitive to the precise values of m and C , there is little doubt that the average transport parameter is enhanced by local stirring arising from bubble dislodgement.

Experiments in the electro-winning configuration.—Two types of experiments were performed in the electro-winning cell with copper cathodes suspended 0.9 cm from facing lead anodes. In the first series, the cell was fed with electrolyte having a known concentration between 0.01 and 0.1M. Typical values of the current efficiency calculated from cathode weight gain are recorded as solid circles in Fig. 8.

The limiting current efficiency at the higher concentrations was found to be 0.965 ± 0.02 . Figure 9 illustrates the bubble distribution observed in the cell. Even at high copper concentrations (Fig. 9A) some oxygen bubbles came in contact with the copper cathode. This may partially account for the observed 3.5% efficiency loss. The hydrogen bubbles given off at the cathode at lower copper concentrations extended far less into the interelectrode space than they did in the isolated-cathode experiments described above. In agreement with results reported by Awakura *et al.*,

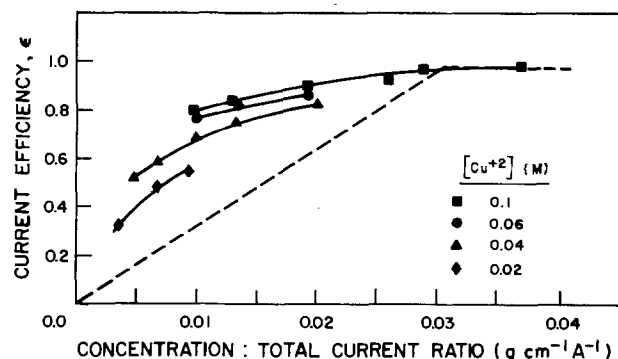


Fig. 7. Current efficiency for electrodeposition of copper at an isolated cathode. The solid lines are calculated using Eq. [6], while the dotted line represents predicted behavior for constant δ .

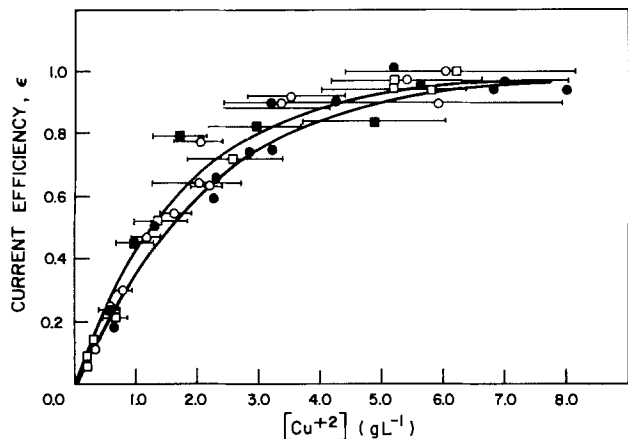


Fig. 8. Current efficiency for electrodeposition of copper. Solid curves are drawn from the expression $\epsilon = 0.965 [1 - \exp(-B'C)]$.

(17), thicker deposits and an upward movement of the electrolyte were observed near the lower part of the isolated cathode. In the electrowinning configuration, however, the deposit was more uniform, and downward electrolyte movement adjacent to the nongassing cathode was observed in agreement with the observations of Ettel, Tilak, and Gendron (13). Figure 9b shows that full turbulence is achieved near the electrodes at low copper concentration, and the downward movement of the electrolyte takes place near the center of the interelectrode region.

The second set of experiments approximated a batch purification process. A small volume (approx. 160 cm³) of electrolyte was constantly recirculated through a single cell compartment, and 0.05 cm³ samples were withdrawn periodically for analysis. Resulting current efficiencies are plotted in Fig. 8. The experimental uncertainty is quite high at the initial copper concentrations since current efficiency must be calculated from small differences in concentration.

The results of this experiment practically coincide with those obtained at constant concentration. Unlike data obtained with the rotating disk electrode which coincided as a function of $C/\Sigma i$ and those obtained at the isolated cathode which showed some enhancement of the transport parameter, the current efficiency in the electrowinning geometry appears relatively independent of current density. With reference to Fig. 8, the current efficiency is closely approximated by

$$\epsilon = 0.965[1 - \exp(-B'C)] \quad [7]$$

here $B' = 0.55 \pm 0.05$ liter g⁻¹ and C is expressed in g liter⁻¹.

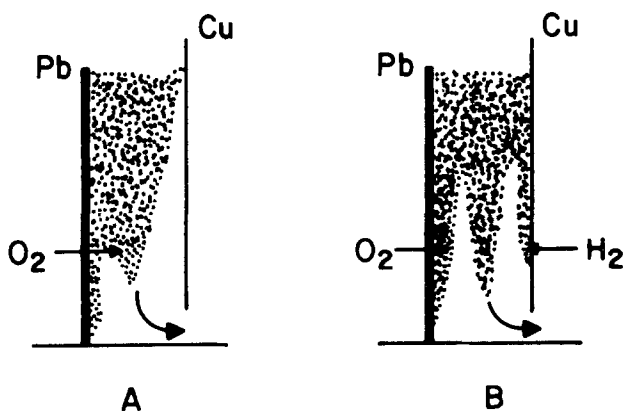


Fig. 9. Gas evolution during copper deposition at 3 mA/cm² at copper ion concentrations above 3.0 g liter⁻¹ (a) and below 1.0 g liter⁻¹ (b).

The apparent inconsistency between the rotating disk (Eq. [4]) and electrowinning cell (Eq. [7]) result is explained if the local transport parameter is directly proportional to the total current. This is reasonable, as the rate of anodic gas evolution is directly proportional to current and it is known that the transport parameter varies directly with air sparging rate (13, 14). Equation [7] may thus be considered a reasonable empirical relationship over the limited current range of practical interest. The parameter B' can be expected to vary with cell geometry, electrolyte viscosity, and temperature.

Conclusion

It has been shown that the current efficiency of metal electrodeposition at electrodes characterized by constant transport parameters is a function of the ratio of metal-ion concentration to the total current. This has been confirmed for the electrodeposition of copper at a rotating disk electrode, where the current efficiency can be adequately reproduced by the expression $\epsilon = \epsilon_{\infty}[1 - \exp(-BC/\Sigma i)]$.

In a typical electrowinning configuration, the experimental results suggest that the parameter B , which includes the local transport parameter, is directly proportional to the total current density, and thus that the current efficiency may be represented by the simple result $\epsilon = \epsilon_{\infty}[1 - \exp(-B'C)]$. This simple two-parameter relationship is found to describe the current efficiency of copper electrodeposition with surprising accuracy.

Acknowledgment

Support of this research by Canadian Industries Limited and by the National Research Council of Canada (through grants to FMK) is gratefully acknowledged.

Manuscript submitted July 16, 1979; revised manuscript received March 24, 1981.

Any discussion of this paper will appear in a Discussion Section to be published in the June 1982 JOURNAL. All discussions for the June 1982 Discussion Section should be submitted by Feb. 1, 1982.

Publication costs of this article were assisted by the Université de Sherbrooke.

LIST OF SYMBOLS

| | |
|---------------------|---|
| C | metal-ion concentration |
| $\Delta E_{1/2}$ | difference in half-wave potentials of processes 1 and 2 = $(E_{1/2})_1 - (E_{1/2})_2$ |
| F | Faraday constant |
| i | current density |
| $i_1 = i_{1L}$ | limiting current density for the desired metal deposition process |
| i_{12} | limiting current density for the competing cathodic process |
| i_1^a, i_1^c | limiting anodic, cathodic current density |
| Σi | total current density |
| i_{H_2} | cathodic current going to hydrogen evolution |
| k | transport parameter |
| α | transfer coefficient |
| ϵ | current efficiency |
| ϵ_{∞} | limiting current efficiency |
| δ | diffusion-layer thickness |

REFERENCES

1. C. L. Mantell, "Electrochemical Engineering," 4th ed., p. 216, McGraw-Hill, Toronto (1960).
2. C. L. Mantell, "Electrochemical Engineering," 4th ed., p. 142, McGraw-Hill, Toronto, (1960).
3. J. O'M. Bockris, Editor, "Electrochemistry for a Cleaner Environment," p. 98, Plenum Press, New York (1972).
4. W. Mueller, *Galvanotechnick*, **67**, 381 (1976).
5. A. B. Tripler, Jr., R. H. Cherry, and G. R. Smithson, Jr., U.S. Environ. Prot. Agency, Off. Res. Dev. (Rep) EPA 670/275-018.
6. J. A. Traiham and J. Newman, *This Journal*, **124**, 1528 (1977); *ibid.*, **125**, 58 (1978).
7. R. Alkire and B. Gracon, *ibid.*, **122**, 1594 (1975).

8. R. Alkire and R. Gould, *ibid.*, **123**, 1842 (1976).
9. R. L. LeRoy, F. M. Kimmerle, F. Routhier, and O. Vittori, *This Journal*, **128**, 1869 (1981).
10. E. Mattsson and J. O'M. Bockris, *Trans. Faraday Soc.*, **55**, 1586 (1959).
11. O. R. Brown and H. R. Thirsk, *Electrochim. Acta*, **19**, 383 (1965).
12. R. Caban and T. W. Chapman, *This Journal*, **124**, 1371 (1977).
13. V. A. Ettel, B. V. Tilak, and A. S. Gendron, *ibid.*, **121**, 867 (1974).
14. N. Ibl, R. Kind, and E. Adam, *Anal. Quim.*, **71**, 1008 (1975).
15. N. Ibl and J. Venczel, *Oberfläche Surf.*, **13**, 1 (1972).
16. L. J. J. Janssen, *Electrochim. Acta*, **23**, 81 (1978).
17. Y. Awakwa, A. Ebata, and Y. Kondo, *This Journal*, **126**, 23 (1979).

Concentration Profiles in Electrowinning Circuits

II. Time and Position Dependence of Metal Ion Concentration

R. L. LeRoy*

Centre de Recherche Noranda, Pointe Claire, Québec, Canada H9R 1G5

F. M. Kimmerle and F. Routhier

Département de Chimie, Université de Sherbrooke, Sherbrooke, Québec, Canada J1K 2R1

and O. Vittori

Université Lyon 1, Claude Bernard, Villeurbanne, France

ABSTRACT

A simple expression has been derived in part I for current efficiency of an electrowinning process as a function of metal-ion concentration: $\epsilon = \epsilon_0 [1 - \exp(-BC)]$. This semi-empirical relationship is used in this paper to predict the concentration variation with time during batch electrolysis, and the steady-state variation of concentration with distance in a flow-through electrowinning circuit. A method of calculation is reported which allows prediction of the transient or steady-state response of a flow-through electrowinning system, for any assumed dependence of the cathodic current efficiency on metal-ion concentration.

The mathematical description of electrowinning and electropurification systems is not unlike recent derivations for flow-through porous electrodes (1-4). A typical purification or electrowinning circuit consists of a series of cascading cell compartments with the electrolyte flowing from one cell to the next. A method for measuring the local mass-transport coefficient in such circuits has been developed by Ettel and his colleagues (5), based on analysis of traces of noble metals which are codeposited with copper ions. However, an analysis which allows calculation of the macroscopic properties of a practical electrometallurgical circuit, in particular the variation of metal-ion concentration with position and time, has not previously been available.

The local current densities during electrodeposition of copper are only uniform at very low current loadings (6). Under the conditions prevailing in an electrowinning or electropurification circuit where the total current density is an appreciable fraction of the limiting current density for metal-ion deposition, the current density is expected to vary as the -0.25 power of the vertical distance. In the latter stages of a purification circuit where applied current may exceed the limiting current density, extensive gas evolution will occur and fully turbulent flow may be expected. Thus *ab initio* calculations of limiting currents are not straight-forward for real systems. Fortunately, it is fairly easy to measure average parameters for narrow electrodes of a given height, and to apply these values to larger systems.

The treatment presented here is based on the fact that the current efficiency at electrowinning cathodes

can be expressed as a function of concentration, and that it seems to be independent of current density over the fairly narrow concentration ranges which are important in industrial systems (7). Electrode dimensions and electrolyte flow may vary to such an extent that neither pure plug flow nor ideally mixed flow can adequately describe the system. It is supposed here that plug flow occurs within parts of the system and, when necessary, that complete mixing occurs before the electrolyte enters the next stage of the circuit. Adequacy of these assumptions is supported by the experimental results.

Theoretical Description of an Electrowinning Circuit

The general equation describing an electrowinning or electropurification circuit is derived by considering the portion of a cell between x and $x + dx$. Geometric parameters are defined in Fig. 1. Conservation of mass requires that the quantity of metal ions brought into the volume element dV by solution flow v in time dt be equal to the quantity carried out by the solution flow, plus the quantity electrowon on the electrode area dS , plus the increase within dV .

The net metal-ion outflow from dV in time dt , is given as $v \partial C / \partial x dt dx$, the gain within the volume element equals $\partial C / \partial t dt dV$, and the quantity electrowon is given as $\epsilon i / nF dS dt$, where the surface element $dS = H dx$ and the electrode height h may vary as a function of distance. The volume element dV is equal to $A dx$, and the local current efficiency ϵ depends on the chemical nature of the process. Thus, the time and space-dependent differential equation can be written as

$$\frac{v \partial C}{\partial x} + \frac{A \partial C}{\partial t} + \frac{\epsilon i h}{nF} = 0 \quad [1]$$

* Electrochemical Society Active Member.

Key words: electrowinning, copper deposition, concentration profiles, dynamic flow system.

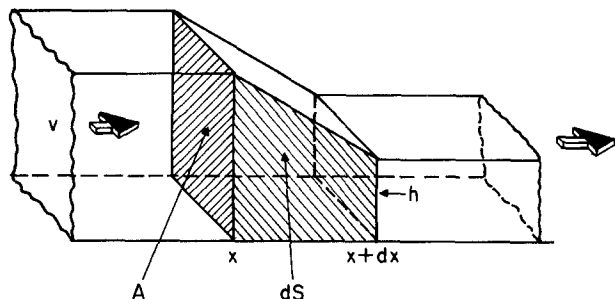


Fig. 1. Volume element of a flow-through electrowinning circuit, defining the geometric parameters.

When steady-state conditions have been attained, $\partial C/\partial t = 0$, and Eq. [1] becomes

$$\frac{v\partial C}{\partial x} + \frac{eh}{nF} = 0 \quad [2]$$

Equations [1] and [2] hold exactly for an infinitely small volume element. The current efficiency ϵ may be conveniently measured using a single cathode as the average current efficiency $\epsilon = \langle \epsilon \rangle$ at an average current density $i = \langle \Sigma i \rangle$. This experimental approach avoids the need to postulate the exact electrolyte and gas-flow characteristics in the interelectrode space. For the electrowinning of copper, we have shown that the current efficiency can be represented as a simple analytical function whose parameters seem to be independent of average current density over the narrow concentration range of interest (7). This facilitates considerably solution of Eq. [1]. However, the general approach remains valid for numerical solutions where current efficiency is only available as a function of copper concentration in tabulated form.

Steady-state profiles.—Solutions of Eq. [2] describe many practical electrowinning situations where the assumptions of ideal plug flow, constant incoming metal-ion concentration C^0 , and uniform transport characteristics are reasonable approximations. To simplify the resulting expressions, it is further assumed that a uniform current distribution exists along an electrode (of constant height h and length l) in a direction perpendicular to the solution flow. Thus $I = i h l$ is the total current passed in the system.

If the current efficiency ϵ is a constant, equal to ϵ_* , Eq. [2] is readily solved to yield

$$C = C^0 [1 - x/x^0] \quad [3]$$

where

$$x^0 = \frac{nFvC^0}{\epsilon_* i h} = \frac{nFvlC^0}{\epsilon_* I}$$

For this limiting case, the metal-ion concentration at the outlet of the cell is independent of the size and geometry of the system.

In the limit of high currents compared to the limiting current density or of low metal-ion concentrations, the current efficiency may be approximated as $\epsilon = \epsilon_* i_l/i$ and solution of Eq. [2] gives

$$C = C^0 \exp(-x/x^*) \quad [4]$$

where

$$x^* = \frac{v}{\epsilon_* k h}$$

The metal-ion concentration decreases much more slowly according to this expression than the prediction of Eq. [3].

At intermediate (and industrially more important) current densities where the current efficiency can be described by the results of part I (7), the differential Eq. [2] becomes

$$\frac{v\partial C}{\partial x} + \epsilon_* \frac{ih}{nF} [1 - \exp(-BC)] = 0 \quad [5]$$

Integration of this expression yields

$$C = \frac{1}{B} \ln \left\{ 1 + \left[\exp\left(\frac{-Bx C^0}{x^0}\right) \right] \left[\exp(BC^0) - 1 \right] \right\} \quad [6]$$

Thus, the concentration initially decreases linearly with increasing distance from the cell inlet, and finally approaches zero in an asymptotic fashion.

Representative concentration profiles are plotted in Fig. 2 for $BC^0 = 1, 2, 3$, and ∞ , as a function of the dimensionless distance parameter x/x^0 . From Eq. [3] it is clear that x^0 corresponds to the distance necessary to deposit all of the metal ions if ϵ has a constant value ϵ_* . The concentration at the exit ($x = l$) will depend on the ratio l/x^0 . Increasing the concentration of the incoming liquor C^0 , or decreasing the current density, will increase x^0 . Current does not appear in Eq. [6], and according to this model (7) will not alter the current efficiency parameter B . Increasing C^0 will move the concentration profile closer to the limiting curve d , but may increase x^0 beyond the length of the purification cell. Optimization of the cell parameters to diminish the exit concentration becomes possible from considerations of results such as those presented in Fig. 2.

Time-dependent profiles.—Equation [1] can be solved by inspection for a closed system where the electrolyte flow rate is equal to zero and the current density is constant. The results are analogous to Eq. [3] and [6]. When the current efficiency has a constant value ϵ_* , the metal-ion concentration decreases as

$$C = C^0 \left(1 - \frac{t}{t^0}\right) \quad [7]$$

where

$$t^0 = \frac{nFVC^0}{\epsilon_* I}$$

In the general case

$$C = \frac{1}{B} \ln \left\{ 1 + \left[\exp\left(\frac{-BtC^0}{t^0}\right) \right] \left[\exp(BC^0) - 1 \right] \right\} \quad [8]$$

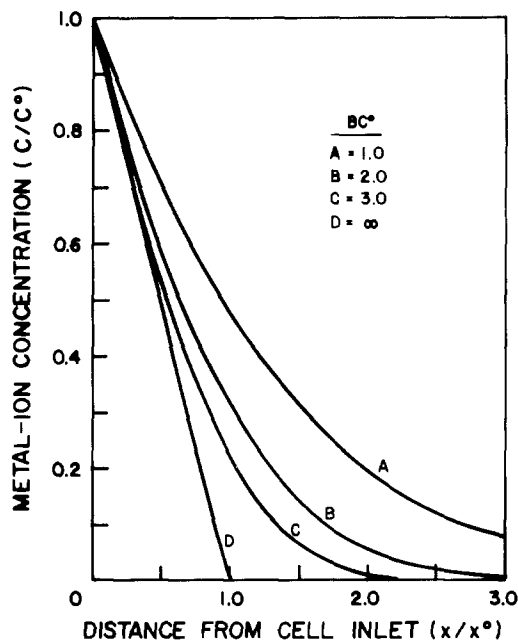


Fig. 2. Steady-state concentration profiles as a function of position in the electrowinning circuit, predicted by Eq. [6].

Thus in a closed system the concentration decreases linearly with time after the electro-winning current is first applied, and then approaches zero asymptotically.

Noting the parallel between Eq. [6] and [8], Fig. 2 can be interpreted as the time variation of metal-ion concentration in a closed system, if the abscissa is read as t/t^0 . In this case t^0 is interpreted as the time required to reduce metal-ion concentration to zero, when the current efficiency assumes a constant value ϵ_c .

The full time-dependent Eq. [1] can be solved numerically, using the Newton Raphson iteration method. The expression is written in finite-difference form as

$$\frac{v([C]_{i,j} - [C]_{i-1,j})}{\Delta x'} + \frac{V([C]_{i,j} - [C]_{i,j-1})}{\Delta t} + \frac{I_e}{nF} = 0 \quad [9]$$

If the number of segments $\Delta x'$ is small, then the iterative solution implicitly assumes ideal plug flow from one segment i to the next segment $i + 1$, followed by ideal mixing within each segment after time interval Δt . If only one segment is considered, then ideal mixing is implicitly assumed within the entire cell. This approach allows treatment of several cells of different volumes and different electrolysis currents which are arranged in series, and it also allows use of an electrolyte-feed solution whose composition varies with time.

Experimental

Experiments were carried out in the 21-electrode model electro-winning cell described in part I (7). As in the earlier work, copper deposition was used as a model system.

For static tests with no solution flow, all of the copper cathodes were connected in parallel, as were all of the lead anodes. Copper concentrations were followed over 3-5 hr intervals, and average results are reported. For dynamic tests where fresh solution was continually pumped into the left compartment of the system and withdrawn from the right, electrical connections to each cathode were made through 0.03 Ω nickel-chrome shunt resistors, so that current could be monitored. Connections to the anodes were through 1.0 Ω 10W resistors. These resistors, together with the high oxygen overpotential, assured a minimum variation in the current flow despite the strong variations of copper concentration with position in the system.

Electrode potentials vs. a saturated calomel electrode were measured with an Orion pH meter using a 1 mm, sulfuric-acid-filled Luggin capillary whose L-shaped tip could approach the cathode without significantly disturbing the electrolyte or gas flow patterns. Overvoltage values were averaged for a number of vertical positions in each cell compartment, and showed a scatter of about 15 mV.

Results and Discussion

Static conditions ($v = 0$).—When the electro-winning cell was operated at no net electrolyte flow, the electrode potentials were observed to vary monotonically as electro-winning progressed. Typical results, recorded in Fig. 3, show that the anode potential remained constant after an initial 2 hr period. The cathode potential shifted to more negative values as the copper ions were depleted. The sharp potential drop corresponded to a rapid drop in cathodic current efficiency and the onset of vigorous hydrogen evolution. This potential shift could be used to control a purification circuit and avoid insipid hydrogen evolution (8).

As indicated in the theoretical development above, the copper-ion concentration profile of Fig. 3A can be predicted by solving Eq. [9] for any given relationship between the current efficiency and copper-ion concentration. Typical examples of such predictions are presented in Fig. 4 in comparison with the experimental data obtained. At 100% current efficiency the

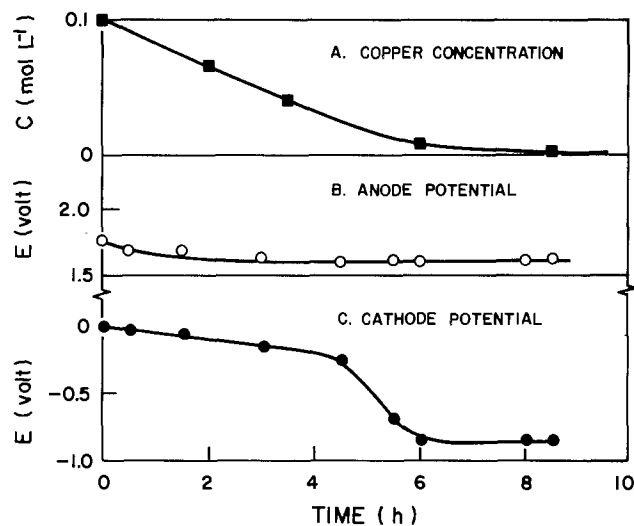


Fig. 3. Time dependence of copper-ion concentration and of the anode and cathode electrode potentials in a static system. Indicated potentials are with respect to the normal hydrogen electrode.

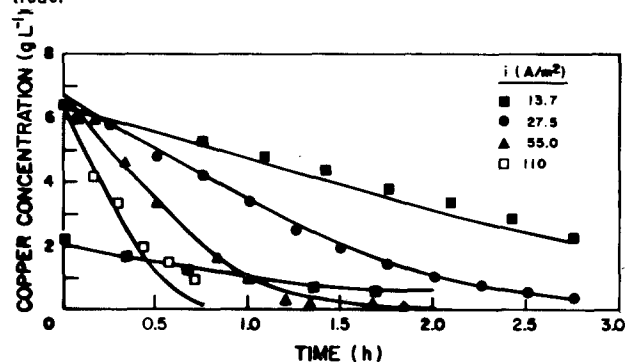


Fig. 4. Copper concentration profiles in a static system. Solid lines are calculated from Eq. [8] for a cell volume of 160 cm³, assuming $\epsilon = 0.965 [1 - \exp(-0.575 C)]$.

copper concentration would decrease linearly with a slope directly proportional to the current (cf. Eq. [7]). However, if the current efficiency can be approximated by the result of part I (7), the quasi-exponential decay predicted by Eq. [8] is to be expected.

The theoretical curves of Fig. 4, based on the model $\epsilon = 0.965 [1 - \exp(-0.575 C)]$ are in very satisfactory agreement with the experimental data.

At the highest current density (110 A m⁻²), the predicted decrease in copper-ion concentration was not quite attained below 2 g liter⁻¹. The deposit in this case was nonadhering and powdery, tending to break off and float about in the cell compartment. The relatively low efficiencies observed are attributed to redissolution of this powder in the presence of the anode gas. At 13.7 A m⁻², the experimental copper concentrations (≈ 4 g liter⁻¹) fell somewhat above the predicted line. There was little cathodic gas formation at this low current density. An appreciable ($\pm 10\%$) vertical concentration gradient was later found to exist in the absence of turbulent mixing at the cathode, and thus a non-negligible sampling error may be reflected in these low current-density results.

Dynamic-flow conditions.—All twenty cell compartments were used in a series of experiments with electrolyte cascading from cell to cell at a steady flow rate. Figure 5 illustrates the concentration profiles in the circuit as a function of the distance from the inlet (or the cell compartment number) and the electrolysis time. The applied current of 7.6A was distributed evenly (0.76 \pm 0.05A) over the ten cathodes, and a constant electrolyte flow rate of 0.41 cm³ sec⁻¹ was imposed throughout the run.

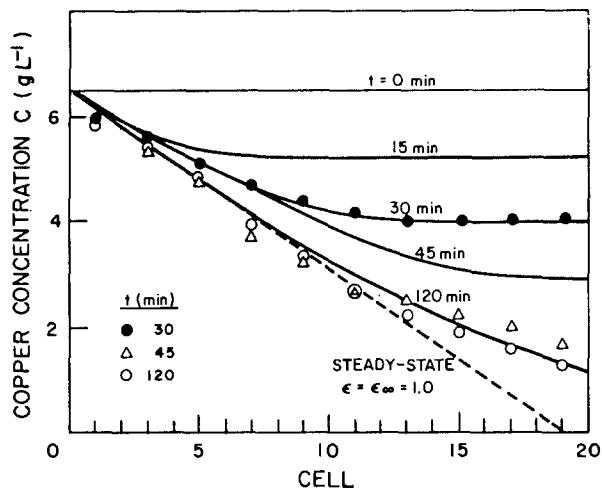


Fig. 5. Concentration profiles in the experimental purification circuit. Solid curves are calculated from Eq. [9] for an initial copper concentration of $6.56 \text{ g liter}^{-1}$, $v = 0.42 \text{ cm}^3 \text{ sec}^{-1}$, total current = 7.6 A , $V = 1.60 \text{ liters}$, and the same efficiency function as used for Fig. 4.

The iterative solution of Eq. [9] is superimposed on Fig. 5, at different electrolysis times. This solution predicts a gradual depletion in copper concentration from the initial constant value of $6.56 \text{ g liter}^{-1}$ to the profile b, c, and eventually reaching the steady-state profile f which is given by Eq. [3]. The electrowinning was clearly less efficient than would be predicted from the simplification $\epsilon = \epsilon_{\infty}$, although this approximation can be useful for copper-ion concentrations above 2 g liter^{-1} .

Assuming ideal plug flow, steady-state conditions should be attained at $t = V/v$, where V is the total volume of the system and v the electrolyte flow rate. The computer program, which assumes mixing within the twenty individual compartments, predicts steady-state profiles (to within 1%) after about 1.6 resistance times. Stable copper-ion concentrations are observed within 15 min in the first cell compartments and after about 2 hr in the last cells.

The agreement between theory and experiment was most satisfactory for the steady-state conditions where sampling could be carried out without interrupting the electrolysis system in any way. Nevertheless, some experimental points were consistently obtained which seemed to indicate greater than 100% current efficiency. The solution in each compartment was by no means homogeneous nor were the current densities uniform from the top to bottom of the cathodes. As was reported in part I (7), gas bubbles and convection currents took on a characteristic pattern which contributed to the scatter of the points in this small-scale electrolysis system.

The electrolyte can be decopperized further within the same cell geometry by several methods: decrease the inlet copper-ion concentration; increase the current density; or reduce the electrolyte flow rate. Any combination of these factors which reduces x^0 (Eq. [3]) to about one-half of the total electrolysis cell distance would decrease the final copper concentration to about 0.1 g liter^{-1} . All three parameters were altered for the experiment reported in Fig. 6. The dotted line in the figure indicates that ten cells would suffice if $\epsilon = \epsilon_{\infty} \approx 100\%$, whereas nearly twenty are actually required when account is taken of the decreased current efficiency with decreasing copper concentration.

Again, despite some experimental scatter attributable to sampling errors, the agreement between the mathematical model and physical reality is striking. A simple expression for the current efficiency involv-

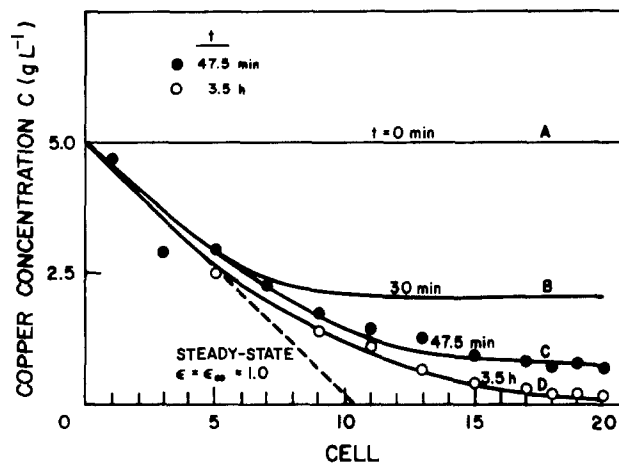


Fig. 6. Concentration profiles in the experimental purification circuit. Solid curves are calculated from Eq. [9] for an initial copper concentration of $5.01 \text{ g liter}^{-1}$, $v = 0.34 \text{ cm}^3 \text{ sec}^{-1}$, a total applied current of 10 A , $V = 1.50 \text{ liters}$, and the same efficiency function as used for Fig. 4.

ing at most two adjustable parameters is able to predict transient and steady-state behavior in a model flow-through electropurification circuit. The parameter ϵ_{∞} is primarily dependent on the chemical composition of the electrolyte and, in the absence of stray current paths, should not be greatly influenced by the cell geometry. The values obtained here fall within the range reported for commercial copper electrowinning systems. The parameter B varied little with current density ($15\text{--}100 \text{ A/m}^2$) but preliminary work indicates that it varies with cell geometry, electrolyte temperature, surface tension, and viscosity, all of which were maintained constant throughout the experiments reported here.

Conclusion

The results obtained in both static and dynamic electrowinning circuits suggest that the two-parameter current-efficiency function $\epsilon = \epsilon_{\infty} [1 - \exp(-BC)]$ is a sufficiently close approximation to reality to be useful in projecting the performance of practical systems. It is likely that relatively simple laboratory experiments which are carried out using electrode spacings and compositions as found in a large-scale electrolysis circuit can be used to yield the values of the parameters ϵ_{∞} and B which are needed to describe the current efficiency. With knowledge of these parameters, and of the cell volume, current, and electrolyte flow, a complete description of the time variation of concentration profiles in a particular electrowinning circuit can be derived.

Acknowledgments

The authors are indebted to Dr. P. L. Claessens for several stimulating discussions concerning the analysis of electrowinning and electropurification circuits. Support of this research by Canadian Industries Limited and by the National Research Council of Canada is gratefully acknowledged.

Manuscript submitted July 16, 1979; revised manuscript received March 24, 1981.

Any discussion of this paper will appear in a Discussion Section to be published in the June 1982 JOURNAL. All discussions for the June 1982 Discussion Section should be submitted by Feb. 1, 1982.

Publication costs of this article were assisted by the Université de Sherbrooke.

LIST OF SYMBOLS

| | |
|--------------|---|
| A, h, S, x | geometric parameters of the electrowinning circuit, defined in Fig. 1 |
| C | metal-ion concentration |
| C^0 | metal-ion concentration at the inlet of the electrowinning circuit |
| F | Faraday constant |
| i | current density |
| i_1 | limiting current density for metal-ion deposition |
| l | length of the electrowinning circuit |
| V | volume |
| v | volume flow rate of electrolyte |
| $x' = x/l$ | dimensionless position in the electrowinning circuit |
| ϵ | current efficiency |
| ϵ_0 | limiting current density |

REFERENCES

1. R. Alkire and B. Gracon, *This Journal*, **122**, 1594 (1974).
2. J. A. Trainham and J. Newman, *ibid.*, **125**, 58 (1978).
3. J. A. Trainham and J. Newman, *ibid.*, **124**, 1528 (1977).
4. R. Alkire and R. Gould, *ibid.*, **123**, 1842 (1976).
5. V. A. Ettel, B. V. Tilak, and A. S. Gendron, *ibid.*, **121**, 867 (1974).
6. Y. Awakura, A. Ebata, and Y. Kondo, *ibid.*, **126**, 23 (1979).
7. F. M. Kimmerle, R. LeRoy, and O. Vittori, *ibid.*, **128**, 1864 (1981).
8. P. E. Mussler, R. S. Olsen, and T. T. Campbell, R18076 Bureau of Mines Report (1975).

Development of BN Felt Separator for Li-Al/MS_x Battery

Robert B. Swaroop* and James E. Battles*

Argonne National Laboratory, Chemical Engineering Division, Argonne, Illinois 60439

ABSTRACT

Boron nitride felts are being developed and evaluated for application as electrode separators in high temperature Li-Al/MS secondary batteries. Boron nitride fabric has been used as the separator material in most Li-Al/MS_x cells fabricated thus far. However, BN felt separators are presently under development because they are more porous and potentially less expensive than the BN fabric separators. As a preliminary evaluation, the physical properties of various BN felts were determined. Subsequently, felts were also tested in experimental cells operated for extended periods (>1000 hr). The tests indicated that the BN felt is compatible with cell components and is stable in the cell environment.

Electrode separators of boron nitride felt are being developed and evaluated for application in advanced secondary batteries. The cells for these batteries, which operate at temperatures of 400°-500°C, consist of lithium-aluminum alloy negative electrodes, FeS or FeS₂ positive electrodes, and molten LiCl-KCl electrolyte (eutectic melting point, ~352°C). The primary function of the separator is to provide electrical and mechanical separation of the electrodes without restricting ionic flow. The separator must fulfill several requirements: (i) low cost, (ii) chemical stability with the electrode materials and electrolyte, (iii) suitable specific gravity, thickness, and porosity chosen to minimize cell weight and resistance, (iv) adequate mechanical strength to accommodate stresses that occur during cell operation, and (v) wettability by the molten LiCl-KCl electrolyte.

The above requirement for a good electrical insulator at temperatures between 400° and 500°C precludes the use of metals or organic/polymeric materials. Thus, the selection of materials for the separator is limited to asbestos or ceramics. However, since asbestos will react with the free lithium in the cell, the choice appears to be limited to ceramic materials, namely, oxides and nitrides. A comparison (1) of the free energies of formation of Li₃N and Li₂O with those of ceramic materials indicated that the following ceramics should be stable at the cell operating temperature: BeO, MgO, Y₂O₃, CaO, BN, AlN, and Si₃N₄. The stability predicted by thermodynamic calculations, however, does not insure that a ceramic will be stable in the cell environment because lithium or sulfur may react with impurities in the ceramic. Therefore, an ex-

perimental program was launched to investigate the stability of ceramic candidate materials in the cell environment. The results (2) indicated that the ceramics most stable for extended periods of time (>1 year) are MgO, BN, and BeO. Of these materials, only BN is commercially available in fibrous form suitable for fabricating into a cloth or felt separator. Cloth or felt forms are desirable because of their flexible nature. Separators of BN cloth (3, 4) are currently being used in developmental cells. This material has the disadvantages of being expensive and technically undesirable because it has a high basic weight (e.g., 110 mg/cm², 2 mm thick) and interstices in the cloth. Therefore, efforts have been directed toward the development of a felt separator (2, 5, 6). Felt separators are more porous, use less material (2/3 less material), are uniform in thickness, and are potentially much less expensive than fabric separators. For the development program, the Kennecott Corporation prepared BN felt which was then evaluated at Argonne National Laboratory.

Preparation of BN felt.—Boron nitride felts for application as separators in Li-Al/metal sulfide cells were developed by the Kennecott Corporation under a sub-contract with Argonne National Laboratory. The process consists of forming a boron nitride fiber and boron oxide fiber slurry into a felt using Fourdrinier paper-forming technology. The final conversion of boron oxide bonds to boron nitride in a nitriding environment results in a boron nitride-bonded BN felt. Further details of the process may be noted elsewhere (7).

Evaluation techniques.—The BN felts were physically characterized in out-of-cell tests; then their stability was assessed in test cells.

* Electrochemical Society Active Member.
Key words: battery, separator, insulator.

Out-of-cell tests.—The felts were characterized by measurements of their thickness, porosity, burst strength, flexibility, and wettability. The thickness was measured with an Ames No. 16 Dial Comparator equipped to provide a contact pressure of 862 Pa. The porosity was calculated from measurements of thickness and weight per unit area (basic weight) of the felt and from the weight fractions and densities of the component materials. The burst strength was measured on a Mullen Burst Tester, Model C.

The wettability by the LiCl-KCl electrolyte was evaluated by the sessile drop technique (8). The felt was gradually heated to 450°C in a helium atmosphere glove box with solid electrolyte pieces on the felt. The wettability was considered to be "good" if the molten electrolyte drop was gradually absorbed into the felt. If evacuation and repressurization of the helium was required to wet the felt, the wettability was characterized as "fair."

In-cell tests.—The functional tests of BN felt as a separator material were performed in unsealed LiAl/LiCl-KCl/FeS prismatic cells; the schematic of this type of cell has been presented elsewhere (2). The cell dimensions were 7.6 × 12.7 × 2.5 cm and the theoretical capacity of each test cell was 48–50 A-hr. The negative and positive electrodes were made by hot pressing the appropriate mixture of LiAl and LiCl-KCl powders or FeS and LiCl-KCl powders, respectively. The electrodes were mechanically and electrically separated by BN-felt separators contained between screens. The cells were assembled in the 50% charged state in a helium-atmosphere glove box and were operated at 450°C in a furnace well attached to the glove box. The break-in of assembled cells before cycling required a special procedure, which was essential in order to assure the wetting of the felt separator by the electrolyte. In the normal procedure the assembled cell was heated gradually under a vacuum from room temperature to 450°C. Once at 450°C, the cell was pressurized with helium gas. One or two vacuum-repressurization cycles were sometimes required to completely wet the separator with electrolyte. This procedure was slightly modified if the separator felt had been treated with the LiAlCl₄ wetting agent (8). In the special procedure, the initial heating of the cell was conducted in helium gas, not under vacuum, and, once the operating temperature of 450°C was reached, one or two vacuum-repressurization cycles were not required.

During operation, the cells were cycled continuously between a discharge cutoff potential of 1.0V and a charge cutoff potential of 1.65V at a constant current density. In most of the cells, both charge and discharge current densities were increased in steps of 20 mA/cm². For lifetime testing, the cells were maintained at either 40 or 60 mA/cm² during the charge-discharge cycles until terminated either because end of test was reached (3000 hr of operation) or because cell performance declined. After termination of cell operation, a post-test examination of the cell was conducted to determine the extent of felt degradation, if any, and its effects on the cell. The examination was generally conducted using optical and scanning electron microscopes and x-ray diffraction equipment.

Results and Discussion

Physical and chemical properties.—The felts produced by the methods described in this paper require a stabilization process in nitrogen at 1750°C. Essentially the stabilization process evaporates the residual boron oxide left in the BN fibers and bonds. Neutron diffraction analyses indicated that unstabilized BN felts from Kennecott contained as much as 5–8% oxygen. After stabilization this oxygen content was generally found to be <1%.

Unstabilized felts were characterized for thickness, basic weight, porosity, burst strength, and deformation behavior. These measured properties are given in Table I. The felts were produced in thicknesses ranging from 1.25 to 3.40 mm with porosities between 92% and 94%. The thickness and porosity are useful in evaluating the resistance of the separator to ionic transport and the ability of the separator to prevent the escape of active materials from the electrodes. Thin felts with high porosity have low resistance to ionic transport, thus high utilization of active material. (This was observed during in-cell testing of felts.) The basic weight (per unit area) was measured to be 22, 34, and 43 mg/cm² for felts of 1.3, 1.9, and 3.1 mm thickness, respectively. The BN material used in the felt is only one-third the material needed to produce BN fabric. The burst strength of a felt indicates whether the material can maintain its integrity when dimensional changes occur in the electrodes during cell operation. The felts were between 3.5 and 5 kPa per millimeter of thickness. Table I also gives the physical properties of the felts after stabilization. As expected, the basic weight decreased because of B₂O₃ evaporation. The burst strength also decreased because of some degradation of the BN bonds. This slightly affected flexibility of the felts; nevertheless, no handling difficulties were experienced during the subsequent cell assembly.

The scanning micrograph of stabilized felt shown in Fig. 1 indicated that this BN felt consisted of large fibers (6–8 μm diam) that were bonded at a few random intersections with BN. The average size of the openings of the felt was approximately 25 μm diam.

The mechanical behavior of the felt was investigated to assess the deformation characteristics of felt at various stress levels. During cell assembly or cell operation, the internal stresses can reach as high as 200–250 kPa (5) which can adversely affect the porous structure of the felt. The stress-strain curves shown in Fig. 2 were measured for 2 mm thick felts. These curves indicate that the deformation behavior of unstabilized and stabilized felt is similar; the felt was reduced to almost half thickness at approximately 150 kPa. The latter finding indicates that at the internally developed stress levels (5) in an operating cell, the reduction in felt thickness could be as much as 50% of the original thickness. Further out-of-cell experiments were conducted to determine the ultimate strength level of the felts. It was found that felts (1.2–3.4 mm thick) were crushed to powder at 690–1035 kPa stress levels. It should be emphasized that such stress levels are not normally observed either during cell assembly or cell operation.

The wettability of untreated BN felt (as-produced and stabilized) by electrolyte was poor. This wettability was improved by the use of vacuum/pressurization cycles or the wetting agent LiAlCl₄ (8). Table II shows the quantity of LiAlCl₄ required to effectively wet BN felt by the electrolyte; the optimum quantity is approximately 10 mg/cm² per separator. The excessive use of this agent is not recommended because LiAlCl₄ dissociates into Al and LiCl at cell operating

Table I. Average properties of BN felt before and after stabilization*

| Felt thickness (mm) | Basic weight (mg/cm ²) | | Burst strength (kPa/mm) | | Porosity (%) | |
|---------------------|------------------------------------|-------|-------------------------|-------|--------------|-------|
| | Before | After | Before | After | Before | After |
| 1.37 ± 0.13 | 21.86 | 20.26 | 5.05 | 4.45 | 92.20 | 92.40 |
| 1.91 ± 0.13 | 34.44 | 29.81 | 4.47 | 1.84 | 92.10 | 93.13 |
| 3.12 ± 0.15 | 42.86 | 40.97 | 3.78 | 1.67 | 93.37 | 93.65 |

* At 1750°C in nitrogen environment for ~8 hr.



Fig. 1. Scanning micrograph of BN felt (400X)

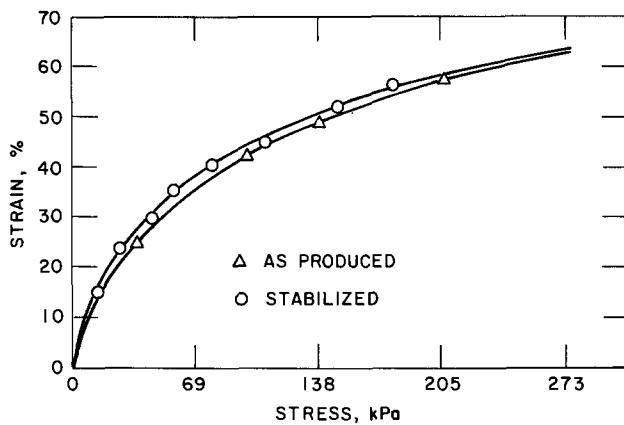


Fig. 2. Stress-strain behavior of BN felt

temperature when in contact with the Li-Al negative electrode. This reaction results in metallic aluminum depositions in the separator that could cause a short circuit. The experiments have shown that a specific procedure should be followed to start a cell which contains felt treated with LiAlCl_4 wetting agent; this procedure was explained in the Experimental section.

In-cell evaluation of felt.—In-cell testing of the separator felt was conducted to determine the material compatibility and adaptability to cell designs and the effects of the separator thickness on active material utilization. The active material utilization of the positive electrode is defined as the ratio of observed discharged capacity at a given current density to the theoretical capacity. The coulombic efficiency (or A-hr

Table II. Predusting of felt with LiAlCl_4

| Cell No. | Concentration loading of LiAlCl_4 per separator (mg/cm ²) | Wetting condition |
|----------|--|-------------------|
| SC-27 | 30 | Good |
| SC-34 | 20 | Good |
| SC-30 | 14 | Good |
| SC-33 | 12 | Good |
| SC-32 | 8 | Poor |

efficiency) is the ratio of observed discharged capacity to the charged capacity at a given current density.

Figure 3 shows both the coulombic efficiency and utilization of positive-electrode active material for a cell (SC-33) which had an unstabilized BN felt separator of 2 mm thickness. The capacity decreased from 77% to 40% as the discharge current density was increased in steps of 20 mA/cm² up to the maximum discharge current density of 120 mA/cm² at cycle 56. From the 56th cycle on, the charge and discharge current densities of the cell were maintained at 60 mA/cm², and the capacity remained steady at 55% for this period. As is shown in this figure, the utilization was sensitive to slight temperature excursion; as the temperature increased, the capacity also increased. The coulombic efficiency of this cell remained steady at 98-100% throughout the operation. At the 140th cycle (~2000 hr), cell operation was terminated because of a sudden decline in coulombic efficiency and utilization.

Figure 4 shows the coulombic efficiency and capacity for a cell (SC-25) that used a 1.25 mm thick stabilized felt. The observed performance was similar to that for cell SC-33. The utilization was 68% at discharge current density of 40 mA/cm². This cell was operated for 98 cycles (1700 hr) before termination. Even though the felt used in cell SC-33 had almost 3-4 times the oxygen content (as boron oxide) as that of the stabilized felt used in cell SC-25, the capacity and

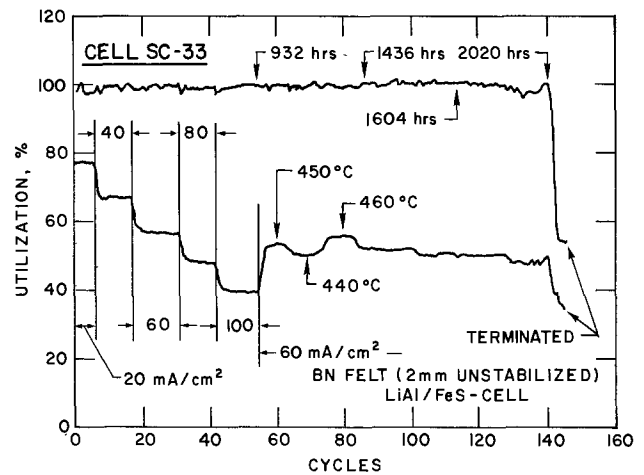


Fig. 3. Electrical performance of cell SC-33, using unstabilized BN felt.

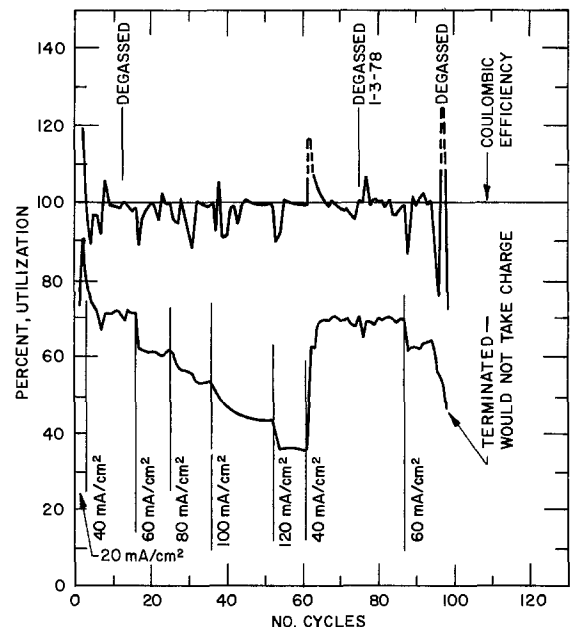


Fig. 4. Electrical performance of SC-25, using stabilized BN felt

Table III. Performance data of separator-test cells

| Cell No. | Separator thickness (mm) | Theoretical capacity (A-hr) | Internal resistance (m Ω) | At 40* mA/cm ² | | |
|----------|--------------------------|-----------------------------|-----------------------------------|---------------------------|---------------------------|-------------------------|
| | | | | Percent utilization | Specific energy (W-hr/kg) | Operational cycles (hr) |
| SC-19 | 2.8 | 50 | 18 | 62 | 55 | 205 |
| SC-25 | 1.25 | 51 | 16 | 72 | 66 | 98 |
| SC-27 | 1.6 | 48.5 | 15 | 69 | 59 | 72 |
| SC-30 | 3.2 | 48 | 18 | 60 | 54 | 90 |
| SC-33 | 2.0 | 50 | 15 | 67 | 62 | 145 |

* Corresponds to approximately 10 hr discharge rate.

coulombic efficiency of these two cells were comparable once the effect of separator thickness on cell capacity and efficiency was taken into account (discussed below). Apparently the high oxide content (>2% oxygen) in the separator after long periods (>3000 hr) of cell operation may cause the cell performance to deteriorate.

Figure 5 shows the effect of the separator thickness on the utilization for cells SC-25, -33, -19, and -30 at various current densities. As indicated, utilization at a given current density was observed to be the best when the separator was the thinnest. Further, the utilization decreased as the current density was increased for any given thickness of felt. The dependence of utilization on felt thickness is further illustrated in Fig. 6. This figure indicates that utilization has a linear

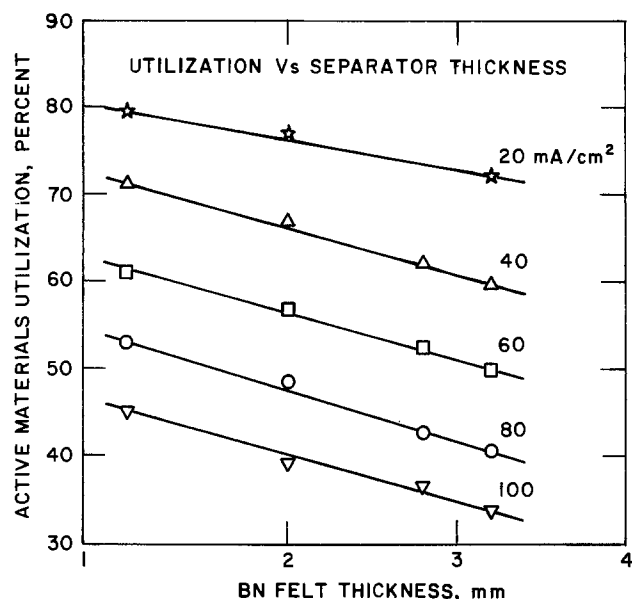


Fig. 5. Utilization performance of various BN felt cells

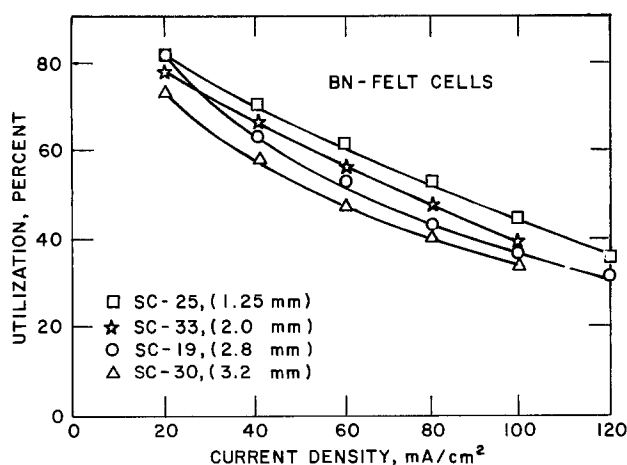


Fig. 6. Effect of felt thickness on utilization performance cells

relationship with the felt thickness. This empirical relationship may be written as $U = mD + C$, where U is the utilization ratio, D is thickness of felt, m is material constant, and C is the discharge-current density constant. The numerical value of m lies between 0.04 and 0.06 (mm)⁻¹. From these test results, it was postulated that thicker separators offer high resistance to ionic transport, thereby decreasing cell utilization.

Table III lists performance data (utilization, specific energy, resistance, and cycle life) for the five separator test cells. The thickness of the felt separator used in these cells ranged from 1.25 to 3.2 mm. These cells were cycled for 1159-3050 hr before termination of operation. The specific energy of a cell at a given current density is the watt-hour output per unit weight of the cell; the average weight of a test cell was 0.75 kg. The highest utilization and specific energy at a given current density were observed with the cell using the thinnest felt (cell SC-25). However, the use of thinner BN felt (<1.25 mm thickness) requires mechanically stronger and denser felts to withstand the internal stresses developed during cell operation. The internal resistance, which includes polarization effects, was measured at 50% state of charge for each cell. Even though a marked difference in internal resistance of these cells was not noticed, internal resistance appeared to increase as the separator thickness was increased.

Post-test examination.—Table IV summarizes the results of post-test examination for the separator test cells. The examinations revealed that BN felt is chemically stable in the cell environment. The felt was observed to be compressed between 30% and 50% of original thickness because of the internally developed stresses during cell operation. These stresses are generally caused by electrode swelling. However, the BN felt was never a cause of failure in these test cells. Most of the cell failures were caused by short circuits resulting from improper cell assembly or electrode swelling and subsequent extrusion of active material. The extrusion of material from one electrode has been eliminated by the use of finer (~200 mesh) retaining screens at the electrodes. Cell SC-33 developed a short

Table IV. Post-test examination of Bn felt cells

| Cell No. | Cause of termination | Suspected reason of failure and felt condition |
|----------|--------------------------------|---|
| SC-19 | Voluntarily | Felt was compressed by ~35% but no chemical attack; cell shorted after third thermal cycle |
| SC-25 | Gradual decline in performance | Migration of fine particle through the felt toward negative electrode; felt was compressed by 45% but no chemical attack |
| SC-27 | Internal short | Positive screen wire was touching against the negative electrode; felt was compressed about 40% but no chemical attack |
| SC-30 | Gradual decline in performance | Probable cause was extrusion of positive electrode due to electrode swelling; felt compressed ~50% but no chemical attack |
| SC-33 | External short | Salt bridging across the terminals |

because evaporated salt had formed a bridge across the terminals. This cause of failure should not be a problem in sealed cells because of negligible salt evaporation.

Conclusions

Results have been reported on an evaluation program for BN felt separators which are being developed for application in Li/MS batteries. The physical characterization of the felts indicated that they have adequate strength, porosity, and handling flexibility for cell assembly and operation. In-cell tests of the felts indicated excellent physical compatibility with chemical stability in the cell environment. Although further development work to improve upon the physical properties of BN felt may be needed, the test results show that BN felt is a viable separator material for Li-Al/MS₂ cells.

Acknowledgments

Authors appreciate the suggestions and encouragement extended by Dr. R. Steunenbergh, Dr. D. Barney, and Dr. P. Nelson during the course of this work. This work was performed under the auspices of the United States Department of Energy (DOE), Division of Energy Storage Systems.

Manuscript submitted Dec. 8, 1980; revised manuscript received March 11, 1981. This was Paper 149

presented at the Los Angeles, California, Meeting of The Society, Oct. 14-19, 1979.

Any discussion of this paper will appear in a Discussion Section to be published in the June 1982 JOURNAL. All discussions for the June 1982 Discussion Section should be submitted by Feb. 1, 1982.

Publication costs of this article were assisted by Argonne National Laboratory.

REFERENCES

1. J. E. Battles, "Critical Materials Problems in Energy Conversion," pp. 769-804, Academic Press, New York (1976).
2. R. B. Swaroop, J. Smaga, and J. E. Battles, in "Proceeding V. Inter-American Conference on Materials Technology, Sao Paulo, Brazil," Nov. 5-10, 1978, pp. 137-145.
3. P. A. Nelson, *et al.*, Argonne National Laboratory Report No. ANL-78-74 (1978).
4. R. A. Sharma, *Ceram. Bull.*, **57**, 1103 (1978).
5. J. P. Mathers, T. W. Olszanski, and J. E. Battles, *This Journal* **124**, 1149 (1977).
6. R. B. Swaroop, C. W. Boquist, and J. E. Battles, Abstract 52, p. 145, The Electrochemical Society Extended Abstracts, Pittsburgh, Pennsylvania, Oct. 15-20, 1978.
7. U.S. Patent 3,423,722.
8. J. G. Eberhart, Argonne National Laboratory Report ANL-79-34 (1979).

Investigation of Nickel Whisker Networks as Electrodes for Hydrogen and Oxygen Evolution

G. L. Cahen, Jr.,* P. J. Moran,*¹ L. L. Scribner, and G. E. Stoner*

Applied Electrochemistry Laboratory, Department of Materials Science, University of Virginia, Charlottesville, Virginia 22901

ABSTRACT

A new concept for the preparation of high surface area electrodes employing polycrystalline nickel whiskers has been demonstrated. Nickel whiskers were fabricated by chemical vapor deposition in the presence of an electromagnetic field. Electrode networks were constructed by a sintering process. The resultant electrodes have been analyzed as hydrogen and oxygen evolution electrodes in potassium hydroxide electrolytes. An improvement of 60-100 mV as compared to conventional nickel screens on an apparent current density basis has been observed for both reactions.

The energy efficiency of electrolytic processes is improved by reducing the overpotentials associated with the occurring reactions. One method of achieving this is by increasing the active electrode surface area. These electrode overpotentials can be represented as

$$\eta = a + b \log i$$

where a and b are constants for the particular electrochemical reaction under consideration. The constant b is commonly referred to as the Tafel slope with i representing the current density and defined as

$$i = I/A$$

where I is the total current and A is the active elec-

trode surface area. Since most electrolytic processes are highly current efficient, the amount of product per unit time is proportional to the total current. In comparison, the electrode overpotentials, which directly influence efficiency, are a function of current density. As the electrode surface area is increased for a constant current, the current density is decreased with a corresponding decrease in electrode overpotentials and increase in efficiency.

A new type of high surface area electrode was examined for conditions of hydrogen and oxygen evolution in 30% by weight potassium hydroxide electrolytes. This is a typical electrolyte for commercial alkaline electrolyzers. Polycrystalline nickel whiskers² can be fabricated into an electrode network by sintering; the resulting high surface area obtained causes a de-

* Electrochemical Society Active Member.

¹ Present address: Department of Materials Science and Engineering, The Johns Hopkins University, Baltimore, Maryland 21218.

Key words: high surface area electrodes, water electrolysis, electrolytic efficiency.

² The technology for the preparation of porous whisker electrodes was developed in Munich, Germany by Mr. Hermann Schladitz, now Research Professor at the University of Virginia School of Engineering and Applied Science.

crease in electrode overpotentials. In the following sections, the fabrication, characterization, and utilization of these electrodes will be discussed.

Whisker Electrode Fabrication and Surface Area Analysis

Polycrystalline nickel whiskers are produced by chemical vapor deposition of nickel tetracarbonyl gas, $\text{Ni}(\text{CO})_4$, in an electromagnetic field. The gas is fed into a chamber which is heated to $300^\circ\text{--}350^\circ\text{C}$ to accomplish gas phase decomposition. The chamber is surrounded by an electromagnet which creates magnetic field lines in the chamber parallel to the chamber's vertical axis. The liberated nickel particles align themselves along the field lines. Further deposition occurs along these aligned "substrates." The resulting whiskers, which have typical grain sizes of $200\text{--}400\text{\AA}$, are very strong, approaching 10^6 psi tensile strength, and possess very low dislocation densities. Diameters and lengths can be varied from 0.1 to $50\ \mu\text{m}$ and from 1 mm to several cm, respectively. The whisker electrodes are then fabricated from these individual whiskers.

Whiskers electrodes (or networks) are constructed by the sintering of individual whiskers at $800^\circ\text{--}1000^\circ\text{C}$ under a pressure of a few psi in a reducing atmosphere for approximately one-half hour. The reducing atmosphere prevents surface oxidation or contamination thereby promoting bonding. The resultant network is porous and fibrous. A 200 mesh nickel screen is used as a substrate in this sintering process. The resultant whisker electrodes obtained from this method are cylindrical disks with a radius of 1.56 cm, a thickness of 0.2 cm, and a weight of about 2.3 g. Porosities of these electrodes are as high as 90% by volume. For the higher porosity networks, the true surface area to volume ratio is $10^4\ \text{cm}^2/\text{cm}^3$ and the true specific surface area is $5 \times 10^3\ \text{cm}^2/\text{g}$ as determined by BET adsorption isotherm techniques. Figures 1 and 2 are scanning electron micrographs of a nickel whisker electrode. The surface roughness of the individual whiskers results from a characteristic nodular type growth (1). This is particularly noticeable on the larger whisker in Fig. 2.

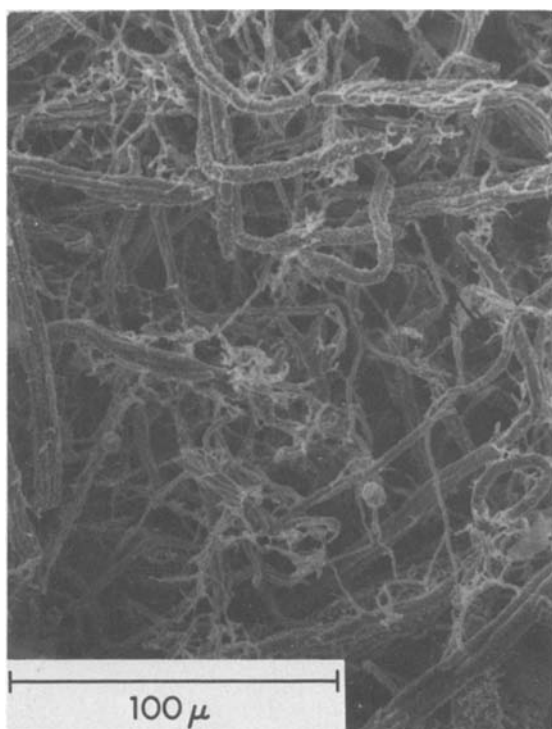


Fig. 1. Scanning electron micrograph of whisker electrode

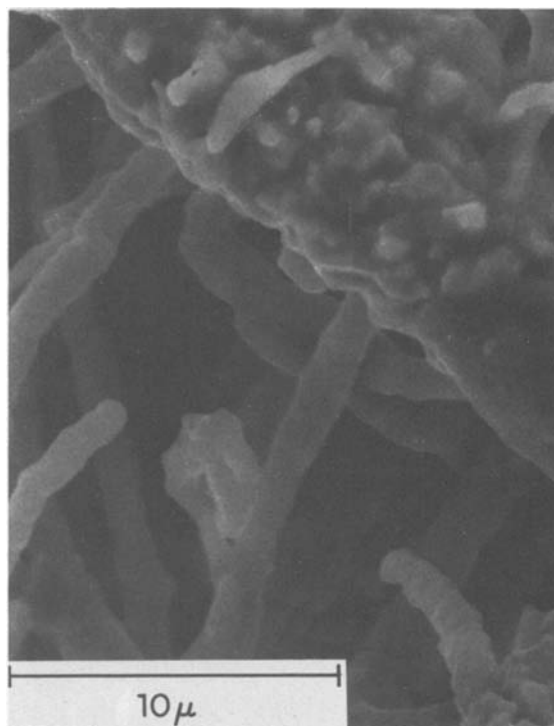


Fig. 2. Scanning electron micrograph of whisker electrode

The roughness factors can be calculated by either of two ways. The first method is by dividing the true surface area by the cross-sectional area of the electrode itself. This yields roughness factors on the order of 2×10^3 to 5×10^3 . The second and more accurate method is to divide the true surface area by the geometric area of the individual whiskers considering them to be smooth cylinders. A distribution of whisker diameters was obtained by examining a collection of micrographs. The results are illustrated in Fig. 3. The following procedure was employed to calculate the roughness factor:

1. Estimate average whisker diameter from distribution graph, $\bar{d} \cong 8\ \mu\text{m}$.
2. Calculate true surface area of the whisker electrode using BET isotherm data. Whisker electrode weight 2.3 g, multiplied by $5 \times 10^3\ \text{cm}^2/\text{g}$, corresponds to $11,500\ \text{cm}^2$ true surface area.

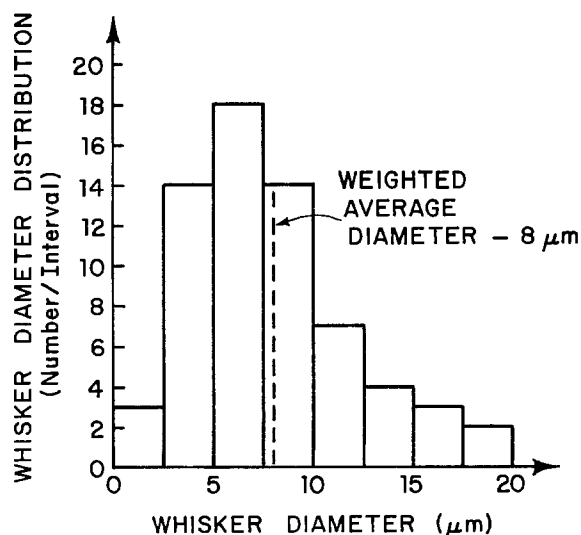


Fig. 3. Distribution of whisker diameters in whisker electrode

3. Calculate surface area of whiskers in electrode assuming one long smooth cylinder of diameter, $\bar{d} = 8 \mu\text{m}$ (from step 1).

4. Step 3 requires a knowledge of the nickel volume in the whisker electrode. 2.3g weight divided by the density of nickel (8.9 g/cm^3) yields 0.258 cm^3 .

5. $V = 0.258 \text{ cm}^3 = \pi r^2 l$ for one long cylinder. Assuming $r = 4 \mu\text{m}$, the length of the cylinder can be calculated

$$l = \frac{V}{\pi r^2} = 5.13 \times 10^5 \text{ cm}$$

6. Whisker surface area can then be calculated $SA = 2\pi r l = 2\pi(4 \times 10^{-4} \text{ cm})(5.13 \times 10^5 \text{ cm}) = 1289 \text{ cm}^2$.

7. The roughness factor is then calculated by dividing the true surface area by the whisker surface area

$$11,500 \text{ cm}^2 / 1280 \text{ cm}^2 = 8.9$$

The model can be improved by various techniques such as better definition of whisker diameter. One such modification was employed by considering two radii intervals and the number fraction of each. The result was sufficiently close to the listed value as to accept the single radius calculation as a useful estimation.

For the sake of comparison, the roughness factor for metal screens composed of drawn wire is about 2 to 3. The actual high surface area of the whisker electrodes is due to a high network porosity and a high roughness factor for the individual whiskers.

A similar technique was applied to the nickel screen electrode to determine its approximate geometric surface area. Wire lengths and diameters were measured with an optical profile projector. The calculated geometric surface area for the screen electrode was approximately 100 cm^2 .

Electrochemical Properties of Whisker Electrodes

The mechanical integrity of sintered components is always a concern, especially where electrolytic gas evolution reactions occur. Whisker electrodes withstood hydrogen and oxygen evolution at current densities (based on electrode cross-sectional area) as high as 1000 mA/cm^2 for 48 hr with no apparent loss in integrity. These apparent current densities are considerably higher than those utilized in industrial electrolytic processes ($200\text{--}500 \text{ mA/cm}^2$) (2-4).

For electrochemical characterization, whisker electrodes were compared to Ni-200 screen electrodes of equal bulk geometry (diameter = 3.13 cm, thickness = 0.2 cm, and mass = 2.3g) for both hydrogen and oxygen evolution reactions in a 30% by weight KOH electrolyte. The Ni-200 screen electrode was fabricated by spot welding together 5 layers of 200 mesh screen. The surface area of the nickel screen electrode as determined by cyclic voltametric surface area analysis was 300 cm^2 . A special Teflon cell was designed and constructed for the electrochemical characterization experiments. The cell schematic is shown in Fig. 4. Simultaneous monitoring of both electrode potentials vs. standard calomel or dynamic hydrogen reference electrodes can be achieved. A 1.0 mm capillary connects the reference electrode chamber to the bottom of the working electrode compartment. This configuration minimizes gas bubble clogging in the capillary and electrolyte contamination from the reference electrodes. The electrolyte used was 30 weight percent KOH prepared from A.C.S. certified Potassium Hydroxide Pellets and distilled water. The electrolyte was pre-electrolyzed for 24 hr prior to experimentation. The electrodes were cleaned by ultrasonic agitation for 10 min in Alconox solution followed by ultrasonic agitation for 10 min in alcohol and concluded by a 5-10 sec dip in 0.01M HCl and final rinsing with distilled water. The electrode leads were masked from

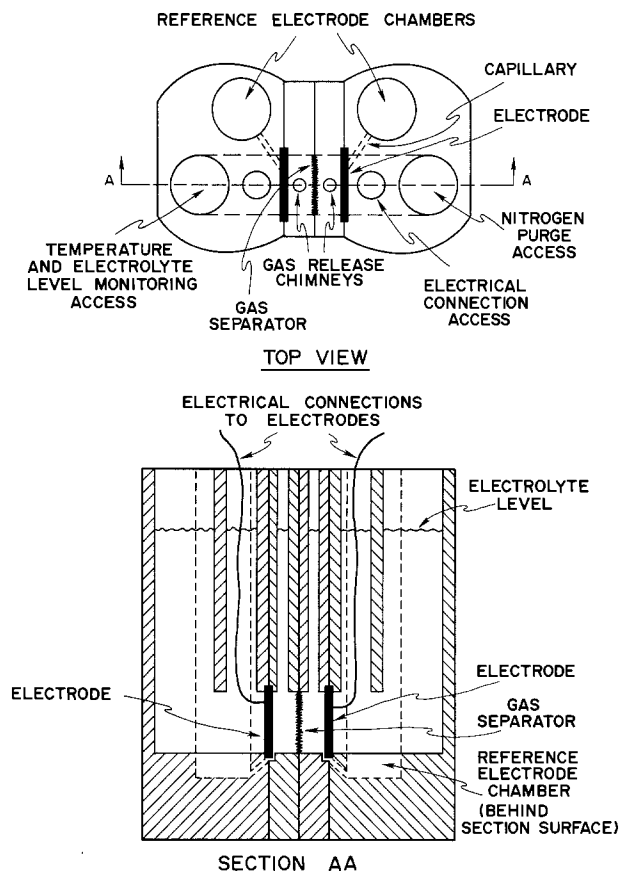


Fig. 4. Cell schematic for electrochemical experimentation with whisker electrodes.

the electrolyte with Teflon shrink tubing and Teflon tape. The experimentation was conducted galvanostatically. A problem of unstable voltages due to time variations in both anodic and cathodic overpotentials, as observed by other investigators was encountered (3, 5, 6, 7). To accommodate these effects, the experiments were conducted at successively higher currents beginning at 1 mA and allowing the electrode potentials to stabilize at each current level. A stable voltage was defined as one which varied less than 1 mV in a 2 min period. The higher currents required longer stabilization times. Results of the experimentation are shown in Fig. 5.

The whisker electrodes exhibited a 60-100 mV lower overpotential (smaller negative number for hydrogen evolution) compared to the screen electrodes in both reactions at equal currents, or apparent current densities (both electrodes have the same cross-sectional area). The reduction in overpotentials represents about a 10% increase in the energy efficiency of water electrolysis. The improvement is presumably due to the higher surface area of the whisker electrodes.

Discussion and Conclusions

The electrochemical characterization of nickel whisker electrodes for hydrogen and oxygen evolution reactions in alkaline electrolytes demonstrates an attractive increase in efficiency by lowering activation overpotentials. The highly porous whisker disks utilized in this investigation are not the most ideal configuration for present day water electrolyzers; thus alternative techniques for affixing them to new or existing commercial electrodes are being considered. Commercial testing of such a whiskerized electrode is anticipated. The technique for growing whiskers directly onto an electrode substrate will prove useful by controlling whisker orientation and by eliminating the need to sinter individual whiskers to each other and/or onto a substrate.

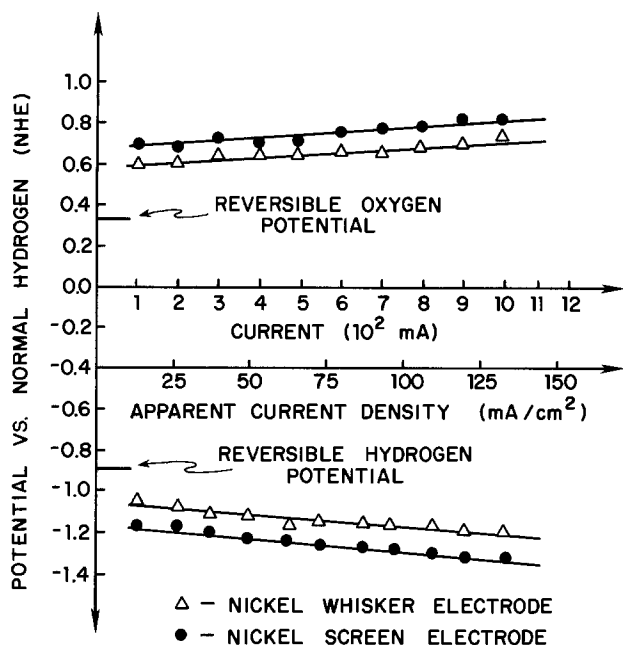


Fig. 5. Comparison of whisker electrodes and screen electrodes under conditions of hydrogen and oxygen evolution.

Acknowledgments

Financial support for this work was provided by the U.S. Department of Energy through Brookhaven National Laboratory, Contract No. 522027-S. One of us (PJM) also wishes to acknowledge NSF, Grant No. DMR-8006688.

Manuscript submitted Sept. 16, 1980; revised manuscript received April 3, 1981.

Any discussion of this paper will appear in a Discussion Section to be published in the June 1982 JOURNAL. All discussions for the June 1982 Discussion Section should be submitted by Feb. 1, 1982.

Publication costs of this article were assisted by the University of Virginia.

REFERENCES

1. T. Moore, M.S. Thesis, University of Virginia (1978).
2. M. Braun, in "Industrial Water Electrolysis," S. Srinivasan, F. J. Salzano, and A. R. Landgrebe, Editors, p. 16, The Electrochemical Society Softbound Proceedings Series, Princeton, NJ (1978).
3. J. N. Murray, J. B. Laskin, and W. C. Kincaide, in "Industrial Water Electrolysis," S. Srinivasan, F. J. Salzano, and A. R. Landgrebe, Editors, p. 39, The Electrochemical Society Softbound Proceedings Series, Princeton, NJ (1978).
4. R. L. LeRoy, M. B. I. Janjua, R. Renaud, and U. Levenberger, in "Industrial Water Electrolysis," S. Srinivasan, F. J. Salzano, and A. R. Landgrebe, Editors, p. 63, The Electrochemical Society Softbound Proceedings Series, Princeton, NJ (1978).
5. P. W. T. Lu and S. Srinivasan, in "Industrial Water Electrolysis," S. Srinivasan, F. J. Salzano, and A. R. Landgrebe, Editors, p. 102, The Electrochemical Society Softbound Proceedings Series, Princeton, NJ (1978).
6. A. Nidola, P. M. Spaziante, and L. Giuffre, in "Industrial Water Electrolysis," S. Srinivasan, F. J. Salzano, and A. R. Landgrebe, Editors, p. 102, The Electrochemical Society Softbound Proceedings Series, Princeton, NJ (1978).
7. C. Kissel, F. Kulesa, C. R. Davidson, and S. Srinivasan, in "Industrial Water Electrolysis," S. Srinivasan, F. J. Salzano, and A. R. Landgrebe, Editors, p. 218, The Electrochemical Society Softbound Proceedings Series, Princeton, NJ (1978).

Cation and Water Diffusion in Nafion Ion Exchange Membranes: Influence of Polymer Structure

H. L. Yeager* and A. Steck

Department of Chemistry, University of Calgary, Calgary, Alberta, Canada T2N 1N4

ABSTRACT

Membrane self-diffusion coefficients for sodium ion, cesium ion, and water have been measured for Nafion® 120 perfluorosulfonate ion exchange membranes. Values have been determined as a function of temperature, and as a function of membrane water content by studying samples in heteroionic forms. The diffusional properties of this polymer are found to differ from those of conventional polystyrenesulfonates in several respects, and the free volume theory which describes ionic diffusion in the latter is inappropriate to treat Nafion. Results indicate that cations may exist in two distinct regions in the polymer; the proportion of total cations in each region may depend on the ions size and charge density. A structural model of Nafion, which correlates the membrane's spectroscopic and diffusional properties, is proposed to explain the results.

Nafion[®] perfluorosulfonate ion exchange membranes (du Pont and Company), as well as similar carboxylate materials, are beginning to be used as separators in industrial electrolytic cell technologies. In particular, their chemical stability and excellent ionic transport capability are essential assets in the harsh en-

vironment of chlor-alkali cells, where hydrogen and chlorine gases and concentrated caustic and brine solutions contact the polymer at elevated temperatures. Several studies of transport, structural, and some thermodynamic properties have now been reported. This research is designed not only to provide a sound basis for the commercialization of these materials but also to learn more about the nature of the unusual ion-

* Electrochemical Society Active Member.
Key words: transport, membrane, chlor-alkali.

clustered morphology of perfluorinated ionomers. The separation of ions and sorbed water into a separate micro-phase in Nafion was first indicated by small angle x-ray scattering (1, 2) and later confirmed by neutron scattering experiments (3, 4). A theoretical basis for the ion clustering phenomenon in Nafion has also been provided (5).

Models based on these experiments and calculations are characterized by an inverse micellar picture of Nafion, in which sulfonate groups at the ends of pendant side chains extend into approximately spherical clusters of water and hydrated cations (2, 5). These clusters are surrounded by fluorocarbon material, which appears to contain microcrystalline regions according to experimental evidence (1, 4, 5). [These microcrystalline regions can be removed for salt forms by heating to 330°C followed by rapid quenching (4).] The cluster-network model of Gierke describes the ionic regions as spherical with interconnecting channels (2), an approach which is reasonably successful in predicting current efficiency in chlor-alkali cells. The more recent approach by Rodmacq and co-workers describes three "phases:" fluorocarbon microcrystallites, ionic-water clusters, and a second ionic region of lower ion content (4). This latter region may be that of sulfonates which have not been formally incorporated into ion clusters.

The extent of sulfonate-counterion interaction is of course an important factor in determining the transport properties of these membranes. Olah and co-workers have shown that Nafion in the hydrogen ion form is an effective solid "superacid" catalyst for a variety of organic reactions (6, 7). Low sulfonate charge density is also indicated in the ion exchange selectivities of alkali metal ions in Nafion 120 (8, 9). Sodium 23 NMR studies do indicate that sodium ion-sulfonate contact ion pairs can form, but this occurs only when the water to sodium ion mole ratio in the polymer has been reduced to about five or less (10, 11). Thus, ion pairing does not appear to be a major factor for Nafion samples which have been equilibrated in dilute aqueous solution.

We have previously reported studies of ion exchange selectivities, membrane water contents (8, 9), and ionic diffusion for Nafion samples in both concentrated (12) and dilute solution environments (13, 14). Unusual alkali metal ion-hydrogen ion exchange selectivities and water sorption were found in comparison to conventional sulfonate ion exchange resins. Unlike the latter cross-linked materials, the water to exchange site mole ratio in the polymer varies widely depending on the counterion, from twelve for sodium ion to about seven for cesium ion forms (1200 equivalent weight polymer). Alkali metal ion diffusion coefficients in Nafion also show interesting differences from those in conventional sulfonate resins. The cesium ion self-diffusion coefficient in Nafion 120 is about twenty times smaller than the respective value for sodium ion; this is in marked contrast to sulfonate resins where the cesium ion-sodium ion diffusion coefficient ratio is about 1.5, as it is in pure water (15). Morphological changes caused by the large difference in water contents was suggested to be a contributing factor (14).

These diffusion measurements have been extended here to include measurements of ionic diffusion as a function of polymer water content and the diffusion of water in the polymer in various counterion forms. These results are discussed in terms of the free volume description of diffusion in water-swollen polymers, and in relation to structural models of Nafion.

Experimental

Two samples of 1200 equivalent weight Nafion (Plastics Department, E. I. du Pont de Nemours and Company, Wilmington, Delaware 19898), manufactured at separate times, were used in this work. The

material has a nominal ion exchange capacity and thickness of 0.83 mequiv./g and 0.025 cm, respectively. Sodium and cesium chloride salts (Fisher Certified) were used as received. The radio-isotopes ^{22}Na and ^{137}Cs (obtained as carrier-free aqueous solutions) and tritium labeled water were obtained from commercial sources.

Details of membrane pretreatment, the measurement of membrane water contents, ion-exchange capacities, and membrane dimensions have been previously described, as well as the procedures involved in the determination of ionic self-diffusion coefficients using radiotracer methods (8, 9, 13, 14). The same general procedures were used to measure membrane self-diffusion coefficients of water, with the exception that tritium labeled water replaced radiotracer labeled 0.05M salt solutions. Standard liquid scintillation techniques were used to count the tritiated water samples. Some membranes were prepared in mixed ionic forms by equilibration in salt solutions of 0.05M total ionic strength and appropriate composition to yield the desired ionic fraction of each component. These solutions were prepared using previously published ionic selectivity coefficients (8, 9); sodium ion and cesium ion contents in the membranes were then accurately determined by flame emission spectroscopy.

Results and Discussion

Self-diffusion coefficients for sodium ion and cesium ion in 1200 equivalent weight Nafion are listed in Table I. Arrhenius plots of some of these data, the slopes of which yield activation energies of diffusion, are shown in Fig. 1. Two separate batches of Nafion were studied. For batch I, previously published diffusion coefficients were redetermined for this work; during the two year interval between measurements the membrane was stored in the dry as-received form. As seen in Fig. 1, results for sodium ion have changed little more than experimental error but cesium ion diffusion coefficients have increased greatly, with a corresponding decrease in the activation energy of diffusion. A second batch of Nafion of recent manufacture was kindly supplied by du Pont; diffusion results for this material are very similar to those of aged batch I for both cations. The water to exchange site mole ratio for sodium ion and cesium ion forms were reported to be 11.9 and 6.6, respectively (8). These water contents were remeasured for aged batch I and batch II samples; no change from these values within experimental error could be found for either material.

These results suggest that batch I has undergone some kind of slow morphological change, a change which affects cesium ion diffusion but not sodium ion diffusion. Results from batch II perhaps indicate an improved annealing process to produce a membrane with constant properties. The importance of these results lies in the difference in the behavior of the two cations to whatever polymer relaxation process did occur. It would appear that cesium ion diffuses in a different manner than sodium ion. Although the acti-

Table I. Ionic self-diffusion coefficients in Nafion 120

| Ionic form | Membrane batch | $\bar{D} \times 10^7 \text{ cm}^2 \text{ sec}^{-1}$ | | | E_{act} (0°-40°C) kJ mol ⁻¹ |
|-----------------|----------------|---|-------|------|---|
| | | 0°C | 25°C | 40°C | |
| Na ⁺ | I ^a | 3.07 | 9.44 | 15.1 | 28.3 |
| | I ^b | 2.78 | 11.2 | 14.9 | 29.8 |
| | II | 3.18 | 9.83 | 14.8 | 27.3 |
| Cs ⁺ | I ^a | 0.038 | 0.520 | 1.58 | 66.1 |
| | I ^b | 0.520 ^c | 1.70 | 3.37 | 38.9 ^c |
| | I ^d | 0.446 | 2.38 | 3.01 | 35.9 |
| | II | 0.363 | 1.88 | 2.67 | 35.4 |

^a Reference (14).

^b After two years in as-received form.

^c Value measured at 5°C.

^d Mixed Na⁺-Cs⁺ form, ionic fraction of Cs⁺ = 0.14.

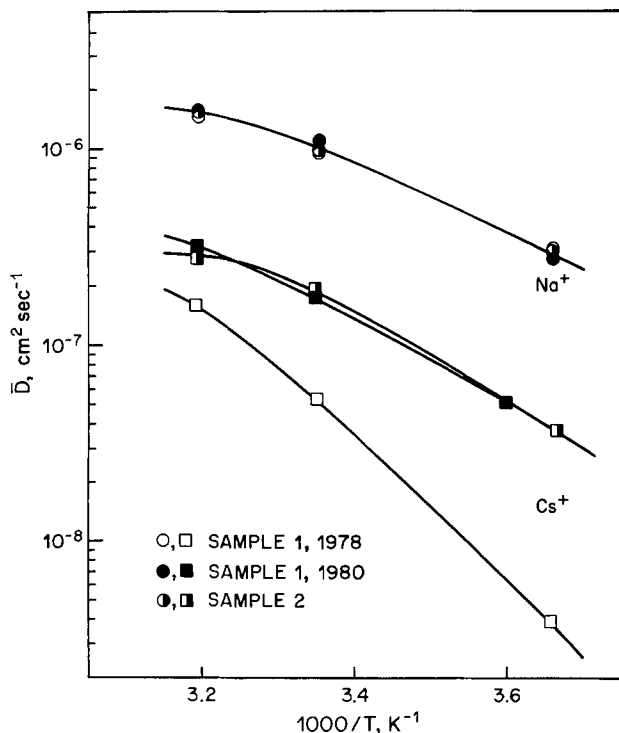


Fig. 1. Logarithm of self-diffusion coefficient vs. reciprocal of absolute temperature for Nafion 120.

vation energy for cesium ion diffusion is reduced to a value more typical of restricted diffusion compared to its original value of 66.1 kJ mol^{-1} , the anomaly in the cesium ion-sodium ion diffusion coefficient ratio remains. The value has increased to about 0.2 from the original value of 0.06 at 25°C , but it is still far from the expected result of about 1.5. Thus the more similar activation energies of diffusion for the two cations now suggests a common mechanism of diffusion but the low absolute magnitude of the cesium ion values still indicates a more tortuous diffusion path for this counterion.

We also wish to explore the dependence of these diffusion coefficients on membrane water content, in order to compare results to the free volume approach of describing diffusional processes. The diffusion coefficient of a molecule in a simple liquid has been represented by the equation

$$D = A \exp(-\gamma v^*/v_f) \quad [1]$$

where v^* is a characteristic volume for diffusion of the species, v_f is the "free volume" per solvent molecule, and γ and A are constants (16). Yasuda and co-workers (17) have adapted this approach to diffusion in water-swollen polymers, and developed an equation of the form

$$\bar{D} = D^0 \exp[-bV_p/(1 - V_p)] \quad [2]$$

Here \bar{D} and D^0 represent the membrane and aqueous diffusion coefficients respectively, V_p is the volume fraction of polymer in the water-swollen material, and b is a constant which is related to the exponent in Eq. [1], where now v_f would represent the free volume of water. Although several assumptions are needed to yield Eq. [2], the authors found that it works well to represent the binary diffusion coefficient of NaCl in a variety of hydrophilic polymer membranes for \bar{D} values ranging over five orders of magnitude.

Fernandez-Prini and Philipp (18) have used Eq. [2] to correlate tracer self-diffusion coefficients of sodium ion and cesium ion in a variety of polystyrenesulfonate resins with excellent success. They find that

the pre-exponential term is also a function of the electrostatic attraction of counterions for the charged matrix though, and that it is difficult to place a simple interpretation on the b coefficient. Lines which these authors found to represent the self-diffusion coefficients for sodium ion and cesium ion in polystyrene sulfonates are shown in Fig. 3, for data where V_p varied from 0.85 to 0.15.

In order to explore the relationship between diffusion coefficients and V_p in Nafion 120, the water content of the membrane must be varied in a controlled manner. Nafion has been found to have different stable water contents for two different treatments: Room temperature soaking, and extended boiling in water followed by room temperature soaking (9). These values are counterion dependent as well. To obtain additional water contents we take advantage of the observation that the membrane water-exchange site ratio in heteroionic forms is essentially a weighted average of the values for the respective homoionic forms, as seen in Fig. 2. Thus membrane samples with varied water contents were prepared for Na^+ - Cs^+ mixed ionic forms, and in successive experiments the membrane diffusion coefficients of both counterions were determined. A possible objection to this approach is that the presence of a second counterion may alter the diffusion characteristics of the reference cation.

Results are shown in Fig. 3 for sodium ion and cesium ion. Values of V_p were calculated from water-exchange site mole ratios (9), the molar exchange site concentration in the swollen polymer, and the partial molar volume of water in condensed systems, which was taken to be 17 ml mol^{-1} (18). Solid symbols are those of normal and boiled homoionic forms. Relatively minor differences exist between results for pure and mixed ion forms, which lends support to this method of varying V_p .

Important differences are seen though for the dependence of these diffusion coefficients on the V_p function, compared to polystyrenesulfonates. Sodium ion has a much higher diffusion coefficient at all water levels. We might attribute this feature, at least partially, to greater organization of exchange sites and water in this ion clustered polymer, in contrast to the more uniform distribution in a cross-linked ion exchange resin. Thus it appears that tortuosity is reduced

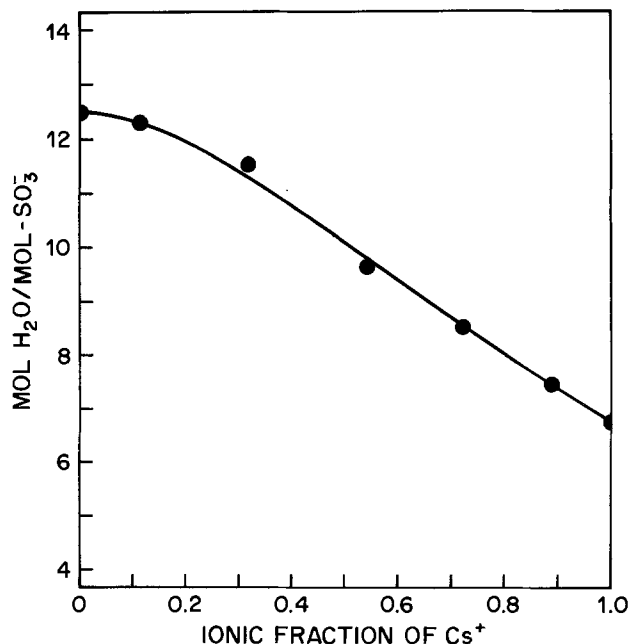


Fig. 2. Molar ratio of sorbed water to exchange site vs. ionic fraction of Cs^+ for Na^+ - Cs^+ heteroionic forms of Nafion 120 at 25°C .

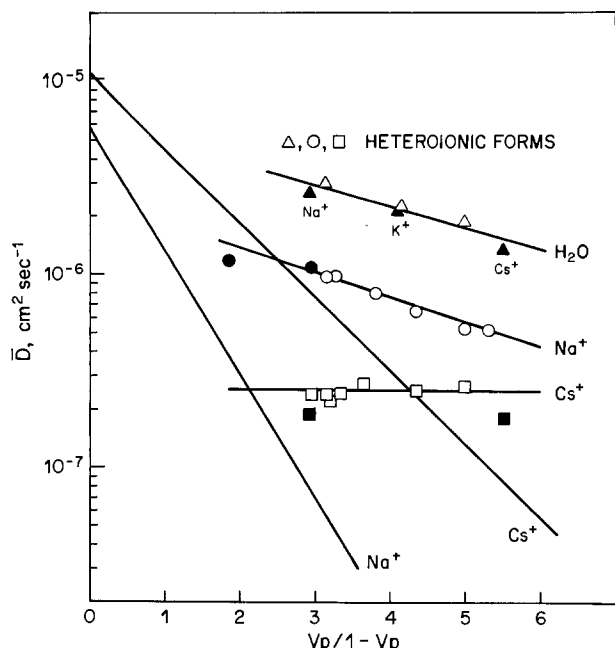


Fig. 3. Logarithm of self-diffusion coefficient vs. polymer fraction function for Nafion 120, 25°C. Na^+ and Cs^+ lines without data points: polystyrenesulfonate behavior, Ref. (18).

with the ion clustered morphology, which would be expected. For cesium ion a similar result is found for the unboiled cesium ion form. But as the water content increases, there is no dependence of the membrane diffusion coefficient on water content. For sodium ion, diffusion does increase with increasing volume fraction of water, but only modestly. (The percentage increases in the self-diffusion coefficients for cesium ion and sodium ion in boiled vs. unboiled membranes are 10 and 20%, respectively; for cesium ion this represents the entire V_p range studied.) In addition, the anomaly of the inverted order of cesium ion to sodium ion diffusion coefficients is not removed at high water contents; indeed the difference becomes greater. In Table I it is seen that the activation energy of diffusion for cesium ion is only slightly changed when the membrane is largely in the sodium form, again indicating that the mechanism of diffusion for this cation is essentially independent of membrane water content.

Self-diffusion coefficients of water in Nafion 120 are listed in Table II for three alkali metal ion forms. Previously reported approximate values of the water diffusion coefficient and activation energy of diffusion in the sodium ion form of 1150 equivalent weight Nafion are in good agreement with the present results (1). Values at 25°C are plotted in Fig. 3, along with self-diffusion coefficients for three sodium ion-cesium ion heteroionic forms. As seen in the figure, water diffusion shows a dependence on V_p , which is similar to that of sodium ion. In general, these self-diffusion coefficients are quite large considering the relatively small fraction of water in the polymer. The activation energies of diffusion are low and similar to those found for water self-diffusion in the hydrogen ion form of an 8% cross-linked polystyrenesulfonate resin, 21.8 kJ mol⁻¹ (19), and in pure water, 17.8 kJ mol⁻¹

Table II. Self-diffusion coefficients of water in Nafion 120

| Ionic form | $\bar{D} \times 10^6, \text{cm}^2 \text{sec}^{-1}$ | | | E_{ACT} (5°-40°C) kJ mol ⁻¹ |
|---------------|--|------|------|---|
| | 5°C | 25°C | 40°C | |
| Na^+ | 1.40 | 2.65 | 3.95 | 21.4 |
| K^+ | | 2.15 | | |
| Cs^+ | 0.815 | 1.32 | 2.37 | 22.0 |

(20) over the same temperature interval. The values for the cesium ion form confirm that there is excellent communication among the aqueous ion clustered regions even when the water-exchange site mol ratio is as low as seven.

In order to interpret the results presented here, two recent spectroscopic studies of Nafion are of particular interest. Lee and Meisel have studied the luminescence quenching of $\text{Ru}(\text{bpy})_3^{2+}$ ($\text{bpy} = 2,2'$ -bipyridine) in Nafion 120 (21). Results indicate that this cation interacts with the fluorocarbon portion of the polymer and not the sulfonate grouping, and that a probable location for the cation is in an interfacial zone between ion clusters and fluorocarbon backbone. This finding may be in part due to the large size and low charge density of this cation, but it suggests that a picture of ion clusters as simple aggregates of water, sulfonate exchange sites, and counterions could be an oversimplification. Falk has made a careful study of the infrared bands of sorbed water in Nafion in the sodium ion form, and was able to draw several conclusions (22). Water exists in two distinct environments. The first is one in which hydrogen bonding strength is about 60% of that in liquid water. About 75% of total sorbed water is in this environment, which is taken to be that of the ionic clusters. The remaining water molecules do not appear to be involved in hydrogen bonding, and thus would be exposed only to fluorocarbon phase. In consideration of the amount of nonhydrogen bonded water, Falk suggests that ion clusters may be nonspherical in shape and have extensive intrusions of fluorocarbon phase (22).

A structural view of Nafion which is consistent with these spectroscopic results and the diffusional properties reported here is diagrammed in Fig. 4. Three regions are indicated: Region A consists of fluorocarbon phase, ionic clusters form region C, and B is an interfacial region between A and C. Region A would contain fluorocarbon backbone material, some of which is in a microcrystalline form, as detected by Rodmacq and co-workers (4). Region C would incorporate sulfonate exchange sites, the majority of sorbed water, and some counterions as well. Region B is viewed as one of relatively large fractional void volume, con-

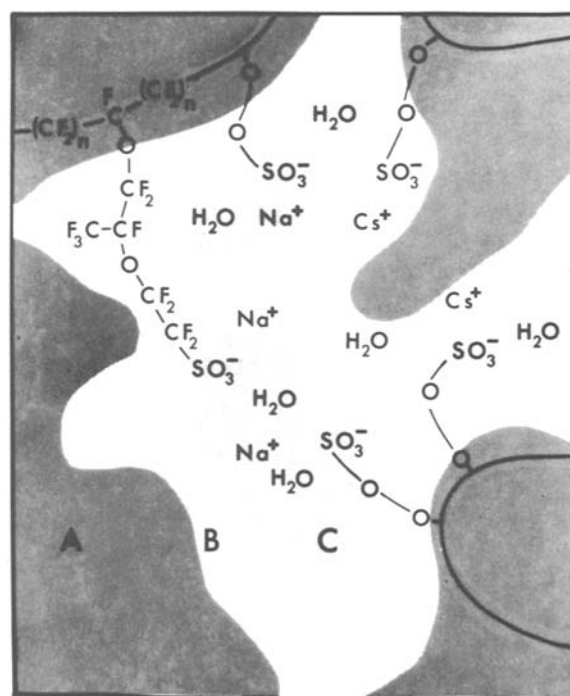


Fig. 4. Three region structural model for Nafion: A, fluorocarbon; B, interfacial zone; C, ionic clusters.

taining pendant side chain material, a smaller amount of sorbed water, some sulfonate exchange sites which have not been incorporated into clusters, and a fraction of the counterions. The relative proportions of counterions in regions B and C would depend upon the size, charge density, and hydration energy of the cation. Ions of low charge density or large size, such as $\text{Ru}(\text{bpy})_3^{+2}$ and Cs^+ , would prefer region B, while ions of larger charge density and hydration energy would localize in the more aqueous ionic clusters. Both types of cations and water would have relatively large microscopic diffusion coefficients in both the ionic clusters and the interfacial regions. As well, region B provides a continuous diffusion path among ionic clusters. While region C is responsible for the peaks which are found in x-ray and neutron scattering studies, both regions C and B contribute to determine the overall diffusional properties of the polymer.

This model provides a reasonable explanation for the results obtained in this work. Cesium ion would have a lower overall diffusion coefficient because of its larger mean-free path in diffusing through the polymer, compared to sodium ion. Both would tend to have larger than expected diffusion coefficients compared to polystyrene sulfonates for a given V_p , because the volume fraction of polymer available for diffusion in region B is not properly taken into account in the calculation of V_p . The insensitivity of cesium ion's self-diffusion coefficient to increased water sorption would result because the majority of increased sorbed water is found in the ionic clusters. Thus the diffusion path of cesium ion would not significantly decrease as the volume fraction of region A increases.

It is interesting to speculate on the causes for the change in diffusional results for batch I of Nafion 120 due to aging of the material. The cesium ion activation energy of diffusion in new samples of batch I is extremely large, and more like values for ionic diffusion in ionic crystal lattices than in swollen polymers (14). This would occur if portions of region B were not originally as well formed as indicated in Fig. 4, but instead included irregular zones and diffusionally isolated regions. These regions would show very high diffusional activation energies. The measured activation energy of diffusion is the weighted average of all environments, and thus cesium ion would be more sensitive to such irregularities than would sodium ion. [All sulfonate sites are available for exchange processes on a long time scale though; the ion exchange capacity of batch I is found to be unchanged in the sodium ion, cesium ion, and other cationic forms (9).] Thus, while the aging process increased the sodium ion diffusion coefficient by 19% without a change in activation energy of diffusion, the cesium ion value increased by more than a factor of three with a new activation energy which is 60% of the original result.

This proposed structural view of Nafion is an extension of those developed by Gierke (2) and Rodmacq and co-workers (4) which provides a unified picture of a variety of observations, including these diffusional results. Additional spectroscopic studies are now needed to probe the microenvironments of ions in the polymer in order to test this model.

Acknowledgment

The authors thank E. I. du Pont de Nemours and Company for samples of Nafion, and Dr. Z. Twardowski

and B. Kipling for useful discussions. Financial support was provided by the University of Calgary and the Natural Sciences and Engineering Research Council of Canada.

Manuscript submitted Nov. 20, 1980; revised manuscript received March 18, 1981. This was Paper 608 presented at the Hollywood, Florida, Meeting of the Society, Oct. 5-10, 1980.

Any discussion of this paper will appear in a Discussion Section to be published in the June 1982 JOURNAL. All discussions for the June 1982 Discussion Section should be submitted by Feb. 1, 1982.

Publication costs of this article were assisted by the University of Calgary.

REFERENCES

1. S. C. Yeo and A. Eisenberg, *J. Appl. Polym. Sci.*, **21**, 875 (1977).
2. T. D. Gierke, Paper 438 presented at The Electrochemical Society Meeting, Atlanta, Georgia, October 9-14, 1977.
3. R. Duplessix, M. Escoubes, B. Rodmacq, F. Volino, E. Roche, A. Eisenberg, and M. Pineri, in "Water in Polymers," Chap. 28, S. P. Rowland, Editor, ACS Symposium Series No. 127, American Chemical Society, Washington, D.C. (1980).
4. B. Rodmacq, J. M. Coey, M. Escoubes, E. Roche, R. Duplessix, A. Eisenberg, and M. Pineri, in "Water in Polymers," Chap. 29, S. P. Rowland, Editor, ACS Symposium Series No. 127, American Chemical Society, Washington, D.C. (1980).
5. K. A. Mauritz, C. J. Hora, and A. J. Hopfinger, in "Ions in Polymers," Chap. 8, A. Eisenberg, Editor, ACS Advances in Chemistry Series No. 187, American Chemical Society, Washington, D.C. (1980).
6. G. A. Olah, J. Kaspi, and J. Bakala, *J. Org. Chem.*, **42**, 4187 (1977).
7. G. A. Olah, G. K. S. Prakash, and J. Sommer, *Science*, **206**, 13 (1979).
8. H. L. Yeager and A. Steck, *Anal. Chem.*, **51**, 862 (1979).
9. A. Steck and H. L. Yeager, *ibid.*, **52**, 1215 (1980).
10. R. A. Komoroski and K. A. Mauritz, *J. Am. Chem. Soc.*, **100**, 7487 (1978).
11. R. A. Komoroski, in "Ions in Polymers," A. Eisenberg, Editor, Chap. 10, ACS Advances in Chemistry Series No. 187, American Chemical Society, Washington, D.C. (1980).
12. H. L. Yeager, B. Kipling, and R. L. Dotson, *This Journal*, **127**, 303 (1980).
13. M. Lopez, B. Kipling, and H. L. Yeager, *Anal. Chem.*, **49**, 629 (1977).
14. H. L. Yeager and B. Kipling, *J. Phys. Chem.*, **83**, 1836 (1979).
15. G. E. Boyd and B. A. Soldano, *J. Am. Chem. Soc.*, **75**, 6091 (1954).
16. M. H. Cohen and D. Turnbull, *J. Chem. Phys.*, **31**, 1164 (1959).
17. H. Yasuda, C. E. Lamaze, and L. D. Ikenberry, *Makromol. Chem.*, **118**, 19 (1968).
18. R. Fernandez-Prini and M. Philipp, *J. Phys. Chem.*, **80**, 2041 (1976).
19. G. E. Boyd and B. A. Soldano, *J. Am. Chem. Soc.*, **75**, 6105 (1954).
20. K. Tanaka, *J. Chem. Soc. Faraday Trans. I*, **71**, 1127 (1975).
21. P. C. Lee and D. Meisel, *J. Am. Chem. Soc.*, **102**, 5477 (1980).
22. M. Falk, *Can. J. Chem.*, **58**, 1495 (1980).

The Effect of Mixing in Paired Dimerizations

D. K. Johnson¹ and R. E. W. Jansson

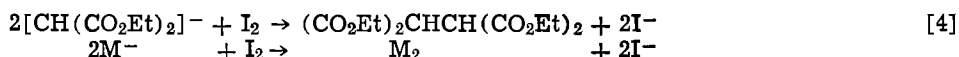
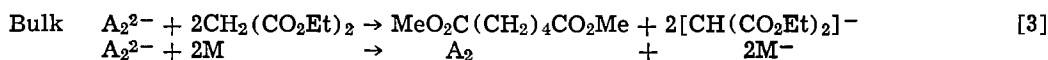
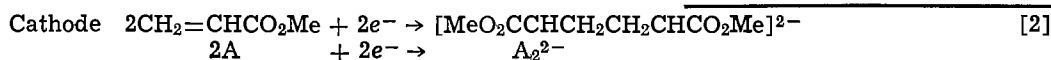
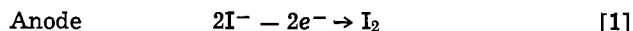
Chemistry Department, Southampton University, Hants, SO9 5NH England

ABSTRACT

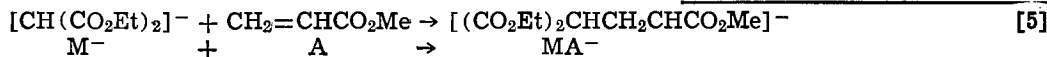
Some paired electrosyntheses involve a sequence of chemical and electrochemical steps. Mixing processes may then be important if the kinetics are not extremely fast, and the physical nature of the cell and its operation may influence the selectivity of the overall reaction. Current efficiency may also be influenced through parasitic reactions which are transport dependent. In the prepilot scale synthesis of ethyl dimalonate and dimethyl adipate, these effects have been studied systematically in a variety of flow cells operated with batch recycling. It has been shown that under conditions of good mixing in all cells the selectivities of the major products are improved. For example, in parallel plate cells, the amount of Michael adduct is inversely proportional to Reynolds number. Similar observations have been made in other prepilot scale operations which strongly affect the choice of the most appropriate cell for a given synthesis.

In paired electrochemical syntheses there are two extreme cases: (i) When it is undesirable for anode and cathode products to be transported to the counter-electrode (e.g., if the electrochemical reactions are reversible); and (ii) when it is necessary for the overall success of the reaction that mixing should occur or intermediates be transported to the region of the counterelectrode. The classical case of (ii) is the epoxidation of alkenes such as propylene using an electro-generated oxidant such as hypobromous acid; with the correct contacting pattern 97% selectivity can be obtained at 95% current efficiency (1). The paired dimerization of methyl acrylate and diethyl malonate also comes into this category. Following the work of Thomas and Lux (2), Baizer and Hallcher (3) investigated the system across a wide range of variables obtaining good performance only when the acrylate and malonate were added dropwise during the electrolysis.

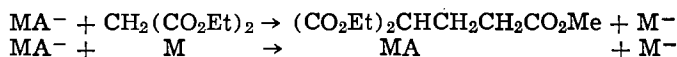
The principal reactions may be summarized as



Even though this is an abbreviated scheme (3) it can be seen that diethyl malonate acts as a proton source, and the dimerization of its anion requires a charge exchange reaction with electrogenerated iodine. A number of competing reactions are also possible, e.g., a Michael reaction between malonate anions and methyl acrylate

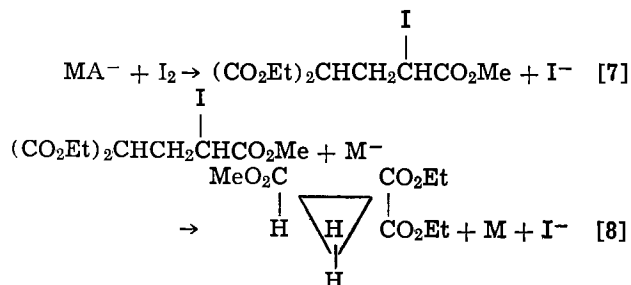


which is important if the acrylate to iodine ratio is high. Malonate acts as a proton source for MA^- giving the normal Michael adduct



Reactions [5] and [6] are therefore autocatalytic and preliminary work (4) has shown that much Michael adduct is made in cells with poor mixing.

If the I_2/M ratio is high, reaction [6] is replaced by a sequence of reactions which can be represented as



giving the cyclopropane form of the Michael adduct by 1,3 elimination. The combined amount of Michael adducts (i.e., MA^-) produced therefore depends on the local ratio of A/I_2 near the cathode, while the ratio of normal to cyclopropane Michael adduct depends on the ratio of M/I_2 .

It is now well established that there may be a high degree of segregation of electrogenerated species in various cells (5-7) so that different cells give different selectivities even though a reaction is carried out under the same nominal chemical conditions in each of them (4,8). Further work on the coupling of chemical and physical variables is the subject of this paper.

The Physical Environments in Various Cells

In parallel plate cells at low Reynolds numbers the flow can be modeled as a creeping layer adjacent to

each electrode, with a faster though still laminar "core" flow in between (5,9). Mass exchange does, of course, take place between these layers, but the effective degree of segregation is high (5,10). At higher Reynolds numbers (>2000) the fluid in most of the channel is turbulent, hence well mixed, but some

¹ Present address: Department of Chemical Engineering, UCLA, Los Angeles, California 90024.

Key words: electrosynthesis, transport, kinetics.

degree of segregation is still evident. In parallel plate cells, then, cross-gap mixing of anode and cathode product is relatively poor, but increases with Reynolds number.

In a disk-stack (capillary gap) cell (11) similar evidence of segregation is seen (7) unless the channel Reynolds number, $Re_{ch} = Q/h\nu$, is very high ($>10^5$), but mixing in a geometrically identical pump cell at the same flow rate is much higher (7) due to the intense tangential shear introduced by rotating alternate electrodes. At all flow rates the fluid in a pump cell approximates to dispersive plug flow, while at low flow rates the segregation in a disk-stack cell approaches that of a parallel plate cell.

The bipolar trickle tower (or trickle bed) exhibits segregation at all flow rates, being modeled best as a reactor with fast and stagnant zones (12), however as the flow rate increases, the relative extent of the fast zone increases, indicating increased mixing (9). Note that the distribution of active zones in space means that the trickle bed approximates to a cross-flow reactor, which can lead to very high selectivities for sequential reactions (1).

The four reactors, parallel plate, pump cell, disk-stack, and trickle bed, represent most of the geometries of cell which have been used in organosynthesis (9).

Experimental

All cells used in this investigation were undivided and were operated in batch recycle mode, the anode and cathode material normally being graphite. The pump cell and disk-stack cell were operated with inter-electrode gaps of approximately 1 mm, the anode and cathode areas each being 50 cm². In the parallel plate cell the interelectrode gap was 3 mm and the electrode area was again 50 cm² of each polarity. The trickle tower reactor consisted of 10 layers of graphite Raschig rings packed in semirandom array (1). Adjacent layers were insulated from each other by polyester nets, electrical continuity being provided by the reaction mixture which fell as a trickling film.

Each cell was inserted in turn into a reaction loop which consisted basically of the cell, a pump where necessary, a throttle valve, flow meter, heat exchanger, hydrocyclone gas disengager, and ports for monitoring temperature and for removing samples.

The composition of the electrolyte was normally 0.1 mol dm⁻³ of methyl acrylate, 0.1 mol dm⁻³ of diethyl

malonate, and 0.05 mol dm⁻³ of tetra n-butyl ammonium iodide, all dissolved in acetonitrile.

Quantitative chemical analyses were carried out on a Perkin Elmer F17 gas chromatograph, using 2m columns of 3% OV-17 on Chromosorb W AW DMCS (80-100 mesh), with a programmed temperature rise of 100° → 290° at 20°C min⁻¹.

Results and Discussion

Laboratory organosyntheses are usually carried out with easily obtainable flow rates (normally in the range 0.5 to 2.5 liters min⁻¹) without regard to Reynolds number in the cell.

Examination of the performance of the malonate/acrylate system in the different cells at a representative high (2.3 liters min⁻¹) and low (0.3 liters min⁻¹) flow rate shows it to be highly sensitive to hydrodynamic conditions. Figures 1 and 2 show the selectivity achieved for production of dimethyl adipate and ethyl dimalonate plotted against theoretical conversion (charge passed ÷ charge required to convert all the starting material to the required product at 100% current efficiency). Although flow rate and composition were fixed, the performance of each cell was otherwise optimized so that best is compared with best.

Providing experiments are not continued much past 80% conversion of ethyl malonate, the major by-products were the two Michael adducts. The decrease in selectivity for dimalonate after this point is due to the further oxidation of the dimer to ethyl ethene tetracarboxylate. The rate of production of Michael adducts decreases with time, which is why the selectivities in both figures are lower at the beginning of experiments but improve with time. The lowest selectivity occurs when using the parallel plate cell at low flow rate, when the degree of mixing is poor ($Re \approx 300$) and large amounts of by-products are produced. On increasing the flow rate, and thus the degree of mixing ($Re \approx 3400$), the selectivity improves substantially. Similarly, in the capillary gap cell a low flow rate ($Re_{ch} \approx 1 \times 10^4$) the flow is almost laminar (13) and so the segregation is high (7) and selectivity is poor. At the higher flow rate ($Re_{ch} \approx 9 \times 10^4$) the fluid is just sub-turbulent (13), consequently the selectivity is much improved. Although the pump cell is geometrically identical to the capillary gap cell, it has an entirely different hydrodynamic environment (14), the degree of mixing depending almost entirely on the ro-

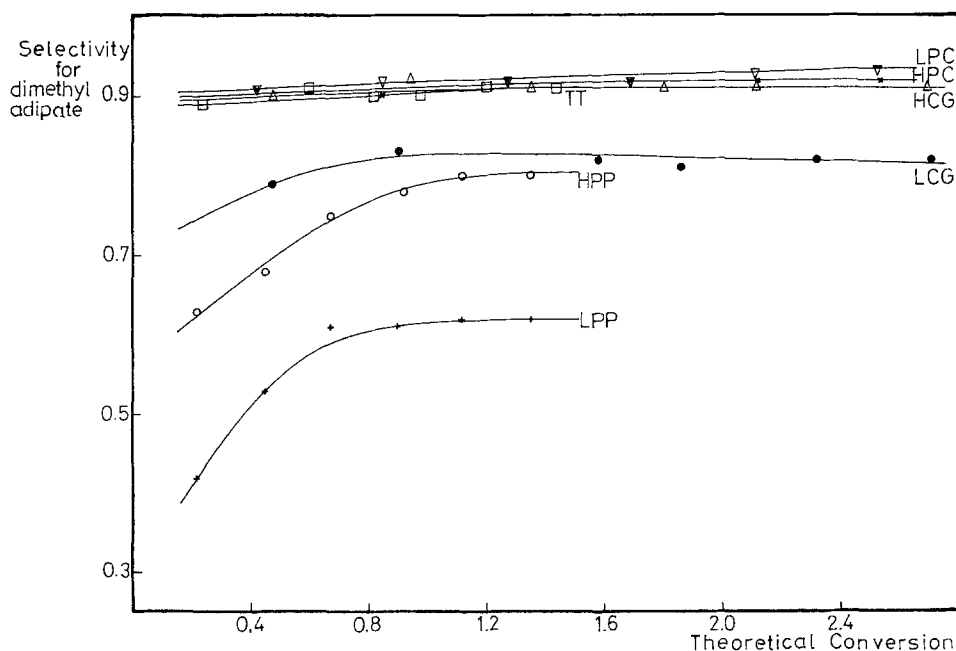


Fig. 1. Selectivity for dimethyl adipate vs. theoretical conversion in different cells. CG, capillary gap cell; PC, pump cell; PP, parallel plate cell; TT, trickle tower; H, high flow rate, 2.3 dm³ min⁻¹; L, low flow rate, 0.3 dm³ min⁻¹.

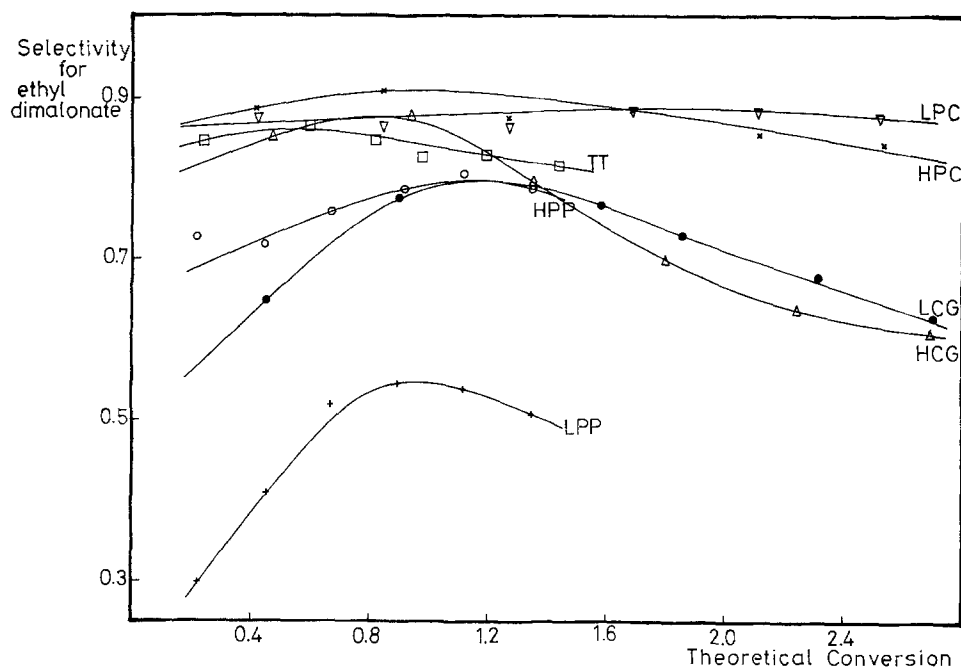


Fig. 2. Selectivity for ethyl dimalonate vs. theoretical conversion in different cells.

tational Reynolds number ($R_\phi = \omega r_o^2/\nu$) and being virtually independent of volumetric flow rate. In these experiments the rotational speed was 2800 rpm ($R_\phi \approx 10^5$) and changes in flow rate were achieved by means of a throttle. Consequently, in the pump cell experiments good selectivities were obtained independently of changes in flow rate, hence residence time and conversion per pass. Unfortunately, the very high mixing also produced an adverse effect since the current efficiency was only about 35-40%, whereas in the disk-stack cell and parallel plate cell operated with high flow rates, current efficiencies of about 60% could be obtained. This loss of current efficiency is due to rapid transport of some of the anodically generated iodine to the cathode where it is reduced back to iodide. The high current density obtained was thus at least partially due to the parasitic I_2/I^- cycle.

In the trickle tower reactor, the net separators between layers provide good mixing near the most active parts of the rings (1) thus giving a high selectivity.

In this paired reaction malonate anions are produced near the cathode; they can then react either with iodine to produce the dimer, or take part in a Michael reaction with methyl acrylate. In cells with segregated

flows the dispersion of malonate anions away from the cathode is slow. At the beginning of the experiment, when the bulk concentration of iodine is low, the Michael reaction proceeds rapidly but as the experiment continues the concentration of iodine builds up, limiting the Michael reaction, until the formation of Michael adduct effectively ceases. When the fluid is less segregated the malonate anions are more quickly dispersed away from the cathode, decreasing the amount of Michael adduct formed. From Fig. 3 it can be seen that in the parallel plate cell and capillary gap cell operated with a low flow rate, i.e., conditions of poorest mixing and greatest segregation, the most Michael adduct is formed. As mixing improves less Michael adduct is produced, the pump cell producing the least. The effect was studied systematically in experiments using the parallel plate cell operated at different Reynolds numbers (Fig. 4). This shows that as the degree of mixing increases the total amount of Michael adduct anion (MA^-), the common intermediate to both propanes decreases, whereas the ratio of cyclopropane adduct to normal Michael adduct generally increases with Reynolds number due to the increased transport of anodically generated I_2 into the reaction zone

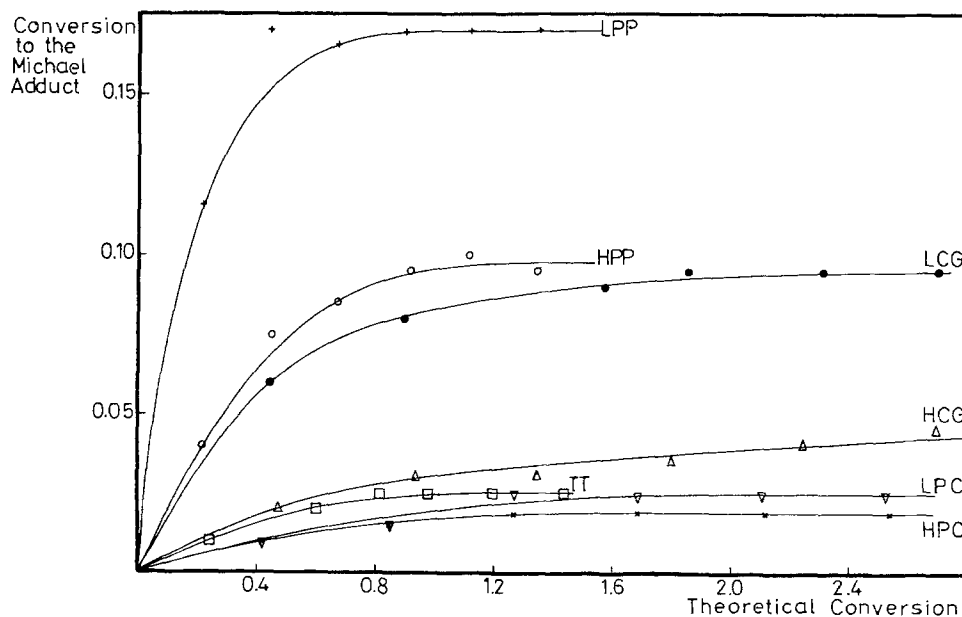
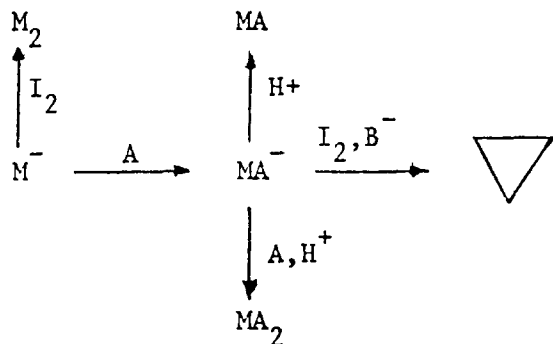


Fig. 3. Conversion to Michael adducts vs. theoretical conversion in different cells.



The cyclopropane adduct may be a valuable product as an intermediate in pyrethroid synthesis, therefore it may be desirable actually to maximize its production. However, from above it can be seen that, while the ratio of cyclo to normal propane increases with Re, the total amount of Michael adduct falls. Figure 4 shows that the optimal Reynolds number is about 3000, in the transitional regime. Alternatively, the production of the cyclopropane may be maximized through choice of a suitable contacting pattern.

A good yield of the cyclopropane requires the production of the anion intermediate (MA^-), in the presence of iodine and the absence of a proton source. Experiments were therefore carried out using a paral-

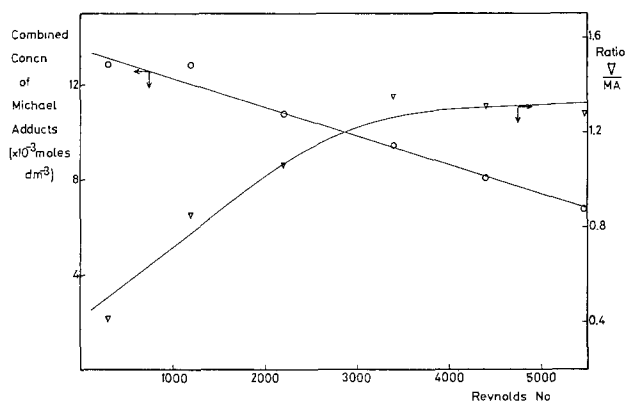


Fig. 4. Combined concentration of Michael adducts and ratio of cyclopropane to normal Michael adduct produced, in experiments run at different Reynolds numbers, in a parallel plate cell.

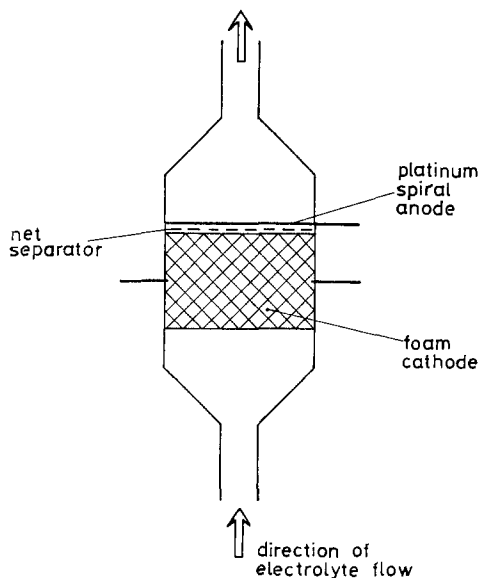


Fig. 5. Diagram of undivided foam cell

lel plate cell and a low flow rate to maximize production of the anion intermediate (MA^-), with the addition of aliquots of the ethyl malonate during the electrolysis to increase the iodine to malonate ratio. This proved unsuccessful as after the initial reduction the acrylate polymerized rather than hydrodimerized, due to the lack of a proton source.

From the reaction scheme it can be seen that if the conversion of ethyl malonate approaches 100% in a single pass through a cell, then in the presence of methyl acrylate and absence of iodine a high yield of the anion intermediate (MA^-) should be produced, since the concentration of proton donor is then low. If the MA^- is then introduced into a region of high iodine concentration the synthesis of the cyclopropane would be facilitated. An attempt to follow this strategy was carried out using the cell shown in Fig. 5, which had a carbon foam cathode. The electrolyte had the same composition as used in the earlier experiments; conversions of about 60% of the ethyl malonate were obtained. Unfortunately, very little of the cyclopropane was produced (material yields of 1% or less). The major product was the normal Michael adduct (material yields of about 30%) with large amounts of the diadduct (material yield of up to 20%) also. The long residence time of the malonate anions in the foam is probably the reason for this. To achieve a 100% conversion of ethyl malonate in a single pass required a flow rate of less than 1.1 ml min^{-1} at a current of 0.2A, or a residence time in the foam of more than 6 min.

At present, work is being carried out with cells of different contacting pattern to maximize the yield of the cyclopropane.

Conclusions

Ethyl dimalonate and dimethyl adipate may be electrosynthesized in good yield and high selectivity in cells capable of being scaled-up, provided that there is a good dispersion of malonate anions away from the cathode. Under conditions of very high cross-gap transport a loss in current efficiency is observed due to the parasitic iodine cycle. Good mixing conditions also favor production of the cyclopropane adduct, the potentially more valuable of the two by-products. By correct choice of reactor design it may also be possible to produce the cyclopropane adduct selectively.

Manuscript received July 15, 1980. This was Paper 432 presented at the St. Louis, Missouri, Meeting of the Society, May 11-16, 1980.

Any discussion of this paper will appear in a Discussion Section to be published in the June 1982 JOURNAL. All discussions for the June 1982 Discussion Section should be submitted by Feb. 1, 1982.

REFERENCES

1. A. V. Bousoulengas, S. Ehdia, and R. E. W. Jansson, *Chem. Ind.*, 670 (1979).
2. H. G. Thomas and E. Lux, *Tet. Lett.*, 965 (1972).
3. M. M. Baizer and R. C. Hallcher, *This Journal*, **123**, 809 (1976).
4. D. K. Johnson and R. E. W. Jansson, *J. Chem. Tech. Biotech.*, **30**, 200 (1980).
5. R. E. W. Jansson and R. J. Marshall, *ibid.*, **00**, 000 (1980).
6. R. E. W. Jansson and R. J. Marshall, *J. Appl. Electrochem.*, **8**, 287 (1978).
7. M. Fleischmann, J. Ghoroghchian, and R. E. W. Jansson, *ibid.*, **9**, 437 (1979).
8. N. R. Tomov and R. E. W. Jansson, *J. Chem. Tech. Biotechnol.*, **30**, 110 (1980).
9. R. E. W. Jansson, "Electrochemical Reaction Engineering," Plenary Lecture at 6th International Symposium on Chemical Reaction Engineering, Nice, France, March 25-27, 1980; *Chem. Eng. Sci.*, **35**, 1979 (1980).
10. R. J. Marshall, Ph.D. Thesis, Southampton University (1980).

11. F. Beck and H. Guthke, *Chem. Ing. Tech.*, **41**, 943 (1969).
12. Z. Ibrisagić and M. Fleischmann, *J. Appl. Electrochem.*, **10**, 157 (1980).
13. G. A. Ashworth and R. E. W. Jansson, *Electrochim. Acta*, **22**, 1295 (1977).
14. G. A. Ashworth and R. E. W. Jansson, *ibid.*, **22**, 1301 (1977).

Electrochemical Reduction of Aromatic Diazonium Salts

I. Electrochemical Behavior of *p*-Tolyl- and *p*-Anisyldiazonium Fluoborates at a Mercury Cathode: Evidence for the Corresponding Hydrazines Formation

Olivier Orange, Claire Elfakir-Hamet, and Claude Caullet*

Laboratoire de Chimie Analytique et Electrochimie,
Faculté des Sciences, BP 67, 76130 Mont-Saint-Aignan, France

ABSTRACT

Reduction of *p*-methyl and *p*-methoxyphenyldiazonium fluoborate in aqueous solutions at mercury micro and macroelectrodes results in formation of a primary hydrazine ArNH-NH₂. The radical ArN = N· formed in the first electrochemical step forms Ar-Hg-Ar; the product of the two electrons reduction forms Ar-NH-NH-Ar in competitive chemical reactions. Low temperature (4°C) and moderate stirring enable minimizing of these side reactions.

Aromatic hydrazines are at present time synthesized by chemical reduction of the corresponding diazonium salts. These chemical reductions involve the use of sodium sulfite (or hydrosulfite) or of stannous chloride as reducing agents which cause various environmental problems. An electrochemical reduction of diazonium salts might be an alternative process to obtain hydrazines.

The electrochemical preparation of aromatic hydrazines by reduction of diazonium salts or hydroxydiazonium compounds has been studied by several authors (1-5) from 1929 to 1940. Using constant-current techniques and various cathode materials, these authors have obtained varying yields of hydrazines (not always properly identified). No attempts were made to elucidate the mechanisms of these processes.

Later investigations (6-20) were restricted to polarographic studies of diazonium salts in various solvents. Two reduction waves were observed in the majority of these studies. The first wave was attributed to a transfer of a single electron and was found to be pH independent, the second was considered to correspond to a transfer of 2, 3, 4, or 6 electrons. The formation of hydrazines was often indicated in the proposed mechanisms, but not proved.

In particular, Wawzonek (8) proposed that the first reduction wave corresponds to the formation of a free radical, with consecutive formation of diphenylmercury and phenylmercuric chloride. The limiting current of the second wave was found to be four times higher than that of the first one. Its half-wave potential depends on pH, and this wave was tentatively ascribed to the direct reduction of the diazonium cation to the corresponding primary hydrazine. However, coulometric measurements at potentials corresponding to the limiting currents of the first and second wave gave the same results.

Elofson and co-workers (6, 13) have furthermore found that, for diazonium concentrations above 10⁻³M, the limiting current of the first wave reaches a constant value independent of concentration, and the occurrence of a polarographic maximum on the second one, which was interpreted by adsorption phenomena. In acidic medium, they have also observed a splitting of the second wave. They assigned the complicated shape of the polarograms to the irreversibility of the process. Using a stirred mercury cathode, the coulometric results obtained at the potential of the limiting current of the first or second wave were not reproducible.

Phenylmercuric chloride was isolated after electrolysis. Controlled potential electrolysis performed at a potential corresponding to the limiting current of the second wave corresponds to a four electrons process. A test reaction with ammonium phosphomolybdate indicates the presence of hydrazine in the electrolyzed solution.

Rüetschi and Trümpler (10) have reported a constant-current method using a mercury-pool cathode and a flowing catholyte, leading to good yields of phenylhydrazine, but did not attempt to investigate the mechanism of this process.

Any attempt to carry out electrochemical synthesis of aromatic hydrazines should be preceded by a critical evaluation of the mechanisms involved and elucidation of the role of adsorption. In particular it should be proved whether the hydrazines formed at very negative potentials operative when the constant current electrolysis is performed are generated in an electrochemical process or by a chemical reduction of diazonium salts by means of the hydrogen formed at the electrode surface.

In the present work, diazonium fluoborates instead of chlorides have been used, in order to avoid the chemical decomposition of the diazonium ions in the presence of halide ions.

* Electrochemical Society Active Member.

Key words: diazonium salts, hydrazine preparation, electrolysis.

Experimental

Reagents.—Stable *p*-methyl- and *p*-methoxyphenyldiazonium fluoborates have been prepared and purified by methods described in the literature (21). High purity commercial products have been used for preparation of supporting electrolytes (KCl, NaClO₄) and buffer solutions (McIlvain and Sørensen) in doubly distilled water.

Apparatus and techniques.—Tacussel instrumentation has been used for all the electrochemical measurements: Three electrode d-c and superimposed a-c polarograph (PRG3), potentiostats (PRT20, PRT40), integrator (IG5N), function generator (GSTP, UAP4), and recorder (EPL). A Telequipment storage oscilloscope DM60 has been used for cyclic voltammetry.

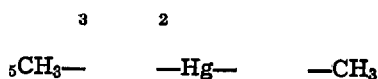
For the coulometric measurements and controlled potential electrochemical reductions, we have used a divided thermostated cylindrical cell. The auxiliary electrode was a platinum grid, parallel to the mercury cathode and separated from it by an inner glass cylinder fitted with a sintered glass disk.

The outer compartment contained the mercury-pool cathode, the tested solution, the saturated calomel electrode (SCE) as reference and the fittings enabling deoxygenation. A relatively slow stirring of the mercury pool is particularly important at the outset of the electrolysis, because of the adsorption phenomena which can cause the partition of the mercury cathode into small balls isolated from each other by the adsorbed film. On the other hand, it is necessary to limit the duration of the electrolysis with a large mercury pool cathode, in order to limit the extent of the chemical side reactions. For the polarographic studies, a thermostated cell was used including SCE, fittings enabling deoxygenation and a platinum wire as an auxiliary electrode. All deoxygenations were done with pure nitrogen ("U" grade from "L'Air Liquide") and the nitrogen flow was kept over the solutions during the measurements.

Procedure.—0.1M NaClO₄ has been used as supporting electrolyte. As diazonium fluoborates are not stable in more basic media, McIlvaine and Sørensen buffers pH 1-7 were used. 0.01M stock solutions of diazonium fluoborates were kept oxygen free and stored at 4°C. All the electrochemical measurements were carried out at 4°C, except for coulometric measurements which were performed both at 4°C and 25°C.

Chemical identification of the products.—Preparative electrolysis were performed in a 500 ml cell, using a 44 cm² mercury-pool cathode.

p-Ditolylmercury has been separated from the acidic electrolyzed solution by CHCl₃ extraction, and recrystallization from benzene. This product has been identified by its melting point (lit. 244°-246°C, found 246°C) microanalysis (C% = 43.32, H% 3.92—Theor. = 43.19, 3.66) and ¹³C NMR spectrum



δ (ppm): C₂ = 137.48, C₃ = 129.48, C₄ = 138.06, C₅ = 20.95

$J(\text{Hg}-\text{C}_2)$: 89.71 ppm- $J(\text{Hg}-\text{C}_3)$: 102.96 ppm

N,N'-Di-*p*-tolylhydrazine has been separated by diethyl ether extraction after elimination of *p*-ditolylmercury and neutralization by sodium carbonate. The diethyl ether solution was dried over magnesium sulfate and saturated with gaseous hydrogen chloride. The resulting white hydrochloride was identified by infrared spectrometry, microanalysis, and NMR. This hydrazine is not electrochemically reducible under experimental conditions used.

p-Tolylhydrazine has been identified in the solution resulting from the controlled potential electrolysis by derivatization with 2,4-dinitrobenzaldehyde. The red hydrazone was recrystallized from acetic acid, and characterized by means of elemental analysis, infrared, NMR, and mass spectrometry; it was identical with the product obtained by reaction of 2,4-dinitrobenzaldehyde with commercial *p*-tolylhydrazine.

Moreover, *p*-tolylhydrazine is electroactive and shows a complex oxidation wave between 0.2 and 0.3V vs. SCE in the acidic medium used for the preparative electrolysis. This oxidation wave has been used, after calibration, for the determination of the concentration of hydrazine produced in electrolysis.

Results and Discussion

The following results have been predominantly obtained in experiments with *p*-methylphenyldiazonium fluoborates. The behavior of the *p*-methoxy derivative is analogous in all aspects with the exception of those obtained in controlled potential electrolysis which are discussed separately.

D-C and superimposed a-c polarography.—Compounds studied are reduced at concentrations of the diazonium salt larger than about 1×10^{-4} M in four waves (*i*₁-*i*₄, Fig. 1) in d-c polarography, and four corresponding peaks (*i*_{s1}-*i*_{s4}, Fig. 1) in a-c polarography. At concentrations lower than 1×10^{-4} M, wave *i*₂ and peak *i*_{s2} are missing.

The electrocapillary and *i-t* curves (Fig. 2) show a strong adsorption occurring at potentials between (*E*_{1/2})₁ and (*E*_{1/2})₃. The shapes of the *i-t* and electrocapillary curves, as well as values of half-wave potentials of waves *i*₁ and *i*₂, are not dependent on pH or concentration changes.

Wave *i*₁ (Table I and II) increases linearly with increasing concentration of the diazonium salt up to 1×10^{-4} M and becomes independent of concentration at higher values.

This observation together with the effect of temperature and a-c polarographic curves indicates that at concentrations above 1×10^{-4} M the height of this wave is governed by adsorption. Wave *i*₁ is thus typical Brdicka prewave.

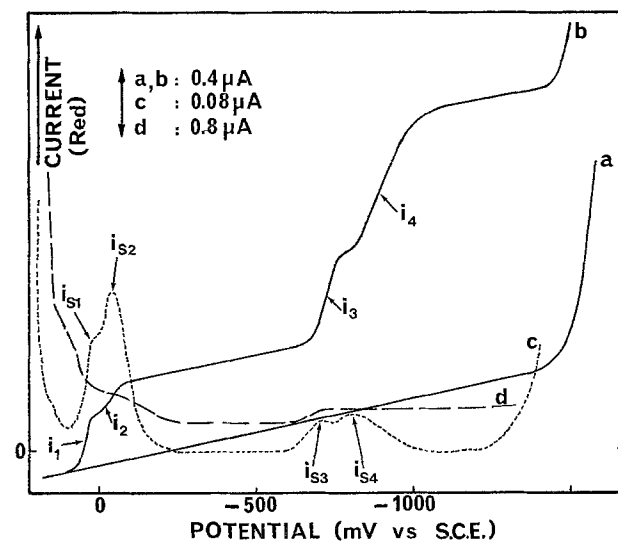


Fig. 1. D-C polarograms (a; b) and a-c polarograms (c; $\phi = 0g$) (d: $\phi = 150g$) of an aqueous solution of paratolylidiazonium fluoborate. McIlvain buffer, NaClO₄ 10^{-1} M, C = 2×10^{-4} M. pH = 5, T = 4°C, h = 65 cm, $\tau = 2$ sec, F = 15 Hz, $\Delta V = 20$ mV. *E*_{1/2}^{*i*1} = +50 mV; *E*₁ = +45 mV; *E*_{1/2}^{*i*2} = -45 mV; *E*_{s2} = -45 mV; *E*_{1/2}^{*i*3} = -730 mV; *E*_{s3} = -775 mV; *E*_{1/2}^{*i*4} = -910 mV; *E*_{s4} = -900 mV (vs. SCE).

Table I. Data obtained by d-c polarography of p-methylphenyldiazonium fluoborate

| Diagnostic test | i_1 | | i_2 | i_3 | i_4 |
|--------------------------------|-------------------------|-------------------------|--------------------|---------------------|--------------------|
| | $C < 1 \times 10^{-4}M$ | $C > 1 \times 10^{-4}M$ | | | |
| $i_d = f(C)$ | $i_1 = kC$ | $i_1 \neq f(C)$ | $i_2 = kC$ | $i_3 = kC$ | $i_4 = kC$ |
| di_d/dT (grad $^{-1}$) | 3% | 0.1% | 2.5-3% | 0.5-1.5% | 2% |
| $i_d = kh^x$ | $x = 0.5$ | $x = 1$ | $x = 0.5$ | $x \cong 0.5$ | $x = 0.5$ |
| $E = f \log \frac{i_d - i}{i}$ | $\alpha n_a = 0.8$ | ^a | $\alpha n_a = 1.0$ | $\alpha n_a = 0.67$ | $\alpha n_a = 0.4$ |
| $dE_{1/2}/dC$ | 0 | 0 | 0 | ^b | 0 |
| $dE_{1/2}/dpH$ | 0 | 0 | 0 | ^b | ^c |

^a Nonlinear dependence.

^b $E_{1/2}$ becomes more negative with increasing concentration of the diazonium salt or increasing pH.

^c $E_{1/2}$ becomes more positive with increasing pH.

Table II. Data obtained by a-c polarography of p-methylphenyldiazonium fluoborate

| Diagnostic test | i_{s1} | | i_{s2} | i_{s3} | i_{s4} |
|-------------------------------|-------------------------|-------------------------|-------------------|-------------------|-------------------|
| | $C < 1 \times 10^{-4}M$ | $C > 1 \times 10^{-4}M$ | | | |
| $i_s = f(C)$ | $i_s = kC$ | $i_s \neq f(C)$ | $i_s = kC$ | $i_s = kC$ | $i_s = kC$ |
| $\Delta EP/2$ | 120 mV | Broad | 100 mV | $i_{s3} < i_{s2}$ | $i_{s4} > i_{s3}$ |
| $i_s = f(\Delta V)^a$ | $i_s = k\Delta V$ | $i_s = k\Delta V$ | $i_s = k\Delta V$ | $i_s = k\Delta V$ | $i_s = k\Delta V$ |
| $\Delta i_s/\Delta(\log F)^b$ | 0.5 | 1 | 0.5 | 0.5 | 0.5 |
| ϕ (gr) | 50 | 77 | 48 | 60 ^c | 30 ^c |
| $\Delta E_s/\Delta C^d$ | 0 | 0 | 0 | <0 | 0 |
| $\Delta E_s/\Delta F$ | 0 | 0 | <0, next > 0 | 0 | 0 |
| $\Delta E_s/\Delta(\Delta V)$ | 0 | 0 | 0 | 0 | 0 |
| $E_s - E_{1/2}$ | <0 | 0 | 0 | -30 to 50 mV | 0 |

^a ΔV = amplitude of the superimposed alternative signal.

^b F = frequency of the superimposed a.c.

^c ϕ decreases with increasing concentration of the diazonium salt.

^d E_s = potential corresponding to the summant current i_s .

The total height of waves i_1 and i_2 is a linear function of concentration and corresponds to a transfer of one electron.

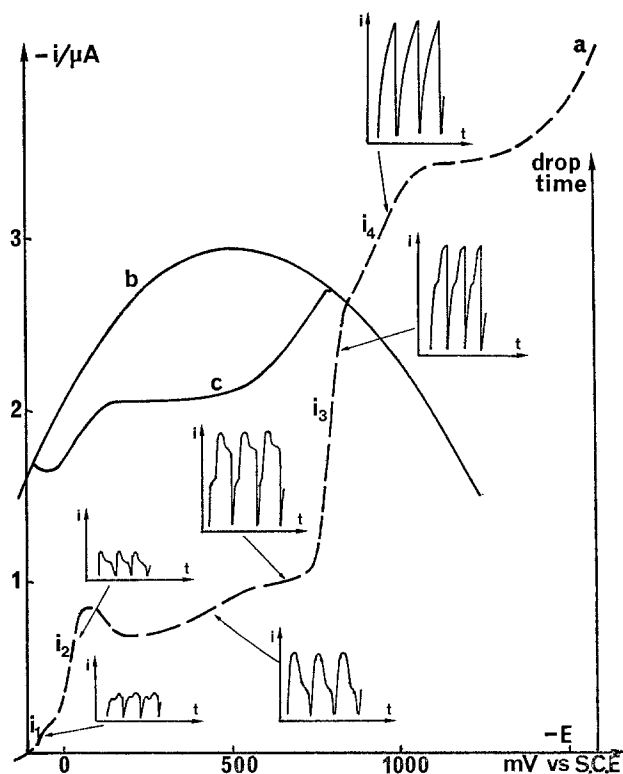
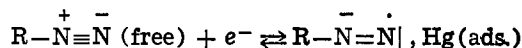


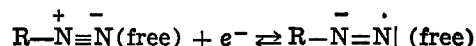
Fig. 2. D-C polarogram (a), electrocapillary curves (b: solvent; c: diazonium solution), and (i, t) curves. pH = 4, $T = 4^\circ C$, $h = 65$ cm, $\tau = 2$ sec. Buffered paratolyldiazonium solution (McIlvain buffer) $NaClO_4$ $10^{-1}M$, $C = 3 \times 10^{-4}M$.

Independence of half-wave potential $(E_{1/2})_2$ of the concentration of diazonium salt, logarithmic analysis yielding a slope of 59 mV, and agreement of the sharp peak ($\Delta E_{s/2} = 100$ mV) potential obtained by a-c polarography with the half-wave potential obtained by d-c polarography indicate reversible, single electron process.

This wave i_1 corresponds to a process



where one-electron reversible reduction of the diazonium cation yields the adsorbed radical. Wave i_2 then corresponds to a reversible reduction of the diazonium cation through the adsorbed film, yielding a free radical



Wave i_3 is proportional to the concentration of the diazonium salt and its height is equal to the sum of limiting currents $i_1 + i_2$ and corresponds thus to a transfer of a second electron. Dependence of i_3 on the height of the mercury column similarly as the electrocapillary and $i-t$ curves (Fig. 2), as well as the a-c polarograms obtained at $\phi = 150g$ (Fig. 1), show that the transfer of the second electron occurs on a surface from which the radical was desorbing. Logarithmic analysis and the shape of a-c polarographic peaks indicate that the electrode process is irreversible and the dependence of the half-wave potential of wave i_3 on pH indicates that proton transfer must occur between the transfer of the first and second electron.

The height of wave i_4 is twice that of wave i_3 . The wave is diffusion controlled and corresponds to a two electron process. Broader and lower a-c polarographic peaks indicate an irreversible process; pH dependence of the half-wave potential of wave i_4 is a proof that

between the transfer of the second and third (and fourth) electron a proton transfer must occur.

Cyclic voltammetry.—The cyclic voltammogram recorded using a triangular potential sweep from +0.1V to -1.3V and back to +0.1V vs. SCE shows, at concentrations of the diazonium salt smaller than 2×10^{-4} M, four cathodic peaks i_{p6} , i_{p1} , i_{p2} , and i_{p3} (Fig. 3, Table III).

Peak i_{p6} corresponds probably to the reduction of the product resulting from the oxidation of the mercury electrode at the starting potential E_1 . This assumption is supported by observation that peak i_{p6} does not appear when the starting potential is slightly more negative.

At sweep-rate slower than 5 Vsec^{-1} only the reduction peak i_{p2} is observed. This peak occurs in the potential range where d-c polarographic waves i_1 and i_2 were observed. At sweep-rate higher than 5 Vsec^{-1} another very broad reduction peak i_{p3} is observed in the same potential range where d-c waves i_3 and i_4 occur. Reduction in this peak i_{p3} is completely irreversible, as no corresponding anodic peak is observed. At sweep rates higher than 5 Vsec^{-1} anodic peak i_{p2}^a is observed, indicating reversibility of the process taking place in peak i_{p2} . Peak i_{p1} is observed only at concentrations of the diazonium salt higher than about 1.5×10^{-4} M, this peak is ill separated from peak i_{p2} and is difficult to measure, but seems to be independent of concentration of the diazonium salt. It may be the adsorption prewave to the process occurring at peak i_{p2} . Indication of a corresponding anodic peak seems to be in agreement with this assumption.

The peak-current i_{p2} increases linearly with the concentration of the diazonium salt up to about 1×10^{-4} M. Deviations from linearity at higher concentrations (Fig. 4) indicate diffusion-controlled electrode process perturbed by adsorption (22, 24), in agreement with conclusions reached for d-c curves i_1 and i_2 . Dependence of the peak potential of peak i_{p2} on concentration of the diazonium salt (Table III) may be due to adsorption and to a consecutive chemical reaction, second order (or higher) in the product of the one-electron transfer (25).

The peak current i_{p3} at sweep rates higher than 5 Vsec^{-1} shows also a nonlinear dependence on diazonium salt concentration. The greater deviation from linearity for i_{p3} than i_{p2} is attributed to the desorption process occurring in this potential range (Fig. 2C). The origin of the dependence of the peak potential of i_{p3} on concentration of the diazonium salt may be similar to that of peak i_{p2} , even when the characteristics (Table III) of these two dependences are different.

Dependence of the reduction peak i_{p2} and the oxidation peak i_{p2}^a on the rate of scanning (Table III, Fig. 5) indicates that a single oxidation-reduction couple is involved. At sufficiently high sweep rates the system is reversible, as indicated by the increase in ratio i_{p2}^a/i_{p2} (Fig. 6) and by variation of the potential of peak i_{p2} with logarithm of the scanning rate (Fig. 7) (25, 26). At slower sweep rates the characteristics indicate the presence of an irreversible chemical reaction following the uptake of the first electron. The

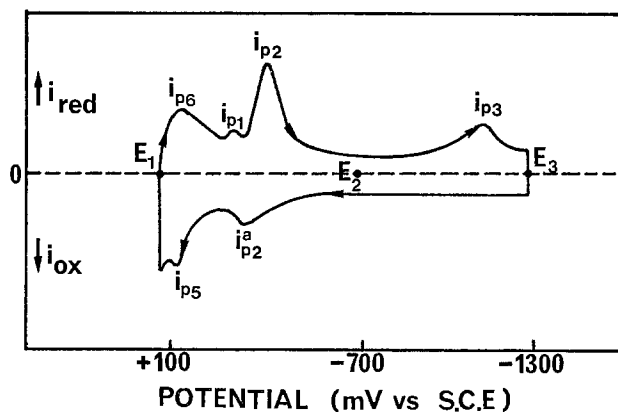


Fig. 3. General shape of the cyclic voltammogram of an aqueous solution of paratolyldiazonium fluoborate. pH = 5, $T = 4^\circ\text{C}$. Buffered paratolyldiazonium solution (McIlvain buffer) NaClO_4 10^{-1} M, $C \leq 2 \times 10^{-4}$ M. $2 \text{ Vsec}^{-1} \leq v \leq 100 \text{ Vsec}^{-1}$. $E_{p1} = +100 \text{ mV}$, $E_{p2} = -700 \text{ mV}$, $E_{p3} = -1300 \text{ mV}$ vs. SCE.

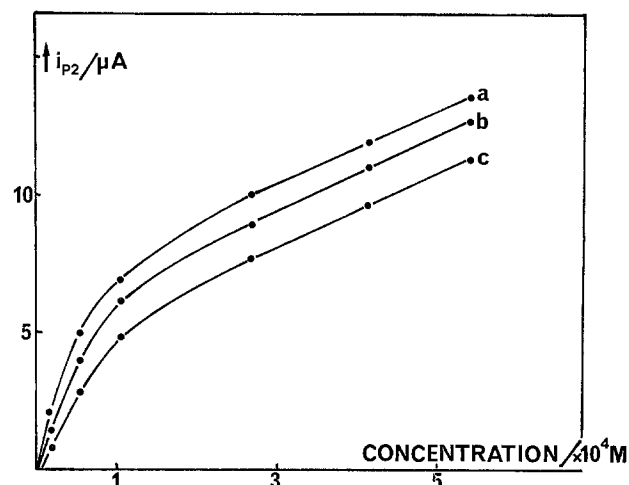


Fig. 4. Evolution of peak i_{p2} with the concentration of the solutions. Paratolyldiazonium solution NaClO_4 10^{-1} M, pH = 4, $T = 4^\circ\text{C}$, $E_1 = +100 \text{ mV}$ vs. SCE. (a): $v = 100 \text{ V} \times \text{sec}^{-1}$; (b): $v = 50 \text{ V} \times \text{sec}^{-1}$; (c): $20 \text{ V} \times \text{sec}^{-1}$.

role of adsorption is reflected in the large slopes of the dependence of the peak-potential on v (Fig. 7).

As frequently observed the shape of the cyclic voltammograms depends on the potential range applied and the direction of the sweep (Fig. 8)

Complete sweeping range: ($E_1 = 100 \text{ mV}$, $E_3 = -1.3 \text{ V}$ vs. SCE). For a forward sweep starting from E_1 toward E_3 (Fig. 8A), the voltammogram has been described above (Fig. 3). For a forward sweep starting from E_3 toward E_1 , i_{p2} and i_{p3} are notably lowered, i_{p4} disappears, and i_{p5} is much increased (compare Fig. 8B and Fig. 8A).

Shortened sweeping range: ($E_1 = 100 \text{ mV}$, $E_2 = -700 \text{ mV}$, $E_3 = -1.300 \text{ V}$ vs. SCE). When the forward sweep starts from E_3 toward E_2 , the peak i_{p3} is not ob-

Table III. Data obtained by triangular sweep voltammetry for p-methylphenyldiazonium fluoborate

| Diagnostic test | i_{p2} | i_{p3} | i_{p4} |
|--|---|---|---|
| $\Delta(i_p \times v^{-1/2})/\Delta v$ | <0 for $v < 40 \text{ V} \times \text{sec}^{-1}$ 0 for $v > 40 \text{ V} \times \text{sec}^{-1}$ | 0 | >0 for $v < 40 \text{ V} \times \text{sec}^{-1}$ 0 for $v > 40 \text{ V} \times \text{sec}^{-1}$ |
| $\Delta E_p/\Delta \log v$ | <0 (-50 mV/decade) | <<0 (-230 mV/decade) | 0 |
| $\Delta E_p/\Delta(\log C)$ | >0 decreases when v increases | 0 when $C < 10^{-4}$ M >0 when $C > 10^{-4}$ M | Unworkable |
| $\frac{i_{p2}^a}{i_{p2}} = f(v)$ | Increases from 0 to 1 with increasing v | | |

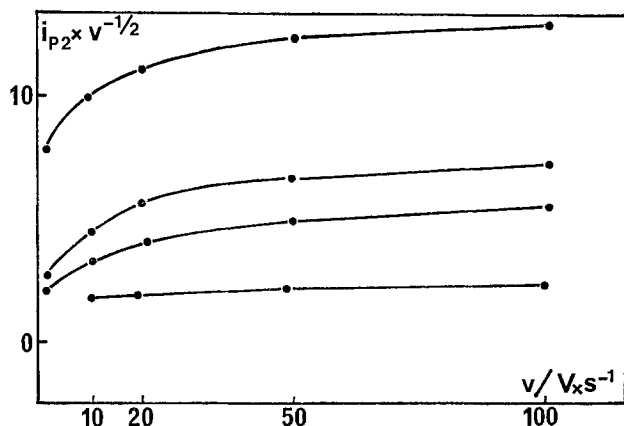


Fig. 5. Influence of the sweep rate. $i_{p2} \cdot v^{-1/2} = f(v)$, NaClO_4 10^{-1} mol · liter $^{-1}$, pH = 4, $T = 4^\circ\text{C}$, $E_1 = +100$ mV vs. SCE. Paratolyldiazonium concentration: (a) $C = 1 \times 10^{-5}\text{M}$; (b) $C = 5 \times 10^{-5}\text{M}$; (c) $C = 10 \times 10^{-5}\text{M}$; (d) $C = 53 \times 10^{-5}\text{M}$.

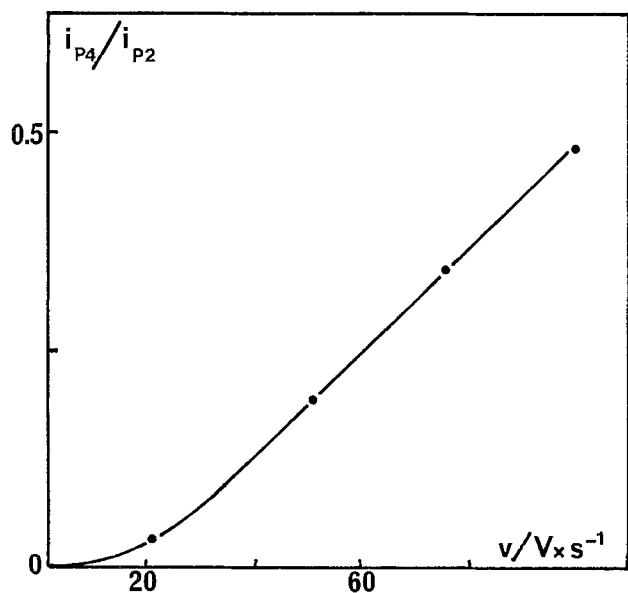


Fig. 6. Evolution of the ratio i_{p4}/i_{p2} with the sweep rate. Paratolyldiazonium solution $C = 1.25 \times 10^{-4}\text{M}$, pH = 4, $T = 4^\circ\text{C}$, NaClO_4 10^{-1}M , $E_1 = +100$ mV vs. SCE.

served. When the forward sweep starts from E_2 toward E_1 , the peak i_{p5} disappears and the peak i_{p2} increases (Fig. 8D). When the forward sweep reversed from E_1 toward E_2 , the peak i_{p4} is again observed, and is much higher than when the sweeping range is extended up to E_3 (Fig. 8C). Oxidation peak i_{p5} appears and disappears simultaneously with peak i_{p3} when the sweeping conditions are modified. Peak i_{p5} is therefore due to oxidation of the species resulting from the reduction step i_{p3} .

A solution of the primary hydrazine $\text{Ar}-\text{NH}-\text{NH}_2$ in a buffered aqueous solution leads to a cyclic voltammogram showing an oxidation peak identical with i_{p5} when the forward sweep starts from E_3 toward E_1 . The formation of hydrazine by the electrochemical reduction of the diazonium salt is therefore highly probable at the potential of the peak i_{p3} .

Controlled potential electrolysis.—Controlled potential electrolysis was carried out at low concentrations of the diazonium salt ($7 \times 10^{-4}\text{M}$) on a small mercury pool cathode (area 5 cm^2) to carry out coulometry and at higher concentrations ($1.2 \times 10^{-2}\text{M}$) with a large mercury pool electrode (area 44 cm^2) and large volume of the solution (300 ml) for electrosynthetic studies.

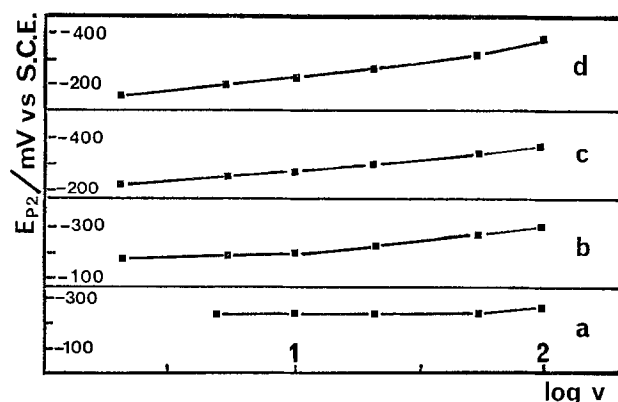


Fig. 7. Variation of peak potential E_{p2} with the sweep rate: $E_{p2} = f(\log v)$ NaClO_4 10^{-1}M , pH = 4, $T = 4^\circ\text{C}$, $E_1 = +100$ mV vs. SCE. Paratolyldiazonium concentration: (a) $C = 1 \times 10^{-5}\text{M}$; (b) $C = 5 \times 10^{-5}\text{M}$; (c) $C = 10 \times 10^{-5}\text{M}$; (d) $C = 53 \times 10^{-5}\text{M}$.

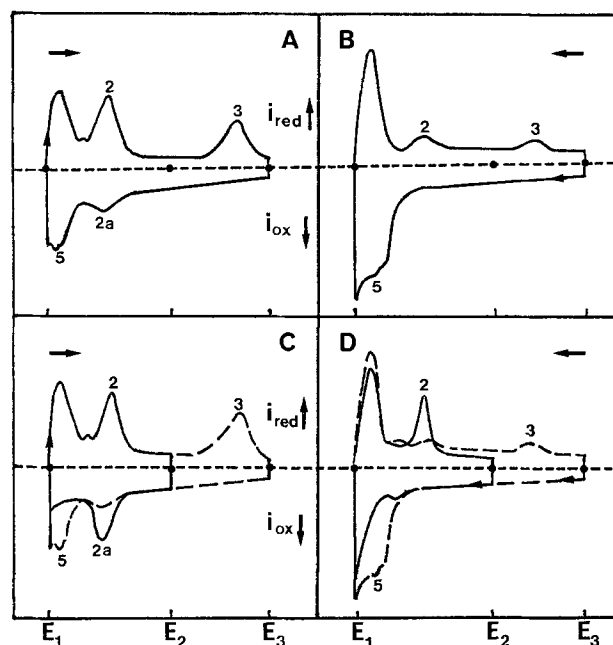


Fig. 8. Evolution of a cyclic voltammogram with sweeping range and direction of sweeping. Paratolyldiazonium solution $C = 1.25 \times 10^{-4}\text{M}$, pH = 4, $T = 4^\circ\text{C}$, NaClO_4 10^{-1}M . (A) $v = 50\text{V} \times \text{sec}^{-1}$, forward sweep from E_1 to E_3 ; (B) $v = 50\text{V} \times \text{sec}^{-1}$, forward sweep from E_3 to E_1 ; (C) $v = 50\text{V} \times \text{sec}^{-1}$ [forward sweep from E_1 to E_2 (solid line)]; [forward sweep from E_1 to E_3 (dashed line)]; (D) $v = 50\text{V} \times \text{sec}^{-1}$ [forward sweep from E_2 to E_1 (solid line)]; [forward sweep from E_3 to E_1 (dashed line)].

Coulometric measurements at potentials corresponding to limiting currents i_1 or i_2 yield $n = 1$. After exhaustive electrolysis all waves i_1 - i_4 disappear simultaneously and no oxidation or reduction wave is formed. The product of the first electron uptake is thus electroinactive under conditions used, probably due to a consecutive chemical reaction such as formation of organomercury compounds.

When the coulometric electrolysis was carried out at the limiting current of wave i_3 the value of n obtained was significantly smaller than 2 (Table IV). This indicates competitive chemical reaction of the product of the one-electron reduction, such as formation of organomercury compounds. Such a reaction is faster for *p*-methyl than *p*-methoxy derivative (Table IV) and is slower at 4°C than at 25°C . Products formed at the limiting current of wave i_3 yield neither oxidation nor reduction waves.

Table IV. Coulometric measurements

| Ar | Wave i_1 Q_1 | | Wave i_2 Q_2 | | Wave i_3 Q_3 | | Wave i_4 Q_4 | | Hydrazine yield | |
|---------------------|------------------------|-----------------------|------------------------|-----------------------|------------------------|-----------------------|------------------------|-----------------------|------------------------|-----------------------|
| | $t = 25^\circ\text{C}$ | $t = 4^\circ\text{C}$ | $t = 25^\circ\text{C}$ | $t = 4^\circ\text{C}$ | $t = 25^\circ\text{C}$ | $t = 4^\circ\text{C}$ | $t = 25^\circ\text{C}$ | $t = 4^\circ\text{C}$ | $t = 25^\circ\text{C}$ | $t = 4^\circ\text{C}$ |
| CH ₃ — | 1 | 1 | 1 | 1 | 1.3 | 1.8 | 2.4 | 3.5 | 5% | 36% |
| CH ₃ —O— | 1 | 1 | 1 | 1 | 1.7 | 1.9 | 3.6 | 3.8 | 32% | 65% |

Similarly, electrolysis at the limiting current of wave i_4 yields the value of n smaller than 4 (Table IV), the value of n being larger for p-OCH₃ than p-CH₃ derivative and in both cases larger at 4°C than at 25°C. Solution of the electrolysis product yields an oxidation wave, identical in wave-shape and half-wave potential with the wave of a corresponding hydrazine Ar-NH-NH₂ recorded under identical conditions.

The height of anodic wave in the solutions electrolyzed at the limiting current of wave i_4 was used to determine yields of the hydrazine (Table IV). These yields were higher for the p-OCH₃ than for the p-CH₃ derivative and in both instances higher at 4°C than at 25°C.

All these experiments indicate that the radical formed in the reduction of the p-methyl derivative is more reactive toward metallic mercury than the corresponding p-methoxy derivative.

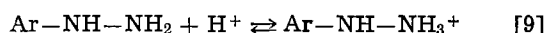
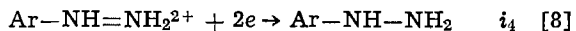
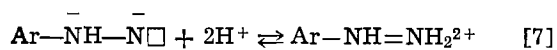
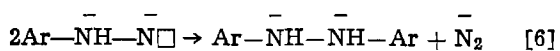
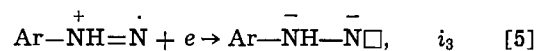
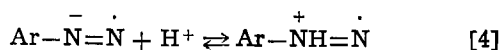
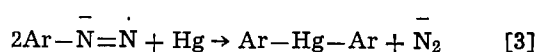
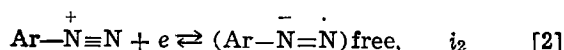
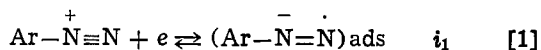
Electro-oxidation at the potential corresponding to the limiting current of the oxidation wave of the hydrazine Ar-NH-NH₂ yielded a solution in which the current-voltage curve obtained with a DME resembled that obtained with a dilute solution of the diazonium salt. The possibility of oxidation of the hydrazine partly to a diazonium salt is being further investigated.

Preparative electrolysis in more concentrated solutions of diazonium salts at the potential corresponding to the limiting current of waves i_1 and i_2 yielded the diaryl derivative Ar-Hg-Ar in 90% yield.

Electrolysis at the limiting current of wave i_4 at low temperature (4°C), with a moderate stirring of the mercury pool (cf. Experimental) in a buffer of pH 2 yielded 10% of the mercury derivative Ar-Hg-Ar, 8% of the symmetrical hydrazine Ar-NH-NH-Ar, and 57% of the primary hydrazine Ar-NH-NH₂ for p-CH₃ and 80% for p-OCH₃ derivatives. When conditions of electrolysis (stirring, temperature) were not optimized, up to 30% of the symmetrical hydrazine was formed.

Conclusion

Experimental evidence indicates the following sequence of reactions



Thus the present paper demonstrates formation of a primary hydrazine derivative by a direct electrochemical reduction of the corresponding diazonium fluoborate.

Lower temperature and the presence of electropositive substituents on the phenyl ring favor formation of hydrazine and minimize the importance of competitive chemical side-reactions. The scaling-up of the electrochemical synthesis of hydrazines and behavior of other substituted aromatic diazonium fluoborate are under investigation.

Acknowledgments

This work has been supported in part by the "Délégation Générale à la Recherche Scientifique et Technique." We gratefully acknowledge Dr. Petr Zuman for his help in rewriting this paper.

Manuscript submitted Feb. 26, 1980; revised manuscript received ca. March 2, 1981.

Any discussion of this paper will appear in a Discussion Section to be published in the June 1982 JOURNAL. All discussions for the June 1982 Discussion Section should be submitted by Feb. 1, 1982.

Publication costs of this article were assisted by the Université de Rouen.

REFERENCES

- R. McClure and A. Lowy, *Trans. Electrochem. Soc.*, **56**, 445 (1929).
- G. Takayanagi, *J. Chem. Soc. Jpn.*, **53**, 430 (1932).
- G. Takayanagi, *ibid.*, **57**, 64 (1936).
- E. W. Cock and W. G. France, *J. Am. Chem. Soc.*, **56**, 2225 (1934).
- F. Fichter and E. Willi, *Helv. Chim. Acta*, **17**, 1417 (1934).
- R. M. L. Eloffson, R. Edsberg, and P. Mecherly, *This Journal*, **97**, 166 (1950).
- E. R. Atkinson, H. H. Warren, P. I. Abell, and R. E. Wing, *J. Am. Chem. Soc.*, **72**, 915 (1950).
- S. Wawzonek, *Anal. Chem.*, **24**, 36 (1952).
- E. R. Atkinson, C. Garland, and A. Butler, *J. Am. Chem. Soc.*, **75**, 983 (1953).
- P. Rüetschi and G. Trümpler, *Helv. Chim. Acta*, **36**, 1649 (1953).
- J. Kochi, *J. Am. Chem. Soc.*, **77**, 3208 (1953).
- C. Calzolari and A. Furlani, *Gazz. Chim. Ital.*, **862** (1957).
- R. M. L. Eloffson, *Can. J. Chem.*, **36**, 1207 (1958).
- D. Coombs and L. L. Leveson, *Anal. Chim. Acta*, **30**, 209 (1964).
- R. M. L. Eloffson and F. F. Gadallah, *J. Org. Chem.*, **34**, 854 (1969).
- F. F. Gadallah and R. M. L. Eloffson, *ibid.*, **34**, 3335 (1969).
- M. Bailes and L. L. Leveson, *J. Chem. Soc. B*, **34**, (1970).
- R. M. L. Eloffson, F. F. Gadallah, and K. F. Schulz, *J. Org. Chem.*, **36**, 1526 (1971).
- H. Clasen and J. Cramer, (Farbwerke Hoechst) Ger. Offen. 2.157.608 cl 07 c, May 24, 1973. Appl. P. 21, 576089 44, Nov. 20, 1971.
- J. Cramer and H. Alt, (Farbwerke Hoechst) Ger. Offen. 2.305.574 cl 07 c, Aug. 8, 1974. Appl. P. 2, 305.574.5, Feb. 5, 1973.
- A. I. Vogel, in "Practical Organic Chemistry," Longman, Editor, pp. 609-611, London (1970).
- E. Laviron, *Bull. Soc. Chim.*, **10**, 3717 (1967).
- E. Laviron, *ibid.*, **5**, 2256 (1968).
- E. Laviron, *ibid.*, **4**, 1637 (1970).
- J. M. Saveant and E. Vianello, *C. R. Acad. Sci.* (1963).
- C. P. Andrieux, "Transferts d'électrons et réactions chimiques associées," Conférence de l'École d'Electrochimie du C.N.R.S., Les Houches (March 1978).

Influence of pH on the Potential Dependence of the Efficiency of Water Photo-oxidation at n-TiO₂ Electrodes

P. Salvador

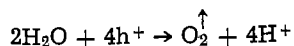
Instituto de Catálisis y Petroleoquímica, C.S.I.C., Serrano, 119, Madrid-6, Spain

ABSTRACT

The measurement of photocurrent *vs.* electrode potential at different electrolyte pH shows the quantum efficiency for water photo-oxidation to be pH dependent. These results are interpreted in terms of surface OH⁻ groups and physisorbed OH⁻ ions acting as intermediates in a double mechanism of hole trapping and charge transfer at the semiconductor/electrolyte interface. The experimental data are analyzed according to Wilson's model for the electrochemical behavior of semiconducting photoexcited electrodes, which introduces as new parameters surface electron transfer and surface recombination rates. This analysis leads to a maximum density of surface centers for charge transfer of the order of 10¹⁴ cm⁻².

The use of n-type wide-bandgap semiconducting materials as photoelectrodes in photoelectrochemical cells has been widely developed since Fujishima and Honda (1) reported in 1972 that water could be photoelectrolyzed at an n-TiO₂ electrode illuminated with u.v. light.

It is well established that water photoelectrolysis in a photoelectrochemical cell (pec) is the result of two processes. First, photons are absorbed by the semiconductor (SC) and generate electron-hole pairs. Those pairs generated within the depletion layer are separated by the electrostatic field, the electrons migrating toward the bulk and the holes toward the surface. The efficiency for the photogeneration of holes at the surface is controlled by the electronic and optical parameters of the SC (2). In a second process the holes reaching the surface react with electrons transferred from reducing species in the electrolyte. The global reaction is



The mechanisms by which the electron exchange between the SC and the electrolyte takes place are not well understood. If O₂ evolution is considered to proceed by electron tunneling through the Helmholtz layer from the electrolyte energy levels to the SC surface, only isoenergetic electron transfer is possible. Since the equilibrium redox level of the O₂/OH⁻ couple lies at the middle of the forbidden band TiO₂ (3), very small overlapping with the valence band should be expected, and very low photocurrents for O₂ evolution should be obtained. However, it is observed experimentally that quantum efficiencies near 100% can be reached (4), which suggests that a different mechanism to that of direct injection of electrons from the electrolyte to the valence band must dominate the charge-transfer process. Most authors explain such a high charge transfer efficiency as being due to surface states overlapping filled states of water molecules (1, 5). The nature of these surface states is not well known. They could be preexisting states on the SC surface inherent to the nature of the solid, e.g., structural defects. However, as suggested by Wilson (6), they could also be considered as electrolyte states sufficiently bound to the surface, so that the isoenergetic restriction on charge transfer could be relaxed.

In this paper we present experimental results dealing with the influence of the electrolyte pH on the

O₂ evolution photocurrents at TiO₂ electrodes. These results provide some new information about the mechanism of charge transfer at the SC/electrolyte interface and on the nature of the surface sites active in water photo-oxidation.

Experimental

The rutile used in this work was obtained from an anatase powder (99.9%, Degussa) by heating at 800°C for several hours. Rutile powder, pressed into a disk of 1 cm² area and 0.05 cm thickness, was sintered in air at 1200°C for 2 hr and then reduced in H₂ atmosphere at 800°C for 20 min. One side of the disk was aluminum-metallized, and a copper wire was attached to it with Ag epoxy. The contact was then sealed with epoxy resin.

The cell, built of Pyrex glass with a quartz window, consisted of the photoelectrode, a platinized Pt counter-electrode, and an SCE reference electrode. Electrolytes, from pH 6.4-13.3, were prepared from a 0.5M Na₂SO₄ solution to which different quantities of a 0.1M KOH solution were added. Bidistilled water and reagent grade chemicals were used. The photoelectrode was illuminated with a 150W Xe lamp followed by a Bausch and Lomb grating monochromator. Steady-state current *vs.* potential curves were obtained, point by point, with a microammeter and a 10⁹Ω digital millivoltmeter. To minimize possible diffusion effects near the electrode surface, the electrolyte was mechanically stirred during the experiments.

Mott-Schottky plots were used to estimate donor concentrations. Capacitance measurements of the photoelectrode/electrolyte/Pt system were carried out with a General Radio 1650A impedance bridge at 1 kHz. The electrode potentials are given *vs.* SCE.

The photon flux reaching the electrode was determined by means of a calibrated E.G. & G. 4000B silicon photovoltaic detector. Reflection losses at the cell window and electrode surface were estimated to be of the order of 10%.

Results

Photocurrent pH dependence.—Figure 1 shows typical photocurrent *vs.* electrode potential curves, at 360 nm, for different pH values. The photocurrent efficiency, η , is defined as

$$\eta = \frac{i_{(\text{light})} - i_{(\text{dark})}}{qI_0}$$

where $i_{(\text{light})}$ and $i_{(\text{dark})}$ are current densities under il-

Key words: interface charge transfer, photoelectrolysis of water, solar energy conversion.

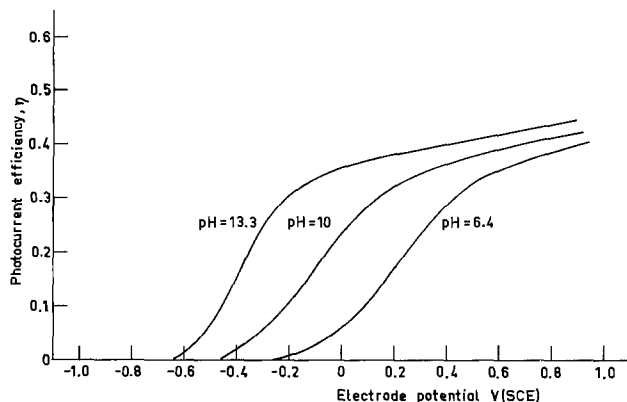


Fig. 1. Steady-state current vs. potential curves for TiO_2 at different electrolyte pH, under illumination with u.v. light ($\lambda = 360 \text{ nm}$). The pH of the electrolyte ($0.5\text{M Na}_2\text{SO}_4$ solution) was adjusted by addition of KOH.

lumination and at dark, respectively, I_0 represents the flux of photons absorbed by the electrode ($I_0 \approx 12 \times 10^{15} \text{ cm}^{-2} \cdot \text{sec}^{-1}$), and q is the electronic charge.

At constant electrode potential, η depends on the electrolyte pH. On the other hand, the potential of zero efficiency shifts toward negative values when the pH is increased. This shift is about -0.4V for a pH increase of 7 units, which is in agreement with the flatband potential shift of $-0.059\text{V}/\text{pH}$ unit expected for metal oxides (7). To compare quantum efficiencies for different pH values the curves in Fig. 1 are replotted by referring the voltage scale to the flatband potential (V_{FB}). Figure 2 shows a plot of η vs. the band bending ($V - V_{\text{FB}}$). Flatband potentials for different pH values were calculated by taking $V_{\text{FB}} = -0.9\text{V}$ vs. (SCE) for pH = 13.3 (7) and assuming that $dV_{\text{FB}}/d\text{pH} = -0.059\text{V}$. The V_{FB} values so obtained agree quite well with those measured from the Mott-Schottky plots. It can be seen in Fig. 2 that for a constant value of the band bending η increases with increasing pH. This effect has a tendency to decrease as the bands are flattened ($V \rightarrow V_{\text{FB}}$). For high band bending the pH effect seems to disappear.

Donor concentration.—For N_{D} a value of 10^{19} cm^{-3} was taken, which represents the average value of the donor concentration calculated from capacitance measurements ($N_{\text{D}} = 8.7 \times 10^{18} \text{ cm}^{-3}$) and from photocurrent spectral distribution ($N_{\text{D}} = 1.4 \times 10^{19} \text{ cm}^{-3}$) (8).

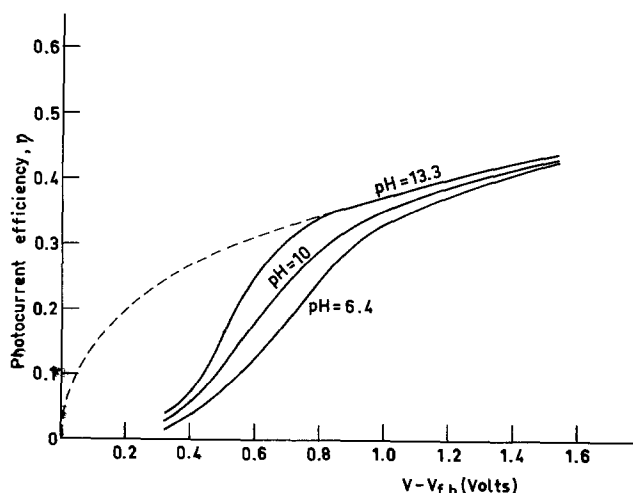


Fig. 2. Plot of photocurrent efficiencies vs. band bending from data of Fig. 1. Dotted line represents the theoretical quantum efficiency for negligible electron-hole bulk recombination (Eq. [18]).

Discussion

The TiO_2 /electrolyte interface.—It is well known that TiO_2 has a great tendency to hydration. According to Munuera *et al.* (9), in a fully hydrated anatase, the amount of adsorbed water is approximately equivalent to a monolayer of hydroxyl groups. About half a monolayer ($\approx 5 \times 10^{14} \text{ H}_2\text{O}/\text{cm}^2$) corresponds to molecular water loosely bound to the surface. Two-thirds of the remaining water ($\approx 3 \times 10^{14} \text{ OH}/\text{cm}^2$) is composed of acidic OH groups and the remaining one-third (about $2 \times 10^{14} \text{ cm}^{-2}$) are the OH^- ions, most strongly attached to the surface, with a marked basic character.

When TiO_2 is in equilibrium with an aqueous medium (electrolyte) the above situation changes. Besides the chemisorbed OH groups, OH^- and H^+ ions, whose bulk concentrations depend on pH, are specifically adsorbed. The point of zero zeta potential (pzpz) represents the pH at which the net surface charge is zero, or the concentration of adsorbed OH^- and H^+ ions is the same. For TiO_2 pzpz ≈ 5.8 (7), i.e., at this pH the potential drop in the Helmholtz layer due to adsorbed H^+ and OH^- ions is zero. Any increase of the pH above the pzpz means an increase of the number of OH^- ions adsorbed, the net surface charge becoming negative. The opposite happens for pH < 5.8, i.e., the net surface charge becomes positive because of the excess of adsorbed H^+ ions. In the first case, the potential drop across the Helmholtz layer is negative, while it is positive in the second case. The result is that the flatband potential shifts by about 0.06V per pH unit (7).

As a first approximation the Helmholtz layer can be considered as a flat capacitor, whose capacity is (10)

$$C_{\text{H}} = \frac{Q_{\text{S}}}{\phi_{\text{H}}} \quad [1]$$

where Q_{S} is the net charge adsorbed and ϕ_{H} the potential drop in the Helmholtz layer. $Q_{\text{S}} = q \cdot \Delta N_{\text{ad}}$ (electronic charge times the surface ion excess) and $\phi_{\text{H}} = \Delta V_{\text{FB}}$, so expression [1] becomes

$$C_{\text{H}} = \frac{q \cdot \Delta N_{\text{ad}}}{\Delta V_{\text{FB}}} \quad [2]$$

It must be remarked that Q_{S} is the result of an excess of both physisorbed and chemisorbed OH^- ions. Therefore, we must write $\Delta N_{\text{ad}} = \Delta N_{\text{chem}} + \Delta N_{\text{phys}}$, distinguishing the excess of surface OH^- groups, ΔN_{chem} , from the excess of physisorbed OH^- ions, ΔN_{phys} .

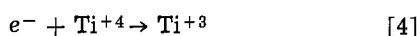
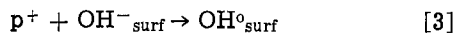
The experience with metals (11) shows that the overall differential capacitance of the double layer has a constant value determined by the oriented sheet of water dipoles in direct contact with the surface. The situation with semiconductors could be different. Recent experiments on TiO_2 electrodes (12) seem to show a small systematic variation of the Helmholtz layer capacitance with pH, from $64 \pm 20 \mu\text{F} \cdot \text{cm}^{-2}$ for pH = 2.7 to $31 \pm 10 \mu\text{F} \cdot \text{cm}^{-2}$ for pH = 13. However, in view of the large standard deviations, any conclusion about these variations is unwarranted. In any case, taking for C_{H} an average value, we can write

$$\begin{aligned} \frac{\Delta N_{\text{ad}}}{\Delta \text{pH}} &= \frac{\Delta N_{\text{ad}}}{\Delta V_{\text{FB}}} \frac{\Delta V_{\text{FB}}}{\Delta \text{pH}} = \frac{C_{\text{H}}}{q} \frac{\Delta V_{\text{FB}}}{\Delta \text{pH}} \\ &= 1.8 \times 10^{13} \text{ cm}^{-2}/\text{pH} \end{aligned}$$

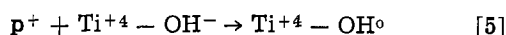
According to this, for an increase of the electrolyte pH from 6.4 to 13.3, the surface excess of OH^- ions increases by $1.2 \times 10^{14} \text{ cm}^{-2}$.

The mechanisms of charge transfer.—Among the mechanisms proposed to explain the generation of photocurrents upon absorption of u.v. light by TiO_2 , the most acceptable is, in our opinion, that in which

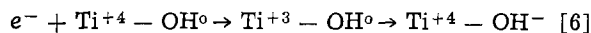
surface OH⁻ groups and Ti³⁺ ions act as hole traps and donor centers, respectively



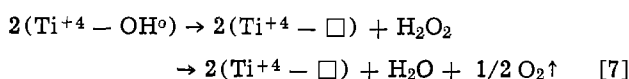
where OH⁰_{surf} denotes adsorbed OH radicals. Reaction [4] represents the bulk majority carrier process. Under high enough anodic polarization electron and holes are efficiently separated by the electric field. Holes reach the hydrated surface



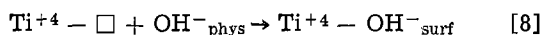
while the electrons migrate toward the bulk. However, near the flatband potential electrons can reach the surface where they could recombine with the holes



If reaction [5] prevails over [6], oxygen is evolved possibly according to the following reaction between surface OH⁰ radicals

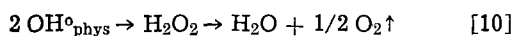
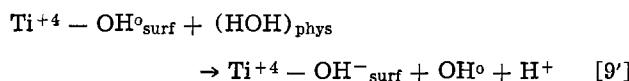
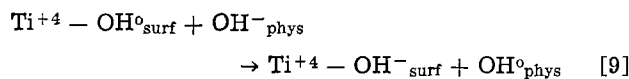


Where \square denotes OH vacancies at the surface. Afterward the vacancies will be filled by physisorbed OH⁻



and the initial state of the surface is reestablished. Experiments of irradiation of hydrated TiO₂ powders give evidence that both H₂O₂ (13, 14) and OH⁰ radicals (15) are formed on the TiO₂ surface, which point in favor of the mechanisms proposed in [5] and [7].

On the other hand, although OH⁰ radicals seem to be loosely bound to the surface (16) and can diffuse bidimensionally, leading to reaction [7], the rehydroxylation process should be too slow to explain the very high turnover number for O₂ evolution. However, this difficulty disappears if instead of surface OH⁰ radicals, either physisorbed OH⁻ or water molecules are considered to participate in a process of charge transfer (17)



According to this alternative model, surface OH⁻ groups act as intermediates for hole trapping, while physisorbed OH⁻ ions must be considered as charge carrier electrolyte species, strongly bound to the surface, participating in a process of charge transfer between the SC and the electrolyte. Electron injection from these species to the SC (surface OH⁰ radicals) could happen directly without necessity of a tunneling process (18).

The photocurrent pH dependence.—Several photoelectrochemical reactions are known where electrolyte composition has a remarkable influence on the intensity of the photocurrents. For α -Fe₂O₃ electrodes, Kennedy and Frese (19) showed that the photocurrent depends on citrate concentration according to: $\Delta\eta \propto \ln[\text{citrate}]$. These authors assumed that the photocurrent's increase was proportional to the surface coverage of citrate ions, θ , which follows a Temkin isotherm (*i.e.*, $\theta = \text{const.} + kT \ln[\text{citrate}]$), but they do not propose any mechanism to explain this effect.

In an attempt to interpret the effect of Na₂S concentration in suppressing corrosion of CdS electrodes, Wilson (20) has given a mathematical model that

treats adsorbed species as surface charge transfer states, which allows a quantitative approach to the role of adsorbed species in the charge transfer process at the SC/electrolyte interface. In addition to the semiconductor physical properties, Wilson's model takes into account, as new parameters to describe the behavior of the SC/electrolyte system, the surface recombination rate, S_r , and the interface electron transfer rate, S_t (6).

At flatband potential S_r is defined by

$$S_r = \int_{E_v}^{E_c} v \sigma_r N_r(E) dE \quad [11]$$

where E_c and E_v are the energies of the low limit of the conduction band and of the upper limit of the valence band, respectively, v is the thermal velocity of the holes, σ_r is the hole capture cross section of the recombination centers, and $N_r(E)$ is the density of recombination centers at the surface. As the band bending increases the electrons are forced to migrate toward the bulk under the space-charge electrical field, and the surface recombination rate decreases. The voltage dependence of S_r is given by (6)

$$S_r = \int_{E_v}^{E_c} \frac{v \sigma_r N_r(E) dE}{1 + \exp(E - E_f)/kT} \quad [12]$$

where q is the electronic charge, k is the Boltzmann constant, T is the absolute temperature, and E_f is the energy Fermi level at the bulk for a given applied voltage.

S_t can be described in terms of a surface density of charge transfer centers, $N_t(E)$, their cross section for interaction with holes in the valence band at the electrode surface σ_t , and the surface hole thermal velocity, v (6)

$$S_t = \int_{E_v}^{E_c} v \sigma_t N_t(E) dE \quad [13]$$

From an electrochemical point of view, N_t is a density of intermediate states for charge transfer, which can be eventually identified with adsorbed species (20).

According to the charge transfer model proposed, in our case N_t should correspond to the density of adsorbed OH⁻ groups (*i.e.*, $N_t = N_{ad}$), this being proportional to the electrolyte pH, that is, to $\log[OH^-]$. If for simplicity we suppose a single energy level for N_t , Eq. [13] can be written

$$S_t = N_{ad} \sigma_t v \quad [14]$$

The fraction of holes reaching the surface that contributes to the photocurrent, P , must be

$$P = \frac{S_t}{S_r + S_t} \quad [15]$$

where we have assumed that all the holes that reach the surface recombine either with bulk free electrons or with electrons from the electrolyte.

An estimation of P from the experimental data of Fig. 2 is not difficult. In fact, according to Eq. [15], P represents the number of holes crossing the interface, relative to the total number of holes, I , reaching the electrode surface

$$P = \frac{\eta I_0}{I} \quad [16]$$

Carrier lifetimes in TiO₂ seem to be determined by a diffusion controlled bulk recombination process, and the hole diffusion length for $(V - V_{FB}) > 0$ is negligible compared to the width of the depletion layer (8). In this case, the holes generated outside the depletion layer will not contribute significantly to the photocurrent. Moreover, as long as the hole lifetime, τ_p , is the reciprocal of the number of collisions between electrons and holes leading to recombination, the value

of τ_p should be larger in the depletion layer than in the bulk, exceeding the respective transit time value. Therefore, all the holes generated within the electrical field region should reach the interface, and I in Eq. [16] could be identified with the number of photons absorbed within the space charge layer

$$I = I_0 [1 - \exp(-W\alpha)] \quad [17]$$

α being the optical absorption coefficient and W the space charge layer width (21)

$$W = \left[\frac{2\epsilon\epsilon_0}{qN_D} (V - V_{FB}) \right]^{1/2} \quad [18]$$

where ϵ is the dielectric constant of the semiconductor and ϵ_0 the vacuum permittivity, the other parameters having been already defined. The dotted line in Fig. 2 is a plot of I/I_0 vs. $(V - V_{FB})$ (Eq. [17]). α has been taken to be 10^5 cm^{-1} at $\lambda = 360 \text{ nm}$.

From the data in Fig. 2, by applying Eq. [16], a plot of P vs. $(V - V_{FB})$ for the three different pH values used is obtained (Fig. 3). As can be seen, at a given pH, P decreases as $(V - V_{FB})$ decreases which was expected according to Eq. [12]. Moreover, for low band bending $S_r > S_t$, which is in agreement with the statement that, in this situation, surface recombination is the dominant reaction (6). By contrast, at high enough band bending, the influence of S_r virtually disappears, and a situation dominated by charge transfer is established. An intermediate situation is that for $S_r = S_t$ ($P = 0.5$), whose analysis is very simple. In fact, from Eq. [15], for $S = S_t$, we can write

$$\left(\frac{dP}{dpH} \right)_{pH=6.4} = \frac{1}{4S_t} \left(\frac{dS_t}{dpH} - \frac{dS_r}{dpH} \right)_{pH=6.4} \quad [19]$$

From Fig. 3 a plot of P vs. pH for different values of $V - V_{FB}$ is shown in Fig. 4. As can be seen the dependence is practically linear.

Let us now analyze with detail the experimental data of Fig. 4 by using Eq. [19]. For $(V - V_{FB}) = 0.6$ and $pH = 7.8$ it is $P = 0.5$ and Eq. [19] becomes

$$\begin{aligned} \left(\frac{dP}{dpH} \right)_{(V-V_{FB})=0.6} &= 0.06 \\ &= \frac{1}{4} \frac{1}{(S_t)_{pH=7.85}} \left(\frac{dS_t}{dpH} - \frac{dS_r}{dpH} \right)_{(V-V_{FB})=0.6} \end{aligned} \quad [20]$$

Equation [19] also applies for $(V - V_{FB}) = 0.5$ and $pH = 12.3$; therefore we can write

$$\begin{aligned} \left(\frac{dP}{dpH} \right)_{(V-V_{FB})=0.5} &= 0.042 \\ &= \frac{1}{4} \left(\frac{1}{S_t} \right)_{pH=12.3} \left(\frac{dS_t}{dpH} - \frac{dS_r}{dpH} \right)_{(V-V_{FB})=0.5} \end{aligned} \quad [21]$$

According to Eq. [14], we know that $dS_t/dpH = dN_{ad}/dpHv$. The hole capture cross section of surface states is, according to Wilson (22), between 10^{-16} and 10^{-17} cm^2 . This value is considerably smaller than that obtained from geometrical considerations if surface states were localized on single atoms, probably due to poor electronic or phonon coupling between the states and the semiconductor (22). A value of $v = 10^7 \text{ cm/sec}$ can be taken for hole thermal velocity. So, we have

$$\frac{dS_t}{dpH} \approx 1.8 \times 10^3 \text{ cm/sec} \quad [22]$$

Experiments with electrodes with different doping levels seem to show that S_t does not depend on the voltage through the surface field. Therefore, Eq. [22] is considered to be valid for any $(V - V_{FB})$ value.

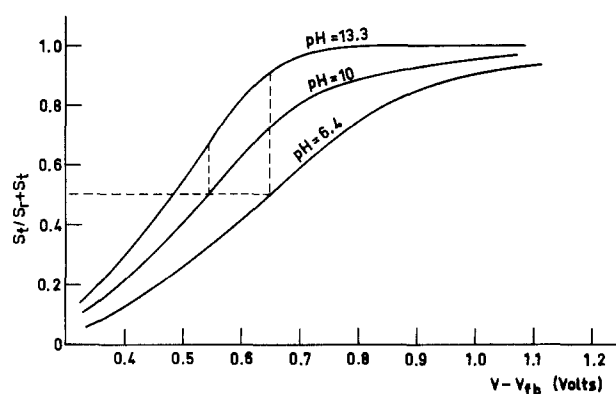


Fig. 3. Plot of the fraction P of holes contributing to the photocurrent (S_t), relative to the number of holes reaching the SC/electrolyte interface ($S_r + S_t$), vs. voltage, for different pH values, calculated from data of Fig. 2.

With respect to dS_r/dpH , the question arising is whether surface states involved in the charge transfer process are, to some extent, responsible for surface recombination. According to Wilson (22), adsorbed species could act as recombination centers, which means that S_r may be increased by adsorption ($dS_r/dpH > 0$). However, there is the possibility that recombination centers were related to preexisting surface states inherent to the solid on which adsorption takes place. In this case, it should be $dS_r/dpH < 0$. In both cases a linear dependence of S_r on pH should be expected. Finally, it could happen that $dS_r/dpH = 0$, i.e., that surface recombination is unaffected by adsorption of electrolyte species.

Let us calculate S_t from Eq. [20] and [21] for different values of dS_r/dpH . This is shown in Table I. As can be seen the only values of dS_r/dpH leading to reasonable values of S_t are those for either $dS_r/dpH = 0$ or $dS_r/dpH > dS_t/dpH \geq 0$. However, the best agreement between $(S_t)_{pH=7.85}$ and $(S_t)_{pH=12.3}$ is obtained for $dS_r/dpH \approx -10^{-3} \text{ cm/sec}$.

On the other hand, for small values of P , i.e., for $S_r \gg S_t$, derivation of Eq. [15] leads to the following approximation

$$\frac{dP}{dpH} = \left(\frac{1}{S_t} \frac{dS_t}{dpH} - \frac{1}{S_r} \frac{dS_r}{dpH} \right) \frac{S_t}{S_r} \quad [23]$$

For $pH = 7.85$ and $(V - V_{FB}) = 0.35$, we have in Fig. 4 $P \approx 0.1$, and Eq. [23] should apply. Therefore we can write

$$\begin{aligned} \frac{dP}{dpH_{(V-V_{FB})=0.35}} = 0.014 &= \left[\left(\frac{1}{S_t} \right)_{pH=7.85} \left(\frac{dS_t}{dpH} \right) \right. \\ &\quad \left. - \left(\frac{1}{S_r} \right)_{pH=7.85} \left(\frac{dS_r}{dpH} \right) \right] \times 0.11 \end{aligned} \quad [24]$$

that can also be used to calculate $(S_t)_{pH=7.85}$. The results are included in the last column of Table I. As we supposed that S_t does not depend on the applied voltage, the correct value of dS_r/dpH should be that giving the best agreement between the two values of $(S_t)_{pH=7.85}$ obtained from Eq. [20] and [23], respectively. This is reached again for $dS_r/dpH \approx -10^{-3} \text{ cm/sec}$. According to Table I the corresponding values for S_t are $(S_t)_{pH=7.85} \approx 10^4 \text{ cm/sec}$ and $(S_t)_{pH=12.3} \approx 2 \times 10^4 \text{ cm/sec}$. Therefore, the maximum value of S_t for $pH = 14$, should be of the order of 10^4 - 10^5 cm/sec , corresponding to a maximum density of surface states for charge transfer $(N_{ad})_{max} \approx 10^{14} \text{ cm}^{-2}$. This value is in quite good agreement with the density of bandgap surface states obtained by Wilson (22), which comes to reinforce the idea that these could be intermediates of the reaction leading to O_2 evolution.

Table I. Values of dS_r/dpH and S_t compared with Eq. [20], [21], and [23], calculated from experimental data of Fig. 4

| | 1 | 2 | 3 | 4 | 5 |
|---|--------------------------------|---|---|---|--|
| | $\frac{dS_r}{dpH}$ (cm/sec) | $(S_t)_{pH=7.85}$ ($V - V_{FB}$) = 0.6 (cm/sec) | $(S_t)_{pH=12.3}$ ($V - V_{FB}$) = 0.6 (cm/sec) | $(S_t)_{pH=12.3}$ ($V - V_{FB}$) = 0.5 (cm/sec) | $(S_t)_{pH=7.85}$ ($V - V_{FB}$) = 0.35 (cm/sec) |
| $\frac{dS_r}{dpH} > \frac{dS_t}{dpH}$ | 10^6 | -4×10^5 | | -5.8×10^5 | -1.6×10^4 |
| $\frac{dS_r}{dpH} = \frac{dS_t}{dpH}$ | 10^4 | -3.4×10^4 | | -4.9×10^5 | 4.7×10^5 |
| $0 < \frac{dS_r}{dpH} < \frac{dS_t}{dpH}$ | 5×10^3 | -1.3×10^4 | | -1.9×10^4 | 8.3×10^5 |
| $0 > \frac{dS_r}{dpH} > \frac{dS_t}{dpH}$ | 1.8×10^3 | 0 | | 0 | 1.07×10^4 |
| | 1.2×10^3 | 2.5×10^3 | 1.05×10^4 | 3.6×10^3 | 1.1×10^4 |
| | 10^3 | 3.3×10^3 | 1.1×10^4 | 4.7×10^3 | 1.1×10^4 |
| | 10^2 | 7.1×10^3 | 1.5×10^4 | 9.0×10^3 | 1.2×10^4 |
| | 10^1 | 7.4×10^3 | 1.5×10^4 | 1.06×10^4 | 1.2×10^4 |
| | 0 | 7.5×10^3 | 1.5×10^4 | 1.07×10^4 | 1.2×10^4 |
| | -10^{-1} | 7.5×10^3 | 1.6×10^4 | 1.06×10^4 | 1.2×10^4 |
| | -10^{-2} | 7.9×10^3 | 1.9×10^4 | 1.1×10^4 | 1.2×10^4 |
| | -10^{-3} | 1.1×10^4 | 2.3×10^4 | 1.7×10^4 | 1.3×10^4 |
| | -1.8×10^{-3} | 1.5×10^4 | 2.3×10^4 | 2.1×10^4 | 1.3×10^4 |
| | -10^{-4} | 4.9×10^4 | 4.3×10^6 | 6.2×10^4 | 1.9×10^4 |
| | -10^{-5} | 4.2×10^5 | | 6.05×10^5 | 8.5×10^4 |

Column 1. Hypothetical values.

Column 2. Values of S_t obtained from Eq. [20].

Column 3. Values of S_t obtained from column 2 by adding $S_t = 8 \times 10^3$ cm/sec.

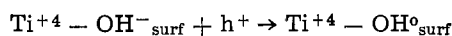
Column 4. Values of S_t obtained from Eq. [21].

Column 5. Values of S_t obtained from Eq. [23].

On the other hand, the maximum value for S_r near flatband must be at least two or three orders of magnitude greater than S_t . This implies a density of states for surface recombination greater than N_{ad} and, probably, the participation of a new type of recombination center, unless $\sigma_r > \sigma_t$. However, if we assume that $\sigma_r = \sigma_t$, the fact that $0 > dS_r/dpH \approx -dS_t/dpH$ seems to indicate that surface recombination centers are destroyed by adsorption of electrolyte species at about the same rate that surface states for charge transfer are formed.

Conclusions

The experimental results reported in this paper, concerning the pH dependence of the photocurrents associated with the process of water photo-oxidation at TiO_2 electrodes, have been used to postulate a mechanism of charge transfer at the SC-electrolyte interface. This mechanism involves two steps. The first step involves surface hydroxyls (basic OH^-) as traps for holes generated by light, giving rise to the formation of OH° radicals according to the reaction



In a second step one electron is transferred from one physisorbed electrolyte species (OH^-)_{phys} to an OH°_{surf} radical

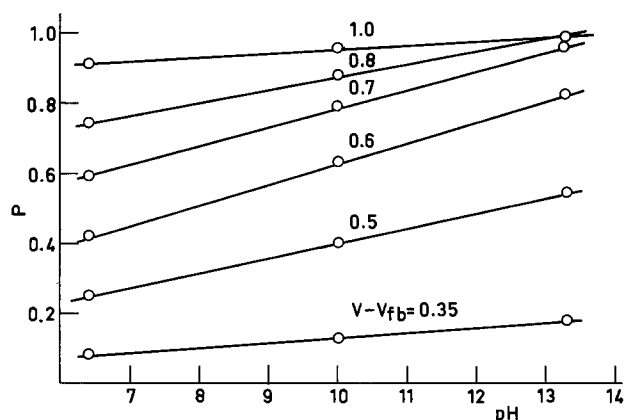
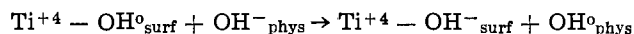


Fig. 4. Plot of P vs. pH for different values of $(V - V_{FB})$ from data of Fig. 3.

followed by reaction among adsorbed OH°_{phys} radicals and evolution of oxygen.

Adsorbed OH^- groups are considered as surface centers for charge transfer. The surface excess of these centers, N_{ad} , depends on the electrolyte pH, which accounts for the pH dependence of the photocurrent. A simple mathematical treatment of these results making use of surface recombination and surface electron transfer parameters as defined by Wilson (6), shows that the maximum surface concentration of such surface centers for charge transfer is of the order of 10^{14} cm^{-2} .

From a recent XPS study of hydrated rutile surfaces (23), evidence of two types of surface OH species (acid and basic) has been obtained. The O 1s and Ti 2p binding energies seem to indicate that the formation of OH° radicals (reaction [1]) is easier from the basic OH^- groups singly bonded to Ti, because of the significant covalent character of this bond. An analogous conclusion about the role of chemisorbed basic OH^- in OH° radical formation is also reached from experiments of photoadsorption-photodesorption of oxygen on TiO_2 hydroxylated surfaces (16). Accordingly, the density of surface centers active in hole capture should be of the order of 10^{14} cm^{-2} (9), which is in agreement with our maximum density of surface centers for charge transfer. On the other hand, it seems reasonable to believe that, due to the higher covalent character of the Ti-OH bond involving basic OH groups, the energy of their valence bonding orbitals should be lowered with respect to the O 2p level of surface oxygens doubly bonded to Ti. Therefore, the energy levels of these surface states should be somewhere in the band-gap, better overlapping the OH^-/O_2 redox level, and so allowing a more efficient isoenergetic charge transfer between SC and electrolyte.

With respect to the nature of surface recombination centers our experimental results do not allow any conclusion. It is probable that adsorbed OH° radicals could behave as surface centers for recombination at or near the flatband situation (22). However, the participation of the other kind of centers, associated for instance to structural defects, in the process of surface recombination is necessary. This type of center seems to be blocked by adsorption of electrolyte species, thus contributing to a more rapid increase of the fraction of holes participating in photocurrent when the electrolyte pH is raised.

Acknowledgments

The author is indebted to Dr. R. H. Wilson for a critical reading of the manuscript. Thanks are due to Dr. J. C. Conesa for helpful discussions.

Manuscript submitted May 12, 1980; revised manuscript received ca. March 12, 1981.

Any discussion of this paper will appear in a Discussion Section to be published in the June 1982 JOURNAL. All discussions for the June 1982 Discussion Section should be submitted by Feb. 1, 1982.

Publication costs of this article were assisted by the Instituto de Catálisis y Petroleoquímica, C.S.I.C.

REFERENCES

1. A. Fujishima and K. Honda, *Nature (London)*, **238**, 37 (1972).
2. H. A. Butler, *J. Appl. Phys.*, **48**, 1914 (1977).
3. R. Memming, in "Semiconductor Liquid-Junction Solar Cells," A. Heller, Editor, p. 38, The Electrochemical Society Softbound Proceedings Series, Princeton, NJ (1977).
4. J. G. Mavroides, D. I. Tchernev, J. A. Kafalas, and D. F. Kolesar, *Mater. Res. Bull.*, **10**, 1023 (1975).
5. H. Gerischer, *J. Electroanal. Chem. Interfacial Electrochem.*, **82**, 133 (1977).
6. R. H. Wilson, *J. Appl. Phys.*, **48**, 4292 (1977).
7. M. A. Butler and D. S. Ginley, *This Journal*, **125**, 228 (1978).
8. P. Salvador, *Solid State Commun.*, **34**, 1 (1980).
9. G. Munuera, V. Rives-Arnau, and A. Saucedo, *J. Chem. Soc., Faraday Trans. 1*, **75**, 736 (1979).
10. H. Gerischer, in "Physical Chemistry: An Advanced Treatise," H. Eyring *et al.*, Editors, p. 475, Academic Press, New York (1970).
11. J. O'M. Bockris and D. M. Dravić, "Electro-Chemical Science," Taylor & Francis Ltd., London (1972).
12. M. Tomkewicz, *This Journal*, **126**, 1505 (1979).
13. S. P. Pappas and R. M. Fischer, *J. Paint. Technol.*, **46**, 65 (1974).
14. R. J. Bickley and V. Vishwanathan, *Nature (London)*, **280**, 306 (1979).
15. H. G. Völtz, G. Kämpf, and H. G. Fitzky, *Farbe U. Kack.*, **78**, 1037 (1972).
16. A. R. González-Elipe, G. Munuera, and J. Soria, *J. Chem. Soc., Faraday Trans. 1*, **75**, 748 (1979).
17. H. Van Damme and W. K. Hall, *J. Am. Chem. Soc.*, **101**, 4373 (1979).
18. F. Williams and A. J. Nozik, *Nature*, **271**, 137 (1978).
19. J. H. Kennedy and K. W. Frese, *This Journal*, **125**, 709 (1978).
20. R. H. Wilson, *ibid.*, **126**, 1187 (1979).
21. H. Gerischer, *Electroanal. Chem. Interfacial Electrochem.*, **58**, 263 (1975).
22. R. H. Wilson, *This Journal*, **127**, 228 (1980).
23. T. K. Sham and M. S. Lazarus, *Chem. Phys. Lett.*, **68**, 426 (1979).

Ruthenium-Based Mixed Oxides as Electrocatalysts for Oxygen Evolution in Acid Electrolytes

R. S. Yeo,^{*1} J. Orehtsky,^{*} W. Visscher,^{*} and S. Srinivasan^{*,2}

Department of Energy and Environment, Brookhaven National Laboratory, Upton, New York 11973

ABSTRACT

Ruthenium oxide, prepared by the thermal decomposition method, has the highest known initial electrocatalytic activity for oxygen evolution in acid electrolyte. However, this material is not stable in the electrolyte and at the same time exhibits a significant increase of oxygen overpotential with time, probably due to a chemical transformation of the oxide from a lower to a higher valence state. Efforts were made to stabilize ruthenium by preparing mixed oxides with Ir and/or Ta using the thermal decomposition method. The electrocatalytic activities for oxygen evolution on these oxides in 1N H₂SO₄ were determined using the potentiostatic method. The surface areas of these oxides were estimated using cyclic voltammetry. Dual Tafel slopes (approximately 30 and 40 mV) were found on most of these oxides. The ternary oxide (RuIr_{0.5}Ta_{0.5}O_x) exhibited a single Tafel slope of 30 mV, had the lowest overpotential, and showed minimum variation of overpotential with time.

Ruthenium oxide, produced by the thermal decomposition method (1), is one of the best electrocatalysts for chlorine evolution (2-5) and is being increasingly used as the anode in chlor-alkali cells (6). Ruthenium oxide exhibits the lowest overpotential initially for oxygen evolution (7-13) but this oxide is not stable in acidic environments and also the oxygen overpotential increases with time (14-16). Numerous plausible explanations have been proposed for these observations. The most likely one involves a consideration of the stoichiometry of this oxide material and of the associated valency state of the ruthenium cations.

Ruthenium oxide produced by the thermal decomposition procedure is suggested to exist in a substoichiometric RuO_x (x < 2) oxidation state (17-19) and the favorable electrocatalytic activity might then result from the mixed Ru³⁺-Ru⁴⁺ cationic valencies present in this substoichiometric oxide. Since the metastable RuO_x is suspected to transform to the stable RuO₂ stoichiometry with its full complement of quadrivalent ruthenium cations, the observed degradation during oxygen evolution conceivably could result from the gradual oxidation of the trivalent ruthenium cations. This explanation appears reasonable since RuO₂ is not a particularly attractive electrode material for oxygen evolution (20). It also implies that a nondegradable electrocatalytically active ruthenium oxide anode can be realized if the ruthenium cation can be stabilized in a mixed III-IV valency state.

* Electrochemical Society Active Member.

¹ Present address: The Continental Group, Incorporated, Energy Systems Laboratory, Cupertino, California 95014.

² Present address: Los Alamos National Laboratory, Los Alamos, New Mexico 87545.

Key words: electrocatalysis, oxygen evolution, ruthenium-based mixed oxides, defect oxides, dual Tafel slopes.

Stabilization of mixed cation valency states frequently occurs in binary or ternary stoichiometric oxide compounds. Unfortunately, there are no reported oxide compounds where the ruthenium cations exist in the III-IV state (21). The objectives of this investigation were to fabricate several potentially promising equilibrium binary and ternary oxide compounds where the ruthenium cations hopefully exist in the mixed III-IV state and then to determine both the electrocatalytic activity and stability of these materials. Selecting the appropriate components for the binary and ternary compounds was a difficult task particularly because very little information is available about oxides that form compounds with ruthenium oxide (21-22) and, of the known compounds, the ruthenium cations usually exist in an oxidation state of four or more. Binary and ternary oxides containing ruthenium, iridium, and tantalum as the cationic constituents were used in this particular study. Tantalum was selected for its potential ability to stabilize the III-IV ruthenium valency state and for its corrosion resistance in an acid electrolytic medium (23). Iridium was chosen because of its reported electrochemical stability during oxygen evolution and because it is a possible agent for alloying tantalum and ruthenium oxides which appear to be immiscible as simple binaries.

Experimental

Electrode preparation.—Six titanium supported oxide electrodes of nominal compositions, RuO_x , IrO_x , RuTaO_x , IrRuO_x , $\text{RuTa}_{0.5}\text{Ir}_{0.5}\text{O}_x$, and $\text{Ru}_{0.5}\text{TaIr}_{0.5}\text{O}_x$ were prepared by the thermal decomposition method, similar to that reported in the patent literature (1) for the DSA anodes used in the chlor-alkali industry. The metal chloride salts were dissolved in the following manner: $\text{RuCl}_3 \cdot 1\text{-}3\text{H}_2\text{O}$ could easily be dissolved in either isopropyl alcohol or water, whereas $\text{IrCl}_3 \cdot 3\text{H}_2\text{O}$ was dissolved in isopropyl alcohol with addition of few drops of H_2O_2 . Some difficulties were found in preparing an aqueous solution of TaCl_5 . However, it could be dissolved in nonaqueous solvents (such as isopropyl alcohol). These metal chloride solutions were then mixed in the appropriate molar proportions to form solutions of the desired electrode compositions. The electrodes were formed by dipping titanium support structures into these solutions, heating the wetted structures over a hot plate to dryness, and then baking the structures in air at 350°C for 5 min. This dipping, drying, and baking procedure was repeated seven times. Each electrode was then heated in air at 350°C for 3 hr. The support structure consisted of a titanium foil $0.5 \times 1.0 \times 0.0025$ cm, that was wet polished on number 600 Emery paper and then spot-welded to a 0.1 cm diam titanium wire. These titanium assemblies were cleaned in acetone and dilute hydrochloric acid before dipping into the appropriate solution for the thermal decomposition treatment. The titanium wire was then masked off with shrinkable Teflon tubing.

For comparative purposes, two proprietary oxygen evolution anode electrocatalysts WE-3 and E-50, provided by the General Electric Company, were also studied. These two materials were supplied in a finely divided powder form and they were fabricated into electrodes by Teflon bonding (24) onto a 52 mesh platinum screen. The dimensions of the screen were 0.8×1.2 cm.

Electrochemical studies.—The kinetic parameters for oxygen evolution were determined on the resulting electrodes in $1\text{N H}_2\text{SO}_4$ solution at 25°C from steady-state potentiostatic measurements employing a PAR 371 potentiostat.³ For each measurement, the current interruptor technique (25) was used to correct for the

IR loss in the electrolyte. The electrolyte was prepared from analytical grade sulfuric acid and double distilled water. Nitrogen was continuously bubbled through the electrolyte. A platinum foil served as the counterelectrode and saturated calomel electrode (SCE) was employed as a reference. The entire electrochemical assembly was housed in a Teflon cell previously described (26).

The surface areas of the electrodes were crudely estimated using the cyclic voltammetric technique, as described in the Results section. The estimated surface areas were used to convert current readings to apparent current density values.

The time variation of electrocatalytic activity of these titanium supported materials during oxygen evolution was evaluated galvanostatically. Each electrode material was maintained at a constant current of 50 mA while the resulting potential was monitored as a function of time.

Results

The Tafel plots for oxygen evolution on the various electrode materials are presented in Fig. 1 and 2, whereas the Tafel parameters are summarized in Table I. The performance of RuO_x electrode is better than that of IrO_x and of the binary oxide electrodes (IrRuO_x and RuTaO_x). On the other hand, the electrocatalytic activity of RuO_x improves as it forms a ternary oxide ($\text{Ru}_{0.5}\text{Ir}_{0.5}\text{TaO}_x$ and $\text{RuIr}_{0.5}\text{Ta}_{0.5}\text{O}_x$) by alloying with both iridium and tantalum. Further, the electrocatalytic activity of the E-50 electrode is less than that of the WE-3 and the mixed oxide electrodes. The $\text{RuTa}_{0.5}\text{Ir}_{0.5}\text{O}_x$ electrode showed a single Tafel slope of 30 mV, while all the remaining electrode materials exhibited dual Tafel slopes (Fig. 1 and 2, Table I). The initial Tafel slope is typically about 30 mV for all the electrodes except IrO_x and the proprietary E-50 anode for which initial Tafel regions had a slope of

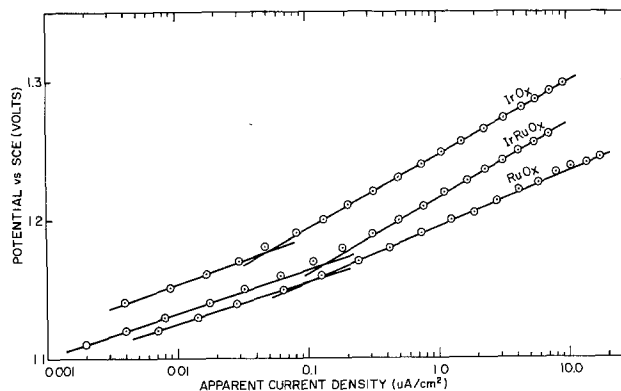


Fig. 1. Tafel plots for oxygen evolution on IrO_x , IrRuO_x , and RuO_x in $1.0\text{N H}_2\text{SO}_4$ at 25°C .

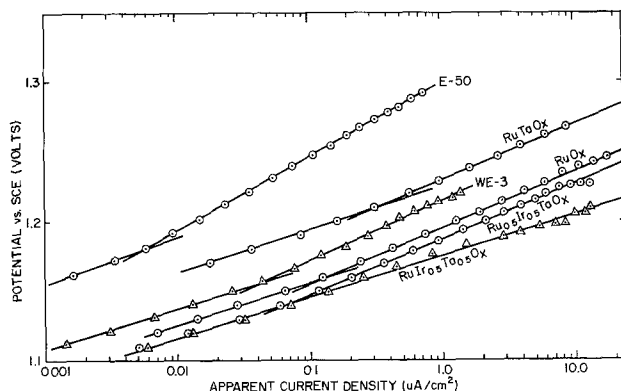


Fig. 2. Tafel plots for oxygen evolution on RuO_x , RuTaO_x , $\text{Ru}_{0.5}\text{Ir}_{0.5}\text{TaO}_x$, and $\text{RuIr}_{0.5}\text{Ta}_{0.5}\text{O}_x$ in $1.0\text{N H}_2\text{SO}_4$ at 25°C .

³ The time taken to reach a pseudosteady current at each potential varied from 5 to 10 min.

Table I. Kinetic parameters for oxygen evolution in 1N H₂SO₄ at 25°C

| Electrode | Tafel slope, mV | | Apparent exchange current density, A/cm ² | |
|--|-----------------|-------------|--|---------------------|
| | Low η | High η | Low η | High η |
| RuO ₂ | 32 | 42 | 7×10^{-13} | 1×10^{-11} |
| RuTaO ₂ | 30 | 40 | 7×10^{-14} | 2×10^{-12} |
| RuIrO ₂ | 30 | 40 | 4×10^{-14} | 2×10^{-10} |
| Ru _{0.5} Ir _{0.5} TaO ₂ | 30 | 40 | 4×10^{-12} | 2×10^{-11} |
| Ru _{0.5} Ta _{0.5} O ₂ | 30 | — | 1×10^{-12} | — |
| IrO ₂ | 35 | 55 | 4×10^{-13} | 3×10^{-11} |
| WE-3 | 30 | 42 | 4×10^{-13} | 9×10^{-12} |
| E-50 | 35 | 55 | 5×10^{-14} | 2×10^{-12} |

about 35 mV. The second Tafel slope is about 40 mV for all the electrodes except IrO₂, RuIrO₂, and E-50, which have a second Tafel region with a slope of 55 mV. The surprising and noteworthy feature of the Tafel plots is that the overpotential for oxygen evolution is greater for the RuTa and RuIr oxides and less for the ternary RuIrTa oxides than it is for ruthenium oxide. This aspect of the data is reflected in the apparent exchange current densities, which have been determined for each electrode by a Tafel slope extrapolation and are also presented in Table I.

The active surface areas of the electrode were estimated using cyclic voltammetry (27). Initially, a potential sweep at 50 mV/sec was performed on each electrode between the hydrogen and oxygen evolution regions and a typical response is presented in Fig. 3. The voltammetric profiles are generally void of any distinctive features and the display did not indicate any obvious double layer charging region, reminiscent of the response on platinum which enables the calculation of true surface area. Cyclic voltammograms, limited to a 50 mV potential range, were employed to obtain a crude estimate of the surface areas of each electrode. The best results, where the anodic and cathodic currents were equal in magnitude and the capacitive current was linear with the sweep rate, were obtained when these limited range cyclic voltammograms were performed around the rest potential of each electrode. A typical sequence of cyclic voltammograms at various sweep rates and the associated current dependence on the sweep rate are presented in Fig. 4 and 5, respectively. The apparent capacitances and the roughness factors of each electrode were evaluated from these cyclic voltammograms and the results are listed in Table II. The roughness factors were determined by assuming a double layer capacitance of $2(10^{-5})$ f/cm² for a smooth surface. It is interesting to note that the roughness factor of these mixed oxide electrodes increases progressively from single to binary to ternary oxides. Also, the roughness factors of both E-50 and WE-3 electrodes are at least ten times higher than that of the mixed oxide electrodes prepared by thermal decomposition method.

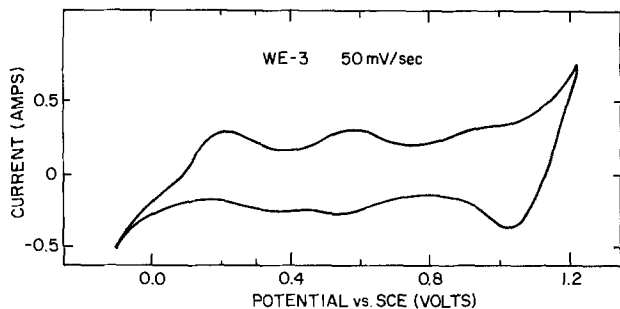
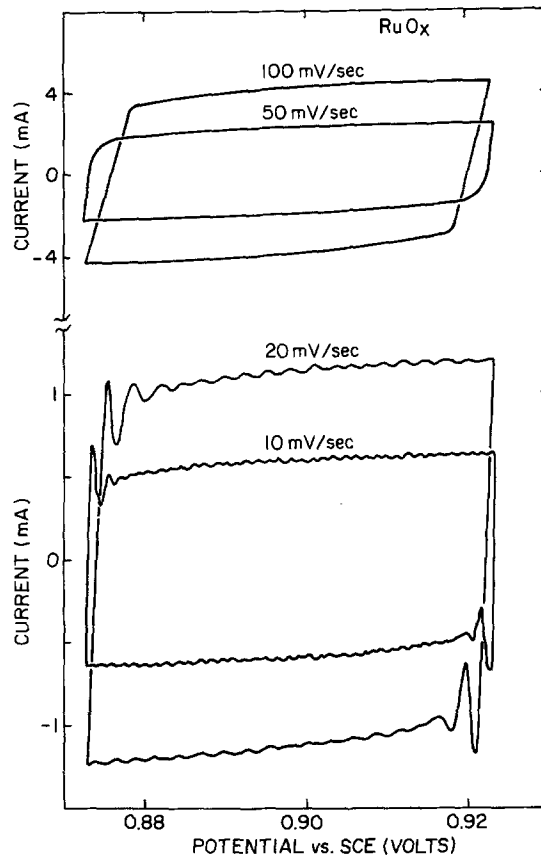
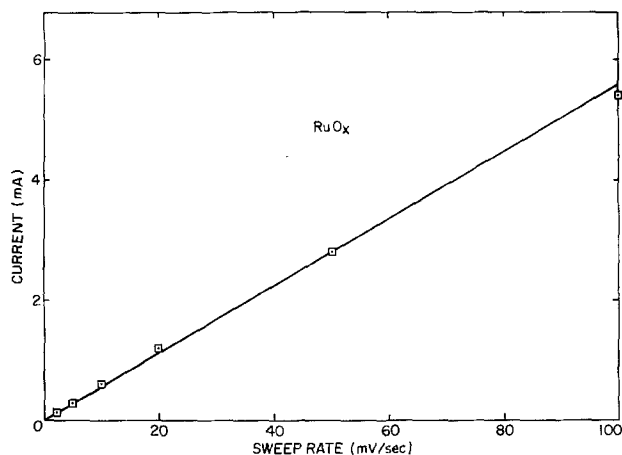

 Fig. 3. Cyclic *i*-V curve for WE-3 electrode in N₂-saturated 1.0N H₂SO₄ at 25°C.

 Fig. 4. Cyclic voltammograms for RuO_x electrode in N₂-saturated 1.0N H₂SO₄ at four sweep rates and at 25°C.


Fig. 5. Capacitive charging current (from Fig. 4) vs. sweep rate.

The time variations of overpotentials for oxygen evolutions on materials at a constant current are presented in Fig. 6. The normalized overpotential is the ratio of overpotential at time *t*, to the initial overpotential at time zero. These plots illustrate that the electrocatalytic activities of both the binary and ternary oxides are considerably more stable than that of ruthenium oxide.

Discussion

Any comparison of the electrocatalytic activity of these anode materials is critically dependent on an accurate determination of the surface area. The surface area of each electrode material was estimated from the limited range cyclic voltammograms. The resulting apparent surface areas, determined by this technique, were unexpectedly and incredibly large. This is evident from our reported roughness factors (Table II), which are sometimes orders of magnitude larger

Table II. Measured capacitance and calculated roughness factor of various electrodes

| Electrode | Capacitance, f/cm ² | Calculated roughness factor |
|--|--------------------------------|-----------------------------|
| IrO _x | 0.04 | 2 × 10 ³ |
| RuO _x | 0.056 | 3 × 10 ³ |
| RuTaO _x | 0.16 | 8 × 10 ³ |
| RuIrO _x | 0.16 | 8 × 10 ³ |
| RuIr _{0.5} Ta _{0.5} O _x | 0.2 | 1 × 10 ⁴ |
| Ru _{0.5} Ir _{0.5} TaO _x | 0.4 | 2 × 10 ⁴ |
| WE-3 | 4.0 | 2 × 10 ⁶ |
| E-50 | 4.0 | 2 × 10 ⁶ |

than the values of 10-700 commonly reported in the literature for thermally decomposed ruthenium oxide (3, 20, 27, 28). The magnitude of our roughness factors are unacceptably high and are not considered to be correct even though the limited range cyclic voltammograms are inversely symmetric and the charging current is linearly related to the sweep rate. The apparent surface areas determined from the cyclic voltammograms are thus considerably higher than the true surface areas, making the calculated exchange current densities considerably smaller than the true current densities which could not be determined. The abnormally large roughness factor probably results from pseudocapacitance, though one may assume that this pseudocapacitance is directly related to the true surface area. The reproducibility of the experiments were supportive of this assumption since different electrodes of the same oxide material with significantly different roughness factors have identical and superimposable potential-apparent current density plots. This suggests that the relative values of the surface areas and roughness factors determined by the cyclic voltammograms are correct even though their absolute values may be incorrect and establish that of all the materials examined for oxygen evolution the two ternary oxides are the best electrocatalysts for oxygen evolution over the entire current range tested.

As is seen from Table II, the surface roughness of both WE-3 and E-50 electrodes are about 100 times larger than that of either RuO_x or IrO_x. The high surface areas of these electrodes probably accounts for the low cell potentials in water electrolyzers using these anode catalysts (29). Also, the better electrocatalytic activity of WE-3 over that of E-50 is consistent with the results reported elsewhere (29).

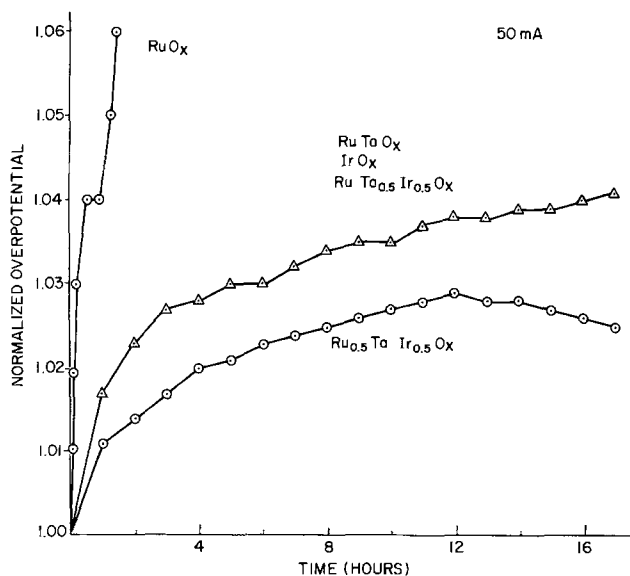


Fig. 6. Normalized overpotential vs. time for various electrodes at 25°C. Normalized overpotential = η_t/η_0 , where η_t and η_0 are overpotential at time t and zero, respectively.

The kinetic parameter that is free from uncertainties in the surface area and can be presented clearly and unambiguously is the Tafel slope. A dual Tafel slope was observed on all the oxide electrodes except for RuTa_{0.5}Ir_{0.5}O_x. Dual Tafel slopes have been observed previously (30) for oxygen evolution on thermally decomposed ruthenium oxide where the initial Tafel slope was reported to be between 30 and 40 mV depending on the pH of the electrolyte. The second Tafel slope was reported to be about 80 mV in an acid electrolyte and this is not at all consistent with our results on ruthenium oxide. The dual 30 and 40 mV slopes, apparent in most of our oxide electrodes containing ruthenium cations, are not consistent with any predicted values associated with the various mechanisms commonly proposed for the oxygen evolution reaction (31). Various mechanistic reaction sequences, consistent with a 30 and 40 mV dual Tafel slope response, are currently being investigated.

Finally, the time variation of overpotential for oxygen evolution at a constant current of 50 mA (Fig. 6) clearly shows that the binary and ternary oxides are electrocatalytically more stable than ruthenium oxide. The time dependence of the overpotential was approximately the same for the other oxide stoichiometries except Ru_{0.5}TaIr_{0.5}O_x which appeared to have a very slight stability advantage.

In conclusion, it is shown that the electrocatalytic activity of ruthenium oxide can be improved and stabilized in acid electrolyte by alloying with iridium and tantalum, probably because the ruthenium cations in these mixed oxides can exist in the III-IV state and remain in such mixed valencies over long periods of time. The existence of III-IV ruthenium cations and its relationship to the electrocatalytic activity awaits a detailed study of both the surface states and the phase diagram of the IrTaRu oxide system.

Acknowledgments

The authors wish to thank Dr. C. R. Davidson and Mr. J. H. Russell of the General Electric Company, Wilmington, Massachusetts for the supply of the proprietary catalyst (E-50 and WE-3) and for their helpful discussions. This work was carried out under the auspices of the United States Department of Energy. Dr. J. Orehtsky and Dr. W. Visscher were Visiting Scientists at BNL in the summer of 1979 from Wilkes College, Wilkes-Barre, Pennsylvania and the Technological University, Eindhoven, The Netherlands, respectively.

Manuscript submitted June 30, 1980; revised manuscript received Jan. 23, 1981.

Any discussion of this paper will appear in a Discussion Section to be published in the June 1982 JOURNAL. All discussions for the June 1982 Discussion Section should be submitted by Feb. 1, 1982.

Publication costs of this article were assisted by Brookhaven National Laboratory.

REFERENCES

- H. B. Beer, South African Pat. 662,667 (1966); 680,034 (1968).
- R. G. Erenburg, L. I. Krishtalik, and V. I. Bystrov, *Elektrokhimiya*, **8**, 1740 (1972).
- A. T. Kuhn and C. J. Mortimer, *This Journal*, **120**, 231 (1973).
- T. Arikado, C. Iwakura, and H. Tamura, *Electrochim. Acta*, **23**, 9 (1978).
- R. S. Yeo, J. McBreen, A. C. C. Tseung, S. Srinivasan, and J. McElroy, *J. Appl. Electrochem.*, **10**, 393 (1980).
- K. J. O'Leary and T. J. Navin, *Chlorine Bicent. Symp.*, 174 (1974).
- S. Trasatti and G. Buzzanca, *J. Electroanal. Chem.*

- Interfacial Electrochem.*, **29**, A1 (1971).
8. P. Ruetschi and P. Delahay, *J. Chem. Phys.*, **23**, 556 (1955).
 9. J. Llopis and M. Vazques, *Electrochim. Acta*, **11**, 633 (1966).
 10. D. Galizzioli, F. Tantardini, and S. Trasatti, *J. Appl. Electrochem.*, **4**, 57 (1974); **5**, 203 (1975).
 11. C. Iwakura, K. Hirao, and H. Tamura, *Electrochim. Acta*, **22**, 329 (1977); **22**, 335 (1977).
 12. D. V. Kokoulina, Y. I. Krasovitskaya, and T. V. Ivanova, *Elektrokhimiya*, **14**, 470 (1978).
 13. M. H. Miles, Y. H. Huang, and S. Srinivasan, *This Journal*, **125**, 1931 (1978).
 14. L. Burke, O. Murphy, J. O'Neill, and S. Venkatesan, *J. Chem. Soc. Faraday Trans. I*, **73**, 1659 (1977).
 15. T. Loucka, *J. Appl. Electrochem.*, **7**, 211 (1977).
 16. L. Elina, V. Gitneva, V. Bystrov, and M. Shmigul, *Elektrokhimiya*, **10**, 68 (1974).
 17. G. Iles and M. Casale, *Plat. Met. Rev.*, **11**, 127 (1967).
 18. F. Cotton and G. Wilkinson, "Advanced Inorganic Chemistry," 2nd ed., Interscience, New York (1966).
 19. S. Pizzini, G. Vuzzance, C. Mari, L. Rossi, and S. Torchio, *Mater. Res. Bull.*, **7**, 449 (1972).
 20. G. Lodi, E. Sivieri, A. DeBattisti, and S. Trasatti, *J. Appl. Electrochem.*, **8**, 135 (1978).
 21. W. Dkomer and D. J. Machin, *J. Less Common Metals*, **61**, 91 (1978).
 22. E. M. Levin, C. R. Robbins, and H. F. McMurdie, "Phase Diagrams for Ceramists," 3rd ed., The American Chemical Society, Columbus, Ohio (1974).
 23. F. S. Galasso, "Structure, Properties and Preparation of Perovskite-Type Compounds," p. 141, Pergamon Press, Oxford (1969).
 24. H. C. Bevan and A. C. C. Tseung, *Electrochim. Acta*, **9**, 201 (1974).
 25. K. R. Williams, "Introduction to Fuel Cells," pp. 57-63, Elsevier, New York (1966).
 26. M. H. Miles, G. Kissel, P. W. T. Lu, and S. Srinivasan, *This Journal*, **123**, 332 (1976).
 27. G. Singh, M. H. Miles, and S. Srinivasan, National Bureau of Standards Special Publication 455, Electrochemicals on Non-metallic Surfaces, Proceedings of Workshop, Gaithersburg, Maryland (1975), p. 289.
 28. W. E. O'Grady, C. Iwakura, J. Huang, and E. Yeager, in "Electrocatalysis," M. W. Breiter, Editor, p. 286, The Electrochemical Society Soft-bound Proceedings Series, Princeton, NJ (1974).
 29. J. H. Russell and L. J. Nuttall, in "Proceedings of the DOE Chemical/Hydrogen Energy Systems Contractor Review," pp. 13-25, (Nov. 1978).
 30. D. V. Kokoulina, Y. L. Krasovitskaya, and T. V. Ivanova, *Elektrokhimiya*, **14**, 470 (1978).
 31. A. Damjanovic, A. Dey, and J. O'M. Bockris, *Electrochim. Acta*, **11**, 791 (1966).

Ring Disk Electrodes with an Impinging Jet

D-T. Chin* and Ravi R. Chandran

Department of Chemical Engineering, Clarkson College of Technology, Potsdam, New York 13676

ABSTRACT

When a jet of electrolyte is impinging perpendicularly on a stationary circular electrode, there is a region of "uniform accessibility" similar to that on a rotating disk electrode. The objective of this study is to develop the impinging jet into a practical tool for electroanalytical applications. This geometry is attractive because there is no mechanical movement and the electrode can be easily adopted for the process streams and closed systems requiring pressure other than the ambient atmospheric pressure. A theoretical and experimental investigation has been made to determine the feasibility of a ring disk arrangement with an impinging jet. The reduction of ferricyanide ion and the cyclic voltammetry of a Cu^{2+}/Cu reaction were used to determine the mass transfer characteristics and the collection efficiencies of platinum and nickel ring disk electrodes located within the uniform accessible regime of the impinged surface. It is found that the rotating ring-disk theory could be used as a first approximation in the numerical computation.

In recent years, the impinging jet has been recognized as an important research tool because it offers a high rate of heat and mass transfer. Among the practical applications are glass toughening, drying of paper, solids leaching, and welding processes. It is commonly used in electrochemical machining and in erosion corrosion.

The impinging jet electrode is composed of a circular disk electrode embedded on a flat plate and a submerged circular jet of electrolyte incident at 90° on the electrode surface. Chin and Tsang (1, 2) have carried out a theoretical and experimental study of mass transfer to an impinging jet electrode; their results can be summarized by the following correlations

(i) for laminar flow ($\text{Re} < 2000$, $0.1 < r_1/d < 0.5$, and $0.2 \leq H/d \leq 6$)

$$\text{Sh}_{\text{disk}} = 1.51 \text{Re}^{1/2} \text{Sc}^{1/3} (H/d)^{-0.055} \quad [1]$$

(ii) for turbulent flow ($4000 < \text{Re} < 16,000$, $0.1 <$

$r_1/d < 1$, and $0.2 \leq H/d \leq 6$)

$$\text{Sh}_{\text{disk}} = 1.12 \text{Re}^{1/2} \text{Sc}^{1/3} (H/d)^{-0.055} \quad [2]$$

where Sh_{disk} is the Sherwood number based upon the inside diameter of the nozzle, d ; Re is the Reynolds number based upon the nozzle diameter and the average velocity of the electrolyte within the nozzle; Sc is the Schmidt number; r_1 is the radius of the electrode; and H is the distance between the nozzle and the electrode surface. These equations confirm the fact that if the disk electrode radius is kept less than one-half of nozzle diameter in laminar flow, and less than one nozzle diameter in turbulent flow, the electrode possesses a "uniform accessibility" to the diffusing species. This property is similar to that of a rotating disk electrode (3). The pattern of fluid flow near the impinging jet electrode also resembles that of the rotating disk.

In view of the foregoing considerations, it is thought that by placing a set of concentric ring and disk electrodes on the impinged surface, one might offer electrochemists an alternative tool for the study of reaction

* Electrochemical Society Active Member.

Key words: convection, mass transport, analysis, voltammetry.

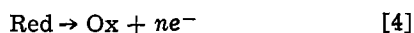
intermediates. Such an arrangement has the advantage that the electrodes are stationary, and the geometry can be adopted for the continuous process streams and the closed electrochemical systems which require a pressure other than the ambient atmospheric pressure. The objective of this study is to determine the mass-transfer rate to the ring, and to measure the collection efficiency of the ring disk combination.

Theoretical Analysis

In order that the ring disk combined with the impinging jet can be used to quantitatively study the reaction intermediate, one must have a knowledge of the collection efficiency at the ring electrode. The collection efficiency, N , is defined as the fraction of a material produced at the disk electrode, being collected at the ring electrode. Let us consider that a species Red is generated at the disk electrode according to the reaction



This species will be carried by convective diffusion to the ring electrode, where the reverse reaction occurs



One may control the potential of the ring electrode such that reaction [4] is limited by the transport of Red to the ring surface. Let us assume that there is an excess inert salt in the electrolyte such that the effect of migration due to the electric field can be neglected. We use the coordinate r as the radial distance from the axis of the impinging jet, and the coordinate z as the perpendicular distance from the impinged surface (Fig. 1). The steady-state axial symmetrical convective diffusion equation for the transport of Red takes the form

$$v \frac{\partial C}{\partial z} + u \frac{\partial C}{\partial r} = D \frac{\partial^2 C}{\partial z^2} \quad [5]$$

where C is the concentration of Red in the flowing electrolyte; D is its diffusivity; and u and v are the velocity components in the r - and z -directions, respectively. The boundary conditions to the differential equation are

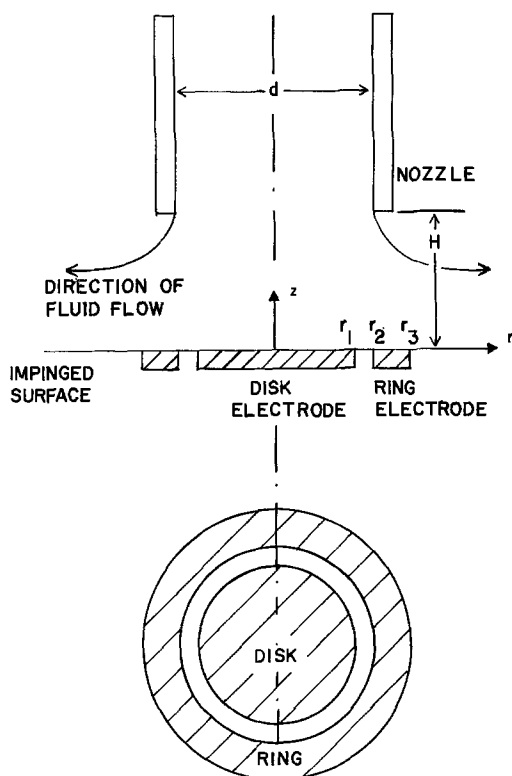


Fig. 1. Ring disk electrodes with an impinging jet

(i) In the bulk of the electrolyte ($r, z \rightarrow \infty$)

$$C = 0 \quad [6a]$$

(ii) On the disk electrode surface ($z = 0, r < r_1$)

$$\frac{\partial C}{\partial z} = \frac{i_{\text{Disk}}}{nFD} \quad \text{or} \quad C = C_{\text{Disk}} \quad [6b]$$

(iii) On the surface of the insulating annulus ($z = 0, r_1 < r < r_2$)

$$\frac{\partial C}{\partial z} = 0 \quad [6c]$$

(iv) On the ring electrode surface ($z = 0, r_2 < r < r_3$)

$$C = 0 \quad [6d]$$

(v) On the insulation plane ($z = 0, r > r_3$)

$$\frac{\partial C}{\partial z} = 0 \quad [6e]$$

For the simplicity of the analysis, we shall assume that the diffusion domain is confined to the stagnation region near the nozzle axis, where the flow boundary layer thickness is uniform, and the radial and the vertical velocity components have the following forms (4, 5)

$$\left. \begin{aligned} u &= ar\phi'(\eta) \\ v &= -2\sqrt{av}\phi(\eta) \end{aligned} \right\} \quad [7]$$

where η is the dimensionless vertical coordinate defined as $z\sqrt{a/\nu}$, and a is an unspecified hydrodynamic constant. The values of a depend upon the nozzle Reynolds number and the dimensionless nozzle height. The stream function, $\phi(\eta)$, has been obtained by Homann (4); its Taylor's series expansion for small η has been found as (1, 2)

$$\begin{aligned} \phi(\eta) &= 0.656\eta^2 - 0.16667\eta^3 + 3.6444 \times 10^{-3}\eta^6 \\ &\quad - 3.9682 \times 10^{-4}\eta^7 + \dots \end{aligned} \quad [8]$$

At high Schmidt numbers (on the order of 1000), the thickness of the concentration boundary layer is much smaller than the thickness of the hydrodynamic boundary layer. Thus, the first term in the Taylor's series expansion of $\phi(\eta)$ would give sufficient accuracy to the solution of the convective diffusion problem, and Eq. [5] can be simplified to

$$1.312 a \sqrt{\frac{a}{\nu}} z \left(r \frac{\partial C}{\partial r} - z \frac{\partial C}{\partial z} \right) = D \frac{\partial^2 C}{\partial z^2} \quad [9]$$

Introducing a new dimensionless vertical coordinate defined as

$$\zeta = \left(\frac{a}{\nu} \right)^{1/2} \left(\frac{1.312\nu}{3D} \right)^{1/3} z \quad [10]$$

Equation [9] becomes

$$3\zeta \left[r \frac{\partial C}{\partial r} - \zeta \frac{\partial C}{\partial \zeta} \right] = \frac{\partial^2 C}{\partial \zeta^2} \quad [11]$$

The boundary conditions to Eq. [11] can be obtained from Eq. [6] as

(i) On the disk ($r < r_1$),

$$\begin{aligned} \frac{\partial C}{\partial \zeta} \Big|_{\zeta=0} &= \left(\frac{\nu}{a} \right)^{1/2} \left(\frac{3D}{1.312\nu} \right)^{1/3} \frac{i_{\text{Disk}}}{nFD} \\ \text{or} \quad C|_{\zeta=0} &= C_{\text{Disk}} \end{aligned} \quad [12a]$$

(ii) On the insulating annulus ($r_1 < r < r_2$),

$$\frac{\partial C}{\partial \zeta} \Big|_{\zeta=0} = 0 \quad [12b]$$

(iii) On the ring ($r_2 < r < r_3$)

$$C|_{r=r_2} = 0 \quad [12c]$$

(iv) In the bulk of the electrolyte

$$C \Big|_{\substack{r \rightarrow \infty \\ r \rightarrow \infty}} = 0 \quad [12d]$$

Equations [11] and [12] are identical to the convective diffusion problem on the rotating ring-disk electrode for which an exact solution has been obtained by Alberly and Bruckenstein (6) and Smyrl and Newman (7). Thus the collection efficiency for the rotating ring-disk electrode is also valid for the ring disk electrode with the impinging jet

$$N = \frac{\text{Total ring current}}{\text{Total disk current}}$$

$$= (A^3 - B^3)^{2/3} \left[\frac{\sqrt{3}}{4\pi} \ln \frac{1 + \theta^3}{(1 + \theta)^3} - \frac{3}{2\pi} \tan^{-1} \left(\frac{2\theta - 1}{\sqrt{3}} \right) + \frac{3}{4} \right] + \frac{\sqrt{3}}{4\pi} \ln \frac{1 + A^3\psi^3}{(1 + A\psi)^3}$$

$$+ \frac{3}{2\pi} \tan^{-1} \left(\frac{2A\psi - 1}{\sqrt{3}} \right) + \frac{1}{4} - A^2 \left[\frac{\sqrt{3}}{4\pi} \ln \frac{1 + \psi^3}{(1 + \psi)^3} + \frac{3}{2\pi} \tan^{-1} \left(\frac{2\psi - 1}{\sqrt{3}} \right) + \frac{1}{4} \right] \quad [13]$$

where

$$\left. \begin{aligned} A &= r_3/r_1, \quad B = r_2/r_1 \\ \theta &= (B^3 - 1)^{1/3} \\ \psi &= \frac{1}{A} \left(\frac{A^3 - B^3}{B^3 - 1} \right)^{1/3} \end{aligned} \right\} \quad [14]$$

Notice that Eq. [13] is only a function of the geometry ratios, r_3/r_1 and r_2/r_1 ; it is independent of the nozzle height as well as the flow conditions in the nozzle. Alberly and Bruckenstein have tabulated the values of N for common values of r_2/r_1 and r_3/r_1 (6).

Experimental

Cell construction and experimental setup.—The construction details of the impinging jet cell are shown in Fig. 2. The cell was made of a Plexiglas tube 15.24 cm in diameter and 10.16 cm in length. The cell had a fixed Plexiglas bottom-plate of 1.26 cm thick and a removable Plexiglas upper plate of 1.26 cm thick. A counter-electrode with a 1.26 cm hole in the center was mounted inside the cell on the bottom plate which had an opening of 9.4 cm to accommodate the nozzle. The nozzle was 0.95 cm ID \times 1.26 cm OD \times 20.32 cm long and was

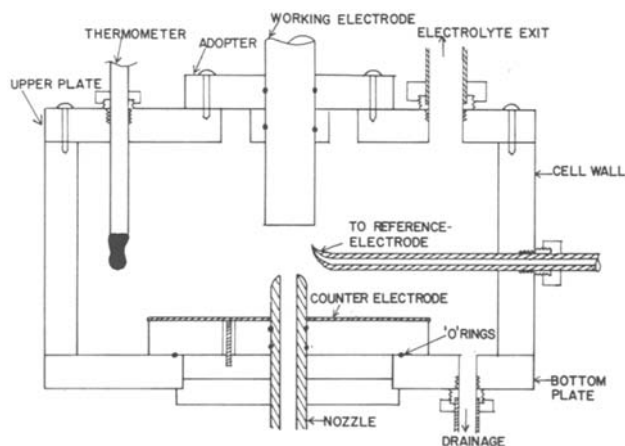


Fig. 2. Schematic diagram of the impinging jet cell

machined to have a tapered end. The electrolyte flowed through the nozzle and impinged perpendicularly on the working electrode surface as shown in the figure. A second nozzle which had a dimension of 0.635 cm ID \times 1.26 cm OD, was also used in the experimental investigation. The nozzle height was adjusted by moving the nozzle up and down and by tightening the nut of the male connector. A Starret micrometer depth gauge (Model 445D-RL) with 0.00254 cm (0.001 in.) precision was used to measure the nozzle height. At 5.08 cm from the bottom plate, a hole was provided to accommodate a Luggin capillary tube. The capillary was connected to an external reference electrode compartment (Fig. 3) with a rubber tubing. A hole of 1.27 cm in diameter was provided on the upper plate for the exit of the electrolyte.

The cell was so designed such that it could adopt different diameters of ring and disk electrodes by changing the electrode adapter. The stationary working electrode with the adapter was mounted on the upper plate over an opening of 4.45 cm in diameter. Four different sizes of ring and ring disk electrodes were used. Two of the electrodes were platinum ring-platinum disk made by Pine Instruments Company; the other two were nickel ring electrodes embedded on a fiberglass resin. The dimensions of these electrodes are listed in Table I.

Figure 3 shows the complete experimental setup. The flow system consisted of a solution tank, a gear pump, a set of rotameters, a flow damper, and the impinging jet cell. These components were connected together with one-half in. polypropylene tube and one-half in. nylon tube fittings. The solution tank was an 11 liter PVC tank; an epoxy gear pump with a Hastelloy-C shaft and a Buna-N impeller were used to circulate the electrolyte. A bypass nylon needle valve and three other nylon needle valves in the upstream of three rotameters were used to control the flow rate of the electrolyte. Three Gilmont F-1500 shielded rotameters were used to measure the flow rate; they were composed of a glass tube and a glass ball to avoid the corrosion problems. The Plexiglas flow damper in the downstream of the rotameters was used to eliminate any turbulences in the electrolyte before it flowed into the impinging jet cell. The electrolyte flowed into the cell through the nozzle tube. It impinged normally on the working electrode and then returned to the storage tank via the exit on the top plate of the cell. All the experiments were performed at a constant room temperature of $24^\circ \pm 1^\circ\text{C}$.

Mass-transfer measurements.—The limiting current measurements for the reduction of ferricyanide ion were used to determine the rate of mass transfer to the ring and the disk electrodes. The solutions used were 0.01M $\text{K}_3\text{Fe}(\text{CN})_6$ and 0.01M $\text{K}_4\text{Fe}(\text{CN})_6$ in a 1M NaOH or 0.5M Na_2SO_4 supporting electrolyte saturated with nitrogen. A Pine Instruments RDE3 potentiostat was used to sweep the potential of the working electrodes

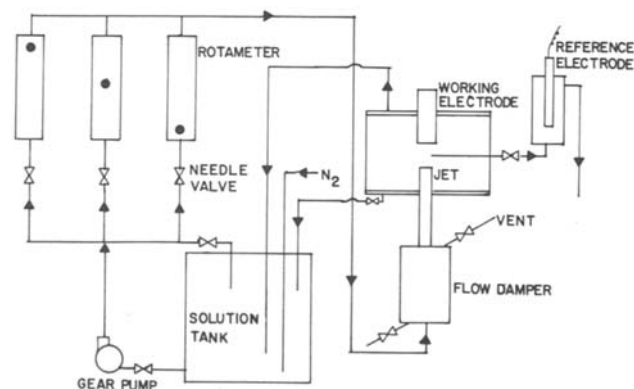


Fig. 3. Schematic diagram of experimental setup

Table I. Dimensions of the ring and the ring disk electrodes

| Electrode | Material | r_1 (cm) | r_2 (cm) | r_3 (cm) |
|-----------------|----------|------------|------------|------------|
| DT-9 ring disk | Platinum | 0.383 | 0.399 | 0.409 |
| DT-21 ring disk | Platinum | 0.250 | 0.276 | 0.358 |
| NIR1 ring | Nickel | — | 0.318 | 0.635 |
| NIR2 ring | Nickel | — | 0.159 | 0.635 |

from 0.25V to $-1.0V$ with respect to a saturated calomel reference electrode. The resulting currents were recorded on a X-Y recorder (Hewlett-Packard 7000 A). In this way the polarization curves and the limiting currents were determined for various flow rates and electrode sizes. The details of the experimental procedures are described in Ref. (8).

Measurement of collection efficiency.—The limiting current measurements for the reduction of ferricyanide to ferrocyanide on the platinum disk electrode, and the oxidation of ferrocyanide to ferricyanide on the platinum ring electrode were used to determine the collection efficiency. A nitrogen-saturated solution containing 0.01M $K_3Fe(CN)_6$ and 0.5M Na_2SO_4 was used for the measurements. The potential of the central disk electrode was swept between 0.2 and $-1.1V$ vs. SCE, whereas the ring potential was controlled at 1.1V vs. SCE. The disk and the ring currents were recorded as functions of the disk potential on two separate X-Y recorders (Hewlett Packard 7000 A and Linseis 1700). The collection efficiency was calculated as the ratio of the ring current (minus any blank current when the disk electrode was at open circuit) to the disk current.

Feasibility test.—To test the ability of the ring disk electrodes with the impinging jet to detect the reaction intermediates, a triangular voltametric sweep was carried out for the Cu^{2+}/Cu reaction. The electrolytes used were: (i) 0.01M $CuCl_2$ plus 0.5M HCl; and (ii) 0.01M $CuSO_4$ plus 0.5M H_2SO_4 . These solutions were saturated with nitrogen before and during the experiments. The potential of the central platinum disk electrode was scanned between 0.4 and $-0.4V$ vs. SCE in the chloride solution and between 0.2 and $-0.2V$ vs. SCE in the sulfate solution. To detect the formation of any intermediate Cu^+ ion during the scan, the potential of the platinum ring electrode was maintained at 0.4V vs. SCE for the chloride system and at 0.58V vs. SCE for the sulfate system. These potential values were the limiting current potentials for the oxidation of cuprous ion to cupric ion (9) at the ring electrode.

Results and Discussion

Mass transfer to ring electrodes.—A set of experiments were first performed to determine the mass transfer characteristics of the ring electrode with the limiting current measurements. The typical results for four different sizes of ring electrodes are shown in Fig. 4 and 5 in the form of $i_{lim,ring}$ vs. $Re^{1/2}$ for two different nozzle heights. All the data were obtained within the stagnation regime of the impinging jet ($r_3d < 0.67$). It is seen that the limiting current density follows a linear relationship in both laminar and turbulent flow regimes, and the straight lines can be extrapolated to the point of origin. This shows that the limiting current density is proportional to $Re^{1/2}$ and thus to the square root of linear velocity of the electrolyte in the nozzle. Each set of data has different slopes in laminar and turbulent regions, and there is a transition flow region in between. The flow transition appears to be in the range of the nozzle Reynolds numbers between 2000 and 4000. This behavior is similar to mass transfer to a circular disk electrode on the impinged surface (1). However, for the disk electrode there is a uniform accessibility and the mass transfer rate is independent of the electrode radius, whereas the limiting current density to the ring decreased with increasing r_3/r_2 ratios. This is because the ring electrode behaved as

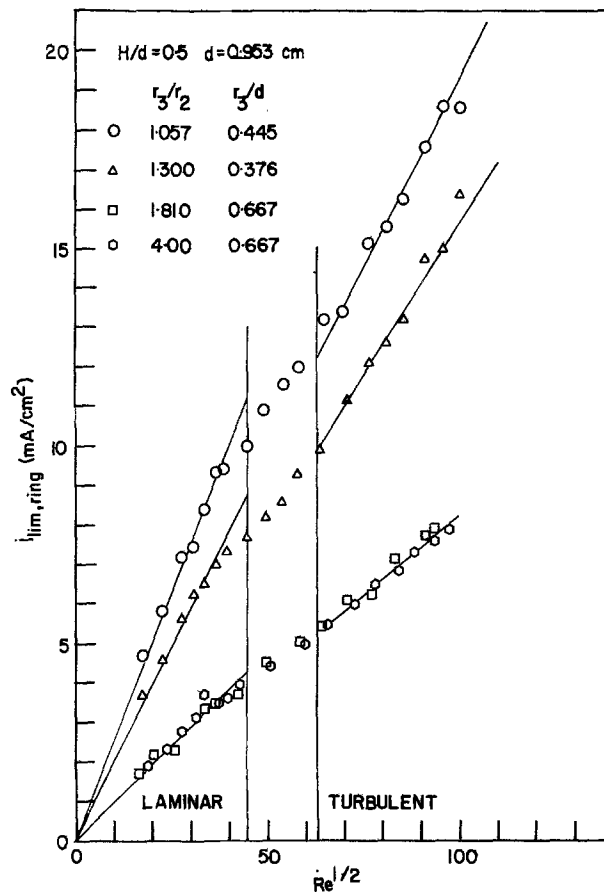


Fig. 4. Dependence of the limiting current density of four different sizes of ring electrodes on the nozzle Reynolds number for $H/d = 0.5$ and $d = 0.95$ cm.

though the central portion of a disk was rendered non-reactive, and the electrode was no longer uniformly accessible to the diffusing ion. The local mass transfer rate was maximum at the inner edge and decreased along the radial direction toward the outer edge. The average mass transfer rate to the ring would be higher than that to a disk. The data for the two ring electrodes with $r_3/r_2 = 1.8$ and 4.0 seem to fall on a single curve as shown in Fig. 4 and 5. This indicates that as the width of the ring increased, the average mass-transfer rate decreased and eventually became the same as that of a disk electrode whose radius would be equal to the outer radius of the ring.

Figure 6 shows the dependence of the limiting current density of a ring electrode on the dimensionless nozzle height for a range of H/d between 0.5 and 6. There was a slight decrease in the mass-transfer rate at various Reynolds numbers; however, the dependence was very small.

For a rotating ring electrode, the mass-transfer rate is related to a geometrical factor, γ , defined as (3, 10)

$$\gamma = \frac{(r_3^3 - r_2^3)^{2/3}}{r_3^2 - r_2^2} \quad [15]$$

It has been found that the ratio of the average limiting current density of a rotating ring electrode to the limiting current density of a rotating disk electrode is equal to γ (10). In the present study, an attempt has been made to normalize the limiting current density of the ring electrode with the limiting current density of a disk electrode having the same radius as the outer radius of the ring under the same flow conditions. The results are plotted in Fig. 7 as a function of the Reynolds numbers for four different sizes of ring electrodes over a range of H/d from 0.5 to 6. The values of $i_{lim,disk}$ used in the figure were calculated from Eq. [1]-[2].

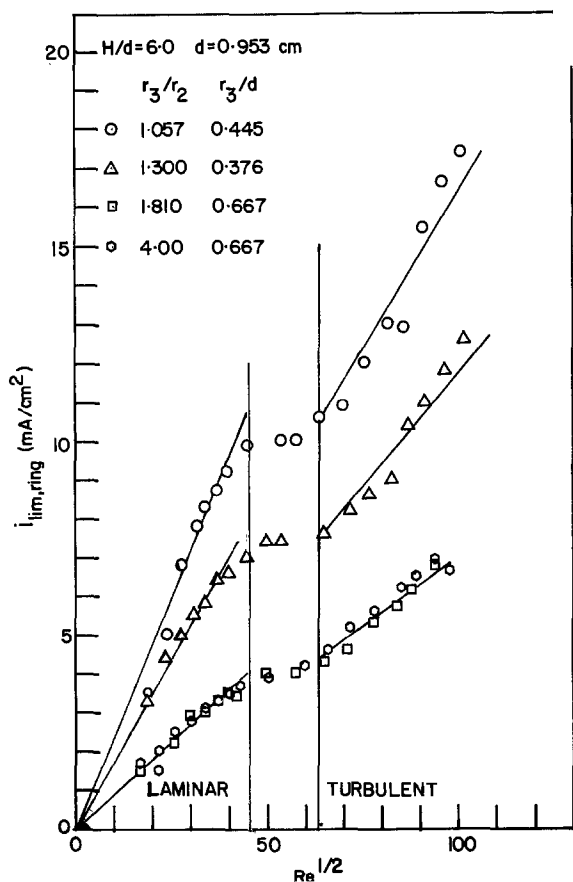


Fig. 5. Dependence of the limiting current density of four different sizes of ring electrodes on the nozzle Reynolds number for $H/d = 6.0$ and $d = 0.953$ cm.

It is interesting to note that the ratio became independent of the Reynolds number and the dimensionless nozzle height; it was only a function of the geometrical factor, γ . A linear regression analysis for all the data obtained ($1 < \gamma < 3$; $r_3/d < 0.67$; $0.5 \leq H/d \leq 6$; $1400 < Sc < 1600$) resulted in the following empiri-

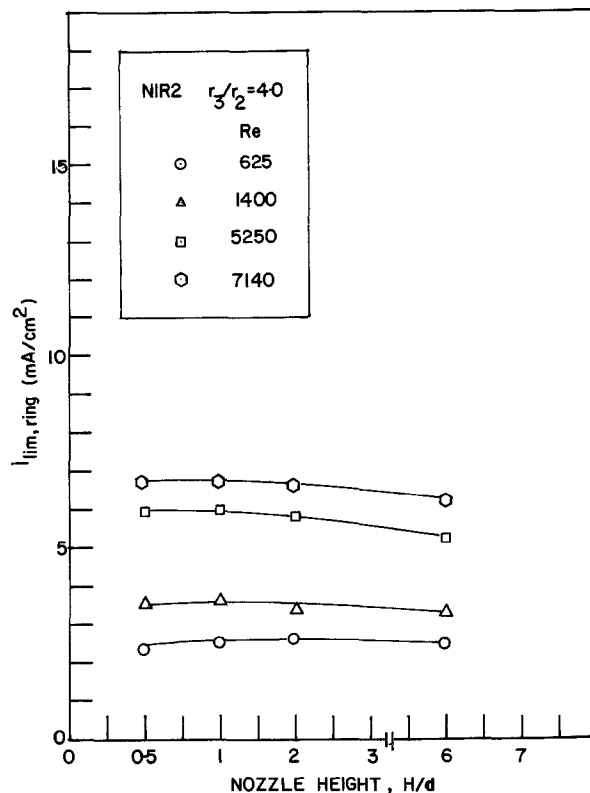


Fig. 6. Dependence of the limiting current density of the NIR2 ring electrode on the dimensionless nozzle height, H/d .

cal correlation for mass transfer to the ring electrode with an impinging jet

$$\frac{i_{lim,ring}}{i_{lim,disk}} = \frac{Sh_{ring}}{Sh_{disk}} = \begin{cases} 0.790 \gamma & (300 < Re < 2000) \\ 0.938 \gamma & (2000 < Re < 11,000) \end{cases} \quad [16]$$

Here $i_{lim,disk}$ and Sh_{disk} are the average limiting current density and the average Sherwood number of a disk electrode whose radius is equal to the outer radius of the ring; these values are calculated from Eq. [1] or [2] obtained previously by Chin and Tsang (1). Figure

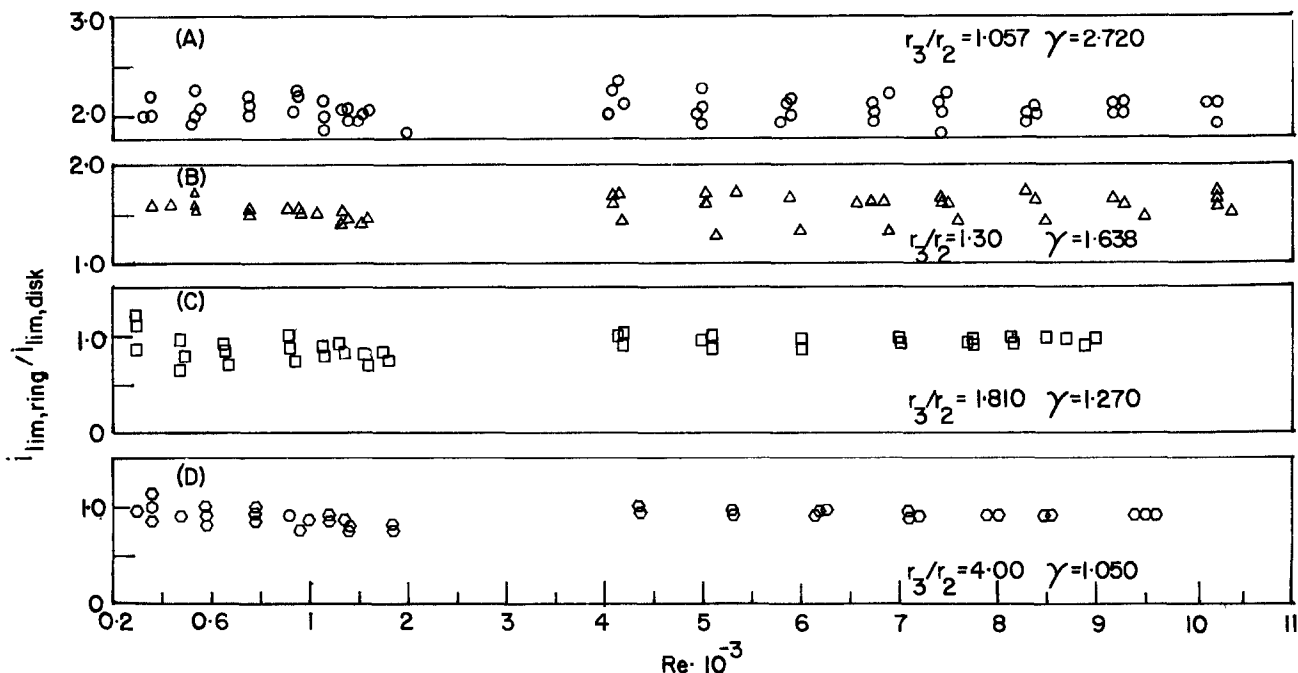


Fig. 7. Dependence of $i_{lim,ring}/i_{lim,disk}$ or Sh_{ring}/Sh_{disk} on the nozzle Reynolds number, for four different sizes of ring electrodes. The values of $i_{lim,disk}$ and Sh_{disk} are calculated from Eq. [1]-[2].

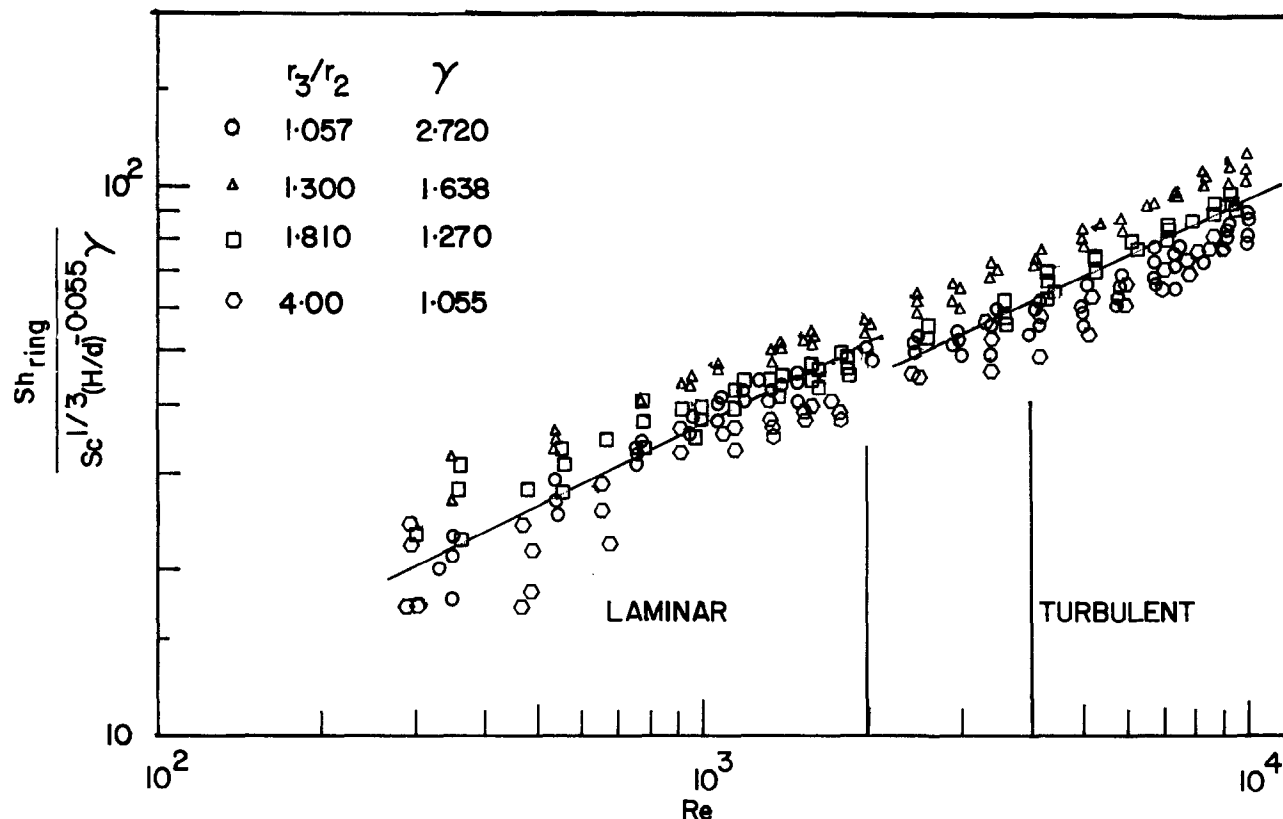


Fig. 8. Summary of mass-transfer data of the impinging jet ring electrodes for $0.5 \leq H/d \leq 6$, and $r_3/d < 0.67$. The solid lines represent the empirical correlation of Eq. [16].

8 shows a log-log plot of $Sh_{ring}/Sc^{1/3}(H/d)^{-0.55} \gamma$ vs. Re for both laminar and turbulent flows. It is seen that Eq. [16] as represented by the straight lines correlated the data well; the agreement was within $\pm 15\%$.

Collection efficiency.—Figure 9 shows the typical recorder traces obtained during the collection efficiency

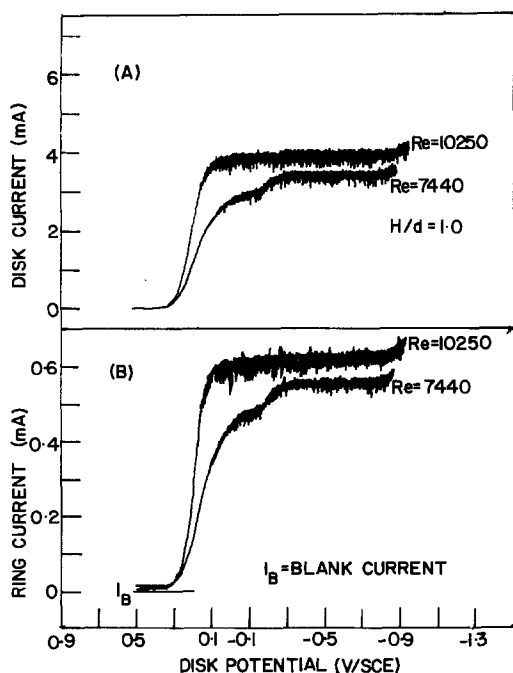


Fig. 9. Recorder traces of the disk and the ring currents as a function of the disk potential for the DT21 platinum ring disk electrodes. The reduction of ferricyanide was carried out at the central disk electrode, whereas the ring potential was kept at 1.1V vs. SCE to reoxidize any ferrocyanide ions reaching the ring electrode. The scan rate of the disk potential was 0.25 V/min, and $H/d = 1.0$.

measurements with the DT21 platinum ring disk electrodes in a solution containing 0.01M $K_3Fe(CN)_6$ and 0.5M Na_2SO_4 . The disk potential was swept toward the cathodical direction, whereas the ring potential was kept at a limiting current potential for the oxidation ferrocyanide to ferricyanide. Figure 9A shows the disk current vs. disk potential for two different Reynolds numbers; the corresponding ring currents are shown in Fig. 9B. The blank current (or background current) at the ring while the disk was at the open circuit is also shown in the figure. The collection efficiency was calculated from the ratio of the ring current minus any blank current, to the disk current. In most cases, the flat portion of the curves in the range of disk potential between -0.3 and $-0.9V$ vs. SCE, was used for the calculation. Since there were fluctuations in the recorded current readings, the maximum and the minimum values of the fluctuations were noted, and the average values of the ring and the disk currents were used to compute the average collection efficiency. Four other ratios, $I_{ring,min}/I_{disk,max}$, $I_{ring,max}/I_{disk,min}$, $I_{ring,min}/I_{disk,min}$, and $I_{ring,max}/I_{disk,max}$, were also computed. Here the suffixes, min and max, denote the minimum and the maximum values of the ring and the disk currents on the flat portion of the recorder traces. These ratios were used to give a statistical representation of the collection efficiency data. It was found that the average collection efficiency was equal to the ratios, $I_{ring,min}/I_{disk,min}$ and $I_{ring,max}/I_{disk,max}$. The fact was supported by the observations during the experiments that the maximum ring current occurred when the disk current reached the maximum of its fluctuations, and conversely the minimum ring current occurred when the disk current was minimum. This suggests that the ratio of the average ring current to the average disk current renders a true representation of the collection efficiency of the ring disk electrodes.

In this way, the collection efficiency for two different sizes of platinum ring disk electrodes (DT9 and DT21) was measured over a range of Reynolds numbers from 300 to 11,000 and for the dimensionless nozzle heights

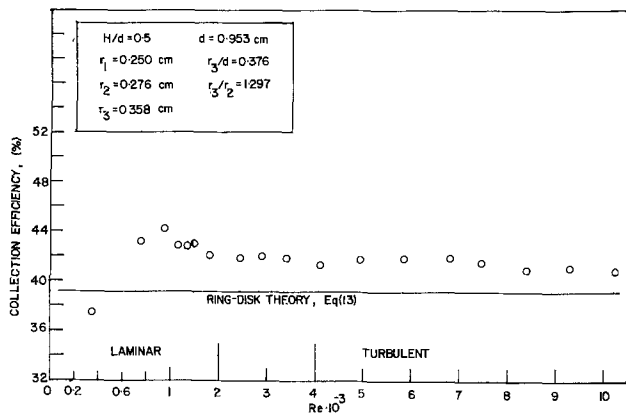


Fig. 10. Dependence of the collection efficiency on the Reynolds number for the DT21 platinum ring disk electrodes.

between 0.5 and 6.0. Figures 10 and 11 show the typical results obtained at $H/d \approx 0.5$ as a function of Reynolds numbers. The data points in the figures are the experimental average collection efficiencies calculated from $I_{\text{ring,ave}}/I_{\text{disk,ave}}$. For comparison, the ring disk theory of Eq. [13] is plotted as the solid horizontal lines. Although there is a scatter in the data, the experimental collection efficiency does not appear to depend on the Reynolds number. For the DT21 electrodes (Fig. 10), the experimental values are consistently higher than the theory prediction, whereas for the DT9 electrodes (Fig. 11), the experimental values are smaller than the theory. However, the difference is small, and the agreement between the ring disk theory and the experiment is within $\pm 10\%$.

Figure 12 shows the dependence of the experimental collection efficiency on the dimensionless nozzle height, H/d , for various Reynolds numbers and r_3/d ratios. It is seen that for the two different sizes of ring disk electrodes shown in the figure, the collection efficiency remained constant in the region of $0.5 < H/d < 2$. At higher values of H/d , the collection efficiency slowly decreased with increasing H/d ratios. This trend was true for both laminar and turbulent flows.

The effect of r_3/d ratio on the collection efficiency was checked by using two different nozzle diameters, and the results are shown in Fig. 12A and B. It appears that an increase in the r_3/d ratio tended to lower the collection efficiency. During the course of completing the present work, a similar paper was published by Du Duc (11) who used an impinging jet ring disk electrode with $r_3/d = 1.55$ and a range of H/d from 0.03 to 3.0. In his experiments, the ring electrode and the part of the disk electrode were located outside the uniform accessible regime of the impinging jet, and the collection efficiency was found to be much smaller

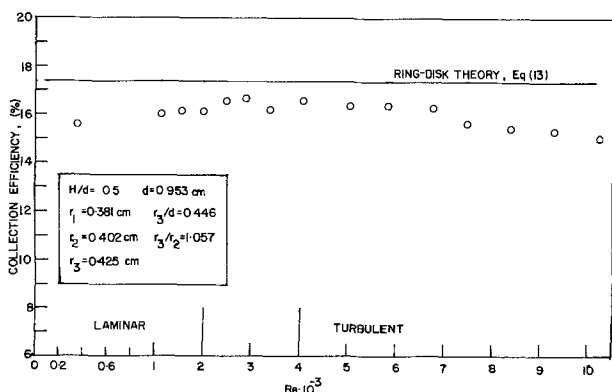


Fig. 11. Dependence of the collection efficiency on the Reynolds number for the DT9 platinum ring disk electrodes.

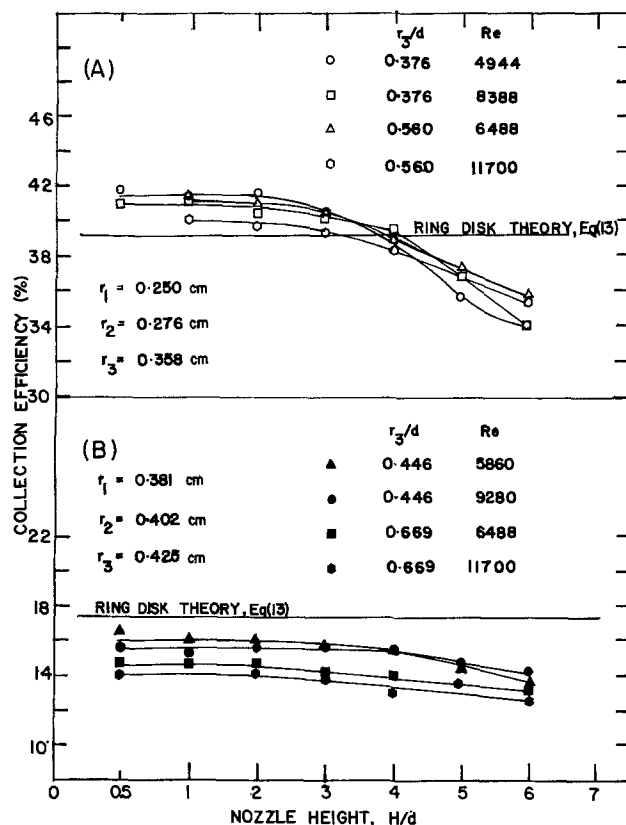


Fig. 12. Collection efficiency as a function of the dimensionless nozzle height for two different sizes of ring disk electrodes at various Reynolds numbers and r_3/d ratios.

than the prediction of the ring disk theory. The present results for $H/d \leq 2.0$ as well as those of Du Duc (11) are summarized in Table II. It appears that if one limits the dimensionless nozzle height to less than 2.0 and the ratio of r_3/d to less than 0.6, the ring disk theory can be used as a first approximation for the prediction of the collection efficiency. However, in view of the complexity of fluid flow in an impinging jet, it is suggested that a cell with fixed H/d , r_1/d , r_2/d , and r_3/d ratios be constructed, and a simple redox reaction, such as the reduction of ferricyanide to ferrocyanide ions be used to calibrate the collection efficiency. The ring disk theory of Eq. [13] can be then used to check the accuracy of the calibrations.

Feasibility test.—The feasibility of the ring disk electrode with an impinging jet to detect a reaction intermediate was tested by detecting an intermediate Cu^+ species in a $\text{Cu}^{++}/\text{Cu}^+$ reaction.

Figure 13 shows the test carried out in a 0.01M $\text{CuCl}_2/0.5\text{M HCl}$ solution with the DT21 platinum ring disk electrodes. The disk and ring currents are plotted against the disk potential for $H/d = 1$ and $\text{Re} = 6970$. The disk current exhibited two reaction waves during the cathodic sweep. The first wave corresponded to the reduction of Cu^{++} to Cu^+ ; within this potential range there was an increase in the ring current which reached a plateau when the disk current reached the limiting current for the $\text{Cu}^{++}/\text{Cu}^+$ reaction. The ratio of the ring current to the disk current gave the collection efficiency and the value agreed with the previous measurements using the ferricyanide/ferrocyanide reaction. The second wave corresponded to the reduction of Cu^+ to Cu ; within this potential range the ring current correspondingly decreased to zero. In the anodic sweep, the copper deposited during the cathodic sweep started to dissolve into the electrolyte, and the disk current increased. It reached a maximum and then sharply decreased once all the copper was dissolved into the electrolyte. There was a correspond-

Table II. Summary of the collection efficiency measurements

| | Dimensions of platinum ring disk electrodes (cm) | | | Nozzle diameter, d (cm) | r_3/d | H/d | Re | Collection efficiency (%) | |
|--------------|--|-------|-------|---------------------------|---------|--------|------------|---------------------------|----------------------------|
| | r_1 | r_2 | r_3 | | | | | Experimental | Ring disk theory, Eq. [13] |
| Present work | 0.250 | 0.276 | 0.358 | 0.95 | 0.376 | 0.5-2 | 900-8390 | 43-41 | 39.4 |
| | 0.381 | 0.402 | 0.425 | 0.95 | 0.446 | 0.5-2 | 1130-5860 | 16-15.6 | 17.4 |
| | 0.250 | 0.276 | 0.358 | 0.635 | 0.564 | 0.5-2 | 800-11,700 | 41.8-40 | 39.4 |
| | 0.381 | 0.402 | 0.425 | 0.635 | 0.669 | 0.5-2 | 800-11,700 | 15.2-14 | 17.4 |
| Ref. (11) | 0.375 | 0.396 | 0.526 | 0.34 | 1.55 | 0.03-3 | 130-19,000 | 30-10 | 40 |

ing increase in the ring current, which simultaneously reached a maximum with the disk current. Again, the ratio of the ring current to the disk current agreed with the measured collection efficiency. This indicates that the main dissolution product of copper in $\text{CuCl}_2\text{-HCl}$ solution is Cu^+ .

Figure 14 shows the cyclic voltammetry of the DT21 platinum ring disk electrodes in a 0.01M $\text{CuSO}_4\text{-0.5M H}_2\text{SO}_4$ solution. In the cathodic sweep the disk current had only one reaction wave. The ring did not detect any Cu^+ species and had a zero ring current. The reason for this is that Cu^+ formed in $\text{CuSO}_4\text{-H}_2\text{SO}_4$ solution was very unstable and immediately converted to Cu . During the anodic sweep, the disk current increased. It reached a maximum and then decreased when all the copper was dissolved. The ring did detect some Cu^+ during the anodic sweep but the ring current was very small as indicated by the μA -scale in Fig. 14B. This implies that the main dissolution product of Cu in $\text{CuSO}_4\text{-H}_2\text{SO}_4$ solution is Cu^{++} and the very small amount of Cu^+ might be the result of a secondary chemical reaction between Cu^{++} and Cu (9). Thus the impinging jet was capable of differentiating the $\text{Cu}^{++}/$

Cu reaction in the $\text{CuCl}_2\text{-HCl}$ solution from that in the $\text{CuSO}_4\text{-H}_2\text{SO}_4$ solution.

Conclusions

A theoretical and experimental study has been made to determine the feasibility of a ring disk arrangement with an impinging jet for electroanalytical applications. The reduction of ferricyanide ion and the cyclic voltammetry of a Cu^{2+}/Cu reaction were used to measure the mass transfer rates and the collection efficiencies of four different sizes of ring disk electrodes over a range of Reynolds numbers from 300 to 11,000. It is found that if one limits the nozzle height to 0.5-2.0 nozzle diameters and the outer radius of the ring electrode to less than 0.6 nozzle diameter, the collection efficiency would be independent of the Reynolds number and the nozzle height for both laminar and turbulent flows. Within these ranges, the rotating ring disk theory can be used as a first approximation in the prediction of the collection efficiency.

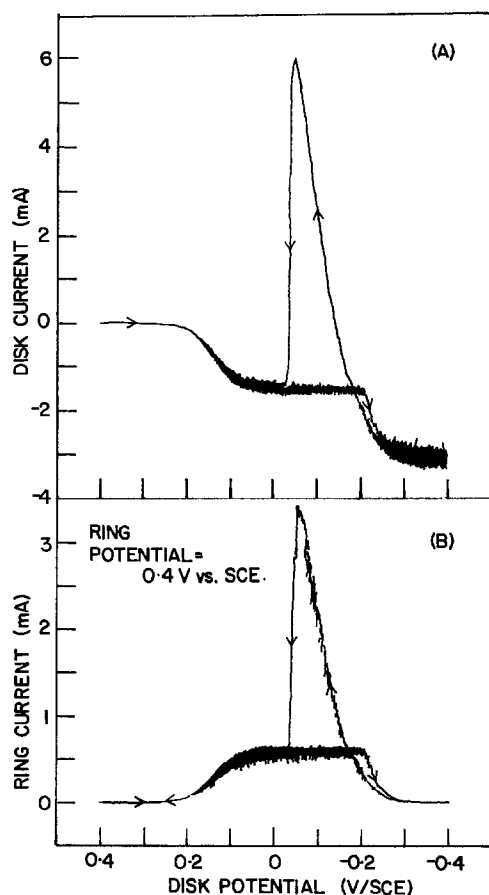


Fig. 13. Cyclic voltammograms of the DT21 platinum ring disk electrodes in 0.01M $\text{CuCl}_2\text{-0.5M HCl}$ solution at $H/d = 1.0$ and $\text{Re} = 6970$. The disk potential was scanned at a rate of 0.25 V/min, and the ring potential was maintained at 0.4V vs. SCE.

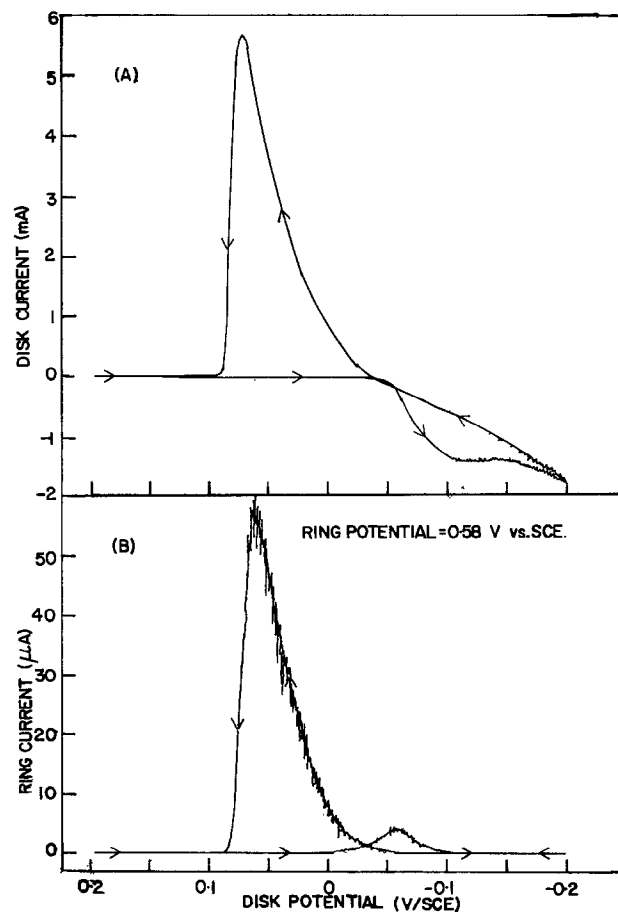


Fig. 14. Cyclic voltammograms of the DT21 platinum ring disk electrodes in 0.01M $\text{CuSO}_4\text{-0.5M H}_2\text{SO}_4$ solution at $H/d = 1.0$ and $\text{Re} = 6070$. The disk potential was scanned at a rate of 0.25 V/min, and the ring potential was maintained at 0.58V vs. SCE.

Manuscript submitted Nov. 17, 1980; revised manuscript received March 9, 1981.

Any discussion of this paper will appear in a Discussion Section to be published in the June 1982 JOURNAL. All discussions for the June 1982 Discussion Section should be submitted by Feb. 1, 1982.

Publication costs of this article were assisted by Clarkson College of Technology.

LIST OF SYMBOLS

| | |
|------------------------|--|
| a | hydrodynamic constant, 1/sec |
| A | r_3/r_1 , dimensionless |
| B | r_2/r_1 , dimensionless |
| C | concentration of the diffusing ion, g-mol/cm ³ or kg-mol/m ³ |
| C_{Disk} | concentration of the diffusion ion on the disk surface, g-mol/cm ³ or kg-mol/m ³ |
| D | diffusivity of the diffusion ion, cm ² /sec or m ² /sec |
| d | diameter of the circular nozzle, cm or m |
| F | Faraday constant, 96,487 C/g-equiv |
| H | nozzle height, cm or m |
| i_{disk} | current density on the disk electrode, A/cm ² or A/m ² |
| i_{ring} | current density on the ring electrode, A/cm ² or A/m ² |
| $i_{\text{lim, disk}}$ | limiting current density on the disk electrode, A/cm ² or A/m ² |
| $i_{\text{lim, ring}}$ | limiting current density on the ring electrode, A/cm ² or A/m ² |
| $I_{\text{disk, ave}}$ | average disk current, A |
| $I_{\text{disk, max}}$ | maximum of the fluctuating disk current, A |
| $I_{\text{disk, min}}$ | minimum of the fluctuating disk current, A |
| $I_{\text{ring, ave}}$ | average ring current, A |
| $I_{\text{ring, max}}$ | maximum of the fluctuating ring current, A |
| $I_{\text{ring, min}}$ | minimum of the fluctuating ring current, A |
| K | average mass transfer coefficient, cm/sec or m/sec |
| N | collection efficiency of the ring disk electrode, dimensionless |
| n | number of electrons transferred in the electrode reaction, g-equiv/g-mol or kg-equiv/kg-mole |
| r | radial coordinate measured from the stagnation point, cm or m |
| r_1, r_2, r_3 | radius of the disk electrode, and the inner and the outer radii of the ring electrode, respectively, cm or m |
| Re | Reynolds number, $d\bar{U}/\nu$, dimensionless |
| Sc | Schmidt number, ν/D , dimensionless |

| | |
|--------------------|--|
| Sh | average Sherwood number, Kd/D , dimensionless |
| Sh_{disk} | average Sherwood number of disk electrode, dimensionless |
| Sh_{ring} | average Sherwood number of ring electrode, dimensionless |
| \bar{U} | average velocity at the nozzle exit, cm/sec or m/sec |
| u | velocity component in the radial direction, cm/sec or m/sec |
| v | velocity component in the axial direction, cm/sec or m/sec |
| z | a coordinate perpendicular to the electrode surface, cm or m |

Greek Letters

| | |
|----------|---|
| γ | geometric factor of ring electrode defined by Eq. [15], dimensionless |
| ξ | dimensionless vertical coordinate defined in Eq. [10] |
| η | a dimensionless variable defined as $\sqrt{a/\nu} z$ |
| θ | a geometrical factor of ring disk electrodes defined in Eq. [14], dimensionless |
| ν | kinematic viscosity of the electrode, cm ² /sec or m ² /sec |
| ϕ | stream function, dimensionless |
| ψ | a geometrical factor of ring disk electrodes defined in Eq. [14], dimensionless |

REFERENCES

- D-T. Chin and C. H. Tsang, *This Journal*, **125**, 1461 (1978).
- C. H. Tsang, M.S. Thesis, Clarkson College of Technology, Potsdam, New York (1978).
- V. G. Levich, "Physicochemical Hydrodynamics," Prentice Hall, Englewood Cliffs, New Jersey (1962).
- F. Homann, *ZAMN* **16**, 153 (1936); *Forsch. Ing. Wes.*, **7**, 1 (1936).
- H. Schlichting, "Boundary Layer Theory," pp. 78-83, McGraw-Hill, New York (1960).
- W. J. Albery and S. Bruckenstein, *Trans. Faraday Soc.*, **62**, 1920 (1966).
- W. H. Smyrl and J. Newman, *This Journal*, **119**, 212 (1972).
- R. R. Chandran, M.S. Thesis, Clarkson College of Technology, Potsdam, New York (1980).
- D-T. Chin, *This Journal*, **120**, 631 (1973).
- A. C. Riddiford, in "Advances in Electrochemistry and Electrochemical Engineering," Vol. 4, P. Delahay, Editor, Interscience, New York (1966).
- H. Du Duc, *J. Appl. Electrochem.*, **10**, 385 (1980).

Oxidation of HCOOH and CH₃OH on Platinum Modified by Foreign Metal Adatoms in 85% Phosphoric Acid

R. R. Adzic,¹ W. E. O'Grady,* and S. Srinivasan*

Brookhaven National Laboratory, Upton, New York 11973

ABSTRACT

The use of underpotentially deposited metal atoms as electrocatalysts suggests a promising route for enhancing the kinetics of oxidation of organic fuels. The electro-oxidation of formic acid and methanol was studied on underpotentially deposited metal atoms on platinum in 85% phosphoric acid. The rates of these reactions were greatly improved. Due to adsorption of phosphate ions, formic acid oxidation rates on underpotentially deposited metal atoms are lower than in perchloric acid. The electrocatalytic activity of the investigated underpotentially deposited metals for formic acid oxidation follows the order Pb > Bi > Tl; for methanol oxidation during the cathodic scan the rates are higher for lower lead concentrations, which is probably due to lower concentration of adsorbed lead and/or oxide. It is proposed that the enhanced reaction rates with underpotentially deposited metal atoms are due to inhibition of hydrogen adsorption and hence of formation of poisoning intermediates such as COH.

The interest in the more efficient use of organic fuels has increased considerably after the energy crisis of 1973. For this reason, the attention of a number of electrochemists has focused on electrochemical energy conversion including the direct oxidation of organic molecules. The oxidation reactions of HCOOH and CH₃OH are of particular interest because these molecules are potential fuels for fuel cells and represent "model molecules" for reactions which serve as a basis for studies of more complex ones. It was recently shown (1-3) that foreign metal adatoms have a striking catalytic effect on these reactions on several noble metals in 1M HClO₄. In this work, the results obtained for the oxidation of formic acid and of methanol on platinum modified by foreign metal adatoms in 85% H₃PO₄, which is one of the most attractive electrolytes for practical fuel cells, are reported.

Experimental

The measurements were made in a three-compartment Pyrex cell. The working electrode was 2 cm² Pt foil. The counterelectrode was also Pt, while the reversible hydrogen electrode served as the reference. The working electrode was first polished to obtain a mirror finish, washed, cleaned with 1:1 volume ratio H₂SO₄-HNO₃, and then rinsed with triply distilled water.

The acid was purified using essentially the procedure of Ferrier *et al.* (4) and Huang *et al.* (5). H₂O₂ was added to reagent grade 85% H₃PO₄ (Mallinckrodt) and this solution was heated to 90°C until gas evolution ceased. The acid was then heated to 160°C to reduce the water content and destroy any remaining traces of H₂O₂. The water content was adjusted and the acid was preelectrolyzed for 24 hr.

Results

Underpotential deposition of Pb, Bi, and Tl on Pt in 85% H₃PO₄.—Figure 1 shows the underpotential deposition (UPD) of Pb. This metal was added in the form of perchlorate, which introduced some HClO₄ and H₂O

into the electrolyte. This, however, negligibly changed the concentration of H₃PO₄. The UPD of Pb considerably suppresses hydrogen adsorption on Pt, but apparently less than in 1M HClO₄. The suppressed hydrogen adsorption peaks are seen in Fig. 1. This behavior and a large pseudocapacitance associated with lead adsorption/desorption process indicate a somewhat smaller electroadsorption valence for Pb_{ad} in this electrolyte. Larger currents for desorption of some other adatoms in the presence of specific adsorption of anions have been ascribed to a desorption of anions which accompanies the UPD (6). It appears that both effects might be present in this particular system. The desorption of Pb_{ad} occurs at less positive potentials than in HClO₄. It appears that these differences are due to the interference of a specific adsorption of phosphate ions with the UPD of Pb. The shift of the lead

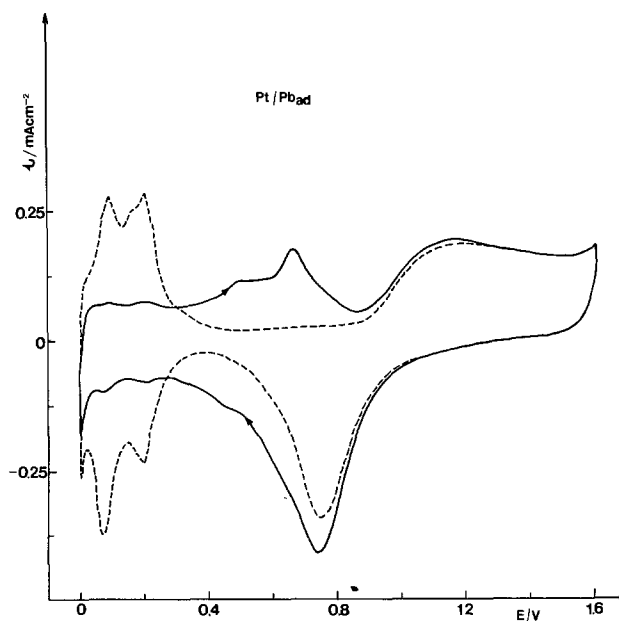


Fig. 1. Underpotential deposition of Pb on Pt in 85% H₃PO₄ (full line). Pt in the absence of Pb (dashed line). Sweep rate 100 mV/sec, 1 × 10⁻³M Pb²⁺.

* Electrochemical Society Active Member.

¹ Visiting Scientist during summer of 1979. Present address: Institute of Electrochemistry, ICTM and Center for Multidisciplinary Studies, University of Belgrade, Belgrade, Yugoslavia.

Key words: formic acid, methanol, oxidation, underpotential deposition.

desorption peak to less positive potentials is equivalent to a reduction in bond strength between metal adatoms and the substrate surface. The interaction of phosphate anions with platinum is stronger than with lead adatoms which hence causes a decrease in bond energy.

Figures 2 and 3 display the UPD of Bi and Tl. The differences found with the UPD of Pb in 1M HClO₄ and 85% H₃PO₄ are also found for the UPD of Bi and Tl. These include a shift of desorption peaks to less positive potentials, i.e., a diminishing of the underpotential deposition effect and a change of the electro-sorption valence. The latter looks negligible with Bi. The peak at 1.3V in Fig. 3 is due to the redox reaction Tl⁺/Tl³⁺.

Oxidation of HCOOH on Pt and Pt modified by foreign metal adatoms.—Figure 4 shows the oxidation of HCOOH on Pt in 85% and 40% H₃PO₄. The voltammogram obtained in 40% H₃PO₄ is essentially the same as that obtained in 1M HClO₄ and H₂SO₄ (1, 6). The oxidation currents are, however, much smaller in 85% H₃PO₄. A very small peak in the anodic scan is noteworthy. The second anodic peak is also different. The lower activity of Pt in 85% H₃PO₄ arises mainly from the decreased H₂O concentration. The specific adsorp-

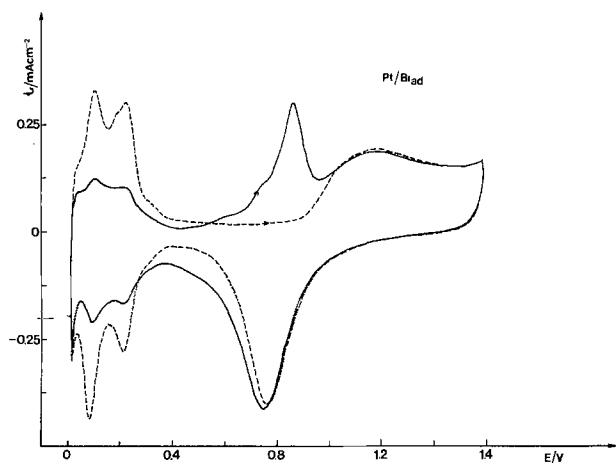


Fig. 2. Underpotential deposition of Bi on Pt in 85% H₃PO₄ (full line). Pt in the absence of Bi (dashed line). Sweep rate 100 mV/sec, 1×10^{-3} M Bi³⁺.

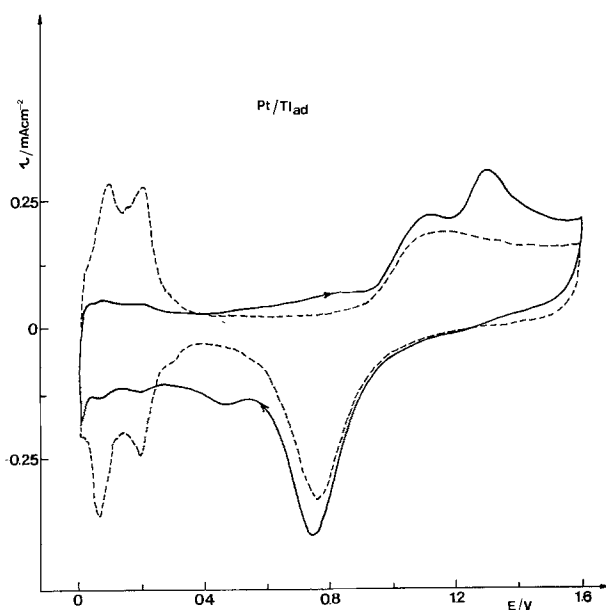


Fig. 3. Underpotential deposition of Tl on Pt in H₃PO₄ (full line). Pt in the absence of Tl (dashed line). Sweep rate 100 mV/sec, 1×10^{-3} M Tl⁺.

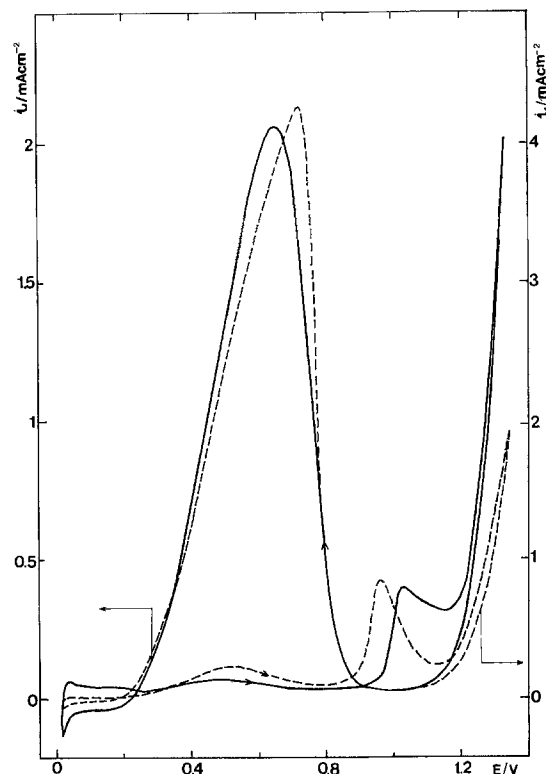


Fig. 4. Oxidation of HCOOH on Pt in 85% H₃PO₄ (full line), in 40% H₃PO₄ (dashed line). 0.5M HCOOH; sweep rate 50 mV/sec.

tion of phosphate ions seems to have a smaller influence.

Figure 5 shows the oxidation of HCOOH on Pt partially covered by lead adatoms (full line). Approximately a 60-fold increase of the peak current in the anodic scan is seen in comparison with the curve for Pt (dashed line). The effect is similar in magnitude to the one observed in 1M HClO₄ (1, 2). The peak at 0.85V is a new feature. It falls exactly between the peak for desorption of Pb and the onset of oxide for-

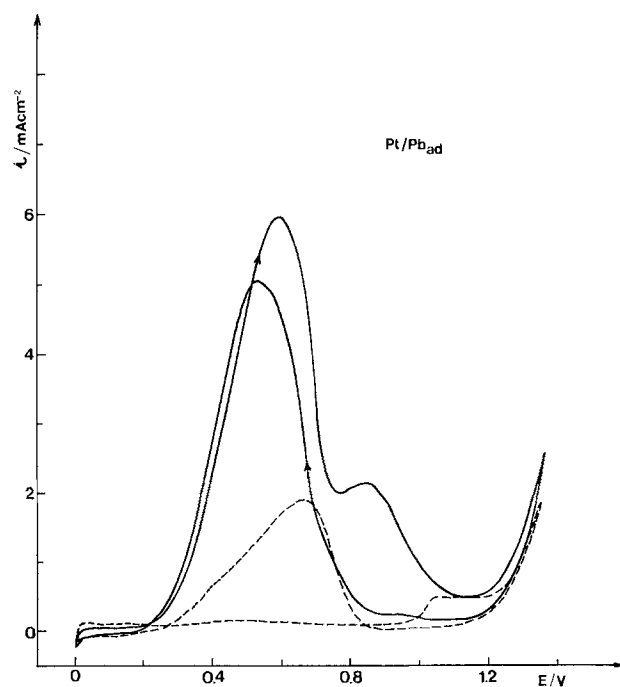


Fig. 5. Oxidation of HCOOH on Pt with Pb adatoms (full line) and on Pt (dashed line) in 85% H₃PO₄. 0.5M HCOOH; sweep rate 100 mV/sec.

mation on Pt (Fig. 1). It appears that after desorption of Pb adatoms, the Pt surface is not completely covered by strongly bound intermediates and thus the oxidation of HCOOH is facilitated. In 1M HClO₄, there is no such window because a complete desorption of Pb coincides with the onset of oxide formation on Pt (1, 2).

Figure 6 displays the results obtained with Bi adatoms. The peak in the anodic scan is increased considerably. It appears, however, at more positive potentials than the peak on Pt without Bi_{ad}. This is caused by an excessive coverage of Bi adatoms at less positive potentials. At smaller concentrations of Bi the peak indeed shifts to less positive potentials. The current at the peak is, however, smaller because it appears at a lower overpotential for HCOOH oxidation. As with Pb adatoms, a second peak in anodic scan appears, but at ~1.0V in this case.

Figure 7 shows the effects of Tl adatoms which are considerable, although smaller than the effects of Pb and Bi. There is agreement with the data obtained in 1M HClO₄ (1, 2). The smaller current density of the peak in the cathodic direction is due to the formation of a high coverage of Tl_{ad}. This decreases the available oxide-free and intermediate-free Pt surface which is otherwise available for the oxidation of HCOOH.

Steady-state measurements (Fig. 8) show striking catalytic effects of Pb adatoms consistent with the linear sweep voltammetry. At 0.4V the effect amounts to three orders of magnitude. A similar effect has been found in 1M HClO₄ (1-3).

Oxidation of CH₃OH.—Figures 9 and 10 show voltammetry curves for the oxidation of CH₃OH on Pt in 85% H₃PO₄ and the effect of a progressive decrease of cathodic and anodic potential limits, respectively. A small oxidation current is seen in the double layer region of Pt for the sweep encompassing the whole potential range. The main oxidation peak coincides with the onset of oxide formation on Pt. Figure 9 shows a surprising current jump when the sweep is reversed at 0.2V which gradually diminishes at more positive potentials. This current spike is not at present clearly understood. It might be connected with the oscillatory phenomena observed in oxidation of organics (26). The currents associated with the sweeps reversed at potentials outside the hydrogen adsorption

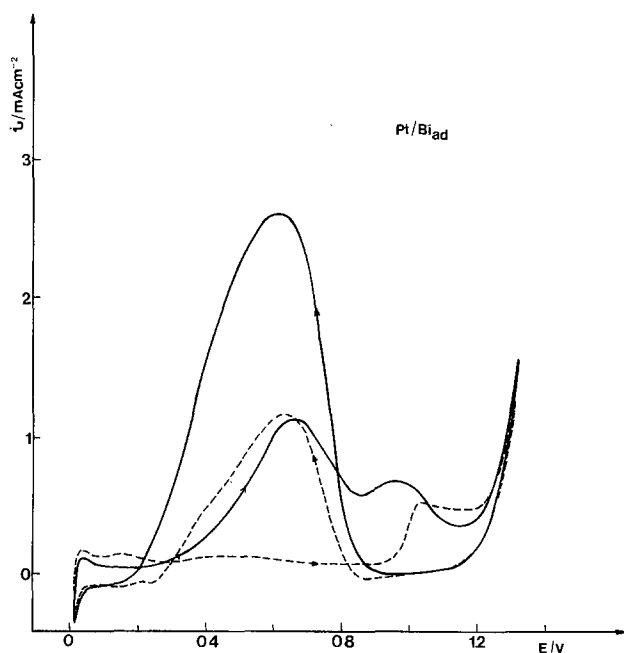


Fig. 6. Oxidation of HCOOH on Pt with Bi adatoms (full line) and on Pt (dashed line) in 85% H₃PO₄, 0.5M HCOOH; sweep rate 100 mV/sec.

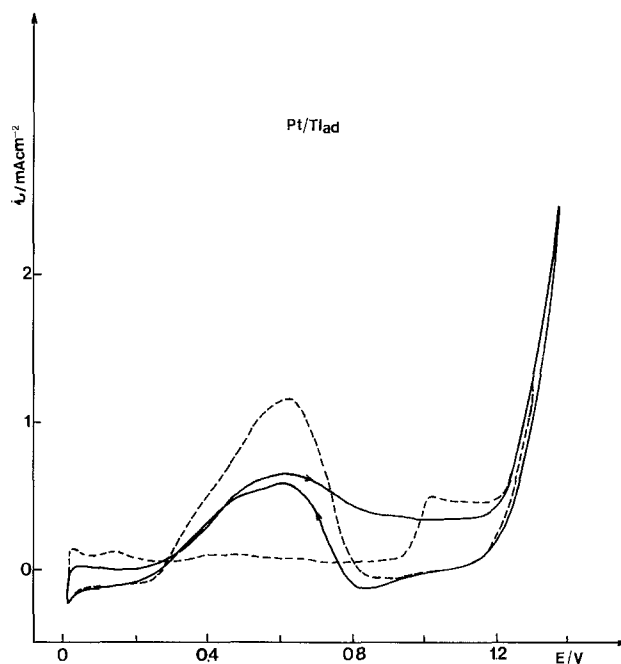


Fig. 7. Oxidation of HCOOH on Pt with Tl adatoms (full line) and on Pt (dashed line) in 85% H₃PO₄, 0.5M HCOOH; sweep rate 100 mV/sec.

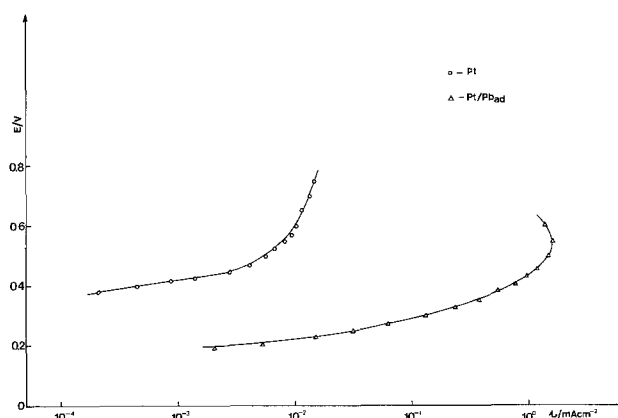


Fig. 8. Steady-state current-potential curve of oxidation of HCOOH on Pt in 85% H₃PO₄, C_{Pb2+} = 1 × 10⁻³M.

are higher than for the sweep which encompasses the whole potential range. The indication is that H_{ad} on Pt has a role in producing strongly bound intermediates in oxidation of CH₃OH on Pt.

A progressive decrease of anodic potential limit (Fig. 10) shows that an incomplete oxidation of strongly bound intermediates leads to a decrease of catalytic activity of Pt.

Figure 11 displays the effect of Pb adatoms on this reaction. The effect is smaller than for oxidation of HCOOH. It is, however, larger than in 1M HClO₄ (3), probably caused by desorption of Pb adatoms before the oxide formation on Pt in 85% H₃PO₄. This view is confirmed by the appearance of the second peak for oxidation of HCOOH (Fig. 5). Platinum is protected from adsorption of strongly bound intermediates by Pb adatoms and after Pb desorption clean Pt surface is available for the oxidation of CH₃OH, since the adsorption of COH can be kinetically controlled. New peaks (solid line) occur at 0.35, 0.5, and 0.8V and the shoulder at 0.65V. The first two peaks and the shoulder are partly caused by the desorption of Pb adatoms. The peak at 0.8V is clearly the catalytic effect, which shifts the oxidation of CH₃OH by 0.2V to less positive potentials. In the cathodic direction an inhibition is ob-

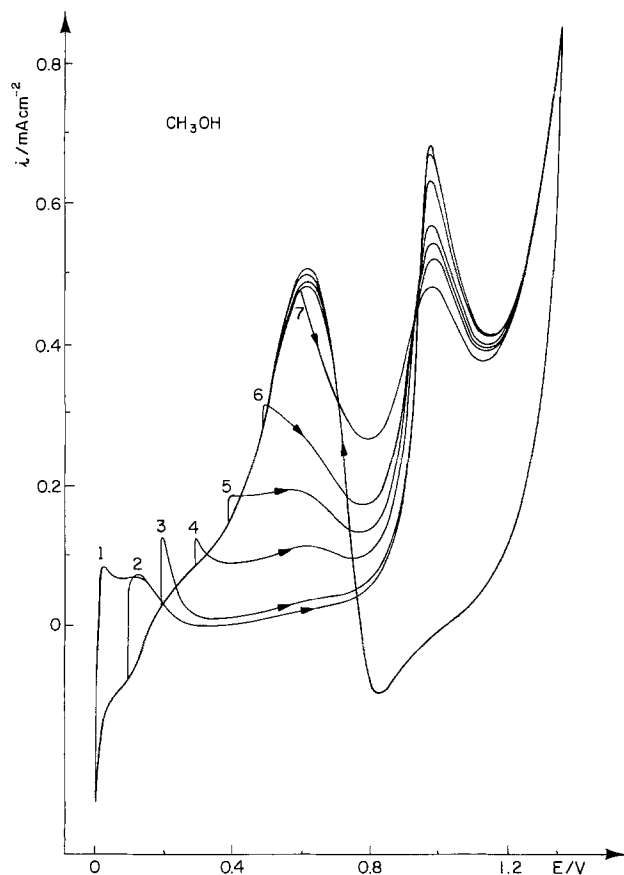


Fig. 9. Oxidation of CH_3OH on Pt in 85% H_3PO_4 . Effects of a progressive decrease of cathodic potential limit. 0.5M CH_3OH ; sweep rate 100 mV/sec.

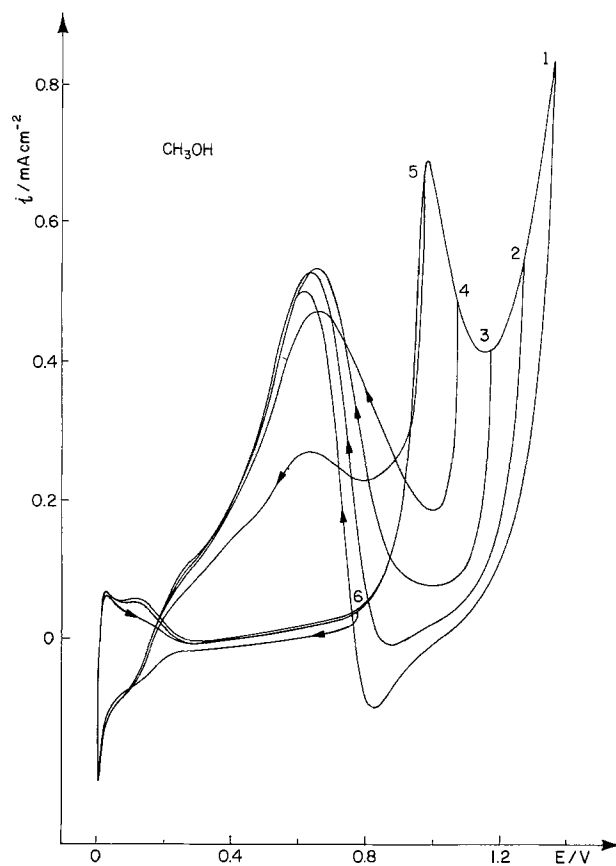


Fig. 10. Oxidation of CH_3OH on Pt. Effects of a progressive decrease of anodic potential limit. Other data as in Fig. 9.

served, caused by an excessive coverage of Pb adatoms formed simultaneously with oxide reduction on Pt. At this high concentration of Pb^{2+} ($C_{\text{Pb}^{2+}}$), a very small portion of the Pt surface is lead- and oxide-free in the cathodic scan. Only on such a surface can the oxidation of CH_3OH occur. For smaller $C_{\text{Pb}^{2+}}$, i.e., smaller θ_{Pb} , both effects are less pronounced (Fig. 11).

Discussion

Oxidation of HCOOH.—The oxidation of HCOOH on Pt has been given considerable attention. The results of various authors differ in details of the reaction mechanism, but agree about the main feature of the reaction, i.e., the formation of strongly bound intermediates which are difficult to oxidize. These intermediates block the surface and reduce the reaction

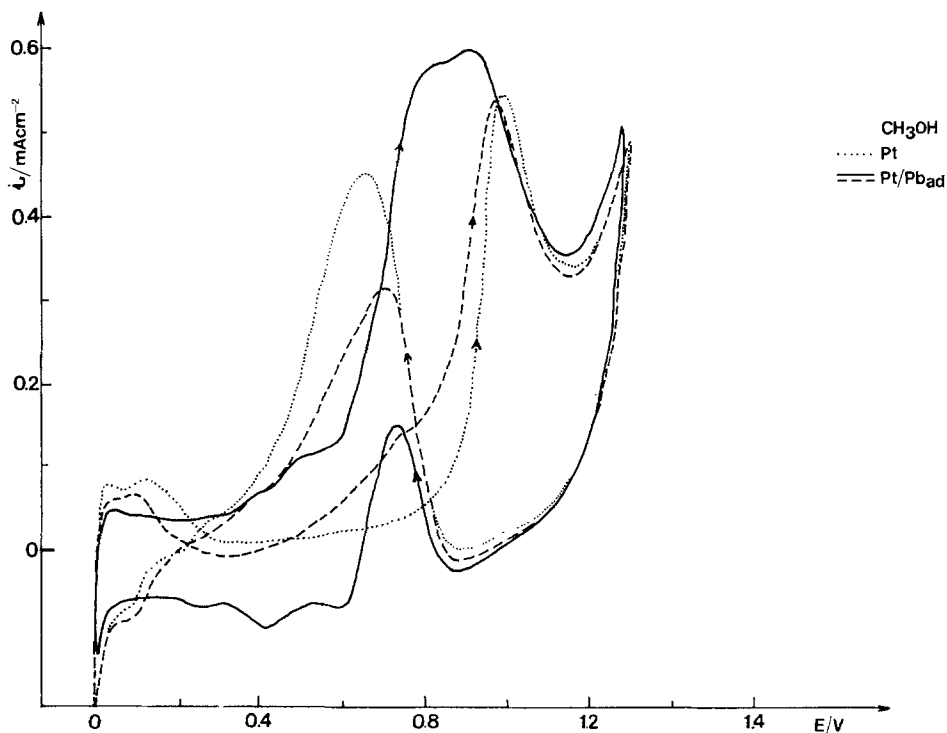
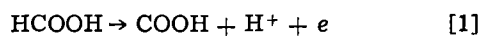


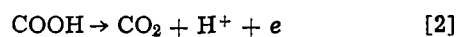
Fig. 11. Oxidation of CH_3OH on Pt (dotted line) and Pt with Pb adatoms (full line and dashed line with 1×10^{-3} and 1×10^{-4} M Pb^{2+} in electrolyte). 0.5M CH_3OH ; 100 mV/sec.

rate. According to a majority of authors, the strongly bound intermediate is the species C OH. [See, for example, the recent reviews by Capon and Parsons (7) and McNicol (8).] In parallel with the reaction leading to the formation of the strongly bound intermediate, a direct oxidation to CO₂ takes place. This apparently occurs only on a small fraction of the surface covered by C OH.

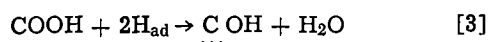
As pointed out above, it appears that there is no major difference between the oxidation of HCOOH in 85% H₃PO₄ and 1N HClO₄, or H₂SO₄. The shape of the voltammogram in 40% H₃PO₄ is the same as in these electrolytes, which suggests the same reaction mechanism. The mechanism given by Capon and Parsons (6) is supported by catalytic effects of foreign metal adatoms. According to these authors, the reaction commences with the oxidative dehydrogenation



followed by further oxidation of carboxy ad-radical

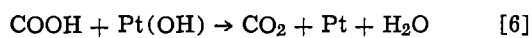
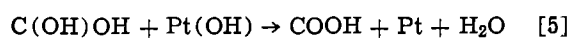
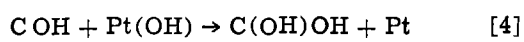


The ad-radical $\overset{\cdot}{\text{C}}\text{OOH}$ also reacts immediately with hydrogen adsorbed on the Pt surface to form the strongly bound intermediate



The species $\overset{\cdot\cdot\cdot}{\text{C}}\text{OH}$ has been postulated by several authors (6,9). The role of H_{ad} in its formation has been clearly illustrated in the work by Capon and Parsons (6). Catalytic effects of foreign metal adatoms provide evidence for the participation of H_{ad} in the formation of $\overset{\cdot\cdot\cdot}{\text{C}}\text{OH}$ (1-3).

The species $\overset{\cdot\cdot\cdot}{\text{C}}\text{OH}$ can be oxidized at higher positive potentials in a reaction with H₂O or OH_{ad} (the peak at 0.9V). On the basis of several sets of data (6, 10, 11), it appears that the reaction with OH_{ad} is more probable



In order to explain all the features of the oxidation of HCOOH on Pt, Capon and Parsons (6) postulated an additional strongly bound intermediate, the species $\overset{\cdot\cdot}{\text{C}}(\text{OH})$ which requires two sites for adsorption. Its oxidation is slow and it eliminates the sites for adsorption of HCOOH causing the peak at 0.5V. It probably occurs in a disproportionation reaction



The existence of such species have also been confirmed by the effects of foreign metal adatoms.

Figure 4 is in agreement with the above considerations based on the analysis of behavior in 1N acid electrolytes. Smaller currents for oxidation of HCOOH are, however, obtained in 40% and especially in 85% H₃PO₄. This is due to the competitive adsorption of phosphate ions which are more strongly adsorbed than ClO₄⁻, or SO₄²⁻ (12,13). A relatively strong specific adsorption of phosphate ions can easily decrease the adsorption of HCOOH and decrease the reaction rate

along the main reaction pathway. It has been shown that Cl⁻ has a detrimental effect on this reaction (15). A shift of the second anodic peak to more positive potentials and its somewhat different shape in 85% H₃PO₄ is caused by the shift of the initial oxide formation on Pt in this electrolyte. This corroborates the view that OH_{ad} is necessary for the oxidation of C OH, rather than adsorbed H₂O. A progressive decrease of cathodic and anodic potential limits supports the mechanism outlined by Eq. [1]-[5].

The adatoms of Pb, Bi, and Tl suppress hydrogen adsorption on Pt (Fig. 1-3). Thus, these adatoms eliminate reaction [3], i.e., the formation of $\overset{\cdot\cdot\cdot}{\text{C}}\text{OH}$ species. This is the primary origin of the catalytic effects of these adatoms. Furthermore, these adatoms also suppress the adsorption of $\overset{\cdot\cdot}{\text{C}}(\text{OH})_2$ intermediate by decreasing

the number of nearest neighbor pairs of Pt atoms necessary for its adsorption. At potentials close to 0.0V, the coverages of Pb, Bi, and Tl adatoms are close to $\theta_M \approx 1$. The oxidation of HCOOH does not take place on such a surface. Hydrogen adsorption is completely suppressed and this prevails into part of the hydrogen adsorption region. At more positive potentials, θ_M commences to decrease and a clean Pt surface is exposed to HCOOH. The reaction can now proceed along the direct oxidation pathway. As long as $\theta_M > 0.5$, the surface is protected from adsorption of $\overset{\cdot\cdot}{\text{C}}(\text{OH})_2$ species because pairs of nearest neighbor

Pt sites are not available. An even distribution of adatoms on the Pt surface is required which appears to be the case for these systems (3).

As θ_M decreases below 0.5, $\overset{\cdot\cdot}{\text{C}}(\text{OH})_2$ commences to adsorb, which decreases the reaction rate. This causes the appearance of the peak in Fig. 6-8, i.e., a decrease of the current, although the overpotential increases.

In the presence of foreign adatoms, the current associated with reaction [1], which appears to be the rate-determining step (6, 15) can be written in the following way

$$i = k(1 - \theta) \exp(1 - \alpha)FE/RT \quad [8]$$

where θ is total coverage of adsorbed species

$$\theta = \theta_M + \theta_{\overset{\cdot\cdot}{\text{C}}(\text{OH})_2} \quad [9]$$

Reaction [2] seems to be fast (6, 15) and therefore the coverage of $\overset{\cdot}{\text{C}}\text{OOH}$ should be negligible. Consequently, it is not taken into account in Eq [9].

If one adatom blocks one Pt site for adsorption of $\overset{\cdot\cdot}{\text{C}}(\text{OH})_2$ then for $\theta_M < 0.5$

$$\theta_{\overset{\cdot\cdot}{\text{C}}(\text{OH})_2} = 1 - 2\theta_M \quad [10]$$

In this case Eq. [8] becomes

$$i = k\theta_M \exp(1 - \alpha)FE/RT \quad [11]$$

When $\theta_M > 0.5$ on the basis of the above discussion, it follows that the rest of the surface will be free from $\overset{\cdot\cdot}{\text{C}}(\text{OH})_2$. Therefore

$$\theta = \theta_M \quad [12]$$

and the current from Eq. [8] is now

$$i = k(1 - \theta_M) \exp(1 - \alpha)FE/RT \quad [13]$$

A semiquantitative calculation based on this model shows that the experimental voltammetry curve for Pt in 1M HClO₄ can be satisfactorily reproduced (2,3). The same is valid for 85% H₃PO₄, except for the peak at 0.85V which has been explained earlier in the text.

Striking catalytic effects obtained in steady-state measurements (Fig. 8) support the view that in the

presence of adatoms, the poisoning intermediate C OH^{***} is not formed, at least by reaction [3]. This species can, however, be formed in the reaction of COOH with HCOOH as shown by reaction [7]. Although lead adatoms are more strongly bound to the surface than C OH, as shown by specular reflectance spectroscopy^{***}

(16), a certain adsorption equilibrium of these two species is established. Besides the equilibrium adsorption of C(OH)₂ takes place at a lower coverage of ad-

atoms. For these reasons, the Pt electrode has lower activity in the steady state than in the transient measurements. The activity is, however, still high and may be of practical interest.

The smaller catalytic effect of Tl adatoms is due to its weaker bond with Pt, which is reflected in its electroadsorption valence (18). Formic acid and its intermediates can therefore affect the adsorption of Tl in the same way as found with Cd (17). Also, partially charged Tl adatoms can induce the adsorption of phosphate ions which would also cause a decrease of the rate of oxidation of HCOOH.

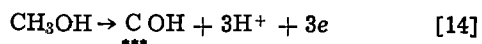
Oxidation of CH₃OH.—The oxidation of CH₃OH apparently leads to the formation of the same strongly bound intermediates as during the oxidation of HCOOH. Frumkin and Podlovchenko (18) have shown that the chemisorption and dehydrogenation of CH₃OH results in formation of C OH. Kazarinov *et al.* (19),^{***}

using a radiotracer technique, have shown that the oxidation of CH₃OH, HCHO, and HCOOH, in both acid and alkaline electrolytes, results in the formation of C OH intermediates. This is in agreement with the re-

sults of Wieckowski (20), Breiter (21), Biegler (22), and Capon and Parsons (7). Vassilyev *et al.* (23) showed how C OH could arise from a whole variety of

organic molecule oxidations. Allen *et al.* (24) using ESCA identified a chemisorbed species as C OH. *In situ*^{***}

identification of this apparently most important intermediate in oxidation of organics would also be desirable. A dehydrogenation of the methyl group leads to the formation of C OH and the oxidation of 3H^{***}



The origin of the catalytic effect of Pb adatoms on this reaction can be explained by a so-called "third body" effect (25). Pb adatoms suppress the adsorption of C OH to a certain extent. The oxidation of CH₃OH^{***}

commences at potentials where θ_M is low, which is the cause of a relatively small catalytic effect. At higher temperatures, the effect should be larger if this explanation is correct, since the oxidation of CH₃OH would shift to lower overpotentials, where θ_M is high enough. In the oxidation of CH₃OH, HCOOH was detected in solution (26). The catalysis of its oxidation probably contributes to the effect observed with CH₃OH. The presence of HCOOH in solution is supported by the role of H_{ad} in oxidation of CH₃OH as seen in Fig. 9.

Motoo *et al.* (10) explained the enhancement of CH₃OH oxidation caused by Ru, Sn, and Ge (27) deposited on Pt as due to a coadsorption of oxygen by these metals. Adsorbed oxygen helps oxidation of COH^{***}

intermediate. Osetrova *et al.* (11) have found that OH coadsorbed on Sn was the active species. Janssen and Moolhuysen (28) and McNicol *et al.* (29) have found that various adatoms modify the adsorption properties of Pt through a ligand effect. There is no indication that Pb, Bi, or Tl coadsorb oxygen or OH species. Ex-

cept for Tl at low coverages, the electroadsorption valence of Pb and Bi on Pt is close to their faradaic valence (18), which supports this view. The modification of uncovered Pt sites by these adatoms, the ligand effect, is not supported by the observation that the foreign metal adatoms do not effect hydrogen adsorption on such sites (17).

Conclusions

Underpotentially deposited metal adatoms on platinum enhance the rates of electro-oxidation of formic acid and of methanol with aqueous phosphoric acid as the electrolyte. The effects are more significant for formic acid oxidation than for methanol oxidation. From the cyclic voltammetric results, it is proposed that the underpotentially deposited metal adatoms (Pb, Bi, and Tl) inhibit the adsorption of atomic hydrogen and hence the formation of the poisoning intermediate. For formic acid oxidation, the electrocatalytic activities follow the order Pb > Bi > Tl. These results can be interpreted on the basis of the higher coverage of the adatoms at lesser positive potentials or due to a weaker bond between the adatoms and the substrate. The magnitudes of the effects of the adatoms are less in phosphoric acid electrolyte than those found previously in perchloric acid, probably due to the specific adsorption of phosphate ions. The use of underpotentially deposited metal atoms as electrocatalysts shows promise for improving the performance of direct organic fuel-air fuel cells.

Acknowledgment

This work was performed under the auspices of the U.S. Department of Energy under Contract No. DE-AC02-76CH00016.

Manuscript submitted May 15, 1980; revised manuscript received March 16, 1981.

Any discussion of this paper will appear in a Discussion Section to be published in the June 1982 JOURNAL. All discussions for the June 1982 Discussion Section should be submitted by Feb. 1, 1982.

Publication costs of this article were assisted by Brookhaven National Laboratory.

REFERENCES

1. R. R. Adzic, D. N. Simic, A. R. Despic, and D. M. Drazic, *J. Electroanal. Chem. Interfacial Electrochem.*, **65**, 587 (1975); **65**, 117 (1975).
2. R. R. Adzic, D. N. Simic, A. R. Despic, and D. M. Drazic, *ibid.*, **80**, 81 (1977).
3. R. R. Adzic, *Israel J. Chem.*, **18**, 166 (1979).
4. D. Ferrier, K. Kinoshita, J. McHardy, and P. Stonehart, *J. Electroanal. Chem. Interfacial Electrochem.*, **61**, 233 (1975).
5. J. C. Huang, R. K. Sen, and E. Yeager, *This Journal*, **126**, 786 (1979).
6. A. Capon and R. Parsons, *J. Electroanal. Chem. Interfacial Electrochem.*, **45**, 205 (1973).
7. A. Capon and R. Parsons, *ibid.*, **44**, 1 (1973).
8. B. McNicol, *Spec. Per. Rep.*, **7**, In press.
9. V. E. Kazarinov and G. Ya. Tsyachnaya, *Elektrokhimiya*, **8**, 292 (1972).
10. S. Motoo and W. Watanabe, *J. Electroanal. Chem. Interfacial Electrochem.*, **69**, 429 (1976).
11. N. V. Osetrova, Yu. B. Vassilyev, and V. S. Bagotsky, *Elektrokhimiya*, **13**, 512 (1977).
12. V. S. Bagotsky, Yu. B. Vassilyev, J. Weber, and J. N. Pirtskhalava, *J. Electroanal. Chem. Interfacial Electrochem.*, **27**, 31 (1970).
13. N. A. Balashova and V. E. Kazarinov, in "Electroanalytical Chemistry," Vol. 3, A. Bard, Editor, p. 135, Marcel Dekker, New York (1969).
14. S. B. Brummer, *J. Phys. Chem.*, **69**, 1363 (1965).
15. S. B. Brummer and A. C. Makrides, *ibid.*, **68**, 1448 (1964).
16. R. R. Adzic and M. M. Podlavicky, *J. Phys.*, **38**, C5-193 (1977).
17. J. W. Shultze and F. D. Koppitz, *Electrochim. Acta*, **21**, 327 (1976).
18. A. N. Frumkin and B. I. Podlovchenko, *Dokl. Akad.*

- Nauk SSSR*, **150**, 349 (1963).
19. V. E. Kazarinov and G. Ya. Tsyachnaya, *Electrokhimiya*, **8**, 731 (1972).
 20. A. Wieckowski, *J. Electroanal. Chem. Interfacial Electrochem.*, **78**, 229 (1977).
 21. M. W. Breiter, *ibid.*, **14**, 407 (1967).
 22. T. Biegler, *J. Phys. Chem.*, **72**, 1571 (1968).
 23. Yu. Vassilyev, V. S. Bagotsky, and O. A. Khazova, *Electrokhimiya*, **11**, 1505 (1975).
 24. G. C. Allen, P. M. Tucker, A. Capon, and R. Parsons, *J. Electroanal. Chem. Interfacial Electrochem.*, **50**, 335 (1974).
 25. H. Angerstein-Kozłowska, B. McDougal, and B. E. Conway, *This Journal*, **120**, 756 (1973).
 26. M. W. Breiter, "Electrochemical Processes in Fuel Cells," Springer-Verlag, New York (1969).
 27. M. Watanabe and S. Motoo, *J. Electroanal. Chem. Interfacial Electrochem.*, **60**, 267 (1975).
 28. M. M. Janssen and J. Moolhuysen, *Electrochim. Acta*, **21**, 801 (1976).
 29. B. D. McNicol, R. T. Short, and A. G. Chapman, *J. Chem. Soc., Faraday Trans. 1*, **72**, 2735 (1976).

Characterization of the Materials Comprising the Reactive Interfaces in the Li(Si)/FeS₂ Primary Battery

Brad J. Burrow, Ken W. Nebesny, and Neal R. Armstrong

Department of Chemistry, University of Arizona, Tucson, Arizona 85721

and Rod K. Quinn* and Dale E. Zurawski

Sandia National Laboratories, Albuquerque, New Mexico 87185

ABSTRACT

Photomicroscopic, electron-microscopic, and surface analytical studies have been conducted on Li(Si)/LiCl · KCl/FeS₂ electrochemical cells before and after discharge, and on individual anode and cathode components. Physical and chemical compositional changes were observed at both the anode and cathode interface that have significance in the discharge mechanism. Oxygen-rich species were found at the surface of the FeS₂ cathode particles and migration of sulfur away from the cathode during discharge was also observed. Thermal shock of FeS₂ single crystals confirmed the tendency for sulfur to move away from the bulk with the application of heat to the surface. Exposure of the Li(Si) alloy to atmosphere and/or thermal shock resulted in the formation of a lithium-rich surface in the carbonate or oxide form. These findings have significance to battery systems that must be stored for long time periods, as well as the possible source of resistive interfaces in charge and discharge cycles.

The Li/FeS₂ primary and Li/FeS secondary batteries are the subject of intense research in several laboratories (1-6). Primary battery applications require that the anode (Li alloys) and the cathode (pelletized FeS₂) be separated by an electrolyte-binder (EB) layer with no membrane separator between them (1). Stacks of these pelletized cells are placed in series to produce the desired operating voltage and the diameter is varied to yield the desired current drain. When operating as a primary power source, the cells normally sit in an inactive state until heated to operating temperatures greater than the melting point of the electrolyte, in times on the order of seconds (or less). Optimization of the operation of these batteries and development of design criteria for future high energy density batteries, must be preceded by a better understanding of the chemical and electrochemical reactions which proceed at each interface. To this end, we have conducted several studies on intact single cells and on individual anode, cathode, and electrolyte components. A typical single cell is discharged as variable currents from 0.1 to 1.0A producing a cell voltage of 1.5-1.9V for periods from minutes to hours using previously described techniques (1). These discharges do not normally consume the entire power capacity of the materials within each cell.

In this paper, we report on the correlation of electron microscopic, photomicroscopic, and various electron spectroscopic surface analysis data to the study of the Li(Si) alloy/electrolyte-binder interface and the FeS₂/electrolyte-binder interface from single cells and battery discharges. Migration of components from both anode and cathode during heating and discharge is noted. Surface analysis of discrete anode and cathode components and of standard materials confirm many of these migration processes.

Experimental Section

The materials used for single cell testing were typical battery compositions (4). The anode pellet was made from an Li(Si) alloy of 40 or 45 weight percent (w/o) Li. Standard particle size was 76-422 μm (-40 to +200 mesh) yielding a typical pellet density of 1.0 g/cm³.

The electrolyte-binder (EB) pellet, used to separate the anode and cathode, was composed of an LiCl · KCl eutectic (45/55 w/o) and a MgO binder (Maglite S, Merck Chemical Company, San Francisco, California). The finely divided MgO acts to immobilize the electrolyte when melted but does not react with either the anode or cathode. The mixture was composed of 70 w/o electrolyte and 30 w/o binder and formed to a density of about 1.7 g/cm³.

The cathode powder was 64 w/o FeS₂, 16 w/o LiCl · KCl eutectic electrolyte, and 20 w/o EB. The EB used

* Electrochemical Society Active Member.

Key words: fused salts, electrode, electron spectroscopy, passivation.

in the cathode was 12 w/o SiO_2 binder and 88 w/o $\text{LiCl} \cdot \text{KCl}$ eutectic. FeS_2 was readily available as granular iron pyrite obtained from Matheson, Coleman, and Bell Manufacturing Company, Norwood, Ohio, with a particle size less than $295 \mu\text{m}$ (50 mesh). Pellets were formed to a density of 2.6 g/cm^3 .

To assemble a cell, the pellets were stacked around a centering post and sandwiched between two stainless steel disks used as current collectors. The assembled cells were then placed between preheated platens to melt the electrolyte, and discharged for various times and at various temperatures and current densities on a standard single cell tester (6).

For microscopic studies, discharged cells were broken through the center and the exposed interface was smoothed with increasingly finer sandpaper. Optical examination before and after sanding showed that the integrity of the diffused material was preserved. Cells from any given series of discharges were assembled as a unit and examined simultaneously under both the optical and the scanning electron microscopes. The interfaces of particular interest in this study involve the electrochemically active $\text{Li}(\text{Si})$ anode and FeS_2 cathode with $\text{LiCl} \cdot \text{KCl}$ electrolyte and MgO binder (all 1 mm thickness).

All experimental apparatus except the Auger electron and x-ray photoelectron spectrometers was located in a "dry room" facility with an atmosphere containing less than 300 ppm water. This unique feature allows cells to be prepared, discharged, and microscopically examined in a relatively water-free environment.

The scanning electron microscope is an International Scientific Instruments Model Super III-A with a resolution of 70\AA . Samples were examined under a $100 \mu\text{A}$ beam current with a 30 keV accelerating voltage. The electron probe microanalysis (EM) using energy dispersive x-ray spectroscopy (XRF) was performed with a Princeton Gamma-Tech XCEL-1000 analyzer. The analyzer used a lithium-drifted silicon detector with a measured resolution of 153 eV and 1000 counts/sec at 5.9 keV. For the elemental analysis, samples were examined under $3000\times$ magnification exposing a surface area of 0.03 mm^2 . The spectra were collected for 30 sec from five different spots on each pellet and then averaged. To quantify the amount of a given element, window integrals were used to measure x-ray counts; the number of counts being proportional to the amount of an element. The x-rays emitted by the element within a given energy range or window were first counted. The number of x-rays in a background window were simultaneously counted; the background window being selected to have the same width and close to the same energy as the elemental window but not containing any x-rays from the element. The elemental x-rays were then divided by the background x-rays resulting in a unitless ratio (S/S° and $\text{Fe}/\text{Fe}^\circ$). The ratio reflects an atomic intensity uncorrected for the fluorescence atomic sensitivity.

The Auger electron spectroscopy (AES) data were taken with a Physical Electronics Auger system with a single-pass, cylindrical mirror analyzer. For a typical spectrum, the electron gun was operated at 2 kV and $5\text{--}20 \mu\text{A}$ and a beam diameter of ca. 0.1 mm was maintained. The pressure was maintained at 5×10^{-10} Torr. The cells were broken in a glove box in high purity argon and transferred quickly to the high vacuum chamber. Careful microscopic examination indicated no visible signs of contamination. This observation is supported by the fact that little or no carbon was observed in the AES spectra. Carbon peaks are typical of most contamination.

X-ray photoelectron spectroscopy (XPS) data were taken from a GCA McPherson ESCA 36 Photoelectron Spectrometer using a 127° electrostatic deflector as an

electron analyzer. The x-ray source emitted $\text{MgK}\alpha$ radiation (1253.6 eV). The spectrometer was interfaced to a PDP 8/e minicomputer, which provided a summation average of the spectra as well as digital control of the analyzer. For all the spectra obtained, pressure was maintained in the $10^{-7}\text{--}10^{-8}$ Torr range.

Results and Discussion

Photomicroscopic and electron microscopic studies.—Figure 1 illustrates a typical voltage-time dependence of a single cell discharged at 100 mA/cm^2 and 520°C . Curve (a) is the total cell potential while curve (b) is the anode-to-reference potential and curve (c) is the cathode-to-reference potential. From these data, the following reproducible features are noted. A positive voltage excursion is observed during the first minute of discharge followed by a nearly constant voltage response of 1.5–1.6V for the next several minutes. A decline in operating voltage is observed after about 20 min for anodes of this composition (i.e., approximately 45 w/o). Small voltage changes observed during discharge have been shown to be due to compositional changes of the lithium alloy (3, 25). Polarization of the cathode is responsible for the steadily declining potential after about 30 min of discharge. Finally, the sharp decline in cell voltage occurs when the anode can no longer support the current drawn, i.e., at about 85% of theoretical Li capacity. However, batteries built with these cells and tested at this current density typically experience end of life due to the internal temperature cooling to $<352^\circ\text{C}$, normally expending less than 50% of the lithium capacity.

Significant compositional changes at the anode/electrolyte interface and at the cathode/electrolyte interface were indicated by study of the photomicrographs of cross-sectioned, discharged single cells. Figure 2 shows the photomicrographs of three single cells which were, (a) held at open circuit for 2 min, (b) discharged at 0.25A for 20 min, and (c) discharged at 0.25A for 80 min—all at 520°C .

Several features were evident in all photomicroscopy studies. These are summarized as follows: (i) a significant change in color and morphology was observed for the anode at the electrolyte interface following discharge; (ii) the FeS_2 particles which comprise the cathode material undergo an apparent phase transformation at their outer perimeter. The transformation is dependent upon the extent of discharge of the single cell and the temperature of the discharge; (iii) a new phase appears as a layer in the electrolyte-binder (EB) region following discharge. The thickness of this

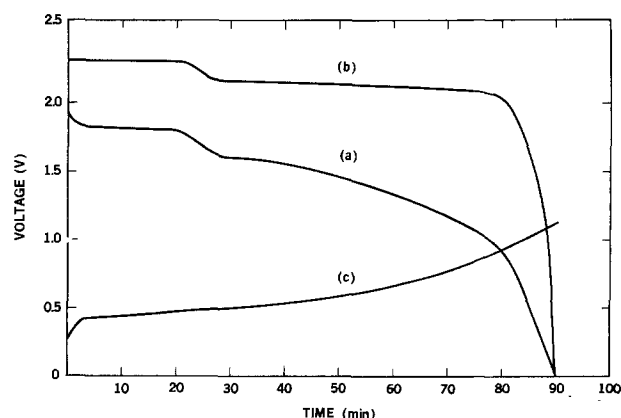


Fig. 1. Discharge curves of a typical $\text{Li}(\text{Si})\text{-FeS}_2$ single cell. Current Drain = 100 mA/cm^2 , temperature = 520°C . Curve (a) cell potential vs. reference as a function of discharge time; curve (b) anode potential vs. reference; curve (c) cathode potential vs. reference.

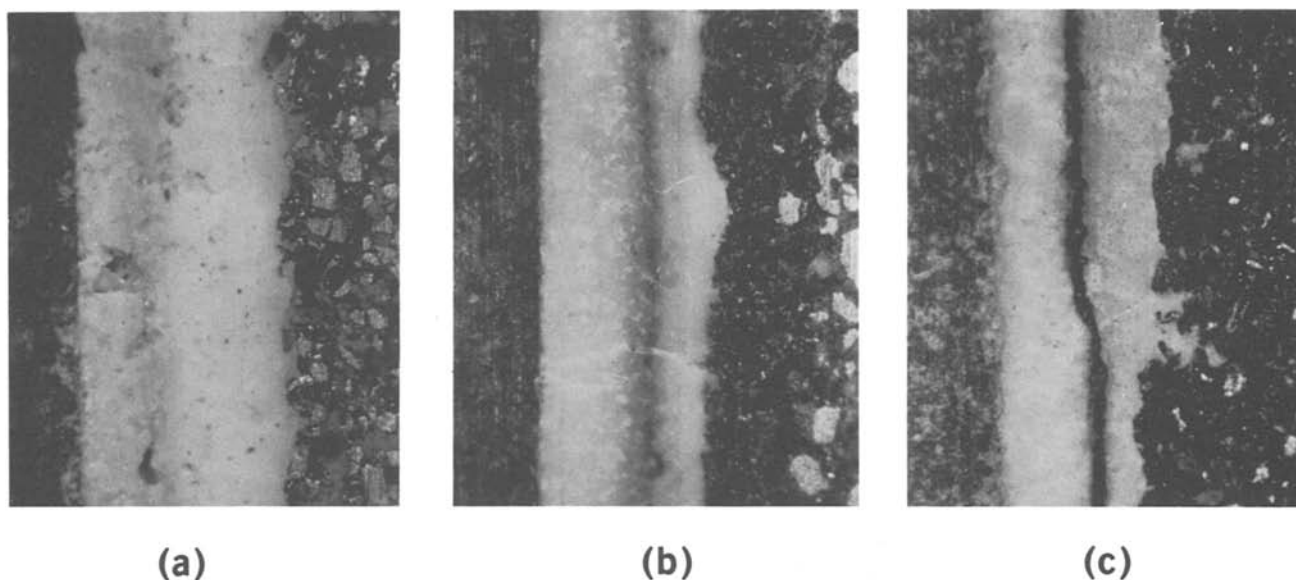


Fig. 2. Photomicrographs of the cross sections of three single cells which were (a) held at open circuit for 2 min at 520°C, (b) discharged at 0.25A for 2 min, and (c) discharged at 0.25A for 80 min. The anode layer is at the left, the EB layer at the center, and the cathode layer is at the right in each photograph.

layer and its proximity to the anode is a complex function of the discharge current, temperature, and voltage. This layer can be seen in the center of Fig. 2(b) and (c). From these photomicrographic studies, it was apparent that stoichiometric changes were occurring at each interface which may have significance

for the performance of these and other lithium-metal sulfide batteries.

Electron microscopic studies of similarly discharged cells were conducted to further study the changes noted above. Figure 3 shows three photomicrographs and the corresponding x-ray fluorescence dot maps

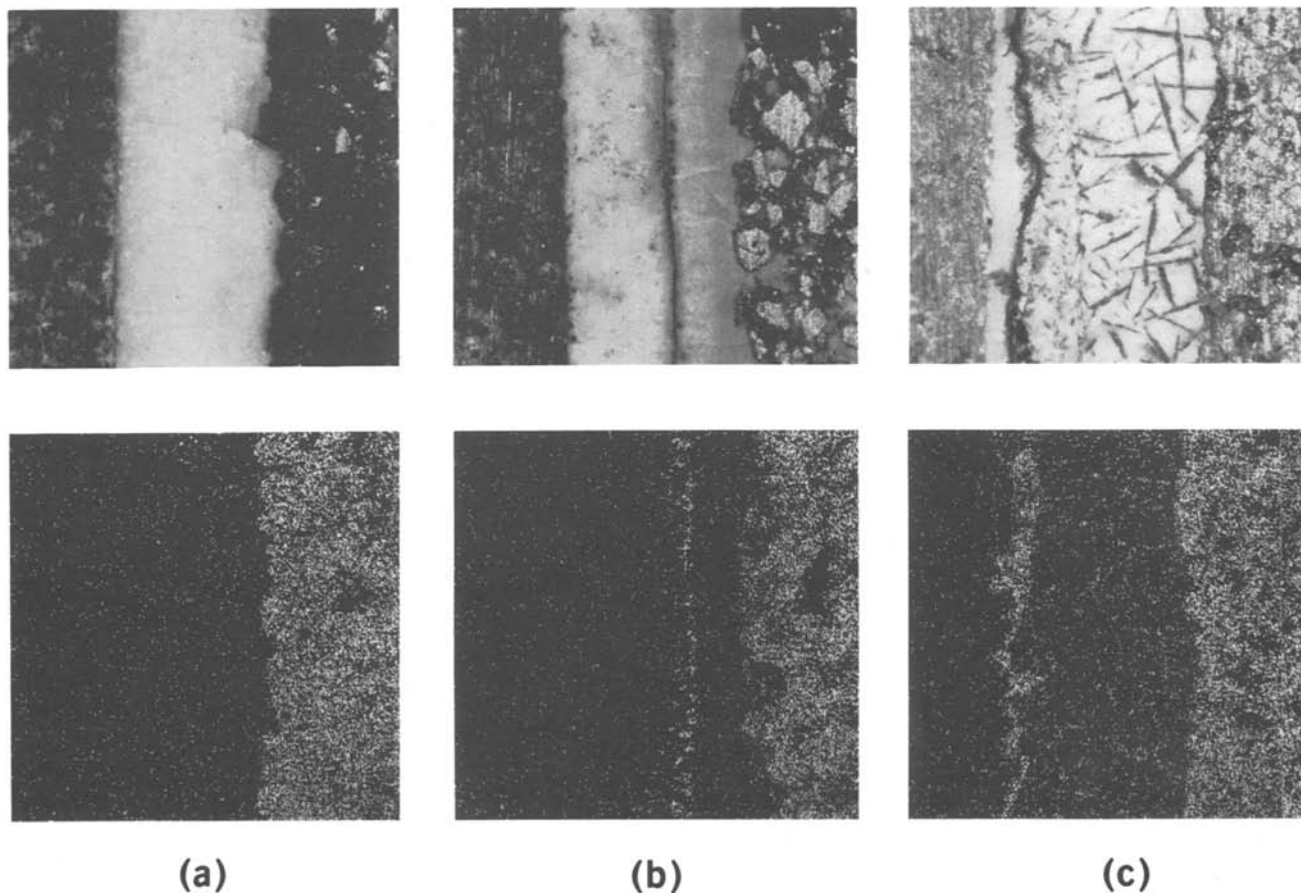


Fig. 3. Scanning electron micrographs and sulfur ($K\alpha$) x-ray fluorescence dot maps of cross sections of three single cells which were discharged at 1.0A for 20 min at (a) 440°C, (b) 520°C, and (c) 600°C. Again the anode, EB layer, and cathode are displayed from left to right.

for sulfur ($K\alpha$ radiation excited at 25 keV) as a function of discharge temperature, from 440° to 600°C. The new phase in the EB layer is transformed from a discrete band to more dispersed linear regions of new material as the discharge temperature increases. The sulfur density maps show the movement of sulfur from the cathode region into the EB layer. Iron (Fe, $K\alpha$) was also detected by the XRF method, in the same region as sulfur. Tables I and II give more information on the stoichiometric changes undergone at the cathode/EB interface. Table I shows the relative increase of both sulfur and iron in the EB layer as a function of discharge time. Table II shows the relative increase in each element with increasing discharge temperature. In all cases the concentrations of sulfur and iron show increases of a factor of two to four by increasing either time or temperature of discharge. TEM and x-ray analysis of the portions of the sulfur-rich phase in the EB layer of cells discharged under high current drain have indicated the presence of lithium sulfide and an Fe containing phase.

Further studies of compositional changes at the anode and cathode/electrolyte interfaces were carried out using Auger electron spectroscopy (AES). AES spectra were recorded on a point-by-point basis as a function of lateral position on nondischarged and discharged single cells and then compared with electron micrographs of similar regions of the single cell. The computation of relative atomic ratios for certain elements as a function of distance is shown in Fig. 4. We have recorded the sensitivity-corrected intensity of each element as a relative atomic ratio with respect to

Table I. Relative sulfur ($K\alpha$) and iron ($K\alpha$) x-ray fluorescence (XRF) intensities in the EB layer of a single cell, discharged at 0.25A, 520°C for the times shown

| Time (min) | S/S° | Fe/Fe° |
|------------|------|--------|
| 2 | 1.3 | 0.94 |
| 10 | 3.4 | 1.0 |
| 20 | 6.3 | 1.2 |
| 40 | 7.2 | 1.4 |
| 80 | 9.8 | 2.7 |

Table II. Relative sulfur ($K\alpha$) and iron ($K\alpha$) XRF intensities in the EB layer of single cells discharged at 1.0A for 20 min at the temperatures shown

| Temp (°C) | S/S° | Fe/Fe° |
|-----------|------|--------|
| 440 | 1.2 | 0.98 |
| 520 | 6.9 | 1.2 |
| 600 | 8.4 | 3.1 |

chlorine. Analysis of the data in this fashion removed many of the uncertainties in the relationship between intensity of the Auger signal and real concentration of the element (7). Chlorine was an ubiquitous component of each single cell. The cathode pellets are a mixture of FeS_2 and the $LiCl \cdot KCl$ eutectic, the EB layer is composed mainly of that same eutectic, and chlorine is found throughout the anodes of cells heated to high temperatures. Fluctuations of the elements noted below are not due to large changes in the chlo-

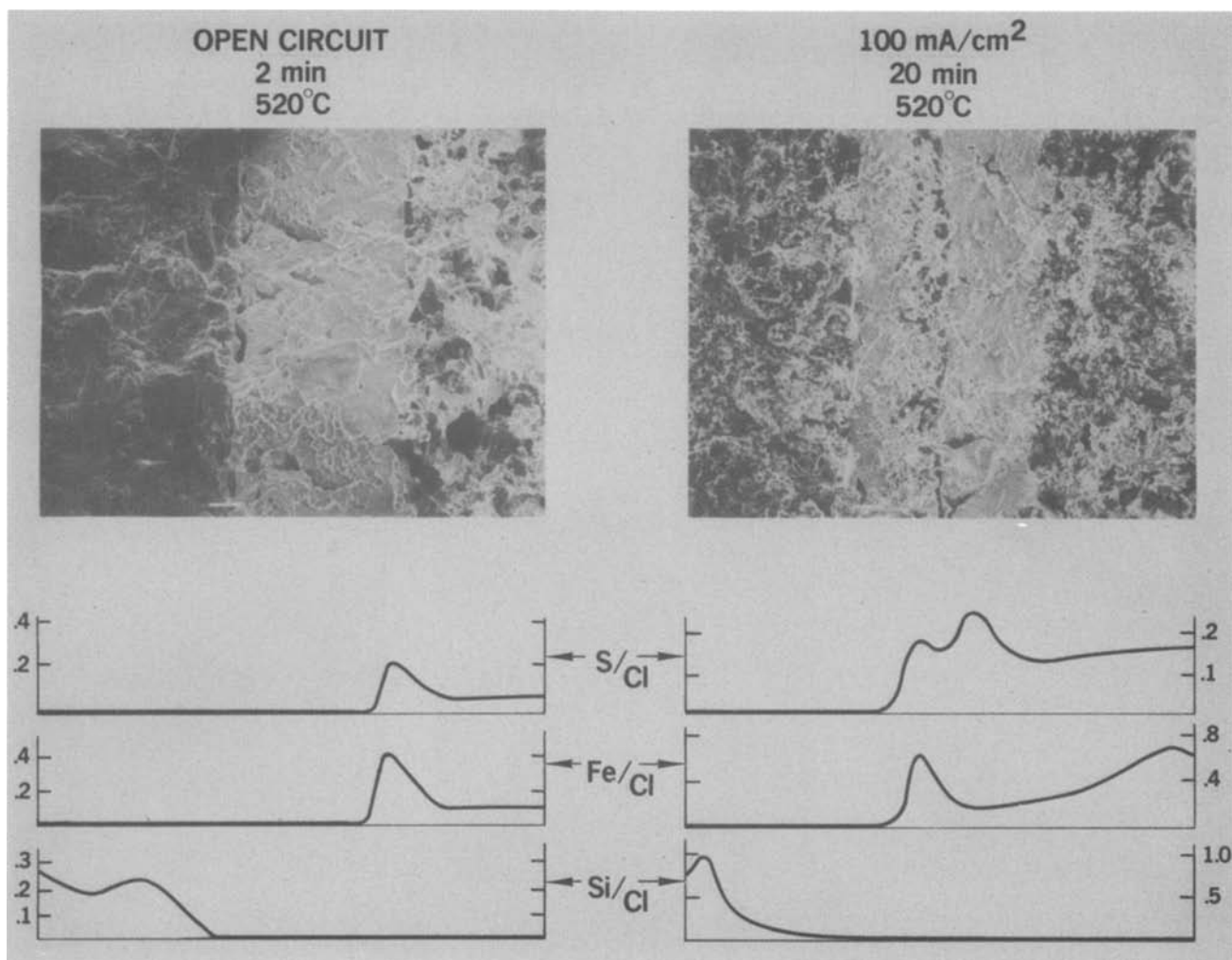


Fig. 4. Scanning electron micrographs and AES/line scans for the relative atomic ratios of sulfur, iron, and silicon in freshly fractured single cells which were (a) held at open circuit for 2 min at 520°C, and (b) discharged at 0.1A for 20 min at 520°C.

rine AES intensity as this intensity remained reasonably constant.

Figure 4a shows the Fe (LMM), S (LMM), and Si (LMM) line profiles for a cell heated to 520°C, but not discharged. There was some variation in the iron and sulfur relative atomic ratios in the cathode layer. Concentrations of iron and sulfur were also detected at the EB interface. It is worth noting that the relative atomic ratio for silicon at the anode/EB interface increases as a function of distance away from that interface. Since the Li/Cl ratio remained constant in this same region, we conclude that some depletion of silicon occurred at the anode/EB interface. The lowering of the silicon content was not due to wetting of the Li(Si) alloy by the LiCl/KCl eutectic. These results are corroborated by other surface analysis studies presented below. Figure 4b shows similar data for a single cell discharged at 520°C for 20 min at 1.0A. The line profiles for this cell clearly show the migration of both sulfur and iron away from the cathode/EB interface. This observation was made several times on different locations along the plane of the single cell, thus it is clearly not an artifact of the fracture procedure. These results confirm the presence of sulfur and of iron in the EB layer as seen by electron microprobe techniques. Figure 4b also confirms the depletion of silicon from the anode/EB interface. It is not yet clear whether this depletion is directly related to the morphological changes observed in the photomicrographs of the anodes which have been heavily discharged.

Surface analysis of individual anode and cathode components.—The discharge behavior of the lithium/silicon-iron disulfide primary batteries is obviously complicated by a variety of morphological and compositional changes. X-ray photoelectron spectroscopy (XPS) and AES, with ion-beam depth profiling, were conducted on the separate anode and cathode materials to help in the elucidation of these changes.

XPS/AES studies of the iron disulfide cathode materials.—The XPS data obtained for the powdered and single crystal iron sulfides and related standard materials are shown in Fig. 5 and 6. Of particular interest is the comparison of the surface compositions of the various FeS₂ materials. Figure 5 shows changes in the

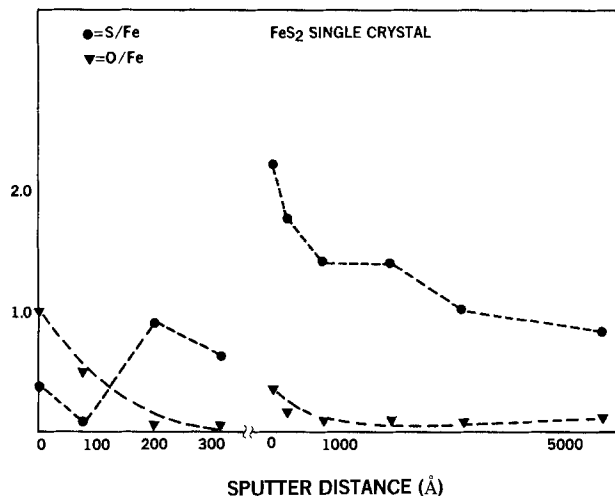


Fig. 6. AES/depth-profile plot of FeS₂ single crystal surface before and after electron beam annealing.

Fe(2p, 1/2, 3/2) peaks of a sample which was synthesized in our laboratory and a commercial FeS₂ sample. Larger amounts of oxygen are present on the surfaces of the commercial samples. Examination of the sulfur (2s) or (2p) peaks in Fig. 6 indicates that the sulfur exists in the form of SO₄²⁻ anions (perhaps SO₃⁻ anions) in addition to the sulfide form (8) on the commercial FeS₂. Further evidence of the different surface features of the two FeS₂ samples lies in the existence of energy-loss peaks of the Fe(2p) transitions of the commercial sample. These peaks indicate the probable presence of Fe(III) on the surface material (9). It is possible that oxygen is bonded directly to iron in both the FeO and Fe₂O₃ forms, as well as in iron sulfates on the commercial FeS₂. The presence of oxygen-rich materials in the cathode may lead to a positive voltage excursion in the initial stages of primary cell discharge (1, 26). This voltage excursion (as shown in Fig. 1) is minimized by using cathode materials that are oxygen-free, and by discharging in an oxygen-free atmosphere (22).

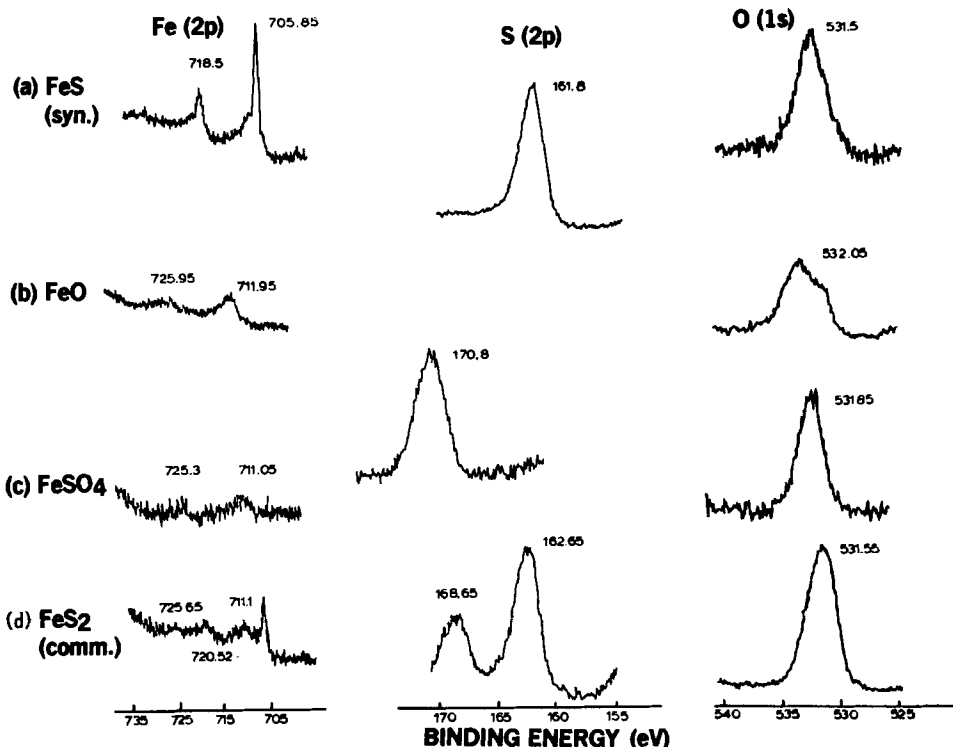


Fig. 5 ESCA spectra of FeS₂ cathode and standard materials, Fe(2p), S(2p), and O(1s) spectral regions. Spectra (a) FeS₂ prepared standard; spectra (b) FeO standard, spectra (c) FeSO₄ standard, and spectra (d) FeS₂ commercial sample.

An AES study was performed on 1 mm slices of single crystals of natural FeS_2 (not polished) to obtain a comparison of surface composition with the XPS data, a depth profile of the crystal, and information on the movement of species through the lattice at the high operating temperatures normally found in the battery during discharge. Single crystal FeS_2 was selected for study as a matter of convenience. It is known that the discharge behavior of single cells using single crystal FeS_2 cathodes is very similar in its initial stages to the behavior observed using pelletized FeS_2 particles (6). The surface compositional changes observed at the FeS_2 single crystal surface can be extrapolated to those observed in the smaller particles.

The AES surface spectra of the FeS_2 surface showed adventitiously adsorbed carbon and oxygen and no other impurities. Brief ion sputtering removed these adsorbed materials and left a surface with an S/Fe ratio of 0.63. This number is corrected for ionization cross section, but does not reflect the true stoichiometry because of the uncertainties in such numbers for both the major sulfur and iron Auger transitions. An electron beam heater was used to thermally shock the FeS_2 samples while still in ultrahigh vacuum. Figure 6 shows the results of an AES/depth profile, before and after treatment of the FeS_2 surface with a 2W electron beam for 30 sec. Following the application of the thermal shock, a large increase in the S/Fe ratio (≥ 2.0) was observed, consistent with the migration of sulfur away from the FeS_2 matrix. Following several thousand seconds of ion sputtering, the original surface composition was achieved.

SEM/EM analysis of the thermally shocked FeS_2 samples confirmed the morphological and chemical changes indicated by the AES studies. A distinct separation of phases was indicated following thermal shock. X-ray fluorescence point analysis indicated a sulfur-rich nonhomogeneous layer on the surface of the crystal (extending to depths of up to 1 μm), and a sulfur-deficient layer underlying. X-ray diffraction of the underlying layer showed it to be mainly $\text{FeS}_{0.9}$ (pyrrhotite). The formation of this phase by simple application of heat is discussed below with regard to compositional changes in the primary battery.

Further studies have shown that prolonged heating (greater than 1 min) under the conditions in Fig. 6

further increased the S/Fe ratio on the single crystal surface. Electron beam heating of the sample under conditions sufficient to cause desorption of sulfur from the surface while at about 10^{-9} Torr caused a decrease of the surface S/Fe ratio back to levels that were seen on the unheated surface. These experiments are described in more detail elsewhere (14).

XPS/AES studies of anode materials.—XPS spectra were obtained from 40 w/o Li(Si) alloy and 45 w/o Li(Si) alloy, and lithium/silicon alloys which had been exposed to atmosphere. The carbon (1s) spectra [as in Fig. 7(c)] indicated the presence of two forms of carbon on the surface of the Li(Si) alloy. This was the case for all lithium metal samples examined. The larger peak at lower binding energy [charge shift corrected to 284.4 eV (7)] was attributed to hydrocarbon contamination of the XPS vacuum system. Comparison of the C(1s) peaks of the alloy to the Li_2CO_3 standard indicated that the rest of the alloy surface carbon was probably present as the carbonate species. As discussed below, this contaminant was not observed in the AES experiments conducted in a cleaner vacuum. It does imply, however, that the carbonate will be a contaminant on samples exposed to normal battery assembly atmospheres.

In attempting to record XPS spectra of Li(Si) alloy samples which had been exposed to atmosphere for long times (10–24 hr) we discovered an interesting technique for examining a freshly exposed Li(Si) alloy surface. Spectra shown in Fig. 7(a) show the C(1s), Si(2s), and Li(1s) regions for surfaces which were atmospherically exposed for 10 hr, loaded into the XPS system, and then had the fresh Li/Si surface exposed just prior to analysis by physical removal of the passive layer which forms on these materials. Figure 7(b) spectra were obtained for the same spectral regions on a sample which had been freshly fractured under argon and then atmospherically exposed for 1–5 min prior to loading in the spectrometer. Spectra illustrated in Fig. 7(c) are for a sample fractured and loaded in atmosphere. Comparison of Fig. 7(a), (b), and (c) indicated that carbonate buildup on the alloy surface is slow at 10^{-7} Torr, but still appreciable over the 24 hr required to achieve operating vacuum. It appears that the first few monolayers

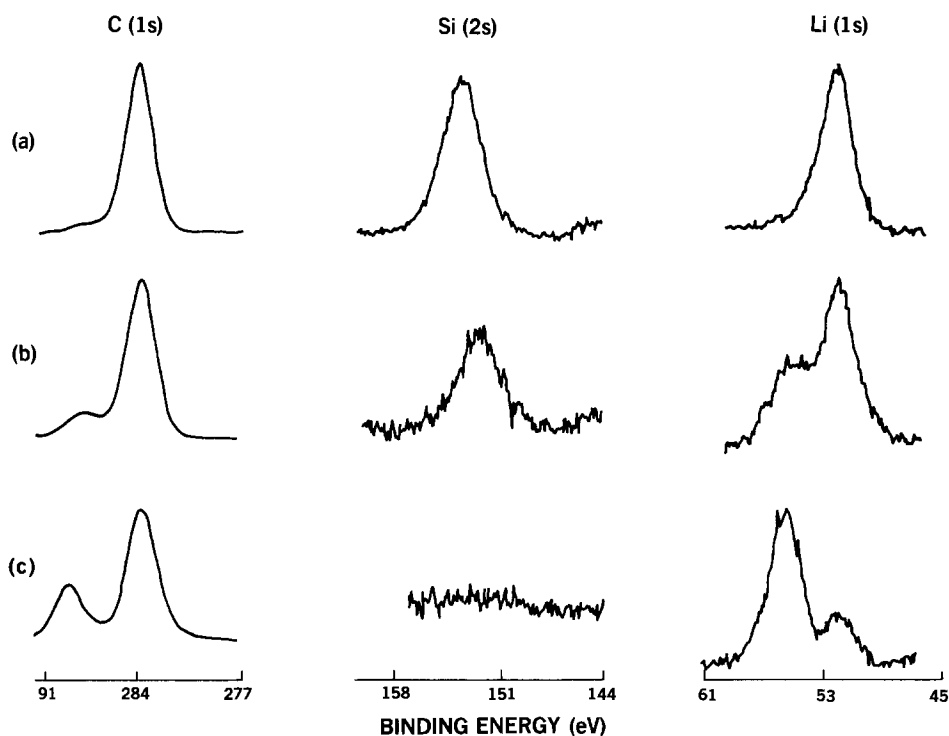


Fig. 7. XPS C(1s), Si(2s), and Li(1s) spectra of 40 w/o Li/Si alloys exposed to atmosphere for various times: (a) the C(1s), Si(2s), and Li(1s) spectra of freshly exposed Li/Si alloy; (b) the C(1s), Si(2s), and Li(1s) spectra of Li/Si alloy exposed momentarily to atmosphere; (c) the C(1s), Si(2s), and Li(1s) spectra of Li/Si alloy fractured and loaded under a normal atmosphere.

were added very quickly (less than a few minutes). Subsequent buildup probably follows an isotherm dependence as observed for other active metals.

The Si(2s) spectrum in Fig. 7(c) showed that no detectable silicon was present on the strongly passivated alloys. Since the escape depth of the Si(2s) electron is about 20-35Å in most solids, this lack of a silicon signal implies a silicon-depleted layer of at least 50-100Å (12, 27). The freshly exposed surfaces showed higher concentrations of silicon. Aging studies discussed below indicate the segregation of lithium and silicon during passivation of the surface.

The Li(1s) spectrum of the freshly exposed Li(Si) surface is shown in Fig. 7(a). The pristine nature of this surface was confirmed by the appearance of only one Li(1s) peak due to lithium metal (13). On those samples which have been partially passivated, two Li(1s) peaks are observed [Fig. 7(b) and (c)]. One might expect that only ionic lithium, with a higher Li(1s) binding energy, would be observed on these samples. Previous studies have shown the reduction of ionic lithium compounds to metallic lithium by the x-ray source (11). Two forms of lithium are always observed in an XPS spectrum of any lithium salt. Figures 7(b) and (c) show an ionic lithium whose concentration roughly correlates to the extent of passivation. Further studies of the kinetics of x-ray photoreduction of these compounds and the kinetics of surface passivation are underway (14).

In studies conducted thus far, no evidence of the formation of Li₃N on the Li(Si) surface has been observed. N(1s) signal intensities were below detectable limits. Although nitrogen will react with lithium at room temperature (15), the reaction is too slow to effectively compete with reactions of the metal with CO₂, H₂O, and O₂. Furthermore, Li₃N decomposes in the presence of H₂O to form Li₂O and NH₃ (16).

Figure 8 shows the AES spectrum of a typical Li/Si alloy (45 w/o). The surface of this material [Fig. 8(a)] showed only lithium, oxygen, and traces of carbon and silicon in the spectrum. The low levels of silicon are consistent with the XPS data; the absence of carbon is likely due to the fact that these materials were freshly fractured under high purity argon and loaded into the AES, UHV system directly. An expanded AES spectrum indicated that the precise energy position and intensity of the lithium Auger transitions are strongly dependent upon chemical form and matrix (17-21), but our data clearly indicate no metallic lithium on the surface (21). Lithium does not possess sufficient core electrons to undergo an intra-atomic, Auger ionization. The detected electron must be donated by neighboring atoms; thus, several Auger transitions are possible, depending on the energy levels of the electrons in the neighboring atoms (18). These AES spectra show transitions consistent with lithium in a fully oxidized form (17).

Following extensive ion sputtering, a larger silicon peak appeared [Si/Li = 0.26, Fig. 8(b)]. The alloy stoichiometry was still not achieved even after prolonged sputtering. We feel that the heating caused by the incident ion beam is also responsible for initiating migration of the lithium away from the bulk alloy (see below). The continued presence of oxygen on the extensively sputtered surface is puzzling. The bulk composition of the alloy does not indicate appreciable oxygen present (22). When the sample in Fig. 8 was exposed to laboratory atmosphere for about 10 min, and then reanalyzed, the spectrum in Fig. 8(c) was obtained. Note the disappearance of silicon in favor of increased lithium and oxygen intensities. This again demonstrates the effect of atmospheric passivation on these alloys.

To approximate the conditions seen by the freshly exposed anode surface in the high temperature battery

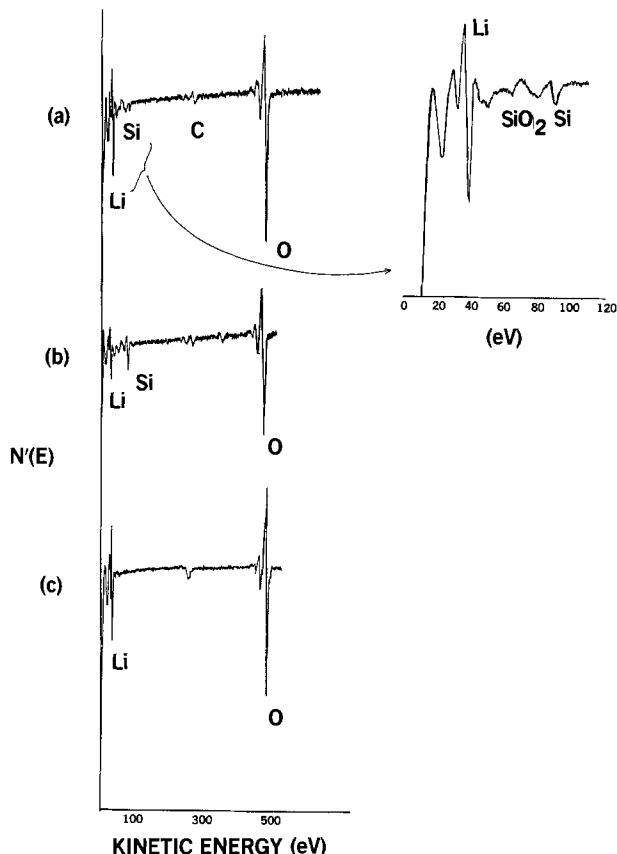


Fig. 8. Auger spectra and ion-beam depth profiling of 45 w/o Li(Si) alloy. (a) Surface scan; (b) surface scan after approximately 5000Å had been ion-beam sputtered, and (c) surface scan after exposure to the atmosphere for 10 min.

environment, a series of experiments was conducted where an ion-sputtered alloy was subjected to thermal shock using an electron-bombardment heater. The alloy surface was ion sputtered until appreciable silicon was present [Si/Li = 0.14, similar to Fig. 8(c)]. The surface was then subjected to E-beam heating of 1W for 1 min and the silicon dropped to below detection limits. Clearly, heating of the sample caused migration of the lithium away from the silicon as was the case for atmospheric passivation. Diffusion of Li into p-type single crystals of silicon at high temperatures has been reported previously (23), supporting this hypothesis.

Discussion

The microscopic examination of the cathode and anode materials before and after discharge leads to the observations that (i) the FeS₂ particle undergoes a chemical and physical change at its surface which likely leads to the migration of a sulfur-rich layer into the EB region of the single-cell; and (ii) there is a color change and a morphological change in the Li(Si) anode during discharge which is likely due to a chemical compositional change. This compositional change is possibly due to the migration of lithium away from the anode bulk, as shown by AES studies. The AES/XPS experiments on the individual components show that (i) there is a significant concentration of oxygen-rich species on the surface on the FeS₂ cathode; (ii) that thermal shock of the cathode material leads to a migration of sulfur away from the bulk and leaves a substoichiometric iron sulfide behind; (iii) a passive oxide/carbonate film forms on the Li(Si) surface following exposure to atmosphere; and (iv) that atmospheric passivation and/or thermal shock of the anode material leave an anode surface that is rich in ionic lithium.

Oxide-rich forms of sulfur and iron on the cathode surface may be responsible for the initial voltage excursion seen in the cathode during single cell discharge. The voltage excursion correlates with the particle size used in the cathode pellet (6). Smaller cathode particles lead to a larger voltage excursion which is consistent with their higher oxide content. Depletion of the oxide-rich layer leads eventually to a more constant discharge voltage.

Thermal or electrochemical migration of sulfur away from the cathode material is not unexpected, especially at the operating temperature of the thermal battery system. Thermal loss of sulfur can cause serious problems in the poisoning of current collectors and unwanted reaction directly with the anode material. In the event that recharging is desired, this loss of volatile sulfur will result in lower charge/discharge capacity. The migration of sulfide from the cathode can be understood in terms of the migration of all anions toward that anode (24). Reasons for the migration of iron are less obvious and may be due to the formation of a nonstoichiometric iron, sulfur, potassium, lithium complex. An X-phase (Li_2FeS_2) and a J-phase ($\text{LiK}_6\text{Fe}_{24}\text{S}_{26}\text{Cl}$) have been identified in discharged Li/FeS₂ batteries following cooling (4). Countering the movement of sulfide is the precipitation of a lithium-sulfur salt in the EB layer. Any precipitation of this type means the removal of current carrying ions from the electrolyte and an addition to the internal cell resistance if the precipitate has low solubility at the operating temperature of the battery.

Movement of lithium at the anode surface can lead to increased resistance toward charge transfer when this migration occurs with the formation of a passive oxide or carbonate layer. Loss of lithium from the anode interface has also been observed through the reduction of the adjacent KCl to metallic potassium, which can volatilize to another part of the sealed battery (1). This type of lithium movement would result in decreased discharge capacity at the anode surface. The kinetics of migration processes at the anode/EB interface are currently under investigation (14).

Further experiments will study the significance of each of these complications in individual half-cells. At the high temperatures of cell operation, the resistance to current flow represented by the reactions noted above may not be restrictive to the near optimum performance of these batteries. If storage of the battery is required before use (especially in adverse environments), or if extended use is required, such as long discharge or several charge and discharge cycles, then these interfacial reactions will be important.

Acknowledgment

This work was supported by the U.S. Department of Energy (DOE) under contract DE-ACO4-76-DP00789.

Manuscript submitted Aug. 5, 1980; revised manuscript received March 26, 1981.

Any discussion of this paper will appear in a Discussion Section to be published in the June 1982 JOURNAL.

All discussions for the June 1982 Discussion Section should be submitted by Feb. 1, 1982.

Publication costs of this article were assisted by Sandia National Laboratories.

REFERENCES

1. R. K. Quinn, A. R. Baldwin, J. R. Armijo, P. G. Neiswander, and D. E. Zurawski, SAND79-0814, Sandia National Laboratories, Albuquerque, N.M. (1979).
2. B. A. Askew and R. Holland, Abstract 27, p. 75, The Electrochemical Society Extended Abstracts, Dallas, Texas, Oct. 5-9, 1975.
3. L. McCoy *et al.*, EPRI-EM-460, Atomic International, Canoga Park, Calif. (1977).
4. P. A. Nelson *et al.*, ANL-76-45, Argonne National Laboratory, Argonne, Ill. (1976).
5. A. Katsuhi and T. Chiki, *This Journal*, **122**, 1322 (1975).
6. D. M. Bush and D. A. Nissen, in "Proceedings of the 28th Power Sources Conf.," p. 81, Atlantic City, N.J. (1978).
7. A. Lin, N. R. Armstrong, and T. Kuwana, *Anal. Chem.*, **49**, 1228 (1977).
8. K. Siegbahn, C. Vordling, A. Barbman, R. Nordberg, K. Hamrin, J. Hedman, G. Johansson, T. Bergmark, S. F. Karlsson, I. Lindgren, and B. Lindberg, "ESCA-Atomic, Molecular and Solid State Structure Studied by Means of Electron Spectroscopy," Almquist and Wiksells, Uppsala, Sweden (1967).
9. J. A. Connor, in "Handbook of X-Ray and Ultraviolet Photoelectron Spectroscopy," D. Briggs, Editor, pp. 183-210, Heyden, Philadelphia (1977).
10. T. Sasaki, T. S. Williams, J. S. Wong, and D. A. Shirley, *J. Chem. Phys.*, **68**, 2718 (1978).
11. A. F. Povey and P. M. A. Sherwood, *Faraday Trans. II*, **70**, 1240 (1974).
12. M. Klasson, A. Berndtsson, J. Hedman, R. Nilsson, R. Nyholm, and C. Nordling, *J. Electron Spectr. Relat. Phenom.*, **3**, 427 (1974).
13. S. P. Kowalczyk, L. Ley, F. R. McNeely, R. A. Pollak, and D. A. Shirley, *Phys. Rev. B*, **8**, 3583 (1973).
14. B. J. Burrow, K. N. Nebesny, and N. R. Armstrong, Unpublished results.
15. C. C. Addison and B. M. Davies, *J. Chem. Soc. A*, 1822 (1969).
16. A. Soliman, *J. Appl. Chem.*, **1**, 98 (1951).
17. R. E. Clausing, D. S. Easton, and G. L. Powell, *Surf. Sci.*, **36**, 377 (1973).
18. H. H. Madden and J. E. Houston, *J. Vac. Sci. Tech.*, **14**, 412 (1977).
19. T. E. Gallon and J. A. D. Matthew, *Phys. Status Solidi*, **41**, 343 (1970).
20. D. G. Lord and T. E. Gallon, *Surf. Sci.*, **36**, 606 (1973).
21. A. J. Jackson, C. Tate, T. E. Gallon, P. J. Bassett, and J. A. D. Matthew, *J. Phys. F.*, **5**, 363 (1975).
22. J. Q. Searcy, Private communication.
23. C. S. Fuller and J. A. Ditzenberger, *Phys. Rev.*, **91**, 193 (1953).
24. C. F. Vallet, D. E. Heatherly, and J. Braunstein, *This Journal*, **127**, 1 (1980).
25. R. N. Seefurth and R. A. Sharma, *ibid.*, **122**, 1049 (1975).
26. S. C. Levy and C. C. Crafts, SAND79-0090, Sandia National Laboratories, Albuquerque, N.M. (1979).
27. L. Lindau and W. E. Spicer, *J. Electron Spectr. Relat. Phenom.*, **3**, 409 (1974).

The Polythiazyl, (SN)_x, Electrode: Surface Modification with Metal Cations

Robert J. Nowak,^{*1} Włodzimierz Kutner,² Judith F. Rubinson,
Anastasios Voulgaropoulos,^{*3} and Harry B. Mark, Jr.^{*}

Department of Chemistry, University of Cincinnati, Cincinnati, Ohio 45221

and Alan G. MacDiarmid^{*}

Department of Chemistry, University of Pennsylvania, Philadelphia, Pennsylvania 19174

ABSTRACT

The covalent, metallic conductor, polymeric sulfur nitride, (SN)_x, has been used as an electrode material in aqueous media. Irreversible redox couples were used as kinetic probes to monitor changes in the (SN)_x electrode surface/solution interface after chemical modification resulting from the strong interaction of (SN)_x with metal cations and/or oxidation of the (SN)_x surface. The iodate reduction and iodide oxidation reactions permitted the study of two different potential regions. Palladium(II) and silver(I) were chemically and/or electrochemically reduced at the (SN)_x surface forming a metallic surface phase. Chromium(III) remained in a cationic form immobilized on parallel (SN)_x surfaces in both potential regions.

Recently there has been a great deal of interest in the chemical modification of electrode surfaces in order to produce electrodes having selective analytical, synthetic, or catalytic properties (1). A few of the applications which have resulted from these chemically modified electrodes are: Electrocatalysis (2), enhancement of surface stability (2d, 2p, 3), spectral sensitization or improved light-electrical energy conversion (2c, 2p, 4), *in situ* analysis (5), reference electrodes for nonaqueous systems (6), or simulation of photosynthetic primary processes (7).

Organosilane chemistry is used extensively in the covalent attachment of different species to electrode materials, thereby introducing a σ -bonded system between the electrode and the electrochemically active group. This increases the electrical resistance and capacitance, making kinetic studies at these chemically modified electrodes more difficult. Direct attachment of metal ions to an electrode surface is less common (2b, k, q; 3b; 4e, g, h, j-m; 5b; 8b; 11) with several instances involving polymers or organic ligands attaching the metal to the electrode surface (2b, k; 4e, g, h; 8a-c). The inorganic metal, polymeric sulfur nitride or (SN)_x, provides functional groups for convenient chemical modification at the surface of this highly conducting material (9). Thus, it is not necessary to introduce insulating species between electrode and active groups. Consequently, systematic fundamental studies have been undertaken (10, 11) in order to determine the electrode characteristics of this unusual material in aqueous solutions.

In order to study the effects of chemical modification on the (SN)_x/solution interface, an electrochemical probe technique (12) was used in the present cyclic voltammetric study. This method employs redox couples which exhibit irreversible behavior at the electrode and, therefore, their electrochemical kinetics are strongly influenced by the nature of the electrode/solution interface. The iodate reduction and iodide oxida-

tion were chosen for this study because these systems: (i) are irreversible, (ii) have been studied extensively with electrodes other than (SN)_x (13), and (iii) provide two different potential regions for study. The qualitative results obtained were compared with the electrochemical behavior of these systems with metal electrodes.

Capacitance studies were not carried out as (SN)_x electrode surfaces are very rough (11) and cannot be polished mechanically (for example, with sandpaper or a polishing powder) without causing considerable damage. In addition, background currents in supporting electrolytes alone exhibit a significant faradaic component (10).

Experimental

All chemicals were of reagent grade. As the redox couples employed in this study were kinetic probes of the nature of the (SN)_x/solution interface, all (SN)_x electrodes did not necessarily yield the same peak potentials for a given couple because of variations in surface characteristics between different (SN)_x electrodes. For example, Fig. 3A and 4A show iodate reduction peaks for two different (SN)_x electrodes. The peak potentials and indeed, the general appearance of the peaks are significantly different for these electrodes. For this reason, comparison of the redox behavior of iodate (or iodide) before and after chemical modification was only meaningful if the same electrode was involved.

Electrodes were prepared as described elsewhere (9). The (SN)_x fiber bundles were either parallel or perpendicular to the electrode/solution interface. Both surfaces exhibited similar electrochemical behavior with respect to the experiments reported here, with the exception of the experiment involving chromium(III).

All other experimental details have been outlined elsewhere (11).

Results and Discussion

Iodate reduction.—Iodate was chosen as one of the systems to probe the nature of (SN)_x surfaces before and after modification for the reasons stated above. Figure 1 illustrates the reduction of 0.040M iodate in 0.5M acetate buffer (pH = 4.75) on platinum and a parallel (SN)_x electrode. The behavior was similar for perpendicular surfaces. The iodate reduction peak re-

^{*} Electrochemical Society Active Member.

¹ Present address: 6130 Naval Research Laboratory, Naval Research Center, Washington, D.C. 20375.

² Present address: Institute of Physical Chemistry, Polish Academy of Sciences, Warsaw, Poland.

³ Present address: Laboratory of Analytical Chemistry, University of Thessaloniki, Thessaloniki, Greece.

Key words: electrocatalysis, adsorption, background currents, breakdown potential, surface functional groups, surface anisotropy.

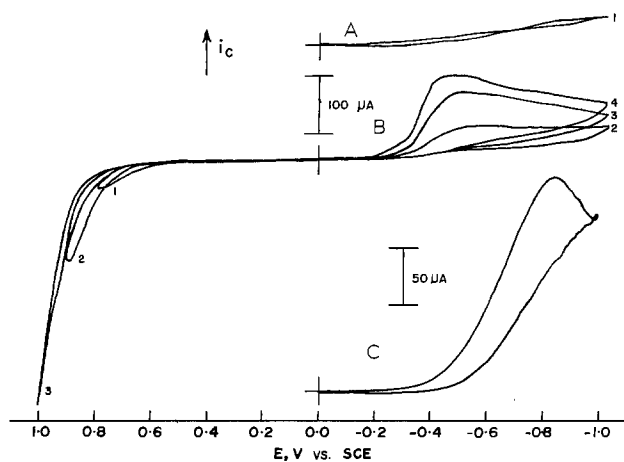
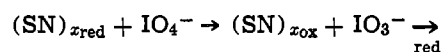


Fig. 1. Dependence of the reduction of 0.04M KIO_3 in 0.5M acetate buffer, pH 4.75 on positive reversal potential at a parallel $(\text{SN})_x$ electrode. Scan rate 0.02 Vsec^{-1} . Numerals refer to scan number. Curves A and B, $(\text{SN})_x$. Curve C, Pt.

recorded with the platinum electrode was concomitant with hydrogen evolution which agreed with chronopotentiometric studies obtained by Anson (14) under similar conditions at platinum electrodes having no surface oxides. The first scan with an $(\text{SN})_x$ electrode (Fig. 1A, curve 1) initiated from 0.0V to negative potentials showed no reduction peak for iodate at potentials similar to those on Pt (Fig. 1C). Only after the potential excursion reached values positive of approximately 0.5V, sufficient to cause oxidation of the surface of $(\text{SN})_x$ (10), (Fig. 1B, curve 1) was the iodate reduction peak observed. The magnitude of the iodate reduction peak was a function of the extent of positive polarization on the preceding scan (Fig. 1B, curves 2-4). If, after obtaining an initial well-defined peak, the scan into positive potentials was reversed at 0.0V on all subsequent cycles, the peak gradually disappeared. Davis (15) has shown that the rate of reduction of iodate on the surface of platinum electrodes, at fixed potential, increases as the amount of platinum oxides on the surface increases. Anson (14) has demonstrated that the reduction of iodate at platinum electrodes having surface oxides present, occurs at potentials 200-600 mV more positive than at electrodes having no surface oxides. The decrease in overvoltage is thought to involve the simultaneous reduction of platinum oxide and the iodate (14). It must be noted that a large excess of iodate (10^3 times the equivalents of platinum oxide) can be reduced at these lower overvoltages (14). The behavior of iodate at $(\text{SN})_x$ electrodes might be explained similarly, *i.e.*, iodates were reduced at relatively low overvoltages at oxidized $(\text{SN})_x$ electrodes. After several scans without positive polarization there were no longer any oxidized surface functional groups and, hence, the iodate reduction no longer occurred at low overvoltages.

To investigate this possibility further, periodate ion was studied in voltammetric experiments with both $(\text{SN})_x$ and platinum electrodes. The results indicate that the periodate ion chemically oxidized the platinum surface, resulting in a positive shift in the iodate reduction potential. The reduction of periodate to iodate precedes the reduction of iodate which takes place at -0.560V at the oxidized platinum electrode. These results are consistent with those previously reported (14). When this process was investigated at $(\text{SN})_x$ electrodes, only one peak was observed at *ca.* -0.60V , in contrast to the behavior at the platinum electrode. Also, there was no need for prior positive polarization, as was required in the iodate experiments described above. Prior polarization to $+0.70\text{V}$ had no effect on the peak current, and the current did not decrease in subsequent scans as was the case with iodate at $(\text{SN})_x$.

Periodate ion apparently oxidizes the $(\text{SN})_x$ surface and the observed peak was simply the reduction of iodate at the oxidized electrode surface. The following CE mechanism may, therefore, be proposed



Such behavior is opposite to that observed with chromic acid preoxidized glassy carbon electrodes (16). These electrodes revealed a loss of reproducibility with respect to iodate reduction and a negative shift in peak potential after oxidation.

Iodate reduction also served as a kinetic probe in experiments involving modification of $(\text{SN})_x$ electrodes with metal cations. Surface modification of $(\text{SN})_x$ consisted of brief immersion (30-60 sec) in solutions containing one of the following ions: silver(I), palladium(II), chromium(III), or periodate. After pretreatment, the electrodes were thoroughly rinsed with distilled water before use. Cyclic voltammograms were recorded in iodate solution before and after pretreatment in order to determine if the nature of the surface had changed for the same $(\text{SN})_x$ electrode under study.

The following study was carried out in the order stated, with the same $(\text{SN})_x$ electrode. After pretreatment with 0.1M AgNO_3 solution (Fig. 2A), a well-defined iodate reduction peak was observed at *ca.* -0.67V , without the need for prior polarization at positive potentials. Subsequent cycling resulted in a decrease in the peak current if the positive reversal potential was 0.0V. If the electrode is polarized at $+0.65\text{V}$ (Fig. 2B) for approximately 15 sec before initiating the negative scan, the iodate potential is shifted to *ca.* -0.48V ; however, on subsequent scans, the peak shifted negatively to its original position with a simultaneous decrease in peak current. The electrode was then immersed in a 0.040M KIO_4 solution followed by negative scanning in iodate solution. The behavior was similar to that after immersion in silver(I) solution (Fig.

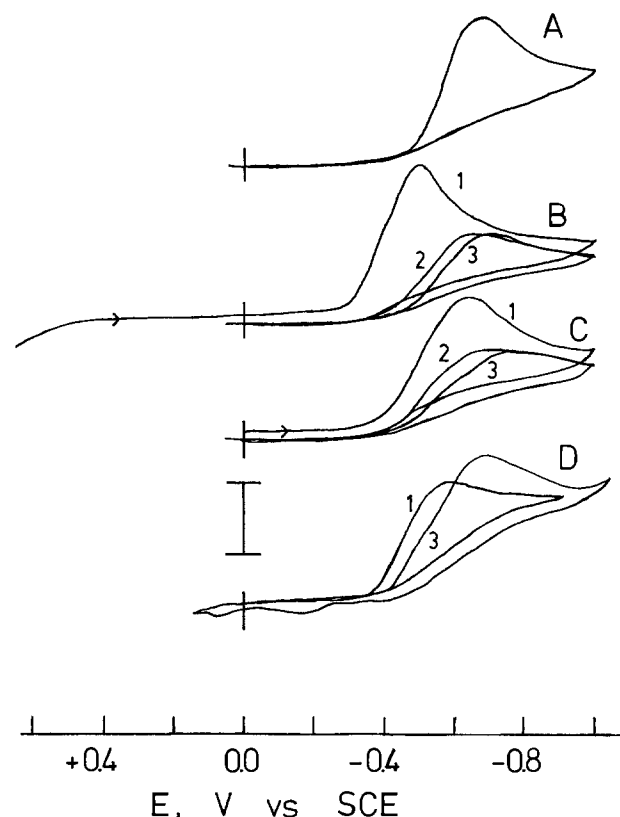


Fig. 2. Influence of (A) pretreatment with 0.1M AgNO_3 , (B) polarization at $+0.65$, (C) pretreatment with 0.04M KIO_4 on $(\text{SN})_x$ electrodes, (D) silver metal electrode. Scan rate: 0.02 Vsec^{-1} (numerals refer to scan number).

2C). The first negative scan from 0.0V showed a positive shift of about 50 mV and a marked increase in current compared to the later scans after silver(I) immersion. However, once again the peak current decreased and there was a negative shift on subsequent scanning. One complete cycle was then made without interruption, beginning positively from 0.0V. The effect of this brief electrochemical oxidation was to produce a peak on the negative scan which was very similar with respect to peak current magnitude and peak potential, to the peak obtained when the electrode was immersed in periodate solution. Finally, the potential was held for 15 sec at +0.65V before scanning, which resulted in a 200 mV positive shift in peak potential from that at an unoxidized (SN)_x electrode and an increase in the current as was observed earlier. Figure 2D (scan 1) shows the behavior of iodate on a silver electrode. The program for the second scan (not shown) was: 0.0 → +1.0 → -1.0 → 0.0V. During this second scan a large split cathodic peak was observed for iodate reduction whose components had the same two peak potentials as those of scans 1 and 3, indicating a partial alteration of the surface. The third scan was initiated negatively from 0.0V without previous positive polarization and resulted in the shift of the cathodic peak potential to more negative values and a marked decrease in the cathodic peak current (when compared to scan 2).

Thus, the electrochemical behavior of iodate at silver electrodes is quite similar to that observed with silver ion pretreated (SN)_x electrodes. Potentiostating at +0.65V, for approximately 15 sec, scanning positively into anodic current regions or periodate pretreatment resulted in the shifting of the iodate reduction peak potential to more positive values with a simultaneous increase in cathodic current. As silver(I) pretreatment is sufficient to yield a well-developed iodate peak without positive polarization and there is similarity between silver(I) pretreated (SN)_x electrodes and silver electrodes with respect to iodate electrochemistry, it might be concluded that silver(I) chemically oxidizes the (SN)_x surface while simultaneously producing metallic silver deposits. The presence of deposits has been verified by scanning electron microscopic investigations.

Iodate studies with (SN)_x electrodes pretreated by brief immersion in 0.02M PdCl₂ or Pd(NO₃)₂ solutions yielded similar results as those with silver ion pretreated material (Fig. 3). Curve A (scans 1 and 2) re-

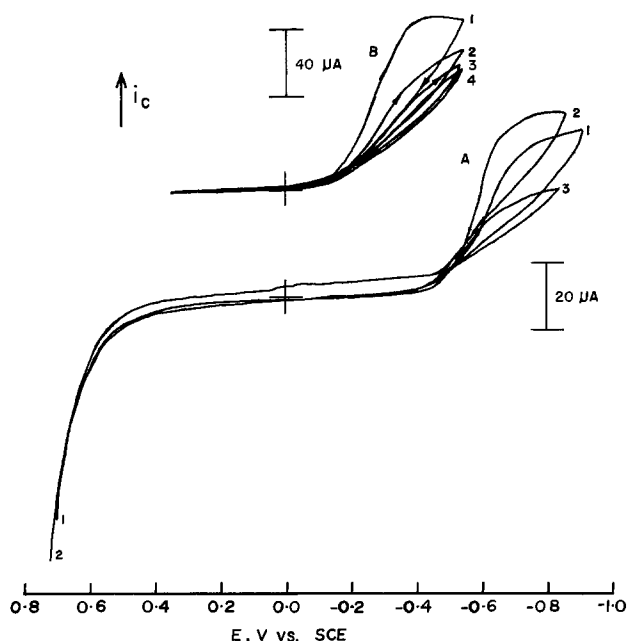


Fig. 3. Influence of (A) prior positive scanning and (B) pretreatment with 0.02M Pd(NO₃)₂ on cyclic voltammetric behavior of an (SN)_x electrode in 0.04M KIO₃, 0.5M acetate buffer, pH 4.75. Scan rate: 0.02 Vsec⁻¹ (numerals refer to scan number).

sulted from an initial scan positively from 0.0V followed by a second complete cycle. When the scan into positive potential was reversed at 0.0V at the end of the second cycle, the diminished reduction peak (scan 3) was recorded. As observed previously, this resulted from the partial reduction of the electrode surface. After the electrode was pretreated with palladium(II), the voltammograms shown in Fig. 4B were obtained. As in the experiments with silver(I) or the periodate pretreatment, a well-defined iodate reduction peak was observed without scanning to positive potentials where a significant quantity of anodic current was passed. The reduction peak potential was shifted by approximately 300 mV to more positive values. As previously shown, there was a decrease in the current with scan number when the positive potential scan reversal was made before significant anodic current flow. When palladium(II) pretreated (SN)_x electrodes are polarized negatively to -0.8V in 0.5M acetate buffer, hydrogen is evolved and there is no hysteresis in the current/potential curves. Untreated (SN)_x electrodes exhibit a current hysteresis at negative breakdown potentials without the evolution of hydrogen (10). This is evidence for the presence of metallic palladium deposits on palladium(II) pretreated (SN)_x electrodes. These deposits can be seen under high magnification.

As silver(I) and palladium(II) are highly oxidizing species and are reduced to metals by (SN)_x in a chemical reaction, chromium(III) was also used to pretreat (SN)_x electrodes. This metal cation was found to be electrochemically inactive at (SN)_x electrodes although its presence in solution significantly decreases background currents caused by surface redox processes (11). It was thought that chromium(III) interacts strongly with (SN)_x and thus, might affect iodate reduction at the surface. This was found to be the case for parallel (SN)_x electrodes (Fig. 4). Iodate behavior on an untreated electrode was as observed previously (Fig. 4A). No reduction peak for iodate was observed on scanning to negative potentials until after scanning into the positive region. After brief pretreatment of this electrode in a 0.1M solution of Cr(ClO₄)₃, the voltammograms shown in Fig. 4B were obtained. The first scan was negative from 0.0V, and was followed by one positive scan and several negative scans with 0.0V as the potential of reversal. A positive shift in peak poten-

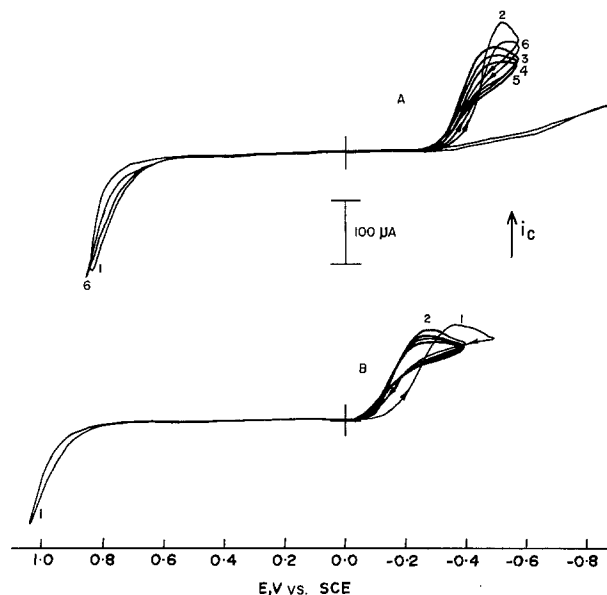


Fig. 4. Influence of (A) prior positive scanning and (B) pretreatment with 0.1M Cr(ClO₄)₃ on cyclic voltammetric behavior at a parallel (SN)_x electrode in 0.04M KIO₃, 0.5M acetate buffer, pH 4.75. Scan rate: 0.02 Vsec⁻¹ (numerals refer to scan number).

tial of approximately 200 mV was observed (Fig. 4B), which is persistent even after multiple cathodic scans initiated at 0.0V. It appears from these data and previous studies (10) that a form of nonmetallic chromium is immobilized on the (SN)_x surface. The valence state of the chromium is unknown at this time.

Iodide oxidation.—The iodine/iodide couple was also used as a probe system to study the surfaces of modified (SN)_x electrodes. As iodide is oxidized at positive potentials at (SN)_x electrodes, this couple offers a different potential region for study. For comparison purposes, cyclic voltammetric studies of iodide at palladium, silver, and hanging mercury drop electrodes were performed.

At low scan rates (0.01–0.05 Vsec⁻¹) the oxidation peak on untreated (SN)_x electrodes was drawn out and not of a diffusion controlled character. Furthermore, on the reverse scan, the reduction peak was often comprised of two ill-defined peaks. The relative height of these two peaks was dependent on scan rate. The more positive peak decreased with a concomitant increase in the second peak with an increase in scan rate until, at 0.500 Vsec⁻¹, only the latter at $E_{pc} = +0.170V$ remained (Fig. 5D). Also the oxidation peak appeared to be diffusion controlled at this scan rate ($E_{pa} = +0.500V$ at 0.500 Vsec⁻¹). The separation between the anodic and cathodic peak potentials increased with increasing scan rate.

As with the iodate studies, (SN)_x electrodes were pretreated by brief immersion in solutions containing cations which might undergo chemical reaction with the surface. Cyclic voltammograms were recorded in iodide solution at two scan rates for untreated, pretreated, and the appropriate metal electrode for comparison.

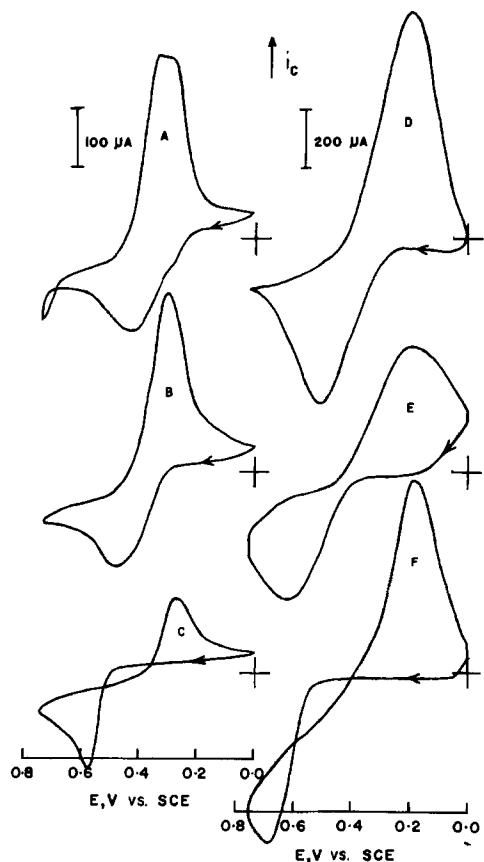


Fig. 5. Influence of palladium(II) pretreatment of (SN)_x electrodes on cyclic voltammetric behavior in 0.05M KI and 0.5M NaClO₄: (A, D) untreated (SN)_x; (B, E) pretreated (SN)_x; (C, F) palladium metal electrode. Scan rate (A–C) 0.1 Vsec⁻¹, (D–F) 0.5 Vsec⁻¹ (numerals refer to scan number).

When an (SN)_x electrode was pretreated with 0.02M Pd(NO₃)₂ voltammograms were obtained in iodide solution (Fig. 5B, E) which had characteristics intermediate between untreated (SN)_x electrodes and a palladium wire electrode. The peak potential for the oxidation of iodide became increasingly positive as one went from untreated to palladium(II) pretreated to palladium metal electrodes for a given scan rate (cf. Fig. 5A, B, C or 5D, E, F). Furthermore, the palladium(II) pretreated (SN)_x electrode exhibited only one (the more positive) of the two reduction peaks at slower scan rates (0.01–0.1 Vsec⁻¹). This may indicate that the palladium(II) pretreated (SN)_x electrode surface consists of regions having palladium metal deposits and other areas of exposed (SN)_x. The electrode process is presumed to occur on both of these surfaces simultaneously.

The potential for the oxidation of electrodeposited palladium metal for an (SN)_x electrode in 5 mM PdCl₂ (17) corresponds to the same potential (ca. +0.60V) for the oxidation of iodide at a palladium(II) pretreated (SN)_x electrode at a scan rate of 0.500 Vsec⁻¹ (Fig. 5E). It is conceivable that metallic palladium present on the (SN)_x surface could be undergoing simultaneous oxidation with iodide in a manner analogous to the reduction of iodates at oxidized metal or (SN)_x surfaces as discussed earlier.

The voltammograms obtained with the palladium wire electrode exhibited a hysteresis of the current upon scan reversal at positive potentials (Fig. 5C, F). At higher scan rates (Fig. 5E) the palladium(II) pretreated electrode exhibited more of a tendency toward hysteresis than the untreated (SN)_x (cf. Fig. 5D).

Qualitatively, the same type of behavior was observed when the (SN)_x was pretreated with 0.1M AgNO₃. However, with silver(I) pretreated electrodes, voltammograms changed with scan number until they appeared to be identical with those obtained with untreated electrodes. Repetitive cycling appears to remove any deposited or immobilized silver. This also was found to be true for mercury in a series of similar experiments, but this was not the case with palladium pretreated (SN)_x electrodes.

Finally, it should be noted that pretreatment of (SN)_x electrodes with chromium(III), europium(III), iron(III), or iron(II) had no effect on I₂/I⁻ redox behavior. This may be due to electrostatic repulsion resulting in the removal of these cations from the surface in such positive potential regions.

In conclusion, pretreatment of parallel or perpendicular (SN)_x electrodes with palladium(II) or silver(I) solutions results in the formation of a metallic phase on the surface. This is expected since they have redox potentials more positive than that of (SN)_x (17). At positive potentials, the metallic palladium is bound more permanently to the (SN)_x surface than silver, as is evidenced by the iodide studies. For a chromium(III) pretreated electrode, the chromium appears to be strongly bound to parallel (SN)_x electrodes in an ionic form, which is logical on the basis of the redox potentials of chromium(III) and (SN)_x (17). The latter modified surface catalyzes the electrochemical reduction of iodate. Periodate, with a redox potential which is more positive than that of (SN)_x, oxidizes the surface of (SN)_x electrodes, thus shifting the potential of iodate reduction to more positive potentials (17).

Acknowledgment

The authors gratefully acknowledge financial assistance received through the National Science Foundation, Grant Number NSF CHE76-04321.

Manuscript submitted Nov. 26, 1980; revised manuscript received March 4, 1981.

Any discussion of this paper will appear in a Discussion Section to be published in the June 1982 JOURNAL.

All discussions for the June 1982 Discussion Section should be submitted by Feb. 1, 1982.

Publication costs of this article were assisted by the University of Cincinnati.

REFERENCES

- For recent reviews, see: W. R. Heineman and P. T. Kissinger, *Anal. Chem.*, **52**, 138R (1980); R. W. Murray, *Acct. Chem. Res.*, **13**, 135 (1980); K. D. Snell and A. G. Keenan, *Chem. Soc. Rev.*, **8**, 135 (1979); and W. Kutner, R. J. Nowak, and H. B. Mark, Jr., *Wiad. Chem.*, **32**, 817 (1978).
- (a) R. A. Adzic and R. Tanasoski, *J. Electroanal. Chem. Interfacial Electrochem.*, **94**, 231 (1978). (b) A. Bettleheim, R. J. H. Chan, and T. Kuwana, *ibid.*, **99**, 391 (1979). (c) J. M. Bolts and M. S. Wrighton, *J. Am. Chem. Soc.*, **101**, 6179 (1979). (d) J. M. Bolts, A. B. Bocarsley, M. C. Palazzotto, E. G. Walton, N. S. Lewis, and M. S. Wrighton, *ibid.*, **101**, 1378 (1979). (e) J. M. Bolts and M. S. Wrighton, *ibid.*, **100**, 5257 (1978). (f) H.-Y. Cheng, E. Strope, and R. N. Adams, *Anal. Chem.*, **51**, 2243 (1979). (g) J. F. Evans, T. Kuwana, M. T. Henne, and G. P. Royer, *J. Electroanal. Chem. Interfacial Electrochem.*, **80**, 409 (1977). (h) H. L. Landrum, R. T. Salmon, and F. M. Hawkridge, *J. Am. Chem. Soc.*, **99**, 3154 (1977). (i) M. R. Van de Mark and L. L. Miller, *ibid.*, **100**, 3223 (1978). (j) R. D. Rocklin and R. C. Murray, *J. Electroanal. Chem. Interfacial Electrochem.*, **100**, 271 (1979). (k) J. P. Collman, M. Marrocco, P. Denisovich, C. Koval, and F. C. Anson, *ibid.*, **101**, 117 (1979). (l) D. C.-S. Tse and T. Kuwana, *Anal. Chem.*, **50**, 1315 (1978). (m) J. B. Kerr and L. L. Miller, *J. Electroanal. Chem. Interfacial Electrochem.*, **101**, 263 (1979). (n) J. B. Kerr, L. L. Miller, and M. R. Van de Mark, *J. Am. Chem. Soc.*, **102**, 3383 (1980). (o) R. Memming, F. Schroepel, and U. Bringmann, *J. Electroanal. Chem. Interfacial Electrochem.*, **100**, 307 (1979). (p) M. A. Fox, F. J. Nobs, and T. A. Voynick, *J. Am. Chem. Soc.*, **102**, 4036 (1980). (q) I. M. Kolthoff and P. Mader, *Anal. Chem.*, **42**, 1762 (1970).
- (a) R. F. Lane and A. T. Hubbard, *J. Phys. Chem.*, **81**, 734 (1977). (b) H. Yoneyama, Y. Murao, and H. Tamura, *J. Electroanal. Chem. Interfacial Electrochem.*, **108**, 87 (1980).
- (a) D. D. Hawn and N. R. Armstrong, *J. Phys. Chem.*, **82**, 1288 (1978). (b) T. Osa and M. Fujihira, Japanese-American Science Seminar, San Francisco, California, May 15-19, 1977. (c) T. Miyasaka, T. Watanabe, A. Fujishima, and K. Honda, *J. Am. Chem. Soc.*, **100**, 6657 (1978). (d) T. Osa and M. Fujihira, *Nature*, **264**, 349 (1976). (e) Y. Umezawa and T. Yamamura, *J. Electroanal. Chem. Interfacial Electrochem.*, **95**, 113 (1978). (f) A. N. Voulgaropoulos, R. J. Nowak, W. Kutner, and H. B. Mark, Jr., *J. Chem. Soc. Chem. Commun.*, 244 (1978). (g) C. D. Jaeger, F.-R. F. Fan, and A. J. Bard, *J. Am. Chem. Soc.*, **102**, 2592 (1980). (h) T. Kawai, K. Tanimuma, and T. Sakata, *Chem. Phys. Lett.*, **56**, 541 (1978). (i) M. S. Wrighton, R. G. Austin, A. B. Bocarsley, J. M. Bolts, O. Haas, K. Legg, L. Nadjo, and M. C. Palazzotto, *J. Am. Chem. Soc.*, **100**, 1602 (1978). (j) W. D. Johnston, H. J. Leamy, B. A. Parkinson, A. Heller, and B. Miller, *This Journal*, **127**, 90 (1980). (k) B. Parkinson, A. Heller, and B. Miller, *ibid.*, **126**, 954 (1979). (l) H. Uchida, H. Yoneyama, and H. Tamura, *ibid.*, **127**, 99 (1980). (m) H. Yoneyama, S. Mayumi, and H. Tamura, *ibid.*, **125**, 68 (1978).
- (a) H. Arwin and I. Lundstrom, *FEBS Lett.*, **109**, 252. (b) J. A. Cox and A. F. Brajter, *Anal. Chem.*, **51**, 2230 (1979). (c) M. F. Dantartas, J. F. Evans, and T. Kuwana, *ibid.*, **51**, 104 (1979). (d) R. F. Lane and A. T. Hubbard, *ibid.*, **48**, 1287 (1976). (e) T. Yao and S. Musha, *Anal. Chim. Acta*, **110**, 203. (f) G. T. Cheek and R. F. Nelson, *Anal. Lett.*, **1978**, All, 393.
- P. J. Peerce and A. J. Bard, *J. Electroanal. Chem. Interfacial Electrochem.*, **108**, 121 (1980).
- D. F. Untereker, J. C. Lennox, L. M. Wier, P. R. Moses, and R. W. Murray, *ibid.*, **81**, 309 (1977).
- (a) A. P. Brown, C. Koval, and F. C. Anson, *ibid.*, **72**, 379 (1976). (b) D. G. Davis and R. W. Murray, *Anal. Chem.*, **49**, 194 (1977). (c) K. Pool and R. P. Buck, *J. Electroanal. Chem. Interfacial Electrochem.*, **95**, 241 (1978). (d) A. Merz and A. J. Bard, *J. Am. Chem. Soc.*, **100**, 3222 (1978). (e) R. F. Lane and A. T. Hubbard, *J. Phys. Chem.*, **77**, 1401 (1973).
- A. G. MacDiarmid, C. M. Mikulski, M. S. Saran, P. J. Russo, M. L. Cohen, A. A. Bright, A. F. Garito, and A. J. Heeger, *Advances in Chemistry Series*, No. 150, "Inorganic Compounds with Unusual Properties," R. Bruce King, Editor, pp. 63-72.
- R. J. Nowak, H. B. Mark, Jr., A. G. MacDiarmid, and D. Weber, *J. Chem. Soc. Chem. Commun.*, 9 (1977); and R. J. Nowak, W. Kutner, H. B. Mark, Jr., and A. G. MacDiarmid, *Ann. N. Y. Acad. Sci.*, **313**, 767 (1978).
- R. J. Nowak, W. Kutner, H. B. Mark, Jr., and A. G. MacDiarmid, *This Journal*, **125**, 232 (1978); and H. B. Mark, Jr., R. J. Nowak, W. Kutner, J. F. Johnson, and A. G. MacDiarmid, *Bioelectrochem. Bioenerg.*, **5**, 215 (1978).
- L. Gierst, E. Nicolas, and L. Tytgat-Vanderberghen, *Croat. Chem. Acta*, **42**, 117 (1970).
- P. G. Desideri, L. Lepri, and D. Heimler, in "Encyclopedia of Electrochemistry of Elements," Vol. 1, Chap. 3, A. J. Bard, Editor, Marcel Dekker, New York (1973).
- F. C. Anson, *J. Am. Chem. Soc.*, **81**, 1554 (1959).
- D. G. Davis, Jr., *Talanta*, **3**, 335 (1960).
- R. J. Taylor and A. A. Humffray, *J. Electroanal. Chem. Interfacial Electrochem.*, **42**, 347 (1973).
- R. J. Nowak, Ph.D. Thesis, University of Cincinnati (1977).



Electrodissolution Kinetics of Iron in Highly Acidic Chloride-Free Solutions

N. L. Nguyen* and Ken Nobe*

Department of Chemical Engineering, UCLA, Los Angeles, California 90024

One of the most important landmarks in the development of the modern science of corrosion has been Bonhoeffer and Heusler's hypothesis of the existence of univalent iron surface intermediates formed by reaction of solution components and iron during corrosion (1). Subsequently, the two classic papers by Bockris and co-workers (2,3), which describe the kinetics and mechanism of iron corrosion, laid the foundation for electrochemical modeling of fundamental metallic corrosion processes.

Both groups reported that the rate of iron electro-dissolution had a negative reaction order with respect to hydrogen ions. Kelly (4), subsequently, confirmed the negative first order result of Bockris and co-workers (2). More recently, McCafferty and Hackerman (5) reported a positive reaction order with respect to hydrogen ions for the rate of iron electro-dissolution in concentrated acidic chloride solutions, in contrast to results obtained for iron in solutions of lower concentrations of hydrogen ions. This positive reaction order was later confirmed by Lorenz *et al.* (6) and Kuo (7). This note reports on studies of iron in concentrated acidic chloride-free solutions. Some preliminary data on this system had been reported previously by Kuo (7).

Experimental

The same rotating disk apparatus, instrumentation, and experimental procedure, as described previously (7), was used in this work. The electrolyte was $\text{HClO}_4\text{-NaClO}_4$ with the ionic strength maintained at 5M while H^+ concentrations were varied from 0.05 to 5M. The test electrodes were prepared from 1.27 cm diam Ferrovac E iron rod. The detailed preparation and pretreatment procedures of the iron electrodes have also been described previously (7). Electrode potentials were corrected for liquid junction potentials and the IR drop.

Results and Discussion

The dependence of the rest potential on hydrogen ion concentration

$$\left(\frac{\partial E_o}{\partial \log [\text{H}^+]} \right) = 0.06 \text{ V/dec}$$

is the same as reported for iron in chloride-free solutions of lower acidity. Figure 1 shows the anodic polarization behavior of iron in the $\text{HClO}_4\text{-NaClO}_4$ solutions within the active region. Linear and parallel anodic Tafel lines of slope 0.04 V/dec, over the entire range of H^+ concentrations (0.05-5M) examined, are obtained. The H^+ reaction order plot, as shown in Fig. 2, gives a negative slope of 1.1. This result shows that the rate of iron electro-dissolution is negative first order at high as well as at low acid concentrations in chlo-

ride-free solutions. Negative first order kinetics and 0.04 V/dec Tafel slopes indicate that the Bockris mechanism of iron electro-dissolution is also valid at high acid concentrations in the absence of chloride ions. On the other hand, in the presence of sufficient concentrations of chloride ions, different kinetic parameters are obtained indicating changes in the mechanism (5-7, 8, 9).

Figure 3 shows the cathodic polarization behavior (hydrogen evolution reaction) of iron in the $\text{HClO}_4\text{-}$

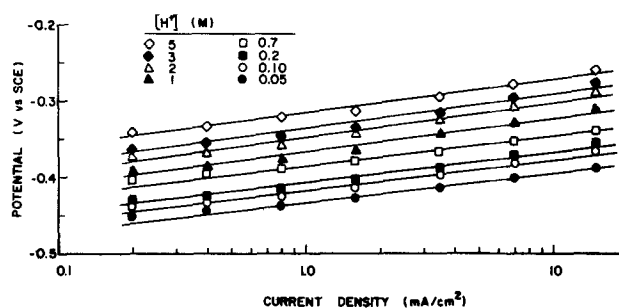


Fig. 1. Electro-dissolution rate vs. potential at various H^+ concentrations. Iron in $x \text{HClO}_4 - y \text{NaClO}_4$ ($x + y = 5\text{M}$).

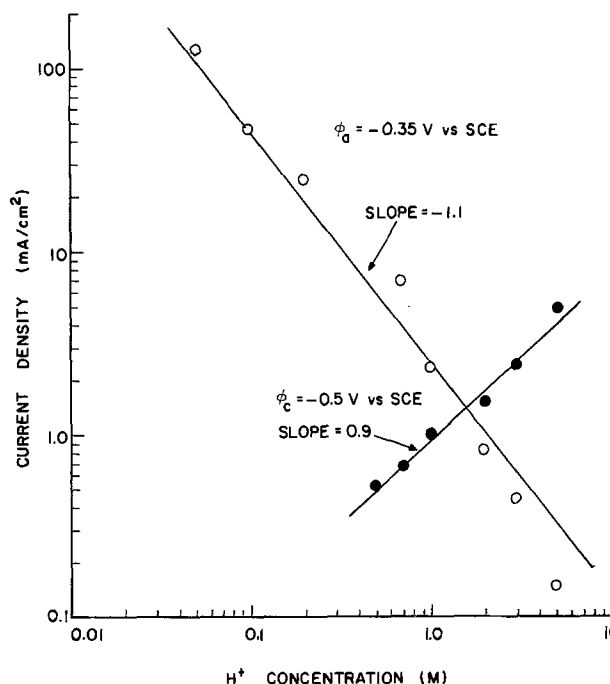


Fig. 2. Reaction order plots for iron electro-dissolution and hydrogen evolution.

* Electrochemical Society Active Member.
Key words: corrosion, electro-dissolution, iron.

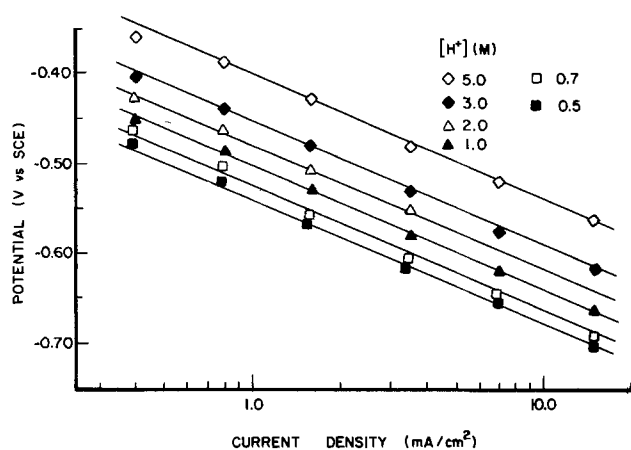


Fig. 3. Hydrogen evolution rate vs. potential at various H^+ concentrations. Iron in $x HClO_4 - y NaClO_4$ ($x + y = 5M$).

$NaClO_4$ solutions. Linear and parallel cathodic Tafel lines of $2 RT/F$ are obtained. The H^+ reaction order plot for the hydrogen evolution reaction (HER) is also shown in Fig. 2 and gives a slope of 0.9 indicating first order kinetics for the HER on iron in highly acidic perchlorate solutions. The same kinetic parameters were obtained for iron in highly acidic chloride solutions (10).

The dependence of the corrosion current on H^+ is

$$\frac{\partial \log i_{\text{corr}}}{\partial \log [H^+]} = 0.5$$

The kinetic parameters for the HER on iron (including

$\partial E_o/\partial \log [H^+]$ and $\partial \log i_{\text{corr}}/\partial \log [H^+]$) are equivalent to corresponding values obtained by Kelly (4) for iron in sulfate solutions of substantially lower ionic strength and acidity.

The results of this work indicate that chloride ions significantly affect the mechanism of iron electrodis-solution but not that of the HER on iron.

Acknowledgment

This work is part of the University of California Sea Water Desalination program.

Manuscript received Nov. 3, 1980.

Any discussion of this paper will appear in a Discussion Section to be published in the June 1982 JOURNAL. All discussions for the June 1982 Discussion Section should be submitted by Feb. 1, 1982.

Publication costs of this article were assisted by the University of California.

REFERENCES

1. K. F. Bonhoeffer and K. E. Heusler, *Z. Electrochem.*, **61**, 122 (1957).
2. J. O'M. Bockris, D. Drazic, and A. R. Despic, *Electrochim. Acta*, **4**, 325 (1961).
3. J. O'M. Bockris and D. Drazic, *ibid.*, **7**, 293 (1962).
4. E. J. Kelly, *This Journal*, **112**, 124 (1965).
5. E. McCafferty and N. Hackerman, *ibid.*, **119**, 999 (1972).
6. N. A. Darwish, F. Hilbert, W. J. Lorenz, and H. Rossowag, *Electrochim. Acta*, **18**, 421 (1973).
7. H. C. Kuo and K. Nobe, *This Journal*, **125**, 853 (1978).
8. W. J. Lorenz, *Corros. Sci.*, **5**, 121 (1965).
9. R. J. Chin and K. Nobe, *This Journal*, **119**, 1457 (1972).
10. H. C. Kuo, Ph.D. dissertation, UCLA (1975).

Procedure for Evaluation of Exchange Current Density and Coverage by an Intermediate at the Reversible Potential in a Process Such as Cl_2 Evolution

B. V. Tilak*

Hooker Chemical Corporation, Hooker Research Center, Grand Island, New York 14072

and D. M. Novak*¹ and B. E. Conway*

Chemistry Department, University of Ottawa, Ottawa, Ontario K1N 9B4, Canada

The electrode kinetics of anodic Cl_2 evolution have, in recent years, become a topic of major interest especially in applications using RuO_2 -based DSA^{®2} electrodes (1-4) employed in the chlor-alkali industry. The kinetics of anodic Cl_2 evolution have also been extensively studied at Pt anodes from a more fundamental mechanistic point of view, commencing from the early work of Chang and Wick (5).

Mechanistic criteria such as reaction order, Tafel slope, and stoichiometric number values were applied

* Electrochemical Society Active Member.

¹ Present address: National Research Council, Division of Chemistry, Corrosion and Metal Oxidation Section, Ottawa, Ontario, Canada.

Key words: adsorbed intermediates, Cl_2 evolution, H_2 evolution, platinum, nonaqueous media.

² DSA[®] is a registered trade mark of Diamond Shamrock Technologies S.A.

to experimental results for Cl_2 evolution at Pt from aqueous Cl^- solutions, e.g., by Yokoyama and Enyo (6) and by Tilak (7). Applications to Cl_2 evolution from molten chloride salts were made by Triaca, Solomons, and Bockris (8). From most of this work (6-10), it was concluded that the recombination of discharged (chemisorbed) Cl^{\cdot} atoms was rate determining, giving rise to a Tafel slope of $RT/2F$ (10) at low overpotentials and an approach to a limiting current at high overpotentials (6, 11, 12). While an approach to limiting current behavior was also observed by Yokoyama and Enyo (6), they concluded that the kinetics were determined by rate-controlling discharge of Cl^- ion, followed by equilibrium recombination/dissociation of $Cl_2(Cl^- \rightarrow Cl^{\cdot} + e; Cl^{\cdot} \rightleftharpoons \frac{1}{2} Cl_2)$. A new method for testing recombination-controlled kinetics

was proposed by Conway and Novak (11, 12) and applied to the anodic Cl_2 evolution on Pt in trifluoroacetic acid and water as solvents in order to evaluate the role of the surface oxide monolayer at Pt anodes with regard to electrocatalysis of the Cl_2 evolution reaction. This method enabled the recombination kinetics to be tested over a wide range of coverages θ by the adsorbed Cl^\cdot intermediate by means of a linear test plot (11, 12) over a wide range of θ_{Cl^\cdot} values from $\theta_{\text{Cl}^\cdot} \rightarrow 0$ to $\theta_{\text{Cl}^\cdot} \rightarrow 1$ as the limiting current is approached.

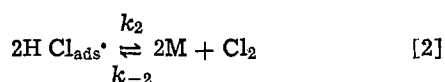
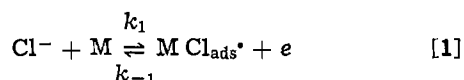
It was demonstrated that the experimental results for Cl_2 evolution from both aqueous and trifluoroacetic acid and water solutions of Cl^- ion gave excellent linear plots of the kind mentioned above except near the reversible potential where the back-reaction component must be taken into account.

It is the purpose of the present communication to show that the data obtained in Ref. (11) and (12) can be treated by a procedure which enables an estimate to be made of the coverage of the adsorbed intermediate in the reaction at the reversible potential. The method also enables the exchange current density to be obtained other than by the usual procedure of extrapolating a Tafel line. Thus, for recombination controlled reactions, e.g., Cl_2 on Pt, this is not always feasible since the overpotential (η) - \log [current-density (i)] plots are continuously curved under most conditions (5, 6, 8, 11, 12) for kinetic reasons rather than diffusion limitations. In the data to be treated below, absence of mass-transfer limitation effects in the observed approach to limiting currents was demonstrated by independence of the η vs. $\log i$ plots on rotation rate at a rotating disk electrode (11, 12).

The experimental conditions for which the data for Cl_2 evolution kinetics at Pt were obtained were fully described in Ref. (11) and (12). Here we shall make some further analysis of these results for anodic Cl_2 evolution kinetics in completely anhydrous trifluoroacetic acid as solvent with RbCl as electrolyte [where no oxide film exists on the electrode (11)] in comparison with the results for aqueous 1M KCl + 0.05M HCl solutions where a significant coverage by a surface oxide monolayer film, with co-adsorbed Cl^- ion, is present (12).

Basis of the Treatment

The following reaction equations [cf. Ref. (8)-(12)] are considered for a discharge/recombination controlled type of two-step reaction sequence such as is well known in the H_2 and Cl_2 evolution processes. The case of Cl_2 evolution will be exemplified here but the treatment will obviously apply to any similar reaction sequence. The steps are



M are the surface sites on the metal (in the anhydrous solution case) or oxide + Cl^- -covered electrode in the aqueous solution case. k_1 , k_{-1} , k_2 , and k_{-2} are the rate constants for the steps [1] and [2] as indicated above. With the recombination step [2] rate controlling, step [1] is assumed to be in quasi-equilibrium.

For brevity, C_{Cl^-} will represent the Cl^- ion concentration in solution and RT/F is represented by h^{-1} . The symmetry factor β in the discharge step is taken as 0.5. η is the overpotential defined as $V - V_{\text{rev}}$ where V is the metal-solution potential difference at finite net current density and V_{rev} that at zero net current density. Double-layer factors are absorbed in the k values and are considered constant for the purposes of the present analysis for constant concentration. θ will

represent the Cl^\cdot coverage at the overpotential η and θ_{rev} that at $\eta = 0$. A term θ_0 is defined as $\theta_0 = \theta_{\text{rev}} / (1 - \theta_{\text{rev}})$.

The quasi-equilibrium assumption for step [1] gives

$$\frac{\theta}{1 - \theta} = \frac{k_1}{k_{-1}} \text{C}_{\text{Cl}^-} \exp(hV) = \theta_0 \exp(h\eta) \quad [3]$$

Since $\theta_0 = \frac{k_1}{k_{-1}} \text{C}_{\text{Cl}^-} \exp(hV_{\text{rev}})$, simple rearrangements result in

$$\theta = \frac{\theta_0 \exp(h\eta)}{1 + \theta_0 \exp(h\eta)} \quad [4]$$

The current density i for the rate-determining Cl^\cdot recombination is given by

$$i = 2F[k_2\theta^2 - k_{-2}(1 - \theta)^2] \quad [5]$$

In terms of the exchange current density, i_0 , and θ_0 defined above through the coverage θ_{rev} at $\eta = 0$, the net current density i is given by

$$i = i_0 \left[\frac{\theta^2}{\theta_{\text{rev}}^2} - \frac{(1 - \theta)^2}{(1 - \theta_{\text{rev}})^2} \right] \quad [6]$$

where the two terms in the brackets correspond to forward and backward rate factors in the reaction velocity near the reversible potential.

Substituting θ in terms of θ_0 from Eq. [4] gives

$$i = i_0 \left[\frac{1}{\theta_{\text{rev}}^2} \left(\frac{\theta_0 \exp(h\eta)}{1 + \theta_0 \exp(h\eta)} \right)^2 - \left(\frac{1}{1 + \theta_0 \exp(h\eta)} \right)^2 \frac{1}{(1 - \theta_{\text{rev}})^2} \right] \quad [7]$$

Rearrangement, following the definition of θ_0 in terms of θ_{rev} , leads to

$$i \left(\frac{1 + \theta_0 \exp(h\eta)}{1 + \theta_0} \right)^2 = i_0 [\exp(2h\eta) - 1] \quad [8]^a$$

By plotting the \ln of each side of this function for various experimental i and corresponding η data, $\ln i_0$ will be obtained as the value of $\ln [i(1 + \theta_0 \exp(h\eta)) / (1 + \theta_0)^2]$ when $\ln [\exp(2h\eta) - 1] = 0$. The required linearity of Eq. [8] will be achieved with the appropriate value of θ_0 , hence giving θ_{rev} , all the other quantities being known. Evaluation of θ_0 can be made either by regression analysis or by numerical evaluation using pairs of data points for η and i . Here we have evaluated θ_0 as the value giving a best linear fit of the data to Eq. [8] in \ln form.

Results

Figures 1 and 2 show \log plots of the left-hand side and right-hand side of Eq. [8] for kinetic data for Cl_2 evolution at Pt in TFA and aqueous solutions of Cl^- ion. The various curves in Fig. 1 and 2 correspond to a range of selected θ_0 values. The plotted graphs indicate that the linear relation expected for the mechanism [1], [2] is only approached as θ_0 is quite near 0, $\theta_0 \simeq 0.01$ for aq. solution, i.e., $\theta_{\text{rev}} \simeq 0$. This is consistent, in the TFA solution case where no oxide film formation is detectable in cyclic voltammetry (11), with the absence of any reversible underpotential deposition of Cl^\cdot species. The anodic current curve on the cyclic-voltammogram goes directly from a double-layer charging current into a continuing faradaic current curve for the Cl_2 evolution without any current

^a For the "electrochemical desorption" case, which does not apply to the present experimental results, the equation equivalent to [8] is

$$i = i_0 \left[\frac{(1 + \theta_0) \exp[h\eta(1 + \beta)]}{1 + \theta_0 \exp(h\eta)} \right] [1 - \exp(-2h\eta)] \quad [8a]$$

Application of the procedure described above to recently discussed results of Khristalik (15) for Cl_2 evolution on RuO_2 electrodes also gives a θ_0 value for Cl^\cdot coverage near to zero. This is consistent with the requirements for Khristalik's mechanism for this electrode.

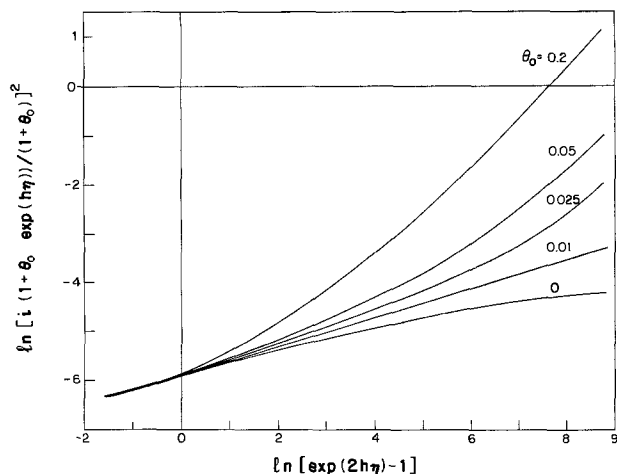


Fig. 1. Plot of $\ln [i(1 + \theta_0 \exp(h\eta))/(1 + \theta_0)]^2$ vs. $\ln [\exp(2h\eta) - 1]$ for the system Pt/0.5M aq. KCl + 0.05M aq. HCl during anodic polarization at room temperature.

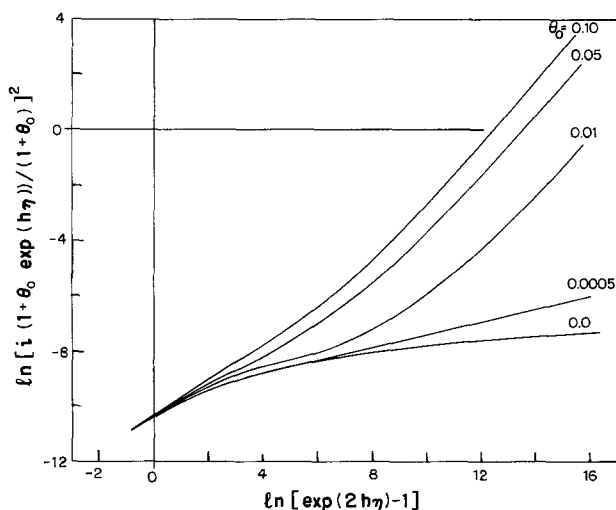


Fig. 2. Plot of $\ln [i(1 + \theta_0 \exp(h\eta))/(1 + \theta_0)]^2$ vs. $\ln [\exp(2h\eta) - 1]$ for the system Pt/100% CF_3COOH + 0.5M RbCl during anodic polarization at room temperature.

due to Cl^\cdot deposition prior to the Cl_2/Cl^- reversible potential (Fig. 3).

As Eq. [8] indicates, $\ln i_0$ values can be estimated from the plots of Fig. 1 and 2. The values are ca. e^{-10} ($=4.5 \times 10^{-5}$) and $e^{-6.2}$ ($=2.03 \times 10^{-3}$) A cm^{-2} , respectively, for TFA and 100% aqueous solutions of Cl^- ion at 0.1M Cl^- . These data are consistent with the differences of k_2 derived from the special linear test plots made in Ref. (11) and (12) for the recombination-controlled kinetics.

Interaction effects in the Cl^\cdot ad-layer.—Hitherto we have not mentioned [but cf. Ref. (11)] that there can be significant lateral interaction effects in the ad-layer of Cl^\cdot , especially when $\theta_{\text{Cl}^\cdot} \rightarrow 1$ as the limiting current is approached. When interaction effects are significant, Eq. [3] may take the form of a Frumkin isotherm (13) where k_1/k_{-1} is replaced by $k_1/k_{-1} \cdot (\exp -g\theta)$, g being the lateral interaction energy parameter (13, 14) characterizing 2-dimensional interactions in the monolayer.

If the “ g ” factor is included in the analysis, Eq. [8] becomes

$$i \left[\frac{1 + \theta_0 \exp(h\eta - g\theta)}{1 + \theta_0} \right]^2 = i_0 [\exp(2h\eta) - \exp(-2g\theta)] \quad [9]$$

Then, of course, the evaluation of θ_0 becomes more

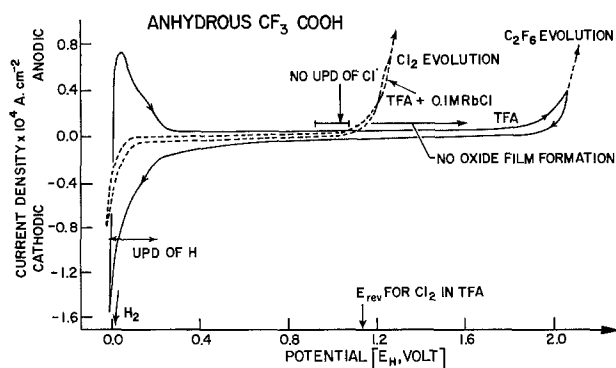


Fig. 3. Cyclic-voltammogram for Pt in 100% anhydrous CF_3COOH with 0.1M CF_3COOH or 0.1M RbCl, showing absence of Pt surface oxide formation or reduction currents, and no detectable upd of Cl atoms.

complex. However, some indication of whether a significant value of g is involved or not can be obtained from the shape of the experimental η vs. $\log i$ curves as the limiting current is approached [see Ref. (11) and (12)].

The equation for i at appreciable η takes the form

$$i = 2Fk_2\theta^2 \exp(2g\theta) \quad [10]$$

When $g > 0$, this gives (i) a limiting current greater than that for Langmuir adsorption ($g = 0$) and (ii) a slower approach of i to its limiting value as $\theta \rightarrow 1$. In fact it is seen that

$$\frac{d \ln i}{d \ln \theta} = 2(1 + g\theta) \quad [11]$$

which is the surface reaction order “in θ .”

Comparison of theoretically calculated $\ln i$ vs. η curves for various small g values in the range of $0 < g < 10$ with the shapes of the experimental curves gives $g \sim 2.5$, near the value found in another way for CF_3COOH solutions in Ref. (11). This enables Eq. [9] to be used to evaluate θ_0 . Small values of θ_0 , near $0 (< 0.05)$ are again found.

An iterative method could also be employed by substituting θ_0 for the condition $g = 0$ (as above) and then using the equation $h\eta = \ln(\theta/1 - \theta) - \ln \theta_0 + g\theta$ to estimate g . A further estimate of θ_0 could then be made with the aid of Eq. [9]. In the light of the limited range of linearity of Fig. 1 and 2 for θ_0 near 0, we have found that the further step is unproductive of exact results for θ_0 for this system. Nevertheless, a low value of θ_0 is still indicated. It is pertinent to note here that Ludwig *et al.* (13) examined the kinetics of H_2 evolution on Pt in 6.1N HCl and observed linearity over 7 decades by plotting η vs. $\log \{i(1 - \exp(2F\eta/RT))^{-1}\}$. This indicates that $\theta_0 = 0$ since Eq. [8] degenerates to the above form (with appropriate sign for η) in the absence of coverage by the adsorbed intermediates on the electrode surface at the reversible potential. Hence, it appears that the mechanism of H_2 evolution on Pt from acid media involves slow recombination of weakly bound H_{ads} , whose coverage is zero near the reversible potential, even though the electrode is already covered with a monolayer of strongly bound adsorbed hydrogen (14).

Acknowledgments

The authors wish to thank Prof. S. K. Rangarajan for his critical comments, the Natural Sciences and Engineering Research Council of Canada for support of part of this work at University of Ottawa, and Hooker Chemical Company for permission to publish this work.

Manuscript submitted Nov. 13, 1980; revised manuscript received March 30, 1981. This was Paper 510 pre-

sented at the St. Louis, Missouri, Meeting of the Society, May 11-16, 1980.

Any discussion of this paper will appear in a Discussion Section to be published in the June 1982 JOURNAL. All discussions for the June 1982 Discussion Section should be submitted by Feb. 1, 1982.

Publication costs of this article were assisted by Hooker Chemical Corporation.

REFERENCES

1. H. B. Beer, "Diaphragm Cells for Chlorine Production," p. 15, Society of Chemical Industry, London (1977).
2. K. J. O'Leary and T. J. Navin, in "Chlorine Bicentennial Symposium," T. C. Jeffrey, P. A. Danna, and H. S. Holden, Editors, p. 174, The Electrochemical Society Softbound Proceedings Series, Princeton, N.J. (1974).
3. D. L. Caldwell, "Comprehensive Treatise on Electrochemistry," Vol. 2, J. O'M. Bockris, B. E. Conway, and E. A. Yeager, Editors, Plenum Press, New York (1981).
4. B. V. Tilak, B. E. Conway, and D. M. Novak, "Modern Aspects of Electrochemistry," Vol. 14, In press. J. O'M. Bockris and B. E. Conway, Editors, Plenum Press, New York (1981).
5. F. T. Chang and H. Wick, *Z. Phys. Chem.*, **A172**, 448 (1935).
6. T. Yokoyama and M. Enyo, *Electrochim. Acta*, **13**, 1631 (1968); **15**, 1921 (1970).
7. B. V. Tilak, *This Journal*, **126**, 1343 (1979).
8. W. E. Triaca, C. Solomons, and J. O'M. Bockris, *Electrochim. Acta*, **13**, 1949 (1969).
9. G. Faita, G. Fiori, and J. W. Augustynski, *This Journal*, **116**, 928 (1969).
10. G. Faita, G. Fiori, and A. Nidola, *ibid.*, **117**, 1333 (1970).
11. B. E. Conway and D. M. Novak, *J. Electroanal. Chem. Interfacial Electrochem.*, **99**, 133 (1979).
12. B. E. Conway and D. M. Novak, *J. Chem. Soc., Faraday Trans. 1*, **75**, 2454 (1979).
13. F. Ludwig, R. K. Sen, and E. Yeager, *Sov. Electrochem.*, **13**, 717 (1977).
14. B. E. Conway in "Electrode Materials and Processes for Energy Conversion and Storage," J. D. E. McIntyre, S. Srinivasan, and F. G. Will, Editors, p. 441, The Electrochemical Society Softbound Proceedings Series, Princeton, N.J. (1977).
15. L. I. Khristalnik, *Electrochim. Acta.*, **26**, 329 (1981).

Calcium Thionyl Chloride High-Rate Reserve Cell

E. Peled,* A. Meitav, and M. Brand

Department of Chemistry, Tel-Aviv University, Tel-Aviv, Israel

Recently, noteworthy progress has been made in the development of a high-rate reserve lithium thionyl chloride cell (1-3). At room temperature, discharge rates as high as 150 mA cm⁻² were obtained with an average discharge voltage above 2.5V (2). At 65°C the rate capability of the cell is improved and a cell with a 0.05 mm thick cathode can deliver 400 mA cm⁻² for a few seconds at a voltage above 2.0V (2).

One of the major obstacles to the development of a high-rate, pile-type (or multi-cell) lithium thionyl chloride battery is its well-known hazard during reversal or charging. Reversal of one or more cells, or the charging of one row of cells by another row connected in parallel, are each likely to happen during deep discharge. The metallic lithium, which deposits under these conditions on either the cathode or the anode, may have a large active surface area. At a high deposition rate, a powder-like lithium deposit can be formed. A mechanism for such a lithium deposition process was recently proposed (4). The presence of lithium powder deposit in a thionyl chloride cell may create a very hazardous condition. Another danger is the formation of an internal short circuit (sometimes accompanied by an internal spark), due to lithium dendrite growth. This will lead to rapid melting, or even evaporation, of the lithium dendrite, thereby initiating a cell explosion.

Replacement of lithium with calcium can solve these safety problems. This is due to the following facts: (i) the melting point of calcium is much higher (838°C); and (ii) the most important safety feature of the Ca/Ca(AlCl₄)₂-SOCl₂ system is the inability to practically deposit calcium on a metallic inert electrode (5), on a carbon cathode or even on calcium itself, as will be shown below.

Recently it was demonstrated (5-7) that calcium thionyl chloride cells can deliver, at low rates, a

capacity comparable to lithium cells. The faradaic yield of a 0.5 mm thick calcium anode at 2.5 mA cm⁻² was found to be 70-80% (7). The electrochemical behavior of calcium in thionyl chloride solutions was recently studied (5, 7). It was found that in thionyl chloride solutions calcium is covered by a passivating layer which acts as a solid electrolyte interphase (SEI). The resistivity of this SEI is (7) 10⁸-10¹⁰ Ωcm, an order of magnitude or more higher than that of lithium in thionyl chloride solutions. The goal of this work was to assess the high-rate capability of a reserve type calcium-Ca(AlCl₄)₂ thionyl chloride cell and to exhibit its excellent safety features.

Hermetically sealed glass cells containing a flat 0.5 mm thick calcium (Roc/Ric) anode and a flat 1.1 mm thick Teflon-bonded carbon cathode were assembled inside a glove box. The carbon cathode had porosity of about 80% and consisted of 90 weight percent (w/o) Shawinigan black and 10 w/o Teflon binder. The electrode area was 5.6 cm². A nonwoven 0.18 mm thick glass separator paper was inserted between the cathode and the anode. The two electrodes were supported by two stainless steel plates held together with four bolts, which tightened at constant force. The cathode was isolated from this support plate by glass separator paper. An electrolyte reservoir was attached to the cell through a Teflon "Rotaflo" stopcock. The electrode compartment was evacuated before the discharge test. The cell was activated by opening the Teflon stopcock and letting the electrolyte fill the cell (about 30 ml) under atmospheric pressure. The cell was loaded as soon as its OCV reached 3.1V. This took 5-20 sec, depending on the temperature and on the composition of the electrolyte. Discharge at 60°C was carried out inside an oven. The cell with the attached electrolyte reservoir was stored at this temperature for 2 hr prior to the discharge test. The procedure for conductivity measurements is described in Ref. (8). Solutions were prepared by vacuum and glove box techniques. Fluke AR AlCl₃ was sublimed under vacuum, Merck AR

* Electrochemical Society Active Member.

Key words: electrodeposition, conductance, electrolysis.

SOCl_2 was twice distilled under vacuum, and Baker AR CaCl_2 was vacuum dried for 24 hr at 250°C .

It was recently found by Staniewicz (5) that the deposition process of calcium on nickel substrate is inefficient and only "little evidence" for calcium deposition was obtained. His experiment was carried out at a current density of 1.25 mA cm^{-2} . Our efforts to electrodeposit calcium on tungsten and Teflon-bonded carbon cathodes at current densities of $1\text{--}30 \text{ mA cm}^{-2}$ all failed. On turning off the current after 15 min of electrolysis of a $0.95\text{M Ca}(\text{AlCl}_4)_2$ solution at 1 mA cm^{-2} , using a tungsten cathode and calcium anode, the OCV of the tungsten reached 1V (*vs.* calcium reference electrode) within 1 sec while a few seconds later it rose to 2.5V . The same results were obtained after 1 min of electrolysis at 10 mA cm^{-2} or 3 min at 30 mA cm^{-2} . In the last two experiments, massive gas evolution (most likely SO_2) was observed on the tungsten cathode. The tungsten overpotential in these experiments rose to 20 and 35V , respectively. The open-circuit voltage of a cathode-limited cell which was overdischarged at 10 mA cm^{-2} for 2 hr rose to 2.5V within 1 sec after turning off the current. This cell contains $0.95\text{M Ca}(\text{AlCl}_4)_2$ thionyl chloride solution. A massive evolution of gas was observed on the cathode during this reversal test. Plots (B) and (C) in Fig. 1 show cell voltage as a function of the current density during a galvanostatic reversal test of fully discharged cells. Cell (B) was galvanostatically discharged at 20 mA cm^{-2} to zero voltage prior to the reversal test. It can be seen that up to a reverse voltage of 15V the current density is rather small, a few mA cm^{-2} only. However, above 15V there is a steep increase in the current and a current density as high as 30 mA cm^{-2} was measured at a reverse voltage of 17.5V . Cell (C) was discharged at 1 mA cm^{-2} to zero voltage prior to the reversal test. This cell can stand a reverse voltage of 30V with no massive current flow. At reverse voltage above 30V the current steeply increases as in the previous case. These results can be explained in the following way. The cathode of a fully discharged cell is passivated by a film of CaCl_2 . The thickness of such a passivating film is below 100\AA (9). This film is a very poor electronic conductor so the reduction of thionyl chloride ceases and the working voltage of the cell is zero. The low current densities measured up to 15V under reversal condition indicates that the deposition process of calcium is also blocked. At a high cathodic over-

potential a very strong electric field, of the order of 10^7 V cm^{-1} , is built up. This strong electric field causes an electrolytic breakdown of the CaCl_2 film, increasing its electronic conductivity and resulting in a massive reduction of the solvent. The electrolytic breakdown process observed for the cathode which was passivated at 1 mA cm^{-2} , took place at a much higher reverse voltage than that observed for the cathode which was passivated at 20 mA cm^{-2} . This indicates that the film which was formed at the low current density is thicker, more compact, and is a better electronic resistor.

It can be seen (Fig. 1, curve A) that the charging current density of a fresh cell is smaller than 0.1 mA cm^{-2} up to 30V . At charging voltage above 40V the current steeply increases and massive gas evolution (most likely SO_2) is observed on the calcium. This test proves that it is practically impossible to "charge" a $\text{Ca-Ca}(\text{AlCl}_4)_2$ thionyl chloride cell. The main cathodic reaction taking place on reversal or on charging of a cell at current densities above 1 mA cm^{-2} is the reduction of the thionyl chloride and there is no indication of calcium deposition. Staniewicz (5) has proposed that the inefficiency of the calcium deposition process results from the fact that the CaCl_2 -SEI is a pure anionic conductor ($t_- \approx 1$), and so the deposition reaction requires the destruction of CaCl_2 at the SEI-metal interface and precipitation of it at SEI-solution interface. It seems that, as in the case of magnesium deposition from thionyl chloride solutions (9), (and in the case of cathodic polarization of passivated inert electrodes), some blocking of the ionic current leads to the development of a very high overpotential and electric field on the SEI. This electric field causes an electrolytic breakdown of the SEI and as a result, large electronic currents start to flow through it, leading to a massive reduction of thionyl chloride and evolution of SO_2 .

The capacity, per square centimeter of cathode, of lithium thionyl chloride reserve cells was found to increase when acidic solutions (excess of AlCl_3) were used (1, 2), instead of neutral solutions. The maximum electrolytic conductivity of LiAlCl_4 thionyl chloride solutions at room temperature is about three times of that of $\text{Ca}(\text{AlCl}_4)_2$ solutions. As high-rate cells require the highest electrolytic conductivity, we studied the effect of temperature and excess of AlCl_3 on the electrolytic conductivity of $\text{Ca}(\text{AlCl}_4)_2$ solutions. The results are summarized in Fig. 2. The total concentration of AlCl_3 was kept constant at 2.2, 2.8, and 3.5M while the concentration of CaCl_2 [or $\text{Ca}(\text{AlCl}_4)_2$] was changed. In general, the conductivity increases with increase in the concentration of CaCl_2 . At 20°C the highest conductivity was measured for 2.2M AlCl_3

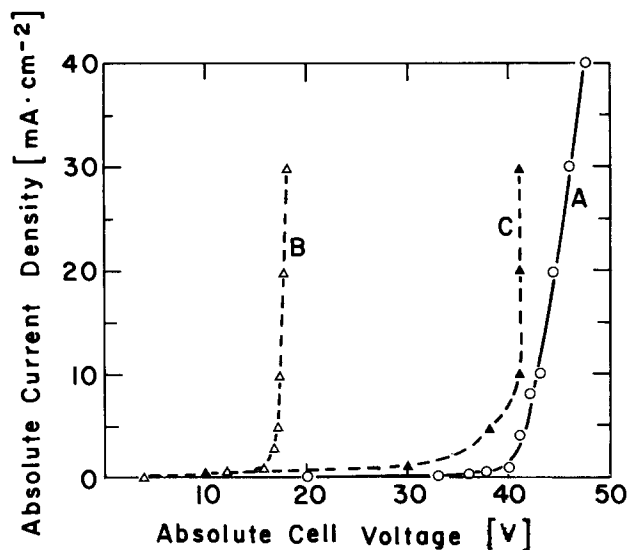


Fig. 1. Cell voltage as a function of the current density during a galvanostatic charging experiment of a fresh cell (A) and during galvanostatic reversal tests of fully discharged cells (B) and (C). Prior to the reversal tests, cell B was discharged at 20 mA cm^{-2} and cell C at 1 mA cm^{-2} . All cells contained $0.95\text{M Ca}(\text{AlCl}_4)_2$.

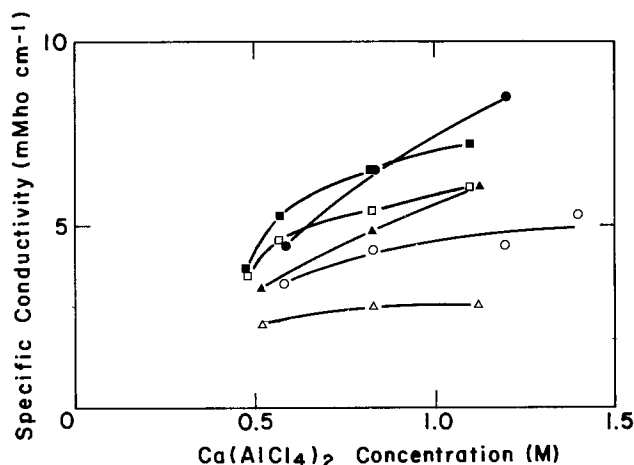


Fig. 2. The effect of CaCl_2 concentration on the specific conductivity of AlCl_3 - SOCl_2 solution for 20°C (empty symbols) and 60°C (full symbols). Triangles, 3.5M AlCl_3 ; Circles, 2.8M AlCl_3 ; Squares, 2.2M AlCl_3 .

solutions and this decreased as the concentration of AlCl_3 was increased. At 60°C for high concentrations of CaCl_2 the highest conductivity was measured for solutions containing 2.8M AlCl_3 . It seems that one of the reasons for the decrease of the specific conductivity of the solution with the increase of the concentration of AlCl_3 is that solutions become more viscous.

The discharge curves of cells containing $0.85\text{M Ca}(\text{AlCl}_4)_2 + 0.4\text{M AlCl}_3$ and $1.2\text{M Ca}(\text{AlCl}_4)_2 + 0.4\text{M AlCl}_3$ at 23° and at 60°C are shown in Fig. 3. All cells were loaded on 8.2Ω resistor as soon as their OCV reached 3.1V . This took 5 sec (from filling the cell) for cell No. 3 and 15–20 sec for the rest of them. Cells No. 1, 2, and 3 exhibited a rather flat discharge curve up to 80% of the discharge time to a cutoff voltage of 1.5V . The discharge plateau at 60°C was about 2.2V while that at 23°C was about 2.0V (for cell No. 2). Higher capacities were obtained at 60°C than at 23°C . At 60°C , cell No. 3, which contained $2.8\text{M AlCl}_3(+1.2\text{M CaCl}_2)$, gave a higher capacity than cell No. 1 which contained $2.2\text{M AlCl}_3(+0.85\text{M CaCl}_2)$. This is due to

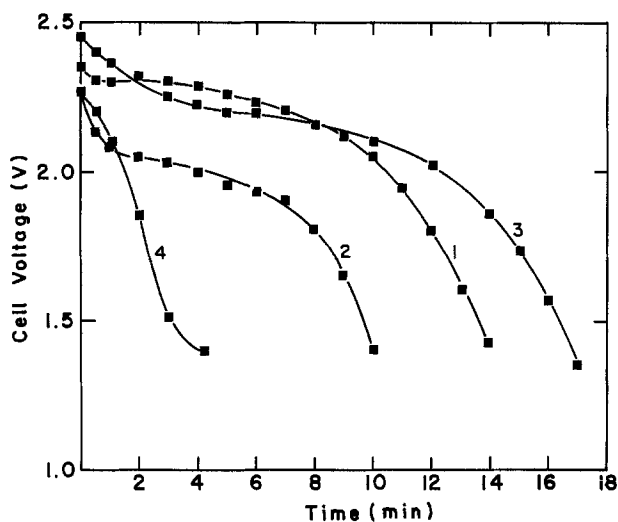


Fig. 3. The effect of temperature and electrolyte concentration on the discharge performance of calcium $\text{Ca}(\text{AlCl}_4)_2$ thionyl chloride reserve cell. Curves 1 and 2, $2.1\text{M AlCl}_3 + 0.85\text{M CaCl}_2$ at 60° and 23°C , respectively; curves 3 and 4, $2.8\text{M AlCl}_3 + 1.2\text{M CaCl}_2$ at 60° and 23°C , respectively.

the better electrolytic conductivity of the more concentrated solution (see Fig. 2). At 23°C the opposite is true. Cell No. 2, which contained only $2.2\text{M AlCl}_3(+0.85\text{M CaCl}_2)$, had a much higher capacity than cell No. 4 which contained $2.8\text{M AlCl}_3(+1.2\text{M CaCl}_2)$. Here again the higher capacity was obtained for the cell which had higher electrolytic conductivity. The current density at 60°C was about 50 mA cm^{-2} . The maximum capacity at this rate was about 12 mA hr cm^{-2} (to a 1.5V cutoff voltage). At 23°C and at a current density of 45 mA cm^{-2} the capacity was about 7 mA hr cm^{-2} (for cell No. 2).

The good discharge performance at a discharge time of 10–15 min, together with the excellent safety features of the $\text{Ca}/\text{Ca}(\text{AlCl}_4)_2$ thionyl chloride cell encourage further investigations of this system as a promising candidate for high-rate multi-cell reserved and nonreserved battery applications.

Manuscript submitted Feb. 17, 1981; revised manuscript received April 23, 1981.

Any discussion of this paper will appear in a Discussion Section to be published in the June 1982 JOURNAL. All discussions for the June 1982 Discussion Section should be submitted by Feb. 1, 1982.

Publication costs of this article were assisted by Tel-Aviv University.

REFERENCES

1. M. J. Domeniconi and K. A. Klinedinst, in "Proceedings of the 28th Power Sources Symposium," Atlantic City, NJ (1978).
2. K. A. Klinedinst, in "Power Sources for Biomedical Implantable Applications and Ambient Temperature Lithium Batteries," B. B. Owens and N. Margalit, Editors, p. 579, The Electrochemical Society Softbound Proceedings Series, Princeton, NJ (1980).
3. M. Babai, U. Meisher, and B. Ravid, in "Proceedings of the 29th Power Sources Symposium," Atlantic City, NJ (1980).
4. E. Peled, *This Journal*, **126**, 2047 (1979).
5. R. J. Staniewicz, *ibid.*, **127**, 782 (1980).
6. R. Huggins and J. S. Cloyd, in "Proceedings of the 29th Power Sources Symposium," Atlantic City, NJ (1980).
7. A. Meitav and E. Peled, in "Proceedings of the 131st ISE Meeting," Venice, Italy, September (1980).
8. E. Peled, M. Brand, and E. Gileadi, *This Journal*, **128**, 1697 (1981).
9. A. Meitav and E. Peled, *ibid.*, **128**, 825 (1981).

Erratum

In the paper "Current Limited by Transport Through the Space-Charge Region of a Semiconductor Electrode" by David L. Ullman which appeared on pp. 1269–1273 of the June 1981 JOURNAL, Vol. 128, No. 6, Eq. [13] is written

$$\frac{1}{2}\sqrt{\phi}\text{Daw}(\sqrt{\phi})$$

but should be written

$$1/(2\sqrt{\phi}\text{Daw}(\sqrt{\phi}))$$



Investigation of Photoelectrochemical Corrosion of Semiconductors

III. Effects of Metal Layer on Stability of GaAs

K. W. Frese, Jr.,* M. J. Madou, and S. R. Morrison

SRI International, Menlo Park, California 94025

ABSTRACT

The effects of displacement plated metal layers on the photoelectrochemical corrosion of the (100) surface of n-GaAs were investigated using the rotating ring disk electrode (RRDE). A large beneficial effect on stability was demonstrated. Measurable improvements in stability were observed for less than a monolayer gold metal coverage. Capacitance/voltage data were consistent with Fermi level pinning caused by metallic deposits.

In view of the current interest in development of photoelectrochemical (PEC) solar cells, the stabilization of semiconductors in contact with electrolytes against photocorrosion is a highly relevant problem. We have been studying fast redox couples that can be effective stabilization agents, as well as the effects of defects (1, 2) on the corrosion process.

In addition to enhancing the stability by fast redox kinetics on the "clean" surface, it is of considerable interest to find other methods to enhance the corrosion stability of semiconductors. A possible way to increase the stability and the solar-electrical conversion efficiency of the semiconductor in a PEC cell is through an effective surface pretreatment. Indeed it has already been shown that pretreatment of n-GaAs electrodes (3) with various metal ions such as Ru^{3+} leads to enhanced solar cell efficiency. However, no quantitative data have been reported about the effect of deposited metals or metal ions on the stability against photoelectrochemical corrosion.

This paper reports some of our results of stabilization efficiency, S , and of capacitance/voltage measurements on (100) single crystal n-GaAs surfaces that have been pretreated with solutions containing metal ions. The technique of displacement deposition from solution is used to obtain the metal deposits. To our knowledge, this displacement technique has not been applied to stabilization of PEC solar cells.

Experimental

The GaAs (100) surfaces were chemomechanically polished with a 1% V/V chlorox (5.25% sodium hypochlorite) solution. The surface was then etched in a 0.05% chlorox solution for ~ 10 min at room temperature. The surface was rinsed successively with H_2O , 1M HCl, and H_2O , and then blown dry.

Solutions of various metal ions were prepared at $\sim 0.01\text{M}$ concentrations. The solutions included acidic RuCl_3 , $\text{Pb}(\text{NO}_3)_2$, $\text{Cu}(\text{NO}_3)_2$, $\text{Fe}(\text{ClO}_4)_2$, H_2PtCl_4 , K_3IrCl_6 , and AuCl_3 . The surface to be treated was

* Electrochemical Society Active Member.

Key words: GaAs, photocorrosion, metal films, corrosion inhibition.

covered with a layer of the solution and then illuminated with a microscope lamp for 3-5 min. The surface was then rinsed with H_2O and blown dry. Finally, the samples were inserted into the rotating disk (RRDE) cell (1) and stabilization measurements were made.

This treatment is known (4, 5) to cause irreversible deposition of metallic gold, silver, copper, and mercury on GaAs and InSb. It was shown in this early work that these deposits could not be removed by successive washing with 1N HNO_3 . We have previously used this plating technique to form gold-back contacts on p-GaAs for electrochemical measurements (6).

Capacitance/voltage curves were obtained using a lock-in amplifier technique with a 10 kHz, constant current a.c. signal of $1 \mu\text{A}$. The ring disk apparatus included a two potentiostat, six electrode system so that the potentials of the ring and disk could be independently controlled. The RRDE consisted of a 5 mm diam GaAs disk, an epoxy insulator, and an amalgamated copper ring. The calculated collection efficiency was 0.36, whereas the experimental value was 0.344 determined (1) in the presence of a highly effective stabilizing agent such as Fe(II) EDTA. The rotation speed was about 1000 rpm. The results were independent of speed in this range. All measurements were done in aqueous solution.

Results and Discussion

The displacement deposition of metals on GaAs occurs by circulating currents where the anodic current corrodes the GaAs, and the cathodic current reduces the metal. Thus in analyzing the deposition process, we look to the energy levels involved in these two processes. Figure 1 shows a diagram of redox energy levels, $-(E_{\text{NHE}}^\circ + 4.48 \text{ eV})$, for various metal ion/metal couples; these levels can be used to thermodynamically predict which metals can deposit on GaAs. On the left the redox energy levels of various couples, including those used in this work, are shown. On the right side the redox level for the anodic corrosion reaction of GaAs in acid solution is shown at -4.40 eV . The metal deposition on the single crystal is assumed

1981

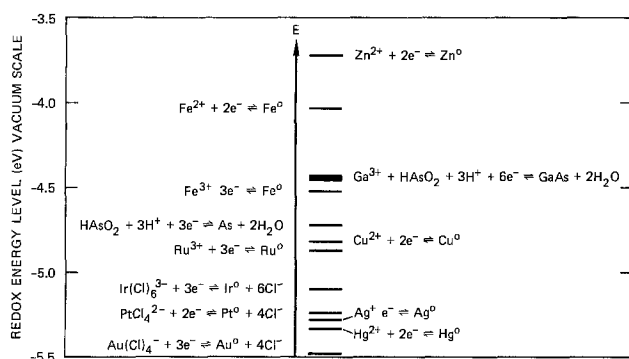


Fig. 1. Redox energy levels for various metal deposition couples and the GaAs corrosion couple in acidic solutions.

to occur via local anodes and cathodes. The sites of corrosion behave as anodes and the sites of metal deposition are the cathodes. On an ideal single crystal surface, no site is preferred for anodic or cathodic current. However, if the n-type surface is illuminated (5), regions of relatively high light intensities become anodes (corrosion occurs) and the dark regions become cathodes (plating occurs). A similar local anode-cathode effect (plating effect) could be caused by surface defects in the absence of illumination.

The metal ion/metal couples shown on the right of Fig. 1 were investigated by Larrabee (4). In the case of Cu^{2+} , Ag^+ , and Hg^{2+} , the metals were irreversibly deposited on GaAs, and Au^{3+} was similarly deposited on GaAs (5) and InSb (4). Importantly, Na^+ ($E^\circ = -1.77$ eV below vacuum) and Zn^{++} did not deposit (4) irreversibly. Note that these two couples have redox energy levels above the corrosion redox level of GaAs. From the chemistry of these semiconductor-metal systems it can be seen that using metal couples with redox energy levels below the corrosion redox level will lead to deposited metal layers and using those above it will not.

We will assume that the above deposition process occurs in the pretreatments described here. Capacitance/voltage data and visual observation support this assumption.

In RRDE measurements, it is found that very low coverages of deposited metals strongly affect GaAs photocorrosion. We will compare results of measurements involving no deposited metal to those involving the various deposited layers.

In the RRDE measurement, the fraction of the photocurrent that leads to reaction with a redox species in solution (stabilizing agent) is found by measuring the current due to reduction of $[\text{Fe(III) EDTA}]^-$. This ratio is termed the stabilization efficiency, S . It is found (1) that S varies with disk photocurrent level, j_p , for a given stabilizing agent concentration. Figure 2 shows results on the stabilization of (100) GaAs in aqueous 0.02M Fe(II)/0.1M Na_2 EDTA, $\text{pH} = 6.7$. The disk potential was 0.0V vs. SCE. Curve (a) refers to the well-etched clean surface. The stabilization decreases rapidly as j_p increases. We note that the level of stabilization presented here is very close to that already observed (1) for the same concentration of stabilizing agent but using the (111) As face. This observation may indicate a small dependence of corrosion rate on crystallographic face.

Curves (b) and (c) show typical S vs. j_p plots for "arsenic-treated" (see below) and iridium-treated surfaces, respectively. Modest but measurable increases in stabilization are found. Curve (d) shows data for a ruthenium-treated surface. A threefold increase in stabilization efficiency is observed. The magnitude of the stability enhancement was similar for Ru and Au. Results with gold will be discussed in more detail later. The data in curve (a) for the "clean surface" could be

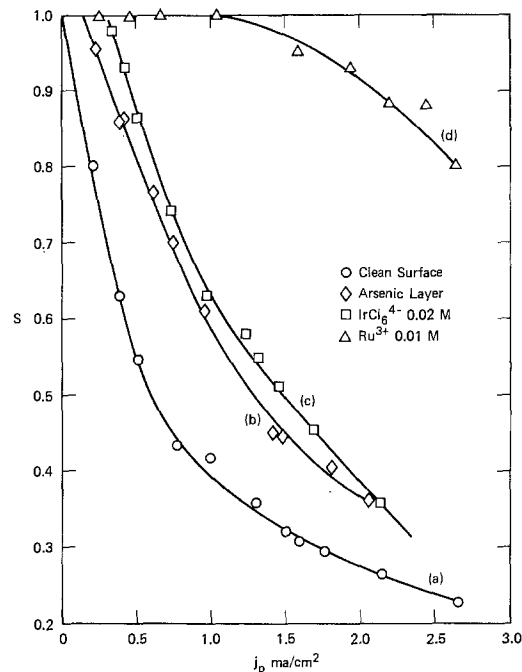


Fig. 2. Stabilization efficiency vs. disk photocurrent for 100-n-GaAs for various surface pretreatments. (a) Clean surface; (b) after 1000Å anodic oxidation (arsenic-rich surface); (c) 0.02M IrCl_6^{3-} ; (d) Ru^{3+} 0.01M. Stabilization experiments in 0.02M Fe(II) in 0.1N Na_2 EDTA $\text{pH} = 6.7$.

reproduced after chemomechanical etching of the previously metallized surface. The coverage by the metals after this preparation is difficult to determine. In our more detailed examination of gold deposits, described below, attempts were made to correlate improvement in stabilization with coverage.

Several other metals were tried, each with much less effectiveness than Ru or Au. For comparison with the data in Fig. 2, the stabilization efficiency at 1 mA/cm^2 and 0.02M Fe(II) EDTA, $\text{pH} = 6.5$, was 0.54 for Pt, 0.59 for Cu, and 0.44 for Fe, whereas for the unmetallized "clean surface" it was 0.41. The value for iron is reasonable since the reduction of Fe^{2+} is thermodynamically unfavorable according to Fig. 1.

The observation that an "arsenic-treated" surface provides increased stability deserves further discussion. The GaAs was not treated with an arsenite solution as could have been assumed from Fig. 1, but the sample was covered with the residue remaining after growth and removal of an anodic oxide. We have good evidence from our work on passivation of GaAs (6, 7) that anodic oxidation of GaAs leads to unoxidized elemental arsenic in the oxide and, importantly, in the GaAs/oxide interfacial region. It was postulated that since semimetallic As may be present on the GaAs surface, growing an anodic oxide and dissolving it with HCl would leave a "semi-metallized" surface rich in elemental, insoluble arsenic. The arsenic surface was thus prepared by growth of a 1000Å oxide by a standard method (6) followed by its removal in HCl. The enhancement in stabilization found by such a treatment is consistent with the As layer model. Attempts to deposit arsenic from arsenite solutions are planned for the future.

Another redox couple was investigated to confirm that the stabilization enhancement was not unique to ferrous EDTA. Figure 3 shows plots of S vs. j_p for 0.1M hydroquinone, H_2Q , ($\text{HQ}^- \sim 0.01\text{M}$) (1), $\text{pH} = 9.0$. The lower curve shows data for a clean well-etched surface and the upper curve (b) shows data for the Au^{3+} -treated surface. In this case, a three to fourfold increase is observed in the stabilization efficiency.

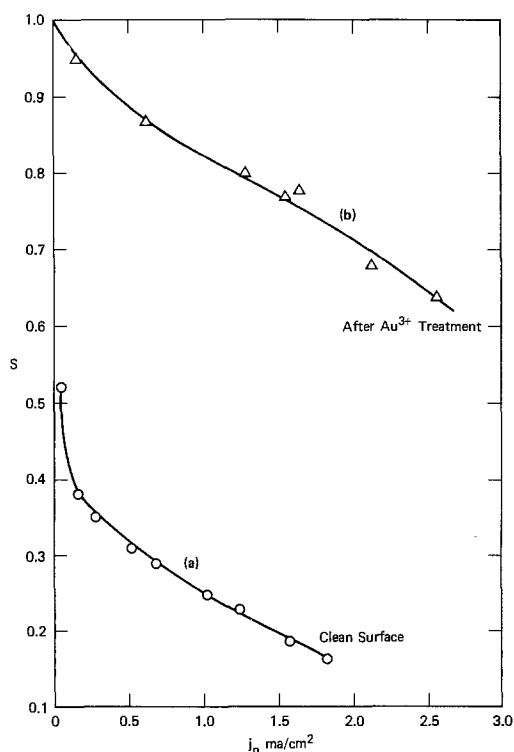


Fig. 3. Stabilization efficiency vs. disk photocurrent for 100-n-GaAs. Stabilization experiments in 0.1M hydroquinone 0.1M KCl pH = 9.0.

In Fig. 4, stabilization efficiency vs. photocurrent is shown for (100) GaAs with varying amounts of gold using 0.02M Fe(II) EDTA. In these studies using auric solutions, an upper limit could be calculated for the amount of gold on the surface. Solutions of $\text{AuCl}_3/0.1N \text{HClO}_4$ were prepared in the concentration range 2.3×10^{-6} to $1.15 \times 10^{-3}M$. By use of micropipettes, $10 \mu\text{l}$ drops containing as low as 2×10^{-11} mol of gold were placed over the whole area of the GaAs electrode. If one assumes a uniform layer of gold and an ideally smooth surface and that all the gold in the drop plates (surface illuminated), then the 2×10^{-11} mol of gold is equivalent to 0.1\AA film thickness or 7×10^{13} atoms/cm². Thus a $2.3 \times 10^{-6}M$ Au solution could ideally give

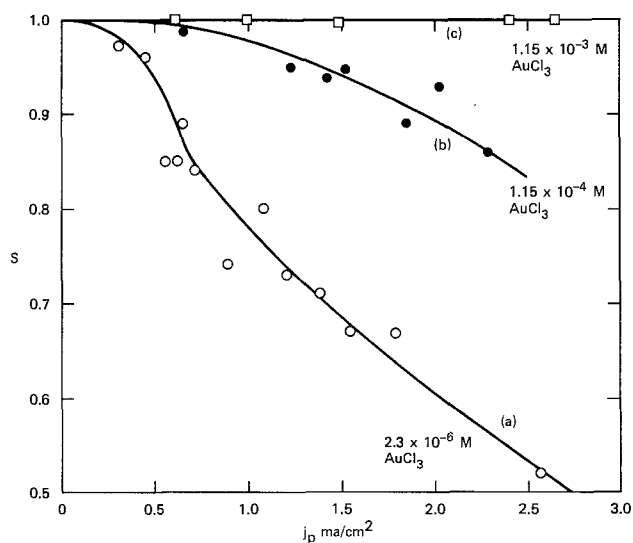


Fig. 4. Stabilization efficiency vs. disk photocurrent for 100-n-GaAs treated with various concentrations of $\text{AuCl}_3/0.1N \text{HClO}_4$. Treatment after 5 min under illumination, electrode area 0.195cm^2 , $10 \mu\text{l}$ samples of Au^{3+} solution. Stabilization experiments in 0.02M Fe(II) in 0.1M $\text{Na}_2 \text{EDTA}$ pH = 6.3.

less than a monolayer coverage whereas $1.2 \times 10^{-3}M$ solution could give 60\AA of gold. Thicknesses calculated in this manner are a convenient index to the maximal amount of Au on the surface. It should be mentioned that even if all the gold plated uniformly, the calculated thickness could still be 50% too large due to possible surface roughness. It cannot be proved from the stabilization data that gold film was uniform (although it appears uniform in Fig. 7 at $20,000\times$). What can be shown is that the stabilization is increased even for a gold deposit equivalent to less than a monolayer.

Curve (a) in Fig. 4 shows the stabilization efficiency vs. photocurrent for a case where the total amount of gold in the plating drop was 2.6×10^{-11} mol. As discussed above, this could only give less than a monolayer coverage if the gold were uniform. Nonetheless, significant increases in stabilization occurred as can be seen by comparing curve (a) in Fig. 2 with curve (a) in Fig. 4. The stabilization efficiency is doubled at j_p of 1mA/cm^2 . Curve (b), Fig. 4, shows a further increase in stabilization where the ideal gold thickness was 6\AA . Finally, the top of Fig. 4 shows points for a gold solution with an ideal film thickness of 60\AA . With this surface treatment the stabilization efficiency was constant and close to unity over a period of at least 2 hr at a photocurrent of 2.5mA/cm^2 . During this extended RRDE experiment, neither the disk photocurrent nor the ring current decayed. If significant amounts of corrosion occurred, films of Ga_2O_3 would be expected to remain on the surface at pH = 6.5. This film would eventually lead to a degradation of the photocurrent that was not observed. It should be noted that in all these experiments only 0.02M Fe(II) EDTA was used. Diffusion limitation of the stabilizing agent could be avoided because of the high rotation speed. The low concentration was necessary to provide a test of the metal additive, for with high concentration of stabilizing agent a metal additive is not required for efficient stabilization. However, metal pretreatment may be needed to give the very high stability needed for practical PEC solar cells. Stabilization efficiencies approaching 100% for the "clean" single crystal surface could be obtained using 0.08-0.1M Fe(II) EDTA (1, 2).

It is desirable to obtain further evidence that metallic layers do indeed form on the surface. This can be done by observing changes in the space charge capacitance/voltage behavior after exposure of the GaAs to metal ions. Figures 5 and 6 show Mott-Schottky plots for clean surface and metal-deposited electrodes. Reasonably linear Mott-Schottky plots were obtained for the "clean" surface over a voltage range of about 1V. The experimental donor densities, $2 \times 10^{18} \text{cc}^{-1}$, were expected from the known electrical properties of the crystals.

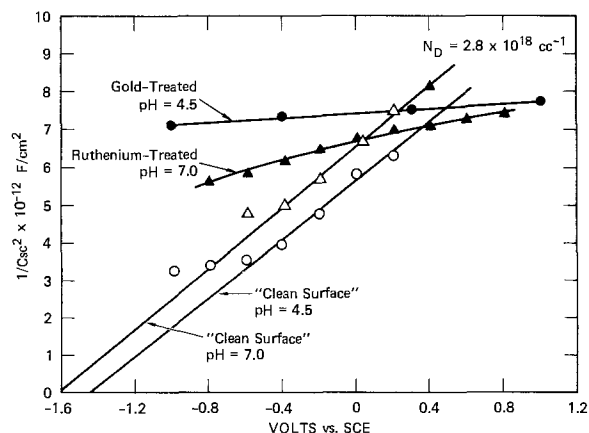


Fig. 5. Mott-Schottky plots for 100 n-GaAs before and after ruthenium and gold ion treatment. Electrolyte 0.1M $\text{Na}_2 \text{EDTA}$ pH = 7.0 and 4.5, respectively.

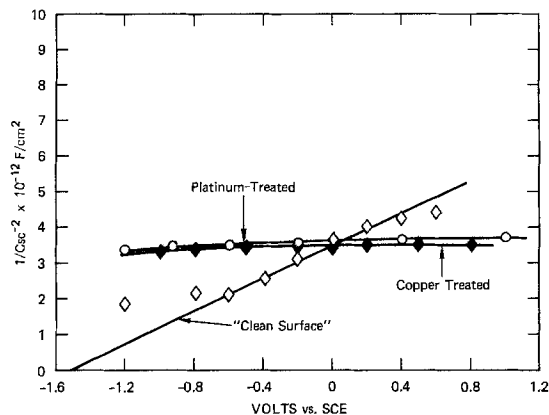


Fig. 6. Mott-Schottky plots for 100-n-GaAs before and after copper and platinum treatment. Electrolyte 0.1M Na₂ EDTA pH = 6.5.

The Mott-Schottky plots changed drastically after exposure of the electrode to the metal ion solution. As shown in Fig. 5 and 6, after treatment the space charge capacitance changes very slowly with electrode potential, indicating that most of the changes in applied potential appear outside the space charge region. Such changes in applied potential could be divided between the semiconductor/metal interfacial layer and the solution Helmholtz layer. Further work is needed to decide the distribution of potential outside the space charge region.

Finally, the oxidation state of the metal deposits is of interest. Our key conclusion from the Mott-Schottky plots is that metallic layers deposit on the surface. This conclusion is reached by analogy to well-known experiments (8) of evaporated metal layers on semiconductors. In such experiments it is concluded that a large density of interface states ($\sim 10^{14} \text{ cm}^{-2} \text{ eV}^{-1}$) cause Fermi level pinning and built-in (space charge) barriers up to 1 eV on GaAs. Similar pinning with large surface barriers is observed here according to the C/V results in Fig. 5 and 6.

On the other hand, if the metal ions were not reduced to metal atoms, two cases could occur. A positive shift in the flatband voltage could occur for sorption of an inert positive ion. The Mott-Schottky plot would have the same slope as the "clean" surface. This effect is completely analogous to the role of protons in shifting the flatband potential of oxide semiconductors. This type of behavior is not observed.

The other case for the positive ion that could account for the pinning observed in that it may act as a surface state and change only its oxidation state to +3 or +2 but not zero. Such a case is rare in semiconductor electrochemistry and can be ruled out for gold and copper since thick, easily visualized metallic films can be grown.

Figure 7 shows a scanning electron micrograph of a 100 n-GaAs surface treated with Au³⁺ to give an ideal film thickness of 60Å. The light region is the gold film, while the dark track is the GaAs surface. The track, which is about 5000Å wide, shows a region where the gold film was scratched in handling. In the adjacent regions of the sample the film looked quite uniform at this magnification.

Conclusions

A very simple method has been demonstrated by which a thin metal layer can be deposited on semiconductors such as GaAs. The layer is formed by simply dipping the illuminated surface of the semiconductor into a dilute solution of the appropriate metal ion. In previous work with metal overlayers (9, 10) evaporated layers were used and gave only qualitative results concerning stability. In addition these authors used H₂O as the reducing agent whereas we are concerned with

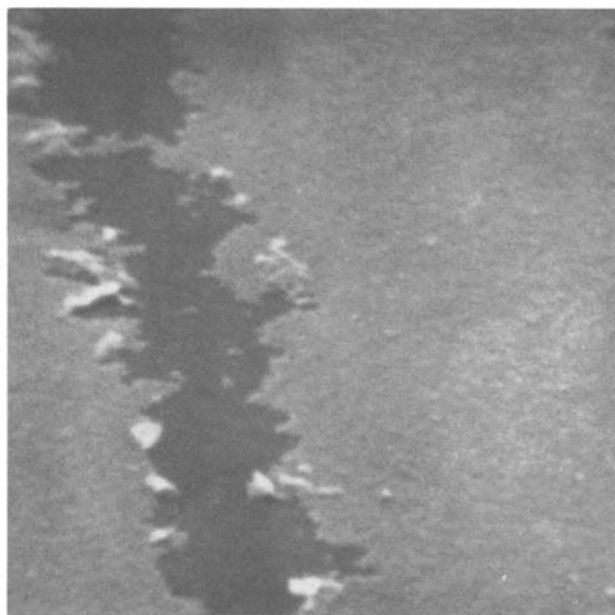


Fig. 7. Scanning electron micrograph of $\sim 60\text{\AA}$ of gold (light region) on (100) n-GaAs. The gold was deposited by a displacement plating technique. The scratch in the gold film is about 5000Å wide and was made during handling.

reducing agents that can effectively capture photogenerated holes. In the present case very substantial increases in the stability of the treated surface (discussed here) were observed with small amounts of metals such as gold or ruthenium.

Several models can be advanced to account for the stabilization results. It is not our purpose to discuss these models in detail, but some general comments are useful in indicating possible explanations.

First, the metal layer can block the electrolyte from contacting the semiconductor directly while still providing a conducting path for photogenerated holes. If the Ga³⁺ and As³⁺ ions formed cannot find OH⁻ or H₂O from the electrolyte, no corrosion product can form. For a sufficiently thick metal layer, field-aided diffusion (the normal mode of oxide growth) should be minimal because of the small zero field in the metal. Therefore, As⁰ and Ga⁰ atoms can be reformed by electrons from the metal, the stabilizing agent, or the GaAs conduction band (recombination). An auxiliary model that could help explain the results makes use of the concept of hot holes in metals. Holes generated at the valence band edge would enter the metal as hot holes since they probably would be several tenths eV below the metal Fermi energy. At such low energies below the Fermi level, the mean-free path for holes can be quite large. For example, the attenuation length for holes in evaporated gold films was found to be 550Å (11) at 0.8 eV below the Fermi energy. This implies that the metal layers used in our experiments are completely transparent to holes.

It may be shown that in certain cases the presence of a metal layer can increase the overlap between filled levels in solution and the hot holes (hot relative to the metal Fermi energy) at the valence band energy because of the potential drop in the metal semiconductor interfacial layer. This model and implications for photoelectrochemical solar cells will be discussed in future publications.

A third mechanism for the increased stability is that the metal atoms (or crystallites) at the surface have a very large effective capture cross section for holes, and so even a fractional monolayer can act as a very effective stabilizing agent. A stabilizing agent must be present in solution to capture the holes from the metal, but

once the hole is captured by the metal it may be rendered ineffective in corroding the host GaAs.

These results with deliberately deposited metal layers seem to explain our previous puzzling results (2) concerning the increase in stabilization efficiency after several minutes of cathodic current passage. In these RRDE/stabilization experiments we used (111) n-GaAs in Fe(II) EDTA. The solutions contained soluble arsenic species and Ga^{3+} (from corrosion) and Fe^{2+} and Fe^{3+} as EDTA complexes. In the cathodic pretreatment one or more of these metals could have been electrodeposited on the GaAs and thus could have given some kind of corrosion protection as observed in the present work.

Acknowledgment

This work was supported by the Solar Energy Research Institute.

Manuscript submitted June 6, 1980; revised manuscript received March 2, 1981.

Any discussion of this paper will appear in a Discussion Section to be published in the June 1982 JOURNAL.

All discussions for the June 1982 Discussion Section should be submitted by Feb. 1, 1982.

Publication costs of this article were assisted by SRI International.

REFERENCES

1. K. W. Frese, Jr., M. J. Madou, and S. R. Morrison, *J. Phys. Chem.*, **84**, 3172 (1980).
2. M. J. Madou, K. W. Frese, Jr., and S. R. Morrison, *This Journal*, **127**, 987 (1980).
3. B. A. Parkinson, A. Heller, and B. Miller, *ibid.*, **126**, 954 (1979).
4. G. B. Larrabee, *ibid.*, **108**, 1130 (1961).
5. R. W. Haisty, *ibid.*, **108**, 790 (1961).
6. K. W. Frese, Jr. and S. R. Morrison, *ibid.*, **126**, 1235 (1979).
7. K. W. Frese, Jr. and S. R. Morrison, *J. Vac. Sci. Technol.*, March/April (1980).
8. S. M. Sze, "Physics of Semiconductor Devices," Wiley-Interscience, New York (1969). See discussion and references contained in Chap. 8.
9. Y. Nakato, K. Abe, and H. Tsubomura, *Ber. Bunsenges, Phys. Chem.*, **80**, 1002 (1976).
10. L. A. Harris, M. E. Gerstner, and R. H. Wilson, *This Journal*, **124**, 1511 (1977).
11. C. R. Crowell, W. G. Spitzer, and H. G. White, *Appl. Phys. Lett.*, **1**, 3 (1962).

RF Sputtering of Yttria on Indium Tin Oxide Substrates

M. P. R. Panicker* and W. F. Essinger*

Sigmatron Nova, Thousand Oaks, California 91311

ABSTRACT

The blackening of indium-tin oxide and tin oxide thin film substrates during rf sputter deposition of yttrium oxide has been investigated to determine the precise conditions and mechanisms effecting this phenomenon. It was determined that at argon pressures below 4 microns and/or with the substrate films grounded, the yttria films deposited were oxygen deficient. The subsequent reduction of the substrate film by the more stable yttria resulted in the blackened appearance of the film. The problem was further compounded when these electrically conductive substrates were of optimum properties (sheet resistance below 20 Ω/sq and light transmission greater than 80%), as these properties can be simultaneously obtained only from a high oxygen deficiency. Based on these results, sputtering conditions are described which effectively deal with the problem.

Degenerate tin oxide ($\text{SnO}_2:\text{SbO}_x$) and indium oxide ($\text{In}_2\text{O}_3:\text{SnO}_x$) are materials commonly used for the electrically conductive (EC) coatings on glass substrates used to make electro-optic devices such as liquid crystal and electroluminescent displays and back-wall-type photovoltaic cells. Low sheet resistance and high optical transmission are two prerequisites for these applications. However, having fixed the dopant concentration and thus the electrical resistivity in an otherwise stoichiometric EC film, these properties are interdependent since lowering the sheet resistance can now be done only by increasing the film thickness resulting in decreased transmission. Under these conditions, the above properties can independently be varied only by reducing the degree of oxidation of the EC film.

In most of the above cited applications, the reduced degree of oxidation of the EC film is not a serious disadvantage either because of the absence of any chemically reactive layer adjacent to it or because of the fact

that the electric fields these films encounter are small. However, such conditions do exist in light emitting thin film (LEF) displays and hence EC coatings with a high oxygen deficiency can present serious problems during the performance of the device.

This paper relates specifically to the problems encountered while sputtering yttria (Y_2O_3) on indium tin oxide and SnO_2 substrates. Yttria is used as the dielectric material in the electroluminescent thin film displays developed by Sigmatron Nova. These yttria films are deposited by radio frequency sputtering. It has been observed that during sputtering the EC coating frequently turned black as a result of the reduction of these films by oxygen-deficient yttria. This made the EC coatings highly unstable leading to display failure during operation, observed as blown holes at random or along the entire length of the conducting lines. Further, this occurred more frequently with ITO substrates than with SnO_2 substrates.

Sigmatron Electroluminescent Thin Film Display

Figure 1 illustrates the structure of the display made by Sigmatron (1). The substrate is ITO- or SnO_2 -

* Electrochemical Society Active Member.

Key words: yttria, rf sputtering, dielectric material, transparent electrodes, ITO, tin oxide EL Film displays.

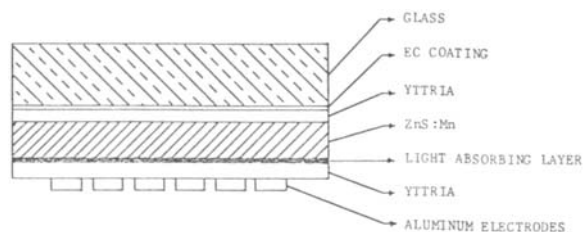


Fig. 1. Sigmatron LEF¹ panel

coated glass on which desired patterns are developed through photolithography. On this a 2000Å thick yttria film is deposited by rf sputtering. This is followed by a one micron thick ZnS:Mn phosphor layer on which a light absorbing layer is deposited (2). The device is then completed by depositing another 2000Å thick yttria layer followed by the deposition of the counter-electrodes.

Experimental

The yttria targets used for the study were obtained from Kema Corporation and were 99.99% pure and hot-pressed to suit the Sloan S-310 sputter gun. The substrates were either ITO-coated soda lime glass obtained from Optical Coating Laboratories, Incorporated, Santa Rosa, with a sheet resistance varying from 10 to 50 Ω per square or SnO₂-coat 7059 glass obtained from Corning, having resistivity in the range of 50-150

¹ LEF is a trademark of Sigmatron Nova.

Ω /sq. Both types of glass had white light transmissions of 75-85%. The substrates used to make the devices had an effective area of 2.5 \times 2.5 cm with a resolution of 22.4 lines per cm. These were cleaned under class-100 environment, degreased, and rinsed in deionized water prior to yttria deposition. Yttria was then rf sputter-deposited on these substrates using a Sloan 310 gun in an argon-oxygen gas mixture at chamber pressures varying from 1 to 10 microns. The oxygen content was varied from 0 to 50%. The substrate temperature was varied from room temperature to 300°C. The chamber was evacuated to about 3 \times 10⁻⁶ Torr using a turbo-molecular vacuum system with a liquid nitrogen trap prior to sputtering.

The resistivity measurements on the EC coatings were done using a four-point probe. Yttria films were tested for their dielectric properties using a capacitance bridge. The annealing of the EC coatings was done in air using a muffle furnace.

Results and Discussion

The effect.—When yttria is rf sputtered on ITO- or SnO₂-coated glass substrates at temperatures above 200°C, often the conductive lines turn black. This indicates that the EC film has been reduced and now has a large oxygen vacancy concentration (3). It has been observed that the effect is not necessarily uniform over an area or along a line. Figure 2a and b are ITO on soda lime, while 2c is SnO₂ on 7059 glass. The net effect of this on the device performance is nonuniform

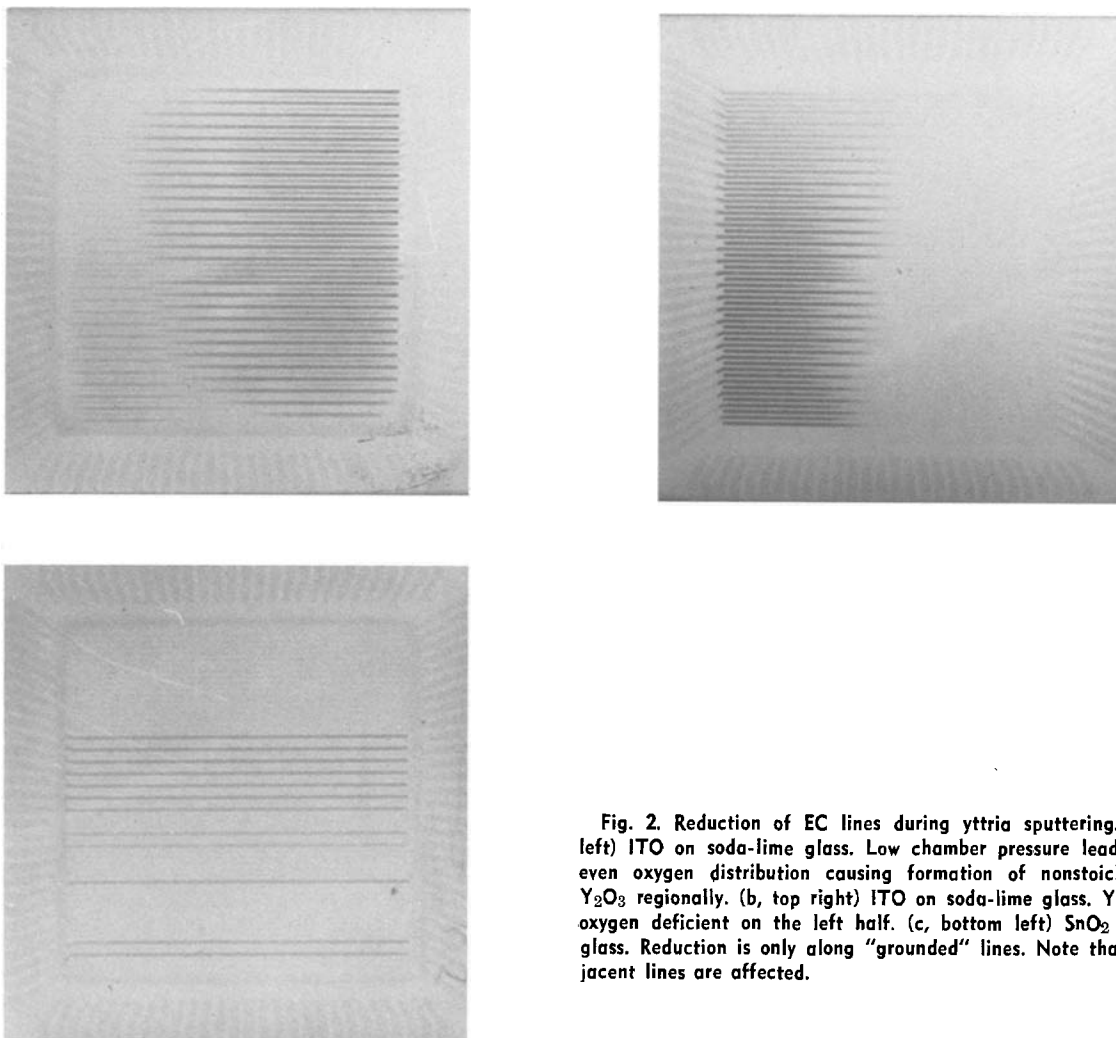


Fig. 2. Reduction of EC lines during yttria sputtering. (a, top left) ITO on soda-lime glass. Low chamber pressure leads to uneven oxygen distribution causing formation of nonstoichiometric Y₂O₃ regionally. (b, top right) ITO on soda-lime glass. Yttria was oxygen deficient on the left half. (c, bottom left) SnO₂ on 7059 glass. Reduction is only along "grounded" lines. Note that no adjacent lines are affected.

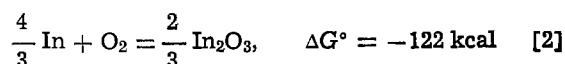
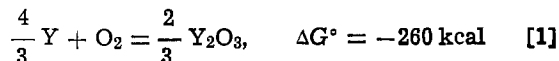
light output, and in extreme cases total failure where the active area is blown away as soon as the voltage is turned on. The latter could be either because these reduced lines, which are thinner and mostly metallic, melt away at the increased current densities ($|i^2R| > \Delta H_{\text{fusion}}$) or because the microcraters and pores that can result from the reduction create highly localized electric fields leading to the breakdown of the films. These black lines are very unstable and dissolve readily even in very dilute acids.

Figure 3a shows a panel where some dark lines were completely dissolved, while 3b shows one in which the dissolution was only partial. The difference is the result of varying degrees of reduction of the ITO because ITO films with varying degrees of oxidation are etched differently in HCl (3) or conversely, varying degrees of oxygen deficiency of the yttria films deposited in those regions. The degree of reduction of the conductive lines varies from line to line, from region to region, and sometimes from run to run.

Figure 4, like 2c, shows an interesting pattern in which the reaction made all alternate lines black. The panel has 56 lines, of which 28 lines originate at each side. Hence, this pattern indicates the reaction was electric field assisted as will be explained later.

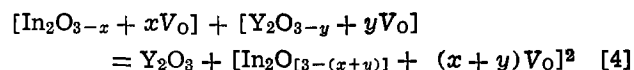
Mechanism.—The EC coating turns black because it loses oxygen to the stronger, but oxygen-deficient

yttria which is being deposited directly on top. This oxygen deficiency stems from the low oxygen partial pressure (7%) we use during sputtering to attain a reasonably high deposition rate. The presence of oxygen vacancy has been indicated by Tallan and Vest (4) and Tsutsumi (5). The substrate temperature during sputtering is about 225°C at which the standard free energies of formation for the three oxides under consideration are as shown below (6)



This shows that in order to replete an oxygen deficiency, yttria can reduce both ITO and SnO₂ at 225°C if the rate is adequate. The rate also seems adequate because oxygen-deficient yttria can pick up oxygen at temperatures as low as 100°C (4, 5). Also, we have observed in our experiments that ITO and SnO₂ increase their surface resistance 2-3 times over 6-8 hr of heating in air at 150°C and that their conductivity increases on annealing in vacuum at 150°C for a few hours.

The extent of reduction and consequently the degree of blackening of the lines depend on the oxygen deficiency in the yttria and ITO. This can be understood by writing the reduction reactions as follows



If ITO has considerably high oxygen deficiency to begin with, even a small amount of oxygen deficiency can cause the ITO to turn black. Thus it is imperative that the ITO should have minimum possible oxygen deficiency.

Factors effecting the reduction.—It can be shown that the reaction is brought about by any or a combination of the following factors:

Chamber pressure.—It was shown earlier that in order to obtain the highest possible film resistivity the optimum oxygen partial pressure during sputtering is 7-10% (7). Hence, experiments were done in this range. Chamber pressure during sputtering is another

² V_O = oxygen vacancy.

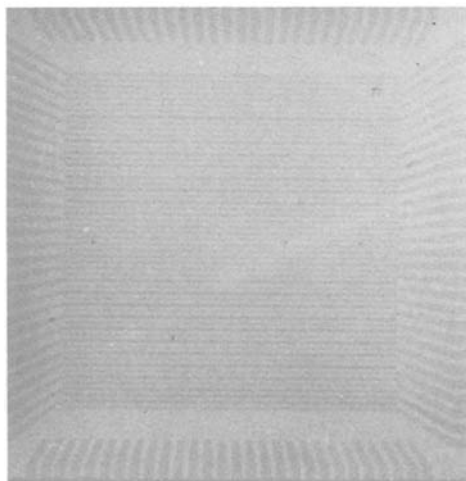
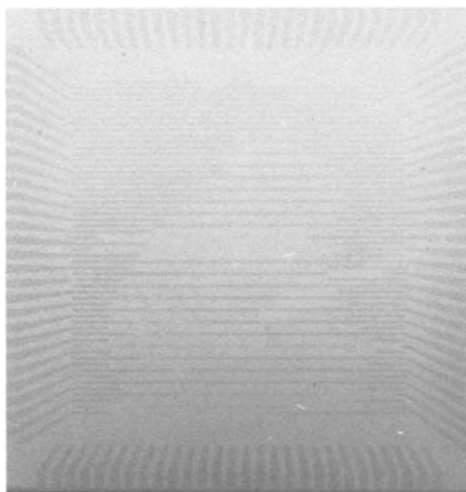


Fig. 3. Dissolution of reduced EC lines in 0.5N H₂SO₄. (a, top) Lines are totally dissolved in certain areas. (b, bottom) The light lines are affected.

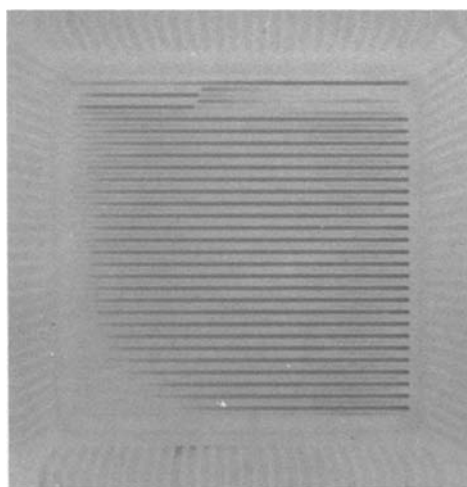


Fig. 4. Reduction of grounded lines. (Note the abrupt change about the discontinuity marked.)

important parameter. As the pressure goes up, the deposition rate falls. However, at very low chamber pressures it is extremely difficult to ensure an even distribution of oxygen over a large substrate area because the mean-free path of the gas molecules at these pressures is very large. The substrate target distance was about 10 cm. Under such circumstances the oxygen inlet design becomes critical. The gas should enter very close to the substrate, well within one mean-free path, less than 2 cm (8), from as many symmetrically placed inlets as possible. Average dissipation factor fell from 0.07 to 0.003 on bringing the gas inlet closer at 2 micron chamber pressure. A slight variation can result in an uneven distribution of oxygen over the substrate which eventually leads to the deposition of oxygen-deficient yttria, the degree of deficiency varying from point to point. Increasing the P_{O_2} did not help solve the problem. Such an oxygen-deficient yttria readily reduces the ITO beneath it, making it black. The result is shown in Fig. 2a where all the lines are black to the left half.

Resistivity of the EC coating.—The allowable electrical resistance along the conducting lines in the LEF display is determined by the driving wave form, the pulse width, and rise time. In order for the display to be efficient the line impedance should be low. High resistance would cause considerable voltage drop along these lines resulting in decreasing light output toward the end of the line. However, considering the dielectric strength of the thin film structure and hence the useful life of the display itself, a high resistance value is desired. Accordingly, the EC lines in our displays have impedances in the range of 400–800 Ω per cm.

The linewidth at 22.4 lines per cm resolution is 0.03 cm. If the starting ITO has a sheet resistance of 100 Ω /sq, the line impedance works out to be 3200 Ω per cm. Line impedance of below 800 Ω per cm can be achieved only if the EC coating has a resistance of less than 25 Ω /sq to start with. However, it was observed that with ITO of low sheet resistivity, such as 10–25 Ω /sq, the reduction effect became very pronounced. Subsequent experiments showed that annealing these low resistivity ITO films at 350°C in air for 4–6 hr prior to sputtering prevented or minimized the problem. Nevertheless, this heat-treatment raised the sheet resistivity of the films from 10 to 20 Ω /sq to 50–100, indicating that the low resistivity ITO was oxygen deficient and that a large part of its high electrical conductivity arose from the abundant oxygen vacancies rather than from the dopant.

Such an oxygen-lean ITO will get reduced further by giving up oxygen to sputter-deposited yttria which is inherently oxygen deficient due to the low P_{O_2} used during sputtering. Figure 5 shows the effect of annealing and the relevant mechanism. Up to point A,

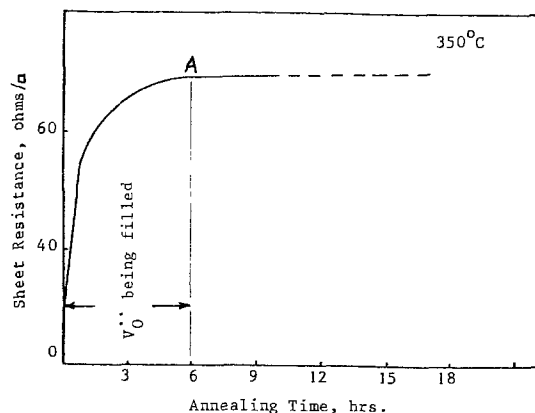


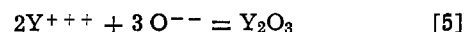
Fig. 5. Effect of air annealing on ITO films

the sheet resistance is a function of the dopant concentration $[D]$ and vacancy concentration $[V_O]$.³ Beyond this point the resistance is essentially a function of $[D]$ and the EC film is fully oxidized.

It is thus imperative that while specifying low sheet resistance for the EC coating this property be achieved during deposition and not by subsequent vacuum annealing. This would mean a trade-off between percentage transmission and low sheet resistance, because once the dopant concentration has been fixed, as is the case with commercial glass, the sheet resistance can be brought down only by increasing the thickness of the coating.

The reduction pattern of oxygen-deficient, low resistivity ITO is similar to that from low chamber pressure. Figure 2b is an example of this. The effect would be all over the area and on all adjacent lines where the resistivity is low. If the entire surface of the glass shows a uniformly low resistance, the glass would be black all over.

Grounding the substrate.—It is necessary to provide a path from the top surface of the glass substrate to the ground during the sputtering (9) of a dielectric because the charge that builds up on the surface reduces the deposition rate, often to zero. However, care should be exercised to ensure that the glass alone is "grounded" and not the conducting lines. It was observed that grounding the conducting lines during sputtering enhanced the probability of the lines being reduced. In other words, grounding the EC lines leads to the deposition of oxygen-lean yttria along these lines. This effect is caused by the electric field. When the lines are grounded some of the O^- ions reaching the electrode surface pick up the necessary electrons from the ground (ITO) instead of combining the Y^{+++} according to the following equation



Effectively, two O^{--} ions pick up four electrons from the ground, along the ITO lines, and form a molecule of oxygen gas which gets pumped out of the chamber. Consequently, oxygen-deficient yttria is deposited along the grounded EC lines which reduces the lines. An example for such reduction is shown in Fig. 2c where the lines are black entirely along the length. Another interesting feature is that the two adjacent lines are not affected at all.⁴ In Fig. 4, it can be observed that the blackening effect stops abruptly at a scratch across the lines. Up to this discontinuity the line is uniformly black, beyond which the line is no more connected to the ground and it is not affected at all, indicating that the effect indeed was an electric-field assisted one.

Thus, the characteristic features of reduction due to the grounded electrode are that it will be along the total length of the lines and that the adjacent lines need not be affected at all. However, if a discontinuity like a scratch exists across the line, the abrupt change described above will be observed. The alternate black lines mentioned in the section "The effect" were due to the fact that the lines from one side were grounded, while those from the other side were open.

Summary

When a strong oxide like yttria is sputter deposited on EC coatings like SnO_2 or ITO, under certain conditions these coatings can get reduced and turn black. Three factors contribute to this effect individually and collectively.

At low chamber pressures the concentration of oxygen over a large area is not uniform and this makes the yttria film oxygen deficient to varying degrees over the substrate. As a result, the EC lines get reduced,

³ This excludes inherent initial $[V_O]$.

⁴ This is because they originate on the opposite side and are not grounded.

manifested as patches of black lines. This problem can be eliminated by carefully designing the oxygen inlet. As a rule of thumb, below 4 microns chamber pressure, oxygen inlet should be as close to the substrate as possible and should ensure an even distribution of the gas over the substrate area.

Commercially available EC coatings with very low sheet resistance (below 20 Ω /sq) and high optical transmission (above 85%) are generally oxygen deficient. When some oxygen-deficient oxides are rf sputter deposited on such EC films, they get readily reduced by these oxides and turn black. Hence, it is necessary to stabilize such EC films prior to sputtering by annealing in air at 350°C for 6 hr.

Grounding the EC lines during rf sputtering leads to the deposition of oxygen-lean yttria along these lines which eventually reduces the conducting lines. Thus care should be taken not to ground these lines during sputtering.

Acknowledgments

We are grateful to Dr. Shiban K. Tiku of Texas Instruments for his useful suggestions during the preparation of this paper. We also thank Robert Bell and Deborah Joiner of Sigmatron Nova for their assistance with the experiments.

Manuscript submitted Dec. 11, 1980; revised manuscript received March 24, 1981.

Any discussion of this paper will appear in a Discussion Section to be published in the June 1982 JOURNAL. All discussions for the June 1982 Discussion Section should be submitted by Feb. 1, 1982.

Publication costs of this article were assisted by Sigmatron Nova.

REFERENCES

1. Joint Army Navy Aircraft Instrumentation Research Report 720903 Technical Report EL-7 (1972).
2. U.S. Pat. No. 3,560,784.
3. V. Hoffman, "The Sputtered Indium Tin Oxide Film," *Optical Spectra*, pp. 60-62, November 1978.
4. N. M. Tallan and R. W. Vest, *J. Am. Ceram. Soc.*, **49**, 401 (1966).
5. T. Tsutsumi, *Jpn. J. Appl. Phys.*, **9**, 735 (1970).
6. T. B. Reed, "Free Energy of Formation of Binary Compounds, An Atlas of Charts for High-Temperature Chemical Calculations," MIT Press, Cambridge, Mass. (1971).
7. M. P. R. Panicker, R. J. Bell, and S. K. Tiku, "Light Emitting Film Panels," *Proc. International Sym. Society of Information Display*, San Diego (1980).
8. "Handbook of Thin Film Technology," L. I. Maissel, I. Maissel, and R. Gilang, Editors, pp. 1-22, McGraw-Hill, New York (1970).
9. "Handbook of Thin Film Technology," L. I. Maissel, I. Maissel, and R. Gilang, Editors, pp. 4-32, McGraw-Hill, New York (1970).

Solid-Phase Epitaxial Crystallization of Amorphous Ge on $\langle 100 \rangle$ Si

B. Y. Tsaur,* J. C. C. Fan,* J. P. Salerno, C. H. Anderson, Jr.,
R. P. Gale,* and F. M. Davis

Lincoln Laboratory, Massachusetts Institute of Technology, Lexington, Massachusetts 02173

E. F. Kennedy

Department of Physics, College of the Holy Cross, Worcester, Massachusetts 01610

and T. T. Sheng

Bell Laboratories, Murray Hill, New Jersey 07974

ABSTRACT

Heteroepitaxial Ge films have been obtained by solid-phase crystallization of amorphous Ge deposited on single crystal $\langle 100 \rangle$ Si substrates. The Si substrates were chemically cleaned by conventional procedures without any attempt to achieve atomically clean surfaces. Epitaxial crystallization of the amorphous Ge films were accomplished by furnace annealing at temperatures of 500°-900°C. The as-crystallized Ge films contain dislocations and twins whose densities decrease with increasing annealing temperature. Significant reduction in twin density has been achieved by using an ion implantation and reannealing treatment. Epitaxial GaAs layers of good crystal quality have been grown by chemical vapor deposition on heteroepitaxial Ge films subjected to this treatment.

The growth of heteroepitaxial Ge films on crystalline Si substrates have been the subject of numerous investigations because of the many interesting electrical and optical properties of Ge-Si heterojunctions (1). Much work has been done by use of liquid-phase epitaxy such as solution growth techniques (2), as well as vapor phase epitaxy such as vacuum evaporation under UHV environment (3, 4) and chemical vapor

deposition (5). Recently, considerable attention has been directed toward the preparation of epitaxial thin films by means of solid-phase crystallization of amorphous deposited layers. For example, epitaxial growth of amorphous Si films deposited on chemically cleaned $\langle 100 \rangle$ Si substrates has been achieved upon furnace annealing at 550°-750°C (6, 7). The solid-phase epitaxial Si layers were found to be comparable in crystal quality to the single crystal Si substrate underneath. The technique of solid-phase epitaxy

* Electrochemical Society Active Member.
Key words: heteroepitaxy, films, twin density.

(SPE) is attractive because of the low processing temperatures required and the ability of using simple experimental apparatus.

In the present work, we investigated the formation of heteroepitaxial Ge films by solid-phase crystallization of amorphous Ge deposited on single crystal $\langle 100 \rangle$ Si substrates. The study was motivated by our recent development of efficient GaAs solar cells with conversion efficiencies exceeding 20% at AM1 that are fabricated on bulk single crystal substrates of Ge (8). It is expected such thin film cells could also be fabricated on crystalline Si substrates with a heteroepitaxial Ge overlayer so that the substrate cost can be markedly reduced. We found that heteroepitaxial Ge films on $\langle 100 \rangle$ Si can be accomplished by the SPE process. The crystal quality of the heteroepitaxial Ge films can further be improved by using an ion implantation and reannealing treatment. The preliminary results of this work have recently been reported (9). In this paper we present detailed results on the effects of preparation of Si substrate surfaces, annealing conditions, as well as Ge film thickness on the crystalline perfection of the SPE Ge films.

Experimental

Amorphous Ge films 1000-3000Å thick were deposited by electron beam evaporation of high purity Ge (99.999% pure) on single crystal $\langle 100 \rangle$ Si substrates. Prior to use the Si wafers were degreased in organic solvents, immersed in a 5 H₂O:NH₄OH:H₂O₂ solution for 10 min, rinsed in DI water, and then immersed in a 6 H₂O:HCl:H₂O₂ solution for 10 min. A final rinse in dilute HF (~10%) was employed immediately before loading in the liquid-nitrogen trapped oil-diffusion-pumped vacuum system. The background pressure was 3×10^{-7} Torr before evaporation and increased to 8×10^{-7} Torr during evaporation. The average deposition rate was about 8 Å/sec. The substrates were not intentionally heated or cooled during deposition.

The Ge/Si $\langle 100 \rangle$ samples were heat-treated in a quartz-tube furnace with flowing forming gas (Ar/H₂) ambient. In each experiment annealing was carried out for 20 min (including the heating period of ~2-3 min) at a constant temperature in the 400°-900°C range at a 100°C increment. Isothermal annealing was performed on a few samples at 400°C up to 120 min. The composition and structure of the annealed samples were analyzed by ⁴He⁺ ion backscattering, Auger spectroscopy, x-ray diffraction, reflection high energy electron diffraction (RHEED), and transmission electron microscopy (TEM).

Results and Discussion

X-ray and electron diffraction measurements showed that the films annealed at temperatures at or above 500°C were single crystalline, while the films annealed at 400°C still contained amorphous materials at the film surfaces. Figure 1 is the (011) RHEED pattern of a typical SPE Ge film, 2000Å thick, annealed at 700°C; similar patterns were obtained for samples annealed at temperatures between 500° and 900°C. The pattern contains strong matrix spots streaked along the (011) azimuth direction, indicating that the film is epitaxial and has a rather smooth surface. Additional weak satellite spots are present due to {111} twinned regions of the crystal. Faint traces of polycrystalline rings were occasionally detected for the 3000Å thick Ge films, but most of the thinner films did not give polycrystalline reflections. For samples annealed at 400°C, RHEED measurements showed amorphous diffraction patterns over the entire surfaces of the Ge films.

The RHEED patterns were generated by diffraction from a region estimated to be a few hundred angstroms in depth. In contrast with the RHEED data, the x-ray patterns for the heat-treated samples were generated by diffraction from a mean depth of several

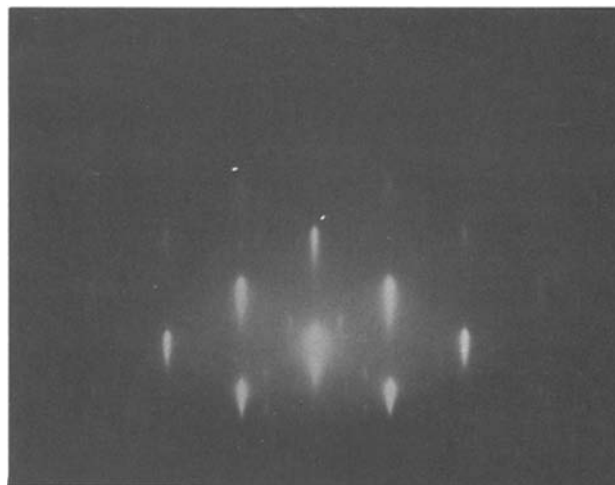


Fig. 1. RHEED pattern for a heteroepitaxial Ge film obtained by solid-phase crystallization of an amorphous Ge film deposited on a $\langle 100 \rangle$ Si single crystal substrate. The annealing was carried out at 700°C for 20 min in a quartz-tube furnace with a flowing Ar/H₂ ambient.

micrometers, so that these patterns contain peaks due to the Si substrate. The (400) diffraction peak intensities for the epitaxial Ge films and those for the single crystal Si substrates have been measured. Figure 2 shows a plot of the ratio of the measured (400) peak intensities for 1000Å thick SPE Ge films vs. annealing temperature. As can be seen in the figure, the ratio increases markedly as temperature increases from 400° to 500°C, which then increases gradually, reaching a maximum at 800°C and falls off at 900°C. The presence of Ge crystalline diffraction peaks for samples after annealing at 400°C for 20 min indicates that epitaxial crystallization already occurs at this temperature. However, the crystallization front advancing from the Ge-Si interface has not reached the film surface during the 20 min annealing period so that the film remains amorphous near surface regions as revealed by RHEED measurements. For samples annealed at 400°C for 30 min, a mixture of single crystalline and amorphous diffraction patterns was detected by RHEED measurements. Each pattern was found on different locations of the sample, indicating that the Ge film was partially crystallized in the form of localized epitaxial islands. Increasing the annealing time leads to successive lateral growth of the epitaxial islands and a uniform epitaxial Ge film is obtained after 60 min of annealing. This growth mechanism is

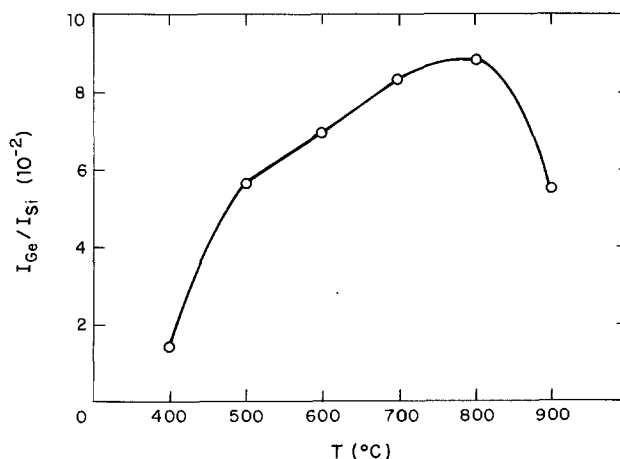


Fig. 2. Ratio of (400) diffraction peak intensities for heteroepitaxial Ge films and those for single crystal Si substrates as a function of annealing temperature.

similar to that recently observed in the epitaxial growth of amorphous Si films deposited on $\langle 100 \rangle$ Si (6).

The decrease in diffraction peak intensity for Ge films annealed at 900°C (Fig. 2) is intriguing. Examination of film surfaces under an optical microscope showed that the films annealed at or below 800°C were mirror smooth, while the films annealed at 900°C were somewhat milky, indicating surface oxidation or contamination during the annealing. Rutherford backscattering measurements showed a significant interdiffusion between Ge and Si for samples annealed at 900°C . Figure 3 is the 2 MeV $^4\text{He}^+$ ion backscattering spectrum of such a sample. The arrows marked in the figure are surface signals due to Ge (channel number ~ 290) and Si (channel number ~ 200). An appreciable amount of Si is observed near the surface region with a peak concentration of approximately 20 atomic percent (a/o) at the surface. Trace Ge, less than 0.4 a/o in concentration, is detected between channels 200 and 250, which is attributed to in-diffusion of Ge into the Si substrate. These results indicate that interdiffusion between Ge and Si is not symmetrical and the process is dominated by outdiffusion of Si toward the surface. Outdiffusion of Si through thin deposited metal overlayers at low temperatures has previously been observed (10). The reaction was attributed to grain-boundary diffusion of Si through the metal film as well as formation of Si oxides on the film surfaces especially in an annealing ambient containing water vapor (10). The solid-phase interdiffusion observed in the present case may be due to a similar cause since our Ar/H_2 annealing ambient may contain some water vapor or oxygen and fast outdiffusion of Si could take place via structural defects contained in the Ge layers. The observation that the Si concentration near the film surface is higher than that in the Ge film (Fig. 3) suggests such a reaction, otherwise a normal diffusion profile (such as an error function) will be expected. The interdiffusion between Ge and Si may explain (in part) the decrease of Ge (400) diffraction peak intensity for samples annealed at 900°C as shown in Fig. 2.

Samples annealed at temperatures between 400° and 800°C have also been examined by backscattering measurements. No broadening of Ge-Si interface was observed for those samples yet faint traces of Si signals were detected on the film surfaces for samples annealed at 700° and 800°C . Figure 4 shows the backscattering spectrum of a sample annealed at 700°C . As

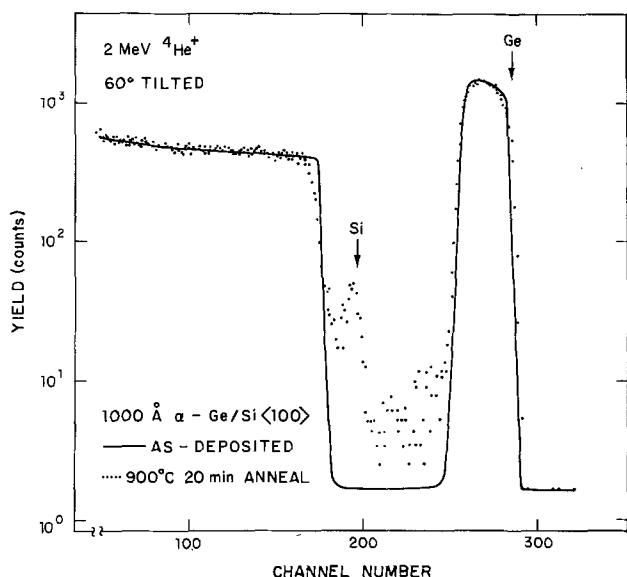


Fig. 3. $^4\text{He}^+$ ion backscattering spectra for a Ge/Si $\langle 100 \rangle$ sample before and after annealing at 900°C for 20 min. Significant interdiffusion between Ge and Si occurs during annealing.

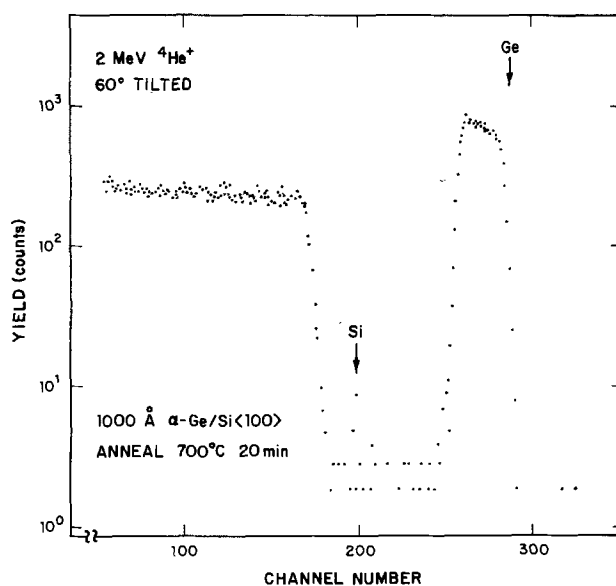


Fig. 4. $^4\text{He}^+$ ion backscattering spectrum for a Ge/Si $\langle 100 \rangle$ sample after annealing at 700°C for 20 min. Trace Si is detected on the surface of Ge film.

can be seen in the spectrum, the Si surface signals (near channel 200) are slightly above the noise level. Again, we attribute outdiffusion of Si (or accumulation of Si on the film surface) to formation of Si oxides on the surface. It should be noted that solid-phase interdiffusion between Ge and Si at this temperature ($\sim 700^\circ\text{C}$) is negligible because of the small diffusion coefficient (11). The outdiffusion of Si is, therefore, presumably defect enhanced and the most probable defects are twin boundaries because twins are the predominant defects observed in the SPE Ge films.

X-ray diffraction analyses have been carried out to obtain a quantitative estimate of the microtwin density. The experiments were carried out in a standard diffractometer with a motor-driven goniometer allowing sample rotation along three perpendicular axes. Details of experimental procedures have been described previously (12). Briefly, the (311) peak intensity for the epitaxial regions of the film was first measured and the sample was tilted by 20° toward a $\{111\}$ plane to maximize the (311) peak for the twinned regions. The ratio of the (311) peak intensities for the twinned and epitaxial regions, which we call the twin index (TI), is a measure of the microtwin density. Our detection limit for TI is about 2×10^{-4} , corresponding to a value of about 6×10^{-4} for the volume fraction of twins. In Fig. 5 the TI values for a

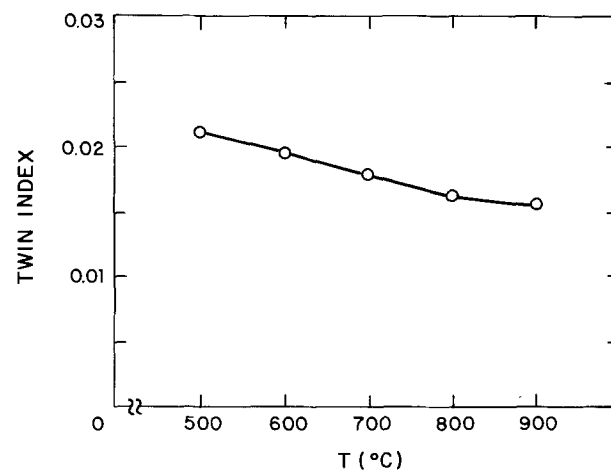


Fig. 5. Twin index (TI) for five SPE Ge films as a function of annealing temperature.

number of SPE Ge films are plotted against annealing temperature. The TI values decrease gradually with increasing temperature. This result is consistent with the gradual increase of (400) diffraction peak intensities with temperature (in the range of 500°-800°C) for epitaxial Ge films as shown in Fig. 2, except for samples annealed at 900°C where interdiffusion between Ge and Si results in a decrease of Ge (400) peak intensity.

Our results demonstrate that epitaxial growth of Ge on Si can be accomplished by solid-phase crystallization in spite of the large lattice mismatch (4%) between the two materials. Marked contamination either at the Ge-Si interface or within the Ge film would be expected to lead to random nucleation in the amorphous Ge films and therefore to extensive polycrystallinity (13). The success of epitaxial growth indicates that electron beam deposition of Ge did not introduce such contamination. This has been confirmed by Auger spectroscopic analysis of both as-deposited and annealed samples. Figure 6 shows the Auger electron spectra obtained from an annealed Ge film (at 700°C) before [Fig. 6(a)] and after [Fig. 6(b)] argon sputter etching. Oxygen and carbon are detected on the surface of annealed films [Fig. 6(a)]. Traces of Si signals due to the KLL transition near 1600 eV and LMM transition near 90 eV (which overlaps with the Ge MNN transition) are also detected. The Si signals were too weak for chemical state identification (*i.e.*, SiO₂ or pure Si). However, the presence of Si on the Ge film surface is consistent with the backscattering observations (Fig. 4) described above. After argon sputter etching, the Auger spectrum of Fig. 6(b) shows that the Si, O, and C signals are within the noise level, indicating their concentrations at or below ~0.1 a/o. Depth-profile measurements showed that the O and C signals were not detected at the original Ge-Si interface either.

The absence of oxygen signals at the Ge-Si interface in Auger spectroscopic analysis suggests that our surface preparations for Si have minimized the formation of native oxide which is known to occur readily in air.

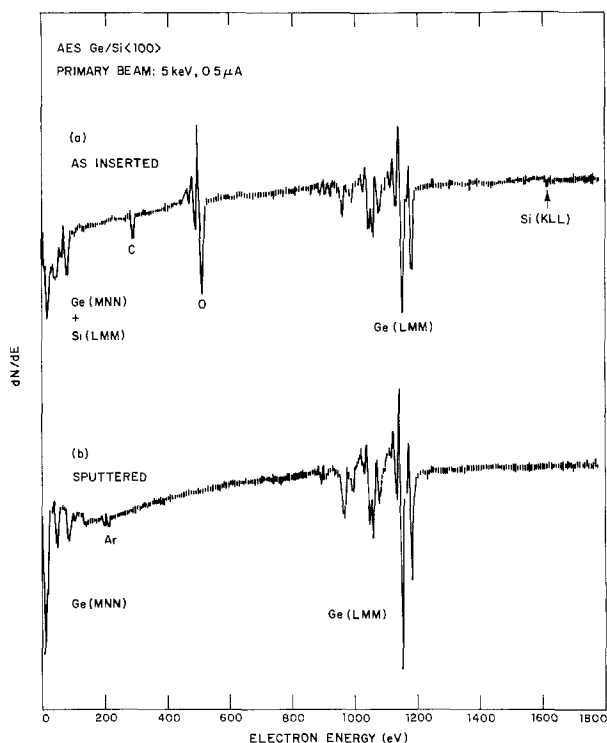


Fig. 6. Auger electron spectra for an SPE Ge film (annealed at 700°C) before (a) and after (b) argon sputter etching. Oxygen, carbon, and Si are detected on the surface of Ge film and they are absent within the detection limit after argon sputter etching.

To test the effects of native oxide on the formation of SPE Ge films, the following HF experiment has been carried out. After the last HF rinse, the Si substrates were deliberately exposed in air for 5-10 min before loading in the vacuum deposition system. The resulting SPE Ge films were found to contain either high densities of twins (with TI value ~ 5% or higher) or random polycrystallites. If the exposure time was increased to 30 min or more, complete polycrystallinity was obtained. Auger analysis indicated the presence of O and C at the Ge-Si interface with amounts just above the noise level for samples that underwent a 5-10 min air exposure and about 0.5-1 a/o for samples that underwent over 30 min air exposure.

As mentioned before, polycrystalline materials were occasionally observed near the surfaces of thick SPE Ge films. The formation of polycrystallites is attributed to either surface or impurity-induced random nucleation due to penetration of impurities into the Ge film from gas ambient (14). Increasing the film thickness increases the probability of polycrystalline formation since random nucleation may occur before ordered transformation is completed by the crystallization front advancing from the film-substrate interface.

We have significantly improved the crystal quality of SPE Ge films on Si substrates by employing a technique suggested by the fact that solid-phase homoepitaxy of Ge (15) and Si (7, 16) has been used to convert amorphous layers to high quality crystalline materials. Following the initial SPE anneal (700°C, 20 min), the Ge film was implanted at liquid nitrogen (LN₂) temperature with Ga⁺ ions, using an ion energy and dose selected to produce an amorphous upper layer about 2/3 the total thickness of the film. For example, a layer about 1200Å thick was produced in a film 2000Å thick by implantation with a dose of $1 \times 10^{14} \text{ cm}^{-2}$ 180 keV Ga⁺ ions in a nonchanneling direction (7° from normal incidence). The p-type Ga ions were used to ensure good ohmic contacts between Ge and GaAs because the presence of Ga is expected to overdope any As (an n-type dopant in Ge) that may diffuse into the Ge during subsequent growth of GaAs layers (8). The Ge/Si sample was then reannealed at 700°C for 15 min, causing the amorphous upper layer of the Ge film to recrystallize by solid-phase homoepitaxy, which was seeded by the lower region of the film that had not been damaged by ion implantation. After reannealing the film surface was as smooth as it had been after the initial annealing.

Figure 7 is the RHEED pattern obtained for an SPE Ge film after ion implantation and reannealing. In comparison with the pattern of Fig. 1 for another portion of the same film subjected only to the initial SPE

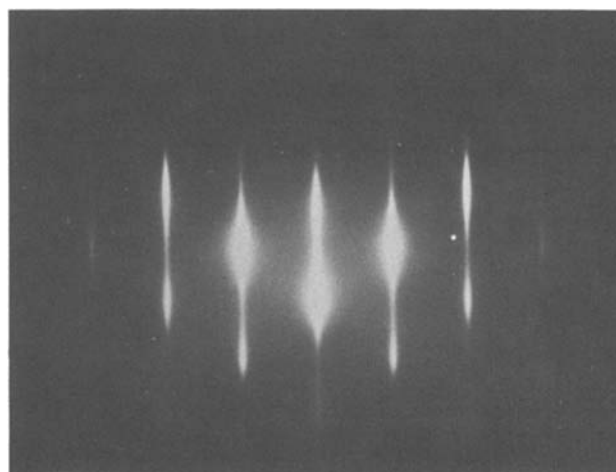


Fig. 7. RHEED pattern for an SPE Ge film after implantation with 180-keV $1 \times 10^{14} \text{ cm}^{-2}$ of Ga⁺ ions and reannealing at 700°C for 15 min.

anneal, the principal diffraction spots are sharper and more elongated, the spots due to (111) twins have disappeared, and the Kikuchi lines are stronger. All these features are evidence for a marked improvement in crystal quality at the surface due to implantation-reannealing treatment. The improvement has been confirmed by TEM observations. Figure 8 shows the cross-sectional TEM micrograph for an SPE Ge film, 2000Å thick, before [Fig. 8(a)] and after [Fig. 8(b)] the implantation-reannealing treatment. {111} primary and secondary twins are present throughout the Ge film after the initial SPE annealing [Fig. 8(a)]. After the implantation-reannealing treatment, the twin density reduces markedly especially in the near-surface region of the film as shown in Fig. 8(b). The TI value for this sample was measured to be 0.004, about a factor of 4 smaller than that (0.016) of this sample before the treatment. Both micrographs show sharp Ge-Si interfaces as expected for the solid-phase crystallization process.

The improvement in crystal quality has also been confirmed by the results of channeling experiments with 1.0 MeV $^4\text{He}^+$ ions. Figure 9 shows the channeling spectra for a 2000Å thick Ge film on $\langle 100 \rangle$ Si after the initial SPE anneal [Fig. 9(a)] and after implantation and reannealing treatment [Fig. 9(b)]. Figure 9(b) also shows the spectrum for a polished $\langle 100 \rangle$ Ge single crystal wafer. The implantation-reannealing treatment results in a decrease of minimum surface yield for the SPE film from 18% in Fig. 9(a) to 4.5% in Fig. 9(b). After the treatment the spectrum for the near-surface region of the film is almost the same as that for the Ge single crystal wafer, indicating that this region of the film is comparable in crystal quality to the bulk crystal. Note that the aligned yield near the interfacial region is much higher than that of single crystal Ge because of the presence of twins and a high concentration of dislocations near this region. Figures 10(a) and 10(b) show the planar bright-field and

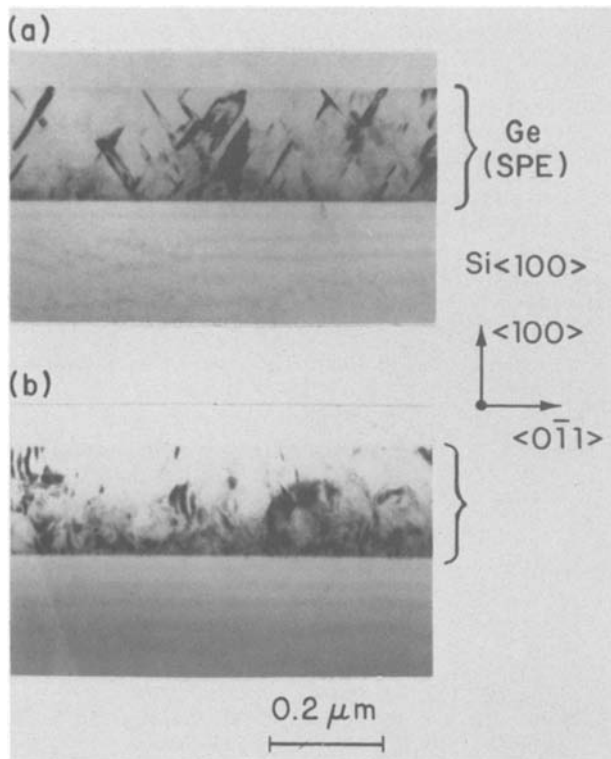


Fig. 8. Cross-sectional TEM micrographs for an SPE Ge film on $\langle 100 \rangle$ Si. (a) After initial annealing at 700°C for 20 min. (b) After subsequent implantation of Ga^+ ions and reannealing at 700°C for 15 min. Significant reduction in twin density in the surface region of Ge film is observed after the implantation-reannealing treatment.

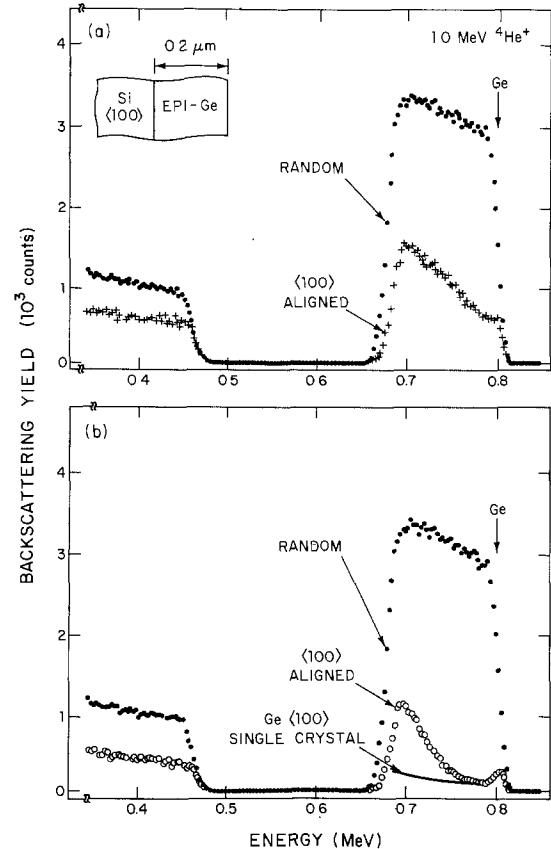


Fig. 9. $^4\text{He}^+$ ion channeling spectra for an SPE-Ge/Si $\langle 100 \rangle$ sample. (a) After initial annealing. (b) After subsequent implantation and reannealing treatment. The TEM micrographs of the sample are shown in Fig. 8a and b, respectively.

weak-beam dark-field TEM micrographs, respectively, for such dislocations. Similar results were obtained for SPE Ge films without the implantation-reannealing treatment. The dislocations are presumably misfit type. They are formed during the growth of heteroepitaxial Ge films to release the interfacial misfit strain originating from the large lattice mismatch ($\sim 4\%$) between Ge and Si. The dislocation density is estimated to be of the order of 10^{10} - 10^{11} cm^{-2} from Fig. 10. Extensive interactions between dislocations are observed, which result in climbing and propagation of dislocations toward the film surface as inclined dislocations. TEM observations on thinner portions (near-surface regions) of the Ge films indicated that the density of inclined dislocations was in the range of 10^8 - 10^9 cm^{-2} , about two to three orders of magnitude lower than that of misfit dislocations near the interface. No significant reduction in dislocation density was observed in Ge films after the implantation-reannealing treatment.

As an initial step in determining the usefulness of SPE Ge films as substrates for the growth of GaAs, undoped GaAs epitaxial layers about 2 μm thick were grown by chemical vapor deposition (CVD) on the SPE Ge films. Details of the deposition procedure, which employs the AsCl_3 -GaAs- H_2 method, have been described elsewhere (8). The GaAs layers were found to be comparable, and in most cases superior, in crystal quality to the underlying Ge films. Figure 11 shows the 1.0 MeV $^4\text{He}^+$ channeling spectrum of a GaAs layer grown on a Ge film that had been subjected to the implantation-reannealing treatment. The minimum surface yield is only 4% indistinguishable within the experimental uncertainty from that of a polished GaAs single crystal. Separate surface peaks due to Ga and As can be distinguished in the aligned spectrum near 0.8 MeV, indicating good crystal quality. For GaAs layers grown on single-step annealed Ge films, the

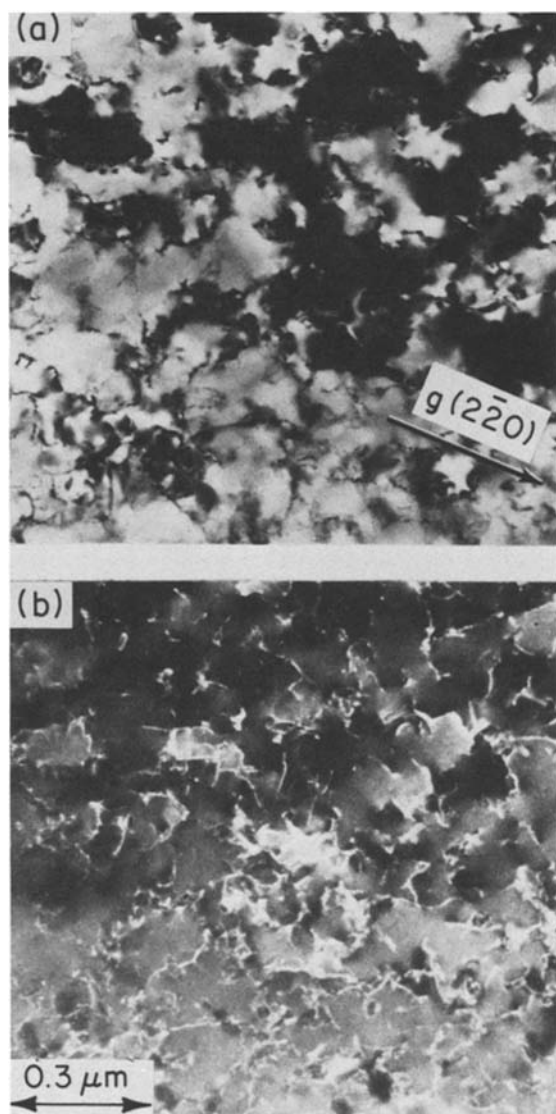


Fig. 10. TEM micrographs of (a) bright-field image and (b) dark-field image under a weak-beam ($g = 220, 3g$) diffraction condition for an SPE Ge film showing the misfit dislocations near the interfacial region.

crystal quality was found to be inferior to that of layers grown on implanted and reannealed Ge films.

Summary

In conclusion, solid-phase epitaxial crystallization of amorphous Ge films deposited on $\langle 100 \rangle$ Si has been achieved upon thermal annealing at temperatures of 500°–900°C. The Si substrates were chemically cleaned by conventional procedures without any attempt to achieve atomically clean surfaces. By minimizing the exposure time of Si substrates after the predeposition chemical etching, the native oxides on the Si surfaces were reduced to a level so that epitaxial crystallization of the amorphous Ge can be achieved by low temperature annealing. Increasing the exposure time increases the probability of native oxide formation which leads to the formation of highly defected epilayers or polycrystalline films.

Structural characterization showed that the SPE Ge films contained dislocations and twins. Significant reduction in twin density has been achieved by implanting the SPE Ge film with 180-keV 1×10^{14} Ga⁺ ions/cm² at LN₂ temperature to produce an amorphous Ge upper layer and then recrystallizing the layer by annealing at 700°C for 15 min. Epitaxial GaAs layers of good crystal quality have been grown by CVD on SPE

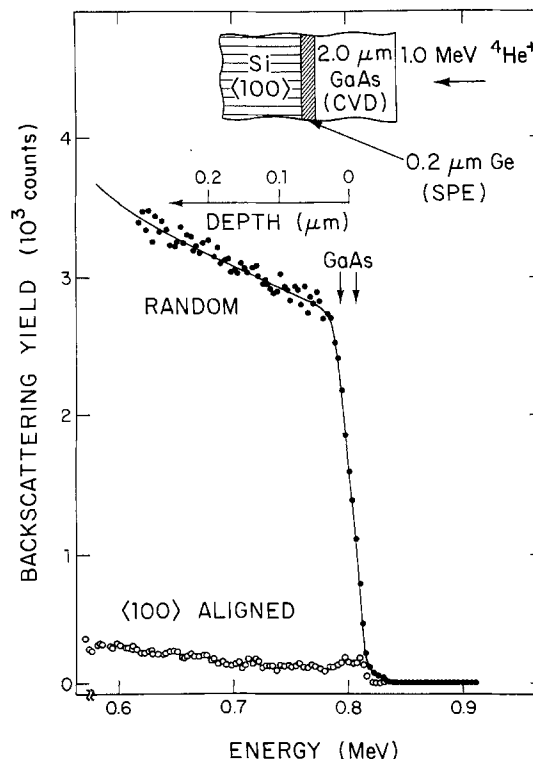


Fig. 11. $^4\text{He}^+$ channeling spectrum for a GaAs layer about 2 μm thick grown by CVD on an SPE-Ge/Si $\langle 100 \rangle$ substrate after the ion implantation and reannealing treatment.

films subjected to this treatment. On the basis of this result, it appears highly probable that GaAs layers suitable for the fabrication of high efficiency thin film solar cells can be grown on SPE-Ge/Si substrates.

Acknowledgments

We acknowledge A. J. Strauss for fruitful discussions, M. C. Finn for performing Auger spectroscopy, E. B. Owens and J. L. Ryan for backscattering, and R. C. Brooks and R. F. Murphy for technical assistance.

The Lincoln Laboratory portion of this work was sponsored by the Department of the Air Force.

Manuscript submitted Jan. 6, 1981; revised manuscript received March 24, 1981.

Any discussion of this paper will appear in a Discussion Section to be published in the June 1982 JOURNAL. All discussions for the June 1982 Discussion Section should be submitted by Feb. 1, 1982.

Publication costs of this article were assisted by the Massachusetts Institute of Technology.

REFERENCES

1. See, for example, A. G. Milnes and D. L. Feucht, "Heterojunctions and Metal-Semiconductor Junctions," Chap. 9, Academic Press, New York (1972).
2. J. P. Donnelly and A. G. Milnes, *This Journal*, **113**, 297 (1966); K. Kurata and T. Hirai, *ibid.*, **115**, 869 (1968).
3. G. O. Krause, *Phys. Status Solidi A*, **3**, 907 (1970).
4. A. G. Cullis and G. R. Booker, *J. Cryst. Growth*, **9**, 132 (1971).
5. A. R. Riben, D. L. Feucht, and W. G. Oldham, *This Journal*, **113**, 245 (1966).
6. M. von Ailmen, S. S. Lau, J. W. Mayer, and W. F. Tseng, *Appl. Phys. Lett.*, **35**, 280 (1979).
7. L. S. Hung, S. S. Lau, M. von Ailmen, J. W. Mayer, and W. F. Tseng, *ibid.*, **37**, 909 (1980).
8. C. O. Bozler, J. C. C. Fan, and R. W. McClelland, *Inst. Phys. Conf. Ser.*, **45**, 429 (1979); J. C. C. Fan, G. W. Turner, R. P. Gale, and C. O. Bozler, in "Proceedings of the 14th IEEE Photovoltaic Specialists Conference," p. 1102, San Diego, Calif. (1980).

9. B. Y. Tsaur, J. C. C. Fan, and R. P. Gale, *Appl. Phys. Lett.*, **38**, 176 (1981).
10. A. Hiraki, E. Lugijjo, and J. W. Mayer, *J. Appl. Phys.*, **43**, 3643 (1972).
11. R. M. Burger and R. P. Donovan, "Fundamentals of Silicon Integrated Device Technology," Vol. 1, p. 205, Prentice-Hall, Inc., New York (1967).
12. J. C. C. Fan, R. P. Gale, F. M. Davis, and G. Foley, *Appl. Phys. Lett.*, **37**, 1024 (1980).
13. S. S. Lau, *J. Vac. Sci. Technol.*, **15**, 1656 (1978).
14. K. Zellama, R. Germain, S. Squelard, J. C. Bourgoin, and P. A. Thomas, *J. Appl. Phys.*, **50**, 6995 (1979).
15. L. Csepregi, R. P. Kullen, and J. W. Mayer, *Solid State Commun.*, **21**, 1019 (1977).
16. S. S. Lau, S. Matteson, J. W. Mayer, P. Revesz, J. Gyulai, J. Roth, T. W. Sigmon, and T. Cass, *Appl. Phys. Lett.*, **34**, 76 (1979).

Evaporation of High Quality In_2O_3 Films from $\text{In}_2\text{O}_3/\text{In}$ Source—Evaporation Chemistry and Thermodynamics

C. A. Pan and T. P. Ma

Department of Engineering and Applied Science, Yale University, New Haven, Connecticut 06520

ABSTRACT

Highly transparent conductive In_2O_3 films can be easily deposited by simple thermal evaporation from an $\text{In}_2\text{O}_3/\text{In}$ source in a low pressure O_2 environment. The important role of In in the evaporation process has been examined. From an analysis of the evaporation chemistry and the thermodynamics of the system, it has been concluded that the incorporation of In in the evaporation source not only significantly enhances the evaporation rate, but also gives rise to a higher concentration of conduction electrons. Many possible reactions in the source region and on the substrate have been considered, and only a few have been found to be of significance, which greatly simplifies the theory. Good qualitative agreement has been found between the theory and several key experimental observations. The theory has also been verified by quantitative comparisons with the experimentally measured film growth rate and the conduction electron concentration.

Optically transparent, electrically conducting films of In_2O_3 are useful in a variety of applications. The most commonly used preparation techniques include sputtering (1-6) and chemical spray deposition (7-9). In two recent publications (10, 11), we showed that high quality polycrystalline In_2O_3 films could be readily produced by a simple thermal evaporation technique. Resistivity of $2 \times 10^{-4} \Omega\text{-cm}$ and optical transmission of 90% in the visible range are typically observed.

The observed optical transparency arises from the relatively wide direct and indirect bandgaps of In_2O_3 , which have been measured to be 3.56 and 2.69 eV, respectively (10). Its high conduction electron concentration ($\geq 4 \times 10^{20}/\text{cm}^3$) is believed to result from the interstitial In atoms (10, 12, 13) or oxygen vacancies (14) in the In_2O_3 structure, which act as shallow donor levels.

As we reported previously (10, 11) the key to the success of this simple evaporation process is the use of a combination $\text{In}_2\text{O}_3/\text{In}$ (approximately 90%:10% by weight) as the source material. Other relevant processing parameters will be described in the next section. It has been found that the incorporation of the metallic In in the evaporation source results in two significant effects. These are (i) a substantial increase of the evaporation rate at the operating temperatures, and (ii) a significant improvement of the film conductivity.

In this paper, the role of In in the present evaporation process is examined. It will be shown that, based on simple evaporation chemistry and thermodynamics, our experimental results can be explained qualitatively as well as quantitatively.

Key words: evaporation rate, In_2O_3 , electron concentration, excess In, vapor transport.

Evaporation Parameters

The evaporation is done in a diffusion-pump vacuum system with a resistance-heated source. As shown in Fig. 1, the evaporation boat consists of an alumina crucible heated by a tungsten heater. A pack of In_2O_3 powder on top of a pack of metallic In (approximately 90% In_2O_3 :10% In by weight) is used as the source material. The substrate is a microscope cover glass slide, and a substrate heater maintains a temperature range from 320° to 350°C during evaporation.

Initially, the vacuum chamber is evacuated to a base pressure in the 10^{-6} Torr range. Pure O_2 is then admitted to the chamber. With the high vacuum remaining open a steady-state chamber pressure ranging from 5×10^{-5} Torr to 2×10^{-4} Torr is rapidly reached and regulated by adjusting the O_2 needle valve. The evaporation rate, monitored by a crystal oscillator, is primarily controlled by the source temperature. Typical source temperature ranges from 800° to 900°C, providing a deposition rate of 20-40 Å/min on the thickness monitor, which is 29 cm above the source. The sheet resistance of the film is also monitored continuously during the evaporation.

The temperatures of the crucible wall and the In_2O_3 powder can be measured by two separate thermocouples, which are used to establish the temperature dependence of the evaporation rate. In a normal run, however, the thermocouples are removed from the source region to minimize the possible contamination sources.

Evaporation Chemistry and Thermodynamics of the System

Figure 2 shows the sheet resistance as a function of thickness during the growth of the In_2O_3 film. It can

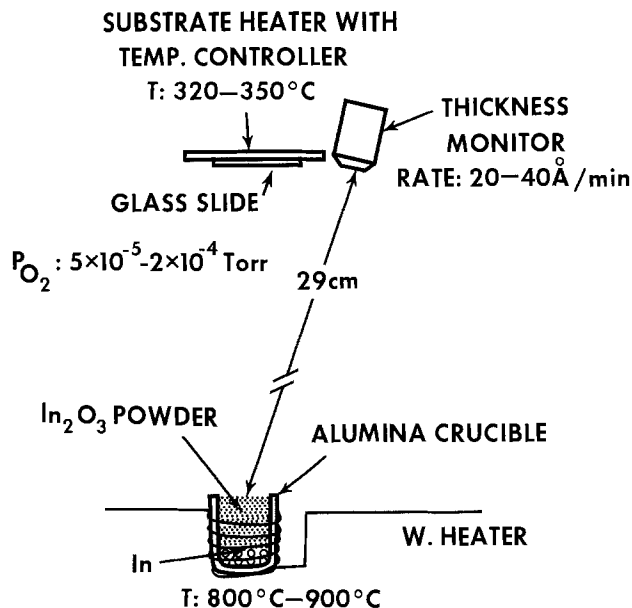


Fig. 1. Source, substrate, and thickness monitor arrangement in the evaporation chamber. Typical evaporation parameters are indicated.

be seen that a sheet resistance of $6.75 \Omega/\square$ is reached at a film thickness of 2700 \AA , corresponding to an average resistivity of $1.8 \times 10^{-4} \Omega\text{-cm}$. From the Hall effect measurement, an average free electron concentration of $4.69 \times 10^{20} \text{ cm}^{-3}$ and a Hall mobility of $74 \text{ cm}^2/\text{Vsec}$ have been determined for this film.

Since no dopant impurity has been introduced into the film, the conduction electrons are believed to arise from the excess In atoms or oxygen vacancies in the structure which act as shallow donor levels (12-14). Assuming each excess In atom gives rise to one donor level, which in turn gives rise to one conduction electron at room temperature, one expects a concentration of $4.69 \times 10^{20}/\text{cm}^3$ for the excess In. Within the accuracy of the given assumption and the experimental uncertainty, a successful theory should therefore be able to predict this result. The enhancement of the evaporation rate due to the presence of In in the evaporation source is another important observation, which should also be contained in the theory.

In the subsequent analysis of the evaporation process, the relevant processing parameters for the film shown in Fig. 2 will be used, which are: (i) Film growth rate = $33 \text{ \AA}/\text{min}$, (ii) O_2 pressure = $1 \times 10^{-4} \text{ Torr}$, (iii) crucible temperature = 860°C (1133 K), and (iv) substrate temperature = 340°C (613 K).

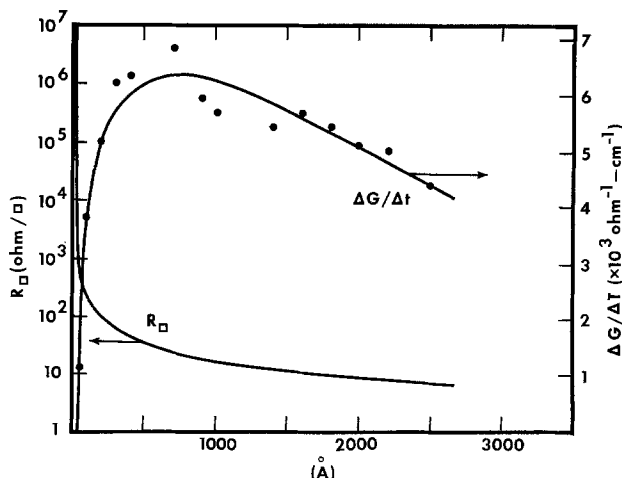
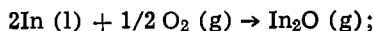
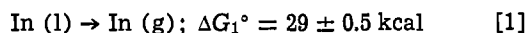
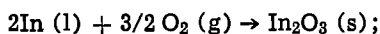


Fig. 2. Sheet resistance R_s and sheet conductance per unit film thickness $\Delta G/\Delta t$ as a function of the In_2O_3 thickness.

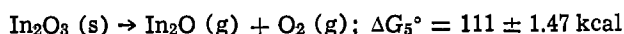
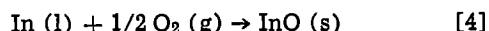
Reactions in the source region.—At a source temperature of 1133 K , a number of reactions involving In_2O_3 , In, and O_2 in the source region may be possible, which are listed below



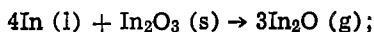
$$\Delta G_2^\circ = -22 \pm 1.4 \text{ kcal} \quad [2]$$



$$\Delta G_3^\circ = -133 \pm 0.45 \text{ kcal} \quad [3]$$



[5]



$$\Delta G_6^\circ = 67.3 \pm 4.2 \text{ kcal} \quad [6]$$

Because of the low melting point of In (430 K at 1 atm), and the low boiling point of In_2O (800 K at 1 atm), In does not exist in the solid phase in the crucible, and In_2O is in its vapor phase. It should also be noted that no gas phase of In_2O_3 has been found in the thermal decomposition experiment performed by Burns *et al.* (15), and the thermal evaporation of In_2O_3 involves gas phase transport of In_2O , In, and O_2 .

The free energy changes, ΔG° in the above equations, have been calculated based on published data and laws of thermodynamics, which are summarized below

$$\Delta G_1^\circ (T) = 58,840 + 3.2T \log T - 35.82T \pm 500 \text{ cal/mol}$$

(Ref. 16, 17) [7]

$$\Delta G_2^\circ (T) = -5000 - 15T \pm 1400 \text{ cal/mol} \quad (\text{Ref. 17, 18})$$

[8]

$$\Delta G_3^\circ (T) = -215,550 + 72.63T \pm 450 \text{ cal/mol}$$

(Ref. 17, 18) [9]

$$\Delta G_5^\circ (T) = \Delta G_2^\circ - \Delta G_3^\circ = 210,550 - 87.63T \pm 1950$$

(From Eq. [2], [3], [5]) [10]

$$\Delta G_6^\circ (T) = 3\Delta G_2^\circ (T) - \Delta G_3^\circ (T) \quad (\text{From Eq. [2],$$

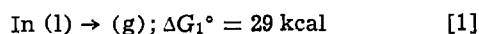
[3], [6]) [11]

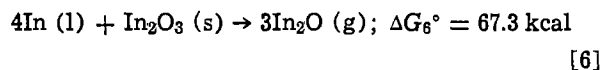
$$= 200,550 - 117.63T \pm 4.2 \text{ kcal}$$

The reactions [2]-[4] all involve the oxidation of In, and they can be neglected because of the very limited supply of O_2 in the crucible. The O_2 partial pressure in the chamber is rather low ($1 \times 10^{-4} \text{ Torr}$) to begin with, and it is expected to be even much lower near the opening of the crucible due to the rapid evaporation of In_2O (see subsequent discussions), which pumps the O_2 away from the source.

Reaction [5] is the thermal decomposition of In_2O_3 . From the value of the free energy change associated with this reaction, $\Delta G_5^\circ = 111 \text{ kcal}$, the partial pressure of In_2O has been calculated to be below 10^{-9} Torr , suggesting that this reaction can also be neglected. It should be mentioned that Burns *et al.* (15) have measured the vapor species over In_2O_3 at elevated temperatures, and they reported a partial pressure of In_2O below 10^{-8} atm at 1200 K , a result consistent with our calculation. This explains why the evaporation rate from the In_2O_3 source (without the presence of In) is negligibly small at a source temperature of 860°C , as we have observed experimentally.

Therefore, only reactions [1] and [6] need to be considered in the source region for our experiment, which are rewritten as





From these two reactions, the equilibrium partial pressure of In and In_2O can be expressed as

$$P(\text{In}) = \exp[-\Delta G_1^\circ(T)/RT] \quad [12]$$

and

$$[P(\text{In}_2\text{O})]^3 = \exp[-\Delta G_6^\circ(T)/RT] \quad [13]$$

At the operating temperature, the numerical values of the partial pressure are

$$P(\text{In}) = 2.2 \times 10^{-6} \text{ atm} = 1.67 \times 10^{-3} \text{ Torr} \quad [14]$$

and

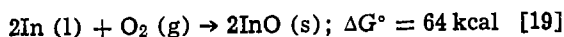
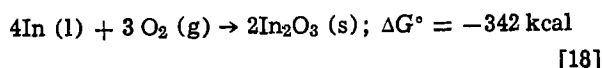
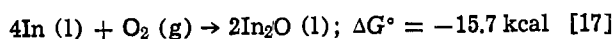
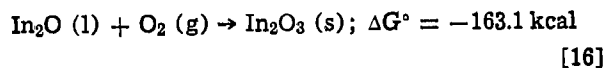
$$P(\text{In}_2\text{O}) = 4.7 \times 10^{-5} \text{ atm} = 3.6 \times 10^{-2} \text{ Torr} \quad [15]$$

In summary, the only two significant vapor species evaporating from the source are In and In_2O , with their respective partial pressures given by [14] and [15]. Thus, the simple theory presented above suggests that the incorporation of the metallic In in the evaporation source should result in several orders of magnitude increase in the evaporation rate. Comparing [14] with [15], it is apparent that the dominating evaporating component is In_2O , and In vapor constitutes approximately 4.6% of the total.

Since our x-ray diffraction analysis indicates that the deposited films are polycrystalline In_2O_3 (10, 11) some chemical reactions must be taking place during the evaporation process, which convert In_2O into In_2O_3 . This process is considered next.

Reactions on the substrate.—The chamber pressure is maintained at 1×10^{-4} Torr (primarily O_2) during evaporation, which corresponds to a mean-free path of 50 cm and is longer than the source-substrate distance. Therefore, reactions with O_2 in the vacuum chamber can be neglected except at the substrate, which is held at 340°C (610 K).

The possible reactions on the substrate are listed below



Note that both In and In_2O are in the liquid phase on the substrate due to their low melting points. Equations [7]-[11] have been used again to obtain the free energy changes in the above equations.

Reaction [16] is the dominant reaction because In_2O is the major evaporating species. Our x-ray diffraction data indicate that the film structure is polycrystalline In_2O_3 , which is also consistent with the outcome of reaction [16].

Equations [17]-[19] all involve the reactions between In and O_2 , which may be neglected based on probabilistic considerations. Because of the low evaporation rate of In, and the low In/ In_2O_3 ratio arriving at the substrate, it is highly unlikely that two or more In atoms could be tightly distributed spatially to react with O_2 in a relatively short period of time.

Thus, the primary reaction taking place on the substrate is the conversion of In_2O into In_2O_3 , according to [16]. The condensation of In_2O on the substrate in its liquid phase may be responsible for the formation of the crystalline phase of In_2O_3 . A small amount of In atoms, however, is incorporated in the film during growth, which gives rise to the conduction electrons. The exact chemical state of the excess In is not clear at the present time. Whether the In atoms indeed occupy the interstitial sites, or form some complexes with the host In_2O_3 , remains to be studied.

Comparison Between Theory and Experiment

In the previous section, we have shown that the theory is in qualitative agreement with our experimental observations. We shall now make a quantitative comparison based on two important experimental observables: (i) the film growth rate, and (ii) the conduction electron concentration.

Film growth rate.—The theoretical growth rate of the In_2O_3 can be calculated given the partial pressures of In_2O and In at the source and the known source-substrate distance. The calculation is as follows.

The average thermal velocity of In_2O at the source temperature ($T = 1133 \text{ K}$) is

$$\bar{v} = \sqrt{\frac{8kT}{\pi m}} = 1.6 \sqrt{\frac{kT}{m}} = 3.13 \times 10^4 \text{ cm/sec} \quad [20]$$

The rate of transported molecules across the effective source surface area A is [see Fig. 3(a)]

$$\frac{dQ}{dt} = A \int f(v) dv^3 | \vec{n} \cdot \vec{v} | \quad [21]$$

where $f(v)$ is the molecular speed distribution function, $f(v) dv^3$ is the average number of molecules per unit volume that has a velocity between v and $v + dv$, and \vec{n} is the outgoing unit vector normal to the surface A .

Evaluating the integral in the upper half of the velocity space

$$\begin{aligned} \frac{dQ}{dt} &= A \int_{\phi=0}^{2\pi} \int_{\theta=0}^{\pi/2} \int_{v=0}^{\infty} f(v) v^3 \cos \theta \sin \theta d\phi d\theta dv \\ &= A\pi \int_0^{\infty} v^3 f(v) dv \quad [22] \end{aligned}$$

On the other hand

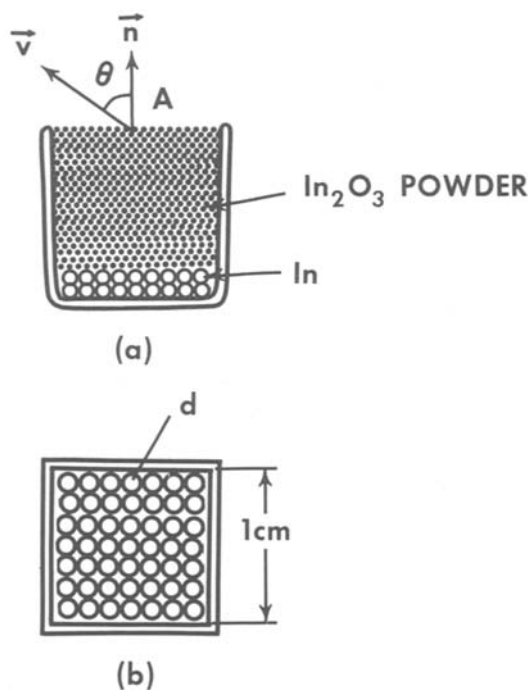


Fig. 3 (a) Schematic of the crucible showing the velocity vector of the vapor particle \vec{v} , surface normal vector \vec{n} , and the angle parameter θ . A is the effective area of the source surface for gas transport, which is the integrated cross-sectional gaps at the surface between the In_2O_3 particles. (b) Schematic top view of a box containing tightly packed spherical particles of diameter d . This is used to calculate the effective area for gas transport.

$$\begin{aligned} \bar{v} &\equiv \frac{1}{N} \int v f(v) dv^3 \\ &= \frac{1}{N} \int_{\phi}^{\pi} \int_0^{2\pi} \sin \theta d\theta d\phi \int_0^{\infty} v^3 f(v) dv \\ &= \frac{4\pi}{N} \int_0^{\infty} v^3 f(v) dv \quad [23] \end{aligned}$$

where N is the total number of In_2O molecules per unit volume. From [22] and [23]

$$\frac{dQ}{dt} = \frac{AN}{4} \bar{v} \quad [24]$$

where $\bar{v} = 3.13 \times 10^4$ cm/sec as given in [20], and N can be calculated from the equation

$$P = NRT \quad [25]$$

At $T = 1133$ K and $P(\text{In}_2\text{O}) = 4.7 \times 10^{-5}$ atm, $N = 5.3 \times 10^{-10}$ mol/cm³. Substituting the values of \bar{v} and N into [24]

$$\begin{aligned} \frac{dQ}{dt} &= A \times 4.15 \times 10^{-6} \text{ mol/cm}^2\text{-sec} \\ &= A \times 1.02 \times 10^{-3} \text{ g/cm}^2\text{-sec} \quad [26] \end{aligned}$$

The evaporation rate of In_2O from the source, therefore, can be obtained once the effective source area, A , is known.

The crucible has a cross-sectional area of 1 cm², but because of the tight packing of the In_2O_3 powder, the effective opening for the evaporating In_2O molecules is reduced [see Fig. 3(b)]. This effective area for the evaporation process can be estimated as follows.

Suppose the In_2O_3 powder is made of spherical particles of diameter d , each giving a cross-sectional area of $\pi d^2/4$. For a 1 cm² cross-sectional area of the crucible, the total area covered by the particles is then $1/(d)^2 \times \pi/4 d^2 = 0.79$ cm², which is independent of the individual diameter of the particles. The effective area for the evaporation process is therefore $A = 0.21$ cm². From the visual examination under a microscope, the particle size in the powder is of the order $d = 10$ μm , and the calculated effective area is in reasonable agreement with the observation.

Substituting $A = 0.21$ cm² into [26], the evaporation rate of In_2O from the source is

$$\frac{dQ}{dt} = 2.15 \times 10^{-4} \text{ g/sec} \quad [27]$$

Since the thickness monitor is at a distance 29 cm from the source, the theoretical deposition rate for In_2O on the crystal monitor is

$$\begin{aligned} 2.15 \times 10^{-4}/2\pi (29)^2 &= 4.06 \times 10^{-8} \text{ g/cm}^2\text{-sec} \\ &= 34.4 \text{ \AA/min (density of In}_2\text{O} \\ &= 7 \text{ g/cm}^3) \quad [28] \end{aligned}$$

Following the same procedure, the theoretical deposition rate for In is calculated to be 1.7 \AA/min . Therefore, the total evaporation rate on the thickness monitor is

$$34.4 + 1.7 \text{ \AA/min} = 36.1 \text{ \AA/min} \quad [29]$$

The agreement between this value and the one recorded by the thickness monitor (33 \AA/min) is better than we expected, especially when one considers the manner in which the effective area was estimated. The result, however, does suggest that the evaporation kinetics is consistent with the assertion that Eq. [6] is the principle reaction in the source region, and that the partial pressure of In_2O at the source is of the order given in Eq. [15].

Conduction electron concentration.—It has been reported that the conduction electrons in the crystalline In_2O_3 arise from the excess In atoms. The electron concentration is therefore expected to be proportional to the concentration of excess In in the crystalline In_2O_3 structure.

From the evaporation rates obtained previously, the molar ratio between In and In_2O in the deposited film is calculated to be 0.06. This suggests an excess In concentration in the In_2O_3 film of $9 \times 10^{20}/\text{cm}^3$. This value is within a factor of two of the experimentally determined free electron concentration, $4.69 \times 10^{20}/\text{cm}^3$.

Since the vapor pressure of In is very sensitive to the temperature (see Eq. [12]), a small error in the experimentally determined crucible temperature could account for the discrepancy. It is also possible that not every excess In atom contributes to a conduction electron. A direct measurement of the In concentration using the composition profiling techniques is necessary to resolve this question, which is unavailable to us at the present time.

Conclusions

From an analysis of the evaporation chemistry and thermodynamics of the system, it has been found that the incorporation of In in the In_2O_3 evaporation source gives rise to two important effects: (i) A great enhancement of the evaporation rate, and (ii) a significant increase in the conduction electrons.

In the source region, the most important reaction involves In and In_2O_3 to form In_2O , which is the dominant vapor species evaporating from the source. On the substrate, In_2O reacts with O_2 to form In_2O_3 , which is the primary end product of this evaporation process. A small amount of In (approximately 6%) is also being evaporated, which is incorporated in the growing In_2O_3 film. These excess In atoms are believed to be the source of conduction electrons.

Acknowledgment

The authors gratefully acknowledge the support of this work by the National Science Foundation under grant numbers ECS-7906933 and ENG-7910888.

Manuscript submitted Dec. 11, 1980; revised manuscript received March 26, 1981.

Any discussion of this paper will appear in a Discussion Section to be published in the June 1982 JOURNAL. All discussions for the June 1982 Discussion Section should be submitted by Feb. 1, 1982.

Publication costs of this article were assisted by Yale University.

REFERENCES

1. R. L. Weiher and R. P. Ley, *J. Appl. Phys.*, **37**, 299 (1966).
2. H. K. Muller, *Phys. Status Solidi*, **27**, 723 (1968).
3. D. B. Fraser and H. D. Cook, *This Journal*, **119**, 1368 (1972).
4. W. W. Molzen, *J. Vac. Sci. Technol.*, **12**, 99 (1975).
5. J. C. C. Fan, F. J. Bachner, and G. H. Foley, *Appl. Phys. Lett.*, **31**, 773 (1977).
6. W. G. Haines and R. H. Bube, *J. Appl. Phys.*, **49**, 304 (1978).
7. R. Groth, *Phys. Status Solidi*, **14**, 69 (1966).
8. R. Clanget, *Appl. Phys.*, **2**, 247 (1973).
9. H. Kostlin, R. Jost, and W. Lems, *Phys. Status Solidi A*, **29**, 87 (1975).
10. C. A. Pan and T. P. Ma, *Appl. Phys. Lett.*, **37**, 163 (1980).
11. C. A. Pan and T. P. Ma, *J. Electron. Mater.*, **10**, 43 (1981).
12. J. H. W. DeWitt, *J. Solid State Chem.*, **8**, 142 (1973).
13. G. Haacke, *Ann. Rev. Mater. Sci.*, **7**, 73 (1977).
14. J. C. C. Fan and J. B. Goodenough, *J. Appl. Phys.*, **48**, 3524 (1977).

15. R. P. Burns, G. DeMaria, J. Drowart, and M. G. Ingraham, *J. Chem. Phys.*, **38**, 1035 (1962).
16. O. Kubaschewski and E. L. Evans, "Metallurgical Thermal Chemistry," 3rd ed., Pergamon Press, Inc., Elmsford, NY (1958).
17. C. A. Pan, Ph.D. Thesis, To be published.
18. D. Chatterji and R. W. Vest, *J. Am. Ceram. Soc.*, **55**, 575 (1972).

Deep Levels Study in Float Zone Si Used for Fabrication of CCD Imagers

L. Jastrzebski*

RCA Laboratories, Princeton, New Jersey 08540

and J. Lagowski*

Department of Material Science and Engineering,
Massachusetts Institute of Technology, Cambridge, Massachusetts 02139

ABSTRACT

The development of a better understanding of the origin of defects which affect device performance requires the characterization of deep levels in Si wafers at various stages of processing. This work reports the results of deep level measurements by standard DLTS (deep level transient spectroscopy) and the newly developed DSPS (derivative surface photovoltage spectroscopy) technique on float zone p-type (10 Ω cm) Si wafers used for the fabrication of CCD imagers. The DSPS measurements revealed the presence of deep centers (in the range of 10^{11} - 10^{13} cm⁻³) around the middle of the energy gap in the as-grown and the heat-treated wafers. The effect of these deep centers on the quantum efficiency and the fixed pattern noise in CCD imagers is discussed.

One of the most challenging problems in VLSI technology is the fabrication of large area defect-free devices. This is particularly true in the case of large area CCD imagers (1 cm² of area or more) for TV applications (in order of 10^5 elements) where any defect locally affecting the generation or recombination current will be visible in the displayed image. In addition to being defect-free, these devices require a long lifetime for minority carriers in order to achieve a good sensitivity and a low background dark current.

Two types of unacceptable cosmetic defects, i.e., localized spots or lines and striation bands, are usually observed in CCD imagers. Most of the lines and spots are caused by electrically active crystallographic defects in the silicon substrate (1-5), while "striations" in the image are generated by inhomogeneities of resistivity and concentration of recombination centers (6). It should be pointed out that the ratio of crystallographic defects, which are electrically active, to the total amount of crystallographic defects as well as striation contrast in the displayed image depends on the heat-treatment involved in CCD imager fabrication (7). Deep levels usually act as recombination centers, therefore their detection after the various stages of processing could provide useful information about mechanisms involved in decoration of crystallographic defects, striation contrast enhancement by heat-treatments, as well as lifetime degradation during processing. Improvement in our understanding of the relationship between defects present in as grown crystals, process-induced defects, and the device performance requires characterization of deep levels in as grown silicon as well as processed wafers.

The characterization of deep levels in semiconductors is most often done with deep level transient spectroscopy (DLTS) (8). This technique relies on the measurement of capacitance changes caused by thermal

emission of the trapped carriers from deep states. Another technique, the newly developed derivative surface photovoltage spectroscopy (9) (DSPS) is based on the measurement of photovoltage changes caused by the photoinjection of carriers from and to deep levels under subband illumination. It should be noted that the thermal activation energy measured by DLTS provides the energy level only for the simple trapping centers as defined within the Shockley-Read recombination model. In general, the ionization of defect centers may involve absorption (emission) of phonons, lattice relaxation, excited states, and/or configurational changes which can be disclosed easier by optical studies (due to strict momentum and energy conservation rules) rather than thermal emission.

The present work reports on the results of deep level measurements by DLTS and DSPS on high quality as-grown and oxidized float zone silicon wafers used for solid-state imager fabrication. The correlation between the deep centers measured by these techniques and other material parameters influencing imager performance will be given.

Experimental Approach

2 in. diam swirls and dislocation-free float zone silicon wafers 10 Ω cm p-type (boron-doped) used for the measurements were bought from Monsanto and Wacker. The wafers were cleaved in half. Schottky diodes were made on one-half of the wafer by Ti evaporation. The second half was oxidized at 900°C in steam + HCl for 2 hr (about 2000Å oxide thickness) and MOS structures were prepared by subsequent Ti or Au evaporation. For DLTS measurements the ohmic contacts were made by alloying gold-germanium, sintering aluminum or soldering indium or tin. For DSPS measurements a second contact was usually made with silver paint and kept in the dark during the experiments. By applying different geometries (i.e., by changing the distance, which photogenerated carriers had to

* Electrochemical Society Active Member.
Key words: defects, DLTS, wafers.

diffuse to the back contact) it was established that it did not influence the measured photovoltage.

The DLTS experiments were performed with a typical system using lock-in detection (8) in the temperature range of 77-320 K and the frequency range of 3-200 Hz. From the slope of the plot of the reciprocal temperature, for which peak of capacitance changes occurs, as a function of the frequency, the position of the energy levels was obtained. The interpolation of this curve to zero frequency allowed the estimation of the capture cross sections. The concentration of the deep centers was estimated from the absolute values of capacitance changes.

The photovoltage experiments were performed in the temperature range 8-300 K using light in the spectral range of 0.5-2.5 eV. The photovoltage was measured with respect to a transparent reference gold electrode, evaporated directly on a semiconductor (MS-configuration) or on an oxide layer (MOS-configuration). The photovoltage transient measurements were performed using square pulses of the incident light (with a frequency adjustable between 0.1 and 500 Hz) and the signal averager. In derivative measurements the wavelength modulation of a constant incident light was provided by a vibrating slit of a double-prism monochromator. Typically $\Delta\lambda/\lambda_0$ was of the order of 10^{-3} . The frequency of wavelength modulation was selected between 1 and 25 Hz. In order to minimize a signal to noise ratio the photovoltage signal generated by wavelength modulation was measured with a lock-in detection. Precautions were taken to eliminate the interference of spurious signals (arising, e.g., from light intensity modulation). The detailed description of the experimental arrangements and the procedure was given elsewhere (10). The procedure presently employed for determination of deep level parameters can be briefly summarized as follows.

1. The low temperature subbandgap photovoltage appears when transition from or to a localized level in the depletion region is taking place. The threshold photon energy corresponds to the difference between the energy level and the conduction or the valence band.

2. The amplitude of the corresponding, low signal steady-state photovoltage, ΔV , depends on the amount of generated carriers Δp

$$\Delta V = C\Delta p \quad [1]$$

where the proportionally constant, C , can be experimentally determined. The Δp can be expressed as

$$\Delta p = I\sigma_1 N_t \tau \quad \text{and} \quad \tau = \frac{1}{K_p p v_t p} \quad [2]$$

where I is the light intensity, N_t is the trap density, σ_1 is the capture cross section for photoionization, τ is the characteristic relaxation time, K_p is the capture cross section for majority carriers, $p = p_0 + \Delta p$ is the majority carrier concentration, and $v_t p$ is the thermal velocity of a hole.

3. The transient of photovoltage V_t for illumination "on" and "off" is given by expressions

$$\Delta V_t/\text{on} = \Delta V(1 - e^{-t/\tau}) \quad \text{and} \quad \Delta V_t/\text{off} = \Delta V e^{-t/\tau} \quad [3]$$

where t is time.

As pointed out above, the spectral dependence of the subband photovoltage enables the determination of the energy levels of deep centers as the threshold energy for which increase in photovoltage takes place. The wavelength modulation measurements of photovoltage derivative allow the establishment of a precise location of the threshold energy and they also enhance a fine structure of photoionization transitions. The measurement of the photovoltage transient allows one to obtain τ and thus the capture cross section K_p . In order to

determine the trap density, N_t , the constant C in Eq. [1] has to be estimated from the dependence of the photovoltage relaxation time on the illumination intensity. Thus, when the amount of generated carriers Δp in Eq. [2] becomes comparable with an equilibrium carrier concentration p_0 , the relaxation time, τ , starts to decrease with increasing light intensity because p in Eq. [2] is no longer p_0 but now $p = p_0 + \Delta p$. Estimating the value of Δp in relation to p_0 and utilizing Eq. [1] the value of C was determined from the measured steady-state photovoltage, ΔV , for high light intensity. This in turn allowed one to obtain a product $\sigma_1 N_t$ from Eq. [1] and [2], knowing ΔV and τ .

To measure the microscopic distribution of the deep centers, a series of parallel and geometrically identical MOS structures were prepared by photolithographic definition of an Al layer evaporated on the oxide. The geometry, spacing, and position of the capacitors in respect to the wafer edge is given in Fig. 1. The photovoltage generated by a monochromatic incident light was measured between a given MOS structure and an electrical contact which was kept in the dark. It has been found that for a reliable assessment of the differences in photoresponse of individual MOS structures, it is necessary to position the structures perpendicularly to a monochromator slit. Positioning of MOS structures parallel to the slit resulted in generation of spurious photovoltage signals similar to that arising from the wavelength modulation of an incident light.

The information about recombination center concentration in the measured wafers was obtained from the measurements of diffusion length by the surface photovoltage technique (11). Nonuniformity in the distribution of recombination centers was obtained from the measurement of the collection efficiency variations of the electron beam induced current (EBIC) collected by the electron-transparent Schottky diodes (12). Under plasma generation condition the variations in the collection efficiency correspond to the recombination centers concentration fluctuations (13). The measurements were performed using beam voltages between 3 and 15 keV and a beam current between 10^{-8} to 10^{-10} A.

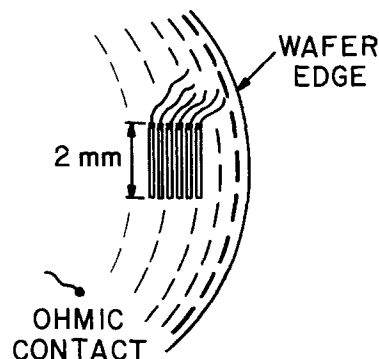


Fig. 1. Geometry of MOS capacitors used to measure microscopic distribution of deep centers.

Experimental Results and Discussion

Deep center parameters.—The typical subband photovoltage spectrum (normalized to light intensity) of MOS structures is shown in Fig. 2. This subband photovoltage is caused by two transitions between valence band and localized states. The photovoltage which is observed in the low energy end of the spectrum involves a center with an energy level of less than 0.5 eV (outside of the spectral range covered by the monochromator). The sharp increase of the photovoltage above 0.56 eV indicates that the additional transition to the state of energy about 0.56 eV above the valence band takes place. The occupation by electrons of any deep levels is rather unlikely in p-type silicon at low temperature; therefore, the photovoltage of Fig. 2 cannot be attributed to the optical transition from deep levels into the conduction band. The precise energy location of the deep level and additional information about its nature is obtained from the derivative surface photovoltage $dV/dh\nu$ spectrum, on Fig. 3b. In addition to the peak corresponding to the 0.56 eV energy level, a series of maxima is observed. These maxima

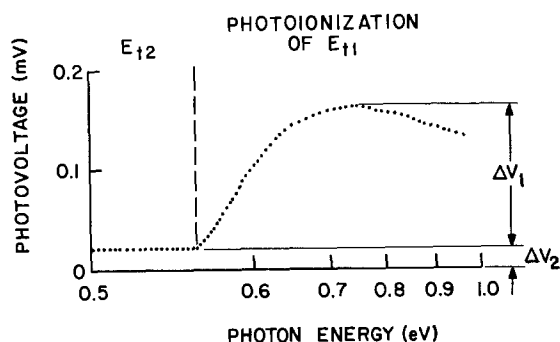


Fig. 2. Spectral dependence of steady-state, subbandgap photovoltage, and the contributions from photoionization of deep levels E_{t1} and E_{t2} . Spectrum was normalized to constant photon flux.

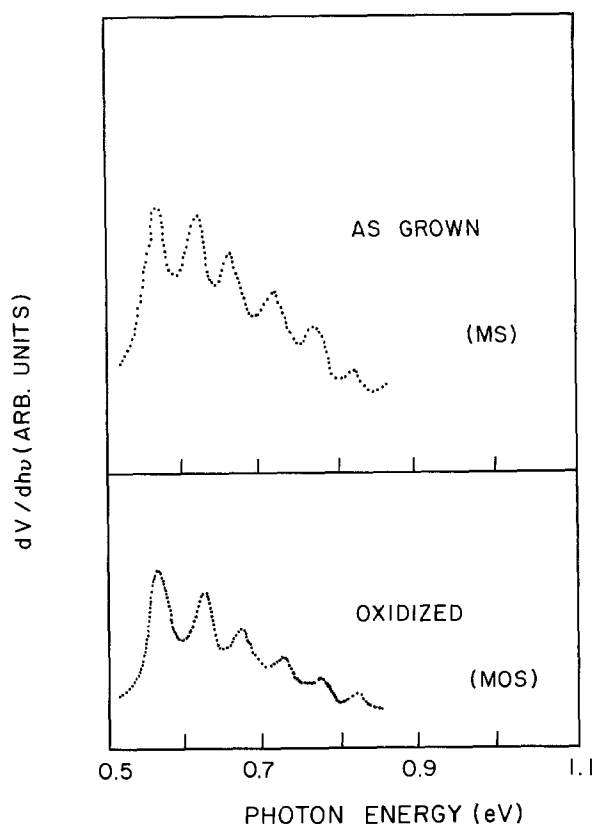


Fig. 3. Subbandgap first derivative photovoltage spectra at 10 K, (a) as grown wafer (MS), (b) oxidized wafer (MOS).

result from the fine structure in the photovoltage, which is not visible in Fig. 2. The separation of the maxima coincides with the energy of the optical phonon 55 meV (14); therefore, it seems to be justified to assume that they are caused by the phonon replica of the optical transitions to the deep level (10). The strong interaction of the deep state with phonons shows a strong coupling of the given state with the lattice, which is characteristic for a recombination center. The same photovoltage spectra (same energy levels) as for the MOS structures on the oxidized wafers were also obtained on the Schottky diodes made on as grown crystals (compare Fig. 3a and 3b). This indicates that the observed levels are not related to the interfacial states but to the states present in bulk of the as grown material and of the oxidized material. (However, note that the oxidation increases the concentration of deep levels, see below.)

The transient photovoltage measurements in the MOS structures for the 0.56 eV level at 12 K give the τ value of about 10 msec. The relaxation time, τ , was found to be independent of the light intensity up to 10^{14} photons per cm^2 . However, above this value it decreased with the light intensity. For example, at 12 K and 2×10^{14} photons per cm^2 (or 0.8 eV) the relaxation time was reduced by about 10%. Accordingly, Δp had to be about $0.1 p_0 \approx 10^8 \text{ cm}^{-3}$ (p_0 at this temperature was estimated to be about 10^9 cm^{-3}). From the value of Δp and the magnitude of photovoltage ΔV (Fig. 2) the factor C in Eq. [1] was estimated. The concentration of deep levels was determined from Eq. [2] (using the value of ΔV from Fig. 2). The required values of photoionization cross section σ_1 ($\sigma_1 \approx 2.5 \times 10^{-18}/E^2$, where E is the energy level). Utilizing the value of the measured time constant, τ , the capture cross section for holes was estimated from $K_p = 1/\tau p_0 v_t^p$. The deep center parameters measured in the two typical MOS samples taken from the wafer center and the same wafer edge are given in Table I. The deep center concentration is about three times higher by the wafer edge than of the wafer center.

As pointed out above, the subbandgap photovoltage spectra similar to that shown in Fig. 2 and 3 were also obtained for Schottky diodes. However, for Schottky diodes the ratio of subbandgap to bandgap photovoltage was found to be about one order of magnitude lower than in MOS structures. This fact suggests that the deep level concentration in the as-grown material is about one order of magnitude below that observed in the oxidized samples (*i.e.*, on the level of 10^{12} cm^{-3}). Consistently, because of an order of magnitude lower concentration of deep levels in as-grown crystals no decrease in the relaxation time with increasing illumination intensity up to 2×10^{15} photons/ cm^2 was observed for the Schottky diodes. Accordingly, the photovoltage transient analysis could not be used for more precise evaluation of N_t in the as-grown material.

The DLTS experiments showed the presence of two levels in the MOS samples (Fig. 4); the hole trap at energy 0.23 eV; hole capture cross sections of about

Table I. Comparison of deep centers parameters measured by DLTS and DSPS

| | DSPS | DLTS |
|------|--|---|
| Edge | $E_1 = 0.56 \text{ eV}$ $N_1 = 2.2 \times 10^{13} \text{ cm}^{-3}$ $\sigma_1 \sim 10^{-14} \text{ cm}^2$ $E_2 < 0.5 \text{ eV}$ $N_2 < 10^{12} \text{ cm}^{-3}$ $\sigma_2 > 2 \times 10^{-15} \text{ cm}^2$ | $E_1 = 0.45\text{-}0.65 \text{ eV}$ $N_1 = 1.5 \times 10^{13} \text{ cm}^{-3}$ σ_1 —not determined $E_2 = 0.23 \text{ eV}$ $N_2 = 9 \times 10^{11} \text{ cm}^{-3}$ $\sigma_2 \sim 10^{-14} \text{ cm}^2$ |
| | Center | $E_1 = 0.56 \text{ eV}$ $N_1 = 9 \times 10^{12} \text{ cm}^{-3}$ $\sigma_1 \sim 10^{-14} \text{ cm}^2$ $E_2 < 0.5 \text{ eV}$ $N_2 < 5 \times 10^{11} \text{ cm}^{-3}$ $\sigma_2 > 2 \times 10^{-15} \text{ cm}^2$ |

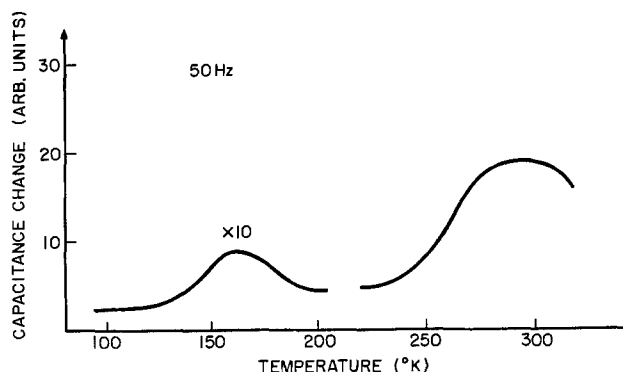


Fig. 4. DLTS spectrum obtained on MOS structure. The high temperature peak corresponds to concentration of about 10^{13} cm^{-3} of deep levels.

10^{-14} cm^2 and concentrations of about $7 \times 10^{11} \text{ cm}^{-3}$ and the second level close to the middle of the energy gap (0.45-0.65 eV range) with a concentration of about 10^{13} cm^{-3} . The capture cross section and precise position of the second level was difficult to determine because a broad band of capacitance changes was observed rather than a sharp peak. This could possibly be caused by the interaction of this level with minority carriers present at this temperature in silicon.

A comparison between DLTS results and the deep level parameters determined from DSPS is presented in Table I and suggests that in both instances we are dealing with the same set of two deep levels located at 0.23 and 0.56 eV above the valence band. DLTS measurements performed on Schottky barriers in as grown crystals showed the deep level concentration to be about one order of magnitude lower (Fig. 6) than in the oxidized wafers, which confirms the DSPS results.

Microscopic distribution of the deep centers.—The important material property affecting the CCD imager performance is distribution of the deep centers on the microscale. Studies on the deep center distribution were performed using a series of geometrically identical MOS capacitors (as shown in Fig. 1). First, uniformity of the MOS capacitors with respect to the photovoltage response was established from the room temperature photovoltage measurements in a region of intrinsic excitation. Under conditions of "back-side" illumination this photovoltage arises due to (i) almost homogeneous generation of electron-hole pairs ($h\nu \simeq E_g$) and (ii) due to "back-surface" excitation of excess carriers ($h\nu > E_g$) and subsequent diffusion of excess carriers across the specimen to the region of the MOS barrier. In case (i) the magnitude of photovoltage probes the lifetime of excess carriers and the value of the interface barrier height. In case (ii) it also probes the interface recombination velocity on the "back surface" in addition to the diffusion lengths of excess carriers. The present results of photovoltage measurements have shown only slight differences between various MOS structures. Typical results of photovoltage vs. incident photon energy are given in Fig. 5 (photovoltage measured between metal electrode of MOS structure and electrical contact to the sample) and it is seen that differences between various structures do not exceed 5%.

It can be concluded from the results of Fig. 5 that homogeneous excitation of excess carriers results in only minor differences between photovoltaic response of individual MOS structures, which can be treated as an indication of negligible differences in potential barrier heights of MOS structures (note that all other factors, i.e., the lifetime, diffusion length, and surface recombination velocity on the back surface are in the present configuration averaged over a relatively large area).

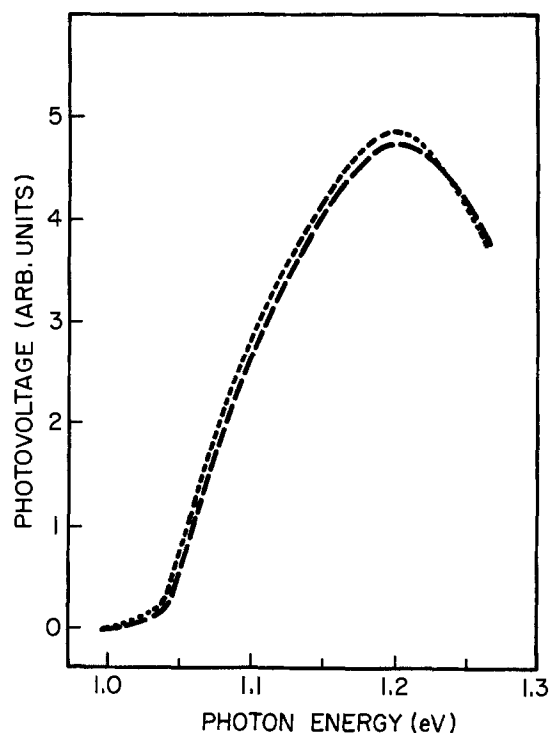


Fig. 5. Comparison of photovoltage generated by band to band transitions of the typical two MOS structures used to measure inhomogeneities in distribution of deep centers. Differences do not exceed 5%.

For a comparison between the concentration of deep levels in wafer regions corresponding to various MOS structures the subband photovoltage spectra were measured at low temperature with respect to a common contact to the sample. The typical results obtained at two temperatures (60 and 100 K) are summarized in Table II. It is seen from this table that the maximum relative difference between the subbandgap photovoltage of different structures is about 20%. These differences reflect primarily different concentrations of deep levels, N_t . As discussed above, the changes of surface barrier height were estimated as not exceeding 5%, i.e., about four times lower than the observed changes in photovoltage due to photoionization of deep levels. Therefore, it can be concluded that deep center concentration variations of at least 20% at distance of a few hundred microns are present in silicon wafers.

Lifetime and inhomogeneity in the recombination center distribution.—The concentration of the deep centers was found to be directly correlated to the lifetime of minority carriers. Figure 6 presents lifetime in the as grown and oxidized silicon (measured by DLTS and DSPS, respectively) as a function of the reciprocal concentration of the deep centers (0.56 eV level) measured, as described earlier. It seems that dependence is linear, which could be described by the expression

$$\tau = \frac{1}{K_e \cdot V_t^e \cdot N_t}$$

where K_e is the capture cross section for electron (minority carriers) and V_t^e is the thermal velocity of an electron. From the slope of the line in Fig. 6, the value of K_e equals $5 \times 10^{-15} \text{ cm}^2$ is obtained. It is not surprising that those centers act as recombination centers and control the lifetime of minority carriers in view of their strong interaction with the lattice demonstrated by the phonon replica in the derivative spectra (Fig. 3).

One of the problems in the CCD imagers used for TV applications is the appearance of a circular striation pattern in the background of the defected video image

Table II. Photovoltaic response of MOS structures at photon energy 0.8 eV
Photovoltage (μV)

| Temperature (K) | Photovoltage (μV) | | | | | | Maximum difference | |
|-----------------|--------------------------------|-------------|-------------|-------------|-------------|---------------|--------------------|--------------|
| | Structure 1 | Structure 2 | Structure 3 | Structure 4 | Structure 5 | Average value | Absolute | Relative (%) |
| 100 | 8.5 | 7.5 | 8.1 | 8.8 | 8.9 | 8.36 | 1.5 | 18 |
| 60 | 21.2 | 18.4 | 20.1 | 22.4 | 22.7 | 21.0 | 4.3 | 20 |

(Fig. 7). It has been established that this pattern reflects nonuniform collection efficiency, caused by inhomogeneous distribution of recombination centers in the silicon substrate (6). The typical fluctuations in the recombination center concentration observed at the edge of the wafer (measured by EBIC under plasma generation conditions) are shown in Fig. 8a. Figure 8b

shows the histogram of recombination center variations obtained by integrating variations presented in Fig. 8a. Figure 8c shows the variations in the concentration of deep centers in the same area, measured by DSPS where EBIC measurements presented in Fig. 8b were performed. Good correlation exists between the distribution of the deep levels measured by DSPS and the distribution of recombination centers measured by EBIC. Therefore, it can be concluded that inhomogeneous distribution of deep levels is responsible for appearance of a striation pattern in the CCD image.

It has to be pointed out that the inhomogeneity of the recombination center distribution can be affected by the heat-treatment. The upper plot in Fig. 9 represents the typical fluctuations in the recombination center concentration observed at the edge of as-grown wafers (measured by EBIC under plasma generation conditions). The lower plot of Fig. 9 represents the fluctuations (measured under the same conditions) in the recombination center concentration observed in the same place in the wafer after oxidation. The periodicity of oscillations is about a few hundred microns in both samples, and their amplitude in the as grown wafer is about 10-15% when in the oxidized wafer it increases to about 20-25%, which indicates that the oxi-

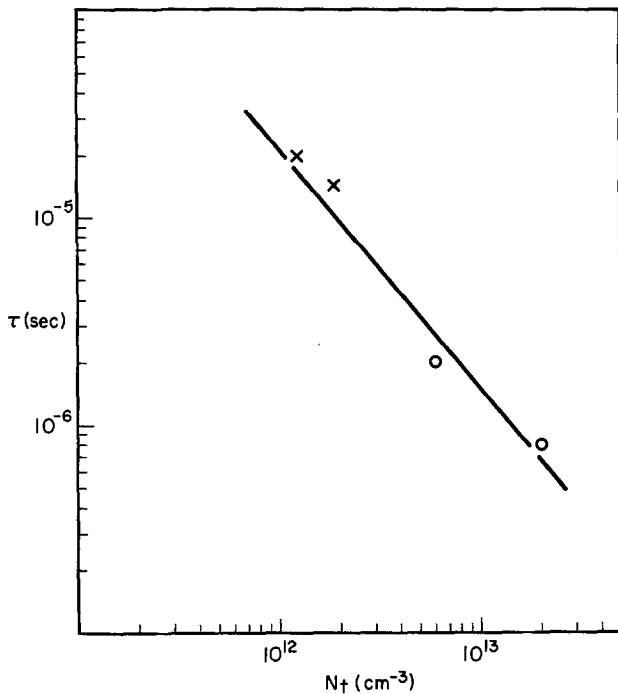


Fig. 6. Lifetime as a function of concentration of 0.56 eV centers. X, as grown (DLTS), O, oxidized (DSPS).



Fig. 7. Striation pattern observed in the video of CCD image

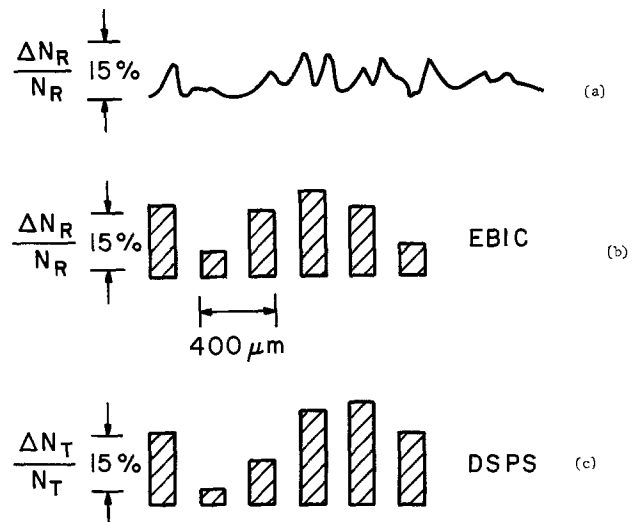


Fig. 8. (a) Distribution of recombination centers measured by EBIC; (b) histogram of recombination centers distribution (EBIC); (c) measured by DSPS histogram of deep centers distribution.

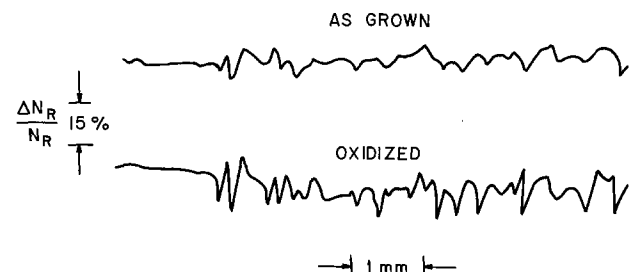


Fig. 9. Distribution of recombination centers measured by EBIC in the virgin wafer and in the same place after oxidation.

dation process enhances the inhomogeneity in recombination center concentration already present in as grown material. The degree of this enhancement for the same heat-treatment was found to differ significantly between the wafers. The observed increase in the inhomogeneity of deep centers during the heat-treatment accounts for the enhancement of striation contrast by processing.¹ The large differences between the striation contrast in the different CCD imagers processed in the same manner (7) can be explained by the observed significant differences in which the heat-treatment influences the inhomogeneity of deep centers in the different wafers.

The second important issue for device performance is the amount of electrically active crystallographic defects which will show up as spots or lines in the displayed image (1-5). Crystallographic defects usually become electrically active after decoration with recombination centers (16). Figure 10 shows observed relationships between the amount of electrically active edge dislocations observed in the image (ratio between the amount of edge dislocations giving white spots and lines and the total amount of edge dislocations observed in the imager area after etching) and the value of the average diffusion length in the silicon. When none of the dislocations were electrically active, the point was placed in the region "no correlation." From the presented plot it is evident that the probability of decoration of edge dislocation increases with the increase of total concentration of deep centers in the crystal (their relationship to lifetime is given in Fig. 6).

The nature and origin of these defects as well as the mechanism responsible for the increase of the deep center concentration and the enhancement of recombination center inhomogeneity after oxidation are not clear at present. Further extensive work is required which would allow one to establish the origin of deep centers and to provide the model describing their behavior during heat-treatment. It is likely that the deep centers are not associated directly with residual chemical impurities but are rather related to the point defect clusters or their complexes with impurities present in as grown float zone crystals. The inhomogeneous distribution of these defects in the crystals could be

¹ Inhomogeneities in the recombination centers concentration, responsible for striation pattern in the displayed image, are from 20 to 200% larger in the processed wafers (with final devices) than in as grown wafers.

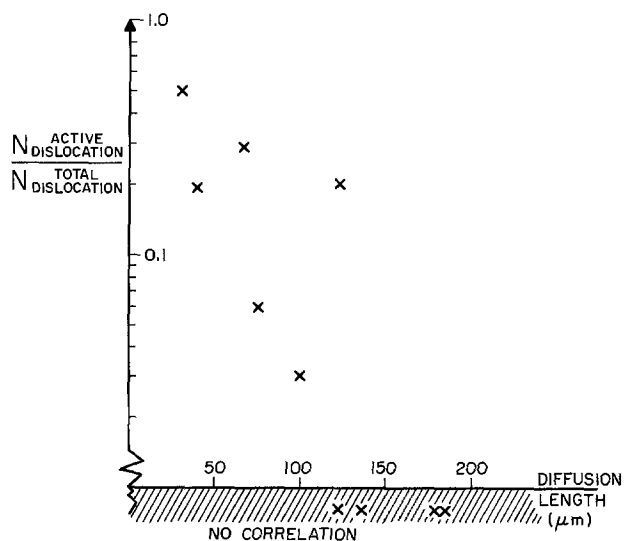


Fig. 10. Ratio of electrically active dislocations observed as white spots in the CCD imagers to total amount of dislocations revealed by etching in the imaging register as a function of diffusion length in silicon. When dislocations did not generate any white spots, the data point was placed in "no correlation" region.

related to the effect of growth kinetics on the formation of point defects on the growing interface. The segregation of point defects during the growth process is affected by the nonequilibrium point defect trapping (17-19), which takes place at the growing interface during growth velocity acceleration (20). The additional explanation of the nonuniform distribution of these defects in the crystals could be the condensation of point defects in the regions with high carbon concentration. This mechanism has been proposed by Foll *et al.* (21) to account for swirls formation. The point defect complexes with impurities or their clusters are probably introduced to the as grown crystals in two different states during the growth process and the subsequent heat-treatment involved in the oxidation affects their concentration in a given state accounting for the increased concentration of deep centers.

Summary

Deep levels in high quality float zone silicon used for fabrication of CCD imagers have been measured by deep level transient spectroscopy and derivative surface photovoltage spectroscopy. These two different techniques revealed presence of two deep levels: 0.23 and 0.56 eV above the valence band in the as grown and oxidized wafers. Their concentration was found to be about 10^{11} - 10^{12} cm^{-3} in the virgin crystal and was increased about one order of magnitude by oxidation. Large macroscopic and microscopic inhomogeneities in the deep level distribution across the wafers have been found.

It has been established that the deep level concentration controls the minority carrier lifetime, a parameter controlling quantum efficiency and dark current in CCD imagers. It was also observed that the probability of crystallographic defect decoration sharply increases with an increase of the average deep level concentration in silicon. It has been found that the non-uniform deep level distribution in the wafers is responsible for the appearance of a striation pattern in the displayed image.

Although the origin of the deep levels and their behaviors during heat-treatments are not fully understood at the present time, the authors believe that the deep levels are introduced by point defect complexes or their clusters with impurities rather than by heavy metals or other simple chemical impurities.

Manuscript submitted Aug. 29, 1980; revised manuscript received Dec. 8, 1980.

Any discussion of this paper will appear in a Discussion Section to be published in the June 1982 JOURNAL. All discussions for the June 1982 Discussion Section should be submitted by Feb. 1, 1982.

Publication costs of this article were assisted by RCA Laboratories.

REFERENCES

1. Y. Hokari and H. Shiraki, *Jpn. J. Appl. Phys.*, **16**, 585 (1977).
2. Y. Hayafuji, T. Shimada, and S. Kawado, in "Semiconductor Silicon 1977," H. R. Huff and E. Sirtl, Editors, p. 750, The Electrochemical Society Softbound Proceedings Series, Princeton, NJ (1977).
3. H. Shiraki, in "Semiconductor Silicon 1977," H. R. Huff and E. Sirtl, Editors, p. 546, The Electrochemical Society Softbound Proceedings Series, Princeton, NJ (1977).
4. H. E. Murphy, "Proceeding of SPIE," Vol. 203, p. 80 (1979).
5. L. Jastrzebski, P. A. Levine, W. A. Fisher, A. D. Cope, E. D. Savoye, and W. N. Henry, Paper 150 presented at The Electrochemical Society Meeting, St. Louis, Missouri, May 11-16, 1980. *This Journal*, **128**, 885 (1981).
6. L. Jastrzebski, P. A. Levine, A. D. Cope, W. N. Henry, and D. Battson, *IEEE Trans. Electron Devices*, **ed-27**, 1694 (1980).
7. E. D. Savoye and W. N. Henry, Unpublished.
8. For review see: C. T. Sah, in "Semiconductor Silicon 1977," H. R. Huff and E. Sirtl, Editors, p. 868,

- The Electrochemical Society Softbound Proceedings Series, Princeton, NJ (1977); G. L. Miller, D. V. Lang, and L. C. Kimerling, *Ann. Rev. Mater. Sci.*, 377 (1977).
9. J. Lagowski, W. Walukiewicz, M. M. Slusarczuk, and H. C. Gatos, *J. Appl. Phys.*, **50**, 5059 (1979).
 10. L. Jastrzebski and J. Lagowski, *RCA Rev.*, **41**, 181 (1980).
 11. Annual Book of ASTM Standards, ASTM, Philadelphia, p. 752 (1974).
 12. For tutorial introduction see: H. J. Leamy, L. C. Kimerling, and S. D. Ferris, "Scanning Electron Microscopy," Vol. 1, p. 717, SEM Inc., AMF O'Hare (1978).
 13. L. Jastrzebski and P. Zanzucchi, Paper 193 presented at The Electrochemical Society Meeting, Minneapolis, Minnesota, May 10-15, 1981. "Semiconductor Silicon 1981," H. R. Huff, R. J. Kriegler, and Y. Takeishi, Editors, p. 138, The Electrochemical Society Softbound Proceedings Series, Pennington, NJ (1981).
 14. K. L. Shaklee and R. E. Nahory, *Phys. Rev. Lett.*, **28**, 942 (1970).
 15. See, for example, P. R. Bratt in "Semiconductors and Semimetals," Vol. 12, Chap. 12, R. K. Willardson and A. C. Beer, Editors, Academic Press, New York (1977), and references quoted therein.
 16. P. M. Petroff, D. V. Lang, J. L. Strudel, and R. A. Logan, "Scanning Electron Microscopy," Vol. 1, p. 325, SEM Inc., AMF O'Hare (1978).
 17. W. W. Webb, *J. Appl. Phys.*, **33**, 1961 (1962).
 18. J. A. VanVechten, *Appl. Phys. Lett.*, **26**, 593 (1975).
 19. L. Jastrzebski, A. E. Bell, and C. P. Wu, *ibid.*, **35**, 608 (1979).
 20. L. Jastrzebski, J. Lagowski, and H. C. Gatos, Paper 410 RNP presented at The Electrochemical Society Meeting, Boston, Massachusetts, May 6-11, 1979. *This Journal*, **128**, 697 (1981).
 21. M. Foll, V. Gosele, and B. O. Kolbensen, *J. Cryst. Growth*, **40**, 90 (1977); Paper 447 presented at The Electrochemical Society Meeting, Hollywood, Florida, Oct. 5-10, 1980.

The Instabilities in the Al-Si Temperature Gradient Zone Melting

Mike F. Chang*

General Electric Company, Syracuse, New York 13221

ABSTRACT

By using the TGZM technique, a job that traditionally needs hundreds of hours of diffusion can be done in minutes. However, various instabilities may be encountered in the application of this new technique. Some of these instabilities and the methods of resolving them are discussed.

The basic physics of temperature gradient zone melting (TGZM) have been investigated by Pfann (1) and others (2-5) for its possible interest to semiconductor applications. For making p-n junctions, solid-state diffusion has been used by the semiconductor industry as a standard technique. Later, the TGZM technique became attractive after Anthony and Cline announced the results of their zone melting studies of KCl-H₂O systems (6). Recently, the Semiconductor Products Department of the General Electric Company started a program to explore TGZM techniques for device fabrication, mainly silicon products (7). Some of the results and analyses are presented in this paper.

The simplified mechanism of TGZM is shown in Fig. 1. In Fig. 1(a), a liquid droplet of Al-Si alloy is embedded in a solid silicon bulk, which has been subjected to a temperature gradient with the lower temperature above the Al-Si eutectic point. According to the phase diagram of the Al-Si system, the upper portion of the droplet, being hotter, will dissolve more silicon than the lower portion, as shown by the solid line in Fig. 1(b). A silicon concentration gradient will be created in the liquid droplet and the silicon atoms will diffuse toward the lower portion at a high liquid diffusion rate. This process, in turn, will create undersaturation and oversaturation conditions in the upper and lower portions of the droplet, respectively, as indicated by the dashed line in Fig. 1(b). Silicon atoms must be supplied by the bulk at the AB interface and deposited back to the bulk at the CD interface. Accordingly, the droplet moves up against the temperature gradient through the bulk. As the droplet moves, it leaves behind a trail of heavily doped p-type silicon whose doping concentration is determined by the solid solubility of aluminum in silicon at the operating temperature.

As compared with the well-established solid-state diffusion process, the TGZM technique has only recently received much attention (7, 9-12). The TGZM technique offers many unique features not found in any other process, yet it still needs some improvement.

Experiments

Theoretically, any system that provides a controllable temperature gradient can be used for TGZM operation. The quartz lamp system shown in Fig. 2 was used in this study (13).

In this paper, we discuss only the Al-Si system, namely, aluminum pattern migrating through silicon. N-type silicon wafers and billets of (111) and (100) orientations were employed. Their resistivity ranges from 10 to 180 Ω cm. The aluminum patterns for migration included straight lines, curves, points, and lumped areas. Since the migration of various patterns are subjected to a common effect of instabilities, a grid-type

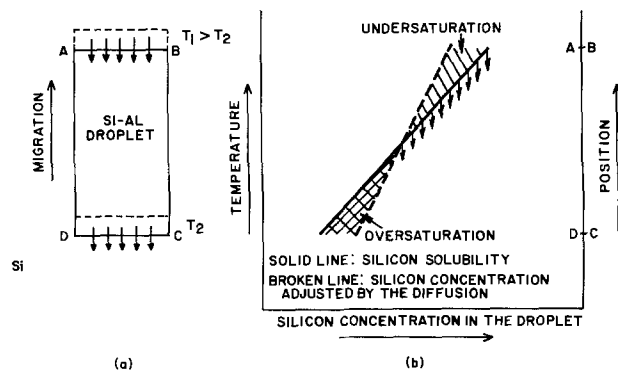


Fig. 1. Simplified mechanisms of an Al-Si droplet migrating in a solid silicon bulk.

* Electrochemical Society Active Member.

Key words: semiconductor, process, defects, thermomigration.

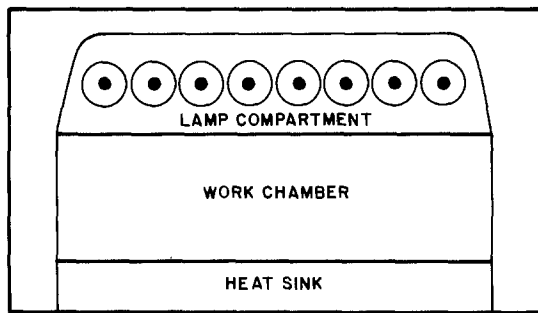


Fig. 2. A schematic diagram of a quartz lamp system for TGZM operations.

pattern is chosen to demonstrate and explain the instabilities of migration without losing generality. The detailed process and variations will be given in a paper to follow.

An aluminum pattern 1-10 μm thick was created on one side of the silicon wafer by evaporation and photolithography. The wafer was placed in the TGZM work chamber with the aluminum pattern facing the heat sink. Radiant energy from quartz lamps heated the wafer from 1000°C up to the melting point of silicon. The molten aluminum pattern reacted with silicon and formed an Al-Si alloy. This liquid alloy pattern migrated toward the hotter side of the silicon wafer and eventually passed through. Figure 3 shows a wafer before and after migration. The migration time depends on the thickness of the wafer and the operating conditions. For example, it took only 8 min to migrate through a 16 mil thick wafer at 1200°C with a temperature gradient around 50°C/cm. Heavily doped p-type trails with abrupt p-n junction borders were left inside the wafer. The doping concentration in the trail is about 1×10^{19} atoms/cm³ and is constantly produced with a temperature range of 950°-1300°C as predicted by Trumbore's curves (8). The concentration profile across a typical TGZM doped trail is shown in Fig. 4.

Results and Discussion

The migration rate of a water droplet in salt has been studied by Anthony and Cline (6). The physics was applied equally well to the Al-Si system (10). There are two opposite forces involved. The temperature gradient is the driving force for the migration of droplets. The surface tension is the retarding force. This retarding force is essential for the stability of migration. Since the surface tension increases as the size of the droplet decreases, the speed of migration

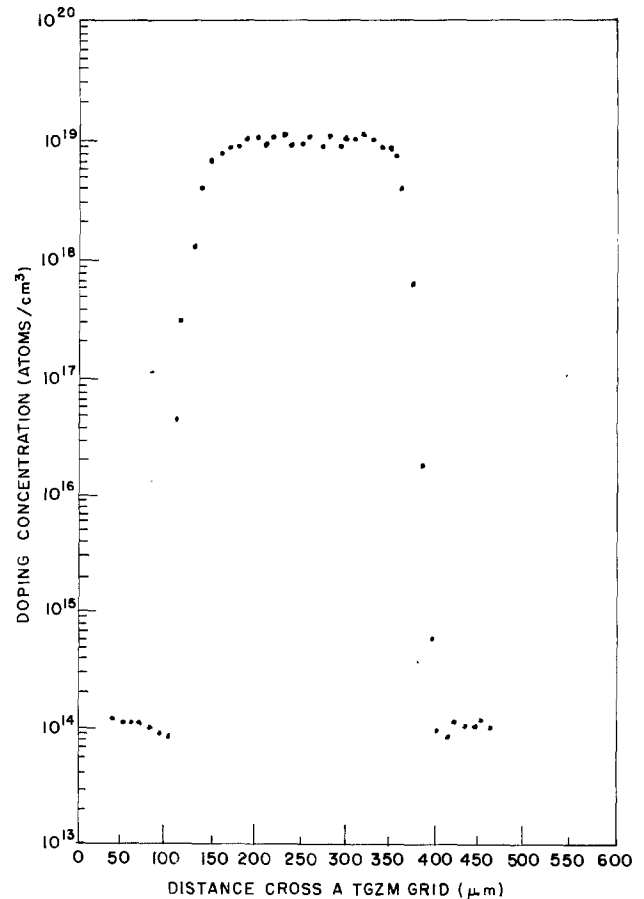


Fig. 4. Doping concentration measured across a TGZM trail

will be reduced as the size of the droplet is reduced. By contrast, as the droplet size is increased, the possibility of disintegration or other instabilities of the droplet increases. Therefore, a speed limit is required in each system to ensure the safety of droplet migration. Fortunately, only a few of the instabilities present difficulties in the area of semiconductor device fabrication. They are discussed below.

Ball up.—In some cases, solid silicon balls (Fig. 5) may be left on the entrance surface of the wafer after migration, creating problems for subsequent photoresist processing. These balls may scratch the mask and damage the photoresist film. The wafer may also be cracked in the mask aligner by the local pressure

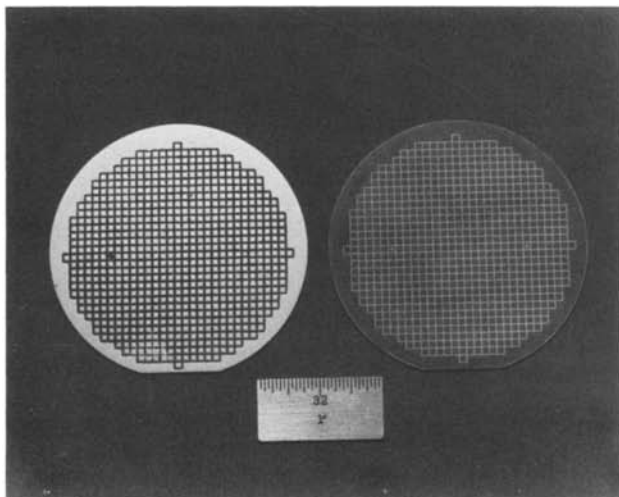


Fig. 3. Aluminum grids on silicon wafers before (right) and after (left) the migration.

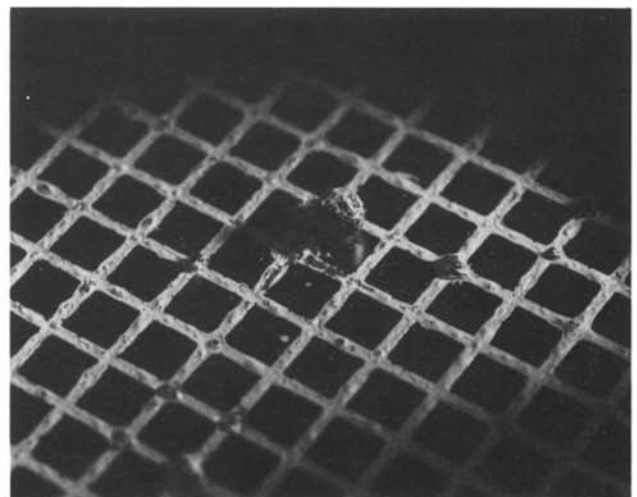


Fig. 5. A solid ball left on the entrance side of a silicon wafer after the migration.

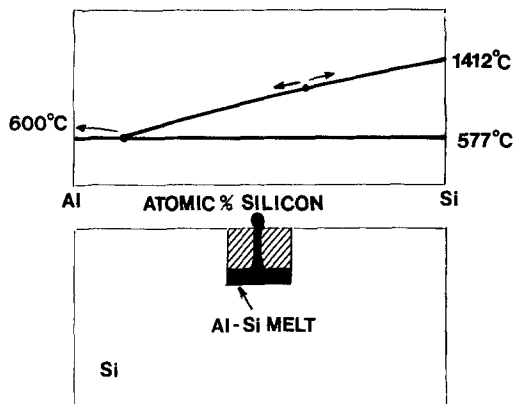
developed from the point contact between the glass mask and balls. Two possible mechanisms of ball formation are considered here. First, the balls may be generated by an excessive operating temperature, *i.e.*, before the temperature gradient has a chance to drive the aluminum-silicon liquid into the silicon bulk, the liquid zone has already been balled up by surface tension. This liquid aluminum ball, in turn, absorbs silicon atoms from the wafer to form an equilibrium Al-Si solution. In this situation, with no parental crystal site or ledge available, the liquid Al-Si melt transforms into a solid silicon ball after the aluminum migrates away. Second, the ball may be induced by a fluctuation in temperature (14). The slope of the Al-Si phase diagram is quite flat at 1200°C. Therefore, the volume of liquid Al-Si droplet is very sensitive to the temperature variation. When the droplet is exposed to a temperature fluctuation, the vigorous change of the volume ejects the excess liquid to the surface to form a ball as depicted by Fig. 6. Thus, a proper and stable temperature is an important factor for a ball-free TGZM operation.

Rough surface.—In most cases, the aluminum pattern is deposited on the surface of the silicon wafer. In the initial stage of migration, the solidified silicon atoms have no crystal ledge to follow, instead they randomly precipitate out of the melt to form a polycrystalline silicon surface that preserves the contour of the former Al-Si liquid surface. Therefore, a flat surface should not be expected. As the droplet moves forward, the single crystal matrix, which originates from the peripheral edges of the droplet, grows wider as illustrated in Fig. 7. Finally, this single crystalline side

band, around the polycrystalline cone, pinches off the polycrystal growth. After this point, all the newly solidified silicon atoms find their depositing ledges and become a part of the parent crystal. For example, KOH etches polycrystalline silicon faster than it etches single crystalline silicon. The etched surface of a (111) silicon wafer leaves a V-shape groove on the TGZM site as shown in Fig. 8. The roughness and the amount of polycrystal material produced are closely related to the temperature and the speed of migration.

Droplet break-up and freeze-in.—An oversized droplet may break into two or more subdroplets as shown in Fig. 9. Generally, this phenomenon of droplet disintegration is caused by the difference in thermal conductivity between the Al-Si droplet and its surrounding solid silicon. This difference generates a higher temperature gradient around the peripheral area of the Al-Si droplet. Thus, the outer portion of the droplet will migrate faster than the center portion. In some cases, the droplet may be torn apart by this nonsynchronized migration if the surface tension of the droplet is not strong enough to hold the droplet together. Figure 10 shows a split grid line. The two split branches migrated as two independent grid lines in parallel. In the KCl-H₂O system, Anthony and Cline reported a higher temperature gradient at the center of each droplet due to the relatively low thermal con-

BALL FORMATION BY TEMP. FLUCTUATION



Liquid squeezed out by excessive pressure

Fig. 6. A schematic diagram explaining the mechanism of ball forming.

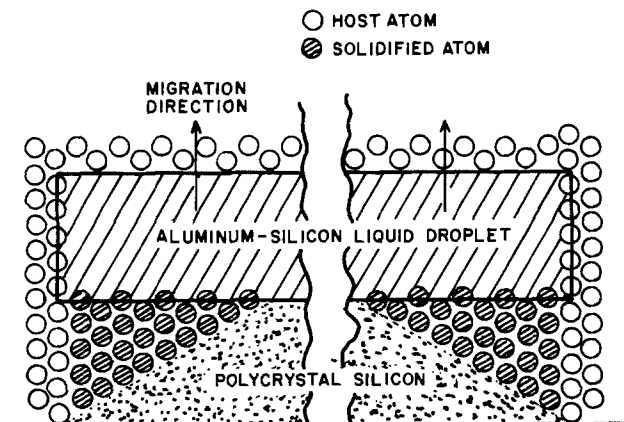


Fig. 7. A schematic diagram explaining the mechanism of polycrystal formation during the early stage of migration.

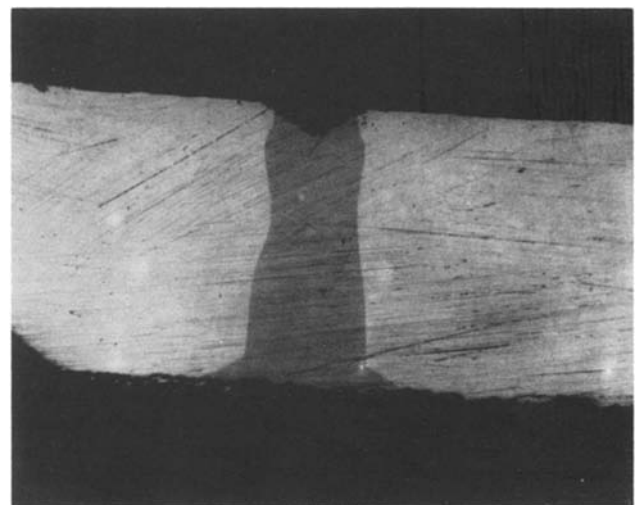


Fig. 8. A V-shape notch on the silicon surface after the polycrystal was etched away by hot KOH solution.

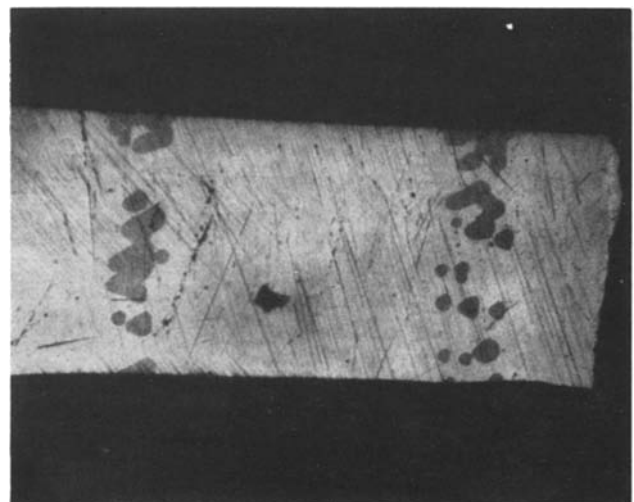
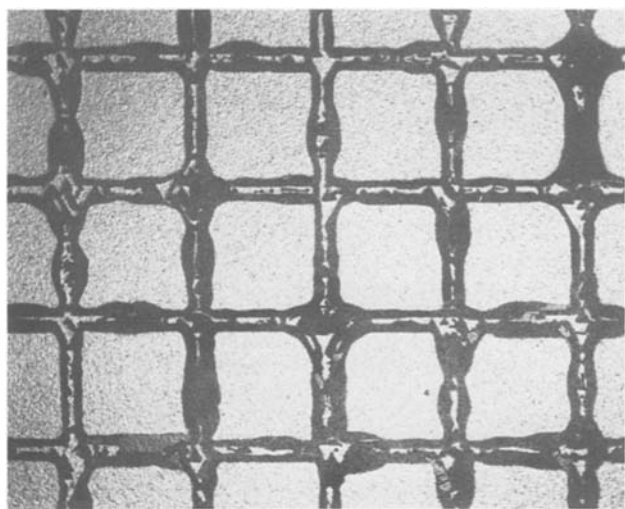
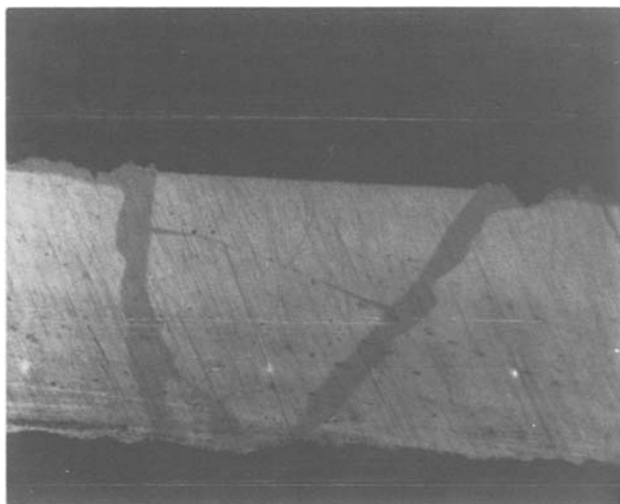


Fig. 9. Lapped and stained sample showing a broken droplet inside a silicon wafer.



a. Pattern of split grid lines on the exit side of a silicon wafer.



b. Lapped and stained sample showing the TGZM trail of a split line.

Fig. 10. Droplet split.

ductivity of the brine droplet (6). Sometimes sub-droplets caused by the droplet break-up may be too small to gain enough momentum to migrate any further and will be left inside the silicon wafer as freeze-in droplets. This droplet freeze-in phenomenon may also happen under two other conditions. In one case, when the TGZM pattern has different sizes of lines, the wider lines will migrate faster than the smaller ones. For a given operating time, the wider lines can migrate through the wafer, but the smaller ones may be only part way through the wafer. In the second case, when the migrating droplet hits a dislocation site, this droplet may be trapped in this energy well and frozen in. The volume of silicon increases when it is solidified from the liquid phase. These freeze-in droplets will generate huge stresses that may crack the wafer. Figure 11 shows a star-shaped crack resulting from a trapped droplet under the area of a registration key. This freeze-in effect makes it difficult for a droplet to migrate into a wafer to a predetermined depth and then to migrate backward out of the wafer. For this application, it is necessary to keep the droplet in the liquid phase for the entire operation period, thus a double heater set is required with one heater on each side of the wafer.

End expansion.—There is a potentially troublesome but interesting phenomenon in TGZM migration. The

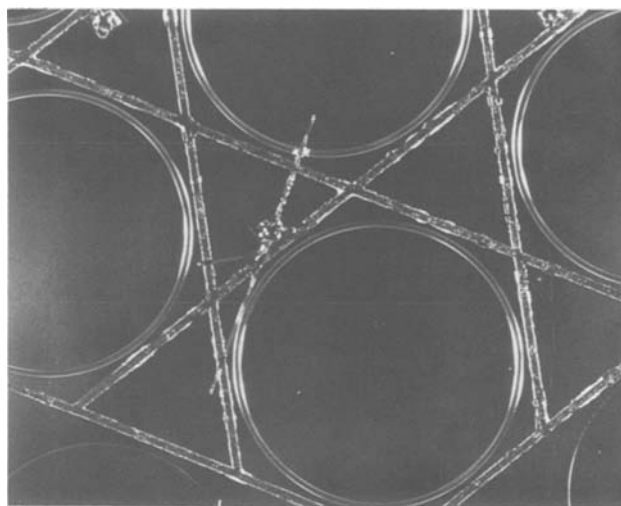


Fig. 11. A star shape crack on the site of an alignment key due to a frozen-in droplet.

stained cross-section picture shows that each migration trail has a cone shape expansion at the exit end as shown in Fig. 12. This phenomenon should be considered for the application of TGZM technique to a two-sided device. The mechanism of this end expansion can be explained by basic TGZM principles. When the droplet reaches the exit surface of the wafer, there are no more solid silicon atoms available at the front surface of the droplet, but the solidifying action at the back interface is still taking place. At this point, the droplet starts to dissolve the solid laterally from the front edges. The result is that the droplet keeps migrating forward by changing its shape, namely, becoming wider and thinner as depicted in Fig. 13. Finally, the droplet migrates out of

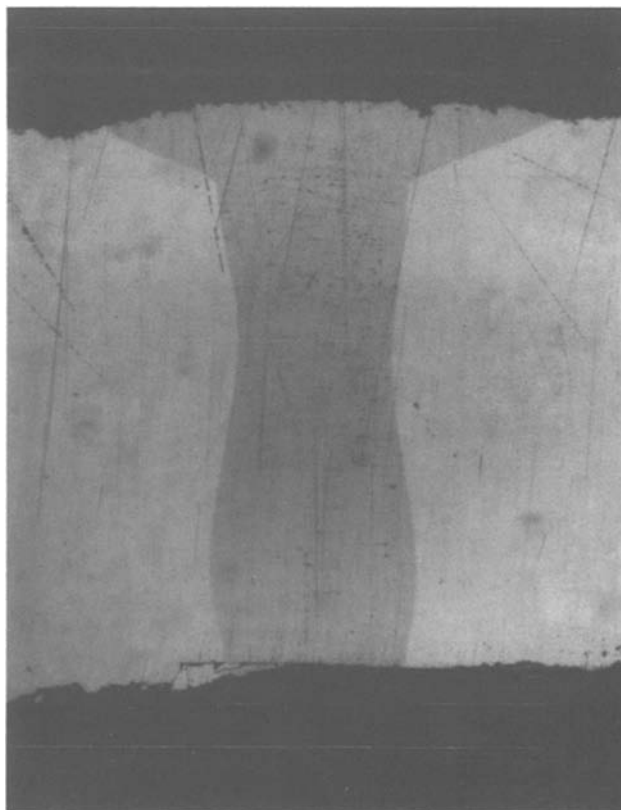


Fig. 12. Lapped and stained sample showing the effect of end expansion.

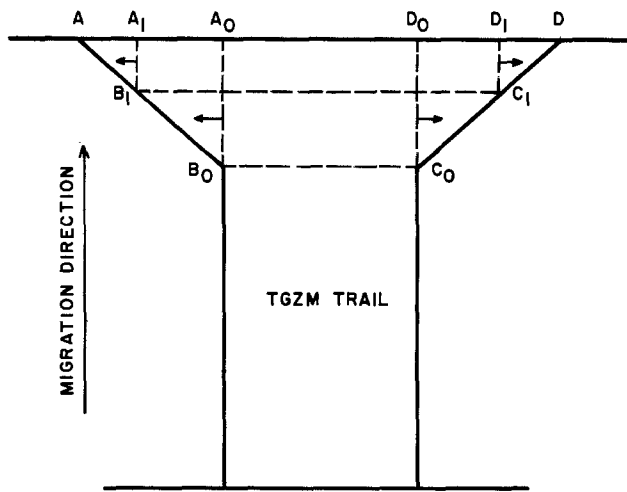


Fig. 13. A schematic diagram explaining the mechanism of end expansion.

the surface and leaves a cone-shaped trail behind. The height of the cone will be the original thickness of the droplet at the migration condition. For example, $10\ \mu\text{m}$ thick aluminum produces droplet thickness of approximately $28\ \mu\text{m}$ at 1200°C and the measured height of the cone is about $26\ \mu\text{m}$. One way to avoid this cone shape end expansion inside the silicon wafer is to supply more silicon to the droplet when it reaches the surface. The phenomenon of lateral surface spreading can also be explained by the above principles. The emerging liquid Al-Si alloy at the surface continues to stretch itself thinner and wider. In other words, the liquid spreads out from the center and eventually may cover the entire surface of a wafer if it is left in the high operating temperature environment long enough. Thus, a beneficial procedure would be to cool the wafers immediately after the liquid droplets reach the surface. Before the droplet has a chance to wet the silicon surface, the aluminum will be frozen out of the liquid as shown by the Al-Si phase diagram.

By avoiding or minimizing these instabilities, we have made several semiconductor devices with the TGZM technique. These devices have a current range from 1 to 600A and a blocking voltage over 2500V. Circular patterns have also been migrated through polysilicon wafers as shown in Fig. 14.

Conclusion

The TGZM technology is a very powerful tool for the manufacture of semiconductors. It has opened a new dimension for device design and process engineers. We have observed various potential instabilities in TGZM operation. A qualitative interpretation of some of these instabilities has been presented for the first time. Through this understanding, TGZM doped structures, which are close to ideal abrupt p-n junctions, can be produced. The fabrication of some actual devices, using this technique, will be discussed in a later paper.

Acknowledgments

The author wishes to express his gratitude to Dave Hartman, Mark Barron, and Richard Kokosa for their

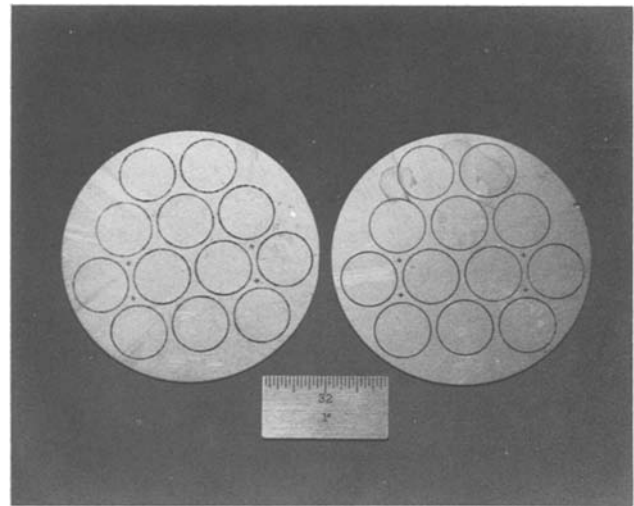


Fig. 14. A circular pattern migrated through polycrystalline silicon wafers. The right-hand side wafer is top side up and the left hand-side wafer is bottom side up.

constant interest and encouragement. He is indebted to H. Cline and T. Anthony for many helpful discussions and encouragement. The manpower support of Dave Smith, Don Foran, Lal Jones, and Ed Lederer is gratefully acknowledged.

Manuscript submitted Aug. 1, 1979; revised manuscript received ca. April 6, 1981. This was Paper 296 presented at the Seattle, Washington, Meeting of the Society, May 21-26, 1978.

Any discussion of this paper will appear in a Discussion Section to be published in the June 1982 JOURNAL. All discussions for the June 1982 Discussion Section should be submitted by Feb. 1, 1982.

Publication costs of this article were assisted by General Electric Company.

REFERENCES

1. W. G. Pfann, "Zone Melting," 2nd ed., John Wiley Sons, Inc., New York (1963).
2. J. H. Wernick, *J. Chem. Phys.*, **25**, 47 (1956).
3. J. H. Wernick, *Trans. AIME*, **209**, 1169 (1957).
4. M. Weinstein and A. I. Mlavsky, *J. Appl. Phys.*, **35**, 1892 (1964).
5. R. W. Hamaker and W. B. White, *ibid.*, **39**, 1758 (1968).
6. T. R. Anthony and H. E. Cline, *ibid.*, **42**, 3880 (1971).
7. T. R. Anthony, J. K. Boah, M. F. Chang, and H. E. Cline, *IEEE Trans. Electron Devices*, ed-23, 818 (1976).
8. F. A. Trumbore, *Bell Syst. Tech. J.*, **39**, 205 (1960).
9. T. R. Anthony and H. E. Cline, *J. Appl. Phys.*, **47**, 2316 (1976).
10. H. E. Cline and T. R. Anthony, *ibid.*, **47**, 2325 (1976).
11. H. E. Cline and T. R. Anthony, *ibid.*, **47**, 2332 (1976).
12. T. R. Anthony and H. E. Cline, *ibid.*, **47**, 2550 (1976).
13. J. K. Boah, U.S. Pat. 4,001,047 (1975).
14. T. R. Anthony and H. E. Cline, Private communication (1977).

Auger Study of the Interface in Evaporated Tin Oxide-GaAs MIS Solar Cells

D. J. Brinker and E. Y. Wang

Department of Electrical and Computer Engineering, Arizona State University, Tempe, Arizona 85281

and W. H. Wadlin and R. N. Legge

Motorola Incorporated, Semiconductor Group, Phoenix, Arizona 85008

ABSTRACT

Auger electron spectroscopy was used to study the interface of vacuum-deposited tin oxide on GaAs substrates. The ratio of oxygen to tin in the tin oxide film, thermally evaporated from SnO₂ powder, was about 1.53. The films are likely a mixture of SnO and SnO₂. A transition region approximately 55Å in width exists between the tin oxide and GaAs substrate, possibly composed of oxides of GaAs and SnO, although the formation of a binary compound (GaSn) is possible. Heating in air further oxidized the tin oxide to SnO₂. Heating in air and vacuum resulted in a Ga-rich surface on the GaAs substrate. Metal-insulator-semiconductor solar cells using vacuum-evaporated tin oxide interfacial layers showed substantial improvement over cells made without the interfacial layer.

Metal-insulator-semiconductor (MIS) and heterojunction solar cells have received considerable interest in recent years. Cells have been developed with efficiencies approaching those of conventional homojunction cells and have the added advantage of ready adaptability to mass production (1-3). However, both types of cells have experienced problems with degradation of their electrical characteristics, leading to life expectancies less than those necessary for practical utilization (4, 5). The degradation of MIS and heterojunction solar cells is due partly to changes at the surface of the semiconductor and in the insulator or interfacial layer. The electrical characteristics of these devices are intimately related to the oxide-semiconductor interface. A study of the interfacial region could yield useful information toward improving solar cell performance as well as understanding degradation mechanisms.

We report the results of a study of tin oxide-GaAs interfaces using Auger electron spectroscopy (AES). Tin oxide was vacuum evaporated on GaAs substrates with electron beam and resistive heating techniques. Depth profiling by AES was employed to determine the composition of the tin oxide layer as well as the tin oxide-GaAs interface. The results show the ratio of oxygen to tin to be approximately 1.53 in the deposited films. Heating in air oxidized the film to SnO₂. Heating in vacuum had little effect on the tin oxide layer. In either case the transition region width was about 55Å. We also present the results of MIS solar cells made by the vacuum evaporation of tin oxide interfacial layers. Open-circuit voltages of 0.765V and efficiencies in excess of 7.0% (without antireflection coatings) were achieved and possible modes of improvement have been identified (6).

Sample Preparation

The substrates used in the study were n-type Te-doped single crystal <100> GaAs with carrier concentration of $5 \times 10^{15} \text{ cm}^{-3}$, epitaxially grown by chemical vapor deposition on GaAs substrates with $N_d > 10^{17} \text{ cm}^{-3}$. After ultrasonic cleaning in trichloroethylene and methanol, the wafers were etched in a 50:1:1 solution of H₂O:H₂O₂ (30%):H₂SO₄ (96%). Fabrication was performed in an LN₂-trapped, oil-pumped vacuum system evacuated to a pressure of less than 3×10^{-6}

Torr. The GaAs wafers were at ambient temperature during deposition. SnO₂ (99.9%) powder was evaporated using an electron beam gun and using a resistance-heated alumina-coated Mo boat at an average rate of 1 Å/sec. Vacuum pressure rose to 3×10^{-5} Torr during deposition and thickness was monitored *in situ* with a quartz crystal thickness monitor. Samples prepared for Auger electron spectroscopy (AES) were fabricated by both electron beam and boat evaporation of the tin oxide. Film thickness was 200Å and sample size was 1.0 cm².

MIS and heterojunction solar cells were fabricated in a similar manner. A back-contact was formed by successive evaporation of Sn and Ag layers and annealing in forming gas. A cell area of 0.07 cm² was delineated by evaporation through a stainless steel mask. The MIS cells were made by evaporation of a thin layer (30-50Å) of tin oxide followed by boat evaporation of 65Å of Au. In addition to the MIS cells, Au-GaAs cells were made with no tin oxide layer. A very thin native oxide present after etching precludes the formation of a true Schottky barrier cell, but does provide for a baseline cell for comparison purposes. Heterojunctions of SnO₂-GaAs were made by deposition of about 900Å of tin oxide and annealing in air at 300°C. Front contact to all types of cells was made with an Ag pad giving a cell active area of 0.06 cm².

Results

Current-voltage characteristics.—Illuminated current-voltage characteristics were taken under simulated AM1 sunlight using an ELH lamp calibrated with a NASA-Lewis silicon standard cell. Figure 1 is the illuminated I-V characteristics of a typical cell of each type—baseline, heterojunction, electron beam MIS, and boat MIS. Short-circuit current density was calculated using the cell active area. The open-circuit voltage enhancement and the consequential increase in efficiency due to the interfacial tin oxide layer in the MIS cells is evident.

The difference in short-circuit current between the two types of MIS cells is due to slight, unavoidable variations in Au-layer thickness between fabrication runs. Variations in GaAs substrate properties between wafers would also contribute to the difference in short-circuit current. The open-circuit voltage of electron beam MIS cells was lower than those of boat MIS cells due to damage caused by the electron beam source to

Key words: solar energy, heterojunctions, interfacial layer.

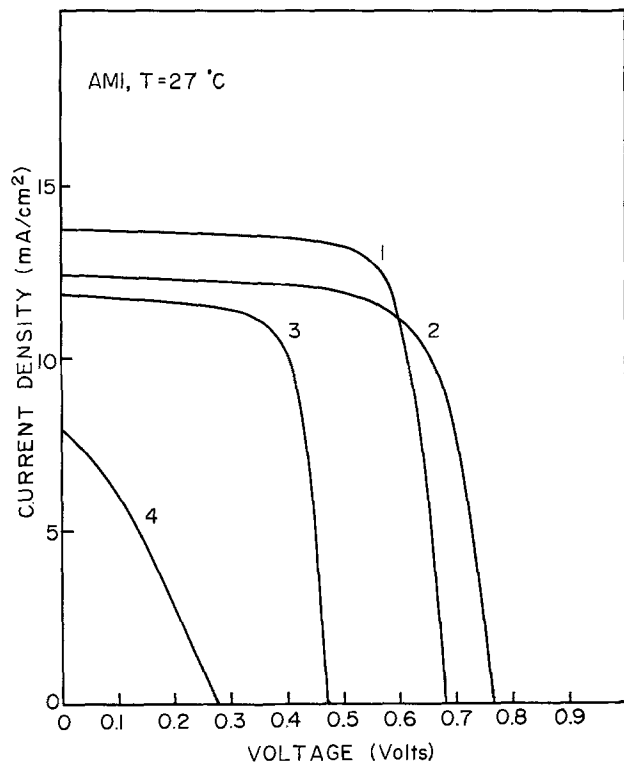


Fig. 1. The illuminated current-voltage curves of: curve 1, electron beam MIS; curve 2, boat MIS; curve 3, baseline; and curve 4, heterojunction solar cells.

the interfacial layer (6). Heterojunction solar cells had the lowest efficiencies and offer the least promise for useful devices fabricated by evaporation techniques.

Auger electron spectroscopy.—Films of electron beam- and boat-evaporated tin oxide on GaAs were depth profiled using Auger electron spectroscopy. A freshly etched GaAs wafer was also analyzed. The Auger depth profiles were obtained using a Physical Electronics thin film analyzer. In this study, the electron beam current was $15 \mu\text{A}$ at 5 KeV with a spot size of about $100 \mu\text{m}$. The ion beam of 2 KeV Ar^+ was rastered over an area of several square millimeters to avoid loss of depth resolution due to crater edge effects and to maintain a slow sputtering rate of about $12 \text{ \AA}/\text{min}$. The sputtering rate and therefore the depth were calibrated using the known tin oxide layer thickness (200 \AA) and the sputtering time necessary to completely penetrate this layer. Tin oxide layer thickness was monitored during deposition with a quartz crystal thickness monitor and checked with ellipsometry.

The AES depth profile of electron beam-evaporated tin oxide on GaAs is shown in Fig. 2. The tin and oxygen atomic concentrations were calibrated with an SnO_2 standard prepared by chemical vapor deposition from $\text{SnCl}_4 \cdot 5\text{H}_2\text{O}$. The atomic concentrations of arsenic and gallium were calibrated with the known stoichiometry of the GaAs substrate. The average error in atomic concentration is $\pm 5\%$. The ratio of oxygen to tin in the tin oxide bulk is 1.53.

Figures 3 and 4 are the AES profiles of electron beam tin oxide samples annealed in air and vacuum, respectively. These samples were from the same specimen as the unannealed sample of Fig. 2. The air-annealed sample was heated at 300°C for 15 min in a small muffle furnace. The effect of the annealing can be seen in the increase in oxygen level throughout the profile. The vacuum-annealed sample was mounted on a stainless steel block heated by a cartridge heater. The temperature was ramped to 300°C , was held there for 15 min, and allowed to cool. Pressure during annealing was 2.2×10^{-6} Torr.

A freshly etched GaAs wafer was also examined to determine the composition and thickness of the resid-

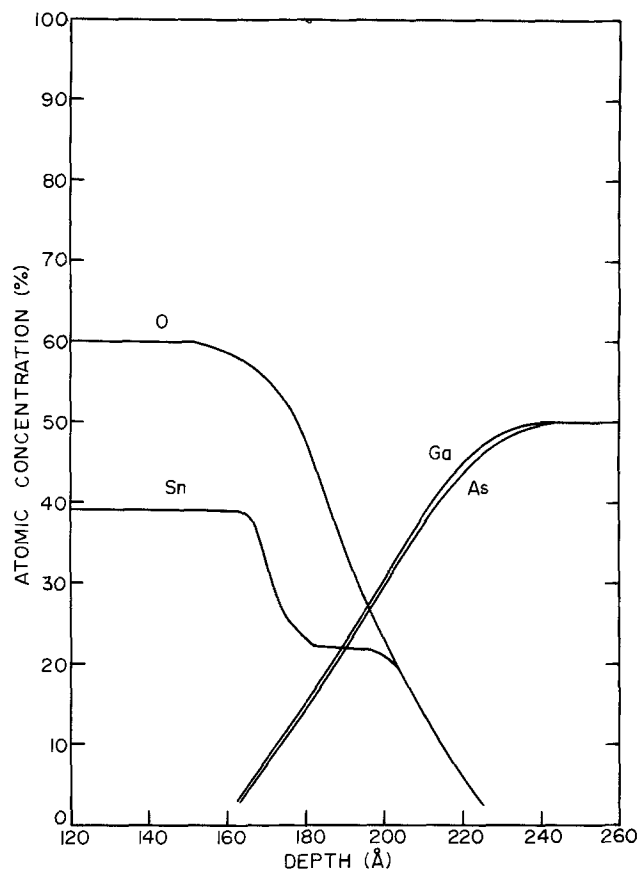


Fig. 2. Auger depth profile of electron beam-evaporated tin oxide on GaAs.

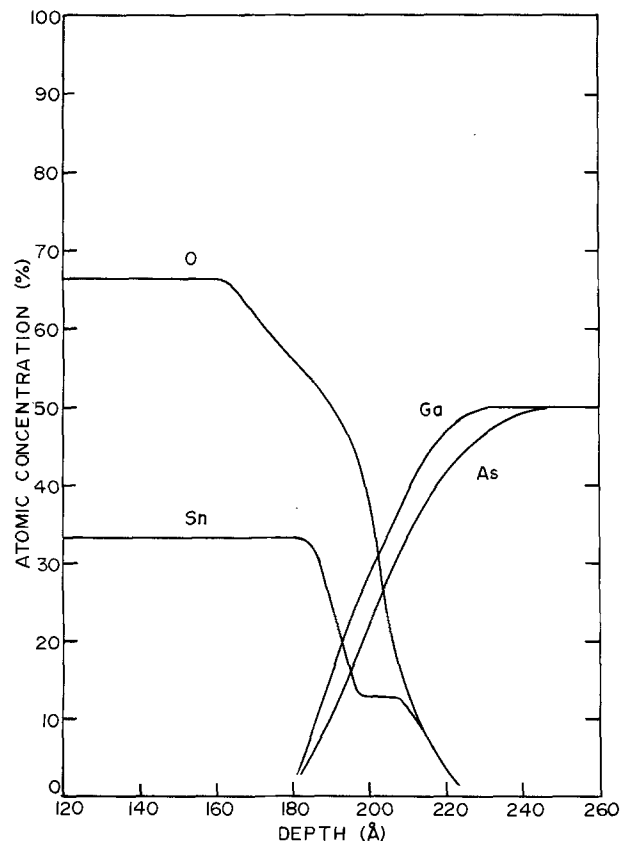


Fig. 3. Auger depth profile of tin oxide-GaAs annealed in air

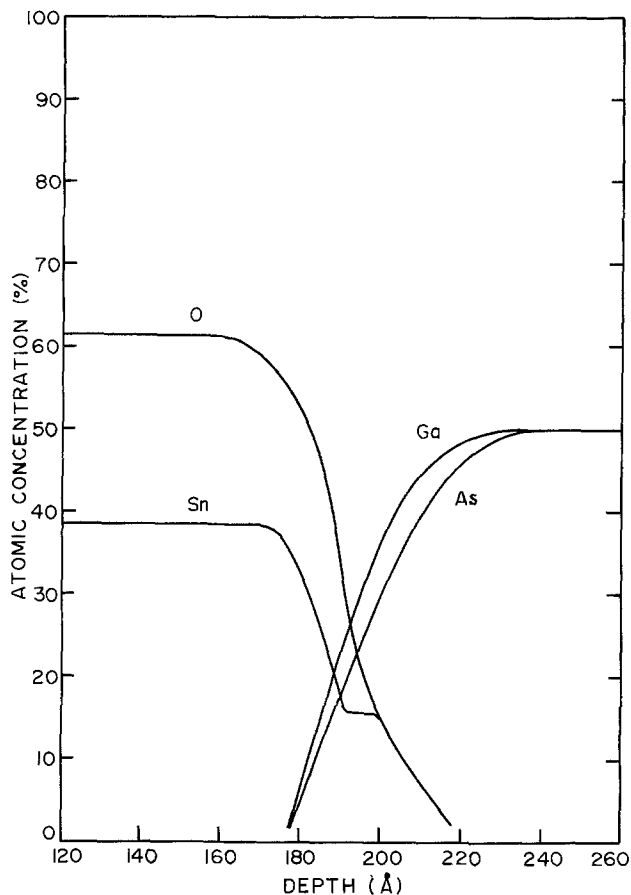
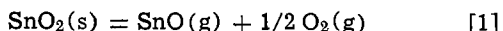


Fig. 4. Auger depth profile of tin oxide-GaAs annealed in vacuum.

ual native oxide layer. Results show a native oxide 17-19Å thick.

Discussion

The stoichiometry of the tin oxide deposited by thermal evaporation of SnO_2 is significantly different than that of the starting material. As seen in Fig. 2, the oxygen to tin ratio is 1.53 in the bulk of the tin oxide layer. Similar analysis of boat-evaporated tin oxide yields a ratio of 1.60. Two oxides of tin exist, stannous oxide (SnO) and stannic oxide (SnO_2); clearly, the deposited films are not composed solely of either of these two oxides. Stannic oxide sublimes upon heating in vacuum and evaporates via the reaction



above 1250 K (7, 8). The oxygen liberated during evaporation is consistent with the tenfold increase in vacuum system pressure. It has been demonstrated that SnO will oxidize to SnO_2 at temperatures as low as 513 K (9). It is likely that a portion of the gaseous SnO produced by the evaporation will reoxidize forming SnO_2 , either before or during condensation on the substrate. The resulting film is a mixture of SnO_2 and SnO .

The transition region from the tin oxide to the GaAs substrate is marked by an increase in the concentration of gallium and arsenic. The width of the transition region is estimated to be approximately 55Å for both the electron beam- and boat-evaporated samples. As seen from Fig. 3 and 4, annealing in either air or under vacuum does not appreciably change the interfacial region width.

As previously mentioned, the etched GaAs wafer was covered with a native oxide about 17-19Å thick. If we assume that a percentage of the oxygen at the interface exists as GaAs oxide, then the ratio of oxygen to tin in the sample of Fig. 2 rapidly decreases from 1.53 to 1.0 as depth increases toward the GaAs sub-

strate. This indicates that the tin oxide layer may change from a mixture of SnO and SnO_2 , to predominantly SnO near the GaAs substrate. A reaction between SnO_2 and GaAs is thermodynamically possible with the reduction of SnO_2 to SnO and further oxidation of the substrate.

Heating in air at 300°C increased the oxygen/tin ratio in the sample of Fig. 3. Although the ratio is equal to 2.0 throughout the tin oxide, it again falls as the depth increases toward the interface. Again assuming that a portion of the oxygen is in the form of GaAs oxide, the oxygen/tin ratio falls to 1.0 as in the unannealed case. Electrical measurements show the annealed SnO_2 to be conductive and of high optical transparency, necessary conditions for efficient heterojunction cells, but SnO_2 -GaAs heterojunction cells fabricated have high series resistance and low fill factor. A change in chemical composition of the interfacial layer or the electrical properties of the interface due to annealing could explain the poor performance of the heterojunction cells.

Another interesting feature of the air-annealed sample is the presence of a Ga-rich surface. This excess of gallium could be due to the outgassing of arsenic from stoichiometric GaAs. In the unannealed electron beam- and boat-evaporated samples as well as the freshly etched wafer, the ratio of As to Ga was unity from the surface through the oxide to the bulk. Because of the excess Ga at the surface of the substrate crystal, the formation of a binary compound of Ga and Sn is possible (10). The eutectic lies at 5 atomic percent Sn at 20°C. The formation of a Ga-Sn eutectic could explain the "shoulder" or flat part of the Sn concentration curve seen in all samples, annealed and unannealed, although such a layer would be quite thin. Formation of such a metallic compound could account for the poor performance of the heterojunction cells; the electrical characteristics would be dominated by a GaSn-GaAs interface rather than an SnO_2 -GaAs interface.

The sample of Fig. 4 was heated to 300°C in a vacuum of 2.2×10^{-6} Torr. The oxygen/tin ratio remains essentially unchanged throughout. Again a Ga-rich surface is seen, possibly allowing the formation of a GaSn compound as in the air-annealed case. The width of the transition region did not change.

In conclusion, the results show that the films of tin oxide deposited by vacuum evaporation of SnO_2 are deficient in oxygen. The films appear to be a mixture of SnO_2 and SnO . Auger electron spectroscopy depth profiling shows that the transition region between the tin oxide and GaAs substrate is approximately 55Å in width. The transition region may be composed of oxides of GaAs and SnO , although the formation of a thin region of a binary compound (GaSn) is possible. Annealing of the films in air further oxidized the tin oxide to SnO_2 , but did not significantly alter the transition region. Annealing in air and vacuum resulted in a Ga-rich surface. The constituents of the 30-50Å interfacial layer of the MIS solar cells was seen to be a mixture of SnO and SnO_2 . The high series resistance and low fill factor of the heterojunction cells can be attributed to changes in the chemical composition or electrical properties of the interface due to annealing.

Manuscript submitted Oct. 22, 1980; revised manuscript received Feb. 2, 1981.

Any discussion of this paper will appear in a Discussion Section to be published in the June 1982 JOURNAL. All discussions for the June 1982 Discussion Section should be submitted by Feb. 1, 1982.

Publication costs of this article were assisted by Arizona State University.

REFERENCES

1. R. J. Stirn, Y. C. M. Yeh, E. Y. Wang, F. P. Ernest, and C. J. Wu, *Tech. Dig. Int. Electron Devices Meet.*, 48 (1977).

2. M. A. Green, R. B. Godfrey, M. R. Willison, and A. W. Blakers, in "Proc. 14th IEEE Photovoltaic Specialists Conf., p. 684 (1980).
3. T. Feng, A. K. Ghosh, and C. Fishman, *Appl. Phys. Lett.*, **35**, 266 (1979).
4. T. R. Nash and R. L. Anderson, *IEEE Trans. Electron Dev.*, **ed-24**, 468 (1977).
5. R. J. Stirn, Nat. Bur. Stand. Spec. Publ., **400-58**, 69 (1979).
6. D. J. Brinker and E. Y. Wang, *IEEE Trans. Electron Devices*, To be published.
7. C. L. Hoening and A. W. Searcy, *J. Am. Ceram. Soc.*, **49**, 128 (1966).
8. J. Drowart in "Condensation and Evaporation of Solids," E. R. Rutner, P. Goldfinger, and J. P. Hirth, Editors, p. 255, Gordon and Breach, New York (1962).
9. C. F. Fink and C. L. Mantell, *J. Phys. Chem.*, **32**, 103 (1928).
10. "Constitution of Binary Alloys," 2nd ed., M. Hansen and K. Anderko, Editors, p. 757, McGraw-Hill Book Company, New York (1958).

An Electron Microscope Investigation of the Effect of Phosphorous Doping on the Plasma Etching of Polycrystalline Silicon

E. A. Irene,* E. Tierney,* J. M. Blum,* C. F. Aliotta, A. C. Lamberti, and B. J. Ginsberg

IBM Thomas J. Watson Research Center, Yorktown Heights, New York 10598

ABSTRACT

The effects of excess phosphorous on plasma etching of polycrystalline silicon were studied by SEM and TEM. The phosphorous levels were altered by the time duration of POCl_3 deposition, by the presence or absence of a phosphosilicate glass layer during high temperature treatments, and by using either an N_2 or O_2 drive-in anneal thereby causing the snow plow effect of oxidation to locally increase the phosphorous levels. Wherever the phosphorous levels were highest (at the poly-Si free surface or at grain boundaries), the extent of plasma etching was greatest. This etching effect was found to cause poly-Si line edge roughening.

The use of dry etching techniques such as plasma etching for delineation of polycrystalline silicon (poly-Si) is becoming widespread in the microelectronics industry. Basically, the plasma etching technique utilizes a fluorine-containing gaseous plasma, to form volatile products that are easily pumped away. It has been our experience that for the plasma etching technique to be described, the presence of phosphorous in the poly-Si greatly enhances the etch rate of poly-Si.

The purpose of the present study is to show definitive scanning electron microscopy (SEM) and transmission electron microscopy (TEM) evidence of the effects of heavy phosphorous doping on the morphology of poly-Si that has been exposed to plasma etching. From the SEM and TEM studies of the various process variables, cause and effect relationships are identified which enable the selection of processing steps that yield high quality delineation of heavily phosphorous-doped poly-Si.

Experimental Procedures

Sample preparation.—Commercially available high quality single crystal silicon wafers were used in this study. All films studied were deposited on the polished side of the wafer. All the poly-Si films were deposited via the decomposition of 100% SiH_4 at 625°C at a total pressure of 4.6×10^{-4} atm and a total flow of 45 sccm onto 90 nm of thermally grown SiO_2 . The phosphorous doping was accomplished by POCl_3 deposition at 870°C using N_2 bubbled through POCl_3 liquid and added to a mainstream carrier of 10% O_2 in N_2 . The resultant phosphosilicate glass (PSG) film was removed chemically using buffered HF (BHF). The drive-in anneal was done at 1000°C for 10 min in either O_2 or N_2 . Any resulting oxide was removed in BHF. For delineation, a 100 nm CVD SiO_2 film followed by photoresist was

deposited on the poly-Si. The photoresist was then exposed through a mask, the resist was developed, and the oxide was chemically removed. Using the resist and/or oxide as the mask, the plasma conditions for etching the POCl_3 -doped low pressure CVD (LPCVD) poly-Si were set at 35W, 0.3 Torr at room temperature ($\sim 23^\circ\text{C}$) in an ambient of $\text{CF}_4 + 8\% \text{O}_2$. The etch rate of the doped polysilicon is 850-900 Å/min. The etching time was adjusted for a 10% overetch when poly-Si lines were to be delineated. For the present study when it was desired to view a partially etched surface, a 1 min etch was used which removed about 40% of the 2500Å polysilicon film.

Electron microscopy.—Scanning electron microscopy (SEM) was performed on samples coated with a thin gold layer. Transmission electron microscopy (TEM) samples were thinned using mixtures of HF and HNO_3 .

Results and Discussions

The phosphorous doping of poly-Si is accomplished using a POCl_3 deposition followed by a P diffusion drive-in. The POCl_3 deposition results in a layer of phosphosilicate glass, PSG, on top of the poly-Si. Typically, the PSG is chemically removed prior to a phosphorous drive-in anneal. The drive-in is done in either O_2 or a relatively inert ambient such as N_2 or Ar. If the drive-in is done in O_2 , SiO_2 will form. It is known that the formation of SiO_2 causes the pile-up of phosphorous at the Si- SiO_2 interface (1, 2) or the so-called "snow plow" effect. The drive-in anneal in N_2 permits excess phosphorous to escape from the poly-Si by evaporation. Therefore, the O_2 anneal will result in more free phosphorous at oxidized grain boundaries and on the oxidized surface of the poly-Si than will the N_2 process.

Figure 1(a) shows the morphology of the poly-Si surface after a 30 min POCl_3 deposition and PSG strip.

* Electrochemical Society Active Member.
Key words: etching, deposition, anneal.

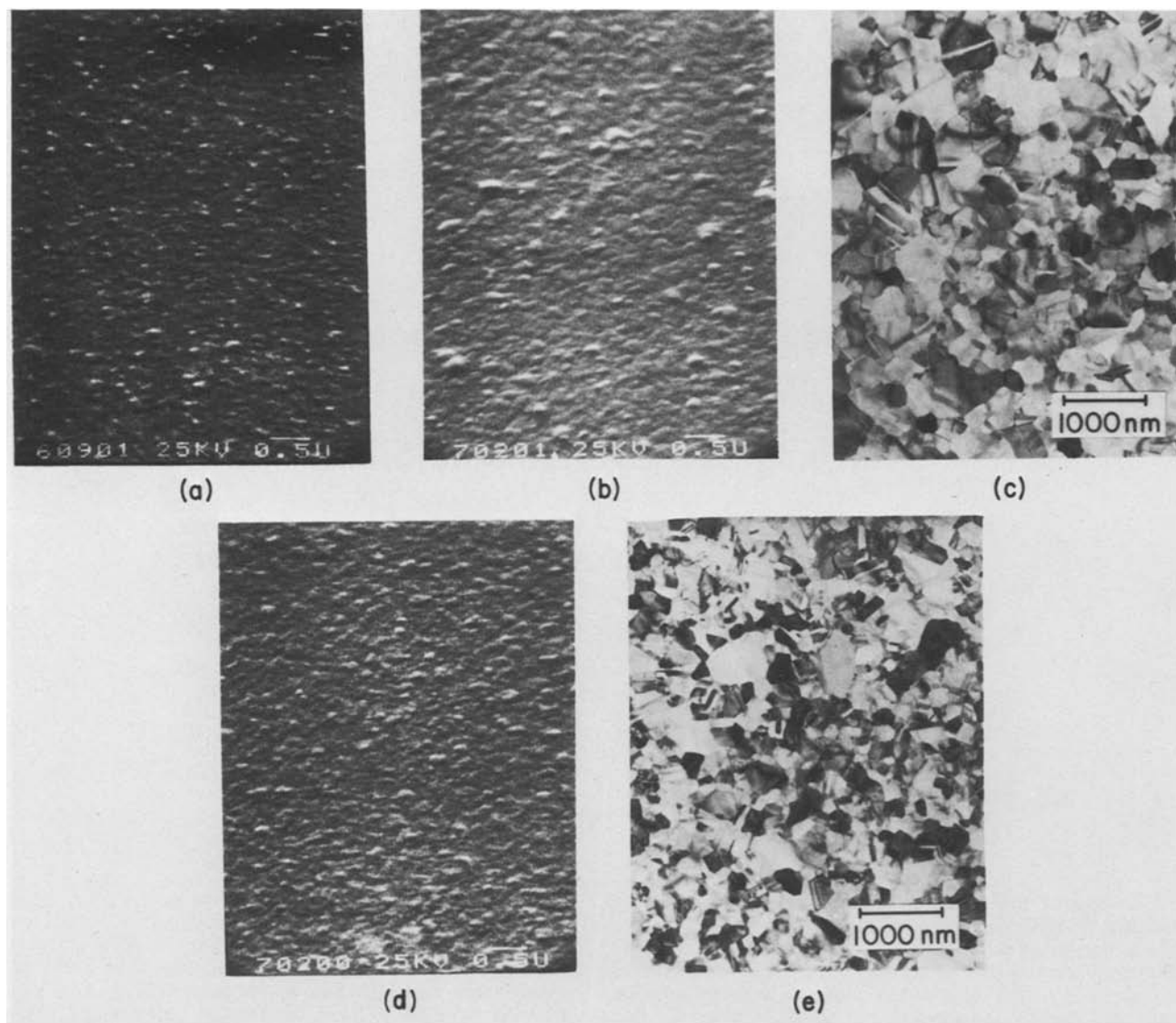


Fig. 1. (a) SEM of blanket poly-Si, 30 min POCl_3 , PSG stripped; (b) SEM of sample in (a) plus O_2 drive-in and BHF strip; (c) TEM of sample in (a) plus O_2 drive-in and BHF strip; (d) SEM of sample in (a) plus N_2 drive-in and BHF strip; (e) TEM of sample in (a) plus N_2 drive-in and BHF strip.

The surface texture is due to the grain morphology (3). The remaining micrographs in Fig. 1 compare the O_2 and N_2 drive-in processes. It is seen that the samples are similar. However, closer examination reveals that the O_2 annealed sample has larger and more dramatically outlined grain boundaries. The larger sized grains are caused by the presence of more phosphorous which causes enhanced grain growth (3). The deeper grain outlines for the O_2 annealed poly-Si are due to the chemical etching (with BHF) of the oxide that formed intergranularly (3). Figure 2 shows the effect of partial plasma etching on the O_2 and N_2 annealed samples. The O_2 annealed sample shows both extensively roughened mid-grain regions and deeply etched grain boundaries. The etched grain boundaries are somewhat difficult to discern in Fig. 2(a) due to the rough surface texture but Fig. 2(b) using TEM clearly shows the thinned grain boundary regions. The intensity variation in Fig. 2(b) across individual grains is due to the surface roughness. The N_2 annealed, plasma-etched sample shown in Fig. 2(c) and (d) shows extensive grain boundary etching but the grain surfaces are smooth. Resistivity measurements of N_2 and O_2 annealed poly-Si samples show no differences in conduction behavior. Therefore, it is concluded that the drastic difference in etching behavior is related to excess electrically inactive phosphorous caused by the snow

plow effect. The phosphorous accumulates in grain boundaries and at the grain-free surfaces and this effect is enhanced, since oxidation occurs at these surfaces and prevents escape of the excess phosphorous.

Based on these findings, it is likely that plasma etching will affect the quality of delineation of poly-Si into conducting lines. Therefore, in order to determine the extent of the line edge roughening, a series of experiments were performed using delineated poly-Si.

The effect of the total amount of phosphorous on line delineation is shown by comparing Fig. 3(a) and (b) with Fig. 4(a) and (b). The only processing difference between the two samples shown in these figures is that the sample in Fig. 3 received a 15 min POCl_3 deposition while that in Fig. 4 received a 30 min POCl_3 deposition. The resistivity of these films was 2.0×10^{-3} and $1.3 \times 10^{-3} \Omega\text{-cm}$ for the 15 and 30 min deposition conditions, respectively. The unmasked portion of both samples was extensively etched to exaggerate any etching effects. It is seen that the masked portion of the sample with 15 min POCl_3 has quite reasonable line edges; the unmasked portion appears somewhat jagged. The sample that received 30 min POCl_3 displays more jagged edges on both the masked and unmasked portions. The masked surface is rougher on the 30 min POCl_3 treated sample. This roughness is attributable to more extensive grain growth at the higher phosphorous levels

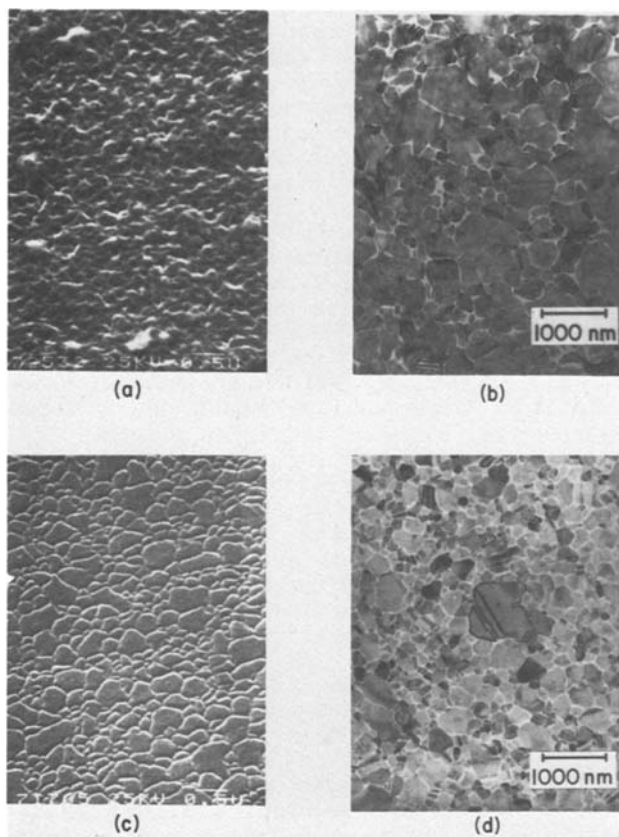


Fig. 2. (a) SEM of blanket poly-Si, 30 min POCl_3 , PSG stripped, O_2 anneal, BHF strip, plasma etch; (b) TEM of (a); (c) SEM of sample same as (a) but N_2 anneal; (d) TEM of sample in (c).

while the unmasked side and the line edges of both sides are roughened by the plasma etching.

Although the PSG layer is usually removed after POCl_3 deposition, the presence of this film as both a capping layer and source of phosphorous is worth considering. Figure 5 compares 15 and 30 min POCl_3 doped samples processed with PSG in place. Both samples are considerably more roughened on masked and unmasked surfaces and at line edges. The masked areas of both samples show mound-like protrusions. These features are common but not always observed in

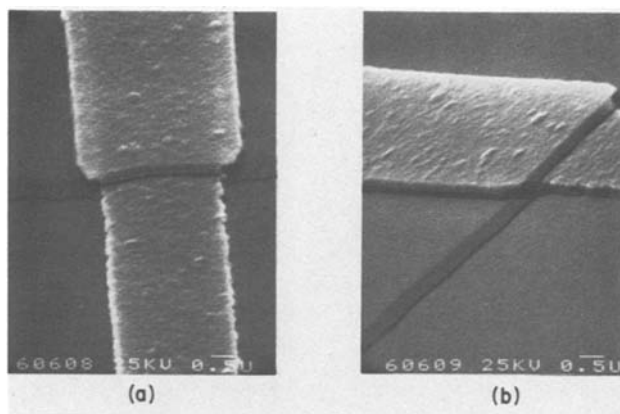


Fig. 3. (a) SEM of delineated poly-Si, 15 min POCl_3 , PSG stripped, O_2 anneal, BHF strip, CVD SiO_2 mask on one-half, plasma etch, top view; (b) same as (a) but side view.

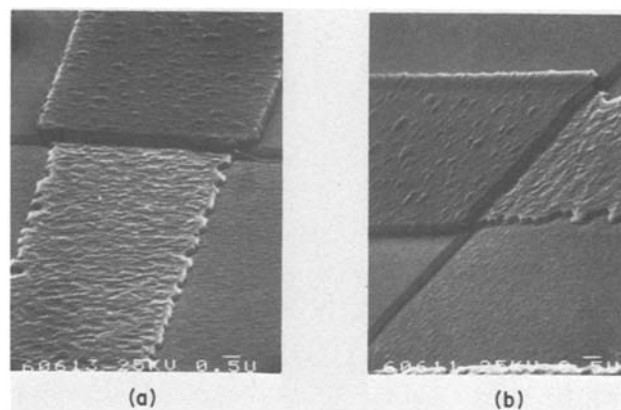


Fig. 4. (a) SEM of delineated poly-Si, 30 min POCl_3 , PSG stripped, O_2 anneal, BHF strip, CVD SiO_2 mask on one-half, plasma etch, top view; (b) same as (a) but side view.

this type sample and energy dispersive x-ray analysis (EDAX) shows no increased phosphorous associated with these features. TEM micrographs which follow (Fig. 6) display nothing relative to these features. Therefore, the protrusions are likely to be the result of extensive surface recrystallization where grains are tilted during growth. This explanation is consistent

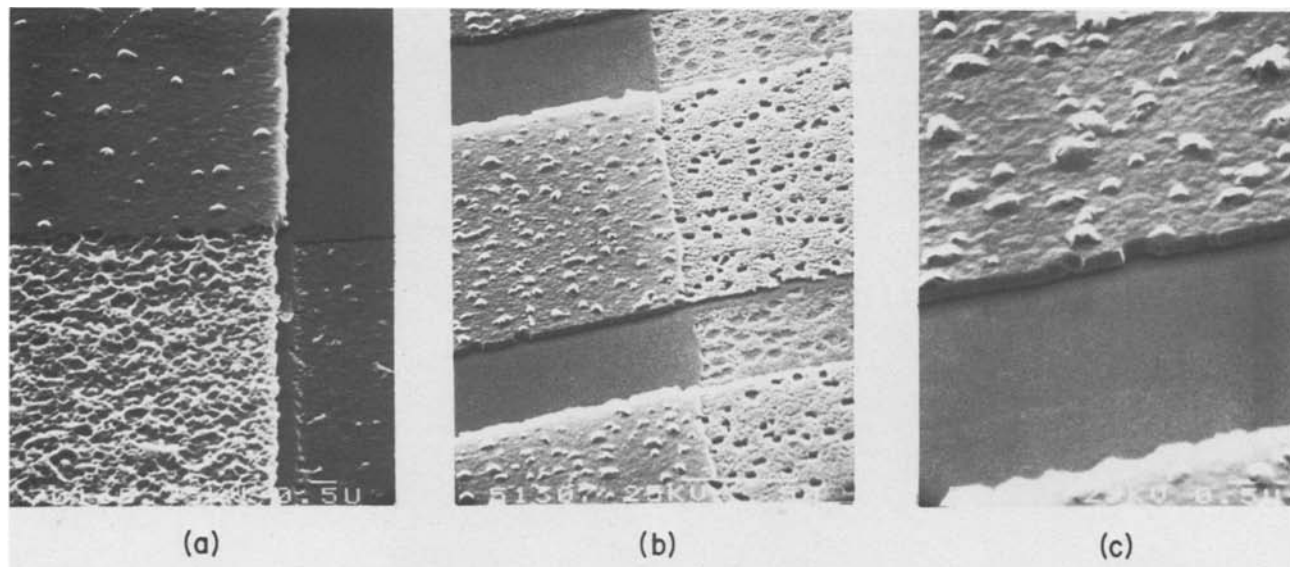


Fig. 5. (a) SEM of delineated poly-Si, 15 min POCl_3 , PSG in place during O_2 anneal, BHF strip, CVD SiO_2 mask on one-half, plasma etch; (b) same as sample (a) but with 30 min POCl_3 ; (c) same as sample (b) higher magnification.

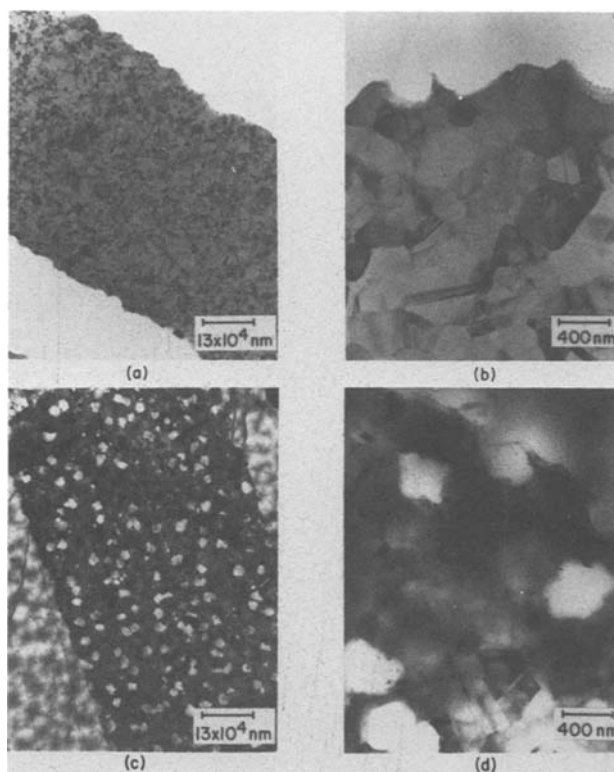


Fig. 6. TEM micrographs of 30 min POCl_3 doped poly-Si annealed with PSG in place of (a) masked, (b) the edge of (a), (c) unmasked, (d) the edge of (c).

with the observation that Si self-diffusion is enhanced in the presence of phosphorous (4). The appearance of jagged line edges and extensive etching of unmasked regions for both the 15 and 30 min POCl_3 doped samples processed with PSG in place demonstrates the importance of removing PSG prior to further processing. For the 30 min POCl_3 treated sample in Fig. 5(b), the shape of the line edge roughness seems to match the holes etched in unmasked mid-line areas. This suggests that entire grains or grain clusters are attacked by plasma etching.

In order to elucidate a possible relationship between the poly-Si grain structure and the edge roughness, TEM was used to observe these features for the 30 min POCl_3 samples treated with PSG in place. Figure 6(a) for the masked side shows the jagged line edges while the higher magnification of 6(b) shows that entire grains and groups of grains were removed from the line edge. Some grains at the line edges display curv-

ature which develops during the plasma etching. Figures 6(c) and (d) show a similar sequence of micrographs for similarly etched lines after the mask was removed and the surface partially plasma etched. This treatment results in extensively etched areas within the poly-Si lines. From these micrographs, it is easily observed that the etched out areas both in the line and at the edge show the angularity associated with the etched out grain boundaries. The location of the removed grains appears to be random. At higher magnification it is also seen that the regions adjacent to the etched holes are thinned. Since the etch rate is quite strongly dependent on the amount of phosphorous present, and since there is likely a random distribution of excess phosphorous at grain boundaries, it is probable that the etching proceeds initially and most vigorously at these randomly distributed highly doped regions leaving a random distribution of holes.

Summary and Conclusions

It has been shown that the presence of excess phosphorous enhances the rate of plasma etching of poly-Si. In the present study, the phosphorous was altered in three ways: simply by the amount of time for the POCl_3 deposition, by the presence or absence of a PSG layer during high temperature anneals, and by drive-in anneals in either N_2 , Ar, or O_2 . The O_2 anneal causes oxidation and pile-up of phosphorous at oxidized surfaces. Whenever a processing step increased the local phosphorous levels at the poly-Si free surface and/or at grain boundaries, the extent of plasma etching was found to be greatest where the phosphorous levels were highest. These etching characteristics affected the poly-Si line edge quality and the quality could be enhanced by a proper choice of processing steps. In particular, those steps which prevented excessive phosphorous pile-up yielded superior poly-Si line edges.

Manuscript submitted Jan. 26, 1981; revised manuscript received March 19, 1981.

Any discussion of this paper will appear in a Discussion Section to be published in the June 1982 JOURNAL. All discussions for the June 1982 Discussion Section should be submitted by Feb. 1, 1982.

Publication costs of this article were assisted by IBM Corporation.

REFERENCES

1. A. S. Grove, O. Leistiko, and C. T. Sah, *J. Appl. Phys.*, **35**, 2695 (1964).
2. B. E. Deal, A. S. Grove, E. H. Snow, and C. T. Sah, *This Journal*, **112**, 308 (1965).
3. E. A. Irene, E. Tierney, and D. Dong, *ibid.*, **127**, 705 (1980).
4. J. M. Fairfield and B. J. Masters, *J. Appl. Phys.*, **38**, 3148 (1967).

Laser Damage Gettering and Its Application to Lifetime Improvement in Silicon

Y. Hayafuji, T. Yanada, and Y. Aoki

SONY Corporation Research Center, 174 Fujitsuka-cho, Hodogaya-ku, Yokohama 240, Japan

ABSTRACT

Lattice defects induced by laser irradiation and their thermal stability during subsequent oxidation were studied by transmission electron microscopy, x-ray topography, and preferential etching. High power laser pulses above 20 J/cm^2 produced dislocation lines and dislocation clusters. Laser pulses of about 15 J/cm^2 also generated dislocation clusters and pseudo-swirl defects in the irradiated region. All of these defects were thermally stable. However, thermally stable defects were not observed when laser pulses of less than 15 J/cm^2 were used, although unstable dislocations were generated. The suppression of defect formation by laser damage gettinger was examined using Sirtl etching. It was found that thermally stable dislocations and pseudo-swirl defects acted as sinks for point defects and prevented the formation of precipitates during a subsequent oxidation. Laser damage gettinger was used to improve generation lifetime in metal-oxide-semiconductor (MOS) capacitors with the result that generation lifetime in the gettered area was improved by two orders of magnitude over that in the ungettered area.

Much work has been reported on the effects of lattice defects on the electrical properties of silicon crystals and on the electrical characteristics of silicon devices. Precipitates, stacking faults, and dislocations induced during the manufacturing process act as generation-recombination centers for carriers (1-4) and degrade the electrical characteristics of p-n junctions (5-8). This degradation is especially noticeable in photosensitive mosaic devices such as CCD imagers where the defects produce generation sites responsible for bright spots and lines in video displays (9-13).

In recent years, one of the major aims of VLSI technology has been the fabrication of large area devices free of lattice defects. For this reason, efforts have been concentrated on the suppression of the formation of process-induced defects in silicon.

The effectiveness of back-side damage gettinger in the reduction of process-induced defects has been reported (14-18). Back-side damage gettinger uses lattice damage, which is capable of eliminating nuclei of defects and absorbing impurities during high temperature processing.

A number of methods of inducing dislocations for gettinger have been proposed, for example, lapping, sand blasting, phosphorus diffusion, and ion implantation. The problem with these methods, however, is that very often the wafers are contaminated with abrasive particles or are subjected to thermal stress. To solve these problems, a method of gettinger which we call laser damage gettinger has been developed (19-22). Laser damage gettinger utilizes laser irradiation damage to generate gettinger sites where a variety of point defects, such as impurities and interstitials, gather. Technological advantages of this method are controllability and room temperature treatment for introducing gettinger sites.

The purposes of the present work are: (i) to examine the lattice defects caused by laser irradiation and subsequent oxidation, (ii) to investigate the suppression by laser irradiation damage of defect formation, and (iii) to study the improvement of generation lifetime in silicon caused by laser damage gettinger.

Experimental Procedure

Silicon wafers with (111) orientation, prepared from a p-type dislocation-free Czochralski-grown crystal

Key words: defects, capacitor, etching, semiconductor, topography.

with oxygen content of about 10^{18} cm^{-2} , were used. The doping impurity was boron and the resistivity range was 3-5 $\Omega\text{-cm}$. Both surfaces of the wafer were mechanochemically polished. The wafers were about $300 \mu\text{m}$ thick and 50 mm in diameter.

Laser damage was induced on the rear surface of the wafer by Q-switched Nd:YAG laser pulses. The laser pulses were scanned in the [110] direction at a pitch of $500 \mu\text{m}$ and with a pulse spot overlap of about 65%. The laser had a CW output power of 5W in the TEM₀₀ mode ($\lambda = 1.06 \mu\text{m}$). The pulse repetition frequency was 10 kHz, the pulse duration time was 150 nsec, and the spot size of the pulses was about $40 \mu\text{m}$. The amount of laser damage induced can be controlled in two ways: one, by varying the pitch of the scanning laser beam and the amount of overlap between spots; and two, by changing the energy density of the laser pulses. In this experiment, the latter method was applied with an energy density from 1630 to 5 J/cm^2 . The energy density was set by moving the samples out of the focal plane and by using an attenuator with an analyzer and a polarizer. Wafers were irradiated on the back surface with laser pulses with an energy density over 30 J/cm^2 and on the front surface outside the active area with laser pulses with an energy density below 30 J/cm^2 . After irradiation, some of the samples were oxidized in a dry oxygen ambient at 1200°C for 1 hr so that the thermal stability of the laser damage could be examined and so that the suppression of defect formation by laser damage could be studied.

In order to study the improvement of generation lifetime through laser damage gettinger, metal-oxide-semiconductor (MOS) capacitors were fabricated as follows. Silicon wafers were irradiated by laser pulses of 1630 J/cm^2 on half of the back surface at a pitch of $500 \mu\text{m}$. After irradiation, chemical vapor deposition of silicon-dioxide 8000\AA thick was carried out at 420°C to make a diffusion mask. A channel-stop region was formed by boron diffusion in wet oxygen at 1000°C for 30 min. Gate oxidation was carried out in wet oxygen at 1000°C for 30 min, followed by annealing in dry nitrogen for 10 min. After aluminum deposition for electrodes, the capacitors were annealed in dry nitrogen at 400°C for 1 hr. MOS capacitors 1.5 mm in diameter with a silicon-dioxide layer 1500\AA thick were then fabricated. In high temperature processes above 900°C , slow insertion and slow retraction of wafers

into and out of furnaces were carried out to heat and to cool the wafers at a rate of about $3^{\circ}\text{C}/\text{sec}$ to avoid dislocation propagation to the front surface.

The capacitance-time curve (transient response) of the MOS capacitors was measured by applying a step input of 15V to the gate electrode at 1 MHz. Generation lifetime t_g was determined from the transient response using the equations derived by Heiman (23).

Lattice defects caused by laser irradiation were examined by transmission electron microscopy (TEM), x-ray topography, and preferential etching. TEM samples about $1\ \mu\text{m}$ thick were prepared by chemical thinning.

Results and Discussion

Lattice defects caused by laser irradiation.—TEM study of the as-irradiated samples established that lattice defects occurred in the samples irradiated by laser pulses with an energy density higher than about $8\ \text{J}/\text{cm}^2$ and that these defects could be classified into three types of configuration. We later found that these three types of configuration were indicative of the configuration of the dislocations they contained. Figures 1a, b, and c are transmission electron micrographs taken of samples exposed to laser pulses of 10, 15, and $22\ \text{J}/\text{cm}^2$, respectively, and show the three types of defect configurations produced by laser irradiation at these three different energy densities. In Fig. 1a, the defects were distributed generally over the periphery of the melted area. We compared the TEM images from different diffraction planes and found that the defects were small dislocations.

In addition to these dislocations, defects of a second type were generated in the samples irradiated by laser pulses of about $15\ \text{J}/\text{cm}^2$, as can be seen in Fig. 1b. This second type of defect grew in fanlike clusters and was also determined by TEM analysis to be dislocations. These fanlike clusters are termed "dislocation clusters." In every trace of a laser spot, dislocation clusters appeared only in the $[\bar{1}2\bar{1}]$ direction. Stereoscopic observation showed that dislocation clusters lay in the $(\bar{1}1\bar{1})$ plane. Contrast analysis of the TEM images revealed dislocation clusters composed of dislocations with a Burgers vector of $a/2\ [110]$, running close to the $[011]$ direction, and dislocations with a Burgers vector of $a/2\ [101]$, running very close to the $[110]$ direction, as can be seen in Fig. 2.

We might expect from these results that dislocation clusters could be generated on any $\{111\}$ plane which approximately coincides with the melt front and we confirmed that the dislocation clusters were, in fact, formed on the $(\bar{1}1\bar{1})$, $(\bar{1}\bar{1}1)$, and $(1\bar{1}\bar{1})$ planes which lay in the $[\bar{1}2\bar{1}]$, $[\bar{1}\bar{1}2]$, and $[2\bar{1}\bar{1}]$ directions, respectively. Dislocation clusters did not appear on the $(\bar{1}\bar{1}1)$ and $(1\bar{1}\bar{1})$ planes in Fig. 2 because they were annihilated by the remelting caused by the following pulse.

A third type of defect was observed after irradiation at a pulse energy density of about $22\ \text{J}/\text{cm}^2$. Defects of this type were long dislocation lines running along the scan direction of the laser pulses, that is, the $[1\bar{1}0]$ direction and lying on the (111) plane parallel to the wafer surface. These defects had a Burgers vector either of $a/2\ [110]$ or of a $a/2\ [101]$. At higher energy densities than $22\ \text{J}/\text{cm}^2$, most defects observed were dislocations of this third type, although laser grooves in excess of $1\ \mu\text{m}$ depth were formed. Only a few of these dislocations were entangled.

TEM observations of the three types of defects after oxidation at 1200°C for 1 hr gave the following thermal stability results. Dislocations of the first type were found to be thermally unstable. After oxidation, there remained no trace of dislocations in the transmission electron micrographs taken of the samples irradiated by $10\ \text{J}/\text{cm}^2$ pulses, which suggests that dislocations of this type were completely annealed out of the surface.

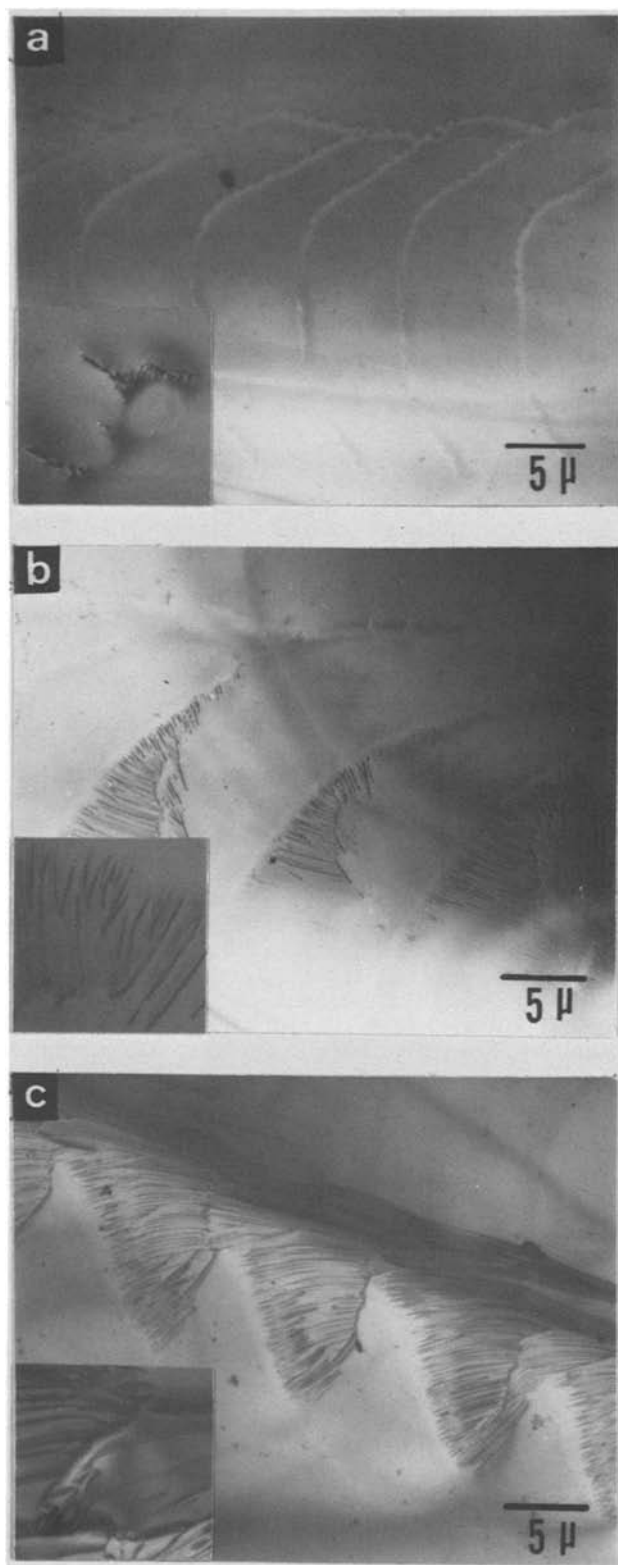


Fig. 1. Transmission electron micrographs showing dislocations induced at laser pulses with an energy density of: a, $10\ \text{J}/\text{cm}^2$; b, $15\ \text{J}/\text{cm}^2$; and c, $22\ \text{J}/\text{cm}^2$.

Some dislocations of the second type proved to be thermally stable because a small part of every dislocation cluster near the bottom of the melted region remained when the other part of the dislocation cluster closer to the surface had been annihilated, as can be seen in Fig. 3a. Figure 3a also shows that oxidation-induced precipitates were generated on dislocations and on other sites. Figures 3b and c are magnified views of the areas marked "d" and "s," respectively,

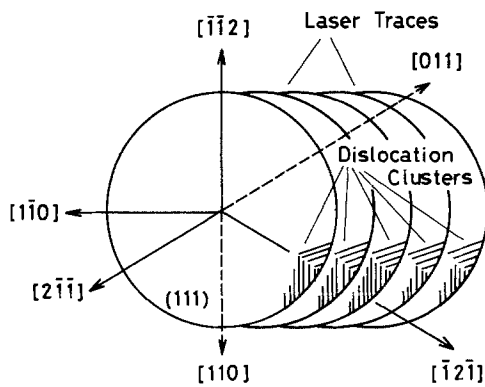


Fig. 2. Position of dislocation clusters

in Fig. 3a. Figure 3b shows that dislocations act as nucleation sites for the precipitates. In Fig. 3c, however, it is not clear what defect the nucleation sites of the precipitates are. These as yet undefined sites may be undetectable microdefects induced by laser irradiation. These microdefects may be clusters of self-interstitials generated during recrystallization after irradiation which are analogous to swirl defects in bulk silicon. For this reason we call these sites "pseudo-swirl defects."

Dislocations of the third type were also thermally stable. Some of these dislocations moved far from the laser grooves and formed networks during subsequent oxidation, as can be seen in the x-ray topographs of Fig. 4. Detailed study using the Secco etching technique showed in the cross section of the sample that dislocation propagation through the wafer toward the undamaged surface did not occur, but stopped two thirds of the way to the wafer surface. Dislocation movement caused by laser damage will be discussed in a separate paper.

Suppression of defect formation by laser damage gettering.—In the previous section, we noted that two types of thermally stable dislocations induced by laser irradiation exist, that is, dislocations which compose a dislocation cluster and dislocations parallel to the scan direction of the laser pulses. Pseudo-swirl defects were also thermally stable. We established that these thermally stable defects act as gettering sites for point defects and suppress the formation of oxidation-induced precipitates outside the irradiated region during subsequent oxidation by examining, using the Sirtl etching technique, the ability of laser damage to getter oxidation-induced precipitates. When low power laser pulses were used, the wafers were irradiated by laser pulses with 10 and 15 J/cm² energy density on the front surface and then oxidized at 1200°C for 1 hr in a dry oxygen ambient. An example of laser damage gettering is exhibited in Fig. 5. Many etch pits of oxidation-induced precipitates, of which composition and structure were not determined by TEM, appeared on the front surface of the wafer without irradiation, as can be seen in Fig. 5a. In Fig. 5b, it can be seen that etch pits also appear with traces of laser pulses of 10 J/cm² energy density and that there has been no gettering effect in this wafer. In Fig. 5c, however, it can be seen that there are no defects in the wafer irradiated with 15 J/cm² pulses, only traces of laser pulses. We can therefore say that laser damage caused by laser pulses with an energy density of 15 J/cm² or more is essential for laser damage gettering.

In another experiment very high power laser pulses were used. Pulses with an energy density of 1630 J/cm², for example, were scanned on half of the back surface at a pitch of 500 μm. The wafer was then oxidized at 1200°C for 1 hr. Figure 6 is a set of optical micrographs taken of the front and the back surfaces after Sirtl etching for 3 min. The optical micrograph

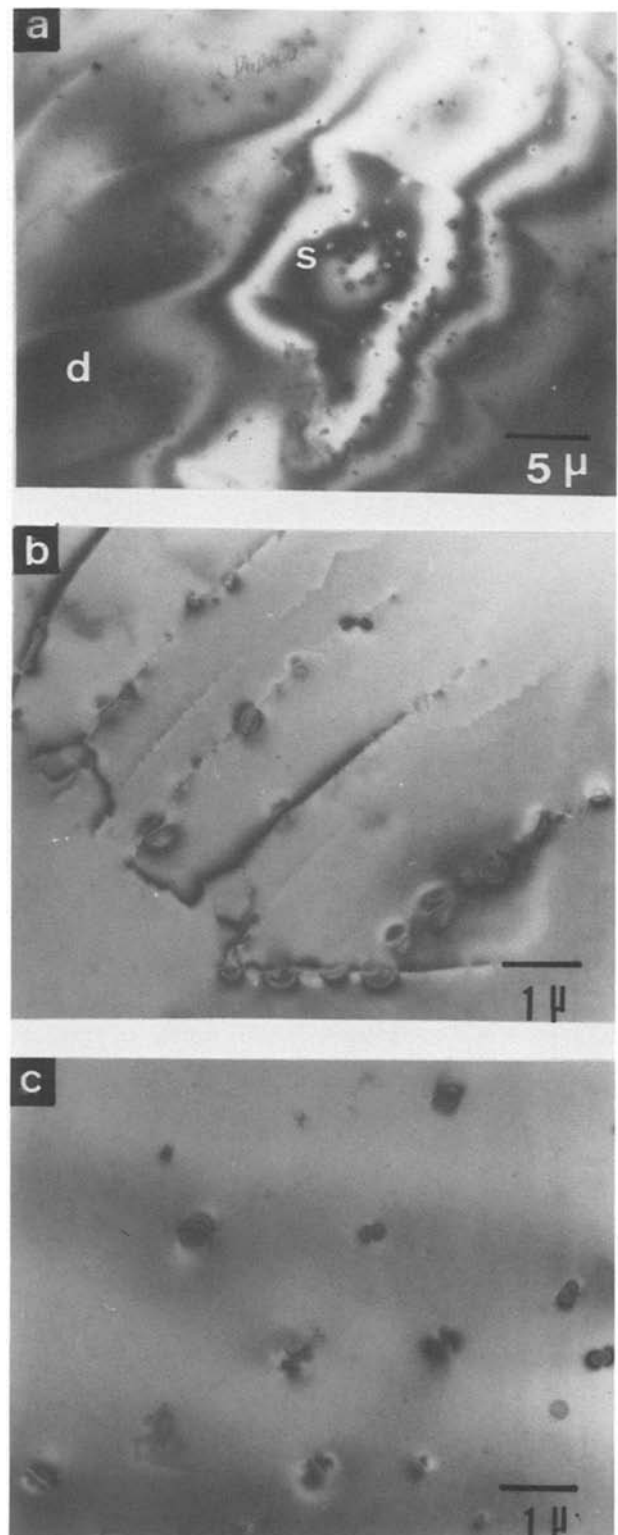


Fig. 3. Transmission electron micrographs of sample oxidized after irradiation by 15 J/cm² pulses. Fig. 3b and c are magnified views which correspond to d and s in Fig. 3a, respectively.

of the front surface shows that the two halves are different. The upper half corresponds to the non-damaged area of the back surface and appears bright because of the scattering of the light by irregularities on the surface. This brightness indicates the existence of oxidation-induced precipitates. The lower half is black, indicating that no lattice defects were formed. We confirmed that laser damage caused by 1630 J/cm² pulses on the back surface prevents defect formation near the front surface, as was the case with laser pulses of 15 J/cm² energy density.

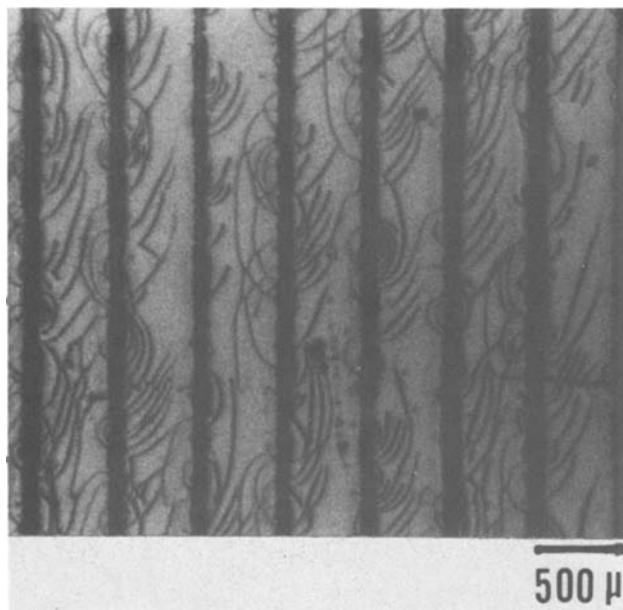


Fig. 4. X-ray topographs taken of oxidized wafer irradiated by 1630 J/cm^2 , showing that dislocations moved far from the laser grooves and formed networks.

On the basis of these observations, the following gettering mechanisms are proposed. When a wafer is irradiated by low-power laser pulses, the near-surface region of the wafer melts. The melt front moves rapidly into the crystal. In the recrystallization of a melt caused by 15 J/cm^2 pulses, dislocations are generated to relieve thermal stress at glide planes so that maximum shear stress occurs. In addition, clusters of self-interstitials supersaturated in the cooling process grow to be pseudo-swirl defects. These dislocations and pseudo-swirl defects are thermally stable so these defects interact with point defects during subsequent oxidation and act as sinks for point defects. The effect of laser damage gettering at low energy is explained by this mechanism, which is illustrated in Fig. 7. In wafers irradiated by laser pulses less than 15 J/cm^2 , the maximum depth of the melt front is shallow. In this case the wafers were not heated long enough to induce thermally stable defects, so gettering is not efficient.

When a wafer is irradiated by high-power laser pulses, thermally stable dislocations are generated around the laser grooves and propagate into the bulk during oxidation to relieve the stress induced by irradiation. These dislocations act as gettering sites for point defects to suppress defect formation. A schematic view of this mechanism is shown in Fig. 8.

Improvement of generation lifetime through laser damage gettering.—Although it is well known that controlled damage on the back surface of the wafer can improve generation lifetime by removal of point defects such as undesirable impurities, it has not been established that laser damage gettering specifically improves generation lifetime.

Results summarizing the effect of laser damage gettering on generation lifetime are plotted in Fig. 9. The generation lifetime in the gettering area was improved by about two orders of magnitude over that in the ungettered area. Generation lifetime in the gettering area tended to level off at about $10^3 \mu\text{sec}$. The plots in the ungettered area, however, were spread between 1 and $100 \mu\text{sec}$. To investigate the reason for the improvement of the lifetime, the surface of the wafer was preferentially etched using the Sirtl etching technique after removal of the MOS capacitors. It was found that lifetime improvement was caused by the

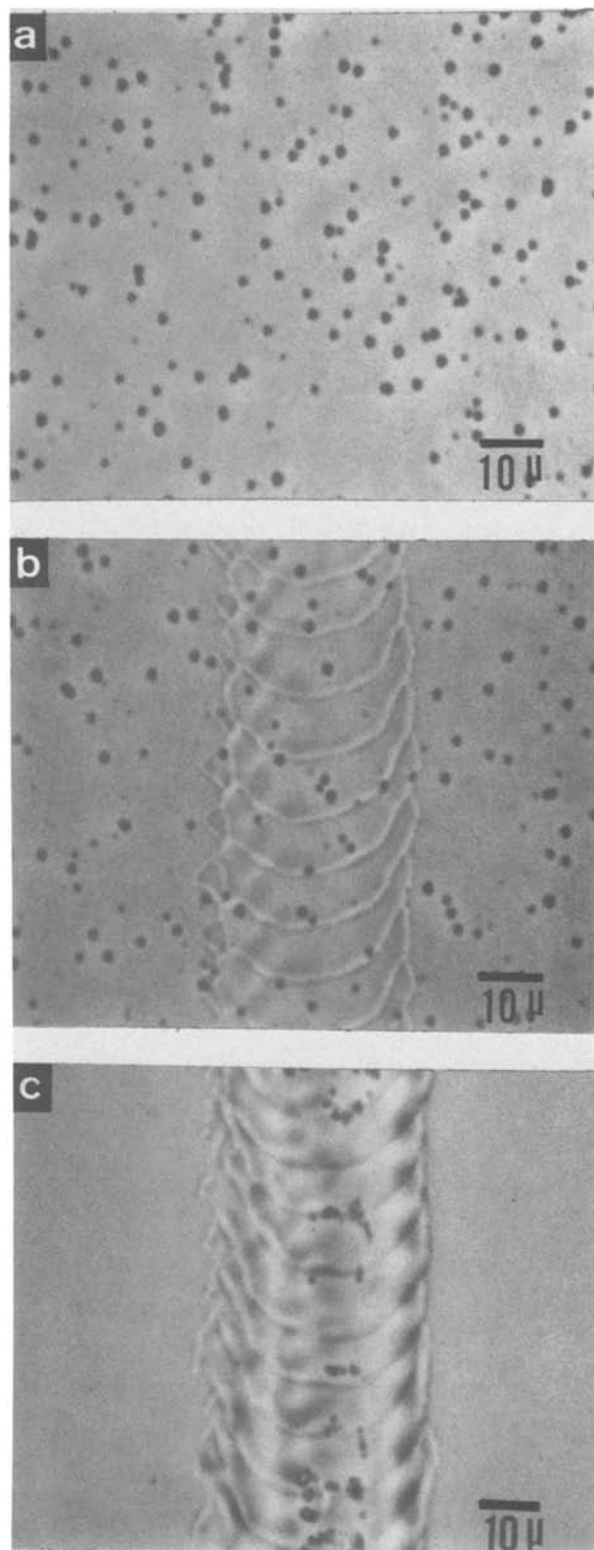


Fig. 5. Etch patterns of the oxidized samples: a, without irradiation, and b and c with irradiation by 10 and 15 J/cm^2 , respectively.

suppression of defect formation by laser damage gettering.

To evaluate the electrical activity of the defects in the ungettered area, the reciprocal of generation lifetime $1/t_g$ was plotted against the density d of defects in Fig. 10. The graph shows that the value of $1/t_g$ is nearly proportional to defect density d . Therefore, $1/t_g$ can be expressed by

$$1/t_g = k \cdot d + 1/t_0$$

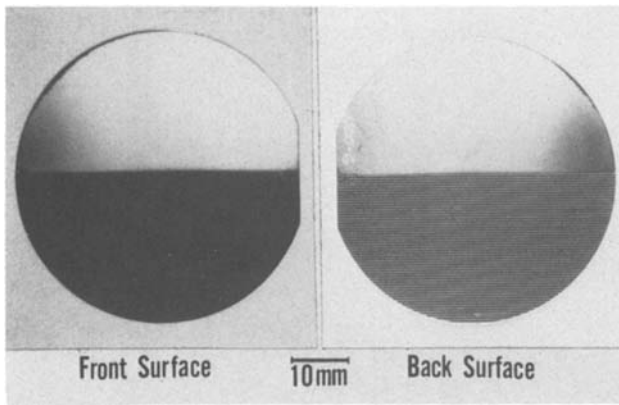


Fig. 6. Optical micrographs of wafer oxidized after irradiation by 1630 J/cm², showing laser damage gettingter suppression of defect formation.

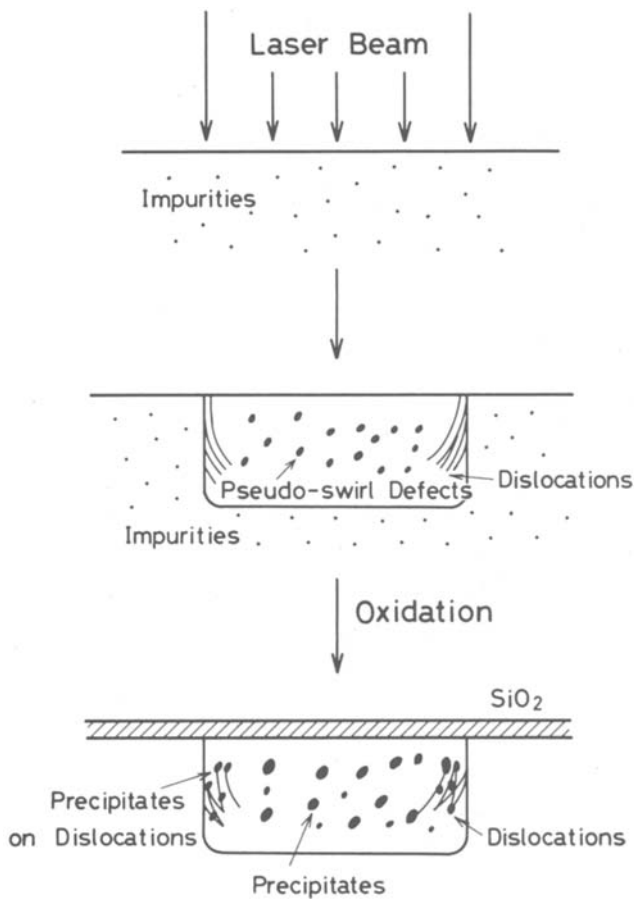


Fig. 7. Mechanism of laser damage gettingter by low-power laser pulses of about 15 J/cm².

where k is the proportional constant which defines the electrical activity of defects expressed in cm²/μsec and t_0 is background generation lifetime expressed in μsec (24). The constant k had a value of 2×10^{-6} in Fig. 10.

Conclusion

A method of gettingter, which we call laser damage gettingter, has been developed to suppress the formation of lattice defects and to improve generation lifetime in silicon. This method utilizes laser irradiation damage as gettingter sites for a variety of point defects, such as impurities and self-interstitials. Summarizing the data, the following conclusions can be drawn.

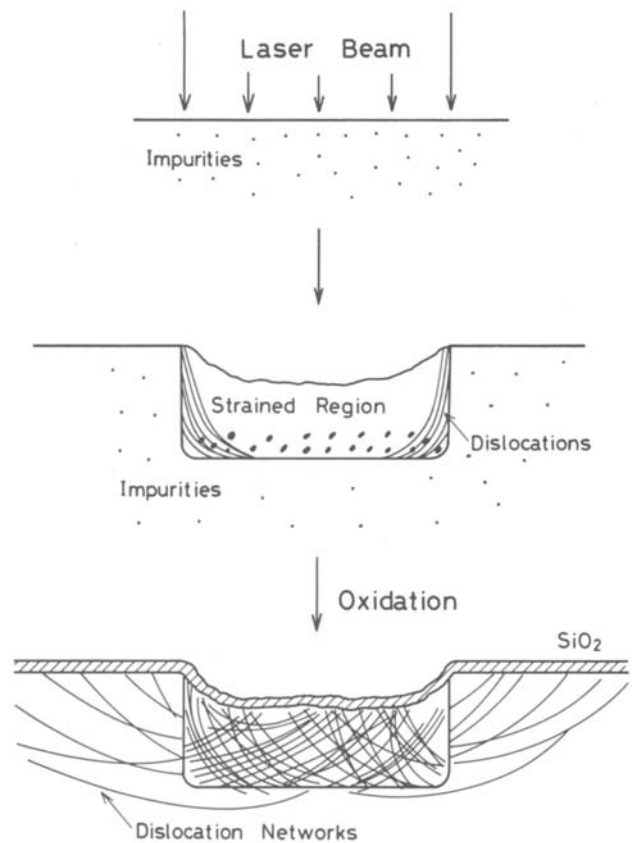


Fig. 8. Mechanism of laser damage gettingter by high-power laser pulses above 20 J/cm².

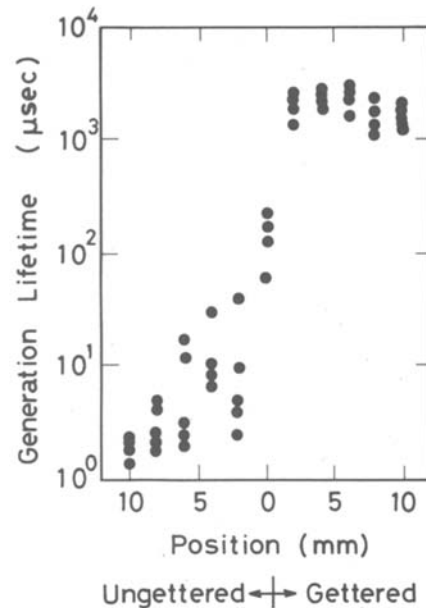


Fig. 9. Distribution of generation lifetime in the gettered and ungettered areas.

1. High-power laser pulses above 20 J/cm² produced thermally stable dislocation lines and dislocation clusters and low-power laser pulses of about 15 J/cm² also generated stable dislocation clusters and pseudo-swirl defects in the irradiated region. However, no generation of thermally stable defects was observed in the case of laser pulses of power lower than 10 J/cm².
2. Thermally stable lattice defects acted as sinks for point defects during subsequent oxidation. Laser damage gettingter prevented the formation of oxida-

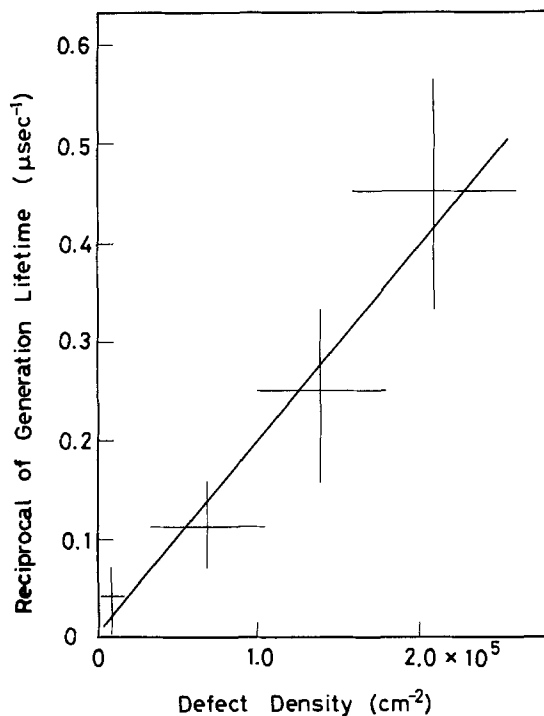


Fig. 10. $1/t_g$ vs. d curve. The tangent of this curve indicates the electrical activity of defects.

tion-induced precipitates. An energy density of at least 15 J/cm^2 was necessary to produce the laser damage which produced effective gettering.

3. Laser damage gettering improved generation lifetime in the gettered area by two orders of magnitude over generation lifetime in the ungettered area. This lifetime improvement was caused by the suppression of defect formation by laser damage gettering.

Acknowledgments

The authors wish to thank Dr. M. Kikuchi and S. Wakayama for their continuous support and encouragement through the course of this research. The authors are also grateful to S. Kawado, Y. Sato, and S. Nakazawa for valuable discussions.

Manuscript submitted Jan. 15, 1981; revised manuscript received April 1, 1981. This was Paper 485 presented at the Los Angeles, California, Meeting of the Society, Oct. 14-19, 1979.

Any discussion of this paper will appear in a Discussion Section to be published in the June 1982 JOURNAL. All discussions for the June 1982 Discussion Section should be submitted by Feb. 1, 1982.

Publication costs of this article were assisted by SONY Corporation Research Center.

REFERENCES

1. A. J. R. de Kock, S. D. Ferris, L. C. Kimerling, and H. J. Leamy, *Appl. Phys. Lett.*, **27**, 313 (1975).
2. A. J. R. de Kock, S. D. Ferris, L. C. Kimerling, and H. J. Leamy, To be published in *J. Appl. Phys.*
3. S. Kawado, Y. Hayafuji, and T. Adachi, *Jpn. J. Appl. Phys.*, **14**, 407 (1975).
4. S. Yoshikawa and J. Chikawa, *Appl. Phys. Lett.*, **23**, 636 (1973).
5. K. V. Ravi and C. J. Varker, *ibid.*, **25**, 69 (1974).
6. K. V. Ravi, C. J. Varker, and C. E. Volk, *This Journal*, **120**, 533 (1973)
7. C. J. Varker and K. V. Ravi, *J. Appl. Phys.*, **45**, 272 (1974).
8. A. H. Plantinga, *IEEE Trans. Electron Devices*, **ed-16**, 394 (1969).
9. C. H. Sequin, D. A. Sealer, W. J. Bertram, Jr., M. F. Tompsett, R. R. Buckley, T. A. Shankoff, and W. J. McNamara, *ibid.*, **ed-20**, 244 (1972).
10. A. J. R. de Kock, *Appl. Phys. Lett.*, **16**, 100 (1970).
11. K. Tanikawa, Y. Ito, and H. Sei, *ibid.*, **28**, 285 (1976).
12. Y. Hokari and H. Shiraki, *Jpn. J. Appl. Phys.*, **16**, 585 (1977).
13. Y. Hayafuji, T. Shimada, and S. Kawado, in "Semiconductor Silicon 1977," H. R. Huff and E. Sirtl, Editors, p. 750, The Electrochemical Society Softbound Proceedings Series, Princeton, NJ (1977).
14. D. Pomerantz, *J. Appl. Phys.*, **38**, 5020 (1976).
15. G. A. Rozgonyi, P. M. Petroff, and M. H. Read, *This Journal*, **122**, 1725 (1975).
16. P. M. Petroff, G. A. Rozgonyi, and T. T. Sheng, *ibid.*, **125**, 565 (1976).
17. C. M. Hsieh, J. R. Mathews, H. D. Seidel, K. A. Pickar, and C. M. Drum, *Appl. Phys. Lett.*, **22**, 238 (1973)
18. G. H. Schwuttke, K. Yang, and H. Kappert, *Phys. Status Solidi A*, **42**, 553 (1977).
19. Y. Hayafuji, Y. Aoki, and S. Kawado, Paper 3p-M-12 presented at the Fall Meeting of the Japan Society of Applied Physics, Osaka, Japan, Nov. 3-5, 1978.
20. C. W. Pearce and V. J. Zaleckas, *This Journal*, **126**, 1436 (1979).
21. Y. Hayafuji, T. Yanada, and Y. Aoki, Paper 485 presented at the Electrochemical Society Meeting, Los Angeles, California, Oct. 14-19, 1979.
22. L. E. Katz, C. W. Pearce, and P. F. Schmidt, Paper 486 presented at the Electrochemical Society Meeting, Los Angeles, California, Oct. 14-19, 1979.
23. F. P. Heiman, *IEEE Trans. Electron Devices*, **ed-14**, 781 (1967).
24. Y. Ichida, T. Yanada, and S. Kawado, ASTM STP 721, American Society for Testing and Materials, p. 107 (1980).

Single Crystal Silicon-on-Oxide by a Scanning CW Laser Induced Lateral Seeding Process

H. W. Lam, R. F. Pinizzotto,* and A. F. Tasch, Jr.*

Texas Instruments Incorporated, Central Research Laboratories, Dallas, Texas 75265

ABSTRACT

A 1 μm thick layer of silicon dioxide is grown on selected areas of a {100} silicon wafer such that the resulting silicon dioxide surface is coplanar with the surface of the silicon wafer. A 0.5 μm thick layer of polycrystalline silicon is deposited onto the silicon wafer using a low pressure CVD process. By scanning a focused CW argon laser beam onto the area where the polycrystalline silicon is deposited directly on the exposed silicon substrate, the polycrystalline silicon is converted into an epitaxial layer by a liquid phase process. By scanning the laser beam from the epitaxial region to the region where the polycrystalline silicon is deposited on the silicon dioxide layer, the polycrystalline silicon is converted into a single crystal through a zone melting process, where the previously formed epitaxial layer is used as the seed. This process is named "lateral seeding." It is found that the resulting area of the single crystal on the silicon dioxide layer is dependent on the temperature of the substrate and the crystallographic direction of the edges of the oxide layer. The best results are obtained with a high substrate temperature and with the edges of the oxide layers aligned along a $\langle 100 \rangle$ direction. Single crystal regions that extended as much as 80 μm from the epitaxial seed region onto the silicon dioxide region have been obtained. It is inferred from the experimental results that a line-shaped beam with a flat intensity profile is preferred for improved lateral seeding results.

Silicon on an insulating substrate (SOI) is an attractive material structure for high speed and high density integrated circuit application. An insulating substrate provides dielectric isolation between devices, so that they can be packed more closely together. The insulating substrate becomes increasingly important in CMOS by eliminating latch-up between devices. The insulating substrate further reduces the parasitic capacitances between devices and interconnecting metal or polycrystalline silicon lines, thus increasing the speed of the circuit. Since the active volume of silicon used in SOI is limited to that in the device islands, the susceptibility of the circuits to α -particles is greatly reduced. The most commonly used SOI material structure is silicon-on-sapphire (SOS) where the silicon epitaxial layer is grown on a sapphire substrate using conventional CVD techniques.

Recently, several laser recrystallization techniques for obtaining large grain SOI were demonstrated. Gat *et al.* (1) demonstrated that by scanning a focused laser beam on the surface of an LPCVD polycrystalline silicon (polysilicon) layer deposited on a thin silicon nitride (nitride) layer on a silicon substrate, very large grain crystallites, typically $2 \times 20 \mu\text{m}$, can be obtained. The orientation of the crystallites is random with a slight preference for {111} (2). Gibbons *et al.* (3) developed a technique for laser recrystallization of polysilicon islands on a nitride substrate. The polysilicon layer is deposited on the nitride using a standard LPCVD technique. The polysilicon islands are defined photolithographically and then formed by etching. For narrow (2 μm wide) islands, {100} single crystal has been obtained. Larger single crystal islands have been subsequently obtained with random orientations (4). Using a scanning laser beam induced graphoepitaxy technique, Geis *et al.* (5) obtained a uniformly oriented silicon film on a quartz substrate with a surface relief grating structure. Several reports of MOSFET devices fabricated in the laser recrystallized silicon-on-insulator material have demonstrated that the surface electron mobility measured in

these devices is as good as or better than those obtainable in SOS (6-12).

Except for the graphoepitaxy approach, control of the resulting orientation of the recrystallized silicon film is not possible. The fact that the grains in the laser recrystallized film are randomly oriented can probably account for the variability in the characteristics observed in devices fabricated in the laser recrystallized SOI material (11).

A silicon bridging epitaxy technique using a Q-switched, pulsed ruby laser annealing (13) was demonstrated where lateral growth of single crystal silicon over silicon dioxide (oxide) was initiated from the single crystal substrate. However, the lateral growth was limited to 1.2 μm beyond the oxide edge. This limited extent of the growth stems from the inability to control the resolidification process with the pulsed laser. Since the lateral growth technique is equivalent to the zone melting process, the control of the melt zone and the melt/solid interface is of paramount importance.

We have developed a method for obtaining large area, controlled orientation, single crystal silicon on a one micron thick oxide substrate using a scanning CW laser induced lateral seeding process involving a micro-zone melting technique. In this technique, silicon dioxide is grown in selected areas of a silicon substrate and polysilicon is deposited onto the surface of the entire wafer. By scanning a focused CW laser beam onto the polysilicon-on-silicon region, epitaxial growth is induced in the polysilicon layer. When the laser beam is scanned from the epitaxial region to the polysilicon-on-oxide region, single crystal growth is induced in the polysilicon by a melting and recrystallization process, where the previously formed single crystal epitaxial layer provides the seed (Fig. 1). This process is called "lateral seeding."

Sample Preparation

Single crystal silicon wafers of {100} orientation were used as the substrate. A 140 nm thick layer of CVD silicon nitride was deposited onto the surface of the wafers. Photoresist was applied to the surface of

* Electrochemical Society Active Member.

Key words: silicon-on-insulator, zone melting, laser induced epitaxy.

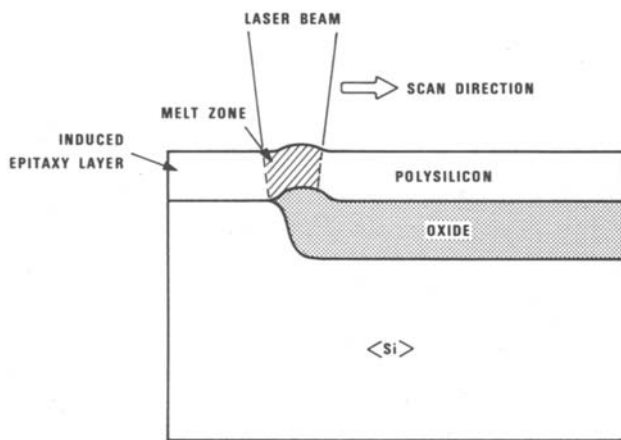


Fig. 1. Schematic representation of the lateral seeding process

the nitride layer and rectangular patterns of various sizes were defined photolithographically. After developing and baking the photoresist, the exposed nitride regions were removed by a plasma etching technique. A $0.55\ \mu\text{m}$ thick layer of the then exposed silicon was removed by an anisotropic plasma etch. After removing the photoresist, the wafers were placed in an oxidation furnace set at 1000°C with a steam ambient, timed to grow a one micron thick layer of oxide, so that the oxide surface was almost coplanar with the original silicon surface. After etching the wafers in a 10% HF solution for 90 sec, the nitride layer was removed by etching in hot phosphoric acid. The wafers were then etched in a 10% HF solution for 30 sec, dried, and loaded immediately into a low pressure CVD reactor, where a $0.5\ \mu\text{m}$ thick layer of polysilicon was deposited at 620°C . A thermal anneal in nitrogen at 1100°C for 1 hr completed the preparation. It was shown that the 1100°C anneal significantly reduces the "etching" (removing) of the polysilicon from the surface of the insulator) of the polysilicon during the laser recrystallization process (6). Without this thermal annealing step, the proper beam power window for the recrystallization of the polysilicon-on-oxide region is typically $\pm 0.5\text{W}$. Furthermore, the beam power for proper liquid phase regrowth of the polysilicon-on-silicon region is higher than the beam power for the recrystallization of the polysilicon-on-oxide region due to the higher thermal conductivity of the polysilicon-on-silicon region. Consequently, a beam power level chosen to induce epitaxial regrowth in the polysilicon-on-oxide region will be excessive for the recrystallization in the polysilicon-on-silicon region and will usually result in the removal of the polysilicon from the oxide surface. The thermal annealing widens the window of beam power for proper recrystallization of the polysilicon-on-oxide area to $\pm 3\text{W}$. The exact mechanism is not presently understood. This thermal annealing step allows the utilization of a single beam power level to be used for both regions simultaneously.

The finished structure is shown in Fig. 2. A step-like oxide substrate was also produced by growing a layer of oxide on a silicon wafer, etching away part of the oxide, and depositing a layer of polysilicon, resulting in a structure shown in Fig. 3.

Laser Processing

The laser-induced recrystallization was performed with a CW argon ion laser system similar to the one described in Ref. (14). Two different lens systems, a single 190 mm focal length spherical lens and a combination of a 300 and a 100 mm focal length cylindrical lenses, were used. Most experiments discussed were performed with the spherical lens. The raster line scan speed was 10.4 cm per sec and the line-to-line step size varied from 5 to $20\ \mu\text{m}$. The wafers were mounted

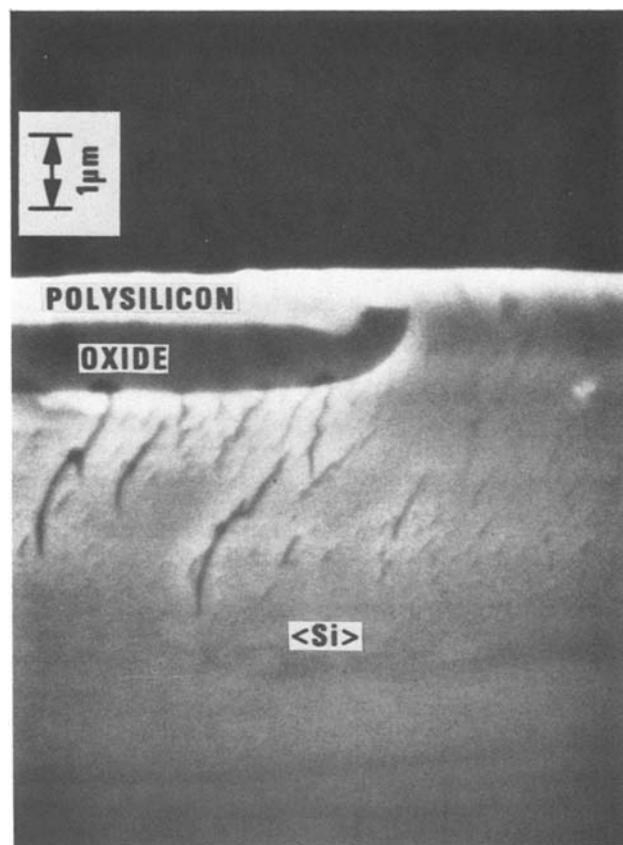


Fig. 2. Cross-sectional electron micrograph of the finished structure. The oxide layer is $0.96\ \mu\text{m}$ thick. The polysilicon layer is $0.5\ \mu\text{m}$ thick. The lines below the oxide region are artifacts of the sample preparation.

such that the lines were scanned parallel and perpendicular to the oxide and single crystal substrate interface. The wafers were held with a vacuum chuck and were heated to a temperature as high as 500°C .

The wafers were studied by optical microscopy, using a Secco etch (15) to decorate the grain boundaries and defects. We have compared the grain boundary patterns observed after Secco etching with TEM studies of the recrystallized SOI material and determined that the pattern obtained after Secco etching is a true representation of the grain structure. Electron channeling was used to study the crystallographic orientation of the laser recrystallized silicon-on-oxide material.

Results and Discussion

An optical interference contrast micrograph of a typical laterally seeded silicon-on-oxide area is shown in Fig. 4. The wafer was etched in a Secco etch for 10 sec to decorate the grain boundaries. It is generally observed that when the silicon-on-oxide area is small, such as the smaller squares at the bottom of the pic-

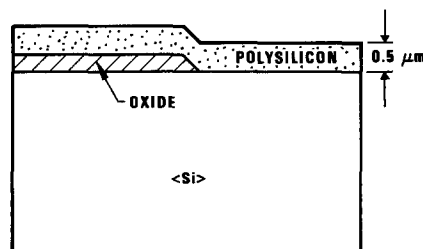


Fig. 3. Schematic representation of a cross-sectional view of a sample with a thin oxide step. The oxide layer is usually thinner than $0.25\ \mu\text{m}$.

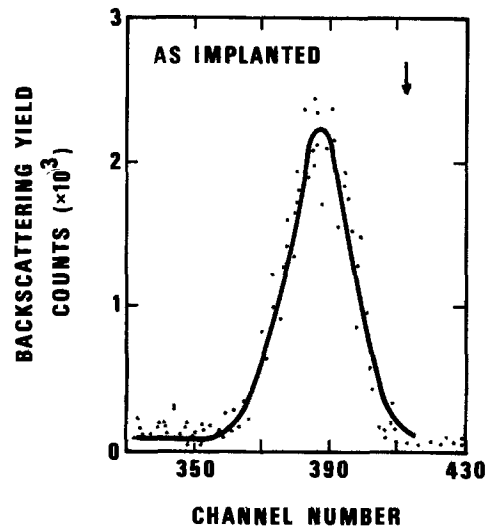


Fig. 4. An optical interference contrast micrograph of a lateral seeding area after etching in a Secco etch for 10 sec. The two large square silicon-on-oxide areas are $70 \times 70 \mu\text{m}^2$ in size. The 13W laser beam scanned from left to right and the lines stepped from top to bottom.

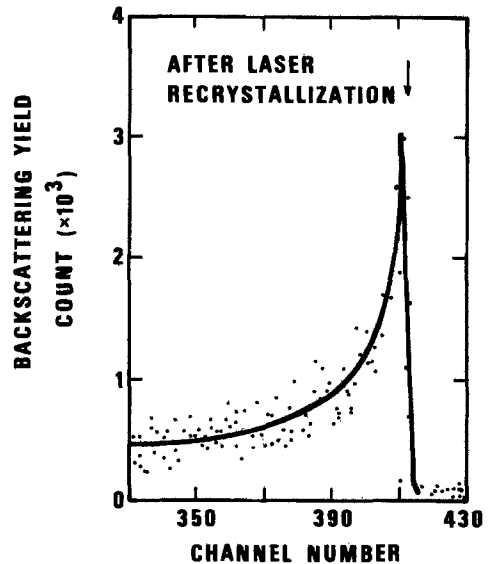
ture, no grain boundaries are observed, indicating that the silicon layer is a single crystal. For the silicon-on-oxide areas that are larger in size, large single crystal regions that are free of grain boundaries are obtained immediately adjacent to the epitaxial regions, but the entire silicon-on-oxide region is not of one orientation.

The laser scan lines are also evident in Fig. 4. It is interesting to note that the single crystal region extended over three successive scan lines, indicating that the single crystal silicon-on-oxide area formed during the first scan served as the seed for the growth during the subsequent scans. Therefore, the single crystal area indeed propagated laterally, using the previously formed single crystal as the seed.

It should also be noted that the smaller square oxide substrates had been displaced from their original position. The displacement is always in the direction of scan of the beam. This displacement is probably caused by the melting of the silicon substrate during the laser process. If the recrystallized layer were to be used for device application, the displacement would cause severe difficulties in placing the device in the SOI region. By measuring the redistribution of implanted dopant after the laser process, we have confirmed that the epitaxial growth in the polysilicon-on-silicon region was induced through the liquid phase. In one wafer, arsenic was implanted into the polysilicon layer at 90 keV to a dose of $5 \times 10^{15} \text{ cm}^{-2}$. The wafer was laser-recrystallized at power levels ranging from 7 to 15W, using conditions similar to those described earlier. Rutherford backscattering spectroscopy was performed in the polysilicon-on-silicon region before and after the laser process and the results are shown in Fig. 5. A very strong segregation of the arsenic was observed at the surface of the laser-recrystallized epitaxial layer, indicating that melting had occurred. As the molten region regrew epitaxially, the implanted arsenic was segregated out at the surface by a process similar to zone refining (16). Furthermore, the arsenic could be detected as far as $2 \mu\text{m}$ into the substrate, indicating that melting occurred beyond the polysilicon-silicon interface and the epitaxial growth proceeded in the liquid phase. Since the thermal conductivity in the polysilicon-on-oxide region is lower than that in the polysilicon-on-silicon region and over 99% of the laser power is absorbed in the $0.5 \mu\text{m}$ thick polysilicon layer, the polysilicon on the oxide substrate is, therefore, also melted by the beam at these power levels.



a. The RBS spectrum of the as-implanted sample with the peak of the profile located 53 nm from the surface.



b. The RBS spectrum of the sample after the laser process with a 12W laser power. A strong segregation at the surface is evident.

Fig. 5. Rutherford backscattering spectra of the arsenic-implanted polysilicon-on-silicon. The arrow in the figures indicates the polysilicon surface.

Figure 4 shows a high etch pit density in the epitaxial region while the etch pits are only sparsely distributed in the single crystal on oxide area. This indicates that the beam power optimized for the silicon-on-oxide region is not optimized for the silicon-on-silicon region and results in damage in the epitaxial layer. Electron channeling experiments which have a resolution of about $2 \mu\text{m}$ were performed and a typical result is shown in Fig. 6a and b. By focusing and rocking a 40 keV electron beam in the laser-recrystallized polysilicon-on-silicon region, a distinct electron diffraction pattern is observed, indicating that the polysilicon has regrown epitaxially on the single crystal substrate. By moving the beam so that the single crystal silicon-on-oxide area was illuminated, a distinct electron diffraction pattern is again obtained. Furthermore, this diffraction pattern indicates that the single crystal silicon-on-oxide area has the same orientation as the substrate.

The behavior of the silicon crystal growth in the lateral seeding process can be understood with the aid of Fig. 7-9. Figure 7 shows a schematic representation

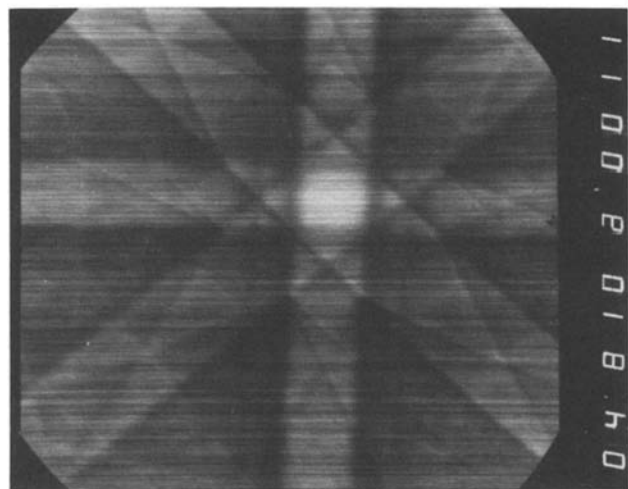
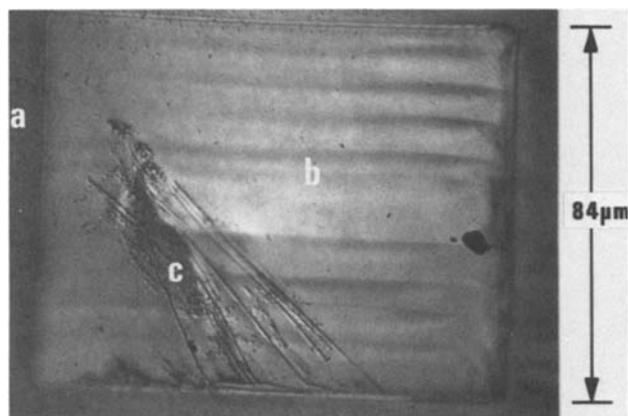


Fig. 6. (a, top) shows an optical interference contrast micrograph of a polysilicon-on-oxide region after the laser process. The electron diffraction pattern shown in b (bottom) is obtained when regions a and b in Fig. 6a are illuminated with the electron beam. Region a is the polysilicon-on-silicon epitaxial layer and region b is the polysilicon-on-oxide which has been converted to single crystal by the laser. The bulging region indicated by "c" is clustered with defects and no electron diffraction pattern is obtained at region c. The rectangular silicon-on-oxide region is 107 μm long \times 84 μm wide.

of a laser beam scanning over a polysilicon-on-oxide region. The silicon region illuminated by the laser beam is melted, forming a small, localized molten zone of silicon on the oxide. As the beam is scanned, the silicon near the trailing edge of the beam cools rapidly. As the molten silicon recrystallizes, it is seeded from the silicon immediately adjacent to the molten zone. Furthermore, the grains grow in a direction normal to the isotherms, namely, in the direction of the thermal gradient which points toward the center of the beam. This is responsible for the chevron-shape grain structure observed (1) (Fig. 8).

The lateral seeding process is represented in Fig. 9. When a laser scan line represented by I is scanned parallel to an interface between a silicon substrate and an oxide layer, with more than 50% of the beam overlapping the oxide layer, the grain growth at the edge of the oxide layer will be seeded by the epitaxial layer. Because of the higher thermal conductivity in the polysilicon-on-silicon region, the epitaxial layer in the region solidifies earlier than the polysilicon-on-oxide region (13). Therefore, the molten silicon on the edge of the oxide layer is seeded with a single crystal epitaxial region and the single crystal propagates into the oxide region along the thermal gradient, as indicated in Fig. 9. The grain growth from the bottom half

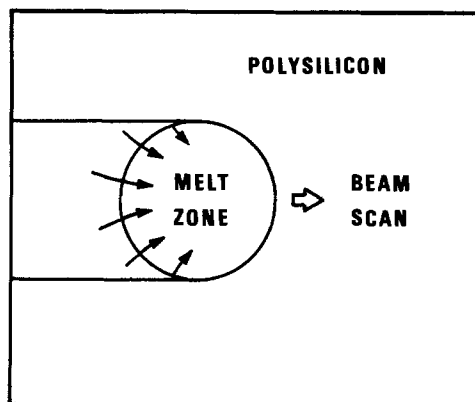


Fig. 7. Schematic representation of a top view of a laser beam scanning over a polysilicon-on-oxide region. The beam induces a zone of molten silicon, which travels as the beam is moved. The molten silicon cools and crystallizes at the trailing edge of the molten zone. The arrows in the diagram indicate the thermal gradient and therefore the directions along which the crystals will grow.

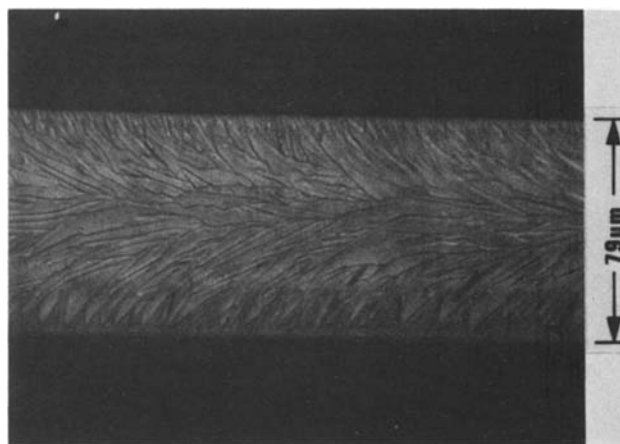


Fig. 8. An optical interference contrast micrograph of a polysilicon-on-oxide region after it is recrystallized by a single scan of the focused laser spot at 13W and then etched in a Secco etch for 10 sec. The laser beam scans from left to right. The chevron-shaped crystals are evident. The width of the recrystallized region is 79 μm .

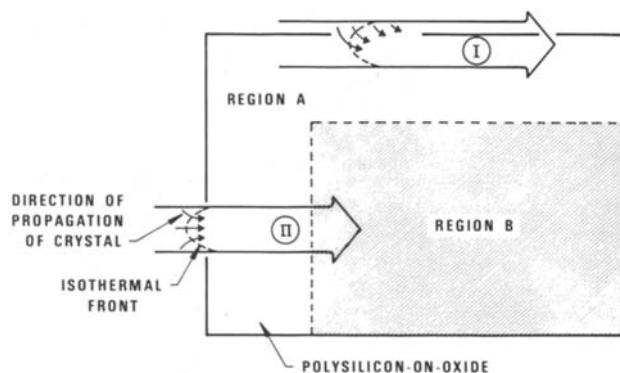


Fig. 9. Schematic representation of lateral seeding. The polysilicon-on-oxide region is surrounded by the polysilicon-on-silicon region. Beam I represents transverse seeding and beam II represents longitudinal seeding.

of the beam is seeded from the polysilicon. On subsequent scans and as long as the scan lines are overlapping by more than 50%, the grain growth from the top half of the molten silicon is seeded by the previously formed single crystal. The successive lateral

seeding process is evident in Fig. 4. Since the single crystal silicon region propagates over the oxide layer from the seed region in a direction transverse to the direction of the scan of the beam, this lateral seeding mode is called transverse seeding. In the case of a scan line represented by II, the crystals again grow normal to the thermal gradient as depicted in Fig. 9. Since the single crystal region propagates into the silicon-on-oxide region from the seed region in the direction of scan of the beam, we call this mode of seeding longitudinal seeding. On oxide layers with a large surface area, the polysilicon in region A is usually converted to single crystal while that in region B is converted to elongated polycrystalline grains.

It has consistently been observed that the transverse seeding mode yields larger single crystal silicon-on-oxide areas than the longitudinal mode, even after multiple scans. It is believed that the shape of the beam, the intensity distribution of the beam, and the isothermal surfaces induced in the silicon are responsible for this result. When the circular laser spot is scanned across the surface of the silicon, the motion of the laser spot induces an elliptically shaped isotherm in the thin silicon layer (17). It is known that thermal stress is induced by a nonplanar solid/melt interface because of the differential rate of contraction across the crystal (18). Furthermore, when a solid/melt interface has a small radius of curvature, point defects can be trapped more easily in the solid, and there is also an increased chance of spurious nucleation (19). In the transverse mode, the crystals are growing normal to an isotherm that has a larger radius of curvature than that of the longitudinal seeding case. Therefore, we would expect that the single crystal growth is more favored in the transverse mode than the longitudinal mode.

Defects are usually formed near the corner where the beam enters the oxide substrate region (Fig. 10). We believe that the clustering of defects, which subsequently leads to the formation of grain boundaries, is probably caused by the crystalline mismatch of the two single crystals propagating in the transverse and the longitudinal directions. In the micrograph shown in Fig. 6, there is significant bulging of the silicon layer where there is a high defect density. This bulging is probably caused by a "snow plow" effect in the laser process where some silicon is "pushed" ahead of the beam. This kind of matter transport is very common in the zone melting process (16) and is due to the expansion in volume in the silicon during solidi-



Fig. 10. An optical interference contrast micrograph of a lateral seeding sample after etching the sample in a Secco etch for 10 sec. The long polysilicon-on-oxide strip in the center of the micrograph is $194 \mu\text{m}$ long \times $55 \mu\text{m}$ wide and is completely converted to single crystal except for a small region near the corner where the beam entered the oxide substrate region. The laser scanned from left to right and the lines stepped from top to bottom.

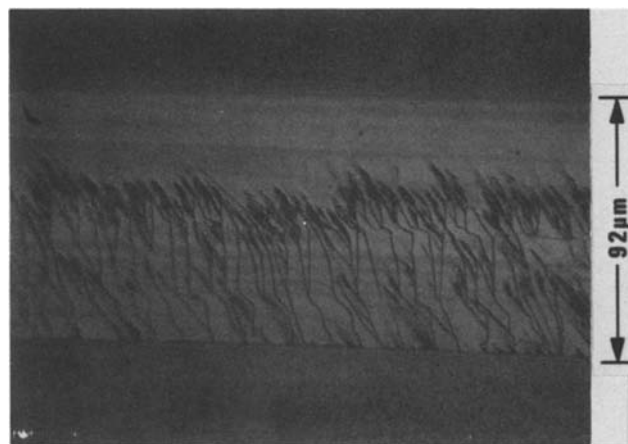


Fig. 11. An optical interference contrast micrograph of the lateral seeding sample after etching the sample in a Secco etch for 10 sec. The laser scanned from left to right and the lines stepped from top to bottom. The silicon-on-oxide strip in the middle of the picture is $92 \mu\text{m}$ wide. The feather-shaped defect clusters are evident. The defect clusters are formed in the silicon after the single crystal extended about $30 \mu\text{m}$ from the epitaxial seed region immediately above the silicon-on-oxide region.

fication. This "snow plow" effect is only observed when the beam power is excessively high. At a power level just sufficiently high enough to induce lateral seeding, no bulging due to matter transport is observed.

Large areas of single crystal SOI have been obtained by using transverse lateral seeding. Figure 10 shows a typical result of a $55 \times 194 \mu\text{m}^2$ silicon-on-oxide region. Our best result to date is a lateral growth of approximately $80 \mu\text{m}$ (Fig. 6). Figure 11 demonstrates that a feather-shaped cluster of defects is commonly formed after the lateral growth has proceeded beyond some critical distance. This distance is found to be proportional to the substrate temperature. There are several possible explanations for this phenomenon. The defects may be caused by thermal stress. A higher substrate temperature reduces the thermal gradients and, thus the stress due to these gradients. Alternatively, the higher substrate temperature may reduce the number of grown-in defects. If a critical dislocation density is needed to destroy crystallinity (20), a longer distance must be traversed before this occurs. A related explanation is that the rate of dislocation formation at the silicon-silicon dioxide interface is inversely proportional to the temperature. Once again, longer growth distances would be needed before grain boundary formation occurs. There is insufficient experimental evidence available to reach any conclusions.

When the nitride patterns are defined such that the resulting oxide layers have their edges along a $\langle 100 \rangle$ direction, the best lateral seeding results were obtained. When the edges of the oxide layers are along a $\langle 110 \rangle$ direction, the extent of the single crystal growth is typically 20 - $30 \mu\text{m}$, while the growth is typically 50 - $80 \mu\text{m}$ in the $\langle 100 \rangle$ case. This result is believed to be a consequence of the fact that, in silicon, growth along the $\langle 100 \rangle$ directions has a higher rate.

We have also performed lateral seeding experiments where the oxide layer was grown on top of the silicon wafer so that there was a step at the edge of the oxide areas. The single crystal growth in those wafers is limited to about $20 \mu\text{m}$, at best, and slip planes are usually observed. Wafers with $\{110\}$ and $\{111\}$ orientations were also used and the results were comparable to those obtained with $\{100\}$ materials.

By using a combination of the two cylindrical lenses to obtain an elliptically shaped beam with its shorter axis along the direction of scan, we have been able to obtain improved results in the longitudinal seeding case. The single crystal typically grows longitudinally

into the oxide substrate region by as much as 50 μm . Since the radius of curvature of the isothermal surfaces is increased with an elliptically shaped beam, it is not surprising that the single crystal area extended further over the oxide layer.

It is apparent from the experimental results that the laser beam, with a Gaussian intensity profile and a trailing edge that is convex to the direction of scan, is not an ideal radiation source for the lateral seeding process. These two attributes of the laser beam promote radial cooling and, therefore, thermal stress in the material and spurious nucleation at the outermost and, therefore, the coolest portion of the scanned region. Therefore, if one can obtain a radiation source that has a trailing edge that is flat or concave to the direction of scan and a "top-hat" intensity profile, these problems can be overcome. This conclusion was also arrived at for traditional zone melting experiments (18). If this radiation source is available, the longitudinal mode of lateral seeding is preferred. From the throughput consideration, the argon laser beam, with a power output limited to about 20W for available commercial sources, is also undesirable since it is estimated that with the scan speed and line-to-line overlap used presently it will take about 30 min to complete a silicon wafer 3 in. in diameter. It is believed that a scanning stripe-shaped electron beam or a scanning focused spot of rod-shaped quartz lamp may be potential alternate sources for the laser.

Summary

We have developed the lateral seeding process to obtain single crystal silicon-on-oxide. This process is similar to the zone melting process, but is performed on a very small scale. Given the beam shape of the focused laser spot, two modes of lateral seeding, transverse and longitudinal, have been distinguished. The best results are obtained when the edges of the oxide substrates are aligned in the $\langle 100 \rangle$ directions in $\{100\}$ oriented wafers, and with the laser scanning in the transverse mode. Furthermore, a higher substrate temperature results in a larger single crystal on oxide region. It has also been shown that the isothermal surfaces induced in the silicon and, therefore, the shape and intensity profile of the beam are the controlling parameters in determining the laterally seeded growth. From the experimental result, it is expected that the ideal radiation source for lateral seeding is one that has a trailing edge that is linear or concave toward the directions of scan and a flat or "top-hat" intensity distribution profile. If this kind of a beam shape and intensity profile can be obtained, probably by a stripe-shaped electron beam or a focused spot of a line-shaped high intensity lamp, then improved lateral seeding results can be obtained by scanning in the longitudinal mode.

It is worth noting that although the single crystal area obtainable in the present experiments is relatively small, this area is large enough for the fabrication of active devices for VLSI applications. The single crystal substrate seed area can be placed adjacent to each of the active device areas in the circuit so that after the lateral seeding process, the active devices can then be fabricated in the single crystal silicon-on-oxide area. Hence, a truly single crystal silicon-on-oxide

IC can be fabricated. Although the laterally seeded area is not free of defects, the etch pits obtained after a Secco etch are only sparsely distributed. A study of the microstructure of the laterally seeded material is underway, and the results will be reported in a later publication.

Acknowledgment

The authors are grateful to Dr. B. Y. Tsaur for performing the Rutherford backscattering experiments. This work is supported in part by the Office of Naval Research (M. N. Yoder) and the Defense Advanced Research Project Agency (Dr. R. Reynolds) through Contract No. N00014-79-C0790.

Manuscript submitted Jan. 13, 1981; revised manuscript received March 12, 1981.

Any discussion of this paper will appear in a Discussion Section to be published in the June 1982 JOURNAL. All discussions for the June 1982 Discussion Section should be submitted by Feb. 1, 1982.

Publication costs of this article were assisted by Texas Instruments Incorporated.

REFERENCES

1. A. Gat, L. Gerzberg, J. F. Gibbons, T. J. Magee, J. Peng, and J. D. Hong, *Appl. Phys. Lett.*, **33**, 775 (1978).
2. T. I. Kamins, K. F. Lee, and J. F. Gibbons, *ibid.*, **36**, 550 (1980).
3. J. F. Gibbons, K. F. Lee, T. J. Magee, J. Peng, and R. Ormond, *ibid.*, **34**, 831 (1979).
4. D. K. Biegelsen, N. M. Johnson, G. T. McKinley, and M. D. Moyer, in "Laser and Electron Beam Processing of Materials," C. W. White and P. S. Peercy, Editors, pp. 569-574, Academic Press, New York (1980).
5. M. W. Gels, D. C. Flanders, and H. I. Smith, *Appl. Phys. Lett.*, **35**, 71 (1979).
6. A. F. Tasch, Jr., T. C. Holloway, K. F. Lee, and J. F. Gibbons, *Electron Lett.*, **15**, 435 (1979).
7. K. F. Lee, J. F. Gibbons, K. C. Saraswat, and T. I. Kamins, *Appl. Phys. Lett.*, **35**, 173 (1979).
8. T. I. Kamins, K. F. Lee, J. F. Gibbons, and K. C. Saraswat, *IEEE Trans. Electron Dev.*, **ed-27**, 290 (1980).
9. H. W. Lam, A. F. Tasch, Jr., T. C. Holloway, K. F. Lee, and J. F. Gibbons, *IEEE Electron Dev. Lett.*, **edl-1**, 99 (1980).
10. J. F. Gibbons and K. F. Lee, *ibid.*, **edl-1**, 117 (1980).
11. H. W. Lam, A. F. Tasch, Jr., and T. C. Holloway, *ibid.*, **edl-1**, 206 (1980).
12. T. I. Kamins and P. A. Pianetta, *ibid.*, **edl-1**, 214 (1980).
13. M. Tamura, H. Tamura, and T. Tokuyama, *Jpn. J. Appl. Phys.*, **19**, L23 (1980).
14. A. Gat and J. F. Gibbons, *Appl. Phys. Lett.*, **32**, 142 (1978).
15. F. Secco d'Aragona, *This Journal*, **119**, 948 (1972).
16. W. G. Pfann, "Zone Melting," Chap. 2, John Wiley & Sons, Inc., New York (1958).
17. Y. I. Nissim, A. Lietoila, R. B. Gold, and J. F. Gibbons, *J. Appl. Phys.*, **51**, 274 (1980).
18. D. C. Bennett and B. Sawyer, *Bell Syst. Tech. J.*, **35**, 637 (1956).
19. W. D. Lawson and S. Nielsen, "Preparation of Single Crystals," p. 191, Academic Press, New York (1958).
20. W. D. Lawson and S. Nielsen, "Preparation of Single Crystals," p. 193, Academic Press, New York (1958).

Open-Tube Diffusion

Mike Chang*

General Electric Company, Syracuse, New York 13221

ABSTRACT

In the power semiconductor industry, aluminum, the fastest diffusion p-type species in silicon, has been used for years but due to the active nature of the process, it was only performed in closed-tube systems. Now, however, aluminum diffusion has been achieved in an open ambient. The related properties of this diffusion technique, together with the characteristics of the devices made with this diffusion process, are described.

Aluminum is the fastest p-type diffusion species for silicon. The diffusion coefficient of aluminum is three times higher than that of gallium and five times higher than that of boron. In the power semiconductor industry, where deep junctions are required, aluminum diffusion has been used for years, but due to the active chemical nature of the process, it can only be achieved in closed-tube systems, as shown in Fig. 1. The resultant surface concentration of aluminum is very low ($\sim 10^{16}$ atoms/cm³) and many researchers have spent considerable time and effort trying to understand this low surface concentration mechanism (1, 2). It is well accepted that aluminum vapor has a strong affinity to silicon dioxide. The presence of SiO₂ can retard the usable aluminum vapor generation. Based on a thermochemical analysis, Rai-Choudhury, Selim, and Takei (3) concluded that in an all-quartz closed-tube system, the surface concentration is low due to an effective reduction of aluminum partial pressure through interactions with SiO₂, SiO, residual moisture, and oxygen. By aluminizing the quartz tube wall, Kao (2) did obtain a higher surface concentration diffusion.

Nevertheless, the closed-tube diffusion is a tedious and expensive process, involving pump-down and seal-off and usually the quartz envelopes must be discarded after each use. It is highly desirable, then, to have an open-tube system for aluminum diffusion. A semi-open tube system was developed by Rosnowski (4), who performed aluminum diffusion in a regular diffusion tube under high vacuum, but strictly speaking, this is still a closed-tube system. Nevertheless, the diffusion tube can be reused many times.

After considerable experimentation, we have successfully performed aluminum diffusion in an open ambient.

Experimental Work

Various types of diffusion sources were used (Fig. 2). Among these, aluminum-coated silicon wafers, aluminum-doped silicon wafers, and elemental aluminum yielded the best results. When source wafers were used, they were loaded alternately with the target wafers, as for BN diffusion, such that every target wafer faces a source wafer; the ambient can be argon or nitrogen. Some hydrogen can also be added if desired. It is important to keep oxygen away from this system; a partial pressure of 0.5% oxygen can severely retard the aluminum diffusion and a partial pressure of 1% can completely shut off the diffusion process. Normally, the source and target wafers were loaded into a quartz boat. The boat and wafers were then placed in a 100 mm quartz tube for diffusion. The diffusion temperature ranged from 1100° to 1250°C. The resultant surface concentration is about 2×10^{18} atoms/cm³ on the target wafers. The aluminum-coated source wafers (ACS) were made by coating 2000Å of pure aluminum onto high resistivity silicon. After diffusion, the surface concentration of the ACS wafers is about 1×10^{19}

atoms/cm³ which is in the range of the solid solubility of aluminum in silicon at the temperature range involved. The aluminum-doped silicon wafers (ADS) were made by pulling a silicon rod from a melt, a process that lends itself to tight control of the doping concentration of aluminum in silicon. Each doped silicon rod can be cut into hundreds of ADS wafers. In the case of the elemental aluminum source, a special sapphire plate and tubes were used. The elemental aluminum chunks were stored in the sapphire tube and this assembly was entered into the diffusion tube at the upper stream of the gas flow. The target wafers were loaded into a lad-

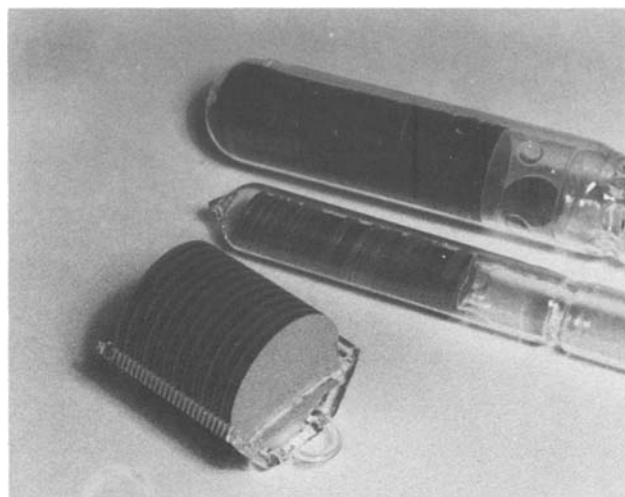


Fig. 1. A comparison of closed and open tube systems

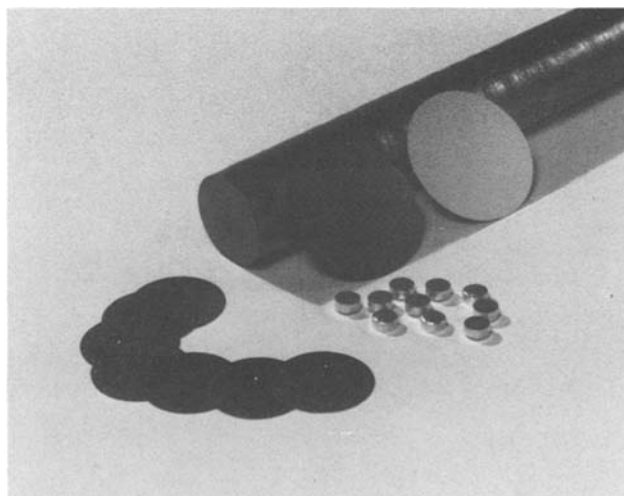


Fig. 2. Various sources for open-tube aluminum diffusion

* Electrochemical Society Active Member.
Key words: aluminum diffusion, semiconductor, device.

der-type boat so that they were parallel to the gas flow, for better uniformity of diffusion. In most cases, the diffusion temperature was about 1200°C or less.

For some applications, a lower surface concentration and graded junction are required for higher reverse junction blocking capability. This type of diffusion profile can be achieved via a two-step process. Wafers were diffused at 1200°C for 2-4 hr to obtain a 15-20 μm deep aluminum diffusion; then a drive-in process without source wafers followed. The drive-in temperature can be higher than 1200°C and the diffusion time depends on the required depth of the device junction. In this case, the ambient can contain some oxygen. If a higher surface concentration is required for better ohmic contact and injection level, a thin layer of aluminum (<1000Å) can be deposited on the target wafers directly. After diffusion, the surface concentration may reach 1×10^{19} atoms/cm³.

Results and Discussion

Figure 3 shows both the lap-and-stain and the spreading-resistance profile photos of a typical 20 hr open-tube aluminum diffusion with ACS source wafers at 1200°C. The diffusion results for a ACS source wafer (direct aluminum diffusion in this case) are shown in Fig. 4. The surface concentration of a direct aluminum diffusion is about five times higher than that from the cross-diffusion for target wafers.

The ACS wafers can be used repeatedly. As a matter of fact, it is better to precondition these source wafers before using them. Normally, we heat-treat the fresh ACS wafers at a higher temperature (~1250°C) for a long time so that the aluminum diffuses deep into the silicon bulk, thus extending their usable lifetime. After this prediffusion treatment, such ACS wafers can be used many times with consistent results; in one experiment, ACS wafers were reused 13 times (each time as a source for diffusion at 1200°C for 15 hr), and there was no noticeable decline of surface concentration of

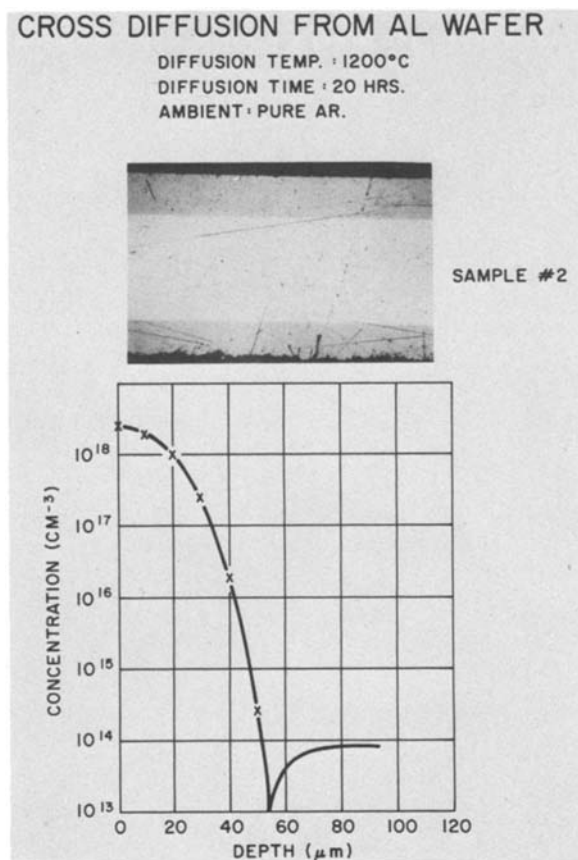


Fig. 3. The doping profile of a target silicon wafer obtained from an open-tube aluminum diffusion.

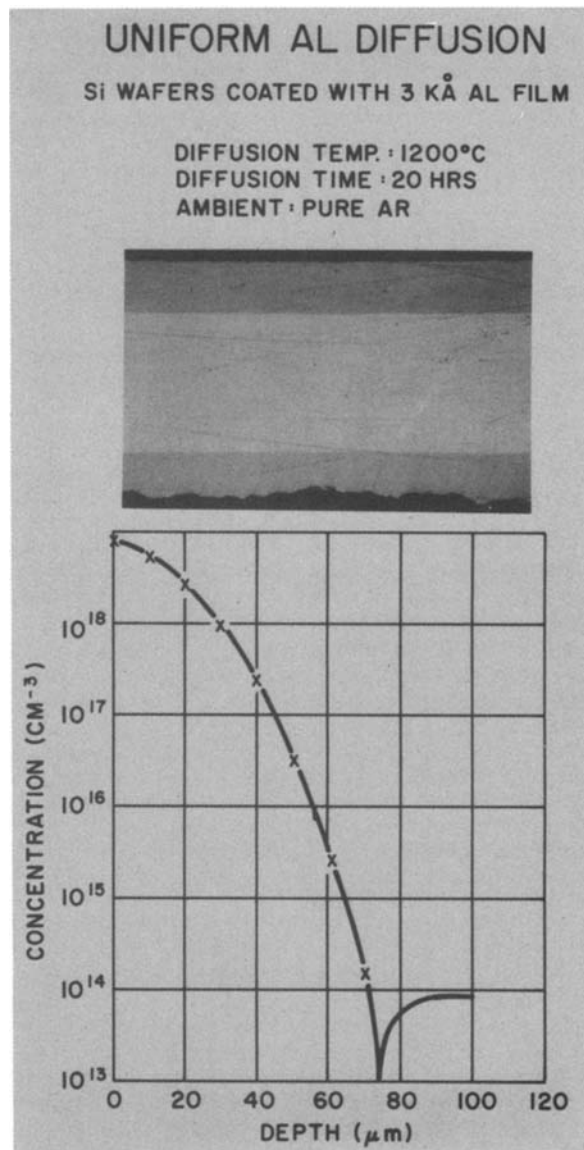


Fig. 4. The doping profile of an aluminum-coated silicon wafer obtained from an open-tube aluminum diffusion.

diffused target wafers (Fig. 5). Without pretreatment, ACS wafers tend to emit lumps of aluminum from their surfaces. Sometimes these lumps may reach target wafers, increasing the local surface concentration. Surface damage can also occur as a result of heavy local aluminum diffusion in target wafers.

Diffusion under these conditions will normally have a consistent erfc profile with a surface concentration of about 2×10^{18} atoms/cm³ at 1200°-1250°C. We found that the surface concentration is not sensitive in the upper diffusion temperature but drops drastically at lower temperatures (<1150°C), as shown in Fig. 6.

The surface concentration increases with diffusion time in the early stages of the process, as shown in Fig. 7. This feature has been utilized to create a diffusion profile of low surface concentration with deep penetration. In this case, a two-step process (predeposition and drive-in) was used to obtain the required profile. This type of process is consistent; for example, in one experiment, the same ACS wafers were used five times to diffuse target wafers. Each time, there was a 2 hr predeposition in argon at 1200°C followed by a 10 hr drive-in in oxygen. The variation in the diffusion results is less than 10% as shown in Fig. 8. This two-step technique has been used to make several diodes and SCR's.

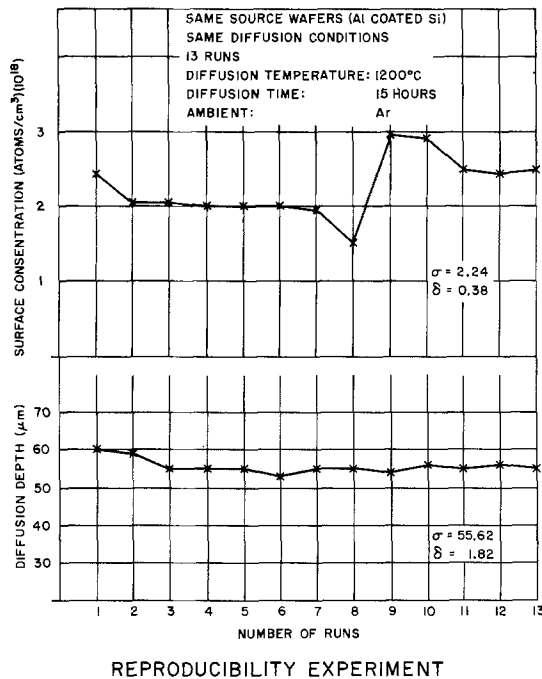


Fig. 5. Diffusion data for 13 runs, using the same source wafers to demonstrate reproducibility.

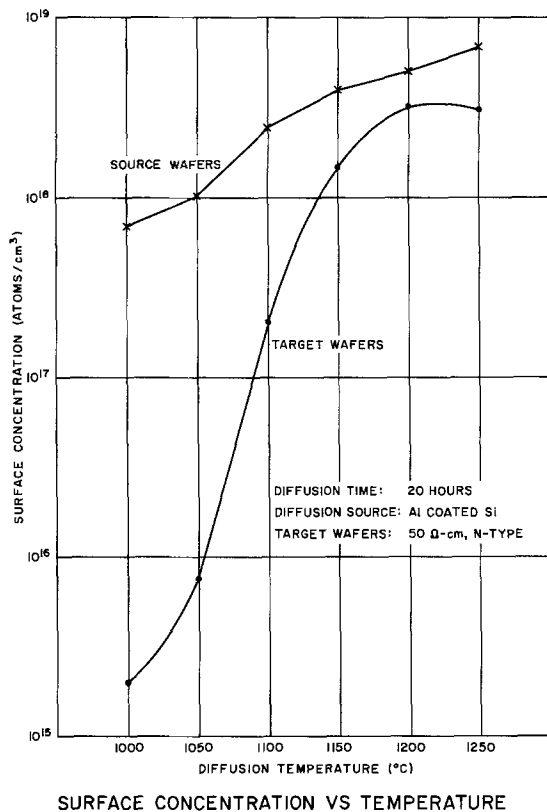


Fig. 6. Diffusion profile as a function of diffusion temperature

In order to compare this open-tube process with conventional boron diffusion, 9 mm diodes were made using the two processes with the resulting profile kept identical for both cases. The starting material was 50-70 Ω-cm, n-type single crystal silicon. It is interesting that the open-tube processed diodes can block up to 1500V, while the boron-diffusion diode can only block up to 1000V. This is due, possibly, to a more favorable lattice match for aluminum atoms in silicon, compared to boron in silicon (6). We also made a direct comparison of gallium diffusion and the open-tube aluminum diffusion. The C441 SCR (silicon control rectifier) was

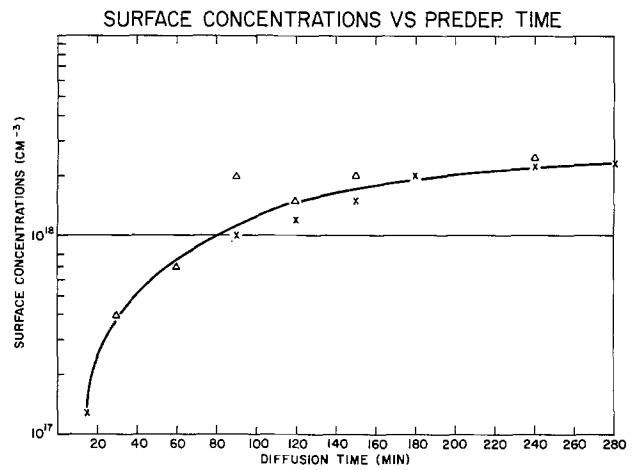


Fig. 7. Diffused surface concentration as a function of diffusion time at 1200°C.

REPRODUCIBILITY

SAME SOURCE WAFERS
 SAME DIFFUSION CONDITIONS
 PRE-DEP CYCLE : 1200°C, 2 HRS., AR.
 DRIVE-IN CYCLE : 1200°C, 10 HRS., O

| | PREDEPOSITION | | DRIVE - IN | |
|------|-----------------|-------|-----------------|----|
| | N _{SP} | μm | N _{SP} | μm |
| 1 ST | 5.0E17 | 15.75 | 6E16 | 47 |
| 2 ND | 2.0E17 | 13.5 | 5E16 | 50 |
| 3 RD | 6.0E17 | 16.0 | 4E16 | 44 |
| 4 TH | 5.0E17 | 17.5 | 5E16 | 50 |
| 5 TH | 5.0E17 | 13.0 | 5E16 | 45 |

Fig. 8. Diffusion data from five consecutive diffusions using the same source wafers.

chosen as a test vehicle. This device is a standard product rated at 1800V and the blocking junction is made via a gallium diffusion step.

Some C441 devices were made with an open-tube aluminum diffusion at 1200°C substituting for the standard 1250°C gallium diffusion. Aluminum has a higher diffusion coefficient at 1200°C than gallium has at 1250°C. Therefore, even at a reduced temperature, the diffusion time was shortened for the open-tube aluminum diffusion, to realize the same diffusion profile. It is well known that the higher the diffusion temperature, the worse the carrier lifetime. The characteristics of these open-tube aluminum C441 devices demonstrate this fact. The open-circuit decay measured carrier lifetime is around 50 μsec. This better lifetime directly reflects on device performance. The forward drop at 1500A is only 1.3V, in contrast to 1.5V for the standard gallium-diffused C441.

Ideally, ADS wafers should do equally as well as ACS wafers. In the case of ADS wafers, a silicon rod is pulled from a melt with precise control of the doping concentration. Each doped silicon rod can then be cut into hundreds of ADS wafers. There are three major advantages in using ADS wafers for the open-tube diffusion process: (i) They are cheaper than the ACS wafers, (ii) they are cleaner, and (iii) they lend themselves more easily to control of the doping concentration. Generally speaking, ADS wafers are also more

desirable for their consistency and reliability. However, at this moment, no silicon vendor can offer the required ADS wafers at a reasonable price. We managed to grow three silicon rods in a Cz puller. The diffusion profiles from these source wafers are good. Hopefully, with more demand, some silicon vendors will soon provide ADS wafers at reasonable prices.

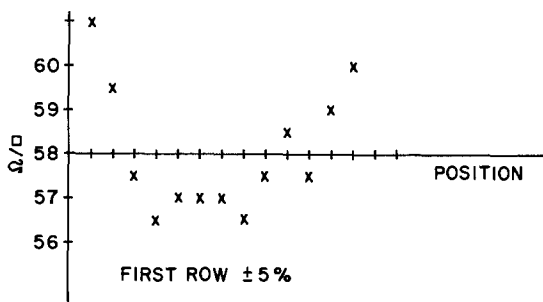
In the case of elemental aluminum diffusion, the source was located in the upper stream and the target wafers were arranged so that they were parallel to the gas flow. In a typical run, 15 wafers were loaded into each row of a 3-row quartz boat. They were diffused at 1200°C for 20 hr. The sheet resistivity was uniform across each row, as shown in Fig. 9. The variation is less than ±5%. However, the two outermost wafers, due to the gas-flow pattern, have a very high resistivity (low diffusion concentration). In production, it would be wise to place two dummy wafers at the outermost position of each row.

The diffusion coefficient of aluminum in silicon has been calculated from many diffusion runs. From this study, it is clear that the diffusion coefficient is also dominated by the surface concentration. For the aluminum-coated source wafers, due to severe surface damage by the aluminum-silicon alloy and the resultant high surface concentration (>10¹⁹), the diffusion coefficient is higher than for the target wafers, as indicated in Fig. 10. In general, the data in this study are quite close to previously published data (5) at higher temperature ranges (>1000°C). However, the diffusion coefficient has a pronounced different slope in the lower temperature ranges. There are no published data in this temperature range. We do not yet have a satisfactory explanation for this phenomenon.

It was also found that a strong interaction between aluminum vapor, quartz, and/or oxygen existed. As the oxygen content in the main flow stream rises to 1%, no cross-aluminum diffusion occurs. We have witnessed the effect of aluminum source depletion in the vicinity of quartz. For most of this study, quartz boats were used to hold the wafers for diffusion. It is also interesting that there was an n-type inversion layer in the spot of target silicon where it touched the slot of the quartz boat. This n-type inversion is clearly a result of the combined effect of aluminum, silicon, and oxygen. We are still studying the exact nature of this phenomenon. A small distance (≅30 mils) away from this spot, the

ELEMENTAL ALUMINUM SOURCE

TEMP: 1200°C
 TIME: 20 HRS.
 AMBIENT: AR.
 ARRAY: 4 ROW x 15 WAFERS



FIRST ROW 57.5 Ω/□
 SECOND ROW 71.5 Ω/□
 THIRD ROW 85.0 Ω/□
 FOURTH ROW 109.0 Ω/□

Fig. 9. Diffusion data across a row of silicon wafers using an elemental aluminum source.

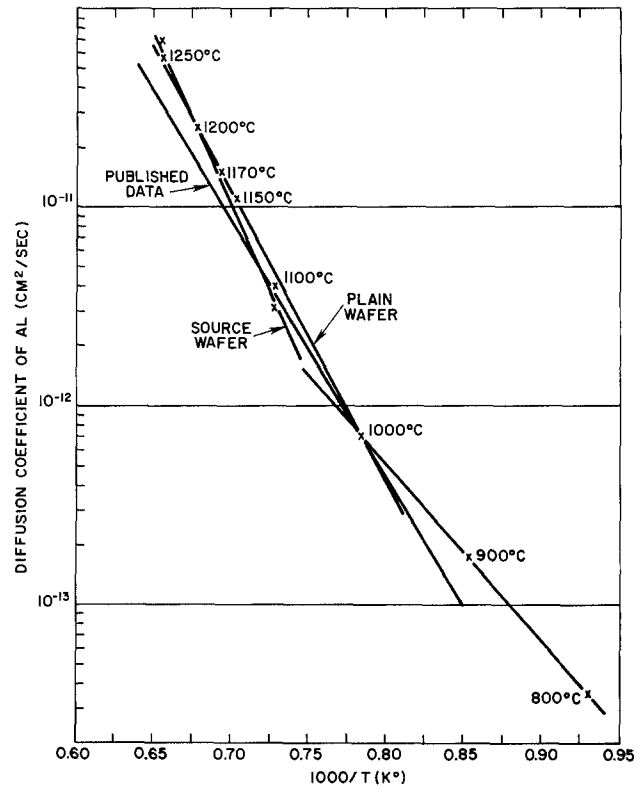


Fig. 10. Measured and calculated aluminum diffusion coefficients compared to published data.

n-type inversion disappears, but the effect of source depletion is still there to reduce the surface concentration of diffusion, as shown in Fig. 11. This source depletion and n-type inversion effect also occurs in other areas of silicon wafers if some silicon oxide is present. For example, a silicon dioxide mask was used in one

DEPLETION OF ALUMINUM SOURCE BY QUARTZ

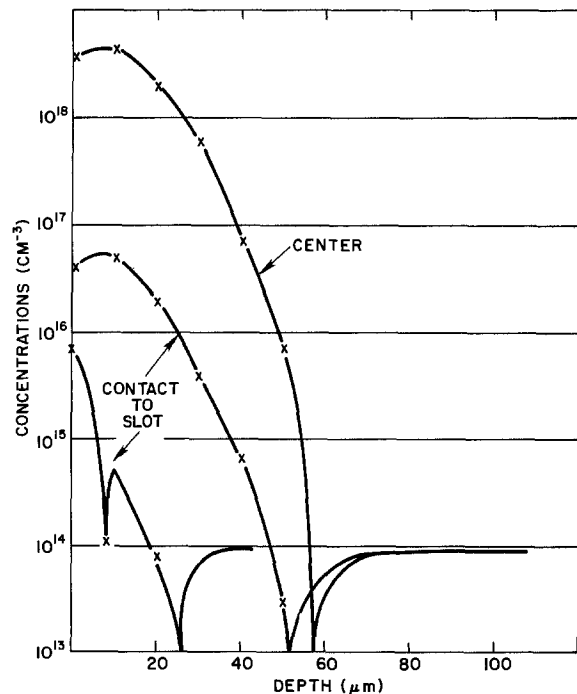


Fig. 11. The anomalous aluminum diffusion resulting from direct contact to a quartz boat.

experiment to mask the aluminum diffusion. While it was shown that silicon dioxide can mask the aluminum diffusion, the presence of the silicon dioxide caused an n-type inversion and a source depletion effect on each aluminum-diffused area where the oxide was removed, as shown in Fig. 12. Silicon tubes and boats have been used to avoid this source-retarding effect, but without success. We found that silicon particles can be evaporated from these silicon wares at temperatures higher than 1200°C under an inert ambient. These evaporated silicon fumes condensed at the end of the tube and formed white film, which proved to be silicon (by atomic emission and absorption analysis).

Another interesting phenomenon is that phosphorus diffusion can slow down aluminum diffusion (reduce the aluminum diffusion coefficient). In one experiment, a short POCl_3 diffusion was done at 1100°C, selectively, onto a silicon wafer, which was masked with an SiO_2 pattern. The oxide pattern was etched away completely after the POCl_3 deposition. These wafers were diffused with ACS wafers at 1200°C for 20 hr. It was clearly shown, by the lap-and-stain photo (Fig. 13), that the

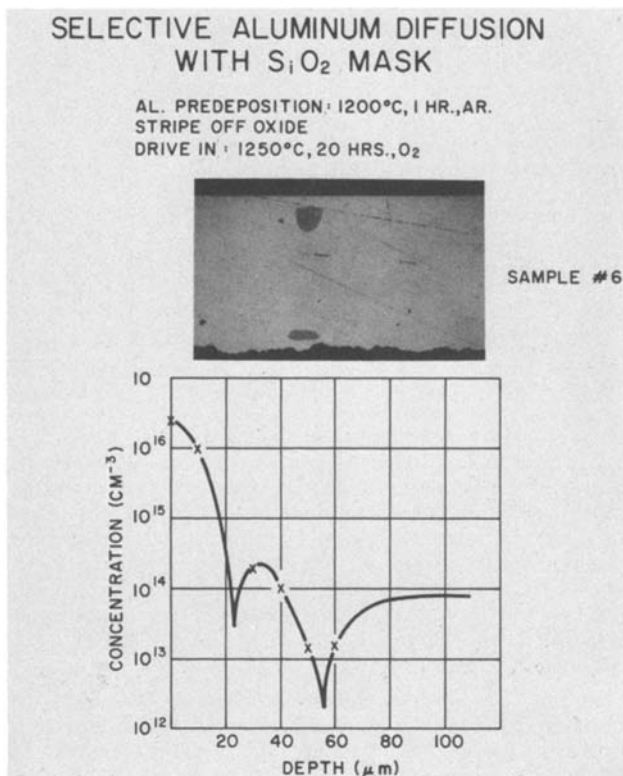


Fig. 12. An inversion layer in the aluminum diffusion due to the presence of silicon dioxide on the silicon surface.

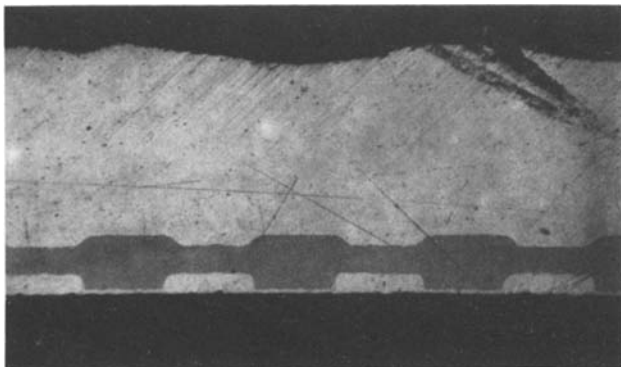


Fig. 13. The retardation effect on aluminum diffusion by a simultaneous phosphorus-aluminum diffusion.

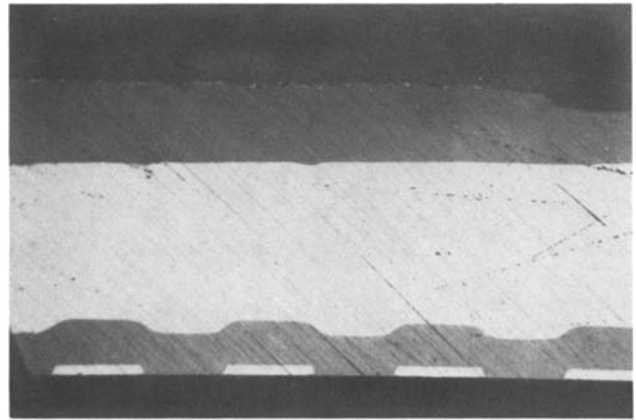


Fig. 14. The enhancement effect on aluminum diffusion by a simultaneous arsenic-aluminum diffusion.

aluminum diffusion was retarded in these areas under the phosphorus deposition. A similar effect also was observed on GaAs simultaneous diffusion.

A reverse effect was found for the aluminum-arsenic diffusion system. The presence of arsenic atoms can locally enhance the aluminum diffusion. In one experiment, arsenic atoms were implanted, selectively, into silicon wafers which were masked with a silicon dioxide pattern. The oxide pattern was etched away completely after the arsenic implantation. The same aluminum diffusion cycle was used on these wafers as in the Al- POCl_3 case. The lap-and-stain photo (Fig. 14) indicates that the aluminum diffusion was enhanced in the arsenic implanted areas. This enhancement effect is not likely due to the surface damage of ion implantation. The implanted surface damage is restricted to a few microns from the surface and should be annealed out completely at the diffusion temperature, which was 1200°C. These effects were not found in the Al-B system.

Conclusion

Open-tube aluminum diffusion was used to replace closed-tube aluminum diffusion. This new technology is not only easier and less expensive, but also offers more process freedom and control. The resultant surface concentration of aluminum diffusion can be selected from 1×10^{16} to 1×10^{19} atoms/ cm^3 . Several devices were made with this technique. The measured device characteristics were far better than those made with the conventional processes. Three types of aluminum diffusion sources were evaluated. The properties and results associated with these sources were discussed. Several new phenomena were discovered and presented in this study.

Acknowledgments

The author wishes to express his gratitude to Dave Hartman and Mark Barron for their constant interest, encouragement, and support. He is indebted to Al Roesch and Ed Mets for many helpful discussions and suggestions. The manpower support from Don Foran, Gladys Holt, and Sally Harrington is gratefully acknowledged. The editorial work done by V. Potoff is deeply appreciated.

Manuscript submitted Aug. 1, 1979; revised manuscript received March 30, 1981. This was Paper 155 presented at the Boston, Massachusetts, Meeting of the Society, May 6-11, 1979.

Any discussion of this paper will appear in a Discussion Section to be published in the June 1982 JOURNAL. All discussions for the June 1982 Discussion Section should be submitted by Feb. 1, 1982.

Publication costs of this article were assisted by General Electric Company.

REFERENCES

1. C. S. Fuller and J. A. Ditzenberger, *J. Appl. Phys.*, **27**, 544 (1956).
2. Y. C. Kao, *Electrochem. Technol.*, **5**, 90 (1967).
3. P. Rai-Choudhury, F. Selim, and W. Takei, *This Journal*, **124**, 762 (1977).
4. W. Rosnowski, *ibid.*, **125**, 957 (1978).
5. R. C. Miller and A. Savage, *J. Appl. Phys.*, **27**, 1430 (1956).
6. S. K. Ghandhi, "Semiconductor Power Device," p. 276, John Wiley & Sons, Inc., New York (1977).

Techniques for Preparing and Grinding Hard and Brittle Diffusion Layers, Application to the Determination of the Nitrogen Diffusion Profile in α -Titanium Nitrided at 1350° and 1450°C

E. Etchessahar, J.-P. Bars, and J. Debuigne

*Laboratoire de Métallurgie et Physico-Chimie des Matériaux,
Institut National des Sciences Appliquées, 35043 Rennes Cedex, France*

ABSTRACT

Grinding techniques and the corresponding metrology are often weak points of the whole process of diffusion measurements. Techniques for preparing and grinding hard and brittle diffusion layers are given in every detail. Application is made of this process to the determination of the diffusion profile of nitrogen in α -titanium and particularly in the vicinity of the α/ϵ interface.

The methods described here were developed for the study of nitrogen diffusion in α -Ti at 1450° and 1350°C (1, 2). The diffusion coefficients are calculated on the basis of concentration-distance curves, the nitrogen concentration being measured by use of nuclear microanalysis (3). The methods of preparation which we describe are very useful for sectioning brittle diffusion layers.

During nitriding of a parallelepipedic sample, the different phases are growing in layers, parallel to the prismatic faces of the sample. Figure 1 shows this configuration on a cross section after nitriding at a temperature above the transition point of titanium.

For the determination of a diffusion profile of nitrogen in the α -phase, we have to choose one of the two interfaces limiting the layer as the origin. The two methods used allow the determination of such a profile for α -layer thicknesses of 80 μm at least. Direct analysis of nitrogen is performed either on planes obtained by parallel sectioning, or on inclined plane crossing of the whole α -layer.

Technological Definitions of Operations

Several samples must be used to work the first method (parallel sectioning). Since hoping to obtain many identical and perfectly nitrided samples is unrealistic, their number was limited to four per temperature considered. Several analyses on each sample are then necessary in that case.

The second method necessitates only one sample, but a long one, in order to spread the concentration gradient as much as possible. The analytical spots must be rigorously located. If in the first method, the surface of the probe is of little importance, the use of the second method implies a probe as small as possible, for in this case the nitrogen distribution is not constant over all the inclined sectioning plane.

Parallel sectioning (first method).—Our parallelepipedic specimens (20 \times 10 \times 8 mm) have their two largest faces plane ground parallel to one another. Two symmetric samples were cut out of each specimen after

nitriding; the cut is a symmetry plane and the sizes of both samples are 20 \times 10 \times 3.5 mm.

Three planes are metrologically defined (Fig. 2): (i) the "S" plane, for the largest nitrided face, (ii) the α/β interface, and (iii) the "R" plane of cut, ground parallel to one another. Plane "R" is the reference plane in each specimen.

In order to facilitate the control of the α/β interface, a lateral face of each sample is submitted to a metallographic polishing down to alumina; after that, the sample dimensions are 20 \times 5 \times 3.5 mm. Parallel grindings through the α -phase are performed by means of a special stage assembly using the "R" plane as reference. The corresponding nitrogen analyses were obtained with the probe always localized in the middle of each plane.

Inclined sectioning (second method).—We have to consider two types of inclined planes, (Fig. 3) for this type of grinding: (i) those which cross the whole

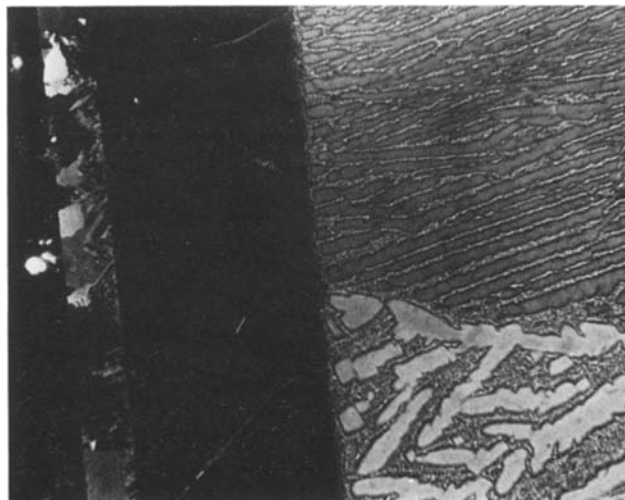


Fig. 1. Cross section after nitriding

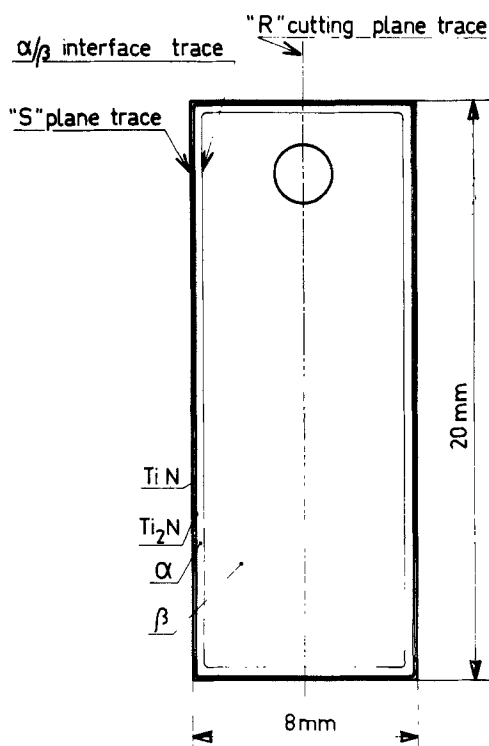


Fig. 2. Schematic representation of the symmetric samples

α -layer, called totally inclined sectioning planes; and (ii) those which reveal only a reduced part of the α -layer, called partially inclined sectioning planes.

The latter type is necessary for a good examination of the layers in the vicinity of the interfaces.

High slope inclined sectioning.—In the case of totally inclined sectioning planes, the special parallelepipedic sample ($22 \times 5 \times 4$ mm) is cut out of a nitrided specimen ($35 \times 10 \times 4$ mm) the largest faces of which were plane ground parallel to each other before nitriding. The “ R_1 ” reference plane is one of these large planes which are in principle parallel to the α/β interface. All lappings and measurements are performed with reference to “ R_1 ”.

By grinding with a $\sin \alpha$ value of 0.00625, metallographic observation on this plane shows from one end of the sample to the other: (i) a 4 mm wide zone, transformed from β ; (ii) a 15 mm α -zone; (iii) a 2 mm ϵ -zone; and (iv) a 1 mm nitride zone. One and a half analysis steps are used on the whole α -zone.

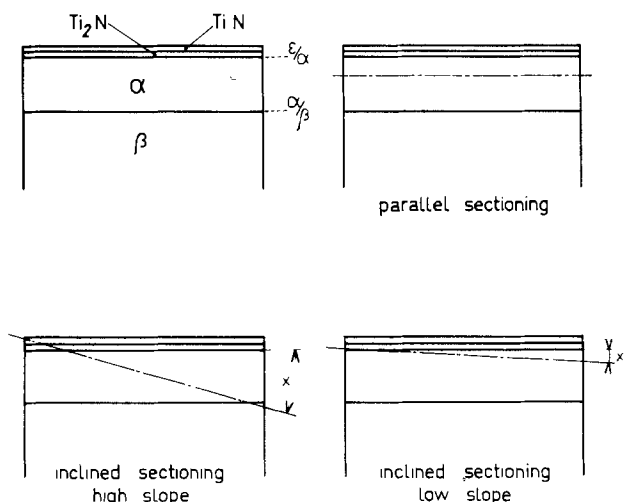


Fig. 3. Schematic representation of the sectioning planes

Low-slope inclined sectioning.—For the study in vicinity of an interface, partial sectioning is used. The samples are then identical to those for parallel sectioning but with grinding slopes corresponding to $\sin \alpha$ values of 0.001384 or 0.0025 with reference to the “ R ” reference surface.

Technique and tool selection.—The technical problem of grinding as described above, presents a double aspect: (i) A macro-geometric one, that is, the precise positioning of the sectioning plane with reference to the reference surface. The machine used must be reliable and precise. (ii) A micro-geometric one corresponding to minimum rugosity of the grinding plane surface.

The grinding technique and tool must be adapted to the material studied. All of these technical requirements were finally satisfied by the choice of a plane rectifying machine equipped with a cubic-boron nitride wheel (wheel specification: CB: 126 Q BB-1.5; flattener: 2R 14 KF 7F; sharpening rod: 38 A; Norton specifications).

The surface profilometry on Fig. 4 shows the very good results obtained with pass depths of $3 \mu\text{m}$ under a very strong cooling fluid jet.

The use of this type of grinding wheel with resinoid binder is rather delicate. For good results, the centering must be very accurate and the ovality less than 0.01 mm. For a good shaping of the grinding wheel, the necessary flattening with a diamond flattener must be done with a maximum $5 \mu\text{m}$ penetration both backward and forward and with alternating the side of flattening rod penetration into the grinding wheel; the cooling liquid jet must be strong.

Flattening is necessarily followed by sharpening to give relief to the abrasive grains by eliminating part of the binder. The abrasive power of the cubic-boron nitride wheels depends on the quality of sharpening. This operation is performed with rods 38 A 150 HV BE ($20 \times 20 \times 200$ mm) (Norton specifications), the wheel rotating as in the normal working conditions, with a slow cooling-jet. Sharpening must be stopped as soon as the rod is consumed at great speed.

TiN and Ti_2N nitrides must be ground before reaching the α -phase; the high hardness of these three phases accounts for the geometric modification of the wheel in the course of work, giving then an alteration of the surface state of the samples. We must therefore control this evolution and then flatten the wheel with the diamond flattener. In our case, this operation is performed after each series of eight to ten abrasions.

Grinding stand and fittings.—For both methods of study (first method, parallel sectioning; second method, inclined sectioning), we have used the same steel stand and it is the way the stand is connected with the rectifying machine which differs. This stand is also used in the preparation of the specimens and for rectifying the “ R ” reference surfaces; it is shown in Fig. 5.

It shows three surfaces, A, B, and C. Faces A and B are parallel to each other (maximum deviation $0.5 \mu\text{m}$). The C groove is parallel to these surfaces.

The specimens are glued to face A; face B is connected with the machine. This operation consists in applying the specimen on face A by using a screw

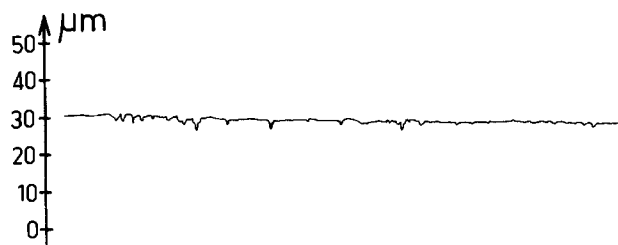


Fig. 4. Example of surface profilometry

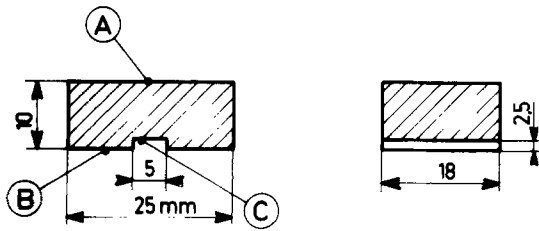


Fig. 5. Schematic representation of the steel stand

clamp with parallel holding jaws, tightened between the C groove and the surface to rectify (see Fig. 6).

The specimen is then stuck to the stand with a low temperature wax ($t_f \approx 50^\circ\text{-}60^\circ\text{C}$). There is no wax between the specimen reference surface "R" and face "A" of the steel stand. This gluing has a good strength under cutting stress for $3\ \mu\text{m}$ grinding passes.

For the first method, the specimen steel stand is connected to the rectifying machine table by means of a magnetic stage with faces ground in parallel with the table.

To perform inclined grindings, the slope of the grinding stand is given by a sinus table, as shown in Fig. 7.

Tests and Measurements

All tests and all thickness measurements are always comparative measurements carried out in a metrology room with the following equipment: metrologic surface-plate, a box of standard thickness gauges, a good comparator with a very sensitive dial giving $1\ \mu\text{m}$ per division and a maximum amplitude of $200\ \mu\text{m}$.

"R" reference surface.—We test the parallelism of "R" compared to "S" and the parallelism of "R" as compared to the α/β interface on a Reichert metallographic bench with cross-carriage stage and ocular micrometer.

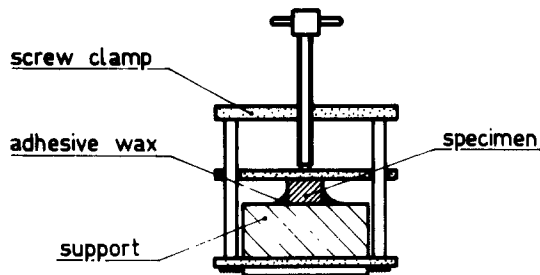


Fig. 6. Experimental setup used for glued-on specimens

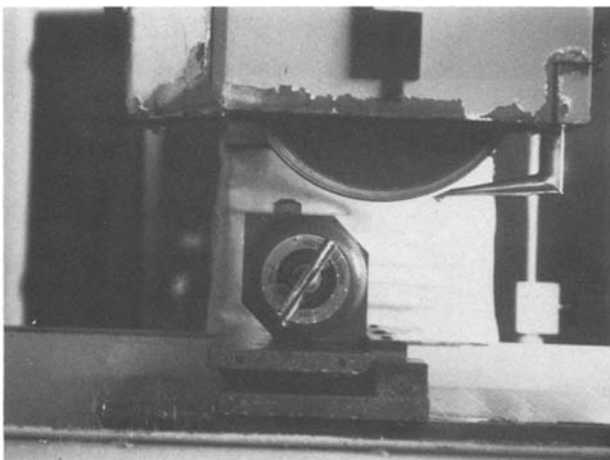


Fig. 7. Rectifying machine equipped with sinus table stage

Parallel grinding.—After grinding of each plane to be analyzed, three series of thickness measurements are performed on the sample: sample with grinding stand, sample alone, and sample alone with a hand precision micrometer in order to avoid gross human errors.

Prior to each thickness measurement, we test the parallelism between "R" and the plane to be analyzed; a surface profilometry is obtained. y_i being the height of ground plane "i" above "R" and $y_{\alpha\beta}$ the height of the α/β interface above "R", we have then

$$d_i = y_i - y_{\alpha\beta}$$

for the distance of the analyzed plane to the α/β interface.

After grinding of a plane close to the α/β interface, the height of this interface above "R" is measured on the metallographic microscope as seen above. The same measure is made also for the plane just ground. By comparing the y_i' obtained on a metallographic microscope and the y_i value for the same plane, obtained by mechanical metrology, we define a correction factor

$$K = \frac{y_i}{y_i'}$$

and we can then calculate

$$y_{\alpha\beta} = Ky_{\alpha\beta}'$$

Inclined grindings.—The measurements are by far easier here. The height above the reference surface on each sample is measured along the ground plane and the value of the height of each interface is noted.

The positions of the probe on the sample being of great importance, a correct initial position of the sample in the reaction chamber is necessary. During the analytical process, the crossing of the interfaces constitutes interesting marks.

Practical example.—Our methodology gives for example Fig. 8, showing the diffusion profile of nitrogen, close to the α/ϵ interface, in the α -phase after nitriding at 1350°C . Very close to the α/ϵ interface, the experimental points correspond to analyses using partial inclined grinding. Over $15\ \mu\text{m}$ from the α/ϵ interface, the analyses use parallel sectioning.

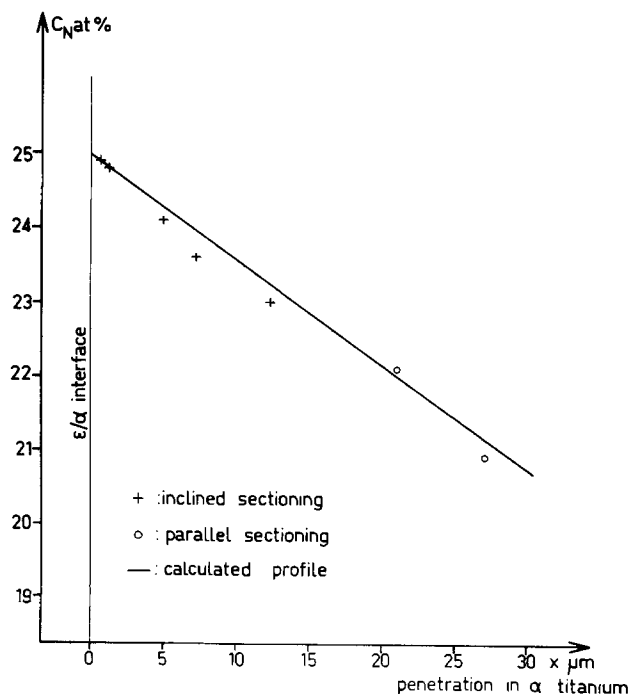


Fig. 8. Diffusion profile of nitrogen in α -titanium (1350°C , 7 hr)

With the hypothesis where only nitrogen diffuses and the diffusion coefficient is constant and independent from nitrogen concentration, we can optimize the adjustment of the experimental profile according to a single curve satisfying the equation

$$\frac{C_{(x_1)} - C_{(o)}}{C_{(x_2)} - C_{(o)}} = \frac{1 - \operatorname{erf} \frac{|x_1 + a|}{2\sqrt{Dt}}}{1 - \operatorname{erf} \frac{|x_2 + a|}{2\sqrt{Dt}}}$$

where $C_{(o)}$ = nitrogen initial concentration in the metal, $C_{(x_1)}$ and $C_{(x_2)}$ = nitrogen concentrations in planes at x_1 and x_2 beneath the α/ϵ solid solution interface, a = cumulated thickness of the preceding layers, corrected, taking into account the Pilling and Bedworth ratios, D = diffusion coefficient of nitrogen in α -Ti, and t = time of nitriding.

We note the good agreement between the experimental points and the theoretical profile calculated for the whole thickness (88 μm) of the solid solution Ti α /N and also the good complementarity of the two grinding techniques.

The advantage of this method is to avoid resorting to concentration values at interfaces deduced from the equilibrium diagrams.

Conclusions

The experimental determinations of diffusion profiles in solid-state materials often use nowadays very so-

phisticated techniques, but in some cases the weak points of the whole process are the preparation of the samples and the mechanical metrology used before the physical measurements which give values for drawing the diffusion profile. We have described in detail the preparation of samples of nitrided titanium (a particularly difficult case) before determining nitrogen concentration by observing a nuclear reaction. This method may be adapted to the grinding of numerous other brittle diffusion couples.

Manuscript submitted July 11, 1980; revised manuscript received Feb. 19, 1981.

Any discussion of this paper will appear in a Discussion Section to be published in the June 1982 JOURNAL. All discussions for the June 1982 Discussion Section should be submitted by Feb. 1, 1982.

Publication costs of this article were assisted by the Institut National des Sciences Appliquées.

REFERENCES

1. D. David, E. A. Garcia, G. Béranger, J.-P. Bars, E. Etchessahar, and J. Debuigne, in Fourth International Conference on Titanium, Kyoto, May 19-22, 1980.
2. D. David, J. P. Bars, E. Etchessahar, and J. Debuigne, To be published.
3. G. Amsel and D. David, *Rev. Phys. Appl.*, **4**, 383 (1969).

Growth of F Center in Zone II as a Function of Electron Injection in Some Potassium Halide Crystals

A. K. Maiti, K. Goswami, S. Choudhuri, and A. Choudhury

Department of Physics, Jadavpur University, Calcutta 700032 India

ABSTRACT

Single crystals of KCl and KBr have been colored by the process of electron injection at different temperatures and voltages. The coloration begins at the onset of zone II. The space charge limited (S.C.L.) injection current and the coloration are found to increase almost linearly in zone II. The efficiency of F-center formation in zone II is determined and is shown to be a function of S.C.L. current.

Mott and Gurney (1) have initiated the analysis of space charge limited injection into an insulator on the assumption that traps are absent in it. Later others (2, 3) put forward some theories for the better understanding of the space charge limited injection process in solid materials of not too high bandgap. Recently the electron injection process in alkali halide crystals found enormous scope although very limited results of the physical parameters are available.

When an electric field is applied to an alkali halide crystal placed between two electrodes and heated at an elevated temperature, a cloud of color centers originates from the pointed cathode and moves toward the flat anode (4). During the injection process the space charge limited (S.C.L.) current in the crystal reveals four distinct zones under suitable experimental conditions. The evolution of electrical current and the color center are intimately related to the applied voltage, temperature of the specimen, and the nature of the crystal (5). It is known (6, 7) that in the first zone (zone I) current remains nearly constant for some

time and characteristically no coloration is produced. Experimental evidence (8-10) suggests that during zone I the process of electrolysis does occur, causing the accumulation of alkali metal at the cathode. Due to this accumulation of alkali metal a fresh ohmic contact at the cathode crystal interface is formed and the nature of zone I current has been attributed primarily to ionic transport (8-10). When the contact is formed, further accumulation of alkali metal ceases and the transport of electrons through the crystal starts (onset of zone II) showing a sharp rise in the electrical current with the formation of color centers. The zone II coloration continues until the color cloud reaches the anode and the entire crystal gets densely colored during which injection current remains practically constant, and this is known as the steady-state situation (zone III). Another zone, known as zone IV, does not participate to form color centers in any way (10).

Most of the current literature is concerned mainly with the growth of space charge limited current and its properties are related to transport processes in solid

Key words: solid electrolyte, injected carriers, color centers.

media under different ambient conditions. In the present experiment some results are reported regarding the growth of injection current at various stages of coloration in some alkali halide crystals under altered conditions of temperature and applied voltages. The efficiency of F-center production (i.e., the energy required to form one F center) has been determined in the space charge region.

Experimental

Crystals of KBr ($0.7 \times 0.4 \times 0.3$ cm) and KCl ($0.65 \times 0.5 \times 0.3$ cm) obtained from the Department of

Atomic Energy, Government of India, were cleaved from the single crystal blocks. An electrical furnace fitted with a flat platinum anode and pointed brass cathode could support a crystal block. The temperature of the furnace was controlled within $\pm 2^\circ\text{C}$. The electron injection was performed under a fixed voltage keeping the temperature of the specimen constant. The injection current flowing through the crystal was measured with a sensitive microammeter at a regular interval of time and at the same time the F absorption was recorded by shining F light normally on a small central part of the crystal. The intensity of the transmitted F light was measured by an RCA IP 28 photomultiplier with conventional electronic circuits.

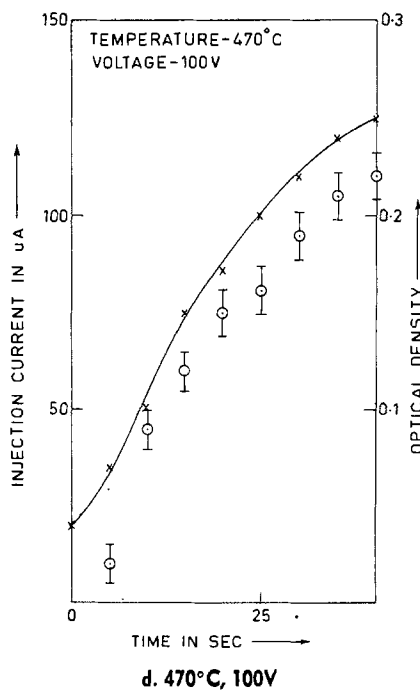
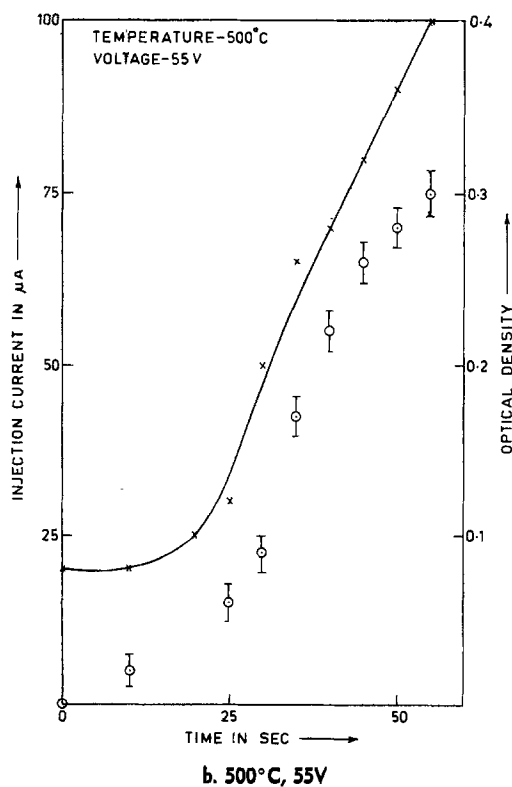
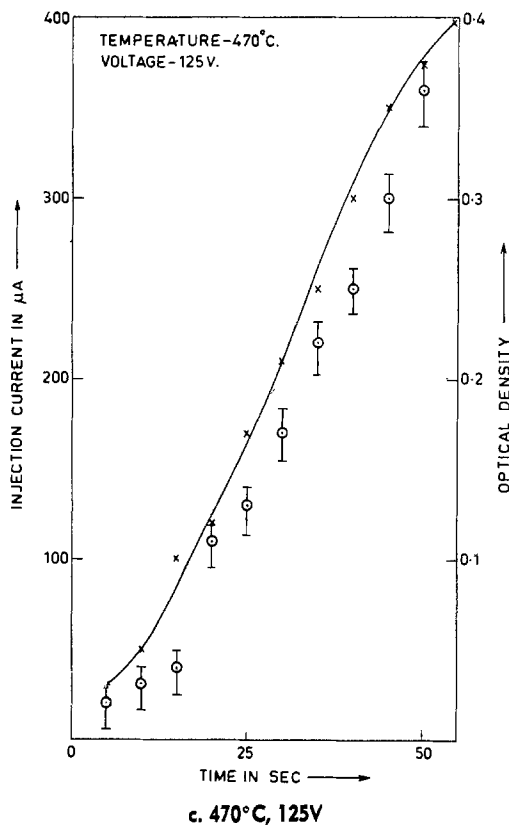
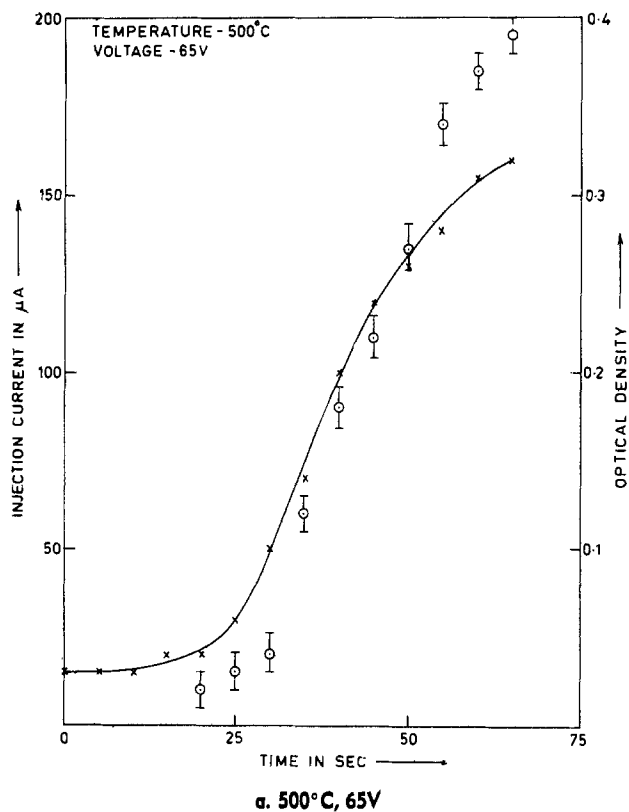
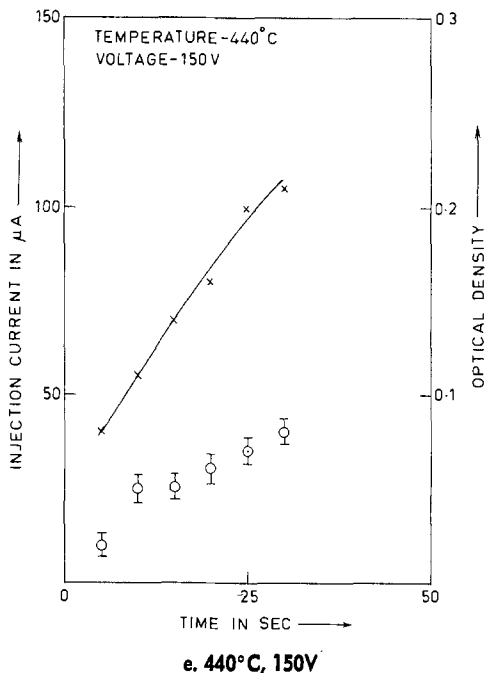


Fig. 1.



e. 440°C, 150V

Fig. 1. Electrical current (continuous line) and optical density (isolated points) vs. time during electrolytic coloration of KBr single crystal at temperature and voltage.

The injection procedure was limited within the third stage where current was found to record more or less a steady value. The coloration so produced in the crystal had been bleached by reversing the polarity of the electrodes under identical conditions. Thus the original transparency of the crystal was retained. The process of electron injection was carried out with a specimen for different temperatures and different voltages.

Results

Injection current and optical density are plotted against time for a particular temperature and voltage for KBr and KCl crystals. Five such sets of KBr and four such sets of KCl crystals for various temperatures and voltages are shown in Fig. 1 and 2, respectively. The error incurred in the measurement of optical density due to coloration is marked in each case (as

shown in Fig. 1 and 2). The plots of optical density and injection current against time are almost linear in the second zone.

The energy necessary to create one F center, i.e., the efficiency (η), is calculated in the following manner.

The number of electrons (N_e) per unit area participating in the formation of color centers is given by

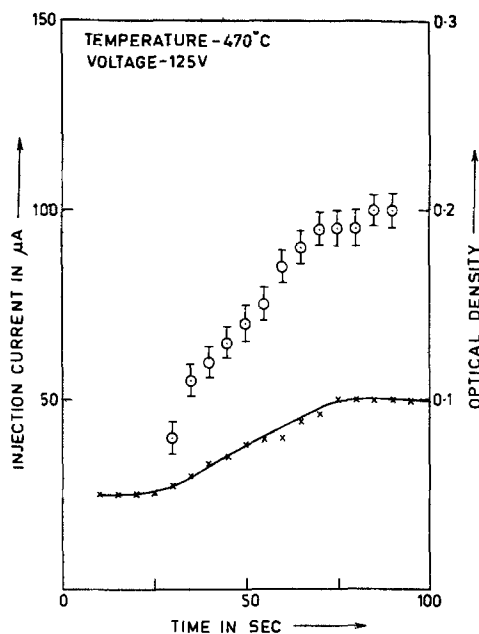
$$N_e = K \int i(t) dt \quad [1]$$

where the constant $K = 6.24 \times 10^{18}$.

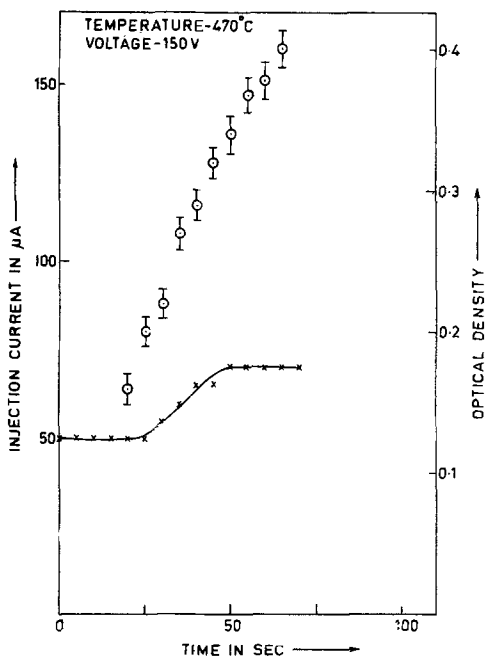
The number of color centers (N_F) per square centimeter is estimated using Smakula Dexter's equation (11) given by

$$N_F = 2.3036K'a \quad [2]$$

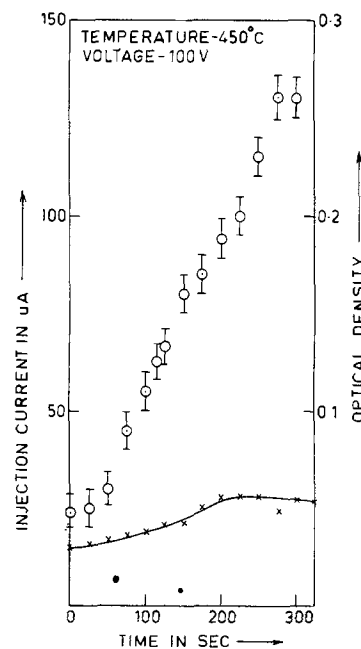
where a is the optical density, K' depends on the refractive index of the specimen, oscillator strength, and half-width ($W_{1/2}$) of the F band. The half-width involved in K' is computed from the equation (12) given by



b. 470°C, 125V



a. 470°C, 150V



c. 450°C, 100V

Fig. 2.

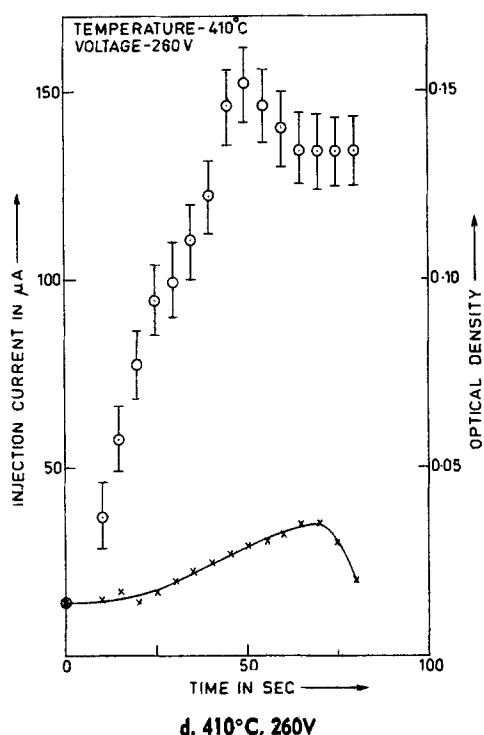


Fig. 2. Electrical current (continuous line) and optical density (isolated points) vs. time during electrolytic coloration of KCl single crystal at temperature and voltage.

$$W_{1/2} = A [\coth(h\nu_g)/2KT]^{1/2} \quad [3]$$

Now defining efficiency (η) of F-center formation as

$$\text{Efficiency } (\eta) = \frac{\text{rate of flow of electrons per cm}^2}{\text{rate of F-center formation per cm}^2}$$

i.e. \times applied voltage per unit length

$$\eta = K'' i(t) \quad [4]$$

where $K'' = 0.4341(K/K') (V/L) 1/da/dt$, K'' is a constant for a particular crystal at a fixed temperature and fixed applied voltage (V), and L is the distance between the two electrodes. Knowing the slope (da/dt) of optical density vs. time graph which is found to be nearly linear in zone II, the efficiency value (η) is calculated for each value of the injection current.

Discussion

The injection current vs. time graphs in Fig. 1 and 2 may be divided into three zones where the zone I contributes no F-center formation which corroborates some earlier work (5, 13). The beginning of coloration causes a sharp rise in zone II injection current and the current will continue to increase until a steady state (zone III) is reached. But the coloration in zone III is still increasing in a regular manner. These lead us to suggest: (i) that current following in zone I is not due to electronic transport, and (ii) that current flowing in zone II is affected by the space charge and this space charge will modify the existing field between the electrodes. The space charge decreases as the coloration as well as current growth during zone II increases with time. Consequently efficiency (η) becomes time dependent.

According to Hadley (14) the use of the pointed cathode facilitates the electron injection due to the high current density at the point tip and therefore to the high accumulation rate of alkali metal at the cathode. If the accumulation rate is faster than that of elimination, a new electrode is obtained and injection begins. From this point of view the start of electron injection

into the crystal is controlled by the ionic current which is a function of temperature. To have appreciable ionic motion sufficient temperature is necessary. It is expected that there will be some lower limit of temperature for coloration.

The efficiency vs. space charge limited current [$\eta - i(t)$] is plotted for KBr and KCl crystals at different conditions of temperatures and voltages as shown in Fig. 3 and 4. It is evident from these figures that the value of the slope decreases with the increase in temperature. It indicates that by lowering the temperature of the crystal larger energy is necessary for the formation of the F center.

The generation of the color center under electron injection is quite different from other modes of coloration. Here the color centers migrate from the cathode toward the anode and the distribution of coloration is not uniform in the close vicinity of the cathode, due to which the optical density records have been made in a localized region of the crystal.

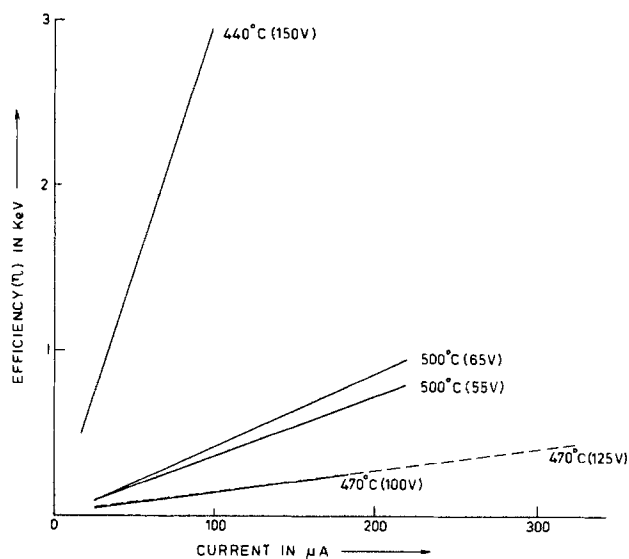


Fig. 3. Efficiency of F-center formation in zone II vs. injection current for KBr single crystal at various temperatures and voltages (dashed line is for 470°C and 125V).

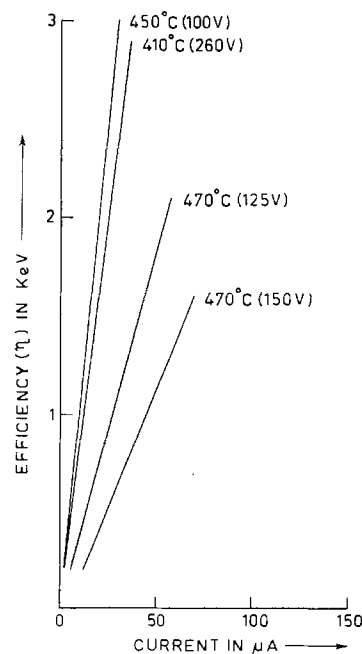


Fig. 4. Efficiency of F-center formation in zone II vs. injection current for KCl single crystal at various temperatures and voltages.

The currents in zone II and zone III are not sharply marked (see Fig. 2), while a theoretical analysis of Many and Rakavy (3) shows a sharp contrast between the two zones. The rounding of zone II and III current in our experiment is quite reasonable because the experimental electrodes are not of identical nature.

Manuscript submitted March 31, 1980; revised manuscript received March 6, 1981.

Any discussion of this paper will appear in a Discussion Section to be published in the June 1982 JOURNAL. All discussions for the June 1982 Discussion Section should be submitted by Feb. 1, 1982.

REFERENCES

1. N. F. Mott and R. W. Gurney, "Electronic Process in Ionic Crystals," 1st ed., Oxford University Press, New York (1940).
2. M. A. Lampert and P. Mark, "Current Injection in Solids," Academic Press Inc., New York (1970).

3. A. Many and G. Rakavy, *Phys. Rev.*, **126**, 1980 (1962).
4. H. N. Hersh and L. Bronstein, *Am. J. Phys.*, **25**, 306 (1957).
5. M. T. Montojo and C. Sanchez, *J. Phys. Chem. Solids*, **35**, 1437 (1974).
6. M. S. Kosman and V. F. Pisarenko, *Sov. Phys. Dokl.*, **2**, 375 (1957).
7. V. F. Pisarenko, *ibid.*, **2**, 391 (1957).
8. M. T. Montojo, F. Jaque, and C. Sanchez, *This Journal*, **122**, 1325 (1975).
9. G. Heiland, *Z. Phys.*, **127**, 144 (1950).
10. M. T. Montojo and C. Sanchez, *Solid State Commun.*, **14**, 485 (1974).
11. J. J. Markham, "F-Centers in Alkali Halides," Academic Press, New York and London (1966).
12. J. H. Schulman and W. D. Compton, "International Series of Monographs on Solid State Physics," Pergamon Press, New York (1962).
13. G. A. Andreev, G. B. Semushkin, and A. N. Tsikin, *Sov. Phys. Solid State*, **9**, 2564 (1968).
14. W. B. Hadley, in "International Symposium on Color Centres in Alkali Halides, Rome," p. 114 (1968).

The Oxidation of Pure Zirconium in Steam from 1000° to 1416°C

R. E. Pawel* and J. J. Campbell

Oak Ridge National Laboratory, Metals and Ceramics Division, Oak Ridge, Tennessee 37830

ABSTRACT

The oxidation of pure, arc-melted crystal-bar zirconium in steam was studied over the temperature range 1000°-1416°C. The early stages of the reaction at all temperatures investigated above 1000°C were characterized by uniform parabolic growth of layers of zirconium oxide and oxygen-stabilized alpha zirconium. Parabolic rate constants were determined for the growth of each layer, and these served as a basis for the calculation of effective chemical diffusion coefficients for oxygen in the growing product phases. These calculations were made on the assumption that this system may be described as an ideal, multiphase, moving boundary diffusion problem. The results and their comparisons with similar data for the oxidation of Zircaloy-4 indicate that this diffusion model is accurate over the temperature range involved. At 1000°C, however, departures from ideal kinetics were observed that were attributed to structural changes in the oxide layer during the course of the reaction.

Recent investigations at this laboratory have examined the oxidation characteristics of Zircaloy-4¹ in steam at temperatures from 1000° to 1500°C. In particular we have studied oxidation kinetics (1), oxide morphology (2), the effect of steam pressure (3) on oxidation rates, oxygen diffusion in the oxide and oxygen-stabilized alpha layers and the applicability of ideal diffusion models (4-6), as well as the effect of the monoclinic-tetragonal transformation in the oxide on transient temperature oxidation behavior (6). Generally, this work has shown that, despite the complexities of the Zircaloy-oxygen system and the intricate structure of the growing oxide, the reaction proceeds by relatively ideal, diffusion-controlled growth of the product phases. Thus, we and others (7-13) have correlated the kinetic data in terms of the parabolic rate constants for the growth of the oxide and oxygen-stabilized alpha phases from the host beta Zircaloy. These data have been used mainly as a basis for developing models suitable for predicting oxidation behavior for a variety of experimental conditions.

* Electrochemical Society Active Member.

Key words: zirconium, high temperature oxidation, oxygen diffusion, parabolic reaction kinetics.

¹ Nominal composition (w/o): Zr-1.60 Sn, 0.25 Fe, 0.12 Cr, 0.12 O, 0.009 C, 0.003 N, and 0.0025 H.

While a considerable amount of new information is available for the high temperature oxidation behavior of Zircaloy, few corresponding data for pure zirconium exist for a critical comparison. Previous experimental efforts here, like the earlier work with Zircaloy, concerned oxidation phenomena at temperatures below 1000°C. Good review articles (14-16) have been published that illustrate the complex nature of the reaction and the large scatter in experimental kinetic data and the different interpretations of the results. For oxidation above 1000°C, Debuigne (17), Pemsler (13), and Rosa and co-workers (14) have presented data and phenomenological descriptions of the oxidation process. Debuigne provided a detailed analysis of the oxidation process for temperatures from 1050° to 1200°C. Pemsler observed parabolic oxidation kinetics for growth of the oxide layer at temperatures from 1100° to 1300°C, but below 910°C (to as low as 750°C) found a complicated kinetic behavior. It was proposed that these complications were due to changing proportions of the monoclinic and tetragonal oxides. Later, Lightstone and Pemsler (19), observed both forms of the oxide growing at 920°C by an *in situ* x-ray examination. Rosa and co-workers (20), for temperatures between 875° and 1050°C, interpreted the growth of the oxide

as parabolic, but only after an initial period of faster growth.

It is clear that both similarities and differences exist when comparing the oxidation behavior of pure zirconium and Zircaloy-4. At the higher temperatures, above about 1100°C, both materials appear to exhibit virtually ideal parabolic growth kinetics. Thus, if measurable differences in the rates exist, they might serve as a basis for defining the mechanism by which the alloying elements in Zircaloy-4 affect oxidation. Our techniques for measuring the kinetics for Zircaloy-4 oxidation proved sufficiently sensitive and self-consistent to detect the small differences associated with different batches of specimen material and also with the presence of oxygen gas in the steam (1). In the present paper, we will report an extension of this work for oxidation of pure zirconium, with the aim of producing data suitable for testing oxidation models and for comparing with data available for Zircaloy-4.

Experimental Procedures

In order to make the comparisons of the oxidation behavior as straight-forward as possible, we utilized experimental techniques that were essentially identical to those reported earlier for the oxidation of Zircaloy-4 (1). Briefly, specimens of zirconium were machined from arc-melted crystal-bar stock² in the form of cylindrical tubes 3 cm long, 1.1 cm diam, and with a wall thickness of 0.075 cm. The outer surfaces were abraded and then chemically polished to remove the cold-worked surface layers. Each specimen was instrumented with three Pt vs. Pt-10% Rh thermocouples on its inner surface and installed between support tubes inside a larger concentric quartz tube that served as the reaction chamber. A slightly positive pressure of helium gas was maintained within the support tube, while steam at atmospheric pressure was allowed to flow in the annular region between the supports and the outer tube. Consequently, oxidation occurred only on the outer surface of the specimen.

A quad-elliptical radiant heating furnace surrounding the reaction chamber heated the specimen according to a programmed temperature cycle. One thermocouple served as a sensor for the programmer-controller-recorder system, while the other two thermocouples, located 180° apart, were connected to a computer-operated data acquisition system that furnished a precise record of the temperature excursions experienced by these points on the specimen. This record was used to normalize the reaction times for sets of experiments conducted at nominally the same reaction temperature. The normalization also included the effective times associated with heating and cooling of the specimen. Specimen heating rates of about 100 K/sec were employed, and the initial cooling rates from the reaction temperature were in this same range. The "isothermal" experiments thus consisted of a rapid heat-up to the desired temperature, a period of constant temperature (generally within $\pm 1^\circ\text{-}2^\circ\text{C}$, followed by a rapid cooling.

The thickness of the oxide and oxygen-stabilized alpha layers at the two monitor thermocouple positions were determined for each oxidation experiment by standard metallographic methods. The mounted specimens were sectioned normal to their axes on a plane containing the thermocouple junctions. Layer thicknesses were measured with a filar micrometer eyepiece on a small bench metallograph. The details of the measurement procedures as well as other experimental items are discussed at length elsewhere (1).

Results and Discussion

The oxidation morphology and the kinetics of layer growth for pure zirconium reacting in steam were stud-

ied at 1000°, 1098°, 1200°, and 1416°C. With the possible exception of the data set at the lowest temperature, the early stages of oxidation conformed to ideal parabolic behavior. The layers of oxide and oxygen-stabilized alpha zirconium were uniform in thickness and, as will be documented below, little evidence of irregular alpha growth into the beta region (alpha "incursions") was observed even for extended oxidation. Consistent with our earlier results for Zircaloy-4, the tetragonal oxide phase is thought to be the product of isothermal oxidation under the conditions of our experiments, except, as noted above, for the data set at 1000°C. These data provided the basis of a diffusion-modeling analysis of the system. The calculated effective chemical diffusion coefficients for oxygen in the product phases were then incorporated into the MULTRAN computer program (5) to examine the influence of several system parameters on the model oxidation behavior.

Oxidation kinetics.—In anticipation of the sensitivity of the reaction kinetics to the oxygen concentration in the beta phase, as evidenced by our previous work with Zircaloy-4 (5), the maximum reaction time at each temperature for those experiments to be used in the determination of rate constants was purposely limited to assure that a semi-infinite geometry condition prevailed. By so doing, the layer growth exhibits wholly parabolic behavior, and a well-defined rate constant can be obtained. This constant is defined by the rate expression

$$\frac{dk}{dt} = \frac{\delta_k^2}{2k} \quad [1]$$

where k is one of the kinetic parameters [ϕ (oxide thickness), α (alpha thickness), or τ (oxygen consumption)] and $\delta_k^2/2$ is the parabolic rate constant. This constant is generally obtained from the slope of the k^2 vs. t plot. Depending upon the nature of the reaction and the experimental procedures, an intercept of 0, 0 may be observed, and this generally indicates that one is dealing with an "ideal" reaction in addition to well-defined experiments.

The squares of the oxide and alpha layer thicknesses, measured for zirconium oxidizing in steam at 1416°C, are plotted in Fig. 1. These data are accurately described by straight lines, and a least squares treatment was used to obtain the rate constant and its statistical uncertainty. The dashed lines in the figure indicate the

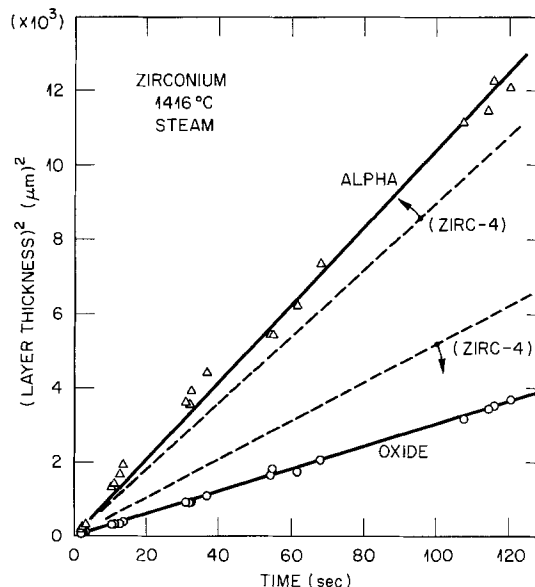


Fig. 1. Growth of zirconium oxide and oxygen-stabilized alpha zirconium layers on pure zirconium in flowing steam at 1416°C. The dashed lines compare the rates for Zircaloy-4 for the same conditions.

² Nominal composition (ppm by wt): Interstitial impurities—(O, C, H, N) to 30 ppm; metallic impurities—30 ppm Hf, other metals 0-10 ppm.

corresponding layer growth for Zircaloy-4. It is observed that the oxide layer on pure Zr grows more slowly than that on Zircaloy-4, while the reverse is true for alpha layer growth. Figure 2 shows a cross section of the product layers after oxidation for approximately 60 sec at 1416°C. While the uniformity of the layer thicknesses is apparent in this micrograph, the detail of the structure is less clear. SEM examination reveals that the oxide is comprised of a thin layer of fine, more-or-less equiaxed grains on its extreme outer surface, with the bulk of the layer consisting of thick (~20 μm) columnar grains each extending through a substantial fraction of the layer thickness. Careful polishing is necessary to discourage grains from popping out during normal specimen preparation; however, the artifacts furnish additional definition of the grain size and nature of the oxide. The alpha layer is also comprised of large columnar grains, and the tendency of this layer to exhibit cracking after cooling and specimen preparation is consistent with its suspected brittle nature. While the prior beta phase has transformed back to alpha upon cooling, it is clearly discernable from the alpha layer stabilized by oxygen at the reaction temperature.

Kinetic and morphological behavior similar to that observed at 1416°C was also found at 1200° and 1098°C. Figure 3 illustrates the excellent conformity of the layer growth to ideal parabolic kinetics at 1098°C. The dashed lines for layer growth on Zircaloy-4 indicate that the differences in growth rates for each layer are larger at the lower temperature.

The oxidation experiments at 1000°C, however, yielded complicated layer growth behavior that differed significantly from the simple behavior observed at the higher temperatures. These measurements are given in Fig. 4. While there is considerable scatter in the data, particularly the oxide thickness values, the dominant features of the first hour of reaction are the apparent changes in kinetics. At one stage, for example, it appears that the oxide layer may actually decrease in thickness as the reaction proceeds. In addition to the uncommon growth behavior for the oxide layer is the sigmoidal shape exhibited for alpha growth. If it is true, as we assume, that the oxidation of zirconium can be described as a multiphase diffusion process, the layer growths would be coupled in precisely this way.

The functional description of the layer growth at short times is not clear from the data in Fig. 4. For oxide growth, we have chosen somewhat arbitrarily to draw a curved line through the initial points, although a straight line segment (parabolic behavior) would seem equally acceptable. Thus, while reasonable esti-

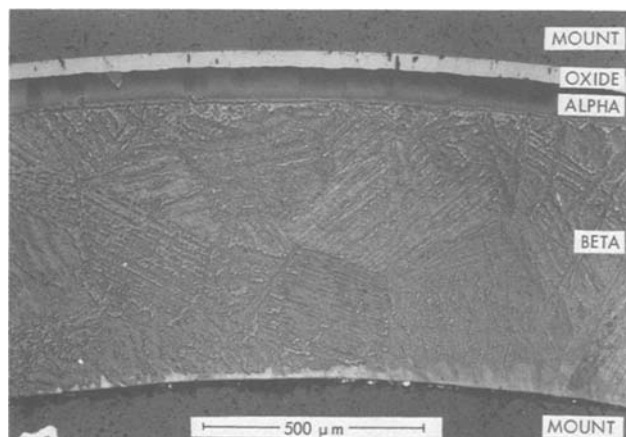


Fig. 2. Cross section of zirconium specimen oxidized in steam for 60 sec at 1416°C. Lightly etched in diluted Kroll's reagent followed by anodization to 20V in 1% KOH. Bright field micrograph.

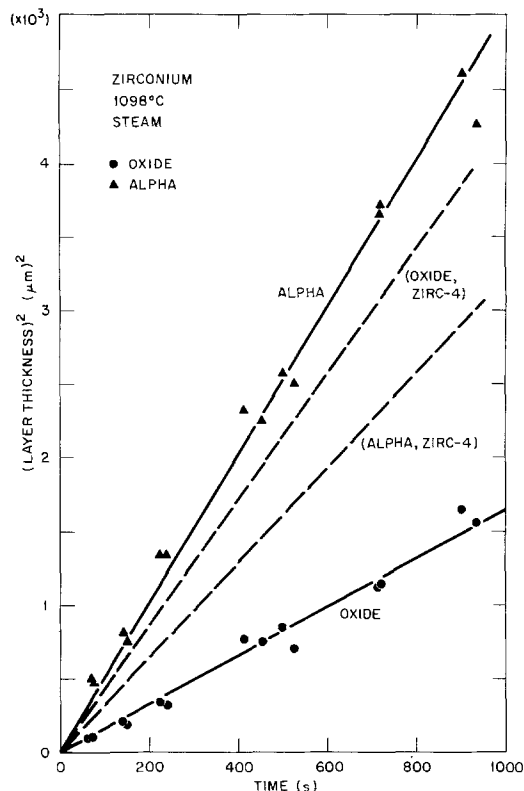


Fig. 3. Growth of zirconium oxide and alpha zirconium layers on zirconium in flowing steam at 1098°C. The dashed lines represent the product growth on Zircaloy-4 for comparable conditions.

mates of "parabolic" rate constants can be obtained, we have omitted these values from the least squares analytical description of the variation in the rate constants with temperature. In any event, the general trend in the differences in layer growth kinetics between Zr and Zircaloy-4 is seen to persist, with complications, at this temperature.

We believe that the kinetic behavior observed during oxidation of Zr at 1000°C constitutes evidence that structural changes take place in the oxide layer during growth and that these changes may be responsible for

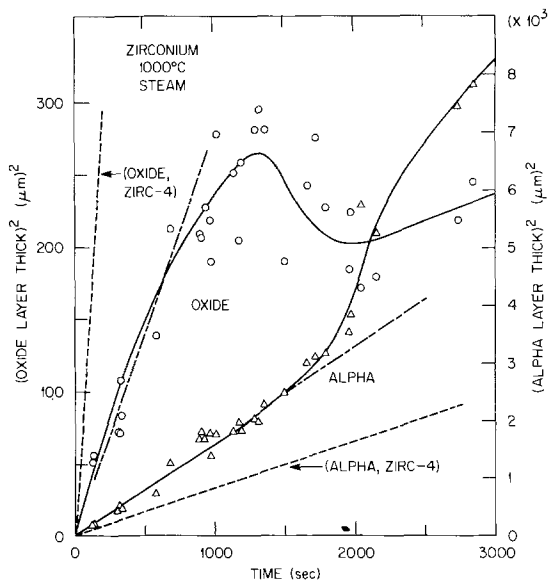


Fig. 4. Growth of zirconium oxide and alpha layers on zirconium in flowing steam at 1000°C showing variations in kinetics presumably due to structural changes within the oxide. Comparable parabolic rates for the early stage ($t < 1100$ sec) oxidation of Zircaloy-4 are given by the dashed lines.

many of the dramatic decreases in growth rates observed in this temperature range. As noted below, extrapolation of the high temperature kinetic parameters down to 1000°C suggests that in the very early stages of oxidation at this temperature, the oxide grows as the tetragonal form despite the fact that the monoclinic form is probably stable (at least for stoichiometric ZrO_2 (27). Pemsler (18) and others have noted that it may be possible to stabilize the tetragonal oxide at lower temperatures by the application of stress, high defect concentrations, or fine grain size. All of these factors are involved during the oxidation reaction.

Thus, a possible explanation for the change in the growth behavior of the oxide layer is the increasing proportion of the monoclinic oxide, which is characterized by a significantly lower oxygen diffusivity. The precise oxidation kinetics in the temperature range where the monoclinic-tetragonal transformation in the oxide is influenced by the metallurgical parameters in addition to its "normal" transformation hysteresis (27) might, therefore, be expected to depend sensitively upon experimental variables. In particular, heating rates, specimen shape, and temperature control would be important. As mentioned earlier, Pemsler (18) accounted for a continuously decreasing oxide growth rate on zirconium in the temperature range 750°-910°C by essentially this same hypothesis, and was later able to observe the existence of at least small amounts of the tetragonal oxide *in situ* at temperatures as low as 500°C (19). (The tetragonal oxide is not generally retained upon cooling to room temperature.) Rosa (20) also observed similar kinetic behavior at 875°-1050°C, but insufficient data were presented to describe the early stages of reaction in a detail sufficient for comparison with the present work.

The parabolic rate constants for layer growth determined in this investigation are given in Table I along with their statistical confidence limits. In addition, the rate constants for oxygen consumption, based on a modeling calculation in which the oxygen in each phase is accounted for consistent with the observed growth rates, are also given. Although, as previously noted, the oxidation does not exhibit precise parabolic kinetics at 1000°C, we nevertheless calculated "apparent rate constants" for the early stages of reaction at this temperature from the slopes of arbitrarily drawn straight lines through the origin of the rate curves using only the first few data points. The range of these values is also given in Table I. It was observed that the maximum value of the rate constant for oxide growth and the minimum value for alpha growth are approximately equal to the extrapolated values of these parameters based on the results of the higher temperature experiments. For the data obtained at the three temperatures above 1000°C, the measured rates conformed surprisingly well to simple Arrhenius behavior, as shown in Fig. 5.

Table I. Parabolic rate constants for oxidation of zirconium in steam^a

| Temperature (°C) | Oxide, $\frac{\delta_\phi^2}{2}$, cm ² /sec | | Alpha, $\frac{\delta_\alpha^2}{2}$, cm ² /sec | | Ox. cons., $\frac{\delta_\tau^2}{2}$, (g/cm ²) ² /sec ^c |
|------------------|---|---------------------|---|---------------------|--|
| | Value | Dev. % ^b | Value | Dev. % ^b | |
| 1416 | 1.522×10^{-7} | 1.6 | 5.193×10^{-7} | 3.3 | 7.95×10^{-7} |
| 1200 | 2.370×10^{-8} | 2.8 | 6.464×10^{-8} | 2.5 | 1.13×10^{-7} |
| 1098 | 8.274×10^{-9} | 8.4 | 2.503×10^{-8} | 6.2 | 3.60×10^{-8} |
| 1000 | $1.1-2.2 \times 10^{-9}$ | ^d | $6.7-8.2 \times 10^{-9}$ | ^d | |

^a Rate constants calculated on basis of $\frac{\delta k^2}{2} = k dk/dt$.

^b Maximum uncertainty at 90% confidence level.

^c Based on modeling calculations with MULTRAN program.

^d Serious departures from parabolic behavior observed after short time at 1000°C.

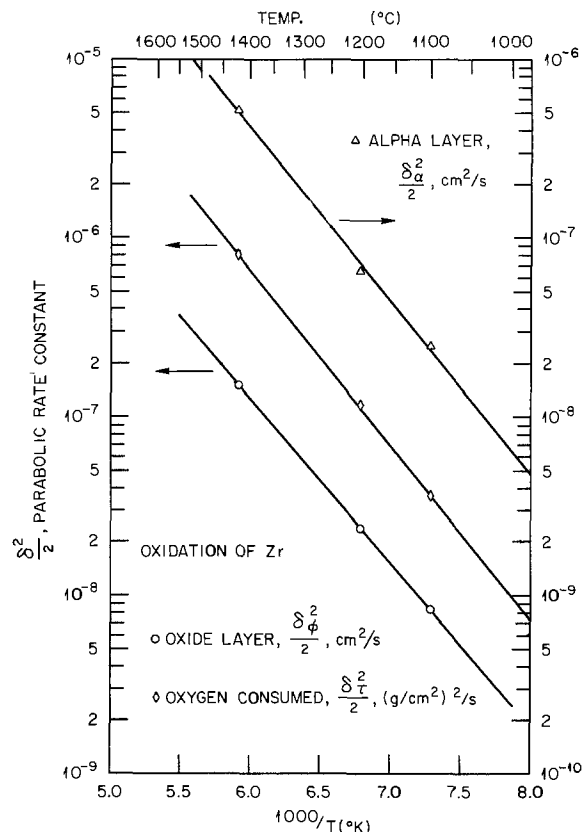


Fig. 5. Parabolic rate constants for oxide layer growth, alpha layer growth, and oxygen consumption. The rate constants for oxygen consumed were determined from a modeling analysis. Rate constants are based on the expression $\delta k^2/2 = k dk/dt$.

The parabolic rate constants for oxide (ϕ) and alpha (α) growth, and for oxygen consumption (τ) are given by

$$\frac{\delta_\phi^2}{2} = 0.04361 \left[\begin{array}{c} +35\% \\ -26\% \end{array} \right] \exp [-176,500 (\pm 2.1\%)/RT] \quad \text{cm}^2/\text{sec} \quad [2]$$

$$\frac{\delta_\alpha^2}{2} = 0.2693 \left[\begin{array}{c} +1350\% \\ -93\% \end{array} \right] \exp [-185,400 (\pm 18\%)/RT] \quad \text{cm}^2/\text{sec} \quad [3]$$

$$\frac{\delta_\tau^2}{2} = 0.4948 \exp (-187,300/RT) \quad (\text{g/cm}^2)^2/\text{sec} \quad [4]$$

The activation energies are expressed in J/gmol, and R is 8.314 J/gmol · K. The small number of data points lead to the wide 90% confidence intervals on the individual terms of the Arrhenius expressions, especially for the rate constant for alpha layer growth. The joint confidence intervals, which estimate the statistical uncertainty on the rate constants themselves, are narrower. At the mean of the reciprocal temperature range involved, they are about $\pm 3\%$ for oxide growth and about $\pm 25\%$ for alpha growth. Confidence intervals are not given for oxygen consumption in Eq. [4] because this parameter was derived from a modeling analysis involving smoothed data rather than directly using experimental measurements. While these expressions are useful for a number of purposes, it should be remembered that each of these rate parameters is influenced by rate (diffusion) processes in more than one phase and, therefore, the kinetics would not be expected to be represented precisely by an Arrhenius expression with a single activation energy.

Oxygen diffusion.—Earlier (4), on the basis of an ideal model in which the oxidation of Zircaloy was considered to be a multiphase, moving boundary dif-

fusion problem, we derived expressions relating the effective chemical diffusion coefficients for oxygen in the oxide and alpha phases to the measured kinetic parameters. In the present work, we have applied these identical equations (essentially Eq. [11] and [18] of Ref. (4)) to the layer growth data for pure zirconium to arrive at diffusion coefficients relevant to this system. Aside from the kinetic data, it is necessary to have information on the Zr-O phase equilibria in order to solve uniquely for these diffusivity values. With the exception of the alpha-beta equilibrium, shown in Fig. 6, we have assumed that there are no significant differences between the zirconium-oxygen and the Zircaloy-oxygen phase diagrams over the temperature range of interest. The interfacial oxygen solubilities shown in Fig. 6 were drawn considering the data of Gebhardt *et al.* (21), Horz *et al.* (22), and Domagala *et al.* (23). The corresponding curves of the pseudo-binary diagram for Zircaloy-4-oxygen are given as the dashed lines taken from the data of Chung *et al.* (24).

For the purpose of various calculations, it is convenient to express the equilibrium oxygen concentration at the various interfaces as functions of temperature. Using the terminology $C_{A/B}$ to represent the oxygen concentration in phase A in contact with phase B, the functions are

$$C_{\phi/\text{gas}} = 1.511 \text{ g/cm}^3$$

$$C_{\phi/\alpha} = 1.517 - 7.5 \times 10^{-5} T(\text{K}) \text{ g/cm}^3 \text{ [Ref. (25)]}$$

$$C_{\alpha/\phi} = 0.4537 \text{ g/cm}^3 \text{ [Ref. (21), (23)]}$$

$$C_{\alpha/\beta} = -2.906 + 5.322 \times 10^{-3} T(\text{K}) - 3.170 \times 10^{-6} T^2(\text{K}) + 6.519 \times 10^{-10} T^3(\text{K}) \text{ g/cm}^3 \text{ [Ref. (21), (23)]}$$

$$C_{\beta/\alpha} = -0.11136 + 7.109 \times 10^{-5} T(\text{K}) + 2.271 \times 10^{-8} T^2(\text{K}) \text{ g/cm}^3 \text{ [Ref. (21), (22), (23)]}$$

The expressions are valid over the temperature range 1200-1760 K. In addition, the diffusivity of oxygen in beta zirconium, D_{β} , was taken as

$$D_{\beta} = 0.0263 \exp[-14,190/T(\text{K})] \text{ cm}^2/\text{sec} \text{ [Ref. (26)]}$$

³ On the assumption that the oxide at the oxide-gas interface is stoichiometric ZrO_2 with a density of 5.82 g/cm^3 .

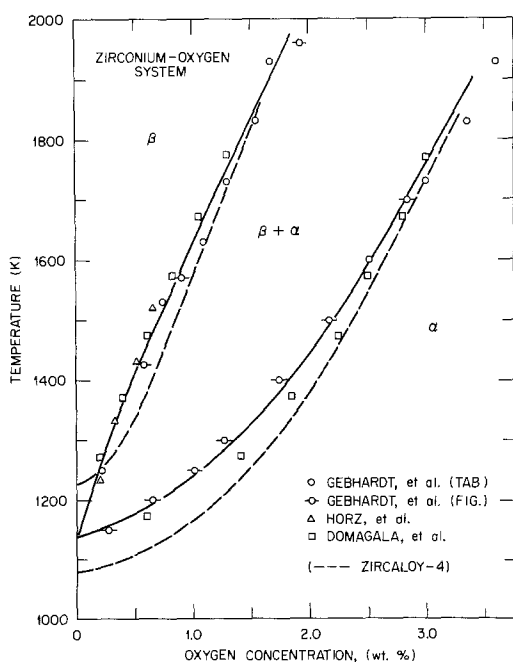


Fig. 6. Phase diagram for the Zr-O system showing the α - β equilibrium. Data are from Gebhardt *et al.* (21), Horz *et al.* (22), and Domagala *et al.* (23). Dashed lines are data for the Zircaloy-4 system from the data of Chung *et al.* (24).

Table II. Oxygen diffusion coefficients in oxide and alpha phases on zirconium during steam oxidation

| Temperature ($^{\circ}\text{C}$) | Oxygen diffusion coefficients, cm^2/sec | |
|------------------------------------|---|--------------------------|
| | Oxide, D_{ϕ} | Alpha, D_{α} |
| 1416 | 2.90×10^{-6} | 1.01×10^{-8} |
| 1200 | 4.90×10^{-7} | 1.01×10^{-7} |
| 1098 | 1.80×10^{-7} | 3.10×10^{-8} |
| 1000 ^a | $2.8-5.0 \times 10^{-8}$ | $6.2-6.7 \times 10^{-9}$ |

^a Calculated using range of "approximate parabolic rates" for the early stages of oxidation at 1000°C .

The effective chemical diffusion coefficients calculated for oxygen in the growing oxide and oxygen-stabilized alpha phases during reaction in steam are listed in Table II and plotted in Fig. 7. The three data points for each diffusivity at the higher temperatures exhibit classical Arrhenius behavior. The data points for 1000°C were calculated from the range of apparent "parabolic rates" assigned to our layer thickness measurements. While the alpha diffusivity is only slightly influenced, the variation of diffusivity indicated for the oxide is appreciably larger and, thus, we have chosen not to include either of these values in the analytical description of the diffusivities. For oxygen diffusion in the oxide phase, D_{ϕ} , the least squares Arrhenius expression is

$$D_{\phi} = 0.4684 \left[\begin{array}{c} +43\% \\ -30\% \end{array} \right] \exp(-168,500 [\pm 2.6\%]/RT) \text{ cm}^2/\text{sec}$$

For oxygen diffusion in the alpha phase, D_{α} , the three data points were judged to belong to the same set as that for Zircaloy-4 (4) and, thus, based on the more extensive latter data set

$$D_{\alpha} = 3.920 \left[\begin{array}{c} +27\% \\ -21\% \end{array} \right] \exp(-213,400 [\pm 1.4\%]/RT) \text{ cm}^2/\text{sec} \text{ [6]}$$

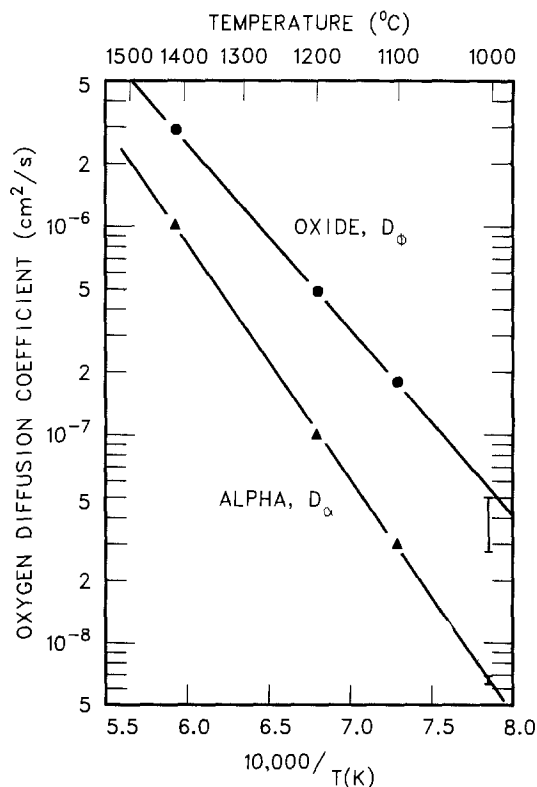


Fig. 7. Arrhenius plot showing temperature dependence of diffusion coefficients for oxygen in the growing oxide phase (D_{ϕ}), and in the alpha phase (D_{α}) on pure zirconium determined in the present investigation.

where, as before, the brackets refer to the 90% individual confidence limits. The joint confidence intervals for both diffusivities at the midpoint of the reciprocal temperature range are about ± 3.5 and $\pm 2.5\%$, respectively.

The experimental result that the calculated diffusion coefficient for oxygen in the alpha phase on zirconium is identical to that found for the alpha phase on Zircaloy-4 is particularly significant. Since one would not expect minor alloy additions to have a large influence on an interstitial diffusion rate, unless the impurities were highly reactive metals, this agreement tends to add confidence to the accuracy of the measurements and the data treatment. Thus, even though both layers grow at different rates on the two materials, all of the differences in the oxidation kinetics of the two systems can be attributed to a difference in the oxygen diffusivities in the oxide phases alone.

Modeling finite-geometry effects for zirconium.—In a recent paper (5), we reported the results of a modeling analysis that described the changes in layer growth kinetics that would be expected when specimens of Zircaloy-4 were oxidized for times sufficient to influence oxygen diffusion in the beta phase through its approach to saturation. The results of this analysis were generally consistent with experimental data, but a completely satisfactory comparison was not possible because irregularities in the alpha-beta interface developed at the longer oxidation times, resulting in a somewhat arbitrary measurement of the alpha layer growth.

In contrast to the behavior exhibited by Zircaloy-4, the oxidation of pure zirconium under similar conditions did not produce alpha "incursions," but uniform growth of both oxide and alpha layers were observed throughout the reaction to the point where virtually no beta phase remained in the specimen. For example, Fig. 8 and 9 show cross sections of zirconium specimens oxidized for approximately 260 and 1040 sec at 1416°C. These specimens show clearly the grain structure and characteristic brittleness of both the oxide and alpha layers. However, despite the fact that very thick layers are involved, and that the shrinking beta phase has become completely oxygen saturated, Fig. 9 shows very uniform layer thicknesses.

The ideal behavior observed here makes the oxidation of zirconium an excellent vehicle to test further this aspect of diffusion modeling. Thus, computer experiments were conducted using the MULTRAN code (5, 28) with diffusivity and equilibrium solubility input appropriate to the oxidation of zirconium in steam. For one-sided oxidation at 1416°C of specimens nominally 0.074 cm thick, the analysis predicts that signifi-

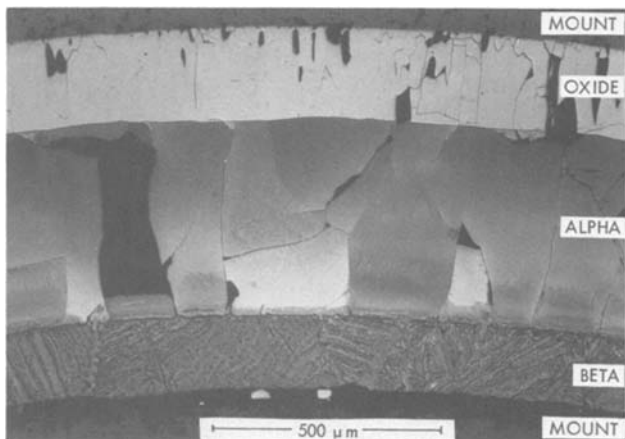


Fig. 8. Cross sections of zirconium specimen oxidized in steam for 260 sec at 1416°C. Coarse, columnar grains in both oxide and alpha layers are apparent.

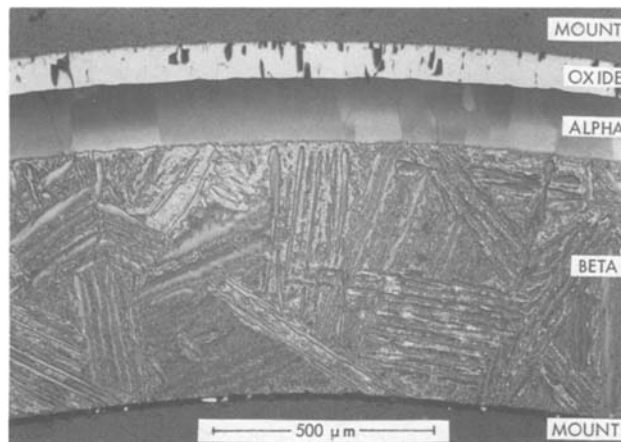


Fig. 9. Cross section of zirconium specimens oxidized in steam for 1040 sec at 1416°C. Growth has continued to be uniform although little beta phase remains. Note brittle response of the oxide and alpha layers to routine polishing.

cant departures from semi-infinite conditions for diffusion in the beta phase will exist by 120 sec and that the beta phase will become saturated at about 600 sec. Over this period of time, the original parabolic growth rates of the product phases increase to values consistent with those of growth into saturated beta. While only a second-order effect is found for growth of the oxide, the rate constant for alpha growth increases by more than a factor of two during this time.

The MULTRAN results for layer growth at 1416°C are shown by the solid curves in Fig. 10. The dashed lines are extrapolations of the short-time parabolic rates from Fig. 1. The comparison graphically illustrates the extent of the rate changes expected from the finite-geometry effect. The individual points are

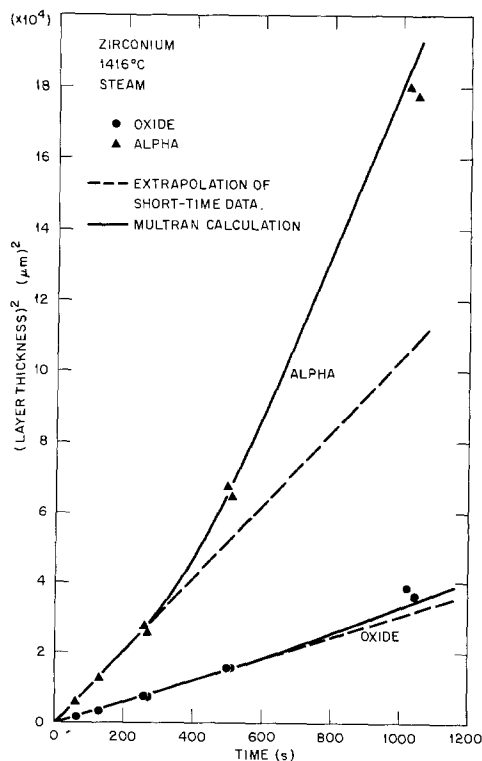


Fig. 10. Growth of oxide and alpha layers on zirconium in steam at 1416°C. The solid curves represent MULTRAN modeling results for a one-sided reaction of a specimen 0.074 cm thick. The dashed lines are extrapolations of the early stage parabolic rates (as in Fig. 1). The data points are experimental measurements.

the experimental data, and the excellent agreement between the predictions and the experimental observations gives additional credibility to the modeling technique. In addition, the extreme sensitivity of the alpha layer growth rate to the specimen thickness and extent of oxidation as well as to the original oxygen concentration points out yet another factor to be considered when evaluating and comparing oxidation behavior in this or a similar system.

Conclusions

1. At temperatures over the range 1098°-1416°C, the oxidation of pure zirconium in steam was characterized by ideal, diffusion-controlled growth of layers of oxide and oxygen-stabilized alpha zirconium.

2. From the parabolic rate constants determined for growth of both product layers, the effective chemical diffusion coefficient for oxygen in each of the phases was determined. These diffusivities exhibited classical Arrhenius behavior, and the alpha phase coefficient was statistically identical to that found earlier for diffusion in alpha Zircaloy-4.

3. A diffusion modeling analysis successfully predicted the changes in layer growth rates observed after "long" periods of oxidation of "thin" specimens. The effects of a finite specimen geometry as well as variation in the original oxygen content of the specimen were shown to be potentially large, particularly for growth of the alpha zirconium layer.

4. At 1000°C, the layer growth during oxidation exhibited complicated behavior. We proposed that this was due to changes in the relative proportions of the tetragonal and monoclinic oxides comprising the growing oxide film at this temperature.

Acknowledgments

We are indebted to J. V. Cathcart for his continuing interest and help in this work and in the preparation of the manuscript. Mrs. Kaye Russell provided specimen preparation and metallography. Suggestions and a critical review of the manuscript were provided by D. O. Hobson.

This research was sponsored by the Division of Materials Sciences, U.S. Department of Energy under contract W-7405-eng-26 with the Union Carbide Corporation.

Manuscript submitted Feb. 2, 1981; revised manuscript received March 23, 1981.

Any discussion of this paper will appear in a Discussion Section to be published in the June 1982 JOURNAL. All discussions for the June 1982 Discussion Section should be submitted by Feb. 1, 1982.

Publication costs of this article were assisted by Oak Ridge National Laboratory.

REFERENCES

1. R. E. Pawel, J. V. Cathcart, and R. A. McKee, *This Journal*, **126**, 1105 (1979).
2. G. J. Yurek, J. V. Cathcart, and R. E. Pawel, *Oxid. Met.*, **10**, 255 (1976).
3. R. E. Pawel, J. V. Cathcart, and J. J. Campbell, *J. Nucl. Mater.*, **82**, 129 (1979).
4. R. E. Pawel, *This Journal*, **126**, 1111 (1979).
5. R. E. Pawel and J. J. Campbell, *ibid.*, **127**, 2188 (1980).
6. R. E. Pawel, J. V. Cathcart, and R. A. McKee, *Oxid. Met.*, **14**, 1 (1980).
7. R. G. Ballinger, W. G. Dobson, and R. R. Biederman, *J. Nucl. Mater.*, **62**, 213 (1976).
8. W. G. Dobson, R. R. Biederman, and R. G. Ballinger, ASTM STP 633, A. L. Lowe and G. W. Parry, Editors, p. 150, ASTM, Philadelphia (1977).
9. V. F. Urbanic, ASTM STP 633, A. L. Lowe and G. W. Parry, Editors, p. 168, ASTM, Philadelphia (1977).
10. V. F. Urbanic and T. R. Heidrick, *J. Nucl. Mater.*, **75**, 251 (1978).
11. S. Leistikow, G. Schanz, and H. V. Berg, *Kernforschungszentrum Karlsruhe, KfK-2587* (March 1978).
12. M. D. Tucker, A. F. Brown, and T. Healey, *J. Nucl. Mater.*, **74**, 41 (1978).
13. A. F. Brown and T. Healey, *ibid.*, **88**, 1 (1980).
14. C. J. Rosa, *J. Less-Common Met.*, **16**, 173 (1968).
15. D. L. Douglass, "The Metallurgy of Zirconium," IAEA, Vienna (1971).
16. B. Cox, in "Advances in Corrosion Science and Technology," Vol. 5, Plenum Press, New York (1976).
17. J. Debuigne, *Met. Corr. Ind.*, **XLII**, 89 (1967).
18. J. P. Pemsler, *Electrochem. Technol.*, **4**, 128 (1966); *This Journal*, **112**, 477 (1965); *ibid.*, **113**, 1241 (1966).
19. J. B. Lightstone and J. P. Pemsler, "Materials Science Research, Vol. 4: Kinetics of Reaction in Ionic Systems," p. 461, Plenum Press, New York (1969).
20. C. J. Rosa and W. C. Hagel, *Trans. Met. Soc. AIME*, **242**, 1293 (1968); C. J. Rosa and W. W. Smeltzer, *Acta Met.*, **13**, 55 (1965).
21. E. Gebhardt, H. D. Seghezzi, and W. Dürschnabel, *J. Nucl. Mater.*, **4**, 255 (1961).
22. G. Hörz and M. Hammel, *ibid.*, **55**, 284 (1975).
23. R. F. Domagala and D. J. McPherson, *Trans. AIME*, **200**, 238 (1954).
24. H. M. Chung and T. F. Kassner, *J. Nucl. Met.*, **84**, 327 (1979).
25. From the phase diagram of R. Ruh and H. J. Garrett, *J. Am. Ceram. Soc.*, **50**, 257 (1967).
26. R. A. Perkins, *J. Nucl. Mater.*, **68**, 148 (1977).
27. C. F. Grain and R. C. Garvie, U.S. Bureau of Mines Report 6619 (1965).
28. S. Malang, guest scientist from Gesellschaft für Kernforschung, Karlsruhe, FRG. Unpublished research, ORNL, 1978). (The MULTRAN code furnishes a finite difference solution to the one-dimensional, multiphase, moving boundary diffusion problem in finite system. It is particularly useful for examining transient-temperature growth effects and other variations in boundary conditions).

Thermodynamic Stability of Beta Alumina

Alain Dubreuil

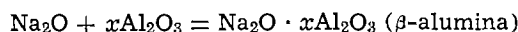
Polyceram Incorporated, C.P. 6079, Succ. "A," Montréal, Québec, Canada H3C 3A7

and Martin Malenfant and A. D. Pelton

Département de génie métallurgique, Ecole Polytechnique, Montréal, Québec, Canada H3C 3A7

ABSTRACT

The Gibbs energy of formation of beta alumina in equilibrium with alpha alumina has been measured over the temperature range 320°-800°C by two different equilibrium emf techniques. The results are well represented by the following equation



$$\Delta G^\circ = -22.0 \times 10^4 - 0.57T \pm 5.5 \times 10^3 \text{J}$$

Chronopotentiometric experiments were performed over the range 85°-140°C. If the observed plateaus are interpreted as representing the dissociation of Na₂O in the beta alumina, results are in agreement with the above equation.

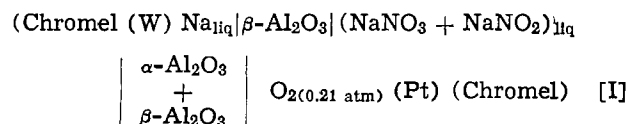
Despite the great interest in the superionic conductor beta alumina in recent years, the thermodynamic stability of this compound still has not been well determined, particularly at lower temperatures. In the present study, the free energy of formation of beta alumina in equilibrium with alpha alumina was determined over the temperature range from 320° to 800°C by two different equilibrium emf techniques and over the temperature range 80°-140°C by chronopotentiometry. Normally, one cannot investigate a solid by this non-equilibrium technique due to the very high ohmic drop. However, the extremely high conductivity of the superionic conductor β-Al₂O₃ permits this method to be used for this material.

Equilibrium Techniques

Experimental.—In the equilibrium techniques, slip-cast high density vacuum-tight beta alumina tubes from Polyceram Incorporated were used. The fabrication of these tubes has been described elsewhere (1). The tubes were approximately 6 cm long × 1 cm diam with a wall thickness of about 0.1 cm.

Approximately half of the tubes were made directly from commercial "Alcoa XB2" powder. Analysis by atomic absorption showed that these tubes had compositions varying from Na₂O · 9.3Al₂O₃ to Na₂O · 9.9Al₂O₃. Hence, according to the phase diagram (2), all the tubes were two-phase α-Al₂O₃/β-Al₂O₃ mixtures. This was confirmed by x-ray analysis of the tubes. For the other half of the tubes, about 25% α-Al₂O₃ powder was added during the grinding step so that these tubes had compositions even further within the two-phase region. No difference in the results obtained from the two sets of tubes was evident. Since Na₂O is the volatile component, slight volatilization losses from the surface of the tubes at high temperature will assure that there is even more of the α-phase at the surface than in the bulk.

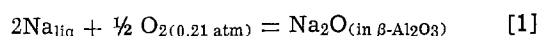
Cell I.—Cell I is shown schematically in Fig. 1. This cell may be represented as



The sodium electrode consisted of a beta alumina tube

containing pure liquid Na. The cell was sealed with an alumina plug and "Cotronix 940"¹ ceramic cement. Contact was made via a tungsten wire which passed through a Pyrex metal/ceramic seal. The tube was sealed with a small amount of tungsten powder inside and the cement was then sintered at 900°C in order to give a gas-tight seal. Several grams of sodium were then titrated coulometrically into the electrode compartment from an NaNO₃-NaNO₂ bath. The oxygen electrode consisted of a two-phase α-Al₂O₃/β-Al₂O₃ tube cemented to an α-Al₂O₃ extension tube open to the air. Electrical contact was made via a platinum wire to the platinized inner surface of the tube. Contact between the two electrodes was via a molten NaNO₃-NaNO₂ bath. The use of the molten salt as an intermediary electrolyte eliminates the possibility of electronic transport between electrode compartments.

The overall cell reaction for cell I is



Hence, the emf of cell I is given by

$$e = -\frac{RT}{2F} \ln \frac{a_{\text{Na}_2\text{O}}}{0.21^{1/2}} - \frac{1}{2F} \Delta G^\circ_{\text{Na}_2\text{O}} \quad [3]$$

where *F* is the Faraday, *R* is the gas constant, *T* is the temperature in Kelvin, *a*_{Na₂O} is the activity of Na₂O in β-Al₂O₃ in equilibrium with α-Al₂O₃, and Δ*G*[°]_{Na₂O} is the standard Gibbs energy of formation of Na₂O. Sub-

¹ Cotronix Corporation, New York, NY 10018.

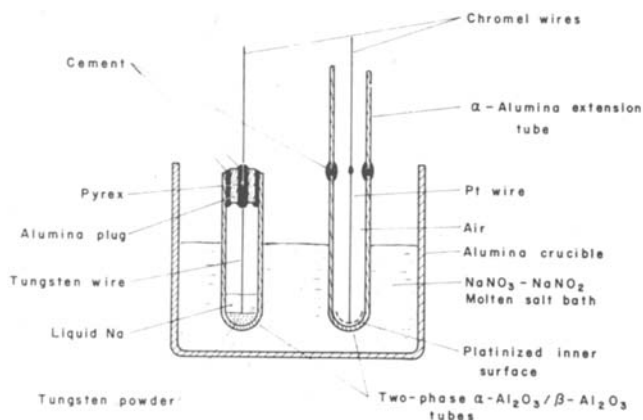


Fig. 1. Cell I

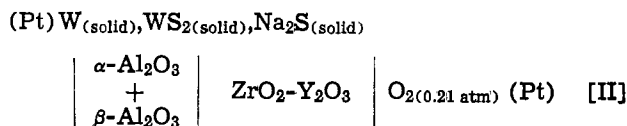
Key words: beta-alumina, thermodynamic properties, solid electrolytes.

stituting into Eq. [2] the value of $\Delta G^\circ_{\text{Na}_2\text{O}} = -405,600 + 128.9T$ in joules obtained from the literature (3) we obtain

$$\log_{10} a_{\text{Na}_2\text{O}} = \frac{-10,080}{T} \epsilon + \frac{21,190}{T} - 7.08 \quad [3]$$

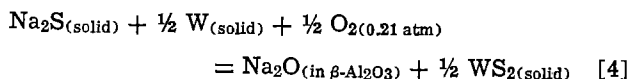
where ϵ is in volts.

Cell II. Cell II which is shown schematically in Fig. 2, may be represented as



A two-phase $\alpha\text{-Al}_2\text{O}_3/\beta\text{-Al}_2\text{O}_3$ tube was filled with a mixture of W, WS_2 , and Na_2S powders.² The compartment was sealed with a highly viscous Kovar glass. The tube rested inside a long $ZrO_2\text{-}Y_2O_3$ tube. Argon was passed inside the $ZrO_2\text{-}Y_2O_3$ tube in order to eliminate the possibility of oxygen traversing the Kovar seal. The exterior of the $ZrO_2\text{-}Y_2O_3$ tube was placed in an atmosphere of air. Electrical contact was made via a Pt electrode attached to the platinized surface. The $W/WS_2/Na_2S$ reference, which establishes a fixed activity of Na, was first used by Liang and Elliott (6). In order that the three-phase equilibrium be established, this reference electrode must be used at temperatures in excess of 550°C.

The overall cell reaction of cell II is



Hence the emf of cell II is given by

$$\epsilon = -\frac{RT}{2F} \ln \frac{a_{\text{Na}_2\text{O}}}{0.21^{1/2}} - \frac{1}{2F} \left(\frac{1}{2} \Delta G^\circ_{WS_2} - \Delta G^\circ_{Na_2S} + \Delta G^\circ_{Na_2O} \right) \quad [5]$$

Substituting into Eq. [5] values for the standard Gibbs energies of formation of WS_2 , Na_2S , and Na_2O from the literature (4, 5, 3) along with their estimated error limits, we obtain

$$\log_{10} a_{\text{Na}_2\text{O}} = -\frac{10,080}{T} \epsilon + \frac{7,210}{T} - 5.31 \pm 1.6 \quad [6]$$

where ϵ is in volts.

Results.—Values of $\log_{10} a_{\text{Na}_2\text{O}}$ calculated via Eq. [3] and [6] from the measured emf's of cells I and II are shown in Fig. 3. For both cells I and II the points

² Alfa Inorganics.

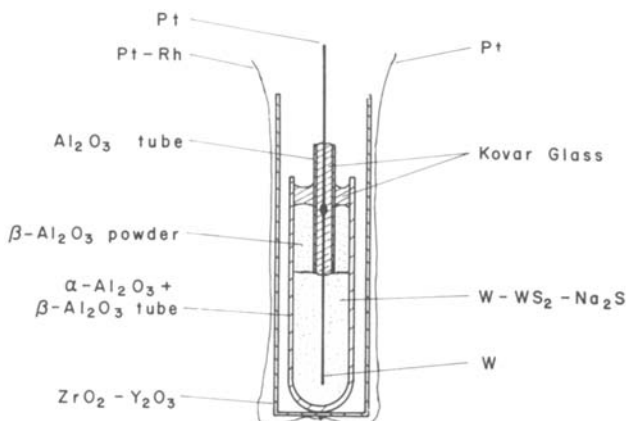


Fig. 2. Cell II

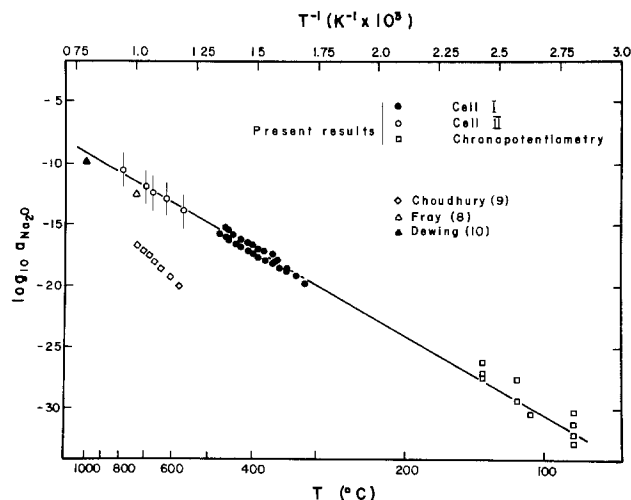
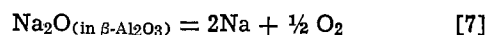


Fig. 3. Activity of Na_2 in $\beta\text{-Al}_2\text{O}_3$ in equilibrium with $\alpha\text{-Al}_2\text{O}_3$

shown were obtained during both heating and cooling cycles. Measured emf's were very stable. If the cells were polarized, the emf quickly returned to within ± 1 mV of its former value within 1 or 2 min. Overall reproducibility is estimated as ± 5 mV. The error bars shown on Fig. 3 for cell II are those given in Eq. [6].

Chronopotentiometry

At lower temperatures, equilibrium techniques can no longer be applied because kinetic barriers to reactions involving the solid state become too great. Consequently, nonequilibrium techniques in which one attempts to force the decomposition of the beta alumina must be used. In these experiments it is assumed that the reaction involved is the decomposition of the sodium oxide in the two-phase $\alpha\text{-Al}_2\text{O}_3/\beta\text{-Al}_2\text{O}_3$ mixture according to



As will be shown later, the final justification for this assumption is that the results agree well with those obtained by the equilibrium techniques discussed in the previous section.

The details of the cell for the chronopotentiometric experiments have been described by Foraison and Souquet (7). A two phase $\alpha\text{-Al}_2\text{O}_3/\beta\text{-Al}_2\text{O}_3$ disk, 3.30 cm in diameter by 1.12 cm thick, was prepared by cold-pressing "Alcoa XB2" beta-alumina powder at 1 t/cm² followed by sintering at 1600°C for 1 hr in a container packed with $\beta\text{-Al}_2\text{O}_3$ powder. Holes for the working, reference, and counterelectrode compartments were made with a diamond drill. The counterelectrode compartment was in the form of an annulus surrounding the working electrode. The reference and counterelectrode compartments were filled with Na-Hg amalgams containing approximately 0.3 weight percent Na. The working electrode compartment contained an amalgam with only a few ppm of sodium. Electrical contact was made via tungsten leads. The entire assembly was maintained under purified nitrogen in a Pyrex tube placed in a thermostated oil bath. A constant current of 1.0 μA was imposed between the working and counterelectrodes, the working electrode being the anode. The voltage between the working electrode and the reference electrode (which was never polarized) was measured as a function of time. A typical curve is shown in Fig. 4. In this figure, the ordinate is the overpotential η defined as

$$\eta = \epsilon - \epsilon(I=0) \quad [8]$$

where ϵ is the measured voltage and $\epsilon(I=0)$ is the voltage measured at open circuit (zero current).

The initial portion of the curve is presumed to correspond to the diffusion of sodium in the working electrode and the formation of a sodium-depleted boundary

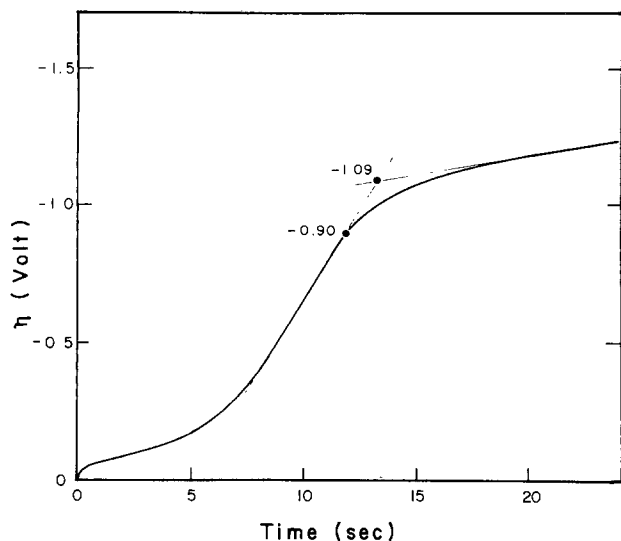


Fig. 4. Experimental chronopotentiometric curve. Conditions: $T = 115^\circ\text{C}$, $\epsilon_{(I=0)} = 0.339\text{V}$, applied current = $1\ \mu\text{A}$.

layer. The plateau which begins between $\eta = -0.9\text{V}$ and $\eta = -1.09\text{V}$ is presumed to result from the decomposition of the $\beta\text{-Al}_2\text{O}_3$ according to Eq. [7]. The actual decomposition overpotential, η_{decomp} , was chosen in Fig. 4 as $\eta = -1.0 \pm 0.1$ which is the average of -0.9 and -1.09V . All the chronopotentiometric curves were interpreted in the same way. From Eq. [8]

$$\eta_{\text{decomp}} = \frac{RT}{F} \left(\ln \frac{a_{\text{Na}(\text{decomp})}}{a_{\text{Na}(\text{ref})}} - \ln \frac{a_{\text{Na}(\text{bulk})}}{a_{\text{Na}(\text{ref})}} \right) \\ = - \frac{RT}{F} \ln \frac{a_{\text{Na}(\text{bulk})}}{a_{\text{Na}(\text{decomp})}} \quad [9]$$

where $a_{\text{Na}(\text{ref})}$ is the activity of Na in the reference electrode, while $a_{\text{Na}(\text{bulk})}$ and $a_{\text{Na}(\text{decomp})}$ are the activities of Na in the bulk of the working electrode at the amalgam/ $\beta\text{-Al}_2\text{O}_3$ interface at the moment when decomposition commences.

In order to calculate the activity of Na_2O in the $\beta\text{-Al}_2\text{O}_3$ it is necessary to know the activity of oxygen dissolved in the working electrode. It may be assumed that the system is saturated in oxygen. That is, the Na and O_2 dissolved in the bulk are in equilibrium with pure Na_2O . Hence

$$K = \frac{1}{a_{\text{Na}(\text{bulk})}^2 P_{\text{O}_2}^{1/2}} = \frac{a_{\text{Na}_2\text{O}}}{a_{\text{Na}(\text{decomp})}^2 P_{\text{O}_2}^{1/2}} \quad [10]$$

where P_{O_2} is the partial pressure of oxygen dissolved the working electrode, $a_{\text{Na}_2\text{O}}$ is the activity of Na_2O in the $\alpha\text{-Al}_2\text{O}_3/\beta\text{-Al}_2\text{O}_3$ mixture, and K is the equilibrium constant for the formation of Na_2O from 2Na and $1/2\ \text{O}_2$. Substitution of Eq. [10] into Eq. [9] gives

$$\eta_{\text{decomp}} = \frac{RT}{2F} \ln a_{\text{Na}_2\text{O}} \quad [11]$$

Hence, $\ln a_{\text{Na}_2\text{O}}$ is given directly from measurement of η_{decomp} .

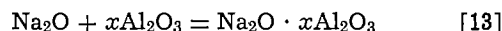
Results of several experiments between 85° and 140°C are shown in Fig. 3.

Discussion

It can be seen from Fig. 3 that the results from the two equilibrium measurements (cells I and II) fall on the same straight line. The equation of the line shown on Fig. 3, which was found by a least squares regression analysis of only the data obtained by the equilibrium measurements, is

$$\log_{10} a_{\text{Na}_2\text{O}} = -11.49 \times 10^3 T^{-1} - 0.03 \pm 0.32 \quad [12]$$

The root mean square deviation of the fit to $\log_{10} a_{\text{Na}_2\text{O}}$ was ± 0.32 . The free energy of formation of $\beta\text{-Al}_2\text{O}_3$ in equilibrium with $\alpha\text{-Al}_2\text{O}_3$ according to



is given from Eq. [12] as

$$\Delta G^\circ_{[13]} = RT \ln a_{\text{Na}_2\text{O}} = -22.0 \times 10^4 \\ - 0.57T \pm 5.5 \times 10^3 \text{J} \quad [14]$$

When the line given by Eq. [12] is extrapolated to lower temperatures, it passes through the experimental points measured by chronopotentiometry as can be seen from Fig. 3. This supports the interpretation of these nonequilibrium measurements given in the previous section.

The present results are in close agreement with the measurement of Fray (8) at 725°C (see Fig. 3) whose cell consisted of a tube of $\beta\text{-Al}_2\text{O}_3$ containing a powdered mixture of $\alpha\text{-Al}_2\text{O}_3$ and $\beta\text{-Al}_2\text{O}_3$ open to the air, immersed in pure sodium.

Choudhury (9) measured the activity of Na_2O in two-phase $\alpha\text{-Al}_2\text{O}_3/\beta\text{-Al}_2\text{O}_3$. The sodium activity was fixed by a mixture of Ni, NiF_2 , and NaF , while the oxygen potential was fixed by a $\text{Cu}/\text{Cu}_2\text{O}$ mixture. All the components were in the solid state. Choudhury's results are also shown in Fig. 3.

Recent calculations and measurements by Dewing (10) (see Fig. 3) are in close agreement with the present study at the higher temperatures.

Conclusions

The free energy of formation of $\beta\text{-Al}_2\text{O}_3$ saturated with $\alpha\text{-Al}_2\text{O}_3$ has been measured over the temperature range $320^\circ\text{-}800^\circ\text{C}$ by two different equilibrium emf techniques. The results are in good agreement with each other. In addition, measurements of the same quantity by chronopotentiometry over the temperature range $85^\circ\text{-}140^\circ\text{C}$ gave results which agree with the values extrapolated from the equilibrium measurements at higher temperatures. However, in view of the many assumptions required, the interpretation of the chronopotentiometric experiments should be regarded as only tentative.

Acknowledgments

Financial support from the Natural Sciences and Engineering Research Council of Canada and a France-Quebec scholarship for one of the authors (A.D.) are gratefully acknowledged.

Manuscript submitted Aug. 4, 1980; revised manuscript received ca. March 2, 1981.

Any discussion of this paper will appear in a Discussion Section to be published in the June 1982 JOURNAL. All discussions for the June 1982 Discussion Section should be submitted by Feb. 1, 1982.

Publication costs of this article were assisted by the Ecole Polytechnique.

REFERENCES

1. M. Rivier and A. D. Pelton, *Am. Ceram. Soc. Bull.*, **57**, 183 (1978).
2. Y. Le Cars, J. Théry, and R. Collongues, *Rev. Int. Hautes Temp. Réfract.*, **9**, 153 (1972).
3. C. B. Alcock and G. P. Stavropoulos, *Can. Met. Quart.*, **10**, 257 (1971).
4. J. P. Hager and J. F. Elliott, *TMS-AIME*, **239**, 259 (1967).
5. JANAF Thermochemical Tables, D. R. Stull and H. Prophet, Editors, U.S. Dept. of Commerce, Washington, DC (1977).
6. W. W. Liang and J. F. Elliott, *This Journal*, **123**, 617 (1976).
7. D. Foraison and J. L. Souquet, *Electrochim. Acta*, **23**, 457 (1978).
8. D. J. Fray, *Metall. Trans.*, **9B**, 153 (1977).
9. N. S. Choudhury, *This Journal*, **120**, 1663 (1973).
10. E. Dewing, Private communication.

Grain Size and Resistivity of LPCVD Polycrystalline Silicon Films

J. P. Colinge

Microelectronics Lab, Université Catholique de Louvain, Place du Levant 3, 1348 Louvain-la-Neuve, Belgium

E. Demoulin*

C.N.E.T., B.P. 42, Chemin du Vieux Chêne, 38240 Meylan, France

F. Delannay

*Groupe de Physico-Chimie Minérale et de Catalyse,
Université Catholique de Louvain, Place Croix du Sud 1, 1348 Louvain-la-Neuve, Belgium*

M. Lobet

Microelectronics Lab, Université Catholique de Louvain, Place du Levant 3, 1348 Louvain-la-Neuve, Belgium

and J. M. Temerson

C.N.E.T., B.P. 42, Chemin du Vieux Chêne, 38240 Meylan, France

ABSTRACT

Measurements have been performed on phosphorous-implanted polysilicon films and TEM investigation has given indications about the mean grain size and about its dependence on the temperature and duration of annealing. Results have also been obtained concerning the sheet resistivity of the films. A semiquantitative model has been derived which attempts to explain the variation in sheet resistivity as a function of the doping level. The observation of both grain size and sheet resistivity suggests that not only segregation to grain boundary and grain growth occur during annealing but that a third phenomenon (a crystallographic relaxation at grain boundary) should occur at a temperature of about 1000°C.

The electrical properties of polycrystalline silicon (polysilicon) have already been extensively investigated for solar cell applications as well as in integrated circuit technology.

The use of that material has given rise to structures such as self-aligned MOSFET's, FAMOS transistors, and charge-coupled devices (1-3). More recently, devices such as diodes, variable resistors, or MOS transistors have been built using polysilicon (4-6), but, until now, polysilicon has been mainly used in the fabrication of passive components such as interconnecting stripes, NMOS gates, or integrated resistors. The resistivity of a polysilicon film varies with the concentration of the dopant atoms in it; it can extend over several decades (from 8 Ω per square up to 10¹⁰ Ω per square). Low resistance polysilicon stripes can be obtained by heavy doping, while small size resistors of high as well as low values can be made in less doped polysilicon.

The main parameters on which the resistivity of polysilicon depends are the temperature of deposition (below 580°C, the deposited silicon is amorphous; above that temperature, it is polycrystalline, with an average grain size increasing with increasing deposition temperature), the average grain size, the doping level, and the annealing cycles to which the material has been submitted.

It is well known that the resistivity of polysilicon varies with the dopant concentration in a way which is very different from that of single crystal silicon.

Several models have been proposed to explain the variation in resistivity of polysilicon, taking the dopant concentration as a parameter, but they all are qualita-

tive models. The basic phenomena that presumably explain the difference between single crystal and polycrystalline silicon are the migration and inactivation of impurity atoms at grain boundaries (7, 8) and carrier trapping at grain boundaries (Seto's model) (9, 10). This last model has generally been found more acceptable.

Since all those models refer to the crystalline texture of the layers, it is important to notice that TEM and SEM investigations have shown that the polysilicon crystallites have a basaltic texture, *i.e.*, that the grains grow with a columnar shape from the substrate up to the top of the layer (11).

It has also generally been assumed that the variation of polysilicon resistivity as a function of the annealing temperature after doping (by implantation of phosphorous in this case) (12) is due to the competition of two phenomena: the segregation of dopant atoms to the grain boundaries below 1000°C and the grain growth above that temperature. One of the goals of this study is to demonstrate that a third phenomenon has to be taken into account: a solid-phase crystallographic relaxation at the grain boundary, at temperatures around 1000°C. Our second goal will be to provide a mathematical model of polysilicon resistivity as a function of the doping level that would give greater consideration to the physical characteristics of polysilicon than previous models (basaltic texture of the grains, film thickness, etc.).

Experimental Procedure and Experimental Results

Sheet resistivity and grain size as a function of annealing cycles.—Resistivity.—The samples were fabricated on <100> 10-20 Ω cm p-type silicon wafers. The wafers were thermally oxidized at 1000°C in dry oxy-

* Electrochemical Society Active Member.

Key words: semiconductor, annealing, diffusion, trapping.

gen, wet oxygen, and dry oxygen to obtain a good oxide surface, a thick oxide, and a good Si-SiO₂ interface, respectively. The oxide thickness was 3000Å to avoid leakage currents. A 5000Å thick polysilicon layer was deposited in a Tempres LPCVD reactor by pyrolysis of silane at 625°C, under a pressure of 180 mTorr. The samples were implanted with phosphorous at an energy of 100 keV at different doses. The polysilicon was then capped with a 3000Å-thick SiO₂ layer deposited at 420°C to avoid dopant outdiffusion and the wafers were annealed at different temperatures, from 800°C up to 1100°C in nitrogen ambient. The annealing time was 30 min, 2 or 12 hr. The capping oxide was then removed and the sheet resistivity was measured by the four-point probe method. The variation in sheet resistivity with annealing temperature is illustrated graphically in Fig. 1.

The sheet resistivity curves show the same shape for various annealing times: a maximum in sheet resistivity is reached at a temperature T_i which decreases when annealing time increases, while the value of this maximum increases with annealing time. For a given higher annealing temperature ($T > T_i$), the longer the annealing time, the lower the sheet resistivity, while the opposite behavior is observed for $T < T_i$.

The dependence of sheet resistance on annealing time is illustrated in Fig. 2 in which one can see that the sheet resistance increases with annealing time for $T < 900^\circ\text{C}$, while it decreases for $T > 900^\circ\text{C}$ and is stable at 900°C.

Grain size.—The samples were annealed for 12 hr and prepared for TEM investigation: a photolithographic

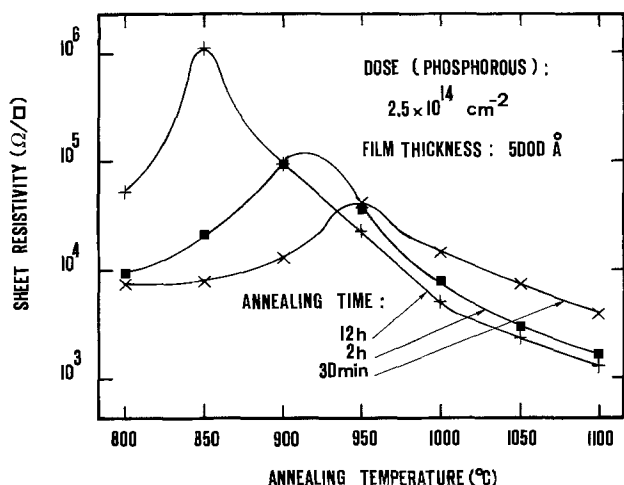


Fig. 1. Variation of sheet resistivity vs. annealing temperature

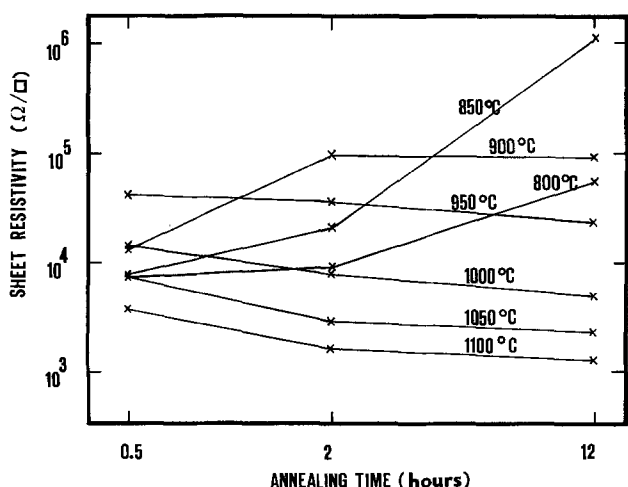


Fig. 2. Variation of sheet resistivity vs. annealing time

step was necessary to create small disks of polysilicon, 3 mm in diameter, which were removed from the wafers by dissolving the subjacent oxide in HF. The small polysilicon disks were observed with a TEM (the accelerating voltage was 100 keV and the magnification was 33,000 or 6,000). Wada's method (13) was used to determine the mean grain size in polysilicon.

It has been observed that the mean grain size is about 1400Å for annealings between 800° and 1000°C. For samples annealed at 1050° and 1100°C, the mean grain size is respectively 4400 and 4700Å (Fig. 3).

Resistivity as a function of the doping level.—The samples were prepared as described above. Phosphorous was implanted with an energy of 100 keV in order to obtain impurity concentrations of 2×10^{18} , 2.4×10^{18} , 2.7×10^{18} , 3.6×10^{18} , 5.5×10^{18} , 10^{19} , 5×10^{19} , and 10^{20} cm^{-3} .

The samples were then capped with a silox oxide and annealed for 30 min at 1000°C. The capping oxide was removed and the resistivity of the samples was measured by the four-point probe method, except for those with the highest resistance, which were measured by the Van der Pauw method. The results are reported in Fig. 9 and will be commented on in the following section under Resistivity of polysilicon.

A New Model for Polysilicon Resistivity

Several models have been proposed to explain the variation of polysilicon resistivity with dopant concentration. The models assuming a trapping of carriers at the grain boundary are generally more accurate than those based on the atom segregation assumption, although evidence of atom segregation to grain boundaries has been found (14). The model of carrier trapping has first been developed by Seto (9) and has been improved by Baccarini, Ricco, and Spadini (15) and by Martinez and Piqueras (16). The improvements of Seto's model these last studies have provided take into account the energy distribution of the trapping centers, but all these models remain qualitative. Furthermore, they take into account neither the real physical shape of the grains (a columnar shape) nor the effect of the film thickness. The present study starts from a columnar-shaped grain, taking into account the fact that a depletion region surrounds the whole grain and "spreads" from the grain boundary to the center of the grain. It also accounts for the effect of the film thickness on the carrier mobility.

The potential barrier.—Let us consider a cylindrical crystallite having a radius R and a height h (the cylindrical shape has been chosen for it is the simplest shape accounting for the basaltic texture of the grain, and it can describe in two dimensions the effect of a depletion region surrounding the crystallite). The grain is as-

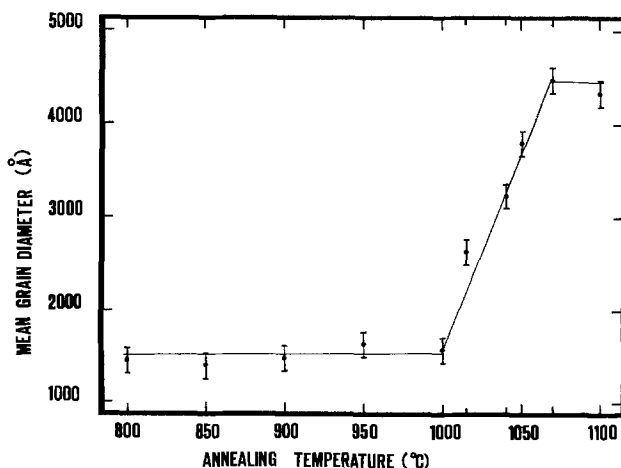


Fig. 3. Mean grain diameter vs. annealing temperature

sumed to be doped with a uniform impurity concentration N_d (cm^{-3}).

Let us also assume a concentration of traps N_t (cm^{-2}) located at the grain boundary (Fig. 4).

These traps are located in the bandgap and trap some carriers. The trapping of carriers gives rise to a depletion region spreading from the grain boundary to the core of the grain. This gives rise to a potential barrier between the grains. If the grain is not too small ($R > 2N_t/N_d$), there is a neutral region at the center of the cylinder; if this is not the case, the whole crystallite is depleted.

Solving Poisson's equation in cylindrical coordinates

$$\nabla^2\Phi = \frac{1}{r} \left[\frac{\partial}{\partial r} \left(r \frac{\partial\Phi}{\partial r} \right) \right] = -\frac{\rho}{\epsilon}$$

yields in the first case ($R > 2N_t/N_d$) a potential distribution

$$\begin{aligned} \Phi(r) &= 0 \quad \text{if } r < r_1 \\ \Phi(r) &= -\frac{qN_d}{4\epsilon} \left\{ r^2 - r_1^2 \left(1 + \ln \frac{r^2}{r_1^2} \right) \right\} \\ &\quad \text{if } r > r_1 \quad [1] \end{aligned}$$

with r_1 being the radius of the neutral region.

Expressing the electrical neutrality of the set grain + grain boundary by

$$(R^2 - r_1^2) \pi h N_d = 2\pi R h N_t$$

we finally obtain the value of the potential barrier

$$V_b = \Phi(R) = -\frac{q}{4\epsilon} \{ 2N_t R + N_d R^2 (1 - 2N_t/RN_d) \ln(1 - 2N_t/RN_d) \} \quad [1a]$$

In the second case ($R < 2N_t/N_d$), the grain is "small" and one obtains

$$V_b = -\frac{qN_d}{4\epsilon} R^2 \quad [1b]$$

One can see that the "smallness" of a grain is (strictly) relative: the importance of the grain size is directly related to the density of traps and to the doping level.

Similar expressions can obviously be derived for holes instead of electrons in the case of a p-type semiconductor.

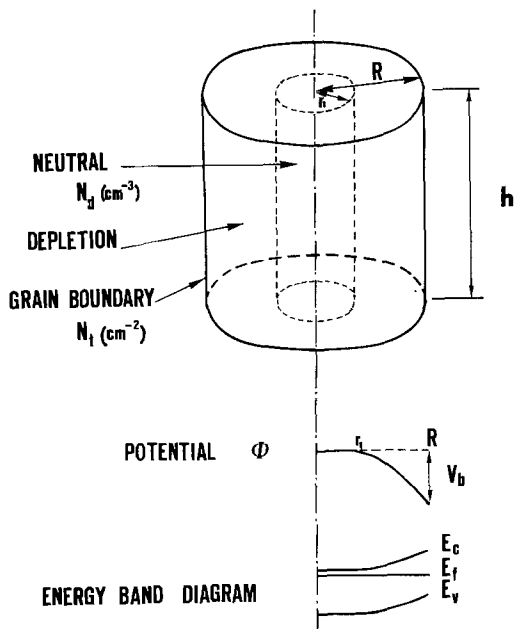


Fig. 4. Grain shape, potential, and energy band diagram in polysilicon.

Current flow through the potential barrier.—The current flowing from one crystallite to another has to overcome the potential barrier. For the sake of simplicity, we now consider a one-dimensional section, although the grains have been previously assumed to be cylindrical. Let $w = R - r_1$ and $dx = dr$ (see Fig. 5).

For a current flow which is assumed to be constant with respect to the x -direction, we have

$$J_n = qD_n \left\{ -n(x) \frac{q}{kT} \frac{\partial\Phi}{\partial x} + \frac{\partial n}{\partial x} \right\}$$

Multiplying that equation by $\exp(-q\Phi(x)/kT)$ and integrating from 0 to w , we obtain

$$J_n \int_0^w \exp\left(-\frac{q\Phi(x)}{kT}\right) dx = qD_n n_0 \left[\exp\left(\frac{qV_r}{kT}\right) - 1 \right] \quad [2]$$

where V_r is the voltage drop applied to the grain.

If one linearizes $\Phi(x)$ between 0 and w , one obtains (Fig. 6)

$$\Phi(x) = -\Phi_b + \left(\frac{x}{w}\right) (\Phi_b - V_r)$$

with Φ_b being the potential at grain boundary.

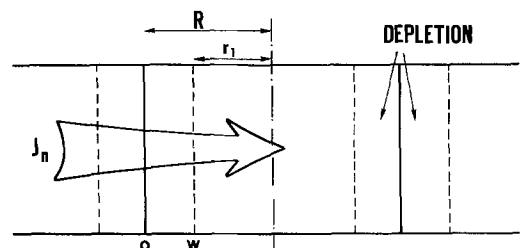
Under this assumption, Eq. [2] may be rewritten

$$J_n = \frac{q^2 D_n n_0}{w k T} (\Phi_b - V_r) \frac{\exp\left(\frac{qV_r}{kT}\right) - 1}{1 - \exp\left(-\frac{q(\Phi_b - V_r)}{kT}\right)}$$

Now, if $V_r \ll \Phi_b$, $\Phi_b \approx V_b$; V_r is equal to the voltage drop applied to the sample divided by the number of grains located between the two contacts. The assumption of $V_r \ll \Phi_b$ (and also $V_b \ll kT/q$) is valid if the grains are relatively small ($R < 1000\text{\AA}$) as is the case in thermally annealed samples.

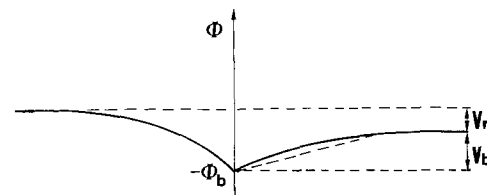
If V_b is small with respect to kT/q , we may estimate the resistivity near the grain boundary as being

$$\rho^{-1} = w \lim_{V_r \rightarrow 0} \frac{J_n}{V_r} = q\mu n_0 \exp\left(-\frac{qV_b}{kT}\right) \quad [3]$$



CURRENT FLOW THROUGH A GRAIN BOUNDARY

Fig. 5. Current flow through a grain boundary



LINEARIZATION OF THE POTENTIAL NEAR THE GRAIN BOUNDARY

Fig. 6. Linearization of the potential near the grain boundary

Carrier mobility.—The last result allows us to define a "boundary mobility," μ_b . We have thus $\mu_b = \mu_0 \exp(-qV_b/kT)$ where μ_0 is the mobility in single crystal silicon. μ_0 has been found to vary as (17)

$$\mu_0 = 80 + 1570 \{1 + (0.77 \times 10^{-17} N_d)^{0.91}\}^{-1} \text{ cm}^2/\text{Vsec}$$

If the crystallites are entirely depleted

$$\mu_{\text{eff}} = \mu_b \quad [4a]$$

If it is not the case, we must consider the neutral region and the barrier region as a serial association of resistors. A brief calculation shows that

$$\mu_{\text{eff}} = \mu_0 \frac{R \exp\left(-\frac{qV_b}{kT}\right)}{R - r_1 \{1 - \exp(-qV_b/kT)\}} \quad [4b]$$

The mobility is also reduced by the effect of the film thickness; one can determine (18) that

$$\mu_{\text{film}} = \mu_{\text{eff}} \frac{3}{4} \left(\frac{t_f}{l_c}\right) \left\{ 0.423 + \ln\left(\frac{l_c}{t_f}\right) \right\} \quad [5]$$

where l_c is the mean free path of electrons (1.95 μm in silicon) and t_f is the film thickness.

Average carrier concentration.—We can estimate the average carrier concentration as follows: If $N_d > 2N_t/R$, the carrier concentration will be

$$\bar{n} = N_d - 2N_t/R \quad [6a]$$

$2N_t/R$ being the amount of carriers trapped at the grain boundary. If $N_d < 2N_t/R$, the carrier concentration can be calculated as follows

$$n(x) = N_c \exp\left(\frac{E_f - E_c + q\Phi(x)}{kT}\right)$$

$$\text{with } \Phi(x) = \frac{-qN_d x^2}{4\epsilon}$$

the average carrier concentration is

$$\bar{n} = \frac{N_c}{\pi R^2} \exp\left(\frac{E_f - E_c}{kT}\right) \int_0^R 2\pi r \exp\left(\frac{-q^2 N_d r^2}{4\epsilon kT}\right) dr \quad [7]$$

If all the traps are located at the same energy level E_t , we have

$$\pi R^2 N_d = \frac{2\pi R N_t}{1 + 2 \exp\{(E_t - E_f)/kT\}} \quad [8]$$

Equations [7] and [8] yield finally

$$\bar{n} = N_c \exp\left(\frac{E_t - E_c}{kT}\right) \frac{8kT\epsilon}{q^2 \left(\frac{2N_t}{R} - N_d\right)} \left[1 - \exp\left(\frac{q^2 N_d R^2}{4\epsilon kT}\right) \right] \quad [6b]$$

A value of $E_c - E_t$ of 0.38 eV has been chosen in order to match the experimental data.

If the doping level is very low, all carriers are assumed to be trapped at the grain boundary, and the average carrier concentration is that of intrinsic silicon

$$\bar{n} = n_i = 1.45 \cdot 10^{10} \quad [6c]$$

if $N_d < 10^{15}$.

The value of 10^{15} has been chosen because Eq. [6b] provides for n a value which is smaller than n_i for impurity concentrations lower than 10^{15} cm^{-3} .

Resistivity of polysilicon.—We have now all the necessary tools to calculate n , μ_{film} , and, thereafter, ρ by $\sigma = nq\mu$, where n is given by Eq. [6a], [6b], or [6c];

μ_{film} is given by Eq. [5] and [4a] or [4b]; and with V_b calculated by [1a] or [1b].

The model gives results in good agreement with the experimental data, although it predicts a too high resistivity for dopant concentration around $2N_t/R$ because of the exponential dependence of the resistivity on the potential barrier. However, Baccarini, Ricco, and Spadini (15) have demonstrated that the potential barrier does not reach values higher than 0.5 eV. This last result has been taken into account to obtain the curves of Fig. 7 and 9.

The numerical values we have chosen to match theoretical values with the experimental data (sheet resistivity, TEM measurements of grain size, and Hall mobility measurements) are (Fig. 7-9): $N_t = 3 \times 10^{12} \text{ cm}^{-2}$, $R = 600 \text{ \AA}$, and $t_f = 5000 \text{ \AA}$.

Discussion

The variation of sheet resistivity with annealing cycles is generally explained (12, 14) by a model in which the dopant atoms begin to diffuse and segregate to the grain boundaries, decreasing the active carrier concentration and thus increasing sheet resistivity. This happens at low annealing temperatures. For higher temperatures, the grain size is supposed to increase with increasing temperature. This diminishes the total grain boundary area and redistributes the dopant atoms to the bulk of the crystallites.

This model explains qualitatively the variation in sheet resistivity with annealing time. For low temperatures, ($T < 900^\circ\text{C}$), phosphorous atoms become electrically inactive for they diffuse toward grain boundaries. This phenomenon causes the resistivity to increase with annealing time.

On the other hand, for higher temperatures ($T > 900^\circ\text{C}$), the longer the annealing time, the lower the sheet resistance, for the grains grow and the boundary area is reduced with annealing time.

However, our measurements of grain size show that this model is not sufficient to explain accurately the decrease of ρ with annealing temperature. For instance, the maximum of resistivity in the case of a 12 hr an-

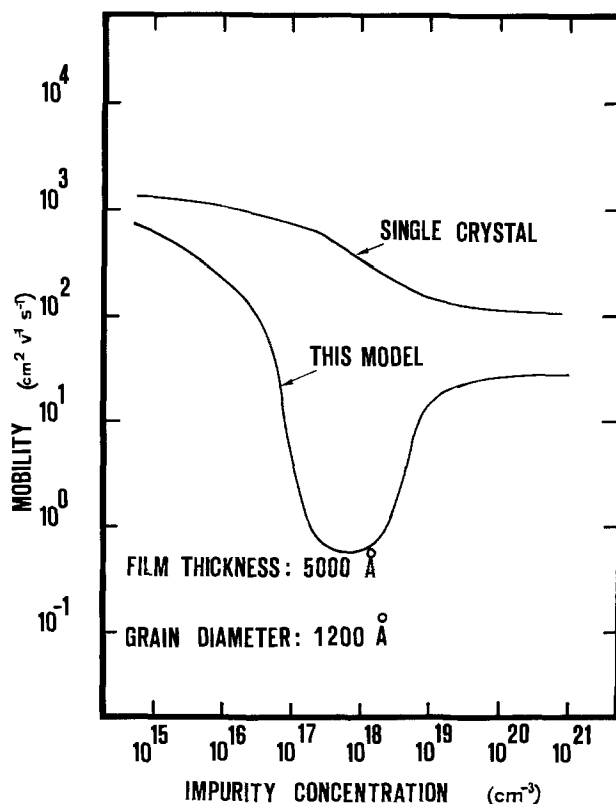


Fig. 7. Mobility vs. impurity concentration

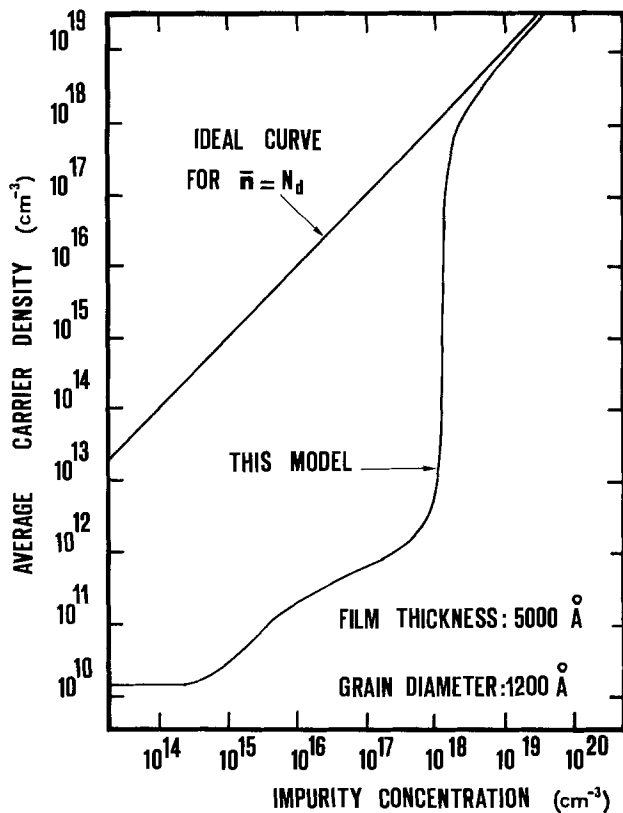


Fig. 8. Average carrier density vs. impurity concentration

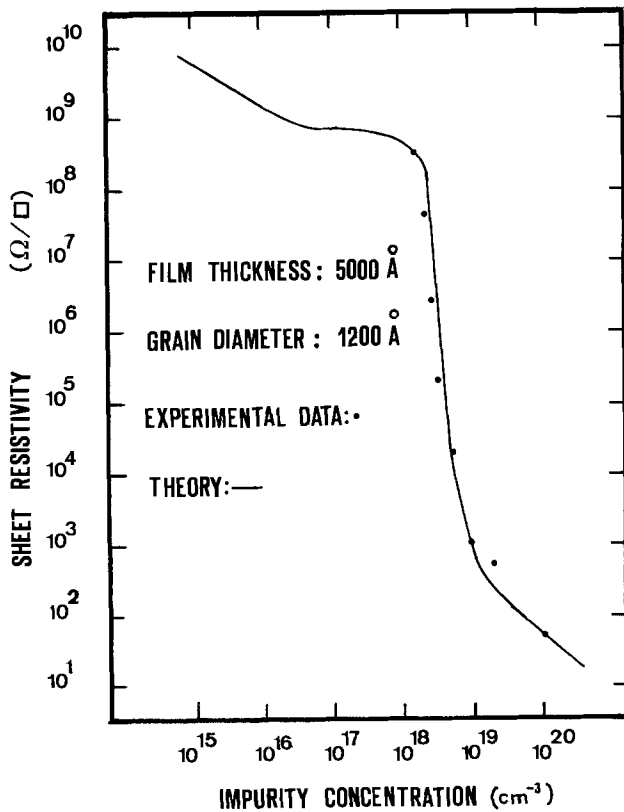


Fig. 9. Sheet resistivity vs. impurity concentration

nealing is reached at about 850°C, while the grain size is still quite unchanged at that temperature, and begins only to increase significantly at 1050°C.

With regard to the dependence of grain size on annealing temperature, our results appear comparable to those of Wada (13); a quantitative difference stems from the fact that we did not work at high doping

levels [$7.5 \times 10^{20} \text{ cm}^{-3}$ in Ref. (13) and $5 \times 10^{18} \text{ cm}^{-3}$ in our study] and our annealing times were different. Our results suggest that another phenomenon must be taken into account. One could assume that three phenomena are in fact competitive at annealing temperatures between 800° and 1100°C. The first one is the segregation of dopant atoms to grain boundaries. This phenomenon is prevalent below 900°C and makes resistivity increase with increasing annealing time.

Above 900°C and below 1050°C, a crystallographic relaxation seems to occur at the grain boundary, removing a part of the defects which trap the carriers. This causes an enhancement of free carriers in polysilicon and causes its resistivity to decrease before the appearance of the grain growth phenomenon. Above that temperature, the grains begin to grow; this reduces the total grain boundary area and further enhances the conductivity. This last phenomenon is increased by a long annealing time.

Summary

This paper reports the results of measurements which aim to explain the variation of resistivity and grain size of polysilicon as a function of annealing cycles and impurity concentration. It suggests a mechanism which would explain the variation of the sheet resistivity with annealing temperature and provides a semiquantitative model of the variation of the sheet resistivity with the doping level.

It also mentions the shortcomings of a previous model which assumed that the decrease in resistivity was directly related to the grain growth.

Acknowledgments

The authors would like to thank the Institut pour l'Encouragement de la Recherche Scientifique et Agricole (I.R.S.I.A.), and all the members of the Laboratoire de Microélectronique of the University of Louvain-la-Neuve (Belgium), and especially Professor Van de Wiele for his support and his encouragement.

Manuscript submitted Jan. 15, 1981; revised manuscript received March 30, 1981.

Any discussion of this paper will appear in a Discussion Section to be published in the June 1982 JOURNAL. All discussions for the June 1982 Discussion Section should be submitted by Feb. 1, 1982.

Publication costs of this article were assisted by the Centre National d'Etudes des Télécommunications.

LIST OF SYMBOLS

- D_n diffusivity of electrons
- E_t energy level of the traps in the bandgap
- h grain height
- J_n electron current density
- k Boltzmann's constant
- l_c mean free path of electrons
- μ_0 mobility of electrons in single crystal silicon
- μ_{eff} mobility in an infinitely thick layer
- μ_{effm} mobility in a thin polysilicon film
- n average carrier concentration
- n_0 $N_c \exp\{(E_f - E_c)/kT\}$ = equilibrium electron concentration
- N_d impurity concentration
- N_t density of traps
- $(-q)$ charge of an electron
- R grain radius
- r_1 radius of the neutral region in the grain
- T absolute temperature
- t_f film thickness
- V_b height of the potential barrier
- V_r voltage drop applied to a grain = the voltage drop applied to the sample divided by the number of grains between the two current-injecting contacts
- $\phi(x)$ potential at any position x
- Φ_b $V_b + V_r$ = potential at grain boundary
- w width of the depletion region ($= R - r_1$)

REFERENCES

- Vadasz, Grove, Rowe, and Moore, *IEEE Spectrum*, **6**, 28 (1969).
- Hamilton and Howard, "Basic Integrated Engineering," p. 572, McGraw-Hill Book Co., New York (1975).
- Sequin and Tompsett, "Charge Transfer Devices," p. 33, Academic Press (1975).
- Dutoit and Sollberger, *This Journal*, **125**, 1648 (1978).
- Iizuka, Nozawa, Muzutani, Kaneko, and Kohyama, *IEDM*, Washington, DC (1979), pp. 370-373.
- Gibbons and Lee, *IEEE Electron. Dev. Lett.*, **edl-1**, No. 6, p. 117 (1980).
- Cowher and Sedgwick, *This Journal*, **119**, 1565 (1972).
- Fripp, *J. Appl. Phys.*, **46**, 1240 (1975).
- Seto, *J. Appl. Phys.*, **46**, 5247 (1975).
- Kamins, *ibid.*, **42**, 4357 (1971).
- Fripp, *ibid.*, **46**, 1240 (1975).
- Tsuchimoto, Yudasaka, and Shirasu, "Ion Implantation in Semiconductors," pp. 605-612, Plenum Press, New York (1974).
- Wada, *This Journal*, **125**, 1499 (1978).
- Mandurah, Saraswat, and Kamins, *Appl. Phys. Lett.*, **36**, 683 (1980).
- Baccarini, Ricco, and Spadini, *ibid.*, **49**, 5565 (1978).
- Martinez and Piqueras, *J. Solid-State Electron.*, **23**, 297 (1980).
- Finetti, Galloni, and Mazzone, *J. Appl. Phys.*, **50**, 1381 (1979).
- H. Wolf, "Semiconductors," p. 287, John Wiley & Sons, Inc., New York (1971).

Diffusion of Cd into InP at 680°C

B. V. Dutt,* A. K. Chin,* and W. A. Bonner

Bell Laboratories, Murray Hill, New Jersey 07974

ABSTRACT

Cadmium was diffused into undoped n-InP at 680°C using elemental mixtures of (Cd,In) and (Cd,P) as starting sources. The depths of the p-n junctions were determined as a function of the Cd-activity, a_{Cd} , of the (In,Cd) alloys, and as a function of the amount of P. The variation of the junction depth with phosphorus vapor pressure indicates the formation of Cd compounds which are the actual diffusion sources on the P-rich side. The diffusion of Cd in InP is interpreted based on the largely accepted interstitial-substitutional model. The charge states of the diffusing interstitial species and the substitutionally incorporated Cd appear to depend on the diffusion conditions. On the In-rich side, at $a_{Cd} < 0.4$, the diffusing interstitial is neutral and Cd is mostly present as a monovalent acceptor. At $a_{Cd} > 0.4$, the diffusing interstitial is doubly ionized and Cd is incorporated as a monovalent acceptor. On the P-rich side, the data suggest a doubly ionized Cd-interstitial as the diffusing species with the Cd largely present in a neutral form.

Diffusion of acceptor impurities such as Cd or Zn for formation of p-n junctions in n-type InP is of technological interest since devices for optical communications are based on the InP/(In, Ga) (As, P) materials system (1).

Tuck and co-workers (2-4) carried out extensive work on chemical and isoconcentration diffusion of Zn into InP. In order to explain the decreasing surface concentration of Zn, or the decreasing solid solubility of Zn with increasing phosphorus vapor pressure, a model was proposed in which Zn is largely present in the form of a complex ($V_PZn_{In}V_P$). The monovalent acceptor species Zn_{In}^+ is present in small concentrations and the fast diffusing species is a neutral interstitial Zn_i^* . From p-n junction depth measurements, Tien and Miller (5) suggested a similar model for Cd in InP, with most of the Cd present as a neutral complex.

Earlier work on diffusion of Zn into III-V compounds by several investigators has been extensively reviewed by Casey (6). Much of the work was interpreted on the basis of an interstitial-substitutional mechanism or dissociative diffusion originally proposed for Cu in Ge by Frank and Turnbull (7) and extended for Zn in GaAs by Longini (8). Tracer diffusion under chemical diffusion conditions showed concentration profiles that were anomalous and different from the error function behavior (6). Isoconcentration diffusion profiles exhibited error function behavior (6). Differences in the interpretation of the largely accepted interstitial-substitutional diffusion model generally pertained to the charge state of the fast-diffusing interstitial.

Recently, formation of $p^+p^-n^-$ junctions in nominally undoped n-type InP with $n = 4 \times 10^{16} \text{ cm}^{-3}$ by a single step diffusion of Cd has been reported (9). Such junctions are suggested to result from the presence of an anomalous diffusion profile. The p^+p^- and p^-n^- junctions were spatially correlated by electron beam induced current (EBIC) profiling with the two diffusion fronts revealed by staining with A-B etch (10). In the present paper, the diffusion studies are extended to understand the diffusion mechanism of Cd in InP. The starting sources for diffusion are mixtures of elemental Cd with either excess In or P. The activity of Cd (the ratio of partial pressure of Cd in the alloy to that of pure Cd) is controlled by (In, Cd) alloys or by phosphides of Cd that appear to readily form at the diffusion temperature. The variations in junction depth with a_{Cd} are interpreted on the basis of an interstitial-substitutional model. On the In-rich side, at $a_{Cd} < 0.4$, the diffusing interstitial is neutral and Cd is mostly present as a monovalent acceptor. At $a_{Cd} > 0.4$, the diffusing interstitial is doubly ionized and Cd is incorporated as a monovalent acceptor. On the P-rich side, the data suggest a doubly ionized Cd-interstitial as the diffusing species. Cd is largely present in a neutral form.

Experimental Conditions

The InP samples used in this study were of $<100>$ orientation cut from boules grown by the liquid encapsulated Czochralski (LEC) technique (11, 12). One surface of the samples was polished using a 1% Br-methanol solution. Most of the diffusion work was done on undoped InP with an electron concentration of $4 \times 10^{16} \text{ cm}^{-3}$ with only a selected set of experiments

* Electrochemical Society Active Member.

Key words: defects, transport properties, p-n junctions, cadmium phosphides, III-V compounds.

REFERENCES

- Vadasz, Grove, Rowe, and Moore, *IEEE Spectrum*, **6**, 28 (1969).
- Hamilton and Howard, "Basic Integrated Engineering," p. 572, McGraw-Hill Book Co., New York (1975).
- Sequin and Tompsett, "Charge Transfer Devices," p. 33, Academic Press (1975).
- Dutoit and Sollberger, *This Journal*, **125**, 1648 (1978).
- Iizuka, Nozawa, Muzutani, Kaneko, and Kohyama, *IEDM*, Washington, DC (1979), pp. 370-373.
- Gibbons and Lee, *IEEE Electron. Dev. Lett.*, **edl-1**, No. 6, p. 117 (1980).
- Cowher and Sedgwick, *This Journal*, **119**, 1565 (1972).
- Fripp, *J. Appl. Phys.*, **46**, 1240 (1975).
- Seto, *J. Appl. Phys.*, **46**, 5247 (1975).
- Kamins, *ibid.*, **42**, 4357 (1971).
- Fripp, *ibid.*, **46**, 1240 (1975).
- Tsuchimoto, Yudasaka, and Shirasu, "Ion Implantation in Semiconductors," pp. 605-612, Plenum Press, New York (1974).
- Wada, *This Journal*, **125**, 1499 (1978).
- Mandurah, Saraswat, and Kamins, *Appl. Phys. Lett.*, **36**, 683 (1980).
- Baccarini, Ricco, and Spadini, *ibid.*, **49**, 5565 (1978).
- Martinez and Piqueras, *J. Solid-State Electron.*, **23**, 297 (1980).
- Finetti, Galloni, and Mazzone, *J. Appl. Phys.*, **50**, 1381 (1979).
- H. Wolf, "Semiconductors," p. 287, John Wiley & Sons, Inc., New York (1971).

Diffusion of Cd into InP at 680°C

B. V. Dutt,* A. K. Chin,* and W. A. Bonner

Bell Laboratories, Murray Hill, New Jersey 07974

ABSTRACT

Cadmium was diffused into undoped n-InP at 680°C using elemental mixtures of (Cd,In) and (Cd,P) as starting sources. The depths of the p-n junctions were determined as a function of the Cd-activity, a_{Cd} , of the (In,Cd) alloys, and as a function of the amount of P. The variation of the junction depth with phosphorus vapor pressure indicates the formation of Cd compounds which are the actual diffusion sources on the P-rich side. The diffusion of Cd in InP is interpreted based on the largely accepted interstitial-substitutional model. The charge states of the diffusing interstitial species and the substitutionally incorporated Cd appear to depend on the diffusion conditions. On the In-rich side, at $a_{Cd} < 0.4$, the diffusing interstitial is neutral and Cd is mostly present as a monovalent acceptor. At $a_{Cd} > 0.4$, the diffusing interstitial is doubly ionized and Cd is incorporated as a monovalent acceptor. On the P-rich side, the data suggest a doubly ionized Cd-interstitial as the diffusing species with the Cd largely present in a neutral form.

Diffusion of acceptor impurities such as Cd or Zn for formation of p-n junctions in n-type InP is of technological interest since devices for optical communications are based on the InP/(In, Ga) (As, P) materials system (1).

Tuck and co-workers (2-4) carried out extensive work on chemical and isoconcentration diffusion of Zn into InP. In order to explain the decreasing surface concentration of Zn, or the decreasing solid solubility of Zn with increasing phosphorus vapor pressure, a model was proposed in which Zn is largely present in the form of a complex ($V_P Zn_{In} V_P$). The monovalent acceptor species Zn_{In}^{\cdot} is present in small concentrations and the fast diffusing species is a neutral interstitial Zn_i^{\cdot} . From p-n junction depth measurements, Tien and Miller (5) suggested a similar model for Cd in InP, with most of the Cd present as a neutral complex.

Earlier work on diffusion of Zn into III-V compounds by several investigators has been extensively reviewed by Casey (6). Much of the work was interpreted on the basis of an interstitial-substitutional mechanism or dissociative diffusion originally proposed for Cu in Ge by Frank and Turnbull (7) and extended for Zn in GaAs by Longini (8). Tracer diffusion under chemical diffusion conditions showed concentration profiles that were anomalous and different from the error function behavior (6). Isoconcentration diffusion profiles exhibited error function behavior (6). Differences in the interpretation of the largely accepted interstitial-substitutional diffusion model generally pertained to the charge state of the fast-diffusing interstitial.

Recently, formation of $p^+p^-n^-$ junctions in nominally undoped n-type InP with $n = 4 \times 10^{16} \text{ cm}^{-3}$ by a single step diffusion of Cd has been reported (9). Such junctions are suggested to result from the presence of an anomalous diffusion profile. The p^+p^- and p^-n^- junctions were spatially correlated by electron beam induced current (EBIC) profiling with the two diffusion fronts revealed by staining with A-B etch (10). In the present paper, the diffusion studies are extended to understand the diffusion mechanism of Cd in InP. The starting sources for diffusion are mixtures of elemental Cd with either excess In or P. The activity of Cd (the ratio of partial pressure of Cd in the alloy to that of pure Cd) is controlled by (In, Cd) alloys or by phosphides of Cd that appear to readily form at the diffusion temperature. The variations in junction depth with a_{Cd} are interpreted on the basis of an interstitial-substitutional model. On the In-rich side, at $a_{Cd} < 0.4$, the diffusing interstitial is neutral and Cd is mostly present as a monovalent acceptor. At $a_{Cd} > 0.4$, the diffusing interstitial is doubly ionized and Cd is incorporated as a monovalent acceptor. On the P-rich side, the data suggest a doubly ionized Cd-interstitial as the diffusing species. Cd is largely present in a neutral form.

Experimental Conditions

The InP samples used in this study were of $<100>$ orientation cut from boules grown by the liquid encapsulated Czochralski (LEC) technique (11, 12). One surface of the samples was polished using a 1% Br-methanol solution. Most of the diffusion work was done on undoped InP with an electron concentration of $4 \times 10^{16} \text{ cm}^{-3}$ with only a selected set of experiments

* Electrochemical Society Active Member.

Key words: defects, transport properties, p-n junctions, cadmium phosphides, III-V compounds.

on samples doped with Sn to $1 \times 10^{18} \text{ cm}^{-3}$. The diffusion anneals were carried out in sealed quartz ampuls for 4 hr at 680°C in a vertical furnace with the diffusion source located at the lower end of the ampul at 675°C in order to prevent condensation on the InP wafer. The sample was held above the diffusion source by a constriction in the ampul. The ampul volume and the amount of Cd were held constant at 5 cm^3 and 3.48 mg , respectively. The diffusion depth was varied by changing the Cd-activity of the (In, Cd) alloy or by varying the excess amount of P added to the ampul. The diffusion fronts were revealed by staining a cleaved edge with A-B etch at room temperature for 5 min (5, 10).

Figure 1(a) shows the typical stained edge of a sample with a doping level of $n = 1 \times 10^{18} \text{ cm}^{-3}$ revealing only a single Cd diffusion front. Figure 1(b) shows the stained edge of a nominally undoped, n-type InP with $n = 4 \times 10^{16} \text{ cm}^{-3}$ after Cd-diffusion. Two diffusion fronts are observed, whereas only one front defining the p-n junction was expected. The delineation of two diffusion fronts by etching has been previously reported (13). The two fronts could arise from either changes in doping density or dopant type since etching reveals both types of variations. Examination of the stained edge with a scanning electron microscope (SEM) showed that a step $\sim 0.2 \mu\text{m}$ deep is delineated at the shallow diffusion front in 5 min of etching. No such step was observed at the deep front even after 30 min of etching.

An SEM image of a typical sample with two diffusion fronts is shown in Fig. 2. The positions of the shallow and deep diffusion fronts obtained from the optical micrograph are indicated by the dashed lines. An electron beam induced current (EBIC) profile is superimposed to demonstrate the nature of the junction. The EBIC signal reaches a peak at the shallow front, remains constant at the peak value for $\sim 3 \mu\text{m}$, and then decreases to a second inflection point at the position of the deep front. The EBIC profile thus reveals the presence of a depletion region bounded by the two fronts. The EBIC profile shown in Fig. 2 is characteristic of a $p^+-p^-n^-$ junction (9, 14, 15).

In order to confirm that the two diffusion fronts are related to Cd diffusion, the region bounded by the two diffusion fronts was investigated by thermal probing and photoluminescence. Thermal probing showed that the surface of a Cd-diffused sample was strongly p-type. Low temperature photoluminescence measurements indicated a high Cd concentration as revealed by the strength of the Cd impurity line at 1.365 eV (16). Then using a 2% Br-methanol solution, a surface layer

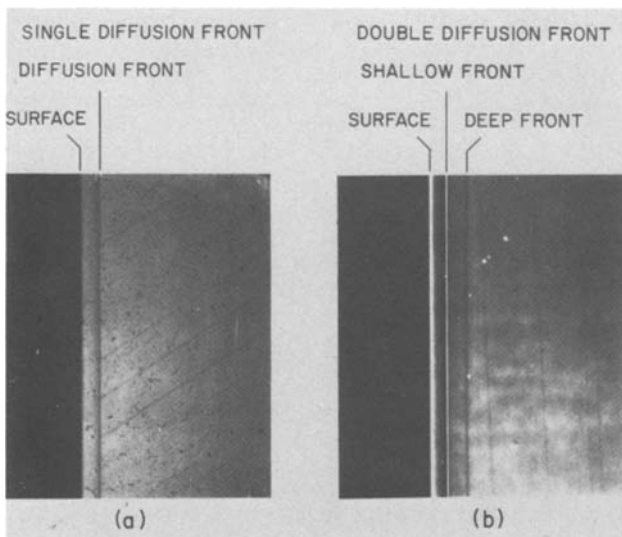


Fig. 1. Single and double diffusion fronts observed in InP. (a) InP:Sn with $n = 10^{18} \text{ cm}^{-3}$, (b) undoped n-InP with $n = 4 \times 10^{16} \text{ cm}^{-3}$.

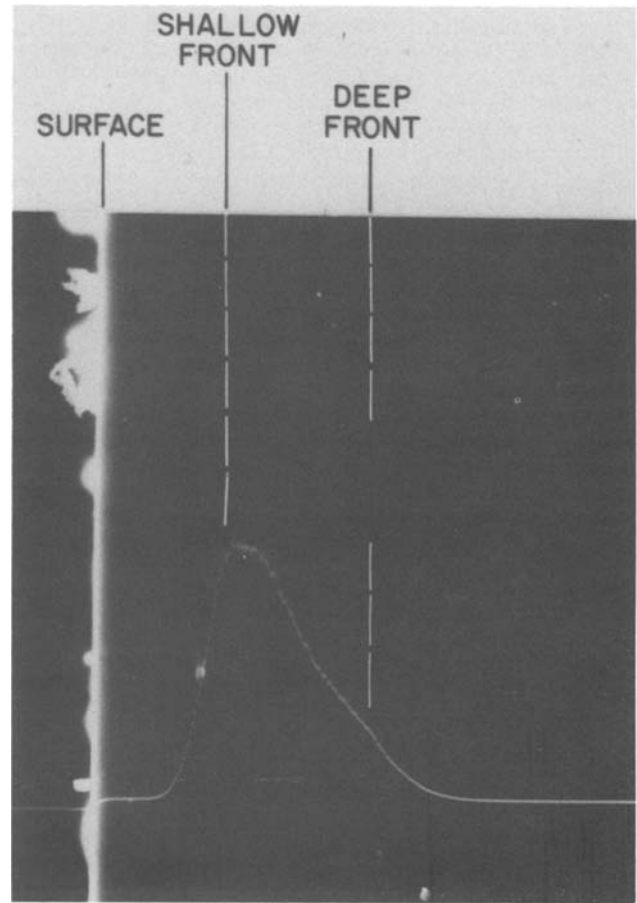


Fig. 2. EBIC profile obtained on a sample showing two diffusion fronts. The positions of the diffusion fronts are indicated by the dashed lines. The EBIC profile is superimposed.

approximately equal to the depth of the deep front was removed. Thermal probing of the etched surface suggested a low doping level but the conductivity type could not be determined. Photoluminescence of the etched surface indicated a much weaker Cd line at 1.365 eV . It is estimated that the amount of Cd is lower by an order of magnitude. These experiments indicate that the two fronts observed are related to Cd diffusion.

Results

Experimental data.—Since the junction depth, x_j , is proportional to $(Dt)^{1/2}$ where D is the diffusion coefficient and t is the time of diffusion, the square of the junction depth is directly proportional to D_{Cd} for a constant t . Figure 3(a) shows the variation of the

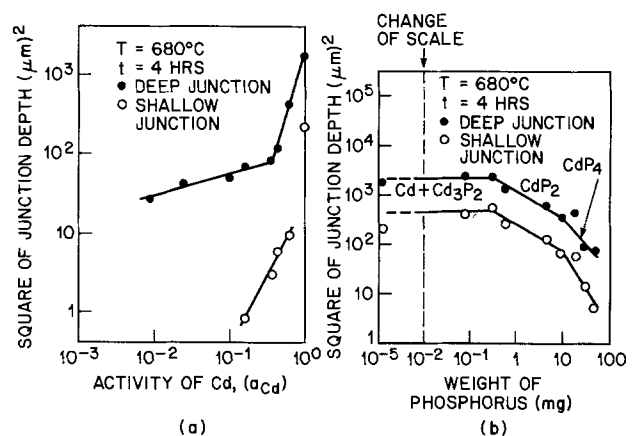


Fig. 3. Variation of diffusion coefficient with (a) a_{Cd} of (In-Cd) alloys and (b) weight of excess P, $W_P(\text{mg})$ in the ampul.

square of the junction depth with a_{Cd} , the Cd activity of the (In, Cd) alloys. The a_{Cd} of the (In, Cd) alloys is estimated from the data of Servis and Munir (17), assuming that the temperature dependence of the activities is weak. In Fig. 3(a), on the In-rich side, the diffusion coefficient for the deep front varies approximately as a_{Cd}^α with $1/3 < \alpha < 1/2$ for $a_{Cd} \lesssim 0.4$ and as a_{Cd}^3 for $a_{Cd} \gtrsim 0.4$. The shallow front starts appearing at $a_{Cd} > 0.15$ and varies as a_{Cd}^2 or a_{Cd}^3 .

On the P-rich side, the behavior is different as shown in Fig. 3(b). Here the square of the junction depth is simply plotted against W_P , the weight of phosphorus, for lack of precise knowledge of the phosphorus partial pressure. Both diffusion fronts are observed within the range of the experiments. The diffusion coefficients responsible for the two fronts are independent of the amount of P for $0 < W_P < 0.33$ mg, vary as $W_P^{-1/2}$ for $0.33 \text{ mg} < W_P < 10$ mg and as W_P^{-1} for $W_P > 10$ mg. Since the volume of the ampul, the amount of Cd, and the temperature were held constant, the vapor pressure of phosphorus would be expected to be a monotonic function of the amount of P. The variations in diffusion coefficient of Cd shown in Fig. 3(b) are thus either due to formation of Cd and P compounds or reflect changes in the diffusion process depending on the amount of P added to the ampul. In the following section, the In-P-Cd ternary phase diagram is qualitatively discussed in order to correlate the changes in diffusion coefficient of Fig. 3 with changes in phase equilibria (17-20).

Thermodynamic considerations.—Figure 4 shows the schematic of the In-P-Cd ternary phase diagram at 680°C based on the data reported in literature (17-20). The locus of our experimental diffusion sources is represented by a small region surrounding the solid InP. The solid lines indicate tie-lines connecting the indicated phases. Applying the phase rule, $f = C + 2 - \phi$, where ϕ = number of phases in equilibrium, C = number of components, to regions A through E, the various condensed phases in equilibrium besides the vapor phase and the degrees of freedom, f , are as follows:

- Region A: Solid InP, (In, Cd) liquid alloy, $f = 2$
- Region B: Solid InP, liquid Cd, and solid Cd_3P_2 , $f = 1$
- Region C: Solid InP, solid Cd_3P_2 , and solid CdP_2 , $f = 1$

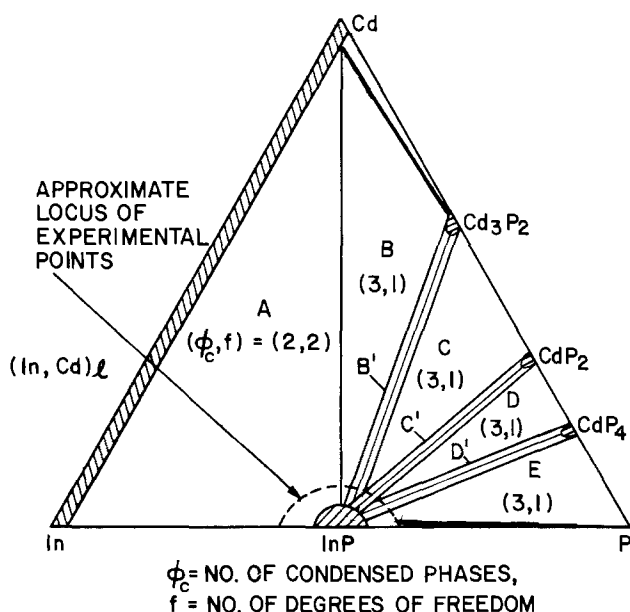


Fig. 4. Schematic of In-P-Cd ternary phase diagram at 680°C. The stability regions of the compounds are shown highly exaggerated. (See text).

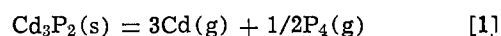
Region D: Solid InP, solid CdP_2 , and solid CdP_4 , $f = 1$

Region E: Solid InP, solid CdP_4 , and solid P, $f = 1$.

Regions B', C', and D': Solid InP is in equilibrium with solid Cd_3P_2 , solid CdP_2 , and solid CdP_4 , respectively. The degrees of freedom in B', C', and D' are two. The widths of the regions B', C', and D' are shown exaggerated to suggest the pressure-temperature stability of the phosphides of Cd.

Considering the region A, the choice of temperature and the activity of Cd can be made independently. The vapor pressures of In and P will then be automatically fixed. In region B, there is only one degree of freedom and the choice of temperature automatically determines the activities of the three constituents. Regions C, D, and E are similar to B. However, in regions B', C', and D', where solid InP is in equilibrium with the phosphides Cd_3P_2 , CdP_2 , or CdP_4 , respectively, both temperature and the vapor pressure of P can be independently chosen.

In the experiments described in "Experimental Conditions" the InP sample is at 680°C and the diffusion source is at 675°C. In such an arrangement, the InP sample initially loses P and the phosphorus vapor pressure in the ampul tends to approach the dissociation pressure of InP at 680°C. The vapor transports phosphorus towards the cooler end kept at 675°C, where the (In, Cd) alloy establishes the Cd and In activities proportional to their respective mole fractions. P-vapor reacts with the alloy forming InP and phosphides of Cd, provided the Cd activity is equal to or larger than the value corresponding to the evaporation of the compounds. For example, the sublimation of Cd_3P_2 occurs by congruent evaporation (19) according to



where (s) and (g) refer to the solid and gaseous phases, respectively. For congruent evaporation, the partial pressures (p) of $Cd(g)$, $P_4(g)$, and $P_2(g)$ are related by

$$p(Cd) = 6p(P_4) + 3p(P_2) \quad [3]$$

The equilibrium constant for Eq. [1] is given (19) by

$$\log_{10} \left(\frac{K_p}{\text{atm}^{7/2}} \right) = - \frac{24,940 \pm 480}{T} + (23.70 \pm 0.39) \quad [4]$$

Using Eq. [4] and the estimated value of the equilibrium constant for Eq. [2] from Stull and Sinke (21), one can estimate K_p (at 680°C) $\approx 3.4 \times 10^{-3} \text{ atm}^{7/2}$ and a $p(Cd) = 0.25 \text{ atm}$, which corresponds to an activity of 0.7, taking the value of the saturated vapor pressure of Cd (21) at 680°C as 0.36 atm. This indicates that at Cd activities higher than 0.7, the formation of Cd_3P_2 which will act as the diffusion source is to be expected.

Correlation of variation of diffusion coefficient with phase changes.—In this section, the variation of the diffusion coefficient is correlated with the different regions of the ternary phase diagram considered above. The diffusion data of Fig. 3(a), obtained by equilibrating InP with different (In, Cd) alloys correspond to region A of Fig. 4. Since the changes in composition of the alloy are continuous, the drastic change in the diffusion coefficient dependence on a_{Cd} shown in Fig. 3(a) is to be interpreted as a change in the diffusion or incorporation process. Alternatively, the system is not entirely in region A for the range of a_{Cd} investigated. In the previous section, we considered the possibility of (In, Cd) alloy with $a_{Cd} > 0.7$ reacting with the P escaping from InP to form Cd_3P_2 to coexist with InP and In-Cd. If this were to happen, there is only one degree of freedom, making temperature the only inde-

pendent variable. The activities of In, P, and Cd will be automatically fixed by the choice of temperature. In such a case the diffusion coefficient varying as the activities would be a constant. However, the diffusion coefficient as shown in Fig. 3(a) does not appear to remain constant at high a_{Cd} on the In-rich side. This rules out the possibility of Cd_3P_2 formation on the In-rich side and suggests that the changes in diffusion coefficient with a_{Cd} should be attributed to corresponding changes in the diffusion process or the incorporation of Cd.

On the P-rich side, D_{Cd} is independent of the amount of P for $W_P < 0.33$ mg. This suggests that the system is now in region B, where liquid Cd is in equilibrium with solids InP and Cd_3P_2 . The partial pressure of Cd is a constant and is nearly equal to the saturated vapor pressure of Cd at 675°C. As the phosphorus content is increased D_{Cd} varies as $W_P^{-1/2}$ and W_P^{-1} or equivalently $p^{-1/2}(P_4)$ and $p^{-1}(P_4)$. We suggest that these two regions of Fig. 3(b) correspond to regions C' and D' of Fig. 4, respectively. In region C', CdP_2 is in equilibrium with InP; the vapor pressure of Cd and phosphorus are related by the dissociation constant $K(CdP_2) = p(Cd) p^{1/2}(P_4)$. Thus, if D_{Cd} varies as $p^{-1/2}(P_4)$, this is equivalent to $D_{Cd} \sim p_{Cd} \sim a_{Cd}$. Similarly, in region D', CdP_4 is in equilibrium with InP and a $p^{-1}(P_4)$ variation of D_{Cd} corresponds to $D_{Cd} \sim a_{Cd}$. Thus the D_{Cd} variations with W_P on the P-rich side can be grouped together into a linear dependence of D_{Cd} on a_{Cd} .

Discussion

Relation between diffusion coefficient and defect concentration.—It is well known that the diffusion coefficient, D_{Cd} of solute Cd in the present case, is a sum of the product of the microscopic diffusivities D_j of the various defect species and their respective concentrations $[j]$. Thus, neglecting correlation effects (6)

$$D_{Cd} = \sum_j D_j [j] \tag{5}$$

At a constant temperature, D_j is a constant and variations of D_{Cd} represent corresponding changes in the concentration of the dominant defect species. The concentration of the defects, $[j]$, in turn depends on the composition of the crystal, the component activities, the pressure, and the temperature.

Defect equilibria.—We shall assume that the system is in equilibrium when InP is heated at 680°C in the presence of Cd, P, or In vapor. Following the approach of Kröger and Vink (22) and also using their symbols for defects, the defect concentrations can be expressed as a function of a_{Cd} , $p^s(P_4)$ or $a_{Cd}^l a_{In}^m$. This activity dependence of the defect species is useful in identifying the diffusion mechanism. Table I lists defect formation reactions of relevance here. Table II lists the values of the exponents l and m for various approximations of the neutrality condition and the Cd balance equation.

Based on Table II, defect isotherms portraying the variation of the defect concentrations as a function of a_{Cd} at a given a_{In} and temperature can be constructed using a log-log plot (22). One such set of isotherms is given in Fig. 5. On the extreme left, where the concentration of Cd in the sample is very low, InP behaves as an intrinsic semiconductor with $p = n = n_i$. In this range, $[Cd'_{In}]$ and $[Cd_i^{\cdot\cdot}]$ vary linearly with a_{Cd} . This range ends when the concentration of $[Cd'_{In}]$ increases to equal n_i , where the extrinsic behavior sets in. The neutrality is approximated by $[Cd'_{In}] = p$ and each of these vary as $a_{Cd}^{1/2}$. All the dissolved Cd concentration in the crystal is approximated by $[Cd'_{In}]$. The neutral Cd-interstitial Cd_i^x and the neutral substitutional Cd'_{In} vary as a_{Cd} in all the three ranges shown. Note that the doubly ionized Cd interstitial concentration rises as a_{Cd}^2 in range II. Eventually a range of self-compensation where $[Cd'_{In}] \approx 2[Cd_i^{\cdot\cdot}]$ may be

Table I. Defect formation reactions and the corresponding mass action relations

| No. | Reaction | Mass action relation |
|-----|--|---|
| 1 | $0 \rightarrow e' + h \cdot$ | $K_i = np$ |
| 2 | $0 \rightarrow V_{In}^x + V_P^x$ | $K_s = [V_{In}^x][V_P^x]$ |
| 3 | $1/4P_4(g) \rightarrow P_P^x + V_{In}^x$ | $K_v = [V_{In}^x]p(P_4)^{-1/4}$ |
| 4 | $InP \rightarrow In(g) + 1/4P_4(g)$ | $K_{InP} = p_{In}p(P_4)^{1/4}$ |
| 5 | $Cd(In - Cd) \text{ alloy} \rightarrow Cd'_{In} + h \cdot + V_P^x$ | $K_{Cd} = \frac{[Cd'_{In}]p[V_P^x]}{a(Cd)}$ |
| 6 | $Cd(In - Cd) \text{ alloy} \rightarrow Cd_i^{\cdot\cdot} + 2e'$ | $K_{Cd_i} = \frac{[Cd_i^{\cdot\cdot}]n^2}{a(Cd)}$ |
| 7 | $Cd_mP_n \rightarrow mCd'_{In} + nP_P^x + (m - n)V_P^x$ | $K_{mn} = \frac{[Cd'_{In}]^m [V_P^x]^{m-n}}{a(Cd_mP_n)}$ |
| 8 | $Cd_mP_n \rightarrow mCd(g) + \frac{n}{4}P_4(g)$ | $K_{Cd_mP_n} = p^m(Cd)p^{n/4}(P_4)$ |
| 9 | $Cd_i^{\cdot\cdot} + V_{In}^x + 2e' \rightarrow Cd'_{In} + h \cdot$ | $K_{is} = \frac{[Cd'_{In}]p}{[Cd_i^{\cdot\cdot}][V_{In}^x]n^2}$ |
| 10 | $n + [Cd'_{In}] = p + [Cd_i^{\cdot\cdot}] + 2[Cd_i^{\cdot\cdot}]$ | |
| 11 | $[Cd]_{tot} = [Cd'_{In}] + [Cd'_{In}] + [Cd_i^{\cdot\cdot}] + [Cd_i^{\cdot\cdot}]$ | |

Table II. Values of exponents l, m of $[j] \propto a^l(Cd)a^m(In)$ for different approximations of the neutrality conditions

| Defect species | Neutrality approximation | | $[Cd'_{In}] = p$ | | $[Cd'_{In}] = 2[Cd_i^{\cdot\cdot}]$ | |
|---------------------|--------------------------|----|------------------|------|-------------------------------------|------|
| | l | m | l | m | l | m |
| Cd'_{In} | 1 | -1 | 1/2 | -1/2 | 1 | -2/3 |
| $Cd_i^{\cdot\cdot}$ | 1 | -1 | 2 | -1 | 1 | -2/3 |
| p | 0 | 0 | 1/2 | -1/2 | 0 | -1/3 |
| n | 0 | 0 | -1/2 | 1/2 | 0 | 1/3 |
| $[Cd'_{In}]$ | 1 | -1 | 1 | -1 | 1 | -1 |

reached. In this range both $[Cd'_{In}]$ and $[Cd_i^{\cdot\cdot}]$ vary linearly with a_{Cd} . This range is hypothetical and has not been observed experimentally.

Models for diffusion and incorporation of Cd.—Models for the diffusion and incorporation of Cd in InP should account for the following summary of experimental results from the junction depth measurements of the "Results" section.

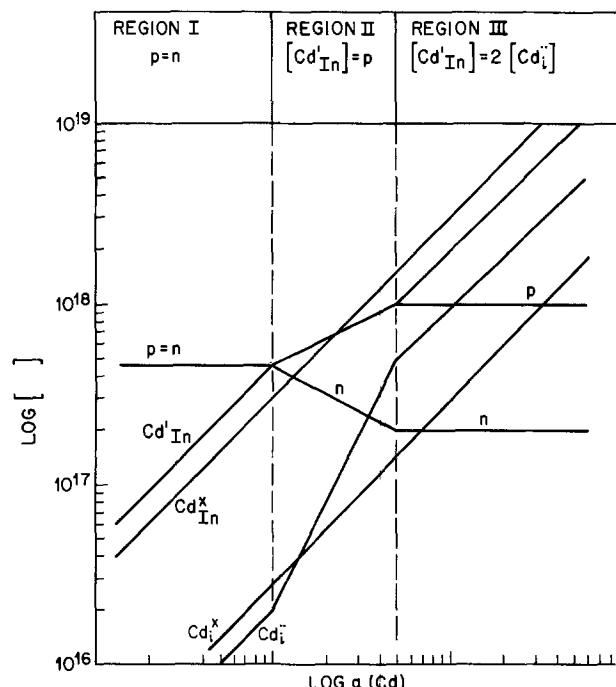


Fig. 5. Defect isotherm at 680°C showing the variation of concentrations of defects with a_{Cd} at a given a_{In} .

1. At low $a_{Cd} < 0.15$ only one diffusion front was observed.

2. The diffusion coefficient of the deep front varies as $\sim a_{Cd}^{1/2}$ for $a_{Cd} \lesssim 0.4$ and as $\sim a_{Cd}^3$ for $a_{Cd} \gtrsim 0.4$ on the In-rich side. The diffusion coefficient of the shallow front at higher a_{Cd} on the In-rich side varies as a_{Cd}^2 or a_{Cd}^3 .

3. On the P-rich side, the diffusion coefficients for both the diffusion fronts are proportional to a_{Cd} .

4. When Cd is diffused into InP doped to $1 \times 10^{18} \text{ cm}^{-3}$, only one diffusion front was observed under conditions where two fronts were observed in undoped InP.

Measurements based on p-n junction depth present several limitations in suggesting models for diffusion and incorporation of Cd in InP. First, the junction depth measurements give the position where the ionized acceptor concentration, in this case that of $[\text{Cd}_{\text{In}}']$, equals or exceeds n , the electron concentration of the InP sample. Secondly, the shallow p^+p^- junction arises due to a sudden change in the ionized Cd-acceptor concentration, presumably resulting from an anomalous profile. This reflects similar changes in the total impurity concentration, which leads us to believe that the Cd diffusion is concentration dependent similar to Zn in III-V compounds. Moreover, the Cd diffusion investigated here is chemical diffusion and whether equilibrium is reached under these conditions is uncertain. Lastly, as the sample is quenched from the diffusion temperature to room temperature, the junction depths measured at 300 K are expected to be different compared to the high temperature values as a result of the redistribution of electrons and holes. This difference is assumed to be negligible.

For a concentration dependent interstitial-substitutional diffusion mechanism, it has been shown (23) that the effective diffusion coefficient is given by

$$D_{\text{eff}} = D_1 \frac{\partial C_1}{\partial C} \quad [6]$$

where C_1 = the concentration of the fast diffusing interstitial and C = total impurity concentration. Both C_1 and C are functions of $a_{Cd}a_{\text{In}}^m$ or $a_{Cd}r^s(P_4)$ as discussed in the previous section. Since a_{Cd} , a_{In} , and $p(P_4)$ are interrelated to each other, Eq. [6] can be rearranged as

$$D_{\text{eff}} = D_1 \frac{\partial C_1}{\partial a_{Cd}} \frac{\partial a_{Cd}}{\partial C} \quad [7]$$

Case 1: Diffusion of Cd from (In, Cd) alloys.—We shall assume that $a_{\text{In}} = 1$ at low a_{Cd} because the amount of Cd in the ampul is considerably smaller than the sample size and the excess In added. This assumption does not hold as a_{Cd} approaches 1, when no In is added to the ampul.

At low Cd activities, under In-rich conditions, the surface concentration of Cd or the solubility of Cd is expected to be low. Assuming that the crystal is extrinsic with $[\text{Cd}_{\text{In}}'] = p$ and $[\text{Cd}]_{\text{tot}} = [\text{Cd}_{\text{In}}']$, the diffusion conditions correspond to column III of Table II which is displayed as range II of the defect isotherm given in Fig. 5. The singly ionized acceptor concentration, $[\text{Cd}_{\text{In}}']$ which is nearly equal to the total impurity concentration C varies as $a_{Cd}^{1/2}$ and the neutral interstitial concentration, Cd_i^x varies as a_{Cd} . Thus the factor $(\partial C_1/\partial a_{Cd})(\partial a_{Cd}/\partial C)$ of Eq. [7] results in $D_{\text{eff}} \sim a_{Cd}^{1/2}$. It is therefore proposed that at low a_{Cd} on the In-rich side, Cd diffuses as a neutral interstitial Cd_i^x and dissolves as a monovalent acceptor Cd_{In}' .

At $a_{Cd} \geq 0.4$, as shown in Fig. 3(a), there is an abrupt change in the dependence of D_{Cd} on a_{Cd} . Thus $D_{Cd} \sim a_{Cd}^{1/2}$ at $a_{Cd} < 0.4$ and changes to $D_{Cd} \sim a_{Cd}^3$ at $a_{Cd} > 0.4$. In addition, the shallow front appears at $a_{Cd} > 0.15$. A D_{Cd} variation of a_{Cd}^3 can be justified by the interstitial-substitutional model if the diffusing inter-

stitial is doubly ionized. Longini (8) originally proposed a doubly ionized interstitial Zn as the diffusing species in GaAs. Later Weisberg and Blanc (26) and Chang and Pearson (23) showed that in the case of an interstitial-substitutional diffusion mechanism, the assumption of a doubly ionized interstitial with most of the impurity present as a monovalent acceptor, the diffusion coefficient varies as the third power of the impurity concentration. Thus in the present case, D_{Cd} would vary as $[\text{Cd}_{\text{In}}']^3$. From Table II and Fig. 5, it can be seen that $[\text{Cd}_{\text{In}}']$ varies as $a_{Cd}^{1/2}a_{\text{In}}^{-1/2}$. Thus $[\text{Cd}_{\text{In}}']^3 \sim a_{Cd}^{3/2}a_{\text{In}}^{-3/2}$. Since a_{In} is proportional to $(1 - x_{Cd})$ or $(1 - a_{Cd}/\gamma_{Cd})$, where γ_{Cd} = activity coefficient of Cd, it can be shown that

$$[\text{Cd}_{\text{In}}']^3 \sim \left(a_{Cd}^{3/2} + \frac{3}{2} \gamma_{Cd}^{-1/2} a_{Cd}^{5/2} + \frac{15}{8} \gamma_{Cd}^{-2} a_{Cd}^{7/2} \right)$$

This is in reasonable agreement with the observed $D_{Cd} \sim a_{Cd}^3$ behavior.

Case 2: $D_{Cd} \sim a_{Cd}$ on the P-rich side.—It has already been suggested that the D_{Cd} variations with the weight of phosphorus shown in Fig. 3(b) can be attributed to formation of phosphides of Cd. Under P-rich conditions, one would expect an increased solubility of Cd, if Cd is occupying the In-sublattice in an unassociated form. Approximating the total Cd concentration by $[\text{Cd}]_{\text{tot}} = C = [\text{Cd}_{\text{In}}^x]$, with $C_1 = [\text{Cd}_i^{\cdot\cdot}] \sim a_{Cd}^2$ and $C = [\text{Cd}_{\text{In}}^x] \sim a_{Cd}$, Eq. [7] leads to $D_{\text{eff}} \sim a_{Cd}$, which is in agreement with the observed behavior.

Some of the Cd-diffused InP samples corresponding to the various regions of Fig. 3(a) and (b) have been examined by transmission electron microscopy (24). On the P-rich side, the samples showed precipitates identified to be Cd_3P_2 and Cd_7P_{10} . On the In-rich side the samples are free from precipitates. It is tentatively suggested that the observation of decreasing p-n junction depths with increasing phosphorus vapor pressure is due to the precipitation of Cd. This leaves in solid solution only a small fraction of Cd in an ionized acceptor form to cause the junction formation. However, if the solubility of Cd in InP is similar to Zn and decreases with increasing vapor pressure of phosphorus as observed by Tuck and Hooper (2), some sort of a neutral complex of Cd whose concentration roughly varies as a_{Cd} is to be invoked to explain the present measurements.

Origin of two diffusion fronts.—The origin of two diffusion fronts observed in the case of the undoped n-InP has been explained (9) assuming an anomalous diffusion profile as shown in Fig. 6. Curve A represents an error function profile, while curve B illustrates an anomalous profile with a sudden change in the concentration of the diffusant. The background doping level is indicated by the dashed line, marked n_B . Assuming that the profiles A and B correspond to ionized impurity species, for the profile A, one would expect a single junction, a p-n junction, to be revealed at a position where the impurity concentration equals the background level. For profile B, two possibilities arise. If the background doping level is above the concave section, again a single p-n junction will be observed. This corresponds to the case of Fig. 1(a) where Cd was diffused into an intentionally doped n-InP with $n \approx 1 \times 10^{18} \text{ cm}^{-3}$. However, when the substrate doping level is below the concave section, as shown by the dashed line, etching reveals two junctions: a deep p^-n^- junction and a shallow p^+p^- junction.

The question that remains to be answered is the origin of the anomalous profile itself in chemical diffusion experiments. It has been suggested (25) that this is due to breakdown of vacancy equilibrium in the interior of the sample, although such equilibrium is presumed to exist at the surface. However, the data of Fig. 3(a) and (b) cannot be satisfactorily interpreted using this explanation. If the vacancy equilibrium

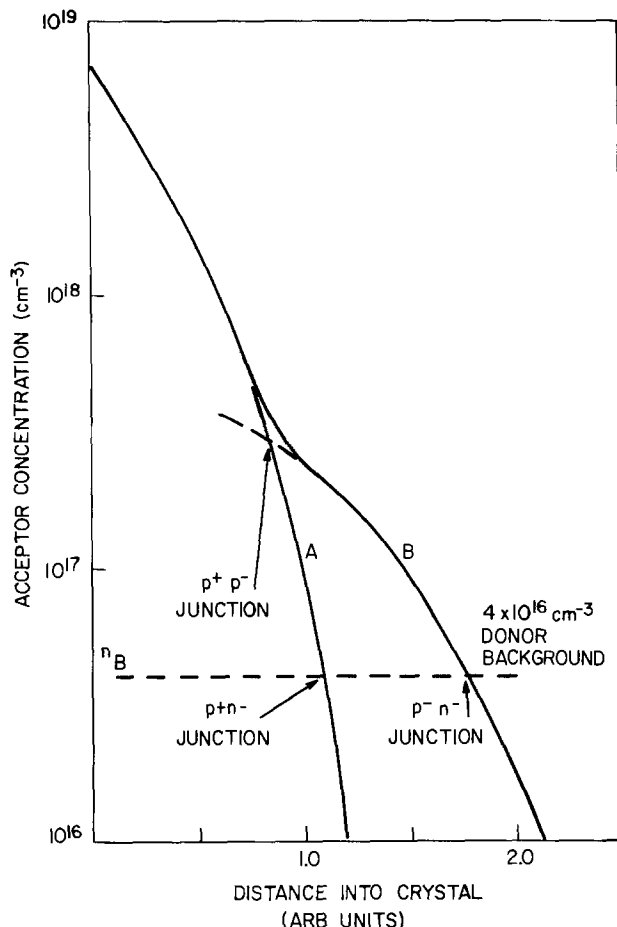


Fig. 6. Schematic of the normal error function diffusion profile (curve A) and the anomalous diffusion profile (curve B). For $n_B = 4 \times 10^{16} \text{ cm}^{-3}$ substrate doping level, one junction (p^+n^-) is formed for normal profile A, whereas two junctions ($p^+ - p^-$) and ($p^- - n^-$) are formed for anomalous profile B.

breaks down in the interior, then the depth of the shallow junction nearer to the surface would be expected to be independent of the deeper junction. The results of Fig. 3 show that the two junctions move parallel to each other. This suggests that equilibrium is probably established in the interior at the same rate as the surface or that there may be cooperative phenomena such as the electric field dependent effects due to the presence of the p-n junction. Further work using tracer diffusion of Cd may throw some light on this problem.

Summary

Normal p-n junctions, as well as $p^+p^-n^-$ junctions could be formed by diffusion of Cd using starting sources of (Cd, In) and (Cd, P) at 680°C. The actual diffusion sources are (In, Cd) alloys and phosphides of cadmium. The linear variation of the diffusion coefficient with activity of Cd on the P-rich side is in good agreement with the generally accepted interstitial-substitutional model. The Cd-transporting species is a doubly ionized interstitial, Cd_i^{2+} , and cadmium is largely present as a neutral species. On the In-rich side, at higher Cd activities, the interstitial-substitutional model is valid with Cd_i^{2+} as the diffusing species and most of the dissolved Cd in a singly ionized acceptor form. At low cadmium activities, the p-n junction depth measurements suggest that Cd is diffusing as a neutral interstitial and is incorporated largely as a singly charged acceptor.

Acknowledgments

We thank B. I. Miller for fruitful conversations. We thank H. Temkin for photoluminescence measurements

and several interesting comments on the manuscript. We benefited from discussions with A. S. Jordan and S. Mahajan. We thank O. G. Lorimor and R. H. Saul for a critical reading of the manuscript.

Manuscript submitted Feb. 24, 1981; revised manuscript received April 14, 1981. This was Paper 347 presented at the Hollywood, Florida, Meeting of the Society, Oct. 5-10, 1980.

Any discussion of this paper will appear in a Discussion Section to be published in the June 1982 JOURNAL. All discussions for the June 1982 Discussion Section should be submitted by Feb. 1, 1982.

Publication costs of this article were assisted by Bell Laboratories.

REFERENCES

1. T. P. Lee, C. A. Burrus, A. G. Dentai, A. A. Ballman, and W. A. Bonner, *Appl. Phys. Lett.*, **35**, 511 (1979).
2. B. Tuck and A. Hooper, *J. Phys. D. Appl. Phys.*, **8**, 1806 (1975).
3. A. Hooper, B. Tuck, and A. J. Baker, *Solid State Electron.*, **17**, 531 (1974).
4. B. Tuck and M. D. Zahari, *J. Phys. D. Appl. Phys.*, **10**, 2473 (1977).
5. P. K. Tien and B. I. Miller, *Appl. Phys. Lett.*, **34**, 701 (1979).
6. H. C. Casey in "Atomic Diffusion in Semiconductors," D. Shaw, Editor, Chap. 6, Plenum Press, New York (1973). See also chap. 1 by D. Shaw for an excellent discussion of diffusion mechanisms in general.
7. F. C. Frank and D. Turnbull, *Phys. Rev.*, **104**, 617 (1956).
8. R. L. Longini, *Solid State Electron.*, **5**, 127 (1962).
9. A. K. Chin, B. V. Dutt, H. Temkin, W. A. Bonner, and D. D. Roccasecca, *Appl. Phys. Lett.*, **36**, 924 (1980).
10. M. S. Abrahams and C. J. Buiocchi, *J. Appl. Phys.*, **36**, 2855 (1965).
11. W. A. Bonner, *Mater. Res. Bull.*, **15**, 63 (1980).
12. W. A. Bonner, *This Journal*, **127**, 1978 (1980).
13. B. I. Miller and P. K. Tien, 21st Electron. Mat. Conf. Meeting, Abstract No. G4, 1979 (unpublished).
14. L. J. Balk, E. Kubalek, and E. Menzel, in IITRI Scanning Electron Microscopy, 448, 1975 (unpublished).
15. M. Aven, E. Eider, R. B. Bolon, and G. W. Ludwig, *J. Appl. Phys.*, **43**, 4136 (1972).
16. A. M. White, P. J. Dean, K. M. Fairhurst, W. Bardsley, E. W. Williams, and B. Day, *Solid State Commun.*, **11**, 1099 (1972).
17. H. J. Servis and Z. A. Munir, *J. Less Common Met.*, **34**, 293 (1974).
18. R. Schoonmaker and K. Rubinson, *J. Phys. Chem.*, **71**, (1967).
19. V. B. Lazarev, J. H. Greenberg, V. J. Shevchenko, S. F. Marenkin, and S. F. Kozlov, *J. Chem. Thermodyn.*, **8**, 61 (1976).
20. V. B. Lazarev, Y. K. Grinberg, S. F. Marenkin, and S. K. Saniev, *Izv. Akad. Nauk SSSR (English Translation) Inorganic Mater.*, **15**, 901 (1979).
21. D. R. Stull and G. C. Sinke, "Thermodynamic Properties of the Elements," Am. Chem. Soc., Washington, D.C. (1956).
22. F. A. Kröger and H. J. Vink, in "Solid State Phys.," F. Seitz and D. Turnbull, Editors, Vol. 3, p. 406, (1956). See also F. A. Kröger, "The Chemistry of Imperfect Crystals," North-Holland Publishing Co., Amsterdam (1964). Briefly, the notation is as follows: [] indicate concentrations expressed as site fractions. Superscript (·) and (′) represent an effective positive and negative charge respectively. Subscript denotes the site occupied.
23. L. L. Chang and G. L. Pearson, *J. Appl. Phys.*, **35**, 1960 (1964).
24. D. Brasen, Private communication.
25. B. Tuck and M. A. H. Kadhim, *J. Mater. Sci.*, **7**, 585 (1972).
26. L. R. Weisberg and J. Blanc, *Phys. Rev.*, **131**, 1548 (1963).

Electrical Properties of Tin Oxide Ultrafine Particle Films

Hisahito Ogawa, Atsushi Abe, Masahiro Nishikawa, and Shigeru Hayakawa

Matsushita Electric Industrial Company Limited, Material Research Laboratory, 1006 Kadoma, Osaka, 571 Japan

ABSTRACT

The film structures and gas sensing properties of tin oxide ultrafine particle films deposited under oxygen pressures between 0.05 and 5 Torr have been studied. The ultrafine particle film having porous columnar structure is found to have high sensitivities in detecting humidity or combustible gases when operated at elevated temperatures. The films can be made selectively sensitive to these gases by choosing the film depositing conditions and the operating temperature.

Tin dioxide, SnO_2 , in its pure form is an n-type metal oxide semiconductor. Its electrical conduction results from the existence of point defects (oxygen vacancies and interstitial tin atoms) which act as donors (1). Some unique properties of SnO_2 make the material useful for many applications such as resistor, NESA glass, and so on. Recently, SnO_2 has attracted special interest as a gas sensor material.

The properties of SnO_2 in the form of sintered polycrystals (2), thin films (3-5), or thick films (6) as gas sensors have been reported. Some of the gas sensors of above types have been put into practical applications for sensing combustible gases. However, the gas sensing mechanism, the change of electrical characteristics by means of gas adsorption, of these sensors has not been explained satisfactorily up to the present time.

Models which have been proposed to explain the conductance modulation in the sensors by gas adsorption are:

1. Electron transfer between adsorbed gas molecules and SnO_2 materials, *i.e.*, change in surface conductance (7).
2. Change of SnO_2 composition, *i.e.*, change in bulk conductance (8).
3. Potential barrier height modulation at the grain boundary of polycrystalline samples (9).
4. Field effect transistor action at the neck parts of polycrystalline samples (10).

In any model, special attention must be paid to the surface quality (proportion of surface to volume) of the gas sensor materials, because the adsorption process responsible for the change in conductance takes place at the boundary between the gaseous and solid states.

We have developed a highly reproducible procedure for preparing the ultrafine particles of the metal oxide and the films (11). The ultrafine particles are grown by the evaporation of the metal in a low oxygen pressure atmosphere where ultrafine particles of metal oxide are deposited and form films having, for example, porous columnar structure on silica glass or silicon substrates covered with SiO_2 thin film. The SnO_2 typical ultrafine particle film fabricated by using this technology has the porous columnar structure constructed from the ultrafine particles having the median particle size of several tens of angstroms (in sintered polycrystalline materials, the particle size is more than several thousands of angstroms):

The unique characteristics of these SnO_2 ultrafine particle films are as follows.

1. Each ultrafine particle has a large specific surface area because of the smallness of its particle size.

Key words: ultrafine particle film structure, gas-evaporation technique, gas sensor, selective detection.

Therefore, the portion of the surface energy in the total energy of the particle becomes large and the surface activity against the adsorbed gases is expected to be increased.

2. The porous columnar structure of the ultrafine particle film makes it easy for gas molecules to enter into the film, so the conductance modulation by gas adsorption in the film is large.

As mentioned above, when the effects of the surface of the materials become noticeable, the conductance modulation by gas adsorption is expected to have unique characteristics, such as gas sensitivity and gas selectivity, which have not been observed in sintered polycrystalline materials, thin films, and thick films.

In the present work, the electrical and gas sensing properties of tin oxide ultrafine particle films were studied in comparison with other reported gas sensors made of sintered polycrystals, thin films, or thick films.

Experiments

Sample preparation.—Two different substrate materials, silica glass (Corning No. 7059) and silicon covered with SiO_2 with the dimension of $2.0 \times 2.0 \times 0.2$ mm were used. There was no substantial difference between the sensors fabricated on these two different substrates. The sensing material, SnO_2 ultrafine particle film, was deposited between the two gold-plated interdigital electrodes (the gap of electrode is 0.02 mm and the total length of electrode is 11.6 mm) on one side of the substrate in the following procedures (11).

Evaporating materials such as Sn, SnO, and SnO_2 , of purity higher than 99.99%, were placed in an evaporator boat. The chamber was pumped down to approximately 2×10^{-6} Torr and then oxygen (about 1 Torr) was introduced into the chamber. The glow discharge of the oxygen was produced by applying the rf power. Then the heating power was supplied to the boat and, after the growth rate of the tin oxide ultrafine particles in the glow discharge of oxygen reached a stable condition, the shutter was opened to deposit the ultrafine particles on the substrate. The deposition was allowed for a few minutes, depending on the thickness of the final ultrafine particle film.

Electrical contacts were made with 0.05 mm gold wires attached to the gold electrodes. The contact resistance between tin oxide ultrafine particle films and gold electrodes was measured at the operation temperature from 25° to 500°C, and was confirmed to be small enough compared with the resistance of the tin oxide ultrafine particle films themselves.

Analytical characterization of SnO_2 ultrafine particle films.—The quality of the ultrafine particles and the films was determined by the depositing condition, oxygen pressure, temperature of evaporator boat, and

others. The mean particle size and composition of the ultrafine particles were determined from x-ray diffraction analysis. The morphology and structure were observed by SEM and TEM. Figure 1 shows the curve of the mean particle sizes of SnO₂ ultrafine particles as a function of the oxygen pressure, and SEM photomicrographs showing three representative film structures at three different oxygen pressures. The mean particle size sublinearly increased as the oxygen pressure increased; the value of the slope was nearly 1/2. When the oxygen pressure was less than 0.05 Torr, the film grew along the direction perpendicular to the surface of the substrate, columnar structure. When the oxygen pressure was 0.5 Torr, derangement in the orientation of the film appeared. The structure was more or less aligned in the columnar direction, but became very much more porous. A structure like this was labeled as porous columnar. As the pressure was 5 Torr, the unidirectional growth of the film disappeared and the structure became spongy in appearance.

Results

Electrical characteristics and gas sensing properties of devices having SnO₂ ultrafine particle gas sensing films prepared by the above technique were studied. A closed stainless steel chamber (5 liters in volume) having a gas inlet port and a liquid (water or alcohol) evaporator was used for the measurement of the device characteristics. The gas in the chamber was circulated by means of a pump.

The circuit voltage (e_1) was applied across the device (the resistance of which is denoted as R_x) and a load resistor (R_L) connected in series. The load voltage (e_o) across the load resistor was measured.

R_x was calculated as follows

$$R_x = \left(\frac{e_1}{e_o} - 1 \right) \times R_L$$

The internal impedance (60Ω) of circuit voltage source was negligible compared to R_x or R_L .

Electrical properties of SnO₂ ultrafine particle films.—In the present work, several kinds of SnO₂ ultrafine particle gas sensing film were prepared at oxygen pressure levels between 0.05 and 10 Torr. Films prepared at different oxygen pressures differed in their mean particle sizes and their film structures. In spite of these differences, most of the ultrafine particle films had a similar thermal hysteresis in conductance-temperature characteristics. A typical example is shown in Fig. 2.

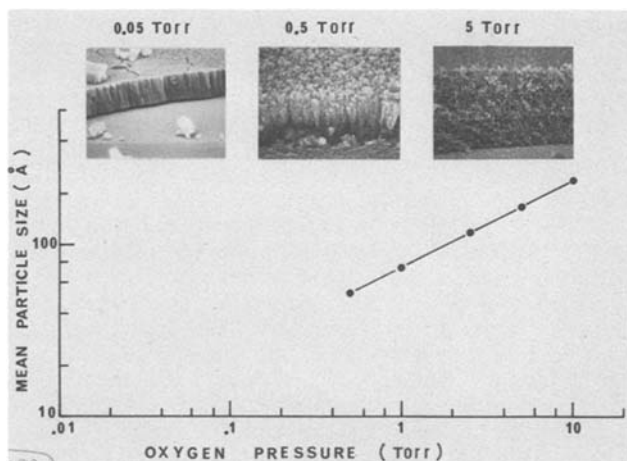


Fig. 1. Mean particle sizes of SnO₂ ultrafine particles and SEM photomicrographs showing the structure of the films deposited onto glass substrates. The structures of the films deposited in oxygen pressure at 0.05, 0.5, and 5 Torr are columnar, porous columnar, and spongy, respectively.

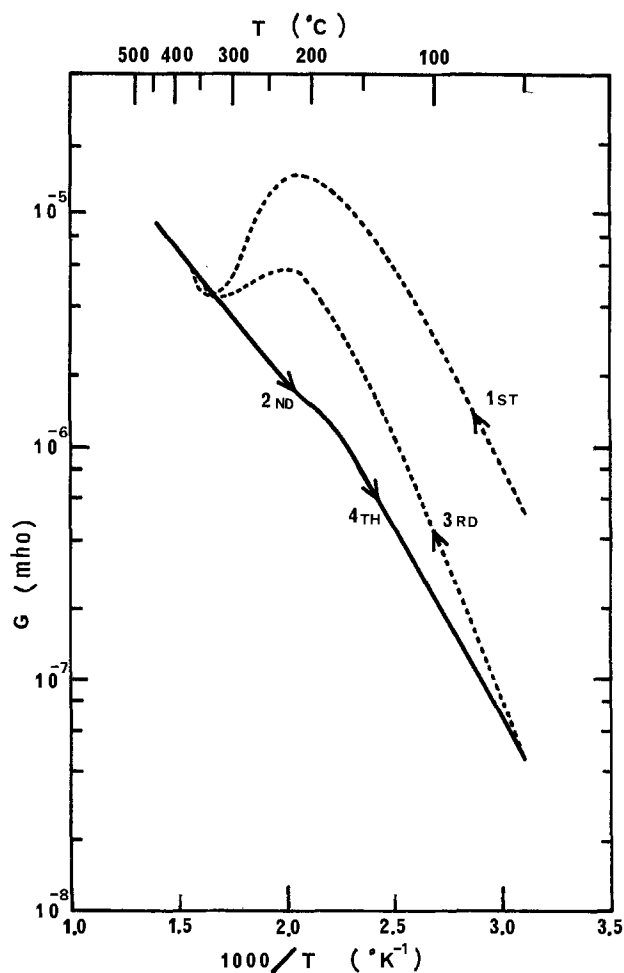


Fig. 2. A typical example of thermal hysteresis in conductance-temperature characteristics of tin oxide ultrafine particle film. The repeat measurements of the conductance done during cooling after the sample was heated to sufficiently high temperatures, agreed rather well.

When the conductance of the ultrafine particle film was measured during heating in air, the measured value depended greatly on preceding temperature-atmosphere history. On the other hand, when the measurement was done during cooling after the sample was heated to sufficiently high temperatures, repeated measurements agreed rather well. This kind of thermal hysteresis of conductance-temperature characteristics has been observed in SnO₂ thick films (6) and ZnO sintered polycrystalline materials (12), and it is considered to be an effect of adsorbed water. In the following measurements, conductance was measured while the sample was cooled down from an elevated temperature, thereby securing a good reproducibility in conductance-temperature characteristics.

When the circuit voltage e_1 was varied from 0.01 to 100V (from 5 V/cm to 5×10^4 V/cm in ultrafine particle films), I - V characteristics of ultrafine particle films obeyed Ohm's law and never showed a non-linearity which was often observed in the sintered polycrystalline materials. The high field I - V characteristics were determined by using a pulse technique with a pulse generator (H.P. Model 214A, pulse width 10 μ sec, repeat time 1 msec).

Figure 3 shows the resistance R as a function of the film thickness t of the SnO₂ ultrafine particle films prepared with three oxygen gas pressures at 0.05, 0.5, and 5 Torr. The film thickness was determined from the SEM observation and the resistance was measured at the operating temperature of 300°C to avoid the effect of the surface adsorbed water. Without distinc-

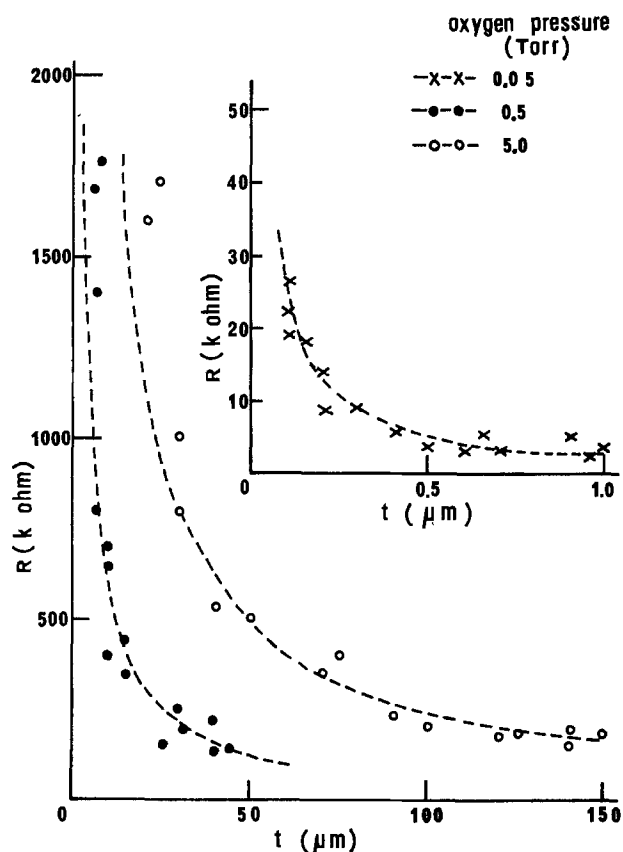


Fig. 3. The resistance R as a function of the film thickness t of the tin oxide ultrafine particle films prepared with three oxygen pressures at 0.05 Torr ($- \times -$), 0.5 Torr ($- \bullet -$), and 5 Torr ($- \circ -$). Most films showed the following relation: $R = k/t$ where k is the constant.

tion of the preparation condition of SnO_2 ultrafine particle films, most films showed the following relation

$$R = \frac{\rho l}{tw} \quad [1]$$

where ρ is the resistivity, l is the gap between the electrodes, t is the film thickness, and w is the total length of the electrode. Only in the region of small t at each group, the observed R became larger than the value calculated in Eq. [1]. It is postulated that this was neither caused by a carrier reflection at the surface of the film nor a carrier dispersion at the grain boundary of the particle, but was due to discontinuities in ultrafine particle films at the initial stage of the growth on the substrate as shown in Fig. 4. The resistivity ρ of the ultrafine particle films was calculated from Eq. [1] using values of R shown in Fig. 3. Calculated values are: $\rho = 60 \Omega\text{-cm}$ at oxygen gas pressure of 0.05 Torr, $\rho = 2 \times 10^5 \Omega\text{-cm}$ at 0.5 Torr, and $\rho = 6 \times 10^5 \Omega\text{-cm}$ at 5 Torr.

Gas sensing properties of SnO_2 ultrafine particle films.—Properties of SnO_2 ultrafine particle films operated as sensors at elevated temperatures and exposed to gases were measured.

Figure 5 shows the conductance of ultrafine particle films, deposited in the oxygen pressure at 0.05, 0.5, and 5 Torr, as a function of the reciprocal of the sensor operating temperature. Solid lines are for the sensor in room air [ambient temperature $T_a = 25^\circ\text{C}$, relative humidity (RH) = 40%], broken lines are in wet atmosphere ($T_a = 25^\circ\text{C}$, RH = 90%), dashed lines are in 100 ppm of ethyl alcohol, $\text{C}_2\text{H}_5\text{OH}$, in room air, and dotted lines are in 1000 ppm of isobutane, $\text{iso-C}_4\text{H}_{10}$, in room air. As the SnO_2 ultrafine particle film is an n-type semiconductor, the conductance in a reductive

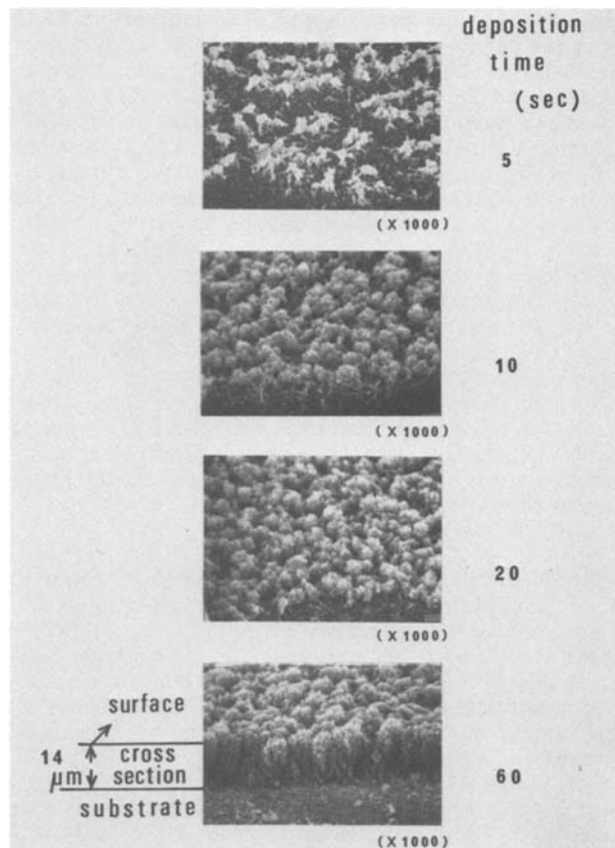


Fig. 4. Scanning electron microscopy examination of the growth of ultrafine particle films deposited in oxygen pressure at 0.5 Torr on glass substrates. Discontinuities in the film at the initial stage of the growth (when the depositing time is shorter than 20 sec) are observed.

gas atmosphere, G , became larger than the conductance in room air, G_0 . The gas sensitivity, S , is defined as the value of $(G - G_0)/G_0$. The sensitivity was strongly related to the operating temperature and the depositing condition of the ultrafine particle films, that is, the composition and mean particle size of ultrafine particles and to the structure of films. For example, the ultrafine particle films made under 0.05 Torr oxygen pressure having columnar structure like that in thin film was very sensitive to humidity, but not sensitive to $\text{iso-C}_4\text{H}_{10}$ gas. In contrast with this, the ultrafine particle films made under 0.5 Torr oxygen pressure (porous columnar structure) exhibited an opposite property; high sensitivity to $\text{C}_2\text{H}_5\text{OH}$ gas and $\text{iso-C}_4\text{H}_{10}$ gas at operating temperatures higher than 200°C and low sensitivity to humidity at the same operating temperatures. The ultrafine particle films made under 5 Torr oxygen pressure (sponge-like structure) had characteristics similar to in nature but less sensitive than those of films made under 0.5 Torr oxygen pressure.

These properties were shown more clearly in Fig. 6 and 7. Figure 6 shows the sensitivity of the SnO_2 ultrafine particle film made under 0.5 Torr oxygen pressure (porous columnar structure) as a function of the sensor operating temperature. The sensor had high sensitivity to humidity at 50°C , to $\text{C}_2\text{H}_5\text{OH}$ gas between 200° and 300°C , and to $\text{iso-C}_4\text{H}_{10}$ gas between 350° and 450°C . Therefore, for example, selective detection of $\text{C}_2\text{H}_5\text{OH}$ gas or $\text{iso-C}_4\text{H}_{10}$ gas could be realized simply by operating the sensor at the temperature of 250° or 450°C , respectively.

Figure 7 shows the sensitivity as a function of oxygen pressure at the time of deposition of the ultrafine particle films. The sensor operating temperature was selected at the temperature where the sensor had the maximum sensitivity to each gas, that is, 50°C for H_2O ,

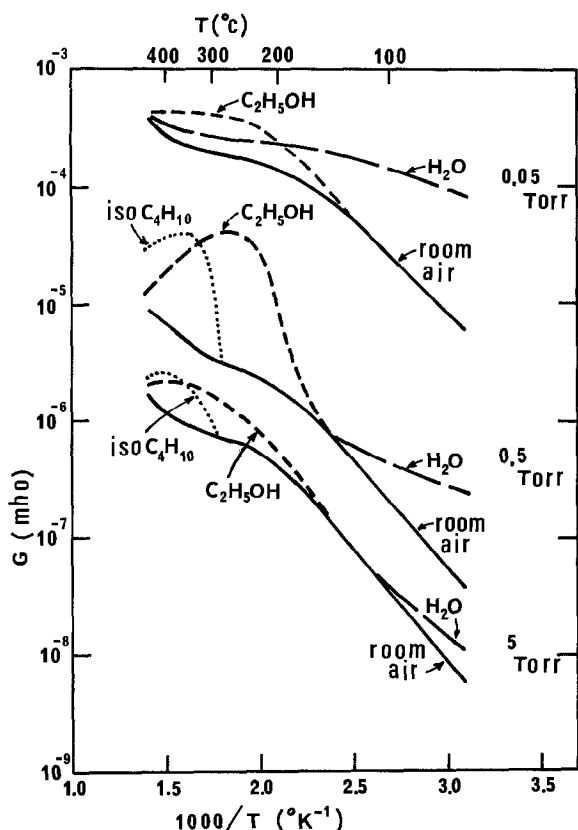


Fig. 5. The conductance of ultrafine particle films, deposited in the oxygen pressure at 0.05, 0.5, and 5 Torr, as a function of the reciprocal of the sensor operating temperature. These measurements were done in the atmosphere of room air (—), wet air (---), 100 ppm of C₂H₅OH (- · - ·), and 1000 ppm of iso-C₄H₁₀ (····).

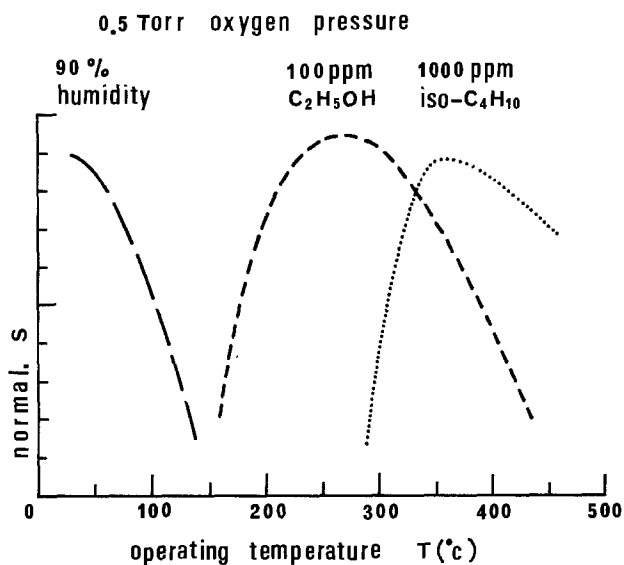


Fig. 6. The sensitivity of the tin oxide ultrafine particle film made under 0.5 Torr oxygen pressure (porous columnar structure) as a function of the sensor operating temperature.

250°C for C₂H₅OH gas, and 350°C for iso-C₄H₁₀ gas. It was found that the SnO₂ ultrafine particle films made under the condition between 0.05 and 0.25 Torr were most sensitive to humidity, between 0.25 and 1 Torr to C₂H₅OH gas, and between 0.5 and 1.5 Torr to iso-C₄H₁₀ gas.

As mentioned above, in the sensor having an ultrafine particle gas sensing film, the sensitivity to various gases could be separated not only by the sensor oper-

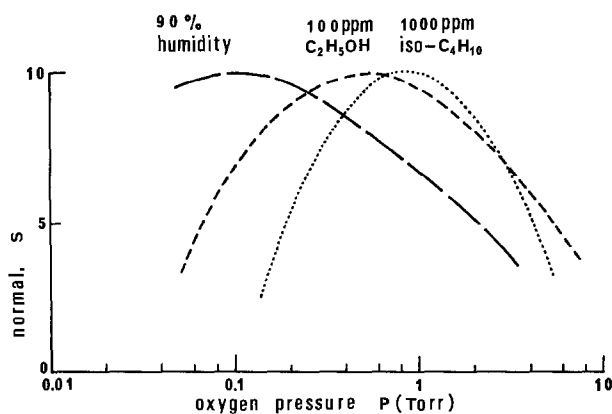


Fig. 7. The sensitivity as a function of oxygen pressure at the time of deposition of the ultrafine particle film. The sensor operating temperature was selected at 50°C for H₂O, 250°C for C₂H₅OH gas, and 350°C for iso-C₄H₁₀ gas.

ating temperature, but also by the depositing conditions of the ultrafine particle films.

This gas-selectivity without using a catalyst is one of the unique characteristics of the ultrafine particle films.

Figure 8 shows the conductance, *G*, of the SnO₂ ultrafine particle gas sensor as a function of the concentration of C₂H₅OH. The film structure of the sensor was porous columnar deposited under oxygen pressure at 0.5 Torr and the sensor operating temperatures were 250° and 400°C. The conductance linearly increased as the C₂H₅OH concentration increased; the slope of the value of conductance was found to be unity at the temperature of 250°C, and nearly 0.5 at 400°C.

Reported values of the slope of conductance of SnO₂ as a function of C₂H₅OH concentration are 0.5 ~ 0.6 (13) for sintered polycrystalline materials having a crystal size of several thousands of angstroms, 0.5 (14)

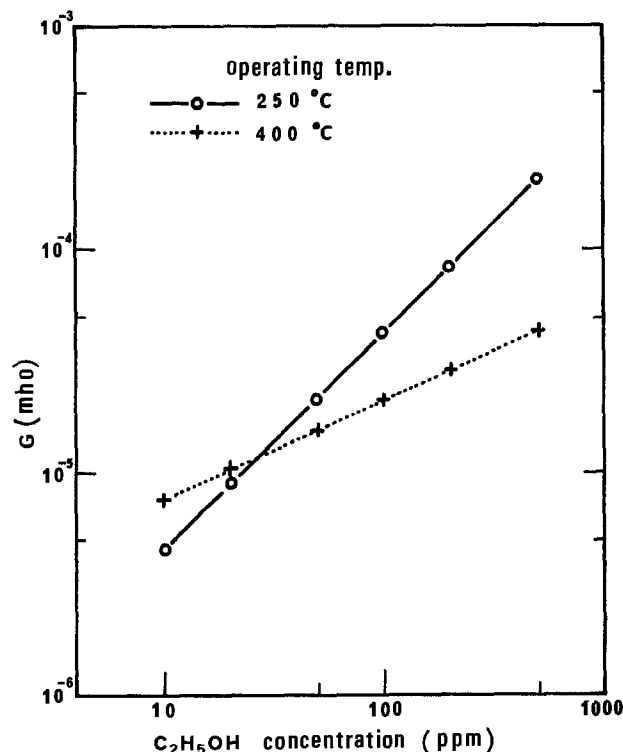


Fig. 8. The conductance, *G*, of the tin oxide ultrafine particle gas sensor as a function of the concentration of C₂H₅OH. The slope of the value of conductance is found to be unity at the temperature of 250°C, and nearly 0.5 at 400°C.

for thin films of several hundreds of angstroms in thickness prepared by the spraying technique, and $0.2 \sim 0.4$ (15) for thin films of several thousands of angstroms in thickness prepared by the sputtering technique. Compared to these reported values, the value of the slope of conductance for SnO_2 ultrafine particle films having particle size of several tens of angstroms, at the optimum operating temperature, 250°C , is nearly twice as large, indicating higher sensitivity.

As shown in Fig. 8, the linear relationship extends down to 10 ppm of $\text{C}_2\text{H}_5\text{OH}$ concentration, indicating a very low limit of detection.

It is considered that the high sensitivity of the ultrafine particle films is realized by the large surface area due to the smallness of the particles and to porosity in the film structure. The specific surface area of the ultrafine particle films is calculated to be several tens of times larger than that of the sintered polycrystalline materials.

Discussion

As it was shown in Fig. 3, the resistivity, $10^4 \sim 10^5 \Omega\text{-cm}$, of the ultrafine particle films, where the structures were porous columnar or sponge-like, was extremely large compared with the value, $0.1 \sim 10^2 \Omega\text{-cm}$, of single crystals, sintered polycrystalline materials, and thin films. Taking into consideration the results of the I - V characteristics and the particle size, several tens of angstroms, of ultrafine particles, the cause for the large resistivity was not a potential barrier of particle boundaries which prevent electrons from moving, but the pores constructed in the ultrafine particle film. That is, with the change of SnO_2 ultrafine particle film structure from columnar to spongy via porous columnar, the number of SnO_2 particles in a unit thickness of the film was decreased.

Figure 9 shows the result of optical transmittance measured with the SnO_2 ultrafine particle film of $175 \mu\text{m}$ in thickness having a spongy structure. In the case of SnO_2 thin films, it is known experimentally that the following relation between the film thickness ($t \mu\text{m}$) and the transmittance ($T\%$) is applicable (16)

$$\log T = \log(0.92) - 0.093t \quad [2]$$

If $T = 0.86$, the transmittance in the wavelength beyond $0.45 \mu\text{m}$, obtained from Fig. 9, is substituted into Eq. [2] then t is found to be equal to $0.3 \mu\text{m}$. That is, the transmittance of SnO_2 ultrafine particle film of $175 \mu\text{m}$ in thickness is equivalent to the transmittance of SnO_2 thin film of $0.3 \mu\text{m}$. This result clearly indicates that the ultrafine particle films have many pores. From the above result, we could estimate that the number of SnO_2 particles packed in ultrafine particle film was about 1/600 times in comparison with the value of SnO_2 thin film in the same thickness.

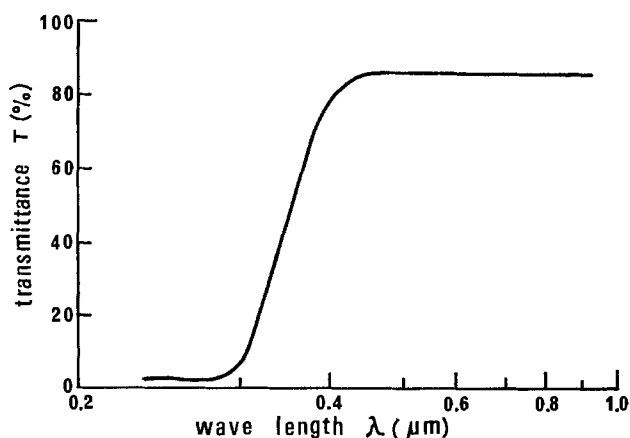


Fig. 9. Optical transmittance measured with tin oxide ultrafine particle film of $175 \mu\text{m}$ in thickness having spongy structure.

Figure 10 shows the curve of the sensitivity, S , to $\text{C}_2\text{H}_5\text{OH}$ as a function of the thickness of ultrafine particle films deposited in the oxygen pressure at 0.05, 0.5, and 5.0 Torr. In the case of 0.05 Torr, the film structure was columnar and was similar to that of thin films.

With the increase of the film thickness, t , the sensitivity, S , decreases.

The reason is suggested to be as follows. Because of low porosity in the film, $\text{C}_2\text{H}_5\text{OH}$ molecules cannot freely enter into the film. Adsorption of $\text{C}_2\text{H}_5\text{OH}$ molecules, which contributes to lower the resistivity of film, is therefore restricted to the surface of the film.

With the increase of the film thickness, the effect of the surface to the resistivity, and to the sensitivity, of the film in total decreases. In the case of 0.5 and 5 Torr, the film structures are porous columnar and spongy, respectively, and the sensitivity, S is independent of the film thickness, t .

In these porous films, $\text{C}_2\text{H}_5\text{OH}$ molecules enter into the film and are adsorbed not only to the surface of the film but also to SnO_2 particles inside the film. Consequently, as shown in Fig. 8, the sensitivity of the ultrafine particle films constructed from porous columnar structure, without addition of any catalyzers such as Pt or Pd, was quite large compared to the values of sintered polycrystalline materials and thin films.

Summary and Conclusion

Three distinct structures of SnO_2 ultrafine particles are observed, depending on the oxygen pressure at the time of deposition.

The characteristics of films having porous columnar or spongy structure are found to be different from those of reported gas sensing materials such as sintered polycrystals or thin films of SnO_2 in the following manner:

1. High gas sensitivity. The high sensitivity of the ultrafine particle film is considered to be caused by (i) a large specific surface area because of the smallness of its particle size, and (ii) the porous film structure which makes it easy for gas molecules to enter into the film and to be adsorbed at the surface of SnO_2 particles.
2. High gas selectivity. When the oxygen pressure at the time of deposition is varied from 0.05 to 0.5 and to 5 Torr, resulting in films of columnar, porous columnar, or spongy structure, respectively, the gas to which the ultrafine particle film is sensitive changes from humidity to $\text{C}_2\text{H}_5\text{OH}$ and to $\text{iso-C}_4\text{H}_{10}$.

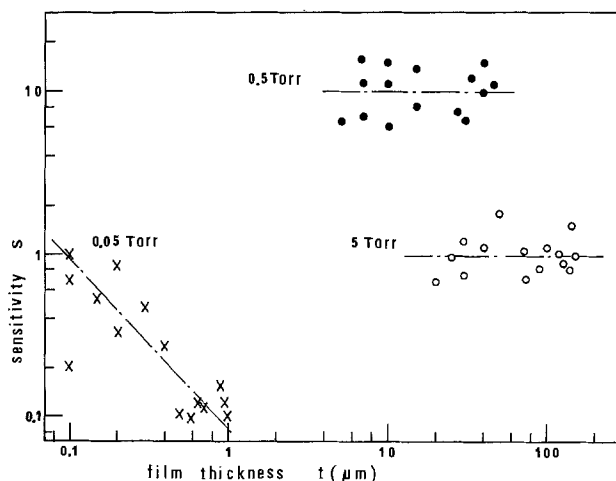


Fig. 10. The sensitivity, S , to $\text{C}_2\text{H}_5\text{OH}$ as a function of the thickness, t , of ultrafine particle films deposited in the oxygen pressure at 0.05, 0.5, and 5 Torr. In the case of 0.5 Torr (porous columnar structure) and 5 Torr (spongy structure), S is independent of t .

That is, the optimum structure of the ultrafine particle film to detect each gas can be obtained by selecting the film deposition condition to be suitable. And, for example, the film having porous columnar structure has a high sensitivity to humidity at operating temperature of 50°C, to C₂H₅OH gas at the temperatures between 200° and 300°C, and to iso-C₄H₁₀ gas between 350° and 400°C. Therefore, selective detection of these gases could be realized simply by sweeping the operating temperature of the sensor from 450° to 50°C.

3. The above-mentioned distinguishing characteristics of the ultrafine particle film are realized without addition of any catalyzers such as Pt or Pd.

Acknowledgments

We would like to express our hearty thanks to Dr. T. Nemoto, Dr. S. Sekido, and Dr. M. Mikoda for their deep interest throughout the progress of the work, and Professor R. Kiriyama, Dr. H. Hozumi, and Dr. L. Ozawa for many useful discussions.

This work was supported by MITI subsidy for important technological research and development.

Manuscript submitted Dec. 2, 1980; revised manuscript received ca. March 16, 1981.

Any discussion of this paper will appear in a Discussion Section to be published in the June 1982 JOURNAL. All discussions for the June 1982 Discussion Section should be submitted by Feb. 1, 1982.

Publication costs of this article were assisted by the Matsushita Electric Industrial Company, Limited.

REFERENCES

1. Z. M. Jarzebski and J. P. Marton, *This Journal*, **123**, 299C (1976).
2. N. Taguchi, U.S. Pat. 3,695,848 (1972).
3. G. N. Advani and A. G. Jordan, *J. Electron. Mater.*, **9**, 29 (1980).
4. H. Windischmann and P. Mark, *This Journal*, **126**, 627 (1979).
5. S. H. Chan, *IEEE Trans. Electron Devices*, **ed-26**, 1875 (1979).
6. M. Nitta and M. Haradome, *ibid.*, **ed-26**, 247 (1979).
7. T. Seiyama, *Zairyo Kagaku*, **8**, 232 (1971).
8. H. Obayashi and T. Kudo, *Jpn. J. Appl. Phys.*, **14**, 330 (1975).
9. K. Ihokura, Paper presented at The ACS/CSJ Chemical Congress in Hawaii, April, 1979.
10. I. Doi, M. Nakagawa, and H. Mitsudo, *Trans. IECE Jpn.*, **EDD-76-42** (1976).
11. H. Ogawa, A. Abe, M. Nishikawa, and S. Hayakawa, *This Journal*, **128**, 685 (1981).
12. M. Takata, D. Tsubone, and H. Yanagida, *J. Am. Ceram. Soc.*, **59**, 4 (1976).
13. S. Sunahara, *Denshi Gijutsu*, **21**, 50 (1979).
14. H. Pink, L. Treitinger, and L. Vite, *Jpn. J. Appl. Phys.*, **19**, 513 (1980).
15. T. Oyabu, *Trans. IECE Jpn.*, **J62-C**, 733 (1979).
16. P. Mark, *J. Chem. Phys. Solids*, **29**, 689 (1968).
17. H. Chon and C. D. Prater, *Disc. Faraday Soc.*, **41**, 380 (1966); H. Chon and J. Pajares, *J. Catal.*, **14**, 257 (1969).

Technical Notes



Properties of CdSe Thin Film Electrodes for Photoelectrochemical Cells

Joseph Reichman* and Michael A. Russak

Grumman Aerospace Corporation, Research Department, Bethpage, New York 11714

Recently, we reported results on n-CdSe thin film photoanodes for use in electrochemical photovoltaic cells (EPC) with aqueous sulfide-polysulfide containing electrolytes which pointed out the relationship between the basic material properties of the various thin film electrodes and their resultant *I-V* performance (1). This paper presents a summary of our more recent efforts on establishing the relationships among thin film processing parameters, electronic properties, and photoelectrochemical performance.

The electrodes under study were deposited onto titanium sheet (0.254 mm thick) and are intended for use in frontwall illuminated electrochemical photovoltaic cells, where the incoming radiation would pass through a transparent window, a thin layer of electrolyte, and then strike the semiconductor electrolyte junction. The CdSe thin films were produced by the simultaneous evaporation of Cd and Se from two independently controlled resistive heated boats. Each source is controlled by a Sloan MDC 9000 Thin Film Deposition Controller (Sloan Technology Incorporated,

Santa Barbara, California). The substrates are clamped onto a copper plate into which cartridge-type heaters have been placed to provide substrate temperature control. The addition of the controllers to the co-evaporation system has improved the reproducibility of the deposition process over that obtained previously (1). The most important deposition parameters were found to be the Se to Cd molar ratio in the evaporant vapor streams, the substrate temperature, and to a lesser extent, CdSe condensation rate. The phase of the as-deposited films could be varied from crystalline to amorphous depending on deposition conditions. The films formed with Se/Cd ratios near one were crystalline (hexagonal) with a strong 001 growth texture at substrate temperature as high as 500°C. At Se/Cd ratios near three (represented as *x* in CdSe_{*x*}) the as-deposited films were amorphous at substrate temperatures up to 200°C above which temperature the films were not adherent to the substrates. These films, however, crystallized with a strong 001 texture upon heat-treatment. In this case, radical chemical, microstructural, and optical changes occurred with crystallization and loss of excess Se as shown in Fig. 1, 2, and 3. This contrasted with the results obtained for films deposited

* Electrochemical Society Active Member.

Key words: CdSe thin films, frontwall photoelectrochemical cells, photovoltaic energy conversion.

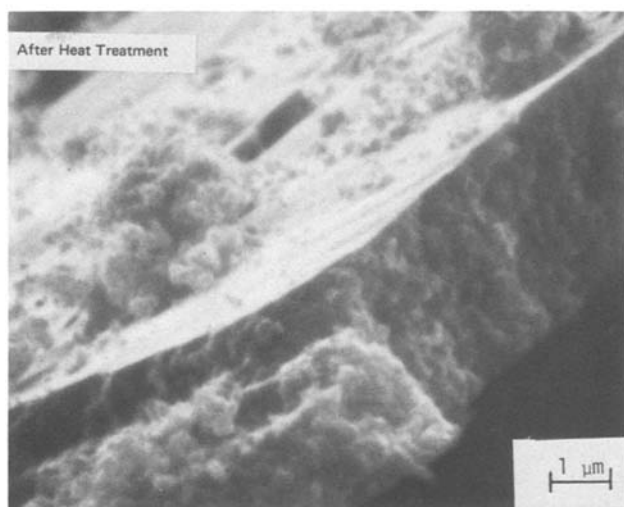
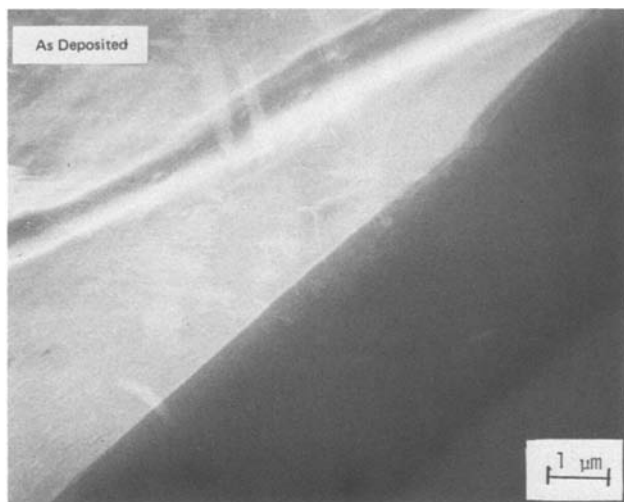


Fig. 1. Microstructural changes observed in a CdSe thin film with Se/Cd ratio of 3 with heat-treatment at 400°C, 15 min in air.

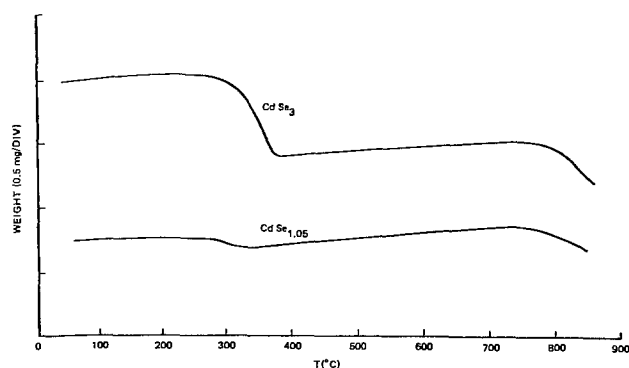


Fig. 2. TGA traces of two CdSe_x as-deposited films in argon (heating rate 10°C/min).

at substrate temperature greater than 200°C, but with Se/Cd ratios near one, where no major microstructural or chemical changes were observed with heat treatment. In almost all cases, however, the photoelectrochemical performance of the as-deposited thin film electrodes was poor, with most films peeling from the substrate. The postdeposition heat-treatment employed was therefore critical to developing good film adherence as well as considerably improved I-V character-

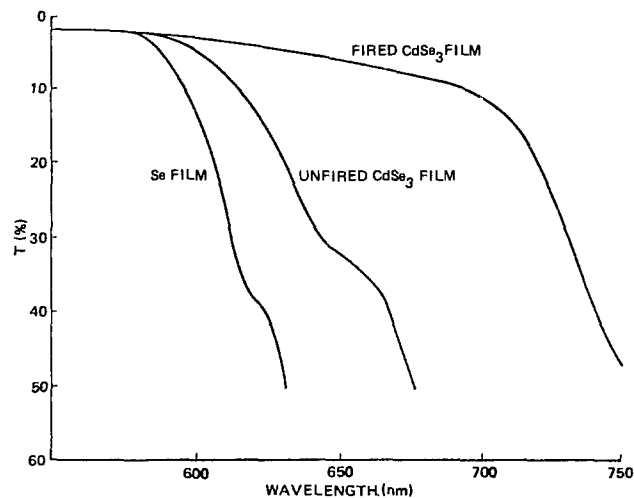


Fig. 3. Optical transmission curves for Se film (1), as-deposited CdSe₃ film, (2) and fired CdSe₃ film (3).

istics. Conventional photoelectrochemical testing procedures described previously were employed (1).

The most promising results to date with electrodes for use in frontwall cells have been obtained with CdSe films deposited at approximately 100°C with Se/Cd ratio of three and then heat-treated in the temperature range of 350°-400°C in air. These films usually had a very fine-grained microstructure after heat-treatment similar to that of Fig. 1 and the resultant electrodes had I-V characteristics with fill factors of 0.60 or greater and high current output. The overall power efficiency of these electrodes was limited by relatively low open-circuit voltages (~0.4V). Power conversion efficiencies at simulated AM2 conditions [W-I ELH lamp discussed in Ref. (2)] from 3 to 5% were obtained consistently with electrodes processed in this manner. Another type of film of interest was deposited on titanium but at substrate temperatures >400°C with a slight excess of Se. It can be seen in Fig. 4 that the microstructure of the films deposited under these conditions was quite different from that of the films produced at lower substrate temperatures and followed by heat-treatment. In particular, the average grain size was significantly larger and the film was columnar with grains that appeared to be continuous throughout the film. Even though these films were deposited at elevated temperatures a postdeposition heat-treatment was required to maximize their I-V performance, as was the case for MIS cells made with CdSe thin films

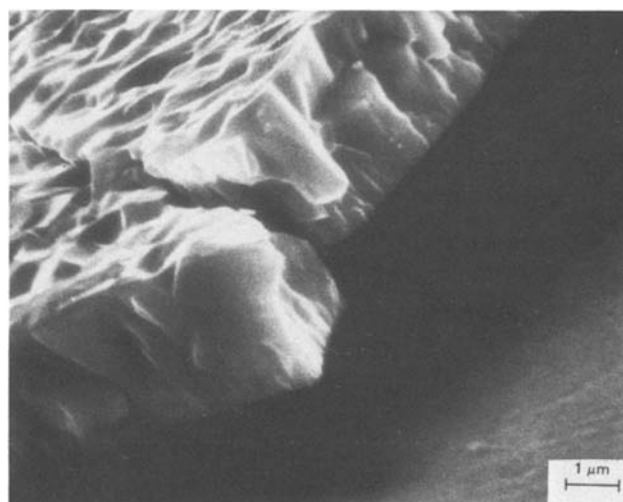


Fig. 4. SEM micrograph of CdSe film deposited at substrate temperature of 425°C.

of this type (3). The interesting feature of films produced in this manner was their higher open-circuit voltage, which was consistently in the range of 0.55 to 0.65V. However, the current output and fill factor were lower than those obtained with the films discussed previously. As a result, the power conversion efficiency of these electrodes was only in the range of 3-4% at 75 mW/cm², AM2 conditions.

Figure 5 compares the *I-V* performance of two thin film electrodes typical of the two types of processing. Curve A is representative of the high substrate temperature film and curve B typifies the film deposited at low substrate temperature and heat-treated. Table I summarizes the pertinent performance parameters for these electrodes. As can readily be seen the *I-V* characteristics of these two films are quite different. The high deposition temperature film, A, has a gradual decline in current with increasing voltage and a tail at the high voltage end. The low deposition temperature film, B, has a flat *I-V* characteristic at low voltages and a sharp drop in current at higher voltages. Some qualitative conclusions relating the resistivity values of these films to their *I-V* characteristics can immediately be made. The film with the higher resistivity, B, shows higher J_{sc} and lower V_{oc} values than those for film A, which had a lower resistivity by more than two orders of magnitude. If it is assumed the difference in the resistivities of the two films is due to changes in free carrier density, N_D , then the difference in the *I-V* characteristics can be explained in the following manner. Since the depletion width, W , is given by $W = (2\epsilon\epsilon_0(V_{FB} - V)/qN_D)^{1/2}$, a lower N_D value would result in a larger depletion width. This then would result in a higher short-circuit current since more carriers would be generated in the depletion layer rather than in the bulk where recombinations are more likely to occur. The initially flat *I-V* characteristic can also be explained as due to the high resistivity film depletion width being sufficiently large so that essentially all generation of electron hole pairs occurs in the space charge region. In contrast, the lower resistivity film's decline of J with V can be explained by narrowing of the depletion width with increasing voltage causing greater generation of holes in the bulk with subsequent recombinations. The differences in V_{oc} of the films is also consistent with their differences in resistivities. As the carrier density decreases, the Fermi level of the CdSe film is lowered. This then makes the flatband potential more positive and results in less band bending. Since the open-circuit voltage is slightly more positive of the flatband potential it decreases as the Fermi level of the film is lowered.

To obtain a more quantitative characterization of the effects of the film properties on the performance characteristics, the theoretical model we have developed (4) was used to analyze experimental *I-V* data. The *I-V* measurements on the two films were made using monochromatic light at a wavelength of 650 nm. The data were reduced to internal quantum efficiency by using measured values of reflectance, correcting for electrolyte absorption, and measuring the incident intensity. The net photocurrent was obtained by using the amplitude of the current resulting from a chopped monochromatic source. This was done to eliminate the effects of dark current on the *I-V* characteristics.

The model used to fit the experimental data was obtained by solving the diffusion equation for minority carriers using boundary conditions relevant to the semiconductor electrolyte junction, that is, the photocurrent is linearly related to the concentration of

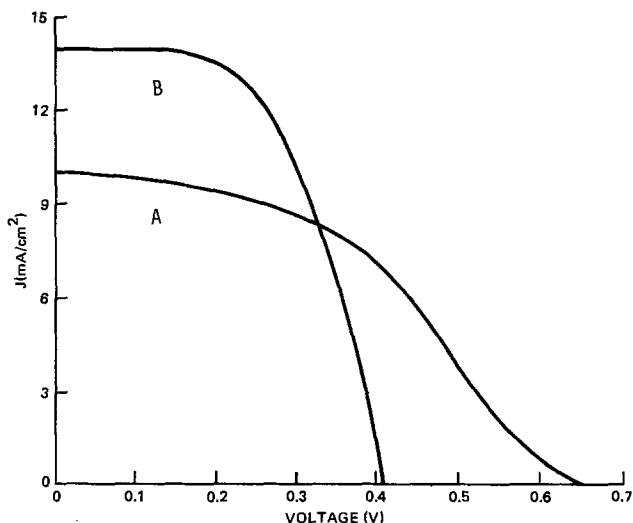


Fig. 5. Comparison of current-voltage curves for CdSe film electrodes discussed in text.

minority carriers at the interface (4). Using this boundary condition and assuming quasi-equilibrium conditions in the depletion region current-voltage relations are derived. The model takes into account losses in current due to recombinations in the depletion region and the bulk of the semiconductor.

The results of the comparison of the model calculations and the experimental *I-V* data are shown in Fig. 6 for the two films. The significant model parameters that were adjusted to fit the data were minority carrier diffusion length, L_p , carrier density, N_D , lifetime, τ , and charge transfer velocity, v_t . The other parameters such as absorption coefficient and flatband potential were obtained from experimental data. The diffusion length was obtained from the low voltage and reverse bias data (not shown) for the high temperature substrate film A. The results indicate that $L_p < 0.02 \mu\text{m}$, which is quite small. The value of N_D also obtained in this voltage region was $3.5 \times 10^{15} \text{ cm}^{-3}$. Values between 10^{15} and 10^{16} have been determined experimentally for films of this type by a modified van de Pauw technique (5). Values of $\tau = 10^{-10}$ sec and $v_t = 5000 \text{ cm/sec}$ were obtained from the data in the region where the current decreases more rapidly with voltage. These parameters characterize the losses due to recombinations in the depletion region. The short lifetime is consistent with the small diffusion length and inferred mobility from the measured resistivity and value for N_D . The fitted value of v_t of 5000 cm/sec is more than an order of magnitude greater than values we have obtained for the same electrolyte using a single crystal CdSe electrode (6). This higher charge transfer velocity for the thin films can explain the finding that the corrosion rate was lower for thin film than single crystal electrodes (7). Since the corrosion rate involves a competition between the decomposition reaction and the redox reaction a higher value of v_t would tend to favor the redox reaction.

The model fit to the low deposition temperature, high resistivity film, (B), data gave a carrier density

¹This charge transfer velocity, v_t , may appear somewhat high when compared to that predicted from theoretical expressions for metal electrodes. It should be noted, however, that values of v_t for metal electrodes refer to the charge transfer velocities of the redox ions, whereas v_t here refers to the holes of the semiconductor with an effective mass at least 5 orders of magnitudes less than the mass of typical redox ions.

Table I. Comparison of film characteristics for two frontwall electrodes (AM2 simulation)

| Film | Thickness (μm) | Grain size (μm) | ρ ($\Omega\text{-cm}$) | V_{oc} (V) | J_{sc} (ma/cm^2) | FF | η (%) |
|------|-----------------------------|------------------------------|-------------------------------|--------------|-------------------------------|------|------------|
| A | 2.0 | 0.7 | 1.1×10^8 | 0.64 | 10 | 0.44 | 3.7 |
| B | 2.3 | 0.05 | 4.2×10^6 | 0.41 | 14 | 0.55 | 4.3 |

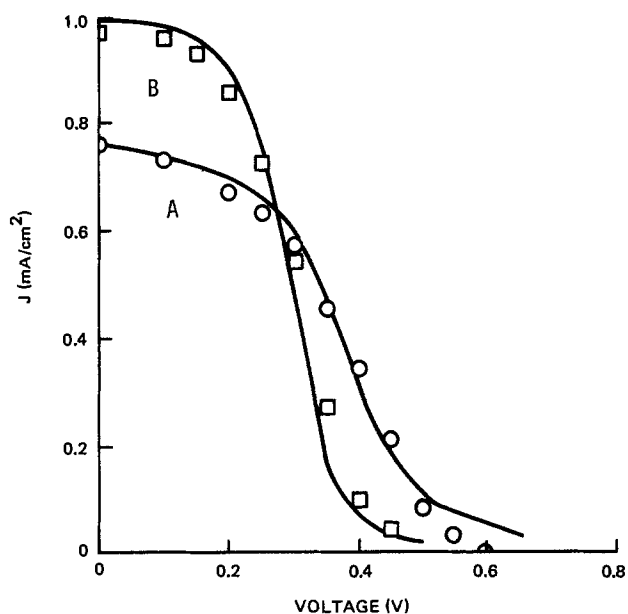


Fig. 6. Experimental monochromatic current-voltage curves (solid lines) and model calculations for electrodes A and B.

of 10^{13} cm^{-3} , in agreement with measured values of 10^{12} – 10^{13} cm^{-3} . This low value indicates that the film is fully depleted, that is, the depletion width extends throughout the thickness of the film. The diffusion length therefore cannot be determined since no measure of absorption in the bulk is available. However, the value of $2 \times 10^{-10} \text{ sec}$ obtained for the lifetime and the resistivity measurement indicates a diffusion length comparable to that of the high temperature films.

Additional confirmation of the analysis of the CdSe thin film properties comes from the spectral response data as shown in Fig. 7. The figure shows that the internal quantum efficiency (ϕ) vs. wavelength characteristics of the two films are quite different. Film B has a measured response further out into the long wavelengths, at sub bandgap energies. This can be explained as being due to absorption from band tail

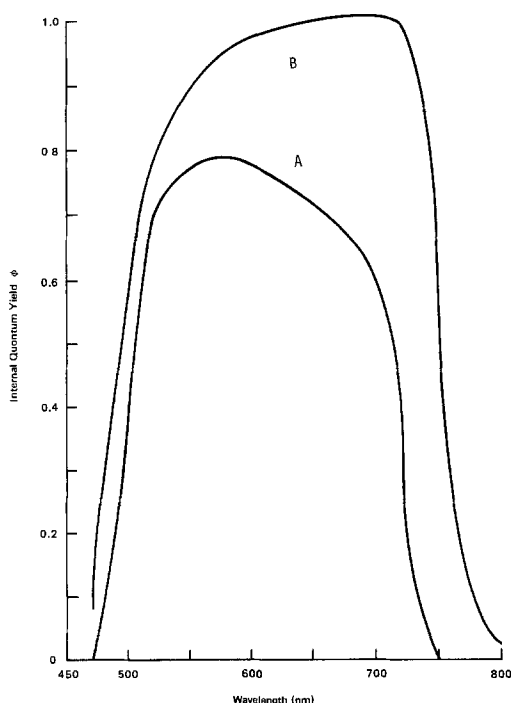


Fig. 7. Spectral response curves for electrodes A and B

states created by charged defects. The large depletion width of this film makes for efficient carrier collection despite the low absorption coefficients in the sub band-gap region. As the absorption coefficient gets larger, and bandgap absorption due to direct interband transitions takes place, the quantum efficiency reaches 100%. At shorter wavelengths the quantum efficiency decreases. This is attributed to photogenerated majority carrier diffusion to the interface where recombination with photogenerated holes takes place (8).

Film A shows a lower quantum efficiency over the entire spectrum due to its smaller depletion width. The falloff in efficiency at short wavelengths, again, is attributed to diffusion of majority carriers to the interface. The peak in efficiency here, however, occurs at a shorter wavelength than for Film B. This is consistent with the higher carrier density of this film. A higher carrier density results in a greater electron field at the interface thereby making diffusion less likely. As a result losses due to diffusion start to occur for carriers generated closer to the interface, *i.e.*, at shorter wavelengths where the absorption coefficient is larger. At longer wavelengths the change in quantum efficiency with wavelength shows the same dependence predicted using the parameters obtained from the analysis of the monochromatic *I-V* data.

In summary, an analysis of the properties of the two CdSe thin film photoanodes using a theoretical model that describes the *I-V* characteristics leads to the following conclusions.

1. Both films appear to have poor diffusion lengths and carrier lifetimes. The larger grain size of the high temperature film does not improve these properties. It seems then that L_p and τ are not limited by grain boundary recombinations but rather by recombinations occurring at point defects or stacking faults within the grains (9).

2. The low substrate deposition temperature films are highly stoichiometric (or highly compensated) with carrier densities of the order of 10^{13} cm^{-3} . This is probably due to the postdeposition heat-treatment of the films that initially contain a high selenium to cadmium ratio. Since the films are fully depleted, high short-circuit currents result. The high substrate deposition temperature films have carrier densities of the order of 10^{15} with depletion widths of $\sim 0.4 \mu\text{m}$. This results in films with lower short-circuit currents but higher open-circuit voltages than the higher resistivity films.

3. The charge transfer velocities of these films are quite high compared to the single crystal. This may be due to the larger surface area caused by highly irregular geometry of the polycrystalline material. As a result reasonably good efficiencies are obtained despite the poor carrier lifetime. The improved kinetics also provide an explanation for the reported higher corrosion resistance of the thin film than the single crystal material.

Acknowledgment

The authors gratefully acknowledge the various contributions of Charles Creter, Jerome DeCarlo, Joseph Havranek, Wayne Gonzales, and Herbert Baker to this work. This work was partially supported by SERI under subcontract XP-9-8002-8.

Manuscript submitted Aug. 12, 1980; revised manuscript received March 30, 1981.

Any discussion of this paper will appear in a Discussion Section to be published in the June 1982 JOURNAL. All discussions for the June 1982 Discussion Section should be submitted by Feb. 1, 1982.

Publication costs of this article were assisted by Grumman Aerospace Corporation.

REFERENCES

1. M. Russak, J. Reichman, H. Witzke, S. K. Deb, and S. N. Chen, *This Journal*, **127**, 725 (1980).
2. K. Yass and H. B. Curtis, NASA Report Number

NASA TM-X-3059, available from NTIS, Springfield, VA 22151.

3. D. Bonnet and E. Rickus, in "Proceedings of the 14th Photovoltaics Specialists Conference," p. 629, New York IEEE, Jan. 1980.
4. J. Reichman, *Appl. Phys. Lett.*, **36**, 574 (1980).
5. F. Chwang, J. Smith, and R. Crowell, *Solid State Electron.*, **17**, 1217 (1974).
6. J. Reichman and M. Russak, "Photoeffects at Semiconductor-Electrolyte Interfaces," ACS Symposium Series 146, chap. 23, p. 359 (1981).
7. D. Cahen, J. Manassen, and G. Hodes, *Solar Energy Mater.*, **1**, 343 (1979).
8. J. Reichman, *Appl. Phys. Lett.*, **38**, 251 (1981).
9. L. L. Kazmerski, W. B. Berry, and C. W. Allen, *J. Appl. Phys.*, **43**, 3521 (1972).

Thin Film CdSe Electrodes for Backwall Photoelectrochemical Cells

Michael A. Russak and Joseph Reichman*

Grumman Aerospace Corporation, Research Department, Bethpage, New York 11714

Considerable success has been achieved in converting light to electrical energy using single crystal electrodes in photoelectrochemical cells (PEC) with conversion efficiencies as high as 14% being reported (1). However, widespread application of these devices will most likely require the use of thin film polycrystalline or amorphous electrodes in order to minimize their cost. Figure 1 shows two basic thin film PEC designs. The difference between these cells is in the configuration of the semiconductor electrode. In Fig. 1a, defined here as a frontwall cell, the semiconductor film is deposited on an opaque conducting substrate and must be positioned in such a way that the incident radiation can reach the semiconductor electrolyte junction. In this case, a transparent window is necessary in front of the electrode and the light must pass through a layer of electrolyte before it strikes the junction. This can result in a significant reduction in the device conversion efficiency due to the highly absorbing nature of the chalcogenide containing electrolytes used to date in most PEC. In addition, it is necessary to have free flow of electrolyte from the photoactive electrode to the counterelectrode. In this configuration, however, semiconductor films of various thickness and a wide range of substrates can be used. Thin film polycrystalline electrodes for use in frontwall cells have been made with efficiencies in the range of 5-8% using CdSe, GaAs, and CdSe-CdTe solid solutions (2-4). Figure 1b, defined as a backwall cell, employs a semi-transparent photoactive electrode that allows irradiation of the

* Electrochemical Society Active Member.

Key words: CdSe thin film electrodes, backwall illuminated cells, photovoltaic energy conversion.

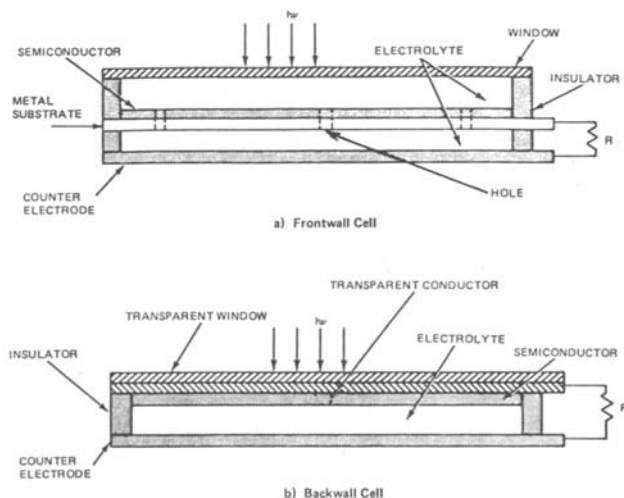


Fig. 1. Thin-film photoelectrochemical conversion cell designs

junction through the semiconductor rather than through the electrolyte, thus eliminating electrolyte absorption. The cell design is also less complex. How-

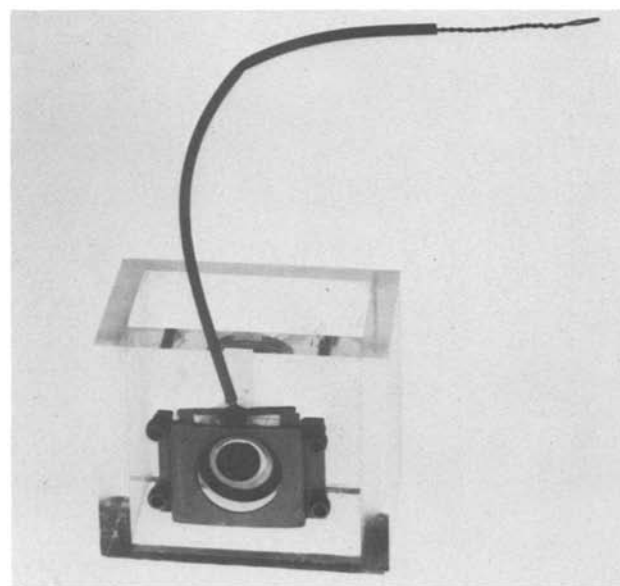
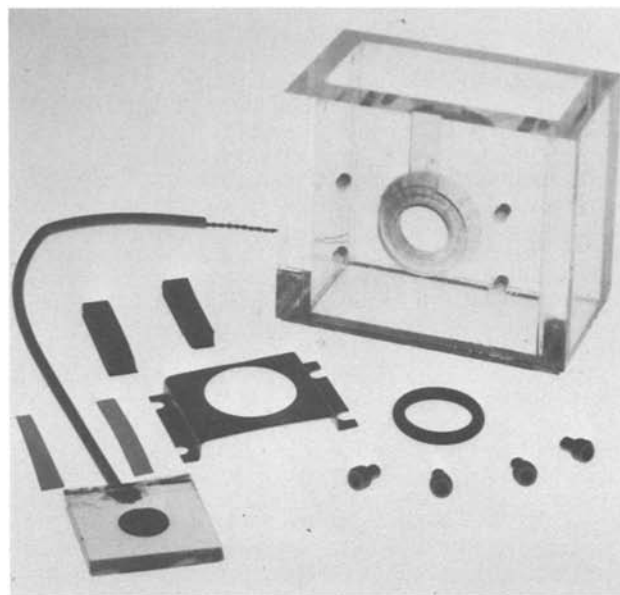


Fig. 2. Cell used for evaluation of backwall illuminated electrodes.

ever, the number of substrate materials is limited due to the transparency requirement. Also, the combination of thin film properties necessary to optimize the performance of such a device is somewhat restricted. It is desirable to have the space charge region extend through the full thickness of the film to promote rapid carrier separation and obtain good collection efficiency (5). In addition, the film thickness should be such that all the incident light of greater than bandgap energy can be absorbed within the film. A calculation of this thickness for CdSe based on the measured values of the absorption coefficient, indicates that, at 500 nm, a film thickness of $0.680 \mu\text{m}$ is sufficient to absorb 99% of the light, whereas, at 700 nm, a thickness of $2.37 \mu\text{m}$ is required. This suggests a film thickness of 2-3 μm to provide an adequate amount of material for the absorption of sunlight. In order to have a space charge layer width of this order, a majority carrier doping density of less than 10^{14}cm^{-3} is necessary (assuming a voltage drop of 0.7V across the space charge layer).

The CdSe electrodes discussed here were deposited by the simultaneous vacuum evaporation of Cd and Se from two independently controlled resistive heated boats onto chemical-spray-deposited, halogen-doped, SnO_2 -coated glass slides. The details of the deposition system employed have been given elsewhere (2, 6). The SnO_2 -coated glass had resistivity in the range of $10 \Omega/\text{square}$ and visible transmission of approximately 80%. Backwall electrode performance was tested in a cell specifically designed for this purpose, (see Fig. 2) which allows irradiation of the CdSe through the substrate glass and transparent conductor. This cell design eliminates the electrolyte absorption loss and allows reasonably quick sample change. A platinum counterelectrode and saturated calomel reference electrode were used in a standard potentiostatic arrangement. The light source was a W-I ELH lamp which simulates an AM2 spectral distribution (7). Narrow bandpass filters were used for monochromatic experiments. The electrolyte was aqueous 2.5M Na_2S , 1M S, 1M KOH.

CdSe films deposited with an Se/Cd atomic ratio of 3, subsequently heat-treated at 400°C in air, produced backwall electrodes with power conversion efficiencies greater than 4% at $75 \text{ mW}/\text{cm}^2$, AM2, as shown in Fig. 3. The short-circuit current density, J_{sc} , of $17 \text{ mA}/\text{cm}^2$ is almost at the theoretical limit for a material with $E_g = 1.7 \text{ eV}$ responding to an AM2 spectrum (8). The thickness of this film is $2.5 \mu\text{m}$ (see Fig. 4) so that all the impinging radiation is absorbed within the film. The open-circuit voltage of 0.45V, while far from the theoretical limit, is such that $V_{oc} \times J_{sc}/\text{intensity}$ still results in a maximum efficiency of 10.3% at $75 \text{ mW}/\text{cm}^2$. It is the low fill factor of 0.42 that limits the effi-

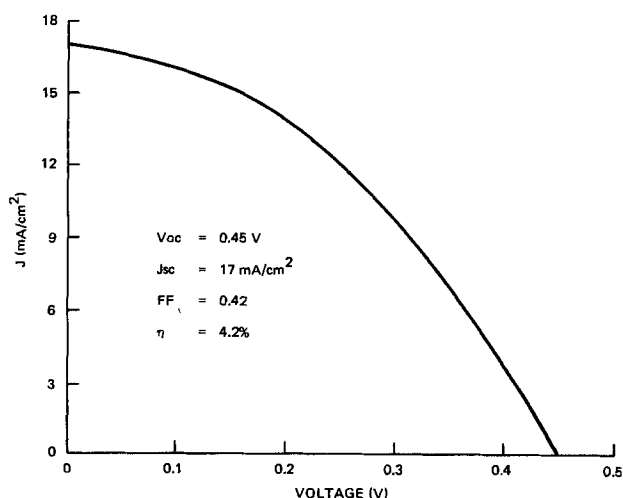


Fig. 3. Current-voltage curve for backwall electrode at $75 \text{ mW}/\text{cm}^2$, AM2 simulation (uncorrected for reflection).

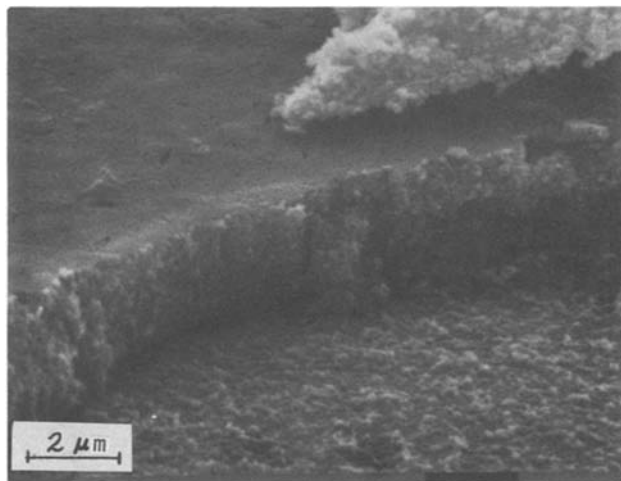


Fig. 4. Microstructure of CdSe film deposited on SnO_2 -coated glass substrate.

ciency of this electrode. The same type of film deposited on a titanium substrate generally has J_{sc} in the range of 12-14 mA/cm^2 , fill factors from 0.55 to 0.65, and V_{oc} from 0.4-0.45 when tested with the same light source.

Hall measurements and direct resistivity measurements on these films (9) indicate the donor densities, N_D , are in the range of 10^{12} - 10^{13}cm^{-3} , majority carrier mobilities, μ , from 10-40 cm^2/Vsec , and resistivities, ρ , from 10^4 to $10^5 \Omega\text{-cm}$. These parameters indicate that the space charge region extends through the entire thickness of the films accounting for the high collection efficiency observed experimentally.

The spectral response and monochromatic I - V behavior of these backwall electrodes were also investigated. The I - V curve for this electrode at 650 nm is shown in Fig. 5. The power conversion efficiency is 9.5% and is limited by a fill factor of 0.52. The maximum $J_{sc} \times V_{oc}$ efficiency is 18.4%. The internal quantum efficiency at short-circuit conditions is 0.95.

The spectral response of another electrode of this type is shown in Fig. 6 (corrected for reflection losses). The response is quite flat and very near unity, with only a small falloff in the blue. This small decrease in quantum efficiency at short wavelengths is attributed to the electric field at the SnO_2 -CdSe contact. Since the contact is ohmic, an accumulation layer exists in the CdSe film. The resultant electric field would therefore tend to oppose diffusion of holes to this interface and

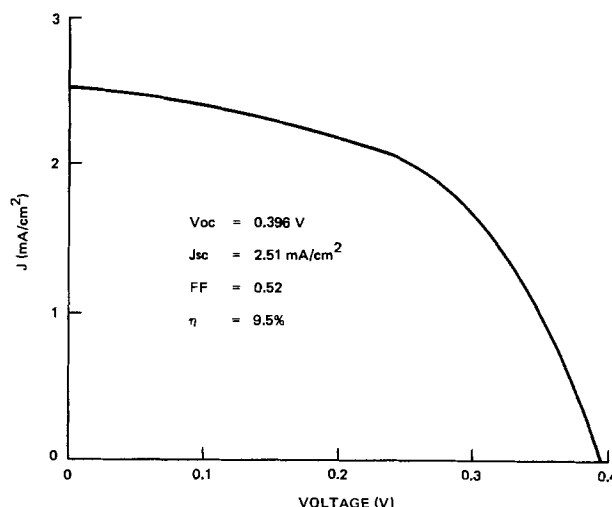


Fig. 5. Monochromatic current-voltage curve for backwall electrode, 650 nm light, $5.3 \text{ mW}/\text{cm}^2$, uncorrected for reflection.

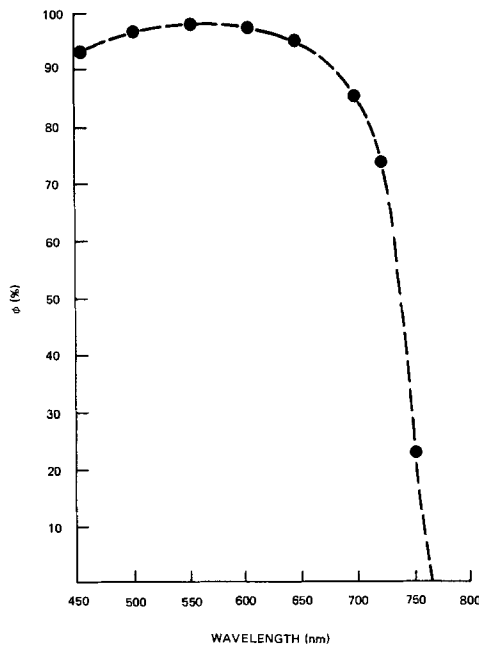


Fig. 6. Internal quantum efficiency vs. wavelength for backwall illuminated electrode.

thereby minimize recombination losses for those carriers generated by the short wavelength radiation.

Analysis of the I - V curves at different wavelengths revealed a significant variation in output power parameters, even though the quantum efficiency was fairly constant. These data are summarized in Table I. This variation is due to the difference in penetration depth of each wavelength radiation into the thin film. When the electrode is in forward bias, and the internal electric field reduced, it is less likely for holes generated closer to the ohmic contact by shorter wavelength light to reach the junction region before recombinations than for those holes generated by longer wavelength light nearer the semiconductor electrolyte interface. This effect is reflected in the observed reduction in fill factor in going to shorter wavelength radiation. This is also supported by the fact that increase in quantum efficiency with voltage in reverse bias is greater for the shorter wavelength curves than for the longer wavelength ones, indicating the additional bias is useful in preventing carrier recombination for radiation absorbed further away from the electrolyte junction.

The origin of the low fill factor of these electrodes, compared to the same film deposited on a metallic substrate, is not completely understood. It has been shown that a high series resistance can significantly reduce the fill factor of a solar cell I - V curve and also reduce the J_{sc} (5, 8). Also, series resistance losses have

Table I. Summary of monochromatic I - V parameters for backwall irradiated electrode

| Wave-length (nm) | Intensity (mW/cm ²) | J_{sc} (mA/cm ²) | V_{oc} (V) | FF | η^1 (%) | ϕ^2 (%) |
|------------------|---------------------------------|--------------------------------|--------------|------|--------------|--------------|
| 450 | 1.08 | 0.30 | 0.35 | 0.41 | 4.0 | 93 |
| 500 | 2.28 | 0.73 | 0.39 | 0.46 | 5.7 | 97 |
| 550 | 4.54 | 1.65 | 0.42 | 0.48 | 7.3 | 98 |
| 650 | 7.62 | 3.02 | 0.44 | 0.50 | 8.8 | 95 |
| 700 | 7.26 | 2.85 | 0.44 | 0.50 | 8.6 | 87 |
| 720 | 6.04 | 2.11 | 0.43 | 0.52 | 7.8 | 74 |
| 750 | 5.52 | 0.61 | 0.39 | 0.51 | 2.2 | 23 |

¹ Power conversion efficiency.

² Quantum efficiency.

Table II. Variation of solar cell parameters for electrode of Fig. 3 with light intensity

| Intensity (mW/cm ²) | J_{sc} (mA/cm ²) | V_{oc} (V) | FF | η (%) |
|---------------------------------|--------------------------------|--------------|------|------------|
| 150 | 33.7 | 0.47 | 0.33 | 3.4 |
| 75 | 16.8 | 0.45 | 0.41 | 4.2 |
| 40 | 8.8 | 0.43 | 0.48 | 4.7 |
| 5.4 | 1.3 | 0.41 | 0.51 | 5.0 |

been reported to give rise to a nonlinear J_{sc} vs. intensity plot for CdSe photoanodes on transparent conducting substrates (10). However, for the electrodes evaluated in this work, the J_{sc} was found to increase linearly to a value of 33.7 mA/cm² at 150 mW/cm² yet, the fill factor and therefore the efficiency increases with decreasing intensity as shown in Table II. The calculated voltage drop attributed to the SnO₂ layer under the collection area for this electrode (see Fig. 2 for electrode construction detail) at a current density of 20 mA/cm² is only 0.01V, indicating ohmic losses are not significant. However, this calculation does not take into account any losses that exist outside the collection area, such as those due to the spreading resistance of the SnO₂ or the wire contact resistance. At present, the low fill factor of these electrodes at AM2 conditions is attributed to the increased recombination of carriers generated by the short wavelength light as well as resistive losses due to the electrode configuration employed.

Recently, the fill factor of this type of film has been improved to 0.56 by minimizing the resistive loss outside the electrode active area and photoetching the electrode. As a result, power conversion efficiencies of 6% have been achieved.

Acknowledgment

We wish to acknowledge the technical assistance of C. Creter and J. DeCarlo in gathering the experimental data and J. Havranek in preparing the thin films. This work was supported by SERI under subcontract XP-9-8002-8.

Manuscript submitted Aug. 12, 1980; revised manuscript received March 30, 1981.

Any discussion of this paper will appear in a Discussion Section to be published in the June 1982 JOURNAL. All discussions for the June 1982 Discussion Section should be submitted by Feb. 1, 1982.

Publication costs of this article were assisted by Grumman Aerospace Corporation.

REFERENCES

- R. Noufi and D. Tench, *This Journal*, **127**, 188 (1980).
- M. Russak, J. Reichman, H. Witzke, S. K. Deb, and S. N. Chen, *ibid.*, **127**, 725 (1980).
- W. Johnston, H. Leamy, B. Parkinson, A. Heller, and B. Miller, *ibid.*, **127**, 90 (1980).
- D. Cahen, G. Hodes, and J. Manassen, "Photoeffects at Semiconductor Electrolyte Interfaces," ACS Symposium Series 146, chap. 24, p. 369.
- B. L. Krauter and R. J. Soukup, *J. Appl. Phys.*, **51**, 2914 (1980).
- J. Reichman and M. Russak, *This Journal*, **128**, 2025 (1981).
- K. Yaas and H. Curtis, NASA Report Number NASA TM-X-3059, available from NTIS, Springfield, VA 22151.
- H. J. Hovel, "Semiconductors and Semimetals, Vol. 11: Solar Cells," Academic Press, New York (1975).
- F. Chwang, J. Smith, and R. Crowell, *Solid State Electron.*, **17**, 1217 (1974).
- C. J. Liu and J. H. Wang, *Appl. Phys. Lett.*, **36**, 852 (1980).

Pulsed E-B Apparatus and Annealing of Ion-Implanted Silicon

T. Itoh,* H. Tamura, D. X. Rao, and Y. Ohkubo

School of Science and Engineering, Waseda University, Shinjuku-ku, Tokyo 160, Japan

The pulsed electron beam (PEB) has been recently used to anneal the disorders in ion-implanted semiconductors and to electrically activate the dopant species (1-4). Also, PEB has been applied to make a suitable metal-semiconductor contact (5). At present, there are few reports on the PEB apparatus. We have developed a single pulsed electron beam processing apparatus consisting of a high density electron source operated by means of pulsed He gas discharge and an accelerating diode. We have tried the annealing of arsenic ion-implanted silicon with $1 \times 10^{16}/\text{cm}^2$ at 50 keV to examine the ability of the apparatus.

The Rutherford backscattering (RBS) measurements with 350 keV $^4\text{He}^+$ were used to analyze the crystallinity and the impurity distribution in ion-implanted layers before and after the single PEB irradiation. Electrical properties of the PEB annealed silicon were evaluated by the carrier concentration and the mobility profiles which were obtained by Hall measurements with successive anodic oxidation and stripping.

Apparatus

The working characteristics of our apparatus are as follows: (i) The structure and operation are relatively simple compared with the scanning E-B annealing system (6, 7), (ii) the energy density of E-B can be controlled by the value of a main capacitor and its charging voltage, (iii) the magnitude of the charging voltage is low in contrast to other works (1), and (iv) E-B parameters can be chosen by a working pressure of He and an acceleration voltage.

Figure 1 shows the schematic diagram of the PEB apparatus. The column consists of two sections: an electron source (section A) and an electron accelerating diode (section B). These two sections are separated with a common mesh electrode that acts as an anode for the section A and a cathode for the section B. Carbon was chosen as the cathode electrode because of its thermal stability. To obtain a stable electron beam, a carbon mesh electrode laminated with aluminum was used for the reduction of its electrical resistivity.

The electron source is assembled as follows. A helical tungsten filament mounted on a metal-lid is used for the thermionic electron emitter. The metal-lid is fixed at the top end of a Pyrex tubing of 100 mm in diameter and 200 mm in length, and a metal flange with the mesh electrode is fixed at the bottom end of the tubing. Capacitor C_s ($1.0 \mu\text{F}$) connecting to the electron source is charged to 3-4 kV. The electron accelerating diode consists of the mesh electrode as a cathode and an aluminum pedestal as an anode. The metal flange is isolated from the ground potential by an insulator made of fluorocarbon polymers, and samples are set on the aluminum pedestal with a distance of 20 mm from the mesh electrode. Capacitors C_a ($1.5 \mu\text{F}$) which are composed of three low inductance type capacitors ($0.5 \mu\text{F}$), are charged to 4-15 kV. These three capacitors are arranged around the column, and connected in parallel with a cylindrical electrode to reduce the lead inductance as shown in Fig. 2.

The density of electrons emitted from the W-filament is multiplied by means of He gas discharged in the electron source. The high density electrons propagate into the electron accelerating diode through the

distributed holes in the mesh electrode, so that these electrons are accelerated to sufficient energy for an-

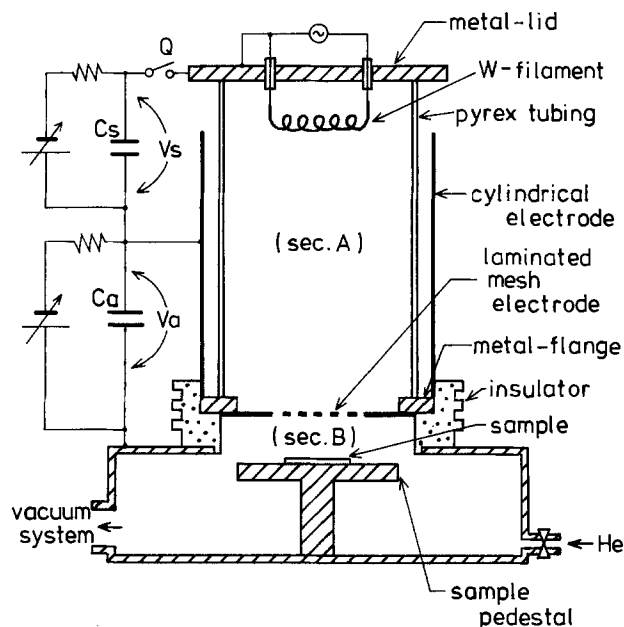


Fig. 1. Schematic diagram of pulsed electron beam apparatus



Fig. 2. Pulsed electron beam apparatus

* Electrochemical Society Active Member.

Key words: pulsed E-B annealing, As implanted Si.

nealing by the electric potential V_a of the capacitors Ca. A mechanical switch Q controls the discharge in the electron source and plays a role of triggering the discharge of the main capacitor.

Experimental and Results

The He pressure P_w and the acceleration voltage V_a are the significant parameters for annealing. Figure 3 shows the suitable working region in these parameters to anneal the arsenic ion-implanted silicon. Arsenic ions were implanted at 50 keV to a dose of $1 \times 10^{16}/\text{cm}^2$ at room temperature into (100) n-type silicon with a resistivity of 60 $\Omega\text{-cm}$. This energy brings the arsenic atoms to a projected range of 322Å and this dose is sufficient to drive the silicon amorphous. After a single PEB irradiation with the parameters shown in Fig. 3 as open circles, the RHEED observations indicated that the implanted layers were singly recrystallized. It is considered that the sufficient energy density to anneal the ion-implanted layers was obtained by taking the parameters below the hatched line in the figure. In all cases, the pulse width determined from the current wave-form measurements was about 1 μsec (FWHM). The width of a pulse is governed mainly by the residual-inductance of the capacitors. The annealed area of 10-20 cm^2 was obtained. Mesa diodes were fabricated to examine the spatial uniformity of the annealed area. The substrates were p-type (100) silicon with a resistivity of 5-8 $\Omega\text{-cm}$. Arsenic ions were implanted at 50 keV to a dose of $1 \times 10^{15}/\text{cm}^2$ into these substrates. Figure 4 shows the diode reverse current vs. the distance from E-B annealed edge. These data indicate that the annealed area is electrically uniform.

Figure 5 shows the energy spectra of 350 keV $^4\text{He}^+$ RBS measurements of as-implanted sample, PEB annealed sample with the parameters at point M shown in Fig. 3 and furnace annealed sample at 1000°C for 30 min. The E-B parameters used here were V_a of 8 kV and P_w of 1×10^{-5} Torr. The minimum yield of the PEB annealed sample was about 5.8%, and this value is slightly higher than that of the bulk silicon. The arsenic yield of the PEB annealed sample detected in

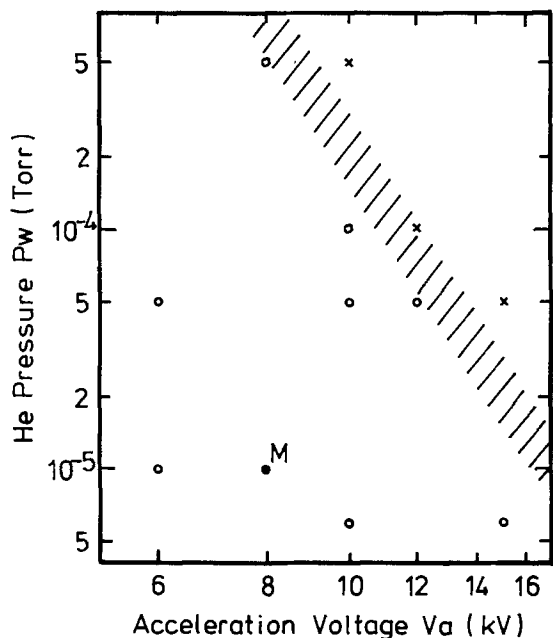


Fig. 3. Suitable working region for E-B parameters of P_w and V_a . Sufficient energy density to anneal ion-implanted silicon was obtained in the region below the hatched line. RHEED observations showed single crystalline pattern after a single PEB irradiation with the parameters shown as open circles (O). Point M (●) denotes the typical parameters of $V_a = 8$ kV and $P_w = 1 \times 10^{-5}$ Torr.

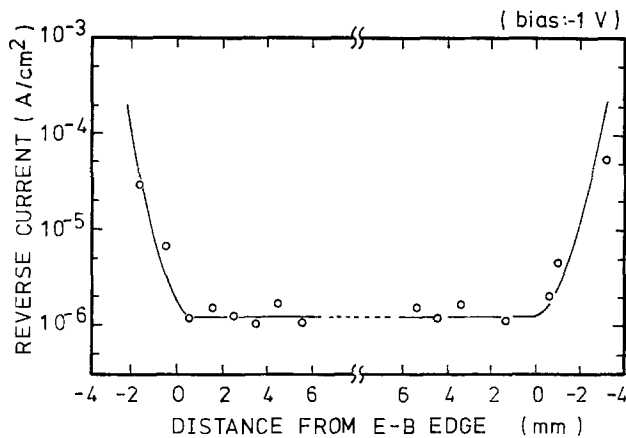


Fig. 4. Electrical uniformity of PEB annealed area. Diode reverse current vs. distance from E-B annealed edge.

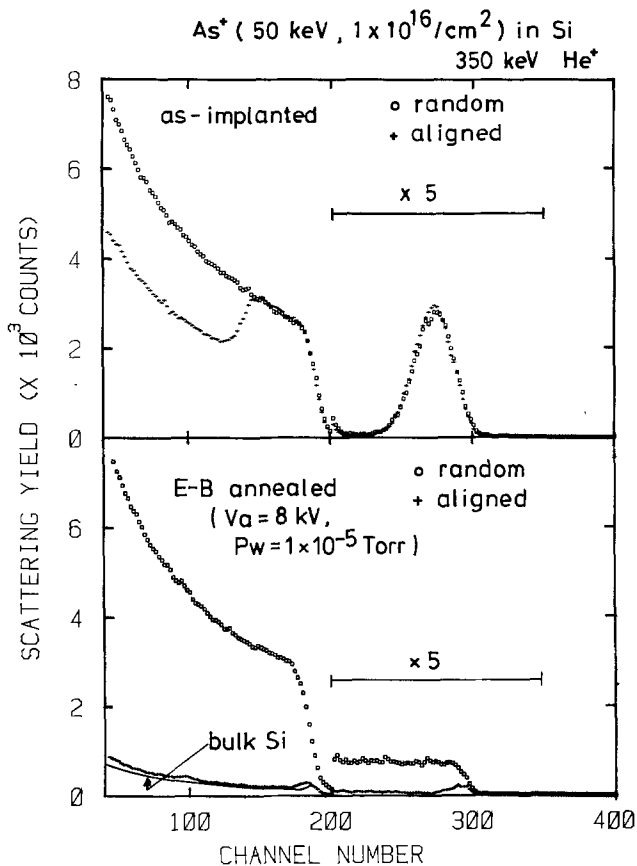


Fig. 5. RBS energy spectra of arsenic ion-implanted (100) silicon before and after PEB irradiation with the parameters at point M shown in Fig. 3. Arsenic ions were implanted at 50 keV to a dose of $1 \times 10^{16}/\text{cm}^2$ at room temperature.

a random direction shows a plateau, which indicates that significant diffusion of arsenic atoms took place. This type of diffusion is said to appear in liquid phase epitaxy (1-3, 8, 9). The arsenic yield ratio of $\langle 100 \rangle$ aligned to random spectra indicates that arsenic atoms more than 80% occupied substitutional lattice sites.

Figure 6 shows the depth profiles of the carrier concentration and the mobility. The profiles were obtained by the Hall measurements by the van der Pauw method with successive anodic oxidation and stripping. The anodic oxidation of silicon was done in a 0.04N solution of KNO_3 in N-methylacetamide (10). A uniform carrier concentration of $3 \times 10^{20}/\text{cm}^3$ was obtained from the surface to the depth of 2000Å. The surface carrier density calculated from this figure was $6.4 \times 10^{15}/\text{cm}^2$. This result indicates that 64% of im-

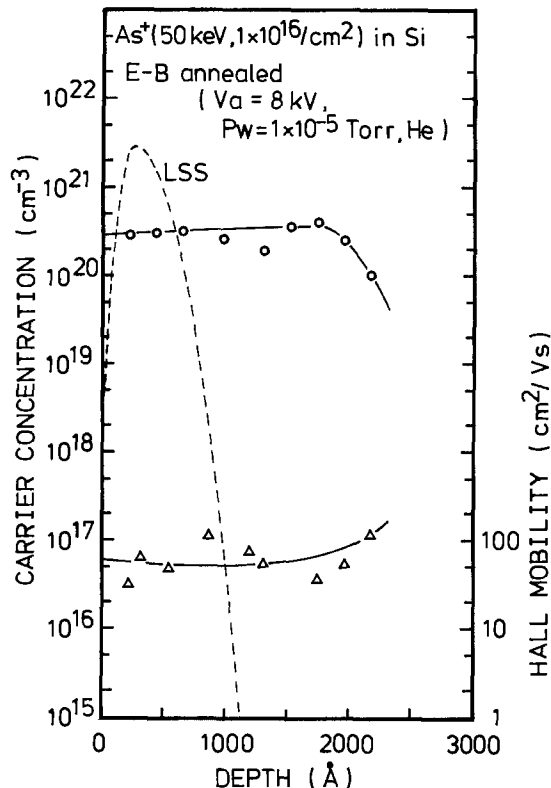


Fig. 6. Carrier concentration (\circ) and mobility (Δ) profiles of arsenic ion-implanted silicon after PEB irradiation with the parameters at point M shown in Fig. 3. As-implanted profile expected from LSS theory is also shown by dashed line.

planted arsenic atoms were electrically activated, and the mobility shows almost the same value as the bulk silicon. The carrier profile shows a redistribution by diffusion of arsenic atoms compared with the theoretical profile expected from the LSS theory (11). This carrier profile is in good agreement with the results of the RBS measurements.

Summary

A low voltage operating PEB apparatus has been developed. The energy density of the electron beam depended strongly on the He pressure and the electron accelerating voltage. Suitable parameters for annealing the ion-implanted silicon were presented. Under the typical condition of $V_a = 8$ kV and $P_w(\text{He}) =$

1×10^{-5} Torr, we performed the annealing of silicon implanted with arsenic ions at $1 \times 10^{16}/\text{cm}^2$ at 50 keV. The ion-implanted layer was recrystallized by a single PEB irradiation, and the minimum yield of 5.8% was indicated from results of RBS measurements. The electrical activation efficiency of 64% was obtained by means of the Hall measurements. The mobility values were almost equivalent with that of the bulk silicon at the same carrier concentration. The redistribution by quick diffusion of arsenic atoms was observed by both measurements, and the redistribution profile suggests that liquid phase epitaxy is the dominant mechanism in these cases.

Acknowledgment

We would like to thank Dr. Y. Yamamoto for useful discussions and encouragement during the course of this experiment.

Manuscript submitted Oct. 6, 1980; revised manuscript received April 3, 1981.

Any discussion of this paper will appear in a Discussion Section to be published in the June 1982 JOURNAL. All discussions for the June 1982 Discussion Section should be submitted by Feb. 1, 1982.

Publication costs of this article were assisted by Waseda University.

REFERENCES

1. A. C. Greenwald, A. R. Kirkpatrick, R. G. Little, and J. A. Minnucci, *J. Appl. Phys.*, **50**, 783 (1979).
2. T. Inada, T. Sugiyama, N. Okano, and Y. Ishikawa, *Electron. Lett.*, **16**, 54 (1980).
3. T. Inada, K. Tokunaga, and S. Taka, *Appl. Phys. Lett.*, **35**, 546 (1979).
4. D. Eirug Davies, J. P. Lorenzo, T. G. Ryan, and J. J. Fitzgerald, *ibid.*, **35**, 631 (1979).
5. J. L. Regolini, T. W. Sigmon, and J. F. Gibbons, Paper 388, p. 981, The Electrochemical Society Extended Abstracts, Los Angeles, California, Oct. 14-19, 1979.
6. J. L. Regolini, J. F. Gibbons, T. W. Sigmon, R. W. Pease, T. J. Magee, and J. Peng, *Appl. Phys. Lett.*, **34**, 410 (1979).
7. R. A. McMahon and H. Ahmed, *J. Vac. Sci. Technol.*, **16**, 1840 (1979).
8. J. C. Wang, R. F. Wood, and P. P. Pronko, *Appl. Phys. Lett.*, **33**, 455 (1978).
9. C. W. White, W. H. Christie, B. R. Appleton, S. R. Wilson, P. P. Pronko, and C. W. Magee, *ibid.*, **33**, 662 (1978).
10. P. F. Schmidt and W. Michel, *This Journal*, **104**, 230 (1957).
11. J. F. Gibbons and S. Mylroie, *Appl. Phys. Lett.*, **22**, 568 (1973).

An Anomalous Effect in Angle Lapping and Staining Ion-Implanted Layers

P. Picco and M. L. Polignano

Divisione MOS, SGS-ATES, 20041 Agrate, Milano, Italy

Techniques for angle lapping and staining ion-implanted layers have recently been reviewed by Wu *et al.* (1).

The interest in these techniques is justified by their usefulness to control semiconductor device fabrication.

In their paper, Wu and co-authors extensively describe the experimental conditions to perform angle lap and stain operations. They claim the reliability of these operations for the determination both of the dop-

ing type of the different layers and of the exact positions of the junctions.

However, they do not mention the possibility of an anomalous effect due to partial compensation near the surface; the appearance of a p-n junction where one does not really exist.

The description of such an effect is the aim of this paper.

Boron-implanted layers were investigated, in view of their use as channel stoppers in MOS circuit technology. 40 KeV boron ions were implanted into 7-10.5

Key words: staining, angle lapping, ion implantation, junction depth.

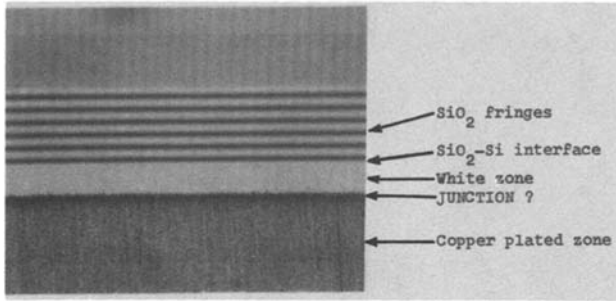


Fig. 1. An example of staining delineation obtained after the process described in the text. The picture has been taken in Na light (fringe distance $\approx 2000\text{\AA}$). Implanted dose = 10^{13} cm^{-2} . All the implanted samples had this appearance.

$\Omega\text{-cm}$, 100 oriented, phosphorus-doped silicon slices, through a 500\AA thick SiO_2 layer (2).

After implantation, without removing the oxide, the slices were first annealed in an inert atmosphere (N_2) for 30 min at 920°C ; then a diffusion was carried out in an oxidizing ambient at the same temperature. The furnaces (normally employed for gate oxidation and successive annealing in device production) were tested for contamination before the described operations.

The behavior of junction depth (x_j) and sheet-resistance (V/I) with respect to the dose was studied to characterize the process. Junction depths were determined following Wu and co-authors (1), using copper sulfate solution.

An example of the staining delineation is shown in Fig. 1 (it corresponds to one of the lowest implanted doses). All the stained samples had this appearance, where the width of the white zone (see Fig. 1) increased with increasing dose. V/I was determined with a four-point probe, at several different low currents ($5\text{-}100\ \mu\text{A}$), in the dark (3, 4). It was found to be both uniform throughout the slice and independent of both direction and magnitude of the current.

Contradictory results were, however, observed: x_j monotonically raised with implanted dose, as expected, but V/I raised too (see Table I; the results of V/I are more widely discussed later).

These results can be explained as follows. The segregation of implanted boron into the growing oxide is so high that the remaining implanted boron in the silicon is not sufficient to completely compensate the substrate doping (such an effect is enhanced by phosphorus accumulation near the surface during oxidation). There is, however, a sufficient photovoltage due to the band bending under illumination, that the reaction



can take place in the noncompensated region of the lapped area. The typical staining delineation of a p-n junction is then observed, as shown in Fig. 1, even if the whole silicon slice is still the same type as before.

The accuracy of this hypothesis is demonstrated by spreading resistance measurements on some samples, whose results are shown in Fig. 2. Our hypothesis is further supported by the behavior of V/I in a wider dose interval, shown in Fig. 3.

Table I. Sheet resistivity and junction depth values after diffusion in oxidizing ambient (final oxide thickness = $1.3\ \mu\text{m}$)

| Dose (B atoms/ cm^2) | $V/I\ (\Omega)$ | $x_j\ (\mu\text{m})$ (determined by staining) |
|--------------------------------|---------------------------|---|
| 5×10^{12} | 35 ± 2 | 0.26 |
| 10^{13} | 150 ± 50 | 0.44 |
| 5×10^{13} | $(2 \pm 0.5) \times 10^3$ | 0.68 |

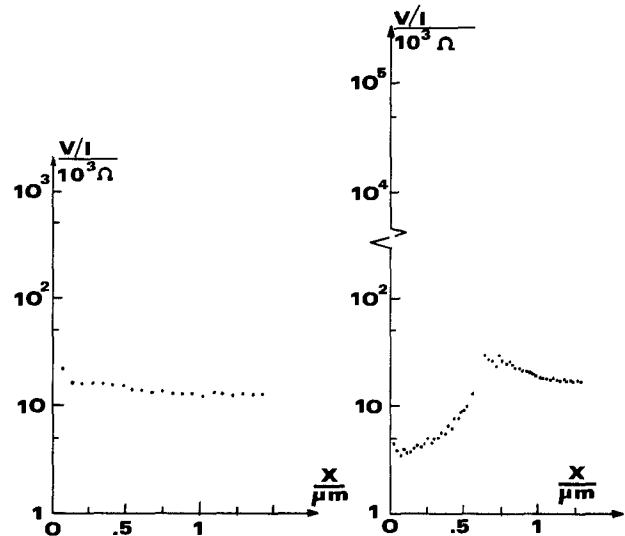


Fig. 2. Spreading-resistance measurements on samples implanted with different doses. (a) $Q = 10^{13}\text{ cm}^{-2}$ (the same sample as in Fig. 1); (b) $Q = 10^{14}\text{ cm}^{-2}$.

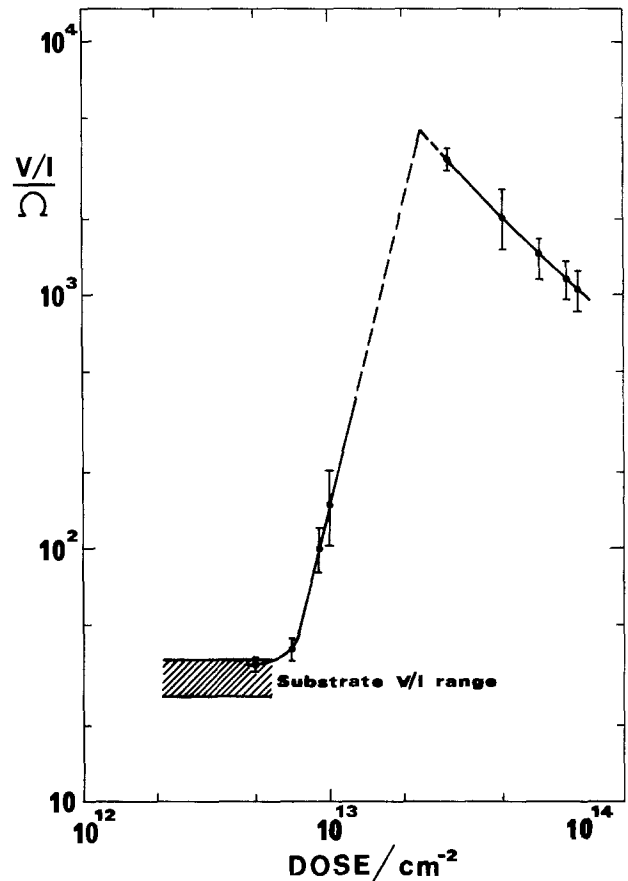


Fig. 3. V/I dependence on implanted dose after the process described in the text.

A critical implant dose \bar{Q} exists; for $Q < \bar{Q}$, V/I increases from the unimplanted substrate value, while for $Q > \bar{Q}$ it regularly decreases. This increase is first of all due to carrier compensation. This effect increases in proportion to the dose $-V/I \propto Q$. Actually, $V/I \propto Q^\alpha$ ($\alpha \approx 4$); this effect can be due to the screening effect of the compensated layer on the more conductive substrate. The decrease ($V/I \propto Q^{-1}$) is the usual one occurring when carriers are added to a conductive layer. In other words, for $Q < \bar{Q}$ the formation of the junction is only apparent, while for $Q > \bar{Q}$ the junction

truly exists. Our value for \bar{Q} ($\approx 2 \times 10^{13} \text{ cm}^{-2}$) is consistent with boron segregation and diffusion data given in the literature (6, 7).

The behavior shown in Fig. 3 can be found every time boron is implanted (in low dose) and diffused into an n-type substrate. When an n-species is implanted on a p-substrate, the described effect ought to occur at much lower doses, because of the opposite roles played by dopant segregation.

In conclusion, we have described an effect that may often occur when low dose boron implantations are made into an n-type substrate. We have described its appearance after angle lapping and staining operations, and its consequences from an electrical point of view. In this case an angle lap and stain operation, as described by Wu *et al.*, is not reliable to correctly identify the layers.

Generally speaking, then, if the doping type of the layer investigated by lapping and staining techniques is not *a priori* known, additional electrical tests must be performed to correctly identify the layers.

Manuscript submitted April 29, 1980; revised manuscript received Oct. 14, 1980.

Any discussion of this paper will appear in a Discussion Section to be published in the June 1982 JOURNAL. All discussions for the June 1982 Discussion Section should be submitted by Feb. 1, 1982.

Publication costs of this article were assisted by SGE-ATES.

REFERENCES

1. C. P. Wu, E. C. Douglas, C. A. Mueller, and R. Williams, *This Journal*, **126**, 1982 (1979).
2. J. F. Gibbons, W. S. Johnson, and S. W. Mylroie, "Projected Range Statistic," Dowden, Hutchinson & Ross, Inc., Stroudsburg, PA (1975).
3. L. H. Garrison, *Solid State Technol.*, **9**, 47 (1966).
4. 1978 Annual Book of ASTM Standard, Part 8, p. 412.
5. D. H. Dickey and J. R. Ehrstein, *Nat. Bur. Stand. Spec. Pub.*, 400-48 (1979).
6. H. G. Lee, R. W. Dutton, and D. A. Antoniadis, *This Journal*, **126**, 2001 (1979).
7. D. A. Antoniadis, A. G. Gonzales, and R. W. Dutton, *ibid.*, **125**, 813 (1979).



Phosphorus Silica Glass as Dopant Source

II. Validity of the Etch Rate Datum

M. L. Polignano, P. Picco, and G. F. Cerofolini

SGS-ATES, 20041 Agrate, Milano, Italy

In a previous paper (1) it was shown that simple profiles, such as Gauss or erfc, cannot be used to describe phosphorus diffusion from highly-doped phosphorus silica glass (PSG). This conclusion was based on the difference between the amounts per unit area as computed from V/I and x_j data and the amounts Q_{Si}^{diff} diffused from PSG as measured by etch rate. This difference was ascribed by us to a complex profile (plateau, kink, tail), though a referee pointed out that "it could equally be argued that the latter datum may be suspect".

To free this datum from any flaws, we have measured the amount diffused into silicon by two independent methods: neutron activation analysis followed by a measurement of β ray activity, and differential resistivity and Hall mobility.

For the analysis we choose the sample diffused at 940 °C for 2 h 15 min in N_2 atmosphere. The amount diffused is given by

$$Q_1^{Si} = (5.1 \pm 0.5) \cdot 10^{15} \text{ cm}^{-2}$$

when evaluated at the Si-PSG interface, and

$$Q_2^{Si} = (5.8 \pm 0.6) \cdot 10^{15} \text{ cm}^{-2}$$

when evaluated at the PSG surface.

Because of the etch-rate procedure, the datum Q_2^{Si} seems more reliable than the corresponding datum Q_1^{Si} .

Within the experimental error $Q_1^{Si} = Q_2^{Si}$ and this result is confirmed by other measurements on samples diffused at 1000 °C and 1050 °C.

The neutron activation analysis was carried out by M. Gallorini (CNR - Center for Radiochemistry and Activation Analysis, Pavia). The sample was irradiated in the central thimble facility of the TRIGA Mark II Research Reactor of the University of Pavia for 10 h; in this position the nominal neutron flux is $9 \cdot 10^{12} \text{ cm}^{-2} \text{ s}^{-1}$. The subsequent β ray activity was monitored by a 2π Geiger counter previously calibrated with silicon samples with the same geometry implanted with several amounts of ^{31}P : $3 \cdot 10^{15}$, $5 \cdot 10^{15}$, $8 \cdot 10^{15} \text{ cm}^{-2}$. The analysis gave the following result:

$$Q_{NAA}^{Si} = (6.4 \pm 0.4) \cdot 10^{15} \text{ cm}^{-2}$$

where the reported error is only due to the statistical fluctuations of the number of counts. This datum is an overestimate of Q^{Si} because of the phosphorus doping of the slice back due to P_2O_5 evaporated during the heat treatment.

Finally, an underestimate of Q^{Si} can be obtained by measuring the amount of electrically active phosphorus atoms diffused into silicon.

This measurement was carried out by M. Finetti and S. Solmi (CNR - Istituto LAMEL, Bologna) by determining differential resistivity and Hall mobility and gave the following result:

$$Q_{act}^{Si} = (5.1 \pm 0.5) \cdot 10^{15} \text{ cm}^{-2}.$$

This value is an underestimate of Q^{Si} because phosphorus atoms may be electrically inactive in the form of interstitials, negatively charged E centers and SiP precipitates.

Keywords: diffusion, junction, resistivity

The situation is summarized in the following table that confirms the validity of the etch rate datum:

| Method | $Q^{\text{Si}} / 10^{15} \text{ cm}^{-2}$ |
|-------------|---|
| Electrical | $\geq 5.1 \pm 0.5$ |
| Etch rate 1 | 5.1 ± 0.5 |
| Etch rate 2 | 5.8 ± 0.6 |
| NAA | $\leq 6.4 \pm 0.4$ |

Reference

(1) M. L. Polignano, P. Picco and G.F. Cerofolini, This Journal 127, 2734 (1980).

A last remark: reference (1) contains two typographical errors.

The first formula of scheme 1 reads

$$Q = C_0 \sqrt{\pi D t} ,$$

and eq. 3 reads

$$C_0 = n_s (1 + 2.04 \cdot 10^{-41} n_s^2)$$

These errors did not affect the computations therein.

Manuscript received June 8, 1981.

Publication costs of this article were assisted by SGS-ATES.

Direct Writing of Refractory Metal Thin Film Structures by Laser Photodeposition

D. J. Ehrlich,* R. M. Osgood, Jr., and T. F. Deutsch

Lincoln Laboratory, Massachusetts Institute of Technology, Lexington, Massachusetts 02173

We have recently described a technique for high-resolution, one-step fabrication of thin-film structures using UV laser photodeposition (1,2). This technique, which makes use of near-ambient-temperature photochemical reactions, provides a means for maskless direct writing of thin-film structures for integrated optics and microelectronics. In this note, we describe results showing that micrometer-wide metal lines can be deposited directly by photodissociation of metal carbonyls, thus showing that the process can be used for deposition of such important refractory metals as Fe, Cr and W. One-step maskless deposition of these refractory metals is important in such diverse microfabrication processes as photolithographic-mask repair or direct writing of silicides and diffused integrated optical waveguides.

UV laser photodeposition requires that the carrier gas have a dissociative continuum extending into the range of available UV laser wavelengths. In the case of many metal carbonyls, molecular fragmentation begins to occur in the near UV at wavelengths greater than 300 nm, although, at least for the longer wavelengths, only one CO ligand is removed after single-photon absorption. As a result, at low laser powers and long laser wavelengths subsequent radiative or collisional events (3,4) are required to completely strip the remaining ligands and release metal atoms from gas-phase molecules.

During the course of our experiment, several laser wavelengths and carbonyl compounds were investigated. Both pulsed (10 nsec) excimer lasers at 248 and 193 nm and a cw, 257-nm, frequency-doubled, Ar-ion laser were used to successfully obtain deposition. The measurements described below were made using the 257-nm beam. Large-area cw photodeposition has also been reported using an ion laser at wavelengths near 350 nm (5).

Key words: Deposition, Lasers

*Electrochemical Society Active Member.

The photodeposition apparatus has been described in detail elsewhere (1,2). Photodeposited lines were "written" by translating a 1-cm-long gas cell, containing the substrate, in a plane perpendicular to the optical axis. The 257-nm beam was focused to a 2.5- μm spot size with a multi-element 3-cm-focal-length lens. The substrates used were Pyrex, fused silica and Si.

Three metal carbonyls $\text{Fe}(\text{CO})_5$, $\text{W}(\text{CO})_6$ and $\text{Cr}(\text{CO})_6$ were investigated; the gas pressure of $\text{Fe}(\text{CO})_5$ was adjusted to ~ 0.5 Torr so that the optical absorption length at 257 nm was ~ 7 cm. The pressures of $\text{W}(\text{CO})_6$ and $\text{Cr}(\text{CO})_6$ were fixed at the room-temperature vapor pressures by simply placing a several-milligram carbonyl crystal in the sample cell. No attempt was made to obtain higher pressures for the latter two compounds by heating the cell, although this would have increased the deposition rates.

Micrometer-scale resolution was obtained in photodeposits from all three gases. Figure 1 shows a series of 2.5- μm -wide

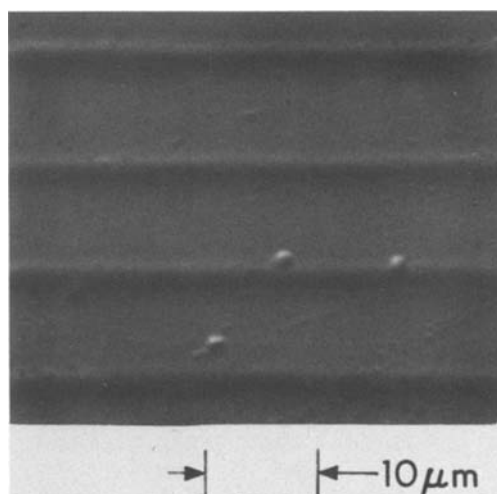


Figure 1. Optical micrograph of tungsten lines on Pyrex produced by single 0.9 $\mu\text{m}/\text{sec}$ scans at a 257-nm power of 0.9 kW/cm^2 .

tungsten features which were made on a quartz substrate. The line width is determined by the laser spot size at the surface and, based on experience with the alkyls, tighter focusing will undoubtedly yield smaller line widths. With $\text{Fe}(\text{CO})_5$, a particulate background, which extended many beam widths away from the central deposit, was sometimes produced. As is shown in Fig. 2, this material consisted of small crystallites; it apparently arises from a gas-phase reaction followed by homogeneous nucleation of the photoproducts occurring at many beam diameters away from the substrate surface. It was found that the amount of this particulate could be reduced to levels undetectable under the optical microscope by reducing the carbonyl dissociation rate per unit volume. This reduction can be accomplished through lowering the laser intensity or $\text{Fe}(\text{CO})_5$ gas pressure; background deposits can also be reduced by the addition of an inert buffer gas such as He or Ar. In the case of $\text{Cr}(\text{CO})_6$ and $\text{W}(\text{CO})_6$, background deposits were never a serious problem.

The relative metal deposition rate was determined by measuring the rate of change in the attenuation of the UV deposition beam. Film thicknesses were estimated from the measured attenuation via the known optical constants of the metals, a procedure shown to be accurate within a factor two in studies of Cd and Zn deposition. Fig. 3 displays the variation of deposition rate versus laser intensity for $\text{Fe}(\text{CO})_5$ and $\text{W}(\text{CO})_6$. Both compounds show a linear dependence of deposition rate on laser intensity at laser intensities less than 200 W/cm^2 . This linearity indi-

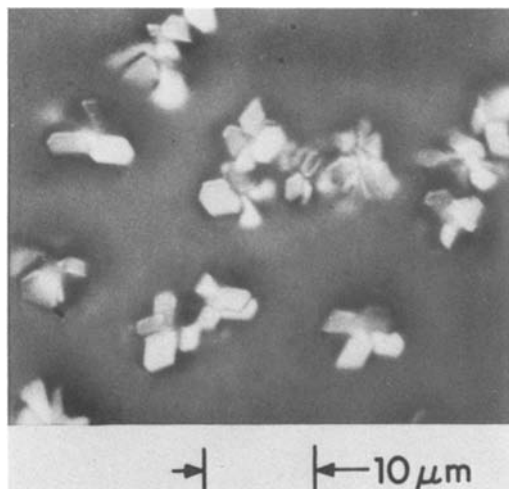


Figure 2. Optical micrograph of the crystalline line deposit from the gas-phase reaction in $\text{Fe}(\text{CO})_5$.

cates that the rate limiting step in the deposition is a single-photon-initiated photochemical reaction. In this low-power linear regime the relative Fe and W deposition rates are approximately in the ratio of the vapor-phase carbonyl absorption strengths at 257 nm. Above 200 W/cm^2 the $\text{Fe}(\text{CO})_5$ rate exhibits a sharp nonlinear increase or "runaway". In this intensity regime the amount of particulate deposit is large and the $\text{Fe}(\text{CO})_5$ gas-depletion rate is rapid. We believe that above the threshold intensity a gas-phase chain reaction is initiated. Evidence of such a reaction has also been seen in the case of pulsed deposition. As suggested above, the onset of this reaction can be controlled by a variation in $\text{Fe}(\text{CO})_5$ and buffer-gas pressure, and UV-laser intensity. However, particulate formation presently limits the Fe deposition rate.

The direct writing of high resolution structures by laser photochemical techniques is of particular importance as a potential means to correct faults or otherwise alter microcircuitry without the use of photolithography. Specifically the photodeposition of refractory metals discussed here provides a means for one-step fabrication of doping (6) and alloying (7) patterns. For example, tungsten-silicide conductors can be written by the technique of Ref. 6. Similarly, photodeposition of Ni and Fe followed by subsequent thermally-activated diffusion into the substrate can enable one to write an optical-waveguide doping pattern directly in LiNbO_3 . Relatively slow rates of deposition are useful for these applications since they require small amounts of atomic

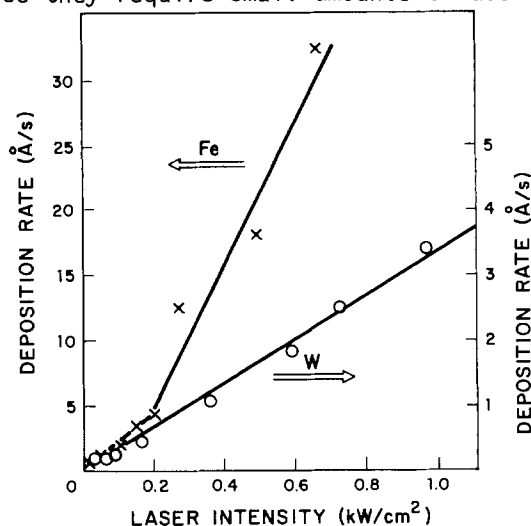


Figure 3. Deposition rate versus laser intensity for $\text{Fe}(\text{CO})_5$ at 0.5 Torr and $\text{W}(\text{CO})_6$ at 0.2 Torr. The substrate is SiO_2 .

dopants. Our results show, however, that an improvement in rate is necessary for applications involving rapid deposition of thick metallic films. Such accelerated rates can be obtained with the use of higher carbonyl pressures in combination with gas diluents, or by the use of a shorter wavelength cw laser.

We would like to acknowledge the important technical contributions of D. Sullivan and B. Duquette to this project.

This work was supported by the Defense Advanced Research Projects Agency and the Department of the Air Force, in part under a specific program sponsored by the Air Force Office of Scientific Research.

REFERENCES

1. T. F. Deutsch, D. J. Ehrlich and R. M. Osgood, Jr., *Appl. Phys. Lett.* 35, 175 (1979).
2. D. J. Ehrlich, R. M. Osgood, Jr. and T. F. Deutsch, *IEEE J. Quantum Electron.*, QE-16, 1233 (1980).
3. Z. Karney, R. Naaman and R. Zare, *Chem. Phys. Lett.* 59, 33 (1978).
4. J. T. Yardley, B. Gitlin, G. Nathanson and A. Rosan, *J. Chem. Phys.* 74, 370 (1981).
5. G. Collins and coworkers (to be published).
6. D. J. Ehrlich, R. M. Osgood, Jr. and T. F. Deutsch, *Appl. Phys. Lett.* 36, 916 (1980).
7. D. J. Ehrlich, R. M. Osgood, Jr. and T. F. Deutsch, *Appl. Phys. Lett.* 38, 399 (1981).

Manuscript received April 1, 1981.

Publication costs of this article were assisted by MIT.

Semiconductor Electrodes

XXXIX. Techniques for Stabilization of n-Silicon Electrodes in Aqueous Solution Photoelectrochemical Cells

Fu-Ren F. Fan,* Bob L. Wheeler,* and Allen J. Bard*

Department of Chemistry, The University of Texas at Austin, Austin, Texas 78712

and Rommel N. Noufi*

Solar Energy Research Institute, Photo Voltaic Division, Golden, Colorado 80401

A number of different approaches have been used in the stabilization of small band gap n-type semiconductors against photocorrosion in photoelectrochemical (PEC) cells. Such stabilization is necessary in the design of practical cells for conversion of solar energy to electricity, and is of critical importance in photoelectrosynthetic systems where the photogenerated holes produce species (e.g. O_2 , Cl_2) at quite positive potentials at the semiconductor surface. 1) One approach involves the utilization of thin films of metals (1) or semiconductors (2) to protect the surface. For example, n-GaAs electrodes can be stabilized in a solution of Fe(II) EDTA by a thin ($\leq 60 \text{ \AA}$) film of gold (3). 2) Use of nonaqueous solvents (4) in PEC cells has been shown to aid in the stabilization of the semiconductor electrode by decreasing the extent of solvation of the oxidation products. A similar approach involves the use of concentrated electrolytes in aqueous solutions. Wrighton and co-workers (5) have recently demonstrated that n-MoSe₂ and n-MoS₂ electrodes are stable in concentrated LiCl solutions even in the presence of chlorine evolution. 3) The deposition of polymer layers on the semiconductor surface can also decrease photocorrosion. Noufi and co-workers (6) have described the stabilization of n-GaAs and n-Si by the electrodeposition of polypyrrole films on the surface.

We demonstrate here that by combining these approaches even better stabilization can be accomplished and describe the photo-oxidation of Fe^{2+} at n-Si electrodes covered by thin gold and thicker polypyrrole film and immersed in a concentrated electrolyte aqueous solution.

Electrodes were fabricated from n-Si single crystals (0.4 to 0.6 Ω cm) donated by Texas Instruments. Ohmic contacts were made with In-Ga alloy. They were connected to a copper wire with silver epoxy cement. The crystals were mounted in a glass tube with all sides insulated with 5 min epoxy and covered by silicone rubber sealant leaving an area of 0.2-0.5 cm^2 exposed. The surfaces of some crystals were polished with sand paper (600 grit), followed by etching in conc. HF for 15-20 sec. This pretreatment gave no improvement, compared with these unpolished electrodes, in the adhesion of the polypyrrole films and in the stability of the polypyrrole-covered n-Si electrodes. Immediately prior to electrodeposition of polypyrrole or Au, the electrodes were etched, if not otherwise mentioned, with an etchant containing HNO_3 :HF:acetic acid (3:3:1) and bromine (one drop of Br_2 per 100 ml of solution) for 10-15 sec and then with conc. HF for 15-20 sec. This etching procedure produced more efficient etching than that simply with conc. HF. The electrodes were then rinsed thoroughly with water, methanol and acetonitrile.

The electroplating of Au on n-Si was carried out at -1.6 V vs. SCE from a gold plating solution that was prepared by mixing 30 ml of VIGOR fine gold plating solution (Vigor Co. New York, NY) with 20 ml of 2.5 M NaCN solution. The polypyrrole films were synthesized potentiostatically (0.75 V vs. SCE) with the electrode surface simultaneously illuminated with the red light ($> 590 \text{ nm}$, 100-150 mW/cm^2) from a 450 W Xe lamp. The solutions used in this electrodeposition, $CH_3CN/0.1 \text{ M}$ tetra-n-butylammonium BF_4^- , were prepared as reported by Noufi et. al. The thicknesses of the polypyrrole and the Au films were estimated from the charge measured during electrodeposition, as discussed by Noufi et. al. (6).

The PEC behavior of naked or modified n-Si electrodes were compared in three different redox solutions: (A) 0.5 M $FeSO_4$ and 0.15 M $Fe_2(SO_4)_3$ in 0.5 M H_2SO_4 ; (B) 0.15 M $FeSO_4$ and 0.15 M $Fe_2(SO_4)_3$ in 0.1 M Na_2SO_4 at pH 1; (C) 0.5 M $FeCl_2$, 0.15 M $FeCl_3$ and 1 M HCl in 11 M LiCl.

For comparison, the light source used in all experiments, if not otherwise mentioned, was a sunlamp, which was separated from the PEC cell by a water IR filter of path length $\sim 14 \text{ cm}$. The light intensity impinging on the window of the PEC cell was 41 mW/cm^2 . The stability of the photoelectrodes was tested here based on two criteria: (A) constant

steady-state photocurrent vs. time of illumination at a load resistance of $10\ \Omega$ and (B) constant fill factor (f.f.) and onset photopotential (V_{on}) (or invariant shape of the photovoltammetric curve) with time of illumination.

The photocurrents of naked n-Si photoelectrodes under the illumination with a light intensity of $41\ \text{mW}/\text{cm}^2$ decayed to small values ($< 20\ \mu\text{A}/\text{cm}^2$) within three potential scan cycles between -0.2 and $0.7\ \text{V}$ vs. SCE at $100\ \text{mV}/\text{sec}$ in solution (A), (B), or (C). The attachment of polypyrrole film ($\sim 3500\ \text{\AA}$) on n-Si electrodes did, as reported by Noufi et al. (6b), decrease the rate of photodegradation of n-Si electrodes in both electrolyte solutions (A) and (B). As shown in Fig. 1(A), the photoelectrodes still showed fairly ideal photovoltammetric curves even after ten potential scan cycles between -0.2 and $0.7\ \text{V}$ vs. SCE. However, the V_{on} shifted in a positive direction with scanning. The photocurrent (through a load resistance of $10\ \Omega$) produced by a PEC cell, composed of a polypyrrole coated single crystal n-Si photoelectrode and a Pt counter electrode in solution (A) or (B), decayed continuously with time, indicating the occurrence of slow passivation of the electrode even under these conditions. (See also curve a in Fig. 2.)

By the addition of $11\ \text{M}$ LiCl to the redox solution (solution C) the suppression of the anodic photodegradation of the photoelectrodes was further improved. As shown in curve b of Fig. 2, the photocurrent decayed initially and then reached a steady state value ($2.1\ \text{mA}/\text{cm}^2$) after 2-3 hrs upon continuous illumination with a light intensity of $41\ \text{mW}/\text{cm}^2$. Parallel to this behavior, the photovoltammetric curves changed continuously during the first 2-3 hrs of illumination and then reached a steady state. (See Fig. 1(B).) The drawn-out character of the steady state photovoltammetric curves shown in curve d of Fig. 1(B) suggests that an insulating layer was formed on the n-Si surface or that the polypyrrole film was photodegraded during the first 2-3 hrs of illumination. The results shown in the following experiments involving a gold underlayer favor the first possibility.

The third type of photoelectrode was prepared by electroplating $10\text{-}20\ \text{\AA}$ of Au on n-Si and then overlaying $\sim 3300\ \text{\AA}$ of polypyrrole on the Au photoelectrochemically. This type of electrode has been tested in solution (C). Very stable photocurrent and photovoltammetric curves were obtained with extended time of illumination. As shown in Fig. 1(D), the fill factor and the onset photopotential were only slightly changed after illumination with $41\ \text{mW}/\text{cm}^2$, giving a steady state photocurrent

density of $3.1\ \text{mA}/\text{cm}^2$ at a load resistance of $10\ \Omega$ for more than 48 hrs. Only a slight decay of the photocurrent was observed, even in the first 2-3 hrs of illumination (see wave c in Fig. 2), indicating that the $10\text{-}20\ \text{\AA}$ of Au underlayer together with the polypyrrole coating suppresses the photodegradation of the n-Si electrodes quite effectively. However, the $10\text{-}20\ \text{\AA}$ of Au layer alone could not stabilize the n-Si electrode even in solution (C).

Under a light intensity of $41\ \text{mW}/\text{cm}^2$, a PEC cell composed of one of the third type of photoelectrodes and one Pt counter electrode in solution (C) gave a short-circuit photocurrent density of $3.5\ \text{mA}/\text{cm}^2$, a fill factor of 0.65 and an open-circuit photovoltage of $0.40\ \text{V}$, corresponding to a power conversion efficiency of 2.3%. Under illumination with a stronger light intensity ($150\ \text{mW}/\text{cm}^2$ from a tungsten-halogen lamp), the photocurrent at a load resistance of $10\ \Omega$ decayed very slowly with time ($\sim 10\%$ decrease of the initial photocurrent, $12\ \text{mA}/\text{cm}^2$, after the first 8-hr illumination and 5% more decrease after the second 8-hr illumination). The decay rate of the photocurrent increased with an increasing temperature of the PEC cell.

In conclusion, polypyrrole films on a metal underlayer on n-Si photoelectrodes substantially improves their stability against photodegradation in an aqueous electrolyte containing $\text{Fe}^{2+}/\text{Fe}^{3+}$ couple. The addition of $11\ \text{M}$ LiCl to the solution further improves the suppression of the anodic photodegradation. The increased stability can be attributed to the following: 1) The highly concentrated LiCl solution substantially decreases the activity of H_2O thus decreasing its reactivity with the electrode surface (5). 2) Li^+ and/or Cl^- may also diffuse into the interstitial regions of the polypyrrole film and decrease penetration of water. 3) Both the gold and polypyrrole serve to remove photo-generated holes rapidly from the silicon surface before degradation occurs. In this way, they are analogous to stabilizing solution redox species (e.g. Se^{2-}) which are rapidly oxidized preferentially. 4) The gold layer improves the adhesion of the polypyrrole to the Si surface and blocks pinholes in the film.

Since the polypyrrole film is highly colored, it blocks some of the light impinging on the electrode surface and thus decreases the efficiency. Improvements should be possible by optimizing the metal and polymer layer thicknesses and by investigating electrolytes other than the $\text{Fe}^{3+}/\text{Fe}^{2+} - \text{LiCl}$ systems to improve both the solar energy conversion efficiency and the stability.

Acknowledgment - This work was supported by a grant from the Solar Energy Research Inst.

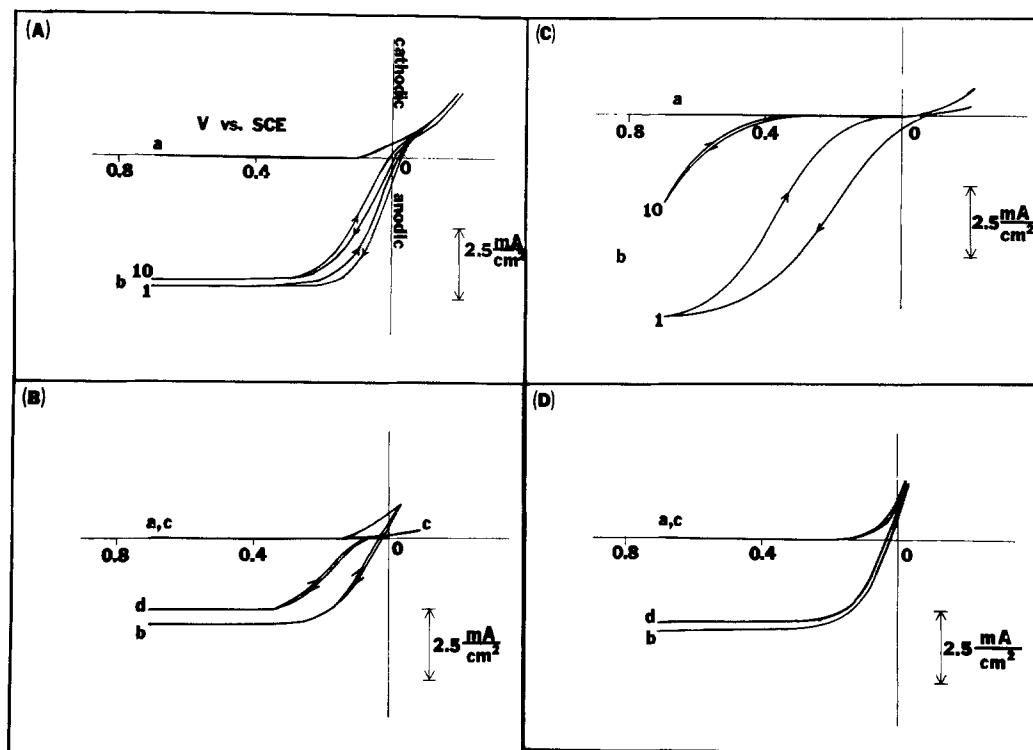


Fig. 1 Voltammetric curves of modified n-Si electrodes in the dark and under illumination (41 mW/cm^2 from a sunlamp). Scan rate 100 mV/sec . (A) n-Si electrode coated with $\sim 3500 \text{ \AA}$ of polypyrrole in 0.5 M FeSO_4 , $0.15 \text{ M Fe}_2(\text{SO}_4)_3$ and $0.5 \text{ M H}_2\text{SO}_4$. (a) dark, (b) under illumination; 1: the first cycle; 10: the tenth cycle. (B) n-Si electrode coated with $\sim 3300 \text{ \AA}$ of polypyrrole in 0.5 M FeCl_2 , 0.15 M FeCl_3 , 1 M HCl and 11 M LiCl . (a) Fresh electrode in the dark, (b) Steady state photovoltammetric curve of fresh electrode, (c) Voltammetric curve of the same electrode after illumination for more than 3 hrs., (d) Steady state photovoltammetric curve of the electrode after illumination for more than 3 hrs. (C) n-Si electrode coated with 20 \AA of Au in 0.5 M FeCl_2 , 0.15 M FeCl_3 , 1 M HCl and 11 M LiCl . (a) dark, (b) under illumination; 1: the first cycle; 10: the tenth cycle. (D) n-Si electrode coated with $\sim 15 \text{ \AA}$ of Au and then with $\sim 3300 \text{ \AA}$ of polypyrrole in 0.5 M FeCl_2 , 0.15 M FeCl_3 , 1 M HCl and 11 M LiCl . (a) Fresh electrode in the dark, (b) Steady state photovoltammetric curve of fresh electrode, (c) Dark voltammetric curve of the same electrode after illumination for 48 hrs., (d) Steady state photovoltammetric curve of the electrode after illumination for 48 hrs.

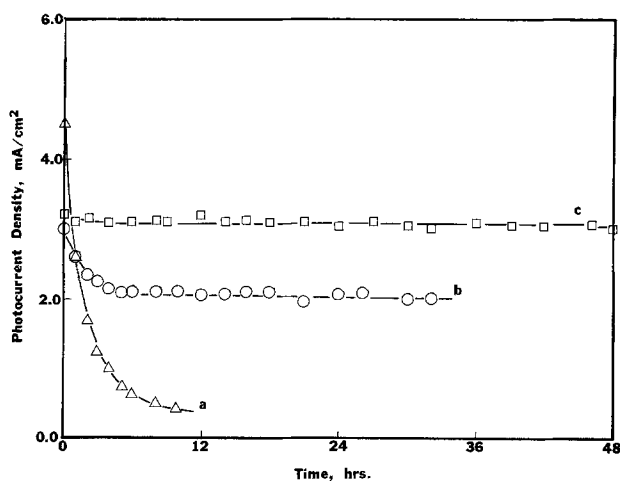


Fig. 2 Photocurrent (at load resistance of 10Ω) vs. time. Light intensity 41 mW/cm^2 from a sunlamp. (a) n-Si electrode coated with $\sim 3500 \text{ \AA}$ of polypyrrole in 0.5 M FeSO_4 , $0.15 \text{ M Fe}_2(\text{SO}_4)_3$ and $0.5 \text{ M H}_2\text{SO}_4$. (b) n-Si electrode coated with $\sim 3300 \text{ \AA}$ of polypyrrole in 0.5 M FeCl_2 , 0.15 M FeCl_3 , 1 M HCl and 11 M LiCl . (c) n-Si electrode coated with $\sim 15 \text{ \AA}$ of Au and then with $\sim 3300 \text{ \AA}$ of polypyrrole film in 0.5 M FeCl_2 , 0.15 M FeCl_3 , 1 M HCl and 11 M LiCl .

References

- e.g. (a) Y. Hakato, T. Ohnishi, and H. Tsubomura, *Chem. Letts.*, **19**, 883 (1975); (b) Y. Nakato, K. Abe, and H. Tsubomura, *Ber. Bunes. Phys. Chem.*, **80**, 1002 (1976).
- e.g. (a) P. A. Kohl, S. N. Frank, and A. J. Bard, *J. Electrochem. Soc.*, **124**, 225 (1977);

- (b) M. Tomkiewicz and J. Woodall, ibid., 124, 1436 (1977).
- (3) K. W. Frese, Jr. and S. R. Morrison, presented in Third Electrochemical Photovoltaic Cells Contractors' Review Meeting, November 10-12, 1980, Denver, CO.
- (4) See e.g. (a) S. N. Frank and A. J. Bard, J. Am. Chem. Soc., 97, 7427 (1975); (b) P. A. Kohl and A. J. Bard, J. Electrochem. Soc., 126, 59, 598, 603 (1979); (c) H. S. White, F.-R. F. Fan, and A. J. Bard, J. Electrochem. Soc., 128, 1045 (1981); (d) G. Nagasubramanian and A. J. Bard, J. Electrochem. Soc., 128, 1055 (1981).
- (5) C. P. Kubiak, L. F. Schneemeyer, and M. S. Wrighton, J. Am. Chem. Soc., 102, 6898 (1980).
- (6) (a) R. Noufi, D. Tench, and L. F. Warren, J. Electrochem. Soc., 127, 2709 (1980) and references therein; (b) R. Noufi, A. J. Frank, and A. J. Nozik, J. Am. Chem. Soc., 103, 1849 (1981).

Manuscript received June 16, 1981.

Publication costs of this article were assisted by the University of Texas at Austin.

Electrocatalytic Properties of Photodeposited Platinum on TiO₂

S. K. Vidyarthi* and N. R. Bharucha*

Noranda Research Centre, Pointe Claire, Québec H9R 1G5, Canada

INTRODUCTION

Recent demonstrations of metallic deposition on TiO₂ powders has created a new variety of catalysts which may find wide applications (1). Many such applications have been studied but await much further development prior to commercial application (2-5). We have found a new application of photodeposited platinum on TiO₂ which may be useful in existing commercial electrolyzers.

Conventional electrolysis appears to be gaining popularity in the production of commercial hydrogen. The energy efficiency of such a process is low primarily as a result of high hydrogen overvoltage on cathodes. The overvoltage can be decreased by additives to the electrolyte, notably platinum in a suitable form. Chloroplatinic acid was used in the past to decrease the operating cell voltage (6) but the electrolytic effect had a short life due to sintering and poisoning of the very active platinum particles deposited on the cathode. We have shown that dispersion of platinum by photodeposition on TiO₂ powder creates a more stable electrocatalyst for the hydrogen producing electrolysis cell.

EXPERIMENTAL

The photodeposition of metallic platinum on TiO₂ powder (MCB, anatase, 99.99% pure and μ particle size) was performed by photolysing the suspension of a known amount of the powder in a 10-25% deaerated aqueous solution of H₂PtCl₆ with a reductant such as acetic acid or dimethyl formamide. The platinized TiO₂ solid was filtered and dried in an oven at 100°C. The detailed procedure has been described by

other workers (1). Weighed amount of the final grey powder was added to hydrogen producing electrolysis cells and the performance was compared with chloroplatinic acid. All cells contained 300 ml of 28% KOH electrolyte, nickel-plated steel anodes and mild steel cathodes in a single compartment. Active cathode surface area was 25 cm². The operating cell voltage ranged from 1.90 to 2.30V at a current density of 51 mA/cm². The cells were operated at room temperature and the electrolyte was continuously stirred with a magnetic bar.

RESULTS AND DISCUSSION

The electrocatalytic activity of the photoplatinized TiO₂ was studied by following its effect upon the operating cell voltage with time. The results are shown in Figure 1. After 170 hours of operation without any additives, 100 mg of TiO₂ with 4% photodeposited Pt equivalent to a concentration of 14 mg/l of the electrolyte, was added to Cell A causing a 230 mV decrease in the cell voltage. The total platinum concentration can be expressed as 0.16 mg cm⁻² of the cathode surface. To compare this performance with that of platinum in another form, a molar equivalent amount of chloroplatinic acid was added to Cell B at 190 hrs. It is evident that the photodeposition of platinum on TiO₂ increases the duration of the electrocatalytic effect from approximately 10 hours for platinum acid to over 250 hours for the Pt/TiO₂ powder. Furthermore, direct addition of chloroplatinic acid causes an anomalous increase in the cell voltage following the treatment compared to the behaviour of the control Cell C (note the increase in Cell B voltage after 220 hours). This was further substantiated by chloroplatinic acid treatment on the control Cell C yielding the similar short-lived electrocatalytic effect followed by a slow rise parallel to that of Cell B. This effect is not usually observed in commercial electrolysis when treated with H₂PtCl₆ (7). A highly resistive film may have formed on the cathode under the conditions of the electrolytic cell.

*Electrochemical Society Active Member
Key words: hydrogen evolution, platinum electrocatalyst

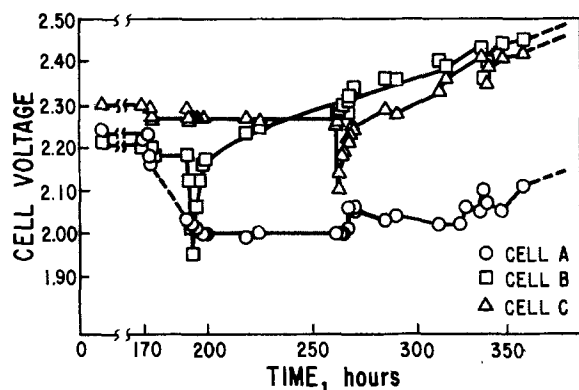


Fig. 1. The electrocatalytic effect of 0.16 mg/cm^2 of platinum as $4\% \text{ Pt/TiO}_2$ (added at 170 hours) on the operating cell voltage of a hydrogen producing electrolysis cell 'A' compared with similar cell 'B' treated with molar equivalent amount of H_2PtCl_6 and a control cell 'C' without any additive. At 260 hours, the control cell 'C' was also treated with H_2PtCl_6 to confirm its short electrocatalytic life as compared to that of photodeposited Pt/TiO_2 .

The mechanism of the electrocatalytic effect observed here may be the migration of charged Pt/TiO_2 particles towards the cathode followed by deposition. This creates a large number of sites for the electrolytic process. The electrostatic nature of the bond between the cathode and the catalyst particles was indicated by a noticeable increase in the cell voltage when the current was interrupted and the electrodes were physically disturbed (at 266 hours, Fig. 1, Cell A). The catalytic activity was recovered in 10 to 15 hours.

Dunn et al. (8) in a recent publication discuss the apparent negatively charged TiO_2 particles produced during the photolysis of a slurry. Interruption of the light source drastically reduces the cathodic current. We believe that this mechanism is not operative in our system. Fully platinised TiO_2 presumably acts as positively charged platinum particles. When partially platinised TiO_2 powder was used, the observed drop in cell voltage was minimal. We believe that TiO_2 acts as an efficient carrier for active platinum and that the potential differences caused by the semiconducting nature of TiO_2 is likely to be minimal in this highly ionic media.

Manuscript submitted Feb. 9, 1981; revised manuscript received ca. May 4, 1981.

Publication costs of this article were assisted by the Noranda Research Centre.

The electrocatalytic effect was enhanced by successive addition of Pt/TiO_2 to the cell as shown in Fig. 2. The decrease in cell voltage reached a plateau after approximately 220 mg of Pt/TiO_2 (4.5% Pt by weight) had been added to the 300 ml electrolyte; further addition of the catalyst had no effect. This indicates a saturation effect caused by a complete coating of the active electrode surface at an approximate platinum coverage of 0.40 mg/cm^2 of the cathode area.

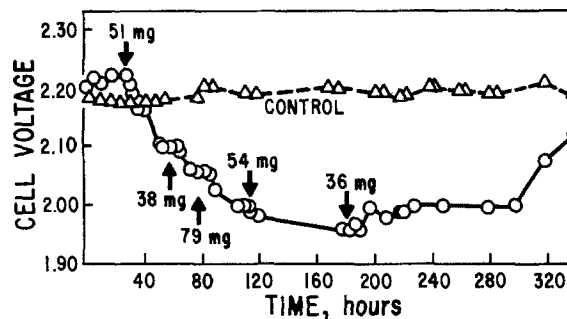


Fig. 2. Dependence of the electrocatalytic activity upon the amount of Pt/TiO_2 added to the cell. Time and amount of catalyst added are indicated by arrows and indicate a saturation of the effect when approximately 220 mg of the catalyst has been added to 300 ml of electrolyte. The active surface area of the cathode was 25 cm^2 .

SUMMARY

In conclusion, the electrocatalytic effect of photodeposited platinum on TiO_2 was demonstrated. The Pt/TiO_2 species appears to be the more suitable form of platinum for the exploitation of its hydrogen overvoltage reduction property. Further optimisation of both the catalyst preparation and electrolysis conditions is required prior to a commercial application of this catalyst.

REFERENCES

1. B. Kraentler and A.J. Bard, *J. Am. Chem. Soc.* **100**, 4317 (1978).
2. B. Kreutler and A.J. Bard, *ibid.*, **100**, 2239 (1978).
3. R.I. Bickley and V. Vishwanathan, *Nature*, **280**, 306 (1979).
4. H.S. Jarrett, H.H.C. Kung and A.W. Sleight, U.S. Patent No. 4,144,147 (1979).
5. H. Reiche and A.J. Bard, *J. Am. Chem. Soc.*, **101**, 3127 (1979).
6. E.A. Zdansky, British Patent No. 797,505 (1958).
7. R. L. LeRoy, Unpublished results.
8. W. W. Dunn, Y. Aikawa, and A. J. Bard, *This JOURNAL*, **128**, 222 (1981).



Reports on Electrochemical Society Summer Fellowship Awards

During the summer of 1980 the following graduate students received \$1,350, \$1,350, and \$1,800, respectively, representing the three Summer Fellowship Awards of The Electrochemical Society.

Mr. Gregory L. McIntire, The University of Delaware, Newark, Delaware, was awarded the Edward Weston Fellowship.

Mr. Robert S. Glass, University of Illinois, Urbana, Illinois, was designated as the recipient of the Colin Garfield Fink Fellowship.

Mr. Richard M. Cohen, The University of Utah, Salt Lake City, Utah, received the Joseph W. Richards Fellowship.

The Summer Fellowship Awards are made "without regard to sex, citizenship, race or financial need, to a fellow or teaching assistant pursuing work between the degrees of B.S. and Ph.D. on a subject in a field of interest to The Electrochemical Society." They are intended to cover a period during which the recipient has no financial support for the continuance of his or her work.

The Edward Weston Summer Fellowship Report

Mr. McIntire's report is given below.

The Effects of Altered Counterions and Counterion Concentrations on the Reductive Electrochemistry of Nitrobenzene in Dodecylsulfate Micelles

Micelles impart a measure of order to systems such that normally insoluble molecules can be solubilized within the micellar aggregate (1). The ability of micelles to solubilize these normally water insoluble species in an essentially aqueous medium as well as the short-range order afforded to the reaction environment by micelles has given rise to the increasing use of these microstructures in a variety of studies including biological (2), synthetic (3), and energy transfer applications (4). Studies in these laboratories have addressed the effects of micelle solubilization on the redox properties (formal potentials) of solubilized substrates (5, 6). In addition, the effects of the micelle solution on the kinetic demeanor of the monoelectronic oxidation and reduction products (radical ions) arising from solubilized substrates have been examined in these systems (5, 6). An earlier report concerned the oxidation of sodium dodecylsulfate (SDS) solubilized 10-methylphenothiazine (MPTH) (5). Voltammetric examination of the oxidation of MPTH in SDS micelles showed that the product of the monoelectronic oxidation, the cation radical, associates with the anionic surfactant (5, 6). The interaction between the cation radical and the anionic dodecylsulfate suggested that negatively charged species arising from the reduction of solubilized neutral substrates might preferentially interact with cationic micelles (7). In contrast to predicted results, reduction of nitrobenzene (NB) to the corresponding anion radical (NB^-) in cationic, nonionic, and anionic micelle solutions indicates that the anion radical is more persistent in the anionic micelle system than in either isotropic aqueous solution or cationic micelles (6, 8). Electron spin resonance (ESR) spectroscopy has confirmed the formation of NB^- in both anionic SDS and nonionic Brij-35 micelles while the existence of NB^- in cationic micelles during the reduction

of NB could not be demonstrated by this sensitive technique. In addition, ESR results suggest that NB^- is resident within the Stern layer of SDS micelles (6, 8). In order to probe the effect of altered Stern layer character on the stability of NB^- , the reduction of NB has been examined in the presence of various counterions as well as varying counterion concentrations in dodecylsulfate micelles. The results are explained in terms of the kinetic demeanor of NB^- .

Experimental Section

Materials.—Sodium dodecylsulfate (SDS, Aldrich) was washed repeatedly with ether, then thrice recrystallized from 95% ethanol. Nitrobenzene (Baker) was passed through a column of activated alumina (400°C, 48 hr) before use. All other reagents were reagent grade or equivalent. All solutions were prepared with deionized distilled water.

Dodecylsulfate surfactants containing various counterions were synthesized as follows. To a stirred solution of 100 ml of ether at 5°C was added 10 ml (0.15 mol) of chlorosulfonic acid (Aldrich) and 28.0g (0.15 mol) of 1-dodecanol (Aldrich). The solution volume was then doubled with ethanol and a sufficient amount of the requisite hydroxide (e.g., LiOH to yield lithium dodecylsulfate) added to ensure complete neutralization. The white, heterogeneous mixture was stirred at room temperature for 1 hr, then filtered and washed repeatedly with ether. Lithium dodecylsulfate (LDS), potassium dodecylsulfate (KDS), tetramethylammonium dodecylsulfate (TMADS), and ammonium dodecylsulfate (ADS) were all synthesized by the above procedure (9). LDS, KDS, TMADS, and ADS were further purified by recrystallization from isopropanol and dried *in vacuo* overnight at room temperature.

Apparatus and technique.—Cyclic voltammetry was performed with a three-electrode potentiostat equipped with circuitry for the compensation of solution resistance (10). Hanging mercury drop electrodes (HMDE's) were produced with a Metrohm E410 drop extruder using triply distilled mercury. Measurements of solution pH were made using a glass electrode, a saturated calomel reference electrode, and a Perkin-Elmer Mettler IV pH meter. All solutions for reductive electrochemistry were oxygen purged prior to use. All electrode potentials are reported relative to the aqueous saturated calomel electrode (SCE).

Results and Discussion

The reduction of NB in anionic SDS micelles at an HMDE is shown in Fig. 1. The two well-resolved processes have been shown to correspond to formation of the anion radical ($\text{NB}^{\cdot-}$) followed by reduction of $\text{NB}^{\cdot-}$ to the dianion which then undergoes protonation and further reduction to phenylhydroxylamine (6, 8). When the potential scan is reversed after only the first wave, that process is seen to be chemically reversible on the 5 sec time scale of the experiment (Fig. 1B). Alteration of the nature of the counterion did not produce a significant effect on the observed peak potential for the formation of $\text{NB}^{\cdot-}$ (Table I). The overall voltammetry of NB in KDS, LDS, and TMADS micelles consists of two well-resolved processes as was observed in SDS micelles (6, 8). KDS micelles cause the second reductive process to occur at more negative potentials than observed in SDS micelles. In ADS micelles, the reduction of NB proceeds as a single chemically irreversible process at potentials anodic of those observed in either isotropic aqueous solution or cationic micelles (6, 8). In the presence of increased counterion concentrations, the peak potential corresponding to formation of $\text{NB}^{\cdot-}$ is shifted to slightly more positive potentials. Addition of 0.7M NaCl to an SDS micellar solution of NB causes the first wave to shift 8 mV (Table II) while the second wave is shifted more than 100 mV in the positive direction (Table II).

Investigations of the effects of micelles on the redox properties of solubilized substrates must consider the thermodynamic and kinetic effects of these media on both substrates and the products of the electron transfer processes. In particular, the kinetic demeanor of the products of the electron transfer processes can affect the observed redox properties of the original substrates (11). Both the anion radical and dianion (second wave) of NB are susceptible to kinetic processes.

Table I. Effect of altered counterion on voltammetric peak potentials for the reduction of nitrobenzene in the presence of dodecylsulfate micelles^a

| Counterion ^b | $E_{p_{c1}}$ | $E_{p_{c2}}$ |
|------------------------------|-------------------------------|-------------------|
| Li ⁺ | -779 (± 3) | -1155 (± 3) |
| Na ⁺ | -766 (± 2) | -1157 (± 5) |
| K ⁺ | -755 (± 6) | -1304 (± 6) |
| TMA ⁺ | -774 (± 2) | -1136 (± 2) |
| NH ₄ ⁺ | -490 (± 10) | a |
| NH ₄ ⁺ | -325 (± 5) ^c | a |

^a pH of bulk solution adjusted to 7.0 (± 0.1) with corresponding hydroxides, peak potentials mV vs. SCE.

^b All solutions 60 mM in respective surfactant, 0.5 mM NB.

^c Cyclic voltammetry acquired at 40°C. All others at 25°C.

^d No second wave evident.

^e pH = 5.10.

Table II. Linear sweep voltammetric peak potentials for the reduction of nitrobenzene in 60 mM SDS with added NaCl^{a,b}

| [NaCl] M | $E_{p_{c1}}$ | $E_{p_{c2}}$ |
|----------------|------------------|-------------------|
| 0 ^c | -772 (± 1) | -1188 (± 4) |
| 0.047 | -769 (± 2) | -1137 (± 4) |
| 0.107 | -766 (± 4) | -1118 (± 3) |
| 0.314 | -764 (± 3) | -1088 (± 3) |
| 0.700 | -764 (± 3) | -1065 (± 3) |

^a All at 50 mV/sec, HMDE radius = 4.6×10^{-2} cm, peak potentials mV vs. SCE.

^b [NB] = 0.001M.

^c No NaCl added, 60 mM SDS.

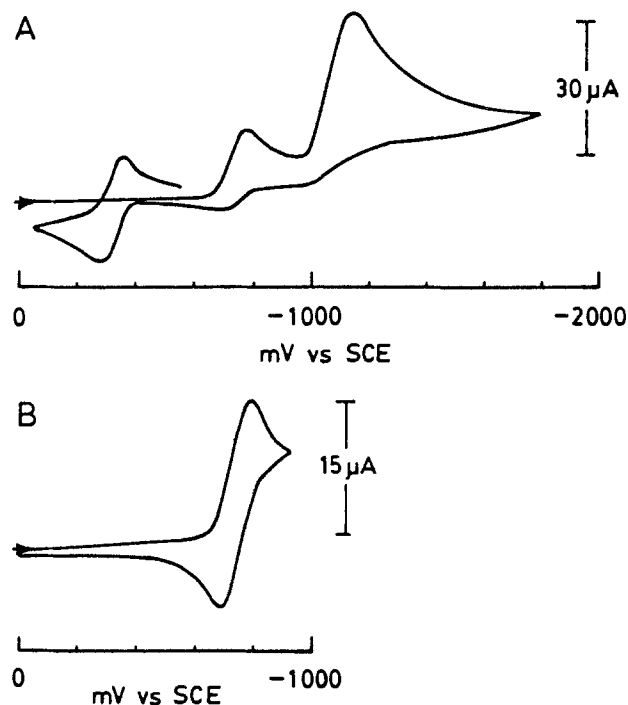
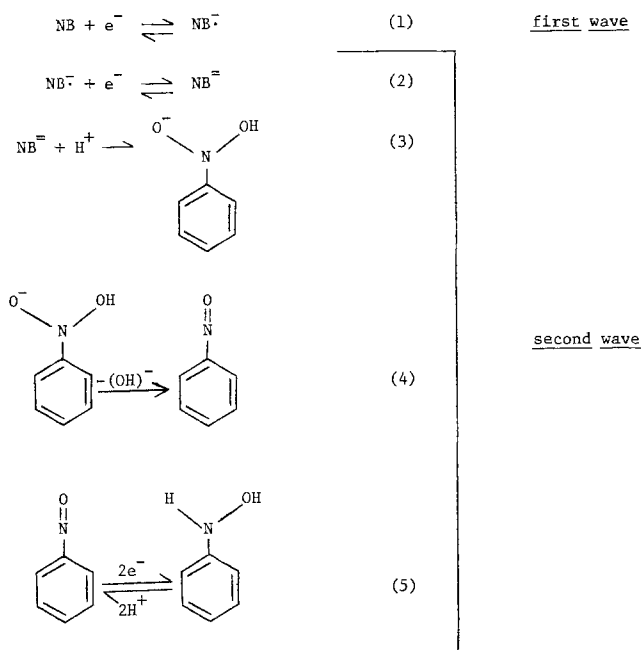
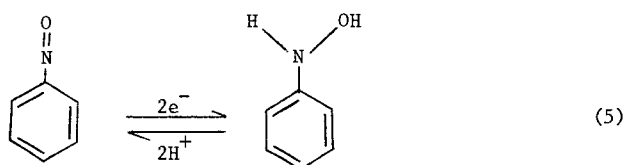
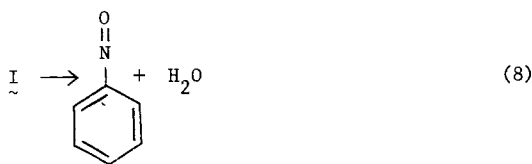
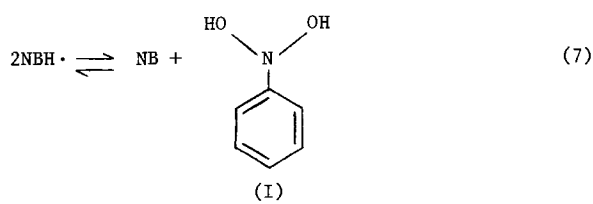


Fig. 1. Cyclic voltammetry of 0.5 mM NB in 50 mM LiCl/50 mM SDS. HMDE radius = 4.6×10^{-2} cm, sweep rate = 50 mV/sec. Arrow indicates initial potential and direction of sweep.

The second voltammetric process (dianion) is composed of a number of electron transfer and chemical reaction steps as shown below (12)



An increase in the rate of the reaction consuming the product of the electron transfer (the dianion) will cause the observed peak potential to shift to more positive potentials (11). In the above reaction sequence, reaction [3] has been reported to be the rate-determining step (12). Alterations of the hydrogen ion concentration will affect the rate of that process and therefore the observed peak potential for reduction of $\text{NB}^{\cdot-}$ to the dianion and ultimately phenylhydroxylamine. In addition, the anion radical of NB is rapidly protonated in aqueous media. The protonated form undergoes disproportionation followed by dehydration to nitrosobenzene which is readily reduced at less negative potentials to phenylhydroxylamine (13) as shown below



It is clear that the products of the reduction of NB are susceptible to kinetic processes that may be responsible for the observed voltammetry of NB in these systems.

Additionally, both NB^- and the dianion of NB have been reported to undergo ion pairing with alkali metal cations (14, 15). The observed electrochemistry of NB in these media may reflect these stabilizing interactions and/or the kinetic processes discussed above. Specifically, if ion pairing of NB^- with micelle counterions is favored over that between the dianion and the micelle counterions, then the formation of NB^- should become more facile (positive shift of observed voltammetric peak potential) while reduction of NB (to the dianion) would become more difficult (negative shift in observed voltammetric peak potential). Conversely, if ion pairing of the dianion of NB is favored over that of NB^- , then the observed voltammetric peak potential for the reduction of NB^- to the dianion would shift in a positive direction (16). The small shift in voltammetric peak potential observed for the NB/ NB^- redox couple together with the relatively large changes observed for the anion radical/dianion redox couple in the presence of weakly pairing cations (K^+ , TMA^+) (13, 14) indicates that ion pairing is not a major factor in these systems.

The reduction of NB in LDS, SDS, KDS, TMADS, and ADS micelles gives rise to phenylhydroxylamine in all cases indicating that protonation of the dianion occurs rapidly in dodecylsulfate micelles (12). The small changes in the observed peak potential for the reduction of NB to NB^- with altered counterion indicate that ion pairing is not the primary stabilizing interaction in these systems. Rather, the observed voltammetry of NB in these systems is dependent on the kinetic properties of NB^- and the dianion in these media. Interaction of NB^- and the dianion with the dodecylsulfate micelles results in retardation of the rate of protonation of these species (12, 13). In the case of NB^- , the stability provided by the micelle renders the observed reduction of NB to NB^- chemically reversible on the cyclic voltammetric time scale. Kinetic stabilization is consistent with observation of NB^- in non-ionic micelles where counterion pairing with NB^- is impossible (6). The dianion is sufficiently reactive that reduction of NB^- to the dianion is chemically irreversible in all dodecylsulfate micelles examined. The nature of the interactions of NB and NB^- with dode-

cylsulfate micelles is the subject of further study in these laboratories (8).

Acknowledgments

The support of The Electrochemical Society through the Edward Weston Fellowship is gratefully acknowledged. In addition, the assistance of D. M. Chiappardi and the continued support and encouragement of Dr. H. N. Blount were essential to this work.

REFERENCES

1. J. H. Fendler and E. J. Fendler, "Catalysis in Micellar and Macromolecular Systems," Academic Press, New York (1975).
2. For example: a) A. Helenius and K. Simons, *Biochim. Biophys. Acta*, **415**, 29 (1975); b) T. Mukherjee, A. V. Sapre, and J. P. Mittal, *Photochem. Photobiol.*, **28**, 95 (1978).
3. E. H. Cordes, *Pure Appl. Chem.*, **50**, 617 (1978).
4. P.-A. Brugger, P. O. Infelta, A. M. Braun, and M. Gratzel, *J. Am. Chem. Soc.*, **103**, 320 (1981).
5. G. L. McIntire and H. N. Blount, *J. Am. Chem. Soc.*, **101**, 7720 (1979).
6. G. L. McIntire and H. N. Blount, in "Solution Behavior of Surfactants: Theoretical and Applied Aspects," K. L. Mittal and E. J. Fendler, Editors, Plenum Press, New York (1981).
7. G. Meyer, L. Nadjjo, and J. M. Saveant, *J. Electroanal. Chem. Interfacial Electrochem.*, **119**, 417 (1981).
8. G. L. McIntire, D. M. Chiappardi, R. L. Casselberry, and H. N. Blount, *J. Phys. Chem.*, Submitted.
9. M. J. Schick, *J. Phys. Chem.*, **68**, 3585 (1964).
10. A. A. Pilla, *This Journal*, **118**, 702 (1971).
11. A. J. Bard and L. R. Faulkner, "Electrochemical Methods," p. 433, Wiley, New York (1980).
12. A. J. Fry, "Synthetic Organic Electrochemistry," p. 226, Harper and Row, New York (1972).
13. K.-D. Asmus, A. Wigger, and A. Henglein, *Ber. Bunsenges. Phys. Chem.*, **70**, 862 (1966).
14. T. M. Krygowski, M. Lipsztajn, and Z. Galus, *J. Electroanal. Chem. Interfacial Electrochem.*, **42**, 261 (1973).
15. W. Kemula and T. M. Krygowski, in "Encyclopedia of Electrochemistry of the Elements," A. J. Bard and H. Lund, Editors, Vol. XIII, p. 77, Marcel Dekker, New York (1979).
16. E. E. Bancroft, J. E. Pemberton, and H. N. Blount, *J. Phys. Chem.*, **84**, 2557 (1980).

The Colin Garfield Fink Summer Fellowship Report

Mr. Glass's report is given below.

Evidence for S-Route Behavior in Electrogenerated Chemiluminescence from the Tris(2,2'-bipyridine)ruthenium(II) System

For several years, workers in the area of electrogenerated chemiluminescence (ECL) have labored to explain the mechanisms of light production in high-energy electron-transfer reactions. It has, in particular, been difficult to find systems which adhere to expectations based upon light production via the "S-route." In these systems, the electron-transfer reaction is energetically sufficient to leave a product in the observed emitting state, and does so directly in the redox event. In systems where the electron-transfer reaction is insufficiently energetic to directly yield an emitting product, the mechanism of light production is assumed to proceed via the T-route. Here triplet intermediates are produced in the electron-transfer event, and triplet-triplet annihilation is invoked to account for production of emitting states. These schemes have been extensively reviewed (1-7).

In mechanistic investigations, the sequential step technique for producing light transients has been widely used (3, 5, 6, 8-11). Results of studies using this technique have, however, not generally been consistent with the above scenarios (6, 12-17).

In the sequential step experimental method, one generates the oxidant and reductant from precursors at a small planar electrode in quiescent solution. In the first step (of duration t_f), the first reagent is produced and diffuses into the solution. At $t = t_f$, the potential of the electrode is switched to a value where the second reagent is produced. It then diffuses into the solution, where it reacts with the first reagent at a total rate (N , moles/sec) that declines with time as the first species is consumed. The reaction rate can be predicted from the laws of diffusion (8, 11). A light transient results from the time dependence of the redox reaction rate N and the kinetics of light-producing processes.

The short-time region of the light transient has been stressed for kinetic evaluation (4, 6, 10, 11, 16), and it has been shown that in this region the light intensity should be linear with $(t_r/t_f)^{-1/2}$, where t_r is time measured into the second step from its start (11). Recently, Kawai *et al.* (18) have reported single transients adhering to this prediction in the anthrylamine charge-transfer systems, but they did not attempt to verify the predicted variations in the slopes and intercepts of the linear plots with step time, nor did they test for the expected invariance in behavior with the sequence of reactant generation.

In the absence of a paradigm showing predictable behavior with respect to all experimental variables, one cannot be sure whether the deviations from non-ideality manifest defects in the experimental approach, significant misconceptions about the fundamental chemistry, or both. Our goal in this work and in a companion study done by Luttmner and Bard (19) is to establish the reaction between $\text{Ru}(\text{bpy})_3^{+1}$ and $\text{Ru}(\text{bpy})_3^{+3}$ (where bpy is 2,2'-bipyridine) as a reasonably well-behaved S-route case under certain conditions. This reaction is simple in comparison to energy-sufficient ion annihilations of aromatics, which can have parallel S and T pathways to emission. Emission arises by phosphorescence from a $d-\pi^*$ metal-ligand charge-transfer triplet of $\text{Ru}(\text{bpy})_3^{+2}$, which is the only excited state with an appreciable lifetime (20, 21). Early studies by Bard and co-workers (22, 23) postulated the direct production of the emitting state of this system in the electron-transfer event. Later work (24, 25) showed that at temperatures below -30°C , the ECL emission yield (photons emitted per redox event) approached the photoluminescence quantum efficiency, which implies 100% efficiency for production of the $d-\pi^*$ triplet in electron transfer.

Even though the key state in this system is a triplet, the description of the kinetics as "S-route" is accurate as this is the emitting state and will be shown to be directly produced in the electron-transfer event. The results from this study are briefly summarized below. More complete details can be found elsewhere (26).

Experimental

Chemicals.— $\text{Ru}(\text{bpy})_3\text{Cl}_2 \cdot 6\text{H}_2\text{O}$ was supplied by G. F. Smith Chemical Company. $\text{Ru}(\text{bpy})_3(\text{ClO}_4)_2$ was prepared from it by metathesis with excess NaClO_4 in H_2O . It was then recrystallized three times from an H_2O -EtOH mixture (4:1), and then dried for 48 hr at 60°C under vacuum.

Tetra-*n*-butylammonium fluoborate (TBABF_4) was used as the supporting electrolyte. It was obtained from Southwestern Analytical Chemicals (Electrometric grade), recrystallized three times from a mixture of ethyl acetate-pentane (5:1), then dried at

95° under vacuum for 48 hr. The electrolyte was stored in a desiccator over CaSO_4 .

N,N-dimethylformamide (DMF), 99% was obtained from Aldrich. The procedure for removal of amine decomposition products and H_2O has been described in detail (14).

Electrochemical cell and sample preparation.—The cell consists of a platinum disk working electrode (3.09 mm^2) and a platinum wire quasi-reference electrode (QRE). The tip of the QRE is placed close (2-3 mm) to the working electrode to minimize uncompensated resistance. A platinum wire was also used as the counterelectrode. All other details of the cell and sample preparation are similar to those described previously (26).

Instrumentation.—Details of the computer interface and instrumentation have been reported elsewhere (26).

The triple-step mode of reactant generation was utilized in this study. The initial potential was always 0V vs. QRE, where $\text{Ru}(\text{bpy})_3^{2+}$ was not electroactive. Two sequential steps of equal duration, t_f , were then used to generate the reacting species. At the end of the second step, the potential of the working electrode was returned to 0V vs. QRE. Uncompensated resistance was compensated for by positive feedback at the 80% level.

Results and Discussion

Electrochemistry and experimental design.—Initial work was performed in acetonitrile. However, both cyclic voltammetry and chronocoulometry revealed severe problems with filming of the electrode. We therefore changed to DMF in hopes of alleviating this obvious solubility problem. Also, in order to suppress the large anodic background seen in DMF at room temperature, the experimental work was performed near -25°C , where the anodic region is fairly clean.

Figure 1 is a cyclic voltammogram of $\text{Ru}(\text{bpy})_3^{2+}$ in DMF at -25° . There are three reduction peaks situated at -1.33 , -1.49 , and -1.74V vs. QRE, which are associated with the production of $\text{Ru}(\text{bpy})_3^{+1}$, $\text{Ru}(\text{bpy})_3^0$, and $\text{Ru}(\text{bpy})_3^{-1}$, respectively. A fourth reduction peak, associated with irreversible ligand loss, is at -2.5V . Good reversible behavior is observed for the first three reductions, the splitting between the anodic and cathodic peaks in each case being 60-70 mV. One oxidation peak appears at 1.31V vs. QRE. It shows quasi-reversible behavior, with a peak separation of $\sim 150\text{ mV}$. At room temperature this oxidation exhibits more reversible character. No problems with deposition onto the electrode surface were noticeable in DMF, and the solubility of the chelate species generally appeared to be much greater in DMF than in acetonitrile.

In the quantitative model developed (11) for analysis of the early portions of ECL light transients, it was

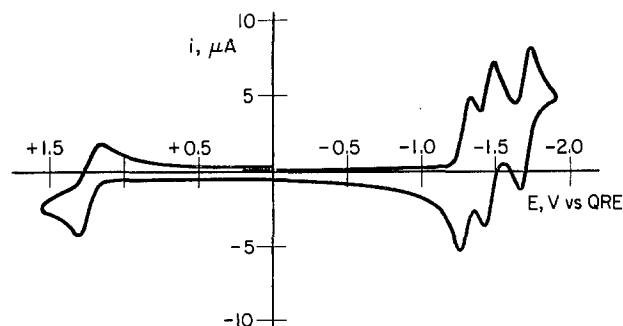
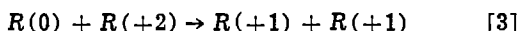
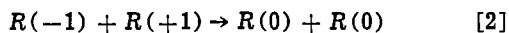
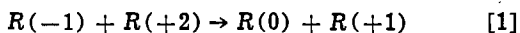


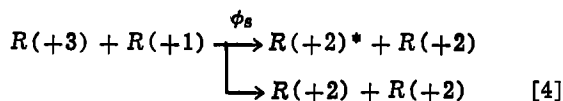
Fig. 1. Cyclic voltammogram of 1 mM $\text{Ru}(\text{bpy})_3^{2+}$ in DMF at -25° . The supporting electrolyte was 0.1M TBABF_4 . Scan begins at 0.0V and first moves negatively.

assumed that diffusion-controlled conditions for generation of the reactants was enforced. However, as seen in Fig. 1, the first and second reduction peaks are closely spaced, and potential oversteps of 200-250 mV past E_p for production of $\text{Ru}(\text{bpy})_3^{+1}$, which are normally used to establish diffusion-controlled conditions for electroreduction, cannot be employed without simultaneous generation of $\text{Ru}(\text{bpy})_3^0$. In such a case, the model relating the light intensity to the redox reaction rate, N , as discussed in the next section will be uninterpretable.

In a different approach to the problem, we employed a triple step program featuring the production of the $\text{Ru}(\text{bpy})_3^{-1}$ species at the electrode in the forward step, and $\text{Ru}(\text{bpy})_3^{+3}$ in the reverse step (27). No control problems were expected in this case because the fourth reduction is so widely separated from the third. During the forward step, $\text{Ru}(\text{bpy})_3^{-1}$ diffuses outward from the electrode and encounters a flux of +2 species, hence the following reactions occur



where the species are designated by the charges on the complexes. The net result is that virtually all of the electrons injected by reduction go to produce $\text{R}(+1)$ in the diffusion layer (except very near the electrode surface). When the second step begins, and $\text{R}(+3)$ is electrogenerated, the ECL reaction is then the usual one



where ϕ_s is the branching ratio for producing the $d - \pi^*$ triplet $\text{R}(+2)^*$. Only in the earliest moments of the second step, when the homogeneous reaction takes place near the electrode, would $\text{R}(+3)$ be able to react with $\text{R}(-1)$ or $\text{R}(0)$.

Theoretical considerations.—For an S-route system, the total light intensity (I , einsteins/sec) is very simply related to N as

$$I = \phi_{\text{ECL}} N \quad [5]$$

where ϕ_{ECL} is the ECL efficiency (photons emitted per redox ion annihilation) and should be independent of time (16). The intensity should therefore be proportional to N .

For the case at hand, an analytical expression has been developed (26) which yields the redox reaction rate in a linearized form. In dimensionless terms, it is given as

$$\omega_n = a(t_r/t_f)^{-1/2} + b \quad [6]$$

where $\omega_n = N t_f^{1/2} / A D^{1/2} C_p^*$, $a = 2.15$, and $b = -1.96$.

This result applies only to the early part of the light decay ($t_r/t_f \leq 0.2$).

Assumptions which are made in deriving the above results are detailed elsewhere (26). In this reference, data are also presented which verify that our basic model of diffusional processes is correct. This verification consists of an examination of faradaic current flow during the second step (11, 16).

The problem was also treated by digital simulation (26). The results for ω_n agreed rather well with the theoretical expression over the time domain of interest ($t_r/t_f \leq 0.2$).

S-route behavior in these experiments would therefore require light transients that show linear plots of intensity vs. $(t_r/t_f)^{-1/2}$ with intercept-to-slope ratios $b/a = -0.91$, regardless of t_f .

Decay curves.—Shown in Fig. 2 are plots of I vs. $(t_r/t_f)^{-1/2}$ for experiments in DMF at -25° with $t_f = 0.1$ -10 sec. It is seen that the plots show good linearity in all cases. The least-squares intercept-to-slope ratios are -1.18 , -1.37 , -1.36 , and -1.62 for $t_f = 0.1$, 1, 5, and 10 sec, respectively. These values are significantly higher in magnitude than the theoretical value of $b/a = -0.91$.

By rearrangement of Eq. [5] and [6], one finds that both the slopes and intercepts of the lines in Fig. 2 should display direct proportionality with $t_f^{-1/2}$, and the plots in Fig. 3 show that the prediction is borne out. The ratio of the slope of line 1 in Fig. 3 to that of line 2 should be $-b/a = 0.91$. In reality, the ratio is 1.15.

The good linearities shown in Fig. 2 and 3 for single transients and among families of transients is concordant with an S-route mechanism of light production. The only remaining discrepancy from the behavior predicted by theory is the consistent tendency of the observed intercept-to-slope ratio $(-b/a)_{\text{obs}}$ to be high. This effect has also been seen by Kawai *et al.* (18) in the ECL of anthrylamine systems, and by Luttmner and Bard (19) in the system of interest here despite a totally different experimental attack.

More ideal values of the intercept-to-slope ratios were observed with shorter t_f and with lower temperatures. For example, from ratios of slopes of plots

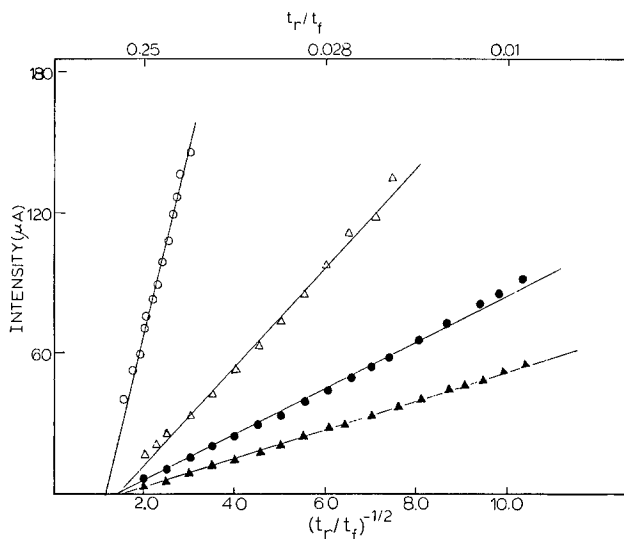


Fig. 2. Plots of I vs. $(t_r/t_f)^{-1/2}$ for experiments with 1 mM $\text{R}(+2)$ in DMF with 0.1M TBABF_4 at -27° . Values of t_f are: Open circles are 0.1 sec; open triangles are 1.0 sec; filled circles are 5.0 sec; filled triangles are 10 sec.

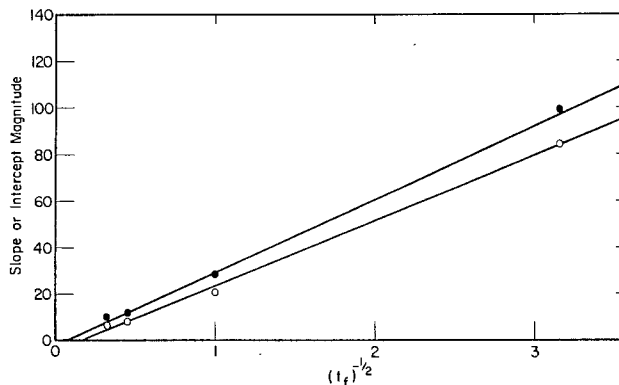


Fig. 3. Slopes (open circles) and intercepts (filled circles) of plots in Fig. 2 vs. $t_f^{-1/2}$.

equivalent to those of Fig. 3, the following trend was observed

| T, °C | (-b/a) _{obs} |
|---------|-----------------------|
| Ambient | 1.58 |
| -25 | 1.09 |
| -35 | 0.96 |

These data were obtained with 0.2M TBABF₄, which was twice the value used in experiments described by Fig. 2 and 3. No effect of electrolyte concentration was discerned.

The high values of (-b/a)_{obs} may be due to side reactions, perhaps with the electrolytic products of the faradaic process occurring in parallel with the oxidation of R(+2). However, the generality of the behavior suggests that there may be a fundamental defect in experimental conformity to the theoretical model. One possibility is the existence of edge diffusion or convective lateral dispersion of the diffusion layer, resulting in losses of the first reactant which would tend to depress the intercepts further and raise -b/a (26).

Conclusions

The following criteria are proposed for S-route behavior.

1. Linearity of plots of I vs. $(t_r/t_f)^{-1/2}$ for $t_r/t_f \leq 0.2$.
2. Plots of the intercepts and slopes of the individual linearized transients that are linear with $t_f^{-1/2}$ and pass through the origin.
3. A ratio of the slopes of the plots in 2 giving $(-b/a)_{obs}$ near the theoretical value.
4. Quantitatively equivalent behavior upon reversal of the order of reactant generation.

With these criteria the essentials of S-route behavior are captured in experimentally realistic terms. It is not felt that strict quantitative observation of the theoretical (-b/a) value should be overstressed, as the observed value may be perturbed by a number of fairly minor experimental defects. It is highly unlikely that a system with a large T-route component would be able to fulfill these criteria (26).

From the data presented here, and in the companion work by Luttmmer and Bard (19), the system at hand has fulfilled all of the above criteria and seems reliable as an S-route model.

Acknowledgments

The support of The Electrochemical Society through the receipt of the Colin Garfield Fink Summer Fellowship is gratefully acknowledged. I would also like to thank Professor Larry R. Faulkner for continued support and guidance. Also, I would like to express my appreciation to Drs. A. J. Bard, K. Itaya, and J. D. Luttmmer for reports on their data in preliminary form.

REFERENCES

1. A. Weller and K. Zachariasse in "Chemiluminescence and Bioluminescence," M. Cormier, D. M. Hercules, and J. Lee, Editors, pp. 169-181, Plenum, New York (1973).
2. K. A. Zachariasse in "The Exciplex," M. Gordon, W. R. Ware, P. de Mayo, and D. R. Arnold, Editors, p. 275, Academic Press, New York (1975).
3. L. R. Faulkner, *Int. Rev. Sci. Phys. Chem. Ser 2*, 9, 213 (1975).
4. L. R. Faulkner and A. J. Bard, *Electroanal. Chem. Interfacial Electrochem.*, 10, 1 (1977).
5. F. Pragst, *Z. Chem.*, 18, 41 (1978).
6. L. R. Faulkner, *Meth. Enzymol.*, 57, 494 (1978).
7. A. I. Bikh, R. F. Vasil'ev, and N. N. Rozhitsky, *Itogi Nauk. Tech. Ser. Rad. Khim. Fotokhim.*, 2 (1979).
8. S. W. Feldberg, *J. Am. Chem. Soc.*, 88, 390 (1966).
9. R. Bezman and L. R. Faulkner, *ibid.*, 94, 3699 (1972).
10. L. R. Faulkner, *This Journal*, 122, 1190 (1975).

11. L. R. Faulkner, *ibid.*, 124, 1724 (1977).
12. R. E. Visco and E. A. Chandross, *Electrochim. Acta*, 13, 1187 (1968).
13. J. Chang, D. M. Hercules, and D. K. Roe, *ibid.*, 13, 1197 (1968).
14. R. Bezman and L. R. Faulkner, *J. Am. Chem. Soc.*, 94, 6317, 6324 (1972); 95, 3083 (1973).
15. E. W. Grabner and E. Brauer, *Ber. Bunsenges. Phys. Chem.*, 76, 106, 111 (1972).
16. P. R. Michael and L. R. Faulkner, *J. Am. Chem. Soc.*, 99, 7754 (1977).
17. P. R. Michael, J. L. Morris, Jr., R. S. Glass, and L. R. Faulkner, Unpublished results.
18. M. Kawai, K. Itaya, and S. Toshima, *J. Phys. Chem.*, 84, 2368 (1980).
19. J. D. Luttmmer and A. J. Bard, *J. Phys. Chem.*, May 1981.
20. J. N. Demas and G. A. Crosby, *J. Mol. Spectrosc.*, 26, 72 (1968).
21. F. E. Lytle and D. M. Hercules, *J. Am. Chem. Soc.*, 91, 253 (1969).
22. N. E. Tokel and A. J. Bard, *ibid.*, 94, 2862 (1972).
23. N. E. Tokel-Takvoryan, R. E. Hemingway, and A. J. Bard, *ibid.*, 95, 6582 (1973).
24. W. L. Wallace and A. J. Bard, *J. Phys. Chem.*, 83, 1350 (1979).
25. K. Itoh and K. Honda, *Chem. Lett.*, 99 (1979).
26. R. S. Glass and L. R. Faulkner, *J. Phys. Chem.*, May 1981.
27. Our experimental attack did not permit a reversal in the order of reactant generation. Producing R(-1) second leads to extremely short-lived transients because the charge-consuming capacity of that species is so great.

The Joseph W. Richards Summer Fellowship Report

Mr. Cohen's report is given below.

Direct Measure of the Esin-Markov Coefficient in Mixed Solutions

The objective of this summer research was to demonstrate the feasibility of using an ion-sensitive field effect transistor (ISFET) to directly measure the Esin-Markov coefficient of ions which specifically adsorb to a polarized gate metal. Gold was chosen as the gate material since it has been studied as a polarized electrode (1-5). For solid materials, the standard technique for finding the Esin-Markov coefficient

$$\left(\frac{\partial E}{\partial \ln a} \right)_{qm} = -RT \left(\frac{\partial \Gamma}{\partial q^m} \right)_a \quad [1]$$

requires measurement of a capacitance-voltage curve in an appropriate base solution to find the potential at the point of zero charge (pzc). One may then integrate the area under the curve to find the charge on the electrode at other potentials. Upon addition of a specifically adsorbing ionic species to the solution, the C-V curve will change; recalculating the potential of the pzc (or any other charge condition on the electrode) allows one to measure the shift in electrode potential as a function of ion activity in solution for a constant charge condition on the metal electrode, yielding the Esin-Markov coefficient.

Experimental

The theory, operation, and construction of ISFET's have been reviewed in detail elsewhere (6). As shown in Fig. 1, a gold gate ISFET is immersed into solution. An external circuit senses the drain current, compares it to a preset value, and adjusts the reference electrode potential to keep the drain current at the preset

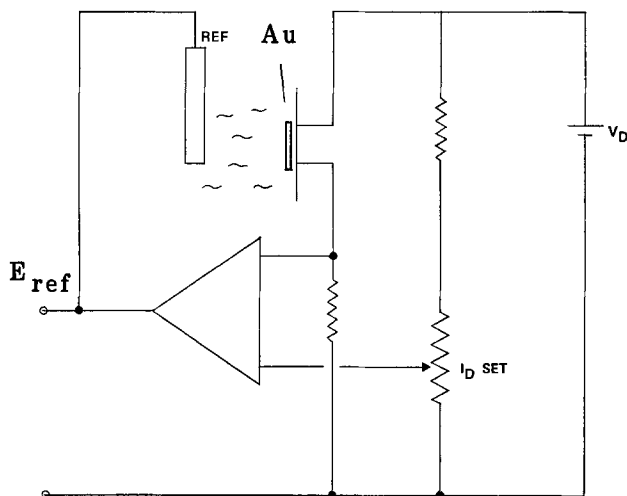


Fig. 1. Circuit for operation of ISFET with constant charge on gold gate.

value. The gold gate is electrically floating so that it makes electrical contact only with the solution.

As long as there are no charge leakage paths to the gold gate, the constant charge condition for measuring the Esin-Markov coefficient is satisfied. If an adsorbing anion is added to solution, positive countercharge must appear at the surface of the gold facing solution. Since this requires a change in charge density on the side of the gold facing the ISFET's conducting channel, the drain current begins to drop. The external circuit senses this change and increases the reference electrode potential sufficiently to maintain constant drain current, and, equivalently, constant potential (and charge density everywhere) on the gold gate. Thus, the change in potential of the reference electrode appears entirely across the gold-double layer region, and directly measures the Esin-Markov coefficient.

The gold gate is a thin film of gold with an area of about 10^{-4} cm². Gold is initially rf sputtered during chip manufacture on top of 200Å of titanium (to bond the gold to the silicon nitride) to form a gate with a thickness of about 0.2 μm. Some experiments were performed on this amorphous gold gate, while others were performed on a polycrystalline gold gate of several microns thick which was formed by using a Bell Laboratories electroplating technique (7) which gives gold of five nines purity.

Deionized, 18 MΩ-cm resistivity, water was passed through a quartz double distillation unit for our use in these experiments. Chemicals used were either Mallinckrodt Reagent grade or Merck Suprapur grade.

The reference electrode used was a double junction type with the compartments separated by porous glass plugs. The upper junction was composed of Ag|AgCl|sat. AgCl in 4M KCl. The lower junction contained electrolyte of the same composition as the base solution under test.

A thermostatted closed test cell at 25°C containing a base solution of 0.9M NaF in water was deaerated by bubbling humid N₂ through the 25 ml of solution for more than an hour before starting any measurements. Gas leaving the cell was passed through a water trap to avoid backflow of oxygen into the system. The ISFET's were entirely encapsulated, except for the gold gates, with EPON epoxy as described elsewhere (6).

For the summer project, iodide was chosen as the specifically adsorbing ion to study. A calibrated, Gilmont 250 μl syringe was used to add NaI to the solution over a concentration range of 10^{-6} - 10^{-3} M.

Devices were cleaned for 10 min or longer in an argon plasma with a background pressure of about 0.3 Torr with 5W of power used to keep the plasma

ignited. After plasma cleaning, the device was removed from the plasma chamber and immediately placed in a container of clean water, moved to the test cell, and placed in the test solution to avoid the possibility of surface contamination. Aqua regia made from electronic grade acids was used to clean other devices. These devices were dipped in the acid for 2-3 sec, plunged immediately into clean water for a minute, and then into the test solution.

Results

After equilibrating a device in solution for an hour to minimize drift and deaerate the solution, the experiment was begun. Nearly all of the 20 devices studied gave a slope of 40-50 mV/decade for both amorphous sputtered gold and polycrystalline plated gold gates (see Fig. 2). Ultrapure chemicals gave the same result as reagent grade chemicals; however, reagent grade chemicals led to a background drift of 5-10 mV/hr. There was no clear difference between cleaning devices in a low power argon plasma and aqua regia.

It is worth noting that these devices hold charge on the gates for days when in air. Early devices held charge only for minutes in air; upon examination of the transistor with ESCA, it was found that a few tens of ppm of titanium on the silicon nitride surface acted as a shunting resistor to drain charge off of the gate. This problem was solved by cleaning the wafer with EDTA solution in ultrasound.

It is desirable to demonstrate the operation of the devices at various charge conditions on the gold. This was done by turning off the feedback circuit, grounding the reference electrode, and applying a potential to the gate to set a known charge density there. This was done either by touching the gold gate with a gold wire set at a desired potential or by applying a potential to a lead which was connected directly to the gold gate when the device was constructed. This applied charge would not stay on the gate for a long enough period of time to make a measure of the Esin-Markov coefficient. The time constant for the charge leakage was about 10 min. Thus, all measurements were made after the charge on the gold gate stabilized. This potential is probably at or near the pzc, and the charge leakage is currently under investigation.

Discussion

Surface cleanliness was clearly an important factor in getting reasonable results; however, the crystallinity of the surface probably also made an important difference. For example, a single crystal face of gold has a well-defined pzc potential, whereas a polycrystalline gold surface has several crystalline faces in contact with solution, each of which has different pzc potentials. Thus, even if a gold gate has zero net charge on its surface, some crystal faces can be expected to have

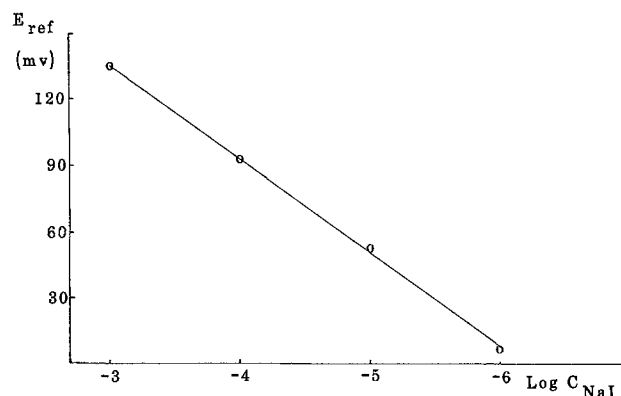


Fig. 2. Result of a direct measure of the Esin-Markov coefficient obtained by adding NaI to a background solution of aqueous 0.9M NaF at 25°C.

a positive surface charge density and others a negative surface charge density. This implies that an adsorbing species will adsorb with different surface concentrations on the various crystalline faces (3, 8) and any measured Esin-Markov coefficient will be a composite of several adsorption isotherms and ought to yield less than 59 mV/decade, particularly at low concentrations of adsorbate.

Due to the existence of a small, but nonzero exchange current density, these floating gate devices could be operated only in the neighborhood of the (averaged) pzc potential. The results demonstrate the feasibility of directly measuring the Esin-Markov coefficient with an ISFET. Extending its use to various surface charge densities is presently under investigation, and the results will be subsequently communicated.

Acknowledgments

Support for this work from The Electrochemical Society's award of the Joseph W. Richards fellowship is gratefully acknowledged. The author wishes to thank

Professor Jiri Janata for his guidance and helpful suggestions, as well as Dr. Scott Collins, Gary Blackburn, and Rosemary Smith for their aid in the laboratory.

REFERENCES

1. J. Clavilier and N. Van Huong, *J. Electroanal. Chem. Interfacial Electrochem.*, **41**, 193 (1973).
2. C. N. Van Huong, J. Clavilier, and M. Bonnemay, *ibid.*, **65**, 531 (1975).
3. A. Hamelin and J. P. Bellier, *Surf. Sci.*, **78**, 159 (1978).
4. C. Hinnen, C. N. Van Huong, A. Rousseau, and J. P. Dalbera, *J. Electroanal. Chem. Interfacial Electrochem.*, **95**, 131 (1979).
5. S. D. Abdulov, A. G. Zelinskii, and R. Y. Bek, *Sov. Electrochem.*, **16**, 559 (1980).
6. J. Janata and R. J. Huber, *Ion Select. Electrode Rev.*, **1**, 31 (1979).
7. R. W. Hodgson and A. H. Szkudlapski, *Plating*, **57**, 693 (1970).
8. C. Hinnen, C. N. Van Huong, A. Rousseau, and J. P. Dalbera, *J. Electroanal. Chem. Interfacial Electrochem.*, **106**, 175 (1980).



Conductivity of KOH Electrolyte Supersaturated with Zincate

Ming-Biann Liu,* Brian R. Faulds,¹ G. M. Cook,* and N. P. Yao*

Argonne National Laboratory, Chemical Engineering Division, Argonne, Illinois 60439

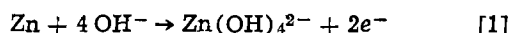
ABSTRACT

The specific conductivity of 7.32N KOH electrolyte with zincate concentrations ranging from 0 to 1.5M has been measured. The electrolyte conductivity was found to decrease with increasing zincate concentration. This finding is consistent with predictions based on the mixture rule. The equivalent conductance of 7.32N potassium zincate of 7 ± 5 mho · cm/equiv. may indicate the formation of neutral associated ion pairs from potassium and zincate ions in the electrolyte. Further calculations indicated that the mixture rule yields predictions of conductivities for the KF-KOH and K_2CO_3 -KOH systems that are in good agreement with experimental data in the literature.

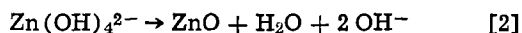
The primary purpose of this study was to obtain specific conductivity data for 7N KOH electrolyte supersaturated with zincate. These fundamental data are needed for engineering analysis of zinc porous electrodes used in alkaline batteries under development for near-term use in electric vehicles. These data also provide a baseline for the evaluation of modifications of battery electrolyte.

The electrolyte in Ni/Zn batteries is initially about 31% KOH (7N) saturated with ZnO. During cell discharge, the concentration of zincate has been observed to rise by three to four times the chemical solubility of ZnO in KOH solution (1-3). Furthermore, the conductivity of the electrolyte at a given concentration and temperature has been found to decrease linearly with an increasing amount of dissolved ZnO up to saturation concentration (4-6). We have determined the conductivity of the KOH electrolyte with zincate concentrations up to twice chemical saturation.

During the discharge of zinc/nickel oxide cells, the reactions for the zinc electrode may be written as follows



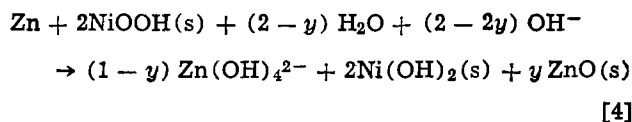
The zincate species may also precipitate to form zinc oxide according to the reaction



For the nickel oxide electrode, the reaction is



Thus, the net reaction of the cell system may be written as



where y is the molar fraction of zincate species precipitating to form ZnO. Reaction [4] suggests that the electrolyte is a ternary system consisting of potassium hydroxide, potassium zincate, and water.

Ternary electrolyte theory developed from the principle of irreversible thermodynamics has been described by Miller (7) and Sunu and Bennion (8). To predict the transport properties of a ternary electrolyte system by using the theory, one has to estimate the values of six solvent-fixed ionic transport coefficients. Miller (7) found empirically that, for seven ternary alkali halide mixtures at total concentrations ranging from 0.5 to 3N, the ionic transport coefficients (l_{ij}) can be closely approximated using l_{ij} data from appropriate binary systems. These estimated values of ternary l_{ij} yield good estimates of transference numbers, conductances, and solvent-fixed thermodynamic diffusion coefficients. In our system, sufficient conductivity data for potassium zincate are lacking. Therefore, this theory cannot be used to analyze our conductivity data. However, the conductance, Λ_{123} , of the seven alkali halide mixtures can also be predicted at low concentrations by the solution mixture rule (7), which states that

$$\Lambda_{123} = X_2\Lambda_{12} + X_3\Lambda_{13} \quad [5]$$

where Λ_{1i} ($i = 2, 3$) is the conductance of the binary electrolyte at the same total equivalent concentration, N , of the mixture and where the equivalent fractions, X_i , are given by

$$X_i = \frac{N_i}{N_2 + N_3} \quad i = 1, 2, 3 \quad [6]$$

$$X_1 = X_2 + X_3 = 1 \quad [7]$$

Substituting Eq. [7] into Eq. [5], one obtains

$$\Lambda_{123} = \Lambda_{13} - (\Lambda_{13} - \Lambda_{12})X_2 \quad [8]$$

In this study, we found that our conductivity data for the KOH- $K_2\text{Zn}(\text{OH})_4$ system and the data for the KOH-KF system (9) and the KOH- K_2CO_3 system (10) are consistent with the solution mixture rule.

* Electrochemical Society Active Member.

¹ Present address: Department of Chemistry, University of Wisconsin, Milwaukee, Wisconsin 53201.

Key words: mixture rule, KOH-KF, KOH- K_2CO_3 .

Experimental

Figure 1 shows the schematic diagram of the experimental apparatus, which consists of (i) zincate generation cell, (ii) electrolyte pump, (iii) power supply, and (iv) electrolyte reservoir. The Lucite zincate generation cell was at room temperature (22°C). The volume of the cell was about 125 ml. The working electrode was an array of four zinc sticks with dimensions of $0.7 \times 0.7 \times 10.5$ cm; these sticks were manufactured by J. T. Baker Chemical Company (Phillipsburg, New Jersey), and had a purity of 99.6%. To prevent the removal of zincate from the electrolyte, a nickel oxide counterelectrode, obtained from Yardney Electric Company (Pawcatuck, Connecticut), was used. A polypropylene separator, purchased from Spectrum Medical Industries, Incorporated (Los Angeles, California), was placed between the two electrodes to prevent electrical shorting. An Hg/HgO reference electrode was used to monitor the electrode potentials. An oxygen-free nitrogen stream was introduced into the cell to eliminate CO_2 from air. The electrolyte reservoir was a 500 ml Pyrex three-necked round-bottomed flask which was kept in a constant temperature water bath at 25°C. The electrolyte was 7.32N KOH (reagent grade) in doubly distilled water which was initially saturated with zinc oxide (0.64M) (analytical reagent quality). No further purification of these materials was attempted. The electrolyte was prepared with doubly distilled water.

At the beginning of the experiment, the cell and the reservoir were filled with the electrolyte. During the discharge of the cell, the electrolyte was continuously pumped by a polypropylene bellow pump, manufactured by Gorman-Rupp Industries (Bellville, Ohio), from the reservoir to the bottom of the cell and then allowed to overflow from the top of the cell back to the reservoir. The flow rate was adjusted so that no gas bubbles were trapped in the overflow stream.

The electrical circuit for the experiment is illustrated in Fig. 1. To maintain a constant current level ranging from 0.6 to 1.2A (about 10-20 mA/cm² on Zn electrode), a dummy resistor was placed between the working electrode (WE) connector and the reference electrode (RE) connector of the Wenking HP72 potentiostat made by G. Bank Elektronik (West Germany). The potential of the cell as well as that of the nickel oxide electrode with respect to the Hg/HgO reference electrode were recorded on a strip-chart

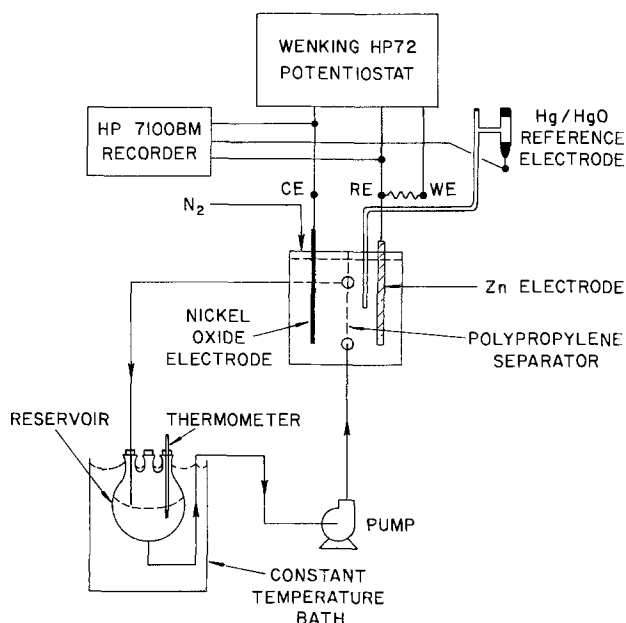


Fig. 1. Experimental apparatus

recorder (Hewlett-Packard 7100 BM). When the recorder indicated that the potential of the nickel oxide electrode had dropped to 0.2V vs. the Hg/HgO electrode, cell discharge and electrolyte circulation were stopped. The nickel oxide electrode was then removed and recharged in fresh electrolyte in a cell using a nickel plate as a counterelectrode. Subsequently, the charged nickel oxide electrode was returned to the zincate generation cell and the zincate generation process continued. This procedure was repeated several times until the desired level of zincate concentration was obtained.

After completion of each discharge, time was allowed for the electrolyte in the reservoir to return to 25°C. Next, 1 ml aliquots of this electrolyte were pipetted for the determination of zincate concentration by titration with 0.1M EDTA (ethylenediaminetetraacetic acid) with Erichrome Black T as an indicator. The specific conductivity of the electrolyte in the reservoir was measured at different zincate concentrations (0-1.52M), using two conductivity cells in conjunction with an a-c conductivity bridge operated at a frequency of 1 kHz. The conductivity cells were Models G50 and G100 Beckman Instruments, Incorporated (Cedar Grove, New Jersey); the conductivity bridge was Model 31, Yellow Springs Instrument Company, Incorporated (Yellow Springs, Ohio). The cell constants were calibrated using 0.1N KCl (specific conductivity 0.11134 mho/cm) (11) and found to be 50.899 cm⁻¹ for the Model G50 and 99.857 cm⁻¹ for the Model G100. To make the conductivity measurement, the electrolyte was sucked into the conductivity cell and a conductance reading completed within 30 sec. In this manner the change in temperature is minimal.

When the concentration of zincate was above 1.3M, white precipitate was observed in the electrolyte. Therefore, several hours were allowed for the precipitate to settle to the bottom of the reservoir. Portions of clear electrolyte were taken for the determination of specific conductivity and zincate concentration; there were at least two measurements made for each determination. For one determination, electrolyte taken from the reservoir was vacuum filtered through 0.2 μm filter paper. The result of this measurement was in agreement with those obtained using clear unfiltered electrolyte. The average uncertainty for all the measurements was 1.5%.

Results and Discussion

The specific conductivity data along with data obtained from other studies (5, 6, 9) under similar conditions are presented in graphical form in Fig. 2. This figure shows that a least squares fit of our specific conductivity data is in agreement with those of the

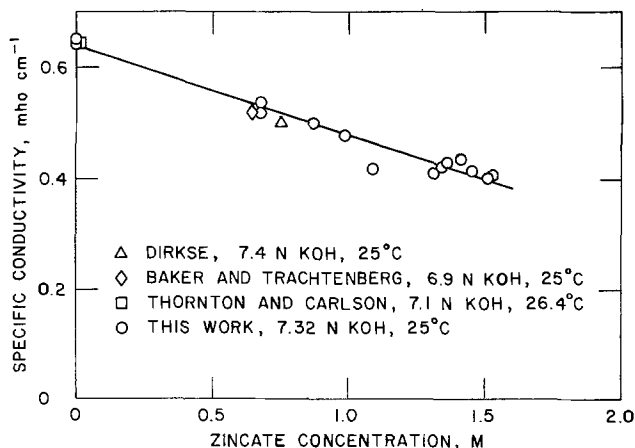


Fig. 2. Specific conductivity of KOH electrolytes as a function of zincate concentration.

other workers. This figure also indicates that the conductance of the electrolyte may be linearly correlated with zincate concentration. A linear relationship for conductivity *vs.* weight percent of ZnO was also observed by Dyson *et al.* (4) up to chemical saturation of ZnO in more concentrated KOH electrolyte (namely, 35-46% by weight or 8.3-11.6N). The linear relationship shown in Fig. 2, between the specific conductivity, k , and the molar concentration of zincate, $C_{Zn(II)}$, can be expressed by the equation

$$k = (0.637 \pm 0.011) - (0.159 \pm 0.009)C_{Zn(II)} \text{ mho/cm} \quad [9]$$

The slope of 0.16 for this equation is higher than the slopes estimated from the data at 25°C given by Dyson *et al.* (4) (slope of 0.13 for 35% KOH, 0.11 for 40% KOH, 0.095 for 46% KOH). These values indicated that the specific zincate conductance decreases with increasing KOH concentration. We also found that the specific conductivity of KOH decreases with increasing KOH concentration ($k = 0.64$ mho/cm at 31% KOH, 0.58 mho/cm at 40% KOH, and 0.45 mho/cm at 46% KOH) (4).

The zincate species in the solution of ZnO in KOH is $Zn(OH)_4^{2-}$ as evidenced by nuclear magnetic resonance (NMR), Raman, and infrared reflection spectroscopic studies (12-14). In the supersaturated solution, Dirkse (12) indicated that the zincate species is also $Zn(OH)_4^{2-}$. However, Briggs *et al.* (1) concluded from their spectroscopic study that the zincate species in the supersaturated state is initially $Zn(OH)_4^{2-}$ and sequentially becomes $[Zn(OH)_3(H_2O)]^-$ and $[Zn(OH)_2(H_2O)_2]$ as the degree of supersaturation increases. If there were any species other than $Zn(OH)_4^{2-}$ in our experiment, a change in the slope of the plot in Fig. 1 would have been detected as was shown in the plots of $emf \text{ vs. } \log_{10}\{[Zn(II)]/[OH^-]^4\}$ given by Briggs *et al.* (1). We find no such evidence in Fig. 1. Therefore, we conclude that the zincate species in the supersaturated solution is the same as that in the solution of ZnO in KOH. Therefore, Eq. [1] is the electrode reaction.

According to Eq. [6]-[8], the concentration of potassium ions is required to apply the mixture rule to our data. The initial concentration of potassium ions was 7.32N. This value may be changed in the dissolution of ZnO and Zn due to possible change in the electrolyte volume and take-up/release of potassium ions by the nickel oxide electrode. We investigated these two possible ways for changing the K^+ concentration and found the change to be negligibly small. In the chemical dissolution of ZnO and anodic dissolution of Zn, the change in the electrolyte volume is small. This is justified by the fact that the additive rule predicts values within 1% of the density data given by Dirkse (5) for the solution of ZnO in KOH electrolytes and values within 3% of the density data given by Eisenberg *et al.* (15) for supersaturated zincate solutions. Experimental evidences (16, 17) indicate that potassium ions are taken up by nickel oxide electrodes during the charge cycle, and released during the discharge cycle. A recent study by Barnard *et al.* (17), indicates that the take-up/release of potassium ions depends on the crystal structure of the nickel oxide electrode: 0.102 mol per $2e^-$ for β -NiOOH and 0.47 mol per $2e^-$ for γ -NiOOH. Harivel *et al.* (18) indicated that the formation of β - and γ -NiOOH depends upon the charging rate, the state of charge, and the electrolyte concentration. In our study, the nickel oxide electrode was charged at 6 mA/cm² up to 20% of theoretical capacity (3 A-hr) in a cell with fresh electrolyte and then discharged in the zincate generating cell. Under such conditions, only β -phase materials are expected to be formed. Therefore, we estimate that 0.102 mol

of potassium ions per $2e^-$ were taken up from the charging cell and released in the zincate generating cell. For our maximum zincate concentration of 1.53M, the concentration of potassium ions is estimated to increase by a maximum of 0.15N or 2% of its original value. Therefore, we may assume that the concentration of potassium ions in the electrolyte throughout the experiment did not change. When divided by the total equivalent concentration (7.32N), Eq. [9] is transformed to

$$\Delta_{123} = (87 \pm 2) - (80 \pm 5) X_2 \text{ mho} \cdot \text{cm}^2/\text{equiv.} \quad [10]$$

where subscripts 1, 2, and 3 designate potassium, zincate, and hydroxide ions, respectively. Thus, from Eq. [8], it can be concluded that $\Delta_{13} = 87 \pm 2$ mho \cdot cm²/equiv. and $\Delta_{13} - \Delta_{12} = 80 \pm 5$ mho \cdot cm²/equiv. In other words, the apparent equivalent conductances are 87 ± 2 mho \cdot cm²/equiv. for potassium hydroxide and 7 ± 5 mho \cdot cm²/equiv. for potassium zincate in the electrolyte. When the mixture rule is applied to the data given by Dyson *et al.* (4), values of about zero are also obtained for the conductance of potassium zincate. This low value of equivalent conductance for potassium zincate indicates that potassium ions and zincate ions are likely to form neutral associated ion pairs in the electrolyte.

If the mixture rule is a valid approximation for concentrated solutions, then it can be used to estimate the conductance of ternary electrolyte systems from the available conductance data of binary electrolyte systems (19). Conductivity data of the KOH-KF system (9) ($7.13 \pm 0.16N$), the KOH-K₂CO₃ system (10) ($8.35 \pm 0.23N$), and our KOH-K₂Zn(OH)₄ system (7.32N) are plotted in Fig. 3 as a function of equivalent fraction. It should be noted that there was a problem with Ref. (10). The data in Ref. (10) were given in both graphical and tabular forms, which was not consistent. It was decided to select that set of data for which the KOH values were consistent with those calculated from the table given in Ref. (19). Results of least squares analyses of these data are shown in Fig. 3 and Table I. As can be deduced for each electrolyte system in Table I, the conductance data of the binary system are in good agreement with those for the ternary system; the maximum difference between the experimental data and the ternary system data (obtained from analyses of binary data using mixture rule) shown in Fig. 3 is six equivalent conductance units for the KOH-KF system and five equivalent conductance units for the KOH-K₂CO₃ system.

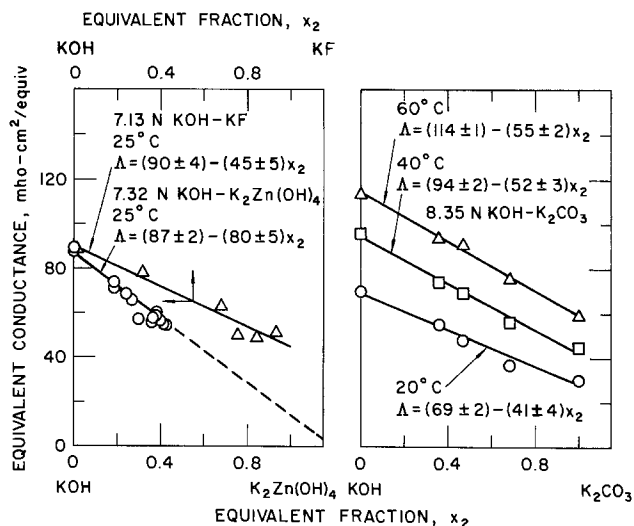


Fig. 3. Equivalent conductances of KOH-K₂Zn(OH)₄ system, KOH-KF system, and KOH-K₂CO₃ system as a function of equivalent fraction.

Table I. Values of Λ_{13} and $\Lambda_{13} - \Lambda_{12}$ obtained from binary system data and least squares analyses of ternary system data using the mixture rule (Eq. [8])

| Electrolyte | Concentration, N | Temperature, °C | Binary system data, ^a mho · cm ² /equiv. | | | Ternary system data, ^b mho · cm ² /equiv. | |
|---|------------------|-----------------|---|----------------|-------------------------------|--|-------------------------------|
| | | | Λ_{12} | Λ_{13} | $\Lambda_{13} - \Lambda_{12}$ | Λ_{13} | $\Lambda_{13} - \Lambda_{12}$ |
| KF-KOH | 7.13 | 25 | 43 | 89 | 46 | 90 ± 4 | 45 ± 5 |
| K ₂ CO ₃ -KOH | 8.35 | 20 | 30 | 70 | 40 | 69 ± 2 | 41 ± 4 |
| K ₂ CO ₃ -KOH | 8.35 | 40 | 44 | 96 | 52 | 94 ± 2 | 52 ± 3 |
| K ₂ CO ₃ -KOH | 8.35 | 60 | 59 | 113 | 54 | 114 ± 1 | 55 ± 2 |
| K ₂ Zn(OH) ₂ -KOH | 7.32 | 25 | — | 88 | — | 87 ± 2 | 80 ± 5 |

^a Obtained from Ref. (9) and (10) and this work except for the value of Λ_{12} for KF, which was calculated from the table given in Ref. (12).

^b Calculated from our data and those from Ref. (9) and (10) [see text for a discussion of the data from Ref. (10)].

Summary

1. The specific conductivity of 7.32N KOH electrolyte at different zincate concentrations was measured. The conductivity of the electrolyte was found to decrease linearly with increasing zincate concentration. This is consistent with predictions based on the solution mixture rule (7).

2. A least squares analysis of our data by using the mixture rule indicates that the equivalent conductances of potassium hydroxide and potassium zincate (7.32N) at 25°C are 87 ± 2 and 7 ± 5 mho · cm²/equiv., respectively. This low value of equivalent conductance for potassium zincate indicates that the potassium and zincate ions are likely to form neutral associated ion pairs in the electrolyte.

Acknowledgments

This work was supported by the U.S. Department of Energy, Division of Electrochemical Energy Storage Systems. We thank Yardney Electric Company for providing nickel oxide electrodes.

Manuscript submitted Jan. 28, 1981; revised manuscript received March 25, 1981.

Any discussion of this paper will appear in a Discussion Section to be published in the June 1982 JOURNAL. All discussions for the June 1982 Discussion Section should be submitted by Feb. 1, 1982.

Publication costs of this article were assisted by Argonne National Laboratory.

REFERENCES

1. A. G. Briggs, N. A. Hampson, and A. Marshall, *J. Chem. Soc. Trans. Faraday Soc.*, **70**, 1978 (1974).
2. A. Langer and E. A. Pantier, *This Journal*, **115**, 990 (1968).
3. R. J. Hoffman, H. F. Gibbard, R. J. Ekern, and B. L. McKinney, Abstract 119, p. 304, The Electrochemical Society Extended Abstracts, Los Angeles, California, Oct. 14-19, 1979.
4. W. H. Dyson, L. A. Schreier, W. P. Sholette, and A. J. Salkind, *This Journal*, **115**, 566 (1968).
5. T. P. Dirske, *ibid.*, **106**, 154 (1959).
6. C. T. Baker and I. Trachtenberg, *ibid.*, **114**, 1045 (1967).
7. D. G. Miller, *J. Phys. Chem.*, **71**, 616 (1967).
8. W. Sunu, Ph.D. Thesis, University of California, Los Angeles (1978).
9. R. F. Thornton and E. J. Carlson, *This Journal*, **127**, 1448 (1980).
10. M. Nitabah, D. Lucesdi, and P. Degobert, *Electrochim. Acta*, **17**, 327 (1972).
11. G. Jones and B. C. Bradshaw, *J. Am. Chem. Soc.*, **55**, 1780 (1933).
12. W. Van Doorne and T. P. Dirkse, *This Journal*, **122**, 1 (1975).
13. G. H. Newman and G. E. Blomgren, *J. Chem. Phys.*, **43**, 2744 (1965).
14. J. S. Fordyce and R. L. Baum, *ibid.*, **43**, 843 (1965).
15. M. Eisenberg, H. F. Bauman, and D. M. Brettner, *This Journal*, **108**, 909 (1961).
16. M. A. Aia, *ibid.*, **114**, 418 (1967).
17. R. Barnard, C. F. Randell, and F. L. Tye, *J. Appl. Electrochem.*, **10**, 109 (1980).
18. H. P. Harivel, B. Morignat, J. Labat, and J. F. Laurent, "Power Sources 1966," D. H. Collins, Editor, p. 239 (1967).
19. D. Dobos, "Electrochemical Data," Elsevier Scientific Publishing Co., New York (1975).

Lithium Incorporation by V_6O_{13} and Related Vanadium (+4, +5) Oxide Cathode Materials

D. W. Murphy,* P. A. Christian,¹ F. J. DiSalvo, J. N. Carides, and J. V. Waszczak

Bell Laboratories, Murray Hill, New Jersey 07974

ABSTRACT

The known vanadium oxides VO_{2+y} ($0 \leq y < 0.5$) have been examined as cathode materials in ambient temperature nonaqueous secondary lithium cells. The discharge products have also been chemically prepared and characterized by x-ray diffraction, thermal analysis, and magnetic susceptibility. The best cathode materials are V_6O_{13} and a slightly oxygen-rich V_6O_{13+y} . Electrochemical and chemical preparations afford $Li_xV_6O_{13+y}$ ($x \leq 8$). The $Li_xV_6O_{13}$ is described as an insertion compound of V_6O_{13} .

A wide variety of inorganic compounds with either two-dimensional van der Waal's bonded layer structures or three-dimensional framework tunnel structures undergo topotactic reactions with lithium (1). Such reactions are often readily reversed, making these materials attractive candidates for the positive electrode in secondary lithium cells (2-5). Most previous work has centered on two-dimensional metal chalcogenides as potential lithium cathode materials, although transition metal oxides with framework structures such as many of the rutiles (6), vanadium oxides (6-10), molybdenum oxides (11), and tungsten oxides (12) have been shown to undergo reversible lithium incorporation both chemically and electrochemical cells. Herein we describe in detail incorporation of lithium by vanadium oxides with stoichiometries between $VO_{2.0}$ and $VO_{2.5}$. In addition to describing the preparation and characterization of the parent vanadium oxides, some of the chemical, thermal, magnetic, spectral, electrical, and electrochemical properties of their chemically derived lithium bronzes are reported.

Experimental

Reagent grade ammonium metavanadate, NH_4VO_3 , (Alfa) was used without further purification. Vanadium pentoxide was prepared by thermal decomposition of NH_4VO_3 (13). Vanadium metal powder (325 mesh, 99.5% pure) was obtained from Cerac and stored under Ar. A solution of $\sim 2.4N$ n-butyllithium in hexane was obtained from Alfa-Ventron and was diluted to $\sim 1.3N$ with hexane. All reactions with n-butyllithium were carried out in an He atmosphere in a Vacuum/Atmosphere glove box. All solvents were reagent grade and were distilled under Ar from the appropriate drying agents.

V_6O_{13} .—Stoichiometric amounts of V_2O_5 and vanadium metal powder were intimately mixed and heated to $600^\circ C$ in an evacuated quartz tube. After 1 day the temperature was increased to $680^\circ C$ for 1-3 days. The resulting microcrystalline product was deep purple in color and exhibited a metallic luster. The vanadium-oxygen stoichiometry was verified by TGA in an oxygen atmosphere. The x-ray powder diffraction pattern of the product was obtained using $CuK\alpha$ radiation and is identical to that reported for V_6O_{13} (14).

V_6O_{13+y} .—Ball milled (1-5 μm), vacuum dried, NH_4VO_3 was thermally decomposed under an Ar stream. In a typical preparation, 38.0-40.0g of NH_4VO_3 was placed in a porcelain boat inside a quartz tube and heated in an Ar stream (140-150 cm^3/min) from

ambient to $500^\circ C$ at a rate of ~ 4 to $4.5^\circ/min$. After 1 hr at $500^\circ C$ the temperature was increased to $550^\circ C$ for 1 hr. The product was slowly cooled to room temperature in an Ar atmosphere. The powder obtained varied in color from blue-gray to navy blue. The stoichiometries of the products were determined by oxidizing the samples to V_2O_5 using TGA and range between $V_6O_{13.5}$ and $V_6O_{13.16}$. The powder x-ray diffraction patterns are similar to that of V_6O_{13} .

$VO_2(B)$.—The procedure of Theobald and co-workers (15, 16) was modified as follows. Finely ground V_2O_5 was reduced in a stream of H_2 ($\sim 200 cm^3/min$) at $320^\circ C$ for 4 days. The resulting black powder was dried at $300^\circ C$ under Ar for 3 days to remove residual water. The overall stoichiometries of the products prepared in this manner were determined by TGA to range from $VO_{1.99}$ to $VO_{2.11}$. The x-ray diffraction powder pattern of the product is consistent with that reported for $VO_2(B)$ (16).

V_4O_9 .—Finely ground V_2O_5 was slowly reduced in a stream of anhydrous SO_2 ($\sim 200 cm^3/min$) at $430^\circ C$ (17). The progress of the reduction was monitored by x-ray powder diffraction. Several intermediate regrindings of the sample were necessary to ensure homogeneity. After 2-3 days' time, the x-ray diffraction pattern was consistent with that reported for V_4O_9 (17).

V_3O_7 .—A mixture of finely ground V_2O_5 (10 mmol) and the required amount of freshly reduced V_2O_3 (2 mmol) was pressed into pellets and heated for 11 days at $550^\circ C$ in an evacuated quartz tube (18). The x-ray diffraction pattern of the dark blue-gray product is consistent with that reported by Thomas *et al.* (19) with only a trace of unreacted V_2O_5 present.

Lithiation of VO_y with n-butyllithium/hexane.—As described previously (20), a 100-250 mg sample of the oxide was treated with a known volume of standardized dilute ($\sim 1.3N$) n-BuLi in hexane. X-ray powder diffraction patterns were measured for lithiated samples mounted in an evacuable holder fitted with a beryllium window.

Delithiation of Li_xVO_y with iodine/acetonitrile (21).—A known volume of $\sim 0.07M$ I_2 in degassed, dry acetonitrile solution was added dropwise to a 100-200 mg sample of the lithium bronze under Ar. The resulting mixture was stirred at room temperature for 10-12 hr. The vanadium oxide was collected by suction filtration and washed with acetonitrile. Titration of the filtrate and washings with a standard $0.1N$ $Na_2S_2O_3$ solution gave the amount of unreacted I_2 and allowed calculation of the residual lithium content. In some cases a solution of DDQ (dichlorodicyanoquinone) was

* Electrochemical Society Active Member.

¹ Present address: Western Electric, Engineering Research Center, Princeton, New Jersey 08540.

Key words: battery, lithium, insertion compound.

added to verify that all of the lithium had been removed.

Electrochemical cells.—Test cells were constructed as previously described (21). Cathodes were powders of the pure vanadium oxide or the oxide mixed with graphite. The electrolyte was generally 1M LiAsF₆ in propylene carbonate. Cells were cycled at constant current between preset voltage cutoffs, generally 3.1V on charge and 1.5V on discharge. Cells typically contained 10-20 mg of the active cathode material.

Results and Discussion

Vanadium oxides with octahedral or distorted octahedral coordination are known for all oxidation states between V⁵⁺ and V²⁺. Furthermore, the energy differences between these different oxidation states are not very great and numerous examples of mixed valence and metallic compounds exist. V₆O₁₃, for example, is metallic with the formal oxidation state assignment: V₄⁴⁺ V₂⁵⁺. The possibility for easy redox chemistry with structures suitable for lithium ion insertion prompted our investigation of lithium insertion chemistry and galvanic cell behavior.

The structures of the vanadium oxides V₂O₅, V₆O₁₃, and VO₂(B) can be viewed as shear structures derived from that of ReO₃ (22, 23). A single shear (Fig. 1) is accomplished by removing every second (200) plane of oxygen atoms and closing the structure up along the shear vector 1/2[101] to give the V₂O₅ structure. The actual structure of V₂O₅ (24) is distorted toward five coordinate V by displacement of V out of the center of each octahedron. A V=O bond is formed which gives a strong IR stretch at 1000 cm⁻¹. Shearing the idealized V₂O₅ lattice by removing every third (020) plane of oxygen atoms and closing the structure along the shear vector 1/2[110] gives the V₆O₁₃ structure. Similarly, removing every second (020) plane of oxygen from V₂O₅ and closing along 1/2[110] gives

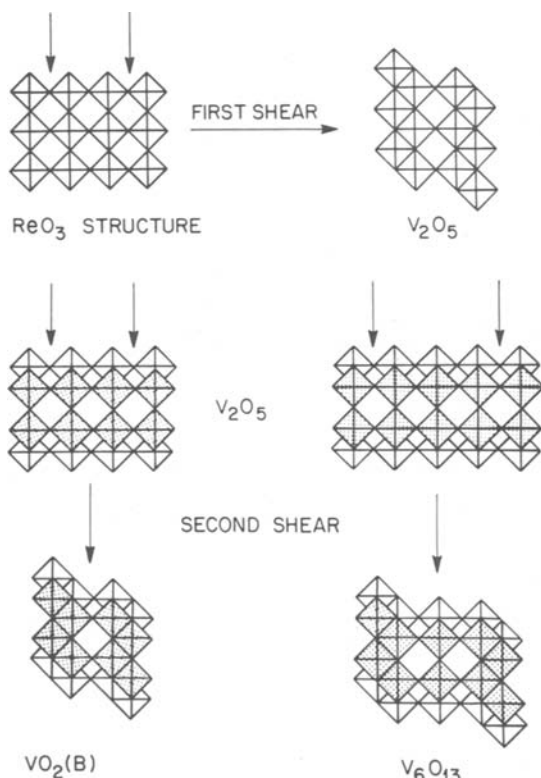


Fig. 1. The idealized V₂O₅ lattice is derived by a shear of the ReO₃ lattice along the planes indicated by arrows. The VO₂(B) and V₆O₁₃ lattices are derived by a shear of the V₂O₅ lattice as indicated.

the VO₂(B) structure. The V₆O₁₃ structure (14) contains only slightly distorted VO₆ octahedra joined by edge sharing into single and double zig-zag chains parallel to [010] and linked together by additional edge sharing into single and double sheets of octahedra parallel to the (100) plane. These sheets are interleaved so that single and double sheets alternate. The stacked sheets are interconnected by corner sharing into a three-dimensional framework. The VO₂(B) structure can be described similarly except that only double sheets of octahedra are present (15). The structures reported for both V₄O₉ (25) and V₃O₇ (18) are very open and cannot be derived by a simple shear mechanism from ReO₃. The structure of V₃O₇ contains both single and double chains of VO₆ octahedra, like V₆O₁₃, as well as some edge-shared zig-zag chains of VO₅ trigonal bipyramids, as in the V₂O₅ structure. Thus, V₃O₇ appears to have an intermediate structure between that of V₆O₁₃ and V₂O₅.

The vanadium oxides V₂O₅, V₃O₇, V₄O₉, and VO₂(B) used in this study were prepared essentially by previously reported methods with slight modifications. Typical reaction conditions are summarized in Fig. 2. Stoichiometric V₆O₁₃ is readily prepared by the solid-state reaction of V₂O₅ and the appropriate amount of V metal in a sealed quartz ampul. A vanadium oxide with a range of stoichiometries approximating V₆O₁₃, an x-ray powder diffraction pattern similar to that of V₆O₁₃, and a transition in magnetic susceptibility at the same temperature as V₆O₁₃ can be prepared by several procedures. Based on reports that "reduced" phases with stoichiometries close to V₆O₁₃ could be obtained by thermal decomposition of [(NH₄)₂V₆O₁₆] *in vacuo* (26), by reducing V₂O₅ with NH₃ at 325°-350°C (27) or by thermally decomposing NH₄VO₃ *in vacuo* at 500°C (22), a procedure involving the thermal decomposition of NH₄VO₃ in a controlled stream of argon was developed. This procedure was utilized to produce slightly nonstoichiometric V₆O_{13+y}. The stoichiometries of the products are typically $\leq 1.5\%$ oxygen-rich, although under more reducing conditions oxygen-deficient products can be generated. If more extensive reduction is desired, additional NH₃ or H₂ can be added to the inert sweep gas. Although the materials prepared in this manner have x-ray powder diffraction patterns very similar to that of V₆O₁₃ there is significant variation in the relative intensities of several of the diffraction peaks as well as a slight shifting of peaks to lower angles. It appears that previously reported V₆O₁₃-related "reduced phases" can be rationalized in terms of nonstoichiometric V₆O_{13±y} compositions. The "D" phase reported

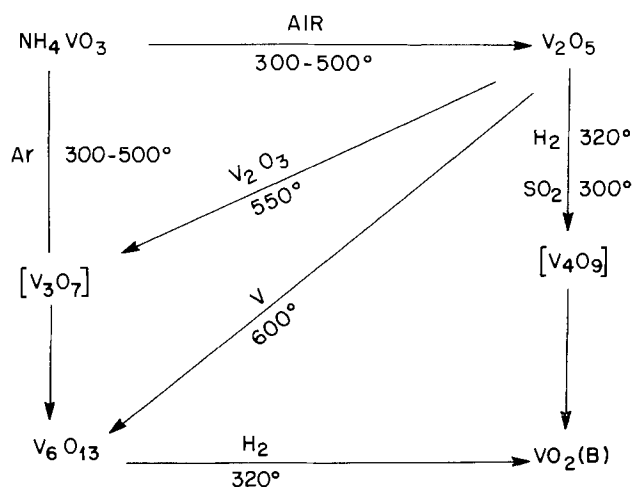


Fig. 2. The reactions used to prepare vanadium oxides are summarized. The reactions of V₂O₅ with V₂O₃ and V are stoichiometric in sealed ampuls. All others use flowing gas.

by Théobald and co-workers (26) exhibits a diffraction pattern with peak intensities comparable to those observed for samples of oxygen-rich V_6O_{13+y} . However, the powder diffraction pattern of the "C" phase reported by the same workers corresponds to that of a sample of oxygen-deficient V_6O_{13-y} prepared in this work below 300°C using H_2 to augment reduction. In this latter sample, the 001 diffraction peaks are greatly diminished in intensity or absent altogether. Differences in x-ray intensities are also sensitive to the maximum temperature reached during the preparation. Heat-treatment at 500°C of samples with weak 001 peaks results in an increase in the intensity of these peaks. Typically the ratio of the intensity of the 002 to the 110 peaks for V_6O_{13+y} discussed below which has been annealed at 550°C is about half that observed for stoichiometric V_6O_{13} . The unit cell parameters determined by a least squares analysis for several samples of V_6O_{13+y} are given in Table I.

The most interesting of the vanadium oxides for secondary cathode materials (vide infra) is the slightly oxygen-rich V_6O_{13+y} ($y \lesssim 0.2$) prepared by the thermal decomposition of NH_4VO_3 in an inert gas stream. The chemical and physical properties of V_6O_{13+y} differ perceptibly from those of stoichiometric V_6O_{13} . The nonstoichiometric V_6O_{13+y} is nearly single phase. Thermal analysis by DSC indicates the presence of ~1-2% VO_2 (endothermic transition at 69°C). Dilute acid or base wash under conditions which would dissolve all higher vanadium oxides does not affect V_6O_{13+y} . The magnetic susceptibility of V_6O_{13+y} is compared to that of V_6O_{13} in Fig. 3. The sharp break in susceptibility at the metal-insulator transition (149 K) characteristic of V_6O_{13} (28, 29) is appreciably broadened in V_6O_{13+y} . Because of the close structural relationship between V_6O_{13} , $VO_2(B)$, and V_2O_5 , a potential lattice defect might involve a stacking disorder in which extra single or double sheets are present. The presence of extra single sheets would correspond to a microregion of V_2O_5 in the structure and result in an oxygen-rich stoichiometry. Similarly, the presence of extra double sheets would correspond to a microregion of $VO_2(B)$ and result in an oxygen-deficient stoichiometry. Such stacking disorders are not uncommon and have been previously observed in related materials. Colpaert and co-workers (30), in their study of the effects of low energy electron bombardment of V_2O_5 , observed the nucleation of V_6O_{13} on the V_2O_5 (010) surface and the presence of shear planes at the boundaries between the V_2O_5 and the V_6O_{13} nuclei. Horiuchi and co-workers (31) have observed regions of $VO_2(B)$ and its twin in areas surrounding small cavities in the V_6O_{13} structure by TEM. Crystallographic shear planes were also observed in the walls of these cavities and substantial stacking faults were present in the regions immediately surrounding the cavities. The relatively small number of extra single or double sheets (<1.5%) required to change the overall stoichiometry of V_6O_{13} would not be expected to significantly alter the bulk powder x-ray diffraction pattern. The presence of stacking faults is also consistent with observed broadening of the metal insulator transition since magnetic susceptibility is highly sensitive to struc-

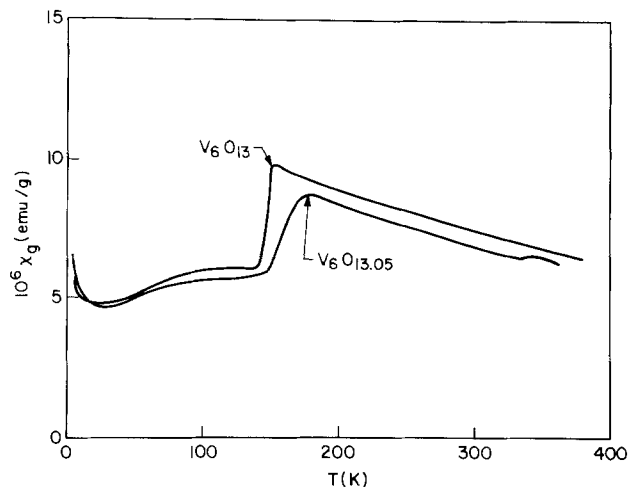


Fig. 3. The magnetic susceptibility of V_6O_{13} and $V_6O_{13.05}$ ($VO_{2.175}$).

tural disorder as well as the presence of interstitial impurities.

Lithium bronzes of V_6O_{13} and V_6O_{13+y} .—Treatment of both solid V_6O_{13} and V_6O_{13+y} with dilute solution of n-butyllithium in hexane at room temperature affords bronzes with the nominal compositions $Li_xV_6O_{13}$ ($0 < x < 4.5$) and $Li_xV_6O_{13+y}$ ($0 < x \lesssim 8$), respectively. The extent and apparent rate of lithium incorporation by V_6O_{13+y} are significantly greater than for V_6O_{13} . At room temperature the stoichiometric material incorporates a maximum of ~0.75Li/V to give a bronze with the composition $Li_{4.5}V_6O_{13}$. Increasing the temperature of the reactants to ~50°C (in a sealed tube) affords a ~30% increase in the maximum lithium stoichiometry to $Li_{5.8}V_6O_{13}$. However, the reaction of an equivalent amount of $V_6O_{13.16}$ with a similar volume of n-butyllithium solution at room temperature is so vigorous that the hexane solvent boils. Even with a more dilute n-butyllithium solution, $V_6O_{13.16}$ incorporates as much as 1.3Li/V to give a bronze with the limiting composition $Li_{7.9}V_6O_{13.16}$. Typically, values of 1.25Li/V are obtained at room temperature with oxygen-rich V_6O_{13+y} compositions. Above room temperature, treatment of V_6O_{13+y} with dilute n-butyllithium solution results in some decomposition. Heat-treatment of V_6O_{13+y} at 650°C *in vacuo* reduces its lithium capacity to approximately that of V_6O_{13} .

Treatment of $V_6O_{13.16}$ with an acetonitrile solution of lithium iodide results in a small amount of lithium incorporation ($Li_{0.35}V_6O_{13+y}$) corresponding to less than 5% of the limiting amount of lithium incorporated by treatment with n-butyllithium. However, treatment of V_6O_{13} with LiI solution at and above room temperature results in negligible (<0.01Li/V) lithium incorporation.

The x-ray powder diffraction data for the lithium bronzes with the compositions $Li_{4.1}V_6O_{13.05}$, $Li_{5.5}V_6O_{13.5}$, and $Li_{7.6}V_6O_{13.16}$ are summarized in Table II. A comparison of the monoclinic unit cell parameters of these bronzes with those of the parent $V_6O_{13.05}$ and $V_6O_{13.16}$ appears in Table III. The detailed structure of the lithium bronzes $Li_xV_6O_{13+y}$, including the nature of the Li sites, is presently unknown. It has been postulated (6, 10) that the lithium ions occupy sites within the tri-capped cube-octahedral cavity generated from the vacant perovskite cavity of ReO_3 in the double shearing process. For both $V_6O_{13.05}$ and $V_6O_{13.16}$ the incorporation of up to 1Li/V results in a 6% or less increase in unit cell volume. The incorporation of more than 1Li/V results in a 15% increase in unit cell volume compared to V_6O_{13} . Diffraction data for $Li_xV_6O_{13+y}$ ($0 < x < 8$) indicate the presence of a nonstoichiometric single phase region for $3.5 < x < 5.5$ in which

Table I. Crystallographic parameters for V_6O_{13+y}

| y | a | b | c | β | V |
|------|--------|-------|--------|---------|-------|
| 0* | 11.922 | 3.680 | 10.138 | 100.87 | 436.8 |
| 0† | 11.918 | 3.680 | 10.135 | 100.82 | 436.6 |
| 0.05 | 11.967 | 3.680 | 10.333 | 102.2 | 438.6 |

* Parameters from Ref. (25).

† Parameters obtained by our least squares analysis.

Table II. X-ray diffraction data for $\text{Li}_x\text{V}_6\text{O}_{13+y}$ *

| hkl | $\text{Li}_{4.1}\text{V}_6\text{O}_{13.05}$ | | $\text{Li}_{5.5}\text{V}_6\text{O}_{13.05}$ | | $\text{Li}_{7.5}\text{V}_6\text{O}_{13.10}$ | |
|-----------------------------|---|---------------------|---|---------------------|---|-------------------|
| | D_{obs} | D_{calc} | D_{obs} | D_{calc} | D_{obs} | D_{calc} |
| 200 | 5.772 | 5.770 | 5.750 | 5.750 | 6.104 | 6.104 |
| 002 | 5.001 | 5.009 | 5.000 | 5.003 | 5.079 | 5.073 |
| 110 | 3.730 | 3.733 | 3.737 | 3.738 | 3.814 | 3.815 |
| 003 | 3.341 | 3.339 | 3.336 | 3.335 | 3.381 | 3.382 |
| $\bar{4}01, 112$ | 2.919 | 2.919, 2.911 | 2.908 | 2.916, 2.909 | — | — |
| 311 | 2.750 | 2.750 | 2.746 | 2.752 | 2.849 | 2.849 |
| 203, 401 | 2.681 | 2.683, 2.645 | — | — | — | — |
| $\bar{3}12, \bar{1}13$ | 2.561 | 2.560, 2.566 | 2.570 | 2.565, 2.570 | — | — |
| 004 | 2.503 | 2.505 | 2.501 | 2.502 | — | — |
| 114 | 2.026 | 2.025 | 2.022 | 2.021 | 2.029 | 2.058 |
| 005 | 2.004 | 2.004 | 2.006 | 2.001 | 2.008 | 2.029 |
| $\bar{5}12, \bar{6}01, 502$ | 1.961 | 1.961, 1.957, 1.962 | 1.957 | 1.962, 1.953 | — | — |
| $\bar{1}06$ | 1.694 | 1.697 | 1.693 | 1.697 | — | — |
| 710, 315, $\bar{3}16$ | 1.524 | 1.521, 1.527, 1.520 | 1.518 | 1.517, 1.522 | — | — |
| 604, 025, 705 | 1.405 | 1.405, 1.406, 1.407 | 1.407 | 1.398, 1.406, 1.409 | — | — |
| 407, $\bar{6}21, 107$ | 1.388 | 1.388, 1.389, 1.389 | 1.390 | 1.391, 1.389, 1.386 | — | — |
| 712, 505 | — | 1.391, 1.391 | — | 1.385, 1.384 | 1.436 | 1.457, 1.436 |

* Unit cell parameters for D_{calc} are given in Table III.

Table III. Comparison of unit cell parameters of $\text{V}_6\text{O}_{13+y}$ and $\text{Li}_x\text{V}_6\text{O}_{13+y}$

| x | y | a | Δa (%) | b | Δb (%) | c | Δc (%) | β | V | ΔV (%) |
|-----|------|--------|----------------|-------|----------------|--------|----------------|---------|-------|----------------|
| 0 | 0.05 | 11.912 | | 3.683 | | 10.119 | | 100.7° | 436.3 | |
| 3.5 | 0.05 | 11.774 | | 3.930 | | 10.180 | | 100.1° | 463.1 | |
| 4.1 | 0.05 | 11.741 | -1.2 | 3.945 | +6.8 | 10.193 | +0.4 | 100.6° | 464.1 | +6.1 |
| 4.5 | 0.05 | 11.731 | -1.5 | 3.947 | | 10.175 | | 100.4 | 463.4 | |
| 5.5 | 0.05 | 11.718 | -1.5 | 3.952 | +7.2 | 10.196 | +0.4 | 100.1° | 463.3 | +6.2 |
| 7.2 | 0.15 | 12.435 | -1.7 | 4.007 | +7.4 | 10.333 | +0.6 | 102.2° | 503.2 | +6.2 |
| 7.6 | 0.15 | 12.420 | +3.9 | 4.016 | +8.9 | 10.322 | +1.8 | 100.6° | 506.1 | +14.7 |
| | | | +3.8 | | +9.1 | | +1.7 | | | +15.4 |

an increase in lithium content results in elongation of the unit cell in the b direction, contraction in the a direction, and virtually no change in the c direction. In addition to the unit cell parameters, other properties of these bronzes including thermal stability, electronic conductivity, magnetic susceptibility, electrochemical potential (OCV), and hydrolytic stability also vary with lithium content. The bronzes $\text{Li}_x\text{V}_6\text{O}_{13}$ and $\text{Li}_x\text{V}_6\text{O}_{13+y}$ are likely metastable relative to disproportionation or irreversible structural transformations. The thermal behavior of the $\text{Li}_x\text{V}_6\text{O}_{13+y}$ bronzes, as determined by DSC, is quite complex. Multiple endothermic and exothermic processes occur during the thermal decomposition of these bronzes. A major irreversible, exothermic structural transformation, which is nearly independent of the lithium content, occurs between 230° and 265°C. Another irreversible transformation observed by DSC at 100°-150°C is more strongly affected by changes in lithium content. At low lithium contents ($x \leq 3$) the transformation is endothermic and occurs at 140°-150°C while at higher lithium contents ($x \geq 4$) it is exothermic and occurs at about 120°-130°C. No change is observed by x-ray diffraction after annealing at 150°C.

The characteristic metal-insulator transition of V_6O_{13} (~140 K) as observed by magnetic susceptibility is influenced by the presence of lithium. This transition is significantly broadened at lithium contents as low as 0.01Li/V (Fig. 4). At lithium contents greater than 0.03Li/V the transition is further broadened and only a smooth increase in slope results. Finally, at lithium contents greater than 0.25Li/V, the susceptibility curve can be fit by a modified Curie-Weiss law. The lack of a transition at 0.03Li/V shows that the Li is homogeneous throughout the material.

Preliminary measurement of the electrical resistivities for pressed powder samples of various $\text{Li}_x\text{V}_6\text{O}_{13}$

suggests that resistivity increases dramatically with increasing lithium content. The resistivity of a fully lithiated material is nearly 10^3 greater than that for unlithiated material ($P \approx 10^{-2} \Omega \text{ cm}$). However, more accurate measurements are required in order to determine the nature of the dependence of the resistivity on lithium content.

The bronzes $\text{Li}_x\text{V}_6\text{O}_{13}$ and $\text{Li}_x\text{V}_6\text{O}_{13+y}$ are stable to oxidation at room temperature in dry air for extended periods of time. Samples stored for more than one year over CaSO_4 exhibit no degradation of their thermal, structural, chemical, or electrochemical properties. These materials can be handled even in humid air for at least several hours without decomposition. Oxidative

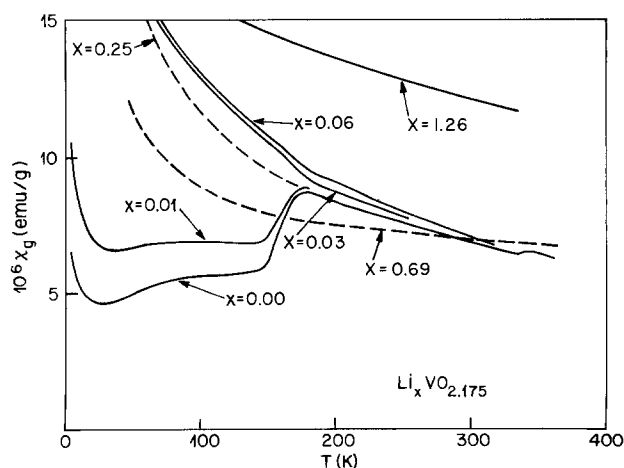


Fig. 4. The magnetic susceptibility of $\text{Li}_x\text{VO}_{2.175}$ as a function of x .

delithiation of $\text{Li}_x\text{V}_6\text{O}_{13}$ and $\text{Li}_x\text{V}_6\text{O}_{13+y}$ with an acetonitrile solution of I_2 removes most of the lithium (80–90%) as soluble lithium iodide. In order to remove the remaining lithium, a stronger oxidizing agent such as dichlorodicyanoquinone (DDQ) must be used (10). Virtually all of the lithium may be removed from $\text{Li}_x\text{V}_6\text{O}_{13}$ or $\text{Li}_x\text{V}_6\text{O}_{13+y}$ by DDQ to recover the host oxide unchanged. This is demonstrated by the reappearance of the metal-insulator transition in the magnetic susceptibility.

V_6O_{13} and $\text{V}_6\text{O}_{13+y}$ cathodes.—Both V_6O_{13} and $\text{V}_6\text{O}_{13+y}$ have been evaluated as active cathode materials for use in nonaqueous secondary lithium cells (9). The capacities of cells containing stoichiometric V_6O_{13} typically range up to 0.6Li/V for the first charge/discharge cycle, then decay slightly on subsequent cycles (Fig. 5). Blending stoichiometric V_6O_{13} with 50% graphite (by weight) does not appreciably increase the initial cell capacity, but such cells retain their capacity longer (Fig. 6). Cells with $\text{V}_6\text{O}_{13+y}$ and graphite exhibit initial capacities of $\approx 1.0\text{Li/V}$ (Fig. 7). Without graphite capacities for $\text{V}_6\text{O}_{13+y}$ cells may be diminished by as much as 50%. This is consistent with the reduced electronic conductivity at high Li concentrations.

Open-circuit potentials (OCV) of Li/LiAsF₆, PC/ $\text{V}_6\text{O}_{13+y}$ and Li/LiAsF₆, PC/ V_6O_{13} cells were measured

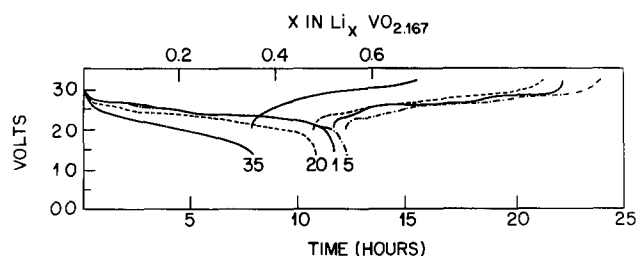


Fig. 5. Voltage vs. time and stoichiometry for a Li/LiAsF₆, PC/ V_6O_{13} cell containing 14.4 mg V_6O_{13} cycled at 0.2 mA between voltage limits of 3.1 and 1.5. No conductive diluents were added. Cycle numbers are indicated.

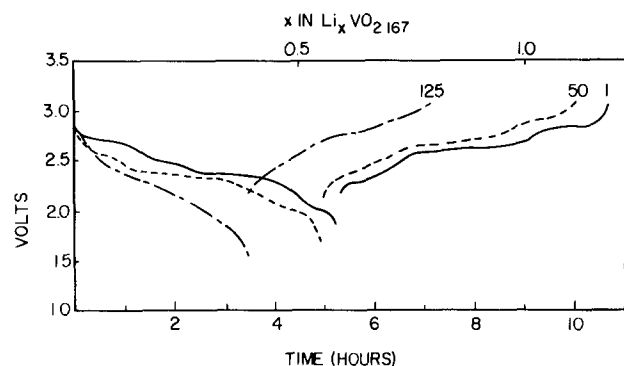


Fig. 6. Cycle data for a Li/LiAsF₆, PC/ V_6O_{13} , C cell containing 5.8 mg V_6O_{13} and 5.8 mg graphite cycled at 0.2 mA.

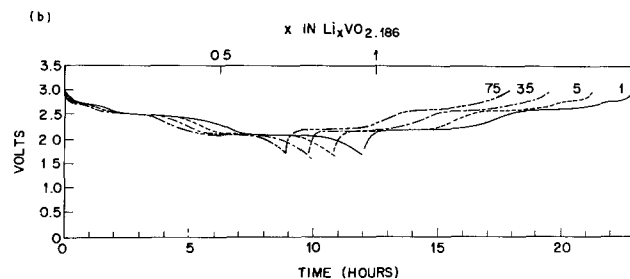


Fig. 7. Cycle data for a Li/LiAsF₆, PC/ $\text{VO}_{2.186}$ C cell containing 8.0 mg $\text{VO}_{2.186}$ and 8.0 mg graphite.

as a function of state of charge. Cells were charged or discharged $\sim 0.05\text{Li/V}$ between measurements. The OCV was taken after the measured value was unchanged for several hours. These results are shown in Fig. 8. The OCV curves are similar to the dynamic discharge curves for these materials.

Several distinct regions are present in these OCV curves. Results of x-ray powder diffraction also indicate the presence of at least three two-phase regions in Li_xVO_y ($0 < x < 1.2$). As x increases diffusion appears to slow down resulting in difficulty in reaching equilibrium at $x > 1.0$ for $y = 2.194$ and $x < 0.5$ for $y = 2.17$. This is also consistent with increased lithiation at elevated temperatures.

Cells containing V_6O_{13} without graphite can be discharged to zero volts briefly (< 2 hr) with no apparent degradation of performance, whereas cells containing $\text{V}_6\text{O}_{13+y}$ rapidly fail after such a discharge. Some protection from low voltage damage is afforded by heat-treating the $\text{V}_6\text{O}_{13+y}$ at temperatures between 575° and 675°C in *vacuo*. At these temperatures, limited sintering of the particles occurs. Although the heat-treated $\text{V}_6\text{O}_{13+y}$ appears to result in less degradation at low voltages, cells containing this material have only 25–45% of the capacity of the untreated material.

In addition to electrolyte and/or cathode decomposition at low voltages, cells containing 1M LiClO₄/propylene carbonate electrolyte are also susceptible to irreversible oxidation by V_6O_{13} above 3.0V during charging. This process appears to be catalytic and once initiated continues as long as current is passed through the cell. This electrolyte oxidation by V_6O_{13} is alleviated by using LiAsF₆ in PC.

The capacities of V_6O_{13} and $\text{V}_6\text{O}_{13+y}$ cells were found to be strongly dependent on the operating temperature. A cell containing V_6O_{13} was cycled at -16° , 0° , 45° , and 70°C (Fig. 9). After five cycles at room temperature the cell capacity had stabilized at $\sim 0.7\text{Li/V}$. When the cell was cooled to -16° the capacity dropped to $< 25\%$ of the room temperature value. At 0° the capacity was nearly 75% of the room temperature value. At 45° the capacity was almost 20% greater than the value at room temperature. Although the cell capacity at 70° was considerably greater than at room temperature, only limited cycling data could be collected since the rate of electrolyte decomposition was also greatly accelerated. At higher temperatures the discharge data of V_6O_{13} resembles that of $\text{V}_6\text{O}_{13+y}$ at room temperature.

$\text{VO}_2(\text{B})$.—The $\text{VO}_2(\text{B})$ prepared by the procedure of Theobald and co-workers (15, 16) exhibited an

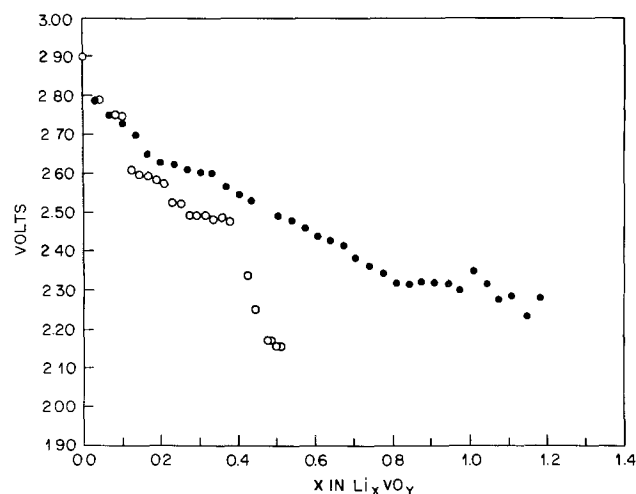
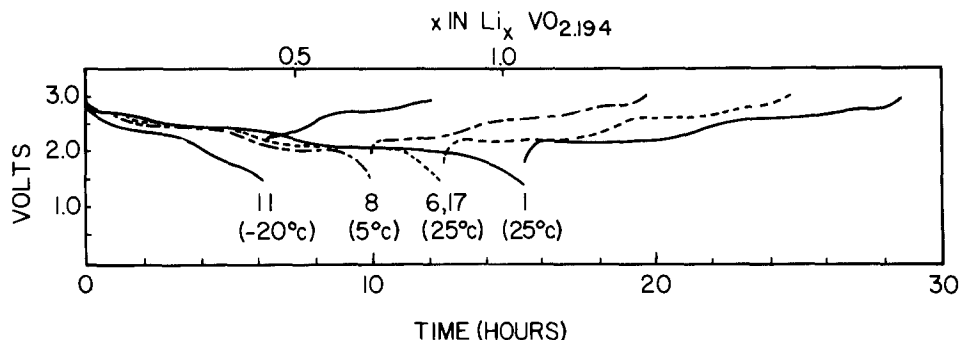


Fig. 8. Open-circuit voltages (OCV) for $\text{VO}_{2.167}$ (open circles) and $\text{VO}_{2.175}$ (closed circles) cells as a function of lithium stoichiometry.

Fig. 9. Cycle data for a Li/LiAsF₆, PC/VO_{2.167}, C cell as a function of temperature.



x-ray diffraction powder pattern which was consistent with that of the oxide B prepared by Sato and Ito (32) and the VO₂ · yH₂O described by Deschanvres *et al.* (33). The compressed powder resistivity of VO₂(B) at room temperature is of the same order of magnitude as that of V₆O₁₃ in contrast to the measurements reported by Sato and Ito (32). Also, the magnetic susceptibility of VO₂(B) exhibits a broad peak at ~250 K as previously reported (32). However, the precise mechanism responsible for producing the peak is not known. Assuming a localized spin ($g = 2$, $S = 1/2$) for the d¹V⁴⁺ ions, the susceptibility for VO₂(B) calculated from the Curie law of $+15.1 \times 10^{-6}$ emu/g is close to the observed value of $+14.2 \times 10^{-6}$ emu/g at 300 K and is nearly twice that of rutile VO₂ ($+7.6 \times 10^{-6}$ emu/g). As previously reported (15) VO₂(B) was observed by DSC to undergo a transformation to the more stable rutile structure when heated in an inert atmosphere above 450°. This transformation has an onset temperature of $440^\circ \pm 20^\circ$ and is exothermic with a heat of -200 ± 25 cal/mol. DSC analysis of samples of VO₂(B) annealed at 500°C revealed the presence of an endotherm at $\sim 69^\circ\text{C}$ characteristic of the metal/insulator transition of rutile VO₂. The x-ray diffraction patterns of these samples are consistent with that of rutile VO₂. Very weak lines assignable to V₆O₁₃ were also present. However, it is not certain whether V₆O₁₃ was produced in the transformation or if it was present as an impurity in the VO₂(B) since

some of the lines of VO₂(B) overlap with those of V₆O₁₃.

Lithium bronzes of VO₂(B).—Treatment of solid VO₂(B) with a dilute hexane solution of n-butyl-lithium at room temperature affords lithium bronzes Li_xVO₂(B) for $0.5 < x < 0.85$. Treatment of VO₂(B) with a solution of LiI in acetonitrile results in some lithium incorporation ($\sim 0.12\text{Li/V}$) at room temperature. Conversely, most of the incorporated lithium ($\sim 80\%$) can be removed from Li_xVO₂(B) by oxidation with a solution of iodine in acetonitrile.

The x-ray powder diffraction data obtained for several Li_xVO₂(B) bronzes are given in Table IV and the calculated monoclinic unit cell parameters in Table V. The powder patterns of these Li_xVO₂(B) bronzes closely resemble that of the parent VO₂(B) as well as Na_{0.2}TiO₂ (34).

The thermal stability of Li_xVO₂(B) bronzes as measured by DSC is somewhat improved over Li_xV₆O₁₃. The Li_xVO₂(B) bronzes are thermally stable up to $\sim 400^\circ$ in an inert atmosphere. Thus, Li_xVO₂(B) is nearly as thermally stable as the parent VO₂(B). This stabilization may arise from the presence of lithium in the cavities. Andersson and Wadsley (34) suggested that the isomorphous Na_{0.2}TiO₂ is stabilized by the presence of the sodium ions. The analogous alkali-free TiO₂(B) and Li_xTiO₂(B) ($x < 0.85$) have recently been reported (35).

Table IV. X-ray diffraction data for Li_xVO₂(B) bronzes

| hkl | Li _{0.52} VO ₂ (B) | | Li _{0.62} VO ₂ (B) | | Li _{0.85} VO ₂ (B) | |
|--------------------------------|--|---------------------|--|---------------------|--|---------------------|
| | D _{obs} | D _{calc} * | D _{obs} | D _{calc} * | D _{obs} | D _{calc} * |
| 001 | 6.125 | 6.132 | 6.164 | 6.141 | 6.134 | 6.139 |
| 200 | 5.731 | 5.715 | 5.776 | 5.769 | 5.742 | 5.761 |
| 201 | 4.997 | 4.953 | 5.036 | 4.943 | 5.002 | 5.018 |
| 201 | 3.706 | 3.685 | 3.725 | 3.725 | 3.718 | 3.686 |
| 002 | 3.064 | 3.066 | 3.070 | 3.070 | 3.063 | 3.070 |
| 111 | 2.958 | 2.954 | 2.978 | 2.977 | — | 2.993 |
| 400 | 2.862 | 2.857 | 2.868 | 2.884 | 2.890 | 2.881 |
| 102 | 2.730 | 2.768 | 2.739 | 2.782 | 2.730 | 2.767 |
| 411 | 2.319 | 2.304 | 2.321 | 2.316 | 2.329 | 2.343 |
| 003 | 2.042 | 2.044 | 2.044 | 2.047 | 2.038 | 2.046 |
| 411 $\bar{5}$ 11, $\bar{6}$ 01 | 2.003 | 1.984, 2.004, 1.989 | 2.005 | 2.004, 2.015, 2.000 | 1.998 | 2.000, 2.035, 2.013 |
| 501, 510, 4403 | 1.962 | 1.965, 1.948, 1.949 | 1.964 | 1.986, 1.966, 1.943 | 1.968 | 1.972, 1.971, 1.970 |
| 103, 600 | 1.921 | 1.919, 1.905 | 1.922 | 1.926, 1.923 | — | 1.918, 1.920 |
| $\bar{5}$ 12, 020 | 1.863 | 1.864, 1.861 | 1.867 | 1.868, 1.876 | 1.869 | 1.894, 1.902 |
| 413 | 1.720 | 1.727 | 1.725 | 1.725 | 1.724 | 1.749 |
| $\bar{7}$ 02, 412 | 1.655 | 1.652, 1.651 | 1.657 | 1.656, 1.667 | 1.660 | 1.674, 1.659 |
| $\bar{4}$ 21, 420 | 1.572 | 1.572, 1.560 | 1.573 | 1.582, 1.573 | 1.568 | 1.602, 1.587 |
| 313, 701, 222 | 1.484 | 1.483, 1.476, 1.477 | 1.486 | 1.495, 1.492, 1.488 | 1.484 | 1.488, 1.483, 1.497 |
| 014 | 1.417 | 1.418 | 1.421 | 1.421 | 1.425 | 1.423 |
| $\bar{2}$ 23, $\bar{3}$ 23 | 1.402 | 1.401, 1.383 | 1.405 | 1.406, 1.387 | 1.404 | 1.422, 1.405 |

* Unit cells used for D_{calc} are given in Table V.

Table V. Comparison of unit cell parameters of $\text{VO}_2(\text{B})$ and $\text{Li}_x\text{VO}_2(\text{B})$

| x | a | Δa (%) | b | Δb (%) | c | Δc (%) | β | V | ΔV (%) |
|------|-------|----------------|-------|----------------|------|----------------|---------|-------|----------------|
| 0 | 12.06 | | 3.685 | | 6.41 | | 106.9 | 272.6 | |
| 0.52 | 11.94 | | 3.723 | | 6.41 | | 106.7 | 272.9 | |
| 0.62 | 12.01 | -1.0 | 3.753 | +1.- | 6.39 | +0.0 | 106.1 | 276.7 | +0.1 |
| 0.85 | 12.08 | -0.4 | 3.805 | +1.8 | 6.43 | -0.3 | 107.4 | 282.0 | -1.5 |
| | | +0.1 | | +3.2 | | +0.3 | | | +3.4 |

Other vanadium oxides.—Of the other vanadium oxides evaluated, $\text{VO}_2(\text{B})$ appears to be the most promising candidate, after V_6O_{13} and $\text{V}_6\text{O}_{13+y}$, for use as a battery cathode material. Nonaqueous lithium cells with cathodes containing $\text{VO}_2(\text{B})$ exhibit lower average voltages, less capacity, and poorer rechargeability than cells containing V_6O_{13} . With a charging voltage limit of 3.1V and a discharging voltage limit of 1.0V, $\text{Li}/\text{LiClO}_4/\text{PC}/\text{VO}_2(\text{B})$ test cells gave initial capacities near 0.5Li/V which decayed slowly with cycling (Fig. 10). After 15 discharge/charge cycles the capacity decreased to ~65% of its value on the initial discharge. Similar performance was observed for cells using a 1.0M LiAsF_6/PC electrolyte. As observed for V_6O_{13} , the addition of graphite to the $\text{VO}_2(\text{B})$ cathodes failed to increase the capacity. The capacity can be increased by heating the cell above room temperature. At ~60°C a cell containing $\text{VO}_2(\text{B})$ and LiAsF_6/PC electrolyte exhibited a 65% increase in capacity. However, prolonged cycling at elevated temperature quickly results in cell failure presumably due to electrolyte decomposition.

The other vanadium oxides evaluated in this study, V_4O_9 and V_3O_7 , were prepared by several methods. Kawashima and co-workers reported that the thermal decomposition of NH_4VO_3 at 500°C *in vacuo* affords V_3O_7 by TGA (22). In this work, the rapid thermal decomposition of NH_4VO_3 in an inert gas stream gave mixtures of V_3O_7 and V_6O_{13} . It has also been reported that V_3O_7 was prepared by reducing V_2O_5 with SO_2 under mild conditions (36). However, we detected no

V_3O_7 in the reaction products for such a reduction. We were most successful in preparing pure V_3O_7 from finely divided V_2O_5 and freshly reduced V_2O_3 by standard solid-state techniques (18, 19). V_4O_9 was prepared by the reduction of V_2O_5 in a stream of anhydrous SO_2 at 400°C. This product exhibits a powder x-ray diffraction pattern which is consistent with that reported by Théobald and co-workers (17) for phase E, Sato and Ito (32) for oxide A, and Kawashima and co-workers (22) for V_4O_9 .

Treatment of V_3O_7 and V_4O_9 with dilute solutions of *n*-butyllithium in hexane at room temperature results in the consumption of ~1.2Li/V by V_3O_7 and ~1Li/V by V_4O_9 . However, less than one-half of this lithium can be removed by oxidation with I_2 . Furthermore, the lithiated materials appear to be amorphous to x-rays. Thus it appears that these oxides do not maintain their basic structural integrity on reaction with lithium.

V_3O_7 and V_4O_9 cathodes.—The capacities of cells containing V_3O_7 or V_4O_9 are considerably less than those typically observed for cells containing V_6O_{13} . A cell containing V_3O_7 blended with 50% graphite (by weight) exhibited an initial discharge capacity of ~0.9Li/V which decreased to ~0.3Li/V after 15 cycles (Fig. 11). This capacity was maintained for over 20 cycles. The initial irreversibility is not unexpected on the basis of the chemical lithiation-delithiation results. Also, the overall shape of the latter discharge curves is distinct from that of the initial curve and resembles that of cells containing heat-treated $\text{V}_6\text{O}_{13+y}$. It appears likely that the initial lithiation of V_3O_7 during the first discharge of the cell converted a substantial amount of the vanadium oxide framework to the $\text{V}_6\text{O}_{13+y}$ structure. Cells made using V_4O_9 deteriorated even more rapidly and no stabilization of capacity was observed.

Conclusion

Of the vanadium oxides evaluated in the course of this work, only cells containing V_6O_{13} and $\text{V}_6\text{O}_{13+y}$ consistently exhibited substantial capacities, good rechargeability, and high average potentials. Because of their exceptional overall performance, both V_6O_{13} and $\text{V}_6\text{O}_{13+y}$ are outstanding candidates for use as active cathode materials in nonaqueous lithium secondary batteries.

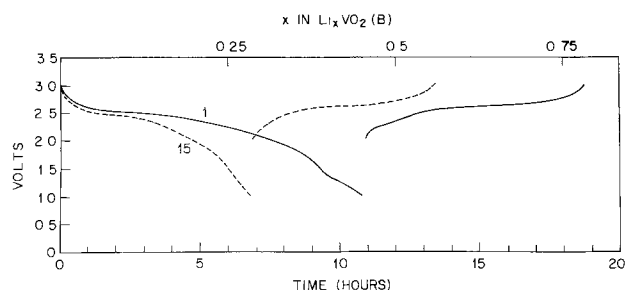


Fig. 10. Cycle data for a $\text{Li}/\text{LiClO}_4/\text{PC}/\text{VO}_2(\text{B})$, C cell containing 14.8 mg $\text{VO}_2(\text{B})$, 14.8 mg graphite, and cycled at 0.2 mA.

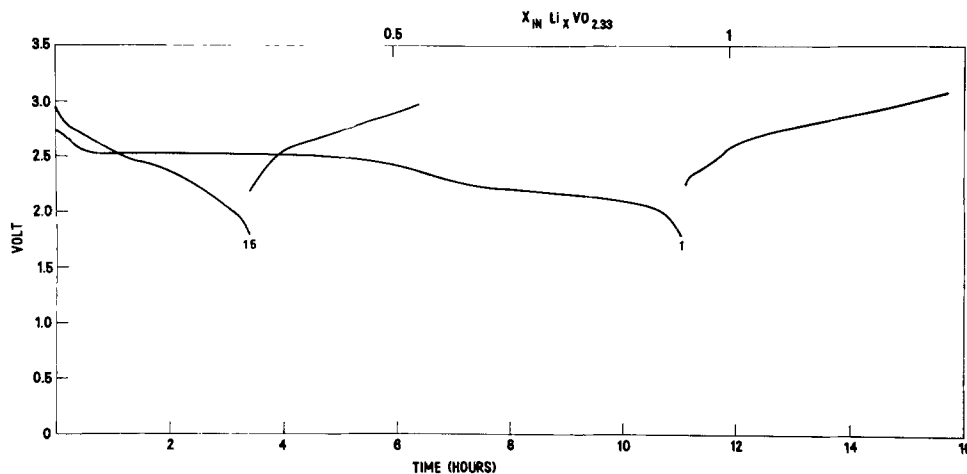


Fig. 11. Cycle data for a $\text{Li}/\text{LiAsF}_6/\text{PC}/\text{V}_3\text{O}_7$, C cell containing 7.9 mg V_3O_7 , 7.9 mg graphite, and cycled at 0.2 mA.

Manuscript submitted Feb. 18, 1981; revised manuscript received April 30, 1981.

Any discussion of this paper will appear in a Discussion Section to be published in the June 1982 JOURNAL. All discussions for the June 1982 Discussion Section should be submitted by Feb. 1, 1982.

Publication costs of this article were assisted by Bell Laboratories.

REFERENCES

1. For a review see M. S. Whittingham, *Prog. Solid State Chem.*, **12**, 41 (1972).
2. M. S. Whittingham, *This Journal*, **123**, 315 (1976).
3. B. C. H. Steele, in "Superionic Conductors," G. D. Mahan and W. L. Roth, Editors, p. 47, Plenum Press, New York (1976).
4. J. D. Besenhard and R. Schöllhorn, *J. Power-Sources*, **1**, 267 (1976).
5. D. W. Murphy and F. A. Trumbore, *J. Cryst. Growth*, **34**, 185 (1977).
6. D. W. Murphy, P. A. Christian, J. N. Carides, and F. J. DiSalvo, Paper No. I-M in "Proc. Cont. on Fast Ion Transport in Solids," Lake Geneva, WI, May 21-25, 1979.
7. D. W. Murphy, F. J. DiSalvo, J. N. Carides, and J. V. Waszczak, *Mater. Res. Bull.*, **13**, 1395 (1978).
8. C. R. Walk and J. S. Gore, Paper 27 presented at The Electrochemical Society Meeting, Toronto, Ont., Canada, May 11-16, 1975.
9. D. W. Murphy, P. A. Christian, F. J. DiSalvo, and J. N. Carides, *This Journal*, **126**, 497 (1979).
10. D. W. Murphy and P. A. Christian, *Science*, **205**, 651 (1979).
11. P. A. Christian, J. N. Carides, F. J. DiSalvo, and J. V. Waszczak, *This Journal*, **127**, 2315 (1980).
12. K. H. Cheung and M. S. Whittingham, *Solid State Ionics*, **1**, 151 (1980).
13. G. Brauer, "Handbook of Preparative Inorganic Chemistry," p. 1270, Academic Press, New York (1965).
14. K.-A. Wilhelm, K. Waltersson, and L. Kihlberg, *Acta. Chem. Scand.*, **25**, 2675 (1971).
15. F. Théobald and J. Bernard, *C. R. Acad. Sci. Paris, Ser. C*, **268**, 60 (1969).
16. F. Théobald, R. Cabala, and J. Bernard, *J. Solid State Chem.*, **17**, 431 (1976).
17. F. Théobald, R. Cabala, and J. Bernard, *C. R. Acad. Sci. Paris, Ser. C*, **269**, 1209 (1969).
18. K. Waltersson, B. Forslund, K.-A. Wilhelm, S. Andersson, and J. Galy, *Acta Crystallogr., Sect. B*, **30**, 2644 (1974).
19. D. Thomas, J. Tudo, and G. Tridot, *C. R. Acad. Sci. Paris, Ser. C*, **265**, 183 (1967).
20. D. W. Murphy, F. J. DiSalvo, G. W. Hull, and J. V. Waszczak, *Inorg. Chem.*, **15**, 17 (1976).
21. D. W. Murphy, J. N. Carides, F. J. DiSalvo, C. Cros, J. V. Waszczak, *Mater. Res. Bull.*, **12**, 825 (1977).
22. K. Kawashima, K. Kosuge, and S. Kachi, *Chem. Lett.*, 1131 (1975).
23. S. Anderson, *Bull. Soc. Chim. Fr.*, 1088 (1965).
24. H. G. Bachmann, F. R. Ahmed, and W. H. Barnes, *Z. Kristallogr.*, **45**, 110 (1961).
25. K.-A. Wilhelm and K. Waltersson, *Acta Chem. Scand.*, **24**, 3409 (1970).
26. F. Théobald, R. Cabala, and J. Bernard, *C. R. Acad. Sci. Paris, Ser. C*, **266**, 1534 (1968).
27. K. Tarama, S. Teranishi, and S. Yoshida, *Bull. Inst. Chem. Res., Kyoto Univ.*, **46**, 185 (1968).
28. S. Kachi, K. Kosuge, and H. Okinaka, *J. Solid State Chem.*, 258 (1973).
29. A. C. Gossard, F. J. DiSalvo, L. C. Erich, J. P. Remeika, and H. Yasuoka, *Phys. Rev. B.*, **10**, 4178 (1974).
30. M. N. Colpaert, P. Clauws, L. Fiermans, and J. Vennik, *Surf. Sci.*, **36**, 513 (1973).
31. S. Horiuchi, M. Saeki, Y. Matsui, and F. Nagata, *Acta Crystallogr., Sect. A*, **31**, 660 (1975).
32. T. Sato and Y. Ito, *Bull. Tokyo Inst. Tech.*, **98**, 1 (1970).
33. A. Deschanvres, G. Novet, and B. Raveau, *C. R. Acad. Sci. Paris, Ser. C*, **261**, 3144 (1965).
34. S. Andersson and A. D. Wadsley, *Acta Crystallogr.*, **15**, 201 (1962).
35. R. Marchand, L. Brohan, and M. Tournoux, *Mater. Res. Bull.*, **15**, 1129 (1980).
36. M. Tachez, F. Théobald, J. Tudo, and G. Laplace, *C. R. Acad. Sci. Paris*, **276**, 1187 (1973).

Anodic Corrosion of Fiber Reinforced Lead Composites for Use in Large Lead-Acid Batteries

C. M. Dacres,* S. M. Reamer, R. A. Sutula,* and I. A. Angres

Naval Surface Weapons Center, Materials Division, Silver Spring, Maryland 20910

ABSTRACT

The corrosion resistance of lightweight, high strength lead metal matrix composites under conditions that simulate their use as grid materials in large lead-acid batteries has been studied. Constant potential testing provides an effective means for holding constant the oxidizing power of a metal-electrolyte system. Data are presented on corrosion currents, effect of exposure time on corrosion rates, dependence of the rate of corrosion on temperature, and the current flow that is proportional to the rate of corrosion.

Corrosion of the positive plate support grids is a major cause of failure in lead-acid secondary batteries. This corrosion problem limits the service lifetime of large lead-acid batteries. These batteries are maintained for most of the time in a fully charged condition. When battery power is needed, they must perform reliably in high rate, deep discharges.

The development of lightweight grid materials made of pure lead reinforced with strong nonmetallic fibers provides a possible solution to the corrosion problem.

Pure lead is resistant to corrosion in sulfuric acid electrolyte, but grids made of pure lead lack adequate mechanical strength and the ability to resist deformation. Improved strength has been achieved by employing metal matrix composites technology to fabricate new experimental grid materials of fiber reinforced lead.

The main purposes of this study are to assess the corrosion resistance of new lead metal matrix composite battery grid materials in sulfuric acid electrolyte and to provide a basis for predicting grid corrosion rates from accelerated corrosion rate data at elevated temperatures obtained in the laboratory.

* Electrochemical Society Active Member.

Key words: corrosion, lead-acid batteries, power.

The shortening of the time for corrosion testing of grid materials used in lead-acid batteries at high temperatures was demonstrated by Willihnganz (1) in his work with cells on float service. However, the anodic corrosion of pure lead was first studied in detail by Lander (2-4). He combined thermodynamic thought with a kinetic approach to relate the mechanism of the positive plate reactions to the actual conditions in battery service. It was demonstrated earlier by Haring and Thomas (5) that the Pb/Ca alloy corroded much slower than Pb/Sb and at a rate comparable to that of pure Pb. Major work was conducted by Weininger and Morelock (6) in which conducting carbon fibers were introduced into the positive grid. An extensive study of lead alloys at high anodic potentials was done by Weininger and Siwek (7) in which Pb/Sb, Pb/Ca, and Pb/Ca/Sn alloys were maintained at constant high float charge, then examined metallographically.

We are reporting here initial corrosion studies. The materials studied were four experimental lead metal matrix composite grid materials, two conventional lead-based alloy grid materials, and pure lead.

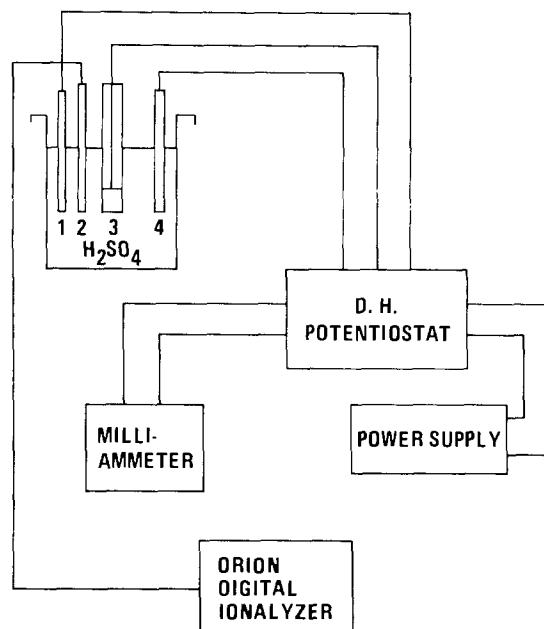
Experimental Procedure

Materials.—Samples of five different materials used in this study were obtained from commercial sources in the form of long, thin rods with lengths between 10 and 25 cm, and cross-sectional areas between 0.25 and 0.1 cm². Descriptive information provided by the suppliers is given in Table I. Samples designated in this report as X1, X2, and X3 were three lead-alumina fiber composite materials (Pb/FP) prepared by three different methods. Samples designated Y were lead-carbon fiber composites. The lead alloy and pure lead samples designated A, B, and L were included in the study for comparison purposes.

Electrochemical corrosion testing.—Corrosion studies were performed in a 1.285 specific gravity sulfuric acid electrolyte at 70°, 60°, and 50°C. The materials were tested in a static constant potential mode. The anode to mercury-mercurous sulfate reference potential was maintained potentiostatically to approximate float service conditions of the battery. A schematic of the experimental arrangement is shown in Fig. 1. The test cells were housed in 10 liter Pyrex glass chromatography jars. The temperature was maintained by immersing the jars in a large constant temperature water bath.

The counterelectrodes were lead grid sheets which lined the walls of the chromatography jars. The working electrodes were those listed in Table I. They were fitted through rubber stoppers which were placed through the Teflon covers of the jar. These electrodes were suspended in the electrolyte towards the center of the cell. Each type of electrode was placed in a separate chromatography jar.

Electrical contacts were made through gold-plated battery clips. A constant potential of 1.226V anodic to



1. WORKING ELECTRODE
2. ION SELECTIVE ELECTRODE
3. REFERENCE ELECTRODE · Hg/Hg₂SO₄
4. COUNTER ELECTRODE · Pb

Fig. 1. Diagram of apparatus for investigating the anodic corrosion of metal matrix materials.

the mercury-mercurous sulfate reference electrode was maintained using a DH Model potentiostat (8). The current flowing between the working electrode and the counterelectrode was recorded as a direct measure of the instantaneous corrosion rate.

Test samples were mechanically cleaned and rinsed with distilled water and acetone. They were dried overnight in a desiccator, then measured and weighed before immersion in the sulfuric acid. After the corrosion period, the test samples were washed and dried with acetone and reweighed. The adhering corrosion products were removed by stripping in a hot hydrazine sulfate-mannitol-hydroxide solution. The samples were studied using the electron microscope.

Results and Discussion

Comparison of corrosion currents vs. time.—A comparison of the current densities of the various samples is shown in Fig. 2 for accelerated testing conditions at 70°C. Most of the corrosion currents were initially high except for pure Pb and Pb/FP-X2. The high corrosion currents declined sharply as the anodic (oxide) layer covered the specimens. At times a sharp rise in current is observed which indicates a rapid breakdown of this

Table I. Composition of grid material samples

| Designation | Material | Preparation method | Composition | | |
|--|------------------------------|---|---|------------------|-------------------------|
| | | | Volume percent Al ₂ O ₃ | Weight percent C | Weight percent Ca Sn |
| Experimental materials | | | | | |
| X1 | Lead-alumina fiber composite | Liquid lead infiltration Fiber bonding method—unknown | 25 | | |
| X2 | Lead-alumina fiber composite | HF mold release agent Liquid lead infiltration Fiber bonding method—unknown | 7.5 | | |
| X3 | Lead-alumina fiber composite | Mold release method—unknown Chemical vapor deposition | 5-6 | | |
| Y | Lead-carbon fiber composite | Fiber bonding method—unknown Chemical vapor deposition | | 4 | |
| Conventional and standard materials | | | | | |
| A | Lead-calcium alloy | Cast | | | 0.07 |
| B | Lead-calcium-tin alloy | Cast | | | 0.065 |
| L | Pure lead | Cast | | | 0.66 |

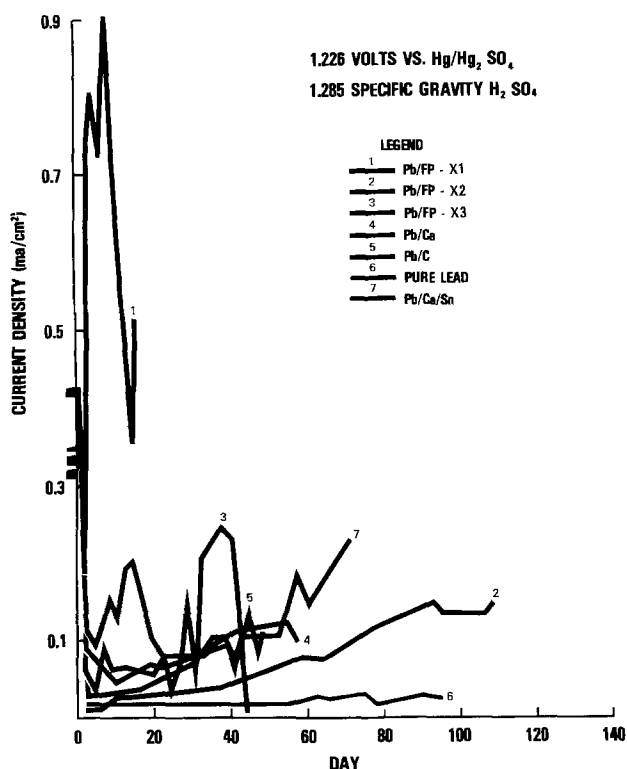


Fig. 2. Measured current densities vs. time at 70°C

oxide film. Corrosion currents for the fiber reinforced materials fell to very low values toward the end of the testing period when the samples physically fell apart and appeared to be no longer capable of conducting any appreciable current. However, the corrosion currents for the alloys increased with time.

The Pb/FP samples frayed at the lower end (Fig. 3) where the electrolyte infiltrated the fibers. The SEM for sample X1 (Fig. 4) shows that the fibers were completely separated from the lead by corrosion products. This indicates insufficient bonding at the lead-fiber interface which allowed electrolyte to diffuse into the interface, thus corroding the lead.

Distortion was peculiar to the graphitic samples (Fig. 5). Also, pitting along the seams where the fibers became exposed was observed. The distortion is attributed to intergranular corrosion whereby the products accumulate along the grain boundaries creating the forces which distort the sample.

Pb/Ca alloy is a conventional grid material for lead-acid batteries and was included in this study for comparison purposes. The surface of these samples was severely etched and stress corrosion cracks developed (Fig. 6). The cracks weakened the sample making it physically incapable of supporting a load.

Accelerated studies on X2 show that the samples were less severely corroded than X1. The reason is believed to be improved bonding of lead to the fibers as

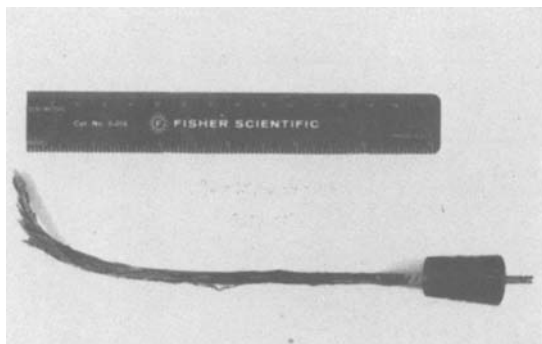


Fig. 3. X1 specimen after corrosion

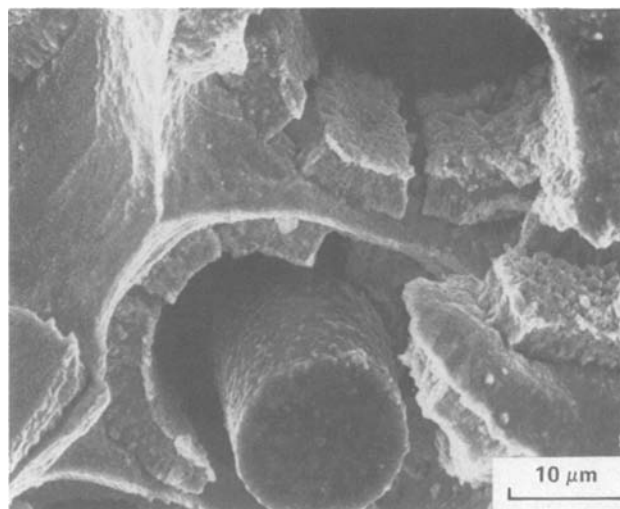


Fig. 4. Micrograph showing a buildup of corrosion products around the fibers in the X1 sample.

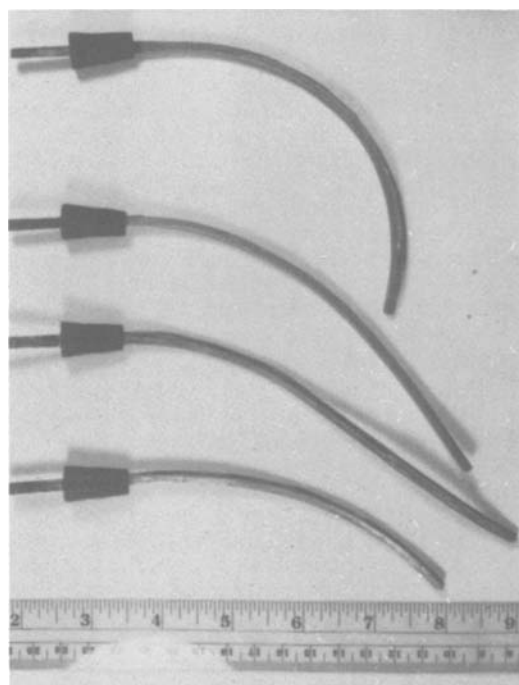


Fig. 5. Y samples after corrosion at 70°C

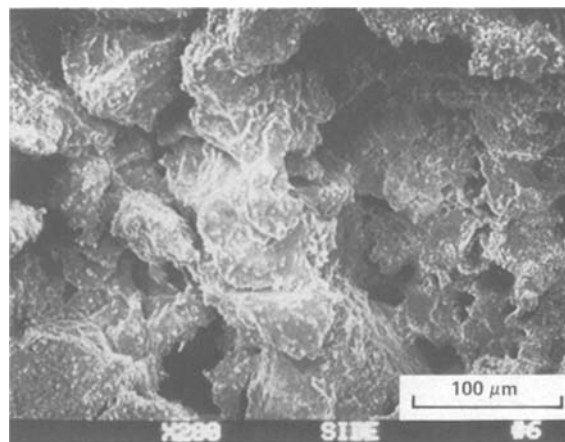


Fig. 6. Corroded surface of sample A

seen in Fig. 7. Also, X1 has 25% volume fiber loading as opposed to 7.5% in X2. This suggests that there is some relationship between the fact that the higher the volume of fibers incorporated in the lead structure, the more susceptible the structure is to corrosion.

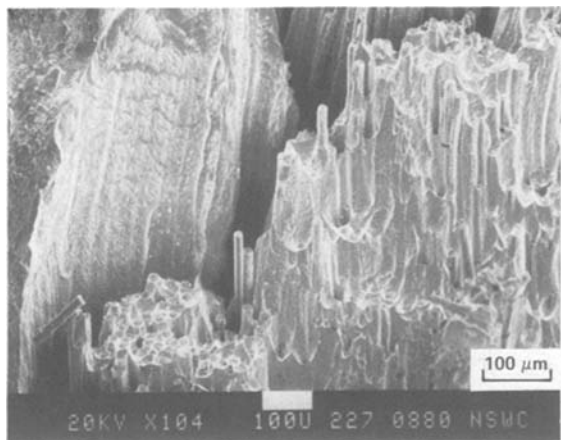


Fig. 7. X2 sample showing improved bonding

Comparison of corrosion rates.—The corrosion rate was determined electrochemically, where the resulting corrosion current densities are converted to corrosion rates through Faraday’s law (9)

$$\text{Corrosion rate (mpy)} = 0.1288I (\mu\text{A}/\text{cm}^2) \frac{\text{eq. wt. (g)}}{\rho (\text{g}/\text{cm}^3)}$$

where I = current density, ρ = specimen density, and eq. wt. = specimen equivalent wt.

The calculation was based on the assumption that the anodic corrosion of lead occurs through the reaction (2)



Figure 8 contains a summary of average corrosion rates in units of mils per year (mpy) of various types of battery grid materials.

Effect of exposure time on corrosion rates.—The effect of exposure time on the corrosion rates of various samples is represented in Fig. 9. The curves A (Pb/Ca) and B (Pb/Ca/Sn) show an increase in corrosion

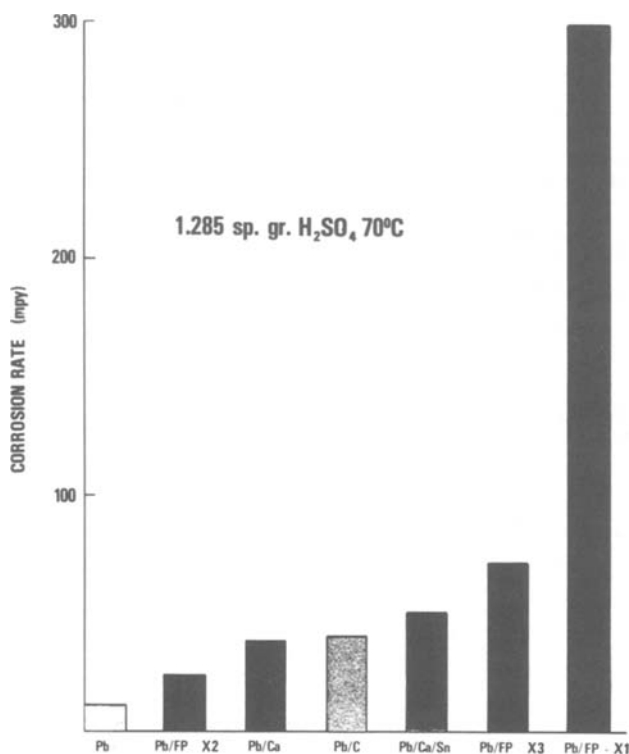


Fig. 8. Relative corrosion rates of lead samples

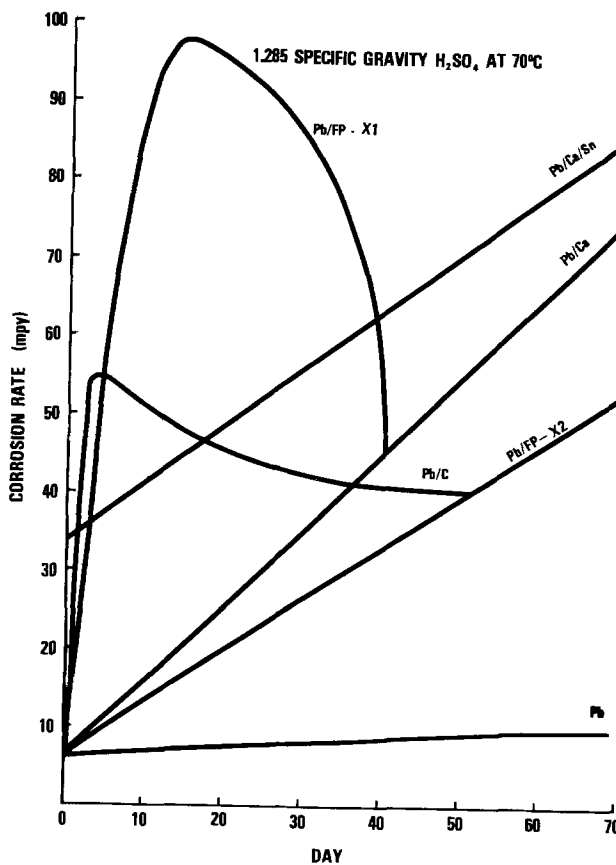


Fig. 9. Effect of exposure time on the corrosion rates of various lead samples.

rate due to acceleration of attack. This can be attributed to the relatively high solubility of the corrosion products in the acidic environment which inhibits the formation of a protective layer.

The corrosion rate curves for X1 (Pb/FP) and Y (Pb/C) show an initial increase due to the acceleration of attack by the alumina and graphitic residue produced initially. This is followed by a decrease in rate as the residue becomes plugged with insoluble corrosion product and carbonaceous debris.

The X2 samples display a corrosion rate/time curve unlike those of other fiber reinforced materials. Its curve appears to be similar to those of lead alloys.

Prediction of corrosion rates.—Corrosion studies have been done on Y and B at 50° and 60°C, and the ratio of corrosion rates has been compared with those at 70°C. Figures 10 and 11 show that at lower temperatures the corrosion of the Y samples is considerably less and the distortions are also less than the distortions seen in Fig. 5. The bonding between the lead and the graphitic fibers remains good even during the corrosion period.

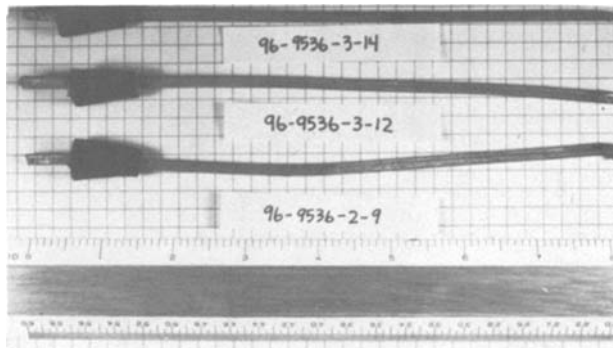


Fig. 10. Photograph showing little distortion of sample Y at 50°C

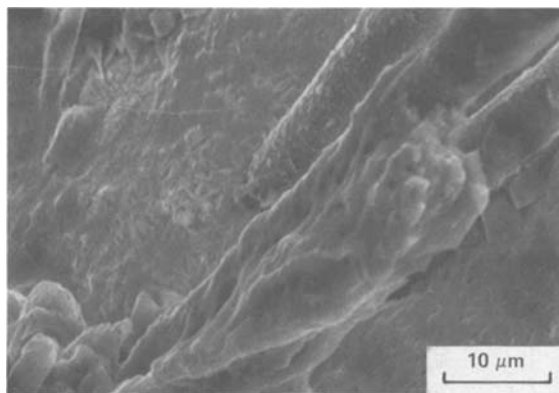
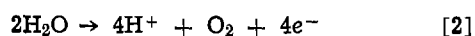


Fig. 11. Micrograph of sample Y after corrosion at 50°C

The corrosion rate data were linear for specimens Y and B. Figure 12 consists of plots of the log of the corrosion rates vs. the reciprocal of Kelvin temperature. These plots were extrapolated to room temperature permitting a prediction of the corrosion rates.

Weight-loss measurements.—The Pourbaix diagrams of reactions in the lead-sulfuric acid system (10) indicate that at the potential used in these studies (1.226V vs. the Hg/Hg₂SO₄ reference) both the oxidation of lead to PbO₂ by reaction [1] and the oxidation of water by the reaction



can occur. The observation of gassing at the surface of the samples strongly supports at least the second of these two reactions. Because some of the current is being used up through reaction [2] it is difficult to make a direct correlation at this time between measured weight changes in the sample and weight changes according to Faraday's law. However, even though the mass loss of the samples may not be directly proportional to the current, a high current will indicate a high rate of corrosion.

Conclusions

On the basis of corrosion studies described in this article, it may be concluded that the equipment and methods employed are suitable for comparing the relative corrosion resistance of candidate grid materials. The major findings of this study in terms of the relative corrosion behavior of the samples studied are:

1. An important need in the selection of corrosion-resistant materials for battery grids is the correlation of laboratory studies with actual grid corrosion performance in battery service. The effects of temperature, float potential, and time on corrosion rates are not yet well enough understood to permit such correlations.

2. All of the samples were severely damaged, deformed, elongated, and weakened by corrosive oxidation in the sulfuric acid electrolyte except X2 and, of course, pure Pb.

3. The extremely severe and rigid corrosion of X1 was apparently a direct result of poor bonding between the lead and the alumina fibers.

4. The greatly improved behavior of X2 confirms the expectation that in fiber reinforced materials the wetting process between the fiber and the metal is extremely critical in the control of corrosion processes.

5. The Pb/Ca alloy, which is representative of a conventional grid material for lead-acid batteries, was severely weakened by etching and stress corrosion cracking.

6. The relationship between volume percentages, weight percentages, and corresponding corrosion rates emphasizes the fact that the ratio of lead to the amount

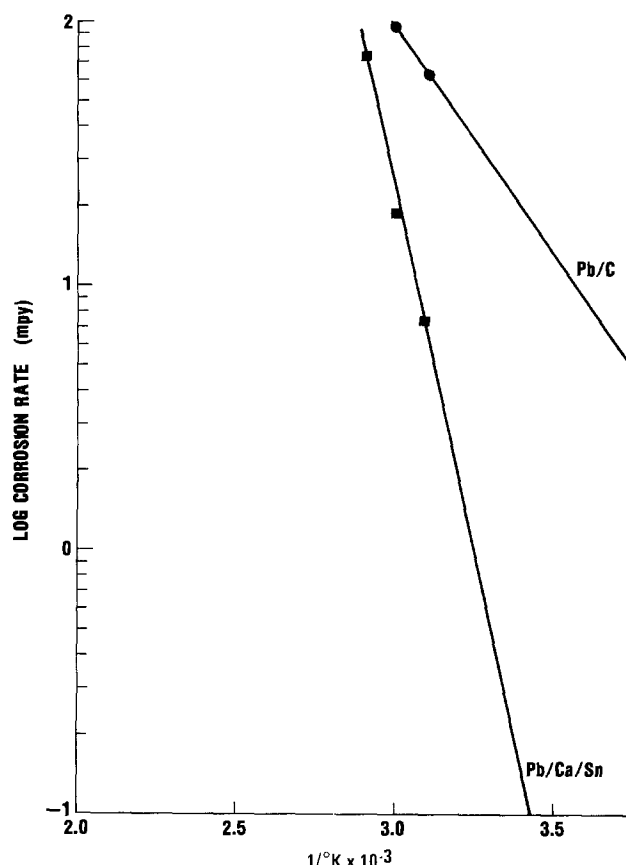


Fig. 12. Log of corrosion rates vs. temperature

of fiber used in strengthening the lead cannot be ignored in utilizing metal matrix materials.

Acknowledgment

The authors thank Benjamin F. Larrick for his very useful contribution in discussing this work and in helping with the preparation of the manuscript.

This work was supported by the Naval Surface Weapons Center, White Oak, Silver Spring, Maryland.

Manuscript submitted Nov. 4, 1980; revised manuscript received March 23, 1981.

Any discussion of this paper will appear in a Discussion Section to be published in the June 1982 JOURNAL. All discussions for the June 1982 Discussion Section should be submitted by Feb. 1, 1982.

Publication costs of this article were assisted by the Naval Surface Weapons Center.

REFERENCES

1. E. Willihnganz, *Electrochem. Technol.*, **6**, 338 (1968).
2. J. J. Lander, *This Journal*, **98**, 213 (1951).
3. J. J. Lander, *ibid.*, **98**, 220 (1951).
4. J. J. Lander, *ibid.*, **103**, 1 (1956).
5. H. E. Haring and U. B. Thomas, *Trans. Electrochem. Soc.*, **68**, 293 (1935).
6. J. L. Weininger and C. R. Morelock, *This Journal*, **122**, 1161 (1975).
7. J. L. Weininger and E. G. Siwek, *ibid.*, **123**, 603 (1976).
8. H. A. Newborn and D. C. Bratlie, "Analysis of Mini-Potentiostat Design Options for Corrosion Research," NSWC/WOL TR 78-129, Sept. 1, 1978.
9. W. H. Ailor, "Handbook of Corrosion Testing and Evaluation," pp. 173-174, John Wiley & Sons, Inc., New York (1971).
10. M. Pourbaix, "Atlas of Electrochemical Equilibria in Aqueous Solutions," pp. 485-492, Pergamon Press, Ltd., New York (1966).

Effect of Sulfide Ions on Caustic Cracking of Mild Steel

Douglas Singbeil and Desmond Tromans*

Metallurgical Engineering Department, University of British Columbia, Vancouver, B.C., Canada V6T 1W5

ABSTRACT

Potentiostatically controlled slow strain rate ($\dot{\epsilon} = 3.3 \times 10^{-6}/\text{sec}$) tensile tests were conducted on AISI 1018 mild steel in hot (92°C) caustic solutions of 3.35M NaOH and 2.5M NaOH + 0.423M Na₂S in a chemically inert cell. Reduction of area was used as a measure of susceptibility to stress corrosion cracking (SCC). The presence of sulfide ions raised the active-passive transition potential to more noble values, and maximum susceptibility to SCC occurred at potentials near the active-passive transition in each environment. Cracking at these potentials was further confirmed by conducting tests on prefatigue cracked double cantilever beam specimens at a known stress intensity, and crack fractography was studied by scanning electron microscopy. Crack liquid pH measurements were obtained with pH indicator paper using a freezing technique. A hydrogen embrittlement mechanism of SCC was eliminated from consideration in both environments on thermodynamic grounds. All observations were reasonably consistent with a dissolution mechanism of SCC involving film rupture events.

Several studies have shown that the caustic stress corrosion cracking (SCC) of mild steels exposed to hot, highly alkaline, aqueous NaOH solutions is associated with a small range of potentials near the active-passive transition potential (1-5). More recently, anodic polarization studies in hot alkaline and alkaline sulfide solutions showed that the presence of sulfide ions raised the active-passive transition potential to more noble potentials relative to the sulfide-free solutions (6, 7). This led to the suggestion (6) that there should be a corresponding change in the potential range for SCC due to the presence of sulfide. Confirmation of this prediction has both fundamental significance with regard to the understanding of SCC and practical consequences for prediction of SCC in hot, industrial alkaline sulfide solutions (white liquors) employed in the Kraft process for producing pulp from wood chips. In fact, some of the results from the present study have already been applied to SCC considerations in the pulp and paper industry (8).

The current program was designed to evaluate the effect of sulfide on the potential regime of SCC susceptibility of mild steel by conducting comparative tests in hot aqueous solutions of NaOH and NaOH + Na₂S, similar to those compositions employed previously (6). Slow strain rate tensile testing techniques (9, 10), conducted under potentiostatic control, were used for the initial evaluation of the potential regimes of SCC susceptibility. Confirmation of SCC in the susceptible regimes was obtained via the techniques of fracture mechanics, whereby potentiostatically controlled SCC propagation tests were conducted on prefatigue cracked double cantilever beam (DCB) specimens at a known stress intensity (K_I). In addition, fractographic studies were conducted on specimens subjected to SCC in the presence and absence of sulfide, and attempts were made to determine the pH of the solution within the stress corrosion crack.

Experimental

Tests were conducted on two batches of AISI 1018 mild steel. One batch was received as cold drawn cylindrical rod of 9.5 mm diam and the second batch was received as cold drawn bar with a square cross section, 31.8 × 31.8 mm. Chemical analyses of the two batches are shown in Table I.

* Electrochemical Society Active Member.

Key words: stress corrosion cracking, strain rate, stress intensity, cantilever beam, white liquor.

Tensile test pieces for slow strain rate tests, machined from the rod, were 254 mm long with threaded ends for grips and a reduced gage section 25.4 mm long and 5 mm in diameter. The gage section was mechanically polished with 320 grit paper, degreased in chloroethane, cleaned in 10 volume percent (v/o) HCl, rinsed in water and alcohol, and dried. Subsequently, each specimen was annealed under vacuum at 920°C for 0.75 hr, air cooled, electropolished for 60 sec at 30V in a solution containing 135 ml CH₃COOH + 0.025 kg Cr₂O₃ + 7 ml H₂O, rinsed in water and alcohol, dried, and tested. The yield stress of the annealed specimens at 92°C was 297 MPa.

Double cantilever beam specimens (DCB) for fracture mechanics SCC testing were prepared from the bar by machining to the configuration shown in Fig. 1. The specimens were crack-line loaded single-edge crack specimens. Beam height (H) was 11.6 mm, specimen length from the loading line (W) was 66.7 mm, and specimen thickness (B) was 25.4 mm. Initial length of machined precrack from the loading line (a) was 25.4 mm. The beams were threaded to receive grips for application of load (P). Brown and Srawley (11) have shown that the stress intensity (K_I) calibration for the DCB specimen is given by Eq. [1] for a/W values up to 0.6, provided $W/H \geq 5$

$$K_I = \frac{P \cdot a}{BH^{3/2}} \left(3.45 + 2.415 \frac{H}{a} \right) \quad [1]$$

Final preparation involved mechanically polishing the faces to 600 grit, followed by washing in ethanol. The machined pre-crack was sharpened and extended a further ~2 mm by fatigue cracking at a K_I level of $12 \pm 11 \text{ MPa} \cdot \text{m}^{1/2}$. All DCB specimens were subjected to SCC in the as-received, cold-worked condition. The yield strength at 92°C was 523 MPa.

Table I. Chemical composition of steels*

| Batch | Element | | | | | | | | |
|-----------------|---------|------|-------|------|------|------|------|----|------|
| | C | Mn | P | S | Si | Ni | Cr | Mo | Cu |
| Cylindrical rod | 0.17 | 0.65 | 0.012 | 0.01 | ND | ND | ND | ND | 0.01 |
| Square bar | 0.17 | 0.67 | 0.015 | 0.02 | 0.22 | 0.08 | 0.16 | ND | 0.16 |

* Weight percentage.
ND = Not detected.

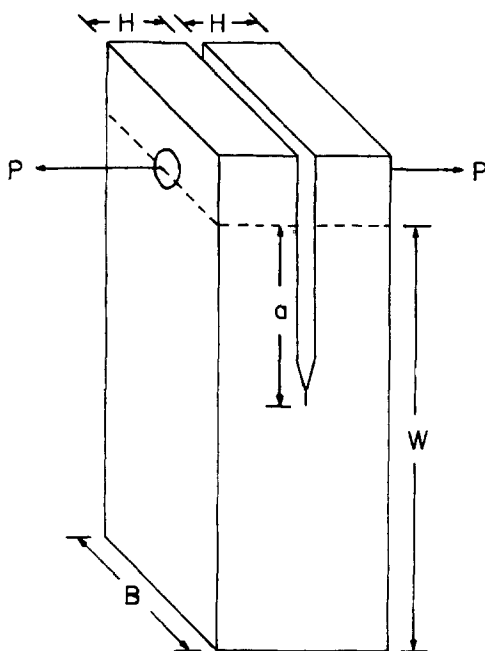


Fig. 1. Specimen geometry of double cantilever beam (DCB) specimen.

Two test solutions, containing (i) 3.35M NaOH and (ii) 2.5M NaOH + 0.423M Na₂S, were prepared from reagent grade NaOH and Na₂S·9H₂O, using distilled water. Total Na⁺ molality in each was 3.35M.¹ Nitrogen purging was employed during preparation and testing to prevent oxidation of sulfide. Calculations (6) showed that the pH of both solutions was near 14 at room temperature and near ~12 at test temperature (92°C).

Potentiostatic control was obtained via a Princeton Applied Research potentiostat (Model 173), equipped with an electrometer probe (Model 178), logarithmic converter (Model 376), and universal programmer (Model 175). Potentials were measured with respect to a room temperature saturated calomel reference electrode connected via a saturated KCl salt bridge to the Luggin capillary, which terminated ~1 mm from the specimen surface. Potential and current were recorded on a Houston Omnigraphic X-Y recorder (Model 2000). All potentials are reported with respect to the standard hydrogen electrode (SHE). No attempt was made to correct for negligibly small potential differences arising from concentration and thermal gradient effects in the salt bridge. All tests were conducted at 92° ± 1°C, corresponding to that usually found in industrial white liquor storage vessels and clarifiers.

Slow strain rate tests, using an Instron tensile machine, were conducted in 550 ml of solution contained within a Teflon cell (PTFE or FEP polymers), as shown in Fig. 2, which contained two graphite counter-electrodes, plus an FEP coated thermistor probe for temperature control. The specimen surface above and below the gage section was protected with PTFE tape. A potential of $-1.01V_{SHE}$ (~120 mV below the corrosion potential, E_{CORR}) was impressed upon the specimen for 120 sec. Thereafter, the potential was raised at 1 mV/sec until the desired test potential was reached. The specimen was then tested to fracture at a strain rate ($\dot{\epsilon}$) of $3.33 \times 10^{-6} \text{ sec}^{-1}$. The percentage reduction in area at final fracture was determined by microscopy and plotted as a function of potential. The potential region of maximum SCC susceptibility was designated by those potentials giving rise to the smallest reduction in area (9, 10). Separate anodic polarization tests

¹Concentration, M, is moles of solute per kg of H₂O.

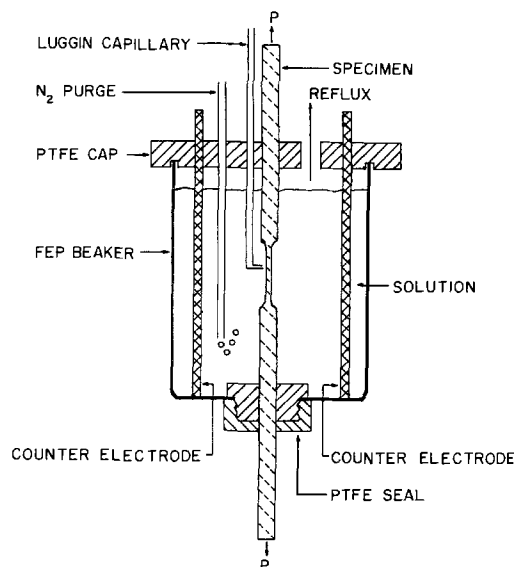


Fig. 2. Schematic diagram of test cell for slow strain rate testing, where *P* represents load applied by tensile machine.

were conducted on unstrained specimens in fresh solutions at scan rates of 1 mV/sec.

Potentiostatically controlled SCC tests were conducted on the DCB specimens in a cell (Fig. 3) of similar size and materials to the slow strain rate cell. The solution was stirred via a Teflon coated magnetic stirrer. The specimen was wrapped in Teflon tape, except for the crack tip region, to minimize total current requirements and changes in solution composition during potentiostatic control. The whole assembly was placed in a horizontally mounted Hounsfield Tensometer tensile machine.

The specimen potential was raised to the preselected value and an initial load (*P*) applied to the specimen to produce a known stress intensity (K_I) value. The SCC test was allowed to run for ~400 hr. During this time the elastic compliance of the test assembly was such that a small change in K_I occurred as a result of crack growth. Aliquots of the sulfide solution were analyzed periodically for sulfide concentration and additions of Na₂S·9H₂O were made to maintain the desired concentration. At the termination of the test, the solution was replaced with liquid nitrogen and the specimen broken by increasing the load (*P*). The fracture surfaces were examined under a travelling microscope, where SCC was clearly distinguishable from the fatigue precrack and brittle (cleavage) overload failure in liquid nitrogen. An average propagation

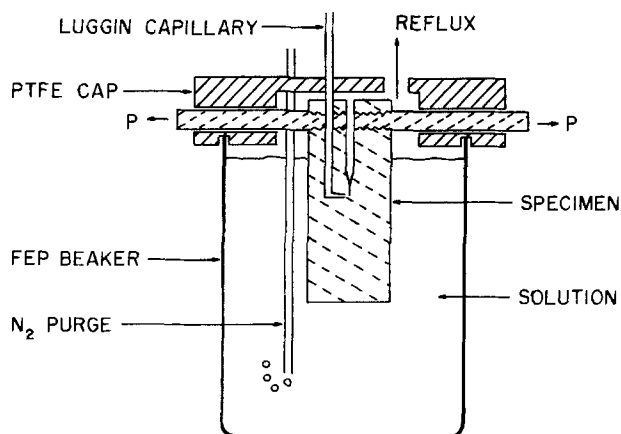


Fig. 3. Schematic diagram of test cell for testing of double cantilever beam (DCB) specimens. The load *P* was applied by means of a horizontally mounted tensile machine.

rate (v) was obtained by dividing the SCC growth increment by the test time.

The pH of the frozen solution remaining near the stress corrosion crack tip of the DCB specimens was determined using the technique of Brown *et al* (12). Commercial pH indicator paper (Hydriion Paper), with colorimetric intervals of 0.5 pH units, was employed.

The stress corrosion crack fractography of the DCB specimens was studied by scanning electron microscopy (SEM). The crack surfaces contained iron corrosion products (6) which were first removed by ultrasonic cleaning in an inhibited solution of 3 ml conc. HCl + 4 ml 35% 2 Butyne-1, 4-diol + 4 ml H₂O that produces no artifacts (13, 14). Following cleaning, the specimens were washed in water and ethanol, dried, and examined in an ETEC Autoscan, using secondary electron imaging mode and 20 keV excitation.

After cleaning, some DCB specimens were sectioned longitudinally normal to the stress corrosion fracture plane, mechanically polished to 1 μ m diamond finish, etched in 2 v/o HNO₃ in ethanol to reveal grain boundaries and pearlite, and then examined by SEM. In this manner, the relationship between grain boundaries and SCC was more easily determined.

Results

Slow strain rate studies.—The effect of potential upon reduction in area is shown for the NaOH solution in Fig. 4 and for the NaOH + Na₂S solution in Fig. 5. These data have been superimposed upon the corre-

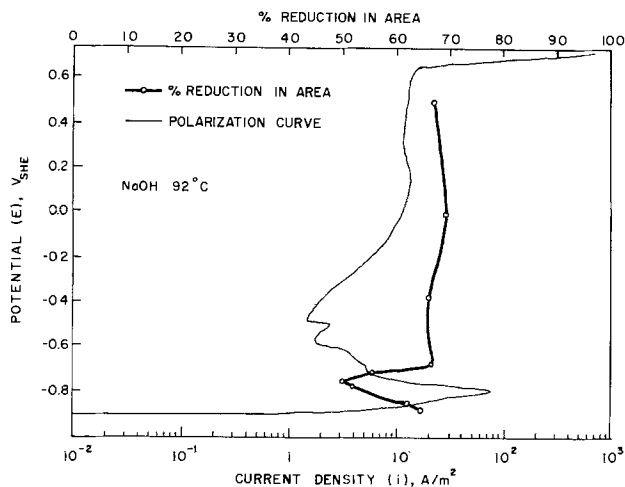


Fig. 4. Effect of potential upon reduction in area at $\dot{\epsilon} = 3.33 \times 10^{-6} \text{ sec}^{-1}$, and superimposed anodic polarization diagram, for mild steel in aqueous 3.35M NaOH.

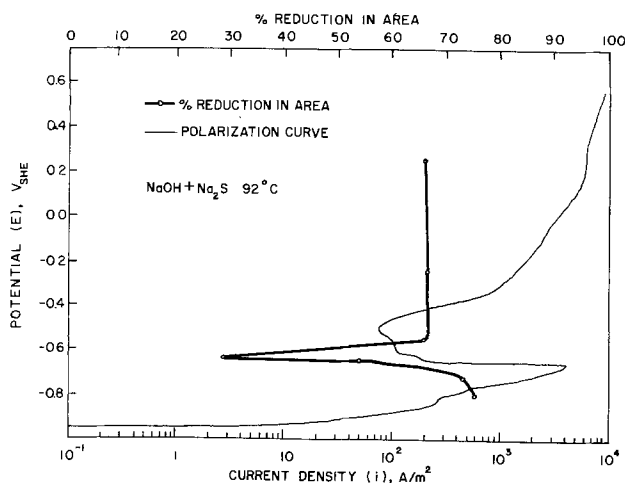


Fig. 5. Effect of potential upon reduction in area at $\dot{\epsilon} = 3.33 \times 10^{-6} \text{ sec}^{-1}$, and superimposed anodic polarization diagram, for mild steel in aqueous 2.5M NaOH + 0.423M Na₂S.

sponding anodic polarization curves, the general characteristics of which are similar to those described previously (6).

Clearly, Fig. 4 and 5 showed that the minimum reduction in area was associated with a potential close to, and slightly above, the active-passive transition potential in each solution. The minimum percentage reduction in area occurred at $-0.76V_{SHE}$ in NaOH and $-0.64V_{SHE}$ in NaOH + Na₂S.

Specimens which were fractured in the potential region giving rise to minimum reduction in area always exhibited numerous secondary surface cracks, as described elsewhere (8), whereas those fractured outside this region did not exhibit surface cracking. Consistent with these observations, the minimum reduction in area must have been associated with environment induced cracking, *i.e.*, SCC. Hence, the variation in reduction of area with potential, as shown in Fig. 4 and 5, was a measure of relative SCC susceptibility.

DCB tests.—Stress corrosion cracking tests were conducted on the DCB specimens at K_I levels near 50 MPa \cdot m^{1/2} and at potentials near the active-passive transition, which the slow strain rate tests had indicated to be the most severe. These were $-0.76V_{SHE}$ in NaOH and $-0.64V_{SHE}$ in NaOH + Na₂S. Cracking occurred in both solutions at average rates of the order of $\sim 1 \times 10^{-9}$ m/sec, the relative rate in NaOH being higher by a factor of two. The results are summarized in Table II, together with the slight variation in K_I which occurred during each test.

pH measurements.—Measurements of pH obtained from the crack liquid near room temperature gave a value of ~ 14 in both solutions. This was the same value as that observed in the bulk solutions at room temperature. Hence, the measurements indicated no significant changes in pH within the crack during SCC.

Fractography.—The stress corrosion cracks in the DCB specimens remained in the initial crack plane with no tendency toward macroscopic crack branching. Longitudinally sectioned and etched specimens showed that the cracks followed a predominantly intergranular path along pearlite/ferrite boundaries and ferrite/ferrite boundaries. Occasionally, transgranular cracks through ferrite and pearlite were observed, the tendency being more noticeable in the NaOH solution. Figures 6a and b illustrate the general features of crack path.

Topographical characteristics of the stress corrosion cracks are shown in the SEM fractographs of Fig. 7a and b. The fractographs were obtained from near the crack tip, where dissolution and etching artifacts due to exposure of crack surfaces to the hot caustic environments were minimized. Intergranular crack topography and secondary microcracks were evident in both environments. In addition, a greater tendency for transgranular crack topography was observed in the NaOH solution, as evidenced in Fig. 7a.

Discussion

General.—The slow strain rate tests have shown that susceptibility to SCC is most pronounced in the passive region at potentials near the active-passive transition for the particular metal/environment combination concerned. The addition of sulfide ions to the NaOH solution raised the active-passive transition potential

Table II. Stress corrosion crack propagation rates (v) at 92°C

| Solution (molality) | Potential (V_{SHE}) | K_I (MPa \cdot m ^{1/2}) | v (m/sec) |
|------------------------------------|-------------------------|---------------------------------------|-----------------------|
| 3.35 NaOH | -0.76 | 48-53 | 2.9×10^{-9} |
| 3.35 NaOH | -0.76 | 49-50 | 1.9×10^{-9} |
| 2.5 NaOH + 0.423 Na ₂ S | -0.64 | 47-50 | 1.5×10^{-9} |
| 2.5 NaOH + 0.423 Na ₂ S | -0.64 | 46-51 | 8.8×10^{-10} |
| | | | 2.4×10^{-9} |
| | | | 1.2×10^{-9} |

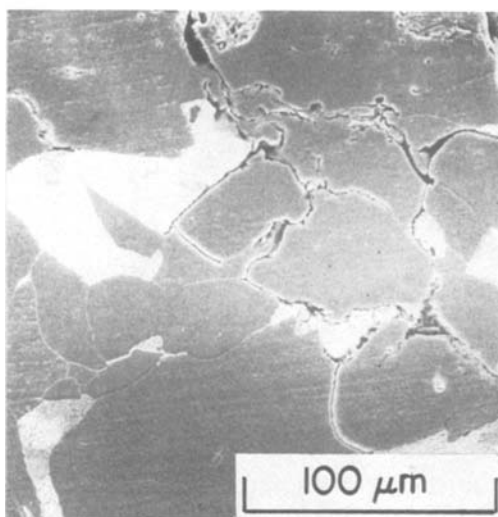


Fig. 6. SEM micrographs of sectioned and etched DCB specimens showing stress corrosion crack path at 92°C. Magnifications as shown in (b). (a, top) 3.35M NaOH, $K_I \approx 50 \text{ MPa} \cdot \text{m}^{1/2}$, $E = -0.76V_{\text{SHE}}$. (b, bottom) 2.5M NaOH + 0.423M Na₂S, $K_I \approx 50 \text{ MPa} \cdot \text{m}^{1/2}$, $E = -0.64V_{\text{SHE}}$.

to a more noble value and produced a corresponding rise in the potential for maximum susceptibility to SCC. Furthermore, the DCB tests confirmed that SCC at these potentials was not a peculiarity of the slow strain rate testing technique. This latter point is important because it has been noted previously by Parkins (15) that it is very difficult to obtain laboratory SCC of carbon steels in hot NaOH solutions, unless slow strain rate testing techniques are employed.

The results of the DCB tests were considered to be representative of plane strain testing conditions, because the K_I levels did not exceed the plane strain limit of $\sim 60 \text{ MPa} \cdot \text{m}^{1/2}$, as defined by the thickness criterion of Brown and Srawley (11) and ASTM (16) testing recommendations, i.e., $B \geq 2.5 (K_I/\sigma_y)^2$, where σ_y is the tensile yield stress. Under these conditions, and K_I levels of $\sim 50 \text{ MPa} \cdot \text{m}^{1/2}$, the results showed that there was a relatively insignificant difference in stress corrosion crack propagation rate between the NaOH and NaOH + Na₂S solutions when tests were conducted at the most susceptible potential for each environment (see Table II).

At the present time, it is not clear whether or not the influence of potential upon SCC susceptibility in NaOH and NaOH + Na₂S solutions, evident from the slow strain rate studies, is exerted primarily on the crack initiation period, the critical stress intensity ($K_{I\text{SCC}}$)

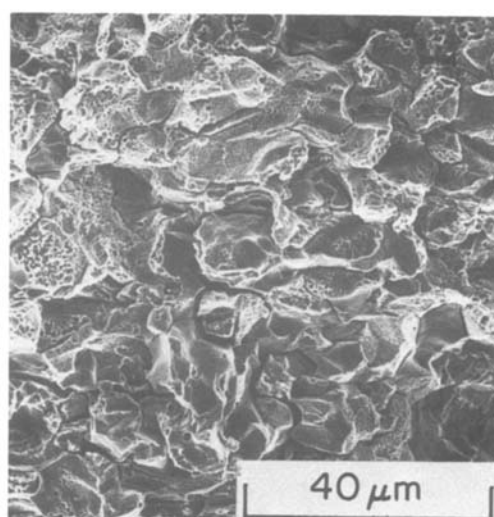
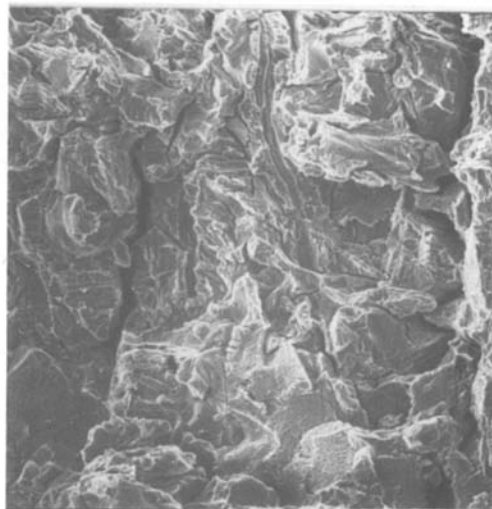


Fig. 7. SEM fractographs of DCB specimens showing stress corrosion crack topography at 92°C. Crack propagation from left to right and magnifications as shown in (b). (a, top) 3.35M NaOH, $K_I \approx 53 \text{ MPa} \cdot \text{m}^{1/2}$, $E = -0.76V_{\text{SHE}}$. (b, bottom) 2.5M NaOH + 0.423M Na₂S, $K_I \approx 51 \text{ MPa} \cdot \text{m}^{1/2}$, $E = -0.64V_{\text{SHE}}$.

for crack propagation, or upon the crack propagation rate itself. This requires further studies utilizing DCB specimens tested over a wider range of K_I levels and electrochemical potentials.

Mechanistic considerations.—The possibility of a hydrogen embrittlement mechanism of SCC in the present studies may be shown to be invalid on a thermodynamic basis. Such a mechanism requires the generation of hydrogen near the crack tip by electrochemical processes during SCC. The work of Biernat and Robins (17) has shown that the thermodynamically reversible potential for hydrogen evolution via reduction of hydrogen ions at 100°C and 1 atm pressure is given by Eq. [2]

$$E_{\text{H}^+/\text{H}_2} = 0.057 - 0.074 \text{ pH}, V_{\text{SHE}} \quad [2]$$

The equation may be considered valid for the test temperature of 92°C without any significant error. The pH of the NaOH and NaOH + Na₂S solutions at 92°C was shown previously to be ~ 12 (6). The crack liquid pH measurements in the current study did not reveal any detectable difference from that of the bulk solution. Hence, the appropriate value of pH to be inserted in Eq. [2] for both the slow strain rate and DCB tests was 12. This showed that the corresponding reversible value of $E_{\text{H}^+/\text{H}_2}$ was $-0.83V_{\text{SHE}}$. The potential of max-

imum susceptibility to SCC during slow strain rate testing was $-0.76V_{SHE}$ in NaOH and $-0.64V_{SHE}$ in NaOH + Na₂S, and SCC occurred at these potentials in the DCB tests. Both potentials were higher (more noble) than the thermodynamically reversible potential for hydrogen evolution. Hence, a hydrogen related mechanism must be dismissed from consideration.

An electrochemical dissolution mechanism of SCC may be considered possible if it can be shown that the maximum anodic dissolution current densities, i_a , occurring at the tip of the propagating cracks were either equal to, or larger than that required to account for the observed crack rates. This approach was first given credence by Parkins (5, 18, 19) and required that the crack rate, v , be equated to the rate of advance of a surface undergoing faradaic dissolution, as shown in Eq. [3]

$$v = \frac{i_a \cdot W}{F \cdot d} \quad [3]$$

where W = equivalent weight of Fe (27.9×10^{-3} kg), F = Faraday (9.65×10^4 A · sec), and d = density of Fe (7.86×10^3 kg · m⁻³).

The maximum value of i_a was assumed to correspond to that associated with the peak anodic current density, i_p , observed at the nose of the anodic polarization curve prior to passivation. This followed from the fact that maximum susceptibility to SCC occurred near the active-passive transition potential and rupture of passive films at the tip of the propagating crack would expose fresh metal to initial (momentary) current densities at least as large as i_p . Accordingly, with reference to Fig. 4 and 5, i_p was ~ 72 A/m² in NaOH and 3.84×10^3 A/m² in NaOH + Na₂S. Thus, with the assumption of a constant current density (i_p) at the crack tip, substitution of these values for i_a in Eq. [3] gave predicted maximum crack propagation rates of 2.6×10^{-9} m/sec in NaOH and 1.4×10^{-7} in NaOH + Na₂S. These rates were equal to or larger than those observed in the DCB tests (Table II).

In reality, once the passive film at the crack tip is ruptured, the exposed metal will tend to re-passivate and the crack tip current density will decrease until the newly formed film undergoes further rupture in the presence of the plastic strain gradient at the crack tip. Thus, there will be alternating cycles of dissolution, re-passivation, and film rupture, where the overall crack propagation rate will be dictated by the time spent in the dissolution stage, together with the time-dependent transient current density operating in this stage. This is the essence of the film rupture dissolution models detailed by Vermilyea (20, 21) and Scully (22).

The most susceptible potentials for SCC in a film rupture-dissolution model are anticipated to be in the passive region near the active-passive transition, as observed, because these conditions represent borderline stability of passive films. Consequently, at these potentials, re-passivation kinetics at freshly exposed surfaces at the crack tip will be relatively slow, thereby allowing a larger increment of metal dissolution (crack advance). Changes in solution composition will affect the re-passivation kinetics, alter the length of the dissolution stage, and cause differences in observed crack propagation rates. Also, the current density in the passive region will be important as this gives an indication of the amount of general dissolution in the presence of the passive film. Higher passive current densities (e.g., in sulfide solutions, c.f. Fig. 4 and 5) will promote more general dissolution in the re-passivation stage and partially blunt the crack. This would lower the local stress concentration, decrease the crack tip strain rate, retard the film rupture process, and decrease the time spent in the crack advance dissolution stage. The conjoint effects of re-passivation kinetics and general dissolution may explain why the sulfide solution did not produce higher crack rates than the sulfide free solution (Table II) despite its larger i_p value.

In principle, the model does not specify an intergranular or transgranular crack path. Intergranular cracking may tend to be favored because of the lattice inhomogeneity represented by the grain boundary, which may affect local film rupture and re-passivation events. However, rupture of the film by slip step emergence can occur elsewhere to promote transgranular cracking. In the present studies, intergranular cracking tended to predominate and transgranular cracking was also observed.

Parkins (15) and Scully (23) have argued that the success of the slow strain rate testing technique for studying SCC lies in the fact that the critical plastic strain increment (creep) necessary to promote film rupture and sustain crack propagation is precisely controlled. Constant load tests on smooth specimens may be unsuccessful because critical local strain rates cannot be maintained. Consistent with this, we were not able to obtain constant load SCC of smooth cylindrical tensile specimens in the current program, even at stresses approaching the ultimate tensile strength. The success of the DCB tests may then be attributed to the fact that the local plastic strain (creep) effects at the tip of the pre-fatigue crack, at the K_I levels employed, were sufficient to promote and sustain the film rupture events necessary for crack propagation.

Overall, the discussion has shown that many facets of the present study were reasonably consistent with the elements of a film rupture-dissolution mechanism of SCC. At this point in time, it does not appear necessary to deviate significantly from this model in order to understand SCC behavior of mild steel in the caustic environments employed.

Conclusions

Potentiostatically controlled caustic cracking studies of AISI 1018 mild steel in aqueous 3.35M NaOH and 2.5M NaOH + 0.423M Na₂S solutions at 92°C were consistent with the following conclusions.

1. The potential regime of maximum susceptibility to SCC occurred at potentials near the active-passive transition in each environment. Maximum susceptibility occurred at $-0.76V_{SHE}$ in NaOH and $-0.64V_{SHE}$ in NaOH + Na₂S.
2. Crack propagation rates were of the order of 1×10^{-9} m/sec at the most susceptible potentials and K_I levels of ~ 50 MPa · m^{1/2}.
3. Cracking generally followed a predominantly intergranular path, with a more noticeable tendency for some transgranular cracking in the absence of sulfide.
4. No detectable change in pH occurred in the liquid contained within the cracks.
5. A hydrogen embrittlement mechanism of SCC was discounted on thermodynamic grounds.
6. The overall studies were reasonably consistent with a mechanism of cracking involving anodic dissolution and film rupture processes.

Acknowledgments

The authors wish to thank the National Science and Energy Research Council of Canada for providing financial support.

Manuscript submitted Jan. 26, 1981; revised manuscript received April 3, 1981.

Any discussion of this paper will appear in a Discussion Section to be published in the June 1982 JOURNAL. All discussions for the June 1982 Discussion Section should be submitted by Feb. 1, 1982.

Publication costs of this article were assisted by the University of British Columbia.

REFERENCES

1. H. Gräfen, *Corros. Sci.*, **7**, 177 (1967).
2. M. Humphries and R. N. Parkins, *Corros. Sci.*, **7**, 747 (1967).
3. K. Bohnenkamp, in "Fundamental Aspects of Stress

- Corrosion Cracking," R. W. Staehle, A. J. Forty, and D. van Rooyen, Editors, pp. 374-382, NACE, Houston (1969).
4. J. E. Reinhoel and W. E. Berry, *Corrosion*, **28**, 151 (1972).
 5. R. N. Parkins, in "Stress Corrosion Cracking and Hydrogen Embrittlement of Iron Base Alloys," R. W. Staehle, J. Hochmann, R. D. McCright, and J. E. Slater, Editors, pp. 601-619, NACE, Houston (1977).
 6. D. Tromans, *This Journal*, **127**, 1253 (1980).
 7. D. A. Wensley and R. S. Charlton, *Corrosion*, **36**, 385 (1980).
 8. D. Singbeil and D. Tromans, in "Corrosion in the Pulp and Paper Industry—1980 Symposium," NACE, Houston, in press.
 9. R. N. Parkins, in "The Theory of Stress Corrosion Cracking in Alloys," J. C. Scully, Editor, pp. 449-468, NATO, Brussels (1971).
 10. "Stress Corrosion Cracking—The Slow Strain Rate Technique," G. M. Ugiansky and J. H. Payer, Editors, STP 665, ASTM, Philadelphia (1979).
 11. W. F. Brown and J. E. Srawley, "Plane Strain Crack Toughness Testing of High Strength Metallic Materials," STP 410, ASTM, Philadelphia (1966).
 12. B. F. Brown, C. T. Fujii, and E. P. Dahlberg, *This Journal*, **116**, 218 (1969).
 13. S. R. Bala and D. Tromans, *Met. Trans. A*, **9**, 1125 (1978).
 14. J. I. Dickson, A. J. Russell, and D. Tromans, *Can. Met. Q.*, **19**, 161 (1980).
 15. R. N. Parkins, in "Stress Corrosion Cracking—The Slow Strain Rate Technique," G. M. Ugiansky and J. H. Payer, Editors, pp. 5-24, STP 665, ASTM, Philadelphia (1979).
 16. ASTM E399-72, ASTM, Philadelphia (1972).
 17. R. J. Biernat and R. G. Robins, *Electrochim. Acta*, **14**, 809 (1969).
 18. P. Lacombe and R. N. Parkins, in "Stress Corrosion Cracking and Hydrogen Embrittlement of Iron Base Alloys," R. W. Staehle, J. Hochmann, R. D. McCright, and J. E. Slater, Editors, pp. 521-523, NACE, Houston (1977).
 19. R. N. Parkins, *Corros. Sci.*, **20**, 147 (1980).
 20. D. A. Vermilyea, in "Stress Corrosion Cracking and Hydrogen Embrittlement of Iron Base Alloys," R. W. Staehle, J. Hochmann, R. D. McCright, and J. E. Slater, Editors, pp. 208-217, NACE, Houston (1977).
 21. D. A. Vermilyea and R. B. Diegle, *Corrosion*, **32**, 26 (1976).
 22. J. C. Scully, *Metal Sci.*, **12**, 290 (1978).
 23. J. C. Scully, in "Stress Corrosion Cracking—The Slow Strain Rate Technique," G. M. Ugiansky and J. H. Payer, Editors, pp. 237-251, STP 665, ASTM, Philadelphia (1979).

Electrochemistry and Reactions of Transition Metal and Oxygen Ions in Dimethyl Sulfoxide

Fred C. Frederick and Keith E. Johnson*

Department of Chemistry, University of Regina, Regina, Canada S4S 0A2

ABSTRACT

Electrochemical studies of oxygen and transition metal ions in dimethyl sulfoxide solution indicate that the O_2/O_2^- , Cu^{2+}/Cu^+ , and Fe^{3+}/Fe^{2+} couples are reversible while the Fe^{2+}/Fe , Co^{2+}/Co , Ni^{2+}/Ni , Cu^+/Cu , and Mn^{2+}/Mn couples are irreversible. The Cr^{3+}/Cr^{2+} and Mn^{3+}/Mn^{2+} systems are difficult to characterize and O_2^{2-} formed from O_2^- undergoes slow degradation. As predicted from the electrode potentials, Cu^{2+} and Fe^{3+} are able to oxidize O_2^- to oxygen. However, the reactions stop with the formation of mixed oxidation state superoxide complexes in solution. Cr^{3+} does not react with O_2^- but forms an insoluble compound with O_2^{2-} .

Dimethyl sulfoxide (DMSO) complexes of transition metal ions may be prepared with tolerable purity, i.e., excess DMSO and perchloric acid can be kept below 5% in most cases (1). When solutions are made up in DMSO, only the perchloric acid impurity is significant, so that electrochemical studies of the Cu(II), Mn(II), Cr(III), Co(II), Ni(II), and Fe(III) complexes should be worthwhile. Previous investigators have employed polarography to study these complexes (2-5), but thorough studies by cyclic voltammetry and coulometry appear to be lacking. In addition to pursuing such studies we have investigated the reactions of several of these compounds and their redox products with electrogenerated superoxide and peroxide ion (6-9).

Experimental

The preparation and analysis of the complexes $M(DMSO)_x(ClO_4)_y$ is described elsewhere (1). Tetraethylammonium perchlorate (TEAP, Eastman Kodak) was recrystallized twice from water and dried *in vacuo*. All solutions for electrochemistry were 0.1M

in TEAP and were purged with O_2 -free N_2 (Cu at 300°).

Electrochemical measurements were carried out with a Princeton Applied Research Model 170 Electrochemistry System with Pt or Au working electrode, Pt counterelectrode, and an aqueous SCE reference electrode, the counter and reference electrodes being isolated in fitted glass compartments.

Results and Discussion

Cyclic voltammograms of DMSO solutions of the complexes of Cr(III), Mn(III), Fe(III), Co(II), Ni(II), and Cu(II) appear as Fig. 1-6. Figure 7 is the voltammogram of oxygen in DMSO. The last traces of oxygen were difficult to remove from the solutions, [cf. (10)] and the voltammogram of O_2 was superimposed on all of the metal voltammograms. For purposes of clarity, all peaks due to O_2 have been omitted from Fig. 1, 3, 4, 5, and 6. In Fig. 2 the combined waves for Mn ions and O_2 are shown for comparable (\sim mM) concentrations. Removal of most of the O_2 leads to current-voltage curves approximated by the inner voltammogram which can be synthesized by subtraction of the

* Electrochemical Society Active Member.

Key words: electrochemistry, oxygen, dimethylsulfoxide, transition metal ions, oxygen ions.

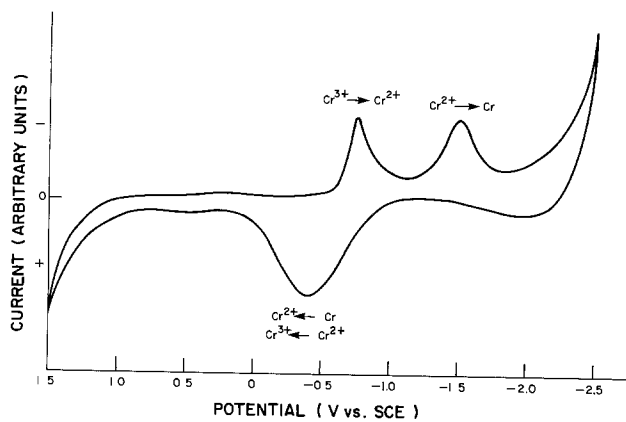


Fig. 1. Cyclic voltammogram of Cr(III) in DMSO solution

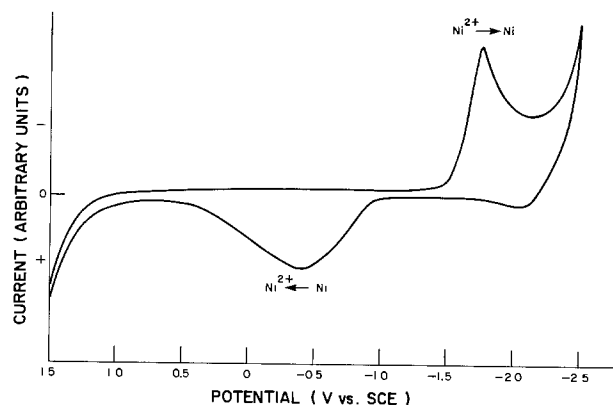


Fig. 5. Cyclic voltammogram of Ni(II) in DMSO solution

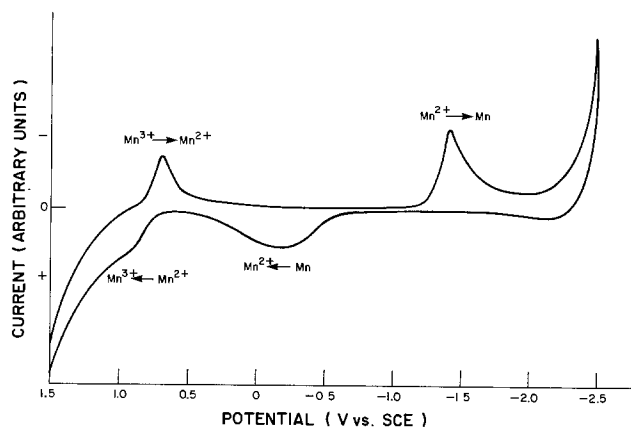
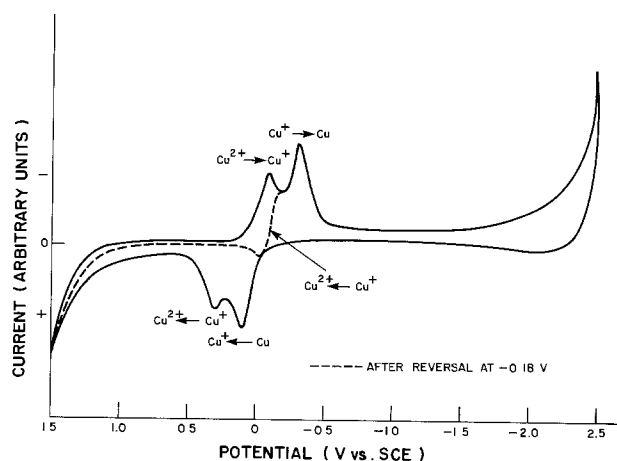
Fig. 2. Cyclic voltammogram of Mn(III) in DMSO solution. Solid line: with O₂ wave included. Broken line: corrected for O₂.

Fig. 6. Cyclic voltammogram of Cu(II) in DMSO solution

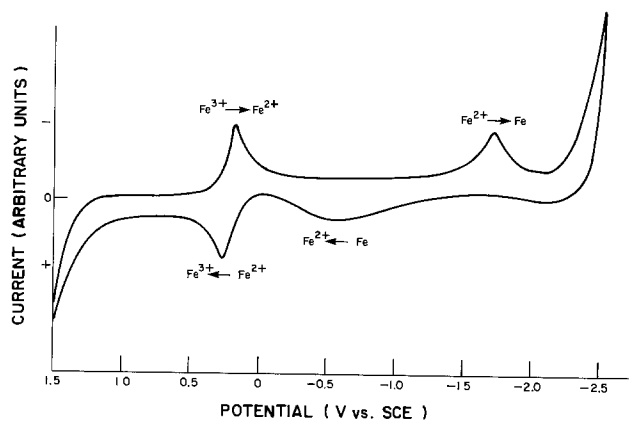


Fig. 3. Cyclic voltammogram of Fe(III) in DMSO solution

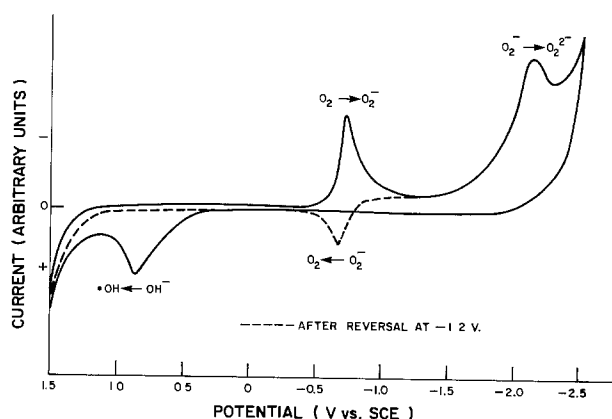
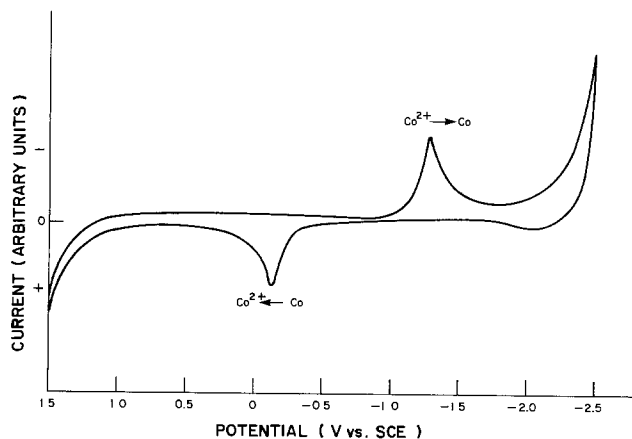
Fig. 7. Cyclic voltammogram of O₂ in DMSO solution

Fig. 4. Cyclic voltammogram of Co(II) in DMSO solution

simple O₂ waves. The scan rate for all voltammograms was 200 mV/sec.

Table I lists the peak potentials. In Table II are presented the results of coulometry applied to the oxygen, Fe(III), and Cu(II) solutions.

Of the electrode processes identified, only the O₂/O₂⁻, Fe³⁺/Fe²⁺, and Cu²⁺/Cu⁺ couples are reversible ($\Delta E =$ difference between reduction and oxidation peak potentials = 60 mV). It should be noted (Fig. 6) that while the Cu²⁺ → Cu⁺ → Cu²⁺ sequence is reversible on platinum, the coating of the electrode with copper changes its redox characteristics. The Cr³⁺/Cr²⁺ peaks are partially masked by the O₂/O₂⁻ system but were discerned by varying the chromium concentration. The Mn³⁺/Mn²⁺ peaks are close to the solvent limit. All the metal ion/metal couples are irreversible. Of special note are the reduction of superoxide to peroxide but

Table I. Cyclic voltammetric peak potentials for dimethyl sulfoxide solutions

| System | Reduction peaks | Oxidation peaks |
|---|--|-------------------------------|
| O ₂ /O ₂ ⁻ | -0.71 (-0.75 ^{10*}) | -0.65 |
| O ₂ ⁻ /O ₂ ²⁻ | -2.13 (-2.02 ^{10*}) | |
| ·OH/OH ⁻ | | +0.90 (+0.75 ^{10*}) |
| Fe ³⁺ /Fe ²⁺ | +0.21 (-0.72 ²) | +0.27 |
| Fe ²⁺ /Fe | -1.70 (-1.44 ²) | |
| Cu ²⁺ /Cu ⁺ | -0.10 (-0.06 ²) | -0.04 |
| Cu ⁺ /Cu | -0.30 | +0.10 |
| Cr ³⁺ /Cr ²⁺ | -0.7 (-0.67 ⁴ , -0.82 ²) | -0.5 |
| Cr ²⁺ /Cr | -1.49 (-1.05 ⁴ , -1.57 ²) | |
| Mn ³⁺ /Mn ²⁺ | +0.7 | +0.8 |
| Mn ²⁺ /Mn | -1.41 (-1.68 ²) | -0.2 |
| Co ²⁺ /Co | -1.26 (-1.4 ^{2,5}) | -0.1 |
| Ni ²⁺ /Ni | -1.75 (-1.1 ² , -1.0 ⁵) | -0.4 |

Potentials in V vs. SCE.

Polarographic half-wave potentials in parenthesis.

* Cyclic voltammetry.

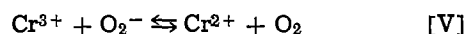
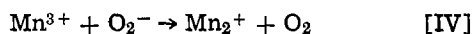
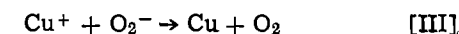
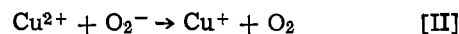
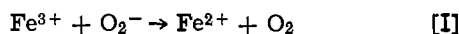
Table II. Coulometry of dimethyl sulfoxide solutions

| Solute | Peak potential (V) | n (Faradays/mol) | Number of trials |
|------------------|--------------------|------------------|------------------|
| O ₂ | -0.71 | 1.12 ± 0.05 | 5 |
| | -2.13 | 2.36 ± 0.16 | 5 |
| Fe ³⁺ | +0.21 | 1.02 ± 0.03 | 3 |
| Cu ²⁺ | -0.10 | 0.87 ± 0.08 | 3 |

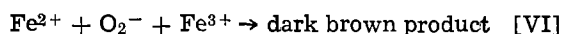
the oxidation of hydroxide ion formed by reaction of peroxide with TEAP and DMSO (11).

Agreement with the polarographic data is good in most instances. However, Burrus (2) probably mistook the O₂/O₂⁻ wave for the Fe³⁺/Fe²⁺ reduction and there are discrepancies between the half-wave potentials and reduction peaks for metal ion/metal couples; differences of 0.1-0.2V would be reasonable.

From the electrode potentials one would anticipate the following reactions might take place

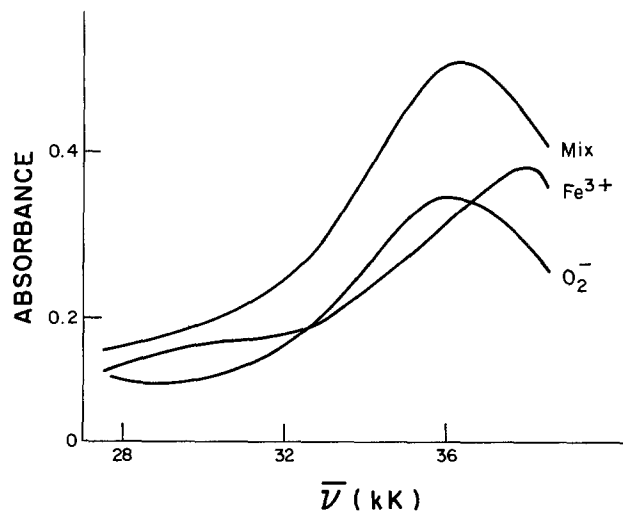
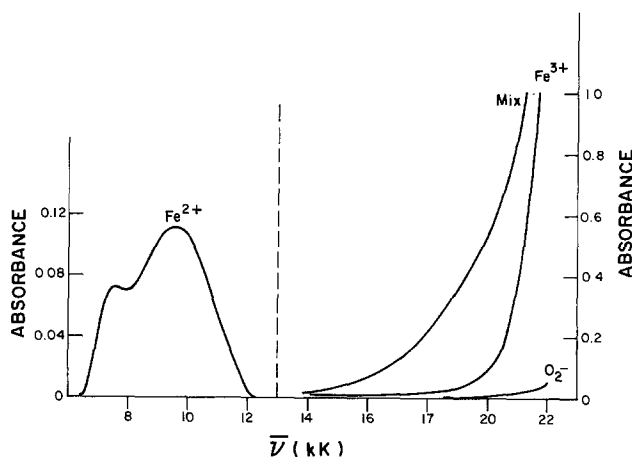


Mixing of electrogenerated superoxide solutions with those of the appropriate metal ion led to oxygen evolution in the case of Fe³⁺ and Cu²⁺, and stabilization of the Mn³⁺, presumably by neutralization of perchloric acid impurity. No copper metal was formed with Cu⁺ and no change whatever occurred for Cr³⁺. However, the solution derived from Fe³⁺ and O₂⁻ (or O₂²⁻) was dark brown and that derived from Cu²⁺ and O₂⁻ green, compared to the yellow Fe³⁺, pale-blue coulometrically generated Fe²⁺ (ν_{max} = 7.46 kK, ε_{max} = 1.41, ν_{max} = 9.61 kK, ε_{max} = 1.93; an appropriate spectrum for high-spin d⁶ in octahedral coordination), and blue Cu²⁺ ions in DMSO solution. The u.v. and visible-near IR spectra of the dark brown solution and the component spectra appear as Fig. 8 and 9. It is clear that a new species is formed involving both ferrous and ferric iron in combination with unoxidized superoxide, i.e., reaction (I) is followed by



Efforts to reach the same equilibrium mixture from Fe²⁺ and O₂ or to drive reaction (I) to completion by bubbling nitrogen gas through the mixture were unsuccessful. A similar situation is believed to occur with reaction (II).

The mixing of DMSO solutions of Cr(DMSO)₆(ClO₄)₃ and electrogenerated peroxide (O₂²⁻) led to the im-

Fig. 8. U.V. spectrum of Fe³⁺/O₂⁻ reaction mixture in DMSO solution.Fig. 9. Visible near IR spectra of Fe³⁺/O₂⁻ reaction mixture, Fe³⁺, O₂⁻, and Fe²⁺ in DMSO solution.

mediate formation of a dark green precipitate. The material was very hygroscopic, evolved oxygen on treatment with aqueous permanganate and analyzed for Cr at 6.0 weight percent (w/o) and ClO₄ at 9.0 w/o (mole ratio ClO₄:Cr ≈ 0.8). When a DMSO solution of Cr(DMSO)₆(ClO₄)₃ was mixed with one of tetraethylammonium hydroxide, a green precipitate formed over a period of hours but this compound did not react with aqueous permanganate. Since some of the immediate reduction product of superoxide can be reoxidized on reversing the direction of scanning the electrode polarization, we conclude that the degradation of peroxide in DMSO solutions of TEAP to form OH⁻, TEA⁺, C₂H₄, (C₂H₅)₃N, and DMSO₂ (11) is not so fast that the peroxide chemistry is necessarily obscured. Thus we suggest that a complex perchlorate of Cr³⁺ and O₂²⁻ is formed; whether or not it contains a variety of other species, besides the coordinating solvent DMSO, remains to be determined. One can speculate that the bonding is of bidentate O₂²⁻ as in CrO₅ or of monodentate O₂H⁻.

These findings indicate that a wealth of coordination and redox chemistry of oxygen ions may be waiting to be uncovered by careful studies in nonaqueous solvents.

Acknowledgment

We are indebted to the National Science and Engineering Research Council for support of this work.

Manuscript submitted Sept. 8, 1980; revised manuscript received May 4, 1981.

Any discussion of this paper will appear in a Discussion Section to be published in the June 1982 JOURNAL. All discussions for the June 1982 Discussion Section should be submitted by Feb. 1, 1982.

Publication costs of this article were assisted by the University of Regina.

REFERENCES

1. F. C. Frederick and K. E. Johnson, *J. Inorg. Nucl. Chem.*, In press.
2. R. T. Burrus, Ph.D. Thesis, University of Tennessee, 1962 (D.A. 23-4524).
3. D. L. McMasters, R. B. Dunlap, J. R. Kuempel, L. W. Kreider, and T. R. Shearer, *Anal. Chem.*, **39**, 103 (1967).
4. V. Gutmann and G. Schober, *Z. Anal. Chem.*, **90**, 897 (1959).
5. I. M. Kolthoff and T. B. Reddy, *This Journal*, **108**, 980 (1961).
6. R. L. Maricle and W. G. Hodgson, *Anal. Chem.*, **37**, 1562 (1965).
7. M. E. Peover and B. S. White, *Chem. Commun.*, 183 (1965).
8. D. T. Sawyer and J. L. Roberts, Jr., *J. Electroanal. Chem.*, **12**, 90 (1966).
9. E. L. Johnson, K. H. Pool, and R. E. Hamm, *Anal. Chem.*, **38**, 183 (1966).
10. J. L. Roberts and D. T. Sawyer, *J. Am. Chem. Soc.*, **103**, 712 (1981).
11. D. T. Sawyer and M. J. Gibian, *Tetrahedron*, **35**, 1471 (1979).

Potentiodynamic Investigation of Cu in Alkaline Phosphate Solutions Containing Added Anions

F. M. Al-Kharafi and Y. A. El-Tantawy

Department of Chemistry, Faculty of Science, Kuwait University, Kuwait City, Kuwait

ABSTRACT

The effect of SO_4^{2-} , Cl^- , and I^- on the intensity of anodic peak currents for the successive processes that occur on Cu in alkaline phosphate media has been studied. At the same sweep rate repeated excursions resulted in a significant anodic current increase for the process corresponding to Cu(I) oxide formation; the anodic peak current of Cu(II) remained unaffected. Also Cu(I) and Cu(II) processes exhibited significant differences in their response to cycling at increasing scan rate. The increase of the anodic current for Cu(I) formation with increasing $[\text{Cl}^-]$ showed a definite tendency to level off. Cu(II) anodic currents exhibited a continuous increase with increasing $[\text{Cl}^-]$. At relatively high $[\text{Cl}^-]$ current oscillations were observed which have been explained. A mechanism of Cl^- attack involving adsorption, interaction with a soluble intermediate, and peptization of the passivating products is discussed. The effect of the Cl^- ion revealed that passivating Cu(II) products were formed, most probably, via a diffusion-controlled pathway.

Studies on the nature and kinetics of the electro-dissolution of Cu are of considerable importance in corrosion, electropolishing, and electrochemical machining. The role of Cl^- on Cu dissolution has received special attention (1-8). It is noted that these investigations were performed in nearly neutral (1, 4, 5, 9) or acidic (3, 6-8) solutions and in flowing (5, 7) or static solutions. There is agreement (3, 5-7) that Cu dissolves as CuCl_2^- and CuCl_3^- , and the dissolution process was reported to be diffusion controlled. In HCl media, it has been reported that a cuprous chloride layer may grow to considerable thickness by a solid-state mechanism (7).

In alkaline media (1) the effect of Cl^- in the electrochemical dissolution of Cu has been investigated by the observation of changes in the overpotential occurring during constant current polarization and after the current was interrupted. Thirsk *et al.* (1) observed "sharp unpredictable fluctuation" in the overpotential curves. They ascribed these variations to "mechanical breakdown" in the otherwise continuous area of the deposit.

The object of the present study is to reveal the nature of the role of the anions SO_4^{2-} , Cl^- , and I^- in the stability of passive films on anodized Cu in alkaline phosphate media. This investigation is also intended to emphasize the role played by these anions during the anodic formation of the passivating salt.

Key words: mechanism, passivity, anion influence, electrode.

Experimental

Chemicals.—The best, commercially available, BDH grade was used. Triply distilled water was employed throughout. Electrodes were of Specpure Johnson Matthey Cu rods with an exposed area of 3.29 cm².

Equipment.—*E-i* and *E-t* traces were obtained with the aid of a Model 350 Princeton Applied Research Set, Model 9700 cell complete with calomel, reference, and auxiliary electrodes and a Model 1201A HP recorder.

Experimental technique.—The value of the anodic current at the first peak (most negative potential) was observed to be significantly and systematically dependent on electrode cycling at the same rate. Therefore, under the same set of conditions the electrode was cycled at least four times. In searching for a trend comparison between scans with the same cycle number is made. Electrodes were cleaned both mechanically and electrochemically (precathodization treatment). The surface treatment of the electrode involved successive polishing with 0,00 and 000 emery paper, degreasing with acetone, washing with triply distilled water, and carefully drying with filter paper. Each half-cycle covered the potential range from -1 to $+0.60\text{V}$. For the same scan rate, the time interval between successive cycles was roughly constant. Electrolytic solutions were deoxygenated by a fine stream of nitrogen gas, purified by passing through two towers containing

acidic vanadous aqueous solutions followed by two towers filled with triply distilled water. Deoxygenation took place before and during the precathodization treatment. All experiments were conducted in a temperature-controlled laboratory at $24^\circ \pm 1^\circ\text{C}$. However, during a run temperature tolerance was not more than $\pm 0.5^\circ\text{C}$. All potential values were recorded *vs.* SCE.

Results

Figure 1a shows a typical potentiokinetic trace for Cu in alkaline phosphate solution of pH value adjusted at 12.50. Three anodic and two cathodic processes are consistently observed. When compared with the behavior in NaOH in the same range of pH, the presence of phosphate ions has practically no effect on peak I but significantly inhibits peak II (10).

Very recent studies employing x-ray photoelectron spectroscopic (XPS) technique have focused attention on the nature and oxidation states of the anodically formed passivating copper oxide (or hydroxide) film (10-12) in alkaline media. These studies (10-12) agree that only Cu(I) and Cu(II) oxide species are formed. However, there is some disagreement on the nature of the Cu(II) species (10-12). Strehblow and Titze (11) stated that in weak alkaline phosphate buffer (pH = 8.0) the anodically formed film was composed for the most part of Cu_2O and $\text{Cu}(\text{OH})_2$. McIntyre *et al.* (12), employing a medium of 1M KOH, reported that the film was composed of a layer of Cu_2O followed by a mixture of cupric oxide and cupric hydroxide. They (12) added that the hydroxide form predominated. Employing a medium of 1M NaOH, El-Tantawy *et al.* (10) reported that only Cu_2O and CuO were formed. In alkaline phosphate media possible formation of insoluble copper phosphate species was excluded on the basis of XPS (11) as well as electrochemical measurements (10, 13). A detailed discussion of the nature of the passivating products and the role of phosphate ion has been given by the authors elsewhere (10).

In the light of the above discussion, processes I, II, and III most probably correspond, respectively, to a solid formation of Cu_2O , CuO , and most probably $\text{Cu}(\text{OH})_2$. The two cathodic peaks represent stepwise reduction of Cu^{2+} (irrespective of its nature) to Cu^+ and Cu^+ to Cu . By comparison with Fig. 1a traces b, c, and d illustrates the effect of mixing Na_2SO_4 , NaCl , and NaI with the passivating phosphate solution. Peak I is the most affected. In terms of the current intensity for the various processes, the addition of I^- gave the largest relative increase of i_p for process I. Chloride ion comes next. The lowest effect is that of SO_4^{2-} . Addi-

tion of sulfate resulted in an initial decrease of $(i_p)_I$. Process III is observed to be significantly suppressed by sulfate and I^- .

Effect of cycling at the same sweep rate.—Table I contains the values of i_p for the anodic and cathodic processes at four consecutive cycles. A number of interesting observations may be noted.

1. i_p values for process I consistently increase on cycling. The magnitude of the increase is dependent on the type of added anion. Also, the mode of increase of i_p for process I is observed to be anion-dependent. While the addition of I^- resulted in the highest initial (cycle I) increase, the rate of increase of $(i_p)_I$ with cycling is seen to be the largest with Cl^- .

2. Cycling is noted to have practically no effect on i_p values for process II. It seems that while process I is very dependent on the changes that may occur on the surface as a result of cycling, process II is not controlled by such changes.

3. In general, peaks IV and V seem to vary very little on cycling. It was consistently noted that the area under peak V was always bigger than that of peak IV.

Cycling is expected to increase surface roughness. In the present case, the increase in surface area is believed to be due to two causes: (i) electrochemical dissolution from preferred sites and (ii) constant attack of selective surface sites by the aggressive anion: the latter occurring even in the absence of an imposed electric field. The dependence of the magnitude of the increase of i_p for process I, Δi_p^I (last column of Table I), on the type of anion reveals the order $\text{Cl}^- > \text{I}^- > \text{SO}_4^{2-}$.

Effect of increasing anion concentration.—The dependence of the values of (i_p) for peaks I, II, IV, and V on increasing additions of the different anions is given in Table II for the first and second cycles. A close look at Table II reveals two interesting features, especially with Cl^- .

1. The i_p values for peaks I and II generally increase with increasing amounts of the added anion. While the increase of $(i_p)_I$ tends to level off, $(i_p)_{II}$ shows a continuous rise.

2. It is observed that the charge accumulated at peak IV and V increases significantly with increasing $[\text{Cl}^-]$. It seems that considerable thickening of the passivating film takes place as the $[\text{Cl}^-]$ is increased.

Figure 2 depicts a redrawn potentiodynamic trace recorded in the presence of an added 1M Cl^- (compare Fig. 1c with 2). Except for the expected increase of the current intensity for the anodic peaks, the form of the potentiodynamic trace shown in Fig. 1c, was always

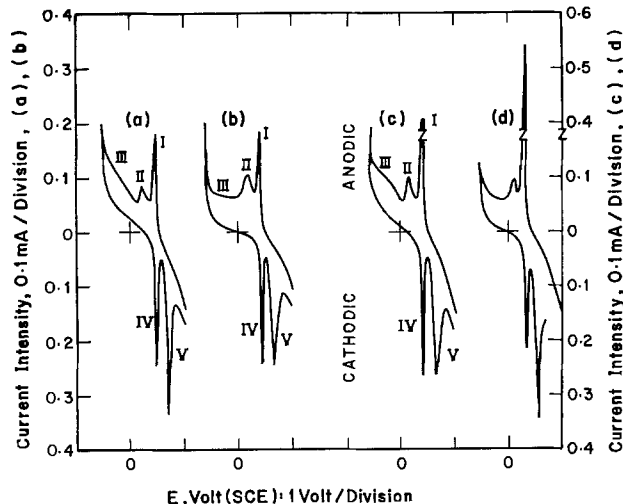


Fig. 1. Representative second cycle potentiodynamic traces at 1 mV sec^{-1} in $0.1\text{M Na}_3\text{PO}_4$ (measured $\text{pH} = 12.50$) plus 0.1M added salt: (a) none, (b) Na_2SO_4 , (c) NaCl , (d) NaI .

Table I. Effect of cycling at the same sweep rate of 1 mV sec^{-1} on the intensity of the peaks of process I, II, IV, and V of Cu in aqueous $0.1\text{M Na}_3\text{PO}_4 + 0.1\text{M X}^n-$

| X^n- | Peak No.* | $i_p/\text{mA}/\text{electrode}$ | | | | Δi_p^I |
|--------------------|-----------|----------------------------------|------|------|------|----------------|
| | | 1 | 2 | 3 | 4 | |
| None | I | 0.17 | 0.18 | 0.21 | 0.25 | 0.08 |
| | II | 0.10 | 0.09 | 0.09 | 0.09 | |
| | IV | 0.36 | 0.24 | 0.22 | 0.22 | |
| | V | 0.34 | 0.33 | 0.33 | 0.33 | |
| SO_4^{2-} | I | 0.10 | 0.18 | 0.21 | 0.32 | 0.22 |
| | II | 0.12 | 0.10 | 0.12 | 0.12 | |
| | IV | 0.19 | 0.24 | 0.30 | 0.27 | |
| | V | 0.22 | 0.24 | 0.26 | 0.27 | |
| Cl^- | I | 0.18 | 0.40 | 0.58 | 0.83 | 0.65 |
| | II | 0.10 | 0.10 | 0.10 | 0.11 | |
| | IV | 0.24 | 0.27 | 0.31 | 0.33 | |
| | V | 0.25 | 0.27 | 0.21 | 0.32 | |
| I^- | I | 0.48 | 0.54 | 0.74 | 0.84 | 0.36 |
| | II | 0.11 | 0.10 | 0.10 | 0.09 | |
| | IV | 0.16 | 0.22 | 0.25 | 0.26 | |
| | V | 0.31 | 0.35 | 0.36 | 0.36 | |

* Peak III appeared as broad sloping shoulder; IV acute, V relatively broader; 1, 2, ... denote cycle number; electrode reactions: I, Cu Cu(I); II, Cu Cu(II); IV, Cu(II) Cu(I); V, Cu(I) Cu, $\Delta i_p^I = (i_p^4 - i_p^1)_I$.

Table II. Effect of increasing $[X^{n-}]$ at constant 0.1M Na_3PO_4 on the intensity of peak currents of I, II, IV, and V of the first and second cycles at 1 mV sec^{-1}

| X^{n-} | C/M | i_p/mA | | | | | | | |
|--------------------|------|-----------------|------|------|------|------|------|------|------|
| | | I | | II | | IV | | V | |
| | | 1 | 2 | 1 | 2 | 1 | 2 | 1 | 2 |
| SO_4^{2-} | 0.04 | 0.10 | 0.15 | 0.10 | 0.09 | 0.14 | 0.15 | 0.17 | 0.17 |
| | 0.10 | 0.10 | 0.18 | 0.12 | 0.11 | 0.19 | 0.24 | 0.22 | 0.24 |
| | 0.40 | 0.12 | 0.34 | 0.09 | 0.11 | 0.18 | 0.23 | 0.21 | 0.26 |
| Cl^- | 0.04 | 0.13 | 0.23 | 0.09 | 0.09 | 0.18 | 0.17 | 0.20 | 0.19 |
| | 0.10 | 0.18 | 0.40 | 0.10 | 0.10 | — | 0.26 | — | 0.26 |
| | 0.30 | 0.38 | 0.48 | 0.12 | 0.12 | 0.20 | 0.22 | 0.26 | 0.28 |
| | 0.50 | 0.42 | 0.15 | 0.15 | 0.14 | 0.29 | 0.33 | 0.35 | 0.38 |
| | 1.0 | 0.42 | 0.68 | 0.29 | 0.29 | 0.31 | 0.42 | 0.46 | 0.48 |
| I^- | 0.04 | 0.36 | — | 0.09 | — | 0.17 | — | 0.26 | — |
| | 0.10 | 0.48 | 0.54 | 0.11 | 0.10 | 0.15 | 0.31 | 0.22 | 0.35 |
| | 0.20 | 0.96 | — | 0.20 | — | — | — | — | — |
| | | | | | | | | | |

observed up to 0.5M Cl^- . At an added $[\text{Cl}^-]$ of 1M, peaks I and II remained practically unaffected (*viz.* their shape). In the potential region of III (0.0-0.7V, SCE) irregular current oscillations were observed. Current oscillations may indicate that the passivating species in a quasi-equilibrium state with the electrode surface do not permanently persist (2).

In presence of both OH^- and Cl^- , the deposition of the electrochemically dissolving Cu^{2+} as an insoluble hydroxide is thermodynamically favored (14). Nevertheless, from a kinetic viewpoint dissolving Cu^{2+} may, through random collisions, interact with Cl^- ions to form a soluble chlorospecies which may then diffuse away into the bulk of solution. Further, due to the probable absorption of Cl^- on the electrode surface, Cu^{2+} would have the chance to dissolve as a chlorospecies. It is probable that Cl^- ions react with the soluble intermediate species (*e.g.*, $\text{Cu}(\text{OH})_n^{1-n}$ or $\text{Cu}(\text{OH})_y^{2-y}$) to form, the more soluble chlorospecies (see Eq. [2]). This would result in a decrease of the concentration of the Cu-hydroxy species, a saturated (or supersaturated) layer of which is necessary to

initiate the deposition of the passivating film. This leads to passivation delay.

In presence of added 1M Cl^- , a heavy gelatinous light-blue precipitate was observed on the electrode surface near the end of the potential region of oscillation. The formation of such a gelatinous deposit is believed to be caused by spontaneous dispersion of the precipitated passivating film to form a colloid as a result of heavy adsorption of Cl^- . This peptization process presumably leads to exposure of the surface of the electrode and the anodic current increases. Therefore, the oscillations observed in Fig. 2 are a result of active \rightleftharpoons passive transitions on the electrode surface.

In the light of the above picture for the role of Cl^- , the increase in i_p values for the cathodic processes IV and V in Table II with increasing $[\text{Cl}^-]$ could result from the formation of thick anodic film deposits that may sustain aggressive attack.

Effect of sweep rate.—Figure 3 illustrates plots of i_p against $v^{1/2}$; v being in mV sec^{-1} . It is true that neither of the curves in Fig. 3 is strictly linear as demanded by purely diffusion-controlled processes (15). At least the deviation from linearity with increase sweep rate for peak II is definitely not as large as that for process I. This difference in behavior toward increasing scan rate is possibly due to a different mechanism for the two processes. Similar behavior at different additions of SO_4^{2-} , I^- , and Cl^- has been observed.

Open-circuit measurements.—In order to gain further insight on the nature of the interaction of halide ions with the various oxides that form along the anodic scan, the cleaned Cu electrode was anodically oxidized at selected constant potential values for long enough to allow the deposition of a film of a particular structure. The electrode was then rapidly transferred, under an inert atmosphere to a solution of only aqueous I^- on Cl^- . For comparison, the potential time behavior of a clean electrode is included in Fig. 4. In aqueous I^- media, irrespective of the past history, the electrode potential values rapidly drift in the direction of the value for a clean electrode, Fig. 4a. It seems that due to an I^- interaction the passivating film is rapidly ruptured. Because of the rapid nature of this interaction, assisted by the strong affinity of copper ions for I^- complexation (16) to form soluble species, it is believed that the potential drift is due to chemical dissolution of the surface film. In aqueous Cl^- media, the electrode potential values for the films precipitated at 0.5 and 0.05V slowly decay toward the open-circuit value. Stripping of the passive films through peptization is expected to occur slowly. Further, Fig. 4b shows

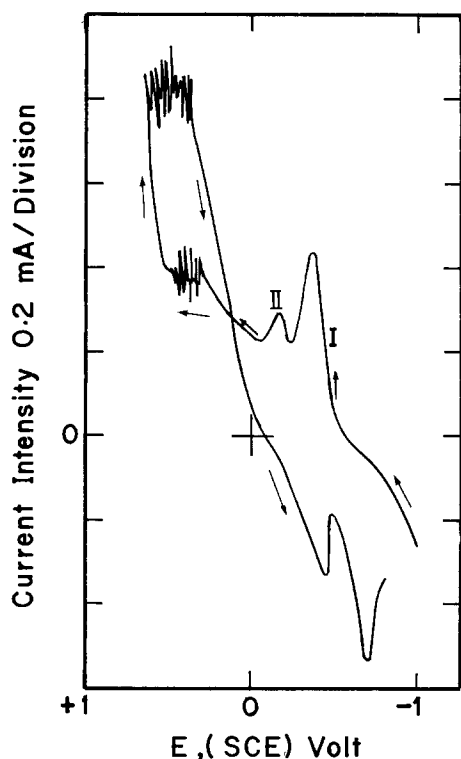


Fig. 2. First cycle redrawn potentiodynamic curve in 0.1M $\text{Na}_3\text{PO}_4 + 1\text{M NaCl}$; current oscillations appear in the potential region of process III; no oscillations were observed at lower $[\text{NaCl}]$.

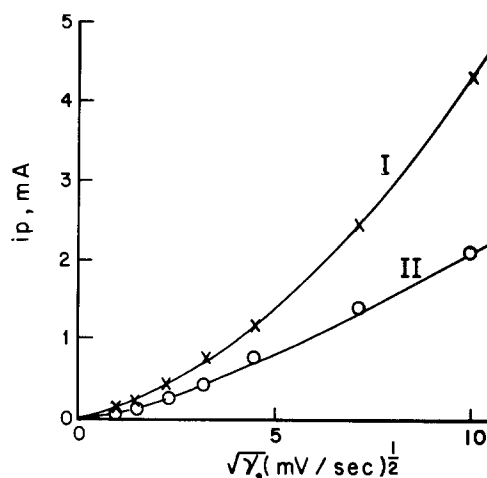


Fig. 3. Mode of response of the current intensities of anodic peaks I and II to increasing sweep rate in the range $1-100 \text{ mV sec}^{-1}$.

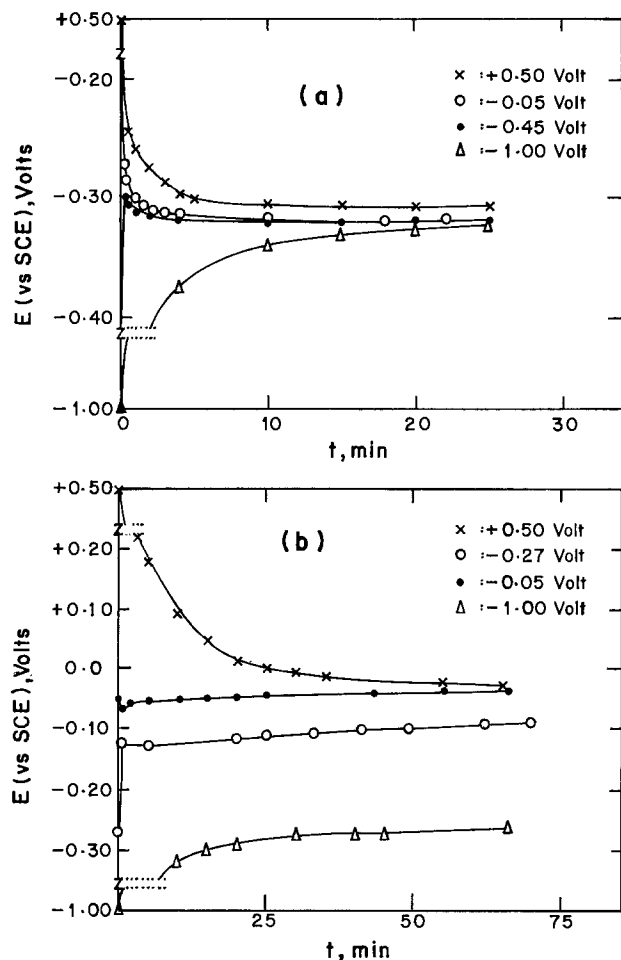


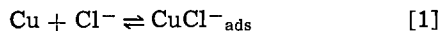
Fig. 4. Mode of potential decay in aqueous (a) 0.2M Cl^- and (b) 0.5M Cl^- .

that the open-circuit potential value of a clean electrode falls well below that of the oxidized surfaces.

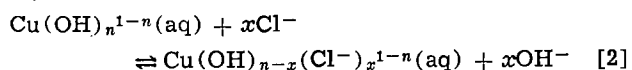
Mechanism and Conclusion

A probable mechanism for the effect of Cl^- ions on the anodic passivation of Cu should conform with the tendency of $(i_p)_I$ to level off with increasing $[\text{Cl}^-]$, as opposed to the observed continual increase of $(i_p)_{II}$. An interesting feature to be accounted for, is the lack of dependence of $(i_p)_{II}$ on voltage cycling, contrary to the significant dependence (increase) of the intensity of the peak current for process I, Table I. Further, the $(i_p)_{II}-v^{1/2}$ plot deviates from linear behavior only slightly compared with that of $(i_p)_I$. For full discussion on the mechanism of the film formation in absence of Cl^- , refer to Ref. (10).

Peak I.—The presence of bulk Cl^- ions furnishes favorable conditions for competitive adsorption of Cl^- with OH^- (or H_2O dipoles) (17) on the Cu surface, in a dynamic step



i.e., increasing $[\text{Cl}^-]$ in the solution bulk favors the electrochemical dissolution of Cu in the form of chlorospecies. Also, increasing $[\text{Cl}^-]$ is expected to necessarily result in the dilution of an intermediate species, the supersaturation of which is needed for crystallization into solid Cu_2O (18, 19)



Equilibria [1] and [2] should lead to leveling off of $(i_p)_I$ with increasing $[\text{Cl}^-]$. $\text{Cu}(\text{OH})_{n-1}$ represents the intermediate soluble species of Cu(I) that crystallizes into the passivating products. The occurrence of

equilibrium [1] should lead eventually to an increase in electrode surface roughness and consequently to the increase in $(i_p)_I$ observed on cycling. Cl^- ions are adsorbed on preferential sites. On starting an anodic excursion, Cl^- adsorbed sites represent potential electrochemical dissolution spots. Preferential site dissolution necessarily results in an increase in the surface roughness and consequently $(i_p)_I$ on cycling. However, after the Cu_2O has deposited it seems that the nature of Cl^- ion attack becomes different. Cl^- attack on the deposited solid was observed to be slow, see Fig. 4. It seems that Cl^- ions attack the precipitated oxide through initial preferential site adsorption which results in local peptization in a colloidal sense. Such a mode of attack may lead to creation of weak spots or perforations in the film structure.

Peak II.—The pronounced difference of $(i_p)_{II}$ form $(i_p)_I$ toward increasing the sweep rate, supported by the complete independence of $(i_p)_{II}$ of cycling (increase of surface area), is consistent with a model controlled mainly by diffusion for process II. At the completion of process I, the surface is nearly covered (19, 20) by Cu_2O and possibly partially blocked with phosphate ions. The only chance for electrochemical generated cupric ions to precipitate is to diffuse through the Cu_2O film to the Cu_2O /solution interphase. This model is further supported by a recently published study (11) where XPS and ISS techniques were employed. There (11), it is reported that in weakly alkaline phosphate buffer of pH 7.0 and 8.0, the passivation of Cu resulted in the formation of Cu(II)-species on top of a Cu(I)-oxide layer. Therefore, the formation of Cu(II) passivating species is believed to be controlled by the rate of passage of soluble Cu^{2+} across the Cu(I) oxide barrier. This rate of ion transport is expected to increase with increasing $[\text{Cl}^-]$, due to the irreversible attack on selective sites as explained in the previous paragraph. Such a model explains the observed continuous increase of $(i_p)_{II}$ with increasing Cl^- .

The increase in $(i_p)_I$ caused by I^- ions is believed to be essentially due to chemical dissolution of the precipitated oxide. This speculation is based on the observations that: (i) the oxidized Cu surface rapidly attains the potential of the clean electrode in aqueous I^- media, (ii) compared with Cl^- or SO_4^{2-} , the increase of $(i_p)_I$ due to I^- addition is usually large for the first cycle, and (iii) surface oxidation of Cu in aqueous I^- medium (nearly neutral) yielded only one anodic peak which did not persist to exhibit a corresponding cathodic process. On reverse half-cycle, the anodic process appeared again. However, the I^- effect needs a detailed study.

Acknowledgments

The authors are gratefully indebted to one of the reviewers for a critical reading of the manuscript, to Mr. Z. Al-Fahd for assistance in the experimental part, and to Kuwait University for financial support under project number SCO12. Particular thanks are due to Dr. D. W. Shoesmith of Atomic Energy of Canada Limited, Pinawa, for his kindness in making available to us manuscripts to be published.

Manuscript submitted Feb. 13, 1981; revised manuscript received April 27, 1981.

Any discussion of this paper will appear in a Discussion Section to be published in the June 1982 JOURNAL. All discussions for the June 1982 Discussion Section should be submitted by Feb. 1, 1982.

Publication costs of this article were assisted by Kuwait University.

REFERENCES

- H. Lal and H. R. Thirsk, *J. Chem. Soc.*, 2638 (1953).
- R. S. Cooper and J. H. Bartlett, *This Journal*, **105**, 109 (1958).

3. T. Hurlen, *Acta Chem. Scand.*, **15**, 1231 (1961).
4. D. J. G. Ives and A. E. Rawson, *This Journal*, **109**, 462 (1962).
5. A. L. Bacarella and J. C. Griess, Jr., *ibid.*, **120**, 459 (1973).
6. C. H. Bonfiglio, H. C. Albaya, and O. A. Cobo, *Corros. Sci.*, **13**, 717 (1973).
7. M. Turner and P. A. Brook, *ibid.*, **13**, 973 (1973).
8. M. Braun and K. Nobe, *This Journal*, **126**, 1666 (1979).
9. G. Faita, G. Fioro, and D. Salvatore, *Corros. Sci.*, **15**, 383 (1976).
10. Y. A. El-Tantawy, F. M. Al-Kharafi, and A. Katrib, *J. Electroanal. Chem. Interfacial Electrochem.*, In press.
11. H. H. Strehblow and B. Titze, *Electrochim. Acta*, **25**, 839 (1980).
12. N. S. McIntyre, S. Sunder, D. W. Shoesmith, and F. M. Stanchell, *J. Vac. Sci. Technol.*, In press.
13. Y. A. El-Tantawy, A. E. El-Kholy, and T. S. E. Kassem, *Corros. Sci.*, **18**, 1065 (1978); *ibid.*, To be published.
14. W. M. Latimer, "Oxidation States of Elements," Prentice Hall, Inc., Englewood Cliffs, NJ (1961).
15. P. Delahay, "New Instrumental Methods in Electrochemistry," p. 124, Interscience, New York (1954).
16. L. G. Sillen and A. E. Martell, "Stability Constants of Metals Ion Complexes," Spec. Publ. No. 17 and Supplement No. 1 Spec. Publ. No. 25 (1971), The Chemical Society, London.
17. H. Leckie and H. Uhlig, *This Journal*, **113**, 1262 (1966).
18. J. Ambrose, R. G. Barradas, and D. W. Shoesmith, *J. Electroanal. Chem. Interfacial Electrochem.*, **47**, 47 (1973).
19. V. Ashworth and D. Fairhurst, *This Journal*, **124**, 506 (1977).
20. D. W. Shoesmith, W. Lee, and M. G. Baily, *ibid.*, **127**, 338C (1980).

Theoretical Treatment of the Transport Equations for Electrons and Ions in a Mixed Conductor

I. Riess

Department of Physics, Technion-Israel Institute of Technology, Haifa, Israel

ABSTRACT

The transport equations for the ions and electrons in a mixed conductor are considered. An exact solution of these equations in the steady state is given for a fixed ion concentration. Explicit analytic expressions are derived for the variation of electron concentration with position and applied voltage. From this, the electron chemical potential variations within the mixed conductor can be obtained. Explicit analytic expressions are also derived for the dependence of the current on the external voltage. The power output and energy conversion efficiency are then calculated for a fuel cell based on a mixed conductor. An example is discussed quantitatively. It is a high temperature fuel cell based on doped ceria and operating at 800°C.

The transport equations for ions and electrons in a mixed conductor were evaluated in parametric form by Choudhury and Patterson (1) and by Tannhauser (2). These calculations resulted in implicit equations for the dependence of the electron concentration and current density on the external parameters. For a fuel cell based on a mixed conductor the power output and efficiency could be calculated numerically.

It is the purpose of this paper to present a solution of the transport equations which yields explicit expressions for the variation of the electron concentration, n , with position and for the dependence of n , of the electric current and of the total current, on the external parameters. We then derive explicit expressions for the power output and the energy conversion efficiency as well as for the maximum power output and maximum efficiency in a fuel cell.

A high temperature fuel cell based on a solid mixed conductor is discussed to demonstrate the results and for comparison with calculations done before (2). Solid electrolytes used in fuel cells are doped oxides which conduct oxygen ions (3). Electronic conductance sets in due to reduction of the oxide on the fuel side. The degree of reduction depends on the oxide used. ZrO₂-10 mol percent (m/o) Y₂O₃ stays "pure" ionic to very low oxygen pressure, P_{O₂}. Its ionic transference number \bar{t}_i is estimated to be 0.5 for P_{O₂} = 10⁻³¹ atm at 1000°C (4). For CeO₂-10 m/o Gd₂O₃, \bar{t}_i = 0.5 for P_{O₂} = 10⁻¹⁶ atm at 800°C (5). Doped ceria is therefore a

mixed conductor due to the low oxygen pressures which prevail on the fuel side of a fuel cell, while doped zirconia can be considered as a "pure" ionic conductor under these conditions. On the other hand, the ionic conductivity of doped ceria is about three times higher than that of doped zirconia at the same temperature and the power density which can be obtained with doped ceria may be higher.

While the discussion is quite general, we shall use the notation relevant to a high temperature fuel cell, namely, the ions will be charged oxygen vacancies and the driving force will be due to a difference in oxygen pressures on both sides of the electrolyte.

Ionic Current vs. Total Current in a Mixed Conductor

Figure 1 shows a mixed conductor solid electrolyte fuel cell (MSEFC) connected to an external voltage V . In general, V can be positive (as shown in Fig. 1) or negative. For normal fuel cell use, the external source, B , is replaced by a load resistance R and $V = IR$, where I is the total current through the mixed conductor solid electrolyte (MSE) and the load. The electrodes A₁, A₂ located at two different oxygen atmospheres are assumed to be nonblocking and reversible, so that there is no voltage drop on the electrodes.

The ionic current through the MSE consists of oxygen vacancies, V_{O'}, which have an effective double positive charge relative to the perfect solid. The ionic current density is

$$j_i = -\frac{\sigma_i}{2q} \nabla \tilde{\mu}_i, \quad \sigma_i = 2q\mu_i N \quad [1]$$

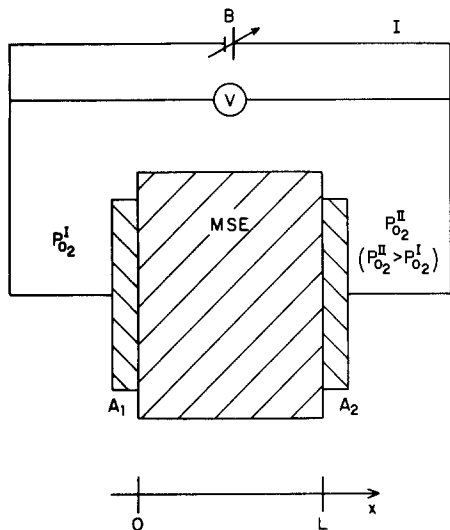


Fig. 1. Schematic representation of a mixed conductor solid electrolyte fuel cell connected to a variable external source B of voltage V .

and the electronic current density of quasi free electrons is

$$j_e = \frac{\sigma_e}{q} \nabla \tilde{\mu}_e, \quad \sigma_e = q\nu_e n \quad [2]$$

where σ denotes conductivity, μ , electrochemical potential, ν mobility, q is the electronic charge, N , n are the concentration of ions and electrons, respectively. ν_e , ν_i are assumed to be constant throughout the MSE, thus independent of concentration.

In the steady state j_i , j_e do not depend on position, x , and Eq. [1], [2] can readily be integrated

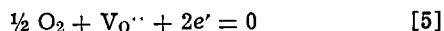
$$\tilde{\mu}_i(A_2) - \tilde{\mu}_i(A_1) = -2qj_i \int_0^L \frac{dx}{\sigma_i} \equiv -2qI_i R_i \quad [3]$$

where R_i is the resistance of the MSE to ionic current I_i . In general R_i may be a function of V . L is the length of the MSE, S its cross section, and $I_i = S j_i$. Similarly

$$\tilde{\mu}_e(A_2) - \tilde{\mu}_e(A_1) = qj_e \int_0^L \frac{dx}{\sigma_e} \equiv qI_e R_e \quad [4]$$

where R_e is the resistance of the MSE to an electronic current, I_e . R_e depends on V . $I_e = S j_e$.

The reaction



takes place at electrodes A_1 , A_2 . The differences between the oxygen chemical potential μ_{O_2} and $\tilde{\mu}_i$, $\tilde{\mu}_e$ at A_1 , A_2 are related by

$$\frac{1}{2} [\mu_{O_2}(A_2) - \mu_{O_2}(A_1)] + [\tilde{\mu}_i(A_2) - \tilde{\mu}_i(A_1)] + 2[\tilde{\mu}_e(A_2) - \tilde{\mu}_e(A_1)] = 0 \quad [6]$$

where

$$\mu_{O_2}(A_2) - \mu_{O_2}(A_1) = kT \ln(P_{O_2}^{II}/P_{O_2}^I) = 4qV_{th} \quad [7]$$

The voltage V is

$$-qV = \tilde{\mu}_e(A_2) - \tilde{\mu}_e(A_1) \quad [8]$$

Substituting Eq. [6], [7], [8] into Eq. [3] and [4] yields

$$V_{th} - V = I_i R_i \quad [9]$$

$$V = -I_e R_e \quad [10]$$

Hence

$$I = I_i + I_e = \frac{V_{th} - V}{R_i} - \frac{V}{R_e} \quad [11]$$

The following limits are immediately obtained

$$a) V = V_{th} \leftrightarrow I_i = 0, \quad I_e = -V_{th}/R_e(V_{th})$$

$$b) V = 0 \leftrightarrow I_e = 0, \quad I_i = V_{th}/R_i(0)$$

c) For $I = I_i + I_e = 0$ the open-circuit voltage is

$$V_{o.c.} = \frac{R_e(V_{o.c.})}{R_i(V_{o.c.}) + R_e(V_{o.c.})} V_{th} \equiv \bar{t}_i V_{th} \quad [12]$$

\bar{t}_i is identified as the average ionic transference number (4). For the MSE, the ratio I_i/I depends on V . From Eq. [9]-[11]

$$-\infty \leq I_i/I \leq 0 \quad \text{if } V_{o.c.} \leq V \leq V_{th}$$

$$0 < I_i/I \leq 1 \quad \text{if } 0 \geq V, \quad V \geq V_{th} \quad [13]$$

$$1 \leq I_i/I \leq \infty \quad \text{if } 0 \leq V \leq V_{o.c.}$$

since R_e , R_i are positive by definition. For normal fuel operation $0 < V < V_{o.c.}$ and I is seen to be smaller than I_i . The total current approaches the ionic one, I_i , only for small values of V .

Exact Solution of the Transport Equations

Solutions of the transport Eq. [1] and [2] were given in an implicit parametric form by Choudhury and Patterson (1) and by Tannhauser (2). Choudhury and Patterson, using Wagner's approach (6), assume that N , the concentration of ions, is uniform throughout the MSE. This assumption is valid for many electrolytes and will be used also here. For doped ceria, for example, the doping fixes the concentration of the ionic charge carrier ($V_{O\cdot}$) and the variation in concentration, δN , due to extra vacancies created by reduction of the oxide, can be neglected. Tannhauser assumed local neutrality and showed that it was consistent with his results. The two assumptions yield similar results when $\delta N \ll N$. Local neutrality means: $2[V_{O\cdot}] = [Gd_{Ce}'] + n$ for $0 \leq x \leq L$, in which case: $2\delta N = n$. Seemingly, Tannhauser's assumption is less restrictive than that used by Choudhury and Patterson. If the ionic current density is rewritten as

$$j_i = -kT\nu_i \frac{dN}{dx} - 2qN \frac{d\phi}{dx} \quad [14]$$

where ϕ is the electrical field, then it is seen that $N(x) = \text{const.}$ leads to $d^2\phi/dx^2 = 0$. On the other hand, the assumption of local neutrality leads, using Eq. [7], to $d\phi/dx = \text{const.}$ and to δN which may vary exponentially with x . However, under fuel cell operation conditions, the concentration of quasi free electrons is low, $n \ll N$, also for a mixed conductor. Since $\delta N \sim \frac{1}{2}n$, hence, $\delta N \ll N$ and Tannhauser's assumption reduces to that of Choudhury and Patterson.

We present now a derivation of the solution of the transport equations for an MSE different from that in [1] and [2], which yields explicit expressions for the dependence of the current densities j_e , j_i , j on the fuel cell voltage V , as well as expressions for the local electron concentration and conductivity as a function of V and x . Then the power generated and the energy conversion efficiency are calculated and compared with that of a "pure" ionic solid electrolyte.

Equations [1] and [2] can be rewritten as

$$j_i = 2q\nu_i \epsilon N \quad [15]$$

$$j_e = kT\nu_e \frac{dn}{dx} + q\nu_e \epsilon n \quad [16]$$

where use was made of the relations: $\mu_e = \text{const.} + kT \ln n$, $\tilde{\mu}_e = \mu_e - q\phi$; T is the temperature, k the Boltzmann constant, and ϵ is the constant field $-d\phi/dx$. Equation [16] is an inhomogeneous linear differential equation of the first order and can readily be integrated. The boundary values of n at $x = 0$ (n_0) and

$x = L$ (n_L) are determined from the oxygen pressure $P_{O_2^I}$, $P_{O_2^{II}}$ at electrodes A_1 , A_2 and from the mass action law $Nn^2P_{O_2^{1/2}} = K_o(T)$, where $K_o(T)$ is the constant of the reaction in Eq. [5] and N is a known concentration. Hence

$$n_o = \sqrt{\frac{K_o}{N}} (P_{O_2^I})^{-1/4} \quad [17]$$

$$n_L = \sqrt{\frac{K_o}{N}} (P_{O_2^{II}})^{-1/4} \quad [18]$$

and (cf. Eq. [7])

$$\frac{n_L}{n_o} = e^{-\beta qV_{th}}, \quad \beta \equiv 1/kT \quad [19]$$

The integration of Eq. [16] yields

$$n(x) = B_o e^{-q\beta\epsilon x} + \frac{J_e}{q\nu_e\epsilon} \quad [20]$$

where B_o and J_e are constants fixed by the boundary conditions n_o , n_L for given ϵ , T , and ν_e .

$$B_o = n_o - \frac{J_e}{q\nu_e\epsilon} \quad [21]$$

and

$$j_e = -q\epsilon\nu_e \frac{n_o e^{-\beta q\epsilon L} - n_L}{1 - e^{-\beta q\epsilon L}} \quad [22]$$

From Eq. [6], [7], [8] and $\nabla\mu_i = 0$, one can express ϵ in terms of the experimental quantities V_{th} , V

$$\epsilon L = V_{th} - V \quad [23]$$

The relation between the cell current density $j = j_i + j_e$ and the cell voltage, readily follows from Eq. [15], [19], [22], [23]

$$j = \frac{V_{th} - V}{L} \sigma_i \left[1 - \frac{\sigma_e L}{\sigma_i} \frac{e^{\beta qV} - 1}{1 - e^{-\beta q(V_{th} - V)}} \right] \quad [24]$$

where $\sigma_e L = q\nu_e n_L$.

$n(x)$ and $\sigma_e(x)$

The variation of the electron concentration with x ($0 \leq x \leq L$), determined from Eq. [19]-[23] is

$$n(x) = n_L e^{\beta qV_{th}} \left[1 - \frac{1 - e^{-\beta q(V_{th} - V)x/L}}{1 - e^{-\beta q(V_{th} - V)}} \right] \quad [25]$$

Since $\sigma_e = q\nu_e n$ and $\mu_e = \text{const.} + kT \ln n$ the dependence of σ_e and μ_e on x and V is readily obtained. For a fixed n_L , $n(x)$ increases with V_{th} due to reduction of the MSE. For $V_{th} \neq 0$ an increase in the applied voltage, V , has a similar effect on the MSE and $n(x)$ increases with V for $0 < x < L$. This is shown in Fig. 2.

Ionic Transference Number

The average ionic transference number \bar{t}_i , as well as the ionic transference number t_i° at the low pressure electrode (A_1), can be determined from the open-circuit voltage $V_{o.c.}$. \bar{t}_i is defined as

$$\bar{t}_i \equiv V_{o.c.}/V_{th} \quad [26]$$

$V_{o.c.}$ is given by Eq. [24] for $j = 0$

$$V_{o.c.} = V_{th} + \frac{kT}{q} \ln \frac{\sigma_e L + \sigma_i}{\sigma_e^\circ + \sigma_i} \quad [27]$$

where $\sigma_e^\circ \equiv q\nu_e n_o$, and we have used also Eq. [19]. At the high pressure side near A_2 , the conductivity is assumed to be mainly ionic, i.e., $\sigma_e L \ll \sigma_i$, hence

$$t_i^\circ \equiv \frac{\sigma_i}{\sigma_e^\circ + \sigma_i} = e^{-\beta q(V_{th} - V_{o.c.})} \quad [28]$$

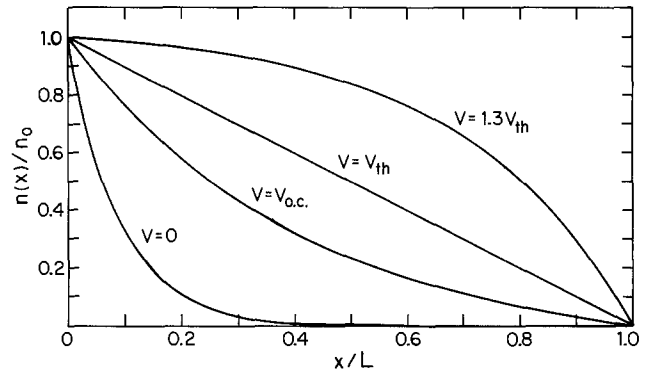


Fig. 2. $n(x)/n_o$ vs. x for various values of V , under the conditions: $V_{th} = 1.03V$, $T = 1073$ K ($n_L/n_o = 1.5 \times 10^{-5}$).

Equations [26] and [28] can be combined to relate \bar{t}_i and t_i°

$$\bar{t}_i = 1 + \frac{kT}{qV_{th}} \ln t_i^\circ \quad [29]$$

This was obtained also by Tannhauser (2) and is implicitly contained in the work of Schmalzried (8). As the oxide is reduced on the fuel side t_i° may be quite small. \bar{t}_i , however, decreases slowly with t_i° . We shall repeatedly consider the following example which can represent a MSEFC made of doped CeO_2 (2, 5)

$$T = 800^\circ\text{C}$$

$$V_{th} = 1.03 \text{ eV} (P_{O_2^I} = 10^{-20} \text{ atm}, P_{O_2^{II}} = 0.21 \text{ atm})$$

$$t_i^\circ = 0.1 \quad [30]$$

For this example, $\bar{t}_i = 0.8$. It should be noticed that a small t_i° is possible though the electron concentration is smaller than the ion concentration since $\nu_e/\nu_i \gg 1$ (2).

Comparison Between a MSEFC and a PSEFC

We compare now the power generated by a fuel cell based on a MSE with the power generated by a pure solid electrolyte fuel cell (PSEFC). To make the comparison meaningful we assume that, except for a difference in the electronic conductivities, all other parameters are the same, namely, σ_i , T , $P_{O_2^I}$, $P_{O_2^{II}}$, L , S , and the rate of fuel consumption (i.e., j_i is the same in both cells). Equations [15] and [23] show that j_i is the same in the two cells if operating with the same voltage V . Hence, the ratio r of the power generated by the MSEFC: VI, to that generated by the PSEFC: VI, is

$$r = \frac{I}{I_1} \quad [31]$$

From Eq. [15], [23], and [24]

$$r = 1 - \frac{\sigma_e L}{\sigma_i} \frac{e^{\beta qV} - 1}{1 - e^{-\beta q(V_{th} - V)}} \quad [32]$$

where we have used $I = Sj$. r can be expressed in terms of the measurable quantities \bar{t}_i , V_{th} , and V using Eq. [19], [28], [29]

$$r = 1 - (e^{\beta q(1 - \bar{t}_i)V_{th}} - 1) \frac{1 - e^{-\beta qV}}{e^{\beta q(V_{th} - V)} - 1} \quad [33]$$

For the normal use of a fuel cell $0 < V < V_{o.c.}$ Table I shows the values of r vs. V/V_{th} and $j_i/j_{i,max}$ for the example given in Eq. [30]. $j_{i,max}$ is the maximum ionic current through the cell obtained under short-circuit conditions ($V = 0$). It is seen that for $V/V_{th} \lesssim 0.6$, $r \lesssim 0.9$, thus under these conditions the power generated by an MSEFC is only a few percent lower than

Table I. ($T = 1073$ K, $V_{th} = 1.03$ V, $t_i = 0.1$)

| V/V_{th} | $j_i/j_{i,max}$ | r | η | $R_1 P/V_{th}^2$ |
|--------------------------|-----------------|------|--------|------------------|
| 0 | 1 | 1.00 | 0.00 | 0 |
| 0.1 | 0.9 | 1.00 | 0.10 | 0.09 |
| 0.2 | 0.8 | 1.00 | 0.20 | 0.16 |
| 0.3 | 0.7 | 1.00 | 0.30 | 0.21 |
| 0.4 | 0.6 | 0.99 | 0.40 | 0.24 |
| 0.5 | 0.5 | 0.97 | 0.48 | 0.24 |
| 0.5 | 0.4 | 0.89 | 0.54 | 0.21 |
| 0.7 | 0.3 | 0.67 | 0.47 | 0.14 |
| 0.787 ($V = V_{o.c.}$) | 0.213 | 0 | 0 | 0 |

that generated by the comparable PSEFC. The decrease in r with V is due to an increase in the electronic component of the current and a decrease in the ionic one. This is shown in Fig. 3.

Efficiency

The efficiency η is defined as

$$\eta = \frac{VI}{V_{th}I_1} \quad [34]$$

and gives that fraction of the change in the oxygen-free energy ΔG which is turned into useful energy. From Eq. [31]

$$\eta = \frac{V}{V_{th}} r \quad [35]$$

Table I shows the calculated values of η . The maximum efficiency η_{max} occurs at $V/V_{th} = 0.6$, where $r = 0.89$. An analytic expression for η_{max} can be obtained. Inserting Eq. [33] into [35] yields

$$\eta = \frac{V}{V_{th}} \left(1 - \alpha \frac{1 - e^{-\beta q V}}{e^{\beta q (V_{th} - V)} - 1} \right) \quad [36]$$

where $\alpha \equiv [\exp\{\beta q (1 - \bar{t}_i) V_{th}\} - 1]$. In the neighborhood of η_{max} , $V \sim 0.5 V_{th}$. If $\beta q V_{th} \gg 1$ then

$$\eta = \frac{V}{V_{th}} (1 - \alpha e^{-\beta q (V_{th} - V)}) \quad [37]$$

From $d\eta/dV = 0$, one finds $V_{m,\eta}$, the value of V for which $\eta = \eta_{max}$

$$V_{m,\eta} = V_{th} - \frac{kT}{q} \ln \{ \alpha (1 + \beta q V_{m,\eta}) \} \quad [38]$$

This implicit equation for $V_{m,\eta}$ can be solved by successive approximations. For $\beta q V_{th} \gg 1$ and $\alpha \lesssim 10$, as for a high temperature fuel cell with conditions similar to those in Eq. [30], two iterations are sufficient to calculate $V_{m,\eta}$ to a very good approximation

$$V_{m,\eta} = V_{th} - \frac{kT}{q} \ln \left\{ \alpha \left(1 + \beta q \left[V_{th} - \frac{kT}{q} \ln \{ \alpha (1 + \beta q V_{th}) \} \right] \right) \right\} \quad [39]$$

This yields $V_{m,\eta}/V_{th} = 0.64$ and $\eta_{max} = 0.54$ for the example in Eq. [30].

Maximum Power

The power output of the cell, $P = VI$, is shown in Table I. The maximum in P occurs at $V_{m,P} \sim 0.5 V_{th}$. To calculate $V_{m,P}$ we write P explicitly using Eq. [24]

$$P = \frac{s\sigma_1}{L} (V_{th} - V)r = \frac{s\sigma_1}{L} (V_{th} - V) V [1 - \alpha e^{-\beta q (V_{th} - V)}] \quad [40]$$

where we have limited V to values near $V_{m,P} \sim 0.5 V_{th}$ and have used $\beta q V$, $\beta q (V_{th} - V) \gg 1$ to obtain an approximation for P . $dP/dV = 0$ yields

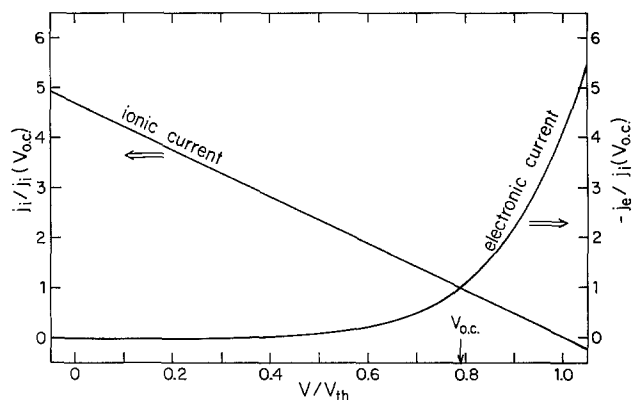


Fig. 3. $j_i/j_i(V_{o.c.})$ and $-j_e/j_i(V_{o.c.})$ vs. V/V_{th} for $V_{th} = 1.03$ V, $T = 1073$ K.

$$V_{m,P} = \frac{1}{2} V_{th} - \frac{1}{2} \alpha e^{-\beta q (V_{th} - V)}$$

$$[V_{th} - 2V_{m,P} + \beta q V_{m,P} (V_{th} - V_{m,P})] \quad [41]$$

This equation can be solved by successive approximations. At the lowest approximation $V_{m,P} = \frac{1}{2} V_{th}$ and the next approximation is

$$V_{m,P} = \frac{1}{2} V_{th} - \frac{1}{8} \alpha e^{-\frac{1}{2} \beta q V_{th}} \beta q V_{th}^2 \quad [42]$$

Equation [42] yields $V_{m,P}/V_{th} = 0.466$ for the example in Eq. [30]. Further iterations in Eq. [41] yield the exact solution $V_{m,P}/V_{th} = 0.480$. The maximum power is $P_{max} = 0.97 \times (0.25 V_{th}^2 / R_1)$, where $R_1 = L / S \sigma_1$ and the efficiency at $V_{m,P}$ is $\eta = 0.46$. These values referring to the MSEFC are only somewhat lower than the corresponding ones for the comparable PSEFC where $P_{max} = 0.25 V_{th}^2 / R_1$ and $\eta = 0.50$. The differences are small since the electronic current is small, compared to the ionic one, for $V \sim \frac{1}{2} V_{th}$ (see Fig. 3).

Conclusions

We have expressed $n(x)$, j_e , J'' , P , η , P_{max} , and η_{max} explicitly in terms of the parameters of the system, namely, V_{th} , V , T , σ_1 , R , L , S , and \bar{t}_i . The characteristics of an MSE are σ_1 and the value of \bar{t}_i for given values of $P_{O_2^I}$, $P_{O_2^{II}}$, and T . If σ_1 and \bar{t}_i are measured, then the expected distribution of electrons in the MSE, as well as the properties of a fuel cell based on the MSE, can be calculated as a function of the remaining parameters. The quantitative example of a fuel cell based on the MSE CeO_2 -10 m/o Gd_2O_3 shows that the maximum power output is only 3% lower than if $\bar{t}_i = 1$, the power output density increases almost linearly with the ionic conductivity of the MSE, and the maximum efficiency is 54%. This is consistent with results obtained before (2).

Acknowledgments

The author thanks D. Tannhauser for many helpful discussions. This work was supported by a grant from the National Council of Research and Development, Israel, and the KFA, Juelich, Germany.

Manuscript submitted Jan. 13, 1981; revised manuscript received April 20, 1981.

Any discussion of this paper will appear in a Discussion Section to be published in the June 1982 JOURNAL. All discussions for the June 1982 Discussion Section should be submitted by Feb. 1, 1982.

Publication costs of this article were assisted by Technion-Israel Institute of Technology.

LIST OF SYMBOLS

| | |
|------------|--|
| I, j | current and current density |
| I_e, j_e | electronic current and current density |
| I_i, j_i | ionic current and current density |
| k | Boltzmann constant |
| L | length of MSE |

| | |
|------------------------------|---|
| MSE | mixed conductor solid electrolyte |
| MSEFC | mixed conductor solid electrolyte fuel cell |
| n | quasi free electron concentration |
| n_0, n_L | n at $x = 0, x = L$, respectively |
| N | ionic (V_o'') concentration |
| P | electrical power |
| P_{\max} | maximum P |
| P_{O_2} | oxygen partial pressure |
| $P_{O_2^I}, P_{O_2^{II}}$ | P_{O_2} near the anode and cathode of the fuel cell, respectively |
| q | absolute value of electronic charge |
| R | load resistance |
| r | I/I_1 |
| S | cross-section area of MSE |
| \bar{t}_i | average transference number |
| t_i° | transference number at $x = 0$ |
| T | temperature |
| V | voltage of fuel cell under load |
| $V_{m,D}, V_{m,\eta}$ | V at maximum power output and maximum efficiency, respectively |
| V_{th} | $kT/4q \ln P_{O_2^{II}}/P_{O_2^I}$ |
| x | position inside the MSE ($0 \leq x \leq L$) |
| ϵ | electrical field ($-d\phi/dx$) |
| σ_e | electronic conductivity |
| $\sigma_e^\circ, \sigma_e^L$ | σ_e at $x = 0$ and $x = L$ |
| σ_i | ionic conductivity |
| η | energy conversion efficiency |
| η_{\max} | maximum η |

| | |
|---------------------------|---|
| μ_e, μ_i, μ_{O_2} | chemical potential of quasi free electrons, ionic charge carriers, and oxygen, respectively |
| μ_e, μ_i | electrochemical potential of quasi free electrons and ionic charge carriers, respectively |
| ν_e, ν_i | electronic and ionic mobilities |
| ϕ | electrical potential |

REFERENCES

1. N. S. Choudhury and J. W. Patterson, *This Journal*, **118**, 1398 (1971).
2. D. S. Tannhauser, *ibid.*, **125**, 1277 (1978).
3. H. Obayashi and T. Kudo, in "Solid State Chemistry and Energy Conversion," J. B. Goodenough and M. S. Whittingham, Editors, pp. 316-363, *Advances in Chemistry Series*, No. 163, American Chemical Society (1977).
4. L. D. Burke, H. Rickert, and R. Steiner, *Z. Phys. Chem. N.F.*, **74**, 146 (1971).
5. T. Kudo and H. Obayashi, *This Journal*, **122**, 142 (1975).
6. C. Wagner, in Proc. Int. Comm. Electrochem. Thermo. and Kinetics (CITCE), 7th meeting Lindau (1955), Butterworth Scientific Publication, London (1957).
7. R. P. Feynman, R. B. Leighton, and M. Sands, "The Feynman Lectures on Physics," Vol. II, p. 6-1, Addison-Wesley Publishing Co., Reading, MA (1975).
8. H. Schmalzried, *Z. Elektrochem.*, **66**, 572 (1962).

Mechanism of the Electrodeposition of Zinc Alloys Containing a Small Amount of Cobalt

Kei Higashi, Hisaaki Fukushima, and Takayuki Urakawa¹

Department of Metallurgy, Kyushu University, Fukuoka 812, Japan

and Takeshi Adaniya and Kazuo Matsudo

Nippon Kokan K.K., Fukuyama Research Laboratories, Technical Research Center, Fukuyama 721, Japan

ABSTRACT

Corrosion resistant Zn-Co alloys were electrodeposited on the steel sheet cathode from an acid galvanizing bath containing a small amount of cobalt sulfate. Under most of the plating conditions studied, the anomalous codeposition and, hence, the preferential deposition of electrochemically less noble Zn occurred. The electrodeposition process of the alloy including the Zn hydroxide formation resulting from the rise in pH in the vicinity of the cathode was estimated by electrochemical and spectroscopic studies.

Since the standard electrode potential of Zn is more negative than that of Fe, Zn has been widely used as an electrochemically protective coating material for steel under ordinary atmospheric conditions. The corrosion resistance of pure Zn coatings is, however, not satisfactory under more corrosive circumstances, particularly in a very humid atmosphere. Recently, a composite electrogalvanizing bath containing a small amount of additive elements has been developed and it was indicated that the addition of Co, Co-Cr, or Co-In considerably increases not only the corrosion resistance but also the subsequent chromating characteristics of galvanized steel (1). The addition of these elements was so effective in the improvement of the surface properties of Zn coatings that these composite baths were employed in commercial galvanized steel production (2).

However, the mechanism which permits the improvement of the surface properties of galvanized

steel is not yet available. This led to a serious drawback for the development of Zn coatings having further superior surface properties. In order to elucidate this mechanism, it is necessary to make clear the electrodeposition processes of the additive elements. In this paper, Co which markedly improved the corrosion resistance of galvanized steel was selected as the additive element and the mechanism of Co codeposition was estimated.

Experimental

Electrodeposition.—Deposits were obtained on the low carbon steel sheet cathode of 4×5 cm² area under coulometric and galvanostatic conditions (80 kcm⁻²). The standard plating conditions were similar to those commonly employed in ordinary electrogalvanizing (1, 2) and are shown in Table I. The deposited metals were weighed and dissolved from the cathode with dilute HCl solution. Co was determined colorimetrically by using the color development between the Co ion and β -nitroso- α -naphthol (3), and the composition of alloys was calculated.

¹Present address: Technical Research Center, Nippon Kokan K.K., Kawasaki 210, Japan.

Key words: electrodeposition, surface pH, film resistance, XPS measurement.

Table I. Standard plating conditions

| Bath composition | | Operating condition |
|---|--|--|
| ZnSO ₄ · 7H ₂ O | 1.739 kmol m ⁻³ (114g liter ⁻¹ as Zn) | Current density 3 kA m ⁻² Temp 50°C |
| CoSO ₄ · 7H ₂ O | 0.170 kmol m ⁻³ (10g liter ⁻¹ as Co) | |
| Na ₂ SO ₄ | 0.352 kmol m ⁻³ | |
| CH ₃ COONa · 3H ₂ O | 0.110 kmol m ⁻³ | |
| Metal-% of Co in bath = 8, pH 4.2 | | |

Measurement of the pH in cathode layer.—The measurement of pH in the vicinity of the cathode during the electrodeposition of Zn-Co alloys was carried out by means of the antimony microelectrode method (4, 5). The experimental setup is shown in Fig. 1. The design of the apparatus permitted the antimony microelectrode of 1 mm diam and reference Ag/AgCl electrode to be placed in position exactly 10 μm from the steel sheet cathode of 4 × 5 cm² area. Figure 2 shows the pH dependence of the antimony microelectrode potential when the pH of the bath used in this work was varied. There existed a linear relationship between the pH and the potential of the antimony microelectrode, indicating the validity of the adoption of this method. Figure 2 was also used as the pH calibration curve.

Solubility measurement of the metal hydroxides.—Two types of solutions were prepared in which Zn or

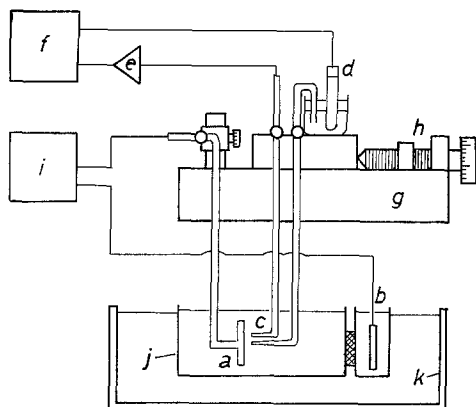


Fig. 1. Experimental setup for the measurement of the pH in the vicinity of the cathode during the electrodeposition of the alloys. a, Cathode; b, anode; c, antimony microelectrode; d, reference Ag/AgCl electrode; e, impedance transducer (10⁷ MΩ); f, potential recorder; g, micrometer; h, micrometer screw; i, d-c constant current power supply; j, cell for electrolysis; k, thermostat.

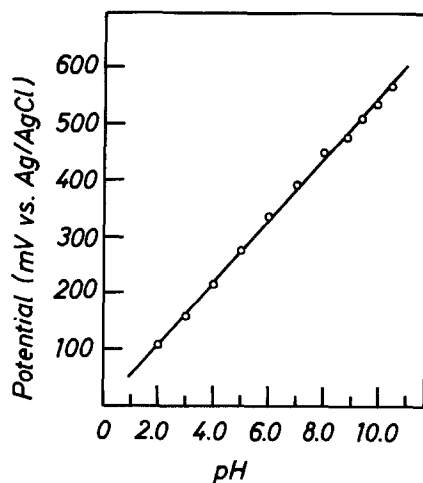


Fig. 2. Relationship between the potential of antimony microelectrode and pH of the solution at 50°C.

Co ion was removed from the standard bath composition and the pH was raised to various values with NaOH solution. The concentration of metal ion still remaining in each solution at 50°C was determined polarographically for Zn and colorimetrically for Co, and the solubilities of Zn and Co hydroxides at various pH's in the bath used were estimated.

Evaluation of the surface film resistance.—In order to confirm the metal hydroxide film formation on the cathode during the electrodeposition of the alloys, the resistance across the cathode surface (steel sheet of 4 × 5 cm² area) and the tip of the capillary bridge of the reference NHE was measured by the interrupter method (6).

A constant current pulse of repetition frequency 18.3 msec, of duty factor 96.42%, and of various current densities was applied to the electrodes, and the cathode potential-relaxation waveform was observed on the oscilloscope, from which the resistance overvoltage was read off. The quotient of the resistance overvoltage by the applied current yields the resistance which consists of the film resistance and the resistance due to the solution between the cathode and the capillary tip of the reference electrode. The solution resistance between the cathode and the capillary tip in this electrode arrangement was also determined by applying the single current pulse of short duration (17.6 msec) where the pH rise in the cathode layer, and hence the formation of metal hydroxide, may be negligibly small. The measurement was carried out for each freshly prepared cathode at various current densities. When neglecting the change in solution resistance during the electrolysis, the change in the gap between the observed resistance and the solution resistance will be anticipated to give the information on the surface film formation.

Measurement of the x-ray photoelectron spectra of the electrodeposited alloys.—Experiments were performed in a Dupont 605 electron spectrometer using MgKα radiation (1253.6 eV), scanning at 0.05 eV sec⁻¹. The binding energies of the elements were referred to the vacuum-deposited gold on copper. The binding energies of Au 4f_{7/2} and Cu 2p_{3/2} lines were taken to be 84.0 and 932.0 eV, respectively. The C 1s binding energy, 285.0 eV, of contamination carbon was used as calibration to compensate for possible charging effects. Ion bombardment of the surface of mechanically polished samples, previously pressed to pellet if in powder form, was carried out for 3 min using prepurified argon prior to the spectra measurement.

Co metal, cobaltous (Co²⁺), and cobaltic (Co³⁺) compounds were used as reference material. The binding energies of Co 2p_{3/2} level in the reference materials examined are listed in Table II and are in good agreement with those reported earlier (7, 8). As is evident from Table II, the chemical shift generally used to distinguish the oxidation states of the element is very small between the cobaltous and the cobaltic compounds. Therefore, it is difficult to clarify the oxidation state of Co in these compounds. However, the chemical shift relative to the binding energy in metallic state is large enough to distinguish the metallic state from the oxidation state of Co.

Table II. Binding energies of Co 2p_{3/2} in different cobalt compounds

| Compound | Binding energy (eV) |
|--------------------------------|---------------------|
| Co ₂ O ₃ | 780.2 |
| Co ₃ O ₄ | 780.3 |
| CoO | 780.7 |
| Co(OH) ₂ | 780.6 |
| Co metal | 778.4 |

Results and Discussion

Deposition behavior of the alloys.—Electrodeposition of Zn-Co alloys is classified into anomalous codeposition by Brenner (9) and is characterized by the anomaly that the less noble metal deposits preferentially.

The effect of the metal percentage of Co in the bath on the Co content of the deposits is shown in Fig. 3. The broken line in the figure indicates the composition reference line (hereinafter simply referred to as CRL) which shows that the weight percentage composition of the alloy just equals the metal percentage of the bath. Figure 3 shows that the Co content of the deposits increased linearly with an increasing metal percentage of Co in the bath. And in all cases studied, the Co content of the deposit lay below the CRL, which indicated the preferential deposition of Zn, although the equilibrium potential of Zn is several tenths of a volt less noble than that of Co.

Figure 4 shows the relationship between the Co content of the deposits and the current density. In the low current density region, the deposit had a larger content of the noble metal Co than the metal percentage of Co in the bath. This indicates that the codeposition appears to be of the normal type. With increasing current density, the deposit rapidly decreased in Co content and above the transition current density contained much more Zn than the metal percentage of Zn in the bath. This transition of the deposition behavior of Co from a normal to an anomalous type occurred in a rather small range of the current density. Further increase in the current density resulted in little change in alloy composition, followed by the

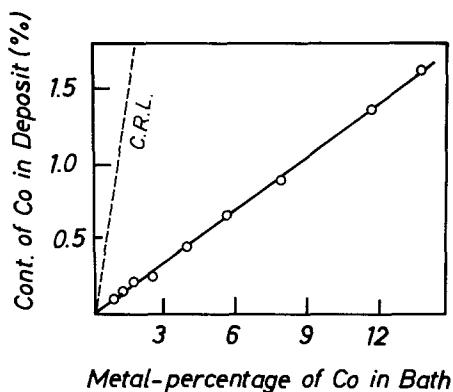


Fig. 3. Effect of metal percentage of Co in the bath on the composition of electrodeposited Zn-Co alloys. Metal percentage of Co = $[\text{wt Co}/\text{total wt (Co + Zn)}] \times 100$.

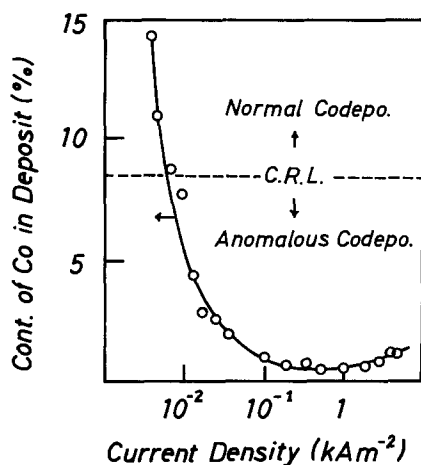


Fig. 4. Effect of current density on the composition of electrodeposited Zn-Co alloys.

trend of Co content slightly upward at still higher current density. Thus, with increasing current density, the Co content of the deposits either decreased, remained constant, or increased, which was the same trend as reported by Brenner (10).

Consequently, the electrodeposition study revealed that the deposition of each metal from the baths used in this work exhibited the characteristics of an anomalous codeposition.

Formation of Zn hydroxide film during the electrodeposition of the alloys.—There is, as yet, no theoretical explanation which satisfactorily describes the mechanism of the anomalous codeposition. Many hypotheses have been proposed so far (11-13) and one of the most plausible mechanisms included the assumption that the pH in the vicinity of the cathode was raised to permit the precipitation of metal hydroxide on the cathode (14-16).

Figure 5 shows the pH dependence of the solubility of Zn or Co hydroxide in the bath used. From Fig. 5, the critical pH values for the precipitation of Zn and Co hydroxides were 5.1 and 6.8, respectively.

Then, the alloys of various composition were electrodeposited at various current densities under the standard plating conditions shown in Table I, and the relationship between the Co content in the deposits and the pH in the cathode layer measured by the antimony microelectrode method was examined. The result is shown in Fig. 6 which also includes the critical pH's for each metal hydroxide precipitation, the pH of the bulk solution, and the CRL. Figure 6 showed that the critical pH for Zn hydroxide precipitation was not achieved in the normal codeposition region although the rise in pH of the cathode layer was observed in all cases. On the other hand, the abrupt rise in the pH was recognized from a value below to a value above the critical pH for Zn hydroxide precipitation when the transition of codeposition from the normal to the anomalous type occurred. In the anomalous codeposition region, the pH of the cathode layer remained in the pH range well below the critical one for Co hydroxide precipitation, probably by the buffering effect due to the Zn hydroxide formation. This indicates that the pH rise in the cathode layer and subsequent Zn hydroxide formation should be closely related to the mechanism of the anomalous codeposition.

Empirical confirmation of the formation of Zn hydroxide film during the electrodeposition of the alloys was also tried under the standard plating conditions by estimating the surface film resistance. Figure 7 shows the change in the resistance obtained by means of interrupter method (6) with the current density. The solution resistance between the cathode surface and the tip of the capillary bridge of the reference electrode was also included in Fig. 7. The resistance

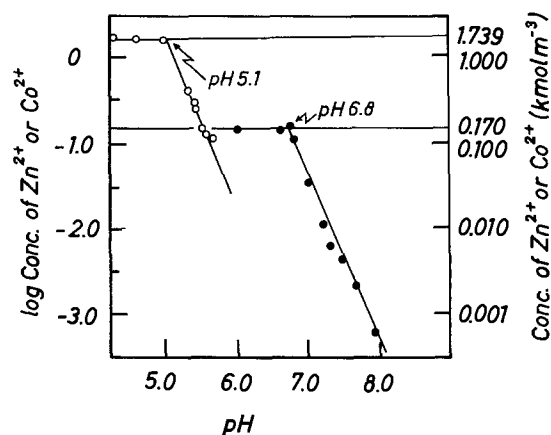


Fig. 5. pH dependence of the solubilities of Zn and Co hydroxides. $\circ = \text{Zn}^{2+}$; $\bullet = \text{Co}^{2+}$.

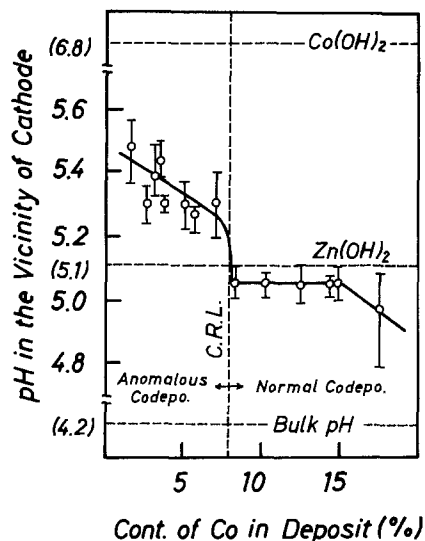


Fig. 6. Relationship between the composition of alloys and the pH in the vicinity of the cathode during the electrodeposition of Zn-Co alloys at various current densities under galvanostatic conditions.

during electrolysis was initially increased and then remained constant with the increased current density. And, at the low current densities where the codeposition of the normal type occurred, the smaller resistance mainly due to the solution was observed. With the increased current density to permit the anomalous codeposition, the larger resistance was observed. These indicate that the resistive component was formed on the cathode with an increase in the current density.

Estimation of the anomalous codeposition process and the confirmation of this mechanism by x-ray photoelectron spectroscopy.—From the results presented above, it becomes possible to propose a mechanism which provides a reasonable explanation for the following features of anomalous codeposition: the preferential deposition of Zn under most conditions of plating although Zn is considerably less noble than Co, the existence of a normal codeposition behavior at low current densities, and the abrupt transition of codeposition from a normal to an anomalous type as the current density is raised.

During anomalous codeposition of Zn with Co, the electrodeposition of Zn proceeds with preceding Zn hydroxide formation on the cathode, which results from a rise in pH in the vicinity of the cathode. On the other hand, since the critical pH for Co hydroxide precipitation is not attained in the cathode layer, Co

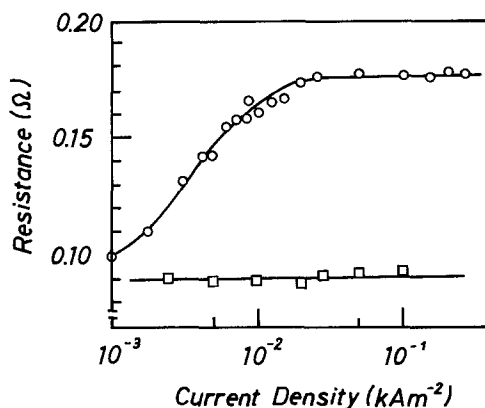


Fig. 7. Effect of current density on the resistance between the cathode surface and the capillary tip of reference NHE. ○ = Resistance during the electrodeposition of Zn-Co alloys; □ = solution resistance.

deposition occurs by the direct discharge of Co^{2+} ions through the Zn hydroxide film, which makes the Co deposition difficult. Consequently, the superiority of Co over Zn in nobility is canceled out by the film resistance of Zn hydroxide, resulting in the preferential deposition of Zn in anomalous codeposition.

Comparison of Fig. 4 with Fig. 7 seems to support the above process of the alloy deposition. In the low current density range, the normal codeposition occurs reflecting the nobility of each metal, since Zn hydroxide neither quite precipitates nor precipitates to such an extent that the Zn hydroxide film exhibits enough resistance to prevent the Co deposition. At about the transition current density, the film resistance increases rapidly to compensate the superiority of Co in nobility, resulting in the abrupt transition of codeposition from a normal to an anomalous type. With further increase in the current density, the alloy composition remains almost constant because the formation rate of Zn hydroxide is balanced by the consumption rate of it due to the electroreduction, which makes the film resistance constant. Thus, the depositing behavior of Co agreed well with the change in the resistance during the electrodeposition of the alloys.

Assuming the alloy deposition occurs in accordance with the above mechanism, Co should be in a metallic state in the deposit. Figure 8 shows the x-ray photoelectron spectra of the deposit obtained under the standard plating conditions shown in Table I. In Fig. 8, spectrum (a) provided no definite peak probably because of the low Co content of approximately 0.9% in the deposit. However, spectrum (b) obtained by integrating 128 times the single scanned intensity using the multichannel analyzer indicated the well-defined peak at the binding energy of 778.2 eV, which is in good agreement with that of metallic state of Co in Table II.

Summary

Zn-Co alloys were electrodeposited from an acid electroplating bath containing a small amount of cobalt sulfate. In a wide range of plating conditions, the deposition behavior of each metal showed the main features of anomalous codeposition. Electrochemical and spectroscopic studies revealed the following mechanism of anomalous codeposition of Co with Zn. The electrodeposition of Zn proceeds with preceding Zn hydroxide formation through which the discharge of Co^{2+} ions occurs. Consequently, the superiority of Co over Zn in nobility is canceled out by the film resistance of Zn hydroxide, resulting in anomalous codeposition.

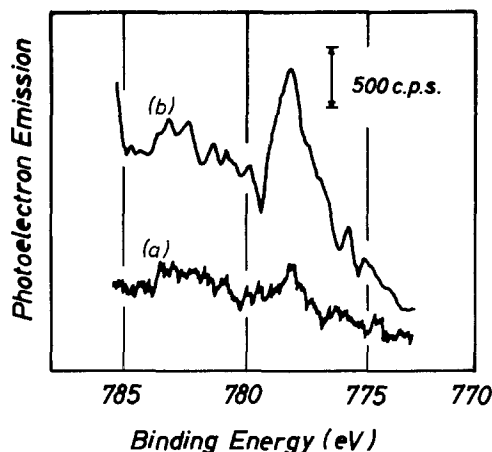


Fig. 8. X-ray photoelectron spectra of the deposit in Co $2p_{3/2}$ level. (a) Single scanned intensity; (b) integrated intensity using multichannel analyzer.

Manuscript submitted Jan. 6, 1981; revised manuscript received ca. April 20, 1981.

Any discussion of this paper will appear in a Discussion Section to be published in the June 1982 JOURNAL. All discussions for the June 1982 Discussion Section should be submitted by Feb. 1, 1982.

Publication costs of this article were assisted by Nippon Kokan K.K.

REFERENCES

1. T. Adaniya and M. Ohmura, Proc. Interfinish 76, p. 5, Amsterdam (1976).
2. K. Matsudo, T. Adaniya, M. Ohmura, and M. Ogawa, *J. Iron Steel Inst. Jpn.*, **66**, 814 (1980).
3. E. B. Sandell, "Colorimetric Determination of Traces of Metals," 3rd ed., Chemical Analysis, A Series of Monographs on Analytical Chemistry and Its Applications, Vol. III, p. 420, Interscience Publishers, Inc., New York (1959).
4. J. Matulis and R. Rlizys, *Electrochim. Acta*, **9**, 1177 (1964).
5. N. Koura, *J. Electrochem. Soc. Jpn.*, **47**, 738 (1979).
6. T. Hayashi and T. Ishida, *J. Metal Finishing Soc. Jpn.*, **17**, 419 (1966).
7. Y. Okamoto, H. Nakano, T. Imanaka, and S. Teranishi, *Bull. Chem. Soc. Jpn.*, **48**, 1163 (1975).
8. H. Konno, *J. Metal Finishing Soc. Jpn.*, **29**, 425 (1978).
9. A. Brenner, "Electrodeposition of Alloys," Vol. I, p. 77 and Vol. II, p. 194, Academic Press, New York and London (1963).
10. A. Brenner, *ibid.*, Vol. I, p. 131.
11. A. Brenner, *ibid.*, Vol. II, p. 221.
12. K. Higashi and H. Fukushima, *J. Jpn. Inst. Metals*, **13**, 865 (1974).
13. M. J. Nicol and H. I. Philip, *J. Electroanal. Chem.*, **70**, 233 (1976).
14. H. Dahms and I. M. Croll, *This Journal*, **112**, 771 (1965).
15. Z. Kovac, *ibid.*, **118**, 51 (1971).
16. E. Raub, *Plating Surf. Finish.*, **63** (2), 29 (1976).

Electrogenerated Chemiluminescence of *trans*-Stilbene Derivatives

James R. Wilson, Su-Moon Park,* and Guido H. Daub

Department of Chemistry, University of New Mexico, Albuquerque, New Mexico 87131

ABSTRACT

Fluorescence maxima, fluorescence quantum yields, electrode potentials, and electrogenerated chemiluminescence (ecl) of 16 *t*-stilbene derivatives such as substituted indenenes and dihydronaphthalenes (DHNP) are reported. Both indenenes and DHNP's were found to have greatly enhanced fluorescence quantum yields in comparison to *t*-stilbene. Twelve single systems of 16 compounds gave ecl mostly attributed to the singlet excited state. With tri-*p*-tolylamine (TPTA) added as a source of cation radical, most of the systems produced ecl having shorter wavelength emission corresponding to the singlet excited state of the *t*-stilbene derivatives and longer wavelength emission attributed to the exciplex. The ecl intensities with respect to the possible applications are discussed.

Electrogenerated chemiluminescence (ecl) is a process where the electrochemically generated radical species, usually cation and anion radicals, annihilate to give an excited state molecule, which subsequently emits light (1, 2). Due to its uniqueness in exciting molecules, several possible applications have been suggested and discussed (3-9). In our continuing effort (10, 11) to discover more efficient ecl, we performed ecl studies on a series of laser dyes structurally related to *trans*-stilbene (*t*-St). Structures of these compounds are shown in Fig. 1. These compounds have been synthesized in one of our laboratories (GHD) as laser dyes (12, 13) and the lasing action of these dyes has been tested (14). As shown in Fig. 1, these dyes are of modified forms of the *t*-stilbene chromophore.

Electron transfer chemiluminescence of *t*-stilbene was first reported by Weller and Zachariasse (15, 16). The mixed system containing tri-*p*-tolylamine (TPTA)(+)/*t*-St(-) was chemiluminescent in THF with the longer wavelength emission attributed to the exciplex (16), while the one containing N,N,N',N'-tetramethyl-*p*-phenylenediamine (TMPD)(+)/*t*-St(-) was nonchemiluminescent (15). Later, Keszthelyi and Bard (17) reported electrogenerated chemiluminescence in the THF solution for the TPTA(+)/*t*-St(-) system, where only exciplex emission was identified as in the chemiluminescence experiment.

In the present report, fluorescence, ecl, and electrochemical potentials of rigid *t*-stilbene analogs, having

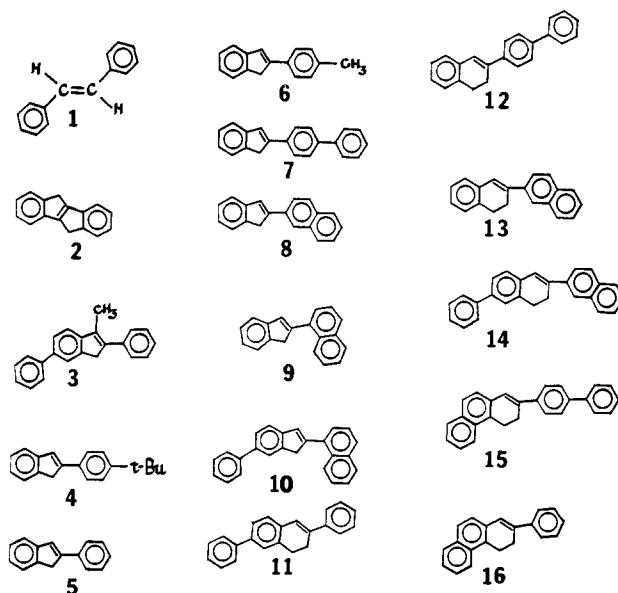


Fig. 1. Structures of compounds used in this study (see Table I for the nomenclature).

* Electrochemical Society Active Member.

Key words: fluorescence, chemiluminescence, organic.

either indene or dihydronaphthalene structures (Fig. 1), have been studied, and the results are reported. In these compounds, the flexibility of the double bond is reduced. Fluorescence studies have shown that a rigid molecular structure reduces the excitation energy loss due to the vibrational and rotational energy loss of the excited molecule, enhancing the fluorescence emission quantum efficiencies (18). The effect of substitution on the fluorescence and ecl has been studied and discussed in this report.

Experimental

Spectrograde acetonitrile (ACN, Eastman Organic), spectrograde benzene (Bz, Aldrich), and polarographic grade *tetra-n*-butylammonium perchlorate (TBAP, Eastman Organic) were purified and dried as described previously (11) and used as solvents and supporting electrolyte, respectively. Spectrograde cyclohexane [Matheson, Coleman, and Bell (MCB)] was distilled under partial vacuum with the middle 30 ~ 40% collected and used as a solvent for the fluorescence measurement. Laboratory quinine sulfate (Fischer Scientific) and scintillation grade *t*-stilbene (MCB) were used as received. TPTA was kindly provided by Professor R. N. Adams of the University of Kansas and used as received. Compounds 2-16 were synthesized and purified in one of our laboratories (GHD) and procedures of syntheses and purifications have been published elsewhere (12, 13).

Solutions for ecl experiments have been prepared in a three-electrode configuration cell as described previously (11). Electrochemical measurements were also made employing a three-electrode cell with a platinum disk working electrode (area ≈ 0.021 cm²). At the conclusion of the electrochemical measurements, the electrode potentials were referenced to a saturated calomel electrode (SCE), which was inserted while the cell was flushed gently with helium.

A Princeton Applied Research (PAR) Electrochemistry Model 173 potentiostat-galvanostat with a PAR Model 175 universal programmer and a PAR Model 176 I/E converter were used for cyclic voltammetric measurements and ecl experiments. Ecl and fluorescence spectra were detected by an Aminco-Bowman spectrophotofluorometer with a Hammamatsu TV R446 photomultiplier tube and recorded on a Plotomatic 815 X-Y recorder. A Cary-14 spectrophotometer was used for the absorption spectrum measurements.

Results and Discussion

Fluorescence maxima, fluorescence quantum yields, electrode potentials, and ecl data for *t*-stilbene derivatives are summarized in Tables I and II. Ecl results for the TPTA/*t*-stilbene derivative mixed systems are listed in Table III. Typical results for selected compounds have been shown in Fig. 2-4. More detailed description of the results follows.

Fluorescence studies.—Fluorescence maxima and fluorescence quantum yields for 15 *t*-stilbene derivatives in cyclohexane solutions are listed in Table I. These quantities were measured with a spectral band pass of 5.5 nm for both excitation and emission and a fluorescer concentration of 1.0×10^{-5} M at room temperature. The fluorescence maxima of these compounds were not dependent on the solvent used, indicating that dipole moments of the excited and ground state molecules may not be significantly different. The fluorescence quantum yields were measured by comparison with a reference compound [i.e., quinine sulfate according to the well-known procedure (18)] and corrected for the refractive index of the solvent used (19). The fluorescence quantum yield for *t*-stilbene has been reported to be 0.04 ~ 0.08 at room temperature in nonviscous solvents, depending on experimental conditions (20-23). The results in Table I show that the

Table I. Fluorescence maxima and quantum yield^a

| Compounds ^b | Fluorescence maximum, nm (eV) | Fluorescence quantum yield, Φ_f ^{c,d} |
|--|-------------------------------|---|
| 1. <i>trans</i> -Stilbene | 361 (3.43) | 0.04 ~ 0.08 ^e |
| 2. 5,10-Dihydroindeno (2,1-a) indene | 371 (3.34) | 0.59 |
| 3. 1-Methyl-2,5-diphenylindene | 390 (3.18) | 0.82 |
| 4. 2-(<i>p</i> -Tert-butylphenyl)indene | 371 (3.34) | 0.70 |
| 5. 2-Phenylindene | 369 (3.36) | 0.78 |
| 6. 2-(<i>p</i> -Tolyl)indene | 371 (3.34) | 0.67 |
| 7. 2-(4'-Biphenyl)indene | 390 (3.18) | 0.86 |
| 8. 2-(2'-Naphthyl)indene | 385 (3.22) | 0.56 |
| 9. 2-(1'-Naphthyl)indene | 404 (3.07) | 0.66 |
| 10. 2-(1-Naphthyl)-5-phenylindene | 416 (2.98) | 0.90 |
| 11. 3,4-Dihydro-2,6-diphenylindene | 397 (3.12) | 0.85 |
| 12. 3-(4-Biphenyl)-1,2-dihydronaphthalene | 398 (3.13) | 0.84 |
| 13. 3,4-Dihydro-2-(2-naphthyl)naphthalene | 390 (3.18) | 0.70 |
| 14. 3,4-Dihydro-2-(2-naphthyl)-6-naphthalene | 410 (3.02) | 0.80 |
| 15. 3,4-Dihydro-2-(4-biphenyl)-phenanthrene | 420 (3.07) | 0.72 |
| 16. 3,4-Dihydro-2-phenylphenanthrene | 404 (3.07) | 0.89 |

^a In cyclohexane. Obtained from uncorrected spectra at room temperature.

^b For structures of these compounds see Fig. 1.

^c Concentrations were 1.0×10^{-5} M in cyclohexane.

^d Determined relative to a quinine sulfate solution in water and corrected for the refractive index.

^e From Ref. (20-23).

stilbene derivatives have generally lower transition energies and enhanced fluorescence quantum yields than *t*-stilbene. These results are consistent with the expectation discussed below. Excitation of *t*-stilbene reduces the double bond character of the ethylene bridge, which subsequently allows the two benzene rings to rotate around the single bond (24). The loss of excitation energy due to the rotation of the benzene rings will be reduced or minimized by substitutions, varying with the size and location of the substituent. When the double bond is made rigid, preventing the rotation of phenyl groups around it after excitation, the energy of the electronic transition is expected to decrease (red shift) and the fluorescence quantum yield should increase (20, 24). Although compound 2 may appear to be planar, it was shown to be the most nonplanar of the compounds when examined by the molecular model. This nonplanarity reduces the resonance between the two phenyl rings, resulting in a relatively high transition energy and a low fluorescence quantum yield in comparison with other compounds. Inspection of Table I and Fig. 1 reveals that compounds having a 6-membered ring around the double bond (3,4-dihydronaphthalene derivatives = DHNP) have generally low transition energies and higher fluorescence quantum yields than the corresponding 5-membered compounds (indene derivatives). This illustrates that the 6-membered ring around the *t*-stilbene double bond is more planar than the 5-membered ring, resulting in higher resonance and conjugation between the two phenyl groups on both sides of the double bond.

Electrode potentials.—Oxidation and reduction potentials of these compounds were measured at a platinum disk electrode using a saturated calomel electrode (SCE) as a reference electrode. The results obtained in ACN and ACN-Bz are reported in Table II.

Inspection of Table II reveals that indene derivatives are generally more difficult to reduce and easier to oxidize than *t*-stilbene. When more aromatic rings are incorporated as in compounds 7, 8, 9, and 10, the reduction is made easier, as expected. Dihydronaphthalenes are generally easier to reduce and oxidize, indicating that phenyl groups on both sides of the double bond communicate better through the six-membered ring configuration, which is consistent with the fluorescence results.

Table II. Electrochemical and ecl data for single systems^a

| Compounds | $-E_{p,r}$ (V vs. SCE) | | $\Delta E_{pc,mV}$ | | $E_{p,o}$ (V vs. SCE) | | $-\Delta H^\circ$, (eV) ^b in ACN-Bz | ECL max, nm (intensity ^c) in ACN-Bz |
|-----------|---------------------------|-------------|--------------------|--------|--------------------------|--------------------------|---|---|
| | ACN | ACN-Bz | ACN | ACN-Bz | ACN | ACN-Bz | | |
| 1 | 2.37 | 2.31 | 197 | 102 | 1.46 | 1.46 | 3.61 | Nil |
| 2 | 2.62 | 2.60 | — | — | 1.14 | 1.22 | 3.66 | Nil |
| 3 | 2.36 | 2.39 | — | — | 1.25 | 1.33 (1.48) ^d | 3.56 | 400 (5.8×10^{-4}) |
| 4 | 2.57 | 2.45 | — | — | 1.27 | 1.32 | 3.61 | 440 (4.5×10^{-5}) |
| 5 | 2.45 | 2.42 | 122 | 122 | 1.36 | 1.40 | 3.66 | 437 (1.8×10^{-6}) |
| 6 | 2.48 | 2.52 | — | — | 1.25 | 1.29 | 3.61 | Nil |
| 7 | 2.24 | 2.23 | 62 | — | 1.29 | 1.30 | 3.37 | 460 (1.3×10^{-5}) |
| 8 | 2.25 | 2.24 | — | — | 1.29 (1.54) | 1.28 | 3.36 | 440 (1.6×10^{-5}) |
| 9 | 2.22 | 2.29 (2.40) | 127 | 90 | 1.29 | 1.32 | 3.45 | 460 (2.0×10^{-5}) |
| 10 | 2.18 | 2.18 | 66 | — | 1.28 (1.45) | 1.27 (1.47) | 3.29 | 430 (2.0×10^{-5}) |
| 11 | 2.26 | 2.30 | 67 | 95 | 1.31 (1.55) | 1.33 (1.60) | 3.47 | 418 (2.3×10^{-5}) |
| 12 | 2.28 | 2.26 | 80 | 151 | 1.30 | 1.33 | 3.43 | 417 (2.8×10^{-4}) |
| 13 | 2.25 | 2.20 | 99 | 62 | 1.25 | 1.33 (1.58) | 3.37 | Nil |
| 14 | 2.18 | 2.15 | 76 | 70 | 1.23 (1.42) (1.68) | 1.30 (1.48) (1.72) | 3.29 | 435 (2.1×10^{-4}) |
| 15 | 2.15 | 2.15 | 71 | 116 | 1.19 | 1.27 (1.56) | 3.26 | 425 (6.9×10^{-5}) |
| 16 | 2.25 | 2.25 | 85 | 64 | 1.25 | 1.28 (1.70) | 3.37 | 387 (3.9×10^{-5}) |

^a Concentrations were about 0.5 mmol. For fluorescence data, see Table I.

^b Calculated from $-\Delta H^\circ = E_{p,o} - E_{p,r} - 0.16$ eV [Ref. (31)].

^c Relative intensities with respect to that of 1.0 mmol 9,10-diphenylamine (DPA).

^d Numbers in parentheses indicate second and third oxidation potentials.

While the reduction of *t*-stilbene was fairly reversible, the reduction of indenenes showed little or no reversal current (Fig. 2). This is probably because radical anions of these compounds cannot obtain a planar structure unless the 5-membered ring is broken. The reduction of DHNP compounds, however, was generally reversible. Here both neutral and reduced molecules may have planar structures through the 6-membered ring structure, leading to lower reduction potentials and higher stability of the radical anion formed.

None of the oxidation processes were reversible with the exception of compound 3 as shown in Fig. 2. This illustrates that the steric effect may be more important than the inductive effect. We see from Fig. 1 that compounds 2 and 3 differ from the rest in that all hydrogens on the olefinic double bond are substituted. The reversibility observed for compound 3 may therefore illustrate the importance of the inductive effects of the methyl group, whose electron-donating property would stabilize the oxidation product, i.e., the radical cation. The oxidation of compound 2 was not reversible, however; the reason may be that the steric effect is more important in making the radical cation stable, since compounds 2 and 3 are practically the same except that the double bond in 2 is tied up by two 5-membered rings around it. Electronic transition energies and the fluorescence quantum yields listed in Table I also demonstrate the importance of the steric effect. As mentioned previously, the molecular model built for compound 2 illustrates that the double bond

bridging the two phenyl rings is out of plane, which reduces the resonance and conjugation through the double bond.

ECL of single systems.—The ecl was obtained by applying potential pulses such that a fluorescer is oxidized and reduced to give the cation radical and the radical anion alternately. The ecl results obtained from the single systems in (1:1) acetonitrile-benzene mixed solvents are summarized in Table II. Fluorescence and ecl spectra are shown for compound 3 in Fig. 3. Several compounds did not produce any ecl, probably a result of the ill-behaved electrochemistry.

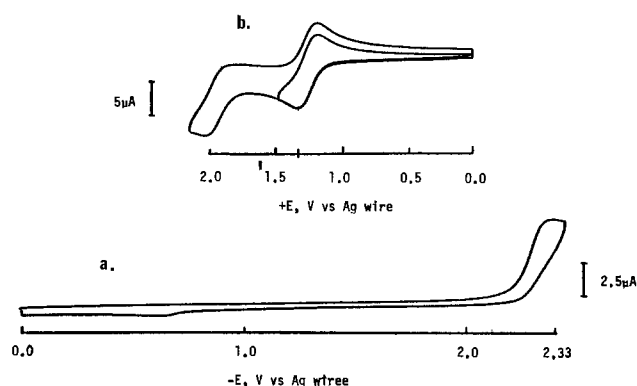


Fig. 2. (a) Cyclic voltammogram for the reduction of compound 3. (b) For the oxidation of compound 3 ($C = 0.38$ mmol). Both were recorded in (1:1) ACN-Bz mixed solvent with 0.1M TBAP as a supporting electrolyte. Scan rate was 100 mV/sec.

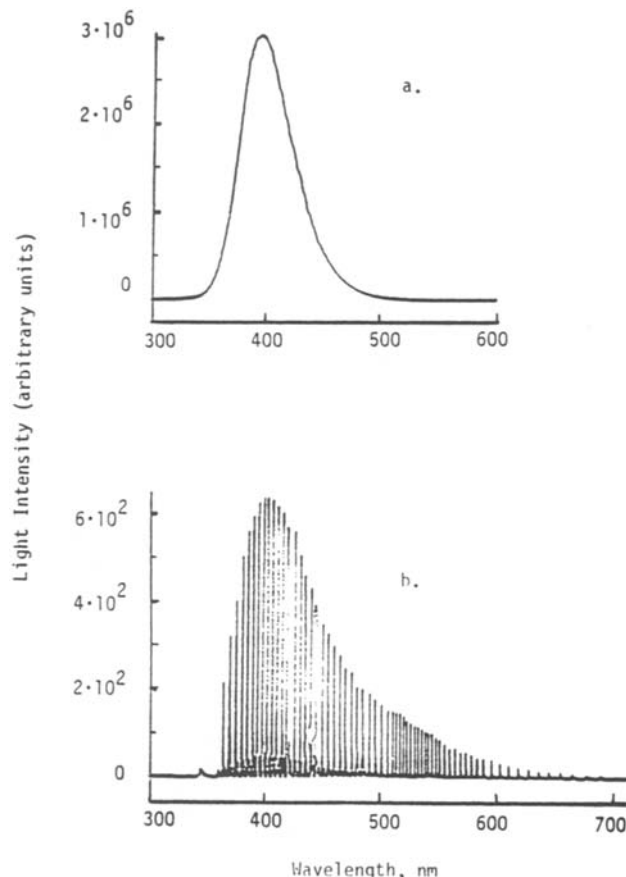


Fig. 3. (a) Fluorescence spectrum of compound 3 (0.67 mmol) in the (1:1) ACN-Bz mixed solvent. Excited at 320 nm. (b) ECL spectrum recorded from the single system of the above solution. Pulse duration was 1 sec.

It is interesting to note that the majority of DHNP's produce ecl corresponding to the fluorescence of the parent compound indicating that the singlet excited molecules are the emitting species. Many of the indene derivatives have ecl emissions which do not correspond to the fluorescence of the compounds studied. Their ecl emissions are at longer wavelengths by approximately 60 ~ 70 nm. The origin of the longer wavelength emission is somewhat unclear. We have carried out routine experiments to rule out the emission from a decomposition product, i.e., fluorescence measurements before and after ecl experiment, frequency dependency of ecl spectra, and detection of impurity current in the cyclic voltammogram recorded before and after ecl experiments, but we have not performed a detailed study such as product analysis. These emissions might have been originated from the eximer, but it is very difficult to rule out emissions from the electrolysis products, since radical species were not stable.

The reaction enthalpies listed for the single systems in Table II indicate that these ecl systems are energy sufficient. Thus, the emitting singlet excited states of DHNP's might have been produced directly from the ionic recombination reaction.

ECL of mixed systems.—Since most of the compounds studied here produced unstable cation radicals upon oxidation, TPTA was added as a source of the stable cation radical. When the cation radical of TPTA and the radical anion of the compounds studied were generated by the double potential step electrolysis, ecl was observed from all systems as summarized in Table III.

The ecl obtained from the TPTA(+)/*t*-St(-) system has only one emission attributable to the exciplex in agreement with the results observed in tetrahydrofuran (THF) by Keszthelyi and Bard (17). Although they were not able to observe it in a polar medium such as ACN or propylene carbonate, in our study ecl was observed in both ACN and ACN-Bz mixed solvent. The emission maximum listed in Table III for the TPTA(+)/*t*-St(-) is red-shifted by 40 ~ 50 nm from that of Keszthelyi *et al.*'s results. This is probably due to a polarity effect of the solvent. A spectral shift of as much as 60 nm, due to the polarity of the solvent used during the ecl experiment (25, 26), has previously been reported for the exciplex emission. Exciplexes between *t*-stilbene and a tertiary amine have also been observed by photoexcitation methods (27).

For many of the systems two emission peaks were observed: a short wavelength emission originating from the singlet excited state of the compound studied

and a long wavelength emission attributable to the exciplex. Typical ecl spectra of the mixed system are shown for compound 8 in Fig. 4. In order to establish that the longer wavelength emission originated from the exciplex, the same experiments described above were carried out. Results from these experiments and the stability of the radical species along with several observations described below support that longer wavelength emissions observed from the mixed systems are attributed to the exciplex.

As mentioned earlier in the TPTA(+)/*t*-St(-) system, the effect of the solvent polarity was remarkable for most of the systems studied. An example is shown in Fig. 4. Note in Fig. 4(a) and (b) that the ecl spectral shape changes greatly when the solvent polarity is changed. There are three main points to be noticed in Fig. 4(a) and (b), when the medium of the ecl experiment is changed from the more polar solvent (ACN) to the less polar one (ACN-Bz mixture). First, the overall ecl intensity went down by changing the solvent from the less polar to the more polar one by at least one order of magnitude. Second, the ratio of the monomer emission peak to that of the exciplex also changed. Finally, the emission energy of the exciplex is lower in a more polar medium (red-shifted). These observations were general for the systems studied with the exception of several systems containing indene derivatives. For systems containing indenenes, the radical anions were frequently unstable and it was difficult to record good, stable ecl. For most of the DHNP's, the radical anions were stable as can be evidenced by the reversal currents observed in the cyclic

Table III. ECL of mixed systems^a

| Compounds | ΔH° , eV ^b | | ECL max, nm (intensity ^c) | |
|-----------|------------------------------------|--------|---------------------------------------|--------------------------------------|
| | ACN | ACN-Bz | ACN | ACN-Bz |
| 1 | 3.01 | 2.99 | 555 (2.0×10^{-5}) | 548 |
| 2 | 3.26 | 3.28 | — | 409, 453 |
| 3 | 3.10 | 3.07 | 368, 500 (3.4×10^{-3}) | 400, 518 |
| 4 | 3.21 | 3.13 | 509 (3.6×10^{-6}) | 595 |
| 5 | 3.09 | 3.10 | 429 (3.6×10^{-6}) | 500 |
| 6 | 3.12 | 3.20 | 507 (3.0×10^{-5}) | 430 |
| 7 | 2.88 | 2.91 | 542 (1.2×10^{-5}) | 388, 502 |
| 8 | 2.88 | 2.92 | 393, 511 (3.8×10^{-4}) | 405, 490 (5.1×10^{-3}) |
| 9 | 2.86 | 2.97 | 390, 530 (2.6×10^{-4}) | 420, 530 |
| 10 | 2.82 | 2.86 | 428, 531 (1.9×10^{-4}) | 437 |
| 11 | 2.90 | 2.98 | 349, 528 (2.8×10^{-4}) | — |
| 12 | 3.59 | 2.94 | 397, 531 (1.9×10^{-4}) | 400, 530 |
| 13 | 2.89 | 2.88 | 405, 562 (2.2×10^{-4}) | — |
| 14 | 2.82 | 2.83 | 418, 534 (3.8×10^{-4}) | 407, 530 |
| 15 | 2.79 | 2.89 | 429 (8.5×10^{-4}) | 410 |
| 16 | 2.82 | 2.86 | 410, 520 (2.3×10^{-4}) | 413, 535 |

^a For TPTA, $E_{p,0} = 0.84V$ vs. SCE.

^b Calculated from $-\Delta H^\circ = E_{p,0,TPTA} - E_{p,r} - 0.16$ eV [Ref. (31)].

^c Relative to that of 1.0 mmol DPA.

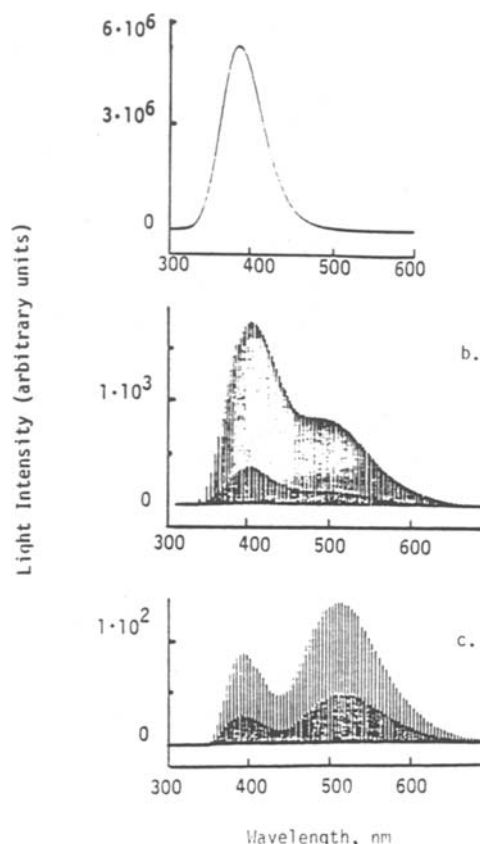
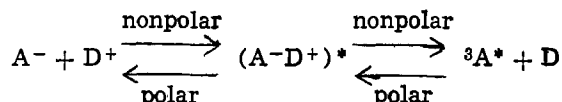


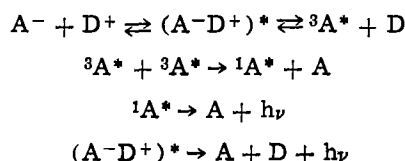
Fig. 4. (a) Fluorescence spectrum of compound 8 (1.0×10^{-5} mmol) in cyclohexane. Excited at 320 nm. (b) ECL spectrum obtained from the TPTA(+)/2-(2'-naphthyl)indene(-) system in the (1:1) ACN-BZ mixed solvent. Pulse duration was 1 sec. The solution was 2.2 mmols in TPTA and 0.96 mmol in 2-(2'-naphthyl)indene. (c) ECL spectrum obtained from the same system in the ACN solution. Pulse duration = 1 sec. TPTA = 1.2 mmols, 2-(2'-naphthyl)indene = 1.2 mmols.

voltammogram. The observations summarized above may be understood with the following equilibrium reaction



where A represents *t*-stilbene derivatives and D, TPTA.

Inspection of Table III indicates that most of the mixed systems are energy deficient with respect to the singlet emitters. While the thermal excitation from the energy potential well of the exciplex to that of the lowest singlet excited state is not impossible (15, 16, 28), it may not be probable. In some cases the energy gap between the two potential surfaces is too large compared with that of kT to allow the thermal crossover. More likely is the dissociation of the exciplex to a triplet excited state of the acceptor, followed by the triplet-triplet annihilation (TTA) to produce the emitting singlet excited state. This process may not occur for *t*-St and several other related compounds due to the short triplet lifetime as pointed out by previous investigators (15-17). Although information about the triplet excited state of most compounds studied here is not available from which to draw any concrete conclusion (with the exception of compounds 1 and 2), the process may be summarized within the framework of our observations as follows



The lowest triplet energy level for compounds 1 and 2 are 2.14 and 2.06 eV, respectively (29). Similar or lower triplet energy levels are expected for other compounds.

We would finally like to comment on the intensity of these ecl systems. Approximate relative ecl intensities with respect to that of 9,10-diphenylanthracene (DPA) are listed in Tables II and III for the single and mixed systems, respectively. Although the compounds studied here have high fluorescence quantum yields and most of them lased (14), ecl intensities are orders of magnitude lower than that of DPA. The ecl of single systems was unstable and weak. By mixing with TPTA, ecl intensities were improved somewhat, but not enough to warrant any practical applications. It appears that those systems having two aromatic rings which are connected through a double bond, as in our present study, give unsatisfactory ecl behavior, compared to the polycyclic aromatic compounds such as benzo[a]pyrene derivatives (30).

Manuscript submitted Feb. 2, 1981; revised manuscript received April 22, 1981.

Any discussion of this paper will appear in a Discussion Section to be published in the June 1982 JOURNAL.

All discussions for the June 1982 Discussion Section should be submitted by Feb. 1, 1982.

Publication costs of this article were assisted by The University of New Mexico.

REFERENCES

- L. R. Faulkner and A. J. Bard, in "Electroanalytical Chemistry," Vol. 10, A. J. Bard, Editor, Marcel Dekker, New York (1976).
- S.-M. Park and D. A. Tryk, *Rev. Chem. Intermediates*, **4**, 43 (1981).
- J. T. Bowman and A. J. Bard, Private communication; see J. T. Bowman, Ph.D. Dissertation, The University of Texas at Austin (1971).
- M. M. Nicholson, *This Journal*, **119**, 461 (1972).
- C. P. Keszthelyi and A. J. Bard, *ibid.*, **120**, 241 (1973).
- E. A. Chandross, in "Chemiluminescence and Bioluminescence," D. M. Hercules, J. Lee, and M. Cormier, Editors, Plenum Press, New York (1973).
- R. M. Measures, *Appl. Opt.*, **13**, 1121 (1974); **14**, 909 (1975).
- C. P. Keszthelyi, *ibid.*, **14**, 1710 (1975).
- C. A. Heller and J. L. Jernigan, *ibid.*, **17**, 61 (1977).
- S. M. Park and A. J. Bard, *J. Electroanal. Chem. Interfacial Electrochem.*, **77**, 137 (1978).
- S. M. Park, M. T. Paffet, and G. H. Daub, *J. Am. Chem. Soc.*, **99**, 5393 (1977).
- M. D. Barnett, G. H. Daub, F. N. Hayes, and D. G. Ott, *ibid.*, **82**, 2282 (1960).
- J. E. Simpson, G. H. Daub, and F. N. Hayes, *J. Org. Chem.*, **38**, 1771 (1973).
- M. E. McIlwain and W. F. Coleman, Private communication; see M. E. McIlwain, Ph.D. Dissertation, The University of New Mexico (1976).
- A. Weller and K. Zachariasse, *Chem. Phys. Lett.*, **10**, 197 (1971).
- K. Zachariasse, Ph.D. Thesis, Vrije Universitat te Amsterdam (1972).
- C. P. Keszthelyi and A. J. Bard, *Chem. Phys. Lett.*, **24**, 300 (1974).
- See, for example, C. A. Parker, "Photoluminescence of Solutions," Elsevier Publishing Co., London (1968).
- J. N. Demas and G. A. Crosby, *J. Phys. Chem.*, **75**, 991 (1971).
- D. Gegion, K. A. Muszkat, and E. Fischer, *J. Am. Chem. Soc.*, **90**, 12 (1968).
- S. Malkin and E. Fischer, *J. Phys. Chem.*, **68**, 1153 (1964).
- D. J. S. Birch and J. B. Birks, *Chem. Phys. Lett.*, **38**, 432 (1976).
- J. L. Charlton and J. Saltiel, *J. Phys. Chem.*, **81**, 1940 (1977).
- R. S. Becker, "Theory and Interpretation of Fluorescence and Phosphorescence," Wiley-Interscience, New York (1969).
- S.-M. Park and A. J. Bard, *J. Am. Chem. Soc.*, **97**, 2978 (1975).
- S.-M. Park and R. A. Caldwell, *This Journal*, **124**, 1859 (1977).
- F. D. Lewis, *Acc. Chem. Res.*, **12**, 152 (1979).
- A. Weller and K. Zachariasse, *J. Chem. Phys.*, **46**, 4984 (1967); *Chem. Phys. Lett.*, **10**, 590 (1971).
- J. Saltiel, G.-E. Khalil, and K. Schanze, *Chem. Phys. Lett.*, **70**, 233 (1980).
- S.-M. Park, *Photochem. Photobiol.*, **28**, 83 (1978).
- L. R. Faulkner, H. Tachikawa, and A. J. Bard, *J. Am. Chem. Soc.*, **94**, 691 (1972).

Electrochemical Investigations of Alkali Metal Intercalation Reactions in Titanium Disulfide: The High Temperature Na/Na₅ErSi₄O₁₂/TiS₂ Cell

T. Palanisamy*¹

University of Dayton, Research Institute, Dayton, Ohio 45469

R. L. Kerr*

Air Force Wright Aeronautical Laboratories, Dayton, Ohio 45433

and J. T. Maloy*

Department of Chemistry, Seton Hall University, South Orange, New Jersey 07079

ABSTRACT

The high temperature Na/Na₅ErSi₄O₁₂/TiS₂ cell has been constructed and its electrochemical properties have been investigated. At 125°C, the open-circuit voltage of this cell is 2.10V. Primary discharge studies indicate that the minimum Na⁺ conductivity of the Na₅ErSi₄O₁₂ is 0.002 Ω⁻¹ cm⁻¹ at this temperature, so that the rate of charge transport within the cell appears to be controlled by the rate of Na⁺ diffusion within the TiS₂. A mathematical model has been developed which predicts the current-time behavior for this kind of cell operating under alkali metal ion diffusion control within the positive plate material. This model predicts that the cell current is given by

$$i(t) = \frac{nFAD^{1/2}\Delta C}{\pi^{1/2}t^{1/2}} \sum_{k=-\infty}^{k=\infty} (-1)^k \exp(-k^2 l^2/Dt)$$

where ΔC represents the difference between the surface and initial bulk concentration of alkali metal ion within the TiS₂ and l is the average grain boundary distance for this material. The observed charge-discharge characteristics of this Na/TiS₂ cell have been examined and interpreted on the basis of this model.

Advanced design secondary batteries are presently under development which employ an alkali metal as the negative electrode, a solid electrolyte as the separator material (1), and a solid solution material as the positive electrode (2, 3). Common to the separator and the positive plate material is a high ionic conductivity of the alkali metal employed in the cell, even though this ionic conductivity is generally higher in separator material than it is in the electrode material. While the electrode must exhibit high electronic conductivity, the electronic conductivity of the separator must be low.

Sodium erbium silicate (Na₅ErSi₄O₁₂) has been synthesized and identified as a solid electrolyte which has high Na⁺ conductivity but low electronic conductivity (4) so that it is suitable as a separator material in a sodium cell. This compound is isotypic with Na₅GdSi₄O₁₂ which has a reported ionic conductivity of 0.3 Ω⁻¹ cm⁻¹ at 300°C (5); this high conductivity is apparently due to the framework structure of the compound in which almost half of the sodium ions are mobile (6). The erbium analog is easily prepared by high temperature synthesis. It may be pressed into pellets and is readily sintered. Because it is relatively stable when exposed to the atmosphere (no observable reaction over a period of several weeks); Na₅ErSi₄O₁₂ was judged to be ideally suited as a solid Na⁺ conductor for a bench study of this type.

Titanium disulfide (TiS₂) is a well-studied (2, 7, 8) positive plate material that is known to intercalate

alkali metal ions; it exhibits high electronic conductivity. Recent studies with chemically prepared Na_xTiS₂ samples indicate that TiS₂ conducts Li⁺ much better than it conducts Na⁺ (9). Nevertheless, the Na/TiS₂ cell has been under recent study (10), and TiS₂ has been found capable of intercalating Na⁺. Thus, TiS₂ is quite acceptable for use in conjunction with a sodium conductor such as Na₅ErSi₄O₁₂ for the charge transport studies described below.

These studies, then, were initially undertaken to investigate the properties of Na₅ErSi₄O₁₂ as a solid electrolyte separator material and the properties of TiS₂ as a solid solution electrode material in a functional, high temperature, Na/TiS₂ cell. The Na/Na₅ErSi₄O₁₂/TiS₂ cell was prepared and subjected to primary and secondary cell testing. As a result of these investigations, it became evident that the charge transport behavior of this cell, both during discharge and during charge, appears to be controlled by the rate of Na⁺ diffusion within the electrode material. Based on this observation, a mathematical model was developed which predicts the current-time behavior of the cell under the influence of solid-state diffusion control within the electrode material. The basis for this development, the development of the model itself, and a critique of the model in comparison with the available experimental data constitute the remainder of this report.

Primary Cell Characteristics

The disassembled Na/TiS₂ cell which was used in these studies is shown in Fig. 1. After this cell had been assembled and sodium had been placed in the cup formed by the quartz cylinder and the solid elec-

* Electrochemical Society Active Member.

¹ Present address: Allied Chemical Corporation, Morristown, New Jersey.

Key words: electrolyte electrode, current, diffusion.

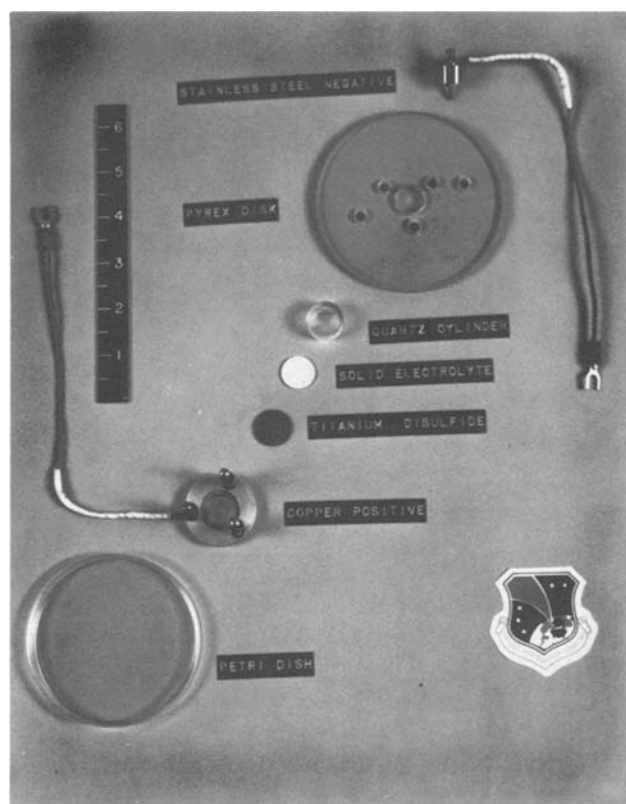


Fig. 1. The disassembled $\text{Na}/\text{Na}_5\text{ErSi}_4\text{O}_{12}/\text{TiS}_2$ test cell. After assembly, molten sodium was contained within the quartz cylinder which was spring-loaded against pressed pellets of $\text{Na}_5\text{ErSi}_4\text{O}_{12}$ and TiS_2 . The assembly was operated under an atmosphere of dry helium. The scale shown is in inches.

trolyte, it was then heated in a glove box under an atmosphere of dry helium; contacts to the stainless steel negative collector and the copper positive collector were made with insulated wires passing through the walls of the glove box to external electronics. After the cell had been heated just beyond the melting point of sodium, it was discharged across a 10 k Ω load, and the initial discharge curve was recorded.

This primary discharge curve at 398 K is shown in Fig. 2. The cell voltage fell immediately to 83% of its open-circuit value during discharge and remained constant during the initial hour of operation; since the load was 10 k Ω this voltage level indicated a maximum

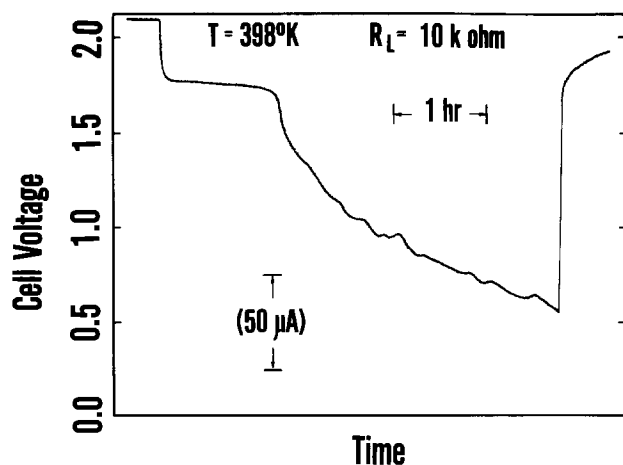


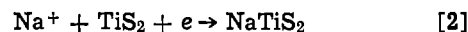
Fig. 2. The Na/TiS_2 primary cell behavior. The open-circuit voltage at the indicated temperature was 2.10V. During discharge this fell to 1.75V and remained constant for more than 1 hr. Thereafter, the cell voltage never exhibited this consistency, even following charge.

initial internal resistance of 2 k Ω . The $\text{Na}_5\text{ErSi}_4\text{O}_{12}$ pellet used in this experiment was 0.100 in. thick; this implies that the minimum conductivity of this material must be at least $0.002 \Omega^{-1} \text{cm}^{-1}$, even at this low temperature. (This approximation is based on the assumption that all internal cell resistance is across the electrolyte; contributions of polarization or interfacial resistances, if measured, would only serve to raise this estimate of Na^+ conductivity within the $\text{Na}_5\text{ErSi}_4\text{O}_{12}$.) Clearly, this material is more than satisfactory as an electrolyte material.

During spontaneous operation, the reaction



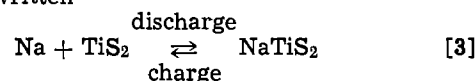
takes place at the negative ($\text{Na}/\text{Na}_5\text{ErSi}_4\text{O}_{12}$) electrode; the reaction which takes place at the positive ($\text{Na}_5\text{ErSi}_4\text{O}_{12}/\text{TiS}_2$) electrode is



Secondary Cell Characteristics

After the initial hour of constant current discharge as a primary cell, the cell never again exhibited this constancy of voltage during discharge. Thereafter, the discharge voltage gradually fell off with time as shown in Fig. 2, even when different load resistors and different temperatures were employed. During a final primary discharge of 14 hr over a 100 Ω load at 418 K in which the available TiS_2 was less than 2% utilized, the cell voltage fell to 0.5V and primary operation was ceased. The cell was then subjected to charge-discharge studies for various times at different temperatures.

Typical results of these secondary cell studies are shown in Fig. 3 at three different temperatures. In these studies, the cell was subjected to 20 min charge-discharge cycles separated by periods of relaxation that were sufficient to obtain constant open-circuit voltage. The net charge-discharge reaction for this secondary cell may be written



Because the cell was prepared initially from pure TiS_2 and then subjected only to shallow discharges result-

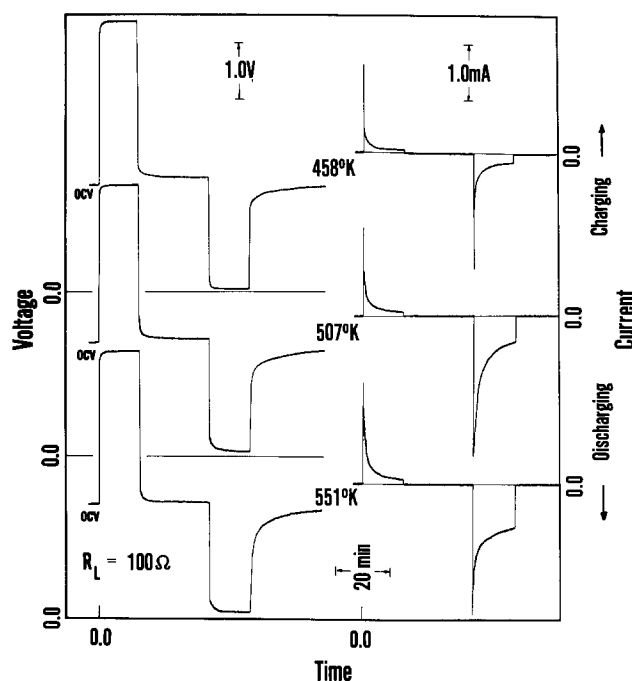


Fig. 3. Secondary cell characteristics at different temperatures. Cell voltages during a 20 min discharge (over a 100 Ω load) are shown at the left, along with voltage transients between charge-discharge periods. Corresponding currents are shown at the right.

ing in minimal Na^+ intercalation, relatively high charging voltages were required to bring about the reversal of Eq. [2]; in each of the curves shown in Fig. 3, 5.0V (2.9V overvoltage) were applied to the cell to bring about charging. Discharge was allowed to take place over a 100 Ω load. Uniform increases in both the charging current and the discharging current are observed with increasing temperature.

The open-circuit voltage transients which were recorded between periods of charge and discharge in experiments such as these were subjected to data analysis. The result of one such analysis is shown in Fig. 4 which relates the open-circuit relaxation voltage to the inverse square root of the relaxation time at four different temperatures. The fact that good linear behavior is obtained, following both periods of charge and periods of discharge, indicates that the relaxation to constant open-circuit voltage is a diffusion-controlled process. Other investigators (11) have used data analysis of this sort to evaluate solid-state diffusion coefficients, but this evaluation requires a knowledge of the Na^+ concentration (that is, evaluation of stoichiometric parameter x in Na_xTiS_2 as a function of position) within the TiS_2 which was unavailable at this point in the experiment. The relatively steeper slopes that are observed in this figure following periods of discharge are probably due to the relatively greater differences in bulk and surface Na^+ concentration within the TiS_2 phase that would be obtained following discharge.

Subsequent secondary cell experiments were carried out at 555 K to investigate the effect of the applied charging voltage on the rate of charge. As evidenced in Fig. 3, much more current passes during a given interval of discharge than is passed during that same interval of charging at 5.0V applied. Therefore, in an effort to maintain a constant average composition of Na_xTiS_2 in the positive plate material it was decided that the time of charge at a given charging voltage should be varied so that the same amount of Na^+ that was injected during discharge would be removed from the electrode during charge. The results of three such experiments for 100 sec discharges through a 100 Ω load are shown in Fig. 5. Only in the vicinity of 15V applied was the average rate of charge equivalent to the rate of discharge. No apparent decomposition of electrolyte materials occurred even at these high charging voltages; subsequent discharge curves were quite repro-

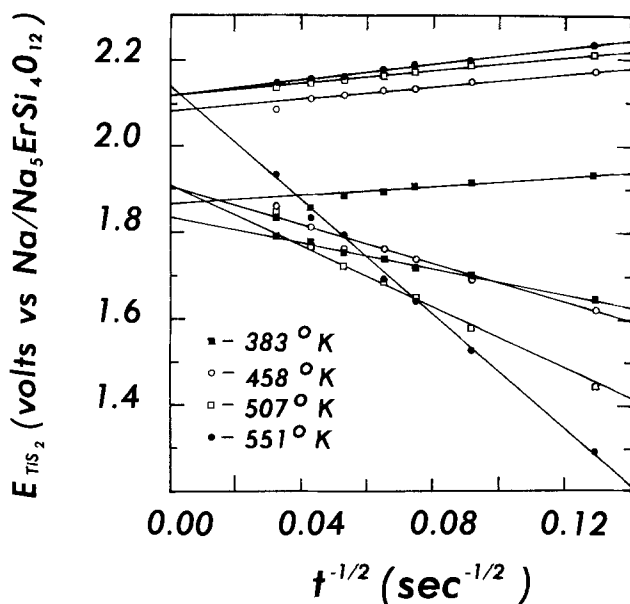


Fig. 4. The open-circuit potential of the TiS_2 electrode as a function of the time of relaxation following charge or discharge. Lines describing behavior following a period of discharge have negative slopes.

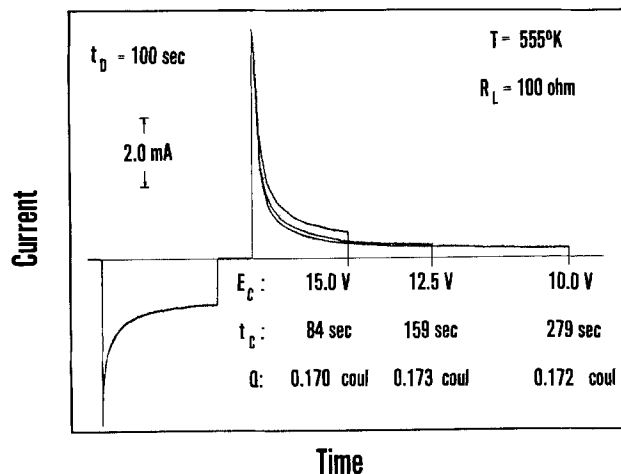


Fig. 5. The effect of charging voltage on the time of charge. Indicated charges passed during the 100 sec discharge. E_c represents the applied charging voltage and t_c represents the time required at that voltage to pass a charge equivalent to the discharge. The discharge curves are superimposed.

ducible as is indicated by the superimposition of the three curves in this figure. The refined data that are presented below confirm the fact that there is no evidence of irreproducibility in the discharge curves that would indicate solid electrolyte material decomposition on the application of charging voltages up to 15V.

Three facts about the $\text{Na}/\text{Na}_5\text{ErSi}_4\text{O}_{12}/\text{TiS}_2$ cell emerge as a result of this preliminary experimentation:

1. Extremely low utilization of the available TiS_2 is achieved during the initial constant current discharge; thereafter, even after recharge, the current during discharge decreases with increasing time so that extremely long times would be required to achieve utilization in excess of 2% of the available TiS_2 .

2. Cell potential relaxation studies following periods of charge and discharge indicate that charge transport is a diffusion-controlled process in this cell; since Na^+ diffusion in TiS_2 is known to be very slow (12) and the Na^+ conductivity of the $\text{Na}_5\text{ErSi}_4\text{O}_{12}$ is high, it is reasonable to assume that the rate-limiting step in this cell is the Na^+ diffusion within the TiS_2 . This hypothesis is supported by the fact that the currents observed in this cell are not independent of time, as would be the case if these currents were limited by the ionic conductivity of the electrolyte.

3. Unusually high charging voltages are required to charge this cell at a rate comparable with the discharge rate; this indication of apparent kinetic irreversibility requires interpretation.

With these facts in mind, then, a model was developed to describe the charge transport processes taking place in this cell. This model was applied to interpret the refined data obtained during the course of the work described above.

Experimental

Reagents.—Metallic sodium (99.95%) was supplied by Gallard Schlesinger Chemicals and used as received. The solid electrolyte $\text{Na}_5\text{ErSi}_4\text{O}_{12}$ was synthesized at 1000°C from stoichiometric amounts of Na_2CO_3 , Er_2O_3 , and SiO_2 . The original mixture was heated at the reaction temperature for approximately 20 hr; the resulting product was then ground in a ball mill and subjected to additional heating. This cycle was repeated until the product achieved a constant weight, usually after three or four cycles. The $\text{Na}_5\text{ErSi}_4\text{O}_{12}$ synthesized in this manner was pressed at 10 kpsi into 0.10 in. pellets of 1.5 cm diam and sintered at 1050°C to produce a rigid separator. Electrochemical grade TiS_2 was prepared by a variation of the method of Holleck (7). Stoichiometric amounts of the elements were placed in the

ends of an evacuated quartz tube and the tube was placed in a two-zone furnace. As the temperature of the sulfur zone was gradually raised from 350° to 500°C, the temperature of the titanium zone was maintained at 700°C. The resulting reaction of the sulfur vapor with the solid titanium produced the stoichiometric amount of gold-green TiS_2 after 16 hr of heating. This material was also pressed into a pellet at 10 kpsi, but the pellet was not sintered. X-ray powder diffraction data for the $\text{Na}_5\text{ErSi}_4\text{O}_{12}$ and the TiS_2 prepared by these methods are given in Table I.

Apparatus.—The unassembled cell used in these experiments has been shown in Fig. 1. Pressed pellets of TiS_2 and $\text{Na}_5\text{ErSi}_4\text{O}_{12}$ as prepared above were spring-loaded against the copper collector by means of a drilled Pyrex disk; the solid electrolyte was held against the TiS_2 with a quartz cylinder which also served as a container for the molten sodium negative electrode. Contact with the sodium metal was maintained with a stainless steel collector which passed through the central hole in the drilled Pyrex disk. The entire assembly was placed in a petri dish so that it could be heated under inert atmosphere.

Equipment.—During experimentation, the cell was placed in a Vacuum Atmospheres Corporation glove box equipped with a Model HE 193-2 Dri-Train and a Model HE-533 vacuum oven. This system routinely maintained the atmospheric water content at less than 2 ppm and the oxygen content at less than 2 ppm. Electrical contact was made through the walls of the glove box to a Trygon Electronics Model HR 20-1.5 d-c power supply used for cell charging. Currents and voltages were measured using precision resistors in conjunction with either a Mosley 7100B strip chart recorder, a Hewlett Packard 2401C integrating digital voltmeter, or a Non-Linear Systems Services X-3 digital voltmeter.

Theory

A schematic representation of the Na/ TiS_2 cell used in these experiments is shown in Fig. 6. Superimposed upon this representation of the cell is a resistance diagram of the components (discussed below). Beneath the diagram is a hypothetical set of concentration profiles that depict the concentration of intercalated sodium at various stages of cell operation. Evidence has been presented above which indicates that the charge transport process is diffusion controlled. Since the TiS_2 is a good electronic conductor (the resistance of the pellet used in these studies was less than 5 Ω), true

Table I. X-ray diffraction data for $\text{Na}_5\text{ErSi}_4\text{O}_{12}$ and TiS_2

| $\text{Na}_5\text{ErSi}_4\text{O}_{12}$ Experimental | TiS_2 | |
|---|----------------|------------|
| | Experimental | Reported* |
| 5.471 (5) | 5.644 (89) | 5.69 (55) |
| 5.215 (6) | 2.940 (3) | 2.95 (2) |
| 4.848 (5) | 2.840 (5) | 2.85 (2) |
| 4.647 (6) | 2.618 (100) | 2.62 (100) |
| 4.484 (8) | 2.047 (54) | 2.05 (45) |
| 4.291 (9) | 1.895 (6) | 1.90 (2) |
| 4.133 (10) | 1.702 (25) | 1.70 (25) |
| 4.004 (31) | 1.631 (8) | 1.63 (8) |
| 3.739 (5) | 1.596 (24) | 1.60 (16) |
| 3.493 (5) | | |
| 3.255 (10) | | |
| 3.043 (100) | | |
| 2.763 (38) | | |
| 2.730 (22) | | |
| 2.637 (59) | | |
| 2.436 (11) | | |
| 2.368 (7) | | |
| 2.243 (10) | | |
| 2.062 (10) | | |
| 1.914 (6) | | |
| 1.859 (35) | | |
| 1.804 (9) | | |
| 1.626 (6) | | |
| 1.585 (24) | | |
| 1.554 (6) | | |

* ASTM Card No. 15-853.

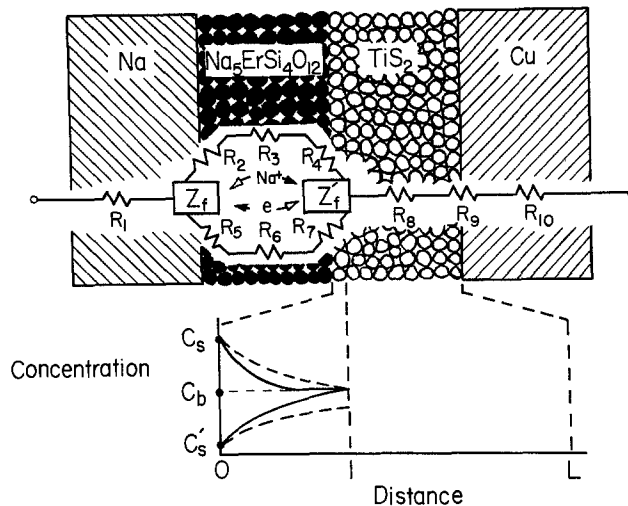


Fig. 6. A schematic representation of the Na/ TiS_2 cell. A discussion of the various resistances and impedances appears in the text. Hypothetical concentration profiles for Na^+ are shown within the first average grain boundary layer (l) of the TiS_2 . C_b represents the initial bulk concentration while C_s and C_s' represent the constant surface concentrations during discharge and charge, respectively. Dashed-line profiles would be obtained after the corresponding solid-line profile. The total thickness of the TiS_2 pellet is represented by L .

sodium ion diffusion could take place within the TiS_2 because the electronic conductivity would maintain local electroneutrality in much the same manner as supporting electrolyte minimizes migration effects in liquid solutions. Thus, sodium ion diffusion within the TiS_2 could provide the mechanism for charge transport control. However, only low utilization of the available TiS_2 is ever achieved; this implies that sodium ion diffusion is confined within a small fraction of the available TiS_2 volume. This confinement could be attributed either to a very slow diffusion process through a continuous solid solution, or to a more rapid diffusion process within a discontinuous medium. Since the former mass transport control mechanism is readily incorporated within a theoretical treatment of the latter, we have elected to base our model on the assumption that solid-state diffusion of the alkali metal ion within the TiS_2 is confined to the average grain boundary distance of the particles that are adjacent to the $\text{Na}_5\text{ErSi}_4\text{O}_{12}$. That is, the cell behaves as a solid-state thin layer cell in which charge transport across the grain boundary is controlled by local ionic conductivity. Thus the ionic concentration profiles shown in Fig. 6 are confined within a thin layer cell having the thickness of the average grain boundary distance, l . Minimal Na^+ transport is assumed to take place into the bulk of the TiS_2 pellet (thickness L).

To treat this model theoretically, one must solve the boundary value problem associated with Fick's second law of diffusion

$$\frac{\partial}{\partial t} C(x, t) = D \frac{\partial^2}{\partial x^2} C(x, t) \quad [4]$$

for the conditions required by this model. Initially, the concentration of Na^+ would be constant throughout the grain boundary layer

$$C(x, 0) = C_b \quad 0 \leq x \leq l \quad [5]$$

During cell operation, the concentration of Na^+ at the interior surface of the solid phase would be maintained a constant, C_s , at the applied potential

$$C(0, t) = C_s \quad t \neq 0 \quad [6]$$

At the grain boundary, the concentration profile would have zero slope as the boundary layer fills with (discharge) or empties of (charge) Na^+

$$\frac{\partial}{\partial x} C(x, t)|_{x=l} = 0 \quad t \neq 0 \quad [7]$$

This boundary value problem may be solved by the Laplace transformation to obtain an expression for the transformed concentration

$$c(x, s) = \frac{C_b}{s} + \frac{(C_s - C_b)}{s(\exp(2l\sqrt{s/D}) + 1)} [\exp((2l-x)\sqrt{s/D}) + \exp(x\sqrt{s/D})] \quad [8]$$

This allows the transform of the current function to be evaluated as

$$i(s) = nFAD \frac{\partial}{\partial x} c(x, s)|_{x=0} \\ = nFAD^{1/2} (C_b - C_s) s^{-1/2} \tanh(l\sqrt{s/D}) \quad [9]$$

The inverse of this transform may be found in at least one compilation of Laplace transforms (13) and the resulting expression for $i(t)$ may be rearranged to give

$$i(t) = \frac{nFACD^{1/2} (C_s - C_b)}{\pi^{1/2} t^{1/2}} \sum_{k=0}^{\infty} (-1)^k e^{-k^2 l^2/Dt} \quad [10]$$

This result is identical (after minor rearrangement) to that obtained by Oglesby *et al.* (14) for the liquid thin layer cell with $C_b = 0$.

This equation predicts that at short times, when the series factor is essentially equal to 1.0, Cottrell behavior will be obtained

$$i(t) = nFAD^{1/2} (C_s - C_b)/\pi^{1/2} t^{1/2} \quad [11]$$

At longer times, when the series factor becomes significantly less than 1.0, deviation from Cottrell behavior will be obtained. The time at which this occurs corresponds to that time at which the system is no longer controlled by semi-infinite linear diffusion of Na^+ within the TiS_2 , that is, when the first appreciable amount of Na^+ (during discharge) reaches the grain boundary and the solid state thin layer cell begins to fill; this reduces the flux of Na^+ into the TiS_2 and causes a corresponding decrease in current. This is illustrated in Fig. 7, which depicts the dimensionless current-time behavior that is predicted by Eq. [10] in the limits as $t \rightarrow 0$ (curve a) and as $t \rightarrow \infty$ (curve b).

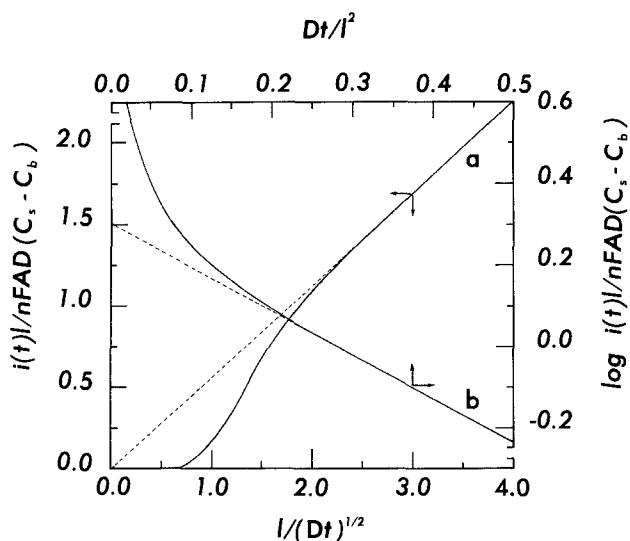


Fig. 7. Theoretical current-time behavior predicted by the solid-state thin layer cell model. Curve a (left and lower axes) shows the Cottrell behavior predicted at short times. Curve b (right and upper axes) shows the linearity obtained at long times. Equation [10] was used to construct both curves.

From curve a in this figure, it is clear that Cottrell behavior will be obtained at times less than $0.25 l^2/D$. At times greater than this, the current falls off so rapidly that linear $\log i(t)$ vs. t behavior is obtained. The equation of the straight line portion of curve b is given by

$$\log \frac{i(t) l}{nFAD (C_s - C_b)} = 0.301 - 1.0717 (Dt/l^2) \quad [12]$$

This limiting equation is numerically equivalent to a solution reported by Weppner and Huggins (15) and obtained for this boundary value problem by Ramana- rayanan and Jose (16) in the long time limit, namely

$$\frac{i(t) l}{nFAD (C_s - C_b)} = 2 \exp(-\pi^2 Dt/4l^2) \quad [13]$$

However, in their treatment of this problem Ramana- rayanan and Jose assumed that solid-state diffusion takes place throughout the entire pellet of solid material (in their investigation, Cu_2S); thus, while Eq. [12] is mathematically equivalent to Eq. [13], it is conceptually different in the definition of l . Obviously, this definition will have implication in the determination of diffusion coefficients by the application of any of these models to physical systems. The implication of selecting the pellet thickness as the distance parameter in diffusion studies of this sort is discussed below.

This proposed thin layer model for mass transport control during electrointercalation, then, predicts the linear $i(t)$ vs. $t^{-1/2}$ behavior during the early stages of both charge and discharge. The magnitude of the observed current will depend on the effective electrode area, the diffusion coefficient (a function of temperature), the average grain boundary distance (a characteristic of pellet preparation procedures), and $\Delta C = (C_s - C_b)$, the difference between the surface and initial bulk concentration of Na^+ within the TiS_2 ; ΔC will depend on the applied potential. Each of those variables also affects the time at which deviation from Cottrell behavior will be observed. Only after this critical time is it predicted that linear $\log i(t)$ vs. t behavior will be obtained. This model may be used in a variety of ways to determine D to whatever degree of accuracy that either one of the necessary spatial parameters (l or A) may be measured. Even in the absence of the information necessary to determine D , however, the model provides a way to investigate the surface concentration of Na^+ as a function of applied charging voltage. This is quite useful in the rationalization of the unusually high voltages necessary to charge the cell in the experimentation described above.

Results

Short time current-time behavior for the $\text{Na}/\text{Na}_5\text{ErSi}_4\text{O}_{12}/\text{TiS}_2$ cell at three different temperatures is displayed in Fig. 8 according to the theoretical model developed above. Excellent agreement with the model is exhibited by the data for all three charging curves (open symbols), and by two of the three discharge curves (filled symbols), namely, that linear $i(t)$ vs. $t^{-1/2}$ behavior which passes through origin is obtained. With the exception of the highest temperature discharge curve, the slope of these Cottrell plots all exhibit the trend that might be expected as the solid-state diffusion coefficient increases with increasing temperature. Since the extent of discharge was never very great during these experiments, $(C_s - C_b)$ would be expected to have a greater absolute value during charge than during discharge at all temperatures. Only the highest temperature discharge curve deviates from the short time behavior predicted by the model; in this case, even though linear $i(t)$ vs. $t^{-1/2}$ behavior is obtained, the current intercept is nonzero (~ 0.8 mA).

This nonzero current intercept is observed in the discharge curves shown in Fig. 9, also. It is quite reproducible. While the model predicts that deviations from

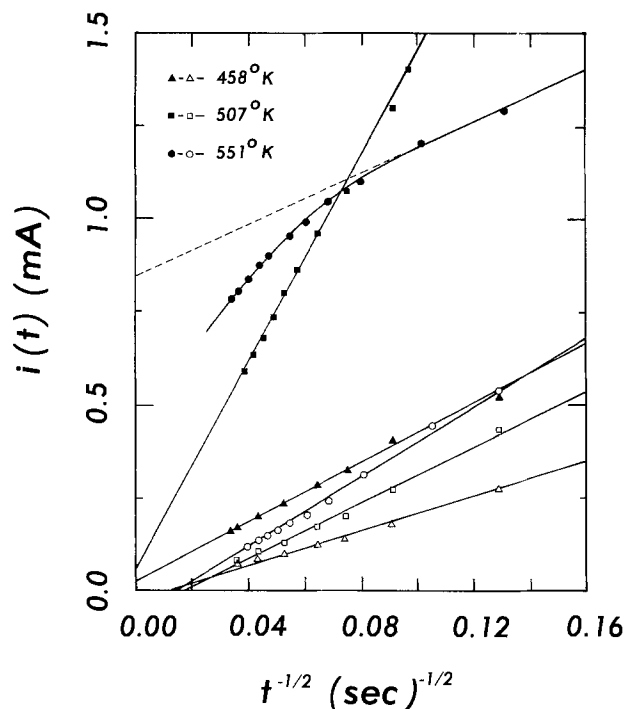


Fig. 8. Experimental current-time behavior for the Na/TiS₂ cell at different temperatures. Charging currents (open symbols) were measured at 5.0V applied. Discharges (filled symbols) were allowed to take place over a 100Ω load. Currents are plotted without regard to electrochemical sign convention.

Cottrell behavior will be obtained at longer times, only negative deviations are predicted on the basis of grain boundary layer saturation with Na⁺. Thus, this experimental observation is unexplained by the model. However, it must be noted that the nonzero current intercept was obtained only after the cell had been heated to 551 K, and the cell had been subjected to several charge-discharge cycles. Na_xTiS₂ is known to exist in several phases (9), with differing charge transport properties (17). It is not altogether unlikely that a high temperature phase transition could result in the

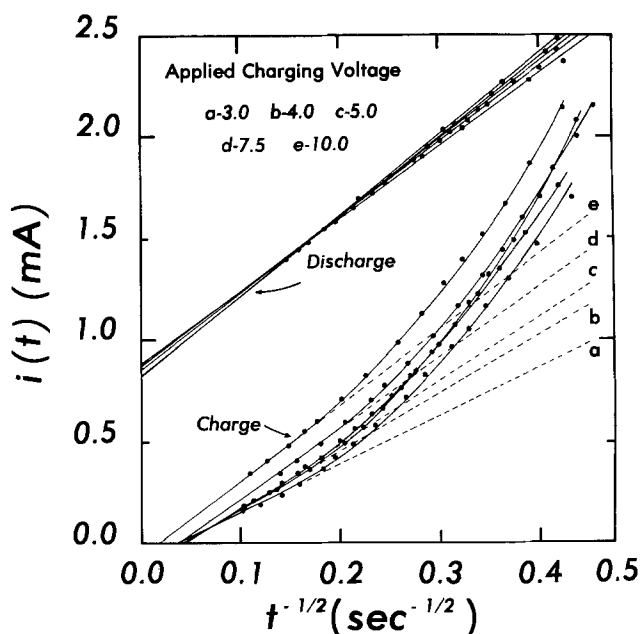


Fig. 9. The Cottrell behavior of the Na/TiS₂ cell at different charging voltages. All runs were made at 550 K. In the manner shown in Fig. 5, the extent of each charge was limited to the extent of the previous discharge.

formation of a surface layer of a different form of Na_xTiS₂ that might react directly with Na⁺ from the solid electrolyte in a manner that would not be controlled by the rate of Na⁺ diffusion within the TiS₂. The current due to a direct surface reaction of this sort would be observed as a background current (the non-zero intercept) on the diffusion-controlled electro-intercalation process. This explanation is made plausible by the fact that some phases of Na_xTiS₂ have been found to be electrochemically irreversible (9); thus, the observed background current is observed only during discharge.

Figure 9 also shows the effect of charging voltage on the rate of charge. Even though nonlinear behavior is obtained during the early states of each charge, good linearity is obtained at times between 25 and 100 sec, the range of Fig. 8. The slope of these linear portions increases, as anticipated, with increasing charging voltage (curves a-e). As the charging voltage is increased, the surface concentration of (Na⁺) is lowered to the point where ΔC during charge is equal in magnitude to ΔC during discharge. When this occurs, the instantaneous rate of charge equals the rate of discharge and the slope of the discharge curve equals the slope on charging. This occurs over the 25 to 100 sec range at an applied charging voltage between 4.0 and 5.0V. This result is significantly different from the conclusion which would have been drawn on the basis of the coulometry times shown in Fig. 5. Clearly, this method of comparing the relative rates of charge transport appears to give more reasonable results.

Discussion

The experimental results presented above agree favorably with the theoretical model developed herein. The fact that negative deviation from Cottrell behavior is not observed indicates that Na⁺ diffusion does not penetrate the TiS₂ to the average grain boundary distance. Thus, the current-time relationship of Eq. [10] is approximated by the Cottrell behavior of Eq. [11] for this system and not by Eq. [13] as might have been inferred from a previous treatment (16). Even if the average grain boundary distance is quite large because of the pressed nature of the TiS₂ pellet (thereby causing $l \rightarrow L$), the validity of the previously suggested approximation of the current-time relationship as expressed by Eq. [13] is not supported by the experimental data for the Na/TiS₂ cell. This is not to say, of course, that Eq. [13] is invalid for all systems; indeed, the data of Ramanarayanan and Jose support its validity for their system. However, this work demonstrates that the exponential approximation is valid only at times greater than those at which Cottrell behavior is obtained, that is, after the diffusing species reaches the interior wall of the thin layer cell represented by the distance l . This distance may be taken as the pellet thickness, L , instead of the average grain boundary distance as in this work, but a necessary consequence of this choice is that a detectable increase in the amount of the diffusing species reaching the pellet-collector interface must take place if the assumptions that $l = L$ and the applicability of Eq. [13] are to be simultaneously valid; this can be verified experimentally. Any overestimation of the size of l will result in an overestimation of the magnitude of D . Ramanarayanan and Jose have determined D for Cu⁺ in Cu₂S to be up to 7.3×10^{-3} cm²/sec at 400°C by assuming that l was the pellet thickness (0.8-2 cm).

In addition to utilizing Eq. [13] to estimate D , the time at which the transition from Cottrell behavior takes place may be used to estimate D , provided that l is known. While this was not possible in this work because the necessary transition to exponential behavior was not observed for this system, concurrent studies of lithium-TiS₂ electrointercalation reactions in liquid electrolyte that have been carried out in these labora-

tories indicate the feasibility of this method. These will be the subject of future communications.

The model developed herein may also be used to investigate the potential dependence of the surface concentration of Na^+ within the TiS_2 (that is, the interfacial stoichiometry of Na_xTiS_2). This arises from the fact that this slope is given by

$$m = nFAD^{1/2} (C_s - C_b) / \pi^{1/2} \quad [14]$$

over the range where Cottrell behavior is obtained so that the ratio of the slope of the Cottrell plot on charge to that on discharge is given by

$$(-m_c/m_d) = (C_s' - C_b) / (C_s - C_b) \quad [15]$$

where C_s' , C_s , and C_b are defined in Fig. 6. Because these experiments were conducted in such a manner that the same state of charge was restored at each charging voltage, C_b may be regarded as a constant. Thus, the slope ratio is equal to one when the surface concentration on charge is lower than C_b by the same amount that it is above C_b on discharge. As shown in Fig. 10, this occurs at an applied voltage of 4.3V. The slope ratio ranges from 0.0 at an applied charging voltage equal to the cell potential (an overpotential of 0.0V) to 1.4 in the limit of high charging voltage. Since these two extremes correspond to the $C_s' = C_b$ and $C_s' = 0$ limits, respectively, it is possible to construct the concentration ratio axis shown on the right in Fig. 10. This allows the determination of the apparent overpotential that is necessary to achieve any relative surface concentration of Na^+ within the TiS_2 at the state of charge represented by C_b . Information of this sort is useful in assessing the reversibility of the kinetics of the electrointercalation reaction. In this case, since very high voltages must be applied to remove the Na^+ injected into the TiS_2 during discharge at the same rate as the discharge process, this reaction appears to exhibit highly irreversible electrode kinetics.

The fact that such high charging voltages can even be employed in this cell with no apparent degradation of the cell components is intriguing. (For example, this characteristic might imply that this cell could be subjected to high voltage charging for rapid recovery applications.) A possible rationalization of this behavior is provided by a consideration of the cell resistance network shown in Fig. 6. In this diagram R_1 , R_6 , R_8 , and R_{10} represent the electronic resistances of the components of the cell; because $\text{Na}_5\text{ErSi}_4\text{O}_{12}$ is a good separator material, R_6 is quite large. The faradaic im-

pedances associated with Eq. [1] and Eq. [2] are represented by Z_f and Z_f' , respectively; each of these impedances is associated with the redox process and not with the transport of charge across the interface. This interfacial resistance is represented by R_5 , R_7 , and R_9 insofar as electronic transport is concerned and by R_2 and R_4 for ionic transport. Electronic conduction across the given interfaces would be quite facile; interfacial ionic conductivity would occur with much more difficulty. The resistance to ionic conduction within the solid electrolyte is represented by R_3 . When the cell is charged, the charging voltage is applied over this network. Since the electronic resistance of the solid electrolyte (R_6) is quite high, the charging current is required to pass primarily through the ionic branch. The actual voltage drop across the solid electrolyte, then, is highly dependent on both the faradaic impedances and the interfacial resistances to ionic conduction (R_2 and R_4). Since these would be quite high, especially at a solid-solid junction like that at the $\text{Na}_5\text{ErSi}_4\text{O}_{12}/\text{TiS}_2$ interface under the influence of concentration polarization, most of the applied voltage would be used to overcome interfacial resistance. Thus, the overpotentials given in Fig. 9 may be regarded as only apparent; each may be in error by an amount proportional to the interfacial resistance. If this is the case, the magnitude of the apparent kinetic irreversibility would be diminished.

Conclusions

A solid electrolyte material has been synthesized and tested in the Na/TiS_2 cell. These experimental results have been compared with a theoretical model which predicts the current-time behavior for a thin layer electrointercalation cell operating under the control of solid-state diffusion; to the extent of experimental feasibility, good agreement has been obtained. The model developed herein is applicable to other electrointercalation reactions, namely, that of lithium from liquid solution. The comparison of this model with experimental results for these systems will be the topic of subsequent publications.

Acknowledgment

This work was supported by the Air Force Systems Command through the sponsorship of the Air Force Office of Scientific Research and the Air Force Wright Aeronautical Laboratories.

Manuscript submitted Oct. 6, 1980; revised manuscript received April 10, 1981.

Any discussion of this paper will appear in a Discussion Section to be published in the June 1982 JOURNAL. All discussions for the June 1982 Discussion Section should be submitted by Feb. 1, 1982.

Publication costs of this article were assisted by Air Force Wright Aeronautical Laboratories.

REFERENCES

1. P. Hagenmuller and W. Van Gool, Editors, "Solid Electrolytes, General Principles, Characterization, Materials, Applications," Academic Press, New York (1978).
2. M. S. Whittingham, in "Materials Science in Energy Technology," G. G. Libowitz and M. S. Whittingham, Editors, Academic Press, New York (1979).
3. D. W. Murphy, P. A. Christian, F. J. DiSalvo, and J. N. Carides, *This Journal*, **125**, 497 (1979).
4. T. Palanisamy, R. L. Kerr, and J. T. Maloy, in "Fast Ion Transport in Solids: Electrodes and Electrolytes," p. 427, New York (1979).
5. R. D. Shannon, H. Y. Chen, and T. Berzins, *Mater. Res. Bull.*, **12**, 969 (1977).
6. B. A. Maksimov, Y. A. Kharitonov, and N. V. Belov, *Sov. Phys. Dokl.*, **18**, 763 (1974).
7. G. L. Holleck and J. R. Driscoll, *Electrochimica Acta*, **22**, 647 (1977).
8. M. S. Whittingham, *This Journal*, **123**, 315 (1976).
9. M. S. Whittingham, in "Fast Ion Transport in Sol-

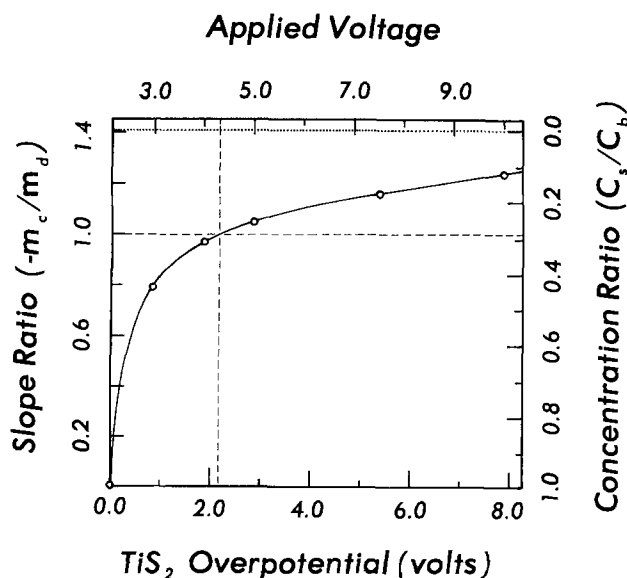


Fig. 10. The charge to discharge slope ratio for the Cottrell plots shown previously as a function of charging voltage.

- ids: *Electrodes and Electrolytes*," P. Vashista *et al.*, Editors, p. 17, North-Holland, New York (1979).
10. G. H. Newman and L. P. Klemann, as reported in Ref. (9).
 11. S. Basu and W. L. Worrell, in "Fast Ion Transport in Solids: *Electrodes and Electrolytes*," P. Vashista *et al.*, Editors, p. 149, North-Holland, New York (1979).
 12. M. S. Whittingham, *Prog. Solid State Chem.*, **12**, 41 (1978).
 13. A. Erdélyi *et al.*, "Higher Transcendental Functions," Chap. 5.9, transform 34, McGraw-Hill, New York (1953).
 14. D. M. Oglesby, S. H. Omang, and C. N. Reilley, *Anal. Chem.*, **37**, 1312 (1965).
 15. W. Weppner and R. A. Huggins, *Ann. Rev. Mater. Sci.*, **8**, 269 (1978).
 16. T. A. Ramanarayanan and P. D. Jose, *This Journal*, **125**, 1684 (1978).
 17. D. A. Winn, J. M. Shemilt and B. C. H. Steele, *Mater. Res. Bull.*, **11**, 559 (1976).

On the Electrolysis of Coal Slurries

G. Okada,¹ V. Guruswamy, and J. O'M. Bockris*

Department of Chemistry, Texas A&M University, College Station, Texas 77843

ABSTRACT

Slurries of anthracite and lignite were used in suspension in 4.15M H₂SO₄. Gas chromatography was used to measure H₂ and CO₂; absorption spectroscopy was used to measure dissolved Fe. Voltammograms were taken of the system solution slurry. Hydrogen was evolved at cell potentials more negative than 0.6V. The limiting current density of this evolution was initially around 5-10 mA/cm² at 80°C. However, when the coal was filtered off from the solution, the current density was around the same. Atomic absorption spectra showed iron dissolved in solution. If coal was sufficiently washed in solution, the limiting current for hydrogen evolution at low potential dropped to around 0.1 mA/cm². The evolution of hydrogen was near 100% in faradaic efficiency. Anode gases were only ~ 10% CO₂ in current efficiency. Results with pure carbon were radically different. Limiting current was low, but anode gases approached 80% CO₂. The essential facts of Coughlin and Farooque's work are confirmed; details are counter-indicated. Coal slurry electrolysis as a method for cheap hydrogen evolution is not in good prospect, because of the low current density available after the removal of Fe. It may be possible to obtain commercially interesting products from the anodic reactions.

The liquefaction and gasification of coal (1-4) are much needed processes for the replacement of gaseous and liquid fossil fuels. However, coal forms grit, which reaches the atmosphere; it contains sulfur, which is expensive to remove to a satisfactory degree. A greater difficulty in realizing liquid or gaseous fuels from coal is that the present processes are high temperature ones. If a low temperature process (5) could be found which would give rise to products of coal liquefaction without the materials problems of high temperature methods, while eliminating the sulfur and grit difficulty, it might become a powerful rival to the classical coal gasification.

A major contribution in this direction was claimed by the work of Coughlin and Farooque (6, 7) who reported that coal slurries could be electrolyzed, giving hydrogen at potentials around 1/3 those necessary for water electrolysis. Little detail was given by Coughlin and Farooque (7) concerning the anodic reactions. The three objectives of the present paper are to:

1. Report a re-examination of the facts of coal slurry electrolysis, bringing out the degree of verification, and bearing any differences between the present work and that of Coughlin and Farooque.
2. Begin work which could lead to the anodic liquefaction of coal.²
3. Investigate the removal of impurities in coal by electrolysis.

* Electrochemical Society Active Member.

¹ On leave of absence from Ehime University, Matsuyama, Ehime, Japan.

Key words: electrolysis, coal, hydrogen, current efficiency, slurry.

² As anthracite is approximately CH, and gaseous or liquid fuels can be represented as CH_n, where n is 2-4, one thinks first of a cathodic liquefaction of coal, the path of most past endeavors which, however, have had a limited success.

Experimental

Suspended coals in sulfuric acid (1M and 4.15M) solution were used as slurry electrolytes. Anthracite and lignite were ground into small particles (-100 mesh) by using a ball mill sieve. Pure carbon (-325 mesh) was also used.

The cells used are shown in Fig. 1(A) (a replica of the cell of Coughlin *et al.*) and 1(B). Cell A was employed for measurements of current as a function of potential. The anode compartment was 600 ml in volume. A Pt plate (3.55 cm²) was the anode, and Pt gauze the cathode. The cathode compartment was separated by a fritted glass disk to prevent coal particles reaching the cathode. The anolyte was agitated, to avoid the settling out of coal particles and to increase the limiting current, by means of a magnetic stirrer. A calomel electrode was used as a reference.

Cell B was employed for analysis of the evolved gases and for long-time electrolysis. The anode was made of Pt foil, rolled into a cylindrical form, 1.25 cm long and about 1.6 cm in diameter (14 cm²). The cathode was a square plate of 1.25 cm²/side. The anode compartment had a volume of 28 ml. The electrolyte temperature in these cells was roughly controlled in the range 25°-80°C by a Corning Hot Plate, PC-101.

The electrolysis of coal was carried out under potentiostatic conditions by using a Stonehart Potentiostat, BC 1200. Voltametry was performed to measure the current/voltage curves by using a Princeton Universal Programmer, Model 175.

Evolved gases were analyzed by an Antec Gas Chromatograph, Model 461-LP. Iron in the coal electrolyte slurry was analyzed, using a Perkin Elmer atomic absorption spectroscopy, Model 306.

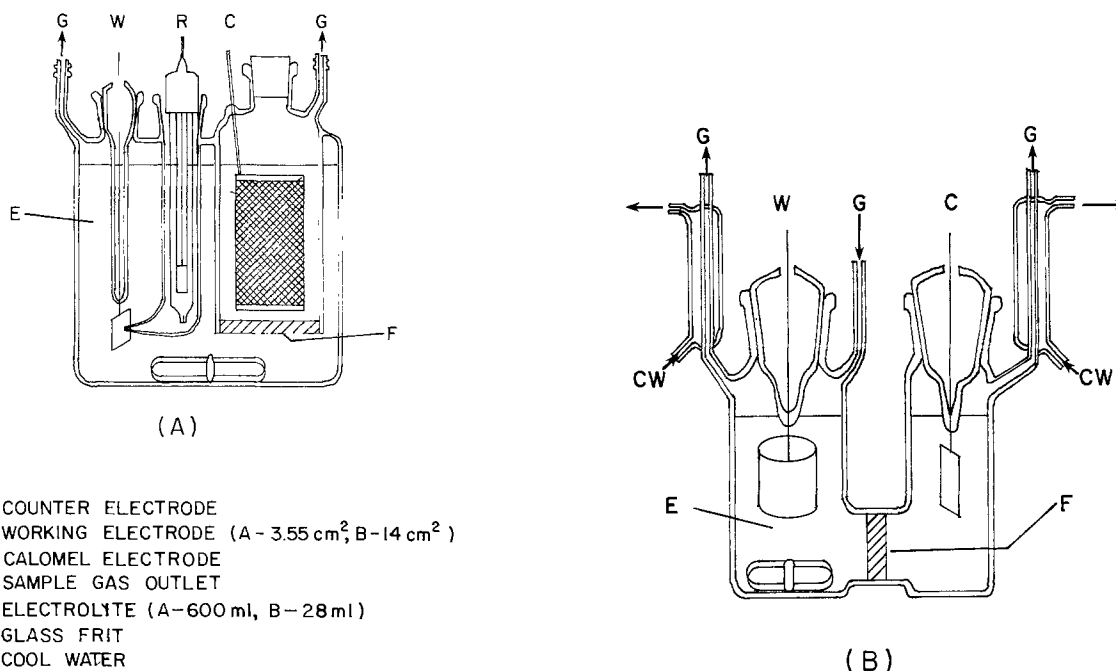


Fig. 1. (A) Electrolytic cell for investigations of coal depolarized hydrogen production—a replica of cell used by Coughlin and Farooque. (B) Electrolytic cell used by gas collection and analysis.

Results

Current/potential relations.—A typical current/potential curve from anthracite slurries (0.136 g/ml, 1M H₂SO₄ solution) is shown in Fig. 2. On the anodic side, the current rises sharply at 0.6 V/NHE, and reaches a limiting value at around 0.8 V/NHE. A limiting current density of 5 mA/cm² at 75°C is observed in the middle region. There is O₂ gas evolution at higher potential than 1.7 V/NHE.

A current/potential curve from lignite slurry (0.475 g/ml, 4.15M H₂SO₄ solution) at 75°C is shown in Fig. 3. The behavior of the current is almost the same as in anthracite, except that the limiting current density is 10 mA/cm² (cf., the difference in concentration of the coal slurry).

To compare with data from the coal slurries, which contain impurities, pure carbon also was used as a slurry electrolyte. The current/potential curve for pure carbon (0.10 g/ml, 1M H₂SO₄ solution) is shown in Fig. 4. The voltamogram shows a maximum at 1 V/NHE, in contrast with the behavior shown in Fig. 2 and 3.

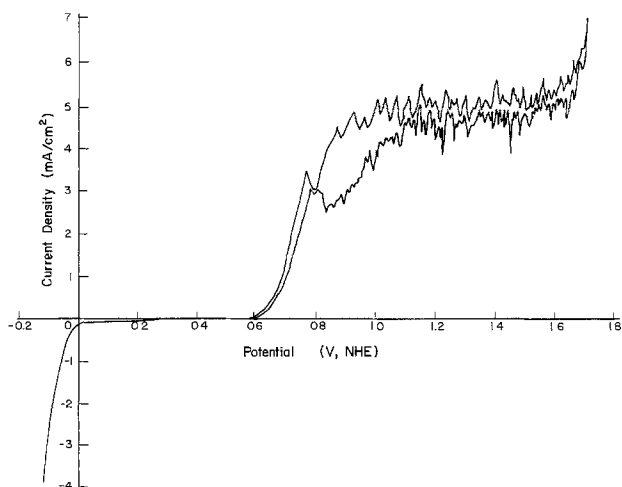


Fig. 2. Current/potential curve for oxidation of an anthracite slurry (0.137 g/ml, 4.15M H₂SO₄ solution) at 75°C. Cathodic potential vs. current density relation is also shown.

Anodic limiting current densities.—The limiting current densities observed in this work were similar to those of Coughlin and Farooque (6). The values depended on coal concentration, electrolyte temperature, and agitation speed. Figure 5 shows that there is an anodic limiting current proportional to the coal concentration.

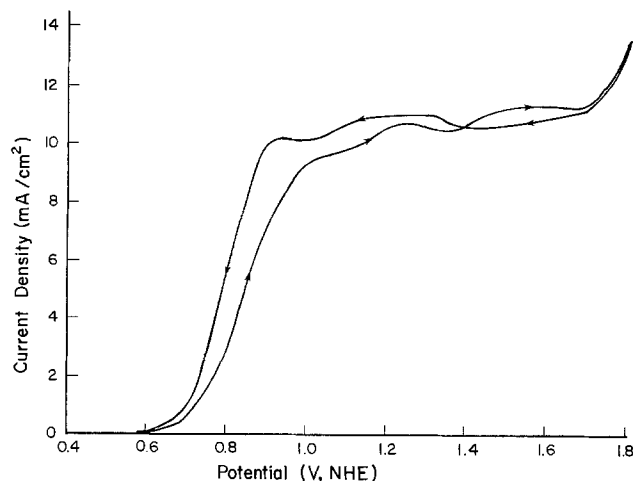


Fig. 3. Current/potential curve for oxidation of a lignite slurry (0.475 g/ml, 4.15M H₂SO₄ solution) at 75°C.

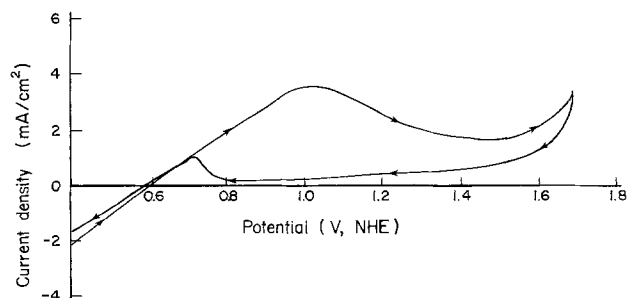


Fig. 4. Current/potential curve for oxidation of pure carbon slurry (0.10 g/ml, 1M H₂SO₄ solution) at 86°C.

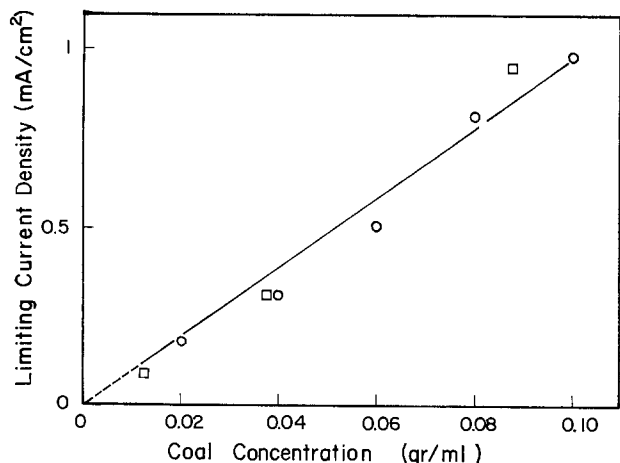


Fig. 5. Effect of coal concentration on the anodic limiting current at room temperature. \square , lignite; \circ , anthracite.

Limiting currents as a function of temperature (22.5°-75.8°C) are shown in Fig. 6. The activation energies for lignite and anthracite slurries are about 16 kcal/mole, as compared to 12-14 kcal, obtained by Coughlin and Farooque (6).

The time dependence of the limiting current on the anodic part of the voltamogram at room temperature after introducing coal into the solution is shown in Fig. 7. Smaller particles give larger currents.

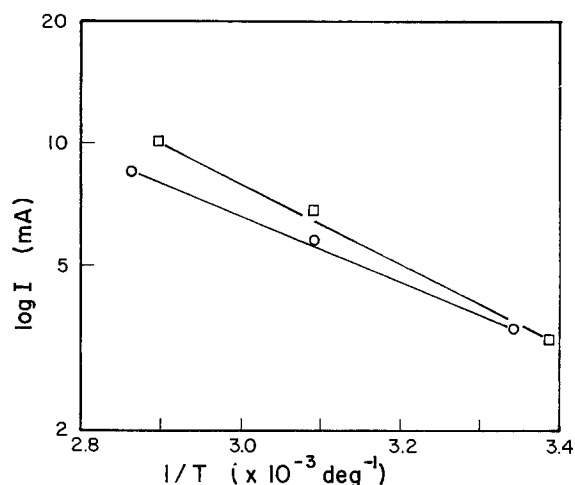


Fig. 6. Anodic limiting current as a function of temperature. \square , lignite (0.088 g/ml); \circ , anthracite (0.20 g/ml).

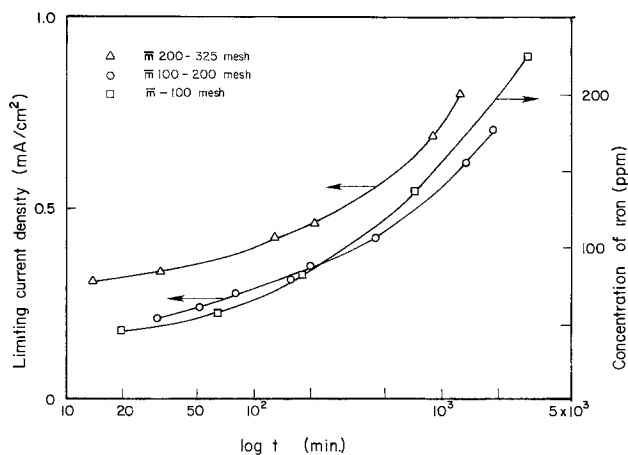


Fig. 7. Time dependence of the limiting currents for dissolution of iron in coal (without continuous electrolysis, at room temperature, anthracite 0.1 g/ml). Δ , 200 ~ 325 mesh; \circ , 100 ~ 200 mesh; \square , 100 mesh.

Effects of iron dissolved in the solution.—Iron is contained as pyrites and magnetite in coal (8). The concentration of the iron dissolved in the electrolyte from coal is shown as a function of time in Fig. 7. The time dependence of this value is similar to that of the limiting current density in the anodic electrolysis of coal.

To examine the effect of impurities, an experiment was made, in which coal had been washed for 20 hr at 75°C by agitation in 1M H_2SO_4 solution. Current/potential curves were thereafter measured at 75°C (Fig. 8), in fresh sulfuric acid containing the washed coal. The value of the limiting current was now only 0.1 mA/cm² at 75°C (5 mA/cm² with virgin coal) and varied little with time, even after 21 hr.

That the difference in limiting current densities between electrolytes containing the virgin and refined coal resulted from the concentration of Fe^{2+} , initially in solution, was evidenced by the fact that the higher limiting current in the former case was recovered (3.7 mA/cm²) by adding FeSO_4 (200 ppm as Fe^{2+}). The current/potential curves and agitation effects thereon in the washed coal slurries to which Fe^{2+} was added were the same as those with unwashed coal. Correspondingly, in sulfuric acid (1M) solution, to which had been added FeSO_4 (500 ppm as Fe^{2+})—no coal—the same kind of current/potential curve was observed (Fig. 9), with around the same limiting current as with unwashed coal slurries.

Evolution of gases.—After degassing by N_2 bubbling, electrolysis was performed. Evolved gases were analyzed by means of a gas chromatograph. After coal was introduced into the electrolyte,³ large volumes of carbon dioxide evolution occurred before any current was switched on. 60 ml of CO_2 was evolved in 7 hr at 75°C from a suspension of anthracite of 0.137 g/ml in cell A and 300 ml in 9 hr from lignite of 0.475 g/ml, also in cell A.

³A reviewer of our paper has pointed out that there may be SO_2 -containing species in the measuring solution, and these could contribute to the overall anodic current.

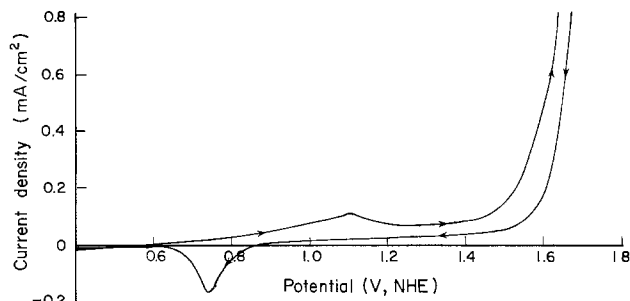


Fig. 8. Current/potential curve for oxidation of washed anthracite slurry (0.17 g/ml, 1M H_2SO_4 solution) at 75°C.

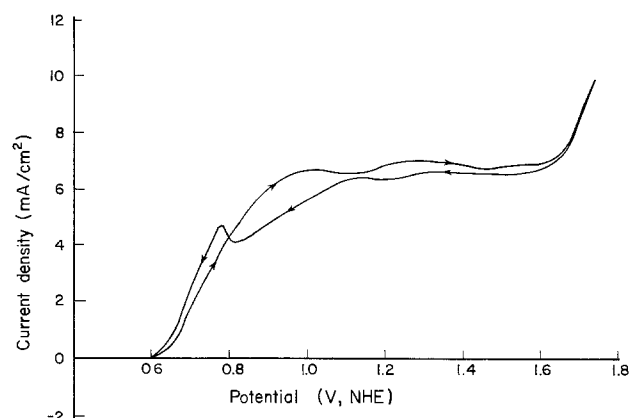


Fig. 9. Current/potential curve for oxidation of FeSO_4 solution (Fe , 500 ppm) at 72°C.

Figure 10 shows the current/time curve at 1V cell voltage in cell B. The current from the anthracite slurry falls with time. After about 100C (17 hr), current of 1.0 mA ($<0.3 \text{ mA/cm}^2$) still remained for the anthracite.

In the cathodic current efficiency measurements using the gas chromatograph, no gas other than hydrogen was observed. By measurement with a flowmeter, the rate of hydrogen evolution observed corresponded to an apparent current efficiency of more than 90%. There is no reason to conclude that the true current efficiency at the cathode was less than 100%.

Evolution rate of CO_2 at the anode is shown in Fig. 11. In calculation of the anode current efficiency for CO_2 evolution, there are two difficulties. First, there is the strong initial chemical reaction which occurs between coal and the 4.15M sulfuric acid used as the electrolyte. After about 1 hr at a temperature of 80°C , this was 0.6 ml per hour from a suspension of anthracite (0.10 g/ml) in cell B. At a corresponding time, when the electrochemical current was 6 mA, the CO_2 at 100% current efficiency would have been of comparable magnitude, namely, about 1.4 ml per hour.

The chemical reaction was allowed to decay for several hours before electrolysis was commenced. In Fig. 11, an example is shown in which electrolysis was started 11 hr after the contact between the coal (anthracite) and the sulfuric acid had begun. The evolution of chemical CO_2 was now about 7×10^{-2} ml per hour. During electrolysis, the most uncertain part of the CO_2 evolution is the degree of the chemical reaction rate. No continuous recording of the chemical CO_2 rate was made after electrolysis was commenced. However, if we assume that the rate of decrease of the chemical CO_2 was exponential with time, it is possible to subtract the chemical reaction rate from the overall reaction rate by calculation, and this has been done for the results of Fig. 11. The value of the resulting current efficiency of CO_2 evolution is shown.

In respect to the influence of iron on the anodic results, strong in the early stages of electrolysis, Fig. 10 shows a plot of current in the absence of coal due to iron and how it varies with time, while the electrode is oxidizing the ferrous iron to ferric. It is, therefore, reasonable to suppose that after a time of some 200

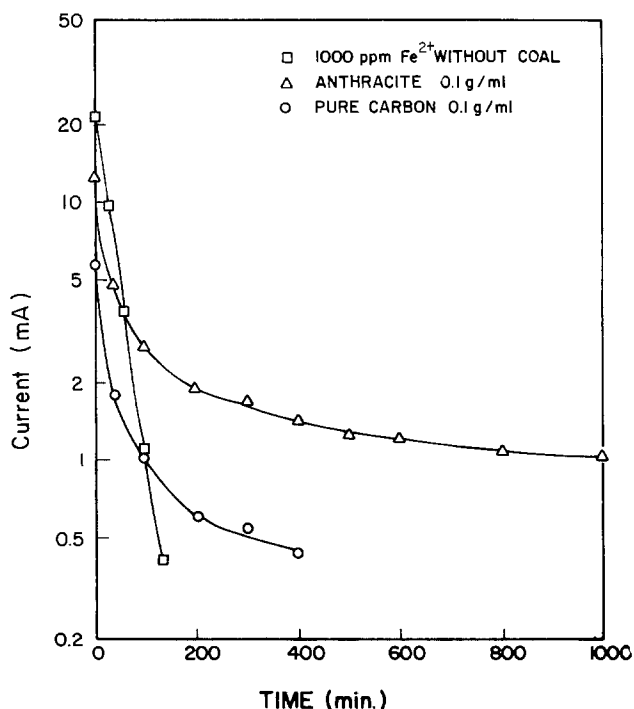


Fig. 10. Anodic current/time curve at 1V cell voltage in 4.15M H_2SO_4 solution (electrode area is 14 cm^2). \square , 1000 ppm Fe^{2+} without coal; \triangle , anthracite 0.1 g/ml, \circ , pure carbon 0.1 g/ml.

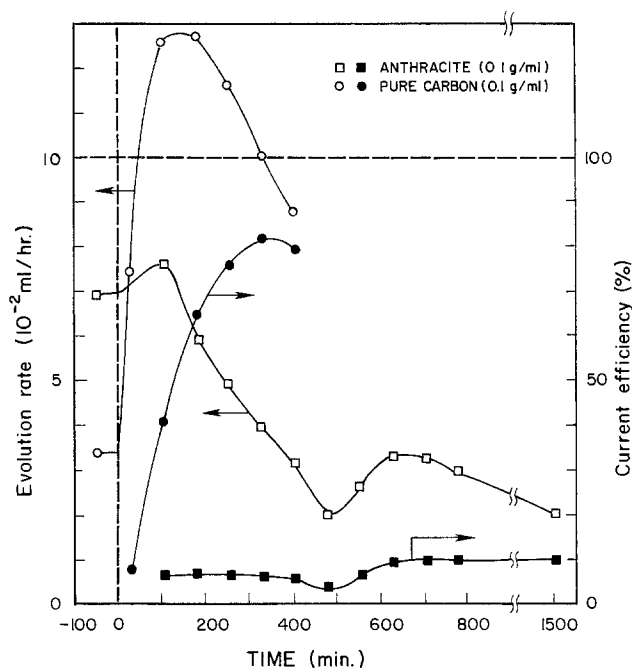


Fig. 11. Evolution rate and current efficiency for CO_2 production as a function of time in 4.15M H_2SO_4 solution at 80°C (cell B). \square , \blacksquare anthracite (0.1 g/ml); \circ , \bullet pure carbon (0.1 g/ml).

min, the effect of Fe^{2+} oxidation is negligible, and this has been assumed in the plots of Fig. 11.

Thus, the current efficiency measurements for CO_2 evolution at the anode are approximate. However, when electrolysis is commenced after 11 hr of contact of the coal with the sulfuric acid solution (4.15M), it is around 5%, rising to around 10% after 25 hr.

Differences in results obtained with pure carbon.—A slurry of pure carbon (2N5, 325 mesh), Alfa Products, was prepared at a concentration of 0.1 g/ml. The current/time curve obtained for these slurries is shown in Fig. 10. The current falls off faster than that for anthracite. The evolution rate of carbon dioxide was almost zero in the early part of the electrolysis, in spite of a current of 5 mA, but the current efficiency rises finally to around 80%. The electrolyte filtered from the carbon slurry revealed only small residual current (0.1 mA/cm^2). The concentration of iron in this electrolyte was less than 12 ppm.

Discussion

Comparisons between data of Coughlin and Farooque (6) and those of the present work are given in Table I. Discussions of these differences follow.

The current/potential relations.—The current in the typical voltammogram (Fig. 2) becomes significantly anodic in the region of $+0.6 \text{ V/NHE}$. This may be compared with the reversible potential of iron ($\text{Fe}^{2+}/\text{Fe}^{3+}$), which is $+0.77 \text{ V}$. Assuming arbitrarily that the

Table I. Comparison between data of Coughlin and Farooque and those of the present work

| Essentially same behavior | Different behavior |
|---|--|
| Cathodic current efficiency | Oxidation rate linear with slurry concentration |
| Initial current | Coughlin and Farooque's current efficiency for CO_2 , 25-50%. Okada, Guruswamy, and Bockris, less than 10%. |
| Potential regions for CO_2 evolution | Pure carbon gives current efficiency for CO_2 around 80%. Currents due to iron-ferrous to ferric oxidation is important in the first few hours of electrolysis. |
| Effect of particle size, temperature, and concentration | Limiting currents in the absence of Fe^{2+} , other impurities $<0.1 \text{ mA/cm}^2$. |

ratio of ferrous to ferric iron at the beginning is about 10^3 , then the reversible potential would become about $+0.6$ V/NHE, and if the i_0 were rather high, this would correspond with the observations made, i.e., the beginning of the current in solutions from which ferrous iron has not yet been removed by electrolysis would be influenced strongly by the ferrous to ferric electrode reaction.

The limiting currents at the anode are largely dependent upon the iron (Fe^{2+}) concentration. From the activation energy value of 16 kcal/mole, such limiting currents are consistent with diffusion of Fe^{2+} in the solution.

On the other hand, the current at which the anodic process begins may also be interpreted in respect to the oxidation of carbon. Taking this as a standard potential at $+0.21$ V for the hydrogen scale, the overvoltage would have to be in the region of 0.4 V for a current of 0.1 mA/cm², and if the Tafel β value is 1/2, this corresponds to an i_0 of 10^{-6} A/cm².

Comparison of the results obtained with slurry electrolysis of pure carbon and those with coal.—The results obtained with pure carbon powder (2N5) and anthracite are compared in Table II. Thus, when the coal has been thoroughly washed, it gives only a small current density, resulting from either further dissolution of impurities from the coal, or, more likely, collision of the coal with the electrode.

Therefore, the high limiting current densities for solutions filtered from the coal slurries are due to impurities which initially dissolve off the coal surface, or a larger amount of dissolved material, in particular, iron. On the other hand, the current from carbon under the same condition is very low. Evidently, in the case of the pure carbon, there is a smaller amount of dissolved impurities, and the current is largely due to the collisional reaction of carbon with the anode. That there is a greater current density from the carbon than from the coal arises from the surface area of the carbon (9). The latter had passed through a 325 mesh entity and the former through a 100 mesh entity. The surface areas were thence 10:1, consistent (spherical particles) with the observations.

The higher efficiency of CO_2 production at the anode from carbon compared with the low efficiency from coal arises because, for coal systems, there are more possibilities for reaction. First, there are impurities (iron, desorbed material); there are also dissolved materials which undergo oxidation reactions, though not to CO_2 . Finally, the coal has carboxyl, nitrogen, and sulfur containing terminal molecules, which could also be reactive centers giving rise to other products. This is consistent with lignite, giving higher currents as it has more terminal groups.

In the early stage of electrolysis, the current efficiencies for CO_2 evolution are small (Fig. 11). Products of electrolysis may be initially adsorbed on the particles (10), reducing apparent current efficiencies, a suggestion made by Coughlin and Farooque (6).

The CO_2 arising in the presence of coal (Fig. 11) reaches 10% after some hours. Competing organic reactions are, therefore, probably present. However, with pure carbon, the possibilities for these are small, and most of the reaction current arises from active carbon sites at the electrode; the efficiency for CO_2 production is, therefore, high.

The decrease of current with time is greater with carbon than with anthracite (Fig. 10). Thus, with carbon, the reaction is the collisional one of carbon with the electrode. The efficiency of this depends on the amount of material adsorbed upon the surface (10, 11). For carbon, some products other than CO_2 , speculatively, formaldehyde, also arise, and these may adsorb upon the carbon increasingly with time, thus reducing the efficiency of reaction in collision. The decrease with carbon would be expected to be faster, because in carbon the predominant mechanism is collisional, affected by adsorption, whereas with coal (because of the lower current efficiency for CO_2 evolution), there must be other organic reactions (12). Even at extended periods of times, the situation is such that organic materials are oxidized by electrode reactions which may (in the anodic region concerned) be less dependent upon the effect of materials which hypothetically adsorb on carbon. Such concepts are, of course, mere speculations, consistent with the results.⁴

General model for the anode reactions.—The situation at the anode is multidetermined, and work needs to be done in finding out what the anode products are and how they depend in respect to current efficiency on potential and electrocatalysts. First, much depends on the time of exposure of the coal in the solution. At short times and high temperatures, the CO_2 -producing reaction is largely chemical. In the first 2 hr of contact of the coal with the solution, its chemical reaction with sulfuric acid gives an amount which would come from electrolysis at a few mA/cm². The chemical reaction decreases rapidly; after about 10 hr at 80°C, it is negligible compared with the electrochemical reactions. The chemical reactions are, therefore, probably connected with removal of surface impurity. Correspondingly, ferrous ions undergo oxidation to ferric ions in about 2 hr of electrolysis (Fig. 10).

Thus, when electrolysis has taken place for this time, iron is removed from contributing to the anodic reaction. The electrode reactions are those with the products of coal, and the collisional reaction of the coal with the electrode. For times in the 10-25 hr region, some 90% of the anodic current is taken up with non- CO_2 -forming organic reactions (12, 14), arising from dissolved products from coal undergoing anodic reactions, and some 10% arises from direct contact, coal electrode-giving CO_2 or CO_2 -forming organic reactions. These conclusions are made in the absence of sufficient analysis of anodic products and insufficient knowledge of the adsorption of CO_2 on coal.

Coal slurries and the production of hydrogen.—Pure hydrogen is produced in the electrolysis of coal slurry, in agreement with Coughlin and Farooque. It arises from water decomposition. From the difference between the anodic and cathodic potential, it is possible to estimate the cell potential. Table III shows the cell potential deduced from Fig. 2. These lower cell potentials in the limiting current region are due to the alternative reactions at the anode, which replaces the evolution of O_2 . The economic question is, "At what rate do such reactions occur in the absence of the consumption of the impurities, e.g., iron?"

⁴ The observation by Coughlin and Farooque, that placing coal samples at 250°C for 6 hr caused a reactivation of the coal, is consistent with our hypothesis of the inhibiting buildup of organic adsorbates, which would be removed upon heating. Further, Fe may diffuse to the surface and be redissolved.

Table II. Comparative behavior of coal and carbon slurries

| Phenomenon | Coal (anthracite) | Carbon |
|--|--|--|
| Current/time at constant applied potential | Decreases | Decreases substantially more quickly than with coal |
| Current efficiency of CO_2 production after 7 hr in 4.15M H_2SO_4 | About 10% | About 80% |
| Currents obtained from solutions which had been filtered free of coal or carbon | High current density, e.g., 5.9 mA/cm ² | Low current density, e.g., 0.1 mA/cm ² |
| Result of remaking slurry with fresh solution of 4.15M H_2SO_4 after washing coal or carbon. | Current density obtained low, e.g., 0.1 mA/cm ² | Current density same as before filtering, e.g., 3.4 mA/cm ² |

Table III. Cell potentials as function of current equivalent to electrolysis of coal slurries to yield hydrogen

| Cell potential (V) | Current density (mA/cm ²) |
|--------------------|---------------------------------------|
| 0.7 | 1.4 |
| 1.0 | 4.9 |
| 1.7 | 4.9 |
| 1.8 | 6.3 |

For unwashed coal, in the first few hours of electrolysis, the current densities were those observed by Coughlin and Farooque, *i.e.*, several mA/cm². However, here, the anodic reaction is the oxidation of ferrous to ferric ion. When the coal has been thoroughly washed and the iron removed, the current density in the region of about 0.6-0.1 V/NHE is only 0.1 mA/cm². This would not give rise to economical hydrogen production, which needs current densities of 100-500 mA/cm².

Depolarization of the anode to obtain H₂ is well known, and it is possible to use more convenient materials than coal. Thus, SO₂ has been used by a number of other workers (15) for obtaining hydrogen at potentials of about 0.8V at 25°C and 100 mA/cm². The situation is more energy efficient than that with slurry electrolysis at about 85°C. Would carrying out the electrolysis at 200°C be effective? The competing chemical reaction at this temperature may offer a difficulty. Electrocatalysis, increase in temperature, decrease in particle size of the coal, and increase in stirring are possible variables. Removing iron, sulfur, and other impurities in coal by removal of Fe²⁺ may be of interest.

Products from anodic reactions in coal slurries.—The evidence that after contact times in the neighborhood of 25 hr, 90% of the current is utilized for non-CO₂-producing electrochemical reactions at 1 V/NHE makes it reasonable to suggest that useful organic chemicals from coal may be produced in this way. The decay of current with time adds caution to this suggestion.

Conclusions

1. In the presence of Fe²⁺ originating from coal, current densities of 5-10 mA/cm² at a cell potential of 0.8V can be obtained for the electrolyte production of hydrogen in 4.15M H₂SO₄ solution at 80°C. The anodic reaction is predominantly Fe²⁺ oxidation and the cathodic reaction is H₃O⁺ + e → 1/2 H₂ + H₂O.

2. In the absence of Fe²⁺, the evolution rate of H₂ is reduced at the low cell potential (*ca.* 0.8V), to the impractical order of 0.1 mA/cm². Anodic reactions involving coal are of two kinds. Direct collision of slurry particles, including pure carbon, with the electrode, gives CO₂ (with pure carbon, the current efficiency for

this reaction is about 80%). However, with lignite and anthracite, the current efficiency for CO₂ generation is reduced to *ca.* 10%. A secondary anodic reaction occurs in the presence of coal and involves the partial anodic oxidation of products dissolved therefrom.

3. The anodic depolarization route to H₂ production using the derivatives of coal to depolarize the anodic reaction (avoiding the evolution of oxygen) would provide H₂ at a lesser moles per watt hour than, say, the use of waste gas SO₂ in a similar concept.

Acknowledgments

The authors acknowledge a discussion with Dr. Coughlin and support of the work by means of a fellowship awarded by the Diamond Shamrock Corporation.

Thanks are due to Lynn McCartney Murphy of Texas A&M University for her assistance in the preparation of this manuscript.

Manuscript submitted Oct. 17, 1980; revised manuscript received *ca.* April 3, 1981.

Any discussion of this paper will appear in a Discussion Section to be published in the June 1982 JOURNAL. All discussions for the June 1982 Discussion Section should be submitted by Feb. 1, 1982.

Publication costs of this article were assisted by Texas A&M University.

REFERENCES

1. W. G. Wilson, C. L. Knudson, G. G. Baker, T. C. Owens, and D. E. Severson, *Ind. Eng. Chem. Prod. Res. Dev.*, **18**, 297 (1979).
2. W. N. Mitchell, K. L. Trachte, and S. Zaczepinski, *ibid.*, **18**, 311 (1979).
3. V. L. Weinberg and T. F. Yen, *Fuel*, **59**, 281 (1980).
4. H. P. Hombach, *ibid.*, **59**, 465 (1980).
5. A. Marzec, M. Juzwa, K. Betlej, and M. Sobkowiak, *Fuel Proc. Tech.*, **2**, 35 (1979).
6. R. W. Coughlin and M. Farooque, *Ind. Eng. Chem. Prod. Res. Dev.*, **19**, 211 (1980).
7. M. Farooque and R. W. Coughlin, *Fuel*, **58**, 705 (1979).
8. J. L. Darryl, H. J. Robert, and E. L. Robert, *Anal. Chem.*, **46**, 239 (1974).
9. R. E. Panzer and P. J. Elving, *Electrochim. Acta*, **20**, 635 (1975).
10. A. G. Dubinin, L. A. Mirking, V. E. Kazarinov, and M. Ya. Fioshin, *Sov. Electrochem.*, **15**, 1337 (1979).
11. B. G. Gaberman and L. N. Yushkova, *Tr. Khim. Met. Inst., Akad. Nauk. Kaz. SSR*, **2**, 101 (1968); **5**, 3 (1969).
12. R. Tomat and A. Rigo, *J. Appl. Electrochem.*, **9**, 301 (1979).
13. D. Benson, "Mechanism of Oxidation by Metal Ions," Elsevier, Amsterdam (1976).
14. W. Juda and D. M. Moulton, *Chem. Eng. Symp. Series*, p. 59 (1972).

An Electrochemical Investigation of Coenzyme A

Michael H. Shiu¹ and Robert D. Braun*

Department of Chemistry, University of Southwestern Louisiana, Lafayette, Louisiana 70504

ABSTRACT

A polarographic, controlled-potential coulometric, and triangular-wave voltammetric study of coenzyme A was undertaken. Coenzyme A is reversibly electrochemically oxidized to dimeric coenzyme A. The pK_a of coenzyme A was estimated from polarographic data to be 9.77. The diffusion coefficient of coenzyme A was determined to be 2.6×10^{-6} cm²/sec. The heterogeneous rate constant for the electrochemical dimerization was estimated from triangular-wave voltammetric data to be 3×10^{-3} cm/sec at pH 6.5.

Coenzyme A (CoA) primarily functions as acyl group carriers in biological systems (1). Its structure is shown in Fig. 1. The active site on CoA is the thiol group to which acyl groups can esterify. For simplicity CoA is symbolically represented throughout much of this paper as RSH where R represents all of the molecule except the thiol group. Many electrochemical studies have been done on compounds which contain a thiol group, but which are structurally simpler than CoA. Typical examples include cysteine (2), butanethiol, benzyl mercaptan, 1-decanethiol, β -phenylethyl mercaptan, and others (3). In most of these cases the compound reacts to form a dimer with linkage through the sulfur atoms. Since CoA is a biologically important compound, and since apparently no thorough electrochemical study of the compound has been done, the present study was undertaken.

Experimental

Chemicals.—Coenzyme A (RSH) and the dimer (RSSR) were obtained from the Sigma Chemical Company, and were used without further purification. The purity of each batch of CoA was spectrophotometrically assayed at 259 nm using a molar absorptivity of 16,400 (4). Typically each batch assayed at 85–90% CoA. The concentrations reported throughout this paper have been corrected for purity of the CoA. Any impurity in the CoA was not electroactive within the potential range used in this study.

The components of the buffer solutions were acetic acid and sodium acetate (pH 4–6), potassium dihydrogen phosphate and dipotassium hydrogen phosphate (pH 6–8), tris(hydroxymethyl)-aminomethane and its protonated salt (pH 8–9), potassium hydrogen carbonate and potassium carbonate (pH 9–11), and dipotassium hydrogen phosphate and potassium phosphate (pH 11–13). Enough of the buffer components were added to the buffer solutions to adjust the ionic strength to 0.5M except when the minor buffer component would have exceeded 0.1M. In those cases the minor buffer component was maintained at 0.1M, and the ionic strength of the solution was adjusted to 0.5M with potassium chloride. The pH 6.5 buffer solution was used for all of the electrochemical studies except the study of the variation of $E_{1/2}$ with pH. It consisted of 0.16M potassium dihydrogen phosphate, 0.10M dipotassium hydrogen phosphate, and 0.04M potassium chloride. The buffer solutions were used as the supporting electrolyte solutions in the electrochemical studies.

Apparatus.—A Model 174a Polarographic Analyzer (EG&G Princeton Applied Research) was used for the polarographic, coulometric, and triangular-wave voltammetric studies. It was coupled to an Omnigraphic 2000 X-Y recorder (Houston Instrument) for the vol-

tammetric studies, and to an Omniscrite strip chart recorder (Houston Instrument) for coulometric studies. A saturated calomel reference electrode and a platinum foil auxiliary electrode were used. The indicator electrode used for the triangular-wave voltammetric studies was a hanging mercury drop electrode (area = 2.2 mm²). The working electrode used for controlled-potential coulometry was a mercury pool. All potentials reported in this paper are relative to the saturated calomel electrode. The water-jacketed, three-compartment cell was maintained at 25.0°C except in the temperature studies. The two outer compartments in the cell were separated from the center compartment by medium-porosity glass frits.

Solutions were deaerated prior to each study with high purity nitrogen which was passed through two wash towers containing acidic ammonium metavanadate and amalgamated zinc, and a final wash tower containing deionized water. Polarographic measurements of diffusion current were made at the end of the drop life, *i.e.*, on the top of the polarographic wave. All pH measurements were made with a Corning Model 7 pH meter. Spectrophotometric studies were done with a Beckman DK-2A spectrophotometer.

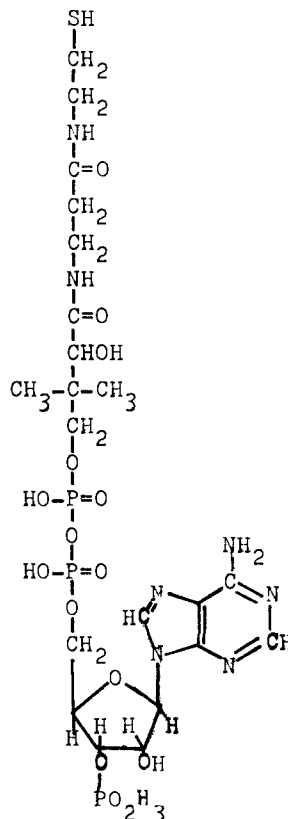


Fig. 1. The molecular structure of coenzyme A

* Electrochemical Society Active Member.

¹ Present address: Morton Chemical Company, New Iberia, Louisiana 70560.

Key words: polarography, voltammetry, electrolysis, oxidation.

Results and Discussion

Polarograms of CoA contain a single anodic wave (Fig. 2) throughout the entire pH range examined in this study (pH 4.7-12.6). At concentrations above 0.7 mM, a maximum of the second kind was associated with the wave. The half-wave potential ($E_{1/2}$) of the polarographic wave of 0.7 mM CoA varied with pH as shown in Fig. 3. The linear portion between pH 4.7 and 8.5 obeyed Eq. [1] (least squares fit, correlation coefficient = -0.999). Between pH 10.9 and 12.6, the $E_{1/2}$ remained constant

$$E_{1/2} = -0.0525 \text{ pH} - 0.0056 \quad [1]$$

at -0.519V. The remainder of the studies were performed at pH 6.5.

The diffusion current (i_d) of the anodic wave increased linearly with the square root of the corrected mercury column height (h_{corr}) for column heights between 38.8 and 100.5 cm, and $i_d/h_{\text{corr}}^{1/2}$ slightly decreased with h_{corr} (slope = -0.015 $\mu\text{A}/\text{cm}$). These results were taken as evidence that the electrochemical reaction obeys the Ilkovic and Koutecky equations, and that the height of the polarographic wave is diffusion controlled.

A polarographic study performed on a 0.8 mM CoA solution at five temperatures ranging from 15° to 35°C revealed no variation in half-wave potential with temperature. This is within the expected range of variation for a reversible electrode process (5a). The corresponding relative temperature coefficient for the diffusion current of the wave was 1.9%/degree, indicating the absence of slow chemical steps (relative to the rate of the polarographic measurement) in the electrochemical oxidation (5b).

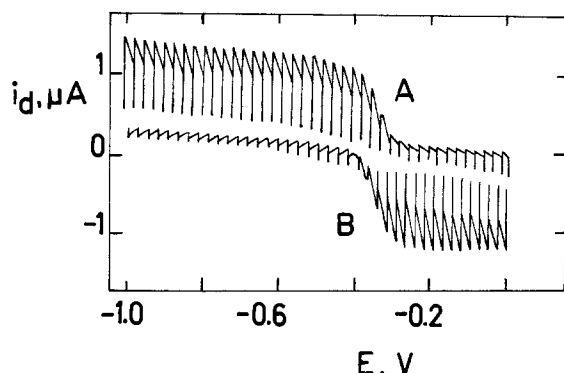


Fig. 2. Polarograms of 0.54 mM coenzyme A before (B) and after (A) exhaustive controlled-potential coulometry on a mercury pool at 0V.

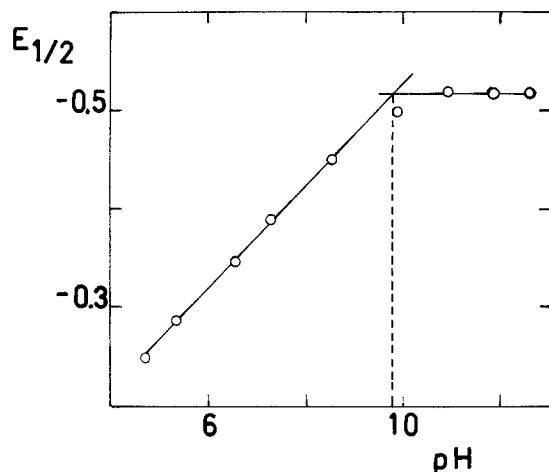


Fig. 3. Variation of the polarographic half-wave potential of 0.7 mM coenzyme A with pH.

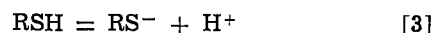
Several log plots were made on the rising portion of the anodic wave assuming different reaction mechanisms in order to deduce the mechanism of the electrochemical reaction. Plots of potential as a function of $\log[(i_d - i)/i]$ were obtained for four samples of varying concentration. These log plots were linear with a slope of -0.050 ± 0.004 V/decade. All uncertainties listed in this paper are expressed as standard deviations. The theoretical slope for an electrochemical reaction of the general form $\text{Red} = \text{Ox} + ne^-$ is $-0.059/n$ V/decade. For a reversible dimerization reaction of the general form $2\text{RSH} = \text{RSSR} + 2\text{H}^+ + 2e^-$, the theoretical slope of a log plot of potential as a function of $\log[(i_d - i)^2/i]$ is -0.030 V/decade. Plots of potential as a function of $\log[(i_d - i)^2/i]$ on the rising portion of four CoA samples of varying concentration were linear with an average slope of -0.030 ± 0.002 V/decade. These data suggest the possibility of a reversible dimerization reaction taking place at the electrode surface.

For a reversible oxidation of the general form $\text{Red} = \text{Ox} + ne^-$, the half-wave potential theoretically should be independent of concentration of the electroactive species and of pH. For a dimerization reaction of the form, $2\text{RSH} = \text{RSSR} + 2\text{H}^+ + 2e^-$, at 25°C the half-wave potential should be dependent on both pH and concentration, i.e., on i_d , as shown in Eq. [2]. As has already been shown, the half-wave potential

$$E_{1/2} = \text{constant} - 0.059 \text{ pH} - 0.030 \log(i_d/2) \quad [2]$$

of 0.7 mM CoA at pH's below 8.5 varied linearly with pH. The slope of a plot of $E_{1/2}$ as a function of pH was -0.053 as compared to the theoretical value of -0.059 predicted by Eq. [2].

Above pH 10, the half-wave potential did not vary with pH indicating that hydronium ion was not involved in the electrochemical reaction. This behavior would be expected for CoA if the CoA were dissociated to yield RS^- rather than RSH at higher pH's (Eq. [3]). The RS^- could then undergo a dimerization reaction of the form $2\text{RS}^- = \text{RSSR} + 2e^-$. Assuming this is the case, the interception of the two extrapolated linear portions of the plot of $E_{1/2}$ as a function of pH should correspond to the pH at which CoA exists as an equimolar mixture of RSH and RS^- . This pH corresponds to the pK_a of CoA. The value



determined from Fig. 3 was 9.77. This value compares favorably with the 9.6 obtained from titrimetric data (6).

A plot of $E_{1/2}$ as a function of $\log(i_d/2)$ for nine solutions of concentration ranging from 0.4 to 3.9 mM was linear with a slope of -0.0386 (least squares fit; correlation coefficient = -0.914). This compares to the theoretical value of -0.030 predicted from Eq. [2] for a dimerization reaction.

Controlled-potential coulometry was performed at 0V on six CoA solutions of varying concentration. The average calculated n was 0.97 ± 0.07 , indicating that a single electron is transferred for each molecule of CoA. A polarogram obtained on a typical sample prior to and after an exhaustive electrolysis is shown in Fig. 2. Polarograms of purchased CoA dimer (RSSR) showed a single cathodic wave at a half-wave potential identical to that observed after the electrolysis of CoA solutions. The half-wave potential of the anodic wave obtained before each electrolysis was within experimental error of the half-wave potential of the cathodic wave obtained after electrolysis.

A sample of the purchased dimer was exhaustively reduced at -1.1V on a mercury pool. The polarogram after the reduction showed a single anodic wave at a half-wave potential identical to that of CoA. These observations lead to the conclusion that, within the time frame of polarographic measurements, CoA is reversibly electrochemically oxidized to the dimer.

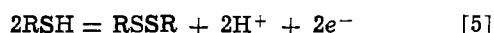
Ultraviolet spectrophotometric studies were performed on CoA, the purchased dimer of CoA, and on the electrolysis product of CoA. In all cases the spectra were nearly identical, and contained a maximum at about 259 nm. This result is to be expected since the absorption is due to the adenine moiety which is not significantly affected by formation of the dimer.

The diffusion current of the polarographic wave increased linearly with concentration. The slope of the plot of diffusion current as a function of concentration was used with the measured capillary characteristics ($m = 1.43$ mg/sec; $t = 4.68$ sec), and the coulometrically determined value of n , to calculate the diffusion coefficient (D) of CoA. This was accomplished by setting the slope of the plot equal to the terms in parentheses in the Ilkovic equation (Eq. [4])

$$i_d = (708 n D^{1/2} m^{2/3} t^{1/6}) C \quad [4]$$

The observed slope was $1.85 \mu\text{A}/\text{mM}$ (12 solutions), and the calculated diffusion coefficient was $2.5 \times 10^{-6} \text{ cm}^2/\text{sec}$.

The results listed earlier in this paper have demonstrated that the overall electrochemical reaction taking place at the electrode surface is that shown in Eq. [5]. In order to determine



the mechanism of this overall reaction, a triangular-wave voltammetric study was undertaken. Five samples of CoA were studied at the hanging mercury drop electrode at six scan rates varying from 0.02 to 1 V/sec. A typical triangular-wave voltammogram is shown in Fig. 4.

The diagnostic criteria of Nicholson and Shain (7) for nondimerization reactions, and the diagnostic criteria of Andrieux, Nadjo, and Saveant (8) for dimerization reactions without complicating chemical steps were applied to five solutions of varying CoA concentration. Typical results obtained using the criteria of Nicholson and Shain are shown in Fig. 5. These results indicate that the reaction mechanism obeyed by CoA consists of a relatively slow preceding chemical equilibrium followed by rapid reversible electron transfer.

Plots of the anodic peak potential as a function of the log of the scan rate, and as a function of the log of the CoA concentration were not those expected for simple dimerization reactions, thereby indicating that the electrochemical reaction was not kinetically identical to any of the dimerization reactions studied by Andrieux, Nadjo, and Saveant. Taken together these data suggest that the dimerization reaction involves a rate-determining dissociation to yield an anion which subsequently reacts at the electrode surface to yield a

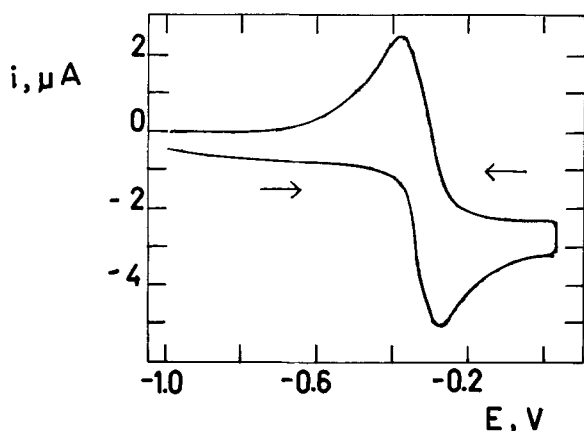


Fig. 4. A triangular-wave voltammogram of 0.98 mM coenzyme A obtained at 0.2 V/sec with a hanging mercury drop electrode at pH 6.5. The scan started at -1V .

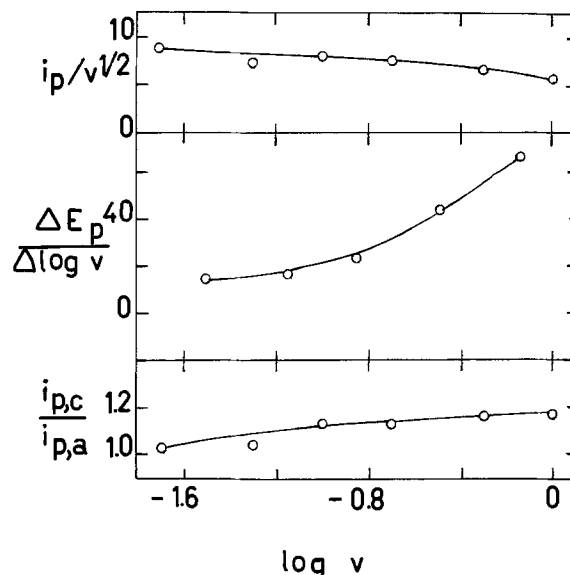
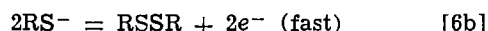
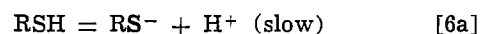


Fig. 5. Application of the diagnostic criteria of Nicholson and Shain (7) to triangular-wave voltammograms of 0.8 mM coenzyme A at pH 6.5.

dimer. The type of dimerization reaction (DIM1, DIM2, etc.) cannot be determined from triangular-wave voltammetric data at pH 6.5. The electrochemical reaction apparently proceeds as shown in Eq. [6] at pH's less than 9.8



and as shown in Eq. [6b] at higher pH's.

The rate of the electrochemical reaction at pH 6.5 is determined by the rate of the dissociation step. The heterogeneous, first-order rate constant for the overall electrochemical reaction at this pH can be estimated at the standard potential of the redox couple from triangular-wave voltammetric data using the method of Nicholson (9). The values of n and D calculated earlier were used in this calculation. A series of five CoA solutions were used at various scan rates for the kinetics study. The calculated rate constant was $(3 \pm 1) \times 10^{-3} \text{ cm}^2/\text{sec}$ (20 trials). This rate constant is for the overall electrochemical reaction as shown in Eq. [5]. The limiting factor in the rate of Eq. [5] is the preceding chemical reaction shown in Eq. [6a].

Manuscript submitted Feb. 6, 1981; revised manuscript received April 15, 1981.

Any discussion of this paper will appear in a Discussion Section to be published in the June 1982 JOURNAL. All discussions for the June 1982 Discussion Section should be submitted by Feb. 1, 1982.

Publication costs of this article were assisted by the University of Southwestern Louisiana.

REFERENCES

1. A. L. Lehninger, "Biochemistry," pp. 249, 344, Worth Publishers, New York (1970).
2. I. M. Kolthoff and C. Barnum, *J. Am. Chem. Soc.*, **62**, 3061 (1940).
3. R. L. Birke and M. Mazorra, *Anal. Chim. Acta*, **118**, 257 (1980).
4. P. D. Boyer, H. Lardy, and K. Myrback, Editors, "The Enzymes," 2nd ed., Vol. 3, pp. 16-17, Academic Press, New York (1960).
5. L. Meites, "Polarographic Techniques," Interscience Publishers, New York (1965). (a) p. 288; (b) p. 139.
6. H. Beinert, R. W. Von Korff, D. E. Green, D. A.

- Buyske, R. E. Handschumacher, H. Higgins, and F. M. Strong, *J. Biol. Chem.*, **200**, 385 (1953).
7. R. S. Nicholson and I. Shain, *Anal. Chem.*, **36**, 706 (1964).
8. C. P. Andrieux, L. Nadjo, and J. M. Saveant, *J. Electroanal. Chem. Interfacial Electrochem.*, **26**, 147 (1970).
9. R. S. Nicholson, *Anal. Chem.*, **37**, 1351 (1965).

Electrochemical Glucose Oxidation on a Platinized Platinum Electrode in Krebs-Ringer Solution

IV. Effect of Amino Acids

José Giner*

Giner, Incorporated, Waltham, Massachusetts 02154

Ljiljana Marincić* and J. Stuart Soeldner

E. P. Joslin Research Laboratory, Department of Medicine, Harvard Medical School,
The Peter Bent Brigham Hospital and The Joslin Diabetes Foundation, Incorporated, Boston, Massachusetts 02215

and Clark K. Colton

Department of Chemical Engineering, Massachusetts Institute of Technology, Cambridge, Massachusetts 02139

ABSTRACT

Physiological amino acids of varied composition in Krebs-Ringer solution both with and without glucose behave qualitatively similarly during fast potential sweeps using platinized platinum electrodes. The degree of observed amino acid electrooxidation and the inhibition of glucose oxidation are strongly related to a parameter which represents the strength of adsorption of the amino acid. This parameter, in turn, is a function of the intrinsic adsorbability of the amino acid and its concentration. A ranking of amino acids according to their ability to inhibit glucose oxidation shows that basic and sulfur-containing amino acids are the most inhibitory. Investigations with lysine and leucine at various concentrations confirm these findings. Amino acid mixtures behave qualitatively similarly to the individual acids, but under certain conditions the mixtures totally inhibit glucose oxidation. Sensitivity to glucose (in the cathodic potential sweep) can be restored by increasing the anodic prepolarization potential, the potential sweep rate, and the real surface area, and by decreasing convective transport to the electrode surface. Mixtures of strongly and weakly inhibiting amino acids (lysine and leucine) behave in the same way as a solution of the single strong inhibiting amino acid (lysine) alone.

In previous publications (1, 2) we have described the concept of an implantable glucose sensor for the determination of glucose concentration in intercellular fluid, with the ultimate goal of controlling glucose levels in diabetics. This sensor is based on the use of high surface area platinum as the glucose sensing electrode. Platinum was selected because of its good cycling characteristics, which provide for good reproducibility over extended periods of time.

As proposed, the glucose sensing electrode is operated in a transient mode using a potentiostat. In this mode the electrode is activated by an anodic prepolarization potential pulse (or pulse sequence), which may be followed by a cathodic prepolarization pulse to remove any oxide (PtO) previously formed. After the anodic/cathodic prepolarization pulses, a potential-step or a potential-time function $E(t)$ is applied to the working electrode, and the current $i(t)$ is measured. A special case of this applied transient potential method involves the use of a continuous trapezoidal $E(t)$ function with constant potential plateaus at high and low potentials, e.g., +1000 mV and -800 mV vs. the saturated calomel electrode (SCE), and with an ascending (anodic) linear potential sweep and a descending (cathodic)

linear potential sweep. Work with Krebs-Ringer solutions containing glucose alone as a reactant has shown (3, 4) that good sensitivity and excellent reproducibility of the current response to changes in glucose concentration can be obtained with platinized platinum or Teflon-bonded platinum electrodes operated in this mode, with or without hydrophilic membranes covering the electrode surface. If this type of sensor and measuring method is to find *in-vivo* application, it is necessary to obtain glucose selectivity with respect to the large variety of coreactants present in physiologic fluids. Interference by macromolecules is eliminated in the proposed sensor by using a membrane which separates the sensing electrode from the body fluids. Interference by low molecular weight species depends on their reactivity and concentration and have to be the subject of study. In a previous publication (5) we have reported the effect of urea on the glucose response using fast linear potential sweeps and have suggested methods to measure glucose concentration in the presence of urea of varying concentrations. The addition of an amino acid mixture to Krebs-Ringer solutions containing glucose has also been shown (6) to greatly modify the voltammogram by providing additional oxidation currents in the anodic sweep at high potentials. This effect is due to amino acid electrooxidation as well as to a substantial inhibition of glucose oxidation.

* Electrochemical Society Active Member.

Key words: anodic oxidation, inhibition, glucose sensor.

Rao *et al.* (7) have investigated the effect of sixteen individual amino acids and a mixture of seven amino acids on the fast potential-sweep voltammogram and on the steady-state current obtained at constant potential using platinum-based electrodes. They used a phosphate buffer as the supporting electrolyte. When investigating individual amino acids using fast potential sweeps, smooth Pt was used as the working electrode and chloride was added to the supporting electrolyte. No chloride was used with the amino acid mixtures nor with any of the steady-state measurements. A platinized platinum electrode was used when testing mixtures with fast potential sweeps, and high surface area Pt-Ni electrodes were used with all steady-state measurements. Based on the results of the steady-state experiments, they classified the amino acids as strongly or weakly inhibiting and speculated that higher inhibition is caused by stronger amino acid adsorption.

Other than the aforementioned study (7), the electrochemistry of amino acids has received little attention when the working electrode is platinum. In contrast, the mercury electrode has been used repeatedly for polarographic investigations of amino acids and for adsorption studies (*i.e.*, measurement of electrocapillary curves) (8-14). These latter studies have been motivated by the zwitterion nature of amino acids. Two factors governed the adsorption properties of amino acids on mercury: the chain length (for the aliphatic amino acids) and the contribution of the zwitterionic amino and carboxylic groups. It has been suggested (14) that near the potential of zero charge of the mercury electrode, the amino acid molecule is adsorbed with its zwitterionic groups as well as the other substituent group in contact with the mercury surface. At more positive or negative potentials, the amino acid adsorption is controlled exclusively by the zwitterionic groups. It is not obvious whether the findings obtained using a mercury electrode are directly applicable to the platinum electrode.

Gold electrode and vitreous carbon electrode were used by Reynaud *et al.* (16) and Malfoy and Reynaud (17). They concluded that out of 20 amino acids examined only six (cystine, cysteine, methionine, tyrosine, tryptophan, and histidine) were specifically oxidized on gold or carbon electrodes. They concluded that on gold the electrochemical oxidation is catalyzed by a labile oxide.

The present investigation was aimed at further clarifying and quantifying the effect of amino acids in the context of the physiological conditions to be encountered when using the glucose sensor we envision, *i.e.*, high surface area Pt electrode, bicarbonate-based buffer with physiologic concentrations of chloride, and fast linear potential sweeps. We have extended the number of amino acids studied individually and have investigated in more detail the effect of amino acid concentration with two amino acids, lysine and leucine, which are representative of strongly and weakly inhibiting species, respectively. Lastly, we have explored possible interactions between amino acids in a simple mixture of lysine and leucine and in a very complex mixture of 24 amino acids.

Experimental

The working electrode was a platinized platinum rotating disk electrode operated at 10 rev/sec. Our previous work (3, 4) established that electrode processes are kinetically controlled at this rate of rotation. The geometrical area of the platinized platinum electrodes was 0.28 cm². The real surface area ranged from 260 to 100 cm² and was measured before each set of experiments using galvanostatic, anodic hydrogen stripping. No significant changes were observed between consecutive measurements. Only two electrodes were used in this study, each with a single platinization which occurred at the start of the investigation. The decay in real surface area was due mostly to mechanical frag-

mentation of Pt crystallites during handling and rotation of the electrode (4). To account for the change in surface area in the interpretation of data from electrodes with different surface areas, results are reported in terms of (i) current densities (currents divided by real surface area), or (ii) relative currents (*i.e.*, ratios of currents or current differences). The reference electrode was a saturated calomel electrode (SCE) and all the reported potentials were determined against this electrode. The supporting electrolyte was a modified (calcium-free) Krebs-Ringer solution equilibrated with a gas mixture containing 95% N₂ and 5% CO₂ (pH = 7.3). The temperature was 37°C. The electrochemical cell and measuring circuit have been described previously (3).

All of the reported data were obtained using single linear potential sweeps following a prepolarization potential sequence. Unless otherwise stated, the potential sweep and prepolarization conditions were as follows: anodic and cathodic linear potential sweeps at 0.5 V/min extending between -600 mV and +1000 mV; cathodic prepolarization prior to an anodic sweep consisting of the application of a 1000 mV pulse for 1 min followed by 1 min at -600 mV; and anodic prepolarization sequence immediately before the cathodic sweep consisting of the application of a -500 mV pulse for 1 min followed by 2 min at 1000 mV.

Voltammograms with supporting electrolyte, glucose, amino acid, and glucose plus amino acid were compared. When doing so the generating sequence of the voltammogram was (i) buffer (B) alone; (ii) amino acid (AA) in buffer; (iii) glucose and amino acid (G, AA) in buffer; (iv) buffer (B) alone (fresh solution); (v) glucose alone (G) in buffer; and (vi) glucose and amino acid (G, AA) in buffer.

The solutions were prepared from concentrated stock solutions of glucose and amino acids by adding 2.5-5.0 ml of stock solution to 250 ml of Krebs-Ringer solution. The test solution was replaced after step (iii) with fresh buffer following a thorough washing and rinsing of all cell parts in contact with the test solution. Excellent reproducibility was observed between steps (i) and (iv) and between steps (iii) and (vi) provided that 1 min was allowed for mixing and equilibrating prior to recording the current-potential curves; this reproducibility confirmed the lack of hysteresis in the voltammogram sequence. The first sweep was not recorded, the following sweep and all consecutive sweeps displayed identical current-potential characteristics. A similar approach was used to investigate simple mixtures of leucine and lysine and more complex amino acid mixtures.

Results

Electrochemical behavior of individual amino acids.—Figure 1 shows anodic and cathodic current-potential curves obtained with fast linear potential sweeps for Krebs-Ringer buffer solution alone (curve A), Krebs-Ringer buffer plus the addition of the amino acid alanine alone (curve B), both glucose and alanine added to the buffer (curve C), and glucose alone added to the buffer (curve D). Similar curves were obtained with the 24 amino acids listed in Table I, each at its normal physiological concentration and also at 3 mg/dl if its physiological concentration was less than 1.7 mg/dl or greater than 3.6 mg/dl. These curves have been used to evaluate the electrochemical behavior of amino acids in pure Krebs-Ringer solution, as well as in glucose-containing Krebs-Ringer solutions.

Electrooxidation and adsorption of individual amino acids.—Comparison of curves A and B in Fig. 1a shows that the second anodic current peak, occurring in the potential range of -250 to +250 mV, for the buffer alone is depressed and shifted by alanine to more positive potentials. It has been previously concluded (15, 3, 4) that this peak is due to the oxidation of "reduced CO₂" formed during the cathodic prepolarization step

Table I. Inhibitory ranking of individual amino acids

| Amino acid | Average physiol. conc., C (mg/dl)† | Molecular weight | Chemical characteristic of substituent group | Sequence of increasing inhibition | |
|--------------------|--|---------------------|--|-----------------------------------|---------------------------|
| | | | | At physi- ologic conc. | At compar- ative conc. |
| Aspartic acid* | 0.16 | 133 | Acidic, hydrophilic | 1 | 7 |
| Taurine* | 0.50 | 125 | Neutral, hydrophilic | 2 | 3 |
| Serine* | 1.2 | 105 | Neutral, hydrophilic | 3 | 8 |
| Citrulline* | 0.50 | 175 | Neutral, hydrophilic | 4 | 14 |
| Leucine | 3.1 | 131 | Neutral, hydrophobic | 5 | 1 |
| Valine | 3.1 | 117 | Neutral, hydrophobic | 6 | 4 |
| Isoleucine | 2.6 | 131 | Neutral, hydrophobic | 7 | 2 |
| Threonine | 2.3 | 119 | Neutral, hydrophilic | 8 | 11 |
| Glutamic acid | 2.4 | 147 | Acidic, hydrophilic | 9 | 5 |
| Proline | 3.6 | 115 | Neutral, hydrophobic | 10 | 6 |
| Methionine* | 0.6 | 149 | Neutral, hydrophobic | 11 | 20 |
| Asparagine* | 1.0 | 150 | Neutral, hydrophilic | 12 | 18 |
| Tyrosine | 1.7 | 181 | Neutral, hydrophilic | 13 | 9 |
| Ornithine* | 0.7 | 132 | Basic, hydrophilic | 14 | 16 |
| Alanine* | 5.0 | 89 | Neutral, hydrophobic | 15 | 10 |
| Tryptophan | 1.7 | 204 | Neutral, hydrophobic | 16 | 12 |
| Glycine | 3.1 | 75 | Neutral, hydrophilic | 17 | 15 |
| Phenylalanine | 2.4 | 165 | Neutral, hydrophobic | 18 | 13 |
| Cysteine + cystine | 0.9 + 2.0 | 121 + 240 | Neutral, hydrophilic | 19 | 22 |
| Lysine | 3.6 | 146 | Basic, hydrophilic | 20 | 19 |
| Arginine | 2.1 | 174 | Basic, hydrophilic | 21 | 21 |
| Histidine | 2.3 | 155 | Basic, hydrophilic | 22 | 23 |
| Glutamine* | 7.3 | 146 | Neutral, hydrophilic | 23 | 17 |

* Amino acids tested at 3 mg/dl.

† A. White, P. Handler, and E. L. Smith, "Principles of Biochemistry," 4th ed., p. 706, McGraw-Hill Book Co., New York (1968).

by the reductive adsorption of carbon dioxide or a related species (e.g., carbonic acid, bicarbonate). The data show that the reduced CO_2 is displaced by chemisorbed amino acid. In the potential sweeps of Rao *et al.* (7) this peak does not appear because phosphate was used instead of bicarbonate buffer. The extent of the decrease in the height of this current peak or its shift toward more positive potentials can be used as a measure of the degree of chemisorption of the amino acid at low potentials. The degree of chemisorption is itself determined by the strength of the intrinsic interaction between the amino acid and the surface as well as by the amino acid concentration. We have chosen to use the relative decrease in the height of the second anodic current peak ($i_B - i_{AA}$)/ i_B as an indication of the degree of electrode coverage by chemisorbed amino acid. Other measures obtained from the current-potential curves might be equally valid. For example, we have also examined the difference in the electrode potential (evaluated at a constant current equal to two-thirds of the background peak current) between

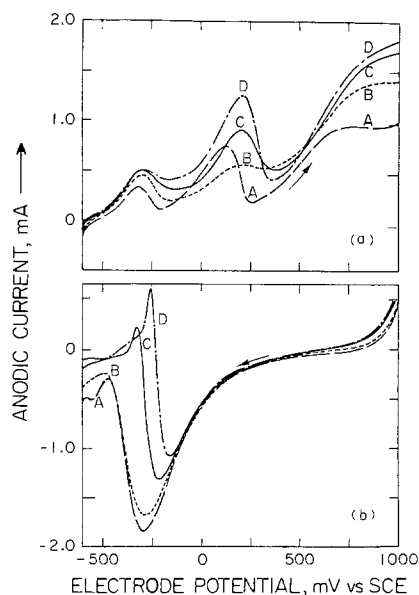


Fig. 1. $i(E)$ curves (at 0.5 V/min). (a) Anodic sweeps; (b) cathodic sweeps. A, Krebs-Ringer (K-R) alone; B, K-R with alanine (5.0 mg/dl); C, K-R with alanine (5.0) + glucose (100); D, K-R with glucose (100).

the results for buffer plus amino acid and buffer alone. In fact, as shown in Fig. 2a, good correspondence exists between these two parametric measures, either of which could be used to characterize the degree of amino acid adsorption. The numbered points in Fig. 2 indicate the specific amino acid corresponding to the numbers in the fifth column of Table I.

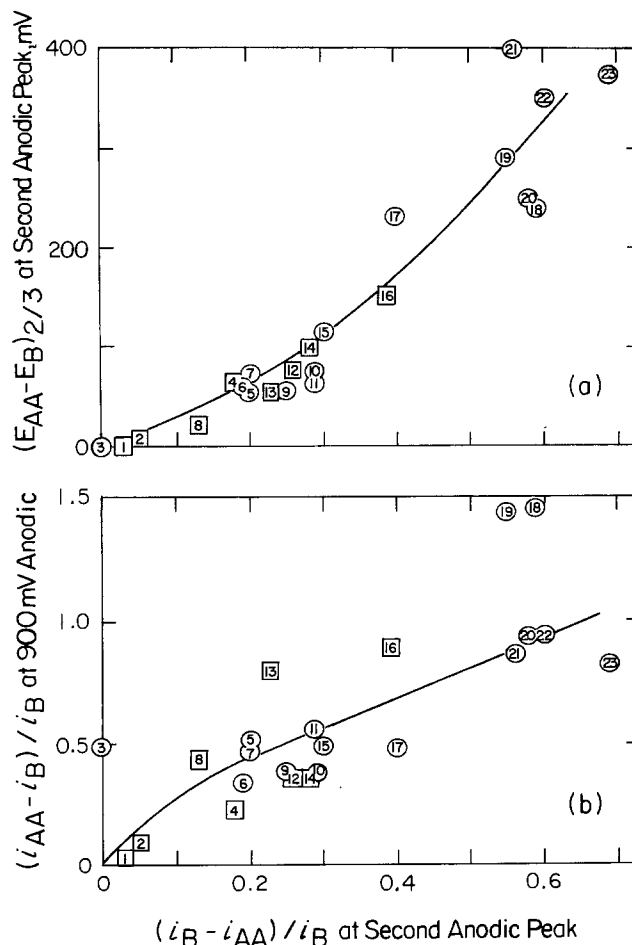


Fig. 2. Dependence of $i(E)$ curve parameters on decrease of second anodic peak for amino acids studied individually (identified by the number in column 5, Table I). Measurements were carried out at physiological amino acid concentrations.

The current plateau observed with Krebs-Ringer buffer solution alone at potentials between 750 and 1000 mV (curve A, Fig. 1a), which results from formation of surface platinum oxides (PtO) or chemisorbed oxygen, is enhanced by the presence of amino acids (curve B). This result indicates that substantial amino acid oxidation occurs at these potentials. The relative increase in current induced by amino acids at 900 mV is plotted in Fig. 2b vs. the relative decrease in the height of the second anodic peak. The correlation suggests that the oxidation current increases with an increase in the degree of adsorption of the amino acid. However, the observed amino acid oxidation current at +900 mV is a transient current which may result largely from oxidation of a previously chemisorbed amino acid and need not reflect oxidation of additional amino acid adsorbed from the bulk solution. It is unclear whether any residual, steady-state current due to bulk amino acid oxidation would be proportional to the degree of amino acid adsorption. Since no steady-state current was measured in this work, this question cannot be answered. The steady-state currents reported by Rao *et al.* (7) are not comparable because they were obtained under very different experimental conditions.

Figure 1b shows the effect of amino acids on the current-potential curve obtained in the cathodic direction. At high potentials (above approximately 300 mV) the small current difference between curves A (buffer alone) and B (buffer plus amino acid) reflects further oxidation of the amino acid after the anodic prepolarization period. The presence of amino acids brings about a small reduction in the magnitude of the PtO reduction peak (at about -300 mV). A small shift in current toward the anodic direction (or less cathodic current) is also observed for potentials more negative than about -450 mV. The effect of amino acid additions in the region of the cathodic PtO reduction peak is different from the effect of urea addition (5) which causes a broadening of the cathodic PtO peak toward negative potentials with the consequent reduction of both the height of the peak and the cathodic currents at potentials negative to the peak. This difference suggests that amino acids slightly inhibit the formation of PtO during the preceding anodic prepolarization while urea inhibits its reduction during the cathodic sweep.

Effect of individual amino acids on glucose electrooxidation.—Comparison of curves C (addition of glucose + amino acid) and D (addition of glucose alone) in Fig. 1a shows that the second current peak of the anodic sweep in the potential range from about -100 mV to about +350 mV is substantially increased in the presence of glucose and that this increase in current is strongly inhibited by the presence of amino acids. Figure 3a shows that there is a good correlation between $i_G - i_{GAA}$, the decrease of the current in the second anodic peak of glucose electrooxidation resulting from addition of amino acid, and the degree of amino acid adsorption. At high potentials (+600 mV), the current obtained when glucose and an amino acid are added together (curve C) is higher than when the amino acid is added alone (curve B), but in general is smaller than with glucose added alone (curve D). Figure 3b indicates that the relative current increase at 900 mV when glucose and an amino acid are added to the buffer, as compared to addition of amino acid alone, is inversely related to the degree of adsorption of the amino acid.

The glucose-dependent "anodically directed peak" observed in the cathodic potential sweep between about -250 and -400 mV has been interpreted (3) as resulting from electrooxidation of glucose after a substantial amount of PtO has been reduced. Comparison of curves C and D in Fig. 1b shows that the presence of amino acids also decreases the height of this peak. The reduction of the height of the anodically directed peak is also accompanied by a shift of the peak toward more negative potentials. This would be expected if less glu-

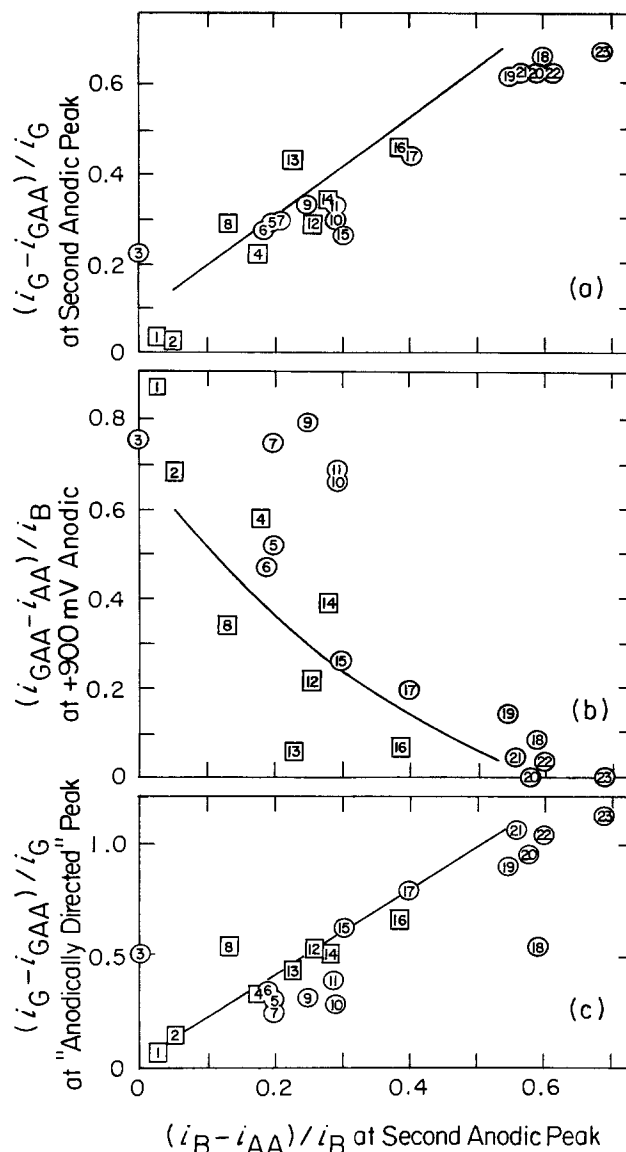


Fig. 3. Dependence of parameters in $i(E)$ curves with glucose and amino acids on amino acid-induced decrease of second anodic peak (amino acid identification same as for Fig. 2). Physiological amino acid concentrations.

cose were electrooxidized simultaneously with PtO reduction. Figure 3c demonstrates a good correlation between the relative decrease in the height of the glucose-dependent anodically directed peak of the cathodic potential sweep resulting from amino acid addition and the degree of adsorption of the individual amino acids.

The effect of amino acids on glucose electrooxidation is summarized in Table I in which the different amino acids are ordered according to their inhibitory power. This sequence was obtained by calculating the average of (i) the degree of amino acid adsorption $(i_B - i_{BAA}) / i_B$ at the second anodic current peak, (ii) the inhibiting power on glucose oxidation at the same current peak $(i_G - i_{GAA}) / i_G$, and (iii) the degree of inhibition of glucose oxidation at the anodically directed current peak in a cathodic sweep, $(i_G - i_{GAA}) / i_G$. The most inhibitory amino acids are those with an excess of basic character imparted by the presence of free NH_2 groups. In addition, there is a suggestion that the presence of sulfur may add to the inhibitory nature of the amino acids.

A brief investigation was conducted to compare the behavior of amino acids with very low (<1.7 mg/dl) or with high (>3.6 mg/dl) physiological concentrations at a constant concentration level of 3 mg/dl. Since the

molecular weight of physiologically significant amino acids in Table I does not differ greatly, the molar concentrations of the different amino acids were also comparable. The results showed that the ranking of the different amino acids according to their inhibitory power changes in some cases (citrulline, methionine, alanine) when comparison is made at comparable concentrations (sixth column of Table I) rather than physiological concentration.

Concentration effects of amino acids and glucose.—Leucine and lysine were selected for further study because, while inhibiting glucose electrooxidation to quite different degrees, their physiological concentration and molecular weight differ only slightly, and both are aliphatic saturated molecules. They differ structurally in their substituent groups, $(\text{CH}_2)_3\text{-NH}_2$ for lysine and $\text{CH}(\text{CH}_3)_2$ for leucine, which make lysine a basic and hydrophilic amino acid and leucine a neutral and hydrophobic amino acid.

Figures 4a and 4b show the effect of increasing concentrations of leucine and lysine, respectively, on the current-potential curves obtained with a fast potential sweep. In these experiments, the sweep rate was 2 V/min, and the electrode prepolarization treatment consisted of a 2 min pulse at -700 mV prior to an anodic sweep and a 2 min pulse at 1150 mV prior to a cathodic sweep. The qualitative effect of increasing amino acid concentration is consistent with the results discussed with respect to Fig. 1. The stronger adsorption of lysine (*vs.* leucine) is consistent with the more pronounced shift of the second anodic peak at about 200 mV and the higher rate of lysine oxidation at the high potentials. A plot of the net amino acid oxidation current density at 950 mV ($i_{AA} - i_B$ divided by real surface area) as a function of amino acid concentration is presented in Fig. 5. There is a higher current density for lysine than for leucine with an indication of saturation in the case of lysine.

Figure 6 is analogous to Fig. 2 and shows the correlations between (i) the electrode potential shift in the second anodic peak at two-thirds of the background peak current, and (ii) the net relative current increase induced by amino acid oxidation at 900 mV in the

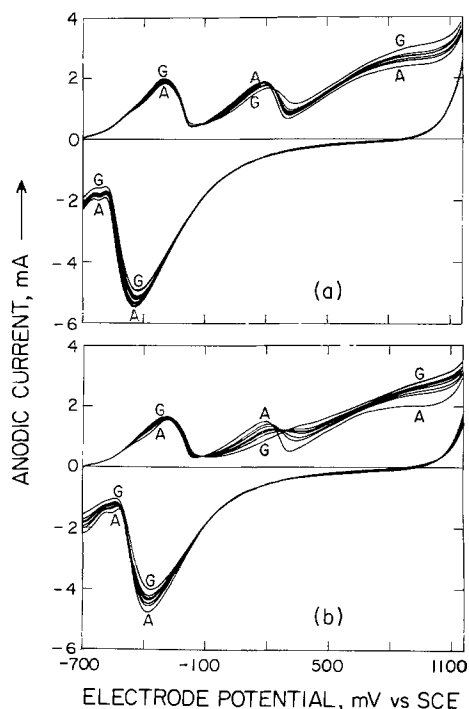


Fig. 4. $i(E)$ curves (at 2 V/min) in K-R buffer. (a) Leucine (roughness factor, $R_f = 518$): 0, 1.2, 1.9, 3.1, 3.7, 5.0, 9.9 mg/dl (A to G). (b) Lysine ($R_f = 411$): 0, 1.4, 2.2, 3.6, 4.6, 5.8, 11.5 mg/dl (A to G).

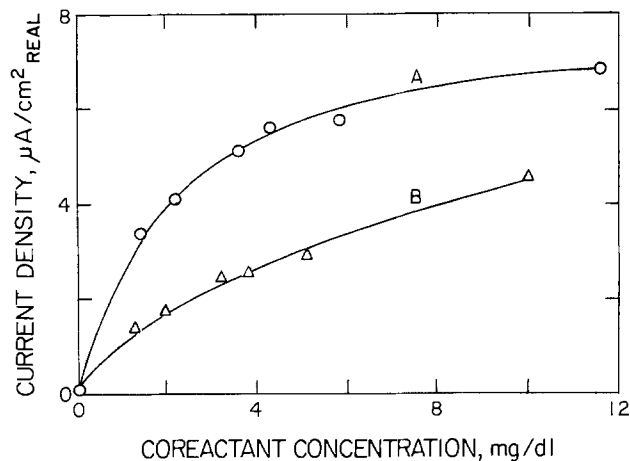


Fig. 5. Net current density at 950 mV during anodic sweep. \circ Lysine ($R_f = 411$); \triangle leucine ($R_f = 518$).

anodic potential sweep as a function of the degree of amino acid adsorption expressed as the relative decrease in the height of the second anodic current peak. The data were obtained with lysine and leucine individually and with simple mixtures of the two at varying concentrations in buffer. The solid curves fitting the data points of Fig. 6a and 6b have been drawn also in Fig. 2a and 2b, respectively. Good agreement is observed for the correlations with the individual amino acid and mixture data obtained at varying concentrations.

Figure 7 contains current-potential curves for a series of different glucose concentrations taken under the following conditions: alone with buffer (Fig. 7a), with 3.1 mg/dl leucine added (Fig. 7b), and with 3.6 mg/dl lysine added (Fig. 7c). Comparison of these three sets of curves demonstrates the decreased electrode sensitivity to glucose concentration changes in both the anodic and cathodic potential sweeps in the presence of added amino acid. The sensitivity is smaller with the more inhibitory lysine than with the less in-

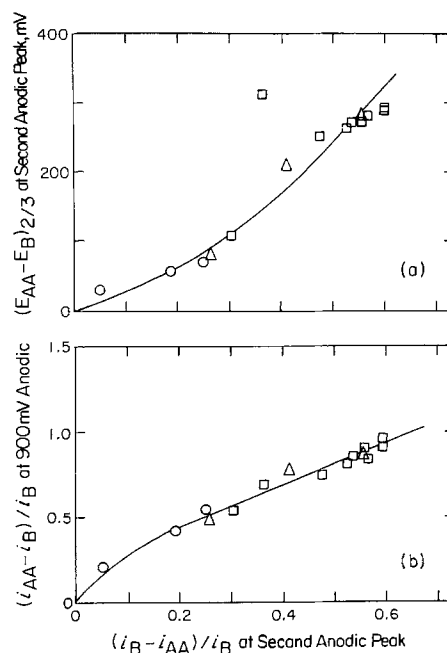


Fig. 6. Dependence of characteristic parameters of $i(E)$ curves (at sweep rate of 0.5 V/min) on amino acid-induced decrease of second anodic peak for leucine and lysine studied individually and in mixtures at different concentrations. \circ Leucine: 1.2, 3.1, 5.0 mg/dl; \triangle lysine: 1.4, 3.6, 5.8 mg/dl; \square leucine + lysine (combinations of above concentrations).

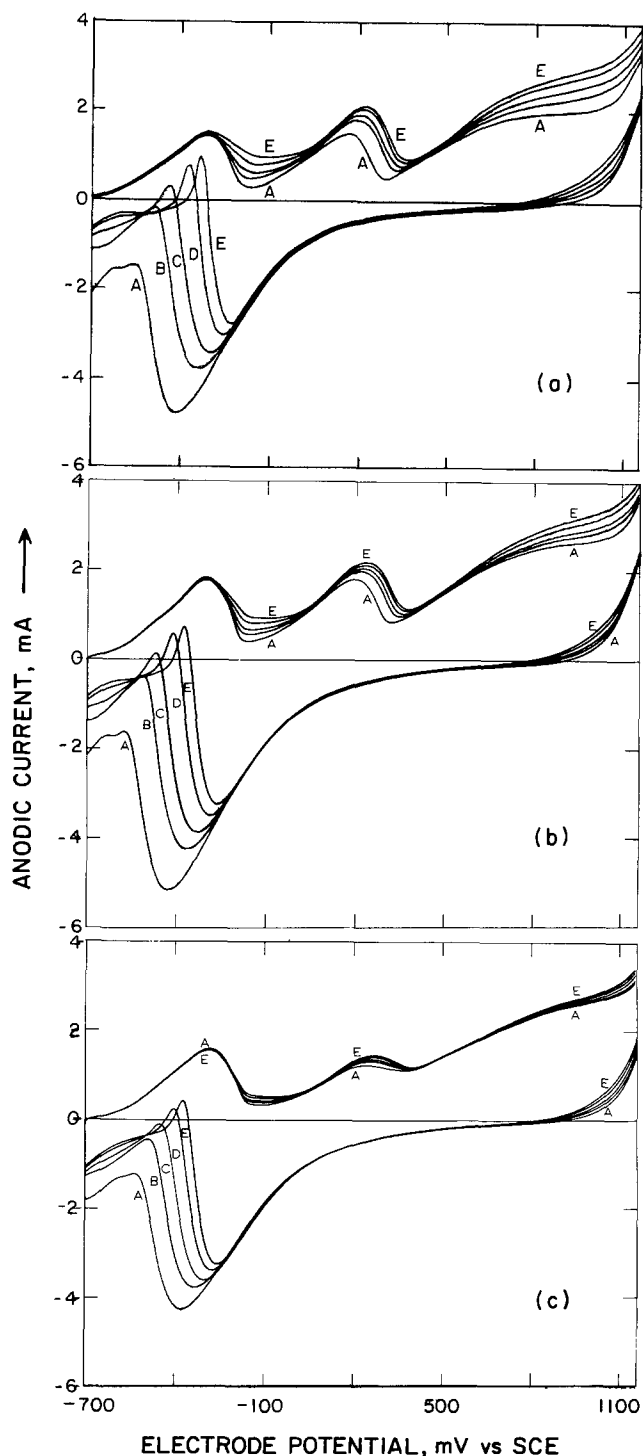


Fig. 7. Effect of glucose concentration on $i(E)$ curves (at 2 V/min). Glucose concentration, 0, 50, 100, 200, 300 mg/dl (A to E). (a) No amino acid present ($R_f = 411$); (b) leucine at 3.1 mg/dl ($R_f = 500$); (c) lysine at 3.6 mg/dl ($R_f = 400$).

hibitory leucine. The effects of glucose and amino acid concentrations on the net glucose oxidation current ($i_{GAA} - i_B$) in the anodically directed peak of the cathodic potential sweep is shown in Fig. 8. The current density is plotted in Fig. 8a as a function of glucose concentration at several concentration levels of lysine and leucine. These data have been replotted in Fig. 8b where the net glucose current is normalized by that measured in the absence of amino acid in order to show the relative decrease in the net glucose oxidation current as a function of coreactant (leucine or lysine) concentration. Each data point is the mean of the data at each glucose concentration plotted in Fig. 8a. The relative decrease of current is independent of glucose

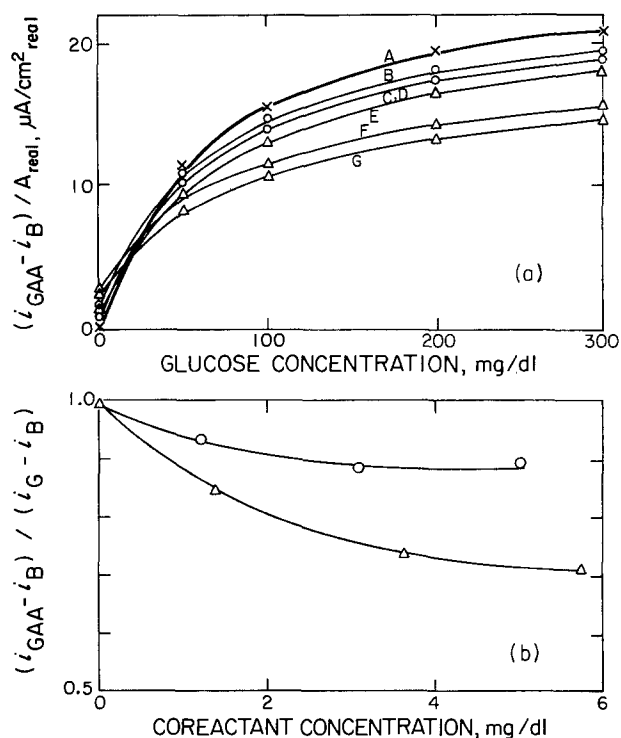


Fig. 8. Dependence of relative glucose current at anodically directed peak of cathodic sweep on glucose and coreactant concentrations at sweep rate of 2 V/min. (a) A, Glucose alone. \circ Leucine at concentrations (mg/dl); B, 1.2; C, 3.1; D, 5.0 \triangle Lysine at concentrations (mg/dl); E, 1.4; F, 3.6; G, 5.8. (b) \circ Leucine, \triangle lysine. Each point is mean of values obtained at glucose concentrations of 50, 100, 200, and 300 mg/dl.

concentration in the range of 50-300 mg/dl. These results show that addition of amino acids decreases the electrode sensitivity to glucose concentration changes.

The normalized net glucose oxidation current at the anodically directed peak is plotted in Fig. 9 as a function of the second coreactant concentration for leucine-lysine mixtures. With a constant physiologic lysine concentration (3.6 mg/dl) and increasing leucine concentrations from 0 to 5 mg/dl, the net current is virtually constant, and the solution behaves as if it contained only the more strongly inhibiting lysine. In contrast, mixtures with a physiological concentration of leucine (3.1 mg/dl) and varying amounts of lysine

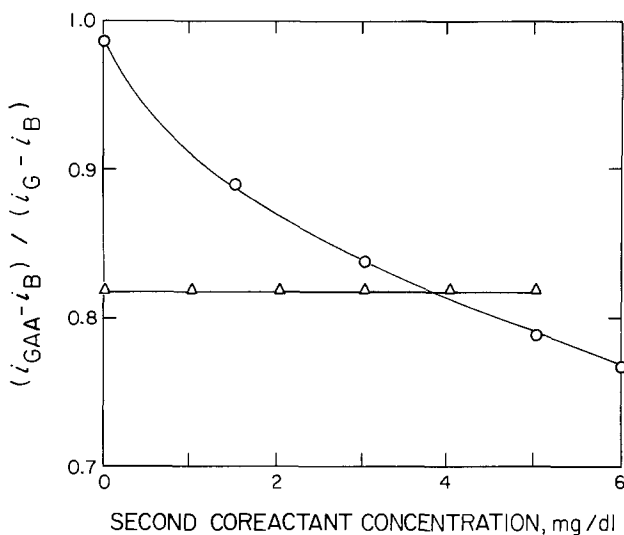


Fig. 9. Net current of anodically directed peak during cathodic sweep, in the presence of both lysine and leucine. Sweep rate 1 V/min. Glucose concentration constant at 100 mg/dl. $R_f = 779$. \circ Leucine (3.1 mg/dl); \triangle lysine (3.6 mg/dl).

show increasing inhibition of glucose electrooxidation with increasing lysine concentration. This again demonstrates that the more strongly inhibiting component controls the behavior of simple amino acid mixtures. Figure 10 relates three measures of the extent of inhibition of glucose electrooxidation to the degree of lysine and leucine adsorption. The data used to construct these plots were taken from current-potential curves obtained with potential sweep rates of 0.5 V/min and with varying concentrations of lysine and leucine studied individually and in mixtures. These plots correlate very well with those in Fig. 3. The solid curves fitting the data points in Fig. 10 are also drawn in Fig. 3; they show the same general trend as the data. The lysine and leucine data obtained at different concentrations agree well with these same curves that correlated a large number of amino acids at their physiological concentration. Although the two mixtures in Fig. 9 behaved very differently, all of the mixture data falls smoothly on the same correlations as that for the individual amino acids in Fig. 6 and 10. This finding further validates the use of the relative current decrease at the second anodic peak as a measure of the degree of amino acid adsorption.

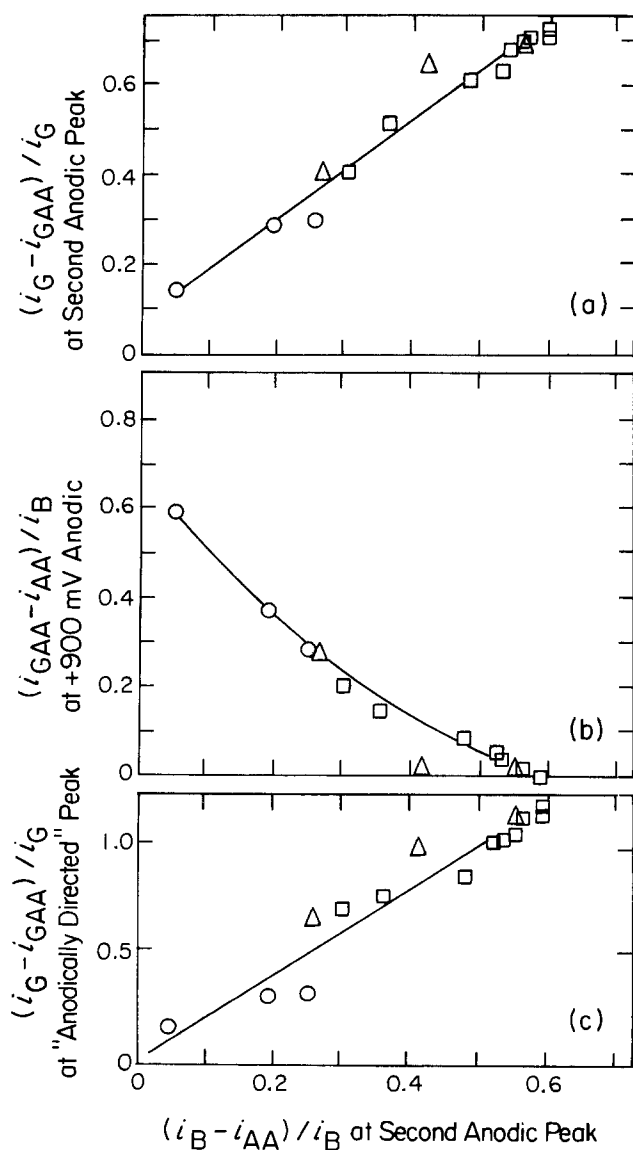


Fig. 10. Dependence of glucose electrooxidation characteristic parameters from $i(E)$ curves at 0.5 V/min on decrease of second anodic peak induced by leucine and lysine. Glucose concentration constant of 100 mg/dl. Symbols and concentrations of leucine and lysine are the same as in Fig. 6.

Table II. Amino acid mixture (AAM)

| Amino acid | Concentration (mg/dl) |
|---------------|-----------------------|
| Glycine | 3.0 |
| Leucine | 7.6 |
| Alanine | 14.9 |
| Histidine | 2.2 |
| Lysine | 3.5 |
| Arginine | 2.0 |
| Serine | 1.1 |
| Glutamic acid | 3.2 |
| Proline | 3.5 |
| Methionine | 0.6 |
| Tryptophan | 1.7 |
| Cysteine | 0.8 |
| Cystine | 2.0 |
| Tyrosine | 3.9 |
| Total | 50.0 |

Electrochemical behavior of complex amino acid mixtures.—In order to assess the behavior of complex amino acid mixtures at physiological concentration, a mixture of 14 amino acids with the composition shown in Table II (total concentration of 50 mg/dl) was used to generate the current-potential curves shown in Fig. 11. Comparison with Fig. 1 shows that the electrochemical response of this mixture and its effect on the glucose current-potential curves is qualitatively similar to that of the individual amino acids. As would be expected, under equivalent conditions of electrode real surface area, prepolarization, and potential sweep rate, the amino acid mixture almost totally inhibits glucose electrooxidation. Further study showed that the sensitivity to glucose in the cathodic potential sweep can be

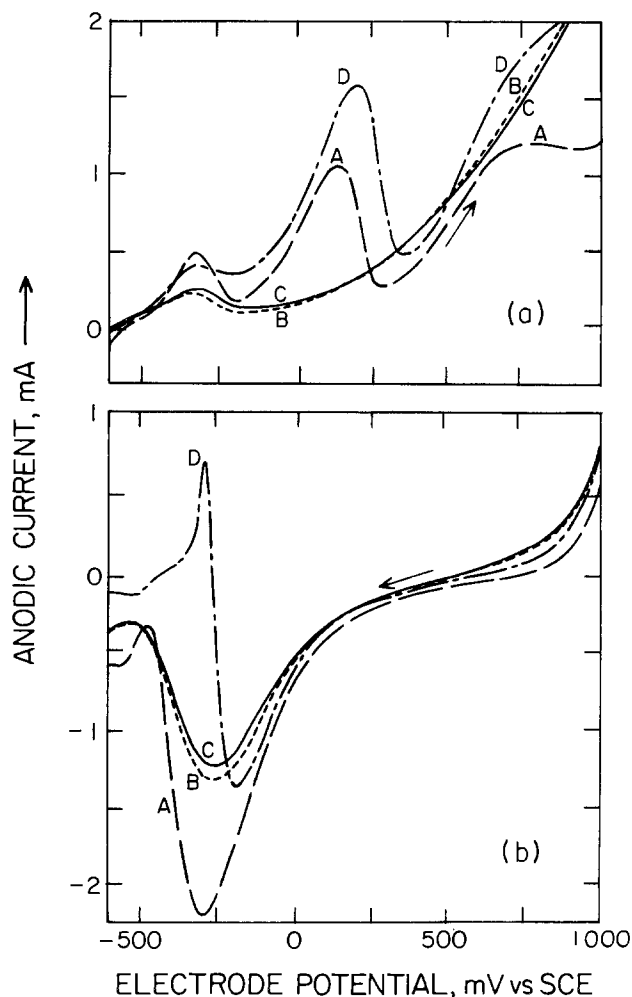


Fig. 11. Current-potential curves (at 0.5 V/min). (a) Anodic sweeps; (b) cathodic sweeps. A, Krebs-Ringer alone; B, K-R with amino acid mixture (Table II, 50 mg/dl); C, K-R with amino acid mixture (50) + glucose (100); D, K-R with glucose (100).

restored by one or more of the following changes: (i) increase of the prepolarization potential from 1000 to 1100 mV; (ii) increase of the potential sweep rate (e.g., from 0.5 to 2 V/min; (iii) increase in the electrode roughness factor; and (iv) reduction of transport to and from the surface by placing a membrane over the electrode. Considerably less effort was spent investigating factors which improve glucose sensitivity in the anodic potential sweep. However, experiments with leucine and lysine mixtures at two sweep rates did indicate that a decreased potential sweep rate can increase glucose sensitivity in the anodic potential sweeps. Figure 12 shows the anodically directed current peak of the cathodic potential sweep obtained with different glucose concentrations in the presence of 50 mg/dl of a commercially available amino acid mixture (Freamine, McGaw Laboratories, Chicago) comparable in composition to the mixture of Table II. Glucose sensitivity is restored by the use of a higher prepolarization potential and a higher sweep rate.

The effect of total amino acid concentration is shown in Fig. 13. The net current density at the anodically directed glucose-dependent peak of the cathodic sweep is plotted vs. glucose concentration for Freamine concentrations of 50 and 85 mg/dl in Fig. 13a. Even at 85 mg/dl there is still considerable glucose sensitivity, but there is also a large effect of amino acid concentration. For example, change in Freamine concentration from 50 to 85 mg/dl causes the current to decrease to one-third of its initial value. The same data are plotted on reciprocal coordinates in Fig. 13b. The good linearity of the data on these coordinates suggests that the net glucose oxidation current density can be represented empirically as a hyperbolic function of glucose concentration. No attempt was made to interpret

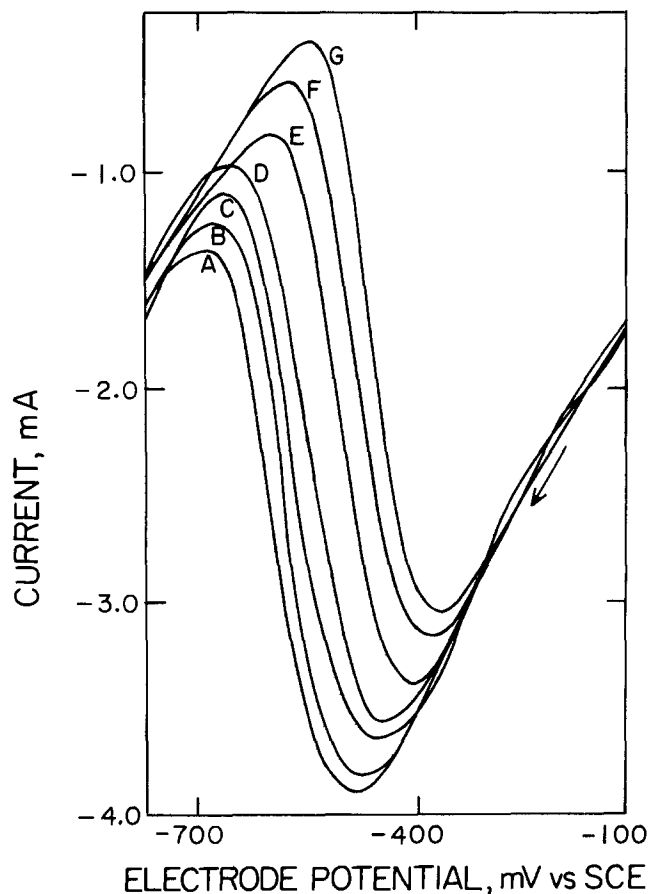


Fig. 12. Anodically directed current peak during cathodic sweep with 50 mg/dl of Freamine amino acid mixture. Prepolarization potential: 1100 mV; sweep rate: 1.8 V/min; $R_f = 600$. Glucose concentrations: 0, 20, 40, 80, 180, 280, 380 mg/dl (A to G).

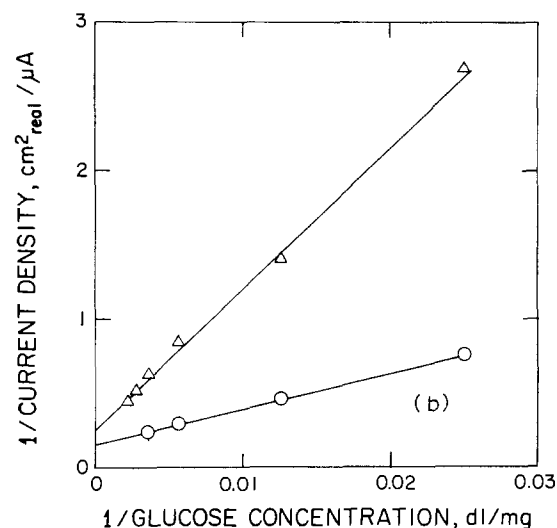
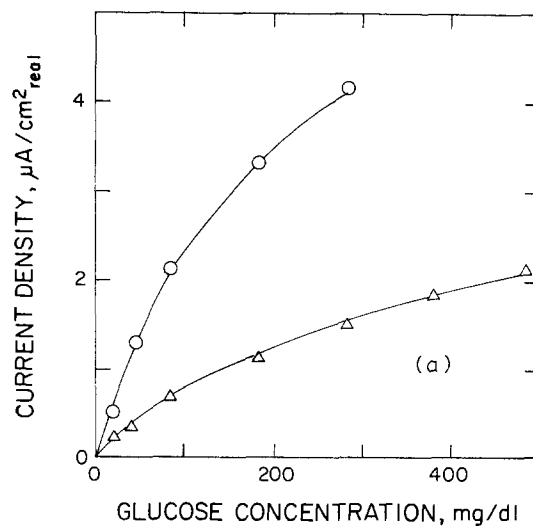


Fig. 13. (a) Net anodically directed peak current density during cathodic sweep as a function of glucose concentration: ○ 50 mg/dl Freamine (from Fig. 12), Δ 85 mg/dl Freamine (experimental conditions as in Fig. 12); (b) reciprocal plot of same data.

kinetically the effect of amino acids on the current since the conditions under which the current is measured involve a number of transient electrode processes such as PtO reduction, glucose oxidation, double layer charging or discharging, and probably some amino acid oxidation.

Conclusions

A number of conclusions can be drawn regarding the effect of amino acids on fast potential sweeps obtained in Krebs-Ringer buffer solutions with and without glucose:

1. In the presence of amino acids the electrochemical activity of the platinum electrode can be reproduced by applying periodic potential-time functions in such a way that no cumulative effect of amino acid action is present. No hysteresis in the sequence of addition of glucose and amino acids is observed.

2. Individual amino acids are adsorbed on platinum at low potentials. They are oxidized at high potentials (above + 650 mV) and inhibit glucose oxidation in all potential regions of glucose activity. Good correlation exists between both the oxidation at high potentials and the glucose inhibition of a given amino acid and a parameter obtainable directly from voltammograms with and without amino acid which indicates the degree of adsorption of the amino acid. These relationships appear to override any effects caused by the variation in chemical composition.

3. Ordering of individual amino acids according to their level of glucose inhibition indicates that the main factor determining their inhibitory power is their basic character. The presence of excess NH_2 groups causes amino acids to be more inhibitory.

4. Lysine and leucine at the same molar concentration display very different behavior in terms of adsorption, oxidation rate, and glucose inhibition. These differences are attributable to the presence of an NH_2 group at the end of the lysine molecule. This result suggests that the adsorption of lysine on the platinum electrode does not occur solely through the zwitterionic groups of the molecule but must also involve the substituent group.

5. Changes in the concentration of lysine and leucine alter their degree of adsorption coverage, the rate of oxidation at high potentials, and the glucose inhibition power. These changes can be described by the same curves which correlate individual amino acid data.

6. Mixtures of amino acids near physiological concentration behave qualitatively as individual amino acids. Under conditions used to study individual amino acids, but with the amino acid mixtures used, the inhibition is so overwhelming that there is no glucose concentration response.

7. Glucose sensitivity in the cathodic potential sweep can be restored by increasing one or more of the following parameters: the prepolarization potential, the potential sweep rate, and the real surface area of the electrode. Reducing the transport rate to the surface can also increase the glucose concentration sensitivity.

8. Mixtures of lysine and leucine behave as individual amino acids with regard to their adsorption, oxidation rate, and glucose inhibition. They fit the same plots relating the various parameters of the $i(E)$ curves for individual amino acids at physiological concentrations and for individual solutions of leucine and lysine at various concentrations.

9. Both leucine and lysine cause a relative decrease in the glucose oxidation current which is nearly independent of the glucose concentration.

10. When leucine is added from 0 to 5 mg/dl to lysine solutions at the physiological concentration of lysine (3.6 mg/dl), the solutions behave with respect to glucose inhibition and to amino acid oxidation as if they contained only lysine.

Manuscript submitted Dec. 24, 1980; revised manuscript received May 5, 1981. This was Paper 529 pre-

sented at the Seattle, Washington, Meeting of the Society, May 21-26, 1978.

Any discussion of this paper will appear in a Discussion Section to be published in the June 1982 JOURNAL. All discussions for the June 1982 Discussion Section should be submitted by Feb. 1, 1982.

Publication costs of this article were assisted by Giner, Incorporated.

REFERENCES

1. D. A. Gough, S. Aisenberg, C. K. Colton, J. Giner, and J. S. Soeldner, in "Blood Glucose Monitoring. Methodology and Clinical Application of Continuous In Vivo Glucose Analysis," Proceedings of a Workshop-Conference held in Freiburg (Germany) March 1976, J. D. Kruse-Jarres and G. D. Molnar, Editors, pp. 9-22, Georg Thieme, Stuttgart (1977).
2. C. K. Colton, J. Giner, H. Lerner, L. Marincić, and J. S. Soeldner, in "Proc. 10th Int'l. Course Transpl. and Clin. Immunol. Excerpta Medica," pp. 165-174 (1979).
3. L. Marincić, J. S. Soeldner, C. K. Colton, J. Giner, and S. Morris, *This Journal*, **126**, 43 (1979).
4. H. Lerner, J. Giner, J. S. Soeldner, and C. K. Colton, *ibid.*, **126**, 237 (1979).
5. L. Marincić, J. S. Soeldner, J. Giner, and C. K. Colton, *ibid.*, **126**, 1687 (1979).
6. D. A. Gough, F. L. Anderson, J. Giner, C. K. Colton, and J. S. Soeldner, *Anal. Chem.*, **50**, 941 (1978).
7. J. R. Rao, G. J. Richter, G. Luft, and F. von Sturm, *Biomat. Med. Dev., Art. Org.*, **6** (2), 127 (1978).
8. E. A. Maksimuk and I. P. Alekseeva, *J. Appl. Chem. USSR*, (English transl.), **38**, 2390 (1965).
9. D. B. Matthews, *J. Biomed. Mater. Res.*, **3**, 475 (1969).
10. B. B. Damaskin, S. Dyatkina, and N. A. Borovaya, *Elektrokhimiya*, (English transl.), **6**, 712 (1970).
11. N. A. Borovaya and B. B. Damaskin, *ibid.*, **7**, 571 (1971).
12. L. M. Baugh and R. Parsons, *J. Electroanal. Chem. Interfacial Electrochem.*, **41**, 311 (1973), also in *Croat. Chem. Acta*, **45**, 127 (1973).
13. G. J. Hills, D. I. Schiffrin, and T. Solomon, *J. Electroanal. Chem. Interfacial Electrochem.*, **41**, 41 (1973).
14. T. Kakiuchi and M. Senda, *ibid.*, **88**, 219 (1978).
15. J. Giner, *Electrochim. Acta*, **8**, 857 (1963).
16. J. A. Reynaud, B. Malfoy, and P. Canesson, *J. Electroanal. Chem. Interfacial Electrochem.*, **114**, 195 (1980).
17. B. Malfoy and J. A. Reynaud, *ibid.*, **114**, 213 (1980).

The Electrosorption and the Potentiodynamic Electrooxidation of Ethane on Platinum at Different Temperatures

V. Solís, A. Castro Luna, W. E. Triaca, and A. J. Arví*

Instituto de Investigaciones Fisicoquímicas Teóricas y Aplicadas, División Electroquímica, Sucursal 4, Casilla de Correo 16, 1900 La Plata, Argentina

ABSTRACT

The electrosorption and the potentiodynamic electrooxidation of ethane on platinized platinum in 1N H₂SO₄ has been studied in the 20°-80°C range. The potentiodynamic *I/E* profiles run immediately after the potentiostatic electrosorption of the hydrocarbon show that three different species participate in the electrooxidation process. The various electrosorbed species are tentatively related to the electrosorbed species which are formed during the electrosorption of both methane and ethylene on platinum. The electrochemical process is discussed through a complex reaction pathway involving electrosorption, interconversion, and electrooxidation processes.

The electrooxidation of ethane on platinum has been studied both in acid and alkaline electrolytes. Data for the electrochemical reaction are reported at different temperatures using conventional galvanostatic and potentiostatic techniques and multipulse potentiodynamic perturbations (1-14). Although the available information is to some extent not straightforwardly comparable, it has been established that the reaction occurs through the participation of different adsorbed species which were denoted as type I species and type II species. The former was assigned to an O-type species and the latter to a CH- α -type species, respectively (15-19). These assignments were made on the basis of triangular potential sweep *I/E* displays which were also compared to those resulting from the potentiodynamic electrooxidation of other related substances and from the charge balances based on the potentiodynamic data (3, 5-9). From the correlation of results obtained for different hydrocarbon electrooxidation on platinum in acid electrolytes various general reaction pathways were postulated (5-8, 12-14).

Recent results on the electrooxidation of ethylene (20, 21) and of methane (22) indicate that the initial stage of the electrochemical reaction is a dissociative electrosorption of the hydrocarbon. For ethylene the principal adsorbed species is assigned to a CH-containing species, while for methane, there are, in principle, two O-containing electrosorbed species predominating on the electrode surface, their relative surface concentration depending on the electrosorption potential and on the electrosorption time (22). These results suggest that for a saturated hydrocarbon such as ethane at least three main adsorbed species could participate in the electrochemical reaction, their relative contributions depending on the physicochemical characteristics of the electrochemical interface and on the potential program applied to the interface.

The present paper deals with the electrosorption and the potentiodynamic electrooxidation of ethane on platinum in acid electrolyte at different temperatures. It shows that three main electrosorbed species contribute to the electrochemical reaction. The potentiodynamic characteristics of these species correlate reasonably well with those derived from ethylene and methane electrooxidation and they suggest the pos-

sibility of presenting a general reaction scheme for the short chain aliphatic hydrocarbon electrooxidations which takes into account the hydrocarbon electrosorption reaction, the possible hydrogenation reactions, the interconversion reactions involving the different electrosorbed species, and the proper electrooxidation of the various adsorbed species yielding CO₂ and hydrogen ions as final products at the platinum anode.

Experimental

A conventional-type three-compartment electrolysis cell was employed. The different cell compartments were connected through cup-type glass stopcocks lubricated with the electrolyte solution. Conventional procedures for the glass cell cleaning were used. The working electrodes consisted of a platinized-platinum electrode prepared as indicated in a previous work (21). The actual electrode areas were evaluated through the charge corresponding to the hydrogen adatom electrosorption current peaks. The potential of the working electrode was measured against a hydrogen reference electrode at 1 atm hydrogen gas saturation pressure in the base electrolyte solution (ethane-free acid electrolyte). The electrode potentials in the text are referred to the reversible hydrogen electrode scale (RHE). The counterelectrode was a large area platinum sheet.

The acid electrolyte (1N H₂SO₄) was prepared from Merck p.a. 95-97% H₂SO₄ and triply distilled water. The electrolyte solution satisfied the purity standards indicated in the literature (22, 23). Runs were made at 20°, 50°, and 80°C in the electrolyte saturated with ethane (C. P. Matheson) at 1 atm pressure. For the sake of comparison blanks were systematically made using the base electrolyte solution under 1 atm nitrogen gas saturation.

Prior to the hydrocarbon adsorption measurements the working electrode was subjected to the pretreatment already described in a recent publication (21). After the electrode pretreatment the potential of the working electrode was held during a preset time, t_{ad} , at a fixed value, E_{ad} , for the ethane adsorption. Immediately afterward a triangular potential sweep was applied from E_{ad} (Fig. 1) either toward the positive (program a) or the negative potential direction (program b), at a potential sweep rate, v . The charge required to electrooxidize the layer of adsorbed hydrocarbon, Q_E , was evaluated by subtracting from the total anodic charge, previously corrected for the double

* Electrochemical Society Active Member.

Key words: ethane electrooxidation, platinum electrodes, ethane electrosorption.

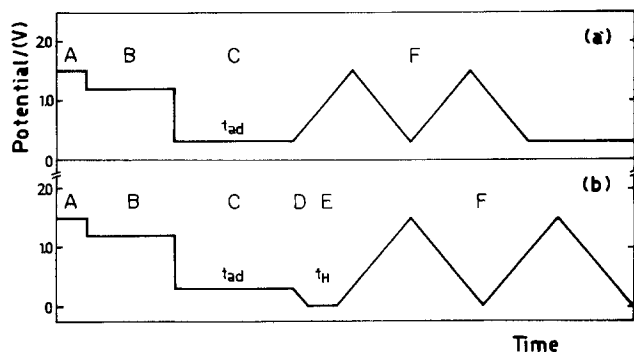


Fig. 1. Potential perturbation programs. Time axis arbitrary scale. Step width: A = 5 sec; B = 60 sec (gas bubbling) + 120 sec (quiescent solution); C = t_{ad} ; D = negative going potential sweep; E = t_H ; F = triangular potential sweep.

layer effect, the cathodic charge pertaining to the electrodesorption of the oxygen-containing layer formed during the anodic scan. In this sense blank experiments served as reference (20). In order to select the suitable v range for the ethane electrooxidation under hydrocarbon readsorption-free condition runs were made at preset values of E_{ad} and t_{ad} between the cathodic ($E_{s,c}$) and the anodic ($E_{s,a}$) switching potentials and different v 's. From the Q_E vs. v plot (20) it was concluded there is practically no ethane readsorption interference when $v \geq 0.3$ V/sec.

The electroadsorption of ethane on platinized platinum was studied at a constant t_{ad} over a reatively wide E_{ad} range ($0.1V \leq E_{ad} \leq 0.6V$) and at a constant E_{ad} over a large t_{ad} range ($5 \text{ sec} \leq t_{ad} \leq 90 \text{ min}$).

Results

The potentiodynamic I/E displays in the ethane-saturated electrolyte.—The potentiodynamic I/E displays depend strongly on the characteristics of each potential perturbation program. Thus, the I/E display resulting from the first potential scan in the positive potential going direction run at $E_{ad} = 0.250V$, $t_{ad} = 10 \text{ min}$, $v = 0.4$ V/sec, and 80°C (Fig. 2) shows that the adsorbed ethane electrooxidation occurs in the range ca. 0.4–1.5V. The process is associated with a composite anodic current peak (peak I) at ca. 0.69V which consists of a doublet and with another composite anodic current peak lying at ca. 1.05V (peak II). The latter overlaps with that related to the oxygen electroadsorption on platinum. Likewise, the appearance of current peaks I and II is related to the remarkable decrease of the current related to the electrooxidation of the hydrogen adatoms, which are located in the 0.25–0.4V range. The negative potential going excursion exhibits the already known cathodic current peak at ca. 0.75V related to the oxygen electrodesorption and the cathodic current related to the initiation of the hydrogen adatom electroadsorption at potentials close to $E_{s,c}$. During the second potential scan the I/E profile rapidly approaches the characteristics obtained in the blanks.

The I/E displays run at a constant E_{ad} and different t_{ad} reveal the doublet structure of current peak I (Fig. 3). Thus, at the shortest t_{ad} 's the current peak component which is located at more positive potentials (peak I_b) predominates over that (peak I_a) which is located at more negative potentials. Likewise, the contribution of current peak II is practically absent.

On the other hand, when $t_{ad} \geq 1 \text{ min}$ the contribution of current peak II becomes appreciable and simultaneously the largest charge contribution to current peak I is due to peak I_a.

At a constant E_{ad} , the total charge related to the electrooxidation of adsorbed ethane attains a limiting value after a certain time, $t_{ad,ss}$. This time can be con-

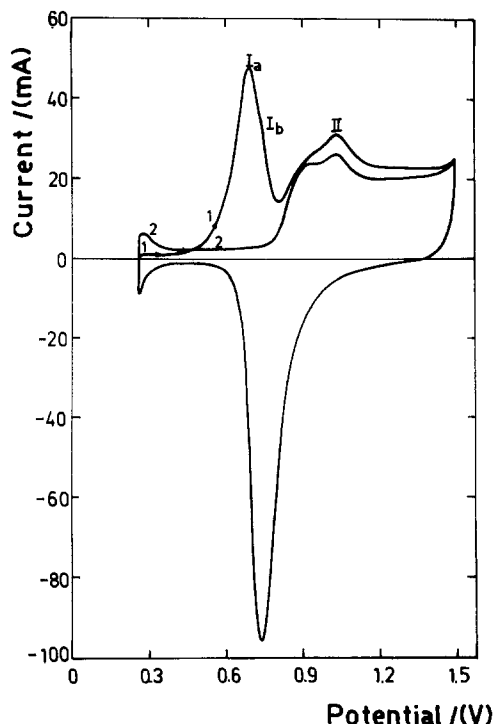


Fig. 2. Potentiodynamic I/E profiles run at 0.4 V/sec using the perturbation program (a) shown in Fig. 1. $E_{ad} = 0.25V$; $t_{ad} = 10 \text{ min}$; 80°C ; real electrode area = 87 cm^2 . Numbers 1 and 2 indicate the first and the second potential scans, respectively. Profile 2 approaches the blank contour (nitrogen saturated electrolyte).

sidered as the minimum time required to reach the stationary surface coverage by the adsorbed species. Thus, at 80° and $E_{ad} = 0.250V$, $t_{ad,ss} = 10 \text{ min}$. Under the same E_{ad} and temperature conditions, within the $1 \text{ min} \leq t_{ad} \leq 7 \text{ min}$ range, Q_E increases linearly with the logarithm of t (Fig. 4). On the other hand, at a constant t_{ad} , the shape of the electrooxidation I/E profile changes with E_{ad} (Fig. 5). Thus, at $E_{ad} = 0.5$ and $0.15V$ the current peak I appears as a small plateau and the contribution of current peak II to the total charge Q_E becomes relatively important. At $E_{ad} = 0.6V$ no ethane adsorption is detected through the potential sweep technique. At $t_{ad} = t_{ad,ss}$, Q_E depends on E_{ad} (Fig. 6). The maximum charge related to the electrooxidation of adsorbed ethane is found at $E_{ad} = 0.250V$, the corresponding charge being $Q_E = 0.27 \text{ mC/cm}^2$ of real area. For this case, the major charge contribution to the total charge Q_E is that of current peak I_a (Fig. 2).

The influence of the electrochemical hydrogenation on the potentiodynamic I/E profiles (Fig. 7) is determined by including a variable potential holding during the time t_H at $E_{s,c} = 0V$ (Fig. 1, program b). Thus, when t_H increases the current peak I becomes thinner and relatively more symmetric, but the corresponding anodic charge remains constant. The peak height to peak width at one-half peak height ratio changes from 7.7 for $t_H = 0.3 \text{ sec}$ to 11 for $t_H = 5 \text{ min}$. Furthermore, after the ethane adsorption at $E_{ad} = 0.25V$, the potential sweep in the negative potential direction reveals a clear and systematic blocking of sites for the electroadsorption of hydrogen atoms, particularly those sites corresponding in the highest hydrogen-platinum adsorption energy. On the other hand, the contribution of current peak II decreases as t_H increases. This indicates that the species related to current peaks I_b and II undergo electrochemical hydrogenation, the former yielding the adsorbed species related to current peak I_a and the latter yielding an apparently nonadsorbable species.

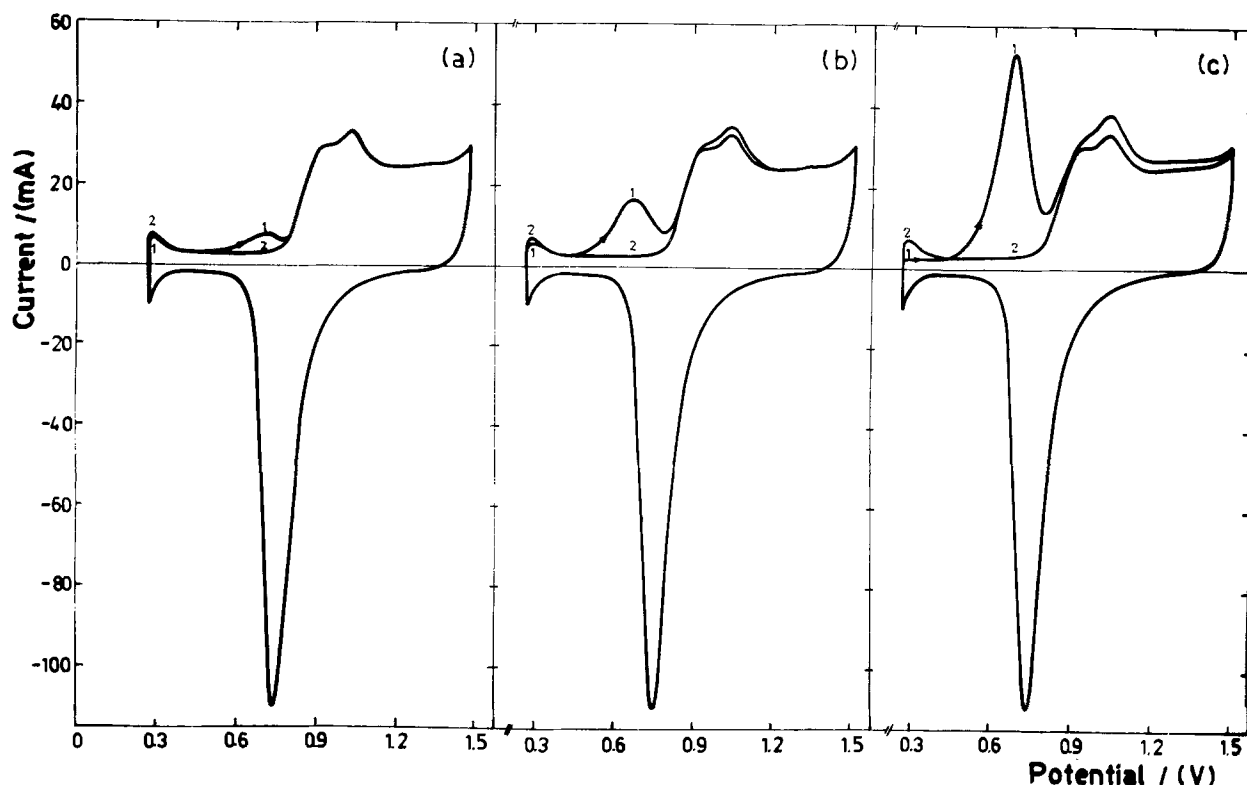


Fig. 3. Potentiodynamic I/E profiles run at 0.4 V/sec using the perturbation program (a) shown in Fig. 1 from $E_{ad} = 0.25V$ at different t_{ad} ; $80^{\circ}C$; real electrode area = 100 cm^2 . (a) $t_{ad} = 15\text{ sec}$; (b) $t_{ad} = 1\text{ min}$; (c) $t_{ad} = 5\text{ min}$.

At constant E_{ad} and t_H the distribution of the anodic current peaks is strongly dependent on t_{ad} (Fig. 8). Thus, for $t_{ad} = 45\text{ sec}$ the current peak I_b becomes the most relevant one, while at $t_{ad} \geq 1.5\text{ min}$ the contribution of current peak I_a becomes progressively more important as t_{ad} increases. Furthermore, as t_{ad} decreases the current peak II appears within a narrower potential range.

The shape of the I/E contour depends also on t_H . Thus, when $t_H \geq 5\text{ min}$ the contribution of current peak II to the total charge Q_E appreciably decreases. After the electrochemical hydrogenation the current related to the oxygen electroadsorption decreases in the 0.75-0.95V range. The corresponding charge decrease may be in part compensated by the charge increase observed in the 0.9-1.5V range, just in the potential range where the current peak II is recorded. The evaluation of the contribution of each reaction occurring in the 0.9-1.5V range exclusively from the potentiodynamic data is not feasible, but independently of it

the possibility that the current peak II results from the sum of the oxygen electroadsorption current and the residual current of peak I should, in principle, be discarded.

The temperature influence.—The same type of experiments already described at $80^{\circ}C$ were also made at 20° and $50^{\circ}C$. In principle, the different current peaks in the potentiodynamic I/E displays are more poorly defined as the temperature decreases because the potential range at which the ethane electrooxidation current peaks are observed becomes significantly more positive when the temperature decreases and, consequently, the potential regions corresponding to the oxygen electroadsorption and to the ethane electrooxidation are partially overlapped (Fig. 9 and 10). At $20^{\circ}C$, the time required to attain the maximum steady surface coverage by adsorbed ethane at $E_{ad} = 0.250V$ extends up to $t_{ad,ss} = 90\text{ min}$. In this case, the current due to the electrodesorption of the hydrogen adatoms becomes appreciable (Fig. 9). The I/E display run at 1 atm ethane saturation pressure at $20^{\circ}C$ resembles that obtained under 1 atm ethylene saturation pressure at $40^{\circ}C$ (20) with the same acid electrolyte. The anodic current peak recorded at $20^{\circ}C$, decreases progressively by electrochemical hydrogenation at 0V when t_H is gradually increased. Therefore, the species formed during ethane electroadsorption on platinum, at $20^{\circ}C$, behaves similarly to that obtained from the electroadsorption of ethylene on the same electrocatalyst at relatively higher temperatures.

The potentiodynamic I/E displays obtained at $50^{\circ}C$ show a behavior which is intermediate between those observed at 80° and $20^{\circ}C$ (Fig. 10). At $50^{\circ}C$ the I/E display presents the current peaks I and II and an appreciable hydrogen adatom electroadsorption current. The time required to attain the steady surface coverage by the adsorbed species from ethane electroadsorption at $E_{ad} = 0.25V$ is $t_{ad,ss} = 30\text{ min}$.

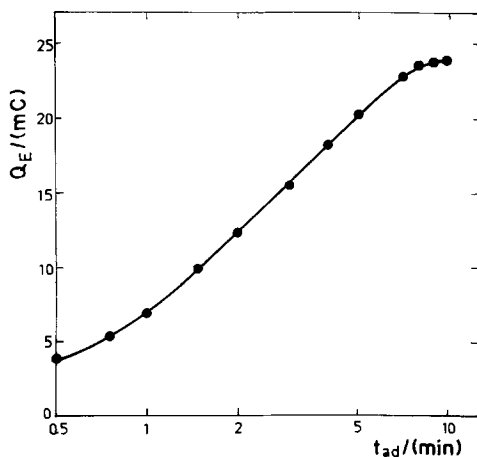


Fig. 4. Dependence of Q_E on t_{ad} at $E_{ad} = 0.25V$; $80^{\circ}C$, real electrode area = 88 cm^2 .

Charge measurements related to the electroadsorption of ethane on platinum.—During the electroadsorption of

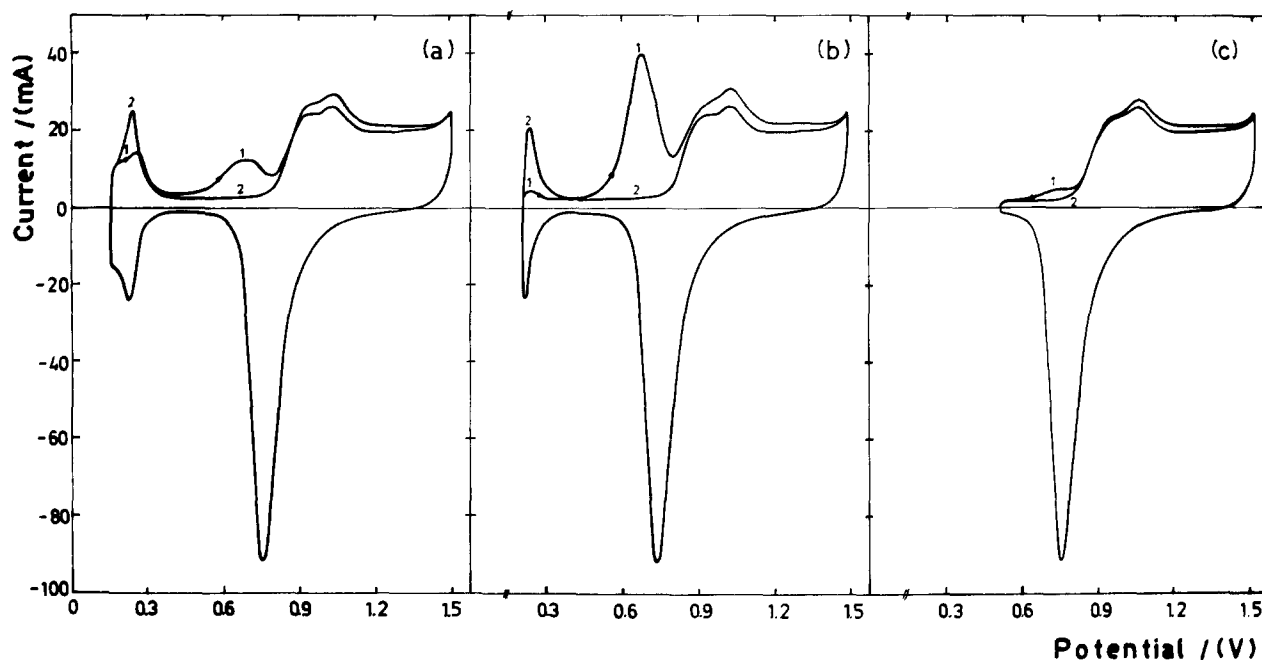


Fig. 5. Potentiodynamic I/E profiles run at 0.4 V/sec using the perturbation program (a) shown in Fig. 1 from different E_{ad} at $t_{ad} = 10$ min; 80°C; real electrode area = 84 cm². (a) $E_{ad} = 0.15V$; (b) $E_{ad} = 0.2V$; (c) $E_{ad} = 0.5V$.

ethane on platinum at 80°C at the maximum electro-sorption potential a current transient is recorded whose integration from $t = 0$ up to the time required to reach the null current (after correction for the baseline) yields the charge (Q_D) associated with the hydrogen ions produced during the electro-sorption process. Immediately after the null current condition is attained a linear potential sweep from E_{ad} up to $E_{s,a}$ is run so that the electrooxidation charge of the electro-sorbed species (Q_E) can be evaluated. Thus, at $E_{ad} = 0.250V$ the Q_D/Q_E ratio is 1.0 ± 0.1 .

Kinetic relationships.—Various relevant kinetic relationships can be derived from the different potentiodynamic I/E profiles. For this purpose the runs made at 80°C are preferred since the different ethane electrooxidation current peaks are more clearly defined. Runs made from $E_{ad} = 0.25V$, after the ethane electro-sorption during $t_{ad,ss}$ show that the height of current peak I, $(I_p)_I$, increases with v (Fig. 11). The low potential sweep data are corrected for the contribution of the ethane readsorption on the basis of the charges recorded in the second successive potential scan at different v . The experimental data fit a slight

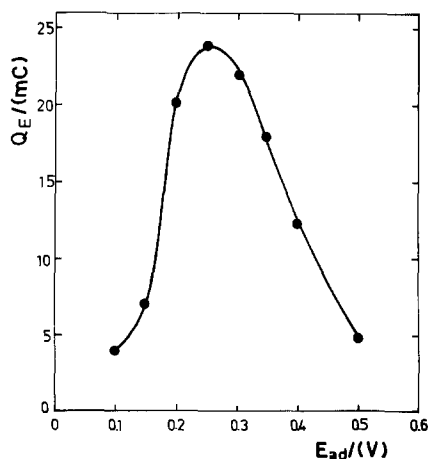


Fig. 6. Dependence of Q_E at $t_{ad,ss}$ on E_{ad} ; 80°C; real electrode area = 88 cm².

curve, approaching a straight line which intercepts the origin of the plot as $v \rightarrow 0$.

The potential of current peak I, $(E_p)_I$, shifts toward more positive potentials as v increases, fitting a linear $(E_p)_I/\log v$ plot (Fig. 12). The slope of the corresponding average straight line is, at 80°, equal to 0.100 V/decade, a value which is intermediate between the $2.3(2RT/F)$ ratio and the $2.3(RT/F)$ ratio.

The $E/\log I$ plots derived from the initial portion of the current peak I (Fig. 13) correspond to smooth curves whose location in the $E/\log I$ plane depends on v . In the low potential range the slope of the $E/\log I$ plots decreases slightly when v decreases. As v decreases, this slope tends to the $2.3(RT/F)$ ratio.

Discussion

The number and possible nature of the adsorbed species.—The potentiodynamic I/E displays related to the electrochemical oxidation of ethane on platinum in 1N HClO₄ at 60°C (3, 5-7) consist of an anodic current peak lying at relatively low potentials and of a broad current maximum which extends from about 0.8V up to 1.2V. According to previously reported data (3, 5-7), the charge of the first current peak remains practically unchanged upon cathodic hydrogenation. The corresponding adsorbed species which are electro-oxidized at near 0.7V behaves apparently similarly to the residual electro-sorbed species observed during the electrooxidation of methane (14). Contrarily, the electro-sorbed species associated with the second current peak is cathodically desorbed through electrochemical hydrogenation. The corresponding species was related to the same adsorbed C₂H₂ species formerly postulated for the ethylene electro-sorption on platinum in the acid electrolyte (7). A comparison of the potentiodynamic electrooxidation of methane, ethylene, and ethane on platinum under hydrocarbon readsorption-free conditions seems to indicate that the electrochemical behavior of the latter is intermediate between that of methane and ethylene. The maximum charge for the electrooxidation of the ethane electro-sorbed species in 1N HClO₄ at 60°C has been estimated as 0.56 mC/cm² (5), a charge which is more than triple of that found for methane adsorbate (14). This is partly due to the fact that ethane is more soluble in aqueous electro-

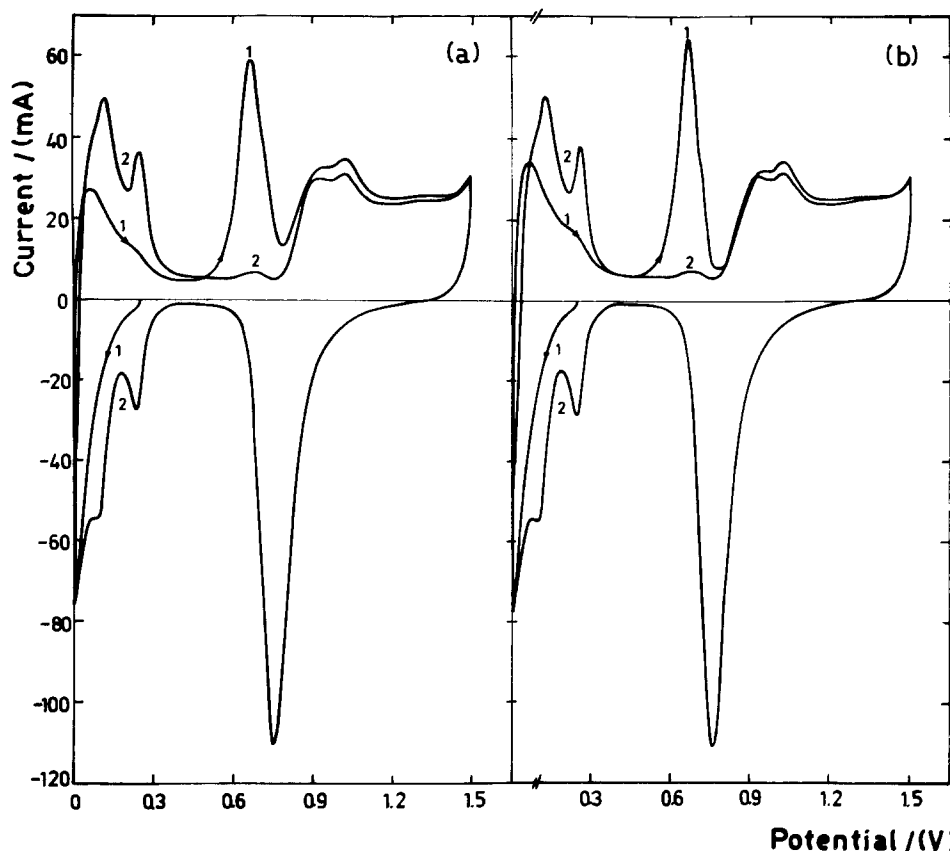


Fig. 7. Potentiodynamic I/E profiles run at 0.4 V/sec using the perturbation program (b) shown in Fig. 1 at different t_H at 0V. $E_{ad} = 0.25V$; $t_{ad} = 10$ min; 80°C; real electrode area = 101 cm². (a) $t_H = 0.3$ sec; (b) $t_H = 5$ min.

lytes than methane. Thus, the ethane solubility in water at 60°C and 1 atm is 1.8×10^{-6} mol/cm³ (5).

The present potentiodynamic I/E displays indicate that at least three different adsorbed species are produced during the electroadsorption of ethane on platinum. The relative surface concentration of the various adsorbed species depends on the temperature, on the electroadsorption potential, and on the duration of the electroadsorption process. Therefore, from the data presented in this paper it seems reasonable to

conclude that the so-called type I species (14) actually corresponds at least to two different adsorbed species, whose relative contributions to the total electrooxidation charge depend on the electroadsorption conditions. Thus, the current peak I appears as the sum of current peaks I_a and I_b . The splitting of current peak I is more evident at 80°C. The previously described experiments also indicate that an interconversion of the adsorbed species related to the current peaks I_a and I_b is feasible through cathodic hy-

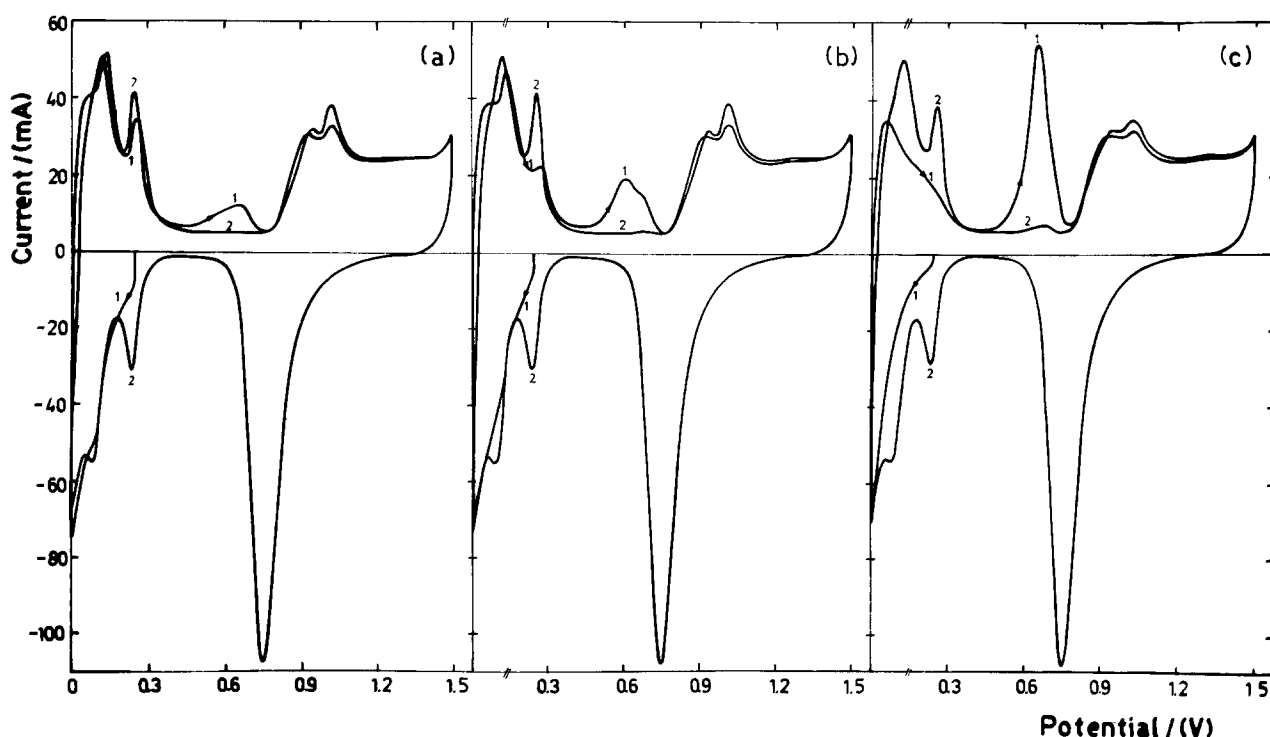


Fig. 8. Potentiodynamic I/E profiles run at 0.4 V/sec using the perturbation program (b) shown in Fig. 1 at different t_{ad} . $E_{ad} = 0.25V$; $t_H = 5$ min at 0V; 80°C; real electrode area = 101 cm². (a) $t_{ad} = 45$ sec; (b) $t_{ad} = 1.5$ min; (c) $t_{ad} = 5$ min.

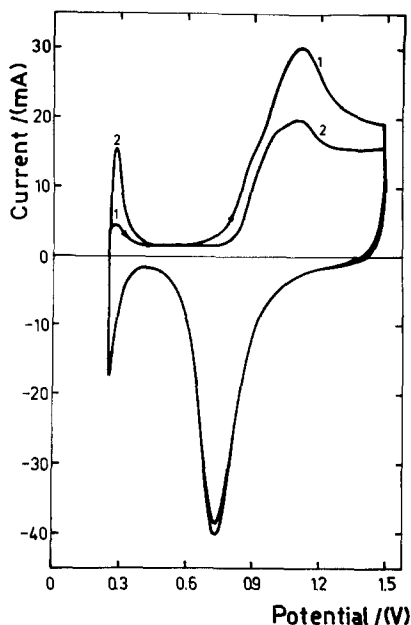


Fig. 9. Potentiodynamic I/E profiles run at 0.3 V/sec using the perturbation program (a) shown in Fig. 1. $E_{ad} = 0.25V$; $t_{ad} = 90$ min; $20^{\circ}C$; real electrode area = 74 cm^2 .

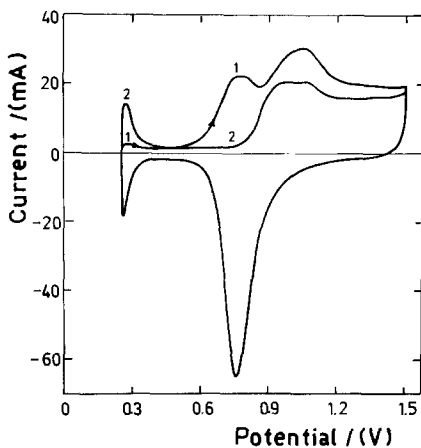


Fig. 10. Potentiodynamic I/E profiles run at 0.3 V/sec using the perturbation program (a) shown in Fig. 1. $E_{ad} = 0.25V$; $t_{ad} = 20$ min; $50^{\circ}C$; real electrode area = 90 cm^2 .

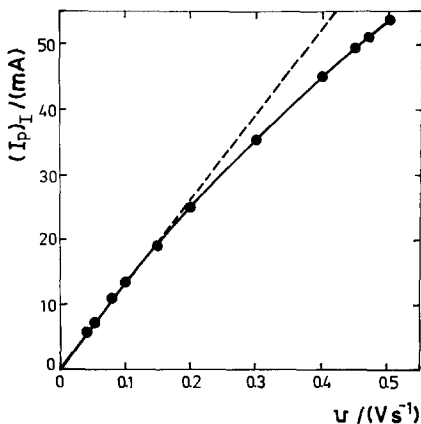


Fig. 11. Dependence of $(I_p)_I$ on v . $E_{ad} = 0.25V$; $t_{ad} = 10$ min; $80^{\circ}C$; real electrode area = 85 cm^2 .

drogenation. The interconversion process is more clearly distinguished in the potentiodynamic runs made at the shortest t_{ad} . These results correlate with those recently discussed for the potentiodynamic electrooxidation of methane on the same electrocatalyst

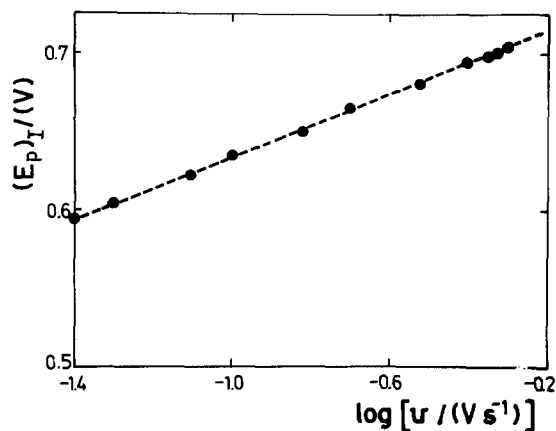


Fig. 12. Dependence of $(E_p)_I$ on $\log v$. $E_{ad} = 0.25V$; $t_{ad} = 10$ min; $80^{\circ}C$; real electrode area = 85 cm^2 . The slope of the dashed line is 0.100 V/decade.

where the current peak I_a was assigned to the electrooxidation of the COH adsorbed species and the current peak I_b was associated with the electrooxidation of the CO adsorbed species (22).

The current peak II obtained during the potentiodynamic oxidation of adsorbed ethane on platinumized platinum in 1N H_2SO_4 coincides with that already observed in the electrooxidation of adsorbed ethylene (20). The latter was earlier attributed to the electrooxidation of a C_2H_2 adsorbed species (20). This species can be cathodically desorbed and it can be assigned to the type II species referred to in the literature (14). The C_2H_2 species seems to be particularly relevant during the electrooxidation of ethane at low temperatures. The relative contribution of type I species and type II species to the total electrooxidation charge is strongly influenced by the temperature. The contribution of the former becomes progressively more relevant than that of the latter as the temperature increases. Therefore, these results show that the potentiodynamic electrooxidation of ethane follows a reaction pattern which is rather more complex than those earlier thought (5, 6, 8, 12, 13), since at least three different adsorbed species can participate in the electrooxidation reaction. However, independently of the number of the adsorbed species the electrooxidation process can be accounted for through the occurrence of electrosorption processes in the early stages

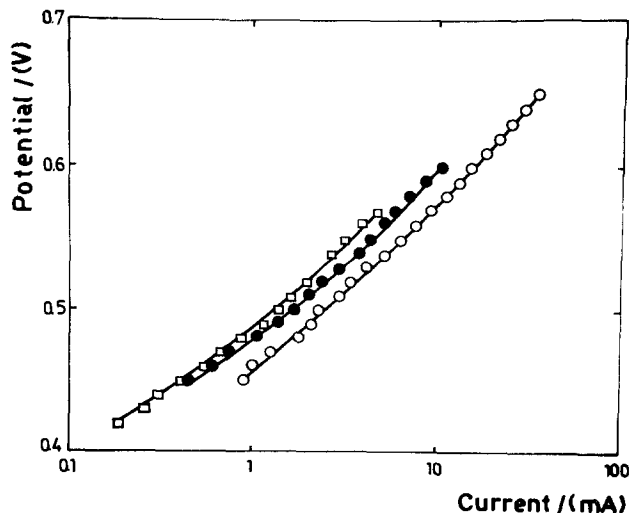
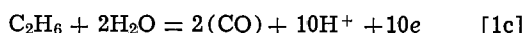
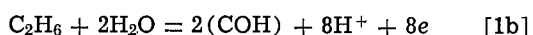
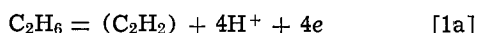


Fig. 13. $E/\log I$ plots derived from potentiodynamic runs at $80^{\circ}C$. $E_{ad} = 0.25V$; $t_{ad} = 10$ min; real electrode area = 85 cm^2 . (\square) $v = 0.05 \text{ V/sec}$; (\bullet) $v = 0.15 \text{ V/sec}$; (\circ) $v = 0.47 \text{ V/sec}$.

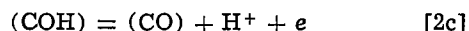
of the reaction, as earlier postulated by other authors (2, 4).

The data derived in this work on the ethane electro-sorption process correlate with the change in the electrode potential with time approaching that of the hydrogen electrode that is observed upon contact of the electrocatalyst with the ethane-saturated electrolyte solution (2, 4). This was formerly explained by assuming that the corresponding open-circuit potential is determined by the equilibrium amount of hydrogen that is formed by dissociative adsorption of ethane on platinum in 5*N* H₂SO₄ at 25°C (2). In agreement with this the cathodic hydrogenation of the electro-sorbed ethane at 25°C yields backward ethane as the main product with small quantities of methane (2).

The electro-sorption and the potentiodynamic electro-oxidation processes.—The results obtained for the ethane electro-sorption at a constant potential and for the potentiodynamic electro-oxidation of the residual electro-sorbed species under ethane-free re-adsorption conditions ($v \cong 0.3$ V/sec) can be interpreted in terms of an electro-sorption process involving at least the following three overall reactions



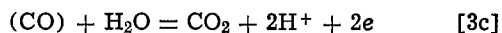
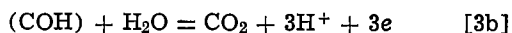
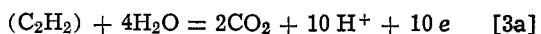
where the parentheses denote the different adsorbed species. The possibility that the different adsorbed species may be linked through interconversion surface processes can be formally expressed in the following way



Reactions [2a] and [2b] are comprised within the reaction formalism earlier proposed for the surface reactions taking part in the electro-oxidation of propane on platinum in 37 mol percent HF at 90°C (24, 25). Otherwise, reaction [2c] has been recently postulated to interpret the cathodic hydrogenation of one of the species formed during the electro-sorption of methane in 1*N* H₂SO₄ at 60°C (22).

As it can be deduced from the potentiodynamic *I/E* profiles the type of adsorbed species predominating on the electrocatalyst surface depends strongly on the temperature. According to the anodic current peak assignment already discussed at low temperatures the C₂H₂ species predominates over the other ones. In contrast, the participation of the CO and COH species in the potentiodynamic electro-oxidation process becomes relatively more important as the temperature increases.

The simultaneous occurrence of three different electro-sorbed species on the electrocatalyst suggests that their potentiodynamic electro-oxidation should be formally interpreted through the following overall reactions



At 80°C, the value of the Q_D/Q_E ratio equal to one indicates that reactions [1b] and [3b] predominate in the electro-sorption and in the potentiodynamic electro-oxidation processes, respectively. Notwithstanding, the slight curvature of the $(I_p)_I$ vs. v plot (Fig. 11) should be related to the existence of more than one adsorbed species on the electrocatalyst. Furthermore, the linear $(E_p)_I$ vs. $\log v$ plot (Fig. 12) indicates that the corresponding electrochemical reaction is highly irreversible. The value of the Tafel slope derived from

the latter which is intermediate between the 2.3(*RT/F*) and the 2.3(2*RT/F*) ratios gives further support to the complexity of the electrochemical reaction.

The possible reaction pathway.—The present results together with the data recently reported (20–22) for the electro-oxidation of ethylene and methane can be correlated through a generalized reaction pathway for the electrochemical oxidation of short chain aliphatic hydrocarbons. This reaction pathway (Fig. 14) involved three main groups of reactions, namely, the hydrocarbon electro-sorption processes, the electro-oxidation processes of the electro-sorbed species, and the interconversion processes of the electro-sorbed species.

From this reaction pathway two limiting cases can immediately be derived. Thus, when either the ethane electro-oxidation reaction proceeds at a low temperature or the reactant is ethylene at any temperature in the 40°–80°C range (20), the main contribution to the electro-sorption process is given by reaction [1a] and the potentiodynamic electro-oxidation is mainly represented by the overall reaction [3a]. Under these circumstances, the group of species of type II, that is, the CH- α -type adsorbed species, predominates on the electrode surface. For the ethylene electro-oxidation the corresponding kinetic equation is associated with a Tafel slope equal to 2*RT/F* (20, 21).

On the other hand, when either the ethane electro-oxidation reaction takes place at high temperature or the reactant is methane the electro-sorption process and the corresponding potentiodynamic electro-oxidation proceed via reactions [1b], [1c], [3b], and [3c] as the main contributions. The principal interconversion process of the adsorbed species is given by reaction [2c] which explains the observed cathodic electro-reduction of the CO-species. In this second limiting case, two

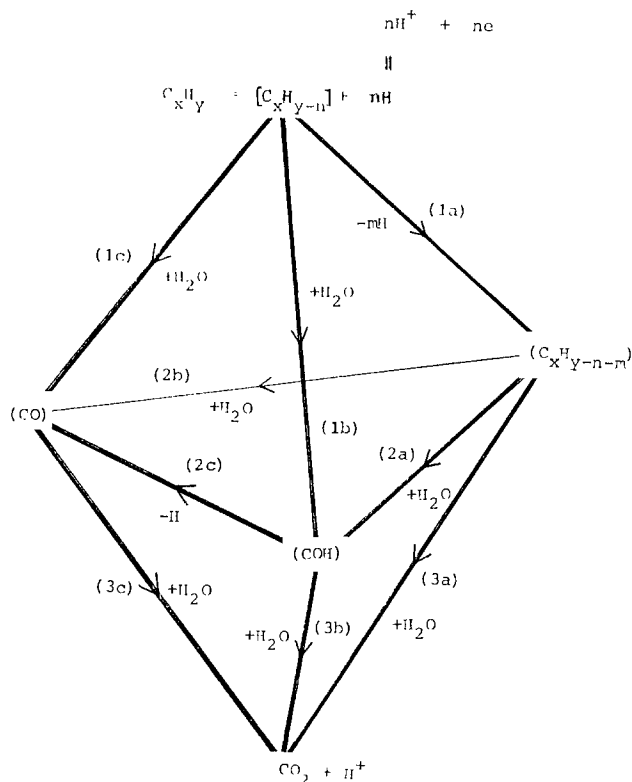


Fig. 14. Possible reaction pathway for the electrochemical oxidation of C_xH_y on platinum. C_xH_y represents either CH_4 , C_2H_4 , or C_2H_6 . $[\text{C}_x\text{H}_y-n]$ corresponds to the intermediate formed in the initial hydrocarbon electro-sorption process. The parentheses denote potentiodynamically detectable adsorbed species. The numbers of the reactions correlate with those given in the text for the particular case of the electrochemical oxidation of ethane.

oxygen-containing adsorbed species are involved in the electrochemical reaction and no simple kinetic law can be obtained. However, at low v the $E/\log I$ plots can be approximated to a straight line with the slope $2.3(RT/F)$ within a relatively low potential range. A similar Tafel slope has been previously reported for the stationary electrooxidation of ethane on platinum (3).

At any situation comprised between the two limiting cases already referred to, particularly under stationary state conditions, the participation of all the above-mentioned reactions should be considered. The relative contribution of each particular reaction depending on the temperature, the applied potential, and the time the hydrocarbon saturated electrolyte is left in contact with the electrocatalyst.

The general scheme applied to the potentiodynamic electrooxidation of adsorbed ethane on platinum indicates that the overall anodic current, i , at any potential is the sum of the contributions of reactions [3a] to [3c]

$$i = i_{3a} + i_{3b} + i_{3c} \quad [4]$$

where the i_{3a} , i_{3b} , and i_{3c} are potential and time dependent terms. The current associated with each adsorbed reactant can be expressed through conventional rate equations involving the interaction energy terms of the adsorbed species. Therefore, in this case it is difficult to derive a more detailed mechanistic conclusion for the electrochemical reaction from the corresponding kinetic data.

The postulated reaction pathway involving different chemisorbed species formed through a combination of consecutive and alternative steps correlates, in principle, with the general reaction scheme recently proposed for the electrooxidation of simple organic substances at platinum group metals (26).

Acknowledgment

INIFTA is sponsored by the Consejo Nacional de Investigaciones Científicas y Técnicas, the Universidad Nacional de La Plata, and the Comisión de Investigaciones Científicas (Provincia de Buenos Aires). This work was partially sponsored by the Regional Program for the Scientific and Technological Development of the Organization of the American States.

Manuscript submitted Aug. 22, 1980; revised manuscript received ca. March 31, 1981.

Any discussion of this paper will appear in a Discussion Section to be published in the June 1982 JOURNAL.

All discussions for the June 1982 Discussion Section should be submitted by Feb. 1, 1982.

Publication costs of this article were assisted by Instituto de Investigaciones Fisicoquímicas Teóricas y Aplicadas.

REFERENCES

1. R. K. Burshtein, V. S. Tyurin, and A. G. Pshenichnikov, in Proc. Fourth International Battery Symposium, Brighton, England (1964).
2. L. W. Niedrach, *This Journal*, **111**, 1309 (1964).
3. L. W. Niedrach, S. Gilman, and I. Weinstock, *ibid.*, **112**, 1161 (1965).
4. R. K. Burshtein, A. G. Pshenichnikov, V. S. Tyurin, and L. L. Knots, *Elektrokhimiya*, **1**, 1268 (1965).
5. S. Gilman, *Trans. Faraday Soc.*, **61**, 2546 (1965).
6. S. Gilman, *Trans. Faraday Soc.*, **61**, 2561 (1965).
7. S. Gilman, in "Hydrocarbon Fuel Cell Technology," B. S. Baker, Editor, Academic Press, New York (1965).
8. S. Gilman, *This Journal*, **113**, 1306 (1966).
9. S. Gilman, *J. Phys. Chem.*, **71**, 2424 (1967).
10. L. W. Niedrach and M. Tochner, *This Journal*, **114**, 17 (1967).
11. G. Aronowitz and R. J. Flannery, *ibid.*, **116**, 938 (1969).
12. V. S. Tyurin, A. G. Pshenichnikov, and R. K. Burshtein, *Elektrokhimiya*, **5**, 1165 (1969).
13. V. S. Tyurin, A. G. Pshenichnikov, and R. K. Burshtein, *ibid.*, **5**, 1168 (1969).
14. E. J. Cairns, in "Advances in Electrochemistry and Electrochemical Engineering," C. W. Tobias, Editor, Vol. 8, Wiley-Interscience, New York (1971).
15. S. B. Brummer, in Preprints of Papers, American Chemical Society, Div. of Fuel Chem., **11**, (No. 3), 178 (1967).
16. S. B. Brummer, J. I. Ford, and M. J. Turner, *J. Phys. Chem.*, **69**, 3424 (1965).
17. S. B. Brummer and M. J. Turner, in "Hydrocarbon Fuel Cell Technology," B. S. Baker, Editor, Academic Press, New York (1965).
18. S. B. Brummer and M. J. Turner, *J. Phys. Chem.*, **71**, 2825 (1967).
19. A. H. Taylor and S. B. Brummer, *ibid.*, **72**, 2856 (1968).
20. W. E. Triaca, T. Rabockai, and A. J. Arvía, *This Journal*, **126**, 218 (1979).
21. W. E. Triaca, A. M. Castro Luna, and A. J. Arvía, *ibid.*, **127**, 826 (1980).
22. M. G. Sustersic, R. Córdova O., W. E. Triaca, and A. J. Arvía, *This Journal*, **127**, 1242 (1980).
23. B. E. Conway, H. Angerstein-Kozłowska, W. B. A. Sharp, and E. E. Criddle, *Anal. Chem.*, **45**, 1331 (1973).
24. E. J. Cairns and A. M. Breitenstein, *This Journal*, **114**, 764 (1967).
25. E. J. Cairns, A. M. Breitenstein, and A. J. Scarpellino, *ibid.*, **115**, 569 (1968).
26. Y. B. Vasiliev, V. S. Bagotskii, and O. A. Khazova, *Elektrokhimiya*, **11**, 1505 (1975).

Analysis of the Current-Voltage Characteristics of Photoelectrolysis Cells

William L. Ahlgren*

Materials Science Department, University of Southern California, Los Angeles, California 90007

ABSTRACT

A theoretical analysis of the current-voltage characteristics of photoelectrolysis cells is presented. The results are used to analyze experimental data for cells using n-type titanium or tungsten oxide semiconductor electrodes in acid electrolyte with platinum counterelectrode. From the i - V characteristics the quantum yield, optimum cell voltage, and maximum electrode efficiency can be derived, as well as the kinetic parameters of the semiconductor electrode (valence and conduction band transfer coefficients and exchange current densities). The theory highlights certain parameters, such as minority carrier exchange current density and diffusion length, which have an important effect on electrode efficiency.

The best-known type of photoelectrolysis cell consists of an n-type semiconductor anode and metal (usually platinum) cathode immersed in an electrolyte solution. When the semiconductor is illuminated and voltage applied to the cell, a family of current-voltage curves such as that shown in Fig. 1 is generated. The convention to be followed regarding sign of cell voltage and direction of current flow are as follows. The cell voltage is that of the semiconductor with respect to the metal and is positive when the semiconductor is the anode. The positive direction of current flow is into the semiconductor from the external circuit (and out of it into the electrolyte). If the electrolyte is only an acid or a base, hydrogen is evolved at the cathode and oxygen at the anode.

The purpose of this paper is to present a theory of these i - V characteristics and to show how it can be used to analyze experimental results. From the experimental i - V characteristics the quantum yield, optimum operating voltage, and maximum efficiency can be derived.

Theory

The theory presented here is due to Dewald (1) and Gerischer (2). The application to photoelectrolysis was developed in detail in (3). It will be assumed that the semiconductor is n-type, however there is no difficulty modifying the theory for p-type semiconductors or p-n cells in which both electrodes are semiconductors (3).

The i - V characteristics of Fig. 1 can be understood qualitatively as follows. When the semiconductor is the cathode (negative cell voltages) it is injecting electrons into the electrolyte. Since these are majority carriers in the n-type material, their concentration is hardly altered by illumination. Consequently the i - V characteristic for negative cell voltages shows no effect of illumination and is exponential, like an ordinary metal electrode. When the semiconductor is the anode (positive cell voltages) it injects minority carriers into the electrolyte. It thus becomes sensitive to illumination, which can alter the minority carrier concentration by orders of magnitude. Minority carrier flow is by diffusion in the bulk of the semiconductor, leading to plateaus in the i - V characteristics for positive cell voltage. These are reminiscent of the common-emitter characteristics of a bipolar transistor, and have a common origin. The limiting current proportional to minority carrier injection is typical of diffusion-controlled transport. The increase in current at high cell voltage

is caused by a transition from minority to majority carrier dominance of charge transport.

To develop this theory quantitatively, the Butler-Volmer equation for semiconductors is postulated.¹ This equation relates the current density at the semiconductor-electrolyte interface to the overpotential η and to the electron and hole concentrations at the surface. These concentrations are then found from continuity conditions, leading to the complete solution for the i - η characteristic of the semiconductor. This is combined with that of the metal to yield the cell i - V characteristics.

The current across the semiconductor-electrolyte interface is

$$i = i_n + i_p \quad [1]$$

where i_n is the current due to charge exchange with the conduction band and i_p with the valence band. An additional term could be included for charge exchange with surface states, but for simplicity this will be subsumed in the valence band current. The relations between these currents and the overpotential at the interface is

$$i_n = i_{no} \left[\exp\left(\frac{\alpha_c p e \eta}{kT}\right) - \frac{n_s^*}{n_s} \exp\left(-\frac{\alpha_v p e \eta}{kT}\right) \right] \quad [2]$$

¹The formulation of this equation for semiconductors is discussed in detail in Ref. (3).

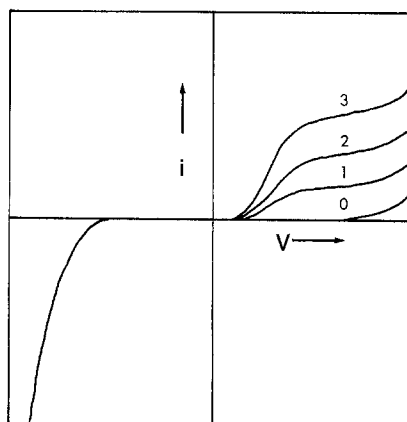


Fig. 1. Typical current-voltage characteristics for photoelectrolysis cells using an n-type semiconductor electrode and a metal counterelectrode. The parameter is light intensity in arbitrary units.

* Electrochemical Society Student Member.

Key words: solar energy, quantum yield, efficiency, titanium oxide, tungsten oxide.

$$i_p = i_{p0} \left[\frac{p_s^*}{p_s} \exp\left(\frac{\overleftarrow{\alpha_{vp} e \eta}}{kT}\right) - \exp\left(-\frac{\overrightarrow{\alpha_{vp} e \eta}}{kT}\right) \right] \quad [3]$$

where i_{p0} is the conduction band exchange current, α_c is the transfer coefficient for electrons crossing the semiconductor-electrolyte interface from electrolyte to semiconductor, $\overrightarrow{\alpha_c}$ is the coefficient for transfer in the opposite direction, ρ is the fraction of the overpotential which occurs in the electrolyte, n_s is the electron concentration at the surface of the semiconductor in equilibrium, and n_s^* is the nonequilibrium value. In Eq. [3] the analogous quantities for the valence band occur (the arrows above the transfer coefficients always indicate the direction of electron transfer; hole transfer is in the opposite direction).

The fraction of the interface potential which occurs in the electrolyte depends roughly on the relative conductivities of the two phases. For a metal, $\rho = 1$ since metallic conductivity is much higher than the electrolyte. For a semiconductor, $\rho = 1$ if the semiconductor surface is accumulated or inverted, but $\rho = 0$ if the surface is depleted.

The currents in Eq. [2] and [3] are due to tunneling of electrons from an ion in the Helmholtz plane of the electrolyte to the surface of the semiconductor. When the surface of a heavily doped semiconductor is depleted the width of the space charge layer may be small enough to permit electrons to tunnel from the electrolyte to the interior of the semiconductor (4). Such tunneling currents would have to be represented by additional terms in Eq. [1]. For present purposes, however, it is not necessary to include these currents in the quantitative model.

The i - V characteristics are obtained by determining the ratios of nonequilibrium to equilibrium carrier concentrations at the surface of the electrode. These are

$$\frac{n_s^*}{n_s} = \frac{n_w^*}{n_o} \exp\left(-\frac{(1-\rho)e\eta}{kT}\right) \quad [4]$$

$$\frac{p_s^*}{p_s} = \frac{p_w^*}{p_o} \exp\left(\frac{(1-\rho)e\eta}{kT}\right) \quad [5]$$

where n_w^*/n_o and p_w^*/p_o are the values at the inside edge of the depletion layer, which is assumed to be of width w . Since electrons are the majority carriers their concentration is hardly changed by illumination, so

$$n_w^* \cong n_o \quad [6]$$

Following Dewald (1), the effect of illumination on the concentration of holes at the inside edge of the depletion layer can be found from the steady-state balance equation for holes within the depletion layer:

Net pair generation rate within depletion layer

= minority carrier flux out of depletion layer

The net generation rate within the depletion layer is the generation due to photon absorption minus the recombination. Dewald assumes that the minority carrier diffusion length is much larger than the width of the depletion region, and consequently within the depletion layer, that surface recombination dominates so that the recombination rate is $v_s(p_w^* - p_o)$, where v_s is the surface recombination velocity. This assumption will be adhered to, although others are possible.

The minority carrier generation due to photon absorption at a depth x in the semiconductor is

$$g(x) = \int_{E_o}^{\infty} \frac{a(E) W(E, x) dE}{E} \quad [7]$$

where $E = h\nu$ is photon energy, E_o is the threshold energy for pair creation, $a(E)$ is the absorption coefficient, and

$$W(E, x) = (1 - R(E)) W_o(E) \exp(-a(E)x) \quad [8]$$

$R(E)$ is the reflectance of the surface (thin film effects are ignored) and $W_o(E)$ is the spectral radiation intensity striking the surface of the semiconductor. As an approximation it will be assumed that

$$g(x) = \frac{\bar{a}\gamma I}{e} \exp(-\bar{a}x) \quad [9]$$

where $\gamma I/e$ and \bar{a} are defined in such a way that [7] and [9] give the same total number of pairs created and also the same number of pairs created within a distance x_o from the surface. The details are given in the Appendix. I is the total radiation intensity ($W \text{ cm}^{-2}$) striking the surface of the semiconductor, e is the elementary charge, and γ is a conversion factor from light intensity to current density (mA W^{-1}). \bar{a} is an average absorption coefficient whose value depends on the depth x_o as specified in the Appendix. The approximation is expected to be most valid when x_o is chosen equal to the depletion layer width.

The minority carrier flux out of the depletion layer is the hole current (i_p) exiting from the semiconductor-electrolyte interface, minus the hole current entering from the bulk. Since minority carrier flow in the bulk is by diffusion, this flux is $J_p = -D_p(dp^*/dx)$, where D_p is the hole diffusion coefficient and the derivative is evaluated at the inside edge of the depletion layer. The minority concentration profile $p^*(x)$ is found from the steady-state minority carrier continuity equation

$$\frac{L_p^2}{\tau_p} \frac{d^2 p^*}{dx^2} - \frac{p^* - p_o}{\tau_p} = -g(x) \quad [10]$$

where L_p and τ_p are the minority carrier diffusion length and bulk lifetime, respectively. These are related to the diffusion coefficient by $D_p = L_p^2/\tau_p$. Equation [10] can be solved subject to the boundary conditions $p^* \rightarrow p_o$ as $x \rightarrow \infty$ and $p^* = p_w^*$ at $x = w$. The solution $p^*(x)$ is then differentiated and the derivative evaluated at $x = w$ in order to find J_p . The result is

$$J_p = \frac{L_p}{\tau_p} (p_w^* - p_o) - \frac{\bar{a}L_p\gamma I \exp(-\bar{a}w)}{e(1 + \bar{a}L_p)} \quad [11]$$

The minority carrier balance on the depletion layer can be expressed as

$$\int_0^w g(x) dx - v_s(p_w^* - p_o) = \frac{i_p}{e} - J_p$$

Using Eq. [9] and [11], this can be solved to yield

$$\frac{p_w^*}{p_o} = 1 + \frac{\gamma\phi_s I - i_p}{i_s} \quad [12]$$

where

$$\phi_s = 1 - \frac{\exp(-\bar{a}w)}{1 + \bar{a}L_p} \quad [13]$$

and

$$i_s = ep_o \left(\frac{L_p}{\tau_p} + v_s \right) \quad [14]$$

ϕ_s and i_s are the saturation values of the quantum yield and dark current density which are approached in the plateau region of the i - V characteristics. The dark saturation current is due to thermal generation of electron-hole pairs, L_p/τ_p representing bulk generation and v_s surface generation.

The i - V characteristics of the semiconductor electrode are obtained by substituting Eq. [2]-[6] and [12] into Eq. [1], and the i - V characteristics of the cell follow from the relations between the electrode overpotentials

and the free energy change for the cell reaction.² For positive cell voltages, $\eta = V - V_{tc}$ where V_{tc} is the threshold voltage for current flow with the metal counterelectrode as cathode

$$V_{tc} = \Delta G/e - \xi_c \quad [15]$$

in which ΔG is the free-energy change per electron transferred and ξ_c is the overpotential at the metal cathode (a negative number). For negative cell voltages, $\eta = V - V_{ta}$, where

$$V_{ta} = -\Delta G/e - \xi_a \quad [16]$$

ξ_a being the overpotential at the metal anode (a positive number).

For cell voltages greater than a few kT/e more negative than V_{ta} , Eq. [1] becomes

$$i(v) = -i_{no} \exp(-\alpha_n(V - V_{ta})e/kT) \quad [17]$$

In this case $\rho \approx 1$ since the surface of the semiconductor is accumulated. Since the metal anode also follows a Tafel law, it can be shown (5) that

$$i(V) = -i_{o,cell} \exp(-A(eV - \Delta G)/kT) \quad [18]$$

where

$$A = \frac{\alpha_n \alpha_a}{\alpha_n + \alpha_a} \quad [19]$$

$$i_{o,cell} = (i_{no})^{A/\alpha_n} (i_o)^{A/\alpha_a} \quad [20]$$

and α_a , i_o are the anodic transfer coefficient and exchange current density at the metal electrode.

For positive cell voltages the semiconductor surface is depleted and $\rho \approx 0$. Equation [1] then becomes³

$$i(V) = \phi(V)\gamma I + i_d(V) \quad [21]$$

where

$$\phi(V) = \frac{\phi_s}{1 + \exp\left(-\frac{\alpha_p e(V - V_{1/2})}{kT}\right)} \quad [22]$$

and

$$V_{1/2} = V_{tc} - \frac{kT}{\alpha_p e} \ln \frac{i_{po}}{i_s} \quad [23]$$

The dark current is

$$i_d(V) = i_s \frac{1 - \exp\left(-\frac{e(V - V_{tc})}{kT}\right)}{1 + \exp\left(-\frac{\alpha_p e(V - V_{tc})}{kT}\right)} \quad [24]$$

This reaches the saturation value i_s for $V - V_{tc}$ greater than a few kT/e . For $V \gg V_{tc}$, however, the dark current increases rapidly for two reasons. When the surface becomes inverted its conductivity increases and ρ approaches unity, i.e., the interface potential drop begins to occur in the electrolyte rather than the semiconductor. The dark current is then

$$i_d(V) = i_s + i_{no} \exp\left(\frac{\alpha_c \rho e(V - V_{tc})}{kT}\right) \quad [25]$$

The increase in dark current is due to majority carriers, which are not limited by diffusion in the bulk of the semiconductor.

Another cause for the increase of dark current is electron tunneling from the electrolyte to the interior

of the semiconductor rather than its surface (4). This is only possible if the surface depletion layer is thin enough and is therefore most likely in heavily doped semiconductors. Electrons can then tunnel from the electrolyte through to empty states in the conduction band in the interior of the semiconductor. This component of the dark current, which is also due to majority carriers, has not been included in the present analysis.

The factors γ and ϕ determine the efficiency of the cell as a solar energy converter. The light-to-current conversion factor γ expresses the fraction of all photons in the solar spectrum which are absorbed by the semiconductor creating electron-hole pairs. Details are given in the Appendix. It depends only on the optical properties of the semiconductor (principally the band-gap and refractive index) and the spectral distribution of the incident radiation. It does not depend on the cell voltage.

The quantum yield ϕ is the fraction of electron-hole pairs created which are collected. It depends on the cell voltage in two ways. Increasing cell voltage decreases the minority carrier concentration at the inside edge of the depletion layer, and thereby decreases surface recombination. This is the effect of the denominator in Eq. [22]. The fraction of minority carriers lost to recombination falls to one-half at $V_{1/2}$, given by Eq. [23]. This is also the voltage at which the photocurrent ($i - i_d$) reaches half its limiting (plateau) value. As the voltage is increased further the minority carrier concentration at the inside edge of the depletion layer and hence the recombination falls to zero. The quantum yield then approaches its saturation value given by Eq. [13]. This equation shows that the limiting value of quantum yield depends on the absorption coefficient, depletion layer width, and minority carrier diffusion length, reflecting the fact that only those holes created in the depletion layer or within a diffusion length from it will be collected.

The cell voltage also affects quantum yield by modulation of the depletion layer width

$$w(V) = \sqrt{\frac{2\epsilon\epsilon_0\psi_b(V)}{eN_D}} \quad [26]$$

where ϵ is the dielectric constant of the semiconductor, ϵ_0 the permittivity of free space, N_D the donor concentration, and $\psi_b(V)$ the voltage barrier height at the surface of the semiconductor. To relate this to cell voltage requires knowledge of the structure of the double layers at both electrodes under nonequilibrium conditions. A detailed solution to this problem will not be attempted. It should be noted, however, that the barrier height and hence the width of the depletion layer will increase with increasing cell voltage, leading to an increasing value of ϕ_s . This is probably the reason why the plateau region of the i - V curves slopes upward rather than being perfectly flat.

Electrode Efficiency

The efficiency of the semiconductor photoelectrode can be defined as the net free energy produced divided by the solar input. The net free energy is the free energy content of the chemical product minus the electric power consumed by the electrode. Thus

$$\text{Efficiency} = \frac{n\Delta G - iA(V - \xi_c)}{IA} = \frac{i(V_{tc} - V)}{I} \quad [27]$$

where n is the rate of production (molecules per second) and A is the area of the photoelectrode. The overpotential ξ_c at the metal counterelectrode has been subtracted from the cell voltage since this loss should not be charged to the photoelectrode.

The electrode efficiency depends on cell voltage through Eq. [21]-[27]. There is an optimum voltage

² Cell resistance and concentration overpotentials in the electrolyte are ignored for simplicity.

³ Substitute [6] and [12] into [2] and [3], and these into [1], making use of $\eta = V - V_{tc}$.

since increasing V increases the quantum yield but also the electric power consumption. Neglecting i_a , which is usually small at low cell voltages where the optimum occurs, it is found that the condition for maximum efficiency is

$$\exp x + x + 1 + \delta = 0 \quad [28]$$

where

$$x = \frac{\leftarrow{\alpha}_p e (V_{\max} - V_{1/2})}{kT} \quad [29]$$

$$\delta = \frac{\leftarrow{\alpha}_p e (V_{1/2} - V_{tc})}{kT} = -\ln \frac{i_{po}}{i_s} \quad [30]$$

and V_{\max} is the cell voltage which maximizes the electrode efficiency.

Application to Experimental Current-Voltage Characteristics

The foregoing theory can be applied to the analysis of i - V characteristics obtained by experiment. As an example the photoelectrolysis cells reported in (6) will be used. These consist of TiO_2 or WO_3 semiconductors immersed in $1\text{M H}_2\text{SO}_4$ with a platinum counterelectrode and illuminated by a xenon lamp (chosen to simulate the solar spectrum). The semiconductor electrodes were prepared by heating the corresponding metal foil in air for 1 hr at $500^\circ\text{--}600^\circ\text{C}$. The cell reaction is $\text{H}_2\text{O} \rightarrow \text{H}_2 + \frac{1}{2}\text{O}_2$, for which $\Delta G = 1.23\text{ eV}$. The i - V characteristics, which are presented in (6), resemble Fig. 1 of the present paper.

With negative cell voltage hydrogen is evolved at the semiconductor cathode and oxygen at the platinum anode. Figure 2 is a plot of $\ln|i|$ vs. $|V|$ which shows that Eq. [18] is obeyed. The kinetic parameters $\rightarrow{\alpha}_n$ and i_{no} , obtained from Fig. 2 using Eq. [18] to [20], are listed in Table I. The kinetic parameters $\leftarrow{\alpha}$ and i_o of the platinum anode were taken from Table II.

When the cell voltage is positive, oxygen is evolved at the semiconductor anode and hydrogen at the plat-

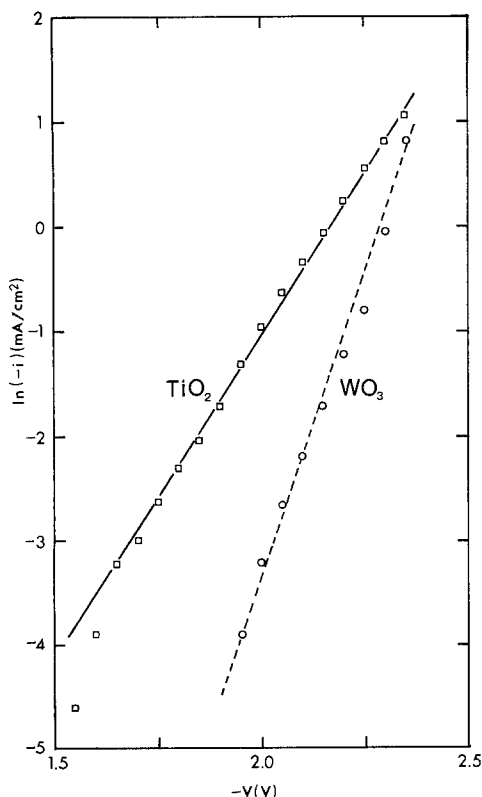


Fig. 2. Plot of $\ln(-i)$ vs. $-V$ for negative cell voltages and currents.

Table I. Kinetic parameters of forward-biased n-type oxidized metal electrodes in $1\text{M H}_2\text{SO}_4$

| Semiconductor | A | $-\log i_{o,cell}$ (mA cm^{-2}) | $\leftarrow{\alpha}_n$ | $-\log i_{no}$ (mA cm^{-2}) |
|----------------|------|---|------------------------|---|
| TiO_2 | 0.16 | 2.6 | 0.22 | 1.1 |
| WO_3 | 0.35 | 5.2 | 0.84 | 3.1 |

Table II. Kinetic parameters of platinum electrode in acid medium

| Electrode function | Gas evolved | α | $-\log i_o$ (mA cm^{-2}) | Overpotential at $i = 1\text{ mA cm}^{-2}$ (V) |
|--------------------|--------------|----------|--|--|
| Cathode | H_2 | 0.5 | 0.1 | -0.01 |
| Anode | O_2 | 0.6 | 6.7 | 0.66 |

num cathode. It will be assumed for the sake of analysis that the overpotential at the platinum cathode, instead of following a Tafel law, remains constant at its value for a current density of 1 mA cm^{-2} , which is -0.01V (from Table II). Thus V_{tc} is also assumed constant and equal to 1.24V .

The quantum yield ϕ can be obtained by plotting current as a function of illumination intensity with cell voltage as a parameter. This yields a family of straight lines with slope dependent on the voltage. The quantum yield is obtained, according to Eq. [21], by dividing this slope by γ

$$\phi(v) = \frac{1}{\gamma} \left. \frac{\partial i}{\partial I} \right|_v \quad [31]$$

The saturation value ϕ_s is obtained by choosing V in the plateau region. Rearrangement of Eq. [22] gives

$$\frac{\phi}{\phi_s - \phi} = \exp \frac{\leftarrow{\alpha}_p e (V - V_{1/2})}{kT} = \frac{i_{po}}{i_s} \exp \frac{\leftarrow{\alpha}_p e (V - V_{tc})}{kT} \quad [32]$$

Figure 3 shows a plot of $\ln \phi / (\phi_s - \phi)$ vs. V for TiO_2 and WO_3 anodes. The values of $\leftarrow{\alpha}_p$ and $\ln i_{po}/i_s$ determined from these plots are listed in Table III.

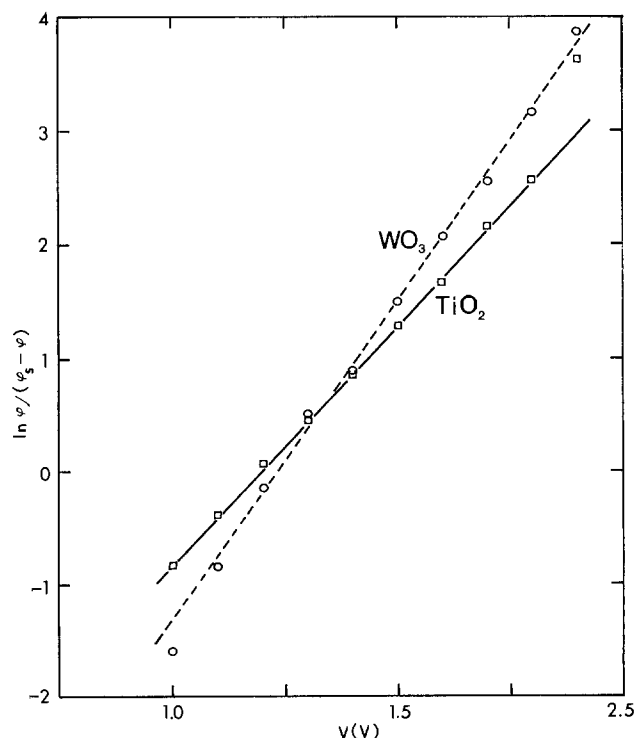


Fig. 3. Plot of $\ln \phi / (\phi_s - \phi)$ vs. V for positive cell voltages

Table III. Kinetic parameters of reverse-biased n-type oxidized metal electrodes in 1M H₂SO₄

| Semiconductor | γ (mA W ⁻¹) | ϕ_s | α_p | $\ln \frac{i_{po}}{i_s}$ | i_s (mA cm ⁻²) | $-\log$ $\frac{i_{po}}{i_s}$ (mA cm ⁻²) | $V_{1/2}$ (V) |
|------------------|--------------------------------------|----------|------------|--------------------------|------------------------------------|--|------------------|
| TiO ₂ | 36.2 | 0.05 | 0.12 | 0.2 | 0.004 | 2.3 | 1.20 |
| WO ₃ | 47.9 | 0.10 | 0.14 | 0.1 | 0.007 | 2.1 | 1.22 |

The current density i_s is the value of the dark current in the plateau region and can be read directly from the i - V characteristic. The hole exchange current for the semiconductor electrode, i_{po} , can then be calculated. The voltage $V_{1/2}$ can also be read directly from the i - V characteristic, or can be calculated using Eq. [23].

The optimum operating voltage can be found using Eq. [28]-[30] and the information in Table III. It is found that for TiO₂, $V_{max} = 0.9V$ and the maximum electrode efficiency is 0.02%. For WO₃ the corresponding values are 1.0V and 0.01%. The low efficiencies are probably caused by the very defective nature of the semiconductor electrodes used, leading to a short hole diffusion length and, hence, low saturation quantum yield ϕ_s . It is instructive to insert some values into Eq. [26] and [13]. Assuming a donor density of 10²⁰ cm⁻³, dielectric constant of 100, and surface barrier of 1V, the depletion layer width is about 10⁻⁶ cm. The absorption coefficient is about 5 × 10⁴ cm⁻¹ (see Appendix). Ghosh and Maruska (7) found the hole diffusion length to be about 10⁻⁴ cm in single-crystal TiO₂. According to Eq. [13], this would lead to $\phi_s \approx 0.8$, sixteen times greater than that observed, and a correspondingly larger efficiency (~ 0.3%), which has been observed with single crystal electrodes. This suggests that the minority carrier diffusion length in TiO₂ prepared by oxidizing the metal foil is about 10⁻⁶ cm, 100 times smaller than that in the single crystal. The minority carrier diffusion length is then about the same as the depletion layer width. Since the two are of comparable magnitude, modulation of the depletion layer width by the cell voltage has a strong effect on the quantum yield, giving the observed upward sloping plateaus in the i - V characteristic. Flatter plateaus are to be expected from the single crystal material.

Discussion

Although Dewald's paper (1) is often cited, the theory embodied in it does not seem to have been applied previously to photoelectrolysis. It is useful to do so since it allows the derivation of quantum yields, optimum operating voltage, and maximum efficiency from experimental i - V curves. It also provides a different viewpoint on the effect of fundamental material parameters on cell performance. Thus, for example, Eq. [22] and [23] indicate that a cell capable of operating at zero cell voltage requires a material with a large minority carrier exchange current density and a small dark saturation current, that is, the ratio of photogenerated holes participating in the cell reaction to those which merely recombine with electrons should be large. A large hole exchange current density means that holes are extracted from the semiconductor rapidly, preventing their recombination. The hole exchange current density may be as important a parameter as the electron affinity, which has been highlighted by previous theories (11). Similarly, Eq. [13] focuses attention on the importance of the minority-carrier diffusion length. If the absorption length of the material is much larger than the width of the depletion layer, a large quantum yield can only be achieved if the diffusion length is large enough

Acknowledgment

This research was performed at the Optical Sciences Center of the University of Arizona, and was supported

in part by the National Science Foundation through the grant of a solar energy traineeship.

Manuscript submitted Nov. 5, 1980; revised manuscript received ca. April 30, 1981.

Any discussion of this paper will appear in a Discussion Section to be published in the June 1982 JOURNAL. All discussions for the June 1982 Discussion Section should be submitted by Feb. 1, 1982.

APPENDIX

The parameters occurring in Eq. [9] are defined as follows. The average absorption coefficient \bar{a} is given by $\exp(-\bar{a}x_0)$

$$\bar{a} = \frac{\int_{E_0}^{\infty} \exp(-a(E)x_0) (1-R(E)) W_0(E) \frac{dE}{E}}{\int_{E_0}^{\infty} (1-R(E)) W_0(E) \frac{dE}{E}} \quad [A-1]$$

where x_0 is an arbitrary length, best chosen equal to the width of the depletion layer (about 10⁻⁶ cm for the electrodes studied in this paper). The light-to-current conversion factor γ is defined by

$$\gamma = \frac{e}{I} \int_{E_0}^{\infty} (1-R(E)) W_0(E) \frac{dE}{E} \quad [A-2]$$

where I is the total radiation intensity striking the surface

$$I = \int_0^{\infty} W_0(E) dE \quad [A-3]$$

To compute \bar{a} and γ it is convenient to approximate the solar spectrum by that of a black body at 5800 K. Thus

$$W_0(E) \propto \frac{E^3}{\exp(E/kT_s) - 1} \quad [A-4]$$

where $kT_s = 0.50$ eV. For $E \gg kT_s$

$$W_0(E) \propto E^3 \exp(-E/kT_s) \quad [A-5]$$

which can be used to evaluate the integrals in Eq.

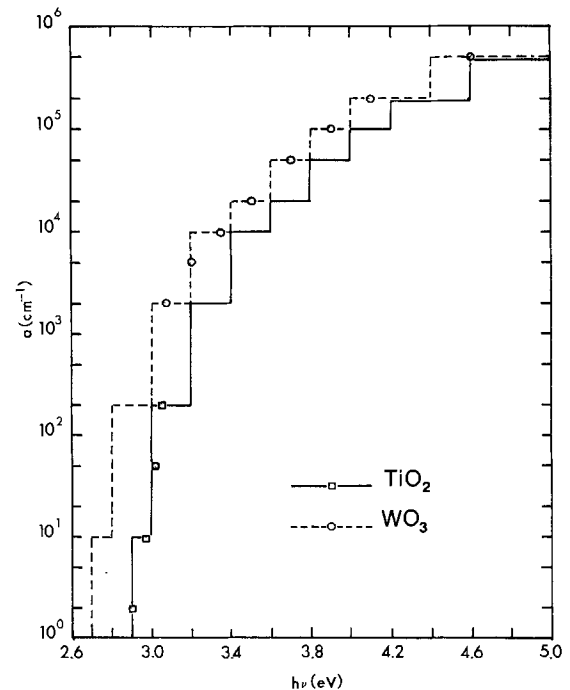


Fig. 4. Absorption coefficient α as a function for photon energy $h\nu$ for TiO₂ and WO₃. Experimental points are taken from Crone-meyer (9) and Deb (10). The lines indicate values assumed in this paper for the purpose of estimating \bar{a} .

[A-1] and [A-2] provided $E_0 \gg kT_s$ (true of wide bandgap semiconductors such as TiO_2 and WO_3).

The reflectance is equal to $(n-1)^2/(n+1)^2$ where n is the refractive index, which is assumed to have no dispersion. Equation [A-1] then becomes

$$\exp(-\bar{a}x_0) = \int_{E_0}^{\infty} \exp(-a(E)x_0) f_{\text{ph}}(E_0, E) dE \quad [\text{A-6}]$$

where

$$f_{\text{ph}}(E_0, E) = \frac{W_0(E)}{E \int_{E_0}^{\infty} \frac{W_0(E)}{E} dE} \quad [\text{A-7}]$$

$f_{\text{ph}}(E_0, E)$ is the fraction of all photons with energy greater than E_0 which have energy E . Equation [A-2] becomes

$$\gamma = \frac{4n}{(n+1)^2} \frac{15e}{\pi^4 kT_s} \left(1 + \left(1 + \frac{E_0}{kT_s} \right)^2 \right) \exp\left(-\frac{E_0}{kT_s}\right) \quad [\text{A-8}]$$

The threshold energy E_0 may be less than the bandgap due to band-tailing and other effects (8). For TiO_2 and WO_3 it is assumed that E_0 is 2.9 and 2.7 eV,

respectively, (6, 9, 10), leading to the γ values listed in Table III when $n = 2.5$.

The absorption coefficients $a(E)$ assumed for TiO_2 and WO_3 are shown in Fig. 4, together with some experimental points from Ref. (9) and (10). With $x_0 = 10^{-6}$ cm, Eq. [A-6] leads to $\bar{a} = 5 \times 10^4 \text{ cm}^{-1}$ for both TiO_2 and WO_3 .

REFERENCES

1. J. F. Dewald, in "Semiconductors," N. B. Hannay, Editor, p. 727, ACS Monograph 140, Reinhold, New York (1959).
2. H. Gerischer, *Z. Phys. Chem., N.F.*, **26**, 223, 325 (1960); **27**, 48 (1961).
3. W. L. Ahlgren, MS Thesis, The University of Arizona, Tucson (1977).
4. P. J. Boddy, *This Journal*, **115**, 199 (1968).
5. J. O'M. Bockris and A. K. N. Reddy, "Modern Electrochemistry," p. 1132, Plenum, New York (1970).
6. W. L. Ahlgren and S. O. Sari, *Surf. Sci.*, **76**, 148 (1978).
7. A. K. Ghosh and H. P. Maruska, *This Journal*, **124**, 1516 (1977).
8. J. I. Pankove, "Optical Processes in Semiconductors," Chap. 3, Prentice-Hall, Englewood Cliffs, NJ (1971).
9. D. C. Cronmeyer, *Phys. Rev.*, **87**, 876 (1952).
10. S. K. Deb, *Philos. Mag.*, **27**, 801 (1973).
11. J. G. Mavroides, J. A. Kafalas, and D. F. Kolesar, *Appl. Phys. Lett.*, **28**, 241 (1976).

The Photoelectrochemical Behavior of Ferric Oxide in the Presence of Redox Reagents

P. Iwanski, J. S. Curran, and W. Gissler*

Commission of the European Communities Joint Research Centre, Ispra Establishment, Varese, Italy

and R. Memming

Philips GmbH Forschungslaboratorium Hamburg, Hamburg, Germany

ABSTRACT

The influence of dissolved sulfide ion and the ferri/ferrocyanide redox system on the photoelectrochemical behavior of iron oxide has been investigated. Particular attention was given to transient behavior and to dark current phenomena. An interpretation of the results is given in terms of a back-reaction of photogenerated species with conduction band electrons via surface states.

Ferric oxide is a potentially interesting semiconductor material for use in semiconductor-liquid junction solar cells. It is very easily produced, resists photo-decomposition, and possesses a flatband potential close to the hydrogen evolution potential. Its bandgap of 2.2 eV allows, in principle, a solar energy conversion efficiency of up to 20%.

Unfortunately ferric oxide always displays a low quantum yield of photocurrent when used as a photoanode. Even single crystal samples showed a quantum yield of only 20% at high anodic polarization (1). One reason for this may be that two optical absorption processes occur in ferric oxide, only one of which leads to electrochemically active holes (2).

Other unusual complexities in the behavior of ferric oxide have been revealed; relatively important transient effects exist (3) which can be modified by preparation (4), and there is strong evidence from anomalous differential space charge capacity behavior of a high

density of a second deep donor level (5, 6). High anodic and cathodic dark currents (7) may be linked with this latter phenomenon.

In the work described below, the influence of redox reagents on the behavior was examined in order to try to establish the role of the electrochemical charge-transfer mechanism in determining the overall behavior of ferric oxide.

Experimental

Electrodes were made by thermal oxidation of "ARMCO" iron in which the total concentration of all the elements C, Mn, P, S, and Si was less than 0.1% and the concentration of Cu less than 0.15%. Iron disks were mechanically polished and maintained for 4 hr at 610°C in air. The resulting oxide films were approximately 30 μm thick, the outer 2 μm consisting of $\alpha\text{-Fe}_2\text{O}_3$. Some experiments were also performed with $\alpha\text{-Fe}_2\text{O}_3$ films on iron prepared by reactive sputtering of ferric oxide of 99.99% purity in an Ar/O_2 atmosphere. The disks were mounted in Perspex holders.

* Electrochemical Society Active Member.

Key words: charge-transfer, solar cells, surface states.

The electrodes were mounted in single compartment cells with a calomel reference and platinum counter-electrodes.

All chemicals used were of Analar Grade. Water was deionized. A PAR Model 173 potentiostat was used in conjunction with a PAR Model 186 lock-in amplifier, a PAR Model 175 Universal Programmer, and a PAR Model 4202 Signal Averager to determine transient behavior. Illumination was from a 500W xenon lamp filtered by 10 cm of water and the light was interrupted by either a PAR Model 192 chopper or a Spindler & Hoyer rapid manual shutter. Capacity measurements were made by superimposing on the potentiostatically controlled d-c voltage an a-c voltage of approximately 100 mV amplitude at 50 or 100 kHz. The a-c amplitude and phase angle were measured in a circuit in which the cell was placed in series with a resistance (8).

Rotating disk electrode experiments were made with equipment supplied by Oxford Electrodes Limited. The absorption of sulfide ion on iron oxide was measured using a Beckman 39610 specific electrode.

Results

The current-voltage dependence of iron oxide electrodes in the presence of sulfide ion and ferrocyanide ion are displayed in Fig. 1, together with the behavior in the blank electrolyte, 1M NaOH. The electrodes were illuminated intermittently in the course of an anodic potential scan (20 mV sec^{-1}) with rather short light pulses, in order to demonstrate general features of their overall behavior (full line). The dashed line shows the photocurrent under continuous illumination with white light. The overall photocurrent is increased markedly in the presence of both redox systems and there is an obvious suppression of the transient effects observed in the blank electrolyte. Simultaneously the anodic dark currents are enhanced at potentials positive of the standard redox potential of the couples concerned. Measurements with ferrocyanide present in lower concentration (5, 7) did not reveal these effects on the photocurrent clearly.

The changes in behavior shown in Fig. 1 are unlikely to be due to the specific adsorption of the charged redox species, as is for example the case with CdS/S²⁻ (9). Differential capacitance measurements and the direct measurement of Sn²⁺ and Fe(CN)₆⁴⁻ adsorption by an Fe₂O₃ powder suspension, in experiments similar to Ginley and Butler's (10) show no evidence of adsorption.

The transient behavior was examined in more detail using the signal averager technique. In Fig. 2 the relaxation of photocurrent is shown for different light intensities using an argon laser ($\lambda = 488 \text{ nm}$). These measurements were performed in solutions free from any redox system at a constant electrode potential ($U_E = +0.2 \text{ V}$). The potential dependence of the relaxation effects is given in Fig. 3 as obtained with and without a reducing agent (Sn²⁺ and [Fe(CN)₆]⁴⁻). This figure shows quite clearly that the transient be-

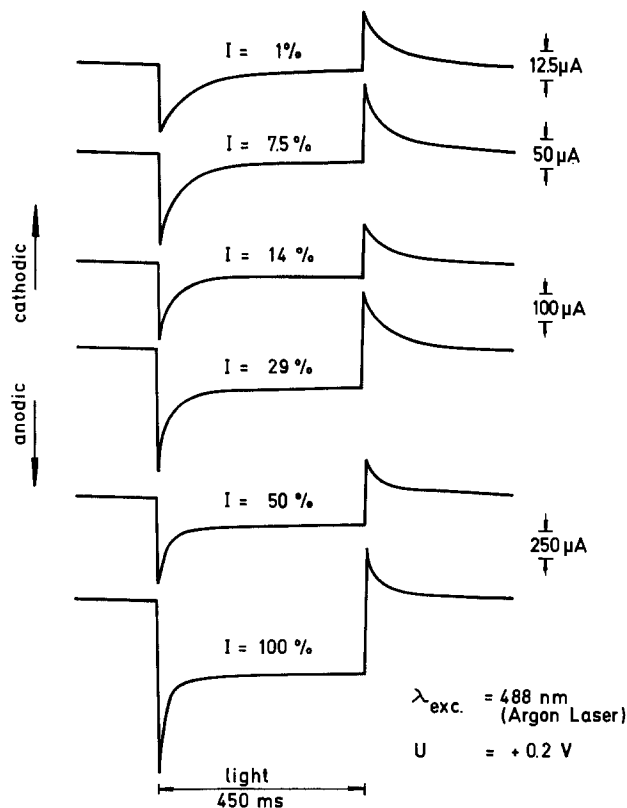


Fig. 2. Relaxation of photocurrent at $U_E = +0.2 \text{ V}$ in 1M NaOH at different light intensities. Light intensity is 100% at 0.7W output power of the argon laser.

havior disappears if a reducing agent is added to the electrolyte.

It is interesting to note that the relaxation phenomena can also be influenced by addition of an oxidizing agent such as [Fe(CN)₆]³⁻ as shown in Fig. 4. According to this figure the decay disappears nearly completely at cathodic potentials with respect to the standard potential of this redox system. The relaxation of the photocurrent is shown in detail for different concentrations of [Fe(CN)₆]³⁻ at an electrode potential of -0.1 V in Fig. 5. In this potential range also a considerable dark current was observed (see Fig. 4). Its concentration dependence is given in Fig. 6. It should be emphasized that these measurements were performed using a rotating disk electrode (rotation speed of 30 rps) so that the current limitation was not due to a limiting ion transport in the solution.

Discussion

The transient characteristic relaxation times reported above are typically in the range of milliseconds. They are thus clearly distinct from those measured in hours or even days which can also be observed with metal oxide electrodes (15). In the latter case Butler

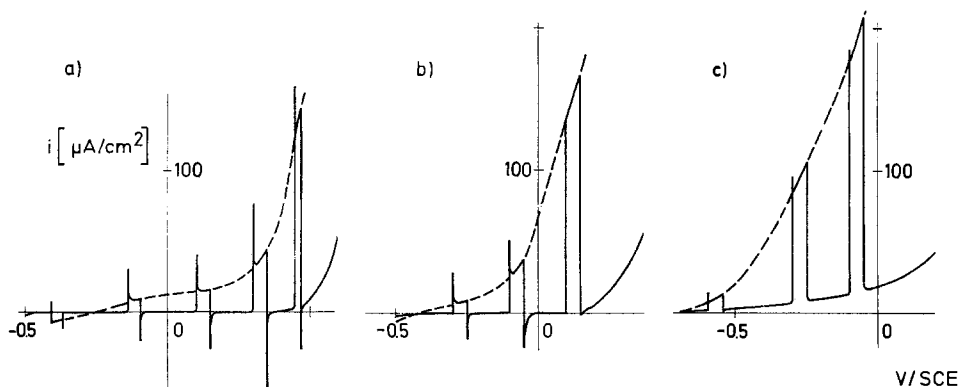
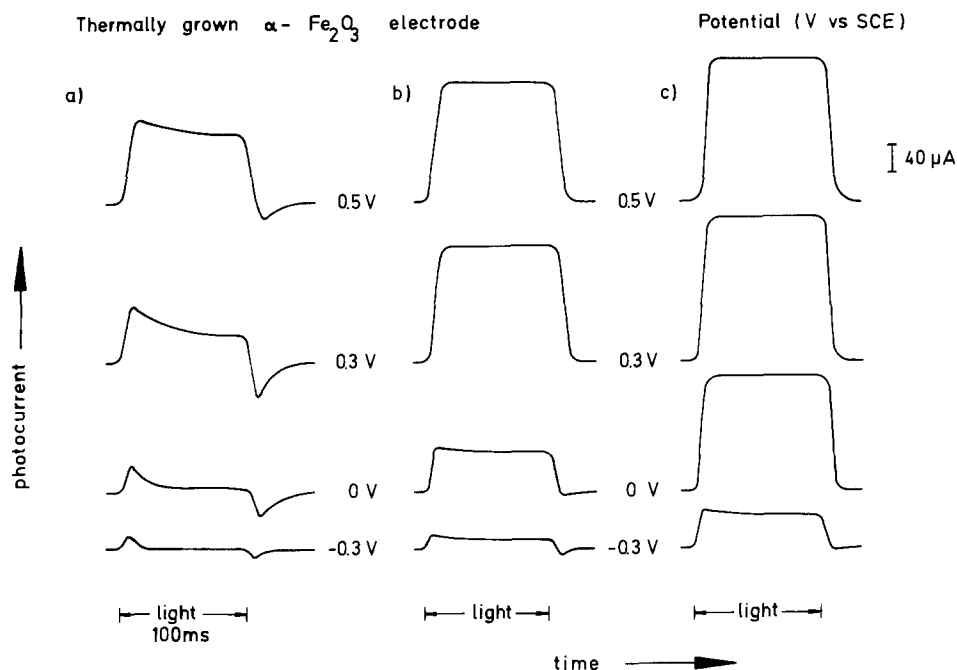


Fig. 1. Potentiostatic current-voltage curves vs. standard calomel electrode for ferric oxide. Anodic scan at 10 mV/sec^{-1} illumination level approximately AM2; solutions as follows: (a) 1 molar sodium hydroxide; (b) 1 molar sodium hydroxide, 0.5 molar sodium sulfide; (c) 1 molar sodium hydroxide, 0.5 molar potassium ferrocyanide. Full line under periodic illumination, dashed line under constant illumination.

Fig. 3. Transient behavior of the anodic photocurrent at illuminated ferric oxide determined using the signal averager technique at fixed electrode potential (vs. SCE). Illumination level approximately AM2, pulse length 100 msec. Solutions used as follows: left, 1 molar sodium hydroxide; center, 1 molar sodium hydroxide, 0.5 molar potassium ferrocyanide; right, 1 molar sodium hydroxide, 0.5 molar sodium sulfide.



has proposed an explanation in terms of electromigration of donors within the space charge layer. In the present work we consider only much more rapid transient behavior.

It has previously been suggested that the transient behavior and the low quantum yield of photocurrent for O_2 -evolution at Fe_2O_3 -electrodes are due to the occurrence of a back-reaction of the photogenerated species with electrons originating from the conduction band (3). Previous work in our laboratory revealed the influence of sample preparation on the transient behavior (4).

We have analyzed the transient behavior now in more detail using the concept of a possible back-reaction involving electrons from the conduction band. Here already problems arise. These are demonstrated by the energy diagrams in Fig. 7a-7c. Figure 7a shows qualitatively the band bending for the equilibrium case assuming as redox system Sn/Sn^{2-} (dashed

curve) and $[Fe(CN)_6]^{3-/4-}$ (full curve), respectively. As shown in Fig. 1b and c the relaxation of the photocurrent disappears if a reducing agent such as Sn^{2-} or $[Fe(CN)_6]^{4-}$ is added to the electrolyte. It disappears, however, only at potentials above the standard potential of the redox system. The band bending at such polarization is shown in Fig. 7b assuming as redox couple $[Fe(CN)_6]^{3-/4-}$. Here the electron hole pairs created by light were well separated by the electric field across the space charge layer. At cathodic potentials with respect to the standard potential, however, a relaxation of photocurrent is still

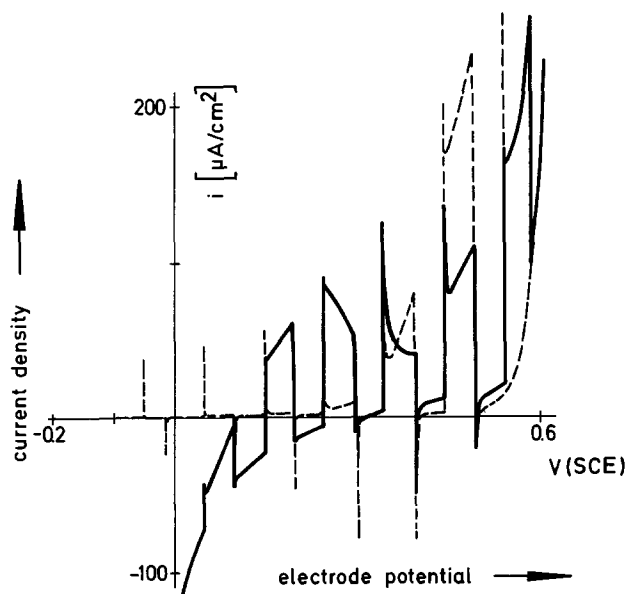


Fig. 4. Potentiostatic current-voltage curve for ferric oxide (vs. SCE) under periodic illumination by white light, level approximately AM2, scan rate 10 mV sec^{-1} . Dashed curve in 1 molar sodium hydroxide solution, solid curve in 1 molar sodium hydroxide, 0.1 molar potassium ferricyanide solution.

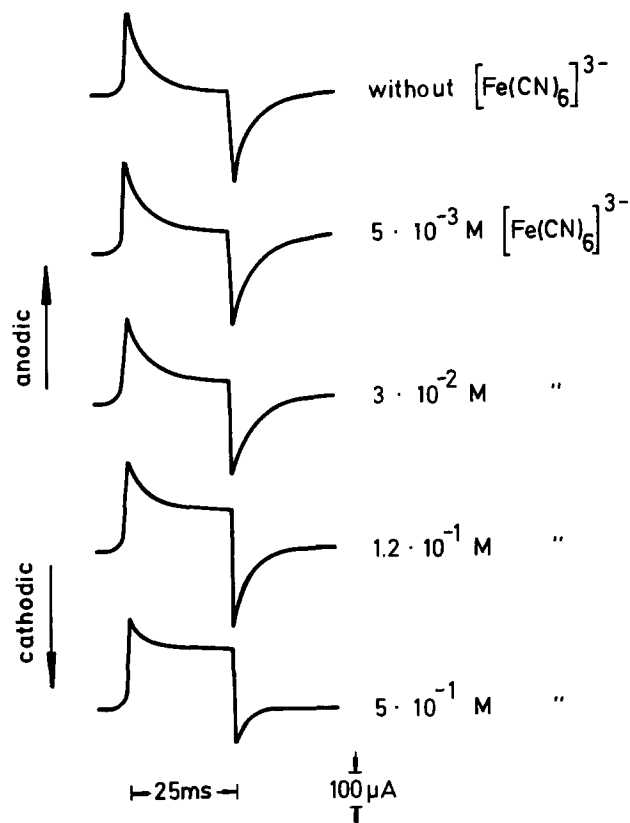


Fig. 5. Relaxation of photocurrent at $U_E = -0.1V$ at different concentrations of an oxidizing agent $[Fe(CN)_6]^{3-}$ in 1M NaOH.

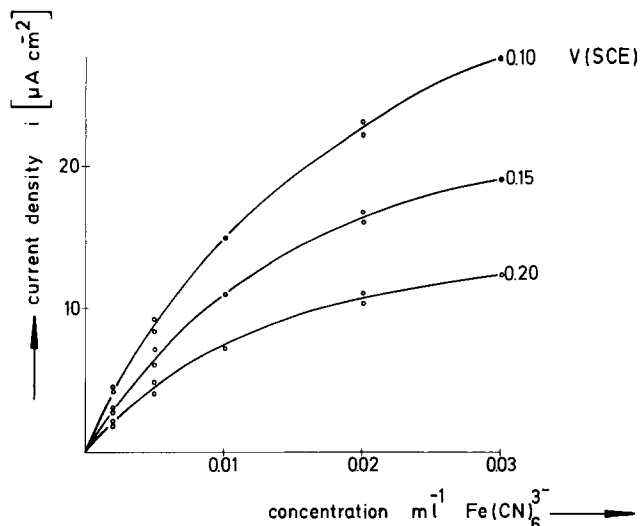


Fig. 6. Cathodic dark currents under potentiostatic conditions at a ferric oxide rotating disk electrode as a function of the concentration of potassium ferricyanide in 1 molar sodium hydroxide solution. Curves labeled with potentials vs. standard calomel electrode. Rotation speed 30 rps.

visible. Assuming the relaxation is due to a cathodic back-reaction, the question arises how electrons from the conduction band can reach the surface. Since the band bending is still very large ($U_{sc} \approx +1.1V$ at the standard potential) the electron density at the surface must be extremely small. The other possibility for electron transfer could be tunneling through the space charge layer as indicated in Fig. 7c. However, this process is also rather unlikely because the thickness of the space charge layer will be far too great (13, 14) (in the order of at least 1000Å) as derived from capacity measurements.

These considerations throw some doubt on the concept of back-reaction by electrons from the conduction band to the photogenerated species. On the other hand, however, we have also observed a large cathodic dark current upon addition of the oxidized species of the redox system $[\text{Fe}(\text{CN})_6]^{4-/-3-}$. According to the relative position of energy levels at the interface this cathodic dark current can only be explained by electron transfer from the conduction band. Consequently, we must conclude that electrons from the conduction band in the bulk of Fe_2O_3 reach the surface somehow. We have no model for this process. Since Fe_2O_3 has not a very well-defined composition one could assume a large density of states within the forbidden zone of the space charge layer and one could speculate that the electrons are transported via these states.

All results are now further analyzed on the basis of this model (Fig. 7c) although we leave open the actual electron transfer mechanism through the space charge region.

Let us first examine the cathodic dark current upon addition of an oxidized species such as $[\text{Fe}(\text{CN})_6]^{3-}$. Since the cathodic current does not linearly increase with concentration (Fig. 6) we have to assume that the electrons used for the reduction of Ox are directly transferred to Ox. Assuming a two-step process via surface states the cathodic current i^- is given by

$$i^- = ek_{ox}fN_Tc_{ox} \quad [1]$$

k_{ox} is the rate constant for the electron transfer from the surface states to Ox, N_T the density of surface states, f the occupation factor of these states and c_{ox} the concentration of Ox. The number of electrons being transferred from the conduction band into surface states is given by

$$dn_e/dt = k_T n_e (1 - f) N_T \quad [2]$$

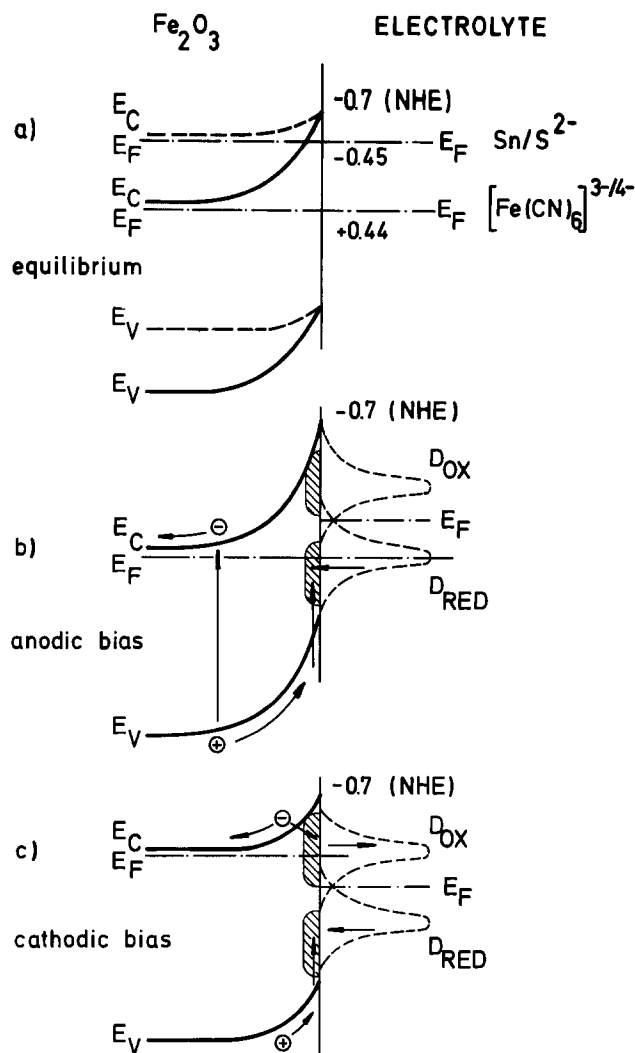


Fig. 7. Energy diagram of a Fe_2O_3 -redox system interface at pH 14. (a) At equilibrium conditions with the Sn/Sn^{2-} (dashed curve) and the $[\text{Fe}(\text{CN})_6]^{3-/-4-}$ redox couple (full curve); (b) at anodic; and (c) at cathodic polarization assuming as redox system the $[\text{Fe}(\text{CN})_6]^{3-/-4-}$ couple. The dashed curve indicates the distribution of the energy levels of the oxidized and reduced states, respectively.

and the number of electrons being transferred to Ox by

$$dn_e/dt = k_{ox}fN_Tc_{ox} \quad [3]$$

Inserting Eq. [2] and [3] into [1] one obtains

$$1/i^- = 1/N_T e [1/k_T n_e + 1/k_{ox}c_{ox}] \quad [4]$$

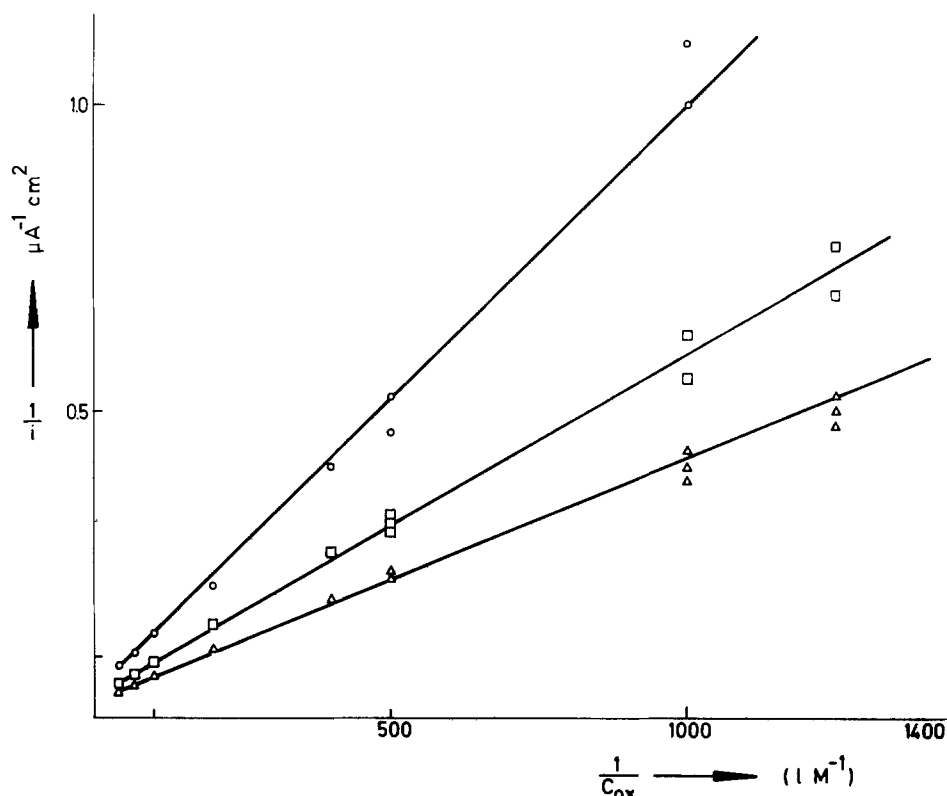
A similar model has also been applied recently to TiO_2 and SrTiO_3 (11).

We replotted the data from Fig. 6 according to Eq. [4] ($1/i^-$ vs. $1/c_{ox}$) and obtained straight lines as shown in Fig. 8. From the intercept with the $1/i^-$ -axis one obtains a value for $N_T k_T n_e$. Since the rate constant k_T is expected to depend on the band bending the intercept should also depend on the electrode potential. In the potential range investigated here the intercept varies only slightly and the average value is given by

$$i^- = eN_T k_T n_e = 2.5 \cdot 10^{-5} \text{ Acm}^{-2}$$

i.e., $N_T k_T n_e = 1.7 \cdot 10^{15} \text{ cm}^{-2} \text{ sec}^{-1}$. The slopes of these curves yield values of $N_T k_{ox}$. They vary from $6.5 \cdot 10^{15}$ to $1.6 \cdot 10^{16}$ liters/mol. It is rather surprising that the k_{ox} depends on the electrode potential. This effect can only be understood if the relative position of the energy levels at both sides of the interface and conse-

Fig. 8. Reciprocal cathodic dark current vs. reciprocal concentration of $[\text{Fe}(\text{CN})_6]^{3-}$. Data from Fig. 6.



quently the Helmholtz layer varies with the electrode potential. The fact that the Mott-Schottky plots of the capacity are not linear with potential (4) may be an indication that the Helmholtz potential is changed.

The relaxation process of the anodic photocurrent as observed with and without redox systems can be interpreted if we include the same cathodic back-reaction as discussed above. An anodic photocurrent i_{ph}^+ occurs immediately after light is turned on (Fig. 1 and 2). In this process either a redox couple or water is oxidized. The products can be either an intermediate in the water oxidation (or oxygen) or the oxidized species (ox) of the redox couple. The latter are reduced by electron transfer from the conduction band leading to the cathodic current i^- . The sum of both currents is given by

$$i_{\text{ph}} = i_{\text{ph}}^+ - i^- \quad [5]$$

The anodic current is assumed to be determined only by the light intensity I and the quantum yield ϕ and to be independent of time, i.e.

$$i_{\text{ph}}^+ = e\phi I \quad [6]$$

whereas i^- is given by Eq. [1].

The kinetics of the formation and decay of Ox are given by

$$dc_{\text{Ox}}/dt = \phi I - k_{\text{ox}}fN_{\text{T}}c_{\text{Ox}} - k_{\text{D}}c_{\text{Ox}} \quad [7]$$

in which k_{D} is the rate constant describing the diffusion of Ox away from the surface. The corresponding term $k_{\text{D}}c_{\text{Ox}}$ is only a rough approximation because normally a diffusion should be described by a concentration gradient. The electron transfer from the conduction band into surface states and from here to Ox is described by

$$N_{\text{T}}df/dt = k_{\text{T}}n_{\text{e}}(1-f)N_{\text{T}} - k_{\text{ox}}fN_{\text{T}}c_{\text{Ox}} \quad [8]$$

in which n_{e} is the electron density in the conduction band and k_{T} the rate constant for the electron transfer from this band into the surface states.

Since it is impossible to give an analytical solution of these differential equations we only consider some limiting cases. Under stationary conditions c_{Ox} and f

and consequently the stationary photocurrent $i_{\text{ph, st}}$ can easily be derived. This current is not a linear function of the light intensity as also found experimentally and displayed in Fig. 9a, where $i_{\text{ph, st}}$ and i_{ph}^+ are replotted from the data of Fig. 2. It should be mentioned, however, that the initial photocurrent i_{ph}^+ does depend linearly on the light intensity as required by Eq. [6]. At very high light intensity the cathodic current i^- is expected to be independent of light intensity. Then one obtains

$$i_{\text{e}}^- = eN_{\text{T}}k_{\text{T}}n_{\text{e}} \quad [9]$$

i.e., the cathodic current is entirely determined by the electron transfer from the conduction band into the surface states. In this case the total stationary photocurrent is given by

$$i_{\text{ph, st}} = i_{\text{ph}}^+ - i_{\text{e}}^- = e(\phi I - N_{\text{T}}k_{\text{T}}n_{\text{e}}) \quad [10]$$

or the ratio of $i_{\text{ph, st}}$ and i_{ph}^+ can be expressed by

$$(1 - i_{\text{ph, st}}/i_{\text{ph}}^+) = (N_{\text{T}}k_{\text{T}}n_{\text{e}}/e\phi)1/I \quad [11]$$

using the data given in Fig. 9a one obtains the curve in Fig. 9b. According to this our light intensity was just sufficient to get a linear dependent of $(1 - i_{\text{ph, st}}/i_{\text{ph}}^+)$ vs. $1/I$. From the slope of the linear part of the curve in Fig. 9b we obtain $N_{\text{T}}k_{\text{T}}n_{\text{e}}/e\phi = 5 \cdot 10^{17} \text{ cm}^{-2} \text{ sec}^{-1}$. Using the value $N_{\text{T}}k_{\text{T}}n_{\text{e}} = 1.7 \cdot 10^{14} \text{ cm}^{-2} \text{ sec}^{-1}$ as obtained from the dark current measurements (see above) then the quantum yield ϕ can be determined. We obtained $\phi \approx 4 \cdot 10^{-4}$ which is an extremely low value. One can check this value by determining ϕ directly from the peak photocurrent i_{ph}^+ . In this case we obtained $\phi \approx 5 \cdot 10^{-4}$ which is in reasonable agreement with the first value. This low quantum yield must be due to strong recombination effects in the bulk of the material.

In principle the relaxation phenomena also give some information about the density of surface states N_{T} . A quantitative determination, however, requires a solution of Eq. [7] and [8].

Conclusions

We have investigated two aspects of the photoelectrochemistry of ferric oxide in detail; the influence of

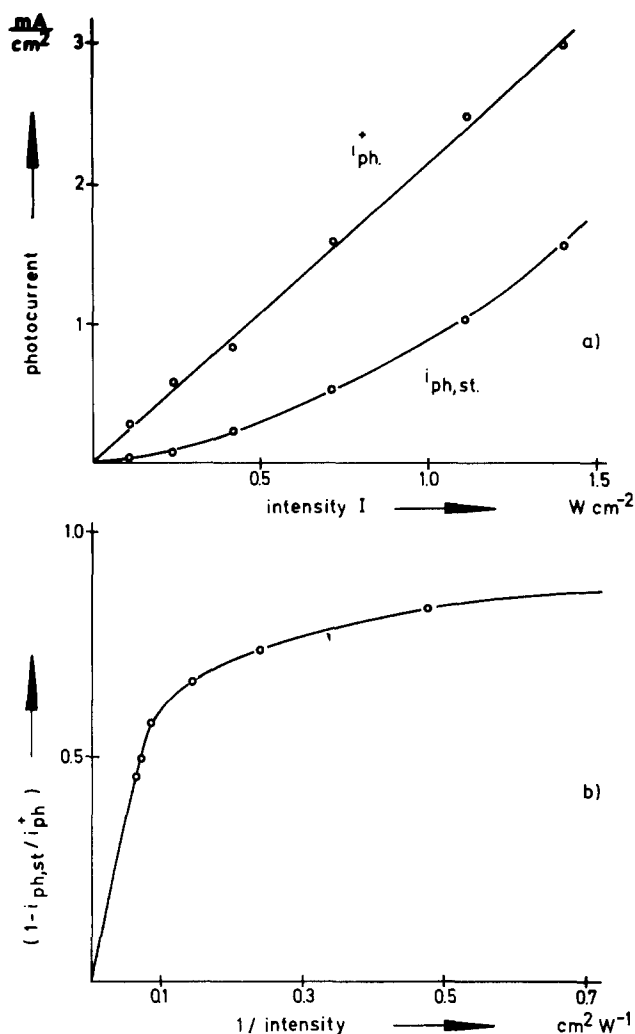


Fig. 9. (a) Peak photocurrent i_{ph}^+ and stationary photocurrent $i_{ph,st}$ (taken from the curves of Fig. 2) vs. the light intensity I . (b) Plot of the function $(1 - i_{ph,st}/i_{ph}^+)$ vs. the light intensity I .

redox reagents on the cathodic dark current and the anodic photocurrent. In the former measurements a nonlinear dependence of the dark current on redox species concentration has been revealed. We take this as evidence for the intervention of surface states. Insofar as photocurrents are concerned, the main observation is that the marked transient behavior is suppressed, if a redox system is added or sufficiently high intensities are used. Especially with redox systems having a rather negative standard potential such as Sn/Sn^{2-} , the relaxation of photocurrent can be avoided over a large potential range. This leads us to an overall interpretation of the photocurrent behavior of this electrode in terms of cathodic back-

reactions of the photogenerated species. The surface states invoked for the explanation of the cathodic dark current behavior are also active in the back-reaction mechanism. The influence of sample preparation on photocurrent transient behavior (4) is consistent with this explanation, since surface-state densities and electron tunneling probabilities are sure to be influenced by crystallinity.

In spite of the fact that the photocurrent relaxation can be virtually eliminated in the presence of the S^{2-} redox species, the Sn/Sn^{2-} redox system is not suitable for use in a solar cell because of the cathodic standard redox potential. Although Fe_2O_3 is an interesting material for a photoanode in a photocell because of its stability against anodic decomposition, the preparation of the material and the surface properties have to be considerably improved in order to avoid the cathodic back-reaction via the conduction band.

Acknowledgments

The authors wish to thank Professor P. Clechet for his valuable comments on the conduct of this work. The technical assistance of Mr. A. Hoffmann and Mr. R. Schubert is gratefully acknowledged.

Manuscript submitted Dec. 10, 1980; revised manuscript received ca. April 13, 1981.

Any discussion of this paper will appear in a Discussion Section to be published in the June 1982 JOURNAL. All discussions for the June 1982 Discussion Section should be submitted by Feb. 1, 1982.

REFERENCES

1. R. K. Quinn, R. D. Nasby, and R. J. Baughman, *Mater. Res. Bull.*, **11**, 1011 (1976).
2. J. H. Kennedy and K. W. Frese, Jr., *This Journal*, **125**, 709 (1978).
3. K. L. Hardee and A. J. Bard, *ibid.*, **124**, 215 (1977).
4. J. S. Curran and W. Gissler, *ibid.*, **126**, 56 (1979).
5. J. H. Kennedy and K. W. Frese, Jr., *ibid.*, **125**, 723 (1978).
6. K. S. Yun, S. M. Wilhelm, S. Kapusta, and N. Hackerman, *ibid.*, **127**, 85 (1980).
7. L. S. R. Yeh and N. Hackerman, *ibid.*, **124**, 833 (1977).
8. W. Gissler, EUR Report 5514E (1978).
9. M. S. Wrighton, A. B. Bocarsly, J. M. Bolbs, A. B. Ellis, and K. D. Legg, in "Semiconductor Liquid-Junction Solar Cells," A. Heller, Editor, p. 84, The Electrochemical Society Softbound Proceedings Series, Princeton, NJ (1977).
10. D. S. Ginley and M. A. Butler, *This Journal*, **125**, 1968 (1978).
11. J. Vandermolen, W. P. Gomes, and F. Cardon, *ibid.*, **127**, 324 (1980).
12. R. H. Wilson, *ibid.*, **127**, 228 (1980).
13. R. Memming and F. Möllers, *Ber. Bunsenges. Phys. Chem.*, **76**, 474 (1972).
14. R. Memming, in "Electroanalytical Chemistry," Vol. 11, A. Bard, Editor, p. 1, Marcel Dekker, Inc., New York (1979).
15. M. A. Butler, *This Journal*, **126**, 338 (1979).

Electrochemical Solar Cells with Layer-Type Semiconductor Anodes: Chemical Treatments of the Crystal Surface

G. Razzini and L. Peraldo Bicelli*

*Centro Studio Processi Elettrodici del C.N.R., Istituto di Elettrochimica,
Chimica-Fisica e Metallurgia, Politecnico di Milan, Milan, Italy*

G. Pini

Sulzer Brothers Limited, Winterthur, Switzerland

and B. Scrosati

Istituto di Chimica Fisica, University of Rome, 00185 Rome, Italy

ABSTRACT

Photoelectrochemical cells based on layer-type semiconductors (*i.e.*, transition metal sulfides and selenides) have gained substantial interest due to their reasonably high solar efficiency and good stability against photocorrosion. However, the performance of this type of cell may be limited by irregularities in the semiconductor, since edges of the van der Waals surface exposed to the electrolyte may act as recombination centers. To control this effect, chemical surface treatments, based on specific agents which perform selectively on the transition metal atoms at the edge sites, have been studied. In particular, the effect of the disodium salt of the ethylene diamine tetracetic acid (EDTA) molecule (as well as that of many other organic molecules) on the performance of an n-MoSe₂/I⁻, I₂/Pt sample cell has been investigated. The treatment with EDTA generally improved both short-circuit current and power output, even if a considerable variation in the response from crystal to crystal was observed. The stability of the EDTA effect under prolonged cell operation was also examined.

In recent years many efforts have been directed to the investigation of new semiconductor compounds suitable for use as electrodes in photoelectrochemical solar cells. In this connection, Tributsch (1-10) has proposed transition metal dichalcogenides (such as MoSe₂, MoS₂, and WSe₂) as stable electrode materials.

Indeed, these layer-type semiconductors are characterized by optical transitions which occur between two d-bands of the metal and do not involve metal and chalcogen bonding orbitals, thus assuring good stability against photocorrosion. Furthermore, the values of the energy gap (1.4-1.8 eV) open possibilities of good energy conversion efficiencies.

Detailed studies have been carried out by various authors on the behavior of these photoanodes in contact with different aqueous redox electrolytes. The results have indicated the I⁻, I₂ system as the optimal redox couple. Using this couple, relatively high efficiencies and long stabilities have been obtained with MoSe₂- and WSe₂-based cells (8).

However, many authors (11-15) have also pointed out that the surface morphology of single crystal layered photoanodes plays a key role in determining the relative photoelectrochemical cell behavior, since surface states and defects greatly increase the rate of electron-hole pair recombination, thus reducing the performance in terms of photovoltage, maximum power output, and thus efficiency.

Unfortunately, even under the most accurate growing procedure, defects (crack-like steps, ruptures, etc.) are inevitably present on the van der Waals surfaces of transition metal dichalcogenide single crystals (12).

In order to assure optimum photoelectrochemical behavior for the layered semiconductors and eventually open the possibility of their use in the polycrystalline state, it is necessary to develop surface treatments

which may act selectively on the recombination sites and which also maintain their effect under the drastic conditions of an illuminated electrode during prolonged anodic operation.

To understand the possible blocking mechanism of a chemical agent, it is necessary to briefly examine the structure of the bonding sites of the semiconductor surface. Let us then consider a "step" as a defect model. Within the step it is possible to have "dangling bonds" of both the transition metals and the chalcogen atoms, which may easily act as bonding points for various ionic species in solution (14). The absorption of a new species onto a surface parallel to the c-axis (reactive surface) by means of free metal bonds may produce new surface states near the conduction band, which determine electron tunneling and high electron-hole pair recombination. Moreover, the contact with the electrolyte of a reactive surface, in addition to the surface perpendicular to the c-axis (van der Waals surface), causes a new space charge region and electric field. These determine a high drift of holes moving toward the semiconductor/electrolyte interphase on the reactive surface, as a consequence of the higher conductivity of the minority carriers along the van der Waals planes (12).

These undesired effects may be limited by specific chemical agents which, upon blocking the free metal bonds situated at the defect sites, prevent the electron-hole pair recombination, thus finally improving the performance of the semiconductor photoanode. Such an approach has been proposed by Parkinson *et al.* (15), who have shown that large organic molecules, such as 4-*tert*-butyl-pyridine, may indeed temporarily block, by a "semi-intercalation" process, the transition metal atoms responsible for the surface state.

In this work we have extended the study by examining the blocking behavior of many organic molecules, using as a typical testing system the n-MoSe₂/I⁻, I₂/Pt cell.

* Electrochemical Society Active Member.
Key words: photoelectrochemical cells, layer-type semiconductors, surface treatments.

Experimental

MoSe₂ single crystals were kindly provided by Dr. F. Lévy of the Ecole Polytechnique Fédérale de Lausanne, Switzerland. These crystals, grown by chemical transport reaction in the vapor phase, using halogens as transport agents (16), were n-type semiconductors with a typical thickness of 0.1-0.3 mm and an apparent surface of 0.2-0.5 cm².

The 1M KI, 0.01M I₂ aqueous electrolyte was prepared using high purity chemicals and distilled water. All the blocking agents tested were high purity chemicals.

The MoSe₂ single crystal was assembled and welded with a conductive silver paste on a brass current collector. This was then embedded with epoxy resin on a Teflon holder in such a way that only the van der Waals surface remained in contact with the electrolyte. The counterelectrode was a platinum wire spirally arranged around the semiconductor photoanode.

The semiconductor surface was illuminated through an optical window situated at the bottom of the cell. The light source was a 100W tungsten iodine lamp with an intensity of 100 mW cm⁻², simulating an AM1 irradiation.

The illumination intensity and uniformity were regularly controlled and measured by a Haenni Solar 118 light intensity meter.

The output characteristics of the cell were obtained by controlling the voltage with a potentiostat driven by a function generator and recording the current-voltage curves with an X-Y recorder.

To test the effect of various surface chemical treatments, the semiconductor crystal was kept in contact with an aqueous solution of a given blocking molecule for periods varying from 1 to 15 hr at room temperature. In the case of polyvinylpyridines an alcoholic solution was used. After washing with distilled water, the crystal was again assembled in the cell and the related current-voltage curves were determined under illumination and in the dark. The results were then compared with those obtained previously with the same untreated crystal.

All the measurements were carried out at room temperature and in air. In certain cases the chemical treatments were also tested at 50-70°C, but the results were not very different from those obtained at room temperature.

Results and Discussion

As already pointed out, the surface of the layer-type semiconductors inevitably presents some defects. However, depending on the amount and the type of these defects, the various single crystal samples may be broadly classified as having "smooth" or "stepped" surfaces.

In the present investigation, to better evidence the effect of the chemical treatments, MoSe₂ crystals with many superficial defects were preferentially considered.

Various organic molecules were tested as possible blocking agents. Among these, by-products of pyridine, with structures similar to the 4-tert-butyl-pyridine investigated by Parkinson *et al.* (15), were examined. As indicated in Table I, where the effects of these products are summarized, some amino-pyridines show certain favorable blocking effects (as indicated by the improvements in the related cell *I-V* characteristics) accompanied, however, by poor stability. Indeed, after short-term operation of the electrode under illumination, drastic decreases in performance were observed. Moreover, the electrode response became frequently worse than that originally offered by the untreated crystal.

This behavior is probably due to a degradation of the amino group, which in turn causes a change in the physicochemical characteristics and in the interaction mechanism with the crystal surface. The change in in-

Table I. By-products of pyridine tested as blocking agents

| Molecule | Improvement of the <i>I-V</i> characteristic | Stability of the blocking agent to the experimental conditions* |
|--------------------------|--|---|
| Pyridine | Yes | Less than 5 hr |
| 2-Aminopyridine | Yes | Less than 1 hr |
| 3-Aminopyridine | Yes | Less than 1 hr |
| 2-Amino-6-methylpyridine | No | — |
| 4-Dimethylaminopyridine | No | — |
| 2-Vinylpyridine | Yes | Less than 1 hr |
| 4-Polyvinylpyridine | No | — |
| 4-Vinylpyridine | Yes | Less than 1 hr |
| 2-Polyvinylpyridine | Yes | Less than 10 hr |

* The blocking agent stability is referred to the power output value.

teraction mechanism may result in the formation of new superficial states which can increase the recombination rate of the electron-hole pairs.

Attention was therefore directed to other molecules having different structure and different bonding mechanism with the semiconductor surface. Particularly interesting appear in this respect the disodium salt of the ethylene diamine tetracetic acid (EDTA), the nitrilo triacetic acid (NTA), and the cyclohexane diamine (1-2)-tetracetic acid (CDTA). These materials, which are well known for their capability to react with transition metal ions to form coordination compounds, acted quite favorably on the performance of "stepped" MoSe₂ crystals.

For instance, as typically illustrated in Fig. 1, a crystal with a high reactive surface and low photovoltage, showed a substantial improvement in power output and dark current, after having been treated with EDTA. Improvements of this kind, even if not to a comparable extent, were also obtained with crystals which, even if with comparable highly defective structure, presented higher photovoltages, *i.e.*, of the order of 400-500 mV.

Also beneficial in terms of electrode response appears to be the treatment of the MoSe₂ crystals with aqueous solutions of CDTA and NTA.

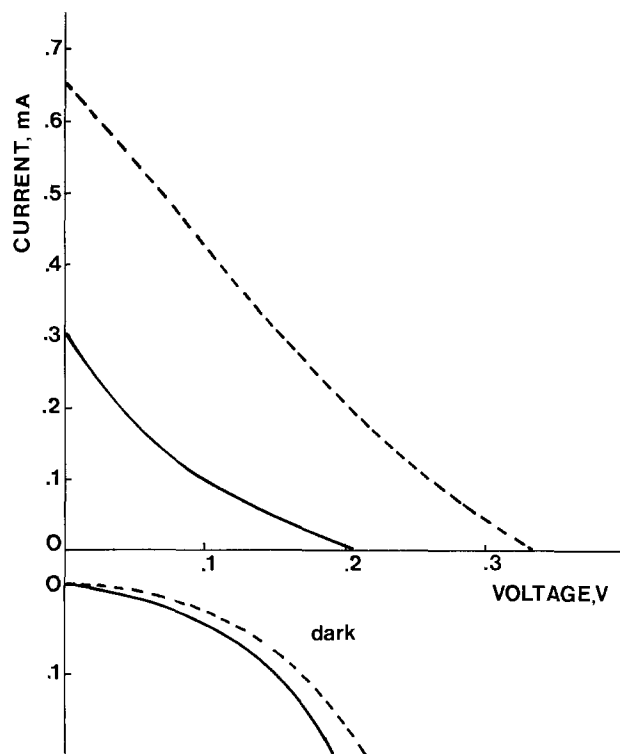


Fig. 1. Illuminated (top) and dark (bottom) current voltage curve before (—) and after (---) surface treatment of n-MoSe₂ with EDTA.

However, it must be emphasized that the effect of EDTA and related compounds, varied consistently from sample to sample of MoSe₂. In fact, some crystals with a highly stepped surface and having original low photovoltages showed appreciable improvements in response after the treatment, while others, still having a comparable defective surface, were affected either a little or not at all.

This discrepancy may be explained on the basis of different impurity levels in the various samples considered. Indeed, low photovoltage values may be due either to superficial defects or to impurities or to both of them. When the low values are prevalently related to surface defects, the blocking action of EDTA may induce consistent improvements, whereas EDTA treatment cannot be effective when the low response is primarily due to impurity levels.

To finally evaluate the EDTA effect on the surface states of layer-type semiconductor photoanodes, the following experiment was carried out. The surface of a crystal, whose output characteristics had been recorded previously, was scratched with the point of a thin needle and the current-voltage curve was again recorded. As shown in Fig. 2, output power and dark current deteriorated (to an extent proportional to the number of scratches), this being further evidence of the great influence of the condition of the surface on the electrode performance. The crystal was then dipped for 15 hr in a concentrated EDTA solution. As again shown in Fig. 2, the performance of the electrode improved after this treatment, but not up to the original level. Therefore, it appears that the EDTA molecules are not capable of blocking all the active sites produced by the scratching procedure.

No attempt to discuss in detail the binding mechanism of EDTA and related compounds is made here. This would require a series of independent measurements, some of which are in progress in our laboratories.

In the present work it has appeared of more immediate interest to evaluate the stability of the EDTA action under prolonged anodic operation at the condition of maximum power output. Figure 3 shows that the EDTA effect decreases with operation time, even if with a rate consistently lower than that reported elsewhere for other types of blocking molecules (15). The observed decay of the EDTA effect is probably related to a modification of its molecular structure, produced by the drastic working conditions, such as those determined by the oxidant medium (iodine), illumination, and anodic oxidation.

Conclusions

Because of the short duration of their action, the treatment with EDTA, CDTA, and NTA, respectively, is

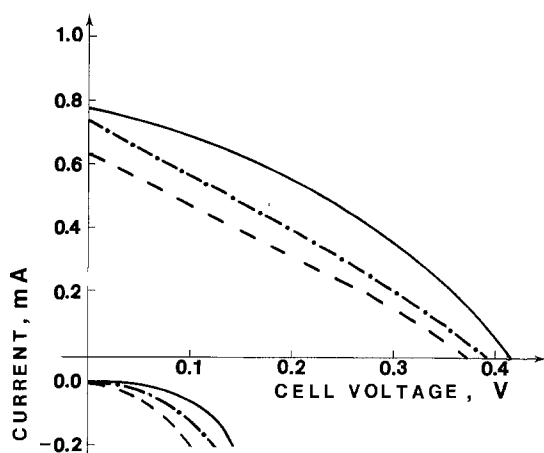


Fig. 2. Illuminated (top) and dark (bottom) current voltage curve before (—) and after (---) surface scratching and subsequent EDTA treatment (- - ● - -) of the scratched surface.

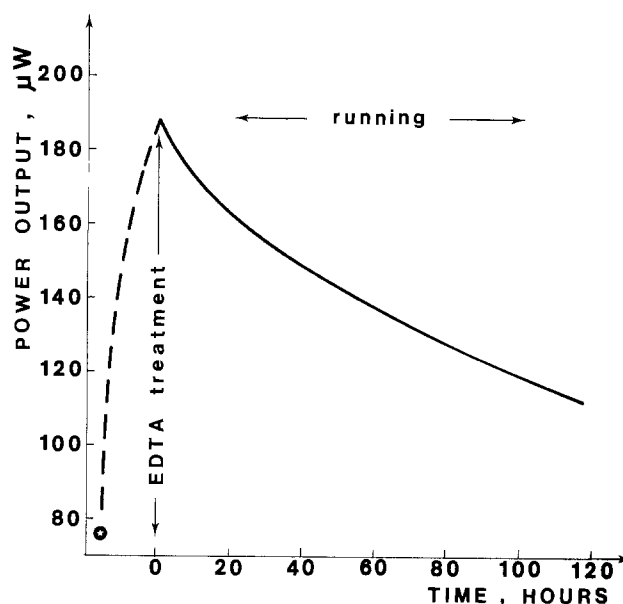


Fig. 3. Time dependence of the power output of an n-MoSe₂/I₂/Pt solar cell monitored during EDTA treatment and illuminated by a 100W tungsten lamp light. ● refers to the power output before EDTA treatment.

certainly of not immediate practical importance. However, the results reported here, in addition to all those concerning other attempts of controlling the surface state of the photoanodes (15), may be useful in this very initial stage of the research on layer-type semiconductor electrochemical solar cells to profitably address future efforts in the development of more effective and stable blocking compounds.

At the present level of knowledge in the field, the properties that such compounds should have appear to be mainly the following: (i) capability of easily reacting with the defective "stepped" surfaces, forming stable and strong bonds at the edge sites; (ii) stability to solar light; (iii) absence of functional groups sensitive to anodic oxidation and/or to oxidizing chemical agents present in the electrolyte; (iv) absence of double bonds in the structure; and (v) low steric hindrance.

Acknowledgments

The authors wish to thank Dr. F. Lévy for kindly providing the MoSe₂ crystal samples. This work has been supported in part by the Finalized Energy Program (Solar Energy) of the National Council of Research (C.N.R.) of Italy and by Sulzer Brothers Limited, Winterthur, Switzerland.

Manuscript submitted Feb. 20, 1981; revised manuscript received ca. May 15, 1981.

Any discussion of this paper will appear in the June 1982 JOURNAL. All discussions for the June 1982 Discussion Section should be submitted by Feb. 1, 1982.

Publication costs of this article were assisted by the University of Rome.

REFERENCES

1. H. Tributsch and J. C. Bennett, *J. Electroanal. Chem. Interfacial Electrochem.*, **81**, 97 (1977).
2. H. Tributsch, *Z. Naturforsch., Teil A*, **32**, 972 (1977).
3. H. Tributsch, *Ber. Bunsenges. Phys. Chem.*, **81**, 361 (1977).
4. H. Tributsch, *ibid.*, **82**, 169 (1978).
5. H. Tributsch, *This Journal*, **125**, 1086 (1978).
6. J. Gobrecht, H. Gerischer, and H. Tributsch, *Ber. Bunsenges. Phys. Chem.*, **82**, 1331 (1978).
7. J. Gobrecht, H. Gerischer, and H. Tributsch, *This Journal*, **125**, 2085 (1978).
8. H. Tributsch, *Solar Energy Mater.*, **1**, 705 (1979).

9. H. Tributsch, H. Gerischer, C. Clemen, and E. Bucher, *Ber. Bunsenges. Phys. Chem.*, **83**, 655 (1979).
10. W. Kautek, H. Gerischer, and H. Tributsch, *ibid.*, **83**, 1000 (1979).
11. S. H. Ahmed and H. Gerischer, *Electrochim. Acta*, **24**, 705 (1979).
12. H. J. Lewerenz, A. Heller, and F. J. DiSalvo, *J. Am. Chem. Soc.*, **102**, 1877 (1980).
13. L. De Angeli, L. Fornarini, F. Galluzzi, M. Lazzari, F. Lévy, L. Peraldo Bicelli, G. Razzini, E. Scafè, and B. Scrosati, *J. Power Sources*, In press.
14. W. Kautek, J. Gobrecht, and H. Gerischer, *Ber. Bunsenges. Phys. Chem.*, **84**, 1034 (1980).
15. B. A. Parkinson, T. E. Furtak, D. Canfield, K. Kan, and G. Kline, *Disc. Faraday Soc.* (September 1980).
16. L. H. Brixner, *J. Inorg. Nucl. Chem.*, **24**, 257 (1962).

The Role of Electron-Hole Recombination at MoS₂ and MoSe₂ Photoelectrodes

M. L. Phillips and M. T. Spitler*

Department of Chemistry, Mount Holyoke College, South Hadley, Massachusetts 01075

ABSTRACT

Analysis of impedance and current-voltage data has revealed that electron-hole recombination plays a significant role in the aqueous photoelectrochemistry of MoSe₂ and MoS₂ single crystals. It is proposed that this recombination shortens the lifetime of the photoproduced hole to such an extent that few solution reductants are able to react with holes at the surface of these electrodes. The role of this recombination in diminishing photocurrents and photopotentials is discussed within the context of the Gerischer model for semiconductor electrochemistry.

Considerable interest has been displayed recently in the use of semiconducting layer-type transition metal dichalcogenides as photoelectrodes in electrochemical cells (1-16). These investigations result from Tributsch's suggestion (1-4) that these materials would be stable against photodecomposition under visible illumination while employed in an electrochemical solar cell. In particular, the group VI dichalcogenides such as MoSe₂, have been studied with regard to stability and energy conversion efficiency (1, 4, 9, 10, 12, 14); the best reported efficiencies of stable photoelectrochemical cells using these materials under simulated solar illumination have been 10.2% for a WSe₂ electrode and 9.4% for MoSe₂ (16), both using I₂/I⁻ as the redox couple. In addition, possibly the single longest continuous operation of a photoelectrochemical solar cell has been made using an MoSe₂ electrode in an I₂/I⁻ electrolyte which ran for ten months with an efficiency of 4-5% (13).

Although it has been demonstrated that the presence of halides, in particular I⁻, profoundly influences the power output of these cells (1, 2, 4), the nature of this effect is not fully understood. An understanding of the electrochemistry of the halides at these electrodes would require the determination on a potential scale of the positions of the semiconductor valence and conduction bandedges over a wide range of electrode bias and a correlation of these energetics with the kinetics of the current producing reactions. Such a complete picture of the system has not yet been established beyond question.

In this work a suitable model was sought to explain the kinetics of photooxidation of reductants at MoSe₂ and MoS₂ electrodes with the hope that some insight might be gained into the interaction of these solids with iodide. Using new results in conjunction with existing data on the photocurrent-voltage and photopotential behavior of these compounds, we have determined that electron-hole recombination plays a significant role in their photoelectrochemistry, a factor which has not been previously discussed for MoS₂ and MoSe₂. We

demonstrate how such a recombination process can be described by a minor extension of the Gerischer model for semiconductor electrochemistry; with this model the photocurrent and photovoltage results lend themselves to a straightforward interpretation. However, the character of the transition metal dichalcogenide/iodide interaction still eludes satisfactory explanation.

Experimental

Crystals of MoS₂ and MoSe₂ grown by vapor transport were obtained from F. Lévy of the Ecole Polytechnique, Lausanne, Switzerland. Through impedance measurements, the donor density of the n-type crystals used in these studies was determined to be $1 \times 10^{17}/\text{cm}^3$ for MoS₂ and 6×10^{17} for MoSe₂.

The thickness of crystals used for electrodes varied but did not exceed 0.5 mm. A razor blade was used to separate single crystals from aggregates and to cut them to an appropriate working size. An electrical contact was made with conductive silver paint between the Van der Waals surface at the back-side of the crystal and a wire; the crystal was then affixed to Teflon mountings with 3M insulating epoxy, leaving an exposed surface area of 4-10 mm². Surfaces were renewed through pressing a piece of adhesive tape onto the crystal and peeling off a thin layer. Before each experiment, electrodes were rinsed for 5 sec in 1M nitric acid followed by deionized water.

All solutions were prepared with Baker analyzed reagent grade chemicals in deionized water. The supporting electrolyte in all experiments with the dichalcogenide electrodes was 0.500M KNO₃. The pH was adjusted with KOH and HNO₃.

The semiconductor electrode was immersed in electrolyte in a Pyrex, three-electrode cell under potentiostatic control with a platinum counterelectrode and an Ag/AgCl reference electrode in 0.5M KCl. The potentials in this work are referenced to this silver/silver chloride electrode. The crystal was illuminated through a Pyrex window with the 578 nm line of a 200W mercury arc lamp which had been passed through a Bausch and Lomb high intensity monochromator set at a bandwidth of 10 nm.

* Electrochemical Society Active Member.

Key words: semiconductor, electrode, energy conversion.

A PAR Model 175 function generator supplied the input potential to a Wenking 70 HVI/90 potentiostat at a sweep rate of 10 mV/sec. Impedance measurements were made with this system using the lock-in technique.

The photopotential measurements represent the potential difference between a Pt button electrode and the semiconductor electrodes under illumination from a 100W tungsten lamp using a 680 nm interference filter with a bandwidth of 10 nm. Before illumination the two electrodes were shorted. The redox potential of the electrolyte was determined using the Pt electrode and the Ag/AgCl reference electrode, except for the cerium solution where the dark potential of the semiconductor electrode was taken as the solution potential.

Results

To gain a better understanding of the photooxidation reactions at MoS₂ and MoSe₂ electrodes, photocurrent and photopotential measurements were made with dilute halides and other reductants at MoS₂ and MoSe₂ electrodes.

Single crystals of these compounds were selected and mounted in such a way as to show maximum photoeffect. In order to insure a constant pH for the duration of a series of experiments, the electrolyte was adjusted to pH 1.0. Halide concentrations were 100 times less than those of the supporting electrolyte to permit resolution of features in the current-voltage curves not distinguishable in the higher concentrations of halide used in most published work in this field.

When positively polarized in 0.50M KNO₃, the MoSe₂ crystals showed an anodic photocurrent in a reaction with water which eventually leads to lattice decomposition, as has been determined by Tributsch and Bennett (5). A typical current-voltage curve for MoSe₂ in the KNO₃ electrolyte is shown in Fig. 1(a). The onset of anodic dark current consistently occurred at +900 mV in the inert electrolyte; photocurrents started at +500 mV and rose with more positive potential to about 800-1000 mV.

For these compounds, the following equation (25) can be used to describe its current-voltage behavior when a depletion layer is formed at the surface of the electrode

$$I = \alpha \cdot [L_p + W(V - V_{FB})^{1/2}] \quad [1]$$

This holds for monochromatic radiation where V is the electrode potential, V_{FB} is the flatband potential, I is the photocurrent, and α is a constant. L_p is the hole diffusion length which for these compounds is $\sim 10^{-4}$ cm (25); W is the width of the depletion region which will be less than 10^{-5} cm when the band bending is less than 0.3V. Given these values for L_p and W it is clear that the photocurrent should be independent of potential once a depletion layer is formed. This behavior has been observed for MoSe₂ and MoS₂ electrodes in electrolytes containing high concentrations of iodide where the onset of photocurrent is marked by a steep climb of the photocurrent to saturation within several tens of millivolts.

The current voltage curves shown here for MoSe₂ do not follow from Eq. [1]. Instead, they show a gradual increase in photocurrent with potential that requires several hundred millivolts to reach a saturation level. It is useful, however, to establish a parameter which will serve to designate the potential at which the slow kinetics of lattice decomposition dominates photocurrents induced by reductants in the electrolyte; this has been done by noting the potential at which the current reaches 20% of its saturation value. These potentials are indicated in Fig. 1 and compiled in Table I for a number of crystals in nitrate solutions.

The effects of 5.00 mM KBr or 5.00 mM KI on dark and illuminated current-voltage curves are shown in Fig. 1(b) and (c). Saturation photocurrents were reached at +780 mV in Br⁻ solution and +900-950 mV

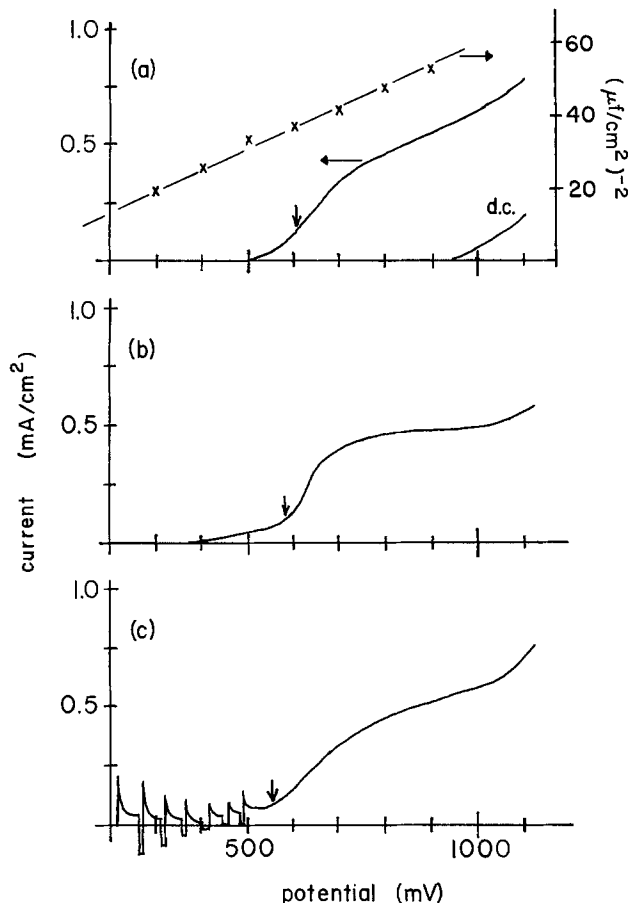


Fig. 1. Current-voltage curves are shown for illuminated MoSe₂ electrodes immersed in: (a) 0.50M KNO₃; (b) 0.50M KNO₃ and 5.0 mM Br⁻; (c) 0.50M KNO₃ and 5.0 mM I⁻. Light intensity was 5 mW/cm² at 578 nm with a solution pH of 1.0 and an Ag/AgCl reference electrode. In (c) illumination was chopped. A current-voltage curve in the dark is also provided (d.c.) in (a). The photocurrent onset parameter is shown as a vertical arrow and denotes the potential at which the photocurrent has reached 20% of its maximum value. Also included in (a) is a Mott-Schottky plot used to derive the flatband potentials from impedance measurements.

in I⁻ solution. The light was chopped as the electrode potential was swept positive to allow comparison of dark and photocurrents. It is seen clearly that photocurrents arose in the presence of halides at potentials substantially negative of the photocurrent onset in the absence of halides. The photocurrent onset potentials for Br⁻ and I⁻ solutions are listed in Table I. No increase in photocurrents was evident upon addition of 5 mM Cl⁻ to the electrolyte.

It is evident that at higher halide concentrations substantial changes in the current-voltage curves do appear; the concentration dependence of these changes has been studied in detail by Tributsch (2). The data here show that in the presence of 5 mM halides, whatever changes that occur in the onset potential for the photodecomposition reaction do not change by more than 50 mV. Therefore we conclude that the energies of the semiconductor bandedges remain fixed with re-

Table I. Photocurrent onset and flatband potentials for MoS₂ and MoSe₂ (vs. Ag/AgCl)

| Photocurrent onset parameter: | MoS ₂ | MoSe ₂ |
|------------------------------------|------------------|-------------------|
| 0.50M NO ₃ ⁻ | 530 (±20) mV | 600 (±15) mV |
| + 5 mM Br ⁻ | 530 (±30) | 550 (±10) |
| + 5 mM I ⁻ | 500 (±20) | 560 (±30) |
| Flatband potentials: | | |
| 0.50M NO ₃ ⁻ | + 150 (±50) mV | - 60 (±50) mV |

spect to energy levels in solution within this 50 mV range.

The n-type MoS₂ crystals were in general of poorer crystalline quality than the MoSe₂ crystals, as evidenced by their appearance and by larger dark currents relative to photocurrents at positive potentials. In the inert electrolyte, the onset of anodic dark current came around +750 mV. From an onset at +300 mV, photocurrents rose to saturation around +920 mV and fell again after +980 mV, while dark currents continued to increase. Current-voltage curves were measured for MoS₂ in inert electrolyte, in 5.0 mM KBr, and in 5.0 mM KI. Only the iodide solution showed any significant photocurrents negative of a bias of +550 mV. The potentials for photocurrent onset using the 20% parameter are listed in Table I.

A closer examination of current-voltage curves for MoSe₂ in electrolytes containing Fe²⁺, Fe(CN)₆⁴⁻, and hydroquinone is shown in Fig. 2 wherein the most positive potential depicted in this figure is still negative of the onset of the current from lattice decomposition.

Photopotential measurements at these electrodes were made in solutions containing a variety of redox couples as have been reported by other authors (4, 8, 9, 11, 12, 15). The results are plotted in Fig. 3, showing the dark potential of the electrode and its potential under illumination as a function of the redox potential of the electrolyte. Solution concentrations for these redox couples were much higher than the 5 mM used in the halide experiments, being 0.1M in the reduced component in most cases. For redox couples with potentials negative of +600 mV, the photopotential of MoSe₂ electrodes attains more negative values than the MoS₂ electrodes.

Through a Mott-Schottky analysis of impedance measurements, flatband potentials were obtained for a number of electrodes used in this study and are to be found in Table I. These results agree fairly well with those values reported by Gobrecht (13). However, the analyses for a number of crystals yielded nonlinear slopes and frequency dispersions. This behavior is not unusual (13, 20) and probably reflects the sensitivity of impedance measurements to defects at the electrode surface which are known to exist for these compounds. A Mott-Schottky plot for MoSe₂ has been included in Fig. 1(a).

Discussion

Electron-hole recombination in MoSe₂ and MoS₂.—Of immediate note in the experimentally observed characteristics of these electrodes is the discrepancy between the photocurrent onset potential and the flatband potential obtained from Mott-Schottky analyses. For MoSe₂ this difference is ~650 mV while for MoS₂ it is only ~400 mV. This observation is not peculiar to these investigations alone as a close examination of the data in the literature (1-15) will reveal it to be the case in most all current-voltage curves reported for these compounds.

With the flatband potentials derived from impedance measurements it is evident that lattice decomposition does not occur until a depletion layer is formed with a maximum band bending of 650 mV for MoSe₂ and 400 mV for MoS₂. This excess band bending can only be explained by a recombination of electrons with holes which is faster than the initial hole transfer step in the lattice decomposition reaction.

At a potential bias of +600 mV, this recombination mechanism must become deactivated so that lattice decomposition occurs. A model which could account for such behavior involves assumption of an electron trap, or distribution of traps, within the energy gap of the semiconductor as is depicted in Fig. 4. When the Fermi level of the electrode is negative of this trap, it is filled by electrons which can recombine with holes faster than the holes can react with the solution reductant. Once the Fermi level becomes more positive than this

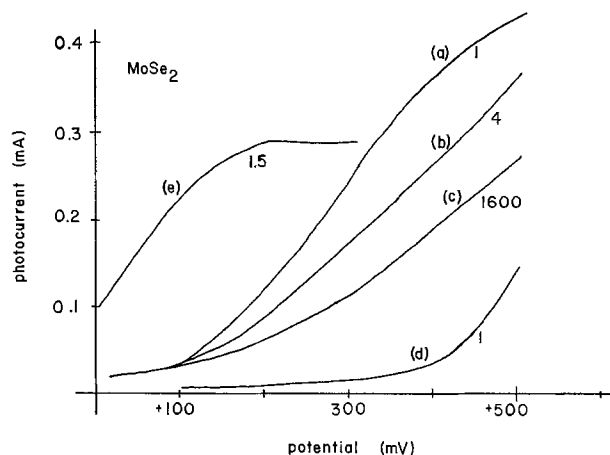


Fig. 2. The potential dependence of photocurrents at MoSe₂ as measured against an Ag/AgCl reference electrode is depicted for solutions containing 0.50M KNO₃ and (a) 50 mM hydroquinone, (b) 50 mM Fe(CN)₆⁴⁻, (c) 15 mM FeSO₄, (d) 30 mM Br⁻, (e) 15 mM I⁻. The solution was maintained at pH 1.0 with illumination conditions as in Fig. 1. The numbers on each curve are the enlargement factors necessary to bring the curves onto the current scale on the left; photocurrent resulting from lattice decomposition does not begin until about +500 mV.

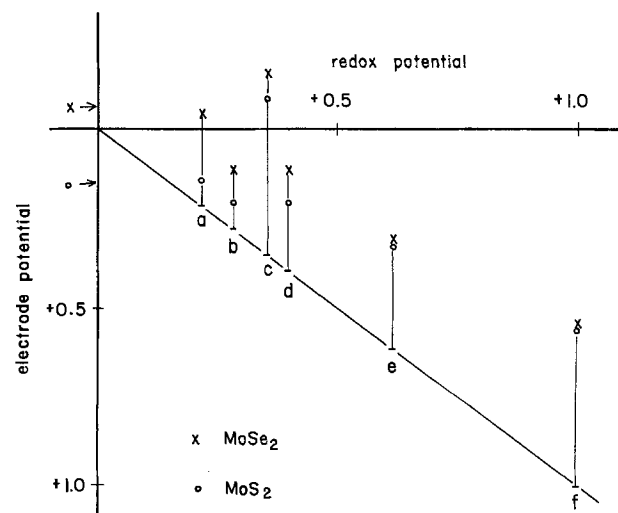


Fig. 3. Along the diagonal line are plotted the measured dark potentials (vs. Ag/AgCl) of MoSe₂ and MoS₂ electrodes immersed in solutions with varying redox couples. Under illumination MoSe₂ (x) and MoS₂ (o) acquire a more negative potential with the former being generally more negative than the latter. The flatband potentials of these electrodes, as determined by impedance measurements, are indicated at the upper left. The electrolyte contains (a) quinone/hydroquinone, (b) Fe(CN)₆^{3-/4-}, (c) I₂/I⁻, (d) Fe^{2+/3+}, (e) Ru^{2+/3+}, and (f) Ce^{3+/4+}, all at pH 1.0.

trap, it is emptied of electrons and recombination ceases. Such a recombination mechanism has been used previously to explain similar phenomena at GaP (21) and WSe₂ (9) electrodes. Heretofore, however, there has been only minimal discussion (13) of the possibility that recombination may play a role at MoS₂ and MoSe₂ electrodes.¹

It is not clear whether this trap is a bulk state as is found in GaP (21) or purely a surface state as is described for WSe₂ in Ref. (9). With these data for MoSe₂ and MoS₂, it is not possible to make a definite statement. However, the effect on the photoelectrochemistry is the same: A fast electron-hole recombination precludes hole oxidation of reductants whenever the Fermi level of the electrode is negative of +600 mV.

¹Note added in proof: This point has also been mentioned in the recent publication F. F. Fan and A. J. Bard, *This Journal*, 128, 945 (1981).

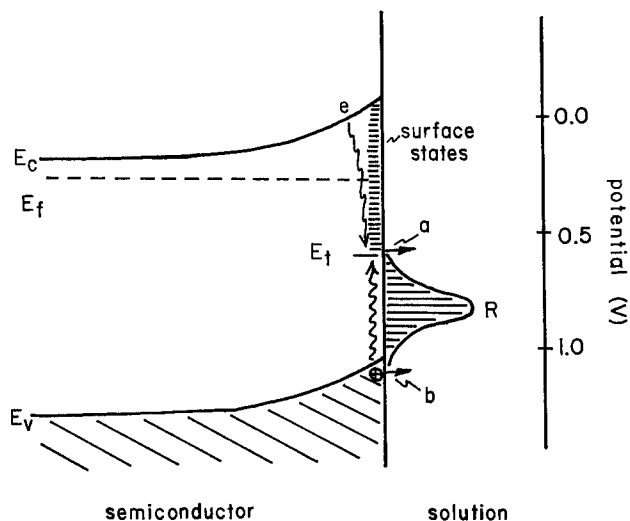


Fig. 4. A schematic representation of the MoSe_2 /electrolyte interface is given here, featuring surface states extending below the conduction bandedge to a level denoted by the energy E_t at $+0.6\text{V}$ (vs. Ag/AgCl). A distribution of occupied energy levels is also depicted for a solution reductant R which may react with holes at the electrode surface. The reductant may be oxidized at level "a" or "b." Recombination of the electron and hole through these surface states appears to compete effectively with the hole oxidation of R as long as the Fermi level, denoted by E_f , is negative of E_t .

Competition between recombination and photooxidation.—With this model, production of anodic photocurrent at a bias negative of $+600\text{ mV}$ is possible only if hole capture by the reductant occurs faster than recombination with an electron. From Fig. 1 (b) and (c) it is evident that Br^- and I^- can do this effectively at MoSe_2 electrodes. A faster recombination may be in effect at the poorer quality MoS_2 electrodes because only I^- photooxidation is evident in this potential range. Photooxidation of hydroquinone, ferrocyanide, and Fe^{+2} is also evident in this region implying that they, too, must capture holes at a rate faster than the recombination can. However, this is not true for Cl^- which produced no detectable increase in photocurrents.

It is unclear, however, at which point in the recombination pathway the reductant captures the hole, at a vacant trap or at the valence band level. It is possible, and indeed likely, that electron exchange occurs at both as is depicted in Fig. 4.

It can be shown in a straightforward manner how recombination can be interpreted in terms of the Gerischer model for semiconductor electrochemistry (22). The discussion here will focus on the domain within this model where the bandedges remain fixed with respect to energy levels in solution. In this situation it is instructive to examine an expression for the current resulting from the oxidation of reductants by holes at the electrode surface

$$I = e \int_{-\infty}^0 k(E) C_{\text{red}} \cdot W_{\text{red}}(E) \cdot D(E) \cdot (1 - f(E)) dE \quad [2]$$

where C_{red} is the concentration of the reductant, $W_{\text{red}}(E)$ is the distribution function for the energy, E , of the electron in the reductant in solution, $D(E)$ is the density of states of the semiconductor; $f(E)$ is the Fermi function, and $k(E)$ is the constant for the electron transfer itself. The product of the last two terms in this integral, $D(E)(1 - f(E))$, represents the concentration of holes, $p(E)$, at the surface with energy E

$$p(E) = D(E) (1 - f(E)) \quad [3]$$

In a steady-state situation, $p(E)$ can also be expressed as the product

$$p(E) = G(E) \cdot \tau(E) \quad [4]$$

where $G(E)$ is the rate of generation of holes with energy E and $\tau(E)$ is the lifetime of the hole at that energy level. $G(E)$ is a complicated function of illumination intensity, electric field strength, hole mobility, and surface hole generation; $\tau(E)$ reflects the kinetics of the phenomena which consume holes, such as electron-hole recombination and electron transfer to the electrolyte, both of which are a function of E .

From Eq. [2], [3], and [4] it is clear that a fast electron-hole recombination will shorten the overall lifetime of the hole at the surface, and if the reductant cannot compete successfully for this hole, that is, if $k(E)$ is not large enough, oxidation will not occur.

With this conclusion, we have found it useful to define a quantum efficiency for oxidation of the reductant by a hole at the valence bandedge (path b in Fig. 4) for the potential depicted in Fig. 2

$$\Phi = k_{\text{et}} / [k_{\text{et}} + k_{\text{rec}}(V)] \quad [5]$$

Here, k_{et} is a pseudo-first order rate constant for electron transfer which includes the concentration of the reductant at the electrode surface, and $k_{\text{rec}}(V)$ is the recombination rate which is a function of potential V . At a particular potential V_0 , within the range spanned in Fig. 2 where $k_{\text{et}} \ll k_{\text{rec}}(V_0)$, this reduces to $\Phi = k_{\text{et}}/k_{\text{rec}}(V_0)$. Consideration of pathway "a" in Fig. 4, where the reductant is oxidized at the trap, changes this result, but as long as the rate constant for oxidation through "a" is much smaller than that through "b," this approximation for Φ will hold. This neglect of pathway "a" is based on the observation (23) that the more exoergic hole oxidation of reductants at semiconductor electrodes proceeds faster than the less exoergic oxidation.

With this formulation for Φ it can be seen that at potentials in Fig. 2 where lattice decomposition does not occur, the relative magnitudes of the photocurrents for the various reductants should reflect their relative k_{et} values quantitatively because $k_{\text{rec}}(V)$ is independent of the nature of the redox couple in solution.

Unfortunately, real information about the rate of the electron transfer is obscured by the concentration term in k_{et} , which reflects, as has been noted in Ref. (15), specific surface interactions, such as adsorption, which disrupt the expected redox potential ordering of the rates of photooxidation at these electrode surfaces.

As the potential of the electrode is changed, $k_{\text{rec}}(V)$ should also change as the Fermi level approaches and passes through the energy levels of the traps responsible for recombination. On the other hand, k_{et} through pathway "b" should not be a function of potential. Consequently, one would expect that the relative ratios of the photocurrents in Fig. 2 would be independent of potential, a prediction which holds to within 10% for curves (a) through (d) between $+100$ and $+400\text{ mV}$.

The exception to this behavior is the current-voltage curve for I_2/I^- which has reached a diffusion limited plateau by $+200\text{ mV}$. Photooxidation of I^- must then proceed very fast, probably assisted by a strong interaction of unknown character between I^- and the crystal surface which has already been shown to have a catalytic effect in the photooxidation of Br^- (15). The high velocity of this reaction is also manifest in the very negative photopotentials depicted in Fig. 3 for these electrodes in I_2/I^- containing solutions.

This is an unexpected result considering the energetics of the hole transfer reaction. The I^- oxidation proceeds much faster than hydroquinone or hexacyanoferrate (II) oxidation even though the latter have more negative redox potentials. One would expect the more exoergic electron transfer to occur faster (23), but this is not the case here. It is likely that a unique mechanism is in operation for the photooxidation of I^- , such as the Fermi level pinning model discussed for this system in Ref. (2) and (12). We can offer no new evi-

dence to support this picture of the I^- interaction, but note that any such model would be compatible with the recombination scheme presented above, so long as it allows a fast hole exchange with iodide that competes effectively with the electron-hole recombination.

Back-reactions at the electrode surface.—Through the $MoSe_2$ data in Fig. 1(c) it can be seen that I^- functions as a recombination agent for the photogenerated holes and electrons. In this figure a net photooxidation of I^- is evident at $MoSe_2$ electrodes polarized negative of +500 mV. However, the chopped illumination reveals that a dark reduction current also flows at these potentials even though they are positive of the flatband potential. Given the observation that there is not a significant change in the flatband potential with the 5 mM I^- used in these experiments, this reduction reaction must proceed through surface states which exist below the conduction band as is shown in Fig. 4.

Thus, the I^- is simultaneously oxidized by holes from the valence band and regenerated through a reduction reaction. The degree to which I^- functions as a recombination center will depend on the quality of the crystal surface; a lesser number of surface defects will result in a diminished dark reduction reaction, an increased photooxidation current, and a greater photopotential. This back-reaction and its effect on the photopotential have been discussed in Ref. (9).

Photopotentials.—Inspection of the photopotential measurements depicted in Fig. 3 reveals that illumination of the semiconductor does not always result in the electrode attaining the flatband potential. These photopotentials are a function of light intensity with more negative potentials possible through an increase in illumination intensity. Consequently, the values presented in Fig. 3 can only be considered as indicative of trends in the photoelectrochemistry of the redox couples at these electrode surfaces. As has often been reported (4, 8, 9, 15), the photopotential appears to plateau for redox electrolytes with potential positive of 0.4V.

The role of recombination in this saturation of the photopotential can be seen through the expression (22) for the photopotential, $\Delta\Phi$, generated at an n-type semiconductor under illumination

$$\Delta\Phi = \frac{kT}{e} \cdot \ln(p^*/p)$$

Here p is the integral of $p(E)$ over all E where p and p^* are the hole concentrations at the surface in the dark and under illumination.

For the redox couples with potentials positive of 600 mV it is clear that the recombination process is responsible for limiting the photopotential of electrodes immersed in these solutions. For these very positive redox systems, once the potential of the electrode under illumination becomes sufficiently negative, this recombination becomes the predominant factor in determining the lifetime, $\tau(E)$, of Eq. [4] and thereby effectively reducing any further increase in p^* . Such a recombination mechanism has also been assumed to play a role in diminishing photopotentials observed with GaAs electrodes (24). Between +0.6V and the flatband potential, the photopotential attained by these electrodes in a redox solution will depend on the relative kinetics of the oxidation and recombination reactions. For redox systems with potentials positive of the energy of the valence band, which is +1.2V for MoS_2 and +0.9V for $MoSe_2$ (25), the dark potential of the electrode should be limited through formation of an inversion layer at

the surface, as has been reported for these electrodes in aprotic solvents (8).

Acknowledgments

The authors would like to thank J. Gobrecht, W. Kautek, H. Tributsch, and J. C. Bennett for their many helpful discussions and A. Friedrichs for her assistance in the laboratory.

This work was supported by a William and Flora Hewlett Grant of the Research Corporation and by the Mount Holyoke College Chemistry Department.

Manuscript submitted Jan. 15, 1981; revised manuscript received April 27, 1981.

Any discussion of this paper will appear in a Discussion Section to be published in the June 1982 JOURNAL. All discussions for the June 1982 Discussion Section should be submitted by Feb. 1, 1982.

Publication costs of this article were assisted by Mount Holyoke College and the Research Corporation.

REFERENCES

- H. Tributsch, *Ber. Bunsenges. Phys. Chem.*, **82**, 169 (1978).
- H. Tributsch, *This Journal*, **125**, 1086 (1978).
- H. Tributsch, *Ber. Bunsenges. Phys. Chem.*, **81**, 361 (1977).
- H. Tributsch, H. Gerischer, C. Clemen, and E. Bucher, *ibid.*, **83**, 655 (1979).
- H. Tributsch and J. C. Bennett, *J. Electroanal. Chem. Interfacial Electrochem.*, **81**, 97 (1977).
- J. Gobrecht, H. Tributsch, and H. Gerischer, *This Journal*, **125**, 2085 (1978).
- W. Kautek, H. Gerischer, and H. Tributsch, *Ber. Bunsenges. Phys. Chem.*, **83**, 1000 (1979).
- W. Kautek and H. Gerischer, *Ber. Bunsenges. Phys. Chem.*, **84**, 645 (1980).
- F. F. Fan, H. White, B. Wheeler, and A. Bard, *J. Am. Chem. Soc.*, **102**, 5142 (1980).
- F. F. Fan, H. White, B. Wheeler, and A. Bard, *This Journal*, **127**, 518 (1980).
- L. Schneemeyer and M. S. Wrighton, *J. Am. Chem. Soc.*, **101**, 6496 (1979).
- L. Schneemeyer and M. S. Wrighton, *ibid.*, **102**, 6964 (1980).
- J. Gobrecht, Ph.D. Dissertation, Technische Universität Berlin (1979).
- H. Lewerenz, A. Heller, and F. DiSalvo, *J. Am. Chem. Soc.*, **102**, 1877 (1980).
- S. Menezes, F. DiSalvo, and B. Miller, *This Journal*, **127**, 1751 (1980).
- D. Canfield and B. A. Parkinson, *J. Am. Chem. Soc.*, **103**, 1279 (1981).
- A. Bard, A. B. Bocarsly, F. F. Fan, E. G. Walton, and M. S. Wrighton, *J. Am. Chem. Soc.*, **102**, 3671 (1980).
- J. Wilson and D. Yoffe, *Adv. Phys.*, **18**, 193 (1969).
- M. A. Butler and D. S. Ginley, in "Semiconductor Liquid Junction Solar Cells," A. Heller, Editor, p. 290, The Electrochemical Society Softbound Proceedings Series, Princeton, NJ (1977).
- H. Tributsch, Private communication.
- M. A. Butler and D. S. Ginley, *This Journal*, **127**, 1273 (1980).
- H. Gerischer, *Adv. Electrochem. Electrochem. Eng.*, **1**, 139 (1961).
- T. Inoue, T. Watanabe, A. Fujishima, and K. Honda, in "Semiconductor Liquid Junction Solar Cells," A. Heller, Editor, p. 210, The Electrochemical Society Softbound Proceedings Series, Princeton, NJ (1977).
- W. D. Johnston, Jr., H. J. Leamy, B. A. Parkinson, A. Heller, and B. Miller, *This Journal*, **127**, 90 (1980).
- W. Kautek, H. Gerischer, and H. Tributsch, *This Journal*, **127**, 2471 (1980).

Modification of Apparent Electrocatalysis for Anodic Chlorine Evolution on Electrochemically Conditioned Oxide Films at Iridium Anodes

J. Mozota*¹ and B. E. Conway*

Chemistry Department, University of Ottawa, Ottawa, Canada

ABSTRACT

Studies of Cl₂ evolution kinetics on iridium anodes on which oxide films of various thicknesses from a monolayer upwards were formed by a potential cycling program, are reported. The multilayer oxide films were of the kind that exhibit reversible reduction/oxidation behavior. The kinetic experiments conducted in aq. KCl at pH 2 give log [current] vs. overpotential relations having a constant Tafel slope of 2.3 RT/F for all anode oxide surfaces prepared, indicating that the Cl₂ evolution mechanism is independent of the thickness of the oxide film produced. However, the apparent exchange current densities increase in an almost linear way with thickness. The latter behavior is attributed to an increase in the real area of the electrode available for Cl⁻ discharge, coupled possibly with improved electrocatalysis, e.g., on account of changes that can arise in the band structure of the oxide. Increases of Cl₂ evolution rates of up to ca. 180× are found. Effects of Cl⁻ adsorption on the development of the initial monolayer of oxide of Ir were also studied and compared with the behavior at Pt. Cl⁻ adsorption is found to inhibit the formation of the thick oxide films at Ir.

The study of the electrochemical properties of metal and metal oxide anodes in reactions such as Cl₂ and O₂ evolution has been a subject of great interest in recent years (1-5), especially since the development by Beer of DSA® electrodes for the chlor-alkali industry (6).

These anodic reactions normally proceed on a surface that is completely or partially covered with an oxide film and it is this oxide that is associated with the electrocatalytic properties of the anode, as shown by Conway and Novak (7) for the case of Pt, in their comparative studies using anhydrous trifluoroacetic acid as solvent which enabled them to obtain oxide-free surfaces for Cl₂ evolution on Pt.

Although, in the case of Pt, the enhanced activity is due only to a monolayer, or less, of oxide, since under normal conditions O₂ evolution takes place before a thicker oxide can develop (8), other metals, such as Ir and Ru, are known to develop, under the proper conditions, anodically formed oxides thousands of angstroms thick (9-14), the characteristics of which can be controlled by means of experimental variables such as growth program, pH, type and concentration of the electrolyte, etc.

In early work, the Cl₂ evolution reaction had been studied by various authors (1-3, 15) on Ir "metal" (presumably bearing some oxide film) and on IrO₂ anodes prepared by thermal methods. Thus, Chang and Wick (15), using the reaction order approach, concluded that the rate-determining step on Ir "metal" was the discharge of Cl⁻ ion in a "Volmer-Heyrovsky" type of mechanism. Consistent with this conclusion they found a Tafel slope of 2RT/3F. Yokoyama and Enyo (1) arrived at a similar conclusion, but they found the rate-determining step to be dependent on the overpotential. Arikado *et al.* (3), studying Cl₂ evolution on IrO₂ anodes, proposed the same mechanism, but Kuhn *et al.* (2) found their data to be consistent with the "Volmer-Tafel" type of mechanism (Tafel slope of RT/2F).

In the above studies, however, the states of the surfaces on which Cl₂ evolution took place were not in any way characterized, e.g., in terms of the thickness and reversibility of the oxide films, or in terms of the oxide interface and changes of its state which may occur during the Cl₂ evolution process.

It is the purpose of this paper to present results which show how the electrocatalytic properties of Ir anodes depend on their surface oxidation history. At Ir, as at Ru (13) or Rh (16), an oxide film of controllable and electrochemically characterizable thickness and state of reversibility can be formed by an anodic/cathodic potential cycling regime. The development of a reversibly oxidizable/reducible state of the oxide film on Ir, very different from the behavior of Pt, was first described by Stonehart, Kozłowska, and Conway (17) and studied by means of reflectivity by Gottesfeld and Conway (18). The formation of such films was studied further by various authors, e.g., Capon and Parsons (9), Otten and Visscher (10), Woods (11, 12), who observed how thickening of the oxide film on Ir is determined by the extent of anodic/cathodic cycling. The apparent thickness of a developed oxide film on Ir can be conveniently characterized by a parameter measuring the extent to which the charge for oxidation of the film in the anodic sweep of a cyclic voltammogram exceeds that for initial monolayer formation on the bare metal. This parameter will be referred to as the "charge enhancement factor" (CEF).

In the present work, Cl₂ evolution kinetics have been studied on a series of oxidized Ir electrodes having varying CEF values and are related to the CEF and other features of the oxide film. Also, as the adsorption of Cl⁻ ions at noble metals is known to influence their surface oxidation (19), the effects of Cl⁻ ion with regard to the development and stability of the anodic oxide film at Cl₂-evolving Ir anodes were studied.

Experimental

General.—Cyclic voltammetry experiments for Ir oxide growth and characterization were performed in the usual way (20). The real area of the Ir electrodes was determined, at the monolayer stage of surface oxi-

* Electrochemical Society Active Member.

¹ CONICIT Scholar, on leave of absence from Universidad Simon Bolívar, Caracas, Venezuela.

Key words: chlorine electrocatalysis, iridium oxide films, electrocatalysis, at Ir oxide films; oxide films.

duction, by integration of the H desorption charge, taking the coverage, θ_H , of H species as 0.65 (21-22) (relative to that for an H monolayer at Pt) for measurements made between potentials of 0.060 and 0.5V E_H , and a charge of 218 $\mu\text{C cm}^{-2}$ for $\theta_H = 1$ (23). Comparison of real and geometric area gave a roughness factor of 2.5-3.

Electrodes.—Oxidized Ir electrodes, with variable but controlled CEF's, were prepared by electrochemical growth of oxide films using a cyclic-voltammetry program with potential varied between 0.060 and 1.460V E_H , at a sweep rate of 100 mV sec^{-1} , in 0.15M H_2SO_4 at 298 K. Electrodes were made from Engelhard high purity grade Ir wires.

The electrodes bearing the conditioned oxide films were then transferred to an all-glass cell (24) which contained 1M KCl + 0.02M HCl and in which the Cl_2 evolution experiments were performed.

IR drop measurements were made by means of a current interruption technique using a Nicolet digital oscilloscope to record the transients; the determined resistances were $\approx 1\Omega$.

Solutions and salts.—A.C.S. analytical grade KCl used in this work was recrystallized twice and dried at 150°C. The KCl solutions at various concentrations were made up with analytical grade aqueous HCl to give solutions 0.02M in the acid. BDH "Aristar" grade H_2SO_4 was used to make up the electrolyte solutions in which the conditioned Ir oxide films were prepared and characterized, and in which effects of added Cl^- ion on oxide film formation were studied. Water used as a solvent was pyrodistilled, following two regular distillations, according to the procedure described previously (25).

Reference electrodes.—For all experiments, a hydrogen electrode in the same solution as that under study was employed. Potentials on this scale are referred to as V " E_H " in this paper.

Kinetic measurements.—In order to determine the electrocatalytic properties of the anode surfaces under study, steady-state current vs. potential relations for anodic Cl_2 evolution were obtained potentiostatically. The potential was stepped in increments of 10 mV by means of a PDP-11/34 computer-based system (26) and held constant for 10 sec at each value to allow current readings to be collected. Currents were recorded for ascending and descending directions of potential change. Cl_2 (g) (1 atm) was bubbled through the solution. All polarization data were corrected for IR drop since most of the electrode surfaces were very active for Cl_2 evolution.

Cl^- ion adsorption.—Chloride ion adsorption experiments at Ir were performed in 0.5M H_2SO_4 by successive additions of known amounts of standard KCl solutions by means of a micrometer pipette fitted with 1 mm Teflon spaghetti tubing terminating in a fine glass tip. The effects of Cl^- adsorption at the monolayer stage of oxidation were evaluated from changes in the Ir surface oxidation charge measured from cyclic voltammograms taken after each addition of Cl^- ion, as previously carried out in work at Pt (27).

Results and Discussion

The states of oxide films at cycled Ir anodes.—The electrochemical behavior of Ir electrodes is characterized by i vs. V profiles that are strongly dependent on the pretreatment and electrochemical history of the electrode (9-12).

Thus, initially, a fresh Ir electrode that has not been repetitively cycled up to potentials higher than 1.2V E_H , behaves like any other noble metal, as shown in Fig. 1 (this state is labeled "A"). Such electrodes exhibit an H adsorption/desorption region between 0.050

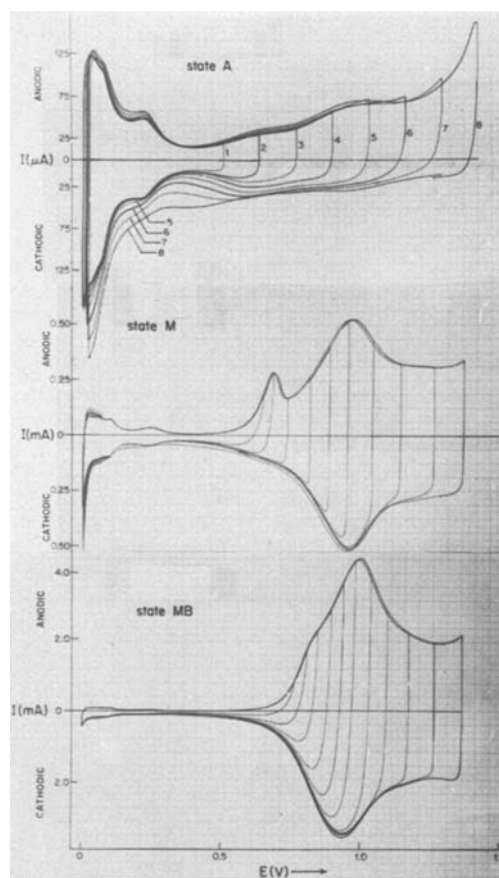


Fig. 1. Cyclic voltammetry i vs. V profiles for Ir electrodes at $5 \times 10^{-2} \text{V sec}^{-1}$, 298 K in 0.5M H_2SO_4 . State A, CEF = 1; state M, CEF = 8; state MB, CEF = 50.

and ca. 0.45V E_H , a double-layer charging region that overlaps with the onset of upd of OH/O species and a region of surface oxidation with two broad peaks that span the potential range 0.5-1.45V E_H . A nominal monolayer of IrOH is completed at 1.1V E_H (10) and that of IrO is nearing completion when O_2 gas evolution starts. On the cathodic sweep, the i vs. V profile shows that the reduction of the IrOH monolayer is relatively reversible but that of the IrO and higher oxide species is quite irreversible, so that there is much hysteresis between the potential ranges for surface oxide formation and reduction, as at Pt (17).

When the potential of this type of electrode is repetitively cycled between anodic limits $E_a > 1.4\text{V}$ (e.g., 1.5 ~ 1.7V) and cathodic limits $E_c < 0.3\text{V}$ E_H , the i vs. V profile undergoes drastic changes, as shown in Fig. 1. The electrode in a state corresponding to Fig. 1 still appears metallic; this state is designated "M." The oxidation/reduction charge increases continuously with extent of repetitive cycling (11), and the i vs. V profile becomes very reversible (9). At the same time, the H charge decreases by about 20% but the double-layer charging current observed between ca. 0.40 and 0.50V remains essentially constant. The latter behavior has been interpreted previously (4, 12, 28) as indicating that no change of real area takes place as the oxide grows.

The fact that the charge for H adsorption also remains almost unchanged is most difficult to account for and has led to conflicting views in the literature; thus Buckley and Burke (13) proposed that an outer layer of the oxide was reduced to Ir metal in the cathodic scan, thus providing sites for H deposition. On the other hand, Woods and others (12, 29) consider that H

deposition takes place on bare metal sites at the metal/metal oxide interface below the oxide film.

As the oxide grows thicker, the first oxidation peak is shifted positively until it overlaps with the main oxidation peak as shown in Fig. 1. This state exhibits a metallic-to-black transition [the electrochromic effect recently described in the literature (30)] and is designated "MB."

In the case of Ir anodes prepared for the study of Cl_2 evolution, with CEF values between 1 and 182, the states of the electrodes span those labeled as A, M, and MB (Fig. 1). The modifications to the oxide are as follows: State A is essentially a monolayer surface oxide state on Ir. In going from A to M or MB, a thicker, phase oxide is formed, consisting (5) probably of an Ir(III)/Ir(IV) hydrated oxide. Once the state M is attained (after a few cycles), the type of oxide does not change further except that the thickness and probably the roughness or porosity increases. As greater film thicknesses are attained (CEF > 100), the film starts to crack macroscopically (Fig. 2).

Although experimental conditions such as rate of growth, pH, nature of electrolyte, etc., also affect the microstructure of these films, in the present work only changes of Cl_2 evolution rates due to an increase in CEF were studied, so that changes of other variables were minimized.

The state of Ir electrode surfaces in H_2O as a function of Cl^- ion concentration.—As mentioned in the section above, in a cyclic voltammetry experiment, an Ir electrode in state A behaves like most other noble metals (31). In this state, when Cl^- is present, the following effects, shown in Fig. 3, are observed: H deposition is blocked by the competitive adsorption of the Cl^- ion, so that the charge under the i vs. V curve decreases and the peak potentials are shifted to less positive values with increasing Cl^- concentration.

Also, a double-layer charging region becomes better resolved since Cl^- ion adsorption shifts the onset of upd of O species towards more positive potentials and of H to less positive ones. This eliminates the overlap between the regions of H ionization and commencement of deposition of oxygen species which otherwise almost obscures the double-layer charging region at Ir [and Ru (28)].

Of particular interest here is the displacement of the surface oxidation region at Ir to more positive potentials by blocking on account of strong competitive adsorption of Cl^- ion, as also occurs at Pt (19, 27) but in a somewhat different manner. This blocking of surface oxide formation is conveniently measured from the

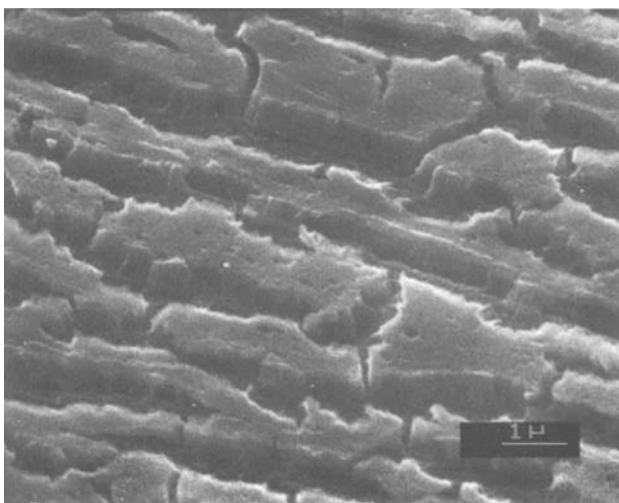


Fig. 2. SEM micrograph of an anodic iridium oxide film CEF \approx 100, showing cracking of the film.

diminution of oxide formation charge on each anodic sweep following successive additions of Cl^- ion [cf. Ref. (27)].

The percent blocking of formation of the monolayer surface oxide as a function of concentration of Cl^- ion is shown in Fig. 4, compared to that observed (27) at Pt under similar conditions. As can be seen, both relations have the same initial slope, but to achieve the same percent blocking, the concentration of Cl^- ion in the case of Ir must be 10 times larger than that for Pt. This is because surface oxidation of Ir starts already at a potential of 0.45–0.5V E_H , making the metal surface less sensitive to competitive adsorption by Cl^- .

The charge isotherm for monolayer surface oxide formation as a function of Cl^- concentration, measured at various end potentials in anodic sweeps, is shown in Fig. 5, which indicates two regions of influence of Cl^- corresponding to the two broad oxidation peaks (previous section) observed in the absence of Cl^- ion.

In the case of Ir anodes on which a thicker oxide has been grown in the absence of Cl^- ion, the addition of this ion produces similar effects in the H region to those observed on the bare metal in that region, as described above.

Figure 6 compares these two situations; with the thicker oxide (curve 1), it is experimentally observed that H deposition is diminished to some extent by the oxide itself so the percent blocking of the H region at low Cl^- concentrations is higher than that (curve 2) for Cl^- adsorption effects at the "bare" metal since the blocking effect is calculated as a percentage of the H charge measured at the "bare" (oxide free) metal. As the Cl^- concentration increases, the behavior of both types of surface referred to above is remarkably similar. This indicates that the oxide film is porous enough to allow the Cl^- ion to reach the "base" metal sites underneath the oxide film. No time effects are experimentally observed in the Cl^- ion blocking effect, so that diffusion-controlled movement of Cl^- ion through the pore system does not seem to be involved in any way.

However, in the oxide region, the Cl^- ion seems to have no effect whatsoever. This is as expected, since the oxide is already deposited (see the previous section) and does not get reduced to bare metal in every cycle (11) as does an oxide film at Pt. For these conditions, therefore, Cl^- ion can have no influence on the oxide film behavior at Ir. Continuous cycling of a previously oxidized Ir electrode in Cl^- solution causes only a slight decrease in the CEF, probably due to some dissolution of the oxide. On the other hand, attempts to continue growing the thick, reversibly oxidizable/reducible film in the Cl^- solution were unsuccessful; this may be for various reasons, e.g., enhanced rate of dissolution of Ir and/or (more likely) interference of adsorbed Cl^- ions with the growth mechanism either by blocking H deposition that could be needed indirectly for the growth (since a minimum potential in the cathodic sweep of ca. 0.2V is required for oxide growth to be maintained in the cyclic regime) or by inhibiting the underlying metal surface from participating in the film growth reaction;² such inhibition is most likely responsible for the observed effect of Cl^- ion in preventing continued oxide film growth at Ir.

Cl_2 evolution kinetics on the conditioned Ir oxide films.—The IR drop-corrected log [current-density] vs. potential curves for Cl_2 evolution on the oxide films at Ir, prepared to various extents of oxidation (CEF), are shown in Fig. 7. As can be seen, the apparent electrocatalytic effectiveness of the surfaces of these electrodes increases with increasing CEF up to a limit, after which the Cl_2 evolution currents become inde-

² A separate paper is in preparation which discusses the kinetics and growth mechanism for formation of thick oxide films on Ir.

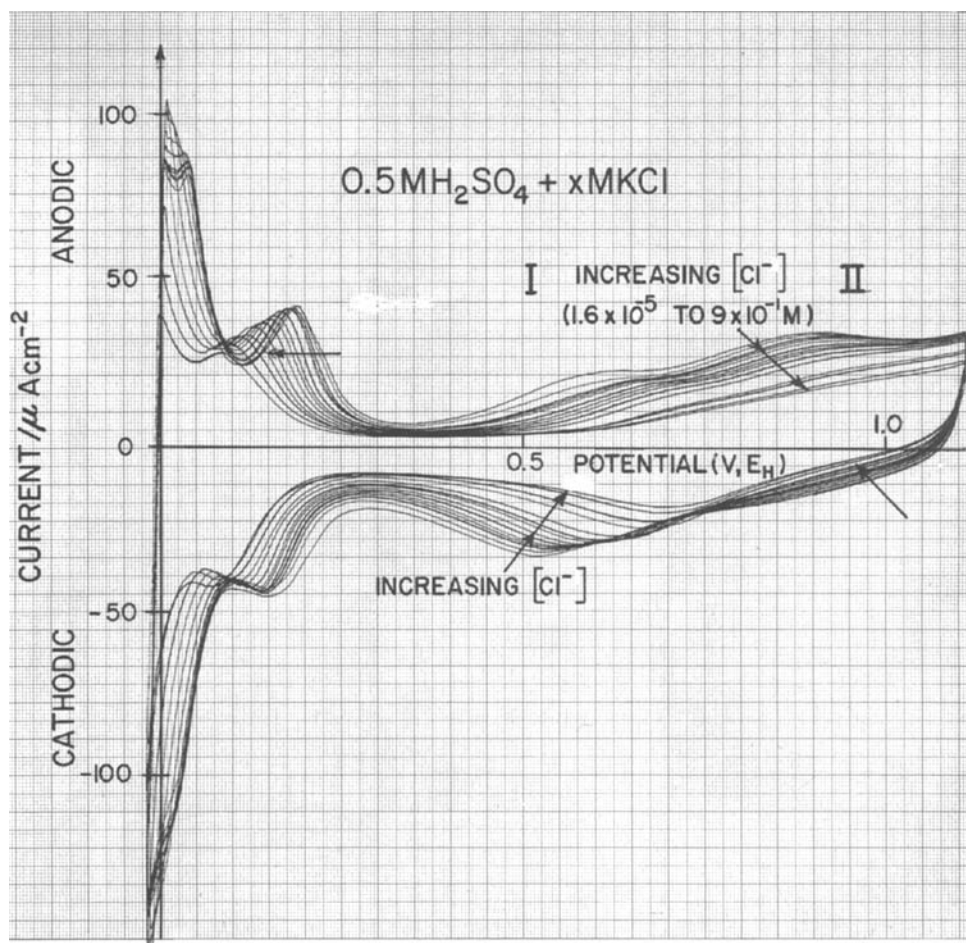


Fig. 3. Series of superimposed cyclic-voltammetry i vs. V profiles for Ir in $0.5M H_2SO_4$, with successive additions of Cl^- ion from 1.6×10^{-5} to $9 \times 10^{-1} mol dm^{-3}$. Arrows show directions of change of curves with increasing $[Cl^-]$.

pendent of the CEF. The relation between current at a given overpotential and CEF can be represented by a linear log-log plot (up to the limit mentioned above), as shown in Fig. 8. This line has a slope close to 1. A similar slope was obtained by Trasatti *et al.* (32) for O_2 evolution on RuO_2 , and was attributed to increasing concentration of defects in the films, although in their case (32) no limiting region was found.

As the overpotential values are quite small, *viz.* < 150 mV from the reversible potential, it is important to

eliminate the influence of the back-reaction in the polarization plots of Fig. 7. When this is done by plotting $\ln i / (1 - \exp[-\eta F/RT])$ vs. η , as in Fig. 9, the data become represented by straight lines the slopes of which are $\alpha F/RT$ and the intercepts of which represent $\ln i_0$. For all of the Ir oxide electrode surfaces, the value of $\alpha F/RT$ was $34 \pm 4V^{-1}$, which corresponds to a value of $\alpha = 1$ (or a Tafel slope RT/F) for the Cl_2 evolution reaction at these surfaces. That the slope remains constant over all the range of CEF values is rather important since such behavior indicates that the mechanism is the same for all the surfaces developed. This allows us to speculate on the reasons for the ob-

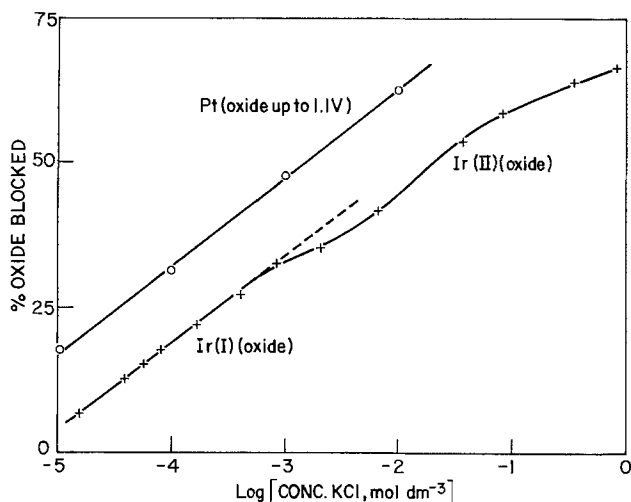


Fig. 4. Percentage of surface oxide, measured as charge for anodic formation, blocked by Cl^- as a function of $\log [Cl^-]$ for Ir as compared to Pt (27). Supporting electrolyte is $0.5M H_2SO_4$ for Ir and $0.1M H_2SO_4$ for Pt. (Regions I and II, respectively, correspond to the two broad peaks indicated in the cyclic-voltammetry curves of Fig. 3).

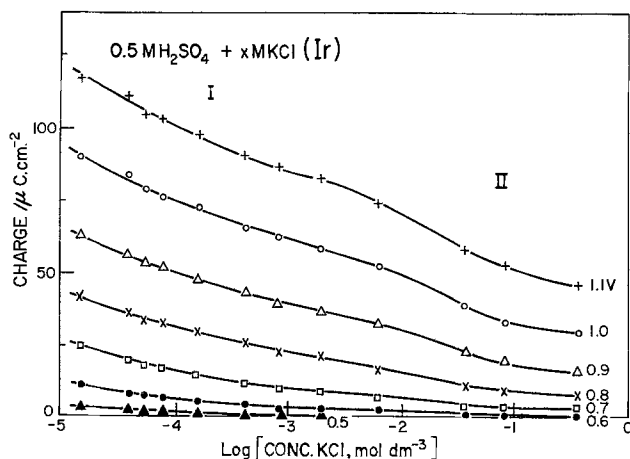


Fig. 5. Surface oxide coverages, as charge, at Ir electrodes in $0.5M H_2SO_4 + xM KCl$ solutions, as a function of $\log [Cl^-]$, evaluated for different potentials of anodic sweeps (regions I and II as for Fig. 3).

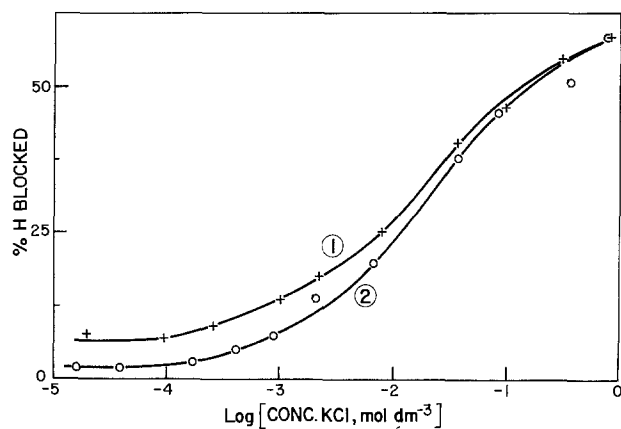


Fig. 6. Percentage of H deposited, measured with respect to initial monolayer H coverage at Ir in state A, which is blocked by Cl^- as a function of $\log [\text{Cl}^-]$ for Ir electrodes. Curve 1, Ir in state M; curve 2, Ir in state A. Supporting electrolyte is 0.5M H_2SO_4 .

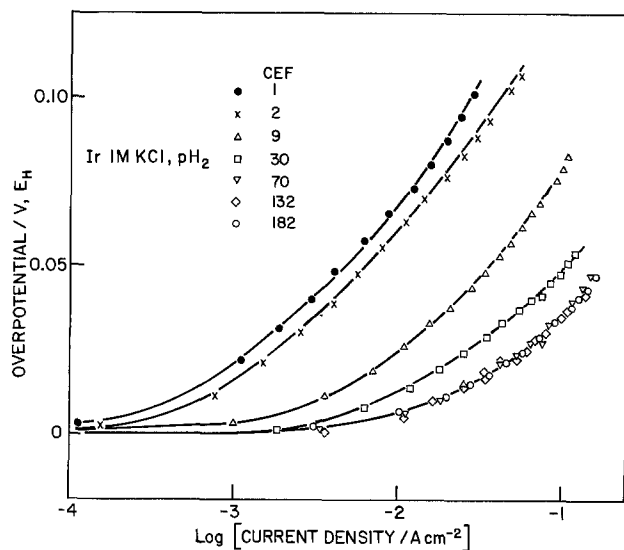


Fig. 7. Steady-state \log [current-density] vs. overpotential relations for anodic Cl_2 evolution on Ir at 298 K in 1M aq. HCl + HCl to pH 2: CEF values as shown.

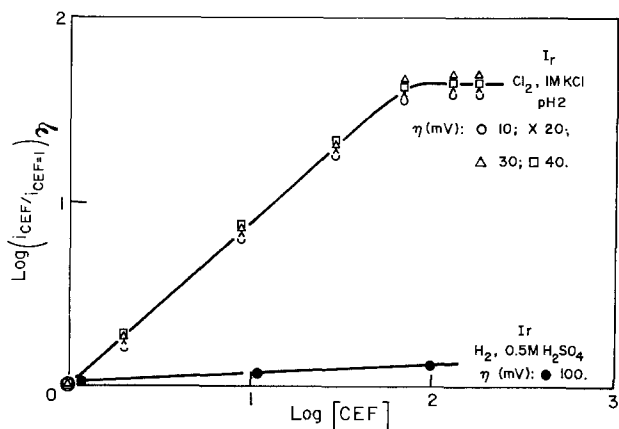


Fig. 8. Plots of Cl_2 and H_2 evolution rates at various indicated constant overpotentials as a function of CEF, expressed relative to currents for CEF = 1, for Ir anodes at 298 K in 1M aq. KCl + HCl to pH 2.

served apparent enhancement of Cl_2 electrocatalysis on a common basis for each of the CEF values and corresponding states of the oxide films.

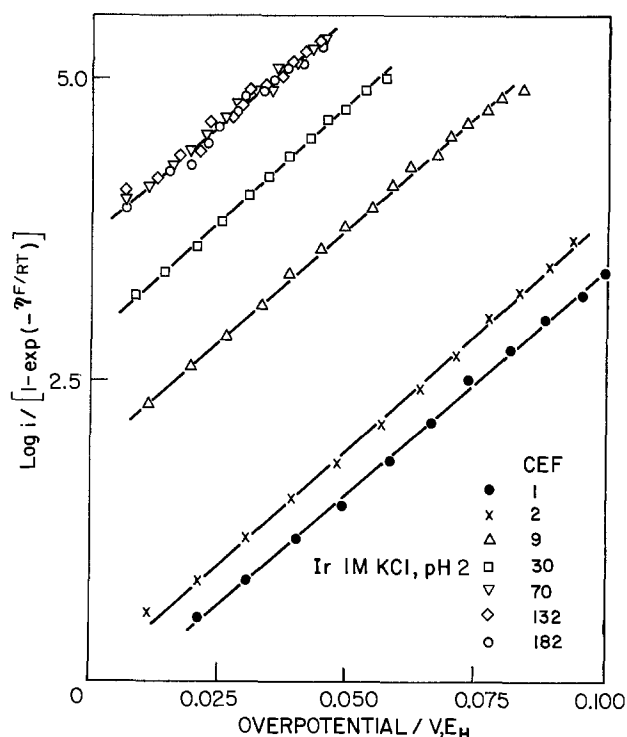


Fig. 9. Steady-state \log [current-density] vs. overpotential plots, corrected for back-reaction current component, for anodic Cl_2 evolution at Ir, as in Fig. 7.

The well-defined Tafel slope of RT/F is an unusual value in electrode kinetics but three types of explanations for such a value have been proposed for other observed examples: (i) The rate is controlled by a heterogeneous chemical recombination step in which "activated" adsorption of the Cl^- intermediate applies (33); (ii) the Cl^- discharge step is followed by a rate-controlling quasi-chemical surface-diffusion step (to sites where Cl^- is desorbed) (34); or (iii) barrierless discharge (35) applies.

We shall not try to argue a preference for applicability of one or other of these mechanisms to the present result except that (iii) is unlikely since a transition to a Tafel slope of ca. $2RT/F$ (β changing from 1 to 0.5) is not found with increasing η (Fig. 9). This then implies that the discharge step is not rate controlling. Also it should be mentioned that Kuhn and Mortimer (2) found Tafel slopes from $RT/2F$ to $2RT/F$ for Cl_2 evolution on RuO_2 , Sr₂ and Mraz (36) the same range for MnO_2 , and Morita *et al.*, (37) the value RT/F for MnO_2 doped with Ir or Ru.

Stability of the Ir oxide films.—From a practical point of view it is important to note that the anodes with bigger CEF were more stable with respect to their activity as a function of time. Thus, an electrode with a CEF of 123, when held at $\eta = 120$ mV (apparent Cl_2 evolution current density = 0.10 A cm^{-2}) for 2 hr, lost only 7% of its activity, measured as Cl_2 evolution current, at a given η . Afterwards a potentiostatic polarization for 60 sec at $0.0 \text{ V } E_H$, restored the activity to within 1% of the original value, without significant change of the CEF as measured by the oxide redox charge. In contrast, electrodes with intermediate degrees of oxide formation were less stable.

Electrodes having a CEF higher than 50 bore a visibly black oxide film when polarized anodically [known electrochromic effect (33)]. This served as a secondary feature enabling flaking of the film, which occurs under certain conditions, to be observed. This phenomenon is quite evident during O_2 evolution in the absence of Cl^- ion, indicating that this reaction is in some way intimately connected with the state of the

oxide film. For Cl_2 evolution at comparable rates, however, no flaking is observed and mechanical intactness is preserved.

Cyclic voltammograms of the anodes taken in 0.5M H_2SO_4 after prolonged Cl_2 evolution indicate that the electrochemical redox behavior of oxides having higher CEF's remained essentially unchanged, as expected, since IrO_2 does not grow on anodic potential holding (17). However, electrodes with intermediate CEF values lost some of their charge (as much as 60%) over a time period of 10 hr of Cl_2 evolution which explains the time effects in their activity for Cl_2 evolution which appear to arise for mechanical reasons due to loss of some oxide material.

SEM examination of the films.—Our own SEM studies on Ir oxide films grown in H_2SO_4 show that as the CEF increases, an apparently macroporous, initially relatively uncracked film (Fig. 10) develops wide cracks in between oxide patches (Fig. 2). This cracking is also observable under the optical microscope with very thick films while they are wet. This rules out the possibility that the cracking is an artifact due to exposure to vacuum in the SEM.

The oxide structure remains unchanged in going from a cycling regime in H_2SO_4 to one in Cl^- solutions. Thus, it appears that Cl^- ion does not chemically attack or modify the film, although it probably enhances its dissolution rate by facilitating the formation of $[\text{Ir}_x\text{Cl}_y]$ soluble complexes.

However, after the Cl_2 evolution experiments, SEM observation of the morphology of the oxide film showed that substantial changes had occurred. The film had developed widespread cracking as shown in Fig. 11 but, under high magnification (Fig. 12), some porosity was still observable. Also the surface was quite homogeneous in terms of its cracked appearance and no oxide fragments had fallen off due to mechanical failure. On the contrary, after O_2 evolution had taken place for 10 min at 50 mA/cm^2 apparent on the same electrode preparation, pieces of oxide film could be seen to have become detached from the surface. The underlying roughened metal is then exposed and the remaining oxide patches appear rough and spongy (Fig. 13). This observation may be understood if O_2 evolution involves, in an intimate chemical way, the O species of the oxide film itself, e.g., as an intermediate.

Electrocatalysis in the Cl_2 evolution reaction at Ir oxides.—In discussing the electrode kinetics of a reaction at an oxide electrocatalyst substrate which is being modified in some way, two factors must be taken into account: (i) The possible change of real area (of

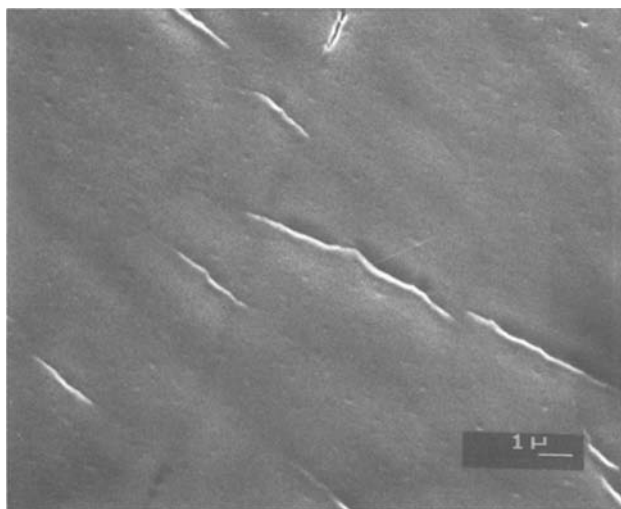


Fig. 10. SEM micrograph of an anodic iridium oxide film, CEF \approx 50, showing macropores and small amount of cracking.

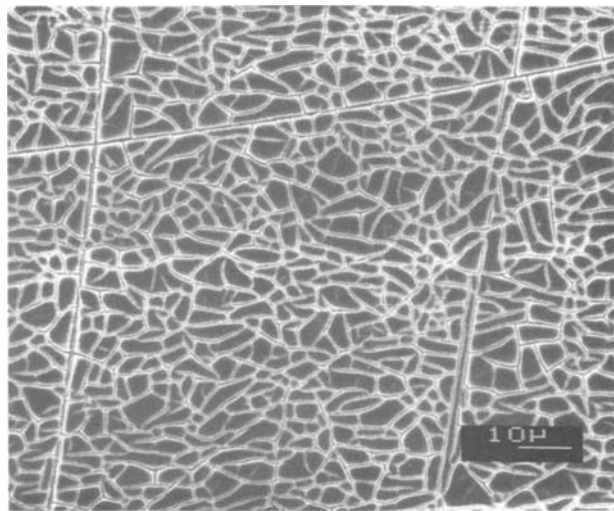


Fig. 11. SEM micrographs of an iridium oxide film of the same thickness as that of the electrode shown in Fig. 10, after being used as an anode for Cl_2 evolution for ca. 10 min at a C.D. of ca. 50 mA cm^{-2} showing widespread cracking.

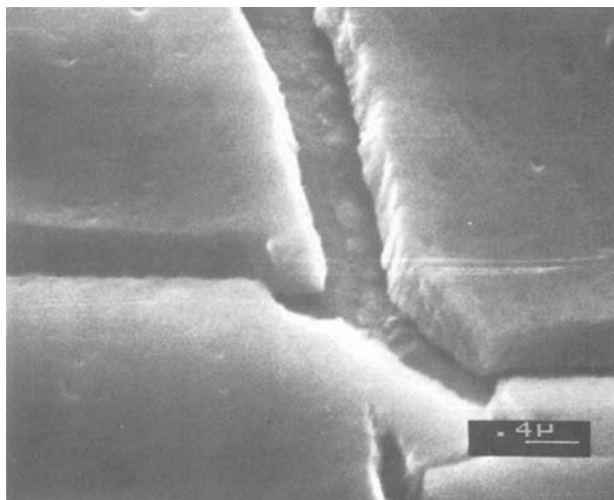


Fig. 12. SEM micrograph, at higher magnification than that in Fig. 11, showing some macroporosity still on the surface and details of cracks.

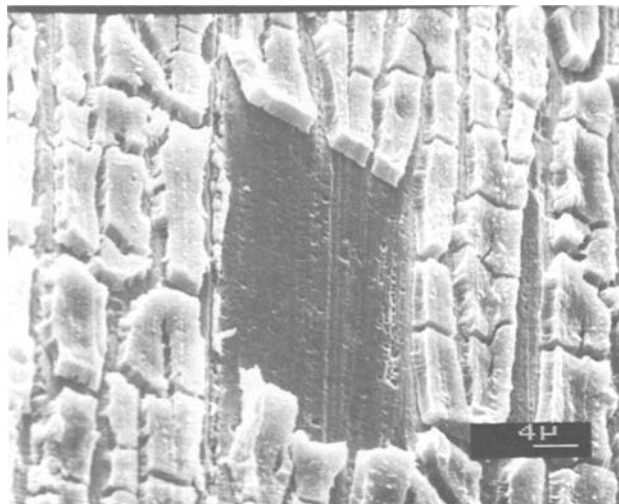


Fig. 13. SEM micrograph of an iridium oxide film, CEF \approx 100, after being used as an anode for O_2 evolution, conditions as in Fig. 11, showing oxide peeled and peeling off from the surface, and roughness of the film.

technological importance) and (ii) changes of intrinsic electrocatalytic activity (of fundamental and technological interest).

Factor (ii) may be due to changes of energy of adsorption of intermediates, changes of transition state of the reaction, modifications of electronic band structure of the material due to changes of valence states of metal ions in the oxide structure, etc. (43).

Cl₂ evolution appears to proceed by either the Volmer-Tafel or Volmer-Heyrovsky types of mechanism (1, 3, 38). The fact that the observed Tafel slopes remain unchanged (Fig. 9) with radically changed thickness of the surface film, means that the mechanism remains unchanged. Although the value of RT/F for the Tafel slope cannot unambiguously be interpreted (see above) in terms of mechanism, it is reasonable to suppose that the surface modification could affect the binding energy of Cl⁻ intermediates in the reaction.

However, the observed changes of rate of the Cl₂ evolution reaction must first be considered in terms of possible changes of real area of the substrate. Although the Ir oxide films are porous and rough, and will thus have an area that tends to increase with thickness, the important parameter that relates the observed currents to an area factor, is the distribution of the applied potential difference across the metal/oxide/electrolyte system, as a function of thicknesses and oxidation state of the film.

Recent a.c. impedance measurements (39) indicate a C_e value of $\approx 60 \mu\text{F cm}^{-2}$ at ca. 0.36V E_H and of $\approx 760 \mu\text{F cm}^{-2}$ at 0.96V E_H (under the capacitance maximum) of the i vs. V profile; thus an area increase would seem to have taken place simply by increasing the oxidation state of the film. At the same time, the conductance of the film was found to change from $10^{-2} \Omega^{-1} \text{cm}^{-2}$ to $10^2 \Omega^{-1} \text{cm}^{-2}$ [units as given in Ref. (39)] in going from the cathodic end potential to the anodic end potential in a cyclic potential change.

These results indicate that the film is not a very good conductor at low anodic potentials; for these conditions, it can therefore be assumed that the applied p.d. is located mainly at the metal/oxide interface. This could provide an explanation for the unchanged H ionization/deposition and double-layer charging potential regions, since the system behaves as Ir metal in contact with electrolyte. The latter would be available at the metal/oxide interface on account of the porous nature of the film. The behavior in the H region is consistent with the observed effect of Cl⁻ ion on the H adsorption/desorption region, discussed earlier, which seems to be independent of the film thickness.

In order to account for the observed results for Cl₂ evolution rates, we propose the following. As the potential increases in the anodic direction, the conductance of the film increases (39) and the oxide becomes a metallic conductor; thus, the oxide film as a whole assumes a potential with respect to the electrolyte as a result of the applied potential difference. Microscopically, of course, in a porous structure, such a situation would require a distribution of oxide-to-solution interfacial potential drops throughout the thick film when it is in the conducting state. The real equivalent circuit for such a situation is then quite complex but elements of it will be like the circuit for a low resistance transmission line. Some potential difference remains, of course, at the metal/oxide interface and a fraction of the applied potential is lost across the film, due to residual IR drop, this amount being a linear function of the film thickness.

This would account for the observed value of C_e under the capacitance maxima (39) ($760 \mu\text{F}$ apparent cm^{-2}) characteristic of a surface of large real area and would be consistent with the optical appearance of the film.

Thus, Cl₂ evolution, which occurs at high positive potentials, takes place under conditions where, in principle, the whole surface of the oxide is available for electron transfer, that is, the outer surface + interface of the pore structure. As the thickness of the film increases, an increasing IR drop, coupled with some mass-transport limitations at the bottom of the pores, restricts the real area available for the reaction.

This model is supported by the behavior of the Fe(CN)₆⁴⁻/Fe(CN)₆³⁻ redox couple at a rotating disk of Ir metal compared with that at a disk of oxidized Ir, as shown by Gottesfeld (40).

Furthermore, the change of location of the applied potential difference with change of conductance of the film, has been confirmed in the present work by carrying out H₂ evolution studies on the same modified Ir anodes.

According to the proposed model, at cathodic potentials, the applied potential difference is located mainly at the metal/oxide interface; thus any increase in real area of the oxide film with increasing CEF is irrelevant for the H₂ evolution reaction, since the oxide cannot support electron transfer at the interfaces of its pore structure if it is essentially nonconducting. Experimental results indicate that the polarization curves for the H₂ evolution reaction remain essentially constant, regardless of the CEF (see curve for H₂ in Fig. 8), and exhibit a Tafel slope of $\approx 2RT/F$.

Related work from this laboratory, to be published elsewhere (41), on the electrocatalytic behavior of oxidized Ru electrodes for Cl₂ evolution showed that a changed state of monolayer surface oxidation could be induced by cycling at that metal, over a restricted potential range, and then Cl₂ evolution rates were enhanced some 30 \times , independently of any area change, which was unambiguously less than 5%. On the other hand, at the thickened oxide films that can be formed at Ru in a similar way to those at Ir, Cl₂ evolution rates are not found to increase with increasing CEF of the Ru oxide film. This is due to the different, impervious character of the oxide film at Ru in comparison with that at Ir as can be observed microscopically.

The rather sharp limit in activity enhancement, which is eventually reached with increasing CEF (Fig. 8), could then be explained in terms of two factors: (i) An increasing IR drop within the film (which would not be included in the experimentally measured IR drop in the solution due to the "RC" coupling in the equivalent circuit of the film itself) with increasing thickness that would account for falloff of the rate of activity increase with CEF, but hardly as sharp an inflexion as observed (Fig. 8); and (ii) a mass-transport problem that renders the innermost regions of the film inactive because of diffusion control limitation in Cl⁻ migration into pores and gas exit.

We can conclude, then, that the apparent large enhancement of electrocatalysis of the modified iridium oxide film for Cl₂ evolution is due mainly to an increase in real, microscopic surface area with increasing CEF. Also, that IR drop across the film, coupled with diffusion limitations, accounts for the leveling off of the activity at CEF's > 100. By comparison with the behavior of RuO₂ films, it is apparent that the d-electron configuration of the Ir oxide films could play some small but perhaps significant role in the electrocatalytic process, along lines suggested by Arikado *et al.* (3) for IrO₂, although compared to the area factor in the present case, it is a minor one. A model for the interfacial potential distribution across the metal/oxide/electrolyte system, dependent on state of oxidation of Ir in the oxide films, has been proposed and will be dealt with in more detail in a forthcoming publication (42).

Acknowledgments

Grateful acknowledgment is made to the Natural Sciences and Engineering Research Council of Canada for support of this work. One of us (J.M.) acknowledges the award of a CONICIT (Venezuela) graduate research scholarship.

We also wish to express our thanks to Mr. R. Myers for carrying out the SEM work and to Drs. H. Angerstein-Kozłowska and V. Birss, for discussions on noble metal surface oxidation.

Manuscript submitted Jan. 6, 1981; revised manuscript received ca. May 1, 1981.

Any discussion of this paper will appear in a Discussion Section to be published in the June 1982 JOURNAL. All discussions for the June 1982 Discussion Section should be submitted by Feb. 1, 1982.

Publication costs of this article were assisted by the University of Ottawa.

REFERENCES

1. T. Yokoyama and M. Enyo, *Electrochim. Acta*, **15**, 1921 (1970).
2. A. T. Kuhn and C. J. Mortimer, *This Journal*, **120**, 231 (1973).
3. T. Arikado, C. Iwakura, and H. Tamura, *Electrochim. Acta*, **23**, 9 (1978).
4. E. J. Frazer and R. Woods, *J. Electroanal. Chem. Interfacial Electrochem.*, **102**, 127 (1979).
5. S. Gottesfeld and S. Srinivasan, *ibid.*, **86**, 89 (1978).
6. H. B. Beer, Neth. Pat. Appl. 216,199 (1957); U.S. Pat. 3,236,756 (1966); U.S. Pat. 3,563,100 (1971).
7. B. E. Conway and D. M. Novak, *J. Electroanal. Chem. Interfacial Electrochem.*, **99**, 133 (1979).
8. A. Damjanović, L. S. R. Yeh, and J. F. Wolf, *This Journal*, **127**, 874 (1980).
9. A. Capon and R. Parsons, *J. Electroanal. Chem. Interfacial Electrochem.*, **39**, 275 (1972).
10. J. M. Otten and W. Visscher, *ibid.*, **55**, 1 (1974).
11. D. A. J. Rand and R. Woods, *ibid.*, **55**, 375 (1974).
12. R. Woods, *Isr. J. Chem.*, **18**, 118 (1979).
13. D. N. Buckley and L. D. Burke, *J. Chem. Soc., Faraday Trans. I*, **71**, 1447 (1975). See also D. N. Buckley, L. D. Burke, and J. K. Mulcahy, *ibid.*, **72**, 1896 (1976).
14. S. Hadzi-Jordanov, H. Angerstein-Kozłowska, M. Vuković, and B. E. Conway, *J. Phys. Chem.*, **81**, 2271 (1977).
15. F. T. Chang and H. Wick, *Z. Phys. Chem.*, **A172**, 448 (1935).
16. L. D. Burke and E. J. M. O'Sullivan, *J. Electroanal. Chem. Interfacial Electrochem.*, **93**, 11 (1978).
17. P. Stonehart, H. Angerstein-Kozłowska, and B. E. Conway, *Proc. R. Soc. London, Ser. A*, **310**, 541 (1969).
18. B. E. Conway and S. Gottesfeld, *J. Chem. Soc., Faraday Trans. I*, **69**, 1090 (1973).
19. M. W. Breiter, *Electrochim. Acta*, **8**, 925 (1963).
20. F. F. Will and C. A. Knorr, *Z. Elektrochem.*, **64**, 258 (1960). See also H. Angerstein-Kozłowska, B. E. Conway, and W. B. A. Sharp, *J. Electroanal. Chem. Interfacial Electrochem.*, **43**, 9 (1973).
21. R. Woods, *ibid.*, **49**, 217 (1974).
22. M. Breiter, H. Kammermaier, and C. A. Knorr, *Z. Elektrochem.*, **60**, 119 (1956).
23. T. Biegler, D. A. J. Rand, and R. Woods, *J. Electroanal. Chem. Interfacial Electrochem.*, **29**, 269 (1971). See also D. A. J. Rand and R. Woods, *ibid.*, **31**, 29 (1971).
24. B. E. Conway, H. Angerstein-Kozłowska, and G. Czartoryska, *Z. Phys. Chem. N.F.*, **112**, 195 (1978).
25. B. E. Conway, H. Angerstein-Kozłowska, W. B. A. Sharp, and E. Criddle, *Anal. Chem.*, **45**, 1331 (1973).
26. J. Mozota, M. Barnett, D. Tessier, H. Angerstein-Kozłowska, and B. E. Conway, *Anal. Chim. Acta. Comp. Techn. and Optim.*, In press (1980).
27. D. M. Novak and B. E. Conway, *J. Chem. Soc. London, Faraday Trans. I*, In press (1981).
28. J. Mozota, M. Vuković, and B. E. Conway, *J. Electroanal. Chem. Interfacial Electrochem.*, In press (1981).
29. J. O. Zerbino, N. R. de Tacconi, and A. J. Arvia, *This Journal*, **125**, 1266 (1978).
30. S. Gottesfeld and J. D. E. McIntyre, *ibid.*, **126**, 742 (1979).
31. H. Angerstein-Kozłowska, B. E. Conway, B. Barnett, and J. Mozota, *J. Electroanal. Chem. Interfacial Electrochem.*, **100**, 417 (1979).
32. G. Lodi, E. Sivien, A. de Battisti, and S. Trasatti, *J. Appl. Electrochem.*, **8**, 135 (1978).
33. J. G. N. Thomas, *Trans. Faraday Soc.*, **57**, 1603 (1961).
34. N. Pentland, J. O'M. Bockris, and E. Sheldon, *This Journal*, **104**, 182 (1957).
35. L. I. Krishtalik, *Elektrokhimiya*, **2**, 624 (1966).
36. V. Srb, R. Mraz, and S. Tichy, Scientific Papers of the Institute of Chemical Technology, p. 93, Prague, B15 (1972).
37. M. Morita, C. Iwakura, and H. Tamura, *Electrochim. Acta*, **24**, 639 (1979).
38. D. M. Novak, B. V. Tilak, and B. E. Conway, in "Modern Aspects of Electrochemistry," Vol. 14, J. O'M. Bockris and B. E. Conway, Editors, In press (1981).
39. S. H. Glarum and J. H. Marshall, *This Journal*, **127**, 1467 (1981).
40. S. Gottesfeld, *ibid.*, **127**, 1922 (1980).
41. M. Vuković, H. Angerstein-Kozłowska, and B. E. Conway, *J. Appl. Electrochem.*, In press (1981).
42. B. E. Conway and J. Mozota, *Electrochim. Acta*, In press (1982).
43. L. F. Mattheis, *Phys. Rev.*, **13**, 2433 (1976).

Characteristic Differences in the Surface Space Charge Layer of the Red and Green Forms of Lutetium Diphthalocyanine

S. C. Dahlberg, C. B. Reinganum, C. Lundgren, and C. E. Rice*

Bell Laboratories, Murray Hill, New Jersey 07974

ABSTRACT

The surface photovoltage of red and green forms of lutetium diphthalocyanine has been measured in a low pressure ($2 \cdot 10^{-9}$ Torr) environment and these two electrochemically interesting compounds have characteristic differences in their surface space charge layers. The green lutetium diphthalocyanine has an electron depletion layer, while the red material, prepared by iodization, has an electron accumulation layer. The photovoltage spectra are distinctive and are correlated with the differing optical absorptions of the colored films. The dependence of the dynamical response of the photovoltage on incident light indicates that photoinduced changes in the electronic populations of slow traps and/or surface states appear to be present.

The unusual electrochemical properties of the rare earth diphthalocyanines were first reported in 1965. Kirin, Moskalev, and co-workers reported that films of lutetium diphthalocyanine in aqueous potassium chloride could be changed from their initial green to either a blue or cinnamon red color with a variation of the applied voltage of less than 2V (1-6). This early work was reproduced by Nicholson and Pizzarello who also discovered several new colors and established that the switching times were on the order of 50 msec and thus were of obvious interest for use in electrochromic displays (7-11). The chemical species responsible for this behavior have not yet been completely established, but EPR observations by Corker *et al.* suggest that changes in the oxidation state of the phthalocyanine rings are responsible for the distinctive color changes (12). Nicholson and Pizzarello have reported that the color changes are sensitive to the presence of ambient gases, particularly oxygen, and that this could be due to the chemical binding of oxygen throughout the bulk of the film (10). Since these materials are organic semiconductors, their color change may be associated with changes in their surface space charge layer. Therefore, in order to further characterize the surface space charge regions of the differently colored forms, we have measured the photovoltaic change in the energy band bending at the surfaces of these films.

Experimental

The synthesis of the lutetium diphthalocyanine followed that reported by Moskalev and Kirin (4), and resulted in a mixture of mono- and diphthalocyanine complexes, which are green and blue, respectively, in DMF solution. The two products were separated by liquid chromatography in DMF on an alumina column, using DMF as eluent. Removal of the solvent from the faster-eluting blue fraction yielded the green form of lutetium diphthalocyanine along with some phthalonitrile starting material. This material was heated to 200°C in flowing N₂ gas to drive off the excess phthalonitrile and thin films were grown by vacuum sublimation ($3 \cdot 10^{-5}$ Torr) on both Ni substrates and glass slides. A red form of lutetium diphthalocyanine containing iodide counterions was prepared by heating the green films to 200°C for a few minutes in flowing I₂/N₂ gas, followed by pure N₂ gas to remove unreacted I₂. Films prepared in this manner appeared reddish-purple under reflected light and brown with trans-

mitted light. This chemical approach to producing the red lutetium diphthalocyanine film is based on the work of Moskalev and Kirin (6), who found that the red films formed by iodization had a spectrum similar to those formed electrolytically. Both the red and green forms appeared to be stable in the air and their photovoltage did not degrade following the 250°C bakeup which was necessary to achieve a low pressure ($\sim 2 \cdot 10^{-9}$ Torr) in the surface photovoltage apparatus.

The retarding potential electron beam technique used for measuring the photovoltage has been described in detail in the literature (13, 14), and involves measuring the optical modulation of the transmission of low energy electrons incident on the surface. Measurement of the photovoltage spectra was obtained with phase sensitive lock-in detection and a mechanically chopped Xenon lamp, while the measurement of the dynamics of the photovoltage response were obtained with signal averaging and a pulsed dye laser. All of the reported photovoltage spectra have been corrected for variations in the relative lamp intensity. Optical absorption spectra were measured with a Cary 14 spectrometer.

Results and Discussion

Figure 1 illustrates the photovoltage spectrum measured for the green lutetium diphthalocyanine film in comparison with the optical absorption spectrum of the film on a glass slide. The optical absorption of the film has maxima at 705 and 670 nm and shoulders at 645 and 620 nm, in fairly close agreement to the 660 nm peak and shoulder reported for the green lutetium diphthalocyanine in solution (12). The photovoltage spectrum, on the other hand, is dominated by the peak at 800 nm, and has smaller maxima at 593 and 445 nm. Discrepancies between optical absorption and photovoltage spectra have been observed for other semiconductors, and are attributed to the fact that the photovoltage spectrum is determined both by the optical absorption and associated exciton creation, and by the subsequent dissociation of these excitons into free charge carriers (15, 16). Since this latter process depends both on the distance of the exciton from the surface and on the "allowed" or "forbidden" nature of the electronic transition, it depends on the wavelength of the light and the photovoltage spectra can thus differ somewhat from the optical absorption spectra. Figure 2 shows the photovoltage spectrum of the red lutetium diphthalocyanine film in comparison with the optical absorption of the yellow-red lutetium diphthalocyanine reported in the literature (12). The photovoltage spectrum has

* Electrochemical Society Active Member.

Key words: photovoltage, spectra, surface states.

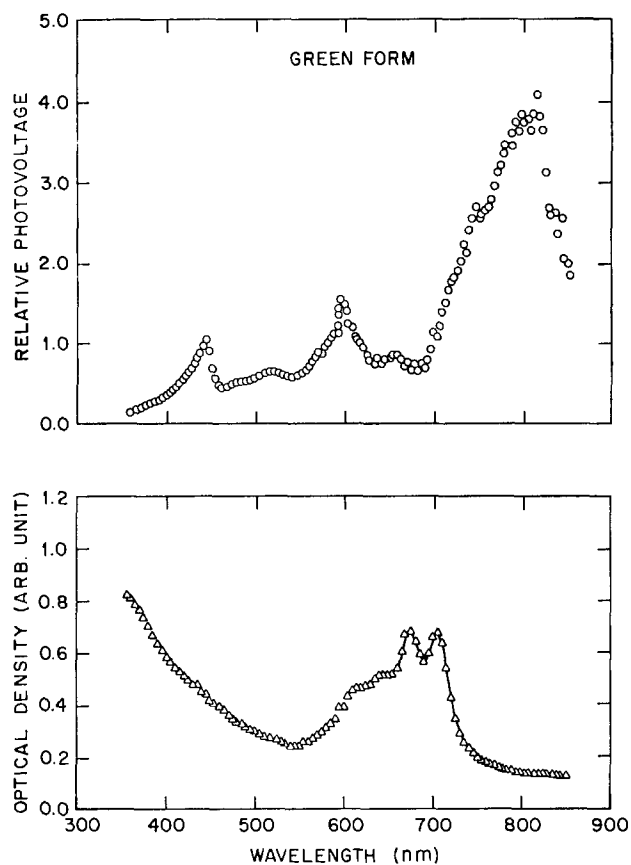


Fig. 1. Comparison between the photovoltage and optical absorption spectra of the green lutetium diphthalocyanine film. The photovoltage spectrum has been normalized to its value at 580 nm.

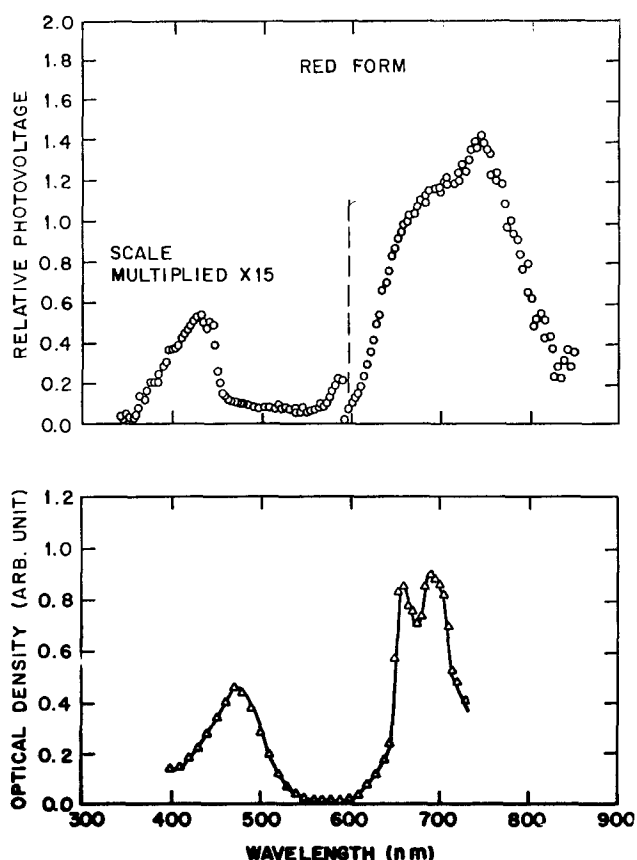


Fig. 2. Comparison between the photovoltage spectrum of the red lutetium diphthalocyanine film and its optical absorption in solution [Ref. (12)]. The photovoltage spectrum has been normalized to its value at 640 nm.

maxima at 742 and 427 nm, which is in reasonable agreement with the optical absorption maxima at 690, 660, and 470 nm. As with the green film, the slight discrepancy is attributed to a wavelength dependence for exciton dissociation. Comparing the data in Fig. 1 and 2 indicates that the distinctive differences in the photovoltage spectra of the two forms are associated with their differing optical absorption spectra.

Figure 3 illustrates the dynamical response of the photovoltage for both the green and red forms of the lutetium diphthalocyanine following 7 nsec laser pulse at time zero. The pulse repetition rate was 7 Hz, which allowed the samples sufficient time to recover a steady-state "dark" signal between pulses. The time dependence in Fig. 3 has the form $PV_0 e^{-t/\tau}$, where PV_0 is the initial response to the laser pulse and τ is a characteristic exponential decay time. A nonlinear least squares fit of this equation to the data was used to obtain the values of PV_0 and τ reported in the figure caption. This exponential form of the photovoltage decay is consistent with the differential equation.

$$\frac{dPV}{dt} = -\frac{1}{\tau} PV \quad [1]$$

It is evident from Fig. 3 that the two forms differ in the sign of PV_0 : The positive signal observed for the green form is consistent with electron depletion at the surface while the negative signal observed for the red form is indicative of electron accumulation at the surface (17).

Figure 3 showed the dynamic photovoltage response at 100% of the laser intensity. This experiment has been repeated for smaller intensities which were achieved with suitable neutral density filters and the

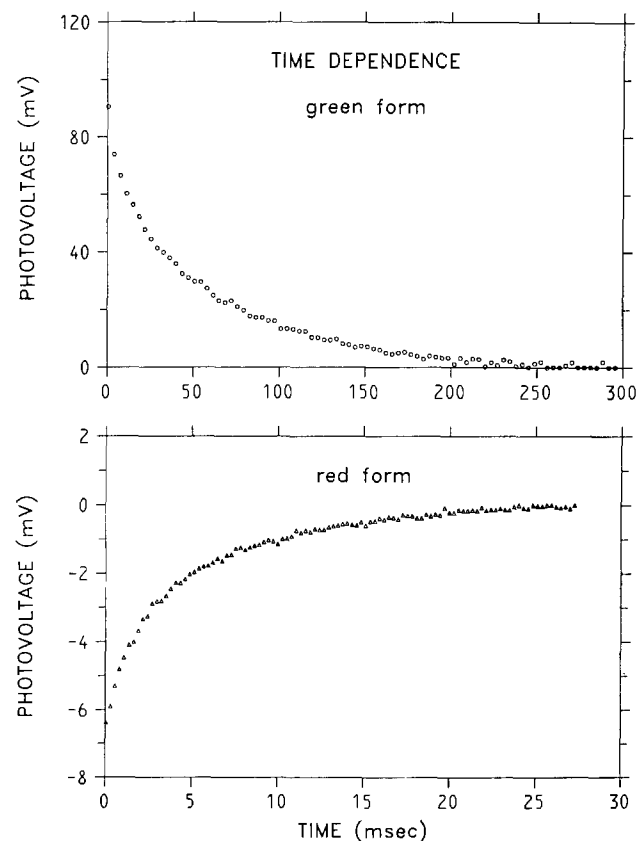


Fig. 3. The exponential decay of the photovoltage signal following a 7 nsec laser pulse at time zero. Because of differences in spectral response, the data for the green form were obtained at 580 nm while the red was at 640 nm. A nonlinear least squares fit was used to fit Eq. [1] to the experimental data: green ($PV_0 = 90.5$ mV, $\tau = 57.3$ msec), red ($PV_0 = -6.4$ mV, 2.3 msec).

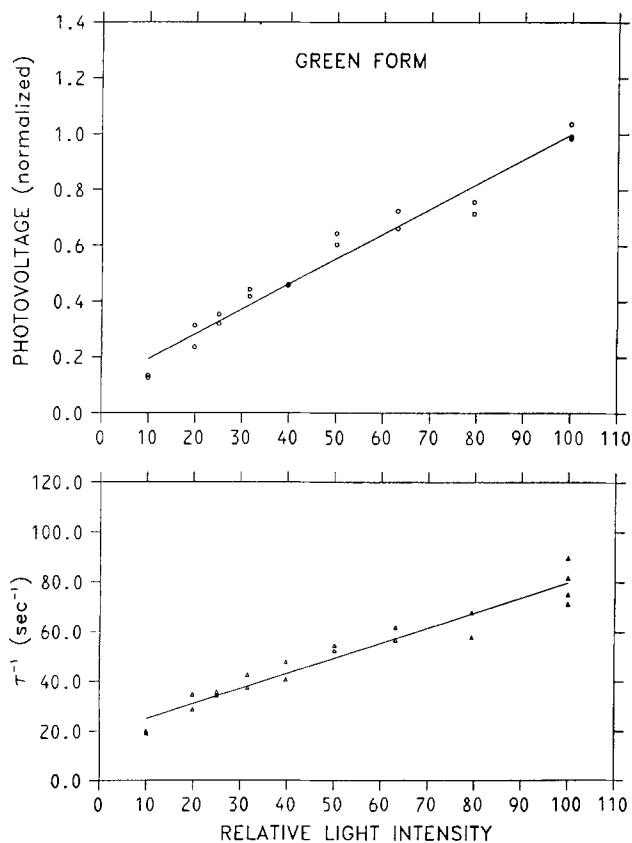


Fig. 4. The dependence of PV_0 and τ on light intensity for the green lutetium diphthalocyanine.

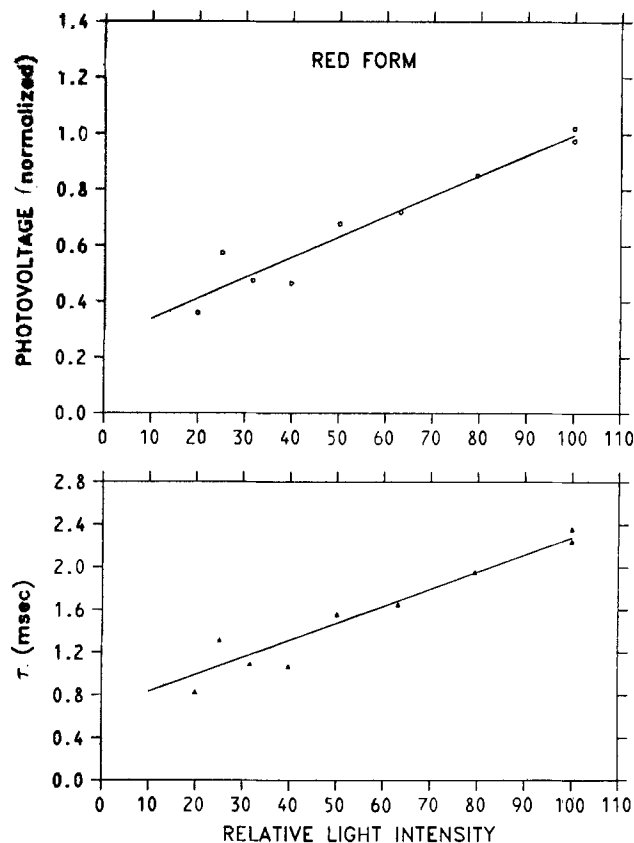


Fig. 5. The dependence of PV_0 and τ on light intensity for the red lutetium diphthalocyanine.

dependence of the resulting PV_0 and τ are illustrated in Fig. 4 and 5. For both the red and green forms of lutetium diphthalocyanine, PV_0 increases linearly with increasing light intensity over the range of intensities examined. This linear intensity dependence is observed when the photovoltaic change in the energy band bending is small compared to the total amount of band bending at the surface (V_d). This corresponds to the situation where the photovoltage is proportional to the minority carrier injection (Δ_{\min}) which, in turn, is proportional to the light intensity (I) (18)

$$PV_0 \propto \Delta_{\min} \propto I \quad \text{for } PV_0 \ll V_d \quad [2]$$

The data in Fig. 4 and 5 indicate, however, that the red and green forms differ in the intensity dependence of τ : τ is directly proportional to light intensity for the red form, but inversely dependent for the green form. In order to understand the underlying mechanism for this difference, it is necessary to consider the decay kinetics for the photoinjected minority carriers in these materials. Combining Eq. [1] and [2] yields

$$\frac{d\Delta_{\min}}{dt} = -\frac{1}{\tau} \Delta_{\min} \quad [3]$$

This phenomenological rate law can be compared to the analogous expression derived from the photovoltage data for polyarene (16) and metal phthalocyanine (19) films

$$\frac{d\Delta_{\min}}{dt} = \frac{-k \cdot PV}{V_d} \cdot \Delta_{\min} \quad [4]$$

where k is determined by the mobility of the minority carrier under flatband conditions. Equation [4] is obtained by assuming that the decay of the photovoltage is determined by the leakage current of minority carriers in the bulk to the surface against the opposing field of the space charge layer. Thus the rate at which photoinjected carriers can reach the surface varies with

time since the electric field in the space charge layer is dependent on the decaying photovoltage. The decay kinetics in Eq. [4] therefore depend linearly on PV and this formula is applicable when PV_0 is appreciable compared to V_d . As noted previously in Eq. [2], however, the experimental results for lutetium diphthalocyanine indicate that PV_0 is small compared to V_d and therefore Eq. [3] is simply the limiting form of Eq. [4] which is appropriate when the electric field in the space charge layer is, to a first approximation, unchanged by the decay of the photoinjected minority carriers. Comparing Eq. [3] and [4] yields

$$\tau \propto \frac{V_d}{k} \quad [5]$$

On the basis of Eq. [5], the dependence of τ on incident light intensity illustrated in Fig. 4 and 5 is simply originating in an intensity dependence of V_d and/or k . Not enough is known about the electrical characteristics of these rare earth diphthalocyanines to be able to predict with any certainty the exact origin of this intensity dependence. One reasonable possibility is that these materials have either bulk traps or surface states which change electronic population on a time scale which is slow compared to the 7 Hz repetition rate used in these experiments. (Faster electronic transitions would cause deviations from the experimentally observed exponential decay.) For example, both the red and green form of lutetium diphthalocyanine could have a photoexcited electronic transition from a filled surface state into the conduction band. For the green form, this would lower the band bending at the depletion layer and thus decrease τ with increasing intensity as seen experimentally in Fig. 4. In contrast, the same transition would increase the band bending at the accumulation layer of the red form and thus increase τ with increasing intensity which is consistent with the observations illustrated in Fig. 5.

Summary

The surface photovoltage of the red and green forms of lutetium diphthalocyanine have photovoltage spectra which are characteristically different and are related to the optical absorptions of these two electrochromic forms. Dynamical measurements indicate that the green form has an electron depletion layer, while the red form has an electron accumulation layer. Both films have a photovoltage which is linearly dependent on light intensity, which implies that the photovoltaic change in the band bending is small compared to the total amount of energy band bending at the surface. The photovoltaic relaxation is linearly dependent on light intensity for the red form and inversely dependent for the green form, and this is shown that this is consistent with the presence of long-lived traps which make the band bending and/or flatband mobility dependent on light intensity.

Manuscript submitted Dec. 11, 1980; revised manuscript received April 24, 1981.

Any discussion of this paper will appear in a Discussion Section to be published in the June 1982 JOURNAL. All discussions for the June 1982 Discussion Section should be submitted by Feb. 1, 1982.

Publication costs of this article were assisted by Bell Laboratories.

REFERENCES

1. I. S. Kirin, P. N. Moskalev, and Y. A. Makashev, *Russ. J. Inorg. Chem.*, **10**, 1065 (1965).
2. I. S. Kirin, Y. L. Shelekin, and P. N. Moskalev, *Sov. Phys. Solid State*, **9**, 1461 (1967).
3. I. S. Kirin, P. N. Moskalev, and Y. A. Makashev, *Russ. J. Inorg. Chem.*, **12**, 369 (1967).
4. P. N. Moskalev and I. S. Kirin, *ibid.*, **15**, 7 (1970).
5. P. N. Moskalev and I. S. Kirin, *ibid.*, **16**, 57 (1971).
6. P. N. Moskalev and I. S. Kirin, *Russ. J. Phys. Chem.*, **46**, 1019 (1972).
7. M. M. Nicholson and F. A. Pizzarello, *This Journal*, **126**, 1490 (1979).
8. M. M. Nicholson and R. V. Galiardi, Final Report, Contract N62269-76-C-0574, AD-A039596, May 1977; *Chem. Abstr.*, **87**, 144073V.
9. M. M. Nicholson and F. A. Pizzarello, *This Journal*, **127**, 821 (1980).
10. M. M. Nicholson and F. A. Pizzarello, *ibid.*, **127**, 2617 (1980).
11. F. A. Pizzarello and M. M. Nicholson, *J. Electron. Mater.*, **9**, 231 (1980).
12. G. A. Corker, B. Grant, and N. J. Clecak, *This Journal*, **126**, 1339 (1979).
13. S. C. Dahlberg, *Surf. Sci.*, **59**, 83 (1976).
14. S. C. Dahlberg and M. E. Musser, *J. Chem. Phys.*, **70**, 5021 (1979).
15. H. E. DeVore, *Phys. Rev.*, **102**, 86 (1956).
16. S. C. Dahlberg and M. E. Musser, *J. Chem. Phys.*, **71**, 2806 (1979).
17. S. C. Dahlberg, *Phys. Rev. B*, **17**, 4757 (1978).
18. E. O. Johnson, *Phys. Rev.*, **111**, 153 (1958).
19. S. C. Dahlberg and M. E. Musser, *J. Chem. Phys.*, **72**, 6706 (1980).

Mechanistic Study of Photoelectrochemical Reactions at a p-GaP Electrode

Kohei Uosaki and Hideaki Kita

Department of Chemistry, Faculty of Science, Hokkaido University, Sapporo 060, Japan

ABSTRACT

The photocurrent-potential relations of a p-GaP electrode in various solutions are studied potentiostatically. Both the cathodic and anodic photocurrents are observed, *i.e.*, the sign of photocurrent changes at a certain potential which we name the potential of zero photocurrent, V_{zp} . The potential of zero photocurrent is close but not equal to the flatband potential. The origin of the anodic photocurrent is presented. The log (photocurrent)-potential relations follow the Tafel line at medium bias potentials and deviate from it at large and small bias potentials. The mechanism of the cathodic reactions is proposed based on the experimental results. The rate-determining step is the supply of photoexcited electrons to the semiconductor surface at large bias potentials and is the electrochemical, *i.e.*, surface, process at medium and small bias potentials. At the small bias potentials, the photocurrent is enhanced by the photoelectrochemical reduction of oxidized species created by holes in valence band.

Photoeffects on electrochemical reactions at semiconductor electrodes have been studied very actively (1-10), particularly after Fujishima and Honda drew attention to the possibility of direct hydrogen production by a photo-driven electrochemical cell without any external electrical energy (11).

However, fundamental aspects of photoelectrochemical reactions such as reaction mechanism seem not to have been well understood. Most theoretical analyses neglected the potential drop in the electrochemical double (Helmholtz) layer (12) and the contribution of the charge transfer process to the overall reaction rate (13), although the importance of these contribu-

tions on the kinetics at semiconductor electrodes was pointed out by Green many years ago (14). We have been stressing the importance of the above contribution (15, 16) and have reported some supporting evidence (17). Recently, Bard *et al.* have used the word "Fermi-level pinning" to express the situation where the entire potential drop occurs within the Helmholtz layer and reported that this situation is not unusual (18).

In this work, we studied the photocurrent-potential relations at p-GaP, which is one of a few stable photocathodes (19), in various solutions to evaluate the reaction mechanism. The photoelectrochemical behavior of p-GaP has been studied very extensively (6, 15, 20-24) and it is reported that the flatband potential

Key words: semiconductor, photoelectrochemistry, energy conversion.

determined by capacitance measurement differs from the so-called critical potential or photocurrent onset potential (20, 21). This difference is usually explained by surface recombination without considering the electrochemical steps (20). The main concern of this paper is to analyze the photoelectrochemical behavior of p-GaP at small potential biases which represent the significant region for practical devices.

Experimental

A Zn-doped p-GaP single crystal wafer was used as a working electrode. The carrier density and the specific resistance of the sample are $6.7 \times 10^{17} \text{ cm}^{-3}$ and $1.3 \Omega \cdot \text{cm}$, respectively. An ohmic contact was made by using In-Zn alloy and a copper wire was attached onto the ohmic contact by soldering. The semiconductor electrode surface was covered with epoxy resin except for (111) face (Ga) and was placed in a PTFE electrode holder. The surface area of the electrode was 0.0315 cm^2 . The electrode surface was etched in $\text{HNO}_3\text{-HCl}$ (1:1) solution before experiment. The electrochemical cell is similar to the one reported previously (15). An Ag/AgCl electrode and a Pt wire were used as a reference and a counterelectrode, respectively. A 500W Xe lamp (Ritsu Oyo Kogaku) was used as a light source and a potentiostat (Wenking Model 68 FRO.5) was used to control the electrode potential. An IRA-20 (Toshiba) filter was placed between the light source and the electrochemical cell to avoid a heat effect. Current-time relations were recorded by using a Toa Model CDR 11A recorder.

All solutions used in this work were prepared with triply distilled water and reagent grade chemicals. Purified helium gas was passed through the solutions for at least 30 min before experiments. All experiments were carried out at room temperature.

Results

The current-time relations of the p-GaP electrode in 1M NaOH at several electrode potentials illuminated with pulsed light are shown in Fig. 1. Steady photocurrents are observed at all potentials investigated, even at potentials very close to the flatband potential, V_{FB} , which is $\sim -0.04\text{V}$ vs. Ag/AgCl (15). Further, the anodic photocurrent, which has not been reported at p-type semiconductor electrodes, is observed here at relatively positive potentials. Thus, the sign of the photocurrent changes at a certain potential. The steady photocurrents of this electrode in various solutions are plotted against the electrode potential in Fig. 2. In all cases, both the cathodic and anodic photocurrents are observed and the photocurrent-potential ($I_{ph}\text{-}V$) relations shift towards more negative potentials when the pH of the solution increases. The addition of methyl viologen changes the shape of the $I_{ph}\text{-}V$ relation drastically.

The effect of time length kept in dark prior to the illumination is also examined. The steady photocurrent is not affected by changing the time length kept in dark at all potentials but the longer the time kept in the dark, the larger the initial photocurrent just after the illumination at potentials close to the flatband potential, as shown in Fig. 3.

Discussion

Origin of anodic photocurrent.—Usually, only a cathodic photocurrent is reported at p-type semiconductors and only an anodic photocurrent is reported at n-type semiconductors with the exception of a cathodic photocurrent observed at TiO_2 (n-type) (25). However, in this work, we found both the cathodic and anodic photocurrents at p-GaP electrode. The origin of the anodic photocurrent and the reason why it has not been reported are as follows.

The anodic currents at a semiconductor electrode in the dark, i_a , and under illumination, i_a^* , are given by Eq. [1] and [2], respectively, with the assumption that

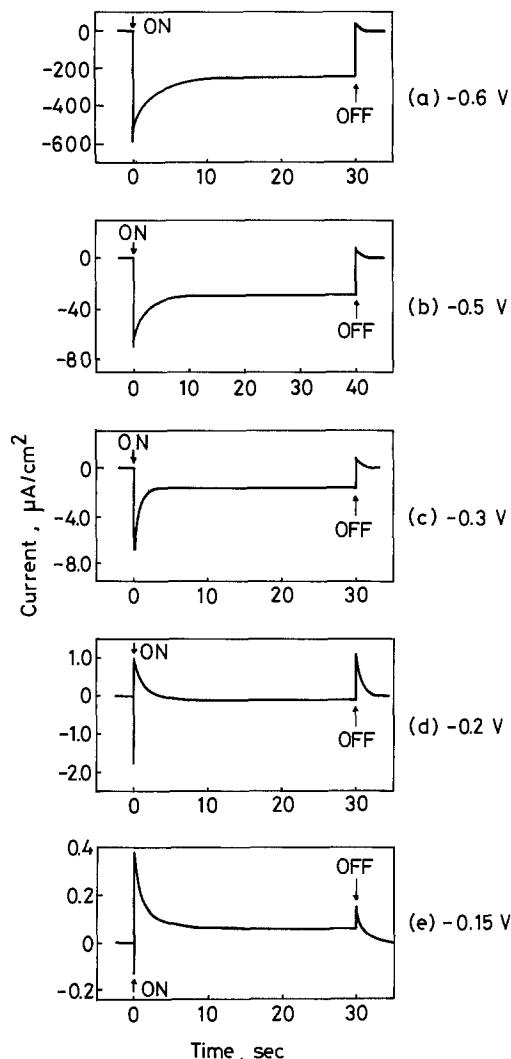


Fig. 1. Current-time relations of p-GaP in 1M NaOH at several potentials illuminated with pulsed light. Currents before illumination were taken as zero. Electrode potentials are with respect to Ag/AgCl.

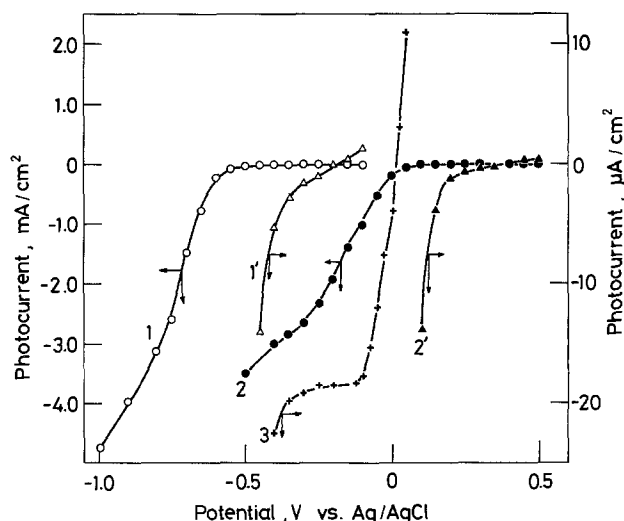


Fig. 2. The photocurrent-potential relation of p-GaP in various solutions with two current scales. 1, 1' in 1M NaOH, 2, 2' in 0.5M H_2SO_4 , 3 in 1M NaOH + 1.7 mM methyl viologen.

the electron transfer takes place in a narrow energy range below the valence band energy, E_v (1)

$$i_a \propto c_{RPs} W(E_v) G_R(E_v) \quad [1]$$

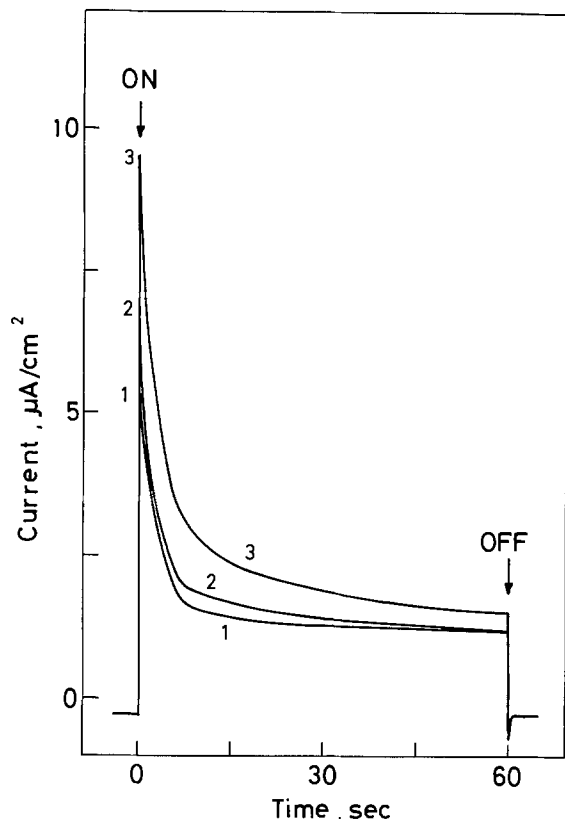


Fig. 3. The current-time relations of p-GaP in 0.5M H₂SO₄ at 0.2V vs. Ag/AgCl, for various lengths of time kept in the dark before illumination. Curve 1, 30 sec; curve 2, 2 min; curve 3, 10 min.

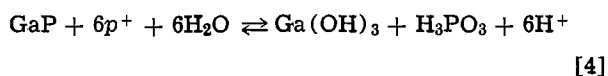
$$i_a^* \propto c_R p_s^* W(E_v) G_R(E_v) \quad [2]$$

where c_R is the concentration of reduced species and p_s and p_s^* are the number of holes at the semiconductor surface in dark and under illumination, respectively, $W(E_v)$ is the tunneling probability at the valence bandedge and $G_R(E_v)$ is the distribution function for finding the reduced species at the energy E_v . Thus, the anodic photocurrent, $i_{a,ph}$, is given by

$$i_{a,ph} = i_a^* - i_a \propto c_R (p_s^* - p_s) W(E_v) G_R(E_v) \quad [3]$$

Therefore, when $p_s^* - p_s > 0$, the anodic photocurrent should be observed at both n-type and p-type semiconductor electrodes. Since holes are the majority carriers of p-type semiconductors, p_s is large and, therefore, anodic dark current is large at the potentials where the anodic photocurrent is expected. Usually $p_s \gg p_s^* - p_s$ and hence $i_a \simeq i_a^*$. This is why anodic photocurrent has not been reported at p-type semiconductor electrodes. For example, in the present work, $i_a = 8.54 \mu\text{A}/\text{cm}^2$ and $i_a^* = 10.0 \mu\text{A}/\text{cm}^2$ at -0.1V vs. Ag/AgCl in 1M NaOH. The small difference between the two could be measured by the potentiostatic method employed in this work but is not possible to be detected by the sweep method which is usually employed in studying the current-potential relations at semiconductor electrodes.

In this system, the anodic reaction is the decomposition of the electrode itself, since no redox reagent is added (6, 26). The anodic decomposition potential of GaP has been calculated only at pH = 7 by assuming the following reaction (24, 27)



We reexamined the thermodynamic data (28-30) and calculated the anodic decomposition potentials of GaP for a wide pH range as shown in Table I. Anodic dissolution occurs at $\text{pH} < 2.56$ and $\text{pH} > 11.7$ and

Table I. The anodic decomposition reactions of GaP and corresponding potentials at various pH

| | |
|--|---|
| pH < 2 | $\text{GaP} + 6p^+ + 3\text{H}_2\text{O} \rightleftharpoons \text{H}_3\text{PO}_3 + 3\text{H}^+$ |
| $E = -0.357 - 0.0295 \text{pH} + 0.00985 \log [\text{Ga}^{3+}] + 0.000985 \log [\text{H}_3\text{PO}_3]$ | |
| $2 < \text{pH} < 2.56$ | $\text{GaP} + 6p^+ + 3\text{H}_2\text{O} \rightleftharpoons \text{Ga}^{3+} + \text{H}_2\text{PO}_4^- + 4\text{H}^+$ |
| $E = -0.337 - 0.0394 \text{pH} + 0.00985 \log [\text{Ga}^{3+}] + 0.00985 \log [\text{H}_2\text{PO}_4^-]$ | |
| $2.56 < \text{pH} < 8.32$ | $\text{GaP} + 6p^+ + 9/2 \text{H}_2\text{O} \rightleftharpoons 1/2 \text{Ga}_2\text{O}_3 + \text{H}_2\text{PO}_4^- + 7\text{H}^+$ |
| $E = -0.315 - 0.0690 \text{pH} + 0.00985 \log [\text{H}_2\text{PO}_4^-]$ | |
| $8.32 < \text{pH} < 11.7$ | $\text{GaP} + 6p^+ + 8 \text{OH}^- \rightleftharpoons 1/2 \text{Ga}_2\text{O}_3 + \text{HPO}_4^{2-} + 7/2 \text{H}_2\text{O}$ |
| $E = -0.233 - 0.0788 \text{pH} + 0.00985 \log [\text{HPO}_4^{2-}]$ | |
| pH > 11.7 | $\text{GaP} + 6p^+ + 11 \text{OH}^- \rightleftharpoons \text{GaO}_3^{3-} + \text{HPO}_4^{2-} + 5\text{H}_2\text{O}$ |
| $E = 0.170 - 0.108 \text{pH} + 0.00985 \log [\text{GaO}_3^{3-}] + 0.0985 \log [\text{HPO}_4^{2-}]$ | |

The thermodynamic values used for calculation are all taken from Ref. (28) for phosphorous compounds and from Ref. (29) for gallium compounds except for $\Delta G_f^\circ(\text{GaP}) = 91.54 \text{ kJ} \cdot \text{mol}^{-1}$ which is taken from Ref. (30).

passive film is formed at $2.56 < \text{pH} < 11.7$. The decomposition potentials are within the bandgap of GaP for all pH range concerned and the reactions expected from the calculation agree with experimental findings (26). The existence of the anodic (dark) currents even at the potentials more negative than V_{FB} suggests that the reaction is very efficient in acid and alkaline solutions (6, 26).

Photocurrent onset potential and flatband potential.—The photocurrent onset potential has a practical importance in a solar energy conversion. However, it is usually defined very vaguely (20, 21) in a similar way to the decomposition potential in electrode processes at metal electrodes which has no theoretical significance. In fact, the value of the photocurrent onset potential varies depending on the current scale chosen, as shown in Fig. 2. We propose here the definition of the photocurrent onset potential as the potential at which the sign of the photocurrent changes. By doing so, no ambiguity is introduced in determining the photocurrent onset potential. To distinguish this potential from the apparent photocurrent onset potential formerly used, we name it the "potential of zero photocurrent," V_{zp} . At V_{zp}

$$i_{ph} = |i_{ph,c}| - |i_{ph,a}| = 0 \quad [5]$$

$$\text{i.e., } |i_{ph,c}| = |i_{ph,a}| \quad [6]$$

Butler and Ginley reported that the difference between V_{FB} and the photocurrent onset potential is 0.7V for p-GaP (20). However, V_{zp} determined in this work are much closer to V_{FB} in various solutions, although there still exists some difference between them up to ca. 200 mV. It is usually believed that one would expect no photocurrent at V_{FB} , because holes and electrons created by illumination recombine easily under the absence of a potential gradient in the semiconductor. However, this is not necessarily true. If the diffusion length of holes is large and the anodic reaction at the valence band is faster than both the cathodic reaction at the conduction band and the surface recombination reaction, the photogenerated hole accepts either an electron from a reduced species in solution or a valence electron of the semiconductor before deactivation. Thus, an anodic photocurrent should be observed at V_{FB} , because the photocurrent observed, i_{ph} , is given by

$$i_{ph} = |i_{ph,a}| - |i_{ph,c}| \propto |c_R (p_s^* - p_s) W(E_v) G_R(E_v)| - |c_o (n_s^* - n_s) W(E_c) G_o(E_c)| \quad [7]$$

where c_o is the concentration of the oxidized species, n_s^* and n_s are the concentration of the electrons at the surface under illumination and in the dark, respectively, $W(E_c)$ is the tunneling probability for the cathodic reaction at the conduction bandedge, and $G_o(E_c)$ is the distribution function of oxidized species at the

energy E_c . Similarly, a cathodic photocurrent should be observed in the corresponding conditions. In other words, only when one of the conditions given in Eq. [8] and [9] is satisfied at V_{FB} , V_{FB} should coincide with V_{zp}

$$p_s^* - p_s = n_s^* - n_s = 0 \quad [8]$$

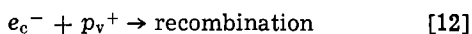
$$|c_R(p_s^* - p_s)W(E_V)G_R(E_V)| \\ = |c_o(n_s^* - n_s)W(E_C)G_o(E_C)| \quad [9]$$

In the present system, the existence of the anodic dark current even at the potential more negative than V_{FB} (6, 26) suggests that the anodic reaction is considerably faster than the cathodic reaction near V_{FB} . Thus, from the above argument the presence of the anodic photocurrent is expected at V_{FB} in this case as experimentally observed.

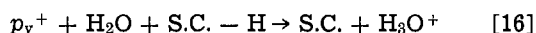
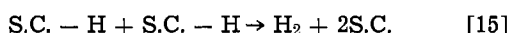
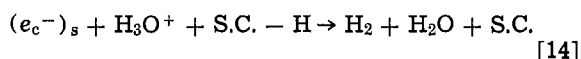
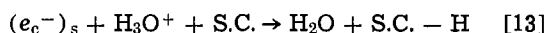
In the solution containing methyl viologen, the V_{zp} is almost identical to the flatband potential. In this case, for the reaction $MV^{++} + e \rightleftharpoons MV^{+\cdot}$ the condition given in Eq. [9] seems to be satisfied.

The photocurrent-potential relations and the reaction mechanism of photoelectrochemical reduction reactions.—The photoelectrochemical processes at cathodically polarized semiconductors are divided into two parts, namely, the bulk and the surface processes. The bulk processes are (i) absorption of photons and photoexcitation of electrons to the conduction band, i.e., photogeneration of electron-hole pairs, (ii) migration of the photoexcited electrons to the semiconductor surface, and (iii) deactivation of the photoexcited electrons to the valence band, in parallel with (ii), i.e., recombination in the bulk including space charge layer of the semiconductor. The surface processes are (i) electron transfer to an oxidized species followed by chemical, electrochemical, and/or desorption processes in some cases, (ii) deactivation of the photoexcited electrons to the valence band at the surface directly or via surface states, i.e., surface recombination.

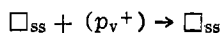
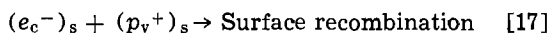
Equations [10]–[12] summarize the bulk processes



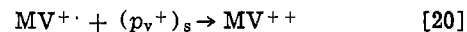
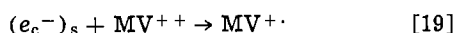
where p_v^+ is the hole in the valence band and $(e_c^-)_s$ and e_c^- are the electrons in the conduction band at the surface and at other places, respectively. The surface processes for hydrogen evolution reaction are



and those for the recombination are



where S.C. is the semiconductor, S.C. - H represents hydrogen atom adsorbed on the semiconductor, $(p_v^+)_s$ is the hole in the valence band at the surface, \square_{ss} is the unoccupied surface state, and \square_{ss} is the occupied surface state. The step expressed in Eq. [18] is the surface recombination via surface state. The combination of step [13] and step [16] could be called the surface recombination via adsorbed hydrogen state (31). For the reduction of methyl viologen, Eq. [13]–[16] should be replaced by the following



To elucidate the mechanism of the photoelectrochemical reduction reactions at the p-GaP electrode in a wide potential range, the photocurrents in logarithmic scale are plotted against the electrode potential in Fig. 4. The $\log(i_{ph}) - V$ relations follow the Tafel line at medium biased potentials ($-0.4 \sim -0.7V$ in 1M NaOH and $+0.2 \sim -0.05V$ in 0.5M H_2SO_4) and deviate from it at large and small bias potentials. It is interesting to note that the slopes of the Tafel line are similar to those of hydrogen evolution reaction at metal (Ga) electrodes (32).

The shape of $\log(i_{ph}) - V$ relations at large cathodic potential biases suggests that the rate-determining step in this potential region is some transport-limited process. The deviation occurs at ca. $-0.7V$ vs. Ag/AgCl in 1M NaOH both with and without methyl viologen. This potential coincides with the apparent photocurrent onset potential determined by $i_{ph}^2 - V$ relation based on a simple Schottky barrier model with the assumption that electrochemical processes are fast and step [11] is the rate-determining process (20). Thus, the supply of the photogenerated electrons to the semiconductor surface seems to be the rate-determining step at the potentials more negative than ca. $-0.7V$ vs. Ag/AgCl in 1M NaOH and ca. $-0.05V$ vs. Ag/AgCl in 0.5M H_2SO_4 .

Butler and Ginley proposed that step [18], i.e., surface recombination via surface state, is responsible for the discrepancy between V_{FB} and the apparent photocurrent onset potential determined by $i_{ph}^2 - V$ relation (20). They concluded from IR photoresponse measurement that the localized state which is ~ 0.7 eV above the top of the valence band acts as the recombination center. According to their model, the photocurrent at steady state, i_{ph} , is given by

$$i_{ph} \propto j - k_r[e_c^-]_s N_{ss}(1 - f_t) \quad [21]$$

where j is the flux of the photogenerated electrons arriving at the surface, k_r is the rate constant of the surface recombination reaction, N_{ss} is the number of surface states, and f_t is the Fermi distribution function

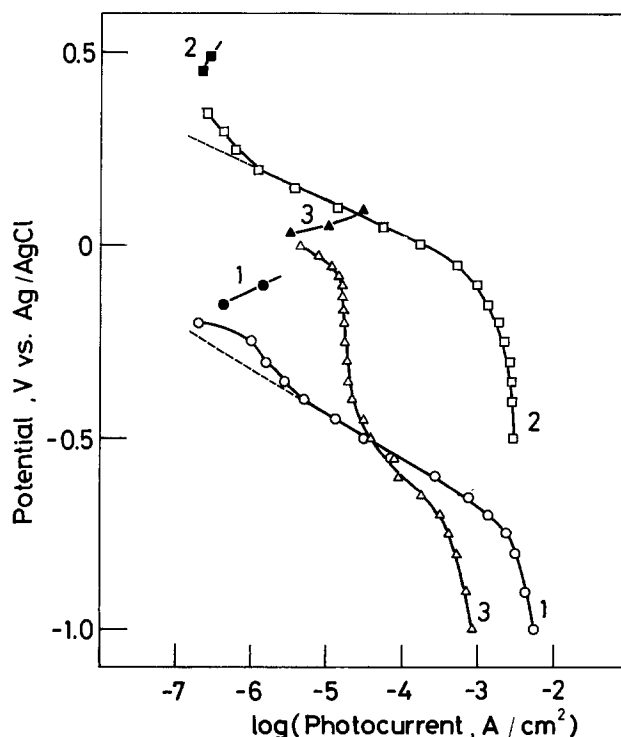


Fig. 4. Tafel plots of the photocurrents of p-GaP in various solutions. Curve 1, 1M NaOH; curve 2, 0.5M H_2SO_4 ; curve 3, 1M NaOH + 1.7 mM methyl viologen.

for the surface states. For the present system, if all potential drop occurs within the semiconductor, f_t is given by

$$f_t = 1/[1 + \exp\{E_t - E_F/kT\}] \\ = 1/[1 + \exp\{0.7 - (V_{FB} - V)/kT\}] \quad [22]$$

where E_t is the energy of the surface states and V is the electrode potential concerned. Since $(1 - f_t)$ changes from 0 to 1 sharply around $-0.7V$ vs. V_{FB} , one would expect sharp change in the photocurrent potential relation at that potential and not be able to explain the potential dependence of the photocurrent at relatively small bias potential (Tafel relation) where $1 - f_t = 1$ by considering the surface recombination via surface states only.¹ The effect of methyl viologen on $i_{ph} - V$ relation gives some clue to evaluate the mechanism. In this case, the photocurrent is larger than that without MV^{++} at low bias potentials. This can be explained as follows.

The rate-determining step of the hydrogen evolution reaction at this potential range is one of the steps expressed by Eq. [13], [14], or [15], i.e., the electrochemical process. The electrochemical reaction rate of MV^{++} is faster than that of hydrogen evolution reaction and therefore much larger current is observed when MV^{++} is added. The fact that V_{zp} with MV^{++} is more positive than that without MV^{++} also supports the fact that the cathodic reaction of MV^{++} is faster than hydrogen evolution reaction. The i_{ph} with MV^{++} is smaller than that without MV^{++} at relatively negative potentials. It is due to absorption of light by MV^{++} created by photoelectrochemical reduction of MV^{++} .

The $\log(i_{ph}) - V$ relations deviate from the Tafel line again at the potentials near V_{FB} , suggesting some faster reaction is involved. At this region, the initial photocurrent just after illumination depends on the length of time kept in the dark prior to illumination, as shown in Fig. 3. Also, the anodic dark current starts to flow at this potential region. Thus, this deviation should be due to the photoelectrochemical reduction of oxidized species created by dark oxidation reaction by holes in the valence band, as shown in Fig. 5. If the reduction of the oxidized species is faster than the hydrogen evolution reaction, much larger current is expected at a given potential. It is essentially the same effect as the addition of MV^{++} . The effect of the time kept in the dark is explained as the accumulation of oxidized species in the dark.²

In the small bias potential region where $\log(i_{ph}) - V$ relation deviates from the Tafel line, the stability

¹ R. H. Wilson proposed a model which takes into account both the surface recombination rate and charge transfer rate for n-type semiconductors (33, 34).

² The fact that the height of the photocurrent spike just after illumination is much smaller when the solution is stirred supports this mechanism.

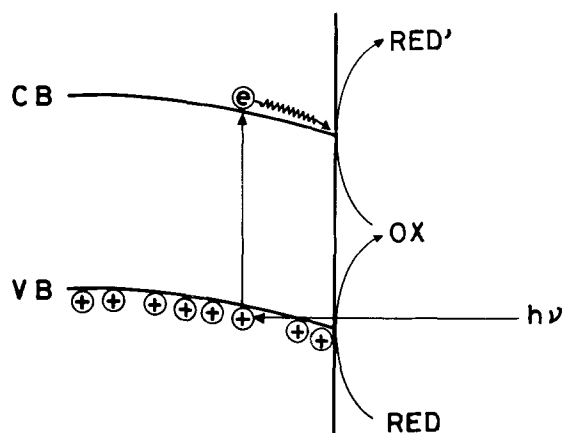


Fig. 5. Contribution of oxidized species created by hole to photocurrent enhancement at relatively small bias potential.

of p-GaP is in doubt even though the net cathodic photocurrent is observed, because the deviation is caused by the photoelectrochemical reduction of oxidized species which is the anodic decomposition product of GaP in this case. Since for practical devices, the potential bias would be small, the stability of p-GaP in this potential region should be studied more in detail.

Acknowledgment

Thanks are due to Dr. K. Akita of Fujitsu Laboratory for the donation of p-GaP single crystals and to Dr. A. Hamnett of Oxford for preprints of his work before publication.

Manuscript submitted March 6, 1981; revised manuscript received ca. May 11, 1981.

Any discussion of this paper will appear in a Discussion Section to be published in the June 1982 JOURNAL. All discussions for the June 1982 Discussion Section should be submitted by Feb. 1, 1982.

Publication costs of this article were assisted by Hokkaido University.

REFERENCES

- H. Gerischer, in "Physical Chemistry: An Advanced Treatise," Chap. 5, Vol. 9A, H. Eyring, D. Henderson, and W. Jost, Editors, Academic Press, New York (1970).
- V. A. Myamlin and Yu. V. Pleskov, "Electrochemistry of Semiconductors," Plenum Press, New York (1967).
- W. P. Gomes, T. Friend, and S. R. Morrison, *Surf. Sci.*, **13**, 201 (1968).
- M. C. Markham and M. C. Upreti, *J. Catal.*, **4**, 229 (1965).
- G. Krüger, *Electrochim. Acta*, **13**, 1389 (1968).
- R. Memming and G. Schwandt, *ibid.*, **13**, 1299 (1968).
- J. O'M. Bockris and K. Uosaki, *Adv. Chem. Ser.*, **163**, 33 (1977).
- G. Campet, M. P. Dare-Edwards, A. Hamnett, and J. B. Goodenough, *Nouv. J. Chim.*, **4**, 501 (1980).
- T. Ohnishi, Y. Nakato, and H. Tsubomura, *Ber. Bunsenges. Phys. Chem.*, **79**, 523 (1975).
- H. Morisaki, T. Baba, and K. Yazawa, *Phys. Rev. B*, **21**, 837 (1980).
- A. Fujishima and K. Honda, *Nature*, **238**, 37 (1972).
- A. J. Nozik, *Appl. Phys. Lett.*, **30**, 567 (1977).
- M. A. Butler, *J. Appl. Phys.*, **48**, 1914 (1977).
- M. Green, in "Modern Aspects of Electrochemistry," Vol. 2, J. O'M. Bockris, Editor, p. 343, Butterworths, London (1959).
- J. O'M. Bockris and K. Uosaki, *This Journal*, **124**, 1348 (1977).
- J. O'M. Bockris and K. Uosaki, *ibid.*, **125**, 223 (1978).
- J. O'M. Bockris, K. Uosaki, and H. Kita, *J. Appl. Phys.*, **52**, 808 (1981).
- A. J. Bard, A. B. Bocarsly, F.-R. F. Fan, E. G. Walton, and M. S. Wrighton, *J. Am. Chem. Soc.*, **102**, 367 (1980).
- J. O'M. Bockris and K. Uosaki, *This Journal*, **124**, 98 (1977).
- M. A. Butler and D. S. Ginley, *ibid.*, **127**, 1273 (1980).
- Y. Nakato, S. Tonomura, and H. Tsubomura, *Ber. Bunsenges. Phys. Chem.*, **80**, 1289 (1976).
- H. Yoneyama, H. Sakamoto, and H. Tamura, *Electrochim. Acta*, **20**, 341 (1975).
- H. Uchida, H. Yoneyama, and H. Tamura, *This Journal*, **127**, 99 (1980).
- M. J. Madon, F. Cardon, and W. P. Gomes, *Ber. Bunsenges. Phys. Chem.*, **82**, 819 (1978).
- H. Morisaki, M. Hariya, and K. Yazawa, *Appl. Phys. Lett.*, **30**, 7 (1979).
- K. Kohayakawa, A. Fujishima, and K. Honda, *Nippon Kagaku Kaishi*, 780 (1977).
- R. Memming, in "Semiconductor Liquid-Junction Solar Cells," A. Heller, Editor, p. 38, The Electrochemical Society Softbound Proceedings Series, Princeton, NJ (1977).
- T. I. Popava, I. A. Bagotskaya, and E. D. Moorhead, in "Encyclopedia of Electrochemistry of the Elements," A. J. Bard, Editor, Vol. VIII, p. 207,

- Marcel Dekker, New York (1978).
 29. A. P. Tomilov and N. E. Chomutov, *ibid.*, Vol. III, p. 1 (1975).
 30. C. D. Thurmond, *J. Phys. Chem. Solids*, **26**, 785 (1965).
 31. M. P. Dare-Edwards, A. Hamnett, and J. B. Good-

- enough, *J. Electroanal. Chem. Interfacial Electrochem.*, **119**, 109 (1981).
 32. H. Kita and T. Kurisu, *J. Res. Inst. Cat. Hokkaido Univ.*, **21**, 200 (1973).
 33. R. H. Wilson, *J. Appl. Phys.*, **48**, 4292 (1977).
 34. R. H. Wilson, *This Journal*, **127**, 228 (1980).

Semiconductor Electrodes

XXXVII. Photoelectrochemical Behavior of p-Type Cu_2O in Acetonitrile Solutions

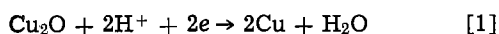
G. Nagasubramanian, Alberto S. Gioda, and Allen J. Bard*

Department of Chemistry, The University of Texas, Austin, Texas 78712

ABSTRACT

The photoelectrochemical behavior of polycrystalline p- Cu_2O in acetonitrile solutions containing a number of redox couples [e.g., phthalonitrile (0/-1), nitrobenzene (0/-1), methyl viologen (+2/+1)] was investigated. The p- Cu_2O , grown by oxidation of Cu metal by thermal methods or anodization, showed stable behavior under optical irradiation in these solutions. The bandgap, estimated from photoacoustic spectroscopy (PAS) and the photocurrent action spectrum in solution, was ~ 2.0 eV and the flatband potential was $\sim +0.16$ V vs. SCE. Scanning electron micrographs of the thermally grown samples reveal well-developed crystallites with distinct boundaries. A PEC cell of the form p- $\text{Cu}_2\text{O}/\text{Ph}(\text{CN})_2/\text{MeCN}/\text{Pt}$ was shown to have an overall optical-to-electrical energy conversion efficiency of only 0.05%. The low efficiency for such a cell is ascribed to rapid recombination processes in the bulk semiconductor and at the interface.

Cuprous oxide (Cu_2O), which crystallizes in a cuprite structure is a catalyst of choice for a diverse variety of chemical reactions (1-4). The optical and electrical properties of p- Cu_2O depend upon the conditions of preparation from Cu and O_2 , i.e., the temperature and oxygen pressure (5). Several workers (6-11) have studied the electrical properties of single crystals of this material and demonstrated that it is a p-type semiconductor whose hole conductivity can be attributed to copper ion vacancies which act as acceptors for electrons from the valence band. Recently, Trivich *et al.* (12) studied solid-state photovoltaic cells based on this material and reported an overall conversion efficiency of optical to electrical energy approaching 1% and stated that efficiencies of 6-12% should be possible. Aqueous photoelectrochemical (PEC) cells involving p- Cu_2O have also been described (13-14). In these cells the p- Cu_2O photocathode is unstable and under irradiation is reduced to Cu metal



Similar instability was observed with CuO electrodes (15). In an aprotic solvent such as acetonitrile (MeCN), however, such a reduction reaction is less favorable because of the unavailability of protons. Since the bandgap is 1.9-2.0 eV, and the reported efficiencies for photovoltaic devices appeared interesting and the material is inexpensive, abundant, and capable of being readily produced in thin film form, we undertook a study of the PEC properties of p- Cu_2O prepared by thermal and anodic oxidation of metallic copper in MeCN. The polycrystalline compacts were prepared by heating a Cu plate in air to minimize the grain boundary effects encountered in the case of sintered powder compacts (16). Studies of the PEC behavior of p- Cu_2O were carried out with MeCN con-

taining several redox couples including phthalonitrile, $\text{Ph}(\text{CN})_2(0/-1)$, nitrobenzene, $\text{PhNO}_2(0/-1)$, and methyl viologen MV (+2/+1). Photocathodes of p- Cu_2O were shown to be stable in these solutions under intense optical irradiation. However, the overall optical-to-electrical energy conversion efficiencies in the PEC cells based on this material were low ($< 0.1\%$).

Experimental

Chemicals.—The procedures for the purification of chemicals and solvent (MeCN) are given elsewhere (17). All compounds were stored inside a helium-filled Vacuum Atmosphere Corporation (Hawthorne, California) glove box. Polarographic grade, tetra-n-butyl ammonium perchlorate (TBAP), dissolved and recrystallized from ethanol thrice and dried under vacuum ($< 10^{-5}$ Torr) for three days, was used as supporting electrolyte. The cell employed was a conventional two-compartment cell of 25 ml capacity containing the p- Cu_2O , a Pt counterelectrode, and a quasi-reference electrode which was an Ag wire immersed in the solution and separated from the main compartment by a medium porosity glass frit. The potential of the electrode was checked against an aqueous saturated calomel electrode (SCE) at regular intervals and was found to be constant. All potentials reported here, unless specified otherwise, are given in V vs. SCE.

P- Cu_2O was prepared by the method of Trivich *et al.* (12, 18). A Cu plate, 0.8 mm thick (Alfa Ventron), was cut to a 2×2 cm square, polished with Al_2O_3 (0.5 μm), washed with acetone, and rinsed thoroughly with double distilled water. The plates were dried and heated in a muffle furnace at about 900°C for 24 hr. Subsequently, the furnace temperature was raised to 1030°C and the samples were heated for an additional 160 hr. The furnace temperature was then reduced to 500°C and at this temperature, the samples were annealed for a day, before quenching them in air at room temperature. Upon quenching, the CuO layer formed

* Electrochemical Society Active Member.

Key words: solar energy conversion, photovoltaics, photoacoustic spectroscopy, nonaqueous electrolytes.

at the surface peels off, exposing the Cu_2O sintered compacts. The resistivity of the material after polishing with an ultrafine emery paper was $\sim 30\text{-}40\ \Omega\ \text{cm}$. An ohmic contact can be formed by either electroplating the back with gold or partial reduction in an H_2 atmosphere at $100^\circ\text{-}125^\circ\text{C}$ for 30 min. A copper wire lead formed the electrical contact and was attached to the gold-coated side with silver epoxy cement (Allied Product Corporation, New Haven, Connecticut). This contact was subsequently covered with 5 min epoxy cement. The assembly was mounted into 7 mm diam glass tubing and was held in position with a silicone rubber sealant (Dow Corning Corporation, Midland, Michigan), which also served as an effective seal against the seepage of electrolyte solution to the rear of the semiconductor electrode. The exposed area of p- Cu_2O was $0.14\ \text{cm}^2$. The etching procedures are given below. The material produced by the Cu-air reaction was shown to be Cu_2O by x-ray diffraction. The x-ray diffraction patterns corresponded to those reported in the literature (ASTM card Index No. 5.0667).

The p- Cu_2O films formed by anodic polarization of a Cu electrode were grown under either linear potential sweep or constant current conditions in aqueous NaOH solutions, mainly, following the procedures described by Marchiano *et al.* (19) and Ashworth and Fairhurst (20). The pretreatment of the Cu electrodes prior to oxidation described in the above papers was employed. Purified N_2 was bubbled for 1 hr through the NaOH solutions, prior to and during the experiments, and an N_2 atmosphere was maintained over the solutions during the anodizations. The potential sweeps were performed at scan rates of 0.02, 0.2, or 1.0 mV/sec with the initial potential at -0.8V (for 0.02 mV/sec) or -1.20V (for 0.2 and 1.0 mV/sec) *vs.* SCE. The galvanostatic runs were performed at the current densities reported in Ref. (20).

Apparatus.—A Princeton Applied Research (PAR) Model 173 potentiostat and PAR Model 175 Universal programmer were used in all experiments with positive feedback *iR*-compensation employed to compensate for solution resistance and internal resistance of the electrode. The *i*-*V* curves were recorded on a Model 2000 X-Y recorder (Houston Instruments, Austin, Texas). In solar cell experiments, the photovoltage and photocurrent between the working electrode and counter-electrode as a function of load resistance were measured with a Keithley Model 179, TRMS Digital Multimeter. The light source was an Oriel Corporation (Stamford, Connecticut) 450W xenon lamp. Differential capacitance was measured with a PAR Model HR 8 lock-in amplifier. All of these solutions were prepared in the glove box and the cell then sealed and removed for the experiments.

Etchants.—(A) For thermally grown p- Cu_2O , the following etchants were tried: (1) 12M HNO_3 , (2) 6M HNO_3 , (3) $\text{H}_2\text{SO}_4\text{:H}_2\text{O}_2\text{:H}_2\text{O}$; 3:1:1 (by volume), (4) $\text{HNO}_3\text{:H}_3\text{PO}_4\text{:acetic acid}$; 17:41.5:41.5 (by volume). In etchants (1), (2), and (3), the etching time was limited to 10-15 sec while for (4) the samples were kept immersed for 15 min. Procedure (1) exposed well-developed large Cu_2O -crystallites while (2) and (3) showed small Cu_2O crystallites. Procedure (4) produced a smooth and shiny surface. (B) The anodically produced films were etched with either (1) 0.01M or (2) 0.1M HNO_3 for 1-2 sec.

Results and Discussion

Capacitance measurements.—The location of the energies corresponding to the edges of the valence and the conduction bands, E_v and E_c , respectively, of the semiconductor electrode with respect to solution energy levels, is useful in the selection of appropriate redox couples for optimizing PEC cell performance. These are usually found by determination of the flatband potential, V_{FB} , by measurement of the electrode capaci-

tance as a function of applied potential. If this capacitance corresponds to the semiconductor space-charge capacitance, V_{FB} and the acceptor density (N_A) can be computed from Mott-Schottky plots (21-23). From these values, the known or estimated effective mass of charge carrier and the bandgap, the band positions (*i.e.*, E_c and E_v) can be located.

A dielectric constant of 7.11 (24) and an effective mass of charge carriers $0.84m_0$ (25) was employed. The bandgap was measured by two methods which are described in the next section; the value determined from the photocurrent action spectrum was employed in the location of the bandedge. The capacitance of p- Cu_2O was measured in MeCN containing TBAP as supporting electrolyte at different frequencies from 100 to 5000 Hz; Mott-Schottky plots are given in Fig. 1. The V_{FB} value determined at low frequencies (100 and 500 Hz) was located $\sim 20\ \text{mV}$ positive of that at high frequencies (2 and 5 kHz). Hence, an average value was taken for computation. These plots were essentially the same after repeated experiments over several hours and were unaffected by the addition of the reducible compound phthalonitrile to the solution. From these plots we estimate V_{FB} as $+0.16\text{V}$ *vs.* SCE and $N_A \cong 4.9 \times 10^{16}\ \text{cm}^{-3}$.

Bandgap.—The bandgap energy, E_g , of p- Cu_2O was determined by two independent methods: From the photoacoustic spectrum of the sample in air (26) and from the photocurrent action spectrum in MeCN/TBAP, $\text{Ph}(\text{CN})_2$. The results of these experiments are shown in Fig. 2(a) and (b). Note that a plot of $(\eta h\nu)^2$ *vs.* $h\nu$ gives a straight line, suggesting that the optical transition in Cu_2O is direct and yields an E_g of 2.00 eV. The photoacoustic spectrum signals an onset of light absorption at 638 nm, corresponding to an $E_g = 1.94\ \text{eV}$. The bandedge energies were obtained by assuming the Fermi-Dirac equation

$$N_A = N_v [1 + 2e^{(E_v - E_f)/kT}]^{-1} \quad [2]$$

$$N_v = 2(2\pi m_p^* kT/h^2)^{3/2} \quad [3]$$

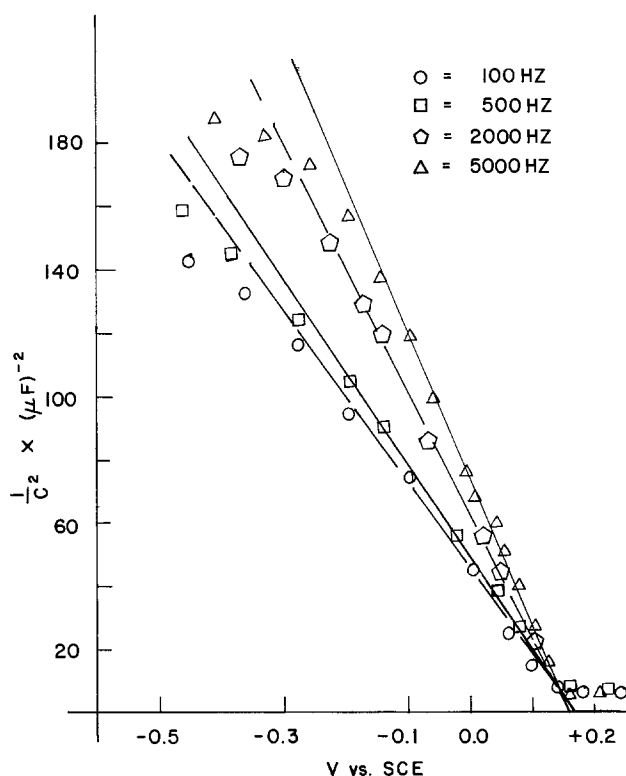


Fig. 1. Mott-Schottky plot of p- Cu_2O , in MeCN containing 0.1M TBAP supporting electrolyte. $\circ = 100\ \text{Hz}$; $\square = 500\ \text{Hz}$; $\diamond = 2000\ \text{Hz}$; and $\triangle = 5000\ \text{Hz}$.

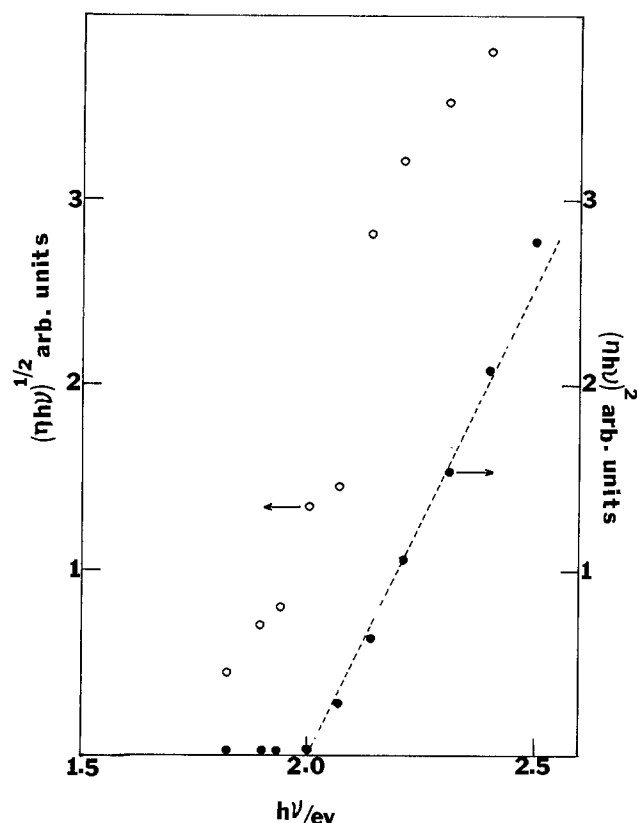


Fig. 2a. Plot of $h\nu$ vs. $(\eta h\nu)^{n/2}$ where $n = 1$ and 4 . The value of η at different wavelengths has been computed from photocurrent action spectrum for p-Cu₂O in MeCN/0.1M TBAP, 10 mM Ph(CN)₂^{0/-1}/Pt solar cell.

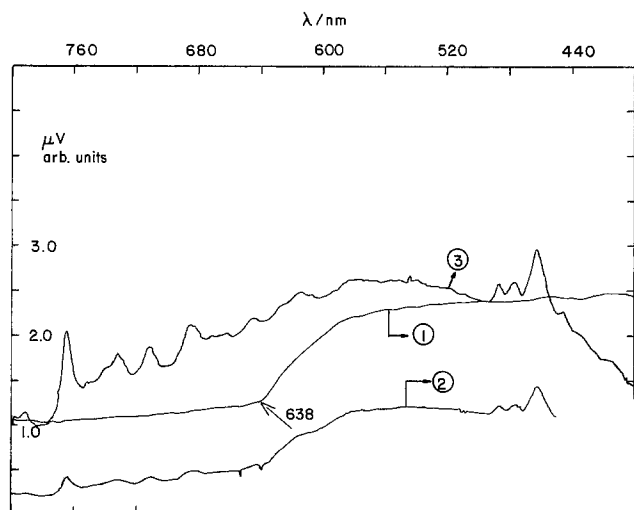


Fig. 2b. Absorption spectrum of p-Cu₂O (photoacoustic technique) (curve 2). Corrected action spectrum of the short-circuit photocurrent of p-Cu₂O (curve 1). Curve 3, background action spectrum of the 2.5 kW xenon lamp.

where N_v is the density of states in the valence band; E_f is the Fermi level energy (corresponding to V_{FB}); and m_p^* is the effective mass of holes. This yielded the position of the VB edge about 0.1 eV below the Fermi level, i.e., at + 0.26V vs. SCE. From the value of E_g , 2.0 eV, E_c is placed at - 1.74V vs. SCE. These levels are shown in Fig. 3, along with the potentials for the solution redox couples employed in this study.

Cyclic voltammetry.—To study the photoinduced electron transfer to reducible molecules in solution, the cyclic voltammetric (CV) response at p-Cu₂O in the dark and under illumination was compared to that ob-

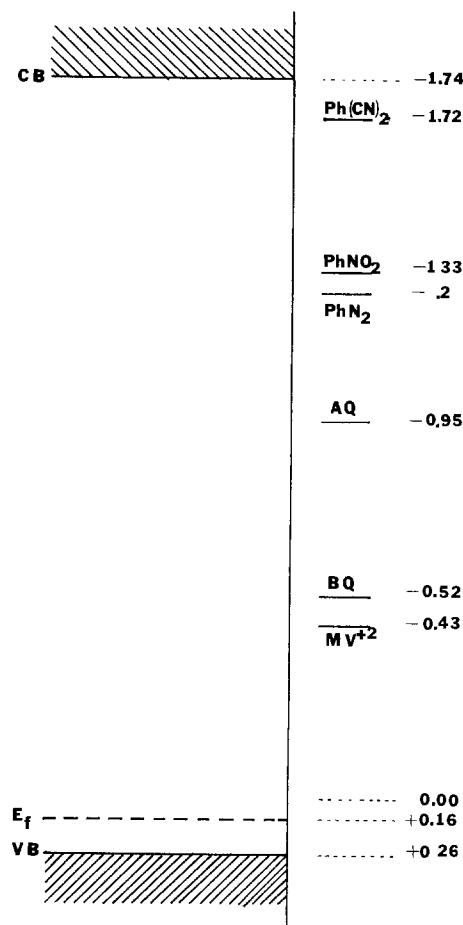


Fig. 3. Schematic representation of the energetic situation at p-Cu₂O/solution interface along with V_{redox} of various redox couples investigated in this work. CB = conduction bandedge; E_f = Fermi level; VB = valence bandedge; Ph(CN)₂ = phthalonitrile; Ph(NO₂) = nitrobenzene; AB = azobenzene; AQ = anthraquinone; BQ = benzoquinone; MV²⁺ = methyl viologen dication.

served for these systems at a platinum electrode. At platinum, near-reversible CV behavior is observed, so that the redox potential of the couple can be obtained. The procedures and interpretations generally followed previous studies from this laboratory (17, 27-29).

The range of stability for the electrode in the absence of an added redox couple was determined from the CV behavior of p-Cu₂O in MeCN containing TBAP alone, as shown in Fig. 4(a). The dark current was very small up to - 1.8V vs. SCE. Under illumination, no photocurrent was observed up to - 1.5V. However, at more negative potentials a small and unstable photo-induced cathodic current was found, which probably involves reduction of the Cu₂O electrode perhaps involving trace impurities (e.g., H₂O) in the solvent.

The addition of a reducible substance to the MeCN/TBAP solution generally did not produce an appreciable increase in the dark cathodic current for potentials up to - 1.60V, demonstrating the expected absence of dark electron transfer to solution species at the p-type semiconductor/liquid interface. Under illumination, however, the photogenerated electrons at energies corresponding to the conduction bandedge can transfer to solution species, and significant photocathodic currents are produced. For example, the CV reduction of phthalonitrile [Ph(CN)₂] on Pt, given in Fig. 4(b), shows a reversible wave for the reduction to the radical anion at - 1.72V vs. SCE. On p-Cu₂O, only a small dark reduction current is seen (Fig. 4c). However, under illumination, significant cathodic current flows with the onset at potentials more positive than those for reduction at Pt (Fig. 4d). Note, how-

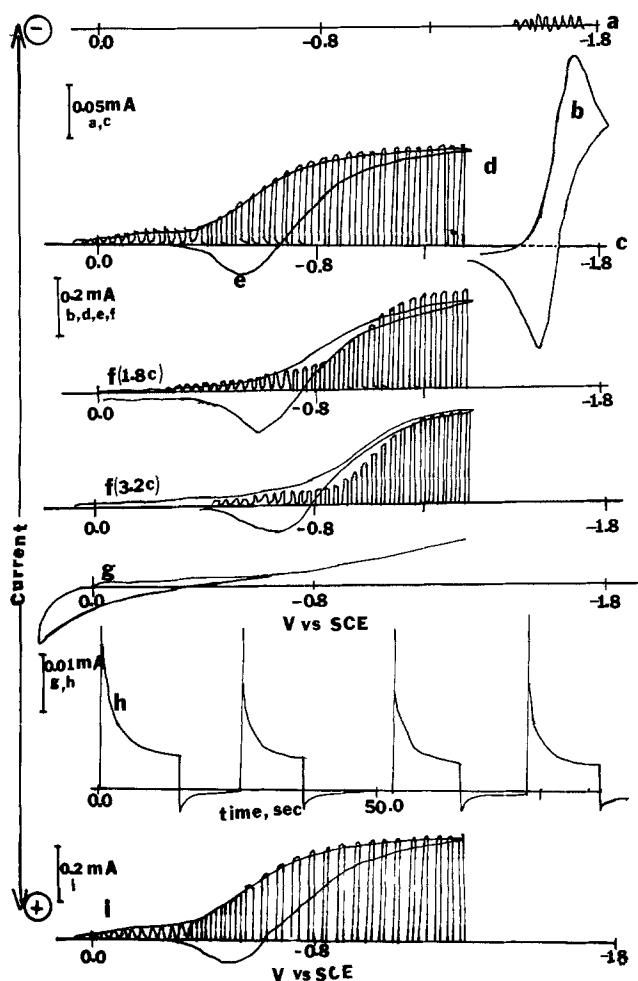


Fig. 4. Voltammetric curves of Pt and p-Cu₂O in MeCN containing 10 mM Ph(CN)₂; 0.1M TBAP (supporting electrolyte). Light source, 450W xenon lamp. Scan rate = 50 mV/sec. (a) C-V curve on p-Cu₂O in dark and under illumination in MeCN containing 0.1M TBAP only; (b) cyclic voltammogram at Pt; (c) dark voltammetric curve on p-Cu₂O; (d) C-V characteristics under chopped light in p-Cu₂O before generating radical anions, in the dark; (e) C-V characteristic curve of p-Cu₂O under continuous illumination; (f) same as in (a-e) but after electrochemically generating anion radicals; (g) C-V curves on p-Cu₂O in dark after electrochemically generating anion radicals; (h) transient *i-t* curves of p-Cu₂O. The electrode was biased at -0.5V vs. SCE; (i) same as in (a-e) but after irradiation for 6 hr, p-Cu₂O electrode was biased at -0.3V vs. SCE.

ever, that although there is a considerable "underpotential" for the start of the reduction of Ph(CN)₂, the cathodic photocurrent rises rather slowly with potential and only attains a limiting value at ~ -0.9V. This slow rise in cathodic photocurrent can be attributed to appreciable oxidation of the photogenerated reduced

species, Ph(CN)₂⁻, at potentials between the onset potential and the limiting one. This oxidation of the reduced form is apparent from the reverse scan (Fig. 4e), where the current crosses the zero current axis at more negative potentials than the original onset potential and the presence of photogenerated radical anion,

Ph(CN)₂⁻ causes an anodic current flow. Similarly, if the initial scan is carried out with a solution that contains both parent and radical anion, the onset potential occurs at more negative values, ~ -0.6V vs. SCE (Fig. 4f). Moreover, as the concentration of radical anion is increased, the onset potential also shifts toward more negative values. In Fig. 4g is shown the effect of radical anion on the behavior of p-Cu₂O in dark. The dark oxidation current begins at -0.6V. Thus the back-

oxidation of Ph(CN)₂⁻ leads to the observed shape of the photocurrent-potential curve and the fact that the photocathodic current remains small up to -0.5V vs. SCE, even though the onset of photocurrent occurs near the flatband potential. The presence of surface recombination or back-reaction below -0.5V vs. SCE is also demonstrated by the transient photocurrent-time behavior of p-Cu₂O in MeCN containing TBAP, Ph(CN)₂^{0/-1} (Fig. 4h). Upon illumination, the cathodic current shows a sharp increase, but then rapidly drops off as radical anion accumulates at the electrode surface. When the light is turned off, the current drops and an anodic current spike appears, representing oxidation of radical anion. At more negative potentials (e.g., -0.9V), only a flat photocathodic current transient appears, with no anodic dark transient. After continuous illumination for 6 hr, with the p-Cu₂O electrode held at -0.3V vs. SCE, the CV behavior was essentially unchanged (Fig. 4i), thus demonstrating the stability of the semiconductor electrode. The behavior of p-Cu₂O with Ph(CN)₂ was typical of that found with other redox couples. From the location of the energy levels of these couples with respect to the band-edges (Fig. 3), one would predict, based on the "ideal" model of the semiconductor/liquid interface, that all of the couples would be photoreduced with the potential of the onset of photocurrent *V*_{on}, located near *V*_{FB}. This was found to be the case for solutions initially containing only the oxidized form of the couple. The values of *V*_{on} and *V*_{redox} are given in Table I. In all cases appreciable photocurrent flowed only at potentials significantly more negative than *V*_{on}. The limiting quantum efficiency for the photogeneration of

Ph(CN)₂⁻, defined as the ratio of the current (in electrons/s-cm²) to the absorbed light flux (in photons/s-cm²), with the p-Cu₂O electrode held at a potential of -1.0V where the limiting current is attained, was estimated at 500 nm. This value of λ corresponds to an energy greater than the bandgap of p-Cu₂O. The 500 nm radiation was obtained by interposing a Jarrel-Ash Company (U.S.A.) monochromator between the PEC cell and the xenon lamp (2500W operated at 1600W); the monochromatic light was focused on the p-Cu₂O electrode. The photocurrent, recorded on a Model 2000 X-Y recorder (Houston Instruments, Austin, Texas), was 0.70 μA/cm². The PEC cell was then replaced and the monochromatic light intensity, measured by a radiometer/photometer, Model 550-1 (Electro Optics Division) was 14.6 μW/cm². These values yield a monochromatic quantum efficiency of ~ 10.5%.

Effect of pretreatment.—The nature of the electrode surface pretreatment, e.g., via etching, is known to affect the behavior and PEC performance of SC electrodes (30, 31). Four different etchants were used in this work, described in the experimental section. Electrodes treated with etchants (2), (3), or (4) gave large dark currents as compared to those with 1 (12M

Table I. Voltammetric data and onset potential of photocurrent

| Redox couple ^a | <i>V</i> _{redox} V vs. SCE | <i>V</i> _{on} V vs. SCE | <i>V</i> _{ph} = <i>V</i> _{redox} - <i>V</i> _{on} |
|--------------------------------------|---|--|--|
| Ph(CN) ₂ ^{0/-1} | -1.72 | +0.02 | 1.74 |
| Ph(NO ₂) ^{0/-1} | -1.33 | +0.03 | 1.36 |
| AB ^{0/-1} | -1.28 | +0.04 | 1.32 |
| AQ ^{0/-1} | -0.96 | +0.04 | 1.00 |
| BQ ^{0/-1} | -0.53 | +0.06 | 0.59 |
| MV ^{+2/+1} | -0.43 | 0.00 | 0.43 |

^a Abbreviations: Ph(CN)₂ = phthalonitrile; Ph(NO₂) = nitrobenzene; AB = azobenzene; AQ = anthraquinone; BQ = benzoquinone; MV = methyl viologen.

HNO_3) (Fig. 5). Generally, electrodes that showed surfaces with large crystallites and grain boundaries, as produced by etching with 12M HNO_3 , showed a better PEC performance than those with smooth and shiny surfaces [e.g., as produced by etchant (4)].

Anodically grown Cu_2O films.—The PEC behavior of p- Cu_2O anodic films depended upon the electrochemical conditions employed for growing the oxide film and the pretreatment of the Cu electrode before film formation. The films produced in aqueous NaOH solutions by linearly scanning the potential showed better photoresponse than those prepared by galvanostatic oxidation. Among the Cu electrode pretreatments tried [etching with 6M HNO_3 , etching with FeCl_3 in EtOH, electropolishing (20), or electropolishing with etching in FeCl_3], etching with HNO_3 produced electrodes which showed the largest photoeffects. Etching, with either FeCl_3 or the electropolished surfaces, yielded Cu_2O films which showed a poor photoeffect. For films grown by linear scans, the photoresponse depended upon the potential scan rate, v , for film growth. Films grown at very small v (0.02 mV/sec) exhibited better PEC behavior than those grown at higher scan rates (0.2 and 1.0 mV/sec). In the linear scan experiments, the formation of Cu_2O was characterized by a peak obtained at -0.4 to -0.5V vs. SCE (20). To avoid conversion of the Cu_2O to CuO , the potential was not scanned beyond -0.35V vs. SCE. Current-potential

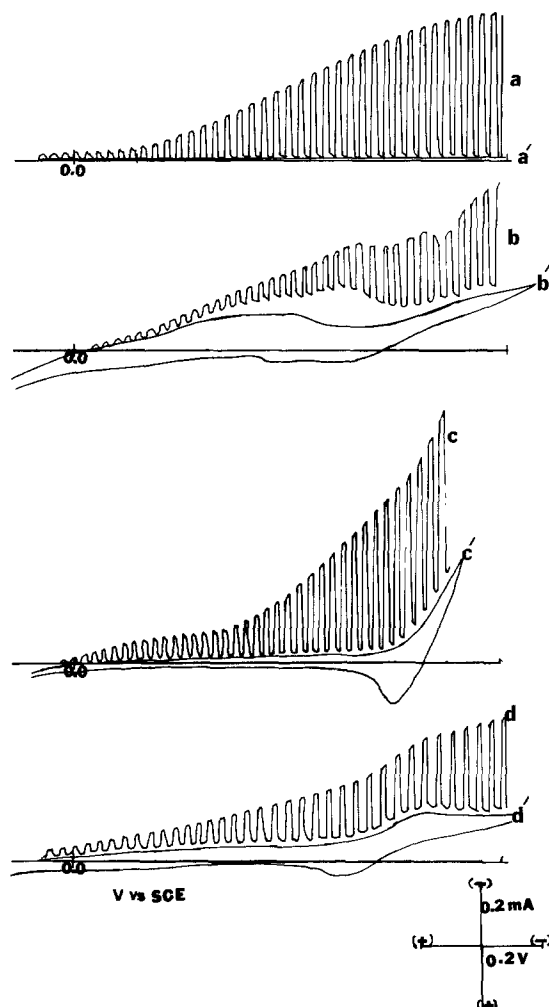


Fig. 5. Current-potential characteristics under chopped light on p- Cu_2O in MeCN containing 0.2M PhNO_2 , 0.1M TBAP (supporting electrolyte). Light source, 450W xenon lamp. Scan rate, 50 mV/sec. (a) p- Cu_2O treated with 12M HNO_3 ; (b) p- Cu_2O treated with 6M HNO_3 ; (c) p- Cu_2O treated with H_2SO_4 : H_2O_2 : H_2O = 3:1:1; (d) p- Cu_2O treated with HNO_3 : H_3PO_4 : acetic acid = 17:41.5:4.15. a', b', c', and d' are in the dark.

curves in the dark and under chopped illumination for p- Cu_2O films (grown at 0.02 mV/sec in 1M and 5M NaOH) in MeCN/TBAP containing $\text{Ph}(\text{CN})_2$ are given in Fig. 6. The photoresponse was clearly much greater for films grown in 5M NaOH. The beneficial effect of slow scan rate and higher NaOH concentration is probably caused by the formation of a less random and thicker film (20). Some improvement in the onset potential and photocurrent was achieved by etching the anodic Cu_2O film with 0.01M HNO_3 for 1-2 sec. Etching with a more concentrated HNO_3 solution (0.1M) destroyed the photoeffect, presumably because dissolution of the Cu_2O film occurred. Films grown in 10M NaOH gave a photoresponse similar to those grown in 5M NaOH at 0.02 mV/sec. Generally, however, the photocurrents at the anodic films were much smaller than those at the thermally grown material for similar solution and illumination conditions.

p- Cu_2O /MeCN PEC cells.—The CV behavior can be used as a guide for the construction of PEC photovoltaic cells, where the open-circuit potential of the semiconductor ideally (in the absence of recombination) approaches V_{FB} and the metal counterelectrode is at V_{redox} . Although the photocurrents found in the CV experiments with p- Cu_2O were rather small, the behavior of actual two-electrode photovoltaic cells is of interest because observed responses under these conditions insure that the effects seen are not merely caused by conductivity changes under illumination and allow an estimation of the actual power conversion efficiency of such devices. From the energy level diagram (Fig. 3) and the voltammetric measurements (Table I), cells containing $\text{Ph}(\text{CN})_2$ would be expected to show the highest open-circuit voltage, V_{oc} , and the best performance. The following cell was constructed: p- Cu_2O /MeCN, TBAP (0.1M), $\text{Ph}(\text{CN})_2$ (10 mM), $\text{Ph}(\text{CN})_2^-$ (0.1 mM)/Pt. The p- Cu_2O photocathode (0.14 cm^2) and the Pt gauze (40 cm^2) counterelectrode were spaced about 1.0 cm, with the p- Cu_2O electrode about <0.1 cm from the cell window. The i - V characteristic of such a cell, obtained with different load resistances, is shown in Fig. 7. The open-circuit photovoltage was 0.3V, the short-circuit photocurrent density was 0.4 mA/cm^2 , and the fill factor was 0.51. Note that this open-circuit voltage is considerably lower than the value predicted from voltammetric measurements conducted with solutions in the absence of appreciable $\text{Ph}(\text{CN})_2^-$. It is, however, about the same as that found with solid-state p- Cu_2O cells (12). From the

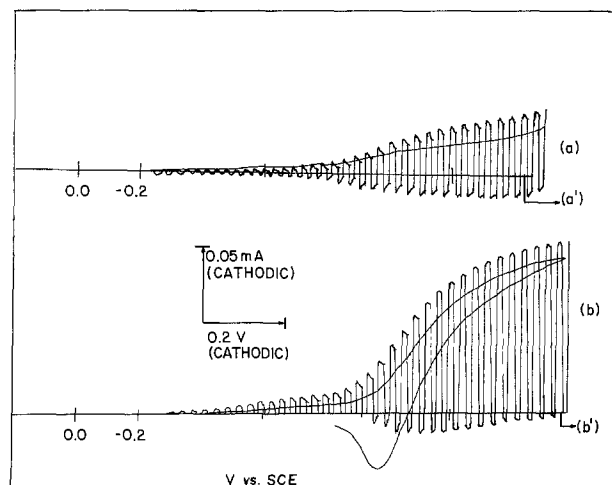


Fig. 6. Current-potential characteristics under chopped light on p- Cu_2O (anodically oxidized) in MeCN containing 10 mM PhCN_2 ; 0.1M TBAP. Light source, 450W xenon lamp. Scan rate, 50 mV/sec. (a) p- Cu_2O prepared in 1M NaOH; (b) p- Cu_2O prepared in 5M NaOH. a' and b' are in the dark.

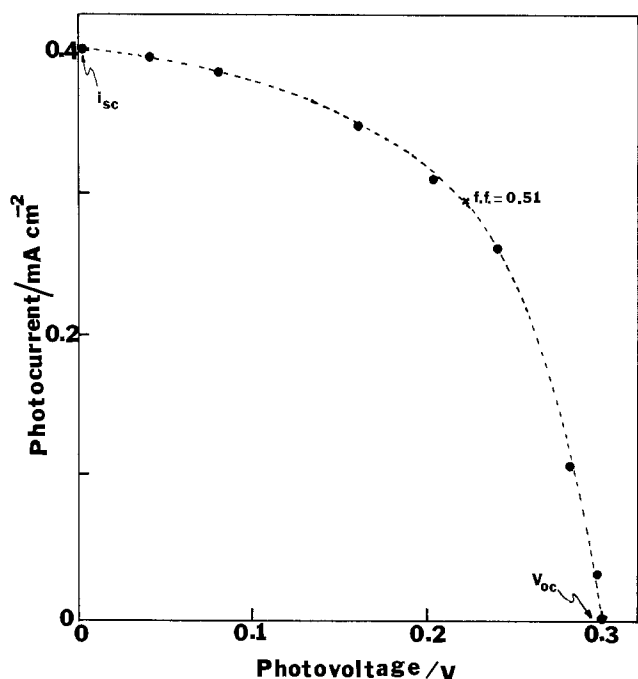


Fig. 7. Photocurrent-photovoltage characteristic of the cell p-Cu₂O/MeCN, 10 mM Ph(CN)₂; 0.1 mM Ph(CN)₂⁻; TBAP, 0.1 M/Pt various load resistances. Irradiation source, 450W xenon lamp.

data in Fig. 7 and the light flux of 120 mW/cm², the overall optical-to-electrical energy conversion efficiency, uncorrected for absorption and reflectivity losses, was calculated to be ~0.05%. This low value can probably be attributed to rapid recombination processes both within the bulk p-Cu₂O and at the interface. The currents were not limited by mass transfer

and were unaffected by stirring. The Ph(CN)₂⁻ was intentionally kept at a low concentration to decrease the light adsorption by this intensely colored species and to minimize the back-reaction at the p-Cu₂O surface. The photocurrent as a function of time is shown in Fig. 8. The photocurrent was fairly stable for at least 6 hr at which time the experiment was terminated.

Scanning electron micrographs of different thermally grown specimens after etching or polishing are given in Fig. 9. Samples etched with HNO₃ (Fig. 9a) showed

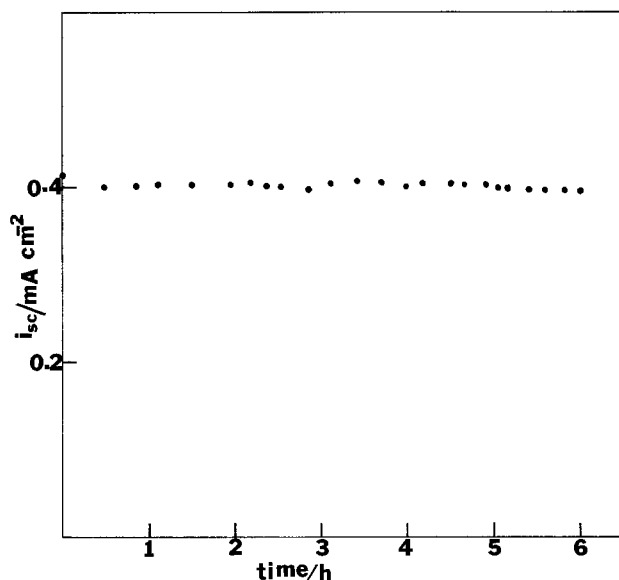


Fig. 8. Plot of photocurrent-output density of the cell p-Cu₂O/MeCN, 10 mM Ph(CN)₂, 0.1 mM Ph(CN)₂⁻; TBAP = 0.1 M/Pt as a function of time. Light source, 450W xenon lamp.

well-developed crystallites with distinct boundaries. While some of the crystallites were rather large, zones of smaller crystallites were also found. There was no marked change in the morphology of p-Cu₂O surfaces after the PEC measurements (Fig. 9b). The surfaces of electrodes either polished with Al₂O₃ (0.5 μm) or etched with HNO₃: acetic acid: H₃PO₄ were smooth (Fig. 9c, d). To test if the small crystallites and numerous grain boundaries found with the 12M HNO₃ etched samples were responsible for the low photovoltages and efficiencies, an electrode was prepared in which all of the small crystallites were covered with silicone rubber sealant, leaving only a single large crystal exposed to the solution. However, PEC measurements with this electrode showed no apparent increase in either the photovoltage or photocurrent density. This suggests that there may be inherent problems in the efficiency of p-Cu₂O itself, and that marked improvement in the efficiency with this material may be difficult.

Conclusions

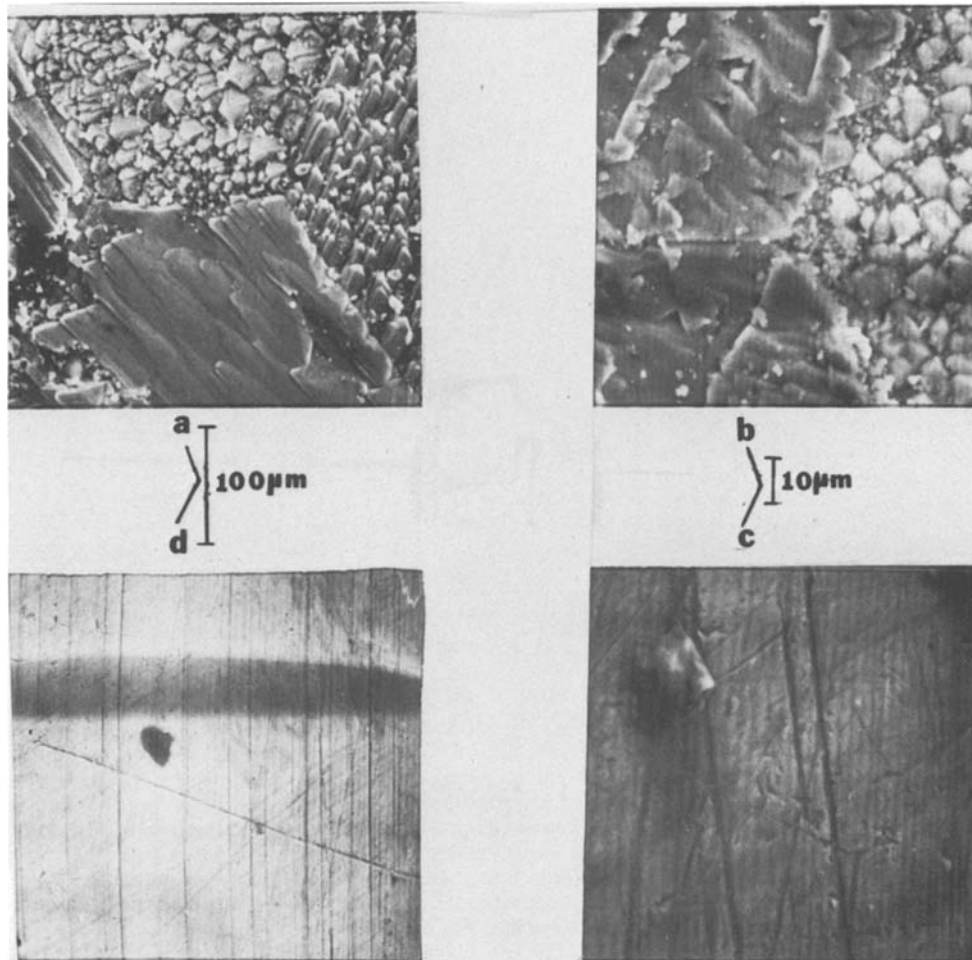
The p-Cu₂O photocathode is stable in MeCN containing a number of different redox couples under irradiation. The photopotential, V_{ph} , equal to $(V_{redox} - V_{on})$, increases linearly with V_{redox} , with a slope near one. The onset of photocurrent is located, for all couples investigated, near the flatband. Pretreatment of the electrode plays an important role on the PEC performance of p-Cu₂O, and etching with 12M HNO₃ was found to give a reasonable photocurrent and small dark cathodic current. The 12M HNO₃ etched surface, which looks matte and polycrystalline with distinct grain boundaries, exhibited better PEC behavior than the one which was shiny and smooth (e.g., produced by an HNO₃: acetic acid: H₃PO₄ etching).

The overall conversion efficiency of optical-to-electrical energy for the PEC photovoltaic cells was low, < 0.1%. A brief comparison of the liquid junction photovoltaic cells with the solid-state cells is in order. Under similar irradiation intensities, the Schottky barrier Cu/p-Cu₂O cells under the best conditions are reported to show an efficiency of 0.8% (12). The observed open-circuit photovoltage (0.30V) and fill factor (0.39) are comparable to the values in the liquid junction cells, so that the lower efficiency can be traced to lower short-circuit photocurrents. Indeed, even in the solid-state cells, encapsulation of the cell with epoxy is required for optimum performance. This encapsulation not only reduced reflection losses but also decreased the observed dark current. Moreover, the resistivity of our p-Cu₂O was ~3-4 times that of the Cu₂O used in the solid-state cells and, in the absence of more promising efficiencies, we did not find it worthwhile to attempt to optimize the semiconductor material. In general, the low photocurrents and efficiencies in the liquid junction cells probably can be attributed to rapid surface and bulk recombination of the photogenerated charge carriers. On the basis of these results and the fact that efficiencies > 1% have not been reported for solid-state cells, unless a significant improvement in the materials, characteristics, and efficiency can be obtained, p-Cu₂O does not seem to be a promising candidate for PEC solar energy conversion devices.

Acknowledgment

The support of this research by the Robert A. Welch Foundation and the Solar Energy Research Institute (in a cooperative project with SumX Corporation) is gratefully acknowledged. We also acknowledge a fellowship to ASG by the Consejo Nacional de Investigaciones Científicas y Técnicas de la República Argentina and a helpful discussion with Professor D. Trivich which assisted in the initiation of this research. The assistance of Victor A. Fishman in obtaining the PAS spectrum of p-Cu₂O is also appreciated.

Fig. 9. Scanning electron micrographs of $p\text{-Cu}_2\text{O}$, thermally grown samples differently etched: (a) Etched with 12M HNO_3 , before PEC measurement. (b) Etched with 12M HNO_3 , after PEC measurement. (c) Al_2O_3 ($0.5\ \mu\text{m}$) polished. (d) Etched with $\text{HNO}_3\text{:H}_3\text{PO}_4\text{:acetic acid} = 17\text{:4}\text{:15}\text{:41}\text{:5}$ by volume.



Manuscript submitted Dec. 22, 1980; revised manuscript received April 9, 1981.

Any discussion of this paper will appear in a Discussion Section to be published in the June 1982 JOURNAL. All discussions for the June 1982 Discussion Section should be submitted by Feb. 1, 1982.

Publication costs of this article were assisted by the University of Texas.

REFERENCES

- B. J. Wood, H. Wise, and R. S. Yolles, *J. Catal.*, **15**, 355 (1969).
- L. L. Holbrook and H. Wise, *ibid.*, **27**, 322 (1972).
- M. O'Keeffe and F. S. Stone, *Proc. R. Soc. London, Ser. A*, **267**, 501 (1962).
- S. R. Morrison, *J. Catal.*, **34**, 462 (1974).
- G. F. J. Garlick, "Photoconductivity," *Handbuch der Physik XIX*, pp. 377-380, Springer, Berlin, West Germany (1956).
- J. A. Assimos and D. Trivich, *Phys. Status Solidi A*, **26**, 477 (1974).
- G. P. Pollack and D. Trivich, *J. Appl. Phys.*, **46**, 163 (1975).
- J. Bloem, *Philips Res. Rep.*, **13**, 167 (1958).
- R. S. Toth, R. Kilkson, and D. Trivich, *Phys. Rev.*, **122**, 482 (1961).
- M. O'Keeffe and W. J. Moore, *J. Chem. Phys.*, **35**, 1324 (1961).
- M. H. Zirin and D. Trivich, *ibid.*, **39**, 870 (1963).
- D. Trivich, E. Y. Wang, R. J. Komp, and F. Ho, *Conf. Rec. IEEE Photovoltaic Spec. Conf.*, **12**, 875 (1976).
- K. Hauße and K. Reinhold, *Ber. Bunsenges. Phys. Chem.*, **76**, 616 (1972).
- U. Bertocci and D. R. Turner, in "Encyclopedia of the Electrochemistry of the Elements," Vol. 2, A. J. Bard, Editor, pp. 457-463 and numerous references therein, Marcel Dekker, New York (1974).
- K. Hardee and A. J. Bard, *This Journal*, **124**, 215 (1977).
- J. S. Anderson and N. N. Greenwood, *Proc. R. Soc. London, Ser. A*, **215**, 353 (1952).
- G. Nagasubramanian and A. J. Bard, *This Journal*, **128**, 1055 (1981).
- R. S. Toth, R. Kilkson, and D. Trivich, *J. Appl. Phys.*, **31**, 1117 (1960).
- S. L. Marchiano, C. I. Elsner, and A. J. Arvia, *J. Appl. Electrochem.*, **10**, 365 (1980).
- V. Ashworth and D. Fairhurst, *This Journal*, **124**, 506 (1977).
- V. A. Myamlin and Y. V. Pleskov, "Electrochemistry of Semiconductors," Plenum Press, New York (1967).
- H. Gerischer, in "Advances in Electrochemistry and Electrochemical Engineering," Vol. 1, P. Delahay and C. W. Tobias, Editors, pp. 139-232, Interscience, New York (1961).
- R. Memming, in "Electroanalytical Chemistry," Vol. 11, A. J. Bard, Editor, pp. 1-84, Marcel Dekker, New York (1979).
- K. Kojendahl, *Z. Phys. Chem.*, **B20**, 54 (1933).
- A. G. Zhilic, J. Halpern, and B. P. Zakharchenya, *Phys. Rev.*, **188**, 1294 (1969).
- V. A. Fishman and A. J. Bard, *Anal. Chem.*, **52**, 1723 (1980), and references therein.
- P. A. Kohl and A. J. Bard, *This Journal*, **126**, 59 (1979).
- P. A. Kohl and A. J. Bard, *J. Am. Chem. Soc.*, **99**, 7531 (1977).
- P. A. Kohl and A. J. Bard, *This Journal*, **126**, 603 (1979).
- B. A. Parkinson, A. Heller, and B. Miller, *ibid.*, **126**, 954 (1979).
- R. L. Van Meirhaeghe, F. Cardon, and W. P. Gomes, *Ber. Bunsenges. Phys. Chem.*, **83**, 236 (1979).



Intermetallic Growth Dependence on Solder Composition in the System Cu-(Pb-Sn Solder)

K. Kumar, A. Moscaritolo, and M. Brownawell¹

The Charles Stark Draper Laboratory, Incorporated, Cambridge, Massachusetts 02139

This study examines the dependence of the growth kinetics of the intermetallic phases Cu_3Sn and Cu_6Sn_5 (formed in the copper, Cu, and lead-tin, Pb-Sn, solder laminated structure that exists in conventional printed circuit boards) on the Pb-Sn solder composition that is employed. We have recently shown that in some of the commercially produced circuit boards, thermally activated growth of the intermetallic regions leads to eventual solder separation at the Cu- Cu_3Sn interphase boundary (1).

To evaluate and reasonably accurately predict the time-dependent performance of these circuit boards during service, it is important to devise accelerated tests at temperatures much in excess of operating temperature. The design of such a test, however, requires a knowledge of growth parameters, principally the activation energy. Its knowledge allows calculation of equivalent time at operating temperature to that used for exposure at the temperature of the test. Since the value of this activation energy is expected to be a function of the composition of the Pb-Sn solder, one needs to know the variation of the activation energy as a function of solder composition, over a reasonably narrow composition range of interest. The solder composition usually used is about 60 weight percent (w/o) Sn. The activation energy variation, therefore, needs to be systematically examined for solder compositions on either side of this value to take into account the effects of variations in plating processes from lot to lot and vendor to vendor. Data generated in earlier studies (2, 3) were considered inadequate in that only discrete, widely separated solder compositions were evaluated. The compositions examined in these earlier studies consisted of solder materials containing 10, 30, 60, and 100 w/o Sn. We have now examined the growth of the intermetallics using solder compositions of 45, 50, 55, 60, 65, and 70 w/o Sn. The samples were fabricated by electrodepositing the selected solder composition on high purity electrolytic grade copper sheets which were about 0.0175 cm thick.

Five specimens, each approximately 1 cm square, were sectioned from each solder-plated copper sheet, using a jeweler's saw. Four of these five specimens were heat-treated for a fixed time (100 hr) at temperatures of 348, 373, 398, and 423 K. The fifth specimen was retained in the as-plated condition. The intermetallic bandwidths in the as-plated samples constituted the starting conditions and these were used to calculate further growth of the bands which resulted from heat-treatments.

All of the as-plated and heat-treated samples were mounted at room temperature (with the copper-solder interface slightly inclined to the plane of polishing)

in a resin containing cast and polished for metallographic examination using standard techniques. The selected angle of tilt of the copper-solder interface allowed amplification of the intermetallic regions, upon polishing, by a factor of ten. The intermetallic regions were photographed on an American Optical Metallograph at 1000 magnification. Figure 1 is typical of what was observed. The intermetallics appeared as a set of two blue bands sandwiched in between the copper substrate and the electrodeposited solder. The two bands, as indicated in Fig. 1, were composed of the phases Cu_3Sn and Cu_6Sn_5 .

The majority of the photographs did not show a clear separation of the intermetallic phases. The Cu_3Sn and Cu_6Sn_5 intermetallics were found to coexist in a narrow region across their interface, with Cu_3Sn particles dispersed in a Cu_6Sn_5 matrix. In this case, the interphase boundary was assumed to exist at the midpoint of this two phase region. The Cu_3Sn -Cu and Cu_6Sn_5 -(Pb-Sn solder) boundaries were also not always smooth. The effective widths were taken as the average of 9 measurements made along each interface. A typical selection criterion for the different boundaries is shown in Fig. 1. The widths of the Cu_3Sn ,

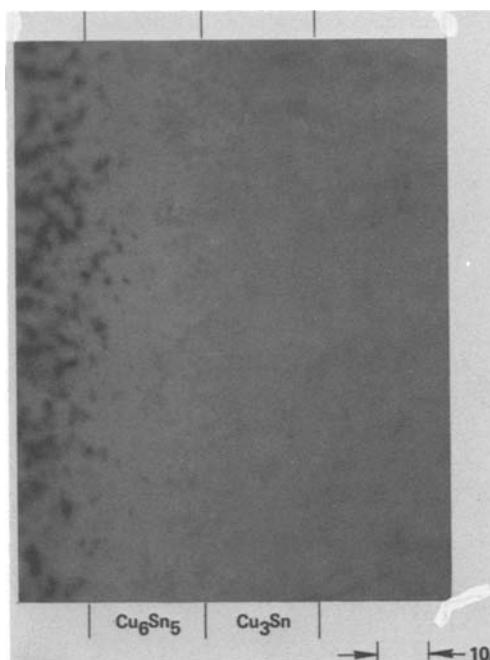


Fig. 1. Typical micrograph showing Cu_3Sn and Cu_6Sn_5 intermetallic regions after polishing on a 10 to 1 bias. (Actual width is less by a factor of ten than what is observed.)

¹Permanent address: Massachusetts Institute of Technology, Cambridge, Massachusetts 02139.

Key words: activation energy, percent Sn variation, Cu_3Sn , Cu_6Sn_5 .

Cu_6Sn_5 , and $\text{Cu}_3\text{Sn} + \text{Cu}_6\text{Sn}_5$ intermetallic regions were all measured separately.

An Arrhenius plot was then constructed with the log values of the widths (of the different intermetallic regions) plotted on the vertical axis, and the reciprocal values of the heat-treatment temperatures plotted on the horizontal axis. Separate plots were obtained for the Cu_3Sn , Cu_6Sn_5 , and $\text{Cu}_3\text{Sn} + \text{Cu}_6\text{Sn}_5$ widths for each composition. The data were made to fit a straight line using a least squares analysis (4).

The equation of this line is given by the expression

$$\ln x = \frac{\ln A}{2} - \frac{E_a}{2RT}$$

where: x [in cm] is the increase in the intermetallic bandwidths for Cu_3Sn , Cu_6Sn_5 , and $\text{Cu}_3\text{Sn} + \text{Cu}_6\text{Sn}_5$, respectively, E_a is the activation energy in cal/mol, R is the gas constant in cal/mol/K, T is the temperature in K, and $A = D_0 t$ in cm^2 (where D_0 is the diffusion constant in cm^2/sec and t is fixed time in sec at temperature).

The activation energy for each solder composition and each intermetallic phase was then calculated from the measured slopes of the various Arrhenius plots using the above expression. The values of the activation energies obtained in this way were then replotted as a function of the weight percent Sn in the solder. The study was then repeated, independently of the first study, and the second set of values of the activation energies were likewise plotted as a function of the solder composition. The two different sets of values of the activation energies were then averaged into one plot (see Fig. 2). The values of the activation energy measured in the second study were all within 10% of the values obtained in the first study. The scatter observed in the data obtained for the Cu_3Sn activation energy plot was partly attributed to the difficulty in determining the position of the Cu_3Sn - Cu_6Sn_5 boundary.

This study shows that the activation energy decreases with increasing amounts of Sn over the range of solder compositions that were examined. This variation of the activation energy was interpreted as being related to the presence of varying amounts of Pb in the solder material. As the reaction between the copper

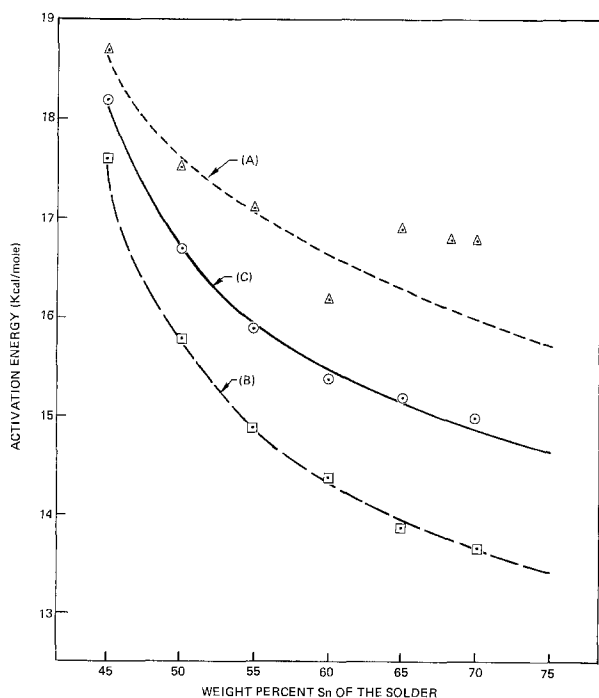


Fig. 2. Activation energy variation with weight percent tin in the solder for (A) Cu_3Sn , (B) Cu_6Sn_5 , and (C) $\text{Cu}_3\text{Sn} + \text{Cu}_6\text{Sn}_5$.

and the solder progresses, most of the Pb is rejected out of the reacted zones into the solder regions close to the Cu_6Sn_5 - (Pb-Sn) solder boundary as a Pb-rich phase (1). The diffusion rate of the Sn through this Pb-rich phase must, therefore, strongly influence the kinetics of the growth of the different intermetallic bands. According to this interpretation, the Pb-rich phase, which accumulates at the Cu_6Sn_5 - (Pb-Sn) solder boundary, must serve as a diffusion barrier to the Sn atoms for growth of the several intermetallics to proceed. Thus the rate of intermetallic growth is directly influenced by the accumulation of this Pb-rich species, which is obviously a function of the overall chemical composition of the solder. The calculated activation energy is, therefore, indicative of the effect of solder composition on intermetallic growth kinetics.

These observations dispute earlier suggestions that the concentration of Pb has little effect in determining the rate of growth of the various compounds (2). Our results also do not show the presence of a maximum value for the activation energy at solder compositions close to 60 w/o Sn, the possibility of which was indicated in Ref. (3). The value for the activation energy of $\text{Cu}_3\text{Sn} + \text{Cu}_6\text{Sn}_5$ at this composition is stated to be 49.64 kJ/mol K (11.86 kcal/mol K) in this reference.

It should be noted that the grain size of the copper sheets used in this study was quite coarse, typically ranging from 20 to 50 micrometers. The grain size present in the copper base that exists in conventional printed circuit boards, on the other hand, is considerably more refined—by at least one order of magnitude. The rate of reaction of the copper base with the Pb-Sn solder in the conventional circuit boards is, therefore, expected to be substantially more rapid than what was observed for the coarse-grained samples of this study. (This grain size effect will show up as a reduced value for the activation energy, in the fine-grained circuit boards, for any given solder composition. In agreement with this analysis we have measured values of about 12.7, 14.4, and 13.5 kcal/mol in commercially produced circuit boards formed with a Pb-Sn solder of nominal 62% Sn composition for the intermetallic phases Cu_6Sn_5 , Cu_3Sn , and $\text{Cu}_3\text{Sn} + \text{Cu}_6\text{Sn}_5$, respectively.) The variation of the activation energy with changes in Sn concentration in the Pb-Sn solder should, however, be similar to what was shown in Fig. 2, since this is believed to primarily depend on the diffusion of Sn through the Pb-rich phase located on the solder side of the Cu_6Sn_5 - (Pb-Sn) solder boundary and this is not expected to be a strong function of the grain size of the copper.

Acknowledgments

The authors wish to thank A. Lattanzi for his continued interest in this activity.

Manuscript submitted Nov. 20, 1980; revised manuscript received March 23, 1981.

Any discussion of this paper will appear in a Discussion Section to be published in the June 1982 JOURNAL. All discussions for the June 1982 Discussion Section should be submitted by Feb. 1, 1982.

Publication costs of this article were assisted by The Charles Stark Draper Laboratory, Incorporated.

REFERENCES

1. K. Kumar and A. Moscaritolo, *This Journal*, **128**, 379 (1981).
2. L. Zakraysek, "Intermetallic Growth in Tin-Rich Solders," *Welding Research Supplement*, 536-s (1972).
3. P. J. Kay and C. A. MacKay, "The Growth of Intermetallic Compounds on Common Basis Materials Coated with Tin and Tin-Lead Alloys," Tin Research Institute, Greenford, England (1976).
4. "Handbook of Chemistry and Physics," 40th ed., p. 308, Chemical Rubber Publishing Company, Cleveland, OH (1959).

Rotating Ring- and Split Ring-Disk Electrodes with Interchangeable Disks

S. Menezes,* L. F. Schneemeyer,* and B. Miller*

Bell Laboratories, Murray Hill, New Jersey 07974

The electrochemical insights gained with ring disk electrodes (RRDE) have generated an enduring interest in making their construction easier and more flexible (1). One such means is to provide a readily demountable disk (2-5) to facilitate many types of RRDE investigations during which one ring material may serve generally. Any study depending on varying the disk composition or morphology, or comparing a series of disk materials in given electrolytes, would be expedited by disk interchangeability. In a prime example of particular current relevance to us, the study of semiconductor disk photoelectrochemistry, these are all prominent requisites. The power of the methodology can be extended in certain complicated systems by use of a split ring variation (SRRDE) which provides two independent monitors of the disk reaction rather than one (6).

We have taken a proven design (6) for making either RRDE or SRRDE's of relatively easy permanent construction, compatible with virtually any 1/4 in. shaft rotator, and modified it to accept demountable disks. Important to us in this development is obtaining a simple interchange (perhaps 15 min of easy steps) without sacrificing any theoretical advantages of the system, such as speed invariant collection efficiency, not found in a most recent demountable electrode design (5). The predecessor permanent version to ours (6) is based on an epoxy adhesive, concentric coupling of a disk (rod) and ring (tube), with the split ring form completed by appropriate subsequent slotting of the tube. Electrodes already constructed of either form, or freshly made up with active disk material omitted, are readily adapted to take a threaded mount for the disk and it is only required to have a solvent-removable, gap-filling polymer of reasonable adhesive quality to have the necessary demountability, as will be shown below.

Demonstration of the practicability of the new electrodes is given for several ring disk combinations, including metal and semiconductor disk examples. Confirmation of theoretical behavior and the demounting, remounting, and replacing of disks are amply examined.

Experimental Section

Apparatus and materials.—The galvanostat-potentiostat (6) and motor control- $\omega^{1/2}$ scanning circuitry (7) have been described earlier. Scans were recorded using an HP Model 7046A X, Y, Y' recorder. Current ratios were obtained with a Burr Brown 4291 analog divider. Electrochemical experiments were performed under an N_2 atmosphere in a three-electrode cell with platinum counterelectrodes and saturated calomel (SCE) reference electrodes. Experiments employing a semiconductor disk utilized a cell with an optical flat bottom, permitting disk illumination with a 100W tungsten-halogen lamp. Electrolytes were prepared with reagent grade chemicals and triply distilled water. Single crystal n-CdS from Cleveland Crystals was etched for a few seconds in concentrated HCl before scans.

Electrodes.—The fabrication of permanent ring disk and split ring disk electrodes has been detailed earlier (6). Easy mounting and demounting of a desired disk have been achieved with modifications shown in Fig. 1. The center rod is drilled and tapped to a convenient

screw size (4-40 in this case) as pictured, following rod-tube alignment and bonding. The active disk material may be machined out of an already constructed electrode and the hole tapped, as was actually done for our electrodes.

Stainless steel Fillister head screws (1/4 in.) with the head machined flat serve as convenient disk mounts. The active disk material is fastened to the screw using solder or conducting silver epoxy. Shaping of the disk may be completed on a lathe with appropriate cutter or abrasive. In the case of the CdS disk, an ohmic contact was formed on the back of the crystal with Ga/In eutectic prior to silver epoxy bonding.

The disk is threaded to approximate planarity to the ring, and then the remaining gap between the ring and the disk is filled with Loctite 430 adhesive (Loctite Corporation, Newington, Connecticut). Cure within minutes was obtained using Loctite Tak Pak Accelerator. Excess adhesive was removed, and the ring and disk made coplanar, by polishing. To demount, the gap-filling adhesive was removed by dipping the electrode assembly in ultrasonically agitated dimethylformamide (DMF) at $\sim 40^\circ\text{C}$ for several minutes, after which it is readily unthreaded. To assure facile removability, the threads were protected from the gap-filling adhesive by coating those nearest the disk with Fluorolube Grease GR-90 before insertion. Care was taken to keep the sides of the ring and disk free of this grease.

Results and Discussion

An Au ring-Pt disk assembled as above was examined in 5 mM $\text{Fe}(\text{CN})_6^{4-}$ + 1M KCl. The disk was

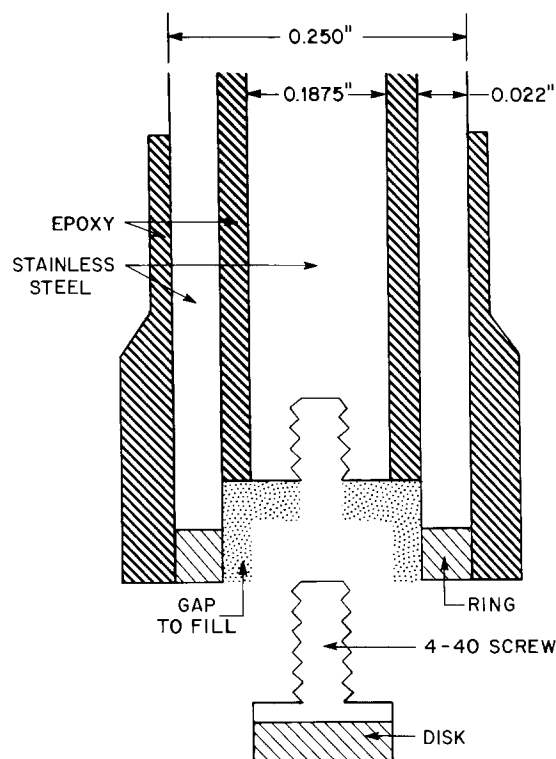


Fig. 1. Schematic diagram of a demountable disk, ring disk electrode.

* Electrochemical Society Active Member.

Key words: ring disk electrodes, demountable disk, electrolytes.

potentiostatted at 0.5V and the ring at $-0.2V$ vs. SCE to oxidize $Fe(CN)_6^{4-}$ and reduce product $Fe(CN)_6^{3-}$ at their respective limiting currents. Figure 2(a) shows Levich plots of the disk and ring-limiting currents, i_D and i_R , vs. $\omega^{1/2}$ for speed scanned at $1 \text{ rpm}^{1/2} \text{ sec}^{-1}$ between zero and 10,000 rpm. Both plots are linear above ~ 400 rpm as expected (8) and the ratio of their slopes yields a collection efficiency of 0.34 in good agreement with that calculated (9) from the nominal geometry of the RRDE in Fig. 1.

To test the RRDE reproducibility after repeated demounting and remounting by the described procedure, the disk electrode was unthreaded after dissolving the adhesive in DMF, reassembled, and polished lightly to assure its planarity. The ring collection experiment of Fig. 2(a) was then repeated. The second set of Levich plots obtained in a fresh solution of the same composition essentially superimposed those of Fig. 2(a). In this run, the constancy of the collection efficiency of the ring disk in the above configuration was examined over the same range of rotation speed by obtaining the ratio of ring to disk current, N , directly with the analog divider in Fig. 2(b). Ring current was corrected for a small measured residual before division. This plot also gives a value of 0.34 for $\omega^{1/2} > 20 \text{ rpm}^{1/2}$.

Figure 3 shows $i_D - E_D$ and $i_R - i_D$ plots obtained in 0.1M $Fe(CN)_6^{4-} + 1M$ KCl at an illuminated n-CdS electrode acting as a photoanode. The higher concen-

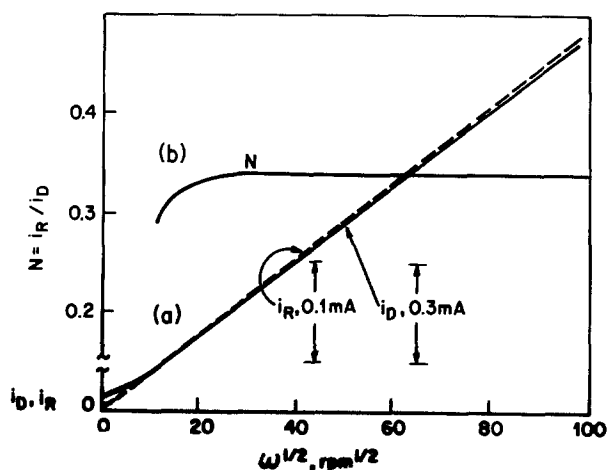


Fig. 2. Pt disk and Au ring potentiostatted at 0.5V and $-0.2V$ vs. SCE, respectively, in 5 mM $Fe(CN)_6^{4-} + 1M$ KCl. Speed scanned at $1 \text{ rpm}^{1/2} \text{ sec}^{-1}$. (a) First mounting of disk, i_D (solid line) and i_R (dashed) vs. $\omega^{1/2}$. (b) Remounting of disk, $i_R/i_D = N$ vs. $\omega^{1/2}$.

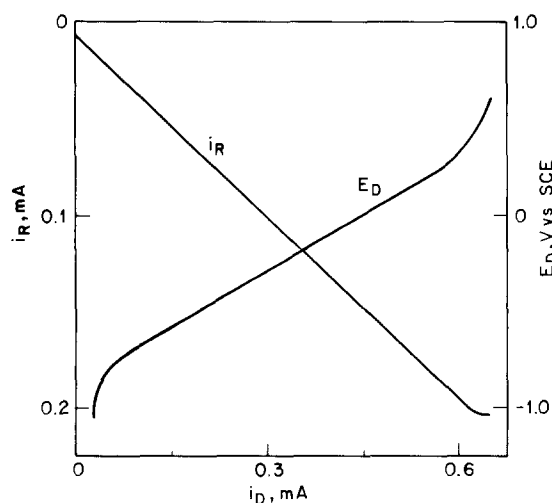


Fig. 3. $i_D - E_D$ and $i_R - i_D$ curves under disk potential scan at 5 mV/sec for illuminated n-CdS disk Pt ring in 0.1M $Fe(CN)_6^{4-} + 1M$ KCl. Ring potential $-0.2V$ vs. SCE, speed 1600 rpm.

tration of $Fe(CN)_6^{4-}$ was employed in this case to suppress the competition of surface corrosion processes under the given illumination intensity. The leveling of i_D above $600 \mu A$ occurs from photon flux limitation. In the accompanying $i_D - i_R$ scan, the ring is held on the reduction wave of $Fe(CN)_6^{3-}$ to collect $Fe(CN)_6^{3-}$ resulting from photo-oxidation at the n-CdS disk. The slope of this trace yields an experimental value for N of 0.32, which compares closely with the calculated 0.34. This agreement of N values indicates that all the anodic photocurrent at n-CdS in the linear region of the plot results from efficient photo-oxidation of $Fe(CN)_6^{4-}$ and the current contribution to surface processes is minimal.

We applied an SRRDE, constructed by mounting the Pt disk used above in a gold split-ring, to a situation where simultaneous monitoring of two oxidation states of a redox species is very helpful in resolving the disk reactions. Figure 4 shows ring collection (product detection) and shielding (reactant removal) measurements during reduction of Cu(II) at a Pt disk. The Pt disk trace shows a two-step reduction, Cu(II) to Cu(I), and Cu(I) to Cu(0), labeled A and B, respectively, before the onset of H_2 evolution. The dashed curves show currents i_R^+ and i_R^- at the two Au half rings which were potentiostatted at $E_R^+ = 0.4V$ and $E_R^- = -0.1V$, respectively. The current in the upper half-ring trace, i_R^+ , results from the oxidation of Cu(I) generated at the disk. For the first reduction wave, it reaches a corresponding limiting value and drops back to zero when the second reduction wave, B, starts. At these potentials, the Cu(II) is reduced further to Cu(0) at the disk and no product reaches the ring. The ring-shielding curve, i_R^- , monitors Cu(II) species at a potential corresponding to the limiting current of the first disk step, A. When no current flows at the disk at positive potentials, i_R^- measures the limiting current of Cu(II) which can be quantitatively related to i_D at A by the relation $i_R^- = 0.52i_D$ for this half-ring geometry. i_R^- decreases by the amount Ni_D when the disk consumes Cu(II) on the A plateau. Since the flux of Cu(II) to the ring is unchanged during the second reduction wave, i_R^- remains constant. The ring and disk curves shown in Fig. 4 are scaled by approximately the geometric factor for a half ring, $N/2$. We note that agreement between the experimental $N/2$ of 0.140 and 0.145 for the two individual methods of detection and the calculated 0.29 for the combined half rings is as expected.

Conclusions

The variety of experiments performed illustrating the desired demountability, interchangeability, and theoretical performance of these electrodes confirms the design objectives. The methylcyanoacrylate gap-filling adhesive selected provided both easy removal in the presence of the primary epoxy mounting and shrink polyethylene tubing used above it, and good

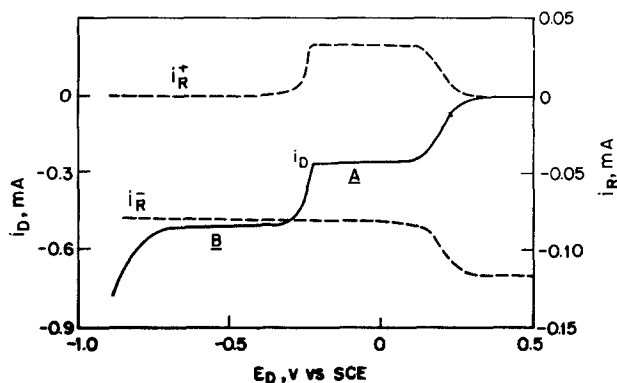


Fig. 4. Pt disk potential scan at 5 mV/sec in 2 mM $CuCl_2 + 0.5M$ KCl with Au split ring. Half rings held at 0.4V (i_R^+) and $-0.1V$ (i_R^-) vs. SCE. Speed 1600 rpm.

evidence of adequate sealing properties and resistance to typical aqueous environments. The savings in time, effort, and cost by having a few basic RRDE or SRRDE structures, as in Fig. 1, to mate with the readily prepared disk-tipped screws can be amply testified to from our own experience with the construction of many dozens of such permanent electrodes.

Acknowledgment

The authors are grateful to S. G. Seger, Jr. for providing the adhesive and information on its use.

Manuscript received March 31, 1981.

Any discussion of this paper will appear in a Discussion Section to be published in the June 1982 JOURNAL. All discussions for the June 1982 Discussion Section should be submitted by Feb. 1, 1982.

Publication costs of this article were assisted by Bell Laboratories.

REFERENCES

1. F. Opekar and P. Beran, *J. Electroanal. Chem. Interfacial Electrochem.*, **59**, 1 (1976), see esp. pp. 75-81.
2. G. V. Zhutaeva and N. A. Shumilova, *Elektrokhimiya*, **2**, 606 (1966).
3. A. N. Doronin, *ibid.*, **4**, 1193 (1968).
4. G. W. Harrington, H. A. Laitinen, and V. Trendaflov, *Anal. Chem.*, **45**, 433 (1973).
5. T. Geiger and F. C. Anson, *ibid.*, **52**, 2448 (1980).
6. B. Miller, *This Journal*, **116**, 1117 (1969).
7. B. Miller, M. I. Bellavance, and S. Bruckenstein, *Anal. Chem.*, **44**, 1983 (1972).
8. B. Miller and M. I. Bellavance, *This Journal*, **120**, 42 (1973).
9. W. J. Albery and S. Bruckenstein, *Trans. Faraday Soc.*, **62**, 1920 (1966).



A Model for Oxidation of Silicon by Oxygen

S. S. Cristy and J. B. Condon

Union Carbide Corporation, Nuclear Division, Oak Ridge Y-12 Plant, Oak Ridge, Tennessee 37830

ABSTRACT

Insights into the transport and deposition of oxygen in silicon oxidation at 700°C have been obtained by isotope labeling and use of the ion microprobe mass analyzer for profiling. The results are consistent with interstitial diffusion of O₂ as the prime support of the interfacial oxidation reaction. Vacancy migration was observed near the surface with a very low diffusion coefficient. The SiO₂-Si interface is found to be diffuse with the interface reaction following a permissive-precipitation model. This model is shown to explain the profile features observed and agrees well with literature data for diffusion coefficient and rate of reaction with silicon.

W. A. Tiller (1) expressed the point of view that the oxidation of silicon is controlled by the migration of O⁼ interstitials. In his treatment, a "free volume supply condition" is assumed to be a problem for the O₂ migration proposed by Doremus (2) since this condition requires greater free energy than O₂ transport and requires large vacancy migration. Significant amounts of vacancy migration have been eliminated by Rosencher, Straboni, Rigo, and Amsel (3) in their article which utilized ¹⁸O₂ labeling and depth profiling with a Van de Graaff accelerator. The depth resolution of this technique, however, is insufficient to obtain profiles usable for modeling of the reaction.

To obtain better profiles for modeling, the ion microprobe mass analyzer (IMMA) was used in a similar isotope labeled study. The resolution of this instrument is sufficient to yield diffusion coefficients that are of the order of those for oxygen in silicon over the temperature range studied by Deal and Grove (4), Law (5), and Irene (6). The conditions of sample preparation were selected to allow a linear rate for most of the reaction. This simplifies the modeling problems and also allows clear inspection of the interface reaction if the model by Blanc (7) is operative.

Experimental Method

The silicon samples were obtained from Electronic Space Products, Incorporated, as 0.25 mm thick, single crystal wafers of about 2 cm diam. The three samples used were a p-type, 100 oriented, with a resistivity of 29.2 Ωcm, a p-type, 111 oriented, with a resistivity of 181 Ωcm, and an n-type, 111 oriented, with a resistivity of 36.3 Ωcm. These samples were oxidized in a tube furnace capable of an ultrahigh vacuum. The temperature chosen for oxidation was 700°C. According to Deal and Grove (4), the oxidation at this temperature is linear for at least 5 days. After evacuation to an ultrahigh vacuum (< 2 × 10⁻⁶ Pa outside the tube furnace area), the container tube was backfilled with 3.3 kPa of ¹⁶O₂ and the reaction allowed to proceed for 10 days. After 10 days, the tube was evacuated and backfilled with 3.3 kPa of ¹⁸O₂ and the reaction allowed to proceed for another ten days.

Key words: oxidation, silicon, ion microprobe, SIMS.

The cooled samples were transferred through air into the IMMA. The depth profiling capability of this instrument was utilized by sputtering with a 5 nA, 21.5 keV N₂⁺ ion beam and measuring the evolved ¹⁶O⁻ and ¹⁸O⁻ ions. The sputtering was confined to a rastered area of 31 by 39 μm. Electronic aperturing minimized etch pit edge effects and maximized the depth resolution. Experience with other samples indicates that the depth resolution of the IMMA for these conditions is better than 10 nm of real distance per decade drop in signal. A sputtering rate of 17.7 nm min⁻¹ in silicon metal was determined for these beam conditions using a boron-implanted silicon calibration standard. This translates into 9.0-15.0 nm min⁻¹ equivalency of silicon metal in SiO₂ depending upon the assumption made. An equivalency rate of 12 nm min⁻¹ was chosen as a compromise until a more accurate calibration is available. (The distance equivalency of silicon metal in SiO₂ is given by 0.47 of real distance since it is assumed that the expansion is constrained by the rigid surface geometry and takes place almost completely in the vertical direction.)

Results

Some typical profiles are shown in Fig. 1. Four main features may be identified in these profiles:

1. A very sharp tailing of the ¹⁸O⁻ signal from the surface inward accompanied by a rise in the ¹⁶O⁻ signal. Some surface enhancements are probably present, but the inward tailing is real since it is reflected in the ¹⁶O to ¹⁸O ratio. If the gradient is due to diffusion of some species, then the diffusion coefficient is between about 3 × 10⁻²³ m² sec⁻¹ for the N(111) sample, and about 1.7 × 10⁻²³ m² sec⁻¹ for the P(111) sample. A diffusion gradient of this magnitude is insufficient to sustain the overall rate of oxidation. (These values were obtained by assuming that the ¹⁸O gradient from the surface was established during the 10 day ¹⁸O₂ exposure. Diffusion equations imply that the natural logarithm of the gradient as shown in the discussion is 1/√πDt for a semi-infinite solid (8) where D is the diffusion coefficient and t is the exposure time.)

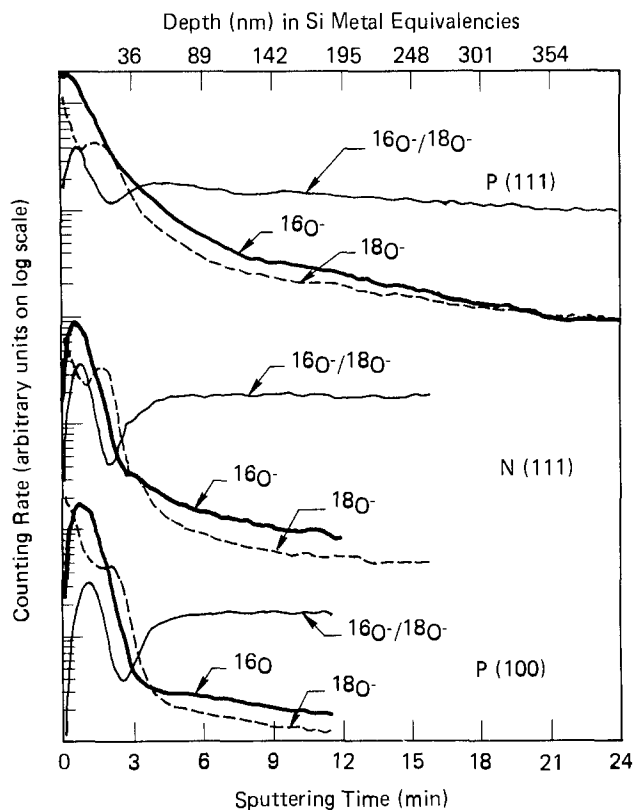


Fig. 1. Typical IMMA depth profiles of oriented silicon wafer which had been oxidized at 700°C with $^{16}\text{O}_2$ for 10 days followed by $^{18}\text{O}_2$ for 10 days. (Actual oxide depth is about twice the silicon metal equivalence depth. The location of x_{st} , the defined transformation boundary, is at about 3 min sputtering time.)

2. An increase in the $^{18}\text{O}^-$ signal at about 20 nm and a maximum at about 30 nm into the sample. This hump was observed in the Van de Graaff experiments (3). However, this is not a sharply defined layer as previously assumed but rather a broadened peak. This cannot be explained by lack of depth resolution of the IMMA profiling which is better than 10 nm real distance per decade of signal drop. Indeed, this apparent lack of resolution can be explained along with the shallow valley of $^{18}\text{O}^-$ at about 20 nm silicon equivalent by the model which will be presented here.

3. A relatively rapid decay of the $^{16}\text{O}^-$ signal at about the position of the $^{18}\text{O}^-$ hump followed by a similar drop in the $^{18}\text{O}^-$ signal. On a linear scale, this decay is S-shaped, and the position of an inflection point may be identified within a 3 nm distance.

4. A very broad tailing of both the $^{16}\text{O}^-$ signal and $^{18}\text{O}^-$ signal into the silicon metal phase. This latter tailing may be interpreted as the decay of oxygen into the metal by diffusion. The calculated diffusion coefficient from this tail is, within experimental error, the expected value from the literature data (9).

Discussion

General feature.—The overall conclusion, which is the same as Rosencher *et al.*, is that the species that migrates through the product layer and supports the interfacial oxidation reaction does not involve oxygen lattice positions. The sharp diffusion gradient in the $^{18}\text{O}^-$ signal at the outer surface, feature 1 described in the results section, is probably the result of vacancy migration on the oxygen sublattice of SiO_2 phase. It is not due to the diffusion gradient of oxygen-bearing species responsible for most of the oxidation, since the diffusion coefficient of $\leq 3 \times 10^{-23} \text{ m}^2 \text{ sec}^{-1}$ is much too low to support the overall reaction rate. Even with a concentration of migrating oxygen of 1.0 mol frac-

tion, a product film of $\leq 7 \text{ nm}$ would be formed in 20 days with this diffusion coefficient.

Elimination of point defect migration mechanisms.—Deduction of the most likely migrating species is accomplished by eliminating possibilities. One possibility is the migration of charged monatomic interstitials where the local equilibrium with oxygen vacancies is assumed as required in the treatment by Wagner (10). Diffusion of these interstitials is from the high concentration region of the gas-product interface to the low concentration region of the product-silicon interface (as required whenever the activity follows the concentration). For this first possibility, it is further assumed that the interstitial concentration profile is too low and flat to be seen by the IMMA. If this second assumption were not true and the feature 1 gradient were indeed due to the interstitial concentration, then the measured diffusion coefficient of $3 \times 10^{-23} \text{ m}^2 \text{ sec}^{-1}$ is insufficient to support the overall reaction rate.

With these assumptions, the feature 1 tailing of the $^{18}\text{O}^-$ signal would be due to exchange of the interstitial oxygen with lattice oxygen by way of formation and filling of vacancies. The local equilibrium condition requires that this process be very fast compared to the diffusion process. The tailing would, therefore, be a reflection of the diffusion gradient. This again yields a diffusion coefficient of $\sim 10^{-23} \text{ m}^2 \text{ sec}^{-1}$ for the overall diffusion of oxygen which is too low to support the overall reaction rate.

Another possibility is to eliminate the local equilibrium condition and allow oxygen gas to react with vacancies on the product surface to yield a charged atomic interstitial. Under these conditions, the flux of vacancies to the surface must equal the flux of oxygen interstitials through the product layer. Again, the observed diffusion coefficient of $\sim 10^{-23} \text{ m}^2 \text{ sec}^{-1}$ for these vacancies is insufficient.

Further evidence for eliminating all atomic interstitials, charged or uncharged, from importance in the reaction arises from the fact that in the parabolic realm the rate is proportional to the oxygen pressure. The only way for atomic oxygen migrant to yield this behavior is for oxygen gas (molecular oxygen in general) to react with a steady and large supply, *i.e.*, constant, of vacancies on the oxygen sublattice. This would yield atomic oxygen interstitials whose concentration is proportional to the oxygen pressure. The IMMA profile yielding a diffusion coefficient of $\leq 3 \times 10^{-23} \text{ m}^2 \text{ sec}^{-1}$ for the vacancies eliminates this possibility.

The conclusion is, therefore, that the mechanism is basically that postulated by Doremus (2), *i.e.*, dissolved O_2 migration, and modeled by Blanc (7) to take into account the complete linear-parabolic behavior. The O_2 must decompose on the silicon metal itself, and other preconditioning of the oxygen on the outer surface such as reaction with vacancies, decomposition to ions, etc., lead to either insufficient rates, incorrect gradients, or scrambled profiles.

Details of the proposed model.—The question raised by the profile shape, especially feature 3, is "why is the ^{18}O hump smeared out?" Since it is concluded that Doremus' model for thick film oxidation is correct, then the assumption that the dissolved O_2 concentration is about 0.01 mol fraction is correct. If one then assumes that the SiO_2 -Si interface is atomically sharp, as assumed by Rosencher *et al.* and by Tiller but not explicitly in Blanc's model, then the tailing is due to draining of the interstitial oxygen. However, there is insufficient oxygen stored up in the oxide film to explain the gradual tailing into the ^{18}O hump. Furthermore, this still does not explain the tailing into the metal phase, that is features 3 and 4, at any concentration of O_2 in the film.

This question can be resolved by assuming that the interface is not sharp, but is rather diffuse as clearly seen from features 3 and 4. Blanc's model is still opera-

tive except that the interface reaction follows the per-
fusive-precipitation model. In this model (11), the O_2
is assumed equilibrated with oxygen dissolved in the
silicon. Precipitation of oxide from the supersaturated
silicon proceeds internally until the metal is distorted
sufficiently to drastically increase the diffusion coeffi-
cient of oxygen. The mathematics of the model have
been derived analytically with some reasonable ap-
proximations by Kirkpatrick (12) and applied to water
oxidation of uranium (13). The equations of interest in
this case are

$$d \ln P/dx|_{x=x_s} = [U_s (\ln U_s)/(1 - U_s)] \sqrt{akU_s/D} \quad [1]$$

where P = the fraction of material that is product
(SiO_2), x = the distance into the sample from gas-solid
surface, x_s = the position where D becomes "large",
i.e., the reaction front, U_s = the mol fraction of metal
remaining at x_s , a = the stoichiometric ratio ($a = 2$
for SiO_2), D = the diffusion coefficient of oxygen in
silicon metal, and k = a microscopic rate constant per
Avrami's limited growth case (14).

The rate constant, k , in some cases can be measured
independently, and U_s should be calculable from the
metal's mechanical properties. U_s in the present case
may be obtained by noting that x_s is the inflection point
(12) of the $^{18}O^-$ profile tailing into the metal. (The
procedure used to obtain this inflection point was as
follows. The total oxygen signal was plotted, point by
point, on a linear scale. The slope of this plot was taken
as the linear connection of each point. The inflection
point was assumed to be between the two points whose
connecting line segments had the greatest negative
slope.) Once the position of the inflection point is
found, the extent of the reaction is calculated as the
ratio of the total oxygen content at x_s (or the average
of the two points on either side of inflection) to the
total oxygen content at the outer plateau or oxygen
maximum. The rate constant, k , may be obtained by
measuring the distance for one decade drop in the log
tangent of the product at the inflection point, $\Delta x_{0.1}$, and
rearranging Eq. [1] to

$$k = (5.3) D (1 - U_s)^2 (\Delta x_{0.1})^{-2} U_s^{-3} (\ln U_s)^{-2} a^{-1} \quad [2]$$

The diffusion coefficient, D , is obtained from the long
tail of oxygen into the metal, feature 4. The concentra-
tion profile for pure diffusion is given by the expression

$$c = c_0 [1 - \operatorname{erf}(x/\sqrt{4Dt})] \quad [3]$$

The slope of the log of the concentration as a function
of depth can, therefore, be shown to be

$$\partial \ln c/\partial x = \partial c/c\partial x = - \exp(-x^2/4Dt)/\sqrt{\pi Dt} [1 - \operatorname{erf}(x/\sqrt{4Dt})] \quad [4]$$

The log tangent of the total oxygen content by a dif-
fusion process as $x \rightarrow 0$ is therefore

$$\partial \ln c/\partial x|_{x=0} = 1/\sqrt{\pi Dt} \quad [5]$$

For determining this tangent from the IMMA output,
it was convenient in this case to define a $\Delta x_{1/2}$ as the
distance over which the tangent line decreased by a
factor of 2. This quantity was estimated graphically
from the output of the IMMA in the feature 4 tail.
This gives the diffusion coefficient as

$$D = 0.66 (\Delta x_{1/2})^2/t \quad [6]$$

A more precise method of determining D does not ap-
pear to be justified for this study. If Eq. [2] and [6]
are combined, it is noticed that the k is independent of
the IMMA depth profiling rate calibration.

The overall linear rate, v_s , may be calculated by the
equation

$$v_s = - (kc_0/\ln U_s) \sqrt{D/akU_s} \quad [7]$$

where c_0 is the dissolved oxygen content at x_s . The
usual method of calculating c_0 is to extrapolate the
ideal solubility law (Sieverts' or Henry's law) beyond
the terminal solubility. According to Logan and Peters
(9), the terminal solubility, c_T — the mol fraction of
oxygen dissolved in silicon metal in equilibrium with
 SiO_2 , is given by the equation

$$c_T = 278 \exp(-26,700/T)$$

The activity of oxygen from SiO_2 is given by

$$P_o = 1.46 \times 10^9 \exp(-108,800/T)$$

according to the listed thermodynamic data (15) on
cristobalite. Extrapolating by ideal solubility

$$c_0 = c_T/(P_{O_2})^{1/2}$$

c_0 thus calculates to be 1.7×10^{10} mol fraction at 100
kPa O_2 pressure, a result which is much too large.
Ideal solubility apparently does not apply in this case,
and an alternate scheme of determining c_0 is required.
This alternate scheme is to back-extrapolate the tail
due to diffusion in the metal to x_s . This extrapolated
value is then divided by the total oxygen content at
the outer plateau and multiplied by 0.67 (i.e., the mol
fraction of O in SiO_2 is 0.67). All of these measure-
ments have a great deal of uncertainty, especially the
 U_s and c_0 . Furthermore, it may be possible that diffu-
sion of O_2 through the product may begin to be a
limiting factor. Nevertheless, the calculated v_s is fairly
close to the v_s observed by the direct measurement to
 x_s . The values for the eight profiles measured are
given in Table I. The diffusion coefficient is in good
agreement with the extrapolated value from Logan and
Peters (9) data, since the extrapolation of their data in-
troduces an uncertainty of a factor of 10^4 (10^{-18} - 10^{-22}
 $m^2 \text{ sec}^{-1}$). The overall rate is in good agreement with
the linear rate by Deal and Grove (4) of 3×10^{-14}
 msec^{-1} , and by Law (5) and Irene (6) for which the
extrapolated values are 1.5×10^{-13} msec^{-1} and $7 \times$
 10^{-14} msec^{-1} . The pressure used in the present study
was about 0.33 that used by Deal and Grove, and Irene,
but about 5000 times that used by Law, yet the linear
rates for all four measurements are about the same.
This is probably indicative of the nonideal oxygen solu-
bility, and that the silicon metal is simply saturated
at x_s even at very low pressures. The value of k of 4
 $\times 10^{-5} \text{ sec}^{-1}$ found is quite low compared to other
oxidation reactions such as copper where k is about
 0.11 sec^{-1} as determined by IMMA, and iron where k
is 150-300 sec^{-1} calculable from data by Turkdogan
et al. (16, 17). It may be that the SiO_2 precipitates are
not formed by the limited isometric growth but rather
formed as needles or platelets.

Given the agreement between the model and ob-
servations of linear rates, it is concluded that the per-
fusive-precipitation model applies. Knowing this, the
shallowness of the valley in the $^{18}O^-$ signal can be ex-
plained without assuming exchange between the mi-
grating interstitials and the oxygen on the oxygen sub-
lattice, although a small amount of exchange may be
present but, as previously demonstrated, unimportant.
The ^{18}O enters into the permanent sublattice by react-
ing with the residual silicon metal which remains un-
reacted after the boundary, at x_s , passes. (The move-
ment of the boundary is very similar to a shock front
which leaves a decaying trail behind it.)

Several problems arise using only the IMMA profiles
to analyze for the various constants needed for the
perfusive-precipitation model. The depth profiling cal-
ibration enters directly into both the calculated and
observed v_s . However, if the calibration changes from
the oxidizing layer to the metal, then the calculated
 v_s is more affected than the observed v_s . The reason
is that the calculated v_s is proportional to (calibration

Table I. Parameters obtained and calculated from IMMA depth profiling of oxidized silicon

| Sample and run | $\Delta x_{1/2}$ (nm) | D ($m^2 \text{ sec}^{-1}$) | c_0 (mole fraction) | $\Delta x_{0.1}$ (nm) | k (sec^{-1}) | U_s (fraction) | v_s calc. (msec^{-1}) | v_s obs. (msec^{-1}) |
|-----------------------------|--------------------------|-----------------------------------|--------------------------|--------------------------|------------------------------|---------------------|---------------------------------------|--------------------------------------|
| P(111)—1 | 89 | 3.1×10^{-21} | 0.038 | 20 | 3.4×10^{-5} | 0.78 | 4.0×10^{-14} | 1.6×10^{-14} |
| P(111)—2 | 140 | 7.7×10^{-21} | 0.020 | 31 | 3.5×10^{-5} | 0.75-0.80 | 3.3×10^{-14} | 1.5×10^{-14} |
| P(111)—3 | 78 | 2.4×10^{-21} | 0.063 | 24 | 3.5×10^{-5} | 0.41-0.73 | 2.8×10^{-14} | 1.6×10^{-14} |
| P(111)—4 | 49 | 9.4×10^{-22} | 0.068 | 24 | 7.7×10^{-6} | 0.75 | 1.6×10^{-14} | 1.4×10^{-14} |
| P(100)—1 | 104 | 4.2×10^{-21} | 0.022 | 11 | 1.2×10^{-4} | 0.85-0.92 | 9.6×10^{-14} | 1.9×10^{-14} |
| P(100)—2 | 86 | 2.9×10^{-21} | 0.006 | 17 | 3.6×10^{-5} | 0.83-0.89 | 9.8×10^{-15} | 2.3×10^{-14} |
| N(111)—1 | 60 | 1.4×10^{-21} | 0.046 | 16 | 2.6×10^{-5} | 0.69-0.82 | 2.5×10^{-14} | 1.7×10^{-14} |
| N(111)—2 | 138 | 7.5×10^{-21} | 0.014 | 12 | 2.6×10^{-4} | 0.69-0.76 | 5.0×10^{-14} | 1.4×10^{-14} |
| Average values | 93 | 3.4×10^{-21} | 0.035 | 19 | 6.9×10^{-5} | 0.8 | 3.7×10^{-14} | 1.7×10^{-14} |
| Calculated from averages | | 2.6×10^{-20} | | | 3.9×10^{-5} | | 4.5×10^{-14} | |
| Literature values (4, 8) | | | | | | | | 3.0×10^{-14} |

in metal)² divided by the calibration in the oxide; whereas the observed v_s is proportional only to the calibration in the oxide to the first power. The selection of the final inflection on the $^{18}\text{O}^-$ signal is difficult. This produces a large uncertainty in U_s which is most serious in the calculation of v_s since the term $(\ln U_s)$ is used. The uncertainty in the position of the inflection point does not greatly affect the position of x_s or the value of $\Delta x_{0.1}$ or c_0 . Uncertainties in the log scale slopes of $\Delta x_{0.1}$ and $\Delta x_{1/2}$ arise mainly from background oxygen signals for which no compensation was made. Background also produces an uncertainty in the value of c_0 . It will cause the measurement of both $\Delta x_{0.1}$ and $\Delta x_{1/2}$ to be high; whereas since c_0 is a back-extrapolated number dependent on both $\Delta x_{1/2}$ and the background in opposite senses, the relationship between c_0 and background is uncertain. One would probably expect the background to produce a high calculated value for v_s ; whereas it had no effect on the observed v_s . The sensitivity of the IMMA to the evolved ions has no effect provided it is equal for both $^{16}\text{O}^-$ and $^{18}\text{O}^-$ which is the normal case.

As a final point of interest, if the presented model is correct, then the linear rates should be calculable at other temperatures. The constant k has been shown for other systems to be relatively temperature insensitive, and the value for c_0 should not change, since it is at the saturation value even at very low oxygen pressures. This leaves only the diffusion coefficient with a significant temperature dependence. This dependence can be obtained using the diffusion coefficient found in this work and the high temperature diffusion coefficient found by Logan and Peters (9) to yield a (H^2/R) of 44×10^3 . The extrapolated calculated linear rate is given in Fig. 2 along with the experimental data. Again, the agreement is good.

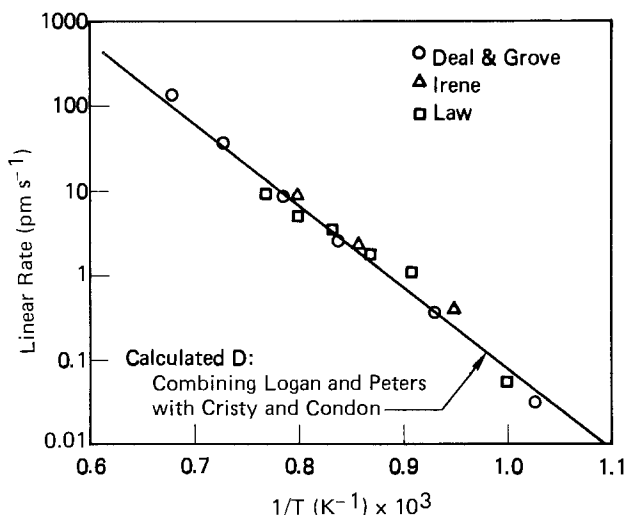


Fig. 2. Comparison of the experimental linear reaction rates for silicon oxidation with the calculated linear rate using a k of $4 \times 10^{-5} \text{ sec}^{-1}$ and diffusion coefficient from combined data of Logan and Peters and the value found from IMMA.

Conclusion

For silicon oxidation at 700°C , it is concluded from IMMA data that:

1. The only migrating species of importance in the product layer is dissolved O_2 .
2. Generally, the kinetics follow the kinetics proposed by Doremus (2) and modeled by Blanc (7).
3. The silicon-oxide interface reaction is a perfusive-precipitation reaction and can be modeled to yield the measured linear rates with no variable parameters.
4. Vacancies in the product oxygen sublattice are probably present at very low concentrations and migrate with a diffusion coefficient of about $10^{-23} \text{ m}^2 \text{ sec}^{-1}$ and are unimportant in the overall reaction kinetics.
5. Atomic ionic oxygen interstitials in the oxidized layer are not present to any great extent since lattice-dissolved O_2 mixing is not observed, and the IMMA profiles may be modeled by the perfusive-precipitation model alone. Furthermore, the reaction order with respect to oxygen in the parabolic range and the limited mobility of vacancies indicates that atomic oxygen interstitials of any type are not relevant to the overall reaction.
6. The values of the kinetic constants obtained from the IMMA profiles are:

$$D(\text{O in Si}) = \text{about } 3.4 \times 10^{-21} \text{ m}^2 \text{ sec}^{-1} \text{ at } 700^\circ\text{C}$$

$$k \text{ (the microscopic, rate constant)} = \text{about } 4 \times 10^{-5} \text{ sec}^{-1},$$

$$U_s \text{ (mole fraction silicon remaining at "interface")} = \text{about } 0.80.$$

These parameters yield a calculated velocity for the interface penetration of about $4 \times 10^{-14} \text{ msec}^{-1}$ which is in good agreement with the observed velocity and the values obtained from the literature.

Manuscript submitted Sept. 30, 1980; revised manuscript received ca. April 27, 1981.

Any discussion of this paper will appear in a Discussion Section to be published in the June 1982 JOURNAL. All discussions for the June 1982 Discussion Section should be submitted by Feb. 1, 1982.

Publication costs of this article were assisted by the Union Carbide Corporation.

LIST OF SYMBOLS

- P fraction of material that is product (SiO_2)
 x distance into the sample from the gas-solid surface
 x_s position where D becomes "large," i.e., the reaction front
 U_s mole fraction of metal remaining at x_s
 a stoichiometric ratio ($a = 2$ for SiO_2)
 D diffusion coefficient of oxygen in silicon metal
 k a microscopic rate constant per Avrami's limited growth case (14)
 $\Delta x_{1/2}$ the distance for the log tangent of total oxygen content to decrease by a factor of 2 in innermost tail

t the total time of oxygen exposure, i.e., 1.7×10^6 sec
 $\Delta x_{0.1}$ the distance for the log tangent of the product at the inflection point to drop by one decade
 v_s overall linear rate or reaction front movement velocity
 c_0 the dissolved oxygen content at x_s
 H^\ddagger activation enthalpy of the oxidation reaction

REFERENCES

- W. A. Tiller, *This Journal*, **127**, 619, 625 (1980).
- R. H. Doremus, *J. Phys. Chem.*, **80**, 1773 (1976).
- E. Rosencher, A. Straboni, S. Rigo, and G. Amsel, *Appl. Phys. Lett.*, **34**, 254 (1979).
- B. E. Deal and A. S. Grove, *J. Appl. Phys.*, **36**, 3770 (1965).
- J. T. Law, *J. Phys. Chem.*, **61**, 1200 (1957).
- E. A. Irene, *This Journal*, **125**, 1708 (1978).
- J. Blanc, *Appl. Phys. Lett.*, **33**, 424 (1978).
- P. G. Shewmon, "Diffusion in Solids," p. 11, McGraw-Hill Book Co., New York (1963).
- R. A. Logan and A. J. Peters, *J. Appl. Phys.*, **30**, 1627 (1957).
- C. Wagner, *Z. Phys. Chem.*, **B21**, 25 (1933); *ibid.*, **B32**, 447 (1936); and C. Wagner and K. Grunewald, *ibid.*, **B40**, 455 (1938).
- J. B. Condon and E. A. Larson, *J. Chem. Phys.*, **59**, 855 (1973).
- J. R. Kirkpatrick, U.S. Government Rep. K/CSD-9 (1977) or in BNL-26523, p. B4 (1978), to be published in *J. Phys. Chem.*
- J. B. Condon, *J. Less-Common Met.*, **73**, 105 (1980).
- M. Avrami, *J. Chem. Phys.*, **7**, 1103 (1939), **8**, 212 (1940), **9**, 177 (1941).
- NSRDS-NBS 37, "JANAF Thermochemical Tables," 2nd ed., D. R. Stull and H. Prophet, Directors, U.S. Department of Commerce-NBS, Washington, D.C. (1971).
- E. T. Turkdogan and J. V. Vinters, *Metall. Trans.*, **3**, 1561 (1972).
- J. H. Swisher and E. T. Turkdogan, *Trans. Metall. Soc. AIME*, **239**, 426 (1967).

Comparison of the Etching and Plasma Characteristics of Discharges in CF_4 and NF_3

N. J. Ianno, K. E. Greenberg, and J. T. Verdeyen*

*Gaseous Electronics Laboratory, Department of Electrical Engineering,
University of Illinois at Urbana-Champaign, Urbana, Illinois 61801*

ABSTRACT

Experiments were performed to explore the correlation (or lack thereof) between the surface effect and plasma characteristics of discharges in CF_4 and NF_3 . The optical emission from excited fluorine can be greatly enhanced by the dilution of these gases with helium, yet the etch rate of Si (or SiO_2) is decreased by this dilution. The effect of biasing the sample with respect to the plasma potential was investigated, and for NF_3 , evidence was found for a reaction involving a negative ion.

There have been many reports on the effects of various additives on the characteristics of discharges used for etching semiconductors. Most of these studies have concentrated on the effects of hydrogen or oxygen as an additive to the various fluorine donor gases such as CF_4 (1-8). Due to the highly reactive nature of free hydrogen or oxygen atoms, it is difficult to determine which of several processes, occurring either on the surface or within the volume of the discharge, affects the etch rate.

Helium was used as a diluent in these experiments since it will not react chemically with either Si, SiO_2 , or Si_3N_4 . In addition, the first excited state of helium is metastable, 19.8 eV above the ground state, which is sufficient to excite, dissociate, or ionize any other gas (with the exception of neon) (9). Thus, while ground state helium is chemically inert, excited helium reacts vigorously in the volume of a discharge.

A d-c hollow cathode discharge (10) was used to excite the gases in order to simplify the diagnostics such as measurements of ion current to the sample. Unlike a positive column discharge, the hollow cathode discharge is an electron beam produced plasma, and thus is capable of producing a stable, uniform, glow discharge in CF_4 and NF_3 (a highly electronegative gas), at low pressures and low power levels.

Figure 1 is a schematic diagram of the hollow cathode used for the experiments. The cathode was a 5 in. long, 1-3/8 in. ID stainless steel nipple. Six stainless steel rods were attached to the aluminum anode plate

and wrapped with nickel wire to form a coaxial metal basket. A retaining plate held a quartz window over a 5/8 in. hole in the anode plate and a Maycor insulator separated the anode from the cathode. The etchant gas flowed into the cathode, past the sample which was mounted on the front of the water cooled probe, and was pumped through a fore line trap and out of the system by a mechanical pump. The pressure was monitored using a capacitance manometer and the optical emission was observed through the quartz window using a McPherson 350 mm monochromator and an RCA 31034 photomultiplier.

During the experiments, the anode was grounded, the cathode was driven negative, and the probe con-

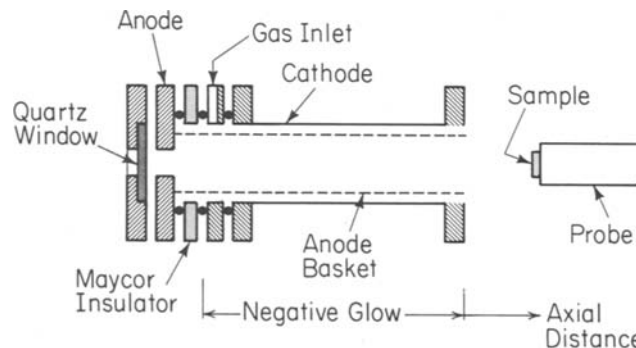


Fig. 1. Schematic of the hollow cathode discharge used in these experiments.

* Electrochemical Society Active Member.

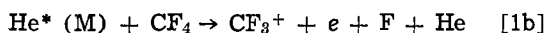
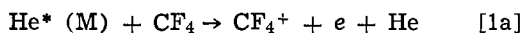
Key words: plasma processing, negative ions, emission enhancement, gas discharge.

taining the sample was biased with respect to floating potential, which was a few tens of volts negative with respect to the anode. The gas flow rate, total pressure, and discharge current were all held constant at 3.3 l/min (STP), 0.25 Torr, and 50 mA, respectively. For these operating conditions, the discharge voltage varied between 300 and 1000V. The remaining controlled parameters were gas mix, probe bias, distance from the plasma, and etch gas (CF_4 or NF_3).

Experimental Results

Optical emission.—In recent years, a strong correlation has been demonstrated between the intensity of the optical emission of excited fluorine from a $\text{CF}_4:\text{O}_2$ discharge and the etch rate (1, 3, 5, 7, 8). To investigate this correlation further, helium was added to a CF_4 discharge.

Figure 2, a partial energy level diagram of helium and CF_4 , illustrates the possibilities afforded by the addition of helium to a CF_4 discharge. The first two excited states of helium, the 2^1S and 2^3S , are both metastable. Either metastable can ionize the CF_4 to create CF_4^+ , or to create CF_3^+ and a free fluorine, via the Penning reactions shown in Eq. [1a] and [1b].



In addition, the 2^1S state has enough energy to simultaneously dissociate and excite a fluorine atom to the 2^2D state, according to Eq. [2], greatly enhancing the fluorine emission at 704 nm (and also the lines of the quartet system) (11)



Figure 3 demonstrates the dependence of the relative intensity of the 704 nm emission and the etch rates of Si and SiO_2 upon the concentration ratio of CF_4 to helium. These data were taken with the sample at floating potential and located at the edge of the negative glow. As illustrated, the 704 nm emission can be

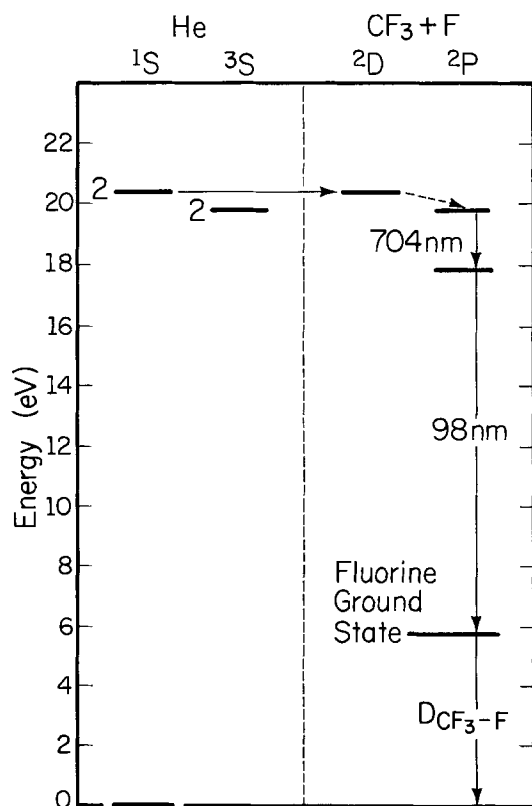


Fig. 2. Partial energy level diagram of helium and CF_4 showing the energy transfer from the helium 2^1S metastable to CF_4 .

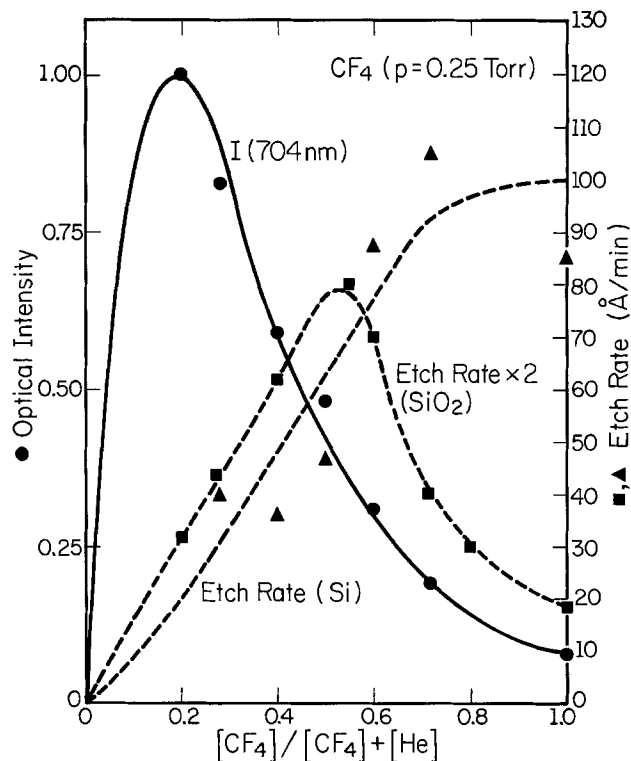


Fig. 3. Variation of 704 nm intensity, Si, and SiO_2 etch rates as a function of the helium partial pressure in CF_4 at a constant total pressure and current density. Note the increase in emission and lack of correlation between it and the etch rates.

enhanced by a factor of approximately 12, using a 5:1 mixture of $\text{He}:\text{CF}_4$. While the optical emission is enhanced and passes through a maximum, the Si etch rate decreases monotonically as the helium concentration increases. Also, it should be noted that while the SiO_2 etch rate is enhanced by the addition of helium, the maximum does not coincide with the fluorine emission peak. These trends are not particular to the $\text{CF}_4:\text{He}$ mixtures as the same general behavior is observed when a more conventional etchant gas mixture, 95% $\text{CF}_4 + 5\% \text{O}_2$, is diluted with helium; the variations of the fluorine emission and the etch rates of Si and SiO_2 with these mixtures are similar to those shown in Fig. 3. Furthermore, these characteristics are not a peculiarity of the electron distribution of the hollow cathode as similar effects are seen when the plasma is excited by an rf induction discharge (12).

There is a point which should be clear from this data: The spectral emission of atomic fluorine is not necessarily correlated with the etch rate of either Si or SiO_2 , for different gas mixtures. Within a particular gas mixture, however, the spectral emission will be indicative of the excitation density of the plasma, and thus, as a discharge parameter affecting the optical emission is varied, the etch rate should correlate well with the emission. For example, the etch rates of Si and SiO_2 and the 704 nm emission were monitored as a function of discharge current, for a constant gas mix. As the current was varied, the optical emission and the etch rates changed in a synchronous manner.

Correlation with ion current.—The relationship between the etch rate and the saturated ion current to the sample was investigated. To measure this current, the sample probe was replaced by a double probe which consisted of an inner conducting rod insulated from an outer tube. A nickel wire mesh covered the open end of the outer tube. By biasing the inner rod 300V negative with respect to the outer case, the electron current to the rod became negligible and only the current carried by positive ions was measured. Therefore, the saturated ion current consisted of ions that

were formed in the discharge and diffused to the nickel mesh.

The data in Fig. 4 were taken by moving the sample and double probes downstream from the edge of the visible glow. As shown, there is an excellent correlation between the etch rate of Si_3N_4 and the saturated ion current to the sample; the etch rate tracks the current over two orders of magnitude. The Si and SiO_2 etch rates behaved quite differently, however. As the sample is moved downstream from the active plasma, the etch rates decrease rapidly at first, and then continue to decline very slowly. It would appear that the dominant etch mechanism for Si_3N_4 is associated with positively charged species impinging upon the sample. For Si and SiO_2 though, it seems that the etch rates close to the discharge are dominated by processes involving positively charged species, whereas neutral species, due to their longer lifetimes, have a greater effect farther away from the active plasma.

To explore the effect of charged species on the etch rate further, the sample probe was maintained in a fixed position at the edge of the negative glow and its bias was varied with respect to the grounded anode (13-15). As shown in Fig. 5, when the probe was biased more negative with respect to floating potential, the positive ion current to the sample increased due to pair production in the sheath. The SiO_2 etch rate tracked this current, implying that positively charged species may contribute to the etch mechanism. When the probe was biased positive with respect to floating potential, an increased current due to negative carriers reaching the sample had no effect on the etch rate.

To determine how much of the etch rate increase could be attributed to physical sputtering when the probe was biased negative with respect to the anode, an argon discharge was used under conditions similar to the CF_4 discharge. When the sample probe was

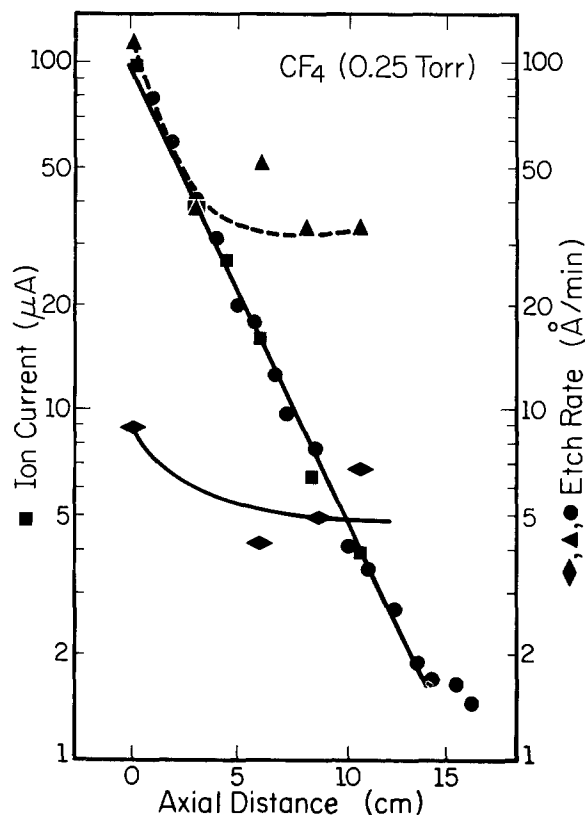


Fig. 4. Variation of the saturated ion current to the sample (■), the etch rate of Si_3N_4 (●), Si (▲), and SiO_2 (◆) as a function of distance from the edge of the visible glow. The Si_3N_4 etch rate tracks the ion current over two orders of magnitude and the etch rates of Si and SiO_2 rapidly become independent of the ion current.

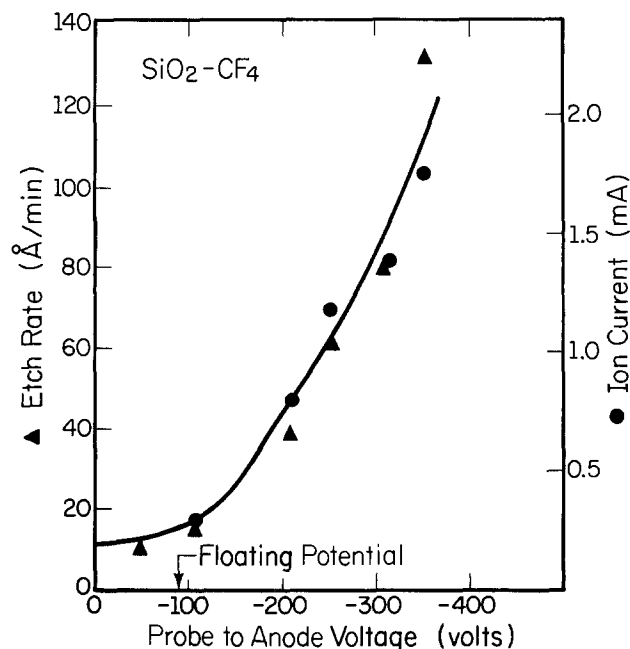


Fig. 5. Etch rate of SiO_2 and ion current to the sample as a function of probe to anode voltage.

biased 300V negative, an etch rate of 100 Å/min was observed. (Etching did not occur in the absence of the bias.) This etch rate is comparable to the enhancement obtained when pure CF_4 was used, indicating that physical sputtering was responsible for the enhanced etch rate as opposed to the decomposition of chemisorbed species or chemical reactions involving the ions (13, 14). This will be discussed in further detail along with the results of the NF_3 experiments.

Etching with NF_3 .—While there have been many papers and discussions associated with the etching characteristics of discharges in CF_4 (and with O_2), comparatively little has been published for NF_3 (16, 17). Some of the practical aspects of etching with this gas are listed below.

1. The etch rates of Si, SiO_2 , and Si_3N_4 are at least a factor of 10 faster with discharges in NF_3 as opposed to CF_4 .
2. The etch rate of Si can be 25 times that of SiO_2 .
3. The products of a discharge attack photoresist very slowly.
4. NF_3 does not etch Si, SiO_2 , Si_3N_4 , or photoresist in the absence of a discharge.

Presumably, much of the contrast in the etch rates of NF_3 and CF_4 can be attributed to the fact that all constituent products of the NF_3 discharge are gases and the problem of carbon build up is nonexistent (13).

The same type of experiments, as described for CF_4 , were performed using NF_3 as the etch gas. The 704 nm emission intensity from a discharge in NF_3 is much larger than from a discharge in CF_4 and can be enhanced as shown in Fig. 6. In contrast to the results using CF_4 , the etch rates of both Si and SiO_2 show a monotonic decrease with an increase of helium concentration.

Figure 7 shows the variation of the etch rates and saturated ion current as a function of distance from the edge of the negative glow. The etch rates of Si and SiO_2 exhibit a slow decrease with distance from the glow, as opposed to the ion current which drops rapidly. Unlike CF_4 , there appears to be no relationship between the ion current and the etch rate, even in the immediate vicinity of the discharge (compare Fig. 7 with Fig. 4 for equal values of distance). This would imply domination of the etch rate by processes involving neutral species, even close to the glow, whereas

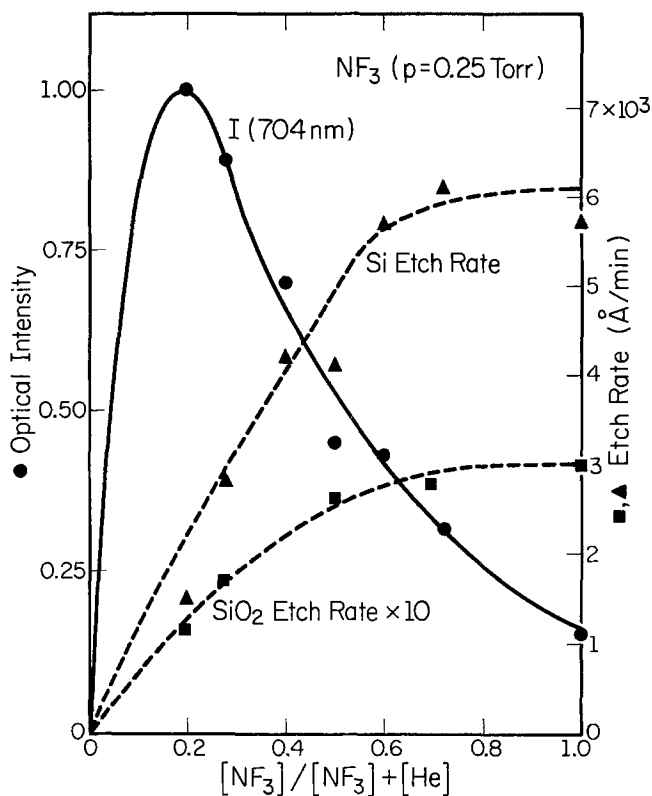


Fig. 6. Variation of 704 nm emission, Si, and SiO₂ etch rates as a function of the He partial pressure in NF₃ at a constant total pressure and current density. There is a large increase in the optical emission, similar to CF₄, yet the etch rates of both Si and SiO₂ decrease monotonically.

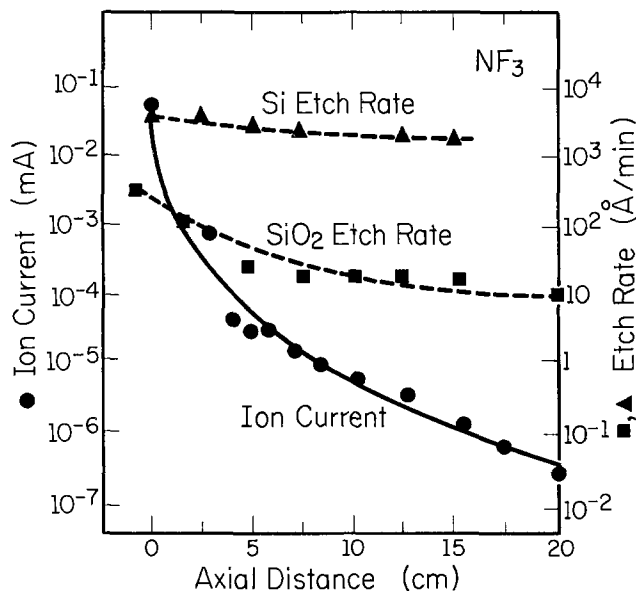


Fig. 7. Variation of the saturated ion current to the sample and etch rates of Si and SiO₂ as a function of distance from the edge of the glow.

CF₄ exhibited a stronger dependence on positively charged species near the discharge.

Although it appears that neutrals play the dominant role in the case of NF₃, it is interesting to note the effect of increasing the flux of charged particles to the sample. As shown in Fig. 8, the etch rate is enhanced for a bias below floating potential and follows the positive ion current similar to the data in Fig. 5 for CF₄. When the probe is driven above floating potential, however, there is a rapid increase in the etch rate which was not observed in CF₄.

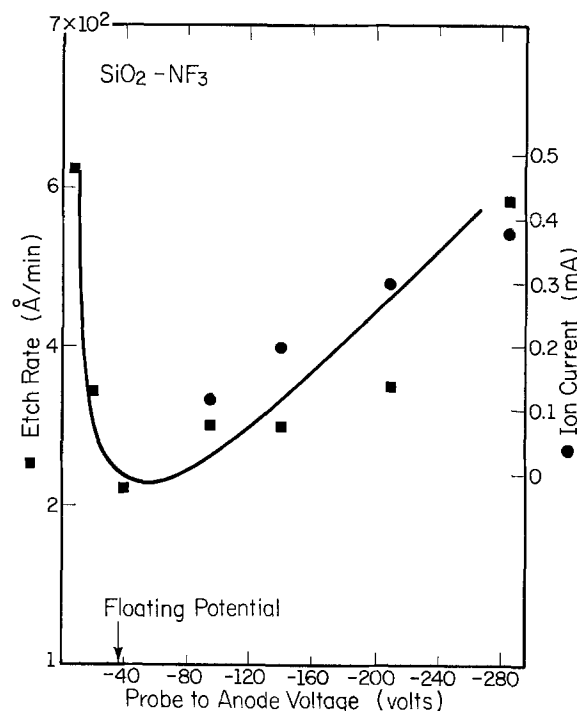


Fig. 8. Variation of the etch rate of SiO₂ and positive ion current to the sample as a function of the probe to anode voltage. There is a large etch rate increase for the small potential change when the probe is driven above floating potential, in contrast to CF₄.

To explore this difference in behavior, a simple cylindrical Langmuir probe was inserted into the discharge. The probe consisted of an 8 mil diam tungsten wire protruding 1/2 cm from the end of a glass support. The end of the wire was placed at the edge of the negative glow.

When biased below floating potential, the probe characteristics are similar for discharges in CF₄ and NF₃; however, when biased positive, there is a distinct difference as shown in Fig. 9. In the CF₄ discharge, the current increases dramatically for a 30V change above floating potential which is indicative of electrons as current carriers. This large increase does not occur in the NF₃ discharge. Instead, the current rises very

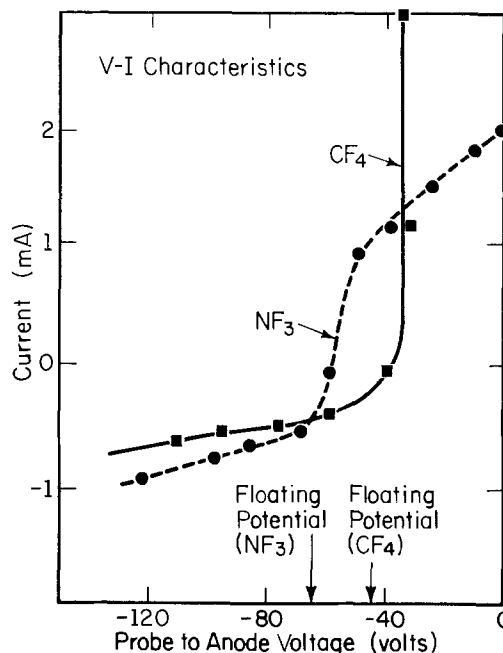


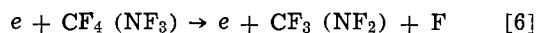
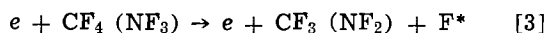
Fig. 9. Variation of the current to a Langmuir probe as a function of anode to probe voltage.

slowly, indicating that the carriers are massive negatively charged ions formed in the discharge. These characteristics are very similar to the probe characteristics of an iodine discharge, as observed by Emeleus and Woolsey, where negative ions are known to exist (18).

Conclusions

The experiments investigating the correlation between the optical emission and the etch rate of the sample show that the addition of helium to NF_3 or CF_4 discharges increases the generation rate, and thus emission, of excited fluorine; nevertheless the etch rate does not correlate with the excited state population. These data are not necessarily in contradiction with previous theories as will be discussed below.

A number of reactions should be considered in formulating a hypothesis to explain these results



Excited fluorine may be produced by the resonant energy transfer from the helium metastable according to Eq. [2] or by direct electron impact as described by Eq. [3] and [4]. On the other hand, ground state fluorine, which can be a major contributor to the etch mechanism (1, 3, 4, 19), may be produced by an electron dissociation (Eq. [6]) in addition to the processes described by Eq. [2] through [4], coupled with Eq. [5].

The dependence of the optical emission on the helium partial pressure could be attributed to a shift in the mean energy of the electron distribution function which, in turn, would affect the excitation rate of either CF_4 (NF_3) or atomic fluorine as described by Eq. [3] and [4]. This is not very likely to occur with the hollow cathode discharge, however, since most of the excitation is caused by high energy electrons which were accelerated through the cathode fall. Even though improbable, this possibility was tested by adding a trace amount of argon to CF_4 (NF_3):He mixtures and monitoring an argon emission line (20, 21). Virtually no dependence of the Ar^* emission upon the helium to fluorine donor concentration was found. Consequently, for creating excited fluorine under the experimental conditions used here, the data in Fig. 3 and 6 indicate that the excitation transfer from helium to CF_4 (or NF_3) via Eq. [2] is much more important than direct electron impact excitation.

The optical emission monitors the excited population (F^*) and not the more numerous fluorine ground state density (which was not measured during these experiments). Thus the data of Fig. 3 and 6 show that the contribution of the excitation transfer (Eq. [2]) to the production of atomic fluorine is small. This can explain why the etch rates of Si and SiO_2 in NF_3 , and Si in CF_4 , behave as shown in Fig. 3 and 6. As the helium concentration increases, the production of fluorine by reaction [6] decreases due to a dilution effect. Even though the fluorine produced via Eq. [6] is diminished, it still overwhelms the amount of fluorine produced by the reactions of Eq. [2]-[5].

The probe biasing experiments show that the etch rate of SiO_2 increases in proportion to the ion current when the probe is biased negative with respect to floating potential, for both NF_3 and CF_4 discharges. In the case of CF_4 , the increase can be attributed to physical sputtering. This does not imply, however, that ions formed in the CF_4 discharge do not contribute to the etch mechanism in other ways. In fact, the saturated ion current data in Fig. 4 indicate that processes involving positive ions dominate the etch rate near the discharge. Since the Langmuir probe characteristics indicate that the plasma potential for the CF_4 discharge is only a few volts above floating potential,

these ions will be nonballistic and contribute to the etch mechanism through a chemical process as opposed to physical sputtering (13, 22).

The probe data for NF_3 also indicate that ions formed in the discharge can contribute to the etch mechanism via chemical processes. When the probe was biased 280V negative with respect to the anode, an etch rate increase of 400 Å/min was observed (Fig. 8). Recalling that an argon discharge yielded an etch rate of only 100 Å/min, it would appear that this increase cannot be accounted for solely by physical sputtering. In addition, when the probe was biased just 20-30V above floating potential, the etch rate was enhanced by 400 Å/min for NF_3 . The Langmuir probe characteristics and electron impact studies both indicate the production of negative ions in the NF_3 discharge (23, 24). Since these negative ions could only gain 20-30V crossing the sheath, it is highly unlikely that sputtering can account for the 400 Å/min enhancement observed. Once again, the ions seem to be reacting chemically at the surface or participating vigorously in the decomposition of chemisorbed species.

In summary, there appear to be a number of processes and etchant species contributing to the etch mechanism for discharges in NF_3 and CF_4 . It is apparent, for both gases, that positive ions have the capability of contributing to the etch mechanism through chemical reactions. In addition, large quantities of negative ions also appear to be formed in NF_3 discharges; there is evidence that these ions can participate vigorously in the etch mechanism.

Manuscript submitted Sept. 19, 1980; revised manuscript received April 21, 1981. This was Paper 107 presented at the St. Louis, Missouri, Meeting of the Society, May 11-16, 1980.

Any discussion of this paper will appear in a Discussion Section to be published in the June 1982 JOURNAL. All discussions for the June 1982 Discussion Section should be submitted by Feb. 1, 1982.

Publication costs of this article were assisted by the University of Illinois.

REFERENCES

1. D. L. Flamm, *Solid State Technol.*, **22**, 109 (1979).
2. J. W. Coburn, *J. Appl. Phys.*, **50**, 5210 (1979).
3. H. F. Winters, J. W. Coburn, and E. Kay, *ibid.*, **48**, 4973 (1978).
4. J. W. Coburn and E. Kay, *Solid State Technol.*, **22**, 117 (1979).
5. C. J. Mogab, A. C. Adams, and D. L. Flamm, *J. Appl. Phys.*, **49**, 3796 (1978).
6. G. Smolinsky and D. L. Flamm, *ibid.*, **50**, 4982 (1979).
7. W. R. Harshbarger and R. A. Porter, *Solid State Technol.*, **21**, 99 (1978).
8. W. R. Harshbarger, R. A. Porter, T. A. Miller, and P. Norton, *Appl. Spectrosc.*, **31**, 201 (1977).
9. G. Herzberg, "Atomic Spectra and Atomic Structure," Chap. 1, Dover Publications, New York (1944).
10. P. F. Little and A. von Engel, *Proc. Roy. Soc. A*, **224**, 209 (1954).
11. This is the reason for its use in the fluorine laser. See J. K. Crane and J. T. Verdeyen, *J. Appl. Phys.*, **51**, 123 (1980).
12. S. T. Griffin and J. T. Verdeyen, *IEEE Trans. Electron Devices*, **ed-27**, 602 (1980).
13. J. W. Coburn, H. F. Winters, and T. J. Chuang, *J. Appl. Phys.*, **48**, 3532 (1977).
14. H. F. Winters, *ibid.*, **49**, 5165 (1978).
15. V. J. Minkiewicz and B. N. Chapman, *Appl. Phys. Lett.*, **34**, 192 (1979).
16. N. J. Ianno and J. T. Verdeyen, Abstract 107, p. 283, The Electrochemical Society Extended Abstracts, St. Louis, Missouri, May 11-16, 1980.
17. K. M. Eisele, Abstract 108, p. 285, The Electrochemical Society Extended Abstracts, St. Louis, Missouri, May 11-16, 1980.
18. K. G. Emeleus and G. A. Woolsey, "Discharges in Electronegative Gases," Chap. 1, Barnes and Noble, New York (1970).

19. D. L. Flamm, C. J. Mogab, and E. R. Sklaver, *J. Appl. Phys.*, **50**, 6211 (1979).
20. S. T. Griffin, Ph.D. Thesis, University of Illinois (1979).
21. J. W. Coburn and M. Chen, *J. Appl. Phys.*, **51**, 3134 (1980).
22. L. D. Bollinger, *Solid State Technol.*, **20**, 66 (1977).
23. R. M. Reese and V. H. Dibeler, *J. Chem. Phys.*, **24**, 1175 (1956).
24. J. C. J. Thynne, *J. Phys. Chem.*, **73**, 1586 (1969).

Dielectric Breakdown and Device Evaluation of Fritted Glass Compositions

D. L. Flowers*

Motorola, Semiconductor Research and Development Laboratory, Phoenix, Arizona 85008

ABSTRACT

Dielectric breakdown studies have been conducted on glass compositions of interest for device passivation. It was found that a 900°C sealing glass, 50 weight percent (w/o) lead oxide, 10 w/o alumina, 40 w/o silica gave dielectric breakdown protection two to three times greater than 1 micrometer of thermal SiO₂ or CVD phosphosilicate glass. The dielectric strength of this glass (168 V/μm) is lower than that of thermal SiO₂ (780 V/μm) or CVD phosphosilicate glass (840 V/μm). When 3% or 11% B₂O₃ is substituted for small amounts of the constituents in a 70 w/o PbO, 20 w/o SiO₂, 10 w/o Al₂O₃ glass, sealing temperature is lowered from 850° to 650° or 560°C, respectively. Dielectric strength is also lowered from 300 to 50 V/μm. It is shown that these low sealing temperatures, low dielectric strength glasses, could protect moat etched devices from arcing with avalanche breakdowns to a targeted 1.3 kV but reverse leakage is quite high, i.e., 300-500 μA at 1 kV. This compares to the 50 w/o PbO glass with 20 μA leakage and the 70 w/o PbO glass (850°C) with 10 μA leakage at 1 kV. In an attempt to obtain lower fusion temperatures and to overcome the high leakage seen with the boron-containing glasses, a new glass without boron was made. It contains 5 w/o GeO₂ and 5 w/o ZnO in place of like amounts of SiO₂ and Al₂O₃ in the 70 w/o PbO glass mentioned above. The fusion temperature was reduced from 850° to 650°C. When used on moat etched devices as a passivant, the new glass protected easily to 1.3 kV with only 10 μA reverse leakage at 1 kV similar to the parent 850°C fusing glass. The properties of this glass make it an excellent candidate as a passivant for devices where a relatively low fusion temperature is required.

Dielectric breakdown of device passivation is of prime importance to the semiconductor industry. Both yield and reliability are directly impacted by the quality and type of passivation used. Dielectric breakdown of thermally grown films of silica and phosphosilicate glass have been reported by Snow *et al.* (1). The effect of processing parameters on the breakdown has also been reported (2). Distefano *et al.* (3) developed a theoretical model which explains the "primary" or electronic breakdown of the films categorized by Fritzsche (4). According to the latter author, there are also "secondary" and "tertiary" breakdown modes. The secondary breakdown mode is postulated to be due to inhomogeneities in the film, perhaps crystallites of quartz in the amorphous silica in the case of SiO₂. The tertiary, lowest voltage breakdown is assumed to be due to pinholes or weak spots in the film.

Passivation of semiconductor devices by fused, fritted glass films has been used extensively in the industry but no studies of the dielectric breakdown behavior of these films on silicon have been reported. It was the purpose of this work to determine the dielectric breakdown of some glass compositions fusing between 560° and 900°C (5). They can be described as derivatives of lead-alumino-silicates containing small amounts of boron, germanium, zinc, and/or cadmium oxides to modify fusion temperature. It was a further objective to determine their limitations for device use. Some unexpected differences in behavior

compared to that of silicon dioxide and phosphosilicate glass passivation were noted.

Experimental

Wafers used in this study were 5.1 cm in diameter, 430 μm thick. They were <100> phosphorus-doped, CZ, 0.001-0.074 Ω-cm material. Cleaning before glass application was done by: (i) 1 min 10:1 H₂O:48% HF at 50°C; (ii) 20 min DI cascade water rinse; (iii) 20 min piranha (85% H₂SO₄, 15% H₂O₂) at 100°C; (iv) 20 min DI cascade water rinse; (v) 1 min 10:1 H₂O:48% HF at 50°C; (vi) 20 min DI cascade water rinse; (vii) blow dry-N₂.

The fritted glass, suspended in an organic solvent-polymeric binder, was spun on the wafers and photolithographically patterned with a conventional contact aligner. They were then fused in an air ambient for 5 min at temperatures noted in the text.

To compare with the dielectric breakdown for the fritted glass compositions, some wafers were steam oxidized at 1000°C and tested. Thicknesses obtained were 550 and 960 nm. In addition CVD passivation was also applied to test wafers and evaluated. The CVD film was a sandwich structure of 200 nm of undoped SiO₂ at the air and silicon interface and 400 nm of 4 weight percent (w/o) phosphorus-doped SiO₂ in the middle. Aluminum dots, 500 nm thick, were evaporated on the glassed wafers through a metal mask (cold substrate.) Two patterns were evaluated to determine the effect of dot size and proximity on the dielectric measurements. These were 500 μm dots, 1240 μm apart, or, 940 μm dots, 6000 μm apart.

* Electrochemical Society Active Member.
Key words: glass, passivity, defects.

Wafers were probed with a Tektronix Model 576 curve tracer with either a standard 2.5 kV or a high voltage 5 kV attachment. Applied voltage was ramped at ~ 100 V/sec until breakdown occurred. Probing was done in the d-c mode with the dots biased positively or negatively as follows: (i) In an air ambient; (ii) wafer surface covered with xylene; (iii) wafer surface dehydrated by a hexamethyl disilazane (HMDS) treatment. This consisted of spinning the material on the wafer (3K rpm, 30 sec) and baking 2 min, 200°C, N₂.

Four of the glasses were tested on p+n moat-etched, high voltage diodes. The moat depth was 80 \pm 5 μ m.

Results and Discussion

Dielectric breakdown of steam oxide and phosphosilicate glass (CVD).—To compare the results of this study of glass compositions, the dielectric breakdown of steam grown SiO₂ and a CVD phosphosilicate glass sandwich was evaluated. The measured dielectric strength of steam SiO₂ was 675 \pm 60 V/ μ m for the 550 nm film and 781 \pm 130 V/ μ m for the 960 nm film. The phosphosilicate glass sandwich had a somewhat higher value, 846 \pm 104 V/ μ m. The dielectric strength for steam oxide is in the midrange of that reported by Klein *et al.* (6, 7) and is somewhat higher than that reported by Deal (8). The higher value for phosphosilicate glass, also observed by Chou and Eldridge (2), is attributed to the phosphorus in the glass.

For device types having high avalanche breakdown voltages, (>1 kV), the use of steam oxide as a passivant is not commercially attractive because the time required to grow very thick oxide is quite long and thick oxide films tend to crack. Also, the inherent positive charge at the oxide interface tends to limit the breakdown (avalanche) that can be achieved. The glass passivation process overcomes these drawbacks of time and positive interfacial charge (9). In addition, the higher dielectric constant ($\epsilon = 10$ -17) of the glasses compared to amorphous SiO₂ ($\epsilon = 3.9$) can drop a greater portion of the applied voltage across the glass thickness to minimize the danger of air ionization.

Dielectric breakdown of 900°C sealing glasses.—The composition of the glasses examined in this section are shown in Table I and results of breakdown studies are shown in Table II. The effect of probe ambient and glass thicknesses on the breakdown properties are also included. It is seen that the breakdown voltage for 5-16 μ m films is much higher than that for commonly used thicknesses of steam oxide or phosphosilicate glass passivation discussed earlier. However, the dielectric strength of the glasses is seen to be lower than that of steam oxide or the phosphosilicate glass sandwich. It is interesting to note that the dielectric strength of these glasses is much greater when measured on thinner films. This is taken as evidence that a higher strength dielectric region above silicon is formed when fusing the glass powder. The nature of the high dielectric strength interface is unknown. If one considers that only 50Å of oxide should be grown on silicon in the 10 min fusion of the fritted glass powder at 900°C in dry oxygen, only about 4V can be added to the breakdown voltage of the film.

The mode of breakdown for these glasses is different than that for steam oxide or phosphosilicate glass. The

Table II. Dielectric breakdown of 900°C sealing glasses

| | Glass thickness (μ m) | Probe ambient | Breakdown voltage (V) | Dielectric strength (V/ μ m) | Breakdown mode |
|------|----------------------------|---------------|-----------------------|----------------------------------|--|
| 1. A | 16.0 \pm 1.5 | Air | 1760 \pm 153 | 110 \pm 10 | Continuous arc |
| | 7.0 \pm 0.5 | Air | 1133 \pm 374 | 162 \pm 47 | Continuous arc |
| | 16.0 \pm 1.5 | Xylene | 2020 \pm 273 | 127 \pm 16 | Continuous arc |
| | 7.0 \pm 0.5 | Xylene | 2005 \pm 335 | 286 \pm 49 | Continuous arc |
| 2. B | 14.0 \pm 2.1 | Air | 1450 \pm 87 | 103 \pm 6 | Continuous arc |
| | 5.5 \pm 1.0 | Air | 1305 \pm 167 | 228 \pm 30 | Continuous arc |
| | 14.0 \pm 2.1 | Xylene | 2133 \pm 34 | 152 \pm 3 | Continuous arc |
| | 5.5 \pm 1.0 | HMDS | 1565 \pm 172 | 284 \pm 31 | Self heal arc at 1300-1400V, arcs continuously |
| 3. C | 17.5 \pm 1.5 | Air | 1730 \pm 177 | 99 \pm 10 | Continuous arc |
| | 15.2 \pm 1.3 | Air | 1300 \pm 200 | 86 \pm 13 | Continuous arc |
| | 17.5 \pm 1.5 | Xylene | 2500 \pm 320 | 143 \pm 18 | Continuous arc |
| | 15.2 \pm 1.3 | Xylene | 2450 \pm 270 | 160 \pm 18 | Continuous arc |
| 4. D | 20.5 \pm 1.5 | Air | 2052 \pm 263 | 100 \pm 13 | Continuous arc |
| | 17.0 \pm 2.0 | Air | 1952 \pm 162 | 115 \pm 9 | Continuous arc |
| | 10.5 \pm 2.0 | Air | 1750 \pm 195 | 165 \pm 18 | Continuous arc |
| | 20.5 \pm 1.5 | Xylene | 2550 \pm 480 | 125 \pm 23 | Continuous arc |
| | 17.0 \pm 2.0 | Xylene | 2167 \pm 167 | 127 \pm 13 | Continuous arc |
| | 10.5 \pm 2.0 | HMDS | 196 \pm 182 | 182 \pm 17 | Continuous arc |

latter two passivants broke down in a single event. This has been attributed by Fritzsche to be ultimate or electronic breakdown occurring between 700 and 900 V/ μ m (4). The deposited glasses however, in the thickness used, break down by a different mechanism, which occurs before the ultimate or electronic breakdown potential is reached. Further, it takes place by an arcing mechanism from the edge of the dot being probed and to several millimeters across the glass. Arcing continues until part of the metal on the dot has burned away, the glass fails, and the device shorts. This manner of breakdown has been described by Klein *et al.* as a single hole event propagating to adjacent sites (6, 7). The ultimate dielectric strength of the glass was not determined because the films were too thick to reach ultimate breakdown before arcing occurred.

By using a xylene film on the wafers being probed, a closer approach to electronic breakdown was made but not reached. Treatment of the glassed wafer surface by HMDS which removes adsorbed water gave effects similar to xylene.

Dielectric breakdown of glasses fusing at or below 850°C.—There is often a need in device technology for passivation glasses fusing well below 900°C, *e.g.*, premetallized wafers, shallow junction devices, etc. A number of such glasses were prepared and their breakdown properties were evaluated and correlated with composition. The glasses, their composition, and fusion temperature are shown in Table III. As can be seen in glass H and glass I, small amounts of boron added to the glass system lead, alumino silicate greatly depress the sealing temperature. As a result these are of great interest in extending device technology.

Dielectric breakdown associated with these glasses is shown in Table IV. The highest dielectric breakdown

Table I. Composition of 900°C sealing glasses

| Glass | Composition |
|-------|---|
| A | 40 w/o SiO ₂ : 50 w/o PbO : 10 w/o Al ₂ O ₃ |
| B | 3 w/o V ₂ O ₅ replacing PbO in A |
| C | 2.8 w/o Mn ₂ O ₃ replacing PbO in A |
| D | 1.3 w/o V ₂ O ₅ + 1.3 w/o Mn ₂ O ₃ replacing PbO in A |

Table III. Composition of glasses fusing below 850°C

| Glass | Composition | | | | | | Fusion temperature (°C) |
|-------|------------------|-----|--------------------------------|-------------------------------|-----|-------|-------------------------|
| | SiO ₂ | PbO | Al ₂ O ₃ | B ₂ O ₃ | ZnO | Other | |
| E | 20 | 70 | 10 | | | | 850° |
| F | 38 | 42 | 10 | | 10 | | 800° |
| G | 20 | 40 | 9 | 20 | 10 | 1 CdO | 750° |
| H | 18 | 70 | 9 | 3 | | | 650° |
| I | 22 | 62 | 5 | 11 | | | 560° |

Table IV. Dielectric breakdown of glasses fusing below 850°C

| Glass thickness (μm) | Probe ambient | Break-down voltage (V) | Break-down strength ($\text{V}/\mu\text{m}$) | Breakdown mode |
|-----------------------------------|---------------|------------------------|--|------------------------------|
| 1. E (850°C) | | | | |
| 7.5 \pm 1.0 | Air | 2223 \pm 86 | 296 \pm 11 | Single spark event breakdown |
| 6.5 \pm 1.0 | Air | 1950 \pm 77 | 301 \pm 12 | Single spark event breakdown |
| 7.5 \pm 1.0 | Xylene | 2333 \pm 92 | 310 \pm 12 | Single spark event breakdown |
| 6.5 \pm 1.0 | Air | 2000 \pm 65 | 309 \pm 10 | Single spark event breakdown |
| 2. F (800°C) | | | | |
| 7.1 \pm 1.0 | Air | 910 \pm 205 | 128 \pm 29 | Continuous arc breakdown |
| 7.1 \pm 1.0 | Xylene | 1450 \pm 165 | 208 \pm 23 | Single spark event breakdown |
| 3. G (750°C) | | | | |
| 13.2 \pm 1.0 | Air | 488 \pm 143 | 37 \pm 11 | Single spark event breakdown |
| 10.7 \pm 1.5 | Air | 400 \pm 55 | 38 \pm 5.0 | Single spark event breakdown |
| 13.2 \pm 1.2 | HMDS | 510 \pm 20 | 39 \pm 1.4 | Single spark event breakdown |
| 4. H (650°C) | | | | |
| 16.5 \pm 1.5 | Air | 844 \pm 163 | 51 \pm 10 | Single spark event breakdown |
| 16.5 \pm 1.5 | HMDS | 1040 \pm 72 | 63 \pm 4.3 | Single spark event breakdown |
| 5. I. (560°C) | | | | |
| 6.0 \pm 1 | Air | 300 \pm 25 | 50 \pm 3.8 | Single spark event breakdown |
| 6.0 \pm 1 | HMDS | 310 \pm 20 | 52 \pm 3.3 | Single spark event breakdown |

strength of the glasses tested in the entire study was seen in glass E. The value of 301 $\text{V}/\mu\text{m}$ is much higher than that of glass A, 162 $\text{V}/\mu\text{m}$. A notable observation separating these glasses from those reported in Table II is that the breakdown mode (except for glass F—air probe ambient) has changed from continuous surface arcing to a single hole or spark event similar to that reported by Fritzche (4). Single event breakdown occurs before surface leakage causing arcing type breakdown. Changing the probe ambient from air to xylene or HMDS changes the measured dielectric strength very little for the boron glasses consistent with single event breakdown. For the zinc containing glass F, however, the use of xylene changed the mode of breakdown from multiple event (arcing) to single event. As such, the breakdown strength was improved 62%. This illustrates how changing constituents in the glass can change the breakdown mode.

Correlation of dielectric strength and fusion temperature with composition.—Figure 1 compares dielectric strength and fusion temperature as they are varied by glass composition. It is seen that the addition of only 3% boric anhydride, to glass A lowers the fusion temperature from 900° to 650°C. However, the dielectric strength is depressed 60%. The addition of 10% zinc oxide, glass F, lowers the fusion temperature 100°C yet depresses the dielectric strength only slightly. Increasing the concentration of lead oxide from 50%, glass A to 70%, glass E, decreases the fusion tempera-

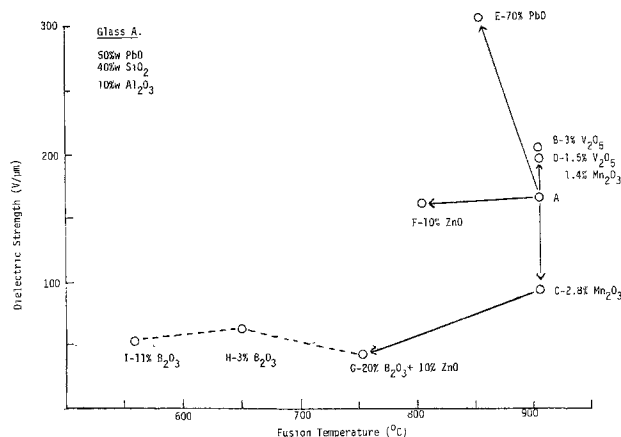


Fig. 1. Dielectric strength and fusion temperature for various glass compositions (ref: Table I and Table III).

ture 50°C but raises the dielectric strength 83%. In the glasses fusing at 900°C, the addition of 3% vanadium pentoxide, glass B, raises the dielectric strength 21% but the addition of 2.8% Mn_2O_3 , glass C, lowers it 44%. These results illustrate an important effect that small changes in glass composition have on fusion temperature and dielectric strength.

Evaluation of moat etched diodes passivated with low temperature fusion glasses.—Because the breakdown voltage of many devices used with glass passivation is considerably higher, $\text{BV} = 1\text{--}2\text{ kV}$, than the observed dielectric breakdown of the passivation, particularly the boron-containing glasses, it was decided to test the 11% boric anhydride glass, I, on a moat-etched, high voltage diode. Comparison with diodes passivated by higher dielectric strength glasses A and E would help qualify the boron-containing, low temperature glasses for high voltage device use. In addition, a glass containing 5% germanium oxide, and 5% zinc oxide to depress the fusion temperature of glass A was also tested, glass 3, 650°C fusion, for potential use if the boron-containing glass failed to qualify. The germanium oxide glass was expected to have better dielectric properties than the boron glass because of germanium's relation to silicon in the periodic table. Results are shown in Table V.

The breakdown voltages at avalanche on the diodes with all four glasses were about the same. The leakage of the boron containing glass I was quite high. This means that boron in the glass is introducing easily activated surface states at the interface. Photosensitivity experiments also confirm the presence of added surface states as shown later. In addition, immediately after sealing, the boron-containing glass evidences some electronic instability which disappears after 24 hr storage at room temperature. The germanium zinc containing glass J with no transient electronic instability has the lowest leakage of all.

Table V. Breakdown (avalanche) properties of moat-etched diodes passivated with selected glass composition

| Glass fusion T (°C) | Composition (w/o) | I_R at 1 kV (μA) | | BV at I_R (μA) (kV) After 24 hr |
|---------------------|---|-----------------------------------|--------------|--|
| | | After fuse | After 24 hr | |
| 1. No glass | ~10A native oxide | Walkout to ~400V, tendency to arc | | |
| 2. A (900°C) | 40 50 10 $\text{SiO}_2\text{-PbO-Al}_2\text{O}_3$ | 20 \pm 8 | 20 \pm 8 | 1.25 \pm 0.04 (20 \pm 5 μA) |
| 3. J (650°C) | 15 5 70 5 5 $\text{SiO}_2\text{-GeO}_2\text{-PbO-Al}_2\text{O}_3\text{-ZnO}$ | 12 \pm 5 | 12 \pm 5 | 1.29 \pm 0.03 (10 \pm 2 μA) |
| 4. I (560°C) | 22 62 11 5 $\text{SiO}_2\text{-PbO-B}_2\text{O}_3\text{-Al}_2\text{O}_3$ | Channel off scale ~500V | 220 \pm 80 | 1.30 \pm 25 (>500 μA) |
| 5. E (850°C) | 20 70 10 $\text{SiO}_2\text{-PbO-Al}_2\text{O}_3$ | — | 10 \pm 2 | 1.28 \pm 0.06 (10 \pm 2 μA) |

In another set of experiments to further qualify and characterize glass J and glass I, the firing temperature of these glasses on moat etched diodes was investigated. Results are shown in Table VI. The breakdown and leakage obtained in both these glasses are improved by raising the firing temperature about 50°C. The wafers were tested with and without a film of xylene on them to determine any change in breakdown voltage or leakage due to the added dielectric film. There was none.

The final point that was briefly studied here concerns photocurrent in the glasses diodes. On first testing it was noted that glass I caused the diodes to become very photosensitive with large channel currents developing. To test the photocurrent in a semiquantitative way, wafers with no glass, glass J, and glass I were probed in darkness and in dimmed room light at 5 and 10V. Details are shown in Table VII.

These data show that the diode without passivation has leakage currents that are enhanced by light due to photosensitive states that are at or near the silicon oxide interface. Passivation with glass J does very little to change that leakage. Glass I, on the other hand, introduces additional surface states illustrated by higher leakage, enhanced by illumination. The reason for these states is evidently related to the boron in the glass. Although not studied in this work, qualitative earlier observations indicated that glass A has light sensitivity similar to glass J.

Summary and Conclusions

Eight glass compositions were studied with respect to their dielectric breakdown behavior. This was done to help characterize fritted glass device passivation and screen new candidates for product use. Fusion temperatures for the glasses tested ranged from 900° to 560°C. To achieve the fusion temperature range noted, the base glass A composition was suitably modified. This was most noticeably effected by varying the composition ratios and by the addition of small amounts of ZnO, B₂O₃, CdO, or GeO₂. The dielectric breakdown of steam oxide and a CVD phosphosilicate glass sandwich were compared with that of the fused glass powders.

It was shown that the dielectric breakdown of glass A, 1.1-1.8 kV, for thicknesses of 1-16 μm, is considerably higher than that of steam oxide (0.73 kV for 1 μm). The application of a film of xylene or HMDS treatment on the surface of the test device did not change the

value of the breakdown voltage of steam oxide or phosphosilicate glass. It did increase the measured breakdown voltage to 2.0-2.3 kV for the tested lead aluminosilicates, glasses A and E.

The mode of breakdown for steam oxide or the phosphosilicate glass sandwich is a single hole event indicative of electronic (primary) breakdown of the passivation. The mode of breakdown for the lead aluminosilicates was distinctively different. Electronic breakdown was not reached before surface arcing occurred. This has been described as a multiple site event with initiation at the probe site followed by propagation (arcing) to adjacent sites. The application of the xylene film or HMDS treatment on the lead aluminosilicates did not change this mode of breakdown. It significantly raised the threshold value. This is taken to mean that surface leakage causing significant voltage drops along the surface is causing arcing. The xylene film or HMDS treatment reduces the leakage and hence raises the threshold voltage for arcing.

The calculated dielectric strength increased for all of the fritted glass powder passivants tested as the thickness decreased. This is taken to mean that a higher dielectric strength region exists between the fused glass film and the silicon wafer. The reason for this is unknown. The highest dielectric strength measured, 305 V/μm, was that of glass E which contains 20 w/o more PbO than does glass A which has a dielectric strength of 168 V/μm, both being measured 6 μm thick. Lowest dielectric strengths were seen with the glasses containing small amounts of boron, 40-50 V/μm. The lead aluminosilicates breakdown in a multiple event without reaching electronic breakdown, while the boro lead aluminosilicates display primary or single event breakdown with the low dielectric strength noted.

To determine if low dielectric strength boron containing glass I fusing at 560°C could be used to passivate high voltage devices, it was applied, patterned, and fused on p⁺n diode wafers with targeted avalanche breakdown to ≧1.0 kV. A new glass, J, was also prepared using germanium and zinc to lower the fusion temperature to 650°C. Probe results showed the boron-containing glass I did allow the diodes to reach stable, high voltages, >1.0 kV, without breakdown of the passivation. Reverse leakage was quite high, however; >300 μA at 1 kV. The germanium-zinc glass also allowed high, stable voltages, >1.0 kV, to be reached with the additional advantage of low reverse leakage, i.e., ~10 μA at 1 kV cf. 20 μA for glass A, the standard 900°C fusing glass.

From these results it is concluded that glasses without boron could be used for high voltage passivation. The new glass, J, using germanium and zinc to lower fusion temperature, is a strong candidate for a lower temperature glass passivant.

Acknowledgments

The author is greatly indebted to Earl Davis of the Ceramics Department for the preparation of the various glasses used in this study. He also wishes to thank Mrs. Eileen Uravitch for help with the glassing process.

Manuscript submitted Nov. 19, 1981; revised manuscript received Feb. 23, 1981.

Any discussion of this paper will appear in a Discussion Section to be published in the June 1982 JOURNAL. All discussions for the June 1982 Discussion Section should be submitted by Feb. 1, 1982.

Publication costs of this article were assisted by Motorola.

REFERENCES

1. E. H. Snow and B. E. Deal, *This Journal*, **113**, 263 (1966).
2. H. J. Chou and J. M. Eldridge, *ibid.*, **117**, 1287 (1970).

Table VI. Comparison of diode breakdown voltage for glass I and glass J fused at different temperatures*

| Glass | Firing temp. (°C) | BV (kV) at I _r (μA) |
|-------|-------------------|-----------------------------------|
| 1. J | 650° | 1.29 ± 0.03 avalanche 10 ± 2 |
| | 700° | 1.38 ± 0.04 avalanche 5 ± 2 |
| 2. I | 560° | 1.30, soft, no avalanche >500 μm |
| | 600° | 1.60, soft, no avalanche 333 ± 28 |

* Evaluated 24 hr after glass fusion.

Table VII. Determination of photocurrent in glass I and glass J

| Glass | Voltage | Reverse current (nA) | | Photocurrent (nA) |
|--|---------|----------------------|------------|-------------------|
| | | Light off | Light on | |
| 1. None | 5 | 100 ± 50 | 800 ± 50 | 700 ± 100 |
| | 10 | 150 ± 50 | 1000 ± 50 | 850 ± 100 |
| 2. J (5% Al ₂ O ₃ , 5% ZnO, 5% GeO) | 5 | 150 ± 33 | 750 ± 50 | 600 ± 88 |
| | 10 | 250 ± 50 | 1050 ± 50 | 800 ± 100 |
| 3. I (11% B ₂ O ₃) | 5 | 450 ± 150 | 1500 ± 200 | 1050 ± 350 |
| | 10 | 550 ± 250 | 1600 ± 100 | 1050 ± 350 |

3. T. H. DiStefano and M. Schatzkes, Abstract 201, p. 514, The Electrochemical Society Extended Abstracts Philadelphia, Pennsylvania, May 8-13, 1977.
4. C. Fritzsche, *J. Agnew. Phys.*, **24**, 48 (1967).
5. D. L. Flowers and K. Ridgeway, Abstract 286, p. 746, The Electrochemical Society Extended Abstracts, Los Angeles, California, Oct. 14-19, 1979.
6. N. Klein, *IEEE Trans. Electron Devices*, ed-13, 798 (1966).
7. N. Klein and H. Gafni, *ibid.*, ed-13, 281 (1966).
8. B. E. Deal, *This Journal*, **110**, 527 (1963).
9. D. L. Flowers and H. G. Hughes, Abstract 240, p. 644, The Electrochemical Society Extended Abstracts, Pittsburgh, Pennsylvania, Oct. 15-20, 1978.

Microstructure and Resistivity of Laser-Annealed Au-Ge Ohmic Contacts on GaAs

O. Aina,* S. W. Chiang,* Y. S. Liu,* and F. Bacon*

General Electric Company, Corporate Research and Development Center, Schenectady, New York 12301

and K. Rose

Rensselaer Polytechnic Institute, Troy, New York 12180

ABSTRACT

The results of a study of laser-annealed Au-Ge ohmic contacts to GaAs are presented. The specific contact resistivity was observed to decrease with increasing laser energy density while the grain size of the polycrystalline microstructure (as observed by transmission electron microscopy) increased. At higher energy densities, both parameters were found to remain constant within the experimental conditions used. Transmission electron micrographs, and sputtering Auger electron spectroscopic data showing Ga, As, and Ge redistribution within the Au-Ge film are also presented.

Recent research has focused on using laser irradiation for making ohmic contacts to GaAs because the localized, short duration heating of a laser beam was expected to result in negligible GaAs decomposition and therefore improve contact quality. Results obtained for laser-annealed ohmic contacts (1, 2) have so far shown no significant improvement in contact properties over contacts made by conventional furnace alloying. A more detailed study of laser-annealed ohmic contacts, focusing on the materials properties, therefore seems necessary.

Transmission electron microscopy (TEM) is useful not only for microstructural study of materials but also for identification of material types and phases. It has been used to study the alloying of thin films of Au (3) and Au-Ge-In (4) on GaAs. However, only the microstructural properties of these contacts were investigated.

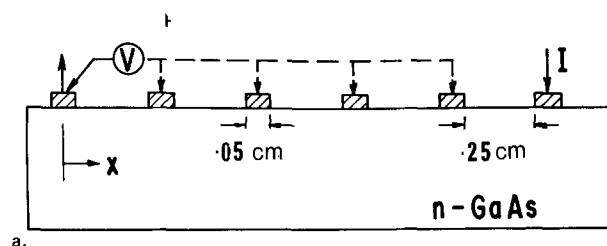
We report here a study of laser-annealed Au-Ge/GaAs ohmic contacts using TEM to correlate the microstructure and the electrical properties as obtained from specific contact resistivity measurements. Specifically, the variation of the specific contact resistivity as a function of the laser energy density was measured and is presented along with variations in the microstructure and the compositional depth profile as measured by Auger electron spectroscopy (AES).

Sample Preparation and Experimental Procedure

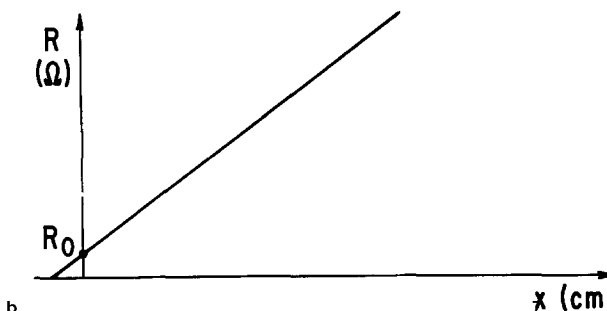
Te-doped (100) n-GaAs substrates of carrier concentration, $2 \times 10^{18} \text{ cm}^{-3}$ were used. They were first cleaned in trichlorethylene, acetone, and methanol. An oxide was then grown in deionized water and etched off with HCl. An Au-Ge layer of 1000Å thickness was deposited in vacuum (2×10^{-6} Torr) from an alloy of eutectic composition [Au-Ge(12%)] which was evaporated to completion in a resistance heated tungsten boat. This deposition was done through a metal evaporation mask of parallel slits that resulted in the contact structure shown in Fig. 1.

Ohmic contacts were formed by single pulse irradiation of the AuGe film with a pulsed Nd-YAG laser of 1.06 micron wavelength, 30 nsec pulse duration, and beam spot diameter of 0.1 cm. The pulse energy density was varied from 0.6 to 3 J/cm².

The ohmicity of the contacts was determined from curve tracer I-V plots while the specific contact resistivity was determined by a four-probe measurement technique as shown in Fig. 1. Current (10 mA) is passed through two of the contact pads while the voltage between one of the current-carrying pads and



a.



b.

Fig. 1. (a) Four-point probe geometry for ohmic contact measurements; (b) resistance measured as a function of distance.

* Electrochemical Society Active Member.

Key words: semiconductor, alloy, contacts, analyses, infrared.

each of the inner pad is measured. The resistance variation as shown in Fig. 1b has been derived by Schuldt (5) by solving Laplace's equation numerically with the ohmic contact plane as a boundary and is given by

$$R(x) = (\rho_B/HW)X$$

$$+ (\rho_B/\pi w) \ln 4 / (1 - \exp(-\pi D/H)) + f\left(\rho_c, \frac{D}{H}\right) \quad [1]$$

where ρ_B is the bulk resistivity, H is the sample thickness, W sample width, D contact length, and $f(\rho_c, D/H)$ is a resistance parameter which is a function of the specific contact resistivity ρ_c and the ohmic contact geometry. Using R_o , the intercept from the four-probe measurements, the specific contact resistivity ρ_c , was obtained from numerical solutions for $f(\rho_c, D/H)$ (5). Prior to the measurements, the sample was scribed into rectangular strips in a direction perpendicular to the Au-Ge stripes. This was to ensure current flow paths only in the planes perpendicular to the contact plane and along the length of the GaAs strip. Equation [1] is valid only for this geometry.

The samples were prepared for TEM examination by chemical jet polishing with bromine methanol from the back side of the substrate so that only the top surface was observed.

Results

Figure 2 shows the I - V characteristics of contacts formed under various conditions. The as-deposited Au-Ge film is a rectifying contact as Fig. 2a shows, but after laser irradiation at 0.6 and 1.1 J/cm², the contact becomes ohmic (Fig. 2b, c). The change in the specific contact resistivity as the laser energy density is varied is shown in Fig. 3. It can be seen that the electrical properties of the contacts are improved at higher laser energy densities. The corresponding microstructural changes are shown in Fig. 4 in which the microstructure of the contact irradiated at 0.6 J/cm² appears similar to that of the as-deposited Au-Ge film. The grain size of the contacts irradiated at 1.1 J/cm² has increased significantly while the grains show features which were not observed in the other contacts fabricated at lower energy densities. The results obtained are summarized in Fig. 5 which compares the measured residual resistance R_o of the contacts and the corresponding grain size. At energy densities higher than 1.1 J/cm², both the specific contact resistivity and the grain size seem to remain constant.

The TEM diffraction patterns also showed changes corresponding to the formation of ohmic contacts by laser irradiation. For example, three rings can be observed in the diffraction patterns of Fig. 4b and c which do not exist in the diffraction pattern of the as-deposited AuGe film shown in Fig. 4a. By matching lattice spacings, these extra rings have been identified with germanium. The dark field image shown in Fig. 6 was obtained with the objective aperture of the TEM on the Ge(111) ring. It indicates segregation of Ge at the grain boundary. The white spots within the grains were also found to be germanium.

Using Auger analysis combined with argon ion sputtering, measurements were made on the as-deposited samples as well as the laser irradiated samples in order to observe the changes in the composition depth profile of the contacts corresponding to the observed electrical and microstructural changes (as a function of laser energy density). The elemental depth distributions of oxygen (503 eV), gallium (1070 eV), germanium (1147 eV), arsenic (1228 eV), and gold (2024 eV) are shown in Fig. 7 for the as-deposited AuGe film. The essential features of this profile (such as the sharp interface) do not change with laser irradiation. There appears, however, to be an increasing redistribution of all the elements present with increasing laser energy density. In Fig. 8, the profiles of Ga and As show a significant redistribution of these two elements.

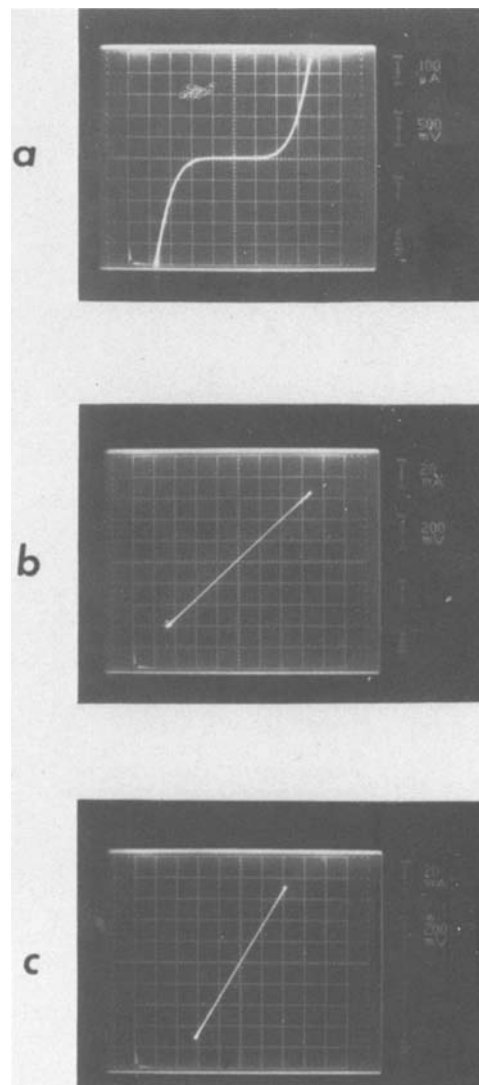


Fig. 2. Current-voltage characteristics of Au-Ge contacts. (a) As-deposited; (b) laser-irradiated at 0.6 J/cm²; (c) laser-irradiated at 1.1 J/cm².

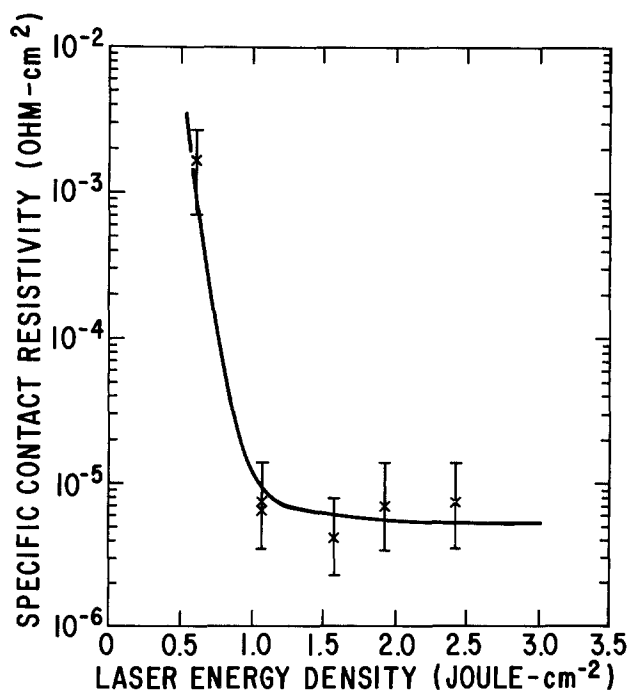


Fig. 3. Specific contact resistivity vs. laser energy density

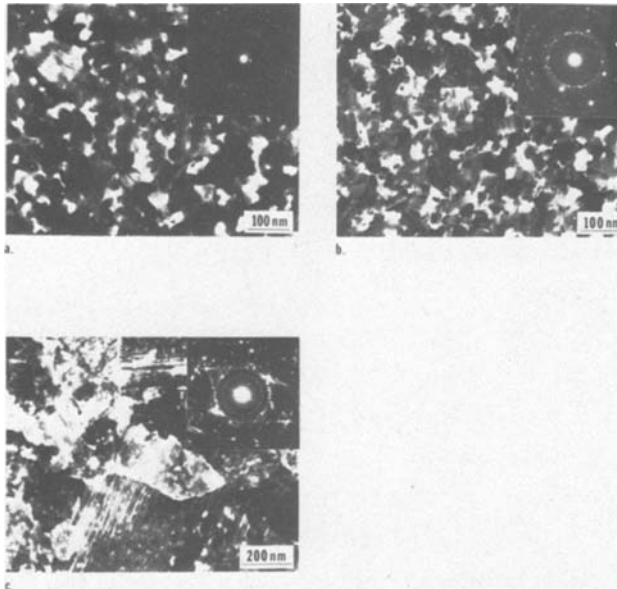


Fig. 4. TEM micrographs and diffraction patterns of Au-Ge contact films. (a) As-deposited; (b) laser-irradiated at 0.6 J/cm²; (c) laser-irradiated at 1.1 J/cm².

Within the energy density range used, this redistribution does not reach the surface and thus no gallium segregation at the surface was observed as was the case with furnace alloyed Au-Ge (and Au-Ge-Ni) ohmic contacts (6). Figure 9 shows a corresponding decrease in the Ge profile which indicates a redistribution of Ge into GaAs. This could not be confirmed by the present AES data because of the coincidence of the arsenic and germanium Auger electron transitions at 1147 eV.

Discussion

It has been observed that pulsed laser annealing of implanted semiconductors results in melting, the dura-

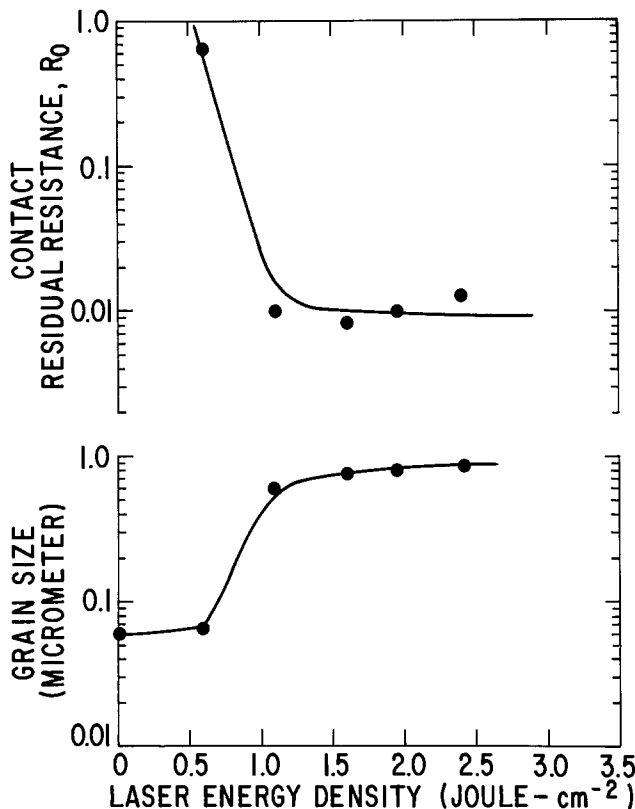


Fig. 5. Variation of the contact resistance and grain size with laser energy density.

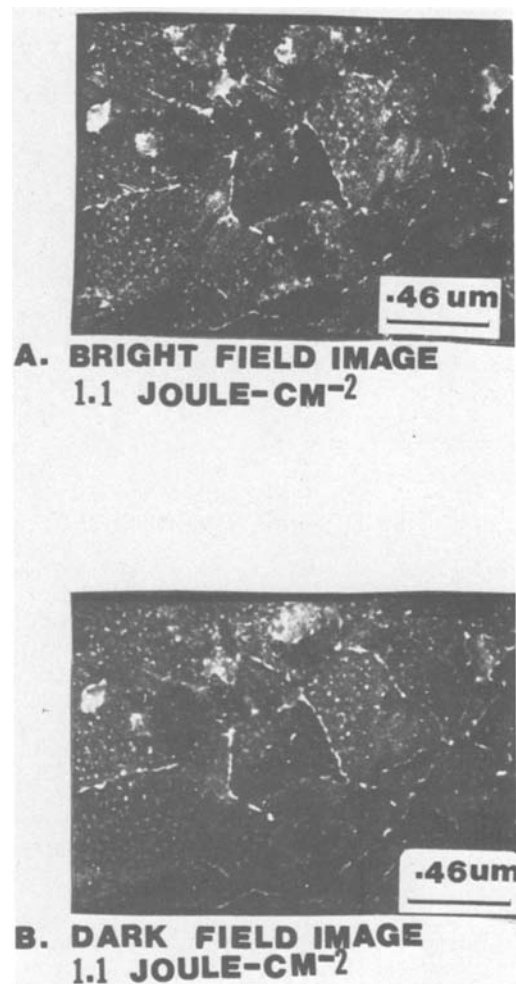


Fig. 6. TEM micrographs of laser annealed Au-Ge film showing Ge segregation at grain boundaries. (a) Bright field image, 1.1 J/cm²; (b) dark field image, 1.1 J/cm².

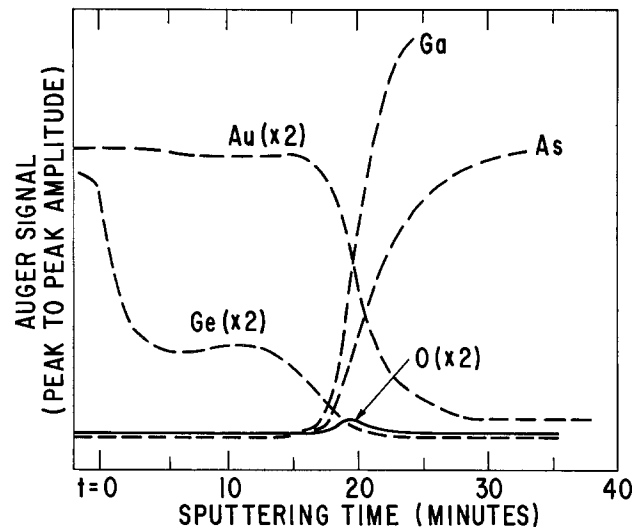


Fig. 7. Sputtered AES profiles for the as-deposited Au-Ge film on GaAs.

tion of which is longer than the pulse width of the laser beam (7, 8). Specifically, it was found that the duration of melting increased with the laser energy density and that for Te-implanted GaAs, the melt duration was approximately 1 μsec at an energy density of 1 J/cm² (7). In view of the short time periods involved in laser annealing, it seems that the drastic change in microstructure observed in this work

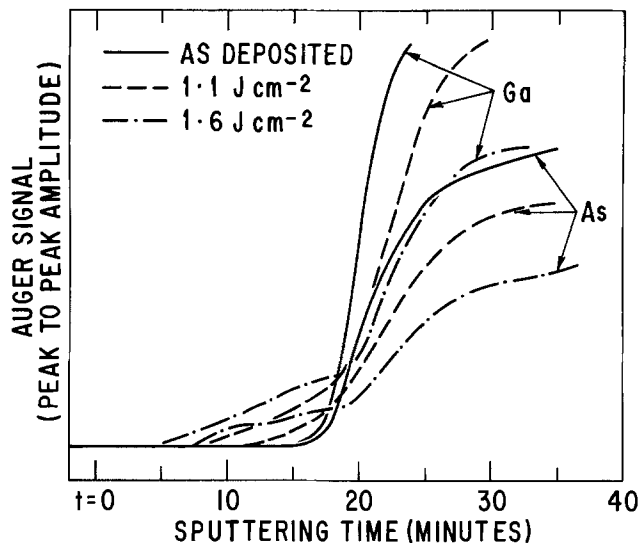


Fig. 8. Sputtered AES profiles for Ga and As before and after laser irradiation.

could not be due to solid-state diffusion (the solid-state diffusion length is much less than the grain sizes observed). This kind of microstructural change is therefore due to melting of the Au-Ge film and an adjacent layer of the GaAs substrate. By analogy with observations of laser annealing of aluminum on silicon (9), this melting is followed by rapid regrowth of Ge-rich GaAs with a top layer of alloys or compounds of Ga-Ge, Au-Ga, and Au-Ge. This kind of structure, consisting of successive layers of GaAs heavily doped with Ge; Au-Ge, Ni-Ga, and Au-Ga alloys and compounds has been observed in furnace alloyed Au-Ge-Ni ohmic contacts (10).

The grain size of a polycrystalline structure which has regrown from a melt is related to a growth parameter which is known to vary inversely as the regrowth velocity (11). The regrowth velocity however, has been shown to also vary inversely as the energy density of the laser beam (7). Thus, the increase in grain size observed in this work may be attributed to an increase in the growth parameter as a result of a decrease in the regrowth velocity with energy density. The decrease of the specific contact resistivity on the other hand may be due to an increased Ge doping of the Ge-rich GaAs layer (12). In GaAs, Ge may go into either Ga or As vacancies depending on the temperature and the vapor pressures (13) of As and Ga. It appears that the constancy of the specific contact resistivity at the higher laser energy densities is due to an increasing concentration of Ge in As sites, instead of in Ga sites as is required for n-type doping.

Our AES results showing limited redistribution of Ga and As are in contrast to previous results obtained for furnace alloyed Au-Ge-Ni ohmic contacts (6) which showed significant Ga and As concentrations at the contact surface. Limited Ga and As segregation as was found here may be due to an incomplete mixing of the melt from which the regrowth takes place. It was found for implanted Si, from numerical calculations, that the melt-front velocity is substantially greater than the velocity of mass diffusion (14). The observed AES profiles for Ga and As are thus probably related to the distribution of Ga and As in the melt which is "frozen" into the ohmic contact layer during solidification.

The observed redistributions of Ga and As can result in Ga and As vacancies in the GaAs substrate. Hence, the substrate concentration of vacancies should be higher in the furnace alloyed contacts than in the laser-annealed ones since there is less redistribution in the latter. One would therefore expect laser-annealed

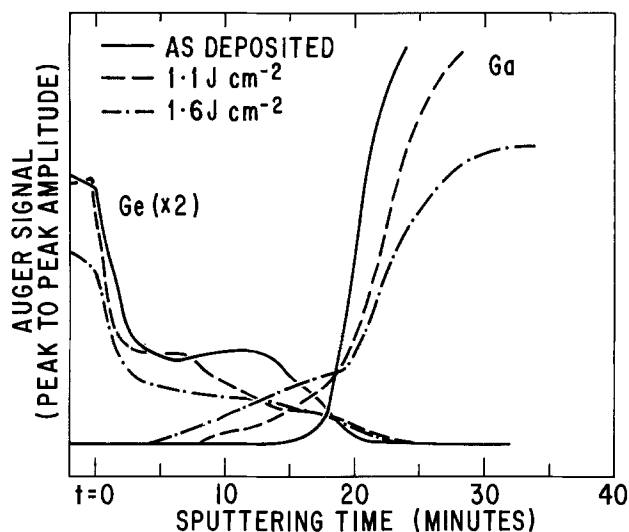


Fig. 9. Sputtered AES profiles for Ga and Ge before and after laser irradiation.

ohmic contacts to have improved contact reliability, since contact reliability has been suggested to depend on vacancy formation in GaAs (15).

Conclusion

We have presented results showing a decrease in the specific contact resistivity with energy density for laser annealed Au-Ge ohmic contacts. We have at the same time shown the correlation between the measured contact resistivity and the microstructure observed by the TEM. In addition, AES results were presented to show the redistribution of Ga and As as a result of the laser annealing.

Acknowledgment

We wish to thank Dr. B. J. Baliga for his interest in this work and Dr. W. Trantraporn for use of his vacuum evaporator and for useful discussions.

Manuscript submitted Dec. 4, 1980; revised manuscript received April 13, 1981. This was Paper 420 presented at the Hollywood, Florida, Meeting of the Society, Oct. 5-10, 1980.

Any discussion of this paper will appear in a Discussion Section to be published in the June 1982 JOURNAL. All discussions for the June 1982 Discussion Section should be submitted by Feb. 1, 1982.

Publication costs of this article were assisted by the General Electric Company.

REFERENCES

1. R. Gold, R. A. Powell, and J. F. Gibbons, 1978 Symposium on Laser-Solid Interaction and Laser Processing, AIP Conference Proceeding, #50, p. 635.
2. G. Eckhardt, C. L. Anderson, L. D. Hess, and C. F. Krumm, 1978 Symposium on Laser-Solid Interaction and Laser Processing, AIP Conference Proceeding, #50, p. 641.
3. T. J. Magee and J. Peng, *Phys. Status Solidi A*, **52**, 695 (1975).
4. J. E. Loveluck, G. M. Rackham, and J. W. Steeds, *Inst. Phys. Conf., Ser. #36*, Chapter 8 (1977).
5. S. B. Schuldt, *Solid State Electron.*, **21**, 715 (1978).
6. G. Y. Robinson, *ibid.*, **18**, 331 (1975).
7. D. H. Auston, J. A. Golovchenko, A. L. Simons, C. M. Surko, and T. N. C. Venkatesan, *Appl. Phys. Lett.*, **34**, 777 (1979).
8. K. Murakami, K. Gamo, S. Namba, M. Kawabe, and Y. Aoyagi, *ibid.*, **35**, 628 (1979).
9. H. G. Parks, PhD Thesis, Rensselaer Polytechnic Institute, Troy, New York (1980).

10. A. Christou, *Solid State Electron.*, **22**, 141 (1979).
11. J. C. Brice, "The Growth of Crystals from the Melt," John Wiley & Sons, Inc., New York (1965).
12. C. Y. Chang, Y. K. Fang, and S. M. Sze, *Solid State Electron.*, **14**, 541 (1971).
13. L. J. Vieland and T. Seidel, *J. Appl. Phys.*, **33**, 2414 (1962).
14. J. C. Wang, R. F. Wood, and P. P. Pronko, *Appl. Phys. Lett.*, **33**, 455 (1978).
15. M. Yoder, *Solid State Electron.*, **23**, 117 (1980).

Transients in the Deposition of Silicon Epitaxial Films in a CVD Reactor

R. Reif*

*Department of Electrical Engineering and Computer Science,
Massachusetts Institute of Technology, Cambridge, Massachusetts 02139*

and M. Vanzi*¹

Integrated Circuits Laboratory, Stanford University, Stanford, California 94305

ABSTRACT

The transients associated with the deposition of silicon epitaxial films in a horizontal reactor have been investigated. An understanding of these transients is important for the fabrication and control of the submicron films that will be required to accommodate VLSI designs. In order to investigate these transients, several experiments were carried out in which the steady-state deposition of epitaxial silicon was perturbed by abruptly varying the flow of silicon species entering the reactor. The response of the epitaxial system to these perturbations was determined by measuring the resulting dopant distribution in the silicon film. A physical model that emphasizes the role of the adsorbed layer on the silicon surface was used to explain and simulate the behavior of the epitaxial system. By comparing theoretical simulations and experimental results, the time constant of the silicon deposition process was estimated to be in the 20-30 sec range.

Submicron silicon epitaxial films are becoming increasingly important with the development of VLSI technology. Epitaxial layer thicknesses in the 0.5-1.5 μm range are needed to accommodate the small cell sizes required for VLSI designs. The transients associated with the first few minutes of growth, however, impose severe limitations on the fabrication of such thin films. As is described elsewhere (1), the dopant incorporation process in a silane/arsine epitaxial system requires several minutes to regain steady state when a perturbation such as a step change in dopant gas flow is imposed on the reactor. Similarly, the dopant incorporation process requires several minutes to reach the expected steady-state condition at the beginning of the deposition step (2). Consequently, the epitaxial dopant concentration reaches the expected doping level only for films thicker than that corresponding to this initial transient. Because this transient period corresponds to a transition layer 1-2 μm thick, the expected steady-state doping level may not be achieved in submicron silicon films.

In addition to the dopant incorporation process, the silicon deposition process must also go through a transient period during the initial stages of growth, i.e., some time is required before the expected steady-state epitaxial growth rate is established. A complete understanding of the transients associated with both the dopant incorporation and silicon deposition processes is critical to the fabrication and control of submicron epitaxial films.

The dopant incorporation process has been the subject of previous investigations (1-4). The work presented here deals primarily with the silicon deposition

process. The main objective of this work was to investigate the transient associated with the establishment of a steady-state silicon growth rate and the effect of this transient on the epitaxial doping level. The simplest technique that could have been used to determine this transient was to carry out a series of depositions for different growth times and then measure the resulting epitaxial layer thicknesses. However, this method is imprecise because very short initial time intervals are needed in order to obtain information on the initial transient. Moreover, the effect of the initial transient on the film thickness could get compensated by that of the final transient, thereby concealing the information being sought. The most desirable approach would be to measure the film thickness continuously as the film is being deposited. Dumin (5) developed an interferometric technique that measured the thickness of silicon films as they were being deposited on sapphire substrates. This technique utilized the infrared emission from the sapphire substrate and from the growing film. The radiation from the sapphire substrate was partially transmitted through the silicon and partially reflected in the silicon, establishing an interference pattern which was used to determine silicon film thickness. Shaw (6), on the other hand, developed a gravimetric technique in which the weight of the growing gallium arsenide crystal was continuously measured. The use of these techniques, however, poses several difficulties when applied to the epitaxial deposition of silicon. The interferometric technique is best suited to cases in which the index of refraction of the film being deposited is different from that of the substrate, while the gravimetric technique measures not only the weight of the substrate but that of the substrate support as well.

In this paper, a different technique is used to investigate the transient associated with the silicon deposition

* Electrochemical Society Active Member.

¹ Present address: Central R & D, SGS, 20041 Agrate, Milano, Italy.

Key words: semiconductor, growth, doping, integrated circuits.

process. As discussed below, it consists of perturbing the steady-state deposition of silicon by abruptly changing the flow of silicon species entering the reactor. This perturbation introduces a transient period during which the silicon growth rate varies with time, thereby affecting the dopant concentration of the growing epitaxial film. By studying the resulting epitaxial dopant profile, the transient in the silicon deposition process can be investigated (7). In the following sections, the experiments carried out to study the transient response of the silicon deposition process are described. Following this, a physical model capable of explaining the results of the experiments is discussed. Finally, epitaxial dopant profiles calculated using the model are compared to measured profiles, and the time constant associated with the transient response of the silicon deposition process is estimated.

Equipment and Experimental Details

The epitaxial reactor used in this work was a horizontal, rf-heated Unipak VI (Sola Basic-Tempres) that operates at atmospheric pressure. The quartz reactor tube has an effective cross section of 26 cm² above the susceptor. The silicon carbide-coated graphite susceptor has the dimensions 56 cm (length) \times 11.4 cm (width) and is tilted at an angle of 1.5°. Hydrogen was used as the carrier gas at a velocity of 67 cm/sec above the susceptor (at room temperature). Silane was used as the silicon source with partial pressures adjusted in the 10⁻⁴ atm range to produce silicon growth rates of 0.34 and 0.17 $\mu\text{m}/\text{min}$. Arsine diluted in hydrogen was used as the dopant source with partial pressures adjusted in the 10⁻¹¹ atm range to produce epitaxial doping levels in the 10¹⁵/cm³ range. The corrected deposition temperature at the wafer surface was approximately 1050°C. The operating conditions used in this work were optimized so that (i) the silicon growth rate was a linear function of the silane partial pressure and (ii) the growth rates and film resistivities along the length of the susceptor were uniform.

The dopant profiles in the epitaxial layers were determined by capacitance-voltage measurements on planar p-n junctions and deep-depletion MOS structures (8). The fabrication details of the C-V structures are explained elsewhere (1). Because of the low diffusivity of arsenic in silicon (9), the heat cycling during the fabrication of these structures produced a diffusion length of only 0.01 μm (1). The epitaxial doping levels used in this study ($\sim 10^{15}/\text{cm}^3$) were low enough to allow the required depth profiling and high enough to produce a relatively short Debye length (10).

Experiments and Results

The experiments carried out to study the transient response of the silicon deposition process are described in this section. These experiments take advantage of the fact that, as illustrated in Fig. 1 (1), the arsenic concentration in an epitaxial film varies with silicon growth rate for a given arsine partial pressure. This growth-rate dependence allows the study of growth-rate variations during silicon deposition by examining the corresponding variations in epitaxial arsenic concentration.

Five experiments are described in this section, each of them addressing a different aspect of the transient phenomena. The first experiment is described with the aid of Fig. 2. At time $t = 0$ (see Fig. 2a) silane and arsine were injected into the reactor tube to begin the deposition. Both flows were adjusted to establish the deposition condition 1 in Fig. 2b, corresponding to a uniform epitaxial arsenic concentration N_1 and a silicon growth rate g_1 . The arsine flow was held constant throughout the entire deposition cycle. At $t = t_0$ the silane flow was abruptly lowered by decreasing the flow setting on the silane rotameter. The new steady-state deposition condition is indicated by 2 in Fig. 2b, corresponding to a uniform epitaxial arsenic concentra-

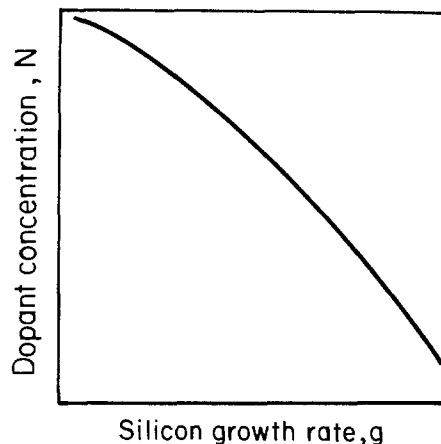


Fig. 1. Dopant concentration of uniformly doped epitaxial layers as a function of growth rate (1).

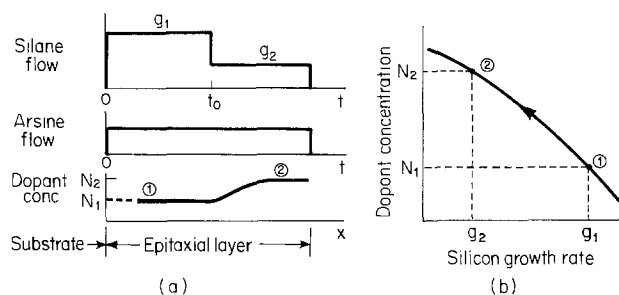


Fig. 2. Experiment to study the transient response of the silicon epitaxial process (see text).

tion N_2 and a growth rate g_2 . The resulting arsenic profile in the epitaxial film (Fig. 2a) contained information on the response of the silicon epitaxial system to the abrupt step change in silane flow. Figure 3 shows the measured arsenic concentration as a function of distance from the surface of the epitaxial film for the decreasing step in silane flow shown in the inset. The epitaxial system gradually moved from one steady-state condition to the next. The transition occurred over a distance of approximately 1 μm , corresponding to several minutes of deposition. Figure 4 shows the result of an experiment similar to that described in Fig. 2, except that the silane flow was abruptly increased rather than decreased as indicated in the inset. The profiles in Fig. 3 and 4 show similar behavior, with the transition occurring approximately over the same distance, and indicate the presence of significant transients in the silicon deposition process. The similarity in the

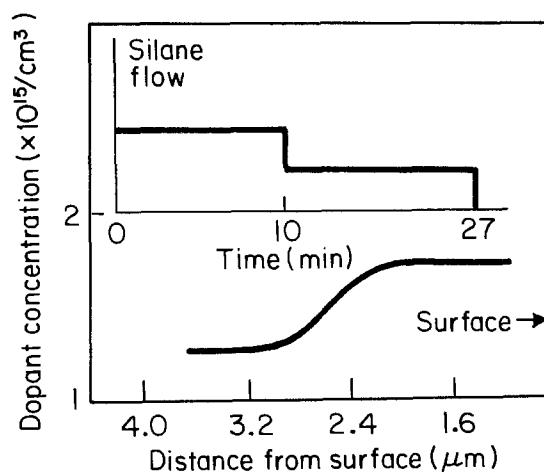


Fig. 3. Experimentally observed dopant concentration as a function of distance from the surface of the epitaxial film for the decreasing step change in silane flow indicated in the inset.

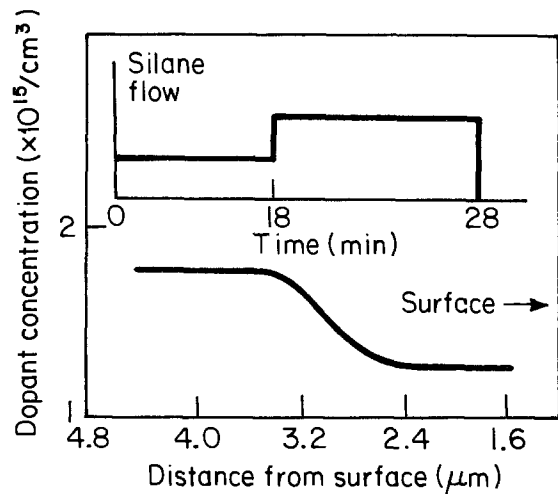


Fig. 4. Experimental dopant profile for an increasing step change in silane flow.

dopant profile for increasing and decreasing silane gas flows suggests the importance of analogous physical mechanisms in the two cases. In an attempt to study the importance of gas flow dynamics, epitaxial dopant profiles were measured at different positions along the length of the susceptor. To this effect, three wafers were used in each of the experiments described above as indicated in Fig. 5, and dopant profiles were measured in each wafer. No differences were observed in the measured profiles from wafer to wafer in a given experiment. The physical mechanisms responsible for the transients observed here are discussed in the following section.

The next experiment is described with the aid of Fig. 6. Silane and arsine were injected into the reactor at $t = 0$. At $t = t_1$, the silane flow was interrupted, and at $t = t_2$ silane was injected back into the epitaxial system. The arsine flow was not interrupted until the end of the second deposition step at $t = t_D$. The dashed line in Fig. 6 represents the response of the silicon growth rate to the abrupt changes in silane flow conditions at $t = t_1$ and $t = t_2$. It considers the fact that the silicon deposition process needs some time to stop after $t = t_1$ and, similarly, that it needs some time to reestablish a steady-state silicon growth rate after $t = t_2$. As a result of these growth-rate variations, the epitaxial arsenic concentration can be expected to increase after $t = t_1$ (see Fig. 6) and decrease after $t = t_2$ until the steady-state epitaxial condition is reestablished. Figure 7 shows the measured epitaxial arsenic profile corresponding to this experiment. The pronounced peak in the arsenic profile clearly indicates the presence of appreciable transients in the silicon epitaxial system.

In the experiments described above the silane flow conditions were varied while the arsine flow was held constant. In the following experiments both the silane and arsine flows were varied with time. The next experiment is described with the aid of Fig. 8. Figure 8a shows the silane and arsine flows as functions of time,

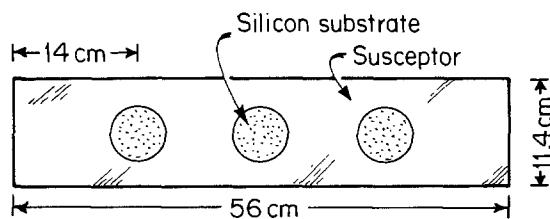


Fig. 5. Experimental arrangement. Dopant profiles were measured in each wafer.

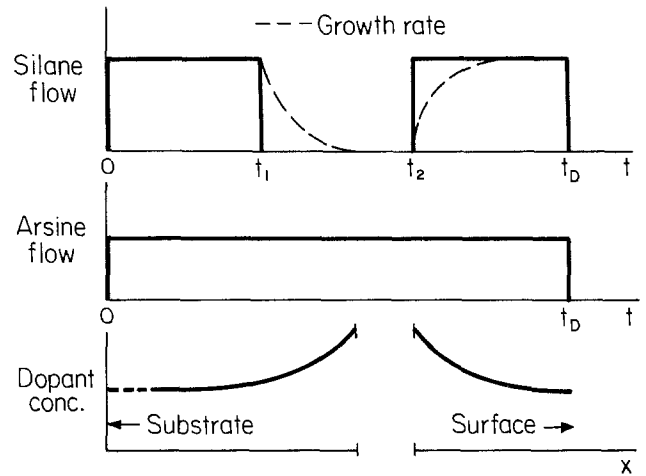


Fig. 6. Experiment to study the transient response of the silicon epitaxial process (see text).

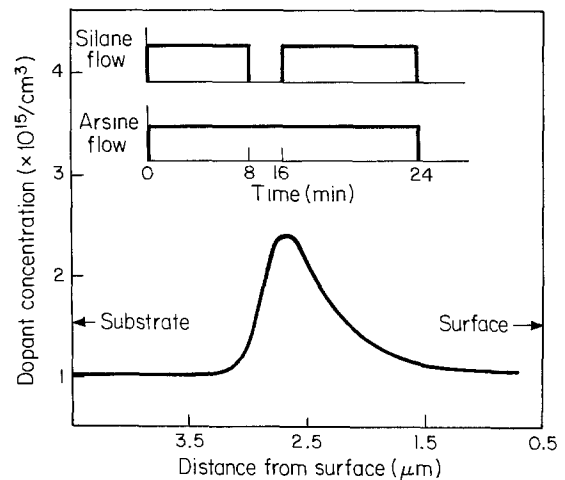


Fig. 7. Experimental dopant profile for the gas flows as functions of time indicated in the inset.

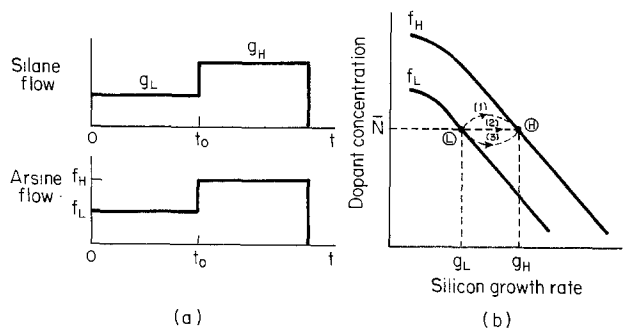


Fig. 8. Experiment to study the transient response of the silicon epitaxial process (see text).

and Fig. 8b shows schematically the variation of epitaxial arsenic concentration with silicon growth rate for two different arsine flows. At $t = 0$ silane and arsine were injected into the reactor tube and their flows were adjusted to produce a silicon growth rate g_L and an arsine flow f_L . This deposition condition is indicated by L in Fig. 8b. The epitaxial system was then allowed to reach steady state and establish a uniform epitaxial arsenic concentration \bar{N} (see Fig. 8b). At $t = t_0$ both the silane and arsine flows were abruptly increased and adjusted to produce a growth rate g_H and a flow rate f_H , respectively. The new deposition condition H (see Fig. 8b) was designed to produce the same epitaxial arsenic concentration \bar{N} . The epitaxial system was expected to change its steady-state operat-

ing condition from L to H following path 1, 2, or 3 in Fig. 8b. Path 2 was expected if the duration of the transient period was negligible, while path 1 or 3 was expected if the transient time was non-negligible. (It is shown in the next section that path 3 is not physically possible in this experiment.) In order to determine which path was followed the dopant profile in the resulting epitaxial film was measured. A peak or dip in the otherwise uniform dopant profile would indicate whether path 1 or 3, respectively, was followed. Figure 9 shows the measured arsenic concentration as a function of distance from the surface of the epitaxial film for this experiment. The corresponding silane and arsine flows as functions of time are indicated in the inset. The profile shows a definite peak, indicating that the epitaxial system went from L to H via path 1 (Fig. 8b). The two steady-state doping levels in Fig. 9 are not the same. This is believed to be due to lack of very accurate control on the flow settings of the rotameters. The presence of a peak in this experiment confirms the existence of non-negligible transients in the silicon epitaxial system.

An experiment similar to that described in Fig. 8 except that the silane and arsine flows were abruptly decreased rather than increased at $t = t_0$ was also carried out. In this case, the operating condition of the epitaxial system was changed from H to L in Fig. 8. As mentioned above, path 2 was expected to be followed if the duration of the transient period was negligible. Figure 10 shows the measured epitaxial dopant profile for the silane and arsine flows as functions of time indicated in the inset. The profile shows a definite dip, indicating that the epitaxial system went from H to L following path 3 (see Fig. 8b) and confirming the presence of significant transients in the silicon epitaxial system. The extent of the dip in Fig. 10 is ap-

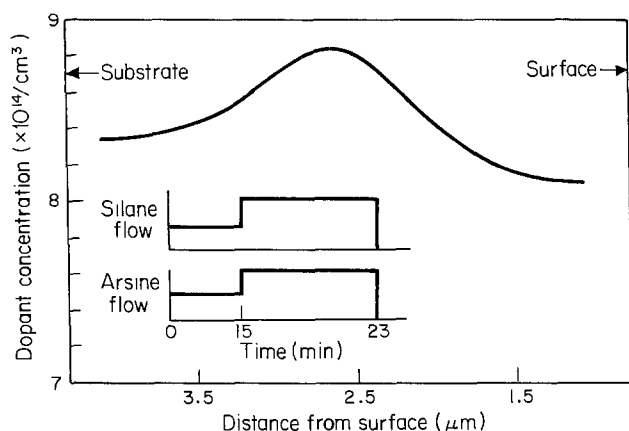


Fig. 9. Experimental dopant profile for the gas flows as functions of time indicated in the inset.

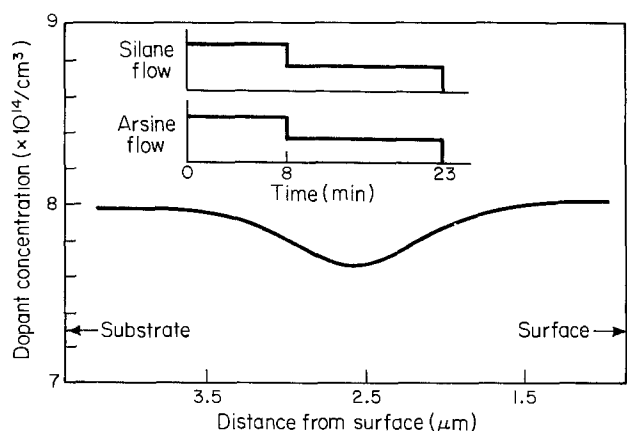


Fig. 10. Experimental dopant profile for the gas flows as functions of time indicated in the inset.

proximately equal to that of the peak in Fig. 9. The magnitudes of the dip and peak, however, differ slightly. This discrepancy in the magnitudes is smaller than $2 \times 10^{13}/\text{cm}^3$ and is believed to be due to artifacts in the measurement technique.

In this section, the experiments carried out to study the transients associated with the silicon deposition process were described. The results of these experiments indicated the presence of transients of non-negligible duration in the silicon epitaxial system. A physical model capable of explaining the results obtained here is discussed in the next section.

Physical Model

In order to explain the experimental results described in the previous section, a physical model of the deposition process is required. The model used here builds on the model for arsenic incorporation in silicon epitaxy reported elsewhere (2, 3). In this section, the basic features of the arsenic incorporation model are reviewed and then used to explain the experimental results.

The arsenic incorporation model can be summarized with the aid of Fig. 11 as follows. When an arsenic-containing species in the gas phase is in the vicinity of the silicon surface (Fig. 11a) it undergoes a process of adsorption. The adsorbed arsenic species diffuses on the surface until it finds an incorporation site to which it can attach. This incorporated arsenic atom is then quickly covered by subsequently arriving silicon atoms. r_1 (Fig. 11) is the rate at which arsenic species are adsorbed on the silicon surface, and is given by (2)

$$r_1(t) = k_{mf} \left[P_D^\circ(t) - \frac{N_s \theta_D(t)}{K_A K_P} \right] \quad [1]$$

where k_{mf} is a kinetic coefficient associated with the rate-limiting step of the arsenic incorporation process (2), P_D° is the input arsine partial pressure, N_s is the surface density of adsorption sites per unit area, θ_D is the fraction of adsorption sites occupied by arsenic species, and K_A and K_P are thermodynamic constants relating the epitaxial arsenic concentration to the concentration of arsenic species in the adsorbed layer and gas phase, respectively (2). r_2 (Fig. 11) is the rate at which arsenic is covered by silicon atoms and is given by (2)

$$r_2(t) = g(t) \frac{N_s \theta_D(t)}{K_A} \quad [2]$$

where g is the silicon growth rate. The adsorbed layer plays an important role in this model. It consists of a population of hydrogen, silicon, and arsenic species occupying adsorption sites and capable of moving on the solid surface. The model assumes that the concen-

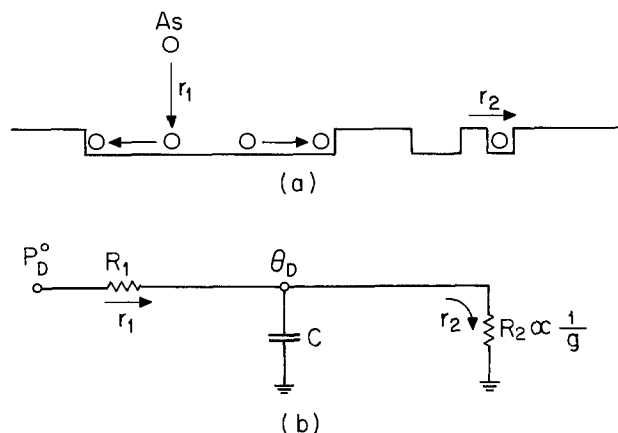


Fig. 11. Simplified model for dopant incorporation into growing silicon epitaxial films: (a) steps taking part in the doping process; (b) equivalent circuit representing the doping process.

tration of arsenic in the growing epitaxial film (N) is proportional to the concentration of arsenic species in the adsorbed layer, i.e. (2)

$$N = \frac{N_s \theta_D}{K_A} \quad [3]$$

In this model, r_1 is viewed as the rate at which the adsorbed layer increases its population of arsenic species. Similarly, r_2 is viewed as the rate at which the adsorbed layer decreases its population of arsenic species due to the silicon-covering step. In steady state, i.e., when the arsine and silane flows entering the reactor have remained unchanged for a "long" time, $r_1 = r_2$. Consequently, θ_D remains unchanged (see Eq. [1] and [2]) and so does N (see Eq. [3]). However, when the arsine and/or silane flows vary with time r_1 and r_2 may not be equal and, as a result, θ_D and N may also vary with time. In this case, the rate of change of θ_D (and N) can be calculated from (2)

$$r_1(t) - r_2(t) = N_s \frac{d\theta_D(t)}{dt} \quad [4]$$

By using Eq. [1], [2], and [3], Eq. [4] can be rewritten as (2)

$$k_{mf} \left[P_D^\circ(t) - \frac{N(t)}{K_P} \right] - g(t)N(t) = K_A \frac{dN(t)}{dt} \quad [5]$$

Equation [5] summarizes the arsenic incorporation model and relates $P_D^\circ(t)$, $g(t)$, and $N(t)$. The redistribution of arsenic in the epitaxial film during silicon deposition was neglected here because of the low diffusivity of arsenic in silicon.

Figure 11b shows an equivalent circuit (3, 4) representing the arsenic incorporation model described above. The "current" in the circuit represents the net flow of arsenic species. R_1 represents the limitation imposed by the rate-limiting mechanism on the flow of arsenic species. R_2 represents the step by which silicon atoms cover arsenic atoms during growth. P_D° represents the "voltage" which drives the current, i.e., the driving force for the arsenic incorporation process. The capacitor accounts for the accumulation of arsenic species in the adsorbed layer. In the equivalent circuit of Fig. 11b, $R_1 \equiv (k_{mf})^{-1}$, $R_2(t) \equiv [g(t)K_P]^{-1}$, and $C \equiv K_A K_P$, and the voltage across the capacitor is proportional to θ_D and N (see the Appendix). Notice that R_2 is proportional to the reciprocal of the silicon growth rate.

The arsenic incorporation model described above can now be used to explain the results of the experiments described in the previous section. Because all experiments can be explained analogously, only the experiment described in Fig. 8 is discussed here with the help of Fig. 12. In that experiment the arsine and silane flows were both adjusted, before and after $t = t_0$, to produce the same epitaxial arsenic concentration N in steady state. The abrupt increase in arsine flow at $t = t_0$ results in an abrupt increase in the rate r_1 at which arsenic species adsorb on the silicon surface (see Eq. [1]). Similarly, the abrupt increase in silane flow at $t = t_0$ increases the silicon growth rate thereby increasing the rate r_2 at which arsenic species in the adsorbed layer are covered by silicon atoms (see Eq. [2], Fig. 12a). If the silicon growth rate reaches the new steady-state rate "instantaneously," then both r_1 and r_2 increase by the same amount and reach the new steady-state rates instantaneously. Consequently, θ_D remains unchanged during the transition (see Eq. [4]) and so does N . This situation corresponds to the epitaxial system moving from L to H via path 2 (see Fig. 8). However, if the silicon growth rate requires some non-negligible time to reach the new steady-state rate, then $r_1 > r_2$ for a brief period of time which results in an increase in θ_D (see Eq. [4]) and, consequently,

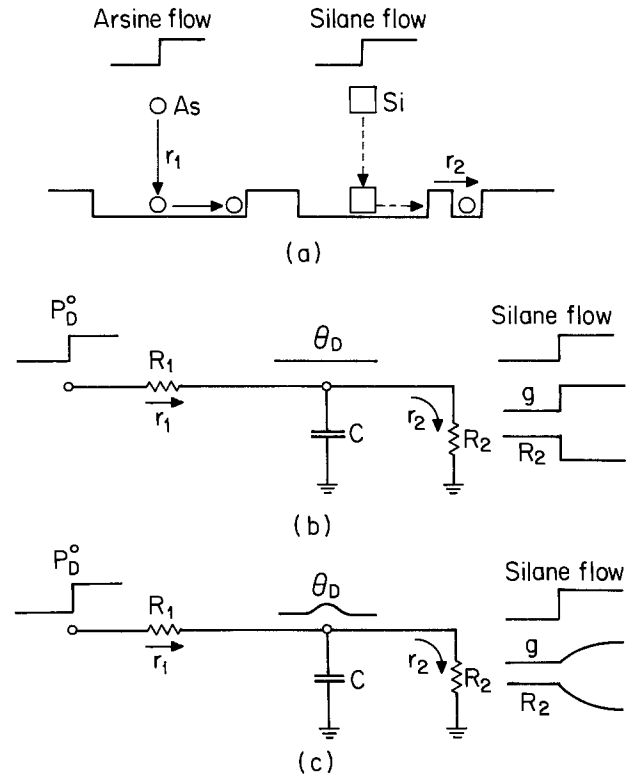


Fig. 12. Physical model used to explain the behavior of the epitaxial system: (a) steps taking part in the doping process and silicon growth; (b) equivalent circuit with R_2 changing "instantaneously;" (c) equivalent circuit with R_2 changing gradually.

an increase in N . Eventually, as the silicon growth rate approaches the new steady-state rate, both θ_D and N gradually fall back to their steady-state levels. The end result is a "peak" in the resulting epitaxial arsenic profile, in agreement with the experimental observation shown in Fig. 9.

The equivalent circuit in Fig. 12 can also be used to explain the experiment. Figure 12b shows the situation that exists when the silicon growth rate reaches the new steady-state rate instantaneously. In this case, R_2 decreases abruptly and, consequently, r_2 increases abruptly compensating the abrupt increase in r_1 . As a result, the amount of charge accumulated in the capacitor (which corresponds to θ_D in the model) remains unchanged. Figure 12c shows the situation that exists when the silicon growth rate approaches the new steady-state gradually. In this case, R_2 decreases gradually and $r_1 > r_2$ for a brief period of time. This increases the amount of charge stored in the capacitor. Eventually, as R_2 reaches its steady-state value, the charge in the capacitor falls back to the steady-state level.

In this section, the arsenic incorporation model was reviewed and then used qualitatively to explain the result of one of the experiments described in the previous section. It was concluded that the experimental results can be explained if it is assumed that the silicon deposition process needs some non-negligible time to regain steady state after a perturbation is imposed on the silane flow. A more quantitative discussion is given in the next section in which arsenic profiles calculated from Eq. [5] are compared to experimental profiles.

Comparison of Theory and Experiments

Equation [5] has been used successfully to simulate epitaxial depositions in which the arsine flow varied with time while the silane flow was kept constant (2). It is shown in this section that Eq. [5] can also be used to simulate epitaxial depositions in which both the arsine and silane flows vary with time. Epitaxial dopant profiles corresponding to the experiments de-

scribed above are computed here using Eq. [5] and are compared to measured profiles.

As discussed by Johnson and Panousis (10), the profiles measured by the capacitance-voltage technique are a closer representation of the majority carrier distribution than they are of the impurity distribution. For this reason, the theoretical profiles shown in this section do not correspond to impurity distributions but to majority carrier distributions. The theoretical majority carrier distributions were obtained by using the impurity distributions obtained from Eq. [5] and computing a one-dimensional solution to Poisson's equation. The computer program SEDAN was used to obtain the Poisson solution (11).

In order to use Eq. [5] to calculate impurity profiles, the silicon growth rate was assumed to respond exponentially to an abrupt change in silane flow. As an illustration, the equations solved numerically to obtain the impurity profiles corresponding to the experiment described in Fig. 8 are given below:

$$0 < t \leq 15 \text{ min}$$

$$k_{mf} \left[P_1 - \frac{N(t)}{K_P} \right] - g'(t)N(t) = K_A \frac{dN(t)}{dt} \quad [6]$$

$$g'(t) = g_1 [1 - \exp(-t/\tau_s)] \quad [7]$$

$$x = \int_0^t g'(t) dt \quad [8]$$

$$15 < t \leq 23 \text{ min}$$

$$k_{mf} \left[P_2 - \frac{N(t)}{K_P} \right] - g''(t)N(t) = K_A \frac{dN(t)}{dt} \quad [9]$$

$$g''(t) = g_1 \exp[-(t-15)/\tau_s] + g_2 \{1 - \exp[-(t-15)/\tau_s]\} \quad [10]$$

$$x = \int_0^{15} g'(t) dt + \int_{15}^t g''(t) dt \quad [11]$$

where τ_s is defined here as the time constant of the silicon deposition process. The values of k_{mf} , K_P , and K_A for a given epitaxial system and operating conditions can be obtained experimentally (2). For the epitaxial reactor and deposition conditions used in this work these values are $k_{mf} = 4.85 \times 10^{19}/\text{cm}^2 \text{ sec atm}$, $K_P = 1.05 \times 10^{26}/\text{cm}^3 \text{ atm}$, and $K_A = 5.7 \times 10^{-5} \text{ cm}$ (2). P_1 , P_2 and g_1 , g_2 were obtained from the corresponding arsine flows and silane flows, respectively. Therefore, the only unknown in the above equations is τ_s . Figure 13 shows measured (solid line) and calculated (dashed and dotted lines) dopant profiles corresponding to this experiment. Three simulations are

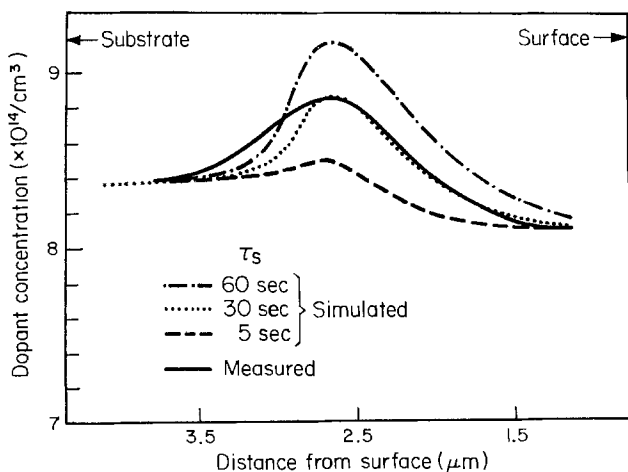


Fig. 13. Solid line: experimental dopant profile. Dashed and dotted lines: simulated dopant profiles for different values of τ_s .

shown, each corresponding to a different value of τ_s . All simulations predict the peak in the dopant profile observed experimentally. In order to fit the steady-state levels of the calculated profiles to those of the measured profile the values of P_1 and P_2 (see Eq. [6] and [9]) were slightly adjusted. The best fit to the measured profile was obtained with $\tau_s = 30 \text{ sec}$.

Figure 14 shows measured (solid line) and simulated (dashed and dotted lines) dopant profiles corresponding to the experiment described in Fig. 10. The equations used in these simulations are similar to Eq. [6]-[11]. Three simulations are shown, each corresponding to a different value of τ_s . All simulations predict the dip in the dopant profile observed experimentally. The best fit to the measured profile was obtained using $\tau_s = 20 \text{ sec}$. The disagreement between the values of τ_s obtained from Fig. 13 and 14 is due to the discrepancy in the magnitudes of the peak and dip, respectively. As mentioned earlier, this discrepancy is believed to be due to limitations in the resolution of the capacitance-voltage technique used to measure the profiles.

The experimental results shown in Fig. 3, 4, and 7 were also simulated using $\tau_s = 20\text{-}30 \text{ sec}$. The simulated and measured profiles were almost indistinguishable, confirming the validity of the physical model and the time constant for the silicon deposition process discussed here.

Summary and Conclusions

In this work, the transients associated with the deposition of silicon epitaxial films in a conventional chemical vapor deposition reactor were investigated. The objectives of this work were (i) to estimate the duration of the transient period that precedes the establishment of a steady-state deposition rate and (ii) to study the effect of this transient on the dopant concentration of the growing epitaxial film. The technique used to investigate these transients consisted of perturbing the steady-state deposition of silicon by abruptly varying the silane gas flow and then studying the effect of this perturbation on the epitaxial dopant concentration. A physical model capable of explaining the behavior of the epitaxial system during the transient period was described. Epitaxial dopant profiles corresponding to the experiments carried out in this work were calculated using the model by assuming that the silicon growth rate responds exponentially to an abrupt variation in silane flow. The theoretical profiles were found to agree fairly well with the measured profiles when the time constant used for the exponential response of the silicon deposition process was in the 20-30 sec range. The physical mechanisms responsible for the transient behavior of the silicon deposition process are currently under investigation. Preliminary results seem to indicate that gas flow dynamics do not play a dominant role, as suggested by the fact that the mea-

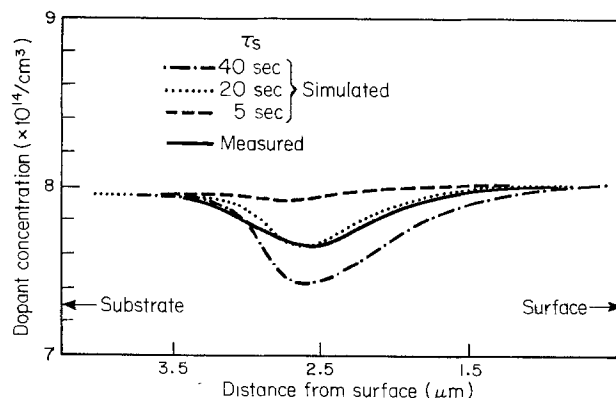


Fig. 14. Solid line: experimental dopant profile. Dashed and dotted lines: simulated dopant profiles for different values of τ_s .

sured profiles shown in Fig. 3 and 4 were independent of the position of the substrate along the length of the susceptor. Equation [5] summarizes the model described here and can be used to design the silane and arsine gas flows as functions of time that produce the desired impurity distribution in the epitaxial film. Therefore, Eq. [5] should allow a better control of the doping level in submicron epitaxial films.

Acknowledgments

The authors thank Professor R. W. Dutton for his encouragement and support and Dr. T. I. Kamins and Dr. K. C. Saraswat for useful discussions. This work was supported by the U.S. Army Research Office (Contract No. DAAG-29-77-C-0006) and was conceived and carried out at Stanford University. R. Reif gratefully acknowledges the financial support provided by the National Science Foundation (Grant No. DMR 78-24185) and by a grant from the IBM Corporation, both through the M.I.T. Center for Materials Science and Engineering, which made the writing of this article possible.

Manuscript submitted Feb. 2, 1981; revised manuscript received May 1, 1981.

Any discussion of this paper will appear in a Discussion Section to be published in the June 1982 JOURNAL. All discussions for the June 1982 Discussion Section should be submitted by Feb. 1, 1982.

APPENDIX

The arsine partial pressure in equilibrium with the epitaxial arsenic concentration is given by (2)

$$P_{D,eq} = \frac{N}{K_P} \quad [A-1]$$

By using Eq. [A-1], Eq. [5] can be rewritten as

$$k_{mf}[P_D^\circ - P_{D,eq}] - gK_P P_{D,eq} = K_A K_P \frac{dP_{D,eq}}{dt} \quad [A-2]$$

which can also be written as

$$\frac{P_D^\circ - P_{D,eq}}{R_1} - \frac{P_{D,eq}}{R_2} = C \frac{dP_{D,eq}}{dt} \quad [A-3]$$

where $R_1 \equiv (k_{mf})^{-1}$, $R_2 \equiv (gK_P)^{-1}$, and $C \equiv K_A K_P$.

By substituting Eq. [3] into Eq. [A-1]

$$P_{D,eq} = \frac{N_s \theta_D}{K_A K_P}$$

REFERENCES

1. R. Reif, T. I. Kamins, and K. C. Saraswat, *This Journal*, **125**, 1860 (1978).
2. R. Reif and R. W. Dutton, *ibid.*, **128**, 909 (1981).
3. R. Reif, T. I. Kamins, and K. C. Saraswat, *ibid.*, **126**, 644 (1979).
4. R. Reif, T. I. Kamins, and K. C. Saraswat, *ibid.*, **126**, 653 (1979).
5. D. J. Dumin, *Rev. Sci. Instrum.*, **38**, 1107 (1967).
6. D. W. Shaw, *This Journal*, **117**, 683 (1970).
7. R. Reif, M. Vanzi, R. W. Dutton, T. I. Kamins, and K. C. Saraswat, Abstract 563, p. 1413, The Electrochemical Society Extended Abstracts, Los Angeles, California, Oct. 14-19, 1979.
8. R. F. Pierret and D. W. Small, *Solid-State Electron.*, **18**, 79 (1975).
9. R. S. Muller and T. I. Kamins, "Device Electronics for Integrated Circuits," p. 44, John Wiley & Sons, Inc., New York (1977).
10. W. C. Johnson and P. T. Panousis, *IEEE Trans. Electron Devices*, **ed-18**, 965 (1971).
11. D. C. D'Avanzo, M. Vanzi, and R. W. Dutton, Stanford Electronics Labs., Stanford University, Tech. Rep. No. G-201-5 (October 1979).

The Application of Temperature Gradient Zone Melting to Silicon Wafer Processing

Mike Chang* and Richard Kennedy

General Electric Company, Syracuse, New York 13221

ABSTRACT

High voltage semiconductor devices fabricated with deep p-type isolation regions are now practical. By employing the temperature gradient zone melting technique (TGZM), structures can now be fabricated that were not possible before using only solid-state diffusion techniques. In this study, various processing alternatives are discussed and analyzed. High voltage SCR devices have been made using the TGZM approach and process limitations, based on the current state-of-the-art, are described. Carrier lifetimes, blocking voltage capabilities, and leakage current levels have been measured and indicate that the processes used are effective.

The temperature gradient zone melting (TGZM) process can yield deep p-n junctions at a much faster rate than conventional solid-state diffusion techniques (1, 2, 6-10). As an example, an aluminum pattern can migrate through a 400 μm thick silicon wafer in just about 10 min at 1200°C. By contrast, conventional boron diffusion would require approximately one month at 1250°C, diffusion simultaneously from both sides, to achieve a comparable structure. This unique feature of the TGZM method allows p-type connections to be made through any thickness of silicon wafer.

In one application, this type of deep connection can be used to join two p-layers, diffused from opposing sides of a silicon slice. Thus, the p-n junctions themselves never extend to the edge of the structure. Separation and passivation of the two blocking junctions can be achieved by etching grooves on one side of the slice to expose the junctions, followed by backfilling the grooves with a suitable passivant. A typical SCR structure fabricated via TGZM isolation is shown in Fig. 1 (2).

It is also of interest that the material presented here can also be used for other applications such as field grids of a field control thyristor (FCT), vertical solar

* Electrochemical Society Active Member.

Key words: semiconductor, devices, thermomigration, process.

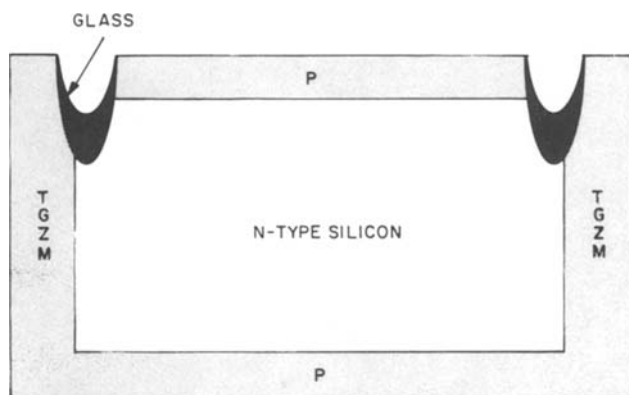


Fig. 1. A typical SCR structure fabricated with TGZM isolation

cells, etc. In this paper, the technique of TGZM isolation, together with its processing characteristics, is described.

Experimental

The TGZM technique was used to introduce an isolation region into a silicon structure. The necessary active p-n junctions were formed by conventional solid-state diffusion processes. The TGZM procedure and the complete structure fabrication process will be described separately. In actual practice, these separate processes can proceed in any sequence.

Migration.—An aluminum-silicon droplet was allowed to migrate through a silicon slice at a given temperature, with a specific temperature gradient through the slice. A quartz lamp system (Fig. 2) was used as a heat source. It performed quite well; however, there are alternative systems, such as a modified epitaxial reactor, that perform equally well. The details of the quartz lamp system have been discussed elsewhere (3) but the wafer supporting mechanism is worth mentioning here.

Any finished surface of a silicon wafer, be it lapped, chemically etched, or mechanically polished, is not microscopically flat, nor is any other solid surface. Therefore, it is impossible for a silicon wafer to lie on another solid surface and maintain a continuous, uniform contact. Rather, there are numerous point contacts, which means that uniform thermal conduction is not possible. In such a situation, the required unidirectional temperature gradient cannot be maintained and the direction of migration will be unpredictable.

The use of an air cushion is the ideal way of achieving uniform thermal conduction. In this work, an air-cushion effect was simulated by using a 3 quartz pin system to support the wafer. The results were reasonably good across the wafer except in the immediate vicinity of the point contacts. The next most likely way of achieving a continuous contact would be to

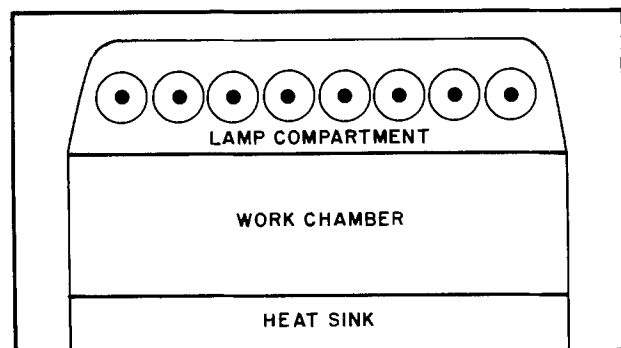


Fig. 2. A schematic diagram of a quartz lamp system for TGZM operation.

use a liquid support system. Molten tin and aluminum support systems are possibilities currently being investigated by the author.

In order to produce a p-type isolation grid in an n-type silicon wafer by TGZM, liquid aluminum-silicon droplets must be migrated through the wafer. A simple calculation shows that 8.128×10^{17} aluminum atoms/cm² is adequate to dope a 400 μm thick silicon wafer to a concentration of 2×10^{19} atoms/cm³. This is equivalent to a 0.1349 μm thick slice of solid aluminum. However, for migration of an aluminum-silicon droplet, approximately 1 μm of aluminum is required. In this study, four methods (Fig. 3) were developed for interfacing an aluminum array with the silicon surface.

Groove method.—A network of grooves 10-20 μm deep is etched into the silicon surface. The aluminum pattern is then introduced into the grooved regions. These grooves contain the aluminum grids and keep the molten aluminum from spreading over the wafer surface during the thermomigration process.

Oxide channels.—An array of windows is opened into an oxidized silicon wafer surface by conventional photolithographic techniques. After the aluminum is patterned into these windows, the oxide borders contain the molten aluminum during processing in much the same way as the grooves.

MOS method.—The aluminum pattern is applied directly to an oxidized silicon surface (4). This investigation showed that the aluminum reacts with the oxide forming a porous material, probably mostly aluminum oxide. The rest of the aluminum then migrates through this porous material and alloys with the silicon forming the aluminum-silicon droplet. This porous oxide has the effect of confirming the aluminum to the patterned area.

Direct application method.—It was determined that none of the above methods are necessary to keep the aluminum from spreading out on the silicon surface during migration, provided that the aluminum pattern is sintered before migration takes place. Thus, the pattern can be applied directly to the silicon wafer surface without any prior surface preparation.

The aluminum pattern can be formed by any of several conventional methods. In one case, the entire surface of the silicon slice is first coated with aluminum, and then the pattern is delineated photolithographically using a suitable aluminum etch. In another photolithographic technique, a photoresist pattern is first formed on the wafer followed by a layer of evaporated aluminum. Then the photoresist material is de-

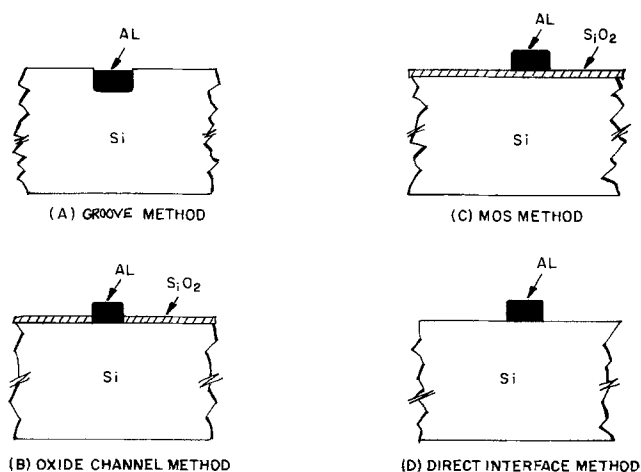


Fig. 3. Four different methods of creating aluminum patterns on the surface of a silicon wafer for TGZM operation.

composed. Since the aluminum adheres only to the uncoated area, the excess aluminum outside these areas can be easily removed. The aluminum pattern can also be formed by evaporation through a metal shadow mask.

The prepared wafers are loaded into the TGZM chamber with the aluminum pattern side facing the heat sink. This study showed that best results were achieved using a three-part temperature cycle, a ramp-up period, a soak period, and a ramp-down period. During the ramp-up period, the aluminum begins to react with the silicon to form the aluminum-silicon solution. By proper manipulation of the ramp-up cycle, the required sintering operation, mentioned earlier, can be instituted. Migration begins during this period, though at a relatively slow rate; it proceeds at its highest rate during the soak period. The aluminum gradually freezes out of the emerged aluminum-silicon droplet on the hot surface of the wafer during the ramp-down part of the cycle. The ramping portion of the cycle has the added benefit of reducing thermal shock stresses. In a typical run, a 10 mil wide pattern with 4 μm thick aluminum will migrate through a 400 μm thick silicon slice using the following cycle: 1 min ramp-up; 8 min soak; 3 min ramp-down. The soak temperature is 1200°C with a temperature gradient around 50°C/cm.

Device fabrication.—Most power semiconductor device fabrication processes involve at least two diffusion operations. For example, an n-base thyristor can be made with a deep p-type diffusion followed by an n-type emitter diffusion. In certain instances, these two diffusion cycles can be combined into a single simultaneous operation. The purpose of TGZM isolation is to connect a diffused p-layer, on one side of the slice, to an opposing p-layer on the other side. Three different sequences of TGZM and diffusion were studied.

Diffusion first.—The TGZM isolation operation is performed after all the diffused junctions have been created. A surface clean-up follows TGZM to remove rough areas. Subsequent operations, such as groove etching, passivation, and metallization, can then proceed.

TGZM first.—The TGZM operation is first performed on the raw silicon wafers, after which the wafers are mechanically lapped or chemically etched (or both) to yield smooth surfaces. Conventional wafer processing operations, i.e., oxidation, diffusion, etc., can now be performed on these wafers treating them as if they were raw silicon slices.

TGZM intermediate.—In some applications, for example, certain power transistor structures, more than two diffusion operations are required. In these cases, it may prove advantageous to insert the TGZM operation after one or more diffusion steps have been performed, but before completion of the entire structure. In this work, TGZM was employed in a power transistor fabrication process just after the initial deep collector diffusion cycle was completed.

During the course of this investigation, SCR (silicon control rectifier), diode, and power transistor structures were fabricated using the TGZM process.

Results and Discussion

Migration results vs. aluminum pattern preparation.

—In the groove method of pattern preparation, the mechanical strength of the silicon wafer is significantly reduced by the etched grooves. This limitation can be devastating to product yield if the groove depth becomes a substantial fraction of the total wafer thickness. This method is, however, the most effective way of keeping the aluminum pattern from surface spreading. The oxide channel and MOS methods do not me-

chanically weaken the structure but do introduce another problem. That is, the material formed by the reaction of molten aluminum with the silicon oxide is extremely tough and difficult to remove. Its presence inhibits the growth of good oxide in those areas during subsequent processing. Because of its abrasive nature, it can decrease photoresist mask life due to mechanical damage. The direct aluminum-silicon coupling eliminates the above mentioned problem. But, it may leave a somewhat bumpy surface (Fig. 4), which can be reduced to a reasonable level by adequate control of migration conditions.

Limitations and problems.—There are some instabilities inherent in the TGZM process (1, 2, 6); ways have been found to overcome some of these and to deal with the others.

Linewidth.—The surface tension of a liquid pattern line varies inversely with the linewidth. If the linewidth decreases to a specific size, the surface tension becomes high enough to cause the liquid line to break up into discrete surface droplets, which may or may not migrate (6-8). Of course, there will be no migration in those areas void of the liquid. The critical point at which breakup occurs depends on TGZM conditions, the thickness of aluminum, and the surface condition and crystal orientation of the silicon. These studies have shown no problems with linewidths greater than 2 mils.

Silicon wafer thickness.—There seems to be no upper limit on wafer thickness for successful migration. Aluminum has been migrated through a 0.25 in. thick slice of silicon in 4 hr with no difficulty whatsoever. However, since the TGZM process, by its very nature, causes damage on the silicon slice that tends to weaken the wafer structure, there probably is a lower limit on wafer thickness. This work shows that wafers less than 8 mils thick are too fragile after TGZM to allow processing without excessive breakage.

Stress and damage.—Even though care is taken to minimize stresses due to thermal shock, TGZM does, after all, employ high temperature and short times, which often leave the silicon stressed and damaged. These defects become visible when the wafer surfaces are etched.

Silicon crystal orientation.—As the width of the aluminum line approaches its lower limit, a critical situation occurs between the silicon crystal orientation and the direction of pattern lines on the wafer (9). If the lines are not properly oriented with the crystal lattice, broken lines, distortions, and other undesirable phe-

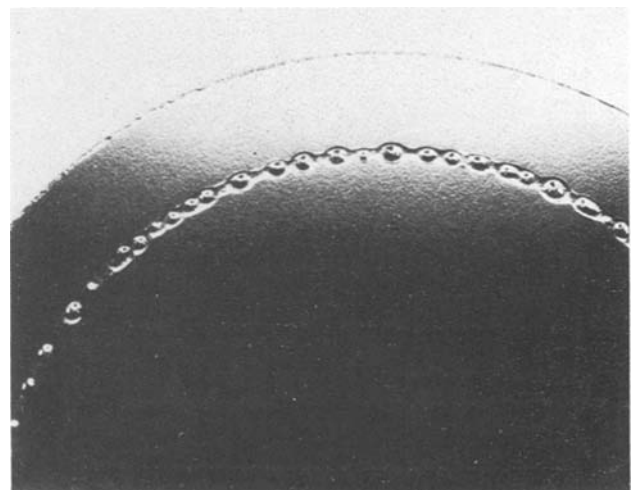


Fig. 4. A picture shows the roughness of TGZM surface in which the TGZM aluminum pattern was directly applied to a bare silicon surface.

nomena will occur. This problem disappears as the width of the line increases. For example, 10-20 mil wide circle patterns have been successfully migrated through polycrystalline silicon which, of course, had many crystal subdomains with different orientations as shown in Fig. 5, where the right-hand side wafer is top side up and the left-hand side wafer is bottom side up.

Silicon surface condition.—When the quartz lamp system is used, the effectiveness of migration depends highly on the reflectivity of the silicon surface. The lower the reflectivity (the greater the absorption), the faster the droplet migrates. Silicon wafers with a rough or darkened surface have a favorable ratio of absorption rate to reflection rate. This investigation has shown that a lapped surface yields faster migration than a chemically etched surface which, in turn, is better than a mechanically polished surface. It was also discovered that a layer of silicon oxide, which acts as an antireflection barrier, provides additional increases in migration rates.

Device fabrication.—In this section the processing sequence experiments, *i.e.*, TGZM first *vs.* diffusion first, are compared and analyzed. This study shows that, when conditions permit, the best approach is to do the TGZM operation first.

"Diffusion first."—In this approach, the TGZM operation is accomplished after all of the semiconductor junctions have been formed. Since the structure is basically complete at this point, it is obvious that the active area of the structure should not be significantly damaged or altered. As noted earlier, TGZM always leaves some surface scars, which must be removed before subsequent processing can proceed. It is almost impossible to remove all of the TGZM damage without adversely affecting the active structure. If all of the damage is not removed, the oxide quality in the TGZM area will be poor, and the remaining rough spots may cause problems in photolithographic processing. Figure 6 shows the process sequences for both "diffusion first" and "TGZM first" methods.

"TGZM first."—When TGZM is performed first on raw silicon wafers, practically all of the TGZM scars can be removed before junction formation takes place. Lapping followed by chemical etching, or lapping alone, has been effective in obtaining acceptable wafer structures after TGZM. All subsequent diffusion, oxidation, and photolithographic processing steps can be performed in the same way as with raw materials. An

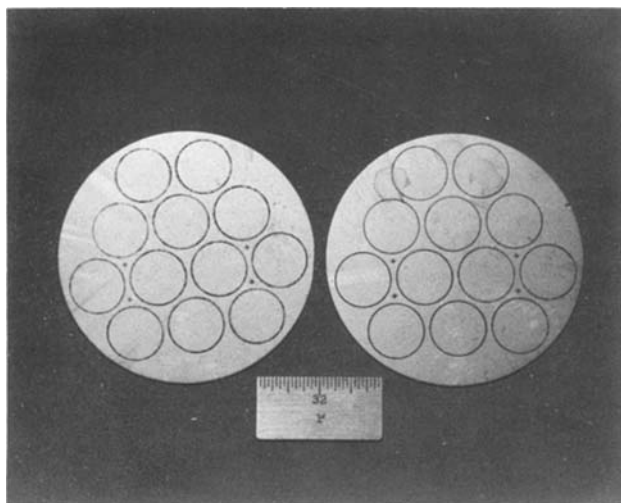


Fig. 5. A circular aluminum pattern migrated through a polycrystalline silicon wafer. The right-hand side wafer is top side up and the left-hand side wafer is bottom side up.

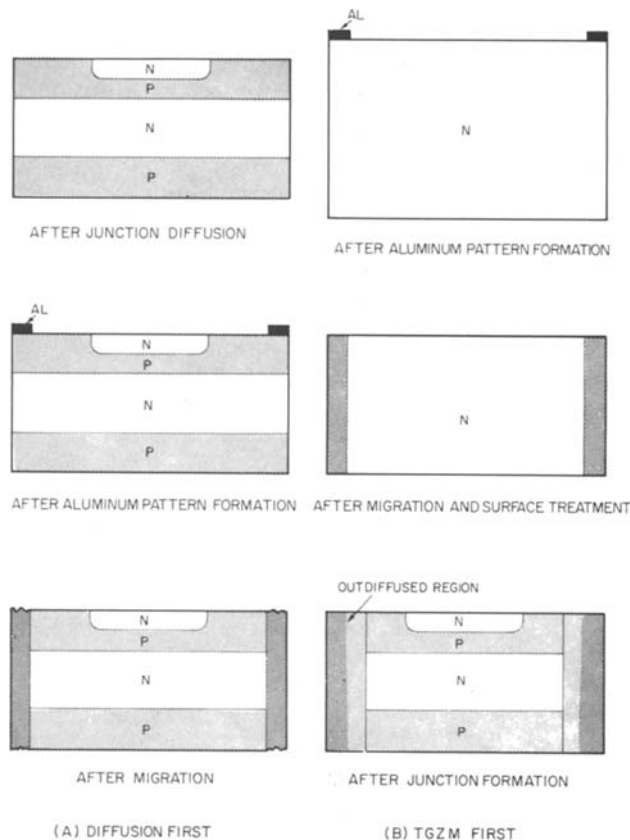


Fig. 6. Process sequences for the "diffusion first" method and the "TGZM first" method.

additional advantage from employing TGZM as a first processing step is the lateral diffusion from the isolation region that occurs during regular junction diffusion. This lateral diffusion expands the TGZM region an additional 10-20 mils on each side (Fig. 7). An abrupt junction is changed to a highly graded junction resulting in a considerably better blocking voltage capability. This diffusion of the TGZM region also tends to close any gaps in the TGZM region that might have occurred during migration. Finally, since the junction has diffused to an area remote from the original border, it is less affected by residual stress or damage in the original TGZM region. In spite of the advantage associated with lateral diffusion, it must be noted that extra area is required, which can be prohibitive in fabricating very small devices.

Out-diffusion of the aluminum atoms during subsequent diffusion operations can also be handled advantageously. In this investigation, out-diffusion has been used with a p-type impurity source, during closed-tube diffusion, to form graded deep blocking junctions. A boron source is also included to enhance the surface concentration of the p-layer. The results of one of these diffusion experiments are shown in Fig. 8. In open-tube diffusion, these out-diffused aluminum atoms can be oxidized and purged away, without affecting diffusion or oxidation results, by providing a sufficient oxygen flow.

An additional advantage from a process yield point of view is that, since TGZM occurs first, the starting thickness of the wafer is not limited. The wafer is reduced to its final thickness only after the TGZM operation has been completed.

Device evaluation.—In this study, TGZM is used only to introduce an extra p-type isolation wall into an existing device, which, obviously, alters the physical structure of the device. Any possible negative effects on device characteristics resulting from the

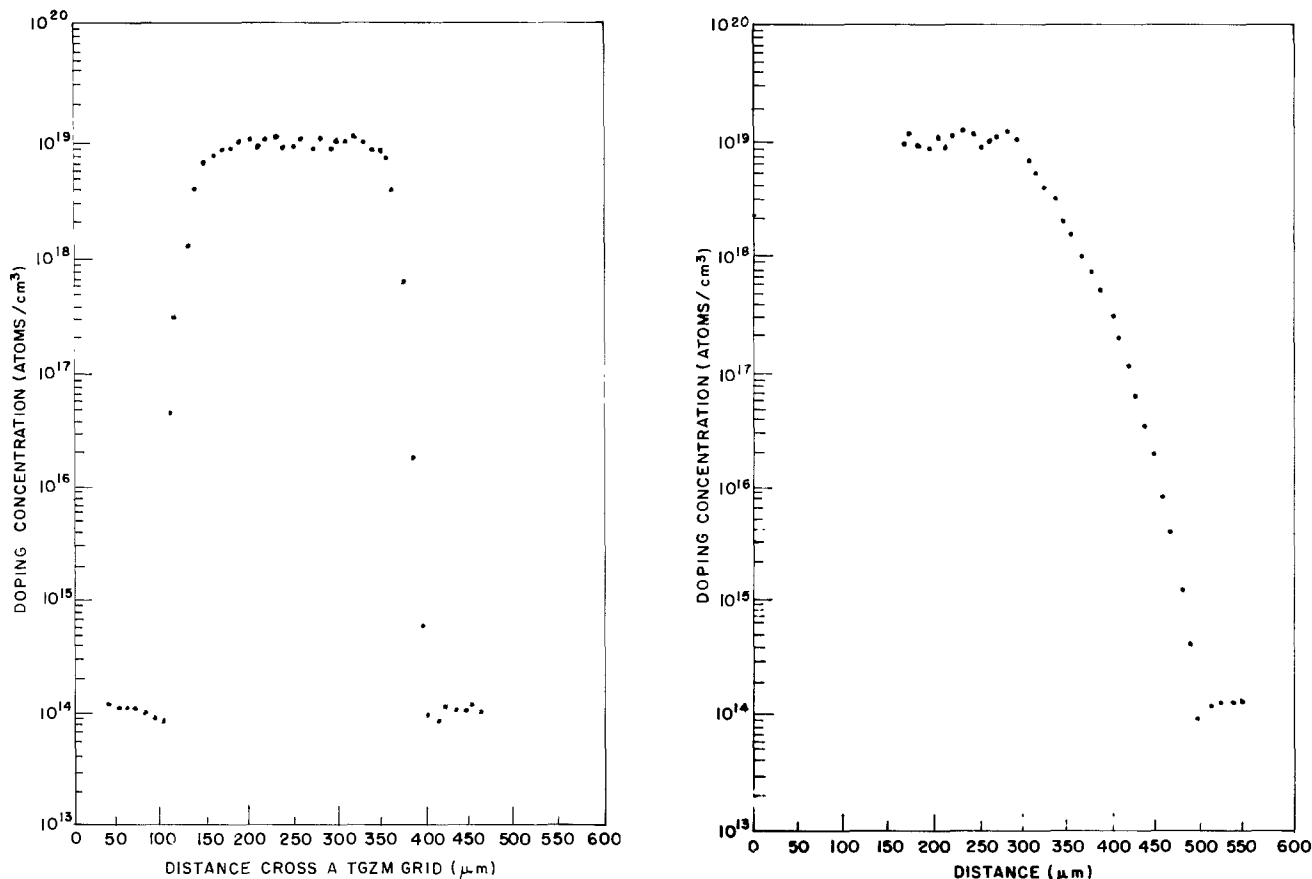


Fig. 7. The effect of side expansion from a post-TGZM diffusion. (a, left) The concentration profile of a TGZM trail before the post-TGZM diffusion; (b, right) the concentration profile after the post-TGZM diffusion.

TGZM operation can be detected by device evaluation. In a typical example, an SCR was fabricated from 50 Ω -cm, 400 μ m thick n-type silicon wafers. The carrier lifetime measurements (open-circuit decay method) showed values of 10-20 μ sec at high injection levels, which is comparable to equivalent devices processed without TGZM. Another way of evaluating the effectiveness of the TGZM operation is to compare blocking-voltage capabilities. These SCR's showed a blocking capability of 1600V in both directions, which is approximately 80% of the theoretical bulk avalanche breakdown voltage for this resistivity range. The leakage current level at 1600V was about 1.5A, as shown in Fig. 9, which suggests a good lifetime. The low leakage is a function of the superior surface passivation obtained with glass. It should be noted that the planar structures studied in this investigation are more adaptable to glass passivation than conventional mesa types.

Various devices have been made with this process. These devices have blocking voltages as high as 2500V and a current-carrying capability of up to 600A. Some of these devices are shown in Fig. 10. Their characteristics are listed in Table I. This table does not imply any limit for devices fabricated by the TGZM technique; it is presented only to indicate the extent of the present work.

Table I. The characteristics of some devices made with TGZM isolation and glass passivation

| Device | Current ratings (RMS) | Blocking (volts) |
|-------------|-----------------------|------------------|
| C106 | 4 | 600 |
| BC57 (C147) | 63 | 1600 |
| C190 | 650 | 800 |
| 40 MM | 950 | >2600 |

Summary

The temperature gradient zone melting technique was used to create deep p-n junctions in silicon at greatly reduced processing times. In this study, TGZM process variations related to power semiconductor structures have been investigated. The specific results of this investigation are summarized as follows.

1. TGZM has proven to be an effective means of fabricating power semiconductor structures that could not be made solely by solid-state diffusion.
2. A method of loading wafers in the TGZM work chamber to assure a unidirectional temperature gradient was demonstrated.
3. Of the four methods of interfacing an aluminum array with a silicon wafer, the direct application approach proved to be the simplest.
4. The introduction of slow heating and cooling segments of the TGZM temperature cycle was effective in reducing thermal shock stresses and eliminated the need for presintering the aluminum pattern.
5. Of the two basic processing sequences studied, the "TGZM-first" approach proved to yield significant advantages.
6. Based on the current state-of-the-art, TGZM is limited to 2 mil aluminum pattern linewidths and silicon wafer thicknesses greater than 8 mils.
7. Alignment of the aluminum pattern to the crystal lattice was shown to be necessary only on very narrow linewidths.
8. It was demonstrated that a rough and darkened silicon wafer surface yielded the highest rate of migration.
9. Characteristics of a typical SCR structure fabricated with TGZM isolation regions have been described.

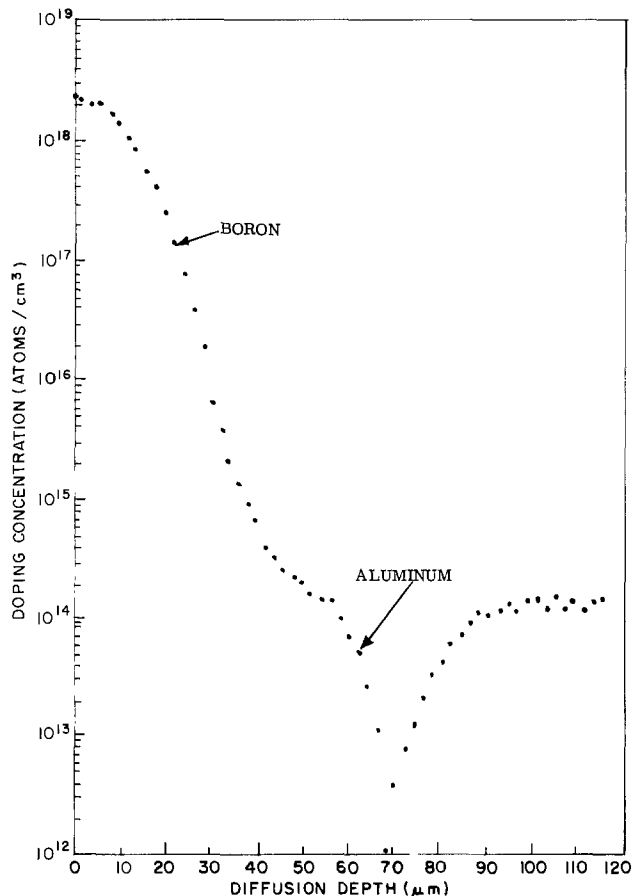


Fig. 8. A plot of a concentration profile shows the result of a closed tube diffusion where the TGZM trails in the silicon wafers served as an aluminum diffusion source and where an extra boron source was added to enhance the surface concentration.

Acknowledgment

The author wishes to express his gratitude to Dave Hartman, Mark Barron, and Richard Kokosa for their constant interest and encouragement. He is indebted to H. Cline and T. Anthony for many helpful discussions and encouragement. The manpower support of Dave Smith, Don Foran, Lil Jones, and Ed Lederer is gratefully acknowledged.

Manuscript submitted Sept. 4, 1979; revised manuscript received ca. April 22, 1981. This was Paper 158 presented at the Boston, Massachusetts, Meeting of the Society, May 6-11, 1979.

Any discussion of this paper will appear in a Discussion Section to be published in the June 1982 JOURNAL. All discussions for the June 1982 Discussion Section should be submitted by Feb. 1, 1982.

Publication costs of this article were assisted by the General Electric Company.

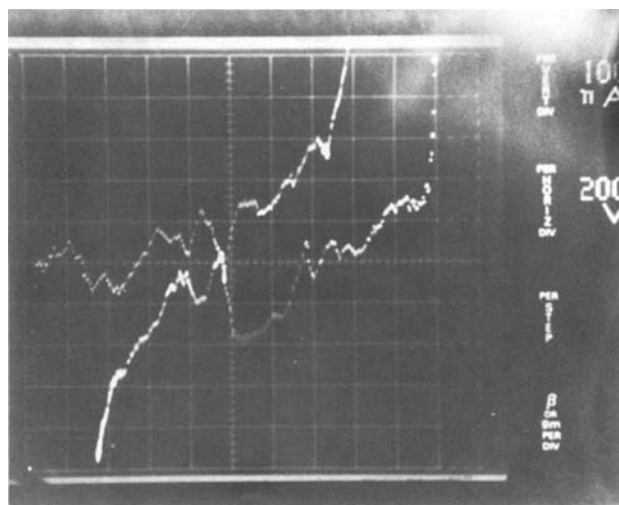


Fig. 9. The characteristics of an SCR made with TGZM isolation and glass passivation.

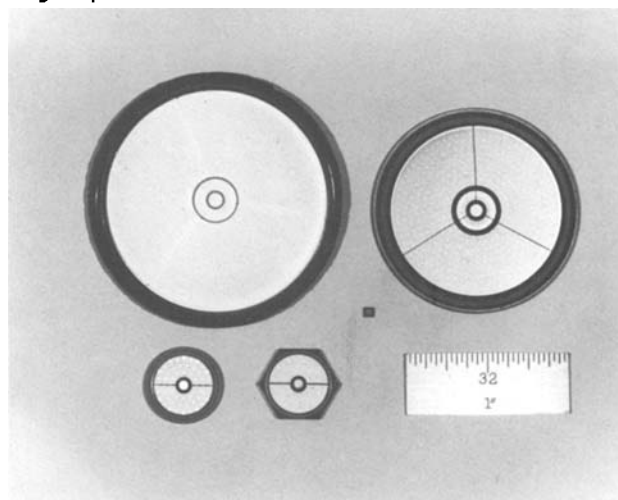


Fig. 10. A picture of some devices made with TGZM isolation and glass passivation.

REFERENCES

1. M. Chang, Paper 296 presented at The Electrochemical Society Meeting, Seattle, Washington, May 21-26, 1978.
2. T. Anthony, J. Boah, M. Chang, and H. Cline, *IEEE Trans. Electron Dev.*, **ed-23**, 818 (1976).
3. J. Boah, U.S. Pat. 4,001,047.
4. M. Chang, T. Anthony, and H. Cline, U.S. Pat. 4,076,559.
5. T. R. Anthony and H. E. Cline, *J. Appl. Phys.*, **42**, 3880 (1971).
6. H. E. Cline and T. R. Anthony, *ibid.*, **43**, 4391 (1972).
7. T. R. Anthony and H. E. Cline, *ibid.*, **47**, 2316 (1976).
8. H. E. Cline and T. R. Anthony, *ibid.*, **47**, 2325 (1976).
9. H. E. Cline and T. R. Anthony, *ibid.*, **47**, 2332 (1976).
10. T. R. Anthony and H. E. Cline, *ibid.*, **47**, 2550 (1976).

Nonequilibrium in Substitutional-Interstitial Diffusion of Zn in GaAs at 850°C

G. Chiaretti

CSELT, Via G. Reiss Romoli, 274, 10148 Torino, Italy

and C. Cognetti

SGS/ATES Componenti Elettronici S.p.A., Via Tolomeo, 1, 20019 Castelletto di Settimo Milanese, Milano, Italy

ABSTRACT

Good control of the diffusion profile on Zn in GaAs is essential in many practical applications. By photoluminescence measurements the Zn distribution obtained in several diffusion runs at 850°C with GaZn:GaAs sources was determined. Under well-defined diffusion conditions, complementary error function distributions of the impurity were found. This is justified admitting that a nonequilibrium in gallium vacancy concentration may be noticeable for a relatively long time (up to 60-90 min); in this case the substitutional-interstitial mechanisms are no longer valid and the diffusion becomes purely substitutional. The coefficient for substitutional diffusion is $D_s = 1.5 \times 10^{-11} \text{ cm}^2 \text{ sec}^{-1}$. Complications due to the source composition and to the surface status of the substrate are also described.

The Zn diffusion mechanism in GaAs can be well understood on the basis of a substitutional-interstitial model (1) in which the equilibrium concentration of Ga vacancies is the controlling factor for the impurity diffusion. The diffusion is explained by means of the existence of a "fast" interstitial ion Zn_i^{m+} ($m = 1, 2$ degree of ionization), which reacts with a gallium vacancy V_{Ga} to produce a "stationary" substitutional ion Zn_s^- and $(m + 1)$ holes



The amount of interstitial Zn_i depends on $[V_{\text{Ga}}]$ and hence from the As partial pressure P_{As_4} through the equilibrium constants K_1 and K_2

$$\frac{[\text{Zn}_i^{m+}]}{[\text{Zn}_s^-]} = \frac{K_1}{[V_{\text{Ga}}]} = \frac{K_2}{[P_{\text{As}_4}]} \quad [2]$$

In this model, the effective diffusion coefficient D is a function of a power of the dopant concentration C_{Zn} , whose exponent goes from zero [very high P_{As_4} (2, 3)] to three [low P_{As_4} , low temperature (4, 5)]. In the first case, for $P_{\text{As}_4} \cong 2 \text{ atm}$, $[V_{\text{Ga}}]$ is so high that $[\text{Zn}_i]$ falls to negligible values (Eq. [2]); only the diffusion of Zn_s is significant and the diffusion process reverts to the substitutional one, with $D_s = \text{const} \cong 10^{-11} \text{ cm}^2 \text{ sec}^{-1}$ even at $C_{\text{Zn}} \cong 10^{20} \text{ cm}^{-3}$ at 900°C. Lowering P_{As_4} , $[\text{Zn}_i]$ increases and interstitial diffusion becomes dominant; if the equilibrium of $[V_{\text{Ga}}]$ exists, D is proportional to C_{Zn}^{m+1} and a "supergaussian" profile is obtained

$$C_{\text{Zn}} = C_s \left(1 - \frac{x}{x_j} \right)^{1/(m+1)} \quad [3]$$

with C_s = surface concentration and x_j = junction depth.

More complex profiles are known with noninteger values of $(m + 1)$ (6, 7) and with a double diffusion front (2, 7).

With properly prepared GaAs substrates, diffusions performed at 850°C and with an As pressure which corresponds to the GaAs dissociation pressure, gave a complementary error function distribution of the Zn ($D = \text{const}$), which apparently contrasts with all

published experimental data. For an interpretation, it is assumed that, in our diffusion conditions, the $[V_{\text{Ga}}]$ is out of equilibrium for a time which is not negligible. This must be taken into account in order to achieve complete control of the diffusion process.

Experimental

In order to optimize a Burrus-type diffused LED, we needed a diffusion process which allowed precise control of the Zn profile, of the Zn surface concentration (between 10^{19} and $4 \times 10^{19} \text{ cm}^{-3}$), and of the junction depth (between 4 and 7 μm).

More than thirty tests were performed on $2 \times 10^{18} \text{ cm}^{-3}$ Si doped GaAs wafers, (100) oriented, dislocation content (EPD) less than 300 cm^{-2} , polished on one side, supplied by Sumitomo. Before Zn diffusion about 70 μm were etched away; by chemical-mechanical polishing employing a solution (1000 H_2O_2 :5 NH_4OH); after the final chemical etching (5 H_2SO_4 : H_2O_2 : H_2O) the correct value of EPD was found, indicating that all work damage was removed.

Slices of 4 cm^2 area were sealed in a quartz ampul of about 70 cm^3 , evacuated at 10^{-6} Torr. The total weight of the source was 1g, with Zn concentrations x_{Zn} between 3.5 and 13 atomic percent (a/o). A quantity of GaAs varying from 0 to 150 mg was added to the source.

Diffusion times varied from 15 min to some hours. The C_s and Zn profiles were measured by photoluminescence (PL) on a bevelled ($\sim 2^\circ$) sample using as excitation light the 6471Å line of a Kr laser, focused to a 5 μm spot.

It is well known that both the peak wavelength λ_m and the full width half maximum $\Delta\lambda$ of the PL spectrum are related to the Zn concentration in GaAs. However, the spectra are rather flat and therefore λ_m cannot be accurately identified and $\Delta\lambda$, in nonuniformly doped samples, depends on the concentration gradient below the excitation spot.

For these reasons we chose a different calibration which is shown in Fig. 1. The normalized PL spectra of four uniformly Zn-doped samples whose carrier concentration was measured by the Hall effect are shown in the figure; the axis labeled d goes through the 80% relative intensity of the spectra and gives the abscissa for the required calibration curve, shown in Fig. 2.

Key words: GaAs technology, photoluminescence measurements on GaAs:Zn, diffusion profiles of Zn in GaAs.

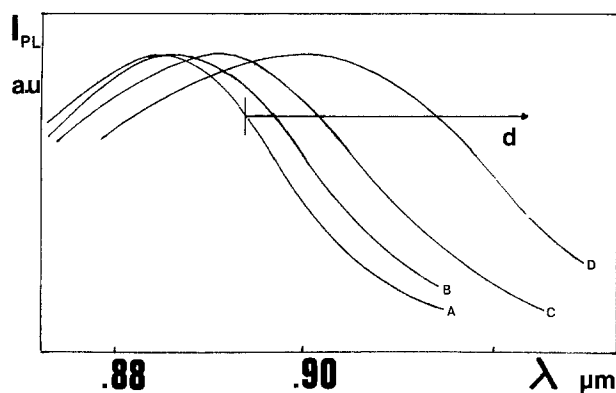


Fig. 1. PL spectra of uniformly doped GaAs:Zn samples. Curves A, B, C, and D refer to doping levels of 10^{18} , 3.5×10^{18} , 9×10^{18} , and $4 \times 10^{19} \text{ cm}^{-3}$, respectively.

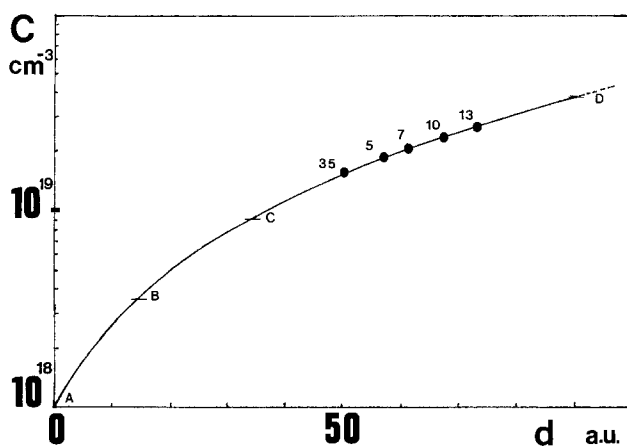


Fig. 2. Calibration curve C_{Zn} vs. d , obtained from Fig. 1. The closed circles are experimental C_s values for diffusions with As-saturated sources having the indicated a/o of Zn content.

Although this choice may be considered empirical, we found that the shift in the low energy side of the PL spectrum is much more sensitive to the doping level variations; furthermore, it is the least affected by the PL contribution arising from the material underlying the point under measurement, which may severely influence the whole PL spectrum, particularly when measurements are made close to the p-n junction (8).

An absolute accuracy better than 10% was estimated for this method.

x_j measurements were made by SEM on reverse biased samples and sheet resistance R_s was measured by the four-point method. The residues of solid GaAs, if present, were removed from the liquid source and weighed to know the final composition of the source.

To understand the importance of surface status, diffusions were added for comparison on intentionally damaged wafers; these were obtained by lapping their surfaces with $5 \mu\text{m Al}_2\text{O}_3$ (measured depth of the damage 40-50 μm) and removing only 10-20 μm by polishing.

Results

Figure 3 shows the relationship between x_j and \sqrt{t} for diffusions performed with more than 100 mg of solid GaAs in the source.

By the procedure illustrated in the preceding section, it was verified that this quantity of GaAs (corresponding to an As content of about 5-6 a/o) was necessary to reach the equilibrium composition of the source at the diffusion temperature, so as to have an As saturated source. This agrees with published experi-

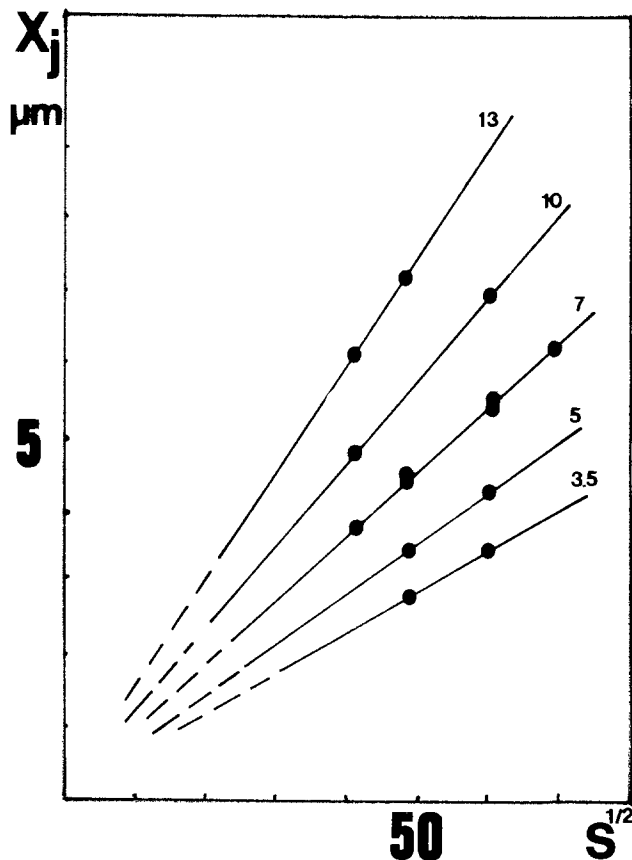


Fig. 3. Plot of x_j vs. \sqrt{t} , at different x_{Zn}^1 , for As-saturated sources.

mental data about the ternary phase diagram GaAsZn (9).

All sources having a lower amount of solid GaAs gave deeper profiles with some single defects on the wafer surface, due to As out-diffusion, and with fair reproducibility of C_s , for constant x_{Zn}^1 and diffusion times.

Figure 4 refers to diffusions with As saturated sources and shows the correct dependence of C_s from $(x_{\text{Zn}}^1)^{1/2}$, C_s being lower than the Zn solubility limit in GaAs (10).

Among the profiles of Fig. 5, A is typical for equilibrium sources with $t \leq 60$ -80 min: It is a complementary error function distribution with $D_s \approx 1.5 \times 10^{-11} \text{ cm}^2 \text{ sec}^{-1}$; diffusion with $t < 60$ min on damaged substrates showed a double front profile (Fig. 5B).

For $t \geq 120$ min, "supergaussian" profiles ($m + 1 = 2$) were always found both for damaged and normally processed wafers. Diffusion conditions and experimental results for the data reported in Fig. 5 are summarized in Table I.

Figure 6 compares the calculated values of R_s for erf and "supergaussian" ($m + 1 = 3$) distributions; experimental points confirm PL profile measurements.

Discussion and Conclusions

Erfc profiles are quite unusual for Zn in GaAs; they are expected for very high As pressures and for C_{Zn}

Table I. Experimental conditions for profiles shown in Fig. 5

| Profile | A | B | C |
|--|------|---------|------|
| Source: x_{Zn}^1 (a/o) | 7 | 7 | 7 |
| GaAs (mg) | 150 | 150 | 150 |
| GaAs residue (mg) | 50 | 50 | 50 |
| Diffusion time (min) | 60 | 60 | 120 |
| C_s ($\times 10^{19} \text{ cm}^{-3}$) | 2.1 | 2.1 | 2.1 |
| x_j (μm) | 5.5 | 6.3 | 8.5 |
| Surface status | Good | Damaged | Good |

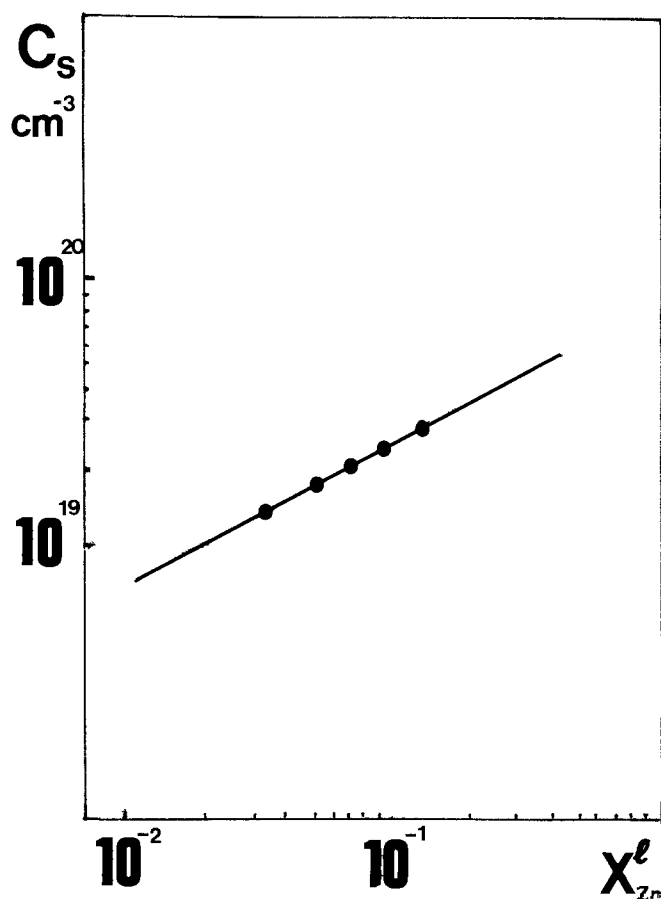


Fig. 4. Surface concentration C_S vs. x_{Zn}^l . The slope of the straight line is 0.5.

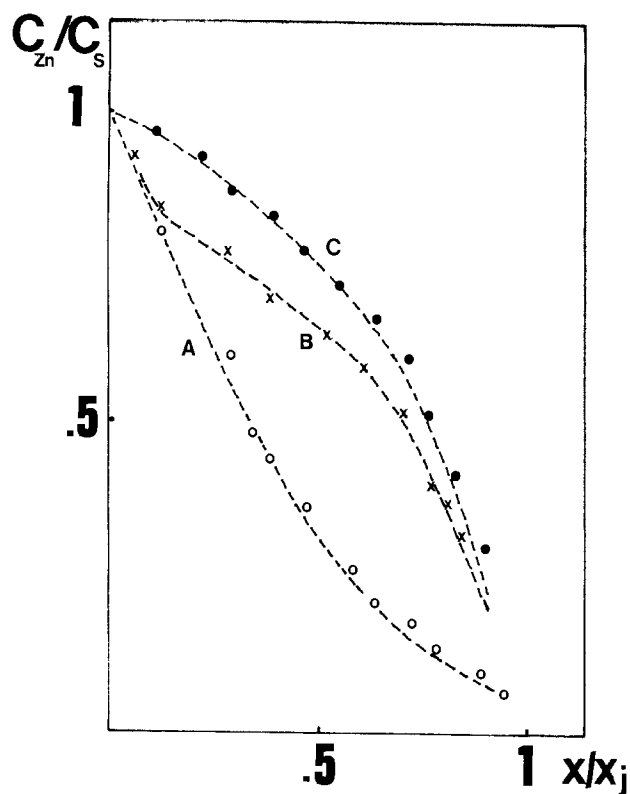


Fig. 5. Dopant profiles for diffusions of Table I

lower than intrinsic carrier concentration n_i [2×10^{17} cm^{-3} at 850°C (11)] possibilities that are excluded in our experiments, where the As partial pressure is 10^{-4} atm or less (12) and $C_{Zn} \gg n_i$.

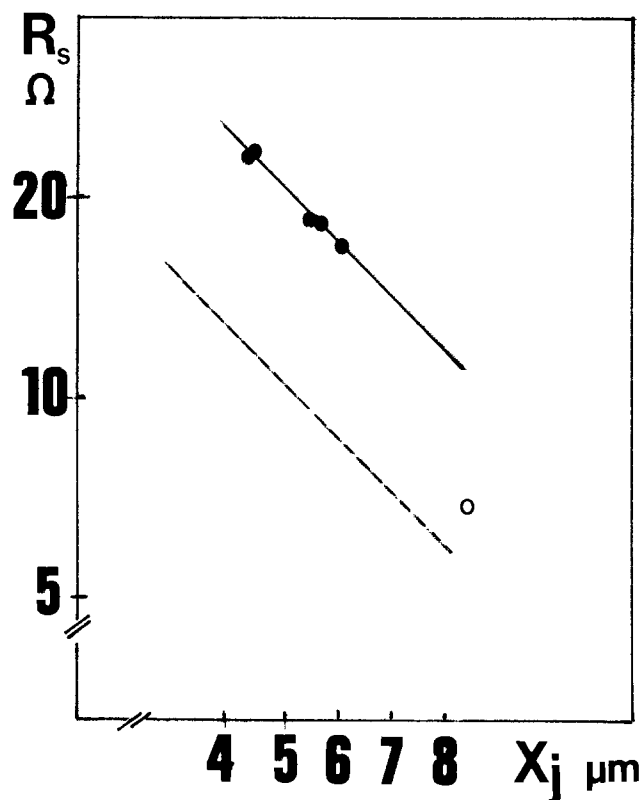


Fig. 6. Calculated dependence of R_S from x_j , for erfc and "super-gaussian" ($n = 3$) distributions at $C_S = 2.1 \times 10^{19}$ cm^{-3} . Closed circles refer to 40, 60, 80 min diffusions with As-saturated source and $x_{Zn}^l = 7\%$. Open circle comes from a 120 min diffusion, with the same source.

However, we observed erfc profiles in more than ten diffusion runs (profile 5A).

On the other hand, with similar sources and the same substrates, double front and "supergaussian" profiles were found also (profiles 5B, 5C).

The main difference between the two sets of diffusions regarded only the treatment of the surfaces and the diffusion times.

The situation can be understood by considering that, if growing and processing the crystals permit the exclusion of consistent sources of Ga vacancies in the bulk, their diffusion from the surface must control the final distribution of Zn_s . Actually, the assumption that $[V_{Ga}]$ is always near its equilibrium value during the diffusion may be correct for highly dislocated crystals and for diffusion times large enough to permit the V_{Ga} equilibrium. However, if the defect content of the substrate is low, V_{Ga} must be considered out of equilibrium in the first step of the diffusion. In this case the reactions [1] and [2] indicate that the slowly diffusing vacancies control the diffusion process by decreasing $[Zn_i]$.

The diffusion becomes a purely substitutional one, with a constant D_s .

From the profile 5A we found $D_s \approx 1.5 \times 10^{-11}$ cm^2 sec^{-1} which is very close to the diffusion coefficient measured for diffusions performed in excess As pressure (2, 3) and agrees with the value 6×10^{-10} cm^2 sec^{-1} at 1000°C (7), if one assumes a decrease of 1-2 orders of magnitude for a temperature reduction from 1000° to 850°C .

By comparison of profiles 5A and 5C, it may be concluded that a time between 60 and 120 min is needed to reach the V_{Ga} equilibrium at 850°C .

A nonlinear relationship between x_j and \sqrt{t} leads to shorter diffusion depth for $t \leq 60$ -80/min; this is in agreement with the conclusions of other works

employing a lower temperature range 600°-750°C (13), and confirms other experimental results at 875°C [Ref. (14), Fig. 3].

We may conclude that in practical applications, when shallow junctions are required, the sublinear dependence $x_j \rightarrow \sqrt{t}$ and the existence of profiles less steep than the "supergaussian" must be taken into account to ensure a good reproducibility of the diffused region.

Acknowledgments

We wish to thank Dr. Ing. M. Conti, Drs. U. Michi and G. Randone for helpful discussions; and Mrs. M. De Grandis and Mr. A. Gabrielli for their assistance in the preparation of samples.

Manuscript submitted Nov. 14, 1980; revised manuscript received ca. March 30, 1981.

Any discussion of this paper will appear in a Discussion Section to be published in the June 1982 JOURNAL. All discussions for the June 1982 Discussion Section should be submitted by Feb. 1, 1982.

Publication costs of this article were assisted by CSELT, Centro Studi e Laboratori Telecomunicazioni S.p.A.

REFERENCES

1. B. Tuck, "Introduction to Diffusion on Semiconductors," Peter Peregrinus LTD, England (1974). This work contains citations of relevant prior works.
2. K. K. Shih *et al.*, *J. Phys. Chem. Soc.*, **29**, 379 (1968).
3. H. Rupprecht and C. Z. Le May, *J. Appl. Phys.*, **35**, 1970 (1964).
4. D. L. Kendall and M. E. Jones, AIEE-IRE DRC, Stanford Univ. (1961).
5. G. L. Pearson *et al.*, *Bull. Am. Phys. Soc.*, St. Louis Meeting (1963).
6. A. Luque *et al.*, *Solid State Sci.*, **123**, 249 (1976).
7. J. Blanc, *J. Appl. Phys.*, **45**, 1948 (1974).
8. E. Daniels, *ibid.*, **44**, 5526 (1973).
9. S. F. Guo, G. L. Pearson, and C. D. Thurmond, *This Journal*, **118**, 486 (1971).
10. H. C. Casey and H. B. Panish, *Phys. Rev.*, **162**, 660 (1967).
11. L. L. Chang and G. L. Pearson, *J. Phys. Chem. Soc.*, **25**, 23 (1964).
12. A. S. Jordan, *Mat. Trans.*, **2**, 1965 (1971).
13. C. H. Ting and G. L. Pearson, *Solid State Sci.*, **118**, 1454 (1971).
14. A. H. Herzog *et al.*, *J. Appl. Phys.*, **43**, 600 (1972).

Low Pressure Vapor Phase Epitaxy of GaAs in a Halogen Transport System

N. Pütz, E. Veuhoff, K.-H. Bachem,* P. Balk,* and H. Lüth

Physikalisches Institut and Institute of Semiconductor Electronics/SFB 56, "Festkörperelektronik," Aachen Technical University, D-5100 Aachen, Germany

ABSTRACT

Deposition of GaAs from the Ga-AsH₃-HCl-H₂ system at 1023 K and pressures from 1 down to 0.01 bar leads to controlled growth rates ranging from 40 to 1 μm/hr. Due to the surface kinetic limitation of the process, very uniform films are obtained at reduced pressures. The background impurity level is low; 77 K electron mobilities of 73,000 cm² V⁻¹ sec⁻¹ were obtained for not purposely doped samples with electron concentrations in the upper 10¹⁴ cm⁻³ region. Using H₂S as a dopant, the electron concentration increases linearly with the H₂S pressure. The sulfur-doped films show the same values for the mobility and the saturation concentration of electrons as layers obtained at atmospheric pressure.

Transport in a chlorine system (1, 2) provides a convenient technique for the preparation of GaAs layers of reproducible thickness and well-defined impurity content. These features make the transport approach attractive for the fabrication of optoelectronic and microwave devices. However, in the classical tube-type reactor, operating at atmospheric pressure, uniform epitaxial growth is only possible on a limited substrate area. Moreover, the rates tend to be of such a magnitude that thickness control in the submicron region presents some difficulties.

Suitably low growth rates of approximately 1 μm/hr may be obtained with the MBE method (3) at the price of using rather complicated equipment. Experience from the silicon technology indicates that both low growth rates and excellent control of film thickness over a substantial number of samples may be obtained by carrying out the deposition of silicon or insulators from the vapor phase at low pressures (4, 5). Such uniform deposition can only be expected if all substrates are exposed to the same gas phase composition, which means that no appreciable depletion of the gas phase should occur in the deposition region. This con-

dition will be met if the growth process is slow, *i.e.*, the growth rate should not be determined by mass transfer (diffusion) in the gas phase, but be limited by the kinetics of the reaction at the surface.

For III-V compound semiconductors the feasibility of the low pressure technique has only been demonstrated for the organometallic chemical vapor deposition (MOCVD) process, using trimethyl gallium and AsH₃. However, in this case the growth process is apparently limited by mass transfer rather than by surface kinetics (6, 7). The study described in the present paper was concerned with the behavior of the inorganic system Ga-AsH₃-HCl-H₂, also at low pressures. It will be shown that for typical experimental conditions the deposition rate is kinetically limited and that a wide range of growth velocities is available by varying the hydrogen pressure.

The Growth Rate for Mass Transport Limited Conditions

The maximum possible growth rate will be obtained for conditions where the process is mass transport controlled in the limiting case of complete removal of the supersaturation in the gas phase. The value of the maximum rate for a given flow rate and surface area

* Electrochemical Society Active Member.

Key words: film growth, kinetics, doping, electron mobility.

of the sample may be calculated from the actual and equilibrium concentrations of the reactive components in the system

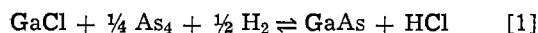


Figure 1 shows the calculated maximum growth rate for a substrate area of 1 cm² and a gas velocity of 0.8 cm/sec (the same value as used in our experiments) as a function of the hydrogen pressure. The GaCl and AsH₃ pressures have been indicated in the figure; they are typical for the operation of this system at atmospheric pressure. The rate exhibits a square root dependence below $2 \cdot 10^{-2}$ bar. At higher pressures the slope decreases because the growth process becomes limited by the amount of gallium available in the gas phase. Therefore, at higher GaCl pressures the curve not only shifts to the right, but the square root dependence also extends to higher hydrogen pressures. It can be recognized from the figure that the rates are in the range of 50-1000 μm/hr. Varying the AsH₃ and GaCl pressures around the values used in Fig. 1 will affect the rate data. However, for the combinations of parameters covered in the experimental part of this study the above-mentioned range still applies for the calculated rate values.

In practical cases the diffusion limitation will lead to slower deposition. For surface limited growth not only lower rates should be observed, but also different pressure dependences than those derived from thermodynamic considerations may be expected.

Experimental

The growth of GaAs in an inorganic chlorine transport system at low pressures presents some specific problems. As shown above, thermodynamic considerations predict that for a given pressure and flow rate of the GaCl and AsH₃ entering the substrate zone the amount of material available for deposition, and thus the growth rate, will decrease when lowering the hydrogen pressure. Due to the increased diffusivity of the gas species at lower pressures, the wall of the reactor downstream of the deposition zone, which is generally at a lower temperature than the substrate, will more effectively compete with the substrate for the reactants. For the same reason one expects the reactor design to become increasingly critical for obtaining efficient reaction between HCl and the Ga source.

With these considerations in mind a low pressure deposition apparatus was designed capable of operating at low gas flows, for example 30 cm³ STP/min at $6.5 \cdot 10^{-2}$ bar through a reactor of 60 mm diam. In our experiments we used a gas velocity of 0.8 cm/sec, which was held constant in all cases. Figure 2 shows a schematic of the reactor. The source chamber was

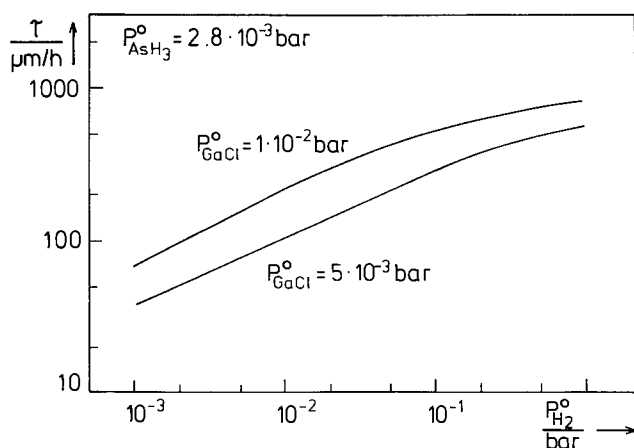


Fig. 1. Calculated dependence of maximum growth rate on H₂ pressure for two GaCl pressures for complete exhaustion of gas phase; surface area: 1 cm²; gas velocity: 0.8 cm sec⁻¹.

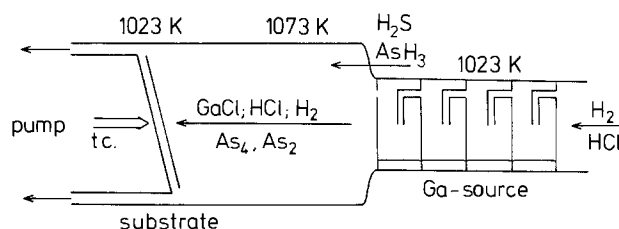


Fig. 2. Schematic diagram of low pressure reactor

constructed to achieve optimum interaction between the Ga melt and the gas phase and thereby efficient production of GaCl. Furthermore, the present design minimizes back-diffusion of AsH₃ to the Ga melt. Similarly, the layout of the deposition chamber is such that diffusion to the colder part of the reactor, where condensation on the walls might take place, is impeded. The temperature of the source was 1023 K in all experiments, that of the substrate was the same except in the experiments where the temperature dependence of the rate was investigated. To allow a high supersaturation of the gas phase without risking deposition at the reactor walls the temperature in the central part of the reactor, where pure AsH₃ was injected, was higher than that at the substrate. HCl was generated by reduction of AsCl₃ with hydrogen at 1023 K and subsequent condensation of the arsenic. The doping gas H₂S was injected together with AsH₃ over a bypass directly into the deposition zone. The sulfur concentration in the gas phase was determined photometrically using the methylen blue method. (8). Total pressures in the range of 0.01-1 bar could be maintained using a rotary pump of 30 m³/hr capacity. Cooling traps and an activated carbon filter between pump and reactor provided adequate protection of the pump against the reactive gases from the deposition system and impeded back-diffusion of oil into the reactor.

Substrates were semi-insulating (100) oriented GaAs wafers which were etched in an H₂O₂/H₂SO₄/H₂O mixture before deposition. The epitaxial system was purged by a number of pumping and flushing cycles, the latter with hydrogen at atmospheric pressure. Before each epitaxial run the substrate was annealed for 5 min in an AsH₃ atmosphere at 1023 K in order to remove residual contaminants such as oxygen and carbon (3) from the surface.

The thickness of the epitaxial layers was determined microscopically after staining (9) to an accuracy of approximately 0.3 μm. Hall mobilities and electron concentrations were measured using the method of van der Pauw (10).

Results

Figure 3 shows the dependence of growth rate on the pressure of the carrier gas (hydrogen), which was varied over a wide range (0.01-1 bar). Below 0.2 bar the growth rate increases linearly with hydrogen pressure (closed circles), whereas at a higher pressure this linearity turns into a square root dependence (open circles). It may be seen that the growth rate can be varied from approximately 1 to 40 μm/hr. In the following figures the dependence of rate on experimental parameters is shown for two hydrogen pressures: one in the linear range at lower pressure and one in the square root range at higher pressures.

The influence of growth temperature on the rate is demonstrated in Fig. 4. The curves exhibit a maximum at the same temperature, independent of hydrogen pressure, but the slope of the low temperature flank is larger in the low hydrogen pressure region.

The dependence of the rate on the GaCl and AsH₃ pressures is shown in Fig. 5 and 6, respectively. In the former case it exhibits a maximum which moves to a higher GaCl pressure for the higher hydrogen pressure region. The rate exhibits a 1/4 order dependence on AsH₃ pressure for both ranges of hydrogen pressure.

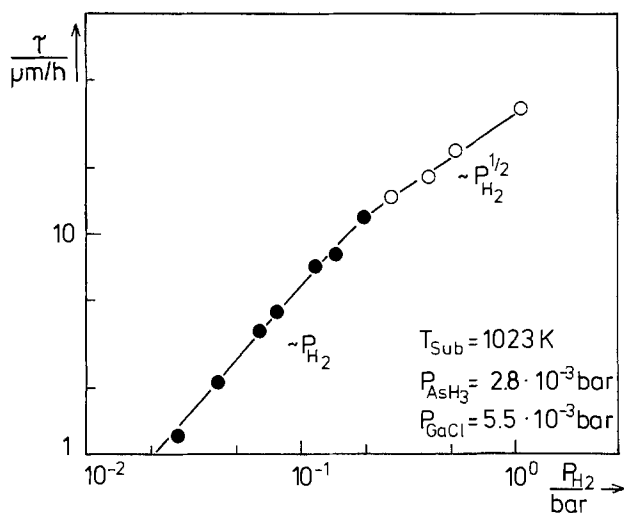


Fig. 3. Growth rate vs. hydrogen pressure

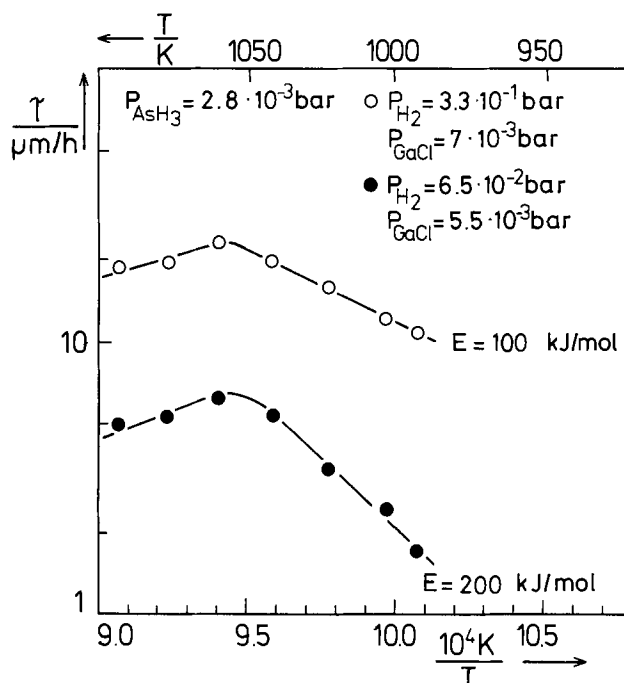


Fig. 4. Growth rate vs. reciprocal growth temperature for two hydrogen pressures.

It reaches a saturation value which shifts to a higher AsH_3 pressure for the higher hydrogen pressure range. In all experiments the substrate was kept at 1023 K. To obtain the higher hydrogen pressure data in Fig. 4, the GaCl pressure was increased from 5.5 to $7 \cdot 10^{-3}$ bar in order to remain in the region of the descending flank to the right of the maximum in Fig. 5. The same change was made to obtain the upper curve in Fig. 6.

A study of the uniformity of film growth obtained in our apparatus indicated within experimental error ($0.3 \mu\text{m}$) the same thickness over the entire sample area of 12 cm^2 for a $6.0 \mu\text{m}$ deposit grown at $6.5 \cdot 10^{-2}$ bar. This should be compared with a thickness variation of $0.7 \mu\text{m}$ on a layer of the same area and $4.7 \mu\text{m}$ total thickness grown at 1 bar.

Besides the influence of the epitaxial parameters on the growth rate, the doping behavior has also been investigated. Figure 7 represents the results of doping experiments in the low pressure system. It shows the electron concentration (n) measured at 77 K as a function of H_2S pressure for two hydrogen pressures. Both curves show a linear increase of n with H_2S pressure and a rather abrupt saturation of the electron concen-

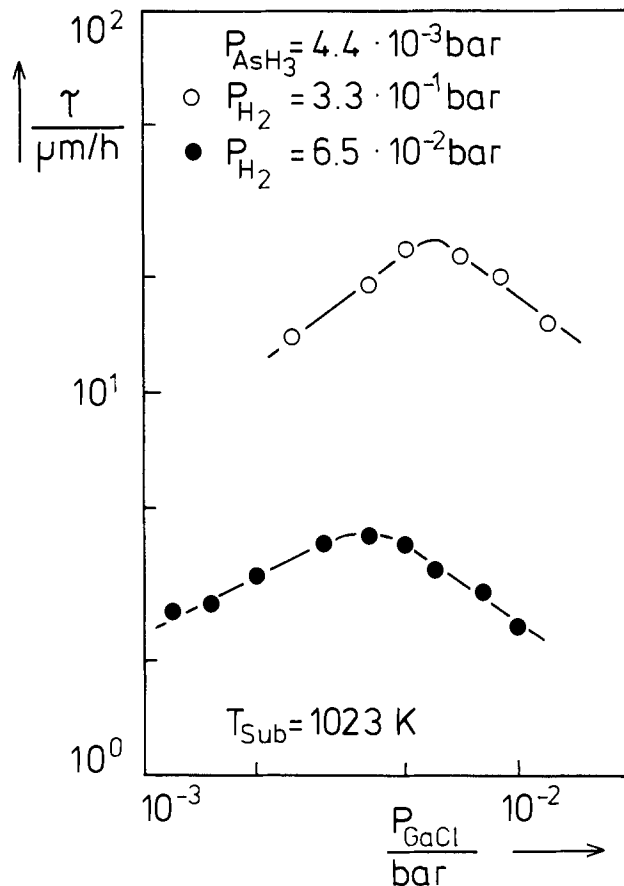
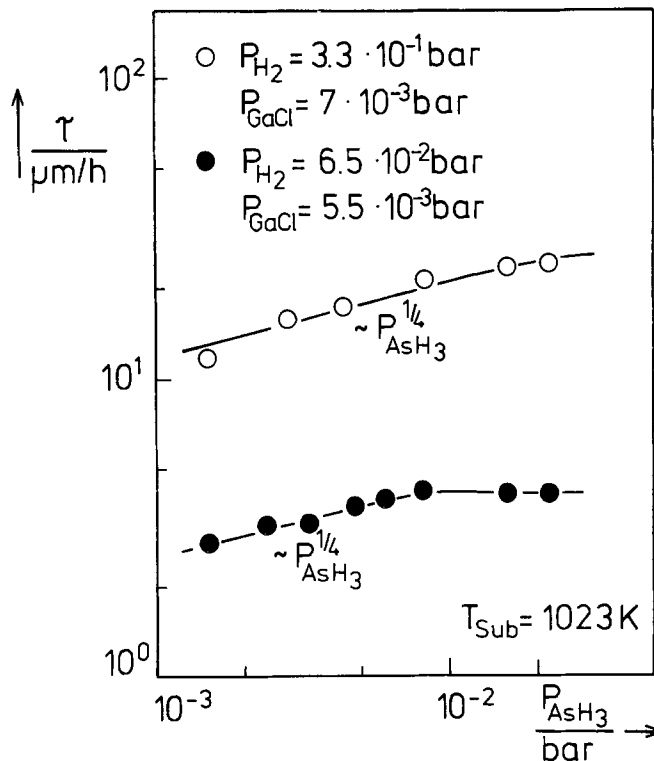


Fig. 5. Growth rate vs. GaCl pressure for two hydrogen pressures

Fig. 6. Growth rate vs. AsH_3 pressure for two hydrogen pressures

tration at approximately $3 \cdot 10^{18} \text{ cm}^{-3}$. A decrease in hydrogen pressure by a factor of 5 requires the same reduction in H_2S pressure in order to obtain films with same electron concentration. However, the saturation value does not appear to be affected by this decrease.

The corresponding Hall mobilities are plotted in Fig. 8 together with the data from Hall measurements for

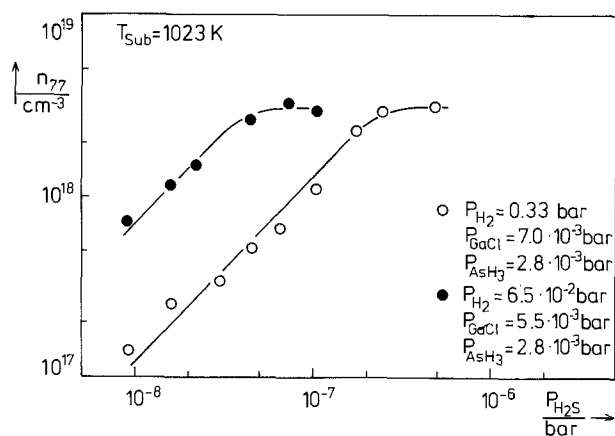


Fig. 7. Electron concentration (77 K) vs. H_2S pressure for low pressure VPE GaAs; parameter: hydrogen pressure.

unintentionally doped material. The solid line represents the phenomenological curve from Ref. (11); it is based on samples grown from the vapor phase at atmospheric pressure. Our data points are close to this curve except at electron concentrations below $2 \cdot 10^{15} \text{ cm}^{-3}$, where the mobility data systematically lie above the curve. Mobilities up to $73,000 \text{ cm}^2/\text{Vsec}$ were obtained for samples with n in the high 10^{14} cm^{-3} region.

Discussion

As may be seen in Fig. 3, the growth rate can be varied over more than one order of magnitude by changing the hydrogen pressure between 10^{-2} and 1 bar. However, the square root dependence expected from thermodynamic considerations (Fig. 1) only appears at higher pressures. The linear relationship at low pressures indicates that the hydrogen molecule is involved in the rate-limiting step. This behavior would fit the simple model that the reduction of adsorbed GaCl to Ga by H_2 is the rate-limiting process in the growth reaction. The same considerations have been made to explain the behavior of a chlorine transport system with a hydrogen-inert gas mixture (12). In this case also a linear relationship was found between rate and hydrogen pressure, but at a hydrogen pressure between 0.2 and 1 bar at a total pressure of 1 bar.

The different slopes of the growth rate above and below 0.2 bar (Fig. 3) suggest that the rate-limiting steps are different in these two regions. This was the reason for studying the dependence of the rate on growth temperature (Fig. 4) for a hydrogen pressure in the linear range and one in the square root range of Fig. 3. The curves show the familiar maximum (13, 14). Especially the increasing growth rate with increasing temperature below 1050 K is indicative of a surface reaction limited regime. The slopes at temperatures below the maximum, i.e., the activation energies, are indeed different in the two regions of hydrogen pressure.

On the other hand, it was reported for the organometallic low pressure system (6, 7) that the growth rate depends neither on growth temperature for any hydrogen pressure nor on the hydrogen pressure itself at a constant molar fraction of trimethyl gallium. Because of these results, and since the rate can only be varied by the flow of trimethyl gallium, it has been concluded that the rate is always limited by the mass transfer of trimethyl gallium.

The model mentioned at the beginning of this chapter implies that adsorbed GaCl plays an important role in the growth mechanism and that at large surface concentrations of this compound blocking of growth may occur. At a low hydrogen pressure the density of adsorbed GaCl molecules at the surface will be higher because less GaCl will be reduced to Ga than at a higher hydrogen pressure. This model is supported by the dependence of the growth rate on GaCl and AsH_3

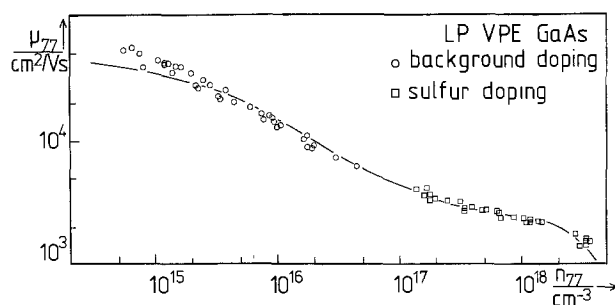


Fig. 8. Hall mobility (77 K) vs. electron concentration; solid line: phenomenological curve from (11).

pressure (Fig. 5 and 6). The maximum in the rate vs. GaCl pressure plot is observed also at atmospheric pressure (13, 14) and has been explained by a similar GaCl adsorption model (15, 16) where growth is assumed to be inhibited by adsorbed GaCl molecules at high GaCl pressures. The maximum value is reached earlier at lower hydrogen pressures, since under these conditions the density of adsorbed GaCl will be higher. Because of this higher density, fewer sites will be available for arsenic adsorption at lower hydrogen pressure, which would lead to a retardation of growth. Indeed, this behavior is observed (Fig. 6). Also, saturation of the growth rate is reached at a lower AsH_3 pressure in the case of a lower than at a higher hydrogen pressure.

A comparison of Fig. 1 and 3 shows that the growth rates, which are calculated assuming the maximum conversion permitted by thermodynamics, exceed the measured rates by more than an order of magnitude. This result and the observed dependence of growth rate on gas phase composition all fit the contention that at temperatures below 1050 K the growth process is kinetically controlled (13, 14). This finding indicates that below 1050 K the chloride growth process meets an important condition for uniform growth. The temperature region above 1050 K was not investigated in this study, since the temperature dependence of the rate in this range points to mass transfer limited growth.

For the fabrication of devices the doping behavior in this low pressure system is equally important. As can be seen from Fig. 7, reproducible doping is possible using H_2S as a doping gas. We have argued in an earlier paper (17) that at atmospheric pressure the sulfur uptake appears to be kinetically determined. Furthermore, we found in the latter case for (100) substrates a linear increase of electron concentration with H_2S pressure, which abruptly saturates at $3 \cdot 10^{18} \text{ cm}^{-3}$, whereas the sulfur incorporation goes on beyond $3 \cdot 10^{18} \text{ cm}^{-3}$. SIMS measurements (17) indicate for this region a continuation of the linear uptake.

The solubility curves from the low pressure system (Fig. 7) thus show the same behavior as those obtained at atmospheric pressure. Therefore, we propose that the incorporation mechanism is the same in both cases. Since H_2S is the dominant sulfur species in the gas phase at our experimental conditions the data suggest that H_2S could react directly with an adsorbed GaCl molecule followed by the incorporation of sulfur at the same site. A lower hydrogen pressure implies a larger density of unreacted GaCl and consequently a larger rate of sulfur uptake would result, as observed in Fig. 7.

Above the saturation of the electron concentration, sulfur probably continues being incorporated as at atmospheric pressure, but in an electrically neutral impurity complex (17). This contention is supported by the strong decrease of the Hall mobility near $3 \cdot 10^{18} \text{ cm}^{-3}$ (Fig. 8).

From Fig. 8 we recognize that the background doping can be reduced to values below 10^{15} cm^{-3} . This

residual impurity level might be predominantly due to silicon, as found for films obtained from VPE systems operating at atmospheric pressure (18), because the material of the epitaxial apparatus and the starting materials are the same in both cases. As discussed in an earlier paper (11) the solid line is based on data for undoped and sulfur-doped VPE samples and represents the "universal" behavior of the mobility in the range $10^{16} \leq n \leq 10^{18} \text{ cm}^{-3}$, independent of growth system and experimental parameters. At higher concentrations the mobility becomes dependent on the type of dopant due to the different solubility limits of donors in GaAs. At lower concentrations the mobility is very sensitive to residual contaminants in the growth system, such as copper (19) or carbon (20), which may cause compensation of the material. The good fit of our experimental data to the phenomenological curve indicates that the layers grown in the low pressure system have the same low compensation as those obtained from systems at atmospheric pressure. Furthermore, the data at low electron concentrations suggest that the level of residual contamination in this system appears to be lower than in those operating at atmospheric pressure.

Conclusions

We have investigated a new method for the growth of GaAs layers, the inorganic chlorine transport system at low pressures. As in the system operating at atmospheric pressure, the growth process as well as the incorporation of the dopant sulfur from H_2S appear to be kinetically controlled. The growth mechanism depends on the hydrogen pressure. The dependence of growth rate on gas phase composition indicates that the rate-limiting step is determined by the specific composition of the gas phase; particularly at low hydrogen pressures the reduction of GaCl to Ga by hydrogen appears to play an important role. The growth rate can be varied continuously over the wide range of 1-40 $\mu\text{m/hr}$; it is constant across a relatively large area.

This behavior of the growth rate indicates that this low pressure system presents some specific advantages compared to the systems operating at atmospheric pressure. The uniformity of the growth rate across larger areas makes the system particularly interesting for production purposes. Furthermore, growth rates, which so far could be obtained only in the very different VPE and MBE systems separately, can in the low pressure approach be achieved in one run in a single system by only varying the hydrogen pressure. This makes feasible the controlled growth of multilayer structures with thicknesses of the single layers differing by more than one order of magnitude. Examples are the growth of a buffer layer followed by the thin active layer for field effect transistors or the growth of laser structures.

The background doping can be reduced to a level below 10^{15} cm^{-3} . Using sulfur as a dopant electron,

concentrations up to $3 \cdot 10^{18} \text{ cm}^{-3}$ are easily obtained. The high 77 K mobility value of approximately $73,000 \text{ cm}^2/\text{Vsec}$ for electron concentrations in the upper 10^{14} cm^{-3} region, is also indicative of the easy purity of the material.

Acknowledgment

The authors are indebted to A. Sauerbrey for support in the experimental part of this study.

Manuscript received Dec. 22, 1980.

Any discussion of this paper will appear in a Discussion Section to be published in the June 1982 JOURNAL. All discussions for the June 1982 Discussion Section should be submitted by Feb. 1, 1982.

Publication costs of this article were assisted by the Institut of Semiconductor Electronics.

REFERENCES

1. J. R. Knight, D. Effer, and P. R. Evans, *Solid State Electron.*, **8**, 175 (1965).
2. J. J. Tietjen and J. A. Amick, *This Journal*, **113**, 724 (1966).
3. K. Ploog, in "Crystals, Growth, Properties and Application," Vol. III, H. C. Freyhardt, Editor, p. 73, Springer, Heidelberg (1980).
4. J. P. Duchemin, M. Bonnet, and F. Koelsch, *This Journal*, **125**, 637 (1978).
5. H. Huppertz and W. L. Engl, *IEEE Trans. Electron Devices*, **ed-26**, 658 (1979).
6. J. P. Duchemin, M. Bonnet, F. Koelsch, D. Huyghe, *J. Cryst. Growth*, **45**, 181 (1978).
7. J. P. Duchemin, M. Bonnet, F. Koelsch, and D. Huyghe, *This Journal*, **126**, 1134 (1979).
8. M. S. Budd and H. A. Bewick, *Anal. Chem.*, **24**, 1536 (1952).
9. D. J. Stirland, *Inst. Phys. Conf. Ser. A*, **33**, 150 (1977).
10. L. H. v.d. Pauw, *Philips Res. Rep.*, **13**, 1 (1958).
11. H. Poth, H. Bruch, M. Heyen, and P. Balk, *J. Appl. Phys.*, **49**, 285 (1978).
12. O. Mizuno and H. Watanabe, *J. Cryst. Growth*, **30**, 240 (1975).
13. D. W. Shaw, *ibid.*, **31**, 130 (1975).
14. E. Veuhoff, K.-H. Bachem, and P. Balk, in "Proc. of the 8th Int. Vac. Conference," Vol. 1, F. Abélès and M. Croset, Editors, p. 575, Société Française du Vide, Thin Films, Cannes, France (1980).
15. J. B. Theeten and F. Hottier, *Surf. Sci.*, **58**, 583 (1976).
16. R. Cadoret and M. Cadoret, *J. Cryst. Growth*, **31**, 142 (1975).
17. E. Veuhoff, M. Maier, K.-H. Bachem, and P. Balk, *J. Cryst. Growth*, **53**, 598 (1981).
18. P. Küpper, H. Bruch, M. Heyen, and P. Balk, *J. Electron. Mater.*, **5**, 455 (1976).
19. H. Martini and P. Balk, *Phys. Status Solidi A*, **57**, 41 (1980).
20. C. E. C. Wood and B. A. Joyce, *J. Appl. Phys.*, **49**, 4854 (1978).

One-Micron Polycide (WSi₂ on Poly-Si) MOSFET Technology

M. Y. Tsai, H. H. Chao, L. M. Ephrath, B. L. Crowder, A. Cramer, R. S. Bennett, C. J. Lucchese,
and M. R. Wordeman

IBM Thomas J. Watson Research Center, Yorktown Heights, New York 10598

ABSTRACT

An n-channel single level polycide (WSi₂ on poly-Si), 22.5 nm gate oxide technology, using electron-beam direct writing for lithography with minimum feature size of 1 μm, has been developed to fabricate NMOS circuits. Low resistance (2.7 Ω/□) polycide interconnections and small dimension (1 μm) devices are the unique features of this process. The overall process is described in this paper. Polycide deposition, annealing, etching, and oxidation are discussed in detail. Cross sections (0.5K to 2K) of polycide dynamic RAM arrays have been successfully fabricated by this polycide technology. The advantage of using low resistance polycide in integrated circuits is demonstrated.

Polycrystalline silicon is commonly used as a gate-electrode and interconnection-line material in MOSFET integrated circuits. Decreasing lithographic dimensions and scaled-down device structures (1) have led to a higher level of integration and increasing importance of interconnection technology. The extendibility of poly-Si to small devices in a VLSI circuit environment is limited by its relatively high sheet resistance (33-50 Ω/□). A metallic silicide layer on poly-Si (called polycide) could reduce the sheet resistance by over an order of magnitude, thereby reducing IR drops and R-C time constants. This composite metal-silicide/poly-Si structure combines the advantages of a well-understood and characterized SiO₂-to-polysilicon interface with a low resistivity silicide. These metal silicides must be able to withstand processing chemicals, high temperatures, and oxidation. In addition, it must be possible to pattern them into fine-line structures. The utilization of evaporated WSi₂ on poly-Si for interconnections in FET's was first proposed by Crowder and Zirinsky (2, 3). Since then, WSi₂, MoSi₂, TaSi₂, and TiSi₂ deposited on poly-Si for interconnection applications have been investigated (4-10). Most of the work has concentrated on the material properties of the silicides or characteristics of single devices, such as a comparison between the polycide and poly-Si devices in terms of resistance in poly-Si lines, flatband voltage, threshold voltages, and gate integrity (2, 6, 7). From these previous studies, it is clear that polycide devices have all the advantages of poly-Si devices and, in addition, much lower sheet resistance. This paper reports the first successful attempt to apply WSi₂ polycide in integrated circuits with minimum feature size of 1 μm. To develop this well-controlled polycide process, it is necessary to gain a detailed understanding of deposition, annealing, etching, and oxidation of polycide. These studies as well as work related to polycide gate integrity are described. Polycide devices and cross sections (0.5K to 2K) of single polycide dynamic RAM arrays (11) have been fabricated by this process. The circuit performance is shown to be greatly enhanced by the low resistance polycide interconnections. The results of this work demonstrate the feasibility and advantages of applying polycide to VLSI with extremely high density circuits.

A 1 μm Polycide Device Process

This process has evolved from a 1 μm single poly-Si process (12) reported before with tighter dimen-

Key words: polycide interconnections, processing, annealing, etching, oxidation, gate integrity, device characteristics.

sional control. Figure 1 shows the schematic of the basic polycide MOSFET along and across the channel length direction. In the cross sections, a composite layer of 150 nm WSi₂/150 nm poly-Si is shown as the gate electrode and interconnection. Electron-beam direct writing for lithography (13), reactive ion etching (RIE) (14), and plasma etching, as well as ion implantation are used extensively throughout the process to achieve control of fabricating small-dimension devices. Six masks are used to fabricate arrays of single polycide dynamic RAM's. Mask 1 is for the alignment marks, which are used for automatic chip alignment during all subsequent mask exposures. This is the first mask level and also the only one defined by optical lithography, because no alignment is required at the first level. The alignment marks, consisting of 200 nm WSi₂, are defined via WSi₂ lift-off. The automatic registration signal in a vector-scan E-beam exposure system (15) is obtained as an averaged signal from many unidirectional beam sweeps across the mark by detecting backscattered high energy electrons (13). The signal acquired by signal averaging from a pedestal of 0.2 μm WSi₂ on an Si substrate is approximately five times larger than that acquired by a pedestal of 0.5 μm poly-Si which was used before (12). The improvement of the alignment signal sub-

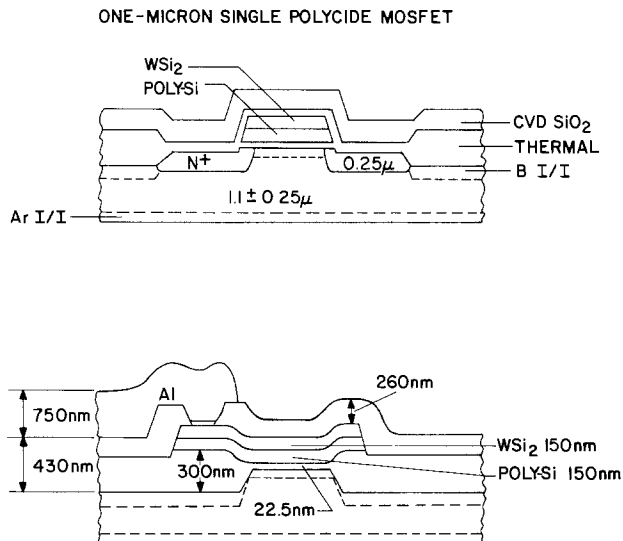


Fig. 1. Schematic cross sections along and across the channel length direction of the basic single polycide MOSFET structure.

stantially reduces the time required for alignment, which, in turn, enhances the throughput of E-beam lithography. An oxidation mask for semi-recessed field oxidation, consisting of nitride on oxide, is etched with mask 2 outside the active device areas. The field threshold-adjustment implant for isolation is performed after patterning and before the semi-recessed oxide is grown. After field oxidation, the oxidation mask is completely removed from the active device areas. Mask 3 defines the area for As⁷⁵ and B¹¹ HiC (high capacitance) implants (16) in the storage region of the dynamic RAM cells. The patterned resist shields the rest of the wafer from the HiC implants. An enhancement channel implant occurs after the gate oxide is grown. WSi₂ is deposited by E-beam co-evaporation onto POCl₃-doped poly-Si. A crystallization anneal is followed by the deposition of a layer of CVD SiO₂. This passivation of WSi₂/poly-Si (polycide) is then followed by a homogenization anneal to obtain a homogeneous WSi₂ film. The polycide gates are patterned by mask 4. The self-aligned source/drain As⁷⁵ implantation is done after gate patterning. The final metal Al is isolated from the polycide and diffusion lines by an oxide stack consisting of both thermal and CVD SiO₂. The contact holes are etched in this isolation stack using mask 5, and the final metal is delineated by mask 6 via lift-off. Table I outlines the process sequence for this polycide technology.

In this process, lithography is achieved by a vector-scan electron-beam exposure system with positive resists. Since exposure areal fraction is kept less than 0.5 at the mask levels to reduce E-beam exposure time, an Al pattern transfer technique is used on masks 2 and 4. A double-layer resist system is exposed and developed first, and an evaporated Al film is then lifted off to obtain the desired pattern. Patterns are etched by reactive ion etching (RIE). Interferometric *in situ* detection of the etching process is utilized (17). The general etching strategy is to etch ~80% of the stack by RIE for near-zero etch bias. The etching is then completed by a selective plasma etch (mask 4 polycide pattern) or wet-etching (mask 2 oxidation mask and mask 5 contact holes). The etching of contact holes was reported before (12), and it is not repeated here.

Polycide Studies

The polycide technology is an enhancement of poly-Si technology. Its major variations from poly-Si technology occur in the deposition, annealing, etching, and oxidation of polycide. These steps have been studied in detail and the results are summarized below. Since polycide gate integrity (dielectric strength)

was found to be different from poly-Si gates under some conditions, it is also discussed in this section.

Deposition of Polycide

In the polycide process, 150 nm poly-Si is deposited on the wafer by LPCVD and doped with POCl₃. A layer of 150 nm WSi₂ is then deposited on this film by dual electron-beam evaporation (9). To ensure a clean interface between poly-Si and WSi₂, the wafers are cleaned and dip etched in a buffered HF solution immediately prior to WSi₂ deposition. To obtain stoichiometric WSi₂, evaporation rates of 0.5 nm/sec for Si and 0.2 nm/sec for W are controlled automatically through a feedback circuit. The Si evaporation rate is low enough to prevent the development of a large thermal gradient in the evaporator hearth, thereby avoiding the "spitting" of Si. The substrate Si wafers are kept at room temperature in a vacuum of 3-6 × 10⁻⁶ Torr during the evaporation. The thickness uniformity is within ±4% and the composition of W and Si is within ±5%. The final thickness of WSi₂ is 75-80% of the sum of the two evaporation components W and Si. It was found that 57 nm tungsten and 143 nm Si form 150 nm WSi₂. It will be shown in the sections "Homogenization Annealing" and "Polycide Gate Integrity" that 150 nm WSi₂/150 nm poly-Si provides sufficient conductivity and good gate characteristics.

Annealing of Polycide

As-deposited tungsten silicide is an amorphous mixture of W and Si and, as a result, post-deposition anneal is essential for controllable processing. The details on the annealing characteristics of tungsten silicide have been reported (10). In this paper, only the process-related studies are discussed. Since silicide films can be prepared with various W-to-Si ratios using the co-evaporation technique, WSi_{1.6}, WSi₂, and WSi_{2.3} films were examined. The annealing of these as-deposited films was performed in a purified Ar or N₂ ambient, but no difference was observed. However, the O₂ and H₂O content in the annealing furnace must be minimized to prevent film corrugation, which is related to the undesired oxidation during film annealing. The normal annealing furnaces and operation procedures were modified to facilitate silicide annealing.

Crystallization.—The as-deposited amorphous tungsten silicide crystallizes after appropriate annealing. Based on x-ray diffraction analysis, the evaporated tungsten silicides with the above three W-to-Si ratios crystallize between 600° and 700°C. The diffraction pattern of tetragonal WSi₂ is clearly observed after the films are annealed above these temperatures (10). However, the Si-rich WSi_{2.3} and WSi₂ films crystallize at the low end of this temperature range (625°C). The W-rich WSi_{1.6} crystallizes at 675°C. It is speculated that the difference lies in the availability of Si atoms near the W atoms in the silicide films.

The reason for crystallizing tungsten silicide is to stabilize the as-deposited film. The as-deposited film is sensitive both to normal processing chemicals (for example, cleaning solutions containing NH₄OH or HCl) and to oxygen at elevated temperatures. Therefore, the crystallization annealing should be done immediately after the film is deposited. Crystallization of tungsten silicide can be achieved by annealing the silicide films above 700°C.

Homogenization annealing.—From He⁺ backscattering analysis, the as-deposited film does not always have a uniform W-to-Si ratio of 1:2 throughout the entire film. A homogeneous WSi₂ film is desirable to obtain controllable etching as described in the next section. In a study of homogenization of WSi_{1.6}, WSi₂, and WSi_{2.3} (10), it was found that the homogenization of WSi_{1.6} can be obtained at 800°C; however, WSi_{2.3}

Table I. Process sequence for 1 μm polycide technology

| |
|--|
| Starting substrate—P-type <100> 4 Ω-cm silicon |
| Back-side I/I—Ar ⁴⁰ I/I for gettering |
| Mask 1—define alignment marks |
| WSi ₂ deposition, lift-off |
| Form nitride/oxide stack |
| Mask 2—define oxidation mask in the active device area |
| Field I/I—low dose B ¹¹ I/I |
| Grow semi-recessed oxide |
| Strip oxidation mask |
| Grow screen oxide |
| Mask 3—define HiC implant mask |
| HiC I/I—low dose As ⁷⁵ and B ¹¹ I/I |
| Form WSi ₂ /POCl ₃ doped poly-Si stack |
| Crystallization anneal |
| CVD SiO ₂ deposition |
| Homogenization anneal |
| Mask 4—define polycide gates |
| Source/drain I/I—high dose As ⁷⁵ I/I |
| Etch back |
| Form thermal oxide, CVD oxide, PSG |
| Mask 5—define contact holes |
| Form a thin metal barrier |
| Mask 6—define Al-Si-Al stack |

requires an anneal at 1000°C. To ensure that the film is homogeneous, 1000°C annealing is carried out.

Annealing of the WSi_2 film also reduces the film resistivity. Figure 2 shows the sheet resistance vs. annealing temperatures and times. The reduction of the resistivity occurs during the first 10 min of the anneal, after which resistivity reaches a saturation-like stage. As shown in Fig. 2, the resistivity of WSi_2 is a strong function of temperature. The minimum resistivity of WSi_2 can be obtained after 1000°C annealing. It is also observed that the resistivity of WSi_2 film is only determined by the highest temperature treatment. As shown in Fig. 2, the samples annealed first at lower temperatures (800° or 900°C) can readily reach low resistivity by a subsequent high temperature (1000°C) anneal. Hence, the various low temperature treatments in a typical process do not affect the final resistivity of the silicide.

The grain size of the silicide film appears to correlate with the resistivity of the silicide. TEM micrographs of WSi_2 annealed at 800°-1000°C are shown in Fig. 3. Small and nonuniform grains are observed in films annealed at 800° or 900°C [Fig. 3(a) and (b)]. Prolonged heat-treatment at these temperatures does not increase the grain size (TEM pictures not shown here). This corresponds well with the saturation-like behavior of resistivity observed in Fig. 2. A 1000°C anneal results in uniform grains ~100 nm [Fig. 3(c)]. This grain size is suitable for fine-line patterning. As is shown in the section "Polycide Etching," 1 μ m polycide lines can be defined with small etching bias.

Surface morphology and adhesion.—The $WSi_{2,3}$ and WSi_2 films have very smooth surfaces even after 1000°C annealing. However, the surface of W-rich $WSi_{1,6}$ film is rougher, more grainy (10), and less adhesive to the underlying poly-Si layer than are the other films. After annealing, the $WSi_{1,6}$ film has a tendency to peel at the edge of the wafer. On the other hand, the Si-rich film, $WSi_{2,3}$, requires a longer annealing time (15-30 min) at 1000°C to become homogeneous. This has an impact on device design due to the diffusion of dopants during the prolonged anneal. Table II summarizes and compares the different compositions. For device fabrication, stoichiometric WSi_2 was chosen rather than W-rich or Si-rich films.

Phosphorus diffusion in polycide.—During annealing, the dopant phosphorus atoms in poly-Si migrate into the WSi_2 . This P migration is observed by SIMS measurements as shown in Fig. 4, where P concen-

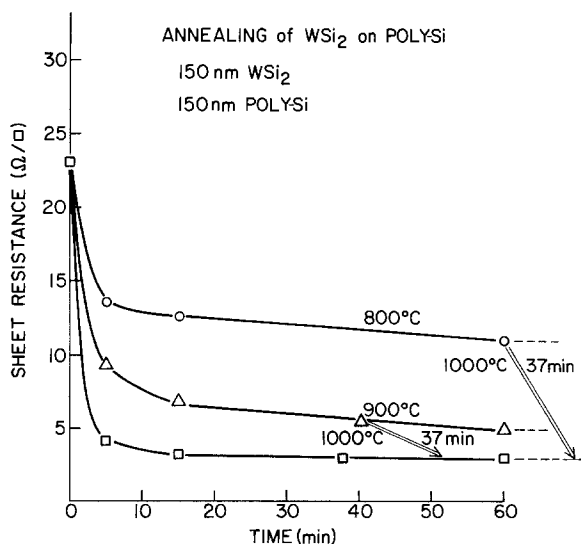


Fig. 2. Resistivity of WSi_2 on poly-Si vs. annealing time and temperature.

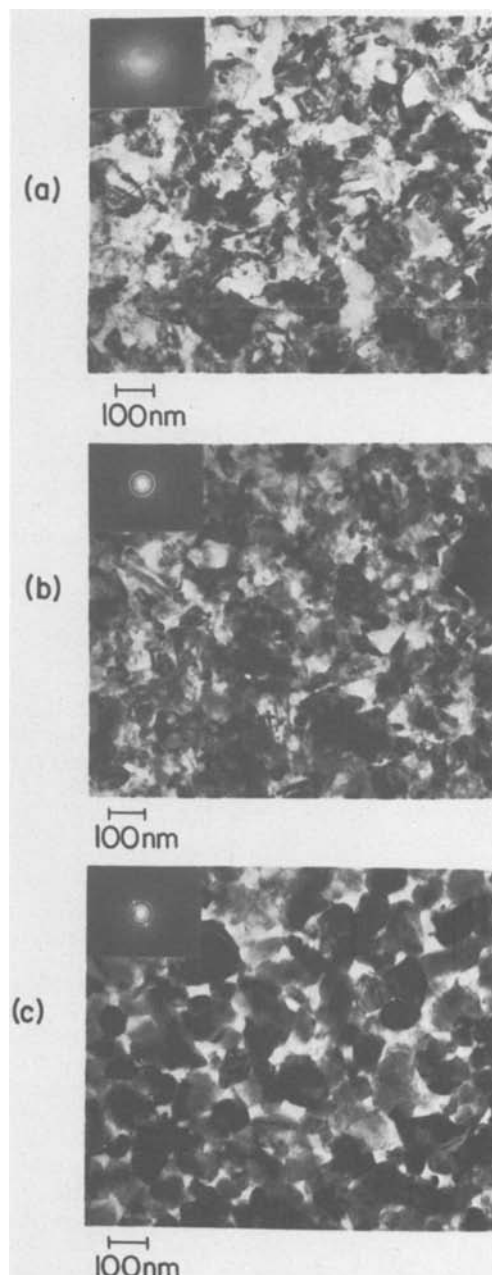


Fig. 3. Bright field TEM micrograph of WSi_2 polycide annealed at (a) 800°C, (b) 900°C, and (c) 1000°C.

trations are plotted vs. the depth from the surface of the WSi_2 /poly-Si stack. All the P atoms are confined to the poly-Si layer prior to annealing. If the polycide is passivated by a thin CVD SiO_2 prior to annealing at 1000°C, the phosphorus atoms diffuse into and accumulate at the surface of the WSi_2 . The CVD SiO_2 effectively prevents P from out-diffusing into the annealing ambient. If the SiO_2 is absent, significant out-diffusing of P from polycide occurs and the dopant is lost to the ambient. This out-diffusion of P has two important effects. First, the concentration of P in WSi_2 has a drastic effect on the plasma etch rate of WSi_2 . Out-diffusion of P atoms results in an uncon-

Table II. Tungsten silicide annealing

| | $WSi_{2,3}$ | WSi_2 | $WSi_{1,6}$ |
|--------------------|-------------|-------------|-------------|
| Crystallization | 625°C | 625°C | 675°C |
| Homogenization | 1000°C | 800°-1000°C | 800°C |
| Adhesion | Good | Good | Peeling |
| Surface Morphology | Smooth | Smooth | Rough |

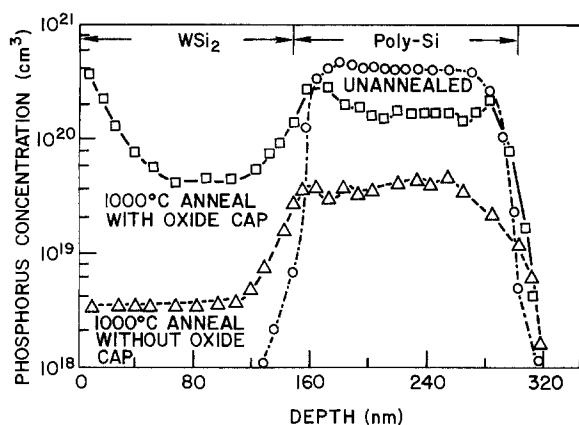


Fig. 4. Atomic distribution of P in WSi_2 polycide. Before annealing, P atoms are confined to poly-Si. After $1000^\circ C$ annealing with an oxide cap layer, P diffuses into WSi_2 . Without the oxide cap, a large amount of P outdiffuses into the annealing ambient. The oxide cap is not shown in this figure.

trollable concentration of P in the polycide, and is an important source of etching variations. Secondly, the P concentration in poly-Si affects the flatband voltage of the MOSFET's. If the remaining activated P in the poly-Si is too low ($<5 \times 10^{19} \text{ cm}^{-3}$), the threshold voltage of the device could shift from the designed value. For these two reasons, a layer of SiO_2 on the polycide during annealing is essential for a controllable polycide process.

Polycide Etching

Polycide etching is a critical step in polycide MOSFET technology, because the channel-length control depends on etch-bias control. In this $1 \mu\text{m}$ FET technology, an etching technique has been developed to achieve a bias of less than $0.1 \mu\text{m}$ per line. In other words, the difference between the etched polycide line and its etch mask is less than $0.05 \mu\text{m}$ per edge. The basic requirement of the process is to etch the WSi_2/n^+ poly-Si stack shown in Fig. 5 selectively to a thin gate oxide. The difficulty in etching polycide has been reported (5, 6). The problem is to etch the top layer of silicide and then poly-Si without a significant loss of definition by overetching the silicide or undercutting the poly-Si. In addition, the thermal oxide must not be attacked. A two-step etching strategy was utilized and the Al pattern transferred from resist lift-off was the mask for etching. This two-step etching technique uses an RIE step to control the linewidth, followed by a plasma etching

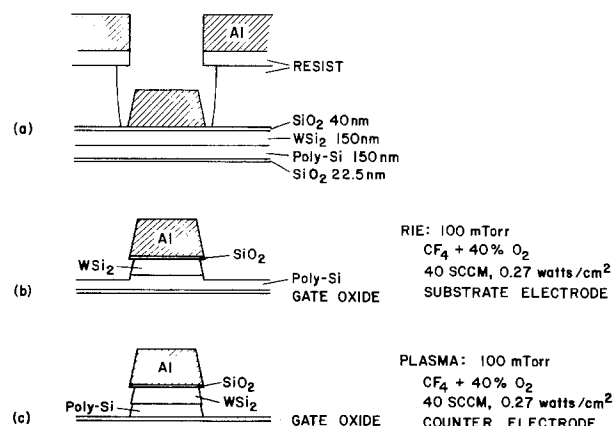


Fig. 5. Schematic diagrams of polycide etching. (a) Al patterns defined via resist lift-off, (b) RIE to etch WSi_2 and half of the poly-Si layer, (c) plasma etching to remove the remaining poly-Si.

step to stop at the underlying oxide. The RIE step removes the top CVD oxide, the WSi_2 film, and about half of the n^+ polysilicon. Plasma etching selectively but isotropically removes the remaining polysilicon. The RIE step was relatively straightforward but the plasma etch rate of WSi_2 varied considerably. After it was found that the O_2 content in the CF_4 etchant gas and the amount of phosphorus remaining in the polycide significantly affect the plasma etch rate of WSi_2 , a well-controlled process was developed. Sequential RIE and plasma etching of polycide is performed in a flexible diode system. The reactor has two independent electrodes, each with a matching network and rf power supply. A more detailed description of the flexible diode system is given elsewhere (18). In this apparatus, RIE and plasma etching can be performed by sequentially powering the substrate and the counterelectrode. This flexible diode etching system is well suited for polycide etching (19).

Reactive ion etching step.—The CVD oxide, WSi_2 film, and approximately half of the poly-Si film are etched by RIE. That is, power is applied to the substrate electrode while the counterelectrode floats. This step is carried out in $CF_4 + O_2$. It is characteristic of RIE that etch rates are insensitive to the doping level, method of deposition, degree of crystallinity, etc. Indeed, the etch rate of WSi_2 was observed to be constant from run to run even though details of the processing varied. The etch profile of the polycide stack is vertical when etching is carried out in 25 mTorr $CF_4 + O_2$. A slope is introduced when the pressure of the etchant gas is raised to 100 mTorr, which is the RIE condition used in this technology as shown in Fig. 5(b), because a sloped polycide etch profile is preferred.

Plasma etching step.—The poly-Si remaining after RIE is etched by plasma etching. That is, rf power is applied to the counterelectrode while the substrate electrode is allowed to float. The underlying gate oxide provides an etch stop because the n^+ poly-Si to SiO_2 etch-rate ratio in this etching mode is 50:1. The final profile of the etched polycide stack depends on the WSi_2 to poly-Si etch-rate ratio during plasma etching. Initially, the ratio was unacceptably large and variable from run to run (between 2.5 and 5 to 1) in $CF_4 + 20\% O_2$ as the result of a variation in the plasma etch rate of WSi_2 . The fast lateral attack of WSi_2 often resulted in a gross undercut with respect to the mask. Based on numerous experiments, it was found that the P concentration in polycide and the O_2 content in the etchant gas are the two critical parameters affecting the plasma etch rate. These effects are discussed next.

Effect of phosphorus concentration in polycide.—As discussed in the section "Phosphorus diffusion in polycide," homogenization annealing causes P to migrate into the WSi_2 (Fig. 4). Since $1000^\circ C$ anneal is normally required to homogenize WSi_2 , this migration is inevitable. As shown in Fig. 4, a 40 nm CVD SiO_2 on the WSi_2 /poly-Si stack provides a barrier against phosphorus out-diffusion. The etch rate of WSi_2 passivated with CVD SiO_2 (solid curve in Fig. 4) is about 60% higher than that without the oxide film (dashed curve in Fig. 4) (333 nm/min vs. 200 nm/min); while the etch rate of the n^+ poly-Si with SiO_2 passivation is only 20% higher than that without SiO_2 (83.5 nm/min vs. 62.2 nm/min). The rapid change of etch rate of WSi_2 suggests that the SiO_2 cap layer is important. The samples without the SiO_2 cap layers have an unstable etch rate of WSi_2 mainly because the out-diffusion of P is not controllable. By adding a CVD SiO_2 top layer on the polycide stack before annealing, reproducible etch rates of WSi_2 and n^+ poly-Si are achieved.

Effect of O_2 content in etching gas.—To better understand the etch rate sensitivity to variations in plasma conditions, the plasma etch rates of both WSi_2 and n^+ polysilicon were obtained for various concentrations of oxygen in CF_4 . Figure 6 plots plasma etch rate vs. the percent of O_2 in CF_4 at constant pressure and incident power with only slight variations in gas flow. The curve indicates a moderate variation in the plasma etch rate of n^+ polysilicon, which reaches a maximum value at approximately 25%. The tungsten silicide etch rate also reaches a maximum at about 25%; however, the increase is much greater. The etch rate ratio of WSi_2 to n^+ polysilicon in the region between 10 and 30% O_2 in CF_4 is much greater than one. The large etch rate ratio during the plasma step is unfavorable since this would result in a substantial pull-back of the WSi_2 with respect to the polysilicon. The etch rate ratio is approximately one in the region between 30 and 35% O_2 in CF_4 . However, the tungsten silicide etch rate in this region is sensitive to the composition of the etchant gas. In the region beyond 35% oxygen in CF_4 , the tungsten silicide etch rate actually drops below that of the n^+ polysilicon, and becomes less sensitive to the percent O_2 in CF_4 . Although the n^+ poly-Si-to- WSi_2 etch rate ratio is about 2:1 in this region, the slope introduced in the RIE step [Fig. 5(b)] minimizes the undercut of poly-Si [Fig. 5(c)]. An SEM micrograph of an etched polycide line is shown in Fig. 7. The sloped sidewall and an etch bias of less than $0.1 \mu m$ are the special features of this polycide etching process.

Oxidation of Polycide

An etch back procedure is required (12) to remove the trapped holes in the field oxide in order to improve the threshold voltage in a MOSFET process. P-etch (12) was utilized to remove ~ 70 nm of SiO_2 in the field region and also the thin gate oxide on the source/drain. In general, to ensure good insulation between the source/drain and gate electrode, a thermal oxidation is required after the etching. In this polycide technology, the oxidation involves polycide as well as Si substrate. The oxidation mechanism of polycide has been studied. It is generally agreed that the underlying silicon diffuses through the WSi_2 film to form SiO_2 on the surface (20). To oxidize polycide structures with a minimum feature size of $1 \mu m$, an inert gas pre-annealing step is essential. This pre-

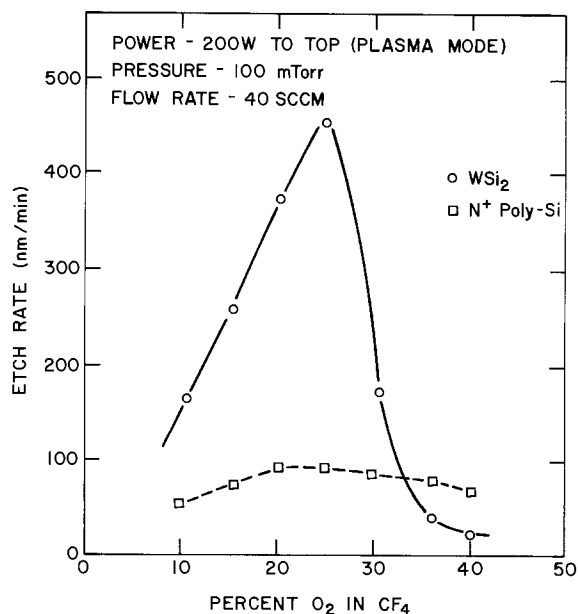


Fig. 6. Plasma etch rate of WSi_2 and poly-Si in CF_4 mixed with various percents of O_2 .

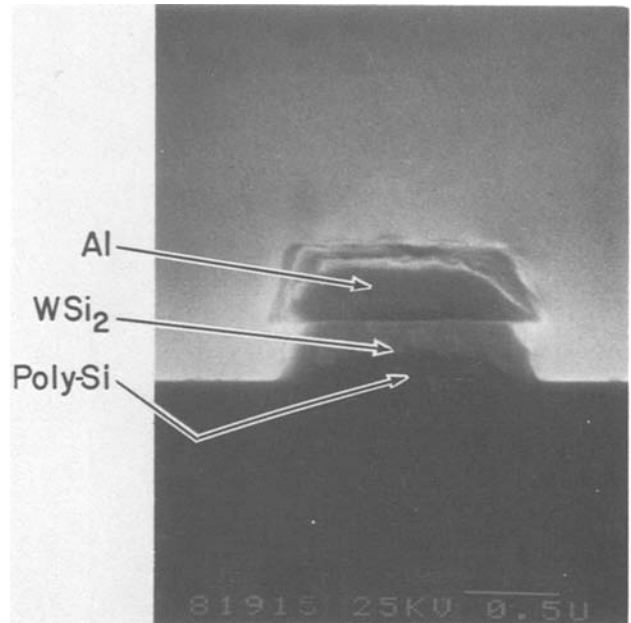


Fig. 7. SEM cross section of an etched polycide line $\sim 1 \mu m$. The etch bias is less than $0.1 \mu m$.

annealing procedure allows the wafers to heat up to a temperature at which Si diffusion through WSi_2 is adequate before oxidation of polycide begins. Exposure of WSi_2 to O_2 at temperatures below $900^\circ C$ usually results in film corrugation caused by the formation of volatile WO_3 or by the stress in the silicide film due to local formation of W-rich phases. With this pre-annealing procedure, $1 \mu m$ polycide lines can be oxidized successfully. Figures 8 and 9 show the cross sections of oxidized polycide lines on both the thin gate oxide and on thick oxide regions. CVD SiO_2 is then deposited conformally on the polycide structures.

The oxidation rate of WSi_2 /poly-Si is roughly 60% of the rate of n^+ poly-Si. The dielectric strength of the oxide on polycide is 2-4 MV/cm which is similar to that of SiO_2 grown on poly-Si. The composite CVD SiO_2 and thermal oxide on polycide form a reliable isolation layer between the Al and devices.

Polycide Gate Integrity

The dielectric strength of gate oxide under the polycide is an important reliability issue in polycide technology. Experiments have been carried out to investigate the dielectric strength (gate integrity) of poly-Si gates vs. polycide gates. It was found that annealing and oxidation of polycide has a minimal effect on the gate integrity. For large area ($1.82 \times 10^{-2} cm^2$) thin oxides (22.5 nm), a polycide gate yield of 95-99% (breakdown voltage > 2 MV/cm) is observed for samples annealed or oxidized at $1000^\circ C$. Therefore, for WSi_2 150 nm/poly-Si 150 nm/ SiO_2 22.5 nm gate electrodes, the gate integrity is identical to poly-Si gate electrodes. However, there are two important factors which degrade polycide-gate integrity. First, the gate integrity depends on the thickness of poly-Si under the WSi_2 film. As shown in Fig. 10, the gate breakdown yield of polycide electrodes is a strong function of the poly-Si thickness, while the poly-Si gates without WSi_2 exhibit no such dependence. In fully processed device runs, 150 nm WSi_2 /150 nm poly-Si/22.5 nm oxide has a yield above 90%. However, thinning down of the poly-Si reduces the yield. Therefore, poly-Si thickness is an important parameter in polycide processing. This observation agrees with the result reported before (8), obtained by measuring MSOS capacitors. Secondly, a buffered

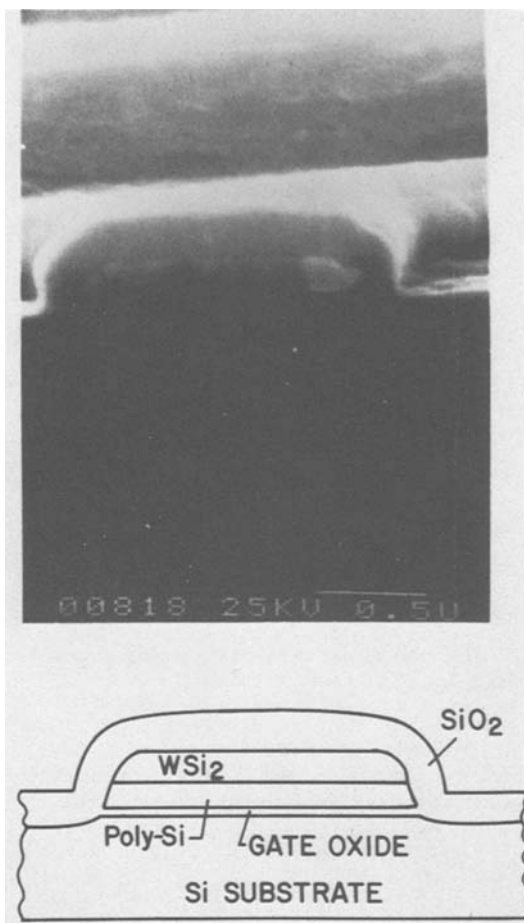


Fig. 8. SEM micrograph and drawing showing a cross section of a WSi_2 polycide-gate FET with $1\ \mu\text{m}$ effective channel length.

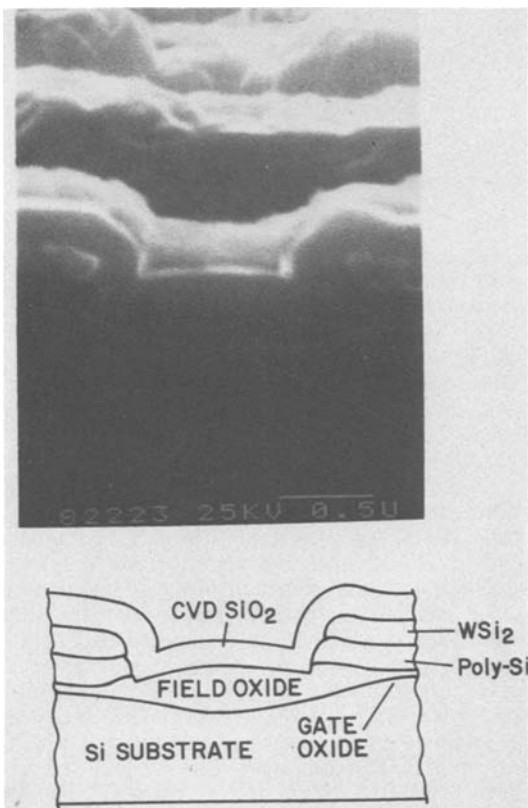


Fig. 9. SEM micrograph and drawing showing a cross section of a WSi_2 polycide-gate structure on the gate oxide and the field oxide.

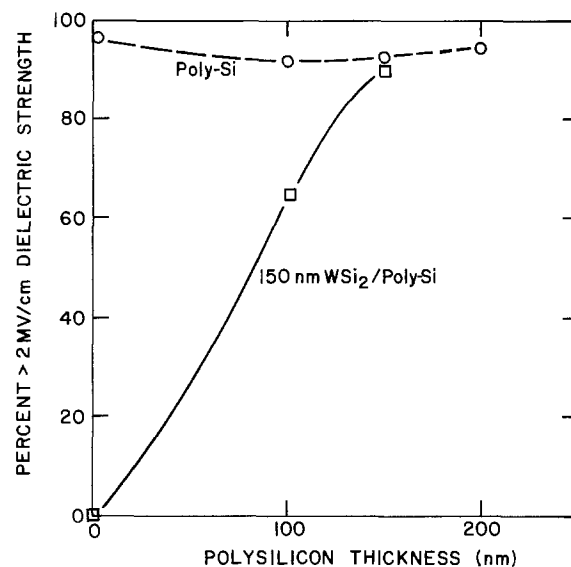


Fig. 10. Percentage of good gate breakdown devices for poly-Si and $\text{WSi}_2/\text{poly-Si}$ electrodes with various poly-Si thickness.

HF (BHF) etch can readily penetrate the polycide stack and attack the thin gate oxide underneath, especially after the polycide is oxidized. Experiments show that samples not exposed to BHF have a polycide-gate yield of 99%. Samples prepared by an identical process, but with the addition of a 30 sec BHF dip on the polycide stack, have a gate yield of only 16%. The conclusion is that exposure of the polycide gate to BHF must be avoided. Since it is standard procedure for contact hole opening to expose wafers to BHF prior to deposition of metal, metal-to-polycide contacts must be located on the field oxide for reliability. In summary, the use of polycide gate electrodes/interconnections places some constraints on the processing to retain the integrity of the gate oxide. If care is taken to process within these constraints, the polycide gate is as reliable as the poly-Si gate.

Device and Circuit Results

This $1\ \mu\text{m}$ polycide FET technology has been successfully applied to fabricate cross sections (0.5K to 2K) of single polycide dynamic RAM arrays (11), which are subsets of a 256K dynamic RAM. From this fully processed run, the sheet resistance of polycide was determined to be $2.72 \pm 0.04\ (1\sigma)\ \Omega/\square$ compared to $38.2 \pm 0.19\ (1\sigma)\ \Omega/\square$ for a poly-Si control. The metal-to-polycide contact resistance is also much lower than metal-to-Si contact resistance. For $1 \times 1\ \mu\text{m}^2$ contacts, the metal-to-polycide contact resistance is $\leq 0.9\ \Omega$ per contact compared to metal-to-Si contact resistance of $\leq 15\ \Omega$ per contact. The ΔL (gate length at mask level-effective channel length) is $0.61 \pm 0.05\ \mu\text{m}\ (1\sigma)$, which is well within the process specification and is indicative of the tight control of this technology. Comparative I_{DS} (drain-to-source current) vs. V_{GS} (gate-to-source voltage) with $V_{SX} = -2\text{V}$ (substrate bias) and $V_{DS} = 0.1\text{V}$ (drain-to-source voltage) are plotted in Fig. 11. The difference between the I - V characteristics of poly-Si and polycide gates is less than 0.1V. It has been observed repeatedly that the threshold voltage of polycide thin gate devices is a little higher than that of poly-Si gates. However, the difference is within 0.1V, which is equivalent to the normal spread of threshold voltages in both the poly-Si and polycide gates. The reason for this difference is not yet known, but the difference is too small to be significant. The short-channel effect and the substrate sensitivity of polycide gate devices are identical to those of poly-Si devices. Hence, poly-

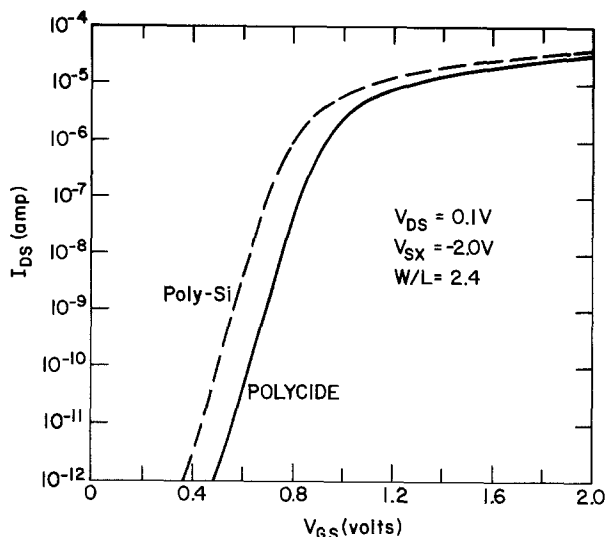


Fig. 11. Log I_{DS} vs. V_{GS} for WSi_2 polycide and poly-Si gate device with $W/L = 2.4$, $V_{DS} = 0.1V$, and $V_{SX} = -2V$.

cide devices are functionally equivalent to the poly-Si devices, even down to $1 \mu m$ dimensions. However, the sheet resistance is improved by a factor of 14 and the contact resistance by a factor of 18. Both of these are important improvements for VLSI circuits where a large number of interconnections and contact holes is utilized. Figure 12 shows an SEM micrograph of the dynamic RAM array. The uniform Al bit lines and clear polycide wordlines demonstrate good process control. No gate shorts are observed, and all of the cross sections (0.5K to 2K) are functional. Figure 13 shows the wordline (128 and 256 bits) risetime improvement achieved by polycide vs. poly-Si. The measured risetime agrees with circuit simulation results. A factor of ten improvement in the risetime of the polycide wordline over the poly-Si wordline clearly demonstrates the circuit advantage of polycide technology.

Conclusions

The $1 \mu m$ polycide (WSi_2 /poly-Si) FET technology has been shown to be viable for VLSI circuits. The

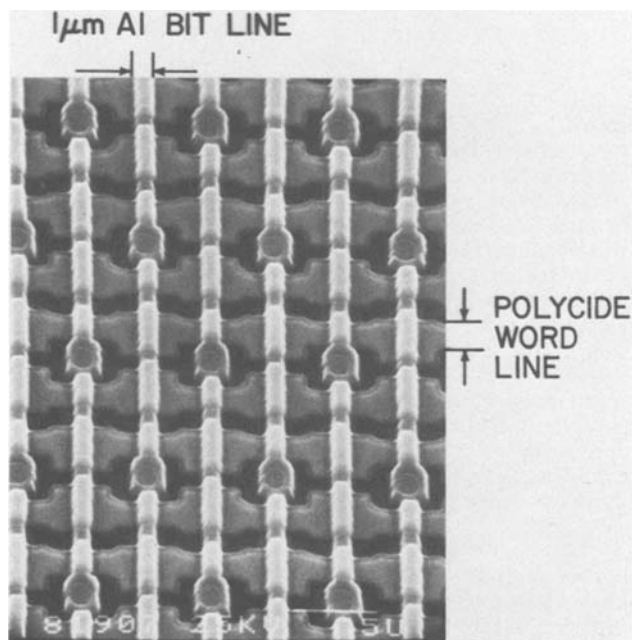


Fig. 12. SEM micrograph of part of a 2K bit dynamic RAM array with WSi_2 polycide wordlines and Al bit lines.

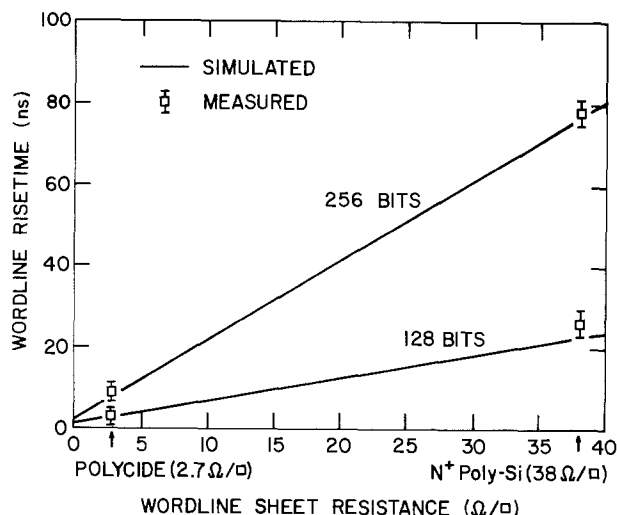


Fig. 13. The wordline risetime vs. sheet resistance in the wordlines. The risetime on the polycide wordline is ten times faster than that on poly-Si wordline. The measured results agree with computer simulation.

resistance of poly-Si interconnection lines is reduced by a factor of 14 by applying silicide on poly-Si. The metal-to-polycide contact resistance is also improved by a factor of 18 in contrast to the metal-to-Si contacts. Due to the reduction in resistance, the wordline risetime in a dynamic RAM array is improved by a factor of ten. The polycide MOSFET is measured to be functionally equivalent to the poly-Si FET even down to $1 \mu m$ dimensions. Functional polycide dynamic RAM arrays clearly demonstrate the validity of this polycide technology and also the circuit advantages of polycide electrodes/interconnections in a VLSI environment. Coupled with advanced lithographic and patterning capabilities, polycide can be used to fabricate dense circuits with low propagation delays for future VLSI.

Although this work is concentrated on single level polycide technology, with some modification, polycide should be applicable to a double poly process. With improvement of lithographic capability, the polycide technology should also be extendible to the submicron technology.

Acknowledgments

The authors would like to thank C. M. Osburn, T. O. Sedgwick, V. L. Rideout, F. M. d'Heurle, and C. S. Petersson for invaluable discussions; the E-beam Lithography group, especially H. Voelker, T. Donohue, W. Grobman; and the Si Fabrication group for processing support. The electrical measurements by R. P. Havreluk, SIMS measurements by R. W. Johnson, and TEM by L. Ng are also greatly appreciated.

Manuscript submitted Jan. 16, 1981; revised manuscript received April 16, 1981. This was Paper 227 presented at the Minneapolis, Minnesota, Meeting of the Society, May 10-15, 1981.

Any discussion of this paper will appear in a Discussion Section to be published in the June 1982 JOURNAL. All discussions for the June 1982 Discussion Section should be submitted by Feb. 1, 1982.

Publication costs of this article were assisted by IBM Corporation.

REFERENCES

1. R. H. Dennard, F. H. Gaensslen, H. N. Yu, V. L. Rideout, E. Bassous, and A. R. LeBlanc, *IEEE J. Solid-State Circuits*, sc-9, 256 (1974).
2. B. L. Crowder and S. Zirinsky, *IEEE Trans. Electron. Devices*, ed-26, 369 (1979).
3. S. Zirinsky and B. L. Crowder, *This Journal*, 463

- RNP, **124**, 338C (1977).
4. S. P. Murarka, in "1979 Int. Electron. Devices Meet. Dig. Tech. Papers," p. 254, Washington, D.C. (1979).
 5. S. P. Murarka, *J. Vac. Sci. Technol.*, **17**, 775 (1980).
 6. A. K. Sinha, W. S. Lindenberger, D. B. Fraser, S. P. Murarka, and E. N. Fuls, *IEEE Trans. Electron. Devices*, **ed-27**, 1425 (1980).
 7. H. J. Geipel, N. Hsieh, M. Ishaq, C. Koburger, and F. White, *ibid.*, **ed-27**, 1417 (1980).
 8. C. Koburger, M. Ishaq, and H. J. Geipel, Abstract 162, p. 428, The Electrochemical Society Extended Abstracts, St. Louis, Missouri, May 11-16, 1980.
 9. M. Y. Tsai, F. M. d'Heurle, C. S. Petersson, L. Ng, and C. J. Lucchese, Paper presented at the Electron. Material Conf., June 1980, Ithaca, NY.
 10. M. Y. Tsai, F. M. d'Heurle, C. S. Petersson, and R. W. Johnson, *J. Appl. Phys.*, August 1981.
 11. H. H. Chao, R. H. Dennard, M. Y. Tsai, M. R. Wordeman, and A. Cramer, in "1981 Int. Solid-State Circuit Conf. Dig. Tech. Papers," p. 152 New York (1981).
 12. W. R. Hunter, L. M. Ephrath, W. D. Grobman, C. M. Osburn, B. L. Crowder, A. Cramer, and H. E. Luhn, *IEEE Trans. Electron. Devices*, **ed-26**, 353 (1979).
 13. W. D. Grobman, H. E. Luhn, T. P. Donohue, A. J. Speth, A. Wilson, M. Hatzakis, and T. H. P. Chang, *ibid.*, **ed-26**, 360 (1979).
 14. L. M. Ephrath, *J. Electron. Mater.*, **1**, 415 (1978).
 15. T. H. P. Chang, A. D. Wilson, A. J. Speth, and C. H. Ting, in "Electron and Ion Beam Science and Technology," R. Bakish, Editor, p. 392, The Electrochemical Society Softbound Proceedings Series, Princeton, NJ (1976).
 16. A. F. Tasch, Jr., P. K. Chatterjee, H. S. Fu, and T. C. Holloway, *IEEE Trans. Electron. Devices*, **ed-25**, 33 (1978).
 17. J. A. Bondur, W. R. Case, and H. A. Clark, Abstract 303, p. 760, The Electrochemical Society Extended Abstracts, Seattle, Washington, May 21-26, 1978.
 18. L. M. Ephrath, in "1980 Int. Electron. Devices Meet. Dig. Tech. Papers," p. 402, Washington, D.C., (1980).
 19. R. S. Bennett, L. M. Ephrath, M. Y. Tsai, and C. J. Lucchese, Abstract 227, p. 570, The Electrochemical Society Extended Abstracts, Minneapolis, Minnesota, May 10-15, 1981.
 20. S. Zirinsky, W. Hammer, F. M. d'Heurle, and J. J. Baglin, *Appl. Phys. Lett.*, **33**, 76 (1978).

Kinetics of High Pressure Oxidation of Silicon in Pyrogenic Steam

Reda R. Razouk,* Liang N. Lie,* and Bruce E. Deal*

*Fairchild Camera and Instrument Corporation,
Research and Development Laboratory, Palo Alto, California 94304*

ABSTRACT

The kinetics of high pressure oxidation of silicon in pyrogenic steam were investigated for ambient pressures of 5-20 atm and for oxidation temperatures of 800°-1000°C. A linear-parabolic model was used in the analysis of the data. Both rate constants of the analytic model were found to be linearly proportional to pressure for the entire range of temperature and pressure. Fixed oxide charge and interface state densities for oxides grown at high pressure were found to be slightly higher at lower temperatures, particularly below 900°C, than for oxides grown at 1 atm. Electron trapping by avalanche injection in oxides grown on (111) Si at 5 atm in pyrogenic steam (800°C) yielded effective trap densities and capture cross sections similar to those obtained at 1 atm.

Higher packing densities and improved device performance are among the requirements for developing VLSI (very large scale integration) technology. In order to achieve these goals, both horizontal and vertical dimensions must be scaled downward. These reduced dimensions imply that better control of dopant diffusion and redistribution will be required and that defect formation during thermal oxidation and other thermal annealing processes must be minimized. In many cases junction movement may have to be reduced to almost zero. The use of high pressure oxidation may have a significant impact on ability to meet the above requirements. Oxidation of silicon in high pressure steam allows the growth of films of the order of 1 μm on (100) substrates at 800°C in less than 2.5 hr, thereby leading the way toward a substantial reduction in dopant redistribution. Furthermore, published reports by Tsubouchi *et al.* (1) and by Katz and Kimmerling (2) indicate a reduction in oxidation induced stacking faults during high pressure oxidation. This reduction may be due to the increased oxidation rate or the reduced oxidation time.

Although high pressure oxidation of silicon was carried out almost 20 years ago (3), commercial units have only recently been available (4) for high pressure oxidation in high volume integrated circuit fabrication.

This report on the kinetics of high pressure oxidation in pyrogenic steam uses the linear-parabolic oxidation relationship (5) to describe the oxide growth and to characterize the pressure dependence of the linear and parabolic rate constants B/A and B . The oxidation parameters under investigation include silicon orientation, (100) and (111), temperature (800°-1000°C) pressure (1-20 atm pyrogenic steam), and time. Electrical properties of pressure grown oxides have been investigated. The dependence of oxide charge densities and trapping properties on oxidation and annealing conditions have been determined and compared with those of oxides produced at 1 atm.

The Thermal Oxidation Process

The thermal oxidation of silicon proceeds by: (i) absorption of the oxidizing species into the outer layer of oxide already formed; (ii) diffusion of the species through the oxide; and (iii) reaction of the oxidizing species with silicon at the Si-SiO₂ interface to produce new SiO₂. The growth kinetics of thermal silicon di-

* Electrochemical Society Active Member.

Key words: rate constants, oxide charges, oxidation, high pressure.

oxide films have been the subject of intensive efforts by many investigators in the last 20 years, and a variety of relationships describing the growth of silicon dioxide films in dry oxygen and in steam have been proposed. The most generally accepted is the linear-parabolic relationship developed by Deal and Grove (5). This relationship is expressed as

$$x_o^2 + Ax_o = Bt + x_i^2 + Ax_i \quad [1]$$

which can be rewritten as

$$x_o^2 + Ax_o = B(t + \tau) \quad [2]$$

where B = parabolic rate constant ($\mu\text{m}^2/\text{hr}$), B/A = linear rate constant ($\mu\text{m}/\text{hr}$), x_i = initial oxide thickness, and $\tau = (x_i^2 + Ax_i)/B$.

The rate constants B and B/A are related to the oxidation process as follows

$$B = 2D_{\text{eff}}C^*/N_1 \quad [3]$$

$$A = 2D_{\text{eff}}(1/k + 1/h) \quad [4]$$

$$B/A = C^*/N_1(1/k + 1/h) \quad [5]$$

where D_{eff} is the effective diffusion coefficient of the oxidizing species and incorporates any enhancements in the transport rates, C^* is the equilibrium concentration of the oxidant in the oxide, N_1 is the number of oxidant molecules incorporated into a unit volume of the oxide layer, h is the gas-phase transport coefficient, and k is a constant dealing with the oxide silicon interface reaction.

The general oxidation relationship as summarized by Eq. [1]-[5] indicates a pressure dependence of both the parabolic rate constant (B) and the linear rate constant (B/A) through their dependence on the equilibrium concentration of the oxidant (C^*) in the oxide which is assumed to be related to the partial pressure by

$$C^* = KP \quad [6]$$

The activation energies of the rate constants have been examined by various authors and found to vary from 0.7 to 0.78 eV for B and 1.83 to 2.05 eV for B/A (5-8). An important aspect of the kinetics of oxide growth under pressure is the dependence of the rate constants on the pressure of the oxidizing species. Although questions about the charge state of the diffusion species are still a matter of controversy, it is known that the permeation of oxygen through fused silica is linearly proportional to oxygen pressure (9), and the dependence of the parabolic rate constant on pressure for oxidation below 1 atm (5) was found to agree quite well with the linearity predicted by a linear parabolic model for both dry O_2 and steam oxidations. Evidence indicates, although not conclusively, that the diffusing species is molecular oxygen in the case of dry O_2 , and for steam oxidation it is some form of water molecule.

In this paper we deal exclusively with the linear-parabolic law of Deal and Grove and test its applicability to the modeling of oxide growth at high pressure and the resultant pressure dependence of the oxidation rate constants. Results published in this area indicate a linear pressure dependence on both rate constants for atmospheric and lower pressure oxidations (5, 10), and up to 10 atm (11). A less than linearly proportional dependence was observed by Tsubouchi *et al.* (1) (steam, 6.4 atm), and by Zeto (12) (dry O_2 , 500 atm). The latter could quite possibly be due to a saturation of the oxygen solubility in the thermal oxide at these pressures.

Experimental Procedure

p-Type (100) and (111) silicon wafers of resistivity 5-9 $\Omega\text{-cm}$ and 1-3 $\Omega\text{-cm}$, respectively, were used in the investigation of the oxidation kinetics as well as for oxide charge determination. The wafers were chem-

mechanically polished on one side and etched on the other. The preoxidation cleaning sequence consisted of hot sulfuric acid, aqua regia, and 1:10 $\text{HF}/\text{H}_2\text{O}$ with appropriate deionized water rinses. The wafers were dried by a spin/dry cycle and subsequently loaded in the oxidation tube in a nitrogen ambient.

The high pressure oxidation system used in the experiments was purchased from GaSronics (Mountain View, California), and can operate at pressures up to 25 atm. The oxidation ambient is obtained by the reaction of hydrogen and oxygen at temperatures exceeding 700°C. All gases are obtained from liquid sources with booster pumps used to increase the pressure to the 1000-1200 psi needed for efficient system operation. Mass flowmeters are used to monitor gas flow. During oxidation the system pressure is increased with the shell pressure maintaining approximately 15 psi differential from the pressure inside the oxidation tube, the shell pressure being higher. Figure 1 illustrates a typical oxidation cycle and indicates the presence of pressure fluctuations when the system is fully pressurized as well as a linear increase in pressure during the initial phase of pressurization. The oxidation temperature was monitored continuously by means of a thermocouple and all experiments were carried out in a 3 in. tube. No temperature instability was observed during pressurization.

The oxidation cycle used in this work is summarized as follows: (i) Wafers are loaded in nitrogen at temperature; (ii) loading door is closed and system activated; (iii) system is purged for 5 min in dry O_2 ; (iv) system is purged for 5 min in steam; (v) pressurization starts with the wafers in the steam ambient; (vi) wafers are oxidized for the preselected time; (vii) depressurization starts. The steam flow terminates and is replaced by nitrogen flow. Depressurization is complete in 3-4 min; and (viii) the wafers are purged in nitrogen for an additional 7 min and pulled from the furnace in N_2 (pull time approximately 2 min). We will refer to this anneal/cool process as nitrogen slow pull or N_2 SP.

Table I indicates the pressurization time required to reach a given pressure. These times are used in the analysis of the data in the next sections. Pressurization in nitrogen was not used in order to avoid any interaction between nitrogen and the substrate at high pressure which could alter the oxidation kinetics.

Oxide thickness was measured by a Gaertner L-116 Automatic Ellipsometer and additional measurements were carried out on a Nanometrics "Nano Spec/AFT" micro spectrophotometer.

Wafers to be used for oxide charge measurements were metallized following oxidation with Al-4% Cu-2% Si by cold flash evaporation and given a postmetallization anneal (PMA) in a 10% H_2 in N_2 ambient at 400°C for 10 min. High frequency and quasistatic C-V

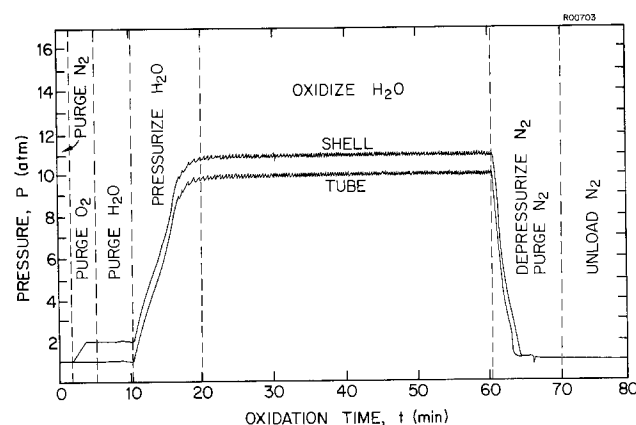


Fig. 1. Typical oxidation cycle in a GaSronics high pressure oxidation system showing the ambients used and the pressure change in both the tube and the shell.

Table I. Pressurization time for various pressures

| Oxidation pressure (atm) | Pressurization time (min) |
|--------------------------|---------------------------|
| 5 | 4 ± 0.5 |
| 10 | 8 ± 0.5 |
| 15 | 10 ± 1 |
| 20 | 13 ± 1.5 |

measurements were used to calculate the densities of fixed oxide charges (N_f) and interface traps or states (D_{it}); bias stress measurements were performed to obtain the mobile ionic charge density N_m . Electron trapping by avalanche injection was used to observe charge trapping in the oxides.

Results and Discussion

Oxide growth data.—Oxide growth data were obtained for 5, 10, 15, and 20 atm in a pyrogenic steam ambient. Temperatures investigated were 800°, 850°, 900°, 950°, and 1000°C. The minimum oxidation time was 30 min, which was selected to allow the system sufficient time to reach pressure and stabilize. Figure 2 shows the kinetic data obtained at a pressure of 20 atm for various oxidation temperatures. The orientation effect is clear and the results show that more than a micrometer of oxide can be grown in less than 30 min at 950° and 1000°C. Figure 3 shows the oxide thickness obtained for oxidations at 900°C at various pressures. The effect of pressure on the parabolic rate constant can be estimated from this graph by noting that a micrometer of oxide requires approximately 11–12 hr at 1 atm, but only 2.3, 1.2, and 0.6 hr at 5, 10, and 20 atm. The oxidation time shown in Fig. 2 and 3 is the time from the onset of pressurization to the onset of depressurization. The latter is carried out in a nitrogen environment.

Rate constant determination.—The determination of the oxidation rate constants is critical to the understanding of the role pressure plays in the oxidation process. Considerable care was taken in the calculation of the rate constants to ensure that the resulting comparisons with the 1 atm data are meaningful.

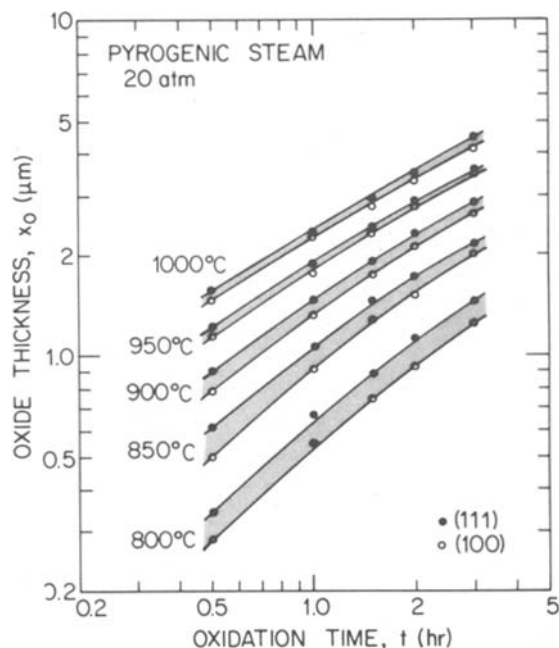


Fig. 2. Oxide thickness vs. oxidation time for (100) and (111) silicon oxidized in pyrogenic steam at a pressure of 20 atm and at temperatures of 800°, 850°, 900°, 950°, and 1000°C. Oxidation time includes pressurization time in steam.

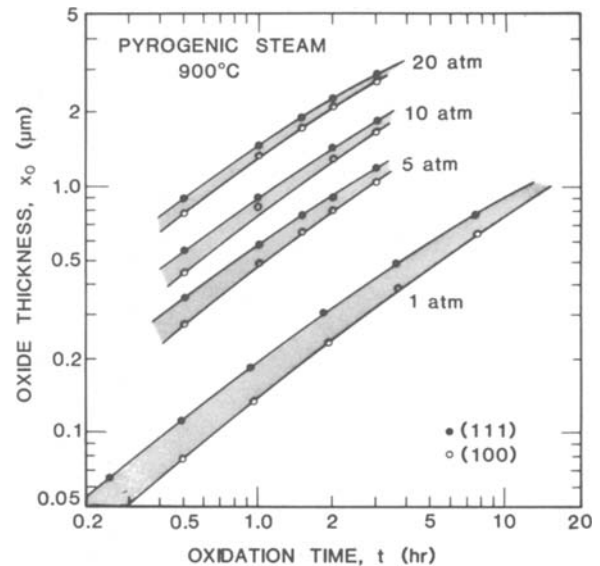


Fig. 3. Oxide thickness vs. oxidation time for (100) and (111) silicon oxidized in pyrogenic steam at a temperature of 900°C and at pressures of 1, 5, 10, and 20 atm. Oxidation time includes pressurization time in steam.

The general oxidation relationship [1] can be rewritten as

$$x_0^2 - x_i^2 + A(x_0 - x_i) = Bt \quad [6]$$

or

$$(x_0 + x_i) + A = B \left(\frac{t}{x_0 - x_i} \right)$$

A plot of $(x_0 + x_i)$ vs. $(t/x_0 - x_i)$ can be used to obtain the rate constants B and B/A . The initial oxide thickness used (x_i) is necessary in order to account for the pressurization time. During that time, pressure increases from 1 atm to the set pressure, resulting in a continuous change in the oxidation rate constants. By using an "initial run" long enough (30 min) for the system to pressurize and stabilize, the initial oxide thickness x_i can be obtained. In all subsequent figures x_i is the oxide thickness following a 30 min oxidation cycle.

Figure 4 shows a plot of $(x_0 + x_i)$ vs. $(t/x_0 - x_i)$ for oxidations at 850°, 900°, and 1000°C at 10 atm. The rate constants B and B/A can be extracted from the slope and intercept of the lines. It should be noted that this technique results in values of B and B/A based upon relatively thick oxides as a result of the minimum time requirements necessary for a reproducible x_i coupled with the fast oxidation rates in steam ambients at high pressure. Figure 4 also indicates that a larger number of data points is needed to obtain accurate values of the rate constants, and that slight variations in the fitting of the data, particularly at low temperatures, can result in considerable differences in the values of the rate constants. The calculation of rate constants based upon high temperature-thick oxide data can result in substantial variations in B/A while in the case of low temperature-thin oxide data large variations in the calculated values of B are obtained.

In view of the preceding discussion, a different approach for calculating the rate constants was taken. This approach allowed us to model the oxidation and supplied us with data on the relationship between B and B/A , allowing us to observe the effect of small variations in one rate constant on the other. In this method the oxidation cycle was divided into several intervals as shown in Fig. 5 with the oxide thickness at the end of each interval identified (x_1 through x_f). Equations were then written for each interval based upon the general oxidation relationship of Deal and Grove

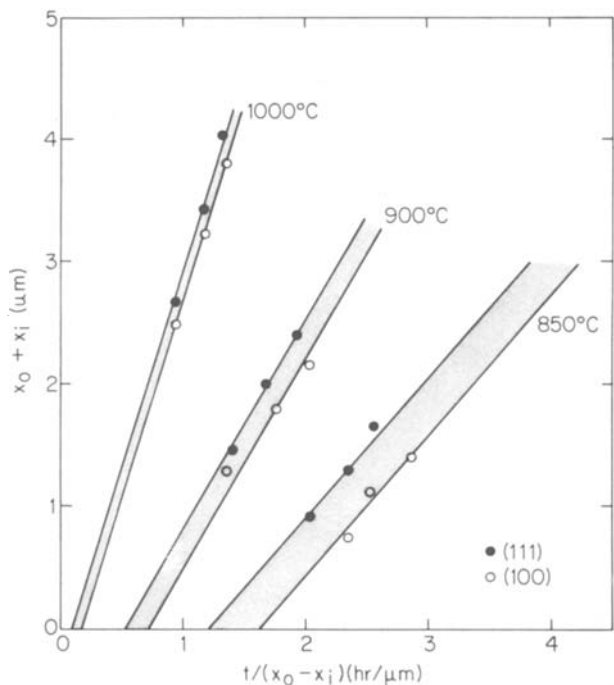


Fig. 4. $(x_0 + x_i)$ vs. $(t/x_0 - x_i)$ for (100) and (111) silicon oxidized at 850°, 900°, and 1000°C in pyrogenic steam at 10 atm. Slope of line is B and intercept is $-A$.

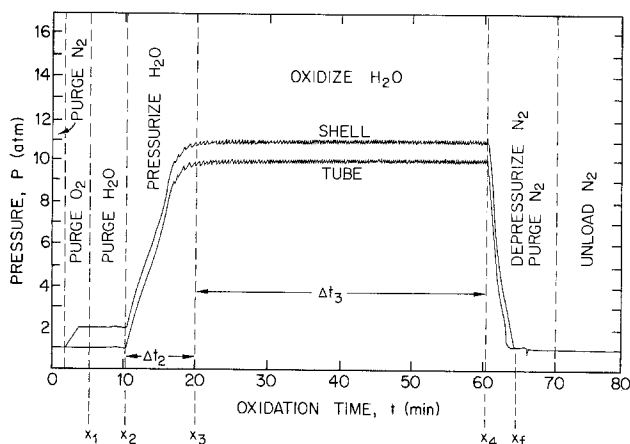


Fig. 5. Typical oxidation cycle showing the various regions considered in modeling the oxidation.

$$x_1 \approx 0 \quad [7]$$

$$x_2 = \frac{1}{2} \left[-A + \sqrt{A^2 + 4B'(t_2 - t_1)} \right] \quad [8]$$

$$x_3 = \frac{1}{2} \left[-A + \sqrt{A^2 + 2B'(t_3 - t_2)(P + 1) + 4x_2^2 + 4Ax_2} \right] \quad [9]$$

$$x_4 = \frac{1}{2} \left[-A + \sqrt{A^2 + 4B'P(t_4 - t_3) + 4x_3^2 + 4Ax_3} \right] \quad [10]$$

$$x_t = \frac{1}{2} \left[-A + \sqrt{A^2 + 2B'(t_f - t_4)(P + 1) + 4x_4^2 + 4Ax_4} \right] \quad [11]$$

where the parabolic rate constant $B = B'P$ and B' = rate constant at 1 atm. The above equations can be simplified by writing for a general oxidation interval

$$\Delta t_i = t_{i+1} - t_i$$

and

$$x_i^2 + Ax_i = B_i \Delta t_i + x_{i-1}^2 + Ax_{i-1}$$

Equations [7]-[11] can then be reduced to

$$x_t = \frac{1}{2} \left\{ -A + \sqrt{A^2 + 4B' \left(\Delta t_1 + \left(\frac{P+1}{2} \right) (\Delta t_2 + \Delta t_4) + P\Delta t_3 \right)} \right\} \quad [12]$$

Results obtained using rate constants determined through the use of Eq. [6] and plots of $(x_0 + x_i)$ vs. $(t/x_0 - x_i)$ are in very good agreement with experimental values for oxidation temperatures greater than 900°C. For lower oxidation temperatures, the rate constants could not be determined with sufficient accuracy by this technique and in some cases were found to model the experimental data poorly. Furthermore, the data suggested the presence of a second activation energy for B and possibly B/A and this result was in need of verification. A more direct method for rate constant determination, with immediate feedback on the modeling of the experimental data was therefore used. In this method, Eq. [7]-[11] are used to calculate the rate constants that would yield the best estimate of oxide thickness over the entire temperature range. The calculation was done by obtaining the locus of B/P and B/AP points that for a given oxidation will yield the experimentally measured oxide thickness. The intercept of the loci for various oxide thicknesses yields the values of B/P and B/AP that would, when used with this model, result in an oxide thickness estimate typically less than $\pm 3\%$ of the experimentally obtained value. An example of this method is shown in Fig. 6 where for each of two oxide thicknesses a band is shown representing variations of $\pm 2\%$.

For a given oxidation condition (temperature, pressure, and silicon orientation) up to five oxide thickness values were used in the manner shown in Fig. 6 to determine the values of B and B/A . The rate constants thus obtained are summarized in Fig. 7 and 8 and include B and B/A values from data at 1, 5, 10, 15, and 20 atm. The solid and dotted lines in the figures represent 5, 10, 15, and 20 times the rate constants at 1 atm, while the data with error bars represent the values of B and B/A which will yield a fit of the experimental oxide thickness within $\pm 3\%$ as determined by Eq. [7]-[11]. These results show that the rate constants

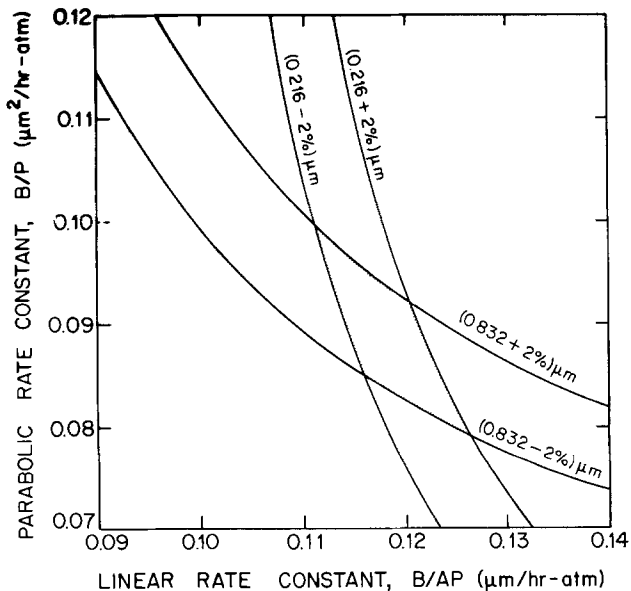


Fig. 6. Parabolic rate constant (B/P) vs. linear rate constant (B/AP). The shaded area represents values of B/P and B/AP which when used with Eq. [7]-[11] will yield oxide thickness values within $\pm 2\%$ of the experimental results.

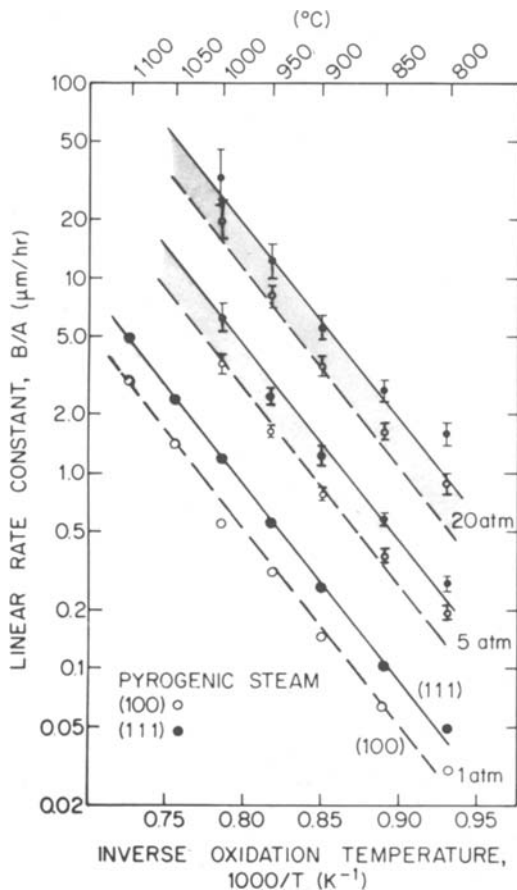


Fig. 7. Linear rate constant B/A vs. $1000/T$ for (100) and (111) silicon wafers oxidized in pyrogenic steam as obtained from 1, 5, and 10 atm data.

are proportional to pressure and indicate the presence of a second activation energy at 900°C and below, particularly in the case of the parabolic rate constant. For B the activation energy increases from 18 kcal/mol (0.78 eV) above 900°C to approximately 27 kcal/mol (1.17 eV) below this temperature, while for B/A the activation energy change is less pronounced and varies from 47.4 kcal/mol (2.05 eV) to about 38 kcal/mol (1.60 eV). This change in activation energy is necessary when modeling the oxide growth by a linear-parabolic relationship. It should be noted that the change occurs at a temperature of 900°C – 950°C and could be indicative of structural changes in the oxide at these growth temperatures, possibly related to the viscous flow postulated by EerNisse (13, 14). The apparent increase in activation energy associated with the parabolic rate constant below 900°C was noted earlier in the results on atmospheric pyrogenic steam oxidation (8).

The normalized values of the parabolic rate constant B are shown in Fig. 9 as a function of pressure. The range shown at each pressure represents data gathered at five different temperatures (800° , 850° , 900° , 950° , and 1000°C). The results indicate clearly that in the range of 1–20 atm the parabolic rate constant is linearly proportional to pressure. Similarly B/A is also proportional to pressure, therefore indicating that the primary pressure effect is on the parabolic rate constant B and that the dependence of B/A on pressure comes about through the dependence of B .

Oxide charges.—High frequency, quasistatic, and bias stress C-V measurements were carried out on p-type (100) and (111) silicon MOS structures. In cases where the oxide thickness was too large to allow for a meaningful C-V plot, the oxide thickness was reduced by etching in a buffered HF solution prior to the evaporation of aluminum fieldplates (by cold flash) on the sur-

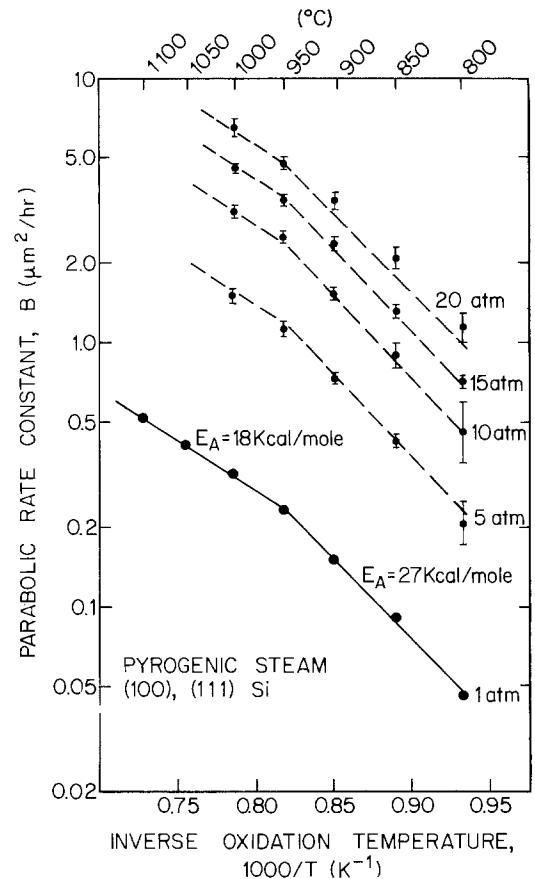


Fig. 8. Parabolic rate constant B vs. $1000/T$ for (100) and (111) silicon wafers oxidized in pyrogenic steam as obtained from data at 1, 5, 10, 15, and 20 atm.

face. Figure 10 shows the fixed oxide charge levels for oxidations at 5, 10, 15, and 20 atm for comparison purposes with those grown in the same tube at 1 atm. All oxides were cooled in N_2 following a 10 min anneal also in N_2 . The high pressure oxides were found to yield higher fixed oxide charge densities particularly for (111) silicon at temperatures below 900°C . Bias stress measurements (300°C , $+50 \text{ V}/\mu\text{m}$, $-30 \text{ V}/\mu\text{m}$)

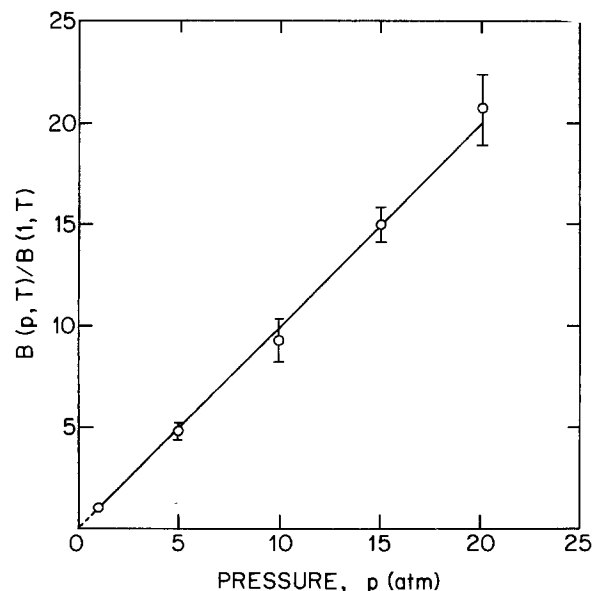


Fig. 9. Normalized parabolic rate constant $B(P, T)/B(1, T)$ vs. pressure for (100) and (111) silicon wafers oxidized in pyrogenic steam at 1, 5, 10, 15, and 20 atm for the temperature range 800° – 1000°C .

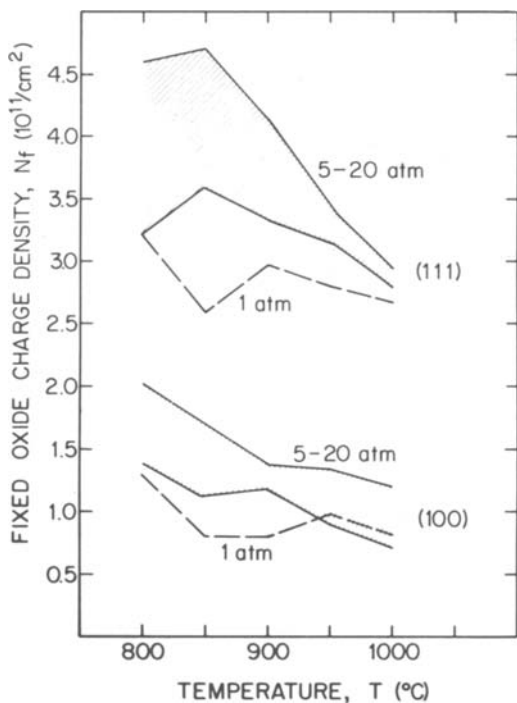


Fig. 10. Fixed oxide charge density vs. temperature for oxides grown on (100) and (111) silicon in pyrogenic steam at 1, 5, 10, 15, and 20 atm.

indicated a mobile ionic charge density (N_m) as low as $2 \times 10^{10}/\text{cm}^2$ and as high as $2.5 \times 10^{11}/\text{cm}^2$ with no particular pressure dependence. Interface state densities at midgap, as measured by the quasistatic technique, were very similar to those obtained at 1 atm and were characteristically low (15). It should be noted that no attempts were made at stabilizing the oxides by phosphorus gettering.

An investigation of the charge annealing characteristics of oxide charges in high pressure grown oxides was conducted in order to examine the differences, if any, in oxide charge annealing properties. Samples were oxidized at 800°C at 1 and 15 atm to grow about 2000Å of SiO_2 . The wafers were cooled and pulled (2 min) in N_2 . Following oxidation, the wafers were annealed in argon at 800°, 900°, and 1000°C for various times, and Fig. 11 presents the resultant anneal curves and indicates no observable difference between 1 and

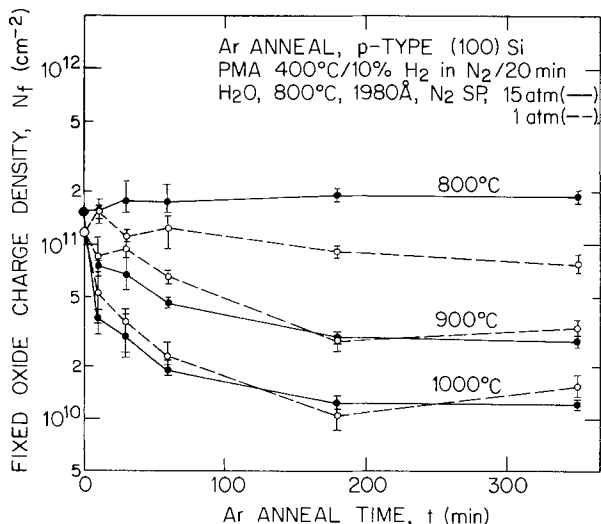


Fig. 11. Fixed oxide charge density vs. postoxidation Ar anneal time. Samples were initially oxidized in steam at 800°C at 1 or 15 atm and subsequently annealed in argon for various times.

15 atm oxides for anneals at 900° and 1000°C. At 800°C, some differences were noted with the 1 atm oxides yielding lower charge densities. Evidence indicates that the higher values obtained at 15 atm can be reduced (10-15%) by an anneal in N_2 at high pressure for 30 min.

It should be pointed out that values of fixed oxide charge are very sensitive to anneal gas purity and that the increasingly higher values of charge density with decreasing temperature may be a reflection of the presence of impurities such as oxygen in the nitrogen anneal ambient.

Electron trapping by avalanche charge injection was carried out on oxides grown on p-type (111) silicon wafers oxidized in pyrogenic steam at 5 atm (800°C, N_2 cooled). Typical flatband voltage shifts obtained are shown in Fig. 12; they first increase and then decrease in a manner typical of steam grown oxides. These results are similar to those obtained at 1 atm in pyrogenic steam at 800°C; values of effective trap densities of $5-6 \times 10^{12}/\text{cm}^2$ and capture cross sections of $2-3 \times 10^{-17} \text{ cm}^2$ can be obtained from the initial charging period.

Summary and Conclusions

The kinetics of high pressure oxidation in pyrogenic steam at temperatures of 800°-1000°C and pressures up to 20 atm have been investigated. A linear-parabolic model was used to analyze the data and a linear pressure dependence is observed for both the linear and parabolic rate constants. These results are in agreement with previous measurements carried out at pressures less than 1 atm (5) and at 10 atm (11).

The deviations from linearity observed by other authors (1, 12) may be due to the effect of pressurization time on the calculation of the rate constants as well as difficulties in obtaining both rate constants simultaneously for some temperature and pressure combinations. For the case of high temperature, high pressure oxidation, B can be calculated accurately whereas B/A values will have large errors. The reverse is true for low temperature situations.

Oxide charge density measurements have been carried out and charge levels compatible with MOS processing technology have been observed. In cases where high charge densities are obtained, they may be effectively reduced by short treatments at higher temperatures. Electron trapping characteristics in oxides grown at 5 atm are the same as those observed in 1 atm oxides.

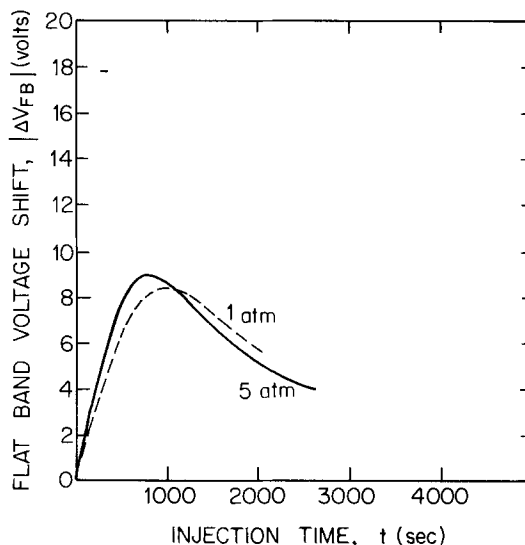


Fig. 12. Flatband voltage shift vs. electron injection time for electron trapping by avalanche charge injection in oxides grown on p-type (111) silicon oxidized at 1 and 5 atm in pyrogenic steam (800Å, $J = 1.5 \times 10^{-5} \text{ A/cm}^2$).

Acknowledgments

The authors would like to thank Edward Dovichi for conducting portions of the experimental work and Dr. M. L. Barry and Dr. J. M. Early for critically reviewing the manuscript. Portions of this work have been sponsored by DARPA Contract No. MDA903-79-C-0257.

Manuscript submitted Dec. 24, 1980; revised manuscript received March 13, 1981.

Any discussion of this paper will appear in a Discussion Section to be published in the June 1982 JOURNAL. All discussions for the June 1982 Discussion Section should be submitted by Feb. 1, 1982.

Publication costs of this article were assisted by Fairchild Camera and Instrument Corporation.

REFERENCES

1. N. Tsubouchi, H. Miyoshi, and H. Abe, *Jpn. J. Appl. Phys.*, **17**, Suppl. 17-1, 223 (1978).
2. L. E. Katz and L. C. Kimberling, *This Journal*, **125**, 1680 (1978).

3. J. R. Ligenza, *J. Phys. Chem.*, **65**, 2011 (1961).
4. R. Champagne and M. Toole, *Solid-State Technol.*, **20**, 61 (1977).
5. B. E. Deal and A. S. Grove, *J. Appl. Phys.*, **36**, 3770 (1965).
6. N. Tsubouchi, H. Miyoshi, A. Nishimoto, and H. Abe, *Jpn. J. Appl. Phys.*, **16**, 855 (1977).
7. M. Maeda, H. Kamioka, and M. Takagi, Paper 178 presented at The Electrochemical Society Meeting, Seattle, Washington, May 21-26, 1978.
8. B. E. Deal, *This Journal*, **125**, 576 (1978).
9. F. J. Norton, *Nature*, **171**, 701 (1961).
10. W. A. Pliskin, *IBM J. Res. Dev.*, **10**, 198 (1966).
11. P. T. Panousis and M. Schneider, Paper 53 presented at The Electrochemical Society Meeting, Chicago, Illinois, May 13-18, 1973.
12. R. J. Zeto, C. G. Thornton, E. Hryckowiaw, and C. D. Bosco, *This Journal*, **122**, 1409 (1975).
13. E. P. Eernisse and G. F. Derbenwick, *IEEE Trans. Nucl. Sci.*, **ns-23**, 1534 (1976).
14. E. P. Eernisse, *Appl. Phys. Lett.*, **35**, 8 (1979).
15. R. R. Razouk and B. E. Deal, *This Journal*, **126**, 1573 (1979).

A New Approach to Liquid Phase Electroepitaxy (LPEE) of III-V Compounds

S. Isozumi,¹ C. J. Herman, A. Okamoto,* J. Lagowski,* and H. C. Gatos*

Department of Materials Science and Engineering,
Massachusetts Institute of Technology, Cambridge, Massachusetts 02139

ABSTRACT

A new configuration of LPEE is described in which the substrate is placed between two wells containing a solution. This configuration eliminates problems associated with the contact to the back-side of the substrate. It also enables simultaneous observation of electroepitaxial growth and dissolution processes on the opposite sides of the substrate, and provides a unique means for *in situ* monitoring of the growth (and dissolution) kinetics.

Increasing efforts have recently been devoted to liquid phase electroepitaxy (LPEE) as a novel approach to the growth of III-V compounds. In this method growth is initiated and sustained by passing an electric current through the growth cell containing the solution and the substrate. In most instances the growth process is primarily controlled by the electromigration of the solute toward the substrate (1). Peltier cooling at the solution interface can provide additional driving force for growth. Thus, the key advantages of electroepitaxy are associated with the direct control of the growth rate by electric current while the overall temperature of the system is maintained constant. These advantages have been demonstrated in the studies of microscopic growth rate (2), dopant modulation (3), composition modulation (4), and the modulation of recombination centers in the crystal (5).

In LPEE systems employed thus far (6) electric current is passed through the solution, substrate, and a metal contact at the back-side of the substrate. A thin metal foil (a) or multilayers (b) have been used for the contact between the substrate and a graphite pedestal. This type of contact to the substrate has a noticeable electrical resistance which can be comparable to the overall resistance of the system at growth temperatures (6). Thus, it leads

to undesirable localized Joule heating, particularly at high current densities. Furthermore, local variations in the contact resistance lead to variations in the thickness of the electroepitaxial layers (6).

In the LPEE configuration developed in this investigation, the substrate is positioned between two identical large segments of saturated solution. Thus, preparation of back-side contact to the substrate is eliminated and the resistance between the metal and the graphite is physically separated from the substrate. Furthermore, *in situ* monitoring of the epitaxial growth process becomes possible through measurements of the resistance changes associated with the growing layer.

Growth System and Experimental Procedure

The apparatus employed in the present work is shown in Fig. 1. A boron nitride (BN) slider is positioned between the two segments of the graphite holder which contains the solution. With the aid of this slider the substrate is brought between the two segments of the solution. A stainless steel current electrode is threaded into each of the two graphite segments and a thermocouple shielded with stainless steel is positioned close to each of these segments (1 mm from the cell wall). The stainless steel shields are in electrical contact with the graphite segments and thus are used to determine the potential drop changes across the solution resulting from changes in the resistance (*i.e.*, thickness) of the growing layer

* Electrochemical Society Active Member.

¹ On leave from Fujitsu Laboratories, Limited, 1015 Kamukodanaka, Kawasaki, Japan.

Key words: LPEE, dissolution, kinetics.

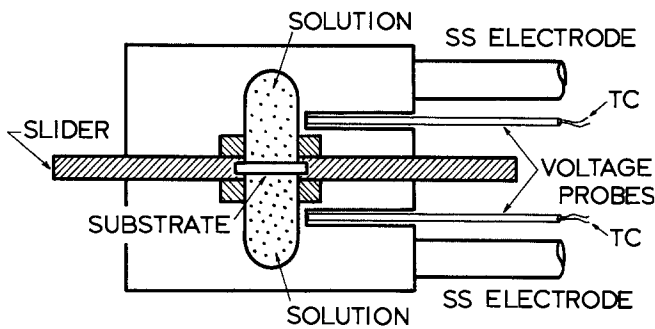


Fig. 1. Top view of apparatus for electroepitaxial growth without back-contact. The holder segments are of graphite and the slider of BN.

(all other electrical resistance components in the system are constant at a constant temperature).

Cr-doped (100) GaAs (500 μm thick) and Si-doped (100) GaAs ($n = 3 \times 10^{18} \text{ cm}^{-3}$, 340 μm thick) were used as substrates. Growth (or dissolution) area was 0.40 cm^2 , and each solution segment contained 9g of Ga saturated with GaAs at 850°C. Undoped layers ($n = 3 \times 10^{16} \text{ cm}^{-3}$) were grown on the Si-doped n^+ substrates, and undoped or Se-doped ($n = 4 \times 10^{18} \text{ cm}^{-3}$) layers were grown on the Cr-doped substrates in an H_2 atmosphere. After saturation of the solution the substrate was brought into position and the electric current was passed through the two solid-solution interfaces. Thus, on the side of the substrate with a positive polarity with respect to the solution growth took place, whereas dissolution took place on the opposite side. The applied current, the temperature of the solution, and the voltage across the solution segments were measured at 1 min intervals and stored by a computerized measurement system.

After 100 min of current flow the substrate was separated from the solutions by the BN slider, and then temperature was rapidly decreased. During the 100 min runs the temperature variations were within 0.5°C. The samples were cleaved and etched in AB etchant for 30 sec for the determination of the thickness and thus for the determination of the average growth or dissolution rate.

Results and Discussion

Resistance measurements.—In order to achieve reliable monitoring of the resistance changes due to changes in thickness of growing layers and/or the substrate the component resistances of the system were determined (and their stability assessed) at the growth temperature (850°C). The resistance of the system including that of the stainless steel electrodes, of the solution and of the electrical contacts were found to be $1.1 \times 10^{-4} \Omega$. The resistance of the growth cell including the resistance of the solution and that of the contacts between the cell walls and the solution was measured employing the stainless steel shields of the thermocouples and was found to be $1.2 \times 10^{-3} \Omega$, while the resistance of the solution was estimated to be less than $3 \times 10^{-4} \Omega$. Thus, the resistance of the stainless steel electrodes is the major part of the resistance of the overall system. All of the above resistances were reproducible and exhibited no variations for extended periods of time at the growth temperature.

The resistances of the substrates at the onset of growth as determined by the stainless shield probes are shown in Fig. 2. These values include the cell resistance of $1.2 \times 10^{-3} \Omega$ pointed out above. Thus, the resistance of the Si-doped (n^+) substrates was $0.9 \times 10^{-3} \Omega$ ($1.1 \times 10^{-2} \Omega\text{-cm}$) and that of the Cr-doped substrates $9.9 \times 10^{-3} \Omega$ ($7.9 \times 10^{-2} \Omega\text{-cm}$). Cr-doped substrates behave as intrinsic ($n = 2 \times 10^{17} \text{ cm}^{-3}$).

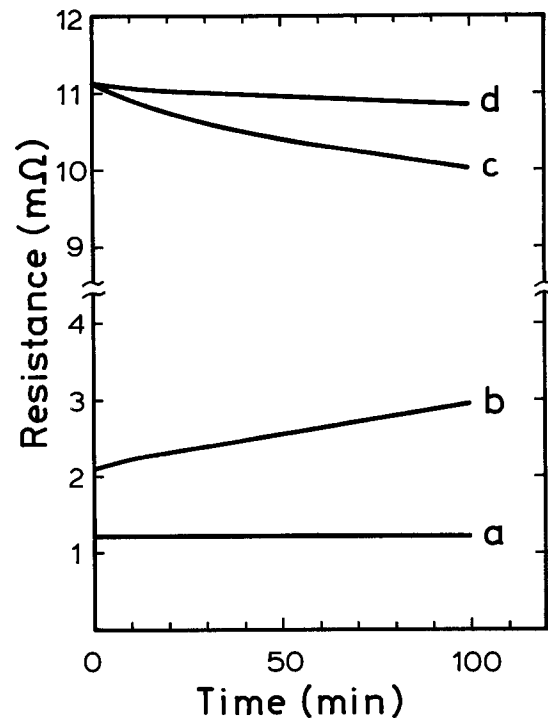


Fig. 2. Changes in the resistance in growth cell during current flow (9 A/cm^2) at 850°C. Each curve represents: (a) no substrate in cell; (b) undoped growth on n^+ substrate; (c) n^+ growth on Cr-doped substrate; (d) undoped growth on Cr-doped substrate.

The resistivity values obtained in the present measurement are quite reasonable.

The changes in resistance of the GaAs material during the growth process are also shown in Fig. 2. It is seen that a significant change in the resistance took place for the n^+ layer growing on Cr-doped substrate and for the undoped layer growing on n^+ substrate. For the undoped layer growing on a Cr-doped substrate, only a small change in resistance is observed.

In the present LPEE configuration, growth takes place on one side of the substrate and, simultaneously, dissolution on the other side. Thus, the resistance changes in Fig. 2 include contributions from both effects. If a growth and a dissolution proceed with velocities v_G and v_D , respectively, the rate of resistance change is

$$\frac{dR}{dt} = v_G \rho_L / S - v_D \rho_s / S \quad [1]$$

where ρ_L and ρ_s are the resistivities of the layer and of the substrate, respectively, and S is the growth area. v_G and v_D exhibit a transient behavior at initial stages of the growth. In general, ρ_L can also vary with time due to impurity segregation effects. It will be shown below that in the absence of interference from Joule heating at the substrate $v_G = v_D$, and the utilization of expression 1 for the analysis of experimental data is simplified.

Growth process vs. dissolution.—The experimental results on the average growth and dissolution rates as a function of electric current density are given in Fig. 3 and 4 for n^+ and Cr-doped substrates, respectively.

It is seen from Fig. 3 that the growth and dissolution rates are similar and increase linearly with current density up to about 12 A/cm^2 . Such behavior is consistent with a theoretical model of electroepitaxial growth kinetics (1). According to this model, in the absence of convection, v_G and v_D can be expressed as

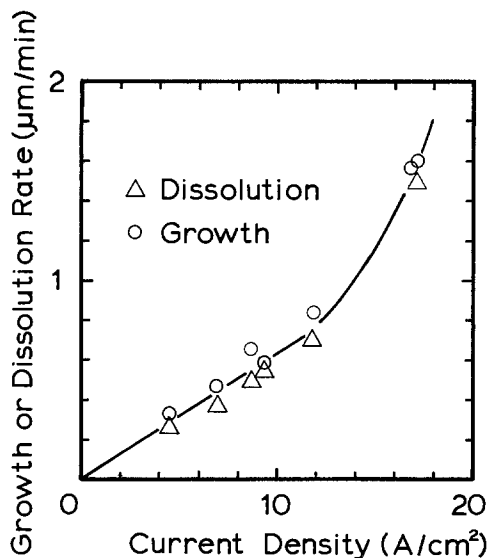


Fig. 3. Dependence of average growth and dissolution rates on current density with n^+ substrate ($340 \mu\text{m}$ thick) at 850°C .

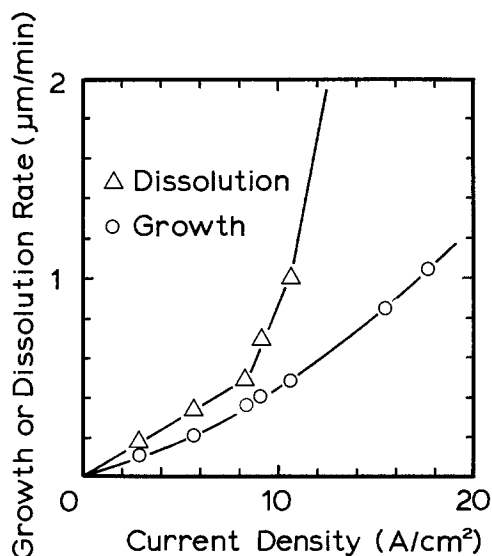


Fig. 4. Dependence of average growth and dissolution rates on current density with Cr-doped substrate ($500 \mu\text{m}$ thick) at 850°C .

$$v_G = \frac{(|\Delta T_p| - \Delta T_j) \frac{dC}{dT} \Big|_L \left(\frac{D}{\pi t} \right)^{1/2} + \mu E \frac{C_o}{C_s - C_o}}{C_s - C_o} \quad [2a]$$

and

$$v_D = \frac{(|\Delta T_p| + \Delta T_j) \frac{dC}{dT} \Big|_L \left(\frac{D}{\pi t} \right)^{1/2} + \mu E \frac{C_o}{C_s - C_o}}{C_s - C_o} \quad [2b]$$

where ΔT_p and ΔT_j are the change of temperature at the interface due to the Peltier effect and Joule heating, respectively; C_s and C_o are the solute concentration in the solid and in the solution, respectively; D is the diffusion coefficient of the solute in the solution, t is the time, μ is the mobility of the solute, and E is the electric field in the solution.

For the polarity employed in the present experiments, ΔT_p corresponds to cooling at the growth interface and to heating at the dissolution interface. Thus, T_j will lead to a decrease in the growth rate and an increase in the dissolution rate. Since up to about 12 A/cm^2 v_G and v_D are approximately the same (Fig. 3), T_j must be insignificant for n^+ substrates.

At higher values of current density both growth and dissolution are significantly enhanced. This behavior can readily be expressed assuming that significant convection is generated in the growth and dissolution segments. In the presence of convection the expressions for v_G and v_D become (1)

$$v_G = \frac{|\Delta T_p| - \Delta T_j}{C_s - C_o} \frac{dC}{dT} \Big|_L \frac{D}{\delta} + \mu E \frac{C_o}{C_s - C_o} \quad [3a]$$

$$v_D = \frac{|\Delta T_p| + \Delta T_j}{C_s - C_o} \frac{dC}{dT} \Big|_L \frac{D}{\delta} + \mu E \frac{C_o}{C_s - C_o} \quad [3b]$$

where δ is the thickness of the boundary layer which decreases with increasing convective flow. Since the values of v_G and v_D remain the same (Fig. 3), ΔT_j is not significant as compared to ΔT_p . Thus, convection is apparently generated by Joule heating from the substrate, e.g., at the solution-graphite contacts.

In the case of Cr-doped substrates, the growth and dissolution rates are different (Fig. 4). Even in the region of linear dependence on current density (up to about 8 A/cm^2) v_D is greater than v_G . At higher current densities the difference between the two rates becomes even more pronounced. This behavior is apparently associated with Joule heating of the Cr-doped substrate, which, at the growth temperature, has a resistivity about one order greater than that of the n^+ substrate. For the geometric configuration of the present cell, the temperature increase at both sides of the substrate with resistance, R , is $\Delta T_j = RI^2/2G_1$ where I is the current and G_1 is the heat conductivity of the solution. The value of G_1 for the Ga-As solution is not known; however, a rough estimate based on the value of liquid Ga near room temperature [$0.09 \text{ cal/sec-cm}^2\text{-}^\circ\text{C}$ (7)], for current density of 10 A/cm^2 and $R = 9 \times 10^{-3} \Omega$, shows that ΔT_j values of the order of 0.5°C can be reached; these values are comparable to the magnitude of the temperature change due to the Peltier effect and account for the observed difference between v_G and v_D .

Above 9.5 A/cm^2 (Fig. 4) the dissolution rate increases precipitously apparently due to turbulent convection caused by increased Joule heating and thus increased thermal gradients. The higher Peltier coefficient of the Cr-doped substrates as compared to that of the n^+ substrates must also be a contributing factor. The observed nonuniform dissolution of the Cr-doped substrates is clear indication of turbulent convection at the substrate-solution interface.

As pointed out in previous studies (1) convective flow can be reduced by decreasing the solution thickness. However, depletion of a solution with reduced thickness would limit the maximum thickness of the LPEE layer. This limitation can be overcome with a multisubstrate configuration in which parallel substrates are positioned between thin solution layers. Joule and Peltier heating can also be reduced by employing thinner wafers. An LPEE cell into which these features are incorporated is currently being tested.

Resistance changes induced by growth.—On the basis of the above analysis of the dissolution and growth processes, the resistance changes shown in Fig. 2 can now be interpreted. In the case of Fig. 2b the resistance change corresponds to the growth of an undoped layer on n^+ substrate. As pointed out earlier, v_G can be here considered equal to v_D . Thus, Eq. [1] reduces to $dR/dt = (\rho_L - \rho_S) v_G/S$ and the overall resistance increase is due to the fact that ρ_L is greater than ρ_S . Indeed, after an initial transient period dR/dt becomes constant indicating that growth and dissolution proceed with a constant rate.

Consistent with the LPEE model (1) this steady-state growth is controlled by electromigration and

$v_G = v_D = \mu EC_0/C_s - C_0$. If $\rho_L \gg \rho_s$, then $dR/dt \simeq \rho_L v_G/S$ and the resistance change provides a direct measure of the growth kinetics. If v_G is known the resistance change can be used for the determination of ρ_L . The results of such measurements are shown in Fig. 5, where the resistance of a growing undoped layer at 850°C is plotted against the layer thickness. For comparison the resistance of Cr-doped GaAs (which behaves as intrinsic material) measured in the cell at 850° is also shown as a function of thickness. It is seen that the resistivity is identical in both cases.

In the case of Cr-doped substrates, a decrease in the total resistance is observed during growth of both undoped and n^+ layers (Fig. 2d and c, respectively). The resistivity of the undoped layer at 850°C is very similar to that of the substrate (both behave as intrinsic material); thus expression [1] can be rewritten as $dR/dt \simeq (v_G - v_D)\rho_s/S$ and the resistance decrease indicates that $v_D > v_G$; this finding is consistent with the results of Fig. 4. A much larger decrease in the resistance takes place for the n^+ layer (Fig. 2b) since here not only $v_D > v_G$, but also $\rho_s \gg \rho_L$. Accordingly, $dR/dt \simeq -v_D\rho_s/S$, and thus the resistance change provides a direct measure of dissolution rate.

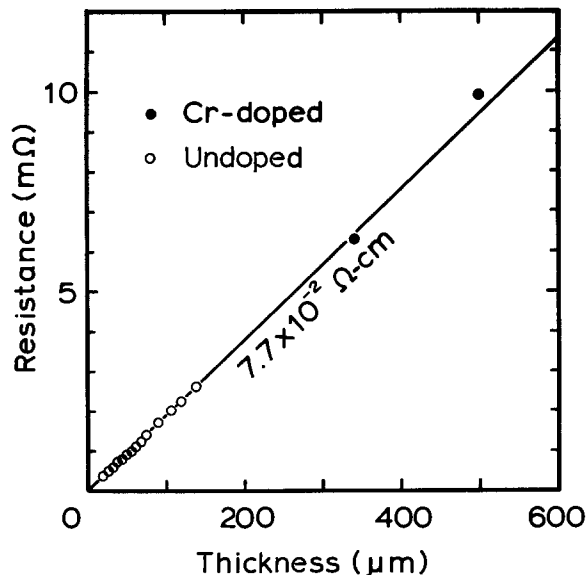


Fig. 5. Resistance of undoped LPE layers grown on n^+ substrate (○), and resistance of Cr-doped GaAs (●).

Summary

A new electroepitaxial configuration was developed in which the back-side electrical contact to the substrate is eliminated, thus rendering electroepitaxy more amenable to practical applications. This configuration can easily be extended to simultaneous growth on a number of parallel substrates separated by relatively thin layers of solution.

Utilizing this new configuration the simultaneous study of growth and dissolution processes on the opposite sides of a substrate became possible for the first time. Experiments with n^+ substrates showed that both processes exhibit the same rates, consistent with the theoretical model of electroepitaxial growth kinetics. In contrast, the high resistance of Cr-doped substrates leads to pronounced Joule heating which promotes dissolution over growth.

Detailed analysis of the resistance components in the growth system showed that *in situ* observation of the growth or dissolution process is possible utilizing the difference in the resistance between the substrate and the LPEE layer at the growth temperature.

Acknowledgment

The authors are grateful to the National Aeronautics and Space Administration and to the National Science Foundation for financial support. They are also grateful to Mrs. K. Isozumi for the evaluation of the samples.

Manuscript submitted March 6, 1981; revised manuscript received May 11, 1981.

Any discussion of this paper will appear in a Discussion Section to be published in the June 1982 JOURNAL. All discussions for the June 1982 Discussion Section should be submitted by Feb. 1, 1982.

Publication costs of this article were assisted by the Massachusetts Institute of Technology.

REFERENCES

1. L. Jastrzebski, J. Lagowski, H. C. Gatos, and A. F. Witt, *J. Appl. Phys.*, **49**, 5909 (1978).
2. M. Kumagawa, A. F. Witt, M. Lichtensteiger, and H. C. Gatos, *This Journal*, **120**, 583 (1973).
3. D. J. Lawrence and L. F. Eastman, *J. Crystal Growth*, **30**, 267 (1975).
4. T. Bryskiewicz, J. Lagowski, and H. C. Gatos, *J. Appl. Phys.*, **51**, 988 (1980).
5. L. Jastrzebski, J. Lagowski, and H. C. Gatos, *This Journal*, **128**, 697 (1981).
6. L. Jastrzebski, Y. Imamura, and H. C. Gatos, *ibid.*, **125**, 1140 (1978).
7. "Liquid Metal Handbook," 2nd ed., Atomic Energy Commission (1954).

Self-Diffusion of Gallium in Gallium Arsenide

Helen D. Palfrey, Margaret Brown, and Arthur F. W. Willoughby*

Mechanical Engineering Department, University of Southampton, Southampton SO9 5NH, England

ABSTRACT

The self-diffusion of gallium in gallium arsenide has been studied over the temperature range 1100°-1025°C using radiotracer techniques. Gallium arsenide samples were diffused with ^{72}Ga evaporated layers under known pressure of arsenic in sealed capsules. Following diffusion, layers were removed from the surface using anodic oxidation followed by oxide dissolution, and the ^{72}Ga concentration in each layer was measured by counting the γ -radiation. This sectioning method, which allows accurate determination of very shallow profiles, has allowed measurements of the diffusion coefficient to be made at lower temperatures than those employed by Goldstein, and the significance of the profile shapes measured is discussed in relation to the existence of possible "tails" in the profiles. It is concluded that there is only evidence for a single diffusion mechanism in the concentration and temperature range studied. Diffusion coefficients obtained in the temperature range 1025°-1100°C are from $3 \times 10^{-15} \text{ cm}^2/\text{sec}^{-1}$ to $9 \times 10^{-15} \text{ cm}^2/\text{sec}^{-1}$ under a constant arsenic pressure (P_{As_2}) of 0.75 atm, and lead to an activation energy of the order of $2.6 \pm 0.5 \text{ eV}$ and a pre-exponential factor of $4 \times 10^{-5} \pm 16 \times 10^{-5} \text{ cm}^2 \text{ sec}^{-1}$. The results are discussed in comparison with previous measurements by Goldstein. The measured diffusion profiles are the first reported under known arsenic pressure and final surface concentration of gallium.

The conspicuous lack of GaAs self-diffusion data and conflict between the little existing data (1, 2) highlighted the need for information in this area of GaAs technology. It is hoped that the present self-diffusion data, carried out under controlled conditions, will help to clarify the native point defect situation and contribute to the understanding of impurity diffusion and redistribution of dopants during device preparation.

Material

GaAs was supplied by M.C.P. Electronics Limited. (100) slices were cut from an undoped Bridgman grown crystal and were n-type with a carrier concentration of $2.2 \times 10^{16} \text{ cm}^{-3}$, mobility of $4270 \text{ cm}^2 \text{ V}^{-1} \text{ sec}^{-1}$, resistivity of 0.068Ω (at 300 K), and an initial etch pit density of 4000 cm^{-2} . The slices were mechanically/chemically polished on both sides, and as x-ray double crystal rocking curves showed the slice to be of good, uniform crystal perfection, it was considered unnecessary to do any further slice preparation. The final slice dimensions were $2.5 \times 2.5 \times 0.05 \text{ cm}$.

Experimental Technique

Capsule design.—In order to prevent loss of arsenic from GaAs to the vapor phase (at temperatures in excess of about 640°C) it was necessary to employ an enclosed annealing technique. This was achieved by enclosing the slices in silica capsules. The capsule design was influenced by factors such as the slice dimensions, ease of loading and unloading, minimizing the capsule volume and thermal mass, heating the slice as little as possible during sealing, and the ability to offer support to the slices at the high annealing temperatures (1025°-1100°C). The final capsule design is presented in Fig. 1. It consisted of a semicylinder formed from silica and open at one end. After loading, an end cap with an outlet to vacuum was sealed onto the main body.

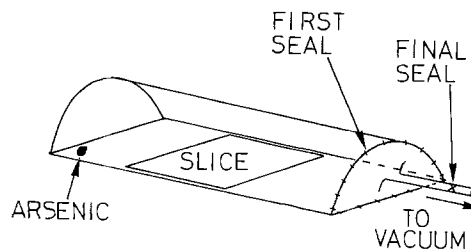
All the capsules were washed in 10% HF for 1/2 hr, followed by repeated rinsing and boiling in deionized water. They were then dried in the diffusion furnace (at the diffusion temperature) for several hours, with high purity nitrogen flowing through the furnace to sweep away any expelled vapors.

* Electrochemical Society Active Member.
Key words: anodic oxidation, radioisotope.

Annealing conditions.—In order to maintain the surface quality of the slices during the long annealing periods of about 24 hr, several factors were found to be of the utmost importance, these were: elimination of water vapor from the silica ware by baking, reduction of temperature gradients in the system to $<1^\circ\text{C}$, the achievement of a good vacuum in the capsule prior to the final sealing, minimizing the volume and thermal mass of the capsules, and the addition of arsenic to create a minimum pressure of 0.75 atm during the anneal (see the Appendix).

Each slice was annealed in the following manner. Radioactive gallium, containing ^{72}Ga , half-life of 14.1 hr (obtained from the Isotope Production Unit, Harwell) was evaporated onto one face of the slice through a circular mask. The slice was introduced into the capsule along with the required amount of arsenic (see the Appendix). The end cap was then sealed onto the main body after which the capsule was flushed with argon then evacuated to about $8 \times 10^{-8} \text{ atm}$ before being finally sealed. The capsule was introduced into the furnace where it remained at the diffusion temperature $\pm 1^\circ\text{C}$ for roughly 24 hr. At the end of the anneal the capsule was allowed to air cool (about $2^\circ\text{C} \text{ sec}^{-1}$). One end of the capsule was locally cooled on a lead block to avoid arsenic condensation on the slice.

Mesa preparation.—In order to obtain absolute Ga concentrations and to avoid high level contamination a



FIRST SEAL: END CAP ONTO MAIN BODY.
FINAL SEAL: CAPSULE SEALED OFF UNDER VACUUM

Fig. 1. Silica capsule design. Capsule length, width, and volume are 9 cm, 2.8 cm, and 24 cm, respectively. Capsule made from 0.2 cm thick silica.

mesa of known area was prepared for profiling, roughly in the middle of the Ga diffused area, after the anneal. However, it became evident during the experiments that the creation of the mesa had not fully achieved its aim and that radioactive Ga was present on the slice outside the mesa area. Contamination problems and the ways in which they were solved are discussed later.

The mesa was masked off by one of two methods. A solution of black wax was sprayed through a circular stencil to give a well-defined area. After careful removal of the stencil the slice was held just above a hot plate to ensure that the black wax coalesced leaving a pinhole-free mask. The slice was then left until the black wax was dry. The alternative was simply to stick a circular piece of polyvinyl chloride (PVC) adhesive tape onto the area to be masked. After masking, the slices were etched for 2 min in freshly prepared 1% $\text{Br}_2/\text{CH}_3\text{OH}$ solution to remove approximately $9\ \mu\text{m}$ from everywhere but the masked area, thus creating the mesa. Since the expected detectable Ga diffusion depth was less than $5\ \mu\text{m}$, the etching procedure should have removed all the radioactive Ga outside the mesa area. The black wax masks were removed after etching by repeated rinsing in trichloroethylene. The PVC masks were also removed by soaking in trichloroethylene, which swelled and lifted off the mask. In both cases the slices were finally thoroughly rinsed in deionized water. Both the wax and PVC masking techniques proved satisfactory. However the PVC mask was favored as it was a cleaner process.

Anodic oxidation.—The mesa area on each slice was profiled using the anodic oxidation technique, reported by Hasegawa and Hartnagel (3), followed by oxide dissolution, to remove thin (typically 250–500Å) parallel layers of GaAs from the mesa area. Hasegawa and Hartnagel (3) reported linear relationships between the anodization voltage, thickness of anodic oxide grown, and thickness of GaAs consumed during oxide growth. Earlier calibration work was in close agreement with these reported values. The thickness of each layer removed from the mesa could therefore be varied and was chosen by using the appropriate anodization voltage. Each anodic oxide had a well-defined interference color which was used to check that the anodization had proceeded correctly.

The equipment used for the anodizations is shown schematically in Fig. 2. It consisted of a hollow cylindrical polytetrafluoroethylene (PTFE) jig which contained a central hole (1.6 cm diam) at one end. The slice was placed on a silicone rubber washer and was

positioned over the hole so the mesa was centrally positioned. The jig was clamped vertically and a circular platinum wire, placed just above the exposed portion of the slice, acted as the cathode. Electrolyte (a buffered 3% aqueous solution of tartaric acid and propylene glycol) was pipetted into the hole until the cathode was well covered ($\approx 2\ \text{cm}^3$). All anodizations were carried out with 60W illumination directly above the jig and were for 7 min each.

After anodization the electrolyte was pipetted from the hole and retained in a $10\ \text{cm}^3$ plastic phial. The anodized area was rinsed with deionized water which was also collected. The slice was then removed from the jig (which was washed and dried before the next anodization) and the oxide color checked against a standard before a few drops of 20% HCl were pipetted onto the anodized area to remove the oxide. This fluid, containing the dissolved oxide, was very carefully poured into the phial via a funnel as was the final rinsing water. The slice was thoroughly washed in deionized water before the next anodization. All phials, pipettes, and funnels were used once only to prevent cross contamination. The electrolyte was retained for measurement as well as the dissolved oxide layer since finite dissolution of gallium and arsenic occurs during the oxidation process.

Radioactivity counting.—The ^{72}Ga present in the liquid collected in the phials following anodization and stripping was counted in a NaI (Tl) well scintillation counter, J. & P. Counter Ratemeter MS310. Absolute values of Ga concentration were obtained by comparison of the radioactivity in each sectioned layer to that of a known standard. The standard consisted of a known weight of irradiated Ga containing ^{72}Ga (specific activity identical to the ^{72}Ga diffusion source) dissolved in a known volume of aqua regia. It was chosen to be in the form of a solution since the radioactive Ga collected from the profiled areas was also in solution.

Observation and prevention of ^{72}Ga contamination outside the mesa area.—As mentioned above, effects due to the presence of ^{72}Ga outside the mesa area were observed during the course of the experiments. These took two forms, namely: type 1, the observation of some anomalously high values of Ga concentration deep in the profile, "spikes"; and type 2, the appearance of low concentration tails in the profiles.

The problem of contamination was not recognized initially since the final surface Ga concentrations were low. Under these circumstances the initial count rates from the sections were relatively low thus preventing deep profiling. Also, radioactive Ga was not present in sufficiently high concentrations to cause noticeable contamination. These conditions resulted from a poor evaporation technique, but when this was improved, and high final surface concentrations were achieved (through a larger quantity of ^{72}Ga diffusion source), type 1 and type 2 contamination effects were observed.

Autoradiographs were obtained from the slices on removal from the furnace and after mesa creation in order to see the radioactive Ga distribution over the slice at these two stages.

On removal from the furnace: The original ^{72}Ga evaporated area was clearly visible, but a high level of ^{72}Ga was also present on two edges of the front face (Fig. 3). ^{72}Ga was also found to be on the back face of the slice.

After mesa creation: The mesa area could be clearly seen. While there was no detectable ^{72}Ga on the back face, some ^{72}Ga still remained on the two edges of the front face.

The ^{72}Ga on the front face, outside the mesa area, was removed by careful lapping. The back face and four sides were also lapped off in order to be sure of complete removal of ^{72}Ga from these areas. After lapping the slice was washed thoroughly and then repeatedly boiled in concentrated HCl (to dissolve any

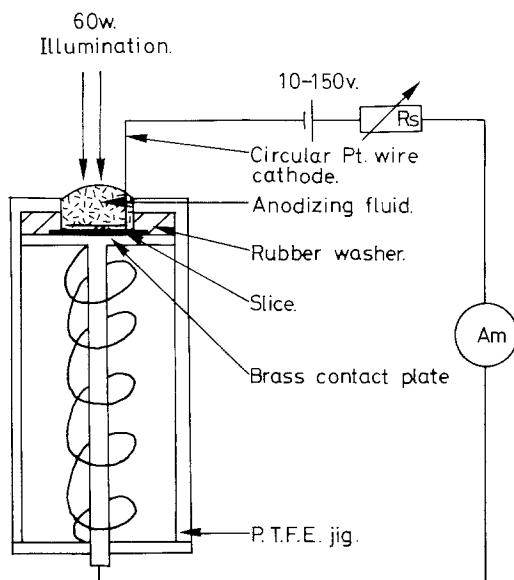


Fig. 2. Anodizing apparatus

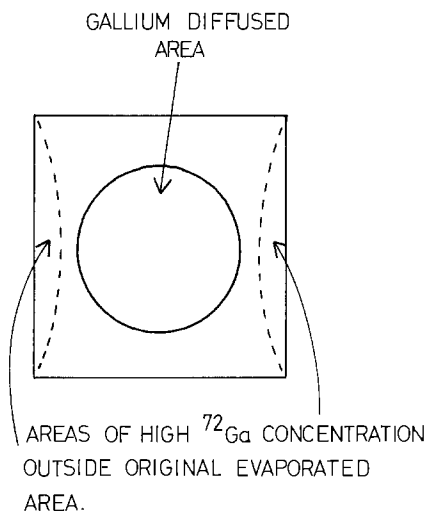


Fig. 3. Schematic representation of slice on removal from furnace

free gallium), until the radioactive level of the concentrated HCl fluids was reduced to near background.

Profiles obtained from slices using this preparation procedure were found to be free of Ga "spikes" (type 1 contamination). However, low Ga concentration "tails" were still apparent. It was thought that the "tails" may have been a result of some systematic but low level contamination. This type of contamination could arise if a proportion of radioactive Ga contained in the 20% HCl etch (used for anodic oxide layer removal) was adsorbed onto the slice. This adsorption phenomenon in acid solutions is well known (4), for example, gold onto silicon and silver and copper onto germanium. The amount of radioactive material adsorbed can be reduced to negligible proportions by addition of suitably large quantities of nonactive material to the acid solution (5). In this work adsorption of ^{72}Ga was minimized by the addition of nonactive GaCl_3 to the 20% HCl solution used during sectioning.

Systematic investigation of contamination showed that the following procedures must be followed in order to obtain a profile unaffected by contamination: (i) The use of autoradiographs to check that ^{72}Ga is present in the mesa area only. (ii) Removal (preferably by mechanical means) of radioactive Ga from all areas other than the mesa. This should be checked again by autoradiographs. (iii) The minimization of radioactive Ga adsorption, from acid solution, onto the slice by the addition of nonactive gallium to the acid solution.

A profile obtained, following these procedures, is presented in Fig. 4. It can be seen that neither type 1 nor type 2 contamination effects are observed. Pits in the original surface, or those that develop at high temperatures, can also give rise to "tails." However, since minimization of ^{72}Ga adsorption eliminated "tails" it appears, that in this case, pitting was not responsible for the observed "tails."

It is clear that great care must be taken to avoid contamination, however, comparison of the diffusion coefficients obtained from profiles affected and unaffected by contamination (24 hr diffusion anneals at 1050°C and $0.75\text{ atm } P_{\text{As}_2}$) shows that the diffusion coefficient was relatively unaffected by both types of contamination effects observed. This is so since the diffusion coefficients were estimated from data covering the first two orders of magnitude drop in Ga concentration where the low level contamination was insignificant and where "spikes" were not observed.

Results and Discussion

The diffusion anneals were carried out over the temperature range 1100°C – 1025°C in order to obtain an estimate for the activation energy of gallium diffusion. Ga profiles ($P_{\text{As}_2} = 0.75\text{ atm}$) are presented in Fig. 4,

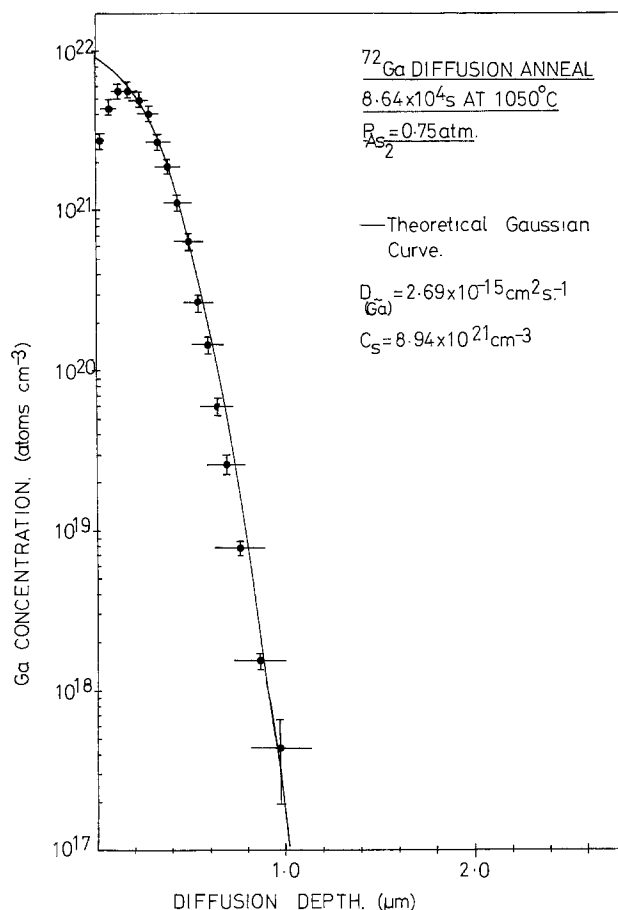


Fig. 4. Diffusion profile at 1050°C

5, 6, and 7. The arsenic pressure was held constant at 0.75 atm in order to observe the temperature dependence of the diffusion behavior. The diffusion coefficient

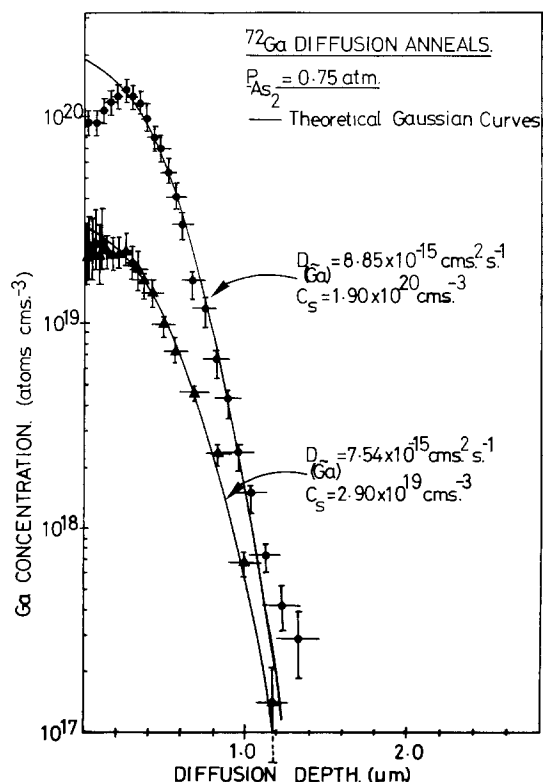


Fig. 5. Diffusion profiles at 1100°C . \blacktriangle , Diffusion time $8.12 \times 10^4\text{ sec}$; \bullet , diffusion time $6.12 \times 10^4\text{ sec}$ and a sixfold increase in evaporated ^{72}Ga layer source compared to \blacktriangle data.

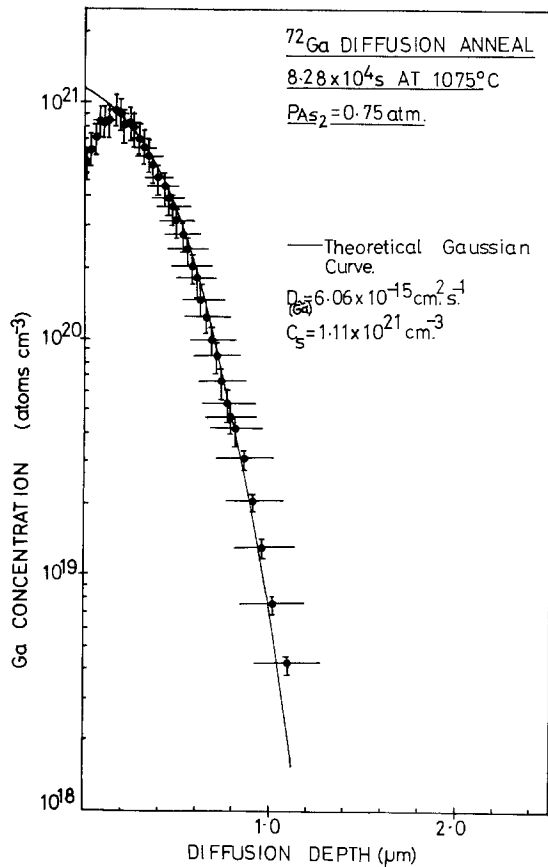


Fig. 6. Diffusion profile at 1075°C

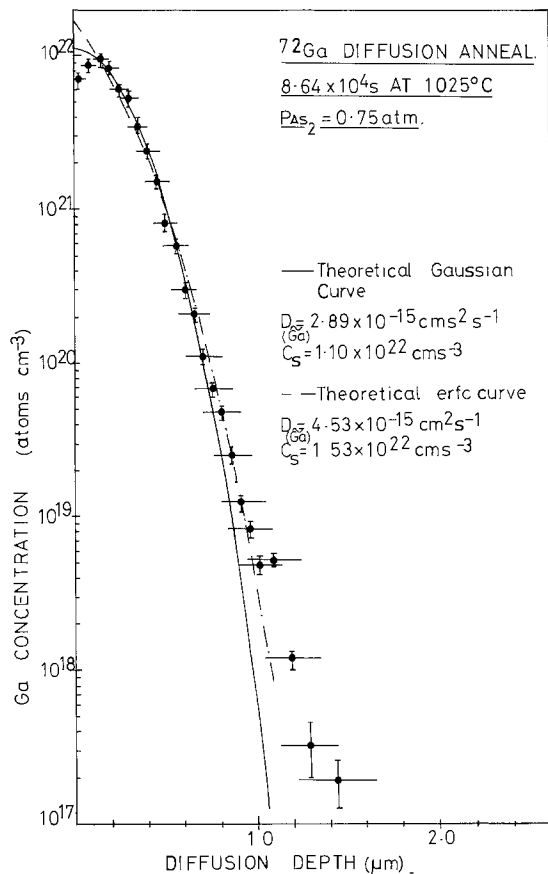


Fig. 7. Diffusion profile at 1025°C

estimated from the profiles by using the method of least squares to obtain the curves of best fit. In most cases the evaporated ^{72}Ga acted as a limited diffusion source so a Gaussian solution was used. When it was unclear whether the source was limited or infinite, both Gaussian and erfc solutions were used to obtain curves of best fit to the experimental data. Diffusion coefficient data obtained in the present work and those reported by Goldstein (1) are plotted vs. $1/T$ and presented in Fig. 8. Q and D_0 values were calculated from a least squares fit to all points using unit weights and were found to be 2.6 ± 0.5 eV and $4 \times 10^{-5} \pm 16 \times 10^{-5} \text{ cm}^2 \text{ sec}^{-1}$, respectively. The errors in Q and D_0 were calculated from the residuals of the least squares fit. It is stressed that the ranges of the calculated errors are only appropriate to the specific experimental conditions used in this work. Further data are required to obtain a more accurate estimate of the activation energy. However, the activation energy is significantly less than that reported by Goldstein (1) for Ga diffusion in GaAs. If Goldstein's experimental data are extrapolated to the temperature range studied in this work, then there is broad agreement between the two concerning the order of the diffusion coefficient. There is, however, a discrepancy between the two observed activation energies which is well outside the range of experimental error. It is known (6) that Goldstein conducted his diffusion anneals at the arsenic-rich side of the phase field, whereas the present results were obtained under comparatively gallium-rich conditions. The discrepancy in activation energies may be due to differences in arsenic pressure conditions and/or a change in the dominant diffusion mechanism.

The very small values of the Ga diffusion coefficients and the high Ga concentrations present in the profiles suggest that a simple interstitial mechanism (i.e., no exchange with lattice vacancies) is not operative, and this seems highly unlikely also on theoretical grounds. Low diffusivity and high activation energies are often

| | D_0 | Q |
|--------------|--|--------|
| GOLDSTEIN | $1 \times 10^7 \text{ cm}^2 \text{ s}^{-1}$ | 5.6 eV |
| PRESENT WORK | $3.9 \times 10^{-5} \text{ cm}^2 \text{ s}^{-1}$ | 2.6 eV |

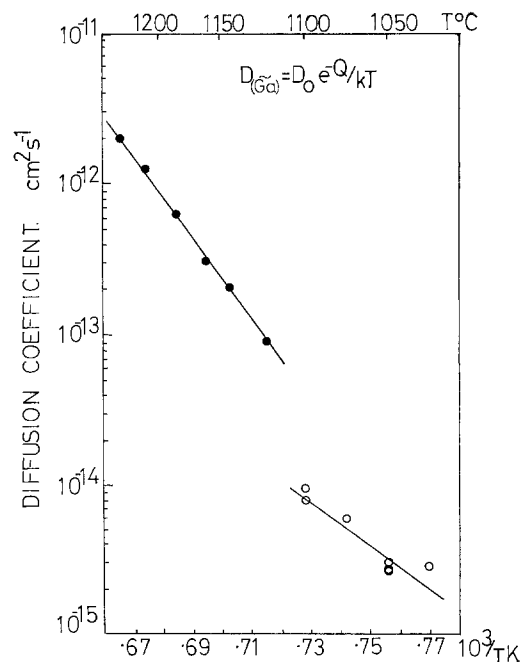
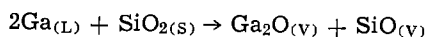
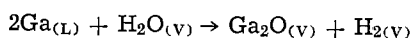


Fig. 8. $D_{(\text{Ga})}$ vs. temperature. ●, Goldstein: $D_0 = 1 \times 10^7 \text{ cm}^2 \text{ sec}^{-1}$; $Q = 5.6$ eV. ○, Present work: $D_0 = 3.9 \times 10^{-5} \text{ cm}^2 \text{ sec}^{-1}$; $Q = 2.6$ eV.

ents, $D_{(\text{Ga})}$, obtained in the temperature range 1100°-1025°C (P_{As_2} of 0.75 atm) were from 8.85×10^{-15} to $2.89 \times 10^{-15} \text{ cm}^2 \text{ sec}^{-1}$. The diffusion coefficients were

associated with diffusion via vacancy mechanisms, and indeed this was the manner in which Goldstein chose to interpret his results. However, a rigorous evaluation of the diffusion mechanism of Ga in GaAs must consider all the possible mechanisms, including diffusion of Ga atoms via vacancies on the gallium sublattice, diffusion of Ga atoms via vacancies on the gallium and arsenic sublattices, and the various interstitial mechanisms such as the interstitialcy mechanism and the interstitial-substitutional (dissociative) mechanism. Although it is not possible yet to discriminate between these possibilities for gallium in gallium arsenide, some comments are possible. Self-diffusion of Ga via gallium and arsenic vacancies requires a significant concentration of anti-structure defects, but Van Vechten (7) has proposed that such defects should be present in significant concentrations in III-V compounds, and Schneider (8) has reported ESR evidence for As_{Ga} defects in GaAs. Regarding the interstitial-substitutional (dissociative) mechanism, it was pointed out by Casey and Pearson (9) that such a mechanism could lead to a relatively slow effective diffusion rate even for a fast interstitial diffusion. Considering next the interstitialcy mechanism, this would seem to be favored by models (10) involving "split-interstitial" gallium defects used to interpret lattice parameter (11) and internal friction (12) measurements on quenched GaAs. The mechanism suggested by Goldstein, namely, diffusion via vacancies on the gallium sublattice, must also be considered. Van Vechten's (7) calculated enthalpy of formation of V_{Ga} is 2.31 eV, and his calculated enthalpy of migration of V_{Ga} via second nearest neighbor sites is 2.7 eV, which would predict an activation energy of self-diffusion by this mechanism of 5 eV, assuming constant composition for the GaAs (compared with our estimate of 2.6 eV). These calculations are not yet well substantiated, however, and it is also extremely unlikely that constant composition was achieved in our experiments by keeping constant arsenic pressure, so we cannot at present rule out this mechanism either. It has also been suggested (2) that AB divacancies might be involved in self-diffusion of III-V compounds. However, it is not believed to be a valid suggestion for GaAs because of the low values of Q and D_0 obtained in this work. The most sensitive way of discriminating between the various possibilities is to investigate the dependence on arsenic pressure at constant temperature.

Two diffusion anneals were carried out at 1100°C ($P_{As_2} = 0.75$ atm) for times of 22.5 and 17 hr, see Fig. 5. Despite a sixfold increase in the amount of ^{72}Ga source, the diffusion coefficients of 8.85×10^{-15} and 7.54×10^{-15} cm² sec⁻¹ were in close agreement with each other. This indicates that the techniques developed are reliable and enable reproducible results to be obtained. On all the profiles a fall in the Ga concentration is observed close to the surface ($\lesssim 0.3$ μm). It is believed that this depletion is a result of preferential removal of Ga from the sample surface. Reactions through which this is achieved are not clear, however it is known (13, 14) that gallium reacts with water vapor and also silica at high temperatures, forming volatile gallium suboxide



If the vapor pressure of this volatile suboxide is relatively high at the diffusion temperature then an appreciable amount of gallium may be removed from the surface in order to fulfill reactions such as those above, resulting in a drop in Ga concentration close to the surface.

Two of the profiles also exhibited low concentration "tails." As discussed above these tails are due to low

level contamination and not a complex diffusion mechanism. The tails may affect the interpretation of the profiles but not the estimate of the diffusion coefficients, since the diffusion coefficients were estimated from data over the first two orders of magnitude drop in Ga concentration where the low level contamination was shown to be insignificant.

No definite conclusion concerning the diffusion mechanism of Ga in GaAs may be drawn from the work carried out so far. However, it does indicate that over the temperature and concentration range investigated there is a single mechanism operative rather than a complex one. There is an obvious need for further information on diffusion, especially at different arsenic pressures. This work is currently in progress. It is clear, however, that Ga diffuses extremely slowly in GaAs even at elevated temperatures, a measurable diffusion depth of about 1 μm being achieved after a 24 hr annealing period at temperatures near 1050°C.

Acknowledgments

The authors would like to thank Dr. P. Fewster and Dr. C. J. Gillham for help and useful discussions concerning this work, and acknowledge the financial support of the Scientific Research Council.

Manuscript submitted Jan. 13, 1981; revised manuscript received May 8, 1981.

Any discussion of this paper will appear in a Discussion Section to be published in the June 1982 JOURNAL. All discussions for the June 1982 Discussion Section should be submitted by Feb. 1, 1982.

APPENDIX

Arsenic Pressure Calculation

The Ideal Gas Law was used to calculate the amount of arsenic needed to create the required arsenic pressure in the capsule. It was assumed that all the elemental arsenic in the capsule went into the vapor phase and that at the diffusion temperature the dominant species was As_2 .

$$\text{Ideal Gas Law} \quad PV = \frac{mRT}{M}$$

where P = arsenic pressure, atm; V = capsule volume, cm³; m = weight arsenic, g; R = Universal Gas constant 82.05 atm cm³ gmol⁻¹K⁻¹; T = absolute temperature K; and M = molecular weight arsenic = 149.84.

REFERENCES

1. B. Goldstein, *Phys. Rev.*, **121**, 1305 (1961).
2. D. L. Kendall, in "Semiconductors and Semimetals," Vol. 4, R. K. Willardson and A. C. Beer, Editors, pp. 163-259, Academic Press Inc., New York (1968).
3. H. Hasegawa and H. Hartnagel, *This Journal*, **123**, 713 (1975).
4. P. J. Holmes, Editor, "The Electrochemistry of Semiconductors," p. 266, Academic Press, New York (1962).
5. M. Brown, Ph.D. Thesis, Southampton University (1977).
6. B. Goldstein, Private communication.
7. J. A. Van Vechten, *Czech. J. Phys.*, **B.30**, 388 (1980).
8. J. Schneider, Paper 15, 11th International Conference on Defects and Radiation Effects in Semiconductors, Sept. 1980, Oiso, Japan (Inst. Phys.).
9. H. C. Casey and G. L. Pearson, in "Point Defects in Solids," Vol. 2, J. H. Crawford and L. M. Slifkin, Editors, Chap. 2, Plenum (1975).
10. P. Fewster, Private communication.
11. H. Potts and G. Pearson, *J. Appl. Phys.*, **37**, 2098 (1966).
12. B. K. Chakraverty and R. W. Dreyfus, *ibid.*, **37**, 631 (1966).
13. C. Frosch and L. Derick, *This Journal*, **105**, 695 (1958).
14. C. Cochran and L. Foster, *ibid.*, **109**, 149 (1962).

Phase Relationships in CaS-Rare Earth Sulfide Systems

H. L. Tsai and P. J. Meschter*

Department of Chemical, Metallurgical and Polymer Engineering,
University of Tennessee, Knoxville Tennessee 37916

ABSTRACT

Phase relationships in the CaS-Y₂S₃, CaS-Dy₂S₃, CaS-Er₂S₃, and CaS-Yb₂S₃ systems have been determined between 800° and 1200°C at $p_{S_2} = 3 \times 10^{-6}$ atm. All four dopants show significant solid solubility in CaS (15-30 m/o at 1200°C). Approximate p_{S_2}/p_{O_2} ratios required to avoid oxygen contamination of the mixed sulfides are derived. Variation of the lattice parameter of the CaS phase with dopant content indicates an increase in size of the dopant ion upon dissolution. The x-ray diffraction pattern of monoclinic β -CaY₂S₄ has been determined. The β -phase may be regarded as a slight distortion of the orthorhombic low temperature α phase.

Calcium sulfide doped with a rare earth sesquioxide such as Y₂S₃ has been proposed as a solid electrolyte system for sensing of sulfur activities by Worrell (1, 2). The dopant cation on a Ca site is effectively positively charged (e.g., Y_{Ca}⁺), and is compensated for by the formation of vacancies on the cation sublattice V_{Ca}^{''}. If enough dopant is added so that the number of extrinsic ionic defects greatly exceeds the number of defect electrons or electron holes over a wide range of temperature and p_{S_2} , then the mixed sulfide has $t_{ion} \approx 1$ over this domain and can in principle be used as a solid electrolyte for sulfur activity or partial pressure measurement.

An effective dopant must have a significant range of solid solubility in CaS. Flahaut *et al.* (3, 4) have identified Y₂S₃, Dy₂S₃, Er₂S₃, and Yb₂S₃ as having extended solutions in CaS, with typical solubilities around 20 mole percent (m/o) rare earth sulfide. Their mixed sulfides were sintered in quartz capsules under vacuum, so that neither the sulfur nor the oxygen chemical potential was well defined. Worrell *et al.* (1) report very limited (<1 m/o) solubility of Y₂S₃ in CaS after heating for 14 hr at 900°C in an H₂-H₂S mixture of unspecified p_{S_2} . Worrell *et al.* attribute Flahaut's results to oxygen and/or carbon impurities in the latter's samples.

In order to resolve this discrepancy, we have determined phase relationships and lattice parameters in the binary systems of CaS with Y₂S₃, Dy₂S₃, Er₂S₃, and Yb₂S₃ containing up to 40 m/o rare earth sulfide over the temperature range 800°-1200°C at a fixed p_{S_2} of 3×10^{-6} atm. The chemical potential of oxygen in the system was approximately controlled by running all experiments in the presence of graphite. We have also determined the x-ray diffraction pattern and lattice parameters of monoclinic β -CaY₂S₄, which is in equilibrium with the saturated CaS solid solution above about 1100°C.

Sample Preparation and Experimental Procedure

Pure CaS (-325 mesh, 99.99%) and the doping materials, Y₂S₃, Yb₂S₃, Dy₂S₃, and Er₂S₃ (-200 mesh, 99.9%) were obtained from Cerac, Incorporated. Samples containing 1-40 m/o rare earth sulfide were prepared by mixing weighed amounts of each dopant powder and CaS powder in the required proportions, cold pressing in a hydraulic die at 90,000 psi, and sintering for 1 day at 1350°C in a purified 1:1 H₂-H₂S mixture. During the sintering, the pellets were surrounded by a bed of powder of the same composition within a graphite boat, which was in turn enclosed in a graphite tube plugged with graphite wool

at both ends. Preliminary experiments showed that these precautions were necessary to prevent contamination of the samples with oxygen from traces of CO₂ or H₂O in the surrounding gas stream. The pellets after presintering were examined by x-ray diffraction to check for completeness of reaction and absence (to <5%) of oxide or oxysulfide phases.

A vertical resistance-wound furnace with a 1½ in. long hot zone ($\pm 1^\circ\text{C}$), controlled to better than $\pm 2^\circ\text{C}$ over any run, was used to equilibrate the samples. Platinum/Pt-13% Rh thermocouples placed near the furnace windings and next to the sample were used, respectively, to control the furnace temperature and measure the sample temperature. The quench tank was a brass cylinder filled with oil fitted directly to the bottom of the vertical reaction tube.

The equilibration atmosphere was a mixture of 99.99% H₂ (major impurity 5 ppm H₂O) and 99.5% H₂S containing nominally 2500 ppm C₂H₆, 800 ppm C₃H₈, 30 ppm (CH₃)₂S, H₂O, and CO₂, and 70 ppm N₂. The gases were purified by passage over successive columns of molecular sieves and P₂O₅. Flow rates and partial pressures of the gases were fixed and measured by constant-pressure-head capillary manometer/flowmeters. The gases were mixed in a column of glass beads before introduction into the furnace.

The presintered pellets were packed into a 1 in. long cylinder in a graphite crucible and the upper end plugged with graphite wool. The crucible was hung from graphite rods in the hot zone of the furnace. To start a run, the furnace was evacuated to check gas-tightness, the H₂S/H₂ mixture introduced, and the furnace heated to the desired temperature. The samples were kept at temperature for times summarized in Table I. To check whether these times were sufficient to achieve equilibrium, additional runs with prolonged holding times were performed at 1200° and 800°C to verify that the lattice parameters were unchanged with time. A run at 700°C, in which equilibrium was not achieved after 400 hr, was excluded. After equilibration, the samples were quenched by releasing the crucible into the oil bath.

Table I. H₂S/H₂ ratios and equilibration times for CaS-R₂S₃ samples

| Temperature (°C) | p_{H_2S}/p_{H_2} | Equilibration time (hr) |
|------------------|-----------------------|-------------------------|
| 800° | 1.13×10^{-1} | 125, 150 |
| 850° | 7.21×10^{-2} | 125 |
| 900° | 4.78×10^{-2} | 100 |
| 1000° | 2.30×10^{-2} | 100 |
| 1050° | 1.67×10^{-2} | 50 |
| 1200° | 7.25×10^{-3} | 20, 100 |

* Electrochemical Society Active Member.

Key words: doping, lattice parameter, x-ray diffraction.

Several preliminary experiments with CaS-Y₂S₃ samples had been done to determine the best equivalent p_{S_2} to use in the gas stream. Runs at 800°C and $p_{S_2} < 10^{-6}$ atm resulted in the formation of a hexagonal phase of stoichiometry Y₂O₂S, while no oxysulfide was found after a run at $p_{S_2} = 3 \times 10^{-6}$ atm and 800°C. Therefore, $p_{S_2} = 3 \times 10^{-6}$ atm was chosen for all equilibration runs. This p_{S_2} corresponds to the H₂S/H₂ ratio at each temperature shown in Table I. X-ray analysis showed minor amounts, at worst, of oxysulfide contaminants after equilibration runs except in the case of CaS-Yb₂S₃, where formation of "Yb₂O₂S" limited valid results to 1050°-1200°C.

The lattice parameters of the CaS solid solution phase present in the quenched samples were determined by a diffractometer method using CuK_α radiation. The parameters were determined from the high angle (620), (622), and (444) reflections of the CaS phase and extrapolation of a lattice parameter *vs.* $\cos^2 \theta$ plot to $\theta = 90^\circ$. A Debye-Scherrer camera with CuK_α radiation was used to determine the diffraction pattern of β -CaY₂S₄ after quenching from 1200°C.

Results and Discussion

The solubility limits for each CaS-rare earth sulfide system were obtained by plotting the lattice parameter of the CaS solid solution *vs.* mol percent dopant as shown in Fig. 1 for CaS-Y₂S₃. The uncertainty in the measured lattice parameter is $\pm 0.001 \text{ \AA}$ for any composition in the CaS phase field. The lattice parameter varies linearly with m/o dopant to $\pm 0.06\%$ (± 3 standard deviations) in any system. The intercepts of the least squares lines at 0% R₂S₃ are all in good agreement ($\pm 0.002 \text{ \AA}$) with the lattice parameter of pure CaS of 5.6948 Å from The Powder Diffraction File. The solubility limits given in Table II were obtained from the intersections of the least squares lines for the single phase CaS solid solutions with the average lattice parameters of the CaS phase in the two-phase samples. The presence or absence of the second phase, which was in all cases

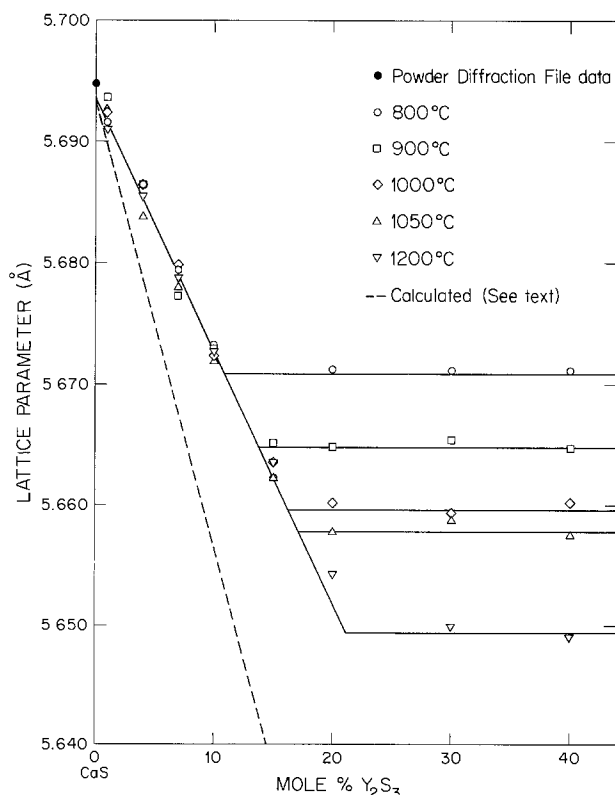


Fig. 1. Variation of lattice parameter with dopant concentration in the CaS-Y₂S₃ system.

Table II. Solubility limits of Y₂S₃, Dy₂S₃, Er₂S₃, and Yb₂S₃ in CaS

| Temperature (°C) | m/o Y ₂ S ₃ | m/o Dy ₂ S ₃ | m/o Er ₂ S ₃ | m/o Yb ₂ S ₃ |
|------------------|-----------------------------------|------------------------------------|------------------------------------|------------------------------------|
| 800° | 10.9 ± 0.1 | — | — | — |
| 850° | — | 9.9 ± 1.2 | 10.5 ± 0.8 | — |
| 900° | 13.8 ± 0.6 | — | — | — |
| 1000° | 16.3 ± 0.5 | — | — | — |
| 1050° | 17.1 ± 0.6 | 12.8 ± 0.9 | 11.4 ± 0.6 | 25.2 ± 0.4 |
| 1200° | 21.1 ± 1.0 | 14.6 ± 0.5 | 17.7 ± 0.7 | 29.0 ± 1.0 |
| Flahaut (4) | 18 | 20 | 22 | — |

CaR₂S₄, was confirmed directly from the diffraction pattern.

The phase diagrams of CaS-CaR₂S₄ systems are all qualitatively similar to the CaS-CaY₂S₄ system shown in Fig. 2. Agreement with Flahaut *et al.* (3,4) for this system is good, although the solubilities of this study are noticeably larger above 1000°C. Flahaut's solubility limits for Dy₂S₃ and Er₂S₃ are larger than ours at 1200°C. Both studies show extended ranges of solid solubility of all dopants in CaS, with solubilities ranging up to 29 m/o Yb₂S₃ in CaS above 1200°C.

The reported solubility of Y₂S₃ in CaS of Worrell *et al.* (1) is much smaller than those found here. These workers had no internal getters near the sample to react with oxidizing impurities in the gas stream, nor did they identify the second phase in equilibrium with their saturated CaS solid solution. Results from our preliminary experiments at 700°-1000°C without graphite getters always showed the existence of hexagonal "Y₂O₂S" in CaS-Y₂S₃ samples. The diversion of yttrium to this compound, which is apparently nearly insoluble in CaS, lowers the apparent extent of the CaS phase field. In ex-

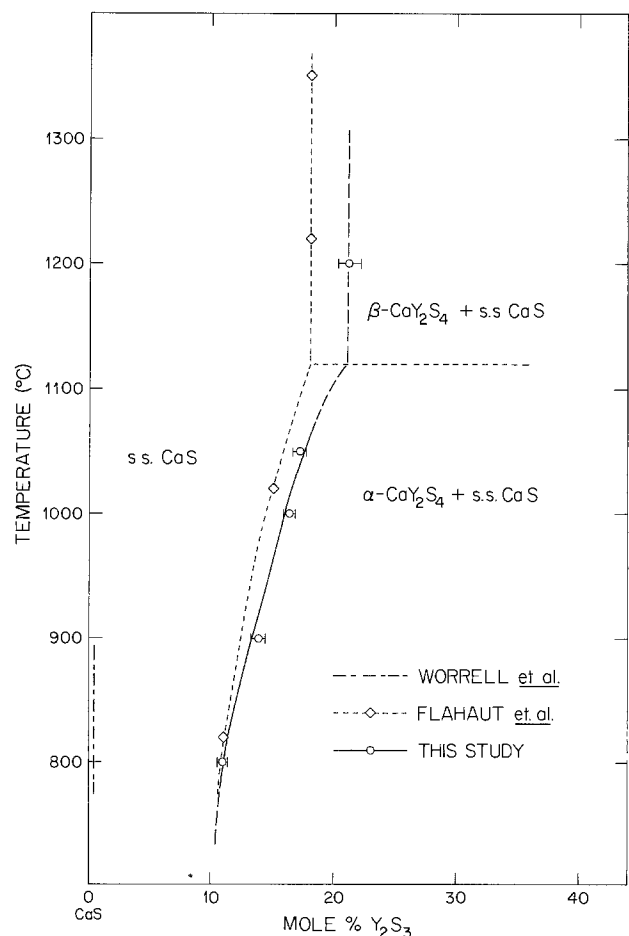


Fig. 2. Phase relations in the CaS-CaY₂S₄ system

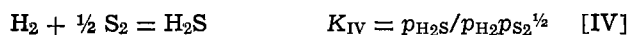
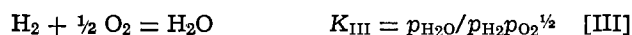
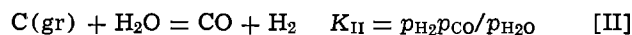
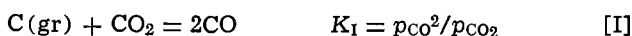
Table III. Least squares analyses of the lattice parameters of CaS doped with Y_2S_3 , Dy_2S_3 , Er_2S_3 , and Yb_2S_3

| Dopant | Dy_2S_3 | Y_2S_3 | Er_2S_3 | Yb_2S_3 |
|---------------------------|-------------------------|-------------------------|-------------------------|-------------------------|
| Observed parameter (Å) | 5.6932-(0.176 ± 0.010)X | 5.6938-(0.210 ± 0.006)X | 5.6946-(0.287 ± 0.015)X | 5.6968-(0.171 ± 0.002)X |
| Calculated parameter (Å) | 5.6938-0.340X | 5.6935-0.371X | 5.6936-0.449X | 5.6935-0.519X |
| Flahaut <i>et al.</i> (4) | 5.6952-0.148X | 5.6904-0.226X | 5.6934-0.274X | — |

X is mole fraction of R_2S_3 .

treme cases, virtually all of the yttrium was found in the oxysulfide and the CaS was nearly pure, thus reproducing the results of Worrell *et al.* (1).

Since the oxygen-sulfur balance in and around the samples during presintering and phase equilibration is critical to successful determination of phase equilibria in these systems, it is of interest to estimate the p_{S_2}/p_{O_2} ratios which obtain in the presence and absence of graphite getters, respectively. This estimation requires simultaneous solution of the reaction equilibria



using reasonable assumptions of concentrations of H_2 , H_2O , H_2S , CO , CO_2 , and O_2 in the incoming gas stream. For example, in our presintering runs at 1350°C, $[p_{H_2}]_i = [p_{H_2S}]_i = 0.5$ atm. Assuming inefficient gettering of the incoming gas as a worst case, one may estimate $[p_{H_2O}]_i = 1 \times 10^{-4}$ atm and $[p_{CO_2}]_i = 3 \times 10^{-5}$ atm, with initial concentrations of CO and O_2 being negligible relative to these. The equilibrium constants K_I and K_{II} are large, so one may assume the function of carbon is to convert essentially all of the CO_2 and H_2O to CO and H_2 . Then $p_{CO} \approx 1.6 \times 10^{-4}$ atm, and using standard thermodynamic data for Eq. [I]-[III], $p_{CO_2} = 6.2 \times 10^{-12}$ atm, $p_{H_2O} = 8.0 \times 10^{-8}$ atm, and $p_{O_2} = 1.2 \times 10^{-24}$ atm are calculated. From the equilibrium of reaction [IV], $p_{H_2} = 0.64$ atm, $p_{H_2S} = 0.36$ atm, and $p_{S_2} = 0.07$ atm. Thus the p_{S_2}/p_{O_2} ratio is about 6×10^{22} . Similar calculations for the equilibration runs at 800°-1200°C yield p_{S_2}/p_{O_2} ratios on the order of 10^{19} - 10^{22} . Small amounts of oxysulfide which appear in some of these runs show that this ratio is close to the ratio required to convert oxysulfide to sulfide. Without a carbon getter, on the other hand, the p_{S_2}/p_{O_2} ratio is about 10^{12} at 1350°C, which is clearly insufficient to produce the mixed sulfide system.

The presence of graphite at unit activity in our experiments raises the question of carbon contamination. In several sample preparation and equilibration experiments the samples had no measurable weight change ($\pm 0.5\%$) during the runs. In experiments where significant amounts of oxysulfides were formed, noticeable weight changes were recorded. Strictly speaking, our results refer to the quaternary Ca-R-S-C system, but it is considered that these results are reasonably representative of the Ca-R-S ternaries.

The least squares analyses of the lattice parameter variation of CaS doped with Dy_2S_3 , Y_2S_3 , Er_2S_3 , and Yb_2S_3 within the solid solubility range are given in Table III. The values marked "calculated" are based on ionic radii derived by Flahaut *et al.* (4) for six-fold coordination from the lattice parameters of pure metal sulfides. These radii are 1.02, 0.93, 0.92, 0.90, and 0.88 Å for Ca^{2+} , Dy^{3+} , Y^{3+} , Er^{3+} , and Yb^{3+} ions, respectively. A radius of 1.824 Å was deduced for S^{2-} from the lattice parameter of pure CaS. Both our observed lattice parameter values and those of Flahaut (line 3 in Table III) are larger than the calculated

values, and are in good agreement with each other (see also Fig. 1).

Because of the large ionic radius of S^{2-} , the formation of interstitial anions is not favored. The difference between measured and calculated lattice parameters thus must be due to a small increase in size of the R^{3+} cation in the solid solutions, compared with the calculated value. The observed value was especially large in comparison with the calculation in the CaS- Yb_2S_3 system. This result may be due to a particularly large expansion of the Yb^{3+} ion, or to diversion of Yb to the oxysulfide, which it was impossible entirely to prevent in this system. It is noteworthy that there is no correlation between solubility limits and the difference in radii between Ca^{2+} and the dopant ion. In fact, the ion Nd^{3+} , which is virtually the same size as Ca^{2+} , has virtually no solubility in CaS (4).

The lattice parameters of α - CaY_2S_4 and β - CaY_2S_4 were calculated from their x-ray diffraction patterns. The lattice parameters of orthorhombic α - CaY_2S_4 quenched from 1000°C ($a = 12.89$ Å, $b = 13.03$ Å, $c = 3.87$ Å) are in agreement with those of Flahaut *et al.* (3) ($a = 12.94$ Å, $b = 13.03$ Å, $c = 3.86$ Å). The x-ray pattern of monoclinic β - CaY_2S_4 taken from the 40% Y_2S_3 in CaS sample quenched from 1200°C is shown in Table IV. The lattice parameters are $a = 12.88$ Å, $b = 13.04$ Å, $c = 4.02$ Å, $\beta = 93.48^\circ$. The β structure may be regarded as a small distortion of the orthorhombic α lattice.

All the CaR_2S_4 compounds but $CaDy_2S_4$ showed conversion to the β -form below 1200°C. The major difference in the two patterns is the existence of the (200) line at small diffraction angles and the non-appearance of the (120), (220), and (130) lines in the β - as compared with the α -form.

Summary

Phase relationships in the CaS- Y_2S_3 , CaS- Dy_2S_3 , CaS- Er_2S_3 , and CaS- Yb_2S_3 systems have been determined at $p_{S_2} = 3 \times 10^{-6}$ atm between 800° and

Table IV. X-ray diffraction pattern for monoclinic β - CaY_2S_4

| Intensity | d_{obs} (Å) | d_{cal} (Å) | Indexes |
|-----------|---------------|---------------|---------------|
| W | 6.43 | 6.43 | 200 |
| VS | 3.60 | 3.60 | 230 |
| VW | 3.42 | 3.42 | 021 |
| * | 3.22 | 3.22 | 400, 211 |
| M | 2.91 | 2.91 | 240, 131 |
| M | 2.85 | 2.85 | 131, 301 |
| * | 2.79 | 2.78 | 311 |
| VS | 2.62 | 2.61 | 321 |
| M | 2.45 | 2.44 | 401 |
| VW | 2.40 | 2.40 | 421, 411 |
| W | 2.184 | 2.186 | 051 |
| VW | 2.170 | 2.167 | 151 |
| M | 2.138 | 2.144 | 151, 160, 600 |
| W | 2.034 | 2.036 | 620 |
| * | 1.989 | 1.983 | 012 |
| VS | 1.927 | 1.928 | 212 |
| VW | 1.883 | 1.881 | 122 |
| S | 1.803 | 1.800 | 460 |
| M | 1.702 | 1.708 | 370 |
| * | 1.661 | 1.660 | 560 |

Indexing based on $a = 12.88$ Å, $b = 13.04$ Å, $c = 4.02$ Å, $\beta = 93.48^\circ$.
 * Intensity uncertain because of coincidence with CaS lines.
 VS = very strong, S = strong, M = moderate, W = weak, VW = very weak.

1200°C. The solubilities of the dopant sulfides are relatively large (15-30 m/o at 1200°C, depending on dopant), in agreement with results of Flahaut *et al.* (4). The much smaller apparent solubilities of Worrell *et al.* (1) are probably the result of oxygen contamination and formation of rare-earth oxysulfides. Variation of lattice parameter of the CaS solid solution indicates an increase in size of the dopant ion over theoretical predictions based on ion sizes in the pure sulfides. The x-ray pattern of β -CaY₂S₄ has been determined, and shows a monoclinic structure which represents a small distortion of the low temperature orthorhombic phase.

Acknowledgment

The authors acknowledge the support of this research by the National Science Foundation under grant No. DMR77-15514.

Manuscript submitted Jan. 21, 1981; revised manuscript received April 30, 1981.

Any discussion of this paper will appear in a Discussion Section to be published in the June 1982 JOURNAL. All discussions for the June 1982 Discussion Section should be submitted by Feb. 1, 1982.

Publication costs of this article were assisted by the University of Tennessee.

REFERENCES

1. W. L. Worrell, V. B. Tare, and F. J. Bruni, in "High Temperature Technology," p. 503, IUPAC, Butterworths, London (1969).
2. W. L. Worrell, *Bull. Am. Ceram. Soc.*, **53**, 425 (1973).
3. J. Flahaut, L. Domange, and M. Patrie, *Bull. Soc. Chim. Fr.*, 105 (1961).
4. J. Flahaut, L. Domange, M. Patrie, A. Bostsarron, and M. Guittard, *Adv. Chem. Ser.*, **39**, 179, (1963).

The Effect of SO₃ Gas on the Surface Tension of Molten Na₂SO₄

G. J. Yurek* and R. E. Deeter

Department of Materials Science and Engineering,
Massachusetts Institute of Technology, Cambridge, Massachusetts 02139

ABSTRACT

The surface tension of molten Na₂SO₄ has been measured as a function of the partial pressure of SO₃ gas in equilibrium with the melt ($10^{-9} \lesssim P_{\text{SO}_3} \lesssim 10^{-1}$ atm) over the temperature range of 1175-1400 K. The surface tension, σ , is independent of P_{SO_3} over the range of partial pressures employed. The temperature dependence of σ is given by

$$\sigma = 2.568 \times 10^{-1} - 6.05 \times 10^{-5}T$$

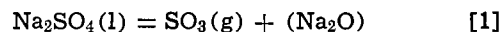
where σ has units of N/m and T is the absolute temperature. The density of Na₂SO₄ is independent of P_{SO_3} for $10^{-9} \lesssim P_{\text{SO}_3} \lesssim 10^{-1}$ atm at 1200 and 1250 K, thereby confirming that Na₂SO₄ is virtually stoichiometric under these conditions.

The surface tension of molten salts has been determined by most investigators under conditions for which the thermodynamic state of the salt was not fixed precisely, *e.g.*, the surface tension of molten Na₂SO₄ has been determined only in the presence of nitrogen gas. Two exceptions to this general statement are noted. Kozakevitch (1) measured the surface tension of liquid FeO at ~1700 K and at 1 atm pressure as a function of oxygen partial pressure. Under these conditions, the composition of liquid FeO varies from about 23 to 24 weight percent (w/o) O as the oxygen partial pressure varies from $\sim 10^{-10}$ to 10^{-8} atm. For this variation in P_{O_2} , the surface tension of liquid FeO decreases from 0.585 to 0.500 N/m, indicating that ferric ions are surface active.

Moiseev and Stepanov (2) measured the surface tension at 1 atm pressure of Na₂CO₃ and Li₂CO₃ melts that were equilibrated with gas mixtures containing varying amounts of N₂, O₂, and CO₂. The surface tension of Na₂CO₃ was not a function of the gas composition, but the surface tension of Li₂CO₃ was higher when the melt was in contact with CO₂ or CO₂-O₂ mixtures by about 0.006-0.008 N/m than when the melt was in contact with air. More significant changes in the surface tension of Li₂CO₃ resulted when additions of Li₂O were made to the melt. In the latter

case, which is discussed more fully later in this paper, an increase in the surface tension with increasing concentration of Li₂O was attributed to the presence of a higher concentration of (O²⁻) anions, which have a higher effective dipole moment than (CO₃²⁻) anions.

Pure molten salts, such as Na₂SO₄, that contain polyatomic ions may be considered quasi-binary thermodynamic systems (*e.g.*, Na₂O + SO₃) if the composition of the salt can be given by a single variable, *e.g.*, the mole fraction of Na₂O, $X_{\text{Na}_2\text{O}}$. The effect of P_{SO_3} on the composition of molten Na₂SO₄ may be described by the following equilibrium



where the parentheses around Na₂O are used to indicate that this component is dissolved in the melt. The equilibrium constant for Eq. [1] is given by

$$K_1 = a_{\text{Na}_2\text{O}} P_{\text{SO}_3} / a_{\text{Na}_2\text{SO}_4} \quad [2]$$

The standard state for SO₃ gas is taken as pure SO₃ gas at 1 atm pressure at the temperature of interest. The thermodynamic state of the quasi-binary Na₂O-SO₃ system is determined fully if the temperature and the activity of either Na₂O or SO₃ are specified. This would be true regardless of the value of $a_{\text{Na}_2\text{SO}_4}$.

At very low P_{SO_3} and at high P_{O_2} , the composition of Na₂SO₄ may change by formation of peroxide

* Electrochemical Society Active Member.

Key words: surface tension, molten salts, Na₂SO₄.

(O_2^{2-}) or superoxide (O_2^-) anions, *i.e.*, by formation of Na_2O_2 or NaO_2 neutral species. At high P_{SO_3} the composition of Na_2SO_4 may change by formation of pyrosulfate anions, ($S_2O_7^{2-}$). If significant quantities of (O_2^-), (O_2^{2-}), or ($S_2O_7^{2-}$) anions were formed at very low or very high P_{SO_3} , respectively, then Na_2SO_4 could not be considered a quasi-binary mixture of $Na_2O + SO_3$.

Molten Na_2SO_4 may be considered a quasi-binary system for P_{SO_3} in the approximate range of 10^{-1} – 10^{-9} atm because its composition does not change significantly in this range even though the activity of Na_2O according to Eq. [1] varies by eight orders of magnitude (3-6). Indeed, Na_2SO_4 is nearly stoichiometric ($x_{Na_2O}/x_{SO_3} = 1.0$) for this range of P_{SO_3} , so that changes in the concentration of (O^{2-}), as well as changes in the concentrations of (O_2^-), (O_2^{2-}), and ($S_2O_7^{2-}$), are very small.

In principle, the surface tension of molten Na_2SO_4 should be a function of P_{SO_3} (i) if the concentration of ions with higher or lower effective dipole moments than (SO_4^{2-}) were changed significantly with a change in P_{SO_3} or (ii) if one or more of those species that change in concentration by a small amount with a change in P_{SO_3} [*i.e.*, (O^{2-}), (O_2^-), (O_2^{2-}), or ($S_2O_7^{2-}$)] were highly surface active. Only the latter possibility could apply in the case of nearly stoichiometric Na_2SO_4 . The purpose of this paper is to present the results of a study of the effect of P_{SO_3} ($10^{-9} < P_{SO_3} < 10^{-1}$ atm) on the surface tension of Na_2SO_4 .

Experimental Procedures

The surface tension of molten sodium sulfate was measured using the double-tube maximum bubble pressure method. The apparatus employed is illustrated schematically in Fig. 1. The general principles involved in the determination of the surface tension of a liquid phase by the maximum bubble pressure method have long been established (7,8). In this method, a gas is forced through a capillary tube that

is partially immersed in a liquid to form a bubble at the tip of the tube. The pressure in the bubble relative to the surrounding pressure may be measured with an oil manometer or other suitable device for measuring pressure. The maximum pressure in the bubble, before the bubble detaches from the tube, comprises a contribution from the hydrostatic head of the liquid and a contribution from the surface forces that oppose an increase in the gas-liquid surface area. Thus, a knowledge of the depth of immersion, the maximum bubble pressure, and the radius of the capillary tube allows the surface tension of the liquid to be calculated. Standard tables are available (9) to correct the calculation for the formation of nonspherical bubbles, which always form unless extremely fine-bore capillary tubes are employed.

In the double-tube maximum bubble pressure method, the maximum bubble pressure is measured in two capillary tubes of different radii that are immersed the same depth in the melt. The difference in the maximum bubble pressures for the two tubes depends only on the radii of the tubes, thereby eliminating the need to measure the depth of immersion of the tubes.

The tubes used in this investigation were Pt-10% Rh that had diameters of approximately 0.1 and 0.3 cm. The tubes were tapered at their tips to provide a well-defined bubble diameter at the point of maximum pressure in the bubble. The inner diameters of the tubes were measured at low magnification (2-7 \times) using a split-image eyepiece that was calibrated against a stage micrometer. The reproducibility of these measurements was good, *i.e.*, the standard deviation from the average measured diameter was always less than 0.25% of the diameter. The change in the diameters of the tubes upon heating was taken into account using the thermal expansivity of the alloy.

The Pt-10% Rh tubes, which were about 17.5 cm long, were welded to stainless steel extension tubes,

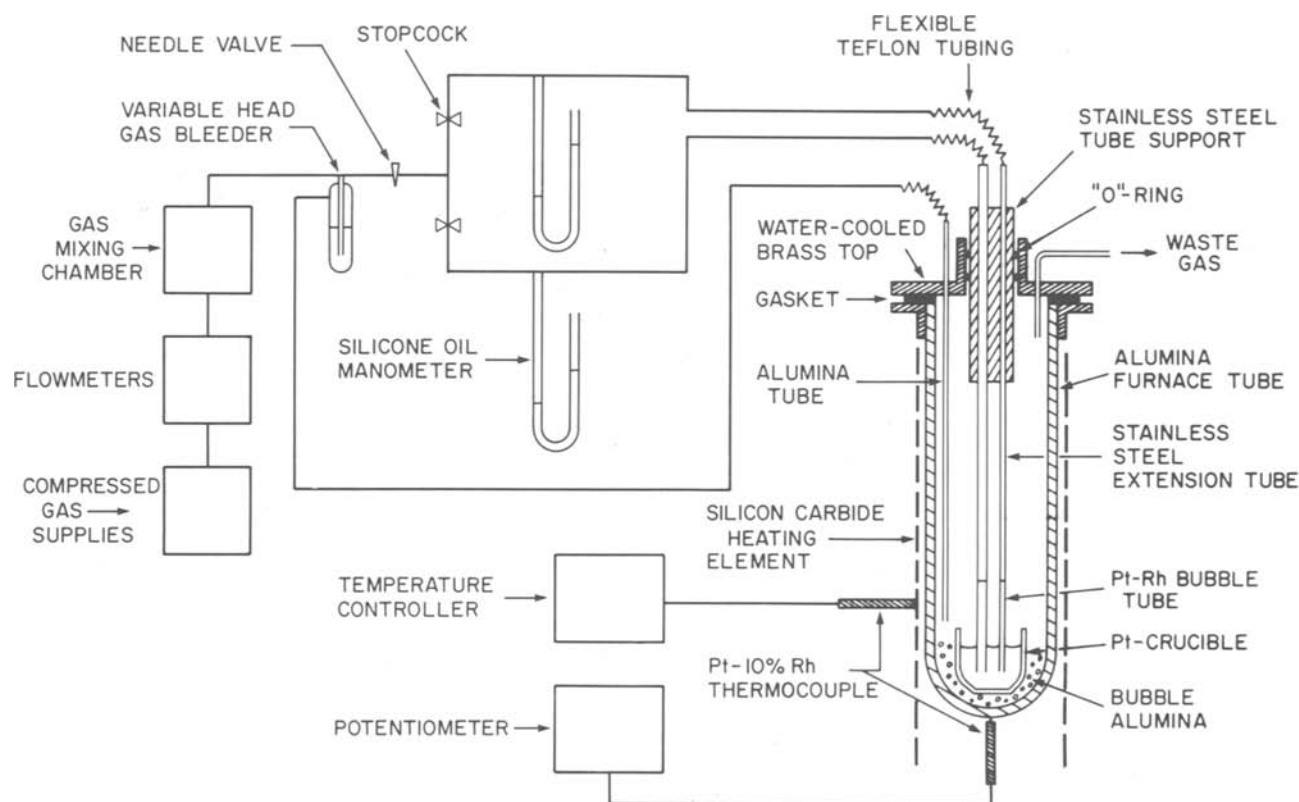


Fig. 1. Schematic illustration of the double-tube, maximum bubble pressure apparatus employed to measure the surface tension of molten Na_2SO_4 .

which, in turn, were connected to the gas-supply line by flexible Teflon tubing. The stainless steel extension tubes were wrapped with Pt foil to prevent corrosion products on the stainless steel from falling into the melt. The bubble tube assembly was cemented firmly into a stainless steel support tube, which served to align the two tubes and maintain the two tubes at equal depths of immersion. The support tube could be moved vertically through the water-cooled brass top of the alumina furnace tube to vary the depth of immersion of the tubes in the melt.

The melt was contained in a Pt crucible at the bottom of the alumina furnace chamber, which was heated by a helical silicon carbide heating element and maintained at a constant temperature by a proportional controller. Although it is not shown in Fig. 1, the region of the furnace chamber between the Pt crucible and the stainless steel tube support contained alumina cylinders that were solid except for holes that were provided for the bubble tubes and a gas injection tube. These alumina cylinders acted as heat shields to help maintain a long constant temperature zone in the furnace chamber. The constant temperature zone, measured from the bottom of the furnace chamber, was about 15 cm long. An extended constant temperature zone helps minimize convective currents, which can cause rather severe fluctuations in the measured bubble pressures. The open ends of the silicone oil manometers depicted in Fig. 1 were actually connected to an alumina tube that was positioned just above the melt in the furnace chamber. Thus, the pressure in the bubbles was measured relative to the pressure in the furnace.

The temperature of the silicone oil manometers was monitored during each experiment using high precision mercury thermometers. Small changes in density of the silicone oil with a change in room temperature were taken into account in calculating the surface tension of the Na_2SO_4 . The change in height of silicone oil in the two legs of the manometers were measured using a cathetometer.

Granular anhydrous Na_2SO_4 (see Table I for analysis) was employed in these experiments. The Na_2SO_4 was dried at 600°-650°C for 1-2 weeks under vacuum. After transferring the Na_2SO_4 to the surface tension apparatus, it was heated under flowing dry Ar at 600°C for about 12 hr before the temperature of the salt was raised above its melting point.

The surface tension of molten Na_2SO_4 at a constant temperature and total pressure of 1 atm was measured as a function of the partial pressures of SO_2 and O_2 (or, equivalently, SO_3) gases that were in equilibrium with the melt. The partial pressure of SO_3 gas in equilibrium with the melt was calculated using the equilibrium constants (16) for the reaction



and the volume fractions of SO_2 and O_2 in the initial gas mixtures. The gas mixtures employed were either premixed Ar- SO_2 - O_2 or mixtures produced by combining pure gases and/or premixed gases using con-

stant-head capillary flowmeters. The compositions of the input gases, the flow rates, and the equilibrium values of P_{SO_3} at 1200 and 1250 K are presented in Tables II and III. Six gas mixtures were employed to measure the surface tension at 1200 and 1250 K for $10^{-9} \lesssim P_{\text{SO}_3} \lesssim 10^{-1}$ atm. Before mixing, the Ar, O_2 , and the Ar- O_2 mixtures were passed through anhydrous $\text{Mg}(\text{ClO}_4)_2$ and P_2O_5 to remove water vapor and through "Ascarite" to remove CO_2 . The SO_2 and Ar- SO_2 - O_2 mixtures were passed through P_2O_5 to remove traces of water vapor.

The oxygen contents of the Ar-970 ppm SO_2 and the Ar-97 ppm SO_2 (Table II) were measured by Matheson Gas Products. We verified the oxygen contents by using a calcia-stabilized zirconia solid electrolyte cell with air as the reference electrode. The uncertainty in the analyses for O_2 and SO_2 in the premixed gases is reported to be less than 2% by Matheson. The gases were not analyzed further by us for the SO_2 content.

The time required to equilibrate SO_2 - O_2 gas mixtures with molten Na_2SO_4 has been measured using sodium β - Al_2O_3 solid electrolyte cells (15). Equilibration is achieved in the presence of a Pt-wire catalyst in 1-2 hr for $10^{-2} < P_{\text{SO}_3} < 10^{-1}$ atm and in ~ 3 hr for $P_{\text{SO}_3} \sim 10^{-3}$ atm. Lin (4) confirmed these times for equilibration using thermogravimetric techniques. Data are not available to indicate the time required to equilibrate molten Na_2SO_4 with a gas phase that has $P_{\text{SO}_3} < 10^{-3}$ atm. In the present investigation, the gases with low equilibrium values of P_{SO_3} were bubbled through the melt via Pt-Rh bubble tubes for at least 15 hr before a measurement was made to ensure that equilibrium was achieved. The surface tension did not change when these gas mixtures were bubbled through the melts for an additional 15 hr or more.

A variable head gas bleeder and a needle valve were located in the gas line after the gas mixing chamber but before the manometers and furnace assembly. These were employed to regulate the flow of gas to the bubble tubes. The rate of bubbling can affect the measurement of pressure in a bubble, and it is usually recommended that the rate of bubbling be in the range of one bubble per second for low viscosity melts and up to 60 sec for more viscous melts (10). In the present study, rates of one bubble per 15-20 sec were found to yield reproducible results.

Excess gas from the bleeder was passed into the furnace and flowed over the surface of the melt. Flowing the gas mixture over the melt during the entire experiment in addition to bubbling the gas mixture through the melt via the bubble tubes before the experiment served to equilibrate the melt with

Table II. Gases employed in this investigation*

| | | | |
|--------|---|--------|---|
| Gas A: | UHP O_2 (99.95% O_2 min); | Gas B: | Anhydrous SO_2 (99.98% SO_2 min); |
| Gas C: | UHP Ar (99.999% Ar); | Gas D: | Ar-4.8% O_2 ; |
| Gas E: | Ar-6.8% SO_2 ; | Gas F: | Ar-970 ppm O_2 -9 ppm O_2 ; |
| | | Gas G: | Ar-97 ppm SO_2 -8 ppm O_2 |

* Matheson Gas Products.

Table I. Analysis* of granular anhydrous Na_2SO_4 used in this work (w/o)

| | | | | |
|------------------|--------------------|--------------|------------------|-------|
| Arsenic | Chloride | Heavy metals | Insoluble matter | Iron |
| 0.0001 | 0.001 | 0.0005 | 0.01 | 0.001 |
| Loss on ignition | Nitrogen compounds | Phosphate | | |
| 0.50 | 0.0005 | 0.002 | | |

* Mallinckrodt analytical reagent grade—manufacturer's analysis.

Table III. Flow rates of input gases and equilibrium SO_3 partial pressures at 1200 and 1250 K (total pressure = 1 atm)

| Gas mixture | Flow rates of input gases, cm^3/min | $\log P_{\text{SO}_3}$ | |
|-------------|---|------------------------|--------|
| | | 1200 K | 1250 K |
| I | 8.16, Gas A: 8.16, Gas B | -1.11 | -1.26 |
| II | 22.83, Gas D: 6.96, Gas E | -3.13 | -3.29 |
| III | 21.76, Gas D: 6.63, Gas F | -5.03 | — |
| IV | 13.60, Gas D: 7.47, Gas F | — | -5.05 |
| V | Gas F | -6.14 | -6.3 |
| VI | Gas G | -7.16 | -7.32 |
| VII | 5.84, Gas C: 2.92, Gas G | -9.13 | -9.3 |

the gas mixture, thereby fixing the thermodynamic state of the salt melt.

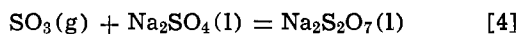
Gas that passed through the needle valve was directed, with the aid of stopcocks, to only one of the bubble tubes. While the pressure was being measured in one bubble tube, gas at approximately the maximum pressure was maintained in the other tube to eliminate changes in the depth of the melt that would occur if the melt moved up the tube that was not in use.

The surface tension apparatus was also used to determine the density of Na_2SO_4 by measuring the maximum bubble pressure in a single tube at two depths of immersion of the tube in the melt. By measuring the surface tension at two depths of immersion of the two tubes in each experiment, the data obtained could also be used to determine the density of Na_2SO_4 .

Results and Discussion

Density of Na_2SO_4 .—At least two measurements of the density of Na_2SO_4 were made at each of six values of P_{SO_3} employed at 1200 and 1250 K. In total, 27 measurements were made at 1200 K and 12 measurements were made at 1250 K. The results are plotted in Fig. 2. Within the precision of the measurements, the density of Na_2SO_4 is independent of P_{SO_3} in the range of 10^{-9} – 10^{-1} atm. The average values of the density are 2.09 ± 0.04 and 2.06 ± 0.02 g/cm^3 at 1200 and 1250 K, respectively, the uncertainties being one standard deviation from the average values.

Constant values of the density of Na_2SO_4 over the range of P_{SO_3} employed indicate that the Na_2SO_4 is virtually stoichiometric over this range of P_{SO_3} . A variation in the density of Na_2SO_4 at higher values of P_{SO_3} could occur, however, by the dissolution of SO_3 in Na_2SO_4 to form pyrosulfate anions according to the reaction



The solubility of SO_3 in Na_2SO_4 at 1200 K varies from ~ 0.1 atomic percent (a/o) $\text{Na}_2\text{S}_2\text{O}_7$ at $P_{\text{SO}_3} = 0.01$ atm to ~ 0.3 a/o $\text{Na}_2\text{S}_2\text{O}_7$ at $P_{\text{SO}_3} = 0.08$ atm (4). Thus, changes in the concentration of ($\text{S}_2\text{O}_7^{2-}$) anions, and corresponding changes in the density of Na_2SO_4 , are expected to be negligible for the low values of P_{SO_3} employed in the present study (maximum $P_{\text{SO}_3} = 0.08$ atm). At low values of P_{SO_3} and high values of P_{O_2} , the composition of Na_2SO_4 , and its density, may change by formation of Na_2O_2 and NaO_2 . Although data are not available for the relative concentrations of the latter oxides of Na in Na_2SO_4 , the observation of constant values of the density of Na_2SO_4 for values of P_{SO_3} as low as 10^{-9} atm indicates that significant quantities of these oxides were not formed.

The densities measured in the present work are about 2% higher than those obtained by Jaeger, who used a hydrostatic weighing technique, which is a much better method to measure densities than the maximum bubble pressure method. Use of the latter method requires a measurement of the maximum bubble pressure in a single tube at two different depths of immersion and a measurement of the difference in the depths of immersion.

In the present investigation, the difference in the depths of immersion was measured using a Vernier scale on a rack and pinion that was used to support the bubble tubes. An error of 2% in the difference in the depths of immersion, which would correspond to about 0.02 cm in the present case, would yield an error of about 2% in the density.

The densities of Na_2SO_4 obtained by Jaeger (11) were employed in the present investigation to calculate the surface tension of Na_2SO_4 using the data obtained with the double-tube maximum bubble pressure method. Jaeger's measurements of the densities of molten salts are generally considered to be accurate (12). In any case, an error in the density of 10% yields an error of less than 0.5% in the surface tension when the double-tube method is employed.

Surface tension of Na_2SO_4 .—The surface tension, σ , of molten Na_2SO_4 was measured at 1200 and 1250 K as a function of P_{SO_3} ($10^{-9} < P_{\text{SO}_3} < 10^{-1}$ atm). The results, which are presented in Fig. 3, demonstrate that σ is not a function of P_{SO_3} for the range of conditions studied.

The reproducibility of the measurements of the surface tension was good, *i.e.*, the largest value of one standard deviation for four measurements of σ at any one P_{SO_3} was $\pm 0.5\%$ (± 0.0009 N/m). The overall uncertainty of the measurements is estimated to be $\pm 1\%$ ($\sim \pm 0.002$ N/m), which includes the uncertainties involved in measuring the diameters of the bubble tubes (± 0.001 cm) and in measuring the maximum pressure in the bubbles with silicone oil manometers (± 0.001 cm in the difference of the height of the legs of the manometer). Thus, the slight apparent variation of σ with P_{SO_3} shown in Fig. 3 is within the limits of the experimental uncertainty of the measurements. The bars around the points in Fig. 3 represent one standard deviation from the average value for two to four measurements at each P_{SO_3} . Each of the three points without bars represents the value of two measurements that yielded the same value of σ .

To test the accuracy of the measurements of the surface tension of Na_2SO_4 , measurements of the surface tension of water at room temperature and of K_2SO_4 at 1400 K were made and compared to well-established values for these quantities. Six measure-

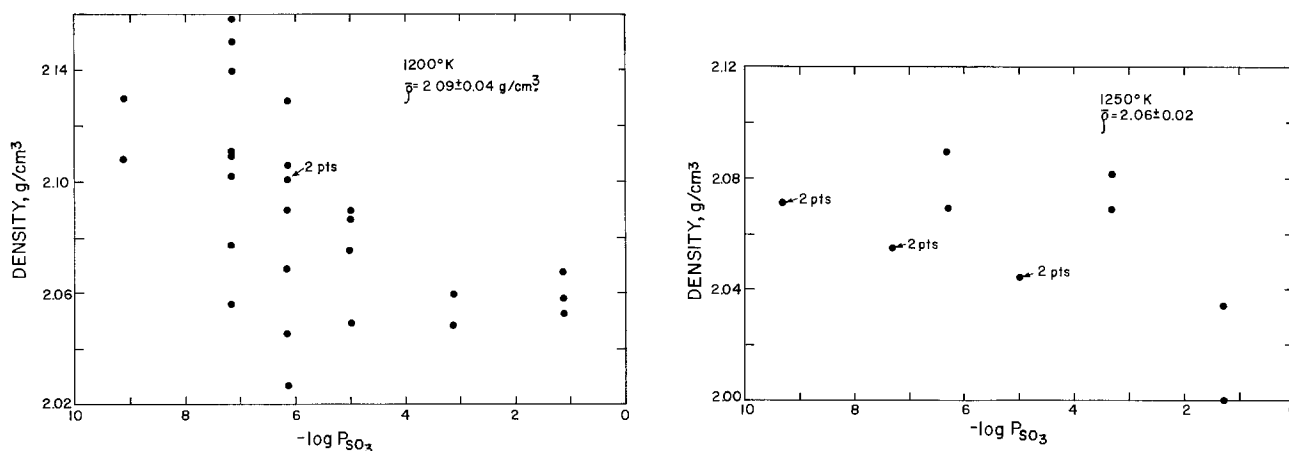


Fig. 2. Dependence of the density of molten Na_2SO_4 on SO_3 partial pressure at (a, left) 1200 and (b, right) 1250 K

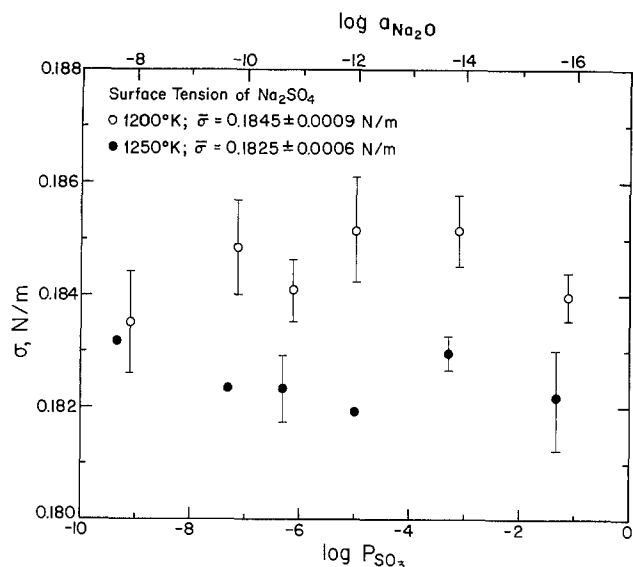


Fig. 3. Dependence of the surface tension of molten Na_2SO_4 at 1200 and 1250 K on the partial pressure of SO_3 gas.

ments of the surface tension of H_2O at 293 K yielded an average value of 0.07265 ± 0.00153 N/m, which is in good agreement with the value of 0.07275 N/m reported in the International Critical Tables (13). Two measurements of the surface tension of K_2SO_4 at 1400 K were made at each of two partial pressures of SO_3 . The average values were 0.1381 and 0.1398 ± 0.0006 N/m at 2.2×10^{-2} and 10^{-5} atm of SO_3 , respectively. Assuming that the surface tension of K_2SO_4 is independent of P_{SO_3} , one obtains an average value for the four measured values of 0.1389 N/m. The latter value agrees within 1% of the value of 0.1381 N/m obtained by Neithammer and Peake (14), who used a single-tube maximum bubble pressure apparatus with nitrogen gas. On the basis of these results, one can conclude that the accuracy of the present measured values of the surface tension of Na_2SO_4 is good.

The average values of σ at 1200 and 1250 K are 0.1845 ± 0.0009 and 0.1825 ± 0.0006 N/m, respectively, which were calculated from all of the measurements made at one temperature based on the conclusion that σ is independent of P_{SO_3} . The latter conclusion should be reserved for the range of values of P_{SO_3} employed in the experiments. At higher P_{SO_3} and lower temperatures, or at lower P_{SO_3} and higher temperatures, Na_2SO_4 may contain sufficient ($\text{S}_2\text{O}_7^{2-}$) or (O^{2-}) anions, respectively, to affect the surface tension.

Moiseev and Stepanov (2) measured the effect of various additives to Li_2CO_3 on its surface tension. Additions of Li_2O to molten Li_2CO_3 at 765°C caused a steady increase in the surface tension of Li_2CO_3 from about 0.242 N/m at 0 mole percent (m/o) Li_2O to about 0.260 N/m at 31 m/o Li_2O . The increase in surface tension was attributed to the increased concentration of (O^{2-}) anions in the melt, which have a higher effective dipole moment than (CO_3^{2-}) anions. Further increases in the concentration of dissolved Li_2O from 31 to 48 m/o caused a decrease in the surface tension, which was attributed to the formation of (LiCO_3^-) complexes in the melt [at 31 m/o Li_2O in Li_2CO_3 there are approximately three (Li^+) cations per (CO_3^{2-}) anion].

By analogy with the results of Moiseev and Stepanov (2), the surface tension of Na_2SO_4 may increase at very low P_{SO_3} in equilibrium with the melt (high $a_{\text{Na}_2\text{O}}$) because of the increased concentration of (O^{2-}) anions. The surface tension of Na_2SO_4 at values of

$P_{\text{SO}_3} < 10^{-9}$ atm has not been measured in the present study because the Pt-Rh bubble tubes and the Pt crucible would be dissolved by the highly basic salt (15).

To determine the temperature dependence of the surface tension of Na_2SO_4 , measurements were made at a constant partial pressure of SO_3 gas equal to 10^{-5} atm over the temperature range of 1175–1400 K. Under these conditions, the activity of Na_2O in Na_2SO_4 varies from 3.1×10^{-13} at 1175 K to 4.3×10^{-9} at 1400 K, which is in the range of $a_{\text{Na}_2\text{O}}$ for which σ is independent of P_{SO_3} (or $a_{\text{Na}_2\text{O}}$) at 1200 and 1250 K. A plot of the surface tension vs. temperature is shown in Fig. 4. The application of linear regression to the data yields,

$$\sigma = 2.568 \times 10^{-1} - 6.05 \times 10^{-5}T \quad [5]$$

where σ has units of N/m and T is the absolute temperature. The correlation coefficient for the linear regression analysis is 0.998. Note that σ changes by only ~ 0.013 N/m over the range of temperature investigated.

Jaeger (11) measured the surface tension of Na_2SO_4 using the single-tube maximum bubble pressure method over the temperature range of 1173–1350 K. His results, which were obtained using nitrogen gas, may be represented by the following quadratic equation (10)

$$\sigma = 4.765 \times 10^{-1} - 5.32 \times 10^{-4}T + 2.43 \times 10^{-8}T^2 \quad [6]$$

Jaeger's values for σ of Na_2SO_4 are about 5% higher than the values measured in the present investigation. Janz *et al.* (10) have pointed out that Jaeger's measurements of the surface tension of molten salts are generally 2–8% higher than measurements made more recently.

The quadratic temperature dependence of σ found by Jaeger (11), if it is real, indicates that the surface tension at higher temperatures is greater than expected by a linear extrapolation of his data obtained at lower temperatures. Higher temperatures and low P_{SO_3} in the gas phase (pure N_2 was used by

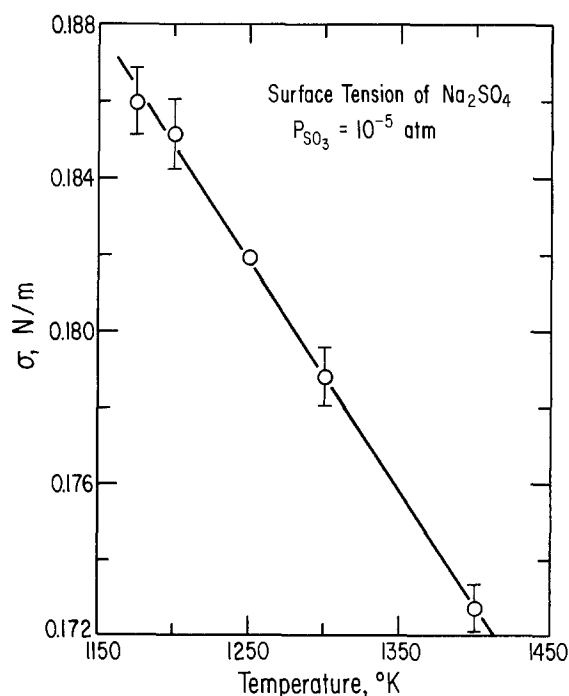


Fig. 4. Dependence of the surface tension of molten Na_2SO_4 on temperature.

Jaeger) causes the reaction in Eq. [1] to move to the right. Thus, it is conceivable that a sufficiently high $a_{\text{Na}_2\text{O}}$ was attained in Jaeger's melts at the highest temperatures to cause a small increase in the surface tension of the Na_2SO_4 . To test this premise, the surface tension of Na_2SO_4 should be measured as a function of temperature for well-defined, low values of P_{SO_3} (high $a_{\text{Na}_2\text{O}}$). In the meantime, the high accuracy of the measurements made in the present investigation indicates that Eq. [6] provides a better representation of the temperature dependence of the surface tension of Na_2SO_4 than that reported by Jaeger.

Summary

The density and the surface tension of Na_2SO_4 are independent of P_{SO_3} for partial pressures in the range of 10^{-1} - 10^{-9} atm at 1200 and 1250 K. The constant value of the density indicates that Na_2SO_4 is virtually stoichiometric for this range of P_{SO_3} . A change in the surface tension of Na_2SO_4 with P_{SO_3} would require either a large change in composition with P_{SO_3} [large change in the concentrations of (O^{2-}) , (O_2^-) , (O_2^{2-}) , or $(\text{S}_2\text{O}_7^{2-})$ with a change in P_{SO_3}], or a small change in the concentration of a highly surface-active species. The concentrations of (O^{2-}) , $(\text{S}_2\text{O}_7^{2-})$, (O_2^-) , and (O_2^{2-}) change by a small amount as P_{SO_3} is changed from 10^{-1} to 10^{-9} atm; however, because the surface tension of Na_2SO_4 is constant for this range of P_{SO_3} , none of these species can be considered to be highly surface active. The surface tension of Na_2SO_4 is a linear function of temperature (1175-1400 K) when P_{SO_3} is held constant at 10^{-5} atm.

Acknowledgments

This work was supported by the Department of Energy (Contract E (49-18)-2295). The authors wish to express their gratitude to Professor J. F. Elliott for his helpful comments and support during the course of this work. They also wish to thank Professor T. B. King for his careful reading of the manuscript.

Manuscript submitted Jan. 6, 1981; revised manuscript received April 20, 1981.

Any discussion of this paper will appear in a Discussion Section to be published in the June 1982 JOURNAL. All discussions for the June 1982 Discussion Section should be submitted by Feb. 1, 1982.

REFERENCES

1. P. Kozakevitch, *Rev. Metall.*, **46**, 505, 572 (1949).
2. G. K. Moiseev and G. K. Stepanov, "Electrochemistry of Molten and Solid Electrolytes," Vol. 4, p. 91, translated by Consultants Bureau, NY (1967).
3. W. W. Liang and J. F. Elliott, submitted to *This Journal*.
4. R.-Y. Lin, Ph.D. Thesis, Massachusetts Institute of Technology (1980).
5. A. W. Coats, D. J. A. Dear, and D. Penfold, *J. Inst. Fuel*, **129** (1968).
6. R. E. Andresen, *This Journal*, **126**, 328 (1979).
7. M. Simon, *Ann. Chim. Phys.*, **33**, 5 (1851).
8. A. W. Adamson, "Physical Chemistry of Surfaces," 3rd ed., John Wiley and Sons, New York (1976).
9. S. Sugden, *J. Chem. Soc. (London)*, **121**, 858 (1922).
10. G. J. Janz, G. R. Lakshminarayanan, R. P. T. Tomkins, and J. Wong, "Molten Salts: Vol. 2, Section 2. Surface Tension Data," NSRDS-NBS 28, Washington, DC (1969).
11. F. M. Jaeger, *Z. Anorg. Allgem. Chem.*, **101**, 1 (1917).
12. G. J. Janz, F. W. Dampier, G. R. Lakshminarayanan, P. K. Lorenz, and R. P. T. Tomkins, "Molten Salts: Vol. 1, Electrician Conductance, Density and Viscosity Data," NSRDS-NBS 15, Washington, DC (1968).
13. "International Critical Tables," Vol. II, McGraw-Hill Book Co., Inc., NY (1926).
14. R. W. Neithamer and J. S. Peake, *J. Chem. Eng. Data*, **6**, 197 (1961).
15. W. Liang, Ph.D. Thesis, Massachusetts Institute of Technology (1976).
16. "JANAF Thermochemical Tables," D. R. Stull and H. Prophet, Project Directors, NBS, Washington, DC, NSRDS-NBS37 (June 1971).

Thermodynamics of Nickel-Aluminum-Oxygen System Between 900 and 1400 K

F. A. Elrefaie* and W. W. Smeltzer*

Department of Metallurgy and Materials Science, McMaster University, Hamilton, Ontario, Canada L8S 4M1

ABSTRACT

Equilibrium oxygen pressures of the univariant systems Ni-NiO-NiAl₂O₄, and Ni-NiAl_{2.54}O_{4.81}-Al₂O₃ were determined between 1123 and 1423 K using galvanic cells with calcia-stabilized zirconia as the solid electrolyte. Slip-cast tubes of a two-phase mixture of β - and α -Al₂O₃ were used as electrolyte in cells to determine the equilibrium oxygen pressures of the univariant Ni-NiAl_{2.54}O_{4.81}-Al₂O₃ between 923 and 1173 K and the dissociation pressure of Al₂O₃ equilibrated with (Ni-Al) alloys containing 0.17, 1.19, and 2.36 atomic percent Al at 1213 K. The free energy of formation of NiAl_{2.54}O_{4.81} was determined between 923 and 1423 K. An electron probe microanalyzer was used to determine the composition of oxides and alloy phases of the ternary Ni-Al-O system that coexist with each other at 1273 K. The Ni-Al-O isotherm at 1273 K and Ni-Al-O equilibrium oxygen pressure diagrams at 1213 and 1273 K are presented.

Equilibrium oxygen pressures of the coexistences of the Ni-Al-O system have not been extensively investigated, probably due to the very low oxygen pressures

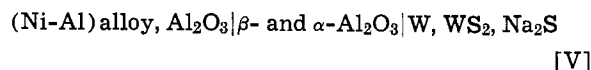
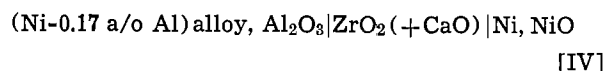
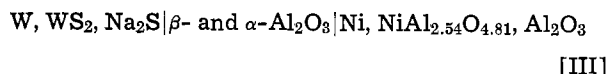
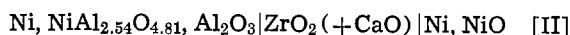
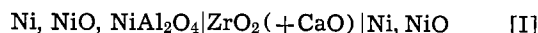
encountered. The free energy of formation of nickel spinel, NiO · (1 + x)Al₂O₃, has been determined at temperatures in the range 973-1673 K using galvanic cells with calcia-stabilized zirconia as solid electrolyte (1-4) or by equilibrating the mixture Ni-NiO ·

* Electrochemical Society Active Member.
Key words: solid electrolyte, emf, equilibrium.

$(1+x)\text{Al}_2\text{O}_3\text{-Al}_2\text{O}_3^1$ with a CO/CO_2 atmosphere (5). Published data, however, are in poor agreement. Aluminum activities in Ni-Al alloys containing between 15 and 60 atomic percent (a/o) Al were studied over the temperature range 1185-1455 K using isopiestic measurements (6). Values of aluminum activities in alloys containing 69.96-99.46 a/o Al at temperatures in the range 956-1200 K have been evaluated from electromotive force measurements with AlCl_3 in $\text{NaCl}\cdot\text{KCl}$ liquid electrolyte (7). Nickel activities in Ni-Al alloys are reported at 1273 K (8, 9). The Ni-Al system is well established (10) and the phase relations in the sub-solidus region of the NiO- Al_2O_3 quasi-binary system are reported between 1273 and 2193 K (11). The lack of compositional data for the ternary Ni-Al-O isotherm and the development of the two-phase mixture of β - and α - Al_2O_3 electrolyte to sense reversibly oxygen pressures as low as those of Al- Al_2O_3 equilibria (12, 13) led us to initiate this work to determine the Ni-Al-O isotherm and the oxygen pressures for equilibria involving alloy and oxide phases at temperatures in the range 923 and 1423 K.

Experimental

Equilibrium oxygen pressures of the coexistences Ni-NiO- NiAl_2O_4 , $\text{Ni}_{(s)}$ - $\text{NiAl}_{2.54}\text{O}_{4.81}$ - Al_2O_3 , and (Ni-Al) alloy- Al_2O_3 were determined from emf measurements on the following cells



A previously described cell assembly (14) that contained a 30 cm long tube of calcia-stabilized zirconia was used to measure the emf's of cells [I], [II], and [IV] between 1123 and 1423 K. The emf of cell [III] was measured between 923 and 1173 K while the emf of cell [V] was measured at 1213 K using a previously described cell assembly (15) which contained a 10 cm long β - and α - Al_2O_3 tube as the electrolytic membrane between the anode and cathode compartments.

A potential shown by cells [I], [II], [III], and [V] at a temperature in the investigated range was very steady, within ± 1 mV or less, for periods investigated up to 45 min. When the temperature was changed, a new steady state was reached after 2-4 hr with furnace temperature stabilization occurring within 20-40 min. Reversibility of cells [I] and [II] was checked by charging or discharging a cell through an external circuit momentarily; the cell emf returned very rapidly to a value within at most ± 1 mV from the original value. A thermal disturbance method was used to check the reversibility of cells [III] and [V]. The cell temperature was cycled several times then fixed at the plateau-attaining temperature; the emf attained its original value, to ± 1 mV, within 5 min and remained at this potential for the investigated period.

Reference Ni,NiO electrodes were tablets pressed from 1:1 mixture of Ni and NiO. The W, WS_2 , Na_2S reference electrodes of cells [III] and [V] were prepared as described previously (16). The working electrodes were fabricated as tablets from mixtures of the metallic and oxide phases. Compositions of mixtures used for preparing tablets to be used as electrodes and for phase composition and identification analyses are given in Table I. Such tablets were annealed for a

¹ Al_2O_3 is used to represent α - Al_2O_3 in the text.

Table I. Starting compositions of coexisting alloy and oxide phases

| Pellet* | The starting contents of the pellets in weight percent | | | | |
|---------|--|-------|-----|------------------------------|------------------------------------|
| | Al | Ni | NiO | NiAl_2O_4 ** | α - Al_2O_3 |
| P-1 | — | 50 | 25 | 25 | — |
| P-2 | — | 50 | — | 25 | 25 |
| P-3 | 0.05 | 49.95 | — | — | 50 |
| P-4 | 0.25 | 49.75 | — | — | 50 |
| P-5 | 0.50 | 49.50 | — | — | 50 |
| P-6 | 1.15 | 48.85 | — | — | 50 |
| P-7 | 6.00 | 44.00 | — | — | 50 |
| P-8 | 11.00 | 39.00 | — | — | 50 |
| P-9 | 13.50 | 36.50 | — | — | 50 |
| P-10 | 15.00 | 35.00 | — | — | 50 |
| P-11 | 17.50 | 32.50 | — | — | 50 |

* P-1 and P-2 tablets were annealed at 1000°C for 60 days while the other pellets were annealed for 30 days at 1000°C.

** NiAl_2O_4 was prepared as we described previously (11).

period of 30-60 days under flowing high-purity argon gettered of oxygen using Zr chips. X-ray analyses confirmed the presence of the desired phases in each tablet after annealing, while compositions of these phases were determined using EPMA (electrode probe microanalysis) technique. Materials used and their sources are listed in Table II.

Results

Cell [I].—Electromotive force values of cell [I], Fig. 1, fit the least squares expression

$$E(\text{mV}) = 0.7(\pm 0.03) + 0.0032(\pm 0.0002) T (\pm 0.1 \text{ mV}) \quad \text{[1]}$$

Cell [II].—Electromotive force values representing the univariant equilibrium Ni, $\text{NiAl}_{2.54}\text{O}_{4.81}$, α - Al_2O_3 are plotted in Fig. 2; the linear plot fits the least squares expression

$$E(\text{mV}) = 64(\pm 2.5) + 0.047(\pm 0.002) T (\pm 1.0 \text{ mV}) \quad \text{[2]}$$

Cell [III].—The variation with temperature of the emf of this cell, Fig. 3, is described by the least squares line

$$E(\text{mV}) = 1117(\pm 3) - 0.444(\pm 0.003) T (\pm 2 \text{ mV}) \quad \text{[3]}$$

Cell [IV].—Unstable emf's were exhibited by this cell; this electrical instability was not amenable to correction by coulometric disturbance or by temperature cycling of the cell.

Cell [V].—The emf of cell [V] was determined only at 1213 K. The investigated working electrodes were Ni containing 0.17, 1.19, or 2.36 a/o Al alloys equilibrated with Al_2O_3 ; the emf values obtained were 19 ± 1 , 119 ± 2 , and 151 ± 1 mV, respectively.

Compositions determined by EPMA for the coexisting oxide and alloy phases at 1273 K are recorded in Table III. The intensity of the Al x-ray signals obtained from the metallic phases of Ni-NiO- NiAl_2O_4 and Ni- $\text{NiAl}_{2.54}\text{O}_{4.81}$ - Al_2O_3 coexistences would not be distinguished from the background intensity which indicates that these phases were essentially pure nickel.

Table II. Materials used in this investigation and its sources

| Material | Source and type |
|------------------------------------|--|
| Nickel powder | Ventron, Alfa Products: 99.9% |
| Aluminum powder | Ventron, Alfa Products: 99.8% |
| Tungsten powder | Fisher Scientific: Purified |
| Nickel oxide powder | Fisher Scientific: 99.8% |
| Aluminum oxide powder (α) | Ventron, Alfa Products: 99.99% |
| Tungsten sulfide powder | Ventron, Alfa Products: Laboratory grade |
| Sodium sulfide powder (anhy.) | Ventron, Alfa Products: Laboratory grade |

Table III. The EPMA analyses of coexisting oxide and alloy phases at 1273 K

| Pellet | Coexisting phases | Aluminum content of the alloy (a/o) | Nickel oxide content of the oxide phase (m/o) |
|--------|--|-------------------------------------|---|
| P-1 | Alloy (γ) | — | — |
| | Nickel oxide | — | 99.0 |
| | Nickel spinel | — | 50.0 |
| P-2 | Alloy (γ) | — | — |
| | Nickel spinel | — | 44.0 |
| | α -Al ₂ O ₃ | — | 2.0 |
| P-3 | Alloy (γ) | 0.17 | — |
| | α -Al ₂ O ₃ | — | 1.9 |
| P-4 | Alloy (γ) | 1.19 | — |
| | α -Al ₂ O ₃ | — | 1.7 |
| P-5 | Alloy (γ) | 2.36 | — |
| | α -Al ₂ O ₃ | — | 1.6 |
| P-6 | Alloy (γ) | 23.1 | — |
| | α -Al ₂ O ₃ | — | 1.3 |
| P-7 | Alloy (β) | 38.1 | — |
| | α -Al ₂ O ₃ | — | 1.1 |
| P-8 | Alloy (β) | 44.6 | — |
| | α -Al ₂ O ₃ | — | 1.0 |
| P-9 | Alloy (β) | 48.6 | — |
| | α -Al ₂ O ₃ | — | 1.0 |
| P-10 | Alloy (β) | 53.7 | — |
| | α -Al ₂ O ₃ | — | 0.8 |

Discussion

Ni-NiO.—This coexistence was used as a reference electrode in cells [I] and [II]. Steele (17) has described the standard free energy of formation of NiO, $\Delta G^\circ_f(\text{NiO})$, by

$$\Delta G^\circ_f(\text{NiO}) = -55,965 + 20.29 T \text{ cal/mol } (\pm 130 \text{ cal}),$$

(900-1400 K) [4]

The equilibrium oxygen pressure of the Ni,NiO coexistence, $P_{\text{O}_2}^*$, is therefore given by

$$\log P_{\text{O}_2}^* (\text{atm}) = -\frac{24,464}{T} + 8.869 \left(\pm \frac{57}{T} \right),$$

(900-1400 K) [5]

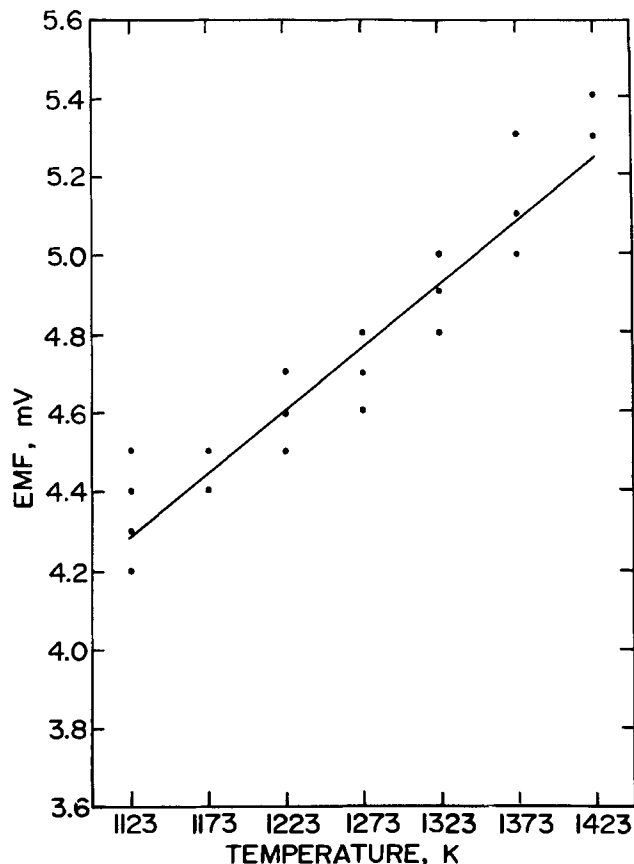


Fig. 1. The variation of emf with temperature for cell [I]

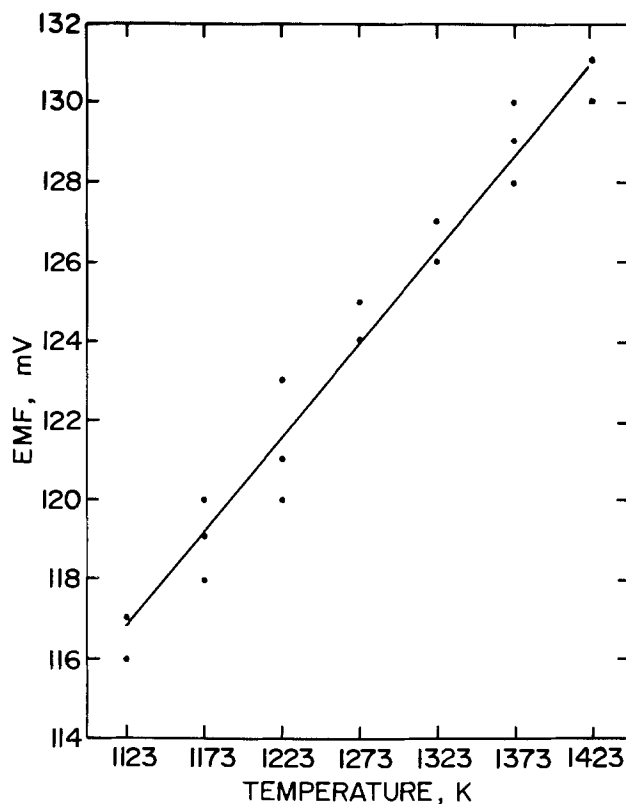


Fig. 2. The variation of emf with temperature for cell [II]

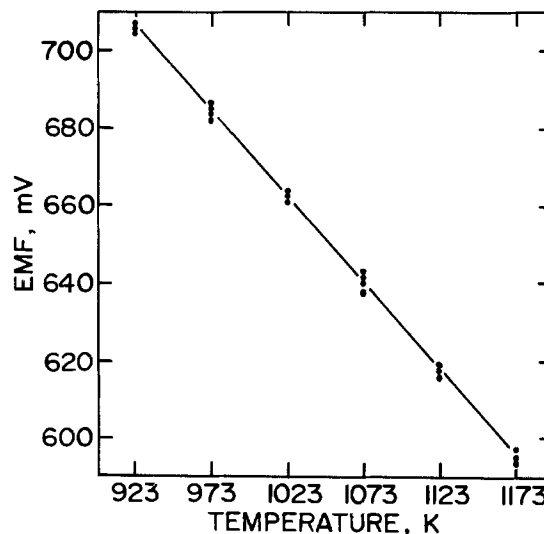


Fig. 3. The variation of emf with temperature for cell [III]

Ni-NiO-NiAl₂O₄ coexistence.—Since the overall reaction in cell [I] can be described by transfer of oxygen from the cathode to the anode compartment, the cell emf is given by

$$E = \frac{RT}{4F} \ln P_{\text{O}_2}^*/P_{\text{O}_2} \quad [6]$$

where P_{O_2} is the equilibrium oxygen pressure of the Ni-NiO-NiAl₂O₄ coexistence. Values of P_{O_2} between 1123 and 1423 K, therefore, were calculated by means of Eq. [1], [5], and [6], and found to follow the relation

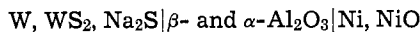
$$\log P_{\text{O}_2} (\text{atm}) = -\frac{24,478}{T} + 8.804 \left(\pm \frac{60}{T} \right),$$

[1123-1423 K] [7]

The oxygen pressure of this coexistence calculated from Eq. [7] at 1273 K is 3.76×10^{-11} atm which is

slightly less than the value of 4.48×10^{-11} atm for the dissociation pressure of NiO equilibrated with Ni. The EPMA analyses of the phases of this coexistence at 1273 K indicated the following: the spinel composition corresponded to the stoichiometric formula NiAl_2O_4 , NiO dissolves approximately 1 mol percent (m/o) of Al_2O_3 , and the metallic phase was essentially pure Ni.

Ni-NiAl_{2.54}O_{4.81}-Al₂O₃ coexistence.—Cells using calcia-stabilized zirconia as electrolyte with a Ni₂NiO reference electrode, cell [II], or the two-phase β - and α - Al_2O_3 electrolyte and W, WS₂, Na₂S as standard electrode, cell [III], were investigated to study this system. The best line through the emf values obtained from cell [II] between 1123 and 1423 K was represented by Eq. [2]. Also the emf data of cell [III] obtained over the temperature range 923–1173 K is found to follow relation [3]. Electromotive force of the cell



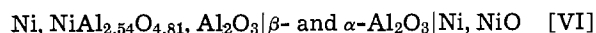
was measured between 923 and 1198 K (15) and found to follow the relation

$$E(\text{mV}) = 1180(\pm 4) - 0.396(\pm 0.004) T (\pm 2 \text{ mV}) \quad [8]$$

By subtracting expression [3] from [8], we obtained

$$E(\text{mV}) = 63(\pm 5) + 0.048(\pm 0.005) T (\pm 3 \text{ mV}) \quad [9]$$

Relation [9] describes the emf dependence of the cell



on temperature. Excellent agreement between Eq. [9] and [2] demonstrates the applicability of using the two-phase β - and α - Al_2O_3 electrolyte in probes to sense oxygen potentials as low as those of the Ni-NiAl_{2.54}O_{4.81}-Al₂O₃ coexistence.

The reaction in cells [II] and [VI] can be written as



where O₂^c and O₂^a are oxygen in the cathode and anode compartments, respectively. Alternatively, the overall cell reaction can be written as



By considering reaction [A], the variation of the equilibrium oxygen pressure of the Ni-NiAl_{2.54}O_{4.81}-Al₂O₃ univariant system with temperature is obtained by combining expressions [2], [5], and [6]; these calculations give

$$\log P_{\text{O}_2} (\text{atm}) = -\frac{25,754}{T} + 7.921 \left(\pm \frac{60}{T} \right), \quad (923\text{-}1423 \text{ K}) \quad [10]$$

where P_{O_2} is the equilibrium oxygen pressure of the Ni-NiAl_{2.54}O_{4.81}-Al₂O₃ coexistence. The value of P_{O_2} at 1273 K equal to 4.90×10^{-13} atm is approximately two orders of magnitude less than the dissociation pressure of NiO equilibrated with Ni. At 1273 K, the spinel in this coexistence was found by EPMA to contain 56 m/o Al₂O₃; therefore, it can be represented by the formula NiAl_{2.54}O_{4.81}. The EPMA results also indicated that Al₂O₃ contains 0.4 a/o Ni but the solubility of Al in Ni necessary to stabilize this coexistence was found to be too small to be determined by this technique.

The variation with temperature of the free energy of formation of NiAl_{2.54}O_{4.81} from its binary oxides, $\Delta G(\text{NiAl}_{2.54}\text{O}_{4.81})$, given by reaction [B], is related to emf values of cell [II] by

$$\Delta G(\text{NiAl}_{2.54}\text{O}_{4.81}) = -2FE \quad [11]$$

Values for the ΔG - T relation obtained by combining relations [2] and [11] are given in Table IV together with those values obtained by various investigators. The temperature coefficient obtained in this investiga-

Table IV. The free energy of formation of nickel spinel, NiO · (1 + x)Al₂O₃, from its binary oxides

| $\Delta G (\text{cal/mol}) =$ | | | | | Temper- ature range (K) | Refer- ence |
|-------------------------------|----------|-----------------|---------|--------------------|-------------------------------|----------------|
| $a + bT$ | $+ CT^2$ | $+ dT \log T$ | $+ e/T$ | | | |
| a | b | $C \times 10^3$ | d | $e \times 10^{-4}$ | | |
| -2,952 | -2.168 | | | | 623-1423 | This work |
| -1,499 | -2.31 | | | | 1000-1400 | (4) |
| -1,560 | -2.44 | | | | 1173-1673 | (5) |
| -5,553 | -0.42 | | | | 1306-1471 | (2) |
| -1,527 | +0.558 | -3.597 | +0.927 | -1.028 | 973-1473 | (3) |

tion, -2.168 cal/deg-mol, is in good agreement with values reported by Jacob and Alcock (4), -2.31 cal/deg-mol, and Lenev and Novokhatskii (5), -2.44 cal/deg-mol.

(Ni-Al)-Al₂O₃ equilibria.—The EPMA results demonstrated that Al₂O₃ coexisted practically with the (Ni-Al) alloy over its entire composition range. The dissociation pressure of Al₂O₃, therefore, decreased from the equilibrium oxygen pressure of the Ni-NiAl_{2.54}O_{4.81}-Al₂O₃ univariant system to values defined by the Al-Al₂O₃ equilibria with increasing Al alloy content. In this investigation, the dissociation pressure of Al₂O₃ equilibrated with Ni-Al alloys containing 0.17, 1.19, 2.36 a/o Al was determined by relating the emf values of cell [V] with thermochemical data of the cell reaction



where O₂ is oxygen of the (Ni-Al)-Al₂O₃ coexistence. For this reaction, we can write

$$\Delta G = 2\Delta G^\circ_f(\text{Na}_2\text{S}) - 2\Delta G^\circ_f(\text{Na}_2\text{O}) - \Delta G^\circ_f(\text{WS}_2) - 2RT \ln a_{\text{Na}_2\text{O}} + RT \ln P_{\text{O}_2} \quad [12]$$

Here, $a_{\text{Na}_2\text{O}}$ is the Na₂O activity of the α -Al₂O₃ and β -Al₂O₃ coexistence and P_{O_2} is the dissociation pressure of Al₂O₃ equilibrated with the (Ni-Al) alloy. Upon substituting $\Delta G = -4FE$ in relation [12] and rearranging, we obtain

$$\log P_{\text{O}_2} = \frac{1}{2.303RT} [2\Delta G^\circ_f(\text{Na}_2\text{O}) + \Delta G^\circ_f(\text{WS}_2) + 2RT \ln a_{\text{Na}_2\text{O}} - \Delta G^\circ_f(\text{Na}_2\text{S}) - 4FE] \quad [13]$$

Values of P_{O_2} of the working electrodes of cell [V] were calculated at 1213 K using Eq. [13], the measured values of E and the thermochemical data reported in our previous publication (15). The obtained values of P_{O_2} are 5.7×10^{-24} , 1.2×10^{-25} , and 3.7×10^{-26} for Ni alloys containing 0.17, 1.19, and 2.36 a/o Al in equilibrium with Al₂O₃, respectively. It is apparent from these results that the electrical instability of cell [IV] can be explained on the basis of electronic conduction in the calcia-stabilized zirconia electrolyte because the oxygen pressures imposed by the coexistence (Ni-0.17 a/o Al)-Al₂O₃ at 1213 K, 5.7×10^{-24} atm, is less than the value of oxygen pressure defined by the lower electrolytic domain boundary of calcia-stabilized zirconia (18).

Thermodynamic properties of Ni-Al alloys.—The Al activity of an alloy, a_{Al} , equilibrated with Al₂O₃ is given by

$$a_{\text{Al}} = P_{\text{O}_2}^{-3/4} \exp \left[\frac{\Delta G^\circ_f(\text{Al}_2\text{O}_3)}{2RT} \right] \quad [14]$$

where P_{O_2} is the dissociation pressure of Al₂O₃ equilibrated with the alloy. Values of a_{Al} given in Table V were calculated using relation [14]. The value of the Al activity coefficient was essentially constant, $\gamma_{\text{Al}} \approx 4 \times 10^{-8}$, at 1213 K over the range 2.36–0.17 a/o Al corresponding to Henrian solution behavior. This value is to be compared with $\gamma_{\text{Al}} = 8 \times 10^{-7}$ reported at 1273 K (9).

Table V. Activity and activity coefficient of Al in Ni-Al alloys (referred to liquid Al as standard state)

| Coexistence | Temperature (K) | a_{Al} | X_{Al} | γ_{Al} |
|---|-----------------|-----------------------|-------------------------------|----------------------|
| (Ni-2.36 a/o Al)-Al ₂ O ₃ | 1213 | 1.0×10^{-9} | 0.0236 | 4.2×10^{-8} |
| (Ni-1.19 a/o Al)-Al ₂ O ₃ | 1213 | 8.0×10^{-10} | 0.0119 | 6.8×10^{-8} |
| (Ni-0.17 a/o Al)-Al ₂ O ₃ | 1213 | 4.0×10^{-11} | 0.0017 | 2.4×10^{-8} |
| Ni-NiAl _{2.54} O _{4.81} -Al ₂ O ₃ | 1213 | 2.0×10^{-18} | $\approx 1 \times 10^{-11}$ * | — |
| | 1273 | 1.0×10^{-17} | $\approx 1 \times 10^{-11}$ * | — |

* These values of X_{Al} were calculated using the relation $X_{Al} = a_{Al}/\gamma_{Al}$.

As emphasized previously, Al alloy contents necessary to stabilize the Ni-NiAl_{2.54}O_{4.81}-Al₂O₃ coexistence were too small to be detected by EPMA. If one considers the values of γ_{Al} at 1213 and 1273 K, an atom fraction of Al equal to $\approx 1 \times 10^{-11}$, i.e., $\ll 1$ ppm of Al, is calculated for stabilization of the Ni-NiAl_{2.54}O_{4.81}-Al₂O₃ coexistence.

Ni-Al-O isotherm at 1273 K.—The isotherm shown in Fig. 4 was compiled from the results reported in Table III. In this diagram, the NiO and Al₂O₃ phase fields have been enlarged to illustrate the very limited solubility of Al in NiO, 1.87 a/o Al, and of Ni in Al₂O₃, 0.4 a/o Ni. A value of 0.051 a/o was reported (10) for oxygen solubility in Ni at 1273 K and molten Al dissolves ≈ 0.005 a/o oxygen (10). Accordingly the curve representing oxygen solubility in the alloy is schematic because of the lack of information to establish a defined boundary. Limiting compositions of the metallic phases were taken from the Ni-Al binary system (10). As the figure indicates, Al₂O₃ equilibrates with Ni-Al alloys essentially over its whole composition range. Nickel solubility in Al₂O₃ decreases with increasing Al content of the alloy: Al₂O₃ equilibrated with Ni-0.17 a/o Al alloy contains 0.38 a/o Ni and 0.16 a/o Ni when equilibrated with a Ni-53.7 a/o Al alloy. The spinel phase, which has a homogeneity range between 50 and 56 m/o Al₂O₃, coexists essentially with pure nickel.

Equilibrium oxygen pressure diagram for the Ni-Al-O system.—Figures 5a and b show the variation of the equilibrium oxygen pressure with the Ni metal atom fraction, $X_{Ni} = n_{Ni}/(n_{Ni} + n_{Al})$, of the solid phases at 1213 and 1273 K, respectively. Dissociation

pressures of pure NiO were calculated using relation [5] while the oxygen pressures of the univariant system Ni-NiO-NiAl₂O₄ and Ni-NiAl_{2.54}O_{4.81}-Al₂O₃ were obtained from relations [7] and [10], respectively. Dissociation pressures of Al₂O₃ equilibrated with alloys containing $X_{Al} \approx 0.0236$ at 1213 K were determined in this investigation while P_{O_2} values corresponding to alloys containing $0.6 \approx X_{Al} \approx 0.05$ were evaluated by considering the following relation

$$P_{O_2} = a_{Al}^{-4/3} \exp \left[\frac{2\Delta G^{\circ}_f(Al_2O_3)}{3RT} \right] \quad [15]$$

Values of a_{Al} used in Eq. [15] to calculate P_{O_2} at 1213 K were calculated by considering the a_{Al} and ΔH_{Al} data reported by Steiner and Komarek at 1273 K over the composition range $0.6 \approx X_{Al} \approx 0.15$; a_{Al} at $X_{Ni} = 0.95$ was calculated from the thermochemical data reported by Schaefer (7) and Hultgren *et al.* (9) at 1273 K. Results given by Schaefer (7) for a_{Al} were used to calculate the dissociation pressure of Al₂O₃ at 1273 K. The diagrams show that the oxygen pressure of the Ni-NiAl_{2.54}O_{4.81}-Al₂O₃ coexistence is less than that of Ni, NiO equilibrium by ≈ 2 orders of magnitude. With increasing Al content of the alloy, the oxygen pressure decreases most markedly over the alloy composition range $X_{Al} < 0.1$ and it subsequently decreases with Al content to the value corresponding to the Al-Al₂O₃ binary equilibrium (19).

Acknowledgments

This research is based on the thesis submitted by F. A. Elrefaie to McMaster University, in partial fulfillment for award of the Ph.D. degree. He gratefully acknowledges awards of an Aluminum Company of Canada Fellowship in Metallurgy and a National Research Council of Canada Graduate Studentship. The authors were indebted to D. A. R. Kay and E. O. Hileman, Jr., for helpful discussions.

Manuscript submitted Jan. 26, 1981; revised manuscript received April 21, 1981.

Any discussion of this paper will appear in a Discussion Section to be published in the June 1982 JOURNAL. All discussions for the June 1982 Discussion Section should be submitted by Feb. 1, 1982.

Publication costs of this article were assisted by McMaster University.

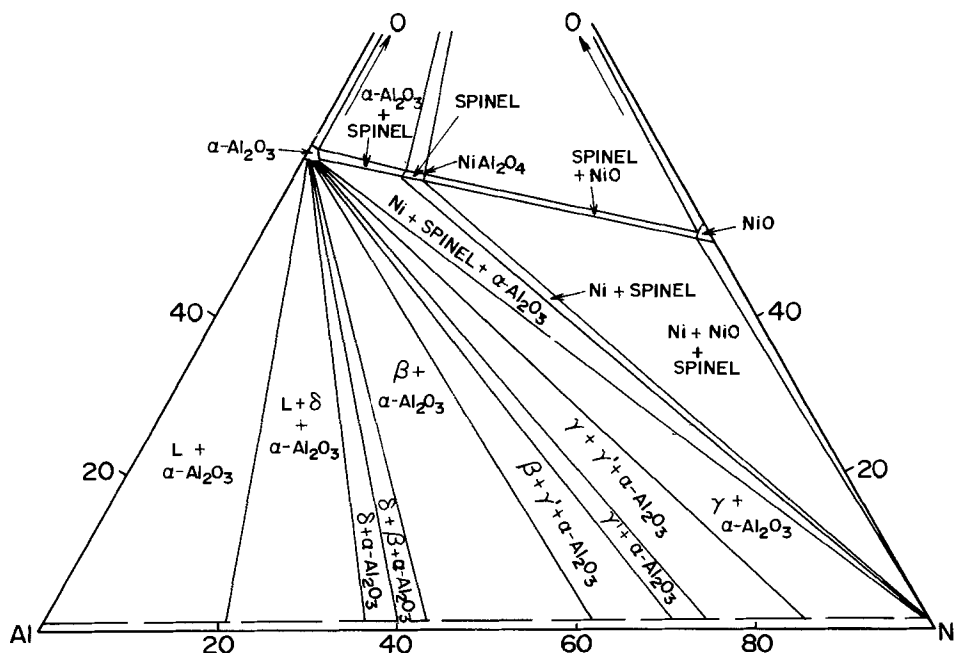


Fig. 4. Ni-Al-O isotherm at 1273 K.

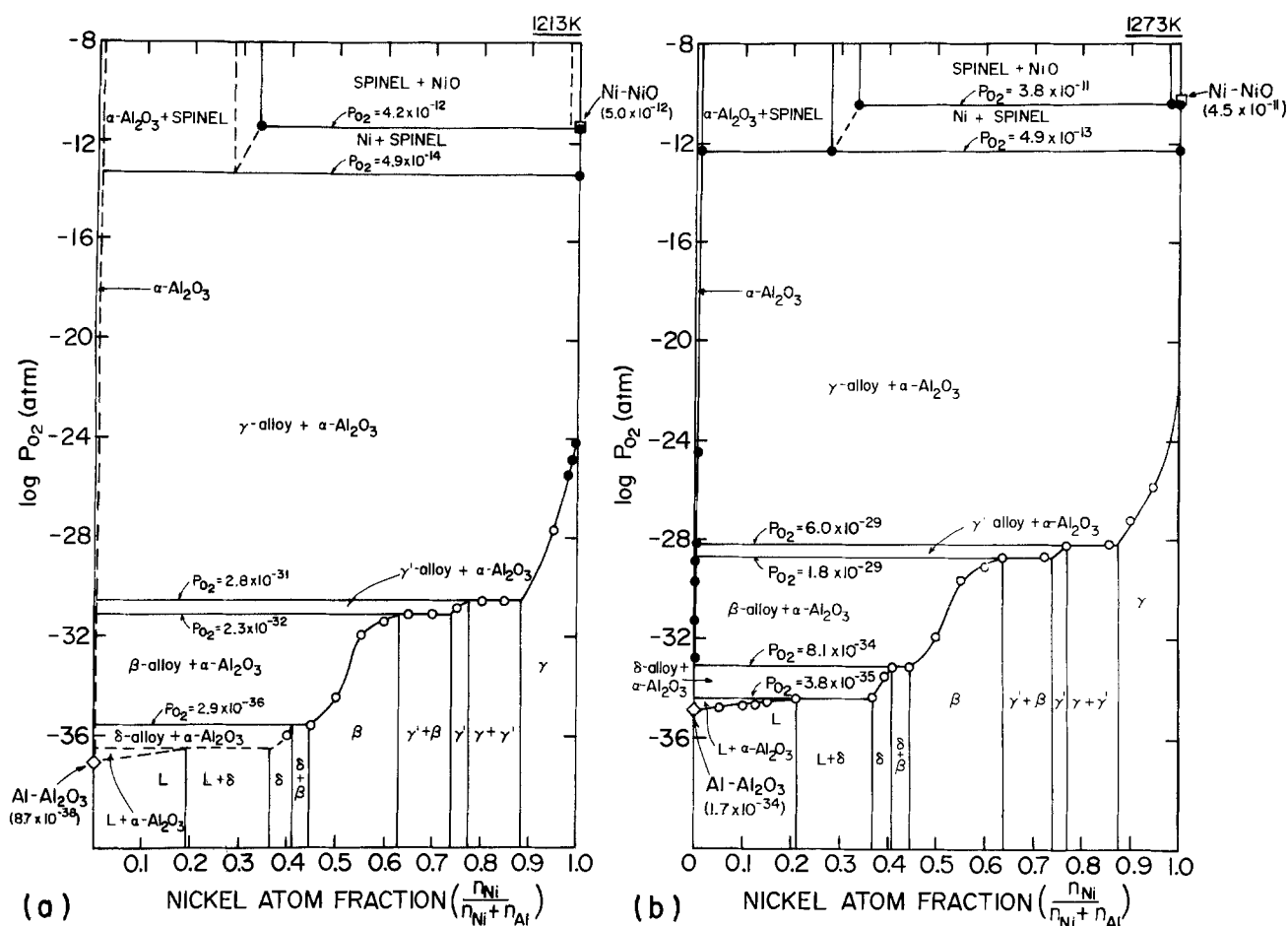


Fig. 5. Ni-Al-O equilibrium oxygen pressure diagram: (a) at 1213 K, (b) at 1273 K

REFERENCES

- J. D. Tretjakow and H. Schmalzried, *Ber. Bunsenges. Phys. Chem.*, **69**, 396 (1965).
- V. A. Levitsky and T. N. Rezukhina, *Neorg. Mater.*, **2**, 145 (1966).
- Grzegorz Rog, *Rocz. Chem.*, **50**, 147 (1976).
- K. T. Jacob and C. B. Alcock, *J. Solid State Chem.*, **20**, 79 (1977).
- L. M. Lenev and I. A. Novokhatskii, *Russ. J. Inorg. Chem.*, **10**, 1307 (1965).
- A. Steiner and K. L. Komarek, *Trans. Metall. Soc. AIME*, **230**, 786 (1964).
- S. C. Schaefer, USA Bur. of Mines, Rep. No. 7993 (1975).
- R. E. Hanneman and A. U. Seybolt, *Trans. Metall. Soc. AIME*, **245**, 434 (1969).
- R. Hultgren, P. D. Desai, D. T. Hawkins, M. Gleiser, and K. K. Kelly, "Selected Values of the Thermodynamic Properties of Binary Alloys," p. 191, American Society for Metals, Metals Park, Ohio (1973).
- M. Hansen, "Constitution of Binary Alloys," McGraw-Hill Book Co., New York (1958).
- F. A. Elrefaie and W. W. Smeltzer, *Oxid. Met.*, In press.
- N. S. Choudhury, *This Journal*, **120**, 1663 (1973).
- F. A. Elrefaie and W. W. Smeltzer, To be published.
- H. Davies and W. W. Smeltzer, *This Journal*, **119**, 1362 (1972).
- F. A. Elrefaie and W. W. Smeltzer, *ibid.*, **128**, 1443 (1981).
- W. W. Liang and J. F. Elliott, *ibid.*, **123**, 617 (1976).
- B. C. H. Steele, in "Electromotive Force Measurements in High Temperature Systems," C. B. Alcock, Editor, p. 3, American Elsevier Publishing Co. (1968).
- J. W. Patterson, *This Journal*, **118**, 1033 (1971).
- JANAF Thermochemical Tables, Second Edition (1971).



Influence of Semiconducting Character of Synthetic PbS Crystals on their Corrosion in Nitric Acid

Claudio Gutiérrez

Instituto de Química Física "Rocasolano," Serrano 119, Madrid-6, Spain

Several contradictory results have been reported on the influence of semiconducting character of synthetic PbS crystals and/or natural galena crystals on its corrosion rate. Simkovich and Wagner (1) found that the corrosion rate in 6M HNO₃ at 60°C for synthetic PbS crystals increased in the order Pb-excess (n)PbS < S-excess (p)PbS < stoichiometric PbS ≈ Bi₂S₃ doped (strongly n) PbS < Ag₂S-doped (strongly p) PbS. The corrosion rate was highest for Ag₂S-doped (strongly p) PbS, and PbS with excess S (p-type) corroded at a slightly higher (30%) rate than Pb-excess PbS (n-type). However, this increase in corrosion rate of PbS with p-semiconducting character was not monotonic. On the other hand, Seltzer and Wagner (2) found that Bi₂S₃-doped (n)PbSe crystals dissolved much more rapidly than Ag₂S-doped (p) or undoped PbSe, a semiconductor very similar to PbS.

Eadington and Prosser (3) worked with PbS powder prepared by addition of a sodium sulfide solution to a lead nitrate solution, after which the nonstoichiometry of PbS was adjusted by heating in a sulfur atmosphere. They found that the oxidation rate by dissolved O₂ of the PbS powder in aqueous suspension increased monotonically with its p-character. On the contrary, Eadington (4) found that the initial dissolution rate of ground galena and synthetic PbS powder in 10⁻⁵M HNO₃ at room temperature increased with the n-character of the sample, although the dissolution rate decreased to a much lower, constant value for all the samples before dissolution of a monolayer had been reached. This author believes that experiments with PbS powder are especially prone to artifacts, as it is known that polycrystalline n-PbS chemisorbs O₂ immediately after exposure to air.

The results reported here, although not quantitative, present a clearcut difference between n- and p-PbS.

Experimental

The synthesis and conditioning of PbS crystals have been described elsewhere (5). PbS powder was obtained by a wet method. Crystals were then obtained by the Bridgman-Stockbarger method in a vertical furnace, with the powder inside an evacuated, sealed silica tube. The semiconducting character of these crystals was changed by heating at 500°C in a controlled sulfur pressure. Resistivities of the crystals were in the range 0.002–0.02 Ω · cm. Unfortunately, the PbS ingot broke easily into small pieces, and the small size of the crystals prevented the measurement of Hall effect and corrosion rates; their semiconducting character was obtained from the sign of the thermoelectric power. The crystals were embedded in Araldit at the end of a length of Pyrex tubing, electrical contact to the inner side being made with mercury. They were polished

Key words: semiconductors, corrosion, potential.

with 5.0 μm alumina (Buehler No. 1) on AB Microcloth (Buehler).

Ultrapure water was obtained from a Milli-RO + Milli-Q system from Millipore. Reagents were of analytical grade. Potentials were measured against a saturated calomel electrode with a Leeds and Northrup pH-meter, Model 7415, input impedance > 10¹³ Ω. Experiments were conducted in the open and without stirring.

Results

1:1 conc. HNO₃:water (6.5M HNO₃).—The n-type crystals acquired in about 1 min a potential of + 270 . . . + 325 mV, and took a black tarnish. On the other hand, the p-samples remained at -40 . . . +20 mV for about 8 min, after which the potential increased to + 250 . . . + 300 mV; the black tarnish was slightly less than for the n-samples.

1:1 conc. HNO₃:acetone (6.5M HNO₃).—After 1 min all the samples had very positive potentials, + 290 to + 350 mV. They took beautiful tarnishing colors, the n-samples more quickly (< 1 min) than the p-samples (> 2 min).

6M HNO₃, 10% in acetone.—The n-samples took in 2 min a potential of + 170 . . . + 330 mV, while the p-samples remained at potentials negative vs. SCE for at least 11 min. The most p-type sample kept a negative potential for 36 min, after which the experiment was interrupted. Correspondingly, it remained shiny, while the other p-samples took beautiful blue and red tarnishing colors. On the other hand, the n-samples became blackish.

1M HNO₃.—In all cases the potential increased with time, but after 10 min the rate of increase only was ≤ 1 mV/min. At 10 min the potential of the n-samples was + 155 . . . + 170 mV, while that of the p-samples was - 10 . . . 0 mV. All samples remained shiny.

10⁻⁴M HNO₃.—After 10 min the potential changed less than 1 mV/min. It was + 270 . . . + 260 mV for the n-samples, and 40 mV for the p-samples. All samples remained shiny.

Deionized water from the Milli-Q + Milli-RO system, with dissolved oxygen as the only oxidant.—After 10 min the potential increase was of only a few mV/min. The potential increased with n-character, from - 130 mV for the more p-type to + 150 mV for the more n-type PbS. All samples remained shiny.

Discussion

For the six solutions studied, the potential of polished PbS crystals increased with n-semiconducting character. At least some of the corrosion products remain on the surface, affecting the value of the potential, which

will not correspond to the intersection of anodic and cathodic lines in an Evans diagram. This makes it impossible to correlate the corrosion mechanism with the potential following the classical study of Gerischer with germanium (6).

The opposite behavior of the potential (potential decrease with increasing n-semiconducting character) was reported previously (7) for PbS pellets sintered at 500°C with a density 80% of that of crystalline PbS. We attribute this difference in the behavior to the porosity of the pellets, as we have now found that the resistivity of n- (and also slightly p-) pellets had changed with time, undoubtedly due to bulk oxidation of PbS by atmospheric oxygen. This is clearly seen in Table I. Only the more p-type sample did not change its resistivity, while that of the more n-type sample increased by 2 orders of magnitude. This is a clear proof that the bulk of the PbS pellets was accessible to oxygen, which reacted with n-type (and also slightly p-type) samples, consuming free electrons.

It becomes obvious that the previous results (7) obtained with sintered PbS pellets could correspond to samples oxidized to a variable extent by atmospheric oxygen.

If it is accepted that larger positive potential increases correspond to higher corrosion rates, the higher

corrosion rate of n-PbS crystals would imply a donation of conduction-band electrons to the oxidant. This does not seem probable, as typical oxidants take electrons from the valence band.

It is remarkable that a difference in corrosion behavior exists at all between n- and p-type PbS, as its bandgap is only 0.41 eV. Apparently there is only one similar case, that of silicon etching in $\text{HNO}_3 + \text{HF}$ aqueous solutions (8), where the corrosion rate was at a maximum for p-Si with a resistivity in the range 0.1-0.001 $\Omega \cdot \text{cm}$. Also a maximum in the thickness-resistivity curve has been reported for the insoluble "surface porous film" that grows on top of a thicker active "porous silicon layer" in the anodic oxidation of p-Si in 50% HF aqueous solution (9).

Acknowledgment

This work has been effected under Project No. 1273 of the Comisión Asesora de Investigación Científica y Técnica, whose help is gratefully acknowledged.

Manuscript received June 9, 1980.

Any discussion of this paper will appear in a Discussion Section to be published in the June 1982 JOURNAL. All discussions for the June 1982 Discussion Section should be submitted by Feb. 1, 1982.

Publication costs of this article were assisted by the Instituto de Química Física "Roscasolano."

REFERENCES

1. G. Simkovich and J. B. Wagner, *This Journal*, **110**, 513 (1963).
2. M. Seltzer and J. B. Wagner, Unpublished results quoted in Ref. (1), p. 515.
3. P. Eadington and A. P. Prosser, *Trans. Inst. Min. Metall. (London)*, **75**, C125 (1966).
4. P. Eadington, *Trans. Inst. Min. Metall. (London)*, **82**, C158 (1973).
5. J. M. Gamboa, C. Gutiérrez, and J. Llopis, *An. Real. Soc. Esp. Fis. Quim.*, **B64**, 679 (1968).
6. H. Gerischer and F. Beck, *Z. Phys. Chem. N.F.*, **23**, 113 (1960).
7. C. Gutiérrez and M. C. López, *This Journal*, **125**, 678 (1978).
8. R. J. Archer, *J. Phys. Chem. Solids*, **14**, 104 (1960).
9. T. Unagami, *This Journal*, **127**, 476 (1980).

Table I. Change with time of the resistivity of PbS pellets, previously sintered at 500°C in vapor of sulfur at the temperature shown

| Sulfur temp./°C | Semicond-type | Resistivity/ $\Omega \cdot \text{cm}$ | | |
|------------------------|---------------|---------------------------------------|---------------|------|
| | | Initial | After 5 years | |
| Increasing n-type ↑ | 67 | n | 0.04 | 3.04 |
| | 80 | n | 0.11 | 2.83 |
| | 90 | n | 0.28 | 0.19 |
| | 104 | p | 9.57 | 1.52 |
| | 110 | p | 1.13 | 1.61 |
| | 130 | p | 0.21 | 0.19 |

Silicon Sheet for Solar Cells

A. Sanjurjo*

SRI International, Materials Research Laboratory, Menlo Park, California 94025

The cost of photovoltaic devices can be lowered substantially if efficient photovoltaic solar cells can be fabricated from polycrystalline, rather than from single crystal, silicon. Polycrystalline silicon substrates for solar cell fabrication can be formed by solidifying molten silicon as unsupported sheets. Typical methods include the Web-Dendritic process (1) and the die-based techniques such as Edge Fed Growth (2) and Stepanov (3). Although solar cells of acceptable quality have already been manufactured from silicon sheet obtained by these techniques, certain problems still remain. Some of the problems result from the difficulty of maintaining constant sheet parameters such as width and thickness during sheet growth. The use of dies helps to minimize this problem, but introduces another problem that stems from the incompatibility of molten silicon with most materials. The use of silica as a die material is precluded because at the temperature of

sheet growth ($\sim 1410^\circ\text{C}$), this material softens and the die loses its shape. Graphite is thermally stable at this temperature, but it reacts with silicon to form SiC. The formation of SiC can be reduced to a layer a few micrometers thick on the graphite surface (Fig. 1) by using high density graphite; however, SiC is soluble in molten silicon, and upon solidification of the sheet, SiC precipitates, thereby degrading the crystallinity of the Si. Attempts to coat the graphite with a variety of inert ceramic coatings—including oxides, nitrides, carbides, borides, and silicides (4)—have only been partially successful because the coatings can be attacked by the molten silicon transferring impurities to the silicon.

This paper describes a method to cast silicon sheet that uses graphite as the construction material for crucibles and dies and uses fused salts, such as NaF, to avoid the reaction between Si and graphite.

The major novelty introduced in this work consists of the development of a coating for the molten silicon,

* Electrochemical Society Active Member.

Key words: silicon sheet, solar cells, sodium fluoride.

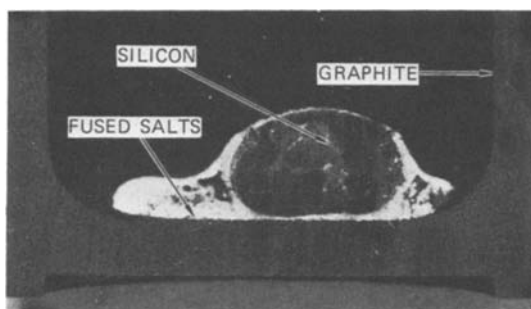


Fig. 1. Silicon melted in a graphite crucible with a liquid barrier coating.

rather than for the die itself. The method relies on favorable values of the surface tensions between molten salts, molten silicon, and graphite (5). For example, when Si and NaF are melted at 1430°C , silicon is strongly wetted by NaF, whereas the NaF does not wet the graphite. This combined surface tension behavior prevents silicon from contacting the graphite (Fig. 1) and thus from reacting appreciably with it. With the NaF coating, liquid silicon can be pressed in a graphite rod-piston system to form a flat pool of silicon that, upon cooling, solidifies into a sheet of silicon protected and separated from the graphite by the molten NaF salt. The sheet can then be removed or allowed to cool further until the salt solidifies. In the latter case, the sheet is removed by dissolving the salt in an aqueous solution. Finally, a brief discussion is presented on the effects of the impurities of the original materials on the purity of the resulting silicon sheet.

Experimental

High purity silicon particles were mixed with reagent grade NaF in proportions ranging from 20 to 50 weight percent (w/o) Si. The silicon particle sizes ranged from 0.1 to 1 cm. A shallow graphite crucible (2.5 mm high, 2.5 cm ID) was loaded with Si-salt mixtures so that the silicon would partially fill the graphite crucible (Fig. 2). Salt mixtures containing NaF- CaF_2 and NaF- Na_2SiO_3 were used in addition to pure NaF. The loaded crucible was covered with a graphite lid to which pressure was applied by means of a metal weight (Fig. 2). Pressures of $0.07\text{--}0.50\text{ Nw/m}^2$ were applied. The ensemble was placed on an alumina pedestal inside a quartz chamber, and heating was provided by induction in the graphite crucible, lid, and metal weight. For each experiment the system was first evacuated and then flushed with argon during actual melting. The temperature was monitored by optical pyrometry. The rate of heating was about 100°C per

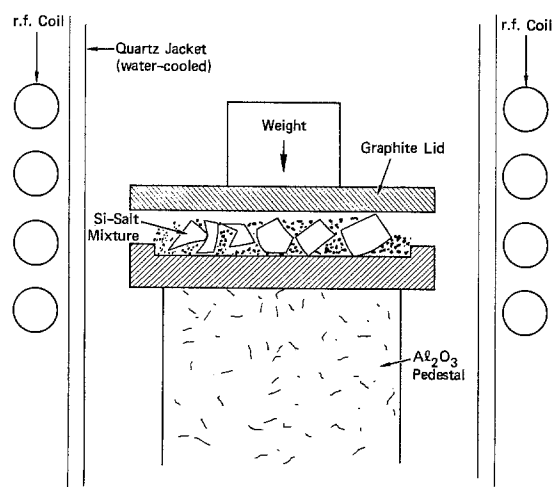


Fig. 2. Silicon pressing system

min and the samples were kept at $1430^{\circ} \pm 20^{\circ}\text{C}$ for 1-3 min to allow the silicon to melt and coalesce into a flat pool under the pressure of the metal weight. The power was then turned off, and the sample temperature was quenched by a rapid flow of argon. The cooling rate was about 300°C per min. After removal from the reactor, the ensemble was immersed in an aqueous acid solution. Typically, the graphite lid could be removed easily; however, the bonding layer of NaF between the Si disk and the graphite crucible required about 30 min in the acid solution before the Si disk could be detached from the crucible.

The surface of the silicon disk was etched and resistivity measurements were made with a four-point probe. In parallel experiments, the level of impurities in silicon before and after melting in contact with NaF was analyzed by plasma emission spectroscopy (PES) and arc emission spectroscopy (AES). X-rays, scanning electron microscopy (SEM), and energy dispersive analysis (EDAX) were also used to characterize the silicon disk and the graphite walls.

The silicon samples for PES analysis were prepared by slow digestion of silicon in an $\text{HNO}_3\text{--HF}$ solution. To minimize interferences of the silicon signal with that of the other impurity elements, the final level of silicon in the acid solution was reduced to less than 100 ppm by weight by concentration in an excess of HF. The solution was then diluted with 1N HCl and injected in the PES system. Blanks of the solution (without silicon) treated in an identical manner were used to calibrate the system. In addition, small, well-determined amounts of silicon (as silicate) were introduced in the blank solution to determine its influence on the peak intensity of other elements. The interferences were very small or negligible. In any case, background blanks were used to correct the final readings.

Results and Discussion

The dimensions of the silicon disks produced by pressing in molten salts (Fig. 3a) ranged from 2 to 3 cm in diameter and 1 to 3 mm in thickness. For a given amount of silicon, the thickness depended basically on the pressure exerted by the metal weight. The mini-

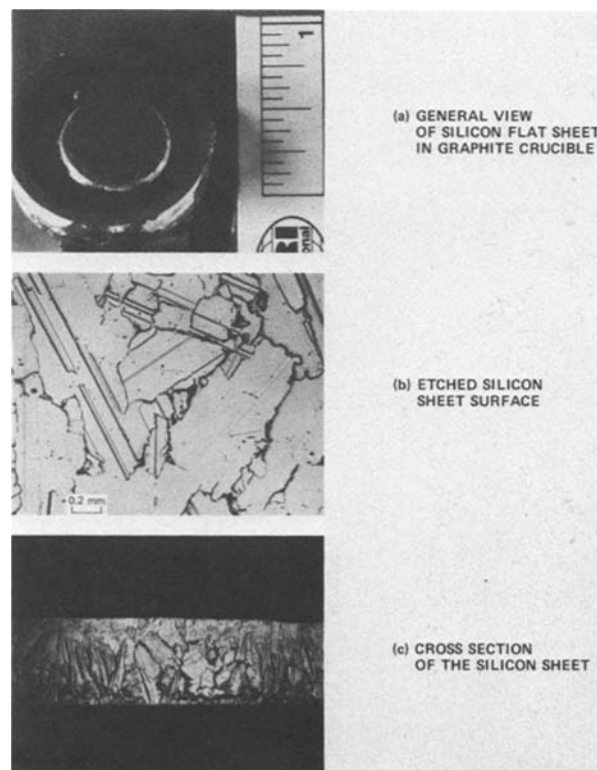


Fig. 3. Silicon sheet

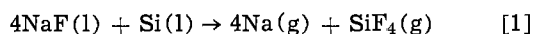
imum thickness was limited by the height of the shallow crucible. Thinner sheets were produced by reducing the height of the crucible, but better control of pressing and temperature is required to obtain more consistent results than those achieved with the system described, which was designed only to demonstrate feasibility. As shown in Fig. 3a, the disks were slightly smaller in diameter than the graphite crucible. As a result of silicon expansion during solidification, it is desirable to reduce the diameter to avoid cracking of the silicon sheet or the walls of the graphite crucible.

Similar results were obtained with pure NaF, Na-CaF₂ (1:1) mixtures, and NaF-Na₂SiO₃ mixtures with up to 10 w/o of Na₂SiO₃. Mixtures with a higher content of Na₂SiO₃ (20 w/o) resulted in the formation of numerous small silicon spheres instead of a single silicon pool and were not used for pressing experiments.

The silicon sheets obtained by this technique were easily detached from the graphite cup by leaching the layer between the Si and the graphite with a 1N HCl solution. The solubility of this layer in HCl solutions indicates the presence of a salt between both phases (Fig. 1) instead of the strongly attached SiC phase that forms when molten silicon contacts high density graphite. SEM and EDAX analyses also showed that a layer of salt separated the silicon from graphite.

Since purity of silicon is a major requirement for good solar cell efficiency, the impurity transfer between Si and NaF was monitored by analyzing the silicon before and after melting in NaF. Emission spectrographic analysis of the starting NaF and plasma emission spectrographic analysis of the starting semiconductor silicon sample are shown in the second and third columns of Table I, respectively. The impurity level for the sample labeled "Semiconductor silicon" represents contamination during handling or limitations of the analytical instrument used, rather than true impurity content in the semiconductor itself. It is used exclusively as a background reference. Comparison with the values in the fourth column shows that some impurities such as B, Al, Cr, Fe, and also Na were transferred to the silicon from NaF.

The mechanism by which Na is transferred from NaF to Si probably starts with the reduction of NaF by Si to produce Na and SiF₄ according to



The generation of SiF₄ when an Si-NaF mixture was heated at 1400°C was experimentally verified by condensing the SiF₄ as a solid using liquid nitrogen and by

Table I. Impurity transfer studies (plasma emission spectrography) (ppm by wt)

| Impurities | NaF* | Semiconductor silicon | | Na-contaminated silicon | |
|------------|--------|-----------------------|---------------|-------------------------|---------------|
| | | Before melting | After melting | Before melting | After melting |
| B | <30 | 0.0 | 7.7 | 4.8 | 4.6 |
| P | — | 0.0 | 0.7 | 0.7 | 0.13 |
| As | — | 0.0 | 0.6 | 0.10 | 0.6 |
| Al | <2.5-5 | 0.7 | 15 | 0.80 | 3.0 |
| Ti | 6 | — | — | — | — |
| V | 5 | 0.0 | 0.1 | 0.04 | 0.06 |
| Cr | <3.5-5 | 0.1 | 3.5 | 1.3 | 3 |
| Mn | <4 | 0.4 | 0.5 | 0.55 | 0.9 |
| Te | <7.30 | 0.5 | 32 | 2.5 | 6 |
| Co | — | — | 2.5 | 0.02 | 0.4 |
| Ni | <8 | 0.0 | 2.6 | 2.4 | 4.5 |
| Cu | <4 | 0.0 | 0.1 | 0.31 | 1.2 |
| Zn | — | 2 | 0.3 | 0.28 | 0.06 |
| Zr | — | — | — | — | — |
| Mo | — | 0.0 | 0.5 | 0.7 | 1.3 |
| Cd | — | 0.0 | 0.1 | 0.02 | 0.33 |
| Pb | 20 | 0.0 | 0.1 | 0.28 | 0.44 |
| Na | — | 0.0 | >4000 | 80 | 3.0 |
| K | — | 0.3 | 1.0 | 0.50 | 4.8 |
| Ca | 10-100 | 0.7 | 1.7 | 0.26 | 0.14 |
| Mg | — | 0.0 | 1.0 | 0.50 | 4.0 |

* Arc emission spectroscopy.

hydrolyzing the collected gas with water to yield HF, H₂SiF₆, and silica gel. As written, reaction [1] has a free energy of reaction of +28.2 kcal/mol Si at 1700 K, as estimated from values from the JANAF tables. Assuming ideal behavior and unity activities for NaF and Si, this free energy corresponds to an equilibrium pressure of Na of 0.2 atm at the Si/NaF interface. Thus, reaction [1] provides a source of Na that can enter the Si phase. Most transition metals such as Fe and Co can be injected in the Si by a similar mechanism. The driving force for the transfer of other impurities such as Al is less clear. Assuming ideal behavior of the impurity fluorides in the molten NaF, the estimated equilibrium activities of the metallic impurities produced by reaction of their corresponding fluorides with silicon are very low and should not be driven into the silicon. Improved models used to explain the transfer of impurities into the silicon should probably include factors such as the presence of silicon surface oxide layers, and the production of silicon subfluorides in addition to SiF₄ (6).

Since impurities play such an important role in the performance of the Si solar cell, it is clear that we must use NaF of purity greater than indicated in Table I. However, the injection of Na will naturally occur with any type of NaF. Accordingly, we examine the ease of distilling the Na out of silicon. Mass spectrometric studies showed that Na is readily removed from silicon heated in vacuum at temperatures as low as 600°C. The removal of Na is much more complete at higher temperatures. For example, heating in vacuum at 1200°C for 5 min yielded silicon with less than 10 ppm of Na. The last two columns in Table I show the analysis of a silicon sample, intentionally doped with 80 ppm of Na, before and after melting under vacuum for 3 min. Although the effect of the Na contamination on solar cell performance is not well known, the residual 3 ppm of Na is not expected to greatly affect the quality of the formed silicon.

The transfer of impurities from NaF to Si affects the Si resistivity. Resistivities of semiconductor (Sm Si) and solar grade silicon (So Si) are substantially decreased after melting in the presence of reagent grade NaF, as shown in Table II. The information in Tables I and II suggest that the decrease in resistivity is due to the injection of boron, sodium in large quantities, and also other impurity elements such as Al and Fe. Since the resistivity of Sm Si doped with a few ppm of B will be around 0.1 Ω cm, and the reduction by two orders of magnitude of the Na content only resulted in a small increase in the resistivity, it seems that B content is the major factor contributing to the drop in resistivity produced by melting silicon in contact with reagent grade NaF. Na and the other impurities seem to exert only a minor effect on the resistivity. This feature could be of practical importance since impurities added to NaF can be used to dope Si and to tailor its resistivity.

It is clear from the above results and discussion that impurities can be easily transferred from the NaF to the silicon phase, and that if solar cells were manufactured from silicon sheets cast in reagent grade NaF, they would exhibit a poor performance. On the other

Table II. Effects of silicon resistivity

| Sample treatment | Sm Si (+ NaF) melt, 3 min, 1450°C | So Si* (+ NaF) melt, 3 min, 1450°C | Si(Na) vac, 7 min, 1400°C | Si(Na) vac, 3 min, 1450°C |
|------------------------------------|-----------------------------------|------------------------------------|---------------------------|---------------------------|
| Resistivity (Ωcm) before treatment | >10 ⁴ | ≈10 ⁴ | 0.07 | 0.09 |
| Resistivity (Ωcm) after treatment | 50 | 1.6 | 0.22 | 0.20 |

* Wacker silicon, with impurity levels at or below 1 ppm, as determined by PES.

hand, it has been shown (6) that when silicon of lower purity (with an impurity content in the hundreds of ppm wt level) is melted with the same type of NaF, most of the metallic impurities concentrate in the salt phase; thus, the final content and distribution of impurities in silicon is very similar to the Sm Si case. These results indicate that the possibility of producing silicon sheet with acceptable impurity levels depends on the initial impurity concentration of the NaF and the relative amount of NaF used during melting.

Conclusion

A technique has been developed to form silicon sheet in a graphite die without the undesirable formation of SiC. Silicon is melted in the presence of a molten salt that wets the silicon, preventing it from reacting with the graphite walls. The silicon coalesces into a pool that is flattened to a disk by a graphite piston. Silicon is solidified in this condition to form flat sheets. High purity NaF can be used as coating salt. Some Na is chemically pumped into the silicon sheet during melting, but it may be readily extracted by vacuum evaporation. With improved mechanical and thermal control and the use of high purity NaF, it may be possible to produce silicon sheet with geometry and structures suitable for solar cell fabrication.

Acknowledgments

The cooperation of Mrs. S. Westphal and Mr. J. Roberts and comments by Drs. L. Nanis, K. Sancier,

and D. Rowcliffe are gratefully acknowledged. This work was funded by SRI International.

Manuscript submitted Aug. 4, 1980; revised manuscript received ca. Dec. 15, 1980.

Any discussion of this paper will appear in a Discussion Section to be published in the June 1982 JOURNAL. All discussions for the June 1982 Discussion Section should be submitted by Feb. 1, 1982.

Publication costs of this article were assisted by SRI International.

REFERENCES

1. R. G. Seidensticker, in "Proc. 12th IEEE Photovoltaic Specialist Conference," pp. 299-302 (1976).
2. L. Vogel, G. Gardner, and E. F. Cave, U.S. Pat. 3, Vol. 124, pp. 489 (1964); T. F. Ciszek, *Mater. Res. Bull.*, **7**, 731 (1972); J. C. Swartz, T. Surek, and B. Chalmers, *J. Electron. Mater.*, **4**, 255 (1975).
3. A. V. Stepanov, *Z. Tekhn. Fiz.*, **29**, 381 (1959).
4. P. E. Grayson and L. A. Addington, Abstract 69, p. 183, The Electrochemical Society Extended Abstracts, Boston, Massachusetts, May 6-11, 1979; R. R. Wills, I. Sekercioglu, J. S. Ogden, C. A. Alexander, and D. E. Niesz, *J. Am. Ceram. Soc.*, **58**, 1198 (1979); T. O'Donnell, M. Leipold, and M. Hagan, LSSA Project Task Report, DOE/JPL, 1012-77/6, March 1, 1978.
5. L. Nanis, A. Sanjurjo, K. Sancier, and R. Bartlett, LSSA Final Report, DOE/JPL 954471 (1980).
6. A. Sanjurjo, To be published.

A New Anodic Etch for the Observation of Dislocations in n-GaAs

Kohei Nagata, Satoshi Komiya, Akihiro Shibatomi, and Sinji Ohkawa

Fujitsu Laboratories Limited, 1015 Kamikodanaka, Nakahara-ku, Kawasaki 211, Japan

There have been many reports on the relation between electrical characteristics of devices and crystal defects in semiconductor materials. It is well known that a threading dislocation in the epitaxial layer can effect the fast degradation of the double heterostructure lasers and light emitting diodes (1, 2). Dislocations in the epitaxial layer are due to dislocation propagation from the substrate crystal (3, 4). It is very important, therefore, to have high quality substrates for good device performance. For this purpose, many methods of revealing crystal growth defects have been developed. The chemical etching method is the simplest one. The AB-etch developed by Abrahams and Buiocchi (5) and Stirland (6) and molten KOH etch as reported by Grabamaier and Watson (7) and Ishii *et al.* (3) are generally used for GaAs but these techniques are more difficult and elaborate. Electrolytic etching techniques of GaAs have been already reported by Tranchart *et al.* (8), and Faktor and Stevenson (9). Green has reported an anodic etch technique using ammonium and hydroxide as a simple method for revealing defects (10).

In this paper, we report a new anodic etch using sulfuric acid for the observation of etch pit in GaAs.

Experimental

Figure 1 shows the experimental arrangement for SAA etching. The dimensions of the container and a cathode of platinum were $8 \times 5 \times 7$ cm³ and $3 \times 4 \times 0.05$ cm³, respectively. The electrolyte in the container was stirred during SAA etching. The composition of the electrolyte was one part of 5% aqueous solution of sulfuric acid and three parts of propylenglycol.

Key words: anodic etch, dislocation, GaAs crystal, etch pit.

Native oxide films of GaAs are dissolved in the solution ($\text{pH} \leq 10$). The pH value of the electrolyte used in this study, therefore, was held to 1.3 in order to etch GaAs crystal anodically. Propylenglycol in the electrolyte was used to make anodic oxidation stable and reproducible (11).

$\langle 001 \rangle$ -oriented n⁺-GaAs wafers with carrier concentrations and defect densities of 10^{18} cm⁻³ and 5000 cm⁻², respectively, were mirror-polished mechanically and chemically after slicing. Then the wafer were etched chemically to remove a 9-11 μm thick layer with 90:5:5 = H₂SO₄:H₂O₂:H₂O. An aluminum ribbon was contacted onto the surface of the wafer as an anodic contact. D-C current was supplied by a constant voltage source through a variable resistor R_s . The etching current was controlled by adjusting the output voltage and the resistance of R_s , which was much higher than the resistance of the electrolyte to keep the etching current constant. The current and voltage between anode and cathode were monitored and recorded by a multi-pen recorder. In this study, all of the SAA etches were carried out in the dark in order to eliminate possible effects of light illumination. The etched surface of the wafer was examined with an optical microscope.

Results and Discussion

Figure 2 shows a typical etch pit pattern revealed on a Si-doped GaAs wafer by the SAA etch under the current density of 1.5 mA/cm². It is clearly observed that there are two kinds of etch pits, that is, the cross-like pit and dot-like pit. The dependence of the shape of these pits on the current density, dopant, and etching time were examined. Current densities of 1-2 mA/

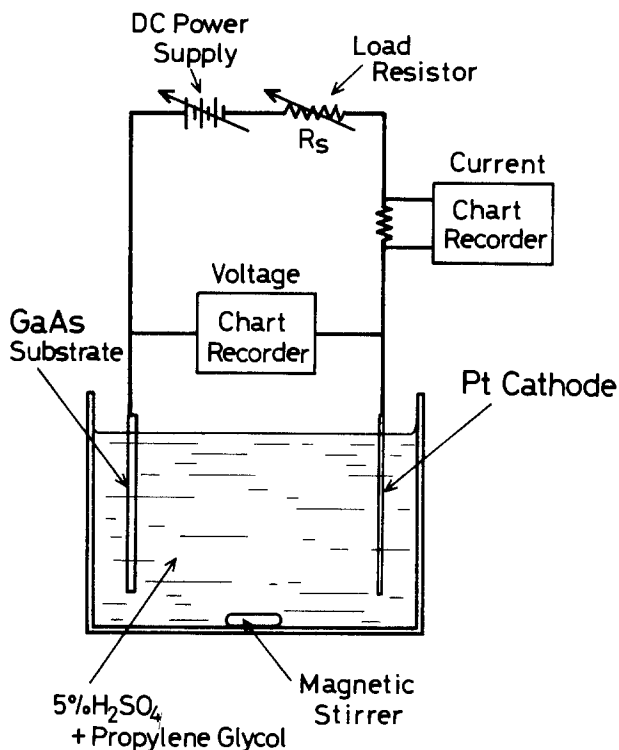


Fig. 1. Experimental setup for an SAA etch

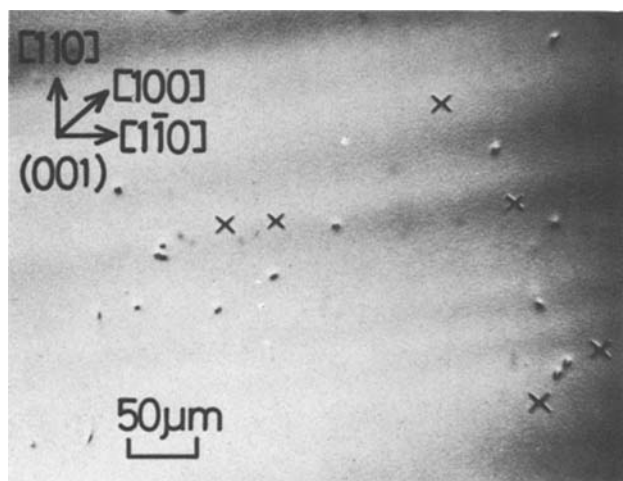


Fig. 2. Etch pit pattern revealed on an Si-doped GaAs wafer by the SAA etch at a current density of 1.5 mA/cm^2 .

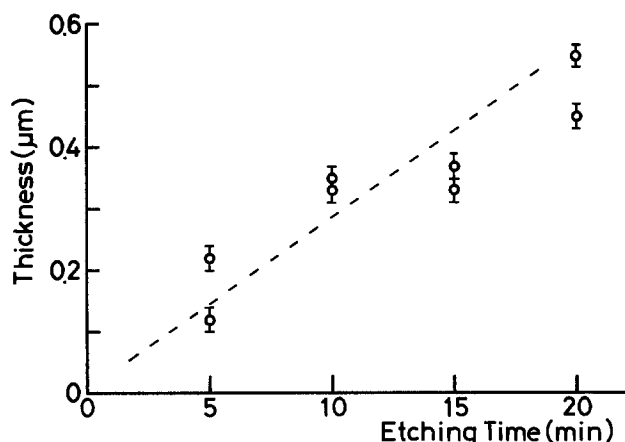


Fig. 3. Mean removed thickness on the area without etch pits on GaAs wafer by the SAA etch.

cm^2 and etching times of 10-15 min are sufficient to reveal defects as the cross-like and dot-like pits, and then the size of the cross-like pit increases with current density.

Figures 3 and 4 show the etching depth and the size of the cross-like pit under the same current density of 1.5 mA/cm^2 as a function of the etching time, respectively. For 10 min etching, the size of the cross-like pit is about $10 \mu\text{m}$ which is easily observed by using an optical microscope. The mean-etched thickness for 10 min is about $0.3 \mu\text{m}$. Therefore, the crystal defects can be detected for the thickness less than $1 \mu\text{m}$.

The etching properties of the SAA etch were examined for Te-, Zn-, and Sn-doped GaAs wafers in addition to Si-doped ones (see Fig. 2). Figure 5 (a)-(c) are the microphotographs of the etch pits on Te-, Zn-, and Sn-doped GaAs wafers, respectively. Both of the cross-like and dot-like pits were observed on the Te-doped GaAs, and no cross-like pit and only low density dot-like pits were observed on the Zn-doped GaAs. The Sn-doped GaAs has similar behavior to the Zn-doped GaAs. This indicates that electrochemical properties of the defect are related to the species of the doped impurities but detail of the interaction between defect and impurity is not clear.

In order to investigate the relation between the etch pits revealed by the SAA etch and crystal defects, these etch pits were compared to the etch pits by the molten KOH.

Si-doped GaAs wafer was etched by the SAA etch. The wafer was chemically polished by $\text{H}_2\text{SO}_4\text{-H}_2\text{O}_2\text{-H}_2\text{O}$ etchant to remove the surface layer of about $10 \mu\text{m}$ in thickness. After that, the wafer was etched by the SAA etch once again in order to examine the reliability of these etch pits, and Fig. 6(a) shows this etch pit pattern. Each blurred shallow pit close to the cross-like pit indicates the afterimage of the corresponding cross-like pit first revealed by the SAA etch. Thus, each of the cross-like and dot-like etch pits was reproducible between the successive SAA etches. Finally, this wafer was etched for 4 min by the molten KOH at 360°C after polishing by $\text{H}_2\text{SO}_4\text{-H}_2\text{O}_2\text{-H}_2\text{O}$ etchant, and the etch pit pattern is shown in Fig. 6(b). From comparison between these etch pit patterns, we can see that both of the cross-like and dot-like etch pits correspond to the etch pits by the molten KOH and dislocations in the GaAs wafer.

Figure 7 shows the detailed shape of the cross-like pit on the etched surface. Four bars which compose the cross-like shape are oriented to the four equivalent $\langle 100 \rangle$ directions on the (001) surface but do not intersect at one point. This detailed shape shows the non-equivalency between the two perpendicular $\langle 110 \rangle$ and $\langle \bar{1}10 \rangle$ directions in the (001) plane of GaAs. The

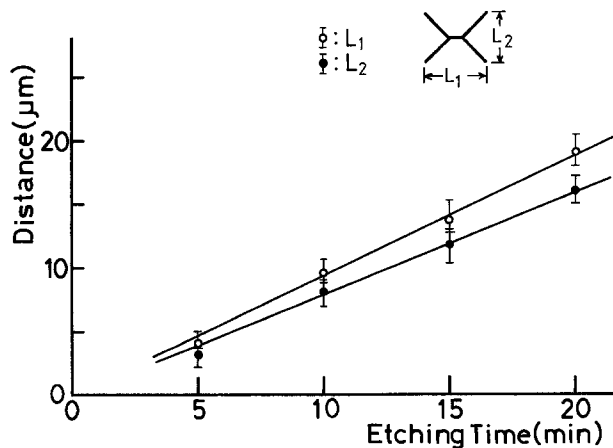


Fig. 4. Two lengths L_1 and L_2 along the two perpendicular $\langle 110 \rangle$ directions of the cross-like pits as a function of etching time.

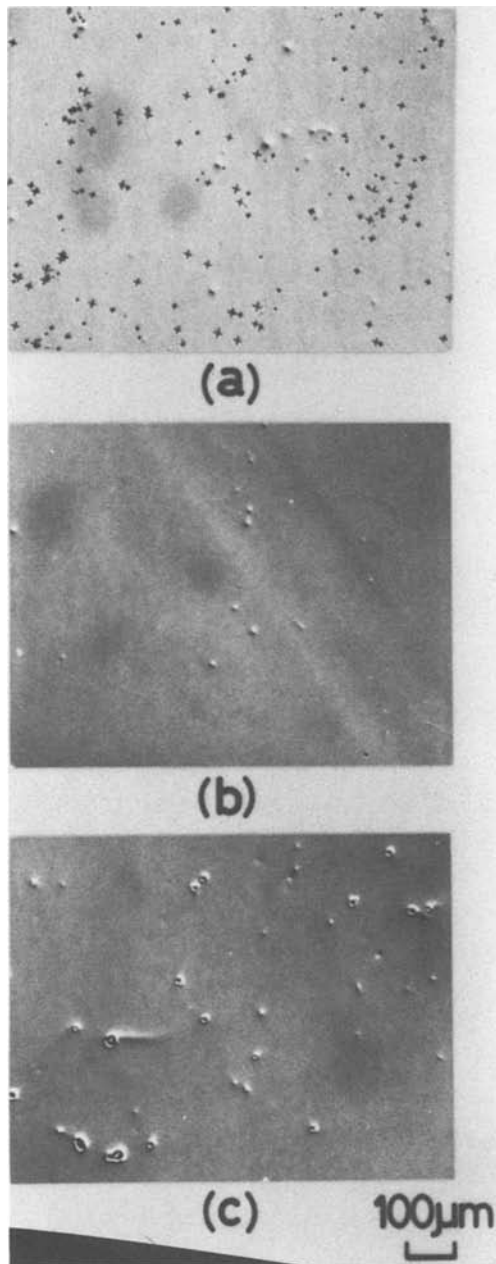


Fig. 5. The dopant dependence of the etching characteristics of the SAA etch. The photographs (a), (b), and (c) are the etch features on the Te-doped, Zn-doped, and Sn-doped GaAs, respectively.

nonequivalency has been observed in various phenomena and mostly attributed to the relation between the (001) face and (111)A or (111)B face (11-13), but the nonequivalency of the cross-like pit is not due to the different polarities between the two (111) planes because of its fine structure described recently. The geometrical relation between a cross-like pit and a hexagonal pit revealed by molten KOH is schematically shown in Fig. 7 (4). In order to examine the inner structure of the cross-like pit, two cleaved {110} surface, A-A' and B-B' in Fig. 8, were observed. It is found that the etched feature is clearly platelike, and these plates consist of the $(10n)$ and $(01n)$ plane because the intersection between their plates and (001) plane are oriented to the $\langle 100 \rangle$ or $\langle 010 \rangle$ direction. The value of n was determined from the angle (θ) between the (001) surface of the wafer and etched plate on the cleaned {110} surfaces. The calculated angle is 35.26° for $n = 1$ and the observed angle is $34 \pm 2^\circ$. The fine structure of the cross-like pit estimated

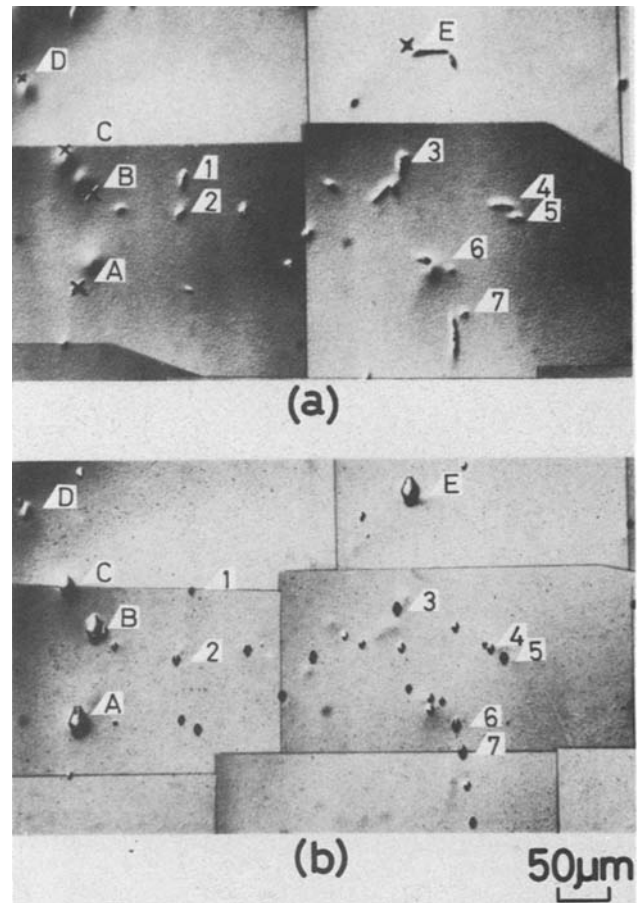


Fig. 6. (a) Etch pit pattern revealed on an Si-doped GaAs by the SAA etch. (b) Etch pit pattern revealed on the same area by the molten KOH etch for 4 min at 360°C , after it was polished by $\text{H}_2\text{SO}_4:\text{H}_2\text{O}_2:\text{H}_2\text{O} = 90:5:5$ for 6 min.

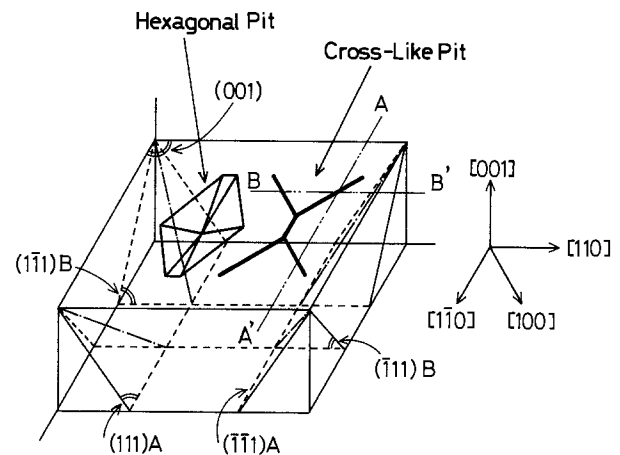


Fig. 7. The geometrical relationship between a cross-like pit and a hexagonal KOH-induced pit on GaAs (001).

from these results is shown in Fig. 8. The platelike erosion progresses into the crystal and the cross-like etch pit consists of five plates, two $\{011\}$, two $\{101\}$, and one $\{110\}$. The $\{101\}$ and $\{011\}$ planes are crystallographically and geometrically equivalent. However, the $(\bar{1}10)$ plate is not etched and only the arrangement of the five plates (as shown in Fig. 8) is revealed, though the two perpendicular (110) and $(\bar{1}10)$ planes to the (001) surface are equivalent to each other. In addition, the formation of this cross-like pit depends on dopants. The etching due to electrochemical process should be related to the distribution of the electrical fields in

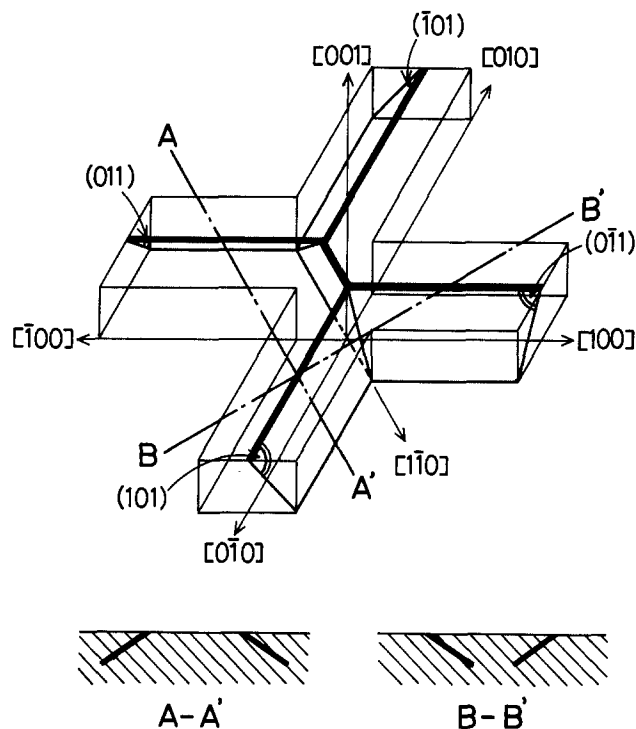


Fig. 8. Illustration of the fine structure of the cross-like pit

neighborhood of dislocations, while a chemical etch pit is frequently related to the (111)A or (111)B plane. However, it is not always clear whether this result means such distribution of dopants is due to interaction between dopants and dislocation.

Conclusion

The etching behavior of pits by the anodic etch using sulfuric acid and propylenglycol (SAA etch) are examined for n^+ -GaAs.

1. Optimum conditions for the SAA etch are current density of 1 mA/cm^2 and pH value of 1.3. Clear etch pits can be revealed with small etching depth of $0.3 \text{ }\mu\text{m}$.

2. The SAA etch reveals two kinds of etch pits. A cross-like pit consists of four lines oriented to $\langle 100 \rangle$ and $\langle 010 \rangle$. The cross-like pit is observed in the SAA-etched n^+ -GaAs wafer doped with Si or Te while no cross-like pit is revealed in Zn- or Sn-doped GaAs. The dot-like pit was found in all GaAs samples.

3. Comparing the SAA-revealed pits with etch pits revealed by the molten KOH, the SAA-etch pit is found to correspond to dislocation.

4. The cross-like pit is formed by etching $\{110\}$ plane selectively and its shape on the (001) surface indicates nonequivalency between the two perpendicular $\langle 110 \rangle$ directions.

Acknowledgment

The authors wish to thank Dr. O. Ryuzan for his encouragement. We also wish to thank Dr. S. Isozumi for providing the sample, and to Mr. K. Odani for his encouragement.

Manuscript submitted May 21, 1980; revised manuscript received May 4, 1981.

Any discussion of this paper will appear in a Discussion Section to be published in the June 1982 JOURNAL. All discussions for the June 1982 Discussion Section should be submitted by Feb. 1, 1982.

Publication costs of this article were assisted by Fujitsu Laboratories Limited.

REFERENCES

1. P. Petroff and R. I. Hartman, *J. Appl. Phys.*, **45**, 388 (1974).
2. O. Ueda, S. Isozumi, T. Kotani, and T. Yamaoka, *ibid.*, **48**, 3950 (1977).
3. M. Ishii, R. Hirano, H. Kan, and A. Ito, *Jpn. J. Appl. Phys.*, **15**, 645 (1976).
4. S. Komiya and T. Kotani, *This Journal*, **125**, 2019 (1978).
5. M. S. Abrahams and C. J. Buiochi, *J. Appl. Phys.*, **36**, 2855 (1965).
6. D. J. Stirland, *Inst. Phys. Conf., Ser. A*, **33**, 150 (1977).
7. J. G. Grabmaier and C. B. Watson, *Phys. Status Solidi*, **32**, K13 (1969).
8. J. C. Tranchart, L. Hollan, and R. Memming, *This Journal*, **125**, 1185 (1978).
9. M. M. Faktor and J. L. Stevenson, *ibid.*, **125**, 621 (1978).
10. L. I. Greene, *J. Appl. Phys.*, **48**, 3739 (1977).
11. H. Hasegawa and H. L. Hatnagel, *This Journal*, **123**, 713 (1976).
12. W. J. Bartels and W. Nijman, *J. Cryst. Growth*, **37**, 204 (1977).
13. G. A. Rozgonyi, P. Petroff, and M. B. Panish, *Appl. Phys. Lett.*, **24**, 251 (1974).
14. T. Fujiwara, N. Takagi, H. Imai, S. Komiya, M. Takusagawa, and T. Misugi, *IEEE J. Quant. Electron.*, **qe-13**, 616 (1977).



ESCA and SIMS Studies of the Passive Film on Iron

S. C. Tjong* and E. Yeager*

Case Laboratories for Electrochemical Studies and the Chemistry Department,
Case Western Reserve University, Cleveland, Ohio 44106

The passivity of iron in borate buffer (pH 8.4) solution has been investigated by many researchers using various techniques (i.e., *in-situ* electrochemical methods, radiotracer measurements, Mössbauer spectroscopy, electro-modulated reflectance, Raman spectroscopy and ellipsometry, *ex-situ* Auger, ESCA and electron diffraction techniques). Discrepancies exist, however, in interpreting these measurements and what they indicate concerning the structure of the passive film on iron. These discrepancies are not surprising in view of the difficulty of carrying out structural measurements on the very thin passive films ($< 50 \text{ \AA}$). The *ex-situ* methods are also complicated by the possibility of structural changes after removal from the passivating medium.

The question of the presence of protons and their chemical form on and in the passive layer of iron is of considerable importance in understanding passivation. Some advocates of the sandwich model (1) have suggested that the outer $\gamma\text{-Fe}_2\text{O}_3$ layer is produced from the inner layer of Fe_3O_4 through the substitution of protons for ferrous ion in the Fe_3O_4 . Protons have been assumed to be the most likely slow charge carriers in the passive film in the a.c. impedance studies of Chen and Cahan (2). The investigations of the existence of H in the passive films have been carried out by radiotracer (tritiated water) measurements. Using this method Okamoto and Shibata (3) showed that bound water was present in the passive film of stainless steel in 0.05 M sulphuric acid. Using a similar method, Kudo et al. (4) estimated the content of bound water in the passive film of iron, formed in sodium borate buffer solution, to be $\text{Fe}_2\text{O}_3 \cdot 1.99 \text{ H}_2\text{O}$. Yolken et al. (5) have also proposed that H in the passive film is present as part of the $\gamma\text{-Fe}_2\text{O}_3$ spinel lattice.

Recently O'Grady (6) used Mössbauer spectroscopy to examine *in-situ* the film on iron and reported that the film was not in any known forms of stoichiometric oxides or hydroxides. He proposed that the passive film was amorphous iron oxides and polymeric in nature. The proposed model consisted of FeO_6 octahedra in a chain-like structure bonded together by di-oxy and di-hydroxy bridging bonds. These chains are linked with each other by water molecules.

In the present work *ex-situ* ESCA and SIMS techniques were used to study the passive films on pure iron. The SIMS studies placed special emphasis on hydrogen in the films using both H_2O and D_2O borate buffer solutions, while ESCA allowed the study of oxygen in the film as OH^- and O^{2-} . Of special interest is the question whether the protons are in the form of OH^- and H_2O in the film. It should be noted that SIMS is mostly a qualitative tool. The yield of various fragments ejected from the specimen during rare gas sputtering is strongly dependent on the chemical and physical properties of the specimens. Large working curve shifts occur even with small changes in chemical composition and physical structure. Calibration is very difficult and with the passive films probably impossible. Nonetheless qualitative identification of various mass fragments and depth profiling for minor constituents can prove quite interesting.

The SIMS measurements were carried out on a 3M Company ISS-SIMS spectrometer with a vacuum of typically 10^{-8} Torr. The operating parameters were: primary ion beam voltage of 3 keV, beam current of 100 nA, and pressure of 2×10^{-5} Torr Ar. The ion beam with FWHM of 670 \mu m was rastered over an area of $3 \text{ mm} \times 3 \text{ mm}$ at a frequency of 1000 Hz in the x-direction and 100 Hz in the y-direction. The signal was gated so that the data were collected for only 4% of the rastered area located centrally. The pure iron specimens were polished with the final step using 0.05 \mu m alumina. They were cathodically reduced at -0.35 V vs. RHE for 20 minutes in the borate buffer (pH 8.4) and then stepped to anodic potentials of 0.65, 1.05 or 1.45 V vs. RHE for

* Electrochemical Society Active Member

Key words: Passivity, borate buffer, ESCA, SIMS.

30 minutes. After passivation, the sample was removed from the electrochemical cell, rinsed with triply distilled water and then stored in a vacuum desiccator until just before introduction into the SIMS spectrometer.

A proton peak was observed in the positive and negative ion spectra although this peak was partially blocked by an instrument artifact. A strong mass 17 peak corresponding to OH^- was found in the negative ion spectrum without any appreciable positive or negative ion mass 18 corresponding to water. The mass OH^- -17 peak was comparable to height to that of O^- -16 peak. The most likely explanation for the OH^- -17 peak is that the film contained protons only in the form of OH^- and not any significant amount of H_2O molecule as such. The failure to observe a positive or negative ion H_2O peak is not associated with any special difficulty in producing such charge species from H_2O or an instability problem. Various workers have observed both H_2O^+ and H_2O^- spectra in SIMS studies of oxide films containing water; e.g. the studies of vanadium oxide by Benninghoven et al. (7). The possibility exists, however, that the protons may be introduced into the film during transfer from the electrochemical cell to vacuum environment or from the vacuum environment and not during the passivation. Even with pre-bake out, the vacuum in the instrument only reached low 10^{-8} Torr because of the high contamination level in the spectrometer with its many users. Furthermore, the samples were in the instrument at higher pressure during the prolonged period necessary to achieve even this modest vacuum (up to 5 hr).

As a check on this question, the pure iron has been passivated in a borate buffer solution made up in 99.8% D_2O . Because of protons in the boric acid and water of hydration in the borax, the final deuterium concentration was only $\sim 98\%$. The passivation film was formed in this solution, rinsed with pure 99.8% D_2O and transferred into the SIMS spectrometer using the same procedure as before. The negative ion spectrum showed only a small mass 2 peak for D^- and a small mass 18 peak but the mass 17 peak remained high. Since no mass 18 peak was observed with the undeuterated buffer, this peak is most likely due to OD^- . Barring some large isotope discrimination effect during the passivation, these observations imply a rapid exchange of the deuterium in the film with protons originating from water in the environment during the transfer and/or in the spectrometer.

To check further into this situation, the passivation of iron in a borate buffer solution was made up from anhydrous sodium borate, boric acid and 99.8% D_2O to obtain an $\sim 99.8\%$ deute-

rated solution. It was then rinsed with D_2O and transferred into a plastic bag directly connected to the sample inlet system of the spectrometer. The bag has been flushed with dry N_2 and the D_2O used for rinsing has been placed in an open beaker within the plastic bag so as to keep the D_2O vapor high compared to that of any H_2O which might diffuse through the plastic into the bag from the outside environment. The SIMS negative ion spectra obtained with this arrangement for the passive film on iron passivated in both the $\sim 98\%$ deuterated borate buffer and $\sim 99.8\%$ deuterated buffer are shown in Figs. 1a, b. The D^- -2 and OD^- -18 peaks are larger than without the glove bag but still much smaller than the corresponding H^- -1 and OH^- -17 peaks. The high OH^- -17 peak and much smaller OD^- -18 peaks undergo a rapid decrease in heights as the film is sputtered away. The OH^- -17 peak decreased to 1/3 of its original height and the D^- -2 and OD^- -18 peak disappear. Simultaneous examination of the Fe^+ , O^- , and FeO^+ peaks indicate that ~ 12 min. is required to sputter away the passivation layer. On the basis of the apparent profile in Fig. 2, most of the D^- , OD^- and OH^- appear to reside on the surface of the film. The residual OH^- -17 after removal of the film is instrumental background.

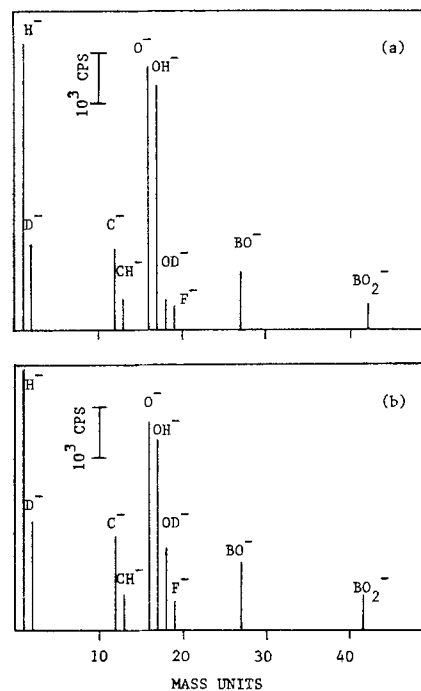


Fig. 1. SIMS negative ion spectra (initial) for iron
(a) Passivated in deuterated borate buffer (98% D) at 0.65 V vs RHE
(b) Passivated in deuterated borate buffer (99.8% D) prepared from anhydrous salt and boric oxide at 0.65 V vs RHE

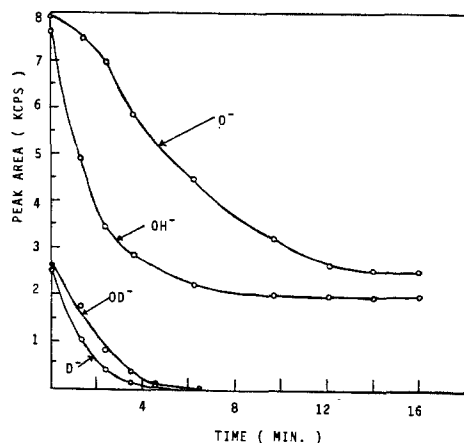


Fig. 2. SIMS peak area vs sputtering time for O^- , OH^- , D^- and OD^- for iron passivated in deuterated borate buffer at 0.65 V vs RHE

On the basis of these results, the deuterium in or on the film appears to be exchanging in some way with protons of the atmosphere or in the vacuum. In the experiments with the plastic bag containing D_2O vapor, the most likely proton source for this exchange is H_2O contamination in the spectrometer. This water vapor in the spectrometer does not contribute any direct OH_2 -18 peak to the spectrum but can adsorb on the surface, exchange protons for deuterium in the film and/or dissociate to yield adsorbed H and OH. An OH^- -17 peak also shows up in the spectrum for iron specimen covered with a Fe_2O_3 layer produced by air oxidation at $450^\circ C$ but it is much smaller than for the passive film produced in borate buffer.

Another factor which may have also contributed to the large OH^- -17 and H^+ -1 peaks for the passivation layers produced in the deuterated borate buffer is possibly a large kinetic effect discriminating against D. For the 98% D - 2% H buffer, a kinetic isotope effect of $\sim 10^2$ would be needed to explain the ratio of OH^- -17 to OD^- -18 in Fig. 1a and even a larger effect for the 99.8% D - 0.2% H in Fig. 1b. Such a large kinetic isotope effect seems unlikely. On the other hand the substantial increment of 3.5 fold in the ratio of OD^-/OH^- for the buffer with close to 100% D vs. that with 98% D (Fig. 1a and b) cannot be explained on the basis of D - H exchange during the transfer or in the SIMS apparatus. It appears that a substantial amount of the OH^- in the films produced in the deuterated buffer originated from the small amount of H in these solutions. This implies a significant kinetic isotope effect but further work is required to confirm this.

The substitution of D for H in the buffer shifts the pH because of changes in the ionization constants K for boric acid as well as water. The extent of the shift has not yet been examined in the present research but would not be expected to be more than a fraction of a pH unit on the basis of the known shift in the pH for H_2O ($pK = 13.9965$) vs. D_2O ($pK = 14.955$ at $25^\circ C$) (8). The apparent pD and pH obtained with a glass electrode were the same within a tenth of a unit but this is not necessarily a direct indication that the D^+ and H^+ activities were the same.

On the basis of the comparison of the SIMS spectra for the films produced in the deuterated and undeuterated buffers with respect to various species (Fe^+ , O^- , FeO^+ , OH^- , OD^-), it does not appear that the deuteration perturbed the properties of the passivation layer significantly other than introducing OD and D on or in the surface layer.

The ESCA measurements were directed to the examination of oxygen in the film and particularly the question of oxygen in the form of OH^- as compared with O^- . The ESCA spectra have been run on a Varian IEE-15 spectrometer. The vacuum on this instrument is in the range 10^{-6} - 10^{-7} Torr. The specimens were handled in the same way as for the SIMS with the exception of the transfer technique. For the ESCA, the samples were transferred in air into the ESCA spectrometer. Fig. 3a shows the $O(1s)$ spectrum for iron passivated at 0.65 V vs. RHE after deconvolution with a DuPont curve resolver. Before any sputtering, two peaks are evident at 532 and 529.4 eV and are assigned to OH^- and O^- , respectively, and a very small peak evident at 533.8 eV which may be due to water physically adsorbed on the surface. With argon ion sputtering, the OH^- peak in the ESCA spectrum at 532 eV decreases and finally disappears after 3 min. of sputtering (Fig. 3b). On the basis of $Fe(2p)$ spectrum as well as that for $O(1s)$ it appears that the passive film has been completely sputtered away at this time. The 529.4 eV peak then approaches a limiting value which does not decrease further with sputtering. This behavior is probably caused by residual oxygen or water in the relatively poor vacuum of the spectrometer.

The 532 eV peak for OH^- is much smaller before sputtering for the film produced at 1.05 V vs. RHE than 0.65 V. This agrees with the decrease in OD^- -18 peak in SIMS negative ion spectrum for iron passivated at 1.05 V. With sputtering the spectrum on this film behaves similarly to that of the sample passivated at 0.65 V although 4 min. is now required to remove the film. It is questionable to reach any

quantitative conclusions concerning the O in the film from the ESCA measurements because of intrinsic oxygen contamination. Nonetheless they lend some support to the results obtained from SIMS.

Both the SIMS and ESCA data obtained with sputtering indicate that the OH in the passive film is principally at or very near the outer surface. While "static SIMS", in principle is sensitive only to one and at the most two atomic layers, this depth resolution is not realized with sputtering in the present study because of the nonuniformity of the sputtering and the possibility of driving species further into the film. Nonetheless very little OH if any appears to be located more than 5 to 10 Å into the film and it is possible that most of the OH is just adsorbed in the surface. The major portion of the film appears to be free of protons in the form of OH or H₂O. Yolken et al. (5) in their radiotracer measurements also found that the H resided in the outer part of the passive film.

A decrease in the OH concentration in the film at more anodic passivation potentials is to be expected on the basis that the protons should tend to migrate out of the film upon standing at relatively anodic potentials. Further, the proton concentration in the film could be expected to be the lowest near the substrate if the protons slowly migrate out of the film into the electrolyte when the film is held at anodic potentials for prolonged periods. It is surprising, however to find the majority of the film so void of OH. One possibility is the loss of water from the film during the extended exposure to the 10⁻⁸ Torr vacuum of the spectrometer.

Acknowledgement

The authors wish to thank the Office of Naval Research for supporting this research.

References

1. M.C. Bloom and L. Goldenberg, *Corros. Sci.*, **5**, 623 (1965).
2. C.T. Chen and B.D. Cahan, submitted to this journal.
3. G. Okamoto and T. Shibata, *Nature*, **206**, 1350 (1965).
4. K. Kudo, T. Shibata, G. Okamoto and M. Sato, *Corros. Sci.*, **8**, 809 (1968).
5. H.T. Yolken, J. Kruger and J.P. Calvert, *Corros. Sci.*, **8**, 103 (1968).
6. W.E. O'Grady, *This journal*, **127**, 55 (1980).
7. A. Benninghoven, C. Plog, H. Fehmer and K.H. Mueller, *Verh. Dtsch. Phys. Ges.*, **6**, 584 (1975).

8. R.C. Weast, "Handbook of Chemistry and Physics", 49th edition, CRC Press, Cleveland (1968).

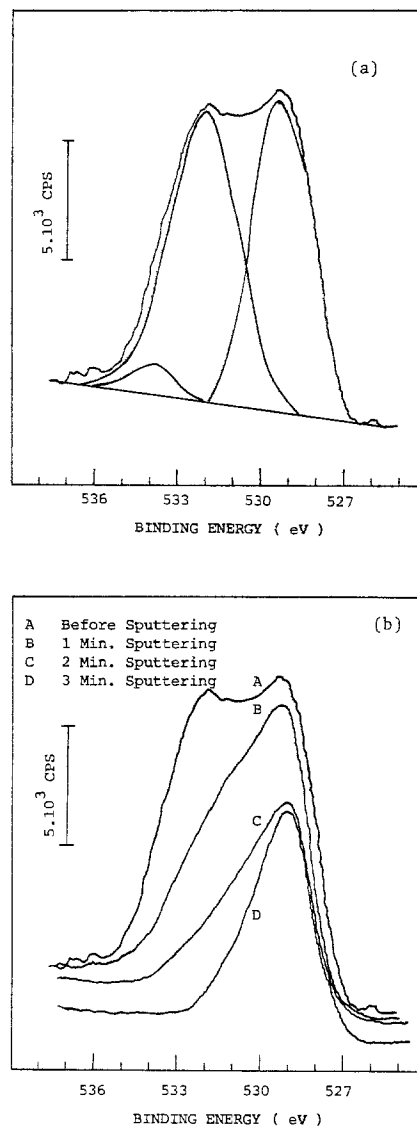


Fig. 3. The O(1s) spectrum for the passive film on iron grown in borate buffer at 0.65 V vs RHE (a) before sputtering (b) before and after sputtering

Manuscript submitted July 14, 1981;
revised manuscript received ca. Aug. 4, 1981.

Publication costs of this article were
assisted by Case Western Reserve University.

Emf Measurements on the Li-Al/FeS Couple in LiF-LiCl-LiBr Electrolyte

Zygmunt Tomczuk,* M. F. Roche,* and D. R. Vissers*

Argonne National Laboratory, Chemical Engineering Division, Argonne, Illinois 60439

In a previous paper (1), the reactions of the FeS electrode of LiAl/LiCl-KCl/FeS cells were determined by a combination of phase studies, cyclic voltammetry experiments, and emf measurements. In this earlier work, six electrochemical reactions were considered, with three of them involving the KCl of the electrolyte to form J phase ($\equiv \text{LiK}_6\text{Fe}_{24}\text{S}_{26}\text{Cl}$). Because of the interference from J phase, it was not possible to experimentally determine the emf vs. temperature curve for the $\text{FeS} \rightarrow \text{Li}_2\text{FeS}_2$ ($\equiv \text{X}$) transition. In this paper we report our measurements on the LiAl/LiF-LiCl-LiBr/FeS cell in which the direct determination of the emf of the $\text{FeS} \rightarrow \text{Li}_2\text{FeS}_2$ transition is possible. Additionally, the emf of the $\text{Li}_2\text{FeS}_2 \rightarrow \text{Li}_2\text{S}$ transition was measured and compared with that obtained for LiCl-KCl eutectic.

The experimental procedure and cell construction were similar to that reported earlier (1). The principal difference was that LiF-LiCl-LiBr (22.1-30.9-47.0 mol %) was used as the electrolyte. The FeS electrode contained a mixture of 3.0 g FeS, 2.0 g Li_2FeS_2 , and 0.5 g Fe powders. The Li_2FeS_2 was prepared by heating an equimolar mixture of FeS and Li_2S at $\sim 800^\circ\text{C}$ in a graphite crucible for several weeks. X-ray diffraction analysis verified that the product was Li_2FeS_2 . Most of the emf measurements for the $\text{FeS} \rightarrow \text{Li}_2\text{FeS}_2$ transition were made without cycling the cell before making measurements; however, some measurements were made after the cell had been discharged once and then charged. All of the $\text{Li}_2\text{FeS}_2 \rightarrow \text{Li}_2\text{S}$ measurements were made after a complete discharge and then partial charge ($\sim 30\%$ of the theoretical capacity). A Keithley model 191 digital multimeter (input impedance $> 10^9 \Omega$) was used for the measurements. As a check on the reproducibility of the results data were obtained for both increasing and decreasing temperatures.

The experimental results are shown in Fig. 1. A linear regression analysis of the data indicated that the $\text{FeS} \rightarrow \text{Li}_2\text{FeS}_2$ data could be fit by

$$E(\text{in mV}) = 1338.9 + 0.0133T \text{ (K)} \quad [1]$$

and the $\text{Li}_2\text{FeS}_2 \rightarrow \text{Li}_2\text{S}$ data by

$$E(\text{in mV}) = 1432.11 - 0.147T \text{ (K)} \quad [2]$$

Equations [1] and [2] were combined to yield the $\text{FeS} \rightarrow \text{Li}_2\text{S}$ transition

$$E(\text{in mV}) = 1385.8 - 0.067T \text{ (K)} \quad [3]$$

The slopes of these three equations are slightly more positive than those reported for measurements in LiCl-KCl eutectic electrolyte. However, the emf's computed from equations [1]-[3] agree with those for LiCl-KCl eutectic electrolyte (see Table 1). This agreement supports our earlier conclusion (1) that the calculated values for the $\text{FeS} \rightarrow \text{Li}_2\text{FeS}_2$ and $\text{FeS} \rightarrow \text{Li}_2\text{S}$ transitions in LiCl-KCl were within several millivolts of the correct values.

The free energy of formation of Li_2S at cell operating temperatures was computed from Equation [3] and the thermodynamic data for LiAl (2) and FeS (3). The computed value is -100.22 kcal/mol at 700 K. The free energy of formation of Li_2FeS_2 was then computed using the derived value for Li_2S and Equation [2]. The resulting value is -125.45 kcal/mol at 700 K. The free energy change for the chemical formation of Li_2FeS_2 from FeS and Li_2S was computed using Equation [1] and [3]. The computed value is -0.45 kcal/mol at 700 K, a value which is in agreement with that computed earlier (1).

* Electrochemical Society Active Member
Key words: fused salts, free energy,
EMF, cell

ACKNOWLEDGEMENT

The authors express their gratitude to R. K. Steunenberg, D. L. Barney, P. A. Nelson and L. Burris for their support and encouragement during this study. This work was conducted under the auspices of the U. S. Department of Energy.

REFERENCES

1. Z. Tomczuk, S. K. Preto and M. F. Roche, *This Journal*, **128**, 760 (1981).
2. N. P. Yao, L. A. Heredy, and R. C. Saunders, *This Journal*, **118**, 1039 (1971).
3. *JANAF Thermochemical Tables*, The Dow Chemical Company (1977).

Table I. Comparison of emf data in LiCl-KCl and in LiF-LiCl-LiBr electrolytes

| Transition | Temp., K | Emf, mV | |
|--|-------------|-----------------------|---------------|
| | | LiCl-KCl ^a | LiF-LiCl-LiBr |
| Li ₂ FeS ₂ → Li ₂ S | 673 | 1334.6 | 1333.1 |
| | 723 | 1325.7 | 1325.7 |
| | 773 | 1316.8 | 1318.3 |
| FeS → Li ₂ FeS ₂ | 673 | 1352.2 | 1347.8 |
| | 723 | 1351.1 | 1348.5 |
| | 773 | 1350.0 | 1349.1 |
| FeS → Li ₂ S | 673 | 1343.0 | 1340.7 |
| | 723 | 1338.0 | 1337.3 |
| | 773 | 1333.0 | 1334.0 |

^aValues taken from ref. 1.

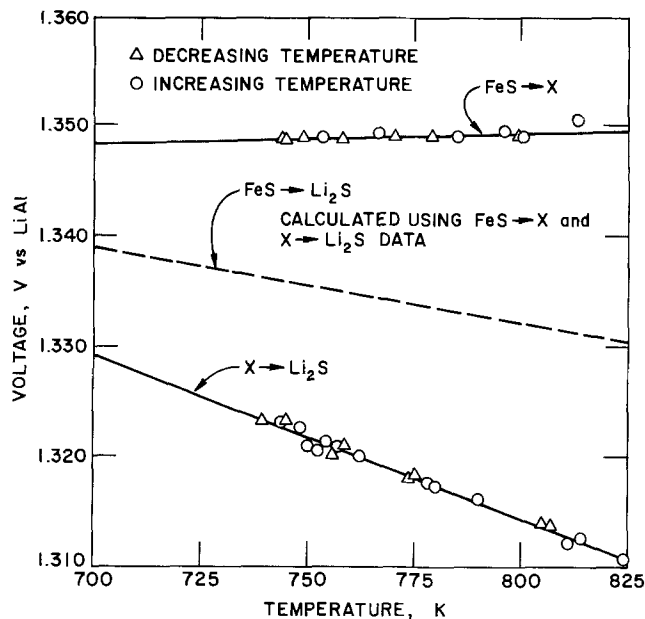


Fig. 1. Emf vs. temperature data for FeS → Li₂FeS₂ (≡X) and X → Li₂S transitions in LiF-LiCl-LiBr electrolyte.

Manuscript submitted April 27, 1981.

Publication costs of this article were assisted by Argonne National Laboratory.



Evaluation of Organic Acids as Fuel Cell Electrolytes

J. Ahmad,* T. H. Nguyen,* and R. T. Foley*

Department of Chemistry, The American University, Washington, D.C. 20016

ABSTRACT

The electrochemical behavior of methanesulfonic acid, ethanesulfonic acid, and sulfoacetic acid as fuel cell electrolytes was studied in a half-cell at various temperatures. The rate of the electro-oxidation of hydrogen at 115°C was very high in methanesulfonic acid. The rate of the electro-oxidation of propane in all three acids was low even at 135°C. Further, there is evidence for adsorption of these acids on the platinum electrode. It was concluded that anhydrous sulfonic acids are not good electrolytes; water solutions are required. Sulfonic acids containing unprotected carbon-hydrogen bonds are adsorbed on platinum and probably decompose during electrolysis. A completely substituted (fluorinated) sulfonic acid would be the preferred electrolyte.

This research was directed toward the investigation of improved fuel cell electrolytes suitable for the low temperature (under 200°C) fuel cell. A comprehensive review of the fuel cell electrolyte problem has been made (1). All of the inorganic acids, phosphoric, sulfuric, hydrochloric, perchloric, and hydrofluoric, as well as the "super acids," are deficient in one or more physical, chemical, or electrochemical property when evaluated in terms of the established characteristics of the "ideal" electrolyte (2). The desired properties of a fuel cell electrolyte are: (i) good ionic conduction; (ii) proper vapor pressure and viscosity characteristics; (iii) a good medium for the oxidation of the fuel; (iv) a good solvent for the active materials and for material transport; (v) chemically and electrochemically stable over the operating temperature range; (vi) noncorrosive to fuel cell container materials; (vii) proper surface tension characteristics (should not wet Teflon bonded electrodes or foam excessively when bubbled with gases).

The shortcomings of inorganic systems have suggested organic acids as alternatives, mainly because it was felt that the ability to alter the structure of an organic molecule allowed for a flexibility not available with inorganic systems. One important property, lacking, for example, in phosphoric acid, was the ability to support the electro-oxidation of propane. For future advancement in the fuel cell field, the development of a direct hydrocarbon-air fuel cell has a high priority.

The first organic acid studied in any depth and also giving promising results was trifluoromethanesulfonic acid used as its monohydrate (3-6). The important finding in this work was to demonstrate convincingly that the development of new improved electrolytes was a route, alternative to electrocatalysis, which could lead to improved fuel cell performance.

A review of the literature and an examination of the physical and chemical properties of certain organic sulfonic acids, namely, methanesulfonic, ethanesulfonic, and sulfoacetic, indicated that these acids warranted further investigation. The specific objective of the pres-

ent research was to evaluate these acids electrochemically, particularly their ability as electrolytes to support the electro-oxidation of hydrogen and propane.

Experimental

Preparation, purification, and analysis of electrolytes.—Methanesulfonic acid, ethanesulfonic acid, and sulfoacetic acid, were evaluated as fuel cell electrolytes, and sulfuric acid and trifluoromethanesulfonic acid monohydrate were used as "reference" electrolytes. Some physical properties of the three acids compared to those of phosphoric acid, sulfuric acid, and trifluoromethanesulfonic acid monohydrate are given in Table I.

The methanesulfonic acid was Eastman 95% practical grade distilled twice under vacuum. The double-distilled acid was further cleaned by maintaining a fuel cell electrode at 0.5V for about 15 hr in the three-compartment cell in which the experiment was to be performed. The methanesulfonic acid was analyzed at three stages to follow the possible oxidation or reduction of the compound: (i) the as-supplied, 95% practical grade; (ii) the double-distilled material; and (iii) the 80% (water) solution of the double-distilled acid which was electrolyzed at 0.9V and 100°C for 20 hr. The analyses were conducted by obtaining nuclear magnetic resonance spectra and gas chromatograms. Analysis by infrared absorption was found to lack sufficient sensitivity. A Varian Associates A60 analytical NMR spectrometer was used for the proton analysis and a Bruker WP-80, ¹³C NMR spectrometer, for the carbon analysis. Deuterium oxide (D₂O) was used as a solvent and tetramethylsilane as an external standard. The tetramethylsilane peak was set at 0.00 ppm after properly phasing and maximizing the resolution and the spectra were run over a 1000 Hz range using a 250 sec sweep time. The gas chromatograms were obtained with a Hewlett-Packard 5830A Gas Chromatograph with a 18850A recorder. A 1% solution of the acid in ether was injected into the column (a 3% OV-225 column). A flame ionization detector was used to obtain a chromatogram of the acid. The experiment was programmed from 50° to 150°C with a 10% per min heating rate.

* Electrochemical Society Active Member.

Key words: fuel cells, electrolytes, electro-oxidation.

Table I. Physical properties of fuel cell electrolytes

| Compound | Melt- ing point | Boiling point | Solubility in water | Specific conduct- ance at 40°C ($\Omega^{-1} \text{ cm}^{-1}$) | Contact angle on Teflon (degrees) | |
|--|-----------------------|--|--------------------------------|--|---|---|
| Methanesulfonic acid, $\text{CH}_3\text{SO}_3\text{H}$ | 19-20 | 167/10 mm | Miscible in all proportions | 0.019 | (98 w/o) | 93.59 (100%) |
| Ethanesulfonic acid, $\text{CH}_3\text{-CH}_2\text{-SO}_3\text{H}$ | -17 | 123/1 mm | Very soluble | 0.009 at 25°C | (98 w/o) | |
| Sulfoacetic acid, $\text{HO}_2\text{S-CH}_2\text{-COOH}$ | 84-86 | 245d | Very soluble | 0.464 | (58% H_2O solution) | 90.15° (58% H_2O solu- tion) |
| Phosphoric acid, H_3PO_4 | 42.35 | $\frac{1}{2} \text{H}_2\text{O}$, 213 | Very soluble | 0.1381 | (85% H_2O solution) | >90 (58% H_2O solution) |
| Sulfuric acid, H_2SO_4 | 10.36 | 338 (98.3%) | Miscible in all proportions | 0.790 | (50% H_2O solution) | >90 (50% H_2O solution) |
| Trifluoromethanesul- fonic acid, monohy- drate $\text{CF}_3\text{SO}_3\text{H} \cdot \text{H}_2\text{O}$ | 33.8 | 217-219 | Miscible in all proportions | 0.01122 0.5750 | (100% (40% H_2O solution) | 72.83 (100%) |

The ethanesulfonic acid was supplied by Aldrich and Company, vacuum distilled to remove impurities, and further cleaned in the cell by electrolyzing at 0.5V with a cleaning electrode for about 15 hr.

The sulfoacetic acid was supplied by Eastman as black crystals in semi-solid form and 98% purity. The acid could be further purified by forming the Pb salt with PbCO_3 and freeing the acid by precipitating PbS. However, the traces of sulfide that remained in solution poisoned the Pt electrode during the electrochemical experiments. The sulfoacetic acid of 98% purity was used in the electrochemical experiments described below.

Electrochemical techniques.—Two types of experiments were performed: (i) polarization studies with argon, hydrogen, and propane in the three electrolytes. The electrical apparatus, the three-compartment cell, the reference system, and the method of pretreatment of the gases have been described in previous publications (2). All potentials reported are *vs.* the dynamic hydrogen electrode (7); (ii) cyclic voltammetry experiments with apparatus and techniques previously described (6).

Results and Discussion

Methanesulfonic acid.—In preliminary experiments the systems were calibrated with polarization curves obtained by the electro-oxidation of H_2 in trifluoromethanesulfonic acid monohydrate over the temperature range of 80°-135°C and cyclic voltammetric scans in 4N sulfuric acid and in trifluoromethanesulfonic acid monohydrate. The results obtained from experiments with the monohydrate were similar to those previously reported in this laboratory (3) and the voltammetric sweeps in sulfuric acid were identical to those reported in the literature (8).

The polarization curves for argon, propane, and hydrogen in an 80% $\text{CH}_3\text{SO}_3\text{H}$ solution at 115° and 135°C are given in Fig. 1. For hydrogen oxidation clear-cut limiting currents were observed, 78.8 and 108 $\mu\text{A}/\text{cm}^2$ at 115° and 135°C, respectively. There was no definite Tafel region in the hydrogen polarization curve. The oxidation currents for argon and propane increased with overvoltage. At an overvoltage of 0.3V the currents for Ar were 0.64 and 1.6 $\mu\text{A cm}^{-2}$ at 115° and 135°C, respectively, while for propane values of 5.5 and 7.5 $\mu\text{A cm}^{-2}$ were obtained. Above 0.65V the current density for Ar and propane increased rapidly and reached peak currents, or limiting currents at about 0.90V *vs.* DHE. At 135°C the peak currents were almost the same for both Ar and propane, suggesting that the oxidation current of the electrolyte, *per se*, exceeded that due to the electro-oxidation of propane.

The inspection of the cyclic voltammograms of the acid taken over a range of temperatures revealed some significant characteristics. At room temperature and up to 80°C, the hydrogen, double layer, and oxygen film

regions were well defined and separated in the positive going part of the curve. At 90°C a strong oxidizing peak at 1200 mV and a shoulder-like peak at 760 mV started to appear; at higher temperature (115° and 135°C) those peaks increased and the hydrogen structure began to lose its fine structure. But the most dramatic change was that, in the cathodic scan, the current crossed into the anodic current domain directly following the reduction of the Pt oxide. This must be characteristic of the presence of an electroactive species. Cyclic voltammograms at 26° and 115°C in Fig. 2 illustrate this behavior. To further study this phenomena, a background voltammogram with 4N H_2SO_4 was run and then a few drops of methanesulfonic acid was added to the cell. A typical cyclic voltammogram for 4N H_2SO_4 was obtained at 80°C (Fig. 3). After addition of a few drops of methanesulfonic acid it was observed that there was no change in the background

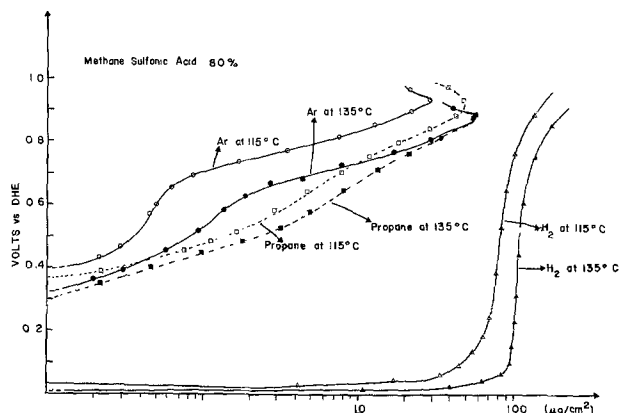


Fig. 1. Polarization curves for argon, propane, and hydrogen in an 80% $\text{CH}_3\text{SO}_3\text{H}$ solution at 115° and 135°C.

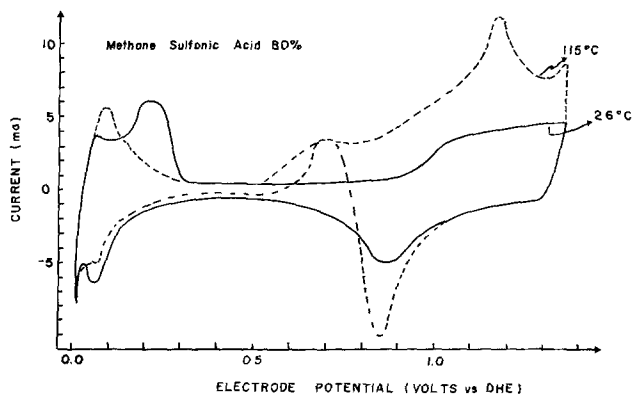


Fig. 2. Cyclic voltammograms in 80% solution of methanesulfonic acid at 26° and 115°C.

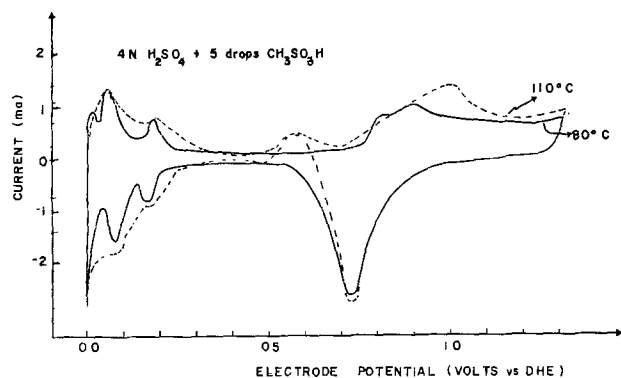


Fig. 3. Cyclic voltammogram in 4N H₂SO₄ to which was added a few drops of CH₃SO₃H.

curve. However, when the solution was heated up to 110°C, the effect of methanesulfonic acid became apparent. A strong oxidizing peak at 1.02V was then observed and in the reverse scan to the cathodic side, the current crossed over to the anodic area after the reduction of the platinum oxide.

From these observations, it is then concluded that methanesulfonic acid is dissociatively adsorbed



At sufficiently large potential, the radical is desorbed and contributes to the high oxidation current. Then, in the reverse scan, after the reduction of the oxide layer on Pt, a product of the higher potential electrolysis reaction is oxidized on the oxide-free platinum surface.

To explain some of these electrochemical results, the methanesulfonic acid was analyzed using ¹H NMR, ¹³C NMR, and gas chromatography techniques, the last being most informative.

The ¹H NMR spectra were recorded employing as-supplied, double-distilled, and electrolyzed samples. In these spectra two peaks were obtained: peak I, attributed to the —CH₃ group and peak II, attributed to the combined effect of the sulfonic group and solvent. The position of peak II changes from sample to sample and the shift is tabulated in Table II. The presence of H₂O in the sample tends to shift the spectrum to a lower ppm value so the shift of peak II to 5.2 ppm is interpreted as the presence of a new structure.

The ¹³C NMR spectra were not particularly informative but seemed to indicate an impurity in all three samples.

These NMR spectra were run at 60°C (proton) and at room temperature (carbon). The gas chromatography analyzed the acid samples at elevated temperature (up to 150°C). The chromatograms obtained from the double-distilled sample of methanesulfonic acid and the acid that had been electrolyzed at 0.9V and 100°C for 20 hr are displayed in Fig. 4 and 5, respectively. It is apparent that the electrolysis at 100°C was effective in producing several fragments or new compounds. These analyses suggest that methanesulfonic acid is unstable at 100°C and 0.9V.

Table II. The positions of the absorption peaks in the ¹H NMR spectra of methanesulfonic acid samples

| Spectrum | *Position of peak I (ppm) | *Position of peak II (ppm) |
|-------------------------|---------------------------|----------------------------|
| As-supplied sample | 1.5 | 4.8 |
| Double-distilled sample | 1.5 | 4.55 |
| Electrolyzed sample | 1.5 | 5.2 |

* These positions are over a 1000 Hz range using a 250 sec sweep time.

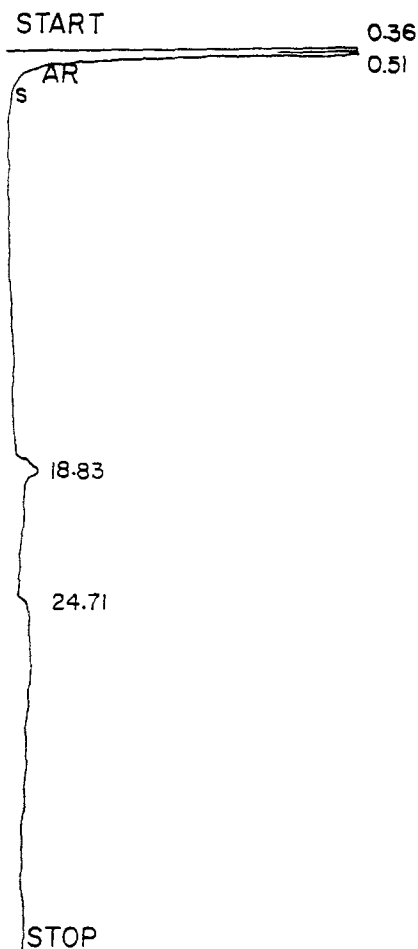


Fig. 4. Chromatogram obtained with a double-distilled sample of methanesulfonic acid.

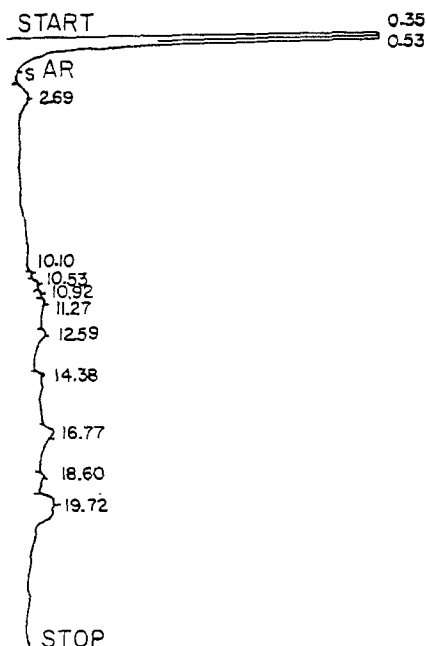


Fig. 5. Chromatograms obtained with a sample of methanesulfonic acid that had been electrolyzed at 0.9V for 20 hr at 100°C.

Ethanesulfonic acid.—Polarization curves were obtained with Ar, propane, and H₂ in a 50% acid-H₂O solution of ethanesulfonic acid. At 115°C, the limiting-current for hydrogen was 27.6 μA/cm², about half of the current obtained with methanesulfonic acid. Also, the polarization curve did not show a distinct Tafel region (Fig. 6). For propane and Ar, there were no

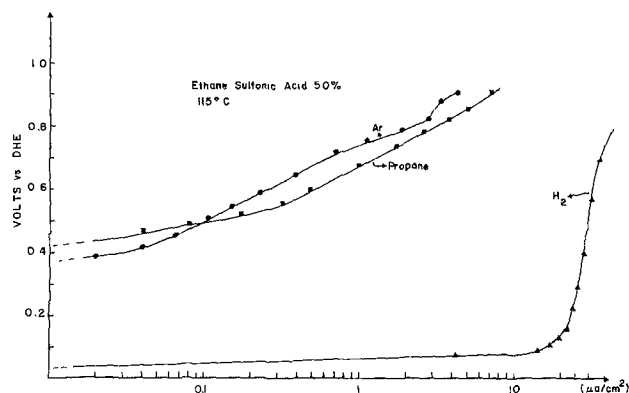


Fig. 6. Polarization curves for argon, propane, and H₂ in 50% solution of ethanesulfonic acid at 115°C.

clear-cut limiting currents but the current density for propane was slightly higher than for Ar. At an overvoltage of 0.3V the current density for propane was $1.2 \mu\text{A}\cdot\text{cm}^{-2}$ compared to $0.65 \mu\text{A}\cdot\text{cm}^{-2}$ for Ar.

The cyclic voltammogram of the 50% acid solution at different temperature is shown in Fig. 7. It is interesting to note that at room temperature, ethanesulfonic acid exhibited electrochemical behavior similar to that of methanesulfonic acid at higher temperatures. This suggests that ethanesulfonic acid is strongly adsorbed on the platinum electrode surface. As we increased the temperature, it is observed that: (i) the oxidation peak-current increases; (ii) the Pt-oxide reduction current slightly decreases; (iii) the electro-oxidation current of the electroactive species increased; and (iv) the definition of the hydrogen peaks decreases and almost completely disappears above 85°C. From those observations, it is concluded that ethanesulfonic acid is strongly adsorbed on the Pt surface and at sufficiently high temperature, inhibits the hydrogen and oxidation reactions. This behavior appears to be characteristic of a platinum electrode in strong concentrated acidic electrolytes.

Sulfoacetic acid.—The polarization curves for argon, propane, and hydrogen in a 50% acid solution are shown in Fig. 8. The current density for hydrogen oxidation at an overvoltage of 0.3V was $38 \mu\text{A}/\text{cm}^2$ at 115°C. The polarization curves for argon and propane did not exhibit a limiting current density but it can be remarked that the current obtained with propane was almost the same as with argon. The voltammogram for the acid shown in Fig. 9 did not show any special behavior. It did not appear that sulfoacetic acid is adsorbed on the Pt electrode from the study of the

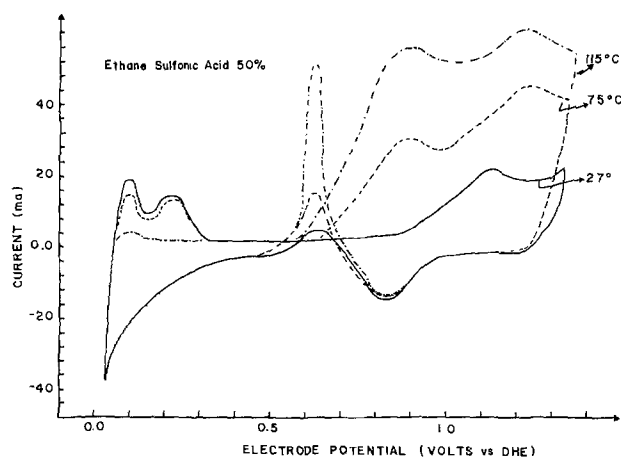


Fig. 7. Cyclic voltammogram in 50% solution of ethanesulfonic acid at 27°, 75°, and 115°C.

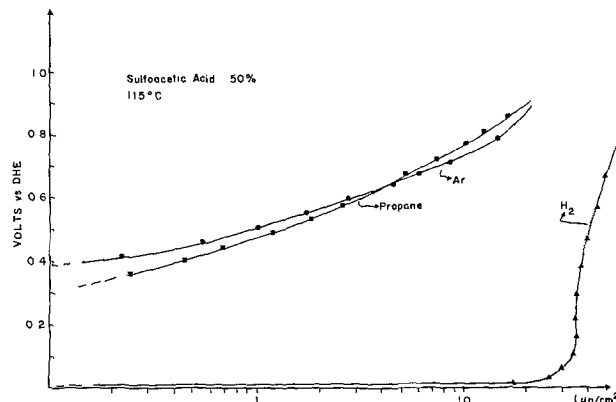


Fig. 8. Polarization curves for argon, propane, and H₂ in 50% sulfoacetic acid solution at 115°C.

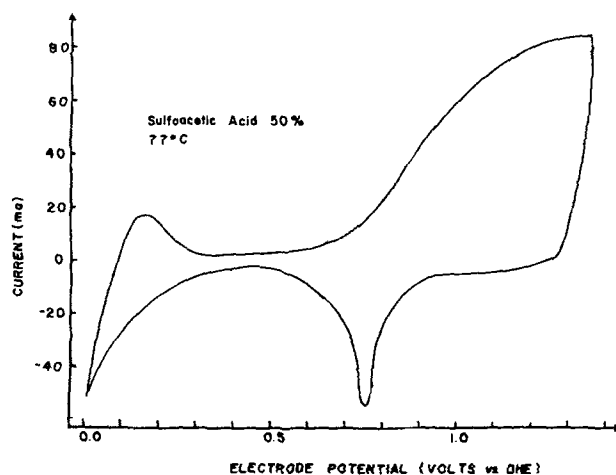


Fig. 9. Cyclic voltammogram in 50% solution of sulfoacetic acid at 77°C.

cyclic voltammogram at different temperature. However, it must be remarked that the commercially available sulfoacetic acid appears to be of uncertain quality to use as an electrolyte and no suitable method of purification has been worked out despite considerable effect to recrystallize the compound using conventional organic chemistry methods.

Conclusions

The three electrolytes are compared by tabulating the current densities achieved with hydrogen, argon, and propane in Table III.

Certain conclusions may be drawn with regard to the three sulfonic acids. The polarization studies indicate that an electrolytic solution, 80% in methanesulfonic acid and 20% in H₂O supports high current densities with H₂, but shows little promise with propane. The results obtained with H₂ agree with results obtained by Rebert *et al.* (9) in a study with platin-

Table III. Summary of current density values obtained in different electrolytes

| Electrolyte | Current densities ($\mu\text{A}/\text{cm}^2$) at 0.3V over potential | | | | | |
|---|--|-------|---------|-------|-------|-------|
| | Hydrogen | | Propane | | Argon | |
| | 115°C | 135°C | 115°C | 135°C | 115°C | 135°C |
| Methanesulfonic acid, CH ₃ SO ₃ H | 78.8 | 108 | 5.5 | 7.5 | 0.64 | 1.6 |
| Ethanesulfonic acid, C ₂ H ₅ SO ₃ H | 27.6 | | 1.2 | | 0.65 | |
| Sulfoacetic acid, HO ₂ SCH ₂ COOH | 38 | | 3.3 | | 6.4 | |
| Trifluoromethanesulfonic acid, monohydrate CF ₃ SO ₃ H · H ₂ O | 122 | 296 | | | | |

ized-platinum rotating disk electrodes. They found that at the same potential and comparable rotation speeds, methanesulfonic acid supports currents that are more than an order of magnitude higher than those obtainable in phosphoric acid. They did not study propane. The practical grade (95%) methanesulfonic acid darkens during electrolysis probably due to further decomposition. The cyclic voltammetry studies indicate that methanesulfonic acid is decomposed at elevated temperatures and high potentials. Analysis of this acid by NMR and gas chromatography also indicates that this acid decomposes into different fragments or forms new compounds during electrolysis, particularly at temperatures 100°C or above.

The polarization studies with ethanesulfonic acid indicate that this acid as an electrolyte does not support high current densities either with H₂ or propane. Ethanesulfonic acid is also completely adsorbed on the Pt electrode. For these reasons this compound does not appear to be a promising fuel cell electrolyte.

From these results it is concluded that sulfonic acids, such as CH₃SO₃H or CH₃-CH₂-SO₃H, containing terminal methyl groups unprotected by fluorination, are strongly adsorbed on the platinum surface and decompose relatively easily during electrolysis. It now appears necessary that the sulfonic acid electrolytes to be evaluated in future studies should be properly substituted to protect the molecule against electrolytic oxidation or reduction.

During the course of the investigation it became apparent that it would be necessary to work with aqueous solutions rather than the anhydrous acids. The anhydrous acids are poor ionic conductors—the conduction process is achieved with hydrated protons. Further, there is evidence that many of these compounds are thermally unstable at temperatures over 100°C.

The commercially available sulfoacetic acid appears to be of uncertain quality to use as an electrolyte and no suitable method of purification has been worked out. Furthermore, the acid is chemically unstable in the 80°-115°C range.

Acknowledgment

The support of the U.S. Army Mobility Equipment Research and Development Command, Fort Belvoir, Virginia under Contract DAAK70-77-C-0080 is gratefully acknowledged.

Manuscript received June 8, 1981.

Any discussion of this paper will appear in a Discussion Section to be published in the June 1982 JOURNAL. All discussions for the June 1982 Discussion Section should be submitted by Feb. 1, 1982.

REFERENCES

1. R. T. Foley, "On the Properties of a Fuel Cell Electrolyte," Final Technical Report, July 10, 1978-January 15, 1979, Contract No. DAAK70-78-C-0128.
2. A. A. Adams and R. T. Foley, "Research on Electrochemical Energy Conversion Systems," Report No. 7, Final Technical Report on Contract No. DAAK02-72-C-0084, December 1975.
3. A. A. Adams and H. J. Barger, *This Journal*, **121**, 987 (1974).
4. A. A. Adams, R. T. Foley, and H. J. Barger, *ibid.*, **124**, 1228 (1977).
5. A. A. Adams and R. T. Foley, *ibid.*, **126**, 775 (1979).
6. T. Sarada, R. D. Granata, and R. T. Foley, *ibid.*, **125**, 1899 (1978).
7. J. Giner, *ibid.*, **111**, 376 (1964).
8. W. Bold and M. Breiter, *Electrochim. Acta*, **5**, 1223 (1964).
9. N. Rebert, B. G. Ateya, T. Poweigha, and L. G. Austin, *This Journal*, **127**, 2641 (1980).

Electrochemical Reactivity of Strong Sulfuric Acid: Some Unusual Behavior at Pt Electrodes

B. E. Conway* and D. M. Novak*.¹

Chemistry Department, University of Ottawa, Ottawa, Ontario, Canada K1N 6N5

ABSTRACT

In very strong, 98%, sulfuric acid cyclic-voltammetry experiments at Pt reveal unusual reduction and oxidation processes as distinct from those associated with electrodeposition and ionization of atomic H, and surface oxide formation and reduction, which are familiar in dilute aqueous solutions of H₂SO₄ at Pt. No reduction processes are observed on a less electrocatalytic metal, Au, under the same conditions. Holding the potential of a Pt electrode near the H⁺/H₂ potential (E_H) in 98% H₂SO₄ gives rise to reduction of the acid, producing a species that is immediately chemisorbed and becomes oxidized in the adsorbed state in a following anodic potential sweep over the "surface oxide formation" potential region. In the succeeding cathodic sweep, a large cathodic current peak follows surface oxide reduction. By means of chemical simulation experiments, it is shown that the reduction behavior is accounted for first by formation of SO₂ or HSO₃⁻ at potentials near E_H , followed by oxidation to a species, possibly adsorbed dithionate (S₂O₆²⁻), or some other chemisorbed sulfur-oxygen species, in a following anodic sweep. This oxidation process cannot be from SO₂ or HSO₃⁻ back to H₂SO₄ or HSO₄⁻ since, in the next cathodic sweep, a re-reduction occurs in a well-defined peak, a little positive to E_H . Experiments at a rotated Pt disk electrode enable distinctions to be made between processes associated with strongly bound chemisorbed species and other species that can be spun off into solution, giving diminished currents in successive cyclic voltammograms. Additions of small quantities of water diminish the reduction reaction observed in 98% H₂SO₄.

In the course of experiments (1) on the surface oxidation of Pt in nonaqueous media containing traces of water, we investigated the behavior of Pt electrodes in very strong 98% sulfuric acid. Some unusual and interesting bulk and surface electrochemical processes are found which are not observed in ordinary aqueous solutions of H₂SO₄. At the 98% level of concentration of H₂SO₄, the medium is essentially a nonaqueous solution with H₃O⁺ and HSO₄⁻ ions as the electrolyte at about 1.1M concentration. Some higher, condensed sulfuric acid species, e.g., H₂S₂O₇, are also present in traces (2).

Studies in very strong acid media are of interest in fuel-cell technology where acids such as H₃PO₄ and CF₃SO₃H are used at ca. 85% concentrations, often at elevated temperatures.

As far as we are aware, no previous studies of the electrochemical surface reactivity of pure H₂SO₄ to give chemisorbed decomposition products at electrode interfaces have been reported except in the work of Arvia *et al.* (3) who investigated electrochemical surface processes at Ir in 96% H₂SO₄. In this work, however, only the usual surface reactions of Ir are revealed with H adsorption and surface oxide formation regions being observed in the normal way, but with displacement of these two processes to more negative and more positive potentials, respectively, due to HSO₄⁻ ion adsorption, as is known in more dilute solutions at Pt with SO₄²⁻ (4) and HSO₄⁻ ion (5), depending on concentration and pH.

An interesting study was also made by Arvia *et al.* (6) on the electrochemistry of fuming sulfuric acid containing various concentrations of SO₃ and small quantities of SO₂, and comparatively on 97.4% H₂SO₄ in the same paper. Most of this work was concerned with the steady-state current-potential behavior arising from reduction of SO₃ at stationary and rotated Pt electrodes, which gives rise to SO₂ and some S.

Also, the cathodic evolution of H₂ and the anodic decomposition to O₂ and persulfuric acid was investigated. The question of adsorbed species that might be involved in the reactions was not treated in this work. In work by Lal *et al.* (7-10) and by Loučka (11-13), however, adsorbed species from SO₂ solutions and S layers formed from H₂S and SO₂ were recognized and investigated. As we discuss later, some of these results are relevant to the interpretation of the experiments in the present work.

Arvia *et al.*, in a series of papers (14), have also reported underpotential deposition of H and surface oxidation of Pt and Ir in KHSO₄ and NaHSO₄/KHSO₄ melts.

In the present paper, we report some unusual reduction and oxidation processes at Pt in 98% H₂SO₄ at ordinary temperatures, studied by means of the linear potentiodynamic sweep method and related procedures. Attempts to identify the principal intermediates involved were made by means of chemical simulation experiments using likely species such as SO₂, dithionite, and dithionate.

Experimental

Method.—A conventional system for applying single and repetitive linear potential sweeps to an electrode was used, employing the equipment and procedure referred to in previous publications (5, 15, 16). In the cyclic-voltammetry mode, the system enables a series of sweeps in an anodic or cathodic direction to be made to successively more positive or more negative potentials, respectively, using the triggering capability for sweep reversal at a constant sweep rate which is provided by a Servomex LF 141 function generator operating on a Wenking potentiostat. This system also allows the potential to be held conveniently at a controlled fixed value (potential "holding" experiment) for recorded times before a following anodic or cathodic sweep is initiated. This type of apparatus enabled current-density (*i*) vs. potential (*V*) profiles to be recorded, as described previously by us

* Electrochemical Society Active Member.

¹ Present address: Research Laboratories, Eldorado Nuclear Limited, Tunney's Pasture, Ottawa, Canada.

(1, 5, 16) and by other authors, e.g., Ref. (15). Most experiments were conducted at 298 K at a Pt disk electrode (Pine Instrument Company) that could be rotated when desired. Some comparative experiments were made at a high purity grade Au wire.

H₂SO₄ electrolyte.—B.D.H. Aristar pure (98%) H₂SO₄ was used as the electrolyte, initially without dilution. This is the acid which gives, at ordinary concentrations (0.5 ~ 1M), the best clean aqueous solution of H₂SO₄ for cyclic-voltammetry experiments at Pt, as we have described in earlier papers (5, 16). In some experiments, where controlled small additions of water are made, pyrodistilled water (16) was used.

Cell.—A small 3-compartment cell capable of being fitted to a rotating disk electrode system was used, as described previously (1). It was provided with a compartment in which either a reversible H₂/H⁺ electrode or an ($\alpha + \beta$)PdH electrode was situated.

Reference electrodes.—A platinized-Pt hydrogen electrode was employed as the reference electrode directly in the strong H₂SO₄. In the 98% H₂SO₄, the potentials are not true reversible potentials but rather steady mixed potentials due to the slow electrocatalytic reduction reaction involving H₂SO₄ which is the subject of this paper. Very satisfactorily steady potentials ($\pm < 1$ mV) could, however, be maintained over an hour or so. In some experiments the ($\alpha + \beta$)PdH reference electrode was used. Potentials on all graphs to be shown below are on the scale of the H₂/H⁺ electrode in the same solution as that in which the working Pt or Au (see below) electrodes were studied. This scale is designated for convenience by E_H.

Potential programs.—The potential-time programs shown in Fig. 1 were applied to the working Pt electrode in 98% H₂SO₄ in order to investigate the nature of the observed electrochemical reactivity of H₂SO₄ and to distinguish the currents from those arising in the normal way [cf. (5, 15, 16)] from underpotential deposition of H, or OH and O species; the potentials employed were adjusted on the function generator and the potentiostat and read with an accuracy of 1 mV on a high impedance digital millivoltmeter. At all times, the latter instrument was used to monitor numerically the various potentials involved at sweep

reversal and in constant potential holding experiments (see below).

(i) **Cyclic-voltammetry at 70 mV sec⁻¹.**—Cyclic-voltammetry experiments were first made by means of a repetitive symmetrical triangular sweep, referred to as program (i) (Fig. 1). Several potential limits to the cathodic and anodic sweeps were employed and are defined on the experimental *i* vs. *V* profiles shown in Fig. 2a and b and Fig. 3a and b. Experiments in this mode established the normal *i* vs. *V* profiles for the surface processes at Pt in 98% H₂SO₄, as shown in Fig. 2 and 3.

(ii) **Cyclic-voltammetry experiments over progressively decreasing ranges of potential.**—These were made by reversing the sweep at successively increas-

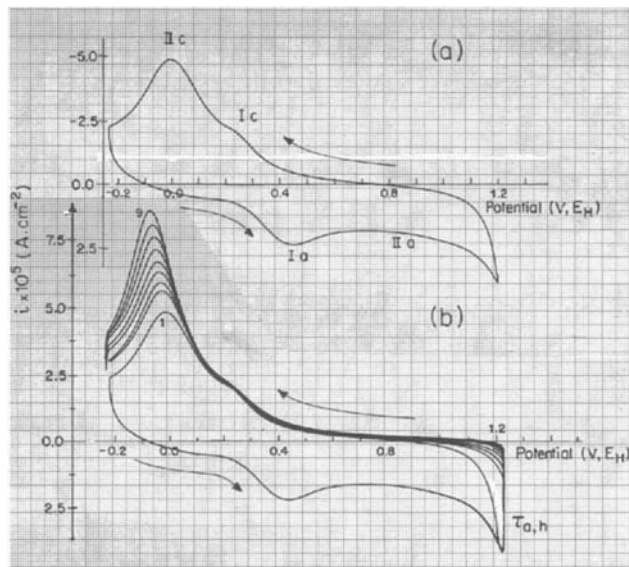


Fig. 2. (a) Cyclic-voltammetry *i* vs. *V* profiles for Pt in 98% H₂SO₄ at 70 mV sec⁻¹ at 298 K, [program (i)]. Designations of principal anodic and cathodic processes are shown. (b) As in Fig. 2 (a) but with holding the potential constant at the positive end of the anodic sweep giving rise to growth of the surface oxide at Pt (70 mV sec⁻¹, 298 K). Curves 1 to 9 for $\tau_{h,a} = 0, 5, 10, 15, 20, 60, 120, 240, \text{ and } 360$ sec.

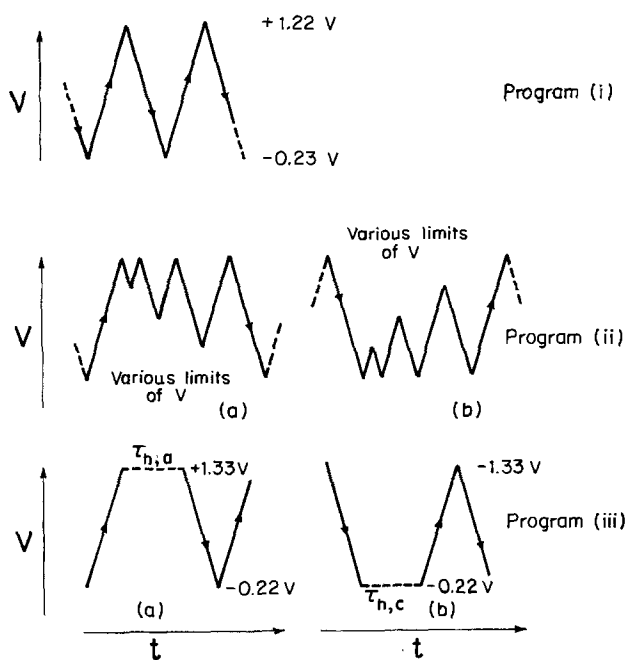


Fig. 1. Potential programs

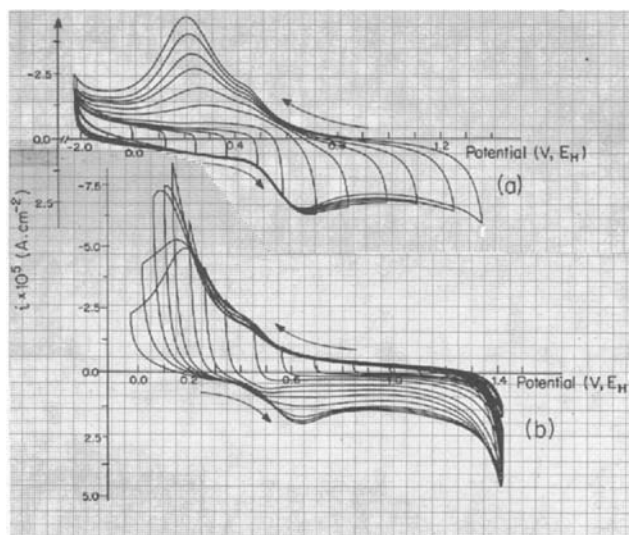


Fig. 3. (a) Cyclic-voltammetry *i* vs. *V* profiles for Pt in 98% H₂SO₄ at 70 mV sec⁻¹ at 298 K showing the effects of reversing the direction of potential sweep at successively more positive potentials in the anodic sweep direction [program (iib)]. (b) As in Fig. 3 (a), but showing the effects of reversing the direction of potential sweep at successively less positive potentials in the cathodic sweep direction [program (iia)].

ing potentials in the anodic or successively decreasing potentials in the cathodic sweep directions. These procedures are illustrated in Fig. 1 and are referred to as programs (iib) and (iia), respectively. These procedures give information on what processes observed in, e.g., a cathodic sweep (where a current peak arises) are conjugate to processes in the prior anodic sweep, or vice-versa, as shown in Fig. 3a and b. The changing potential limits in the programs (iia) and (iib) are evident from the potentials of reversal of the series of curves shown in Fig. 3a, b.

(iii) *Potential holding experiments.*—Holding the potential at either the end of an anodic sweep for a time $\tau_{h,a}$ [program (iia)] or at the end of a cathodic sweep for a time, $\tau_{h,c}$ [program (iib)] followed by initiation of a further cathodic or anodic sweep, respectively, enabled the formation and reactivity of products of slow processes to be followed. It was in these experiments, with cathodic holding of the potential near ($-0.2V E_H$) the steady-state hydrogen electrode potential (see above), that the unusual reactivity of H_2SO_4 was observed. The potentials at which cathodic or anodic holding for times τ_h was maintained are shown later in the respective figures.

After each change of conditions, e.g., potential holding, the electrode was allowed to return to the reproducible state generated initially as in section (i) above by repetitive anodic/cathodic cycling [program (i)] until the initial *i vs. V* curve, corresponding to the cyclic-voltammetry profile shown in Fig. 2, was recovered. This *i vs. V* profile, under continuous cycling, was exactly reproducible from one experiment to another and between different Pt electrodes with normalization to the same real area. It was also virtually identical with the initial anodic and cathodic *i vs. V* profile observed when an electrode, precycled in 1M aq H_2SO_4 , was transferred to the 98% H_2SO_4 .

Real electrode area.—The real area of the disk Pt electrode used in most of the experiments was determined, in the usual way, from the charge for desorption of the underpotential deposited H layer measured separately in 0.05M aq H_2SO_4 , using the figure 2.10 C m^{-2} for the H monolayer at Pt [cf. (17)]. After several days' experiments in the 98% H_2SO_4 , the real area of the electrode determined by the H accommodation remained unchanged within 0.5%.

Experiments at Au.—In order to establish how specific the observed H_2SO_4 reduction was to Pt, comparative experiments were carried out on a noble metal less electrocatalytic than Pt, viz., Au.

Reflectance experiments.—In order to see if chemisorbed intermediate species which arise, as shown later, in the reduction of H_2SO_4 can be distinguished from other, e.g., surface oxide, species on the electrode, relative reflectivities ($\Delta R/R$) were measured in the cyclic-voltammetry experiments using the apparatus and procedures previously described (18).

Results and Discussion

Phenomenology of the effects.—*Cyclic-voltammetry and potential-holding experiments: programs (i) and (iii).*—The unusual electrochemical reactivity of H_2SO_4 at Pt arises in the cathodic holding experiments, (iib). However, it is first necessary to show the normal behavior of a Pt electrode in 98% H_2SO_4 under conditions where the unusual reactions either do not take place significantly in the time scale of an anodic/cathodic sweep at 25 mV sec^{-1} or at all, if the potential range in the sweep is adjusted appropriately.

Figure 2a shows the *i vs. V* profiles for a Pt electrode in 98% H_2SO_4 over the potential range -0.244 to $+1.210V E_H$ and with cycling over successively diminished ranges of potential in the anodic (Fig. 3a)

or cathodic (Fig. 3b) sweeps. These figures define the general behavior of Pt in the 98% H_2SO_4 without any further added water. Characteristic regions of the *i vs. V* profile are designated by Ia, IIa, Ic, IIc, etc., where "a" and "c" denote anodic and cathodic processes, respectively.

Under the above conditions, the observed currents are predominantly for surface processes since the reduced current densities, *i/s*, (viz., the apparent pseudo-capacitance per unit area) are almost constant with changing sweep rate, *s*, after a given holding period, $\tau_{h,c}$.

The *i vs. V* profiles for Pt in 98% H_2SO_4 under the conditions of Fig. 2 and 3 differ substantially from those well known (5, 15, 16) for Pt in dilute ($\sim 0.05M$) aqueous H_2SO_4 . Principally, no region of underpotential deposition of H is seen, i.e., before H_2 is evolved at the most negative end of a cathodic potential sweep. This is presumably due to strong adsorption of H_2SO_4 molecules and HSO_4^- ions and to the changed nature of the solvent. The regions Ia, IIa (Fig. 2a) of the anodic sweep, which are presumably attributable in the usual way to surface oxidation (since, e.g., the charge in the reduction peak increases logarithmically with time of holding at the positive end of the anodic sweep and the hysteresis between formation and reduction regions increases with time of anodic holding), are broad and almost structureless, showing less well-resolved states than are observed in a dilute aqueous solution (15, 16) of H_2SO_4 .

An oxide reduction region, which appears to be conjugate with the broad surface oxidation region, Ia, IIa, shows a peak (IIc) and a shoulder (Ic). A similar behavior is only resolved in more dilute H_2SO_4 solutions under special low temperature conditions (19) or with weakly adsorbed anions, e.g., ClO_4^- . That the currents in the region Ia,c and IIa,c correspond to surface processes is indicated by approximate constancy (to 5%) of the charges under the curves in experiments conducted at various sweep rates.

Application of the potential holding program (iia) at the positive end of an anodic sweep gives the results shown in Fig. 2b. Only growth of the surface oxide occurs, as indicated by the increasing reduction charges with time, $\tau_{h,a}$, in the cathodic sweep which increase logarithmically in $\tau_{h,a}$. This is the normal kind of behavior, e.g., as observed (20, 21) in dilute solutions at Pt.

It is under the cathodic holding program (iib) that the unusual behavior of H_2SO_4 is observed. When the potential is held at the negative end of a cathodic sweep at $-0.244V, E_H$ for various times, $\tau_{h,c}$, an increasing anodic current appears initially over the surface oxide region in a following anodic sweep (Fig. 4). With increasing $\tau_{h,c}$, the currents in following anodic sweeps after the holding period: (a) initially increase but eventually reach a saturation limit; (b) are independent of solution mass-transfer rate at a rotated electrode [see the following section]; also, (c) a component of anodic current in these anodic sweeps appears at a lower than usual (Fig. 2) anodic potential, giving a shoulder. IIIa, (Fig. 4), on the anodic *i vs. V* profiles after holding for more than 20 sec.

As this shoulder current appears and increases with increasing $\tau_{h,c}$, the oxide reduction current profile (Ic, IIc) diminishes and a new cathodic current peak (IIIc) appears and progressively increases with increasing $\tau_{h,c}$, eventually reaching saturation. This behavior is illustrated in the succession of *i vs. V* profiles shown in Fig. 4 for various times of holding.

The dependence of the extra anodic currents which appear over the oxide formation region and of the new cathodic currents which appear in the cathodic sweep, and also of the oxide reduction charges, on time of cathodic holding, $\tau_{h,c}$, is shown as integrated charges in

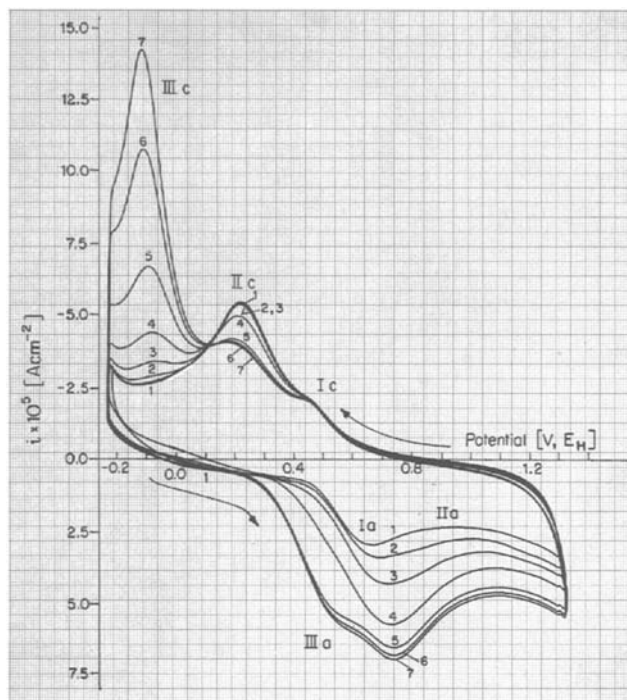


Fig. 4. A series of anodic followed by cathodic cyclic-voltammetry curves for Pt in 98% H₂SO₄ at 298 K after various times $\tau_{h,c}$ of holding the potential constant at $-0.244E$. Sweep rate 70 mV sec⁻¹; times $\tau_{h,c}$: curve 1, 0; curve 2, 5; curve 3, 10; curve 4, 15; curve 5, 20; curve 6, 40; and curve 7, 80 sec.

Fig. 5. There appears to be some induction period in the formation of whatever species (see later) that gives rise to the extra cathodic peak in the cathodic sweep which follows the first anodic sweep after holding. All the charges derived from integration of the currents over various regions of the i vs. V profiles correspond, in order of magnitude (see Fig. 5), to values

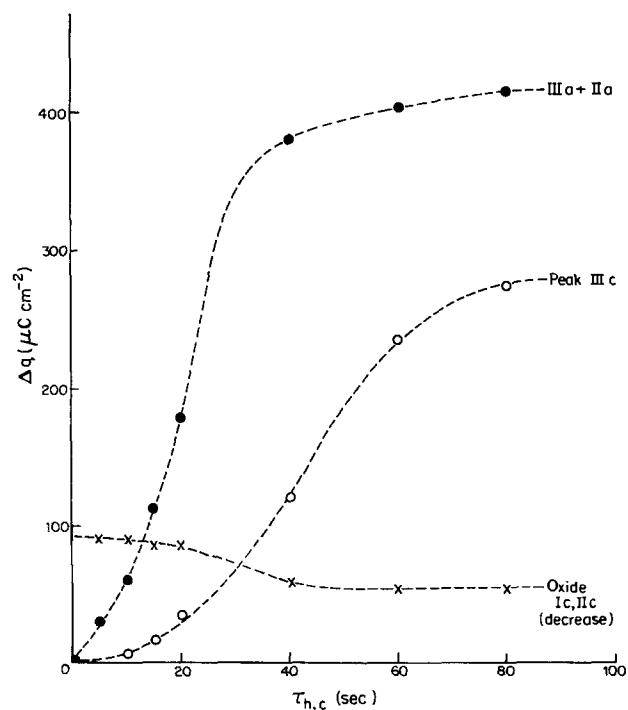


Fig. 5. Changes in $\mu\text{C cm}^{-2}$ for the three principal time-dependent processes in the curves of Fig. 4 as a function of cathodic holding time $\tau_{h,c}$ sec. \circ Charges for process IIIc; \bullet charges for processes in the region IIIa + IIa; and \times charges in the surface oxide reduction region Ic, IIc.

for monolayer processes, suggesting the role of chemisorption in the reactions involved.

If, after the experiment at a series of successively increasing cathodic holding times, the electrode is allowed to be freely cycled [cyclic-voltammetry mode (i)], the new cathodic peak IIIc gradually diminishes, the currents over the surface oxidation region diminish, and the surface oxide reduction region eventually recovers to its initial charge and peak currents. As this recovery takes place (slowly, as shown in Fig. 6), an isopotential point (22) is observed between the series of decreasing current peaks at 0.05V for process IIIc and the series of increasing surface oxide reduction currents Ic and IIc. This suggests that there is a coupling between the processes, Ic, IIc, and the reduction process, IIIc, probably through adsorption and occupancy of surface sites on the Pt electrode by two species.

Behavior at the rotated Pt electrode.—If the experiments corresponding to the results shown in Fig. 4 and 6 are performed at a rotating Pt disk electrode (1000 ~ 3000 rpm), the initial ($\tau_{h,c} = 0$) i vs. V profile shown in Fig. 2a remains unchanged. If, however, the cathodic holding experiment is carried out under rotation conditions, the development of the enhanced anodic and new cathodic currents in following sweeps (as shown in Fig. 4) is retarded, but eventually, as $\tau_{h,c} \rightarrow 90$ sec (Fig. 7) the same (saturation) anodic current profiles are attained as in the static solution with $\tau_{h,c} \approx 45$ sec (curve for IIa + IIIa in Fig. 5). This result suggests that (a) the immediate product of reduction becomes spun-off into solution, but (see below) may become re-adsorbed after its formation; and (b) the primary reduction process involves H₂SO₄ rather than another species such as H₂S₂O₇ (2) at low concentration, since electrode rotation retards rather than enhances the reduction process; thus, if the reduction effects observed in 98% H₂SO₄ were, in fact, due to a small concentration of electroactive H₂S₂O₇, rotation would tend to enhance rather than diminish the observed reduction effects, due to the expected facilitation of mass transfer of H₂S₂O₇ molecular to the electrode surface under rotation conditions.

An experiment in which the cathodic holding is conducted at a stationary Pt disk electrode, but the

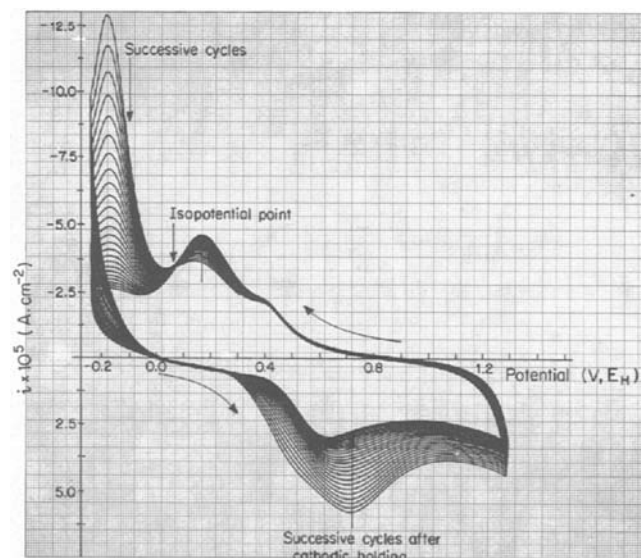


Fig. 6. "Recovery" of initial cyclic-voltammetry i vs. V profile [Fig. 3(a)] after a series of 25 repetitive potential sweeps at 70 mV sec⁻¹, following a period $\tau_{h,c}$ of holding the potential at $-0.244V E_H$. Time scale of the succession of the 25 curves is determined by the sweep rate of 70 mV sec⁻¹ and the potential range of 1.54V.

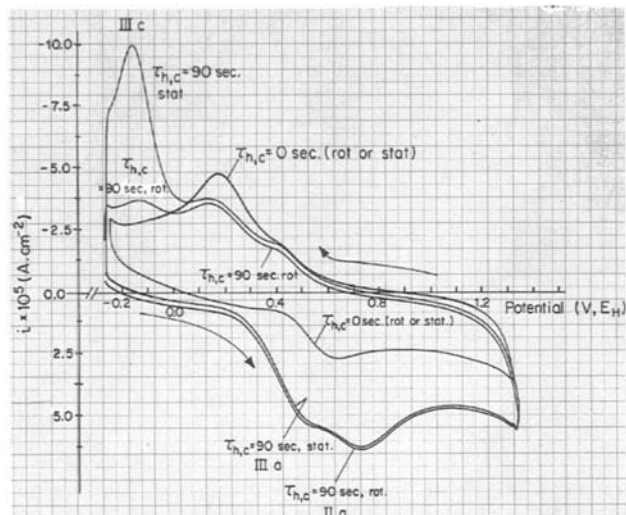


Fig. 7. Cyclic-voltammetry i vs. V profiles for a Pt disk electrode in 98% H_2SO_4 at 70 mV sec^{-1} after 0 and 90 sec cathodic holding, with ("rot") and without ("stat") electrode rotation at 3000 rpm. Current-density profiles in regions IIIa, IIa are independent of electrode rotation.

following anodic sweep is taken with or without rotation at 3000 rpm, shows (Fig. 7) that the profiles of the extra anodic currents that pass at the rotated electrode on the anodic sweep immediately following the reduction during the time $\tau_{h,c}$, are identical with those observed at the stationary electrode under otherwise the same conditions. This suggests that, although the immediate product (say "X") of reduction in the cathodic holding experiment may be a species weakly adsorbed and hence able to be spun away into solution (as indicated by the result referred to in the previous paragraph), eventually a strongly bound species (say "Y") becomes, and remains, chemisorbed up to a saturation limit (Fig. 4 and 5) at the Pt electrode during the subsequent anodic sweep.

If, however, after cathodic holding for 80 sec without rotation, free potential cycling is allowed to occur as in Fig. 6, but now with electrode rotation, the cathodic peak currents marked IIIc and the extra anodic currents (marked IIIa and IIa) which overlap with the original surface oxide formation region Ia + IIa, rapidly decay (as shown in Fig. 7) almost to the level of currents in the initial i vs. V profile (cf. Fig. 1a) without holding. This shows that while the species (Y, say) which originates from the species X produced in the cathodic holding treatment is a chemisorbed species, it can, however, following oxidation on the surface in processes Ia + IIa + IIIa (Fig. 4), be spun away into the bulk solution after reduction and slow desorption in the next cathodic sweep, so that currents in subsequent cathodic and anodic sweeps progressively diminish; Y itself and its products of oxidation in IIIa and IIa are bound species unaffected by mass-transfer conditions (Fig. 7).

The reduction process in IIIc appears to be associated with a species that arises from IIc and is loosely bound on the surface since electrode rotation eliminates most of the reduction current in this region almost from its commencement in the IIIc region (Fig. 7), yet the remainder of the anodic and cathodic i vs. V profile is independent of rotation, e.g., after $\tau_{h,c} = 90$ sec. However, under successive cycling conditions (Fig. 6) after $\tau_{h,c} = 90$ sec with no rotation, it then takes ca. 20 cycles (ca. 400 sec) for the peak current at IIIc to decay to the level in Fig. 7 after 1 cycle with rotation, so that the species being reduced at the surface in IIIc remains in some loose attachment to the Pt sufficient for reoxidation immediately in the following anodic sweep with little loss of the level

of currents over the regions IIIa, and Ia (Fig. 4). (Possibly a polymeric form of S or a polysulfide is involved.) The latter result indicates clearly that the species generated at the end of the cathodic sweep through the IIIc region (e.g., the top curve, Fig. 6) is the same as that formed in the initial holding period for $\tau_{h,c}$ sec.

Possible mechanism of the effects: elucidation by chemical simulation experiments.—The results of Fig. 4, 5, and 6 suggest that a product, X, derived from the sulfuric acid is first formed by reduction near the H_2/H^+ steady potential. Some of X, probably in a further reduced chemisorbed state Y (see below), then becomes oxidized to a species Y_0 in the following anodic sweep. The reduction of H_2SO_4 to form detectable X and Y, as indicated by its subsequent oxidation to Y_0 and the following reduction of Y_0 in the next cathodic sweep, is quite slow, requiring ca. 20 sec for formation of a detectable adsorbed intermediate at 298 K.

In the next cathodic sweep, following formation of Y_0 by oxidation of Y derived from X, Y_0 is reduced to a species "Z", giving (Fig. 4) the substantial peak IIIc on the cathodic i vs. V profile near the H_2/H^+ potential. The reduction current giving Z depends on how much X, and hence Y (and thus Y_0 from Y), were produced in the cathodic holding.

The observation of the reduction peak IIIc producing Z, after oxidation of X and Y to Y_0 species in the previous anodic sweep, means that the process of oxidation of X or Y is not re-formation of H_2SO_4 or HSO_4^- ion (i.e., Y_0 is not one of these species) since H_2SO_4 (or HSO_4^-) itself is not rapidly reduced in a single cathodic sweep, as follows from the behavior in Fig. 2, and from the fact that the primary reduction process which takes place during cathodic holding is quite slow.

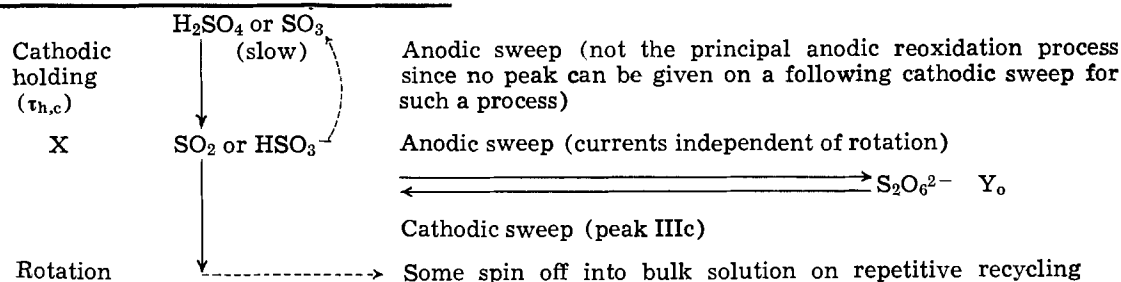
Consideration of the chemistry of 98% H_2SO_4 suggests that the first reduction product X is likely to be SO_2 or HSO_3^- produced either from H_2SO_4 molecules or any dissolved SO_3 present [cf. Ref. (6)]. However, the latter possibility is quite unlikely since the concentration of SO_3 in 98% H_2SO_4 (ca. 1M in H_2O) is known to be vanishingly small (2). The effects are unlikely to be due to other adventitious impurities since we have found previously (16) with this B.D.H. acid, and in the present work, that its solutions in pyrodistilled water give excellent cyclic voltammograms for Pt without any impurity problems. This is also indicated by the behavior of Au (see later) in this acid.

Since only monolayer magnitudes of intermediates in the H_2SO_4 reduction are produced in the experiments (e.g., see Fig. 5), direct chemical analyses and characterizations were not feasible, especially in excess of 98% H_2SO_4 . However, chemical simulations of the behavior of several likely intermediates, by addition of known sulfur compounds in trace amounts, were found to be profitable for the purpose of indicating some of the initial processes that take place.

First, in order to test the possibility that X is SO_2 (or HSO_3^-), a small amount of SO_2 was added (as SO_3^{2-} in a crystal of Na_2SO_3) to the 98% H_2SO_4 in which the potential of the Pt electrode was being cycled as in Fig. 2a (full potential range). Immediately the characteristics of Fig. 4 were developed, including quantitatively the finer details. Therefore, the initial reduction of H_2SO_4 is evidently to SO_2 or HSO_3^- . However, it is known [e.g., Ref. (7)] that SO_2 itself can be reduced at Pt to sulfur species in lower oxidation states, e.g., H_2S or S. This could explain the initial effects of electrode rotation in the cathodic holding experiment; thus, SO_2 (X) is first produced and some can be spun away, but some more strongly bound reduced species Y, such as one-site

and two-site chemisorbed S and corresponding SO species (7, 8) are eventually built up on the surface from the SO₂ and give rise the anodic saturation

(23): $2\text{SO}_3^{2-} \rightarrow \text{S}_2\text{O}_6^{2-} + 2e$. This suggests an alternative pathway for the reduction and reoxidation processes observed in 98% H₂SO₄ at Pt, as follows:



currents for partial reoxidation of these species in regions IIa + IIIa (Fig. 4, 5, and 7) when $\tau_{h,c}$ is sufficiently long (90 sec). The subsequent oxidation of these strongly bound species, or of the SO₂ initially produced, in the anodic sweep following the time $\tau_{h,c}$ cannot be back to H₂SO₄ or SO₃, otherwise no further facile reduction of Y₀ to Z in the next cathodic sweep would be observed, as we mentioned earlier.

There is some induction time in the development of the species (Y) that is oxidized in the anodic sweeps after cathodic holding and after this induction time an extra anodic current shoulder (IIIa) appears on the anodic sweep. It is when this shoulder is developed that the re-reduction peak, IIIc, on the subsequent cathodic sweep is developed (Fig. 4). The efficiency of the production of Y and Y₀ from X depends on the mass-transport conditions and these determine the induction time.

The chemistry of the oxy- and thio-oxy-acids of sulfur is very complex (23) and a number of possibilities exists for the identity of the species Y and Y₀. Generally speaking, there are two types of species that may be involved: (a) thio-oxy-acid or anion species that may be produced in an adsorbed state on the electrode, but correspond stoichiometrically to known molecules or ions; or (b) chemisorbed species, not necessarily known molecules, derived from reduction of SO₂ (produced initially from the H₂SO₄) and from the reoxidation of these species on the electrode surface, e.g., Ref. (7, 8). First, we shall deal with possibilities of type (a).

The experiment with added SO₂ as SO₃²⁻ gives the unambiguous conclusion that the initial product (X) of electrochemical reduction of H₂SO₄ at Pt is SO₂ or HSO₃⁻. Products of further reduction could be dithionite (X', see below), and of subsequent reoxidation in the following anodic sweep, they could be SO₂ (or HSO₃⁻) or dithionate (S₂O₆²⁻), or the corresponding acids or acid anions. Sulfoxylate or sulfoxylic acid, S(OH)₂, is unlikely to be the species Y₀ as the S in this compound is in a lower valence state than that of S in SO₂ or HSO₃⁻ and is very unstable (23).

A first possibility for consideration is that, initially, after short periods of cathodic holding, SO₂ can, in fact, be to some extent reoxidized back to H₂SO₄ (or SO₃) in an anodic sweep, but, during longer times of reduction, $\tau_{h,c}$, SO₂ can be reduced further to dithionite ion, S₂O₄²⁻. This could be then reoxidized on the following anodic sweep to the species Y₀ that can be re-reduced in the cathodic peak IIIc. Thus Y₀ would be SO₂ and Z S₂O₄²⁻ again.

A chemical simulation experiment with addition of dithionite (as Na₂S₂O₄) was unproductive as the S₂O₄²⁻, or the corresponding acid, is immediately decomposed by 98% H₂SO₄ to SO₂, and some H₂S and colloidal S. Only the characteristics of added SO₂ are observed. S₂O₄²⁻ appears therefore to be too unstable to be a likely intermediate giving rise to Y as SO₂.

The electrolytic oxidation of SO₂ or SO₃²⁻ to dithionate, however, is reported in the early literature

Here it is supposed that the species Y₀ (which cannot be H₂SO₄ or SO₃) is S₂O₆²⁻, formed in the anodic sweep over regions Ia and IIa from X (SO₂ or HSO₃⁻), and that S₂O₆²⁻ can be reduced with facility back to SO₂ or HSO₃⁻ in the cathodic sweep (peak IIIc), following its formation from SO₂ or HSO₃⁻.

A further simulation experiment was performed in which S₂O₆²⁻ (as the Na⁺ salt) was added at the beginning of the surface oxidation region (Ia) in an anodic sweep. No enhancement of anodic currents is observed under these conditions, but on the following cathodic sweep, the cathodic current peak IIIc near the H₂ reference potential is observed, as in the experiments with slow reduction of the H₂SO₄ (Fig. 4) in the absence of an added compound. A subsequent anodic/cathodic cycle gave a substantial increase in this cathodic peak; the behavior of added S₂O₆²⁻ is illustrated in Fig. 8.

These observations are consistent with Y₀ being an adsorbed form of S₂O₆²⁻ (or HS₂O₆⁻ or dithionic acid) since if Y₀ is S₂O₆²⁻ and it is added at the beginning of the surface oxidation region, no extra anodic currents should be observed; this is as found. Moreover, if Y₀ is S₂O₆²⁻ formed from the SO₂ or HSO₃⁻ produced in the reduction experiments in H₂SO₄, then it could be reduced back to SO₂ or HSO₃⁻ (or some other species such as H₂S) in the cathodic peak sweep (peak IIIc); this is observed in the simulation experiment (Fig. 8).

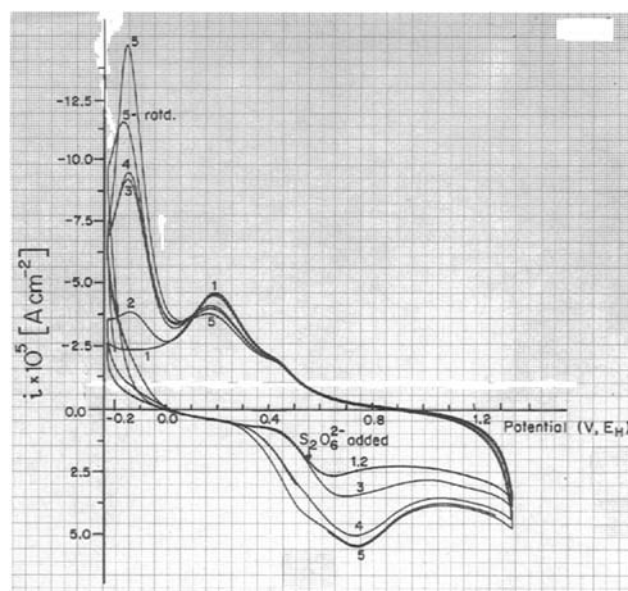


Fig. 8. Cyclic-voltammograms at 70 mV sec⁻¹ for Pt in 98% H₂SO₄ with dithionate added on the anodic sweep at 0.48V E_H. Curve 1, initial anodic sweep *i* vs. *V* profile without holding and without addition of S₂O₆²⁻. Curve 2 (beyond 0.48V), after addition of 10⁻⁴ mol S₂O₆²⁻ (no change). Curves 3, 4, 5 *i* vs. *V* profiles for successive potential sweeps after completion of 1, 2 following addition of the dithionate.

It should be noted that most of the thio-oxy-acids of S, and their anions, are unstable in acid medium but $S_2O_6^{2-}$ is known to be the least unstable (23). It does, however, decompose in H_2SO_4 with evolution of SO_2 , as was observed in the present experiments. Since this SO_2 could form Y_0 on the anodic sweep, whatever Y_0 is, another simulation experiment was carried out by cycling the electrode only over the potential range up to the onset of surface oxidation (0.48V) (Fig. 8), i.e., over the range where Y_0 could be reduced on a following cathodic sweep, but where no oxidation peaks for any species such as SO_2 formed from some decomposition of added $S_2O_6^{2-}$ would be observed. $S_2O_6^{2-}$ was added and again gave, under these conditions, a reduction peak on the cathodic cycle, similar to that observed in the experiments on reduction of H_2SO_4 or with added SO_2 or HSO_3^- .

These results suggest that the intermediate Y_0 could be $S_2O_6^{2-}$ (or $HS_2O_6^-$ or dithionic acid) or, more likely, $S_2O_6^{2-}$ in an adsorbed state. We next consider (b), chemisorbed species.

Possible chemisorbed species.—Not all the features of the reduction behavior of H_2SO_4 can be accounted for simply in terms of plausible, "stable" chemical intermediates such as dithionite or dithionate species, even if they are chemisorbed. It has already been mentioned that the lack of an effect of electrode rotation rate on the anodic *i vs. V* profile observed after reduction of the H_2SO_4 to SO_2 for times $\tau_{h,c}$ indicates that a species in a chemisorbed state is derived from SO_2 (X) and saturation coverage can be attained as measured by the subsequent oxidation current profile (IIIa + IIa). This opens up a number of possibilities for the identity of species Y_0 , or Z, other than in terms of known chemical intermediates of the kind considered above.

Some insight into the nature of the chemisorbed species that evidently might be involved in the reduction of H_2SO_4 can be gained from the work of Lal *et al.* (7-10) and of Loučka (11-13) who studied chemisorbed S-containing species at Pt, derived from H_2S and SO_2 in aqueous medium. Both Loučka (11, 13) and Lal *et al.* (7, 8) concluded that an oxygenated S species arose in chemisorption from either SO_2 or H_2S solutions (9) at Pt when the Pt surface was subjected to an anodic sweep. Bridged and linear "Pt-S-O" species (valencies and bonding not defined) were proposed, based on cyclic-voltammetry experiments on 0.5M aq H_2SO_4 solutions containing SO_2 and H_2S . Doubly and singly bound S and S_2 species produced in successive reduction stages from SO_2 were also postulated. Species such as "Pt-S-O" would be qualitatively consistent with the observation that the reduction peaks in the "surface oxide" region, observed in the present work, are related in some coupled way to the reduction process IIIc nearer the H region, as indicated by the isopotential point (Fig. 6). When the species X and some derived oxidized form Y_0 is produced on the electrode, the bound surface oxide reduction charge on the following cathodic sweep is diminished, but the charge associated with the "re-reduction" process at IIIc is increased. The process IIIc can evidently produce a product which is desorbed as indicated by the experiments at a rotated electrode (Fig. 7). This product is unlikely to be regenerated SO_2 since the results show that at potentials near the cathodic side of the peak IIIc, SO_2 is strongly adsorbed. Possibly the step IIIc involves reduction of the previously adsorbed species to H_2S . At the moment the nature of the various chemisorbed species remains speculative.

An attempt was made by means of relative reflectivity measurements to distinguish qualitatively between the surface oxide species generated in the regions Ia, IIa, and the species associated with the extra

currents observed in this region and IIIa (Fig. 4) after cathodic holding. Thus the surface oxide monolayer formed at Pt normally gives an increasingly negative ($\Delta R/R$) signal with increasing positive potential.

Figure 9 shows how ($\Delta R/R$) varies with potential in anodic and cathodic sweeps following cathodic holding. The potential range is the same as that in Fig. 4, so that both the regions where extra anodic currents pass in IIIa, + Ia + IIa, and the region where the cathodic peak IIIc arises are covered in this diagram.

Figure 9 shows that the general shape of the ($\Delta R/R$) vs. *V* relations remains the same while the chemisorbed reactive species produced on cathodic holding is removed by successive anodic/cathodic cycling, but the intensity of the ($\Delta R/R$) signal falls

as less of the species remains on the electrode. In the anodic direction, the reflectivity features of surface oxidation are not lost despite the development of extra oxidation charge (~ 4.20 C m^{-2} , Fig. 5) over the surface oxide formation region. This suggests [cf. Ref. (7, 8, 11, 13)] that the adsorbed species generated by cathodic holding and oxidized in the following sweep, is in a state intimately connected with the development of the surface oxide film as we have implied earlier in discussing the cyclic voltammograms and the isopotential point observed therein.

Relation to surface oxide formation and reduction.—

The diminution of the surface oxide reduction peak as larger extents of reduction of H_2SO_4 are allowed to take place (Fig. 4) during cathodic holding, probably arises because the surface oxide participates, during the anodic sweep after holding, in the oxidation of SO_2 or of a reduced and/or chemisorbed (7-13, 24) form, to $S_2O_6^{2-}$ or to other adsorbed species such as -S-O (9), so that less oxide is formed during the time of that anodic sweep. The experiment where cathodic holding was carried out at the stationary and

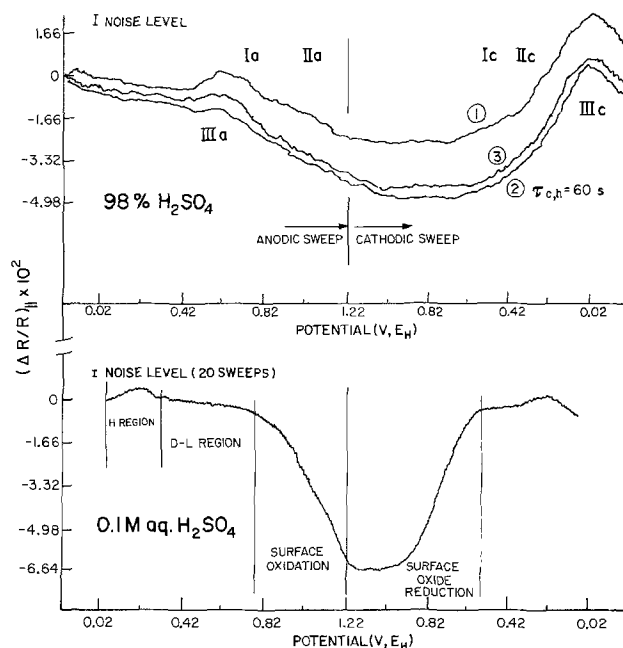


Fig. 9. Relative reflectivity ($\Delta R/R$) profiles for Pt in 98% H_2SO_4 as a function of potential (sweep rate 70 mV sec^{-1} , 298 K) at Pt in the presence of the adsorbed species generated by cathodic holding for 60 sec and in its absence during a repetitive sweep or during its decline after holding. Designations as in Fig. 2(a). Curve 1, behavior on repetitive cycling, as in Fig. 2(a); curve 2, after 60 sec holding at cathodic end of sweep, one cycle; curve 3, third cycle after the 60 sec cathodic holding; lower curve for $0.1M$ aq H_2SO_4 for comparison.

rotated electrode, showing that rotation had no effect on anodic currents observed on the subsequent anodic sweep, implies that S₂O₆²⁻ or S-O-species are being formed in an adsorbed state, thus competing with formation of some of the surface oxide that would otherwise have been produced on the anodic sweep as in Fig. 2 without any reduction of H₂SO₄. The complete absence of an observable upd region for H at Pt (Fig. 2a) indicates that strong adsorption of H₂SO₄ molecules and/or HSO₄⁻ ions is occurring as well.

The conclusions concerning S₂O₆²⁻ or S-O-adsorption are supported by the behavior observed when the potential is held constant for some time at the end of the anodic sweep, following slow reduction of H₂SO₄ during cathodic holding: then a normal quantity (cf. Fig. 2) of surface oxide becomes again observable. It was also concluded by Geronov *et al.* (25), that reduction of SO₂ at Pt, in this case in CH₃CN, leads to formation of an adsorbed species that rapidly transforms into a passivating film of dithionate (*sic*; probably dithionite in their case).

Role of water.—Following the work described above in "98%" H₂SO₄, some experiments were performed with controlled additions of water to give concentrations of 0.275, 0.55, and 1.10M of added H₂O in the 98% H₂SO₄. As shown in the series of *i vs. V* profiles in Fig. 10, addition of water allows some upd of H to arise before significant H₂ evolution currents appear. Also, in the presence of added water, cathodic holding, followed by an anodic cathodic sweep, produces less of the reduced and reoxidizable species as the water content is increased. Eventually normal behavior of an aqueous H₂SO₄ solution is recognized where reduction effects are insignificant.

Since, with relatively small additions of water, the reduction reaction is considerably diminished, yet the concentration of H₂SO₄ is still *ca.* 17M, this behavior suggests that the reduction to SO₂ and another intermediate does not take place from molecular H₂SO₄ but possibly from the small concentration² of H₂S₂O₇ that is present at equilibrium with H₂SO₄ molecules (2). The added water of course, even at the highest concentration of 1.1M could only produce 1.1M of extra H₃O⁺ and HSO₄⁻ ions, *i.e.*, *ca.* 5.8 mol percent, so that most of the H₂SO₄ remains as un-ionized molecules.

Behavior at Au.—In order to examine if the reduction of H₂SO₄, or H₂S₂O₇ contained in it, is a simple electron-transfer process or one requiring chemisorption and electrocatalysis, the behavior of a gold electrode in 98% H₂SO₄ was examined comparatively. An excellent cyclic-voltammetry profile is obtained at Au, with no evidence of impurity effects [cf. Ref. (5, 16)], confirming the high degree of purity of B.D.H. Aristar H₂SO₄. The general features of this curve for Au are similar to those for Au in aqueous H₂SO₄. Cathodic holding for up to 2 min at the same potential as at Pt revealed absolutely no indication of any reduction of the H₂SO₄. The subsequent anodic and cathodic sweeps were identical with those under repetitive cycling conditions. Under the same conditions as at Pt, addition of SO₂ (as SO₃²⁻) also gave no reaction currents, either in anodic or cathodic sweeps. This is contrary to what has been found in aqueous solutions (24) and the absence of such an effect here must be attributed presumably to the strong adsorption of H₂SO₄ [cf. Ref. (5)] at Au and the different effective cathodic range of potentials therefore involved. Adsorption and reactivity of S (as S²⁻) at Au are also known (26).

It is therefore to be concluded that the reaction of H₂SO₄ reduction observed at Pt is associated with the

² However, the rotation experiments mentioned on p. 2265 on behavior at the rotated Pt electrode would not support this conclusion unless the rotation effect is more connected with spin-off of SO₂, restricting further reduction and/or chemisorption to Y.

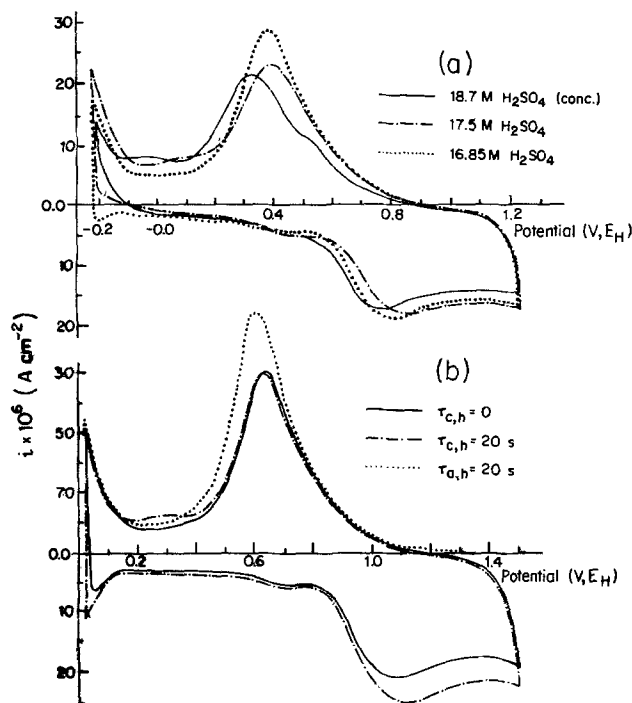


Fig. 10. Cyclic-voltammetry *i vs. V* profiles for Pt in 98% H₂SO₄ with small additions of extra water. Sweep rate 58 mV sec⁻¹; 298 K. (a) Anodic/cathodic cyclic-voltammograms without cathodic holding. (b) Behavior after cathodic holding for 20 sec or, separately, anodic holding for 20 sec. Concentrations of H₂SO₄, after additions of water, as indicated.

catalytic and adsorptive properties of this metal and that H₂SO₄, or H₂S₂O₇, is not easily reduced in an electron-transfer process not involving chemisorption and electrocatalysis.

Conclusions

98% H₂SO₄ can be reduced at Pt electrodes near the steady potential of a hydrogen electrode in the same solution. Chemical simulation experiments demonstrate that the identity of the initial product of the observed slow reduction of H₂SO₄ is SO₂ or HSO₃⁻. A chemisorbed species derived from SO₂ is oxidized in a following anodic sweep not back to H₂SO₄ or SO₃ but to an adsorbed intermediate Y₀ that is reduced back to a species that is relatively easily desorbed into solution at the end of a subsequent sweep near the H₂/H⁺ steady potential. Simulation experiments show that it is possible that the species (Y₀) derived from SO₂ is dithionate or dithionic acid, probably stabilized in some state by adsorption at the Pt electrode. It is most likely that chemisorbed intermediates, derived from SO₂, or from the added S₂O₆²⁻, which are not normal stable compounds, are involved.

No reduction of 98% H₂SO₄ or electroactivity of SO₂ (or HSO₃⁻) is observed at Au under the same conditions as at Pt. By comparison, therefore, the observation of reactions which take place at Pt indicate that an electrode surface, where electrosorption and electrocatalysis can occur, is required for the initial stage of reduction of H₂SO₄ to SO₂.

Acknowledgments

Grateful acknowledgment is made to the Natural Sciences and Engineering Research Council of Canada for support of this work. One of us (D.M.N.) acknowledges a Leave of Absence for Specialization from the Laboratory of Physicochemical Separations, Centre for Marine Research, Ruder Bosković Institute, Zagreb, Yugoslavia. We thank Mr. J. C. Ku in our laboratory for carrying out the reflectivity experiments.

Manuscript submitted Sept. 12, 1980; revised manuscript received May 12, 1981.

Any discussion of this paper will appear in a Discussion Section to be published in the June 1982 JOURNAL. All discussions for the June 1982 Discussion Section should be submitted by Feb. 1, 1982.

Publication costs of this article were assisted by the University of Ottawa.

REFERENCES

- B. E. Conway and D. M. Novak, *J. Phys. Chem.*, **81**, 1459 (1977); see also B. E. Conway and D. M. Novak, *J. Electroanal. Chem. Interfacial Electrochem.*, **99**, 133 (1979).
- R. J. Gillespie and E. A. Robinson, in "Non-Aqueous Solvent Systems," T. C. Waddington, Editor, Chap. 4, Academic Press, New York (1965).
- J. O. Zerbino, N. R. de Tacconi, and A. J. Arvia, *This Journal*, **125**, 1266 (1978).
- N. A. Balashova and V. E. Kazarinov, *Elektrokhimiya*, **1**, 514 (1965); *Dokl. Acad. Nauk SSSR*, **157**, 1174 (1964).
- B. E. Conway, H. Angerstein-Kozłowska, B. Barnett, and J. Mozota, *J. Electroanal. Chem. Interfacial Electrochem.*, **100**, 417 (1979).
- J. S. W. Carrozza, H. A. Garrera, and A. J. Arvia, *Electrochim. Acta*, **14**, 205 (1969); **13**, 771 (1968).
- A. Q. Contractor and H. Lal, *J. Electroanal. Chem. Interfacial Electrochem.*, **93**, 99 (1978).
- A. Q. Contractor and H. Lal, *ibid.*, **96**, 175 (1979).
- R. Jayaram, A. Q. Contractor, and H. Lal, *ibid.*, **87**, 225 (1978).
- A. Q. Contractor and H. Lal, *ibid.*, **103**, 103 (1979).
- T. Loučka, *ibid.*, **31**, 319 (1971).
- T. Loučka, *ibid.*, **36**, 366, 369 (1972).
- T. Loučka, *ibid.*, **44**, 221 (1973).
- J. O. Zerbino, N. R. Tacconi, A. J. Calandra, and A. J. Arvia, *ibid.*, **77**, 379 (1977); A. J. Calandra, N. R. de Tacconi, and A. J. Arvia, *ibid.*, **49**, 145 (1974); N. R. de Tacconi, A. J. Calandra, and A. J. Arvia, *ibid.*, **51**, 25 (1975); N. R. de Tacconi, A. J. Calandra, and A. J. Arvia, *ibid.*, **57**, 267, 325 (1974). See also F. Colom, A. de la Plaza, and R. Gancedo, *Anal. Quim.*, **71**, 985 (1975).
- E.g., see F. G. Will and C. A. Knorr, *Z. Elektrochem.*, **64**, 258 (1960).
- B. E. Conway, W. B. A. Sharp, H. Angerstein-Kozłowska, and E. E. Criddle, *Anal. Chem.*, **45**, 1331 (1973).
- M. W. Breiter, *Z. Elektrochem.*, **60**, 37, 119 (1956); see also S. B. Brummer, J. I. Ford, and M. J. Turner, *J. Phys. Chem.*, **69**, 3424 (1965).
- S. Gottesfeld and B. E. Conway, *J. Chem. Soc., Faraday Trans. 1*, **69**, 1090 (1973).
- H. Angerstein-Kozłowska, B. E. Conway, and W. B. A. Sharp, *J. Electroanal. Chem. Interfacial Electrochem.*, **43**, 1 (1973).
- D. Gilroy and B. E. Conway, *Can. J. Chem.*, **46**, 875 (1968).
- P. Stonehart, H. A. Kozłowska, and B. E. Conway, *Proc. R. Soc. London, Ser. A*, **310**, 541 (1969).
- D. F. Untereker and S. Bruckenstein, *Anal. Chem.*, **44**, 1009 (1974).
- H. Remy, "Treatise on Inorganic Chemistry," pp. 720-726, Elsevier Publishing Co., Amsterdam (1956).
- Z. Samec and J. Weber, *Electrochim. Acta*, **20**, 402 (1975).
- Y. Geronov, R. V. Moshtev, and B. Puresheva, *J. Electroanal. Chem. Interfacial Electrochem.*, **108**, 335 (1980).
- D. G. Wierse, M. M. Lohengrel, and J. W. Schultze, *ibid.*, **92**, 121 (1978).

Reactions of Scratched Copper Electrodes in Aqueous Solutions

G. T. Burstein* and R. C. Newman¹

Department of Metallurgy and Materials Science, University of Cambridge, Cambridge CB2 3QZ, England

ABSTRACT

The behavior of copper electrodes scratched under potential control in aqueous electrolytes is presented. In alkaline solution the metal surface shows the presence of two distinct types of oxidized monolayer, ascribed to CuOH and Cu₂O, each formed over a unique potential range well below the reversible potential for bulk Cu₂O formation. The Cu₂O monolayer is a necessary precursor to passivation of the metal, and in sulfuric acid solution only the CuOH monolayer is observed. This monolayer acts as an intermediate layer in both the dissolution and passivation processes and probably also exists during steady-state hydrogen evolution. Addition of ammonia to alkaline electrolytes modifies the CuOH monolayer, probably by incorporation of NH₃, rendering formation of Cu₂O more difficult.

Determination of the kinetics of reaction between scratched metal electrodes and aqueous electrolytes gives quantitative information on fast electron transfer steps (1-6). The scratched iron electrode (1) reacts very rapidly to form an Fe(I) species adsorbed to complete coverage to the metal surface. Given the nominal composition of FeOH, this monolayer is affected by some anions in the electrolyte such as Cl⁻ and H₂PO₄⁻ (2). Silver has been shown to react anodically with the formation of single adsorbed monolayers of AgOH and Ag₂O (3, 4). These monolayers are formed at po-

tentials well below the reversible potential for bulk Ag₂O formation and the behavior is in complete accord with results obtained from fast potential sweeping and potential pulsing experiments on polished silver surfaces (3). Thus, at least in the case of silver, these underpotential reactions are not uniquely a property of the heavily cold-worked scratch surface. Further, at pH 14, scratched silver shows a small potential range in which no oxidation reaction occurs: Under these conditions it is possible to determine the zero charge potential of the unreacted metal surface (3, 7).

The fast electron transfer reactions that occur from scratched surfaces have been used to interpret the rate of stress-corrosion cracking in some systems (5, 6, 8). The relevance of bare surface reaction kinetics

* Electrochemical Society Active Member.

¹ Present address: Brookhaven National Laboratory, Upton, New York 11973.

Key words: copper anode, copper polarization, scraped copper, underpotential monolayers.

to mechanically assisted corrosion processes such as stress-corrosion cracking and corrosion fatigue has prompted investigation of dissolution and passivation processes on dynamically strained wire electrodes (9); however, the ill-defined rate of bare surface generation in this type of experiment renders difficult the quantification of this type of result.

The ohmic potential drop to potentiostatically controlled scratched electrodes in relatively resistive solutions has been calculated (10): This type of calculation is necessary because of the very large current densities that flow from the freshly generated metal surface. It is worthy of note that when pure copper is scratched in solutions containing NO_2^- in open circuit, reduction of the anion to NH_3 occurs (11, 12).

In the present paper we examine the behavior of potentiostatically controlled scratched copper electrodes and describe the effects of ammonia on the reactions that occur.

Experimental

Rotating disk electrodes (8 mm diam) were prepared from pure Cu (Johnson-Matthey, 99.999%) by mounting into Perspex and sealing with Araldite. The technique used to scratch potentiostatically controlled rotating disk electrode was described previously (1-6). The diamond stylus tracked with a weight of ~ 2 g, creating a shallow scratch ~ 3 μm deep and 40 μm wide at a rotation rate of 100 Hz and a linear scratching velocity of ~ 2 msec^{-1} . The contact times of the stylus varied from 0.2 to ~ 1 msec. By using the slope of the rising current transient during the actual scratching process to calculate the bare surface current density i_s the resulting value is independent of the contact time of the stylus and also independent of any small irregularities occurring in the scratch width. Thus

$$i_s = \frac{1}{2\pi r \omega y} \frac{dI}{dt}$$

where dI is the change in current on the electrode in time dt due to scratching, r is the distance of the scratch from the center of rotation, ω is the rotation rate of the disk, and y the scratch width. The maximum scratch depth is small compared with its width and is thus ignored. The total charge density q_s required to bring the scratch back to a steady state was also measured; this was calculated from the total area under the current transient, and is given by

$$q_s = \frac{1}{2\pi r \omega y t_c} \int_0^\infty I dt$$

where t_c is the contact time of the stylus. The quantity $2\pi r \omega y t_c$ is the area of the scratch surface. Where re-equilibration of the scratch surface took longer than 5 msec, the q_s values quoted are for 5 msec after initial contact of the stylus.

The potential of the working electrode was measured relative to a saturated calomel electrode via a Luggin capillary probe positioned ~ 40 mm below the working electrode. All potentials are presented relative to the normal hydrogen electrode and have been corrected for the liquid junction potential between the working and reference electrolytes. Corrections have also been made for the ohmic potential drop in the electrolyte due to the current from the scratch using calculations and measurements of the resistance to flow of current to narrow strip electrodes (10).

The counterelectrode was a circular platinum foil, 30 mm diam, containing a small concentric hole through which the Luggin capillary probe emerged. Electrolytes were prepared from analytical grade reagents and doubly distilled water and were purged with deoxygenated nitrogen before and during experiments. Ammoniacal electrolytes were made up to a constant

concentration of $(\text{NH}_3 + \text{NH}_4^+)$ at 1.0M, the latter being added as $(\text{NH}_4)_2 \text{SO}_4$. Where necessary Na_2SO_4 was added as supporting electrolyte to give approximately constant ionic strength. Measurements were made at a temperature of 293 ± 2 K. Potentials were controlled with a Wenking potentiostat (Type OPA 69). Current transients were recorded in a transient recorder (Datalab Type DL 905) and displayed on an oscilloscope or chart recorder.

Results

Bare surface polarization curves and charge density curves for copper in 1.0M KOH are shown in Fig. 1. The anodic reaction is accelerated by orders of magnitude at all potentials above -900 mV (NHE) when compared with the steady-state current densities i_b (also shown in Fig. 1). At potentials more negative than -900 mV (NHE) the cathodic reaction, representing the evolution of hydrogen, is also greatly accelerated. Both anodic and cathodic branches of the bare surface polarization curves do indeed represent electron transfer reactions and are not accounted for by non-faradaic double layer charging processes, since the bare surface charge densities, q_s , are too large at all potentials to represent the latter process. Only in the region of the bare surface mixed potential E_{ms} , at $E_{ms} \pm 25$ mV, does q_s fall below 100 $\mu\text{C cm}^{-2}$, accounted for quite clearly by the fact that the anodic and cathodic reactions occur at comparable rates over this small range.

Anodic current density plateaus occur between -800 and -550 mV (NHE) and between -500 and -350 mV (NHE). These correspond to plateaus in charge density q_s , at 145 ± 26 and 378 ± 58 $\mu\text{C cm}^{-2}$, respectively; although the latter is rather poorly defined it is in quantitative agreement with that found for the

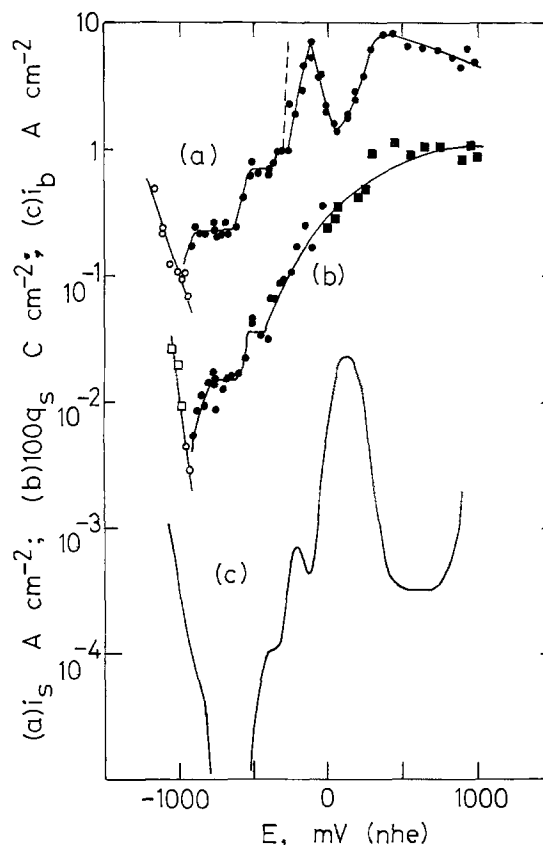


Fig. 1. Bare surface electrochemistry of copper in 1.0M KOH. (a) i_s . (b) q_s after complete re-equilibration (\bullet), or 5 msec after first stylus contact (\blacksquare). (c) i_b obtained from potential sweeping at 10 mV sec^{-1} . Broken line denotes i_s corrected for ohmic drop (10). Black points anodic; white points cathodic. $\omega = 100$ Hz.

silver electrode in the same electrolyte (3) (see below). Between -120 and $+80$ mV (NHE) i_s decreases with increase in E . This potential range corresponds to a rise in the steady-state current density i_b , where copper dissolves anodically to give CuO_2^{2-} in solution prior to passivation of the metal by CuO . It should be noted that during this process q_s increases continuously. The maximum anodic current density observed on the scratch surface is 8 A cm^{-2} . Typical current transients obtained at different potentials in 1.0M KOH are shown in Fig. 2.

Further bare surface polarization curves measured in nonammoniacal electrolytes are shown in Fig. 3-5. In $1.0\text{M H}_2\text{SO}_4$ the maximum anodic current density, i_s , is 1 A cm^{-2} , and q_s shows a maximum at $208 \pm 58 \mu\text{C cm}^{-2}$ covering the long potential range -250 to $+250$ mV (NHE). The second plateau in i_s and q_s does not occur in this electrolyte. Figures 4 and 5 also show plateau anodic charge densities in borate solutions.

Results obtained for ammoniacal electrolytes at three pH values are shown in Fig. 6-8. The diagrams show regions in which both i_s and q_s are independent of E . Regions of potential are also shown where i_s decreases with increase in E , although there is no parallel decrease in q_s . The potential range over which the latter effect occurs commences with the onset of anodic activity of the electrode as a whole, as can be seen by inspecting the appropriate values of i_b in Fig. 6-8. These features of the bare surface polarization curves are discussed below.

The bare surface mixed potentials E_{ms} are plotted in Fig. 9 as a function of pH, together with the reversible potentials for stable equilibrium reactions given by Pourbaix (13) for copper in noncomplexing solutions. Solution species are plotted at a concentration of 10^{-6}M . The values of E_{ms} , which represent potentials at which the rates of oxidation of copper and reduction of hydrogen on the scratch are equal, all lie well below the thermodynamic equilibrium potentials. The anodic reactions on the scratch are thus

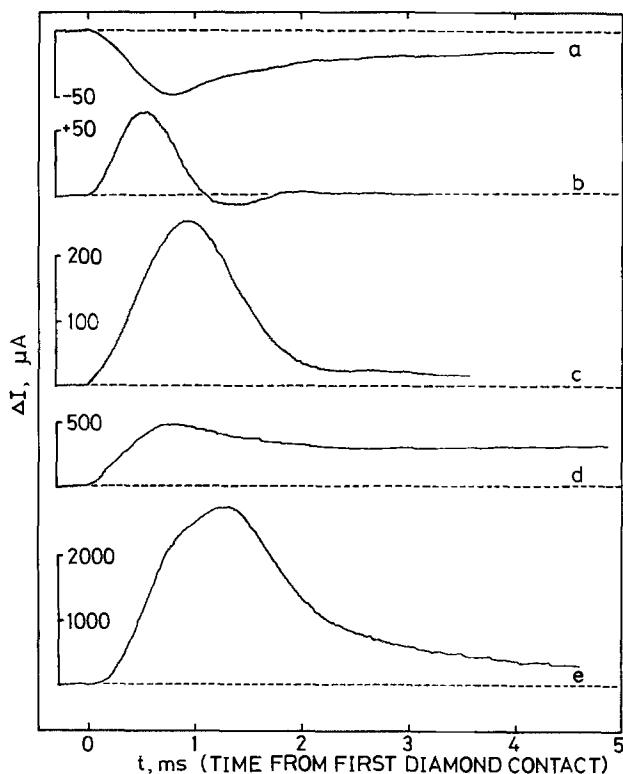


Fig. 2. Current transients obtained from scratching copper in 1.0M KOH at the following potentials in mV (NHE): (a) -1060 , (b) -760 , (c) -385 , (d) $+65$, (e) $+540$.

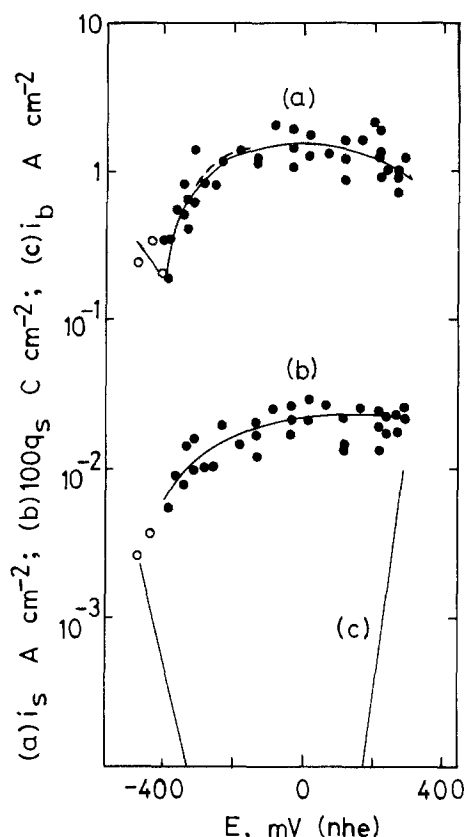


Fig. 3. Bare surface electrochemistry of copper in $1.0\text{M H}_2\text{SO}_4$. (a) i_s . (b) q_s . (c) i_b . Broken line denotes i_s corrected for ohmic drop (10). Black points anodic; white points cathodic. $\omega = 100 \text{ Hz}$.

occurring at an underpotential compared with the equilibrium potentials for bulk reactions. In the non-ammoniacal electrolytes two regions of pH dependence occur: For $\text{pH} < 8$, $\partial E_{ms}/\partial \text{pH} = -57 \text{ mV}$, while for $\text{pH} > 11$ the bare surface mixed potential is indepen-

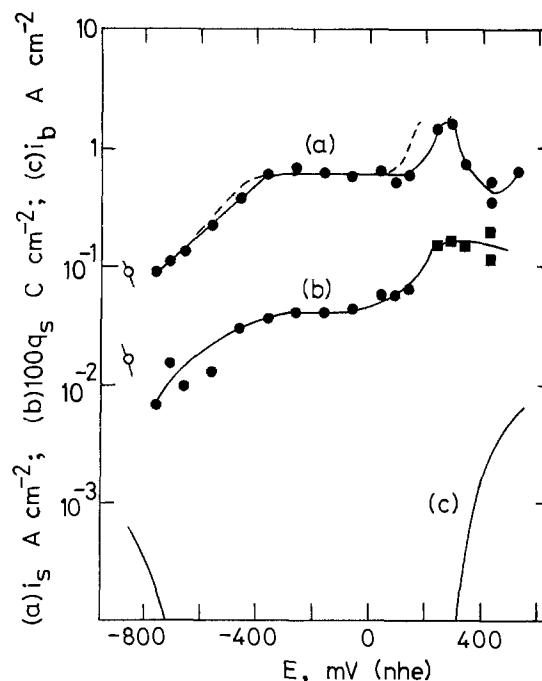


Fig. 4. Bare surface electrochemistry of copper in $0.5\text{M Na}_2\text{SO}_4 + 0.05\text{M (H}_3\text{BO}_3 + \text{Na}_2\text{B}_4\text{O}_7)$, $\text{pH} = 7.3$. (a) i_s . (b) q_s after complete re-equilibration (\bullet), or 5 msec after first stylus contact (\blacksquare). (c) i_b . Broken line denotes i_s corrected for ohmic drop (10). Black points anodic; white points cathodic. $\omega = 100 \text{ Hz}$.

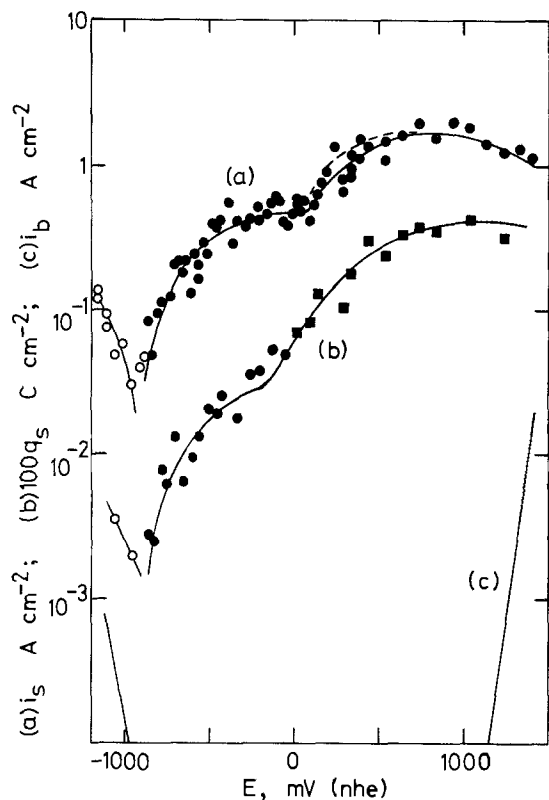


Fig. 5. Bare surface electrochemistry of copper in 0.5M $K_2B_4O_7$, pH = 9.8. (a) i_s . (b) q_s after complete re-equilibration (●) or 5 msec after first stylus contact (■). (c) i_b . Broken line denotes i_s corrected for ohmic drop (10). Black points anodic; white points cathodic. $\omega = 100$ Hz.

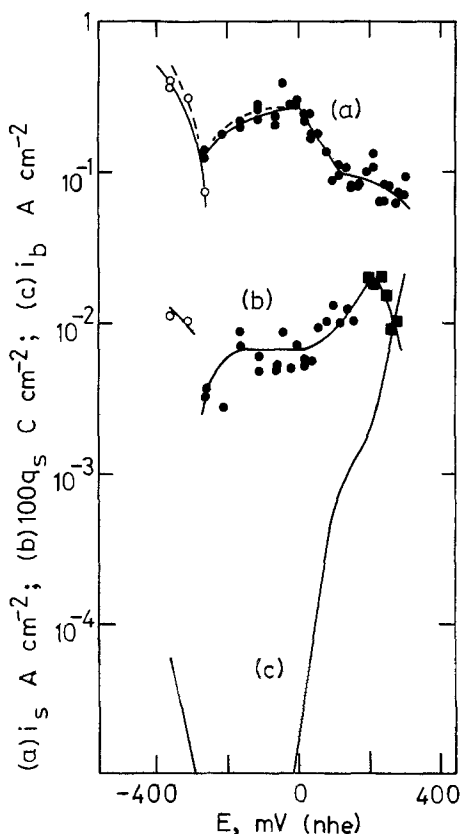


Fig. 6. Bare surface electrochemistry of copper in 1.0M $(NH_3 + NH_4^+)$, pH = 7.25. (a) i_s . (b) q_s after complete re-equilibration (●) or 5 msec after first stylus contact (■). (c) i_b . Broken line denotes i_s corrected for ohmic drop (10). Black points anodic; white points cathodic. $\omega = 100$ Hz.

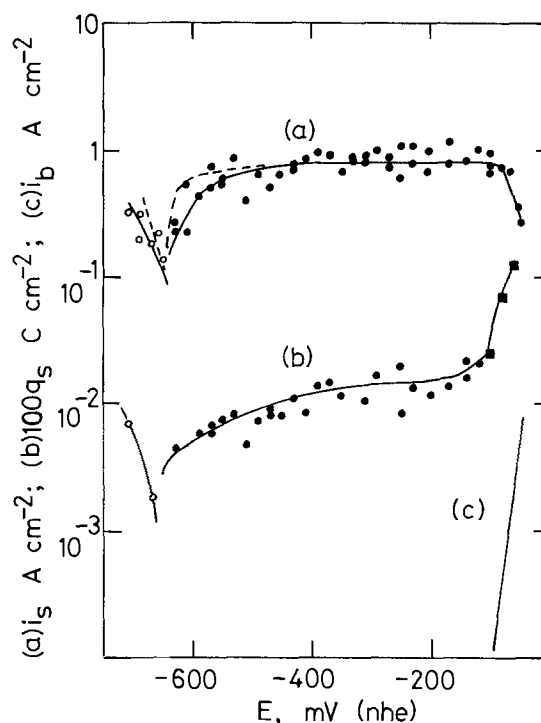


Fig. 7. Bare surface electrochemistry of copper in 1.0M $(NH_3 + NH_4^+)$, pH = 9.5. (a) i_s . (b) q_s after complete re-equilibration (●) or 5 msec after first stylus contact (■). (c) i_b . Broken line denotes i_s corrected for ohmic drop (10). Black points anodic; white points cathodic. $\omega = 100$ Hz.

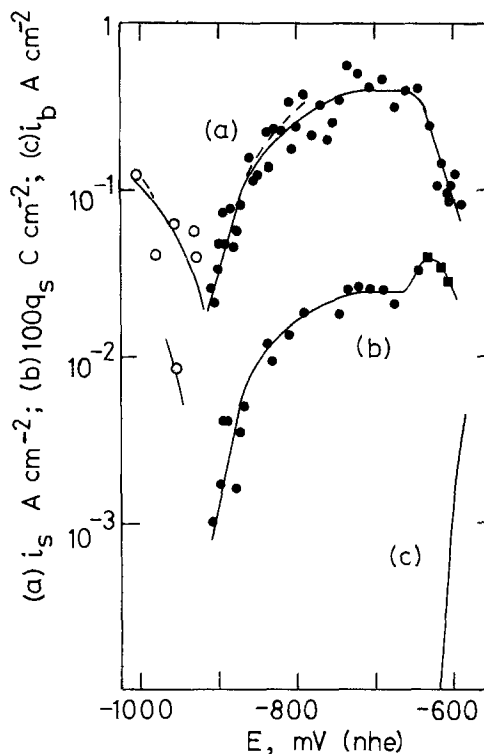


Fig. 8. Bare surface electrochemistry of copper in 1.0M $NH_3 + 0.5M Na_2SO_4$, pH = 11.6. (a) i_s . (b) q_s after complete re-equilibration (●) or 5 msec after first stylus contact (■). (c) i_b . Broken line denotes i_s corrected for ohmic drop (10). Black points anodic; white points cathodic. $\omega = 100$ Hz.

dent of pH. In ammoniacal electrolytes the values of E_{ms} are more positive and give for pH < 10, $\partial E_{ms}/\partial pH = 137$ mV, but this also tends toward pH independence at high pH.

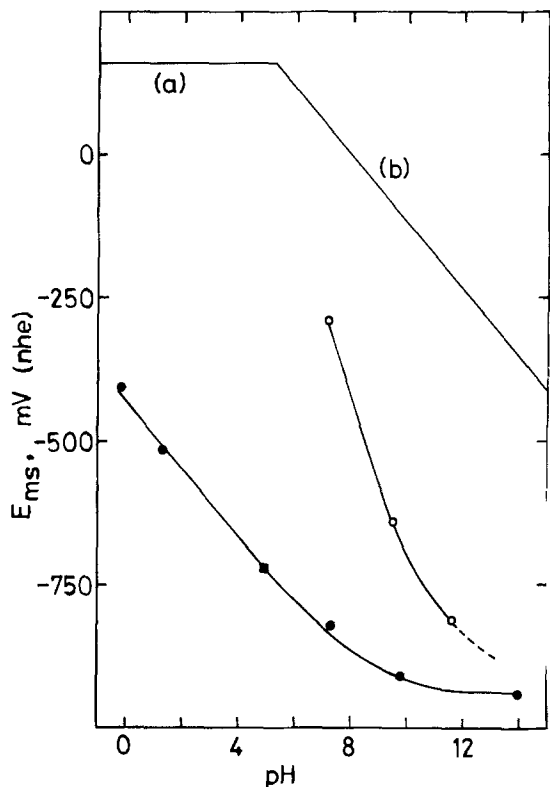


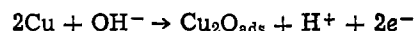
Fig. 9. Bare surface mixed potential E_{ms} of copper as a function of pH. Black points from nonammoniacal electrolytes; white points from ammoniacal electrolytes containing 1.0M $(\text{NH}_3 + \text{NH}_4^+)$. (■) from an acetate buffer solution containing 0.5M HOAc + 0.5M NaOAc. Also shown are the following equilibrium lines from Pourbaix (13): (a) $\text{Cu} = \text{Cu}^{2+} + 2e^-$ with $(\text{Cu}^{2+}) = 10^{-6}\text{M}$, (b) $2\text{Cu} + \text{H}_2\text{O} = \text{Cu}_2\text{O} + 2\text{H}^+ + 2e^-$.

Discussion

Nonammoniacal electrolytes.—In a previous paper we showed that the current and charge densities passed on scratched silver surfaces in 1.0M KOH were not significantly different from those obtained by potential pulsing or rapid potential sweeping experiments on unscratched silver surfaces. Two different adsorbed oxidized monolayers, designated AgOH and Ag_2O , were proposed to account for anodic charge densities of ~ 150 and $\sim 378 \mu\text{C cm}^{-2}$, respectively, obtained by all three techniques; these monolayers were shown to exist over two consecutive potential ranges, both well below the potentials at which anodic activity of the metal is expected (13). The fact that all three techniques showed similar behavior indicates that these observations are not influenced significantly by the highly defective nature of the surface produced by scratching. Figure 1 shows that copper behaves in a very similar way when scratched in 1.0M KOH, with two distinguishable plateaus in the anodic q_s vs. E curve (145 and $378 \mu\text{C cm}^{-2}$, respectively) at low potentials. It is not possible to compare these results obtained on scratched copper directly with those obtained from rapid potential sweeping or potential pulsing experiments owing to interference from the hydrogen electrode reaction. Thus no zero charge potential is observed for scratched copper [as was obtained for silver (3)] owing either to formation of adsorbed hydrogen or oxidation of Cu, or both, at all potentials around the bare surface mixed potential. The two plateau charge densities in the anodic region are ascribed to formation of single adsorbed monolayers of CuOH and Cu_2O , respectively. One would expect a monolayer of Cu_2O to contain approximately twice as many Cu^+ ions per unit area as CuOH, in line with comparisons of other oxide-hydroxide molar density ratios. Both of these monolayers occur at potentials well below the

equilibrium potentials required for multilayer oxide formation (13).

The full sequence of reactions exhibited by the scratched Cu electrode in 1.0M KOH is given in Table I. At -350 mV (NHE) q_s rises above $378 \mu\text{C cm}^{-2}$, representing growth of a multilayer film of Cu_2O , in full agreement with the value of $E_o = -356$ mV (NHE) (13). Dissolution as CuO_2^{2-} also occurs and this contributes to the rise in i_b . Formation of Cu_2O and CuO on the bare surface in Table I is described in terms of the net reactions, and the mechanisms are unknown. Thus for example the underpotential monolayer of Cu_2O may occur in one step



or may form from the previously formed CuOH monolayer



The effects of scratching on the oxygen evolution reaction ($E_o = +400$ mV (NHE)] are also unknown because of interference from the copper oxidation reactions.

The results obtained in 1.0M H_2SO_4 (Fig. 3) differ from those shown in Fig. 2 in that q_s is almost constant at $208 \mu\text{C cm}^{-2}$ over a large potential range. This charge density is consistent with, although slightly greater than that assigned to formation of a monolayer of CuOH in the alkaline solution, and the monolayer of Cu_2O is not formed. In the borate electrolytes (Fig. 4 and 5) the higher charge density plateau, at 300 to $400 \mu\text{C cm}^{-2}$, is observed although plateaus at around $150 \mu\text{C cm}^{-2}$ are obscure. The full analyses of these charges are given in Table II, together with those obtained from the ammoniacal electrolytes.

It is important to realize that in 1.0M H_2SO_4 only the CuOH monolayer is formed. The monolayer of adsorbed Cu_2O , which is apparent at potentials below the Cu/bulk Cu_2O reversible potential in neutral and alkaline solutions, was not found in acid solution. Inspection of the i_b vs. E curve for the acid electrolyte (Fig. 3) shows that there is no tendency for the metal to passivate. Clearly, the first monolayer of Cu_2O is a necessary precursor for passivation, whereas the adsorbed CuOH monolayer acts as an intermediate layer in both the dissolution and passivation processes. Indeed, the CuOH layer probably participates in the hydrogen evolution reaction as well, since Fig. 1-5 indicate that the layer is present at potentials where hydrogen evolution occurs in the steady state. It is for this reason, of course, that the hydrogen evolution reaction is accelerated on scratching. In the regions where i_s is cathodic in Fig. 1-5 values of q_s show that more than a monolayer of hydrogen is reduced on the scratch surface before a steady state is reestablished.

Ammoniacal electrolytes.—The introduction of 1.0M $(\text{NH}_3 + \text{NH}_4^+)$ into neutral electrolytes (Fig. 6) profoundly affects the behavior of the scratched copper electrode. Values of q_s in the potential range -150 to $+50$ mV (NHE) were $62 \mu\text{C cm}^{-2}$, compared with $388 \mu\text{C cm}^{-2}$ in the absence of ammonia (see Table II). The Cu_2O monolayer is thus not formed in the ammoniacal solution. Indeed, the values of q_s are even smaller than that expected for a monolayer of CuOH, and it is clear that NH_3 must be incorporated into the monolayer lattice, so that the number of copper atoms required to form the oxidized monolayer is decreased. The proposed monolayer for ammoniacal electrolytes is $\text{Cu}(\text{NH}_3)\text{OH}$, in which the cation is now $\text{Cu}(\text{NH}_3)^+$, occupying a greater surface area per cation than Cu^+ for nonammoniacal electrolytes. The formation of the ammonia-containing monolayer might be expected to hinder further reaction to produce the Cu_2O monolayer and thus impede passivation of the metal at higher po-

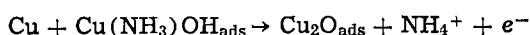
Table I. Reactions of scratched copper in 1.0M KOH and steady-state surface composition as a function of E

| E , mV (NHE) | Bare surface reactions | Steady-state surface composition |
|----------------|---|---|
| < -900 | $\text{H}_2\text{O} + e^- \rightarrow \text{H}_{\text{ads}} + \text{OH}^-$ | $\theta_{\text{H}} \ll 1$ |
| -900 to -550 | $\text{Cu} + \text{OH}^- \rightarrow \text{CuOH}_{\text{ads}} + e^-$ | $\theta_{\text{CuOH}} = 1$ |
| -550 to -500 | $\text{Cu} + \text{OH}^- \rightarrow \text{CuOH}_{\text{ads}} + e^-$ | $\theta_{\text{CuOH}} + \theta_{\text{Cu}_2\text{O}} = 1$ |
| -500 to -350 | $2\text{Cu} + \text{OH}^- \rightarrow \text{Cu}_2\text{O}_{\text{ads}} + \text{H}^+ + 2e^-$ | $\theta_{\text{Cu}_2\text{O}} = 1$ |
| -350 to -150 | $2\text{Cu} + \text{OH}^- \rightarrow \text{Cu}_2\text{O}_{\text{s}} + \text{H}^+ + 2e^-$ | Cu_2O (multilayer) |
| > -150 | $\text{Cu} + \text{OH}^- \rightarrow \text{CuO}_{\text{s}} + \text{H}^+ + 2e^-$ | CuO (multilayer) |

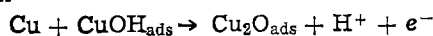
Table II. Analysis of plateau charge densities passed on a bare copper surface in several electrolytes. Error limits are standard deviations over the number of points given. The adsorbed surface monolayers give the proposed stoichiometries, each at complete monolayer coverage.

| Electrolyte | pH | E , mV (NHE) | q_s ($\mu\text{C cm}^{-2}$) | Number of points | Adsorbed surface monolayer |
|---|-------|----------------|---------------------------------|------------------|---|
| 1.0M KOH | 14 | -800 to -600 | 145 ± 26 | 9 | CuOH |
| 1.0M KOH | 14 | -500 to -400 | 378 ± 58 | 4 | Cu_2O |
| 0.5M $\text{K}_2\text{B}_4\text{O}_7$ | 9.8 | -250 to -200 | 352 ± 25 | 2 | Cu_2O |
| 0.5M Na_2SO_4 + 0.05M (H_3BO_3 + $\text{Na}_2\text{B}_4\text{O}_7$) | 7.3 | -450 to -50 | 388 ± 55 | 5 | Cu_2O |
| 1.0M H_2SO_4 | -0.16 | -250 to +275 | 208 ± 58 | 26 | CuOH |
| 1.0M NH_3 + 0.5M Na_2SO_4 | 11.6 | -490 to -350 | 233 ± 33 | 6 | CuOH |
| 1.0M (NH_3 + NH_4^+) + SO_4^{2-} | 9.5 | -390 to -170 | 133 ± 32 | 10 | $\text{CuOH} + \text{Cu}(\text{NH}_3)\text{OH}$ |
| 1.0M (NH_3 + NH_4^+) + SO_4^{2-} | 7.25 | -150 to +50 | 62 ± 15 | 12 | $\text{Cu}(\text{NH}_3)\text{OH}$ |

tentials, since the process



requires removal of NH_4^+ rather than H^+ , as in the reaction



This is reflected in the far higher steady-state dissolution current densities i_b shown for ammoniacal electrolytes (compare Fig. 6-8 with Fig. 1, 4, and 5). In this respect it is noteworthy that the main product of steady-state anodic dissolution of Cu in these ammoniacal electrolytes is $\text{Cu}(\text{NH}_3)_2^+$, which is soluble to the extent of 0.05M in equilibrium with Cu_2O (14).

For higher pH, on the other hand, the values of q_s shown in Table II for ammoniacal electrolytes are higher; this is probably due to reversion of the monolayer to CuOH with increase in hydroxide concentration. This is also reflected in the E_{ms} vs. pH curve (Fig. 9): at high pH E_{ms} approaches the same constant value for both types of electrolytes. Values of the dissolution current density i_b , however, are not a direct consequence of whether the initial monolayer is CuOH or $\text{Cu}(\text{NH}_3)\text{OH}$, since formation of the monolayer is not the rate-determining step in the total dissolution process. Subsequent steps also clearly involve complexing ligands. This has already been described for the scratched iron electrode in chloride and bicarbonate electrolytes (2). Both Cl^- and HCO_3^- cause pitting of iron, but only Cl^- enters the formation of the initial monolayer.

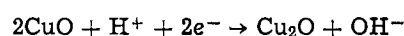
Effects of electrolyte resistance.—Many of the bare surface polarization curves shown in Fig. 1 and 3-8 exhibit regions in which i_s decreases as E becomes more positive. The feature is shown most dramatically in Fig. 1 and 6-8 and is invariably associated with a rise in i_b , representing an increasing rate of anodic dissolution of Cu from the unscratched surface. It is not seen in electrolytes in which Cu is passive (Fig. 4 and 5); nor is it seen in the sulfuric acid system. The effect is associated invariably with ohmic potential drops (10) which occur on and near the scratched surfaces owing to a combination of high electrolyte resistance and high anodic scratch current densities. The consequence of this is to superimpose on the anodic

current transient emanating from the scratch, a cathodic current transient resulting from a lowering of the electrode potential on an area surrounding the scratch when the electrode as a whole is dissolving or carries a readily reducible film. The effect may include two components: a decrease in the rate of steady-state anodic dissolution of the area surrounding the scratch, or electrochemical reduction of surface oxidized species. Thus for example, in Fig. 1 in the potential region in which steady-state dissolution as Cu(II) (in the form of CuO_2^{2-}) occurs from the electrode as a whole, scratching the electrode causes a transient reduction in the rate of steady-state dissolution on an area surrounding the scratch, giving an apparent lowering of the value of i_s with increasing E . The further possible effect of the ohmic potential drop is to reduce oxidized ions on the surface, for example by the following reactions:

on the scratch



on the surrounding surface



Either or both mechanisms may explain the effect as it is observed in 1.0M KOH (Fig. 1) since it occurs in a potential region [commencing at -150 mV (NHE)] where both CuO_2^{2-} and CuO can form (13). The effect has also been observed for the scratched silver electrode (3) at potentials where AgO is reduced transiently to Ag_2O on the area surrounding the scratch.

In 1.0M H_2SO_4 (Fig. 3) the ohmic potential drop effect is not observed, despite overall dissolution of the electrode, since the ohmic resistance of the electrolyte is small, and the values of i_s are themselves lower. In the ammoniacal environments, however, where the electrolyte resistance is high, the effect is clearly observed where the entire electrode is dissolving as $\text{Cu}(\text{NH}_3)_2^+$.

Previous work on scratched and rapidly strained brass electrodes in ammoniacal electrolytes (8, 15) has overlooked these effects and thus obtained values of i_s which are too low. While the effect has not yet been fully quantified, it is clear that the electrode surface

area over which it extends is large compared with the scratch area since i_s is large compared with i_b . It follows that an increase in the ratio of the scratch area to the total electrode area would decrease the ohmic potential effect, and this has indeed been demonstrated by the use of lacquered and partially lacquered electrodes. Appropriate positioning of the Luggin capillary probe would also be of some benefit, but this is impracticable because (i) the proximity of the scratching stylus and (ii) the diameter of the probe tip which would have to be small compared with the scratch size.

Conclusions

1. Scratching of Cu electrodes at constant potential results in greatly accelerated anodic oxidation and cathodic reduction current densities. Up to 8 A cm⁻² of anodic reaction have been recorded.

2. Copper carries two surface oxidized monolayers at potentials very much more negative than the Cu/Cu₂O reversible potential. These underpotential monolayers are designated as CuOH and Cu₂O and account for anodic charge densities of ~150 and 300-400 μC cm⁻² on the scratch surface, each occurring to complete coverage. The former exists at the lowest accessible anodic potentials on the scratch and probably even into the region where hydrogen evolution is the dominant electrode reaction.

3. The Cu₂O monolayer occurs only in neutral and alkaline solutions and is a necessary precursor to passivation of the metal at higher potentials by a thicker film of Cu₂O.

4. The steady-state anodic dissolution of Cu occurs through an adsorbed monolayer of CuOH at complete coverage. The steady-state evolution of hydrogen on Cu also occurs through this monolayer, at least at low cathodic overpotentials.

5. The presence of 1.0M (NH₃ + NH₄⁺) in the electrolyte results in formation of an adsorbed monolayer of Cu(NH₃)OH in the neutral pH range at potentials very much more negative than the Cu/Cu₂O reversible potential. This monolayer is not readily converted to a Cu₂O monolayer, and results in dissolution of the metal as Cu(NH₃)₂⁺ at higher anodic potentials.

6. The scratched copper electrode does not yield a potential of zero charge since electron transfer occurs at all potentials for all pH.

Acknowledgment

We are grateful to the British Petroleum Company Limited for the award of a research studentship to R.C.N.

Manuscript submitted Nov. 19, 1980; revised manuscript received March 31, 1981.

Any discussion of this paper will appear in a Discussion Section to be published in the June 1982 JOURNAL. All discussions for the June 1982 Discussion Section should be submitted by Feb. 1, 1982.

REFERENCES

1. G. T. Burstein and D. H. Davies, *This Journal*, **128**, 33 (1981).
2. G. T. Burstein and D. H. Davies, *Corros. Sci.*, **20**, 1143 (1980).
3. G. T. Burstein and R. C. Newman, *Electrochim. Acta*, **25**, 1009 (1980).
4. G. T. Burstein and R. C. Newman, *ibid.*, **26**, 1143 (1981).
5. F. P. Ford, G. T. Burstein, and T. P. Hoar, *This Journal*, **127**, 1325 (1980).
6. R. C. Newman and G. T. Burstein, *Corros. Sci.*, **21**, 119 (1981).
7. T. N. Andersen, J. L. Anderson, and H. Eyring, *J. Phys. Chem.*, **73**, 3562 (1969).
8. D. J. Lees and T. P. Hoar, *Corros. Sci.*, **20**, 761 (1980).
9. T. P. Hoar and J. C. Scully, *This Journal*, **111**, 348 (1964).
10. H. J. Pearson, G. T. Burstein, and R. C. Newman, *ibid.*, **128**, 2297 (1981).
11. S. P. Pednekar, A. K. Agrawal, H. E. Chaung, and R. W. Staehle, *ibid.*, **127**, 701 (1980).
12. R. C. Newman and G. T. Burstein, *ibid.*, **127**, 2527 (1980).
13. M. Pourbaix, "Atlas of Electrochemical Equilibria in Aqueous Solutions," p. 393, Pergamon/CEBELCOR, Oxford (1966).
14. T. P. Hoar and G. P. Rothwell, *Electrochim. Acta*, **15**, 1037 (1970).
15. J. J. Podesta, G. P. Rothwell, and T. P. Hoar, *Corros. Sci.*, **11**, 241 (1971).

Protective Coatings by Anodic Coupling Polymerization of o-Allylphenol

Giuliano Mengoli, Paolo Bianco, Sergio Daolio, and Maria Teresa Munari

Istituto di Polarografia ed Elettrochimica Preparativa del C.N.R., Corso Stati Uniti 4, 35100 Padova, Italy

ABSTRACT

The anodization of Fe sheets in hydroalcoholic solutions of o-allylphenol containing allylamine leads to *in situ* formation of coherent coatings. These coatings consist of thermosetting polyoxyphenylenes which after thermal curing have good adhesion and impart corrosion protection to the substrate. The anodization time and electric power consumption are comparable with those typical of a conventional electrophoretic coating.

A route for achieving the *in situ* formation of thick (10-20 μm) polyoxyphenylene coatings, having possible applications for metal protection, has been recently outlined (1, 2). The process may be realized by anodizing, at the metal surface to be coated, hydroalcoholic solutions of phenol containing a suitable amine [allylamine gave the best performances (2)]. However, the data so far reported have shown that

Key words: film, corrosion, organic, electrolysis.

the process is not yet competitive with other conventional "painting" techniques. In comparison with the electrophoretic deposition (3) of preformed polymers, the major handicaps were: extended electrolysis times; limited corrosion resistance of the coatings (from salt fog tests), and poor adhesion under stress (from conical mandrel and drawing tests).

The fact that the electrolysis time was too long was mainly related to the low useful electrolysis current

(<10 mA/cm²). *In situ* phenol polymerization, in fact, did not tolerate high applied voltages,¹ because either passivation of the substrate occurred especially when Fe sheet anodes were coated, or rupture of the film being formed took place. The limited corrosion resistance and poor adhesion were likely related to the structure of the polymer. The polymer probably was, *ab initio*, exceedingly branched and cross-linked and thus could neither take appreciable advantage from thermal curing nor have elasticity enough to tolerate stresses and deformations. Through the utilization of *o*-allylphenol instead of phenol we now have overcome such handicaps.

The aim of this paper is to describe both the features of *o*-allylphenol/allylamine *in situ* polymerization onto Fe sheet anodes and the protective performances of the resulting coatings.

Experimental

Apparatus and procedure.—The coating runs were performed in a single compartment cell described previously (1, 4) by applying a constant voltage between the sample of Fe sheet (anode) and a Pt coil (cathode) facing the sheet. Physical properties of the coated specimens were determined according to ASTM methods. The composition of the polymeric material, once recovered from the substrate, was investigated by instrumental analytical techniques, including pyrolysis coupled to mass spectroscopy (5) and thermogravimetry. Information on the molecular weights and their distribution was obtained by vapor pressure osmometry and gel permeation chromatography. Other experimental details are reported in either the tables or the captions of the figures.

Chemicals.—All compounds used in this study were commercially available reagent grade chemicals. The reaction medium consisted of water/alcohol mixtures. The preferred standard composition was: *o*-allylphenol 6 ml, allylamine 6 ml, cellosolve 2 ml, KOH 0.5g, all dissolved in a standard 100 ml of H₂O/CH₃OH (equal volumes). The Fe sheets [23.5 × 2.5 × 0.05 cm (1, 2)] were dipped in alkaline cleaning bath prior to coating.

Results

Characteristics of the electrolytic process.—The formation of coatings on Fe sheet anodes from the *o*-allylphenol/allylamine system bears many similarities to systems based on phenol as described in preceding papers (1, 2). Thus, the coating material is produced by a yield not far from 2F/mol of monomer consumed. An oxidative coupling process is therefore strongly supported, whereas the engagement of the allyl group in an electrolytic polymerization must be discarded.

The formation of a coherent and homogeneous coating is indicated, during electrolysis, by a smooth continuous current decrease. Such current transients are qualitatively affected by experimental variables such as monomer and amine concentration, temperature, composition of the medium, and applied voltage.

However, it must be noted that the high voltages applied here (≅ 15V) do not cause the dramatic passivation phenomena observed elsewhere (1, 2). This behavior is illustrated in Fig. 1 and 2. Figure 1 shows the current transients obtained during the coating process for various applied voltages. In each case the sheets were uniformly coated: The high residual current tested at the highest voltage is due to the relatively low electrical resistance of the wet film. Figure 2 shows the current-potential curves obtained potentiodynamically on a rotating Fe microdisk. Anode insulation by filming is evident here only for very

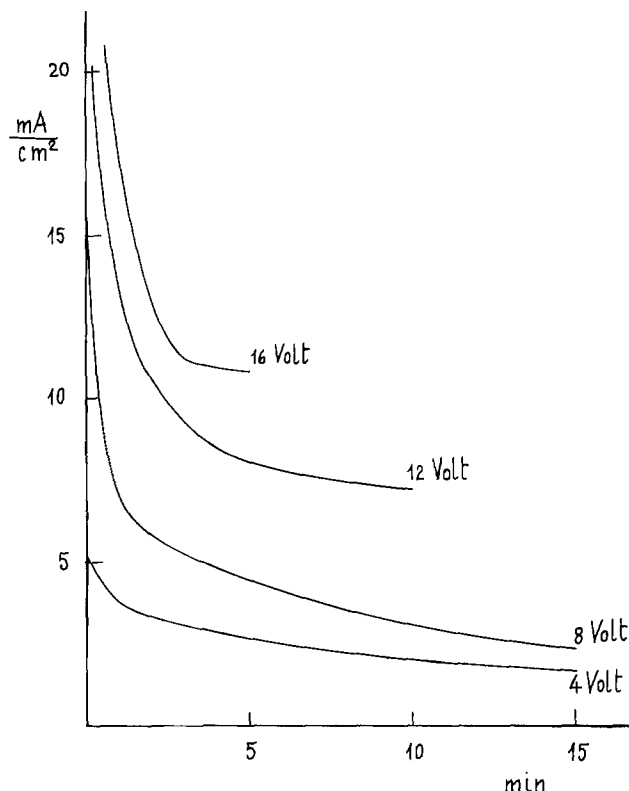


Fig. 1. Current transients during the anodization of Fe sheets in the standard composition (*o*-allylphenol 0.456 mol liter⁻¹, allylamine 0.800 mol liter⁻¹, cellosolve 0.200 mol liter⁻¹, KOH 0.09 mol liter⁻¹, in H₂O/CH₃OH at *t* = 25°C) for increasing applied voltages.

low potential sweep rates (*i.e.*, long electrolysis times).

As mentioned before, the fact that the *o*-allylphenol/allylamine system tolerates far higher voltages than phenol-based systems is very important from a practical point of view, as faster coating operations are achieved. This may be deduced from the data of Table I. The decrease of coulombic yield taking place as the voltage is increased to 16V is quite acceptable considering that both coating thickness (mg/cm²) and deposition time become typical of a conventional electrophoretic process.²

Molecular weights.—In previous work, the coating material obtained from phenol, when dried, partially dissolved only in trifluoroacetic acid. By contrast the (uncured) products from allylphenol consist of a major fraction soluble in common organic solvents (acetone) and a minor insoluble fraction. The latter, which constitutes the inner layer in contact with the metal, may become important in some experimental conditions.

Table II shows how the experimental variables influence both \bar{M}_n and the ratio of soluble to insoluble fractions. Constancy (in the range 2000-3000) of \bar{M}_n obtained for different conditions indicates that the termination step is mainly determined by insolubility of the chains, which cannot thus undergo further anode oxidation. The higher \bar{M}_n resulting either at a high percentage of methanol (runs 8-9) or with ethanol and propanol instead of methanol (runs 20-21), therefore takes into account the increased solubility of the polymer in the medium, whereby chain precipitation takes place for higher degrees of polymerization. The inverse dependence of \bar{M}_n on monomer concentration which seems indicated by runs 1

¹Not more than 3.5V could be generally applied to an electrolyzer having a cell constant ~20 cm, and for solutions having $\chi = 3.8$ msec (1).

²The current passed is about ten times higher here than in electrophoresis, but power consumption ($i \times t \times v$) is of the same order.

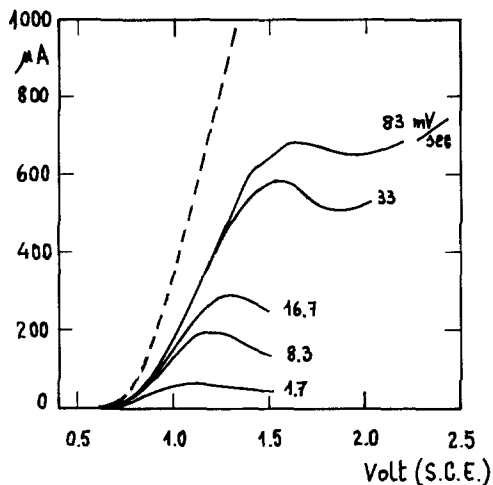


Fig. 2. Current-potential (vs. SCE) curves obtained from the standard composition by a rotating (1000 r/min) Fe microanode (area 0.03 cm²). The dashed line refers to the oxidation of the background system alone; the other curves refer to increasing sweep rates (mV sec⁻¹).

and 5-7 is not surprising when considering that polymer chains are built up step by step at the anode and that the probability of oxidizing and coupling the same chains again increases with monomer dilution. The formation of the insoluble fraction seems to be favored by the highest temperatures, methanol concentrations, and electrolysis times, but depends inversely on the amine concentration (runs 17-19). Neither applied voltage nor charge transferred has any influence.

Molecular weight distributions were estimated, using polystyrene as a standard, by gel permeation chromatography, as shown in Fig. 3.

Table I. Features of electrolytic coating process for various voltages applied*

| Applied Voltage (V) | Time (min) | Charge (C) | I initial (mA/cm ²) | I final (mA/cm ²) | Current yield (mg/C) |
|---------------------|------------|------------|---------------------------------|-------------------------------|----------------------|
| 3.0 | 50 | 81 | 2.78 | 0.59 | 0.577 |
| 5.0 | 15 | 78 | 8.52 | 1.89 | 0.564 |
| 10.0 | 8 | 86 | 23.33 | 5.00 | 0.477 |
| 16.0 | 3 | 74 | 31.48 | 10.55 | 0.400 |

* Conditions: o-allylphenol 0.456 mol liter⁻¹; allylamine 0.800 mol liter⁻¹; cellosolve 0.200 mol liter⁻¹; H₂O/CH₃OH 50% by volume; t = 25°C. The coating yield (mg/cm²) ranged from 1.7 (3V) to 1.3 (16V).

Table II. Features of the coating and molecular weight of the product for various experimental conditions

| Run No. | Temp (°C) | Alcohol (%) | o-Allylphenol (mol/liter) | Allylamine (mol/liter) | Voltage (V) | Electr. time (min) | Coulombs | Yield (mg/C) | Insoluble (%) | \bar{M}_n * | |
|---------|-----------|-------------|---------------------------|------------------------|-------------|--------------------|----------|--------------|---------------|---------------|------|
| 1 | 25 | Methanol | 50 | 0.456 | 0.800 | 4.0 | 65 | 100 | 0.60 | 17.7 | 2660 |
| 2 | 25 | Methanol | 50 | 0.456 | 0.800 | 8.0 | 18 | 100 | 0.52 | 10.0 | 2320 |
| 3 | 25 | Methanol | 50 | 0.456 | 0.800 | 12.0 | 9 | 100 | 0.42 | 10.0 | 2110 |
| 4 | 25 | Methanol | 50 | 0.456 | 0.800 | 16.0 | 4 30 sec | 100 | 0.40 | 7.0 | 2420 |
| 5 | 25 | Methanol | 50 | 0.110 | 0.200 | 8.0 | 38 | 22 | 0.30 | 27.6 | 3030 |
| 6 | 25 | Methanol | 50 | 0.228 | 0.400 | 8.0 | 49 | 60 | 0.53 | 8.9 | 2630 |
| 7 | 25 | Methanol | 50 | 0.684 | 1.200 | 8.0 | 5 | 60 | 0.62 | 5.2 | 2030 |
| 8 | 25 | Methanol | 85 | 0.228 | 0.400 | 8.0 | 20 | 60 | 0.15 | 63.7 | 3220 |
| 9 | 25 | Methanol | 70 | 0.228 | 0.400 | 8.0 | 46 | 60 | 0.20 | 20.8 | 3050 |
| 10 | 25 | Methanol | 35 | 0.228 | 0.400 | 8.0 | 10 | 60 | 0.65 | 7.4 | 2160 |
| 11 | 45 | Methanol | 50 | 0.456 | 0.800 | 8.0 | 47 | 100 | 0.60 | 56.3 | 2520 |
| 12 | 35 | Methanol | 50 | 0.456 | 0.800 | 8.0 | 23 | 100 | 0.60 | 20.8 | 2670 |
| 13 | 13 | Methanol | 50 | 0.456 | 0.800 | 8.0 | 13 | 100 | 0.54 | 0.1 | 1630 |
| 14 | 25 | Methanol | 50 | 0.456 | 0.800 | 8.0 | 44 | 200 | 0.53 | 6.7 | 2280 |
| 15 | 25 | Methanol | 50 | 0.456 | 0.800 | 8.0 | 2 | 30 | 0.65 | 5.8 | 2000 |
| 16 | 25 | Methanol | 50 | 0.456 | 0.800 | 8.0 | 1 | 15 | 0.68 | 4.3 | 2360 |
| 17 | 25 | Methanol | 50 | 0.456 | 0.270 | 8.0 | 34 | 100 | 0.54 | 28.5 | 2700 |
| 18 | 25 | Methanol | 50 | 0.456 | 0.132 | 8.0 | 60 | 100 | 0.50 | 45.1 | 2500 |
| 19 | 25 | Methanol | 50 | 0.456 | 0.066 | 8.0 | 40 | 40 | 0.58 | 56.4 | 2500 |
| 20 | 25 | Propanol | 50 | 0.456 | 0.800 | 8.0 | 18 | 100 | 0.39 | 8.6 | 3750 |
| 21 | 25 | Ethanol | 50 | 0.456 | 0.800 | 8.0 | 27 | 100 | 0.49 | 5.0 | 3220 |

* Determined by vapor pressure osmometry in acetone at 40°C.

Reproducibility of coating performances.—Figure 3 refers to samples selected from a series of 50 sheets, all coated one after the other, with the same 100 ml of standard solution. The good independence of molecular weights on the progressive number of the sheets constitutes a first test of reproducibility for the system.

Confirmation is provided by the constancy of the coulombic yield (mg/C \approx 0.55) observed during the coating process for all these 50 sheets. However, in a limited volume of solution, repeated coating runs lead to a kinetic decline. This is shown in Fig. 4 where the coating yield (mg/cm²) obtained on each sheet after 30 min of electrolysis (i.e., average coating rate) is plotted vs. the progressive number of sheets. This behavior is determined by progressive impoverishment of the monomer from the solution (compare dashed curves a and b of Fig. 4). For the same voltage and electrolysis time, a concentration decrease in effect results in a reduced transfer of current. However, since from a practical point of view it is very easy to achieve automatic control of both monomer concentration in solution and thickness of coatings formed (by the coulombs passed), it may be concluded that system features³ are such as to allow application in continuous processes.

Protective features of the coatings.—When withdrawn from the anodization bath, the coated sheets appear homogeneous and coherent, their color varying from pale yellow to brown yellow.

Wet film adhesion to the substrate is good enough to allow rinsing in running water before drying. When the samples are cured in an oven at 150°-155°C for 20-30 min a fine gloss is obtained. Thermal treatment further improves resistance toward chemicals and organic solvents as well as any other protective feature.

Table III shows the properties of samples obtained on varying either o-allylphenol/allylamine concentrations or electrolysis voltages. Each sample was prepared with the same current passed. The very good results of the conical mandrel and drawing tests, evidencing strong adhesion coupled to elasticity, are to be noted. Remarkable improvements are furthermore shown in the salt fog tests: the time scale of resistance to salt corrosion, especially for samples prepared by fast electrolysis (high voltages), is now more than an order of magnitude higher than the data

³The gas chromatographic analysis of the solutions after repeated coating operations performed on different days showed only dimers as by-products; however, these are easily engaged in the anodic coupling.

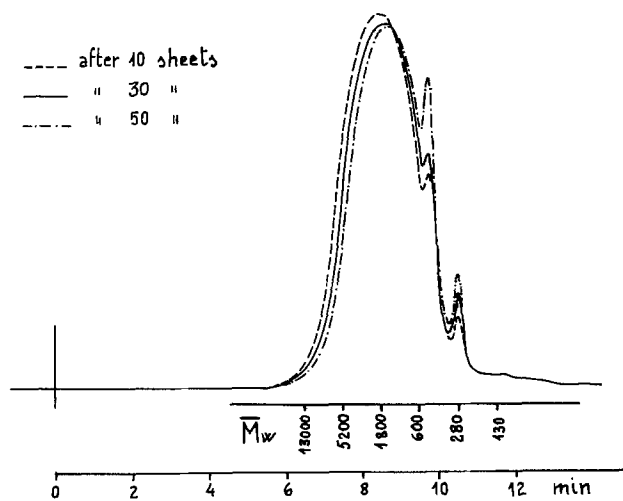


Fig. 3. Gel permeation of unpurified coating samples obtained from a solution utilized for repetitive coating runs. Progressive number of the sheet equal to: - - - 10; — 30; - · - 50. Chromatographic conditions: column μm Styragel 500 A; solvent THF 1 ml/min; detector u.v. 254 nm.

previously reported (800 hr as against 24 hr (1) and 48 hr (2)).

Table IV shows the influence on physical properties of either the temperature of the electrolytic bath or the amount of current passed. An increase in temperature seems to increase the resistance to salt corrosion, while the number of coulombs passed (which controls the thickness of the polymer film) improves that resistance until the coating is between 10–15 μm thick. As regards the influence of the medium on physical properties, it must be mentioned that in nearly methanolic solvent (85%) only thin films (1–2 μm) are obtained, by a low current yield. During the electrolysis these films rapidly passivate the substrate, but when submitted to physical tests, neither give (making due allowance for their thinness) improved protection to the metal nor benefit from curing. The reason for this is discussed below.

Composition of the coating material.—The elemental compositions of either the soluble or the insoluble fractions are not far from the theoretical provisions of an allylsubstituted polyoxyphenylene, although some nitrogen is present (see Table V). With respect

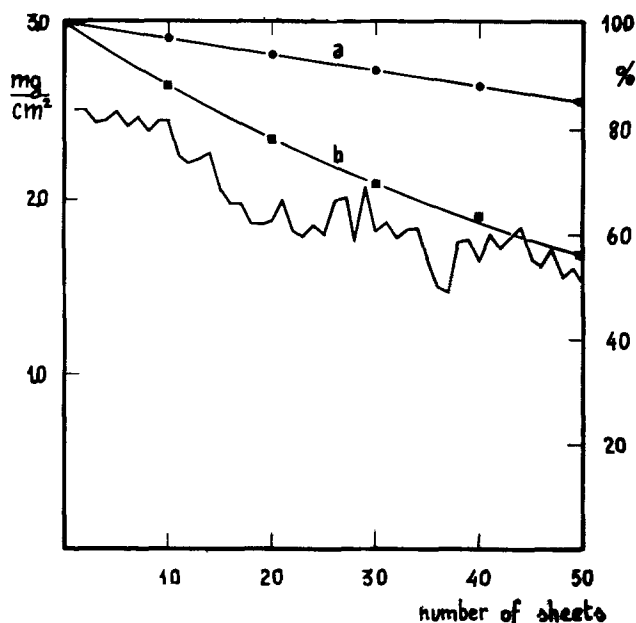
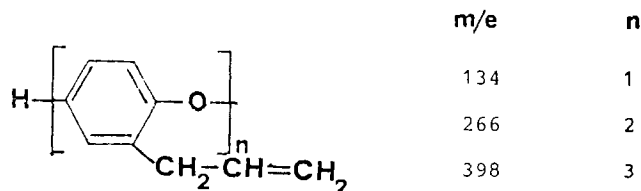


Fig. 4. Left-side scale: polymer yield (mg/cm^2) obtained after a fixed electrolysis time as a function of the number of the samples coated. Right-side scale: curve a, volume decrease (%); curve b, o-allylphenol decrease (%).

to this fact it must be noted that the amount of nitrogen (which derives from the amine) is many times higher in the coatings obtained from phenol (2.5–6%). Similarity for both the soluble and insoluble fractions also exists in the infrared and mass spectroscopy patterns. The second technique, after pyrolysis of the samples at $t \geq 260^\circ\text{C}$ and ionization by a 70 eV electron beam, mainly shows peaks of the structure:



The thermal curing reaction was examined by both infrared and thermogravimetry.

Table III. Physical properties of samples obtained for various o-allylphenol concentrations and applied voltages

| o-Allylphenol (mol/liter) | 0.228 | 0.456 | | | | 0.684 | 0.608 |
|-----------------------------|-----------|-----------|-----------|-----------|-----------|-----------|-----------|
| Allylamine (mol/liter) | 0.400 | 0.800 | | | | 1.200 | 0.533 |
| Voltage (V) | 8.0 | 4.0 | 8.0 | 12.0 | 16.0 | 8.0 | 8.0 |
| Thickness (μm) | 10 | 18 | 14 | 12 | 10 | 14 | 16 |
| Cross cut adhesion | Very good | Very good | Very good | Very good | Very good | Very good | Very good |
| Microholes/ cm^2 | 0 | 0 | 0 | 2 | 10 | 0 | 0 |
| Conical mandrel (ASTM test) | Very good | Very good | Very good | Very good | Very good | Good | Good |
| Drawing (ASTM test) | Very good | Very good | Very good | Very good | Very good | Good | Good |
| Hardness* | 6H | 6H | 6H | 6H | 6H | 6H | 6H |
| Salt fog resistance (h)** | 200 | 150 | 170 | 500 | 800 | 180 | 220 |
| U.V. resistance (h) | >300 | >300 | >300 | 240 | 240 | >300 | >300 |

* Determined by graphite standards.

** ASTM method B117.

Table IV. Physical properties of samples obtained for various temperatures and coulombs

| Temperature ($^\circ\text{C}$) | 13 | 35 | 45 | 25 | 25 | 25 | 25 | 25 |
|----------------------------------|-----------|-----------|-----------|-----------|-----------|-----------|------|------|
| Coulombs | 100 | 100 | 100 | 15 | 30 | 60 | 150 | 200 |
| Thickness (μm) | 14 | 18 | 15 | 2.5 | 4 | 9.5 | 25 | 30 |
| Microholes/ cm^2 | 0 | 0 | 0 | 50 | 20 | 0 | 0 | 2 |
| Hardness | 6H | 6H | 6H | 6H | 6H | 6H | 6H | 6H |
| Adhesion + elasticity | Very good | Very good | Very good | Very good | Very good | Very good | Good | Good |
| Salt fog resistance (h) | 120 | 280 | 500 | 70 | 280 | 400 | 150 | 120 |

The anodization solution had the standard composition.

On comparing infrared spectra obtained from samples before and after thermal curing, the following variations may be outlined: (i) The uncured samples show three bands in the range 3000-2840 cm^{-1} , typical of allyl C-H stretching, and a sharp band at 1640 cm^{-1} , which may be ascribed to $-\text{HC}=\text{CH}_2$ stretching; (ii) in the cured samples, the morphology of the bands between 3000-2840 cm^{-1} changes, although the respective ν do not. At the same time the band at 1640 cm^{-1} becomes very feeble, and a new absorption appears between 1750-1650 cm^{-1} (maximum at 1715 cm^{-1}), which may be ascribed to $\text{C}=\text{O}$.

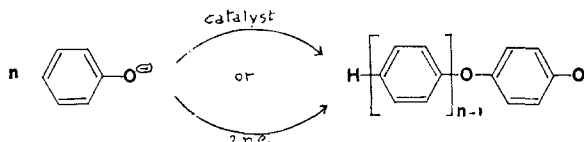
Different results are obtained from the thermogravimetric analysis when the experiments are performed in either nitrogen or air. Under N_2 a slow weight loss takes place up to pyrolysis conditions; at 285°C an exothermic reaction occurs (by DTG). Under air, the weight of the samples increases from 140°C, the reaction reaching its maximum at 170°C; pyrolysis occurs at 230°C.

An oxidative cross-linking is thus strongly supported as the main curing process. It must also be noted that since the polymer has a T_G at 328 K, it passes through a viscous quasi-melting state in the oven before reacting with oxygen.

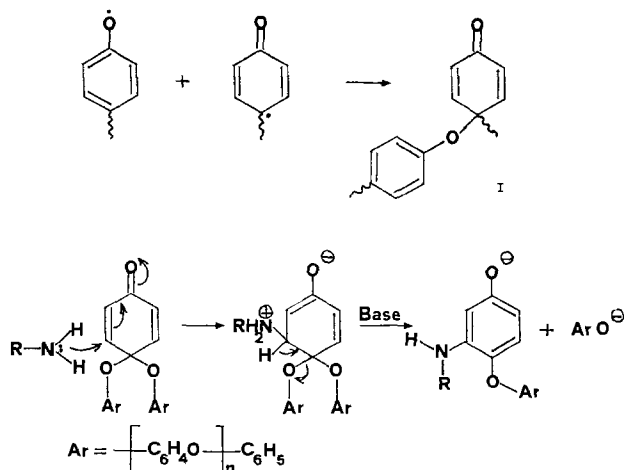
Discussion

In order to explain the results shown by *o*-allylphenol, it seems useful to summarize the mechanism of *in situ* coating formation.

In the electrochemical coupling of phenoxide anions, the anode substitutes the copper salt amine complex catalyst (6)



For the chemical polymerization the exhausted (reduced) copper catalyst is continuously restored (oxidized) by oxygen; electrochemically the continuity of the oxidation is provided by the anodic potential. The polymerization reaction is not limited to head-to-tail coupling, but also involves the ortho positions: For this reason 2,6-dimethylphenol is usually used for obtaining technologically useful linear polymers (6). We have also shown (2) that during anodic coupling of phenol in the presence of amines,⁴ a side reaction frequently takes place between quinol-ether polymeric (I) intermediates (6-8) and amine according to the following scheme



⁴ The amine has a fundamental role as inhibitor of Fe oxidation in the anodic formation of polyoxyphenylene coatings onto Fe sheets (2).

Table V.

| | Elemental analysis | | |
|-------------------------|--------------------|------|------|
| | C | H | N |
| Theoretical composition | 81.2 | 6.7 | — |
| Soluble fraction | 79.2 | 5.31 | 0.70 |
| Insoluble fraction | 77.8 | 4.65 | 0.78 |

The reaction with amines is favored by the electron-attracting ortho substituents which increase the electrophilicity of quinol-ether meta positions. It is probable that other nucleophilic molecules or ions such as OH^- may attack the same positions. In this last case, the newly formed phenolic group might be engaged in the oxidative coupling, thus contributing strongly toward cross-linking. As regards *o*-allylphenol, the *o*-allyl group reduces the occurrence either of coupling in ortho or attack in meta by amine and OH^- . Branching and cross-linking are therefore strongly reduced with respect to phenol polymers. The linearity of the chains leads to two consequences: Uncured coatings have good solubility; and in the oven, before curing, the coating material may melt, thus achieving complete and homogeneous spreading onto the substrate.

However, the same should also hold for other alkyl substituted phenols, whereas we have observed the formation of poorly adhering coatings from, for instance, 2,6-dimethylphenol. The reason for the peculiar behavior of *o*-allylphenol is thus to be found in a strong interaction of the allyl group with the substrate, which causes adsorption of the monomer and bonding to the metal of the polymer as it is formed.

These considerations seem strongly supported by the following macroscopic evidence:

1. High voltages are tolerated during deposition. This fact is also related to the linearity of chains which, swollen by solution, do not cause excessive electric resistance.
2. There is strong adhesion of the polymeric material to the substrate. Such adhesion (which may also be related to the morphology of the chains as determined by the allyl group) cannot be due to some product of the oxidative cross-linking because films dried below 100°C adhere strongly. In addition the reactivity of the allyl group allows thermal curing, whereby the molecular complexity is increased so as to obtain good resistance to chemical and physical agents.
3. Furthermore, since polyoxyphenylene chains are cross-linked in this way through nonrigid bridges composed of several aliphatic carbon atoms, the cured coatings retain sufficient elasticity to cope with any stress or deformation of the substrate.

Concluding Remarks

From the low electrical resistance of the wet films (Fig. 1) it may be deduced that "throwing power" is rather low. Indeed by varying some experimental conditions (e.g., by increasing either temperature or methanol percentage) throwing power may increase, but the benefits generally are lower than the disadvantages. From this point of view, therefore, *in situ* electropolymerization of allylphenol is at a disadvantage compared to classical electrophoretic coatings. Another hindrance to practical applications is the fact that inorganic pigments cannot be entrapped in the film during its *in situ* formation. Such pigments often contribute significantly to the life of the electrophoretic coatings.

The advantages of preparing the polyoxy-(allyl)-phenylene coatings by the electrolytic process presented in this paper are: (i) good corrosion resistance

of the coatings; (ii) simplicity of the electrolytic process; (iii) stability of the solutions (the electrophoretic bath instead is a metastable colloidal system); (iv) strong adhesion, which likely originates from interactions existing *ab initio* between monomer and substrate (for this same reason the substrate does not require, apart from cleanness, any particular pretreatment); and (v) good ability of bonding organic overpaintings.

Acknowledgment

The authors are indebted to Mr. F. Furlanetto for experimental support. This work was done in collaboration with Centro Ricerche Fiat, 10043 Orbassano, Torino, Italy.

Manuscript submitted Oct. 21, 1980; revised manuscript received May 22, 1981.

Any discussion of this paper will appear in a Discussion Section to be published in the June 1982 JOURNAL.

All discussions for the June 1982 Discussion Section should be submitted by Feb. 1, 1982.

Publication costs of this article were assisted by the Istituto di Polarografia ed Elettrochimica Preparativa del C.N.R.

REFERENCES

1. G. Mengoli, S. Daolio, U. Giulio, and C. Folonari, *J. Appl. Electrochem.*, **9**, 483 (1979).
2. G. Mengoli, S. Daolio, and M. M. Musiani, *ibid.*, **10**, 459 (1980).
3. R. L. Yeats, "Electro-painting," Robert Draper Ltd., Teddington (1970).
4. G. Mengoli, *Adv. Polymer Sci.*, **33**, 1 (1979).
5. G. Mol, R. J. Gritter, and G. Adams, in "Applications of Polymer Spectroscopy," E. G. Brame, Jr., Editor, p. 257, Academic Press, New York (1978).
6. A. S. Hay, *Adv. Polymer Sci.*, **4**, 496 (1967).
7. G. D. Cooper and J. G. Bennett, *J. Org. Chem.*, **37**, 441 (1972).
8. G. D. Cooper, H. S. Blanchard, G. F. Endress, and H. L. Finkbeiner, *J. Am. Chem. Soc.*, **87**, 3996 (1965).

Substrate Effects on Zinc Deposition from Zincate Solutions

I. Deposition on Cu, Au, Cd and Zn

M. G. Chu,* J. McBreen,* and G. Adzic*¹

Brookhaven National Laboratory, Department of Energy and Environment, Upton, New York 11973

ABSTRACT

The deposition of zinc on Cu, Au, and Cd from alkaline zincate solutions has been investigated using cyclic voltammetry, potential pulse methods, x-ray diffraction, and scanning electron microscopy. Deposits on Zn were examined by scanning electron microscopy and x-ray diffraction. In the case of Au and Cu approximately a monolayer of zinc is formed in the underpotential deposition region prior to bulk deposition. The respective underpotential shifts of Au and Cu are 0.45 and 0.22V and are in good agreement with the difference in work function between zinc and the substrate. Electrodeposited zinc forms an undetermined surface brass phase on Cu and two alloys (Au₃Zn and AuZn₃) with Au. The deposits on all substrates are oriented preferentially parallel to the basal plane.

In a recent study of inorganic oxide additives in pasted zinc electrodes it was found that in many cases the oxide was reduced to the metal prior to deposition of zinc (1). Thus the effect the additives have on the zinc electrode could be due to a substrate effect. Accordingly, an investigation of zinc deposition on various substrates was carried out. Work on Ag substrates has been reported (2). In this case zinc deposition is a complex process involving underpotential deposition, alloy formation, and growth of bulk zinc.

Most morphological studies on zinc electrodeposition have been carried out on either Zn (3-9) or Cu (10-13) substrates. Detailed treatment of deposition habits on single crystal Zn has been carried out in both sulfate (10) and zincate (4, 9) electrolytes. In the latter case at low overvoltages (50 mV) layered deposits were found. There have been two detailed studies of zinc deposition on single crystal Cu from sulfate solution (10, 11). The zinc deposits are of the layered or ridge type with an orientation parallel to the basal plane. Oxley and Fleischman studied zinc

deposition on Zn, Cu, Ag, and Cd under conditions of activation control and diffusion control (14, 15). In the case of diffusion-controlled deposition the initiation period for dendrite growth appeared to be a function of the substrate. In the case of activation-controlled deposition the weight of nonadherent deposit for 27C of Zn/cm² varied with the substrate according to Cu > Zn > Ag > Cd. For an identical quantity of deposit under diffusion control the weight of nonadherent deposit decreased in the order Cu > Ag > Zn > Cd. Cadmium-plated current collectors have been used in zinc-ferrocyanide (16) and nickel-zinc batteries (17).

Despic (13) has investigated the deposition of zinc on Cu and Au in sulfate solutions. In both cases he found underpotential deposition of zinc and a low nucleation overvoltage for bulk deposition. Kolb, in his review (18), mentions underpotential deposition of zinc from sulfate solution on Au.

It is well known that copper turns to a gray color when coupled with zinc in alkaline solutions (19, 20). This apparently is due to alloy formation.

Even though it is known that the substrate greatly affects the adherency of zinc deposits in alkaline electrolyte and that in some cases there is evidence for

* Electrochemical Society Active Member.

¹ Present address, Institute of Chemical Power Sources, ICTM, Beograd, Yugoslavia.

Key words: amalgam, battery, electrodeposition, nucleation.

alloy formation with the substrate, no systematic study has been carried out on the effects of various substrates on zinc deposition. The purpose of the present work was to elucidate the reasons for the substrate effect on the morphology and dissolution behavior of zinc deposits in alkaline electrolyte.

In the present study the deposition of zinc on polycrystalline substrates of Cu, Au, Cd, and Zn was investigated using cyclic voltammetry, potential pulse methods, scanning electron microscopy, and x-ray diffraction. The data were analyzed for evidence of underpotential deposition of zinc, alloy formation, and deposit morphology and orientation.

Experimental

Cell.—The cell was the same as that used for deposition on Ag (2).

Working electrode.—Two types of working electrodes were used. One was a simple "flag" type sheet electrode (1×1 cm); the other was a machined disk electrode (0.686 cm²). The electrodes were polycrystalline and were at least 99.998% pure. The preparation of the electrodes is given below. No common electrode preparation method could be used because of the differences in the metallurgical and chemical properties of the metals.

Copper.—Copper sheet electrodes were first immersed in dilute HNO₃ for a few seconds and then washed with triply distilled water. Copper disk electrodes were mounted in the holder and polished successively with 600 grit SiC paper, Microcut sheets (Buehler Limited), 5 and 0.5 μm alumina. The electrodes were then washed with triply distilled water prior to incorporation into the cell.

Gold.—Gold sheets were degreased in acetone and washed with triply distilled water.

Cadmium.—Cadmium sheet electrodes were first immersed in a solution of 75% fuming nitric acid and 25% water for 5-10 sec, then washed with triply distilled water. The cadmium disk electrodes were polished successively with 600 grit SiC and Microcut sheets and were rinsed with triply distilled water.

Electrolytes.—The electrolytes were prepared from triply distilled water, reagent grade KOH, and ZnO (New Jersey Zinc USP-19).

Electrochemical studies.—After assembly, the solutions were deaerated by bubbling nitrogen through the solution for 15 min prior to the start of measurements. The nitrogen was purified by passage through molecular sieves. The cyclic voltammetry studies were made in voltage envelopes that were more negative than $-0.63V^2$ for copper and $-1.1V$ for cadmium. At no time, except for cyclic voltammetry on Au, did the voltage go into a potential region where the substrate could oxidize.

In the case of Cu and Au two types of potential step experiments were carried out. In one case electrodes were held initially at a potential of $-1.0V$ and then pulsed to potentials between -1.1 and $-1.25V$ for 100 sec. This was followed by an anodic pulse to $-1.0V$. The purpose of this potential profile was to quantify the charge associated with underpotential deposition of zinc. Measurement of the charge on the anodic pulse gives more accurate results because of the smaller contribution of hydrogen evolution to the total current. In the other experiments the electrodes were held initially at $-1.0V$ and then pulsed to increasingly negative potentials between -1.30 and $-1.46V$ for 100 sec. This was followed by an anodic pulse to $-1.25V$ for 100 sec, followed by a second anodic pulse to $-1.0V$. The purpose of the latter po-

tential profile was to quantify the charge associated with bulk zinc deposition and alloy formation. The cathodic potential which first yielded anodic charge on pulsing to $-1.25V$ was taken to indicate the onset of zinc deposition. The difference between this potential and the Nernst potential is the nucleation overvoltage. In the case of Cd the potential profile was first to hold the electrode at $-1.1V$ then pulse to potentials between -1.25 to $-1.46V$ for 100 sec and a final pulse to $-1.1V$. In all the experiments particular care was taken to prevent dissolution of the substrate during the course of the experiments.

Scanning electron microscopy and x-ray diffraction.—Sample preparation for the scanning electron microscopy and the x-ray diffraction studies was as follows: The zinc was deposited on the "flag" sheet electrodes until a required number of coulombs was deposited. The electrode was immediately removed from the electrolyte, washed repeatedly in distilled water, rinsed in acetone, air dried, and stored in a desiccator until mounted in either the scanning electron microscope or the x-ray goniometer. The x-ray diffraction pattern was determined using Cu-K α radiation. The samples prepared for the morphology and deposit orientation studies were deposited from 8.4M KOH + 0.74M ZnO. Four samples on Cu, Au, and Cd substrates were prepared. The deposition conditions were 0.5 C/cm² at $-1.40V$, 2 C/cm² at $-1.42V$, 5 C/cm² at $-1.44V$, and 2 C/cm² at 15 mA/cm². On Zn only 2 C/cm² samples deposited at 15 mA/cm² were examined.

Results

Cyclic voltammetry.—Figure 1 shows cyclic voltammograms on Cu sheet in the voltage envelope -0.6 to $-1.4V$ in 1M KOH + $10^{-3}M$ ZnO. There is a well-defined underpotential deposition pattern at $-1.08V$. There are two other dissolution peaks at -1.18 and $-1.32V$. On the anodic sweep there is a small cathodic current peak at $-1.0V$.

The cyclic voltammograms on Au were very dependent on the positive limit of the voltage envelope. When the positive limit was $-0.45V$ no clear underpo-

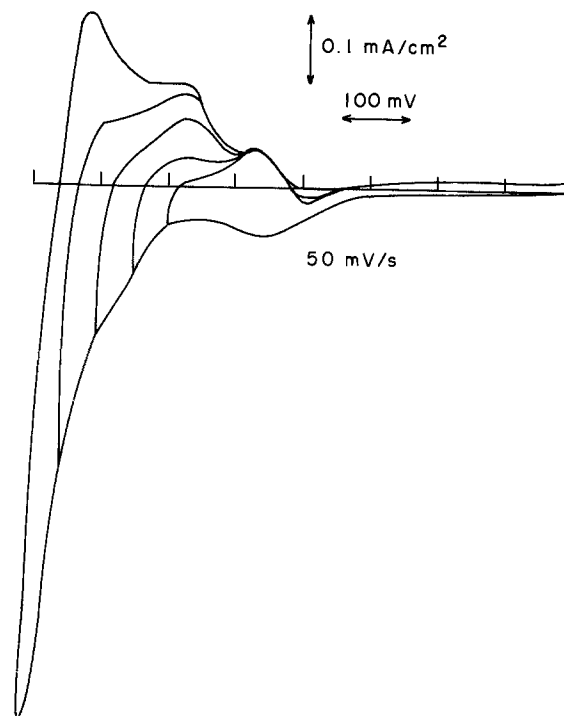


Fig. 1. Cyclic voltammograms on Cu sheet in 1M KOH + $10^{-3}M$ ZnO in the potential envelope -0.6 to $-1.4V$; sweep rate 50 mV/sec.

² All potentials are with respect to an Hg/HgO reference electrode in the same electrolyte.

tential deposition pattern could be observed. However, when the positive limit was extended into the oxide region (Fig. 2) a clear underpotential deposition pattern was found at -0.85V . The results are very similar to those found by Despic in sulfate solutions (13).

Figure 3 is a cyclic voltammogram on Cd in $1\text{M KOH} + 0.08\text{M ZnO}$ in the voltage envelope -1.1 to 1.42V . There was no evidence of underpotential deposition or alloy formation. The current pattern can be ascribed simply to zinc deposition and dissolution.

Investigations were also carried out in $6\text{M KOH} + 0.8\text{M ZnO}$ and in $8.4\text{M KOH} + 0.74\text{M ZnO}$. The overall features of the cyclic voltammograms were similar to those reported here.

Potentiostatic pulse studies.—Figures 4-6 show the current transients for cathodic and anodic pulses on Cu, Au, and Cd substrates in $8.4\text{M KOH} + 0.74\text{M ZnO}$. All anodic pulses were at -1.25V .

Figure 7 shows a comparison of anodic stripping charges for two potentiostatic pulse profiles on Cu and Au in $8.4\text{M KOH} + 0.74\text{M ZnO}$. The results indicate that in both cases at -1.25V approximately a monolayer of underpotential deposited zinc is formed prior to bulk deposition. In the case of bulk deposition most of the deposit is stripped at -1.25V . When deposition is carried out at more negative potentials, the second anodic pulse to -1.0V results in the dissolution of additional zinc (up to 30 monolayers).

Figure 8 shows the results on Cd. The results are consistent with simple deposition of zinc with a high nucleation overvoltage. Complete dissolution of the bulk deposit occurs at -1.25V and no additional anodic dissolution was observed at -1.1V .

X-ray diffraction.—In addition to the diffraction lines for Zn and Cu, the deposit on zinc had diffraction peaks at $2\theta = 24.8^\circ, 37.7^\circ, 42.1^\circ,$ and 57.7° . The strong diffraction peak at 42.1° could be attributed to the hexagonal Cu-Zn brass phase, and the peak at 37.7° to the γ brass phase. Unfortunately, the other strong reflections for these phases coincide with those of copper. In the case of the deposit on Au there were many reflection peaks that could not be attributed to Au or Zn. These were $2\theta = 22.7^\circ, 25.5^\circ, 27.9^\circ, 32.3^\circ, 46.2^\circ, 47.7^\circ, 49.2^\circ, 52.0^\circ, 53.4^\circ, 54.8^\circ, 63.7^\circ,$ and 67.3° .

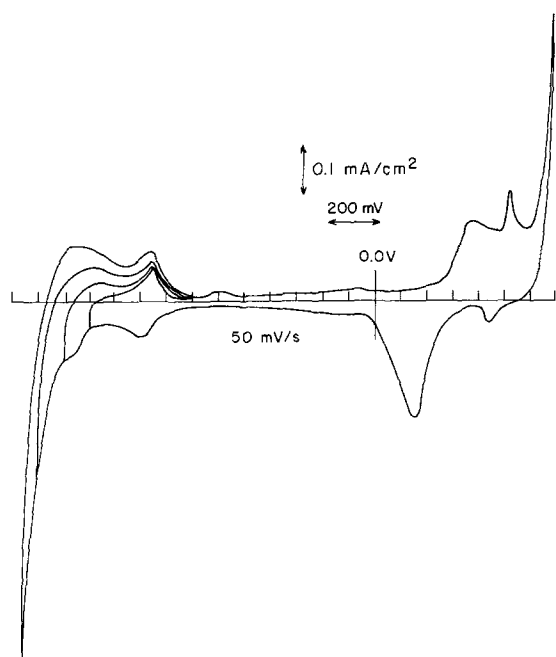


Fig. 2. Cyclic voltammograms on Au sheet in $1\text{M KOH} + 10^{-3}\text{M ZnO}$ in the potential envelope 0.7 to -1.35V ; sweep rate 50 mV/sec .

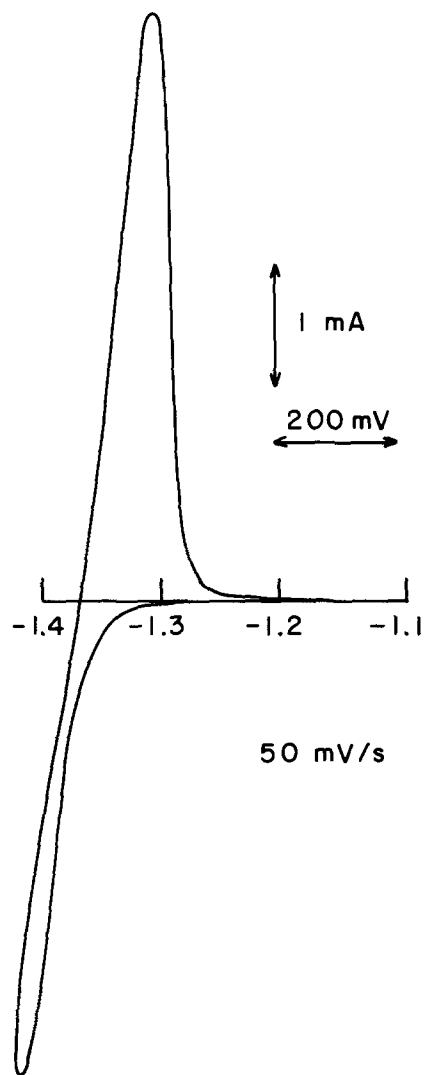


Fig. 3. Cyclic voltammogram on Cd disk (0.686 cm^2) in the $1\text{M KOH} + 0.08\text{M ZnO}$ in the potential envelope -1.1 to -1.42V ; sweep rate 50 mV/sec .

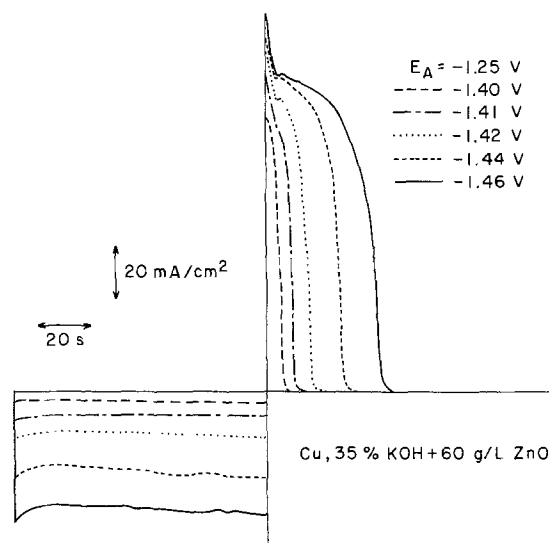


Fig. 4. Current transients for zinc deposition on Cu sheet at various potentials for 100 sec , followed by an anodic stripping pulse at -1.25V .

Some of the peaks ($22.7^\circ, 27.9^\circ, 32.3^\circ, 47.7^\circ,$ and 49.2°) could be attributed to the cubic $\gamma_1\text{-AuZn}_3$ phase ($49.2^\circ, 52.0^\circ, 53.4^\circ, 54.8^\circ,$ and 67.3°) while others could be attributed to the tetragonal $\alpha\text{-Au}_3\text{Zn}$ phase. The diffrac-

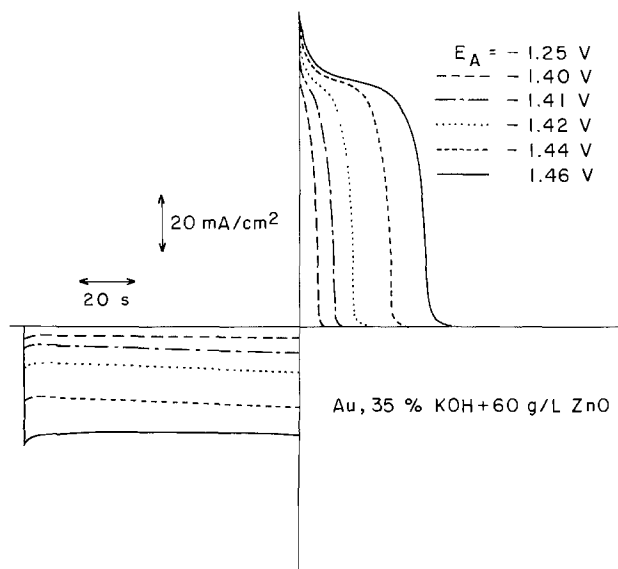


Fig. 5. Current transients for zinc deposition on Au sheet at various potentials for 100 sec, followed by an anodic stripping pulse at -1.25 V.

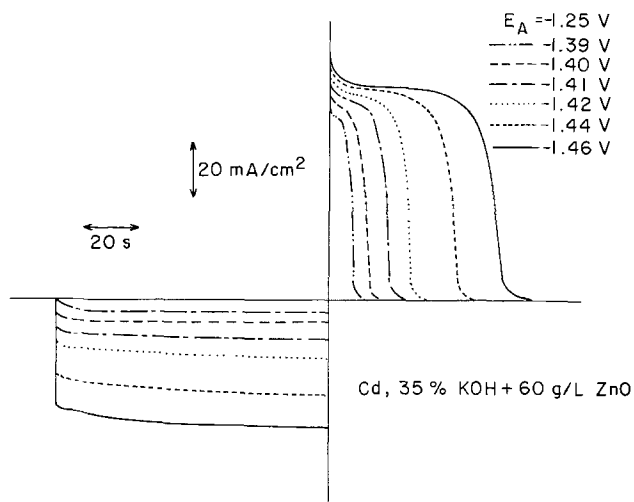


Fig. 6. Current transients for zinc deposition on Cd sheet at various potentials for 100 sec, followed by an anodic stripping pulse at -1.25 V.

tion peak at 46.2° is common to both phases. In the x-ray pattern for the deposit on Cd only reflections that could be attributed to either Cd or Zn were found.

Deposit orientation and morphology.—The deposits on all four substrates had an orientation that was preferentially parallel to the basal plane. The morphology of the deposits on Cu, Au, and Cd are shown in Fig. 9-11. On Cu, Au, and Cd the deposit consisted of hexagonal platelets. On Cd the platelets were layered and more compact than those of Cu. On Zn the morphology was identical to that found by Bockris *et al.* (9) and the orientation was parallel to the basal plane. Deposit orientation and morphology did not vary with the deposition conditions investigated.

Discussion

Quantitative treatment of the cyclic voltammograms and the cathodic current transients is essentially impossible because of the unknown contribution of the hydrogen evolution reaction. Nevertheless the electrochemical results yield valuable information which complements the results of the scanning electron microscopy and x-ray diffraction analysis.

Underpotential deposition of zinc.—The results in Fig. 1, 2, and 7 indicate that approximately a mono-

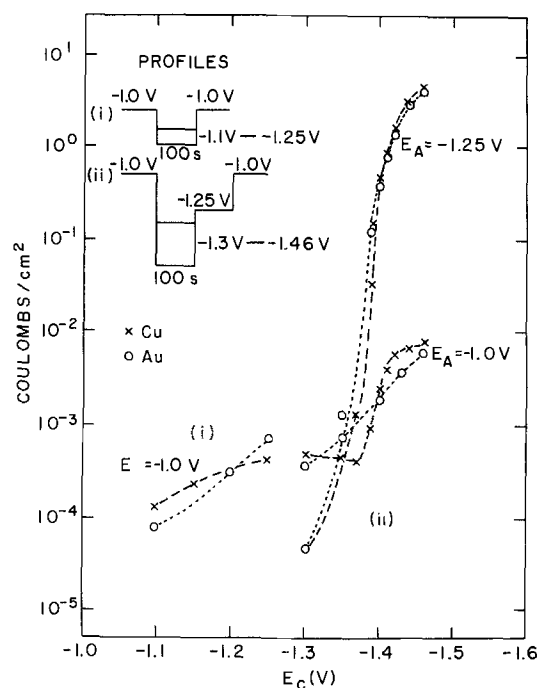


Fig. 7. Anodic stripping charge vs. deposition potential for zinc on Cu and Au sheet in 8.4M KOH + 0.74M ZnO. Potential profiles are given in figure. Deposition time, 100 sec.

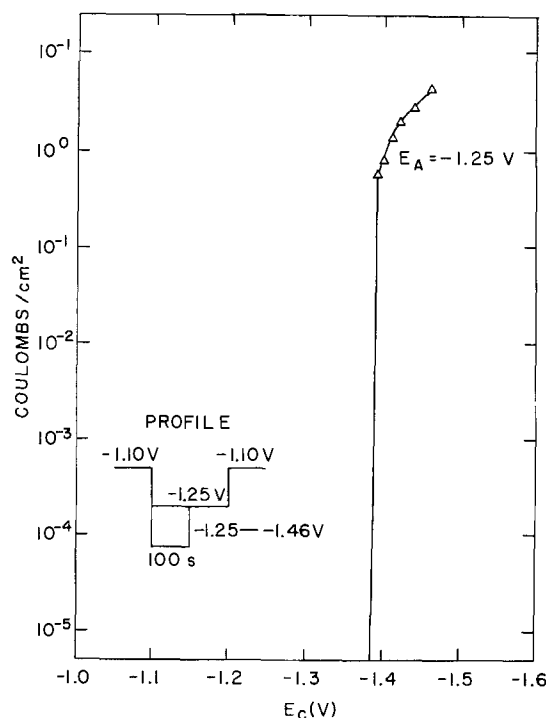


Fig. 8. Anodic stripping charge vs. deposition potential for zinc and Cd sheet in 8.4M KOH + 0.74M ZnO. Potential profile is given in figure. Deposition time, 100 sec.

layer of underpotential deposited zinc is formed on Au and Cu, at -1.25 V, prior to bulk deposition. If one takes the underpotential shift as the difference between the bulk and monolayer stripping peaks (18), then the respective underpotential shifts on Au and Cu are 0.45 and 0.22 V. These are in good agreement with the difference in work function between zinc and the substrate (18). According to Trasatti (21) the work function for Cd is lower than that of Zn and in agreement with the empirical relationship (18); no underpotential was observed on Cd.

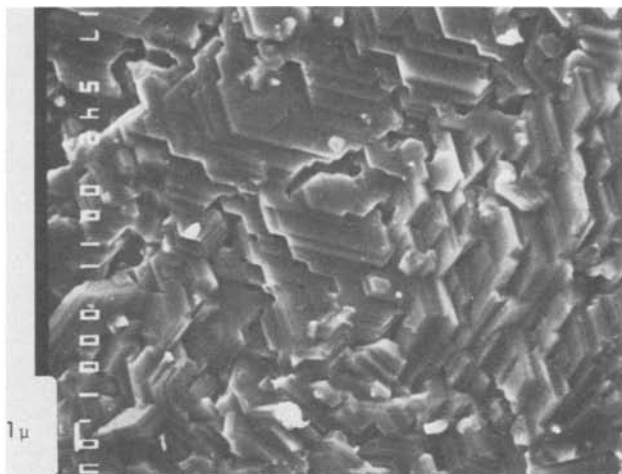


Fig. 9. Scanning electron micrograph of zinc deposit on Cu sheet. Deposit conditions were 2 C/cm^2 at 15 mA/cm^2 from $8.4\text{M KOH} + 0.74\text{M ZnO}$. Magnification $5400\times$.

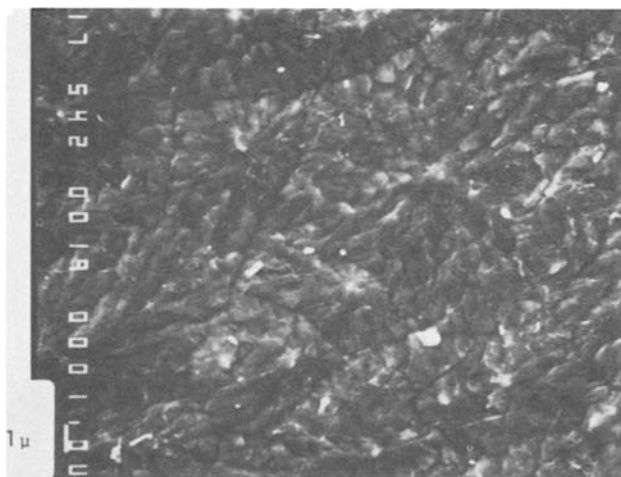


Fig. 10. Scanning electron micrograph of zinc deposit on Au sheet. Deposit conditions were 2 C/cm^2 at 15 mA/cm^2 from $8.4\text{M KOH} + 0.74\text{M ZnO}$. Magnification $5400\times$.

The cyclic voltammogram on Cu (Fig. 1) is fairly complex. Apart from the underpotential deposition pattern with a current peak at -1.08V , there is a shoulder on the cathodic current scan between -1.2 and -1.35V . On going to more negative potentials, an anodic current peak develops at -1.18V . When the cathodic scan goes into the zinc deposition region, a third anodic peak appears at -1.32V . This behavior is very similar to that found for cadmium deposition on Au in acetate buffered CdSO_4 electrolyte (22). The cathodic current shoulder between -1.2 and -1.35V and the anodic peak at -1.18V can be ascribed to alloy formation in the potential region between the Nernst potential and the underpotential deposition region. The anodic peak at -1.32V can be ascribed to dissolution of bulk zinc.

One peculiar feature of the cyclic voltammogram on Cu is the small cathodic current at -1.0V on the anodic sweep. This can be explained by the inhibition of hydrogen evolution by the adsorbed zinc layer. Such inhibition by underpotential deposited layers is well known (23, 24). On the anodic sweep, when the layer is stripped, hydrogen evolution occurs and the current makes an excursion into the cathodic region at approximately -1.0V .

The behavior of zinc on Au is very similar in some respects to zinc on Cu. In addition to underpotential deposition of zinc, there is evidence for alloy forma-

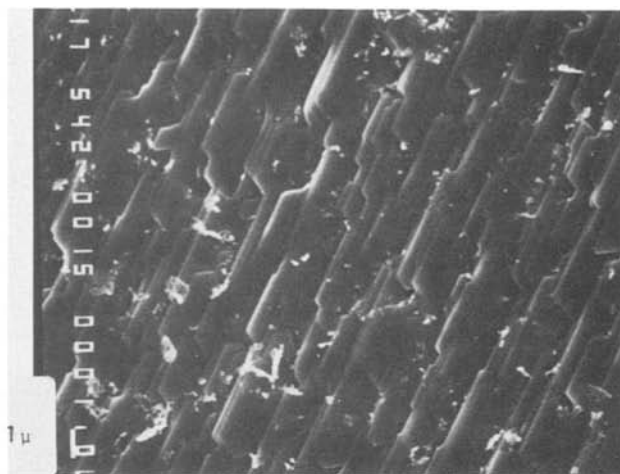


Fig. 11. Scanning electron micrograph of zinc deposit on Cd sheet. Deposit conditions were 2 C/cm^2 at 15 mA/cm^2 from $8.4\text{M KOH} + 0.74\text{M ZnO}$. Magnification $5400\times$.

tion as the cathodic scan is extended to potentials between the underpotential deposition region and the Nernst potential. Underpotential deposition of zinc on Au is enhanced by extending the cyclic voltammograms into the oxide region. This may be due to a re-ordering of the Au surface. Also, it has recently been found that the adsorption behavior of metals can be modified by extended polarization at a preset potential (25). One proposed mechanism is that the adsorption behavior is modified by adsorbed or absorbed oxygen. A similar mechanism may apply here.

Bulk deposition and alloy formation.—As in the case of Ag (2), there is no discernible nucleation overvoltage for zinc deposition on Cu and Au substrates (Fig. 7). Similar results were found by Despic (13, 26) for zinc deposition on Cu and Au in sulfate solutions. However, in this present case there is evidence for alloy formation between the underpotential deposition potential and the Nernst potential, and this may account for the apparent absence of a nucleation overvoltage.

The cyclic voltammetry, potential pulse studies, and x-ray diffraction analysis confirm alloy formation in the case of both Cu and Au. In the case of Cu diffraction peaks that could be attributed to either a γ -brass or a hexagonal Cu-Zn brass phase were observed. The overlap of the other strong lines of these phases with those of copper precluded unequivocal determination of the alloy phase. In the case of Au the situation is much clearer since several diffraction peaks could be uniquely attributed to either the AuZn_3 or the Au_3Zn phase. These two alloys are probably found at different depths in the substrate. The results in Fig. 7 indicate the formation of an alloy to a depth of at least 30 monolayers in both cases.

The cyclic voltammetry, potential pulse, and x-ray analysis measurements on Cd are consistent with simple zinc deposition with a high nucleation overvoltage. The absence of alloy formation is in agreement with the finding that the solubility of Zn in Cd is practically nil at 100°C (27).

Deposit morphology and orientation.—The basal orientation of the deposit on Cu is in agreement with that found on single crystal copper in sulfate solutions and with that found when zinc is condensed on Cu from the vapor phase (28). The hexagonal growth habit is typical for growth of a hexagonal close-packed crystal structure oriented parallel to the basal plane (29). Visual inspection of the scanning electron micrographs of the deposits obtained on Cu, Ag (2), and Cd indicates that the density of the zinc deposit

increases in the order $\text{Cu} > \text{Ag} > \text{Cd}$. This is the order of decreasing peak current for the anodic stripping pulse at -1.25V (Fig. 7). It is also the order of increasing deposit adhesion that was found by Oxley and Fleischman (14, 15). Copper substrates in particular encourage the growth of an active hexagonal deposit with many kink sites and edges. This encourages the growth of a deposit whose surface area increases with thickness. This also results in an increase in the dissolution activity of the deposit with increasing thickness.

Summary

1. Approximately a monolayer of zinc is formed on polycrystalline Cu and Au prior to bulk deposition. There is excellent agreement between the underpotential shift and the difference in work function between the substrate and zinc.

2. Alloy formation of zinc with the substrate was found in the case of Cu and Au. Copper forms an undetermined brass phase, and Au forms Au_3Zn and AuZn_3 .

3. Bulk deposition proceeds without any detectable nucleation overvoltage on Cu and Au. On Cd the nucleation overvoltage is high. In all cases the deposits are preferentially oriented parallel to the basal plane.

Acknowledgments

This work was supported by the U.S. Department of Energy (Contract No. DE-AC02-76CH00016) and the Naval Ship Engineering Center (NAVSEC). The authors acknowledge helpful discussions with A. Himy of NAVSEC, O. C. Wagner of the U.S. Army Electronics Research and Development Command (ERADCOM), Professor B. E. Conway of the University of Ottawa, and W. E. O'Grady, R. R. Adzic, W. Visscher, and S. Srinivasan of Brookhaven National Laboratory (BNL). The authors wish to thank O. Kammerer (BNL) for the x-ray analysis and R. L. Sabatini (BNL) for the scanning electron microscopy. One of the authors (G.A.) had financial support from the Research Fund of Serbia, Yugoslavia, during the course of this work.

Manuscript submitted Dec. 4, 1980; revised manuscript received ca. June 1, 1981.

Any discussion of this paper will appear in a Discussion Section to be published in the June 1982 JOURNAL. All discussions for the June 1982 Discussion Section should be submitted by Feb. 1, 1982.

Publication costs of this article were assisted by the Brookhaven National Laboratory.

REFERENCES

1. J. McBreen, E. Gannon, and M. G. Chu, Abstract 91, p. 248, The Electrochemical Society Extended Abstracts, Hollywood, Florida, October 5-10, 1980.
2. G. Adzic, J. McBreen, and M. G. Chu, *This Journal*, **128**, 1691 (1981).
3. R. W. Powers, *Electrochem. Technol.*, **5**, 429 (1970).
4. R. D. Naybour, *Electrochim. Acta*, **13**, 763 (1968).
5. R. D. Naybour, *This Journal*, **116**, 520 (1969).
6. F. Mansfield and S. Gilman, *ibid.*, **117**, 588 (1970).
7. F. Mansfield and S. Gilman, *ibid.*, **117**, 1154 (1970).
8. F. Mansfield and S. Gilman, *ibid.*, **117**, 1521 (1970).
9. J. O'M. Bockris, Z. Nagy, and D. Drazic, *ibid.*, **120**, 30 (1973).
10. J. M. Keen and J. P. G. Farr, *ibid.*, **109**, 668 (1962).
11. M. F. Ahmed, B. S. Shuhadri, and F. Pushpanaden, *J. Mater. Sci.*, **12**, 549 (1977).
12. K. I. Popov, D. N. Keca, and M. D. Andjelic, *J. Appl. Electrochem.*, **9**, 19 (1978).
13. A. R. Despic, in "Electrode Processes," S. Bruckenstein, J. D. E. McIntyre, B. Miller, and E. Yeager, Editors, pp. 235-245, The Electrochemical Society Softbound Proceedings Series, Princeton, NJ (1979).
14. J. E. Oxley and C. W. Fleischman, Third Quarterly Report to NASA Contract No. NA85-9591, Leeson Moss Laboratories, Great Neck, NY, March 1966, NASA Assession No. 66-26870.
15. H. G. Oswin and K. F. Blurton, in "Zinc Silver Oxide Batteries," A. Fleischer and J. J. Lander, Editors, John Wiley & Sons, New York (1971).
16. E. L. Littauer, Private communication.
17. M. Knaster, Abstract 92, p. 250, The Electrochemical Society Extended Abstracts, Hollywood, Florida, October 5-10, 1980.
18. D. M. Kolb, in "Advances in Electrochemistry and Electrochemical Engineering," Vol. 11, H. Gerischer and C. W. Tobias, Editors, John Wiley & Sons, New York (1978).
19. J. M. Booe, *This Journal*, **99**, 197C (1952).
20. T. P. Dirkse and E. G. Vrieland, *ibid.*, **106**, 997 (1959).
21. S. Trasatti, *J. Electroanal. Chem. Interfacial Electrochem.*, **33**, 351 (1971).
22. J. W. Schultz, F. D. Koppitz, and M. M. Lohregel, *Ber. Bunsenges. Phys. Chem.*, **78**, 693 (1974).
23. R. R. Adzic, A. V. Tripkovic, and N. M. Markovic, *J. Electroanal. Chem. Interfacial Electrochem.*, In press.
24. F. Furuya and S. Motoo, *ibid.*, **98**, 195 (1979).
25. H. Siegenthaler and E. Schmidt, Extended Abstracts, 31st ISE Meeting, Venice, Italy, September 22-26, 1980, Abstract No. A44.
26. A. R. Despic, Abstract 402, p. 1013, The Electrochemical Society Extended Abstracts, Hollywood, Florida, October 5-10, 1980.
27. W. Boos, *Metallwirtschaft*, **11**, 603 (1932).
28. O. Haase, *Z. Naturforsch.*, **11**, 862 (1956).
29. I. Sunagawa, in "Crystal Growth and Characterization," R. Ueda and J. B. Mallin, Editors, pp. 347-359, North Holland Publishing Co., Amsterdam (1975).

Substrate Effects on Zinc Deposition from Zincate Solutions

II. Deposition on Pb, Tl, Sn, and In

J. McBreen,* M. G. Chu,* and G. Adzic*¹

Brookhaven National Laboratory, Department of Energy and Environment, Upton, New York 11973

ABSTRACT

The deposition of zinc on Pb, Tl, Sn, and In has been investigated using cyclic voltammetry, potential pulse methods, x-ray diffraction, and scanning electron microscopy. There is no evidence of underpotential deposition on any of the substrates and the nucleation overvoltage is 30-40 mV. Thallium forms a surface alloy with zinc and there is evidence that zinc diffuses into Pb. In the case of Sn and Tl the deposit had an intermediate orientation and on Pb and In the deposit was oriented perpendicular to the basal plane. Deposit orientation has been correlated with the degree of mismatch of zinc with the substrate. The morphology of the zinc was dense on all substrates and there was no evidence for the hexagonal type of deposit that is usually found on Zn and Cu.

The deposition of zinc on Sn and Pb has been investigated by Oxley and Fleischman (1, 2). They found that the deposits were more adherent than on Cu, Ag, or Cd, with the best adherency being on Pb.

There is an extensive literature on the effect of Pb and Sn ions on zinc deposits in alkaline electrolyte (3-7). Initial work was carried out by Kudryatzev (3). Since then several investigators have confirmed that Pb (4-6) and Sn (7) ion additions inhibit zinc dendrite growth. It has also been shown that Pb ion additions affect the specific area of the zinc deposit, suppress self-discharge, and improve the mechanical and discharge characteristics of the electrodes (5). The effect of Pb ion additions on zinc deposits in aqueous zinc chloride and zinc sulfate electrolytes has been investigated (8, 9). In both cases additions of Pb ions change the deposit and promote zinc growth perpendicular to the basal plane.

In recent years there have been several reports on the effect of PbO, Tl₂O₃, SnO₂, SnCl₂, H₂O, In₂O₃, and In(OH)₃ additions to the pasted battery zinc electrodes (10-13). It has been found that in the case of PbO and Tl₂O₃ additions to zinc electrodes in nickel-zinc cells that the oxides are reduced to the metal prior to zinc deposition on the first charge (13). The mechanism by which these additives modify the electrode has been attributed to a substrate effect.

The present study was part of an investigation of substrate effects on zinc deposition on several metals from zincate solution. The techniques used were cyclic voltammetry, potential pulse methods, scanning electron microscopy, and x-ray diffraction.

Experimental

Cell.—The cell for the electrochemical studies is described elsewhere (15).

Working electrode.—Two types of working electrodes were used. One was a simple "flag" type sheet electrode (1 × 1 cm); the other was a machined disk electrode (0.686 cm²). The electrodes were polycrystalline and were at least 99.998% pure. The preparation of the Pb, Tl, In, and Sn electrodes is given below; no common electrode preparation method could be used.

Lead.—Lead sheet was first immersed in a solution of 20% hydrogen peroxide and 80% glacial acetic acid

for 15 sec, then washed with triply distilled water (14). The lead disk electrodes were first polished with 600 grit SiC paper and then chemically etched in a solution of 80% glacial acetic and 20% hydrogen peroxide for 15 sec. Finally the electrode was rinsed with methanol.

Thallium.—The preparation of thallium sheet was the same as that for lead sheet electrode. The thallium disk electrodes were polished with 600 grit SiC and then washed in 6N KOH followed by a rinse in triply distilled water.

Indium.—Indium electrodes were first washed in acetone and rinsed with triply distilled water.

Tin.—Tin sheet electrode was only washed with triply distilled water. The tin disk electrodes were first polished with 600 grit SiC paper and then washed with triply distilled water.

Electrolytes.—The electrolytes were prepared from triply distilled water, reagent grade KOH, and ZnO (New Jersey Zinc USP-19).

Electrochemical studies.—After cell assembly, the solutions were deaerated by bubbling nitrogen through the solutions for 15 min prior to the start of measurement. The nitrogen was purified by passage through molecular sieves. The cyclic voltammetry was made in voltage envelopes that were more negative to -0.84V for Pb, -0.9V for Tl, -1.15V for In, and -1.2V for Sn. At no time did the voltage scan go into a potential region where the substrate could oxidize. Double cathodic-anodic pulse measurements were made in an effort to quantify the amount of the deposit, determine the nucleation overvoltage, and obtain further evidence for alloy formation. This procedure consisted of a cathodic pulse for 100 sec at increasingly negative potentials between -1.25 and -1.46V followed by an anodic pulse at -1.25V for 100 sec and a final pulse to a potential slightly negative of the dissolution potential of the substrate. In the case of Pb, Tl, In, and Sn, the respective potentials of the final anodic pulses were -1.0, -1.0, -1.19, and -1.15V. The cathodic deposition potential which first yielded an anodic charge at -1.25V was taken to indicate the onset of zinc deposition. The difference between this potential and the Nernst potential is the nucleation overvoltage. Any additional dissolution that occurred on stepping to potentials more positive to -1.25V was ascribed to zinc that had alloyed or diffused into the substrate.

* Electrochemical Society Active Member.

¹ Present address: Institute of Chemical Power Sources, ICTM, Beograd, Yugoslavia.

Key words: electrodeposition, alloy, SEM.

Scanning electron microscopy and x-ray diffraction.—Sample preparation for the scanning electron microscopy and the x-ray diffraction studies was as follows. The zinc was deposited on the "flag" sheet electrodes at a fixed potential until a required number of coulombs was deposited. The electrode was immediately removed from the electrolyte, washed repeatedly in distilled water, rinsed in acetone, air dried, and stored in a desiccator until mounted in either the scanning electron microscope or the x-ray goniometer. The diffraction pattern was determined using Cu-K α radiation. The sample prepared for the morphology and deposit orientation studies was deposited from 8.4M KOH + 0.74M ZnO. Four samples on each substrate were prepared. The deposited conditions were 0.5 C/cm² at -1.40V, 2 C/cm² at -1.42V, 5 C/cm² at -1.44V, and 2 C/cm² at 15 mA/cm².

Results

Cyclic voltammetry.—Figure 1 is a cyclic voltammogram on a Pb disk electrode in 1M KOH + 0.08M ZnO in the potential envelope -0.83 to -1.45V. The cathodic current has a distinct nucleation loop with no zinc deposition occurring on the cathodic sweep till a potential of -1.4V is reached. Cyclic voltammograms with negative limits at -1.43V displayed one anodic current peak at -1.28V. When the negative limit was extended to -1.45V a second anodic peak appeared at -1.35V (Fig. 1); when the limit was -1.55V a third anodic peak appeared at -1.3V. Results in Fig. 2 show the effect of various voltage arrests on the anodic behavior of the cyclic voltammogram. Figure 3 shows cyclic voltammograms for thallium in 1M KOH + 0.08M ZnO in the voltage envelope -0.9 to -1.4 and -1.45V. There is no evidence of underpotential deposition on Tl. At -1.4V there is no zinc deposition. At 1.45V there is deposition and a very distinct nucleation loop. Figure 4 shows cyclic voltammograms for more negative limits down to -1.65V. When the negative limit is -1.65V another anodic peak is observed -0.8V. The main feature of zinc deposition on Tl is that there is no underpotential deposition; there is evidence of a nucleation overvoltage for zinc deposition. The behavior of Sn is shown in Fig. 5. There is no evidence of underpotential deposition or alloy formation. Almost identical results were found on In substrates.

Potentiostatic pulse studies.—Figures 6-9 show the current transients for cathodic and anodic pulse on Pb,

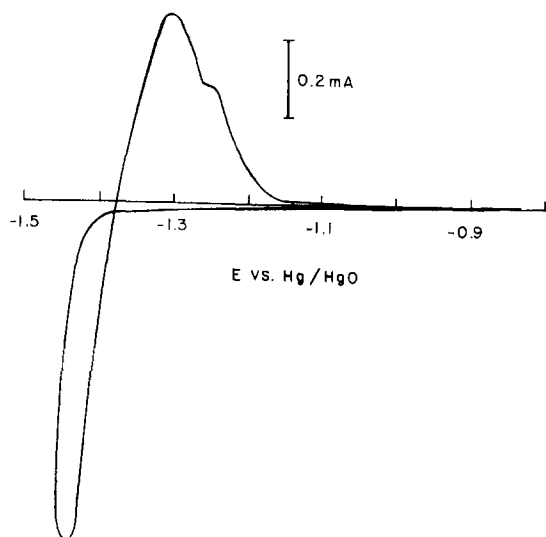


Fig. 1. Cyclic voltammogram on Pb disk (0.686 cm²) in 1M KOH + 0.08M ZnO; sweep rate 100 mV/sec. Negative limit -1.45V.

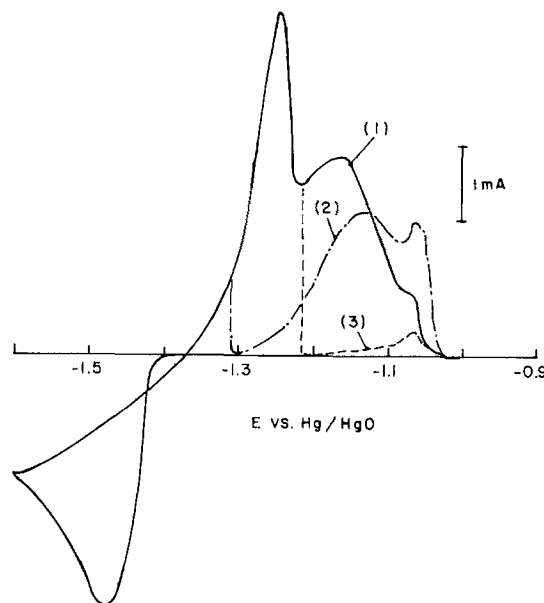


Fig. 2. Cyclic voltammograms on Pb disk (0.686 cm²) in 1M KOH + 0.08M ZnO; sweep rate 10 mV/sec. (Curve 1) continuous cyclic voltammograms, (curve 2) with a 5 sec anodic arrest at -1.3V, (curve 3) with a 5 sec anodic arrest at -1.21V.

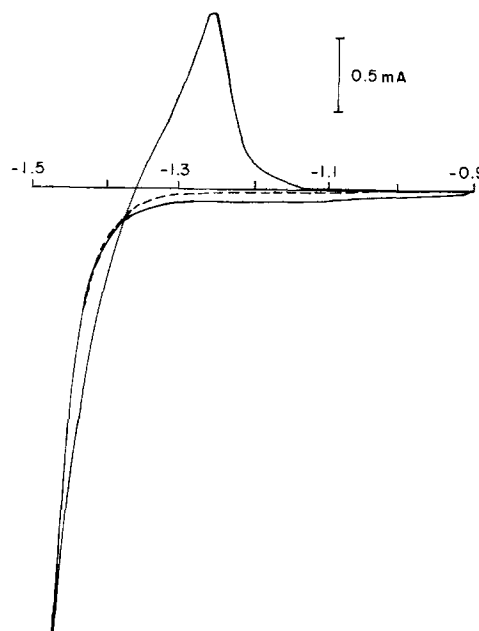


Fig. 3. Cyclic voltammograms for Tl disk (0.686 cm²) in 1M KOH + 0.08M ZnO; broken line for a negative limit at -1.4V; solid line for a limit at -1.45V. Sweep rate 100 mV/sec.

Tl, Sn, and In substrates (1 × 1 cm) in 8.4M KOH + 0.74M ZnO. Cathodic pulses vary from -1.40 to -1.46V. All anodic pulses were at -1.25V.

Figures 10 and 11 show the anodic stripping charge for various potentiostatic pulse profiles in 8.4M KOH + 0.74M ZnO for Pb, Tl, In, and Sn, respectively. On Pb and Tl substrates, most of the dissolution of bulk deposit occurs at -1.25V; the remainder of the deposit is stripped at -1.0V. On In and Sn substrates, all of the dissolution of bulk deposit occurs at -1.25V; no dissolution was observed at the higher potential.

X-ray diffraction result.—In the case of the Tl sample prepared for morphology and deposit orientation studies strong diffraction peaks at $2\theta = 23.5^\circ, 26^\circ, 27.2^\circ, 31^\circ, 38.5^\circ,$ and 48.5° were observed. In the case of Pb, In, and Sn, all the diffraction peaks could be attributed to either zinc or the substrate.

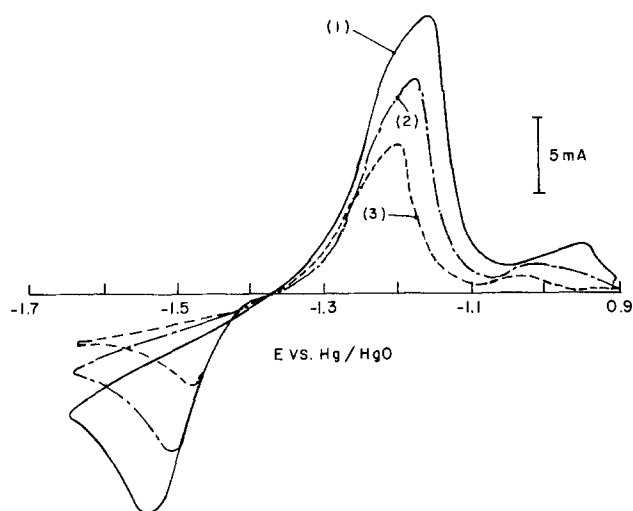


Fig. 4. Sweep rate dependence of cyclic voltammograms on Tl disk (0.686 cm^2) in $1\text{M KOH} + 0.08\text{M ZnO}$. Sweep rates: (curve 1) 100 mV/sec , (curve 2) 50 mV/sec , (curve 3) 20 mV/sec .

Deposit orientation and morphology.—The zinc deposits on both Pb and In were oriented perpendicular to the basal plane. On Tl and Sn the deposit had an intermediate orientation. Figures 12 to 15 show scanning electron micrographs of zinc deposits on each substrate. There is no evidence of the hexagonal structures found on Ag (15), Cu and Cd (16). On In and Sn the deposits had a very dense appearance.

Discussion

Zinc deposition.—No underpotential deposition was observed on any of these substrates. This is to be expected since the work function for Sn is only 0.05 eV higher than that of zinc and for the other metals is considerably lower (17). The nucleation overvoltage is high on all metals. Thallium was the only material with which zinc formed an alloy. This was confirmed by the additional anodic peak, at approximately

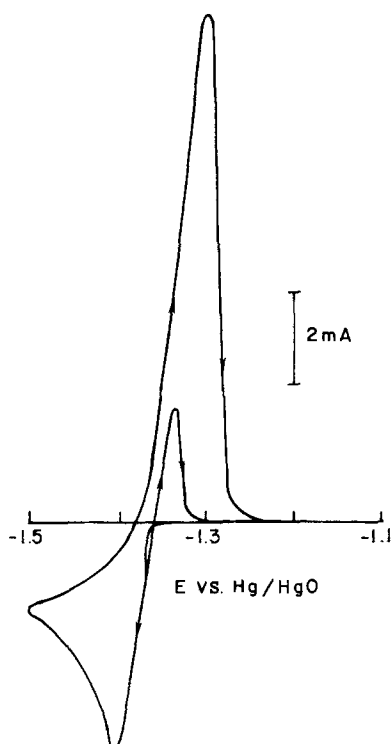


Fig. 5. Cyclic voltammograms on Sn disk (0.686 cm^2) in $1\text{M KOH} + 0.08\text{M ZnO}$; sweep rate 50 mV/sec .

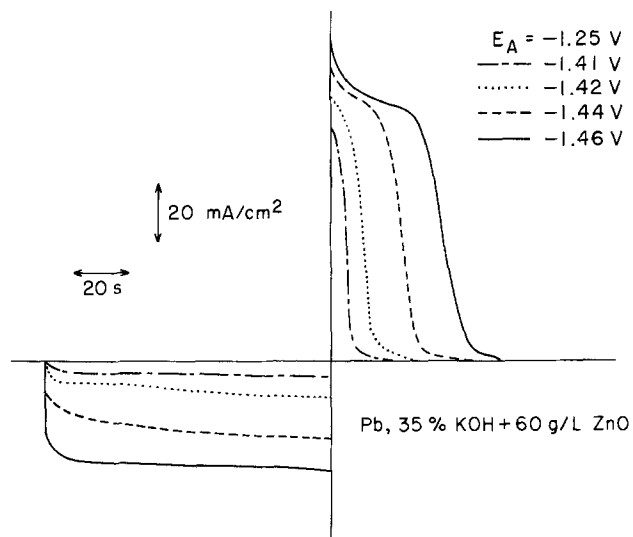


Fig. 6. Current transients for double cathodic/anodic pulse experiments on Pb sheet in $8.4\text{M KOH} + 0.74\text{M ZnO}$. Deposition potentials are indicated on the figure. Anodic pulses were to -1.25V .

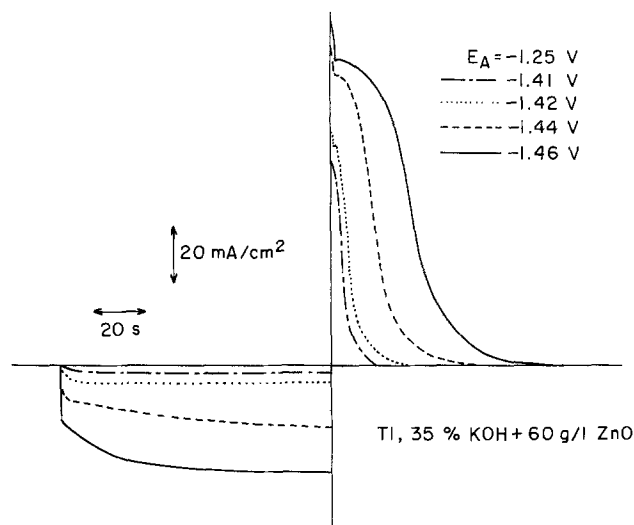


Fig. 7. Current transients for double cathodic/anodic pulse experiments on Tl sheet in $8.4\text{M KOH} + 0.74\text{M ZnO}$. Deposition potentials are indicated on the figure. Anodic pulses were to -1.25V .

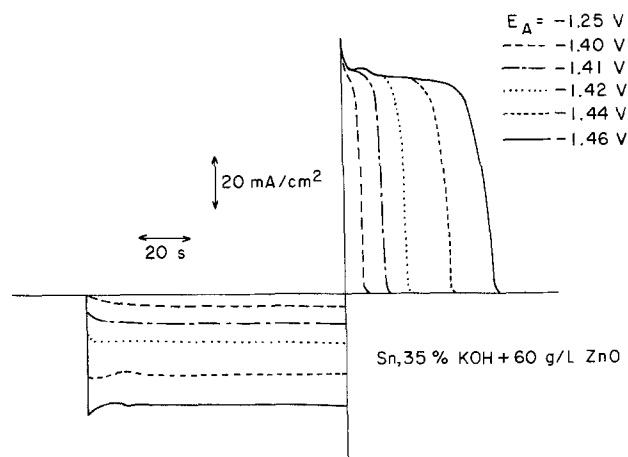


Fig. 8. Current transients for double cathodic/anodic pulse experiments on Sn sheet in $8.4\text{M KOH} + 0.74\text{M ZnO}$. Deposition potentials are indicated on the figure. Anodic pulses were to -1.25V .

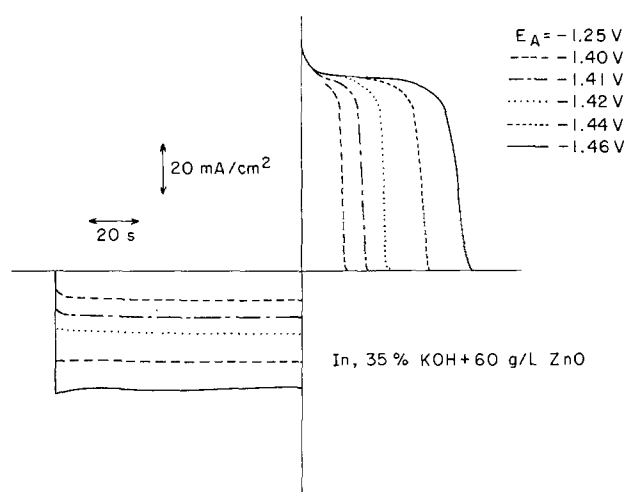


Fig. 9. Current transients for double cathodic/anodic pulse experiments on In sheet in 8.4M KOH + 0.74M ZnO. Deposition potentials are indicated on the figure. Anodic pulses were to -1.25V .

-1.0V , in the cyclic voltammograms (Fig. 5). The double anodic pulse also showed additional dissolution on going to -1.0V . This additional dissolution was observed on the cyclic voltammograms at slow sweep rates and in the potential pulse measurements after holding the electrode at -1.25V for periods as long as 300 sec. Thus it could not be ascribed to residual passivated zinc. In addition, the x-ray diffraction results showed several diffraction peaks that could not be ascribed to either Zn or Tl. No literature data for x-ray patterns of Zn-Tl alloys could be found.

The cyclic voltammetry results (Fig. 4 and 5) and the double anodic pulse measurements (Fig. 11) indicate that alloy formation of zinc with Tl is quite different than alloy formation with Ag (15), Au or Cu (16). There is no evidence for alloy formation at potentials positive to the Nernst potential. Actually the cyclic voltammogram displays a nucleation loop (Fig. 4) and no zinc is deposited at potentials more positive

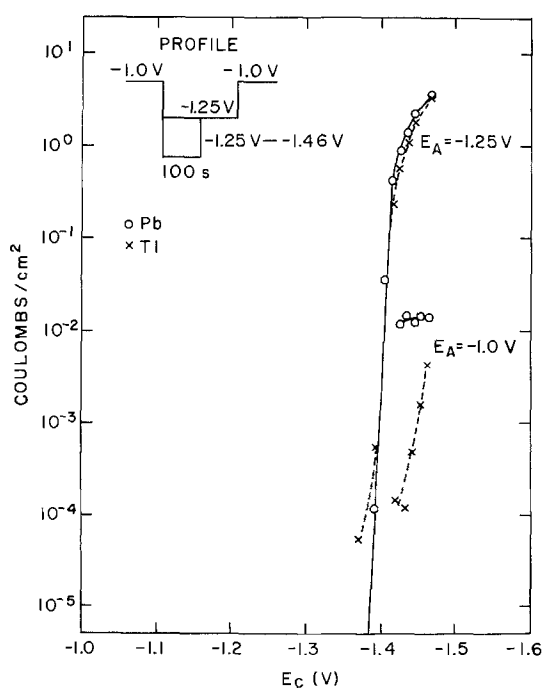


Fig. 10. Anodic stripping charge vs. deposition potential for Pb and Tl sheet in 8.4M KOH + 0.74M ZnO. Deposition time was 100 sec. Potential profiles are indicated on the figure.

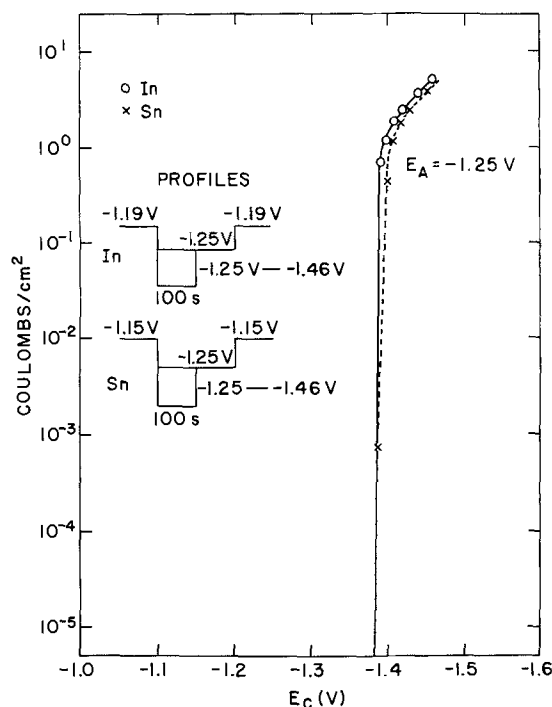


Fig. 11. Anodic stripping charge vs. deposition potential from Sn and In sheet in 8.4M KOH + 0.74M ZnO. Deposition time was 100 sec. Potential profiles are indicated on the figure.

to -1.4V . Apparently the presence of bulk zinc is required on the Tl surface before alloy formation. There is a possibility that in the case of Ag, Au, and Cu, the underpotential deposited layer catalyzes alloy formation at potentials positive to the Nernst potential. It is difficult to quantify the amount of alloy formation from the double anodic pulse measurements. On pulsing to -1.25V , the current tailed off (slowly) over a long period of time (Fig. 7). This may be due to some alloy dissolution at -1.25V after stripping the bulk deposit.

The behavior of zinc on Pb is very complex as indicated by the cyclic voltammetry and potential pulse measurements. The behavior was similar in some respects to that observed with substrates that alloyed with zinc. However, no Pb-Zn alloy is known and the x-ray diffraction data showed only reflections for Pb and Zn. The cyclic voltammograms indicate that there are at least three dissolution processes. This could be rationalized on the basis of dissolution of nonepitaxial

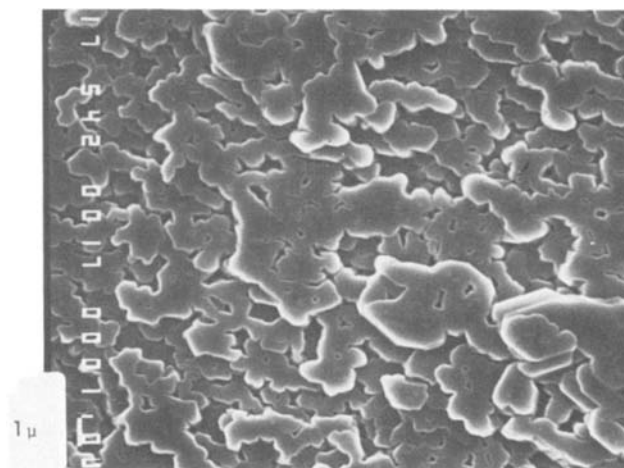


Fig. 12. Scanning electron micrograph of a zinc deposit on Pb sheet. Electrolyte was 8.4M KOH + 0.74M ZnO. Deposition conditions were $2\text{C}/\text{cm}^2$ at $15\text{mA}/\text{cm}^2$. Magnification $5400\times$.

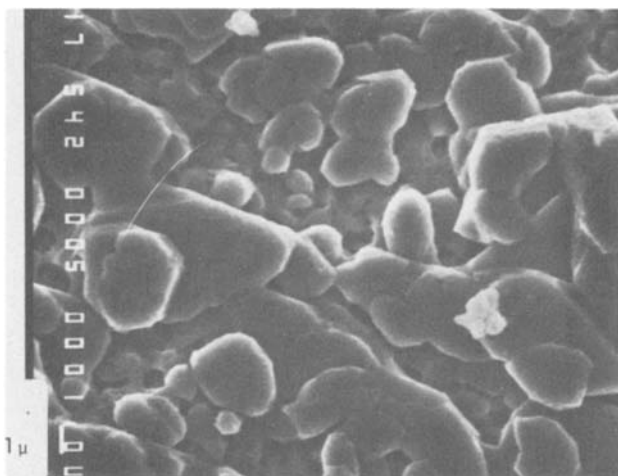


Fig. 13. Scanning electron micrograph of a zinc deposit on Tl sheet. Electrolyte was 8.4M KOH + 0.74M ZnO. Deposition conditions were 2 C/cm² at 15 mA/cm². Magnification 5400×.

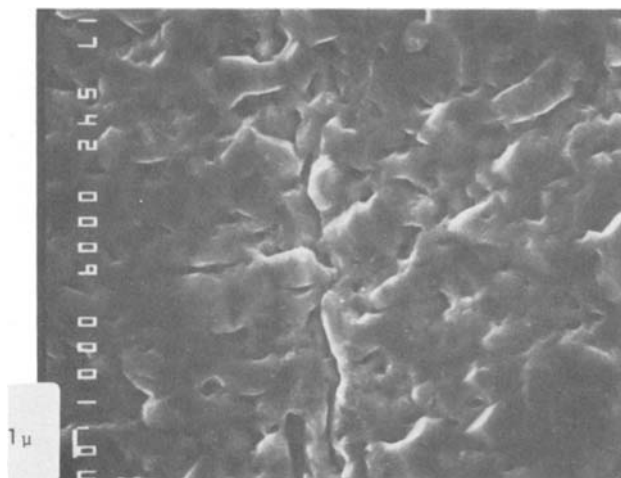


Fig. 14. Scanning electron micrograph of zinc deposit on Sn sheet. Electrolyte was 8.4M KOH + 0.74M ZnO. Deposition conditions were 2 C/cm² at 15 mA/cm². Magnification 5400×.

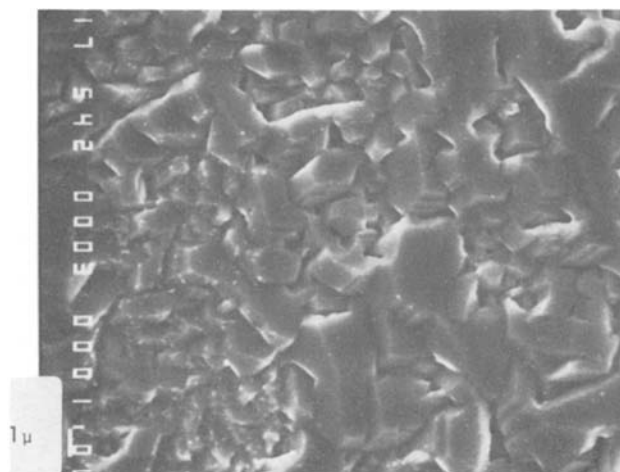


Fig. 15. Scanning electron micrograph of zinc deposit on In sheet. Electrolyte was 8.4M KOH + 0.74M ZnO. Deposition conditions were 2 C/cm² at 15 mA/cm². Magnification 5400×.

growth, epitaxial growth, and zinc that diffuses into the lead. The concept of the dissolution of epitaxial and nonepitaxial growth has been invoked to explain the dissolution of Cd deposits on Cu (18), and a simi-

lar mechanism may be operative here. It is known that the diffusivity of Zn in Pb is abnormally high (19, 20). It is about six orders of magnitude higher than the self-diffusion of Pb in Pb. Extrapolation of the data of Ross *et al.* (19) indicates a diffusivity of 8.24×10^{-11} cm² sec⁻¹ for Zn in Pb at 25°C. If one assumes that the area under curve 3, Fig. 3 is due to dissolution of zinc that diffuses into Pb, then the amount of Zn in the substrate is 1.4×10^{-3} C. The total zinc that diffuses into the Pb is given by

$$Q = 4FAC_0 \left(\frac{Dt}{\pi} \right)^{1/2}$$

where *F* is the Faraday constant, *A* the electrode area, *D* the diffusivity of Zn in Pb, *C*₀ the concentration of zinc directly beneath the Pb surface, and *t* the time the substrate was covered with Zn (21). The total time *t*, including the arrest time, was 78 sec. This yields a value of *C*₀ of 0.06 atom percent Zn in Pb, a value that is reasonably close to the theoretical solubility of Zn in Pb (22).

The electrochemical behavior of the zinc deposit on In and Sn was unique in that the deposit activity does not increase with deposit thickness (Fig. 9 and 10). The limiting discharge current on stepping to -1.25V does not change with thickness. This would indicate that the surface area of the zinc remains constant as the deposit grows. This may be a feature associated with epitaxial growth perpendicular to the basal plane. The stripping current behavior also differed from that of Pb and Tl in that there was no tailing of the current. This is consistent with no interaction of the zinc with the substrate bulk.

Deposit morphology and orientation.—The zinc deposits on Pb, Tl, In, and Sn differed from those found on Ag (15), Cu, Au, Cd, and Zn (16) in that the deposits were not oriented parallel to the basal plane. Consequently the deposits did not display the usual hexagonal platelets that are obtained from growth in a direction parallel to the basal plane.

The only correlation that can be made is that substrates with atomic radii close to that of zinc encourage growth parallel to the basal plane, and substrates with atomic radii much larger than zinc encourage growth perpendicular to the basal plane. The latter deposits tend to be more dense. Table I summarizes data on the interatomic distances in the substrates investigated (23) and give the degree of mismatch with the basal plane spacing of zinc. It is best to compare substrates that do not form alloys with zinc such as Cd, Sn, In, and Pb, since alloy formation certainly must rearrange the atoms of the substrate. In going from Cd to Sn to In and Pb the deposit changes from a basal to an intermediate and then to a perpendicular orientation. According to Finch and his co-workers (24), the critical mismatch is about 15%. This appears to be the case here.

Summary

1. The nucleation overvoltage for zinc on Pb, Tl, Sn, and In in alkaline zincate solutions is 30-40 mV.

Table I. Substrate interatomic distance in comparison to interatomic distances in the zinc basal plane

| Metal | Interatomic distance (Å) | Differences with interatomic distance of Zn in basal plane (%) |
|-------|--------------------------|--|
| Cu | 2.556 | -4.1 |
| Ag | 2.889 | 8.4 |
| Au | 2.883 | 8.1 |
| Cd | 2.979, 3.293 | 11.78 |
| Sn | 3.02, 3.17 | 13.32 |
| In | 3.24, 3.37 | 21.57 |
| Tl | 3.401, 3.456 | 29.68 |
| Pb | 3.500 | 31.3 |
| Zn | 2.665, 2.912 | |

2. Thallium is the only metal that alloys with Zn during deposition.

3. As opposed to the deposits found on Ag, Cu, Au, Cd, and Zn, the deposits were not oriented parallel to the basal plane. On Sn and Tl the deposit had an intermediate orientation and on In and Pb the deposit was oriented perpendicular to the basal plane. Deposit orientation and morphology has been correlated with the degree of mismatch of Zn with the substrate.

Acknowledgments

This work was supported by the U.S. Department of Energy (Contract No. DE-AC02-76CH00016) and the Naval Ship Engineering Center (NAVSEC). The authors acknowledge helpful discussions with A. Himy of NAVSEC, O. C. Wagner of the U.S. Army Electronics Research and Development Command (ERADCOM), Professor B. E. Conway of the University of Ottawa, and W. E. O'Grady, R. R. Adzic, W. Visscher, and S. Srinivasan of Brookhaven National Laboratory (BNL). The authors wish to thank O. Kammerer (BNL) for the x-ray analysis and R. L. Sabatini (BNL) for the scanning electron microscopy. One of the authors (G.A.) had financial support from the Research Fund of Serbia, Yugoslavia, during the course of this work.

Manuscript submitted Dec. 4, 1980; revised manuscript received ca. June 1, 1981.

Any discussion of this paper will appear in a Discussion Section to be published in the June 1982 JOURNAL. All discussions for the June 1982 Discussion Section should be submitted by Feb. 1, 1982.

Publication costs of this article were assisted by the Brookhaven National Laboratory.

REFERENCES

1. J. E. Oxley and C. W. Fleischman, Third Quarterly Report to NASA, Contract No. NA85-9591, Leeson Moos Laboratories, Great Neck, NY, March 1966, NASA Assession No. 66-26870.
2. H. G. Oswin and K. F. Blurton, "Zinc Silver Oxide

- Batteries," A. Fleischer and J. J. Lander, Editors, John Wiley & Sons, New York (1971).
3. N. T. Kudryatzev, *Tr. Konf. Korr. Metal*, **2**, 119 (1943).
 4. J. W. Diggle and A. Damjanovic, *This Journal*, **117**, 65 (1970).
 5. K. L. Hampartzumiam and R. V. Moshtev, in "Power Sources 3," D. H. Collins, Editor, pp. 495-510, Oriel Press, Newcastle upon Tyne (1971).
 6. F. Mansfield and S. Gilman, *This Journal*, **117**, 588 (1970).
 7. F. Mansfield and S. Gilman, *ibid.*, **117**, 588 (1970).
 8. D. J. Mackinnon, J. M. Brannen, and V. I. Lakshmannan, *J. Appl. Electrochem.*, **9**, 603 (1979).
 9. D. J. Mackinnon, J. M. Brannen, and R. C. Kerby, *ibid.*, **9**, 55 (1979).
 10. O. Wagner and A. Himy, in "Proceedings of 27th Power Sources Conference," p. 135, The Electrochemical Society, Princeton, NJ (1976).
 11. A. Himy and O. C. Wagner, U.S. Pat. 4,084,047.
 12. S-P Poa, G-M.C. Chiang, and T-C Lin, *Science Development Monthly (Taiwan)*, **6**, 1013 (1978).
 13. J. McBreen, S. Gannon, and M. G. Chu, Abstract 91, p. 248, The Electrochemical Society Extended Abstracts, Hollywood, Florida, Oct. 5-10, 1980.
 14. W. G. McQ. Tegart, "Electrocatalytic and Chemical Polishing of Metals," Pergamon Press, Oxford (1959).
 15. G. Adzic, J. McBreen, and M. G. Chu, *This Journal*, **128**, 1691 (1981).
 16. M. G. Chu, J. McBreen, and G. Adzic, *This Journal*, **128**, 2281 (1981).
 17. S. Trasatti, *J. Electroanal. Chem. Interfacial Electrochem.*, **33**, 351 (1971).
 18. J. N. Jovicevic, D. M. Drazic, and A. R. Despic, *Electrochim. Acta*, **22**, 589 (1977).
 19. R. A. Ross, H. B. Vanfleet, and D. L. Decker, *Phys. Rev. B*, **9**, 4026 (1974).
 20. D. L. Decker, R. A. Ross, W. E. Evenson, and H. B. Vanfleet, *ibid.*, **15**, 507 (1977).
 21. W. Seith, "Diffusion in Metallen," p. 8, Springer Verlag, Berlin (1955).
 22. G. Lumsden, *Discuss. Faraday Soc.*, **4**, 62 (1948).
 23. R. W. G. Wyckoff, "Crystal Structures," Vol. 1, John Wiley & Sons, New York (1963).
 24. G. J. Finch, H. Wilman, and L. Yang, *Discuss. Faraday Soc.*, **1**, 144 (1947).

Electrodeposition of Silicon from Solutions of Silicon Halides in Aprotic Solvents

A. K. Agrawal* and A. E. Austin*

Battelle, Columbus Laboratories, Columbus, Ohio 43201

ABSTRACT

Amorphous silicon has been electrodeposited from nonaqueous baths using SiHCl_3 as the silicon source. A typical bath composition was 1.0M SiHCl_3 in propylene carbonate containing 0.1M tetrabutyl ammonium chloride as the supporting electrolyte. Deposits were made potentiostatically at around -2.5V vs. Pt reference at temperatures $35^\circ\text{--}145^\circ\text{C}$ under an argon atmosphere. A variety of materials including Pt, Ti, Ti-6Al-4V alloy, n-Si, and indium-tin oxide coated fused silica were used for the substrate. The as-deposited silicon contains some hydrogen bonded as SiH_2 or SiH. The quality and hydrogen content of the deposits are controllable by selecting the proper bath composition and operating temperature. The electrodeposition process offers an inexpensive route for producing α -Si films for possible solar cell applications.

The successful development of low cost solar cells for large-scale terrestrial power generation calls for new technology for attaining required cost reductions of 30-fold from the present. Amorphous silicon films

produced by various vapor phase deposition processes are being actively considered for solar cell applications (1). We investigated electrodeposition as a process for producing silicon directly on low cost metal substrates. As is well known, silicon cannot be electrodeposited from aqueous electrolytes because of hydrolysis of its salts and very large negative potentials

* Electrochemical Society Active Member.

Key words: amorphous silicon, solar cell, electrodeposition, nonaqueous bath.

required for the cathode. The use of a wide range of nonaqueous organic solvents was investigated. Appropriate media were found to be solutions of silicon halides in dipolar aprotic organic solvents that are essentially anhydrous (2). The process yielded amorphous silicon of 1-5 μm thickness on a variety of substrates. Process details, deposit quality, and composition of the electrodeposited α -silicon are discussed here.

System Development

Initially a number of solutes (silicon source—chloro and bromo silanes mainly), nonaqueous solvents, and supporting electrolytes (tetraalkyl ammonium salts) were investigated for the process. The screening was done by cyclic voltammetry experiments and followed by electrodeposition onto a platinum or Ti-6Al-4V substrate [see Ref. (2)]. After extensive trials the most suitable choices for the solute, solvent, and supporting electrolyte were trichlorosilane, propylene carbonate (PC), and tetraalkyl ammonium chlorides, respectively. The main considerations in the selection were stability of various components in the bath at operating cathode potentials in the anticipated temperature range of 35°-150°C, and the product quality.

Although SiHCl_3 is quite soluble ($>1\text{M}$) in PC, the SiHCl_3 is barely ionized in the solvent. As a result the solution conductivity is extremely low ($35 \mu\text{mho cm}^{-1}$) for an efficient operation of the cell. Tetraalkyl ammonium chlorides were therefore added to the cell to increase the conductivity of the bath and thereby reduce the operating cell voltages.

Cyclic voltammetry.—Preliminary cyclic voltammetry experiments were done on platinum electrodes in PC with tetrabutyl ammonium chloride (TBAC) as the supporting electrolyte but without any SiHCl_3 present. This was done to check the inertness of the bath and also to determine the safe working potential range. In the voltograms no current waves, either cathodic or anodic, were observed in the potential range +0.8 to -3.0V vs. Pt . This indicated an absence of reactions and proved the inertness of the bath. However, when the scanning was extended beyond the above potentials, in separate experiments, large current waves resulted at both ends. These waves were due to the breakdown of the bath constituents. The potential range beyond -3.0V vs. Pt was therefore considered unsafe for the cell operation but safe between +0.8 and -3.0V vs. Pt . Chloride ion oxidation starts beyond $+0.8\text{V vs. Pt}$.

A cyclic voltagram for SiHCl_3 in PC and TBAC is shown in Fig. 1. Two reduction waves at cathodic potentials near -1.2 and -2.3V vs. Pt are evident. During scanning in the positive direction from the most negative potential -2.7V vs. Pt , no anodic waves corresponding to either of the cathodic waves were observed. This implies that the cathodic reactions are highly irreversible. The first wave at -1.3V vs. Pt is thought to be from the reduction of trace amounts of HCl present in the bath. This HCl results from a re-

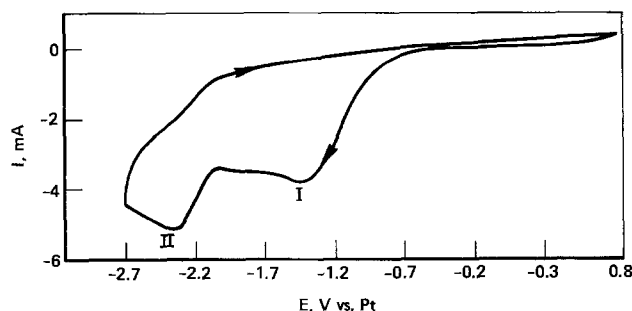


Fig. 1. A cyclic voltammogram of platinum substrate at 35°C in PC containing 0.1M TBAC and 0.2M SiHCl_3 .

action between SiHCl_3 and H_2O , which finds its way as a trace impurity in PC or TBAC. In the second cycle the first wave completely disappeared, probably because of an exhaustion of HCl from the bath. Formation of HCl by hydrolysis of chlorosilanes, e.g., $\text{R}_3\text{SiCl} + \text{H}_2\text{O} \rightarrow \text{R}_3\text{SiOH} + \text{HCl}$, and the reduction of HCl on electrolysis in nonaqueous solvents have been reported by Corriu *et al.* (3).

The second wave in the voltagram in Fig. 1 is from the reduction of SiHCl_3 to α -Si. The current peak is located at -2.3V vs. Pt . Repeated cycling of the potential between +0.8 and -2.7V vs. Pt produced a gradual shrinking of the peak and also a slight negative shift of the peak potential in successive cycles. These changes are thought to be from a buildup of α -Si deposit on the substrate during each cycle and the resulting IR drop therein. The presence of only a strong single peak, after the HCl removal, suggests that the reduction of SiHCl_3 is essentially a one-step process. Multiple peaks corresponding to stage-wise reduction of SiHCl_3 were never observed.

Experimental

All experiments including screening experiments were done inside a dry glove box under an argon atmosphere. Initially a reagent grade PC after careful drying over molecular sieves and purification by vacuum fractional distillation was used for the solvent. The distillate was kept at all times under an argon atmosphere. Gas chromatographic analysis of the distillate gave a maximum of 10 ppm H_2O and 100 ppm propylene glycols. The conductivity of the distillate was 0.5-1.0 μmho . Later, high purity, very low water, glass distilled PC from Burdick and Jackson Laboratories was used in all experiments, without any further treatment. Cyclic voltammetry results and the quality of deposits with the latter PC justified its use. Trichlorosilane used as solute was from Silar Corporation. Tetraalkyl ammonium chlorides, i.e., tetraethyl (TEAC), tetrapropyl (TPAC), TBAC, tetrapentyl (TPnAC), and tetrahexyl (THAC) were obtained from the Ventron Corporation and these were purified by recrystallization under argon atmosphere according to the procedures described in Mann (4).

Electrodeposition experiments were carried out potentiostatically in Teflon cells using an internal platinum reference electrode. A Teflon cell of 15 ml capacity used with 2 cm diam substrates is shown in Fig. 2. The counterelectrode was made from vitreous carbon, whereas a variety of substrates were used for the cathode, including Pt, Ti-6Al-4V alloy, commercially pure titanium, n-silicon, and transparent indium-tin oxide on fused silica. All metallic substrates were mechanically polished to a mirror smooth finish for

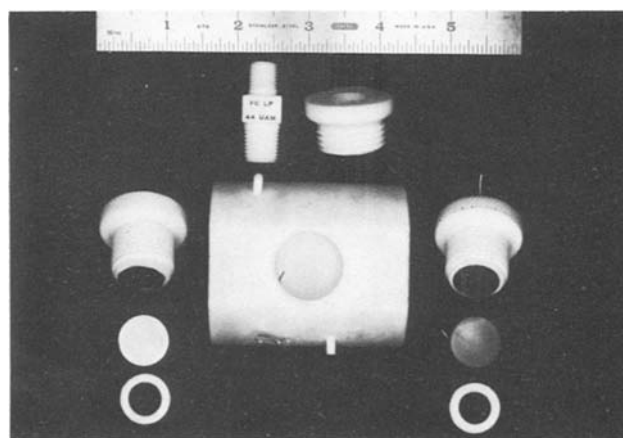


Fig. 2. A Teflon cell used in electrodeposition experiments shown disassembled.

use as a cathode. These were cleaned with deionized water and rinsed off with acetone prior to use. A deposition potential around $-2.5V$ vs. Pt was used in most of the experiments.

Deposits were made at 35° - $145^{\circ}C$. Experiments above $35^{\circ}C$ required a heated pressure chamber for the cell because of the high volatility of $SiHCl_3$ (bp $33^{\circ}C$). For runs at high temperatures the Teflon cell after assembling and filling with the solution was sealed in the chamber. The chamber was then pressurized with argon. The pressure was maintained at 20-30 psi (140-210 kPa) above the vapor pressure of $SiHCl_3$ at the operating temperature of the cell, e.g., 110 psig (800 kPa) for a $90^{\circ}C$ run. This prevented the loss of $SiHCl_3$ from the cell.

During deposition the cell current was monitored, and in most cases a digital integrator was also used to show the cumulative charge passed at any time. Deposit thickness was calculated using Faraday's law assuming 4 electron transfer reduction, 100% current efficiency, and a deposit density of 2.0 g/cm^3 . The thickness was checked in a few instances by weight gain of the substrate and a measurement of the tapered section of the deposit with SEM. A good correspondence between the calculated thickness and measured thickness supported the assumptions.

Results and Discussion

In very early experiments a tank-type 300 ml capacity bath was used as a cell. The bath was reused 3 or 4 times for the deposition without changing the solution but after replenishing the $SiHCl_3$. It was noticed that the starting currents in subsequent runs, under identical operating conditions, were smaller than in the previous runs. It was reasoned that some by-product is generated during the $SiHCl_3$ reduction. This by-product adsorbed on the cathode surface in competition with the active $SiHCl_3$ species and hindered the reduction process. As a result, the practice was changed to using a fresh bath for each deposit. However, in order to save on expensive chemicals the cell design was changed and the volume was reduced to ~ 15 ml solution for a 2 cm diam substrate. All the results described here are for the later practice using the new cell.

A typical deposit made on Ti-6Al-4V substrate at $35^{\circ}C$ is shown in Fig. 3. A typical bath contained 0.1M TBAC and 0.25M $SiHCl_3$. The starting currents in general were 2-5 mA/cm², but decayed rapidly after about 0.5 min at a rate proportional to $t^{-1/2}$ to t^{-1}

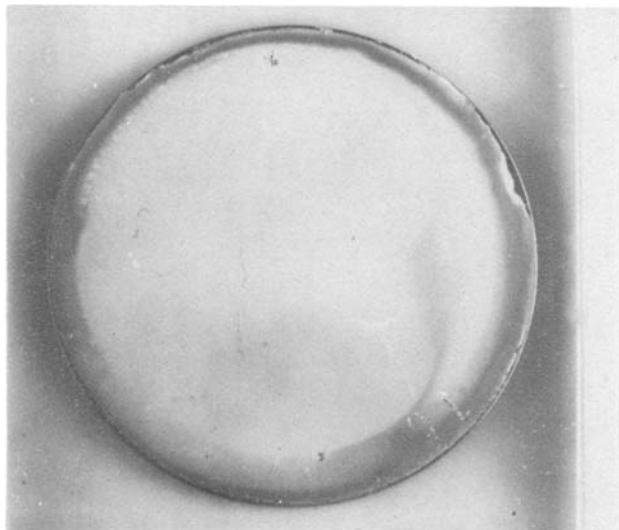


Fig. 3. Photomicrograph of silicon deposit on titanium alloy ($4\times$).

(where t is time) with thickening of the deposit (see Fig. 4). The drop in current with time was partly due to the IR drop in the growing film, and for the rest the reasons are not completely understood at this time. A $1\text{ }\mu\text{m}$ thick deposit required more than 1000 min. The process was subsequently improved to give better yields. The effect of process variables, such as solute concentration, temperature, and the size of cation in the supporting electrolyte are discussed below. The supporting electrolyte used in most of the experiments was TBAC at 0.1M concentration unless mentioned otherwise.

Temperature.—Increasing the temperature above $35^{\circ}C$ resulted in a higher starting current which remained higher during the course of deposition. The electrodeposition currents for two temperatures of 35° and $70^{\circ}C$ are shown in Fig. 4 for comparison. It should be noted in the figure that although the current for the $70^{\circ}C$ run is higher by at least a factor of two over most of the deposition period, the rate of decay for the two runs is almost identical. The identical nature of two curves suggests that the deposition process in both cases is the same. The activation energy for the process was calculated from the Arrhenius plots of i vs. $1/T$ shown in Fig. 5, for the temperature range 35° - $90^{\circ}C$. Three time intervals 0.1, 1, and 100 min were chosen for the calculations, but all three gave the same value of activation energy 2 ± 0.2 kcal. The low activation energy for the process suggests that the rate-determining step is probably an electroadsorption process. Higher temperatures usually resulted in thicker and smoother deposits. Deposit thickness of $\sim 1\text{ }\mu\text{m}$ could be obtained in about 1000 min by operating the cell at $70^{\circ}C$, as opposed to $\sim 0.5\text{ }\mu\text{m}$ at $35^{\circ}C$.

Solute concentration.—The solute concentration in the bath in the range 0.1-1.0M had a significant effect on the rate of current decay as well as on the quality of deposit. The rate of decay, particularly in the first 10 min, was considerably retarded with increasing $SiHCl_3$ concentration. Consequently a deposit of $1\text{ }\mu\text{m}$ thickness could be produced in about an hour or less with 1.0M $SiHCl_3$ in the bath at $50^{\circ}C$ or higher. The deposits were also more uniform and smoother in texture than those made with lower concentrations of $SiHCl_3$. Concentrations above 1M $SiHCl_3$ offered no further improvements.

Although the rate of current decay was affected by the solute concentration, the starting current changed little with the increasing $SiHCl_3$ concentration. The starting current was strictly dependent upon the type of substrate used for the cathode.

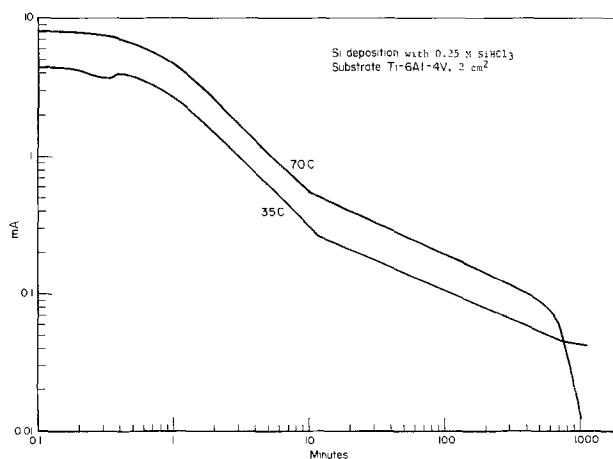


Fig. 4. Comparison of the electrodeposition current for two temperatures, 35° and $70^{\circ}C$ at $-2.5V$ vs. Pt with 0.25M $SiHCl_3$. Substrate area: 2 cm^2 .

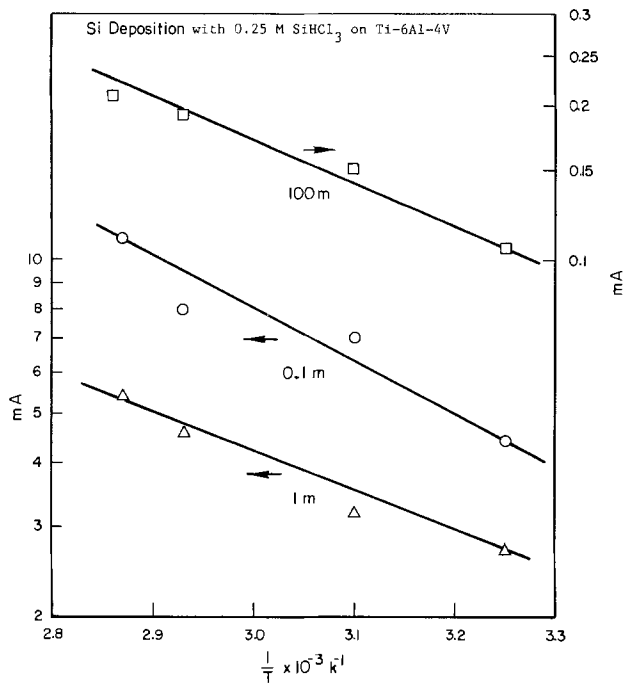


Fig. 5. Arrhenius plots of i vs. $1/T$ at 0.1, 1, and 100 min

Supporting electrolyte.—From the low activation energy and the current decay behavior during the deposition, it was hypothesized that the process is adsorption controlled. It was, therefore, concluded that by changing the cation size of the supporting electrolyte in the bath, the deposition rate and the quality of the deposit, particularly the morphology, could be controlled. As a result, silicon deposition was experimented using different supporting electrolytes of the tetraalkylammonium chloride series. The tetraalkylammonium chlorides used in the experiments were TEAC, TPAC, TBAC, TPnAC, and THAC. The concentration of the supporting electrolyte in each of the experiments was kept constant at 0.1M. The nominal bath temperature was 35°C and the SiHCl₃ concentration 0.5M.

The morphology of the Si deposit and the deposition current decay both were strongly affected by the size of the cation in the bath. In general, the deposits were coarser with increasing cation size; with smaller cations TEAC and TPAC the deposits were very smooth, at 2000 magnification with SEM no separate nodules could be detected. With THAC, the deposits were extremely coarse and loosely adherent to the titanium substrate. The adherence appeared to improve with lowering of the cation size in the bath.

The starting current on the Ti substrate in all the cases was 2.6 ± 0.2 mA/cm², irrespective of the cation size. However, after a few monolayers of Si deposition the current decay was greatly affected by the cation size. The smaller the cation in the bath, the higher was the rate of current decay. The current decay with TEAC was so rapid that deposit thickness was limited to only ~ 0.3 μ m before the deposition rate reached to nearly zero (~ 0.01 mA/cm²) value. With THAC, on the other hand, the rate of decay was very small, and the current stayed with deposition at about 1 mA/cm². The starting current of 2.6 mA/cm² appears to be controlled only by the number of active sites available on the Ti substrate for the adsorption of active SiHCl₃. It is only after the first few monolayers that the cation size of the supportive electrolyte became important.

In order to improve the morphology of electrodeposited silicon, mixed supporting electrolytes of TBAC and TPAC were tried in the bath. Typical experiments with the mixed TBAC and TPAC electro-

lyte were made at 50°C and cathode potential of -2.6 V vs. Pt. The total concentration of the mixed electrolyte in the bath was always maintained at 0.1M with 1.0M SiHCl₃. The TPAC:TBAC compositions tried were 1:100, 10:100, 50:50, 100:10, and 100:1. The optimum composition for TPAC:TBAC was found to be 100:10. With this TPAC:TBAC ratio good deposits of about 1 μ m could be obtained in less than 2 hr. With any other mixture the rates were significantly lower.

The nodule size in the deposits in general decreased with the increasing proportion of TPAC in the mixture. For comparison purposes, four deposits from different bath compositions are shown in Fig. 6. The lower two of the deposits in Fig. 6 are from pure electrolytes TPAC and TBAC, whereas the upper ones are from 10:100 TPAC to TBAC and 10:100 TBAC to TPAC ratios. The deposit from the bath with 10:100 TBAC to TPAC ratio is fine grained and smoother in comparison to the others. Table I gives the deposit thickness and their resistivity, as measured in the solution, from different electrolyte mixtures. The resistivity generally increased with decreasing nodule size and increasing smoothness.

Composition and properties.—Silicon deposits were analyzed for composition with EDAX, Auger spectrometer, and SIMS. The EDAX analysis showed no other metallic element besides Si. Transfer of specimens from the deposit dry box to the Auger chamber resulted in surface oxidation of deposits. This produced insulating film on the specimen surface, and subsequently presented problems with Auger analysis because of the electron charging. Auger analysis after argon sputtering showed Si_{1LL} peak at 92 eV. Analyses with SIMS indicated Si, oxygen ($\approx 3\%$ SiO), and less than 0.01% of trace impurities C, Mg, Al, K, and Na in the deposits. Chlorine was not detected with either SIMS or Auger in any of the deposits analyzed.

The deposits contain some hydrogen, which is driven off on annealing with a threshold at 350°C and a peak of evolution at 470°C. The amount of hydrogen in the deposits varied with the deposition tem-

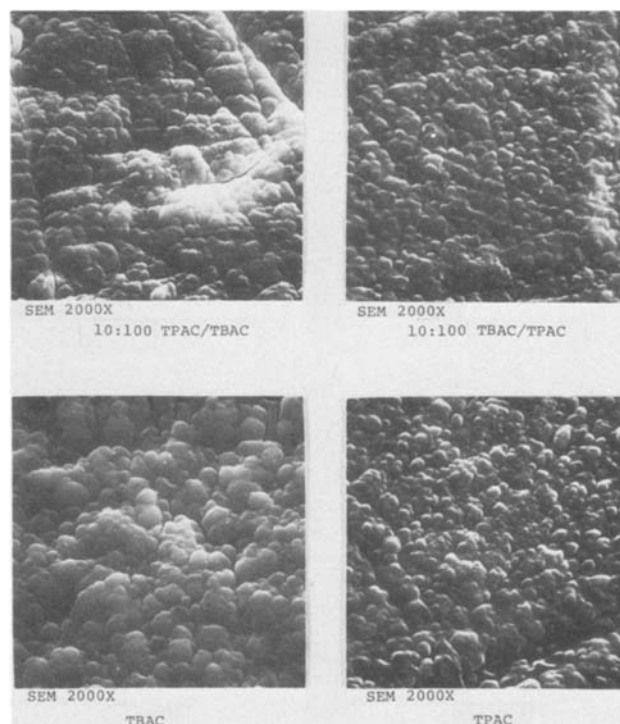


Fig. 6. Micrographs of silicon deposits made with varying supporting electrolyte ratio of TBAC and TPAC on titanium substrate at 50°C.

Table I. α -Si characteristics from mixed TBAC and TPAC electrolyte baths

| Ratio TBAC:TPAC | Thickness (μm) | Resistivity ^a ($\Omega\text{-cm} \times 10^7$) |
|--------------------|--------------------------------|--|
| 0:100 | 0.36 | 12 |
| 1:100 | 0.68 | 12 |
| 10:100 | 0.91 | 1.5 |
| 50:50 | 0.51 | 7.5 |
| 100:10 | 1.36 | 3.9 |
| 100:1 | 1.07 | 2.3 |

^a Resistivity as measured in deposition cell using a Wayne-Kerr bridge.

perature. The hydrogen in deposits made at 35°C was determined by thermal evolution in mass spectrometer, whereas other deposits were analyzed by nuclear reaction with ¹⁵N beam (5). The hydrogen content was estimated to be 35% in deposits made at 35°C, 20% at 50°C, and only 16% at 90°C.

There is indication from infrared spectra that the hydrogen in deposited silicon is chemically bonded in the form of SiH, SiH₂, and SiH₃, mostly as SiH₂ (6, 7). The nature of bonding changes from SiH₂ to SiH as the temperature of the deposition bath is raised; the change was detected by a shift in the IR absorption spectra at 2100 cm⁻¹ and appearance of absorption band at 650 cm⁻¹. The IR absorption spectra of electrodeposited silicon was interpreted in the light of work by Lucovsky *et al.* (8) with amorphous silicon produced by other techniques.

The electrodeposited silicon showed photoconduction as well as photovoltaic properties. The nature of hydrogen bonding in the deposits and some of their photoelectric properties are subjects of another paper (9).

Amorphous nature of the deposits was determined with x-ray diffraction and transmission electron diffraction. X-ray diffraction of silicon deposits produced no crystalline pattern but only a broad diffused band, indicative of amorphous material. Transmission electron diffraction at 100 kV of free silicon films that were lifted off from the substrate, gave also diffused rather than a crystalline pattern. At 100 kV any microcrystallinity of the order of 10-20Å would have been easily revealed. For the present purposes, the deposited material is therefore considered amorphous.

Conclusions

Amorphous silicon can be deposited from a non-aqueous bath containing PC as solvent, SiHCl₃ as

solute, and tetraalkyl ammonium chlorides as the supporting electrolytes. The deposit growth is nodular 1-3 μm in size. An increase in bath temperature ($35^\circ \leq T \leq 145^\circ\text{C}$) and solute concentration ($0.1 \leq C \leq 1.0\text{M}$) favors faster deposition rates, more uniform and smoother deposits. Nodule size and therefore smoothness can also be controlled by using a mixed supporting electrolyte from the tetraalkyl ammonium chloride series.

As deposited α -silicon contains some bonded hydrogen as SiH₂ or SiH. The hydrogen is driven off on annealing at temperatures $\sim 470^\circ\text{C}$. The electrodeposition process offers an inexpensive route for producing α -Si films for possible solar cell applications.

Acknowledgment

This research was supported by Battelle Memorial Institute, the Northwest Mutual Life Insurance Company, the U.S. Department of Energy under Contracts DE-AC03-78-ET-20521 and SERI Subcontract XS-9-8249-1. The authors wish to thank Dr. W. A. Lanford of State University of New York for supplying hydrogen analyses.

Manuscript submitted Dec. 12, 1980; revised manuscript received June 5, 1981. This was Paper 363 presented at the St. Louis, Missouri, Meeting of the Society, May 11-16, 1980.

Any discussion of this paper will appear in a Discussion Section to be published in the June 1982 JOURNAL. All discussions for the June 1982 Discussion Section should be submitted by Feb. 1, 1982.

Publication costs of this article were assisted by Battelle Memorial Institute.

REFERENCES

1. J. I. B. Wilson and D. Weaire, *Nature*, **275**, 93 (1978).
2. A. E. Austin, U.S. Pat. 3,990,953 (1976).
3. R. J. P. Corriu, G. Dabosi, and M. Martineau, *J. Chem. Soc. Chem. Commun.*, 457 (1979).
4. C. K. Mann, in "Electroanalytical Chemistry," Vol. 3, A. J. Bard, Editor, Marcel Dekker, Inc., New York (1979).
5. W. A. Lanford, *Solar Cells* **2**, 351 (1980).
6. A. E. Austin, A. K. Agrawal, and G. T. Noel, Final Report, November 8, 1979, DOE/ET/2052C4.
7. A. E. Austin, A. K. Agrawal, and G. T. Noel, "Electrodeposited Amorphous Silicon for Solar Cell Applications," Final Report to DOE/SERI, September 30, 1980.
8. G. Lucovsky, R. J. Nevranch, and J. C. Knights, *Phys. Rev. B.*, **19**, 2064 (1979).
9. A. E. Austin, To be published.

Resistance to Flow of Current to Scratched Electrodes

H. J. Pearson,¹ G. T. Burstein,* and R. C. Newman

Department of Metallurgy and Materials Science, University of Cambridge, Cambridge CB2 3QZ, England

ABSTRACT

The electrolyte resistance to flow of current to a scratched electrode is calculated assuming the scratch to be shallow and represented by a rectangular planar strip. The resulting equation agrees with experimentally measured ohmic resistances to long, narrow rectangular strip electrodes. Also presented are corrections to the previously published formula for the ohmic resistance to a disk electrode due to finite dimensions of the counterelectrode and the electrochemical cell for systems with radial symmetry.

Rapid mechanical scratching or abrasion of potentiostatically controlled metal electrodes in aqueous electrolytes provides a method of examining the electrochemical properties of metal surfaces initially free from oxide films (1-10). Under external potential control, initially passive electrodes can react at very high anodic current densities on scratching before reverting to the passive state. Important features of an experimental device for studying scratched electrodes are a rapid rate of bare surface generation, an accurately known bare surface area, and minimal surface heating during abrasion. These criteria are satisfied most closely by a device which creates a single narrow shallow scratch on a rotating disk electrode (6-10). The purpose of the present paper is to consider the effects of electrolyte resistance during electrochemical reactions at scratched electrodes under potentiostatic control, where the current passing on the scratched surface flows to a counterelectrode. The related problem of the open-circuit potential distribution across a scratch in a passive film has been investigated by Doig and Flewitt (11) and Melville (12). However, the use of similar open-circuit results to criticize the soundness of the potentiostatic scratching technique (11) is not valid since the current distribution in the two cases is quite different. Many potentiostatic scratching experiments are performed on specimens whose overall surfaces are not coated: the area of exposed metal carries a slow steady-state reaction. Ohmic potential changes occurring around the scratch due to high current densities from the scratch itself can interfere with measurements of scratch current densities. This has been observed when the electrode as a whole is active or carries a readily reducible oxide film (7, 9).

Newman (13) has presented a calculation of the ohmic potential drop due to current flow between a rotating disk electrode embedded in an insulating surface and a counterelectrode at infinity. He solves the Laplace equation for the potential distribution by transforming to rotational elliptic coordinates (oblate spheroidal coordinates). This exact method of solution is only possible because of the symmetry of the problem and is not available for more general electrode geometries. Here we show that knowledge of the approximate form of the current distribution near the electrode leads to accurate expressions for the ohmic potential drop for various electrode shapes, in particular a thin strip of finite length representing a scratch in a passive film. The technique also allows calculation of the corrections required for counterelectrodes of finite size and distance from a rotating

disk working electrode. Confirmation of the calculations is obtained by measuring the ohmic resistance to segments of narrow strip electrodes using a double galvanostatic pulse technique.

Mathematical Model

Consider a plane counterelectrode situated at a position $z = 0$ (where z is the axis perpendicular to the planes of the counter and working electrodes), and a plane working electrode of given geometry embedded in an insulating plane at $z = d$. The Laplace problem for the ohmic component of the potential given by

$$\nabla^2\phi = 0 \quad [1]$$

may be considered as having the following boundary conditions

$$\phi = 0 \text{ at } z = 0 \quad [2a]$$

$$\frac{\partial\phi}{\partial z} = \frac{1}{\sigma} f(x, y) \text{ at } z = d \quad [2b]$$

where x and y are the axes parallel to the counter and working electrode surfaces. $f(x, y)$ is zero on the insulated portion of the plane $z = d$ and represents the current distribution at the surface of the working electrode. The exact value of $f(x, y)$ is such that the value of ϕ is constant on the surface of the electrode. However, calculation will proceed by assuming forms of $f(x, y)$ close to, but not necessarily identical to, the real expression. The first class of geometries that we consider will use an infinite plane counterelectrode at $z = 0$. A further idealized calculation will yield estimates for the corrections due to finite counterelectrode and cell size. The model deals first with the disk electrode as considered by Newman (13) and proceeds to an electrode geometry representing that of a finite, long, narrow, rectangular scratch.

Disk working electrode with plane counterelectrode of infinite size.—Here the boundary value problem is solved by Fourier-Bessel transform in the radial direction. Details are given in Appendix A. For comparison with the results of Newman (13) we consider two current distributions on the disk electrode of radius a

$$f(x, y) = ai_0(a^2 - r^2)^{-1/2} \text{ for } r < a \quad [3a]$$

$$f(x, y) = i_0 \text{ for } r < a \quad [3b]$$

where

$$x^2 + y^2 = r^2 \quad [4]$$

The distribution represented by Eq. [3a] is the same as that for the exact problem solved with the counterelectrode and probe at infinity. Equation [3b] is an artificial distribution included to show the relative insensitivity of the ohmic resistance to the precise form of the current distribution on the electrode. For $d \gg a$ Eq. [3b] gives

* Electrochemical Society Active Member.

¹ Present address: Department of Applied Mathematics and Theoretical Physics, University of Cambridge, Cambridge, England.

Key words: disk working electrode, plane counterelectrode, rectangular strip working electrode.

$$R = \frac{V}{I} \approx \frac{1}{4a\sigma} \left(1 - 2\beta \frac{a}{d} \right) \quad [5]$$

where $\beta = \ln(2/\pi) = 0.2206$. This gives a small correction to the result of Newman (13)

$$R = \frac{1}{4a\sigma} \quad [6]$$

due to the finite distance of the counterelectrode. For Eq. [3a] the potential varies across the disk. Taking the potential at the center of the disk as representative we find

$$R_o = \frac{V_o}{I} = \frac{1}{\pi a \sigma} \left(1 - 2\beta \frac{a}{d} \right) \quad [7]$$

Taking the potential at the edge of the disk as representative we find

$$R_a = \frac{V_a}{I} = \frac{2}{\pi^2 a \sigma} \left(1 - 2\beta \frac{a}{d} \right) \quad [8]$$

Thus any suitable average of Eq. [7] and [8] gives a similar result to Eq. [5], for example

$$R = \frac{1}{2a\sigma} \left(\frac{1}{\pi} + \frac{1}{\pi^2} \right) = \frac{1}{3.6a\sigma} \quad [9]$$

A constant current distribution also clearly gives a reasonable value for the ohmic resistance.

Disk working electrode with plane counterelectrode of finite size.—This uses a disk-shaped counterelectrode of radius p , coaxial with the working electrode and distance d from it. For this case we also define the cell as a coaxial cylinder of radius c . Using cylindrical polar coordinates (r, θ, z) the Laplace Eq. [1] is solved subject to the following boundary conditions

$$\frac{\partial \phi}{\partial z} = \frac{1}{\sigma} f(r, \theta) \text{ at } z = 0, d \quad [10a]$$

$$\frac{\partial \phi}{\partial r} = 0 \text{ at } r = c \quad [10b]$$

This now restricts current flow to within the finite cell and specifies the current distribution on the counter and working electrodes. The problem given by Eq. [1] and [8] with distribution of the form [3a] is solved in the manner given in Appendix B using a Fourier-Bessel series expansion. The solution is

$$R = \frac{d}{\pi \sigma c^2} + \frac{1}{\pi \sigma} \sum_{n=1}^{\infty} \frac{1}{\lambda_n^2 J_0^2(\lambda_n)} \left[\frac{\sin(\lambda_n a/c)}{a} + \frac{\sin(\lambda_n p/c)}{p} \right] \quad [11]$$

where the λ_n are the positive solutions of the equation $J_1(\lambda_n) = 0$. The first term on the right-hand side of Eq. [11] is simply the electrolyte resistance within the cylindrically shaped cell. The second and third terms are the end corrections for the finite size of the working and counterelectrodes, respectively. For $a/c \ll 1$ the second term is the resistance found previously for the disk electrode with c and d infinite (section above). The first and third terms, being independent of a , should represent a good estimate of the correction for finite cell geometry for small scratches as well as disk electrodes and, hence, will be negligible for small scratches. Note that for $p/c = 0.5$ the third term is half the first term.

Rectangular strip working electrode and plane counterelectrode.—We now consider the ohmic resistance to flow of current between a finite length rectangular strip electrode (length $v = 2b$, width

$w = 2a$, $b > a$) and a planar counterelectrode. This shape of working electrode is selected since it most accurately represents a rectangular scratch of negligible depth in a metal surface. Details of the calculation are given in Appendix C for the following current distributions analogous to those used above

$$f(x, y) = ai_o(a^2 - x^2)^{-1/2}, \quad -a \leq x \leq a, \quad -b \leq y \leq b \quad [12a]$$

$$f(x, y) = i_o, \quad -a \leq x \leq a, \quad -b \leq y \leq b \quad [12b]$$

For distribution [12a] we have for $d \gg b > a$

$$R = \frac{1}{2\pi \sigma b} \ln \{ 2[(1 + b^2/a^2)^{1/2} + b/a] \} \quad [13]$$

For the additional inequality that $b \gg a$, Eq. [13] simplifies to

$$R = \frac{1}{2\pi \sigma b} \ln(4b/a)$$

For current distribution [12b], and for $d \gg b \gg a$

$$R = \frac{1}{2\pi \sigma b} [\ln(2b/a) + 1] \quad [14]$$

Equation [13] will be used for comparison with the experimentally determined ohmic resistances (see below).

Experimental

The apparatus used for scratching potentiostatically controlled rotating disk electrodes has been described previously (6-10). The electrochemical cell used for measurement of the ohmic potential drop was similar in design and dimensions; its internal diameter was 10.5 cm and its capacity 1000 cm³.

The working electrodes were designed to simulate rectangular scratches and were made in the following way. Rotating electrodes were prepared in which the edges of copper foils of various thicknesses were exposed to the electrolyte, as shown in Fig. 1. Three foil thicknesses were used: 39, 126, and 936 μm . The foils were set in epoxy resin so that the rectangular edges were exposed, with the insulating resin forming the rotating disk (8 mm diam). Surfaces were abraded to a 1200 grit finish, cleaned ultrasonically, and degreased. Different lengths of the resulting straight, narrow, rectangular strip copper electrodes were exposed by applying a thin mask of lacquer to insulate varying proportions of the electrode length. Rotation at 33 Hz was used for convenience to remove bubbles adhering to the working electrode surface; however, electrode rotation had no effect on the measured ohmic potentials.

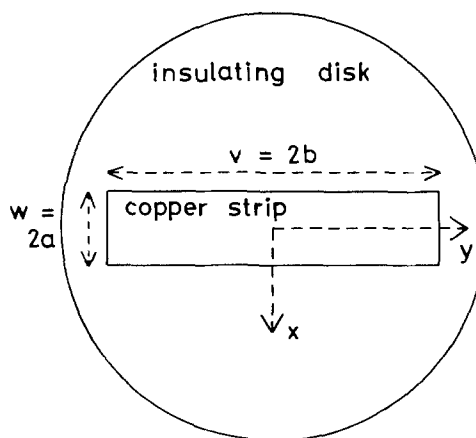


Fig. 1. Schematic diagram of rectangular strip electrode embedded in an insulating rotating disk.

The counterelectrode was a circular platinum disk of 5 cm diam mounted symmetrically below the working electrode surface at a distance of 6 cm. A small hole cut through the center of the counterelectrode allowed a Luggin probe to emerge through it from the bottom of the cell. The probe tip of ~ 1 mm internal diameter was positioned 4 cm vertically below the working electrode surface. This probe distance is effectively infinite within this cell geometry. Potentials were measured with respect to a saturated calomel reference electrode.

Electrolytes were prepared from analytical grade reagents and distilled water. Their conductivities were measured to $\pm 2\%$ with a conductivity bridge (Wayne-Kerr B642 Auto-Balance Universal Bridge).

The ohmic resistances were measured using a double galvanostatic pulse technique, delivered from a potentiostat (Wenking Type OPA 69, response time 1 μsec) programmed to operate as a galvanostat. Square current pulses were generated by feeding the output of a waveform generator (Chemical Electronics Type WG 01) into the potentiostat. Double current pulses, each of 3 msec duration, were used, both in the anodic direction. The initial current density was zero, and the first pulse (A) was adjusted to give an anodic current density of ~ 2 A cm^{-2} . The second pulse (B) was adjusted to increase the anodic current density to ~ 4 A cm^{-2} . Pulse A allowed fast electrode processes such as double layer charging to approach completion; the instantaneous potential change, which occurred as a result of the current pulse B, was used as a measure of the ohmic potential drop in the electrolyte. This was checked by measuring the ohmic potential drop as a function of the current amplitude of pulse B for constant electrode length and width, demonstrating that the relationship was indeed ohmic (see below). Electrode response to the double pulse was stored in a transient recorder (Datalab Type DL 905) and displayed oscillographically. The working electrode was resurfaced between measurements to prevent significant recession of the metal surface into the epoxy resin mount due to anodic dissolution.

All experiments were performed at 291 ± 2 K.

Results and Discussion

Figure 2 shows the relationship between the measured potential change ΔE , due to current pulse B and the pulse amplitude ΔI , for constant amplitude of pulse A. The relationship is ohmic and the slope gives

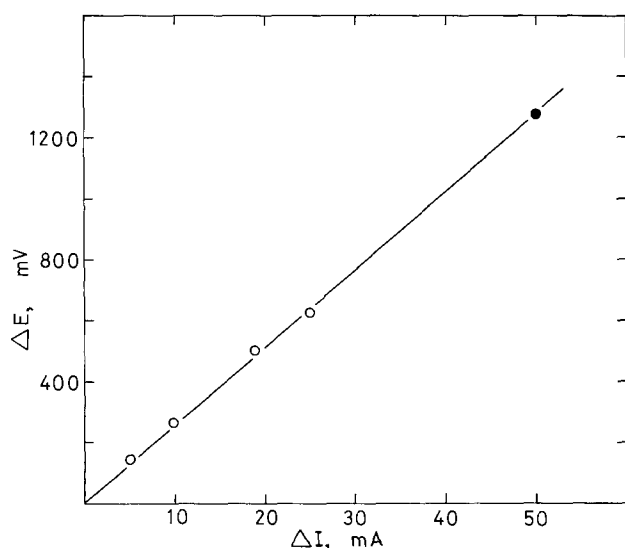


Fig. 2. Measured potential change as a function of applied current pulse (B) amplitude (○). Also shown is one point (●) from pulse A. Electrolyte: 1M KOH, $\sigma = 15.4 \Omega^{-1} \text{m}^{-1}$. Strip electrode, $w = 39 \mu\text{m}$, $v = 5.48$ mm.

the electrolyte resistance R (25.3Ω measured from Fig. 2; 23.9Ω calculated from Eq. [13]). Figure 2 also shows one measurement for a different amplitude of pulse A, which yields a similar value of R .

The resistance to flow of current through an acetate buffer solution (0.75M HOAc, 0.75M NaOAc) to rectangular electrodes of three different widths, w ($= 2a$), is plotted as a function of inverse electrode length v^{-1} ($v = 2b$) in Fig. 3. The solid lines in Fig. 3 represent the theoretical electrolyte resistance predicted from Eq. [13] using the measured electrolyte conductivity. Deviation from the predicted behavior occurs for the widest electrode ($w = 936 \mu\text{m}$) for $v^{-1} > 0.4$. This represents the condition $v/w = b/a < 2.5$ and is, in fact, expected from Eq. [13], which is not symmetrical in a and b . Apart from this the experimental data are in excellent agreement with the theoretical predictions. Similar behavior is shown in Fig. 4 for different electrolytes of several conductivities: again significant deviation from the predicted behavior occurs only for $v/w < 2.5$.

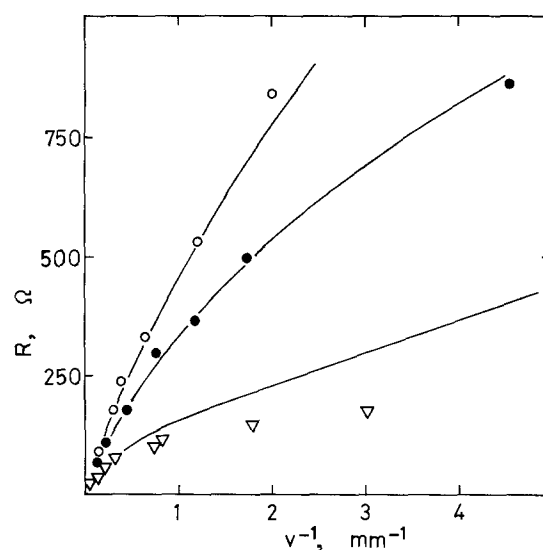


Fig. 3. Electrolyte resistance as a function of electrode length for 0.75M HOAc, 0.75M NaOAc, $\sigma = 3.3 \Omega^{-1} \text{m}^{-1}$. ○, $w = 39 \mu\text{m}$; ●, $w = 126 \mu\text{m}$; ▽, $w = 936 \mu\text{m}$. The lines shown are the theoretical lines calculated from Eq. [13].

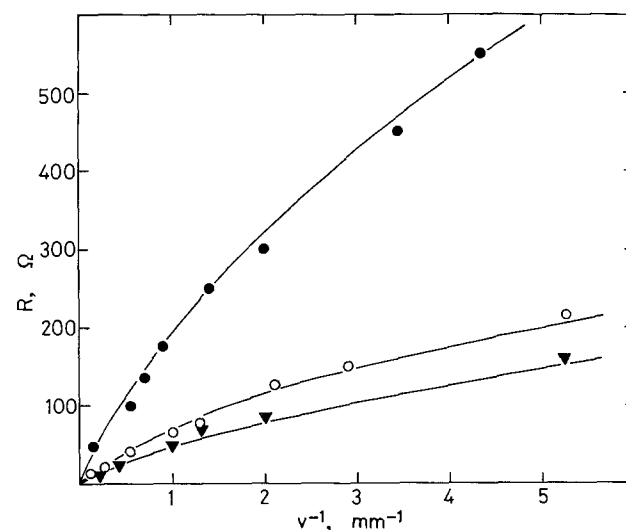


Fig. 4. Electrolyte resistance as a function of electrode length. ●, 0.53M $(\text{NH}_4)_2\text{SO}_4$, $\sigma = 7.0 \Omega^{-1} \text{m}^{-1}$, $w = 58 \mu\text{m}$; ○, 1M KOH, $\sigma = 15.4 \Omega^{-1} \text{m}^{-1}$, $w = 126 \mu\text{m}$; ▽, 1M H_2SO_4 , $\sigma = 32.8 \Omega^{-1} \text{m}^{-1}$, $w = 39 \mu\text{m}$. The lines shown are the theoretical lines calculated from Eq. [13].

The predicted dependence on electrode width using Eq. [13] is shown in Fig. 5 for $b \gg a$ ($v \gg w$), and agreement is obtained with the measured data. Measurements were also made in several different electrolytes as a function of solution conductivity, and these are shown in Fig. 6 together with the theoretical lines from Eq. [13]. The graph shows that the measured resistance is indeed inversely proportional to the electrolyte conductivity, and the data are in accord with Eq. [14]. Figure 6 also shows that the measured ohmic potentials lie across the electrolyte and are not due to any surface film on the electrode.

However, in electrolytes in which a highly resistive film grows on the metal surface during current pulse A, one would expect the measured ohmic resistances to be higher than those predicted from Eq. [13] by

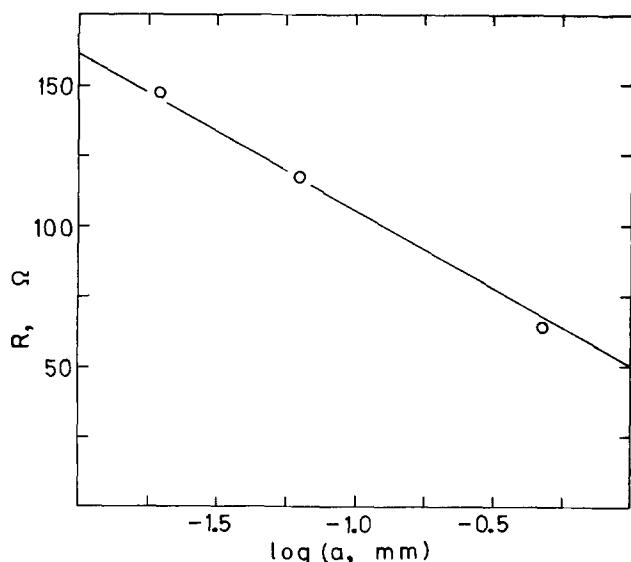


Fig. 5. Dependence of electrolyte resistance on width of strip electrode for constant length (4.0 mm). 0.75M HOAc, 0.75M NaOAc, $\sigma = 3.3 \Omega^{-1} \text{ m}^{-1}$. The line shown is that calculated from Eq. [13].

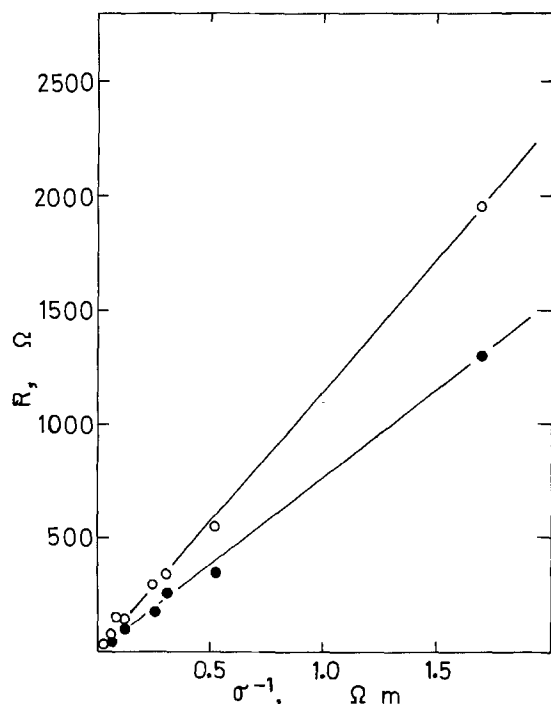


Fig. 6. Electrolyte resistance as a function of conductivity for $v = 1.6$ mm. \circ , $w = 39 \mu\text{m}$; \bullet , $w = 126 \mu\text{m}$. The lines shown are calculated from Eq. [13].

an amount equal to the ohmic resistance of the film. Two such cases are shown in Fig. 7. In both of these electrolytes (1M K_2CO_3 , pH 11.6 and 0.5M K_2CO_3 , 0.5M KHCO_3 , pH 9.8) the copper electrode surface was green after galvanostatic pulsing, owing to formation of a copper carbonate film. In both these cases the measured resistances were considerably higher than those predicted from Eq. [13]. Furthermore, successive galvanostatic double pulses in these electrolytes without resurfacing the electrode between measurements gave ohmic resistances which increased with the number of pulses, showing that film thickening occurred. Whether this increased resistance is due to the film lattice itself or to the electrolyte resistance within pores in the film is not known. Clearly, however, a working electrode which does not produce salt films in carbonate electrolytes, such as Pt or Au, could be used to determine the ohmic resistances of these solutions.

It is clear from Eq. [13] (and Eq. [14]) that for a rectangular scratch in a rotating disk electrode the minimum ohmic potential drop across the electrolyte is achieved when the scratch length and width are both minimum, since the total current $I (= vwi)$ decreases more rapidly with decrease in scratch area than does R , and thus the product IR also decreases. Practical limitations on the scratch area, however, arise from the ability to detect very small current transients arising from very small scratches. The technique which has been employed in recent experiments to scratch rotating disk electrodes (6-10) used a diamond stylus assembly which was allowed to fall under its own inertia onto the disk creating a long (~ 2 mm), narrow ($\sim 40 \mu\text{m}$) scratch at a distance of ~ 2 mm from the center of the disk, at a rate determined by the electrode rotation rate. This has simplified the calculation by imposing the inequality $b \gg a$ (see above). It also ensures that the scratch is of constant width, thereby approximating rectangularity. The ends of the scratch, which are the contact-making and contact-breaking regions, are tapered: Under the above conditions they comprise only $\sim 5\%$ of the total scratch area. As b approaches a , not only must Eq. [13] be used in its full form, but the scratch ceases to be approximately rectangular, and the equation becomes inaccurate. Thus a long narrow scratch, of sufficiently large area to provide a detectable current transient, provides the most quantifiable reaction

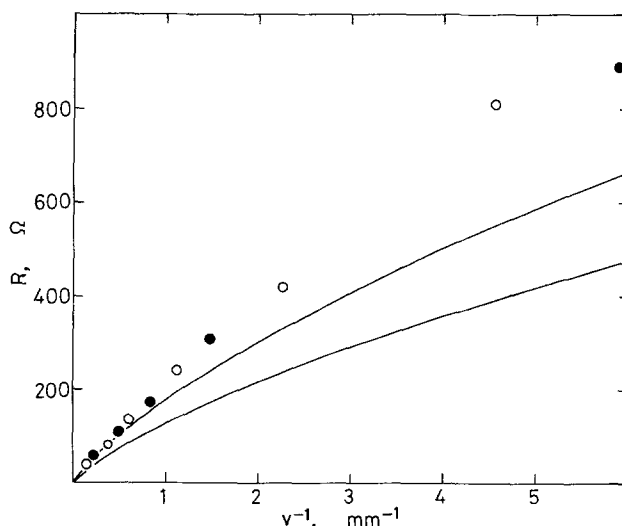


Fig. 7. Measured resistance as a function of electrode length (for $w = 39 \mu\text{m}$) for carbonate electrolytes. \circ , upper line: 0.5M K_2CO_3 , 0.5M NaHCO_3 , $\sigma = 8.2 \Omega^{-1} \text{ m}^{-1}$. \bullet , lower line: 1M K_2CO_3 , $\sigma = 11.4 \Omega^{-1} \text{ m}^{-1}$. The lines shown are calculated from Eq. [13].

parameters of the freshly generated metal surface. The model described above also assumes that the scratch has no depth. For the experiments described (6-10) the scratch depth of $\sim 3 \mu\text{m}$ was small compared with the width, and was thus negligible.

Doig and Flewitt (11) have criticized the scratched electrode technique using calculations made for the ohmic potential drop to a scratch in a metal surface under open-circuit conditions. In that case the current from the scratch as anode flows to the unscratched area of the same specimen acting as cathode. It is fallacious to apply that calculation directly to a potentiostatically controlled scratched disk, however, since the current now flows to a counterelectrode and not to other parts of the working electrode. That this is so is demonstrated by the ability to record a current transient: if all the current from the scratch flowed to other parts of the working electrode no transient would be detectable. Doig and Flewitt showed that for a scratch current density of 0.3 A cm^{-2} flowing from a scratch $10 \mu\text{m}$ wide to the surrounding unscratched metal surface in a solution of conductivity $10 \Omega^{-1} \text{ m}^{-1}$ the ohmic potential drop could be as high as 500 mV. However, under the potentiostatic conditions actually used in these experiments, and with a scratch length of 2 mm, Eq. [13] gives the ohmic potential drop as only 6 mV.

Acknowledgment

We are grateful to the British Petroleum Company for the financial support of R.C.N.

Manuscript submitted Aug. 29, 1980; revised manuscript received March 28, 1981.

Any discussion of this paper will appear in a Discussion Section to be published in the June 1982 JOURNAL. All discussions for the June 1982 Discussion Section should be submitted by Feb. 1, 1982.

APPENDIX

A. Disk Working Electrode with Plane Counterelectrode of Infinite Size

The problem to be solved is

$$\nabla^2 \phi = 0 \tag{A-1}$$

$$\phi = 0 \text{ for } z = 0 \tag{A-2}$$

$$\left. \frac{\partial \phi}{\partial z} \right|_d = \begin{cases} \frac{1}{\sigma} f(r) & \text{for } r < a \\ 0 & \text{for } r > a \end{cases} \tag{A-3}$$

In cylindrical polar coordinates (r, θ, z) we have axial symmetry and may take

$$\phi = \int_0^\infty A(k) J_0(kr) \sinh(kz) dk \tag{A-4}$$

where J_0 is the zero order Bessel function of the first kind. This form of ϕ satisfies [A-1] and [A-2]; the transform $A(k)$ is determined by [A-3] through the relation

$$\left. \frac{\partial \phi}{\partial z} \right|_d = \int_0^\infty k A(k) J_0(kr) \cosh(kd) dk$$

Inverting this expression gives

$$\sigma \cosh(kd) \cdot A(k) = \int_0^a r f(r) J_0(kr) dr$$

which is then substituted in [A-4] to give an expression for ϕ .

(a) For

$$f(r) = ai_0(a^2 - r^2)^{-1/2}$$

then

$$\sigma A(k) = \frac{ai_0}{\cosh(kd)} \frac{\sin(ak)}{k}$$

thus

$$\sigma \phi(r, d) = i_0 a \int_0^\infty \frac{\sin(ak)}{k} J_0(kr) \tanh(kd) dk$$

In order to find the ohmic drop we evaluate V/I , where V is the potential at the disk electrode, given by $\phi(O, d)$ and I is the total current flowing. The latter is given by

$$I = \int_0^a 2\pi r f(r) dr = 2\pi a^2 i_0$$

Evaluating V we have

$$\sigma \phi(O, d) = i_0 a \int_0^\infty \frac{\sin(ak)}{k} \tanh(kd) dk \tag{A-5}$$

For $d \gg a$, that is to say, the counterelectrode many disk radii away from the working electrode, $\tanh(kd)$ differs from unity, while $(\sin(ak))/k$ is given to a good approximation by the constant value a . So we may write [A-5] as

$$\begin{aligned} \sigma \phi(O \cdot d) &= i_0 a \int_0^\infty \frac{\sin(ak)}{k} dk \\ &\quad - i_0 \int_0^\infty a^2 (1 - \tanh(kd)) dk + i_0 a O\left(\frac{a}{d}\right)^3 \\ &= i_0 a \left[\frac{\pi}{2} - \ln \frac{2a}{d} + O\left(\frac{a}{d}\right)^3 \right] \end{aligned}$$

$$R = \frac{V}{I} \approx \frac{1}{4a\sigma} \left[1 - \frac{2 \ln 2}{\pi} \left(\frac{a}{d}\right) \right]$$

and the correction for the finite counterelectrode distance to the Newman result (13)

$$R = (4a\sigma)^{-1}$$

is of the order a/d ($\ll 1$) as might be expected. $O(a/d)^3$ represents all terms of order $(a/d)^3$.

(b) For $f(r) = i_0$

by similar arguments to above

$$\begin{aligned} \sigma \phi(O, d) &= ai_0 \int_0^\infty \frac{J_1(ak)}{k} \tanh(kd) dk \\ &\approx ai_0 \left(1 - \ln \frac{2a}{d} \right) \end{aligned}$$

and so

$$R_o = \frac{1}{\pi a \sigma} \left(1 - \ln \frac{2a}{d} \right)$$

Also

$$\sigma \phi(a, d) = \frac{2ai_0}{\pi} \left(1 - \ln \frac{2a}{d} \right)$$

whence

$$R_a = \frac{2}{\pi^2 a \sigma} \left(1 - \ln \frac{2a}{d} \right)$$

B. Disk Working Electrode with Plane Counterelectrode of Finite Size

The problem to be solved is

$$\nabla^2 \phi = 0 \tag{B-1}$$

$$\left. \frac{\partial \phi}{\partial z} \right|_d = \frac{1}{\sigma} f_1(r) \text{ at } z = d \tag{B-2}$$

$$= \frac{1}{\sigma} f_2(r) \text{ at } z = 0$$

$$\left. \frac{\partial \phi}{\partial r} \right|_c = 0 \text{ at } r = c \tag{B-3}$$

A suitable representation of ϕ satisfying [B-1] and [B-3] is

$$\sigma \phi = A_0 z + \sum_{n=1}^\infty \left[A_n \exp\left(-\frac{\lambda_n z}{c}\right) \right]$$

$$+ B_n \exp\left(\frac{\lambda_n z}{c}\right) \Big] J_0\left(\frac{\lambda_n r}{c}\right) \quad [\text{B-4}]$$

where the λ_n 's are the positive roots of $J_1(\lambda_n) = 0$. We take

$$\begin{aligned} f_1(r) &= i_0 a (a^2 - r^2)^{-1/2} && \text{for } r < a \\ &= 0 && \text{for } c > r > a \\ f_2(r) &= i_0 a^2 p^{-1} (p^2 - r^2)^{-1/2} && \text{for } r < p \\ &= 0 && \text{for } c > r > p \end{aligned}$$

Then, as in Appendix A

$$\begin{aligned} \sigma A_0 &= \frac{2a^2 i_0}{c^2} \\ \sigma A_n &= \frac{2i_0}{\lambda_n^2 J_0^2(\lambda_n)} \\ &\frac{\frac{a^2}{pc} \sin\left(\frac{\lambda_n p}{c}\right) \exp\left(-\frac{\lambda_n d}{c}\right) - \frac{a}{c} \sin\left(\frac{\lambda_n a}{c}\right)}{1 - \exp\left(-\frac{2\lambda_n d}{c}\right)} \\ \sigma B_n &= \frac{2i_0}{\lambda_n^2 J_0^2(\lambda_n)} \\ &\frac{\frac{a^2}{pc} \sin\left(\frac{\lambda_n p}{c}\right) \exp\left(\frac{\lambda_n d}{c}\right) - \frac{a}{c} \sin\left(\frac{\lambda_n a}{c}\right)}{\exp\left(\frac{2\lambda_n d}{c}\right) - 1} \end{aligned}$$

for $n = 1, 2, 3 \dots$

If $d/c > 1$ and a/p is not too small, then the first term in the expansion for A_n and the second term in the expansion for B_n are both small and may be ignored, giving

$$\begin{aligned} R &= \frac{\phi(d, 0) - \phi(0, 0)}{I} = \frac{d}{\pi \sigma c^2} \\ &+ \frac{1}{\pi \sigma} \sum_{n=1}^{\infty} \frac{1}{\lambda_n^2 J_0^2(\lambda_n)} \left[\frac{\sin\left(\frac{\lambda_n a}{c}\right)}{a} + \frac{\sin\left(\frac{\lambda_n p}{c}\right)}{p} \right] \end{aligned}$$

C. Rectangular Strip Working Electrode and Plane Counterelectrode

The problem to be solved is

$$\nabla^2 \phi = 0 \quad [\text{C-1}]$$

$$\phi = 0 \quad \text{at } z = 0 \quad [\text{C-2}]$$

$$\frac{\partial \phi}{\partial z} = \frac{1}{\sigma} f(x, y) \quad \text{at } z = d \quad [\text{C-3}]$$

The rectangular strip is given by $|x| \leq a, |y| \leq b$; $f(x, y) = 0$ outside these limits.

The solution is found in terms of a double Fourier transform in x and y

$$\sigma \phi = \frac{1}{4\pi} \int_{-\infty}^{\infty} \int_{-\infty}^{\infty} A_1(k_1) A_2(k_2) \exp i(k_1 x + k_2 y) \sinh(kz) dk_1 dk_2$$

where

$$k^2 = k_1^2 + k_2^2$$

This form satisfies [C-1], [C-2], and [C-3] and yields

$$\begin{aligned} f(x, y) &= \frac{1}{4\pi^2} \int_{-\infty}^{\infty} \int_{-\infty}^{\infty} \exp i(k_1 x + k_2 y) \\ &A_1(k_1) A_2(k_2) k \cosh(kd) dk_1 dk_2 \quad [\text{C-4}] \end{aligned}$$

(a) Suppose the current density on the rectangular strip is constant, i_0

$$I = 4abi_0$$

Inverting [C-4] gives

$$\begin{aligned} &A_1(k_1) A_2(k_2) k \cosh(kd) \\ &= i_0 \int_{-a}^a \int_{-b}^b \exp -i(k_1 x + k_2 y) dx dy \\ &= 4i_0 \frac{\sin(k_1 a)}{k_1} \frac{\sin(k_2 b)}{k_2} \end{aligned}$$

Therefore

$$\begin{aligned} \sigma \phi(0, 0, d) &= \frac{i_0}{\pi^2} \int_{-\infty}^{\infty} \int_{-\infty}^{\infty} \frac{\sin(k_1 a)}{k_1} \frac{\sin(k_2 b)}{k_2} \frac{\tanh(kd)}{k} dk_1 dk_2 \end{aligned}$$

To evaluate this integral we transform to polar coordinates: $k_1 = k \sin \theta, k_2 = k \cos \theta, dk_1 dk_2 = k dk d\theta$, and note that only a very small error is made by putting $\tanh(kd) = 1$. Then

$$\begin{aligned} \sigma \phi(0, 0, d) &= \frac{4i_0}{\pi^2} \int_0^{\infty} \int_0^{\pi/2} \frac{\sin(ak \sin \theta) \sin(bk \cos \theta)}{k^2 \cos \theta \sin \theta} dk d\theta \end{aligned}$$

The k integration gives

$$\begin{aligned} &\frac{\pi b}{2 \sin \theta} && a \sin \theta > b \cos \theta \\ &\frac{\pi a}{2 \cos \theta} && a \sin \theta < b \cos \theta \end{aligned}$$

leading to a final answer of

$$\sigma \phi(0, 0, d) \approx \frac{\pi}{2} a i_0 \left[\ln\left(\frac{2b}{a}\right) + 1 \right]$$

for a long thin strip, where $b \gg a$. This gives

$$R = \frac{1}{2\pi \sigma b} \left[\ln\left(\frac{2b}{a}\right) + 1 \right]$$

(b) For the more realistic current distribution

$$f(x, y) = a i_0 (a^2 - x^2)^{-1/2}, \quad |x| < a, \quad |y| < b$$

the calculation is similar, with $(\sin(k_1 a))/k_1$ replaced by $J_0(ak_1)$. The final result for this case is

$$R = \frac{1}{2\pi \sigma b} \ln \left\{ 2 \left[\left(1 + \frac{b^2}{a^2}\right)^{1/2} + \frac{b}{a} \right] \right\}$$

for $d \gg b > a$.

LIST OF SYMBOLS

| | |
|-------------|--|
| a | radius of disk-shaped working electrode; half-width of strip working electrode |
| $A(k)$ | transform of potential |
| A_n | coefficient in expansion for potential |
| b | half-length of strip working electrode |
| B_n | coefficient in expansion for potential |
| c | radius of cylindrical cell |
| d | distance between working and counterelectrodes |
| E | electrode potential |
| i | current density |
| I | current |
| J_0 | zero order Bessel function |
| J_1 | first order Bessel function |
| k | wave number |
| O | terms of order . . . |
| p | radius of counterelectrode |
| r | polar coordinate |
| R | resistance |
| v | length of strip working electrode |
| V | potential difference |
| w | width of strip working electrode |
| x | cartesian coordinate |
| y | cartesian coordinate |
| z | polar, cartesian coordinate |
| β | $\ln(2/\pi)$ |
| θ | polar coordinate |
| λ_n | positive roots of equation $J_1(\lambda_n) = 0$ |
| σ | electrolyte conductivity |
| ϕ | potential |

REFERENCES

1. E. Kunze and K. Schwabe, *Corros. Sci.*, **4**, 109 (1964).
2. T. Hagyard and W. B. Earl, *This Journal*, **114**, 694 (1967).
3. N. D. Tomashov and L. P. Vershinina, *Electrochim. Acta*, **15**, 501 (1970).
4. T. R. Beck, *ibid.*, **18**, 807 (1973).
5. T. R. Beck, *ibid.*, **18**, 815 (1973).
6. F. P. Ford, G. T. Burstein, and T. P. Hoar, *This Journal*, **127**, 1325 (1980).
7. G. T. Burstein and R. C. Newman, *Electrochim. Acta*, **25**, 1009 (1980).
8. G. T. Burstein and D. H. Davies, *Corros. Sci.*, **20**, 1143 (1980).
9. R. C. Newman and G. T. Burstein, *ibid.*, **21**, 119 (1981).
10. G. T. Burstein and D. H. Davies, *This Journal*, **128**, 33 (1981).
11. P. Doig and P. E. J. Flewitt, *Philos. Mag.*, **38**, 27 (1978).
12. P. H. Melville, *This Journal*, **126**, 2081 (1979).
13. J. Newman, *ibid.*, **113**, 501 (1966).

Conductivity of Beta-Alumina Highly Doped with Iron

John H. Kennedy and Susan M. Stuber

Department of Chemistry, University of California, Santa Barbara, California 93106

ABSTRACT

Complex plane impedance diagrams were used to determine the ionic conductivity of Fe-doped β -alumina over the composition range $\text{Na}_{1.3}\text{Al}_{9.88}\text{Fe}_{1.14}\text{O}_{17.15}$ (10% Fe by weight) to $\text{Na}_{1.3}\text{Al}_{7.18}\text{Fe}_{3.82}\text{O}_{17.15}$ (30% Fe by weight). The influence of starting material [Fe_2O_3 , $\text{Fe}_2(\text{C}_2\text{O}_4)_3 \cdot 6\text{H}_2\text{O}$, $\text{Fe}(\text{C}_2\text{O}_4) \cdot 2\text{H}_2\text{O}$, $\text{Fe}(\text{NO}_3)_3 \cdot 9\text{H}_2\text{O}$] upon grain boundary and bulk properties was studied. The ionic conductivity of all doped materials increased over that of undoped β -alumina. The best materials obtained resulted from doping with $\text{Fe}(\text{C}_2\text{O}_4) \cdot 2\text{H}_2\text{O}$. At the 10% doping level, bulk conductivity reached a maximum coinciding with a minimum in activation energy. Electronic conductivity was investigated by a "floating" blocking technique. The electronic conductivity was small at the 15% dopant level, representing $<10^{-3}\%$ of the total conductivity, but increased rapidly and at the 30% dopant level was $\sim 0.1\%$ of the total conductivity. Preliminary Mössbauer studies showed a steady increase in the Fe(III)/Fe(II) ratio as dopant levels increased.

A previous study of β -alumina doped with small amounts of iron [ca. 2 weight percent (w/o)] investigated the oxidation states and site symmetry of the iron dopant and concluded that both Fe(II) and Fe(III) were present after air sintering (1). Conductivity results for iron-doped β -alumina containing up to 8 w/o Fe showed an increase in bulk conductivity up to 4 w/o Fe while 8 w/o material was of lower density and conductivity when the same sintering conditions were used (2). It becomes apparent that sintering conditions must be adjusted as the dopant level changes in order to achieve the maximum density and conductivity particularly when higher doping levels are attempted.

In the present study iron doping of 10-30 w/o has been carried out, and changes in bulk and grain boundary conductivity are reported. The influence of starting material and sintering conditions on the properties of the sintered pellets has also been studied. It was anticipated that high doping levels of iron in β -alumina could be attained because Fe_2O_3 and Al_2O_3 form solid solutions across the whole composition range and β -alumina analogs of the type $\text{MFe}_{11}\text{O}_{17}$ are also known (3, 4).

Experimental

Sodium β -alumina (Alcoa XB-2 "Superground") was doped with iron using Fe(III) nitrate, Fe_2O_3 , Fe(II) oxalate, and Fe(III) oxalate as starting materials. In some of the samples investigated, Na_2CO_3 was added as a starting material in order to see the influence on the final Na^+ concentration. The presence of Na_2CO_3 seemed to have no effect on the outcome. However, the important factor for maintaining sample control with regard to Na^+ concentration in-

involved a fresh packing of coarse β -alumina powder surrounding the pellets. All samples were packed in 300 mesh β -alumina during sintering. Details of the doping and firing procedures have been published previously (1).

Pellets of approximately 1.27 cm diam and 0.2 cm thickness were isostatically pressed and then sintered. Sintering time and temperature necessary to yield highest density material (typically 3.15-3.25 g/cm³) were determined for each iron concentration. Material of the highest density invariably also exhibited the highest conductivity. In general, 0-10 w/o Fe material could be sintered at 1600°C for 3 hr while 15-25 w/o Fe was sintered at 1540°C for 3 hr. Recent measurements with more highly doped iron (>25%) indicate that sintering temperature must be decreased to about 1500°C to achieve optimum results. When pellets are fired at too high a temperature they shrink to a small diameter but are porous and are of low density, mechanical strength, and conductivity. All samples were fired in air.

The sintered disks were prepared for electrode deposition by polishing with successively finer grades of silicon carbide paper. Finishing was accomplished by polishing with 9, 6, and 3 μm diamond impregnated lapping wheels. The polishing solvent was ethanol. The polished samples were then ultrasonically cleaned in acetone. The disks were then heated at 300°C for 24 hr before electrodes were applied.

Electrodes were deposited on the disks by a Technics, Incorporated Hummer Sputtering and Deposition instrument using a gold target. The electrodes were nominally 2.5 μm thick.

Complex impedance/admittance diagrams were recorded between 25° and 325°C by placing the sample in a furnace which was inside a helium-filled glove box (Overly P-100). Accurate temperature control

was achieved by a digital setting Eurotherm controller. Measurements from 10^{-4} to 10^{+6} Hz were made using a Schlumberger-Solartron 1174 Frequency Response Analyzer interfaced to a Hewlett-Packard 9845-S desktop computer. Most often impedance measurements were taken directly and inversion of the data to the admittance mode, if desired, was part of the 9845 program. The computer was programmed to accept measurements from the frequency response analyzer in the a,b (cartesian coordinates) mode and generally 16 data points per decade of frequency were taken, although this feature was programmable. In addition to tabulating the results, the program output was in the form of a complex plane plot which could then be fit to a series of semicircles and straight lines by curve fitting routines (5). An example is shown in Fig. 1.

A correction program was incorporated to compensate for inductive and capacitive effects observed at high frequency (10^5 - 10^6 Hz). The signal across the sample was normally 100 mV but other signals may be selected as part of the computer program.

X-ray diffraction patterns were obtained using a diffractometer to determine percentage of β'' -alumina present.

Sodium analysis was accomplished by dissolving the samples in boiling, concentrated phosphoric acid and analyzing the solution by atomic absorption. Exchangeable sodium was also determined by ion exchanging the samples with molten AgNO_3 and measuring the mass change (2).

Results

An equivalent circuit which approximates polycrystalline β -alumina has been reported (2, 6) which allows the calculation of bulk and grain boundary effects from complex plane diagrams. Values reported here were determined using the techniques reported previously (2) plus computer program curve-fitting routines developed since the previous study (5).

The conductivity in all doped samples increased compared to undoped β -alumina. However, differences were observed depending on the starting material used for doping. Densities, sodium content, conductivities, and activation energies were all sensitive to the starting composition. Because firing resulted in decomposition of all starting materials to the oxide form but the observed final Fe(II/III) ratio was dependent on firing conditions, these differences were attributed to differences in particle size and attainment of homogeneity. In general it was found that doping with Fe(II) oxalate gave pellets with the highest density and conductivity at each doping level investigated. Therefore, results with this particular dopant starting material will be emphasized. Results are shown in Table I for all Fe(II) oxalate compositions. In addition, other materials with data of particular interest discussed in the text are also presented.

A maximum bulk conductivity, σ_b , was observed at ~10 w/o Fe followed by a steady decrease in the conductivity values up to the highest levels investigated to date (30 w/o). At the same time the activation energy for bulk conductivity was a minimum at the 10 w/o doping level. These trends can be seen in Fig. 2 and Fig. 3. At first it was thought that the decrease in conductivity reflected less-than-optimum sintering conditions as was experienced for early work with 8 w/o iron doped β -alumina (2). However, densities near theoretical were obtained for several samples and all attempts to improve the density and conductivity over those shown in Table I have failed.

Table I. Properties of Fe-doped β -alumina

| Nominal composition dopant | Nominal formula (iron as +3) | Density (g/cm ³) | % Na | | β : β'' (%) | Fe(III)/Fe(II) | $\sigma_{0.25^\circ}$ (Ω cm) ⁻¹ | $\sigma_{0.300^\circ}$ (Ω cm) ⁻¹ | $\sigma_{600.25^\circ}$ (Ω cm) ⁻¹ | E_a (bulk) (kcal/mol) | E_a (gr) (kcal/mol) | σ electronic (Ω cm) ⁻¹ |
|------------------------------------|--|------------------------------|------|----------|-------------------------|----------------|--|---|--|-------------------------|-----------------------|--|
| | | | AA | Ag exch. | | | | | | | | |
| 20%/Fe(II) oxalate | $\text{Na}_{1.3}\text{Al}_{1.6}\text{Fe}_{0.4}\text{O}_{7.35}$ | 3.05 | 6.76 | 4.57 | 99%:1% | 4 | 6.71×10^{-3} | 7.76×10^{-3} | 3.38×10^{-3} | 3.02 | 6.44 | |
| 20%/Fe(III) oxalate | $\text{Na}_{1.3}\text{Al}_{1.6}\text{Fe}_{0.4}\text{O}_{7.35}$ | 2.92 | 5.21 | | | | 1.78×10^{-3} | 4.71×10^{-2} | 1.01×10^{-3} | 4.047 | 4.77 | |
| 25%/Fe(II) oxalate | $\text{Na}_{1.3}\text{Al}_{1.6}\text{Fe}_{0.5}\text{O}_{7.15}$ | 2.96 | 4.76 | 5.3 | 98%:2% | 7 | 3.95×10^{-3} | 5.8×10^{-2} | 2.59×10^{-3} | 3.32 | 6.65 | |
| 25%/Fe ₂ O ₃ | $\text{Na}_{1.3}\text{Al}_{1.6}\text{Fe}_{0.5}\text{O}_{7.15}$ | 2.72 | 6.17 | | | | 0.88×10^{-3} | 37×10^{-3} | 2.23×10^{-3} | 7.38 | 2.43 | 1.1×10^{-8} |
| 30%/Fe(II) oxalate | $\text{Na}_{1.3}\text{Al}_{1.6}\text{Fe}_{0.5}\text{O}_{7.15}$ | 3.29 | | | 80%:20% | | 3.3×10^{-5} (?) | 8.2×10^{-3} | 8.4×10^{-6} | 3.97 | 8.34 | 3×10^{-8} (0.1% of total) |
| 30%/Fe ₂ O ₃ | $\text{Na}_{1.3}\text{Al}_{1.6}\text{Fe}_{0.5}\text{O}_{7.15}$ | 3.27 | | | | | 2.17×10^{-3} | 3.7×10^{-3} | 2.54×10^{-4} | 5.32 | 5.64 | 1.07×10^{-6} (0.047% of total) |

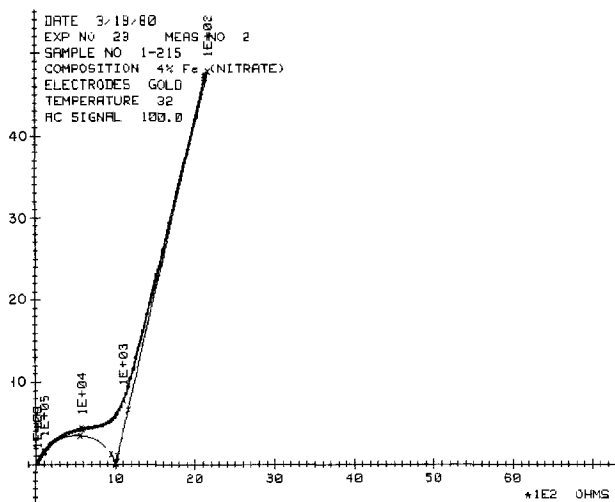


Fig. 1. Impedance diagram showing experimental data and mathematical fitting into semicircle and straight line components.

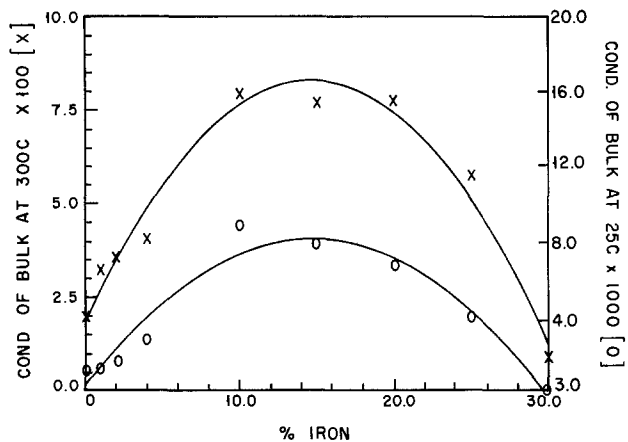


Fig. 2. Bulk conductivity at 25° and 300°C as a function of iron content.

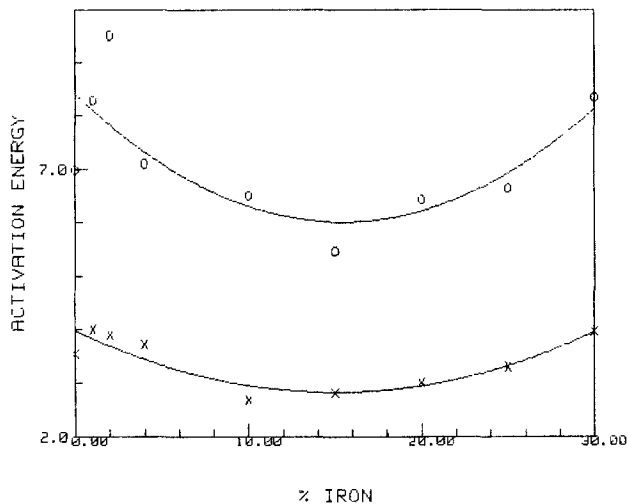


Fig. 3. Activation energy of bulk (X) and grain boundary (O) as a function of iron content.

The grain boundary conductivity also reached a maximum but the actual peak value was observed at 15 w/o Fe as shown in Table I and Fig. 4. The activation energy showed the same small trend toward lower values in the 10-20 w/o doping region as did the activation energy for bulk conductivity.

Grain boundary contribution to the total resistance of a sample at 300°C was so small that measured

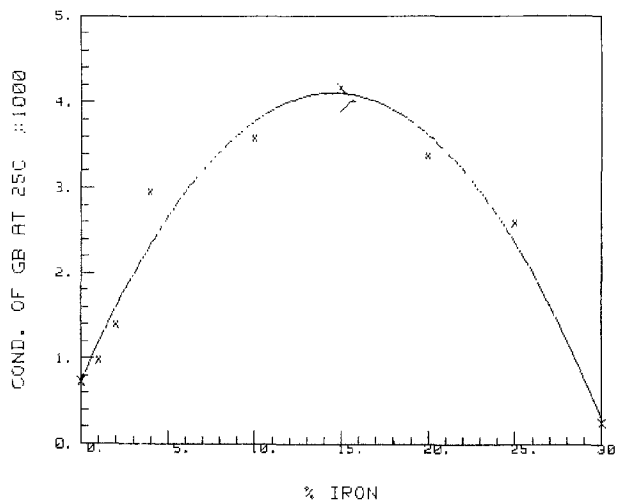


Fig. 4. Grain boundary conductivity at 25°C as a function of iron content.

values are not very meaningful. The cross-over temperature above which bulk resistance was the dominant factor occurred a little above room temperature (<80°C for most materials). Below this temperature grain boundary resistance was greater than the bulk resistance.

Admittance diagrams in the 10^{-2} - 10^{-4} Hz frequency range gave no evidence for the existence of any appreciable electronic conductivity, i.e., the lowest frequency semicircle had a real-axis intercept of zero mhos (infinite resistance) within experimental accuracy (Fig. 5). This conclusion was supported by d-c measurements with gold blocking electrodes (Fe-doped β -alumina is not stable in the presence of sodium so that the traditional Wagner blocking technique was not possible). A reasonably stable steady-state current was reached after 1-2 days at each applied voltage, and a plot of current vs. applied voltage is shown in Fig. 6. The slope of the line indicated a resistance of $2.3 \times 10^6 \Omega$ which translated to a conductivity value of $1.2 \times 10^{-7} (\Omega\text{-cm})^{-1}$ for 15% Fe-doped β -alumina. Since true equilibrium may not have been reached, this probably represents a maximum value for electronic conductivity in this "floating" system (i.e., no reference potential as in a Wagner blocking technique). The bulk conductivity for this material was $7.9 \times 10^{-3} (\Omega\text{-cm})^{-1}$ at 25°C so that electronic conductivity contributed 10^{-3}% of the total conductivity. As can be seen from Table I the

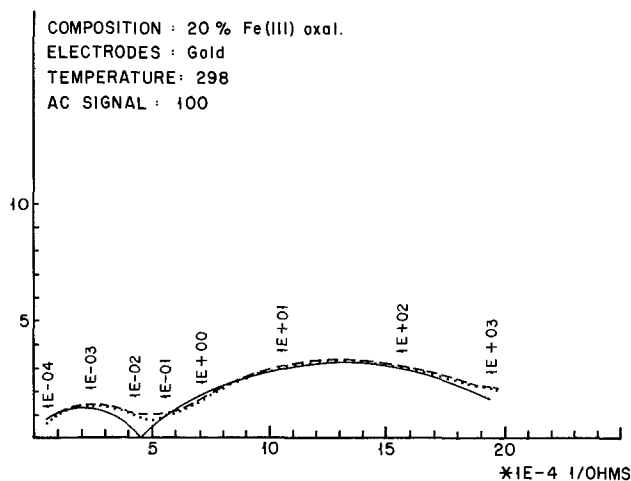


Fig. 5. Admittance diagram for 20% Fe in β -alumina doped from Fe(III) oxalate. Low frequency intercept of zero (within experimental uncertainty) gives no evidence for electron hopping.

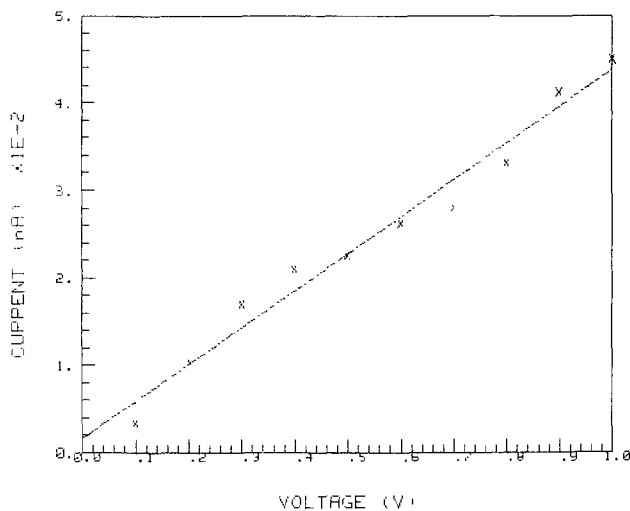


Fig. 6. Plot of current vs. applied voltage for 15% Fe in β -alumina doped from Fe(II) oxalate.

percentage electronic conductivity increased rapidly to nearly 0.1% when the iron content reached 30%. Roland reported (7, 8) that electronic conductivity in iron-doped β -alumina was significant at these doping levels and projected that at 53 w/o Fe electronic conductivity would equal ionic conductivity. Results from this study show that the percentage electronic conductivity does increase with increasing Fe content but the point at which $t_i = t_e$ would not be reached until at least 60 w/o Fe were present assuming the observed trend continued. This point will be discussed further later on.

A critical factor in the electrochemical properties of iron-doped β -alumina is the Fe(III)/Fe(II) ratio. It is well known that metal ions in the plus two oxidation state tend to increase the conductivity of β -alumina, probably by incorporating more conductive Na⁺ and/or by decreasing the concentration of O²⁻ interstitials needed for charge compensation. A Mössbauer study of low iron doping showed the existence of both Fe(II) and Fe(III) in nearly equal proportions (1). A more accurate calculation based on peak areas attributable to Fe(II) and Fe(III) shows that the Fe(III)/Fe(II) ratio was about 1.7 at the 2.95 w/o doping level. Higher doping levels also showed the existence of Fe(II), but preliminary results indicated that the Fe(III)/Fe(II) ratio increased to 4 at 20 w/o Fe and to 7 at 25 w/o Fe. Details of the Mössbauer study will be published later. Similar results showing an increase in the Fe(III)/Fe(II) ratio at higher doping levels were also reported by Burzo and Ardelean in their work with iron-doped glasses (9).

Another factor which was considered to play a role in the electrochemical properties of Fe- β -alumina was the possible presence of β'' -alumina. Low doping levels of Fe reported previously showed only single phase β -alumina (1, 2). However, Mg²⁺ stabilizes the β'' -form and perhaps other M²⁺ ions could play the stabilizing role to produce compositions of the type Na_{2-x}M_{1-x}Al_{10+x}O₁₇. X-ray diffraction patterns of β -alumina doped with at least 10 w/o Fe generally indicated the presence of the β'' -phase. The amount of β'' -phase remained small even at high doping levels which may be a result of the small amount of Fe(II) in highly doped Fe- β -alumina. Amounts of β'' -phase estimated from diffraction line intensities are given in Table I. The technique for estimating β/β'' involved comparing diffractometer peak heights for the following d -spacings: $d = 2.039$ and $d = 1.939$ for β compared to $d = 1.978$ for β'' ; $d = 2.687$ and $d = 2.514$ for β compared to $d = 2.605$ for β'' . The peak heights were normalized to the peak heights reported for pure β

and β'' -alumina. It should be noted that the material showing the highest bulk conductivity [10 w/o from iron(II) oxalate] also contained the highest concentration of β'' -alumina.

Discussion

Previous work involving M(II) doping showed that conductivity increases correlated well with M(II) content and also with sodium content (2). One possible charge compensation mechanism involves replacement of an Al(III) by an M(II) in the spinel block with incorporation of an additional sodium ion in the conduction plane. When β -alumina is doped with iron, some of the iron is present as Fe(II) and, therefore, this mechanism would be possible. However, unlike other plus two metal dopants such as Mn, Co, and Ni, the sodium content did not continue to increase as the dopant level increased (2). In Table I it can be seen that with higher doping levels the sodium content did not correlate well with doping level and, if anything, was no higher than undoped β -alumina.

These results are not unexpected when one considers the Mössbauer results. As the dopant level increased the percentage Fe(II) decreased so rapidly that the concentration of Fe(II) in 25 w/o Fe was less than in 20 w/o Fe (3 vs. 4%). The maximum concentration of Fe(II) probably occurred in the 10-20 w/o region which correlates well with conductivity.

Another charge compensation mechanism involves a decrease in blocking oxide interstitials as the M(II) concentration increases. One would predict a decrease in activation energy for this mechanism and no necessary change in sodium content. As can be seen in Fig. 3, the lowest activation energies were observed with 10-20 w/o Fe, but, if anything, a slight increase at low doping levels compared to undoped β -alumina [data taken from Ref. (2)]. Thus, it appears that at low doping levels (<5 w/o Fe) a significant amount of Fe(II) is present which incorporates additional sodium ions resulting in an increase in bulk conductivity. At higher doping levels the amount of Fe(II) reaches a maximum in the 10-20 w/o region and this doping is at least partially charge compensated by a decrease in oxide interstitials leading to a lower activation energy. At doping levels >20 w/o Fe the amount of Fe(II) drops, and the conductivity begins to fall as the activation energy begins to increase.

This simple picture is clouded by the presence of β'' -phase. One would expect a higher conductivity for β'' -form compared to β , and this may account for some of the increased conductivity in the 10-20 w/o region. However, β'' -phase was also found in the 30 w/o material so that the previous argument involving Fe(II) concentrations probably predominates.

The increasing electronic conductivity at high doping levels most likely reflects the shorter average distance between iron atoms. If an electron hopping mechanism exists it would be necessary to maintain a significant amount of Fe(II) in the structure at high doping levels. It was shown in a previous study (1) that Fe(III) may be reduced to Fe(II) in β -alumina by treatment with 90% N₂/10% H₂ at 1200°C. An increase in the Fe(II) content at high doping levels may result in a substantial increase in electronic conductivity making these materials potentially valuable mixed conductors. The Fe(III)/Fe(II) ratio is most probably a sensitive function of sintering temperature and sintering atmosphere and this fact could explain the higher electronic conductivity values reported by Roland (7, 8). However, no information on the Fe(III)/Fe(II) ratio is available for his materials. At present we are continuing these studies of β -alumina highly doped with iron to investigate the possibility of increasing the electronic conductivity (and possibly the ionic conductivity as well) by increasing the amount of Fe(II).

Acknowledgment

The authors acknowledge financial support of this project by the National Science Foundation, Grants DMR 77-24562 and DMR 8002676. The authors also thank Professor Paul Barrett of the Physics Department for the use of his Mössbauer equipment and helpful discussions.

Manuscript submitted Aug. 4, 1980; revised manuscript received ca. April 3, 1981.

Any discussion of this paper will appear in a Discussion Section to be published in the June 1982 JOURNAL. All discussions for the June 1982 Discussion Section should be submitted by Feb. 1, 1982.

Publication costs of this article were assisted by the University of California.

REFERENCES

1. J. R. Akridge, B. Srouf, C. Meyer, Y. Gros, and J. H. Kennedy, *J. Solid State Chem.*, **25**, 169 (1978).
2. J. H. Kennedy, J. R. Akridge, and M. Kleitz, *Electrochim. Acta*, **24**, 781 (1979).
3. A. T. Howe and G. J. Dudley, *J. Solid State Chem.*, **30**, 157 (1979).
4. T. Takahashi and K. Kuwabara, *ibid.*, **29**, 27 (1979).
5. M. Kleitz and J. H. Kennedy, "Proceedings of Fast Ion Transport in Solids," P. Vashishta, J. N. Mundy, and G. K. Shenoy, Editors, pp. 185-188, Elsevier-North Holland, Inc., New York (1979).
6. A. Hooper, *J. Phys. D. Appl. Phys.*, **10**, 1487 (1977).
7. J. P. Roland, Ph.D. Thesis, Purdue University (1978).
8. J. P. Roland, T. Y. Tseng, and R. W. Vest, *J. Am. Ceram. Soc.*, **62**, 567 (1979).
9. E. Burzo and I. Ardelean, *Mater. Res. Bull.*, **14**, 1425 (1979).

Effects of Cadmium Impurities on the Electrowinning of Zinc

F. R. Foulkes,* J. W. Smith, R. Kalia, and D. W. Kirk*

Department of Chemical Engineering and Applied Chemistry,
University of Toronto, Toronto, Ontario, Canada M5S 1A4

ABSTRACT

A study was carried out on the effect of cadmium, a major impurity in commercial zinc electrolytes, on the zinc plating current efficiency in acid sulfate baths. The synthetic electrolyte ($200 \text{ g} \cdot \text{dm}^{-3} \text{ Zn}^{++}$ and $0\text{-}100 \text{ mg} \cdot \text{dm}^{-3} \text{ Cd}^{++}$) was continuously circulated through the electrolysis cell. The electrolysis was carried out with a current density of $480\text{-}490 \text{ A} \cdot \text{m}^{-2}$ at 37°C . Hydrogen overpotential, potential sweep, atomic absorption, x-ray diffraction, and electron microscopy were used to determine the effect of cadmium on the behavior of the zinc plate. The results indicate that cadmium may either increase or decrease the zinc plating current efficiency. For Cd^{++} less than $20 \text{ mg} \cdot \text{dm}^{-3}$, increasing cadmium concentrations in the electrolyte reduce the hydrogen overpotential and the zinc plating current efficiency. For Cd^{++} greater than $20 \text{ mg} \cdot \text{dm}^{-3}$, increasing cadmium concentrations cause a refinement in the structure of the zinc plate with subsequent increase in the hydrogen overpotential and in the zinc plating current efficiency. The incorporation of cadmium into the zinc plate neither significantly alters the crystal orientation of the deposit nor alters the hydrogen evolution mechanism.

The effects of metallic ion impurities on the electrowinning of zinc from acidic sulfate solutions have been the subject of a large number of investigations (1-3). Metallic impurities are known to affect the current efficiency, deposit morphology, and product purity. In general, metal impurities more noble than zinc and having less negative hydrogen overvoltages tend to reduce the current efficiency (4) and accelerate the rate of dissolution of the electrodeposited zinc in both acidic and alkaline media (5, 6). Although lead is a more noble metal, lead ions are recognized to either increase or not affect the zinc plating current efficiency (1, 7). This effect is attributed to a more negative hydrogen overvoltage on lead [-1.09V for Pb, -0.75V for Zn in H_2SO_4 at 16°C and $1 \text{ A} \cdot \text{m}^{-2}$ (8)]. Similarly, magnesium also is known to retard the corrosion of zinc (9).

Cadmium also has a large hydrogen overvoltage, but there is disagreement in the literature concerning its effects on zinc electrodeposition. It has been reported that cadmium increases (10), does not affect (11), and decreases (1, 7) the current efficiency. It

also has been reported that cadmium retards zinc corrosion (12-14) as well as accelerates it (15). The present work was undertaken to clarify the effects of cadmium impurities on the electrowinning of zinc.

Experimental

Cell.—The experimental cell (Fig. 1) was constructed of Lucite. The grooves in the side walls permitted the maintenance of a uniform and reproducible electrode gap of 3.7 cm. The electrical connections were sealed at the gastight lid, so that the rate of hydrogen evolution during deposit dissolution could be measured using a soap-bubble flowmeter at outlet G when the spent electrolyte outlet (F) was closed.

The cathodes were cut from 0.35 mm thick aluminum foil. Before use, they were treated for 2 min with 2.0M NaOH solution, washed with distilled water, treated with 0.05M H_2SO_4 solution, washed again with distilled water, and dried in an oven at 100°C . This cathode pretreatment procedure was found to be essential in order to obtain reproducible results. The backs, edges, and upper faces of the cathodes were masked with "invisible sellotape." By so decreasing the effective area of the cathode compared with that of the anode, a uniform deposit was obtained. The anode,

* Electrochemical Society Active Member.

Key words: electrodeposition, cathode, impurity, current efficiency.

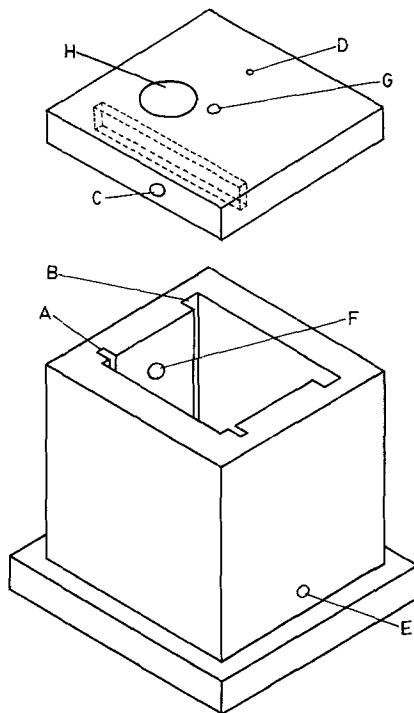


Fig. 1. Electrolytic cell. A, slot for cathode; B, slot for lead anode; C, electrical connection to cathode; D, electrical connection to anode; E, inlet; F, outlet; G, hydrogen outlet to flowmeter; H, opening for reference electrode.

made from lead containing 2% silver, was anodized in 2M H_2SO_4 for 1 hr at $360 \text{ A} \cdot \text{m}^{-2}$ before use.

Reagents.—The electrolyte was prepared by dissolving Fisher certified ZnSO_4 ¹ and H_2SO_4 in double distilled water to yield a solution containing $62 \text{ g} \cdot \text{dm}^{-3}$ Zn and $200 \text{ g} \cdot \text{dm}^{-3}$ free acid. Cadmium sulfate (Analar, B.D.H.) was used for making a stock solution containing $2.0 \text{ g} \cdot \text{dm}^{-3}$ Cd^{++} which was further diluted as required to be added as 5 cm^3 aliquots to 500 cm^3 of zinc electrolyte.

Measurements.—A cathodic current density of $480\text{--}490 \text{ A} \cdot \text{m}^{-2}$ was maintained during all the electro-deposition experiments. Cathodic voltages were measured against a saturated calomel electrode (SCE)² using a Corning pH meter, Model 7. Fresh electrolyte was pumped to the cell at a constant rate of $2.0 \text{ cm}^3 \cdot \text{min}^{-1}$ using a Teflon-lined solution metering pump. The temperature of both the cell and electrolyte was maintained at $37^\circ \pm 1^\circ\text{C}$ in a constant temperature bath.

Unless otherwise specified, the electrolysis was carried out for 90 min. For current efficiency determinations the cathode was removed from the cell immediately after a run, washed with distilled water, dried at 60°C , and weighed to constant weight. For cathode dissolution experiments the pump was shut off immediately after the electrolysis, the cell outlet closed, and the rate of hydrogen evolution measured with a soap-bubble gas flowmeter.

The current efficiency determinations were reproducible to $\pm 0.3\%$, while the time required to dissolve the deposit in a sulfuric acid solution varied by ± 10 min for apparently identical plates.

Results and Discussion

The effect of cadmium on the zinc plating current efficiency is shown in Fig. 2. The electrolyte contained $200 \text{ g} \cdot \text{dm}^{-3}$ H_2SO_4 and $62 \text{ g} \cdot \text{dm}^{-3}$ Zn^{++} with varying cadmium concentrations. It can be seen from

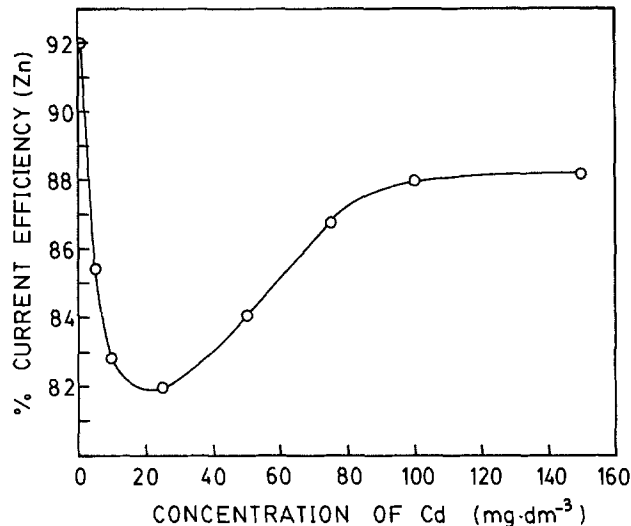


Fig. 2. Effect of cadmium concentration on zinc plating current efficiency. Electrolyte: H_2SO_4 $200 \text{ g} \cdot \text{dm}^{-3}$, Zn $62 \text{ g} \cdot \text{dm}^{-3}$. Temperature 37°C .

the figure that the current efficiency has a minimum at about $20\text{--}25 \text{ mg} \cdot \text{dm}^{-3}$ Cd^{++} . Increasing cadmium concentrations to this level causes a decrease in the zinc plating current efficiency, while increasing cadmium concentration above this level causes an increase in the zinc plating current efficiency. This behavior is undoubtedly the cause of some of the confusion concerning cadmium effects on current efficiency. In the range $0\text{--}20 \text{ mg} \cdot \text{dm}^{-3}$ Cd^{++} , Kerby and Ingraham (1) reported a decrease in the zinc plating current efficiency from 92% to 80% with increasing cadmium concentration. Similarly Nikiforov (16) has reported increasing current efficiency with decreasing cadmium concentration for concentrations less than $6 \text{ mg} \cdot \text{dm}^{-3}$. These observations are in agreement with our work.

For a greater concentration range Turomshina and Stender (9) reported no change in the zinc plating current efficiency with $10 \text{ mg} \cdot \text{dm}^{-3}$ Cd^{++} . As can be seen from Fig. 2, the current efficiency is very sensitive to small concentrations of Cd^{++} and a small concentration of Cd^{++} impurity would result in there being no apparent difference in the current efficiency with the $100 \text{ mg} \cdot \text{dm}^{-3}$ Cd^{++} solution. Figure 2 also shows that at concentrations greater than $\sim 100 \text{ mg} \cdot \text{dm}^{-3}$ cadmium does not seem to greatly alter the current efficiency and it is possible to speculate that the reduction in zinc plating current efficiency reported by Turomshina and Stender (9) for a $1000 \text{ mg} \cdot \text{dm}^{-3}$ Cd^{++} was the result of increased cadmium plating.

Since the major competing reaction with zinc deposition at low impurity levels is hydrogen evolution, the effect of cadmium on the hydrogen overpotential was studied. Zinc deposits from the electrolytes containing various cadmium concentrations were immersed in a sulfuric acid bath ($200 \text{ g} \cdot \text{dm}^{-3}$ without Zn^{++} or Cd^{++} present) at 37°C . The cathodic potentials required to yield a current density of $480 \text{ A} \cdot \text{m}^{-2}$ were recorded. Using the calculated value for the reversible hydrogen potential for this solution at 37°C (-0.2576V vs. SCE; see Appendix A), the hydrogen overpotentials were calculated and the results plotted in Fig. 3. The results show that the magnitude of the hydrogen overpotential η_c displays a maximum for the zinc deposit obtained from an electrolyte containing $20 \text{ mg} \cdot \text{dm}^{-3}$ Cd^{++} . It is clear that the minimum for the zinc plating current efficiency observed in Fig. 2 is related to the maximum in the hydrogen overpotential observed in

¹ Impurities: \leq Fe 0.0003%, Pb 0.0008%, As 0.2 ppm, Mn 1 ppm.
² All voltages are reported vs. SHE unless otherwise noted.

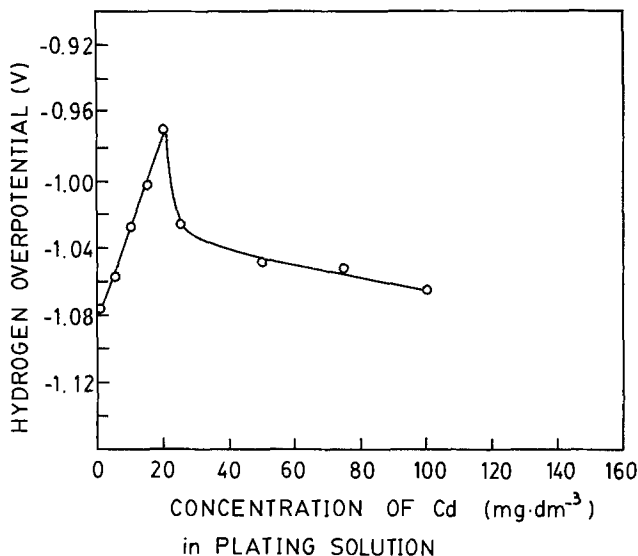


Fig. 3. Hydrogen overpotential for zinc plated from solutions containing various cadmium concentrations. Electrolyte: 2M H_2SO_4 . Temperature = 37°C. $E_{\text{rev}} = -0.2576\text{V}$. Current = 480 $\text{A} \cdot \text{m}^{-2}$.

Fig. 3. At low cadmium concentrations ($\leq 20 \text{ mg} \cdot \text{dm}^{-3}$) increasing cadmium concentrations cause a decrease in the magnitude of the hydrogen overpotential and hence cause an increase in the rate of hydrogen evolution. This results in a lower zinc plating current efficiency. Conversely, increasing cadmium concentrations greater than $20 \text{ mg} \cdot \text{dm}^{-3}$ cause an increase in the magnitude of the hydrogen overpotential which improves the zinc plating current efficiency as observed in Fig. 2.

In order to elucidate the effect of cadmium on the hydrogen overpotential of the zinc deposits, polarization profiles were measured for pure zinc and pure cadmium plates electrodeposited from solutions without added impurities and tested in a sulfuric acid electrolyte without Zn^{++} or Cd^{++} present. The results are shown in Fig. 4. For current densities less than $10 \text{ A} \cdot \text{m}^{-2}$ the profile for zinc remains horizontal at the potential -0.75V . This portion of the curve reflects the equilibrium potential of 0.76V for the reaction $\text{Zn}^{++} + 2e^- \rightarrow \text{Zn}$ at 35°C. At greater current densities the evolution of hydrogen begins. From 30-800 $\text{A} \cdot \text{m}^{-2}$ a second linear region is found. The Tafel slope of -0.105 results from the kinetics of the hydrogen evolution reaction on zinc. The transfer co-

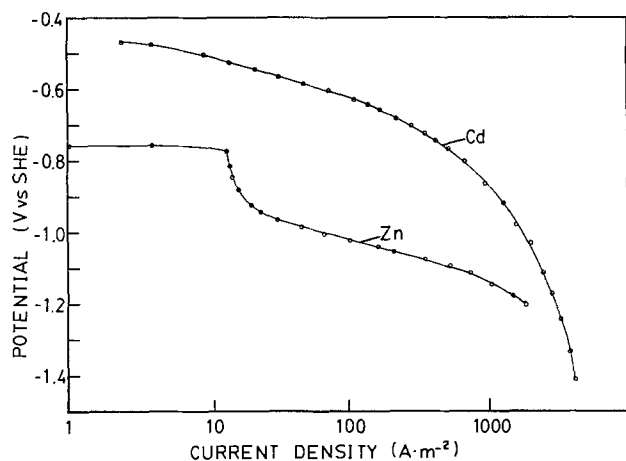


Fig. 4. Polarization plot of pure zinc plate and pure cadmium plate from solutions containing only zinc or cadmium ions, respectively. Electrolyte: $200 \text{ g} \cdot \text{dm}^{-3} \text{H}_2\text{SO}_4$. Temperature = 37°C.

efficient, α , calculated from the Tafel slope is 0.58 and indicates that $\text{H}_3\text{O}^+ + e^- \rightarrow \text{H}_{\text{ads}} + \text{H}_2\text{O}$ is the rate-determining step (17). This finding is in agreement with that of other workers (6, 18-20). Measurement of the hydrogen evolution transfer coefficient in pure sulfuric acid solutions for zinc plates obtained from solutions with cadmium concentrations from 0 to $100 \text{ mg} \cdot \text{dm}^{-3}$ produced an average transfer coefficient of 0.498 with a deviation of ± 0.078 . These measurements show that the transfer coefficient does not change significantly with the addition of cadmium to the plating bath. Thus the rate-determining step for the hydrogen evolution reaction does not change with the addition of cadmium to the plating bath and cannot be the cause of the maxima observed in Fig. 2 and 3.

The polarization plot in Fig. 4 reveals that higher current densities can be sustained on pure cadmium plate than on pure zinc plate for the same potential. There is some variance in the literature concerning this point. Values of hydrogen overpotential on zinc and cadmium in 2N H_2SO_4 at 25°C are reported to be 0.926 and 1.211V at $500 \text{ A} \cdot \text{m}^{-2}$, respectively (21). Mantell (22) gives values of 1.06 and 1.22V at $100 \text{ A} \cdot \text{m}^{-2}$ for zinc and cadmium in 2N H_2SO_4 at 25°C. These indicate that cadmium has the greater overpotential in contrast to that shown in Fig. 4. However, hydrogen bubble overvoltages reported by Glasstone (23) for Zn and Cd are 0.70 and 0.48V in 1N sulfuric acid at room temperature. More recent data by Pickett (24) at 25°C give values of 0.94 and 0.90V at $100 \text{ A} \cdot \text{m}^{-2}$ for Zn and Cd, respectively. These differences may reflect the effect of different impurity levels in the zinc and cadmium plates. From the experimental results of Fig. 4 it is clear that, for the zinc and cadmium plates obtained from the synthetic electrolytes, zinc has a higher hydrogen overpotential than cadmium. The approximate exchange current densities estimated from Fig. 4 (by extrapolation of the linear portion of the V vs. $\log i$ plot) are 0.4 and $1.5 \text{ A} \cdot \text{m}^{-2}$ for zinc and cadmium, respectively, again indicating that the hydrogen is more easily evolved on cadmium than on zinc. While these values are quite different from theoretical exchange current densities, they are in good agreement with those reported ($0.2 \text{ A} \cdot \text{m}^{-2}$) by Lowenheim (8). The results indicate that for plating baths in the absence of other deliberate impurity additions, the incorporation of cadmium into the zinc plate should cause an increase in the hydrogen evolution rate. Thus the zinc plating current efficiency should decrease with increasing cadmium content in the zinc plate. This would explain the initial decrease in the current efficiency observed in Fig. 2. To confirm that cadmium was being incorporated into the zinc plate, the zinc deposits were analyzed for their cadmium content.

The results of the atomic absorption analysis are shown in Fig. 5. In order to ensure complete ionization of the sample, ionization was carried out using either a flame or a graphite furnace. Comparable results were obtained in either case. It is clear from Fig. 5 that the percent of cadmium in the deposit increases monotonically with cadmium concentration in the electrolyte. The increase is linear for cadmium concentrations less than $\approx 50 \text{ mg} \cdot \text{dm}^{-3}$. This behavior simply demonstrates that at these concentrations cadmium is under limiting diffusion current control. Calculations (see Appendix B) show that the limiting diffusion currents are: $i_{\text{H}^+} \approx 17,000 \text{ A} \cdot \text{m}^{-2}$; $i_{\text{Cd}^{++}} \approx 0.6 \text{ A} \cdot \text{m}^{-2}$ (maximum at a concentration of $100 \text{ mg} \cdot \text{dm}^{-3}$); $i_{\text{Zn}^{++}} \approx 670 \text{ A} \cdot \text{m}^{-2}$. Thus under these conditions, the partial current for cadmium plating ($i_{\text{Cd}^{++}}$) is proportional to the cadmium concentration in the bulk of the electrolyte (25).

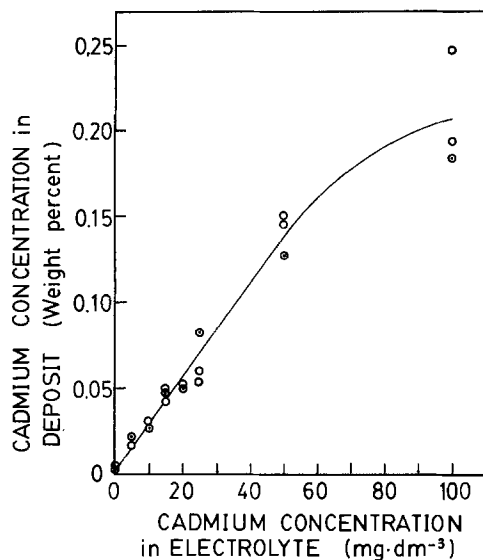


Fig. 5. Cadmium content of zinc plate from electrolytes with various cadmium concentrations, by atomic absorption analysis. Deposits from electrolyte: $200 \text{ g} \cdot \text{dm}^{-3} \text{ H}_2\text{SO}_4$, $62 \text{ g} \cdot \text{dm}^{-3} \text{ Zn}$. Current density $480 \text{ A} \cdot \text{m}^{-2}$. Temperature 37°C . Sample ionization, by flame \odot ; by graphite furnace \circ .

An increase in cadmium concentration in the electrolyte results in a zinc plate with a greater cadmium content, which promotes the hydrogen evolution reaction and decreases the zinc plating current efficiency. While this explains the current efficiency and overpotential behavior at low cadmium concentrations ($\leq 20 \text{ mg} \cdot \text{dm}^{-3}$) seen in Fig. 2 and 3, the behavior at greater cadmium concentrations ($> 20 \text{ mg} \cdot \text{dm}^{-3}$) is not explained by this model.

In order to study other possible changes in the reaction, cyclic potential sweep measurements were conducted for the zinc plates in a sulfuric acid bath ($200 \text{ g} \cdot \text{dm}^{-3}$). Some typical potential scans are shown in Fig. 6. A relatively high sweep rate ($100 \text{ mV} \cdot \text{sec}^{-1}$) was used to reduce the effect of changing surface area during the measurement. The samples were masked so that the same geometrical area was represented. From the potential scans it is clear that there are no hydrogen adsorption peaks. This is consistent with the fact that hydrogen does not strongly adsorb on zinc (6). The composition of the plate does, however, affect the rate of hydrogen evolution at any potential. In Fig. 7 the variation of the cathodic current density with plate composition is shown at various potentials. These measurements were conducted at room temperature (23°C) and again show that a maximum cathodic current density (hydrogen evolution rate) is found for the zinc plates obtained from solutions with $20 \text{ mg} \cdot \text{dm}^{-3} \text{ Cd}^{++}$. No obvious changes in the hydrogen evolution reaction mechanism are apparent from these measurements. To determine whether any macroscopic change in the zinc deposit was caused by changes in the cadmium content, scanning electron micrographs were taken. The results are shown in Fig. 8. It is clear from the photographs that a certain amount of grain refinement does take place with increasing cadmium content. This grain refinement of the zinc plate has also been reported by Mackinnon, Brannen, and Kerby (26) for increasing cadmium content in industrial acid sulfate baths. Other changes in zinc plate morphology from the presence of impurities have also been reported. The concentration of lead in the plating solution has been shown to alter both morphology and orientation (27). Antimony and glue additions will likewise alter the surface plate characteristics (4). In addition to impurities, overpotential

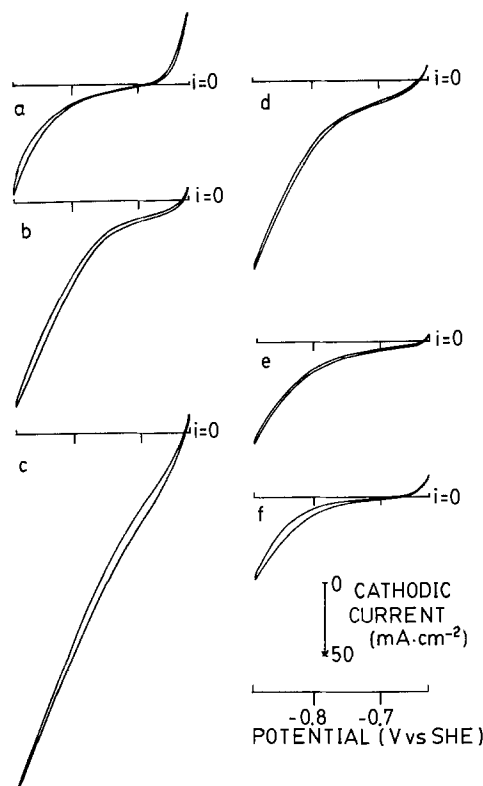


Fig. 6. Potential sweep profiles of zinc plates. Electrolyte: H_2SO_4 $200 \text{ g} \cdot \text{dm}^{-3}$. Temperature = 22.5°C . Sweep rate = $100 \text{ mV} \cdot \text{sec}^{-1}$. Zinc plates obtained from synthetic industrial electrolyte containing $200 \text{ g} \cdot \text{dm}^{-3} \text{ H}_2\text{SO}_4$, $62 \text{ g} \cdot \text{dm}^{-3} \text{ Zn}$, and (a) $0 \text{ mg} \cdot \text{dm}^{-3} \text{ Cd}$; (b) $15 \text{ mg} \cdot \text{dm}^{-3} \text{ Cd}$; (c) $20 \text{ mg} \cdot \text{dm}^{-3} \text{ Cd}$; (d) $25 \text{ mg} \cdot \text{dm}^{-3} \text{ Cd}$; (e) $50 \text{ mg} \cdot \text{dm}^{-3} \text{ Cd}$; (f) $100 \text{ mg} \cdot \text{dm}^{-3} \text{ Cd}$.

can have an important role in the type of crystal growth (28). The work of Vagramyan, Leach, and Moon indicated that at low overpotentials metal deposition causes crystal growth to take place along close-packed crystal directions while at higher overpotentials more random growth occurs. X-ray diffraction patterns of the zinc plates were measured to determine whether there were any changes resulting from the differences in cadmium content. The analysis of the patterns showed no change in the orientations with the exception of the weakening of the (102) with greater cadmium concentrations. The preferred

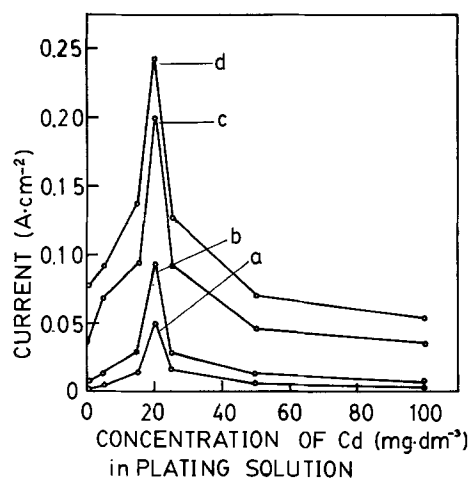


Fig. 7. Cathodic current density for zinc plated from solutions containing various cadmium concentrations. Electrolyte $200 \text{ g} \cdot \text{dm}^{-3} \text{ H}_2\text{SO}_4$. Temperature = 22.5°C . Potential: (a) 0.7V ; (b) 0.758V ; (c) 0.858V ; (d) 0.888V .

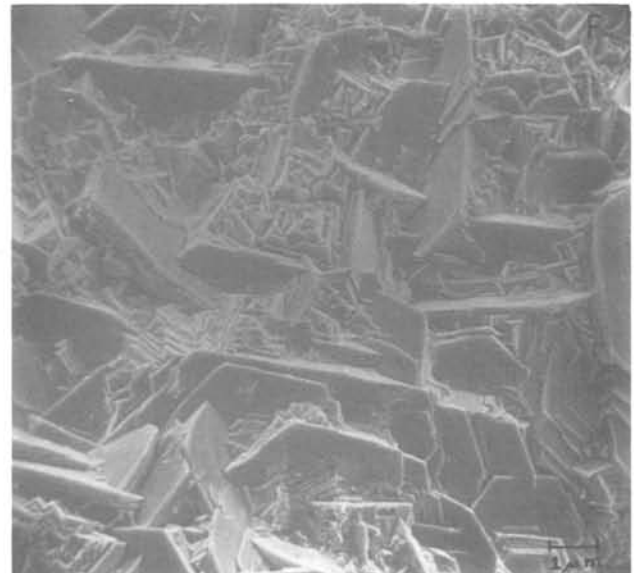
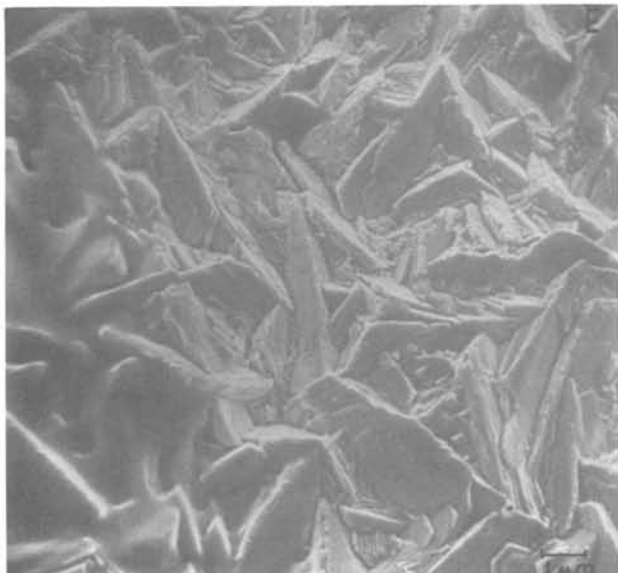
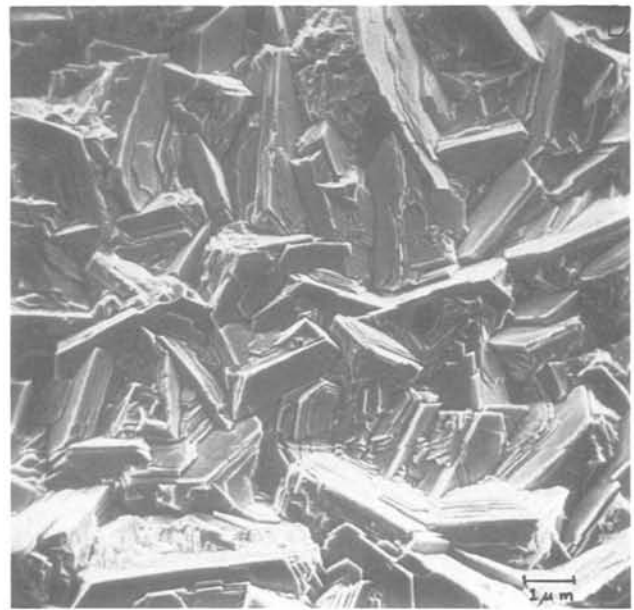
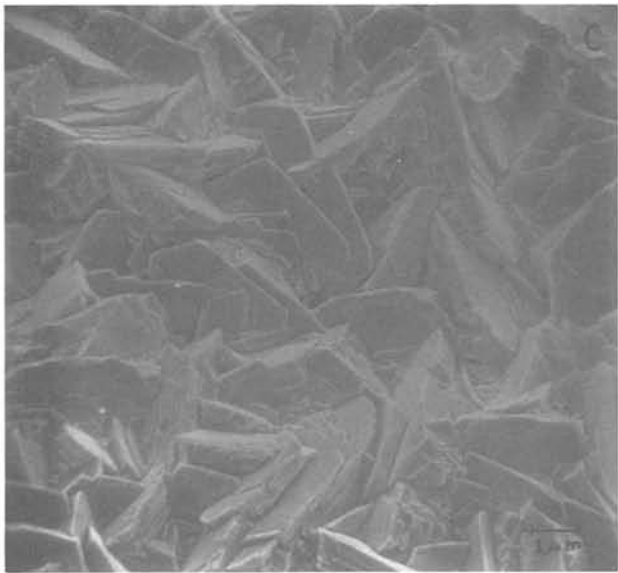
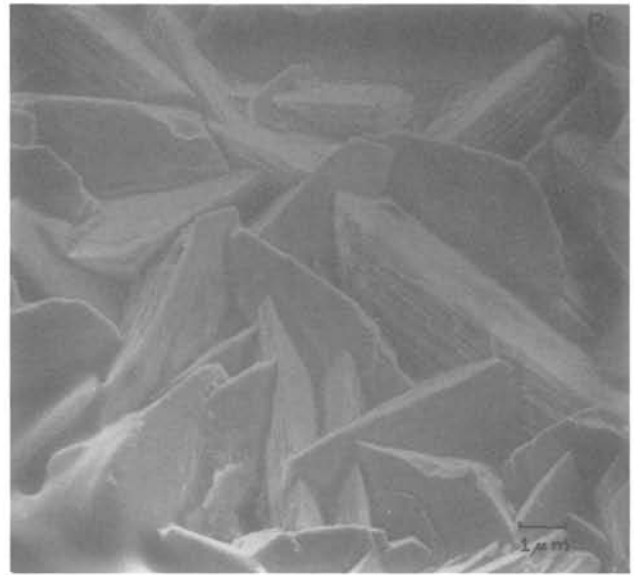
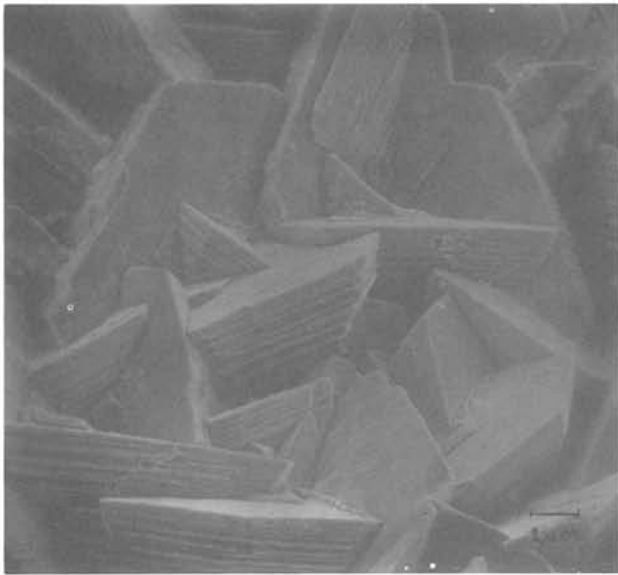


Figure 8 continued on next page

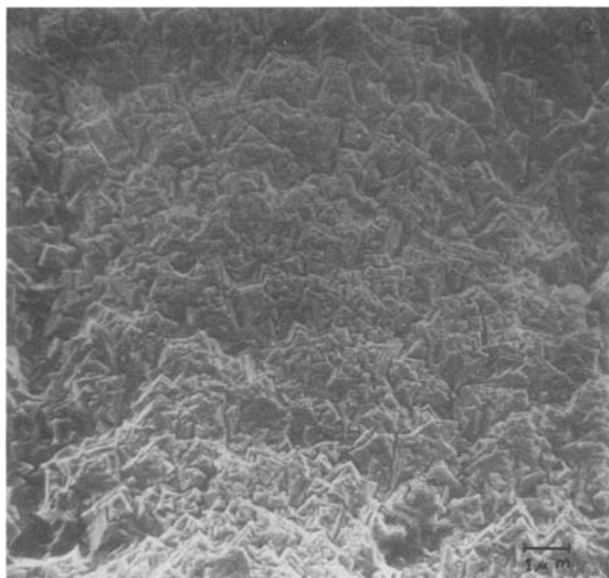


Fig. 8. Scanning electron micrographs of deposit morphology. Zinc deposit from solution containing $200 \text{ g} \cdot \text{dm}^{-3} \text{H}_2\text{SO}_4$ + various cadmium concentrations. Temperature = 37°C . Current density $480 \text{ A} \cdot \text{m}^{-2}$. A, 0 Cd^{++} ; B, $10 \text{ mg} \cdot \text{dm}^{-3} \text{Cd}^{++}$; C, $15 \text{ mg} \cdot \text{dm}^{-3} \text{Cd}^{++}$; D, $20 \text{ mg} \cdot \text{dm}^{-3} \text{Cd}^{++}$; E, $25 \text{ mg} \cdot \text{dm}^{-3} \text{Cd}^{++}$; F, $50 \text{ mg} \cdot \text{dm}^{-3} \text{Cd}^{++}$; G, $100 \text{ mg} \cdot \text{dm}^{-3} \text{Cd}^{++}$.

orientations (112), (002), and (103) were not affected, but the patterns from the zinc plates with greater cadmium concentrations were more continuous with less spread in the diffraction bands. This change resulted from the fine grain size at higher cadmium concentrations. Changes in crystal structure orientation can be ruled out as the cause of the increase of hydrogen overpotential with cadmium concentration.

One change that is apparent (from Fig. 8) with increasing cadmium concentrations is the increase in the number of crystallites and finer grain size in the zinc plates. The change in crystallite size causes a change in the surface area of the sample. Based on a fixed geometrical area, a decrease in the surface area would result in an increase in the current density and hence a greater apparent overpotential. It is partially due to this effect that shiny platinum has a greater hydrogen overpotential than platinized platinum. From the scanning electron micrographs in Fig. 8 it is clear that increasing cadmium concentrations cause smoother deposits and hence the surface roughness factor should decrease. The variation of overpotential with surface morphology has been studied by Bockris and Raxumney (29). They found that the transition in surface morphology from large pyramidal crystal structures to finer polycrystalline structures was accompanied by an increase in overpotential. During zinc deposition, increasing overpotential has been found to cause smaller crystallites (28). For the deposition of copper, the magnitude of the increase of the overpotential was reported to be $\approx 120 \text{ mV}$ (29). From Fig. 2, the increase in the magnitude of the hydrogen overpotential is about 92 mV and therefore it is not unreasonable to assign the cause of the increase to the change in morphology of the zinc plates. Although the change in morphology does not affect the reaction mechanism (since the transfer coefficient did not change with zinc plate composition), the exchange current density could be affected. The hydrogen exchange current density depends on surface activity as well as on the effective surface area. If surface area change is ignored for the moment, a decrease in the exchange current density would increase the overpotential. The decrease

in the exchange current density could be caused by the transition to fine grain deposits (29). Thus three factors must be considered to explain the overpotential behavior. The first is the co-deposition of cadmium with zinc. This initially results in a surface with a greater hydrogen exchange current density. The second factor is the increased number of nucleation sites resulting from the cadmium co-deposition. This results in a finer grained deposit. The third factor is the decrease in the hydrogen exchange current density resulting from the change in surface morphology. Thus a maximum would be expected in the hydrogen exchange current density for the zinc deposit with increasing cadmium content. Support for this behavior is given in Fig. 9. The hydrogen exchange current density determined from potential sweep data in sulfuric acid ($200 \text{ g} \cdot \text{dm}^{-3}$ without Zn^{++} or Cd^{++} present) at 22.5°C is plotted against cadmium concentration in the plating bath. An average of 10 runs was used for each point. A distinct maximum is formed at $20 \text{ mg} \cdot \text{dm}^{-3} \text{Cd}^{++}$. Although data from potential sweeps at $100 \text{ mV} \cdot \text{sec}^{-1}$ must be viewed with some caution, the relative behavior of the zinc deposits is clear. An advantage of the data from the potential sweeps is that there is little area change during the course of the measurement. From Fig. 9 the exchange current density does increase initially with increasing cadmium content up to about $20 \text{ mg} \cdot \text{dm}^{-3} \text{Cd}^{++}$. At greater cadmium concentrations the exchange current density decreases as a result of the change in morphology (finer deposits) and the decrease of the effective area. The magnitude of the change in the exchange current density is much larger than would be predicted by a surface area changes and must be primarily due to the increase of activity of the fine grained deposits.

Conclusions

The effect of cadmium on the zinc plating current efficiency in acid sulfate baths is dependent on cadmium concentration. At less than about $20 \text{ mg} \cdot \text{dm}^{-3} \text{Cd}^{++}$, increasing cadmium concentrations lower the zinc plating current efficiency by decreasing the hydrogen overpotential on the zinc plate. This effect is superseded at greater cadmium concentrations by the refinement of the zinc plate and subsequent in-

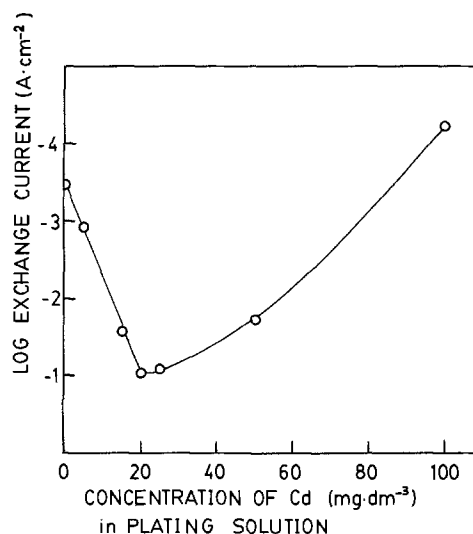


Fig. 9. Hydrogen exchange current density for zinc plated from electrolytes containing various cadmium concentrations. Data from potential sweep measurements. Electrolyte H_2SO_4 $200 \text{ g} \cdot \text{dm}^{-3}$. Temperature = 22.5°C . Sweep rate = $100 \text{ mV} \cdot \text{sec}^{-1}$. (Average of 10 runs per determination.)

crease of the hydrogen overpotential as a result of the morphology change and surface area decrease. The incorporation of cadmium into the zinc plate does not cause any significant change in the crystal orientations of the zinc plate nor does it alter the mechanism of hydrogen evolution.

Acknowledgments

We would like to express our appreciation for the assistance given by Powesland Engineering Limited, Texasgulf Canada Limited, and Canadian Electrolytic Zinc and also for the financial assistance provided by the Natural Sciences and Engineering Research Council of Canada. Our thanks also go to Dr. A. Iribarne for the atomic absorption analysis and to J. W. Dowkes for the photographs of the zinc plate micrographs.

Manuscript submitted Feb. 13, 1981; revised manuscript received May 24, 1981.

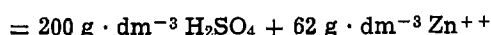
Any discussion of this paper will appear in a Discussion Section to be published in the June 1982 JOURNAL. All discussions for the June 1982 Discussion Section should be submitted by Feb. 1, 1982.

Publication costs of this article were assisted by the University of Toronto.

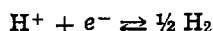
APPENDIX

A. Theoretical Hydrogen Voltage

Electrolyte



$$\text{pH} = 0.35$$



$$\epsilon_{\text{H}} = \epsilon_{\text{H}}^\circ - \frac{RT}{F} \ln \frac{(P_{\text{H}_2})^{1/2}}{a_{\text{H}^+}}$$

$$= -\frac{RT}{F} \ln (P_{\text{H}_2})^{1/2} + \frac{2.303 RT}{F} \log_a \text{H}^+$$

at $P_{\text{H}_2} = 1 \text{ atm}$, $\epsilon_{\text{H}} = -0.0215 \text{ V}$ vs. SHE at 37°C and at 37°C SCE = 0.2361 V vs. SHE (30) and $(\epsilon_{\text{H}})_{37^\circ\text{C}} = -0.2576 \text{ V}$ vs. SCE.

The contribution of the liquid junction potential for the SCE in this solution is estimated as follows. The Planck-Henderson theory (31) gives

$$E_j \approx \left(\frac{2.303 RT}{F} \right) \left[\frac{\sum_i \lambda_i (M_{\text{Ls}} - M_{\text{Rs}})}{\sum_i \lambda_i |Z_i| (M_{\text{Ls}} - M_{\text{Rs}})} \right] \log \left[\frac{\sum_i \lambda_i |Z_i| M_{\text{Rs}}}{\sum_i \lambda_i |Z_i| M_{\text{Ls}}} \right]$$

where E_j = liquid junction potential, λ_i = equivalent conductivity for ion i , M_{Rs} = concentration of ion i in reference electrolyte, M_{Ls} = concentration of ion i in solution, and Z_i = charge on ion.

The concentrations of the $[\text{H}^+]$, $[\text{HSO}_4^-]$, $[\text{SO}_4^{=}]$, and $[\text{Zn}^{++}]$ are calculated in Appendix B, $[\text{K}^+]$ and $[\text{Cl}^-]$ are assumed to be completely dissociated at saturation at 37°C .

Equivalent ion conductivities (λ_i) at infinite dilution + 37°C were obtained by graphical interpolation of data given by Quist and Marshall (32).

Walden's Rule was used to extend the data to the concentrated solutions. From this the above equation yields the value $E_j \approx 0.0183 \text{ V}$ indicating that the overpotentials may be in error by this amount.

B. Limiting Current Density Calculations

Electrolyte $2.04 \text{ M H}_2\text{SO}_4 + 0.948 \text{ M ZnSO}_4$ at 37°C $\text{pH} = 0.35$. The limiting current densities may be estimated from the equation (17)

$$i_{\text{lim}} = \frac{ZFDC^\circ}{(1-t)S}$$

where Z is the charge on the ion, F is Faraday's constant, D is the diffusion coefficient, C° is the concentra-

tion of the ion in the bulk of the solution, t is the transport number, and S is the diffusion layer thickness.

The concentrations of $[\text{SO}_4^{=}] + [\text{HSO}_4^-]$ were calculated knowing the dissociation constant for H_2SO_4 .

For $2 \text{ M H}_2\text{SO}_4$, $[\text{SO}_4^{=}] = 0.7$, $[\text{HSO}_4^-] = 1.3$, $K_2 = 7.24 \times 10^{-3}$ at 37°C (33, 34)

$$K_2 = \frac{\gamma_{\text{H}^+} \cdot \gamma_{\text{SO}_4^{=}} \cdot (\text{H}^+) \cdot (\text{SO}_4^{=})}{\text{HSO}_4^- \cdot (\text{HSO}_4^-)} \approx 0.01 \frac{(\text{H}^+) \cdot (\text{SO}_4^{=})}{(\text{HSO}_4^-)}$$

$$[\text{H}^+] = 1.92, [\text{HSO}_4^-] = 2.17, [\text{SO}_4^{=}] = 0.821,$$

$$[\text{Cd}^{++}] \approx 0, [\text{Zn}^{++}] = 0.948$$

The transport number

$$t_i = \frac{i_i}{i_T} = \frac{Z_i C_i \lambda_i}{\sum Z_i C_i \lambda_i}$$

using $\lambda_{37^\circ\text{C}}^\circ$ [equivalent conductivity ($\Omega^{-1} \cdot \text{m}^2 \text{equiv}^{-1}$)] $t_{\text{H}^+} = 0.60$, $t_{\text{Zn}^{++}} = 0.10$, $t_{\text{Cd}^{++}} \approx 0$, $t_{\text{HSO}_4^-} = 0.17$, $t_{\text{SO}_4^{=}} = 0.13$ and using $\delta \approx 0.03 \text{ cm}$, i.e., boundary layer thickness with some stirring from gas evolution

$$i_{\text{H}^+} \approx 17,000 \text{ A} \cdot \text{m}^{-2}, i_{\text{Zn}^{++}} \approx 670 \text{ A} \cdot \text{m}^{-2}$$

for

$$[\text{Cd}^{++}] = 5 \text{ mg} \cdot \text{dm}^{-3} \quad i_{\text{Cd}^{++}} \approx 3 \times 10^{-2} \text{ A} \cdot \text{m}^{-2}$$

$$[\text{Cd}^{++}] = 100 \text{ mg} \cdot \text{dm}^{-3} \quad i_{\text{Cd}^{++}} \approx 0.6 \text{ A} \cdot \text{m}^{-2}$$

Despite the assumptions in using λ_i° for λ_i and a diffusion layer thickness 0.03 cm it is clear that Cd^{++} will be diffusion controlled.

REFERENCES

- R. C. Kerby and T. R. Ingraham, Mines Branch Rep. R243, Dept. of Energy, Mines and Resources, Ottawa (1971).
- D. R. Fasnacht, Ph.D. Thesis, University of Missouri-Rolla (1978).
- H. Fukubayashi, Ph.D. Thesis, University of Missouri-Rolla (1972).
- B. A. Lamping and T. S. O'Keefe, *Metall. Trans. (B)*, **7**, 551 (1976).
- A. G. Pecherskaya and V. V. Stender, *Zh. Prikl. Khim.*, **23**, 920 (1950).
- R. J. Brodd and V. E. Leger, "Encyclopedia of Electrochemistry of the Elements," Vol. V, Marcel Dekker Inc., New York (1976).
- V. F. Turomshina and V. V. Stender, *Zh. Prikl. Khim.*, **28**, 372 (1955).
- F. A. Lowenheim, "Modern Electroplating," p. 15, John Wiley & Sons, Inc., New York (1963).
- M. Saloma and H. Holtan, Sr., *Acta Chem. Scand. Ser. A*, **28**, 86 (1974).
- G. C. Bratt, *Electrochem. Technol.*, **2**, 323 (1964).
- B. Peyer, M. Micho, S. Vasil, and S. Georgi, *Rubsdoliv Mat. (Sofia), Met.*, **21**, 28 (1966).
- R. Piottelli, *Chim. Ind. (Milan)*, **22**, 109 (1940).
- Z. Wada and K. Makamura, *Rep. Inst. Sci. Tech. Univ. Tokyo*, **8**, 63 (1954).
- J. E. Oxley and J. R. Humphrey, NASA Contract Rep. 1968, NASA-CR-100814.
- S. Stanislav, *Rudodoliv Met. (Sofia)*, **21**, 25 (1966).
- A. F. Nikiforov, *Tsvetn. Met.*, **4**, 28 (1975).
- J. O'M. Bockris and A. K. N. Reddy, "Modern Electrochemistry," Plenum Press, New York (1970).
- A. L. Rotenyan, N. P. Fedotieff, and L. U. Sok, *Zh. Fiz. Khim.*, **31**, 1295 (1957).
- G. M. Westrip, *J. Chem. Soc.*, **125**, 112 (1924).
- A. N. Frumkin, V. S. Bagotskii, Z. A. Iofa, and B. N. Kabanov, "Kinetics of Electrode Processes," *Izd. Moskow Gos. Univ.* (1952).
- M. Knobel, "International Critical Tables," Vol. 6, p. 329.
- C. L. Mantell, "Industrial Electrochemistry," p. 1969, McGraw Hill Book Co., New York (1950).
- S. Glasstone, "Introduction to Electrochemistry," p. 443, Van Nostrand Co. Inc., New York (1942).
- D. S. Pickett, "Electrochemical Reactor Design," p. 71, Elsevier Publishing Co., Amsterdam (1977).
- A. Brenner, "Electrodeposition of Alloys: Principles and Practice," Vol. 3, pp. 94-96, Academic Press, New York (1963).

26. D. J. Mackinnon, J. M. Brannen, and R. C. Kerby, *J. Appl. Electrochem.*, **9**, 71 (1979).
27. D. J. Mackinnon, J. M. Brannen, and R. C. Kerby, *ibid.*, **9**, 55 (1979).
28. T. Vagramyan, J. S. Leach, and J. R. Moon, *J. Mater. Sci.*, **14**, 1170 (1979).
29. J. O'M. Bockris and G. A. Razumney, "Fundamental Aspects of Electrocrystallization," Plenum Press, New York (1967).
30. M. Lavallee, O. F. Schanne, and N. C. Herbert, Editors, "Glass Microelectrodes," John Wiley & Sons, Inc., New York (1969).
31. J. S. Newmann, "Electrochemical Systems," p. 126, Prentice-Hall, Englewood Cliffs, NJ (1973).
32. A. S. Quist and W. L. Marshall, *J. Phys. Chem.*, **69**, 2984 (1965).
33. T. F. Young, *Rec. Chem. Prog.*, **12**, 81 (1951).
34. R. A. Robinson and R. H. Stokes, "Electrolyte Solutions," 2nd ed., p. 382, Butterworths, London (1970).

Effects of the Brine Impurities on the Cell Performance of the Diaphragm-Type Chlor-Alkali Cell

F. Hine,* M. Yasuda,* and K. Fujita[†]

Nagoya Institute of Technology, Nagoya 466, Japan

ABSTRACT

A laboratory cell equipped with the deposited asbestos diaphragm was operated with impure brine to investigate the effects of the hardness on the cell performance. The concentration distribution of NaOH in the diaphragm was established by three factors: diffusion, migration, and the hydraulic flow. It is pointed out that the migration flux was larger than the diffusion flux under the operating conditions of the diaphragm cell.

The amalgam process is best for producing chlorine and pure caustic. However, no new constructions using amalgam cells are being announced at present, and many amalgam cell plants are being converted to diaphragm cells, especially in Japan, due to environmental concerns with mercury pollution (1). It is estimated that now about 70% of the world production of chlorine and caustic comes from diaphragm cells.

Although the diaphragm cell process has a long history, innovations were delayed by a poor market for the impure caustic and the relatively high consumption of energy, both electricity and steam.

Recently, the invention of dimensionally stable anodes (DSA) by Beer (2), and the development of the modified asbestos diaphragms (3, 4), for example, the HAPP of Hooker and the TAB of Diamond Shamrock, have brought a new phase in diaphragm-type chlor-alkali technology.

The d-c electric power for cell operation and steam for evaporating the weak caustic liquor are major energy requirements, thus the overall consumption of energy by these factors must be minimized.

Consumption of electric power could be optimized by the reduction of several factors: the anode overvoltage (2, 5); the cathode overvoltage, (6-11); the solution IR drop, especially the bubble effects of chlorine and hydrogen gases (12-24); and the IR drop through the diaphragm (16). This paper deals with this last factor.

The brine is fed to the electrolytic cells after purification and under pH control, if necessary. Even so, the hardness (Mg^{2+} and Ca^{2+}) in the anolyte may plug the porous diaphragm, resulting in a gradual increase in the cell voltage for long-time operation. This also decreases the brine flow rate because the hydraulic resistance of the porous diaphragm increases.

The transport of OH^- through the diaphragm is by diffusion, migration, and hydraulic flow. All these

factors are affected significantly by plugging of the diaphragm with precipitates. This causes changes in the operating conditions affecting cell performance (17).

In this paper the limitations on hardness of the feed brine based on experimental results of an accelerated test are discussed. The transport phenomena of NaOH through the diaphragm was also studied.

Experimental

A small "Lucite" cell as shown in Fig. 1 was used. A titanium sheet, 2 cm long, 2 cm wide, and 0.5 mm thick, coated with a thermally deposited mixture of RuO_2 and TiO_2 was used as the anode. The cathode was made of Ni sheet (2×2 cm). A modified asbestos mat was used as the diaphragm. Chrysotile fiber [5g of Hooker, Grade H-1, 0.4g of E-CTFE powder (Allied Chemical, "Halar 5004"), and a small amount of surfactant in 2M NaOH] was vacuum-deposited on a steel mesh, dried at 120°C for 1 hr, peeled off from the mesh, then heated at 270°C for 3 hr for setting. The thickness was about 4 mm, and the effective area was 19.6 cm^2 (5 cm diam).

Two Luggin-Haber probes were located about 0.5 mm from the diaphragm to measure the IR drop. A

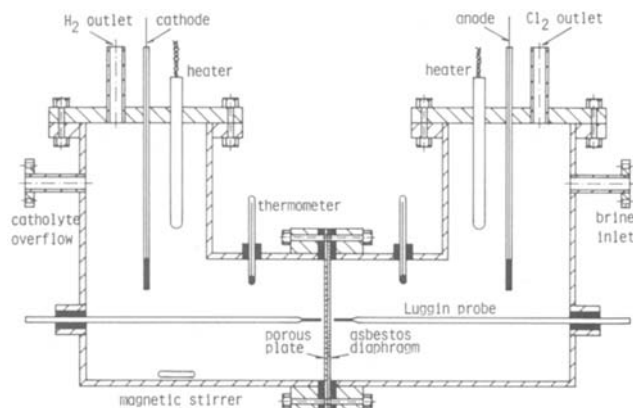


Fig. 1. An experimental electrolytic cell

* Electrochemical Society Active Member.

[†] Present address: Niihama Works, Sumitomo Chemical Industry Company, Niihama, Japan.

Key words: current efficiency, flow rate, diffusion, electrical resistance, migration.

saturated calomel electrode, $\text{Hg}/\text{Hg}_2\text{Cl}_2/\text{satd. KCl}$ (at 30°C), was used as a reference electrode for the anode Luggin, and a mercuric oxide electrode, $\text{Hg}/\text{HgO}/3.5\text{m NaOH}$ (at 30°C), was employed for the cathode Luggin.

Electric heaters were located in both the anode and the cathode compartments to maintain the solution temperature. A magnetic stirrer was located under the cathode compartment.

A saturated NaCl solution, 5.1m NaCl prepared with pure salt and distilled water, in the brine reservoir (ca. 50 liters) was pumped up to the level tank (ca. 10 liters) located about 3m above the cell. The brine was fed to the anode compartment at a given rate. The electrolytic solution passed through the diaphragm and flowed out of the cathode compartment to the catholyte reservoir by gravity.

Chlorine liberated at the anode was collected in a gas holder (ca. 5 liters) located about 3.5m above the cell and was sent to an absorption column containing caustic soda solution. Hydrogen generated at the cathode was purged to the air after a water wash.

The required amounts of MgCl_2 or CaCl_2 were added to the brine reservoir to investigate the effects of these brine impurities.

The rate of feed brine was adjusted to yield a 50% decomposition with respect to pure brine. The flow rate decreased and the NaOH concentration in the catholyte increased when an impure brine was fed to the cell.

The current density was kept constant during each experiment.

The amperage and the IR drop were recorded continuously whereas the flow rate of the electrolyte was measured at certain intervals, say every 30 min. The catholyte effluent was titrated every 24 hr. Thus the current efficiency for production of caustic soda (C.E. in percent) was calculated by Eq. [1]

$$\text{C.E.}(\%) = \frac{\text{Practical amount of NaOH produced}}{\text{Theoretical amount of NaOH to be produced}} \times 100 \quad [1]$$

A three-compartment cell illustrated in Fig. 2 was employed to determine the diffusion and migration of OH^- . The cell was equipped with a cation exchange membrane ("Nafion 390") between the anode compartment and the center compartment to eliminate transport of OH^- and Cl^- as well as hydraulic flow of the electrolytic solution. Each compartment has a volume of about 300 cm. The alkali strength in the cathode compartment was kept constant at 2.2m NaOH during the experiment, whereas 5m NaCl ($\text{pH} \approx 2$) was fed to the center compartment at the start-up time. The NaOH concentration in this room increased with time due to diffusion of OH^- . Thus the "superficial" diffusion coefficient of OH^- through the diaphragm can be evaluated.

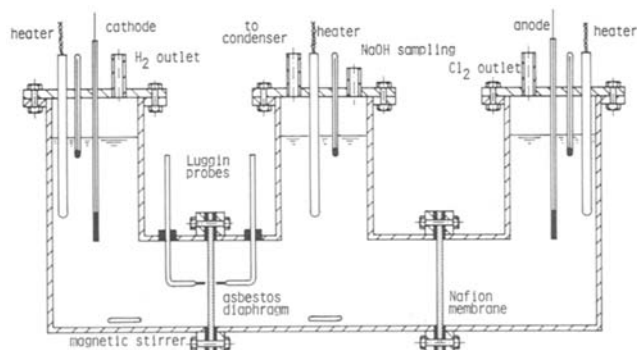


Fig. 2. A three-compartment electrolytic cell

The electrolyte level was equalized to avoid a hydraulic pressure between adjacent compartments. A reflux condenser was located on the top of each compartment to minimize the change of the solution composition by evaporation.

The anode, cathode, and reference electrodes were the same as for the cell shown in Fig. 1.

The potential drops between the Luggin probes were recorded continuously. The electrolytic solutions in the three compartments were titrated at intervals to obtain the transport of OH^- . The pH of the anolyte was unchanged during the experiments.

The diaphragm thickness was varied: 1.2, 2.4, and 4.8 mm. The material was the same as in the cell in Fig. 1. The current density ($0 \sim 25 \text{ A}/\text{dm}^2$) and the solution temperature ($30^\circ \sim 90^\circ\text{C}$) were varied.

Results and Discussion

Effects of the brine hardness.—It was confirmed that the flow rate of brine, the IR drop, the NaOH concentration, and the current efficiency were unchanged for 10 days or more when the purified brine was fed to the electrolytic cell.

Figure 3 shows the results obtained during electrolysis of brine containing 100 mg/liter Mg^{2+} at 10 A/dm^2 current density. For three days, all the data were unchanged during the electrolysis of a pure brine. When an impure brine was fed to the anode compartment of the cell, the flow rate decreased with time due to plugging of the diaphragm, which results in a rise in the caustic strength in the catholyte. Also the IR drop increased gradually. The current efficiency decreased, presumably due to the enhancement of diffusion. Similar results would be obtained with impure brines containing different amount of the hardness, either Mg or Ca.

On the other hand, the IR drop decreased, as shown in Fig. 4, when the brines containing hardness of a high concentration were electrolyzed at relatively high current densities. The caustic strength of the catholyte increased considerably. A significant reduc-

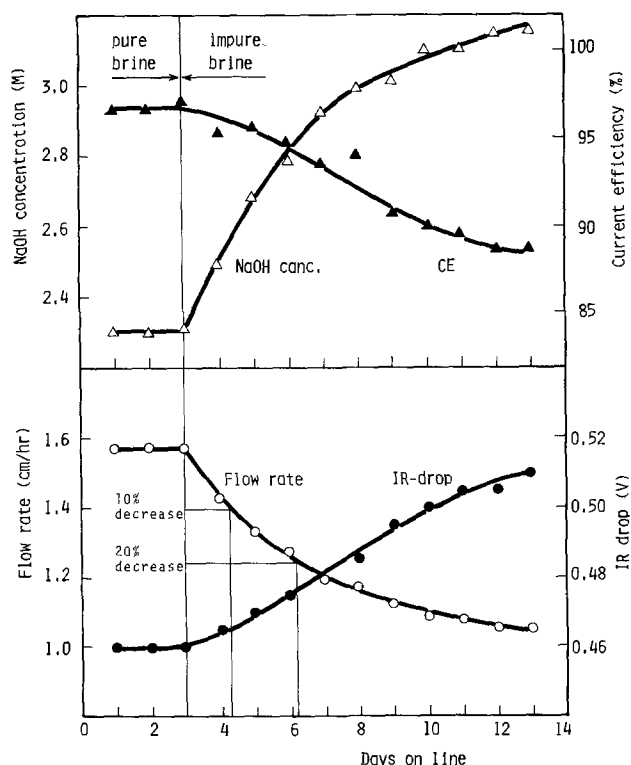


Fig. 3. Flow rate, IR drop, NaOH concentration, and current efficiency. Conditions: current density = 10 A/dm^2 ; Mg^{2+} concentration = 100 mg/liter.

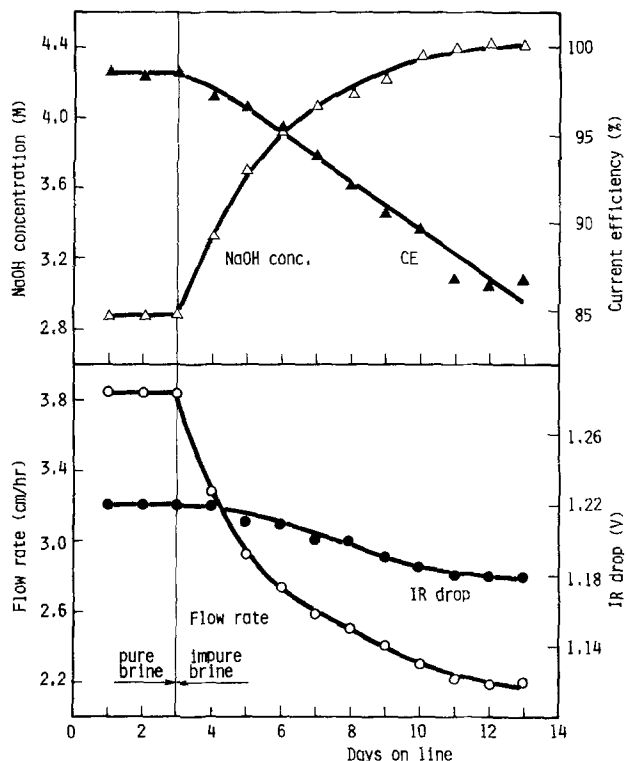


Fig. 4. Flow rate, IR drop, NaOH concentration, and current efficiency. Conditions: current density = 30 A/dm²; Mg²⁺ concentration = 80 mg/liter.

tion in the electrical resistivity of the diaphragm is due to a rise in the caustic strength (see Table I). The brine flow, the NaOH concentration, and the current efficiency are affected by the brine hardness, but the IR drop depends on the solution composition in the diaphragm and the operating temperature rather than on the clogging of the diaphragm.

Since the flow rate of electrolyte decreases gradually with time due to plugging, and influences the cell performance, it can be used as a parameter for evaluating the effects of hardness in feed brine. In Fig. 3, for example, the flow rate decreased by 10% for 1.3 days and by 20% for 3.2 days after switching the feed brine.

The diaphragm of the laboratory cell was plugged more quickly compared to commercial cell operation since the feed brine contained Mg²⁺ at a relatively high concentration (100 mg/liter) in this experiment. The operable period is, of course, extended when the brine hardness is decreased. Figure 5 illustrates the operable period vs. Mg content based on the accelerated test with relatively high contents of Mg in the feed brine (10 ~ 100 mg/liter). Experiments were conducted, using the galvanostatic method, at 10, 20, and 30 A/dm². The dotted line shows the 10% decrease of the flow rate and the solid line the 20% decrease. It is clear that the operable period is reciprocally proportional to the Mg content. Plugging occurs quickly at high current densities since the flow

Table I. Resistivity of mixed solutions of NaCl and NaOH at 50°C

| Composition (M) | | Resistivity (Ω-cm) |
|------------------|------|--------------------|
| NaCl | NaOH | |
| Satd. (ca. 5.1M) | | 3.06 |
| 2.5 | | 3.79 |
| 2.5 | 2.5 | 2.05 |
| 5 | 1 | 2.21 |
| 4 | 2 | 2.04 |
| 3 | 3 | 1.91 |
| 2 | 4 | 1.76 |

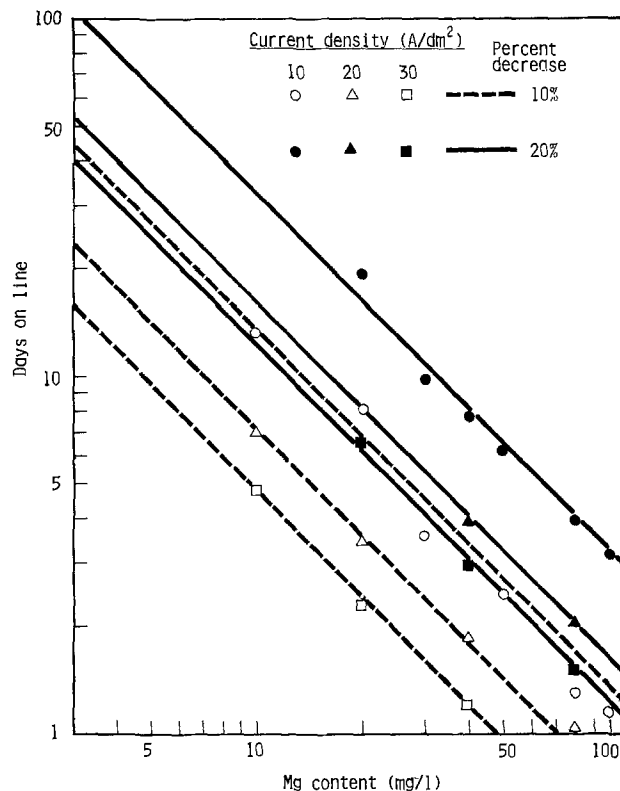


Fig. 5. Days on line vs. Mg content as functions of the percent reduction of the brine flow and the current density.

rate of the brine is large to yield a given decomposition (50%); but the product of period (d) and current (i) was almost constant (Table II). Magnesium in the feed brine precipitates as hydroxide and is collected or filtrated on the asbestos mat. Magnesium hydroxide is a typical compressible precipitate (18, 19), and hence the rate of brine flow may decrease appreciably within a short time if the pressure drop is high. Since the pressure differential through the diaphragm is small, say one tenth of the brine filter, the effect of the compressibility of precipitate on the flow rate seems to be small.

Figure 6 illustrates similar results for Ca in the feed brine, which are essentially the same as for Mg. However, it is important that the $i \times d$ increases with an increase in the current density (see Table II), probably due to a different mechanism of plugging of the diaphragm by Ca precipitate than by Mg precipitate. Although these results were obtained by the accelerated test by electrolysis of brines containing a very high hardness concentration, they agreed

Table II. Operable periods with impure brine at various current densities. Hardness: 10 mg/liter Mg²⁺ or Ca²⁺

| Brine impurity | Percent reduction of brine flow | Current density, i (A/dm ²) | Days (d) | $i \times d$ | |
|----------------|---------------------------------|---|----------|--------------|-------|
| Mg | 10 | 10 | 13.5 | 135 | |
| | | 20 | 7.0 | 140 | |
| | | 30 | 4.7 | 141 | |
| | | | | (avg) | 138.7 |
| | 20 | 10 | 32.3 | 323 | |
| | | 20 | 16.1 | 322 | |
| | | 30 | 12.0 | 360 | |
| | | | | (avg) | 335.0 |
| | Ca | 10 | 10 | 20.5 | 205 |
| 20 | | | 15.2 | 304 | |
| 30 | | | 11.7 | 531 | |
| 20 | | 10 | 53.0 | 530 | |
| | | 20 | 36.0 | 720 | |
| | | 30 | 27.0 | 810 | |

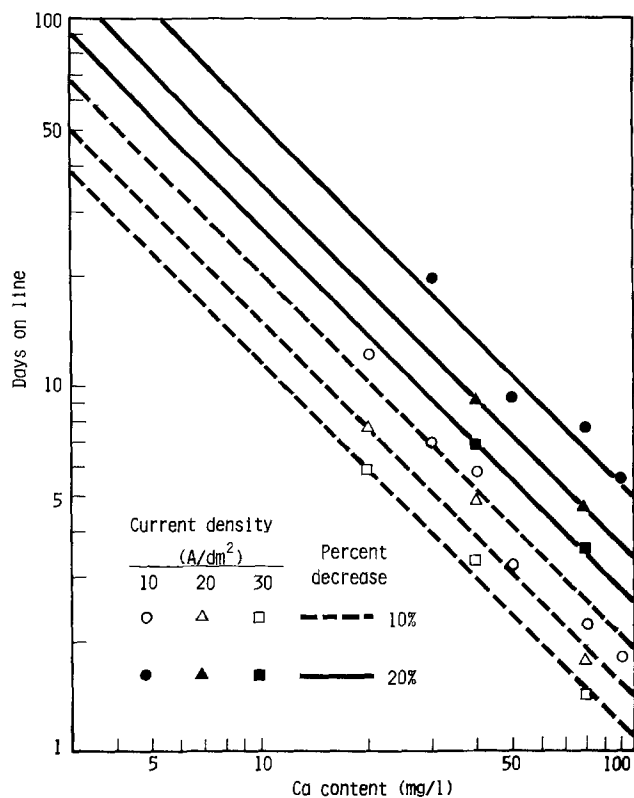


Fig. 6. Days on line vs. Ca content as functions of the percent reduction of the brine flow and the current density.

well with our plant experiences. In practical operation, the brine level is varied in accordance with the permeability of the diaphragm so as to keep the flow rate and, hence, the percent decomposition constant.

The flow rate of the brine containing 2.5 mg/liter Ca through a commercial diaphragm cell operated at 31 A/dm² would decrease by about 20% when the brine level is unchanged for 100 days of operation, which agrees with Fig. 6.

In conclusion, we believe that Fig. 5 and 6 are applicable as a guide to commercial cell operation.

The concentration distributions of Mg and Ca in the diaphragm were determined since their behavior seems to differ. A diaphragm mat after electrolysis was sliced into four equal sections (1 mm thick each). Each segment was immersed in dilute HCl (1 ~ 3N HCl depending on the amount of precipitate), and the Mg content in the filtrate was measured by atomic absorption spectrochemical analysis. Because a small amount of Mg from the chrysotile fiber is dissolved by the acid solution, this effect was calibrated for. A large amount of magnesium hydroxide is deposited in the first and the second segments on the anode side as shown in Fig. 7 since the asbestos mat became completely alkaline due to back-migration of OH⁻. On the contrary, Ca was precipitated more uniformly throughout the porous mat.

Since the Mg content in the brine was high, an amount of Mg(OH)₂ was deposited on the surface of diaphragm, whereas Ca did not do so. This is clearly a filtration mechanism associated with chemical reaction. According to chemical analysis, the catholyte contained 0.2 ~ 0.5 mg/liter Mg or 1.5 ~ 2.5 mg/liter Ca, due to leakage since the brine hardness was significantly higher.

MacMullin states in a private letter that "magnesium deposits on the diaphragm surface facing the anodes and penetrates to a lesser extent in the calcium. Calcium is deposited throughout the diaphragm and Hine's work indicates that at low value of calcium might be expected that calcium washed through. Mag-

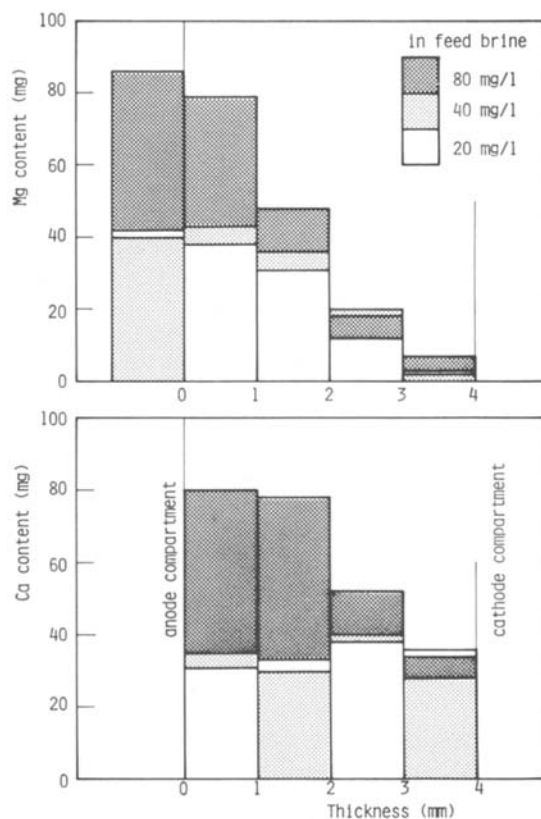


Fig. 7. Distribution of magnesium and calcium precipitates in the diaphragm (5 cm diam and 0.4 cm thick) after electrolysis.

nesium hydroxide is considerably less soluble than calcium hydroxide."

Permeation of the brine without electrolysis.—Experiments without electrolysis were conducted so as to separate diffusion from migration of alkali. The catholyte consisting of NaCl and NaOH was circulated between the reservoir (ca. 60 liters) and the cathode compartment to keep the solution composition constant. The hydraulic head between the anolyte and the catholyte was kept constant at 60 cm, which corresponded to the flow rate required for electrolysis of pure brine at 50% decomposition and 15 A/dm². A small current (1 A/dm²) was switched on briefly at certain intervals to determine the IR drop through the diaphragm.

As is shown in Fig. 8, the flow rate decreased gradually, and the electric resistance of the diaphragm became larger due to plugging, whereas the anolyte pH was unchanged during experiment. The phenomena were the same for electrolysis, but blocking was rapid because of a different distribution of precipitates in the mat as shown in Fig. 9. Both Mg and Ca deposited closely to the cathode side.

Since Mg²⁺ deposits as Mg(OH)₂, the concentration distribution of Mg indicates the OH⁻ distribution in the porous mat. Consequently, the experimental results would show that the contribution of migration for an overall permeation of alkali during electrolysis is significant compared with diffusion.

Experiments with a three-compartment cell.—An example of the results obtained with the three-compartment cell (Fig. 2) is shown in Fig. 10. The NaOH concentration in the cathode compartment and in the center compartment increased almost proportionally to the time of electrolysis.

It is well known that the diffusion flux under steady-state conditions is represented by the equation

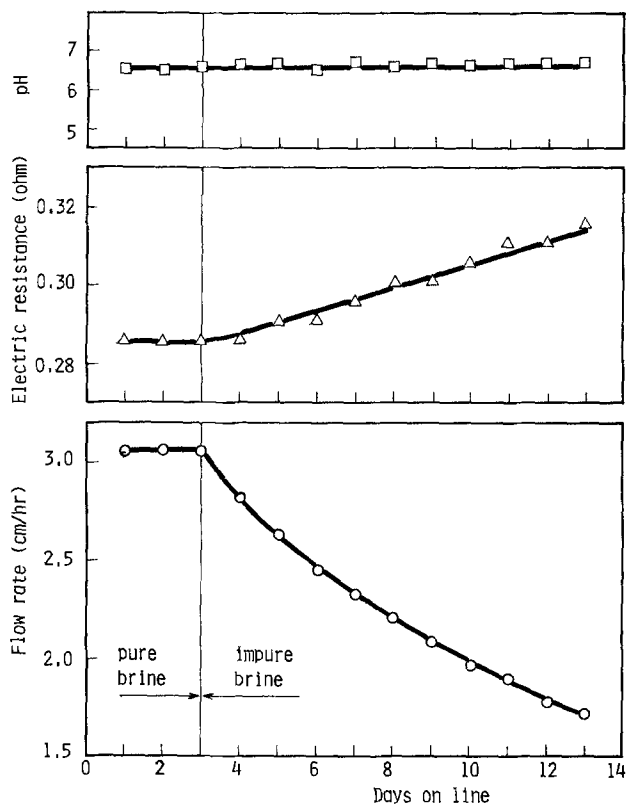


Fig. 8. Flow rate, electric resistance of the diaphragm, and the pH of anolyte at zero current. Mg^{2+} concentration = 50 mg/liter.

$$j = -DA \frac{dC}{dx} \quad [2]$$

Assume that dC/dx is equal to $\Delta C/L$, where ΔC is the difference of the OH^- concentration between two sides. Thus the diffusion coefficient D can be obtained by Eq. [2].

Figure 11 shows the Arrhenius plots for diffusion. The activation energy is evaluated to be about 3 ~ 4 kcal/mol.

It is well known that the diffusion coefficient for electrolytes at room temperature is in the order of 10^{-5} cm^2/sec (20) whereas the experimental results in Fig. 11 show it to be in the order of 10^{-6} cm^2/sec because of limitations of mass transport through the diaphragm. The diffusion flux through the porous medium depends on the formation factor, F_c , of the medium

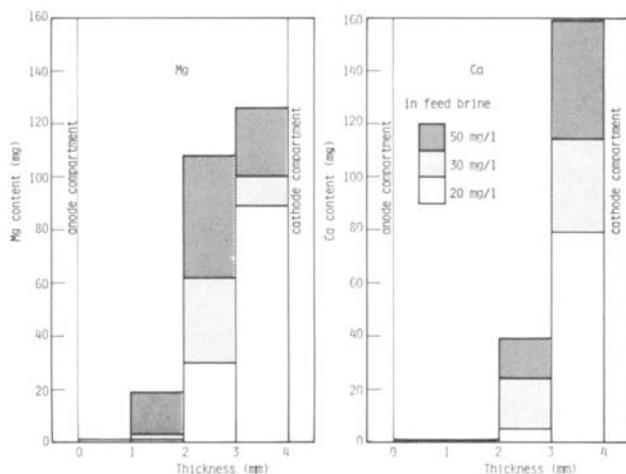


Fig. 9. Distribution of magnesium and calcium precipitates in the diaphragm (5 cm diam and 0.4 cm thick) without electrolysis.

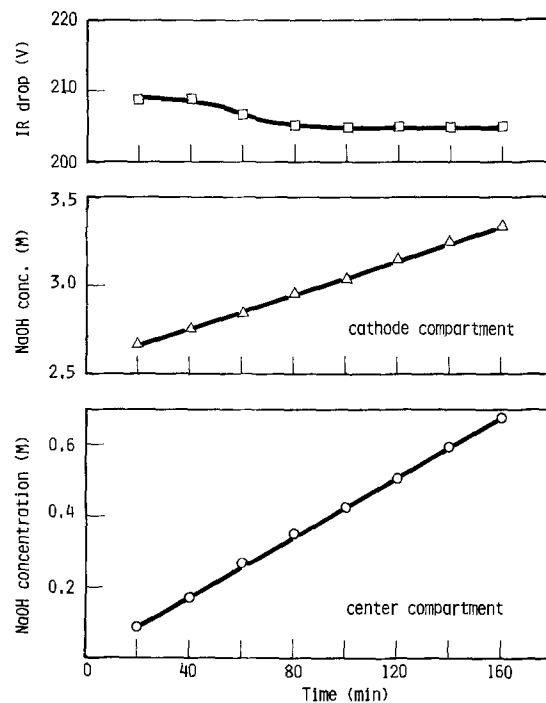


Fig. 10. NaOH concentration and IR drop as functions of the time of electrolysis. Conditions: diaphragm thickness = 2.4 mm. Temperature = 70°C. Current density = 20 A/dm².

$$F_c = \frac{D^\circ}{D} = \frac{x^2}{e} \quad [3]$$

An equation for D° vs. t ($^\circ C$) was established by the method of least squares. The data listed in the International Critical Tables (20) were employed. Thus D° at 30°C was calculated to be 1.88×10^{-5} cm^2/sec , compared to 0.55×10^{-5} cm^2/sec for D (see Fig. 11).

Substituting these data into Eq. [3]

$$F_c = \frac{1.88}{0.55} \approx 3.42$$

On the other hand, F_c can also be obtained by the ratio of the specific resistances as follows (17)

$$F_c = \frac{\rho}{\rho_0} \quad [4]$$

where ρ is the superficial resistivity of the porous medium in $\Omega \cdot cm$ and ρ_0 is the resistivity, also in $\Omega \cdot cm$, of the electrolyte. From Fig. 10, the electric resistance of a porous diaphragm of 19.6 cm^2 in area and 0.4 cm

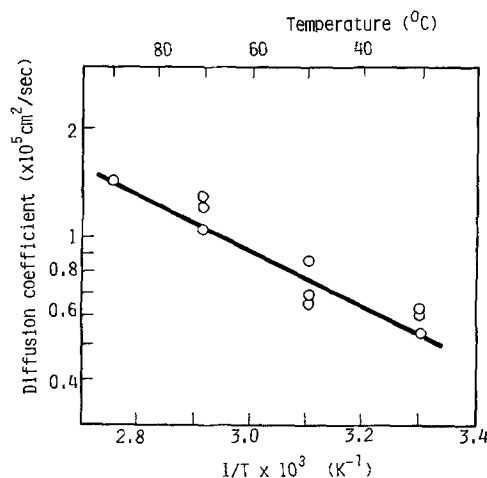


Fig. 11. Diffusion coefficient as a function of the temperature

thick filled with 2.5m NaCl is estimated to be 0.28Ω . Therefore

$$\rho = \frac{0.28 \times 19.6}{0.4} \approx 13.72 \Omega \cdot \text{cm}$$

The specific resistance of 2.5m NaCl is $3.79 \Omega \cdot \text{cm}$ (see Table I). Thus, we have F_c as follows

$$F_c = \frac{13.72}{3.79} \approx 3.62$$

It is clear that both calculations agree well with each other.

Mass transport through the diaphragm.—The mass transport problems through the diaphragm in chlor-alkali cells have been investigated by many authors [see Ref. (17)].

Stender *et al.* have calculated the mass transport of OH^- , j_{OH} (24)

$$j_{\text{OH}} = -D \frac{dC}{dx} + UC \quad [5]$$

$$U = \frac{F D}{RT \kappa} i - v \quad [6]$$

Integrating Eq. [5] with the boundary conditions

$$C = C^\circ \quad \text{at} \quad x = 0 \quad (\text{at cathode side})$$

and

$$C = 0 \quad \text{at} \quad x = \delta \quad (\text{at anode side})$$

Equations [7] and [8] are obtained

$$j_{\text{OH}} = \frac{C^\circ U}{1 - \exp\left(-\frac{U\delta}{D}\right)} \quad [7]$$

and

$$\frac{C}{C^\circ} = \frac{1 - \exp\left(-\frac{U}{D}(\delta - x)\right)}{1 - \exp\left(-\frac{U}{D}\delta\right)} \quad [8]$$

where the thickness of the alkaline zone δ is assumed to be equal to the thickness of diaphragm L . Also the current efficiency for OH^- is

$$\text{C.E.}(\%) = \frac{1}{1 + \frac{U}{v} \left(1 - \exp\left(-\frac{U\delta}{D}\right)\right)^{-1}} \times 100 \quad [9]$$

When a thin diaphragm is employed, $U\delta \ll D$. Therefore

$$\text{C.E.}(\%) = \frac{1}{1 + \frac{U}{v\delta}} \times 100 \quad [10]$$

When $U > 0$, the C vs. x curves become convex as shown in Fig. 12 (see Eq. [8]). When $U < 0$, on the other hand, the curves are concave. Assume that $D = 10^{-5} \text{ cm}^2/\text{sec}$, $\delta = 0.5 \text{ cm}$, $v = 10^{-3} \text{ cm/sec}$, $\kappa = 0.5 \text{ mho/cm}$, $T = 373 \text{ K}$, and $i = 0.2 \text{ A/dm}^2$, therefore for practical operation, we have

$$\frac{U\delta}{D} \approx -7$$

Consequently, the C vs. x curves are clearly concave, and the reduction of current efficiency is controlled by migration and diffusion of OH^- .

The flux of alkali through a unit area of the diaphragm ($A = 1$ in Eq. [2]) in a three-compartment cell, j_{OH} , can be represented by the sum of the diffusion flux, $j_{\text{OH}}(d)$, and the migration flux, $j_{\text{OH}}(m)$, since there is no flow of brine

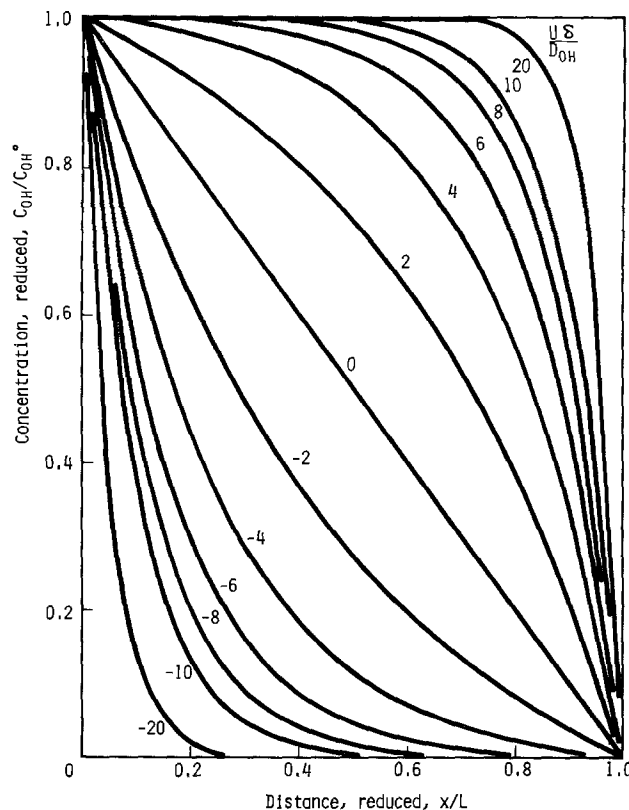


Fig. 12. Distribution of the NaOH concentration in the diaphragm

$$j_{\text{OH}} = j_{\text{OH}}(d) + j_{\text{OH}}(m) \quad [11]$$

$$j_{\text{OH}}(d) = -D \frac{dC}{dx} \quad [12]$$

$$j_{\text{OH}}(m) = \frac{F D}{RT \kappa} Ci = -\frac{F}{RT} DC \frac{d\phi}{dx} \quad [13]$$

Assuming that

$$\frac{dC}{dx} = \frac{C}{\delta} \quad \text{and} \quad \frac{d\phi}{dx} = \frac{\Delta\phi}{\delta}$$

we have

$$K = \frac{j_{\text{OH}}(m)}{j_{\text{OH}}(d)} \approx \frac{F}{RT} \Delta\phi \quad [14]$$

where K is the ratio of $j_{\text{OH}}(m)$ to $j_{\text{OH}}(d)$. The diffusion flux $j_{\text{OH}}(d)$ can be obtained by experiment without electrolysis, whereas the OH^- flux during electrolysis is the sum of $j_{\text{OH}}(d)$ and $j_{\text{OH}}(m)$. Thus $j_{\text{OH}}(m)$ can be evaluated. Factor K , calculated by Eq. [14], is listed in Table III and is in good agreement with experiment. The K is proportional to the IR drop, but the line in Fig. 13 is independent of other factors.

Since the IR drop through the diaphragm in practical cells is $0.3 \sim 0.4\text{V}$, $j_{\text{OH}}(m)$ is one order of magnitude greater than $j_{\text{OH}}(d)$. Therefore, $j_{\text{OH}}(m)$ must be minimized to improve the current efficiency. Operation at high temperatures is feasible for this purpose because D and κ increase. Use of a thin diaphragm decreases K since $j_{\text{OH}}(d)$ increases, whereas $j_{\text{OH}}(m)$ remains constant because $\Delta\phi/\delta$ is unchanged.

At high current densities, both $\Delta\phi$ and K become large. On the other hand, the flow rate of the brine is increased proportionally to the current density to keep the brine decomposition constant. Since the effect of the flow rate on the current efficiency is larger than that of other factors under operating conditions, operation at high current densities, say $25 \sim 35 \text{ A/dm}^2$, is desirable to improve the current efficiency.

Table III. Mass transfer of OH⁻ through the diaphragm.
Diaphragm thickness = 2.4 mm (an example).

| Temp (°C) | Current density (A/dm ²) | IR drop (mV) | OH ⁻ flux $j_{OH(m)} + j_{OH(d)}$ (g-ions/liter hr) | $j_{OH(m)}/j_{OH(d)}$ | |
|-----------|--------------------------------------|--------------|--|-----------------------|------------|
| | | | | Experimental | Calculated |
| 30 | 0 | | 0.015 | | |
| | 1 | 26 | 0.025 | 0.67 | 1.0 |
| | 5 | 95 | 0.065 | 3.3 | 3.6 |
| 50 | 0 | | 0.020 | | |
| | 1 | 18 | 0.030 | 0.50 | 0.65 |
| | 5 | 80 | 0.080 | 3.0 | 2.9 |
| | 10 | 150 | 0.120 | 5.0 | 5.4 |
| 70 | 0 | | 0.030 | | |
| | 1 | 14 | 0.055 | 0.17 | 0.47 |
| | 5 | 60 | 0.090 | 2.0 | 2.0 |
| | 10 | 110 | 0.135 | 3.5 | 3.7 |
| | 15 | 158 | 0.180 | 5.0 | 5.4 |
| | 20 | 205 | 0.255 | 7.7 | 6.9 |
| 90 | 0 | | 0.035 | | |
| | 1 | 11 | 0.040 | 0.14 | 0.35 |
| | 5 | 50 | 0.085 | 1.4 | 1.6 |
| | 10 | 100 | 0.135 | 2.9 | 3.2 |
| | 15 | 138 | 0.190 | 4.4 | 4.4 |
| | 20 | 190 | 0.260 | 6.4 | 6.1 |
| | 25 | 235 | 0.290 | 7.3 | 7.5 |

Conclusion

The performance of diaphragm-type chlor-alkali cells is related closely to the transport phenomena of OH⁻ and the physicochemical properties of the diaphragm. The overall mass-transfer through the diaphragm is composed of the diffusion flux, the migration flux, and the hydraulic flow. Of these, diffusion and migration have been discussed in this paper.

The concentration distribution of alkali in the diaphragm without electrolysis differs greatly from that with electrolysis because the migration flux is significantly large. Also the OH⁻ concentration distribution varies with the current density for the same reason.

Hardness in the feed brine deposits in the porous diaphragm and affects the electrical conduction and mass transport through the diaphragm. Cell performance as measured by the current efficiency and the cell voltage becomes less favorable as the diaphragm is plugged. The limits of hardness in the feed brine have been discussed with the results obtained by an accelerated test involving electrolysis of brines containing high hardness concentrations.

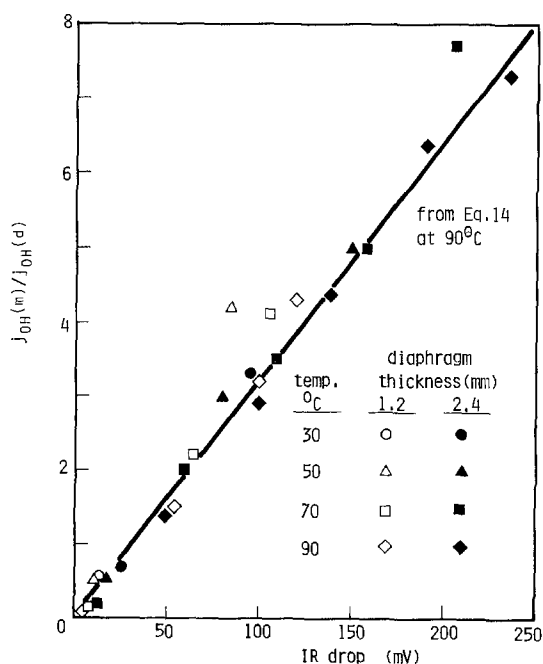


Fig. 13. The ratio of the migration flux to the diffusion flux vs. IR-drop curve under various conditions of the diaphragm thickness and the solution temperature.

Acknowledgments

The authors wish to express many thanks for useful discussions with Dr. W. C. Gardiner and Mr. R. B. MacMullin. Also thanks are due to M. Nozaki, Y. Takahashi, M. Inosaka, and K. Nakamoto for their efforts on experimental work and discussion.

Manuscript submitted March 20, 1981; revised manuscript received June 9, 1981. This was Paper 411 presented at the Minneapolis, Minnesota, Meeting of the Society, May 10-15, 1981.

Any discussion of this paper will appear in a Discussion Section to be published in the June 1982 JOURNAL. All discussions for the June 1982 Discussion Section should be submitted by Feb. 1, 1982.

Publication costs of this article were assisted by F. Hine.

LIST OF SYMBOLS

| | |
|--------------------|---|
| A | area (cm ²) |
| C | concentration (mols/cm ³) |
| C ^o | concentration of OH ⁻ in catholyte (mols/cm ³) |
| C.E. | current efficiency with respect to OH ⁻ (%) |
| D | diffusion coefficient in diaphragm (cm ² /sec) |
| D ^o | diffusion coefficient in solution (cm ² /sec) |
| d | days on line (days) |
| F | Faraday's constant (23,060 kcal/g-equiv. · V) |
| F _c | formation factor |
| i | current density (A/cm ²) |
| j | flux (mols/cm ² · sec) |
| j _{OH} | overall flux of OH ⁻ (mols/cm ² · sec) |
| j _{OH(d)} | diffusion flux of OH ⁻ (mols/cm ² · sec) |
| j _{OH(m)} | migration flux of OH ⁻ (mols/cm ² · sec) |
| K | ratio j _{OH(m)} /j _{OH(d)} |
| L | thickness of diaphragm (cm) |
| R | gas constant (1.987 cal/mol · K) |
| T | temperature (K) |
| U | see Eq. [6] (cm/sec) |
| v | flow rate (cm/sec) |
| x | distance (cm) |
| δ | thickness of alkaline zone (cm) |
| ε | void fraction |
| κ | electrical conductivity (mho/cm) |
| ρ | electric resistivity of diaphragm (Ω · cm) |
| ρ _o | electric resistivity of electrolyte (Ω · cm) |
| φ | potential (V) |
| Δφ | potential difference (V) |
| χ | tortuosity |

REFERENCES

1. F. Hine, N. Yokota, and T. Takasaki, *Int. Chem. Eng.*, **17** (1), 1 (1977).
2. Belgian Pat. 710,551; British Pat. 6490/67.
3. R. W. Fenn and A. D. Babinsky, Paper 340 presented at The Electrochemical Society Meeting, Toronto, Ontario, Canada, May 11-16, 1975.
4. D. J. Harvey and J. R. Fowler, *Chem. Eng. Progr.*, **72** (4), 47 (1976).
5. M. P. Grotheer and C. J. Harke, in "Chlorine Bicentennial Symposium," T. C. Jeffery, P. A. Dana, and H. S. Holden, Editors, p. 209, The Electrochemical Society Softbound Proceedings Series, Princeton, NJ (1974).
6. C. A. Melendres, Paper 345 presented at The Electrochemical Society Meeting, Toronto, Ontario, Canada, May 11-16, 1975.
7. D. W. Carnell and C. R. S. Needs, Paper 260 presented at The Electrochemical Society Meeting, Boston, Massachusetts, May 11-16, 1979.
8. W. W. Cariin and W. B. Darlington, Paper 261 presented at The Electrochemical Society Meeting, Boston, Massachusetts, May 11-16, 1979.
9. I. Malkin and J. R. Brannan, Paper 262 presented at The Electrochemical Society Meeting, Boston, Massachusetts, May 11-16, 1979.
10. M. C. Man and A. C. Tseung, Paper 263 presented at The Electrochemical Society Meeting, Boston, Massachusetts, May 11-16, 1979.
11. S. Matsuura, Y. Ozaki, K. Motani, Y. Ohhashi, and Y. Onoue, Paper 417 presented at The Electrochemical Society Meeting, St. Louis, Missouri, May 11-16, 1980.
12. F. Hine, M. Yasuda, R. Nakamura, and T. Noda,

- This Journal* **122**, 1185 (1975).
13. F. Hine and T. Sugimoto, Paper 459 presented at The Electrochemical Society Meeting, Seattle, Washington, May 21-26, 1978.
 14. F. Hine and K. Murakami, *This Journal*, **127**, 292 (1980).
 15. F. Hine and K. Murakami, *This Journal*, **128**, 64 (1981).
 16. F. Hine, M. Yasuda, and T. Tanaka, *Electrochim. Acta*, **22**, 429 (1977).
 17. F. Hine, *Soda and Chlorine (Japanese)*, **31**, 219 (1980).
 18. F. Hine, S. Yoshizawa, and S. Okada, *Kogyo Kagaku Zasshi (J. Chem. Soc. Jpn., Ind. Chem. Section)*, **62**, 769, 773 (1959).
 19. F. Hine, T. Sugimori, S. Yoshizawa, and S. Okada, *ibid.*, **62**, 955 (1959).
 20. "International Critical Tables." Vol. 5, p. 67 (1929).
 21. R. B. MacMullin and G. A. Muccini, *AIChE J.*, **2**, 393 (1956).
 22. K. S. Spiegler, *This Journal*, **113**, 161 (1966).
 23. F. A. L. Dullien, *AIChE J.*, **21**, 820 (1975).
 24. V. V. Stender, O. S. Ksenzhek, and V. N. Lazarev, *Zh. Prikl. Khim.*, **40**, 1293 (1967). English translation was supplied by R. B. MacMullin.

Growth of Thick Anodic Oxide Films on Nickel in Borate Buffer Solution

B. MacDougall* and M. J. Graham

Division of Chemistry, National Research Council of Canada, Ottawa, Ontario, Canada K1A 0R9

ABSTRACT

Anodic galvanostatic charging of nickel in pH 7.65 borate buffer solution produces a finely porous oxide film which is distinctly different from the passive film of NiO. The porous film which is probably NiOOH can grow to thicknesses in excess of 1000Å. It is reduced to a lower oxidation state during galvanostatic reduction, giving a distinct cathodic potential arrest. The oxide, however, remains on the surface during the cathodic treatment and reapplication of the anodic charging current results in an anodic arrest that is almost the mirror image of the cathodic arrest. The reversible conversion charge increases with increasing time of polarization in the O₂ evolution region, in conjunction with an increase in porous film thickness as determined by x-ray emission and Auger electron spectroscopies. In fact, the conversion charge is a close monitor of porous film thickness over a wide range of thicknesses and has been used to study film growth kinetics as a function of temperature, charging rate, and prior electrode treatment. The kinetics of porous oxide growth are interpreted in terms of an outer porous film growing on top of an inner compact film, the latter probably being the passive film. It is suggested that breakdown and repair events in the compact inner film generate the Ni²⁺ which is incorporated into the porous film, and that the stability of the passive film thus determines the growth rate of the porous film. This model explains the influences of temperature and electrode surface condition on oxide growth rate as well as the existence of breakaway-type kinetics and its dependence on charging rate.

The anodic oxidation of nickel in the passive potential region has been extensively studied in a variety of electrolytes, e.g., borate buffer solution (1-3) and neutral and acid sulfate solutions (1, 4-22). The composition of the passive oxide film formed in neutral and acid solutions is generally thought to be NiO with a maximum thickness reported anywhere from 12Å (4, 13, 23, 24) to 18Å (1, 9). In borate electrolyte, considerably thicker oxide films can be grown at potentials in the oxygen evolution region (1-3, 25, 26). The oxide formed in this potential region is a higher oxide of nickel, probably NiOOH (26). Unlike the passive film of NiO, this oxide gives a distinct galvanostatic reduction arrest which is believed to be associated with its conversion to a lower oxide of nickel, e.g., Ni(OH)₂ (or NiO). Subsequent anodic charging of the lower oxide also gives a distinct potential arrest as the lower oxide converts back again to the higher oxide (1, 27). This electrochemical conversion reaction is similar to that proposed for charging and discharging the nickel electrode in the nickel alkaline battery (27, 28), and while extensive research has been published in this area [cf., for example, (29)], little work has appeared concerning the kinetics and

mechanism of anodic growth of thick conversion oxide films on nickel surfaces by direct oxidation of the metal. The present investigation considers the factors influencing the growth kinetics of thick anodic oxide films on nickel in pH 7.65 borate buffer solution, and a model will be suggested for the mechanism of film growth.

Experimental

Polycrystalline specimens, 1 × 2.5 × 0.02 cm thick, were prepared from Materials Research Corporation zone-refined nickel sheet of 99.996% purity (4). They were degreased with benzene, chemically polished, electropolished for 2 min at 23°C in a 57 volume percent sulfuric acid solution at 0.5 A cm⁻², and then annealed at 800°C in a vacuum of 10⁻⁸ Torr. The specimens were again electropolished immediately before use in an experiment. Potentials quoted in this paper are referred to the saturated calomel electrode which is 0.245V with respect to the standard reversible hydrogen electrode. Electropolished nickel electrodes were galvanostatically anodized without cathodic reduction of the prior oxide film. Solutions were de-aerated pH 7.65 borate buffer, and were analyzed for Ni²⁺ by carbon rod atomic absorption spectroscopy, the lower limit of detection by this method being 0.2 μg cm⁻² (sample area = 5 cm²; cell volume = 50

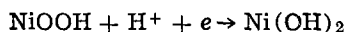
* Electrochemical Society Active Member.

Key words: electrode, passivity, oxidation, conversion, defects.

ml). X-ray emission (30, 31) and Auger electron spectroscopies (Physical Electronics Incorporated Model 590) were used to determine oxide film thicknesses.

Results

Cathodic and anodic galvanostatic charging profiles.—Figure 1 shows the cathodic and anodic charging profiles for electropolished nickel electrodes anodized for various times at $80 \mu\text{A cm}^{-2}$ in the oxygen evolution region [potentials $>0.95\text{V}$ (25, 26)]. Anodic charging generates a species which, when the charging polarity is switched from anodic to cathodic, undergoes reduction and gives a distinct potential arrest at $\sim 0.75\text{V}$. When reduction of this species is complete, the potential rapidly shifts into the hydrogen evolution region. Upon immediate reapplication of the anodic charging current, an anodic arrest occurs at about the same potential as the cathodic arrest; the cathodic and anodic arrest charges are equivalent. Oxides formed at potentials in the passive region do not give rise to this reversible arrest since the $\sim 12\text{\AA}$ thick passive film of NiO (4, 13, 23, 24) is inert to both conversion to a higher oxide of nickel and to cathodic reduction. During anodic charging in the oxygen evolution region, a very finely porous (26) higher oxide of nickel is generated, perhaps NiOOH as has been previously suggested by a number of workers (1, 3, 27). The charge-consuming reaction would thus be associated with interconversion of the nickel ion in the oxide between the 3+ and 2+ oxidation states *e.g.*, by a reaction such as



The term "conversion charge" will denote the cathodic arrest charge associated with this reaction.

To investigate the kinetics of the conversion reaction, a constant quantity of higher oxide was formed (*e.g.*, by anodizing at $80 \mu\text{A cm}^{-2}$ for 24 hr at 25°C) and this was reduced and reoxidized at charging rates of 4, 80, and $200 \mu\text{A cm}^{-2}$. The conversion charge was constant ($6.6 \pm 0.3 \text{ mC cm}^{-2}$) at all three charging rates indicating that the conversion reaction is a rapid, reversible process under activation rather than diffusion control. A fixed quantity of porous oxide gives the same conversion charge at all electrolyte temperatures from 5° to 45°C so that the kinetic results obtained for growth of the conversion oxide at different temperatures may be directly compared.

Oxide film examination.—The degree of hydration of oxides in the above conversion reaction is still open to question. Electrodes removed from solution in the oxidized state were blue-black in color, but this color-

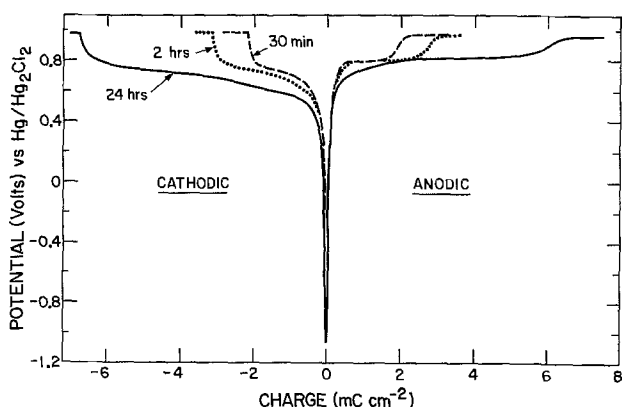


Fig. 1. Cathodic and anodic galvanostatic charging profiles, at $80 \mu\text{A cm}^{-2}$, for nickel electrodes anodized at $80 \mu\text{A cm}^{-2}$ for various times in the O_2 evolution region: (---) 30 min; (···) 2 hr.; (—) 24 hr. The charging current was switched from cathodic to anodic as soon as the potential shifted into the H_2 evolution region (*i.e.*, -1.06V); for comparison, the profiles are centered at the point of transition from cathodic to anodic charging.

ation slowly disappeared and the oxide film eventually became transparent. (This is exactly what happens when an oxidized electrode is cathodically reduced in solution, *i.e.*, the dark color becomes less distinct during the cathodic conversion arrest and at the end of the arrest the film is transparent.) Because the films change with time, difficulties are presented in attempting phase identification of the oxide in the oxidized state; reflection electron diffraction of a thick oxide film did confirm, however, the presence of $\beta\text{-NiOOH}$ in addition to NiO. Oxide films in the reduced state examined by electron diffraction and Auger spectroscopy appeared to be NiO rather than Ni(OH)_2 . It may be, though, that the porous film in the reduced state is Ni(OH)_2 , but that this species dehydrates in the vacuum system, *i.e.*, $\text{Ni(OH)}_2 \rightarrow \text{NiO} + \text{H}_2\text{O}$. In any event, the conversion reaction of $\text{Ni}^{3+} \rightarrow \text{Ni}^{2+}$ involves a 1-electron transfer, and assuming a current efficiency of 100%, the amount of oxide can be estimated from the conversion charge. The conversion charge increases with increasing time in the oxygen evolution region (Fig. 1), and thus the measured conversion charge can be used to determine the kinetics of porous oxide growth, provided that the relationship between conversion charge and quantity of porous oxide is constant over a wide range of film thicknesses. To check this, electrodes anodized at $80 \mu\text{A cm}^{-2}$ for 30 min and 24 hr (at 25°C) were removed from the solution and analyzed for oxygen content. The conversion charges for the 30 min and 24 hr treatments were 2.2 mC cm^{-2} and 6.6 mC cm^{-2} , respectively, compared with an increase in oxygen content (as determined by x-ray and Auger techniques) from $0.54 (\pm 0.05)$ to $1.27 (\pm 0.13) \mu\text{g oxygen cm}^{-2}$ (25). This increase in oxygen thus correlates reasonably well with the conversion charge increase. The relationship holds even for very thick films ($\equiv 10 \mu\text{g oxygen cm}^{-2}$), indicating that the oxide growth kinetics can be determined from galvanostatic charging experiments.

Kinetics of porous oxide growth.—Figures 2 and 3 show the increase in conversion charge with time of anodic charging at 4, 80, and $200 \mu\text{A cm}^{-2}$ for electrolyte temperatures of 5° , 25° , and 45°C . It is immediately evident that the temperature at which the oxide is grown plays a much more important role than

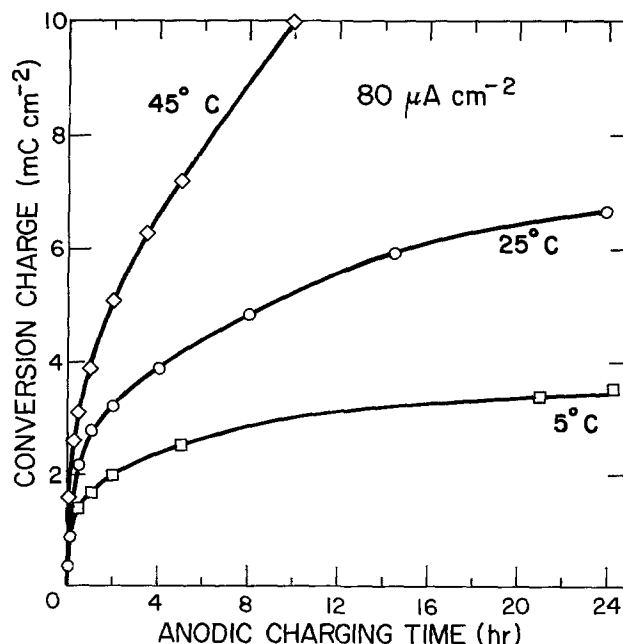


Fig. 2. Increase in conversion charge with time of anodic charging at $80 \mu\text{A cm}^{-2}$ at various temperatures: (—□—) 5°C ; (—○—) 25°C ; (—◇—) 45°C .

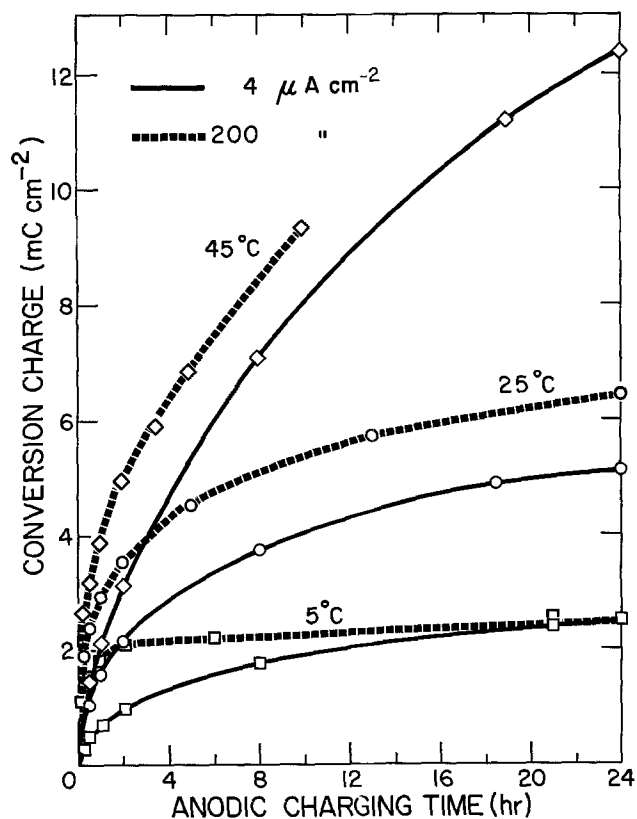


Fig. 3. Increase in conversion charge with time of anodic charging at 4 (—○—) and 200 (---□---) $\mu\text{A cm}^{-2}$ at various temperatures. (—□—) 5°C; (—○—) 25°C; (—◇—) 45°C. The conversion charge was determined by cathodic charging at 80 $\mu\text{A cm}^{-2}$.

the anodizing current. Obviously, the current efficiency for oxide growth is higher at the lower charging rate, but the values are $\leq 1\%$ at all charging rates and temperatures with most of the charge being consumed by oxygen evolution (25). When the film is sufficiently thick, breakaway-type kinetics are observed with the oxide growth rate increasing rapidly (Fig. 4 and 5). It is also seen in Fig. 5 that oxide growth is much faster on etched nickel (electropolished and then etched for 60 sec in 5% HNO_3) than on electropolished nickel.

Discussion

Previous electrochemical and Auger results suggest that the conversion oxide has a porous structure, and that the porosity is on too fine a scale to be detected by electron microscopy (25). It is difficult to explain the conversion charge kinetic curves (Fig. 2-5), where the rate slows and then increases dramatically, on the basis of growth processes of the porous oxide alone. A more reasonable model of the oxidation

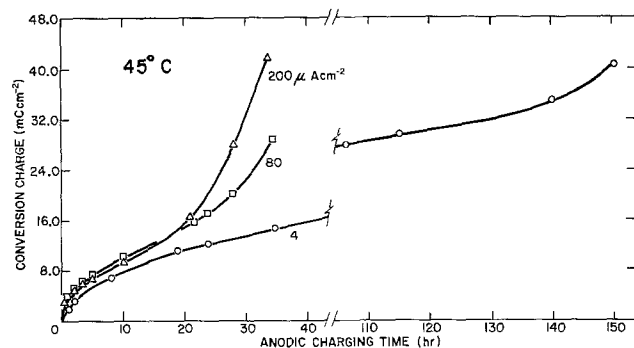


Fig. 4. Increase in conversion charge with time of anodic charging at 45°C using different charging rates: (—○—) 4 $\mu\text{A cm}^{-2}$; (—□—) 80 $\mu\text{A cm}^{-2}$; (—△—) 200 $\mu\text{A cm}^{-2}$.

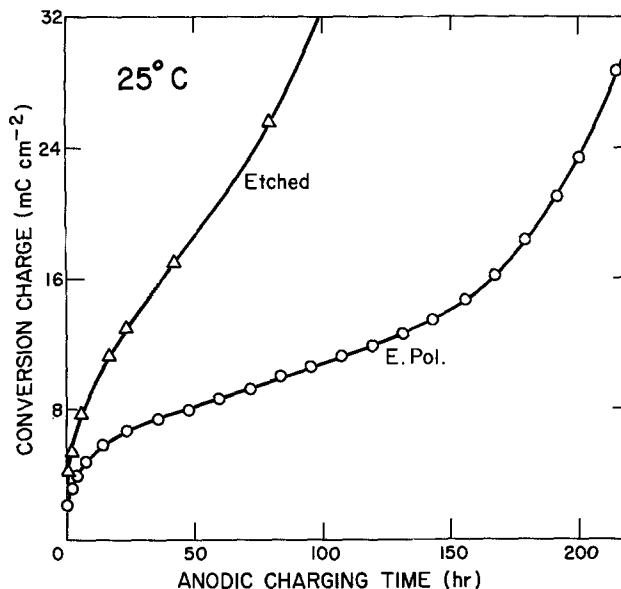
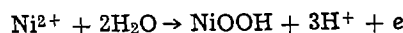


Fig. 5. Increase in conversion charge with time of anodic charging at 80 $\mu\text{A cm}^{-2}$ at 25°C for electropolished nickel (—○—) and etched nickel (—△—). Etching was in 5% HNO_3 for 60 sec.

mechanism would involve the presence of a compact oxide film beneath the outer porous film. It is suggested that the compact film is the 9-12Å passive film of NiO as illustrated schematically in Fig. 6. It is known from previous work that the passive oxide has a defect character and the local breakdown of the film, in the passive potential region, generates Ni^{2+} in solution. In the oxygen evolution potential region, the Ni^{2+} arising from passive film breakdown could be oxidized to a higher oxide of nickel and this would give rise to the porous film, perhaps by the reaction



An alternative reaction would be



which has a reversible potential of 0.2V (vs. Hg_2Cl_2). In the proposed model for porous film formation, growth would be controlled solely by the frequency of breakdown events in the passive film which would depend on the stability of the passive film as well as

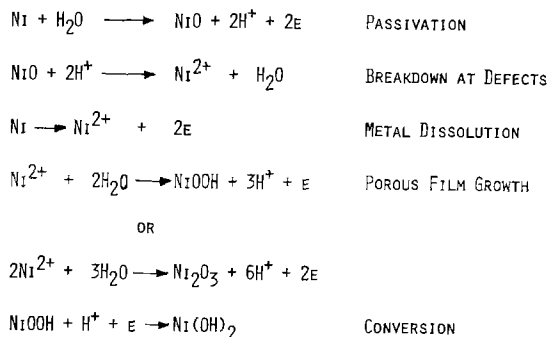
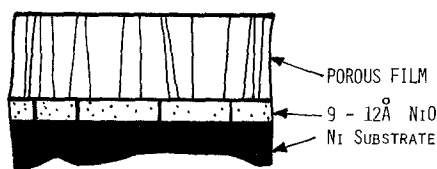


Fig. 6. Schematic illustration of the growth of the thick porous film on top of the compact passive film of NiO. The reaction sequence indicates the possible mechanisms for growth and conversion of the porous film.

the electrolyte environment. It is known that the state of perfection of the passive film increases and the anodic corrosion current (due mainly to $\text{Ni} \rightarrow \text{Ni}^{2+} + 2e$) decreases with time of anodization after a potential step into the passive region, the decrease being rapid at first and then quite slow (24). It may be that the initial rapid decrease of anodic current with time correlates with the initial slowing down of the oxide growth kinetics in the oxygen plateau region (Fig. 2-4). That is, as the passive film becomes more perfect, less Ni^{2+} is generated so less porous film can form. The linear-type kinetics (cf. Fig. 5, E. Pol.) could be associated with the passive film reaching a virtual steady state of perfection and therefore having a constant breakdown frequency, after some time of anodization in the oxygen region. This would correlate with the almost constant corrosion current in the passive potential region after long times of potentiostatic holding. The results then suggest that the changes in the corrosion current with time of potentiostatic holding in the passive potential region are similar to the changes in the nickel dissolution current in the oxygen plateau region during galvanostatic oxidation.

The breakaway kinetics (Fig. 4 and 5), observed after the porous film has reached a significant thickness, can be explained by a localized pH decrease at the base of the porous film, i.e., in the vicinity of the passive film. This arises because the oxidation reaction generates protons which must diffuse out from the body of the porous film for pH equilibration. When the porous film is too thick, the protons are not able to diffuse out rapidly enough for pH equilibration, so that a local decrease in pH occurs [cf. (32)-(35)]. The frequency of breakdown events at the passive film is highly dependent on the solution pH with the result that a decrease in pH causes this frequency to increase. This results in more rapid generation of Ni^{2+} and consequently a more rapid growth of the porous film. Growth kinetics at 4, 80, and 200 $\mu\text{A cm}^{-2}$ support this interpretation (Fig. 4), breakdown occurring at a lower porous film thickness at 200 $\mu\text{A cm}^{-2}$ since the higher charging current is generating a more rapid, local pH change. At 4 $\mu\text{A cm}^{-2}$, a much thicker oxide film is required before breakaway-type kinetics are observed.

This model of porous oxide film growth readily explains the previously noted thickness anisotropy¹ from grain to grain on polycrystalline nickel electrodes (25). It has been established in a number of earlier papers that the defect character of the passive oxide film is highly dependent on the crystal orientation of the substrate (23), the passive film on some grains being more defective than on others. Thus, with a polycrystalline sample, those grains with the most defective passive film will have the highest growth rates for the porous film. The rate of the porous film growth on a particular metal grain is therefore a monitor of the stability of the passive film on that grain.

The proposed model also explains the observations regarding temperature, anodic charging rate, and the influence of surface pretreatment on porous oxide growth kinetics. With increasing temperature, the porous film growth rate increases dramatically (Fig. 2 and 3). To quantify this increase with increasing electrolyte temperature, the extensive linear-type growth region can be used (cf. for example, Fig. 5). Growth kinetics for the porous film in this region are (charging rate 80 $\mu\text{A cm}^{-2}$): 0.6 \AA hr^{-1} at 25°C and 5.5 \AA hr^{-1} at 45°C. This compares with an increase of the corrosion current in the passive potential region from 0.01 $\mu\text{A cm}^{-2}$ at 25°C to 0.1 $\mu\text{A cm}^{-2}$ at

45°C. Thus, the increase in the porous film growth rate with temperature follows the increase in current measured in the passive potential region, a result to be expected if the dual oxide model is correct. The observation that the anodic charging rate has little influence on the growth kinetics of the porous film is also to be expected since the anodic charging current should have little or no influence on the defect character of the underlying passive film. With increased anodic current, the oxygen plateau potential shifts in the anodic direction and the extra charge is consumed by oxygen evolution. The influence of surface pretreatment on the growth rate of porous films (Fig. 5) is understandable in terms of the much less stable prior oxide film on etched nickel (36). Since the prior oxide is less stable, the anodic corrosion current is higher with more Ni^{2+} available for incorporation into (and therefore growth of) the porous film. In the proposed model where the passive film persists beneath the porous oxide, any factor which increases the corrosion rate of the passive film also increases the growth rate of the porous film.

Summary

Anodic galvanostatic charging of nickel in pH 7.65 borate buffer solution produces a finely porous oxide film whose thickness is dependent on the time of charging and the electrolyte temperature. The anodically formed porous film is probably β -NiOOH which undergoes a facile cathodic reduction to a lower oxidation state, likely $\text{Ni}(\text{OH})_2$. The conversion from the higher to lower oxide, and vice versa, gives a distinct galvanostatic arrest structure; the arrest charge is related to the quantity of porous oxide and can thus be used to study the kinetics of porous film growth. The kinetics are explained by a model which suggests that the compact passive film persists beneath the porous film and controls the latter's growth. Factors which increase the corrosion rate of the passive film (e.g., increasing temperature and different surface pretreatment) also increase the growth rate of the porous film, suggesting that breakdown and repair events in the underlying passive film provide Ni^{2+} which is anodically incorporated into the porous film. In fact, the measured corrosion current of the passive film appears to directly determine the growth rate of the porous film.

Manuscript submitted Feb. 23, 1981; revised manuscript received ca. June 5, 1981.

Any discussion of this paper will appear in a Discussion Section to be published in the June 1982 JOURNAL. All discussions for the June 1982 Discussion Section should be submitted by Feb. 1, 1982.

Publication costs of this article were assisted by the National Research Council of Canada.

REFERENCES

1. J. L. Ord, J. C. Clayton, and D. J. DeSmet, *This Journal*, **124**, 1714 (1977); also J. Ord in "Proceedings of the Fourth International Symposium on Passivity," R. P. Frankenthal and J. Kruger, Editors, p. 273, Airlie, Virginia, Published by The Electrochem. Society, Princeton, NJ (1978).
2. M. Okuyama and S. Haruyama, *Corros. Sci.*, **14**, 1 (1974).
3. N. Sato and K. Kudo, *Electrochim. Acta*, **19**, 461 (1974).
4. B. MacDougall and M. Cohen, *This Journal*, **121**, 1152 (1974).
5. N. Sato and G. Okamoto, *ibid.*, **110**, 605 (1963).
6. N. Y. Bune, *Zasch. Met.*, **3**, 50 (1967).
7. A. Jouanneau, M. Keddani, and M. C. Petit, *Electrochim. Acta*, **21**, 287 (1976).

¹ This thickness anisotropy is also evident during cathodic charging of a thick, dark porous film; the oxide on some grains becomes transparent long before that on other grains.

8. R. M. Latanision and H. Opperhauser, *Corrosion*, **27**, 509 (1971).
9. T. Dickinson, A. F. Povey, and P. M. A. Sherwood, *J. Chem. Soc. Faraday Trans. I*, **73**, 327 (1977).
10. P. Marcus, J. Oudar, and I. Olefjard, *J. Microsc. Spectrosc. Electron.*, **4**, 63 (1979).
11. T. Ohtsuka and K. E. Heusler, *J. Electroanal. Chem. Interfacial Electrochem.*, **100**, 319 (1979).
12. J. Siejka, C. Cherki, and J. Yahalom, *This Journal*, **119**, 991 (1972); also *Electrochim. Acta*, **17**, 161 (1972).
13. B. MacDougall and M. Cohen, *This Journal*, **123**, 191 (1976); also **124**, 1185 (1977).
14. M. Zamin and M. B. Ives, *ibid.*, **126**, 470 (1979).
15. U. Ebersbach, K. Schwabe, and K. Ritter, *Electrochim. Acta*, **12**, 927 (1967).
16. M. Turner, G. E. Thompson, and P. A. Brook, *Corros. Sci.*, **13**, 985 (1973).
17. J. Mieluch, *Rocz. Chem. Ann. Soc. Chim. Polonorum*, **49**, 365 (1975).
18. W. Paatsch, *Corros. Sci.*, **37**, 59 (1973).
19. L. N. Yagupol'skaya and A. A. Gordonnaya, *Zashch. Met.*, **4**, 712 (1968).
20. R. D. Armstrong, *J. Electroanal. Chem. Interfacial Electrochem.*, **28**, 221 (1970).
21. J. R. Vilche and A. J. Arvia, in "Proceedings of the Fourth International Symposium on Passivity," R. P. Frankenthal and J. Kruger, Editors, p. 861, Airlie, Virginia. Published by The Electrochemical Society (1978).
22. B. Droste and H. G. Feller, *ibid.*, p. 802.
23. B. MacDougall and M. Cohen, *ibid.*, p. 827.
24. B. MacDougall, D. F. Mitchell, and M. J. Graham, *Isr. J. Chem.*, **18**, 125 (1979).
25. B. MacDougall, D. F. Mitchell, and M. J. Graham, *This Journal*, **127**, 1248 (1980).
26. B. MacDougall, D. F. Mitchell, and M. J. Graham, *Corrosion* **81**, Toronto, Canada, April 1981, Pub. by NACE, In press.
27. M. A. Hopper and J. L. Ord, *This Journal*, **120**, 183 (1973).
28. J. L. Ord, *Surf. Sci.*, **56**, 413 (1976).
29. G. W. D. Briggs, in "Electrochemistry—Special Periodical Reports," Vol. 4, p. 33, published by the Chemical Society (1974).
30. D. F. Mitchell and P. B. Sewell, *Thin Solid Films*, **23**, 109 (1974).
31. P. B. Sewell, D. F. Mitchell, and M. Cohen, "Developments in Applied Spectroscopy," Vol. 7A, pp. 61-79, Plenum Press, New York (1969).
32. S. Gottesfeld and S. Srinivasan, *J. Electroanal. Chem. Interfacial Electrochem.*, **86**, 89 (1978).
33. S. Gottesfeld and J. D. E. McIntyre, *This Journal*, **126**, 742 (1979).
34. S. Gottesfeld, J. D. E. McIntyre, G. Beni, and J. L. Shay, *Appl. Phys. Lett.*, **33**, 208 (1978).
35. S. Gottesfeld, M. Yaniv, D. Laser, and S. Srinivasan, *J. Phys.*, **38**, C5-145 (1977).
36. B. MacDougall and M. J. Graham, *Electrochim. Acta*, **26**, 705 (1981).

Effect of Surface Etching and Morphology on the Stability of CdSe/S_x⁼ Photoelectrochemical Cells

Gary Hodes* and Joost Manassen

Department of Plastics Research, The Weizmann Institute of Science, Rehovot, Israel

and David Cahen*

Department of Structural Chemistry, The Weizmann Institute of Science, Rehovot, Israel

ABSTRACT

The stability of single crystal CdSe photoelectrodes in polysulfide electrolyte is shown to be a function of the etching treatment used. This is explained by changes in real electrode surface area caused by different etchants, leading to a variation in real photocurrent density. The effect of photocurrent density on stability is measured, and used to semiquantitatively explain the observed variation in stability with etching. The effect is shown to be consistent for three different crystal faces, and is extended to polycrystalline electrodes.

Since the earliest reports showing that polychalcogenide electrolytes can stabilize n-Cd-chalcogenides as photoanodes in a photoelectrochemical cell, PEC, (1-3), it has become apparent that this stability is very ill defined. For example, the stability of the CdSe/polysulfide system has been reported to vary between minutes (4) to months (5). The variables which have been shown to affect the degree of stability are: electrode crystal structure and exposed crystal face, electrolyte composition, stirring, and photocurrent density (5-8).

In the CdSe/S_x⁼ system it has been shown that stabilization of the photoanodes is connected with the exchange of Se from the CdSe by S from the electrolyte leading to a polycrystalline CdS layer on top of the CdSe (1,4-6, 9-11). Under favorable circumstances

cell output is stable because the CdS layer stops growing after reaching a certain thickness (probably less than ~100Å), at which point Se/S exchange is replaced by S/S exchange. If, however, Se/S exchange continues, even at a much reduced rate, the CdS layer continues to grow. This thicker layer will start to impede the transfer of minority carriers from the bulk solid to the solution phase, leading to increased deactivation. The resistance to the transfer of the minority carriers can be due to blocking by the higher bandgap CdS layer and/or reduced electrical conductivity of this layer. However, the similar stability behavior of CdS, where such a blocking layer is not expected, suggests that the degradation in output is due primarily to the increased polycrystallinity of the surface CdS layer, leading either to trapping and recombination of holes at the grain boundaries (8, 10, 11) or if the surface layer is porous and inactive, impeding the dissolution of

* Electrochemical Society Active Member.
Key words: CdSe photoelectrodes, photoelectrode surface area, photoetching.

photogenerated S [which is the rate-determining step (12)] away from the active surface through the porous CdS layer (8, 9).

Therefore photocorrosion is related to the competition between several possible reactions by the photo-generated holes: oxidation of polysulfide from the solution (the desired reaction); oxidation of the freshly formed CdS layer, which renews the solid/solution interface; or oxidation of the CdSe itself, which is the photocorrosion reaction and leads to increased S/Se substitution, and eventually, degradation of the output. Any change in conditions which facilitates the overall electrochemical oxidation of polysulfide and removal of the reaction photoproducts from the surface, should change the balance of the competitive reactions in favor of decreasing exchange, and thus increasing stability. We have shown that polycrystalline electrodes are more stable than single crystal ones, and explain this by the higher real surface area of the less smooth polycrystalline electrodes, leading to a lower real photocurrent density (5) which has previously been shown to cause increased stability (6). This follows from the competitive nature of the possible reactions (13); if the photocurrent density is not too high, the oxidation of polysulfide (actually the dissolution of S from the surface) can occur as fast as (or faster than) the hole flux to the surface. At higher photocurrent densities (i.e., greater hole fluxes), if the overall polysulfide oxidation step cannot keep up with the arrival of holes at the surface, we expect degradation according to the principles previously discussed.

This picture is, however, too simple, and the purpose of the work reported here is to investigate more fully than previously the effect of real surface area of CdSe photoelectrodes, together with the influence of several etching treatments, on the output stability of these electrodes in polysulfide electrolyte. By trying to achieve a picture, that is as complete as possible, of the various factors influencing the output stability of such PEC's, it may become feasible to manipulate the variables influencing these factors in such a way so as to achieve stable PEC's with output stability under normal day/night conditions, that is constant for years.

Experimental

All the CdSe crystals were cut from the same boule, which was "as-grown" (from Dr. W. Giriat, IVIC, Caracas), with an approximate resistivity of 15 Ω cm. Crystals were cut along the (0001), (10 $\bar{1}$ 0), and (11 $\bar{2}$ 0) faces. All orientations were checked by x-ray diffraction. Using the anomalous dispersion factors the (0001) face was shown to be the Cd-one (14). Polycrystalline CdSe electrodes were prepared by painting an aqueous slurry of CdSe (Alfa 99.999%) mixed with a ZnCl₂ flux onto a Ti substrate, and annealing 10 min at 630°C in argon (15). Single crystal electrodes were all polished to a mirror finish using alumina polishing suspension down to 0.3 μ m. The different etching treatments on these polished electrodes were, all at room temperature:

1. Dip in 4% Br₂ in MeOH for 5 sec; rinse with polysulfide (S_x²⁻) and then with water. Repeat. Br₂/MeOH.
2. Dip in CrO₃:HCl:H₂O in 6:10:4 w/w ratio, for 5 sec; rinse with S_x²⁻ and then with water. Repeat. "CrO₃."
3. Dip in fresh aqua regia, 15 sec; rinse with S_x²⁻, then with water. Repeat. AR.

4. AR followed by "CrO₃," i.e., as 3, followed by 2.
5. AR followed by photoetch, i.e., as 3, followed by illumination in HNO₃:HCl:H₂O (0.3:9.7:90) electrolyte, short circuited to a carbon counterelectrode in the same electrolyte, under AMI illumination for 4-5 sec; then rinsing in S_x²⁻ and H₂O (16). The polycrystalline electrode was etched for 4-5 sec in 3% HNO₃ in HCl (aqua regia was too vigorous an etchant for these thin

layers), rinsed in S_x²⁻ and water, and photoetched as above.

The electrolyte in all cases was 1M each KOH, Na₂S, and S in deionized water. The experiments were all carried out using the same bulk solution stored under argon. Each stability run was obtained using a fresh quantity of this solution. The stability runs were carried out potentiostatically under essentially short-circuit conditions using Pt counter and reference electrodes. The cell was thermostated in a water bath at 35°C, and no stirring was employed. Illumination was by a stabilized quartz-iodine lamp, and illumination was controlled to give the required photocurrent density in all cases. In some cases, where the photocurrent density initially increased with time for constant illumination, which often happens in this system, the illumination intensity was reduced slightly to maintain the initial current, (otherwise a meaningful comparison could not be made).

Results and Discussion

It has been shown previously (6) that the (0001) face of a CdSe crystal is less stable as a photoanode in S_x²⁻ than the (11 $\bar{2}$ 0) face. Since we wished to compare the effect of change in surface roughness by use of different etchants, which could preferentially expose planes other than that initially chosen, we had to verify that the various etchants did not expose any crystal face(s) preferentially. Therefore, we investigated three different faces, namely (0001), (10 $\bar{1}$ 0), and (11 $\bar{2}$ 0), assuming that, if preferential exposure of a more stable face did occur upon etching, the dependence on etchant of these three faces would be different. Figures 1 and 2 show the photocurrent densities of these faces after the various etching treatments, as a function of time, plotted on a logarithmic scale. The (0001) and (10 $\bar{1}$ 0) faces behaved identically (within experimental error). The interesting result is that, in spite of entirely different stabilities of the (11 $\bar{2}$ 0) face on the one hand and the (0001) and (10 $\bar{1}$ 0) faces on the other hand, they respond very similarly to the various etching treatments. Stabilization by a factor of ~50 is obtained when going from the entirely smooth surface to one that has been photoetched. This behavior indicates that we are not dealing with preferential exposure of more or less stable faces by the different etchants used.

To correlate these results with the effects of the various etchants on the real surface area, we show in

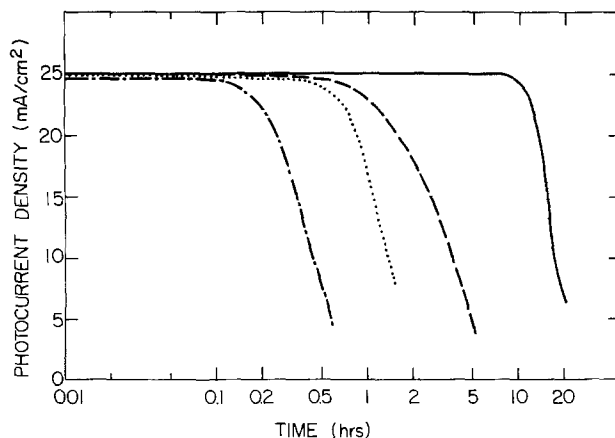


Fig. 1. Output stability of the (10 $\bar{1}$ 0) face of a CdSe crystal in a polysulfide electrolyte (1M each KOH, Na₂S, and S) at 35°C. —····· Polished and Br₂/MeOH (for (0001) face) or "CrO₃" (for (10 $\bar{1}$ 0) face) etched; aqua regia (AR) etch followed by "CrO₃" etch; - - - - - AR etch; ——— AR etch followed by photoetch. An essentially identical picture was obtained for the (0001) (Cd) face.

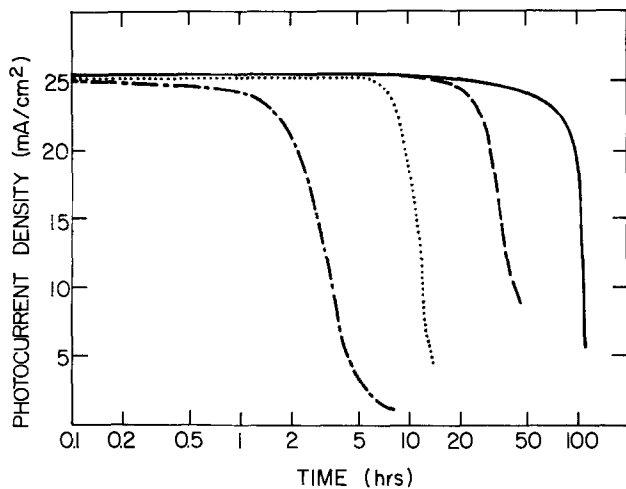


Fig. 2. As Fig. 1, but for the $(11\bar{2}0)$ face

Fig. 3-11 SEM pictures of the surfaces of the 3 faces, each after 3 different etching treatments. (SEM pictures of the Br₂/MeOH or "CrO₃" only, etches are not shown, since these surfaces were all mirror-smooth, and featureless under the SEM.)

Figures 3, 4, and 5 show AR + Br₂/MeOH, AR, and AR + photoetch for the (0001) face of CdSe. We can see an increase in surface roughness going from Fig. 3 to 5. Figures 6, 7, and 8 [for the (10 $\bar{1}0$) face] and 9, 10,

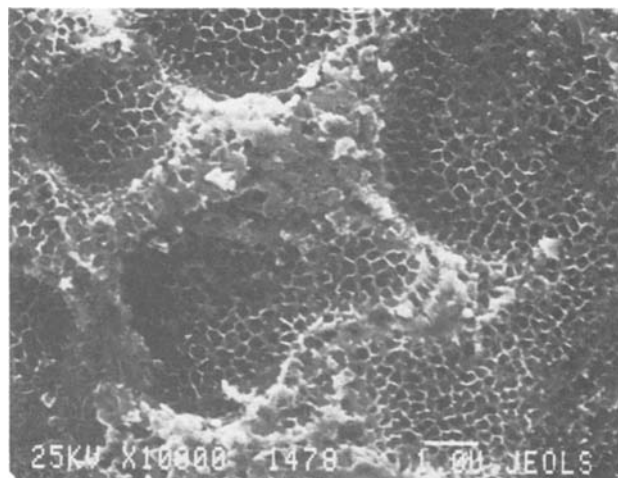


Fig. 5. SEM micrograph of (0001) face after AR + photoetch

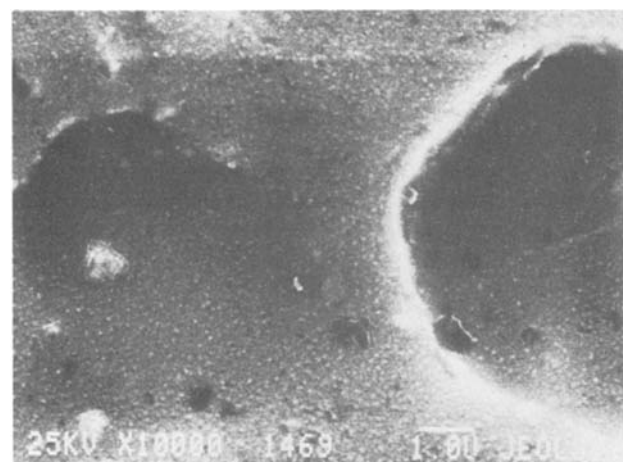


Fig. 3. SEM micrograph (10,000 times magnification) of the (0001) face after AR followed by Br₂/MeOH etch.

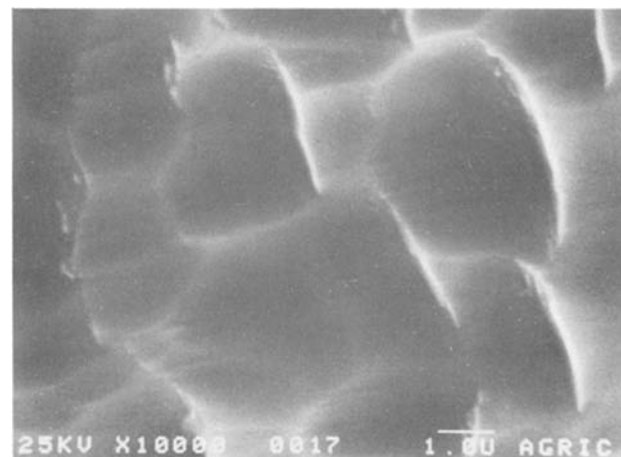


Fig. 6. SEM micrograph of (10 $\bar{1}0$) face after AR + "CrO₃" etch

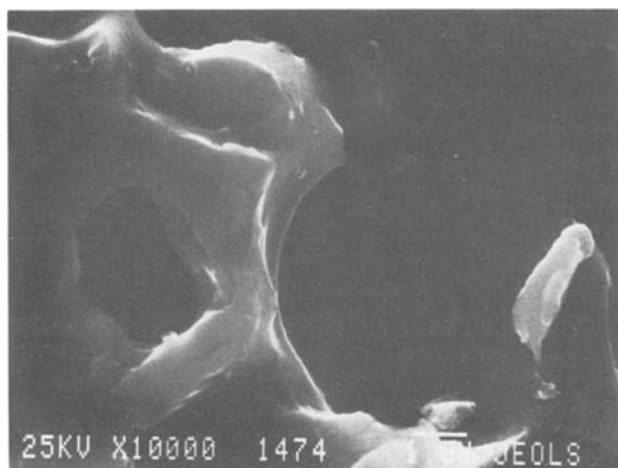


Fig. 4. SEM micrograph of (0001) face after AR etch

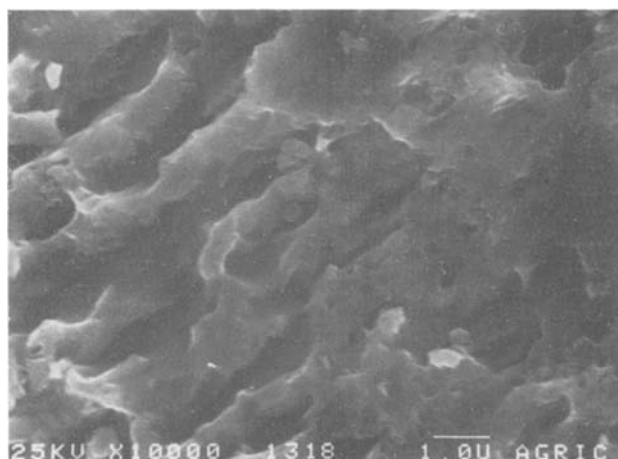


Fig. 7. SEM micrograph of (10 $\bar{1}0$) face after AR etch

and 11 [for the $(11\bar{2}0)$ face] show precisely the same trend, although the etch patterns vary from one face to another. Figure 12 shows a photograph of the (1120) crystal face with 3 differently etched regions. Even such a visual observation of the surface shows the strikingly different effects of different etchants.

Thus, the increase in stability in going from left to right in Fig. 1 and 2 correlates with an increase in surface area, in agreement with our reasoning given previ-

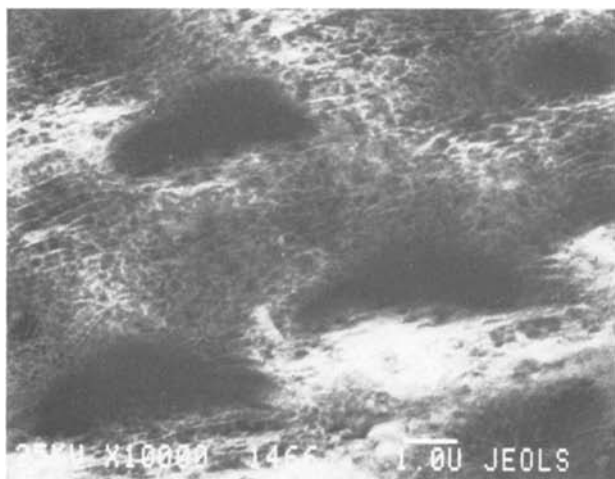


Fig. 8. SEM micrograph of $(10\bar{1}0)$ face after AR + photoetch

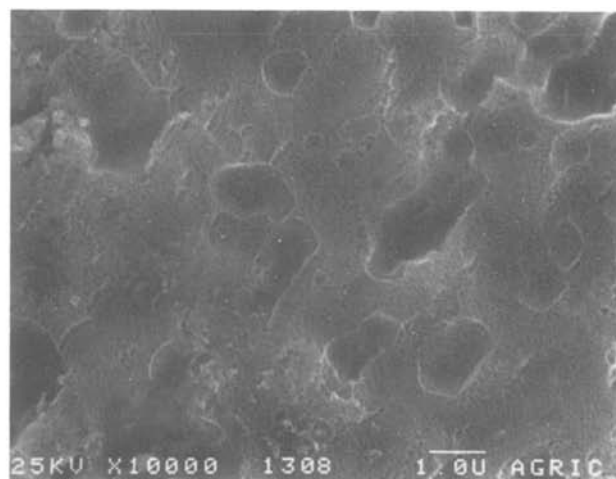


Fig. 11. SEM micrograph of $(11\bar{2}0)$ face after AR + photoetch

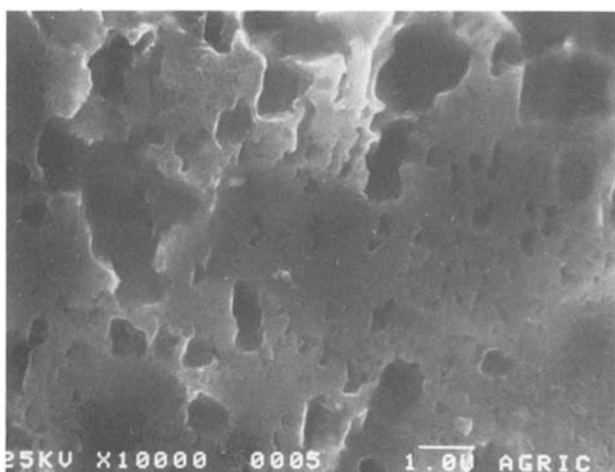


Fig. 9. SEM micrograph of $(11\bar{2}0)$ face after AR + "CrO₃" etch

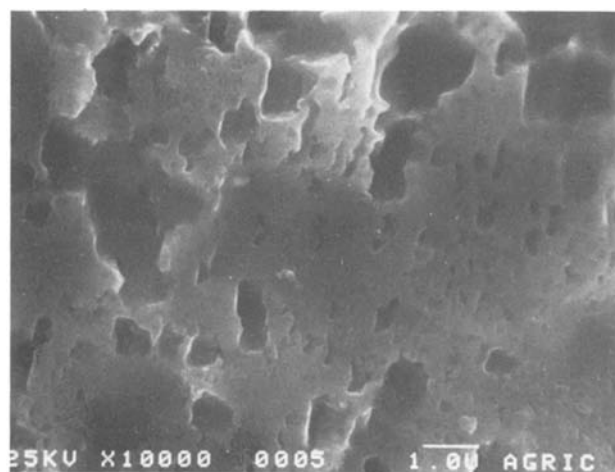


Fig. 10. SEM micrograph of $(11\bar{2}0)$ face after AR etch

ously on the basis of the difference between single crystal and polycrystalline CdSe.

Although we have not yet developed a method, reliable enough to measure these variations in surface area quantitatively (but diffuse reflectance together with photoacoustic measurements do show some promise in this respect), and in any case, such measurements would be of limited value, since an increase in real surface area by a certain factor need not reflect an in-

crease in the active surface area by the same factor, it is of interest to see if such variation is sufficient to explain the effect of stability. Figure 13A shows the effect of photocurrent density on stability for the smooth, Br₂/MeOH etched, (0001) face (we have given the x-axis in time, and not coulombs, in order to facilitate comparison with other figures). In Fig. 13B these and similar data are used to show directly the dependence of the amount of photocharge that can be passed, as a function of initial photocurrent density.

Because of the long measuring times at lower current densities, the curve could not be extended in this direction. But based on general experience we expect the curve to straighten out and to give a practically infinite lifetime at some finite lower (<10 mA/cm²) current density. The strong dependence of stability on the initial photocurrent density, also described in Ref. (6),

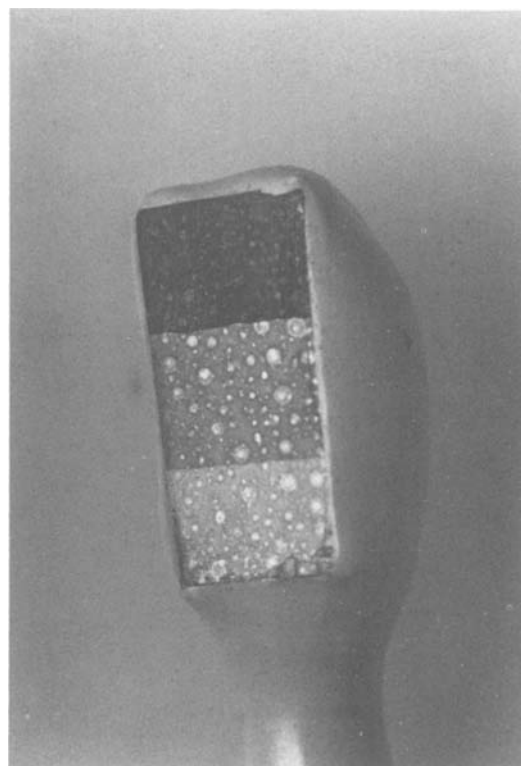


Fig. 12. Photograph (10× magnification) of a $(11\bar{2}0)$ face of a CdSe crystal. The three different regions are obtained after: AR followed by "CrO₃" etch (lightest region); AR etch alone (middle region); and AR followed by photoetch (darker region).

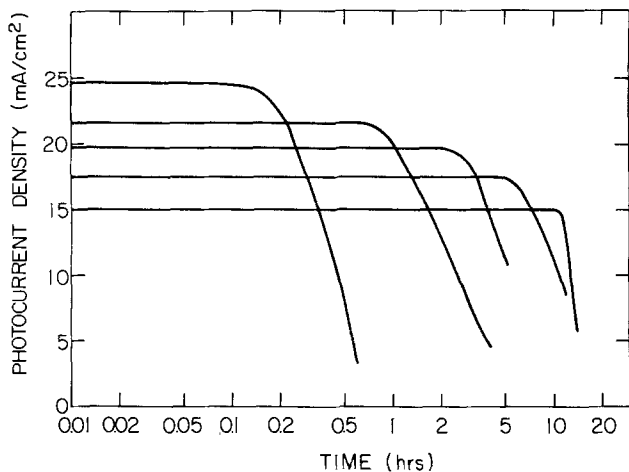


Fig. 13A. Effect of photocurrent density variation (by varying illumination intensity) on stability of polished, and subsequently Br_2/MeOH etched, (0001) CdSe crystal at 35°C .

can be seen clearly. Using Fig. 13A we can understand the results shown in Fig. 1 and 2. Those were obtained at an initial current density of 25 mA/cm^2 . We see from Fig. 13A that a roughness factor of ~ 1.6 ($24.5\text{ mA}/15\text{ mA}$), which would decrease real current density to $\sim 15\text{ mA/cm}^2$, would increase the lifetime by a factor of about fifty. The SEM pictures in Fig. 3-11 show that the range of roughness factors resulting from the different treatments are probably much higher and the most logical explanation for the increased stability is therefore this increase in surface area with concurrent decrease in real current density.

As mentioned earlier, the increase in active surface area need not be the same as the increase in real surface area, and will probably be smaller, since the presence of small pores of other surface irregularities may lead to transport problems which could partially offset

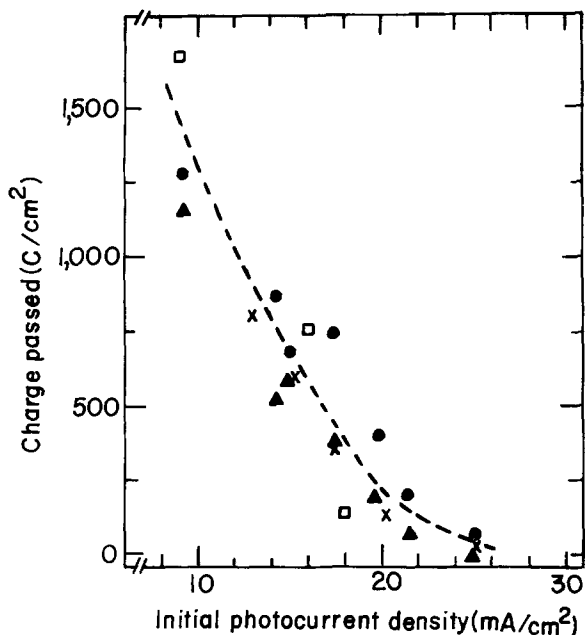


Fig. 13B. Dependence of the amount of photocharge, that can be passed through a CdSe electrode (as in 13A) until destabilization, on the initial photocurrent density. The data are from Fig. 13A (\bullet , \blacktriangle) and similar ones obtained with crystals cut from the same boule (\times , \circ). \bullet , \times , \square : Only photocharge passed until the current density decreases to 5 mA/cm^2 is taken into account, because of varying behavior and long measuring times at lower current densities. \blacktriangle : As \bullet , but for the photocharge passed at constant current density (= initial current density), i.e., while the electrode is 100% stable.

the gain due to increased surface area. This makes it very difficult to treat the above effect in any more quantitative detail.

Since our original reasoning for the effect of surface area on stability came from the comparison between single crystal and thin layer polycrystalline CdSe (5), it is of interest to see how the most stable form of a single crystal photoetched (11 $\bar{2}$ 0) face compares in stability with photoetched thin layer electrodes. This is shown in Fig. 14. Note the high photocurrent densities used here (50 mA/cm^2) in order to measure a degradation in a reasonably short period of time. While there is a definite difference in stability between the two electrodes, the difference is considerably less than that noted earlier in comparing polycrystalline CdSe with the AR-etched (0001) face of CdSe, for what are now obvious reasons. The main difference is in the slow and diminishing rate of deactivation of the polycrystalline electrode, compared with the single crystal. This slow rate of deactivation is characteristic of our polycrystalline electrodes. It may be due to the very large degree of surface irregularity of these electrodes (see Fig. 15). Some areas will be photoelectrochemically more active than others. Thus, the more active ones may deactivate first, since the local current density at them will be relatively high. As the photocurrent falls,

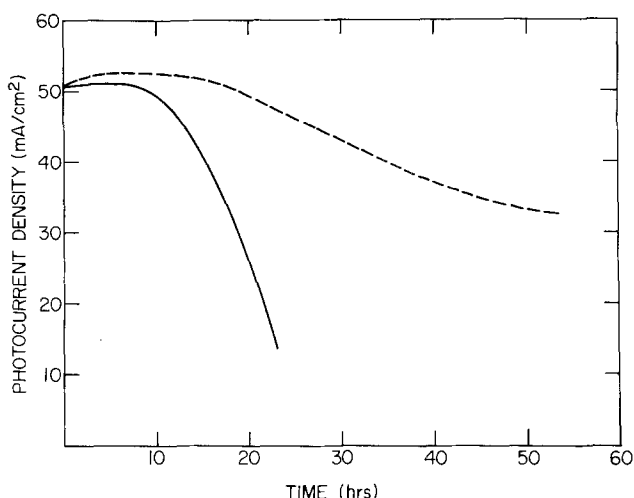


Fig. 14. Comparison of stability of thin layer polycrystalline painted CdSe (3% HNO_3 in HCl etch followed by photoetch) (broken line), and (11 $\bar{2}$ 0) face of single crystal CdSe (AR followed by photoetch) (solid line).

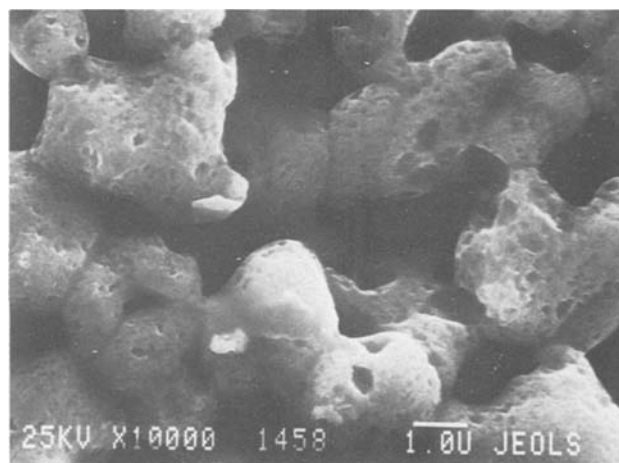


Fig. 15. SEM micrograph (10,000 \times magnification) of a painted polycrystalline CdSe electrode after 3% HNO_3 in HCl etch and use in $S_x=$ solution.

the previously less active areas now become (relatively speaking) the most active, but at a lower current density, hence a slower rate of deactivation. While this explanation is admittedly rather simplistic, it can serve as a basis for explaining the slow and decreasing rate of deactivation of polycrystalline electrodes.

It should be noted that the electrolyte used here (1M each OH^- , S^{2-} , S) is far from being the most stabilizing electrolyte for this system. Therefore, the stability results shown here should not be interpreted as reflecting the maximum attainable stability of this system. In a more stabilizing electrolyte, the stability will in fact be much greater (8).

Although not the main point of this study, it is of interest to attempt to understand the difference in stability of the various faces. A possible reason may be found by considering the number of bonds that have to be broken to free a Cd^{2+} ion from the surface. In the (11 $\bar{2}$ 0) plane there are two in-plane bonds and one into the bulk phase. The (10 $\bar{1}$ 0) plane has only one in-plane bond and one or two into the bulk phase, while the (0001) plane has no in-plane bonds but one or three into the bulk phase. Thus, one could argue that the (11 $\bar{2}$ 0) plane is more stable since always three bonds need to be broken in order to free a Cd ion. If this is so, then the decomposition potential of a semiconductor photoelectrode must be dependent on the crystal face exposed. The different bonding at the surface may also influence the electrochemical reaction through different surface-solute interaction, and thus change the relative energetics of the two competing processes. In this case, the decomposition potential need not necessarily change. Finally, if photocorrosion is connected with the diffusion of Cd^{2+} through the bulk to the surface, such as has been reported to occur for CdTe photoanodes (17), then the varying stability of different faces may be due to varying rates of diffusion (or migration in the space charge layer) of the Cd^{2+} in the different crystal directions.

According to the strong dependence of lifetime on current density, we might expect the electrode at constant illumination to be less stable at short circuit than at maximum power, because of the higher current density passed. But according to our experience this is not true and we find that at constant illumination, most of our electrodes are more stable at short circuit than at maximum power. We shall deal with this interesting phenomenon in a subsequent publication. Suffice here to note that apparently, current density is not the only parameter influencing stability, but the electrode potential under the actual working conditions plays a

role as well. In view of the rate-determining dissolution of sulfur, it is likely that changes in electrode potential influence the stability through variations in surface potential (or changes in the Helmholtz layer), rather than simply by a change in band bending.

Acknowledgments

This work was supported by the U.S.-Israel Binational Science Foundation, Jerusalem, Israel, and by Ormat Turbines, Yavne, Israel. We thank L. Leisero-witz for help with the x-ray diffraction measurements, and W. Gariat for supplying the crystals.

Manuscript submitted Feb. 26, 1981; revised manuscript received May 28, 1981.

Any discussion of this paper will appear in a Discussion Section to be published in the June 1982 JOURNAL. All discussions for the June 1982 Discussion Section should be submitted by Feb. 1, 1982.

Publication costs of this article were assisted by the Weizmann Institute of Science.

REFERENCES

1. G. Hodes, J. Manassen, and D. Cahen, *Nature*, **261**, 403 (1976).
2. A. B. Ellis, S. W. Kaiser, and M. S. Wrighton, *J. Am. Chem. Soc.*, **98**, 1635 (1976).
3. B. Miller and A. Heller, *Nature*, **262**, 680 (1976).
4. R. N. Noufi, P. A. Kohl, J. W. Rogers, Jr., J. M. Whilte, and A. J. Bard, *This Journal*, **126**, 949 (1979).
5. D. Cahen, G. Hodes, and J. Manassen, *ibid.*, **125**, 1623 (1978).
6. A. Heller, G. P. Schwartz, R. G. Vadimsky, S. Menezes, and B. Miller, *ibid.*, **125**, 1156 (1978).
7. M. A. Russak, J. Reichman, H. Witzke, S. K. Deb, and S. N. Chen, *ibid.*, **127**, 725 (1980).
8. G. Hodes, J. Manassen, and D. Cahen, *Solar Energy Mater.*, In press.
9. K. T. L. DeSilva and D. Haneman, *This Journal*, **127**, 1554 (1980).
10. H. Gerischer and J. Gobrecht, *Ber. Bunsenges. Phys. Chem.*, **82**, 520 (1978).
11. D. Cahen, B. Vainas, and J. Vandenberg, *This Journal*, **128**, 1484 (1981).
12. D. Lando, J. Manassen, G. Hodes, and D. Cahen, *J. Am. Chem. Soc.*, **101**, 3969 (1978).
13. D. Cahen, J. Manassen, and G. Hodes, *Solar Energy Mater.*, **1**, 343 (1979).
14. E. P. Warekois, M. C. Lavine, A. N. Mariano, and H. C. Gatos, *J. Appl. Phys.*, **33**, 690 (1962).
15. G. Hodes, J. Manassen, D. Cahen, and M. David, *This Journal*, **127**, 2252 (1980).
16. R. Tenne and G. Hodes, *Appl. Phys. Lett.*, **37**, 428 (1980).
17. C. Vazquez-Lopez et al., *J. Appl. Phys.*, **50**, 5391 (1979).

The Relationship of Transport Properties and ^1H NMR Spectra to the Structure of Molten Methylpyridinium Halides

David S. Newman,* Rick R. Rhinebarger,* David Siconolfi,* and Olumuyiwa A. Banjoko*

Department of Chemistry, Bowling Green State University, Bowling Green, Ohio 43403

ABSTRACT

The equivalent conductance, viscosity, and ^1H NMR spectra of several molten symmetric and asymmetric methylpyridinium halides were measured as a function of temperature. From these measurements, correlations between structure, spectra, and transport properties were made. From these correlations conclusions about the dynamics of motion in these and in other organic melts were drawn.

Molten pyridinium salts alone or in combination with molten aluminum halides are of considerable importance as the electrolyte in batteries and as the solvent for synthetic and mechanistic studies of organic and inorganic compounds. In recent years they have also become important as a possible heat storing media in solar heating and air conditioning systems as well as solvents for coal solubilization and decomposition reactions (1). In addition to these practical considerations, molten pyridinium salts offer a convenient vehicle for understanding the nature of the molten state because their relatively low melting points make them accessible to NMR techniques as well as to conventional transport measurements. This, combined with the myriad different pyridinium salts that are easily synthesized, makes it possible to observe the effects of small structural changes, such as moving a methyl group from the 4 to the 3 position on the pyridine ring, on both transport and spectral properties. From these effects a qualitative understanding of molecular motion in these and probably other molten organic liquids can be obtained.

In an earlier study (2) we reported the equivalent conductance, Λ , of 4-methylpyridinium bromide to be about 8% lower than the conductance of N-methylpyridinium bromide over approximately the same temperature range. We attributed this surprising result to complex formation in the 4-methyl salt which reduces the number of charge carriers per unit volume relative to the N-methyl salt. The complex probably forms by means of hydrogen bonding between the nitrogen proton and the bromide ion and this, of course, cannot occur in the N-methyl salt (3-5). The ^1H NMR spectrum of 4-methylpyridinium bromide showed no line width broadening greater than 0.02 ppm, over a nearly 50° temperature range, indicating the barrier to complex formation is less than about 40 kJ/mol (1). There is, however, a change in proton chemical shift, as the anion changed from Br^- to Cl^- , that correlates well with the conductance data and this is discussed later. Herein we extend our investigation to include other symmetrical methylpyridinium salts as well as the asymmetrical methylpyridinium halides. We also assess the nature of the complex species in 4-methylpyridinium chloride and in 4-methylpyridinium bromide and estimate the magnitude of their association constants. In addition, we comment on the mechanism of molecular motion in methylpyridinium melts.

Experimental Details

All transfer operations were carried out in a dry box in which N_2 gas was circulated over molecular

* Electrochemical Society Active Member.

Key words: molten pyridinium salts, transport properties, ^1H NMR spectra.

sieves to remove water. A fiber optic light pipe was used to conduct light into the Dow Corning 710 oil which served as the heat bath. The flexible light pipe greatly facilitated the density and viscosity measurements. The bath was held constant to $\pm 0.1^\circ\text{C}$. A Varian CFT-20 NMR machine with variable temperature capability was used to obtain the ^1H NMR spectra.

The preparation of the salts, conductivity measurements, density measurements, viscosity measurements, and ^1H NMR techniques are all described in detail elsewhere (6-9).

Results

The density, ρ , the specific conductance, κ , the viscosity, η , and the ^1H NMR spectra of molten 2-methylpyridinium chloride (2-mepyr/HCl), 2-methylpyridinium bromide (2-mepyr/HBr), 3-methylpyridinium chloride (3-mepyr/HCl), and 3-methylpyridinium bromide (3-mepyr/HBr) were measured as a function of temperature over an approximately 50°C temperature range. These salts, together with their melting points, are shown in Fig. 1. The η 's of 4-methylpyridinium bromide and chloride as well as the η of N-methylpyridinium chloride (N-mepyr/Cl) were measured as a function of temperature. The κ of molten 4-mepyr/HCl was also measured as a function of temperature. The values of ρ used to compute η and Λ for the symmetric salts were taken from an earlier study (7). The ^1H NMR spectra of the three molten 4-methylpyridinium halides were obtained relative to an external standard of either $(\text{CH}_3)_2\text{SO}$ or $(\text{CH}_3)_2\text{SO}_2$. Figure 2 shows the spectrum of 4-mepyr/HI at 172°C relative to $(\text{CH}_3)_2\text{SO}_2$. Figures 3 and 4 show the spec-

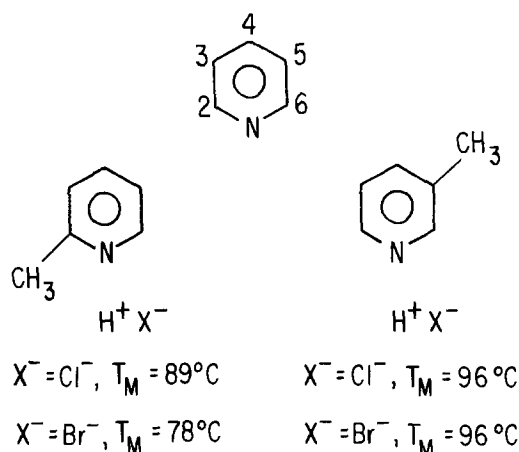


Fig. 1. The asymmetric methylpyridinium halides, their melting points, and the numbering system used in this study.

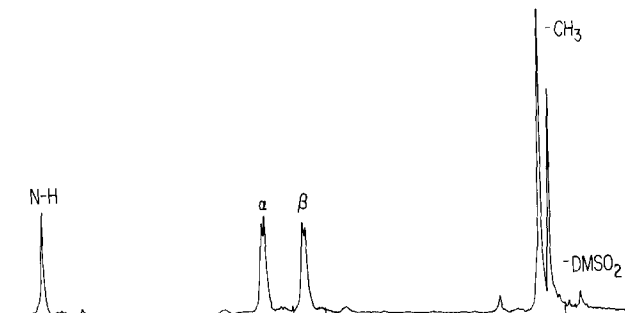


Fig. 2. The HNMR spectrum of 4-mepyr/HI relative to $(\text{CH}_3)_2\text{SO}_2$ at 172°C .

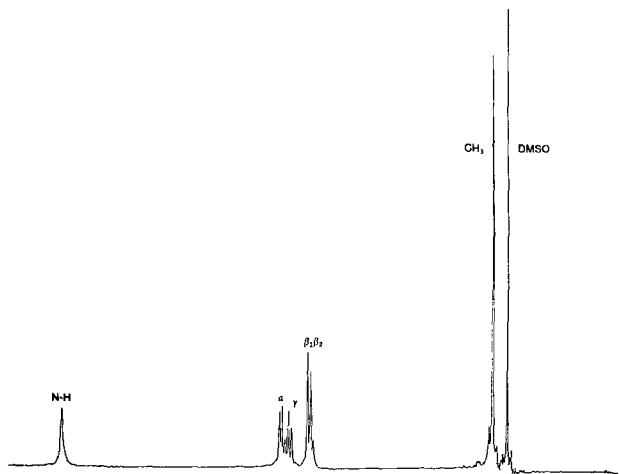


Fig. 3. The HNMR spectrum of 2-mepyr/HCl relative to DMSO at 100°C .

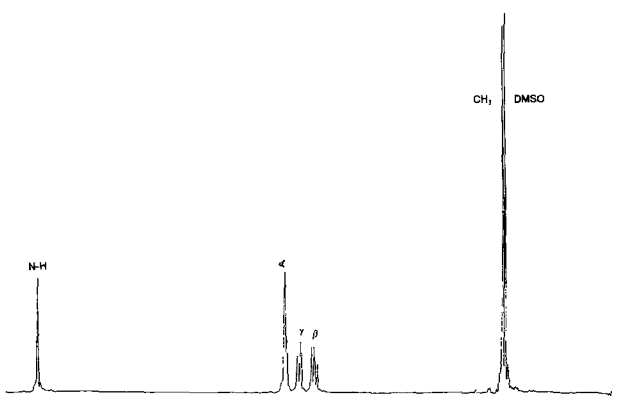


Fig. 4. The HNMR spectrum of 3-mepyr/HCl relative to DMSO at 100°C .

tra of 2-mepyr/HCl and 3-mepyr/HCl, respectively, at 100°C relative to DMSO. There was no discernable peak narrowing or chemical shift change as a function of temperature greater than 0.02 ppm in any of the melts so only one spectrum of each cation need be shown.

Table I lists the chemical shifts, δ , for the several asymmetric methylpyridinium salts studied, relative to a standard of DMSO. Table II lists the δ 's for the symmetric methylpyridinium salts relative to an external standard of $(\text{CH}_3)_2\text{SO}_2$. The $(\text{CH}_3)_2\text{SO}_2$ peak is 0.45 ppm downfield from DMSO. Table III lists the densities of the asymmetrical melts.

Figure 5 is a graph of $\ln \eta$ vs. T^{-1} for the four asymmetric salt melts and it should be noted that there is a slight, but distinct, curvature in the plots. Figure 6 shows the $\ln \eta$ vs T^{-1} behavior of the symmetric melts and here the graphs are linear over the temperature

Table I. The proton chemical shifts of the asymmetric pyridinium halides relative to DMSO

| Salt | -CH ₃ | α | γ | β | N-H |
|-------------|------------------|----------|----------|---------|-------|
| 2-mepyr/HCl | 0.42 | 6.43 | 5.58 | 6.21 | 13.62 |
| 2-mepyr/HBr | 0.63 | 6.51 | 5.76 | 6.43 | 13.28 |
| 3-mepyr/HCl | 0.09 | 6.54 | 5.68 | 6.15 | 13.87 |
| 3-mepyr/HBr | 0.28 | 6.71 | 5.90 | 6.34 | 13.30 |

Table II. Proton chemical shifts, δ , of 4-methylpyridinium halides in ppm relative to an external standard of $\text{CH}_3\text{SO}_2\text{CH}_3$

| Melt | α | β | CH ₃ | N-H | $\Delta(\text{H} - \alpha)$ | $\Delta(\alpha - \beta)$ |
|------------|----------|---------|-----------------|-------|-----------------------------|--------------------------|
| 4-mepyr Cl | 6.25 | 5.28 | -0.18 | 13.68 | 7.43 | 0.97 |
| 4-mepyr Br | 6.42 | 5.44 | 0.03 | 12.66 | 6.24 | 0.98 |
| 4-mepyr I | 6.62 | 5.67 | 0.19 | 11.66 | 5.04 | 0.95 |

Table III. Density of asymmetric pyridinium salts as a function of temperature ρ (g/cm^3) = $a + bT(\text{K})$

| Salt | a | $-(b \times 10^3)$ | Temperature range (K) |
|-------------|-------|--------------------|-----------------------|
| 2-mepyr/HCl | 1.334 | 0.5657 | 363-408 |
| 2-mepyr/HBr | 1.711 | 0.7279 | 350-395 |
| 3-mepyr/HCl | 1.329 | 0.5525 | 374-419 |
| 3-mepyr/HBr | 1.690 | 0.6890 | 370-415 |

range studied. Figure 7 shows $\ln \Lambda$ vs. T^{-1} for the four methylchlorides while Fig. 8 is a plot of $\ln \Lambda$ vs. T^{-1} for the four methyl bromide isomers. It is obvious from Fig. 7 that N-mepyr/Cl is a much better conductor than the 4-methyl salt and that this unexpected phenomenon first observed in the bromide melts is even more pronounced in the chloride melts.

Discussion

To validly compare properties of one melt with those of another, the melts must be in the same state. In order to ensure they are in the same state, a reference state must be agreed upon. Historically, most authors, including us, have used the salt's normal melting point, T_M , as the reference state and compared properties at a convenient multiple of T_M . This is tantamount to saying that each salt is in the same state if it is the same relative distance into its liquid range on a p vs. T plane. This, of course, assumes that the start of the liquid range is T_M , but recent evidence has called this assumption into question, especially for complicated salts like the methylpyridinium halides (10).

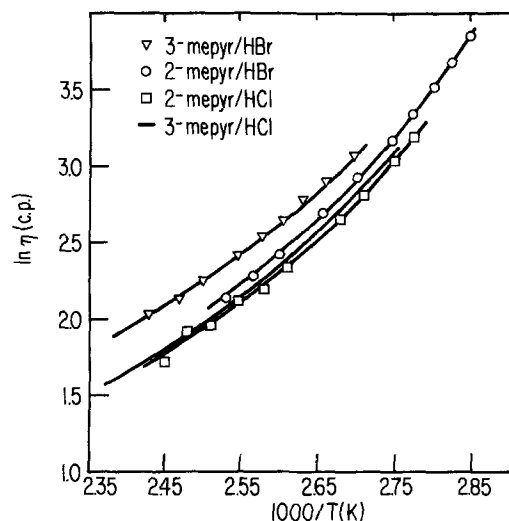


Fig. 5. Log of the viscosity (in cp) vs. $1000/T$ for each of the asymmetric methylpyridinium halides.

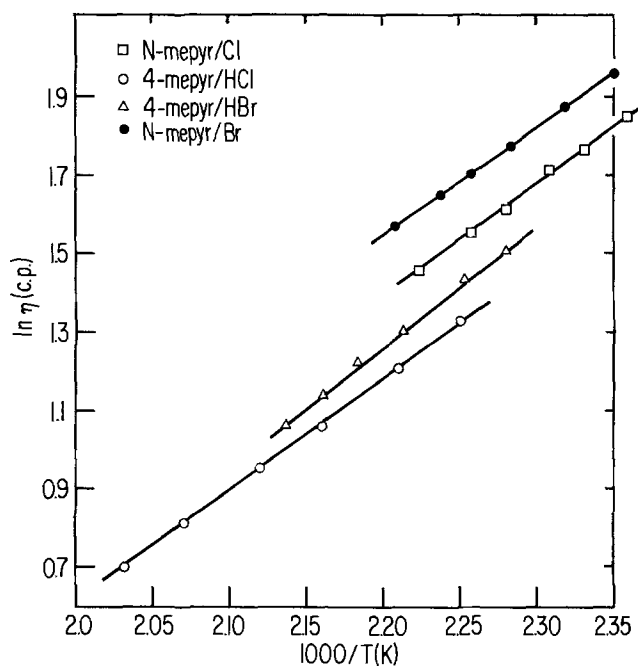


Fig. 6. Log of the viscosity (in cp) vs. $1000/T$ for each of the symmetric methylpyridinium halides.

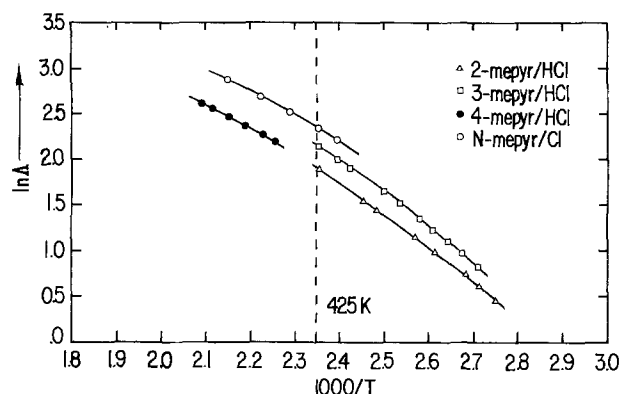


Fig. 7. Log of the equivalent conductance vs. $1000/T$ for the four methylpyridinium chlorides.

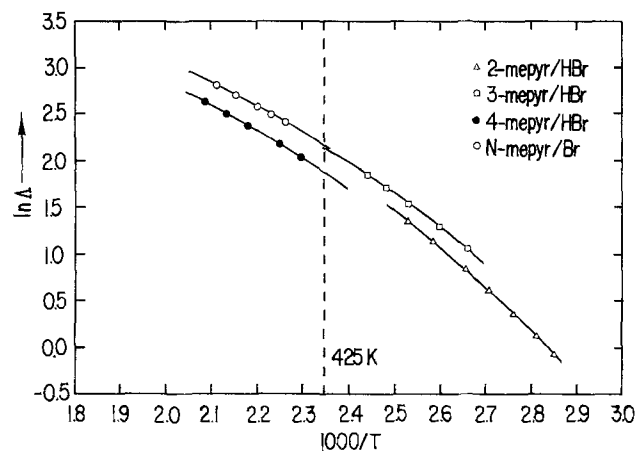


Fig. 8. Log of the equivalent conductance vs. $1000/T$ for the four methylpyridinium bromides.

For these systems, a more appropriate standard state is either the boiling point, T_b , or the glass transition temperature, T_g . Since we do not know the T_g 's for our salts and many of them dissociate before they boil, we have selected a "common temperature" of 425 K as the reference state.

Table IV lists viscosities, densities, equivalent conductances, and Walden products of the eight salts at 425 K. This choice of reference implies that all of the compounds have the same liquid range and, *mutatis mutandis*, that T_g is a more reliable approximation to the start of the liquid state than is T_M .

Enough evidence from measurements of the liquid ranges of disubstituted benzenes exists to support our choice of reference state. To site one example, the *o*-, *m*-, and *p*-fluorotoluenes boil at 388, 387, and 385 K, respectively, have T_g 's of 120, 122, and 123 K, respectively, but have T_M 's of 211, 185, and 216 K, respectively (10).

Evidence for the existence of complex species.—Comparing the equivalent conductance of an N-methyl salt with the equivalent conductance of the corresponding 4-methyl salt, over the entire temperature range, indicates that the N-methyl salt is the better conductor. Because isomers are being compared, and the N-methyl melts are slightly more dense than the 4-methyl melts, suggesting motion is relatively more restricted, the most plausible explanation for this difference in Λ is that there are fewer charge carriers per unit volume in the 4-methyl salts than in the corresponding N-methyl salts because complex species are present. The alternative explanation, that there are the same number of charge carriers per unit volume, but they move slower, is still possible, but based on the spectroscopic data and observed viscosities is far less likely. The formation of a complex almost certainly involves hydrogen bonding between the nitrogenic proton and the halide ion, which means we should obtain further evidence for the existence of a complex from the ^1H NMR spectra of the three 4-methylpyridinium ions (Fig. 2 and Table II). In these melts the ring and methyl protons are deshielded more by the I^- than by Br^- , and more by Br^- than by Cl^- , so that there is actually a sign reversal of δ for CH_3 relative to the dimethylsulfone external standard. On the contrary, the nitrogenic proton is deshielded more by the Cl^- than by the Br^- and more by the Br^- than the I^- . This dramatic change in chemical shift order correlates very well with the conductivity data and is compelling evidence for believing that the N-H^+ forms a stronger hydrogen bond with Cl^- than it does with Br^- . It probably does not hydrogen bond to I^- at all (5). In an isolated methylpyridinium ion, the proton is well shielded by the nitrogen's lone pair of electrons, presumably located in an sp^2 orbital. The halide ion strongly attracts this proton, partially dislodging it from the protection of its shielding electrons, and causes it to resonate at a lower frequency. This phenomenon is more pronounced in the Cl^- melts than in the Br^- melts due to the larger charge to volume ratio in Cl^- than in Br^- . This same trend is present in the asymmetric chlorides and bromides as well. The reasons why the ring protons respond to the halide differently are still not perfectly clear, but it is very likely that hydrogen bonding is not the major factor. Probably exigencies of packing are responsible for the observed chemical

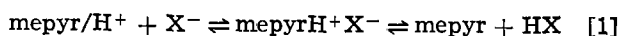
Table IV. Transport properties, densities, and Walden products of the four isomers of methylpyridinium chloride and the four isomers of methylpyridinium bromide at 425 K

| Isomer | Λ ($\text{cm}^2(\Omega \text{equiv.})^{-1}$) | η (cp) | ρ (g/cm^3) | $\Lambda\eta$ |
|-------------|--|-------------|-----------------------------------|---------------|
| 2-mepyr/HCl | 6.68 | 3.90 | 1.093 | 26.1 |
| 3-mepyr/HCl | 8.58 | 3.87 | 1.094 | 33.2 |
| 4-mepyr/HCl | 6.61 | 5.06 | 1.094 | 33.5 |
| N-mepyr/Cl | 10.5 | 6.24 | 1.137 | 65.5 |
| 2-mepyr/HBr | 7.76 | 4.78 | 1.401 | 37.1 |
| 3-mepyr/HBr | 8.41 | 6.65 | 1.397 | 55.9 |
| 4-mepyr/HBr | 6.55 | 5.41 | 1.405 | 35.4 |
| N-mepyr/Br | 9.00 | 7.27 | 1.445 | 65.4 |

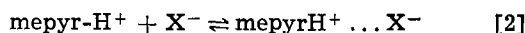
shifts. The crystal structure of pyridinium iodide indicates the I^- is sandwiched between the π clouds of two pyridinium rings (11) and it is not unlikely that this sort of structure would tend to persist in molten 4-mepyr/HI. On the other hand, the Cl^- ion, by virtue of its strong tendency to form hydrogen bonds with the nitrogenic proton, will reside much of the time at the $N-H^+$ end of the molecule, as it does in solid pyridinium/HCl (12). The Br^- will occupy an intermediate position, on the average. This means the I^- ion perturbs the pyridine ring current more than the Br^- and the Br^- perturbs it more than the Cl^- . The ring current, which diamagnetically shields protons, will be least effective in the iodide, next least effective in the Br^- melts, and most effective in the Cl^- melts at shielding protons on neighboring molecules; hence the observed order of deshielding of the ring protons and CH_3 groups (13). These phenomena taken together, account for the observed chemical shifts in a qualitative way and when correlated with the conductivity data yield fairly decent evidence for the existence of some sort of complex species in these melts.

The $N-H^+$ contribution to the conductivity.—Before discussing the nature of the complex, we comment on the protonic contribution to the conductivity. It is obvious that the 2- and 3-methylpyridinium chlorides have about the same viscosities, but the 3-methyl salt's equivalent conductance is 22% greater. The most likely reason for this, since the molecular dimensions, densities, and molecular geometry are so similar, is that there is a greater protonic contribution to the conductivity of the 3-methyl salt, than to the conductivity of the 2-methyl salt (3, 4, 14). The 3-methylpyridine is less basic than the 2-methylpyridine (15), so its proton is held less tightly and can make a greater contribution to the conductivity. The $-CH_3$ group at the 2 position of the ring would also interfere with facile proton transfer (or complex formation for that matter) thus further reducing the proton's contribution to the 2-methyl salt's conductivity. A similar protonic contribution is probably occurring in the bromide melts, as well, though here it seems less pronounced. At this point it is unclear if an actual Grotthuss mechanism occurs (Fig. 9b), in which there is a transfer of charge or virtual movement without an actual proton diffusion, or a hopping mechanism occurs, in which a given proton hops from site to site, and during one of its excursions reaches an electrode. Nevertheless, there is almost certainly some protonic contribution to the conductance and this contribution seems to be greater in the chloride melts than in the bromide melts.

The nature of the complex species and equilibria in the melts.—The spectroscopic and conductivity data suggest that in melts containing $N-H^+$, an equilibrium of the sort



is present with the proton oscillating within its double minimum potential well. This sort of equilibrium has been suggested by Shuppert and Angell to exist in pyridinium HCl melts (4). Since neither spectral measurements nor chemical analysis has turned up any evidence of free methylpyridine or HX, we think these species are present in very low concentration and consequently the principal equilibrium is simply



A rough estimate of the association constant, K_A , for $4\text{-mepyr}H^+ \dots X^-$ can be made using the following line of reasoning. If there were no complex formation in the 4-methyl melts, their conductivities would be similar to those of the corresponding N-methyl melts because the respective molecular sizes, densities, and

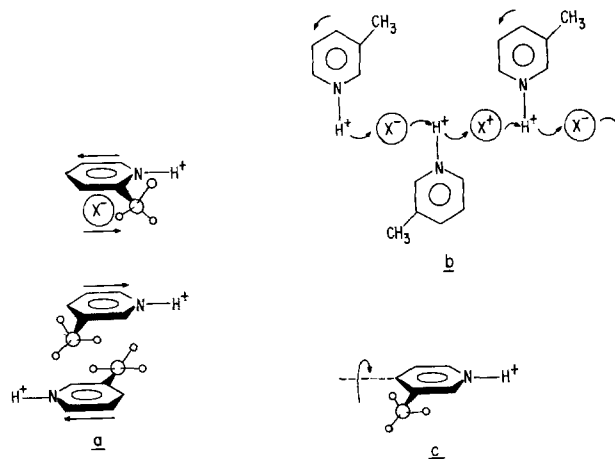


Fig. 9. Contributions to molecular motion in methylpyridinium melts. a, Methyl groups interfering with each other as ions pass each other (in plane); b, possible Grotthuss mechanism; c, out of plane rotation about the C...N axis.

symmetries are similar. We therefore assume that to a first approximation the measured Λ 's for the N-methyl salts are the Λ 's the corresponding 4-methyl salts would have if they were completely dissociated. We next attribute the lower conductance of the 4-methyl salts to formation of the complex species described by Eq. [2]. The degree of dissociation can be approximated, as it is in the case of weak electrolyte solutions, by the Arrhenius notion.

$$\alpha \approx (\Lambda_{4\text{-meth}}/\Lambda_{N\text{-meth}})_{425\text{ K}} \quad [3]$$

K_A is then given by the expression

$$K_A = \frac{[4\text{-mepyr}H^+ \dots X^-]}{[4\text{-mepyr}\cdot H^+][X^-]} = \frac{1 - \alpha}{c\alpha^2} \quad [4]$$

where c is the average concentration in moles per liter at 425 K. It is possible to further correct the $\Lambda_{4\text{-meth}}$ for protonic contribution by assuming this protonic contribution is roughly the same as it is in the 3-methyl melt. The protonic contribution to the 3-methyl melt's conductance is estimated in the following manner. If the difference in conductivity between the 3-mepyr melts and the corresponding 2-mepyr salts is mostly due to the protonic contribution, and if this contribution is negligible in the 2-methyl salts for the reasons mentioned earlier, then at T_c the protons contribute $1.90 (\Omega \text{ equiv.})^{-1} \text{ cm}^2$ to the 3-mepyr/HCl conductance and $0.65 (\Omega \text{ equiv.})^{-1} \text{ cm}^2$ to the 3-mepyr/HBr conductance. Subtracting these values from the appropriate $\Lambda_{4\text{-meth}}$'s gives a corrected conductance $\Lambda'_{4\text{-meth}}$ which contains only contributions from the methylpyridinium ion and the halide ion. The value of Λ' for the chloride is $4.71 \text{ cm}^2 (\Omega \text{ equiv.})^{-1}$ and for the bromide it is $5.90 \text{ cm}^2 (\Omega \text{ equiv.})^{-1}$. Values for K_A , α , and ΔG , the free energy of complex formation, are listed in Table V.

Although the method for estimating the K_A 's is somewhat convoluted, the values obtained give at least correct order of magnitude association constants. The greater basicity of the 4-methylpyridine than the 3-methylpyridine almost certainly reduces the protonic contribution to the 4-methyl melt's conductivity, but this is compensated for because if there

Table V. Association constants for 4-mepyr/HCl and 4-mepyr/HBr

| Salt | α | K_A | ΔG (kJ/mol) |
|-------------|----------|-----------------------|------------------------|
| 4-mepyr/HCl | 0.448 | 3.81×10^{-2} | 3.4 |
| 4-mepyr/HBr | 0.655 | 9.9×10^{-3} | 8.2 |

were no labile protons and no hydrogen bonding the conductance of the 4-methyl salt should be a bit higher than that of the N-methyl salt (which serves as the Δ_0 in the Arrhenius equation) because of lower density. Moreover, the K_A of the Br^- melt is smaller than that of the Cl^- melt, as is expected based on the differences in charge density of the halide. These K_A 's represent a significant complex ion contribution to the structure of the 4-methyl chloride and bromide melts and certainly will influence transport properties.

Comparison between asymmetric and symmetric salts.—The most obvious difference between the symmetric and asymmetric isomers of a given salt is the melting point; the symmetric salts melting considerably higher than the corresponding asymmetric salts (this difference also persists in the iodide melts) (16). A second difference is that the $\ln \eta$ vs. T^{-1} graphs for the asymmetric salts exhibit some curvature while the $\ln \eta$ vs. T^{-1} graphs for the symmetric melts are linear.

In contrast to these differences, both symmetric and asymmetric salts of a particular halide ion have similar viscosities at a common temperature. For example, at the standard temperature, 425 K, which is just above the high temperature end of the asymmetrical salt's liquid range, and just below the symmetrical salts' melting point, 4-mepyr/HCl has an extrapolated η of about 4.5 cp whereas the 2- and 3-mepyr/HCl have η 's equal to about 4.6 cp. The conductivities of the salts are also relatively unaffected by symmetry *per se*. For instance, the conductances of 2- and 4-methylpyridinium chloride lie on essentially the same curve. Taking these data in the aggregate, we conclude that symmetry, *per se*, has relatively little effect on transport properties or spectral properties, but manifests itself mainly through differences in observed melting points and protonic contributions to the melt's conductivity. Far and away, a more significant factor in determining relative values of transport properties is the presence or absence of hydrogen bonding. This conclusion is in sharp contrast to one reached earlier (8, 9) where we suggested symmetry, rather than H-bonding, was the most important factor in determining transport properties in pyridinium melts. Our earlier conclusion was arrived at using a melting point reference state, and the difference between the two conclusions dramatically illustrates the importance of the particular reference state used.

The role of hydrogen bonding.—We can now assemble the diverse results of our experiments into a fairly coherent pattern and assess the contribution of hydrogen bonding to structure and to ionic motion.

The equivalent conductance of the symmetrical chloride and bromide melts decreases 37% and 27%, respectively, when the methyl group is moved from the nitrogen to the 4 position of the ring. At the same time η decreases 19% and 25%, respectively. The only plausible explanation for these results is the one we suggested earlier and that is that complex formation reduces the number of charge carriers per unit volume thereby lowering the conductivity. These same complexes reduce the melt's viscosity by, in effect, lowering interionic friction and shortening the length of the hydrogen-bonded species along the $\text{C}_4\text{-N-H}^+\text{-X}^-$ axis relative to the separated ions (17, 18). Therefore, the H-bonded salts are poorer conductors, but less viscous than the N-methyl melts.

Undoubtedly, additional factors are also contributing to the differences in transport properties between the two types of melt. For example, within the time frame of diffusional motion, the N-methyl melt may still have vestiges of its crystal structure in which the halide ion is above and to one side of the ring (as it is

in the N-mepyr/I crystal (19). This fluctuating asymmetry will increase the interionic friction due to one melt layer interfering with another and consequently increase the viscosity relative to the hydrogen bonded melts. However, these factors are difficult to isolate and seem much less important than hydrogen bonding itself.

We think the fact that the corresponding N-H⁺ containing chlorides and bromides have such similar Δ 's is one more indication of the importance of hydrogen bonding. The Cl^- ion forms stronger hydrogen bonds than the Br^- ion, and consequently has its mobility considerably reduced. What might be considered "normal" behavior is exhibited by the N-methyl salts, in which there is a 14% decrease in Δ between the Cl^- and the Br^- melts and a 13% decrease between the Br^- and I^- melts (2, 16).

Details of ionic motion and melt structure.—The principal charge carrier in all of the pyridinium melts studied is the halide ion. This is consistent with our earlier results and those of King and co-workers (20, 14, 2). Attractive forces and steric factors dominate, hence the relatively low ratio of about 1.1 for E_η to E_Δ and the likely, very little if any, expansion upon melting. Bloom and Reinsborough (21) found Pyr/HCl expands only 2% on melting and preliminary results in our laboratory indicate 3-methylpyridinium chloride actually contracts when it melts. This should be contrasted with typical inorganic salts which expand 15-25% on melting and have E_η/E_Δ ratios of between 2 and 5 (22, 23).

It is difficult to identify particular modes of motion that are favored over others because there is no special difference between symmetrical and asymmetrical salts with regard to their transport properties and relatively little difference between viscosity and conductivity with regard to energies of activation. The best one can say is it looks as if inplane rotation, or rocking back and forth about an axis perpendicular to the plane of the molecule, may be favored over out of plane rotation (Fig. 9c). In other words, the cations translate as rotating or rocking weighted disks rather than rotating weighted cylinders. The reason for arriving at this conclusion is that all of the cations sweep out about the same area, but the asymmetric cations sweep out considerably larger cylindrical volumes, rotating out of plane (9c), than do the symmetric cations. Since the asymmetric ions require greater volumes, and space is at a premium, they should have higher viscosities and higher energies of activation. This is contrary to our experimental results. Because the planar area of the disklike cation is considerably greater than half the area of an edge, and because only one end is charged, the ion is prevented from freely rotating. Consequently it is unlikely that the cations are translating as rotating spheres as are the halide ions.

The E_η/E_Δ ratio of ~ 1.1 further implies that viscosity and conductivity meet with the same sort of barriers. (24). Ions are moving past each other, Fig. 9a, and it matters little whether two cations pass each other or a cation and anion pass each other, the energies required are quite similar.

Errors and comparison with other workers.—Comparing our proton chemical shifts in the 2-mepyr/HCl melt with the chemical shifts in the same melt reported by Angell and Shuppert (25) we agree within experimental error on the location of the α , β , γ , and methyl peaks, but differ by -0.85 ppm on the N-H⁺ chemical shift, ours being 16.2 ppm and theirs being 17.05 corrected to TMS. One possible reason for this discrepancy is that a trace of water may still be present in our melts, but not in theirs. This water molecule would tend to lie on, or near, the N-H⁺ and shield it

from the magnetic field. On the other hand, they used an internal standard of $(\text{CH}_3)_4\text{NCl}$ which exchanges with H^+ and with other CH_3^+ groups (25), but also increases the Cl^- concentration which would deshield the N-H^+ proton and cause it to resonate at lower frequencies. There does not seem to be any other melt spectra in the literature to compare our data with. Our melting point of 89°C for 2-methylpyridinium chloride is identical to the one reported by Angell, Hodge, and Cheeseman for the same compound and our specific conductances are within $\pm 2\%$ of theirs (3). Our conductivity data for the N-mepyr/Cl is within $\pm 2\%$ of the values reported by King and co-workers (20).

Overall, we estimate our equivalent conductance data to be correct to $\pm 2\%$ and our viscosity data to be accurate to $\pm 3\%$. Our analyses of the pyridinium salts were in all cases $99\pm\%$.

Perhaps the largest error in this study is the assumption that all the melts have the same liquid range, but since no conclusion depends on an exact knowledge of T_g or T_b , this error should not seriously affect our conclusions.

Conclusion

By systematically varying the structure of the methylpyridinium cation and changing the anion, correlations between structure, spectra, and transport properties in molten pyridinium salts can be made in a relatively simple and straightforward manner. From these correlations, several conclusions can be reached about the structure of the melt and its relation to transport properties. The conclusions drawn are the following:

1. Hydrogen bonding exerts a strong influence on transport properties, species present, and melt structure.
2. Symmetry of the cation, *per se*, has little influence on either melt structure or transport properties.
3. The anion is the principal charge carrier in the methylpyridinium melts.
4. There are complex species in the 2-, 3-, and 4-methylpyridinium chloride and bromides.
5. There is probably a protonic contribution to the conductivity of those melts in which the N-H^+ is present. The protons move either through a Grotthuss mechanism or through a hopping mechanism.
6. In the molten pyridinium halides, and probably in molten organic salts generally, attractive forces dominate over repulsive forces, and there is very little free space, hence the E_η/E_A ratio of 1.1.

Acknowledgment

The authors wish to thank C. Austen Angell for his helpful discussions.

Manuscript submitted Aug. 25, 1980; revised manuscript received ca. May 12, 1981. This was Papers 331 and 332 presented at the Pittsburgh, Pennsylvania, Meeting of the Society, Oct. 15-20, 1978.

Any discussion of this paper will appear in a Discussion Section to be published in the June 1982 JOURNAL.

All discussions for the June 1982 Discussion Section should be submitted by Feb. 1, 1982.

Publication costs of this article were assisted by Bowling Green State University.

REFERENCES

1. D. S. Newman, R. Winans, and R. L. McBeth, Paper 660 presented at The Electrochemical Society Meeting, Hollywood, Florida, Oct. 5-10, 1980.
2. D. S. Newman, R. T. Tillack, D. P. Morgan, and W. C. Wan, *This Journal*, **124**, 856 (1977).
3. C. A. Angell, I. M. Hodge, and P. A. Cheeseman, in "International Symposium on Molten Salts," J. P. Pemsler, J. Braunstein, K. Nobe, D. R. Morris, and N. E. Richards, Editors, p. 139, The Electrochemical Society Softbound Proceedings Series, Princeton, NJ (1976).
4. J. W. Shuppert and C. A. Angell, *J. Chem. Phys.*, **67**, 3050 (1977).
5. N. Goldstein and J. L. Ragle, *ibid.*, **70**, 5072 (1979).
6. M. S. Rozhdestvenskii and L. M. Brode, *J. Appl. Chem. USSR*, **10**, 722 (1937).
7. D. S. Newman, D. P. Morgan, and R. T. Tillack, *J. Chem. Eng. Data*, **21**, 279 (1976).
8. D. S. Newman and O. A. Banjoko, Paper 332 presented at The Electrochemical Society Meeting, Pittsburgh, Pennsylvania, Oct. 15-20, 1978.
9. D. S. Newman, R. R. Rhinebarger, and D. Siconolfi, Paper 331 presented at The Electrochemical Society Meeting, Pittsburgh, Pennsylvania, Oct. 15-20, 1978.
10. J. Wong and C. A. Angell, "Glass-Structure by Spectroscopy," Chap. 1, Marcel Dekker, Inc., New York (1976).
11. H. Hart, *Acta Crystallogr.*, **31**, 178 (1975).
12. C. Rerat, *ibid.*, **15**, 427 (1962).
13. J. Robinson, R. C. Dugle, H. L. Chum, D. Koran, and R. A. Osteryoung, *J. Am. Chem. Soc.*, **101**, 3776 (1979).
14. D. S. Newman, W. Rohr, D. Kirklín, and H. D. Frame, *This Journal*, **119**, 797 (1972).
15. A. Albert and E. P. Serjeant, "Ionization Constants of Acids and Bases," p. 145, Methuen and Co., Ltd., London (1962).
16. D. S. Newman and R. M. Stevens, in "Third International Symposium on Molten Salts," G. Mammantov, Editor, The Electrochemical Society Softbound Proceedings Series, Princeton, NJ (1981).
17. J. Gordon, "The Organic Chemistry of Electrolyte Solutions," p. 400, John Wiley & Sons, Inc., New York (1975).
18. K. Bauge and J. W. Smith, *J. Chem. Soc. (A)*, 616 (1966).
19. R. A. Lalancette, W. Furey, J. N. Costanza, P. R. Hemmes, and F. Jordan, *Acta Crystallogr., Sect. B*, **34**, 2950 (1978).
20. R. A. Carpio, L. A. King, R. E. Linstrom, J. C. Nardi, and C. H. Hussey, *This Journal*, **126**, 1644 (1979).
21. H. Bloom and V. C. Reinsborough, *Aust. J. Chem.*, **21**, 1525 (1968).
22. J. O'M. Bockris and A. K. N. Reddy, "Modern Electrochemistry," Vol. 1, p. 525, Plenum/Rosetta Editions, New York (1973).
23. H. Bloom and E. Heymann, *Proc. R. Soc. London, Ser. A*, **188**, 392 (1947).
24. G. J. Janz, R. D. Reeves, and A. T. Ward, *Nature (London)*, **204**, 1188 (1964).
25. C. A. Angell and J. W. Shuppert, *J. Phys. Chem.*, **84**, 538 (1980).

The Kinetics and Mechanism of the Electroreduction of Sulfur Dioxide in Nonaqueous Media

I. Reduction in Solutions of Tetraethylammonium Perchlorate in N,N-Dimethylformamide

C. L. Gardner* and D. T. Fouchard*

Defence Research Establishment Ottawa, Ottawa, Ontario, Canada K1A 0Z4

and W. R. Fawcett*

The Guelph-Waterloo Centre for Graduate Work in Chemistry (Guelph Campus),
Department of Chemistry, University of Guelph, Guelph, Ontario, Canada N1G 2W1

ABSTRACT

Polarographic studies of the electroreduction of sulfur dioxide in dimethylformamide containing 0.1M tetraethylammonium perchlorate have shown that at 20°C, the mechanism of electroreduction is given by the reactions

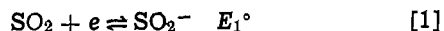


The standard rate constant for the electron transfer reaction [1] has been found to be 1.0 ± 0.2 cm/sec. This rate of electron transfer is very fast, being of the same order of magnitude as that observed for reduction of aromatic hydrocarbons (21). The association constant, K_2 , for reaction [2] has been found to be 8400 ± 2000 dm³ mol⁻¹. This is an order of magnitude larger than the association constant measured in bulk solution using ESR spectroscopy (20). In addition to formation of the complex, S_2O_4^- , the results show that a second follow-on reaction is also important. Evidence is presented that this follow-on reaction is the disproportionation of SO_2^- to form SO and SO_3^{2-} . The equilibrium constant for this reaction has been found to 0.6 ± 0.4 . The dimerization of SO_2^- to form dithionite is not important during the initial stages of reduction at room temperature and over the range of SO_2 concentration (1×10^{-4} – 5×10^{-3}) used in these experiments. However, at low temperatures, the formation of dithionite is favored.

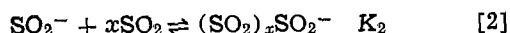
In recent years considerable effort has gone into the development and commercialization of the lithium-sulfur dioxide battery. While these efforts have resulted in successful exploitation of this battery system, there remain a number of environmental (1) and safety (2) problems to be solved.

By contrast, work reported on the basic chemistry and electrochemistry of the reduction of sulfur dioxide has been limited. While it is generally agreed that the major product formed during the discharge of the lithium-sulfur dioxide battery is lithium dithionite, previous work has indicated that the reduction mechanism is influenced by the choice of solvent and electrolyte.

It is generally agreed that the initial one-electron transfer step



is followed by one or more follow-on reactions. In N,N-dimethylformamide (DMF), a stable, blue paramagnetic product is formed (3-7) which has been ascribed to a complex of the form

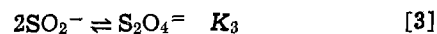


The number, x , of neutral SO_2 molecules in the complex has been the subject of some controversy. Thus,

* Electrochemical Society Active Member.
Key words: high energy density batteries.

Dinse and Mobius (5) concluded that $x = 2$ by measuring the ratio of the concentrations of $(\text{SO}_2)_x\text{SO}_2^-$ and SO_2^- using ESR spectroscopy. On the other hand, Rinker and Lynn (4) concluded that $x = 1$. The recent work of Kastening and Gostisa-Mihelcic (6) which was based on ESR measurement of the $[(\text{SO}_2)_x\text{SO}_2^-]/[\text{SO}_2^-]$ ratio coupled with direct electrochemical measurement of the SO_2 concentration has shown that the complex has the stoichiometry S_2O_4^- (i.e., $x = 1$). This is also in agreement with kinetic measurements made by the same authors (8). K_2 was determined to be 230 dm³ mol⁻¹ at 25°C. The larger value of $x = 2$ obtained by Dinse and Mobius appears to be the result of their failing to correct for the change in the bulk SO_2 concentrations after electrolysis. However, since details of the experiments are not given in their paper this cannot be confirmed.

In addition to the formation of the complex species, S_2O_4^- , dimerization of the SO_2^- to form dithionite has also been shown to be important (9)



Reaction [3] is the major follow-on reaction in dimethylsulfoxide solution, the value of K_3 being 10⁵ dm³ mol⁻¹ at 55°C.

In view of the potential importance of studies of the basic electrochemistry and chemistry of the reduction process in helping to resolve some of the remaining

problems of the primary lithium-sulfur dioxide battery and in indicating directions for further improvement of the system (e.g., the development of a rechargeable Li/SO₂ battery), we have recently undertaken a systematic study of the effect of solution composition on the kinetics and mechanism of the electroreduction of sulfur dioxide in nonaqueous media. In this paper, we describe results that we have obtained for the electroreduction of SO₂ in solutions of 0.1M tetraethylammonium perchlorate (TEAP) in DMF. Additional work on the effect of solvent and electrolyte on the kinetics and mechanism of the electroreduction of SO₂ will be described in another paper as will results of simultaneous electrochemical-electron spin resonance measurements.

Experimental

Current-potential data were obtained using a PAR Model 170 Electrochemistry System. All measurements were made in a jacketed 3-electrode glass cell. The working electrode was normally a dropping mercury electrode except in the cyclic voltammetric experiments where a hanging mercury drop electrode was used. The counterelectrode was a platinum cylinder and the reference electrode a silver wire in a solution of 0.05M AgNO₃ and 0.05M TEAP in DMF. This solution was changed daily because of photoreduction of the Ag⁺. The solution in the reference electrode compartment was isolated from the working solution by fritted glass disks.

Kinetic data for the electron transfer process were obtained using the phase sensitive a-c admittance method described previously (10). Admittance data were obtained as a function of d-c potential in the vicinity of the d-c half-wave potential over the frequency range from 160 to 1050 Hz using a 10 mV (peak-to-peak) a-c signal. Pulse polarographic measurements were also made for many of the systems. In these experiments, a potential pulse is applied for 45 msec at the end of the drop life, the average current being measured during the final 5 msec.

The procedures followed for purifying and drying the DMF (Aldrich Spectrophotometric grade) and TEAP (Eastman) have been described previously (10-12). Anhydrous SO₂ was used as received from Matheson. A stock SO₂ solution was prepared by bubbling SO₂ in DMF. The concentration of the stock SO₂ solution (~0.5M) was determined by titration. All solvents, salts, and stock solutions were stored in a controlled atmosphere glove box (Vacuum Atmospheres Limited) where the argon atmosphere was continually purged of oxygen and water. Further dilution of the stock SO₂ solution to prepare the working solutions (0.1-5 mM) was carried out in the glove box and all solutions were bubbled with argon to remove traces of oxygen. The experiments were conducted in the same glove box. The temperature of the cell was maintained constant by passing methanol, controlled at the desired temperature, through an outer jacket surrounding the working compartment of the cell.

Results

Cyclic voltammetry.—Reduction of sulfur dioxide in a 0.1M TEAP/DMF solution gives a well-defined cyclic voltammogram as shown in Fig. 1. The presence of a follow-on reaction is indicated by the appearance of more than one oxidation peak on the reverse sweep and the ratio of the peak anodic to the peak cathodic currents for the reduction reaction which is less than one (13). These results are in qualitative agreement with those reported earlier by Martin and Sawyer (3).

D-C polarography.—In order to study the reduction process in more detail, d-c polarographic measurements were made as a function of both SO₂ concentration and temperature. These polarograms are broader than is expected for a simple one-electron transfer

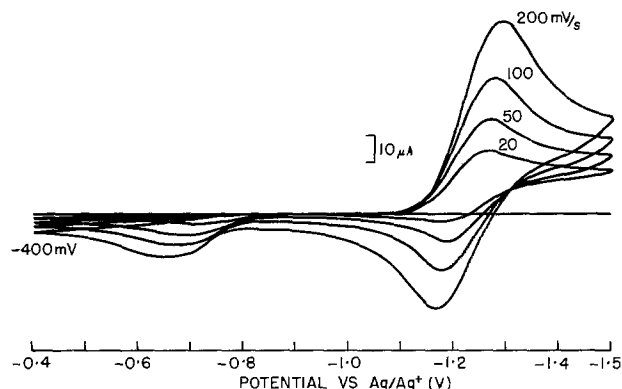


Fig. 1. Cyclic voltammogram for the reduction (forward sweep) of 10⁻²M SO₂ at a hanging mercury drop electrode in N,N-dimethylformamide containing 0.1M tetraethylammonium perchlorate with varying sweep rates as indicated.

reaction, plots of $\log(i/i_d - i)$ having nonlinear slopes greater than 59 mV per decade. In addition, the half-wave potential is dependent both on SO₂ concentration and temperature.

The effect of concentration on the half-wave potential is shown in Fig. 2 and on the plots of $\log(i/i_d - i)$ vs. E in Fig. 3. It is seen that, as the concentration is increased, there is a positive shift of the half-wave potential and a marked increase in the curvature of the $\log(i/i_d - i)$ plots. There is also a linear variation of the limiting current, i_d , with concentration. The half-wave potential and shape of the polarograms were found to be independent of drop time in the range from 1 to 5 sec.

Figure 2 also shows that decreasing the temperature causes a positive shift of the half-wave potential. As one might expect, there is also a marked decrease in the limiting current. The plots of $\log(i/i_d - i)$ vs. E (Fig. 4) show that the polarograms are sharpened as the temperature is decreased.

A-C polarography.—A-C admittance measurements were made on each of the SO₂ solutions in order to measure the rate of electron transfer (10). Above 0°C, the a-c admittance data give good Randle's plots (Fig. 5). At lower temperatures deviation from linearity is observed. Analysis of the a-c data allows (10) both the standard rate constant for the electron transfer reaction and the diffusion coefficient to be determined (see Table I). In calculating these parameters, allowance has been made for the fact that, at the standard electrode potential, E_1° , the SO₂ concentration is less than half the bulk SO₂ concentration as a result of the follow-on reaction. The actual concentration was determined from the d-c polarograms.

The a-c peak potential (as measured from the peak of the out-of-phase component of the a-c admittance) was found to be 20-50 mV negative with respect to the half-wave potentials from d-c polarography and independent of concentration and temperature, having a constant value of -1.30V against the Ag/Ag⁺ reference electrode.

Pulse polarography.—Pulse polarography was used to study the reduction process for times intermediate between those used for the d-c and a-c measurements.

Table I. A-C polarography analysis

| Temp (°C) | k_s (cm sec ⁻¹) | D (cm ² sec ⁻¹) × 10 ⁶ |
|-----------|-------------------------------|--|
| 30 | 1.2 | 8.68 |
| 25 | 1.0 | 6.76 |
| 20 | 0.9 | 5.23 |
| 10 | 0.7 | 3.03 |
| 0 | 0.5 | 1.69 |
| -10 | 0.4 | 0.90 |

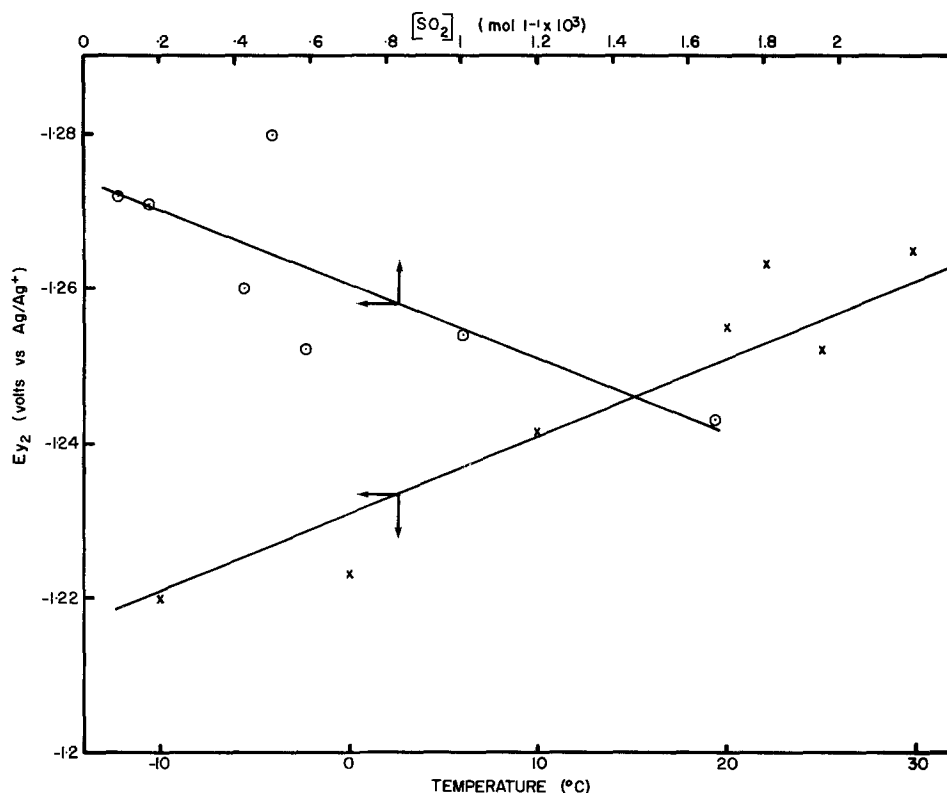


Fig. 2. Effect of reactant concentration and temperature on the half-wave potential for the electroreduction of SO_2 in the same solution as Fig. 1.

More specifically, the current was sampled at the end of a 45 msec pulse. This can be compared with times in the 1-6 msec range used in the a-c measurements and the 2 sec drop time used for most of the d-c measurements. Pulse polarography measurements were made using both cathodic and anodic sweeps.

Pulse polarograms obtained for solutions of SO_2 in 0.1M TEAP/DMF using a negative sweep give half-wave potentials which are negative with respect to the d-c half-wave potentials. In addition, the plots of

$\log (i/i_d - i)$ vs. E (Fig. 6) are more linear and have slopes closer to 59 mV per decade.

When the potential is swept positively from a point on the reduction wave, the pulse polarogram has two distinct waves (Fig. 7): one at -1.3V and one at -0.7V . The relative heights of the two waves depend both on concentration and initial potential. Table II gives the heights of the two waves as a function of initial potential for several different concentrations of SO_2 . At the higher concentrations ($\geq 10^{-3}\text{M}$) a slight

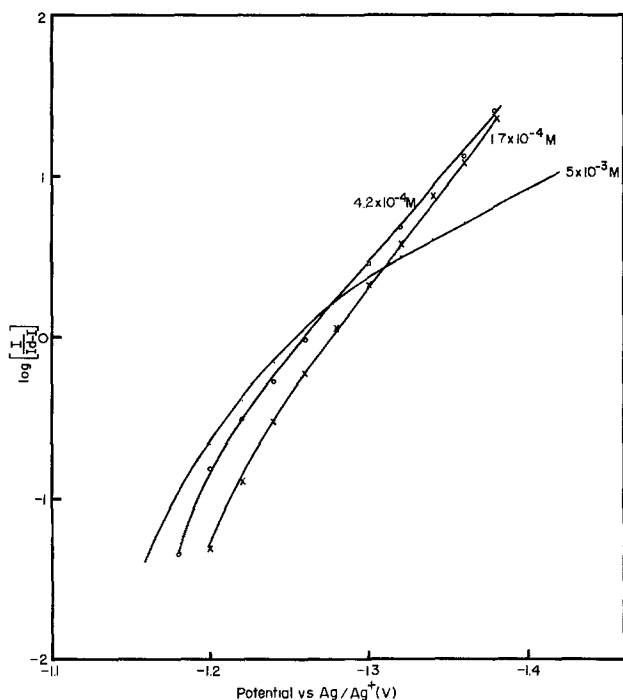


Fig. 3. Plots of $\log [i/i_d - i]$ against electrode potential on the basis of d-c polarographic data for the electroreduction of SO_2 with varying concentration of SO_2 as indicated. Electrolyte as in Fig. 1.

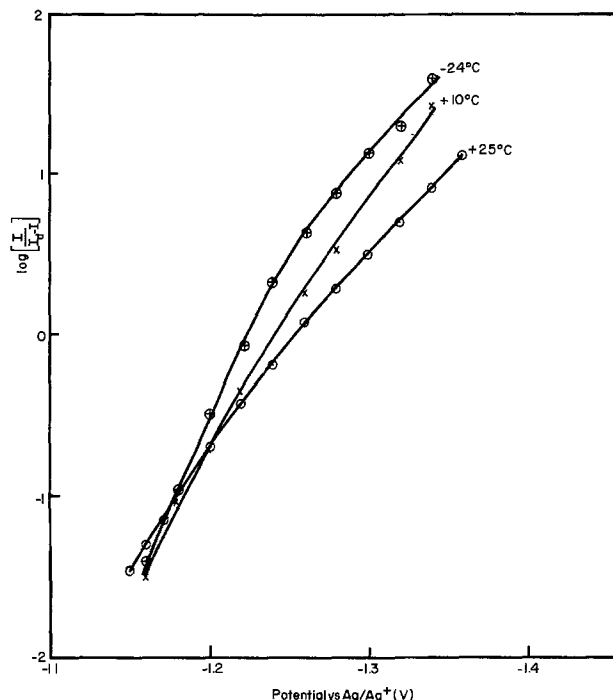


Fig. 4. Plots of $\log [i/i_d - i]$ against electrode potential on the basis of d-c polarographic data for the electroreduction of SO_2 with varying temperature of the electrochemical cell as indicated. Electrolyte as in Fig. 1.

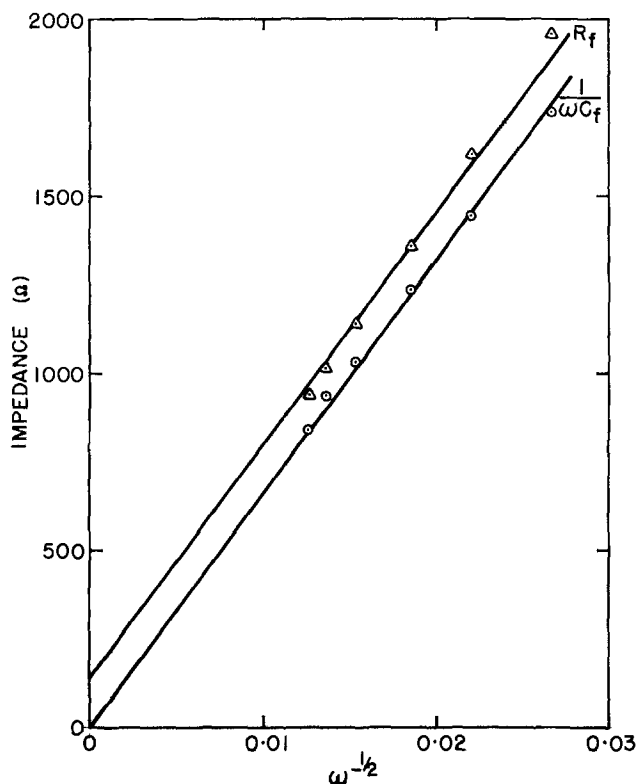


Fig. 5. Randle's plot of a-c admittance data for the electroreduction of 10^{-3}M SO_2 in the same system as Fig. 1.

maximum is observed in the wave at -0.7V suggesting that weak adsorption is taking place (14).

Discussion

As discussed earlier, previous work has shown that the SO_2^- produced in the primary electron transfer step can undergo the two follow-on reactions [2] and [3]. In the discussion that follows, the experimental results are discussed initially in terms of reactions [1] to [3] assuming $x = 1$ (i.e., the complex is assumed to have the stoichiometry S_2O_4^-).

Information regarding the mechanism of the electroreduction of SO_2 in TEAP/DMF solutions can be obtained by comparing the experimental polarograms with theoretical predictions based on the proposed mechanism. In our description of the shape of the d-c polarograms, we assume that reactions [2] and [3] are

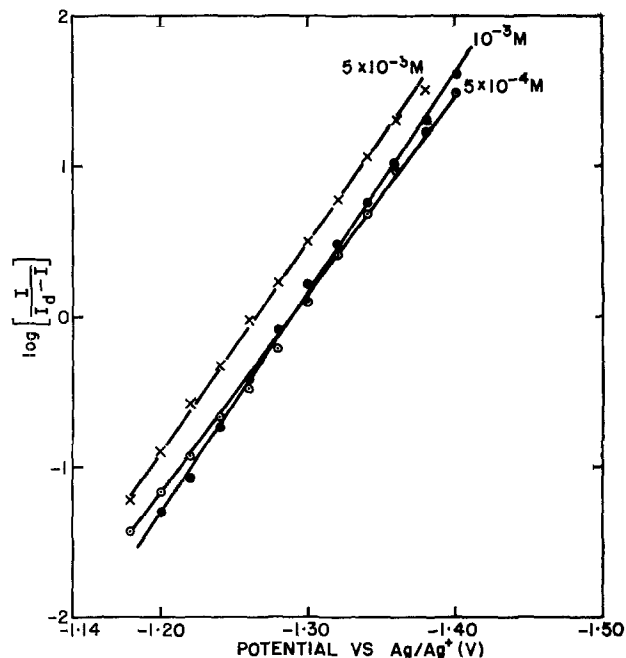


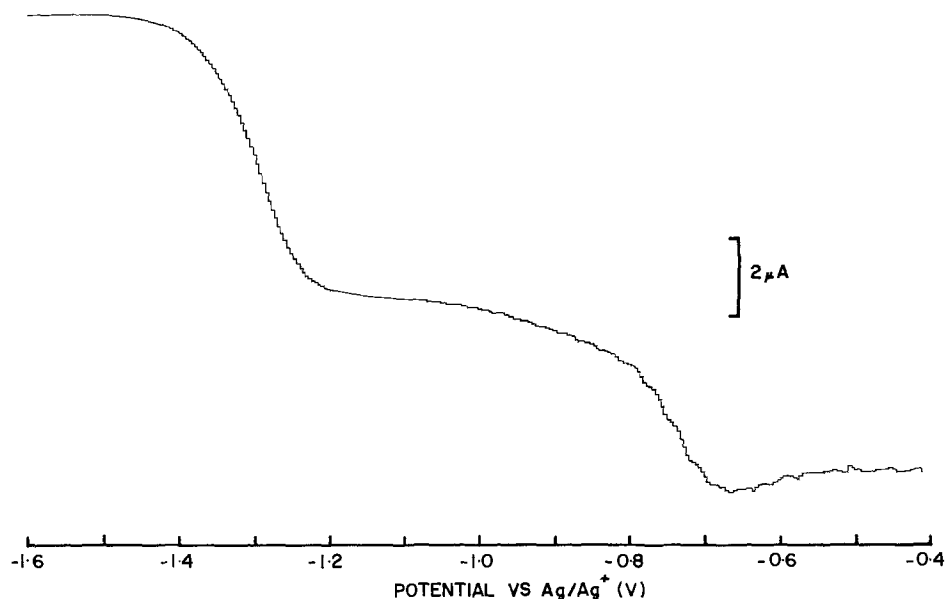
Fig. 6. Plots of $\log [i/i_d - i]$ against potential for pulse polarographic data obtained with varying SO_2 concentrations as indicated. Other conditions as in Fig. 1.

at equilibrium.¹ This assumption is supported by the observation that the measured half-wave potentials are independent of drop time. The present approach differs from that of Bonnetterre and Cauquis (9) who have described their cyclic voltammetric and rotating disk studies of the reduction of SO_2 in dimethylsulfoxide in terms of dimerization of SO_2^- using a reaction layer approximation. If it is assumed that the Nernst and Ilković equations hold, then the following general expression can be derived (see Appendix) which describes the shape of the d-c polarogram

$$E - E_1^\circ = \frac{RT}{F} \ln \left\{ \frac{1}{2} \left(\frac{i_d - i}{i} \right) \left\{ \left(1 + K_2 \left(\frac{i_d - i}{i} \right) \right) + \left[\left(1 + K_2 \left(\frac{i_d - i}{i} \right) \right)^2 + \frac{4K_3 i}{g} \right]^{1/2} \right\} \right\} \quad [4]$$

¹This assumption is not valid on the time scale used for the a-c, pulse polarographic, and cyclic voltammetric measurements.

Fig. 7. Pulse polarogram for the oxidation of the reduction products of a 10^{-3}M SO_2 solution with an initial potential for the positive sweep of -1.6V vs. the reference electrode. Other conditions as in Fig. 1.



where i_d is the limiting current and g the Ilković constant.

It is of interest to consider the simpler situations where either reaction [2] or [3] predominates.

When $K_3 = 0$ (i.e., complex formation is the dominant follow-on reaction), Eq. [4] can be simplified to give

$$E - E_1^\circ = \frac{RT}{F} \ln \left\{ \left(\frac{i_d - i}{i} \right) \left[1 + K_2 \left(\frac{i_d - i}{g} \right) \right] \right\} \quad [5]$$

In this case it can be shown that the follow-on reaction [2] causes a shift of the polarogram to positive potentials and broadens the wave so that plots of $\log(i/i_d - i)$ vs. E have slopes greater than 59 mV per decade.

If, on the other hand, it is assumed that dimerization of SO_2^- according to [3] is the major follow-on reaction (i.e., $K_2 = 0$), then Eq. [4] can be simplified to give

$$E - E_1^\circ = \frac{RT}{F} \ln \left\{ \frac{1}{2} \left(\frac{i_d - i}{i} \right) \left(1 + \sqrt{\frac{4K_3 i}{g}} \right) \right\} \quad [6]$$

In this case, a positive shift of the polarograms is also predicted, but the polarographic waves are sharpened so that slopes of less than 59 mV per decade are obtained from plots of $\log(i/i_d - i)$ vs. E .

It follows that the qualitative behavior of the d-c polarograms (Fig. 3) obtained for the reduction of SO_2 in 0.1M TEAP/DMF solutions at room temperature corresponds to the predictions based on Eq. [5].

The experimental shift of the half-wave potential with respect to the standard potential for the $\text{SO}_2/\text{SO}_2^-$ couple can be compared with theoretical predictions. Thus substituting the relationships that, at the half-wave potential

$$i = \frac{i_d}{2} = \frac{g[\text{SO}_2]^\circ}{2} \quad [7]$$

then, from Eq. [5], the dependence of the half-wave potential on SO_2 concentration can be written

$$E_{1/2} - E_1^\circ = \frac{RT}{F} \ln \left(1 + \frac{K_2[\text{SO}_2]^\circ}{2} \right) \quad [8]$$

Thus, a plot of $\exp((E_{1/2} - E_1^\circ)F/RT)$ against $[\text{SO}_2]^\circ$ should be linear with a slope of $K_2/2$ and unit intercept. A value of $E_1^\circ = -1.30\text{V}$ is obtained^{2,3} from the peak potential of the out-of-phase component of the a-c admittance. Figure 8 shows values of $\exp((E_{1/2} - E_1^\circ)F/RT)$ plotted against $[\text{SO}_2]^\circ$. From the slope, a value of $K_2 = 8400 \pm 2000 \text{ dm}^3 \text{ mol}^{-1}$ is obtained for the association constant for reaction [2]. On the other hand, the intercept is found to be 2.5 ± 0.8 , that is, not unity as predicted by Eq. [8]. The large value of the intercept suggests that some other reaction is contributing to the shift of the half-wave potential.

Some support for this conclusion is obtained from the pulse polarographic experiments. Regarding the two distinct waves observed on the positive sweep, the first at -1.3V is ascribed to the oxidation of SO_2^- . The second wave at -0.7V has been ascribed previously by Martin and Sawyer (3) and ourselves (15) to oxidation of the complex species S_2O_4^- . As mentioned previously, the relative heights of these two waves are dependent on both SO_2 concentration and initial potential (Table II). From these results it is seen that

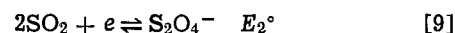
² The assumption is made that the diffusion coefficients for SO_2 and SO_2^- are equal.

³ As discussed later in the paper, on the time scale used for the a-c measurements, the follow-on reaction is sufficiently slow that the reaction can be considered as a simple one-electron transfer reaction. In this case, the peak of the out-of-phase component of the a-c admittance will occur when the surface concentrations of $[\text{SO}_2]$ and $[\text{SO}_2^-]$ are equal. The situation in this case is similar to that described by Fawcett and Lasia (10).

Table II. Pulse polarography—*anodic sweeps*

| $[\text{SO}_2]$ mol dm ⁻³ $\times 10^{-3}$ | Initial potential volts vs. Ag/Ag ⁺ | wave 2 wave 1 |
|---|---|------------------|
| 5.0 | -1.4 | 0.31 |
| 1.67 | -1.6 | 0.54 |
| 1.0 | -1.6 | 0.61 |
| 0.70 | -1.6 | 0.77 |
| 0.58 | -1.6 | 0.56 |
| 0.5 | -1.6 | 0.60 |
| | -1.36 | 0.58 |
| | -1.24 | 1.0 |
| | -1.20 | 1.83 |
| 0.20 | -1.6 | 0.93 |
| 0.167 | -1.6 | 0.79 |
| 0.10 | -1.4 | 1.18 |

the relative intensity of wave 2 with respect to wave 1 decreases with increasing SO_2 concentration instead of increasing linearly with increasing SO_2 concentration as one would anticipate on the basis of S_2O_4^- being formed by reaction [2]. In addition, an estimate of the standard potential E_2° for S_2O_4^- oxidation can be obtained from the association constant K_2 . On the basis of fundamental thermodynamics, the standard potential for the reaction



is given by

$$E_2^\circ - E_1^\circ = \frac{RT}{F} \ln K_2$$

Assuming $K_2 = 8400 \text{ dm}^3 \text{ mol}^{-1}$, it is found that standard potential for the $2\text{SO}_2/\text{S}_2\text{O}_4^-$ couple is 226 mV more positive than that for the $\text{SO}_2/\text{SO}_2^-$ couple whereas a 600 mV difference is observed between the two oxidation waves in the pulse polarogram.

For these reasons it is concluded that the assignment of the wave at -0.7V to oxidation of S_2O_4^- is incorrect. The failure to observe an oxidation wave for S_2O_4^- can be explained by reaction [2] being sufficiently labile that the S_2O_4^- is completely removed during the 45 msec pulse due to oxidation of the SO_2^- (reaction [2]).

The wave at -0.7V must therefore be ascribed to the oxidation of another product produced during the reduction of sulfur dioxide. Since this reaction causes a potential shift that is independent of SO_2 concentration, it is concluded that the reaction is first or pseudo-first order. The following suggestions can be made:

(a) Formation of a cation complex



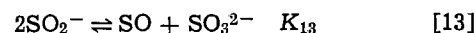
(b) Formation of an anion complex



(c) Formation of a solvent complex

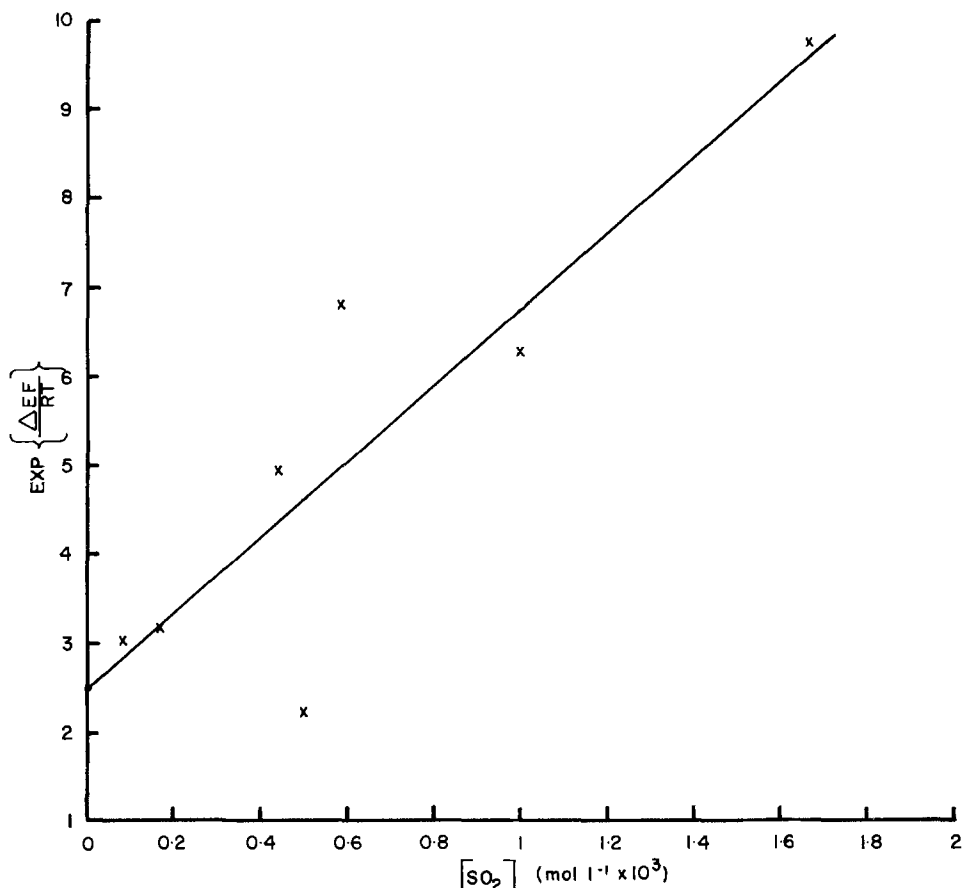


(d) Disproportionation



The formation of a complex between SO_2^- and either the cation or the anion of the supporting electrolyte (reactions [10] and [11]) can be eliminated since the ratio of the two waves in the anodic pulse polarogram has been found to be independent of the concentration of the supporting electrolyte. The two waves were also observed at the same potential in hexamethylphosphoramide indicating that the reaction does not involve formation of a complex with the solvent. However, the results are consistent with a disproportionation of the SO_2^- according to reaction [13]. In this scheme the wave at -0.7V can be attributed to the oxidation of SO_3^{2-} . If it is assumed that the equilibrium for this reaction is established slowly compared to the 45 msec

Fig. 8. Graphical determination of the association constant K_2 and the disproportionation constant K_{13} according to Eq. [15] from plots of the exponent of the shift in half-wave potential from the standard potential against the bulk SO_2 concentration.



pulse then it is clear that two oxidation waves corresponding to oxidation of SO_2^- and SO_3^{2-} will be observed. In addition, at low SO_2 concentrations where the formation of the S_2O_4^- complex is negligible, the ratio of the SO_3^{2-} wave to the SO_2^- wave should be constant.

As the SO_2 concentration is increased, the ratio of the SO_3^{2-} wave to the SO_2^- wave should decrease because the contribution that the complex makes to the SO_2^- wave will increase. This is observed experimentally where the ratio of the two waves goes from 1.2 in a 10^{-4}M SO_2 solution to 0.3 in a $5 \times 10^{-3}\text{M}$ SO_2 solution. Using data for the free energy of formation of Li_2SO_3 and SO_3 , it has been estimated (16) that E° for the system $2\text{Li} + \text{SO}_3 \rightarrow \text{Li}_2\text{SO}_3$ is $\sim 3.7\text{V}$. The corresponding value for $2\text{Li} + 2\text{SO}_2 \rightarrow \text{Li}_2\text{S}_2\text{O}_4$ is about 3.0V. This indicates that the oxidation wave for SO_3^{2-} should occur approximately 700 mV more positive than the oxidation wave for SO_2^- . This is in reasonable agreement with the experimentally observed potential shift (600 mV).

The SO formed in reaction [13] is expected to further disproportionate (17) to form elemental sulfur and SO_2 . This mechanism is supported by the work of Rinker and Lynn (18) who have shown that both sulfite and elemental sulfur are formed during the reduction of SO_2 in DMF at sodium amalgam. Similar reactions have been postulated for the decomposition of dithionite in aqueous media (19). Experiments to measure the oxidation potential of SO_3^{2-} directly were unsuccessful because of the low solubility of the available sulfite salts.

It is easily shown that, when the disproportionation reaction is included in the reaction scheme, the shape of the d-c polarogram is given by the expression

$$E - E_1^\circ = \frac{RT}{F} \ln \left[\left(\frac{i_d - i}{i} \right) \left(1 + 2K_{13}^{1/2} + K_2 \left(\frac{i_d - i}{g} \right) \right) \right] \quad [14]$$

and the corresponding shift in half-wave potential by the relationship

$$E_{1/2} - E_1^\circ = \frac{RT}{F} \ln \left(1 + 2K_{13}^{1/2} + K_2 \frac{[\text{SO}_2]^\circ}{2} \right) \quad [15]$$

Equation [15] is of the same general form as Eq. [8]; however, in this case a plot of $\exp(E_{1/2} - E_1^\circ)F/RT$ against $[\text{SO}_2]^\circ$ should give a linear plot with intercept $1 + 2K_{13}^{1/2}$ and a slope equal to $K_2/2$ as before. From the experimental intercept (Fig. 8) of 2.5 ± 0.8 , a value of $K_{13} = 0.6 \pm 0.4$ is obtained. At low concentration the ratio of the two waves in the anodic pulse polarogram should be approximately $1/K_{13}^{1/2}$. Using the value of $K_{13} = 0.6$ obtained above, it is seen that the ratio of the two waves should be about 1.3 at low SO_2 concentrations. Experimentally, a ratio of 1.2 is observed for a 10^{-4}M solution, the lowest concentration measured.

An estimate of K_2 can also be obtained by measuring the surface concentration of SO_2 at the equilibrium potential. As a result of the follow-on reactions, the surface concentrations of SO_2 and SO_2^- are less than half of the bulk concentration at the standard potential. It can be shown (Appendix) that the following relationship holds

$$K_2 = \frac{[\text{SO}_2]^\circ - 2(1 + K_{13}^{1/2})[\text{SO}_2]_{E=E_1^\circ}}{[\text{SO}_2]_{E=E_1^\circ}^2} \quad [16]$$

It follows that a plot of $[\text{SO}_2]^\circ/[\text{SO}_2]_{E=E_0}$ against $[\text{SO}_2]_{E=E_0}$ should give a straight line with slope equal to K_2 and intercept $2(1 + K_{13}^{1/2})$. A plot of these data are shown in Fig. 9 from which the estimates $K_2 = 2400 \pm 2000$ and $K_{13} = 0.4 \pm 0.1$ are obtained. The value for K_{13} is in agreement with the potential shift analysis, but the K_2 value does not agree with the previous estimate. On the whole, however, we feel the potential shift analysis is more reliable as it is less affected by distortions which occur on the upper part

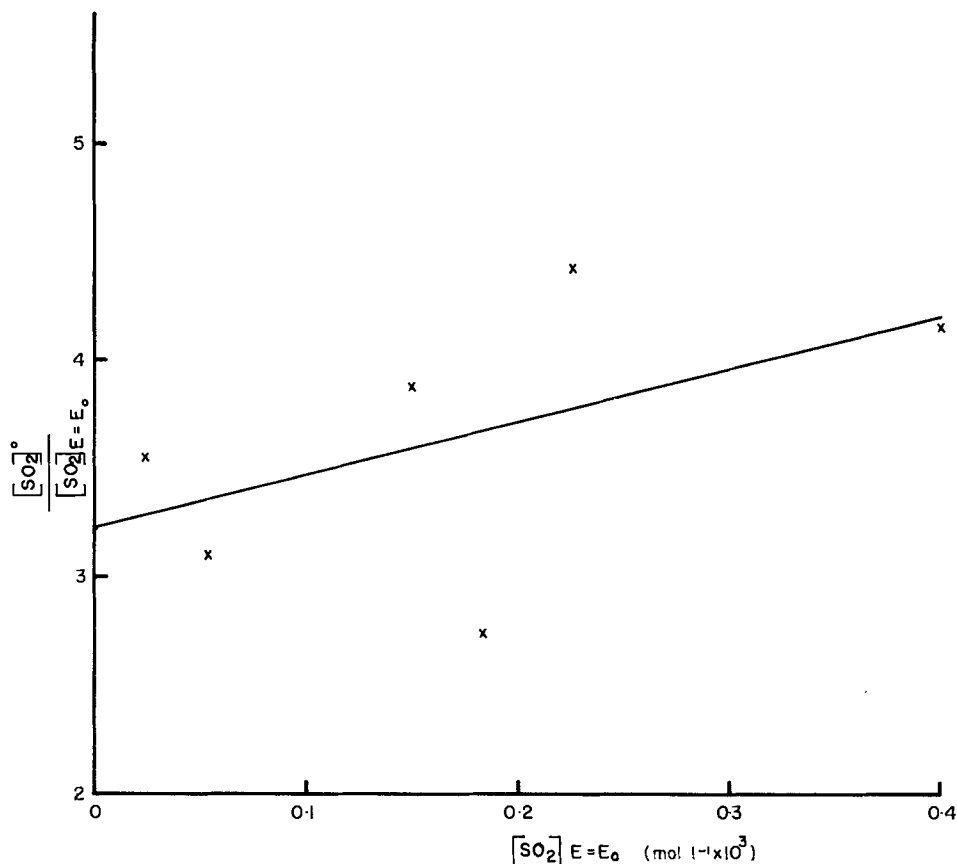


Fig. 9. Graphical determination of the association constant K_2 and the disproportionation constant K_{13} from a plot of the ratio of the bulk SO_2 concentration $[\text{SO}_2]^\circ$ to the SO_2 concentration at the electrode surface at the standard potential $[\text{SO}_2]_{E=E_0}$ against $[\text{SO}_2]_{E=E_0}$ according to Eq. [16].

of the wave and which become more significant as the SO_2 concentration is increased. This distortion is probably due to a second reduction process.

The values of K_2 obtained from these measurements are at least an order of magnitude higher than the value of $600 \text{ dm}^3 \text{ mol}^{-1}$ determined by Laman *et al.* (20) in TEAP solutions and of $230 \text{ dm}^3 \text{ mol}^{-1}$ determined by Kastening *et al.* (6) in tetraethylammonium bromide solution using ESR spectroscopy.

The reason for the large difference in the value of K_2 obtained by the two methods is not clear. It is interesting to note, however, that ESR transients measured using a constant current pulse (20) can only be simulated if the larger (*i.e.*, electrochemical) value of K_2 is used. This suggests that the ESR measurement underestimates the value of K_2 for some reason.

As the temperature is decreased, considerable changes occur in the reaction mechanism. Positive shifts in the half-wave potential along with a sharpening of the d-c polarogram all point to an increasing contribution of the dimerization reaction (reaction [3]) to the reduction mechanism as the temperature is lowered. This suggestion is confirmed by the observation that the intense ESR signal due to the paramagnetic complex S_2O_4^- in a partially reduced 0.05M SO_2 solution completely disappears when the sample is cooled to 77 K . At room temperature, our own results as well as those of Kastening and Gostisa-Michelcic (6) indicate that the contribution of the dimerization reaction is not significant. From Ref. (6) it can be shown from the ratio of the two paramagnetic species and the SO_2 concentration measured after electrolysis that very little if any of the SO_2^- formed during the initial stages of the electroreduction of SO_2 dimerizes to form S_2O_4^- at room temperature.

Dithionite is, of course, the major product when the electroreduction is carried to completion (*i.e.*, one electron per SO_2 molecule). In addition, other complex species such as $\text{S}_3\text{O}_6^{2-}$ have been observed by Martin and Sawyer (3) during the later stages of the electroreduction.

Analysis of the d-c polarographic limiting current data yields a diffusion coefficient of $1.52 \times 10^{-5} \text{ cm}^2 \text{ sec}^{-1}$ at 20°C . A least squares fit of the limiting current data as a function of temperature yields an activation energy of $8.5 \pm 0.3 \text{ kJ mol}^{-1}$ for the diffusion process.

Analysis of the pulse polarograms recorded using a cathodic sweep (Fig. 6) show clearly that the follow-on reactions have much less influence on the shape of the pulse polarogram than on the d-c polarogram. Thus, the half-wave potentials are closer to the standard electrode potential and plots of $\log(i/i_d - i)$ against E are much more linear and have slopes closer to 59 mV . Systematic deviations remain, however, indicating that one or more of the follow-on reactions are fast enough to influence the shape of the pulse polarograms.

In order to obtain information on the kinetics of the electron transfer reaction, phase sensitive a-c admittance measurements were made. For temperatures above 0°C , the a-c admittance data give linear Randle's plots as shown in Fig. 5. These results indicate that, under these conditions, the follow-on reaction is sufficiently slow that the reaction can be considered as a simple one-electron transfer reaction on the time scale used for these measurements. In addition, the half-wave potentials are considerably more negative than those determined from d-c polarography and are independent of concentration. These results indicate that, by using a-c polarography, the primary electron transfer step can be studied without interference from follow-on reactions. The observation that deviations from linearity are observed in the Randle's plots for frequencies less than about 160 Hz in the 10^{-3}M solution provides a crude estimate of the half-life of the SO_2^- radical which must be about 10 msec under these conditions. The influence of the SO_2 concentration on the rate of conversion of SO_2^- into S_2O_4^- can be seen by the fact that deviations from linearity are observed at higher frequencies as the concentration of the SO_2 is increased.

The results indicate that the electron transfer rate is very fast. At 25°C , $k_s = 1.0 \pm 0.2 \text{ cm/sec}$. The uncer-

tainty in determining k_s is high as rates of this order of magnitude are at the limit of the a-c admittance technique. Analysis of the effect of temperature on the rate of electron transfer allows an activation energy of 20.4 kJ/mol to be determined. Electron transfer rates for the electroreduction of aromatic hydrocarbons are of the same order of magnitude (21) as those measured for the reduction of SO_2 .

Acknowledgment

The authors wish to thank Dr. A. S. Baranski for his helpful discussions and suggestions.

Manuscript submitted Sept. 24, 1980; revised manuscript received April 10, 1981. This was Paper 43 presented at the Los Angeles, California, Meeting of the Society, Oct. 14-19, 1979.

Any discussion of this paper will appear in a Discussion Section to be published in the June 1982 JOURNAL. All discussions for the June 1982 Discussion Section should be submitted by Feb. 1, 1982.

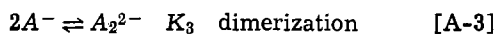
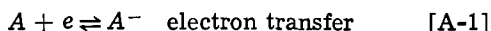
Publication costs of this article were assisted by the Defence Research Establishment Ottawa. This article was issued as DREO Report No. 848.

APPENDIX

Shape of the d-c Polarogram

In describing the shape of the d-c polarogram it is assumed initially that:

(a) The mechanism of reaction is as follows



(b) That reactions [A-2] and [A-3] are in equilibrium; therefore

$$K_2 = \frac{[A_2^-]}{[A][A^-]} \quad [\text{A-4}]$$

and

$$K_3 = \frac{[A_2^{2-}]}{[A^-]^2} \quad [\text{A-5}]$$

(c) That the A/A^- couple determines the electrode potential and that the Nernst equation holds

$$\frac{[A]}{[A^-]} = P = \exp \left\{ \frac{(E - E_0)F}{RT} \right\} \quad [\text{A-6}]$$

(d) That the Ilkovič equation holds; it follows that

$$i = g([A]^\circ - [A]_0) \quad [\text{A-7}]$$

and

$$i_d = g[A]^\circ \quad [\text{A-8}]$$

where $[A]^\circ$ is the bulk SO_2 concentration and $[A]_0$, the concentration at the surface.

(e) That the system is at steady state (i.e., flux in = flux out); thus

$$g_A \{ [A]^\circ - [A]_0 \} = g_A [A^-]_0 + 2g_{A_2^-} [A_2^-]_0 + 2g_{A_2^{2-}} [A_2^{2-}]_0 \quad [\text{A-9}]$$

and assuming

$$g_A = g_{A^-} = 2g_{A_2^-} = 2g_{A_2^{2-}} = g \quad [\text{A-10}]$$

we then find that

$$\frac{i_d}{g} = [A]^\circ = [A]_0 + [A^-]_0 + [A_2^-] + [A_2^{2-}] \quad [\text{A-11}]$$

Substituting [A-4] to [A-10] into [A-11] we find that

$$\frac{i_d}{g} = \frac{(i_d - i)}{g} + \frac{(i_d - i)}{gP} + K_2 \frac{(i_d - i)^2}{g^2P} + K_3 \frac{(i_d - i)^2}{g^2P^2} \quad [\text{A-12}]$$

The equation for P is

$$P = \frac{1}{2} \left\{ \frac{i_d - i}{i} \right\} \left\{ \left(1 + K_2 \frac{(i_d - i)}{g} \right) + \left[\left(1 + K_2 \frac{(i_d - i)}{g} \right)^2 + \frac{4K_3 i}{g} \right]^{1/2} \right\} \quad [\text{A-13}]$$

From [A-6]

$$E - E_0 = \frac{RT}{F} \ln P \quad [\text{A-14}]$$

The above expression describes the shape of the polarogram in the general case where both reactions [A-2] and [A-3] are important. It is also of interest to consider the special cases where:

(a) $K_3 = 0$ (i.e., complex formation is the dominant follow-on reaction). In this case, Eq. [A-4] can be simplified to give

$$E - E_0 = \frac{RT}{F} \ln \left[\left(\frac{i_d - i}{i} \right) \left(1 + K_2 \frac{(i_d - i)}{g} \right) \right] \quad [\text{A-15}]$$

At the half-wave potential $i = i_d/2$. Substitution of this relationship into [A-15] allows the following relationship to be obtained for the shift of the half-wave potential with respect to the standard potential

$$E_{1/2} - E_0 = \frac{RT}{F} \ln \left(1 + \frac{K_2 [A]^\circ}{2} \right) \quad [\text{A-16}]$$

Measurement of the shift of the half-wave potential thus allows K_2 to be determined.

An estimate of K_2 can also be obtained from the concentration of A at E_0 which can be obtained from the d-c polarogram using the Ilkovič equation at $E = E_0$, $P = 1$ and $[A]_{E_0} = [A^-]_{E_0}$. Substitution into [A-11] thus yields

$$[A_2^-]_{E_0} = [A]^\circ - 2[A]_{E_0} \quad [\text{A-17}]$$

therefore

$$K_2 = \frac{[A_2^-]}{[A][A^-]} = \frac{[A]^\circ - 2[A]_{E_0}}{[A]^2_{E_0}} \quad [\text{A-18}]$$

(b) $K_3 = 0$ (i.e., dimerization is the major follow-on reaction). In this case Eq. [14] can be simplified to give

$$E - E_0 = \frac{RT}{F} \ln \left\{ \frac{1}{2} \left(\frac{i_d - i}{i} \right) \left[1 + (1 + \sqrt{4K_3 i/g}) \right] \right\} \quad [\text{A-19}]$$

REFERENCES

1. K. Crumrine, E. Juergens, and C. Colburn, "Investigation of the Environmental Consequences of the Disposal of the Lithium/Organic Electrolyte/ SO_2 Battery," Versar Inc. (1978) AD A059512.
2. A. N. Dey, "Safety Studies of Lithium-Sulphur Dioxide Cells," P. R. Mallory and Co. Inc. (1978) AD A062708.
3. R. P. Martin and D. T. Sawyer, *Inorg. Chem.*, **11**, 2644 (1972).
4. R. G. Rincker and S. Lynn, *J. Phys. Chem.*, **72**, 4706 (1968).
5. K. P. Dinse and K. Mobius, *Z. Naturforsch., Teil A*, **23**, 695 (1968).
6. B. Kastening and B. Gostisa-Mihelcic, *J. Electroanal. Chem. Interfacial Electrochem.*, **100**, 801 (1979).
7. F. Magno, G. A. Mazzocchin, and B. Bontompelli, *ibid.*, **57**, 89 (1974).
8. B. Kastening, B. Gostisa-Mihelcic, and J. Divisek, *Faraday Disc.*, **56**, 341 (1973).
9. R. Bonnatere and C. Cauquis, *Electroanal. Chem.*, **32**, 215 (1971).
10. W. R. Fawcett and A. Lasia, *J. Phys. Chem.*, **82**, 1114 (1978).
11. W. R. Fawcett, P. A. Forte, R. O. Loutfy, and J. Prokipcak, *Can. J. Chem.*, **50**, 263 (1972).
12. A. S. Baranski and W. R. Fawcett, *J. Chem. Soc. Faraday Trans. I*, **76**, 1962 (1980).
13. R. S. Nicholson and I. Shain, *Anal. Chem.*, **36**, 706 (1964).

14. J. B. Flanagan, K. Takahashi, and F. C. Anson, *J. Electroanal. Chem. Interfacial Electrochem.*, **85**, 257 (1977).
15. C. L. Gardner, D. T. Fouchard, F. C. Laman, and W. R. Fawcett, in "Power Sources for Biomedical Implantable Applications and Ambient Temperature Lithium Batteries," B. B. Owens and N. Margalit, Editors, p. 545, The Electrochemical Society Softbound Proceedings Series, Princeton, NJ (1979).
16. G. E. Blomgren, V. Z. Leger, T. Kalnoki-Kis, M. L. Kronenberg, and R. J. Brodd, Proc. 11th Internat. Power Sources Symposium, 1978.
17. A. N. Dey and P. Bro, *This Journal*, **125**, 1574 (1978).
18. R. G. Rinker and S. Lynn, *Ind. Eng. Chem. Prod. Res. Dev.*, **8**, 338 (1969).
19. R. Pointeau, in "Nouveau traité général de minéralogie," Vol. 13, P. Pascal, Editor, Part II, pp. 1184-1196, Masson, Paris, (1956-1963).
20. F. C. Laman, C. L. Gardner, and D. T. Fouchard, In preparation.
21. A. C. Aten, C. Buthker, and G. J. Hoijtink, *Trans. Faraday Soc.*, **55**, 324 (1959).

The Kinetics and Mechanism of the Electroreduction of Sulfur Dioxide in Nonaqueous Media

II. Effects of Electrolyte and Solvent on the Mechanism of Reduction

C. L. Gardner* and D. T. Fouchard*

Defence Research Establishment Ottawa, Energy Conversion Division, Ottawa, Ontario, Canada K1A 0Z4

and W. R. Fawcett*

*Guelph-Waterloo Centre for Graduate Work in Chemistry,
Department of Chemistry, University of Guelph, Guelph, Ontario, Canada N1G 2W1*

ABSTRACT

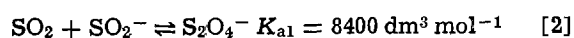
The effect of solvent and supporting electrolyte on the mechanism of the electroreduction of SO₂ has been studied using polarography. It has been found that both the solvent and the electrolyte have a strong influence on the course of the reduction process. The reduction proceeds via the free radical intermediate S₂O₄^{•-} in systems containing large cations but leads directly to S₂O₄⁼ when the system contains small cations. In addition, it has been shown that the stability of the S₂O₄^{•-} decreases with increasing basicity of the solvent. These effects have been interpreted in terms of ion pairing in the system.

The reduction of sulfur dioxide is industrially important for both the operation of the newly developed (1) high energy density lithium/sulfur dioxide battery and for the manufacture of dithionite salts (2) which are used in large quantities as an industrial reducing agent. In a previous paper (3), polarographic studies of the electroreduction of SO₂ in 0.1 mol dm⁻³ solutions of tetraethylammonium perchlorate (TEAP) in N,N-dimethylformamide (DMF) have been described. In agreement with earlier work (4-8) it was found that, in this medium, the reduction process proceeds via a stable, blue paramagnetic complex of SO₂ and SO₂⁻ having a 1:1 stoichiometry. Both ESR (9) and Raman (10) spectroscopic studies indicate that this species is a loosely bonded charge transfer complex. The polarographic studies have shown that the initial stages of the electroreduction process in 0.1 mol dm⁻³ TEAP/DMF can be explained in terms of the following reactions

(a) Electron transfer

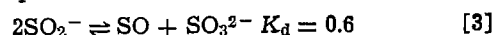


(b) Complex formation



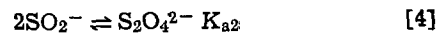
and

(c) Disproportionation



At later stages of the reduction process a red complex that has been ascribed (4) to the complex species SO₂ · S₂O₄²⁻ and finally dithionite are formed (10).

There are indications, however, that the choice of solvent and electrolyte has an important effect on the reduction mechanism. For example, Bonnetterre and Cauquis (11) concluded that the major follow-on reaction in dimethylsulfoxide solution is the dimerization of SO₂⁻ to form dithionite according to the reaction



In the present paper, we report results of studies that we have carried out to examine the effects that both the solvent and the electrolyte have on the mechanism of the electroreduction of sulfur dioxide in nonaqueous media.

Experimental

The electroreduction of dilute solutions (~10⁻³ mol dm⁻³) of sulfur dioxide has been studied using three different solvents and six different supporting electrolytes. The solvents, which were chosen for their different solvating abilities, included N, N-dimethylformamide (DMF) (Aldrich Spectrophotometric grade), acetonitrile (AN) (Aldrich Spectrophotometric grade), and hexamethylphosphoramide, HMPA, (Sigma). The

* Electrochemical Society Active Member.

Key words: sulfur dioxide, high energy density batteries.

supporting electrolytes, which were chosen for variation of cation size, included tetraethylammonium perchlorate (TEAP) (Eastman), tetrabutylammonium perchlorate (TBAP) (Eastman), potassium perchlorate (Fisher), sodium perchlorate (Analar), and lithium perchlorate (Research Inorganic Chemical Company). The procedures followed for purifying and drying the solvents and salts have been described previously (12-14).

All potential measurements given in this paper were measured against a reference electrode that consisted of a silver wire in a solution of $0.05 \text{ mol dm}^{-3} \text{ AgNO}_3$ and $0.05 \text{ mol dm}^{-3} \text{ TEAP}$ in the solvent being used for the experiment. The reference electrode solution was changed daily due to photodecomposition of Ag^+ in DMF. Other details of the electrochemical methods used to make the electrochemical measurements have been described in the first part of this study (3). Electron spin resonance measurements were made using a Varian E-Line spectrometer. The electrochemical ESR cell used for these measurements was similar to that designed by Goldberg and Bard (15). This cell was filled and sealed in the glove box to exclude moisture and air and ESR measurements were then made after partial electrolysis of the solution.

Results and Discussion

Effects of cation on the mechanism of reduction in DMF.—The results to be described in this section show that the mechanism of reduction of SO_2 becomes more complex when supporting electrolytes other than TEAP or TBAP are used in DMF solvent.

A comparison of the cyclic voltammograms in different electrolytes shows a transition from a quasi-reversible reduction in TBAP and TEAP to an irreversible reduction when a small cation such as Li^+ is used. The cyclic voltammograms of SO_2 in TBAP are almost identical to those presented earlier for TEAP (3). These voltammograms show a quasi-reversible peak at -1.3 V and a minor oxidation peak at about -0.7 V , the latter being ascribed (3) to the oxidation of SO_3^{2-} produced from reaction [3]. When LiClO_4 is used as electrolyte (Fig. 1), the reduction reaction is essentially irreversible, the SO_2 being removed rapidly by a follow-on reaction. In this case, there is evidence for the formation of an additional major product which is oxidized at more positive potentials (-1.0 V). Only a small oxidation peak is observed at -0.7 V . In TEAP and LiClO_4 solutions, a linear relationship is observed between i_p , the peak current of the reduction wave, and $\nu^{1/2}$ where ν is the sweep rate.

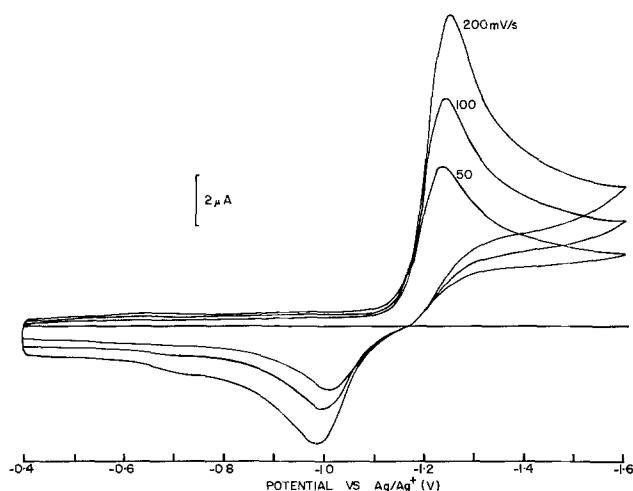


Fig. 1. Cyclic voltammograms for the reduction (forward sweep) of $10^{-3} \text{ mol dm}^{-3} \text{ SO}_2$ at a hanging mercury drop electrode (HMDE) in *N,N*-dimethyl formamide (DMF) containing $0.1 \text{ mol dm}^{-3} \text{ LiClO}_4$ with varying sweep speeds as indicated.

The cyclic voltammograms of SO_2 in $0.1 \text{ mol dm}^{-3} \text{ KClO}_4$ and NaClO_4 (Fig. 2 and 3) are more complex. The distinct prewave and large oxidation wave on the reverse sweep seen in KClO_4 solution is characteristic (16) of product adsorption.

For both NaClO_4 and KClO_4 , $i_p/\nu^{1/2}$ decreases with increasing ν . This behavior is ascribed to product adsorption in both electrolytes. This suggestion is confirmed by d-c and pulse polarographic measurements as discussed later. Because of product adsorption, interpretation of the number and position of the oxidation peaks observed in KClO_4 and NaClO_4 is difficult. Qualitatively, however, it appears that the cyclic voltammogram of SO_2 in KClO_4 most closely resembles that in TEAP while the voltammogram in NaClO_4 more closely resembles that in LiClO_4 .

In order to study the reduction process in more detail, d-c polarographic measurements were also made on all of the solutions. Both the shape and the half-wave potential were dependent on the nature of the base electrolyte. This is illustrated in Fig. 4 where plots of $\log(i/i_d - i)$ vs. E are presented. The half-wave potentials and limiting current constants, based on maximum currents, are given in Table I.

The d-c polarogram of SO_2 in TBAP is virtually identical with that in TEAP which has been described in detail previously (3). The d-c polarographic data are consistent (3) with the reduction proceeding via reactions [1]-[3] in both electrolytes.

The shape of the d-c polarogram for SO_2 in LiClO_4 or LiBr is quite different (Fig. 4) from that described above for SO_2 in TEAP. In this case, the follow-on reaction causes the polarogram to be sharpened so that plots of $\log(i/i_d - i)$ vs. E have a slope of about 45 mV per decade, the half-wave potential

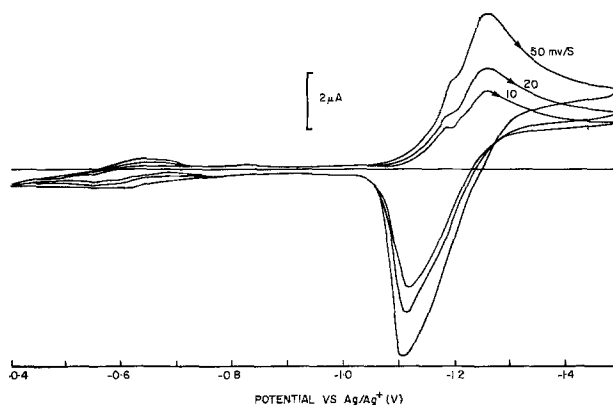


Fig. 2. Cyclic voltammograms for the reduction of $10^{-3} \text{ mol dm}^{-3} \text{ SO}_2$ at an HMDE in DMF containing $0.1 \text{ mol dm}^{-3} \text{ KClO}_4$ with varying sweep speeds as indicated.

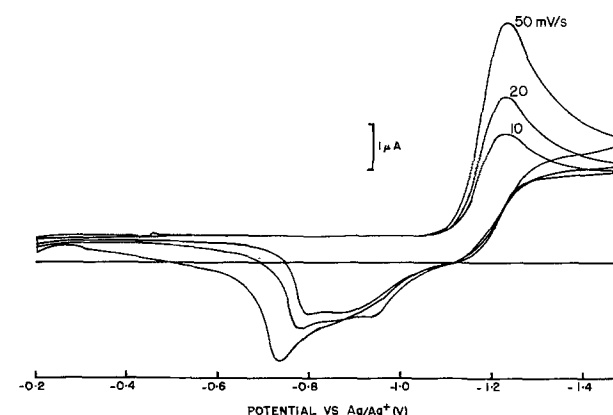


Fig. 3. Cyclic voltammogram for the reduction of $10^{-3} \text{ mol dm}^{-3} \text{ SO}_2$ at an HMDE in DMF containing $0.1 \text{ mol dm}^{-3} \text{ NaClO}_4$ with varying sweep speeds as indicated.

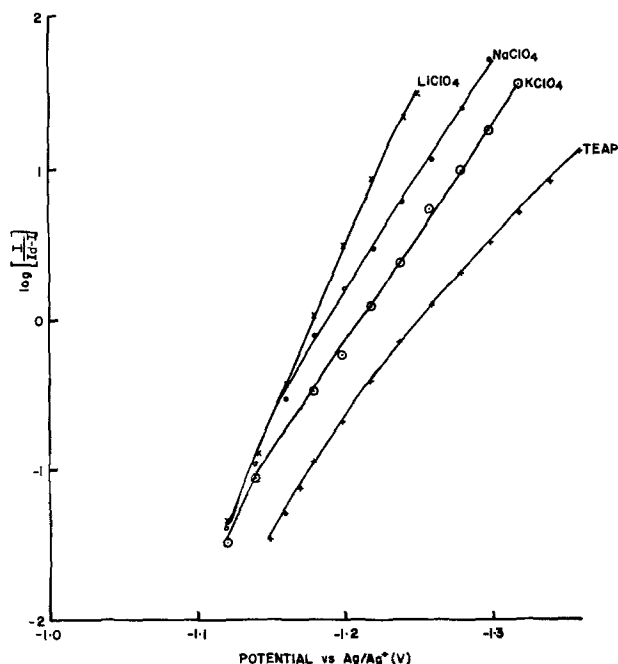


Fig. 4. Plots $\log(i/i_d - i)$ against electrode potential on the basis of d-c polarographic data for the electroreduction of SO_2 in DMF containing different electrolytes as indicated.

being -1.18V . The effects of temperature on the half-wave potential and limiting current constant are shown in Table II.

This behavior is consistent (3) with a change of mechanism so that dimerization of the SO_2^- to form dithionite (reaction [4]) becomes the major follow-on reaction, i.e.



Dithionite is known (17) to be the major product in the discharge of the lithium/sulfur dioxide battery.

If it is assumed that reaction [4] is at equilibrium on the time scale used to make the d-c polarographic measurements and that the Nernst and Ilkovic equations hold then the shape of the d-c polarogram is described (3) by the equation

$$E - E^\circ = \frac{RT}{F} \ln \left\{ \frac{1}{2} \left(\frac{i_d - i}{i} \right) \left(1 + \sqrt{\frac{4K_{a2}}{g}} \right) \right\} \quad [5]$$

where E° is the standard electrode potential for the $\text{SO}_2/\text{SO}_2^-$ couple, i_d is the limiting current, and g is the Ilkovic coefficient. At the half-wave potential, Eq. [5] reduces to

Table I. D-C polarographic data. Reduction of SO_2 in DMF using various supporting electrolytes

| | TEAP | KClO ₄ | NaClO ₄ | LiClO ₄ |
|--|--------|-------------------|--------------------|--------------------|
| Half-wave potential (volts vs. Ag/Ag ⁺) | -1.263 | -1.212 | -1.187 | -1.183 |
| Limiting current constant ($i_d/\text{cm}^{2/3}t^{1/3}$) | 2.532 | 2.576 | 2.509 | 2.873 |

Table II. D-C polarographic data. Reduction of SO_2 in 0.1M LiClO₄/DMF at various temperatures

| Temp (°C) | Half-wave potential (volts vs. Ag/Ag ⁺) | Limiting current constant ($i_d/\text{cm}^{2/3}t^{1/3}$) |
|-----------|---|--|
| -10 | -1.22 | 2.135 |
| 0 | -1.21 | 2.322 |
| 20 | -1.195 | 2.873 |

$$E_{1/2} - E^\circ = \frac{RT}{F} \ln \left\{ \frac{1}{2} \left(1 + \sqrt{2K_{a2} [\text{SO}_2]^\circ} \right) \right\} \quad [6]$$

Taking the value of $E^\circ = -1.30\text{V}$ estimated from a-c polarographic measurements as described later, then from the half-wave potential of -1.18V at 24°C a value of $23.3 \times 10^6 \text{ dm}^3 \text{ mol}^{-1}$ is obtained for K_{a2} .

ESR measurements support this change in reduction mechanism in changing from TEAP to LiClO₄ solutions. In LiClO₄ solutions no paramagnetic intermediates are detected even at relatively high SO_2 concentrations ($\sim 10^{-2}\text{M}$). Under similar conditions an intense ESR signal is detected (6, 7, 9) for the polarographic complex S_2O_4^- in TEAP solutions. The measurement of diffusion-limited currents for the reduction of SO_2 in TEAP and LiClO₄ also reflects the difference in reduction mechanism. In TEAP the limiting currents (and hence the apparent diffusion coefficient of SO_2) are significantly lower (Fig. 5) than the LiClO₄ solutions. This is undoubtedly caused by the scavenging of SO_2 by SO_2^- to form S_2O_4^- .

Interpretation of the d-c polarograms for SO_2 in KClO₄ and NaClO₄ solutions is more difficult. In both systems distinct adsorption prewaves are observed. This is in agreement with the cyclic voltammogram for SO_2 in KClO₄ solutions which also showed effects due to product adsorption (Fig. 1). At 53°C , the polarogram for the reduction in NaClO₄ solution shows a distinct kinetic maximum. From the cyclic voltammetric and d-c polarographic data, it appears that the situation in KClO₄ and NaClO₄ solutions is intermediate between that in TEAP and LiClO₄. It is thus probable that both S_2O_4^- and $\text{S}_2\text{O}_4^{=}$ are formed by reactions [2] and [4] in these solutions. Pulse polaro-

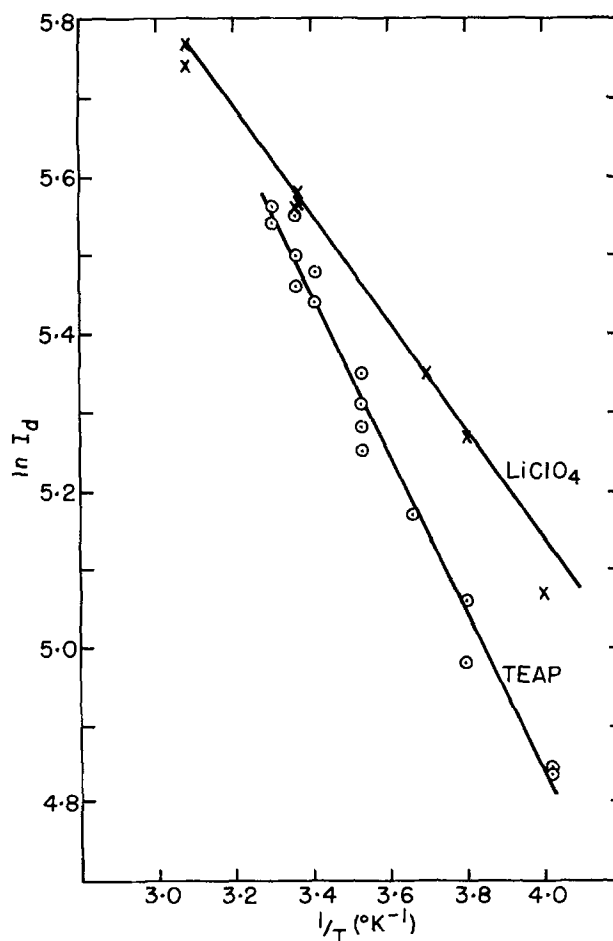


Fig. 5. Effect of temperature on the limiting current constant for the reduction of SO_2 in DMF containing TEAP and LiClO₄ as indicated.

graphic measurements support this conclusion. Using a negative potential sweep, the pulse polarogram for SO_2 in all of the electrolytes consists of a single wave that gives a linear plot of $\log(i/i_d - i)$ vs. E (Fig. 6). It is seen that there is a regular increase in slope of these curves from 68 to 46 mV per decade in going from TEAP to LiClO_4 . This change of slope can be attributed to the shift in mechanism from formation of the free radical complex S_2O_4^- in TEAP to the formation of dithionite in LiClO_4 . The theoretical description of the shape of the d-c polarogram when both reactions [2] and [4] contribute has been given previously (3). It can be shown that this gradual change of slope is consistent with the transition from one product to the other (i.e., S_2O_4^- to $\text{S}_2\text{O}_4^{2-}$).

The pulse polarographic data obtained using a positive potential sweep from various points on the reduction wave provide some information regarding the reaction mechanism. As has been discussed in detail previously (3), the pulse polarogram of SO_2 in TEAP solutions obtained using a positive potential sweep shows two distinct waves, one wave at -1.3V that is attributed to the oxidation of SO_2^- , and a second wave at -0.7V that is attributed to oxidation of SO_3^{2-} . The failure to detect a wave due to oxidation of S_2O_4^- was attributed to the labile equilibrium that exists between SO_2^- and S_2O_4^- . It is believed that this equilibrium is sufficiently rapid that all of the S_2O_4^- is depleted through oxidation of SO_2^- before the current is sampled at the end of the 45 msec pulse.

The anodic pulse polarograms of SO_2 in KClO_4 (Fig. 7) and NaClO_4 are more complex, the polarograms exhibiting large maxima. This behavior has been described by Flanagan and co-workers (18) who have shown that this effect is caused by product adsorption. This is in agreement with the d-c polarographic and cyclic voltammetric results which have also indicated that product adsorption is taking place as discussed previously. It is interesting to note that, when the initial potential is set just at the foot of the d-c polarogram, a small wave at -0.7V is observed. This indicates that the disproportionation of SO_2^- to form SO_3^{2-} takes place in these solutions as well.

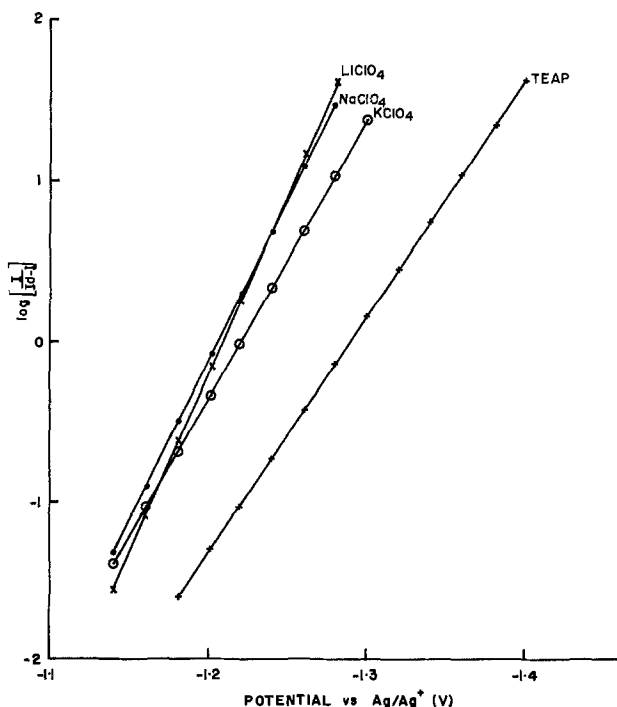


Fig. 6. Plots of $\log(i/i_d - i)$ against electrode potential on the basis of pulse polarographic data for the electroreduction of SO_2 in DMF containing different electrolytes as indicated.

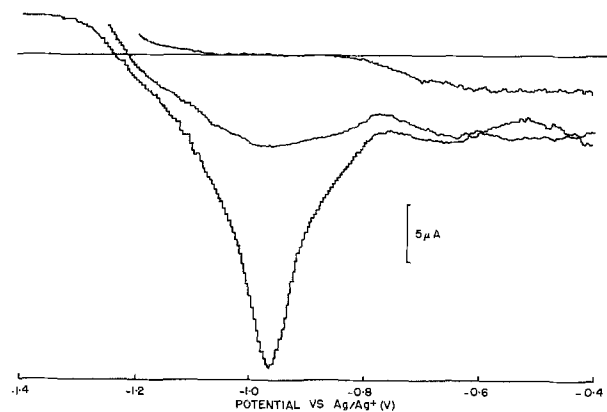


Fig. 7. Pulse polarogram for the oxidation of the reduction products of a 10^{-3} mol dm^{-3} SO_2 in DMF containing 0.1 mol dm^{-3} KClO_4 with initial potential as indicated.

In LiClO_4 solutions (Fig. 8), the anodic pulse polarogram shows three distinct waves at -1.3 , -1.0 , and -0.7V . At -1.3V the net current flowing is cathodic indicating that the SO_2^- produced in the primary reduction is completely removed during the 45 msec pulse. The major oxidation wave occurs at -1.0V and probably results from oxidation of dithionite which is thought to be the major product from the follow-on reactions. A small wave is also observed at -0.7V indicating that some SO_3^{2-} is also produced.

The experiments described above indicate that the electrolyte cation has a strong influence on the course of the electroreduction process. Thus, in TEAP solutions, the reduction process proceeds via the free radical complex S_2O_4^- as well as a red complex that has been ascribed to $\text{SO}_2 \cdot \text{S}_2\text{O}_4^{2-}$ on route to dithionite on complete electrolysis. In LiClO_4 solutions, on the other hand, dithionite is formed directly by dimerization of SO_2^- . The influence of electrolyte cation on the mechanism of reduction can be explained in terms of the effect of ion pairing on the position of the various equilibria (19). It appears that the formation of dithionite is favored when strong ion pairing occurs in solutions containing a small cation such as lithium. On the other hand when a large cation such as TEA^+ is used and ion pairing is expected to be weak, the formation of the complex species is favored. With Na^+ and K^+ in solution, the degree of ion pairing is expected to be intermediate between these two extremes.

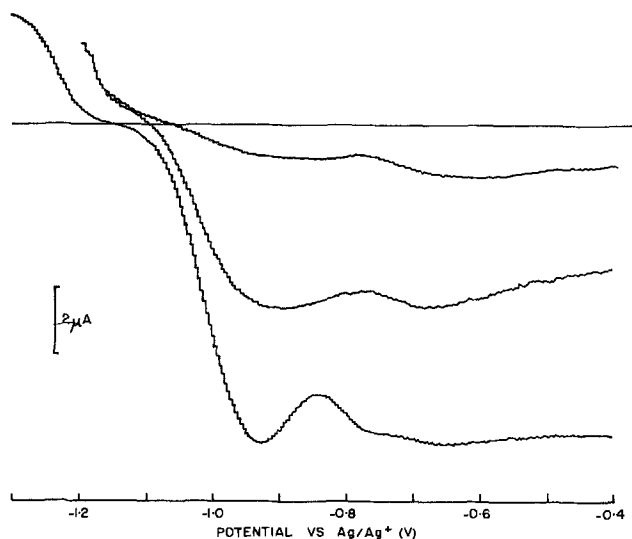


Fig. 8. Pulse polarogram for the oxidation of the reduction products of 10^{-3} mol dm^{-3} in DMF containing 0.1 mol dm^{-3} LiClO_4 with initial potential as indicated.

Effects of solvent on the mechanism of reduction.—As mentioned previously, the electroreduction of sulfur dioxide has been studied in three different solvents (DMF, HMPA, and AN) of varying solvating ability to examine the effect of solvent on the mechanism of reaction. Measurements have been made in each of these solvents using TEAP, NaClO₄, and LiClO₄ as electrolyte.

The d-c polarographic data for the reduction of SO₂ in 0.1 mol dm⁻³ solutions of TEAP in each of the three solvents are shown in Fig. 9. The shapes of the log (*i*/*i*_d - *i*) plots are very similar in HMPA and DMF. On the other hand, in AN a marked broadening of the curve occurs at negative potentials similar to that seen at high SO₂ concentrations in DMF (3). It is possible that this broadening is due to a second reduction process such as the direct reduction of S₂O₄²⁻. It was also noted that there is a fairly large variation in limiting current which can be related to the variation in diffusion coefficient due to a corresponding variation in solvent viscosity.

The general features of the polarograms in all solvents with TEAP as electrolyte suggest that the reduction of SO₂ in these systems proceeds via reactions [1]-[3]. In this case the shift in the half-wave potential can be related (3) to the equilibrium constants *K*_{a1} and *K*_d by the relationship

$$E^{1/2} - E^{\circ} = \frac{RT}{F} \ln \left\{ 1 + 2K_d^{1/2} + \frac{K_{a1}}{2} [\text{SO}_2]^{\circ} \right\} \quad [7]$$

where [SO₂][°] is the bulk SO₂ concentration.

Using the method described earlier (3), the disproportionation constant *K*_d was determined to be 1.5 in HMPA. The pulse polarogram for SO₂ in AN (Fig. 10) obtained using a positive potential sweep is quite different than that obtained in DMF or HMPA. In AN, a fairly weak broad wave is observed at about -0.85V which is absent when the initial potential is held at the foot of the reduction wave. This indicates that SO₃²⁻ is not produced in this reaction and that *K*_d = 0.0 in AN. The broad wave at -0.85V is tentatively assigned to the oxidation of S₂O₄²⁻.

An estimate of the standard potential for the process SO₂ + *e* ⇌ SO₂⁻ was obtained from the peak

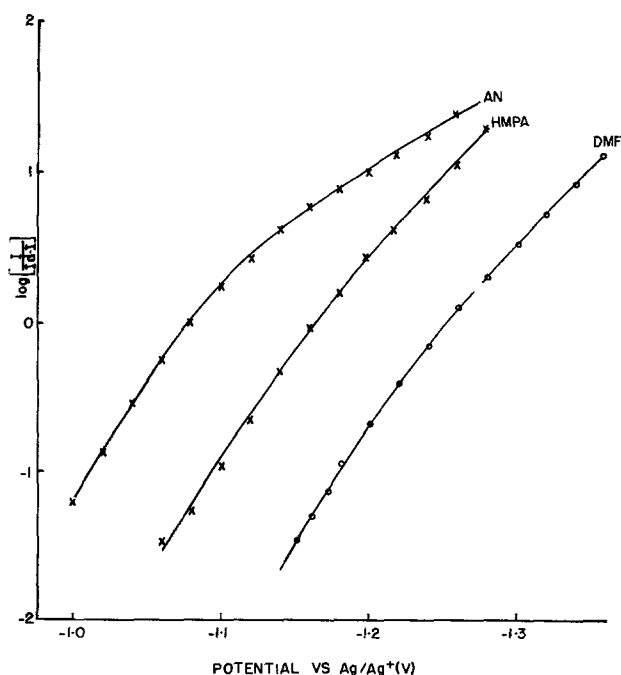


Fig. 9. Plots of log (*i*/*i*_d - *i*) against electrode potential on the basis of d-c polarographic data for the electroreduction of SO₂ in various solvents as indicated containing 0.1 mol dm⁻³ TEAP.

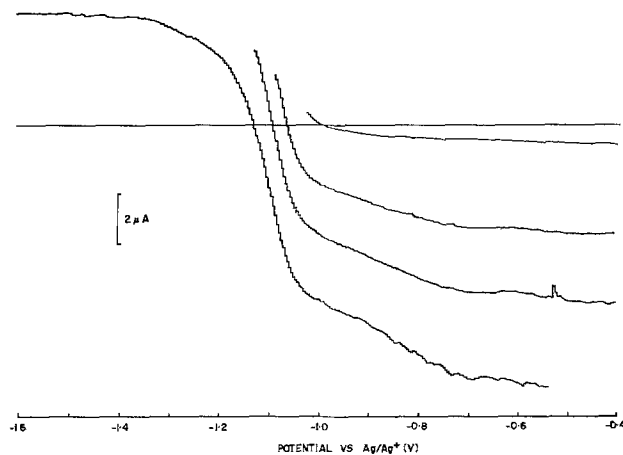


Fig. 10. Pulse polarogram for the oxidation of the reduction products of 10⁻³ mol dm⁻³ SO₂ in AN containing 0.1 mol dm⁻³ TEAP with initial potential as indicated.

potential of the out-of-phase component of the a-c admittance. Using the measured d-c polarographic half-wave potentials and Eq. [7], values of *K*_{a1} = 0, 8400, and 17,000 dm³ mol⁻¹ are obtained in HMPA, DMF, and AN, respectively. From these results, it is seen that the solvent has an important effect on the stability of the complex and thus the reaction mechanism. These results provide further evidence of the importance of ion pairing in determining the position of equilibrium among the various components of the reacting system. As the basicity of the solvent decreases (20) (HMPA > DMF > AN) the ability of the cation in the system to interact with negatively charged components of the reaction system increases; thus, it appears that the negatively charged complex S₂O₄²⁻ is most stable in AN where it can most strongly interact with the cation, in this case, TEA⁺.

The electroreduction of SO₂ was also studied in 0.1 mol dm⁻³ solutions of LiClO₄ and NaClO₄ using each of the three solvents. In these electrolytes, the experimental results are complicated by the apparent kinetically limited reduction in HMPA and extremely strong adsorption of product in AN. Because of these complications, very few conclusions regarding the effect of solvent on the reaction mechanism could be reached. Perhaps the most revealing results are the data obtained by pulse polarography recorded using a negative sweep with 0.1 mol dm⁻³ LiClO₄ electrolyte (Fig. 11). From these curves it is concluded that the formation of dithionite is the major follow-on reaction in AN and DMF. In HMPA (Fig. 11) the slope of the log (*i*/*i*_d - *i*) plot is much larger (~ 91 mV per decade) and the half-wave potential is considerably more positive than that measured using d-c polarography. It is suggested that this behavior is the result of a kinetic limitation of the reduction of TEA in this system.

The very strong product adsorption that occurs in AN leads to some curious results. In LiClO₄ or NaClO₄ solutions, it is not possible to record a d-c polarogram because the electrode becomes blocked by the adsorbed product. As shown in Fig. 12, the normal pulse polarogram recorded in 0.1 mol dm⁻³ solution of LiClO₄ in AN using an anodic sweep also shows dramatically the effects of adsorption. In this case a large adsorption peak is observed at very positive potentials rather than the normal oxidation waves seen when HMPA or DMF are used as the solvent (Fig. 12). This gives the normal pulse polarogram a very unusual appearance.

Conclusions

These studies have indicated that the choice of solvent and electrolyte has a major effect on the

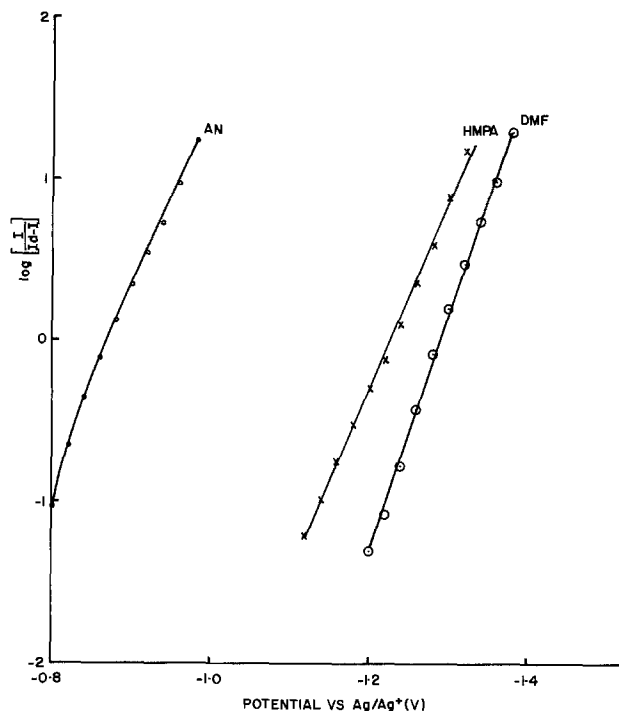


Fig. 11. Plots of $\log(i/i_d - i)$ against electrode potential on the basis of pulse polarographic data for the electroreduction of SO_2 in various solvents as indicated containing 0.1 mol dm^{-3} LiClO_4 .

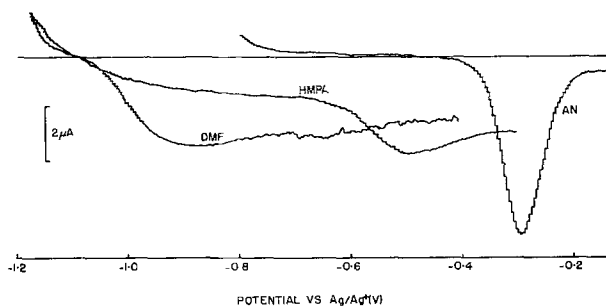


Fig. 12. Pulse polarogram for the oxidation of the reduction products of $10^{-3} \text{ mol dm}^{-3}$ SO_2 in various solvents as indicated containing 0.1 mol dm^{-3} LiClO_4 .

mechanism of reduction of sulfur dioxide in nonaqueous media. The influence of solvent and electrolyte on the reaction mechanism can be interpreted in terms of ion pairing in the system.

In DMF solution, it has been shown that, in solutions containing a large cation such as TEA^+ which leads to relatively weak ion-pairing, the reduction

process proceeds via the free radical complex S_2O_4^- during the initial stages of electrolysis. When a small cation such as Li^+ is used, on the other hand, dithionite is formed directly by dimerization of the primary reduction product SO_2^- . In addition, it has been shown that the stability of S_2O_4^- decreases with increasing basicity of the solvent.

Manuscript submitted Feb. 9, 1981; revised manuscript received May 29, 1981.

Any discussion of this paper will appear in a Discussion Section to be published in the June 1982 JOURNAL. All discussions for the June 1982 Discussion Section should be submitted by Feb. 1, 1982.

Publication costs of this article were assisted by the Defence Research Establishment Ottawa. This article was issued as DREO Report No. 849.

REFERENCES

1. W. P. Kilroy, in "28th Power Sources Symposium," p. 198, June 12-15, 1978, The Electrochemical Society, Princeton, NJ (1978).
2. R. G. Rinker and S. Lynn, *Ind. Eng. Chem. Prod. Res. Dev.*, **8**, 338 (1969).
3. C. L. Gardner, D. T. Fouchard, and W. R. Fawcett, *This Journal*, **128**, 2337 (1981).
4. R. P. Martin and D. T. Sawyer, *Inorg. Chem.*, **11**, 2644 (1972).
5. R. G. Rinker and S. Lynn, *J. Phys. Chem.*, **72**, 4706 (1968).
6. K. P. Dinse and K. Mobius, *Z. Naturforsch. Teil A*, **23**, 695 (1968).
7. B. Kastening and B. Gostisa-Mihelcic, *J. Electroanal. Chem. Interfacial Electrochem.*, **100**, 801 (1969).
8. F. Magno, G. A. Manochin, and G. Bontempelli, *ibid.*, **57**, 89 (1974).
9. F. C. Laman, C. L. Gardner, and D. T. Fouchard, *J. Phys. Chem.*, Submitted for publication.
10. W. A. Adams, C. L. Gardner, and D. T. Fouchard, Proc. 7th International Raman Conf., Ottawa, 1980, North/Holland Publishing Co., Amsterdam, p. 202.
11. R. Bonnetterre and G. Cauquis, *J. Electroanal. Chem. Interfacial Electrochem.*, **32**, 215 (1971).
12. W. R. Fawcett and A. Lasia, *J. Phys. Chem.*, **82**, 1114 (1978).
13. W. R. Fawcett, P. A. Forte, R. O. Loutfy, and J. Prockipcak, *Can. J. Chem.*, **50**, 263 (1972).
14. A. S. Baranski and W. R. Fawcett, *J. Chem. Soc. Faraday Trans. I*, **76**, 1962 (1980).
15. I. B. Goldberg and A. J. Bard, *J. Phys. Chem.*, **75**, 3281 (1971).
16. R. H. Wopschall and I. Shain, *Anal. Chem.*, **39**, 1514 (1967).
17. P. Bro, H. Y. Yang, C. Schlaikjer, and H. Taylor, Tenth IECEC Conference, p. 423 (1975).
18. J. B. Flanagan, K. Takahashi, and F. C. Anson, *J. Electroanal. Chem. Interfacial Electrochem.*, **63**, 257 (1977).
19. "Ions and Ion Pairs in Organic Reactions," M. Swarc, Editor, Wiley, New York (1972).
20. W. R. Fawcett and T. M. Krygowski, *Can. J. Chem.*, **54**, 3282 (1976).

Electrocatalysis for Chlorine Electrode Reaction on RuO₂ Electrode in NaAlCl₄ Melt

I. Uchida,* H. Urushibata, and S. Toshima

Department of Applied Chemistry, Faculty of Engineering, Tohoku University, Aramaki-Aoba, Sendai 980, Japan

ABSTRACT

In molten AlCl₃-NaCl with near equimolar compositions, electrocatalysis of the chlorine electrode reaction ($2\text{Cl}^- = \text{Cl}_2 + 2e^-$) on RuO₂ electrodes has been investigated at 175°C. Melt-stable RuO₂ electrodes were prepared by a thermal decomposition method on semiconductive SnO₂ films deposited on Pyrex substrates. Tafel relationships for chlorine evolution and reduction were studied as functions of $p\text{Cl} (= -\log a_{\text{Cl}^-})$ and partial pressure of Cl₂, and several kinetic parameters including reaction orders with respect to Cl⁻ and Cl₂ were determined. The mechanistic analysis based on the theoretical kinetic derivatives revealed that the chlorine electrode reaction on RuO₂ obeys a Volmer-Tafel type mechanism under the activated Temkin condition: $\text{Cl}^- = \text{Cl}_{\text{ad}} + e^-$ (fast), $\text{Cl}_{\text{ad}} + \text{Cl}_{\text{ad}} \rightleftharpoons \text{Cl}_2$ (slow). The exchange current density at the standard condition ($p\text{Cl} = 1.1$, $P_{\text{Cl}_2} = 1$ atm) was $132 \pm 22 \mu\text{A}/\text{cm}^2$, and this figure was found to be 15-20 times larger than that on glassy carbon electrodes. The difference of this electrocatalytic activity was ascribed to the mechanistic difference between the two electrode materials and not to the difference of electrode roughness. Capacity data to check this viewpoint were also presented.

Electrocatalysis of the chlorine electrode reaction in molten salt systems is of special interest from the viewpoint of developing molten salt batteries and electrolytic metal winning processes. The only anode material available so far is carbon, which is not sufficiently stable in chloroaluminate melts, showing considerable swelling and disintegration (1, 2). In previous works (3, 4), we have shown that Sb-doped tin oxide acts as stable working electrodes for chlorine evolution. Highly doped SnO₂ having carrier densities of the order of 10^{20} cm^{-3} behaves as an electron-tunneling electrode which allows the electron to pass through the space charge layer formed at the semiconductor/melt interface (5). The comparative study carried out on SnO₂ and glassy carbon (GC) electrodes showed that the polarization behavior for chlorine evolution on SnO₂ increasingly approached that on GC with increasing carrier density (4). In this case, however, electrocatalytic activity would not be expected for SnO₂ electrodes because the electron tunneling process governs the chlorine evolution. Considering that SnO₂ can be utilized as a catalyst support and a current collector, we have proposed the possibility of developing DSA-type, SnO₂-based electrocatalysts usable in melts by applying the oxide-coating techniques employed in the production of DSA.

DSA-type electrodes used for the electrolysis of brine have a multilayer structure consisting of the upper layer of electrocatalyzers such as RuO₂ and the intermediate layer of titanium dioxide acting as the catalyst support which is formed on the underlying titanium substrate (6), and their physicochemical properties and electrochemical behavior have been studied extensively (7-12). Specially for chlorine evolution, a number of studies have been carried out with various electrochemical techniques (13-17). Iwakura *et al.* studied the reaction mechanism and catalytic activity for chlorine evolution on several kinds of metal oxides (RuO₂, IrO₂, MnO₂ etc.) on the basis of crystal field theory (18, 19). Kazarinov *et al.* reported the double layer structure on Ru-Ti oxide anodes in various electrolyte solutions (20), and Rolison *et al.* investigated the electrochemical behavior of

RuO_x electrodes in organic solvents (21). Although there are so many works concerning ruthenium oxide anodes, no workers have reported the electrocatalytic effect of ruthenium oxide on chlorine evolution in molten salt systems.

One of the problems for the use of so-called DSA-type anodes in chloride melts is the instability of Ti substrates. If the oxide anode has a pinhole or a crack and Ti metal comes into contact with melt, anodic dissolution of Ti will take place vigorously. To avoid this problem, ruthenium oxide used in this work was prepared on SnO₂ films on Pyrex substrates. With the electrodes thus prepared, we examined the electrocatalytic effect for chlorine evolution and the reduction in this melt system at 175°C and carried out the mechanistic study using kinetic parameters collected under various conditions. In comparison with the kinetic behavior of the chlorine electrode reaction on glassy carbon electrodes in the same melt system (22), the salient feature of ruthenium oxide as the electrocatalyzer has been demonstrated.

Experimental

Melt preparation.—The AR grade NaCl and AlCl₃ which was rendered iron free by sublimation were mixed under a dry nitrogen atmosphere. After melting the mixture, a sequence of purification procedures (HCl gas treatment, Al displacement, and preelectrolysis) was performed as described previously (23, 24).

Electrodes.—Ruthenium oxide was prepared on Sb-doped tin oxide films with thermal decomposition of RuCl₃. The SnO₂ films were prepared on rectangular Pyrex glass plates by a spray method using tin(IV) chloride solution containing 5 mol percent (m/o) SbCl₃ (23). A dilute n-propanol solution of RuCl₃ · 3H₂O (0.02M) was applied to the thin SnO₂ film by the dip coating method, and then the liquid film of RuCl₃ on the SnO₂ substrate was dried in an oven at 120°C for 30 min and heated in air at 500°C for 20 min. This procedure was repeated 20 times to attain uniform coating of the oxide film, and finally the electrode thus prepared was annealed for 10 hr at 500°C in air.

Visual inspection showed that the SnO₂ film was covered with a blue-black, compact layer with satis-

* Electrochemical Society Active Member.

Key words: fused salts, Tafel slope, electrocatalysis, anode.

factory uniformity. SEM observation revealed a pore-free structure, and x-ray analysis showed the presence of all the principal RuO_2 peaks in comparison with those of ASTM cards (File No. 21-1171). The underlying SnO_2 film acts as a catalyst support as well as a current collector. The adhesion of RuO_2 to SnO_2 was proved quite satisfactory. No damage was observed when the electrode was subjected to gentle scraping or thermal shocks.

The electrical contact with the electrode was made through a gold layer which was printed on the SnO_2 film by using a gold paint (C-5040, Sumitomo Mining Company). The unnecessary part of the oxide surface and the gold contact were insulated with a thick layer of Teflon coating (30-J, Mitsui Fluorochemical Company). These techniques were described in previous paper (23). Details of the electrode construction are shown in Fig. 1. Hereafter this type of electrode is called the SnO_2 -based RuO_2 electrode.

Prior to experiments, the electrode surface was slightly polished with fine alumina powder ($0.3 \mu\text{m}$, Buehler Limited) and degreased with a methanol solution of NaOH . Then, it was soaked in a mixed acid of concentrated HNO_3 and H_2SO_4 for 1 hr and washed thoroughly with distilled water. After the above surface conditioning, the electrode was dried in an oven (120°C) for 12 hr.

Glassy carbon electrodes (GC) were sealed into Pyrex tubes as described previously (25). Their surface conditioning was similar to that of the RuO_2 electrode. The counterelectrode was a W sheet with a large area.

Two types of reference electrodes, whose constructions were described previously (22), were used: the Al reference electrode confined in a Pyrex bulb (membrane type) and the chlorine electrode on a large area GC rod under an atmospheric pressure of chlorine (gas electrode type). The melt composition of the reference room was an NaCl -saturated NaAlCl_4 melt. All the potentials quoted without description are given with respect to the gas electrode.

Apparatus and procedures.—Experiments were performed in a Pyrex vessel at 175°C . The electrochemical cell assembly equipped with gas delivering systems (N_2 and Cl_2) and a temperature control system were essentially the same as that in previous works (22,

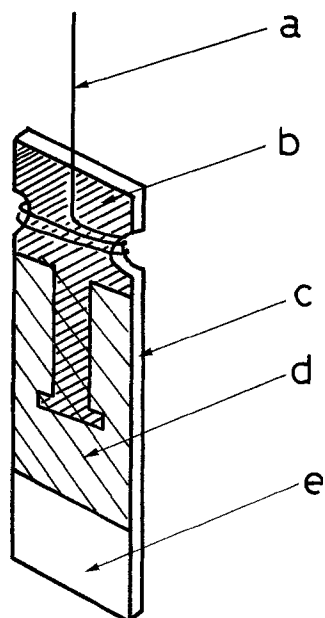


Fig. 1. Electrode construction of the SnO_2 -based RuO_2 electrode. a, Au lead; b, printed Au layer; c, Pyrex; d, SnO_2 -based RuO_2 covered with Teflon; e, SnO_2 -based RuO_2 electrode surface.

23). Nitrogen gas was rendered oxygen free by passing it through heated copper fibers and drying it with anhydrous $\text{Mg}(\text{ClO}_4)_2$ and P_2O_5 . Chlorine gas was dried by passing it through concentrated H_2SO_4 and anhydrous $\text{Mg}(\text{ClO}_4)_2$. The gas delivering system had a gas mixing chamber where N_2 and Cl_2 were mixed at a desired ratio. The gas mixture was blown into the melt for 1 hr and allowed to flow over the melt during the experiments. The gases sampled from the mixing chamber were subjected to iodometry for determination of the partial pressure of chlorine (22).

The concentration of chloride ion depends on the melt composition ($\text{NaCl} + \text{AlCl}_3$). At the equimolar composition, chloride ion activity determined by the acid-base equilibrium of Eq. [3] is $10^{-2.54}$ ($-\log a_{\text{Cl}^-} = 2.54 = p\text{Cl}$) (29). The highest activity of Cl^- ($p\text{Cl} = 1.1$) is attained in the melt saturated with NaCl (49.75 m/o AlCl_3) which is used as the standard state in this melt (29). All the measurements carried out in this work were, therefore, started with this standard condition, and then $p\text{Cl}$ was changed by partial electrolysis. Part of chloride ion in the cell compartment which was separated from a counterelectrode with a fritted disk was removed coulometrically by chlorine evolution, and the exact $p\text{Cl}$ value was determined from the shift of chlorine electrode potential. The use of the off-gas reaction to change $p\text{Cl}$ and of the gas electrode as a $p\text{Cl}$ indicator electrode were described previously (22).

Measurements of voltammograms and differential capacities were carried out as described previously (22-24). For measurements of Tafel relationships, a logarithmic amplifier (Philbrick Nexas, 4350) was used for curve tracing. Tafel plots were always started from the rest potentials with a scan rate of 1 mV/sec and were recorded on an X-Y recorder (Watanabe Denki, WX 4401).

Results and Discussion

Electrode roughness.—Many workers observed large background current levels of the order of several mA/cm^2 in aqueous systems with their RuO_2 electrodes prepared on Ti substrate (8-12), ascribing the anomaly to electrode roughness. The surface roughness is an important factor in calculation of the exchange current density, which is a measure of the electrocatalytic activity to be examined in this study. In order to check the roughness of our RuO_2 electrodes prepared on SnO_2 , the differential capacity and background cyclic voltammograms were measured and compared with those of metal electrodes as shown in Fig. 2 and 3. The anodic limit of the melt is chlorine evolution taking place at potentials positive to ca. 2.1V vs. Al, and we have the double layer region at less noble potentials. The capacity value of the SnO_2 -based RuO_2 electrode in the double layer region was 25-30 $\mu\text{F}/\text{cm}^2$ on the basis of geometric area, which is comparable to those of Pt and W electrodes, while the GC showed large discrepancy. Fellner *et al.* reported that the double layer capacity on Hg electrodes in the melt at 160°C is 14-20 $\mu\text{F}/\text{cm}^2$ at a potential range from 0.1 to 0.7V vs. Al (26). Adopting Fellner's value as a true capacity of the double layer, we may conclude that the roughness factor of our RuO_2 electrode is 1.5-2.0, while that of GC is 6-8. This feature was confirmed by the background voltammograms shown in Fig. 3.

The background current levels for GC observed in the double layer region were several times as large as those for the RuO_2 electrode, whereas the anodic current due to chlorine evolution increased more rapidly on the RuO_2 electrode than on GC despite its lower roughness, indicating the marked catalytic activity of the RuO_2 electrode. It is widely accepted that the roughness of Ti-supported RuO_2 electrodes largely

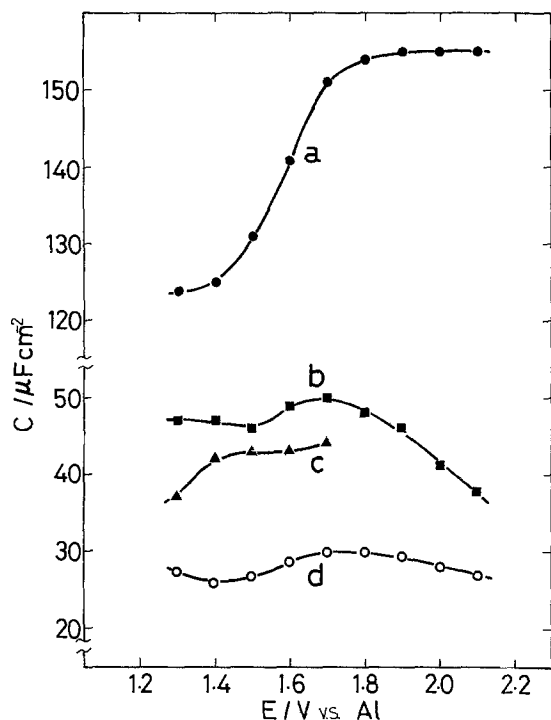


Fig. 2. Capacity vs. potential curves for different electrode materials in the melt of $p\text{Cl} = 1.1$ at $f = 1$ kHz. a, GC; b, W; c, Pt; d, SnO_2 -based RuO_2 .

depends on coating methods and annealing conditions (7-12). The estimated values of their roughness factor show large scattering; below 10 (21) and 8-20 (10) for compact RuO_2 electrodes and 60-200 (10) and above 200 (9) for porous RuO_2 electrodes. Rolison *et al.* prepared Ti-supported RuO_x electrodes with low roughness factors below 10 and observed low background current levels less than $100 \mu\text{A}/\text{cm}^2$ (21), which are comparable to the background current levels obtained in this work. Similarly low current levels were also observed in aqueous solutions with SnO_2 -based RuO_2 electrodes (27). All the evidence collected with SEM observation, capacity measurements, and background voltammograms, therefore, indicates

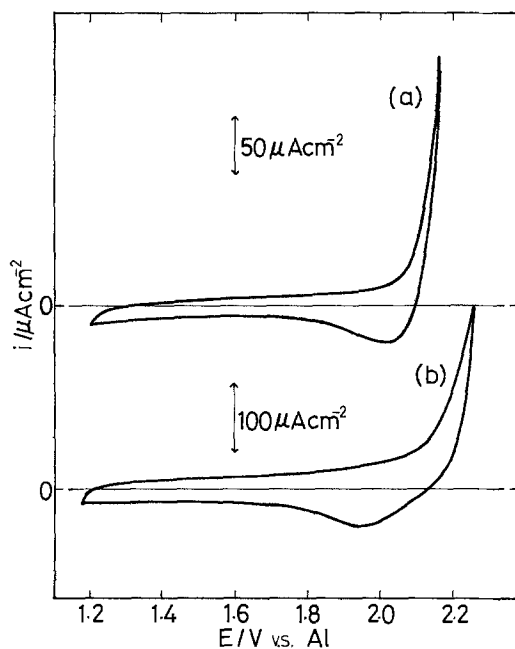
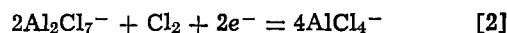
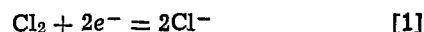


Fig. 3. Background cyclic traces in the melt of $p\text{Cl} = 1.1$ at $v = 50$ mV sec^{-1} . (a) SnO_2 -based RuO_2 electrode, (b) GC electrode.

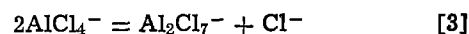
that the real surface area of our RuO_2 electrode is not considerably different from the geometric area, the ratio of the real to the geometric area being estimated to be two at most. The causes of the low roughness can be attributed partly to the optically flat surface of the Pyrex substrate, the use of dilute coating solutions (0.02M RuCl_3), and the relatively long annealing time (10 hr at 500°C).

Comparison of Tafel plots between SnO_2 -based RuO_2 and GC electrodes.—Figure 4 shows the Tafel plots for chlorine evolution and reduction in the melt of $p\text{Cl} = 1.1$ on (a) GC and (b) RuO_2 electrodes. At low overpotentials chlorine evolves from free chloride ions whose activity is specified by the $p\text{Cl}$ value, and the current plateau is ascribed to the diffusion process of Cl^- (28), because the limiting value depends on $p\text{Cl}$, irrespective of electrode materials. The cathodic limiting current is due to the diffusion of Cl_2 (22), depending on the partial pressure of Cl_2 .

There are two overall reactions concerning chlorine evolution



The standard potential of reaction [2] is located at 0.62V positive to the potential of reaction [1] ($p\text{Cl} = 1.1$, $p\text{Cl}_2 = 1$ atm) according to the thermodynamic calculation using the equilibrium constant ($K = 1.06 \times 10^{-7}$) of the following acid-base reaction (29)



In the present study, we are concerned with reaction [1], which is the primary reaction taking place at low $p\text{Cl}$ and low overpotentials.

The polarization behavior obtained during reverse scanning is not shown in Fig. 4 for simplicity. Deep scanning ($\eta \sim 500$ mV) resulted in so-called hysteresis curves and subsequent scanning showed different results. However, those changes in the polarization easily recovered to the original one by agitating the bulk melt, and irreversible changes indicating surface degradation were not observed. The hysteresis effect is ascribed to the change in $p\text{Cl}$ at the electrode surface.

The chlorine evolution on semiconductive SnO_2 electrodes is less reversible than that on GC as reported previously (4). Hence, the reversible be-

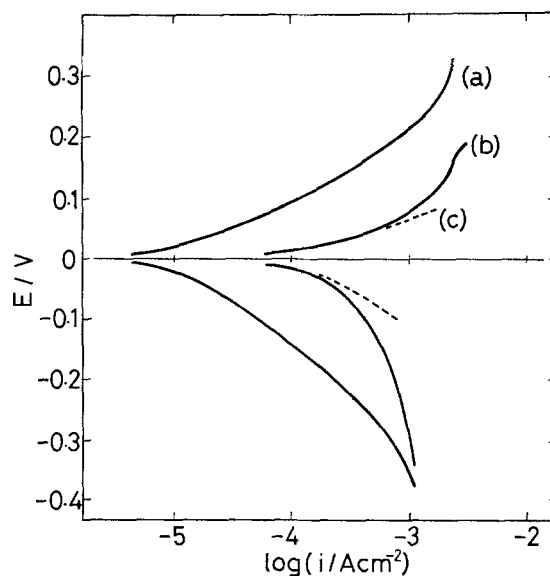
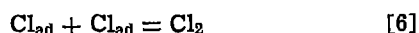
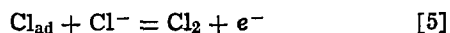
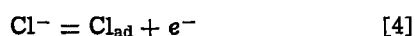
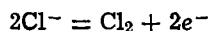


Fig. 4. Comparison of Tafel plots between SnO_2 -based RuO_2 and GC electrodes in the melt of $p\text{Cl} = 1.1$ under an atmospheric pressure of Cl_2 . (a) GC electrode, (b) SnO_2 -based RuO_2 electrode, (c) curve (b) corrected for concentration overpotentials.

havior of curve (b) is obviously ascribed to the activity of the electrocatalyzer prepared on SnO_2 . Because of the improved reversibility, the Tafel region of the RuO_2 electrode is narrow and largely curved, showing a great participation of the diffusion process. In order to obtain kinetic parameters, the concentration overvoltage was corrected with the conventional method described by Vetter (30). The dotted line in Fig. 4 shows the corrected Tafel plots. The anodic (b_+) and cathodic (b_-) Tafel slopes were 72 ± 8 and -105 ± 8 mV/decade, respectively, and the exchange current density (i_0) based on the geometric area was $132 \pm 22 \mu\text{A}/\text{cm}^2$ for several experiments. The i_0 value on GC was $8.9 \mu\text{A}/\text{cm}^2$ based on the geometric area, being in good agreement with the previous result, $8.6 \pm 0.8 \mu\text{A}/\text{cm}^2$ (22). Comparing the two i_0 's it is seen that the former value is 15 times larger than the latter value, or more if taking into account the higher roughness of GC electrodes. The electrocatalytic activity of the RuO_2 electrode is therefore quite noticeable.

The reaction mechanism on RuO_2 electrode.—For the overall reaction [1], the following elementary reactions have been proposed (1, 22, 31-33)

overall



Using the stoichiometric number (ν) defined by reaction [7], one can specify possible combinations of the above elementary reactions

$$\nu = \frac{nF i_0}{RT} \left(\frac{\partial E}{\partial i} \right)_{E \rightarrow 0} \quad [7]$$

Near-equilibrium polarization behavior (i vs. E) obtained in the melt of $p\text{Cl} = 1.1$ is shown in Fig. 5, the so-called polarization resistance, $(\partial E / \partial i)_{E \rightarrow 0}$, being easily determined. The ν value calculated from the i_0 and the $n (= 2)$ values was 0.94, being close to unity. Therefore, the reaction mechanisms corresponding to the fact that $\nu = 1$ are three combinations of them

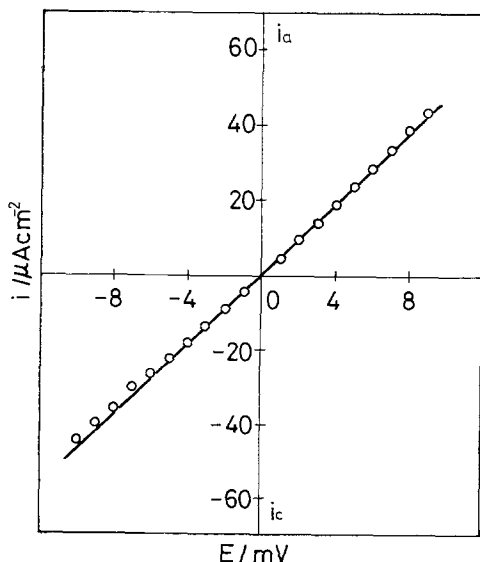


Fig. 5. Micropolarization behavior of SnO_2 -based RuO_2 electrode in the melt of $p\text{Cl} = 1.1$ under $p_{\text{Cl}_2} = 1$ atm.

(A) fast, reaction [4] + slow, reaction [5]

(B) fast, reaction [4] + slow, reaction [6]

(C) fast, reaction [5] + slow, reaction [4]

The rate equations for the above reaction schemes have to involve some adsorption isotherm which the adsorbed intermediate obeys. Langmuir, nonactivated Temkin, and activated Temkin isotherms are applied in formulating the rate equations, and then the theoretical kinetic parameters are subjected to comparison with the experimental values to determine which reaction scheme is the most probable. Mechanistic analysis based only on Tafel slopes, however, would fail in the determination because some of the isotherms yield the same Tafel slope for the different schemes. In connection with this, kinetic analyses based on reaction orders are quite informative. In a previous study (22), the reaction orders with respect to Cl^- and Cl_2 played decisive roles in determining the reaction mechanism of chlorine electrode reaction on GC electrode in the melt.

Figures 6 and 7 show the dependence of Tafel plots on $p\text{Cl}$ and P_{Cl_2} (partial pressure of Cl_2), where the concentration overvoltages are corrected for each plot. Cathodic Tafel plots showed slightly curved features which were presumably due to experimental uncertainty of the cathodic diffusion current (i_{dc}). The correction term $(1 - i/i_{\text{dc}})$ is very sensitive to the i_{dc} value because available i values are limited only to one order range below the i_{dc} . Using those data, we can obtain six kinetic parameters; three reaction orders of i_0 , i_a , and i_c with respect to Cl^- , and also similar three parameters with respect to Cl_2 . The former three parameters were calculated from Fig. 8, where anodic current values (i_a) at $E = 0.105\text{V}$, cathodic current values (i_c) at $E = -0.030\text{V}$, and i_0 values are plotted against $-p\text{Cl}$ ($= \log a_{\text{Cl}^-}$) at a constant P_{Cl_2} ($= 1$ atm). The latter ones were obtained from Fig. 9 where i_a and i_c at $E = \pm 0.080\text{V}$ and i_0 were plotted against partial pressures of Cl_2 at a constant $p\text{Cl}$ ($= 1.1$). The reaction orders thus collected are summarized in Table I.

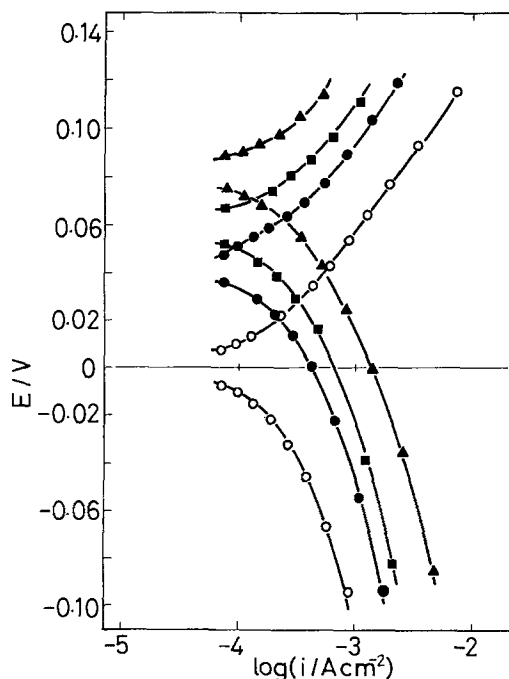


Fig. 6. $p\text{Cl}$ dependence of Tafel plot for chlorine electrode on SnO_2 -based RuO_2 in NaAlCl_4 melts under an atmospheric pressure of Cl_2 at 175°C . (\circ) $p\text{Cl} = 1.1$, (\bullet) $p\text{Cl} = 1.58$, (\blacksquare) $p\text{Cl} = 1.78$, (\blacktriangle) $p\text{Cl} = 2.02$.

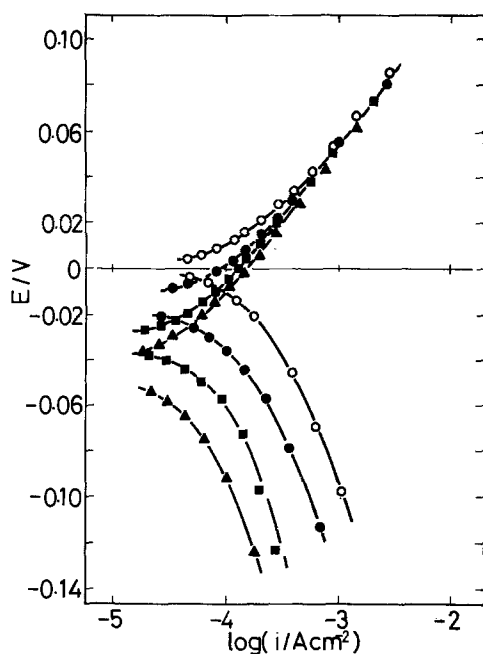


Fig. 7. P_{Cl_2} dependence of Tafel plot for chlorine electrode on SnO_2 -based RuO_2 in a $NaAlCl_4$ melt of $p_{Cl} = 1.1$ at $175^\circ C$. (\circ) $P_{Cl_2} = 1$ atm, (\bullet) $P_{Cl_2} = 0.52$ atm, (\blacksquare) $P_{Cl_2} = 0.22$ atm, (\blacktriangle) $P_{Cl_2} = 0.11$ atm.

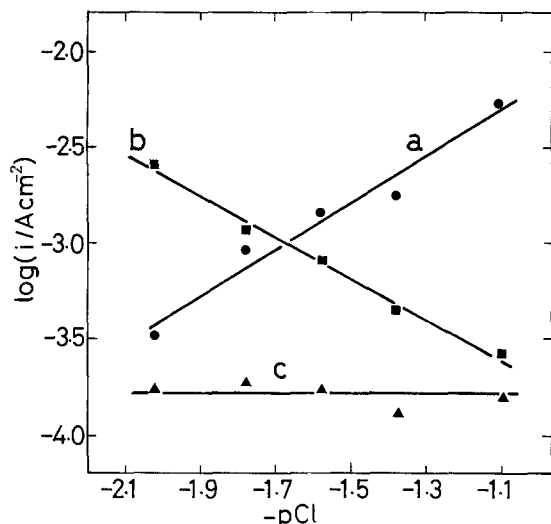


Fig. 8. p_{Cl} dependence of current (i) under a constant $P_{Cl_2} (= 1$ atm). a, Anodic current densities at $E = 105$ mV; b, cathodic current densities at $E = -30$ mV; c, exchange current densities.

The data shown in Table I were inspected first from the viewpoint of the i_0 derivatives, which must be the most reliable parameters because their definition does not involve any arbitrary choice of electrode potential. The theoretical i_0 derivatives with respect to p_{Cl} and P_{Cl_2} are tabulated in Table II for the mechanism (A), (B), and (C) with the three adsorption

Table I. Experimental reaction orders with respect to Cl^- and Cl_2 on a RuO_2 electrode in $NaAlCl_4$ melt at $175^\circ C$

| | |
|--|------|
| $(\partial \log i_0 / \partial \log a_{Cl^-})_{P_{Cl_2}}$ | 0 |
| $(\partial \log i_0 / \partial \log P_{Cl_2})_{p_{Cl}}$ | 0.6 |
| $(\partial \log i_a / \partial \log a_{Cl^-})_{E, P_{Cl_2}}$ | 1.2 |
| $(\partial \log i_c / \partial \log a_{Cl^-})_{E, P_{Cl_2}}$ | -1.1 |
| $(\partial \log i_a / \partial \log P_{Cl_2})_{E, p_{Cl}}$ | 0 |
| $(\partial \log i_c / \partial \log P_{Cl_2})_{E, p_{Cl}}$ | 1.0 |

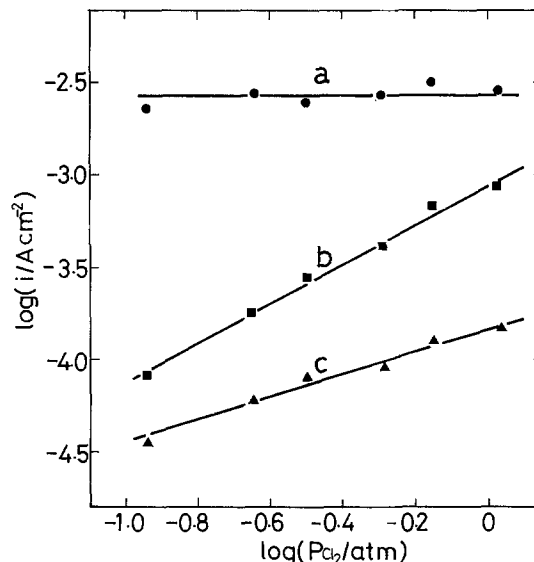
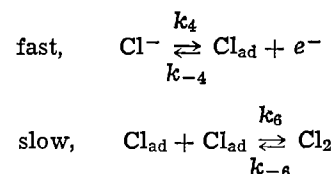


Fig. 9. P_{Cl_2} dependence of current (i) at a constant $p_{Cl} (= 1.1)$. a, Anodic current densities at $E = 80$ mV; b, cathodic current densities at $E = -80$ mV; c, exchange current densities.

isotherms. The table was constructed on the bases of our calculations described previously (22) and literature (34). Since the experimental i_0 derivatives are 0 with respect to Cl^- and 0.6 with respect to Cl_2 , it is seen at first glance that mechanism (B) under the activated Temkin isotherm is the most probable scheme.

The validity of the Temkin condition can be seen in the anodic and cathodic reaction orders with respect to Cl^- . Table III shows both theoretical reaction orders for mechanism (B) with the different isotherms (22, 35). Apparently, only the activated Temkin isotherm gives a tendency consistent with the results shown in Table I. This mechanistic conclusion was also confirmed by comparison between the theoretical and experimental reaction orders with respect to Cl_2 . As shown in Table IV, the former values for the anodic and cathodic processes are 0 and 1, being in excellent agreement with the experimental values.

For mechanism (B) under activated Temkin condition, the following rate equation is derived (22, 36), assuming a quasi-equilibrium state for the fast process, reaction [4]



$$i = 2Fk_6(K_4)^{2(1-\beta)}a_{Cl}^{-2(1-\beta)} \exp [2(1-\beta)fE] - 2Fk_{-6}(K_4)^{-2\beta}a_{Cl}^{-2\beta}P_{Cl_2} \exp (-2\beta fE) \quad [8]$$

where $K_4 = k_4/k_{-4}$, $f = F/RT$, β is the symmetric factor of the adsorption process, and E is the potential difference from the reference electrode. Neglecting the backward reaction, we obtain Tafel relationships for the anodic and cathodic processes

$$\ln i_a = \ln (2Fk_6) + 2(1-\beta) \ln (K_4) + 2(1-\beta) \ln (a_{Cl^-}) + 2(1-\beta)fE \quad [9]$$

$$\ln i_c = \ln (2Fk_{-6}) - 2\beta \ln (K_4) - 2\beta \ln (a_{Cl^-}) + \ln (P_{Cl_2}) - 2\beta fE \quad [10]$$

The kinetic derivatives shown in Table IV are easily obtained from reactions [9] and [10]. Some of the reaction orders involve the parameter β , which is usu-

Table II. The theoretical reaction orders (i_0 derivatives) with respect to Cl^- and Cl_2 in the chlorine electrode reaction

| Mechanism | Langmuir | | | | Nonactivated Temkin | | Activated Temkin | |
|-----------|--------------------|------|--------------------|-------|---------------------|------|------------------|-----|
| | $\theta \approx 0$ | | $\theta \approx 1$ | | x | y | x | y |
| | x | y | x | y | | | | |
| (A) | 0.5 | 0.75 | 0.5 | 0.25 | 0.5 | 0.75 | 0.5 | 0.5 |
| (B) | 0 | 1 | 0 | 0 | 0 | 1 | 0 | 0.5 |
| (C) | 0.5 | 0.25 | 0.5 | -0.25 | 0.5 | 0.25 | 0.5 | 0 |

In calculations, symmetry factor of electron transfer step (α) and adsorption step (β) were assumed as 0.5. $x = (\partial \log i_0 / \partial \log a_{\text{Cl}^-})_{P_{\text{Cl}_2}}$, $y = (\partial \log i_0 / \partial \log P_{\text{Cl}_2})_{P_{\text{Cl}^-}}$.

Table III. The theoretical reaction orders with respect to Cl^- for mechanism (B) under different adsorption isotherms

| Reaction order | Langmuir | | Nonactivated Temkin | Activated Temkin* |
|--|--------------------|--------------------|---------------------|-------------------|
| | $\theta \approx 0$ | $\theta \approx 1$ | | |
| $(\partial \log i_a / \partial \log a_{\text{Cl}^-})_{E, P_{\text{Cl}_2}}$ | 2 | 0 | 2 | 1 |
| $(\partial \log i_c / \partial \log a_{\text{Cl}^-})_{E, P_{\text{Cl}_2}}$ | 0 | -2 | 0 | -1 |

* $\beta = 0.5$.

Table IV. Theoretical Tafel slopes and reaction orders for mechanism (B) under activated Temkin condition

| | |
|--|--------------------|
| $(\partial \log i_0 / \partial \log a_{\text{Cl}^-})_{P_{\text{Cl}_2}}$ | 0 |
| $(\partial \log i_0 / \partial \log P_{\text{Cl}_2})_{P_{\text{Cl}^-}}$ | $1 - \beta$ |
| $(\partial \log i_a / \partial \log a_{\text{Cl}^-})_{E, P_{\text{Cl}_2}}$ | $2(1 - \beta)$ |
| $(\partial \log i_c / \partial \log a_{\text{Cl}^-})_{E, P_{\text{Cl}_2}}$ | -2β |
| $(\partial \log i_a / \partial \log P_{\text{Cl}_2})_{E, P_{\text{Cl}^-}}$ | 0 |
| $(\partial \log i_c / \partial \log P_{\text{Cl}_2})_{E, P_{\text{Cl}^-}}$ | 1 |
| $(\partial E / \partial \log i_a)$ | $1/2(1 - \beta)f'$ |
| $(\partial E / \partial \log i_c)$ | $-1/2\beta f'$ |

* $f' = F/2.3RT$.

ally regarded as 0.5 as assumed in the foregoing sections. Thus the β value, which can be calculated with the data shown in Table I, may be used to evaluate the consistency of our conclusion. The calculated β was 0.4 from the i_0 derivative, and 0.4 and 0.55 from the reaction orders with respect to Cl^- . Using the average value of β ($= 0.45$), we can also calculate the theoretical Tafel slopes; $b_+ = 80.9$ mV and $b_- = -98.9$ mV, being in good agreement with the experimental results ($b_+ = 72 \pm 8$ mV and $b_- = -105 \pm 8$ mV). Thus there is no inconsistency in our mechanistic analysis.

The polarization behavior of the RuO_2 electrode shown in Fig. 4 is again represented in a different manner, taking into account the presented reaction mechanism. The rate equation [8] can be rewritten as follows

$$i/[1 - \exp(-2f\eta)] = i_0 \exp[2(1 - \beta)f\eta] \quad [11]$$

where η is the overvoltage. In this case the reference electrode is the reversible chlorine electrode ($p_{\text{Cl}} = 1.1$, $P_{\text{Cl}_2} = 1$ atm), hence $\eta = E$ for the condition of Fig. 4. Since the backward reaction is not omitted in reaction [11], the plot of $\log \{i/[1 - \exp(-2f\eta)]\}$ vs. η describes the polarization behavior corrected for the backward reaction rate over a broad range of current density (37) and gives a straight line with the slope of $2(1 - \beta)F/2.3RT$. Figure 10 shows this relationship in a potential range where the concentration overvoltage can be negligible. The β value

($= 0.45$) obtained from the slope and the i_0 value at $\eta = 0$ again coincided with the above values.

Consequently, the chlorine electrode reaction on RuO_2 in NaAlCl_4 melt with near equimolar compositions occurs according to a Volmer-Tafel mechanism, where the Tafel reaction (atom-atom recombination) is a rate-determining step for both anodic and cathodic reactions. This mechanism is in contrast with that on GC, which obeys a Volmer-Heyrovsky type mechanism involving the Heyrovsky reaction (atom-recombination) as a rate-determining step, i.e., mechanism (A) as revealed previously (22). Mechanisms (A), (B), and (C) are analogous to the mechanism of hydrogen electrode in aqueous systems. It is widely accepted that in acidic solutions the hydrogen evolution on highly catalytic substrates such as Pt obeys the Volmer-Tafel mechanism, while the Volmer-Heyrovsky mechanism prevails on other metals such as Au and Ni, giving smaller exchange current densities (38). Similar kinetic correlation seems to be applied to chlorine evolution in aqueous systems. Several authors suggested that the rate-determining step of the chlorine evolution is the Tafel reaction on RuO_2 electrodes (6, 16, 39) and the Heyrovsky reaction on vitreous (39) and graphite electrodes (40). The electrocatalytic activity of RuO_2 electrodes in the melt, which is associated with the Tafel reaction, may be understandable from this phenomenological aspect.

Conclusions

Ruthenium oxide electrodes have a noticeable electrocatalytic effect on the chlorine electrode reaction in molten NaAlCl_4 . The exchange current density at the standard conditions ($p_{\text{Cl}} = 1.1$, $P_{\text{Cl}_2} = 1$ atm, at 175°C) is $132 \pm 22 \mu\text{A}/\text{cm}^2$, while the corresponding i_0 on GC is $8.9 \mu\text{A}/\text{cm}^2$. The chlorine evolution obeys a Volmer-Tafel type mechanism under the activated Temkin condition

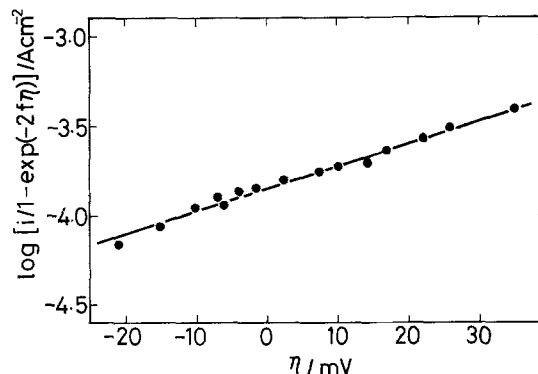
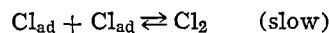
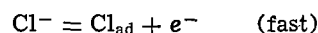


Fig. 10. Polarization behavior of SnO_2 -based RuO_2 electrode corresponding to the data of Fig. 4. The data were plotted according to Eq. [11].

The rate-determining step is the combination (Tafel) reaction. The chlorine reduction also obeys the same mechanism in the reverse direction.

Acknowledgment

Part of the experimental data has been obtained by Mr. Isao Sato during his undergraduate research training.

Manuscript submitted June 24, 1980; revised manuscript received May 22, 1981.

Any discussion of this paper will appear in a Discussion Section to be published in the June 1982 JOURNAL. All discussions for the June 1982 Discussion Section should be submitted by Feb. 1, 1982.

Publication costs of this article were assisted by Tohoku University.

REFERENCES

- G. L. Holleck, *This Journal*, **119**, 1158 (1972).
- U. Anders and J. A. Plambeck, *Can. J. Chem.*, **47**, 3055 (1969).
- I. Uchida and S. Toshima, *J. App. Electrochem.*, **9**, 647 (1979).
- I. Uchida, H. Urushibata, and S. Toshima, *This Journal*, **127**, 757 (1980).
- I. Uchida, K. Niki, and H. A. Laitinen, *ibid.*, **125**, 1759 (1978).
- G. Bianchi, *J. App. Electrochem.*, **1**, 231 (1971).
- Ya. M. Kolotykin, *Denki Kagaku*, **47**, 390 (1979).
- D. Galizzioli, F. Tontardini, and S. Trasatti, *J. App. Electrochem.*, **4**, 57 (1974); **5**, 203 (1975).
- L. D. Burke, O. J. Murphy, J. F. O'Neill, and S. Venkatesan, *J. Chem. Soc., Faraday Trans. I*, **73**, 1659 (1977).
- G. Lodi, E. Sivieri, A. De Battisti, and S. Trasatti, *J. App. Electrochem.*, **8**, 135 (1978).
- L. Burke and O. J. Murphy, *J. Electroanal. Chem. Interfacial Electrochem.*, **96**, 19 (1979).
- D. V. Kokoulina, T. V. Ivanova, Yu. I. Krasovitskaya, Z. I. Kudryavtseva, and L. I. Krishtalik, *Élektrokhimiya*, **13**, 1511 (1977).
- R. G. Erenburg, L. I. Krishtalik, and V. I. Bystrov, *ibid.*, **8**, (1972).
- R. G. Erenburg, L. I. Krishtalik, and I. P. Yaroshenskaya, *ibid.*, **11**, 1072 (1975).
- L. J. J. Janssen, L. M. C. Starmans, J. G. Visser, and E. Barendrecht, *Electrochim. Acta*, **22**, 1093 (1977).
- I. R. Burrows, D. A. Denton, and J. A. Harrison, *ibid.*, **23**, 493 (1978).
- D. A. Denton, J. A. Harrison, and R. I. Knowles, *ibid.*, **24**, 521 (1979).
- T. Arikado, C. Iwakura, and H. Tamura, *ibid.*, **23**, 9 (1978).
- M. Inai, C. Iwakura, and H. Tamura, *ibid.*, **24**, 993 (1979).
- V. E. Kazarinov and V. V. Andreev, *Elektrokhimiya*, **14**, 577 (1978).
- D. R. Rolison, K. Kuo, M. Umana, D. Brundage, and R. W. Murray, *This Journal*, **126**, 407 (1979).
- H. Urushibata, I. Uchida, and S. Toshima, *J. Electroanal. Interfacial Electrochem.*, **117**, 43 (1981).
- I. Uchida, H. Urushibata, and S. Toshima, *ibid.*, **96**, 45 (1979).
- I. Uchida, H. Urushibata, and S. Toshima, *This Journal*, **127**, 995 (1980).
- H. A. Laitinen, Y. Yamamura, and I. Uchida, *ibid.*, **125**, 1450 (1978).
- P. Fellner, M. Chrenková-Paučířová, A. Silný, and K. Mantiasovský, *Electrochim. Acta*, **25**, 189 (1980).
- H. Urushibata and I. Uchida, Unpublished data.
- G. Letisse and B. Tremillon, *J. Electroanal. Chem. Interfacial Electrochem.*, **17**, 371 (1968).
- L. G. Boxall, H. L. Jones, and R. A. Osteryoung, *This Journal*, **120**, 223 (1973).
- K. J. Vetter, "Electrochemical Kinetics," p. 163, Academic Press, New York (1967).
- S. Sernger, I. Galasiu, and D. Geana, *Electrochim. Acta*, **24**, 115 (1979).
- R. Tunold, H. M. Bø, K. A. Paulsen, and J. O. Yttredal, *ibid.*, **16**, 2101 (1971).
- W. E. Triaca, C. Solomons, and J. O'M. Bockris, *ibid.*, **13**, 1949 (1968).
- B. E. Conway, "Theory and Principles of Electrode Processes," p. 174, Ronald Press, New York (1965).
- G. Fanta, G. Fiori, and J. W. Augustynski, *This Journal*, **116**, 928 (1969).
- T. Yokoyama and M. Enyo, *Electrochim. Acta*, **24**, 997 (1979).
- P. Delahay, "Double Layer and Electrode Kinetics," p. 163, Interscience, New York (1965).
- J. O'M. Bockris and A. K. N. Reddy, "Modern Electrochemistry," Vol. 2, p. 1250, Plenum Press, New York (1970).
- B. V. Tilak, *This Journal*, **126**, 1343 (1979).
- L. J. J. Janssen and J. G. Hoogland, *Electrochim. Acta*, **15**, 941 (1970).

Electrochemical Photovoltaic Cells Based on n-GaAs in Propylene Carbonate

M. E. Langmuir,* P. Hoenig, and R. D. Rauh*

EIC Laboratories, Incorporated, Newton, Massachusetts 02158

ABSTRACT

Electrochemical photovoltaic cells (EPC's) have been characterized based on n-GaAs and propylene carbonate electrolytes. Photovoltages are limited to ~0.7V due to electrode corrosion and lack of specific adsorption by the redox systems studied. Polarization of photo and counterelectrodes, resulting from low redox solubilities and electrolyte conductivities, are responsible for lower fill factors and short-circuit photocurrents for nonaqueous compared to aqueous EPC's. Potentially, these losses can be offset by higher voltages and long-term stabilities, particularly if specifically adsorbing redox couples can be found.

Nonaqueous electrolytes hold the promise of enhancing long-term stability in electrochemical photovoltaic cells (EPC's). In this paper we characterize

n-GaAs, propylene carbonate (PC) based EPC's with regard to limitations on photovoltage and photocurrent.

Propylene carbonate has been chosen as a representative solvent for its wide anodic and cathodic stability range, and because we have established procedures for

* Electrochemical Society Active Member.
Key words: photoelectrochemistry, propylene carbonate, gallium arsenide.

its effective drying and purification (1). In addition, PC supports a stable Li^+/Li reference electrode (2) which is simple to use and which can be employed without danger of solution contamination. We note, however, that the low conductivity of PC electrolytes (relative to H_2O) probably prevents its use in practical devices as currently conceptualized. Nevertheless, the aspects of photoelectrochemical operation discovered in PC can be generalized to other nonaqueous systems.

We will first ask: What are the limits to the photovoltage in such a cell? In the ideal two-electrode EPC, the counterelectrode senses the rest potential of the solution and is thus equivalent to V_{redox} . The photoelectrode has a maximum onset voltage corresponding to its flatband potential, V_{FB} , leading to the relation

$$V_{\text{oc}} = V_{\text{FB}} - V_{\text{redox}} \quad [1]$$

This simple relation is fundamental to EPC operation. The relation is meaningless, however, if the redox couple in the cell is not oxidized or reduced by the photoelectrode so as to stabilize it against photocorrosion. Thus, we further specify the limiting photovoltage in a stable cell by

$$V_{\text{oc}}(\text{max}) = V_{\text{FB}} - V_{\text{c}} \quad [2]$$

where V_{c} is the anodic or cathodic corrosion potential of the photoanode or photocathode, respectively. One of the potential advantages of nonaqueous solvents is to allow the maximization of Eq. [1] through the maximization of Eq. [2] assuming that corrosion reactions are rendered more difficult than in H_2O .

Two factors appear to complicate the use of Eq. [1] as a simple predictor for cell design. The first is that V_{FB} is influenced by the redox couple when specific adsorption occurs. For example, in the aqueous-based $\text{CdX}/\text{X}_n^{-2}$, X^{-2} cells ($\text{X} = \text{S}, \text{Se}, \text{or Te}$), V_{FB} is shifted negative by such adsorption (3). Most documented cases of this kind of influence on V_{FB} occur in protic media due to acid-base equilibria involving surface OH or XH groups (4). Thus, we might be able to test Eq. [1] in aprotic media like PC without this additional variable.

The other complicating factor involves the observation that half-cell photovoltages equivalent to V_{FB} are often unattainable. In solid-state Schottky barrier devices, this is often ascribed to the intermediacy of "surface states" (5). The latter may be viewed as surface-bound redox centers which act as very efficient captors of electrons or holes. As a result, such centers "pin" the Fermi level, thus restricting the photovoltage. It may be possible to modify, chemically, such states. Improvements in cell operation due to certain semiconductor etching treatment, oxidation, hydrogenation, or treatment with Ru^{+3} have been ascribed to such surface-state modification (6-9). Recent observations by Wrighton, Bard and co-workers suggest Fermi level pinning at some semiconductor liquid junctions (10).

The other major question regarding cell operation concerns the factors which influence the photocurrent. The effects on photocurrent yields of redox potential, interaction of the electrolyte with the electrode surface states, and the doping, orientation, and crystalline quality of the photoelectrode are little understood. Surface states can, for example, influence the voltage onset and sharpness of the rise of photocurrent-voltage curves. Recombination via the surface has been used to explain the so-called "foot problem" in EPC i - V curves, characteristic of inefficient electrodes with low fill factor (3, 11).

Experimental

Materials preparation and handling.—Several different redox couples were employed in this study. Acetyl ferrocene (acFc), ferrocene (Fc), and NN'-tetramethyl-*p*-phenylenediamine (TMPD) were sublimed before use. I_2 was also sublimed *in vacuo* before use. Both KI and tetrabutylammonium bromide (Eastman)

were dried *in vacuo* over P_2O_5 . Bromine (Ventron, ultrapure) was used as received. The propylene carbonate (PC), LiAsF_6 electrolyte preparation and purification were described previously (1).

All manipulations were carried out in an Ar-filled glove box containing <10 ppm H_2O . The acFc^+ , Fc^+ , and TMPD^+ were produced by electrolysis of acFc, Fc, and TMPD solutions at constant current. Concentrations were verified spectrophotometrically.

Electrochemical cell and reference electrode.—Most experiments were carried out in a demountable thin layer photoelectrochemical research cell shown in Fig. 1. The cell has a liquid path length of ~ 0.4 mm. Irradiation occurs through an optically transparent electrode of tin oxide (NESATRON) or indium-tin oxide (NESATRON).

The electrodes are mounted in a Macor machinable glass block. Filling was carried out in the glove box (<10 ppm H_2O , Ar atmosphere) through the holes containing the demountable Pt electrodes. The photoelectrode is provided with an ohmic contact and a Ni lead wire and is sealed into the block using an epoxy cement previously tested for solvent compatibility. All the desired electrochemical and photoelectrochemical measurements can be made in this cell. Typically, one of the Pt electrodes served as a reference electrode, placing V_{redox} at 0 volts in each cell.

As the supporting electrolyte in the cells was LiAsF_6 , we were able to calibrate the internal reference electrode *vs.* Li^+/Li (in a separate measurement), since PC is compatible with Li metal. The Li^+/Li potential is known *vs.* aqueous SCE in a variety of nonaqueous solvents. The liquid-junction corrected value of $E^\circ(\text{Li}^+/\text{Li})$ is -2.94V *vs.* $(\text{SCE})_{\text{aq}}$ in PC (12). The potentials of some of the specific redox solutions in PC which we have employed are listed in Table I.

Electrode materials.—All investigations were carried out on the $<100>$ face of an n-GaAs crystal ($0.11 \Omega\text{-cm}$, partially Zn compensated) of 0.07 cm^2 area. Usually the n-GaAs surface was etched prior to each experiment according to the procedures of Kohl and Bard (13), which produced a shiny surface with a nonuniform distribution of etch pits (etch A). In several experiments on the effects of surface preparation on n-GaAs photoelectrodes, the matte etching procedure of Parkinson, Heller, and Miller was employed, which produced a high area, nonreflective surface (etch B). Etch B followed by treatment for 30 sec in a 0.01M RuCl_3 , 0.1M HNO_3 solution is denoted as etch C.

Photoelectrochemical measurements.—Illumination of the working electrode was achieved with a 150W xenon lamp, the output of which was passed through a water filter with Pyrex windows. Light intensity was measured using an EG&G Model 450 Radiometer/

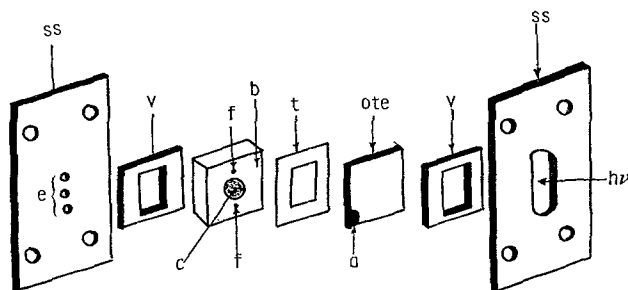


Fig. 1. Demountable thin layer photoelectrochemical research cell. The crystal (c) is mounted in a Macor block (b), which also contains holes (f) for filling and auxiliary wire electrodes. The optically transparent counterelectrode (OTE) is separated by a Teflon spacer (t), and has an Ag epoxy reinforced electrode contact (a). The package is confined using Viton rubber spacers (v) and stainless steel front and back plates (ss) with holes for electrodes (e). The plates are secured with bolts and wing nuts through the four corner holes.

Table I. Measured redox potentials for couples in propylene carbonate

| Couple* | V_{redox} (vs. SCE _{aq})** |
|----------------------------------|--|
| Br ₂ /Br ⁻ | +0.96 |
| acFc ⁺ /acFc | +0.59 |
| Fc ⁺ /Fc | +0.34 |
| I ₂ /I ⁻ | +0.16 |
| TMPD ⁺ /TMPD | -0.01 |
| Li ⁺ /Li | -2.94 |

* acFc: acetyl ferrocene. Fc: ferrocene. TMPD: tetramethylphenylenediamine.

** Liquid junction corrected values.

Photometer at a constant distance from the source. The cell was then always placed at that distance. The intensity was adjusted using various neutral density filters. Although the Xe source yields an imperfect representation of the solar spectrum, it is a convenient white light source and is used here to compare results under typical broad band radiation.

Current-voltage curves were obtained with a Wenking LT73 potentiostat. A function generator specially designed for voltammetry provided a linear voltage scan with a preset starting voltage and adjustable scan rate. The current-voltage curves were measured on an X-Y recorder.

Half-cell measurements were made with respect to one of the Pt internal reference electrodes, using the window OTE as the counterelectrode. For solar cell measurements, the OTE was either shorted to the Pt reference electrode, or was used as both the counter and reference electrode. Both configurations gave equivalent results.

Linear sweep voltammograms of the redox couple on n-GaAs were obtained for different light intensities using a Pyrex filter to eliminate the u.v. component below 320 nm of the 150W Xe arc spectrum. The scan rate was 20 mV/sec for all cases. The reported data are not corrected for reflection or light absorption by the OTE or the solution and therefore give a true picture of the efficiency of the cell operated as a solar cell. Measurements of output stability of the solar cells were made at the potential yielding the maximum power on the cell's figure of merit *i*-*V* curve.

Results and Discussion

Factors influencing the photovoltage.—A typical series of current-voltage curves are shown in Fig. 2 for the cell

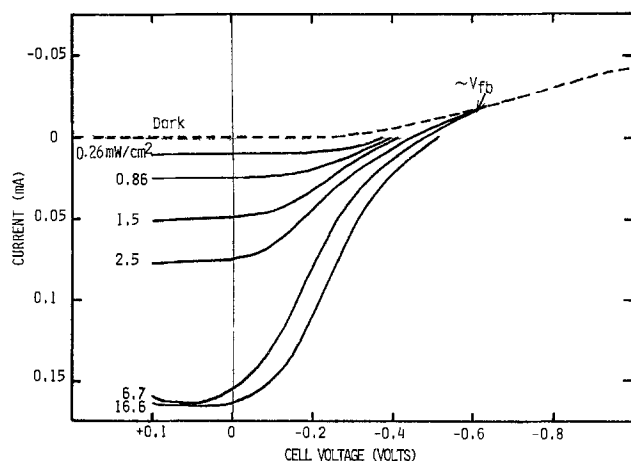
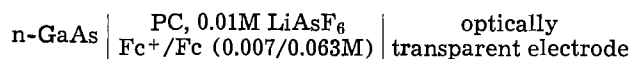


Fig. 2. Current vs. voltage at various light intensities for the photoelectrochemical cell n-GaAs (0.07 cm²)|Fc⁺(0.007M), Fc (0.063M), LiAsF₆(0.1M), PC|NESATRON OTE. Light source is an Xe arc, Pyrex filter.

In this cell, which contains a rather dilute redox electrolyte, the mechanisms of current and voltage control are evident. In the dark, no anodic current flows. However, a dark cathodic current is observed with an onset of around -0.2V^1 vs. Pt/redox. The magnitude of this current is proportional to the concentration of oxidized species. Its onset is considerably positive of the flatband potential of n-GaAs (see below).

The positive onset of dark current with respect to V_{FB} is indicative of a process involving the tunneling of electrons from the conduction band through the space charge region. We have measured this onset as a function of V_{redox} . In Fig. 3, the voltage onset of dark current (V_{dark}) is plotted vs. V_{redox} , both on the aqueous SCE scale. In the region from 0 to +1V vs. SCE, V_{dark} is directly proportional to V_{redox} . This result would be consistent with a surface-state controlled barrier potential, which would render $V_{\text{FB}} - V_{\text{redox}}$ independent of V_{redox} . It is also possible that the dark reaction occurs via a few metal-like areas on the crystal surface.

Returning to Fig. 2, we see next that, on irradiation, an anodic photocurrent is produced. The onset of photocurrent at each intensity corresponds to the open-circuit voltage, V_{oc} . It occurs at the voltage where dark and photocurrents are exactly equal. Thus, the dark current-voltage behavior of the photoelectrode is important in determining the open-circuit voltage of the cell. If V_{dark} always occurred at the same potential, we might hope to adjust V_{redox} to minimize the dark current effect. This is, however, not the case, as seen in Fig. 3.

Even though a dark current always opposes the photocurrent, regardless of V_{redox} , cells studied here with large separations between V_{redox} and the apparent flatband voltage (see below) still have larger open-circuit voltages. In Fig. 4, the open-circuit photovoltages of these cells are plotted vs. V_{redox} . Note that these are photovoltages of two-electrode cells in which the counterelectrode is the OTE. The measurements were made at a high light intensity, where the photovoltage exhibits saturation. For the couples studied, the variation of V_{oc} at saturation is quite linear with V_{redox} for any given crystal and surface preparation. For crystals cut from the same slice, but for different runs of the same polishing/etching regime, photovoltages are reproducible to about $\pm 10\%$.

¹ Electrochemical measurements were made in both two- and three-electrode configurations. For the cell featured in Fig. 2, the counterelectrode has been shown to be more polarizable than the n-GaAs, and due to its larger area has a negligible contribution to the total cell polarization at the current levels employed. In other systems where the redox reactions have kinetic limitations, such as in I⁻/I⁻ cells, this is not always the case.

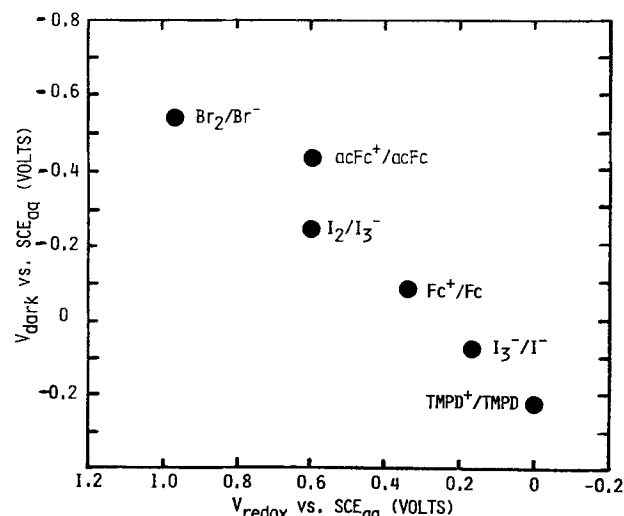


Fig. 3. Variation of voltage onset of cathodic dark current (V_{dark}) with redox potential (V_{redox}) for the half-cell n-GaAs/redox couple, 0.1M LiAsF₆, PC.

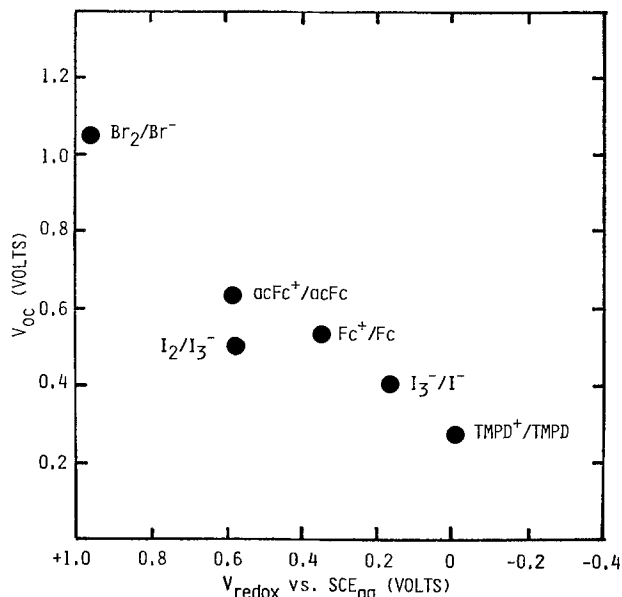
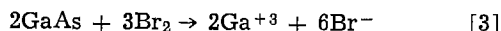


Fig. 4. Variation of open-circuit voltage (V_{oc}) with redox potential (V_{redox}) for the photoelectrochemical cell n-GaAs redox couple, 0.1M LiAsF₆, PC|NESA OTE. Illumination is 150W Xe source, 55 mW/cm².

An important point concerning photovoltages in photoelectrochemical cells is illustrated by the case of the Br₂/Br⁻ couple, which is an exception to the above discussion. With Br₂ present, GaAs corrodes even in the dark according to the reaction



Hence, the redox couple is ineffective in stabilizing the semiconductor. In these cases, the cell exhibits a voltage in the dark, approximately given by the difference $V_{redox} - V_c$. This bucking voltage acts in series with the photovoltage, which is now $V_{FB} - V_c$. The difference $V_{FB} - V_{redox}$ can be made large by choosing any redox couple, but the resulting photovoltages cannot be related to the band bending in the photoelectrode unless it is established that the redox couple is indeed photoelectrochemically oxidized or reduced.

In Fig. 5, V_{oc} and V_{dark} of the semiconductor are summarized along with V_{redox} , but with all potentials presented on the aqueous SCE scale. It is seen that V_{oc} under high light intensities is about -0.2V for the n-GaAs half-cell regardless of the redox couple in solution. This either represents the flatband potential of n-GaAs, or is the effective potential of a surface level which, when reduced at more negative potentials, is totally effective in quenching the photocurrent.

Also shown in Fig. 5 are the values of V_{oc} for each cell at the lowest light intensity used, 0.26 mW/cm².

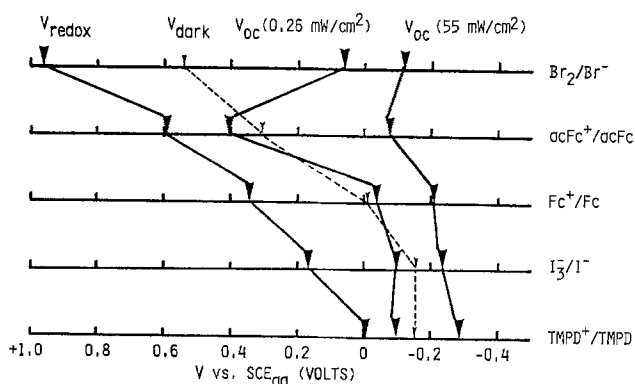


Fig. 5. Diagram showing variations of V_{dark} and V_{oc} at low and high light intensity, with redox couple potential for n-GaAs photoelectrochemical cells in PC.

Except for the case of Br₂/Br⁻, these are close to the voltage onsets of cathodic dark current. The trend is toward a larger difference between high and low intensity V_{oc} 's with increasingly positive V_{redox} (discounting, again, Br₂/Br⁻). The slopes $dV/d(\log I)$ in the linear region of these plots are revealed in Table II. In a classical photodiode, this slope is 59 mV, but in these cells it is usually somewhat larger. This phenomenon has been noted recently by Sakata *et al.* (14) for some other photoelectrochemical cells. They assign a value of δ to the ratio $59 \text{ mV}/(dV/d(\log I))$. A small value of δ means that the photocurrent is effective in overcoming the dark current, as is certainly expected under conditions of large band bending. In general, the onset of dark current is more likely to determine the onset of photocurrent at low intensity. However, the onset of photocurrent tends toward V_{FB} at saturation. Hence, measurements made at low intensity are more likely to show "Fermi level pinning," since V_{dark} is proportional to V_{redox} (Fig. 3).

One major issue to be resolved in these and other n-GaAs cells is the true position of the flatband potential. Capacitance-voltage analysis obtained in the dark indicates a flatband potential for n-GaAs in PC of $-1.1 \pm 0.2\text{V}$ vs. SCE, in agreement with Kohl and Bard in acetonitrile (13), although considerable frequency dependence characterizes the slope of the Mott-Schottky plots. However, other estimates of V_{FB} can be made by observing the intersection of dark and light i - V curves (cf. Fig. 2) or by measuring the bias voltage at which the instantaneous photovoltage, obtained using a pulsed dye laser, is zero (Fig. 6). Both methods give a V_{FB} of about -0.2V vs. SCE. In addition, the plot of V_{oc} vs. V_{redox} shown in Fig. 4 extrapolates to the same value of V_{FB} . Comparison with Table II indicates that, if the more positive values of V_{FB} are accepted, then the redox couples employed all have potentials lying within the n-GaAs gap. If the value of -1V is accepted, then several of the couples lie beneath the valence bandedge, and it would be surprising if they could react with photogenerated holes.

We have tested the stability of the n-GaAs cell with all the couples and found over several hours operation at 1 mA/cm² that only the Br₂/Br⁻ cell shows significant degradation of photocurrent or change in electrode surface morphology as determined by microscopic examination. Furthermore, in all cases except Br₂/Br⁻, the photoelectrochemical oxidation of the redox species can be observed visually at the n-GaAs surface. Although this does not prove total stabilization, it does indicate that hole transfer to the reduced redox species is by far the dominant process except with Br⁻. Experiments with just Br⁻ in the electrolyte show no visual evidence of Br₂ production at the irradiated n-GaAs surface.

Therefore, the accumulated results cast doubt on the validity of C-V measurements for predicting V_{FB} in this case. It is possible that surface states accessible only at potentials $< -0.2\text{V}$ vs. SCE influence the capacitance at cathodic voltages, leading to anomalously negative values for V_{FB} determined in this manner.

Photocurrents, fill factors, and cell efficiencies.—The other important features of Fig. 2 are related to the photocurrents. For light intensities of up to 2.5 mW/

Table II. Variations of photovoltage with light intensity for the cell n-GaAs | PC, redox, 0.1M LiAsF₆ | NESA OTE

| Solution | V_{redox} (meas) | $dV/d(\log I)$ (mV) | $\delta = \frac{59 \text{ mV}}{dV/d(\log I)}$ |
|----------------------------------|--------------------|---------------------|---|
| Br ₂ /Br ⁻ | (0.01/0.05M) | 0.96 | 50 |
| acFc ⁺ /acFc | (0.007/0.03M) | 0.59 | 170 |
| Fc ⁺ /Fc | (0.007/0.063M) | 0.34 | 125 |
| I ₂ /I ⁻ | (0.01/0.05M) | 0.16 | 88 |
| TMPD ⁺ /TMPD | (0.01/0.09M) | -0.01 | 55 |

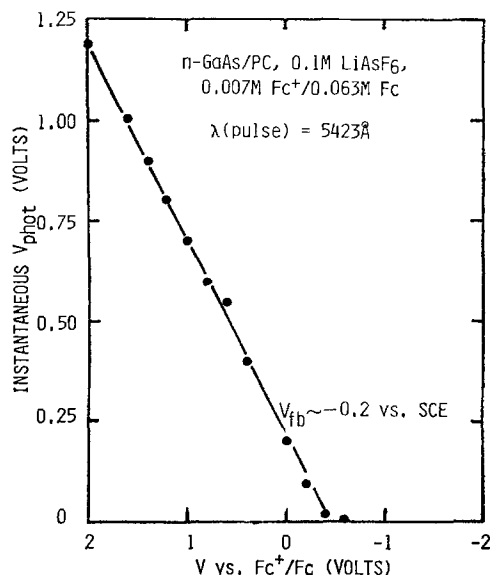


Fig. 6. Instantaneous photovoltage as a function of electrode bias on internal reference scale.

cm^2 , the photocurrents are limited by the number of photons absorbed by the n-GaAs and thus by the number of holes produced. At the higher intensities, the photocurrents become limited by the supply of ferrocene to the electrode surface. An approximation of the steady-state diffusional current is given by Eq. [4] (16)

$$i(\text{mA}/\text{cm}^2) = \frac{1000nFCD}{d} \quad [4]$$

where d is the electrode separation (~ 0.04 cm), C is the concentration (in mols/cm^3), and D the diffusion coefficient. In the present case, $C = 6.3 \times 10^{-5}$ mols/cm^3 and 10^{-5} is a reasonable value for D (15). The resulting limiting current is ~ 1.5 mA/cm^2 . Experimental results of the limiting photocurrents observed for oxidation of 0.05M I^- and 0.032M acFc at n-GaAs are plotted as a function of light intensity in Fig. 7.

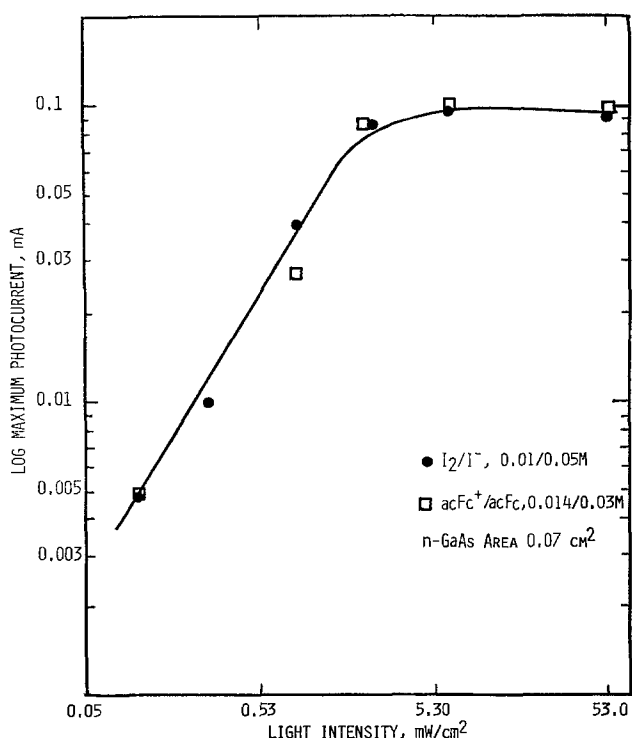


Fig. 7. Limiting photocurrent as a function of light intensity for n-GaAs in PC, 0.1M LiAsF_6 , redox couple, NESAs counterelectrode.

The diffusion-limited current density in both cases is ~ 1.4 mA/cm^2 , attained at light intensities >5 mW/cm^2 for these concentrations, close to that predicted by Eq. [4].

The fill factor or "squareness" of the current-voltage curves in the region between 0 volts and V_{oc} is an important variable in determining cell efficiencies. As shown in Fig. 8, contributions to the final curve arise from polarizations at the photoelectrode and counterelectrode, as well as from solution resistance. The production of photocurrent is also sensitive to the efficiency of light absorption and to lifetime of minority carriers. Cells based on n-GaAs/propylene carbonate, Fc^+/Fc ($0.007/0.063\text{M}$) have been tested in which we have varied the counterelectrode, the concentration of supporting electrolyte, and the surface treatment of the n-GaAs. Some of the results are summarized in Table III, and indicate some of the limitations of the present system.

All cells listed in Table III exhibited diffusionally limited currents at high light intensities. Efficiencies in the range where currents were limited only by the hole flux, i.e., $0-2$ mW/cm^2 white light, were $4-8\%$ while efficiencies at solar intensities were $<1\%$. Kohl and Bard (13) have reported the same type of decrease in efficiency with increasing intensity for n-GaAs/acetoneitrile-based systems. Short-circuit photocurrents were enhanced by $25-30\%$ by employing a black matte etched GaAs surface rather than a reflective shiny surface. Another increase in photocurrents was observed by decreasing the sheet resistance of the optically transparent counterelectrode. NESAs glass (SnO_x , 150 $\Omega\text{-cm}$) gave short-circuit currents which were about 50% less than the more conductive, though $\sim 20\%$ less transmissive, NESATRON ($\text{SnO}_x \cdot \text{In}_2\text{O}_{3-x}$, 5 $\Omega\text{-cm}$). Fill factors and efficiencies were also enhanced in the NESATRON cells, despite a reduction in voltage which may relate to NESATRON's higher optical absorption. An attempt to decrease the surface recombination velocity by adsorbing Ru^{+3} on the n-GaAs surface proved unsuccessful (surface treatment C, in the table). In the original work by Heller and co-workers, a pretreatment in $\text{Se}^{-2}/\text{Se}_n^{-2}$ aqueous electrolyte was employed (6, 7). We have demonstrated in other work that such pretreatment is also necessary for observation of the Ru^{+3} effect in nonaqueous electrolytes (17).

At high light intensity, concentration polarization develops for all these cells over the first minute of cell operation. This effect is demonstrated in Fig. 9 for a cell based on 0.007M Fc^+ , 0.063M Fc , and is due, at least in part, to the limiting concentration of Fc achievable in PC. The wavelength of the incoming light has a significant effect on the cell efficiency. This is due to the wavelength dependence on solution and semiconductor absorbances, as well as that of photocurrent production due to differences in light penetration depth into the semiconductor. For the GaAs cell, sev-

Table III. Effects of n-GaAs surface treatments on performance of the EPC n-GaAs| Fc^+ (0.007M), Fc (0.053M), LiAsF_6 (0.1M), PC|NESAs OTE. Figures in parentheses are for NESATRON OTE.

| | Source intensity (mW/cm^2) (150W Xe arc, 300-1200 nm) | | |
|---------------------------------------|--|------|-------------|
| | 0.9 | 6.7 | 53 |
| Etch A | | | |
| V_{oc} (V) | 0.53 | 0.55 | 0.59 |
| i_{sc} (mA/cm^2) | 0.17 | 1.7 | 1.7 |
| P_{max} (mW/cm^2) | 0.04 | 0.23 | 0.28 |
| η (%) | 4.4 | 3.4 | 0.5 |
| Etch B | | | |
| V_{oc} (V) | 0.55 (0.46) | 0.58 | 0.59 (0.54) |
| i_{sc} (mA/cm^2) | 0.23 (0.40) | 1.7 | 2.1 (2.91) |
| P_{max} (mW/cm^2) | 0.06 (0.07) | 0.26 | 0.44 (0.7) |
| η (%) | 6.9 (7.8) | 3.9 | 0.8 (1.32) |
| Etch C | | | |
| V_{oc} (V) | 0.52 | — | 0.54 |
| i_{sc} (mA/cm^2) | 0.14 | — | 1.65 |
| P_{max} (mW/cm^2) | 0.04 | — | 0.24 |
| η (%) | 4.4 | — | 0.45 |

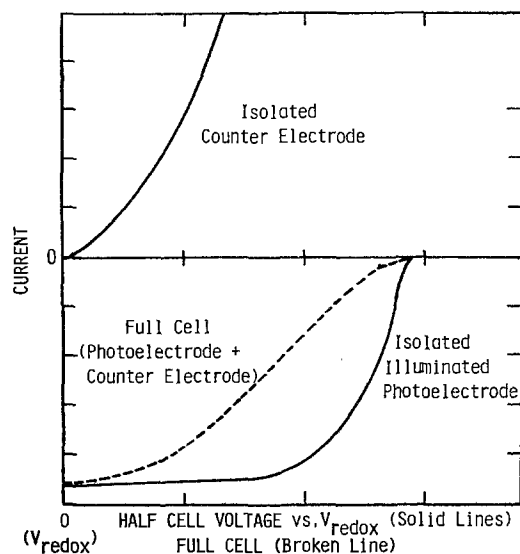


Fig. 8. Hypothetical steady-state current-voltage curves illustrated for half-cell components of an electrochemical photovoltaic cell (solid line) and for the resulting full cell (broken line).

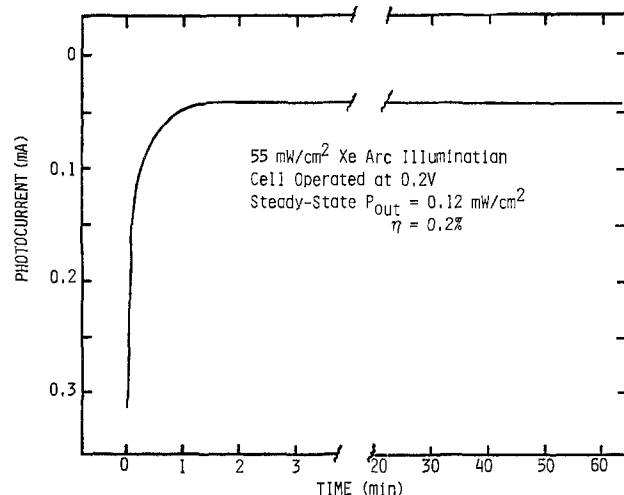


Fig. 9. Output and stability of photoelectrochemical cell n-GaAs (0.07 cm²)|Fc⁺ (0.007M), Fc (0.063M), LiAsF₆ (0.5M) PC|NESATRON OTE under high intensity white light illumination.

eral experiments were done with monochromatic light using a 765 nm interference filter and a power of 0.9 mW/cm². At this wavelength, absorbance by Fc⁺ is small, and the cell action spectrum is nearly maximized. As shown in Fig. 10, instantaneous conversion efficiencies of 14% were obtained, followed by relaxation to a somewhat lower steady-state value of 9% due to electrode polarization. These values are comparable with those reported by Kohl and Bard for GaAs in acetonitrile using red light. White light from the Xe source of the same intensity gave ~6.6% conversion efficiency.

Conclusions

Measurements of n-GaAs photoelectrodes with a variety of redox couples in PC electrolytes have indicated several limiting factors in EPC devices. Photovoltages were sensitive to the position of V_{redox} , but were limited to $< \sim 0.7V$ by decomposition of the semiconductor. Redox couples which lie too positive of V_{FB} , are likely to act as etchants; indeed, Br₂ is a common etchant for GaAs. Furthermore, the redox couples explored in this work appear not to have adsorptive effects on the onset of photocurrent, which occurred at a common potential of $\sim -0.2V$ vs. SCE in all the PC-based systems. In aqueous solutions, negative shifts of V_{FB} due to adsorption of redox species can provide an

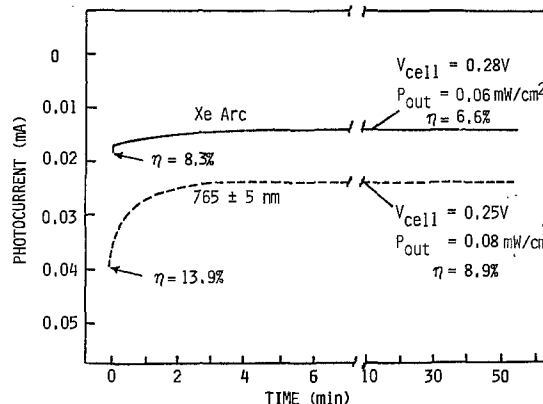


Fig. 10. Output and stability of photoelectrochemical cell n-GaAs (0.07 cm²)|Fc⁺ (0.007M), Fc (0.063M), LiAsF₆ (0.5M) PC|NESATRON OTE under white light (—) and monochromatic (---) illumination of 0.9 mW/cm². Cells operated at voltages (V_{cell}) yielding maximum power.

increased range of photovoltages, e.g., n-GaAs/aqueous Se₂⁻², Se⁻² devices. Although more positive-lying redox couples can stabilize GaAs in PC than in water (e.g., ferrocene, I₃⁻), photovoltages are no greater in the nonaqueous systems due to the lack of such adsorptive effects. Nevertheless, nonaqueous systems do have the advantage of allowing a wider variety of stabilizing redox couples than aqueous solutions. We anticipate that less noxious electrolytes than alkaline Se₂⁻²/Se⁻² can be developed in nonaqueous systems.

We have shown that efficiencies degrade seriously with increasing light intensity in PC-based electrolytes. We assume these losses to be related to limited redox electrolyte solubility and low electrolyte conductivity. Such losses are accumulated at both cell electrodes and are manifested as reductions in short-circuit currents and fill factors. We note that even the most conductive nonaqueous electrolytes, such as those based on acetonitrile, are still at least ten times more resistive than their aqueous counterparts. Nevertheless, if high photovoltages can be achieved in nonaqueous systems because of their increased stabilizing range, then high efficiencies can be achieved even with reduced currents, i.e., $P_{max} = 10 \text{ mA/cm}^2 \times 1V$, rather than $P_{max} = 20 \text{ mA/cm}^2 \times 0.5V$. However, surface adsorbed redox couples in nonaqueous electrolytes or other semiconductor surface modifications may be necessary to achieve such high voltages.

Acknowledgment

This work was supported by the Solar Energy Research Institute under contract to the Department of Energy, Subcontract No. XP-9-8002-7.

Manuscript submitted March 11, 1981; revised manuscript received ca. May 11, 1981.

Any discussion of this paper will appear in a Discussion Section to be published in the June 1982 JOURNAL. All discussions for the June 1982 Discussion Section should be submitted by Feb. 1, 1982.

REFERENCES

1. R. D. Rauh, T. F. Reise, and S. B. Brummer, *This Journal*, **125**, 186 (1978).
2. J. N. Butler, in "Advancement in Electrochemical and Electrochemical Engineering," Vol. 7, P. Delahay, Editor, pp. 106-114, Interscience, New York (1970).
3. A. B. Ellis, S. W. Kaiser, J. M. Bolts, and M. S. Wrighton, *J. Am. Chem. Soc.*, **99**, 2839 (1977).
4. M. A. Butler and D. S. Ginley, *This Journal*, **125**, 228 (1978).
5. S. M. Sze, "Physics of Semiconductor Devices," pp. 363 ff., Wiley-Interscience, New York (1969).
6. B. Parkinson, A. Heller, and B. Miller, *Appl. Phys. Lett.*, **33**, 521 (1978).

7. W. D. Johnson, H. I. Leamy, B. A. Parkinson, A. Heller, and B. Miller, *This Journal*, **127**, 90 (1980).
8. H. Hovel, in "Solar Cells: Semiconductors and Semimetals," Vol. 11, R. K. Willardson and A. C. Beer, Editors, Academic Press, New York (1975).
9. C. H. Seager and D. S. Ginley, *Appl. Phys. Lett.*, **34**, 337 (1979).
10. A. J. Bard, A. B. Bocarsly, F. F. Fan, E. G. Walton, and M. S. Wrighton, *J. Am. Chem. Soc.*, **102**, 3671 (1980).
11. R. H. Wilson, *J. Appl. Phys.*, **48**, 4292 (1977).
12. N. Matsuura, K. Umimoto, and Z. Takeuchi, *Bull. Chem. Soc. Jpn.*, **47**, 813 (1974).
13. P. A. Kohl and A. J. Bard, *This Journal*, **126**, 603 (1979).
14. T. Sakata, T. Kawai, and K. Tanimura, *Ber. Bunsenges. Phys. Chem.*, **83**, 486 (1979).
15. D. Sawyer, "Experimental Electrochemistry for Chemists," John Wiley & Sons, Inc., New York (1975).
16. R. Parsons, "Handbook of Electrochemical Constants," Butterworths, London (1959).
17. M. E. Langmuir, R. H. Micheels, and R. D. Rauh, Paper IX-18, Third International Conference on Photochemical Conversion and Storage of Solar Energy, Boulder, Colorado, Aug. 3-8, 1980.

Photoelectrochemical Evaluation of the n-CdSe/Methanol/Ferro-Ferricyanide System

Rommel Noufi,^{*1} Dennis Tench,^{*} and Leslie F. Warren^{*}

Rockwell International, Microelectronics Research and Development Center, Thousand Oaks, California 91360

ABSTRACT

Factors limiting the short-circuit photocurrent for the n-CdSe/methanol/ferro-ferricyanide system to 17.5 mA/cm² have been identified. The principal limiting factor is apparently specific adsorption of hexacyanoferrate species on the electrode surface, which occurs at higher redox couple concentrations and slows the overall charge transfer process. Ion pairing also occurs, resulting in a low mass transport rate (smaller diffusion coefficients and increased solution viscosity), and probably enhances the degree of specific adsorption.

In a previous publication (1), the systematic development of a nonaqueous ferro-ferricyanide electrolyte for stabilization of n-CdSe photoanodes was described. Selection of the solvent was discussed in terms of inherent stability provided, the rate of the redox reaction, the tendency toward specific adsorption of the redox species, and the equilibrium potential of the redox couple with respect to the flatband potential (attainable open-circuit voltage). Results were presented for cells of the type n-CdSe/methanol, Fe(CN)₆^{3-/4-}/Pt which had been operated for up to 700 hr at 6 mA/cm² with no detectable degradation in either the electrode surface or the photoresponse.

Although the Fe(CN)₆^{3-/4-}/methanol system itself was subsequently found to be photolytically unstable (substitution for cyanide slowly occurs), additional work was warranted since this system serves as a prototype for stabilizing nonaqueous redox electrolytes. In the present paper, the factors limiting the attainable photocurrent for n-CdSe in this system are discussed.

Electrolyte Preparation

Tetraethylammonium ferricyanide was prepared by the metathesis of Ag₃Fe(CN)₆ with Et₄NBr (where Et = ethyl) in methanol (2), recrystallized twice from an acetonitrile-acetone mixture, and then subjected to high vacuum to remove traces of solvent. Tetraethylammonium ferrocyanide was prepared as an off-white crystalline powder by anaerobic neutralization of H₄Fe(CN)₆ (3) with excess Et₄NOH (Southwestern Analytical Chemicals) in water, treated *in vacuo* to remove the solvent, and recrystallized from an i-propanol/acetone mixture in an inert atmosphere. This chemical procedure for preparing the air-sensitive

(Et₄N)₄Fe(CN)₆ is faster and less tedious than the electrochemical synthesis used previously (1). Tetraethylammonium fluoroborate was precipitated from a solution of Et₄NBr and 48% fluoroboric acid in ethanol by addition of i-propanol, and was then recrystallized twice from ethanol. The methanol solvent (Baker Analyzed) was refluxed over Mg, and then fractionally distilled under an inert atmosphere.

Electrodes

Reference electrodes were isolated in a separate compartment which was connected to the main cell through a medium glass frit. Both Ag/AgCl and saturated calomel reference electrodes were used with comparable results.

The Pt disk electrode (0.13 cm²) used to study the kinetics of the Fe(CN)₆^{3-/4-}/Pt reaction was mounted concentric and flush with the end of a 12 mm diam Kel-F cylinder by hot pressing. After mounting, the electrode was polished on successively finer aqueous alumina powder slurries to 1 μm particle size, and was then cleaned ultrasonically in water. Before each use, the electrode was further cleaned by immersion in boiling concentrated nitric acid.

The n-CdSe electrodes (0.18 cm² × 1 mm thick) were cut from rods supplied by Cleveland Crystals, Incorporated (Cleveland, Ohio) and had from 10¹⁶ to 10¹⁸ carriers/cm³. Ohmic contacts were made with an In-Ga alloy. Before use, n-CdSe electrodes were polished to 0.05 μm particle size, then etched in 3M nitric acid or a 1:25 mixture of concentrated nitric and hydrochloric acids (with comparable results). For long-term studies, n-CdSe electrodes were mounted in Kel-F by hot pressing. Results for electrodes mounted in silicone adhesive/sealant (Dow Corning Corporation, Midland, Michigan) were comparable.

^{*} Electrochemical Society Active Member.

¹ Present address: Solar Energy Research Institute, Golden, Colorado 80401.

Key words: semiconductor photoanodes, nonaqueous solvents, performance characteristics.

Electrochemical Measurements

All electrochemical measurements were made in Pyrex glass cells inside an inert atmosphere dry box using a PAR Model 173 Potentiostat/Galvanostat in conjunction with a PAR Model 175 Universal Programmer. The effects of solution resistance were always eliminated by electronic iR compensation. Electrodes were illuminated by a tungsten-halogen lamp through a quartz window. The illumination intensity was measured with a Pyroelectric Radiometer (Molelectron, Sunnyvale, California).

Results and Discussion

Performance characteristics were measured for n-CdSe photoanodes in methanol solutions as a function of the ferro-ferricyanide redox couple concentration. The best output parameters (5.5% conversion efficiency, $FF = 0.47$) were obtained for electrodes with 5×10^{16} carriers/cm³ in solutions containing 0.25M each of chemically prepared $Fe(CN)_6^{3-/4-}$ species. A typical power curve is shown in Fig. 1. The measured open-circuit voltage is very close to the maximum value expected for this system (0.7V). Photocurrent measurements as a function of light intensity indicated that the maximum stable short-circuit current is 17.5 mA/cm² in stirred solutions and 7.5 mA/cm² in unstirred solutions (at 95 mW/cm²). Transient photocurrents were larger at higher light intensities but rapidly decayed to the steady values. Currents of 17.5 mA/cm² were passed for as long as 2 hr.

Possible causes for such photocurrent limitations include decreased redox reaction rate and/or inadequate mass transport of the redox species in the electrolyte caused by ion pairing and/or specific adsorption of one or both of the electroactive species. The inherent electrode kinetics for the ferro-ferricyanide couple in methanol were studied by cyclic voltammetry at a rotating Pt disk electrode (4). Kinematic viscosity measurements were made as a function of the redox couple concentration so that the relative effects of changes in the fluid flow characteristics, reactant diffusion coefficients, and electron transfer rate could be ascertained. The dependence of the

photocurrent for n-CdSe photoanodes on light intensity was determined in both the methanol/ferro-ferricyanide and the established aqueous polysulfide systems as a means of detecting solid-state limitations.

Figure 2 shows plots of the diffusion-limited currents (i_L) for the ferro-ferricyanide reaction at a rotating Pt disk electrode as a function of the redox couple concentration. For both the anodic and cathodic branches, i_L goes through a maximum at about 0.15M $Fe(CN)_6^{3-/4-}$. Also, at concentrations above 0.05M, specific adsorption becomes significant, as indicated by higher Tafel slopes (180-250 mV/decade) than obtained at lower concentrations (~120 mV/decade). The decrease in i_L at higher concentrations could result from a decrease in the diffusion coefficient of the hexacyanoferrate species, stemming from increased ion pairing, and/or an increase in the electrolyte viscosity. That i_L is practically diffusion limited at all redox couple concentrations is shown by the Levich plots (4) in Fig. 3.

Figure 4 shows plots of the diffusion coefficients for the $Fe(CN)_6^{3-/4-}$ species (calculated from the Levich equation) and the electrolyte kinematic viscosity (measured with a Cannon-Fenske viscometer) vs. the redox couple concentration. The viscosity is practically constant at low $Fe(CN)_6^{3-/4-}$ concentrations but increases sharply at about 0.2M, which corresponds approximately to the maximum in the diffusion-limited current for the redox reaction (0.15M). However, the diffusion coefficient decreases by almost an order of magnitude (from 28×10^{-6} to 3×10^{-6} cm²/sec) from 0.01 to 0.1M $Fe(CN)_6^{3-/4-}$, indicating that considerable ion pairing occurs even at relatively low redox couple concentrations. Ion pairing of hexacyanoferrate species with tetraalkylammonium cations in solvents with low acceptor numbers has also been detected polarographically (2).

The relative effects of the electrolyte kinematic viscosity (ν) and the diffusion coefficients (D) in reducing the diffusion-limited currents can best be seen by plotting $D^{2/3}$ and $\nu^{-1/6}$, which are the terms appearing in the Levich equation (4)

$$i_L = 1.94 \times 10^7 C_R D_R^{2/3} \nu^{-1/6} \omega^{1/2}$$

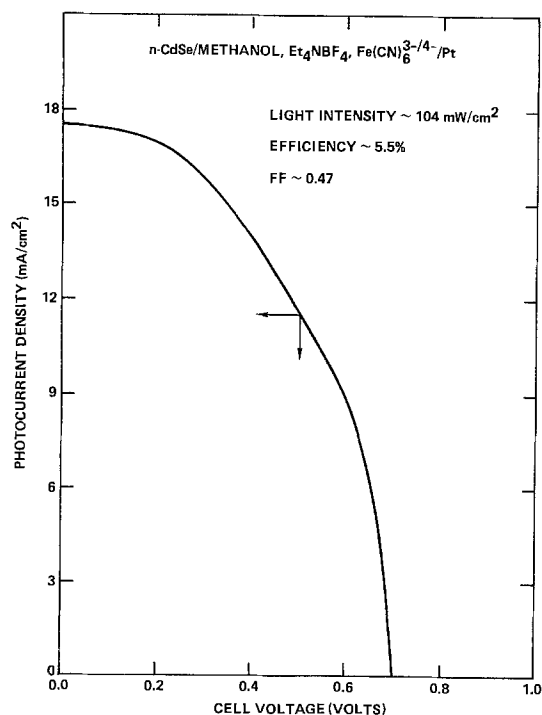


Fig. 1. Photocurrent density vs. voltage for the cell n-CdSe/methanol, 0.25M $Fe(CN)_6^{3-/4-}$, 0.1M Et_4NBF_4 /Pt under illumination at 104 mW/cm².

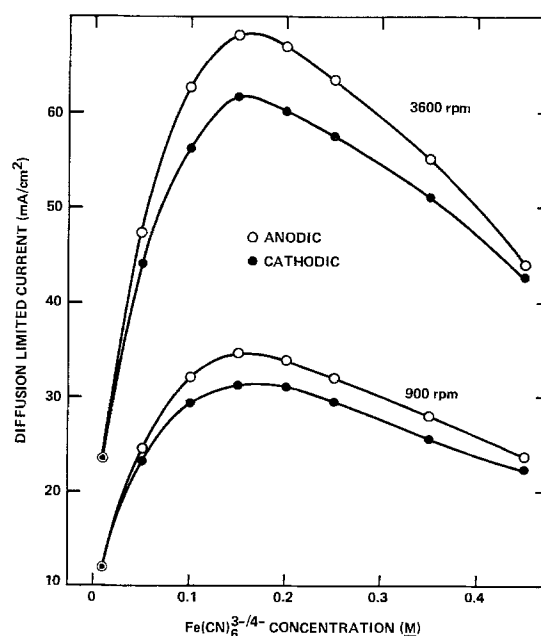


Fig. 2. Diffusion-limited currents vs. the $Fe(CN)_6^{3-/4-}$ concentration for a rotating 0.13 cm² Pt disk electrode in methanol/0.1M Et_4NBF_4 electrolyte containing equal concentrations of the oxidized and reduced species. The scan rate was 20 mV/sec and i_L was determined at an overvoltage of 1.00V in each case.

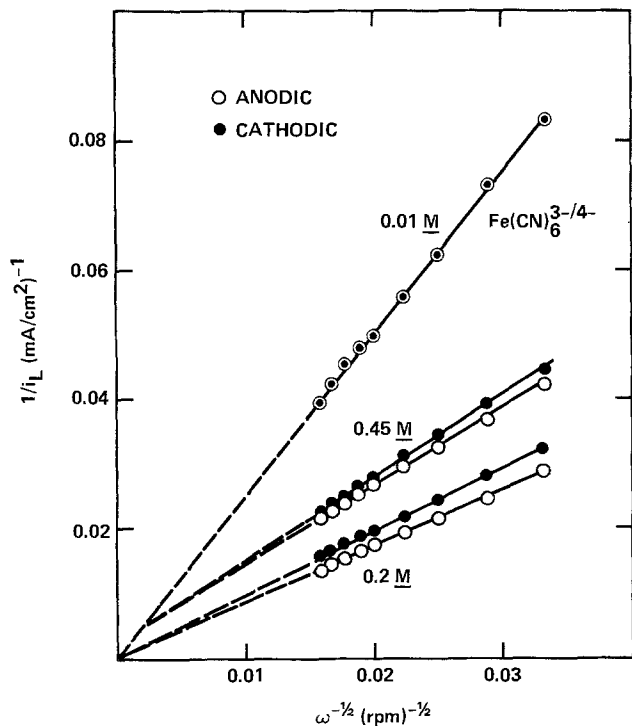


Fig. 3. Levich plots (4) for the $\text{Fe}(\text{CN})_6^{3-/4-}$ reaction at a rotating Pt disk electrode in methanol/0.1M Et_4NBF_4 (conditions same as for Fig. 2).

where i_L is in mA/cm^2 , C_R is the concentration of reactant in mol/ml, D_R is the reactant diffusion coefficient in cm^2/sec , ν is the electrolyte kinematic viscosity in cm^2/sec , and ω is the disk electrode rotation rate in rpm. Such plots are shown in Fig. 5, where $\nu^{-1/6}$ is seen to decrease linearly and relatively slowly (note scale difference) with $\text{Fe}(\text{CN})_6^{3-/4-}$ concentration,

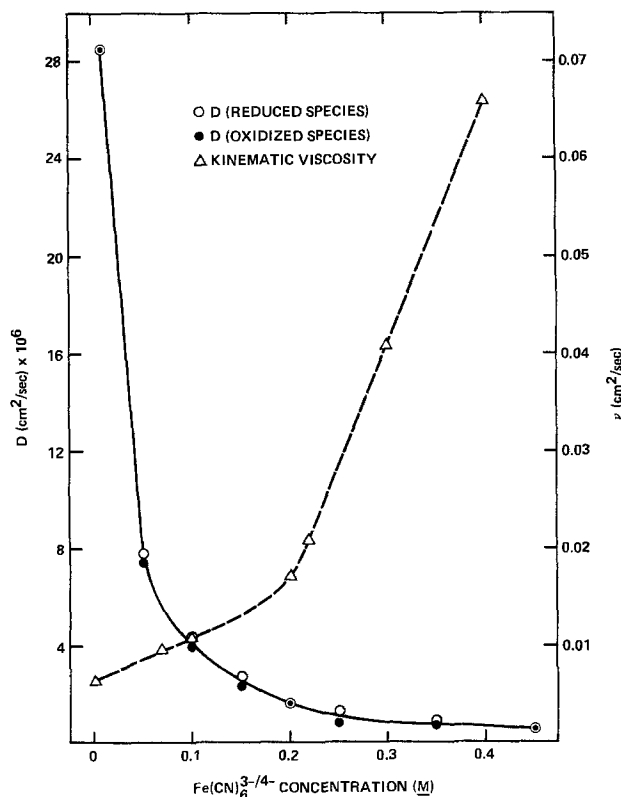


Fig. 4. Plots of the diffusion coefficients (D) of $\text{Fe}(\text{CN})_6^{3-/4-}$ species and the kinematic viscosity of 0.1M Et_4NBF_4 /methanol solutions as functions of the $\text{Fe}(\text{CN})_6^{3-/4-}$ concentration.

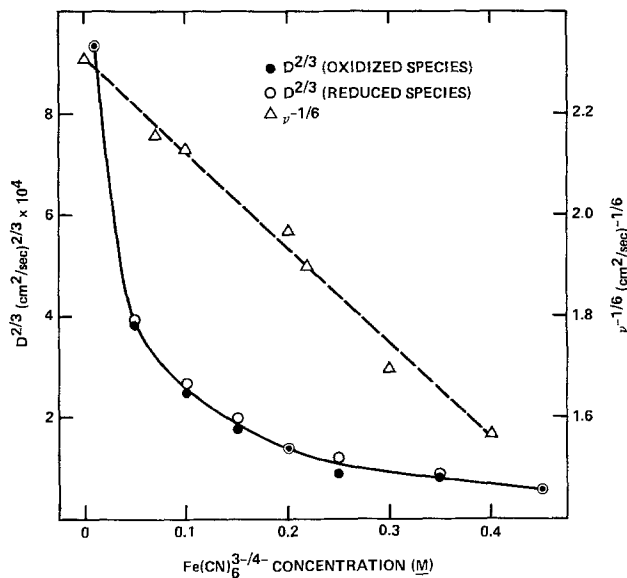


Fig. 5. Plots of $D^{2/3}$ and $\nu^{-1/6}$ for the data in Fig. 4

whereas $D^{2/3}$ decreases sharply to about 0.1M and then more gradually. Thus, the decrease in i_L at concentrations above 0.15M results from a combination of the effects of $\nu^{-1/6}$ and $D^{2/3}$.

Plots of the short-circuit photocurrent at single crystal n-CdSe photoanodes in 0.25M $\text{Fe}(\text{CN})_6^{3-/4-}$ /methanol and in aqueous polysulfide electrolyte vs. light intensity are shown in Fig. 6. The linear plot (passing through the origin) for the aqueous system indicates that solid-state limitations are not predominant. Therefore, the nonlinearity in the methanol/ $\text{Fe}(\text{CN})_6^{3-/4-}$ plot and the upper limit of 17.5 mA/cm^2 for the steady-state photocurrent are apparently associated with electrolyte effects. The data can be adequately explained by assuming the occurrence of strong specific adsorption of a ferricyanide species, which is the product of the photoelectrochemical redox reac-

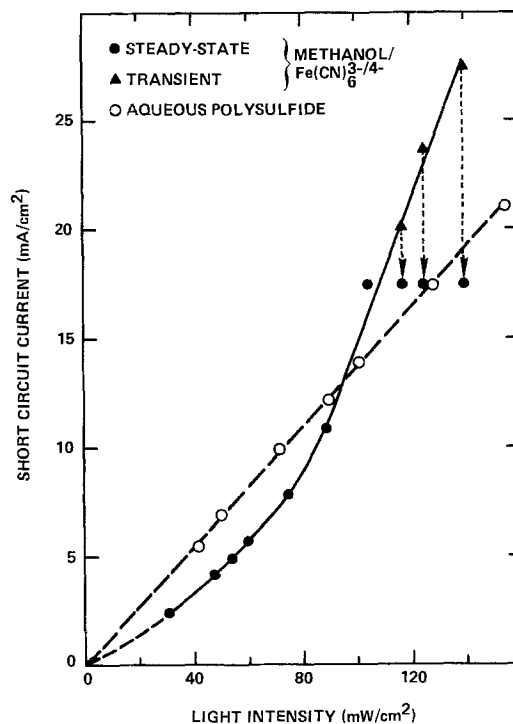


Fig. 6. Short-circuit currents vs. light intensity (tungsten-halogen lamp) for n-CdSe electrodes in 0.25M tetraethylammonium $\text{Fe}(\text{CN})_6^{3-/4-}$ /0.1M Et_4NBF_4 /methanol and in aqueous 2.2M Na_2S /0.1M S/0.1M NaOH electrolytes.

tion. Thus, at the lower light intensities, for which the currents are lower, the reaction rate is under mixed electron transfer/product desorption control, i.e., the rates of electron transfer (which is determined by the availability of photoholes in the semiconductor) and product desorption are comparable. As the light intensity (and consequently the current) is increased, the electron transfer rate increases and product desorption becomes the slow reaction step. In this case, higher currents can be passed for a short time but product accumulation on the electrode surface ultimately limits the current to a constant value determined by the rate of desorption. This model is consistent with the transient photocurrents (at the higher light intensities) decaying to the steady-state value (Fig. 6), and with the higher Tafel slopes (on Pt) for higher redox couple concentrations. The adsorbed species may be either the ferricyanide species normally present in solution or some reaction intermediate, and it may be ion paired since the viscosity data indicate that ion pairing is prevalent at $\text{Fe}(\text{CN})_6^{3-/4-}$ concentrations above 0.1M. Note that specific adsorption is known to also occur for the aqueous polysulfide system but would not affect the linearity of the corresponding plot in Fig. 6 if adsorption/desorption is fast compared to the electron transfer step, which involves two electrons.

Summary and Conclusions

The photocurrent for n-CdSe photoanodes in the methanol/ferro-ferricyanide system is limited to 17.5 mA/cm², apparently by specific adsorption of ferri-

cyanide redox species. Ion pairing in this system also has a pronounced effect on the redox couple diffusion coefficients and the electrolyte viscosity at higher redox couple concentrations. Such factors would be expected to be of general importance in photoelectrochemical cells employing nonaqueous electrolytes.

Acknowledgment

The authors gratefully acknowledge support of this work by the Solar Energy Research Institute under Subcontract No. XG-0-9276.

Manuscript submitted March 23, 1981; revised manuscript received ca. June 8, 1981.

Any discussion of this paper will appear in a Discussion Section to be published in the June 1982 JOURNAL. All discussions for the June 1982 Discussion Section should be submitted by Feb. 1, 1982.

Publication costs of this article were assisted by Rockwell International.

REFERENCES

1. R. Noufi, D. Tench, and L. F. Warren, *This Journal*, **127**, 2709 (1980).
2. E. Gritzner, K. Danksagmuller, and V. Gutmann, *J. Electroanal. Chem. Interfacial Electrochem.*, **72**, 177 (1976).
3. G. Bauer, "Handbook der Preparativen Anorganischen Chemie," F. Enke, Verlag, Stuttgart (1960).
4. V. G. Levich, "Physicochemical Hydrodynamics," Prentice-Hall, Englewood Cliffs, NJ (1962).

Technical Notes



Kinetics of Electroless Copper Plating

V. Mass Transport at Cylindrical Surfaces

Francis M. Donahue*

Department of Chemical Engineering, The University of Michigan, Ann Arbor, Michigan 48109

In a previous communication, properties of mass transport in electroless copper plating baths were presented for the common case of linear transport (1). Since some studies have been performed on cylindrical samples (2-4), it is worthwhile to determine the effects of this geometry on mass transfer phenomena.

The steady-state mass balance for a transporting species, "j," for cylindrical geometry in the absence of a homogeneous reaction and with concentration variation only in the radial direction is

$$\frac{d^2c_j}{dR^2} + \frac{1}{R} \frac{dc_j}{dR} = 0 \quad [1]$$

The boundary conditions for the case considered here are

$$c_j = c_{sj} \quad \text{at} \quad R = R_o \quad [2a]$$

and

$$c_j = c_{bj} \quad \text{at} \quad R = R_o + \delta \quad [2b]$$

The solution of Eq. [1] for these boundary conditions is

$$c_j = c_{bj} + (c_{sj} - c_{bj}) \frac{\ln\left(\frac{R_o + \delta}{R}\right)}{\ln\left(\frac{R_o + \delta}{R_o}\right)} \quad [3]$$

The flux of the transporting species at the sample-solution interface is

$$N_j = -10^{-3} D_{jm} (dc_j/dR)_{R=R_o} \quad [4]$$

Differentiating Eq. [3] and setting $R = R_o$, the flux becomes

$$N_j = (10^{-3} D_{jm}/\delta) (c_{sj} - c_{bj}) \frac{\delta/R_o}{\ln(1 + \delta/R_o)} \quad [5]$$

Comparing Eq. [5] with Eq. [1a] of Ref. (1) shows that the flux at a cylindrical sample reduces to that for linear transport when the ratio of the boundary layer thickness to the sample radius is less than 0.1.

* Electrochemical Society Active Member.
Key words: mass transport, baths, plating.

The boundary layer thickness for rotating cylinders can be computed from the macroconvection mass transfer coefficient (1) and the diffusivity. The boundary layer thickness for the cylinders used by Dumesic and co-workers (3) at the lowest rotation speed (150 rpm) was computed using Donahue's corrected value of the macroconvection mass transfer coefficient (1) and their diffusivity for cupric ion. Since the ratio, δ/R_o , was less than 0.01, the flux of cupric ion was correctly described by the authors in terms of the linear transport equation.

When microconvection controls the transport process (e.g., in the absence of forced convection, but the presence of gas evolution), the boundary layer thickness is a function of the plating rate (1), i.e.

$$\delta = 0.026 r_p^{-0.53} \quad [6]$$

Insertion of Eq. [6] in Eq. [5] provides some insight into the roles of plating rate and sample radius under these conditions. However, it is more convenient to define an "effective" mass transfer coefficient, k_{cj}' , by

$$k_{cj}' = \frac{10^3 N_j}{c_{sj} - c_{bj}} \quad [7]$$

or, from Eq. [5]

$$k_{cj}' = \frac{D_{jm}/R_o}{\ln(1 + \delta/R_o)} \quad [8]$$

which can be rearranged to

$$\frac{k_{cj}'}{D_{jm}} = \frac{1/R_o}{\ln(1 + \delta/R_o)} \quad [9]$$

where the right-hand side of the equation is a function of the plating rate and sample radius and independent of the transporting species. Figure 1 shows the behavior of the left-hand side of this equation as functions of sample radius and plating rate. From this figure one concludes that the stationary cylinders of Dumesic and co-workers (3) exhibited linear transport even at the lowest plating rates. On the other hand, the wire samples of Donahue and co-workers (2, 4), i.e., $R_o = 0.016$ cm, exhibit substantial deviation from the linear transport line even at the highest plating rates. Therefore, when computing interfacial concentrations, they cannot use the linear transport equations given previously (1), but must use Eq. [5].

Acknowledgment

This material is based upon work supported by the National Science Foundation under Grant No. ENG-7511869.

Manuscript submitted Nov. 7, 1980; revised manuscript received March 16, 1981.

Electrodeposition of Palladium on Iron and Steel for Electrochemical Hydrogen Permeation Studies

R. Driver*

CSIRO Division of Applied Physics, Sydney, Australia 2070

In the highly sensitive electrochemical technique for studying hydrogen permeation in metals (1, 2), a thin test membrane acts as a bipolar electrode in a two-compartment cell. A fraction of the hydrogen produced at the cathodically polarized (inlet) side diffuses through the membrane and is oxidized as it reaches the

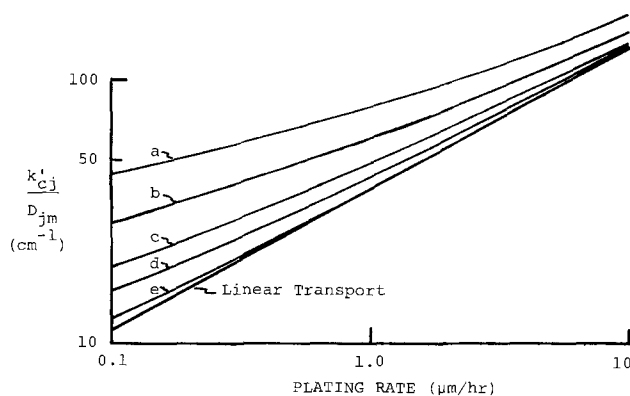


Fig. 1. Relationship between k_{cj}'/D_{jm} and electroless copper plating rate for microconvection conditions.

| Symbol | R_o (cm) |
|--------|------------|
| a | 0.01 |
| b | 0.02 |
| c | 0.05 |
| d | 0.10 |
| e | 0.50 |

Any discussion of this paper will appear in a Discussion Section to be published in the June 1982 JOURNAL. All discussions for the June 1982 Discussion Section should be submitted by Feb. 1, 1982.

Publication costs of this article were assisted by the National Science Foundation.

LIST OF SYMBOLS

| | |
|-----------|---|
| c_j | concentration of species "j" (M) |
| c_{bj} | bulk concentration of species "j" (M) |
| c_{sj} | interfacial concentration of species "j" (M) |
| D_{jm} | diffusivity of species "j" in the solution (cm ² /sec) |
| k_{cj}' | "effective" mass transfer coefficient of species "j" (cm/sec) |
| N_j | flux of species "j" (mol/cm ² -sec) |
| R | radial distance (cm) |
| R_o | cylinder radius (cm) |
| r_p | plating rate (μm/hr) |
| δ | mass transfer boundary layer thickness (cm) |

REFERENCES

1. F. M. Donahue, *This Journal*, **127**, 51 (1980).
2. F. L. Shippey and F. M. Donahue, *Plating*, **60**, 43 (1973).
3. J. Dumesic, J. A. Koutsky, and T. W. Chapman, *This Journal*, **121**, 1405 (1974).
4. F. M. Donahue, K. L. M. Wong, and R. V. Bhalla, *ibid.*, **127**, 2340 (1980).

* Electrochemical Society Active Member.
Key words: membrane, permeation, metals.

anodically polarized (exit) side. To obtain meaningful permeation rate data, it is necessary to ensure that ionization of hydrogen at the exit surface occurs much faster than the competing, nonelectrochemical, hydrogen atom recombination reaction, and that the measured ionization current is free of any spurious components associated with anodic dissolution or passivation of the exit surface.

In principal, these objectives may be achieved by coating the exit surface with a very thin layer of palladium, an inert and highly permeable material which has virtually no effect on the overall rate of hydrogen transport. Electrolytic deposits have usually been employed, but descriptions of the plating methods are both meager and conflicting and very little attention has apparently been directed at monitoring the thickness or integrity of the coatings. As pointed out by Heidersbach *et al.* (3), there is wide variation in existing hydrogen permeation data and this could be due partly to poor control of the palladium deposits applied to membrane exit surfaces.

The present work was undertaken to establish a simple and reliable laboratory method for obtaining good quality palladium electrodeposits on iron and steel, the materials most commonly used in hydrogen diffusion studies. A simple porosity test was used to determine the minimum deposit thickness for complete coverage. The chemical factors underlying the operation of the plating bath are discussed briefly.

Experimental

Sample preparation.—Plating experiments were performed on coupon specimens of surface area 4–10 cm², cut from Johnson Matthey "Specpure" iron sheet, 1.0 mm thick, and from bright mild steel sheet, 0.78 mm thick. After degreasing in hot petroleum (bp 100°–120°C), any rust or oxide bloom was removed by treatment with a commercial acid-based rust remover, or alternatively, by appropriate pickling in 0.5M H₂SO₄. The former procedure had the advantage of leaving a brilliantly clean surface, almost free of etching. The samples were then rinsed in distilled water, dried with alcohol, and finally polished with steel wool.

Plating solution.—The alkaline plating electrolyte was prepared from palladium diammine dinitrite, Pd(NH₃)₂(NO₂)₂ ("Palladium P Salt"), using the composition recommended by Hedrich and Raub (4), *i.e.*, 0.1M Pd(NH₃)₂(NO₂)₂, 100 g/l NH₄NO₃, and 10 g/l NaNO₂, with addition of sufficient ammonia to adjust the pH between 8 and 10. It is convenient to dissolve the palladium complex in ammonia solution before adding the other constituents. The solution is then diluted approximately to volume and pH adjusted (using graduated indicator paper) either by further addition of ammonia or by warming the solution to expel the excess. The question of the optimum bath pH is discussed later. The same bath may be prepared just as conveniently by substituting 0.1M palladium nitrate, Pd(NO₃)₂, for the nitrite complex, in which case the required sodium nitrite concentration is 24 g/liter.

Electroplating procedure.—Experiments to establish a satisfactory plating procedure were performed in a simple beaker cell. The current source was a Wenking Model POS73 scanning potentiostat operated in galvanostatic mode with an external control resistor. The anode was a sheet of bright platinum foil, the area of which was comparable with that of the cathode specimen. The cell was first filled with 0.5M H₂SO₄ and the specimen was activated by anodic polarization at 5 mA/cm² for 30 sec. The cell and electrodes were then rinsed quickly with dilute ammonia to ensure complete removal of hydrogen ions, the plating solution introduced, and deposition commenced immediately, without stirring, at a current density of 20 mA/cm². The current was maintained at this value for 30 sec, and then reduced uniformly at 0.5 mA/cm² sec to a constant value of 5 mA/cm² and deposition continued for a further 18 min. Plated specimens were dried with alcohol, and the coating thickness was determined from the gain in mass. All experiments were conducted at 22°C.

Porosity test.—Porosity was assessed using a method based on the Ferroxy test for detecting pinholes in

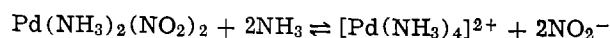
tinplate (5). Specimens were just submerged in a solution containing 0.2M K₃[Fe(CN)₆] and 0.0025M KCl. Exposed iron is rapidly attacked, and within a few minutes, the presence of pores is revealed by telltale spots of "blue rust" formed by reaction between ferrous and ferricyanide ions.

Results and Discussion

Although various plating solutions have been mentioned for palladium (6), the above formulation is better suited to laboratory applications and under appropriate conditions is capable of yielding smooth deposits with a high gloss, even from an unstirred bath. The given procedure yielded pore-free coatings 1.5–1.6 μm in thickness for a total plating time of about 19 min, corresponding to a current efficiency of 55–60% (at 100% current efficiency, the Pd deposition rate at 5 mA/cm² is 0.138 μm/min). Deposits generally displayed some porosity at thickness < 1.3 μm, although this could be as little as 1–2 pores/cm² at about 1 μm. Sample cleanliness is essential for the attainment of pore-free deposits. Except in the case of extremely thin foil specimens, a palladium coating of about 2 μm will not materially affect the hydrogen permeation kinetics.

The relatively high initial current density was designed to obtain more or less complete coverage as soon as possible. This procedure was prompted by the gradual formation of an unidentified precipitate containing iron during deposition attempts at current densities < 1 mA/cm². Initial plating densities exceeding 20 mA/cm² are not recommended, as the deposit structure may suffer due to increasing hydrogen content (7). The follow-up plating density of 5 mA/cm² was chosen to maximize current efficiency and to minimize the degree of hydrogen ion buildup at the anode, the effects of which are discussed later.

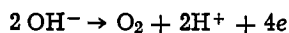
With this bath, discharge of palladium takes place from the tetrammine palladium (II) ion, formed according to the equilibrium



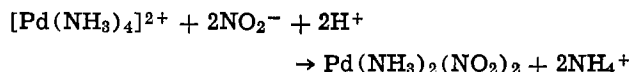
and hence the performance is very dependent on the pH. As the pH is lowered, the tetrammine gradually reverts to the insoluble diammine complex and palladium deposits (7) obtained at pH 7–8 reportedly contain occluded Pd(NH₃)₂(NO₂)₂. This can eventually lead to blistered coatings at pH < 7. As the pH increases, reduction of the [Pd(NH₃)₄]²⁺ ion occurs at more negative potentials which favor discharge of hydrogen. These effects determine the recommended operating range of pH 8–9. Since the bath loses ammonia continuously on exposure to the atmosphere, regular pH checks are essential.

The low current efficiency of this bath, even under optimum conditions of pH and current density, is apparently due to reduction of nitrite and/or nitrate ions (4), rather than hydrogen discharge, which only becomes important at high pH or at current densities > 30 mA/cm². The efficiency of the unstirred bath also depends on the palladium concentration, which should be maintained fairly close to the recommended value of 0.1M. When the palladium content had been depleted by 20–30%, the observed current efficiency dropped below 50%, and more importantly, deposits of given thickness were significantly more porous than those from a relatively fresh solution. Efficiency and performance were fully restored by appropriate evaporation. Alternatively, the bath may be replenished by addition of the palladium complex dissolved in dilute ammonia. In the absence of proper pH control, the bath can be depleted very rapidly by crystallization of Pd(NH₃)₂(NO₂)₂ on the anode, where the dis-

charge of hydroxyl ions causes a substantial drop in local pH, i.e.



followed by



At 5 mA/cm², crystallization was only observed at pH ≤ 8, but higher current densities might be expected to exacerbate this problem.

Conclusion

Good quality palladium electrodeposits on iron and steel may be readily obtained from an unstirred bath at room temperature. Complete coverage and passivation of these substrates requires an electroplated coating >1 μm and preferably 1.5-2 μm thick. A palladium layer of these dimensions will not affect the rate of hydrogen transport through ferrous specimens. The coatings should be individually checked for porosity as this could vary with different substrates.

Dependence of Flatband Potentials of n-TiO₂ on Electrolytes and Electrolyte Concentrations

James R. Wilson and Su-Moon Park*

Department of Chemistry, University of New Mexico, Albuquerque, New Mexico 87131

The flatband potential of a semiconductor electrode is an important parameter in designing a photoelectrochemical cell. The importance of the flatband potential of a given semiconductor material in locating energy levels of the conduction and valence bands (1-3), and for predicting its stabilities has been discussed elsewhere (4-6). Flatband potentials have been reported to be dependent on the pH of the medium (1, 3). The pH dependency of flatband potentials has been characterized by a straight line with a slope of 59 mV/pH according to the equation

$$E_{\text{FB}} = E_{\text{FB}}^{\circ} - 0.059 \text{ pH}$$

where E_{FB}° is the value at pH = 0. The pH dependency is ascribed to the adsorption of the hydroxyl ion at the electrode surface (1), which in turn is dependent on the pH of the medium.

In the present note, we report the effect of electrolytes and electrolyte concentrations on the flatband potential of an n-TiO₂ electrode. This study was carried out on the assumption that electrolyte species other than the hydronium or hydroxyl ion could also be the potential determining species at the semiconductor-electrolyte interface.

Reagents used were of reagent or analytical reagent grade and obtained from Baker, Eastman Organic, Mallinckrodt, or Merck. Most reagents were used as received, but a few salts were recrystallized from double distilled water. A Princeton Applied Research (PAR) 175 Universal Programmer, a PAR 173 potentiostat-galvanostat, and a PAR 176 I/E converter have been used to control the potential at the working electrode and to record the photocurrent. A Tectronics Model 5115 storage oscilloscope was used to record faster measurements such as the capacitance current produced by applying a small triangular a-c signal (± 10 mV) superimposed on a d-c bias potential. An Oriel

Manuscript received March 24, 1981.

Any discussion of this paper will appear in a Discussion Section to be published in the June 1982 JOURNAL. All discussions for the June 1982 Discussion Section should be submitted by Feb. 1, 1982.

Publication costs of this article were assisted by CSIRO.

REFERENCES

1. J. O'M. Bockris and M. A. V. Devanathan, Tech. Report 4, Office of Naval Research, NR 036-028 (1961).
2. M. A. V. Devanathan and Z. Stachurski, *Proc. Roy. Soc. London, Ser. A*, **270**, 90 (1962).
3. R. Heidersbach, J. Jones, and M. Surkein, 2nd Intern. Congr. on Hydrogen in Metals, p. 1, Paris (1977).
4. H. D. Hedrich and C. J. Raub, *Metalloberflaeche*, **31**, 512 (1977).
5. P. Hersch, J. B. Hare, A. Robertson, and S. M. Sutherland, *J. Appl. Chem.*, **11**, 246 (1961).
6. J. Fischer and D. E. Weimer, "Precious Metal Plating," p. 213, Robert Draper Ltd., Teddington (1964).
7. H. D. Hedrich and C. J. Raub, *Surf. Technol.*, **8**, 347 (1979).

450W Xe arc lamp powered by an Oriel 8540 Universal power supply was used as a light source. Monochromatic light was produced by an Oriel 7240 monochromator (bandpass = 20 nm). The illumination intensity was measured with the International Light Model 700 Radiometer. The pH was monitored by a Cambridge 5-700 combination electrode with a Sargent-Welch Model NX Digital pH meter. The photocurrent was recorded on a Houston Model 2000 X-Y recorder.

The electrolyte concentration was controlled by dispensing small volumes of a concentrated electrolyte solution from a buret. This has the advantage of maintaining the same electrode position in the solution throughout the experiment.

An n-TiO₂ electrode, furnished by Dr. Mike A. Butler, Sandia Laboratories, was cut from a large single crystal perpendicular to the c-axis. The TiO₂ electrode was doped in a quartz tube furnace under the hydrogen atmosphere at 450°C for 2 hr, whenever necessary. The electrode thus doped had a donor density of $\sim 1.0 \times 10^{19}/\text{cm}^3$, as measured from the slope of a Mott-Schottky plot (1, 2).

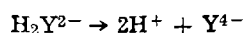
Due to the irreproducibilities encountered in flatband potential measurements by the Mott-Schottky method (7, 8), a photoresponse method (9) was used. This method is based on a measurement of the photocurrent (I) as a function of the applied potential (E). From the I - E measurements, a plot of I^2 vs. E was obtained. The flatband potential was then obtained from the intercept of the E -axis. Since the results obtained from this method were found to be affected by experimental parameters such as the voltage scan rate and the wavelengths of light illuminated (10), we employed a scan rate of 1 mV/sec and a wavelength of 360 nm for electrode illumination. The illumination intensity was about 0.71 mW/cm². In order to check the reproducibility of this method, the pH dependency of the flatband potential was obtained; an extremely well-correlated straight line with a slope of -53 mV/pH was observed.

* Electrochemical Society Active Member.

Key words: flatband potential, complexation effect, n-TiO₂.

Of eight inorganic salts studied, only one showed a slight concentration effect on the flatband potential. Compounds such as NaCl, KCl, NaI, KNO₃, Na₂SO₄, K₂SO₄, and NaClO₄ did not show any effects. The values of flatband potentials of TiO₂ were the same in solutions of these salts and independent of their concentrations. Addition of NaH₂PO₄ to water moved the flatband potential to a more positive value, which would be expected from the resultant change in pH. While the flatband potential varied slightly with NaH₂PO₄ concentration, E_{FB} values corrected against the corresponding change in pH were constant.

The fact that most inorganic salts did not exert any effects on flatband potentials indicates that both cations and anions of the salts studied did not show significant specific adsorption toward the electrode material. A small change in the flatband potential when NaH₂PO₄ was added has been ascribed to the change in pH due to the hydrolysis of the salt. Thus, we decided to perform the same study for complexing agents. Complexing agents used were NaCN, sodium citrate, ethylenediaminetetraacetic acid (EDTA), and 8-hydroxyquinoline. Of these, neither NaCN nor sodium citrate showed any significant effects, while EDTA and 8-hydroxyquinoline did. The effect of the concentration of EDTA on the flatband potential of n-TiO₂ is shown in Fig. 1. Note that the measurements were made in solutions of pH's 11 and 12. The intercept of the two curves shown in Fig. 1 was identical with the E_{FB} values that were obtained at pH = 11 and 12 without EDTA present for its pH-dependence studies. The effects shown in Fig. 1 were not observed at lower pH's. This indicates that the dissociated form (Y⁴⁻) of EDTA (H₂Y²⁻) according to the equilibrium reaction



is important as a potential determining species at the electrode surface. Indeed, when the shift in the flatband potential is normalized by dividing it by the molar concentration of the dissociated form of EDTA ([Y⁴⁻]), it was approximately constant with about 9% average deviation. The normalized shift thus calculated was ~ 0.36 V/M Y⁴⁻. The fact that Y⁴⁻ is a potential determining species also implies that the complexation of Y⁴⁻ with surface ions may be responsible for the observed results.

For 8-hydroxyquinoline, the results were similar. No effects were observed at low pH, whereas the flatband

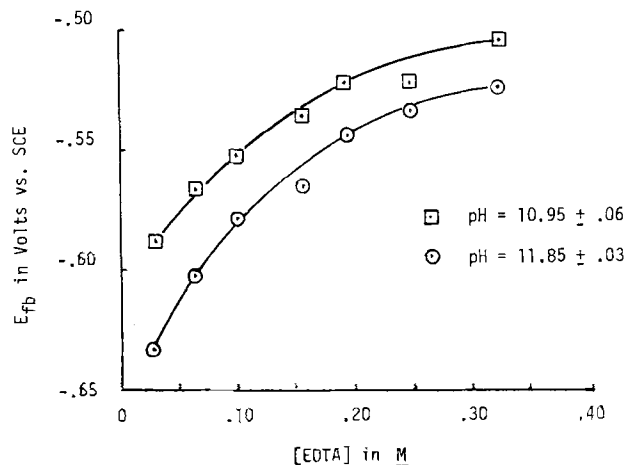


Fig. 1. The flatband potential of an n-TiO₂ electrode as a function of the EDTA concentration. Wavelength of light illuminated was 360 nm.

potential shifted to a more positive direction at high pH, where hydroxide on the 8-hydroxyquinoline (8-HQ) molecule would be dissociated. The shift in the flatband potential was to the extent of 0.14V at a 8-hydroxyquinoline concentration of 27 mM. At a higher 8-HQ concentration, no photocurrent was observed.

We attribute the observed behavior to the complexation of donor ions such as Ti³⁺ at the semiconductor surface. When EDTA or 8-hydroxyquinoline is present in the solution, the dopants at the surface may be complexed, shifting the energy levels of the electron donor ions. We believe that the surface complexation affects the energy level of the semiconductor more than of the solution side. This will shift the flatband potential in a more positive direction. The complexation effect was more dramatic for 8-HQ, probably because it forms the insoluble complex (precipitate), possibly blocking the electrode surface.

The reason that the addition of cyanide and citrate did not affect the flatband potential may be that these ions are not strong enough complexing agents toward Ti³⁺. It is readily predicted that both EDTA and 8-hydroxyquinoline would be stronger complexing agents than citrate and cyanide for Ti³⁺, although no quantitative data except for EDTA are available in the literature (11). Further work is in progress in our laboratory along the lines described.

Acknowledgments

Financial support of this research by Sandia Corporation through the Sandia-University Research Program (SURP), New Mexico Energy and Mineral Department, and the Research Allocations Committee is gratefully acknowledged. We also express our gratitude to Dr. Michael A. Butler of Sandia Laboratories for providing us a TiO₂ single crystal.

Manuscript submitted March 16, 1981; revised manuscript received May 11, 1981.

Any discussion of this paper will appear in a Discussion Section to be published in the June 1982 JOURNAL. All discussions for the June 1982 Discussion Section should be submitted by Feb. 1, 1982.

Publication costs of this article were assisted by the University of New Mexico.

REFERENCES

- H. Gerischer in "Physical Chemistry—An Advance Treatise," Vol. IXA, H. Eyring, D. Handerson, and W. Yost, Editors, Academic Press, New York (1970).
- V. Myamlin and R. V. Pleskov, "Electrochemistry of Semiconductors," Plenum Press, New York (1967).
- J. M. Bolts and M. S. Wrighton, *J. Phys. Chem.*, **80**, 2641 (1976).
- H. Gerischer, *J. Electroanal. Chem. Interfacial Electrochem.*, **82**, 133 (1977).
- A. J. Bard and M. S. Wrighton, *This Journal*, **124**, 1706 (1977).
- S.-M. Park and M. E. Barber, *J. Electroanal. Chem. Interfacial Electrochem.*, **99**, 67 (1979).
- E. C. Dutoit, F. Cardon, and W. P. Gomes, *Ber. Bunsenges. Phys. Chem.*, **80**, 475 (1976).
- R. DeGryse, W. P. Gomes, F. Cardon, and J. Vennick, *This Journal*, **122**, 711 (1975).
- M. A. Butler, *J. Appl. Phys.*, **48**, 1914 (1977).
- J. R. Wilson, Ph.D. Dissertation, The University of New Mexico (1980).
- L. G. Sillen and A. E. Martell, "Stability Constants of Metal-Ion Complexes," The Chemical Society, London, 1964 and volumes thereafter.

Photoactivity of Polycrystalline α -Fe₂O₃ Electrodes Doped with Group IVA Elements

John H. Kennedy,* Menahem Anderman, and Ruth Shinar

Department of Chemistry, University of California, Santa Barbara, California 93106

Success in obtaining significant photocurrents with polycrystalline, SiO₂-doped α -Fe₂O₃ photoanodes (1) gave rise to a study of the photoelectrochemical properties of other group IVA elements as dopants. Recently, photochemical properties of SnO₂- and CaO-doped α -Fe₂O₃ electrodes were investigated elsewhere (2) but only 1 and 5% doping levels were studied.

In the present work α -Fe₂O₃ material was mixed with 0.002-5 atomic percent (a/o) GeO₂ and SnO₂ and with 0.01-5 a/o (initial composition) PbO₂. Emission spectroscopy and x-ray diffraction were used to check the initial and final doping levels and for the possible presence of two-phase materials. Photoelectrochemical results were compared to those obtained at Si(IV)- and Ti(IV)-doped α -Fe₂O₃ electrodes.

Experimental

Electrodes were prepared from high purity, 99.999% α -Fe₂O₃ (Alfa Products) by mixing with the dopant powder, pressing, and sintering as described elsewhere (1). The dopants were Alfa Products 99.9% GeO₂, B and A 99% SnO₂ or Alfa Products 99.9% SnO₂, and Research Organic/Inorganic Chemical Corporation 95% PbO₂ or Apache 99.9% PbO₂.

Pressed pellets were sintered at 1250°-1370°C for 3-40 hr. Table I summarizes the dopant concentrations, sintering temperatures, and sintering times needed to prepare the best electrodes. The electrodes were 1.29 cm diam when initially pressed but some shrinking occurred during sintering so that final electrodes were \sim 1 cm².

Electrical connections were made using silver epoxy as previously described (3). Densities were 75-90% of the theoretical value, and resistances measured at 1 kHz with a conductivity bridge were usually 50-2500 Ω .

Samples containing Ca²⁺ (starting material: Matheson, Coleman & Bell CaCO₃) and Pb²⁺ (starting material: Mallinckrodt, Analytical Reagent PbO) were also prepared. 0.5 a/o Ca²⁺-doped α -Fe₂O₃ pellets were sintered at 1370°C for about 15 hr and at 1330°C for 70 hr. In both cases the resistances were very high (>200 k Ω). 0.5 a/o Pb²⁺-doped electrodes were sintered at 1370°C for 5 hr. Resistances were \sim 2 k Ω .

Pellet weight was checked before and after sintering. Differences between starting and final dopant concentration were also determined by emission spectroscopy. Both powders and ground sintered pellets of pure and doped α -Fe₂O₃ were analyzed by a Norelco x-ray diffractometer.

The cell arrangement, and optical and electrochemical measurement procedures were described previously (1). Lamp intensity was measured with a Yellow Springs Instrument Company Kettering Model 65A radiometer, and the photocurrent spectra were normalized to the lamp output spectrum. When using a monochromator light intensities in the range 350-560 nm were 4-18% mW/cm². The lamp intensity at the electrode surface was about 300 mW/cm² when no monochromator was employed. This was reduced to about 180 mW/cm² when a filter was used (pass light <540 nm).

Results

No loss of weight during sintering was observed in the case of pure α -Fe₂O₃, Si⁴⁺-, Sn⁴⁺-, and Ge⁴⁺-

* Electrochemical Society Active Member.

Key words: semiconductor electrode, polycrystalline, doped α -Fe₂O₃, photoactivity.

(sintered at 1300°C) doped electrodes, but some loss of weight was observed in Ge⁴⁺-doped pellets sintered at \sim 1350°C, probably due to some evaporation of GeO₂ at high sintering temperatures (4).

A significant weight loss was observed in the Pb⁴⁺-doped pellets as expected, since PbO₂ decomposes at 290°C and PbO, the final decomposition product, melts at 888°C and evaporates appreciably (4).

Emission spectroscopy confirmed the above results. Si⁴⁺-, Ge⁴⁺-, and Sn⁴⁺-concentrations in the ground pellets (after sintering) were the same, within experimental error, as in the mixed powders (before sintering). In the case of Ge⁴⁺-doped pellets a reduction in the final concentration of the dopant was observed when sintered at relatively high temperatures. For example, the final doping level of the 0.5 a/o Ge(IV) sample sintered at 1350°C for 13 hr was \sim 0.1 a/o. It should be kept in mind that emission spectroscopy is not a highly accurate analytical technique but significant differences between initial and final composition could be readily observed. For the lead-doped electrodes only low levels of lead (\sim 200 ppm) were observed in the final sintered pellets independent of initial concentration, sintering temperature, or sintering time.

X-ray patterns of ground sintered pellets indicated the existence of single phase α -Fe₂O₃ even at doping levels of 5 a/o GeO₂ and SnO₂. On the other hand, x-ray diffraction of the starting mixtures containing as little as 0.5 a/o GeO₂ and SnO₂ clearly showed the presence of dopant phases along with α -Fe₂O₃. Also, no evidence for the presence of other phases was found for electrodes containing up to 2 a/o SiO₂.

Most of the photoactivity experiments were carried out on low doping level electrodes. High doping levels were used mainly to check for possible weight loss during sintering and for the presence of two-phase materials.

To ensure homogeneity in the electrodes some pellets were sintered at elevated temperatures for very long periods (>3 days) compared to the time required to obtain pellets of relatively low resistance. No noticeable change in the photoactivity could be observed by the long sintering cycle. In addition, some sintered samples were ground and resintered. Occasionally densities were slightly improved but no significant changes in the photoactivity were observed.

Photocurrent density vs. applied potential at 400 nm for α -Fe₂O₃ electrodes doped with group IVA elements is shown in Fig. 1. The indicated doping levels are those of the final electrodes. Initial concentration for the lead-doped electrode is given in parentheses.

The photocurrent was measured in 1F NaOH. Results for 0.05 a/o Ti⁴⁺-doped electrodes are also shown for comparison. Dark currents in the range shown were always lower than 8 μ A/cm². As can be seen the elec-

Table I. Composition and sintering conditions for group IVA-doped α -Fe₂O₃ electrodes

| Dopant | Doping level (a/o) | Sintering temperature, °C | Sintering time, hr |
|------------------|--------------------|---------------------------|--------------------|
| SiO ₂ | 0.25-2 | 1350 | 20-30 |
| GeO ₂ | 0.002-0.01 | 1300 | 5-20 |
| SnO ₂ | 0.002-0.01 | 1300-1370 | 8-15 |
| PbO ₂ | 0.05-0.2 (initial) | 1330-1370 | 7-30 |

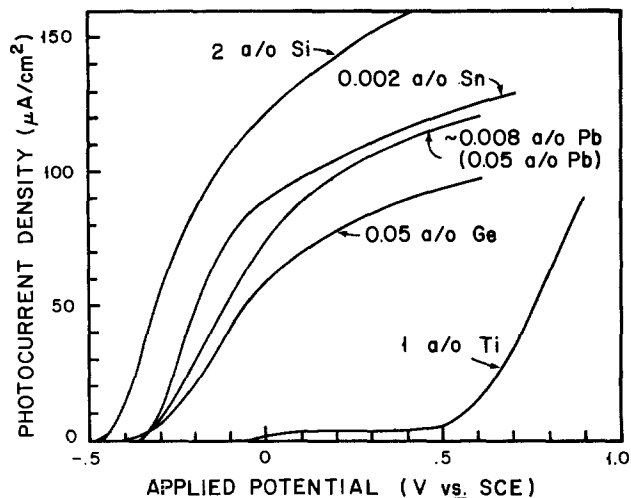


Fig. 1. Photocurrent density as a function of applied potential at 400 nm for $\alpha\text{-Fe}_2\text{O}_3$ electrodes doped with group IVA elements and with TiO_2 . Solution: 1F NaOH.

trodes doped with group IVA elements exhibited significant photocurrents even at 0V vs. SCE in a basic solution. The highest photocurrents at relatively low potentials (<0.5V vs. SCE) were observed at 2 a/o Si^{4+} -doped electrode. Although there were differences in photocurrents at low applied potentials among the different electrodes the photocurrent plateau values reached at higher potentials ($\sim 1\text{V}$ vs. SCE) were about the same for nearly all electrodes.

Figure 2 shows the spectral response for the photocurrent (quantum) efficiency in 1F NaOH for several electrodes. In general there was no significant difference between the effect of GeO_2 and SnO_2 as dopants. Both of the lower doping levels 0.002-0.01 a/o showed higher photocurrent densities at 0V vs. SCE than those obtained at higher (>0.05 a/o) doping levels. At doping levels >1 a/o the photocurrents at 0V vs. SCE were negligible for both dopant types. This doping level effect is demonstrated in Fig. 3 for Sn(IV)-doped electrodes. It should be noted that this effect was not observed for SiO_2 -doped electrodes and we did not succeed in preparing TiO_2 -doped electrodes at a level lower than 0.05 a/o. Photoelectrochemical performance of all electrodes reported was stable for long periods (>3 days at 0.4-1.8 mA) of irradiation. The onset of photocurrent spectral response (\sim bandgap) of all group IVA-doped electrodes was the same within experimental error. A value of ~ 2.2 eV was obtained by plotting $(\eta h\nu)^{1/2}$ vs. $h\nu$, where η is the photocurrent

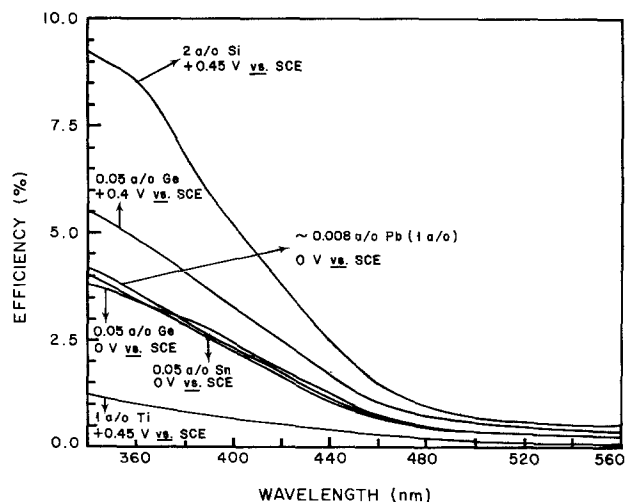


Fig. 2. Spectral response for photocurrent efficiency (uncorrected for reflection losses at the cell window and the electrode surface) of doped $\alpha\text{-Fe}_2\text{O}_3$ electrodes in 1F NaOH.

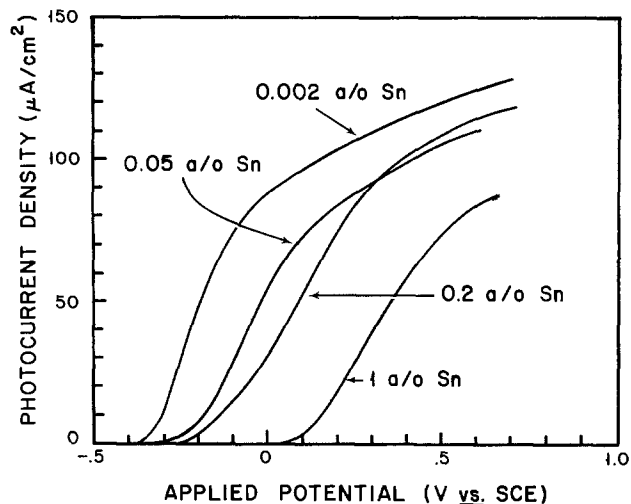


Fig. 3. Photocurrent density as a function of applied potential at 400 nm for $\alpha\text{-Fe}_2\text{O}_3$ electrodes doped with various amounts of Sn(IV). Solution: 1F NaOH.

(quantum) efficiency. An example for SiO_2 - and GeO_2 -doped electrodes is shown in Fig. 4.

The turn-on voltage for several SiO_2 -, GeO_2 -, and SnO_2 -doped electrodes was measured as a function of pH as shown in Fig. 5 for the SiO_2 - and GeO_2 -doped electrodes. Straight lines were obtained for each electrode with slopes in the range of $-(60-68)$ mV/pH. These results were within experimental error of -59 mV/pH, the value expected for the pH dependence of the flatband potential. Although the turn-on voltage does not correspond exactly to the flatband potential (3) the pH dependence is usually identical. The turn-on voltage shifted to negative potentials as the dopant level decreased, as can be seen in Fig. 3 for Sn(IV)-doped electrodes.

It had been observed previously (1, 5) that dipping Si(IV)- and Ti(IV)-doped electrodes in 1F KI at pH 9 improved photocurrents observed in strong base solution. However, dipping Ge(IV)- and Sn(IV)-doped electrodes did not significantly improve the photocurrent. Soaking in KI solution appears to be effective only for electrodes showing less than optimum photoactivity perhaps by removing surface recombination sites. It should be noted that undoped high purity $\alpha\text{-Fe}_2\text{O}_3$ was highly resistive and exhibited no photocurrent during the tenure of our experiments.

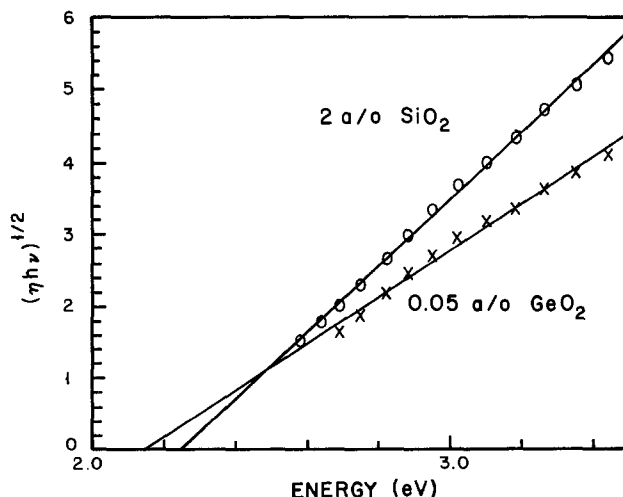


Fig. 4. $(\eta h\nu)^{1/2}$ vs. $h\nu$. (o) 2 a/o Si(IV); (x) 0.05 a/o Ge(IV)-doped $\alpha\text{-Fe}_2\text{O}_3$ electrodes. E_g : 2 a/o Si(IV) = 2.25 eV; 0.05 a/o Ge(IV) = 2.15 eV.

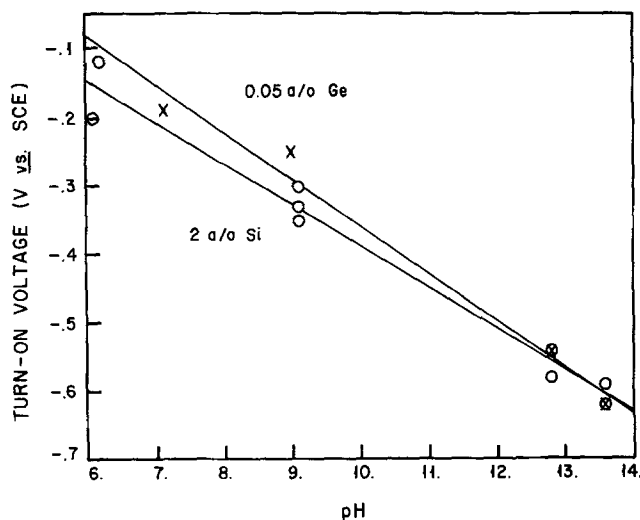
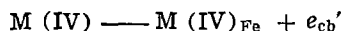


Fig. 5. Turn-on voltage vs. pH. (o): 2 a/o Si(IV); (x): 0.05 a/o Ge(IV)-doped α -Fe₂O₃ electrodes. Slopes: 2 a/o Si(IV) = -60 ± 3 mV/pH; 0.05 a/o Ge(IV) = -68 ± 5 mV/pH.

Discussion

It appears that all IVA elements are effective dopants for α -Fe₂O₃ photoanodes. This is consistent with the general aliovalent doping concept that the +4 ion introduces an electron into the conduction band



One could argue that group IVB elements should be equally effective whereas the experimental evidence indicates that titanium is not as effective as silicon. The difference may lie in the additional energy levels introduced by the aliovalent metal ion centers present. A Ti_{Fe}^x center may trap an electron to form Ti_{Fe}^x, i.e., a Ti(III) ion. Such centers may also act as electron hole recombination sites thereby decreasing photocurrent efficiency. Lower members in group IVB may not display this behavior, and recently Horowitz (6) showed that single crystal Fe₂O₃ doped with ZrO₂ was more effective than titanium doping.

A second conclusion is that photocurrent decreases at a given applied potential as the doping level increases as shown in Fig. 3 for SnO₂-doped electrodes. This is expected when one considers the effect of donor density on space charge layer thickness. As the donor density increases the space charge layer becomes thinner and fewer photons are absorbed in the space charge region. Photons may still be absorbed at a greater depth in the Fe₂O₃ electrode but hole mobility is so low that few reach the space charge region to be driven to the surface. The apparent shift in turn-on voltage to more anodic values with increasing doping level is not expected although this point was observed and discussed in a previous paper (3).

However, it must be kept in mind that the dopant may play other roles besides introducing electronic

defects especially at high doping levels. For example, they may act as traps and recombination centers leading to lower photocurrent efficiency at high doping levels.

The results with lead-doped electrodes are more difficult to explain because the final oxidation state is not +4 as with the other dopants. In fact, doping with PbO gave electrodes with photoelectrochemical properties similar to PbO₂-doped electrodes. Doping with a +2 ion could lead to p-type material although doping with Ca(II) produced only highly resistive electrodes. However, the behavior of lead-doped α -Fe₂O₃ electrodes indicates that it is n-type like other members of group IV. Because doping levels need not be high, and in fact, better performance is observed with lower doping levels (Fig. 3) it may be that traces of Pb(IV) account for the photoelectrochemical behavior. Fredlein and Bard (7) also observed n-type behavior for single crystal α -Fe₂O₃ grown from a PbO melt. The Pb content was 1-10 a/o, but photocurrents were small unless heat-treated. These authors assumed that lead was present as Pb(IV) because the electrodes were n-type. All electrodes were stable for long periods of illumination with many electrodes being studied over periods of several weeks with no significant change in photoelectrochemical properties.

Acknowledgment

This work is supported by the Division of Chemical Sciences, Office of Basic Energy Sciences, v.s. Department of Energy.

Manuscript submitted Feb. 26, 1981; revised manuscript received May 5, 1981.

Any discussion of this paper will appear in a Discussion Section to be published in the June 1982 JOURNAL. All discussions for the June 1982 Discussion Section should be submitted by Feb. 1, 1982.

Publication costs of this article were assisted by the University of California.

REFERENCES

1. J. H. Kennedy, R. Shinar, and J. P. Ziegler, *This Journal*, **127**, 2307 (1980).
2. M. Gori, H. R. Grüniger, and G. Calzaferrri, *J. Appl. Electrochem.*, **10**, 345 (1980).
3. J. H. Kennedy and K. W. Frese, Jr., *This Journal*, **125**, 723 (1978).
4. G. V. Samsonov, Editor, "The Oxide Handbook," IFI/Plenum Data Corporation, New York (1973).
5. J. H. Kennedy, R. Shinar, and J. P. Ziegler, Paper X-3 presented at the Third International Conference on Photochemical Conversion and Storage of Solar Energy, University of Colorado, Boulder, Colorado, August, 1980.
6. G. Horowitz, Paper IX-6 presented at the Third International Conference on Photochemical Conversion and Storage of Solar Energy, University of Colorado, Boulder, Colorado, August, 1980.
7. R. A. Fredlein and A. J. Bard, *This Journal*, **126**, 1892 (1979).



Environmental Stability and Failure Mechanisms of Chromated Lead/Tin Alloy Joints Bonded with an Ethylene-Acrylic Acid Copolymer

I. Acidic Conditions

Fumio Yamamoto, Shinzo Yamakawa, and Makoto Wagatsuma

*Nippon Telegraph and Telephone Public Corporation,
 Ibaraki Electrical Communication Laboratory, Tokai, Ibaraki 319-11, Japan*

ABSTRACT

The environmental stability and the failure mechanisms of a cathodically chromated lead/tin (38/62) alloy joint bonded with an ethylene-acrylic acid (EAA) copolymer have been investigated in acidic solutions. Immersion of the joint in acidic solutions causes rapid decrease in peel strength and finally interfacial separation. ESCA analysis of the peeled surfaces shows that this decrease in peel strength is due to an interfacial degradation between the chromate film and the underlying alloy (consisting both of lead and tin phases). The retention time, during which a joint retains the initial peel strength, decreases with increasing anode current density of the alloy in acidic solutions or with decreasing polarization resistance. This result suggests that the interfacial failure at the chromate-alloy interface results from anodic dissolution of the underlying alloy. A failure mechanism of the chromated alloy joint in acidic solutions has been proposed: The degradation at the chromate-alloy interface occurs through rapid anodic dissolution of the lead phase and slow anodic dissolution of the tin phase.

The long-term exposure of metal joints bonded with ethylene-acrylic acid (EAA) copolymers to humid environments causes the loss in joint strength (1-4). We have reported that cathodic chromate treatments of lead/tin alloys greatly enhances the environmental stability of the alloy joints bonded with an EAA copolymer and that the joint strength is kept unchanged in distilled water for more than 2 years (5, 6). However, these joints seem to have poor environmental stability in acidic solutions since both lead and tin metals are rapidly corroded in acidic solutions (7). This paper is concerned with the environmental stability in acidic solutions and the failure mechanisms of a cathodically chromated lead/tin alloy joint bonded with an EAA copolymer.

Experimental

The preparation of T-peel specimens consisting of adherend (0.5 mm)-adhesive (0.2 mm)-adherend (0.5 mm) and the T-peel testing were described elsewhere (5). The adherend used was a cathodically chromated lead/tin (38/62) alloy. The adhesive used was an EAA copolymer (1) supplied by Union Carbide Company (melt index 50 g/10 min, acrylic acid content 20 weight percent, density 0.96 g/cm³, glass transition temperature 31°C). To evaluate the environmental stability of the joints, the peel specimens were immersed in acidic solutions, and the T-peel strength was mea-

sured at 25°C immediately after immersion. The pH range of the solutions was 0.8-5.6, and the temperature range was 20°-70°C. The acidic solutions were 2-HOCOC₆H₄COOK-HCl (pH 0.8, 2.5, and 3.2), CH₃COONa-HCl (pH 4.5), 2-HOCOC₆H₄COOK-NaOH (pH 5.0), and CH₃COOH-CH₃COONa (pH 5.6) buffers.

The corrosion resistance of untreated and chromated alloy sheets in acidic solutions were evaluated from anode current density (I_p) by a potentiostatic method or from polarization resistance (R_p) (8-10) by a coulometric method (11-15). The potentiostatic measurements were made using a Hokuto potentiometer, and the anode current density was measured at an overpotential of 50 mV under nitrogen gas. The surface area of untreated and chromated alloy sheets used as the working electrodes was ca. 2 cm². A platinum sheet of ca. 2 cm² and a saturated calomel electrode were used as the counter and reference electrodes, respectively. The anode current density decreased with time of applying overpotential and leveled off after 30-60 sec. The leveled-off anode current density was recorded as an I_p value. The coulometric measurements were made using a Hokuto galvanostat connected with a pulse generator (pulse width 10 μsec) without removing dissolved oxygen. The overpotential-time curves were displayed on a storage oscilloscope. The amount of charge density applied was 0.1-0.3 μC/cm², and the induced initial overpotentials were in the range 2-10 mV. The polarization resistance calculated from the overpotential-time curves decreased with

Key words: ESCA, anodic dissolution, interfacial degradation, metal-polymer joint.

water immersion of alloy sheets and leveled off after ca. 20 min immersion. The leveled-off polarization resistance was recorded as an R_p value. To check the validity of the R_p values measured by the coulometric method, R_p values of alloy sheets in various acidic solutions were also measured from polarization curves. In this case, R_p values were calculated using $R_p = \beta_a \beta_c / I_0 (\beta_a + \beta_c)$, where β_a and β_c are anodic and cathodic Tafel slopes, respectively, and I_0 is corrosion current density. The R_p values measured from the coulometric measurements were in agreement with those from the polarization curves within an error of 20%. The amount of oxides on the alloy surfaces was measured by electrolytic reduction in an aqueous solution of 0.1 mol/liter NH_4Cl at a constant current density of $90 \mu\text{A}/\text{cm}^2$ under nitrogen gas, in the same way as in the previous work (5).

The original chromated alloy and EAA surfaces before bonding and the fractured surfaces of the joints were analyzed by x-ray photoelectron spectroscopy (ESCA). ESCA spectra were recorded on an A.E.I. ES 200 spectrometer using $\text{Al } k_{\alpha_1, \alpha_2}$ radiation. Typical operating conditions were: x-ray gun, 10 kV, 20 mA; pressure in the sample chamber, 1×10^{-7} Torr. The binding energies were calibrated with respect to the carbon 1s electron peak at 284.9 eV due to residual pump oil on the sample surface. Electron probe x-ray microanalysis (XMA) was also used for the surface analysis of chromated alloy sheets. XMA was carried out using a Shimadzu EMX-SM7. XMA data were taken at a probe operating voltage of 15 kV and a sample current of 1 nA.

Results and Discussion

Chromate films on a lead/tin alloy surface.—Figure 1 shows an SEM micrograph and lead and tin images of a lead/tin (38/62) alloy surface cathodically chromated for 5 sec. The presence of a chromate film on the alloy surface was not detected by XMA analysis because its film thickness was much thinner (ca. 100Å) (5) than the XMA sampling depth (several micrometers), whereas it was detected by ESCA and IMA (ion microanalyzer) (5). From the lead and tin images (Fig. 1), it is apparent that the alloy surface consists both of lead and tin phases. The XMA analysis showed that the tin content in the lead phase and the lead content in the tin phase were less than a few percent.

It is well known that most chromate films deposited on metals have considerable cracks (16). Figure 2 shows the changes in oxygen 1s ESCA spectrum of the chromated alloy surface with heating. The chromated alloy sheet was heated in ESCA chamber for 20 min at each temperature, and ESCA spectra from its alloy surface were measured immediately at the same temperature. The intensity of oxygen 1s decreases with increasing heating temperatures and after heating at 180°C reaches ca. 70% of that heated at 60°C. The disappeared oxygen 1s peak at 532.3 eV has been assigned to adsorbed oxygen or water by Ansell *et al.* (17). Figure 3 shows the changes in the amount of alloy oxides of the chromated alloy surface with heating for 20 min at each temperature. The amount of oxides on the chromated alloy surfaces corresponds to that of the underlying alloy oxides at cracks of the chromate film. The amount of oxides increases gradually with heating at temperatures of more than 100°C and then increases rapidly with the rupture of chromate film due to the melt of the underlying alloy at ca. 183°C. These results indicate that many cracks, which are probably formed by contraction in volume due to escaped water, are present in the chromate film on the alloy surface heated at temperatures of more than 100°C. Since chromated alloy joints were prepared by heating for 5 min with a hot press at 120°C (5), the chromate film in the joints should have many cracks.

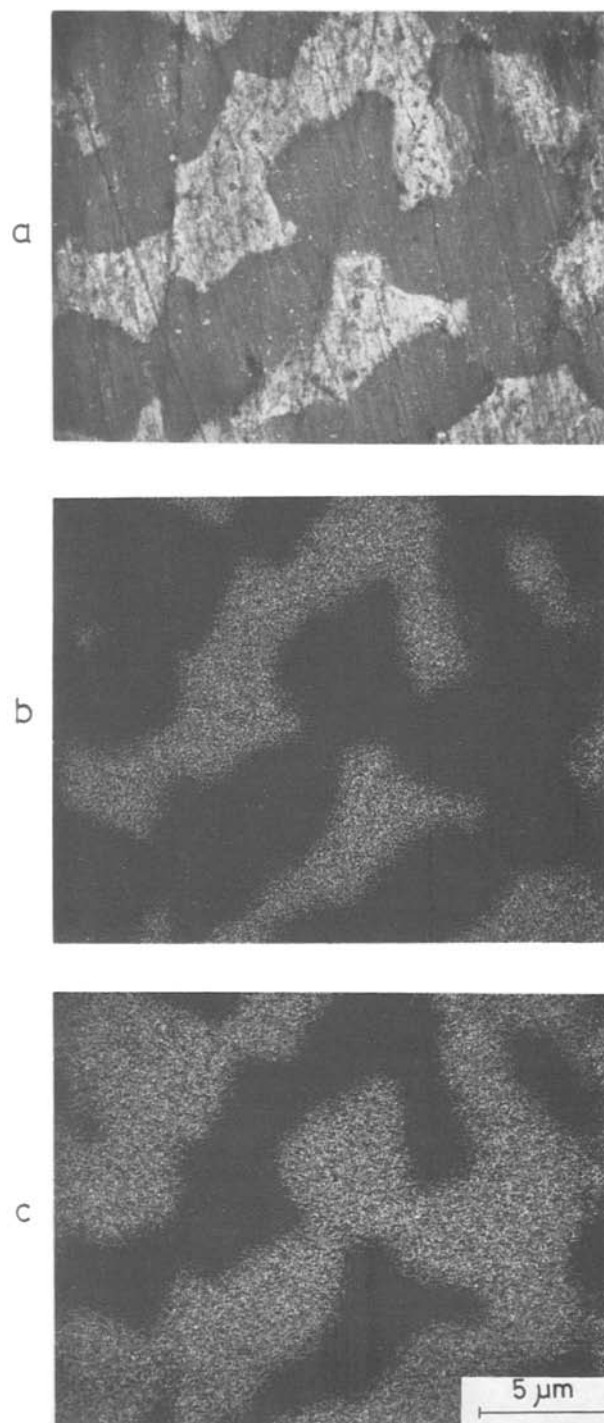


Fig. 1. An SEM micrograph (a) and lead (b) and tin (c) images of a chromated lead/tin (38/62) alloy surface.

Bond durability.—Figure 4 shows the changes in peel strength with immersion in a $\text{CH}_3\text{COONa-HCl}$ buffer (pH 4.5) for a chromated alloy joint. Figure 5 shows the change in peel strength retention time (during which the initial peel strength is kept unchanged) with immersion temperature. The peel strength retention time decreases with increasing immersion temperature and was only 5 days at 70°C. On the other hand, the peel strength retention time of the chromated alloy joint immersed in distilled water at 50°C was more than 2 years (6). Apparently, the joint deteriorates more rapidly in the acidic solution than in distilled water. SEM observations of fractured surfaces showed that the small areas or spots of peel strength $\approx 0 \text{ kg}/\text{cm}^2$, different in peel strength from the surrounding area of peel strength which was 6.0–6.5 kg/cm^2 .

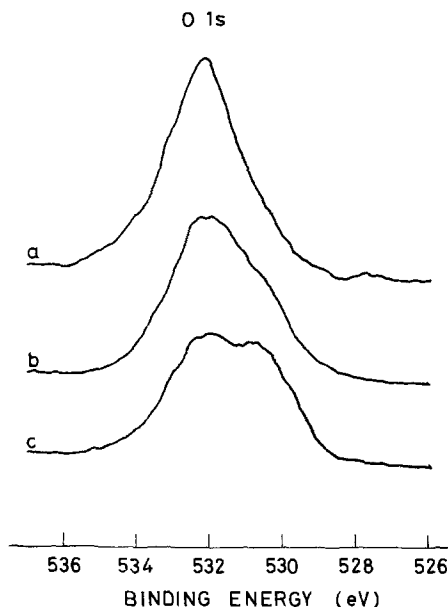


Fig. 2. Changes in oxygen 1s ESCA spectrum with heating for a chromated alloy surface. The alloy was heated in ESCA sample chamber for 20 min at each temperature. Heating temperatures were: (a) 60°C, (b) 120°C, (c) 180°C.

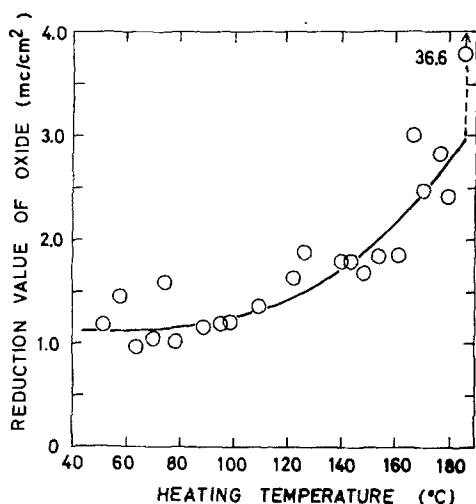


Fig. 3. Changes in amount of oxides with 20 min heating for a chromated alloy surface measured by electrolytic reduction in an aqueous solution of 0.1 mol/liter NH_4Cl at a constant current density of $90 \mu\text{A}/\text{cm}^2$.

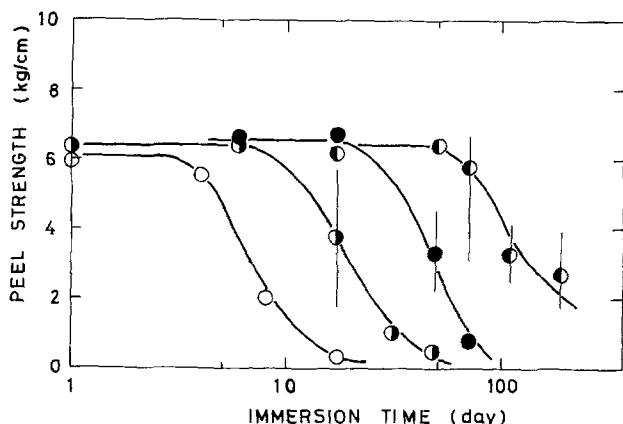


Fig. 4. Changes in peel strength with immersion in a $\text{CH}_3\text{COONa-HCl}$ buffer (pH 4.5) for a chromated lead/tin (38/62) alloy joint bonded with an EAA copolymer. Immersion temperatures were: (●) 40°C, (●) 50°C, (○) 60°C, (○) 70°C.

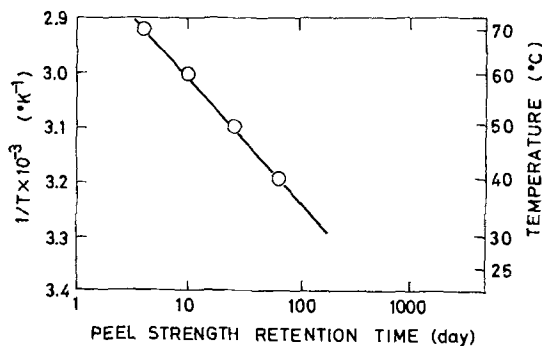


Fig. 5. Arrhenius plot for peel strength retention time of a chromated alloy joint in a $\text{CH}_3\text{COONa-HCl}$ buffer (pH 4.5).

cm, appeared over the whole part of the interface, the area and number of the spots increased gradually with immersion, and then finally an interfacial separation occurred.

Table I summarizes the peel strength retention times of the chromated alloy joint in various acidic solutions. In most cases, the peel strength retention time decreases with decreasing pH of acidic solutions. However, there are some exceptions: the peel strength retention time in a $\text{CH}_3\text{COONa-HCl}$ buffer (pH 4.5) at 50°C and that in a $2\text{-HOCOC}_6\text{H}_4\text{COOK-HCl}$ buffer (pH 3.2) at 50°C.

Locus of failure.—Figure 6 shows ESCA spectra of fractured chromated alloy and EAA surfaces of chromated alloy joints peeled with low peel strength after immersion in a $\text{CH}_3\text{COONa-HCl}$ buffer (pH 4.5), together with those of original chromated alloy and EAA surfaces. Each fractured surface peeled with low peel strength after immersion in the other buffers showed ESCA spectra similar to those in Fig. 6. The fractured alloy surface shows the increase in tin intensities (metal peak, 484.3 eV; oxide peak, 486.5 eV), the decrease in oxygen intensity (532.3 eV), and the disappearance of chromium oxide (577.0 eV). On the other hand, the fractured EAA surface shows the decrease in carbon intensity (285.0 eV), the remarkable increase in oxygen intensity, and the appearance of tin and chromium oxides. Apparently, the exposure of tin and chromium oxides on the fractured EAA surface is due to the transfer from the chromated alloy surface. Further, the remarkable increase in oxygen intensity on the fractured EAA surface is due to the transfer of the chromate film from the alloy surface. On the other hand, the increase in tin intensities on the fractured alloy surface is probably due to exposure of the underlying lead/tin alloy by the transfer of the chromate film to the EAA surface. These results indicate that the failure occurs between the chromate film and the underlying alloy, although it is not clear whether the failure occurs at the chromate-underlying alloy oxide layer interface, in the alloy oxide layer, or at the alloy oxide layer-alloy metal interface. On the other hand, the water absorption of the EAA copolymer was as low as ca. 0.44 w/o in the pH 4.5 buffer at 50°C. This value

Table I. Peel strength retention time in various acidic solutions

| Acidic solution | pH | Temperature (°C) | Peel strength retention time (days) |
|---|-----|------------------|-------------------------------------|
| $2\text{-HOCOC}_6\text{H}_4\text{COOK-HCl}$ buffer | 0.8 | 50 | 30 |
| $2\text{-HOCOC}_6\text{H}_4\text{COOK-HCl}$ buffer | 2.5 | 50 | 40 |
| $2\text{-HOCOC}_6\text{H}_4\text{COOK-HCl}$ buffer | 3.2 | 50 | 40 |
| $\text{CH}_3\text{COONa-HCl}$ buffer | 4.5 | 70 | 4 |
| $\text{CH}_3\text{COONa-HCl}$ buffer | 4.5 | 60 | 10 |
| $\text{CH}_3\text{COONa-HCl}$ buffer | 4.5 | 50 | 26 |
| $\text{CH}_3\text{COONa-HCl}$ buffer | 4.5 | 40 | 64 |
| $2\text{-HOCOC}_6\text{H}_4\text{COOK-NaOH}$ buffer | 5.0 | 50 | >900 |
| $\text{CH}_3\text{COOH-CH}_3\text{COONa}$ buffer | 5.6 | 70 | 75 |
| $\text{CH}_3\text{COOH-CH}_3\text{COONa}$ buffer | 5.6 | 40 | 600 |

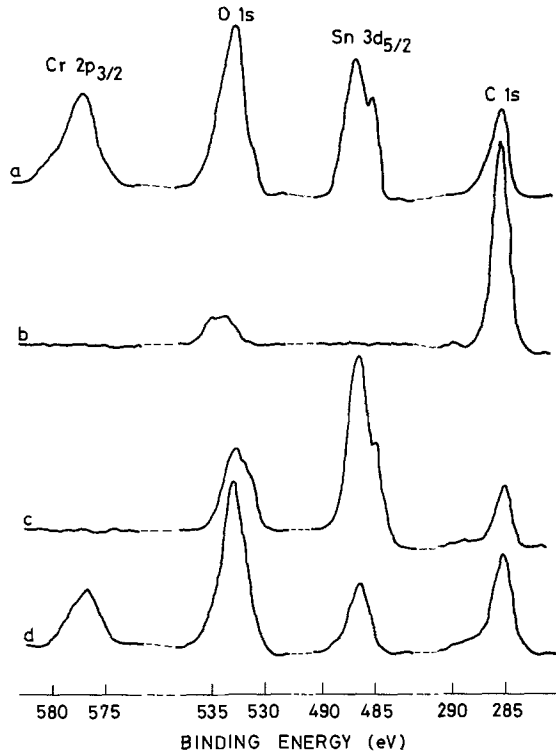


Fig. 6. ESCA spectra of original chromated alloy (a) and EAA (b) surfaces and fractured chromated alloy (c) and EAA (d) surfaces of a chromated alloy joint peeled with low peel strength after immersion in a CH₃COONa-HCl buffer (pH 4.5).

was nearly equal to that (0.36 w/o) in distilled water. Therefore, the mechanical properties of EAA copolymer such as stress-strain and failure behavior were not affected by immersion in acidic solutions. As a result, as long as the failure occurred cohesively in the EAA copolymer, the initial peel strength was kept unchanged (6). Thus, the decrease in peel strength occurs in acidic solutions with the change in locus of failure from the EAA copolymer to the chromate-underlying alloy interface.

Relationship between bond durability and alloy corrosion.—It seems likely that the interfacial failure between the chromate film and the underlying alloy in acidic solutions is due to anodic dissolution of the underlying alloy. To clarify the relation between the decrease in peel strength and the chromated alloy corrosion, the anode current density (I_p) from the potentiostatic method and the polarization resistance (R_p) from the coulostatic method were measured for untreated and chromated alloys in acidic solutions, in which immersion tests of chromated alloy joints were carried out. Figure 7 shows the changes in I_p value

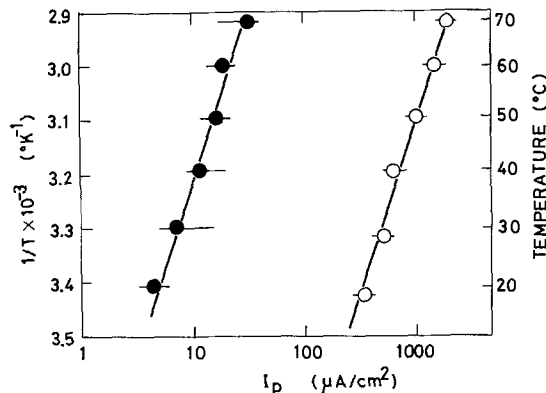


Fig. 7. Arrhenius plots for I_p values of untreated (○) and chromated (●) alloy sheets in a CH₃COONa-HCl buffer (pH 4.5).

with immersion temperature for untreated and chromated alloy sheets in a CH₃COONa-HCl buffer (pH 4.5). On both the surfaces, the I_p value increases with increasing immersion temperature. The I_p values on chromated alloy are ca. 1/500 times those on untreated alloy. Since the chromate film itself is corrosion-resistant, the I_p values measured on chromated alloy surfaces mean those on regions uncovered with the chromate film [e.g., grain boundaries (5) and cracks in the chromate film]. The I_p values on untreated and chromated alloy surfaces show the same temperature dependence (Fig. 7). This fact also supports the view that the I_p value on chromated alloy surfaces measures a leak current density from the underlying alloy. Therefore, the corrosion properties of chromated alloys depend on both the area uncovered with the chromate film and the corrosion of the underlying alloy itself. In this paper, since the chromate treatment was carried out under the same conditions, the area uncovered with the chromate film is thought to be the same for all chromated samples. Accordingly, since the corrosion resistance of the chromated alloy can be related to that of untreated alloy, the I_p and R_p values of untreated alloy in acidic solutions were compared with the peel strength retention time of chromated alloy joints in acidic solutions.

Figures 8 and 9 show log-log plots of I_p and R_p of untreated alloy vs. peel strength retention time for chromated alloy joints at various immersion temperatures in various acidic solutions. In spite of the use of different acidic solutions and different immersion temperatures, the peel strength retention time is inversely proportional to the I_p value and proportional to the R_p

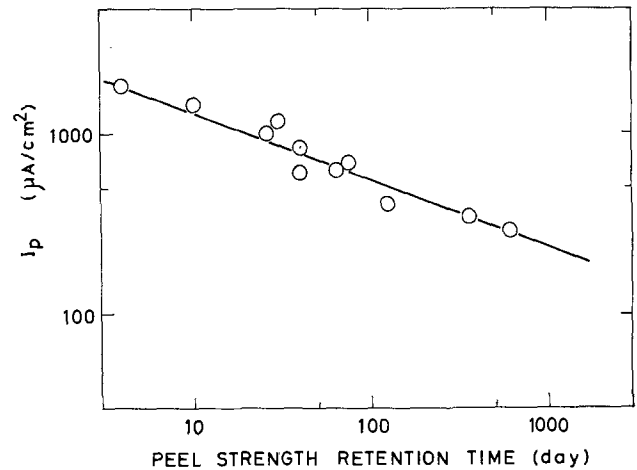


Fig. 8. Log-log plot of I_p vs. peel strength retention time of chromated alloy joints at various immersion temperatures in various acidic solutions.

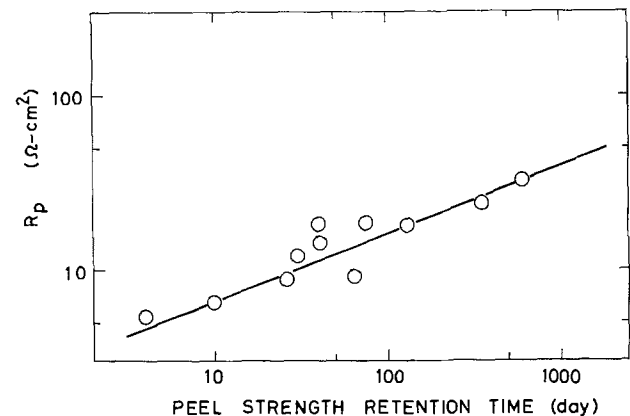
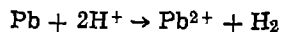


Fig. 9. Log-log plot of R_p vs. peel strength retention time of chromated alloy joints at various temperatures in various acidic solutions.

value. In other words, the peel strength retention time increases with decreasing anodic dissolution of the underlying alloy, i.e., decreasing I_p value or increasing R_p value. Thus, it is concluded that the decrease in peel strength is due to the anodic dissolution of the underlying alloy.

Failure mechanism in acidic solutions.—Figure 10 shows a schematic diagram of chromated lead/tin alloy-EAA interfaces degraded in acidic solutions. The alloy surface consists both of lead and tin phases (Fig. 1). Since the lead phase was corroded more rapidly than the tin phase when untreated alloy sheets were immersed in acidic solutions, the lead phase-EAA interface of chromated alloy joints are assumed to degrade rapidly in acidic solutions by anodic dissolution of lead according to the reaction.



Therefore, the joint strength of chromated alloy joints is due mainly to interfacial forces at the tin phase-EAA interfaces. In chromated alloy joints immersed in acidic solutions, hydrogen ions diffuse into the adhesive joints along the lead phase-chromate film interfaces and reach the tin phase-chromate film interfaces. At the same time, hydrogen ions may diffuse through the EAA copolymer, pass through the cracks (Fig. 2) of chromate film, and then reach the tin phase-chromate film interfaces. Subsequently, at the tin phases in contact with the chromate film, the growth of tin oxide layer and the anodic dissolution occur gradually according to the reaction



The decrease in peel strength occurs simultaneously

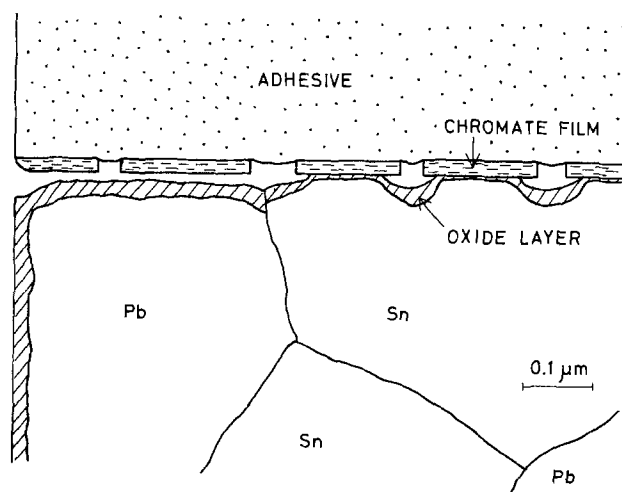


Fig. 10. Schematic diagram of chromated lead/tin alloy-EAA interfaces degraded in acidic solutions.

with anodic dissolution of the tin phases. After complete anodic dissolution of all the tin phases in contact with the chromate film, interfacial separation occurs between the chromate film and the underlying alloy. In conclusion, the environmental stability of chromated lead/tin alloy joints in acidic solutions depends on the corrosion properties of the tin phase in acidic solutions, and the failure of chromated alloy joints proceeds with anodic dissolution of the tin phases.

The I_p and R_p values of untreated alloy were 1.0 $\mu\text{A}/\text{cm}^2$ and 3.2 $\text{k}\Omega\text{-cm}^2$ in distilled water, respectively. It is estimated from Fig. 8 and 9 that the peel strength retention time of chromated alloy joints is more than 10 years in distilled water. This estimation is in fair agreement with an experimental result (6) that the decrease in peel strength of chromated alloy joints does not occur even after immersion in distilled water for 2 years.

Acknowledgment

The authors wish to thank Dr. K. Kudo and Mr. S. Tsuru for many helpful discussions.

Manuscript submitted March 4, 1980; revised manuscript received June 25, 1981.

Any discussion of this paper will appear in a Discussion Section to be published in the June 1982 JOURNAL. All discussions for the June 1982 Discussion Section should be submitted by Feb. 1, 1982.

Publication costs of this article were assisted by Nippon Telegraph and Telephone Public Corporation.

REFERENCES

- H. G. Frank, M. C. McGugh, and W. E. Ropp, 17th Int. Wire and Cable Symposium, Atlantic City, NJ (1968).
- B. Wargotz, *J. Appl. Polym. Sci.*, **13**, 1965 (1969).
- W. H. Smarook and S. Bonotto, *Polym. Eng. Sci.*, **8**, 41 (1968).
- B. Wargotz, *J. Appl. Polym. Sci.*, **12**, 1873 (1968).
- F. Yamamoto and S. Yamakawa, *ibid.*, **25**, 2479 (1980).
- F. Yamamoto, S. Yamakawa, and M. Wagatsuma, *ibid.*, **25**, 2731 (1980).
- H. H. Uhlig, "Corrosion Handbook," John Wiley & Sons, Inc., New York (1948).
- K. Kanno, M. Suzuki, and Y. Sato, *Boshoku Gijutsu*, **26**, 697 (1977).
- E. J. Simmons, *Corrosion*, **11**, 255t (1955).
- W. J. Schwerdtfeger and O. N. McDorman, *This Journal*, **99**, 407 (1952).
- P. Delahay, *J. Phys. Chem.*, **66**, 2204 (1962).
- P. Delahay, *Anal. Chem.*, **34**, 1161 (1962).
- P. Delahay, *Anal. Chim. Acta*, **27**, 90 (1962).
- W. H. Reinmuth and C. E. Wilson, *Anal. Chem.*, **34**, 1159 (1962).
- W. H. Reinmuth, *ibid.*, **34**, 1272 (1962).
- F. W. Eppenstein and M. R. Jenkins, *Metal Finishing*, No. 9, 29 (1975).
- R. O. Ansell, T. Dickinson, A. F. Povey, and P. M. A. Sherwood, *This Journal*, **124**, 1360 (1977).

Environmental Stability and Failure Mechanisms of Chromated Lead/Tin Alloy Joints Bonded with an Ethylene-Acrylic Acid Copolymer

II. Alkaline Conditions

Fumio Yamamoto, Shinzo Yamakawa, and Shinji Tsuru

*Nippon Telegraph and Telephone Public Corporation,
Ibaraki Electrical Communication Laboratory, Tokai, Ibaraki 319-11, Japan*

ABSTRACT

The environmental stability and the failure mechanisms of a cathodically chromated lead/tin (38/62) alloy joint bonded with an ethylene-acrylic acid (EAA) copolymer (20 weight percent acrylic acid) have been investigated in alkaline solutions. The environmental stability has been compared with that of the alloy joint bonded with an ethylene-ethyl acrylate copolymer grafted with acrylic acid (EEA-g-AA). The peel strength of the EAA joint decreases rapidly with immersion in alkaline solutions. This decrease in peel strength results from stepwise swelling of the EAA adhesive layer from the edges of the joint to the inside, which swelling occurs by alkaline ions diffusing into the joint inside. On the other hand, the decrease in peel strength of the EEA-g-AA joints occurs from stepwise interfacial degradation from the joint edges, with no swelling of the EEA-g-AA adhesive layer. The interfacial failure mechanism is discussed in comparison with that of the EAA joint.

Cathodically chromated lead/tin alloy joints bonded with an ethylene-acrylic acid (EAA) copolymer have high peel strength in dry conditions (1) and show high environmental stability in distilled water (2). However, immersion of the joints in acidic aqueous solutions causes a rapid decrease in peel strength and finally an interfacial separation (3). This decrease in peel strength is due to an interfacial degradation or failure between the chromate film and the underlying alloy. This interfacial failure is due to anodic dissolution of the underlying alloy. In alkaline solutions, on the other hand, lead/tin alloys are corroded since both lead and tin are amphoteric metals (4). Therefore, it is interesting to see whether the interfacial failure of lead/tin alloy joints occurs in alkaline solutions via the same mechanism as that in acidic solutions or via the other failure mechanism. This paper is concerned with the environmental stability in alkaline solutions and the failure mechanism of a cathodically chromated lead/tin (38/62) alloy joint bonded with an EAA copolymer used in previous papers (1-3). The failure mechanism in alkaline solutions is compared with that of the alloy joint bonded with an ethylene-ethylacrylate copolymer grafted with acrylic acid (EEA-g-AA).

Experimental

The preparation of T-peel specimens consisting of adherend (0.5 mm)-adhesive (0.2 mm)-adherend (0.5 mm) and the T-peel testing were described elsewhere (1). A cathodically chromated lead/tin (38/62) alloy sheet was used as the adherend. An EAA copolymer sheet (EAA-1), used in previous works (1-3), was used as the adhesive in this work, together with an ethylene-ethyl acrylate copolymer grafted with acrylic acid (EEA-g-AA). The EEA copolymer, supplied by Nippon Unicar Company, was homogeneously grafted with acrylic acid in benzoyl peroxide-containing xylene solutions at 120°C under nitrogen gas (5). The properties of ethylene copolymers investigated in this work are given in Table I. To evaluate the environmental stability of the joints, the peel specimens were

immersed in alkaline solutions at temperatures of 40°-70°C, and the T-peel strength was measured at 25°C immediately after immersion. The alkaline solutions used were: H₃BO₄ + KCl-NaOH (pH 8.0 and 8.5), NaHCO₃-NaOH (pH 10.0), Na₂HPO₄-NaOH (pH 11.0), and KCl-NaOH (pH 12.0 and 13.0) buffers, and 0.1N NaOH solution (pH 14.0). The locus of failure of these joints was determined from analysis of the fractured surfaces by x-ray photoelectron spectroscopy (ESCA) and scanning electron microscopy (SEM).

Results and Discussion

Water immersion test.—Figure 1 shows the changes in peel strength with immersion at various temperatures in an NaHCO₃-NaOH buffer (pH 10.0) for an EAA-1 joint. Figure 2 shows the changes in peel strength with immersion in various alkaline solutions at 50°C for the same EAA-1 joint. The peel strength decreases rapidly at relatively high pH values and temperatures as in acidic solutions (3). The peel strength retention time (during which the initial peel strength is kept unchanged) decreases with increasing immersion temperature or pH of alkaline solutions. Figure 3 shows the changes in peel strength in various alkaline solutions at 50°C for an EEA-g-AA joint. The peel strength retention time also decreases with increasing pH of alkaline solutions. However, the peel strength retention times of the EEA-g-AA joint is

Table I. Properties of acrylic acid-containing copolymers

| Sample | Melt index (ASTM D1238) (g/10 min) | Acrylic acid content (w/o) | Ethyl acrylate content (w/o) | Density (g/cm ³) | Glass transition temperature (°C) |
|-----------|------------------------------------|----------------------------|------------------------------|------------------------------|-----------------------------------|
| EAA-1* | 50 | 20 | — | 0.96 | 31 |
| EAA-2* | 9.0 | 8 | — | 0.932 | 12 |
| EAA-3* | 11.0 | 3.5 | — | 0.925 | -5 |
| EEA-g-AA† | 6.4 | 4.7 | 18 | 0.931 | -27 |

Key words: ESCA, interfacial degradation, metal-polymer interface, adhesive joint.

* Ethylene-acrylic acid copolymer.

† Ethylene-ethyl acrylate copolymer grafted with acrylic acid.

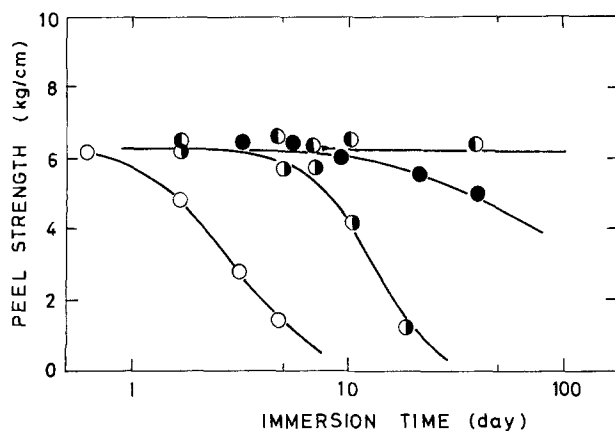


Fig. 1. Changes in peel strength with immersion in an NaHCO_3 - NaOH buffer (pH 10.0) for an EEA-1 joint. Immersion temperatures were: (●) 40°C; (●) 50°C; (◐) 60°C; (○) 70°C.

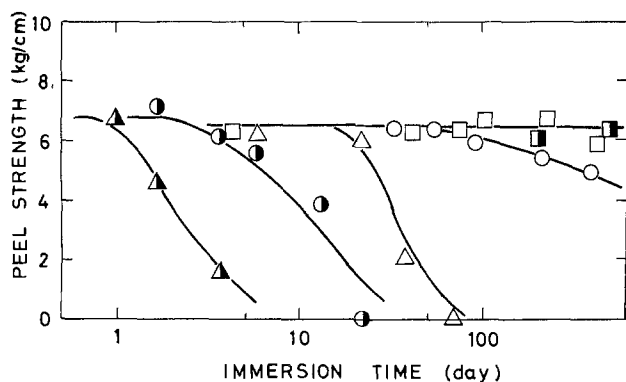


Fig. 2. Changes in peel strength with immersion in various alkaline solutions at 50°C for an EEA-1 joint. Alkaline solutions were: (▲) 0.1N NaOH solution, pH 14.0; (●) KCl-NaOH buffer, pH 12.0; (△) Na_2HPO_4 - NaOH buffer, pH 11.0; (○) NaHCO_3 - NaOH buffer, pH 10.0; (□) H_3BO_4 + KCl-NaOH buffer, pH 8.5; (◻) H_3BO_4 + KCl-NaOH buffer, pH 8.0.

longer than those of the EEA-1 joint when both the joints are immersed in the same alkaline solution; the EEA-g-AA joint is more stable in alkaline solutions than the EEA-1 joint.

Locus of failure.—The peel strength of the EEA-1 joint decreases as rapidly in alkaline solutions as in acidic solutions. However, the progress of the interfacial failure in alkaline solutions has been found to be significantly different from that in acidic solutions. Immersion of the joint in acidic solutions causes first the small areas or the spots of peel strength ≈ 0 kg/cm over the whole part of the interface, next the increases in the area and the number of the spots, and finally an interfacial separation (3). In alkaline solutions, on the other hand, the failure initiates from the edges of the joint in contact with the alkaline solutions and proceeds into the joint inside with water immersion. Figure 4 shows SEM micrographs of fractured chromated alloy and EAA surfaces of the EEA-1 joint peeled after immersion in an NaHCO_3 - NaOH buffer (pH 10.0). The SEM micrographs show a distinct front of failure on both the peeled surfaces. On the peeled alloy surface, the part of smooth surface corresponds to the undegraded region of the joint inside, which was peeled with a high peel strength similar to the initial peel strength. The part of rough surface corresponds to the degraded region of the joint edges, which was peeled with a low peel strength of ca. 0 kg/cm. The rough surface topography results from the residual adhesive, which had been transferred from the adhesive side to the alloy side through the cohesive

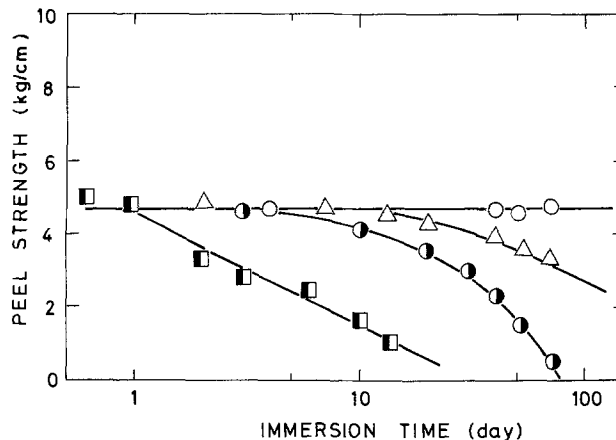


Fig. 3. Changes in peel strength with immersion in various alkaline solutions at 50°C for an EEA-g-AA joint. Alkaline solutions were: (■) KCl-NaOH buffer, pH 13.0; (●) KCl-NaOH buffer, pH 12.0; (△) Na_2HPO_4 - NaOH buffer, pH 11.0; (○) NaHCO_3 - NaOH buffer, pH 10.0.

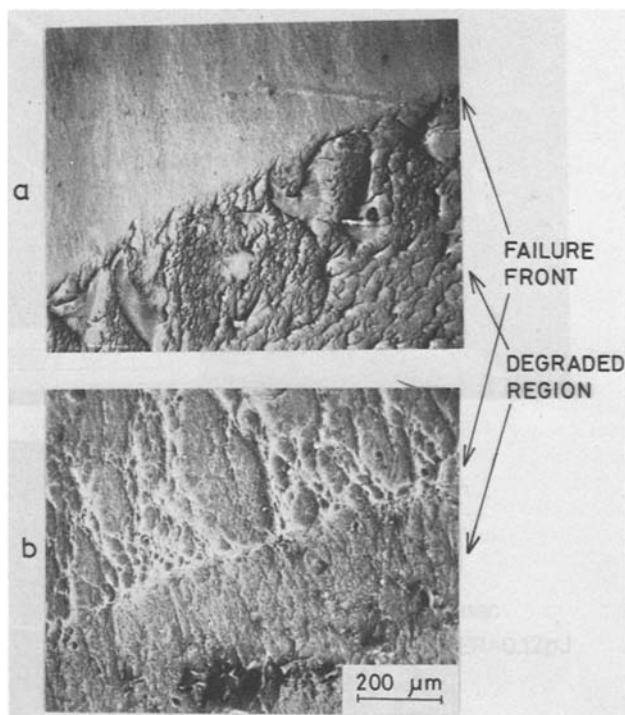


Fig. 4. SEM micrographs of fractured chromated alloy (a) and EAA (b) surfaces of an EEA-1 joint peeled after immersion in an NaHCO_3 - NaOH buffer (pH 10.0).

failure of the adhesive layer. On the other hand, on the peeled EAA side, remarkable swelling of the EAA adhesive was observed on the degraded region. The front of swelling coincided approximately with the front of the interfacial degradation. The undegraded EAA surface, peeled with high peel strength, shows a rough surface topography similar to that peeled in dry conditions (1). This rough topography results from plastic deformation of the adhesive.

Figure 5 shows ESCA spectra of the fractured chromated alloy and EAA surfaces corresponding to those of Fig. 4, together with those of original chromated alloy and EAA surfaces. The degraded parts of both the peeled surfaces show an overall ESCA spectrum similar to that of the original adhesive surface, although there is a slight ESCA peak of tin. This ESCA result and the presence of the residual adhesive on the degraded alloy surface (Fig. 4a) indicate that the failure of the degraded region of the joint occurs within the adhesive when the joint is peeled. On the

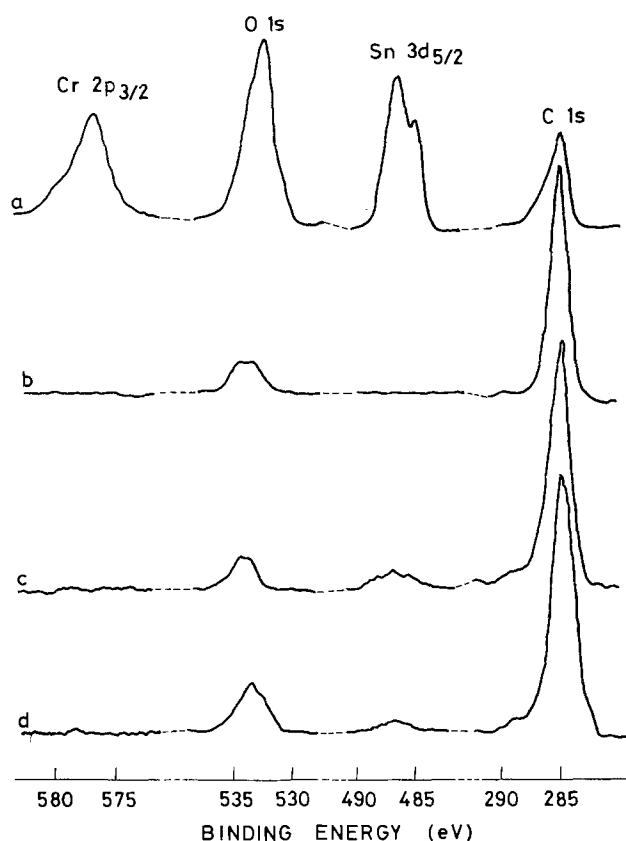


Fig. 5. ESCA spectra of original chromated alloy (a) and EAA (b) surfaces and fractured chromated alloy (c) and EAA (d) surfaces of an EAA-1 joint peeled with low peel strength after immersion in an $\text{NaHCO}_3\text{-NaOH}$ buffer (pH 10.0).

other hand, peeled alloy and EAA surfaces of the dry joint (1) and the undegraded region of immersed joints showed ESCA spectra similar to those (c, d) of Fig. 5. This result indicates that the locus of failure in the dry joint or in the undegraded region of the joint inside, in which the initial peel strength is kept unchanged, also is the cohesive failure of the adhesive itself. In other words, both the undegraded and degraded regions of the EAA-1 joint result in cohesive failure within the adhesive in spite of the significant difference in peel strength. This fact suggests that the decrease in peel strength of EAA-1 joints results from the decrease in mechanical or cohesive strength of the EAA adhesive, but not from anodic dissolution of the underlying alloy (3, 6-8) and from displacement of the adhesive by water (9).

Failure mechanism of EAA-1 joints in alkaline solutions.—The anode current density (I_p) (3) at an overpotential of 50 mV and the polarization resistance (R_p) (3) of a lead/tin (38/62) alloy in the alkaline solutions used were of the order of $100 \mu\text{A}/\text{cm}^2$ and $500 \Omega\text{-cm}^2$, respectively. The estimated peel strength retention time in alkaline solutions, which was obtained from the above I_p and R_p values using the relation between peel strength retention time and I_p or R_p in Fig. 8 or 9 of the previous paper (3), is more than 10 years. In fact, however, the joint degrades rapidly in alkaline solutions; the measured peel strength retention time is of the order of 10-100 days (Fig. 1 and 2). This disagreement indicates that anodic dissolution of the underlying alloy is not the prime cause for the joint deterioration in alkaline solutions, although it is the prime cause for the joint failure in acidic solutions.

Table II shows water absorption test results of EAA-1 and EEA-g-AA copolymer sheets (used as adhesives in this paper) immersed in an $\text{NaHCO}_3\text{-NaOH}$

Table II. Water absorption test of acrylic acid-containing copolymer sheets (0.5 mm thick) immersed in an $\text{NaHCO}_3\text{-NaOH}$ buffer (pH 10.0) in the range $40^\circ\text{-}70^\circ\text{C}$

| Sample | Acrylic acid content (w/o) | Water absorption (w/o) | | | |
|-----------|----------------------------|------------------------|--------------------|--------------------|--------------------|
| | | 40°C | 50°C | 60°C | 70°C |
| EAA-1* | 20 | 26.2 | 61.0 | 128.2 | 190.4 |
| EAA-2* | 8 | <0.01 | ~0.08 | 0.1 | 0.3 |
| EAA-3* | 3.5 | <0.01 | ~0.03 | ~0.06 | 0.2 |
| EEA-g-AA† | 4.7 | 5.2 | 6.2 | 8.2 | 11.2 |

* Ethylene-acrylic acid copolymer.

† Ethylene-ethyl acrylate copolymer grafted with acrylic acid.

buffer (pH 10.0) in the temperature range $40^\circ\text{-}70^\circ\text{C}$ until there was not further increase in weight. Table III shows those immersed in three buffers of pH 8.5-12.0 at 50°C . Tables II and III also include those of two other EAA copolymers (EAA-2 and EAA-3) containing lower acrylic acid contents. EAA-1 sheets show much higher water absorption values than those of EAA-2, EAA-3, and EEA-g-AA sheets, corresponding to its high acrylic content [20 weight percent (w/o)]. Furthermore, the water absorption of the EAA-1 copolymer increases with increasing immersion temperature and pH of alkaline solutions. Also, it was observed that EAA-1 sheets were significantly swollen and became mechanically weak at relatively high water absorption, whereas EAA-2, EAA-3, and EEA-g-AA sheets were not swollen. The significant swelling of EAA-1, which is probably due to ionization or dissociation of carboxyl groups in the copolymer, also indicates that the deterioration of EAA-1 joint in alkaline solutions occurs with decreasing mechanical strength of the bulk EAA due to its remarkable swelling.

Figures 6 and 7 show the degraded depth from the edges of T-peel specimen vs. the square root of immersion time in an $\text{NaHCO}_3\text{-NaOH}$ buffer (pH 10.0) at various temperatures and in various alkaline solutions at 50°C , corresponding to Fig. 1 and 2, respectively. The degraded depth corresponds to the region peeled with low peel strength of ca. $0 \text{ kg}/\text{cm}$ and to the swollen region of the EAA-1 adhesive layer. In other words, the degradation or failure front of the interface coincides with the swelling front of the EAA-1 adhesive layer. In an $\text{NaHCO}_3\text{-NaOH}$ buffer (pH 10.0) at 40° and 50°C (Fig. 6 and 7) and in an $\text{H}_3\text{BO}_4 + \text{KCl-NaOH}$ buffer (pH 8.5) at 50°C (Fig. 7), the degraded depth is proportional to the square root of immersion time. This result indicates that failure of the EAA-1 joint occurs with swelling of the EAA adhesive layer by alkaline ions diffusing into the joint inside through the adhesive layer.

On the other hand, in an $\text{NaHCO}_3\text{-NaOH}$ buffer (pH 10.0) at 60° and 70°C (Fig. 6), in a 0.1N NaOH solution (pH 14.0) at 50°C , in a KCl-NaOH buffer (pH

Table III. Water absorption test of acrylic acid-containing copolymer sheets (0.5 mm thick) in three buffers of pH 8.5-12.0 at 50°C

| Sample | Acrylic acid content (w/o) | Water adsorption (w/o) | | |
|-----------|----------------------------|------------------------|-----------|----------|
| | | pH 8.5* | pH 10.0** | pH 12.0† |
| EAA-1‡ | 20 | 43.0 | 61.0 | 174.2 |
| EAA-2‡ | 8 | <0.01 | ~0.08 | 0.2 |
| EAA-3‡ | 3.5 | <0.01 | ~0.03 | ~0.03 |
| EEA-g-AA§ | 4.7 | 6.0 | 6.2 | 5.2 |

* $\text{H}_3\text{BO}_4 + \text{KCl-NaOH}$ buffer.

** $\text{NaHCO}_3\text{-NaOH}$ buffer.

† KCl-NaOH buffer.

‡ Ethylene-acrylic acid copolymer.

§ Ethylene-ethyl acrylate copolymer grafted with acrylic acid.

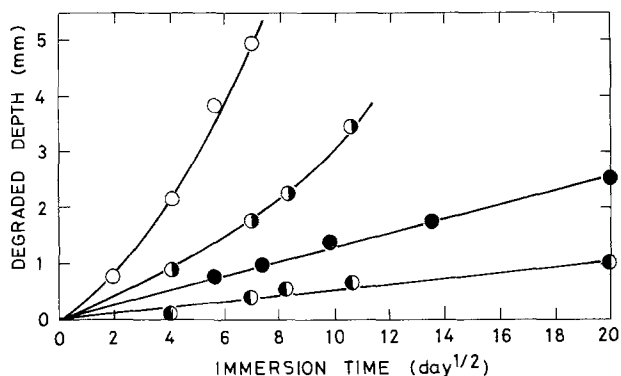


Fig. 6. Degraded depth from the edges of T-peel specimen vs. the square root of immersion time. An EAA-1 joint was immersed in an $\text{NaHCO}_3\text{-NaOH}$ buffer (pH 10.0) at various temperatures: (●) 40°C; (●) 50°C; (●) 60°C; (○) 70°C.

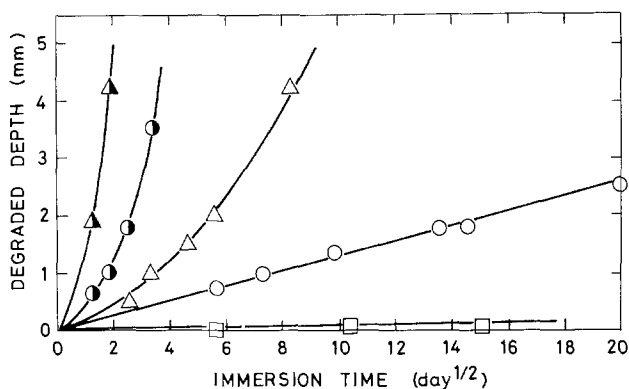


Fig. 7. Degraded depth from the edges of T-peel specimen vs. the square root of immersion time. An EAA-1 joint was immersed at 50°C in various alkaline solutions: (▲) 0.1N NaOH solution, pH 14.0; (●) KCl-NaOH buffer, pH 12.0; (△) $\text{Na}_2\text{HPO}_4\text{-NaOH}$ buffer, pH 11.0; (○) $\text{NaHCO}_3\text{-NaOH}$ buffer, pH 10.0; (□) $\text{H}_3\text{BO}_4 + \text{KCl-NaOH}$ buffer, pH 8.5.

12.0) at 50°C, and in an $\text{Na}_2\text{HPO}_4\text{-NaOH}$ buffer (pH 11.0) at 50°C (Fig. 7), the degraded depth deviates from the linear relation with the square root of immersion time and accelerates with immersion time. In these cases, the two adherends were bent outside from each other by a remarkable swelling of the EAA copolymer adhesive (see Tables II and III) sandwiched by the two adherends. This waved swelling caused gaps between the adherend and the adhesive. Although the degraded depth values in Fig. 7 deviate from the linear relationship with the square root of immersion time, they give linear lines when replotted against immersion time (Fig. 8). This linear relationship indicates that alkaline solutions easily reach the failure front of EAA joints (or the swelling front of EAA adhesive layer) through above-mentioned gaps between the adherend and the adhesive.

Failure mechanism of EEA-g-AA joint in alkaline solutions.—The water absorption of EEA-g-AA sheets having a low acrylic acid content is low in alkaline solutions (Table II) and does not increase appreciably with increasing pH of alkaline solutions (Table III), whereas that of EAA-1 sheets is high and increases appreciably with increasing pH. The EEA-g-AA sheets are not swollen in alkaline solutions, whereas the EAA-1 sheets are appreciably swollen. These results indicate that alkaline ions diffuse into the bulk EAA-1, but do not diffuse into the bulk EEA-g-AA copolymer. However, it has been observed that the failure of the EEA-g-AA joint also initiates from the edges of the joint and proceeds gradually into the joint inside in a manner similar to that of EAA-1 joint. Figure 9 shows

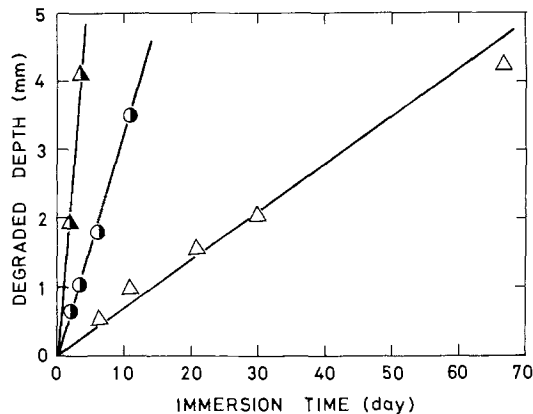


Fig. 8. Degraded depth from the edges of T-peel specimen vs. immersion time. An EAA-1 joint was immersed at 50°C in various alkaline solutions: (▲) 0.1N NaOH solution, pH 14.0; (●) KCl-NaOH buffer, pH 12.0; (△) $\text{Na}_2\text{HPO}_4\text{-NaOH}$ buffer, pH 11.0.

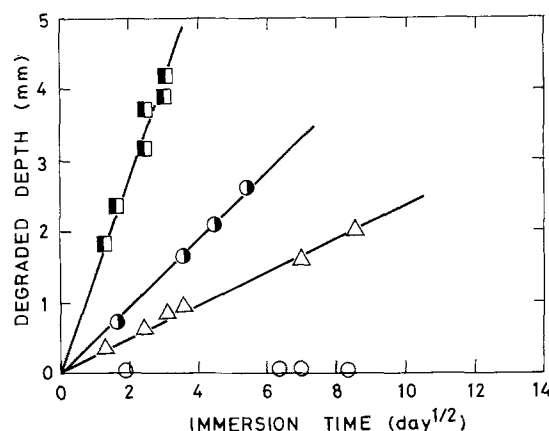


Fig. 9. Degraded depth from the edges of T-peel specimen vs. the square root of immersion time. An EEA-g-AA joint was immersed at 50°C in various alkaline solutions: (■) KCl-NaOH buffer, pH 13.0; (●) KCl-NaOH buffer, pH 12.0; (△) $\text{Na}_2\text{HPO}_4\text{-NaOH}$ buffer, pH 11.0; (○) $\text{NaHCO}_3\text{-NaOH}$ buffer, pH 10.0.

the relation between the degraded depth from the edges of T-peel specimen and the square root of immersion time in various alkaline solutions at 50°C. The degraded depth is proportional to the square root of immersion time. The bulk EEA-g-AA copolymer sheet has low water absorption values in these alkaline solutions, and its use as an adhesive results in no gap between the adherend and the adhesive. All the results suggest that the rate of the joint failure also is controlled by diffusion of alkaline ions along the alloy-adhesive interface.

Based on the well-documented phase structures of multiphase polymers such as block and graft copolymers, polymer blends, and interpenetrating networks (10), it is reasonable to assume that the grafted poly(acrylic acid) within EEA-g-AA undergoes phase separation. The presence of the grafted poly(acrylic acid) phase domains at the alloy-adhesive interface is responsible for the high peel strength ($\geq 4 \text{ kg/cm}$) of the chromated alloy-EEA-g-AA joint (Fig. 3), because the base EEA copolymer before grafting gives only low peel strength (ca. 0.5 kg/cm). In analogy with the above-mentioned failure mechanism of EAA-1 joints, it is tempting to assume that the decrease in peel strength of alloy-EEA-g-AA joints in alkaline solutions occurs with swelling of the poly(acrylic acid) domains at the interface by alkaline ions diffusing into the joint inside along the interface. We discuss in more details the failure mechanism of EEA-g-AA joints in a later paper.

Acknowledgment

The authors wish to thank Dr. K. Kudo and Mr. M. Wagatsuma for many helpful discussions.

Manuscript submitted March 4, 1980; revised manuscript received June 25, 1981.

Any discussion of this paper will appear in a Discussion Section to be published in the June 1982 JOURNAL. All discussions for the June 1982 Discussion Section should be submitted by Feb. 1, 1982.

Publication costs of this article were assisted by Nippon Telegraph and Telephone Public Corporation.

REFERENCES

1. F. Yamamoto and S. Yamakawa, *J. Appl. Polym. Sci.*, **25**, 2479 (1980).
2. F. Yamamoto, S. Yamakawa, and M. Wagatsuma, *ibid.*, **25**, 2731 (1980).
3. F. Yamamoto, S. Yamakawa, and M. Wagatsuma, *This Journal*, **128**, 2374 (1981).
4. H. H. Uhlig, "Corrosion Handbook," John Wiley & Sons, Inc., New York (1948).
5. S. Tsuru, S. Yamakawa, and F. Yamamoto, *Kobunshi Ronbunshu*, **36**, 759 (1979).
6. B. Wargotz, *J. Appl. Polym. Sci.*, **12**, 1873 (1968).
7. B. Wargotz, *ibid.*, **13**, 1965 (1969).
8. R. F. Wegman, *Appl. Polym. Sci.*, **19**, 385 (1972).
9. R. A. Gledhill and A. J. Kinloch, *J. Adhesion*, **6**, 315 (1974).
10. J. A. Mauson and L. H. Sperling, "Polymer Blends and Composites," Plenum Press, New York (1976).

Kinetics for the Reaction of Hydrogen with a Plutonium-1 Weight Percent Gallium Alloy Powder

Jerry L. Stakebake

Rockwell International, Golden, Colorado 80401

ABSTRACT

Kinetics for the reaction of hydrogen with plutonium-1 w/o gallium were measured using powder prepared "in situ." The rates obeyed a first-order rate law and were independent of temperature from -29° to 355°C . A pressure dependence proportional to $P^{1/2}$ was observed at pressures less than 1 kPa. From 1 to 70 kPa the pressure dependence rapidly decreased. Total pressure dependence could be accurately described by a Langmuir equation. Results indicate an adsorption-controlled reaction at low pressures and a reaction-controlled process at high pressures.

Plutonium hydride is frequently employed as an intermediate for preparing the metal or nitride powder and as such plays an important role in the nuclear industry. Even though a number of experimental studies have been carried out to describe the physicochemical properties of the plutonium-hydrogen system, several areas are still poorly defined. Earlier studies (1-7) have described in detail the equilibrium behavior and thermodynamic properties of plutonium hydride. Much less information, however, is available on the kinetics of the reaction of hydrogen with plutonium. Some kinetic data for the reaction of hydrogen with plutonium coupons have been reported by Bowersox (8,9) and Colmenares *et al.* (10). A recent report (11) has also described the decomposition kinetics of plutonium hydride in both the two-phase region below $\text{PuH}_{0.95}$ and in the nonstoichiometric region between $\text{PuH}_{1.95}$ and PuH_3 . Much of the early experimental kinetic data were influenced by oxide films on the metal coupons which increased the importance of hydride nucleation in the reaction. Hydrogen diffusion also plays a role in coupon hydriding and this process is likewise not understood. Therefore, additional work is required in order to fully understand the kinetics of plutonium hydriding as well as the factors which influence the kinetics.

Hydrogen reacts rapidly and exothermally with plutonium metal. The reaction is, however, strongly influenced by impurities in the gas phase hydrogen or on the plutonium metal surface. When impurities are present the reaction is characterized by a period of inhibition followed by a nucleation process on the plutonium surface. Elimination of the effect of impure

hydrogen can be accomplished through gas purification techniques. Oxide films on the surface are more difficult to eliminate. To accomplish this successfully the sample must be prepared *in situ* without exposure to air. The problem of a surface film contaminant was dealt with in another way by Bowersox (8,9). Plutonium coupons were heated under vacuum to about 300°C . During such a treatment the PuO_2 surface film is converted to PuO or more likely a $\text{Pu}(\text{C},\text{O})$ phase (12). This material is catalytic and enhances the dissociation of hydrogen thus promoting the hydriding reaction. When plutonium coupons were treated in this manner, hydride nucleation sites were rapidly generated and inhibition caused by the oxide film was nearly zero. The problem with this type of approach was that the true plutonium-hydrogen reaction was not being studied. The approach used in the present investigation was to purify the hydrogen gas and then prepare a plutonium powder *in situ*. This procedure results in a relatively clean sample with a high surface area.

A second problem in measuring plutonium hydriding kinetics arises from the exothermic nature of the reaction. The heat of formation of plutonium hydride varies from -38 to -50 kcal/mol depending on the composition of the hydride (3). Self-heating of the sample during reaction makes it difficult to obtain isothermal kinetic data. Use of a heat sink bonded to the plutonium coupon can alleviate the problem to a degree (8,9). However, this was not practical in the present investigation. The significance of not maintaining strictly isothermal conditions will be discussed later.

This paper describes the results from an investigation of the hydriding kinetics of a plutonium-1 weight

percent (w/o) gallium alloy powder. The metal powder was used because it could be prepared with a clean surface and any bulk hydrogen diffusion effects would be minimal. Measurements were carried out over a temperature range of -29° – 355° C and at hydrogen pressures of 20 Pa to 67.96 kPa. Kinetic data were evaluated with the reaction model used for uranium powder (13).

Experimental

Materials.—Plutonium metal used in this investigation was a plutonium-gallium alloy which was stabilized in the delta phase. The gallium concentration was 1.03 w/o. There was a total of 1335 ppm of metallic impurities including 855 ppm of americium. Americium is present as a radiolytic decay product of plutonium-241. Coupons for this study were machined to a thickness of 3 mm from cast rods. Individual samples weighed about 1.5g. They were cleaned by mechanically polishing the surface and immediately loaded on the vacuum microbalance.

Ultrapure hydrogen (99.999%) and argon (99.999%) were used in this investigation. These gases were introduced into the system through a bed of uranium hydride to further minimize oxygen contamination. However, surface reactions between hydrogen and the stainless steel walls of the vacuum system still produced some water vapor contamination.

Apparatus.—The experimental apparatus used for this investigation has been described in detail elsewhere (13). A Cahn Model 100 microbalance was incorporated into a stainless steel vacuum system. Minimum pressures attainable were in the 10^{-6} Pa (10^{-8} Torr) range. Hydrogen pressures during reaction were controlled with a Granville-Phillips pressure controller and could be varied from 10^{-4} Pa to 10^5 Pa. Pressures were measured with an ionization gauge or a capacitance manometer. Sample temperatures were varied with a resistance heater controlled with a power proportioning programmer. The thermocouple for measuring the sample temperature was located beside the sample and inside the vacuum system. Output from the microbalance, thermocouples, and pressure meters were collected with a data acquisition system and processed using a computer.

Procedure.—Plutonium powder was prepared by hydriding and then dehydriding a 1.5g plutonium coupon. Hydride sites were nucleated on the coupon by exposure to 6.65 kPa of hydrogen at 20° C for 2 min. Bulk hydriding was then performed slowly in 67 Pa of hydrogen at 20° C. Although slow, this process produced the highest surface area for the powder. Dehydriding was accomplished by heating the sample at 450° C under vacuum. The objective during dehydriding was to attain a reasonable rate and still minimize any sintering of the powder. Surface areas for the powders were calculated from the argon adsorption isotherm, obtained at -196° C, using the BET (14) method. Powder hydriding rates were then measured over a range of temperatures (-29° – 355° C) and pressures (0.020–67.96 kPa). Following each run the sample was dehydrided at 450° C and reused for the next hydriding run. A total of fifteen different plutonium samples were used throughout the course of this investigation.

Reaction Kinetics

The reaction model used to describe the reaction of hydrogen with plutonium metal powder is called the "Progressive Conversion" model (15). This model assumes that once hydrogen is adsorbed on the surface diffusion into the bulk is very rapid and not rate determining. Thus, the reaction takes place uniformly throughout the particle and not strictly at the metal/hydride interface. The general reaction equation is

$$W_t = W_m \{1 - [1 + k(n-1)M_o^{(n-1)}t]^{1/(1-n)}\} \quad [1]$$

where W_t = hydrogen reacted in time, t ; W_m = total hydrogen reacted; k = rate constant; n = order of the reaction; and M_o = milligram atoms of metal initially available. In the special case where the reaction is first-order ($n = 1$), Eq. [1] becomes

$$W_t = W_m (1 - e^{-kt}) \quad [2]$$

This equation was used throughout this study to evaluate rates of reaction.

Results and Discussion

Plutonium powder characterization.—Gallium metal present in this plutonium alloy powder is nonreactive with respect to hydrogen. The role of gallium is to stabilize the plutonium in the delta phase. This metal phase is more reactive with respect to hydrogen than the room temperature alpha phase found in pure plutonium. The most logical reason for the increased reactivity is the greater metal-metal atomic spacing in the delta alloy. In this structure the f-electrons are more localized and are not involved in metallic bonding (16). Thus, it has been proposed that they are available for the rapid chemisorption of hydrogen during the hydriding reaction (17). One initial concern was that gallium would become segregated during the hydriding/dehydriding cycles. This would result in a mixture of alpha and delta phase material. X-ray diffraction analysis of the metal powder showed that the metal was in the delta phase and there was only a trace of alpha plutonium. Apparently the gallium remains uniformly distributed throughout the powder.

When the initial hydriding of a plutonium coupon was carried out in 26.6 kPa of hydrogen at 200° C the reaction was very rapid. Powder formed in this manner contained large particles (Fig. 1). Additional hydriding and dehydriding did not reduce the particle size because of the high temperature (450° C) required for dehydriding. For this investigation the initial coupon was nucleated in 6.65 kPa of hydrogen at 20° C for about 2 min. During this stage about 1% of the total reaction took place. The remainder of the coupon hydriding was carried out at 20° C in 67 Pa of hydrogen over a period of about 5 hr. Powder formed by this method was finer and more uniform than that prepared by rapid, high temperature hydriding (Fig. 2).

Particle sizes of the powder used were measured with a Quantimet 720 particle analyzer. The particle size distribution is shown by a log-normal plot in Fig. 3. The count mean diameter (CMD) was $5.0 \mu\text{m}$, while the standard deviation, σ_g , was 13.4. Total surface areas

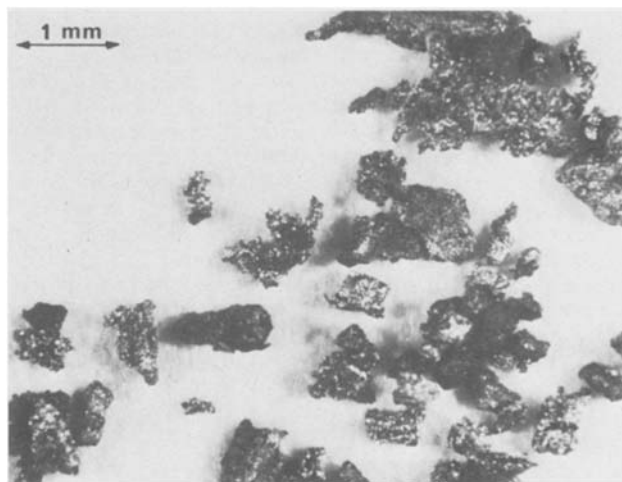


Fig. 1. Plutonium-1 w/o gallium powder prepared at 200° C in 26.6 kPa of hydrogen.

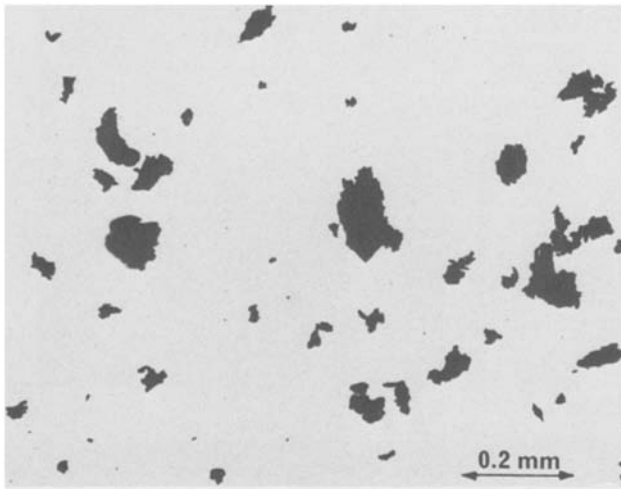


Fig. 2. Plutonium-1 w/o gallium powder prepared at 20°C in 0.067 kPa of hydrogen.

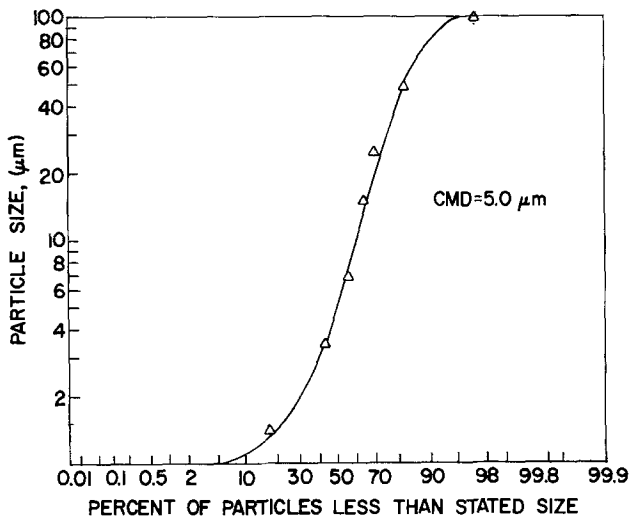


Fig. 3. Log-normal size distribution of plutonium alloy powder. The count median diameter for the particles was 5.0 μm and the geometric standard deviation σ_g was 13.4.

of the samples were measured with the BET (14) technique using argon adsorption at -196°C . The surface area of this powder was calculated to be $0.16\text{ m}^2/\text{g}$. All of the powders used in this study had surface areas on the order of $0.1\text{--}0.2\text{ m}^2/\text{g}$. This range was too small to establish any surface area dependence for the reaction.

Kinetic evaluation of powder hydriding.—The applicability of the "Progressive Conversion" model discussed earlier was evaluated under all of the conditions of this investigation. A typical evaluation is illustrated in Fig. 4. This particular hydriding run was made at an initial temperature of 30°C in 1.06 kPa of hydrogen. Because of the heat of reaction the average temperature of this run was 130°C . It is evident that both Eq. [1] and [2] fit the data quite well. Using Eq. [1] the rate constant, k , was 1.60 min^{-1} and the calculated order was 0.91. Equation [2] for a first-order reaction produced a rate constant of 1.46 min^{-1} . For the purpose of this investigation all data were evaluated using Eq. [2].

Effects of temperature on powder hydriding.—Hydriding of plutonium metal released significant amounts of heat. With the experimental set-up being used, this heat could not be dissipated and the net result was an increase in sample temperature. This effect is shown in Fig. 5. Because of the rapid heat release thermal

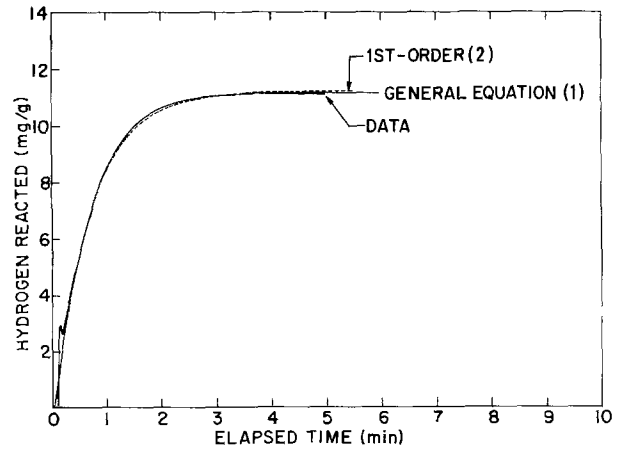


Fig. 4. Evaluation of plutonium powder hydriding rates at 30°C and 1.06 kPa using Eq. [1] and [2].

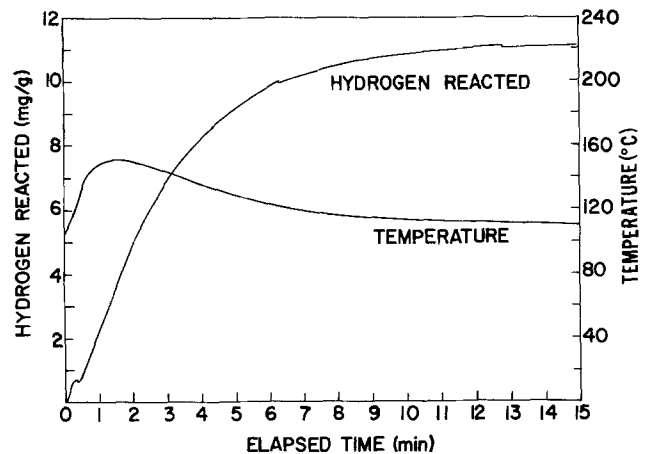


Fig. 5. Exothermic behavior of plutonium powder hydriding at 100°C in 0.067 kPa of hydrogen.

gradients were established between the sample and the wall of the chamber. These gradients, which were most pronounced at low pressures and temperatures, are believed to cause the discontinuities observed in Fig. 4 and 5 through their effect on the microbalance. Discontinuities have been observed at about $0.1\text{--}0.2\text{ min}$ after the start of a run for all experiments at temperatures less than 140°C and pressures less than 1.33 kPa .

When the main purpose of an investigation is the measurement of reaction rates, the inability to maintain isothermal conditions could present a problem. Table I summarizes data obtained over a range of temperatures for two pressure levels, 0.067 and 26.6 kPa (0.5 and 200 Torr). Temperatures being reported

Table I. Effect of temperature on the hydriding rate of plutonium-1 w/o gallium alloy powder

| Run | Pressure (kPa) | T_0 ($^\circ\text{C}$) | T_{Max} ($^\circ\text{C}$) | T_{Avg} ($^\circ\text{C}$) | k (min^{-1}) |
|-----|----------------|----------------------------|---------------------------------------|---------------------------------------|---------------------------|
| 827 | 0.067 | 68 | 140 | 126 ± 9 | 0.45 |
| 830 | 0.067 | 55 | 127 | 119 ± 13 | 0.40 |
| 831 | 0.067 | 77 | 162 | 156 ± 8 | 0.40 |
| 832 | 0.067 | 218 | 266 | 261 ± 8 | 0.47 |
| 833 | 0.067 | -33 | 27 | 5 ± 13 | 0.42 |
| 834 | 0.067 | 6 | 62 | 35 ± 16 | 0.48 |
| 835 | 0.067 | 233 | 323 | 315 ± 14 | 0.41 |
| 838 | 0.067 | 30 | 80 | 73 ± 8 | 0.40 |
| 839 | 0.067 | 30 | 83 | 76 ± 8 | 0.40 |
| 864 | 26.60 | 30 | 142 | 103 ± 28 | 1.78 |
| 865 | 26.60 | 244 | 372 | 355 ± 9 | 1.69 |
| 866 | 26.60 | 120 | 226 | 193 ± 17 | 2.10 |
| 867 | 26.60 | -96 | 47 | -29 ± 43 | 2.68 |
| 869 | 26.60 | 24 | 148 | 106 ± 27 | 2.02 |
| 870 | 26.60 | -31 | 109 | 50 ± 35 | 2.38 |
| 871 | 26.60 | 175 | 315 | 277 ± 22 | 2.25 |
| 872 | 26.60 | 48 | 184 | 129 ± 30 | 2.42 |

were gas-phase temperatures measured next to the sample. Because of the significant self-heating during reaction, an average temperature was calculated for each run. In the first set of experiments at 0.067 kPa, an attempt was made to hold the temperature near its maximum. With the exception of the low temperature runs 833 and 834, heat was supplied to the sample with a furnace and temperature programmer. The effectiveness of this approach is shown by the standard deviations of the temperature. This technique was not used for the higher pressure experiments. The lack of temperature programming coupled with reaction rates which were nearly five times larger resulted in significantly higher standard deviations for the average temperatures.

Since actual powder temperatures were unknown, no attempt was made to evaluate the temperature dependence for powder hydriding using the Arrhenius equation. Examination of the gas-phase temperatures shown in Table I indicate that temperature apparently has little effect on the hydriding rate. This is indicative of a very small activation energy. Additional work is required, however, to measure actual powder temperatures and to evaluate the nonisothermal kinetics.

Studies made with plutonium coupons have shown some temperature dependence. Activation energies have been reported to range from 2 to 6 kcal/mol (8-10, 18). Since in the case of bulk coupons such processes as nucleation and diffusion play a significant role, activation energies may be associated with these processes and not the direct reaction between plutonium and hydrogen.

Effects of hydrogen pressure on powder hydriding rates.—Experimental runs were conducted at pressures of 20 Pa (0.15 Torr) up to 67.96 kPa (510 Torr). Temperatures were nonisothermal and the variation during the investigation ranged from an average of -29° to 355°C . Earlier in this discussion it was shown that hydriding rates were essentially independent of temperature. Only a slight inverse temperature dependence was noted at higher pressures, e.g., 26.6 kPa. This type of behavior was attributed to the role of adsorption at low temperatures and hydride decomposition at high temperatures. The decomposition reaction becomes significant at about 350°C (11). Because of this temperature influence at the temperature extremes, runs at temperatures less than 0°C or greater than 350°C were not used in evaluating pressure effects on hydriding rates.

Data from all runs at various pressures are listed in Table II. These data were analyzed using the equation

$$k_{\text{hyd}} = k_0 P^n \quad [3]$$

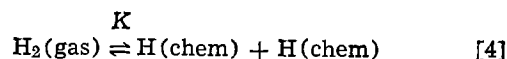
where k_{hyd} is the first-order rate constant, P the hydrogen pressure in kPa, k_0 is a constant, and n is the order of the hydrogen pressure dependence. A plot of the data using this equation is shown in Fig. 6. A discontinuity is noted at about 1 kPa (8 Torr) indicating the pressure dependence might be evaluated for two pressure ranges. For the pressure range 0-1 kPa (0-8 Torr) n is equal to 0.45 while for pressures greater than 1 kPa n is 0.11.

In the low pressure region the rate is proportional to $P^{1/2}$. This relationship is typical for dissociative adsorption of hydrogen. For pressures greater than 1 kPa the pressure dependence of the reaction is proportional to 0.11 or very nearly equal to zero. This type of behavior is similar to the Langmuir adsorption isotherm and suggests that hydrogen adsorption may play a major role in the overall hydriding kinetics.

Using Langmuir's kinetic derivation (19) for the adsorption isotherm, θ is the fraction of the surface covered with hydrogen and $1 - \theta$ is the fraction bare. If hydrogen is adsorbed dissociatively

Table II. The effect of pressure on the rate of hydriding of plutonium-1 w/o alloy powder

| Run | Pressure (kPa) | k (min ⁻¹) | T_{Avg} (°C) |
|-----|----------------|--------------------------|-----------------------|
| 862 | 0.020 | 0.25 | 76 ± 8 |
| 827 | 0.067 | 0.45 | 126 ± 9 |
| 830 | 0.067 | 0.40 | 119 ± 13 |
| 831 | 0.067 | 0.40 | 156 ± 8 |
| 832 | 0.067 | 0.47 | 261 ± 8 |
| 833 | 0.067 | 0.42 | 5 ± 13 |
| 834 | 0.067 | 0.48 | 35 ± 16 |
| 835 | 0.067 | 0.41 | 315 ± 14 |
| 838 | 0.067 | 0.40 | 73 ± 8 |
| 839 | 0.067 | 0.40 | 76 ± 8 |
| 853 | 0.075 | 0.41 | 94 ± 16 |
| 844 | 0.120 | 0.64 | 61 ± 6 |
| 849 | 0.250 | 0.86 | 105 ± 15 |
| 854 | 0.332 | 0.84 | 103 ± 15 |
| 840 | 0.665 | 1.23 | 164 ± 7 |
| 841 | 0.665 | 1.23 | 84 ± 12 |
| 842 | 0.665 | 1.22 | 100 ± 11 |
| 843 | 1.064 | 1.46 | 130 ± 9 |
| 848 | 2.128 | 1.68 | 145 ± 14 |
| 850 | 2.128 | 1.60 | 105 ± 19 |
| 847 | 3.19 | 1.80 | 106 ± 20 |
| 855 | 3.42 | 1.52 | 107 ± 19 |
| 859 | 5.32 | 1.70 | 96 ± 16 |
| 809 | 6.65 | 1.68 | 238 ± 17 |
| 810 | 6.65 | 1.69 | 144 ± 24 |
| 812 | 6.65 | 1.86 | 63 ± 24 |
| 860 | 13.30 | 2.06 | 107 ± 18 |
| 864 | 26.60 | 1.78 | 103 ± 28 |
| 866 | 26.60 | 2.10 | 193 ± 17 |
| 869 | 26.60 | 2.02 | 106 ± 27 |
| 870 | 26.60 | 2.38 | 50 ± 35 |
| 871 | 26.60 | 2.25 | 277 ± 22 |
| 872 | 26.60 | 2.42 | 129 ± 30 |
| 861 | 67.96 | 2.21 | 108 ± 20 |



The rate of adsorption may then be written as

$$v_1 = k_1 P (1 - \theta)^2 \quad [5]$$

and the rate of desorption is

$$v_{-1} = k_{-1} \theta^2 \quad [6]$$

At equilibrium the rates are equal and

$$\frac{\theta}{1 - \theta} = \left(\frac{k_1 P}{k_{-1}} \right)^{1/2} = (KP)^{1/2} \quad [7]$$

Upon rearranging Eq. [7] becomes

$$\theta = \frac{(KP)^{1/2}}{1 + (KP)^{1/2}} \quad [8]$$

The pressure dependence of the surface coverage is shown in Fig. 7. At high pressures θ is independent of pressure while at low pressures $\theta \approx (KP)^{1/2}$.

In considering the hydriding of plutonium powder

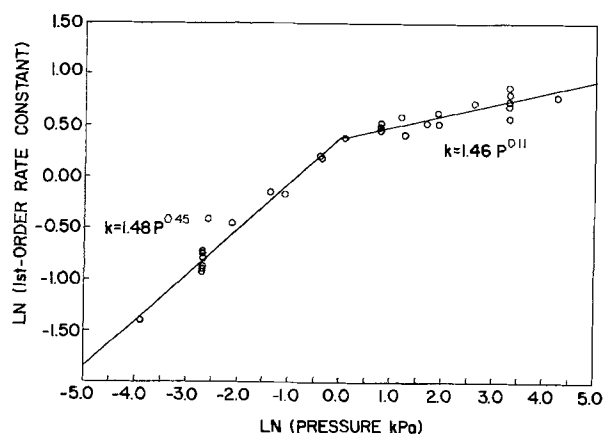
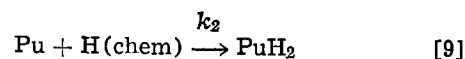


Fig. 6. Effect of hydrogen pressure on plutonium powder hydriding rates with temperatures varying between 5° and 315°C .

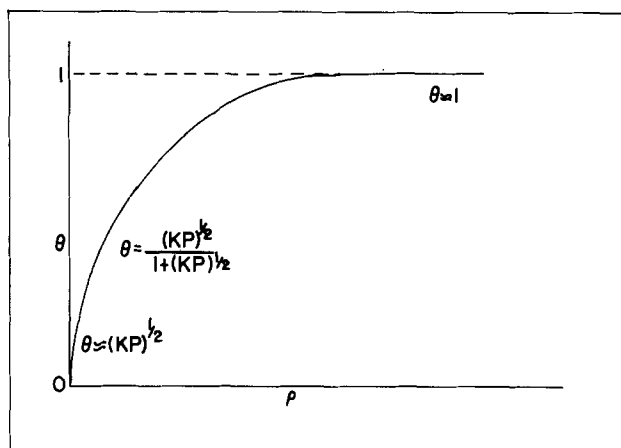


Fig. 7. Variation in surface coverage as a function of pressure for Langmuir-type adsorption.

the temperatures were kept sufficiently low so that the reverse decomposition reaction was negligible. The rate of hydriding has been found to follow a first-order process. If the rate of hydriding is proportional to the hydrogen surface coverage the first-order rate is

$$k_{\text{hyd}} = k_2 \theta \quad [10]$$

or

$$k_{\text{hyd}} = \frac{k_2 (KP)^{1/2}}{1 + (KP)^{1/2}} \quad [11]$$

The relationship given in Eq. [11] has exactly the same form as seen in Fig. 7. At pressures less than 0.02 kPa $(KP)^{1/2} < 1$, Eq. [11] becomes

$$k_{\text{hyd}} = k_2 (KP)^{1/2} \quad [12]$$

where the rate of hydriding is proportional to $P^{1/2}$ and adsorption is rate determining. At high pressures (>1000 kPa) where $(KP)^{1/2} > 1$ Eq. [11] becomes

$$k_{\text{hyd}} = k_2 \quad [13]$$

Under these conditions the hydriding rate is equal to k_2 and is independent of hydrogen pressure. This behavior has been observed for the hydriding of plutonium-1 w/o gallium powder as illustrated in Fig. 6.

Equation [11] can be tested for the hydriding of plutonium powder by rearranging to the form

$$\frac{P^{1/2}}{k_{\text{hyd}}} = \frac{1}{k_2 K^{1/2}} + \frac{P^{1/2}}{k_2} \quad [14]$$

Plotting $P^{1/2}/k_{\text{hyd}}$ against $P^{1/2}$ gives a straight line with the slope $1/k_2$. Such a plot is shown in Fig. 8. From an evaluation of the data k_2 was found to be 2.69

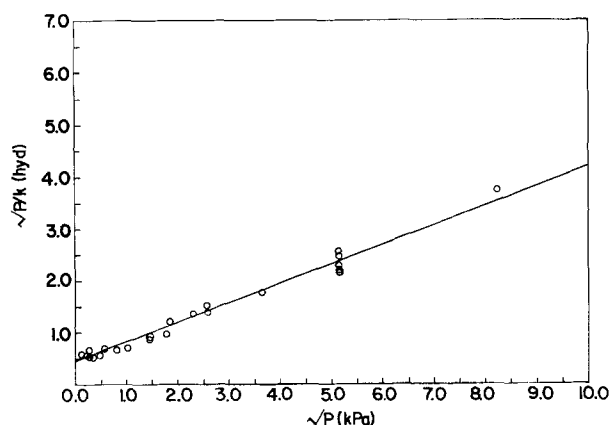


Fig. 8. Modified Langmuir plot for the pressure dependence of plutonium-1 w/o gallium hydriding rates on the hydrogen pressure.

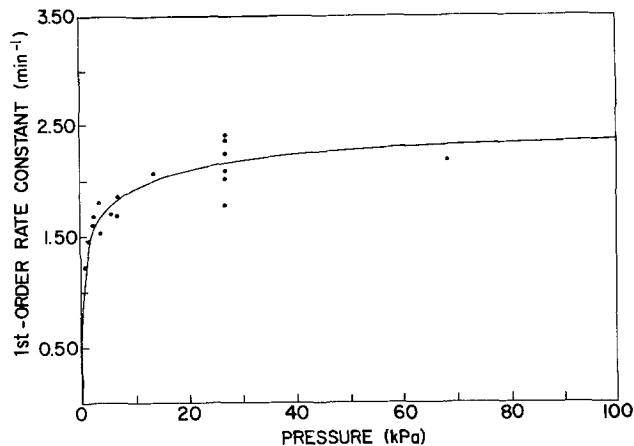


Fig. 9. Variation of experimental and predicted plutonium-1 w/o gallium powder hydriding rates with pressure.

min^{-1} and K was equal to 0.66 kPa^{-1} . Using these constants hydriding rates have been predicted over the pressure range 0-100 kPa. Results are shown by the solid line in Fig. 9. Predicted rates obtained from Eq. [11] are in good agreement with the experimental values from 0 to 70 kPa.

Conclusions

The reaction kinetics for the hydriding of plutonium-1 w/o gallium were measured using a metal powder prepared "in situ." This technique successfully minimized oxide formation which introduces a predominant hydride nucleation and growth step in the reaction sequence. Powder hydriding was found to be independent of temperature from -29° to 355°C . Hydriding rates exhibited a hydrogen pressure dependence which could be described by a modified Langmuir equation. At pressures less than 1 kPa rates were proportional to $P^{1/2}$ indicating dissociative adsorption of hydrogen was rate controlling. Above 1 kPa the pressure dependency decreased with complete independence being predicted at about 1000 kPa. In the high pressure region the rates are reaction controlled.

Acknowledgment

This work was performed under the auspices of U.S. Department of Energy Contract DE-AC04-76DP03533.

Manuscript submitted Jan. 13, 1981; revised manuscript received May 22, 1981.

Any discussion of this paper will appear in a Discussion Section to be published in the June 1982 JOURNAL. All discussions for the June 1982 Discussion Section should be submitted by Feb. 1, 1982.

Publication costs of this article were assisted by Rockwell International.

REFERENCES

1. R. N. R. Mulford and G. E. Sturdy, *J. Am. Chem. Soc.*, **77**, 3449 (1955).
2. R. N. R. Mulford and G. E. Sturdy, *ibid.*, **78**, 3897 (1956).
3. J. M. Haschke, A. E. Hodges III, C. M. Smith, and F. L. Oetting, *J. Less-Common Metals*, **73**, 41 (1980).
4. S. Takeuchi and K. Suzuki, *Trans. Jpn. Inst. Metals*, **3**, 41 (1962).
5. C. Colmenares and C. Alexander, "Heat of Formation of Plutonium Hydrides," U.S. AEC Report UCID-16799, Lawrence Livermore Laboratory, Livermore, CA (1975).
6. I. B. Johns, "Plutonium Hydride and Deuteride," U.S. AEC Report MDDC-717, Argonne National Laboratory, Argonne, IL (1944).
7. M. I. Ivanov and N. S. Podol'skaya, *Russ. J. Phys. Chem.*, **45**, 1682 (1971).
8. D. F. Bowersox, "The Reaction between Plutonium and Deuterium Part I. Rate Measurements by

- Pressure Changes," U.S. AEC Report LA-5515-MS, Los Alamos Scientific Laboratory (1974).
9. D. F. Bowersox, "The Reaction between Plutonium and Deuterium Part II. Rate Measurements by Weight Changes," U.S. AEC Report LA-6681-MS, Los Alamos Scientific Laboratory (1977).
 10. C. A. Colmenares, Lawrence Livermore National Laboratory, Unpublished data (1980).
 11. J. M. Haschke and J. L. Stakebake, in "The Rare Earths in Science and Technology," Vol. 2, G. J. McCarthy, J. J. Rhyne, and H. B. Silber, Editors, p. 577, Plenum Publishing Co., New York (1980).
 12. D. T. Larson and J. M. Haschke, *J. Inorg. Chem.*, In press.
 13. J. L. Stakebake, *This Journal*, **126**, 1596 (1979).
 14. S. Brunauer, P. H. Emmett, and E. Teller, *J. Am. Chem. Soc.*, **60**, 309 (1938).
 15. J. L. Stakebake and G. E. Bixby, "Evaluation of Reaction Kinetics for Gas-Powder System," U.S. DOE Report RFP-2849, Rockwell International, Golden, CO (1979).
 16. C. Bonnelle and G. Lachere, in "Plutonium 1975 and Other Actinides," H. Blank and R. Linder, Editors, North-Holland Publishing Co., Amsterdam (1976).
 17. J. W. Ward, Personal communication (1980).
 18. J. M. Haschke, Personal communication (1980).
 19. M. Langmuir, *J. Am. Chem. Soc.*, **40**, 1361 (1918).

Effects of Heat-Treatment on Indium-Tin Oxide Films

F. T. J. Smith* and S. L. Lyu

Eastman Kodak Company, Research Laboratories, Rochester, New York 14650

ABSTRACT

Highly conductive and transparent films of indium-tin oxide have been sputter-deposited from an oxide target. The effects of annealing in oxidizing or reducing atmospheres on the electrical and optical properties of these films have been determined. The electron concentration and related optical properties are reversible functions of the oxygen partial pressure in the annealing atmosphere. The form of this relationship is consistent with a defect model in which most of the Sn dopant is present in neutral complexes with interstitial oxygen. The Hall mobility and refractive index are changed irreversibly by annealing as a result of subtle changes in film structure.

Highly transparent and electrically conducting thin films are useful in a wide variety of applications, for example, transparent Joule heating elements, infrared-reflecting coatings transparent in the visible, and transparent electrodes allowing optical and electrical access to solid-state devices. The oxides of Cd, In, Sn, and Sb have usually been found to have the best combination of properties (1). In particular, films of indium oxide containing some tin oxide are widely used where sheet resistances of less than 10 Ω /sq are required.

Films of indium-tin oxide (ITO) can be prepared by spray hydrolysis, but for most electronic applications, sputtering, evaporation, or chemical vapor deposition methods are necessary to achieve the required uniformity. Sputtered films have been prepared by using either conventional sputtering from hot-pressed oxide targets (2) or reactive sputtering from metal targets (3). With oxide targets the optimum composition has been reported to be 5-20 mol percent (m/o) SnO₂ in In₂O₃ (4).

The properties of these films are sensitive to the preparation conditions, in particular the oxygen partial pressure in the sputtering atmosphere (5). Film properties can also be modified by annealing in either oxidizing or reducing atmospheres. It would therefore be desirable to develop an understanding of the effects of film structure and stoichiometry on electrical conductivity and optical transmission. This has been achieved to some extent for pure In₂O₃ films (6, 7). In the presence of Sn, however, the situation is much more complex. Precipitation of metallic clusters (8) or possibly an Sn₃O₄-like phase (9) has been reported in some situations. Although the presence of tin leads to a higher conductivity, it is not clear what its role is or

what the mechanism is for the changes in conductivity observed when these films are annealed.

We will present results obtained for films deposited by rf sputtering from a hot-pressed oxide target. Deposition parameters have been optimized to yield films having high electrical conductivity and transparency. We will not describe the dependence of film properties on sputtering parameters in detail, since our results are similar to those reported previously (10). Instead, the results of annealing ITO films at various partial pressures of oxygen will be discussed. We will show that, if the films are not reduced to the point of producing a metallic phase, the effect of annealing on conductivity is a reversible function of oxygen partial pressure. These changes in conductivity can be interpreted in terms of the formation of neutral clusters of tin with interstitial oxygen. Annealing also affects the optical properties of these films, in some cases reversibly, as a result of their relationship to the free-carrier concentration.

Experimental Methods

An rf diode sputtering system was used (Fig. 1). It has two notable features. First, the target is placed below the substrate so that material sputtered upward is collected. Second, the substrates were loaded through an evacuable load lock, thus avoiding exposure of the target to the atmosphere and preventing adsorption of moisture by the target material, which is somewhat hygroscopic. As a result the run-to-run reproducibility was very high after initial outgassing and presputtering of new targets. The sputtering chamber is a stainless steel cylinder pumped by an oil diffusion pump with a cold trap. System pressures of 1×10^{-7} to 5×10^{-8} Torr were typically obtained between runs. During sputtering, a throttle valve of fixed diameter was used to limit pumping speed, and both argon and

* Electrochemical Society Active Member.

Key words: conductance, transmittance, sputtering.

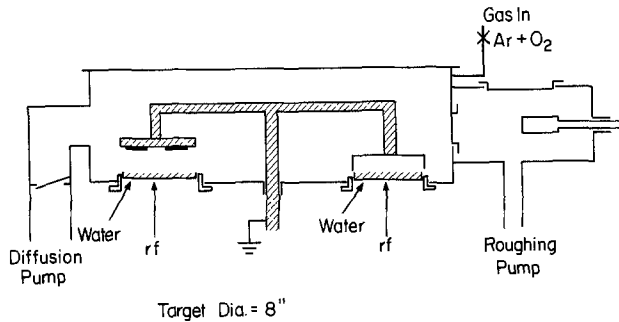


Fig. 1. RF diode sputtering system

oxygen of high purity were introduced to the chamber through metering valves.

A 20 cm diam hot-pressed disk of In_2O_3 containing 9 m/o of SnO_2 was used as a target. This was bonded to a water-cooled copper plate. The substrates were clamped into recesses in a 3 mm thick aluminum disk which in turn was bolted to a 12 mm thick copper plate. This plate acted as a heat sink. Either the substrates or a stainless steel shield could be rotated into position over the target. The target-to-substrate distance was 3.5 cm. To stabilize the system, presputtering onto the stainless steel shield was always done for 30 min before deposition onto the substrates. With a new target, presputtering for 8-12 hr was necessary before film properties became reproducible from run to run. An increased outgassing rate was observed during the first few hours of this procedure.

Polished fused quartz disks 5 cm in diameter and 0.05 cm thick were used as substrates. These were cleaned using ammonia-hydrogen peroxide and hydrochloric acid-hydrogen peroxide mixtures (11).

Optical measurements were made at near-normal incidence using a Cary 14 two-beam spectrophotometer in the visible and near-infrared region and a Beckman AR10 spectrophotometer in the 2-10 μm range. Sheet resistances were measured using a four-point tungsten probe, and both sheet resistance and Hall coefficients were measured by the van der Pauw method. Good agreement ($\pm 5\%$) was found between the two methods for sheet resistance. For the van der Pauw measurements the films were etched into a cloverleaf pattern by using conventional photolithography with hot hydriodic acid as an etchant (12). Silver paste contacts were used.

The measurements were made using a-c current and a d-c magnetic field of 4.3 koe. In some cases electrical measurements were made at high temperatures at various oxygen partial pressures, also by the van der Pauw method. To do this the samples were enclosed in a quartz tube in a furnace placed between the poles of an electromagnet. Mixtures of argon with traces of oxygen were passed through the tube, and the oxygen concentration in the exit gas was measured with a commercial solid-state oxygen meter. For these high temperature measurements, pressure contacts were made by spring-loaded nickel wires. Film thickness was measured by using a profilometer to determine the average height of an etched film edge. Annealing was done in a horizontal tube furnace. The annealing ambient was established by placing the samples in a quartz tube and flowing the appropriate gas over them at ~ 0.5 cm/sec.

Results and Discussion

A series of films 5000-10,000Å thick were deposited while sputtering parameters such as gas composition and pressure, power, and substrate-target spacing were varied so as to optimize film properties. That is, these parameters were varied to obtain the highest ratio of visible-wavelength transmission to sheet resistance for films in this thickness range.

Films sputtered in an atmosphere containing a few percent of oxygen had a high resistivity. For example, films $\sim 7000\text{\AA}$ thick deposited at a power of 500W in an argon plus 5% oxygen atmosphere at a total pressure of 2×10^{-2} Torr had a sheet resistance of $2.5 \times 10^3 \Omega/\text{sq}$. In contrast, films of this thickness deposited in pure argon under the same conditions had a sheet resistance of $\sim 5 \Omega/\text{sq}$. Sheet resistance decreased with increase in sputtering power, as reported previously (10). Thus the sheet resistance of films $\sim 7000\text{\AA}$ thick deposited from pure argon at 2×10^{-2} Torr decreased from $\sim 9 \Omega/\text{sq}$ at 200W to $\sim 4 \Omega/\text{sq}$ at 600W.

Repeated presputtering and deposition in pure argon gradually reduced part of the target surface, as evidenced by the development of a very dark metallic appearance. Films deposited from such a target had sheet resistances a factor of two or more higher than those from a fresh target surface obtained by abrading away the darkened surface layers. Similar observations have been reported elsewhere (2). Presputtering at a reduced power of 300W in a 50% O_2 plus 50% Ar atmosphere prevented this darkening, apparently by reoxidation of the target surface. Presputtering was therefore always carried out under these conditions for 30 min before each deposition run. Changing the presputtering atmosphere to pure argon for 1-10 min before film deposition had no effect on film properties. Several hours of deposition in pure argon were required before significant reduction of the target occurred, so that only minor changes in target condition would be expected during a single deposition run.

On the basis of these results, all subsequent films were deposited at 500W in a pure argon atmosphere, pressure 2×10^{-2} Torr, after presputtering in an argon-oxygen mixture as described. The oxygen flow was stopped ~ 3 min before deposition was begun. With this procedure, sheet resistances were reproducible to within $\pm 5\%$ from run to run. Figure 2 shows the sheet resistance of deposited films and the optical transmission at 500 nm, after averaging interference fringes, both as functions of the total deposition time. Under these conditions the deposition rate was 8.5 Å/sec, so that the film thickness increased from 5100Å after 10 min to 30,600Å after 60 min. The sheet resistance correspondingly decreased, reaching a value of less than 1 Ω/sq after 60 min. The transmission, on the other hand, increased for the first 25 min of deposition and at this point was limited only by the reflectivity of the film. The decrease in transmission of thicker films is presumably due to bulk absorption adding to reflection losses. The decrease at short times is not understood.

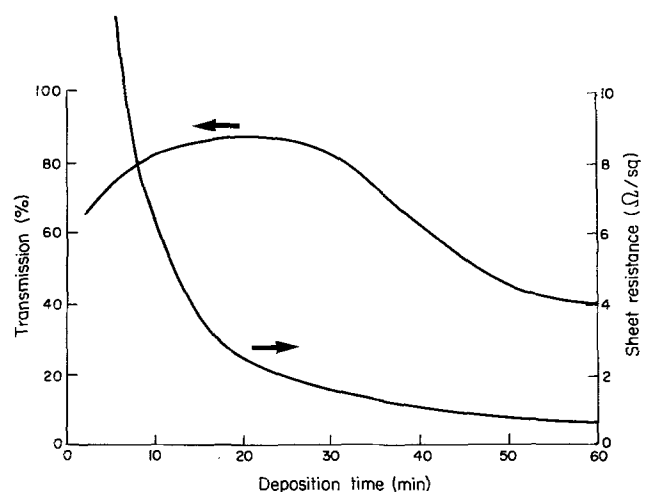


Fig. 2. Dependence of sheet resistance and transmission at 500 nm on total deposition time in 2.0×10^{-2} Torr Ar at 500W power.

If the higher resistivity of films deposited in Ar-O₂ mixtures were due only to differences in carrier concentration resulting from differences in oxygen content, it should be possible to bring all films to the same resistivity by equilibrating them with the same oxidizing or reducing atmosphere. This should take place at a temperature sufficient to allow rapid oxygen diffusion within the bulk of the film. In fact, when films were annealed at 200°C, the resistivity did change and equilibrium was reached within ~30 min. Figure 3 shows the sheet resistance of a relatively resistive film as a function of time at 200°C in nitrogen containing ~20 ppm of oxygen. This film was deposited in an Ar + 5% O₂ mixture. The equilibrium sheet resistance for several films is shown in Fig. 4 as a function of anneal conditions. These data were obtained using films ~8000Å thick deposited in pure argon, giving an as-deposited sheet resistance of 3.5 Ω/sq (curves a), and at oxygen levels of 5% (curves b) and 10% (curves c), resulting in as-deposited sheet resistances of ~2200 and 7000 Ω/sq, respectively. The coated disks were cleaved into halves, and the halves were annealed in either N₂ + 200 ppm O₂ (broken lines in Fig. 4) or N₂ + 10% H₂ + 50 ppm H₂O (solid lines). Anneals were carried out for 30 min at 100°C and repeated at 100°C intervals above this. The sheet resistances decreased with increasing anneal temperature, approaching each other and reaching a minimum at 300°-500°C. At higher temperatures the sheet resistance increased rapidly and the films acquired a dark metallic appearance, indicating reduction of the oxides to a metallic phase. The fact that all samples did not reach the same resistivity indicates that simple differences in initial oxygen stoichiometry do not entirely explain the increase in resistivity for films deposited at the higher oxygen levels. Differences in structure were therefore looked for which could explain these differences in resistivity.

Figure 5 is an SEM picture of the surface of a film ~8000Å thick. This particular film was deposited in

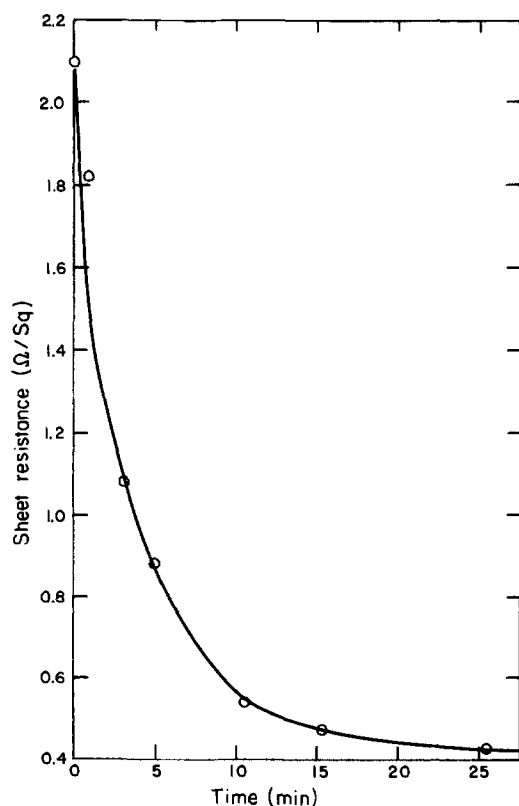


Fig. 3. Dependence of sheet resistance on anneal time at 200°C in nitrogen.

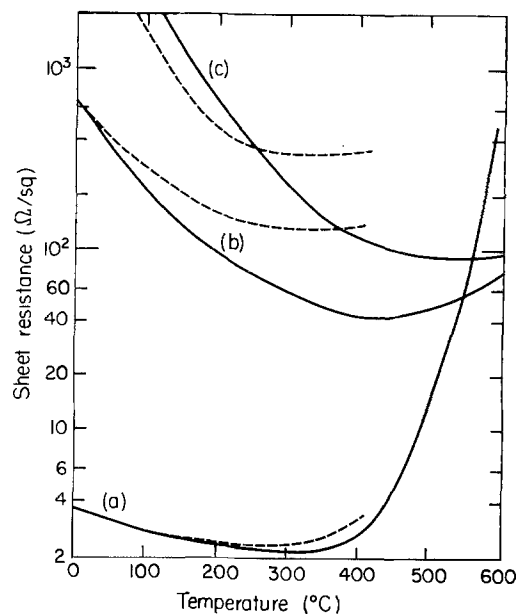


Fig. 4. The equilibrium sheet resistance as a function of temperature for films annealed in N₂ (broken lines) or N₂ + 10% H₂ (solid lines).

pure Ar, but an apparently identical surface morphology is seen for films sputtered in Ar-O₂ mixtures. The films consist of crystallites 1000-2000Å in diameter which form the rounded hillocks seen in Fig. 5. This structure is very similar to that reported by Fraser and Cook (2) for d-c-sputtered films. Cleaved cross sections of similar films were also examined by SEM. Although this instrument was operating near the limit of resolution, a columnar grain structure could be seen with grain boundaries extending perpendicularly from the film surface to the substrate. X-ray diffraction spectra show the films to have the bcc In₂O₃ structure. All films had a predominantly [100] texture with a lesser tendency to a [111] orientation. The O₂ level in the sputtering atmosphere had no effect on this surface appearance or orientation. Both [111] (2) and [100] (4) orientations have been reported. The lattice parameter was 10.17Å for all ITO films, as compared with 10.12Å for In₂O₃ deposited from a pure In₂O₃ target in the same system. Fan *et al.* (5) found the lattice parameter $a = 10.23\text{Å}$ for highly transparent films and an apparently different phase with $a = 10.15\text{Å}$ in dark films deposited at low oxygen level. These authors used a target containing 15 m/o SnO₂ compared with 9 m/o in the present work. The present films presumably correspond with their transparent films, the re-

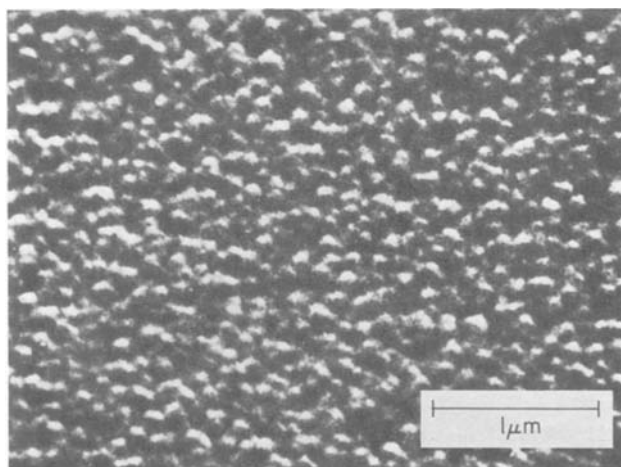


Fig. 5. SEM micrograph of film surface

duction in a from 10.23 to 10.17Å resulting from the reduced Sn concentration. Anneals at 400°C in either N₂ or O₂ for 30 min had no effect on either the surface appearance or the x-ray diffraction patterns of any of the films. Thus the differences in resistivity (Fig. 4) for films deposited at various oxygen levels and then all annealed at 400°C in the same atmosphere apparently result from differences in structure which are beyond the resolution of the methods we have used.

Hall coefficient measurements were made to characterize further the effects of annealing on low resistivity films. All films were n-type. The carrier concentration n was obtained from the Hall coefficient R , using the expression $R = r/ne$. The Hall factor r has been approximated by unity in view of the high electron concentrations. In any case, the absolute value of n is not critical to interpretation of the results. In early experiments it was observed that for a given film, if it was not reduced to a metallic phase, e.g., by heating in hydrogen at temperatures above 400°C, n is a reproducible function of the annealing atmosphere. For example, a series of anneals were carried out at 400°C on a single film ~12,000Å thick under reducing, then oxidizing, and then again reducing conditions. The results are given in Table I. Annealing in reducing conditions increased n as compared with the as-deposited film. Annealing in oxygen reduced n to below its initial value. Subsequent anneals in mildly oxidizing, neutral, and reducing conditions increased n until it reached essentially the same value it had after the first anneal in reducing conditions. These changes in n could not be attributed to changes in the film or grain boundary structure, since such changes would not be reversible. On the other hand, the mobility decreased in most instances after annealing in either oxidizing or reducing atmospheres; this could be attributed to structural changes.

To determine whether surface effects are important to the annealing behavior, as has been suggested (13), measurements were made on films of various thicknesses. If the observed changes in n were due to a surface phenomenon, they would decrease in magnitude linearly with increases in film thickness. Figure 6 shows n for films ranging in thickness from ~3000 to ~18,000Å. Results for both as-deposited films and films annealed at 400°C for 30 min in N₂ + 5% H₂ are shown. Before annealing, the results are quite strongly dependent on the film thickness. This is probably due to relatively small changes in the actual oxygen partial pressure during sputtering. An initial adsorption of oxygen from the sputtering atmosphere followed by a gradual release has been reported (5) in a similar system. At some point an optimum oxygen level was apparently reached, giving rise to the maximum in n observed. This variation is almost totally removed by the anneal, indicating the result of such anneals to be a bulk effect for these films. However, note that, although the dependence of n on deposited-film thickness can be removed by annealing, variations in doping level from substrate to surface could exist. It has been reported that the surface of as-deposited ITO films may be tin-rich (9). This could be true for our annealed films but only if the tin-rich layer increased in

Table I. Results of a series of anneals at 400°C on an ITO film 12,000Å thick

| Atmosphere | Time (min) | Electron concentration (cm ⁻³) | Mobility (cm ² /Vsec) |
|------------------------------------|------------|--|----------------------------------|
| As deposited | | 5.69 × 10 ²⁰ | 27.9 |
| N ₂ + 5% H ₂ | 30 | 1.18 × 10 ²¹ | 18.8 |
| O ₂ | 150 | 1.96 × 10 ²⁰ | 4.81 |
| N ₂ + 1% O ₂ | 60 | 2.37 × 10 ²⁰ | 5.24 |
| N ₂ | 120 | 3.75 × 10 ²⁰ | 4.97 |
| N ₂ + 5% H ₂ | 120 | 1.21 × 10 ²¹ | 2.16 |

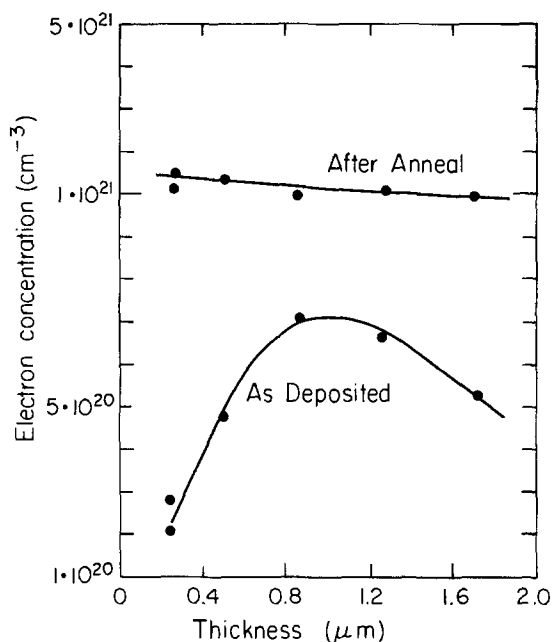


Fig. 6. Electron concentration vs. film thickness for both as-deposited films and films annealed for 30 min at 400°C in N₂ + 5% H₂.

thickness linearly with increases in total film thickness so that the average value of n remained constant, the result shown in Fig. 6.

To summarize these observations, n is uniquely determined by the temperature and composition of the annealing ambient for a particular film, if it is not reduced enough to cause a phase change, for example, by annealing under strongly reducing conditions above 450°C. Furthermore, the changes in n caused by annealing result from a bulk effect. To determine n as a function of the oxygen partial pressure p_{O_2} , conductivity and Hall coefficient were measured by the van der Pauw method at high temperatures while samples were held in a flowing argon-oxygen mixture. The range of temperatures over which measurements could be made was small, because below 250°C changes occurred too slowly and above 450°C the films were easily reduced and darkened or developed cracks after a few hours at high temperature. Figure 7 shows equilibrium values of n as a function of p_{O_2} at 320° and 400°C for a film 8300Å thick. The mobilities at these temperatures were 15.3 and 14.3 cm²/Vsec, respectively, and were independent of n . Over a wide range of p_{O_2} , n is proportional to $p_{O_2}^{-m}$. Measurements at intermediate temperatures overlap these but are of the same form with $m = 0.14 \pm 0.01$. The same type of relationship but with $m = 0.166$ has been reported for pure sintered In₂O₃ powder above 600°C (13). The values of n reported for pure In₂O₃ are, however, several orders of magnitude below those shown in Fig. 7 for a tin-doped film.

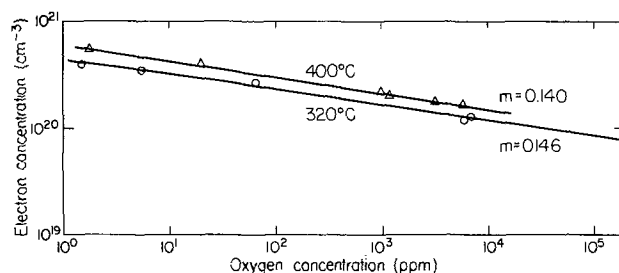
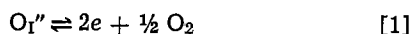


Fig. 7. Equilibrium carrier concentration as a function of oxygen partial pressure for a film 8300Å thick. Lines show fit to $n \sim p_{O_2}^{-m}$ with values of m given.

In undoped In_2O_3 this behavior was attributed to the presence of oxygen vacancies which act as doubly ionized donors and are the dominant contributors to n (13). In the present case this is obviously not the situation since the presence of Sn in the lattice has increased n substantially. On the other hand, if all of the Sn simply substituted for In and donated one electron, then n would be equal to the total tin concentration, i.e., $n = [\text{Sn}_{\text{In}}] = [\text{Sn}]_{\text{T}} \approx 1.4 \times 10^{21}/\text{cm}^3$, and independent of p_{O_2} . In fact, the measured values of n are much less than the total tin concentration, as noted previously for tin concentrations above a few percent (14). In the In_2O_3 structure, O^{2-} ions occupy only $3/4$ of the tetrahedral interstices formed by the In^{3+} ion lattice. It might be expected, therefore, that additional oxygen ions could be accommodated easily into the remaining interstices and act as double acceptors to compensate any Sn^{4+} ions introduced onto In^{3+} sites. The oxygen partial pressure would then influence n through the reaction

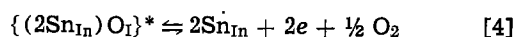


$$K_1 = \frac{n^2 p_{\text{O}_2}^{1/2}}{[\text{O}_I'']} \quad [2]$$

Since $n \ll [\text{Sn}]_{\text{T}}$, i.e., $n \ll 1.4 \times 10^{21}/\text{cm}^3$ over the range of our measurements, most of the Sn_{In} is compensated, therefore, $2[\text{O}_I''] \approx [\text{Sn}]_{\text{T}}$. Substituting this into Eq. [2] gives

$$n \approx \left(\frac{K_1 [\text{Sn}]_{\text{T}}}{2} \right)^{1/2} p_{\text{O}_2}^{-1/4} \quad [3]$$

Obviously the value of $m = 1/4$ predicted by this model does not agree with our results. Making the assumption that interstitial oxygen can accept only one electron leads to $n \sim p_{\text{O}_2}^{-1/2}$, in even worse agreement with experiment. On the other hand, if the Sn^{4+} ions form pairs in association with the extra oxygen ion to form a neutral complex of local stoichiometry Sn_2O_4 , this could be reduced at low oxygen levels to give pairs of Sn_{In} donors



$$K_2 = \frac{[\text{Sn}_{\text{In}}]^2 n^2 p_{\text{O}_2}^{1/2}}{\{[(2\text{Sn}_{\text{In}})\text{O}_I]\}} \quad [5]$$

Since most of the Sn is not electrically active, $\{[(2\text{Sn}_{\text{In}})\text{O}_I]\} \approx [\text{Sn}]_{\text{T}}/2$, and since on the other hand Sn_{In} is the dominant donor, $n \approx [\text{Sn}_{\text{In}}]$. Substituting these approximations into Eq. [5] gives

$$n \approx \left(\frac{K^2 [\text{Sn}]_{\text{T}}}{2} \right)^{1/4} p_{\text{O}_2}^{-1/4} \quad [6]$$

i.e., $m = 0.125$, in reasonable agreement with the value 0.14 ± 0.01 obtained from our high temperature measurements. Clusters of more than two Sn^{4+} ions may be expected at higher Sn levels until a distinct separate SnO_2 phase is formed. The fact that the conductivity of films deposited at a high oxygen level can never be increased by annealing to as high a value as for films deposited in pure argon could be attributed to a much greater degree of formation of large SnO_2 -like complexes of this type during deposition as a result of the greater oxygen ion availability. Fan *et al.* (5) have shown in detail the effect on n of oxygen level in the sputtering atmosphere. They report n to decrease very steeply with increases in oxygen partial pressure in the region where highly transparent single phase deposits were obtained, also indicating the formation of neutral complexes under oxidizing conditions.

All films were highly transparent in the visible region. The transmission spectrum for a film $\sim 8000\text{\AA}$

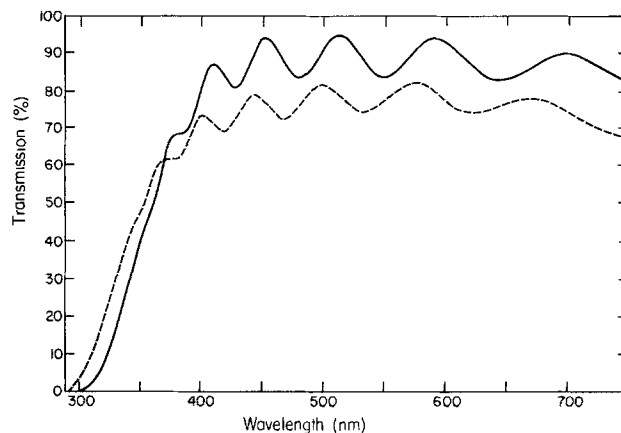


Fig. 8. Transmission spectrum for film $\sim 8000\text{\AA}$ thick, as-deposited (solid line) and after 30 min anneal at 400°C in $\text{N}_2 + 10\% \text{H}_2$ (broken line).

thick (Fig. 8) shows an absorption edge at 300-350 nm and interference fringes at longer wavelengths. Figure 8 also shows the spectrum after this film was annealed in $\text{N}_2 + 10\% \text{H}_2$ at 400°C for 30 min. This anneal increased n from 5.76 to $11.2 \times 10^{20}/\text{cm}^3$. It also reduced the optical transmission, shifted the absorption edges, and shifted the interference fringes. Transmission was reduced as a result of any anneal in either oxidizing or reducing atmospheres. The refractive index, calculated from the spacing between interference fringes, was also reduced by any annealing procedure. Figure 9 shows the refractive index for both the as-deposited and annealed films of Fig. 8. The reduction in index resulting from annealing is surprisingly large.

The shift in the short-wavelength absorption edge depended on the nature of the annealing atmosphere in the same way that n does, i.e., anneals in reducing and oxidizing atmospheres gave shifts in opposite directions. Figure 10 shows the shifts in the absorption edge of a single film resulting from a series of anneals and the electron concentrations resulting from each anneal. At values of α above 10^3 cm^{-1} , the square of the absorption coefficient is linearly proportional to the photon energy. A relationship of this sort is expected for direct allowed transitions and has been reported for pure In_2O_3 films (15). By extrapolating the linear regions to zero absorption coefficient, values of the apparent direct gap were obtained. Figure 11 shows these results as a function of electron concentration. A linear relationship is observed between $n^{2/3}$ and the apparent gap, as would be expected if this shift can be attributed to the Moss-Burstein effect (16). In the case of parabolic bands the shift $\Delta E = \frac{\hbar^2}{8m} \left(\frac{3n}{\pi} \right)^{2/3}$.

If the effective electron mass m_e is much smaller than the effective hole mass, then $m \approx m_e$. With this assumption, the data of Fig. 11 give $m_e = 0.64 m_0$. This

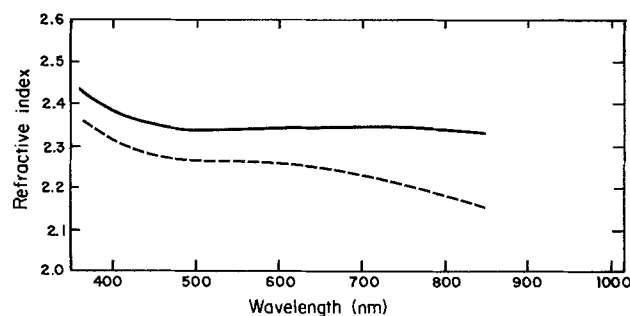


Fig. 9. Refractive index of film $\sim 8000\text{\AA}$ thick, as deposited (solid line) and after 30 min anneal at 400°C in $\text{N}_2 + 10\% \text{H}_2$ (broken line).

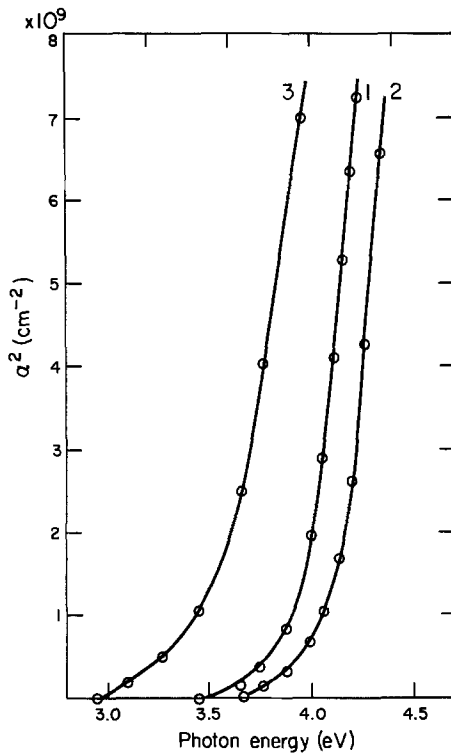


Fig. 10. Energy dependence of square of absorption coefficient for film $\sim 8000\text{\AA}$ thick. Curve 1: as deposited, $n = 5.76 \times 10^{20}/\text{cm}^3$; curve 2: after 30 min 400°C anneal in $\text{N}_2 + 10\% \text{H}_2$, $n = 11.2 \times 10^{20}/\text{cm}^3$; curve 3: after 150 min 400°C anneal in O_2 , $n = 1.96 \times 10^{20}/\text{cm}^3$.

can be compared with somewhat lower reported values of $0.54 m_0$ (14) and $0.5 m_0$ (17) obtained by varying the Sn concentration to vary n . Since Sn doping at the high levels used would be expected to shift the absorption edge to shorter wavelengths (as a result of the alloying effect), by an amount proportional to the Sn concentration (Vegard's law) this method would be expected to underestimate m_0 . Recently a value of $0.55 m_0$ was reported by others also using the annealing method to vary n (18).

The optical properties in the infrared depend strongly on n . Figure 12 shows the transmission and reflection spectra of an as-deposited film $\sim 4000\text{\AA}$ thick having $n = 3.8 \times 10^{20}/\text{cm}^3$. As discussed in detail

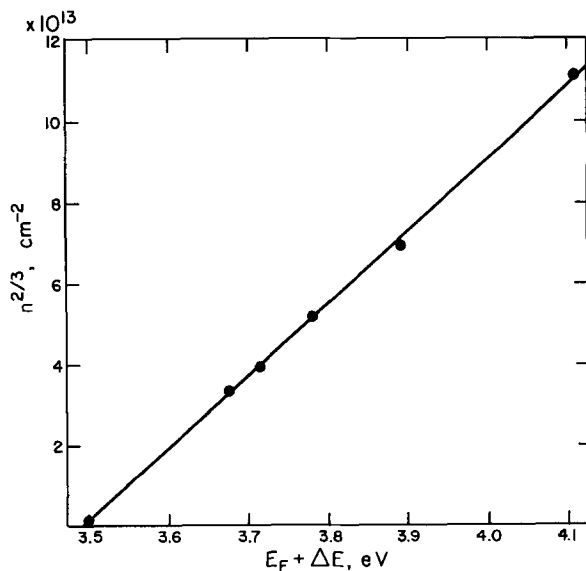


Fig. 11. Dependence of absorption edge on $n^{2/3}$

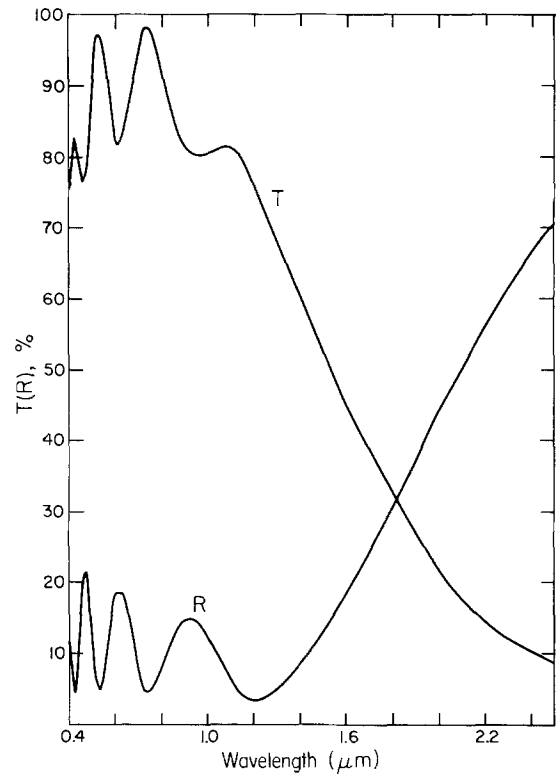


Fig. 12. Transmission T and reflectivity R in the infrared for a film $\sim 4000\text{\AA}$ thick with $n = 3.8 \times 10^{20}/\text{cm}^3$.

previously (10, 14), free-carrier absorption dominates the optical properties at wavelengths longer than the plasma wavelength, which is $\sim 1.8 \mu\text{m}$ for this particular film.

From the reflectivity and transmission data for both as-deposited and $\text{N}_2 + \text{H}_2$ annealed films, the value of the optical absorption coefficient α was calculated over a range of photon energies of 0.5-4.5 eV (Fig. 13). Both the Moss-Burstein shift at higher energies and

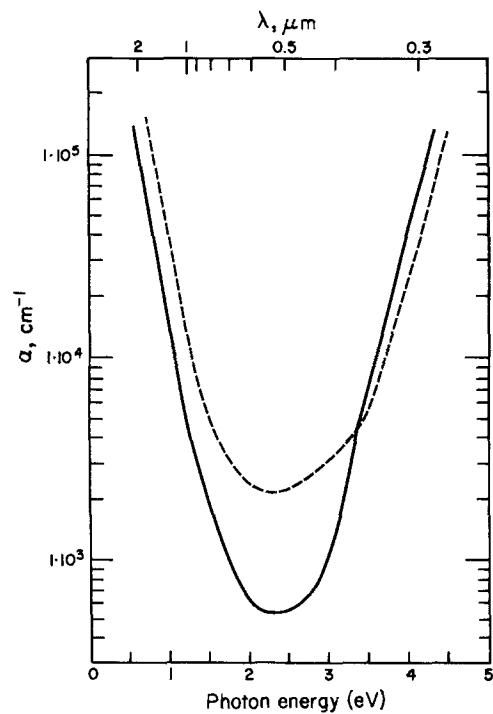


Fig. 13. Absorption coefficient α as a function of photon energy for as-deposited films (solid line) and after 30 min 400°C anneal in $\text{N}_2 + 10\% \text{H}_2$ (broken line).

the opposite shift at low energies due to the change in plasma frequency are illustrated.

Conclusions

Highly conductive and transparent films of ITO can be deposited from an oxide target by maintaining the target surface in an oxidized condition but depositing films from a pure argon ambient. The electron concentration in these films and properties which depend on it, such as the absorption edges, are affected reversibly when the films are annealed in mildly reducing or oxidizing conditions. This behavior can be rationalized in terms of the formation of neutral complexes of Sn with oxygen interstitials. Other properties, such as the electron Hall mobility and the refractive index, change nonreversibly, apparently because of permanent structural changes.

Acknowledgments

We are grateful to L. R. Spaulding for the x-ray diffraction results and to L. E. Brady for application of the SEM.

Manuscript submitted June 3, 1980; revised manuscript received June 4, 1981.

Any discussion of this paper will appear in a Discussion Section to be published in the June 1982 JOURNAL. All discussions for the June 1982 Discussion Section should be submitted by Feb. 1, 1982.

Publication costs of this article were assisted by Eastman Kodak Company.

REFERENCES

1. J. L. Vossen, in "Physics of Thin Films," Vol. 9, G. Hass, M. F. Francombe, and R. W. Hoffman, Editors, Academic Press, New York (1977).
2. D. B. Fraser and H. D. Cook, *This Journal*, **119**, 1368 (1972).
3. W. W. Molzen, *J. Vac. Sci. Technol.*, **12**, 99 (1975).
4. J. L. Vossen, *RCA Rev.*, **32**, 289 (1971).
5. J. C. C. Fan, F. J. Bachner, and G. H. Foley, *Appl. Phys. Lett.*, **31**, 773 (1977).
6. R. Groth, *Phys. Status Solidi*, **14**, 69 (1966).
7. H. K. Müller, *ibid.*, **27**, 723 (1968).
8. W. G. Haines and R. H. Bube, *J. Appl. Phys.*, **49**, 304 (1978).
9. J. C. C. Fan and J. B. Goodenough, *ibid.*, **48**, 3524 (1977).
10. J. C. C. Fan and F. J. Bachner, *This Journal*, **122**, 1719 (1975).
11. W. Kern and D. A. Puotinen, *RCA Rev.*, **31**, 187 (1970).
12. G. Bradshaw and A. J. Hughes, *Thin Solid Films*, **33**, L5 (1976).
13. J. H. W. deWit, G. van Unen, and M. Lahey, *J. Phys. Chem. Solids*, **38**, 819 (1977).
14. H. Kostlin, R. Jost, and W. Lems, *Phys. Status Solidi*, **29**, 87 (1975).
15. R. L. Weiher and R. P. Ley, *J. Appl. Phys.*, **37**, 299 (1966).
16. T. S. Moss, "Optical Properties of Semiconductors," p. 46, Butterworths, London (1959).
17. V. M. Vainshtein and V. I. Fistul, *Sov. Phys. Semicond.*, **1**, 104 (1967).
18. Y. Ohhata, F. Shinoki, and S. Yoshida, *Thin Solid Films*, **59**, 255 (1979).

On the Limits of the Filter Concept for Color TV Screens

K. Carl

Philips GmbH Forschungslaboratorium Aachen, 5100 Aachen, Germany

J. A. M. Dikhoff

N. V. Philips' Gloeilampenfabrieken, Eindhoven, The Netherlands

W. Eckenbach

Philips GmbH Forschungslaboratorium Aachen, 5100 Aachen, Germany

and H. G. Junginger

N. V. Philips' Gloeilampenfabrieken, Heerlen, The Netherlands

ABSTRACT

The image contrast of color television tubes is reduced by the diffuse reflection of ambient light at the tube face. A recent method used to compensate this effect makes use of color filters, which are transparent to the phosphor light and absorb the rest of the visible spectrum. The subject of this paper is an investigation of the fundamental optical capability of the color filter concept. The main emphasis is placed on the sandwich system, involving a filter layer between the phosphor layer and the screen glass. Experiments were performed on 5×5 cm² test samples, using a spectrophotometer for the reflection measurements and a scanning electron microscope for measuring the phosphor light output. They yield a gain in brightness contrast performance (BCP) of 15-28% for combinations of red or blue phosphors with commercially available inorganic filter pigments. The corresponding increase of brightness can be twice as high if the contrast is held constant. Model calculations, assuming isotropic light scattering within the powder layers and linear superposition of multiple reflections between adjacent layers, show good agreement with the experimental results. Ideal square filters yield a BCP gain of 100-120%, whereas a shift of real phosphor spectra or filter spectra along the wavelength axis only yields a gain of a few percent. The conclusion drawn is that the inorganic filter pigments used set a practical limit to the gain in BCP that can be achieved with the color filter concept. Some results on mixtures of phosphors and filters are included. The experimentally found BCP gain amounts to about 7-10%, i.e., only about one-half of the sandwich gain. A simplified model leads to approximately the same values. The different optical behavior of a color pigment in sandwich and mixture arrangements is apparently due to differences in the effective optical path length for ambient light and phosphor light.

Brightness and contrast are important parameters determining image quality in color television. Both can be improved by an enhanced light output. A further improvement of contrast, i.e., the ratio of useful (image) light to disturbing (reflected ambient) light becomes possible by lowering the tube reflection. This can be achieved, for example, by blackening the screen glass or by filling the empty space between phosphor areas with a black powder. A third method, which has recently come into use (1-3), involves spectral filtering. Each of the three phosphors (red, green, and blue) is combined with a suitable filter material, which is transparent in the spectral region of phosphor emission and absorbent in the rest of the visible spectrum. In this way the phosphor light is hardly if at all attenuated, while the ambient light is strongly reduced after being reflected at the tube face.

The color filter concept is explained in more detail in Fig. 1. In a normal, nonfilter tube (on the left) high-energy electrons out of the vacuum penetrate into the phosphor layer, where they are absorbed and generate visible light, which reaches the observer through the glass of the screen. The thin aluminum backing functions as a definite electrode and serves as a mirror for

the visible light. In the sandwich-type filter tube an additional filter layer is placed between each phosphor layer and the screen glass, which must be traversed by the phosphor light as well as by the light from the surrounding. These filter layers, usually inorganic color pigments, have to be applied with exactly the same geometry as the three-color phosphor dots or lines.

A filter effect similar to the sandwich arrangement can be achieved by mixing each phosphor with its corresponding color pigment. The mixture-type filter tube is preferred in practice because of its technological simplicity. Besides contrast improvement, the color filter concept offers the advantage of enlarging the selection of phosphors, because unsuitable chromaticity coordinates can to some extent be corrected by the filter. The quality gain as a result of color filtering is usually (1) expressed in terms of the brightness contrast performance (BCP), which is defined for the red, green, and blue color components, respectively, as follows

$$\text{BCP} = \left(\frac{B}{\sqrt{R}} \right)_{\text{filter}} \text{ with} / \left(\frac{B}{\sqrt{R}} \right)_{\text{filter}} \text{ without} \quad [1]$$

Here B stands for the tube brightness per color and R

Key words: cathodoluminescence, inorganic, reflectance, solids.

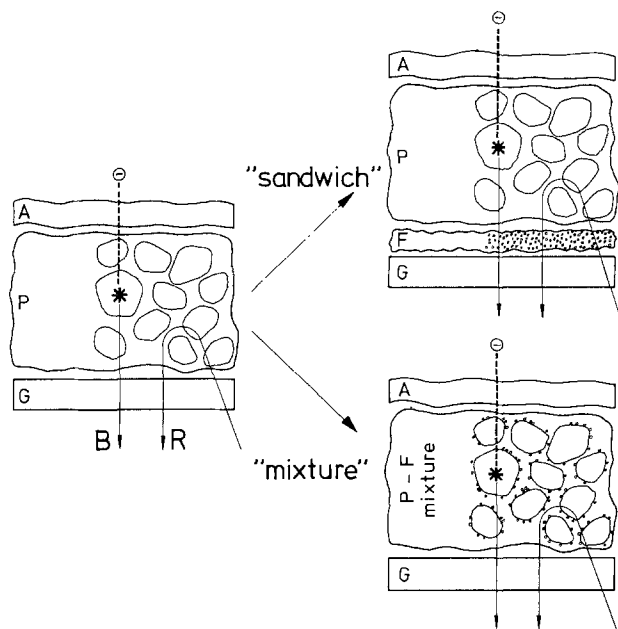


Fig. 1. Filter concept. Light-generating system of a normal, i.e., nonfilter tube (left) and of filter tubes with sandwich or mixture arrangement (right). A = aluminum, P = phosphor, F = filter, G = glass.

denotes the diffuse reflection of the tube for white ambient light, with the specular reflection at the first glass surface excluded. Both B and R are measured with a photopic detector.

The subject of this paper is an investigation of the fundamental optical capability of the color filter concept in color television. The main emphasis is on the sandwich system, results of which have not yet been published. Though somewhat less advantageous for fabrication than the mixture, the sandwich can be regarded as a model system with a more easily understandable mode of operation.

The measurements of the complete color filter systems are assisted by optical model calculations, based on spectrometer measurements on simplified systems, i.e., pigment layers on glass in the case of a sandwich and thick powder layers of pigmented phosphor in the case of a mixture. In the case of the mixture, satisfactory agreement between theory and experiment has not yet been achieved, probably because of greater complexity and additional interaction between phosphor and pigment particles. In the sandwich case, which generally shows greater BCP gains, reasonable agreement between theory and experiment is obtained. This agreement supports further predictions of the theory, i.e., selection of suitable color pigments and their appropriate concentration ranges and an estimate of the theoretical limits of the color filter concept.

Experimental

Sample preparation.—All experiments were made with small test samples of 5×5 cm² with clear glass slides as substrates. Layers of phosphor or pigment were prepared by several techniques, the simplest one being sedimentation of a particle suspension in an organic liquid. Electrophoretic deposition is used especially for pigment suspensions, applying charging additives and an upward electrical field. In the lacquer technique some polymer, e.g., nitrocellulose, is incorporated in the suspension, so that a lacquer film can be prepared by centrifuging. Polyvinylalcohol plus ammonium dichromate (pva, adc) is another example of a lacquer material, which can be photohardened in the usual way (4), thereby facilitating the preparation of sandwiches.

Mixtures are prepared by coating the surface of the phosphor particles with pigment. The adherence of the pigment particles (typical diameter 0.1 μ m) on the phosphor particles (diameter about 5–10 μ m) is usually improved by the addition of latex. On top of the phosphor layer an aluminum film about 0.2 μ m thick is evaporated, supported by an auxiliary nitrocellulose film. Finally all volatile, organic components are removed by baking out at 430°C.

Investigated pigments are commercially available types of cobalt blue, ultramarine blue, cobalt green, green chromium oxide, cadmium red, and red iron oxide. Standard blue/green/red phosphors are used: ZnS:Ag/(Zn,Cd)S:Cu or Y₂SiO₅:Tb/Y₂O₂S:Eu.

Optical measurements.—The light paths shown in Fig. 1 are only schematic. In reality pigment as well as phosphor particles strongly scatter light. Reliable measurements of their optical properties can therefore only be performed with goniophotometers or with spatially integrating detectors. We used the Zeiss DMR 21 automatic spectrophotometer including a 150 mm diam integrating sphere.

The measurements consisted of reflection of complete color filter systems of sandwich or mixture type (compare Fig. 1), reflection and transmission of pigmented layers on glass slides, and reflection of pigmented phosphor in 5 mm glass cuvettes (so-called R_e). Reflection values are related to the reflectivity of the BaSO₄ standard. If necessary the influence of the cover glass is eliminated, according to the theory in the section on Theory Sandwich.

Measurements usually extend from 380 to 800 nm wavelength. With respect to phosphor emission and eye sensitivity the range from 700 to 800 nm is of less importance, but it serves as an additional control, providing nearly absorption-free regions. The continuous measurement values are digitized every 10 nm and fed into a computer.

Brightness measurements.—The brightness of the "glass-filter/phosphor-Al film" samples under cathode-ray excitation was measured in a scanning electron microscope (type: Philips PSEM 500). The excitation conditions were chosen in such a way as to simulate a "TV-like" phosphor load see (Table I). The light output, i.e., the brightness, was measured with a photopic detector (type: Osram-Si-V_λ cell), the spectral sensitivity of which is well matched to the "eye sensitivity." This detector was incorporated into the PSEM and mounted close to the sample.

Theory Sandwich

The optical action of a sandwich-type color filter tube takes place in the four-layer sandwich glass-filter-phosphor-aluminum (GFPA); compare Fig. 1. The main experimental variations concern the F-part. Because of the difficult preparation of a GFPA sandwich, an FG sandwich is a much more favorable test sample. In the following a model is presented, which

Table I. Conditions of electron beam excitation

| | PSEM 500 | 30 AX tube |
|-------------------------------|---|---|
| High voltage* | 25 kV | 25 kV |
| Beam current | 0.1 μ A | 300 μ A |
| Spot diameter | 30 μ m | 1.5 mm |
| Scanned area | 4.8 \times 3.6 mm ² | 50 \times 40 cm ² |
| Number of lines | 62.5 | 625 |
| Line frequency | 15 kHz | 15 kHz |
| Current density* in the spot | $\sim 1.4 \times 10^{-2}$ A/cm ² | $\sim 1.7 \times 10^{-2}$ A/cm ² |
| Excitation time* [†] | 0.42 μ sec | 0.2 μ sec |

* Parameters relevant for comparison of PSEM 500 with 30 AX tube.

[†] Excitation time per phosphor element and frame scan, calculated from spot diameter divided by line frequency and length of scanned area.

allows the evaluation of the BCP of a GFPA sandwich from reflection and transmission measurements of an FG sandwich.

The model involves (i) the interrelation between the optical properties of single layers and sandwiches; (ii) averaging according to the eye sensitivity V_λ , the phosphor emission spectrum E_λ , and the ambient illumination N_λ ; and (iii) normalizing of "tube with filter" relative to "tube without filter." Assumptions are (a) one-dimensional calculation, i.e., no lateral or angular effects; (b) addition of light intensities, i.e., no interference effects, which should be allowed for diffusely scattering phosphor and pigment layers; and (c) no optical contact between glass and powder layer, in other words a small gap between them.

Let ρ_1, ρ_2, τ_1 , and τ_2 be the reflection and transmission of two homogeneous layers. If the two layers are combined to form a sandwich, a geometric series of multiple reflections between adjacent surfaces occurs (see Fig. 2a). The overall transmission τ_{12} and reflection ρ_{12} therefore follow

$$\begin{aligned} \tau_{12} &= \tau_1 \tau_2 (1 + \rho_1 \rho_2 + \rho_1^2 \rho_2^2 + \dots) \\ &= \tau_1 \tau_2 / (1 - \rho_1 \rho_2) \end{aligned} \quad [2]$$

$$\begin{aligned} \rho_{12} &= \rho_1 + \rho_2 \tau_1^2 (1 + \rho_1 \rho_2 + \rho_1^2 \rho_2^2 + \dots) \\ &= \rho_1 + \rho_2 \tau_1^2 / (1 - \rho_1 \rho_2) \end{aligned} \quad [3]$$

From Eq. [2] and [3] it is evident that the overall transmission is commutative, but not the overall reflection, i.e.

$$\tau_{12} \equiv \tau_{21}, \quad \rho_{12} \neq \rho_{21} \quad [4]$$

If the single layers are not homogeneous, but have a reflection which depends on the direction of light incidence, Eq. [3] has to be replaced by

$$\rho_{12} = \rho_1' + \rho_2 \tau_1^2 / (1 - \rho_1 \rho_2) \quad [3a]$$

ρ_1 and ρ_1' being the reflection of layer No. 1 from the right and the left side, respectively.

The properties of a single layer can be determined from the sandwich properties by resolving Eq. [2] and [3], e.g.

$$\rho_1 = (\tau_2^2 \rho_{12} - \rho_2 \tau_{12}^2) / (\tau_2^2 - \rho_2^2 \tau_{12}^2) \quad [5]$$

$$\tau_1 = \tau_2 \tau_{12} (1 - \rho_2 \rho_{12}) / (\tau_2^2 - \rho_2^2 \tau_{12}^2) \quad [6]$$

A different problem arises if layer No. 1 is a planar light source. The transmission of light emitted by this light source through a filter layer (No. 2) in front of it follows similarly (see Fig. 2b) as

$$\begin{aligned} \tau_{(1)2} &= \tau_2 (1 + \rho_1 \rho_2 + \rho_1^2 \rho_2^2 + \dots) \\ &= \tau_2 / (1 - \rho_1 \rho_2) \end{aligned} \quad [7]$$

Equation [2], [3], and [7] can be extended for more than two layers by splitting, e.g.

$$\tau_{123} = \tau_{12/3} = \tau_{12} \tau_3 / (1 - \rho_{21} \rho_3) \quad [8]$$

with τ_{12}, ρ_{21} according to Eq. [2] and [3]. The kind of splitting has no influence, i.e., $\tau_{12/3} \equiv \tau_{1/23}$.

The reflection of the TV-sandwich GFPA is obtained by splitting into GF and PA

$$\rho_{GFPA} = \rho_{GF} + \rho_{PA} \tau_{GF}^2 / (1 - \rho_{FG} \rho_{PA}) \quad [9]$$

based on Eq. [3a]. ρ_{GF} is calculated from ρ_{FG} and τ_{FG} using Eq. [5] and [6]. By the same kind of splitting, for the transmission of the planar light source AP through the sandwich FG (in front of it) it follows from Eq. [7] that

$$\tau_{(AP)FG} = \tau_{FG} / (1 - \rho_{FG} \rho_{PA}) \quad [10]$$

Tube reflection R and relative brightness T are obtained by spectral averaging

$$R = \int \rho_{GFPA} V_\lambda N_\lambda d\lambda / \int V_\lambda N_\lambda d\lambda - r \quad [11]$$

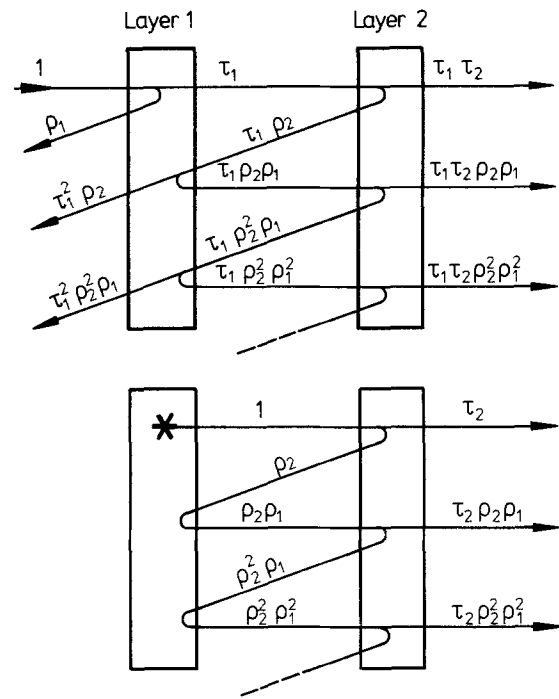


Fig. 2. Light intensities induced by multiple reflections in a sandwich. (a, top) τ_{12} and ρ_{12} , (b, bottom) $\tau_{(1)2}$.

$$T = \int \tau_{(AP)FG} V_\lambda E_\lambda d\lambda / \int V_\lambda E_\lambda d\lambda \quad [12]$$

The specular reflection r at the first glass surface usually amounts to 0.04. T is proportional to brightness B , so that on the grounds of definition [1] BCP becomes

$$\text{BCP} = \left(\frac{T}{\sqrt{R}} \right)_{\text{filter}} \bigg/ \left(\frac{T}{\sqrt{R}} \right)_{\text{without filter}} \quad [13]$$

The screen "without filter" forms a three-layer sandwich GPA, which can be evaluated similarly to GFPA. Its characteristic values R and T are determined by ρ_{PA} and by the glass properties ρ_G and τ_G , which are connected with internal glass transmission θ and first surface reflection r

$$\rho_G = r + \theta^2 (1 - r)^2 r / (1 - r^2 \theta^2) \quad [14]$$

$$\tau_G = (1 - r)^2 \theta / (1 - r^2 \theta^2) \quad [15]$$

The computer model described permits the introduction of artificial filter-phosphor combinations as well. Several cases are of interest: (i) Real spectra of filter or phosphor may be shifted along the wavelength axis in order to obtain better coincidence. (ii) Square filters represent the ideal case. With suitable cut-on and cut-off wavelengths they form the theoretical limit of the color filter concept. (iii) A further idealization results from narrow-band or even monochromatic phosphors.

The chromaticity coordinates, X, Y of the three television phosphors must obey international standards. Since the chromaticity may be influenced by color filters, a control is necessary. For this purpose X and Y of each phosphor-filter combination are calculated in the known way by forming three integrals of $E_\lambda \cdot \tau_{(AP)FG}$ multiplied by the three color-matching functions, followed by normalization (5). Small color variations can quantitatively be expressed in multiples of "just noticeable difference," represented by the so-called MacAdam ellipse (6) in the X, Y plane.

Results

Results are given for the measured optical properties of the subsystem "filter glass" (FG), the calculated optical properties of the complete system "glass-

filter-phosphor-aluminum" (GFPA) including the model BCP, and the experimentally determined BCP. Figures 3 and 4 show two typical examples of red pigments Cd(S,Se) and α -Fe₂O₃. In Fig. 3a transmission τ_{FG} and reflection ρ_{FG} spectra of thin pigment layers on glass are to be seen. Because of the scattering nature of the pigment particles the curves of transmission and reflection closely resemble each other, i.e., in regions with low absorption both transmission and reflection are high, and vice versa.

Figure 3b shows the reflection ρ_{GFPA} of the complete sandwich GFPA and the transmission $\tau_{(AP)FG}$ of the light source AP through the filter FG in front of it. They are calculated from Fig. 3a assuming a constant

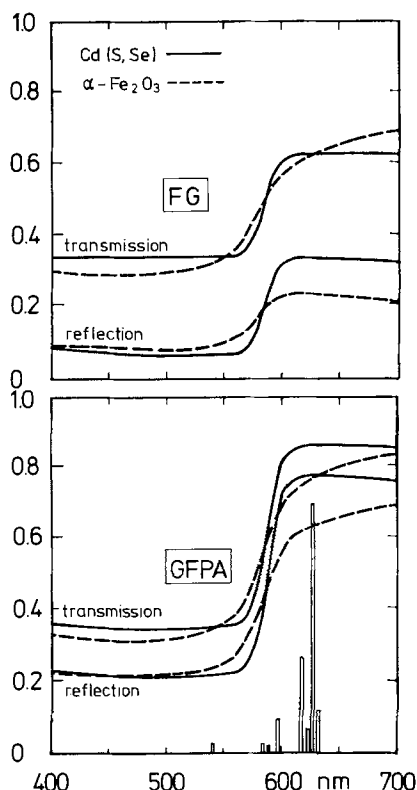


Fig. 3 (a, top) τ_{FG} and ρ_{FG} of two red pigment layers on glass, measured in a spectrometer; (b, bottom) $\tau_{(AP)FG}$ and ρ_{GFPA} calculated from (a), together with E_{λ} of red phosphor Y₂O₂S:Eu.

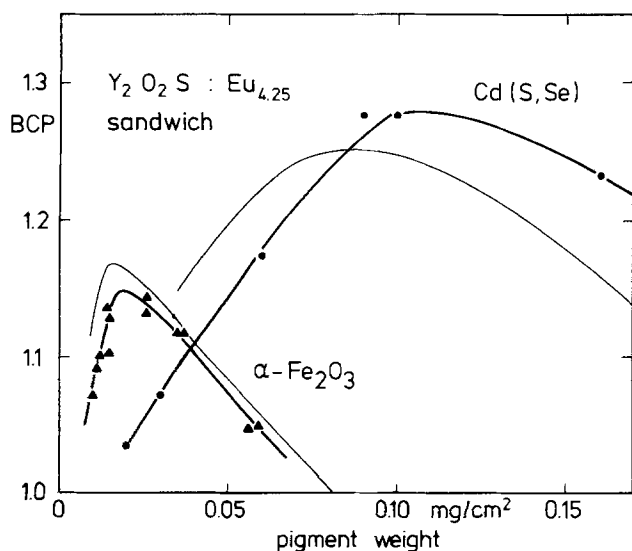


Fig. 4. BCP as a function of pigment weight in a sandwich filter system. The two red pigments are cadmium red and iron oxide. Thin lines refer to model calculations.

Table II. Theoretical R , T , and BCP values of color filter sandwiches with two typical red pigments*

| Filter | mg/cm ² | R | T | BCP |
|--|--------------------|-------|-------|------|
| Cd(S,Se) | 0.099 | 0.323 | 0.800 | 1.25 |
| α -Fe ₂ O ₃ | 0.016 | 0.306 | 0.727 | 1.17 |
| No filter | — | 0.763 | 0.984 | 1 |

* Calculated on the basis of spectrometer measurements of pigment layers on glass substrate.

$\rho_{PA} = 0.80$ and no glass blackening. The main feature is a steepening of the absorption edges due to the mirror action of the PA-double layer. Averaging with the emission E_{λ} of Y₂O₂S:Eu_{4.25} phosphor and a "white" ambient light N_{λ} delivers theoretical values for the tube reflection R , relative brightness T , and BCP, listed in Table II.

The superior behavior of Cd(S,Se) pigment compared to α -Fe₂O₃ pigment, evidently caused by the steeper absorption edge, appears correspondingly in the thickness dependence of BCP (Fig. 4, thin lines). Experimental BCP values of complete color filter sandwich systems, determined by reflection and brightness measurements, are included in Fig. 4. They exhibit good agreement with the theoretical values for both maximum BCP and optimum filter thickness.

An example for a blue pigment is shown in Fig. 5 and 6, arranged as for Fig. 3 and 4. A cobalt blue layer of 0.22 mg/cm² thickness in combination with E_{λ} of ZnS:Ag phosphor yields model values $R = 0.350$, $T = 0.869$, and BCP = 1.30. Figure 5b contains additionally the measured reflection curve of a complete sandwich with a comparable thickness of 0.21 mg/cm². The agreement with the calculated ρ_{GFPA} is satisfactory; larger deviations below 420 nm originate in the assumption of a constant ρ_{PA} . Still better agreements can be achieved by taking into account a slight glass absorption and the angular dependence of glass reflection.

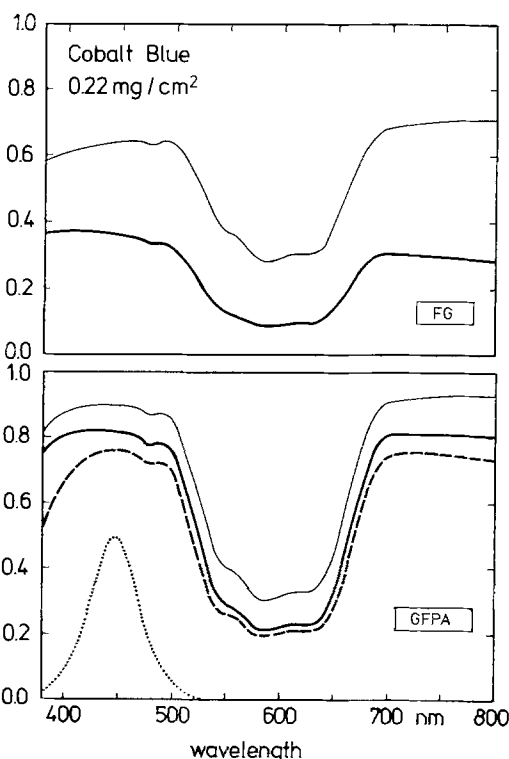


Fig. 5. (a, top) τ_{FG} (thin line) and ρ_{FG} of a cobalt blue layer on glass, (b, bottom) $\tau_{(AP)FG}$ (thin line) and ρ_{GFPA} calculated from (a), together with E_{λ} (dotted line) of blue phosphor ZnS:Ag. The thick dashed line is the measured reflection ρ_{GFPA} .

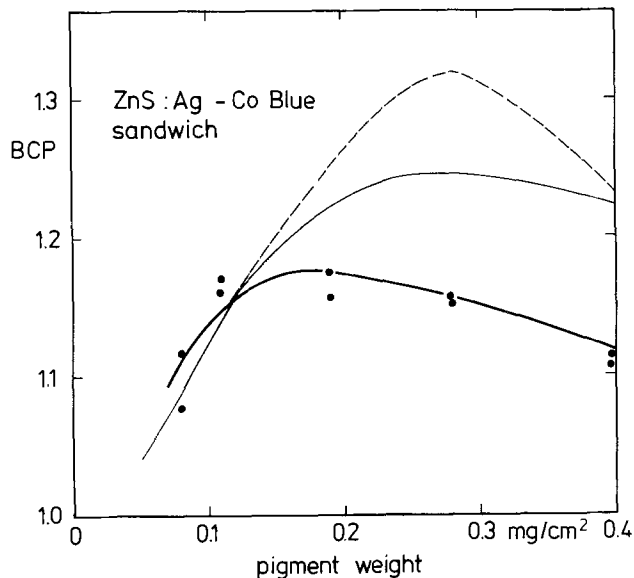


Fig. 6. BCP as a function of cobalt blue pigment weight in a sandwich filter system. The two thin, dashed and full lines refer to model calculations, based on differently deposited pigment layers.

The thickness dependence of BCP is plotted in Fig. 6, for both model calculations and experimental values. The agreement is not so good as with the two red pigments, which may be an effect of pigment processing. The strong influence of preparation technique can be seen by comparing the two thin lines: the dashed and the full ones correspond to different methods of depositing the pigment.

Figure 7 presents results of a green pigment. In this example a layer of 0.06 mg/cm² cobalt green in combination with the green phosphor (Zn,Cd)S:Cu yields $R = 0.520$, $T = 0.764$, and $BCP = 0.94$, i.e., only a loss. There is little hope of finding a filter-phosphor combination with a clear BCP gain, either with line-emitting or broad-band phosphors, simply because of the high eye sensitivity in the green spectral region.

The results obtained so far with color filter sandwiches are summarized in Table III, the BCP maxima of real filter-phosphor combinations ranging from 1.15 to 1.45. Among the blue pigments cobalt blue is exceeded by ultramarine blue. Unfortunately, however, the latter has poor temperature stability. As expected, idealized square filters offer much higher BCP gains, as illustrated in Fig. 8. While the usual green phosphor (Zn,Cd)S:Cu even with an ideal square filter exhibits only 1.09, the line-emitting green phosphor Y₂SiO₅:Tb with a 20 nm square filter yields a surprisingly high BCP of 1.65. Narrow-band phosphors with the ability to transmit their whole light output through 10 nm square filters would offer BCP values of 3.39, 2.74, and 4.02 for the red, green, and blue regions, respectively.

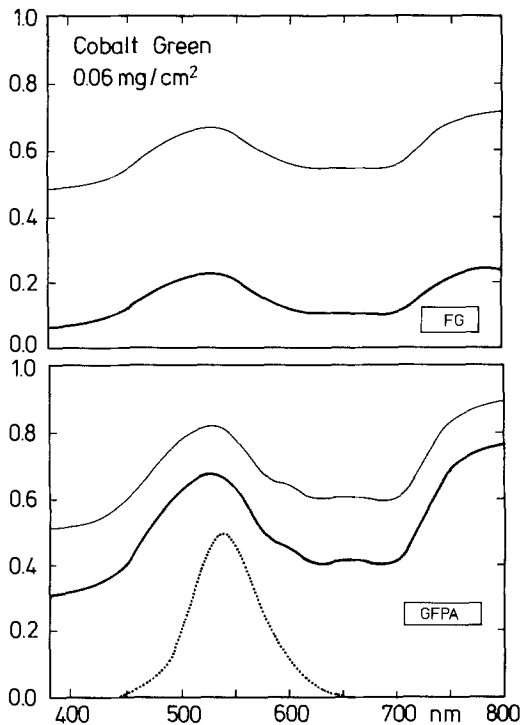


Fig. 7. (a, top) τ_{FG} (thin line) and ρ_{FG} of a cobalt green layer on glass; (b, bottom) $\tau_{(AP)FG}$ (thin line) and ρ_{GFPA} calculated from (a) together with E_λ of green phosphor (Zn,Cd)S:Cu (dotted line).

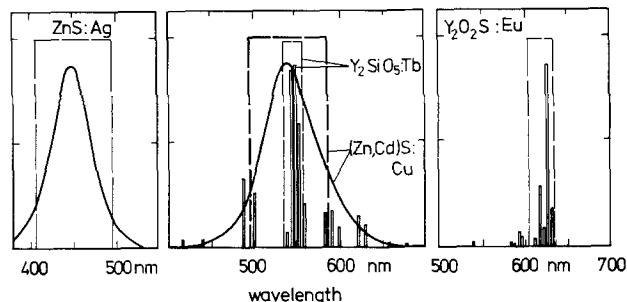


Fig. 8. Emission spectra E_λ of blue, green, and red phosphors, together with transmission τ_F of ideal square filters.

The influence of the pigment on the phosphor chromaticity is expressed in the changes ΔX , ΔY of the chromaticity coordinates (see Table III). Up to optimum pigment thicknesses there is only a small shift, providing a slight expansion of the accessible color triangle toward the purple line [about 1 or 2 steps of "just noticeable difference" (6) for the two blue pigments and about 3 or 4 steps for the two red pigments, respectively, exceeding the standardized E.B.U. toler-

Table III. Summary of color filter sandwiches. Maximum BCP obtained by experiment and by model calculation of real and idealized filter phosphor combinations, respectively

| Phosphor | Filter | | BCP _{max} ^{model} | BCP _{max} ^{exp} | ΔX^* | ΔY^* |
|--|--|-------------------------|-------------------------------------|-----------------------------------|--------------|--------------|
| Y ₂ O ₂ S:Eu ₄₋₂₅ | Cd(S,Se) | 0.13 mg/cm ² | 1.27 | 1.28 | 0.0098 | -0.0096 |
| Y ₂ O ₂ S:Eu ₄₋₂₅ | α -Fe ₂ O ₃ | 0.02 mg/cm ² | 1.16 | 1.15 | 0.0069 | -0.0068 |
| Y ₂ O ₂ S:Eu ₄₋₂₅ | "Ideal" | 605-635 nm | 1.99 | | | |
| Monochrom. 620 nm | "Ideal" | 10 nm width | 3.39 | | | |
| ZnS:Ag | Co-Blue | 0.28 mg/cm ² | 1.32 | 1.17 | 0.0002 | -0.0017 |
| ZnS:Ag | Ultramarine | 0.25 mg/cm ² | 1.45 | | 0.0002 | -0.0034 |
| ZnS:Ag | "Ideal" | 405-495 nm | 2.18 | | | |
| Monochrom. 450 nm | "Ideal" | 10 nm width | 4.02 | | | |
| (Zn,Cd)S:Cu | Co-Green | - | <1 | | | |
| (Zn,Cd)S:Cu | "Ideal" | 495-585 nm | 1.09 | | | |
| Y ₂ SiO ₅ :Tb | Co-Green | - | <1 | | | |
| Y ₂ SiO ₅ :Tb | "Ideal" | 535-555 | 1.65 | | | |
| Monochrom. 540 nm | "Ideal" | 10 nm width | 2.74 | | | |

* Filter-induced chromaticity displacements ΔX and ΔY according to CIE 1931 (5).

ances (7) by no more than a factor of 2]. On the other hand, this shift can be used to compensate the green shift of certain high efficiency red or blue phosphors. For example, Y_2O_3S phosphor with 3 instead of 4.25% Eu exhibits a chromaticity displacement ($\Delta X = -0.0093$, $\Delta Y = 0.0086$), which is largely canceled by $0.13 \text{ mg/cm}^2 \text{ Cd(S,Se)}$.

Pigment as well as phosphor materials frequently exist in the form of mixed crystals, and compositional variations can be simulated by shifting real spectra along the wavelength axis. Our model calculations reveal, however, that no essential BCP improvements can be obtained in this way. In the case of filter variation, BCP increases by only about 1% at the most. Shifting of phosphor spectra yields up to 5% additional BCP gain, but at the cost of an intolerable chromaticity change ($\Delta X = 0.015$, $\Delta Y = -0.033$ for $ZnS:Ag$).

Discussion

The experimentally determined BCP of sandwich-type filter tubes ranges from about 1.15 to 1.25 for commercially available red or blue pigments. Up to now no gain has been found for the green color. The filter-induced chromaticity changes exceed the perception threshold only slightly. They can be used either for a slight increase of color gamut or for the green shift compensation of certain high efficiency phosphors.

Reasonable agreement is obtained between experiments and sandwich model calculations, regarding both maximum BCP value and optimum pigment layer thickness. From this fact the other model predictions acquire a higher probability, too. The model thus helps one in making a selection from among numerous commercial pigments. Those presented belong to the best ones according to model calculations.

Another important model prediction concerns the wavelength shifts of real spectra. Only about 1% additional BCP gain appears to be possible, unless excessive chromaticity displacements take place. Therefore, essential improvements cannot result from variations of mixed crystals. The most important point is the slope of absorption edges. In this respect commercial pigments are probably optimized, because in accordance with color theory (8) the most saturated colors are those with rectangular spectral characteristics, the so-called optimal colors. The conclusion is therefore drawn that the present filter pigments form a practical limit and essentially higher BCP gains are not to be expected.

Ideal square filters yield BCP values of 2-2.2 for the red and the blue, i.e., a gain of 100-120%, while the portion achieved by real filters amounts to about 1/4 to 1/3. This is another indication of the limiting character of the present pigments, since square responses are, of course, quite unrealistic. A further, even more utopian BCP improvement results from narrow-band phosphors with 10 nm square filters.

For all three stages, i.e., real filters, square filters, and narrow-band phosphors with 10 nm square filters, the same sequence green, red, and blue of increasing BCP is observed. This is evidently due to the increasing wavelength distance (about 15, 70, 105 nm) from the maximum of eye sensitivity, which facilitates the discrimination between passband and rejection band. At the third stage, however, differences between green, red, and blue would disappear if the bandwidth approaches zero. In this case, with $T = 0.984$ and $R = 0.037$, BCP arrives at its absolute limit 4.55, as long as antireflection coatings are excluded.

As already stated, blackening of screen glass is frequently used for contrast improvement. From Eq. [7] one can see that brightness or relative brightness T is approximately proportional to glass transmission τ_G . From Eq. [3] it follows that tube reflection R varies approximately as a function of τ_G^2 . So indeed contrast,

which is proportional to B/R , increases approximately as $1/\tau_G$, but at the cost of a loss in B . On the other hand, BCP, forming a kind of geometric means of contrast and brightness, to a first approximation does not depend on τ_G , since τ_G and square root of τ_G^2 cancel out.

A given BCP gain can lead to different results, depending on the choice of τ_G . If, for example, τ_G of the filter tube is increased so that R (with filter) equals R (without filter) then B (with filter) becomes B (without filter) times BCP. Alternatively, τ_G of the filter tube can be chosen so that contrast remains constant, whereby the brightness ratio becomes approximately BCP squared. As the BCP criterion cannot decide which of these alternatives is to be preferred, we propose a new criterion, as demonstrated in Fig. 9. Relative brightness T is plotted as a function of tube reflection R . The curve is obtained by variation of internal glass transmission ϑ from 1 (i.e., no glass blackening) to 0 (total glass blackening). The absolutely best combination of T and R is no doubt $T = 1$ and $R = 0$.

We now put forward the hypothesis that a real combination (T, R) is the better the shorter its distance from the "ideal point" ($T = 1, R = 0$). From this the optimum ϑ for the tube without filter turns out to be $\vartheta_{op} = 0.66$, corresponding to $\tau_G = 0.61$, which agrees surprisingly well with the quality maximum known from practice. For sandwich filter tubes with 0.03 and $0.1 \text{ mg/cm}^2 \text{ Cd(S,Se)}$, ϑ_{op} equals 0.79 and 0.89, respectively, agreeing with the experience that the more filter elements (color pigments or also black matrix between phosphor areas) are already present, the lower the optimum glass blackening. Of course, this is not an absolute criterion, which would require detailed physiological knowledge, but it can help one to find a reasonable compromise between brightness and contrast, especially if supplemented by empirical calibration points.

Outlook for Mixture Systems

Typical results of mixture-type color filter systems are shown in Fig. 10. BCP of the combination $\alpha\text{-Fe}_2\text{O}_3$

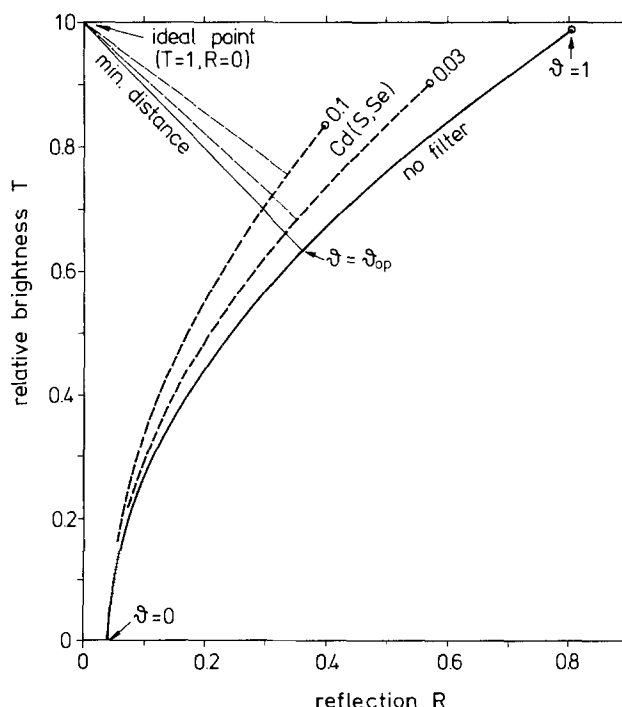


Fig. 9. Relative brightness T vs. reflection R (inclusive specular component) for a nonfilter tube and two sandwich filter tubes with 0.03 and $0.1 \text{ mg/cm}^2 \text{ Cd(S,Se)}$, calculated from τ_{FG} and ρ_{FG} measurements by variation of the internal glass transmission ϑ . At $\vartheta = \vartheta_{op}$ the distance from the ideal point passes through a minimum.

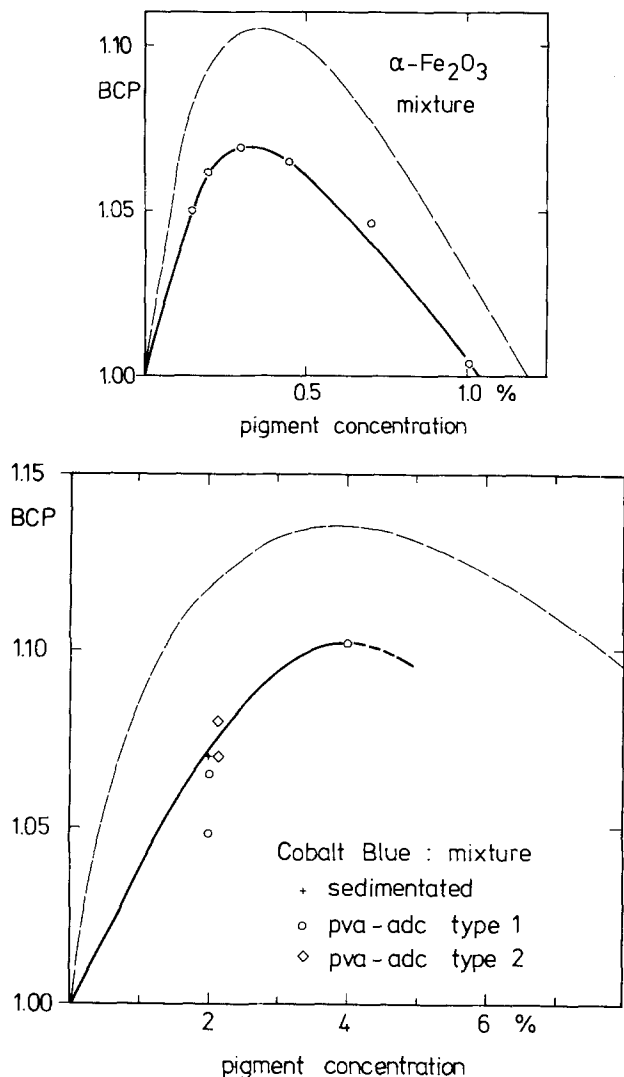


Fig. 10. BCP as a function of pigment concentration in a mixture filter system. The dashed lines refer to model calculations. (a, top) Red pigment $\alpha\text{-Fe}_2\text{O}_3$; (b, bottom) cobalt blue.

with $\text{Y}_2\text{O}_3\text{:Eu}$ phosphor reaches 1.07 at about 0.3% pigment concentration. For cobalt blue with ZnS:Ag phosphor a maximum BCP value of about 1.1 is achieved at about 4% pigment concentration. In both examples the mixture yields only about half the BCP gain of the sandwich (see Fig. 4 and 6, and Table III).

Converted to the phosphor layer thicknesses of about 3.5 mg/cm^2 for the red and 3 mg/cm^2 for the blue, the optimum pigment concentration corresponds to layer thicknesses of about 0.12 mg/cm^2 for cobalt blue and 0.01 for $\alpha\text{-Fe}_2\text{O}_3$, which are again only about half of the optimum thickness values of the sandwiches. This implies that at low pigment quantities the BCP of sandwiches and of mixtures rises in approximately the same way, but that the BCP of sandwiches continues to rise up to about twice as high a pigment quantity as with mixtures.

A qualitative explanation for this behavior can be derived from electron absorption by the filter pigment instead of the phosphor, which occurs in mixtures only. But in view of the low actual pigment concentration it is clear that this mechanism is not sufficient. The main cause is probably the simple fact that the filter layer in a sandwich system has to be crossed twice by the ambient light, but only once by the phosphor light, whereas in a mixture system the paths for both kinds of light are approximately equal. For a final understanding the different mechanisms of light scattering in sandwiches and mixtures have to be taken into account. In mixtures with a small pigment concentration

the optical interaction between phosphor and pigment proceeds mainly by scattering at the phosphor particles, which are large compared to the light wavelength. In sandwiches the filter-relevant light scattering happens among subwavelength pigment particles within the pigment layer.

The essential experimental findings can be reproduced by a simplified empirical model, the results of which are included as dashed lines in Fig. 10. It is assumed that light generation takes place only in a thin surface region of the phosphor layer adjacent to the aluminum film. By formally regarding the layer with the phosphor-filter mixture as a filter layer and combining a virtual light-emitting layer with the aluminum film, it is possible to treat a mixture-type color filter system with the same computer program as the sandwich.

Transmission and reflection of this type of "filter" layer are determined on the basis of the Kubelka-Munk theory (9), which enables a weakly absorbing, scattering material to be described with the aid of an absorption coefficient K and a scattering coefficient S . Measurements of R_∞ , the reflection of an "infinitely" thick powder layer, yield the ratio K/S . S can be evaluated, for example, from reflection measurements of layers with different finite thicknesses. S depends, as stated above, mainly on the phosphor. This is confirmed by our measurements, which give values of about $500 \text{ cm}^2/\text{g}$ for the blue phosphor and $400 \text{ cm}^2/\text{g}$ for the red one, nearly independent of pigment addition and wavelength. So a relatively simple measurement of R_∞ is generally sufficient to obtain a reasonable prediction of the BCP of a complete mixture system.

Conclusion

The action of color filters in color television tubes can be understood with the help of relatively simple models, especially in the case of sandwiches. BCP gains up to about 25% have been obtained in sandwiches with commercial filter pigments. This appears to be a practical limit, which could not be essentially exceeded. Mixture-type color filters, though more favorable for production, exhibit only about one-half of the sandwich BCP gain.

Acknowledgment

The authors wish to thank W. Czarnojan, E. Klein, and H. Lade who conducted most of the experimental work.

Manuscript submitted May 15, 1981. This was Paper 226 presented at the St. Louis, Missouri, Meeting of the Society, May 11-16, 1980.

Any discussion of this paper will appear in a Discussion Section to be published in the June 1982 JOURNAL. All discussions for the June 1982 Discussion Section should be submitted by Feb. 1, 1982.

Publication costs of this article were assisted by Philips GmbH Forschungslaboratorium Aachen.

REFERENCES

1. S. S. Trond, Abstract 329, p. 817, The Electrochemical Society Extended Abstracts, Seattle, WA, May 21-26, 1978.
2. T. Takahara, T. Wakatsuki, and T. Nishimura, Abstract 219, p. 564, The Electrochemical Society Extended Abstracts, St. Louis, MO, May 11-16, 1980.
3. W. Möller, W. de Rave, and H. Widmann, Abstract 225, p. 576, The Electrochemical Society Extended Abstracts, St. Louis, MO, May 11-16, 1980.
4. S. Larach and A. E. Hardy, *Proc. IEEE*, **61**, 915 (1973).
5. G. Wyszzecki and W. S. Stiles, "Color Science," John Wiley & Sons, Inc., New York (1967).
6. D. L. MacAdam, *J. Opt. Soc. Am.*, **32**, 247 (1942).
7. "E.B.U. standard for chromaticity tolerances for studio monitors," E.B.U. Tech. 3213-E, August 1975.
8. E. Schrödinger, *Ann. Phys.*, **62**, 603 (1920).
9. P. Kubelka and F. Munk, *Z. Tech. Phys.*, **12**, 593 (1931).

Phosphorus-Doped Molybdenum Silicide Films for LSI Applications

S. Inoue,* N. Toyokura, T. Nakamura, and H. Ishikawa*

Fujitsu Laboratories Limited, 1015 Kamikodanaka, Nakahara-ku, Kawasaki, Japan

ABSTRACT

The properties of phosphorus-doped molybdenum silicide as a gate electrode, interconnecting material, and impurity diffusion source for LSTs have been studied. The phosphorus-doped molybdenum silicide films were deposited by co-sputtering using specially designed Mo and Si targets in a PH_3/Ar atmosphere. PH_3 decomposed to P and H_2 during sputtering and the phosphorus combined with Mo and Si. Typically, a phosphorus concentration of $1.5 \times 10^{21} \text{ cm}^{-3}$ in the films was used. As-deposited films ($\text{Mo/Si} \leq 0.5$) had amorphous structure and high resistivity. After the films were annealed at temperatures above 800°C , they became polycrystalline and resistivity was decreased. The resistivity of the film with a Mo/Si ratio of 2 to 1 was $7.5 \times 10^{-5} \Omega\text{-cm}$ with annealing at 1000°C in N_2 . Phosphorus was able to diffuse from the doped molybdenum silicide films to the Si substrate during annealing in O_2 . After high temperature annealing up to 1100°C , the contact resistance between the molybdenum silicide and the silicon substrate was below $2 \times 10^{-6} \Omega\text{-cm}^2$. The reliability of doped molybdenum silicide gate MOSFETs is as good as polysilicon gates and the threshold voltage shift is within $\pm 20 \text{ mV}$ under stress conditions of 2.5 MV/cm for 1000 hr at 150°C .

As LSI device dimensions continue to decrease, the conductivity of the polysilicon used for interconnections and gates is beginning to limit the circuit performance.

Previous investigators have explored the use of refractory metals such as Mo and W for gate electrodes and interconnections in MOSFET circuits (1-6). These metals have significantly higher conductivity than polysilicon, but do not have the ability to withstand the chemical reagents and oxidizing ambient used in LSI fabrication.

In order to overcome these disadvantages, the refractory metal silicides, such as MoSi_2 and WSi_2 , have been proposed because of their resistance to oxidizing ambient and chemical reagents (7-11). It has been reported that the contact resistance between the molybdenum silicide and the silicon substrate was increased by high temperature annealing, but this problem has never been solved completely (12, 13). Moreover, as the contact region cannot be doped through the silicide, it must be doped prior to gate electrode deposition. Sometimes, a slight shift of threshold voltage appears due to the mobile ions in the oxide films when silicide is used as the gate electrode (7).

We have developed phosphorus-doped molybdenum silicide films in order to overcome just these problems. This film has several advantages for LSI fabrication.

In this paper we discuss the properties of these phosphorus-doped molybdenum silicide films, the composition of films, the behavior of the phosphorus in the films, the electrical properties of the contact between the silicide and the silicon substrate, and MOS device characteristics.

Deposition of Phosphorus-Doped Molybdenum Silicide Film

The phosphorus-doped molybdenum silicide film was deposited by a d-c magnetron co-sputtering technique. A conceptual diagram is given as Fig. 1. The deposition was performed from specially designed Si and Mo targets as shown in Fig. 2. A larger proportion of the Mo target (99.95%, 150 mm diam) was covered with fan-shaped high-purity Si.

* Electrochemical Society Active Member.

Key words: molybdenum silicide, contact resistance, diffusion, MOSFET.

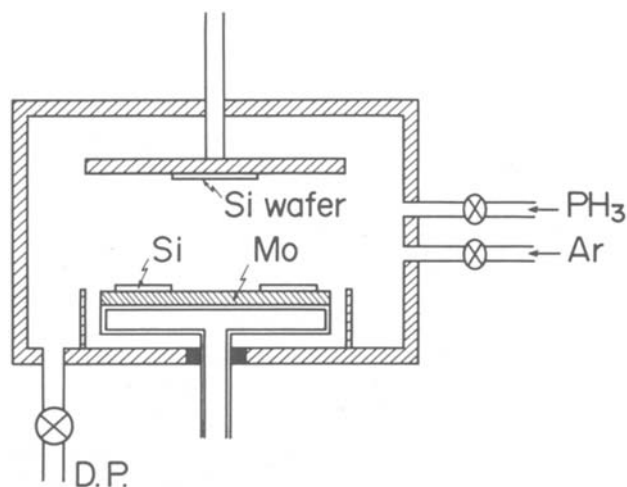


Fig. 1. Conceptual diagram of the phosphorus-doped co-sputtering apparatus.

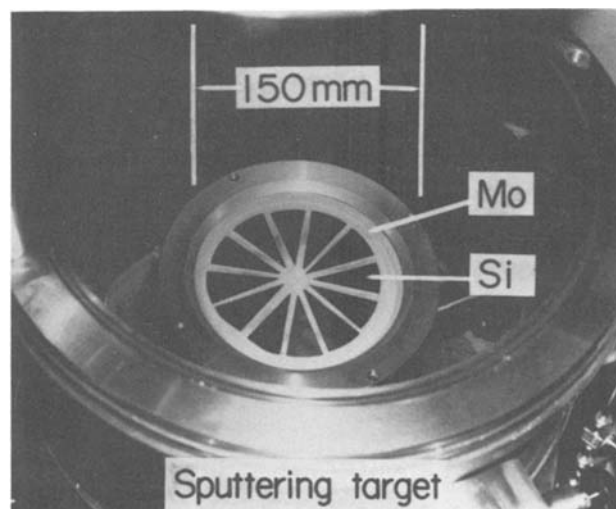


Fig. 2. Photograph of the specially designed Si and Mo targets

The chamber was pumped down to 4×10^{-7} Torr (5.3×10^{-5} Pa) and backfilled to sputtering pressure, 6×10^{-3} Torr (0.8 Pa), by introducing Ar and PH_3 . Typically, PH_3 partial pressure of 1.1×10^{-3} Torr (0.15 Pa) was used. The ratio of Mo to Si in the deposited films could be varied by changing the positions of the Si and the sputtering pressure. The phosphorus concentration is varied by controlling the ratio of PH_3 and Ar in the sputtering gas. The deposition rate was 10-15 Å/sec and d-c power was 160-220W.

Crystal Structure

Silicide films of various Mo/Si ratios were deposited on the thermally grown SiO_2 . The Mo/Si ratio in the film was measured by Rutherford backscattering using $^4\text{He}^+$ ions at 330 keV and $^3\text{He}^{++}$ ions at 300 keV. Structure information was obtained using x-ray diffraction techniques. When the Mo/Si ratio was lower than 0.5 as-deposited films were an amorphous structure. The amorphous film became a polycrystalline structure after high temperature annealing. The relation between annealing temperature and x-ray diffraction traces is shown in Fig. 3. The Mo/Si ratio in this film was 0.45 (Mo:Si = 1:2.2). This figure shows that the silicide film is crystallized at annealing temperatures above 800°C and exhibits a tetragonal MoSi_2 structure (JCPDS cards 6-0681).

On the other hand, as-deposited films with Mo/Si ratios higher than 0.5 were crystallized a little as shown in Fig. 4. Figure 4(a) shows the Mo_3Si phase for an Mo/Si ratio of 2.7, and Fig. 4(b) shows MoSi_2 (hexagonal structure) for an Mo/Si ratio of 0.9. After annealing above 800°C, the MoSi_2 structure changes from hexagonal to tetragonal.

X-ray diffraction traces for various Mo/Si ratios are shown in Fig. 5. The silicide films on SiO_2 were annealed at 1000°C for 20 min in N_2 . Figure 5(a) shows the simple phase Mo_3Si for an Mo/Si ratio of 2.7 (Mo:Si = 1:0.37). When the Si ratio in the film is increased, the film produces Mo_5Si_3 and MoSi_2 , as shown in Fig. 5(b) for an Mo/Si ratio of 0.9 (Mo:Si = 1:1.1). The MoSi_2 phase is for an Mo/Si ratio of 0.5 (Mo:Si = 1:2) only, as shown in Fig. 5(c). When the Mo/Si ratio falls 0.35 (Mo:Si = 1:2.9), as in Fig. 5(d), the film has the MoSi_2 phase only.

Composition of the Films

The depth concentration profile of the samples before and after annealing was obtained by Rutherford

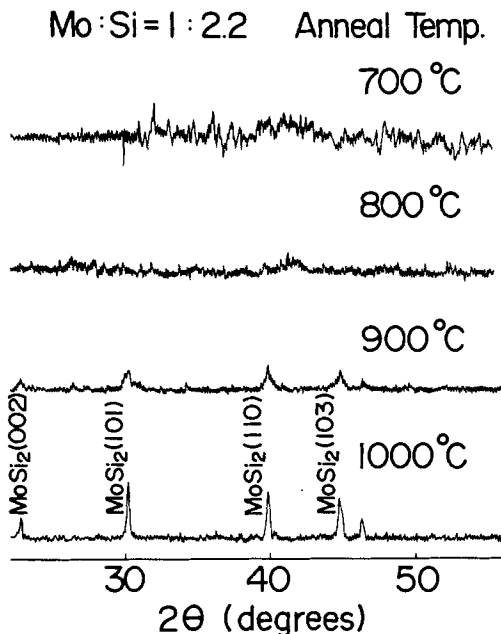


Fig. 3. X-ray diffraction traces as a function of the annealing temperatures. The Mo/Si ratio is 0.45.

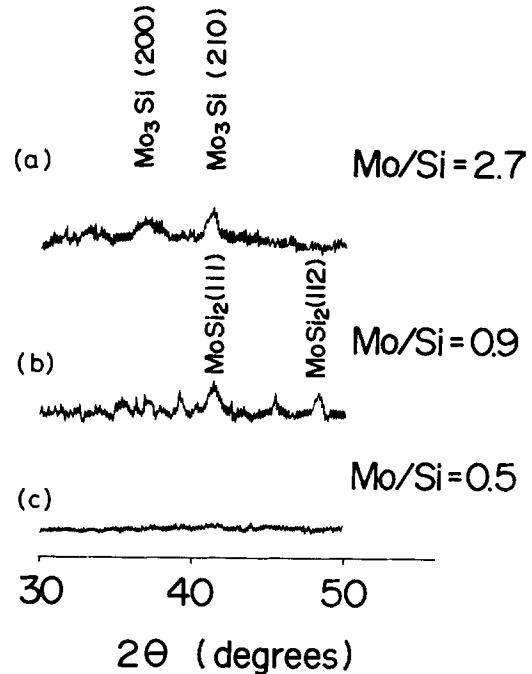


Fig. 4. X-ray diffraction traces of as-deposited films for various Mo/Si ratios: (a) 2.7, (b) 0.9, and (c) 0.5.

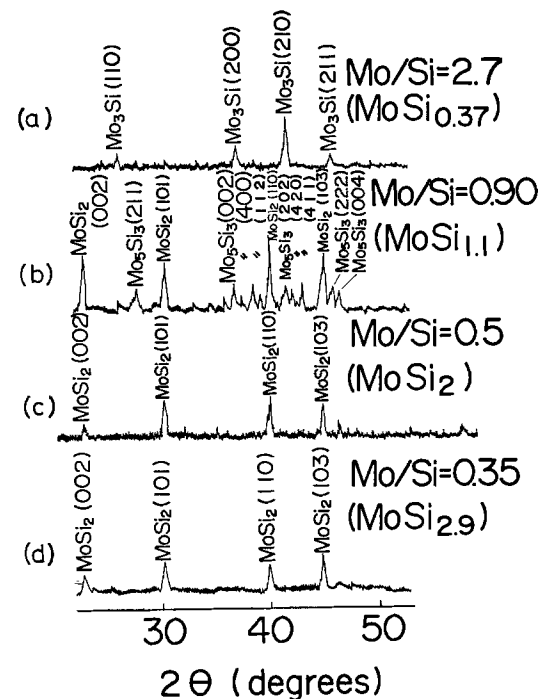


Fig. 5. X-ray diffraction traces of annealed films for the various Mo/Si ratios. The films were annealed at 1000°C for 20 min in N_2 .

backscattering spectra analysis. The silicide films deposited on SiO_2 and Si were annealed for 20 min at 1000°C in N_2 . The Mo/Si ratios of the samples were 0.35 (1:2.9) and 0.82 (1:1.2) for Si-rich silicide and Mo-rich silicide films, respectively, as compared to MoSi_2 . The film thickness was 780Å.

Figure 6 shows the backscattering spectra of the sample before and after annealing. The sample was Si-rich silicide film deposited on SiO_2 . In the spectra of the annealed sample, the center of the Mo spectra is slightly higher than one side, and the shoulder is broad. This indicates that the ratio of Mo decreased slightly at both the silicide surface and at the silicide/ SiO_2 interface. A model of this is shown in the upper right-hand corner of Fig. 6.

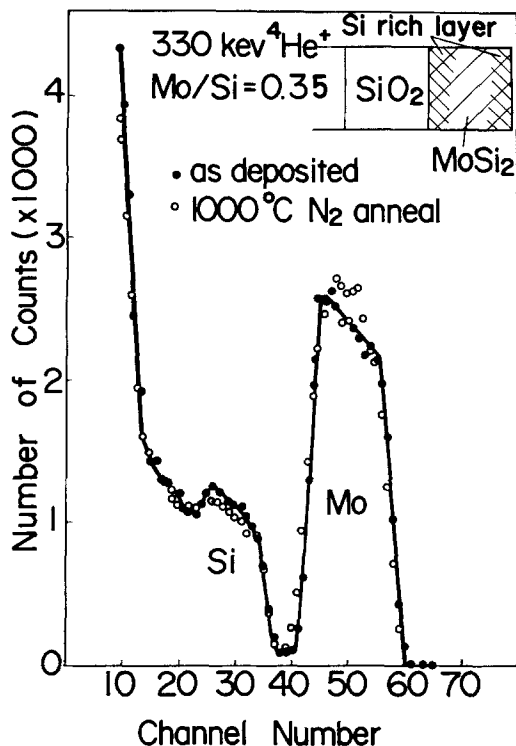


Fig. 6. Backscattering spectra of the thin film on SiO₂ before and after annealing at 1000°C for 20 min in N₂. The Mo/Si ratio is 0.35.

Figure 7 shows the backscattering spectra of the Si-rich silicide on Si before and after annealing. After annealing, the presence of the phase is confirmed by the height of the respective "step" in the backscattering spectra, indicating a region with a 1:2 Mo/Si ratio. The width of the Mo spectra is decreased and the interface between the silicide and Si moves toward the surface after annealing. This indicates that excess Si in the film is precipitated at the silicide/Si interface and

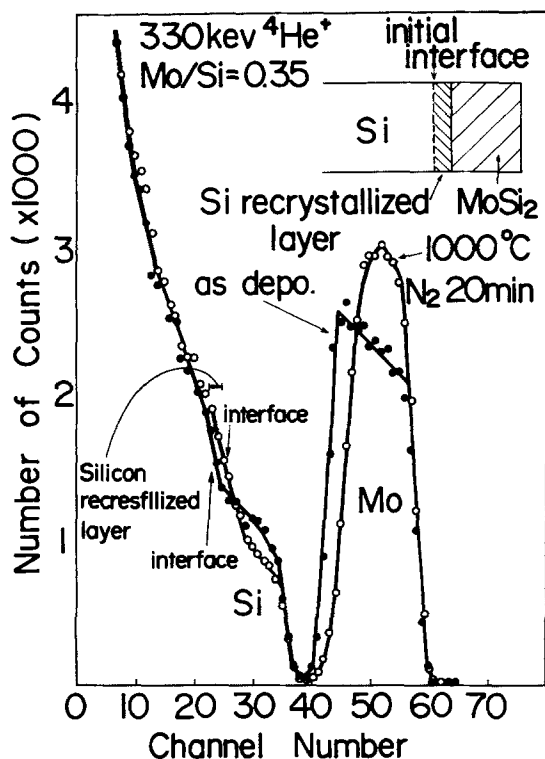


Fig. 7. Backscattering spectra of the film on Si before and after annealing at 1000°C for 20 min in N₂. The Mo/Si ratio is 0.35.

the film is recrystallized as a double layer of MoSi₂ and Si, as shown in the upper righthand corner of Fig. 7.

The spectrum of the Mo-rich silicide film on SiO₂ is shown in Fig. 8. This spectrum shows that the ratio of Mo increases at the surface and at the silicide/Si interface, and the Mo/Si ratio at the middle of the film approaches MoSi₂ after high temperature annealing. A model of this is shown at the top of Fig. 8.

The spectra of the Mo-rich film on Si are shown in Fig. 9. The spectrum of the annealed film indicates that Si diffuses into silicide from the Si substrate and forms a 1:2 Mo/Si ratio. The film thickness increases until the composition changes to MoSi₂ as shown in Fig. 9.

These backscattering spectra indicate the following results. The composition profile of the as-deposited sample is uniform from the silicide surface to the silicide/SiO₂ or Si interface. The composition profiles of the films on SiO₂ vary from the middle of the film to the surface or the silicide/SiO₂ interface. The middle of the films approaches 1:2 Mo/Si ratio.

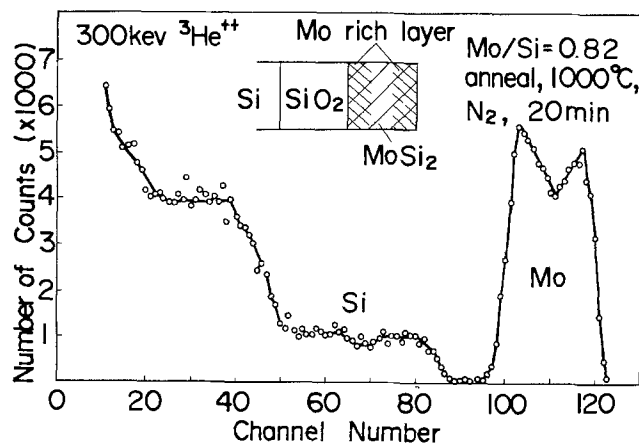


Fig. 8. Backscattering spectrum of the film on SiO₂ after annealing at 1000°C for 20 min in N₂. The Mo/Si ratio is 0.82.

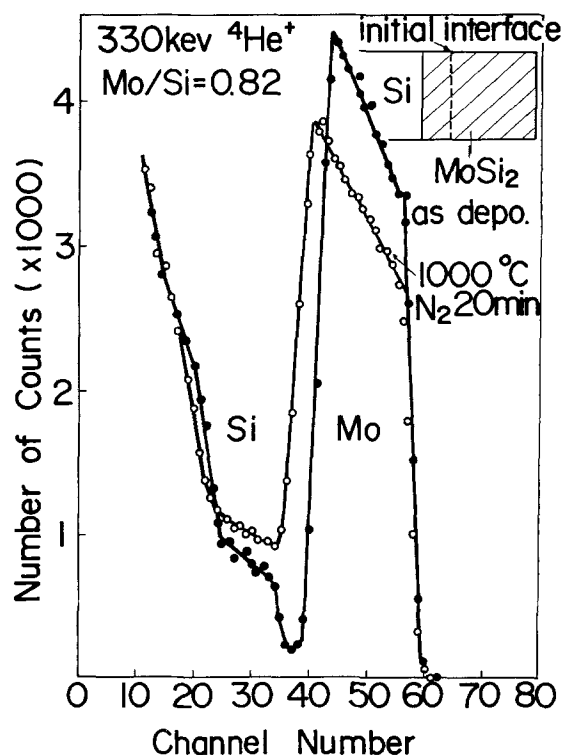


Fig. 9. Backscattering spectra of the film on Si before and after annealing at 1000°C for 20 min in N₂. The Mo/Si ratio is 0.82.

Behavior of Phosphorus in Molybdenum Silicide Films

The sputtering gas was analyzed by a mass analyzer. The mass spectra of the sputtering gas are shown in Fig. 10. Before sputtering, H₂O, P, PH₁, PH₂, PH₃, and Ar signals were observed in the atmosphere. During sputtering, P, PH, PH₂, and PH₃ signals disappeared, and the H₂ signal increased. Thus, it is clear that PH₃ gas decomposes into P and H₂, and the phosphorus is combined with Mo and Si during the deposit.

Phosphorus-doped molybdenum silicide films with various Mo/Si ratios were deposited on thermally grown SiO₂. The film thickness was about 3000Å. The phosphorus concentration was measured by neutron activation analysis (14). The doped silicide films on SiO₂, were irradiated for 6 hr in the center of a nuclear reactor at a flux of 3.7×10^{12} n/cm² · sec. Subsequently the phosphorus was chemically separated and then precipitated. The precipitate was β-counted several times during the next 30 days to determine the amount of radioactive P-32. The weight of phosphorus in the film was measured through this radioactive tracing process.

Figure 11 shows the relation between the phosphorus concentration in the as-deposited films and the Mo/Si ratio when the film was deposited by sputtering under PH₃ at 1.1×10^{-3} Torr. When the Mo/Si ratio is less than 0.5, the phosphorus concentration in the film is about 1.5×10^{21} cm⁻³. When the Mo/Si ratio is greater than 0.5, the phosphorus concentration decreases. These films were slightly crystallized as described in the previous section. The phosphorus concentration may be related to the crystallization of as-deposited films. When the total pressure was 6×10^{-3} Torr and the PH₃ partial pressure was below 1.1×10^{-3} Torr, the phosphorus concentration appeared to be proportional to the exponent of the PH₃ partial pressure as shown in Fig. 12.

The doped silicide films were annealed in O₂ and N₂ from 800° to 1000°C for 20 min. The phosphorus concentration in the film was measured by neutron activation analysis. Figure 13 shows the relation between the phosphorus concentration and the annealing temperature. When annealing above 900°C in N₂, the phosphorus concentration decreases to a level of 2.5×10^{18} cm⁻³ at 1000°C for 20 min. On the other hand, in O₂ annealing, the phosphorus concentration remained almost the same as before annealing. Moreover, when the doped silicide film covered with CVD SiO₂ of 2000Å was annealed in N₂, the phosphorus concentration was almost the same as before annealing. Therefore, thermal oxide film formed by O₂ annealing on the silicide prevents the out-diffusion of phosphorus from the doped film.

The chemical state of phosphorus was investigated by x-ray photoelectron spectroscopy (XPS).

Typical XPS spectra of phosphorus 2p core level in the doped silicide film is shown in Fig. 14. For comparison, XPS spectra of phosphorus in the doped molybdenum film, doped polysilicon film, and phosphorus evaporated film are also shown in Fig. 14. All spectra were calibrated by the carbon C_{1s} as a line at 285.0 eV. The doped molybdenum film was deposited on SiO₂ by sputtering with red phosphorus on the Mo targets. The

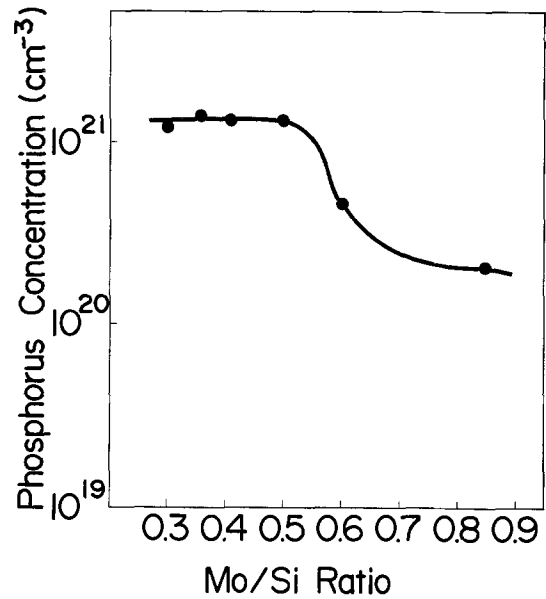


Fig. 11. Phosphorus concentration in the as-deposited films for various Mo/Si ratios.

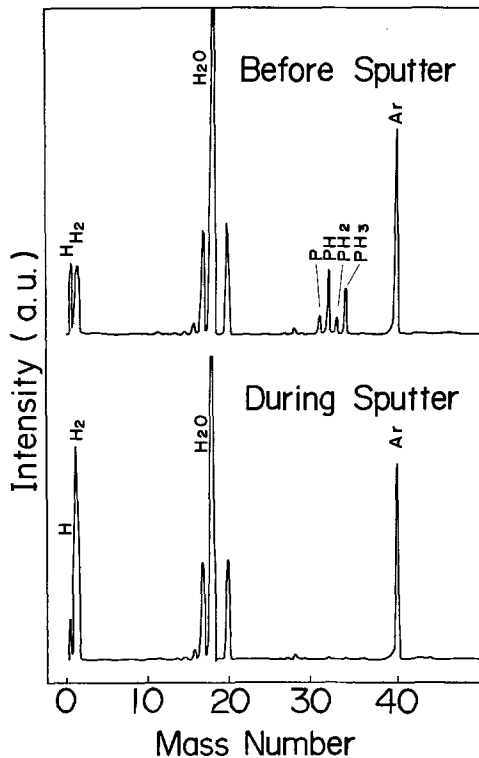


Fig. 10. Mass spectra in the sputtering gas before and during sputtering.

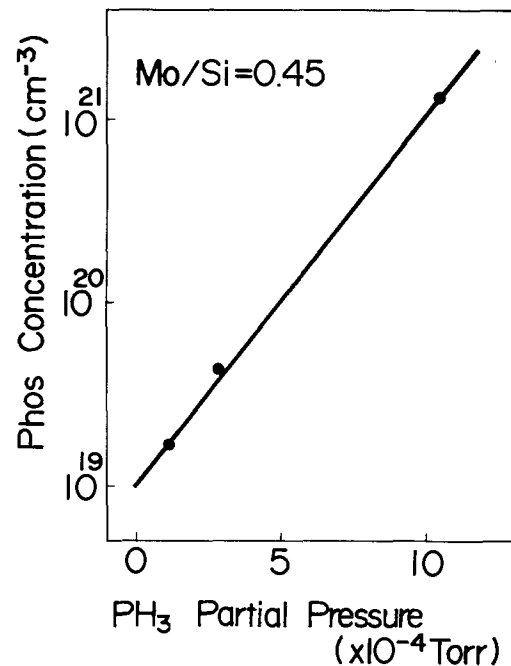


Fig. 12. Phosphorus concentration in the films as a function of the PH₃ partial pressure. The Mo/Si ratio is 0.45.

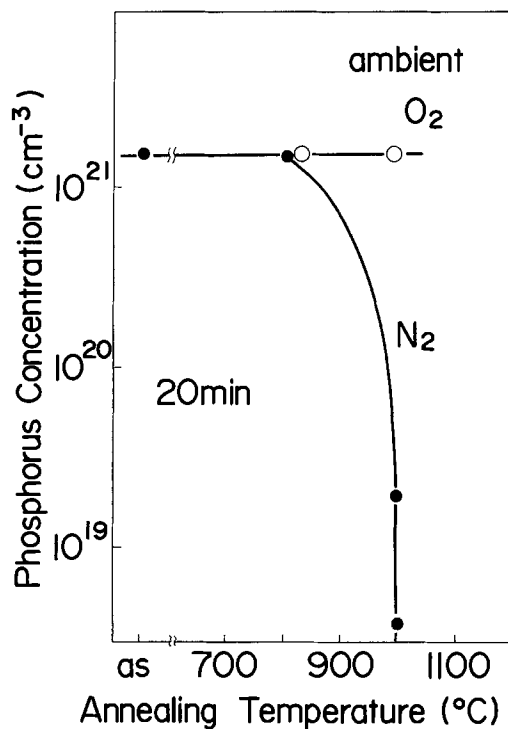


Fig. 13. Phosphorus concentration in the film after annealing in N_2 and O_2 .

doped polysilicon was deposited by CVD with PH_3 , SiH_4 , and N_2 gas at $700^\circ C$. The phosphorus film was evaporated on SiO_2 from a red phosphorus source with a tungsten heater. The phosphorus spectra in as-deposited silicide film has a peak at 129.5 eV (E_1), as shown in Fig. 14. The peak value of phosphorus 2p in

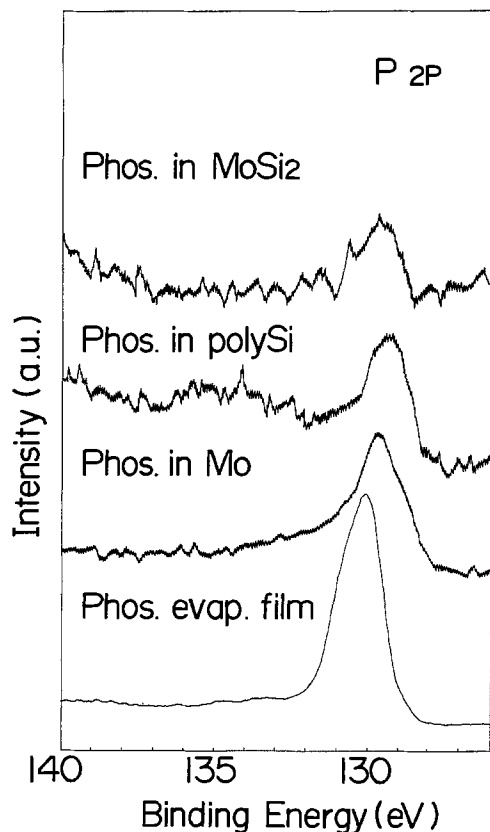


Fig. 14. X-ray photoelectron spectra of the phosphorus 2p electron core level in the doped molybdenum silicide film, doped polysilicon film, doped molybdenum film, and phosphorus evaporation film.

doped molybdenum film and doped polysilicon was observed to be the same. The peak value of phosphorus 2p in the evaporated phosphorus film is 130.1 eV (E_2), as shown in Fig. 14. This value is the same as that for red phosphorus as reported by Pelavin (15).

This chemical shift is not fully understood. The peak value of phosphorus in molybdenum film and in doped polysilicon is the same as in the doped silicide film, but is different from that of red phosphorus. Therefore, it is thought that the phosphorus in the film was incorporated interstitially, as in phosphorus implanted into SiO_2 (16).

Figure 15 shows the phosphorus 2p spectra of the film before and after annealing. The film was annealed at $1000^\circ C$ for 20 min in O_2 and was etched off the thermally grown SiO_2 on the silicide. The annealed film displays the two peaks such as E_1 (129.5 eV) and E_2 (130.1 eV).

The line shape of spectra E_2 is corresponding to red phosphorus. This indicates that some phosphorus in the film may be gathered at the grain boundary after high temperature annealing because the film was crystallized. Then the phosphorus formed the metallic state of red phosphorus. These two peaks are tentatively interpreted as due to the interstitial state (corresponding to E_1) and metallic state (corresponding to E_2) of phosphorus.

Phosphorus Diffusion into Si Substrate

Phosphorus-doped molybdenum silicide was deposited on p-type (100) Si and the diffusions were performed in O_2 at the nominal diffusion temperature. The thickness of the films was 3000 \AA , the Mo/Si ratio was 0.45 (Mo:Si = 1:2.2), and the phosphorus concentration was $1.5 \times 10^{21}\text{ cm}^{-3}$. The phosphorus concentration profiles were determined by the incremental sheet resistivity method using the anodic oxidation technique. The profiles for various diffusion times at $900^\circ C$ and various diffusion temperatures for 20 min are shown in Fig. 16 and 17, respectively.

These profiles are similar to those obtained from other diffusion sources such as doped polysilicon (17), or PSG. High surface concentrations are obtained with relatively low temperature diffusion. XPS and Auger analysis confirmed that sufficient phosphorus is always supplied at the silicide/Si interface and a high surface concentration is obtained. Therefore, this is a very attractive technique for fabricating MOS LSI's.

Ohmic Contact with Si Substrate

The major advantage of polysilicon gate technology is the excellent ohmic contact between the gate electrode and the Si substrate in a buried contact. The same advantage is required if silicide gate technology

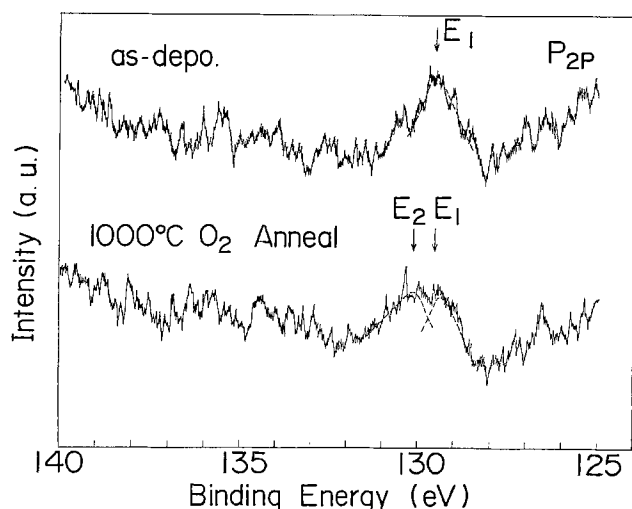


Fig. 15. X-ray photoelectron spectra of the phosphorus 2p electron core level in the films before and after annealing.

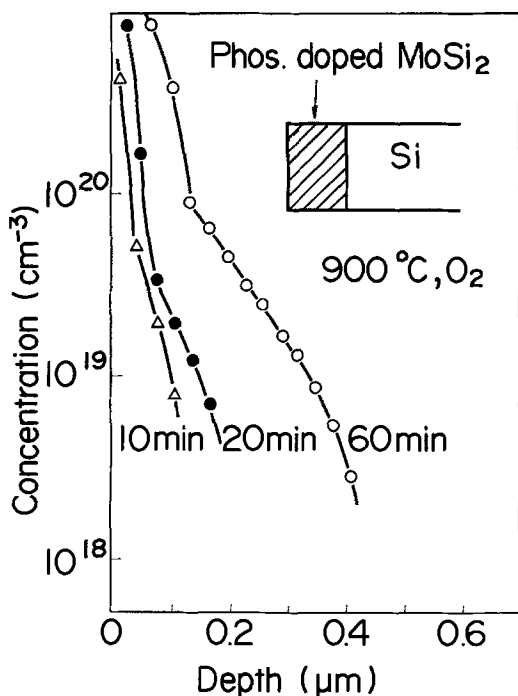


Fig. 16. Phosphorus depth profiles diffused from doped molybdenum silicide into Si substrate at 900°C for 10, 20, and 60 min in O_2 .

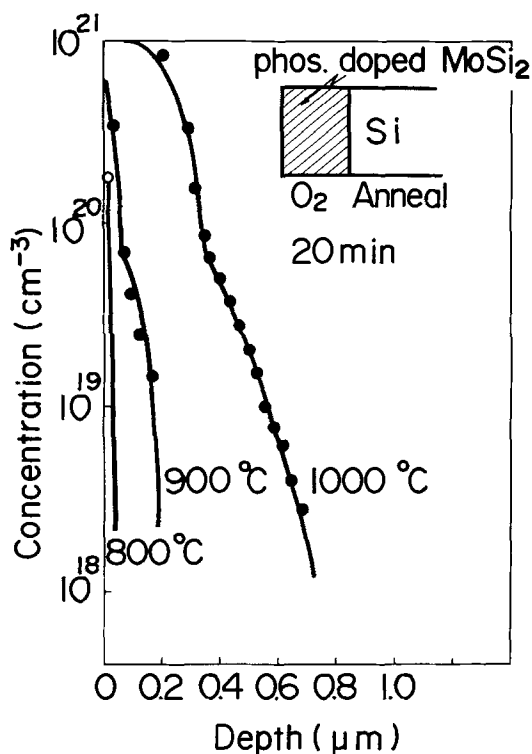


Fig. 17. Phosphorus depth profiles diffused from doped molybdenum silicide into Si substrate at 800°, 900°, and 1000°C for 20 min in O_2 .

is to replace polysilicon technology. However, the contact resistance between the molybdenum silicide and Si often becomes high due to a highly resistive layer formed during annealing at the silicide/Si interface (12) or related to film deposition and stress (13).

The measured contact resistance between the silicide and silicon n^+ layer is shown in Fig. 18 as a function of annealing temperature in O_2 . The Mo/Si ratio in the film was 1:2.0 ($MoSi_2$). The contact resistance was measured by a 1000 contact hole chain with a contact area of $4 \times 4 \mu m^2$. The contact resistance between

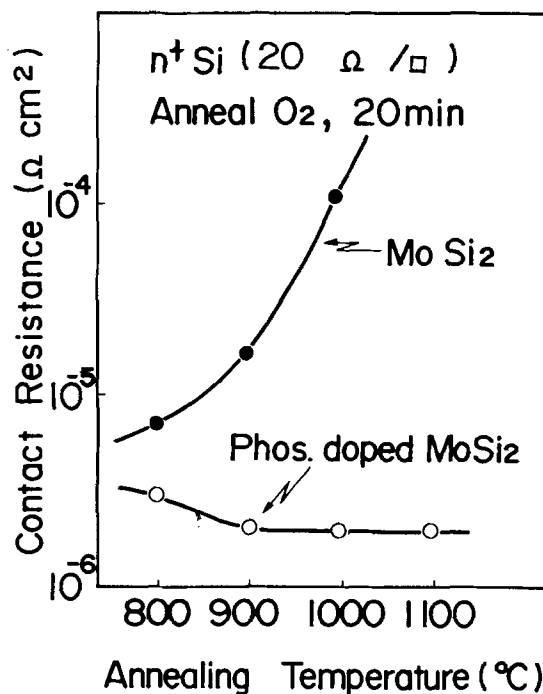


Fig. 18. Contact resistance between the molybdenum silicide and the n^+ Si after annealing for 20 min in O_2 .

nondoped silicide and the n^+ Si layer increased with higher annealing temperatures, while the contact resistance of the doped silicide and the n^+ Si layer was below $2 \times 10^{-6} \Omega\text{-cm}$, up to 1100°C. These results may be explained as follows. When the nondoped silicide/Si was annealed at high temperature, the donor impurity of the Si surface decreased and a highly resistive layer was formed at the silicide/Si interface. The presence of enough phosphorus in the doped silicide films prevented the formation of a high resistive layer, even after annealing at temperature up to 1100°C.

Resistivity

The effect of the Mo/Si ratio on film resistivity was evaluated. The resistivity of as-deposited films is quite high. As the annealing temperature increases, the resistivity decreased. The relation between the resistivity of annealed films and the Mo/Si ratio is shown in Fig. 19. The films were annealed for 20 min at 1000°C in N_2 . The resistivity decreases as the Mo/Si increases. The resistivity of $MoSi_2$ is $7.5 \times 10^{-5} \Omega\text{-cm}$. This value is lower than that of $MoSi_2$ obtained from hot press targets. Because hot press targets have a significant level of impurities such as carbon, oxygen, and alkali ions, its impurities raise the film resistivity (18, 19).

Phosphorus concentration had no influence on the resistivity of the films.

MOS Device Characteristics

V_{FB} dependence on the Mo/Si ratio.—Using various Mo/Si ratios for the gate electrodes, MOS diodes having a $5 \times 10^{-3} \text{ cm}^2$ gate area were fabricated on thermally oxidized p-type (100) Si, with $1 \times 10^{16} \text{ cm}^{-3}$ doping density. The gate oxide was 400Å thick and was grown in dry O_2 at 1000°C.

The samples were annealed at 1000°C in N_2 for 20 min to reduce the resistivity and to crystallize the film, and then annealed at 450°C in forming gas (5% H_2 , 95% N_2) for 30 min to minimize surface states.

Capacitance was measured as a function of gate voltage at a frequency of 1 MHz. The flatband voltage, V_{FB} , was measured from the C-V plot. The V_{FB} of the silicide gate is shown in Fig. 20 as a function of the Mo/Si ratio. The figure also shows the V_{FB} of the molybdenum and n^+ polysilicon gate. The V_{FB} of the MOS

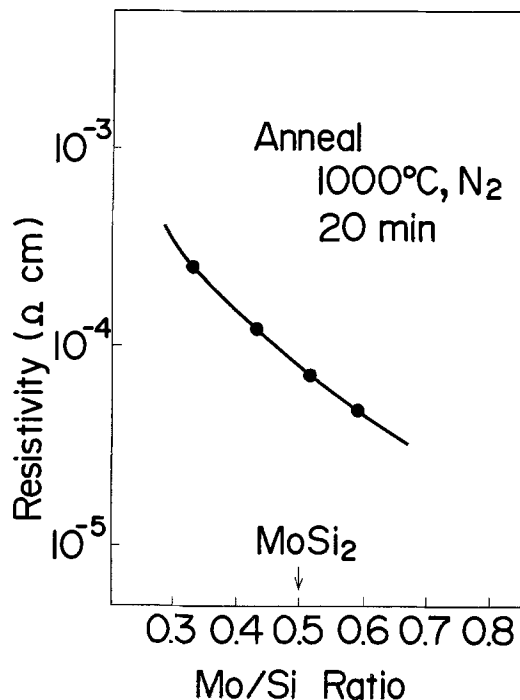


Fig. 19. Resistivity of the molybdenum silicide films as a function of the Mo/Si ratios. The films were deposited on SiO₂ and annealed for 20 min at 1000°C in N₂.

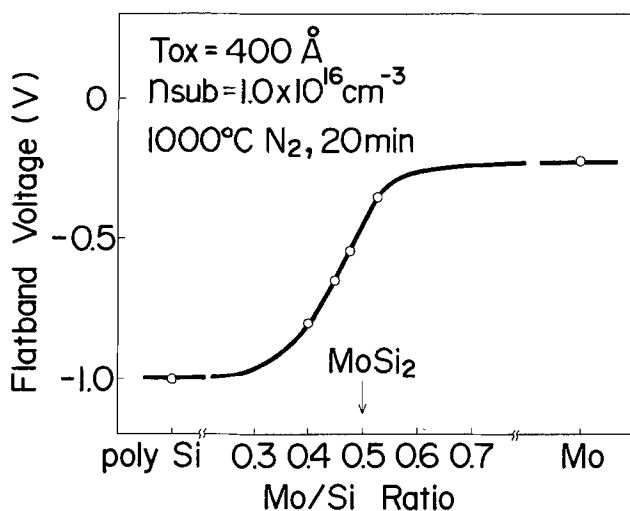


Fig. 20. Flatband voltage for various Mo/Si ratios after annealing for 20 min at 1000°C in N₂.

diode gradually increases from -1.0 to -0.2 V as the Mo/Si ratio increases. When the Mo/Si ratio decreases, the V_{FB} of the annealed silicide gate rises to the value for an n⁺ polysilicon gate. If the Mo/Si ratio increases, V_{FB} approaches the value for a molybdenum gate. The V_{FB} of the MoSi₂ gate is -0.45 V.

From measuring with the quasi static C-V method (20), the surface state density in the midgap was found to be below 3×10^{10} eV⁻¹ cm⁻² and was constant for various Mo/Si ratios. Further, the fixed charge in the oxide did not vary with different Mo/Si ratios. Thus, the V_{FB} shifts observed for the MOS diodes were mainly due to the difference of the effective work function for molybdenum silicide. As described in the previous section, the excess Si or Mo in the silicide films on the SiO₂ moves toward the silicide/SiO₂ interface and then forms an Si-rich or Mo-rich layer after high temperature annealing. It is confirmed that the effective work function of the silicide films is determined by the Mo/Si ratio at the silicide/SiO₂ inter-

face, however, this phenomenon is not completely understood.

Mobile ions.—Mobile ions in the gate oxide were measured by the triangular voltage sweep (TVS) method with a temperature of 230°C and voltage sweep velocity of 33 mV/sec (21). The mobile ion density as a function of annealing temperature for nondoped and phosphorus-doped silicide gates is given in Fig. 21. The Mo/Si ratio in this test was 1:2.

Mobile ion density was about 1×10^{11} cm⁻² in the nondoped silicide gates annealed below 900°C, and density decreased to 5×10^{10} cm⁻² after 1000°C annealing. Mobile ion density of doped silicide gates annealed above 900°C in O₂ were below the TVS sensitivity level ($<10^9$ cm⁻²). After high temperature annealing, phosphorus diffuses slightly from the doped silicide to the SiO₂ surface, and its oxide surface layer includes phosphorus and had a strong mobile ion gettering effect as in a phosphosilicate glass.

Reliability of MOSFET's.—MOSFET's were fabricated using doped silicide for the gate electrode. The Mo/Si ratio was 1:2 (MoSi₂), a 7 Ω-cm CZ p-type Si wafer was used as the substrate, and the gate oxide thickness was 400 Å. The doped silicide film of 3000 Å was deposited and patterned by plasma etching. Arsenic was ion-implanted in the source and drain regions, and CVD SiO₂ film of 8000 Å was deposited for surface passivation. The doped MoSi₂ was annealed at 1000°C for 20 min together with activation of the source and drain implanted layers. Aluminum-containing silicon was metallized through contact holes and annealed at 400°C for 10 min in forming gas.

The current-voltage characteristics of the MOSFET's are shown in Fig. 22. Effective channel length and width are (a) 20 and 100 μm, and (b) 2 and 19 μm, respectively. Threshold voltage, V_{th} , for long channel (20 μm) is 0.5 V and for short channel (2 μm) is 0.3 V. Size effect of V_{th} is observed for channel lengths smaller than 3.0 μm.

The V_{th} shifts of the MOSFET after bias and temperature stress (BT stress) are listed in Fig. 23, where + and - indicate the gate bias polarities with respect to source, drain, and substrate. The test MOSFET had a channel length of 20 μm and width of 100 μm. The electric field was ± 2.5 MV/cm and the temperature was 150°C. After \pm BT stress for 1000 hr, shifts of V_{th} were within ± 20 mV. Nonionic V_{th} shifts were not observed under these stress conditions. Effective electron mobility was 620 cm²/V·sec and had no influence before and after BT stress. This indicates that the phosphorus-doped MoSi₂ gate MOSFET is very stable, as in the polysilicon gate structure.

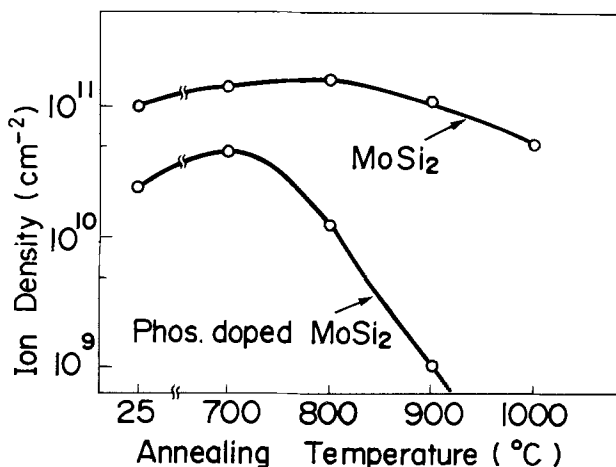


Fig. 21. Mobile ion density in the gate oxide films as a function of annealing temperatures.

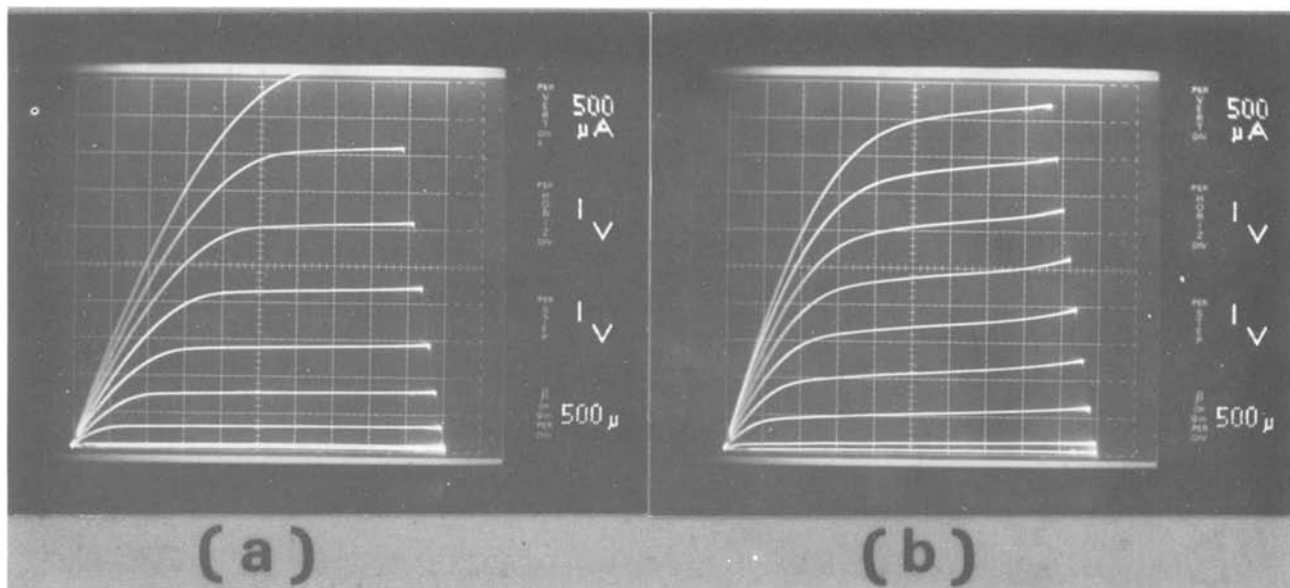


Fig. 22. Current-voltage characteristics of the phosphorus-doped molybdenum silicide gate MOSFET's. Effective channel length and width are (a) 20 and 100 μm , (b) 2 and 19 μm , respectively.

Conclusion

Phosphorus-doped molybdenum silicide was deposited by co-sputtering Mo and Si in Ar containing PH_3 . PH_3 was decomposed to P and H_2 , and the phosphorus combined with Mo and Si. As-deposited films ($\text{Mo/Si} \leq 0.5$) exhibited amorphous structure and the resistivity was high. At high annealing temperatures the films became polycrystalline and resistivity was decreased. After annealing at 1000°C for 20 min, the resistivity of film with a Mo/Si ratio of 1:2 was $7.5 \times 10^{-5} \Omega\text{-cm}$. This value is one order of magnitude lower than that of polysilicon. As the proportion of Si increases in the film, the resistivity also increases.

After high temperature annealing, the excess Si in Si-rich silicide film on SiO_2 and the excess Mo in Mo-rich silicide on SiO_2 move to the surface and the silicide interface both. At these locations, Si-rich or Mo-rich silicide layers were formed.

The silicide films on Si with various Mo/Si ratios are changed in composition to a MoSi_2 after high temperature annealing.

When the silicide is covered with SiO_2 , phosphorus can diffuse from the films into the Si substrate as in doped polysilicon, so the contact region need not be doped prior to gate electrode deposition.

Good ohmic contact between the phosphorus-doped molybdenum silicide and Si substrate is maintained because the phosphorus prevents the formation of a highly resistive layer at the silicide/Si interface during high temperature annealing. Contact resistance

was below $2 \times 10^{-6} \Omega\text{-cm}^2$ after annealing at temperatures up to 1100°C.

V_{th} shifts are within ± 20 mV under stress conditions of ± 2.5 MV/cm for 1000 hr at 150°C and mobile ions in the film were no longer detectable after annealing. The reliability of phosphorus-doped molybdenum silicide gate technology is comparable to polysilicon gate technology.

These important advantages make doped molybdenum silicide material technology a viable alternative to polysilicon in LSI fabrication.

Acknowledgments

The authors wish to thank Dr. T. Misugi, Dr. Y. Fukukawa, and H. Hashimoto for helpful discussion; S. Tatsuta for backscattering analysis; and M. Shiraki, T. Shinoki, T. Fukano, and H. Horie for help with measurement.

Manuscript submitted Nov. 14, 1980; revised manuscript received March 9, 1981.

Any discussion of this paper will appear in a Discussion Section to be published in the June 1982 JOURNAL. All discussions for the June 1982 Discussion Section should be submitted by Feb. 1, 1982.

Publication costs of this article were assisted by Fujitsu Laboratories Limited.

REFERENCES

1. D. M. Brown, W. E. Engler, M. Garfinkel, and P. V. Gray, *Solid-State Electron*, **11**, 1105 (1968).
2. A. K. Sima, T. E. Smith, T. T. Shange, and N. N. Axelrod, *J. Vac. Sci. Technol.*, **10**, 436 (1973).
3. M. Kondo, T. Mano, H. Yanagawa, H. Kikuchi, T. Amazawa, K. Kiuchi, and H. Yoshimura, *ISSCC Dig. Tech. Papers*, 158 (1978).
4. M. Koyanaki, T. Hayashida, N. Yamamoto, and H. Hashimoto, Abstract 153, p. 409, The Electrochemical Society Extended Abstracts, Boston, Massachusetts, May 6-11, 1979.
5. F. Yanagawa, K. Kiuchi, T. Hosoya, T. Tsuchiya, T. Amazawa, and T. Mano, *Tech. Dig. IEDM*, 362 (1979).
6. H. Ishikawa, M. Yamamoto, H. Tokunaga, N. Toyokura, F. Yanagawa, K. Kiuchi, and M. Kondo, *IEEE Trans. Electron Devices*, **ed-27**, 1586 (1980).
7. T. Mochizuki, K. Shibate, T. Inoue, and K. Ohuchi, *Jpn. J. Appl. Phys.*, **17**, Suppl. 17-1, 37 (1978).
8. B. L. Crowder and S. Zirinsky, *IEEE J. Solid-State Circuits*, **sc-14**, 291 (1979).
9. S. P. Muraka, *Tech. Dig. IEDM*, 454 (1979).
10. K. C. Saraswat, F. Mohammadi, and J. D. Meindl, *ibid.*, 462 (1979).

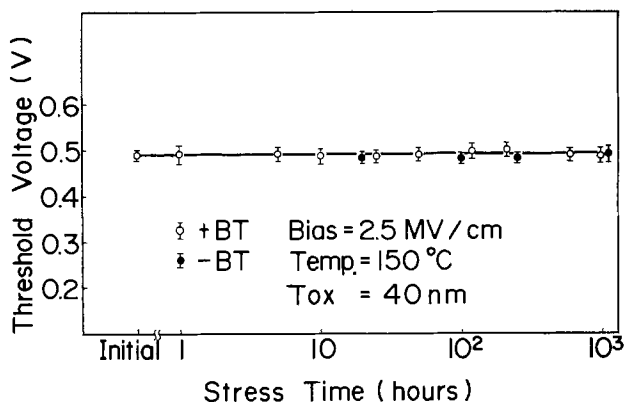


Fig. 23. Threshold voltage shifts of MOSFET's with effective channel length of 20 μm after bias and temperature stress.

11. T. P. Chow, A. J. Steckl, M. E. Motamedi, and D. M. Brown, *ibid.*, 458 (1979).
12. T. Mochizuki, M. Kashiwagi, and Y. Nishi, 700 RNP, *This Journal*, 126, 457C (1979).
13. P. Shah, D. Laks, and A. Wilson, *Tech. Dig. IEDM*, 465 (1979).
14. K. Chow and L. G. Garrison, *This Journal*, 124, 113 (1979).
15. M. Pelavin, D. N. Hendrickson, J. M. Hollander, and W. Ljolly, *J. Phys. Chem.*, 74, 1116 (1970).
16. A. Saxena, in "Proceedings of International Topical Conference on SiO₂ and Its Interface," p. 195, Pergamon, New York (1978).
17. M. Takagi, K. Nakamura, C. Terada, and H. Kamioka, *Jpn. J. Appl. Phys.*, Suppl. 101 (1973).
18. C. Koburger, M. Ishag, and H. Geipel, Abstract 162, p. 428, The Electrochemical Society Extended Abstracts, St. Louis, Missouri, May 11-16, 1980.
19. R. S. Nowicki and J. F. Moulder, Abstract 163, p. 431, The Electrochemical Society Extended Abstracts, St. Louis, Missouri, May 11-16, 1980.
20. M. Kuhn, *Solid-State Electron.*, 13, 873 (1970).
21. M. Yamin, *IEEE Trans. Electron Devices*, ed-13, 79 (1966).

Shaping of Bulk Semiconductor Samples by Photolithography and Chemical Etching

J. S. Blakemore, R. S. Mand,¹ and E. H. Wishnow

Oregon Graduate Center, Beaverton Oregon 97006

ABSTRACT

Semiconductor bulk samples, suitable for characterization of electronic properties, have been made by simultaneous deep patterned mesa etching from opposing faces of polished wafers. Outlines of the samples to be produced were delineated by areas of hard-baked photoresist on those faces, with mirror-image masks aligned for the two opposing faces. Sample outlines thus created included the well-known "bridge-shaped" and "clover-shaped" forms used for electrical characterization. The etching action was quenched when canyons etched from the two faces met, releasing individual sample shapes. An H₂SO₄/H₂O₂/H₂O etch was used in making GaAs samples, from polished wafers of (100), (110), (111), and (211) orientations; wafers of thickness in the range 0.2-0.5 mm could be used without excessive undercutting. Preliminary results are reported for silicon samples made by this method, using an HNO₃/HF/H₂O etch.

Numerous techniques have been developed for the characterization of (nominally homogeneously doped) bulk semiconductor materials (1). When the electrical resistivity is moderate (no more than a few hundred Ω cm), some basic properties of isotropic monocrystalline materials can be assessed with reasonable accuracy from measurements on a bulk ingot or sliced complete wafer, using contactless or temporary probe methods. However, many characterization methods require a bulk sample of specific size and shape. There are special problems associated with the interpretation of data for an anisotropic solid (2, 3), for material with inhomogeneous doping (4), or for a porous ceramic sample (5). However, the concern of the present work was simply to arrive at desired sample shapes for isotropic monocrystalline semiconductors, with a primary interest in semi-insulating GaAs.

Intricate sample shapes can be produced, in principle, by mechanical, chemical, and electrochemical methods of attack. For the high resistivity GaAs of interest to us, electrochemical attack by spark erosion cutting was not possible. This method has been used for highly conducting semiconductors (6), though is more traditionally thought of as a method for shaping metallic samples (7).

Mechanical shaping techniques include use of a diamond cut-off wheel, string saw, airborne abrasive particle stream, and ultrasonic impact cutter head. For semiconductors which do not cleave excessively readily (such as Ge and Si), complex sample shapes have been made in many laboratories using a liquid slurry of abrasive particles, directed by an ultrasonic tool with a "cookie-cutter" impact head (8). Since a thin GaAs

wafer is prone to cleavage on {110} planes, impact cutting is much less attractive for that material, if the desired sample shape is to include arms with narrow necks. We have been able to use mechanical methods for making bulk GaAs samples in simple shapes such as a filamentary one without sidearms; but attempts to use impact cutting for shapes with narrow sidearms had relatively poor success.

At that point, we were encouraged (by Dr. P. K. Bhattacharya) to attempt sample shaping by unusually deep mesa etching, using photolithographic delineation for the areas to be protected from etching. A shallower version of this is, of course, a common procedure for electrical isolation of a thin conducting layer on a semi-insulating substrate (9), or one separated from the underlying material by a p-n junction.

This paper reports on a procedure we have found satisfactory for making GaAs samples, with simultaneous mesa etching from the opposing faces of a wafer of thickness up to approximately 0.5 mm. The etching action produced an array of "canyons" into the two faces. The etching action was quenched when the canyons from the opposing faces met, an event signalled by the release of individual sample shapes.

Some samples have similarly been made of silicon, and Fig. 7 and 8 will show the appearance of these. Whereas the procedure for GaAs has become a routine in this laboratory, that for silicon is preliminary and not optimized.

Some Useful Sample Shapes

The simplest shape for measurements of the basic electronic transport parameters of a semiconductor (conductivity, Hall effect, etc.) is an elongated filamentary bar, of uniform cross section. If this cross section is rectangular, then the rectangular parallelepiped

¹Present address: School of Applied Physics, University of Bradford, Bradford, England.

Key words: sample shape, mesa etching, gallium arsenide, silicon.

shape can be simply made with a series of cuts by a diamond wheel or string saw. That shape was used in Pearson and Bardeen's 1948 investigation (10) of carrier transport in doped silicon, with electroplated areas on ends and sides for current contacts and potential probes.

It is advantageous to have potential contacts removed from the region of current flow. This led to the adoption of more intricate sample shapes, often cut by impact grinding (8) through a parallel-faced wafer. Among these shapes one of the most useful has been the "bridge-shaped" one; a filamentary bar with sidearms. Those sidearms were "dumb-bell" shapes as utilized and illustrated by Pearson and Suhl (11) and by Debye and Conwell (12). Such dumb-bell shapes can provide large areas for minimization of contact resistance, though are not necessary if the contacting procedure provides an adequately small specific contact resistance, in $\Omega\text{-cm}^2$.

Figure 1 illustrates a bridge-shaped sample we have made by the procedure of photolithography and chemical etching described in the present paper. The sample shape of Fig. 1 uses simple rectangular sidearms; the shape analyzed by Jandl *et al.* (13) as a "double-cross." Jandl *et al.* showed that relatively short rectangular arms could permit adequate isolation of the contact pad areas from the current flow in the main bar. Thus current density and electric field strength are essentially constant throughout the volume being analyzed, for a bridge-shaped or double-cross sample of semiconductor material which is isotropic and uniformly doped.

In contrast, some other geometries cause the equipotential surfaces to be markedly nonplanar, and unequally spaced. That is not a problem for some semiconductor materials, particularly if measurements are to be made exclusively of low field transport in the dark. However, some semiconductors are less tolerant of field nonuniformity, especially if high electric fields and/or a photoconductive response is to be involved.

The sample shapes most commonly used for which the field pattern is markedly nonuniform are based on the theorem of van der Pauw (14, 15) for the resistance of a flat sample with peripheral contacts. These shapes include the simple rectangular slab with corner contacts (16), the "Greek cross" (17), and the "clover" shape² that van der Pauw proposed and illustrated

²This shape has attracted many names in the ensuing literature, including "iron cross," "papal cross," "Maltese cross," and others.

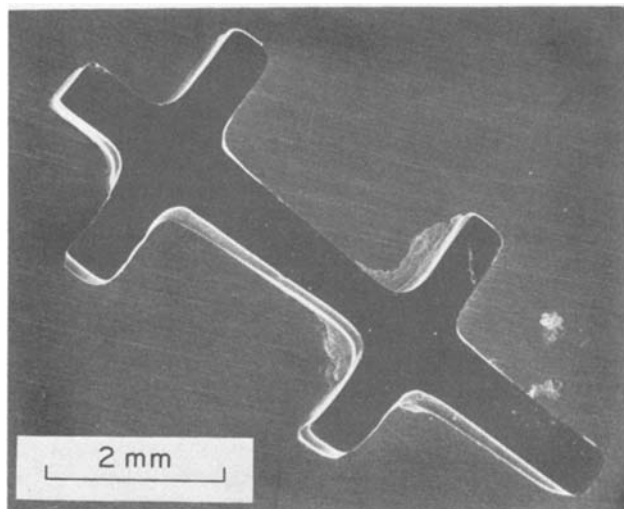


Fig. 1. A bridge-shaped sample of chromium-doped semi-insulating GaAs, created from a polished 0.45 mm thick wafer of (211) orientation, by etching inwards from both faces while the designated sample area was protected by photoresist. Etching was carried out in $(2)\text{H}_2\text{SO}_4\text{-(1)H}_2\text{O}_2\text{-(1)H}_2\text{O}$ at 80°C.

(14, 15). Figure 2 illustrates a clover-shaped sample of GaAs, made by the method described in the present paper, and prior to the evaporation of Au:Ge contact areas in the outer corners.

Experimental Procedures for GaAs Samples

As noted in the introduction, the procedure we evolved consisted of removal of unwanted bulk material surrounding designated sample outlines by chemical etching, this action proceeding from both faces of a wafer simultaneously. Meanwhile, the sample areas themselves were protected with hard-baked photoresist. This section describes the procedure as evolved for making GaAs bulk samples of satisfactory outline shape and profile.

Many factors determine the outcome when parts of a semiconductor wafer are protected by photoresist, and adjacent unprotected portions are chemically etched. Thus, etching may be carried out in a plasma chamber, or in a liquid. Our work as reported here used aqueous etches.

The etching rate in aqueous solution depends on the strength and freshness of the ingredients, on the solution temperature, and often on crystal orientation (18, 19). Highly preferential etching can sometimes be turned to advantage; thus, Otsubo *et al.* (20) used citric acid/peroxide etches into {100} GaAs to create flat-bottomed holes, and grooves of "tsuzumi" (hand-drum) profile. [An even more dramatic anisotropy of the etching rate has been demonstrated in the work of Kendall (21) with {110} silicon, using KOH-based etches to make deep narrow grooves.] However, our preference was for an etch that would work with more or less facility for GaAs wafers of various orientations.

The etch composition and strength that we have found particularly useful for the present purpose with GaAs of various orientations has been $(2)\text{H}_2\text{SO}_4\text{-(1)H}_2\text{O}_2\text{-(1)H}_2\text{O}$, used in the temperature range 70°-80°C. Iida and Ito (22) showed that the $\text{H}_2\text{SO}_4/\text{H}_2\text{O}_2/\text{H}_2\text{O}$ system includes some compositions that are highly selective, but found that the above-mentioned composition gave good polishing action for most low index planes of GaAs with, of course, an inferior response for the gallium (111A) plane. This has been our experience also. When the above-cited etch composition is used at 80°C for a (111) GaAs wafer, the attack rate on the (111A) plane is only about 30% slower than on

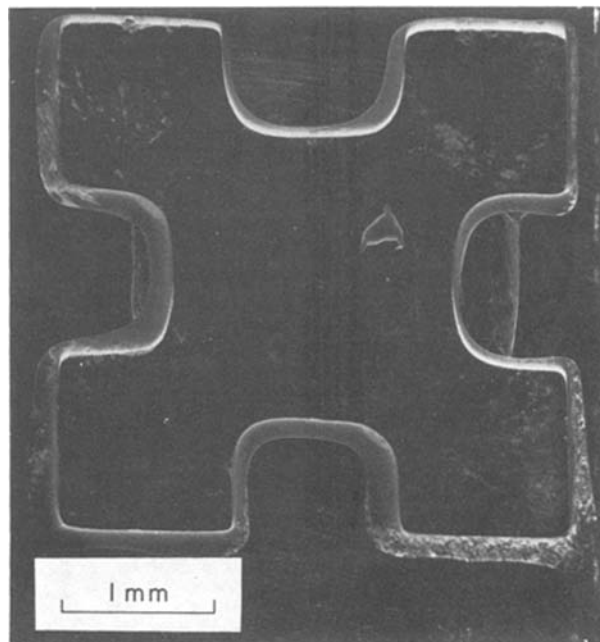


Fig. 2. A clover-shaped sample of semi-insulating GaAs, made by the same method as the sample of Fig. 1. The polished starting wafer here was of (100) orientation, 0.53 mm thick.

the (111B) plane ($7 \mu\text{m}$ per min, compared with $10 \mu\text{m}$ per min), but microscopic examination of a partly consumed wafer shows the attacked (111A) surface to be much more pitted than the opposite face.

Figure 3 illustrates the effect of various etching times on the total thickness reduction of wafers with orientations of (100), (110), (111), and (211), determined from microscopic measurement of the decrease of distance between bottoms of opposing etched canyons. These measurements, the consequences of using the above-cited etch at 80°C , correspond to an etching rate of some $(10 \pm 1) \mu\text{m}/\text{min}$ for fresh etch acting on a GaAs surface with any orientation other than (111A). That rate, and the reduction of some 30% for (111A), is in general agreement with the findings of Iida and Ito (22) for etching rate vs. composition, orientation, and temperature. Figure 3, and similar results obtained with other wafers, shows no signs of any pre-etching induction period. Provided the etching solution is freshly prepared, and of large enough quantity so that reaction products do not slow the action, then etching reduces thickness at an essentially linear rate until sample separation occurs. For a wafer 0.5 mm thick, this requires about 25 min for most orientations, and perhaps 28–30 min for a {111} wafer.

The wording of the preceding paragraph was chosen to indicate that reliable etching at a constant rate was obtained when the etch (i) was used fresh, and (ii) was of volume sufficient to minimize the effects of dissolved etching products on the continuation of the process. Thus, for a part-wafer of area 5 cm^2 and thickness 0.5 mm , one may need to etch away about 0.75 g of GaAs to separate out individual samples. It would be our practice not to attempt this with less than 100 ml of mixed etch, with vigorous stirring of the etch throughout to minimize the buildup of etch products near the surfaces under attack.

Since the procedure required that a wafer remain in the etch for a time of up to half an hour at a temperature of $70^\circ\text{--}80^\circ\text{C}$, it was extremely important that the photoresist over designated sample areas adhere as strongly as possible. That called for some changes from the photoresist procedures normally encountered in

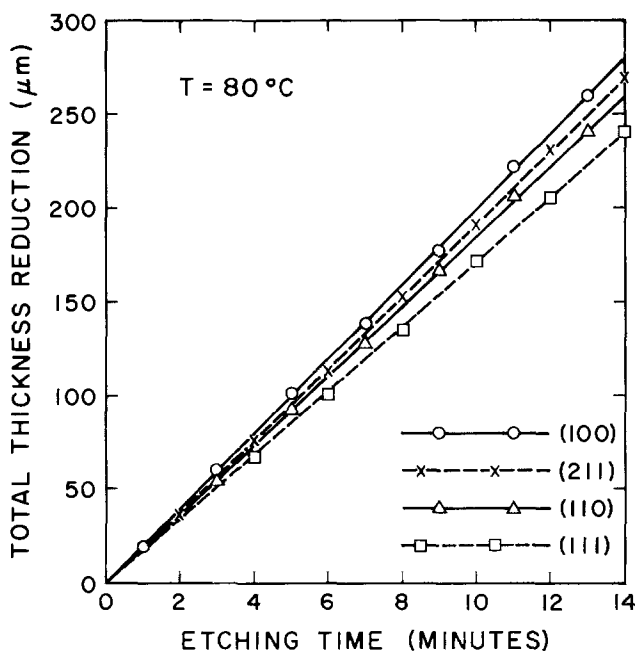


Fig. 3. Total reduction in wafer thickness (sum of amounts thinned from opposing sides) vs. etching time, for GaAs in $(2)\text{H}_2\text{SO}_4\text{--}(1)\text{H}_2\text{O}_2\text{--}(1)\text{H}_2\text{O}$ at 80°C . These are representative data for wafers etched in large quantities of the etchant, with ample stirring, so that effects of etchant exhaustion and/or poisoning were minimized. The results for (100), (110), and (211) are all essentially the same. The total thinning rate is smaller for (111) wafers because of the slower attack rate for the (111A) face.

the integrated circuit industry, where etch depths are typically no more than a few micrometers, and etch durations quite short.

Our objectives of etching completely through wafers up to a considerable thickness also placed requirements on the layout of any sample shape on the mask, that this allow for inevitable undercutting. Resist adhesion and undercutting are related, since any tendency of the resist to "lift off" around the edges will open up new territory for undercutting.

Figure 4 shows part of a (211) GaAs wafer bearing a repetitive array of hardened photoresist areas (each of the van der Pauw clover shape) after etching for 1 min. The unprotected areas have been etched to a depth of some $10 \mu\text{m}$. It will be observed that the resist has curled up from one corner, and is showing signs of doing so at two adjacent corners. That lack of adherence is unacceptable in view of the 20 or more minutes of additional etching time that would be necessary to complete separation of samples from each other.

The results of etching a wafer for a longer period of time are exemplified by the almost edge-on view shown in Fig. 5. The wafer here was of (100) orientation, patterned on both faces with photoresist, etched at 80°C for 7 min, and cleaved to permit study of the profiles of the canyons etched from the opposing faces. Note in Fig. 5 that (i) overhanging ledges of photoresist jut out above the canyon walls, (ii) the canyon

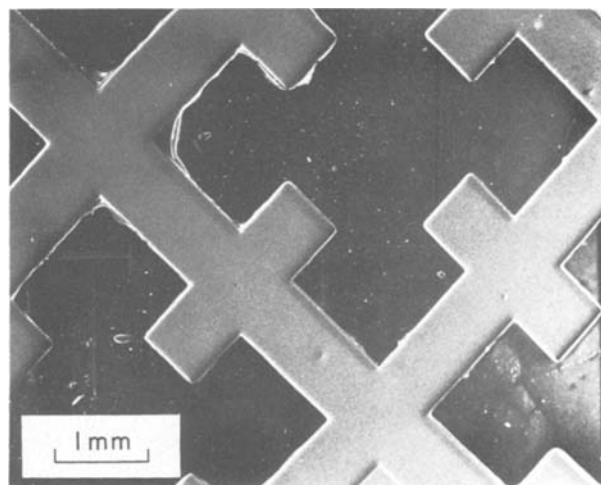


Fig. 4. Part of a repetitive pattern for making clover-shaped samples, as formed into hardened resist areas on the surface of a (211) GaAs wafer. One minute in the $\text{H}_2\text{SO}_4/\text{H}_2\text{O}_2/\text{H}_2\text{O}$ etch has removed some $10 \mu\text{m}$ of material from the unprotected areas. Note that poor adherence of the photoresist for this wafer has already led to curling back from some outer corners.

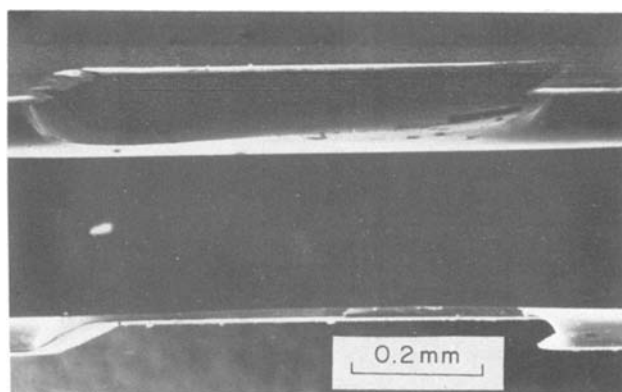


Fig. 5. An edge-on view of a $400 \mu\text{m}$ thick (100) GaAs wafer, which had been (a) patterned with hardened resist so that resist edges would lie along $\langle 011 \rangle$ directions, (b) etched at 80°C for 7 min, and then (c) cleaved to permit the edge-on view.

floors are essentially flat and parallel, and (iii) the canyon walls curve in a manner appropriate for complete nonselectivity of etching action. Somewhat to our surprise, we have found the canyon wall shapes to curve in essentially the same fashion for any (100) wafer (whether the edges of the resist are aligned with $\langle 010 \rangle$ or $\langle 011 \rangle$ types of orientation), and also for wafers of other orientations including (111).

The literature provides ample citations for etch pits produced in GaAs [and other zincblende structure solids such as InSb (23)] which show marked facets of preferential etching. Thus Iida and Ito (22) showed that slow action of an $\text{H}_2\text{SO}_4/\text{H}_2\text{O}_2/\text{H}_2\text{O}$ etch on (100) could produce a flat-bottomed pit of trapezoidal cross section (overhanging canyon walls) when the edge of the resist-protected area was parallel to $\langle 010 \rangle$ or $\langle 001 \rangle$. We have not observed this to happen with the relatively speedy etching action of the 2:1:1 composition at 80°C. With any orientation of the wafer and any alignment of the mask pattern, the canyon wall shows a curved profile such as that in Fig. 5. Incidentally, that figure shows undercutting to have proceeded by some 40 μm at a stage when the canyon floor lies some 75 μm below the original wafer surface plane.

Through the courtesy of M. Pope and M. Wright, photographic masks were made for us through which photoresist could be exposed. These masks had repetitive patterns for sample shapes (such as bridge-shape and clover-shape). It was necessary to have pairs of masks which were mirror images of each other, so that a matched pair placed to sandwich a prepared wafer would register the same pattern on both surfaces of that wafer. A simple mechanical fixture was constructed which enabled the pair of masks to be aligned with respect to each other, in respect of x , y , and θ .

Mask pairs of these kinds were made with opaque/transparent patternings suitable for use with positive resist, and additional pairs of the converse opacity for use with negative resist. Our first crude attempts at sample separation were made using a negative resist³ on the wafer faces, and were (not surprisingly) accompanied by frequent failures owing to resist detachment during the lengthy etching. There can be little doubt that the procedure can be made to work perfectly well with negative resist applied and baked properly; but we have not persisted with this approach. For since it happened that we were successful rather soon in persuading positive resist⁴ to stay in place until etching was complete, all our subsequent work has been based on the positive resist approach. Thus, for this we have been using masks with opaque areas where designated sample areas are to be protected from the etching action.

Photoresist as used in the integrated circuit industry is applied typically by spinning, with a resist layer thickness of perhaps 1 μm , and an emphasis on the ability to create narrow linewidths (24). Our requirements were quite different. High spatial resolution was not important, but a tenacious and adherent resist layer on both faces was very important. These requirements were met most readily by dip coating of suitably prepared wafers, at a temperature ($T \approx 20^\circ\text{C}$) and viscosity that would provide a hardened film thickness in the range 12-17 μm .

Our wafer preparation now requires that both faces of the wafer be polished. That admittedly involves extra work, but we have found that undercutting progresses more slowly under photoresist that is firmly adherent to a polished face.

Thus the procedure as it has evolved comprises mechanical polishing of both faces, degreasing, baking dry at 90°C, cooling to room temperature, photoresist application by dip coating, a 1 hr "soft bake" at 90°C, cooling to 25°C, exposure to u.v. radiation through a

matched pair of facing masks, development in diluted (Shipley AZ-351) resist developer, water rinse, air dry, and then a 2 hr "hard bake" at 160°C. When cooled for handling, the wafer is then ready for etching.

Two physical arrangements have been used for etching. In one of these, the wafer (and its eventual daughter samples) is supported above a glass frit in the etching solution, while bubbled nitrogen gas is supplied from below to provide agitation. The other arrangement uses a magnetic stirrer within the beaker of etch on a hotplate. (The latter arrangement simplifies positive control of the temperature.) The clover-shaped sample of Fig. 2 happened to have been made using the first of these systems, while the bridge-shaped sample of Fig. 1 was made using the magnetic stirring system.

The clover-shaped sample of Fig. 2 came from a wafer 0.53 mm thick. Thus one might expect the periphery of the top and bottom sample surfaces to retreat by some 200-250 μm if etching and undercutting were completely isotropic. A comparison of this sample with mask dimensions shows that the upper periphery has actually been cut back by (215 ± 10) μm . However, Fig. 6 shows a magnified edge-on view of one corner of this sample, and one may see that the cusped profile protrudes by only ~ 100 μm . This was obtained by allowing the etching to continue for some 30 sec after the first sample was seen to "calve" from the parent wafer. Now such a sample would normally have the resist stripped from top and bottom faces (with acetone and/or Shipley 1112A "photoresist stripper"), and then be etched over its entire surface prior to contacting, in order to remove the mechanical damage associated with the prior polishing procedures. That additional etching would further reduce the peripheral protuberance before the sample was ready for electrical measurements.

A clover-shaped sample with a protuberant profile as just described and illustrated is in technical violation of a requirement of van der Pauw's theorem (14, 15), that a sample be of constant thickness over its entire current-bearing area. However, a protuberance of the size described appears to involve an error in the analysis of van der Pauw resistivity and Hall measurements of less than 3% by direct measurement; an error in the (expected) sense of making the resistivity (using van der Pauw's expression) appear slightly low. That estimate of the error involved was obtained by first measuring a sample as resulting from

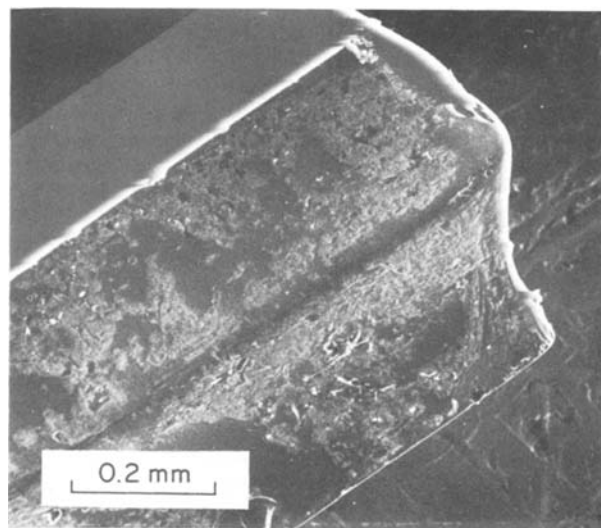


Fig. 6. A magnified edge-on view of one corner of the clover-shaped sample of Fig. 2. This shows details of the edge profile resulting from undercutting prior to sample separation, and the partial rounding off of this cusped protuberance during an additional 30 sec of etching after separation.

³ MOS-Grade Negative Photoresist, available from KTI Chemicals, of Sunnyvale, California.

⁴ AZ-1350J Positive Resist, available from the Shipley Company, of Newton, Massachusetts.

the photolithography/etching process, and then using an abrasive particle stream to "trim up" the re-entrant portions of the sample periphery.

The GaAs bridge-shaped sample of Fig. 1 shows similar imperfections of profile. In that case, these would be enough to require that the usual conversion [$\sigma = (L/wt)(I/V)$] from resistance to bulk conductivity be modified to take account of the slightly non-rectangular cross section of the bar. Whereas the bridge sample of Fig. 1 has a thickness $t = 0.45$ mm, we have usually resorted to thinner wafers when the desire was for Hall data with GaAs bridges of more nearly perfect geometry. Of course, a sample shape and profile such as that of Fig. 1 is perfectly adequate for photoconductive or various relative measurements.

Thus, for most of our purposes in measuring GaAs of resistivity up to the semi-insulating range, the procedure as described above needs little further optimization.

Preliminary Results with Silicon Samples

A procedure for making silicon samples by simultaneous etching from both sides of a masked wafer has not been tested by us so far beyond the stage of crude feasibility. Results we obtained show that the etch we used, of (2)HNO₃-(2)HF-(1)H₂O composition (25), was not ideal for this purpose.

Figure 7 shows a clover-shaped silicon sample, made from a (100) wafer that had been polished on both faces, equipped with patterned photoresist as described in the previous section, and etched in the HNO₃/HF/H₂O solution until individual samples separated. With the etch brought to a temperature of 30°C prior to the introduction of the wafer, separation of individual samples from a wafer ~0.4 mm thick would occur in approximately 3 min. As is well known (19, 25), this is a fast-acting etch.

It will be apparent from Fig. 7 that the periphery of this sample (of 0.37 mm thickness) was undercut much more severely than for the GaAs samples previously illustrated. The extent of the undercutting is shown clearly in the enlarged edge-on view Fig. 8 provides of one corner of that sample. In this instance, etching action was quenched with water as soon as possible after the release of individual samples was spotted, thus the cusp tip was not appreciably eroded. However, note also in Fig. 8 that the edge of the sample blends toward the upper and lower surface faces in convex arcs. This shows that the etching action had preferentially attacked the wafer/photoresist interface.

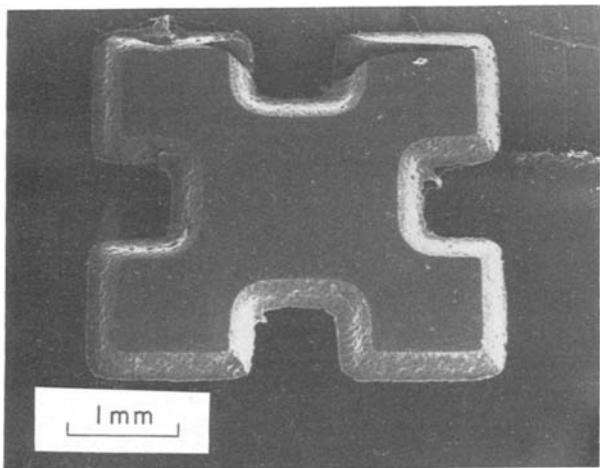


Fig. 7. A silicon clover-shaped sample, made by photomasking and chemical etching of a polished (100) wafer 370 μm thick. Etching was carried out in (2)HNO₃-(2)HF-(1)H₂O at $T \approx 30^\circ\text{C}$, and sample separation occurred (with severe undercutting as may be seen) after etching from both faces simultaneously for 150 sec.

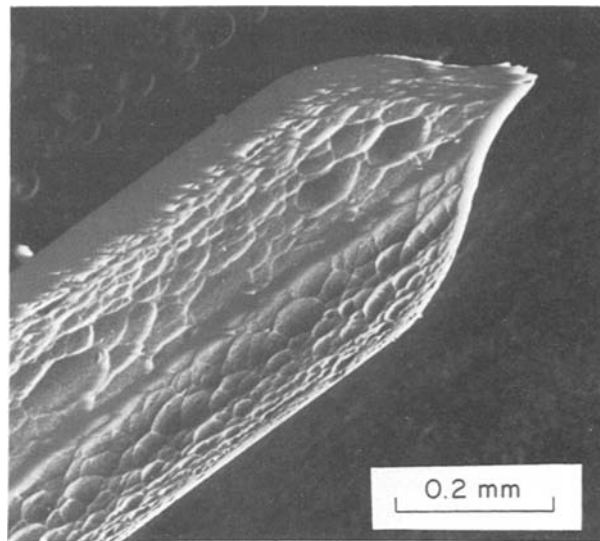


Fig. 8. An enlarged edge-on view of one corner of the silicon sample of Fig. 7. The convex curvature of the edge surface adjacent to the top and bottom faces indicates that the etch had preferentially attacked the (SiO₂-rich) silicon surface under the edge of the resist layer.

That preferential attack is inherent in the mechanism by which an etch of the HNO₃/HF/H₂O family attacks silicon (19, 25), because the inevitable SiO₂ layer on the silicon surface is attacked by HF, the complexant in the mixture. That promotes undercutting, and lift-off of the photoresist shapes. When we have attempted to make silicon samples, but with the etch solution cooled, to slow down the reaction rate, the photoresist has always lifted off before the canyons from the two faces have had an opportunity to meet.

Thus one can envisage preferable etching approaches for making silicon samples. One possibility is that the wafer might first receive a quick dip in HF (to remove SiO₂ from the exposed areas), then be rinsed, and placed for an extended period in an etch (such as an alkaline one) that has a preference for dissolution of Si itself rather than SiO₂.

Acknowledgments

We wish to thank Morgan Pope and Mel Wright of Tektronix, Incorporated, for their splendid cooperation in making masks patterned to meet our various needs. We should also like to thank Pallab Bhattacharya and Robert Rugh for helpful discussions. This work has been supported in part by the National Science Foundation, through Grant DMR 79-16454.

Manuscript submitted Dec. 18, 1980; revised manuscript received May 7, 1981.

Any discussion of this paper will appear in a Discussion Section to be published in the June 1982 JOURNAL. All discussions for the June 1982 Discussion Section should be submitted by Feb. 1, 1982.

Publication costs of this article were assisted by the Oregon Graduate Center.

REFERENCES

1. See, for example, W. R. Runyan, "Semiconductor Measurements and Instrumentation," Chap. 3, Texas Instruments, Inc., Dallas, TX (1975).
2. L. J. van der Pauw, *Philips Res. Rep.*, **16**, 187 (1961).
3. H. C. Montgomery, *J. Appl. Phys.*, **42**, 2971 (1971).
4. See, for example, R. T. Bate, in "Semiconductors and Semimetals, Vol. 4," R. K. Willardson and A. C. Beer, Editors, p. 459, Academic Press, New York (1968); also, J. S. Blakemore, *J. Appl. Phys.*, **52**, 840 (1981).
5. H. J. Juretschke, R. Landauer, and J. A. Swanson, *ibid.*, **27**, 838 (1956).

6. B. I. Stavitsky, *Elektron. Obra. Mater.*, **4**, 3 (1969).
7. R. H. Packwood and R. W. Smith, *J. Sci. Instrum.*, **44**, 1057 (1967).
8. W. L. Bond, *Phys. Rev.*, **78**, 646 (1950).
9. C. M. Wolfe, G. E. Stillman, and E. B. Owens, *This Journal*, **117**, 129 (1970).
10. G. L. Pearson and J. Bardeen, *Phys. Rev.*, **75**, 865 (1949).
11. G. L. Pearson and H. Suhl, *ibid.*, **83**, 768 (1951).
12. P. P. Debye and E. M. Conwell, *ibid.*, **93**, 693 (1954).
13. S. Jandl, K. D. Usadel, and G. Fischer, *Rev. Sci. Instrum.*, **45**, 1479 (1974).
14. L. J. van der Pauw, *Philips Res. Rep.*, **13**, 1 (1958).
15. L. J. van der Pauw, *Philips Tech. Rev.*, **20**, 220 (1958).
16. R. Chwang, B. J. Smith, and C. R. Crowell, *Solid-State Electron.*, **17**, 1217 (1974).
17. W. Versnel, *ibid.*, **22**, 911 (1979).
18. B. Tuck, *J. Mater. Sci.*, **10**, 321 (1975).
19. W. Kern, *RCA Rev.*, **39**, 278 (1978).
20. M. Otsubo, T. Oda, H. Kumabe, and H. Miki, *This Journal*, **123**, 676 (1976).
21. D. L. Kendall, *Appl. Phys. Lett.*, **26**, 195 (1975).
22. S. Iida and K. Ito, *This Journal*, **118**, 768 (1971).
23. H. C. Gatos and M. C. Lavine, *This Journal*, **107**, 433 (1960).
24. See, for example, A. B. Glaser and G. E. Subak-Sharpe, "Integrated Circuit Engineering," Section 5.10, Addison-Wesley, Reading, MA (1977).
25. H. Robbins and B. Schwartz, *This Journal*, **106**, 1020 (1959); B. Schwartz and H. Robbins, *ibid.*, **123**, 1903 (1976).

Parameter Dependence of RIE Induced Radiation Damage in Silicon Dioxide

L. M. Ephrath,* D. J. DiMaria, and F. L. Pesavento

IBM T. J. Watson Research Center, Yorktown Heights, New York 10598

ABSTRACT

Radiation damage in silicon dioxide films exposed to reactive ion etching (RIE) in CF_4 has been investigated. Capacitance-voltage ((C-V) and photo-current-voltage (photo I-V) techniques were used to monitor charge trapping and location after the films were incorporated into MOS capacitors. Blanket etched films were used to study the trapping characteristics of bulk, neutral, radiation-induced traps as a function of position in the reactor, rf peak-to-peak voltage, and pre-RIE high temperature annealing. The trapping characteristics of films etched in a $\text{CF}_4 + \text{H}_2$ mixture were also studied. Oxide films etched in $\text{CF}_4 + \text{H}_2$ show reduced trapping when compared with oxides etched in CF_4 . The ability of gate electrode materials to shield an underlying oxide during RIE was also tested. It was determined that aluminum and n^+ polysilicon are effective in shielding oxide from RIE induced radiation damage.

Reactive ion etching (RIE) is a directional, dry etching technique that has been used in our laboratory to fabricate micron dimension FET logic and array chips (1, 2). RIE is used at several levels of processing including definition of recessed oxide isolation, polysilicon gate electrodes, and contact holes to polysilicon and diffused regions. Extensive use of RIE is required for the delineation of fine lines and openings with no undercut of the etch mask. RIE is, however, carried out in a radiation environment; substrates are subjected to bombardment by electrons, ions, and photons. For this reason, experiments have been carried out to determine the effect of RIE on the reliability of devices. RIE induced trapping was characterized by exposing a blanket oxide film to RIE, incorporating the etched oxide into an MOS device, and injecting charge into the conduction band of the oxide by avalanche injection. The numbers and cross sections of the traps, the density of trapped charge, and the centroid of the trapped charge distribution were determined by C-V and photo I-V techniques (3). Three distinct trapping sites were observed (4). The first was a buildup of positive charge at the silicon-silicon dioxide interface. These positive trapped charges present a coulombic capture cross section for electrons in the range of 10^{-12} and 10^{-13} cm^2 and have a density of about 10^{12} positive charges/ cm^2 . These trapped positive charges are believed to be holes which were generated initially by ionization across the bandgap of the oxide. Some of the free positive charges in the silicon dioxide valence band are subsequently trapped at pre-existing sites

near the interfaces. The second type of trapping site is created by ion implantation damage within about 5 nm of the surface. These traps are observed only when a nonetching gas such as O_2 is used to clean the surface. Presumably, an etching gas such as CF_4 removes its damage as it is produced leaving only a residual when etching is stopped. The third type of trap is a neutral trapping center. These sites are distributed approximately uniformly throughout the bulk of the oxide. The electronic capture cross sections of these traps are between 10^{-14} and 10^{-17} cm^2 and their density is between 10^{11} and 10^{12} cm^{-2} . These traps are very similar to those observed by Aitken, Young, Pan, and Ning (5-7) for oxides exposed to much higher energy radiation than in the present case (20-25 keV x-rays or electrons). In the comparatively low energy environment of RIE, the occurrence of trapping in the bulk suggests, by process of elimination, the involvement of photons which are sufficiently energetic to penetrate the oxide. Ion energies are not sufficient to penetrate the oxide, and energetic electrons would not reach the cathode because of its negative bias. High energy photons, though, would be created in the reactor when secondary electrons which are accelerated across the cathode dark space strike ground planes. Photons generated by secondary electrons in an rf sputtering configuration have been shown to degrade the stability of MOS devices (8). Secondary electrons vary in energy depending on when they are emitted during the rf cycle, but some may have energies corresponding to the full peak-to-peak voltage. Photon energies, then, could also approach this value. The trapped positive charge and the ion implantation damage were not studied beyond their initial characterization (Table I).

* Electrochemical Society Active Member.

Key words: reactive ion etching, plasma etching, radiation damage.

Table I. Summary of trapping center data

| Trapping center | Cross section (cm ²) | Density (cm ⁻²) | Source | Anneal T°C |
|---------------------|--------------------------------------|------------------------------------|---------|------------|
| Positive charge | 10 ⁻¹² -10 ⁻¹³ | 10 ¹² | Photons | 400 |
| Implantation damage | 10 ⁻¹⁴ -10 ⁻¹⁵ | 10 ¹³ | Ions | 1000 |
| Neutral center | 10 ⁻¹⁴ -10 ⁻¹⁷ | 10 ¹¹ -10 ¹² | Photons | 600 |
| Background | 10 ⁻¹⁷ | 10 ¹² | — | — |

The trapped positive charge is annealed at a low temperature of 400°C on the aluminum gated structures used in this study. The implantation damage can be eliminated by dip etching the oxide since the damage is confined to the surface or by avoiding the use of a nonetching gas. The neutral traps, however, are present throughout the bulk of the oxide and an anneal of 600°C or more is required for their removal. Thus, they must be avoided or annealed before aluminum metallurgy is in place.

In the present study, the RIE parameter dependence of the neutral traps was studied. The RIE parameters that were varied include position of substrate in the reactor, rf voltage, and composition of etching gas. Finally, the ability of gate electrode materials to shield an underlying oxide from RIE radiation damage was evaluated by etching oxide films masked with aluminum or n⁺ polysilicon patterns.

Experimental

RIE system.—The reactive ion etching system used in this work is shown in Fig. 1. The substrates were loaded onto an 18 cm diam aluminum plate. The aluminum plate was mechanically and electrically connected to the water-cooled copper rf cathode. A perforated anode plate which is attached to the grounded chamber was placed 3.3 cm from the cathode in order to prevent backspattering of aluminum sputtered from the substrate holder. A perforated anode plate was used so that wafers could be monitored visually during etching, and also to ensure an adequate and uniform supply of etchant in the vicinity of the wafers. The chamber was evacuated with a 6 in. oil diffusion pump and then backfilled with 40 sccm CF₄ to establish a dynamic pressure of 3.33 Pa (25 milliTorr). During etching, 0.25 W/cm² is delivered to the cathode. Under these conditions, the peak-to-peak voltage is 800V. The d-c voltage at the cathode is approximately one-half of the peak-to-peak voltage (9). The etch rate of silicon dioxide in CF₄ is about 50 nm/min.

Sample preparation.—Dry silicon dioxide films of 150 nm thickness were grown on boron-doped, <100> orientation, 0.1-0.5 Ω-cm resistivity p-type silicon substrates. The oxide films were then exposed to a CF₄ or CF₄ + H₂ plasma to etch approximately 50 nm of silicon dioxide. The wafers were then cleaned to remove metals and hydrocarbons from the surface of the oxide

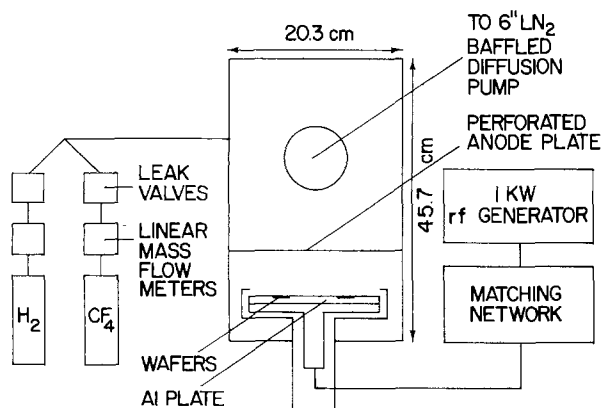


Fig. 1. Schematic of RIE reactor

in alkali and acid peroxide solutions using a procedure similar to that used by Irene (10), but without HF. Some wafers received a buffered HF dip at this point in order to remove ~10 nm from the surface of the oxide. After cleaning, some wafers were annealed in an N₂ ambient for 30 min. Annealing temperatures ranged from 600° to 1000°C. Circular aluminum dots, 13.5 nm in thickness and 5.2 × 10⁻³ cm² in area, were then evaporated in vacuum from resistively heated tantalum boats or rf heated crucibles. Finally, the backs of the wafers were stripped and metallized, and a forming gas anneal at 400°C for 20 min was carried out.

Techniques.—To investigate the enhanced electron trapping characteristics of silicon dioxide layers exposed to plasmas in an RIE system, avalanche injection (11, 12) and internal photoemission (13-15) techniques were used to inject electrons from the contacts of the MOS structures into the oxide. The experimental apparatus for avalanche injection (16) and internal photoemission (17) have been described in other publications. As the electrons traverse the film in the presence of an applied electric field, some of the carriers are trapped into sites created during RIE. This trapping is not particularly sensitive to the mode of carrier injection: avalanche injection from the silicon or internal photoemission from the aluminum or silicon. The trapping rate is not particularly sensitive to the average field in the oxide layer which is consistent with the weak field dependence of the capture process for radiation induced neutral traps recently reported by Ning (7). This weak field dependence is in contrast to the strong field dependence of electron capture on trapped holes (3, 7, 18).

The buildup of this trapped charge is sensed through the internal electric field it creates near the contacts by the capacitance-voltage (C-V) (19, 20) and photocurrent-voltage (photo I-V) (18, 21, 22) techniques which are well described in the literature. The voltage shifts between the C-V curves depend on the product $\bar{x}Q$ where Q is the charge per unit area and \bar{x} is the centroid of trapped charge in the oxide layer measured with respect to the aluminum-oxide interface (19, 20). The voltage shifts between photo I-V data for both positive and negative polarity allow separate determination of \bar{x} and Q (18, 21). The combination of the C-V and photo I-V techniques can also be used to separate silicon-silicon dioxide interface trapping from bulk oxide trapping (18, 21, 22). Also by studying charge buildup as a function of time, electron capture cross sections σ_c and areal trap densities N_t can be determined (3). These quantities (\bar{x} , Q , σ_c , and N_t) are used to characterize the different traps created by the exposure to RIE plasmas in the following sections. Only a very small amount of trapping was seen for the charging conditions used on samples fabricated in an identical manner, but not exposed to RIE (4). The results were reproducible for different locations within a sample, and for samples fabricated over a time span of several months.

Results and Discussion

RIE parameter dependence.—It was suggested earlier that the neutral traps are created in the relatively low energy environment of RIE by photons. To substantiate this view, substrates were loaded onto the grounded perforated plate with the oxide film facing away from the cathode. In this way, the oxide film is no longer subjected to bombardment by energetic ions. The oxide film is also protected from secondary electrons from the cathode by the silicon substrate. The oxide film is, however, still exposed to photons that are created when secondary electrons strike the walls of the reactor. A plot of the volume density of trapped charge as a function of avalanche injection time (Fig. 2) shows that the oxide etched

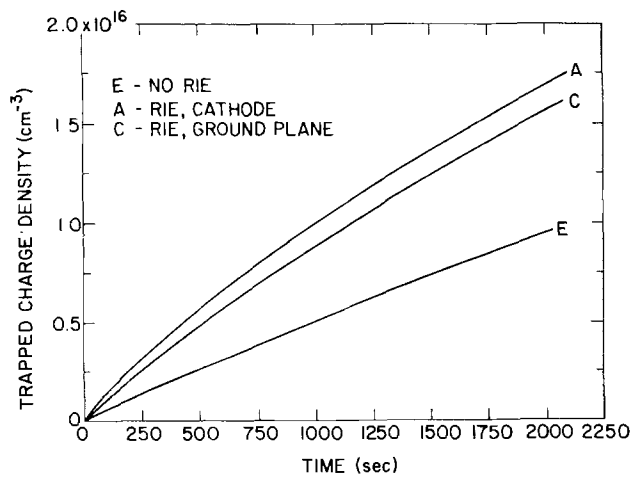


Fig. 2. Volume trapped charge density as a function of avalanche injection time for oxides exposed to RIE on the electrode and on a ground plane. Constant avalanche current = 8×10^{-9} A.

by RIE and the oxide exposed only to energetic photons show enhanced trapping relative to that measured in the control. Data points are taken at 44 sec intervals and so are represented by a solid line. The error bars included for data plotted against an expanded scale in Fig. 7 are representative of data shown in Fig. 2-6.

In the second experiment, the rf power was varied in order to vary the rf peak-to-peak voltage. Etch times were increased as voltage was decreased so that the amount of oxide removed was constant. The purpose of this experiment was to determine whether the introduction of traps exhibited a threshold in the regime of power and pressure that is appropriate for RIE. As can be seen in Fig. 3, enhanced trapping was observed for all oxides etched by RIE even though rf peak-to-peak voltage was reduced by more than a factor of two, from 730 to 330V. Thus, radiation damage is not avoided by etching for longer times at lower rf voltages. It is not possible to carry out RIE at lower voltages. RIE requires low pressures to maintain vertical etching and a low pressure discharge could not be sustained at voltages below 330V. It is possible, however, to reduce voltage if the requirement for directional etching is suspended. For the third experiment, pressure was increased to simulate plasma etching. Oxygen was added to CF_4 so that a direct comparison could be made with oxides etched in a commercial barrel plasma etcher. The pressure of the $CF_4 +$

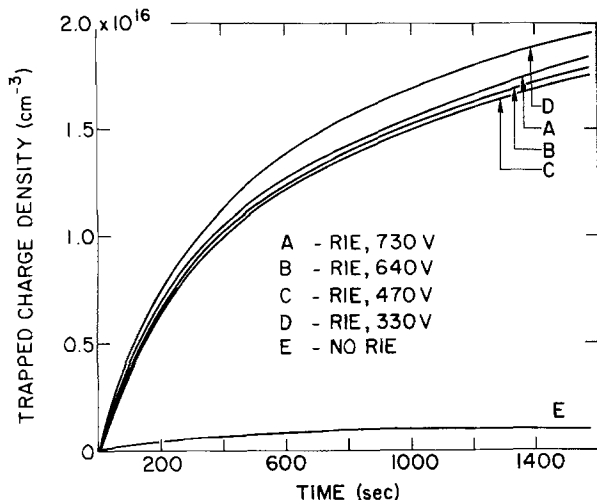


Fig. 3. Volume trapped charge density as a function of avalanche injection time for oxides exposed to RIE with rf peak-to-peak voltages between 730 and 330V. Constant avalanche current = 2×10^{-9} A.

20% O_2 etching gas was increased to 0.5 Torr which results in an rf peak-to-peak voltage of 120V. The trapping data (Fig. 4) show that neutral traps are not created during plasma etching or during etching under plasma etching-like conditions in the RIE reactor. For completeness, an oxide was etched by low pressure RIE in the $CF_4 + O_2$ mixture to assure that the addition of O_2 was not the significant factor. As expected, this oxide shows the presence of neutral traps with a trap density that is approximately equal to that of an oxide etched in CF_4 .

The fourth and last experiment carried out with blanket etched oxide films was to add H_2 to CF_4 . This experiment was suggested by speculation that the neutral traps were created by breaking or relaxing bonds in the lattice of the oxide (6). If correct, the diffusion of atomic hydrogen into silicon dioxide might anneal neutral traps in a way that is analogous to the reduction in dangling bond density in amorphous silicon by atomic hydrogen (23). The data in Fig. 5 show that the addition of H_2 does lead to a significant reduction in trapped charge when compared with an oxide etched in CF_4 alone. A peak-to-peak voltage of 810V was measured. This value is slightly higher than that measured during RIE in CF_4 . While the effect of adding H_2 is reproducible and consistent with annealing of traps by atomic hydrogen, it was not possible to reduce trap density by introducing hydrogen in other ways. Trapping was not reduced by exposing oxides to a hydrogen plasma before or after RIE in CF_4 or by annealing oxides in forming gas (90% $N_2/10\% H_2$) at 1000°C before RIE in CF_4 .

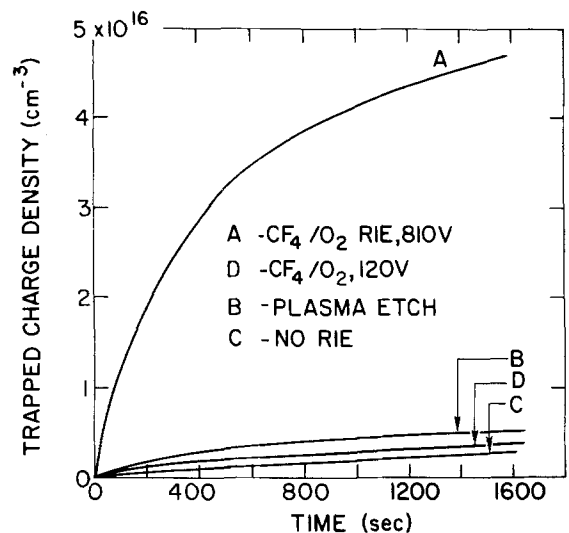


Fig. 4. Volume trapped charge density as a function of avalanche injection time for oxides exposed to RIE in $CF_4 + O_2$ and plasma etching in RIE and barrel-type plasma reactors. Constant avalanche current = 2×10^{-9} A.

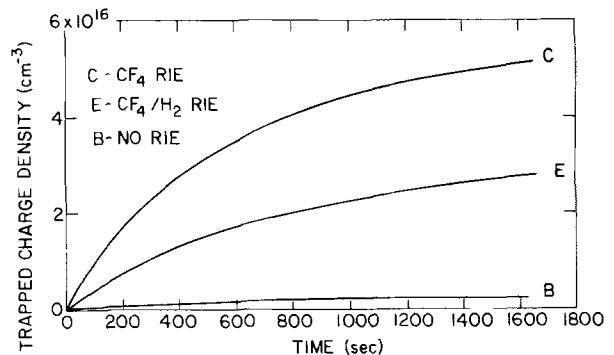


Fig. 5. Volume trapped charge density as a function of avalanche injection time for oxides exposed to RIE in CF_4 and $CF_4 + H_2$. Constant avalanche current = 2×10^{-9} A.

Gate shielding.—The purpose of experiments carried out with blanket oxide films is to understand the nature and parameter dependence of the neutral traps. During FET processing, however, the gate oxide is covered by the material that is used as a gate electrode. With this fact in mind, the ability of polysilicon and aluminum to shield an underlying gate oxide from the introduction of neutral traps was tested.

The procedure used to fabricate the samples begins with the same cleaning and oxidation steps described earlier. After the oxide was grown, a 350 nm thick film of silicon was deposited by chemical vapor deposition on some substrates and then doped n^+ by the deposition and drive-in of POCl_3 . The polysilicon plus 50 nm of oxide was etched using patterned photoresist to delineate 32 mil diam dots. On other oxidized substrates, 32 mil diam, 400 nm thick aluminum dots were evaporated by resistive heating. 50 nm of oxide was then etched by RIE. Appropriate control wafers were included to determine background trapping in the oxide, to provide a reference for the degree of shielding by the gate electrode, and to provide a comparison with wet etching of polysilicon. The data in Fig. 6 show that 400 nm of aluminum does shield the oxide. The shielded oxide exhibits the same increase in trapped charge density as the control, while the unshielded oxide again shows enhanced trapping. The trapping data for oxides covered by polysilicon plus resist during RIE also show that the oxide has been effectively shielded (Fig. 7). The trapped charge density for the reactive ion etched structure is shown on an expanded

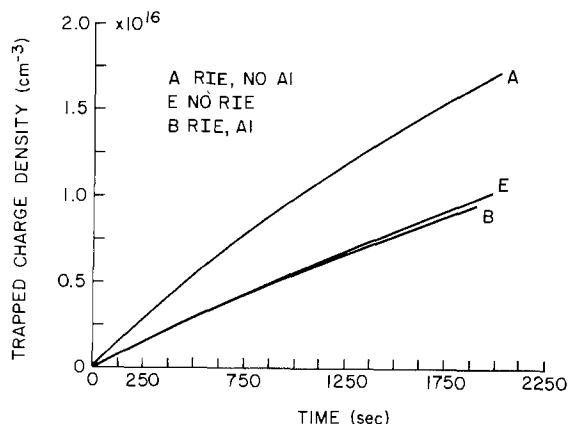


Fig. 6. Volume trapped charge density as a function of avalanche injection time for oxides exposed to RIE with and without an aluminum etch mask. Constant avalanche current = 8×10^{-9} A.

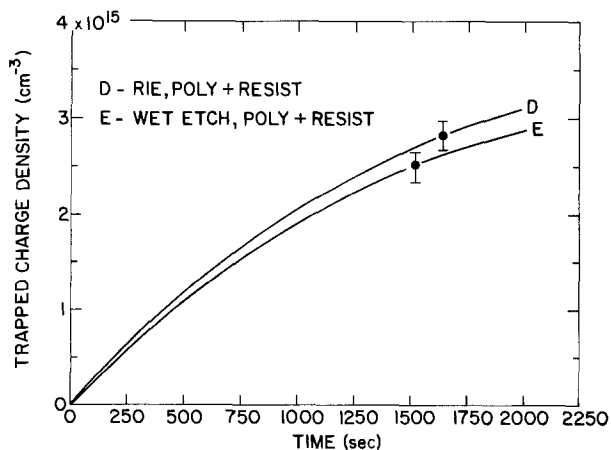


Fig. 7. Volume trapped charge density as a function of avalanche injection time for oxide after RIE of polysilicon electrode. Sample in which polysilicon was wet etched serves as a control. Constant avalanche current = 8×10^{-9} A.

scale with the trapped charge density obtained for a structure that was wet etched. The two samples show the same low density of trapped charge. In fact, the trapped charge density measured for both samples is approximately half that measured on similar structures with aluminum electrodes. This reduction is attributed to a decrease in background oxide trapping as a result of the high temperature deposition and doping of the polysilicon films. Other differences in plots of the trapped charge density as a function of the avalanche injection time on the Al-gated controls (compare Fig. 2 and 6 with Fig. 3, 4, and 5) are due to differences in the magnitude of the avalanche current used.

Summary

The parameter dependence of neutral traps introduced during RIE has been investigated under worst case conditions of blanket etching and also with a gate electrode in place. During blanket RIE of silicon dioxide, neutral traps are created. These traps are removed by a 600°C anneal and so are of concern only if an RIE step occurs after aluminum metallurgy is in place. The trap density is reduced by adding H_2 to the etching gas. Neutral traps were not introduced when the reactor was operated under plasma etching-like conditions. Finally, it is concluded that oxide is effectively shielded during RIE by a polysilicon or aluminum gate electrode.

Acknowledgments

The authors wish to acknowledge the critical reading of this manuscript by J. M. Aitken, and the preparation of samples by the Silicon Process Studies Group. This research was supported in part by the Defense Advanced Research Projects Agency, and was monitored by the Deputy for Electronic Technology (RADC) under contract number F19628-78-C-0225.

Manuscript submitted March 20, 1981; revised manuscript received June 4, 1981.

Any discussion of this paper will appear in a Discussion Section to be published in the June 1982 JOURNAL. All discussions for the June 1982 Discussion Section should be submitted by Feb. 1, 1982.

Publication costs of this article were assisted by IBM Corporation.

REFERENCES

- H. N. Yu, R. H. Dennard, T. H. P. Chang, C. M. Osburn, V. DiLonardo, and H. E. Luhn, *J. Vac. Sci. Technol.*, **12**, 1197 (1975).
- W. R. Hunter, L. M. Ephrath, W. D. Grobman, C. M. Osburn, B. L. Crowder, A. Cramer, and H. E. Luhn, *IEEE J. Solid-State Circuits*, **sc-14**, 275 (1979).
- D. J. DiMaria, "The Physics of SiO_2 and Its Interfaces," S. T. Pantelides, Editor, Pergamon Press, New York, p. 160 and references therein (1978).
- D. J. DiMaria, L. M. Ephrath, and D. R. Young, *J. Appl. Phys.*, **50**, 4015 (1979).
- J. M. Aitken and D. R. Young, *ibid.*, **47**, 1196 (1976).
- J. M. Aitken, D. R. Young, and K. Pan, *ibid.*, **49**, 3386 (1978).
- T. H. Ning, *ibid.*, **49**, 4077 (1978).
- W. D. Ryden, E. F. Labuda, and J. T. Clemens, Abstract 55, p. 149, The Electrochemical Society Extended Abstracts, Washington, DC, May 2-7, 1976.
- H. R. Koenig and L. I. Maissel, *IBM J. Res. Dev.*, **14**, 168 (1970).
- E. A. Irene, *This Journal*, **121**, 1613 (1974).
- A. Goetzberger and E. H. Nicollian, *J. Appl. Phys.*, **38**, 4582 (1967).
- E. H. Nicollian and C. N. Berglund, *ibid.*, **41**, 3052 (1970).
- R. Williams, *Phys. Rev.*, **140**, A569 (1965).
- B. E. Deal, E. H. Snow, and C. A. Mead, *J. Phys. Chem. Solids*, **27**, 1873 (1966).
- A. M. Goodman, *Phys. Rev.*, **144**, 588 (1966).
- D. R. Young, D. J. DiMaria, and W. R. Hunter, *J. Electron. Mater.*, **6**, 569 (1977).
- D. J. DiMaria and P. C. Arnett, *IBM J. Res. Dev.*, **21**, 227 (1977).

18. D. J. DiMaria, Z. A. Weinberg, and J. M. Aitken, *J. Appl. Phys.*, **48**, 898 (1977), and references therein.
 19. A. S. Grove, "Physics and Technology of Semiconductor Devices," Chap. 9, Wiley, New York (1967).
 20. S. M. Sze, "Physics of Semiconductor Devices," Chap. 9, Wiley-Interscience, New York (1969).
 21. D. J. DiMaria, *J. Appl. Phys.*, **47**, 4073 (1976).
 22. R. J. Powell and C. N. Berglund, *ibid.*, **42**, 4390 (1971).
 23. M. H. Brodsky, *Thin Solid Films*, **54**, 159 (1978).

Ion Beam Analysis of Molecular Beam Epitaxy InAlAs/InGaAs Layer Structures

D. V. Morgan,¹ H. Ohno,² C. E. C. Wood, L. F. Eastman, and J. D. Berry

*School of Electrical Engineering and National Research and Resource Facility for Submicron Structure,
Cornell University, Ithaca, New York 14853*

ABSTRACT

In this paper the Rutherford backscattering technique combined with channeling is used to study the stoichiometry and perfection of molecular beam epitaxial layers of InAlAs and InGaAs. Corroborative evidence from SIMS and Auger profiling are used to supplement the RBS studies.

In recent years molecular beam epitaxy (MBE) has emerged as a valuable tool for the growth of electronic quality epitaxial layers of many compound semiconductors (1, 2). The improvement of layer quality depends critically on the development of analytical techniques with which to characterize the material properties. These include parameters such as mobility, conductivity, doping profile, deep level densities and energy levels, and crystal perfection. In this paper we consider the application of Rutherford backscattering (RBS) in evaluating the structure and quality of molecular beam epitaxial InGaAs and InAlAs layer structures. We also consider the use of ion beam channeling for the measurement of crystal perfection, with particular interest in the interfaces between heteroepitaxial MBE layers. RBS has many limitations in the present context including: (i) Poor sensitivity in the measurement of light elements such as aluminum in matrixes incorporating relatively heavy atoms such as indium; and (ii) the inability to resolve neighboring atoms in the periodic table (*i.e.*, such as gallium and arsenic). In order to resolve any ambiguities arising from these limitations, complementary studies have been conducted with secondary ion mass spectrometry (SIMS) and sputter/auger profiling.

Experimental Procedures

Lattice matched $\text{In}_{0.53}\text{Ga}_{0.47}\text{As}$ layers were grown on (100) InP substrates by MBE. Substrates were heat cleaned *in situ* under stabilizing arsenic fluxes at 505°C for 2 min (3). A concentric double cell was used for gallium and indium to improve the spatial and depth composition uniformity of InGaAs layers, while separate aluminum and indium cells were used for growth of InAlAs alloys. Lattice mismatching to InP substrates measured by x-ray diffraction were $\Delta a/a_0 < 1 \times 10^{-3}$ for InGaAs and $\Delta a/a_0 < 2 \times 10^{-3}$ for InAlAs. Layers grown on GaAs substrates were not lattice matched. Typical substrate temperatures (T_s) = 490°C for InGaAs and $T_s = 510^\circ\text{C}$ for InAlAs. Low field electron mobilities of unintentionally doped InGaAs layers were as high as $\mu_{300} = 8800 \text{ cm}^2/\text{Vsec}$ with $n_{300} = 1 \times 10^{16} \text{ cm}^{-3}$ and $\mu_{77} = 15,000 \text{ cm}^2/\text{Vsec}$ with $n_{77} = 8.5 \times 10^{15} \text{ cm}^{-3}$, while unintentionally doped InAlAs layers were of high resistance ($\rho > 3 \times 10^{-3} \Omega \text{ cm}$). Single

crystal epitaxial aluminum layers were grown on some of the samples (below 120°C) without exposure to air to obtain Schottky barriers.

The basic principles underlying the RBS/channeling techniques have been discussed extensively in the literature (4-7) and consequently, only a brief summary will be provided here. A collimated beam of 2-2.5 MeV He^+ ions is directed onto the crystal surface and the energy distribution of particles scattered through an angle θ degrees is measured using a surface barrier nuclear particle detector. This energy spectrum of the backscattered ions yields information on the mass and depth distribution of the scattering ions (5). When the ion beam is incident in a random crystal direction, the near surface composition of the crystal may be deduced from the Rutherford scattering law (6). The relative concentration N_A and N_B of species A and B may be deduced from the respective yields Y using the approximate equation (5)

$$\frac{N_A}{N_B} = \frac{Y(A)}{Y(B)} \cdot \frac{[S]_A}{[S]_B} \left(\frac{Z_B}{Z_A} \right)^2 \quad [1]$$

where Z_A and Z_B are the atomic numbers for the atoms A and B and the $[S]$ terms are the compound stopping powers in the crystal for scattering from the species A or B, respectively, given by the expression (5)

$$[S]_A = k_A^2 [S]_{\text{in}} + \frac{[S]_{\text{out}}}{\cos(\theta)} \quad [2]$$

k_A^2 is the kinematic factor for the atoms A (or B) and θ is the scattering angle defined in the inset of Fig. 1. The stopping powers $[S]_{\text{in}}$ and $[S]_{\text{out}}$ correspond to the ingoing and scattered beam. For the compounds used in this work $[S]$ was obtained from the stopping powers of the elements concerned by the use of the Bragg law (4, 8).

Results and Discussion

The straightforward use of RBS in the measurement of the elemental composition (8) was of value to the present study. Figure 1 shows a spectrum obtained for random incidence from an $\text{In}_x\text{Al}_{(1-x)}\text{As}$ layer 1.5 μm thick ($x = 0.4$) grown on GaAs. The random spectra were obtained by aligning the crystals to the $\langle 100 \rangle$ axis and then carefully misaligning to find a random direction. In this figure we show both the compound (raw) RBS spectrum obtained by scatter-

¹ Permanent address: Department of Electrical and Electronic Engineering, University of Leeds, Leeds, England LS2 9JT.

² Permanent address: Sakaki Laboratory, Institute of Industrial Science, University of Tokyo, Tokyo, Japan.
Key words: channeling, MBE, RBS studies.

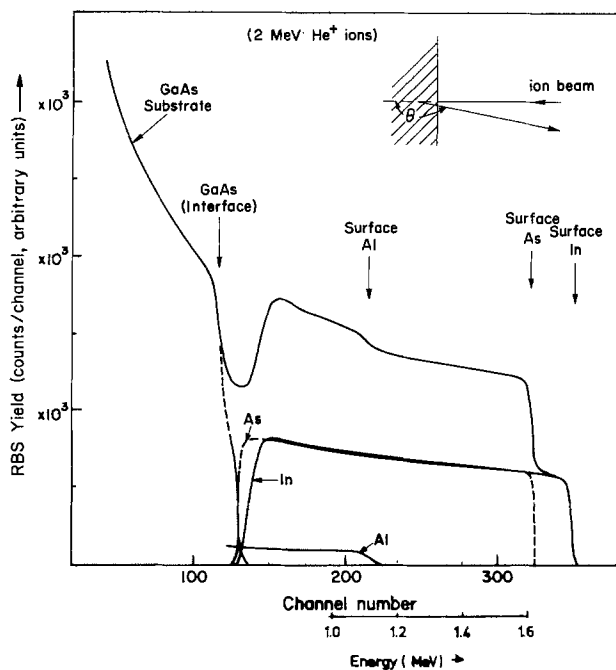


Fig. 1. Rutherford backscattering spectrum (RBS) obtained from an $\text{In}_x\text{Al}_{1-x}\text{As}$ crystal ($x = 0.4$) grown on a GaAs substrate. (Incident helium ion energy $E_i = 2.0$ MeV scattering angle $\theta = 168^\circ$.) Both the composite spectrum and its component parts are shown.

ing 2 MeV He^+ ions through 168° , together with the individual component spectra from the indium, arsenic, and aluminum and the substrate GaAs. In order to estimate the component spectra, a simple iterative procedure (9a) based upon the work of Ref. (9b) was used. For each component spectrum an increase in yield with depth was obtained by normalizing the surface yield of each of the spectra to unity and using the Rutherford scattering relationship [i.e., yield \propto (energy) $^{-2}$] to generate the depth dependence of the spectrum. In InAlAs grown on GaAs, for example, the GaAs substrate spectrum would be extracted first. The procedure described above would then be used for the In spectrum, followed by the As and finally the Al spectra. The heavier indium atoms give the clearest near-surface spectrum, while the much lighter aluminum spectrum superimposed on the relatively large background is more difficult to resolve and hence has the largest uncertainty. From this spectrum the value of x from the indium spectrum and $(1-x)$ from the aluminum spectrum may readily be obtained.

RBS spectra have been obtained for a range of $\text{In}_x\text{Al}_{1-x}\text{As}$ samples with x ranging between 0 and 1. The values of x and $(1-x)$ and the arsenic concentration obtained from the corresponding RBS spectra are shown by the circular and triangular points in Fig. 2 as a function of the values predicted from the molecular beam cell fluxes. The full lines are the best straight lines through the experimental points. The arsenic concentration is stoichiometric (i.e., at 50%) in all the layers grown with x varied between 0 and 1. This is as expected from thermodynamic considerations. Observation of the indium concentration again confirms that the x values measured by RBS agree well with those estimated from the MBE flux monitor (3). The one departure from this behavior is that of a layer with $x = 0.2$ (Fig. 3); here RBS estimates a value near to $x = 0.1$, which is confirmed by repeated measurements at different areas over the crystal surface. Another interesting feature of this spectrum is the appearance of a surface indium peak where the local x value rises to near the predicted $x = 0.2$. The reproducibility of the surface indium peak across the

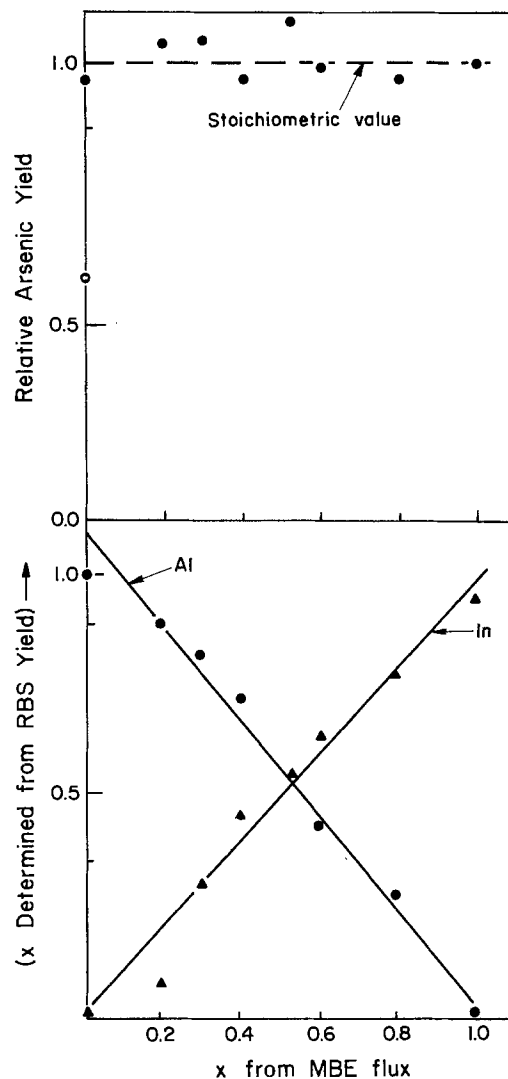


Fig. 2. A summary of the results obtained from a series of crystals grown with the value of x in $\text{In}_x\text{Al}_{1-x}\text{As}$ varied from 0 to 1. The upper graph shows the normalized (stoichiometric value = 1.0) arsenic concentration as a function of x . In the lower graph the RBS values of x for indium and $(1-x)$ for aluminum are plotted as a function of the predicted MBE flux values.

surface, confirms that it is not a local segregation of indium [as would be expected with spitting from the indium or aluminum source (10)]. The surface indium peak in this case arises from the surface accumulation of indium [or preferential incorporation of $\text{Al}(\text{Ga})$] in the nucleation stages, during growth at high substrate temperatures or low As_4 fluxes. Further confirmation comes from SIMS studies (Fig. 3 inset) where results show that the indium concentration falls by about 10% at about 0.5 micron inside the surface. The spatial uniformity of the surface indium accumulation was also confirmed by the SIMS studies. (Note that the very high arsenic yield near to the surface is an artifact of the present SIMS technique possibly associated with residual surface oxide persisting during the erosion process.) In comparison with the SIMS profiles, RBS spectra are relatively easy to interpret and they yield quantitative data. However, the problem of obtaining an aluminum profile from the spectrum shown in Fig. 3 is not tractable, making complementary SIMS profiles invaluable.

The ability of the backscattering technique to measure indium profiles is again indicated in Fig. 4(a) which shows an RBS spectrum of a $1.5 \mu\text{m}$ lattice matched InGaAs crystal grown on an InP substrate. The indium profile extracted from this spectrum shows two regions of different composition, one at the surface

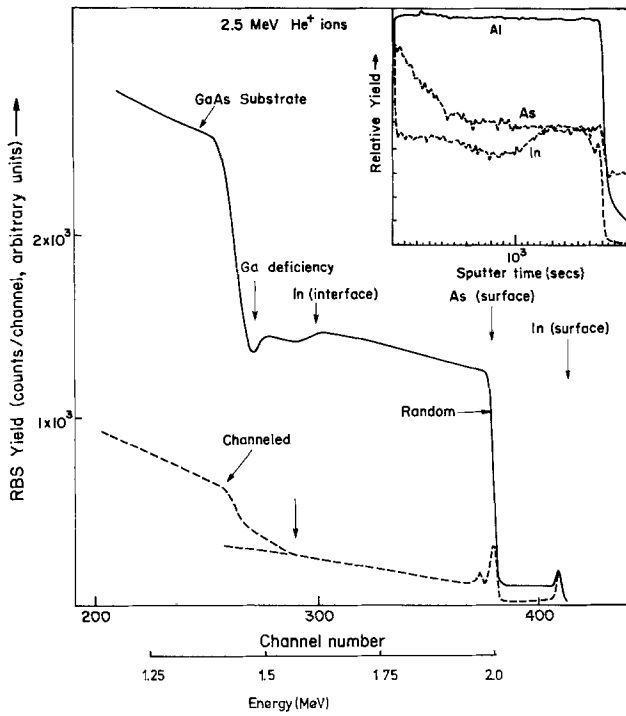


Fig. 3. RBS spectrum from an InAlAs crystal ($x = 0.2$) grown on a GaAs substrate. In this case $E_i = 2.5$ MeV and $\theta = 170^\circ$. Both the channeled $\langle 100 \rangle$ and random spectra are shown. Also shown in the inset is the corresponding SIMS profile.

and a second peak approximately $0.3 \mu\text{m}$ inside the crystal. This indium fluctuation was the result of indium surface segregation at the relatively high growth temperature (489°C). This was done to determine the upper temperature limit to the growth and to identify the growth problems that occur in this high temperature regime. We note that the surface indium concentrations indicate an almost 100% increase over the bulk indium value. Note also that the close proximity of the gallium and arsenic atomic masses makes it difficult for the profiles to be separated unambiguously from this spectrum. The reverse situation, namely a drop in indium concentration at the surface, was associated with an instability in the indium effusion cell temperature control and is clearly shown in Fig. 4(b) where the indium concentration in InAlAs falls from the value corresponding $x = 0.8$ to $x = 0.72$. Note

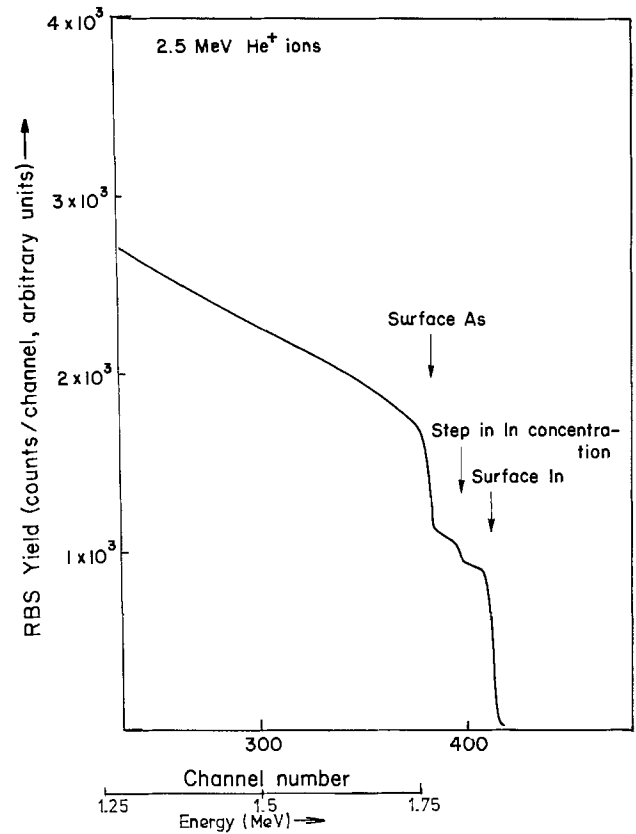


Fig. 4(b). RBS spectrum from an InAlAs crystal ($x = 0.8$) grown on a GaAs substrate. ($E_i = 2.5$ MeV, $\theta = 170^\circ$.)

also that it becomes more difficult to identify fluctuations unambiguously where the indium and arsenic spectra overlap.

In some potential device applications where the device active layer is of a composition that does not lattice match that of the substrate used, it is necessary to grade the ratio of the component elements to reduce mismatch strain and strain induced defects etc. (i.e., x in $\text{In}_x\text{Al}_{1-x}\text{As}$). Such structures provide good test vehicles for material characterization techniques. RBS alone can provide information on the compound composition and its depth dependence. When complemented by channeling measurement, however, information on crystal quality may also be obtained. This latter point is discussed later. The crystal analyzed in Fig. 5(a) is an $\text{In}_x\text{Al}_{1-x}\text{As}$ sample where x was stepped down from 1.0 at the interface in 20% steps to 0 at the surface. To avoid oxidation of the AlAs surface region a thin InAs layer was deposited on the top surface. This is seen as the near surface peak at the high energy end of the spectrum of Fig. 5(a). From the main spectrum the indium yield is readily obtained by extracting the arsenic profile, which is known to be a constant from thermodynamic considerations and is also confirmed from sputter Auger and SIMS profiling studies. The indium profile lies close to that predicted by the growth parameters and is again confirmed by the Auger and SIMS results. The steps in the composition are apparent only for In_x (x stepped from 1.0 to 0.8) which is also confirmed by Auger sputtering profiles. The 20% steps from $x = 0.8$ down to $x = 0$ are reduced due to mismatch strain-induced interdiffusion at the high growth temperature (480°C). This strain becomes apparent in the channeling measurements discussed later in this paper. It is interesting to note that the Auger sputter profiling of the inverse layer structure (i.e., where x was stepped in 20% increments from 0 at the interface to 1.0 at the surface) grown at 375°C [inset shown in Fig. 5(b)] shows discrete steps, although this is not observed on the cor-

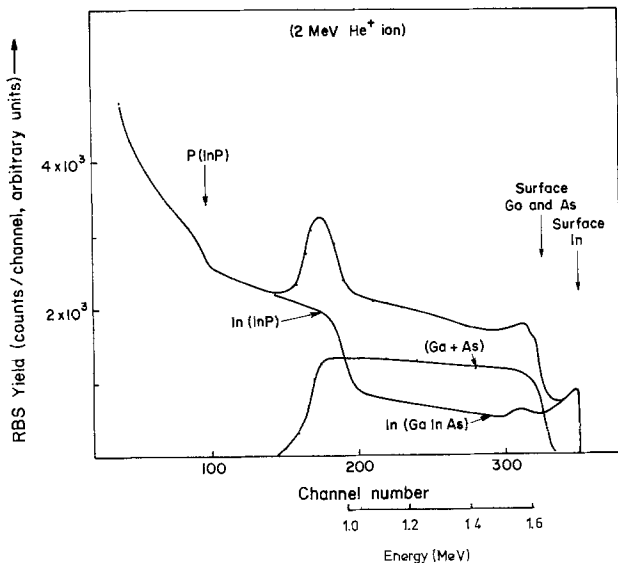


Fig. 4(a). RBS spectrum from an InGaAs crystal grown lattice matched to an InP substrate. ($E_i = 2$ MeV (He ions) $\theta = 168^\circ$.)

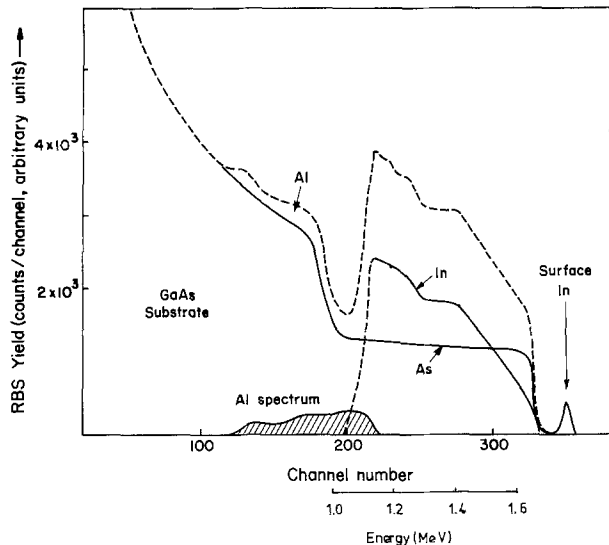


Fig. 5(a). RBS spectrum from an InAlAs crystal where the indium concentration x is varied from 1.0 at the interface in 20% steps to 0 at the surface. The AlAs surface is protected from oxidation by the growth of a thin InAs layer. [$E_i = 2.0$ MeV (He) and $\theta = 168^\circ$.]

responding RBS spectrum as the ion beam energy and incident angle were not optimized for the best depth resolution. The RBS spectrum again illustrates the difficulty of extracting the aluminum profile. The extracted indium and aluminum signals are compared to the Auger profiled results in Fig. 5(b) inset. Here both techniques confirm the relative integrity of the individual alloy layers and interface regions when grown at the lower temperature.

So far we have considered only the basic RBS technique. The following considers the use of the channeling process (6) to investigate bulk layer crystal quality and more importantly the crystalline perfection of interfaces. Figure 6 shows two RBS spectra obtained for aligned and random incidence from a multilayer structure consisting of an InGaAs (2500Å)/InAlAs (1000Å)/InP (substrate). Using the channeling technique there are two basic measures of crystal quality, the minimum yield χ_{\min} and the dechanneling rate α ($= dx_{\min}/dz$) where z is the depth of the penetration

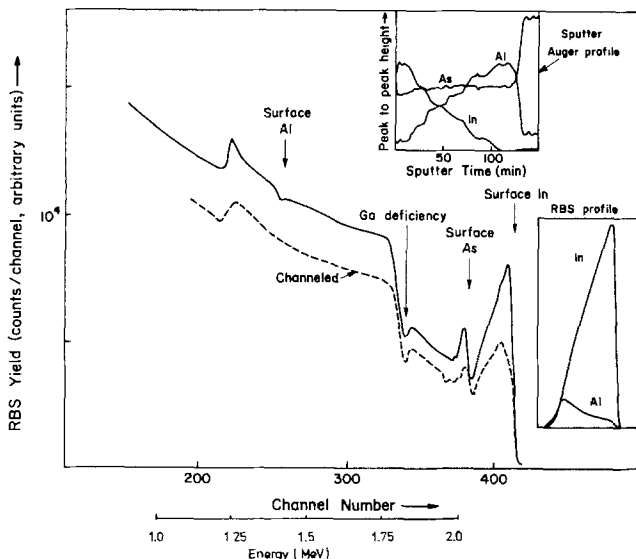


Fig. 5(b). The channelled ($\langle 100 \rangle$ axis) and random spectra from an $\text{In}_x\text{Al}_{1-x}\text{As}$ crystal where the indium concentration x is varied from 0 at the interface in 20% steps to 1.0 at the surface. [$E_i = 2.5$ MeV (He ions), $\theta = 170^\circ$.] Also shown in the inset is the corresponding sputter Auger profile.

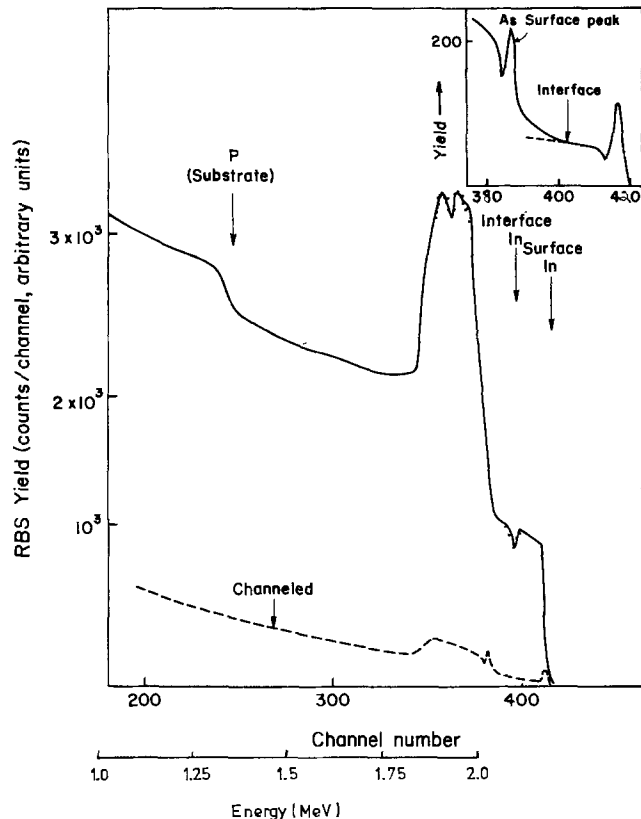


Fig. 6. The RBS spectrum for channelled and random incidence from an InGaAs/InAlAs/InP crystal, where the two epitaxial layers are grown lattice matched to the InP. [$E_i = 2.5$ MeV (He ions), $\theta = 170^\circ$, axis for channeling $\langle 100 \rangle$.] The inset shows an enlarged version of the near surface channelled spectrum.

in the crystal (11). These parameters provide only a relative measure of crystal quality. In order, therefore, to provide a standard we note that for channeling along the $\langle 100 \rangle$ axis in a good quality GaAs layer values of $\chi_{\min} \approx 0.04$ and $\alpha \approx 10^{-4} (\text{nm})^{-1}$ are typical. For the crystal shown in Fig. 6 (i.e., channeling along the $\langle 100 \rangle$ axis) we obtain near surface values of $\chi_{\min}(\text{In}) = 0.04$ and $\alpha(\text{In}) = 5 \times 10^{-4} (\text{nm})^{-1}$. The minimum yield shows excellent agreement with the best GaAs experimental results (12). In the case of the dechanneling rate α , this result is a factor five larger than that typical of premium grade GaAs. However there are two reasons why this is reasonable. In the first instance dechanneling is a much more sensitive parameter than the minimum yield. Wood and Morgan (12), for example, have observed fourfold increases in α in GaAs epitaxial layers at a growth interface. A second important consideration arises from the disparity in the atomic numbers of the component atoms—indium, arsenic, and aluminum. A large disparity gives rise to a much larger intrinsic dechanneling rate. In the case of planar channeling, computer simulation (13) results show that this factor alone could result in a 300% increase in going from GaAs to a material such as InAlAs. In view of these considerations it is concluded that the value of $\alpha = 5 \times 10^{-4} (\text{nm})^{-1}$ is comparable to those obtained for high-grade epitaxial layers and indicates that the uppermost InAlAs layer exhibits a high degree of perfection, justifying the care in lattice matching to the substrate InP.

A second interesting feature of these spectra may be more clearly seen in the inset to Fig. 6, which shows an enlarged plot of the near surface indium peaks (i.e., the indium in the InAlAs and the InGaAs). At the interface between these two layers the indium channeling curve undergoes an abrupt transition resulting in a fourfold increase in the dechanneling parameter

$\alpha(\text{In})$ (i.e., α increases from 5×10^{-4} to 20×10^{-4} $(\text{nm})^{-1}$). This indicates that the lattice structures are strained at the interface, presumably a result of imperfect matching, local segregation, or diffusion of group III elements within the alloy sublattice across the interface. It is clear that such strain can result in undesirable deep levels which could adversely affect the performance of FET's made from such layers. Further clarification of the interface strain may be gained from the random spectrum of Fig. 6. At the interface the indium yield decreases indicating that a deficiency of indium occurs during the transition from the growth of InGaAs to InAlAs. The indium deficiency at the interface is further evidence for accumulation of indium in these two ternary alloys growing under conditions of low As₄ fluxes or high temperature substrates. The total indium deficiency at the interface corresponds to a total equivalent of 1.5 monolayers of pure indium. Because of the limited depth resolution ($\sim 200\text{\AA}$) it is not known how localized this deficiency is.

A third measure possible from a channeling spectrum is the area under the surface indium, gallium, and arsenic peaks (9). These peaks give the ratio of unscreened components in the surface disordered layer. From the $\langle 100 \rangle$ channel spectrum shown in the inset of Fig. 1 we obtain a value of $N(\text{In})/N(\text{Ga} + \text{As}) = 0.63$ which is significantly larger than the expected bulk value of 0.36. One of the difficulties of this measurement is that the Ga and As peaks cannot be separated and hence the source of the nonstoichiometry cannot be identified. Before leaving the topic of interfaces we note in the random spectrum in Fig. 3 that there exists a dip in the gallium yield when InAlAs is grown on a GaAs substrate which is explained by an Al/Ga exchange and redistribution reaction during growth of the first few atomic layers of any aluminum-containing alloy or compound on any gallium-containing alloy or compound. It is also observed that the dechanneling curve in Fig. 3 undergoes an abrupt increase as the interface between InAlAs and the GaAs substrate is approached. This is presumably a result of the interface strain expected since this interface is not lattice matched. The dechanneling results indicate that this strain extends some 2000Å into the epitaxial layer.

In order to further investigate the value of channeling measurements, studies have been carried out on the range of samples studied earlier (i.e., those with $\text{In}_x\text{Al}_{1-x}\text{As}$ for x ranging from 0 to 1). The clear trend in these results is that the best channeling (i.e., lowest χ_{min}) was obtained in crystals with $x \simeq 0.5$ (i.e., the InP lattice matched system). We note also that layers grown on GaAs (not lattice matched) give poorer channeling. For example, in the case of $x = 0.8$ [Fig. 4(b)] the crystal structure is so poor that it is very difficult to observe any channeling dips with any degree of certainty. The same conclusions may be drawn for other crystals with variable x [Fig. 5(b)], the near surface $\chi_{\text{min}}(\text{In}) = 0.52$, confirming that the crystallinity is very poor.

Another example of the value of this technique is shown in Fig. 7 in the spectrum from a lattice matched layer of InGaAs/InP. This layer exhibited a very low mobility compared to normal. The reason for this low mobility is apparent from the RBS spectra shown in Fig. 7. Consider first the random spectrum. This shows a series of peaks in the indium concentration culminating with a large surface accumulation (i.e., a 15-20% increase over the average bulk value). These oscillations occur and can be seen even when the indium and GaAs spectra overlap. Clearly any variation in indium concentration must be matched by a complementary change in the gallium. Of particular interest is the

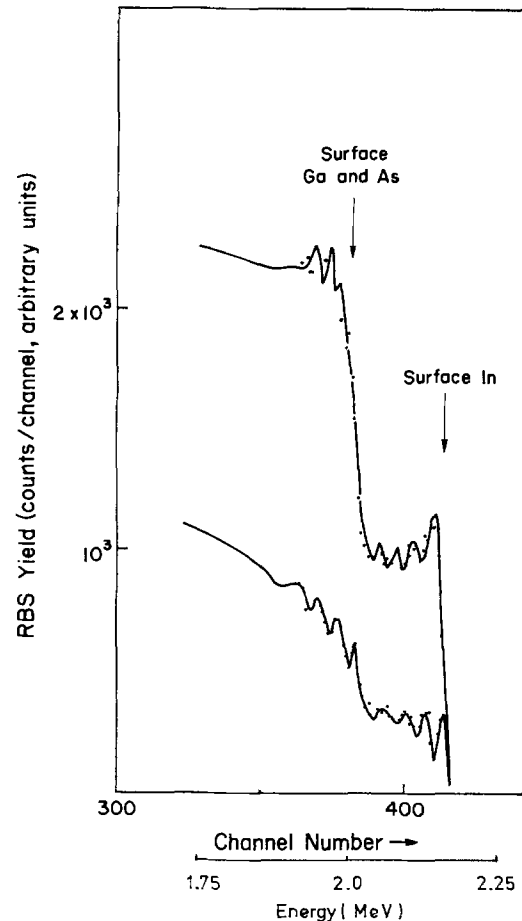


Fig. 7. RBS spectrum of an InAlAs grown on a GaAs substrate [$E_i = 2.5$ MeV (He ions), $\theta = 170^\circ$].

channeled spectrum; here the oscillations are greatly amplified (i.e., a maximum of 100% change). The reason for this greater sensitivity lies in the nature of the channeling process. The channeled component of the beam is screened from violent collisions. However, when the indium concentration increases, the channel becomes distorted and some channeled ions are no longer screened, resulting in the increased backscattering. In this way the effect of the indium fluctuations are amplified (i.e., 10% variation in the random RBS spectrum becomes a 100% change).

Conclusions

Both random and channeling RBS have been used with complementary sputter Auger and SIMS techniques to study epitaxial InAlAs and InGaAs multilayer structures on (100) InP and GaAs substrates.

Results indicate that at higher temperatures or reduced arsenic fluxes indium accumulates on the surface during growth of both InGaAs and InAlAs alloys. The net effect is to leave an indium deficiency at near substrate layer interface regions. The effect was confirmed by observing depth fluctuations of the In/Ga ratio in layers grown with intentionally fluctuating arsenic fluxes. A further effect seen only by RBS was the preferential exchange of aluminum for gallium at the nucleation stage of InAlAs on GaAs substrates or on InGaAs layers.

Acknowledgments

The authors are grateful to L. Rathbun for the sputter Auger data, to G. Morrison for SIMS data, and to Ms. Elma Weaver and Mrs. C. Edmondson for preparation of the typescript. We also acknowledge Dr. J. M. Poate (Bell Laboratories) and Professor G. Carter (University of Salford, UK) for the use of their RBS machines and the planning committee of NRRFSS for permission to use the MBE machine.

³ The background correction procedure used to extract the surface peaks was that described by Morgan and Wood in Ref. (11).

Manuscript submitted Oct. 27, 1980; revised manuscript received April 23, 1981.

Any discussion of this paper will appear in a Discussion Section to be published in the June 1982 JOURNAL. All discussions for the June 1982 Discussion Section should be submitted by Feb. 1, 1982.

Publication costs of this article were assisted by Cornell University.

REFERENCES

1. A. Y. Cho and J. R. Arthur, in "Progress in Solid State Chemistry," G. Somorjai and J. McCaldin, Editors, Pergamon, New York (1975).
2. C. E. C. Wood, in "Physics of Thin Films," Haff and Francombe, Editors, p. 35, Academic Press, New York (1980).
3. G. Davies, R. Heckingbottom, H. Ohno, C. E. C. Wood, and A. R. Calawa, *Appl. Phys. Lett.*, **37**, 290 (1980).
4. W. K. Chu, J. W. Mayer, M.-A. Nicolet, T. M. Buck, G. Amsel, and F. Eisen, *Thin Solid Films*, **17**, 1 (1973).
5. W. K. Chu, J. W. Mayer, and M.-A. Nicolet, "Backscattering Spectrometry," Academic Press, New York (1978).
6. D. V. Morgan, *Solid State Electron Devices*, **1**, 37 (1977).
7. D. V. Morgan, Editor, "Channeling: Theory Observation and Applications," Wiley-Interscience, London (1973).
8. P. Blood, K. L. Bye, and J. S. Roberts, *J. Appl. Phys.*, **51**, 1790 (1980).
9. (a) C. J. Madams, Ph.D. Thesis, University of Leeds (1978); (b) J. Zeigler and W. K. Chu, IBM Report No. R.C. 4288 (1973).
10. C. E. C. Wood, H. Ohno, D. Desimone, and L. F. Eastman, *J. Cryst. Growth*, Accepted for publication.
11. D. V. Morgan and D. R. Wood, *Proc. Roy. Soc. London, Ser. A*, **335**, 509 (1973).
12. D. R. Wood and D. V. Morgan, *Phys. Status Solidi A*, **17**, K143 (1973).
13. D. V. Morgan and D. P. Jackson, *Radiat. Eff.*, **29**, 99 (1976).

Plasma Oxide FET Devices¹

A. K. Ray* and A. Reisman*

IBM T. J. Watson Research Center, Yorktown Heights, New York 10598

ABSTRACT

Plasma oxidation techniques described in this issue (1, 2) by the authors were employed alone, or in conjunction with thermal oxidation processes in the fabrication of n-channel polysilicon gate field effect transistors. Horizontal dimensions were delineated using optical lithography, and ranged from 2.5 μm minimum dimensions up, to enable assessment of device parameters. The characteristics of 500°C plasma oxidized structures were compared to those fabricated in a conventional manner at 1000°C. Gate oxides were 35 nm thick and field planar oxide regions were 350 nm thick. Using wafers of a given resistivity, the thick and thin oxide thresholds of plasma oxide structures were higher than their thermal counterparts due, it is believed, to the absence of surface boron depletion in plasma oxidized regions. In line with this, threshold sensitivity to substrate bias (substrate sensitivity) was greater in plasma oxidized structures for a given starting background substrate doping level. Also because of the absence of impurity spreading, the sheet resistivity of n⁺ junctions was higher in plasma oxidized structures. Aside from doping level effects which can be advantageously accommodated for by appropriate device design, plasma oxidized devices are otherwise quite comparable to their thermal counterparts. They exhibit obvious device design and process control attributes due to shorter processing time at high temperatures, i.e., absence of oxidation induced stacking faults, confinement of junctions, and absence of surface impurity depletion. In n-channel devices, the absence of boron depletion during plasma oxidation has enabled the fabrication of surface and junction ion-implanted devices with lower boron doses and lower substrate sensitivity.

In the fabrication of micron or submicron device structures, there is an increasing interest in the use of lower processing temperatures to minimize impurity redistribution and defect generation effects. Oxidation is a key process in semiconductor device fabrication. High temperature oxidation is accompanied in addition to the problems mentioned above by surface depletion of impurities (3), oxidation enhanced diffusion (4), generation of stacking faults (4, 5), and so-called bird's beak generation (6). In Parts I and II the authors have described a low temperature plasma oxidation process (1, 2) in which uniform thickness oxides exhibiting excellent physical and electrical properties can be grown on 57 mm diam silicon wafers. In the process described, an oxygen plasma is generated at pressures above 10 mTorr in an electrodeless fused

silica reaction chamber using a 3 MHz rf generator and a 1 kW power output. The system is pumped continuously during oxidation and the oxygen pressure is varied by varying the oxygen flow rate. Silicon wafers are placed on either side of an rf coil, mounted perpendicular to the direction of gas flow, with the silicon surfaces to be oxidized facing away from the plasma. Oxide grows primarily on the silicon surfaces facing away from the plasma, while much thinner oxide grows on the silicon surfaces facing the plasma. The temperature of the wafers during plasma oxidation is about 500°C, and is measured by a Chromel-Alumel thermocouple placed adjacent to the wafers. The plasma oxides can be grown at rates less than, equal to, or greater than that obtainable via dry thermal oxidation processes at 1000°C, depending upon oxygen partial pressure, wafer position relative to the rf coil, temperature, and generator output power. The high-low thickness uniformity of the grown oxide was better than $\pm 5\%$ and the standard deviation was of the order 1-3%. The etch rate and refractive index

* Electrochemical Society Active Member.

¹ See Parts I and II prior to reading this paper: *This Journal*, **128**, 2460, 2466 (1981).

Key words: silicon, oxygen plasma, boron depletion, substrate sensitivity.

of the as-grown plasma oxides were comparable to thermal oxides grown at 1000°C. The as-grown oxides exhibited large negative flatband voltages with high interface trap density ($3 \times 10^{12}/\text{cm}^2 \text{ eV}$). However, after a conventional low temperature postmetallization anneal (400°C, 20 min, forming gas), the interface charge and trap densities decrease to 6×10^{10} . The electrical breakdown strength (3-4 MV/cm) was somewhat lower than the thermal counterpart. However, after a postoxidation heat-treatment at 1000°C for 15 min in dry O_2 , followed by 5 min in Ar, the breakdown strength improved to 7-8 MV/cm and the interface charge and trap densities dropped further to the 2×10^{10} . The properties of plasma grown oxides after a short anneal at 1000°C are thus comparable to the thermal oxides grown at 1000°C. The thickness change associated with this annealing treatment is less than 5 nm. In addition, boron depletion effects are absent, as are oxidation-induced stacking faults and bird's beak effects (2). Elimination of the bird's beak is due solely to the fact that an oxide pad is not required under the oxidation mask to avoid defect generation during the low temperature plasma oxidation. Based on these results, the present study was conducted to evaluate plasma oxides in terms of polycrystalline silicon insulated gate FET device characteristics.

Experimental Techniques

Polysilicon gate FET devices were fabricated using optical lithographic techniques in conjunction with the plasma oxidation process alone, or in combination with thermal oxidation. For the present studies, plasma oxide growth rates considerably faster than 1000°C dry oxidation rates were employed. For example, 35 nm gate oxides were grown in 5 min and 350 nm field oxides were grown in 330 min. The comparable times for dry thermal oxidations at 1000°C would have been 38 and 1220 min, respectively. The plasma oxides were all grown at 500°C, 30 mTorr system partial pressure, 1 kW generator output power, and a generator frequency of 3 MHz. As mentioned, the growth of these plasma oxides occurs on the surfaces of the wafers facing away from the plasma which was described earlier (2). No external bias was applied to the wafers. There were three oxidation steps involved in the device fabrication; field isolation oxidation, gate insulator oxidation, and simultaneous source-drain:gate electrode oxidation. Four groups of wafers, two in each group, were employed in the experiments. These included: (A) wafers with plasma field, plasma gate insulator, and plasma source-drain:gate electrode oxidations, (B) wafers with plasma field, plasma gate insulator oxidations, and thermal gate electrode:source-drain oxidation, (C) wafers with plasma field oxidation, thermal gate insulator, and thermal gate electrode:source-drain oxidations, and (D) control wafers with thermal field, thermal gate insulator, and thermal source-drain:gate electrode oxidations. In order to keep the device fabrication process as simple as possible, no field or channel tailoring implants were employed in this first series of experiments, and source and drain regions were formed by diffusion. In addition, field regions were planar (as opposed to semi-ROX configurations). 0.5 $\Omega\text{-cm}$ p-type ($B \sim 3.2 \times 10^{16}/\text{cm}^3$) Czochralski grown silicon wafers were used as substrates. About 350 nm of blanket field oxides were grown over the entire wafer using either plasma or thermal oxidation techniques as the starting point. Field regions were subsequently defined using standard photolithographic techniques. Gate oxides (35 nm) were then grown using plasma or thermal oxidation processes. Wafers with plasma gate insulators were given a postoxidation heat-treatment at 1000°C for 15 min in dry O_2 followed by 5 min in Ar. As mentioned before, this heat-treatment reduces the interface traps and charge density, and improves the breakdown strength of

plasma oxides. During this postoxidation heat-treatment, as mentioned, about 5 nm of thermal SiO_2 is grown in addition to the 30 nm of plasma gate oxide already present on the wafers. If the postoxidation annealing of the plasma oxides is conducted only in an inert atmosphere (argon), the interface electrical properties of the oxides are essentially equivalent to those obtained using the procedure described (2). The breakdown strength of the oxides following inert gas annealing does not improve however, although it is still adequate for device applications. Our normal procedure is to use the two-step annealing procedure so as to obtain the higher breakdown strength oxides. Wafers with conventional thermal oxides received a 1000°C, 5 min Ar postoxidation heat-treatment. After growing field and gate oxides, about 350 nm of undoped polysilicon films were deposited over the wafers and subsequently doped with phosphorus. Polysilicon gate electrodes, source, and drain regions were defined by photolithography. Source and drain were then formed by phosphorus diffusion. Following source-drain diffusion, 100 nm of oxides were grown over these regions using plasma or thermal oxidation processes. Subsequent device fabrication steps, e.g., CVD SiO_2 deposition (250 nm), PSG formation, contact metallurgy, pre (500°C, 30 min, forming gas) and post (400°C, 20 min, forming gas) metallization anneals were common to all wafers.

Results and Discussions

Threshold voltage comparisons of FET devices were made using a standard I - V technique. Measurements were made on devices with a 10.8 μm channel length and an 89.5 μm channel width, unless otherwise specified. About ten devices on each wafer were measured to obtain the average threshold voltage. Figure 1 shows the I - V characteristics of FET devices in wafer type A which were fabricated using only plasma oxidation steps. Threshold measurements were made with a source-substrate bias of -1V with the source grounded and 0.1V applied between the source and drain. The threshold voltage as determined from the straight line portion of the curves was $0.88 \pm 0.07\text{V}$. Figure 2 shows the I - V characteristics of FET devices in control wafer, type D. The threshold voltage of FET devices made by conventional processes was $0.74 \pm 0.065\text{V}$. Comparing slopes of the straight lines in Fig. 1 and 2, it is seen that the channel transconductance of FET devices fabricated with plasma oxidation processes is essentially the same as those fabricated by conventional thermal techniques. The thermal oxide devices exhibited lower threshold voltages, but the spread in threshold voltages is essentially the same for the two types of wafers. This spread is quite

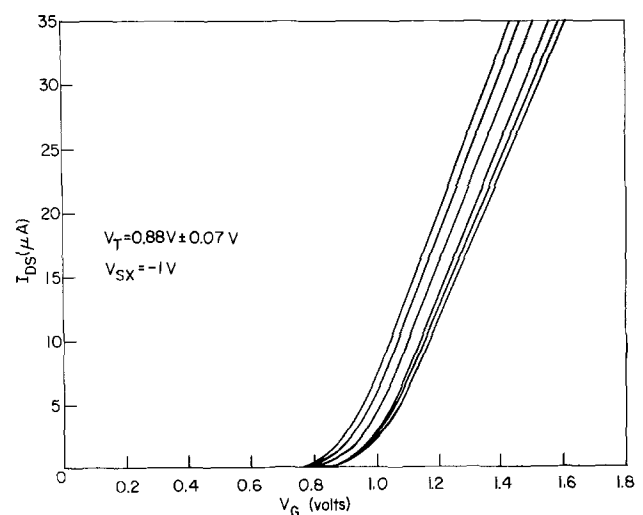


Fig. 1. I - V characteristics of FET devices fabricated using only plasma oxidation steps.

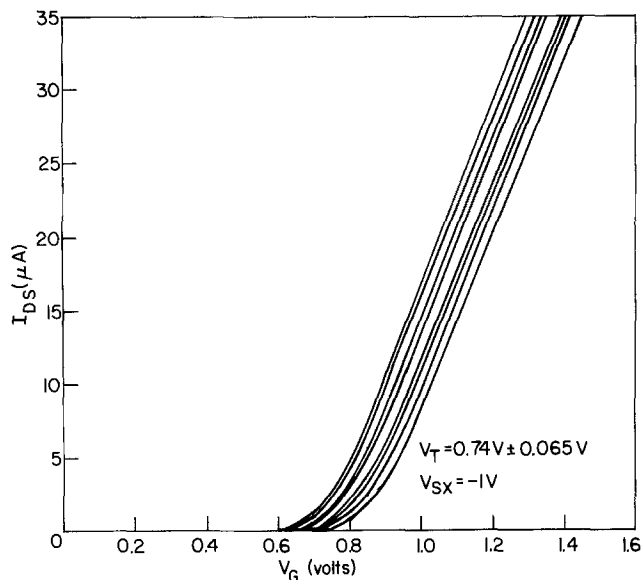


Fig. 2. I - V characteristics of FET devices fabricated using only thermal oxidation steps.

common in devices which do not have channel implant tailoring and is due to bulk doping variations. Figure 3 shows the variation of the threshold voltage with channel mask length for the four types of wafers being examined. The effective channel length for each device size which would differ from the mask length by a value Δl could not be determined from the mask set employed, because the device width was different for each channel length. The channel etch tolerance for all devices should, however, be the same and the Δl value would depend then on junction diffusion spreading in each wafer type. Consequently, the comparison of similar devices in Fig. 3 is of less value than device-to-device comparison along each curve, and the relative position of one curve to the others. Devices on all the wafers showed the expected short channel effect below $L = 3.5 \mu\text{m}$. The straight line portions for the wafer types A and B may have a slight upward slope, because the large devices ($L = 50.8 \mu\text{m}$, $W = 508 \mu\text{m}$) in both wafer types A and B exhibit thresholds of 1.1-1.2V compared to values around 0.88V for somewhat smaller devices ($L = 10.8 \mu\text{m}$, $W = 89.5 \mu\text{m}$). Corresponding devices on wafer types C and D, both of which have thermal gate insulators show no such effect. If we now examine the curves for wafer types C and D of Fig. 3, it is seen that devices on wafer type D appear to show a lower threshold than corresponding devices on wafer type C. This is believed to be due to surface boron depletion (7) in wafer type D which underwent thermal field oxidation as compared to wafer type C which underwent plasma field oxidation. Since wafer types C and D both received a thermal gate insulator oxidation sequence, the relative threshold difference cannot

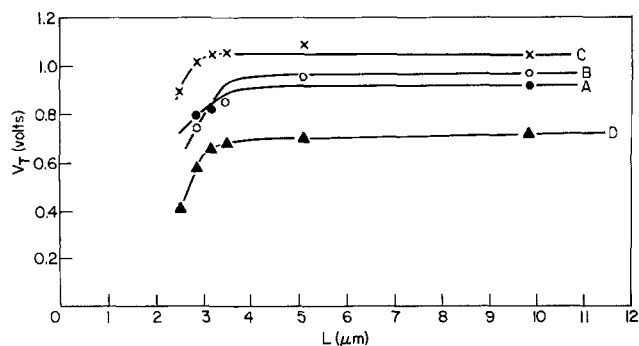


Fig. 3. Variation of thin oxide threshold voltage with channel mask length.

be due to gate insulator thickness difference between them. This was verified via C-V measurements on capacitor pads present on the device wafers on which flatband values were also determined to insure that the difference could not be attributed to difference in insulator charge levels. More definitive boron depletion experiments which confirmed the above are discussed more fully below.

Figure 4 shows the variation of thin oxide threshold voltage as a function of substrate bias voltage. It is seen that the control wafer D exhibits slightly lower substrate sensitivity than the plasma oxidized devices. This is also consistent with the existence of a boron depletion effect in the control wafers. The boron depletion effect is even more pronounced in the substrate sensitivity curves for Al gated thick oxide devices (Fig. 5). Thermal thick oxide devices (D) have much lower thresholds compared to plasma thick oxide devices (A, B, and C), again consistent with boron depletion effects in the former. The slight variation in thresholds of thick plasma oxide devices in wafer types A, B, and C is probably due to variation in oxide thickness (493, 507, and 509 nm, respectively) or bulk substrate doping level variations.

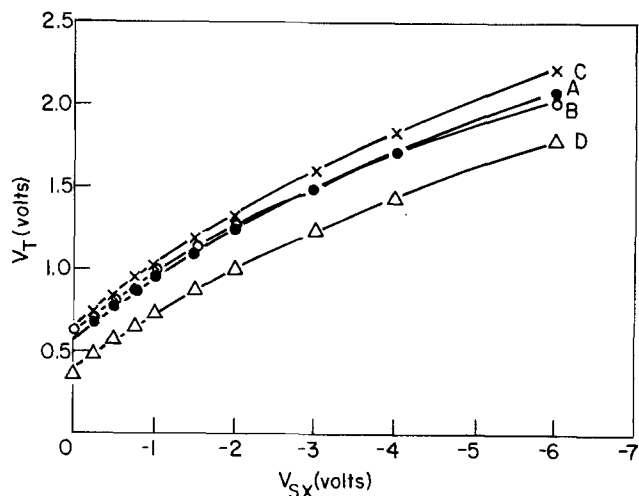


Fig. 4. Variation of thin oxide threshold voltage as a function of substrate bias voltage.

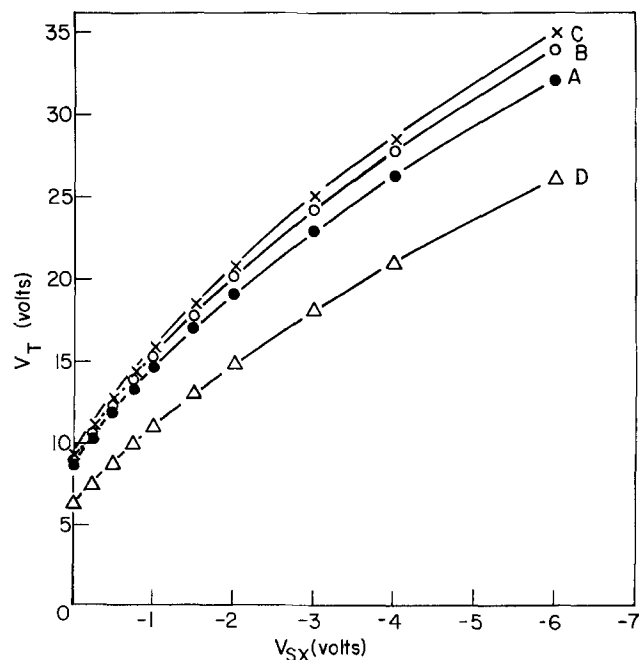


Fig. 5. Variation of thick oxide threshold voltage as a function of substrate bias voltage.

The absence of boron depletion effects during plasma oxidation was confirmed via pulsed $C-V$ measurements on polysilicon gated capacitors in separate experiments. 350 nm of SiO_2 was grown on $2 \Omega\text{-cm}$ p-type ($B \sim 8 \times 10^{15}/\text{cm}^3$) silicon wafers using either plasma oxidation at 500°C or thermal oxidation at 1000°C . These thick oxides were grown to enhance boron depletion effects, if present, as they would be in a conventional field oxidation. The thick oxides were then stripped off, and thin oxides (35 nm) were grown on the same wafers by plasma or thermal oxidation processes. Polysilicon gated capacitors were formed on this thin oxide, and the boron concentration profile near the Si-SiO_2 interface was determined via the pulsed $C-V$ technique. Figure 6 shows the boron concentration profile near the Si-SiO_2 interface after plasma oxidation, indicating the absence of boron depletion effects. Figure 7 shows the boron concentration profile after thermal oxidation. The boron concentration gradually decreases from its bulk value as the Si-SiO_2 interface is approached. In Fig. 6 and 7 the profile is shown to within $2L_D$ of the Si-SiO_2 interface, ($L_D = \text{Debye length}$), because at $<2L_D$ the pulsed $C-V$ data are not considered reliable. The sheet resistivity of n^+ junctions for devices with thermal source-drain: gate electrode oxidation was lower ($30 \Omega/\square$) than devices with plasma source-drain: gate electrode oxidation ($41 \Omega/\square$). This is an indication of the formation of deeper junctions during the thermal source-drain: gate electrode oxidation step at the higher temperatures employed, since the same doping cycle was used for all the wafers during initial source-drain formation. The sheet resistivity of polysilicon gate electrodes ($25 \Omega/\square$) was essentially the same for all wafers.

The results of the first device test run led to the fabrication of a second device test run to test semi-ROX plasma field oxides against thermal field oxides. Plasma oxidation was used only to grow field oxides in this test run with the gate oxides being grown ther-

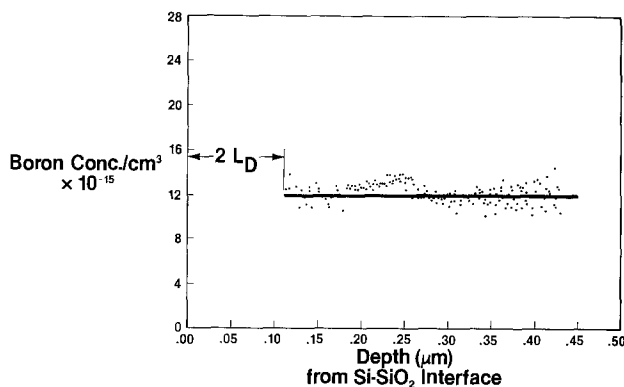


Fig. 6. Boron concentration in silicon as a function of depth from the Si-SiO_2 interface after plasma oxidation.

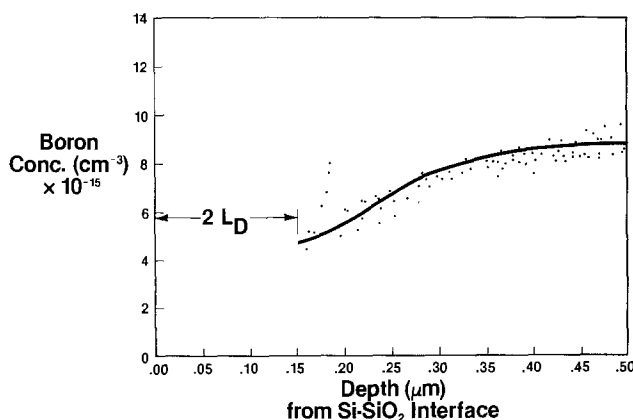


Fig. 7. Boron concentration in silicon as a function of depth from the Si-SiO_2 interface after thermal oxidation.

mally at 800°C . During the gate oxide growth at 800°C , we would expect minimal surface boron depletion. The absence of boron depletion during plasma oxide growth should enable the fabrication of ion-implanted devices with lower boron field doses than that used in conventional processing. The use of lower boron doses in field ion implantation should also result in lower junction capacitance and lower substrate sensitivity. Field ion implantation conditions were chosen so as to obtain the same thick oxide thresholds for the plasma and thermal thick oxide devices with -0.75V on the substrate. For the plasma field oxides, boron implantation dosage was 1.15×10^{12} and 80 keV while that for thermal field oxides was 7.5×10^{12} and 65 keV . About 450 nm of semi-ROX plasma field oxides were grown on wafer type E at 550°C , 15 mTorr system pressure, and 1 kW generator output power in 6.5 hr. 200 nm of MgO on top of 5 nm of SiO_2 was used as an oxidation mask. About 450 nm of thermal field oxides were grown on wafer type F at 950°C . As mentioned above, gate oxides (22.5 nm) were grown on all wafers by thermal oxidation at 800°C . Channel tailoring ion implantation ($B \sim 1.1 \times 10^{12}$, 34 keV) was employed in this test run, and source-drain regions were formed via ion implantation. Other device fabrication steps were essentially the same as described before. Figure 8 shows the thick oxide thresholds for polysilicon gate plasma (wafer E) and thermal (wafer F) thick oxide devices as a function of substrate voltage. At -0.75V substrate bias voltage, the threshold for the thermal thick oxide devices is about 1V higher than the plasma oxide devices. It is seen from Fig. 8 that the plasma oxide devices have much lower substrate sensitivity compared to the thermal oxide devices because of the lower boron dosage required for field ion implantation. It is thus possible to obtain desired threshold voltage accompanied by lower substrate sensitivity in plasma oxide devices by adjusting ion implantation conditions, since no boron is lost to the grown oxide via a boron depletion effect.

Since the thin oxides in both types of wafers were grown thermally at 800°C , and same channel tailoring ion implantation was used, we expected the thin oxide threshold voltages to be the same for both wafers. Figure 9 shows the variation of thin oxide threshold voltage as a function of substrate bias voltage for the two types of wafers. Thin oxide devices have similar thresholds and substrate sensitivity. Threshold measurements were made on devices with nominal dimensions ($L = 10.8 \mu\text{m}$, $W = 89.5 \mu\text{m}$). Since plasma field oxides were grown at much lower temperature compared to thermal field oxides, there will be less

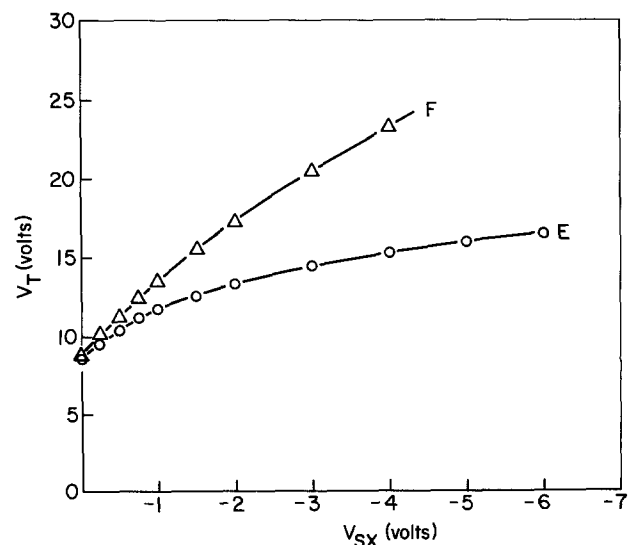


Fig. 8. Variation of plasma and thermal thick oxide threshold voltage as a function of substrate bias voltage.

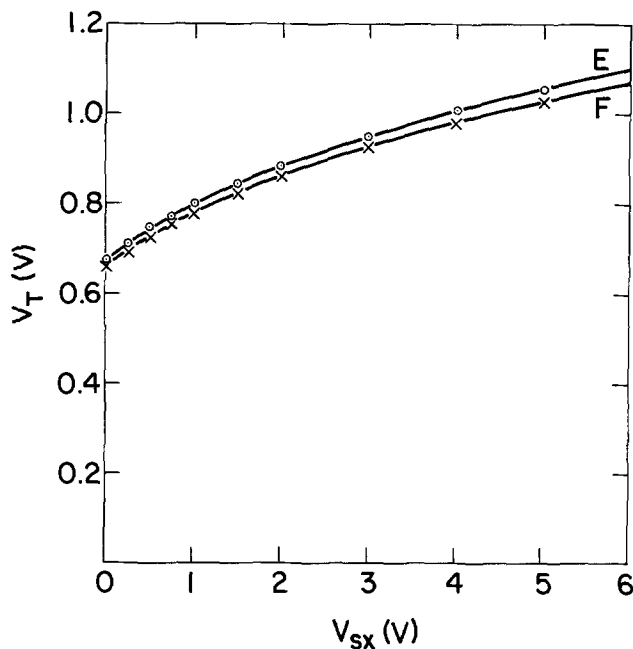


Fig. 9. Variation of thin oxide threshold voltage as a function of substrate bias voltage for plasma and thermal field oxide structures.

dopant redistribution in plasma oxidized structures and as a consequence, the boron concentration near the semi-ROX edges may be less for plasma field oxides compared to thermal field oxides. This could lead to leakage along the width of an FET channel often called "sidewalk leakage." This effect would be more pronounced for narrow width devices. In order to examine this phenomenon, the subthreshold characteristics of thin oxide FET devices with nominal dimensions $L = 3.18 \mu\text{m}$ and $W = 3.18 \mu\text{m}$ were determined. Figure 10 shows the subthreshold I - V characteristics of FET devices with plasma (E) and thermal (F) field oxides. Both devices exhibit similar subthreshold behavior with no indication of abnormal leakage current, *i.e.*, normal subthreshold conduction characteristics are observed.

Conclusions

The characteristics of FET devices fabricated using plasma oxidation processes were found to be normal and comparable to devices fabricated in conventional manner. With a given starting substrate resistivity, the threshold voltages of plasma oxide devices are higher than thermal oxide devices because of the absence of boron depletion effects during plasma oxidation. A higher observed substrate sensitivity of plasma oxide devices is also consistent with the absence of the boron depletion effect. The higher sheet resistivity of n^+ junctions in plasma oxide devices is presumably due to the formation of shallower junctions because of the lower source-drain:gate electrode oxidation temperature. The doping level employed during source-drain formation can be adjusted for desired junction sheet resistivity. It has been demonstrated

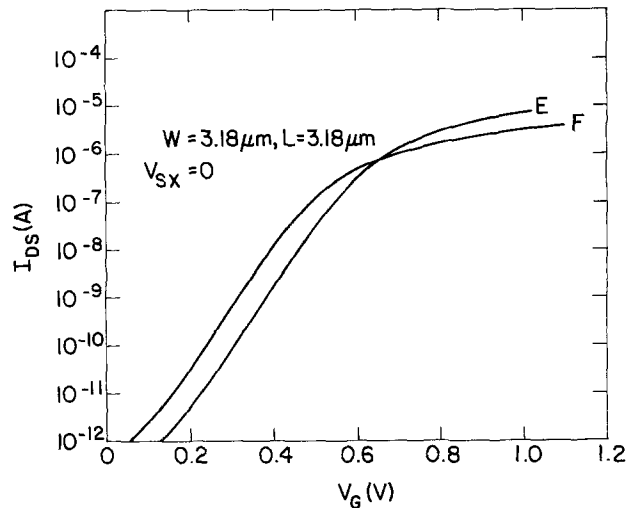


Fig. 10. Subthreshold I - V characteristics of thin oxide FET devices with plasma and thermal field oxides.

that a required threshold voltage and lower substrate sensitivity in the field regions can be achieved in plasma oxide devices by using lower dosage implants, since no excess boron is lost to the grown oxide via a boron depletion effect. A similar but smaller effect would occur in the channel regions. In general, then, plasma oxide devices have advantages over thermal oxide devices in terms of lower processing temperatures, absence of defects, absence of surface dopant depletion and junction depth containment, as well as minimization of "bird's beak" phenomena.

Acknowledgments

The authors are indebted to R. H. Dennard and C. M. Osburn for helpful discussions. The authors would like to thank G. Hu for impurity profile simulation and R. P. Havreluk for electrical measurements.

Manuscript submitted Jan. 30, 1981; revised manuscript received June 11, 1981. This was Paper 234 presented at the Minneapolis, Minnesota, Meeting of the Society, May 10-15, 1981.

Any discussion of this paper will appear in a Discussion Section to be published in the June 1982 JOURNAL. All discussions for the June 1982 Discussion Section should be submitted by Feb. 1, 1982.

Publication costs of this article were assisted by IBM Corporation.

REFERENCES

1. A. K. Ray and A. Reisman, *This Journal*, **128**, 2460 (1981).
2. A. K. Ray and A. Reisman, *ibid.*, **128**, 2466 (1981).
3. B. E. Deal, A. S. Grove, E. H. Snow, and C. T. Sah, *ibid.*, **112**, 308 (1965).
4. S. M. Hu, *J. Appl. Phys.*, **45**, 1567 (1974).
5. S. P. Murarka, *ibid.*, **48**, 5020 (1977).
6. E. Bassous, H. N. Yu, and V. Maniscalco, *This Journal*, **123**, 1729 (1976).
7. D. L. Critchlow, R. H. Dennard, and S. E. Schuster, *IBM J. Res. Dev.*, **17**, 430 (1973).

A Modified SEM Type EB Direct Writing System and Its Application on MOS LSI Fabrication

Y. Iida* and K. Mori

Nippon Electric Company, Limited, Basic Technology Research Laboratories, Takatsu-ku, Kawasaki 213, Japan

ABSTRACT

A modified SEM type electron beam exposure machine adopts an auto-registration function and it is converted to a direct writing purpose system. One-chip-one field and chip-by-chip registration scheme is adopted to increase the field size and to eliminate stage-related problems, such as laser interferometric control complexity and stage movement slowness. 2 μm rule 64 k ROM, shrunk to 4/10 from the original design, is used as a device for testing the developed EB system capability. 0.8 μm high, 2 μm wide, L-shaped step made from bulk Si is used as registration marks and $\pm 0.1 \mu\text{m}$ of 2 level overlay accuracy is achieved. Although no special optimization or device design modification is done on the shrinkage, the device fabricated by all EB direct writings and dry etching process shows no noticeable difference in electric functions from one made by photolithographic (DSW) processes. The system is stable without intensive maintenance jobs and overlay accuracy through the process (7 exposing levels) is better than $\pm 0.25 \mu\text{m}$, although the registration mark structure is changed by the fabrication processes. It becomes clear that this kind of direct writing machine is very useful for research of EB lithography and the LSI development.

Master mask fabrication using electron beam exposure has become usable on the factory level. A raster scanning machine is most popular for this purpose (1-3).

However, it is not clear yet which is the best system for direct writing and there is no commercial machine used for production. For a while the electron beam direct writing machine was used as an experimental or LSI development purpose tool, due to the small throughput from its serially exposing nature but quick turn around time. The system under these circumstances should have the following characteristics to compete with ever improving photolithographic machines (4): (i) Achievability of highly accurate re-registration, even though the wafer is distorted (5) and the registration mark is degraded by the fabrication processes; (ii) reasonable throughput to fabricate developing devices; (iii) high stability and high up-time ratio; and (iv) connection to computer aided design system is possible.

To satisfy (i), a vector scanning electron beam exposure is one of the best ways, because of its scheme to register the writing pattern on a chip by chip basis, using registration marks on each chip corner. If chip by chip registration is possible, necessary stage movement accuracy becomes less and reregistration could be realized even without laser interferometric control. It also reduces the EB system cost and complexity.

About (ii), a one-chip-one field strategy for large field would be one of the better choices, since it can reduce the stage movement time, which could be a large part of exposing time after the advent of high resolution high speed DAC for steering the electron beam. While this technique results in bigger writing field distortion, if all the exposure is accomplished by the same machine, there should not be any problem including overlaying.

To satisfy (iii), magnetic field scan and separation of main scan and correction for reregistration are important. About (iv), PG-3000 format¹ could be an interface.

The system developed in this research is a vector scanning type using pre-lens double deflection correc-

tion for registration and post-lens main scanning. Field size is relatively large, 5 mm. It can accommodate various developing test devices like 64 K ROM, 4 k static RAM, 256 k bubble device, SAW device, etc. It could give important information for larger scale integration, which is often an ally of these devices (6). A testing tool selected for clarifying the system characteristics through its direct writing application is a 64 k ROM which simply reduced the conventional 5 μm rule into the 2 μm rule. Emphasis was placed on determining degradation in registration marks on the wafer by the process chosen to fabricate the 64 k ROM. The technologies used in the process were not only a direct writing, but reactive sputtering in combination with beam resists.

System Description

A vector scan electron beam system² is modified for direct writing by the adoption of auto-registration system. A block diagram of the system is shown in Fig. 1. The electron beam column has a main post-lens magnetic scanning coil and an additional small pre-lens double deflection coil for registration purposes. Main scan is achieved by a combination of positioning purpose high accuracy 16 bit DAC and fill-in mode high speed 12 bit DAC. Accelerating voltage is set at 20 kV, but is adjustable from 2.5 to 30 kV. A tungsten filament is used for its high stability. Also, a single crystal LaB₆ is used sometimes for tests. The modified machine is balanced to operate at an equivalent 0.5 MHz data rate with electron resist sensitivities of 5 $\mu\text{C}/\text{cm}^2$ for W filament and 30 $\mu\text{C}/\text{cm}^2$ for single crystal LaB₆. The column can provide a minimum beam diameter less than 500 Å at 56 mm working distance. Typical probe size used for this work is 0.25-0.40 μm . Beam blanking is electrostatic. A scintillator system is used to provide video signals for setup and registration. Registration has been accomplished in two stages.

First, the wafer is roughly registered in the stage movement direction and writing field, using large wafer registration mark. Next, the writing field is finely and automatically registered on a chip by chip basis using chip registration mark. Figures 2 and 3 show the wafer setting errors in shift and rotation, respectively, without preregistration to the cassette. Both errors

* Electrochemical Society Active Member.

Key words: electron beam exposure, direct writing system, auto-registration, MOS LSI process, registration mark.

¹ A pattern data format, proposed by David W. Mann Company.

² LEBES, ETEC Corporation, Hayward, CA 94544.

LEBES SYSTEM DIAGRAM

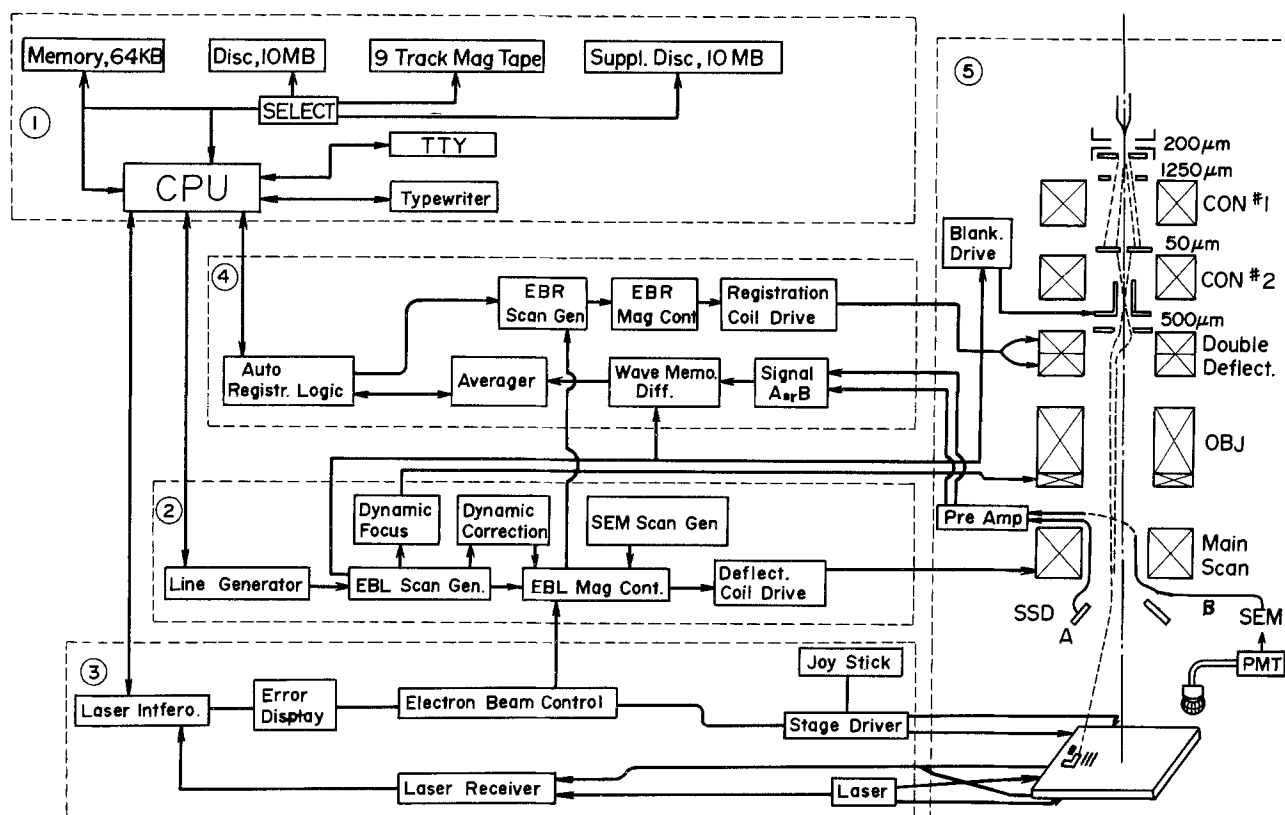


Fig. 1. LEBES system diagram

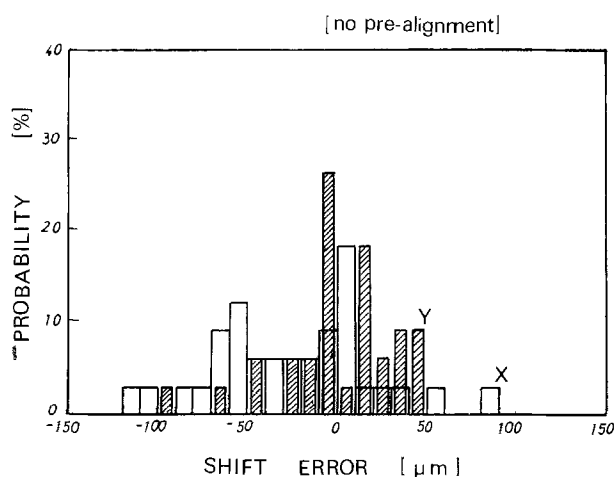


Fig. 2. Wafer setting error (shift); blank (X direction), shadowed (Y direction).

include that of wafer to cassette and that of cassette to column. They are fundamentally gaussian distribution. From the data, the auto-registration system correction range was designed to shift $\pm 150 \mu\text{m}$ and rotate $\pm 2.5^\circ$ at maximum. Field size is adjustable $\pm 2\%$. Any correction is accomplished by 12 bit multiplication DAC in X and Y directions, separately. Resolutions are $0.073 \mu\text{m}$ in shift, and 0.045 and $0.039 \mu\text{m}$ at the field corner in rotation and magnification, respectively. Drive amplifier for registration correction has high level response, close to 10 MHz. After registration pattern writing commences, the system can select a data file to expose, and multiple chip fabrication is possible aiming at small volume but quick fabrication.

Patterns are exposed in serpentine, rectangular, or raster format with pattern generation providing several primitive shapes such as rectangles, parallelograms, and triangles. Proximity correction has not been

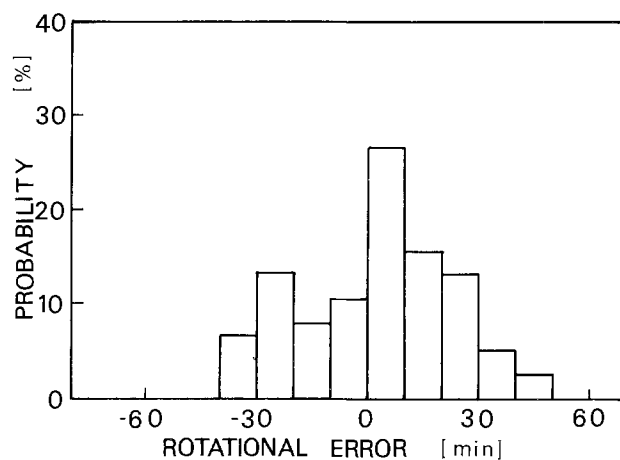


Fig. 3. Wafer setting error (rotation)

included, because of the relatively large design rule employed.

Writing Method and Hysteresis

To minimize the settling time, jumping distance from one pattern to another is restricted through subfield sorting (7). For this method, a basketweave shift between subfields is the best (8). However, it causes a hysteresis error at the connection point of each subfield stripe. This error comes from magnetization of stage parts in the column by leakage field.

This problem is partially alleviated by shielding with Permalloy, as shown by the dotted line in Fig. 4. However, a system aiming at a large field, like the present one, cannot escape from the error completely. Stripe raster shift should be adopted. Using this method, the error is completely eliminated. A drawback is that longer settling time (typically 20 times the subfield jump time) is needed when the subfield is shifted from one corner to the other of a stripe. It is, however, only 10 msec (field jump settling time) \times 20

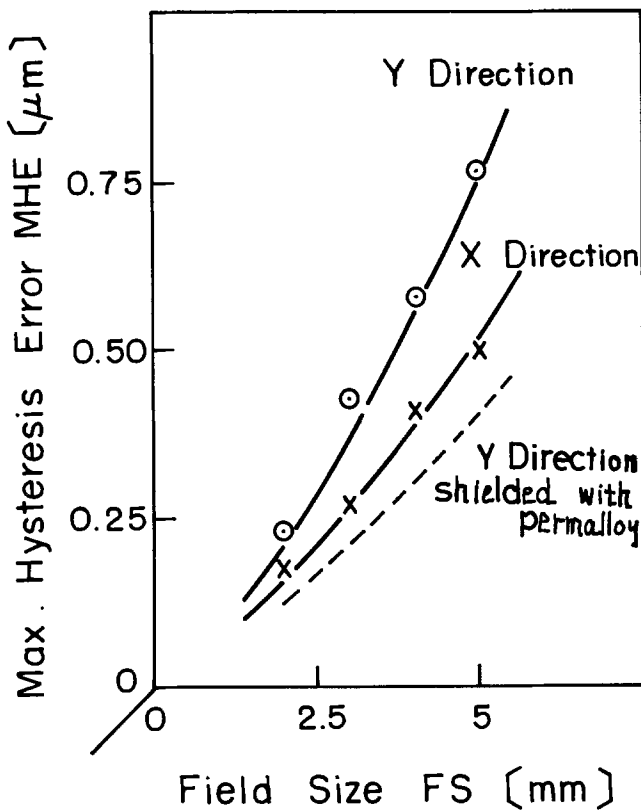


Fig. 4. Maximum hysteresis error as a function of field size

(number of stripes), making 200 msec. There is no problem compared with writing time, typically 3 min/chip for 64 k ROM.

Pattern Data Preparation

The pattern data are first created in an interactive computer aided design (CAD) system, and are output in PG-3000 format. The shapes are sorted to minimize long jumps between shapes using a large computer system (ACOS-700).

Consequently, pattern writing time will contain minimum overhead necessary for settling the deflection system. This is achieved by first sorting the chip data into subfields through which the writing will progress in a stripe raster fashion.

The typical size of a subfield is 1/20 of the field size. Within a subfield, the shapes are connected to compact the data. The resulting set of sorted records is then translated into code in the format required by the modified E-beam machine. Typical CPU time to treat 100 k data is about 10 min.

Resist Process

A key to this work is the resist system, which must provide high durability against reactive sputter etching and adequate sensitivity. Commercial availability of resists might be another important factor in order to make the fabrication process reliable. AZ-2400⁸ was chosen as a positive electron resist (9) and NER-1 was chosen as a negative electron resist. The former is a well-known photoresist. The latter is made from narrow molecular weight dispersion polystyrene, which is easily available as molecular weight standard synthesized by living polymerization. Selection of negative resist molecular weight is important. The higher the molecular weight is, the greater the severity of the swelling problem and the "kissing" problem between lines, while soaking in the developer. A 4:1 tetrahydrofuran-ethanol mixture was selected as a low swelling developer. However, the smaller the molecular weight, the stronger the tensile stress and the more

* Shipley Company, Newton, MA.

Table I. Direct writing resist characteristics

| RESIST | NER-1 (polystyrene) | | AZ-2400 | |
|------------------------------|--|--|-------------------------------|--|
| TYPE | NEGATIVE | | POSITIVE | |
| ETCHED MATERIAL | Si ₃ N ₄ | Poly-Si | Al | SiO ₂ |
| ETCHING GAS | CF ₄ +H ₂ 0.09 Torr | CCl ₃ F+O ₂ 0.04 Torr | CCl ₄ 0.35 Torr | CF ₄ +H ₂ 0.08 Torr |
| ETCH RATIO (MATERIAL/RESIST) | 4.3 | 2.1 | 6.5 | 2.8 |
| TYPICAL PATTERN | | | | |

severe the distortion in the L-shaped pattern results. This is due to the polymer cross-linking by exposure and concomitant volume shrinkage.

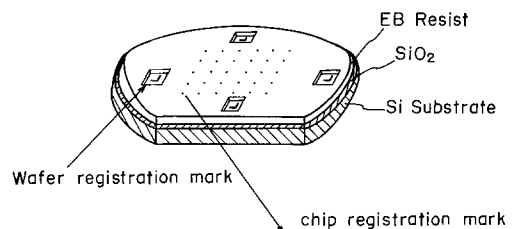
Relatively large 600 k molecular weight was chosen to optimize swelling and shrinking problems. It is called NER-1. Table I shows a summary of characteristics for both resists.

Linewidth Control and Registration Mark

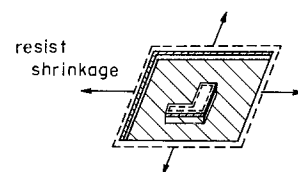
All EB direct writing process is practically usable when the device patterns are directly etched by EB resist mask; without metal mask transfer step the registration mark is compatible with the process. Delineation accuracy values, when using SiO₂, Si₃N₄, poly-Si, and Al are ±0.15, ±0.15, ±0.15, and -0.25 ± 0.15 μm, respectively. It is achieved by using reactive sputter etching (10) and highly durable EB resist against dry etching mentioned above.

For accurate registration, it is desirable to fabricate registration marks using electron beam exposure. The registration marks used in this work are 0.8 μm high silicon pedestals, which are completely compatible with the silicon process. The fabrication process is illustrated in Fig. 5. There are several advantages to the process: (i) There is no foreign material like refractory metal, CVD poly-Si, etc.; (ii) the resist area for the registration mark is small and resist deformation caused by dry etching does not affect pattern accuracy.

1. Electron Beam Exposure and Development



2. Dry Etching of SiO₂ and Si



3. Remove resist and wash out SiO₂

Fig. 5. Si pedestal registration mark fabrication process with EB resist mask and dry etching.

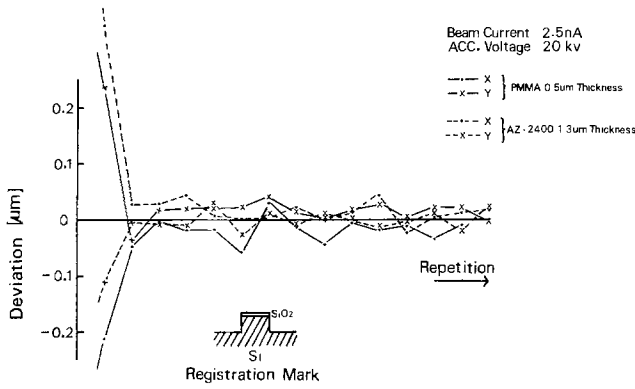


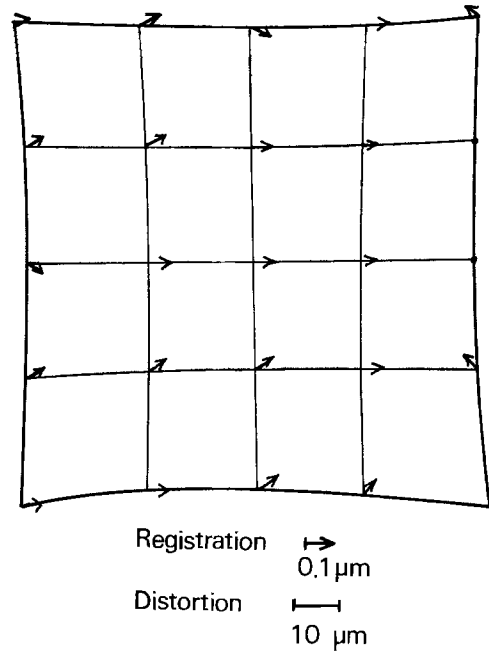
Fig. 6. Deviation in detected position from desired position

The larger the continuous resist area, the more critical the pattern deformation or positional shift. (iii) Device area; cleanliness is protected by the SiO₂ during the process. The SiO₂ is etched away after the process. Figure 6 shows the X direction and Y direction detection accuracy for the registration mark coated by different thickness resists. There is no notable difference between them. After two scans, the detection accuracy is better than 0.1 μm. Though the reason for relatively large error in the first scan is not clear, it could be because of resist deformation by the first beam scan. It is desirable to practice dummy scanning before the detection. Figure 7 shows an example of the two layer registration accuracy for the 5 mm field. Since the system has field distortion, the registration condition shown by the arrows is slightly different for different positions. They are, however, within ±0.1 μm.

Direct Writing Process and the Function of the Fabricated Device

The direct writing process is fundamentally an n-channel polysilicon MOS process. Figure 8 shows key steps in the etching process. Table II shows exposure and doping processes. After registration mark patterning, device areas were isolated by boron diffusion in the field and by the local oxidation of silicon (LOCOS). Threshold voltages for driver enhancement transistor and load depletion transistor are adjusted by boron ion and arsenic ion implantations, respectively. Gate insulator thickness was 400Å; 5000Å CVD polysilicon was used as gate metallization. The polysilicon was covered by 1600Å CVD Si₃N₄. Arsenic ions were implanted to form the self-aligned source and drain. Wafers were annealed at 1000°C in a steam atmosphere to form the sidewall insulator of the polysilicon gate

5mm Field OVERLAY ACCURACY



| Exposure level | Shift (μm) | | Rotation (min) |
|----------------|------------|--------|----------------|
| | X | Y | |
| 1 | -112.8 | 93.4 | -12.9 |
| 2 | 27.6 | -112.9 | -25.2 |

Fig. 7. 5 mm field overlay accuracy

and thick silicon dioxide on the source and drain by heavily doped arsenic enhancing oxidation. After Si₃N₄ removal, phosphorous was thermally diffused into the polysilicon. Double layers of phosphorous silicate glass and CVD SiO₂ were used as an insulator. PSG made it possible to topographically smooth the device surface, preventing discontinuing the Al metallization and thin SiO₂ eliminated the wetting and poor resist adhesion problems of PSG. Contact holes were etched into the double layer to write ROM information. Phosphorous-doped polysilicon 0.2 μm thick and 1.2 μm Al

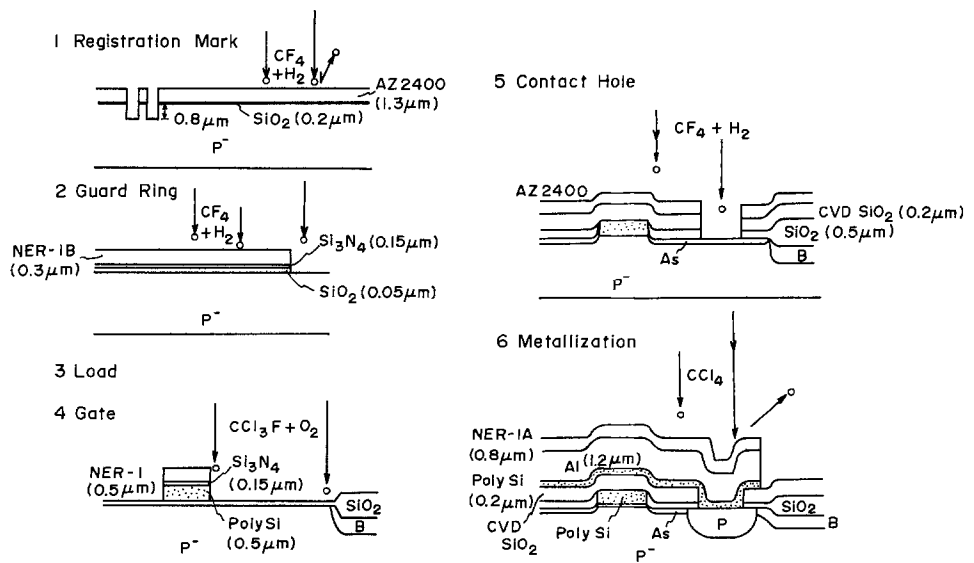


Fig. 8. Fabrication step drawings.

Table II. N-MOS process parameters used for the experiment

| | |
|-------------------|---|
| starting material | P-type, 50 Ω -cm (511) |
| exposure [1] | registration mark (2 μ m) |
| exposure [2] | locos pattern (2 μ m) |
| field I/I | $^{11}\text{B}^+$, 100 KeV, $2 \times 10^{13} \text{ cm}^{-2}$ |
| locos oxidation | 1000°C, 4hr, 0.8 μ m SiO ₂ |
| gate oxidation | 950°C, 85 min dry O ₂ , 400 \AA |
| channel I/I | $^{11}\text{B}^+$, 150 KeV, $3 \times 10^{11} \text{ cm}^{-2}$ 40 KeV, $5 \times 10^{11} \text{ cm}^{-2}$ |
| exposure [3] | Load pattern (5 μ m) |
| depletion Tr I/I | $^{75}\text{As}^+$, 150 KeV, $2 \times 10^{12} \text{ cm}^{-2}$ |
| exposure [4] | Direct contact |
| exposure [5] | Gate pattern (2 μ m) |
| S/D I/I | $^{75}\text{As}^+$, 150 KeV, $5 \times 10^{15} \text{ cm}^{-2}$ |
| exposure [6] | Contact pattern (2.5 μ m) |
| exposure [7] | Al pattern (2 μ m space) |
| exposure [8] | Pad pattern |

were continuously deposited and etched as interconnectors. Annealings to remove the irradiation damage were carried out in H₂ atmosphere at 450°C.

Figure 9 shows an overall view of the fabricated 64 k ROM and enlarged views. The 2.5 μ m contact hole is centered in 3 μ m width Al metallization. It is clear that the registration mark is kept well through the fabrication processes. Details are discussed in the following section.

Figure 10 shows a function of the device fabricated by all E-beam direct writing. As can be seen, the rise-time for the fall time of the signal are unbalanced. It was, however, assumed that the input and output buffer is not optimized, although high reduction (4/10) has been accomplished. The same design rule device, fabricated by photolithographic process (DSW), has shown very similar results (11).

Overlay Accuracy

Table III shows an example of overlay accuracy through the process. The Vernier method was adopted to measure the accuracy. On the table, for example, GR-load shows overlay accuracy for load I/I pattern on the guard ring pattern.

The overlaid pattern always has little X and Y shift and distribution. The shift error origin is not clear, but the registration mark structure change caused by unbalanced resist or material coating of the mark are considered reasons. Similar phenomena are often discussed on Al metallization coverage.

Table III. Overlay accuracy through the all EB direct writing process

| | X [μ m] | | Y [μ m] | |
|---------------|--------------|----------|--------------|----------|
| | \bar{X} | σ | \bar{Y} | σ |
| GR- Load | -0.02 | 0.13 | -0.05 | 0.13 |
| GR- D.Contact | 0.12 | 0.03 | -0.04 | 0.12 |
| GR- Gate | 0.13 | 0.06 | 0.07 | 0.12 |
| Gate- Contact | 0.08 | 0.08 | 0.02 | 0.03 |
| Contact- Al | 0.07 | 0.07 | 0.09 | 0.06 |

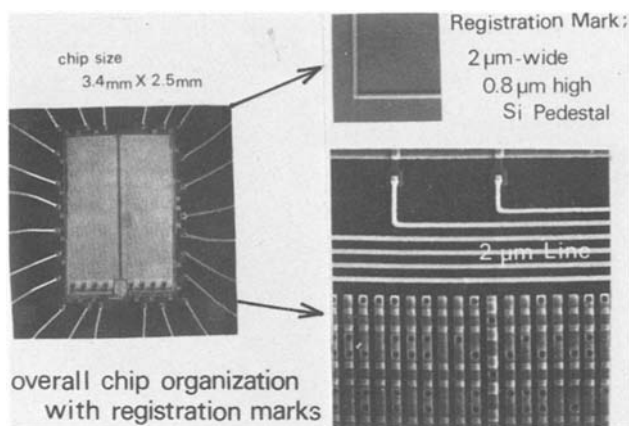


Fig. 9. Overall and magnified view of 64 k ROM

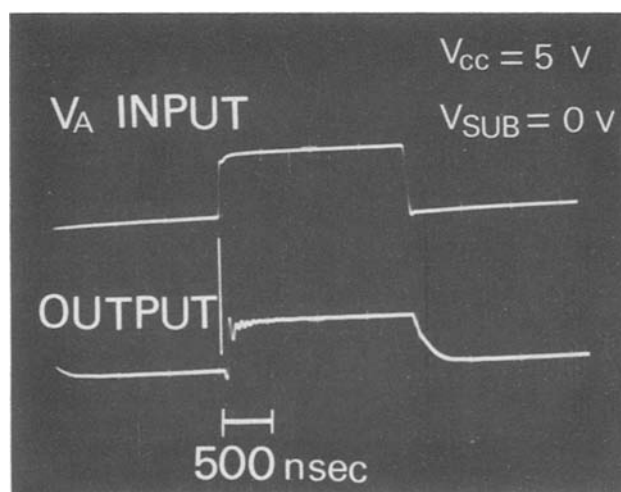


Fig. 10. An example of output waveform

Even considering shift and distribution, the results shows that the system well satisfied the required $\pm 0.25 \mu$ m overlay accuracy, using registration mark damaged by various coating and etching processes.

Conclusion

The systems described here are a fundamentally modified SEM machine, not those machines which could be fabricated only by a huge company laboratory. The systems are easily modified to research fundamental electron optics and new strategy to write pattern, such as double deflection correction, hysteresis, and stripe scanning. It has, however, enough capability to fabricate LSI such as 64 k ROM by all direct writing process. The beam is focused into a small diameter area, less than 500 \AA .

The system could be used for quick fabrication of a wide variety of devices, like bubble memories, Josephson circuits, GaAs FET, etc. It is also used for new resist evaluation, research in physics related to electron beam damage, electron scattering, and delineation limitation.

Acknowledgment

The authors wish to thank Drs. D. Shinoda and K. Muta for their encouragement. They would like to thank Messrs. S. Ishida, M. Tajima, and K. Kamimura for their technical assistance. They also thank Drs. Y. Okuto, Y. Ohnishi, and K. Suzuki, and Messrs. H. Mizumura, Y. Kurogi, M. Morimoto, and N. Endo for informative discussions.

Manuscript submitted Dec. 9, 1980; revised manuscript received May 13, 1981.

Any discussion of this paper will appear in a Discussion Section to be published in the June 1982 JOURNAL. All discussions for the June 1982 Discussion Section should be submitted by Feb. 1, 1982.

Publication costs of this article were assisted by Nippon Electric Company, Limited.

REFERENCES

1. D. R. Herriott, *IEEE Trans. Electron Devices*, **ed-22**, 385 (1975).
2. N. C. Yew, *Solid State Technol.*, **20**, 86 (1977).
3. J. A. Doherty, *ibid.*, **20**, 83 (1977).
4. G. L. Resor, *Microelectron. J.*, **10**, 18 (1979).
5. L. D. Yau, *IEEE Trans. Electron Devices*, **ed-26**, 1299 (1979).
6. K. Suzuki, M. Morimoto, N. Endo, H. Ishiguro, K. Kurogi, Y. Iida, and K. Mori, in "Proceedings of 1980 Custom Integrated Circuits Conf.," p. 8, New York (1980).
7. T. H. P. Chang, A. J. Speth, C. H. Ting, R. Viswanathan, M. Parikh, and E. Munro, in "Electron and Ion Beam Science and Technology," R. Bakish, Editor, p. 377, The Electrochemical Society Soft-bound Proceedings Series, Princeton, NJ (1976).
8. W. D. Grobman, H. E. Luhn, T. P. Donohue, A. J. Speth, A. Wilson, M. Hatzakis, and T. H. P. Chang, *IEEE Trans. Electron Devices*, **ed-26**, 360 (1979).
9. M. Hatzakis and J. W. Shaw, in "Electron and Ion Beam Science and Technology," R. Bakish, Editor, p. 301, The Electrochemical Society Soft-bound Proceedings Series, Princeton, NJ (1978).
10. N. Endo and Y. Kurogi, *IEEE Trans. Electron Devices*, **ed-27**, 1376 (1980).
11. N. Endo, Private communication.

MOS Device Fabrication Using X-Ray Lithography

K. Suzuki and J. Matsui

Nippon Electric Company, Limited, Basic Technology Research Laboratories, Takatsu-ku, Kawasaki 213, Japan

and T. Ono and Y. Saito

*Nippon Telegraph and Telephone Public Corporation,
Musashino Electrical Communication Laboratory, Musashino, Tokyo 180, Japan*

ABSTRACT

X-ray lithography has been applied to fabricate n-MOS devices such as transistor matrixes, ring oscillators, and MOS capacitors. A propagation delay time as low as 200 psec/gate, and about 0.12 pJ power-delay product were obtained from the ring oscillator with 0.7 μm effective gate length. From the threshold voltage measurements of the transistor matrixes, it was found that the standard threshold voltage deviation in MOSFET's with 1.5 μm effective gate length in a chip and the deviation in a wafer were as low as 5 and 7 mV, respectively.

X-ray lithography has been expected to be useful as a fine pattern replicating technique, because of its high resolution and productivity. Recently, a high power x-ray lithographic system using a water-cooled rotating Si anode for x-ray source and a beam vibration method for mask alignment has been developed and its performance was demonstrated (1, 2). An SiN/SiO₂/SiN sandwich structure membrane mask (3) has also been developed and was applied to fabricate poly-Si gates in ring oscillators (2).

In this experiment, MOS devices have been fabricated using the above-mentioned x-ray lithographic system for four mask levels. The present paper describes the x-ray lithography process followed by dry etching, and also the device characteristics.

X-Ray Lithography Process

The IC chips which have been fabricated in this experiment contain transistor matrixes, ring oscillators, and MOS capacitors. Of the five lithographic steps, local oxidation of silicon (LOCOS) (4), gate, contact hole, and metallization were processed by x-ray lithography. Only the channel doping step was processed by photolithography. In order to examine the x-ray exposure influences on the devices, a few wafers in the lot were processed by photolithography through all lithographic processes.

A water-cooled rotating Si anode x-ray source was operated at 20 kW (20 kV, 1A) electron beam input power, which generates about 6×10^{-5} W/Sr SiK α x-ray radiation.

Key words: fine pattern, x-ray mask, dry etching, transistor matrixes.

X-ray masks (3) consisting of an SiN (0.2 μm)/SiO₂ (1.0 μm)/SiN (0.2 μm) sandwich structure were prepared by CVD for SiN and by rf-sputtering for SiO₂, respectively. The membranes have as high as 85% transparency for both the SiK α line and visible light. X-ray absorber patterns, consisting of a 0.8 μm thick gold, were fabricated by a double lift-off method (5), in which 1.2 μm thick polyimide spacer patterns are used for gold plating masks.

Details of the x-ray lithographic levels are shown in Table I. In three mask levels, i.e., LOCOS, gate, and metallization, negative resist SEL-N¹ has been used. Figure 1 shows a scanning electron micrograph of 2 μm gate patterns exposed in a 0.8 μm thick SEL-N. The SEL-N patterns show trapezoidal cross sections. This is caused by the swelling of SEL-N patterns in a developer followed by shrinking in rinsing solution and postbaking process. The swelling magnitude changes,

¹ SEL-N is produced by Somar Industry Corporation, in Japan.

Table I. X-ray lithographic levels

| Level | Film | Resist | Etching method | Gas | Etch rate ratio (film/resist) |
|---------------|------------------------------|----------------------------|--------------------------|-------------------------------|-------------------------------|
| LOCOS | SiO ₂ | SEL-N (0.7 μm) | Wet etching | — | — |
| Gate | Poly-Si (0.4 μm) | SEL-N (1.0 μm) | Reactive sputter etching | CBrF ₃ | 3.5 |
| Contact | PSG (0.8 μm) | FBM (1.0 μm) | Reactive sputter etching | C ₂ F ₆ | 1.3 |
| Metallization | Al (0.8 μm) | SEL-N (1.5 μm) | Plasma etching | CCl ₄ | 1.0 |

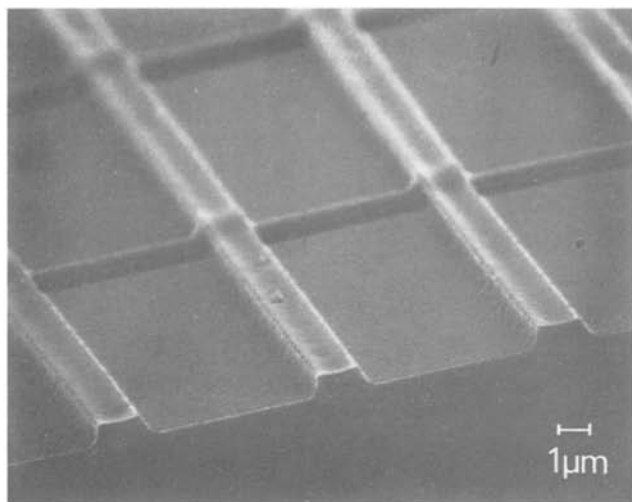


Fig. 1. Scanning electron micrograph of 2 μm gate patterns exposed in a 0.8 μm thick SEL-N.

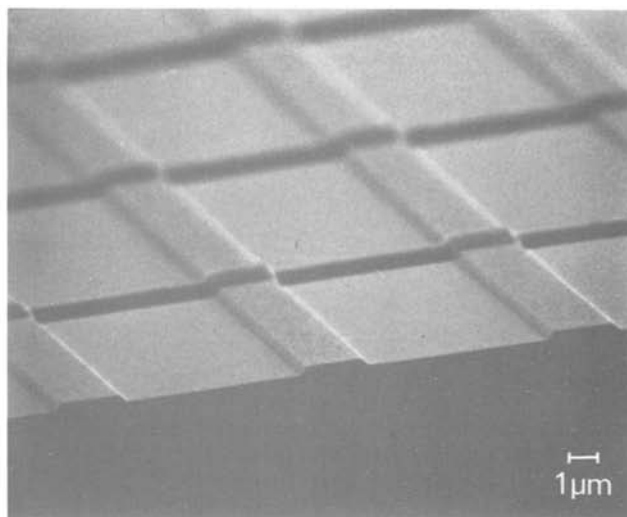


Fig. 3. Reactive sputter etched 2 μm poly-Si gates

depending on the resist volume, and also on the kind of developer. In this experiment, methyl alcohol was used for developer, which resulted in rather small swelling. However, in contact hole level, negative resists, including SEL-N, are hard to use because of the large resist-covered area that leads to conspicuous swelling (narrowing or plugging up of the contact holes). In this level, therefore, a positive resist poly hexafluorobutyl metacrylate (FBM) (6) was used, which showed little swelling in the developer. A scanning electron micrograph of 4 μm wide contact holes, exposed in a 1.3 μm thick FBM, is shown in Fig. 2. FBM contact holes preserved squarish shoulders, and the side walls were inclined from the surface at 75 degrees.

Dry etching has been employed for constructing gates, contact holes, and wiring. The etching method after each lithographic step is presented in Table I with gases used, and film to resist etch rate ratio. A scanning electron micrograph of 2 μm poly-Si gates etched by reactive sputter etching (7) is shown in Fig. 3. Side walls of the poly-Si gates show 45° ~ 50° tilts, which reflect SEL-N pattern profile used for etching mask. Figure 4 is an SEM photograph, which indicates good step coverage of the poly-Si gate at the 0.5 μm guard ring projection.

Figure 5 shows the appearance of aluminum metallization in the transistor matrix after plasma etching. Although the etch resistance of SEL-N against plasma

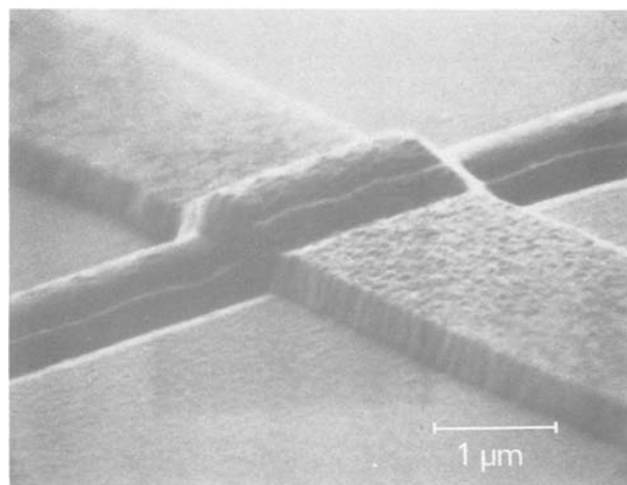


Fig. 4. Scanning electron micrograph showing good step coverage at the 0.5 μm step.

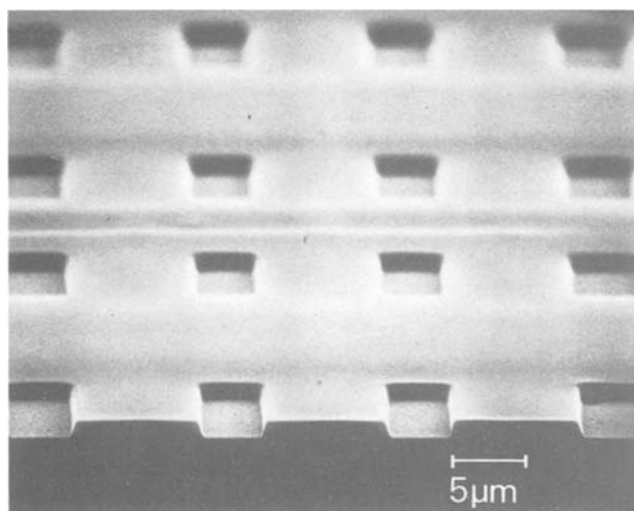


Fig. 2. Scanning electron micrograph of 4 μm wide contact holes exposed in a 1.3 μm thick FBM.

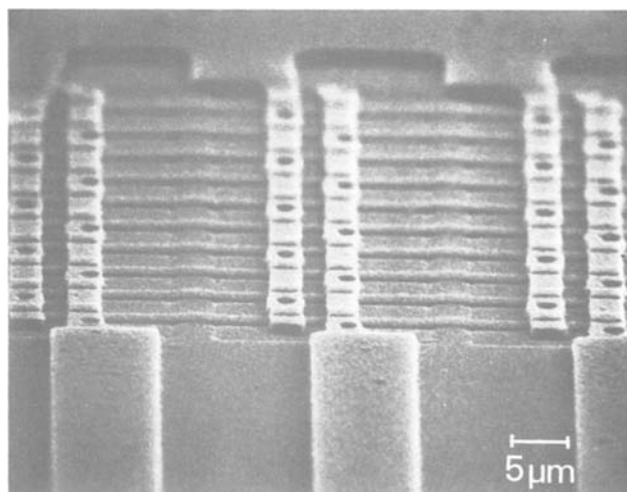


Fig. 5. 3 μm wide aluminum metallization in a transistor matrix

etching using CCl_4 is the same as that of aluminum, a considerably thick ($\sim 1.5 \mu\text{m}$) SEL-N resist layer is required for x-ray exposure of the metallization level, because the decrease in the resist thickness at the shoulder of contact holes is significant. In this case, 0.8 μm thick, 3 μm wide, 2 μm gap aluminum metallization is successfully fabricated, as shown in Fig. 5.

The x-ray masks were aligned to the wafer using the beam vibrating method (1, 8). The alignment marks on the wafer were made by preferential etching using hydrazine solution. It was found that the S/N of this mark was not changed through the five lithographic processes. Therefore, the same mark was used for all lithographic processes without any protection. The total alignment error by the above-mentioned method was found to be less than $0.3 \mu\text{m}$ (2σ) in a 2 in. diam wafer, from measurements using vernier patterns which were made in each lithographic process.

Device Characteristics

An example of the threshold voltage (V_{th}) distribution for transistor matrixes with $1.5 \mu\text{m}$ effective gate length is shown in Fig. 6. The upper numeral in each of the sixteen squares shows V_{th} , the average values of the V_{th} of 120 FET's in the transistor matrix. The lower numeral shows σ_0 , the standard deviation in the V_{th} . The average value of σ_0 , over all chips in the wafer, represented by $\bar{\sigma}_0$, is 5.0 mV. The standard V_{th} deviation in the wafer, σ_1 is 6.7 mV. Other wafers show a similar tendency. These results show highly uniform characteristics in devices made by x-ray lithography followed by dry etching.

Figure 7 is a photomicrograph of the ring oscillator fabricated by x-ray lithography. The ring oscillator is a 31-stage E/D mode unit with a fan-in and fan-out ratio of 1. Effective channel length is $0.7 \mu\text{m}$ in the driver transistors, and $2.3 \mu\text{m}$ in load transistors.

The output waveform for the ring oscillator at $V_{\text{dd}} = 5\text{V}$ is shown in Fig. 8. The oscillation period is 12.5 nsec, which corresponds to 202 psec/gate propagation delay time. The power-delay product is about 0.12 pJ/gate.

The C-V curve for the MOS capacitor, fabricated using x-ray lithography for four mask levels and that by using photolithography for all mask levels, is shown in Fig. 9. Both MOS capacitors have the same design, and have been made in the same lot, except for the lithographic processes. There was no special annealing process after the x-ray lithographic process. Figure 9 shows that there is no x-ray radiation-induced damage in the MOS capacitor, when every standard process is over. It is reported, however, that the C-V curves from MOS capacitor irradiated by $\text{AlK}\alpha$ (8.3\AA) shift from the original state (9-11). It is considered that, in the

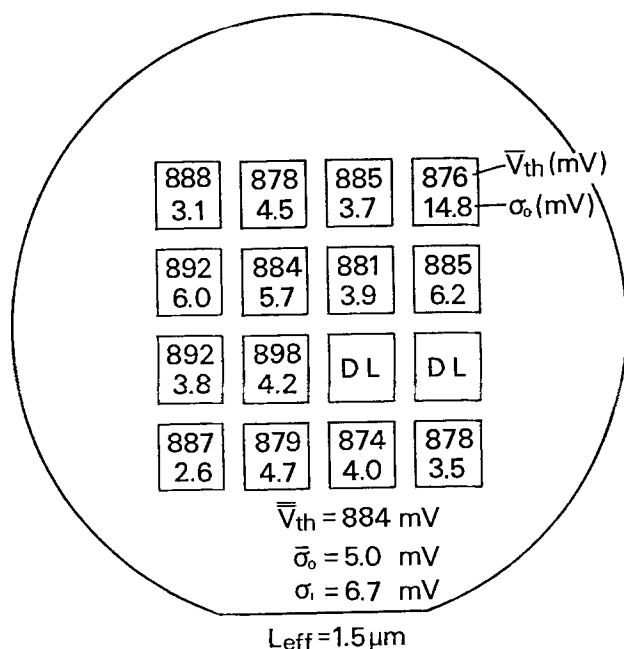


Fig. 6. An example of V_{th} distribution map in the wafer

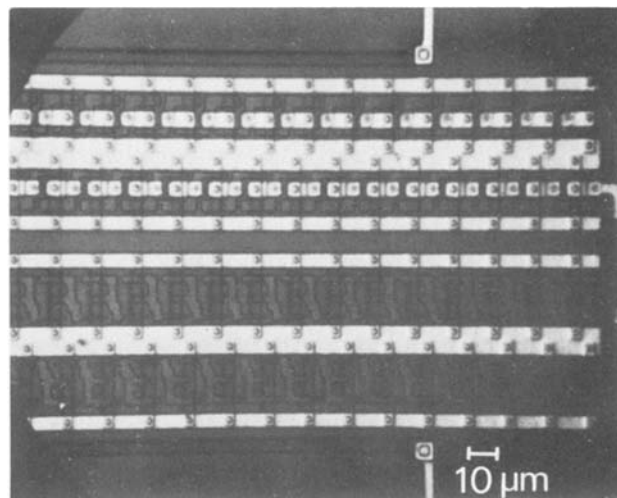


Fig. 7. Ring-oscillator fabricated by x-ray lithography

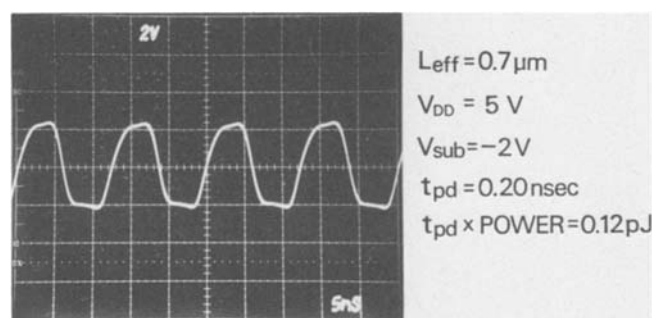


Fig. 8. Waveform of ring-oscillator fabricated by x-ray lithography.

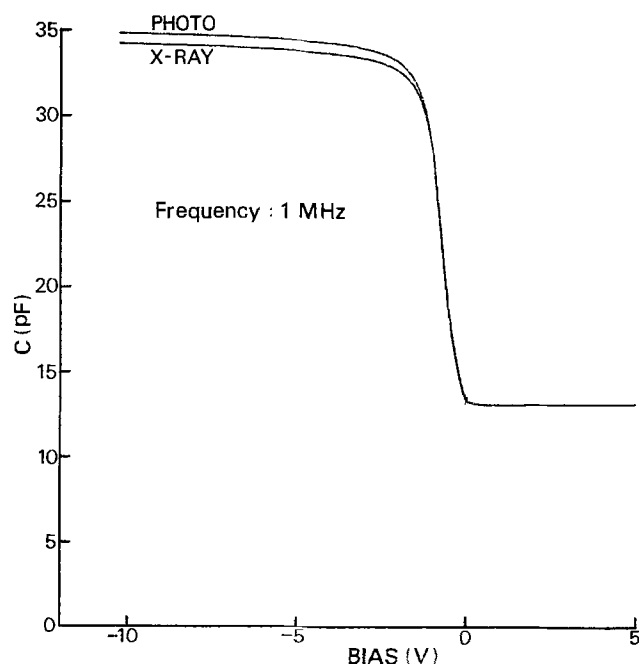


Fig. 9. C-V curve for MOS capacitor fabricated by x-ray lithography and that by photolithography.

present experiment, radiation-induced damage was annealed out at the high temperature processes, such as impurity diffusion, oxidation, and CVD.

Conclusions

MOS devices, such as transistor matrixes with $1.5 \mu\text{m}$ effective channel length, ring oscillators with $0.7 \mu\text{m}$ effective channel length, and capacitors for C-V

measurements, have been fabricated using x-ray lithography, including automatic mask alignment.

Results obtained from the present study are as follows.

1. High contrast x-ray masks with 0.8 μm thick gold patterns have been prepared on SiN/SiO₂/SiN membrane by double lift-off method.

2. Alignment marks made by preferential etching work well through all mask processes without any protection.

3. High registration accuracies, better than $\pm 0.3 \mu\text{m}$ (2σ) on 2 in. wafers, were realized.

4. Dry etching is successfully applied to fabricate poly-Si gates, PSG contact holes, and aluminum metalizations.

5. Standard deviation in V_{th} as low as 5 mV in a chip, about 6.7 mV in a wafer, was realized.

6. Propagation delay time reaching 202 psec/gate, and the power-delay product of 0.12 pJ/gate were obtained from the ring oscillator.

7. No x-ray exposure damage in devices has been observed from the C-V measurements, without any special annealing after the x-ray lithography processes.

Acknowledgment

The authors wish to thank Drs. S. Asanabe, D. Shinoda, and H. Muta of Basic Technology Research Laboratory, Nippon Electric Company, Limited, and Drs. S. Yamazaki and S. Nakayama of Musashino Electric Communication Laboratory, N.T.T. for their discussions and encouragement. The members of Polymer Section

of Electric Communication Laboratory, N.T.T. are also thanked for the supply of FBM resists.

Manuscript submitted Feb. 10, 1981; revised manuscript received April 17, 1981.

Any discussion of this paper will appear in a Discussion Section to be published in the June 1982 JOURNAL. All discussions for the June 1982 Discussion Section should be submitted by Feb. 1, 1982.

Publication costs of this article were assisted by Nippon Electric Company, Limited.

REFERENCES

1. S. Yamazaki, S. Nakayama, T. Hayasaka, and S. Ishihara, *J. Vac. Sci. Technol.*, **15**, 987 (1978).
2. S. Yamazaki and T. Hayasaka, *Jpn. J. Appl. Phys.*, **19**, Suppl. 19-1, 35 (1980).
3. K. Suzuki, J. Matsui, T. Kadota, and T. Ono, *Jpn. J. Appl. Phys.*, **17**, 447 (1978).
4. J. A. Appels, E. Kooi, M. M. Paffen, J. J. H. Schatorjé, and W. H. C. G. Varkuylen, *Philips Res. Rep.*, **25**, 118 (1970).
5. T. Ono and A. Ozawa, *Jpn. J. Appl. Phys.*, **19**, 2311 (1980).
6. M. Kakuchi, S. Sugawara, K. Murase, and K. Matsuyama, *This Journal*, **124**, 1648 (1977).
7. S. Matsuo, *Appl. Phys. Lett.*, **36**, 768 (1980).
8. S. Yamazaki, S. Nakayama, S. Ishihara, and S. Sasayama, *Bull. Jpn. Soc. Prec. Eng.*, **14**, 137 (1980).
9. S. E. Bernachi, Doctoral Thesis, Harvard University (1975).
10. H. L. Stover, F. L. Hause, and D. McGreevy, *Solid-State Technol.* Aug, **95** (1979).
11. M. Peckerar, R. Fulton, and P. Blaise, *J. Vac. Sci. Technol.*, **16**, 1658 (1979).

Measurement of the Diffusion Coefficient of Gallium in Molten Germanium

E. D. Bourret,¹ J. J. Favier, and O. Bourrel

Laboratoire d'Etude de la Solidification,
Centre d'Etudes Nucleaires de Grenoble, 85X, 38041 Grenoble Cedex, France

ABSTRACT

The diffusion coefficient of ⁷²Ga in molten germanium has been measured at $T = 1219 \text{ K}$ using the shear-cell technique. The concentration profile was obtained from the intensity of the γ -emission detected in the range 0.740-0.900 MeV. The diffusion coefficient was found to be $2.1 \times 10^{-8} \text{ m}^2\text{sec}^{-1}$ at this temperature.

The accurate determination of diffusion coefficients of solute in the liquid phase (D_L) is becoming more and more important for the understanding of solidification in metallurgical processes as well as in crystal growth. Up to now, very few measurements of these coefficients have been made (1). In the germanium-gallium system, the lack of data for D_L has been pointed out by different authors (2, 3). In order to relate the diffusion phenomenon to the segregation during solidification, an accurate value of the diffusion coefficient near the solidus temperature is badly needed. This is of prime importance for determining the type of mass transport which took place during the growth of Ge-Ga crystal in a microgravity environment (2, 4). This paper reports the measurements of D_L at 1219 K.

The melting point of pure germanium is $T_m = 1210.4 \text{ K}$.

Experimental Procedure

Measurements were made using the shear-cell technique developed by Potard *et al.* (5). The shear-cell consists of several graphite disks mounted coaxially in which three off-center holes (1.5 mm diam) are drilled to form three capillaries when they are aligned. As shown in Fig. 1, solvent and solvent + solute metals were kept separate until an experiment was begun by aligning the upper and the lower capillaries in a vertical position. After diffusion, the disks were rotated so that the liquid columns were sheared. This last rotation of the disks avoids subsequent change of concentration due to solidification; thus there was no need for quenching the samples. Upper capillaries were filled with pure germanium and lower capillaries contained the dilute alloy germanium-gallium. Diffusion occurs from bottom to top for preventing additional

¹ Present address: Department of Materials Science and Engineering, Massachusetts Institute of Technology, Cambridge, Massachusetts 02139.

Key words: shear-cell technique, gallium, diffusion.

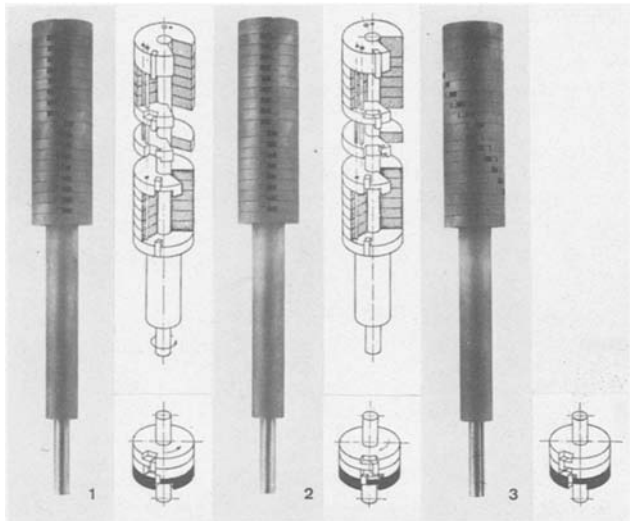


Fig. 1. The shear-cell: 1, filling; 2, diffusion; 3, shearing

effects due to segregation of gallium. Densities of gallium and germanium are, respectively, 5.91 and 5.32 g/cm³. In order to obtain a direct and precise concentration measurement of the samples, ⁷²Ga was used as a radioactive tracer. Under irradiation by thermal neutrons, gallium of normal isotopic composition, which contains 39.8% of ⁷¹Ga, produces ⁷²Ga. ⁷²Ga emits β⁻ particles with a maximum energy of 2.54 MeV, followed by γ-emission with a maximum energy (96%) of 0.835 MeV. One gram of gallium was irradiated for 700 sec under a neutron flux of 1.6 × 10¹⁹ nm⁻³ sec⁻¹.

The active gallium was then melted with pure germanium to obtain a Ge-Ga alloy containing about 600 ppm of Ga.

Diffusion occurs at 1219 K, a "stabilizing" gradient of 100 K m⁻¹ being maintained between the bottom and the top of the cell to reduce convection.

Results

A practical diffusion time was determined from theoretical considerations to be 20 min. A preliminary experiment, using nonactive gallium, confirmed that this time was correct. The gallium was found to diffuse over 4 disks. Concentration measurements which were made, in this case, by x-ray fluorescence cannot be used to evaluate the diffusion coefficient since, due to the small size of the samples, the surface of integration is very small and induces large experimental errors. In the shear-cell configuration, the boundary value problem is that of diffusion between a pair of semi-infinite solids. A solution of Fick's second law $\left(\frac{\partial C}{\partial t} = D \frac{\partial^2 C}{\partial x^2}\right)$, with the boundary conditions $C = C_0$ at $x > 0$ at $t = 0$ and $C = 0$ at $x < 0$ at $t = 0$ is given by

$$C(x,t) = \frac{C_0}{2} \left(1 + \operatorname{erf} \frac{x}{2\sqrt{Dt}} \right)$$

Knowing x , t , and $C(x,t)$, D is given by

$$D = \frac{1}{4b^2t}$$

b being the slope of

$$\operatorname{erf}^{-1} \left(\frac{2C}{C_0} - 1 \right) = \frac{x}{2\sqrt{Dt}}$$

The gallium concentration is proportional to the intensity of the γ-rays emitted with an energy in the range 0.740-0.900 MeV. Each measurement was corrected to account for the weight of the sample and the intensity of the ⁷²Ga peak as a function of time ($t_{0.5} = 51,000$ sec for ⁷²Ga). If the intensity of the source at t is I_t , then at $t + \Delta t$, it will be

$$I_{t+\Delta t} = I_t \exp(-\lambda \Delta t) \quad [1]$$

λ being the disintegration constant, $\lambda = 0.693/t_{0.5}$. The mean intensity during Δt is

$$\bar{I} = I_t \frac{1}{\Delta t} \int_0^{\Delta t} \exp(-\lambda t) dt \quad [2]$$

and then

$$I_t = \bar{I} \frac{0.693 \Delta t/t_{0.5}}{1 - \exp(-0.693 \Delta t/t_{0.5})} \quad [3]$$

The intensity represents the accumulated counts per time units. Every measurement is corrected using a reference time; in this case, the reference time is $t = 0$ at the beginning of the countings.

Another correction is made to account for the dead time of the detector. To account for the dead time, an apparent half-life is determined using the decreasing curve of the activity of ⁷²Ga ($\log N = -\lambda t$) (Fig. 2). This curve exhibits three different slopes corresponding to three apparent half-lives, as shown in Table I. The apparent half-lives are used to calculate the intensity of accumulated counts per time unit (Eq. [3]). The concept of apparent half-lives is used because the correlation (Table I) with straight lines is good enough so that specific corrections for each count rate according to Fig. 2 are not necessary and the corrective calculations are then simplified. Finally, the diffusion coefficient obtained from the measurements reported in Fig. 3 is $D_L = 2.1 \times 10^{-8}$ m²sec⁻¹ at $T = 1219$ K. The coefficient of determination for the straight line is 0.999.

In earlier studies, Schmidt and Verhoeven (6) measured this diffusion coefficient at $T = 1303$ K. The method used was the capillary-reservoir technique and led to the value of 2.4×10^{-8} m²sec⁻¹.

Considering an activation energy of 0.32 eV given by Kodera (3), this value, corrected to 1219 K, becomes 2.0×10^{-8} m²sec⁻¹, which is in good agreement with our direct measurements at this temperature.

The shear-cell technique is a very appropriate one for direct measurement of the interdiffusion coefficient in the vicinity of the liquidus temperature (less than 10 K above) and should be used before investigating

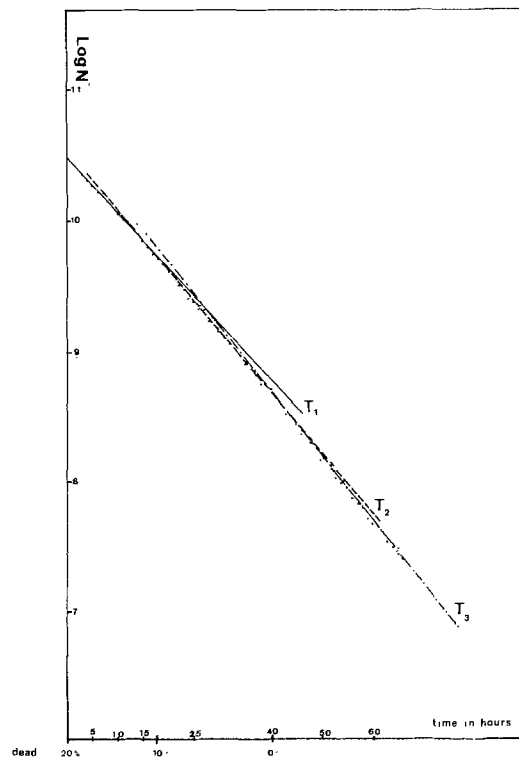


Fig. 2. Decreasing curve of the ⁷²Ga activity

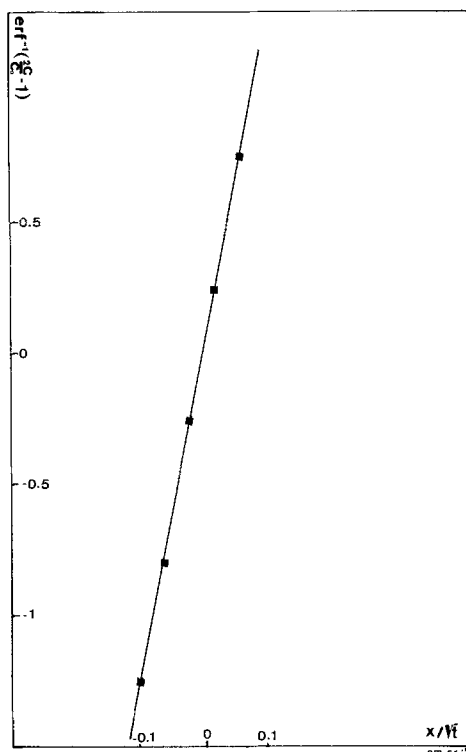


Fig. 3. Diffusion profile. Experimental data. Slope = 34.68 = $1/2 \sqrt{D_L}$; $T = 1219$ K.

solidification problems for which mass transport takes place partly by diffusion.

Table I. Correction due to the amount of dead time

| Dead time | λ | Coefficient of determination | Apparent half-life (hr) |
|-----------|-----------|------------------------------|-------------------------|
| 10-20% | 0.0425 | 0.999 | 16.3 |
| 0-10% | 0.0465 | 0.998 | 14.9 |
| 0 | 0.0491 | 1 | 14.1 |

Acknowledgments

The authors are indebted to Dr. C. Potard for his advice about the shear-cell technique.

Manuscript submitted Jan. 26, 1981; revised manuscript received April 20, 1981.

Any discussion of this paper will appear in a Discussion Section to be published in the June 1982 JOURNAL. All discussions for the June 1982 Discussion Section should be submitted by Feb. 1, 1982.

Publication costs of this article were assisted by the Centre d'Etudes Nucleaires de Grenoble.

REFERENCES

1. J. B. Edwards, E. E. Huckle, and J. J. Martin, *Met. Rev.*, **120**, Parts I and II (1968).
2. A. F. Witt, H. C. Gatos, M. Lichtensteiger, and J. C. Herman, *This Journal*, **125**, 1832 (1978).
3. H. Kodera, S. Iida, and S. Tauchi, *Jpn. J. Appl. Phys.*, **2**, 227 (1963).
4. J. J. Favier, *J. Cryst. Growth*, **49**, 373 (1980).
5. C. Potard, A. Teiller, and P. Dusserre, *Mater. Res. Bull.*, **7**, 583 (1972).
6. R. L. Schmidt and J. D. Verhoeven, *Trans. Met. Soc. AIME*, **239**, 148 (1967).

A Mathematical Assessment of Chemical Diffusion Measurements in Transition Metal Oxides

François Morin*

Institut de Recherche d'Hydro-Québec, Varennes, Québec, Canada J0L 2P0

ABSTRACT

The relaxation method lends itself to the measurement of chemical diffusion coefficients in transition metal compounds. By means of various mathematical calculations, it is shown that the significance of experimental results can be greatly improved. A better insight into the interrelations between physical parameters like nonstoichiometry, defect mobility, and electrical conductivity should be gained by proper consideration of various experimental parameters. The effects of many parameters such as slow surface reaction, large departure from stoichiometry, and varying defect mobility, are reviewed. The electrical conductivity is perfectly equivalent to weight measurements when properly applied to relaxation experiments. Moreover, in some cases, it may contain some specific information regarding the interrelation between electronic and ionic defects.

Chemical diffusion in transition metal compounds is a common phenomenon. It has already been associated with various important physical processes like oxide growth and sintering of ceramics. There is also a renewal of interest in the search for new battery electrode materials. Various formalisms have already been developed in order to describe the basic mechanisms involved in the course of chemical diffusion (1-7), most of them largely based on C. Wagner's transport theory. Besides, most of our point defect theory originates

from Wagner and Schottky (8). Wagner *et al.* also applied the simple mass action law to point defects for several oxides (9-11). This last approach was considerably developed and also described with a convenient notation by Kröger and Vink (12-13). There are a few widely accepted examples, like CoO and Cu₂O, where the diffusion and the point defect theories merge in a simple manner (14). Such a simple picture is also commonly transferred to other compounds.

Several controversial arguments were set forth in the recent years, regarding either coulombic interactions (15) or the prevalent existence of clustered de-

* Electrochemical Society Active Member.
Key words: defects, dielectrics, diffusion, kinetics.

fects (16-17) and nonrandom walk diffusion (18). In view of those complex considerations, the usual treatment of experimental data looks rather crude. Any comparison of experimental data with a more sophisticated theory would be faced with a crucial problem regarding the actual precision of those data. Thus, experimental diffusion phenomena would require a degree of accuracy that is neither intrinsically available for certain types of experiments nor has been completely evaluated in a peculiar experimental method.

The relaxation method might be one of the most suitable means for studying chemical diffusion with both a high precision and a simple procedure. The compound is first equilibrated with the outer atmosphere, whether pure oxygen or an oxidizing-reducing mixture. The compound must thus possess a nonnegligible electronic conductivity. The chemical activity of that atmosphere is suddenly changed from its original value to a different one and the evolution of the defect within the compound is normally recorded as a variation in weight or electrical conductivity *vs.* time. Dünwald and Wagner (19) also formulated the analytical solutions for various sample shapes such as plates, cylinders, and spheres. An equivalent solution has been described by Newman for brick-shaped samples (20). A few comprehensive reviews on the subject are available (21-23). The precision commonly reached with the relaxation method might suffice normally if the aim were simply to verify a largely accepted diffusion mechanism coupled with a very simple defect model. However, if one wants to make full use of this method, further consideration must be given to the various sources of error. Certain criteria have already been suggested by J. B. Wagner *et al.* (21, 23, 24) such as the equivalence between oxidation and reduction runs, the effect of graded sample sizes or diluted atmospheres for nonnegligible surface reactions, and also some preference for thermogravimetry instead of electrical conductivity. Such criteria deserve a complete mathematical analysis of all experimental parameters as has already been described (25). The basic simplicity of relaxation experiments is not an impairment of the significance of their results. Analysis of the relaxation method is considerably refined and more completely described here.

The Relaxation Technique and Its Analytical Solution

The chemical diffusion coefficient \tilde{D} is unequivocally defined by Fick's first law

$$j_i = -\tilde{D} \cdot \frac{\partial c_i}{\partial x} \quad [1]$$

where c_i is the concentration of the chemical species, but can also sometimes be considered as a point defect concentration, and j_i is the flux of the same species. In the case of a transient concentration state, the preceding equation becomes, according to the mass conservation law

$$\frac{\partial c_i}{\partial t} = \frac{\partial}{\partial x} \left(\tilde{D} \cdot \frac{\partial c_i}{\partial x} \right) \quad [2]$$

which is equivalent to Fick's second law of diffusion. If \tilde{D} is concentration independent, Eq. [2] then reads

$$\frac{\partial c_i}{\partial t} = \tilde{D} \cdot \frac{\partial^2 c_i}{\partial x^2} \quad [3]$$

The following set of time and boundary conditions fully describes the normally expected conditions for relaxation experiments

$$\begin{aligned} c_i(x, 0) &= c_o \quad \text{at } t = 0 \\ c_i(0, t) &= c_f \quad \text{at } t > 0 \end{aligned}$$

where c_o is the initial equilibrium concentration within the sample, c_f is the final equilibrium concentration,

and x is the length along the diffusion axis. Equation [3] can be extended to a three-dimensional case. According to Newman (20), the concentration c_i in a prism with overall dimensions equal to $2a_1$, $2a_2$, and $2a_3$ is expressed by the following relation

$$c_i(X, T) = c_o \cdot f(X_1, T_1) \cdot f(X_2, T_2) \cdot f(X_3, T_3) \quad [4]$$

where

$$f(X, T) = \frac{2}{\pi} \sum_0^{\infty} \frac{(-1)^n}{n + \frac{1}{2}} \cdot \exp \left\{ -T \left(n + \frac{1}{2} \right)^2 \pi^2 \right\} \cdot \cos \left\{ \left(n + \frac{1}{2} \right) \pi \cdot X \right\}$$

$$T = \frac{\tilde{D}t}{a^2}$$

$$X = x/a$$

The reduced coordinate X varies from zero to one while T varies from zero to infinity. The average concentration \bar{c} is a more readily accessible parameter than the local concentration $c_i(X, T)$ so that

$$\bar{c} = c_f - (c_f - c_o) \int_0^1 \int_0^1 \int_0^1 f(X_1, T_1) \cdot f(X_2, T_2) \cdot f(X_3, T_3) \cdot dX_1 \cdot dX_2 \cdot dX_3 \quad [5]$$

Again, \bar{c} can be transformed to a dimensionless parameter

$$c_r = (c_f - \bar{c}) / (c_f - c_o) \quad [6]$$

By introducing Eq. [6] into Eq. [5] and integrating

$$c_r = g(T_1) \cdot g(T_2) \cdot g(T_3) \quad [7]$$

where

$$g(T) = \frac{2}{\pi^2} \sum_0^{\infty} \frac{1}{(n + \frac{1}{2})^2} \cdot \exp \left\{ -T \cdot \left(n + \frac{1}{2} \right)^2 \cdot \pi^2 \right\}$$

For equilibration runs, c_r is usually interpreted in terms of weight or electrical conductivity variation *vs.* time. Therefore, both a relative weight W_r and a relative electrical conductivity have to be defined

$$\sigma_r = (\sigma_f - \bar{\sigma}) / (\sigma_f - \sigma_o) \quad [8]$$

$$W_r = (W_f - W) / (W_f - W_o) \quad [9]$$

In most cases, W_r can be shown to be strictly equivalent to c_r . But σ_r is identical to c_r only when a linear relationship between σ and c_i is obeyed and when the average conductivity is measured perpendicular to the diffusion axis. Any approximation of Eq. [7] or any actual departure from the ideal case should be assessed in comparison with that solution. A correction parameter, $\Delta\tilde{D}/\tilde{D}$ is accordingly defined

$$(\Delta\tilde{D}/\tilde{D}) = (\tilde{D}_{\text{true}} - \tilde{D}_{\text{apparent}}) / \tilde{D}_{\text{apparent}} \quad [10]$$

so that

$$\tilde{D}_{\text{true}} = \tilde{D}_{\text{apparent}} [1 + (\Delta\tilde{D}/\tilde{D})]$$

The significance of \tilde{D}_{true} and $\tilde{D}_{\text{apparent}}$ is two-fold. First, if all conditions are fulfilled for the exact application of Eq. [7], \tilde{D}_{true} is derived directly from that equation and $\tilde{D}_{\text{apparent}}$ comes out from the approximations usually encountered with the same equation. Second, if any departure from the ideal relaxation case occurs, \tilde{D}_{true} is then derived from a more appropriate exact numerical solution. Then, $\tilde{D}_{\text{apparent}}$ comes out from the normal analytical equation since that equation is often assumed to still correctly apply to the experimental case.

A Detailed Approach to Various Errors on \tilde{D}

There are several potential error sources associated with the relaxation method. The precision of \tilde{D} and, consequently, its physical significance can be enhanced only if those error sources are properly identified and controlled. The most common ones are listed in Table I. Mathematical handling is straightforward for types one and two while numerical integration is required for the third type. It has been found convenient to illustrate each case numerically. Generally speaking, values of $\Delta\tilde{D}/\tilde{D}$ can be extrapolated readily up to about 10%. All errors do not add up necessarily, but the maximum uncertainty criterion may prove to be useful for type two. Not all the error sources mentioned in Table I lend themselves to a global statistical analysis based on the least squares fit. Some of those errors always behave in a systematic manner. Others would vary randomly from one relaxation run to another, but would systematically affect any single experiment. The graphical representation of \tilde{D} vs. c_r bears much significance in finding potential error sources and also in evidencing unexpected phenomena.

Consequently, a normalized representation of $\Delta\tilde{D}/\tilde{D}$ vs. c_r has been developed and is used throughout the present analysis.

Mathematical approximations.—The most common tendency when handling a large number of relaxation data within any single run, is to use a linearized graphical fit of these data and to measure the resulting slope. Equation [7] does not lend itself readily to that operation unless some approximation is made. In fact, the summation represented by $g(T)$ rapidly reduces to its first term as c_r tends toward zero. Hence, a linear relationship between $\ln c_r$ and T should work properly at low c_r values (19-21) and it also corresponds to the common practice. For the three-dimensional case

$$\tilde{D}t = \frac{\ln(512/\pi^6) - \ln(c_r)}{\frac{\pi^2}{4} \left(\frac{1}{a_1^2} + \frac{1}{a_2^2} + \frac{1}{a_3^2} \right)} \quad [11]$$

Analogous relationships can also be easily deduced for one- and two-dimensional processes. By comparing such equations with the reference analytical equation, one gets the results shown in Fig. 1. One-, two-, and three-dimensional approximations, such as in Eq. [11], are illustrated by means of specific examples. All corresponding curves were identified with their respective dimensional ratios. The worst approximation usually pertains to the three-dimensional equation. Under certain unfavorable geometrical conditions, Eq. [11] would even lose all of its original sense.

Another common approximation consists of neglecting either one or two diffusion axis out of the three possible ones. This is illustrated in Fig. 2. Equation

Table I. Identification of most common error sources in relaxation experiments

| Classification | Description |
|--------------------------------|---|
| 1. Mathematical approximations | Reduction to a two- or a one-dimensional diffusion process Reduction to a simple logarithmic equation |
| 2. Experimental uncertainties | Uncertainties on c_0 , c_r , and \bar{c} , respectively Uncertainties on time and dimensions Uncertainties on temperature and partial pressure |
| 3. Nonanalytical conditions | Slow surface reaction Initial gas exchange period Large departure from stoichiometry; moving boundaries Concentration dependent mobility Temperature and pressure fluctuations during reequilibration |

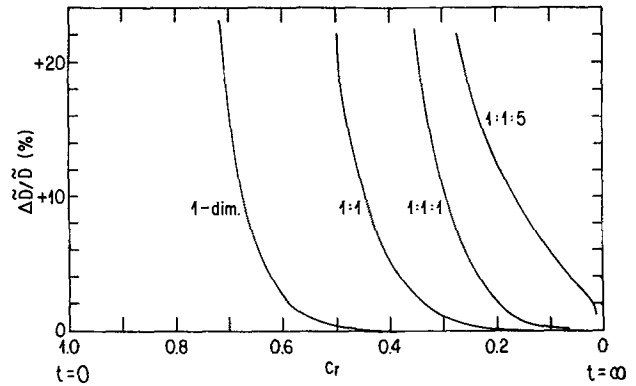


Fig. 1. Validity range for the use of a simple logarithmic relationship between c_r and T . One-, two-, and three-dimensional cases are considered.

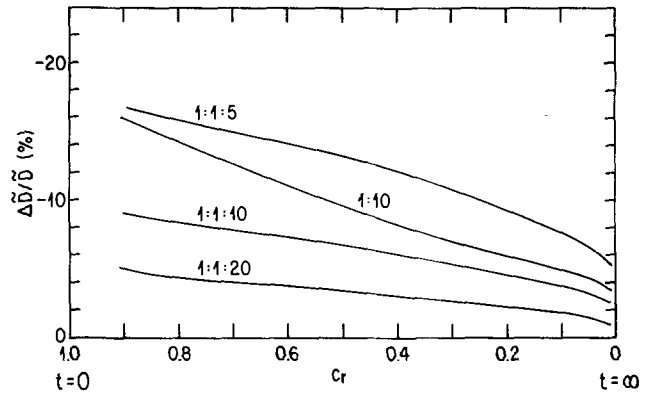


Fig. 2. Application of the full analytical equation, reduced to a two- or a one-dimensional diffusion process. The last figure, for any ratio, corresponds to the specifically neglected sample dimension.

[7] has been successively applied to the full and to the approximated sample geometries. The last figure appearing in any one ratio, corresponds actually to the neglected dimension. In contradistinction with Fig. 1, the correction factor $\Delta\tilde{D}/\tilde{D}$ never completely disappears. Only for the most favorable cases does it remain within acceptable limits.

Actual uncertainty on c_r .—Most of the accuracy of \tilde{D} relies on a precise determination of c_r during the re-equilibration process. A crude estimate of the uncertainty of \tilde{D} , due to c_r , is a mathematical derivation of the reference equation and is shown in Fig. 3, mainly reflecting the mathematical behavior of Eq. [7]. Based on this behavior, it is often believed that the best pre-

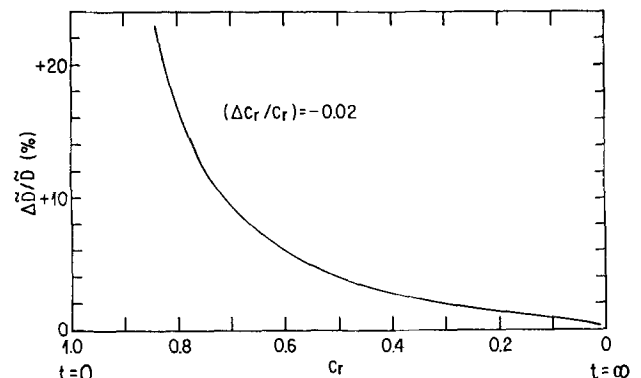


Fig. 3. Effect of the relative uncertainty $\Delta c_r / c_r$ on the correction factor $\Delta\tilde{D}/\tilde{D}$, for a one-dimensional diffusion process.

cision of \tilde{D} might be obtained for the lowest c_r values, i.e., the longest diffusion times. However, the overall uncertainty of c_r is normally not constant due to its definition given by Eq. [6]. In fact, the relative concentration c_r is the combination of three experimentally independent variables: c_0 , the initial defect concentration, \bar{c} , the evolving average defect concentration and c_f , the final defect concentration. An optimum c_r

range for the determination of \tilde{D} becomes evident when those three terms are dealt with separately as in Fig. 4. That range is more or less defined by the flattened portion of those three curves. It should vary somewhat from one experimental case to another but, roughly speaking, it will extend from about $c_r = 0.55$ to $c_r = 0.1$. By averaging within such a region, the precision of \tilde{D} values will be increased.

Other experimental parameters.—In Eq. [7], the uncertainty of T is rather simply estimated more directly

by considering \tilde{D} , t , and a^2 and adding the uncertainties for those terms together. A high degree of accuracy can be readily achieved on the measurement of time except for the absolute determination of the origin $t = 0$ at the startup of the experiment. Mathematically speaking, that uncertainty is readily calculated. In practice, however, there is some risk that the lack of precision on $t = 0$ be inadvertently used as a fitting parameter for the whole experimental curve. Slow pressure changes are more specifically dealt with

later on. The expected uncertainty of \tilde{D} due to sample dimensions is very easily deduced for the simplest cases. For a one-dimensional diffusion process, it is equal to $2(\Delta a/a)$, and equal to $6(\Delta a/a)$ for a perfectly cubic sample. $\Delta a/a$ is the uncertainty on one single dimension.

For any intermediate sample geometry, $\Delta\tilde{D}/\tilde{D}$ would stand somewhere between the two former values.

Finally, \tilde{D} is also intrinsically influenced by temperature, and more occasionally, by partial pressure. With a perfect constancy of these two parameters during any single run, the uncertainty of \tilde{D} is limited to the lack of precision on temperature. It is rather insensitive to an exact absolute value of the partial pressure.

For example, \tilde{D} varies by about 0.9% for a 1°C variation in CoO at 1000°C. Much greater attention should be paid to the temperature or the partial pressure fluctuations during the course of a single reequilibration experiment; c_r is then appreciably affected through its experimentally fluctuating \bar{c} and c_f components. The surface concentration c_f is instantaneously modified

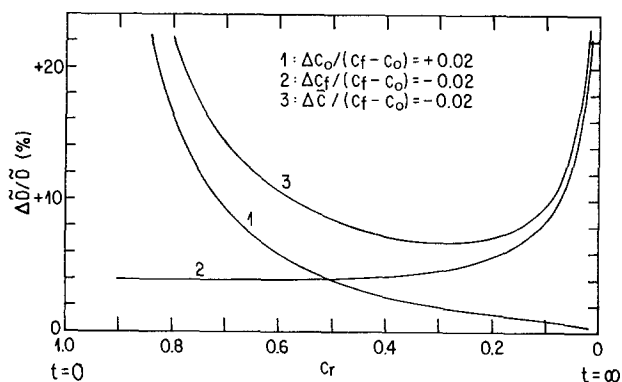


Fig. 4. Reconsideration of the uncertainty on c_r in view of its experimental components c_0 , c_f , and \bar{c} for a one-dimensional diffusion process.

while \bar{c} is influenced more progressively. The true diffusion coefficient is only slightly affected compared to the estimated \tilde{D} . That also explains why the usefulness of the experimental data become severely limited at c_r close to zero, i.e., at the largest values of t .

Departure from the analytical solution.—The third type of error, in Table I, is related to the occurrence of nonanalytical experimental conditions. Mathematical solutions for various specific sets of conditions can be developed by means of numerical analysis and, more precisely, with Crank-Nicholson's method (26). Little would normally be added to our present aims by dealing with two and three diffusion axes. Emphasis is placed on the one-dimensional process. Two- and three-dimensional diffusional processes are expected to behave in quite an analogous manner and this has been checked already for a few cases.

Initial partial pressure modification.—According to Eq. [7], the surface concentration must be abruptly modified at time $t = 0$, which is a condition difficult to achieve. The gas handling operation is a time-consuming process and slow surface reactions are also likely to occur. The use of pure oxygen appreciably simplifies the rapid establishment of new partial pressures, but limits the physically achievable partial pressure ranges. In many circumstances, gas mixtures must be employed, which implies either an additional gas flushing or gas sweeping operation. A specific example

is depicted in Fig. 5. The greatest effect on $\Delta\tilde{D}/\tilde{D}$ appears immediately after emptying out the gas mixture. More explicitly, the value $T = 0.0015$ is approximately equivalent to $t = 10$ sec for a 1 mm thick CoO sample at 1000°C. For the quite common case where no flushing operation is used, the gas composition changes only very progressively, in a more or less logarithmic manner, even with a rapid switching between different mixtures. This process can be accelerated by faster sweep rates, but with an appreciable penalty on thermogravimetric measurement accuracy. Close attention to the initial partial pressure modification is especially important with faster reequilibrating compounds.

Slow surface reaction.—At the beginning of the relaxation process, the incoming defect flux in the first few layers of the solid sample is, theoretically, extremely large. The surface reaction may not be fast enough to accommodate such a flux, with the resultant occurrence of some deviation from the true surface equilibrium concentration. This departure from the ideal reequilibration process vanishes more or less rapidly as the relaxation process goes on, but the actual

determination of \tilde{D} remains affected for longer times. In the following somewhat simplified model, the surface reaction rate is assumed to be proportional to the surface concentration departure from equilibrium

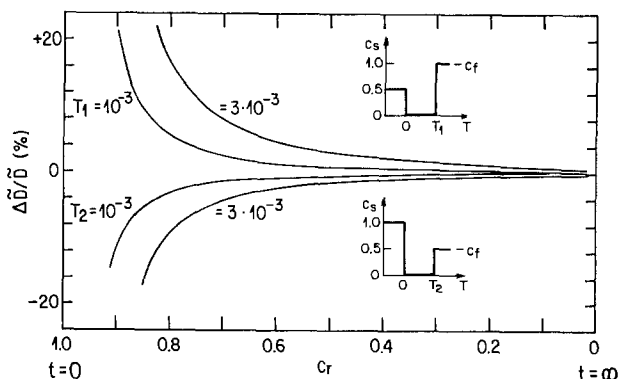


Fig. 5. Effect of a gas emptying operation for two distinct cases. c_s is the instantaneous surface concentration.

with the outer atmosphere. Hence

$$j(0, t) = A\{c_1(0, t) - c_f\} \quad [12]$$

By combining with Fick's first equation

$$\left(\frac{\partial c_1}{\partial x}\right)_{x=0} = B \cdot \{c_1(0, t) - c_f\} \quad [13a]$$

where C is defined as $(c_1 - c_0)/(c_f - c_0)$. Consequently

$$\left(\frac{\partial C}{\partial x}\right)_{x=0} = B\{1 - C(0, t)\} \quad [13b]$$

where $j_1(0, t)$ is the flux at the gas-solid interface, A is a constant specific to the gas mixture, and B is

equal to $(A \cdot a/\tilde{D})$. Equation [12] is analogous to the drying process already discussed by Newman (27) and the wustite surface reaction model used by Landler and Komarek (28) for a combined surface and volume rate-limited process. Other models have also been described and discussed at some length (29-31). But the main purpose of the present approach is to quantify the effect of a surface rate-limited reaction on the determination of \tilde{D} rather than identifying the exact surface mechanism responsible for that rate-limiting action. Equation [13b] has been introduced as a boundary condition for the numerical integration of Fick's second

law. The results for $\Delta\tilde{D}/\tilde{D}$ are shown in Fig. 6. To scale up the phenomenon, various values were attributed to B , e.g., $B = 25$ leads to a limiting surface flux equal to the flux that would be theoretically observed at $c_r = 0.976$ in the absence of a slow surface reaction. Since the individual curves uniquely depend on the magnitude of B , the present numerical solution is concentration independent. In contradistinction to Fig. 5, and to the error on the estimation of time at $t = 0$, there is a largely persistent effect of the surface reaction on $\tilde{D}_{\text{apparent}}$, even at very low c_r values.

Oxidizing-reducing mixtures like $\text{H}_2/\text{H}_2\text{O}$ and CO/CO_2 are quite susceptible to the kind of phenomenon presently discussed. Experimental results on wustite have been discussed at some length by J. B. Wagner *et al.* (24). Even pure oxygen should theoretically not be overlooked for a partly surface rate-limiting action.

Large stoichiometric variations.—Several compounds like FeO , MnO , and UO_2 exhibit large departures from stoichiometry. Large concentration variations have often been applied to those compounds for relaxation experiments. On fundamental grounds, the effect of a large stoichiometric variation within any single relaxation experiment is two-fold: (i) the outer crystal surface cannot be considered any more as a fixed boundary, in the case of a mobile cationic sublattice;

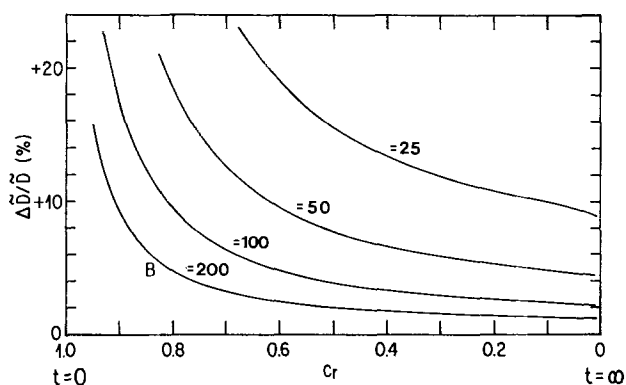


Fig. 6. Effect of a slow surface reaction on $\Delta\tilde{D}/\tilde{D}$. B is used here as a scaling parameter and it is proportional to the surface reaction rate constant.

and (ii) there should be a stress-induced effect due to the concentration gradient. Case one must be numerically integrated. The apparent value of σ_r (see Eq. [8]), i.e., its value obtained without correcting the initial sample dimensions for the continuously advancing boundaries, departs from the actual value of σ_r or, else, c_r . It can be shown that

$$c_r = 1 - (a_f/a)[1 - (\sigma_r)_{\text{app}}] \quad [14]$$

where a is the instantaneous sample dimension and a_f , the final one. Weight and apparent conductivity variations vary in exactly the same way, so that a strictly equivalent equation also holds for W_r . The correction to be brought *vs.* c_r , to compensate for the departure

from the true \tilde{D} value, is shown in Fig. 7. The other effect, concerning internal stresses in the course of diffusion, has been theoretically discussed at some length elsewhere (32-33). Practically speaking, there is no absolute need for large stoichiometric variations except for more sensitivity in a few thermogravimetric experimental procedures.

Concentration-dependent diffusion coefficient.—The eventual defect mobility variation, which has sometimes been reported for transition metal compounds (22, 34), is a rather controversial problem. That phenomenon is likely to be accompanied by either a change in the defect nature or by defect interactions. Taking

into account the sole effect of \tilde{D} variation and numerically integrating Fick's second law lead to the results shown in Fig. 8. In that solution, $\tilde{D} = f(c_i)$ was defined as follows

$$\tilde{D}(c_i) = \tilde{D}_{\text{min.}} + (\tilde{D}_{\text{max.}} - \tilde{D}_{\text{min.}}) \cdot (c_i/c_{\text{max}}) \quad [15]$$

Because \tilde{D} is concentration dependent and should likewise vary continuously during the course of the re-

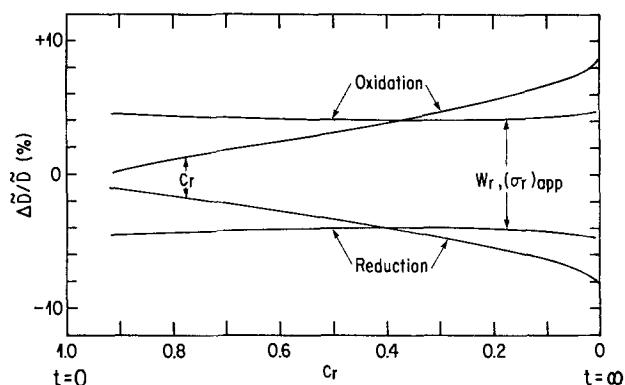


Fig. 7. Description of a large departure from stoichiometry in MeO_{1+y} . Here, y varies between 0 and 0.05.

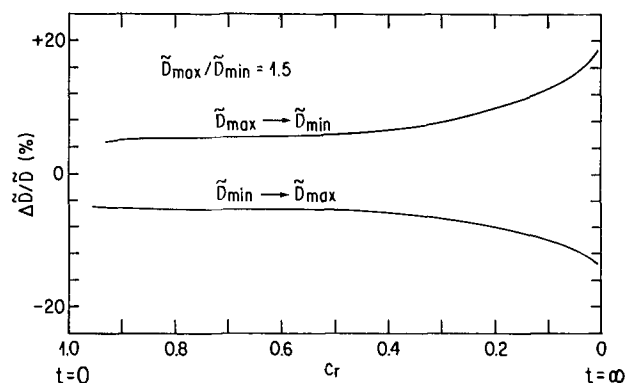


Fig. 8. Study of a chemical diffusion coefficient linearly dependent on concentration.

laxation process, \tilde{D}_{true} is arbitrarily taken as equal to its arithmetic mean, $(\tilde{D}_{\text{max}} + \tilde{D}_{\text{min}})/2$. Whenever the correction factor $\Delta\tilde{D}/\tilde{D}$ is applied to the analytically calculated \tilde{D} values, the corrected \tilde{D} value becomes identical to the preceding arithmetic mean. From Fig.

8, the analytical \tilde{D} values should be slightly biased either positively or negatively depending on reequilibration being an oxidation or a reduction process. The expected analytical deviation during the course of a single experiment is somewhat smothered both by the actual diffusion process and by the use of the arithmetical average on \tilde{D} . A true \tilde{D} variation vs. concentration would consequently be more easily detected by several small successive concentration changes over a desired range, instead of a single large concentration variation.

Thermogravimetric and Electrical Conductivity Measurements

One last and major point of interest in relaxation experiments is the physical means used in measuring the concentration evolution within the sample. Weight and electrical conductivity are the most suitable and the most widely used physical properties. The preference for either of these must be discussed on its respective merits. Theoretically speaking, one major advantage in using weight is that it always relates more directly to a chemical component activity than conductivity would, in agreement with a perfectly general thermodynamical formulation of diffusion. However, structural interpretation of defects is usually done currently, hence invalidating the preceding argument. Experimentally speaking, thermal noise, simple buoyancy, and gas flow effect limit the useful sensitivity of weight measurements. These factors can be quite well controlled in carefully designed experiments. An additional difficulty may come from the initial gas handling procedure associated with a rapid weight variation. The accuracy of thermogravimetric measurements depends on the magnitude of the absolute concentration change. Weight variations are thus easily recorded for large stoichiometric changes but at the same time, they become rather less sensitive at low defect concentrations.

For the counterpart, electrical measurements can intrinsically be made very precise so that their accuracy is usually limited by external factors like temperature and partial pressure control. The relative error made in conductivity measurements being generally constant, makes them very suitable for extended defect concentration ranges. The electrical conductivity is related to c_e , the free electron concentration or else the electron hole concentration in the following way

$$\sigma_e = \mu_e \cdot q_e \cdot c_e \quad [16]$$

where μ_e is the electron mobility, q_e is the elementary charge, and the mobility μ_e is normally considered to be constant. The mobility is quite often temperature dependent, but to a much lesser degree than the departure from stoichiometry. Four different conductivity types have been accordingly distinguished in Table II. The first two types, showing a linear relationship between electronic and ionic defects, are readily compatible with relaxation experiments. Type IV is the main exception to the use of electrical conductivity measurements. The conditions for types I and II do not need to be strictly obeyed to be used for relaxation experiments because the electrical conductivity is intimately related to defect concentration and to defect nature. In fact, σ only needs to be unequivocally related to the departure from stoichiometry. The effect of an eventual nonlinear relationship between σ_r and c_r can be readily evaluated by numerical integration of

Table II. Electrical conductivity in nonstoichiometric compounds in relation to the relaxation method

| Conductivity type | Example | Ref. |
|--|---------|------|
| I. Electrical conductivity is directly proportional to departure from stoichiometry; electronic mobility is temperature dependent | CoO | (36) |
| II. Electrical conductivity is directly proportional to departure from stoichiometry; electronic mobility is temperature independent | MnS | (36) |
| III. Electrical conductivity is dependent on nonstoichiometry; a mixed defect state prevails for a certain oxygen activity range. | MnO | (37) |
| IV. Electrical conductivity is identified with metallic conduction; it is independent of nonstoichiometry | NbO | (38) |

that relationship. A power law between equilibrium values of σ and c_i is taken here as an example

$$\sigma = \text{constant} \cdot c_i^r \quad [17]$$

In this type of equation, c_i is normally dealt with as a defect concentration. The present treatment partly resembles that described by Campbell and O'Keefe (35), and r can either be thought of as an arbitrary exponent or it can be deduced from already existing experimental data on σ and c_i . For example, $r = 3/4$ may also be interpreted in terms of n_σ equal to 4 and n_x equal to 3. One other example is that of r equal to 0.5. Again, that may also correspond to $n_\sigma = 8$ and $n_x = 4$ in Me_2O . Typical calculations, reported in Fig. 9 and 10, have been performed for various r and c_f/c_o ratios. Oxidation and reduction processes are identified by c_f/c_o greater or smaller than unity, respectively. These results can also be summarized as follows:

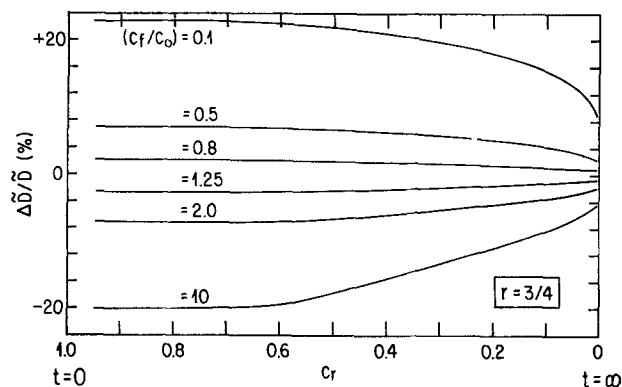


Fig. 9. Nonlinear dependency between electrical conductivity and concentration. The effect is shown for various concentration ratios, during both oxidation and reduction runs.

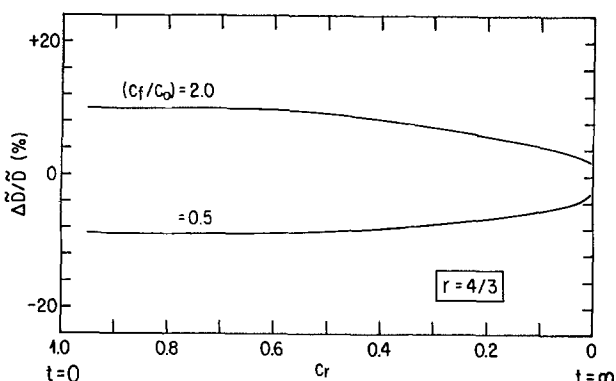


Fig. 10. Nonlinear dependency between electrical conductivity and concentration. Effect of an inverted power law coefficient on the correction factor $\Delta\tilde{D}/\tilde{D}$.

1. The effect on $\Delta\tilde{D}/\tilde{D}$ is most important during about the first half of the relaxation run; it diminishes asymptotically at the very end of the experiment.

2. The greater the departure of r from unity, the greater the correction factor $\Delta\tilde{D}/\tilde{D}$; $\Delta\tilde{D}/\tilde{D}$ reverses sign when r goes from $r < 1$ to $r > 1$.

3. $\Delta\tilde{D}/\tilde{D}$ increases with increasing c_f/c_0 departure from unity; that effect is symmetrical for low enough $\Delta\tilde{D}/\tilde{D}$ values.

4. The nonlinearity effect on \tilde{D} tends to become negligible as r or c_f/c_0 tend toward unity.

Other empirical relationships between σ and c_i have also been tested. The observations are quite analogous to those previously formulated. Therefore, the $\Delta\tilde{D}/\tilde{D}$ behavior is not specifically tied to a peculiar relationship, but is generally dependent on (i) the degree of curvature between σ and c_i , combined with the magnitude of the concentration change and on (ii) the absolute sign of that curvature.

Finally, Fig. 11 is an exact representation of the most generally accepted defect model in cuprous oxide. Neutral cation vacancies are assumed to be the major defects and electrical conduction would come from the simultaneous and minor existence of electron holes and singly ionized cation vacancies (14). The present calculations provide the guidelines for correcting eventual relaxation experiments in Cu_2O or for probing the actual existence of the preceding model.

In brief, the effect of a nonlinear relationship between σ and c_i is predictable. The calculations involved in that process can either be used to correct diffusion coefficient measurements or, inversely, to detect the existence of a nonlinear relationship between those two fundamental parameters.

Electrode configuration.—The electric conductivity technique should normally be quite attractive. Nonetheless, there is a very common source of discrepancies which is directly related to the electrode configuration. For relaxation experiments, there should be two basic types of electrode configuration as illustrated in Fig. 12. According to type a, the electric current is perfectly parallel to the diffusion axis through the whole sample. Hence, the average conductivity is related to the average defect concentration by the following equation

$$\bar{\rho} = \text{constant} \cdot \int_0^a (1/c_i) \cdot dx \quad [18a]$$

or, since $\bar{\sigma} = 1/\bar{\rho}$

$$\bar{\sigma} = \text{constant} / \int_0^a (1/c_i) \cdot dx \quad [18b]$$

where $\bar{\rho}$ is the average sample resistivity. The electrode is simultaneously assumed to be perfectly porous and

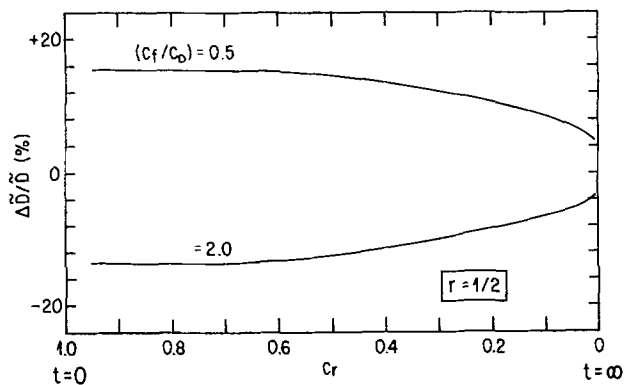


Fig. 11. Characterization of the cuprous oxide model behavior during relaxation runs with electrical conductivity.

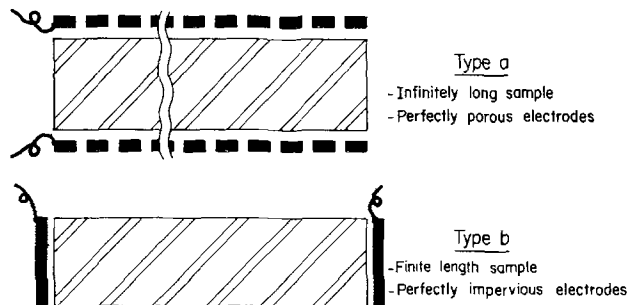


Fig. 12. Idealized electrode arrangements for relaxation runs

perfectly conducting. In type b, the current flow is strictly perpendicular to the diffusion axis and the electrodes are assumed to be completely impervious to diffusion. Hence

$$\bar{\sigma} = \text{constant} \cdot \int_0^a c_i \cdot dx \quad [19a]$$

or

$$\bar{\sigma} = \text{constant} \cdot \bar{c} \quad [19b]$$

The two preceding sets of equations represent a perfectly linear relationship between σ and c_i . The difference between Eq. [18b] and [19a] is obvious. Thus, directly substituting c_r for σ_r would lead to erroneous results in the first case. Regarding type a configuration, the assumption that the electrode layer is perfectly porous is hardly feasible. Type b is to be preferred. The use of electric conductivity measurements would thus be limited to one- and two-dimensional processes. Any intermediate configuration would lead to a nonohmic interpretation of the measurements. Wrapping the diffusion samples with electrode wires at a finite length from one another is one such case. It leads to at least partially incorrect results unless a full specific mathematical treatment is allowed for it. Such a treatment would be rather lengthy and cumbersome. The electrode configuration suggested here is simpler and more reliable.

Final Comments

The relaxation method has been discussed here from the experimentalist's point of view. All calculations were based on a very few fundamental equations or else on very simple assumptions. These calculations were developed to let the relaxation method gain more potential regarding the study of defect diffusion and point defect behavior in transition metal compounds. The actual significance of \tilde{D} has not been discussed outside its basic definition given by Eq. [1]. That would naturally be the next important step in discussing present diffusion theories.

A graphical representation of \tilde{D} vs. c_r is suggested to give a better statistical weight to all data during any single experiment and to make use of all the information contained within any data set. Several numerical examples have been worked out in order to obtain more specific ideas about the actual effects of the most common error sources. Those examples were mostly done in dimensionless parameters so that they might be transferred to the practical design or assessment of experiment. Moreover, an optimum range for c_r that would lead to more accurate \tilde{D} values has been indicated.

The electrical conductivity measurements applied to the reequilibration method were thoroughly discussed. As long as there is a nonstoichiometric dependency of electrical conductivity, this measurement technique appears to be useful for all defect concentration ranges. Large concentration changes should generally be avoided. Nevertheless, the electrical conductivity may then, on the base of preceding calculations, be a useful

means of detecting some eventual nonlinear relationship between σ and c_i .

Finally, experimental papers on the relaxation method are still very representatively described by Childs *et al.* (23). Quite surprisingly, there is only a limited number of works in the field and there is ample room for further experimental development. The most useful aspect of the present mathematical analysis is in redesigning relaxation experiments so that not only more precise and reproducible data are made available, but also the experimental observations keep in pace with the constantly developing defect theory. In that sense, relaxation experiments have been performed recently on CoO and they are reported extensively elsewhere (39). Not only do we observe a clear tendency for \tilde{D}_{CoO} to vary with the oxygen activity but any discrepancy with previous assumptions on \tilde{D}_{CoO} is explained by the present analysis.

Manuscript submitted Dec. 18, 1980; revised manuscript received May 15, 1981. This was Paper 357 presented at the Hollywood, Florida, Meeting of the Society, Oct. 5-10, 1980.

Any discussion of this paper will appear in a Discussion Section to be published in the June 1982 JOURNAL. All discussions for the June 1982 Discussion Section should be submitted by Feb. 1, 1982.

Publication costs of this article were assisted by the Institut de Recherche d'Hydro-Québec.

REFERENCES

1. C. Wagner, *Z. Phys. Chem., Teil B*, **11**, 139 (1930).
2. C. Wagner, *ibid.*, **21**, 25 (1933).
3. C. Wagner, *ibid.*, **32**, 447 (1936).
4. L. S. Darken, *Trans. AIME*, **175**, 184 (1948).
5. C. Wagner, *Adv. Electrochem. Electrochem. Eng.*, **4**, 1 (1966).
6. D. E. Coates and A. D. Dalvi, *Oxid. Met.*, **2**, 331 (1970).
7. W. Weppner and R. A. Huggins, *This Journal*, **124**, 1569 (1977).
8. W. Schottky and C. Wagner, *Z. Phys. Chem., Teil B*, **11**, 163 (1930).
9. H. Dünwald and C. Wagner, *ibid.*, **22**, 212 (1933).
10. H. H. V. Baumbach and C. Wagner, *ibid.*, **24**, 59 (1934).
11. C. Wagner and H. Hammen, *ibid.*, **40**, 197 (1938).
12. F. A. Kröger and H. J. Vink, *Solid State Phys.*, **3**, 307 (1956).
13. F. A. Kröger, "The Chemistry of Imperfect Crystals," p. 313, North-Holland Publishing Co., Amsterdam (1966).
14. P. Kofstad, "Nonstoichiometry, Diffusion, and Electrical Conductivity in Binary Metal Oxides," pp. 138, 328 ff., Wiley-Interscience, New York (1972).
15. C. Wagner, *Prog. Solid State Chem.*, **10**, 3 (1975).
16. M. S. Seltzer and R. I. Jaffee, Editors, "Defects and Transport in Oxides," Battelle Institute Materials Science Colloquia, Columbus (1973), Published by Plenum Press, New York (1974).
17. C. R. A. Catlow, W. C. Mackrodt, M. J. Norgett, and A. M. Stoneham, *Philos. Mag. A*, **40**, 161 (1979).
18. R. A. McKee, *Phys. Rev. B*, **21**, 4269 (1980).
19. H. Dünwald and C. Wagner, *Z. Phys. Chem., Teil B*, **24**, 53 (1934).
20. A. B. Newman, *Trans. AICHE*, **27**, 310 (1931).
21. J. B. Wagner, in "Mass Transport in Oxides," NBS Special Publication No. 296, p. 65, Washington, DC (1968).
22. P. E. Childs and J. B. Wagner, in "Heterogeneous Kinetics at Elevated Temperatures," G. R. Belton and W. L. Worrell, Editors, pp. 269-342, Plenum Press, New York (1970).
23. P. E. Childs, L. W. Laub, and J. B. Wagner, *Proc. Br. Ceram. Soc.*, **19**, 29 (1971).
24. L. W. Laub and J. B. Wagner, *Oxid. Met.*, **7**, 1 (1973).
25. F. Morin, *Can. Met. Quart.*, **14**, 97 (1975).
26. J. Crank, "Mathematics of Diffusion," p. 186, Clarendon Press, Oxford (1956).
27. A. B. Newman, *Trans. AICHE*, **27**, 203 (1931).
28. P. F. J. Landler and K. L. Komarek, *Trans. AIME*, **236**, 138 (1966).
29. S. Stotz, *Ber. Bunsenges. Phys. Chem.*, **70**, 769 (1966).
30. C. Wagner, *ibid.*, **70**, 775 (1966).
31. H. J. Grabke, K. J. Best, and A. Gala, *Werkst. Korros.*, **21**, 911 (1970).
32. J. C. M. Li, R. A. Oriani, and L. S. Darken, *Z. Phys. Chem.*, **49**, 271 (1966).
33. R. H. Campbell, Ph.D. Thesis, Arizona State University (1969).
34. F. Morin, *Can. Met. Quart.*, **14**, 105 (1975).
35. R. H. Campbell, W. J. Kass, and M. O'Keefe, in "Mass Transport in Oxides," NBS Special Publication No. 296, p. 173, Washington, DC (1968).
36. J. P. Delmaire and H. LeBrusq, *C.R. Acad. Sci. Paris, Series C*, **284**, 635 (1977).
37. J. P. Bocquet, M. Kawahara, and P. Lacombe, *C.R. Acad. Sci. Paris*, **265**, 1318 (1967).
38. J. A. Roberson and R. A. Rapp, *J. Phys. Chem. Solids*, **30**, 1119 (1969).
39. F. Morin and R. Dieckmann, Paper submitted to *Z. Phys. Chem.*

Comparison Between C.V.T. of Titanium Diboride by Different Transport Agents: Experimental Results and Application of Two Thermodynamic Models

C. Bernard*

Laboratoire de Thermodynamique et Physico-Chimie Métallurgiques,
E.N.S.E.E.G., B.P. 44, 38401 Saint Martin d'Herès, France

and G. Constant* and R. Feurer

Laboratoire de Chimie Minérale et Cristallographie,
E.N.S.C.T., 118, Route de Narbonne, 31077 Toulouse, Cedex, France

ABSTRACT

In order to explain the differences experimentally observed in the chemical vapor transport of titanium diboride by various transporting agents we have used thermodynamics to model the process. Two different calculating methods have been undertaken. The first one is based upon the consideration of the transport process as two successive thermodynamic equilibria whose chemical compositions have been obtained by minimization of the Helmholtz free energy. The second one refers to the Richardson and Nörling model and accounts for the mass transport by calculating the flux functions of the vapor phase constituents. The comparison between experiments and results of each calculating method shows that the two models give fuller information, contribute to a satisfactory explanation of the experiments, and allow one to choose available transporting agents.

In order to grow titanium diboride single crystals of a relatively large size (about a few millimeters), we have undertaken a set of chemical vapor transport experiments in sealed tubes using a great variety of transport agents:¹ halogens, hydrogen halides, titanium and boron halides, tellurium tetrachloride. While doing these long-lasting experiments we could reveal very different behaviors for each transport agent (1, 2). This is the set of results we use to test predictive models based upon thermodynamic considerations. Two different types of approaches are tested in this way. As both use the minimization of a thermodynamic function of the system, their simultaneous implementation is very easy. The comparative study of their respective pros and cons points out how pertinent a simultaneous use of both models is in predicting the transport phenomenon in closed tubes.

Experimental

Experiments have been carried out in silica sealed tubes (6 mm diam 100 mm long, and 12 mm diam 100 mm long). The starting materials are industrial titanium diboride powder (> 99%), halogen, and halides. The quantities are about 300 mg of TiB₂ (an excess) and 6×10^{-4} mol of t.a. per 10 cm³. The tube is air evacuated to 10^{-5} Torr for 6 hr then sealed under low pressure transport agent. The ampuls are heated by electric horizontal furnaces in temperature gradient of 10 deg. cm⁻¹ for one month.

Experiments have been carried out for nine transport agents and transport was observed except in the case of TiI₄. The transport occurs from the cold to the hot end of the tube with some t.a., from the hot to the cold end with the others. Table I gives the experimental observations with an average evaluation of the amount transported in each case.

Chemical analyses have been made by spectrophotometric measurements on the transported crystals.

* Electrochemical Society Active Member.

Key words: chemical vapor transport, flux function, thermodynamic model, titanium diboride, transport agent.

¹ t.a. in the following text.

They show a variation in the boron-titanium ratio when changing the transport agent.

After cooling of the ampul, in most cases the tube was unpolished showing an etching of silica at the source end. Gaseous or liquid halides remain on the tube and except in the case of tellurium halides no solid compound other than TiB₂ appears at the sink end.

First Thermodynamic Model: Equilibria in Closed Tubes

The model consists in decomposing the transport process into two successive equilibria. The first one is at the source end of the tube at temperature T_1 taking into account the powdery titanium diboride, the transport agent, and the silica of the tube. The composition of this system at equilibrium is determined by minimization of the Helmholtz free energy.² The gas phase of this equilibrium causes the transport.

The second equilibrium system consists of the gas phase taken at the sink end of the tube together with silica at T_2 temperature. A second minimization of the Helmholtz free energy gives the composition of the sink system at equilibrium.

² The computer program used for the minimization is a slightly modified version of the one used for the minimization of the Gibbs free energy (3).

Table I. Data and results for TiB₂ transported from T_1 to T_2

| t.a. | T_1 (K) | T_2 (K) | TiB ₂ transported (mg/month) |
|----------------------|-----------|-----------|---|
| T_1 I ₂ | 1125 | 1225 | 50 |
| | 1050 | 1200 | 50 |
| | 1075 | 1225 | 10 |
| T_2 ^ | 1255 | 1125 | 150 |
| | 1255 | 1125 | 150 |
| | 1235 | 1105 | 150 |
| T_1 < | 1270 | 1125 | 20 |
| | 1320 | 1270 | 10 |
| | 1300 | 1190 | 0 |

Such systems are of great complexity because of the number of chemical reactions which are feasible between halogen, titanium, boron, silicon, and oxygen but the number of constituents is not limited in the calculation method. The only limit is the knowledge of the thermodynamic values of all the compounds. All the values used in the calculations are reported at the end of the text in the Appendix.

The Helmholtz free energy is minimized; that is, the very one which falls to a minimum at equilibrium in a sealed tube (under constant V and T). Let us consider a system involving Γ phases, each phase itself involving N_γ constituents. The Helmholtz free energy is

$$F = G - PV$$

after the Euler's theorem

$$G = \sum_{i=1}^{N_\gamma} n_i \bar{G}_i$$

with $\bar{G}_i = \left(\frac{\partial G}{\partial n_i} \right)_{P,T} = \mu_{i\gamma}^0 + RT \ln P_i$ (for one gaseous species for example

$$\frac{F}{RT} = \sum_{\gamma=1}^{\Gamma} \sum_{i=1}^{N_\gamma} n_i^\gamma \left[\frac{\mu_{i\gamma}^0}{RT} + \phi_\gamma \ln P_i + (1 - \phi_\gamma) \ln a_i^\gamma \right] - \frac{1}{RT} \sum_{\gamma=1}^{\Gamma} \sum_{i=1}^{N_\gamma} \phi_\gamma n_i^\gamma RT$$

$$\frac{F}{RT} = \sum_{\gamma=1}^{\Gamma} \sum_{i=1}^{N_\gamma} n_i^\gamma \left[\frac{\mu_{i\gamma}^0}{RT} + \phi_\gamma \left(\ln \frac{RT}{V} + \ln n_i^\gamma - 1 \right) + (1 - \phi_\gamma) \ln a_i^\gamma \right]$$

with $n_i^\gamma =$ mols of the i th species in γ th phase; $\mu_{i\gamma}^0 =$ standard chemical potential of the i th species in the γ th phase; $\phi_\gamma = 1$ if a gaseous phase; $\phi_\gamma = 0$ if nongaseous phase; $a_i^\gamma =$ activity of the i th species in the γ th nongaseous phase; and $V =$ volume of the tube.

The nongaseous phases are assumed to be pure, their activity is taken equal to 1, and the chemical potential gradients are contingent on the temperature. The gaseous compounds are assumed to follow the ideal gas law.

The compositions of the two equilibria have been calculated for the following conditions: temperature gradient 1200-1300 K (or vice versa), transport agent 6×10^{-4} mol, volume of the tube 10 cm³ and with five series of transport agents: (i) halogen Cl₂, Br₂, I₂; (ii) hydrogen halides HCl, HBr; (iii) tellurium halides TeCl₄; (iv) titanium halides TiCl₄, TiBr₄, TiI₄; (v) boron halides BCl₃, BBr₃, BI₃.

The set of calculations provides a number of indications. The whole set of numerical results gives too many tables, so we have limited the presentation to one series of transporting agents, the boron halides for example (Table II). This table shows the complexity of the vapor phase and the non-negligible role of silica; as to the presence of titanium diboride at the sink it means the suitability of the chosen temperature gradient (if the gradient is not in the good direction we do not obtain TiB₂ at the sink).

In the order to determine the amount of TiB₂ expected at the sink when the equilibrium state has been reached, we have reported in Table III the calculated values which indicate the tendency of the system to transport TiB₂, together with experimental results when obtained. The poor agreement between the two sets of results is obvious. So, while TiCl₄ is

Table II. Compositions in mols of source and sink equilibria by minimization of the Helmholtz free energy for BCl₃, BBr₃, and BI₃ as transport agents

| Source 1<TiB ₂ > + 1<SiO ₂ > + 60.10 ⁻⁴ BX ₃ T ₁ = 1300 K (mol) | | | Sink Gas phase of the I ⁺ equilibrium + 1<SiO ₂ > T ₂ = 1200 K (mol) | | |
|--|-----------|--------------------|---|-----------|--------------------|
| BCl ₃ | | | | | |
| TiCl ₄ | 1.77 | × 10 ⁻⁶ | TiCl ₄ | 6.9 | × 10 ⁻⁷ |
| TiCl ₃ | 1.4 | × 10 ⁻⁷ | TiCl ₃ | 3 | × 10 ⁻⁸ |
| BCl ₃ | 2.2791 | × 10 ⁻⁴ | BCl ₃ | 2.0082 | × 10 ⁻⁴ |
| BCl ₂ | 3 | × 10 ⁻⁸ | SiCl ₄ | 2.9327 | × 10 ⁻⁴ |
| BClO | 3 | × 10 ⁻⁸ | SiCl ₃ | 7.11 | × 10 ⁻⁶ |
| SiCl ₄ | 2.6630 | × 10 ⁻⁴ | SiCl ₂ | 1.3 | × 10 ⁻⁷ |
| SiCl ₃ | 1.815 | × 10 ⁻⁶ | <SiO ₂ > | 9.9998144 | × 10 ⁻¹ |
| SiCl ₂ | 5.0 | × 10 ⁻⁷ | <B ₂ O ₃ > | 1.238 | × 10 ⁻⁵ |
| <TiB ₂ > | 9.9999805 | × 10 ⁻¹ | <TiB ₂ > | 1.19 | × 10 ⁻⁶ |
| <SiO ₂ > | 9.9971803 | × 10 ⁻¹ | | | |
| <B ₂ O ₃ > | 1.8796 | × 10 ⁻⁴ | | | |
| P = 5.46 atm | | | P = 4.95 atm | | |
| BBr ₃ | | | | | |
| Br | 2 | × 10 ⁻⁸ | Br | 1 | × 10 ⁻⁸ |
| TiBr ₄ | 4.3 | × 10 ⁻⁷ | TiBr ₄ | 3.7 | × 10 ⁻⁷ |
| TiBr ₃ | 6 | × 10 ⁻⁸ | TiBr ₃ | 3 | × 10 ⁻⁸ |
| BBr ₃ | 6.362 | × 10 ⁻⁵ | BBr ₃ | 4.790 | × 10 ⁻⁵ |
| BBrO | 2 | × 10 ⁻⁸ | BBr ₂ | 1 | × 10 ⁻⁸ |
| SiBr ₄ | 4.0141 | × 10 ⁻⁴ | SiBr ₄ | 4.1358 | × 10 ⁻⁴ |
| SiBr ₃ | 7.7 | × 10 ⁻⁷ | SiBr ₂ | 1.6 | × 10 ⁻⁷ |
| <TiB ₂ > | 9.9999948 | × 10 ⁻¹ | <SiO ₂ > | 9.9998841 | × 10 ⁻¹ |
| <SiO ₂ > | 9.9959781 | × 10 ⁻¹ | <B ₂ O ₃ > | 7.7 | × 10 ⁻⁶ |
| <B ₂ O ₃ > | 2.6810 | × 10 ⁻⁴ | <TiB ₂ > | 9 | × 10 ⁻⁹ |
| P = 4.98 atm | | | P = 4.55 atm | | |
| BI ₃ | | | | | |
| I ₂ | 1.291 | × 10 ⁻⁶ | I ₂ | 1.439 | × 10 ⁻⁶ |
| I | 9.17 | × 10 ⁻⁸ | I | 1.692 | × 10 ⁻⁸ |
| TiI ₄ | 2.08 | × 10 ⁻⁸ | TiI ₄ | 2.02 | × 10 ⁻⁴ |
| BI ₃ | 1.6 | × 10 ⁻⁷ | TiI ₃ | 2 | × 10 ⁻⁶ |
| SiI ₄ | 4.3852 | × 10 ⁻⁴ | BI ₃ | 1.3 | × 10 ⁻⁷ |
| SiI ₂ | 1.04 | × 10 ⁻⁶ | SiI ₄ | 4.3327 | × 10 ⁻⁴ |
| <TiB ₂ > | 9.9999787 | × 10 ⁻¹ | SiI ₂ | 6.30 | × 10 ⁻⁶ |
| <SiO ₂ > | 9.9956041 | × 10 ⁻¹ | <SiO ₂ > | 1 | |
| <B ₂ O ₃ > | 2.9305 | × 10 ⁻⁴ | <B ₂ O ₃ > | 0 | |
| | | | <TiB ₂ > | 2 | × 10 ⁻⁸ |
| P = 4.57 atm | | | P = 5.05 atm | | |

Table III. Number of mols of TiB₂ "deposited" at sink when gas is first equilibrated with TiB₂ at source and experimentally transported amounts (after one month)

| Transport agent | Calculated values (mol) | Experimental (mg TiB ₂) |
|-------------------|-------------------------|-------------------------------------|
| HBr | 7.0 × 10 ⁻⁶ | — |
| TiCl ₄ | 2.0 × 10 ⁻⁶ | 0 |
| HCl | 1.7 × 10 ⁻⁶ | 10 |
| TiBr ₄ | 1.5 × 10 ⁻⁶ | 10 |
| BCl ₃ | 1.2 × 10 ⁻⁶ | — |
| TeCl ₄ | 1.1 × 10 ⁻⁶ | 150 |
| Cl ₂ | 6.6 × 10 ⁻⁷ | 20 |
| BBr ₃ | 9 × 10 ⁻⁸ | 150 |
| Br ₂ | 4 × 10 ⁻⁸ | — |
| BI ₃ | 2 × 10 ⁻⁸ | 50 |
| I ₂ | 2 × 10 ⁻⁸ | 50 |

Table IV. Percentages of silicon halides in the source vapor phase

| t.a. | ΣSiXn | t.a. | ΣSiXn |
|------------------|----------------------|-------------------|----------------------|
| | ΣN | | ΣN |
| BI ₃ | 0.95 | TeCl ₄ | 0.30 |
| BBr ₃ | 0.86 | 4Br | 0.128 |
| BCl ₃ | 0.55 | HCl | 0.09 |
| I ₂ | 0.54 | TiBr ₄ | 0.013 |
| Br ₂ | 0.51 | TiCl ₄ | 0.004 |
| Cl ₂ | 0.30 | | |

ΣSiXn : number of mols of all silicon halides.
 ΣN : total mol number of the gaseous phase.

expected to work a hundred times better than BI_3 , it is the latter which produces experimental transport.

In Table IV the relative importance of the silicon halides in the vapor phase is reported. These values represent maximum limits of silica etching never reached in facts because of the passivation of the tubes.

So this first model gives the appropriate transport direction, accounts for the silica etching, but does not enable us to anticipate the importance of mass transport. In such experiments in which weak transport occurs (few milligrams a month), it seems interesting to implement a method which optimizes, or at least provides indications about the speed of transport; that is the reason why we refer to the Richardson and Noläng model.

Second Model

In his thesis (6) Richardson has demonstrated (4, 5) the influence on the transport rate of all the vapor species, even when they had very low partial pressures. Moreover, when studying the transport of SnO_2 by iodine and sulfur (4), he points out the competition between two tin halides that constitutes a case similar to ours in which the titanium is present in the gas phase as TiX_3 and TiX_4 , both responsible for the transport of TiB_2 (in a few cases TiX_2 also appears).

We have applied this model to our systems to predict the rate of chemical transport. The principal assumptions are that the gaseous diffusion follows the laminar flow model, that the system has reached a

steady state, and that the total pressure is equal to the average value of the pressures at sink and source calculated by the first method. Then, the reactions of the walls of the ampul are assumed infinitely kinetically hindered so that the fluxes are position independent. It is therefore necessary to neglect all the products of reactions with silica. The Gibbs free energy of the systems $\text{TiB}_2/\text{t.a.}$ is minimized at the assumed pressure successively at source and sink temperature. The results of these minimizations for a number of transport agents experimentally tested are reported in Tables V-XII, the compositions of the equilibria are given as partial pressures (atm) for the gaseous species and number of mols for the solid ones. These partial pressure values allow us to obtain the flux functions of the various species.

In the approximation of the experimental model the flux function of a species can be written as

$$\phi_i = \frac{1}{RT} \left(\frac{P_0}{P} \right) \left(\frac{\bar{T}}{T_0} \right)^\alpha \left[\bar{P}_i \left(\sum_t \lambda_{ir} \frac{\Delta P_t}{\Delta T} / \sum_t \lambda_{ir} \bar{P}_i \right) - \frac{\Delta P_i}{\Delta T} \right]$$

$$= \frac{1}{RT} \left(\frac{P_0}{P} \right) \left(\frac{\bar{T}}{T_0} \right)^\alpha [f(i)]$$

with

$$\bar{P}_i = \frac{P_{i1} + P_{i2}}{2}$$

Table V. I_2 6×10^{-4} mol, $\langle \text{TiB}_2 \rangle$ 1 mol, $T_1 = 1200$ K, $T_2 = 1300$ K, $P = 3.3$ atm

| Compositions of source (1) and sink (2) equilibria | | | $\frac{P_{i2} - P_{i1}}{T_2 - T_1}$ | \bar{P}_i |
|--|-------------------------|-------------------------|--|-----------------------|
| Gas phase | P_{i1} (atm) | P_{i2} (atm) | | |
| TiI_4 | 1.7878 | 1.1674 | -6.204×10^{-3} | 1.477 |
| TiI_3 | 2.325×10^{-3} | 4.471×10^{-3} | 2.146×10^{-5} | 3.4×10^{-5} |
| BI_3 | 4.628×10^{-2} | 5.602×10^{-2} | 9.97×10^{-5} | 5.11×10^{-2} |
| I_2 | 1.1876 | 1.5066 | 3.19×10^{-3} | 1.347 |
| I | 2.759×10^{-1} | 5.655×10^{-1} | 2.89×10^{-3} | 4.21×10^{-1} |
| Solid phases | n_{i1} (mol) | n_{i2} (mol) | | |
| $\langle \text{TiB}_2 \rangle$ | 9.9978×10^{-1} | 9.9983×10^{-1} | $\frac{P_{i2} - P_{i1}}{T_2 - T_1}$ | |
| $\langle \text{B} \rangle$ | 4.26×10^{-4} | 3.25×10^{-4} | $\frac{\sum \lambda_{ir} (P_{i2} - P_{i1})}{T_2 - T_1} = -1.65 \times 10^{-3}$ | |
| | | | $\frac{\sum \lambda_{ir} \bar{P}_i}{\sum \lambda_{ir} \bar{P}_i}$ | |

Table VI. Cl_2 6×10^{-4} mol, $\langle \text{TiB}_2 \rangle$ 1 mol, $T_1 = 1300$ K, $T_2 = 1200$ K, $P = 3.4$ atm

| Compositions of source (1) and sink (2) equilibria | | | $\frac{P_{i2} - P_{i1}}{T_2 - T_1}$ | \bar{P}_i |
|--|--------------------------|--------------------------|--|----------------------|
| Gas phase | P_{i1} (atm) | P_{i2} (atm) | | |
| TiCl_4 | 1.07333 | 1.10326 | -2.993×10^{-4} | 1.0883 |
| TiCl_3 | 5.996×10^{-2} | 3.10×10^{-2} | 2.986×10^{-4} | 4.5×10^{-2} |
| BCl_3 | 2.26641 | 2.26656 | -1.6×10^{-6} | 2.2665 |
| Solid phases | n_{i1} (mol) | n_{i2} (mol) | | |
| $\langle \text{TiB}_2 \rangle$ | 9.99879×10^{-1} | 9.99880×10^{-1} | $\frac{P_{i2} - P_{i1}}{T_2 - T_1}$ | |
| | | | $\frac{\sum \lambda_{ir} (P_{i2} - P_{i1})}{T_2 - T_1} = -2.72 \times 10^{-5}$ | |
| | | | $\frac{\sum \lambda_{ir} \bar{P}_i}{\sum \lambda_{ir} \bar{P}_i}$ | |

Table VII. HCl 6×10^{-4} mol, $\langle \text{TiB}_2 \rangle$ 1 mol, $T_1 = 1200$ K, $T_2 = 1300$ K, $P = 5$ atm

| Compositions of source (1) and sink (2) equilibria | | | $\frac{P_{i2} - P_{i1}}{T_2 - T_1}$ | \bar{P}_i |
|--|--------------------------|--------------------------|--|------------------------|
| Gas phase | P_{i1} (atm) | P_{i2} (atm) | | |
| TiCl_4 | 4.8217×10^{-1} | 4.3795×10^{-1} | -4.42×10^{-4} | 4.60×10^{-1} |
| TiCl_3 | 1.729×10^{-2} | 3.271×10^{-2} | 1.54×10^{-4} | 2.500×10^{-2} |
| BCl_3 | 8.9738×10^{-1} | 8.3116×10^{-1} | -6.62×10^{-4} | 8.64×10^{-1} |
| HCl | 1.1144 | 1.3613 | 2.469×10^{-3} | 1.2379 |
| BHCl_2 | 1.0154×10^{-1} | 1.099×10^{-1} | 8.45×10^{-5} | 1.058×10^{-1} |
| Solid phases | n_{i1} (mol) | n_{i2} (mol) | | |
| $\langle \text{TiB}_2 \rangle$ | 9.99949×10^{-1} | 9.99952×10^{-1} | $\frac{P_{i2} - P_{i1}}{T_2 - T_1}$ | |
| | | | $\frac{\sum \lambda_{ir} (P_{i2} - P_{i1})}{T_2 - T_1} = -1.09 \times 10^{-4}$ | |
| | | | $\frac{\sum \lambda_{ir} \bar{P}_i}{\sum \lambda_{ir} \bar{P}_i}$ | |

Table VIII. TeCl_4 6×10^{-4} mol, $\langle \text{TiB}_2 \rangle$ 1 mol, $T_1 = 1300$ K, $T_2 = 1200$ K, $P = 7$ atm

| Compositions of source (1) and sink (2) equilibria | | | $\frac{P_{i_2} - P_{i_1}}{T_2 - T_1}$ | P_i (atm) |
|---|---------------------------|------------------------|--|--|
| Gas phase | P_{i_1} (atm) | P_{i_2} (atm) | | |
| TiCl ₄ | 1.9660 | 2.2038 | -2.378×10^{-3} | 2.085 |
| TiCl ₃ | 9.158×10^{-2} | 4.893×10^{-2} | 4.265×10^{-4} | 7.02×10^{-2} |
| BCl ₃ | 4.1151 | 4.5056 | -3.905×10^{-3} | 4.3103 |
| TeCl ₂ | 2.52×10^{-3} | 8.80×10^{-4} | 1.64×10^{-5} | 1.71×10^{-3} |
| Solid phases | n_{i_1} (mol) | n_{i_2} (mol) | | |
| <TiB ₂ > | 9.997589×10^{-1} | 9.997595 | $\frac{P_{i_2} - P_{i_1}}{T_2 - T_1}$ | |
| <Te> | 4.069×10^{-4} | 5.486×10^{-4} | $\frac{\sum \lambda_{i,r} (P_{i_2} - P_{i_1})}{T_2 - T_1}$ | |
| | | | | $\frac{\sum \lambda_{i,r} P_i}{\sum \lambda_{i,r} P_i} = -9.26 \times 10^{-4}$ |

Table IX. TiCl_4 6×10^{-4} mol, $\langle \text{TiB}_2 \rangle$ 1 mol, $T_1 = 1300$ K, $T_2 = 1200$ K, $P = 6$ atm

| Compositions of source (1) and sink (2) equilibria | | | $\frac{P_{i_2} - P_{i_1}}{T_2 - T_1}$ | \bar{P}_i |
|---|--------------------------|--------------------------|--|--|
| Gas phase | P_{i_1} (atm) | P_{i_2} (atm) | | |
| TiCl ₄ | 5.4203 | 5.6685 | -2.48×10^{-3} | 5.5444 |
| TiCl ₃ | 4.830×10^{-1} | 2.762×10^{-1} | 2.07×10^{-3} | 3.796×10^{-1} |
| BCl ₃ | 9.664×10^{-2} | 5.525×10^{-2} | 4.14×10^{-4} | 7.59×10^{-2} |
| Solid phases | n_{i_1} (mol) | n_{i_2} (mol) | | |
| <TiB ₂ > | 9.99995×10^{-1} | 9.99997×10^{-1} | $\frac{P_{i_2} - P_{i_1}}{T_2 - T_1}$ | |
| | | | $\frac{\sum \lambda_{i,r} (P_{i_2} - P_{i_1})}{T_2 - T_1}$ | |
| | | | | $\frac{\sum \lambda_{i,r} \bar{P}_i}{\sum \lambda_{i,r} \bar{P}_i} = -1.06 \times 10^{-4}$ |

Table X. TiBr_4 6×10^{-4} mol, $\langle \text{TiB}_2 \rangle$ 1 mol, $T_1 = 1300$ K, $T_2 = 1200$ K, $P = 6$ atm

| Compositions of source (1) and sink (2) equilibria | | | $\frac{P_{i_2} - P_{i_1}}{T_2 - T_1}$ | \bar{P}_i |
|---|--------------------------|--------------------------|--|--|
| Gas phase | P_{i_1} (atm) | P_{i_2} (atm) | | |
| TiBr ₄ | 5.3474 | 5.6560 | -3.086×10^{-3} | 5.502 |
| TiBr ₃ | 5.4136×10^{-1} | 2.8612×10^{-1} | 2.55×10^{-3} | 4.14×10^{-1} |
| TiBr ₂ | 1.925×10^{-3} | 4.46×10^{-4} | 1.48×10^{-5} | 1.18×10^{-3} |
| BBr ₃ | 1.0894×10^{-1} | 5.737×10^{-2} | 5.15×10^{-4} | 8.31×10^{-2} |
| Solid phases | n_{i_1} (mol) | n_{i_2} (mol) | | |
| <TiB ₂ > | 9.99994×10^{-1} | 9.99997×10^{-1} | $\frac{P_{i_2} - P_{i_1}}{T_2 - T_1}$ | |
| | | | $\frac{\sum \lambda_{i,r} (P_{i_2} - P_{i_1})}{T_2 - T_1}$ | |
| | | | | $\frac{\sum \lambda_{i,r} \bar{P}_i}{\sum \lambda_{i,r} \bar{P}_i} = -1.32 \times 10^{-4}$ |

Table XI. BI_3 6×10^{-4} mol, $\langle \text{TiB}_2 \rangle$ 1 mol, $T_1 = 1200$ K, $T_2 = 1300$ K, $P = 4.7$ atm

| Compositions of source (1) and sink (2) equilibria | | | $\frac{P_{i_2} - P_{i_1}}{T_2 - T_1}$ | \bar{P}_i |
|---|--------------------------|-------------------------|--|--|
| Gas phase | P_{i_1} (atm) | P_{i_2} (atm) | | |
| TiI ₄ | 2.8663 | 2.0252 | -8.41×10^{-3} | 2.4457 |
| TiI ₃ | 3.323×10^{-3} | 6.772×10^{-3} | 3.45×10^{-5} | 5.05×10^{-3} |
| BI ₃ | 6.595×10^{-2} | 8.468×10^{-2} | 1.87×10^{-4} | 7.53×10^{-2} |
| I ₂ | 1.5038 | 1.9843 | 4.80×10^{-3} | 1.744 |
| I | 3.1051×10^{-1} | 6.490×10^{-1} | 3.38×10^{-3} | 4.80×10^{-1} |
| Solid phases | n_{i_1} (mol) | n_{i_2} (mol) | | |
| <TiB ₂ > | 9.99855×10^{-1} | 9.9972×10^{-1} | $\frac{P_{i_2} - P_{i_1}}{T_2 - T_1}$ | |
| | 1.281×10^{-3} | 1.151×10^{-3} | $\frac{\sum \lambda_{i,r} (P_{i_2} - P_{i_1})}{T_2 - T_1}$ | |
| | | | | $\frac{\sum \lambda_{i,r} \bar{P}_i}{\sum \lambda_{i,r} \bar{P}_i} = -1.43 \times 10^{-5}$ |

Table XII. BBr_3 6×10^{-4} mol, $\langle \text{TiB}_2 \rangle$ 1 mol, $T_1 = 1300$ K, $T_2 = 1200$ K, $P = 5$ atm

| Compositions of source (1) and sink (2) equilibria | | | $\frac{P_{i_2} - P_{i_1}}{T_2 - T_1}$ | \bar{P}_i |
|---|--------------------------|--------------------------|--|---|
| Gas phase | P_{i_1} (atm) | P_{i_2} (atm) | | |
| TiBr ₄ | 6.407×10^{-2} | 6.107×10^{-2} | 3.0×10^{-5} | 6.26×10^{-2} |
| TiBr ₃ | 4.694×10^{-3} | 1.999×10^{-3} | 2.69×10^{-3} | 3.34×10^{-3} |
| BBr ₃ | 4.9305 | 4.9367 | -6.24×10^{-5} | 4.934 |
| Br | 4.67×10^{-4} | 9.5×10^{-5} | 3.7×10^{-6} | 2.81×10^{-4} |
| Solid phases | n_{i_1} (mol) | n_{i_2} (mol) | | |
| <TiB ₂ > | 9.99991×10^{-1} | 9.99992×10^{-1} | $\frac{P_{i_2} - P_{i_1}}{T_2 - T_1}$ | |
| | 2.72×10^{-6} | 2.50×10^{-6} | $\frac{\sum \lambda_{i,r} (P_{i_2} - P_{i_1})}{T_2 - T_1}$ | |
| | | | | $\frac{\sum \lambda_{i,r} \bar{P}_i}{\sum \lambda_{i,r} \bar{P}_i} = 1.14 \times 10^{-5}$ |

mean partial pressure value between the two equilibria

$$\frac{\Delta P_i}{\Delta T} = \frac{P_{i_2} - P_{i_1}}{T_2 - T_1}$$

$$\bar{T} = \frac{T_1 + T_2}{2}$$

α is a constant used in the relationship $\bar{D} = \bar{D}_0 (P_0/P)$

$(T/T_0)^\alpha$ to describe the temperature and total pressure variation of the diffusion coefficient. Its value lies between 1.5 and 2.

λ_{ir} is the stoichiometric coefficient of the r th element in the i species where r is present only in the vapor phase (here r is the halogen). The relation between ϕ_i and the flux of the i species is

$$J_i = \bar{D}_0 \phi_i \frac{\Delta T}{\Delta x}$$

in which Δx is the length of the tube and \bar{D}_0 the mean diffusion coefficient; this single average value replaces the diffusion coefficients D_0 .

Richardson and Nörläng (4, 5) wished to optimize the flux function, in this paper we shall only compare the values of this function for different transport agents.

The transport of TiB_2 , for the titanium part, being due to TiX_3 and TiX_4 , we can write

$$\begin{aligned} \phi[\text{TiB}_2] &= \phi[\text{TiX}_3] + \phi[\text{TiX}_4] \\ &= \frac{1}{RT} \left(\frac{P_0}{P} \right) \left(\frac{\bar{T}}{T_0} \right)^\alpha [f(\text{TiX}_4) + f(\text{TiX}_3)] \end{aligned}$$

The different values obtained (Table XIII) show that, with the exception of BBr_3 , the functions ϕ of the halides have opposite signs. Therefore, there is a competition between them and only one is responsible for the transport.

A means of comparison of the transport agents in spite of the different values of \bar{P} and D_0 is the consideration of the ratio

$$R = - \frac{\text{flux of the transporting halide}}{\text{flux of the second halide}}$$

When the ratio tends toward 1 (equal fluxes), infinitely slow transport is expected. The values of R for the various transport agents are reported in Table XIII against the amounts experimentally transported. There is now a very good agreement between the two series of results except for TeCl_4 and Cl_2 .

These two transport agents will be studied together with TiBr_4 and TiCl_4 , all of them producing an R value close to 1. Let us consider the case of Cl_2 : For that carrier, just like for TiCl_4 and TeCl_4 , there appears neither boron (unlike the cases of BI_3 , BBr_3 , and I_2) nor BHCl_2 (unlike the case of HCl) and, as Cl_2 acts only as a solvent and is completely consumed, the relation between the partial pressures results in

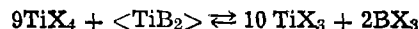
$$P_{[\text{TiCl}_3]} + P_{[\text{TiCl}_4]} = \frac{1}{2} P_{[\text{BCl}_3]}$$

and

$$P_{[\text{BCl}_3]} = \frac{2}{3} P_{\text{total}}$$

The model assumes the same pressure at source and sink and, in the absence of chemical potential gra-

dient, transport becomes impossible. The same phenomenon occurs in the case of TeCl_4 (with transport of tellurium in the process). In the cases of TiBr_4 and TiCl_4 , transport can be described by the equation



and as we started from TiX_4 , we necessarily have

$$P_{[\text{TiX}_3]} = 5P_{[\text{BX}_3]}$$

which gives for the flux functions

$$\phi_{[\text{TiX}_3]} = 5\phi_{[\text{BX}_3]}$$

now

$$\phi_{[\text{TiB}_2]} = \phi_{[\text{TiX}_3]} + \phi_{[\text{TiX}_4]} + \frac{1}{2} \phi_{[\text{BX}_3]}$$

In the absence of solid boron we shall have

$$\phi_{[\text{TiX}_4]} = -4,5 \phi_{[\text{BX}_3]}$$

and

$$\frac{\phi_{[\text{TiX}_3]}}{\phi_{[\text{TiX}_4]}} = \frac{5}{4,5} = -1,11 \quad (\text{cf., Table XIII})$$

These few equations explain why the Richardson model predicts no transport in these cases. To understand why two of these transport agents still give experimental transport, it is necessary to come back to the first model and to consider Table IV showing the side reactions with silica of the tube. In the case of TiCl_4 and TiBr_4 , there is almost no attack so that the restraints on the partial pressures remain and, as predicted, there is no transport. On the contrary, in the case of Cl_2 and TeCl_4 , silicon halides are formed by attack of the tube, and the restraints fall down, and the transport becomes possible.

Conclusion

The application of thermodynamics and flux functions, while pointing out their limitations, provides a useful insight into investigating transport system.

The grouping of the two submitted models brings an approach of the complicated chemical processes which occurs. From that approach we deduce the transport direction and the importance of the wall etching as well as its influence on the transport. Lastly, it allows one to make *a priori* choice between the different transport agents.

Manuscript submitted Nov. 7, 1980; revised manuscript received April 6, 1981. This was Paper 425 presented at the Los Angeles, California, Meeting of the Society, Oct. 14-19, 1979.

Any discussion of this paper will appear in a Discussion Section to be published in the June 1982 JOURNAL. All discussions for the June 1982 Discussion Section should be submitted by Feb. 1, 1982.

Publication costs of this article were assisted by the Ecole Nationale Supérieure de Chimie.

Table XIII. Results of calculations after the Richardson model

| t.a. | BBr_3 | BI_3 | I_2 | HCl | TiBr_4 | TiCl_4 | TeCl_4 | Cl_2 |
|-------------------|---------------------------------|-----------------------|-----------------------|-----------------------|------------------------|-----------------------|-----------------------|-----------------------|
| $f(\text{TiX}_4)$ | -3×10^{-5} | 4.9×10^{-3} | 3.8×10^{-3} | 3.9×10^{-4} | 2.3×10^{-3} | 1.9×10^{-3} | 4.5×10^{-4} | 2.7×10^{-4} |
| $f(\text{TiX}_3)$ | -2.7×10^{-5} | -3.4×10^{-5} | -2.7×10^{-5} | -1.6×10^{-4} | -2.60×10^{-3} | -2.1×10^{-3} | -4.9×10^{-4} | -3.0×10^{-4} |
| t.h.* | $\text{TiBr}_3 + \text{TiBr}_4$ | TiI_4 | TiI_4 | TiCl_4 | TiBr_3^{**} | TiCl_3 | TiCl_3 | TiCl_3 |
| R^{***} | 142 | 138 | 138 | 2.25 | 1.11 | 1.11 | 1.1 | 1.1 |
| exp. (mg) | 150 | 50 | 50 | <10 | <10 | 0 | 150 | 20 |

* t.h. = halide effective in the transport.

** = + TiBr_3 with $f(\text{TiBr}_2) = -1.5 \times 10^{-5}$.

*** = defined in the text as: $f(\text{TiX}_4)/f(\text{TiX}_3)$.

APPENDIX

The various constituents taken into account in equilibria calculations are:

| | | | | | | | |
|-----------------------------------|-----|----------------------|-----|--|-----|------------------------------------|-----|
| Cl | (a) | Br | (a) | <Te> | (e) | <TiH ₂ > | (a) |
| Cl ₂ | (a) | Br ₂ | (a) | Te | (e) | <TiB ₂ > | (a) |
| TiCl | (a) | BBr | (a) | Te ₂ | (e) | <TiB> | (a) |
| TiCl ₂ | (a) | BBr ₂ | (a) | TeCl ₂ | (e) | <Ti> | (a) |
| TiCl ₃ | (a) | BBr ₃ | (a) | TeCl ₄ | (d) | Ti | (a) |
| TiCl ₄ | (a) | TiBr | (a) | <TiTe ₂ > | (f) | TiO | (c) |
| <TiCl ₂ > | (a) | TiBr ₂ | (a) | TiTe | (e) | TiO ₂ | (c) |
| BCl ₃ | (a) | TiBr ₃ | (a) | TeO | (e) | <Ti ₂ O ₃ > | (c) |
| BCl | (a) | TiBr ₄ | (a) | TeO ₂ | (e) | <Ti ₃ O ₅ > | (c) |
| SiCl ₄ | (b) | <TiBr ₂ > | (a) | Te ₂ O ₂ | (e) | | |
| SiCl ₃ | (a) | SiBr ₄ | (d) | | | <SiO ₂ > | (a) |
| | | | | | | (cristobalite) | |
| SiCl ₂ | (b) | SiBr ₂ | (d) | | (a) | <Si ₃ Ti ₅ > | (d) |
| SiCl | (a) | BBrO | (a) | BO ₂ | (a) | SiO ₂ | (a) |
| BClO | (a) | HBr | (a) | B ₂ O ₂ | (a) | SiO | (a) |
| TiClO | (a) | BHBr ₂ | (a) | B ₂ O ₃ | (a) | <Si> | (a) |
| TiCl ₂ O | (a) | | | (B ₂ O ₃) | (a) | Si | (a) |
| ClH | (a) | I | (a) | H ₂ | (a) | O ₂ | (a) |
| ClH ₃ HSi | (a) | I ₂ | (a) | H | (a) | H ₄ Si | (a) |
| Cl ₂ H ₂ Si | (a) | BI | (a) | BH ₂ | (a) | H ₂ O | (a) |
| ClH ₃ Si | (a) | BI ₂ | (a) | BH ₃ | (a) | | |
| ClHO | (a) | BI ₃ | (a) | B ₂ H ₆ | (a) | | |
| BHCl ₂ | (a) | TiI | (a) | B ₁₀ H ₁₄ | (a) | | |
| | | TiI ₂ | (a) | BH ₃ O ₃ | (a) | | |
| | | TiI ₃ | (a) | B ₃ H ₃ O ₃ | (a) | | |
| | | TiI ₄ | (a) | BH ₂ O ₂ | (a) | | |
| | | <TiI ₂ > | (a) | BHO | (a) | | |
| | | SiI ₂ | (d) | | | | |
| | | SiI ₄ | (d) | | | | |

(a) JANAF thermochemical tables, U.S. Department of Commerce, N.B.S., 2nd ed., Dow Chemical Co, Midland, MI (1971).

(b) JANAF thermochemical tables, U.S. Department of Commerce, N.B.S., supplement (1974).

(c) JANAF thermochemical tables, U.S. Department of Commerce, N.B.S., supplement (1975).

(d) I. Barin, O. Knacke, and O. Kubaschewski, "Thermochemical Properties of Inorganic Substances," Springer Verlag, Berlin, Heidelberg, New York, supplement (1977).

(e) K. C. Mills, "Thermodynamic Data for Inorganic Sulfides, Selenides and Tellurides," Butterworths, London (1974).

(f) For <TiTe₂> the following thermodynamic values have been used: $\Delta f_{298}^\circ = -50900 \text{ cal mol}^{-1}$, after Mills (e), $S_{298}^\circ = 28 \text{ cal. deg.}^{-1} \text{ mol}^{-1}$, estimated by the Latimer's method (e), the function $G_T - H_{298}/T$ has been estimated to $35.1 \text{ cal. deg.}^{-1}$ at 800 K (e) and the approximations of the method being taken of, it has been considered as a linear function of the temperature: $G_T - H_{298} = 23.785 - 0.01414T$.

REFERENCES

1. R. Feurer, C. Bernard, and G. Constant, *C.R. Acad. Sci. Paris*, **282**, 1117 (1976).
2. R. Feurer, G. Constant, and C. Bernard, *J. Less-Common Met.*, **67**, 107 (1979).
3. C. Bernard, Y. Deniel, A. Jacquot, P. Way, and M. Ducarroir, *ibid.*, **40**, 165 (1975).
4. B. I. Nöläng and M. W. Richardson, *J. Cryst. Growth*, **34**, 198 (1976).
5. B. I. Nöläng and M. W. Richardson, *ibid.*, **34**, 205 (1976).
6. M. W. Richardson, *Acta Univ. Upsaliensis*, 464 (1978).

Vacuum Plasma Electron Beam Melting of Reactive and Refractory Metals and Their Alloys

One Step Melting of Low Oxygen Content Titanium Scrap by Using VPEB

S. Kashu, K. Watanabe, M. Nagase, and C. Hayashi

Vacuum Metallurgical Company, Limited, P.O. Box 11, Yachimata, Inba-gun, Chiba 289-11, Japan

and Y. Yoneda

ULVAC Corporation, 2500, Hagizono, Chigasaki-shi, Japan 253

ABSTRACT

Vacuum plasma electron beam (VPEB) melting with a hot hollow cathode gives satisfactory results for recovery of low oxygen content titanium scraps and Zircaloy-2 scraps. The yield of relatively high vapor pressure elements, such as Cr, can be controlled easily to meet with the tolerance. The VPEB has a high energy density and purification effect which is similar to that of high voltage electron beam melting. Power input of the VPEB to a target of a molten pool is by far more stable and the yield of materials throughout the melting of reactive and refractory metals and their alloys is quite satisfactory compared to those of high voltage EB or the vacuum arc melting process. The VPEB process is also safer, easier to operate, and suitable for automation. Three examples of VPEB application at VMC-ULVAC are described in this paper.

A simple recycle process of reactive metal and alloy scrap to sound ingots is aimed at. Low oxygen content, loose-shape titanium scraps (Fig. 1), the chemical composition of which is shown in Table I, are melted by using VPEB. Oxygen content of the VPEB melted ingots satisfied the high quality level of JIS Grade-1 specification. One-step melting of high purity reactive metal scrap by using VPEB is feasible both technologically and economically.

Figure 2 illustrates a VPEB one-step recycle furnace. A schematic drawing of the furnace is shown in Fig. 3. By using a 200 mm diam water-cooled copper crucible and an ingot pulling mechanism, a 1m length of titanium ingot (weight 130 kg) is produced. Melt stocks of titanium scraps, which are represented in Table II, are charged to a material feeding chamber and moved over the lip of the crucible. An 18 in. gate valve is attached to the furnace for semicontinuous feeding of the melt stock. A 20 in., 8 m³/sec oil ejector pump, a 1 m³/sec mechanical booster pump, and a rotary piston pump with a capacity of 7 m³/min are equipped in series. A d-c power supply of 100V and 3 kA maximum output is used as the VPEB power source.

Figure 4 illustrates the melting operation. An example of operating parameters are represented in

Key words: VPEB, titanium, metals.

Table I. JIS* chemical composition of Ti in ppm

| | H | O | N | Fe |
|---------|------|-------|------|-------|
| Grade 1 | <150 | <1500 | <500 | <2000 |
| Grade 2 | <150 | <2000 | <500 | <2500 |
| Grade 3 | <150 | <3000 | <700 | <3000 |

* JIS H 4670.

Table III. Figure 5 illustrates the surface of the one-step melted titanium ingot. Table IV represents the

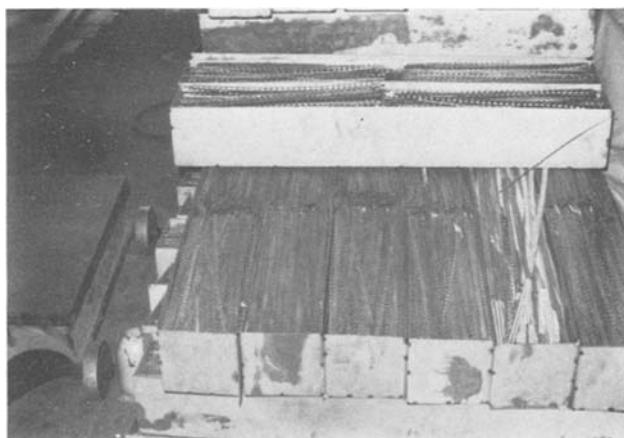


Fig. 1. Loose shape titanium recycle scraps

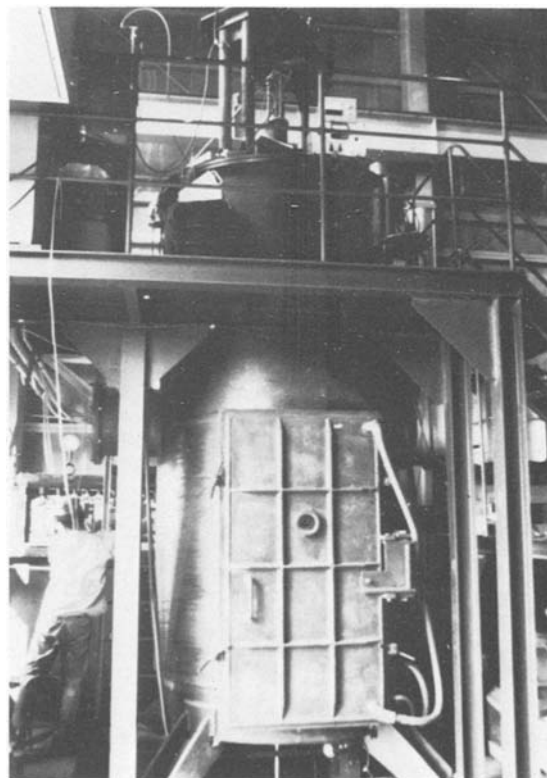


Fig. 2. Overall view of the VPEB one-step recycle furnace

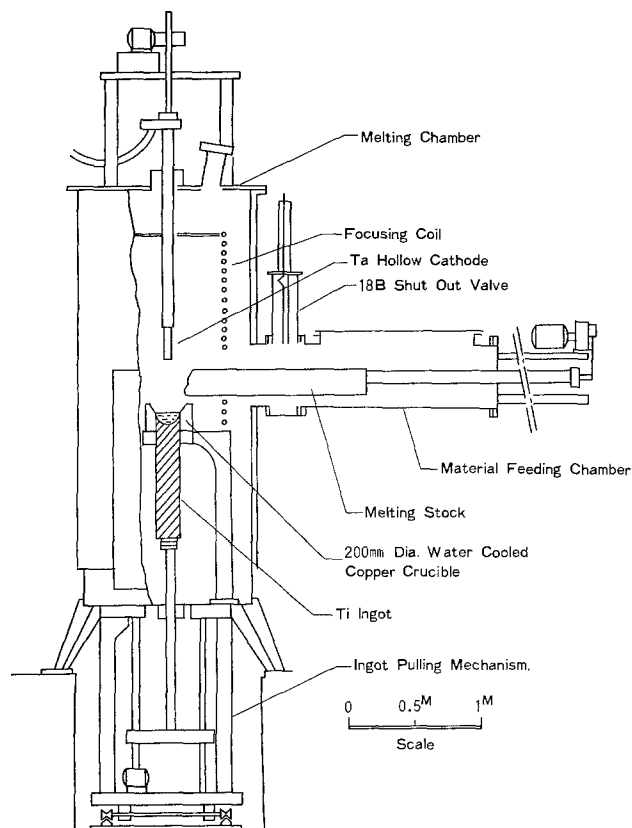


Fig. 3. Schematic drawing of VPEB one-step recycle furnace

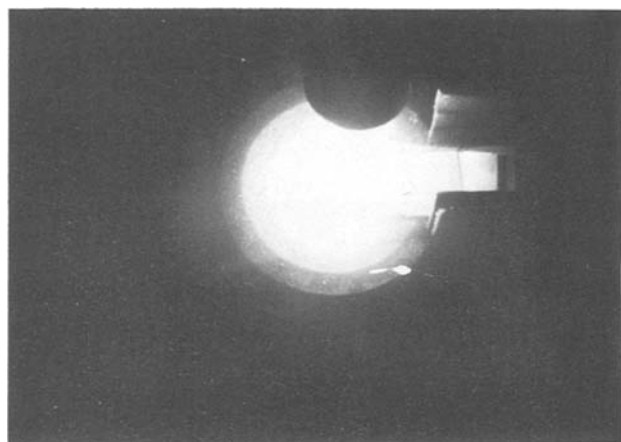


Fig. 4. Molten pool of titanium is bombarded by means of VPEB

results of the oxygen level of the recycled ingot. Table V represents the results of the chemical analysis of the 3 mm diam titanium wire which is forged and drawn from an ingot made by the VPEB process. A standard chemical analysis value of a commercially used high

Table II. Typical value of oxygen content

| Ti scraps | O (ppm) |
|-----------|---------|
| No. 1 | 630 |
| No. 2 | 750 |
| No. 3 | 790 |
| No. 4 | 830 |
| No. 5 | 500 |

Table III. Operating parameter of VPEB for Ti scrap melting

| | |
|--------------------------|-----------|
| Operating pressure (Pa) | 6.7 ~ 9.3 |
| VPEB out put Voltage (V) | 80 ~ 85 |
| Current (kA) | 1.8 ~ 2.0 |
| Wattage (kW) | 140 ~ 170 |
| Melting rate (kg/hr) | 23 |

Table IV. Typical value of oxygen content

| Ingot No. | O ₂ content (ppm) | | |
|-----------|------------------------------|--------|------|
| | Material | Ingot* | |
| 11 | 650 | T | 750 |
| | | B | 1070 |
| 12 | 580 | T | 710 |
| | | B | 950 |
| 13 | 670 | T | 750 |
| | | B | 1040 |
| 14 | 750 | T | 770 |
| | | B | 1030 |
| 15 | 580 | T | 610 |
| | | B | 680 |

* T: Top of the ingot. B: Bottom of ingot.

Table Va. Chemical analysis of 3 mm od Ti wire

| Lot No. | Impurity content (ppm) | | |
|---------------|------------------------|-----|-----|
| | O | Fe | C |
| W-1 | 750 | 490 | 130 |
| W-2 | 710 | 300 | 110 |
| W-3 | 690 | 410 | 93 |
| W-4 | 730 | 430 | 140 |
| W-5 | 670 | 360 | 75 |
| Average value | 710 | 400 | 110 |

Table Vb. Impurity level of JIS Grade-1 Ti wire

| | Impurity content (ppm) | | |
|-------------|------------------------|-----|-----|
| | O | Fe | C |
| Lower limit | 400 | 200 | 50 |
| Average | 650 | 450 | 100 |
| Upper limit | 850 | 600 | 150 |

Table VI. Chemical composition of Zircaloy-2

| Sn | Fe | Cr | Ni |
|-----------|-----------|-----------|-----------|
| 1.20-1.70 | 0.07-0.20 | 0.05-0.15 | 0.03-0.08 |

Table VII. Preliminary test of VPEB melt

| | I | II | III | VI | Raw material |
|----------------------------|-------|-------|-------|-------|--------------|
| Operating pressure (Ar Pa) | 1.2 | 1.1 | 1.2 | 5.3 | |
| Melting time (min) | 7 | 0.5 | 2 | 2 | |
| VPEB melting power (kW) | 50.4 | 51.6 | 52.8 | 51.4 | |
| Charged weight (g) | 1049 | 1466 | 1322 | 1458 | |
| Weight loss (g) | 2 | 2 | 1 | <1 | |
| Chemical analysis (%) | | | | | |
| Sn | 1.27 | 1.38 | 1.35 | 1.39 | 1.40 |
| Ni | 0.052 | 0.053 | 0.054 | 0.054 | 0.057 |
| Cr | 0.023 | 0.060 | 0.018 | 0.058 | 0.097 |
| Fe | 0.104 | 0.120 | 0.117 | 0.124 | 0.139 |

Table VIII. Operating parameter of VPEB

| | |
|--------------------|-----------------------------|
| Operating pressure | Ar 1.9-2.0 Pa |
| Voltage | 44-50 (V) |
| Current | 1500-1700 (A) |
| Melting power | 70-80 (kW) |
| Melting speed | Approx. 1.6 (kg/min) |
| Hearth size | w 125 × D 135 × L 1650 (mm) |

Table IX. Operating parameter of VAR

| | |
|--------------------|------------------|
| Operating pressure | 0.7-1.3 Pa |
| Voltage | 32 (V) |
| Current | 5700 (A) |
| Melting power | 182.4 (kW) |
| Melting speed | 5.2-5.8 (kg/min) |
| Crucible size | ID 250 (mm) |

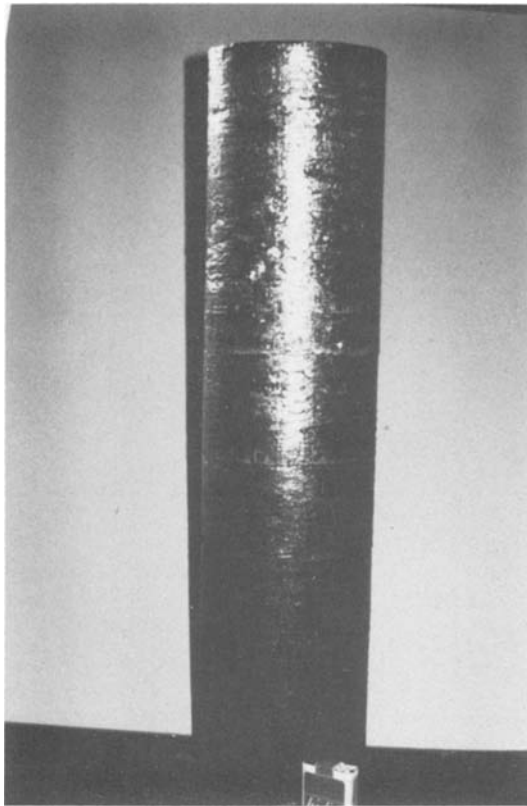


Fig. 5. One-step melted titanium ingot

purity grade titanium wire is also shown as the reference.

A low oxygen content 200 mm diam titanium ingot can be produced by VPEB one-step melting. Results are shown as follows: (i) The increase of the oxygen content level by one-step melting is less than 100 ppm. (ii) The melting rate of titanium one-step melting is 0.2 kg/kA · min. This value is acceptable in practical application. (iii) Variations of pressure, voltage, and current are very small so that extremely stable operation continues throughout melting. (iv) Argon gas consumption for VPEB discharge is small and can be neglected. It is, however, possible to recycle the argon, if required. (v) Operating experience has proved that the VPEB process is economically advantageous.

Direct Recovery of Zircaloy-2 Scrap by Using VPEB

Zircaloy (Table VI) scraps are conventionally shipped back to a chemical processing plant. In this

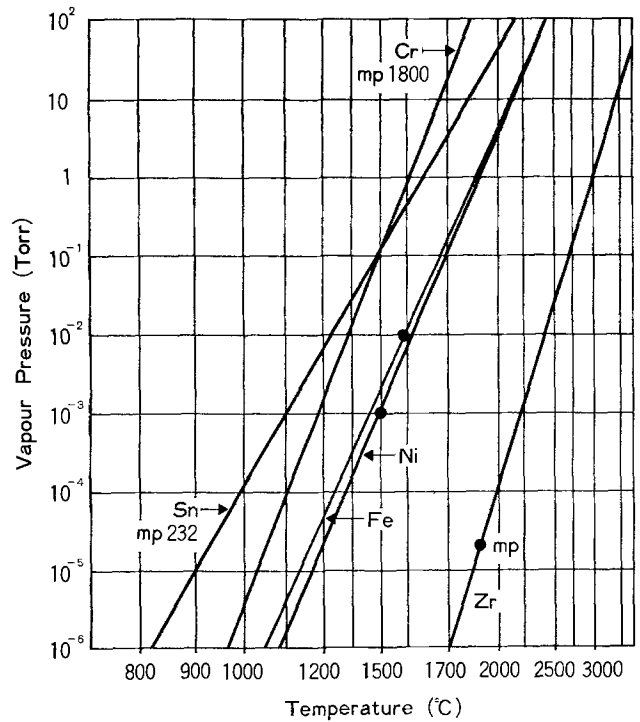


Fig. 6. Vapor pressure of additional elements of Zircaloy-2

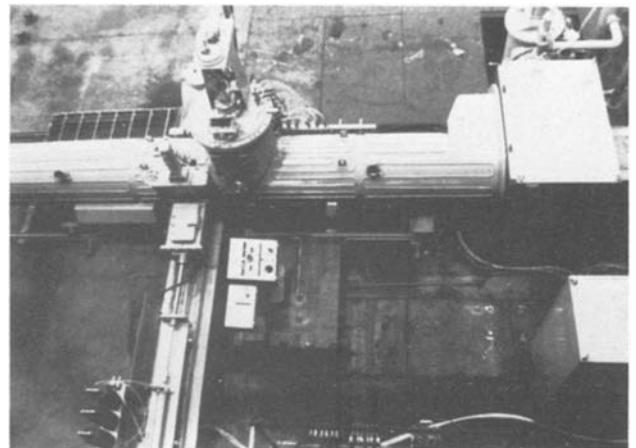


Fig. 7. General view of the VPEB scrap recycle furnace

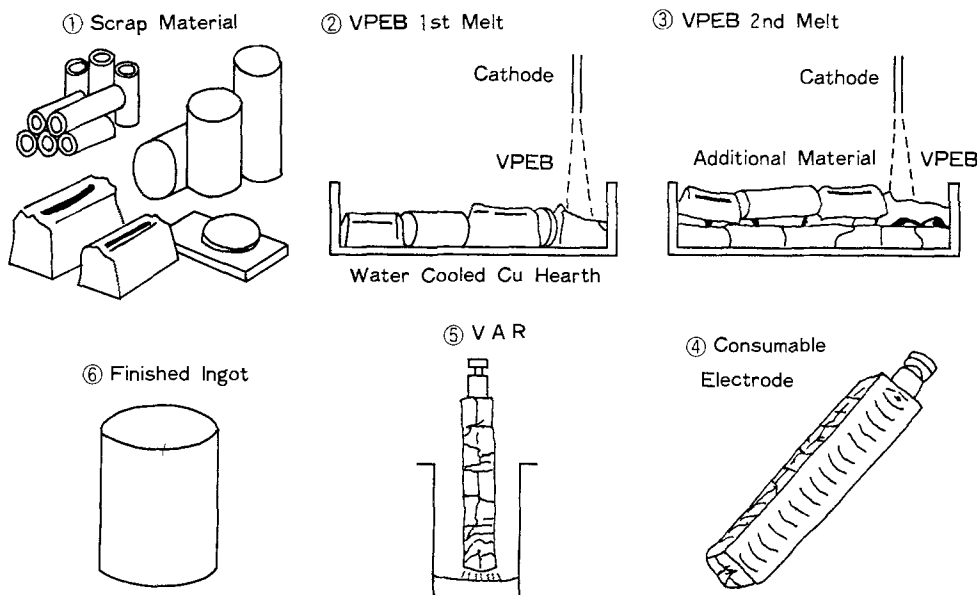
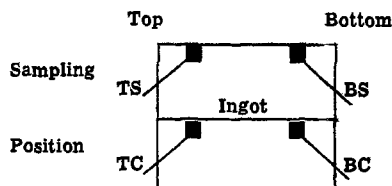


Fig. 8. Process of direct recovery of Zircaloy scrap.

Table X. Chemical analysis of finished ingot (%)

| ASTM B-350 | Sn 1.20-1.70 | Fe 0.07-0.20 | Ni 0.03-0.08 | Cr 0.05-0.15 | Rate of Cr addition | |
|------------|-----------------|-----------------|-----------------|-----------------|------------------------|-------|
| Ingot 1 | Raw material* | 1.49 | 0.139 | 0.051 | 0.082 | |
| | TC-1 | 1.59 | 0.149 | 0.060 | 0.122 | 0.059 |
| | TS-1 | 1.35 | 0.142 | 0.053 | 0.124 | 0.059 |
| | BC-1 | 1.52 | 0.136 | 0.049 | 0.120 | 0.059 |
| | BS-1 | 1.48 | 0.141 | 0.046 | 0.123 | 0.059 |
| Ingot 2 | Average | 1.53 | 0.142 | 0.051 | 0.122 | 0.059 |
| | TC-2 | 1.67 | 0.149 | 0.060 | 0.151 | 0.061 |
| | TS-2 | 1.59 | 0.140 | 0.054 | 0.142 | 0.061 |
| | BC-2 | 1.50 | 0.116 | 0.046 | 0.134 | 0.061 |
| | BS-2 | 1.48 | 0.106 | 0.043 | 0.125 | 0.061 |
| Ingot 3 | Average | 1.56 | 0.127 | 0.051 | 0.138 | 0.061 |
| | TC-3 | 1.52 | 0.144 | 0.054 | 0.102 | 0.025 |
| | TS-3 | 1.49 | 0.138 | 0.052 | 0.098 | 0.025 |
| | BC-3 | 1.46 | 0.125 | 0.047 | 0.091 | 0.025 |
| | BS-3 | 1.45 | 0.110 | 0.045 | 0.100 | 0.025 |
| Ingot 4 | Average | 1.48 | 0.129 | 0.049 | 0.098 | 0.025 |
| | TC-4 | 1.69 | 0.127 | 0.060 | 0.087 | 0 |
| | TS-4 | 1.66 | 0.123 | 0.059 | 0.087 | 0 |
| | BC-4 | 1.54 | 0.098 | 0.047 | 0.073 | 0 |
| | BS-4 | 1.53 | 0.095 | 0.047 | 0.072 | 0 |
| Average | 1.60 | 0.110 | 0.054 | 0.080 | 0 | |

* Average value of 10 sampling.



paper, however, a new process for direct recovery of Zircaloy scrap is proposed. Surface-cleaned Zircaloy

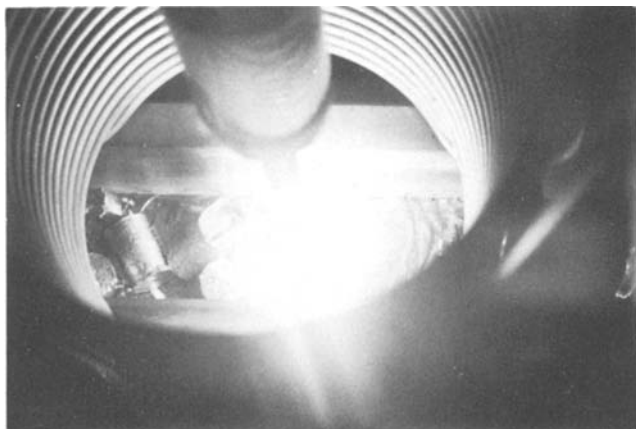
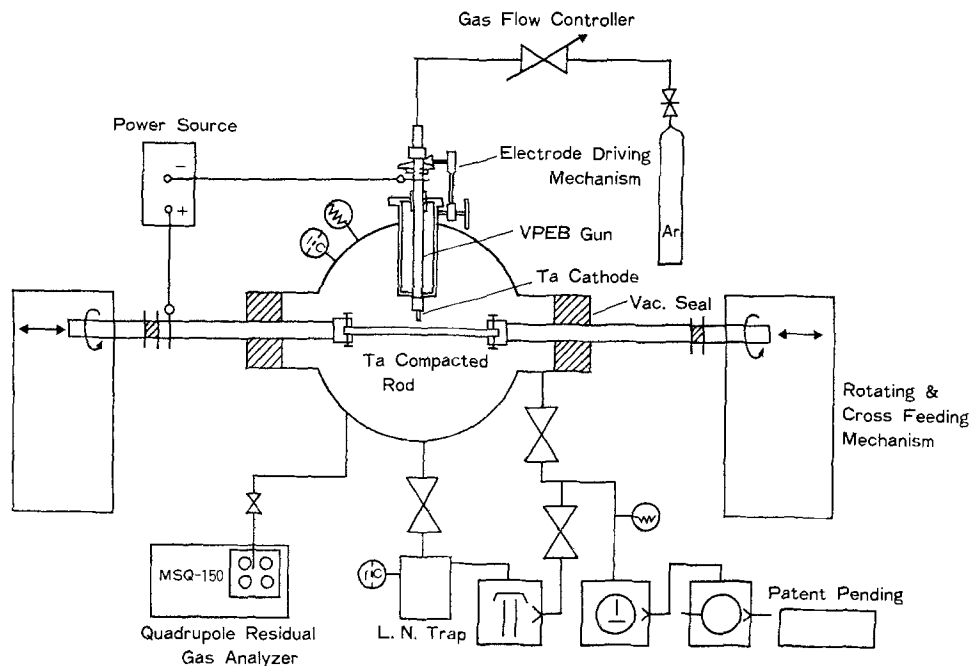


Fig. 9. VPEB melting of Zircaloy scrap for electrode

scraps are converted in a specially designed vacuum plasma electron beam furnace to an electrode for vacuum arc remelting which is a part of a conventional process. Sufficient mechanical strength and electrical conductivity are the two factors required with the VPEB processed electrode, while compensation for chromium loss (Fig. 6) during the melting was considered. The result of the development work is satisfactory and the new process can be a big improvement.

Figure 7 illustrates the specially designed VPEB scrap recovery furnace. Scraps are laid on a water-cooled copper hearth which has dimensions suitable for electrode to successive VAR. The hearth is movable back and forth in the vacuum chamber while VPEB bombards the surface of the scraps. A simple scanning mechanism is equipped for the VPEB gun. A chromium charging mechanism feeds the necessary addition of chromium granules following the first melt down. A larger charging mechanism feeds Zircaloy scraps over the first melt for additional second melting as is illustrated in Fig. 8. VPEB melting in this ap-

Fig. 10. Schematic drawing of the VPEB melting equipment.



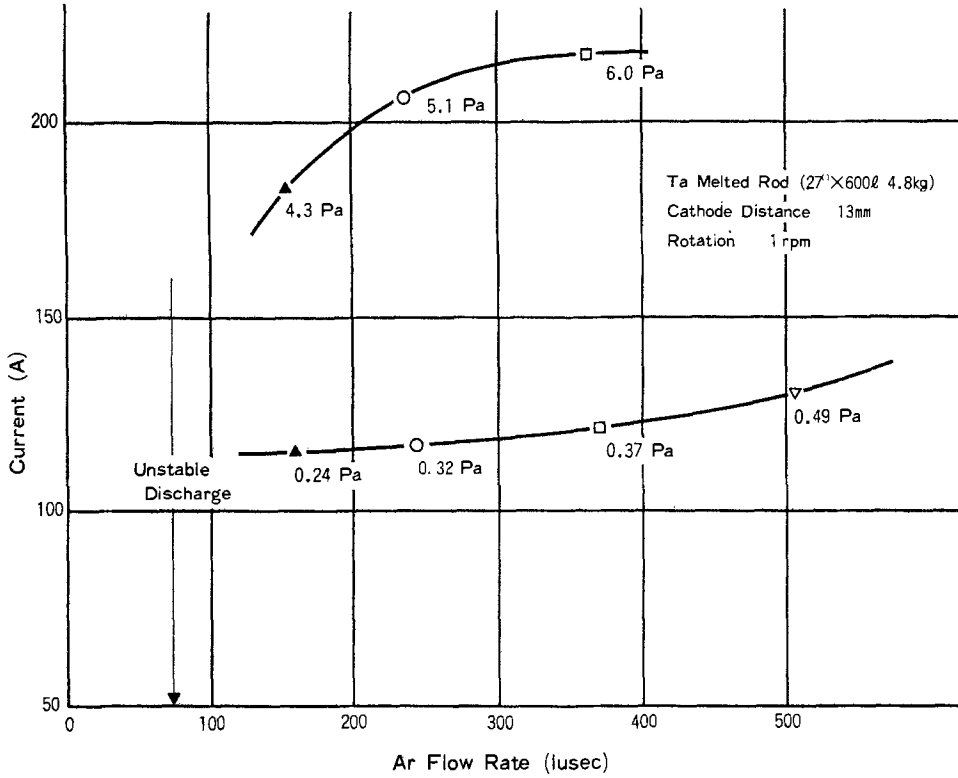


Fig. 11. Minimum current for Ta melting.

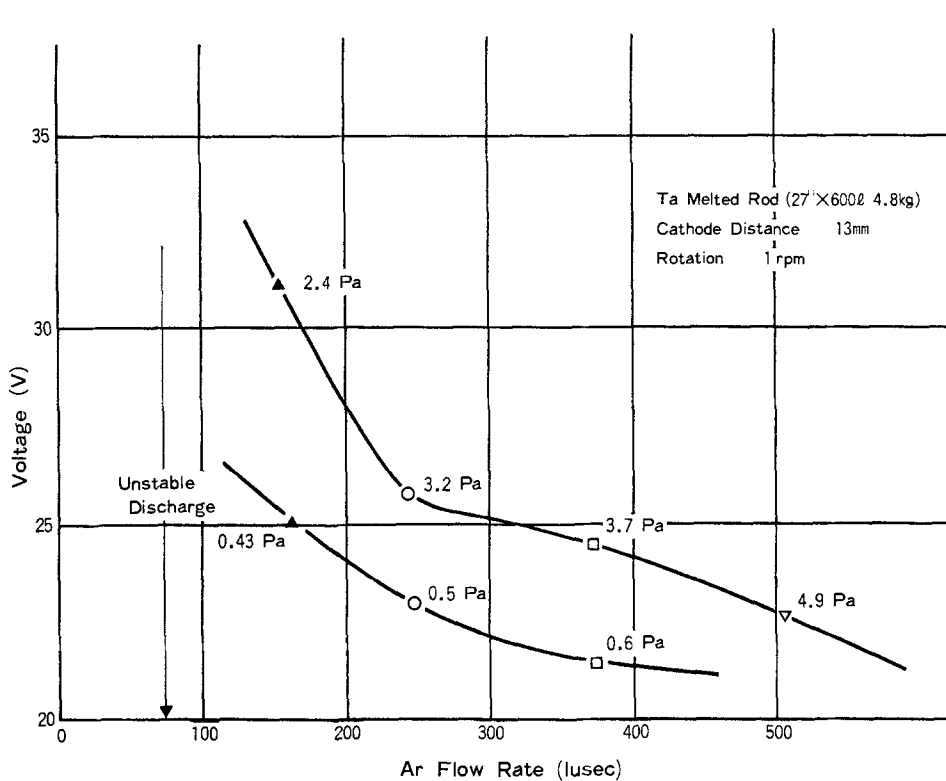


Fig. 12. Corresponding voltage for Ta melting.

plication is aimed at joining scraps to a satisfactory electrode, so a complete melt down of the charge is not required. Figure 9 illustrates melting operation. An example of the operating parameters are represented in Tables VII and VIII. Table IX represents the parameters for successive VAR operation. Table X represents the results of chemical analysis of the finished ingot.

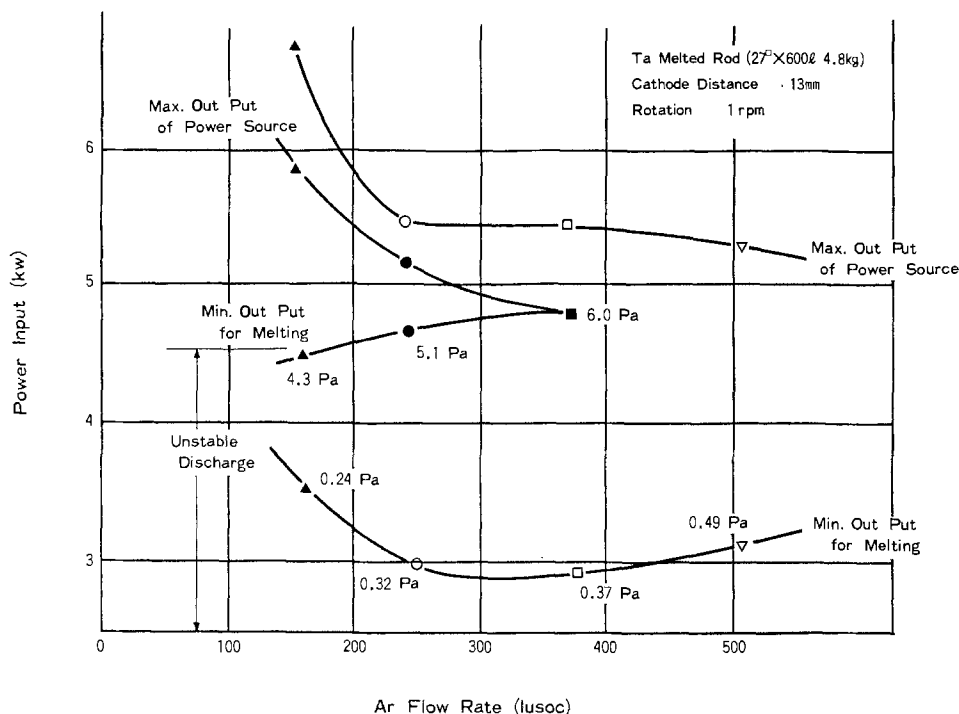
The addition of chromium is not required at least for several recyclings. This is a favorable result for actual production. Chromium loss as a whole is kept small because of the relatively short thermal history of the electrode. However, it will be required to add chromium if, for example, all scraps charged are of chips and thin sheets.

The VPEB is considered to be the ideal heat source for the direct recovery of Zircaloy scraps. VPEB is operable at low voltage and medium to high vacuum. There is no danger of damage to the water crucible with sufficient power density to melt down refractory metals. Power input can be controllable and maintained constant for as much time as is required. Practically any shape of raw stock can be charged.

Melting Tantalum by Using VPEB

Tantalum ingot is conventionally produced by using either a vacuum arc (VA) furnace or high voltage electron beam (HVEB) furnace. A vacuum sintering (VS) furnace has been an alternative for producing smaller rod shapes. An example of VPEB melting,

Fig. 13. Electrical power input vs. operating flow rate.



which is new, economical, versatile, easy for maintenance and operation, and produces a similar grade of purification to that of HVEB, is presented in this paper.

Figure 10 illustrates a schematic of the equipment. Melting and purification of a tantalum rod or ingot by using the VPEB is aimed at. A mechanical drive gives rotation and push-pull transfer motion to the tantalum rod through vacuum-tight seals while VPEB melts the surface. A quadrupole residual gas analyzer (RGA) is used for dual purpose: monitoring the purity of background environment and gaseous or vapor composition degassed during the melting. Partial pressure of any active gases or vapors which may react with hot tantalum must be kept below a certain level. Argon pressure to keep VPEB is roughly between 3×10^{-1} and 10 Pa measured in the vacuum chamber. Figures

11 and 12 illustrate the minimum current and corresponding voltages required for melting the tantalum surface, respectively. Shift of operating pressure was made by changing pumping speed and argon flow rate.

Figure 13 represents electrical power input vs. operating flow rate. Table XI summarizes a comparison of operating parameters at the two typical conditions. Details of basic experiment and data were published elsewhere (1, 2). Table XII represents some of the purification effects obtained for surface melting of powder compacts $22 \text{ mm } \phi \times 500 \text{ mm L}$, 76% density made by hydrostatic compaction of 100 mesh Ta. Carbon powder was additionally mixed for the No. 02 series in order to promote oxygen removal by CO reaction. The result indicates that partial pressure of H_2O and the total pressure played a major role in this case. Figures 14 and 15 represent monitored gas composition during the processing.

A new product, SMTR (3) (surface melted tantalum rod) is an example of optimized use of VPEB. The SMTR has pure, dense, and sound surface made by VPEB melting while the inside (central portion) of the rod is composed of sintered smaller density tantalum. Figure 16 represents an example of the process flow. Figure 17 illustrates the purification effect at the surface. Figure 18 illustrates radial density variation from the surface to the center. Average density before and after surface melting is 76% and 88%, respectively. The fabricated square rod $5 \times 5 \text{ mm}$ cross section and annealed at 1200°C 1 hr showed mechanical properties represented in Table XIII, which is, by far, over the specification JIS H4701. Similar surface treat-

Table XI. VPEB operating parameters

Ta melted rod ($22\phi \times 500 \text{ L}$ 3.15 kg)

| Ar flow rate (1 μsec) | Pressure (Pa) | Power input | Pool depth (mm) | Pool diameter (mm) |
|-----------------------------------|---------------|-------------------|-----------------|--------------------|
| 250 | 4.3 | 220A (5.15 kW) | 1.2-1.5 | 3-4 |
| 250 | 0.27 | 220A (5.45 kW) | 5.0-7.0 | 15-17 |

Cathode: Ta $7\phi \times 8\phi \times 55 \text{ L}$. Cathode distance: 13 mm. Rotating speed: 1 rpm.

Table XII. Surface purification effect of SMTR

| Sample No. | Surface before melting O_2 ppm C ppm | Surface after melting O_2 ppm C ppm | Surface hardness after melting Hv (1 kg) | Pressure (Pa) | $P_{\text{H}_2\text{O}}$ (Pa) before melting ↓ melting | P_{O_2} (Pa) before melting ↓ melting |
|------------|---|--|---|---------------|--|--|
| 01-5 | 810 | 490 | 172 | 5.1 | 0.05 | 7×10^{-4} |
| 02-1 | 47 | 8 | 172 | 5.1 | 0.13 | 7×10^{-4} |
| | 920 | 420 | 175 | 5.1 | 0.05 | |
| 01-7 | 410 | 30 | 175 | 5.1 | 0.13 | 5×10^{-5} |
| | 870 | 111 | 86 | 0.33 | 0.009 | |
| 02-3 | 42 | 6 | 86 | 0.33 | 0.01 | 4×10^{-4} |
| | 940 | 142 | 82 | 0.33 | 0.008 | 8×10^{-5} |
| | 530 | 24 | 82 | 0.33 | 0.01 | 4×10^{-4} |

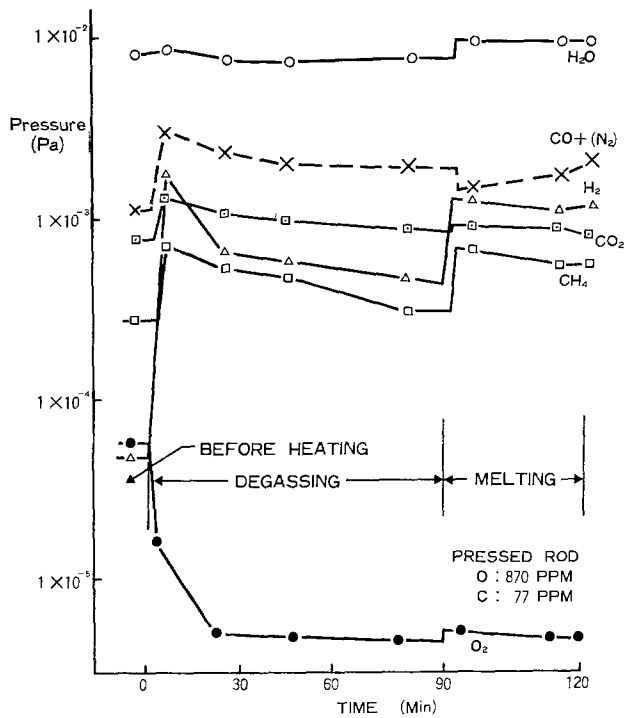


Fig. 14. Gas composition during Ta melting (1)

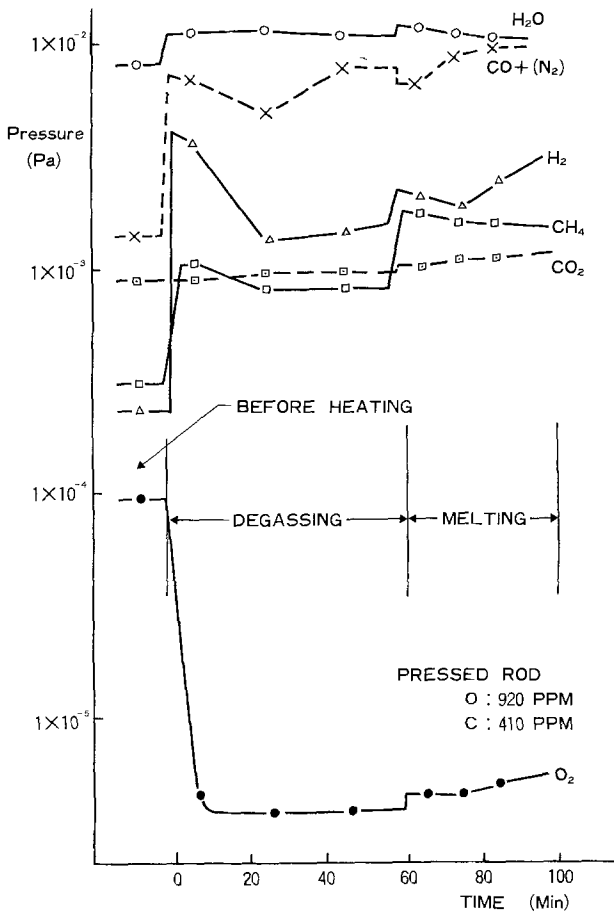


Fig. 15. Gas composition during Ta melting (2)

ment applied for VA melted ingot eliminates surface machining and results in more utilization of the precious metal. A few percent of evaporation loss which is unavailable in the case of HVEB purification is not necessarily the case for SMTR: That is also valuable for saving tantalum metal.

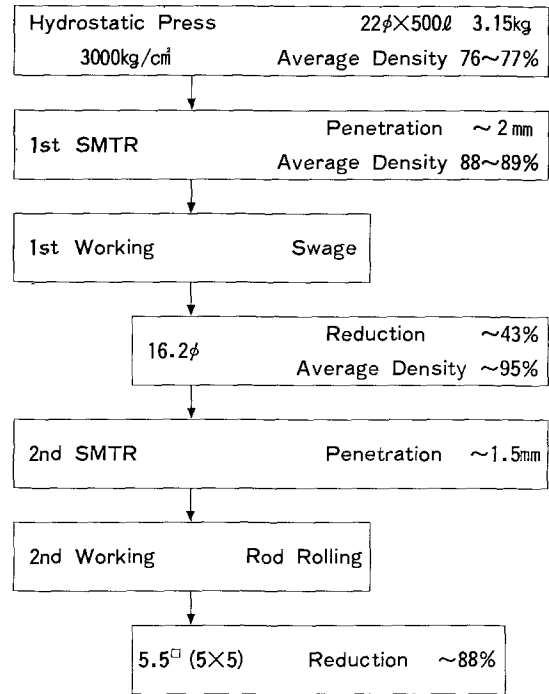


Fig. 16. Process of SMTR

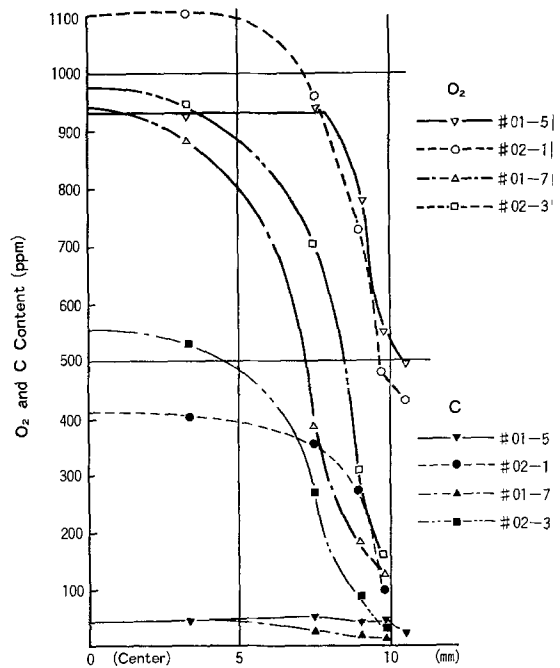


Fig. 17. Purification effect at the surface of the SMTR

Major operating parameters to be considered in the VPEB are listed as follows: (i) voltage, (ii) current, (iii) cathode to target distance, (iv) flow rate of operating gas, (v) vacuum pressure of operating gas, and (vi) impurity levels of residual gases. Geometrical configurations of structures inside the vacuum cham-

Table XIII. Mechanical properties of SMTR processed Ta rod*

| Tensile strength (kg/mm ²) | | Elongation (%) | |
|--|---------|----------------|---------|
| 46.4 | Average | 57 | Average |
| 46.9 | 46.7 | 53 | 47 |
| 46.8 | | 31 | |

* Size: 5 × 5 mm. Heat-treatment: 1200°C × 1 hr. JIS specifications: JIS H4701: Tap-0, tensile strength (kg/mm²) >25; elongation (%) >25; and Tap-1/4 H, tensile strength (kg/mm²) >35; elongation (%) >20.

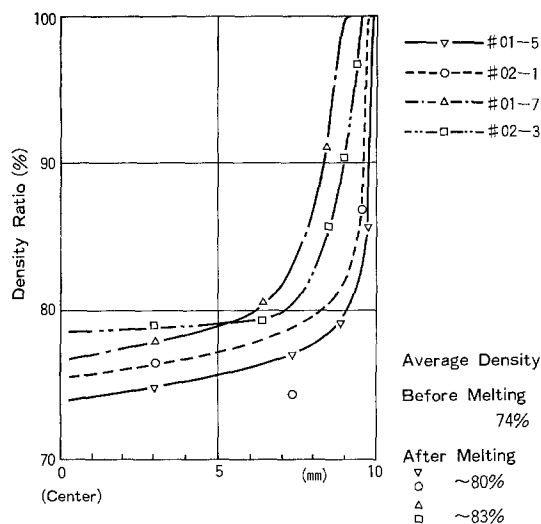


Fig. 18. Radial density variation of SMTR

ber should be paid due consideration with respect to gas flow pattern and electrical field distribution. Magnetic confinement can improve concentration of the plasma, with additional expense.

In summary, application of VPEB requires careful design of system. Operation of VPEB, however, has big advantages in reliability (stability) and safety over VA or HVEB. VPEB is usable for producing both large ingots and small diameter rods starting from

powder compact, sponges, or any shape of raw stock. It is also usable for controlled heating which varies application in a variety of heat-treatments. Energy density at a target surface can be as high as 10^4 kW/cm², which is sufficient for surface melting of refractory metals and alloys. VPEB can often be an alternative short-cut process of an existing production line; valuable for rationalization or saving labor, energy, and thus cost.

Acknowledgments

The authors are indebted to Mr. H. Takei and his group, ULVAC Corporation, for the design and manufacture of the VPEB scrap recycle furnace. Mr. K. Yoshida, Vacuum Metallurgical Corporation, gave helpful advice throughout this study.

Manuscript received May 7, 1980. This was Paper 300 presented at the St. Louis, Missouri, Meeting of the Society, May 11-16, 1980.

Any discussion of this paper will appear in a Discussion Section to be published in the June 1982 JOURNAL. All discussions for the June 1982 Discussion Section should be submitted by Feb. 1, 1982.

Publication costs of this article were assisted by the Vacuum Metallurgical Company, Limited.

REFERENCES

1. S. Kashu, S. Nishino, and C. Hayashi, in Trans. 10th Vac. Met. Conf., pp. 771-798 (1967).
2. S. Kashu, S. Nishino, and C. Hayashi, in Trans. 3rd Intern. Conf. Electron and Ion Beam Science and Technology, pp. 221-235 (1968).
3. Patent pending.

The Formation of SiO₂ in an RF Generated Oxygen Plasma

I. The Pressure Range Below 10 mTorr

A. K. Ray* and A. Reisman*

IBM Thomas J. Watson Research Center, Yorktown Height, New York 10598

ABSTRACT

This paper deals with the formation of SiO₂ on silicon in an rf generated oxygen plasma in the pressure range below 10 mTorr. A companion paper describes the behavior of the oxide growth process in the pressure range above 10 mTorr. The oxide was formed in an open-tube pumped fused silica system without substrate biasing. Oxide formation rate was studied as a function of substrate temperature, conductivity type, resistivity, distance from the end of the plasma generating coil, oxygen pressure, and generator power output. Based on the results obtained on masked substrates, using the silicon-mask interface as a marker, it was determined that within the limits of experimental error, all the oxide formed in the pressure range studied was deposited on the surface and not a result of oxidation. The rate of deposition increased with increasing power, decreasing pressure, and decreasing wafer to plasma generation zone distance. This rate was temperature independent and was unaffected by substrate parameters. Excellent uniformity was obtained over 56 mm diam wafers, $\pm 3-5\%$. The properties of the oxide deposited at 600°C and above are only slightly poorer than thermal oxides grown at 1000°-1100°C. They exhibit somewhat higher fixed charge and interface state density while the breakdown strength, etch rate, and refractive index are essentially the same as thermal oxides. A key observation of the plasma process conducted at pressures below 10 mTorr is that the oxide always forms on the silicon surface facing the plasma. This is opposite to the results obtained at higher pressures described in Part II of this study.

It is to be anticipated that as semiconductor devices are scaled to smaller dimensions, i.e., less than 1 μm ground rules, currently employed chip processing tem-

peratures will tend to become incompatible with desired device designs, because impurities present in shallow junctions and/or in surface threshold adjusting layers will tend to redistribute. The problem will be compounded further by surface depletion of im-

* Electrochemical Society Active Member.
Key words: silicon, plasma, oxidation, SEM.

purities during oxidation (1), oxidation enhanced diffusion effects (2), and the generation of substrate defects (2, 3). Two of the primary high temperature processes to be contended with are oxidation, and ion implantation damage annealing and activation.

As a first step in evolving a lower temperature processing sequence, the authors have focused on the oxidation process. One might assume, initially, that the lower the temperature at which one can conduct an oxidation process, the better. This is not necessarily true from a stress point of view. If, for example, the intrinsic stress at the oxide formation temperature tends toward zero, then any temperature excursions above this temperature will force the oxide into tension, making it susceptible to cracking at mask opening corners. To minimize this problem, oxidation processes should be conducted at the highest possible temperature consistent with impurity redistribution, surface depletion, and defect generation constraints.

High pressure and plasma oxidation processes both offer potential for use at lower temperatures. The high pressure approach (4, 5) is in current use, but for large areas (5) is conducted only in wet oxygen ambient atmospheres, and at moderate pressures, up to 25 atm. In dry oxygen, pressures in excess of 100 atm would be required (4) to achieve oxidation rates comparable to wet oxidation. Such a pressure-temperature combination is not achieved readily on a practical basis for a variety of technical reasons which will be discussed by us at a later time. Very high oxidation rates have, however, been reported using plasma anodization approaches (6-15) at temperatures as low as 170°C (12). Two general problems encountered in using plasma approaches have been the difficulty in achieving uniform growth over areas greater than 1-2 cm² (6, 7) and the generally poor electrical and defect characteristics of the oxides (7, 12). Partial resputtering of the grown oxides has been considered by Kraitchman (8) and others (12, 13), but none of the reports considered seriously the possibility of sputtering from the walls of the reaction chamber onto the wafer surface as an effect to be contended with. In addition, using presumably similar experimental techniques, different workers have obtained significantly different results. Lingenza (6) reported power and temperature dependencies, but no substrate bias voltage dependency on oxidation rate. He also found parabolic growth behavior for biased oxidations and non-parabolic growth in unbiased oxidations. Skelt and Howells (7) and Kraitchman (8), however, saw no temperature dependency, and Kraitchman implied that there was no power dependency. Furthermore, Kraitchman found parabolic growth behavior for both biased and unbiased oxidations, even when constant current biasing (as opposed to constant voltage) was employed. Pulfrey and Reche (12), on the other hand, observed linear kinetics in constant current anodizations.

The present study was prompted by the noted discrepancies among the reported results and by a desire to see if uniform growth could be achieved over large areas. In addition, it was desired to operate in an electrodeless system to avoid possible electrode sputtering contamination effects. It was felt also that the plasma and sample temperatures should be independently controllable to a degree at least, by separating the plasma generation and oxidation zones, and that the effects of temperature and power on both oxide quality and growth kinetics required better understanding. Independent temperature control was accomplished by separating the plasma generation and oxidation zones, with the sample being placed at predetermined distances from the plasma generation zone in a resistance-heated portion of a reaction chamber. Excited species drift from the plasma generation region to the oxidation zone at the drift velocity of the low pressure flowing gas.

This paper deals with the pressure regime below 10 mTorr while a companion paper, Part II, is concerned with the pressure regime > 10 mTorr for reasons which will become obvious.

Experimental Techniques

The experimental setup for plasma oxidation in the pressure regime below 10 mTorr is shown schematically in Fig. 1. Ultrahigh purity bottled oxygen (99.999%) was purified further by heating to 1000°C in a quartz chip bed to decompose any hydrocarbons present to CO₂ and H₂O. These contaminants were removed subsequently in a liquid nitrogen trap. The liquid nitrogen trap could be used to remove CO₂ and H₂O without liquefying the oxygen because the oxygen pressures employed (2-100 mTorr) were less than the vapor pressure of oxygen at the boiling point of nitrogen. The vapor pressures of CO₂ and H₂O at liquid nitrogen temperature are estimated to be of the order of 10⁻⁵ and 10⁻⁸ mTorr, respectively. For an operating pressure of 10 mTorr, this corresponds to maximum values of 1 ppm of CO₂ and 1 ppb of H₂O in oxygen, assuming equilibrium obtains. The purified oxygen was used to generate an oxygen plasma in the 80 mm ID, 100 cm long fused silica reaction chamber by a variable frequency (0.5-8 MHz) rf generator. All experiments were conducted at 0.5 MHz unless otherwise specified. Electrical coupling to the system was effected by a six turn coil of 0.25 in. OD Cu tubing placed around the reactor tube and connected to the rf generator by appropriate cables. In our experimental system, only the generator output power was known. An estimate of the power input to the plasma could not be made. Hence, a variation of the generator output power was considered as a variation of the power input to the plasma. The coupling mechanism was assumed not to change with power and pressure variations. The system was pumped continuously during the experiments, and the pressure in the chamber was controlled by regulating the oxygen mass flow into the reaction chamber using a mass flow controller. The pressure in the reaction chamber was measured by a thermocouple gauge located at the exit end of the reaction tube. In order to avoid coupling to the rf field, the thermocouple gauge was placed remote to the plasma generating region. Most of the silicon wafers used were 56 mm diam p-type with a nominal resistivity of 10 Ω cm. The wafers were cleaned prior to an experiment by a process described elsewhere (16). A wafer was placed, on a quartz sample holder, perpendicular to the direction of gas flow. The temperature of the wafer was, as mentioned above, varied and controlled by an external resistance heated furnace. The temperature of the wafer was measured by a Chromel-Alumel thermocouple placed adjacent to it. SiO₂ film thickness was measured using an IBM 7840 Film Thickness Analyzer (17). The IBM 7840 F.T.A. measures combined reflectance of the films and substrate in the wavelength range of 380-750 nm and computes the thickness of the film from the optical constants of

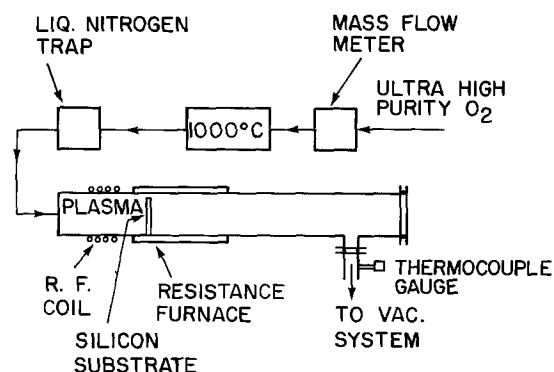


Fig. 1. Schematic diagram of the experimental plasma oxidation system.

the film and substrate. The film thicknesses measured by the F.T.A. were checked with the values obtained ellipsometrically and found to agree to better than $\pm 5\%$. Since the IBM 7840 F.T.A. can be programmed to measure oxide thickness automatically at 21 predetermined locations over the entire wafer, and is much more rapid in use than the ellipsometric measurement available to us, it was used to gather the uniformity data. The electrical properties of plasma SiO_2 were determined by measurements of fixed charge density, surface-state density, and electrical breakdown strength in conventional fashion, *i.e.*, C-V measurements and ramp voltage breakdown measurements.

Results and Discussions

In an initial experiment, a silicon wafer was placed perpendicular to the direction of gas flow 20 cm downstream from the end of the rf induction coil. The temperature of the wafer was maintained at 650°C . An oxygen plasma was generated at 5 mTorr and a generator output power of 4.5 kW at 0.5 MHz. About 50 nm of SiO_2 was formed in 4 hr on the surface of the wafer facing the plasma. No SiO_2 was formed on the other side of the wafer. Thickness uniformity of the SiO_2 film formed was better than $\pm 5\%$. Under the same conditions, but with increasing pressure in the chamber, the thickness of SiO_2 formed decreased significantly. Consequently, to study the effect of pressure on oxide formation, the generator output power was subsequently increased to 7 kW to increase oxide thickness to reasonable values. Figure 2 shows the thickness of SiO_2 formed in 4 hr as a function of system oxygen pressure at 7 kW. The pressure was changed simply by changing the rate of oxygen input to the system. Since pressure was found to vary linearly with oxygen input rate in the pressure range studied, the flow rate and, therefore, the linear gas stream velocity were constant. The oxygen flow rate was $2.1 \text{ scm}^3/\text{min}$ at 30 mTorr pressure, and the linear gas stream velocity was 20 cm/sec. As seen in Fig. 2, the oxide thickness obtained after 4 hr shows two distinct regimes when plotted in log-log fashion. The oxide thickness decreases from 350 nm in 4 hr at 1.5 mTorr to 40 nm in 4 hr at 7 mTorr with approximately a 1.4 power dependency on pressure. Above 7 mTorr, the rate decreases much more slowly, *i.e.*, to the 0.1 power. Even with the high (7 kW) output power employed, the SiO_2 thickness at 30 mTorr is only 34 nm in 4 hr. If one wants rapid growth, it is evident from Fig. 2 that the operating pressure should be as low as possible in the experimental configuration described. An operating pressure of 2.5 mTorr was then chosen for the low pressure studies, because below 2.5 mTorr

it was difficult to ignite and maintain an oxygen plasma. The behavior at this pressure is representative of the range up to about 10 mTorr. The variation of oxide thickness with position of the silicon wafer outside the confines of the rf coil was studied at 650°C , 2.5 mTorr and 4.5 kW generator output power. Figure 3 shows the data obtained in a 2 hr series of growth experiments. The oxide thickness decreases sharply with increasing distance up to 12 cm. At distances greater than 12 cm, the oxide thickness remains more or less constant. As the thickness uniformity was found to vary more in the region from 7-12 cm than in the region greater than 12 cm, a distance of 20 cm from the end of the rf coil was then chosen for most of the experiments. Experiments were also conducted with the wafer in a horizontal position. The rate of SiO_2 formation was greatly reduced compared to vertical mounting, and a significant SiO_2 thickness gradient was generated across the axial direction of the wafer.

The effect of generator output power on the thickness of oxide formed in 1 hr was studied at 650°C and 2.5 mTorr, the wafer being placed vertically at a distance of 20 cm from the end of the rf coil. With increasing power, the oxide thickness increases linearly with power up to 6 kW and above 6 kW, the oxide thickness increases as $(\text{power})^{4.5}$, Fig. 4, but as might be expected from the large slope of the curve, the thickness uniformity of the SiO_2 formed was poor at the higher power. An output power of 4.5 kW yields a reasonable oxide formation rate and good thickness uniformity. With the preceding as a basis for choosing a usable set of experimental conditions, the kinetics of SiO_2 formation were studied at 2.5 mTorr O_2 pressure, 4.5 kW of generator output power, and the silicon wafer placed vertically at a distance of 20 cm from the end of rf coil. Figure 5 shows the thickness of SiO_2 formed at 600°C as a function of time. It is seen from Fig. 5 that the oxide thickness varies linearly with time in the entire oxide thickness range up to 160 nm. Thermal oxidation of silicon at high temperatures in dry oxygen, of course, follows linear parabolic kinetics to a first approximation. The proposed model of a conventional thermal oxidation process (18) is that there are three basic steps: (i) the transfer of oxidant from the gas phase to SiO_2 at the gas- SiO_2 interface; (ii) the transport of oxidant through the SiO_2 to the Si- SiO_2 interface and (iii) the reaction of oxidant with Si to form SiO_2 at the Si- SiO_2 interface. In a film growth process, the step (i), depending on the temperature, linear gas stream velocity, and the film thickness, may or may not be rate limiting (19). In a conventional thermal oxidation process, step (i)

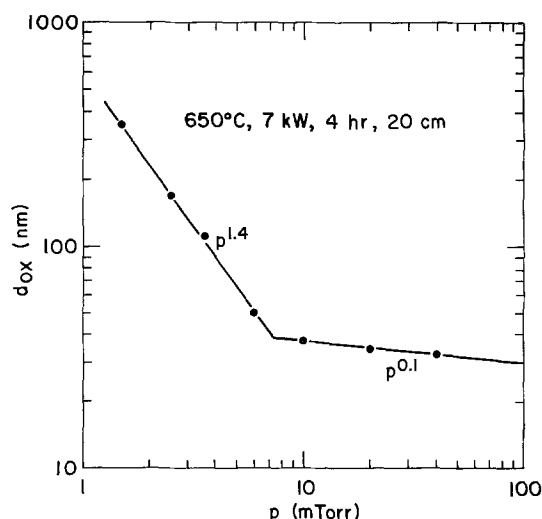


Fig. 2. Thickness of SiO_2 formed at 650°C in 4 hr as a function of system oxygen pressures.

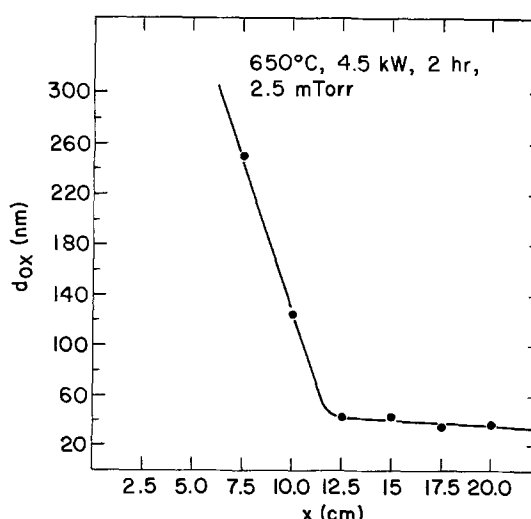


Fig. 3. Thickness of SiO_2 formed at 650°C in 2 hr as a function of distance of the wafer from the end of rf coil.

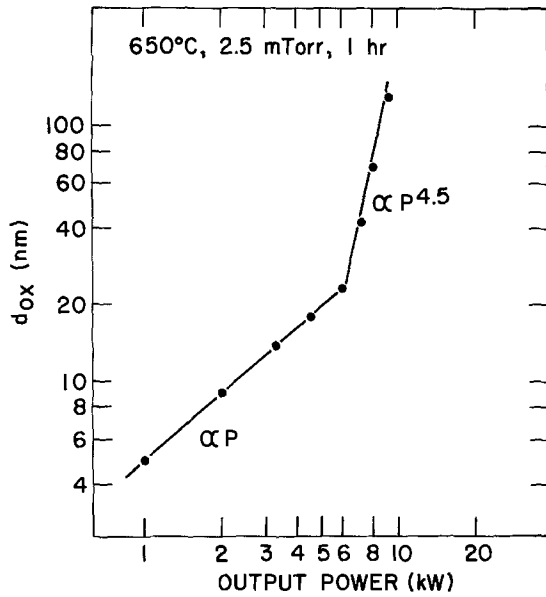


Fig. 4. Thickness of SiO₂ formed at 650°C in 1 hr as a function of generator output power.

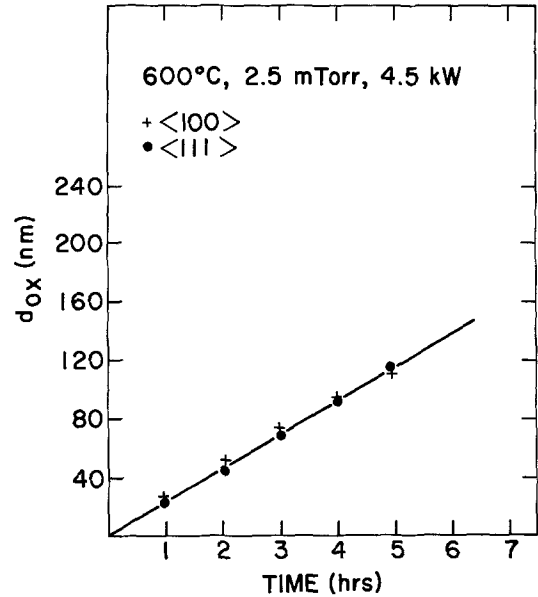


Fig. 6. Thickness of SiO₂ formed at 600°C as a function of time for <111> and <100> oriented silicon wafers.

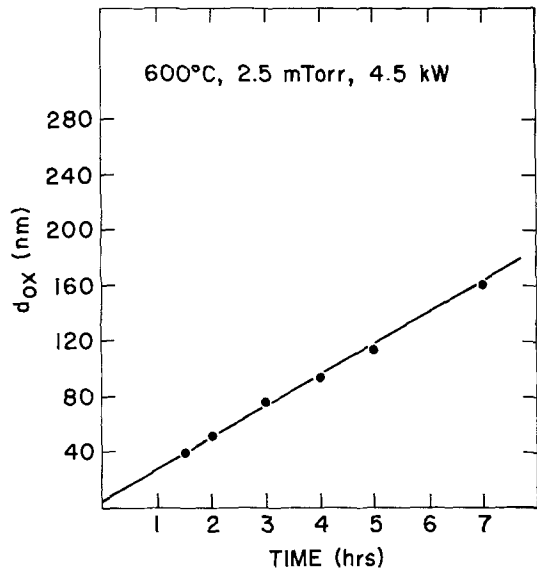


Fig. 5. Thickness of SiO₂ formed at 600°C as a function of time

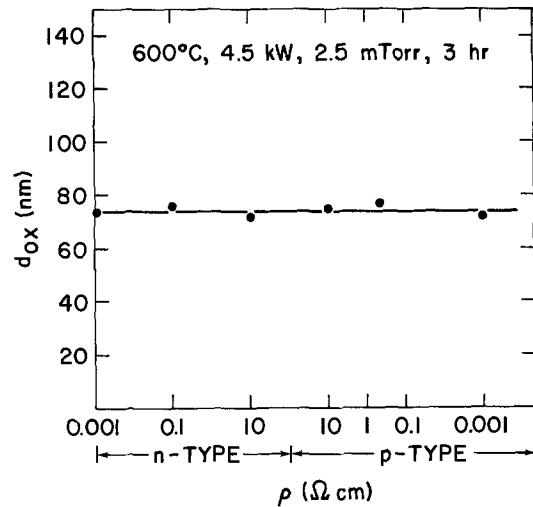


Fig. 7. Thickness of SiO₂ formed at 600°C in 3 hr for wafers of different resistivities.

is usually not rate limiting. The step (ii), if it is a diffusion-controlled process, follows parabolic kinetics. The third step determines the oxidation rate and follows linear kinetics. If step (iii) alone determines the rate of oxidation, then the rate of oxidation should depend on the temperature, the orientation, and the doping level of silicon wafers and should not depend on oxide thickness.

Figure 6 shows the thickness of SiO₂ formed at 600°C as a function of time for <111> and <100> orientated Si wafers. The rate of SiO₂ formation on <111> surfaces is seen to be the same as that on <100> Si wafers while both are seen to be linear with time. Oxide formation was found not to depend on silicon dopant concentration either. Figure 7 shows the thickness of oxide formed in 3 hr at 600°C for both p- and n-type wafers of different resistivities. Oxide formation rate was found to be independent of temperatures also. Figure 8 shows the thickness of SiO₂ formed as a function of time for three different temperatures. In another series of experiments, about 307.5 nm of dry thermal SiO₂ were first grown at 1000°C on Si wafers, and these wafers were then used as substrates for subsequent plasma experiments. Figure 9 shows the oxide thickness of these wafers as a function of time of ex-

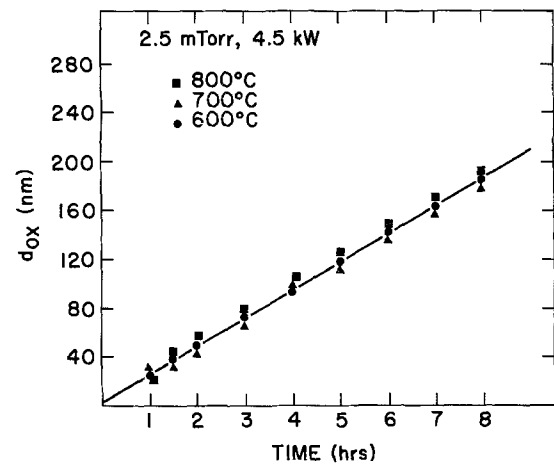


Fig. 8. Thickness of SiO₂ formed as a function of time at 600°C, 700°C, and 800°C.

posure to the oxygen plasma. The oxide thickness still increases linearly with time, and the rate of increase is the same as that observed for bare silicon wafers. The data for bare silicon wafers is taken from Fig. 8. From

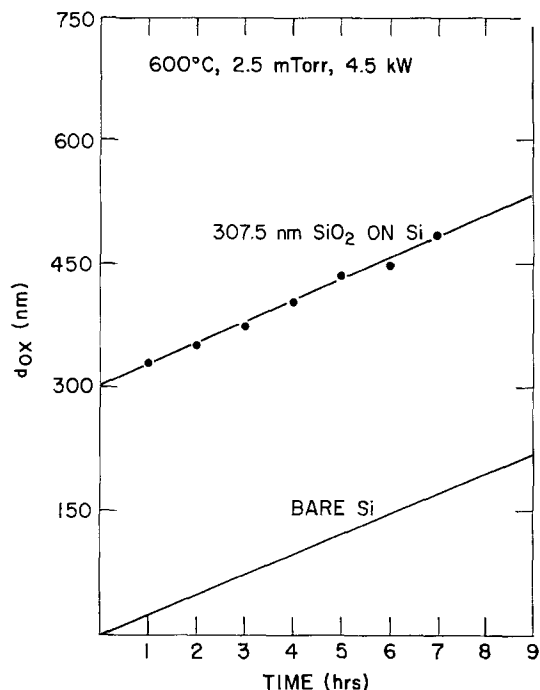


Fig. 9. Thickness of SiO₂ formed at 600°C as a function of time for starting silicon wafers with 307.5 nm of dry thermal SiO₂.

the above experimental results, it would appear that the second process does not determine the rate of formation of SiO₂ under the growth conditions studied. Furthermore, the temperature, wafer orientation, and resistivity independence of oxide formation rate made questionable the possibility that the linear kinetics observed are due to a combination of steps (i) and (iii) and raised the possibility that the oxide formed in our experiments was not the result of a reaction between silicon and oxygen, but was due to a deposition of SiO₂ in the fused silica reaction chamber at the high rf generator output power and low operating pressure employed. The possibility existed that SiO₂ or a silicon oxygen species, e.g., SiO sputtered from the wall of the reaction chamber, could react with oxygen and deposit SiO₂ on the silicon wafers. In order to test this hypothesis, a silicon wafer was partially masked with Al (400 nm thick) and then exposed to the plasma under the standard set of conditions described. After about 800 nm of SiO₂ was formed, the wafer was cleaved, the Al was etched in dilute HCl, and the cross section was examined in an SEM. It is clear from the

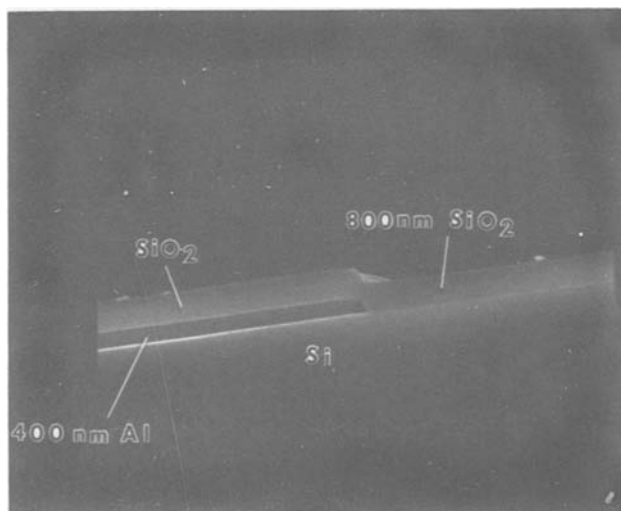


Fig. 10. SEM micrograph of the cross section of a silicon wafer after SiO₂ formation.

SEM micrograph (Fig. 10) that SiO₂ formed on both the exposed Si surface as well as over the Al, indicating that the SiO₂ is deposited oxide. Using the silicon-aluminum interface as a marker, it appears that very little, if any, silicon is oxidized during this process. Whether SiO₂ molecules are sputtered as such, and then deposited, or whether a species such as SiO is sputtered which reacts with oxygen homogeneously or at the silicon surface to form SiO₂ could not be determined. We consider the direct sputtering of SiO₂ to be unlikely since the properties of the deposited SiO₂ are quite different from those of conventionally sputtered silica (20). The refractive index of oxides deposited at 600°C and at lower temperatures was measured by ellipsometry at 632.8 nm and was in the range 1.461-1.465. The etch rate of the plasma deposited SiO₂ was comparable to that of dry thermal SiO₂ grown at 1000°C. The etch rates were compared by etching simultaneously the thermal and plasma oxides in 1:9 (49% HF:40% NH₄F) solution at room temperature. The etch rate was determined by measuring the change in oxide thickness during etching. The etch rates at room temperature were in the range of 74-76 nm/min. In order to evaluate the electrical properties of the plasma-deposited SiO₂, about 75 nm of plasma deposited SiO₂ was formed on 2 Ω cm p-type <100> oriented Si wafers at 600°C. No other high temperature heat-treatment was given to the oxide. Aluminum dots 32 mil in diameter were evaporated on the oxide through a metal mask. Aluminum was also evaporated on the back side of the wafers for electrical contact. A post-metallization anneal in forming gas at 400°C for 20 min was given to the capacitors. Figure 11 shows the high frequency C-V curve of these capacitors. The high frequency C-V curve was obtained at 1 MHz with a voltage ramping rate of 0.2 V/sec. Well-defined inversion and accumulation regions were obtained. The hysteresis effect observed between the inversion and accumulation regions may be due to the presence of a large number of surface states. Surface-state density measured by the quasi-state technique was about 10¹²/cm² eV at midgap. With surface-state density so high, the expression for V_{FB} in terms of fixed positive charge becomes complicated. So effective charge density (Q_f) was calculated from the flatband voltage (V_{FB}) determined via the high frequency C-V curve according to the formula

$$V_{FB} = \phi_{ms} - \frac{Q_f}{C_{ox}}$$

where ϕ_{ms} = work function difference between Al and the semiconductor, taken as -0.7V for 2 Ω cm p-type silicon, C_{ox} = oxide capacitance per unit area, and Q_f = effective charge per unit area.

The calculated effective charge density from the V_{FB} is 1.3×10^{-3} C/m² which is equivalent to 8×10^{11} /cm² singly charged centers. A high temperature (1000°C) postoxidation heat-treatment was given to some wafers, but this did not reduce effective charge density appreciably. Electrical breakdown strength was measured on one hundred Al-SiO₂-Si capacitors in accumulation. Figure 12 is a histogram showing the

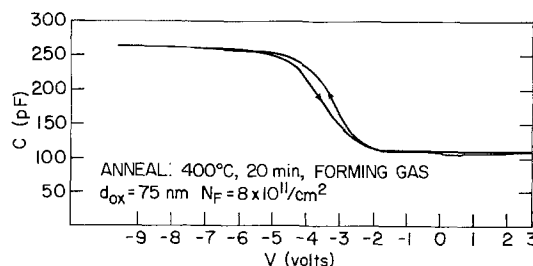


Fig. 11. High frequency C-V curve of plasma deposited SiO₂ capacitors after postmetallization anneal in forming gas at 400°C for 20 min.

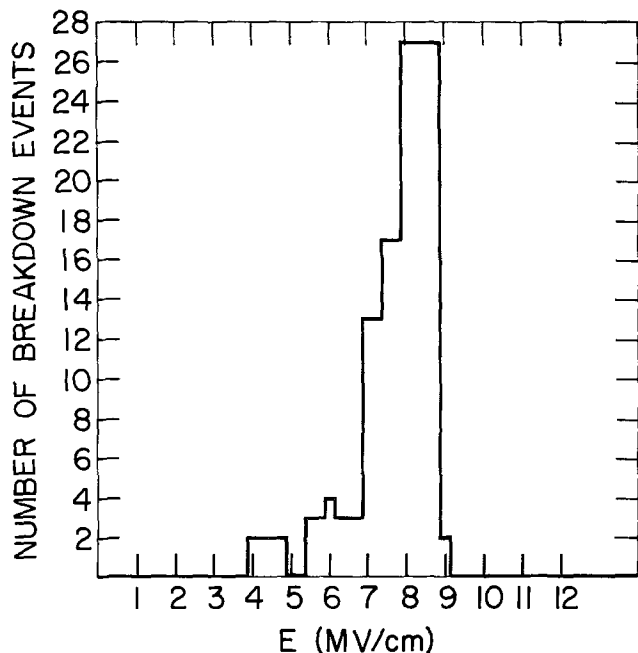


Fig. 12. Histogram showing the number of breakdown events at different breakdown strengths for one hundred plasma SiO₂ capacitors.

number of breakdown events at different breakdown strengths. The breakdown strength is high and there are few low field breakdown events.

Conclusions

From our experimental results, it can be concluded that the SiO₂ formed on the surface of a silicon wafer facing the plasma in a low pressure (<10 mTorr) oxygen plasma is deposited oxide. The deposited oxide is believed to be sputtered material from the wall of the quartz reaction plasma. The exact mechanism (sputtering or reactive sputtering) of SiO₂ formation is not clear. Since the properties of the deposited oxide bear more of a resemblance to thermal oxides grown at 1000°C than sputtered oxide, we believe that reactive sputtering is the mechanism of oxide formation. The rate of oxide deposition increases with increasing power input to the plasma and decreasing pressure and distance of the wafer from the plasma. The increase of oxide formation rate with decreasing pressure is due to the fact that at pressures less than 10 mTorr, wall sputter deposition appears to be the primary mechanism of oxide formation. The sputtering phenomenon leading to deposition rather than oxidation is a function of pressure only and does not depend on the distance of the wafer from the plasma generating zone. Clearly, however, the rate of deposition in such a process will depend on the distance. Very uniform deposits are obtained only under certain experimental conditions. The use of high power or positioning the wafer

too close to the plasma results in less uniform deposits. The properties of the deposited oxide are probably related to the purity of the quartz reaction chamber. Refractive index, etch rate, and electrical breakdown strength of the oxides deposited at 600°C are comparable to those of thermal SiO₂ grown at 1000°C. Fixed charge and surface state densities are higher. Limited results indicate that the oxides deposited at lower temperatures have properties similar to those deposited at 600°C. This technique thus may have potential for forming passivation layers for interconnections where conventional high temperature CVD methods cannot be used. The companion paper that follows describes the plasma system behavior at pressures greater than 10 mTorr which is dramatically different from that described here.

Manuscript submitted Dec. 18, 1980; revised manuscript received April 27, 1981. This was Paper 167 presented at the St. Louis, Missouri, Meeting of the Society, May 11-16, 1981.

Any discussion of this paper will appear in a Discussion Section to be published in the June 1982 JOURNAL. All discussions for the June 1982 Discussion Section should be submitted by Feb. 1, 1982.

Publication costs of this article were assisted by IBM Corporation.

REFERENCES

1. B. E. Deal, A. S. Grove, E. H. Snow, and C. T. Sah, *This Journal*, **112**, 308 (1965).
2. S. M. Hu, *J. Appl. Phys.*, **45**, 1567 (1974).
3. S. P. Murarka, *ibid.*, **48**, 5020 (1977).
4. R. J. Zeto, C. G. Thornton, E. Hryckowian, and C. D. Bosco, *This Journal*, **122**, 1409 (1975).
5. H. Mioshi, N. Tsubouchi, and A. Nishimoto, *ibid.*, **125**, 1824 (1978).
6. J. R. Ligenza, *J. Appl. Phys.*, **36**, 2703 (1965).
7. E. R. Skelt and G. M. Howells, *Surf. Sci.*, **7**, 490 (1967).
8. J. Kraitchman, *J. Appl. Phys.*, **38**, 4323 (1967).
9. J. R. Ligenza and M. Kuhn, *Solid State Technol.*, **b33** (December 1970).
10. M. A. Copeland and R. Pappu, *Appl. Phys. Lett.*, **19**, 199 (1971).
11. D. L. Pulfrey, F. G. M. Hathorn, and L. Young, *This Journal*, **120**, 1529 (1973).
12. D. L. Pulfrey and J. J. H. Reche, *Solid State Electron.*, **17**, 627 (1974).
13. R. Dragila, L. Bardos, and G. Loncar, *Thin Solid Films*, **34**, 115 (1976).
14. L. Bardos, G. Loncar, I. Stoll, J. Musil, and F. Zacek, *J. Phys. D. Appl. Phys.*, **8**, L195 (1975).
15. J. Musil, F. Zacek, L. Bardos, G. Loncar, and R. Dragila, *ibid.*, **12**, L61 (1979).
16. E. A. Irene, *This Journal*, **121**, 1613 (1974).
17. IBM 7840 Film Thickness Analyzer, Product Information.
18. B. E. Deal and A. S. Grove, *J. Appl. Phys.*, **36**, 3770 (1965).
19. A. Reisman and M. Berkenblit, *This Journal*, **113**, 146 (1966).
20. W. A. Pliskin, P. D. Davidse, H. S. Lehman, and L. I. Maissel, *IBM J. Res. Dev.*, **11**, 4, 461 (1967).

The Formation of SiO₂ in an RF Generated Oxygen Plasma

II. The Pressure Range Above 10 mTorr

A. K. Ray* and A. Reisman*

IBM Thomas J. Watson Research Center, Yorktown Heights, New York 10598

ABSTRACT

This paper describes the formation of SiO₂ in an rf generated oxygen plasma in the pressure range above 10 mTorr. The experimental setup used for this study is the same as that described in Part I of this study. Using the silicon-mask interface as a marker and examining the cross section of silicon wafers after oxide formation, it was concluded that the mechanism of oxide formation in the pressure range 10-100 mTorr is growth of SiO₂. A unique and unexpected result of the plasma process conducted at pressures greater than 10 mTorr is that oxide growth occurs primarily on the surface of the wafer facing away from the plasma, in sharp distinction to the observations made at pressures less than 10 mTorr where the oxide forms only on the surface facing the plasma. A key experimental parameter is the confinement of the plasma by the wafer which was observed only at pressures greater than 10 mTorr and at generator frequencies from 0.5 to 3 MHz. Oxide growth rate was studied as a function of pressure, power, frequency of the applied field, and substrate parameters to determine the optimum growth conditions. The etch rate, refractive index, stress, fixed charge, interface states, and breakdown strength of plasma oxides grown at 500°C compare very favorably to thermal oxides grown at 1100°C.

In Part I of this study (1), it was concluded that the SiO₂ formed in a low pressure oxygen plasma is a deposited oxide. The deposited oxide is believed to result from the sputtering of SiO₂ or an oxygen-silicon species from the wall of the fused silica reaction chamber. Because of the long mean free path at low pressures, it is possible for the sputtered material to deposit on a wafer placed as far as 20 cm from the plasma generating region. The sputter yield is therefore expected to be minimized with increasing pressure and decreasing power input to the plasma. In this paper, we describe the *in situ* oxidation of Si at higher pressures and lower power in the plasma system. The results are unique in that at elevated pressures, not only does deposition cease, but oxidation occurs primarily on the silicon surface facing away from the plasma.

Process and Kinetic Studies

When the operating pressure was increased to 30 mTorr and power output from the generator was reduced to 1 kW, no detectable SiO₂ was formed on a silicon wafer placed at a distance of 20 cm from the end of the rf coil. Consequently, for experiments in the high pressure regime (>10 mTorr), the wafer was placed closer (2 cm) to the coil. Under this condition, surprisingly, the plasma was confined by the wafer and the bulk of the SiO₂ was formed on the surface of the wafer facing away from the plasma (the wafer back side) while a much thinner oxide was formed on the surface facing the plasma (the wafer front side). The high-low thickness uniformity of the oxide formed on the back side was better than $\pm 5\%$ and the standard deviation was of the order of 1-3%. The thin oxide formed on the front surface was much less uniform. For example, on a 56 mm diam silicon wafer, there is a region around the wafer periphery where oxide thickness is considerably greater than in the central area. This region of greater oxide thickness increases with increasing oxidation time. After about 5 hr of oxidation at 540°C, there was a region 6 mm wide around the periphery where oxide thickness was about 200 nm as

compared to an average oxide thickness of about 65 nm in the central area. During the same oxidation time, about 300 nm of SiO₂ was formed on the back side. An initial explanation for this observation that came to mind was that the oxide formed in equal amounts on both surfaces, but that the SiO₂ formed on the surface facing the plasma was resputtered. In addition, it was to be determined whether the oxide films formed were wall-sputtered oxides, as was the case at low pressures, grown oxides, or combinations of the two with resputtering complicating the picture. To resolve these questions, the results required analysis according to the schematic representation depicted in Fig. 1. In Fig. 1, the expected wafer cross section is depicted for the possible cases, *in situ* growth only,

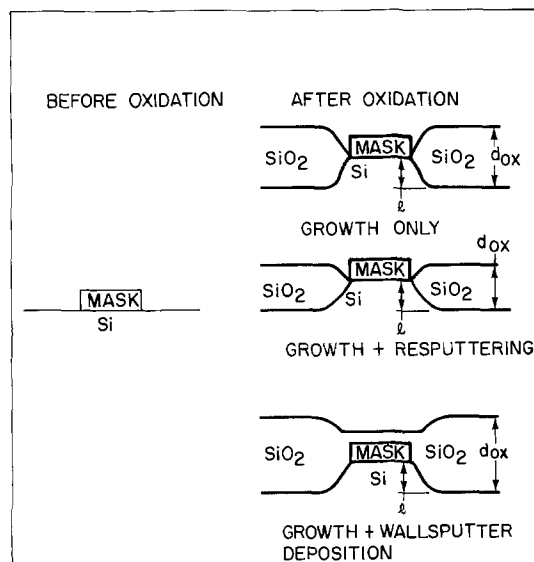


Fig. 1. Schematic representation of the cross section of a silicon wafer for the possible cases, growth only, growth + resputtering, and growth + wall-sputter deposition.

* Electrochemical Society Active Member.
Key words: silicon, plasma, oxidation, SEM.

growth plus resputtering, and growth plus wall-sputter deposition. On the left-hand side of Fig. 1 the situation before oxide formation is shown where part of the silicon area is masked against oxide formation. Using the silicon-mask interface as a marker, it is possible to distinguish among the possible cases mentioned earlier. If the Si-SiO₂ interface is below the original silicon surface (silicon-mask interface), then clearly some of the SiO₂ at least is being formed by a growth mechanism because silicon is consumed from the substrate during the oxide formation process. The thickness of SiO₂ would be approximately twice the distance (l) of the Si-SiO₂ interface below the silicon-mask interface. This value should equal the measured oxide thickness (d_{ox}) if resputtering and deposition are both absent. If growth and resputtering take place simultaneously and the rate of resputtering is less than the rate of growth, then for the same amount of oxidation, as in the case above, the Si-SiO₂ boundary will be at the same distance (l) from the Si-mask interface, but the measured oxide thickness (d_{ox}) will be less than $2(l)$ and there will be thickness asymmetry relative to the marker. If growth and wall-sputtering take place simultaneously, then oxide would form over the mask as well as on the silicon substrate. As a result, the apparent thickness of the masking layer would change after oxide formation, and the SiO₂ boundary would again be unsymmetrical with respect to the silicon-mask interface. If the resputtering rate is greater than the growth rate, no oxide would be detected and the unmasked silicon surface would drop below the silicon-mask interface. Finally, if all processes occur simultaneously, *e.g.*, deposition, oxidation, and resputtering, mask thickness would increase, and asymmetry around the mask level would result except in the unlikely event that the resputtering rate and deposition rate are identical. 200 nm thick MgO was used as a mask to examine these possibilities. The reason for selecting MgO as a mask is discussed later. Figure 2 is an SEM micrograph of the cross section of a silicon wafer after oxide formation on the MgO masked silicon surface which faces away from the plasma. It is evident from the picture that oxide formed on this surface is grown oxide and not deposited oxide. There is also no evidence of resputtering or wall-sputtering. Figure 3 shows the cross section of the wafer after oxide formation on the MgO masked silicon wafer surface which faces the plasma. Even though the oxidation was carried out for the same length of time as for the back side, the distance of the Si-SiO₂ interface from the original silicon surface is much less compared to that in Fig. 2, indicating that oxidation has taken place to a much lesser extent on the front surface. However, the oxide is symmetrical around the original silicon surface. Consequently, it may be concluded that the thinner oxide grown on the front surface is due to a reduced oxidation rate, and not due to growth plus simultaneous resputtering of oxide. Further, there is no evidence of deposition on either surface of the wafer. The difference in oxidation rate, for the back side and front side oxidations is believed to be due to self-biasing of the wafer in the plasma. This phenomenon is being examined currently and will be discussed when our experiments are completed. Further interesting observations are as follows.

When two silicon wafers are placed one behind the other, greater than 5 mm apart, the oxide thickness on the back side of the wafer closest to the plasma is uniform and significantly greater than that on the back side of the second wafer. For separation distances less than 5 mm, the oxide thickness uniformity on the first wafer degrades significantly. When the two wafers are placed in direct contact with each other, the back side of the second wafer only is oxidized. The design of the wafer holder was found to be critical for obtaining uniform oxide growth. In order to get uniform growth over an entire wafer, the wafer has to be mounted vertically and supported only at its base. Other mount-

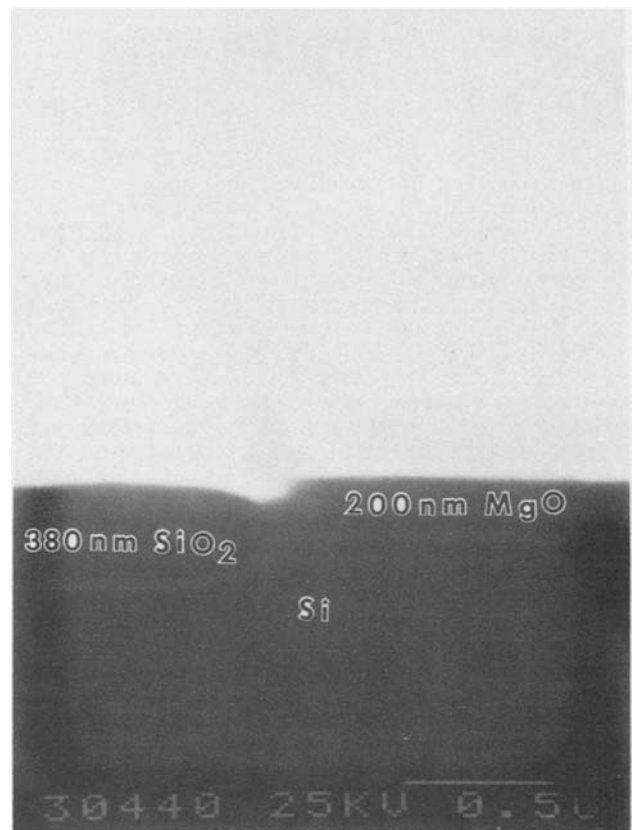


Fig. 2. SEM micrograph of the cross section of a silicon wafer after SiO₂ formation on an MgO masked silicon surface which faces away from the plasma.

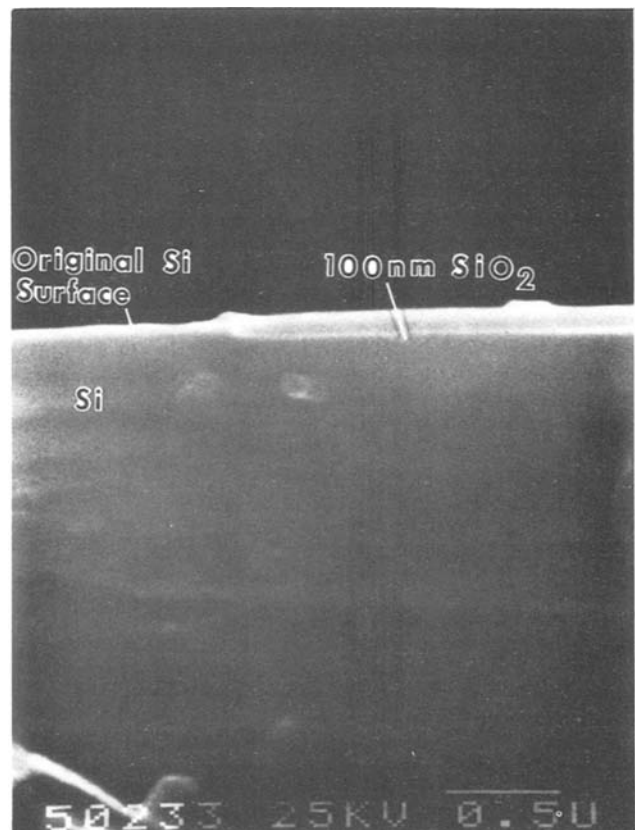


Fig. 3. SEM micrograph of the cross section of a silicon wafer after oxide formation of an MgO masked silicon surface which faces the plasma.

ing configurations, e.g., horizontal placement, wafer support on its bottom and edges, etc. lead to nonuniform growth.

Our process of plasma oxidation involves placing the silicon wafer vertically perpendicular to the direction of the gas flow with the surface to be oxidized facing away from the plasma. This is true for a wafer located on either side of the rf induction coil. Thus, two wafers can be oxidized simultaneously using this plasma oxidation technique. The rate of oxidation is a strong function of the position of the wafer relative to the edge of the coil, decreasing sharply with increasing distance. For the experimental results to be discussed below, the wafer(s) was placed at a distance of 2 cm from the end of the rf coil. Since the wafer lies adjacent to the plasma generation region, the temperature of the wafer is determined to some extent by plasma heating. It takes about 15 min for the temperature of the wafer to stabilize when the plasma is ignited. To study the kinetics of oxidation at a particular temperature, the wafer was brought to an initial temperature using the resistance heat furnace and then a helium plasma was struck at the desired pressure. When the wafer temperature stabilized, the gas input was changed over to oxygen. The latter step takes about a minute. A control wafer was heated in a helium plasma for 30 min to determine whether any oxide is formed during the preheating stage due to contaminants. No detectable amount of SiO_2 formed. The temperature of the resistance heated furnace was varied to obtain the desired oxidation temperature, independent of the power used to generate the plasma. To study the kinetics of oxide formation on two surfaces of a wafer simultaneously, wafers polished on both sides were oxidized for different lengths of time. As mentioned before, the oxide thickness on the front side is less uniform. The average oxide thickness on the front side was computed from the thickness measurements on a 4 cm diam central area of the wafer. Figure 4 shows the thickness of oxide grown at 540°C on the back and front sides of a wafer as a function of time. Oxide thickness on the back side was about 4-5 times the oxide thickness on the front side. In order to analyze the kinetics of oxidation, the data was plotted as $\log d$ vs. $\log t$ (Fig. 5). Both curves follow essentially the same behavior. The oxide thickness appears to increase as t in the initial oxidation phase and as $t^{1/2}$ for longer oxidation times. It is interesting to note that for the back side of the wafer, the $t^{1/2}$ law is obeyed at an oxide thickness of 150 nm whereas for the front side, the $t^{1/2}$ law prevails at an oxide thickness of 40 nm. If neutral species are responsible for oxidation, then the onset of

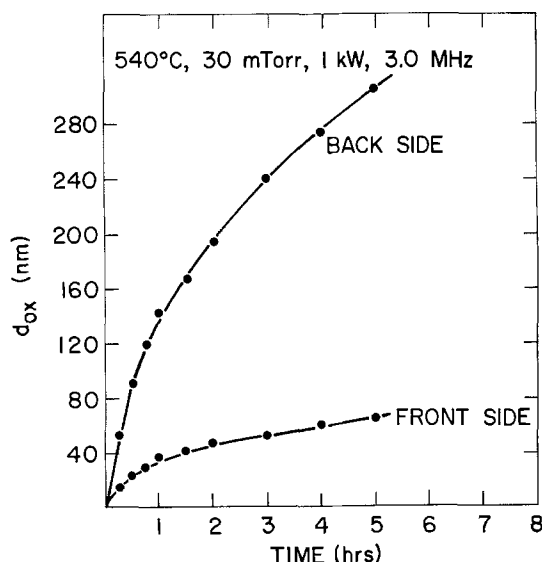


Fig. 4. Thickness of SiO_2 grown at 540°C on the back and front sides of a wafer as a function of time.

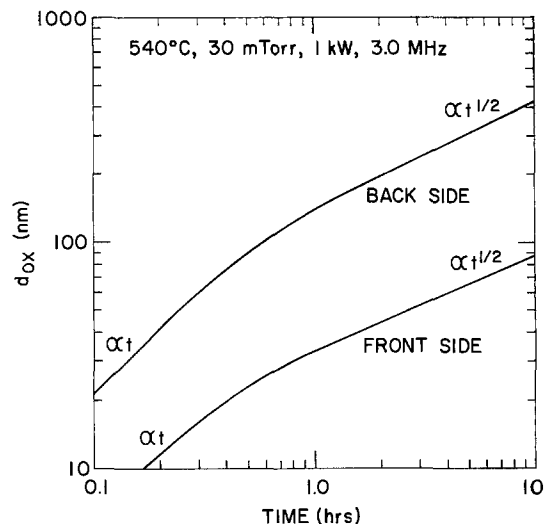


Fig. 5. Thickness vs. time for the data shown in Fig. 4 plotted as $\log d$ vs. $\log t$.

a parabolic law for two different oxide thicknesses would imply that oxidation on the two surfaces is due to different species being responsible for oxidation on each side of the wafer. If we assume that plasma oxidation follows linear-parabolic kinetics (2), then in the parabolic regime $d_{\text{ox}} \propto C_0^{1/2}$ and in the linear regime $d_{\text{ox}} \propto C_0$ where d_{ox} is the oxide thickness grown in a fixed time and C_0 is the concentration of oxidizing species in the gas phase. The two lines in Fig. 5 are more or less parallel indicating that the difference in the oxidation behavior of the two surfaces cannot be explained on the basis of different concentrations of oxidizing species present on either side of the silicon wafer. However, if the oxidizing species is charged, then in addition to the oxidizing species itself, the electric field (V/d_{ox}) would affect the rate of oxidation and the onset of parabolic behavior (3). V is the applied or built in potential difference across the oxide. Studies are in progress to examine such built in potentials and the role they play in the plasma oxidation mechanism.

Figure 6 shows the thickness of the oxide grown on the back side of a wafer in 1 hr at 425°C as a function of oxygen pressure in the reaction chamber. Below 10 mTorr, the oxide thickness is seen to increase sharply with increasing pressure while above 10 mTorr,

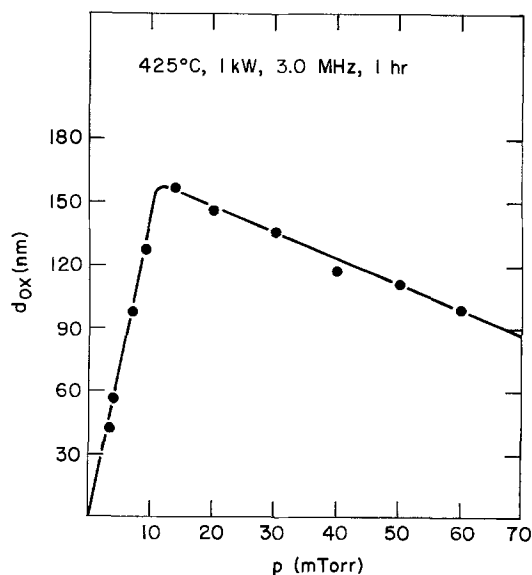


Fig. 6. Thickness of SiO_2 grown at 425°C as a function of oxygen pressure in the reaction chamber.

it decreases slowly with increasing pressure. The effect below 10 mTorr may be explained by the increase in concentration of the oxidizing species with increasing pressure and the effect above 10 mTorr may be explained by the loss of oxidizing species due to an increase in recombination rate with increasing pressure. It is to be recalled from the previous paper that at pressures less than 10 mTorr, when wall-sputtering is the primary mechanism for oxide formation, the rate of oxide formation on the front side of a wafer decreases with increasing pressure. This is a completely different phenomenon than that shown in Fig. 6, which refers only to the process of oxidation taking place on the back side of a wafer. Concomitant with the process of oxidation shown in Fig. 6, at pressures below 10 mTorr, deposition of oxide is taking place on the front side of a wafer in accordance with the discussion in Part 1. If an experiment is conducted, however, at pressures in excess of 10 mTorr, the front side deposition ceases and, of course, the process described in Fig. 6 continues to occur. One other point with respect to Fig. 6 which describes back-side oxidation is that the experiments were conducted at generator output powers in which the front-side deposition rate was very small compared to the rate of oxidation. This point is important because in the experiments to be described at a later date, it will be shown that the back-side oxidation rate is affected by the thickness of an oxide on the front side. One other important aspect of the pressure effect is at pressures less than 10 mTorr, the plasma is not well confined by the silicon wafer, while at pressures greater than 10 mTorr, the visible plasma is totally confined by the wafer. This confinement phenomenon which is striking to observe depends not only on the pressure but also on the frequency of the applied field. The confinement is readily obtained from 0.5 to 3 MHz and very difficult to obtain at 13.6 MHz. When confinement is not obtained, the back-side oxidation rate is dramatically decreased. Figure 7 shows the thickness of oxide grown as a function of time for two generator output powers. Since with increasing power from 1 to 2 kW, there is only a small increase in oxide thickness, most of our experiments were carried out with 1 kW power. The effect of the frequency of the applied field on the thickness of the grown oxide as a function of time is shown in Fig. 8. With increase in frequency from 0.5 to 3 MHz, there is about a 20% increase in oxide thickness. The higher frequency was used in most experiments to obtain higher growth rates. As shown in Fig. 9, the thickness of oxide grown in a fixed time experiment was found

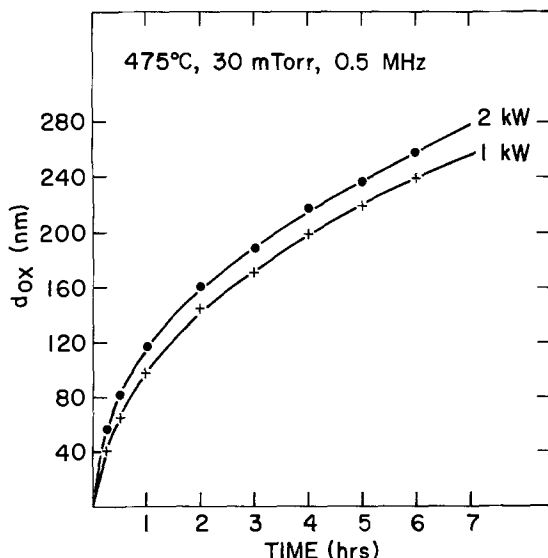


Fig. 7. Thickness of SiO₂ grown at 475°C as a function of time for 1 and 2 kW generator output powers.

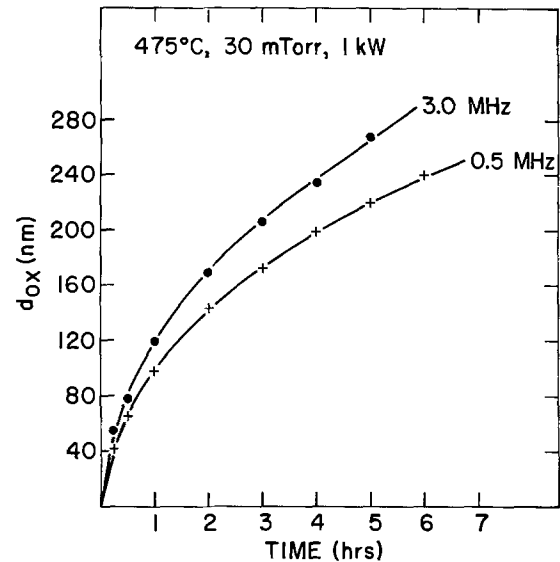


Fig. 8. Thickness of SiO₂ grown at 475°C as a function of time for applied field frequencies of 0.5 and 3 MHz.

not to depend on the resistivity of a silicon wafer. At these low oxidation temperatures, dopants are practically immobile and they are not expected to play a role in the oxidation rate. Oxide thickness as a function of time for <111> and <100> orientation silicon wafers is shown in Fig. 10. Oxide thickness was found to be independent of silicon orientation also, supporting the rate data which indicate a mass transport limited growth process. Since the linear regime, if at all present in our experiments, was probably confined to times less than 10 min, no distinction between the two silicon orientations was possible for the initial stage of the growth process. The effect of temperature on the thickness of oxide grown as a function of time is shown in Fig. 11. Temperature has more of an effect in the parabolic regime than in the initial regime. If we define a parabolic rate constant K_p as $d_{ox}^2 = K_p t$ for the parabolic regime, then the activation energy of K_p is found to be 0.16 eV compared to 1.3-2.3 eV (4, 5) observed for the thermal oxidation of silicon. This is, of course, expected in view of the low temperatures at which we are able to effect oxidation. It should be noted, based on the above, that at 540°C, growth rates comparable to dry thermal oxidation at 1100°C can be achieved by plasma oxidation, but the oxidation rate is strongly limited by the wafer distance from the plasma zone.

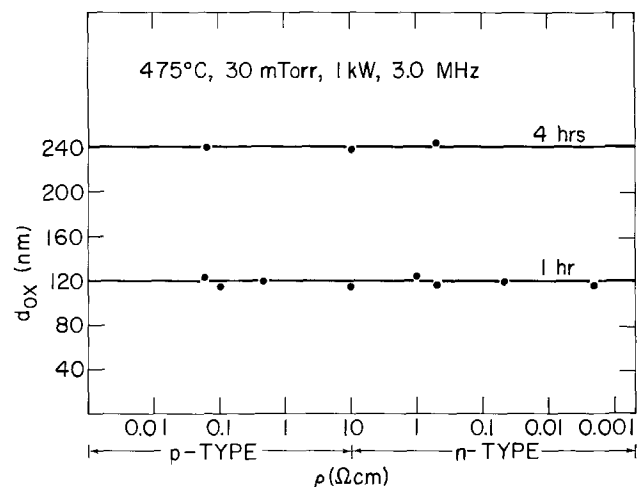


Fig. 9. Thickness of SiO₂ grown at 475°C for silicon wafers of different resistivities.

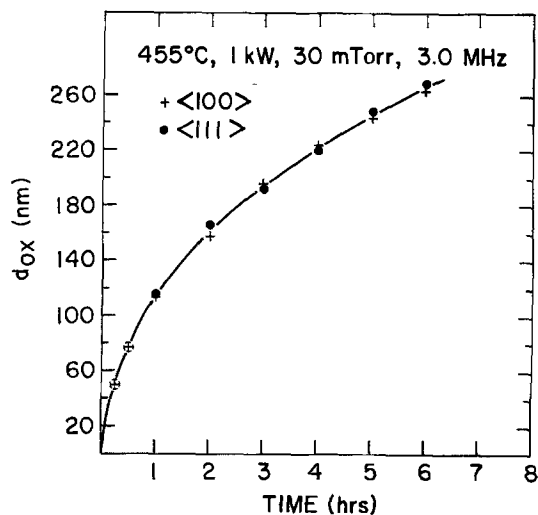


Fig. 10. Thickness of SiO₂ grown at 455°C as a function of time for <111> and <100> oriented silicon wafers.

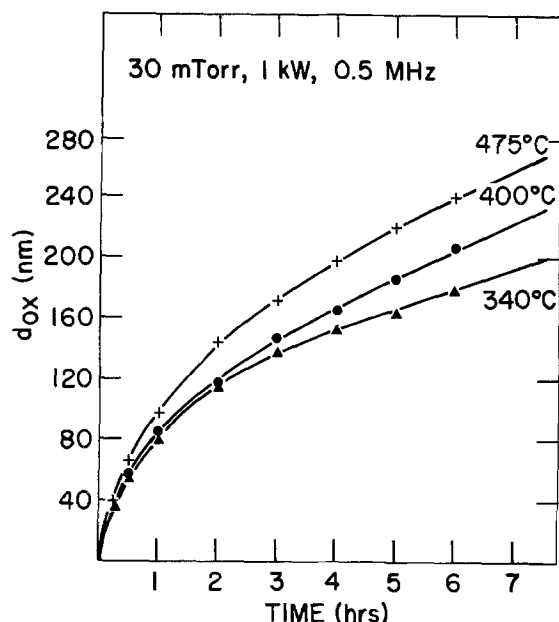


Fig. 11. Thickness of SiO₂ grown as a function of time at 340°, 400°, and 475°C.

Masking Studies

Some interesting observations were also made when a mask material was used. Ligenza (6) reported using Al as an oxidation mask. However, in our case, Al oxidized preferentially to Si and the rate of silicon oxidation, when 50% of the wafer was uniformly masked with Al, was a factor of approximately three less than that of an unmasked silicon wafer. This behavior indicates a large sticking coefficient on the Al of the oxidizing species and is reminiscent of epitaxial growth behavior on Ge and ZnO reported previously by one of the authors (7-9). However, when MgO was used as a mask material, exposed Si areas oxidized at the same rate as that of a blanket silicon wafer. Si₃N₄ was also found to be an effective oxidation mask material and like MgO did not affect growth rate on unmasked surfaces. However, difficulty was encountered in etching Si₃N₄ preferentially to SiO₂ after plasma oxidation using this masking material. SIMS studies indicated that the surface of the Si₃N₄ is oxidized, probably to SiO_xN_y, during plasma oxidation. The bird's beak effect described by Bassous *et al.* (10) was examined using 200 nm of MgO as a mask. After about 380 nm of plasma oxide was grown, the MgO was dissolved in a saturated ammonium oxalate solution at

room temperature, and the Si-SiO₂ interface was examined using SEM. It is evident from Fig. 12 that the bird's beak effect is apparently absent in plasma oxidation. Si₃N₄ directly on top of silicon surface may minimize the bird's beak effect in conventional oxidation but the stress at the Si₃N₄-Si interface damages the underlying silicon at high temperatures. In order to avoid the generation of dislocations and other defects, a pad oxide must be used between the Si₃N₄ and the silicon surface. This pad oxide provides a diffusion path for oxidation and gives rise to a bird's beak. The ability to plasma oxidize silicon at lower temperatures enables one to place the oxidation mask in direct contact with silicon and thereby eliminate bird's beak formation.

Properties of Plasma Grown SiO₂

The properties of plasma SiO₂ grown at 500°C were studied and were compared to thermal SiO₂ grown at 1100°C. The results are summarized in Table I. The refractive indexes were determined at 632.8 nm using ellipsometry. The etch rates of plasma and thermal SiO₂ were compared by etching simultaneously the two types of oxide in 1:9 (40% HF:49% NH₄F) solution at room temperature. The stress (σ_F) at the Si-SiO₂ interface was calculated knowing the film thickness (t_f), substrate thickness (t_s), and the radius of curvature of the silicon substrate (R), using the formula

$$\sigma_f = \frac{E_s}{6(1-\gamma_s)} \frac{t_s^2}{t_f} \cdot \frac{1}{R}$$

where E_s = Young's modulus of the silicon substrate and γ_s = Poisson's ratio.

In order to get an accurate measurement of the radius of curvature, 7 mil thick wafers polished on both sides were used. About 450 nm of SiO₂ were grown by plasma oxidation or by thermal oxidation at 1100°C. Oxide was then etched from one surface of the wafers. The compressive stress in SiO₂ results in elas-

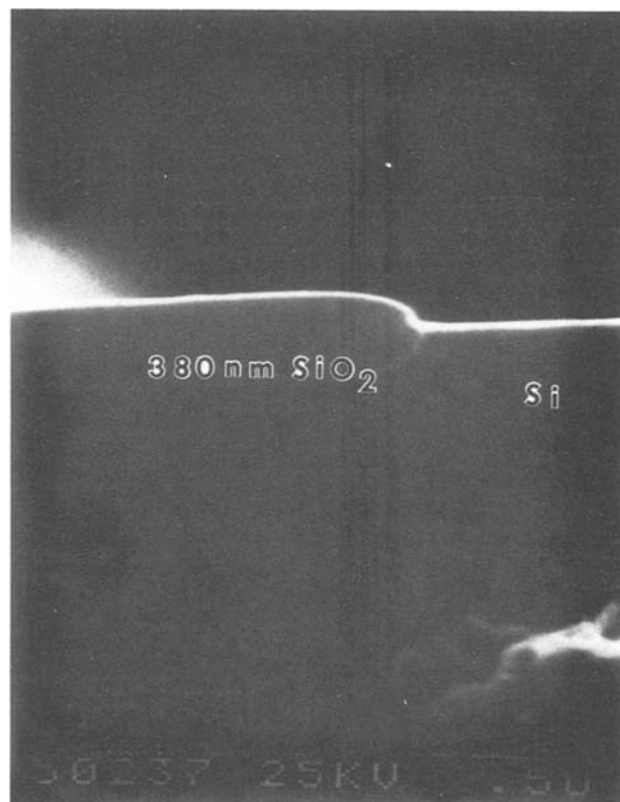


Fig. 12. SEM micrograph of the cross section of a silicon wafer after oxide growth showing the apparent absence of bird's beak effect.

Table I. Properties of plasma SiO₂ grown at 500°C compared to thermal SiO₂ grown at 1100°C

| Properties | Plasma SiO ₂ 500°C growth temperature | Thermal SiO ₂ 1100°C growth temperature |
|---|--|--|
| Etch rate in 1:9 BHF (nm/min) | 74-76 | 75 |
| Refractive index | 1.461-1.465 | 1.462 |
| Stress (dynes/cm ²) | 1.5-1.6 × 10 ⁹ | 3.1-3.4 × 10 ⁹ |
| Fixed charge (No./cm ²) | 2-6 × 10 ¹⁰ | 2 × 10 ¹⁰ |
| Interface states (No./cm ² eV) | 2-6 × 10 ¹⁰ | 2 × 10 ¹⁰ |
| Retention time (sec) | ~100 | >500 |
| Breakdown strength (MV/cm) | 4-8 | 10 |
| Boron depletion | Absent | Present |
| Bird's beak effect | Absent | Present |
| Oxidation-induced defects | Absent | Present |

tic bending of the wafer. The radius of curvature of the silicon wafer was determined by an automatic x-ray diffraction technique described by Segmuller *et al.* (11). The stress for plasma oxide was determined to be 1.5-1.6 × 10⁹ dynes/cm² and that of thermal oxide was 3.1-3.4 × 10⁹ dynes/cm². The difference in stress can be explained by the different growth temperatures and the subsequent cooling to room temperature. If we assume that strain at the Si-SiO₂ interface is proportional to the difference in thermal contraction of Si and SiO₂ during cooling from the growth temperature, and that the intrinsic stress at the growth temperature is negligible, then we can write strain ∝ (α_{Si} - α_{SiO₂}) ΔT where α_{Si} and α_{SiO₂} are the coefficients of expansion of Si and SiO₂, respectively, and ΔT is the difference between the growth temperature and room temperature. Thus, the ratio of stress in plasma oxide (500°C) and thermal oxide (1100°C) is expected to be (1100 - 23)/(500 - 23) = 2.27, close to 2.1, the ratio of the experimentally determined stress values. Since the deformation in silicon is elastic in nature as evidenced by the absence of slip in the oxidized wafers, the rate of cooling from the growth temperature to room temperature is not important.

Fixed charge and interface-state density for oxides grown on <100> Si wafers were determined using high frequency and quasi-static C-V techniques. As-grown oxides exhibited large negative flatband voltages and high surface-state density (3 × 10¹²/cm² eV). Figure 13 shows high frequency (solid line) and quasi-static (dotted line) C-V curves of Al-SiO₂-Si capacitors with only a standard postmetal anneal (400°C, 20 min, forming gas). No high temperature postoxidation heat-treatment was given to these capacitors prior to metallization nor were they premetal annealed at a

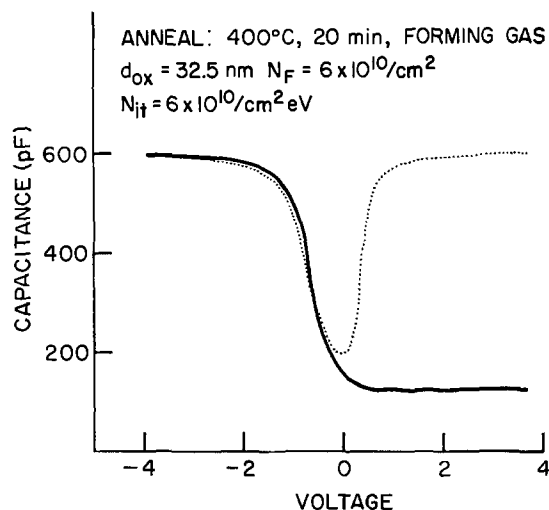


Fig. 13. High frequency and quasi-static C-V curves of plasma SiO₂ capacitor after postmetallization anneal in forming gas at 400°C for 20 min.

lower temperature. The postmetal anneal fixed charge density calculated from the flatband voltage was 6 × 10¹⁰/cm², and the surface-state density at midgap was found to be 6 × 10¹⁰/cm² eV. When, in addition to the standard postmetallization anneal, a postoxidation heat-treatment (1000°C, 20 min, Ar) was given, both the fixed charge and surface-state density values dropped to 2 × 10¹⁰. Another postoxidation heat-treatment at 1000°C for 15 min in dry O₂ followed by 5 min in Ar also reduced the fixed charge and surface-state density to the same value. However, the postoxidation heat-treatment in dry O₂ also improved the breakdown strength of plasma oxides considerably. A breakdown strength histogram on one hundred capacitors with different postoxidation heat-treatments is shown in Fig. 14. Plasma oxides without any postoxidation heat-treatment exhibited breakdown strengths of 3-4 MV/cm. The postoxidation heat-treatment at 1000°C in Ar did not change this breakdown histogram. However, after postoxidation heat-treatment in oxygen, the breakdown strength increased to 7-8 MV/cm. During the heat-treatment in oxygen, another 5 nm of thermal SiO₂ were formed in addition to the 35 nm of plasma oxide already present on the wafer. The improvement in breakdown strength cannot be accounted for by this additional 5 nm of thermal SiO₂. The improvement is also not due to the densification of SiO₂ at high temperature since the argon anneal at the same temperature did not improve breakdown characteristics. It is possible that some kind of stoichiometric change in plasma oxide takes place during annealing in oxygen. One aspect of our experimental technique which is suspect is the use of liquid nitrogen baffled mechanical pumping to maintain desired pressures during oxidation. This is accompanied unavoidably by oil back streaming which may incorporate carbon into the oxide films. The oxygen treatment may remove these defects.

In order to establish the presence or absence of oxidation-induced stacking faults and other defects, about 400 nm of plasma SiO₂ were grown on a silicon wafer, the oxide was subsequently stripped in BHF and the silicon surface was etched in Wright etch for 40 sec. The etched silicon surface was then examined using optical microscopy. No oxidation-induced stacking faults or other defects were observed. Plasma oxidation thus has definite advantages over thermal oxidation from the defect and bird's beak elimination point of view, both of which advantages arise because of the lower oxidation temperatures employed.

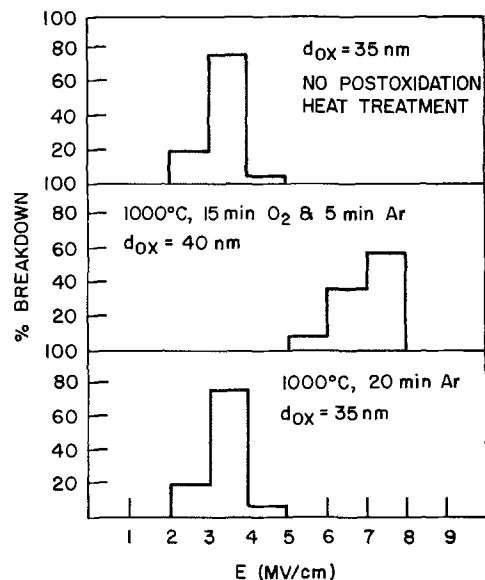


Fig. 14. Breakdown histogram of plasma SiO₂ capacitors with different postoxidation heat-treatments.

Conclusions

From the experimental results described in this paper, we can conclude that oxide formation in an oxygen plasma in the pressure range above 10 mTorr is solely due to silicon oxidation. The process of oxidation involves placing the wafer surface to be oxidized facing away from the plasma, close to the plasma generation region, and perpendicular to the direction of gas flow. The oxide thickness grown in a fixed time experiment increases with increasing power, temperature, frequency of the applied field, and decreases with increasing pressure and distance of the wafer from the plasma. Oxide thickness was found to be independent of the resistivity and crystallographic orientation of the wafer. The growth rate and properties of SiO₂ grown in an oxygen plasma at 500°C were comparable to thermal SiO₂ grown at 1000°-1100°C. Low fixed charge and interface-state densities were obtained following only a low temperature postmetallization anneal. Following a short postoxidation anneal in argon or oxygen, these values improved further by a factor of three. Breakdown strength improved considerably following a brief postoxidation heat-treatment at 1000°C in dry O₂, but not in argon. Bird's beak and oxidation-induced defects were both found to be absent in plasma grown oxides.

Manuscript submitted Dec. 18, 1980; revised manuscript received April 27, 1981. This was Paper 167 pre-

sented at the St. Louis, Missouri, Meeting of the Society, May 11-16, 1980.

Any discussion of this paper will appear in a Discussion Section to be published in the June 1982 JOURNAL. All discussions for the June 1982 Discussion Section should be submitted by Feb. 1, 1982.

Publication costs of this article were assisted by IBM Corporation.

REFERENCES

1. A. K. Ray and A. Reiman, *This Journal*, **128**, 2460 (1981).
2. B. E. Deal and A. S. Grove, *J. Appl. Phys.*, **36**, 3770 (1965).
3. U. R. Evans, "The Corrosion and Oxidation of Metals," p. 823, Edward Arnold, Publisher, London (1960).
4. E. A. Irene and Y. J. Vander Meulen, *This Journal*, **123**, 1380 (1976).
5. E. A. Irene and D. W. Dong, *ibid.*, **125**, 1146 (1978).
6. J. R. Ligenza, *J. Appl. Phys.*, **36**, 2703 (1965).
7. A. Reisman, M. Berkenblit, S. A. Chan, and J. Angilello, *J. Electronic. Mater.*, **2**, 177 (1973).
8. M. Berkenblit and A. Reisman, *Met. Trans.*, **2**, 803 (1971).
9. V. J. Silvestri and T. O. Sedgwick, *This Journal*, **117**, 198 (1970).
10. E. Bassous, H. N. Yu, and V. Maniscalco, *ibid.*, **123**, 1729 (1976).
11. A. Segmuller, J. Angilello, and S. J. LaPlaca, *J. Appl. Phys.*, **51**, 6224 (1980).

Preparation and Electrical Properties of V₂O₃ Single Crystals of Controlled Stoichiometry

S. A. Shivashankar,¹ R. Aragón,² H. R. Harrison, C. J. Sandberg, and J. M. Honig

Purdue University, West Lafayette, Indiana 47907

ABSTRACT

V₂O₃ crystals have been grown by the skull-melting technique and subsequently annealed in CO₂/CO atmosphere to produce crystals of controlled stoichiometry. Crystals were characterized by x-ray Laue back-reflection photography, lattice parameter refinement, polarized reflected light microscopy, neutron and gamma ray diffraction, and thermogravimetric analysis. Deviations from strict stoichiometry, V_{2-y}O₃, were found to follow the relation $y \sim f_{O_2}^{3/4}$ in the dependence on oxygen fugacity. The dependence of electrical resistivity on temperature was measured for two different samples, and the variation of the temperature of metal-insulator transition with sample composition was determined.

As is by now well recognized, V₂O₃ and its dilute alloys with other transition metal sesquioxides undergo a variety of spectacular metal-insulator transitions, which can be drastically altered by small changes in sample composition. Approximately 400 publications have been catalogued by us which deal with various aspects of this problem. It has also been known for some time that small departures from the 3/2 ratio of oxygen/vanadium considerably affect the physical properties of V₂O₃ or its alloys. While there is general agreement concerning the overall effects, various workers in the field differ from each other in their detailed findings. This points up the need for a method that permits precise control to be achieved over the exact oxygen stoichiometry. The object of the present publication is to report on progress in this particular area.

A variety of techniques have been used to obtain samples of nonstoichiometric vanadium sesquioxides; these may be briefly summarized as follows: For polycrystalline samples, treatment of V₂O₅ or of other vanadium oxides in CO₂/H₂ or CO₂/CO mixtures at high temperatures (1-3), generation of ceramic sintered bodies by reaction of V₂O₃ with a small quantity of V₂O₅ or of VO in evacuated quartz ampuls (4-8), reduction of VO₂ whiskers under a variety of low partial pressures of oxygen at 1500°C (9); for growth of single crystals, use of TeCl₄ or HCl as a chemical transport agent in a gradient furnace (5, 8, 10-12), and growth of bulk single crystals by the Verneuil flame-fusion technique (13, 14), utilizing different H₂/O₂ ratios, and by the Reed tri-arc technique (15, 16).

Physical investigations carried out on the resulting ceramic specimens include phase equilibria studies (1, 3, 4, 15, 17), heat capacity measurements at ordinary temperatures (9) and in the cryogenic temperature range (10), lattice parameter determinations by x-ray diffraction techniques (2, 5, 8, 11), magnetic susceptibility investigations (2, 4, 6, 8, 14), electrical resistivity

¹Present address: IBM Thomas J. Watson Research Center, Yorktown Heights, New York 10598.

²Present address: Departamento de Física, Universidad Nacional de La Plata, La Plata, Pcia. de Buenos Aires, Argentina.

Key words: electrical properties of V₂O₃, preparation of V₂O₃ single crystals, annealing procedures for V₂O₃.

measurements (4, 5, 8, 11-14), Seebeck coefficient studies (13), optical measurements (9), electron microscope imaging (12), NMR and Mössbauer techniques (7, 8), and inelastic neutron spin-flip scattering investigations (7).

Growth of Single Crystals

The common deficiency in most of the techniques for growing single crystals is the lack of adequate control over the ambient. This is manifested in a recent investigation on V₂O₃ single crystals grown in this laboratory either by the Reed tri-arc technique (15, 16) or by CVT, using TeCl₄ as the transporting agent (16). With the aid of polarized reflected light microscopy Aragón (18) has demonstrated the occasional presence of higher oxide phase domains in these V₂O₃ single crystals, even though they appear to be single phase and homogeneous in x-ray diffraction patterns. To remedy this problem, and to obtain a homogeneous sample of precisely defined stoichiometry, thin slices cut from single crystalline boules were annealed in a variety of different CO₂/CO buffering atmospheres. By altering the CO₂/CO ratio one may precisely control the equilibrium fugacity of oxygen, f_{O_2} , and thereby achieve the variations in oxygen stoichiometry discussed below.

Single crystals of V₂O₃ were grown in a skull-melting apparatus; the principles, techniques, and operating procedures have been repeatedly described elsewhere (19-26). Provision was made for operation in a vacuum/gas chamber (volume ~ 125 liters) for control of the ambient (25, 26). The charge for each skull-melter run consisted of approximately 500g of V₂O₃ powder obtained by reducing 99.9% Cerac/Pure V₂O₅ (placed in alumina boats) in flowing hydrogen at 1000°C for 10 hr. Traces of water present in the hydrogen used for reduction were removed by passing the gas over copper mesh at 0°C. A susceptor is required to initiate the melting of the V₂O₃ powder in the skull melter; it was found that a relatively small polycrystalline piece (10-20g) of previously produced V₂O₃ served this purpose very well. Two separate runs with CO₂/CO mixtures in the ratio of 25/75 were carried out, employing gas flow rates in the range 5-10 l/min at different stages of the melting process. Although these experiments had to be terminated early because of technical difficulties arising from the high electrical conductivity of V₂O₃ at elevated temperatures, single crystals as large as 10 × 6 × 5 mm³ were nevertheless obtained in the center of the boules. These crystals were singularly free of voids and cracks that often blemish V₂O₃ crystals grown by the tri-arc (Czochralski) technique. This material then served as the starting point for the annealing process described below.

Subsolidus Annealing Procedures

Specimens grown by the above process were annealed under controlled CO₂/CO atmospheres at temperatures below their melting point. Figure 1 provides information on the stability range of the various vanadium oxides; the upper part of this phase diagram is taken from the compilation by Okinaka *et al.* (27) of experimental results published by Katsura and co-workers (1, 3). The V₂O₃/VO/V boundaries were calculated by us from data on the free energies of formation collected by Reed (28). As the data incorporated in the phase diagram (Fig. 1) are taken from different sources, the phase boundaries as indicated are not considered to be precise. Included in this diagram is a set of well-calibrated f_{O_2} values corresponding to a variety of different CO₂/CO mixtures, as specified by Deines *et al.* (29). It is seen that as one lowers the ratio $r \equiv CO_2/(CO_2 + CO)$, the volume percentage of CO₂ in the mixture, from approximately 90% to about 5%, one should be able to generate V₂O₃ compositions bordering from the most oxygen-rich to the most oxygen-poor.

Most of the annealing runs were carried out at 1200°C in a horizontal resistance furnace 60 cm in length, under a typical gas flow of 20-50 cm/min. Provision was made for rapid quenching of the specimens at the end of the run in the controlled atmosphere. Gas flow was carefully regulated by utilizing two-stage regulators on the gas cylinders. The desired CO₂/CO ratio and mixing of the gases was achieved with a Matheson 7372 gas proportioner equipped with precision NRS flow-control valves. V₂O₃ single crystals, cut into thin plates by use of a low-speed diamond wheel saw, were placed in a silica tube plugged loosely with silica wool. Silica wool by its baffling action aids the equilibration of the sample with the flowing gas mixture. Calculations (30) based on estimated cation diffusion rate constants for Al₂O₃, Cr₂O₃, and Fe₂O₃ (31) showed that annealing times of ~75-100 hr should suffice to generate a uniform oxygen stoichiometry in plates of 300 micron thickness of V₂O₃ at 1200°C. Annealing times of 75 hr were generally used.

A few runs were also carried out in a vertical resistance furnace at 1400°C; however, because of large temperature gradients and fluctuations the annealing conditions could not be regulated as closely.

Several annealing experiments were also carried out with solid buffers: VO/V₂O₃, Fe/FeO, FeO/Fe₃O₄, and Ni/NiO, corresponding to values of log f_{O_2} (atm) = -21.4, -14.8, and -10.1, respectively at 1000°C (32). Specimens to be annealed were cut into plates approximately 250 microns in thickness and placed in a silica tube with roughly five times their weight of the solid buffer mixture. The tube was then evacuated, sealed, and placed in a furnace at 1000°C for 100 hr, and finally quenched to room temperature.

Characterization

Samples were characterized by several different techniques.

X-ray Laue back-reflection photography.—Laue photography was used primarily to confirm that the dominant phase present in the annealed single crystals was the corundum V₂O₃ phase. At 1200°C the corundum phase covers the range $-7.7 \geq \log f_{O_2} \geq -14.7$ (nominal).

X-ray lattice parameter refinement.—Lattice parameters of annealed single crystals were determined and refined with an ENRAF NONIUS CAD-4 diffractometer, controlled by a PDP-8/e minicomputer. Molybdenum K α_1 and K α_2 radiation was used, with a graphite monochromator in the detector arm. Within the detection limit of roughly 2-5%, no extraneous phases were found in single crystals annealed under the conditions specified above.

Polarized reflected light microscopy.—Annealed single crystals were examined by polarized reflected light microscopy which is a sensitive technique for detecting extraneous phases. Samples annealed in the solid-solid buffer mixtures mentioned above showed evidence of phase segregation. By contrast, samples annealed under CO₂/CO proved to be consistently monophasic in the range $-7.7 \geq \log f_{O_2} \geq -14.7$ (nominal, 1200°C). All electrical measurements were carried out on single crystals annealed in these gaseous buffered atmospheres.

Neutron and gamma ray diffraction.—Skull-melter V₂O₃ crystals annealed in CO₂/CO have recently been examined by neutron and gamma ray diffraction (33). Compared to unannealed V₂O₃ grown by the tri-arc technique, these samples showed very much narrower and taller diffraction peaks. The annealed samples also proved to be of very homogeneous composition.

Thermogravimetric analysis.—The oxygen content of the samples annealed at various oxygen partial pressures was determined by thermogravimetric tech-

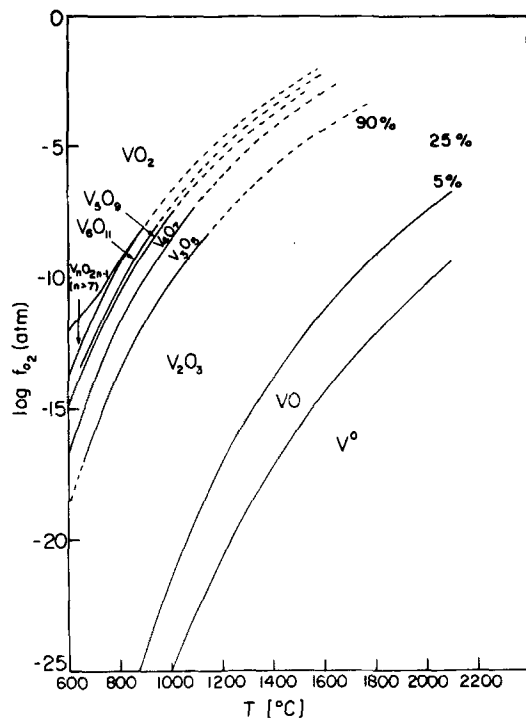
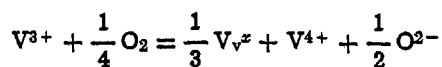


Fig. 1. Stability diagram of part of the V-O system in $\log f_{O_2}$ -temperature representation. Solid lines (with dashed extrapolations) are phase boundaries; dotted lines, CO_2/CO gas mixtures; numbers are volume percentages of CO_2 , i.e., $CO_2/(CO + CO_2)$. Note melting point of $V_2O_3 = 1967^\circ C$.

niques. A single crystal weighing approximately 200 mg was annealed at a series of different f_{O_2} in the range $-8.0 \geq \log f_{O_2} \geq -12.0$ at $1200^\circ C$ for 80 hr, quenched at the end of each annealing run, and weighed with a precision of $\pm 1 \mu g$. As a final step, the sample was annealed at a value of $\log f_{O_2} = -11.0$ at $1200^\circ C$ and reweighed; this is thought to correspond to the condition required to achieve stoichiometry (1). The sample was then oxidized in pure oxygen to V_2O_5 at $670^\circ C$ in a du Pont 951 Thermogravimetric Analyzer. This instrument is capable of 0.4% accuracy in differential weight measurements. It was thus determined for the sample annealed at $\log f_{O_2} = -11.0$ at $1200^\circ C$ that the final composition was given by $V_{2-y}O_3$, with $y < 0.001$. From the mass determinations at the different f_{O_2} values it was possible to establish a correspondence between composition and equilibrium oxygen fugacity at a given temperature.

The results so obtained are shown in Fig. 2 as a plot of $\log y$ (in $V_{2-y}O_3$) vs. $\log f_{O_2}$ (oxygen fugacity) at $1200^\circ C$; least-squares fitting of the data yields a straight line with a slope of 0.74. This power law may be understood in terms of the simple point defect scheme (34)



where, in the Kröger-Vink notation, V_v^{\cdot} denotes a neutral vanadium vacancy. This scheme predicts an equilibrium vacancy concentration

$$[V_v^{\cdot}] = K(T) \frac{[V^{3+}]}{[V^{4+}]} f_{O_2}^{3/4}$$

where $K(T)$ is the equilibrium constant and concentrations are taken to be equivalent to the corresponding

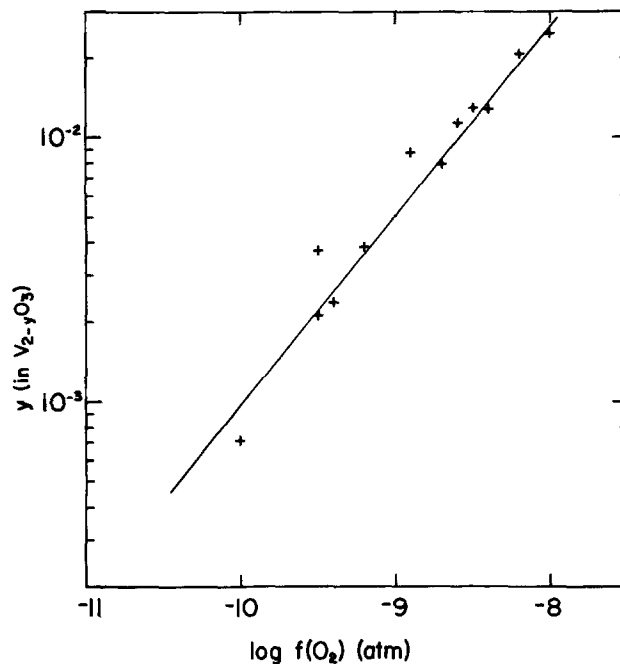


Fig. 2. Deviation from stoichiometry (y in $V_{2-y}O_3$) as a function of $\log f_{O_2}$ for V_2O_3 at $1200^\circ C$.

activities. This is equivalent to the observed relation $y \sim f_{O_2}^{3/4}$ (34, 35).

Electrical Measurements

We conclude with a brief report on the variation of the electrical properties of $V_{2-y}O_3$ with increasing y , prepared as described above. Figure 3 shows the variation of the electrical resistivity ρ with temperature T for samples with $y = 0.0$ and 0.017 , displaying the sharp, first-order transition from metallic (M) to the antiferromagnetic insulating (AFI) phase. While the progressive lowering of the transition temperature (T_t) in $V_{2-y}O_3$ with increasing y has been previously reported (4, 8), new features emerge from the present investigation. Transition temperatures as low as 14 K have been observed, in contrast to the previously lowest transition temperature of ~ 50 K reported earlier

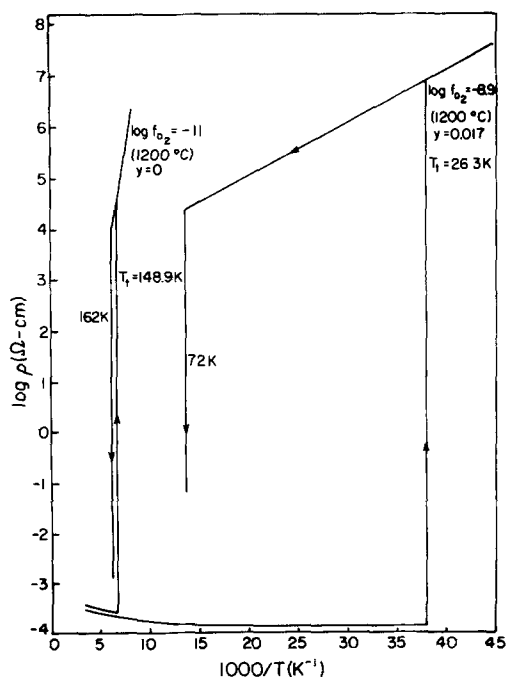


Fig. 3. Metal-insulator transition in $V_{2-y}O_3$ for single crystals of widely different stoichiometry, $\log \rho$ vs. $1/T$. (a) $y = 0.0$, $T_t = 152$ K; (b) $y = 0.017$; $T_t = 26$ K.

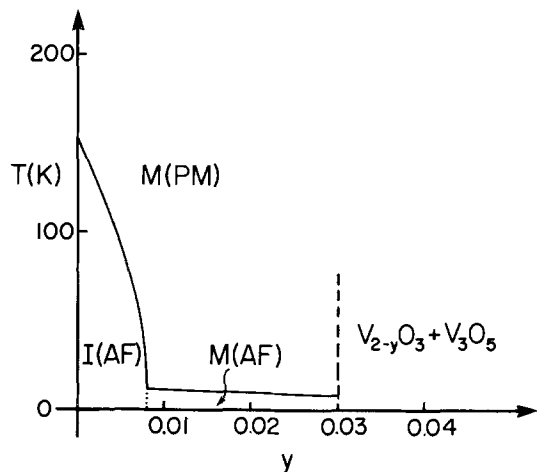


Fig. 4. Phase diagram for $V_{2-y}O_3$, T_t vs. y . M(PM) = metal (paramagnetic), M(AF) = metal (antiferromagnetic), I(AF) = insulator (antiferromagnetic).

(8). The resistivity discontinuity remains large for all y ; indeed $\Delta\rho$ increases from about $10^8 \Omega\text{-cm}$ at $y = 0$ ($T_t = 152 \text{ K}$) to about $10^{12} \Omega\text{-cm}$ at $y \approx 0.017$ ($T_t = 14.0 \text{ K}$). At the same time the hysteresis in the transition temperature (ΔT_t) increases from 12 to 63 K. Earlier studies showed constant values of $\Delta\rho$ and ΔT_t independent of the deviation from stoichiometry (8).

Figure 4 shows a phase diagram for $V_{2-y}O_3$ based on electrical resistivity measurements. This provides a modification of the phase diagram given by Ueda *et al.* (8), by extending the M-AFI boundary to $\sim 11 \text{ K}$ for $y \approx 0.017$. T_t declines at first rather slowly with increasing y , until a range approaching $y \approx 0.014$ is reached; there is then a precipitous decline in T_t with further departures from strict stoichiometry. The M-AFI transition disappears altogether at a critical value of $y \approx 0.018$; for greater departures from the 3/2 ratio of O/V, the material remains metallic at all temperatures and undergoes antiferromagnetic ordering below 11 K. This AF ordering, investigated earlier by Ueda *et al.* (6) through Mössbauer studies, was confirmed in our present studies by the observations of anomalous behavior of electrical resistivity near the magnetic ordering temperature. A more detailed discussion of these findings will be provided elsewhere.

Acknowledgments

The authors wish to thank Mr. S. Chen and Professor R. W. Robinson for their x-ray characterization of several samples. This work was supported by NSF-MRL Grant DMR77-23798.

Manuscript submitted Dec. 1, 1980; revised manuscript received ca. June 4, 1981.

Any discussion of this paper will appear in a Discussion Section to be published in the June 1982 JOURNAL. All discussions for the June 1982 Discussion Section should be submitted by Feb. 1, 1982.

Publication costs of this article were assisted by Purdue University.

REFERENCES

1. T. Katsura and M. Hasegawa, *Bull. Chem. Soc. Jpn.*, **40**, 561 (1967).
2. M. Nakahira, S. Horiuchi, and H. Ooshima, *J. Appl. Phys.*, **41**, 836 (1970).
3. M. Nakahira and T. Katsura, *Metall. Trans.*, **1**, 369 (1970).
4. D. B. McWhan, A. Menth, and J. P. Remeika, *J. Phys. (Paris)*, **32**, C-1079 (1971).
5. K. Nagasawa, Y. Bando, and T. Takada, *J. Cryst. Growth*, **17**, 143 (1972).
6. Y. Ueda, K. Kosuge, S. Kachi, S. Shinjo, and T. Takada, *Mater. Res. Bull.*, **12**, 87 (1977).
7. Y. Ueda, K. Kosuge, S. Kachi, H. Yasuoka, H. Nishihara, and A. Heidemann, *J. Phys. Chem. Solids*, **39**, 1281 (1978).
8. Y. Ueda, K. Kosuge, and S. Kachi, *J. Solid State Chem.*, **31**, 171 (1980).
9. N. Kimizuka, M. Ishii, M. Saeki, M. Nakano, and M. Nakahira, *Solid State Commun.*, **12**, 43 (1973).
10. D. B. McWhan, J. P. Remeika, J. P. Maita, H. Okinaka, K. Kosuge, and S. Kachi, *Phys. Rev. B*, **7**, 326 (1973).
11. M. Pouchard and J.-C. Launay, *Mater. Res. Bull.*, **8**, 95 (1973).
12. J.-C. Launay, M. Pouchard, and R. Ayroles, *J. Cryst. Growth*, **36**, 297 (1976).
13. V. N. Novikov, B. A. Tallychik, E. I. Gindin, and V. G. Prokhorov, *Soviet Phys. Solid State*, **12**, 2061 (1971).
14. V. G. Zubkov, J. I. Matveenko, B. A. Tallychik, and P. V. Gel'd, *ibid.*, **13**, 2885 (1972).
15. J. C. C. Fan and T. B. Reed, *Mater. Res. Bull.*, **7**, 1403 (1972).
16. H. Kuwamoto, Thesis, Purdue University, May 1978, unpublished.
17. J. Springer, *J. Less-Common Metals*, **1**, 14 (1965).
18. R. Aragón, Tech. Rept. "Status Report on the Growth and Characterization of Some Oxide Crystals from the Melt," Purdue University, January 1979, unpublished.
19. D. Michel, *Rev. Int. Hautes Temp. Refract.*, **9**, 225 (1972).
20. V. I. Aleksandrov, V. V. Osiko, A. M. Prokhorov, and V. M. Tatarintsev, *Vest. Akad. Nauk SSSR*, No. 12, 29 (1973).
21. J. F. Wenckus, M. L. Cohen, A. G. Emslie, W. P. Menashi, and P. F. Strong, Tech. Rept. AFCRL-TR-75-0213 (1975).
22. V. I. Aleksandrov, V. V. Osiko, A. M. Prokhorov and V. M. Tatarintsev, in "Current Topics in Materials Science," Vol. 1, E. Kaldis, Editor, pp. 421-480, North-Holland, Amsterdam (1978).
23. D. Michel, M. Perez y Jorba, and R. Collongues, *J. Cryst. Growth*, **43**, 546 (1978).
24. J. E. Keem, H. R. Harrison, S. P. Faile, H. Sato, and J. M. Honig, *Am. Ceram. Soc. Bull.*, **56**, 1022 (1977).
25. H. R. Harrison and R. Aragón, *Mater. Res. Bull.*, **13**, 1097 (1978).
26. H. R. Harrison, R. Aragón, and C. J. Sandberg, *ibid.*, **15**, 571 (1980).
27. H. Okinaka, K. Kosuge, and S. Kachi, *Jpn. J. Appl. Phys.*, **9**, 224 (1970).
28. T. B. Reed, "Free Energy of Formation of Binary Compounds: An Atlas of Charts for High-Temperature Chemical Calculations," MIT Press, Cambridge, MA (1971).
29. P. Deines, R. H. Nafzinger, G. C. Ulmer, and E. Woerman, "Temperature-Oxygen Fugacity Tables for Selected Gas Mixtures in the System C-H-O at One Atmosphere Total Pressure," Bulletin of the Earth and Mineral Science Experiment Station No. 88, The Pennsylvania State University, University Station, PA (1974).
30. J. Crank, "The Mathematics of Diffusion," 2nd ed., p. 50, Clarendon Press, Oxford (1975).
31. C. E. Birchenall, in "Mass Transport in Oxides," N.B.S. Special Publication **296**, pp. 119-127 (1968).
32. J. S. Huebner, in "Research Techniques for High Pressure and High Temperature," G. C. Ulmer, Editor, pp. 123-177, Springer Verlag, New York (1971).
33. S. A. Werner, Personal communication.
34. P. Kofstad, "Non-stoichiometry, Diffusion and Electrical Conductivity in Binary Metal Oxides," pp. 177-178 and 27-46, Wiley-Interscience, New York (1972).
35. M. Wakihara and T. Katsura, *Metall. Trans.*, **1**, 363 (1970).

p-Type NiO as a Photoelectrolysis Cathode

F. P. Koffyberg* and F. A. Benko

Department of Physics, Brock University, St. Catharines, Ontario L2S 3A1, Canada

ABSTRACT

From an experimental study of p-type $\text{Ni}_{0.98}\text{Li}_{0.02}\text{O}$ as a cathode for the photoelectrolysis of water, we have determined its flatband potential [$+0.1\text{V}$ (SCE) at a pH of 9.2] and its bandgap (3.47 eV, indirect). The electron affinity of NiO is only 1.4 eV, which is unusually small compared to most other oxides; this is due to the valence band being mainly nickel-3d type instead of the usual oxygen-2p type. The relevance of 3d valence bands to the performance of semiconducting photoelectrodes is discussed.

The photoelectrolysis of water using semiconducting electrodes has been the subject of intensive research recently (1, 2). For solar applications, electrode materials must have the following properties (apart from being good conductors): (i) A bandgap larger than 1.23 eV but smaller than 3 eV; (ii) a flatband potential which is sufficiently negative (for n-type photoanodes) or positive (for p-type photocathodes) so that a depletion layer of the proper sign is formed without the need for an external bias, and (iii) excellent chemical stability, both in the dark and under illumination. The last requirement limits the field of possible materials to oxide semiconductors. Nearly all oxide materials investigated so far have been n-type.

Stoichiometric NiO is an insulator, but it can be doped with lithium to give a good conducting p-type material. The conductivity mechanism has been a subject of some controversy, but an exhaustive review (3) of experimental data shows that the free holes move, with low mobility, in a narrow valence band made up mainly of 3d-type wavefunctions originating from the Ni^{2+} ions. Because of the low mobility, heavy doping is necessary to achieve acceptable conductivity; this, in turn, will produce narrow depletion layer widths so that the efficiency of an NiO photocathode is expected (and found) to be low. However, since both flatband potential (4) and band-gap data (5) are available, we thought it worthwhile to measure the properties of NiO as a photocathode.

In this paper we report the photocurrent-potential characteristics and the spectral quantum efficiency of $\text{Ni}_{0.98}\text{Li}_{0.02}\text{O}$. From the data we obtain the flatband potential and bandgap, which are in good agreement with the literature values. We then calculate the electron affinity of NiO, which is much smaller than the values reported for most other oxides; we propose that this is due to the d-type valence band. Finally, the implications of our results for the search for suitable solar photoanodes are discussed.

Experimental

Polycrystalline samples of $\text{Ni}_{0.98}\text{Li}_{0.02}\text{O}$ and $\text{Ni}_{0.95}\text{Li}_{0.05}\text{O}$ were prepared by thoroughly grinding NiO powder (Fischer Reagent Grade) moistened with the appropriate quantity of LiNO_3 solution. After drying, disks (area 1.2 cm^2 , thickness 0.1 cm) were pressed and subsequently fired at 1000°C for 12 hr in air. The disks were then reground, re-pressed, and finally fired for 24 hr at 1450°C , during the final firing the disks were embedded in NiO(Li) powder to prevent lithium loss by evaporation. Disks so prepared had reproducible and stable photoelectrolytic properties. If the final firing was done at a lower temperature, then photocurrents slowly decreased in time; we ascribe this to lithium leaching. Qualitatively

the polycrystalline samples with 2 and 5% Li, and a single crystal sample with 0.2% Li, showed the same behavior; the 2% Li samples (with a resistivity of $9 \pm 1 \Omega\text{cm}$) showed the largest photocurrents, and all data reported are for this composition.

Experiments were performed in a one-compartment cell; solutions (from reagent-grade materials) were flushed continuously with hydrogen or oxygen. The counterelectrode was 7 cm^2 of platinized Pt. All potentials are with respect to SCE; measurements were made potentiostatically. Photocurrent measurements were made with pulsed light from a 150W xenon arc (0.81 W/cm^2 intensity at the sample); the time dependence was recorded with a digital storage oscilloscope. For the quantum efficiency (η) measurements the monochromatic light pulses were shaped such that only the instantaneous photocurrents were measured with a lock-in amplifier. For a given sample the η values were reproducible to $\pm 3\%$, but variations of $\pm 20\%$ were found between different samples.

Results

On exposing the sample, in hydrogen-flushed 0.1M Na_2HPO_4 solution, pH = 9.2, to "white" xenon arc light the cell current increased within one msec to a maximum value; it then decayed relatively slowly to a smaller steady-state value. We define (Fig. 1) i_m as the instantaneous photocurrent and i_s as the steady-state photocurrent, both corrected for the dark current i_d . These currents are shown in Fig. 2 as a function of sample potential. This general behavior was observed in 0.1M phosphate solutions ranging in pH from 1 to 12, in 0.2M solutions of Na_2SO_3 , Na_2HPO_3 , Na_2CO_3 , and in 0.01M KOH. Changing the counter-

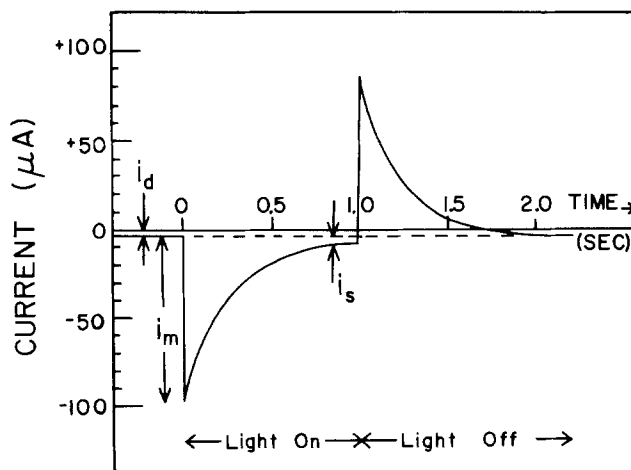


Fig. 1. The current response of $\text{Ni}_{0.98}\text{Li}_{0.02}\text{O}$ to a light pulse. Electrolyte: 0.1M Na_2HPO_4 , pH = 9.2, H_2 flushed. Sample potential -0.45V (SCE).

* Electrochemical Society Active Member.

Key words: semiconductor, electrode, photoelectricity, electrolysis.

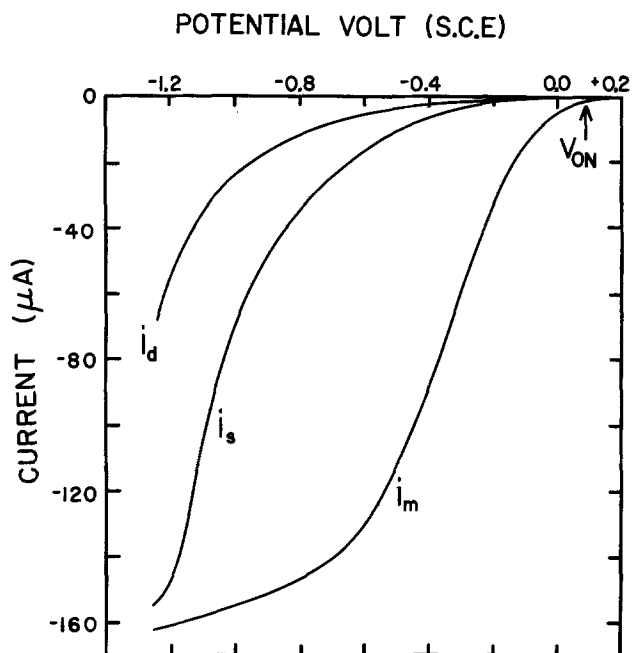


Fig. 2. The instantaneous photocurrent i_m , the steady-state photocurrent i_s , and the dark current i_d of $\text{Ni}_{0.98}\text{Li}_{0.02}\text{O}$ as a function of sample potential $V(\text{SCE})$. Electrolyte: $0.1\text{M Na}_2\text{HPO}_4$, $\text{pH} = 9.2$, H_2 flushed.

electrode from Pt to metallic $\text{La}_{0.9}\text{Sr}_{0.1}\text{CoO}_3$ made no difference. Only in 0.01M KOH solutions flushed with oxygen was i_s much larger, approximately 90% of i_m in the potential range of 0 to -1.0V . In phosphate solutions the onset potential V_{ON} , defined where i_m equals $1 \mu\text{A}$ (Fig. 2) was equal to $+0.07 \pm 0.05\text{V}$ (SCE) at $\text{pH} = 9.2$; it shifted regularly $0.056 \pm 0.005 \text{V/pH}$ unit more positive with decreasing pH . The quantum efficiency η (defined as the ratio of the instantaneous photocurrent density and the incident photon flux) is shown as a function of the photon energy ($h\nu$) in Fig. 3. η is proportional to the optical absorption coefficient α if the depletion layer width and the minority carrier diffusion length are both

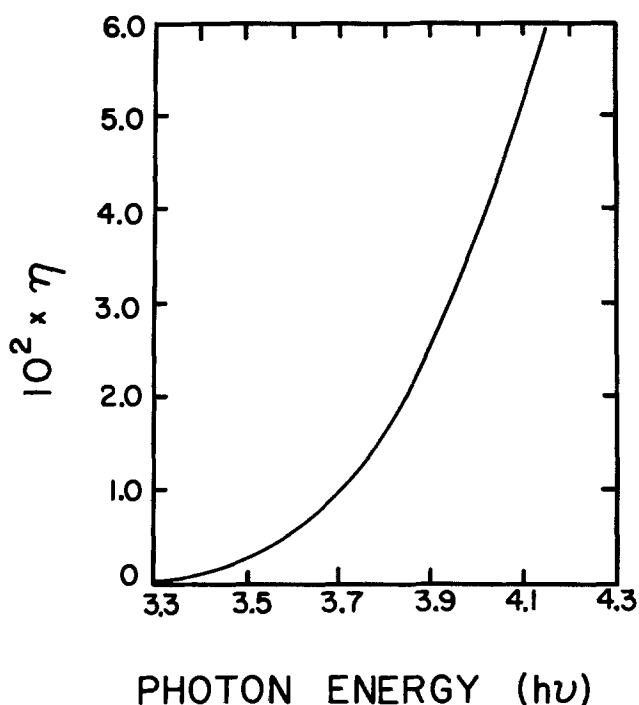


Fig. 3. The quantum efficiency η as a function of photon energy $h\nu$, at an electrode potential of -0.7V (SCE).

smaller than α^{-1} (6); these conditions are met in our heavily doped samples. Then the bandgap E_g can be determined from a linear plot of $(\eta h\nu)^{1/2}$ vs. $h\nu$; the most linear plot was obtained with $n = 2$ (Fig. 4), indicating that the optical transition from the valence to the conduction band is indirectly allowed. E_g was found to be equal to $3.47 \pm 0.04 \text{ eV}$ (average for five samples).

Discussion

The value of the bandgap for NiO found by us is at the lower end of the range (3.4–3.7 eV) of values determined from absorption measurements (5). The spread in the reported values for E_g is probably due to the existence of strong crystal field absorption and lithium-induced optical absorption in the visible, which overlaps the bandgap absorption (7). These complications are unimportant for the photoelectrolysis experiment, which is sensitive only to that part of the overall absorption spectrum in which electron-hole pairs are produced by photon absorption.

At least two reactions are possible at the NiO cathode: hydrogen generation by photoelectrolysis and reduction of NiO according to $\text{NiO} + \text{H}_2\text{O} + 2e^- \rightarrow \text{Ni} + 2\text{OH}^-$. The decomposition potential for the latter reaction is -0.62V (SCE) at $\text{pH} = 9.2$; the rapid rise in the dark current i_d for sample potentials less than -0.9V (Fig. 2) suggest that there the NiO reduction contributes substantially to the cell current. However, in the potential range -0.9 to $+0.1\text{V}$ the instantaneous photocurrent i_m is large with respect to i_d ; we assume that here the dominant reaction is photoelectrolysis.

The rapid rise in the photocurrent, on exposing the sample to light, and its subsequent slow decay to a lower steady-state value have been observed previously for the n-type photoanodes TiO_2 and Fe_2O_3 . Hardee and Bard (8) have proposed the following explanation for this behavior: On exposure to light an intermediate electrolysis product is formed by a fast forward (cathodic) reaction; this intermediate is unstable at the applied electrode potential and is subsequently re-oxidized in a slower back-reaction. The back-reaction slows down with increasing cathodic potential, so that at sufficiently negative potential i_s will be equal to i_m . This explanation may be valid for p-type NiO as well, but our experimental

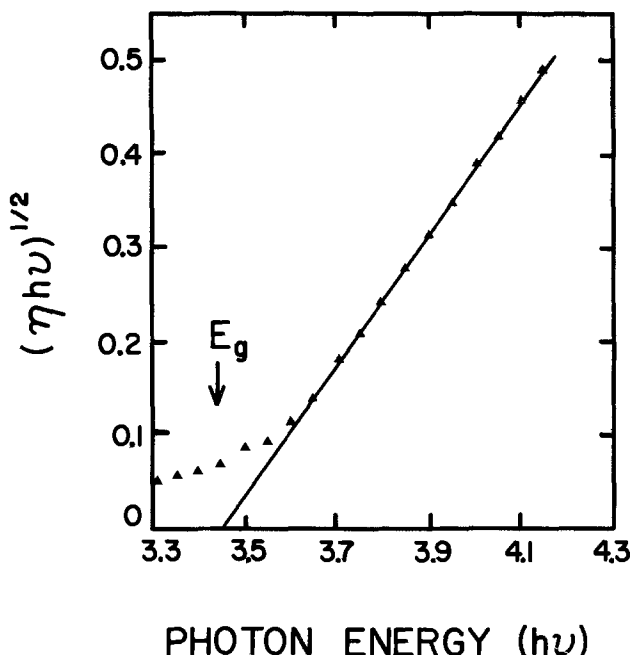


Fig. 4. Determination of the bandgap E_g for $\text{Ni}_{0.98}\text{Li}_{0.02}\text{O}$ from a plot of $(\eta h\nu)^{1/2}$ vs. $h\nu$.

results give no indication of the nature of the intermediate species. However, the i_m vs. V curve (Fig. 2) has the characteristic shape of a photoelectrolysis curve, and we take the flatband potential V_{FB} of NiO equal to or slightly more positive than the onset potential V_{ON} . At $pH = 9.2$, V_{FB} is therefore $+ 0.1 \pm 0.05V$ (SCE).

A possible objection can be raised against this identification of V_{FB} with V_{ON} , since in some p-type materials [LuRhO₃ (9), GaP (10)] V_{ON} is not identical to V_{FB} . The clearest case is p-GaP, where V_{ON} is 0.7V more negative than the V_{FB} determined from a Mott-Schottky plot of the differential capacitance. This is due to the presence of an active electron-hole recombination center situated 0.7 eV above the valence band; evidence for this is a small maximum in the quantum efficiency spectrum at a photon energy 0.7 eV less than the bandgap energy. We consider it very improbable that a similar situation exists for NiO, for the following reasons. First, a careful search for a small maximum in η at photon energies less than E_g was a failure. Secondly, our V_{FB} value, extrapolated from $pH = 9.2$ to $pH = 1$ by 0.059 mV/pH unit, is $+0.58V$; this is very close to the value ($+0.64V$ SCE) found previously (4) from a Mott-Schottky plot. Therefore we take $V_{FB} = +0.1V$ at $pH = 9.2$.

We can now calculate the electron affinity EA of NiO from the relation (10)

$$EA = eV_{FB} - E_g + e\Delta E_F + eV_H + 4.74 \quad [1]$$

Here ΔE_F is the energy difference between the Fermi level and the top of the valence band, and V_H is the potential drop in the Helmholtz layer due to adsorbed H^+/OH^- ions; we take the SCE level 4.74 eV below vacuum (Fig. 5). ΔE_F , calculated (3) from the hole concentration and the hole effective mass ($6 m_0$) is less than 0.1 eV for our samples, and can be neglected. In general V_H is pH dependent according to $V_H = 0.059 (pH - P_0)$ where P_0 is the pH of zero charge for the NiO-solution interface. From electrophoresis experiments (11) P_0 has been estimated as 10.2 for NiO, with a probable accuracy of one pH unit. At $pH = 9.2$, V_H is therefore unlikely to be larger than 0.1V, and it can be neglected as well. Taking all uncertainties into account, we find therefore $EA = 1.4 \pm 0.2$ eV (Fig. 5).

In NiO the valence band is therefore located 4.9 eV below the vacuum level; for most other oxides the valence band lies 7.0-7.5 eV below vacuum (12, 13). This is due to the fact that in NiO the valence band is made up mainly from Ni-3d type wave functions (3), instead of O-2p wave functions as for

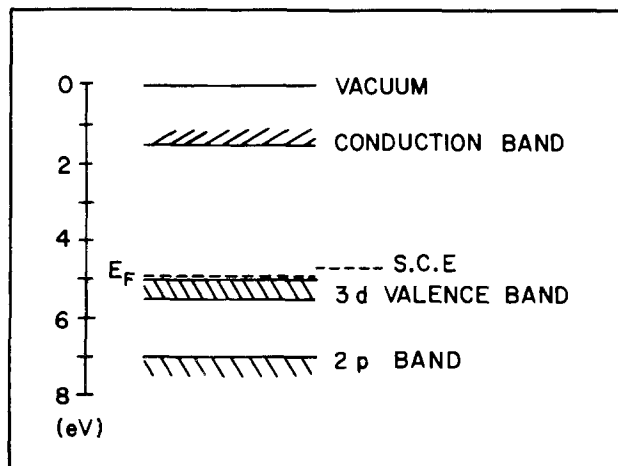


Fig. 5. Energy band scheme for NiO. The width of the 3d valence band is uncertain [Ref. (3)].

most other oxides. Photoemission experiments (14) indeed show a p-bandedge approximately 2 eV below the d-bandedge. The O-2p band is therefore at its usual position of 7 eV below vacuum, but it is not the valence band in NiO.

Butler and Ginley (15) have proposed a scheme to calculate both P_0 and EA for a compound from the electronegativities of the constituent atoms. For NiO such a calculation leads to a predicted P_0 of 8.5 (in fairly good agreement with the experimental value of 10.2), and an EA of 4.01 eV, (in contrast with the experimental value of 1.4 eV) which would place the valence band at 7.5 eV below the vacuum level. This is very close to the position of the O-2p band, and it suggests strongly that the predictions from the Butler and Ginley scheme will be correct for oxides with O-2p valence bands, but will be incorrect for materials with d-type valence bands.

It is clear from our results that p-type NiO is not a good photocathode for solar photoelectrolysis; although the spontaneous band bending is sufficiently large (0.8V), its large bandgap and the back-reaction render it unsuitable. However, materials which, like NiO, have $EA + E_g \approx 5.0$ eV could be good photoanodes if they had n-type conductivity. For the presently known n-type oxide photoanodes the sum of EA and E_g seems to be 7-7.5 eV (12), so that materials with suitably small E_g do not operate spontaneously, but need an external bias to form the depletion layer. Our results show that n-type oxides with a 3d valence band could have the desirable combination of both small E_g and small EA , if the 3d valence band lies at least 2 eV above the O-2p band. Regrettably we cannot test this prediction with NiO, since it cannot be doped n-type.

From the review (2) of the data presently available, it is already clear that not all 3d semiconducting oxides will have suitable valence bands; for example, the oxides containing Fe^{3+} (3d⁵) and Zn^{2+} (3d¹⁰) ions have a valence band approximately 7 eV below vacuum. However, photoemission data for Cu_2O (3d¹⁰) indicate a valence band 5.3 eV below vacuum (16); this value is confirmed by photoelectrolysis experiments on Cu_2O (17). Preliminary experiments by us on CuO (3d⁹) also indicate a valence band at approximately 5 eV. Therefore, as a speculation, we suggest that oxides based on Cu^+ , Cu^{2+} , Ni^{2+} , and possibly Co^{2+} , if they can be made n-type, may be promising materials for bias-free solar photoanodes.

Summary

The flatband potential of p-type NiO, determined from the potential dependence of the instantaneous photocurrent of an NiO/electrolyte/Pt cell, is $+0.1V$ (SCE), in good agreement with the literature value; the NiO bandgap, determined from spectral quantum efficiency data, is 3.47 eV. Taken together, these two parameters indicate that the conduction band in NiO lies unusually high, only 1.4 eV below the vacuum level. This, in turn, is due to the fact that the valence band is made up of mainly 3d-type wavefunctions, instead of oxygen-2p type wavefunctions as is the case for the majority of oxides investigated so far. If materials with 3d valence bands can be made n-type, then they offer the possibility of constructing solar photoelectrolysis cells which would operate without an externally applied bias.

Acknowledgment

We are grateful to the National Science and Engineering Research Council of Canada for financial support of this research.

Manuscript received March 9, 1981.

Any discussion of this paper will appear in a Discussion Section to be published in the June 1982 JOURNAL.

All discussions for the June 1982 Discussion Section should be submitted by Feb. 1, 1982.

Publication costs of this article were assisted by Brock University.

REFERENCES

1. A. Nozik, *Ann. Rev. Phys. Chem.*, **29**, 189 (1978).
2. L. A. Harris and R. H. Wilson, *Ann. Rev. Mater. Sci.*, **8**, 99 (1978).
3. A. J. Bosman and H. J. van Daal, *Adv. Phys.*, **19**, 1 (1970).
4. T. O. Rouse and J. L. Weininger, *This Journal*, **113**, 184 (1966).
5. J. B. Goodenough, in "Progress in Solid State Chemistry," H. Reiss, Editor, Vol. 5, p. 272, Pergamon Press, Oxford (1971).
6. F. P. Koffyberg, K. Dwight, and A. Wold, *Solid State Commun.*, **30**, 433 (1979).
7. R. Newman and R. M. Chrenko, *Phys. Rev.*, **114**, 1507 (1959).
8. K. L. Hardee and A. J. Bard, *This Journal*, **124**, 215 (1977).
9. H. S. Jarrett, A. W. Sleight, H. H. Kung, and J. L. Gillson, *J. Appl. Phys.*, **51**, 3916 (1980).
10. M. A. Butler and D. S. Ginley, *This Journal*, **127**, 1273 (1980).
11. G. A. Parks, *Chem. Rev.*, **65**, 177 (1965).
12. H. P. Maruska and A. K. Ghosh, *Solar Energy Mater.*, **1**, 411 (1979).
13. D. E. Scaife, *Solar Energy*, **25**, 41 (1980).
14. D. E. Eastman and J. L. Freeouf, *Phys. Rev. Lett.*, **34**, 395 (1975).
15. M. A. Butler and D. S. Ginley, *This Journal*, **125**, 228 (1978).
16. J. A. Assimos and D. Trivich, *Phys. Status Solidi A*, **26**, 477 (1974).
17. J. F. Kos, Private communication.

Investigations into the Electrochromism of Lutetium and Ytterbium Diphthalocyanines

David Walton, Brian Ely, and George Elliott

Marconi Research Laboratories, Great Baddow, Chelmsford, Essex, England

ABSTRACT

A comparison was made between the infrared, electronic, and electron spin resonance spectroscopic properties of lutetium and ytterbium diphthalocyanines, in the solid state as analytically pure powders, and after vacuum sublimation as thin deposited films. No significant differences were observed. Spectroscopic analysis of the sublimed films during electrochromic changes showed that the lutetium and ytterbium complexes behaved in a similar manner. Both gave identical variations in their electronic spectra with potential. Electron spin resonance data demonstrated that the oxidative color change is not associated with a change in paramagnetism, although the shape of the signal from the lutetium complex was altered upon oxidation. The ytterbium complex displayed no ESR signal before or after electro-oxidation.

Diphthalocyanine complexes of rare-earth elements are of interest in view of their electrochromic properties (1-3). The lutetium complex displays four colors (orange, green, blue, and purple), when an applied potential is varied between $\sim \pm 1.5V$ (*vs.* aqueous Ag/AgCl reference) in a suitable electrolytic system. Similar results are obtained whether the complex is deposited as a thin film on an electrode surface (3) or in solution in dimethylformamide (4).

Recent investigations into the electrochromic changes of the Lu complex have concerned the variation in ESR spectrum of solutions in dimethylformamide (4), the charge transport phenomena during oxidation (5-7) and attempts to isolate the oxidized species (8). In this paper we wish to report the results of some electrochemical and spectroscopic studies made on lutetium and ytterbium diphthalocyanines. Comparisons are made between the infrared, visible, and electron spin resonance spectra of the analytically pure solids and sublimed films of the complexes deposited on to conducting glass for electro-optical devices. The voltammetry and the changes in the visible and electron spin resonance spectra of the deposited films during the electrochromic transformations are also investigated.

Experimental

Preparation.—The complexes are prepared by the reaction of the rare-earth acetate salt with excess of phthalonitrile, according to the method of McKay (9).

Key words: electrochromism, rare-earth diphthalocyanines, electronic spectra, electron spin resonance spectra.

The required product was isolated from the mix by extraction into chloroform. Solvent evaporation gave a green powder which was carefully washed with organic solvents (acetic anhydride, methanol, acetone) to remove traces of a persistent impurity.

The residual deep-green powder gave elemental analyses for the empirical formula $M Pc_2H$ where $M = Lu, Yb$, and $Pc = C_{32}H_{16}N_8$.

Thus:

| | |
|---------------------------------|------------------------------|
| LuPc ₂ H theoretical | C, 64.00; H, 2.77; N, 18.65% |
| found | C, 64.15; H, 2.79; N, 18.57% |
| YbPc ₂ H theoretical | C, 64.10; H, 2.77; N, 18.69% |
| found | C, 64.01; H, 2.79; N, 18.85% |

Yields 30-40%.

This procedure is advantageous since no lengthy chromatographic purification is employed, and the product is obtained in an unsolvated condition. The empirical formula is in agreement with the results of a recent x-ray structural analysis on neodymium diphthalocyanine (10) though the presence of the unique proton has not been established unequivocally, and its role in the bonding of the molecule is not clear.

Film deposition.—15 mg of the powdered diphthalocyanine complex was placed in a silica crucible, 15 cm above which a 50 cm² square of commercially available tin-oxide coated conducting glass was positioned. The conducting glass was a standard commercial product,

Nesa glass, of 80-100 Ω /square, supplied by PPG Industries Incorporated, Pittsburgh. The apparatus was evacuated to $\sim 10^{-5}$ Torr and the crucible heated indirectly to $\sim 450^\circ\text{C}$. Sublimation of the complex occurred, giving a uniform film, pale green in color, of thickness $\sim 2000\text{\AA}$.

Apparatus.—Infrared spectra were recorded on Pye-Unicam Model SP3-100 spectrometer, and visible spectra on a Hitachi Perkin-Elmer Model 204, all recorded at room temperature. ESR spectra were recorded on a Varian Model E3 spectrometer. Film thicknesses were measured by the interference fringe method on a Reichert Zetopan research microscope.

Electrolyses were performed using a laboratory-built solid-state potentiostat, based on operational amplifier circuits, and operating in a conventional three-electrode mode. The working electrode comprised a slide of tin-oxide coated conducting glass with a working area 2×1 cm, upon which the diphthalocyanine complex had been deposited by sublimation. This was suspended in an aqueous electrolyte, containing either 5% Na_2SO_4 or 5% KCl , at pH 6-7, degassed with argon. An EIL standard aqueous silver/silver chloride reference electrode was employed in all instances. A suitable counterelectrode was a 1 cm^2 piece of platinum foil.

For cyclic voltammetry, the potential sweep was driven by a Commodore PET personal computer employing a Hewlett Packard 59303A digital to analogue converter working on an IEEE 448 bus through the external input of the potentiostat. Scans could be initiated at any intermediate potential between the preset positive and negative limits, and the potential could be varied linearly between the limits starting in either initial sweep direction. Current/potential curves were recorded on a Philips PM8131 X-Y recorder. Potentials were monitored on a Fluke series 8600A digital multimeter.

Electrolysis procedure.—The duration of electrolysis and the potential required varied with thickness of the diphthalocyanine film. Electrolyses were continued until the color change was complete. Similar results were obtained whether the potential was stepped directly to the final value or progressively varied to this value over a period of several seconds. Typically at $+1.5\text{V}$ the initially green-colored film became orange over a period of a few seconds, with the passage of an electric current. The orange species was air stable over several hours. The slide could be removed from the electrolysis cell, washed with distilled water, dried in a stream of nitrogen gas, and placed in a spectrometer. By this means the ESR spectra of the oxidized species were recorded. By returning the slide to the electrolysis cell and maintaining a potential of $\sim 0\text{V}$, the green coloration returned. Reduction at $\sim -0.8\text{V}$ gave a blue species. This was not air stable and returned uniformly to green over a period of a few minutes on removing from the cell. Further reduction at $\sim -1.3\text{V}$ resulted in the formation of a deep purple coating. This also was unstable in air, and on removal from the cell it reverted uniformly to blue over a period of a few seconds, and then to green in a few minutes. The purple and blue species could also be converted to green within the electrolysis cell, in the absence of air, by the application of a small positive potential. To obtain the visible spectra of the reduced species, the electrolysis was performed in an especially adapted cell with windows of optical glass, placed directly in the beam.

All reagents and chemicals were of analytical grade, purified by conventional methods.

Results

Spectral properties of thin films of diphthalocyanine complexes.—The infrared, visible, and electron spin resonance spectra of sublimed films of the diphthalo-

cyanine complexes were compared with the corresponding spectra of the solid powders and no significant differences were observed.

The infrared spectrum of a lutetium diphthalocyanine film sublimed directly onto a potassium bromide disk is given in Fig. 1. The ytterbium complex gives an almost identical spectrum. The characteristic peaks at 1320 cm^{-1} , 1112 cm^{-1} , and 724 cm^{-1} are observed in the nujol mulls of the powder samples. [The presence of absorptions at 2220 cm^{-1} , 1515 cm^{-1} , 1361 cm^{-1} , 760 cm^{-1} , and 631 cm^{-1} (sharp) in the crude product, obtained directly from chloroform extraction, shows the presence of a persistent impurity, removed by careful solvent washings.]

Comparison with other published infrared spectra shows a very close correspondence in the prominent lines for other rare earth complexes, as shown in Table I, which lists the results of MacKay *et al.* (9), Kirin *et al.* (11), Kirin *et al.* (12), Moskalev and Kirin (13), and Misumi and Kasuga (14). There are some discrepancies, for example, we do not find a line in the region of $1070\text{--}1078\text{ cm}^{-1}$, and it is possible that this only appears in the blue form of the rare-earth complex. Some of the other workers have listed several other minor peaks, which we did not detect in our analysis. It is possible that some of the spectra could indicate the presence of impurities; a particular example is the spectrum published by Corker *et al.* (4), which would indicate a high proportion of the colorless persistent by-product which we found in our crude preparation, and also reported by MacKay *et al.* (9).

The visible spectrum of a green sublimed ytterbium diphthalocyanine film on conducting glass slide is shown in Fig. 2, curve (a), and displays a broad main peak at 668 nm , the half peak width being 55 nm , and a distinctive weak and broad peak at 463 nm . The shape of this spectrum is very similar to that of green solutions of the complex as powder dissolved in a range of organic solvents, though the peaks are narrower in solution. Thus, in chloroform: lutetium complex main peak 660.5 nm ($\epsilon = 1.71 \times 10^5$), half peak width 19 nm , and weak broad peak at 458 nm ; ytterbium complex, 661 nm ($\epsilon = 1.59 \times 10^5$) half peak width 19 nm , 457 nm (weak). Solvatochromic effects do not appear to be pronounced in the visible spectra of the green complexes, and the wavelengths of maximum absorption, λ_{max} , of the lutetium (ytterbium) complex in methanol solution is 657 nm (658 nm), and in dimethylsulfoxide solution is 661 nm (661.5 nm).

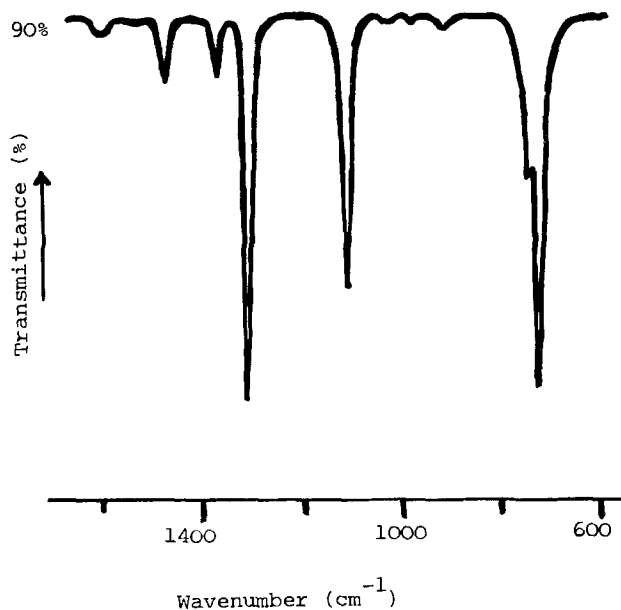


Fig. 1. Infrared spectrum of lutetium diphthalocyanine, as sublimed film on potassium bromide disk.

Table I. Prominent infrared lines (cm^{-1})

| This paper LuPc ₂ H | Ref. (9) GdPc ₂ H | Ref. (11) NdPc ₂ H | Ref. (12) Nd ₂ Pc ₃ | Ref. (13) | | | Ref. (14). Only "metal sensitive" lines listed | | | | | | |
|-----------------------------------|---------------------------------|----------------------------------|--|---------------------|--------------------|---------------------|--|---------------------|---------------------|---------------------|---------------------|---------------------|--|
| | | | | NdPc ₂ H | YPc ₂ H | ErPc ₂ H | LaPc ₂ H | CePc ₂ H | NdPc ₂ H | EuPc ₂ H | ErPc ₂ H | YbPc ₂ H | |
| 724 | 725 | 726 | 725 | 726 | 728 | 729 | | | | | | | |
| 740 | 741 | 740 | 740 | 738 | 743 | 743 | | | | | | | |
| 778 | 778 | 772 | 771 | 768 | 780 | 783 | | | | | | | |
| 882 | 881 | 878 | 880 | 874 | 883 | 884 | 880 | 884 | 881 | 885 | 886 | 887 | |
| 1060 | 1054 | 1060 | 1060 | 1056 | 1052 | 1057 | 1059 | 1050 | 1056 | 1062 | 1063 | 1064 | |
| — | 1070 | 1075 | 1075 | — | — | — | 1084 | 1070 | 1072 | 1077 | 1075 | 1078 | |
| 1112 | 1110 | 1112 | 1114 | 1106 | 1110 | 1113 | | | | | | | |
| 1320 | 1314 | — | 1326 | 1321 | 1321 | 1327 | | | | | | | |
| 1370 | — | — | 1360 | — | — | — | | | | | | | |
| 1450 | 1440 | — | 1448 | — | — | — | | | | | | | |
| 1600 | 1600 | — | 1604 | — | — | — | | | | | | | |

These solvents span a wide range of dielectric constants (Table II). These results suggest the ground and excited states of the transition to be similar in polarity, unlike, e.g., merocyanine dyes where a change of dielectric produces a considerable shift in wavelength of maximum absorption (20).

The electron spin resonance spectrum of solid, analytically pure, lutetium diphthalocyanine powder at room temperature displays a single resonance at 3390G, the half peak width being 9.7G. This is slightly sharpened by cooling to liquid nitrogen temperatures, but no structure is observed. Similar structureless signals are obtained in chloroform and purified dimethylformamide solutions. The sharp single line at $g \sim 2$ indicates that the unpaired electron is located on the porphyrin ring and not on the metal.

When a sublimed film of lutetium diphthalocyanine on tin-oxide coated glass is suspended in the beam, the same signal is observed, though broader, the half peak width being 22.0G.

Ytterbium diphthalocyanine shows no ESR signal at all, whether in the solid state, in solution, or as a sublimed film.

Electrochemical transformations using cyclic voltammetry.—Figure 3 shows the current/potential curve for a sublimed film of lutetium diphthalocyanine on conducting glass, suspended in 5% aqueous sodium sulfate solution. Potentials are referred to aqueous silver/silver chloride, and the sweep rate was 10 mV/sec.

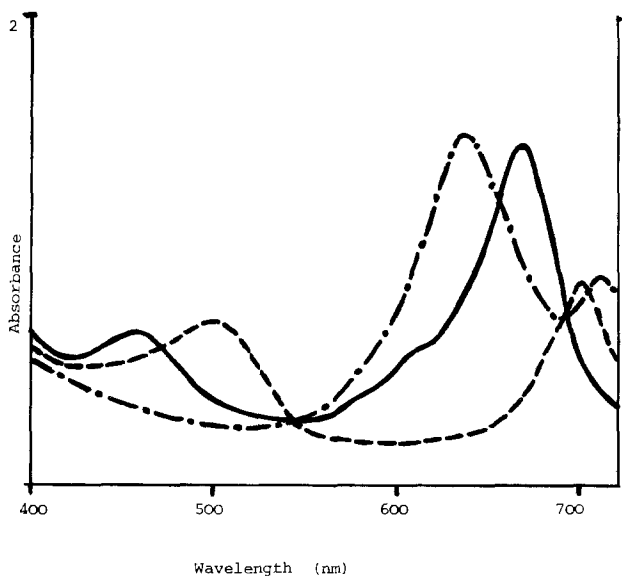


Fig. 2. Electronic spectrum of ytterbium diphthalocyanine as sublimed film on conducting glass. Variation with electrode potential. (a) — green form ($\sim 0\text{V}$); (b) - - - electro-oxidized orange species ($\sim +1.5\text{V}$); (c) —●— electroreduced blue species ($\sim -0.8\text{V}$). (Electrolyte 5% aqueous KCl, potentials w.r.t. aqueous Ag/AgCl reference film thickness $\sim 2000\text{\AA}$).

Table II.

| Solvent | Dielectric constant ϵ | Dipole moment μ | Absorption max LuPc ₂ H (nm) | Absorption max YbPc ₂ H (nm) |
|------------------------------------|--------------------------------|---------------------|---|---|
| CHCl ₃ | 4.81 | 1.15 | 660.5 | 661 |
| CH ₃ OH | 32.7 | 2.87 | 657 | 658 |
| (CH ₃) ₂ SO | 46.7 | 3.9 | 661 | 661.5 |

Curve (a) shows the first full oxidation/reduction cycle, starting with an initially green film at 0V. At +1.5V the color becomes orange and an oxidation current is passed. No reduction current is observed in this region upon scan reversal and the potential is swept to -0.2V before the green color reappears and a reduction current is observed. The shape and definition of these waves depend very much upon the sweep rate, and faster scan rates are unsatisfactory. The green/orange change is color reversible but the difference of $\sim 1.7\text{V}$ between the oxidative and reductive reactions suggests that chemical processes are associated with the electron transfer reactions. Further reduction to -1.0V produces a blue coloration with the passage of a reduction current. Scan reversal produces an oxidation wave at -0.2V with the reappearance of the green color. These results are reproducible over several cycles.

Curve (b) displays the first blue/green reductive cycle, limiting the voltage sweep between 0 and -1.6V, starting from green at 0V, and demonstrates that this change is independent of the orange/green transformation. It is less sensitive to scan rates and good peaks of similar "quasi-reversible" shape are obtained at 140 mV/sec. There is a linear rise of current with scan rate, and a close to linear increase in the peak separation potential within the range of scan rates 10 mV/sec \rightarrow 140 mV/sec.

Further reduction at potentials beyond -1.6V results in a purple coloration in the film, but an ill-

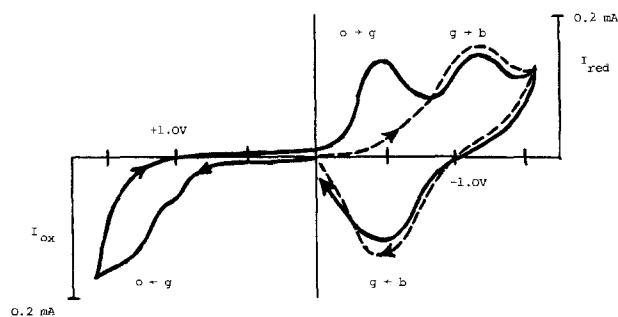


Fig. 3. Lutetium diphthalocyanine as sublimed film on conducting glass. Cyclic voltammetry in 5% aqueous KCl vs. aqueous Ag/AgCl reference, film thickness 2000\AA , slide area $\sim 2\text{ cm}^2$. Scan rate 10 mV/sec, 1st cycle. Letters refer to color changes, g = green, o = orange, b = blue. (a) — full oxidation reduction cycle: start 0V, initial sweep anodic. (b) - - - reduction cycle only: start 0V, initial sweep cathodic.

defined wave is observed together with current due to solvent breakdown and is not shown in the figure.

The above results are for a film thickness $\sim 2000\text{\AA}$. Variations in the film thickness affect the voltammetry, particularly of the green/orange transformation.

Electronic spectra.—Figure 2 shows the visible spectrum of a single film of ytterbium diphthalocyanine sublimed on to conducting glass in (a) the initial green, (b) the oxidized orange, and (c) the reduced blue forms. All spectra were recorded *in situ* in an electrochemical cell fitted with optical glass sides, and the potentials employed were 0V, +1.5V, -0.8V , respectively (*vs.* aqueous Ag/AgCl reference, 5% aqueous KCl electrolyte). The results from the lutetium complex are very similar and the sets of data from both complexes are given in Table III.

These spectral changes are of a similar form to those obtained from electrochemical transformations of a solution of lutetium diphthalocyanine in carefully purified dimethylformamide (4). Purification of the solvent is necessary because green solutions of lutetium and ytterbium diphthalocyanines in dimethylformamide gradually become blue on standing in the absence of an electrode potential. The mechanism of this change is not clear though it has been reported that green solutions of gadolinium diphthalocyanine became blue upon the addition of base (9), and that Russian workers have added hydrazine to solutions of lutetium diphthalocyanine in DMF to improve solubility, giving deep blue solutions (8, 15, 16).

We have established that the addition of triethylamine to green solutions of lutetium and ytterbium diphthalocyanines in dimethylsulfoxide, methanol, acetone, and freshly purified dimethylformamide (vacuum distilled from anhydrous CuSO_4), produces an immediate blue coloration. It has not been shown with certainty that this base-produced blue color is due to the same species as that produced by electrochemical reduction. There are similarities in the electronic spectra of both species. The spectrum of the electroreduced blue species is given in curve (c) of Fig. 2. A distinctive twin peak is observed, that at shorter wavelength being more intense than that at long wavelength. A similar shape is observed in basified solutions though in these instances there is some distortion in the shape of the long wavelength peak, and also a weak "shoulder" at $\sim 560\text{ nm}$ that is not present in the spectrum of the electrochemically reduced form. Comparative data for blue species in methanol, acetone, dimethylsulfoxide, and dimethylformamide solutions, compared to the electroreduced blue species as a thin film are given in Table IV. Blue solutions in the above solvents are air stable. Solutions in dimethylformamide have retained their color over several months, and evaporation yields dark crystals which are solvated (12). The electrochemically produced blue coloration in thin solid films is unstable in air, and returns to the green form over a period of a few minutes.

Color changes which parallel the electrochemical color changes can be induced by chemical oxidants

Table III. Electronic spectra of lutetium and ytterbium diphthalocyanines as sublimed films on conducting glass. Variation with electrode potential

| Potential ^a (V) | Color | Metal complex | Characteristic absorptions, λnm (absorbance ^b) |
|----------------------------|--------|---------------|---|
| 0 | Green | Lu | 668 nm (1.32) 463 (weak, broad) |
| 0 | Green | Yb | 668 nm (1.46) 465 (weak, broad) |
| +1.5 | Orange | Lu | 698 nm (0.56) 493 (broad, 0.43) |
| +1.5 | Orange | Yb | 700 nm (0.60) 496 (broad, 0.48) |
| -0.8 | Blue | Lu | 634 nm (1.30) 714 (0.60) |
| -0.8 | Blue | Yb | 637 nm (1.42) 713 (0.66) |

^a Potentials *vs.* aqueous Ag/AgCl reference, 5% aqueous KCl electrolyte.

^b Both films $\sim 2000\text{\AA}$ in thickness.

Table IV. Electronic spectra of blue forms of lutetium and ytterbium diphthalocyanines

| Medium | Metal complex | λ_1 | λ_2^b | Abs (λ_1) |
|---|---------------|-------------|---------------|---------------------|
| | | | | Abs (λ_2) |
| Solution in DMF ^a | Lu | 614 | 693 | 1.91 |
| | Yb | 616 | 688 | 1.95 |
| Solution in MeOH ^a | Lu | 617 | 696 | 1.89 |
| | Yb | 619 | 689 | 2.06 |
| Solution in Acetone ^a | Lu | 609 | 691 | 1.90 |
| | Yb | 611 | 687 | 1.94 |
| Solution in DMSO ^a | Lu | 617 | 692 | 1.91 |
| | Yb | 619 | 690 | 1.93 |
| Thin film in aqueous $\text{Na}_2\text{S}_2\text{O}_4$ (2%) / Na_2SO_3 (2%) | Lu | 635 | 705 | 1.70 |
| | Yb | 637 | 703 | 1.43 |
| Thin film at -0.8V electroreduced (5% KCl) | Lu | 634 | 714 | 1.88 |
| | Yb | 637 | 713 | 1.82 |

^a Solutions were prepared by dissolving the green solid complex in the required solvent and were converted to blue by the addition of a trace of Et_3N .

^b This peak is somewhat misshapen on the spectra of solutions prepared as above. Sharper definition is observed in the spectrum of a DMF solution that has been eluted from a chromatographic column packed with neutral alumina [see Ref. (17)].

and reductants. Figure 4 displays the visible spectra of a film of lutetium diphthalocyanine on a glass slide in (a) initially green form, (b) oxidized to orange after $\sim 1\text{ min}$ in 4% (w/v) aqueous acidified ceric sulfate solution, (c) reduced to blue after $\sim 1\text{ min}$ in a mixture of 2% sodium dithionite/2% sodium sulfite solution, (d) purple after 2 min in 4% aqueous sodium dithionite solution. The orange species is air stable but the blue and purple forms revert to green on removal from solution. The spectra were recorded in a cell with optical glass sides using a Grubb-Parsons experimental spectrometer based on a D2 monochromator unit. The data from the chemically reduced blue species are included in Table IV for comparison. The difficulty in arresting the reduction process at the blue stage reflects the difference between chemical reduction and electrochemical reduction, where a precise potential can be applied to achieve maximum effect in a system where species can exist in several oxidation states.

Electron spin resonance.—In the green form lutetium diphthalocyanine has a single ESR absorption [Fig. 5, curve (a) for a thin film on conducting glass]. Upon electro-oxidation at +1.8V in 5% aqueous sodium sulfate (*w.r.t.* aqueous Ag/AgCl reference) for several minutes, the absorption remains of similar amplitude but has become much sharper [Fig. 5, curve (b)]. The

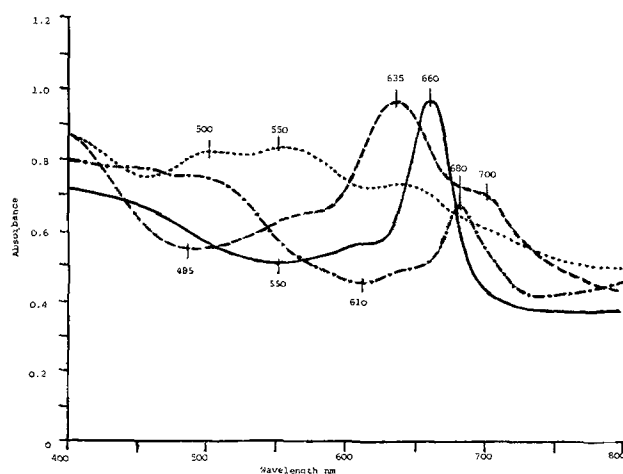


Fig. 4. Electronic spectrum of lutetium diphthalocyanine as sublimed film on to glass. Color changes induced by chemical oxidants/reductants. (a) — initial green form; (b) —●— orange after $\sim 1\text{ min}$ in 4% aqueous ceric sulfate solution; (c) - - - blue after $\sim 1\text{ min}$ in aqueous mixture of 2% sodium sulfite + 2% sodium dithionite; (d) ···· purple after $\sim 5\text{ min}$ in 4% aqueous sodium dithionite solution.

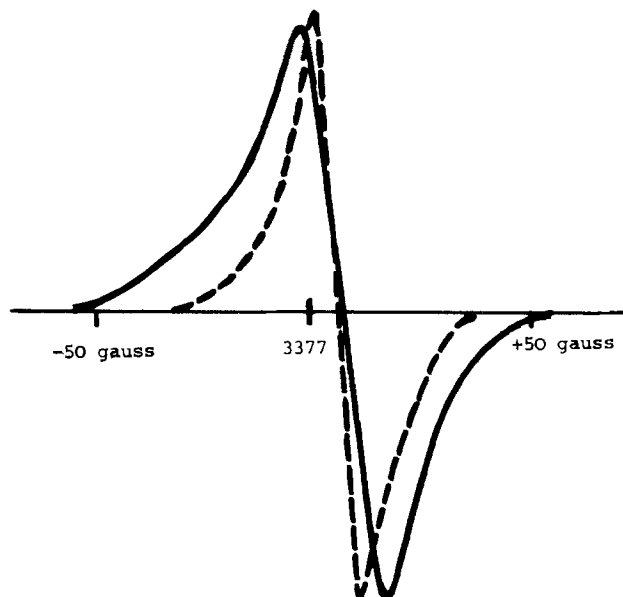


Fig. 5. Lutetium diphthalocyanine as sublimed film on conducting glass. Change of electron spin resonance spectrum with oxidation potential. (a) — green form ($\sim 0V$); (b) - - - orange form ($\sim +1.5V$). (Electrolyte 5% aqueous Na_2SO_4 , potentials vs. aqueous $Ag/AgCl$ reference. Instrumental conditions: room temperature, modulation amplitude 5G, power 2 mW).

color of the film is orange. The color change is, therefore, not associated with a loss of paramagnetism in the system. If electro-oxidation is continued for 1 hr, a 30% loss in intensity of the sharp signal is observed, but on returning to the green form at 0V, the broader absorption reappears at its full intensity. The slide was removed from the electrochemical cell, washed, and dried before placing in the cavity of the spectrometer at room temperature.

In 5% aqueous KCl electrolyte a more rapid narrowing of the signal is observed, concomitant with the rapid appearance of the orange coloration. Further electrolysis for $\sim \frac{1}{2}$ hr results in the total loss of the sharp signal, but, on returning to the green form at 0V the full intensity of the initial broad absorption is restored.

It seems that exhaustive electrolysis results in a total loss of signal. We have confirmed that this occurs in solutions of lutetium diphthalocyanine that are electro-oxidized in DMF/0.1M tetrabutylammonium tetrafluoroborate, as has been recorded (4), but the color change from green to orange is associated with a sharpening of the signal, not a loss of paramagnetism. This result is supported by the behavior of films of ytterbium diphthalocyanine. This complex is ESR inactive in the green form. It remains inactive after electro-oxidation to orange at $+1.8V$ even after ~ 1 hr of electrolysis, though the color change occurs in less than 1 min. No change of paramagnetism occurs in this system.

Some comparative, but less detailed measurements were made on holmium and europium diphthalocyanines. Solid samples showed ESR signals that, compared with lutetium, were only 0.01 times the value in the case of holmium and 0.1 times the value in the case of europium; the ytterbium signal was virtually zero. Thin films of Ho and Eu did not show sufficiently large signals to enable differences to be observed between the green and orange forms of the complex, the glass substrate giving a small residual signal which masked the small responses due to the rare earth compounds.

Discussion

The observation of ESR signals from both the initially green and the electro-oxidized orange forms of

lutetium diphthalocyanine is in accord with the evidence of Nicholson and Pizzarello (5, 6) who measured an approximately two-electron change from charge-transport data during electro-oxidation, employing aqueous sodium sulfate and potassium chloride electrolytes. These results do not necessarily conflict with those of Corker *et al.* (4) who reported that in dimethylformamide solution with tetrabutylammonium tetrafluoroborate support electrolyte, the electro-oxidation to a "yellow-red" species was concomitant with a loss of ESR signal and the removal of one electron, since the experimental conditions were different in this latter instance.

If the electro-oxidation is a multi-stage reaction in which the color change and modification of the ESR signal are distinct from the eventual loss of the ESR signal, then the relative rates of these processes may differ in solution compared to a solid film, particularly if ionic migration (5, 6) as well as electron transfer is important during the transformation. Furthermore, the behavior of lutetium diphthalocyanine in dimethylformamide solution appears to be complicated, and the nature of all species that may be present is not certain. Analytical data published by Kirin *et al.* (12) suggests that a blue product obtained from dimethylformamide solution may have the composition $R_2Pc_3 \cdot 3DMF$, where R is the rare-earth atom.

The difference in behavior of the ESR signal in sodium sulfate solution as compared to potassium chloride solution is paralleled by the observations of Nicholson and Pizzarello (18) who also noticed a difference between these electrolytes. They showed that the propagation of the anodic reaction boundary in a thin film of lutetium diphthalocyanine depended on the nature of the ambient gas, and that the boundary ceased to move in sodium sulfate electrolyte if oxygen was excluded, but this was not true in potassium chloride electrolyte. It was concluded that oxygen was bound in the red form of the diphthalocyanine prepared in sodium sulfate electrolyte. Raynor *et al.* (19) have studied the origin of ESR signals in diamagnetic phthalocyanines of Zn, Ni, Pd, and Pt and have suggested that oxygen is the cause of a substantial part of the signal, but is not present as a simple radical with the unpaired electron localized on the oxygen. We conclude that the difference in ESR behavior of the lutetium complex in aqueous sodium sulfate and potassium chloride electrolytes may represent the differential uptake of oxygen following an initial two-electron change to the orange species. However, the existence of the original ESR signals in the green lutetium complex, and the much lower ESR responses from the holmium, europium, and particularly ytterbium complex are not easily explained by this simple model, and further work is required to elucidate the structure of these species.

Acknowledgments

This paper is published by permission of the Technical Director, GEC-Marconi Electronics Limited.

We wish to thank Professor G. R. Luckhurst and the Southampton University Chemistry Department for performing the electron spin resonance measurements; the Chelmsford College Science Department for the use of their u.v./visible spectrometer, and Mr. I. Forster for producing a program for the PET computer to perform voltammetry.

Manuscript submitted Feb. 2, 1981; revised manuscript received May 12, 1981.

Any discussion of this paper will appear in a Discussion Section to be published in the June 1982 JOURNAL. All discussions for the June 1982 Discussion Section should be submitted by Feb. 1, 1982.

REFERENCES

1. P. N. Moskalev and I. S. Kirin, *Opt. Spectrosc.*, **29**, 220 (1970).

2. P. N. Moskalev and I. S. Kirin, *Russ. J. Phys. Chem.*, **46**, 1019 (1972).
3. M. M. Nicholson and R. V. Galiardi, Final Report Contract N 62269-76-C-0574-AD-A039596; *Chem. Abstr.*, **87**, 144073V (1977).
4. G. A. Corker, B. Grant, and N. J. Clecak, *This Journal*, **126**, 1339 (1979).
5. M. M. Nicholson and F. A. Pizzarello, *ibid.*, **126**, 1490 (1979).
6. F. A. Pizzarello and M. M. Nicholson, *J. Electron. Mater.*, **9**, 231 (1980).
7. M. M. Nicholson and F. A. Pizzarello, *This Journal*, **127**, 821 (1980).
8. P. N. Moskalev, G. N. Shapkin, and A. N. Darovskikh, *Russ. J. Inorg. Chem.*, **24**, 188 (1979).
9. A. G. MacKay, J. F. Boas, and G. J. Troup, *Aust. J. Chem.*, **27**, 955 (1974).
10. K. Kasuga, M. Tsutsui, R. C. Petterson, K. Tatsumi, N. VanOpdenbosch, G. Pepe, and E. F. Mayer, Jr., *J. Am. Chem. Soc.*, **102**, 4835 (1980).
11. I. S. Kirin, P. N. Moskalev, and Yu. A. Makashev, *Russ. J. Inorg. Chem.*, **12**, 369 (1967).
12. I. S. Kirin, P. N. Moskalev, and N. V. Ivannikova, *ibid.*, **12**, 497 (1967).
13. P. N. Moskalev and I. S. Kirin, *ibid.*, **15**, 7 (1970).
14. S. Misumi and K. Kasuga, *Nippon Kagaku Zasshi*, **92**, 335 (1971).
15. P. N. Moskalev, G. N. Shapkin, and Yu. S. Misko, *Radiokhimiya*, **20**, 343 (1978).
16. P. N. Moskalev and G. N. Shapkin, *Elektrokhimiya*, **14**, 574 (1978).
17. I. S. Kirin, P. N. Moskalev, and Yu. A. Makashev, *Russ. J. Inorg. Chem.*, **10**, 1065 (1965).
18. M. M. Nicholson and F. A. Pizzarello, *This Journal*, **127**, 2617 (1980).
19. J. B. Raynor, M. Robson and A. S. M. Torrens-Burton, *J. Chem. Soc. Dalton Trans.*, **23**, 2360 (1977).
20. L. G. S. Brooker, G. H. Keyes, and D. W. Haseltine, *J. Am. Chem. Soc.*, **73**, 5350 (1951).

Technical Note



Excitation into Charge Transfer Band of $Y_2O_3:Eu$

Lyuji Ozawa*

Matsushita Electric Industrial Company, Limited, Central Research Laboratories, Moriguchi, Osaka, Japan

This note describes the mode of excitation into the charge transfer band of $Y_2O_3:Eu$ phosphor. In general, the radiative transition impurities (*i.e.*, activator ions) in crystals can be optically excited in three ways; by (i) direct excitation into absorption of the ions (direct), (ii) excitation into associated activator-host absorption (*i.e.*, charge transfer band, CTB), and (iii) indirect excitation via absorption of host lattice (host), *i.e.*, radiative recombination of mobile electron-hole pairs (radiation-induced carriers) at activator ions. This can be seen comprehensively in excitation spectrum giving rise to luminescence. Figure 1 shows, for instance, the excitation spectrum of the Eu^{+3} luminescence line at 627 nm ($^5D_0 \rightarrow ^7F_2$ transition) of $Y_2O_3:Eu$; the spectrum consists of the small and narrow direct excitation lines ($4f^6$ transition), and a broad and strong CTB overlapped partially with a host band (shadowed). It has been believed that the CTB excitation belongs to the host excitation (1) because the CTB partially overlaps with the host absorption band and the hole photoconductivity has been suggested in $Y_2O_3:Eu$ under the CTB radiation (2). It has then been said that the CTB is an essential necessity to obtain the efficient cathodoluminescence phosphors (3). A question is raised as to whether the CTB belongs to the host excitation.

An experimental difficulty in determining the excitation mode of the CTB is that by either way of the photoexcitations, the activator ions emit the same characteristic activator luminescence even though the excitation mechanisms involved are quite different. Thus, the ambiguity always remains in the discussion of the CTB excitation if the study has been made with the measurements of the luminescence or excita-

tion spectra alone. It has recently been shown that the concentration dependence (CD) curve of activator luminescence provides us with a powerful tool to clarify the excitation mode of activator ions (4). There are two excitation modes to be considered for the luminescence study in the first-order approximation: (i) direct excitation and (ii) indirect excitation through mobile carriers. The mode of the excitations can be clearly distinguished if the measurements of the CD curves are made on powdered phosphor

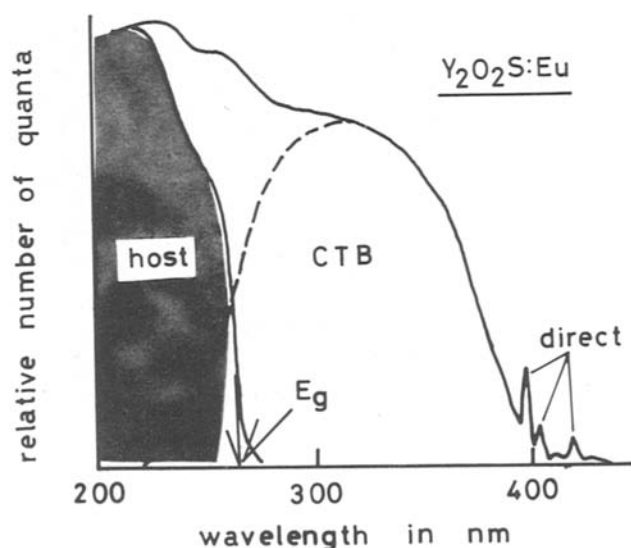


Fig. 1. Excitation spectrum of $Y_2O_3:Eu$ (0.01) giving rise to luminescence line at 627 nm ($^5D_0 \rightarrow ^7F_2$ transition). The spectrum consists of host absorption band (host), charge transfer band (CTB), and direct excitation lines of Eu^{+3} (direct).

* Electrochemical Society Active Member.
Key words: luminescence, phosphor.

screens. For direct excitation of activator ions, the time-averaged luminescence intensities from phosphor screen, obtained under constant intensity, has a linear dependence on activator concentration "C" in the concentration region where the concentration quenching mechanisms are neglected, and the normalized CD curve exhibits no crystal size effect (5). When the activator luminescence is due to the radiative recombination of the mobile carriers (created by host lattice absorption) at activator ions, the CD curve has two slopes, depending on C, in which C^* at the discontinuity (i.e., inflection of the curve) shows the crystal size effect due to the mobile carriers; C^* decreases as the crystal size increases (4-6). We use this distinguishable different appearance in the CD curves to clarify the mode of the CTB excitation of $Y_2O_3S:Eu$.

Figure 2 shows the CD curves of the Eu^{+3} luminescence line at 627 nm of $Y_2O_3S:Eu$ under irradiation of electron beam (CL), host-photoexcitation using the 200 nm radiation (PL-host), CTB excitation by the 320 nm radiation (PL-CTB), and direct photoexcitation using the 417 nm radiation (PL-direct). We used the 200 nm radiation for the PL-host to keep away from the entanglement of the CTB in the excitation. It can be seen that the CD curve of the PL-host is almost identical with that of CL, because the activator ions in both cases are predominantly excited through the mobile carriers created in the crystal (6). Both curves have two slopes and the value of C^* shows the crystal size effect. The normalized curve for the PL-direct fits in with the theoretical curve of $C(1 - C)^{12}$ (unity slope below $C = 1 \times 10^{-2}$ and optimum $C = 8 \times 10^{-2}$) (5) and the curve exhibits no crystal size effect.

Referring the CD curves of the PL-host and PL-direct, it has been revealed that the mode of the CTB excitation actually belongs to the direct excitation. The CD curve for the CTB has unity slope, instead of two slopes, in the region below $C = 3 \times 10^{-3}$ and exhibits no crystal size effect. There is no evidence to show that the luminescence process at the Eu^{+3} is determined by the mobile carriers. The curve obtained clearly indicates that the CTB excitation falls under the category of direct excitation by incident radiation rather than the category through host-lattice excitation

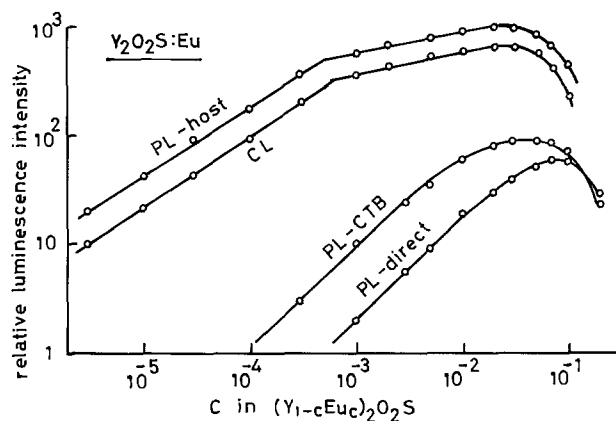


Fig. 2. Concentration dependence curves of Eu^{+3} luminescence of $Y_2O_3S:Eu$ under irradiation of various excitation modes; electron beam (CL), host photoexcitation using 200 nm radiation (PL-host), charge transfer photoexcitation with 320 nm radiation (PL-CTB), and direct photoexcitation using 417 nm radiation (PL-direct).

Irradiation of the CTB radiation of $Y_2O_3S:Eu$ probably creates an Eu^{+2} and a hole as a consequence of the electron (charge) transfer from anion (O^{-2} or S^{-2}) to Eu^{+3} . Since hole photoconductivity has been suggested in $Y_2O_3S:Eu$ under irradiation of the CTB radiation (2), the Eu^{+2} may be stable at room temperature and does not release the electron; the luminescence may occur as the Eu^{+2} captures the free hole (4). Because Eu ions in the crystal never move out from their occupied lattice sites during the luminescence process, the absorption (and subsequent luminescence) is definitely limited in the volume where the CTB radiation has been penetrated. In other words, the place at which the luminescence occurs is not determined by the free holes which move out from the location created. The penetration of the CTB radiation into the powdered phosphor screen is determined by $(\alpha + \beta)^{-1}$ where α and β are absorption and scattering coefficients, respectively. The value of α changes with C; i.e., $\alpha = kC$ where k is expressed in cm^{-1} and depends only on the oscillator strength of the absorption. When the activator concentration is below 3×10^{-3} , $\alpha \ll \beta$, and the penetration volume is determined by β^{-1} and the cross section of the radiation beam; both are constant, resulting in the linear dependence of luminescence intensities on C (5). The penetration depth is decreased with increasing activator concentrations beyond 3×10^{-3} ($\alpha \gtrsim \beta$); subsequently, the apparent optimum activator concentration moves to $C = 5 \times 10^{-2}$ (5).

The results of the CD curves suggest that the CTB and host absorption bands possibly occur at different levels, and the partial overlap in the excitation spectrum (Fig. 1) is not real; they are apparently overlapped. If it is so, the band model may be inadequate to explain the luminescence process of the Eu^{+3} in $Y_2O_3S:Eu$ which has been considered (1, 3).

In conclusion, it has been shown that the excitation into the charge transfer band falls under the category of the direct excitation by the incident radiation, which the excitation is restricted in the penetration volume of the incident radiation. Therefore, it can be said that the presence of the charge transfer band is not essential to obtain the efficient cathodoluminescence phosphors. The efficient activator cathodoluminescence is predominantly due to the radiative recombination of the mobile electron-hole pairs at the activator ions, and the number of the electron-hole pairs created in the penetration volume would be about 100 times the number of the direct excitation of the activator ions by the incident electrons.

Manuscript received May 26, 1981.

Any discussion of this paper will appear in a Discussion Section to be published in the June 1982 JOURNAL. All discussions for the June 1982 Discussion Section should be submitted by Feb. 1, 1982.

Publication costs of this article were assisted by Matsushita Electric Industrial Company, Limited.

REFERENCES

1. C. W. Struck and W. H. Fonger, *Phys. Rev. B*, **4**, 22 (1971).
2. W. I. Dobrov and R. A. Buchanan, *Appl. Phys. Lett.*, **21**, 201 (1972).
3. D. J. Robbins, B. Cockyane, J. L. Glasper, and B. Lent, *This Journal*, **126**, 1222 (1979); H. Yamamoto and T. Kano, *ibid.*, **126**, 305 (1979).
4. L. Ozawa, *ibid.*, **128**, 140 (1981).
5. L. Ozawa, *ibid.*, **126**, 106 (1979).
6. L. Ozawa and H. N. Hersh, *Phys. Rev. Lett.*, **36**, 683 (1976).

Erratum

Concentration Profiles in Electrowinning Circuits

I. Current Efficiency

F. M. Kimmerle, R. L. LeRoy, and O. Vittori

(This Journal, Vol. 128, No. 9, pp. 1864-1869)

Due to the Canadian postal disruptions, proofs of this article were not received in time for correction. Figure 2 was mislabelled, and should be replaced by the following

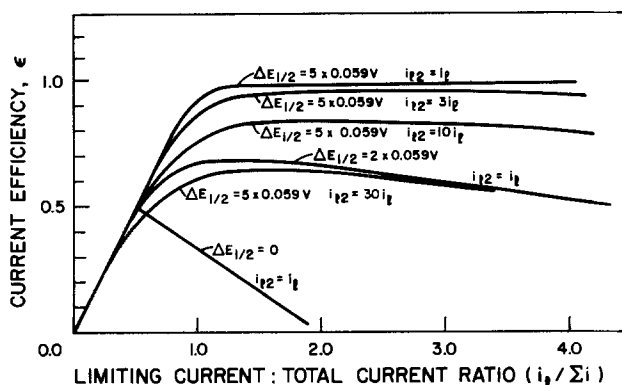


Fig. 2. Current efficiency variation for kinetic parameters characteristic of metal deposition in competition with hydrogen evolution, $(\alpha n)_1 = 2.0$ and $(\alpha n)_2 = 0.5$.

In the discussion of Fig. 1 and 2, case 1 should have stated that efficiency approaches the asymptotic value $\epsilon_\infty = 1$ when the current density is *much less than* the limiting current density, in situations where the transfer coefficient for metal deposition is less than that for the competing reaction.

Before Eq. [3], the requirement for a function describing current density should have read that it must vary in a monotonic fashion from case 1 to case 2, and that

$$\lim_{C \rightarrow \infty} \epsilon = \epsilon_\infty \quad \text{and} \quad \lim_{C \rightarrow 0} \epsilon = 0$$

In the discussion of Fig. 5, the statement concerning the dependence of current efficiency on $i_1 / \Sigma i$ should have noted that it can be approximated by two straight-line portions at concentrations above 0.01M.



Determination of the Measurable Low P_{O_2} Limits of Oxygen Ion-Conducting Solid Electrolytes

T. A. Ramanarayanan*

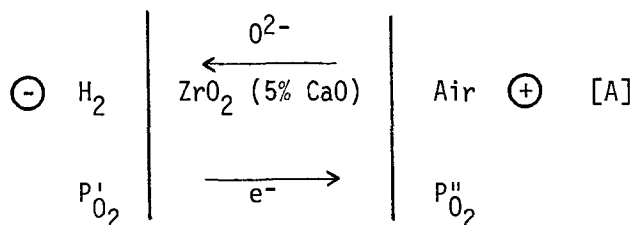
Exxon Research and Engineering Company, Corporate Research-Science Laboratories, Linden, New Jersey 07036

Oxygen ion-conducting solid electrolytes based on ZrO_2 and ThO_2 are widely used for the measurement of oxygen chemical potentials in high temperature gaseous environments, melts and solid phases (1). These electrolytes have also applications in determining the kinetics of diffusion-controlled processes (2) and the rates of surface reactions (3).

In most applications of oxygen-conducting solid electrolytes, the ionic transference number of the electrolyte, t_{ion} , must be unity. At extremely low P_{O_2} values, the ionic transference number of the electrolyte is decreased by the introduction of excess electronic conduction. Thus, especially for low oxygen partial pressure measurements, there is a need to establish the low P_{O_2} limits (above which $t_{ion} > 0.99$) as a function of temperature. Since these low P_{O_2} limits are extremely sensitive to the presence of minute impurity levels in the electrolyte (4), the measurable low P_{O_2} limits can vary between two electrolytes of nearly identical chemical composition.

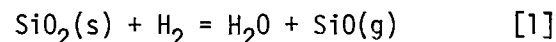
In the present communication, a simple experiment for the determination of the low P_{O_2} limits of an oxide-ion conducting electrolyte is discussed. The technique has been used for establishing the low P_{O_2} limits of ZrO_2 (~5% CaO) solid electrolyte tube purchased from Degussa.

The electrochemical cell used in the present experiments may be represented as:



in which the left hand electrode is extremely pure hydrogen. It would be nearly impossible

experimentally to obtain a $P_{O_2} = 0$ in the hydrogen electrode. For one thing, even the best purification ensures only a finite extremely low P_{O_2} level. Secondly, a reaction between the H_2 gas and the quartz tube in which the electrochemical cell was placed is possible in principle:



At a temperature of 1100°K, which is in the middle of the temperature range used in the current study, the equilibrium constant, K_1 , for reaction [1] equals 2.05×10^{-16} . Assuming that both H_2O and SiO are generated by reaction [1] only, one can assume that $P_{H_2O} \approx P_{SiO}$. With this assumption, one calculates at 1100°K a P_{H_2O} value of 1.43×10^{-8} atm. This amount of water vapor in H_2 would correspond to a P_{O_2} of 3.6×10^{-34} atm, which is extremely low. It is not suggested here that the reaction [1] proceeds to equilibrium, but only that even if it did, the P_{O_2} in the hydrogen stream would be very low.

According to Schmalzried (5,6), the Emf of cell A under these conditions is given by,

$$E = \frac{nRT}{4F} \ln \left[\frac{P_{\theta}^{1/n+P'} \cdot 1/n}{P_{\theta}^{1/n+P''} \cdot 1/n} + \frac{P_{\theta}^{1/n+P''} \cdot 1/n}{P_{\theta}^{1/n+P'} \cdot 1/n} \right] \quad [2]$$

where $n = 4$ for a stabilized zirconia electrolyte, P_{θ} and P_{θ} refer to the P_{O_2} values at which the ionic conductivity of the electrolyte equals the positive hole conductivity and excess electronic conductivity respectively. As discussed by Schmalzried (5,6), for $P_{\theta} \gg P''_{O_2} \gg P_{\theta} \gg P'_{O_2}$, equation [2] reduces to

$$P_{\theta} = P''_{O_2} \exp(-4 EF/RT) \quad [3]$$

Equation [3] applies to cell [A] and the P_{θ} values can be determined from the measured open circuit Emf values as a function of

*Electrochemical Society Active Member.

temperature. From the P_{O_2} values, the limiting low P_{O_2} values which can be measured using a ZrO_2 ($\sim 5\%$ CaO) Degussa electrolyte can be calculated as follows.

The excess electronic transference number, t_e , of the electrolyte at low oxygen partial pressures is given by,

$$t_e = \frac{\sigma_e}{\sigma_e + \sigma_{ion}} \quad [4]$$

where σ_e and σ_{ion} are the excess electronic conductivity and ionic conductivity, respectively. For stabilized zirconia electrolytes, at a given temperature, σ_{ion} is a constant and $\sigma_e = \sigma_e^0 P_{O_2}^{-1/4}$ where σ_e^0 is a constant (1). Thus, Eq. [4] can be rewritten in the form,

$$\frac{1}{t_e} = 1 + k P_{O_2}^{1/4} \quad [5]$$

where $k = \sigma_{ion}/\sigma_e^0$. By definition, $P_{O_2} = P_{O_2}$, when $t_e = 0.5$. Upon substitution into Equ. [5],

$$k = (P_{O_2})^{-1/4} \quad [6]$$

hence

$$\frac{1}{t_e} = 1 + \left(\frac{P_{O_2}}{P_{O_2}^L} \right)^{1/4} \quad [7]$$

If the lowest P_{O_2} value measurable with the ZrO_2 -based electrolyte is denoted by $P_{O_2}^L$, then,

$$t_e = 0.01 \text{ for } P_{O_2} = P_{O_2}^L \quad [8]$$

Equation (8) corresponds to the generally agreed ionic transference number of >0.99 for an acceptable solid electrolyte. Upon substitution of Eq. [8] in Eq. [7],

$$P_{O_2}^L = 99^4 P_{O_2} \quad [9]$$

The experimental cell arrangement used in the present study is shown in Fig. (1). A degussa ZrO_2 ($\sim 5\%$ CaO) solid electrolyte tube ($3/8''$ O.D. x $1/4''$ I.D.) was platinized over a 1" length on the inside and outside using platinum paste (Engelhard #6082). The paste was thinned with xylene and brushed on to the cleaned solid electrolyte surface. The coated portion was heated gradually to $800^\circ C$ in a furnace, held at this temperature for one

hour and furnace-cooled to room temperature. A series of four coatings was applied in this manner. Platinum lead wires were used to contact the inside and outside Pt paste. A slow stream of dry air was circulated through the inside of the electrolyte tube using a small alumina tube. The electrolyte tube was surrounded by an outer quartz tube. The outer surface of the electrolyte tube was exposed to a stream of high purity hydrogen. High purity hydrogen gas from a gas cylinder was further purified by passing through an Engelhard platinum catalyst (for conversion of any O_2 to H_2O); the water vapor was subsequently absorbed in a series of magnesium perchlorate towers.

The electrochemical cell was heated in a non-inductively wound tube furnace. A grounded Inconel tube was used around the quartz tube to eliminate stray Emfs. The cell was initially heated to a temperature of $750^\circ C$ ($\pm 1^\circ C$). The open circuit Emf developed across the cell was measured using a Hewlett Packard electronic voltmeter. The cell Emfs were observed to increase slightly with the flowrate of H_2 ; the flowrate dependence vanished beyond a certain flowrate. The actual flowrate where this occurred was not measured since no flowmeter was placed in the system. The flowrate independent Emf was taken to be the correct Emf value. An Emf reading was considered steady if the random variation over a two hour period was within ± 1 mV. Emf readings were taken at $50^\circ C$ intervals up to $950^\circ C$.

The experimentally measured Emf values are shown as a function of temperature in Fig. 2. Shown in Fig. 3 are the P_{O_2} values calculated using Eq. [3]. The temperature dependence of P_{O_2} follows the expression:

$$\log P_{O_2} = 4.77 - \frac{35,130}{T} \quad [10]$$

Fig. 3 also contains the P_{O_2} values reported by Patterson (7) and by Schmalzried (6) for the ZrO_2 (7 1/2% CaO) electrolyte. In Fig. 4, the limiting low P_{O_2} values, $P_{O_2}^L$, obtained using Eq. [9] have been plotted as a function of temperature. The temperature dependence of $P_{O_2}^L$ can be expressed by the relation:

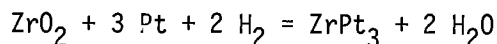
$$\log P_{O_2}^L = 12.75 - \frac{35,130}{T} \quad [11]$$

Also shown in Fig. 4 are the limiting P_{O_2} values of the ZrO_2 (7 1/2% CaO) electrolyte according to Patterson (7). In Fig. 4 are

also shown the coexistence P_{O_2} values of two commonly used metal-metal oxide reference electrodes, the Fe-FeO electrode and the Cr-Cr₂O₃ electrode. It is readily seen that the Degussa ZrO₂ (5% CaO) electrolyte can accurately measure the P_{O_2} of the Fe-FeO electrode, but not the Cr-Cr₂O₃ electrode.

There are a few points which must be mentioned in connection with measurements involving cells of the type A. First of all, since the electrolyte exhibits some electronic conduction under conditions involved in measurements with cell A, even under open circuit conditions, there is electronic transport through the electrolyte from the low P_{O_2} side to the high P_{O_2} side. Such transport is accompanied by oxygen ion transport in the opposite direction. It is conceivable that the oxygen arriving at the left hand electrode of cell A by transport through the electrolyte raises the P_{O_2} at the left hand electrode/electrolyte interface locally. This effect should be more serious at low flow rates; at the higher flow rates, the oxygen is rapidly carried away in the hydrogen stream. This would in principle explain why the cell Emf would increase with flow rate in a certain range.

Another effect to be concerned about is the possibility of a chemical reaction between ZrO₂ and Pt at the left hand electrode where conditions are reducing. Meschter and Worrell (8) have determined the Gibbs' energy of formation of the intermetallic compound ZrPt₃ using electrochemical measurements involving a ThO₂-Y₂O₃ electrolyte. They have estimated that the reaction,



is possible at 800°C at P_{O_2} values below $\sim 10^{-25}$ atm. No ZrPt₃ could be detected by X-ray diffraction on the platinized surface of the electrolyte tube after completion of experiments with cell A.

Shores and Rapp (9) have reported on the possibility of proton conduction in ThO₂ base electrolytes in the presence of H₂-H₂O environments. However, no such conduction has been reported for ZrO₂ based electrolytes. Wagner (10) found the solubility of water vapor in ZrO₂ containing 8 or 17% Y₂O₃ in the temperature range, 900°C-1000°C to be extremely small, of the order of 13-30 ppm. Thus, it is assumed in the present study that there is no significant proton conduction in the ZrO₂ (5% CaO) electrolyte.

ACKNOWLEDGEMENTS

The author expresses his appreciation to Professor R. Rapp for helpful suggestions.

REFERENCES

- (1) R. A. Rapp and D. A. Shores, "Solid Electrolyte Galvanic Cells," Chapter in "Physicochemical Measurements in Metals Research," Part 2, ed. by R. A. Rapp, Interscience Publishers, 1970, p. 123.
- (2) T. A. Ramanarayanan and R. A. Rapp, *Met. Trans.*, **3**, 1972, 3239.
- (3) V. B. Tare and H. Schmalzried, *Trans. Met. Soc. AIME*, **236**, 1966, 444.
- (4) T. A. Ramanarayanan and W. L. Worrell, *Canad. Met. Quart.*, **13**, 1974, 325.
- (5) H. Schmalzried, *Z. Physik. Chem. (N.F.)*, **38**, 1963, 87.
- (6) H. Schmalzried, *Z. Elektrochem.*, **66**, 1962, 572.
- (7) J. W. Patterson, *J. Electrochem. Soc.*, **118**, 1971, 1033.
- (8) P. J. Meschter and W. L. Worrell, *Met. Trans.*, **7A**, 1976, 299.
- (9) D. A. Shores and R. A. Rapp, *J. Electrochem. Soc.*, **119**, 1972, 300.
- (10) C. Wagner, *Ber. Bunsenges. Phys. Chem.*, **72**, 1968, 778.

Manuscript submitted Nov. 5, 1980;
revised manuscript received March 24, 1981.

Publication costs of this article were assisted by Exxon Research and Engineering Company.

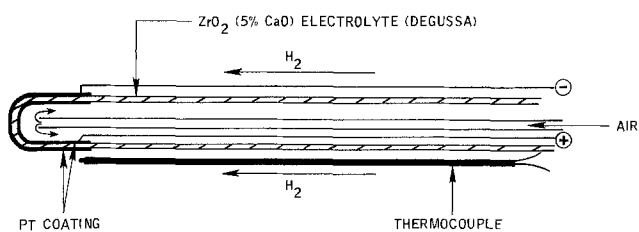


Fig. 1. Experimental cell arrangement for the determination of low P_{O_2} limits of oxygen ion conducting solid electrolytes.

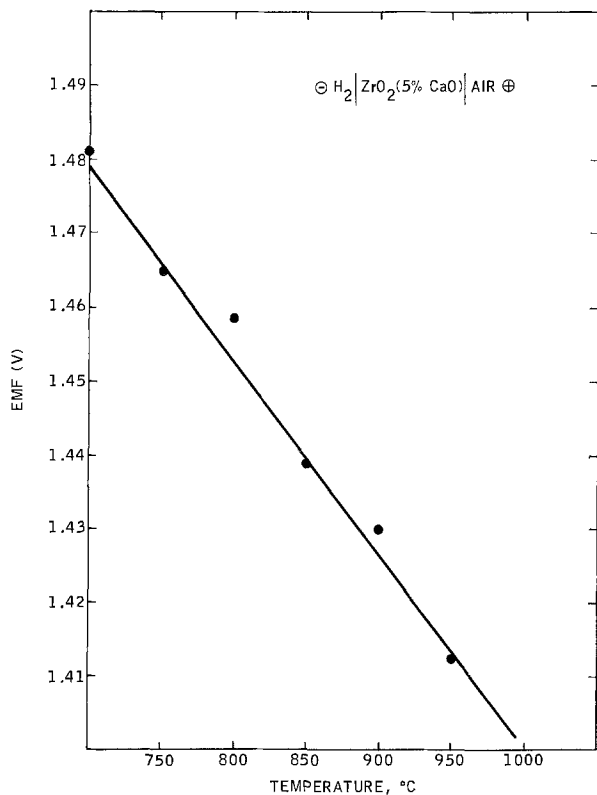


Fig. 2. The open circuit Emf of cell A as a function of temperature.

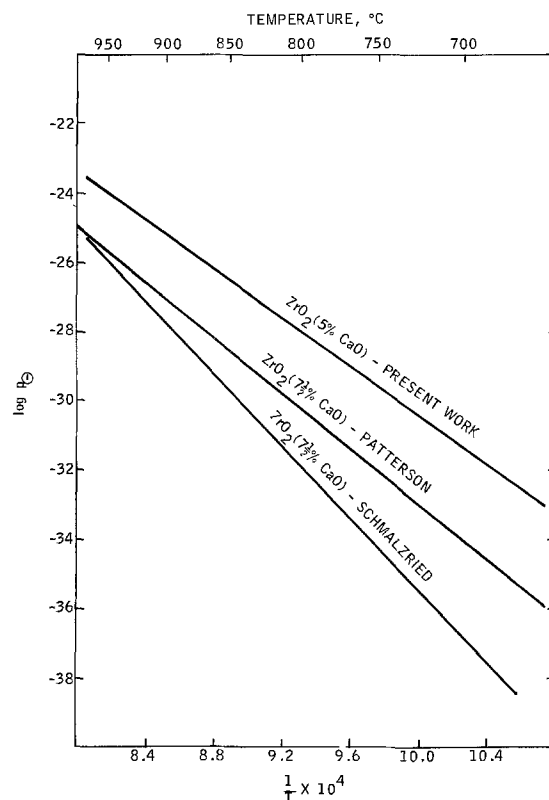


Fig. 3. P_{O_2} values as a function of temperature.

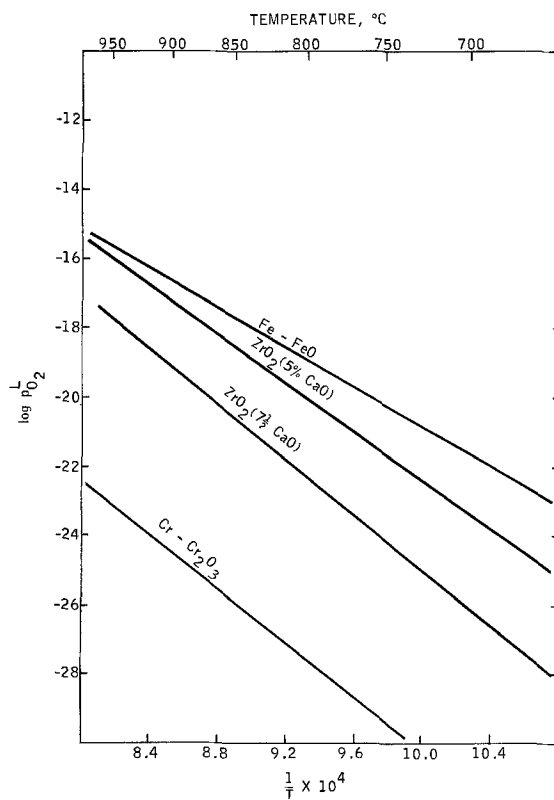


Fig. 4. Limiting P_{O_2} values as a function of temperature.

Direct Observation of Surface States at the TiO₂ Electrolyte Interface

Withana Siripala and Micha Tomkiewicz*

Department of Physics, Brooklyn College of CUNY, Brooklyn, New York 11210

Relaxation Spectrum Analysis was suggested⁽¹⁾ as a general technique for measurements of charge accumulation modes and their corresponding relaxation times at the space charge layer of a semiconductor with strong emphasis on semiconductor liquid junction interfaces. Among all the reported results⁽²⁻⁴⁾, none was, as yet, confirmed by an independent technique.

We wish to report here, evaluation of parameters of surface states that were observed on the surface of single-crystal TiO₂ in contact with an aqueous electrolyte, using the Relaxation Spectrum Analysis technique and subband gap spectral response.

Fig. 1 shows the impedance spectrum of single crystal TiO₂ in contact with phosphate buffer. For detailed explanation of the experimental technique, the reader is referred to reference (1).

The equivalent circuit was found to consist of two parallel passive capacitive elements with distinctive relaxation times. The dependence of the capacitive elements on the electrode potential is shown in fig. 2. The space charge capacitance C_{sc}, obeys the Mott-Schottky

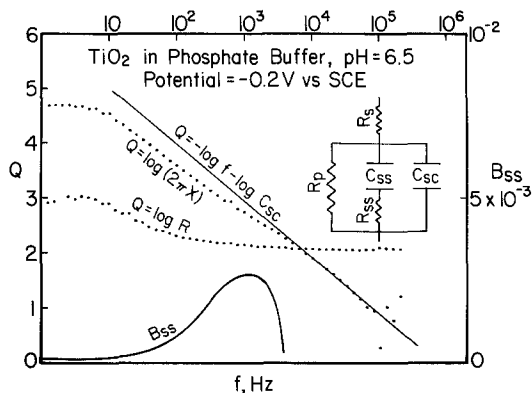


Fig. 1. Impedance response curves for n-type TiO₂ in 0.33 M phosphate buffer. On the right-hand corner is the equivalent circuit constructed from the curves in the manner explained on ref. (1). Area = 0.07 cm².

* Electrochemical Society Active Member

relation over an extended range of potentials, from which the flatband potential and the doping level of the crystal were evaluated. The dependence of C_{SS} on the electrode potential, also shown in fig. 2., is more complex. It is dominated by a single gaussian distribution, centered around 0 V vs SCE. Similar behavior was found with surface states that were introduced on purpose by chemical modification of TiO₂⁽⁵⁻⁶⁾ and by unmodified TiO₂ under certain surface preparation conditions². The difference between the states observed here and those that were previously reported is that the relaxation times of the surface states in the previously reported examples were all fast and limited by the series resistance of the electrolyte. This resulted in our inability to distinguish the surface state capacitance from the space charge layer capacitance. The surface state capacitance in those reports was evaluated from the deviations of the observed capacitance from the expected Mott-Schottky behavior. In the present case the states are much slower and their relaxation time clearly distinguishable from that of the space charge layer. The possible origin of the gaussian distribution of the surface states was previously reported⁽⁵⁻⁶⁾. From the maximum amplitude of the gaussian distribution coverage of $1.8 \times 10^{13}/\text{cm}^3$ was

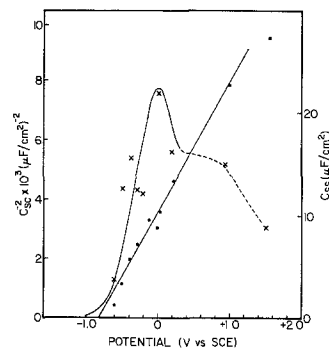


Fig. 2. Mott-Schottky plot of C_{sc} (left scale) and the variation of C_{SS} with potential (right scale). o - C_{sc}, X - C_{SS}. The solid lines are theoretically based on linear behavior of the Mott-Schottky plot and gaussian lineshape for C_{SS}.

estimated. From the potential of the maximum of the gaussian distribution and from the intercept of the Mott-Schottky plot, we can infer that the surface states are located around 0.8 eV from the bottom of the conduction band, or approximately 2.2 eV above the top of the valence band.

The influence of the surface states on the band gap light induced current voltage behavior will be discussed in the full manuscript which will follow this letter. Fig. 3 shows the spectral response of subband gap illumination with a clearly distinctive peak at 550 nm which is equivalent to photon energy of 2.2 eV. This can only be due to light induced electron ejection from the top of the valence band to the surface states. From fig. 1. it is observed that the states are relatively fast states with relaxation times in the millisecond range and can efficiently communicate with the bulk of the semiconductor.

Full analysis of these results, their implication on the photoelectrochemical behavior of TiO_2 and the relation between the surface states reported here and those that were reported in the literature will be discussed in subsequent publications.

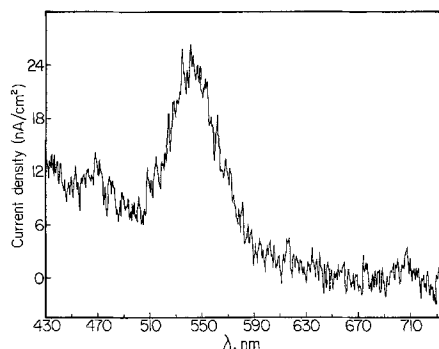


Fig. 3. Subband gap spectral response of the same crystal as in fig.1 and 2.

REFERENCES

- (1) M.Tomkiewicz: J. Electroch. Soc. 126, 2220 (1979).
- (2) M.Tomkiewicz: J. Electroch. Soc. 126, 1505 (1979).
- (3) M.Tomkiewicz, in "Semiconductor Liquid Junction Solar Cells", A.Heller, ed. p. 92, The Electrochemical Society Softbound Proceedings Series, Princeton, N.J. (1977).
- (4) M.Tomkiewicz, J.K.Lyden, R.P.Silberstein and F.H.Pollak: Proc. of the ACS Symposium on "Photoeffects at Semiconductor Electrolyte Interfaces", A.J.Nozik, ed. 146, 267 (1981)
- (5) M.Tomkiewicz: J. Electroch. Soc. 127, 1518 (1980).
- (6) M.Tomkiewicz: Surf. Sci. 101, 286 (1980).

ACKNOWLEDGMENT:

This work was supported by NASA Grant# NAG1-44.

Manuscript submitted May 1, 1981; revised manuscript received July 10, 1981.

Publication costs of this article were assisted by Brooklyn College of CUNY.



Rechargeable Lithium/Vanadium Oxide Cells Utilizing 2Me-THF/LiAsF₆

K. M. Abraham,* J. L. Goldman,* and M. D. Dempsey

EIC Laboratories, Incorporated, Newton, Massachusetts 02158

ABSTRACT

Vanadium oxides of various compositions were synthesized and evaluated as rechargeable cathodes in cells of the type Li/2Me-THF/LiAsF₆/V-oxide, C. The most useful compositions were found to be VO_{2.17}, VO_{2.19}, and the Fe or the Cr substituted oxide of apparent composition, M_{0.13}V_{0.87}O_{2.17}. In high capacity cells, VO_{2.17} exhibited a capacity of ~0.55 electrons/vanadium (e⁻/V) at current densities of 0.5, 1, and 2 mA/cm² and 0.45 e⁻/V at 4 mA/cm². The excellent rechargeability of this oxide in practical cells within cycling limits of 3.0 and 1.9V was demonstrated by extended cycling of a cell with an average cathode utilization of ~0.52 e⁻/V in over 200 cycles. The first discharge of VO_{2.19} resulted in a capacity of ~1 e⁻/V at current densities as high as 2 mA/cm². In the first charge of this oxide a loss in capacity of 15-20% of the first discharge occurred even at charge current densities as low as 0.1 mA/cm². Moreover, in extended cycling, the capacity of this oxide slowly declined in early cycles, diminishing to ~0.70 e⁻/V by about the 15th cycle and remaining fairly steady thereafter. These performance characteristics of VO_{2.19} were reproduced in a 5 A-hr prismatic cell. Both types of oxide require carbon in the cathode for acceptable performance with the result that the oxides have only moderate volumetric energy densities. Incorporation of metals such as Cr or Fe into the vanadium oxide lattice appears to be a useful approach to the synthesis of new and useful cathode materials.

Lithium secondary battery technology has been actively pursued for more than 20 years (1). Some striking advances have been made in the past ten years. These have been made possible by the discoveries (2) of new organic solvent/Li salt systems in which the Li electrode can be recharged with high efficiency. Especially noteworthy are the EIC System (3), 2Me-THF/LiAsF₆, and the Exxon electrolyte (4), 1,3-dioxolane/LiClO₄. Unfortunately, the 1,3-dioxolane/LiClO₄ system shows a tendency to detonate upon impact and therefore has been abandoned (5). Recently, we have demonstrated 100-200 deep discharge cycles in high capacity Li/TiS₂ cells utilizing 2Me-THF/LiAsF₆ electrolyte (6).

Considerable progress has also been made in the development of rechargeable cathode materials (7). The most extensively studied and promising materials are solid-state cathodes which undergo intercalation or topochemical reactions with Li. Among these, only TiS₂ has received any significant developmental effort. Our recent studies (6) demonstrated the excellent reversibility and chemical compatibility of TiS₂ in practical Li cells utilizing 2Me-THF/LiAsF₆. Despite its impressive performance characteristics, TiS₂ does not have the energy density required for many potential applications of secondary Li cells. Therefore, new materials with improved energy densities are of great interest.

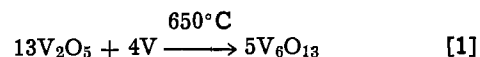
A potentially attractive group of materials are the transition metal oxides. Preliminary studies of several

rutile and perovskite-related oxides have been carried out recently by Murphy and co-workers (8,9). These studies have indicated that several vanadium oxides, particularly V₆O₁₃, are potentially attractive materials as high energy density cathodes for Li cells. The reaction of V₆O₁₃ with n-BuLi results in an uptake of ~8Li per mol of V₆O₁₃ leading to a theoretical specific energy of ~850 W-hr/kg (8). However, there has not been a clear demonstration of the performance characteristics of the oxide in practical cells. In view of the recent demonstration from this laboratory (3,6) that 2Me-THF/LiAsF₆ is a highly desirable electrolyte for rechargeable Li cells, we have investigated in detail the performance characteristics of V₆O₁₃ and related oxides in high capacity cells utilizing this electrolyte. The results are presented in this paper.

Experimental

Synthesis and Characterization of Vanadium Oxides

Stoichiometric V₆O₁₃; (VO_{2.17}).—The oxide was prepared according to the reaction shown in Eq. [1]



In a typical preparation, an intimate mixture consisting of 11.82g (65 mmols) of V₂O₅ (Alfa-Ventron) and 1.02g (20 mmols) of powdered V (Alfa-Ventron, -325 mesh) was heated in an evacuated, sealed quartz tube for 24 hr at 650°C. An x-ray pattern of the dark powder was in satisfactory agreement with that reported by *Wilhelmi et al.* (10). Samples were

* Electrochemical Society Active Member.

Key words: battery cathodes, cycling, energy density.

also prepared using heating times 8 and 16 hr (11). Although all the samples exhibited very similar x-ray patterns, the relative intensities of the lines in the pattern of the 24 hr sample, listed in Table I, exhibited the best match to the data of Wilhelmi and co-workers. Therefore we consider the 24 hr sample to be the most desirable. This was further borne out by cycling data (*vide infra*). A scanning electron micrograph of the 24 hr sample is shown in Fig. 1. The material is highly crystalline, the crystals being 10-40 μm long and 5-10 μm wide. The crystal size distribution, however, varied from one preparation to the other and had no apparent effect on cathode utilization. This material will be referred to as V_6O_{13} (S).

Nonstoichiometric V_6O_{13} ; ($\text{VO}_{2.19}$).—In a typical preparation, 17.33g NH_4VO_3 contained in a graphite boat were heated in a flowing argon atmosphere (flow rate, 450 cm^3/min) with the following temperature regime: Initially the temperature was raised from 25° to 400°C in about 1/2 hr. The temperature was then increased to 450°C and the sample was kept at this temperature for another 2 hr. Finally, the material was annealed at 550°C for 1 hr. The dark product weighed 12.73g. The composition of the oxide was calculated to be $\text{VO}_{2.19}$. Its x-ray pattern (Table I) is very much similar to that of the stoichiometric oxide. The SEM of the material revealed it to be composed of 4-5 μm particles. The material will be referred to as V_6O_{13} (NS).

Other vanadium oxides from NH_4VO_3 .—In optimizing the synthesis of $\text{VO}_{2.19}$ from NH_4VO_3 , it was found that a very careful control of the Ar flow rate was of utmost importance in obtaining the desired product. The Ar flow rate controls the residence time of the liberated NH_3 , the reducing agent which determines the V to O ratio in the oxide product. In different preparations with Ar flow rates significantly lower than 450 cm^3/min ,¹ oxides of the compositions $\text{VO}_{1.98}$, VO_2 , $\text{VO}_{2.04}$, and $\text{VO}_{2.08}$ were obtained at the same temperature ranges. X-ray patterns of these oxides (11) were different from those of $\text{VO}_{2.19}$. All these oxides exhibited electrochemical characteristics inferior to those of $\text{VO}_{2.19}$ (*vide infra*).

Metal substituted vanadium oxides, ($\text{V}_{0.87}\text{M}_{0.13}\text{O}_{2.17}$); M = Cr, Mo, or Fe².—Following the synthesis of $\text{VO}_{2.17}$ from V_2O_5 and V, metal substituted vanadium oxides with an overall metal to oxygen ratio of 1:2.17 were prepared by heating V_2O_5 (65 mmols) with Cr, Mo, or Fe (20 mmols) at 650°C for 24 hr. X-ray pat-

¹ The Ar flow rate required to obtain $\text{VO}_{2.19}$ may vary with sample size and the container tube size.

² This formulation is based on analogy to the synthesis of V_6O_{13} (S) as shown in Eq. [1].

Table I. Debye-Sherer x-ray patterns of $\text{VO}_{2.17}$ and $\text{VO}_{2.19}$

| $\text{VO}_{2.17}$ | | $\text{VO}_{2.19}$ | | V_6O_{13} (Wilhelmi,* [Ref. (10)]) | |
|--------------------|--------|--------------------|--------|---|--------|
| d(obs), Å | I(obs) | d(obs), Å | I(obs) | d(obs), Å | I(obs) |
| 5.85 | W | 5.81 | W | 5.85 | W |
| 5.40 | VW | 4.94 | W | 4.97 | VW |
| 4.87 | W | 3.49 | S | 3.51 | VS |
| 4.52 | VW | 3.28 | S | 3.32 | S |
| 3.46 | VS | 2.91 | M | 2.96 | M |
| 3.29 | S | 2.66 | M | 2.67 | S |
| 2.93 | M | 2.47 | W | 1.99 | M |
| 2.65 | M | 1.98 | S | 1.98 | M |
| 2.47 | W | 1.83 | S | 1.84 | S |
| 1.98 | S | 1.70 | M | 1.61 | M |
| 1.83 | M | 1.61 | M | 1.56 | W |
| 1.69 | VW | 1.54 | M | 1.54 | S |
| 1.65 | VW | 1.49 | W | 1.51 | VW |
| 1.60 | W | 1.40 | W | | |
| 1.54 | W | 1.35 | M | | |
| 1.50 | W | | | | |

* Lines identified as "VWV" are not listed here.

Table II. Debye-Sherer x-ray patterns of metal-substituted vanadium oxides

| $\text{V}_{0.87}\text{Cr}_{0.13}\text{O}_{2.17}$ | | $\text{V}_{0.87}\text{Fe}_{0.13}\text{O}_{2.17}$ | | $\text{V}_{0.87}\text{Mo}_{0.13}\text{O}_{2.17}$ | |
|--|--------|--|--------|--|--------|
| d(obs), Å | I(obs) | d(obs), Å | I(obs) | d(obs), Å | I(obs) |
| 5.60 | M | 5.01 | M | 4.69 | W |
| 4.79 | W | 4.39 | W | 3.86 | W |
| 4.29 | VS | 3.52 | VS | 3.17 | S |
| 4.02 | M | 3.34 | S | 2.68 | W |
| 3.36 | S | 2.98 | M | 2.41 | M |
| 2.85 | S | 2.69 | M | 2.13 | W |
| 2.73 | W | 2.50 | W | 2.01 | VW |
| 2.58 | M | 2.00 | S | 1.86 | W |
| 2.13 | W | 1.84 | M | 1.65 | M |
| 1.98 | M | 1.72 | VW | 1.59 | W |
| 1.90 | M | 1.70 | VW | 1.52 | VW |
| 1.85 | W | 1.61 | W | 1.43 | W |
| 1.77 | M | 1.59 | VW | | |
| 1.74 | W | 1.55 | W | | |
| 1.64 | W | 1.51 | W | | |
| 1.55 | VW | | | | |
| 1.51 | W | | | | |
| 1.48 | W | | | | |

terns of these materials are given in Table II. The SEM photograph of the iron derivative is shown in Fig. 2. These data confirmed the crystallinity of these materials.

Lithium Cell Studies

The oxides were evaluated in cells of the type

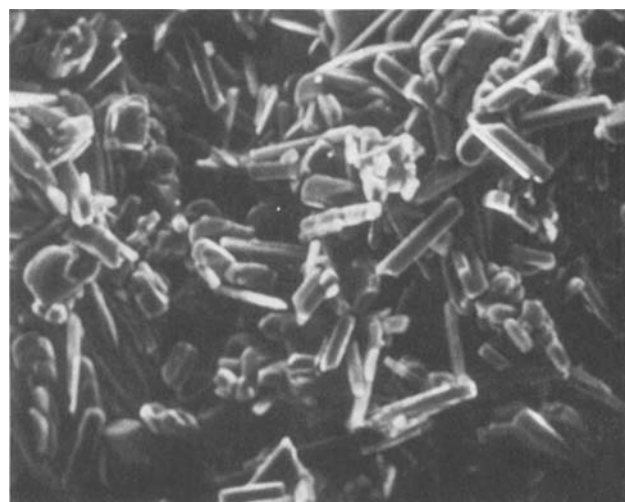
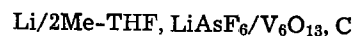


Fig. 1. SEM photograph of stoichiometric V_6O_{13} . Magnification 1000 \times .



Fig. 2. SEM photograph of Fe substituted vanadium oxide. Magnification 1000 \times .

Electrolyte preparation.—2-Methyltetrahydrofuran, 2Me-THF, obtained from Aldrich Chemical Company, was distilled over CaH₂ on a spinning band fractionating column (Perkin-Elmer 251) in an Ar atmosphere at a 5:1 reflux ratio. The middle 70% fraction was collected. The distilled solvent was treated with neutral alumina (Fisher Scientific Company) and a 1.5M LiAsF₆ electrolyte was prepared by adding an appropriate amount of LiAsF₆ (U.S. Steel Agri-Chemicals, electrochemical grade) to cooled (<0°C) 2Me-THF. The cooling is necessary to minimize possible decomposition (12). The solution was preelectrolyzed between two Li electrodes (~1 mA/cm² for ~16 hr) prior to use.

Cathode preparation.—The cathodes were prepared as pressed powder electrodes. An intimate mixture consisting of 70 weight percent (w/o) V₆O₁₃, 20 w/o C (Shawinigan 50% compressed), and 10 w/o Teflon was prepared in a blender. The mixture was pressed on either side of an expanded Ni screen (Exmet Corporation 5Ni7-4/0) at a pressure of 1000 lb/in.². The electrodes typically had a thickness of 1-2 mm, depending on the loading capacities.

Test cells.—Most of the experiments were carried out in a prismatic glass cell (11). In these cells, the electrode package comprised one cathode flanked on either side by an Li electrode, wrapped in 1 mil thick Celgard 2400 (Celanese Corporation) separator. The Li electrode was fabricated from a 15 mil thick Li foil (Foote Mineral Company) by pressing the foil to one side of an expanded Ni screen. Each electrode had an area per side of 8 cm² (3.2 × 2.5 cm). The cell was completed with an appropriate amount of 2Me-THF/1.5M LiAsF₆.

Tests were also carried out in hermetically sealed laboratory cells (11). The electrode package in these cells comprised two cathodes and three anodes, arranged in an alternating fashion with Li forming the outer electrodes in the stack. The cell typically had a capacity of ~500 mA-hr based on a theoretical capacity of 1 e⁻/V. The Li capacity was ~2.7 A-hr.

Large hermetically sealed prismatic cells (5 A-hr capacity) were constructed and tested with nonstoichiometric V₆O₁₃ as the cathode material. The cell contained a stack of rectangular electrodes. The cell consisted of deep drawn stainless steel (SS-316) with the following dimensions: width, 5.76 cm; depth, 1.97 cm; height, 5.59 cm; wall thickness, 0.057 cm. The cover contained two glass-to-metal compression seals for electrical terminals. Other cell specifications were as follows: cathode: 16.1g nonstoichiometric oxide (70 w/o), 20 w/o C, and 10 w/o Teflon. Theoretical cathode capacity was 5 A-hr (based on 1 e⁻/V). The cell had seven cathodes; each cathode was 5.0 × 3.75 cm per side; total area, 265 cm². The anode was 5.18g Li (20 A-hr). The cell had eight anodes; each was 5 × 3.75 cm. Total area was 265 cm². The separator was Celgard 2400, double wrap. The electrolyte was ~20g, 2Me-THF/1.5M LiAsF₆; the cell weight was 115g (about half of this weight is due to cell can and cover).

Cells were cycled galvanostatically or potentiostatically using standard instrumental techniques similar to those described previously (13, 14). For extended cycling of the cells, a microprocessor controlled galvanostat cycler, built in-house, was used. Data collection and retrieval were done with a Bascom-Turner Series 8000 Recorder equipped with microprocessor accessories.

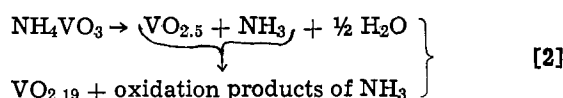
Results and Discussion

Synthesis and Characterization of the Oxides

The synthesis of V₆O₁₃ (S) was optimized and we found that heating for 24 hr at 650°C was the most

desirable. Reduction reactions of V₂O₅ similar to those in Eq. [1] have also been carried out with Cr, Mo, or Fe to obtain what are believed to be the corresponding metal derivatives of V₆O₁₃, namely, M_{0.78}V_{5.22}O₁₃. Although the x-ray patterns of the mixed metal oxides have not been indexed, the absence of oxide phases corresponding to the metal reductants suggests these materials to be mixed metal oxides produced by the insertion of the metal reductants into the vanadium oxide lattice. The formulation suggested here for the mixed metal oxides are based on analogy to the synthesis of VO_{2.17}. Alternatively, the materials can be formulated as M_xV₂O₅, where x = ~0.31, as in the case of the previously reported Fe_{0.33}V₂O₅ (15). Indeed, our x-ray data for the Fe derivative closely resemble those for Fe_{0.33}V₂O₅. The structural similarities between V₆O₁₃ and Fe_{0.33}V₂O₅ are discussed in Ref. (15). The noticeable differences in the x-ray patterns of the mixed metal derivatives shown in Table II seem to suggest that they are structurally not identical. It should be noted that structures such as Na_{2-2x}Mo₂V₆O₁₅ have been identified (16) in which Mo⁺⁶ ions enter the oxide structure, substituting V⁺⁵ ions. The elaborate x-ray studies needed for the full structural characterization of the mixed metal oxides were beyond the scope present study since our work emphasized their electrochemical properties in Li cells. Nevertheless, the present work opens up possibilities for the synthesis of new and useful cathode materials.

The formation of VO_{2.19} from NH₄VO₃ apparently follows the reactions depicted in scheme [2], with NH₃ reducing the initial decomposition product, VO_{2.5}

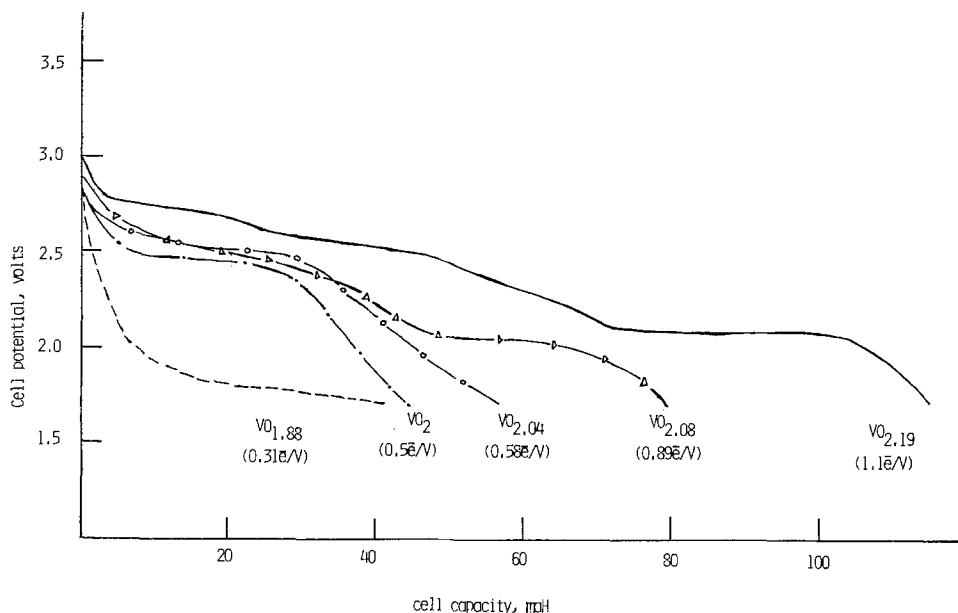


Because of the very complicated phase relations in the V-oxygen binary system, and the narrow compositional and stability ranges of the V₆O₁₃ phase (17, 18), it is necessary to maintain a strict control of the residence time of the liberated NH₃ over the oxide to obtain the desired product. In our synthesis of VO_{2.19}, we achieved this by maintaining an Ar flow rate of 450 cm³/min. By maintaining Ar flow rates considerably lower than this, we have synthesized VO_{1.88}, VO₂, VO_{2.04}, and VO_{2.08} whose x-ray pattern and electrochemical properties were significantly different from those of VO_{2.19}. Some of these lower oxides probably are not homogeneous oxide phases (17, 18). We also note that even with the optimized synthesis, different preparations of V₆O₁₃ (NS) yielded materials with V to O ratios from 1:2.18 to 1:2.20.

The crystal structure of V₆O₁₃ (S) was described by Wilhelmi and co-workers (10) and recently by Murphy and co-workers (8). This structure contains two perovskite cavities per V₆O₁₃ structural unit. Each cavity contains 15 distorted square pyramidal sites which belong to two groups comprising 3 and 12 sites, respectively. It is not known how the slightly oxygen-rich structure of V₆O₁₃ (NS) differs from that of V₆O₁₃ (S). We have found that when V₆O₁₃ (NS) is heated in vacuum at 650°C, it is converted to a more crystalline material whose electrochemical properties approach that of V₆O₁₃ (S). In analogy with V₂O₅, which loses oxygen when heated at 600°C in vacuum (17), it is possible that heating of V₆O₁₃ (NS) leads to the loss of the additional oxygens and transforms it to the more stable V₆O₁₃ (S).

Discharge characteristics of NH₄VO₃ decomposition products.—The primary discharges of the oxides, VO_{1.88}, VO₂, VO_{2.04}, VO_{2.08}, and VO_{2.19}, obtained galvanostatically at 0.5 mA/cm², are shown in Fig. 3. The data indicate that the cathode capacities and the potentials at which the discharges proceed depend on

Fig. 3. Galvanostatic discharges of various vanadium oxides synthesized by the thermal decomposition of NH_4VO_3 . Current = 8 mA (0.5 mA/cm^2).



the composition of the oxide. Thus for $\text{VO}_{1.88}$, although the discharge begins at $\sim 2.8\text{V}$, the cell polarizes rapidly to $\sim 1.8\text{V}$, at which potential most of the discharge proceeds. The discharges of VO_2 and $\text{VO}_{2.04}$ show a voltage plateau at $\sim 2.45\text{V}$. The discharge curve for $\text{VO}_{2.08}$ shows two potential plateaus at ~ 2.45 and $\sim 2.05\text{V}$. The discharge of $\text{VO}_{2.19}$ is characterized by two voltage plateaus at ~ 2.70 and 2.50V , a downward sloping potential region at $\sim 2.3\text{V}$, and another plateau at 2.1V . The highest capacity is exhibited by $\text{VO}_{2.19}$ with $1.1 \text{ e}^-/\text{V}$ to a 1.7V cutoff. The potential profiles observed here for $\text{VO}_{2.19}$ are identical to those reported by Murphy (8), for V_6O_{13} , prepared from NH_4VO_3 .

Walk and Gore have studied the discharge characteristics of $\text{Li}/\text{V}_2\text{O}_5$ cells (19). In the first discharge of V_2O_5 about 20% of the capacity occurs at potentials above 3.0V . Thus the primary discharge characteristics of the oxides with their unique potential profiles appear to be useful in evaluating material purity.

Cycling behavior of $\text{V}_6\text{O}_{13}(\text{NS})$.—The first two cycles of a cell utilizing this oxide are shown in Fig. 4. The discharge proceeds in discrete potential steps, indicating that Li incorporation is accompanied by phase transitions of the oxide lattice. The discharge shows a fairly sharp cutoff to 1.9V with a capacity of $\sim 1.0 \text{ e}^-/\text{V}$ in the first discharge. In the first charge, typically only 80–85% of this capacity is recharged. The capacity in the second cycle is nearly 100% of that in the first charge.

The potential plateaus in the first discharge occur at the approximate Li compositions in $\text{Li}_x\text{V}_6\text{O}_{13}$ of $0 < x \leq 0.95$, $0.95 < x \leq 2.75$, $2.75 < x \leq 3.65$, and $3.65 < x \leq 6.05$. A capacity of nearly $4\text{Li}/\text{V}_6\text{O}_{13}$ is obtained at potentials $> 2.1\text{V}$. This may involve the occupation of 2Li per cavity in the perovskite structure of the oxide. Of the additional two Li discharging at $\sim 2.1\text{V}$, one is

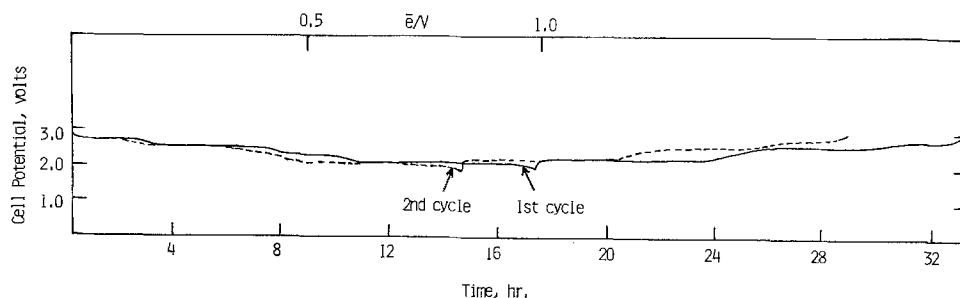
probably taken up by each cavity. It should be noted that with $n\text{BuLi}$, nearly 8Li can be incorporated into $\text{V}_6\text{O}_{13}(\text{NS})$, suggesting that the maximum Li capacity in $\text{V}_6\text{O}_{13}(\text{NS})$ is 4Li per cavity (8, 11).

The 15–20% capacity loss in the first charge was independent of the current densities between 0.10 and 2.0 mA/cm^2 . This fraction appears to involve mostly the capacity at the higher voltage regions, i.e., primarily from the 2nd and 3rd phase regions. With continued cycling between 1.9 and 3.0V , the relative ratios of the capacities involved in the various phase regions of 2nd discharge are maintained. Because of the distinct changes in the potential profiles of the first and second discharges, we ascribe the capacity loss to Li which occupies irreversibly some sites in the oxide lattice. This is further substantiated by our observation that a similar irreversibility is not exhibited by $\text{V}_6\text{O}_{13}(\text{S})$; *vide infra*. It should be noted that prior studies from this laboratory have clearly demonstrated (3, 6, 12) the electrochemical stability of the electrolyte in the region of 1.9 – 3.0V .

Cycling behavior of $\text{V}_6\text{O}_{13}(\text{S})$ and related oxides.—The first two cycles of a cell utilizing $\text{V}_6\text{O}_{13}(\text{S})$ are shown in Fig. 5. The discharge proceeds in three distinct voltage steps corresponding to a capacity of $\sim 0.55 \text{ e}^-/\text{V}$. The end of discharge is indicated by a very small plateau at $\sim 2.0\text{V}$ and then a clear potential drop to 1.9V . In the present cell the three upper plateaus occur to the approximate Li compositions in $\text{Li}_x\text{V}_6\text{O}_{13}$ ternary of $0 < x \leq 0.75$, $0.75 < x \leq 1.5$, and $1.5 < x \leq 3.0$. Practically 100% rechargeability is observed in the first charge. Moreover, very few changes in the voltage profiles or capacities occur with continued cycling between voltage limits of 1.9 and 3.0V (*vide infra*).

Figure 6 compares the first cycles of three different samples of $\text{V}_6\text{O}_{13}(\text{S})$ obtained using heating times

Fig. 4. The first two cycles of nonstoichiometric V_6O_{13} . Current density = 0.5 mA/cm^2 .



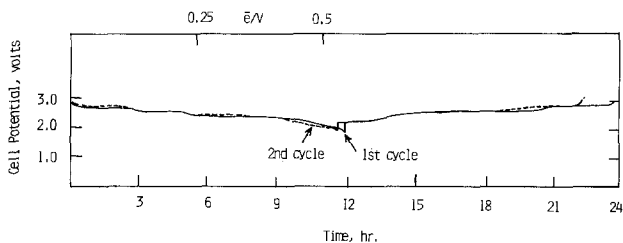


Fig. 5. The first two cycles of stoichiometric V_6O_{13} . Current density = 0.5 mA/cm^2 .

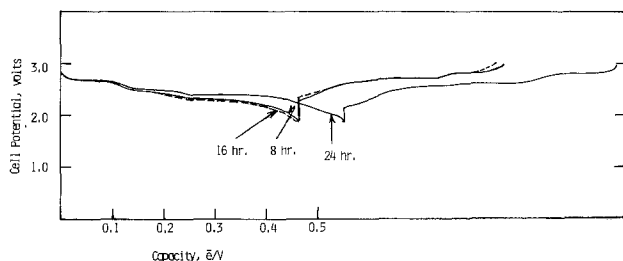


Fig. 6. The first cycles of $V_6O_{13}(S)$ samples prepared at 650°C using heating times of 8, 16, and 24 hr. Current density = 0.5 mA/cm^2 .

respectively of 8, 16, and 24 hr. There is very little difference in the potential profiles of the cycles of the three materials. However, the 24 hr sample exhibited the highest specific capacity. Moreover, the capacities of the 8 and 16 hr samples decreased with cycling while that of the 24 hr sample remained practically unchanged. The SEM data revealed the 24 hr sample to have the most uniform crystal size distribution. It was also found from x-ray data that although these materials had similar x-ray patterns, the relative intensities of the lines at 3.52 and 3.32Å showed a systematic variation with heating time, with the pattern of the 24 hr sample exhibiting the best match to the data reported by Wilhelmi (10). It appears that the inferior electrochemical performance, i.e., the lower capacities and diminishing utilization with cycling, of the 8 and 16 hr samples are due to crystal imperfections. The nature of these crystal imperfections is not clearly understood, however. The effect of a heating time longer than 24 hr has not been evaluated in our studies.

The significant difference between the $V_6O_{13}(S)$ and $V_6O_{13}(NS)$ at ambient temperature is the absence of the plateau in the discharge of the latter at $\sim 2.1\text{V}$. Consequently, $V_6O_{13}(S)$ exhibits approximately $0.33 \text{ e}^-/\text{V}$ less capacity than $V_6O_{13}(NS)$. The maximum capacity of the stoichiometric oxide determined by the $n\text{BuLi}$ reaction is $4\text{Li}/V_6O_{13}$ or $0.66 \text{ e}^-/\text{V}$ (7). This corresponds to the incorporation of 2Li per cavity in the oxide lattice.

The maximum capacity of 4Li per $V_6O_{13}(S)$ at ambient temperature appears to be determined by kinetic factors. This was indicated by the observation that by discharging the cell at 60°C , an additional capacity of $0.33 \text{ Li}/\text{V}$ was obtained with the extra capacity appearing at $\sim 2.1\text{V}$, as in $V_6O_{13}(NS)$. However, the recharge at 60°C was only 85% of the discharge, i.e., $0.72 \text{ e}^-/\text{V}$. This resembles the ambient temperature behavior of $V_6O_{13}(NS)$ and suggests that similar irreversibility mechanisms are probably operative in both cases. When the cell was returned to room temperature, its behavior resembled that prior to the cycle at 60°C . But it appeared that the high temperature discharge had induced an irreversibility in the oxide with the result that the ambient temperature cathode utilization after the discharge at 60°C showed

a declining trend, falling below $0.4 \text{ e}^-/\text{V}$ after a few cycles.

Typical cycles of the cells containing the metal substituted vanadium oxides are depicted in Fig. 7 and 8, respectively. The first discharge of the Fe substituted oxide resulted in a capacity of $0.49 \text{ e}^-/\text{mol}$ of total metal. The discharge, although it shows a close similarity to that of $V_6O_{13}(S)$, does not exhibit well-defined potential plateaus as observed in the latter. The first recharge was nearly 100% efficient. With continued cycling there was very little change in the potential profiles of the cycles although the capacity gradually decreased with utilizations of $0.34 \text{ e}^-/\text{metal}$ at the 15th and $0.24 \text{ e}^-/\text{metal}$ at the 50th cycles. The close similarities in the potential profiles of the cycling of $V_6O_{13}(S)$ and the Fe derivative seem to indicate that the two oxides have very similar crystal structures. Indeed, they have very similar x-ray patterns. Since the capacity of the Fe-V oxide was not better than that of $\text{VO}(S)$, we did not investigate the mixed metal oxide in any great detail as a cathode material. The specific energy of the oxide corresponding to the first discharge is 320 W-hr/kg .

The first discharge of the Cr derivative to 1.9V proceeded at two major potential plateaus. The upper plateau region occurred at $\sim 2.3\text{V}$ and involved a capacity of $0.56 \text{ e}^-/\text{mol}$ of the total metal. The second plateau occurred at $\sim 2\text{V}$ and involved a capacity of $0.22 \text{ e}^-/\text{total metal}$. In the first charge only the upper plateau region was rechargeable. In the second cycle, the discharge involved a capacity of 0.5e^- with a recharge efficiency of $\sim 85\%$. With continued cycling, this capacity decreased, and the cathode utilizations were 0.42 and 0.33 e^- at the 16th and 38th cycles. The specific energy of the oxide corresponding to the second discharge was 350 W-hr/kg .

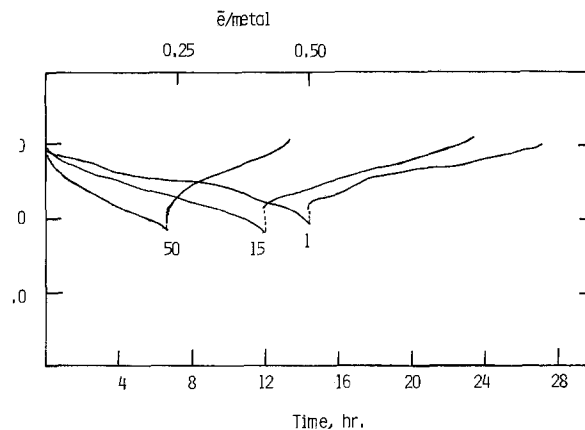


Fig. 7. Typical cycles of Fe substituted vanadium oxide cathode. Current density = 0.25 mA/cm^2 .

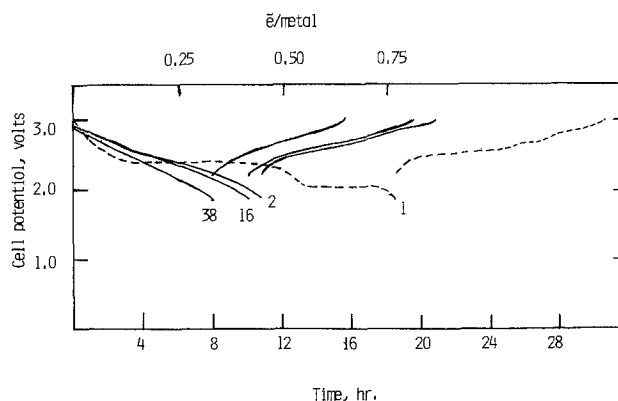


Fig. 8. Typical cycles of Cr-substituted vanadium oxide. Current density = 0.25 mA/cm^2 .

The discharge capacity of the Mo oxide was only $0.2 e^-/\text{mol}$ of total metal. This low capacity, though practically not interesting, was quite reversible.

Attempts to modify the structure of V_6O_{13} by metal substitution resulted in new materials. Their electrochemical properties were not superior to those of V_6O_{13} itself. However, the results are promising. A systematic study is presently underway to further evaluate mixed metal oxides as cathode materials.

Rate-capacity behavior of V_6O_{13} .—Figure 9 shows the discharges of a 51 mil thick cathode utilizing $V_6O_{13}(S)$ at current densities ranging from 0.5 to 8 mA/cm². The cathode, based on $1 e^-/V$, had a capacity density of 20.9 mA-hr/cm². A capacity of $\sim 0.55 e^-/V$ was obtained at current densities of 0.5, 1.0, and 2.0 mA/cm². At 4 mA/cm², the capacity was 0.45 e^-/V . With an Li cycling efficiency of 97%, the volumetric energy density, calculated using the practical electrode dimension is $\sim 260 \text{ W-hr/dm}^3$ at current densities $\leq 4.0 \text{ mA/cm}^2$. However, this does not take into account the volume required for the electrolyte.

Similar behavior was exhibited by $V_6O_{13}(NS)$. At current densities $\leq 2.0 \text{ mA/cm}^2$, a capacity between 1 and 1.1 e^-/V was obtained in the first discharge. At 4 mA/cm², the initial cathode utilization was 0.87 e^-/V . As discussed in the next section these capacities decreased with cycling.

These results suggest that Li cells with V_6O_{13} cathodes potentially have high rate capabilities. An amount of $\sim 20 \text{ w/o}$ carbon in the cathode matrix appears to be sufficient for obtaining these high rate performances. The diffusion coefficient of Li^+ in V_6O_{13} seems not to have been determined. The present data suggest that it is quite high, probably approaching those found in layered compounds such as TiS_2 which exhibit high rate discharge capabilities in Li cells (20).

At lower temperatures, i.e. $< 0^\circ\text{C}$, the cells exhibited relatively poorer rate characteristics. For example, at 0°C , a cell with $V_6O_{13}(S)$ and 2 Me-THF/1.5M LiAsF_6 exhibited a capacity of 0.41 e^-/V at 0.25 mA/cm², but practically no capacity at 0.5 mA/cm². Although not investigated in detail, it appears that at lower temperatures, the rate is primarily limited by the electrolyte.

Rechargeability of V_6O_{13} .—A detailed study (11) of the factors which affect the rechargeability of the vanadium oxides revealed the following: (i) High capacity cathodes utilizing both types of V_6O_{13} require carbon in the electrode matrix to obtain even an acceptable primary discharge. It was determined

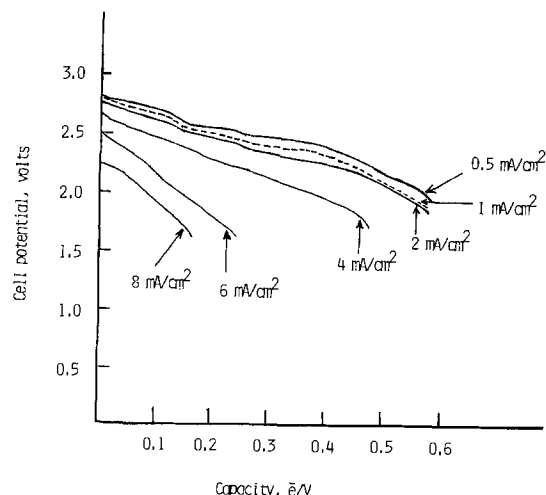


Fig. 9. Capacities of a $\text{Li}/V_6O_{13}(S)$ cell at various current densities. Cathode has 313 mA-hr, $1 e^-/V$ capacity. Cathode thickness = 51 mils.

that an optimal amount of carbon which would permit high rate discharges was about 20% by weight of the cathode mix. (ii) Control of the lower voltage limit of cycling is of utmost importance especially with $V_6O_{13}(NS)$ to avoid irreversible reduction of the oxides.

Potentiostatic discharges of cathodes utilizing $V_6O_{13}(S)$ and $V_6O_{13}(NS)$ were performed to evaluate the nature of electrode processes at potentials between 1.3 and 1.9V. Each cathode was initially discharged at 1.9V and then the potential was lowered to 1.3V at 0.1V intervals. At each potential the current was allowed to decay to $< 10 \mu\text{A}$. The results are tabulated in Table III. The capacity at the 1.9V discharge corresponded to 1.17 e^-/V for $V_6O_{13}(NS)$ and 0.71 e^-/V for the $V_6O_{13}(S)$. At 1.8 and 1.7V only little additional capacities were obtained. At 1.6V, however, additional capacities of 1.49 e^-/V for $V_6O_{13}(S)$ and 0.71 e^-/V for $V_6O_{13}(NS)$ were found. This substantial difference seems to suggest that the discharge process at 1.6V is due to the cathode material and not the solvent. The electrolyte itself did not show any substantial current on a carbon electrode down to 1.3V (21). The integrated capacities of the two oxides for discharges at 1.9, 1.8, 1.7, and 1.6V were remarkably close being equivalent to $\sim 14 e^-/V_6O_{13}$ formula. This would correspond to the reduction of all the V in the oxide to V^{+2} . The high capacity reduction at 1.6V in both of the oxides occurred at the low rate of $\sim 0.06 \text{ mA/cm}^2$.

After the high capacity reduction the cathode exhibited little rechargeability even potentiostatically. Also, in agreement with the results of the potentiostatic studies, we found that the cathode performance degraded significantly during galvanostatic cycling with lower voltage limits $\leq 1.5V$. The rate of degradation, however, was less in $V_6O_{13}(S)$ than in $V_6O_{13}(NS)$.

The average oxidation states of V in V_6O_{13} , $\text{Li}_4V_6O_{13}$, $\text{Li}_6V_6O_{13}$, and $\text{Li}_8V_6O_{13}$, respectively, are +4.33, +3.66, +3.33, and +3.0. Our data suggest $V^{+4.33} \rightleftharpoons V^{+3.33}$ as the redox limits with least structural irreversibility.

$V_6O_{13}(S)$ exhibits excellent rechargeability between cycling limits of 3.0 and 1.9V. Figure 10 shows a plot of cathode utilization vs. cycle number for a hermetically sealed laboratory cell utilizing $V_6O_{13}(S)$. The cell with a cathode capacity density of 12 mA-hr/cm² and a total capacity of $\sim 500 \text{ mA-hr}$, based on $1 e^-/V$, was cycled at a current density of 1.0 mA/cm² for both discharge and charge. The average cathode utilization in over 200 cycles was $\sim 0.52 e^-/V$. Some typical cycles are shown in Fig. 11. The mid-discharge potentials show no change when going from the first to the 200th cycle, although the later discharges exhibit more of a linear, but sloping, voltage profile. The latter indicates that minor structural perturbations of the oxide lattice may occur in the cycling, but has no effect on its performance as a cathode. Indeed, when the current density was lowered to 0.5 mA/cm² at the 198th cycle, the capacity increased to 0.6 e^-/V and remained nearly constant in the next 10 cycles at the same rate. The cell was cycled 260 times before it was terminated. These cycles were obtained in a period of more than 5 months, indicating the excellent system compatibility at ambient temperature.

Table III. Potentiostatic discharges of V_6O_{13}

| Oxide | Capacity (e^-/V) at volts | | | | Total capacity, e^-/V |
|-----------------|-------------------------------|-------|-------|-------|-------------------------|
| | 1.9 | 1.8 | 1.7 | 1.6 | |
| $V_6O_{13}(S)$ | 0.784 | 0.020 | 0.074 | 1.493 | 2.371 |
| $V_6O_{13}(NS)$ | 1.160 | 0.173 | 0.342 | 0.707 | 2.383 |

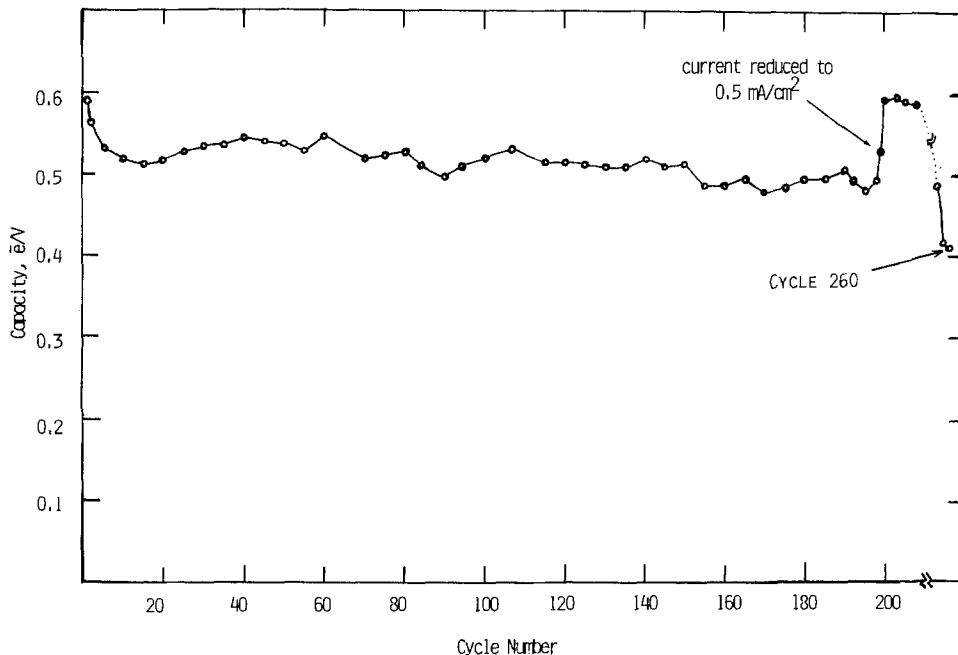


Fig. 10. Cathode utilization vs. cycle number for a hermetic laboratory test cell utilizing $V_6O_{13}(S)$. Current density = 1 mA/cm^2 . Cathode area = 40 cm^2 . Cathode capacity = 500 mA-hr (based on $1 \text{ e}^-/\text{V}$).

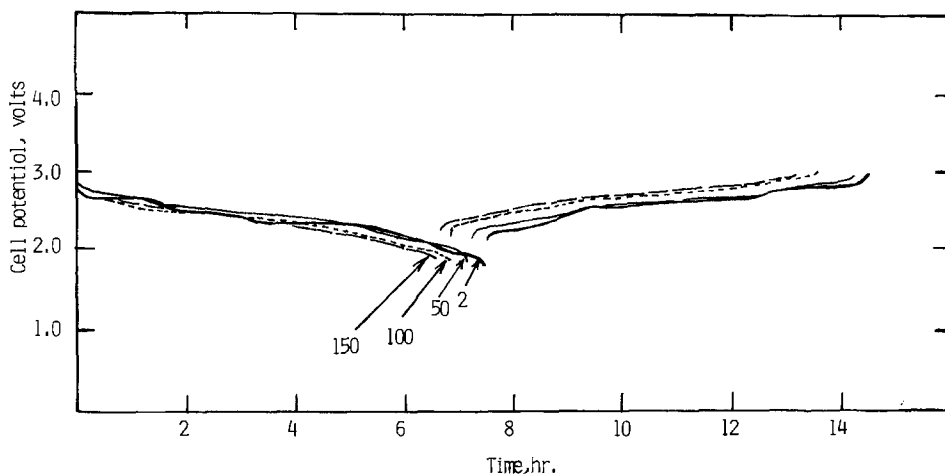


Fig. 11. Typical cycles of the cell shown in Fig. 10.

The Li cycling efficiency has exceeded 96%, as we found previously in Li/TiS_2 cells (6).

Figure 12 shows a plot of cathode utilization vs. cycle number for a cell with $V_6O_{13}(NS)$. The cathode based on $1 \text{ e}^-/\text{V}$ had a capacity density of 5.6 mA-hr/cm^2 . In the first discharge at 1.0 mA/cm^2 the capacity was $1.1 \text{ e}^-/\text{V}$. In the second discharge the capacity decreased to $0.88 \text{ e}^-/\text{V}$. With further cycling the capacity showed a continued, but slow, decline, diminishing to $\sim 0.65 \text{ e}^-/\text{V}$ at the 19th discharge. There was very little change thereafter up to the 40th cycle. A probable reason for the decline in capacity in the early cycles may be related to the insulating characteristics of lithiated phases, $\text{Li}_x\text{V}_6\text{O}_{13}$, $x > 4$ (8). In each cycle a small fraction of the highly lithiated oxide phases probably gets isolated in the electrode matrix and loses electronic contact with the bulk of the material. The electronically isolated material is electrochemically not utilized. Supporting this view is the fact that after the second cycle the potential plateaus of the cycles remain the same despite the lower capacities (see below). The average capacity achievable in high capacity nonstoichiometric oxide cathodes appears to be $\sim 0.7 \text{ e}^-/\text{V}$, corresponding to a specific energy of 450 W-hr/kg . The actual energy densities achieved in practical cells are discussed below.

With both of the oxides there were only small effects of discharge current densities up to 2.0 mA/cm^2

on cathode utilization. However, it appeared that good rechargeability is achieved with a charge current density of $\leq 1.0 \text{ mA/cm}^2$.

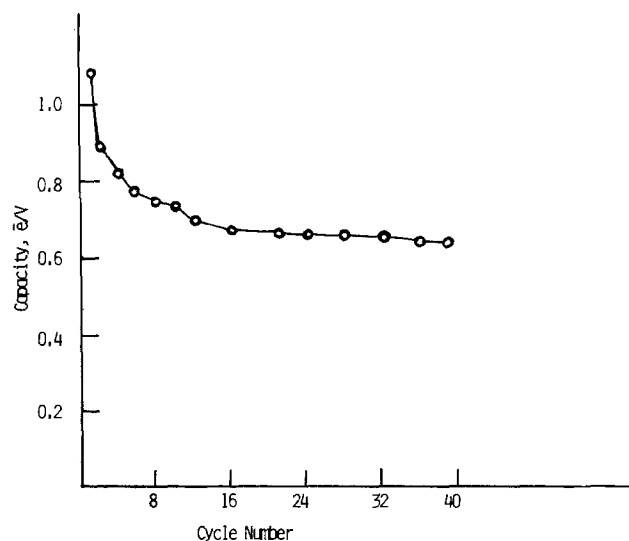
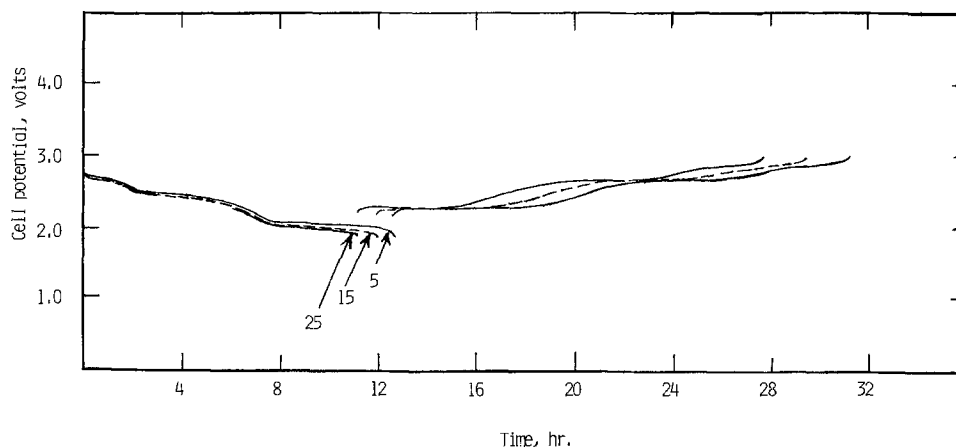


Fig. 12. Cathode utilization vs. cycle number for a cell utilizing $V_6O_{13}(NS)$. Cathode area = 16 cm^2 . Cathode capacity = 100 mA-hr (based on $1 \text{ e}^-/\text{V}$). Current density = 1 mA/cm^2 .

Fig. 13. Typical cycles of the 5 A-hr nominal capacity prismatic cell. Discharge current = 300 mA. Charge Current = 200 mA.



Performance characteristics of high capacity prismatic cells.—Approximately 5 A-hr capacity, hermetic prismatic cells were fabricated with V_6O_{13} (NS). Some typical cycles are shown in Fig. 13. The 5 A-hr nominal capacity cell reproduced the performance characteristics achieved in the small laboratory cells. For example, the capacity in the first discharge at a current of 140 mA (0.5 mA/cm^2) was 5.04 A-hr. The first charge at the same current was 83% efficient, with a capacity of 4.17 A-hr. From the second cycle onward the cell was cycled with currents of 300 mA for discharge and 200 mA for charge. The decrease in capacity with cycling in this cell occurred at a much slower rate than in the laboratory cell with V_6O_{13} (NS). The capacities were 3.66 A-hr in the 10th cycle, 3.51 A-hr in the 20th cycle, and 3.2 A-hr in the 40th cycle. The gravimetric and volumetric energy densities which correspond to these capacities are shown in Table IV. Testing of the cell was discontinued when it developed a partial short at the 45th cycle, manifested by a longer charge input than the previous discharge. The partial short results from dendrite penetration through the separator. We had previously identified this as a major failure mode also in 0.5 A-hr Li/TiS₂ cells (6). In the latter, however, this occurred at a much later stage in the cycling, i.e., typically after 100-150 deep discharge cycles.

Conclusions

Specific capacities, potential profiles, and rechargeabilities of vanadium oxide cathodes are highly dependent on the oxide composition. The compositions, $VO_{2.17}$ and $VO_{2.19}$ have properties suitable for fabricating rechargeable, nonaqueous Li cells. Whereas the specific capacity of $VO_{2.17}$ is lower than that of $VO_{2.19}$, it cycles more reversibly. Performance characteristics identified in low capacity laboratory cells can be reproduced in high capacity practical cells. The system Li/2Me-THF/LiAsF₆/V₆O₁₃ has acceptable stability at ambient temperature for many practical applications, as evidenced by extended cycling studies.

Table IV. Energy densities* achieved in a hermetically sealed prismatic cell†

| | 1st dis-charge | 2nd dis-charge | 10th dis-charge | 20th dis-charge | 40th dis-charge |
|---|----------------|----------------|-----------------|-----------------|-----------------|
| Capacity, A-hr | 5.04 | 4.07 | 3.66 | 3.51 | 3.2 |
| Gravimetric energy density, W-hr/kg | 102 | 81 | 73 | 70 | 64 |
| Volumetric energy density, W-hr/dm ³ | 183 | 146 | 131 | 126 | 115 |

* About half of the cell weight (115g) is due to the can and cover. Cell volume = 64 cm³.

† The cell utilizes nonstoichiometric V₆O₁₃ with 5 A-hr (1 e⁻/V) capacity.

A performance-limiting characteristic of these cells was identified to be irreversible reduction processes at potentials below 1.7V. In a high capacity (5 A-hr) prismatic cell utilizing $VO_{2.19}$, a specific energy of 102 W-hr/kg and an energy density of 183 W-hr/dm³ were achieved. These energy densities were reduced by 17% in the second discharge and ~30% in the 20th discharge. With the highly reversible $VO_{2.17}$, based on the same cell design, the specific energy would be ~60 W-hr/kg and the energy density would be ~115 W-hr/dm³.

The two major factors limiting the volumetric energy densities are the amount of carbon required for fabricating an acceptable cathode and the amount of Li required to achieve a specified number of cycles. Considerable improvements in volumetric energy density may be possible by the use of metallic conductive additives to the V_6O_{13} and by improvements in the Li cycling efficiency.

Acknowledgment

This work was supported by the U.S. Army Electronics Research and Development Command under Contract DAAK20-79-C-0267.

Manuscript submitted Jan. 23, 1981; revised manuscript received ca. June 8, 1981.

Any discussion of this paper will appear in a Discussion Section to be published in the June 1982 JOURNAL. All discussions for the June 1982 Discussion Section should be submitted by Feb. 1, 1982.

REFERENCES

- S. B. Brummer, K. M. Abraham, V. R. Koch, and G. L. Holleck, Final Report, Contract 4503510 to Lawrence Berkeley Laboratory by EIC Laboratories, Inc., August 1980.
- V. R. Koch, in Final Report, Contract 4503510 to Lawrence Berkeley Laboratory by EIC Laboratories, Inc., August 1980, Chap. II.
- V. R. Koch and J. H. Young, *Science*, **204**, 499 (1979).
- M. S. Whittingham, *ibid.*, **192**, 1126 (1976).
- G. H. Newman, R. W. Francis, L. H. Gaines, and B. M. L. Rao, *This Journal*, **127**, 2025 (1980).
- G. L. Holleck, K. M. Abraham, and S. B. Brummer, in "Proceedings of the Symposium on Power Sources for Biomedical Implantable Applications; Ambient Temperature Lithium Batteries," B. B. Owens and N. Margalit, Editors, p. 384, The Electrochemical Society Softbound Proceedings Series, Princeton, NJ (1980).
- K. M. Abraham, *J. Power Sources*, **1**, 1 (1981).
- D. W. Murphy and P. A. Christian, *Science*, **205**, 651 (1979).
- D. W. Murphy, P. A. Christian, F. J. Disalvo, and J. W. Carides, *This Journal*, **126**, 497 (1979).
- K. Wilhelmi, K. Waltersson, and L. Kihlberg, *Acta. Chem. Scand.*, **25**, 2675 (1971).
- K. M. Abraham, J. L. Goldman, M. D. Dempsey, and G. L. Holleck, Final Report, Contract ERADCOM DAAK20-79-C-0267, October 1980.

12. J. L. Goldman, R. M. Mank, J. H. Young, and V. R. Koch, *This Journal*, **127**, 1461 (1980).
 13. K. M. Abraham, R. D. Rauh, and S. B. Brummer, *Electrochim. Acta.*, **23**, 501 (1978).
 14. K. M. Abraham, L. Pitts, and R. Schiff, *This Journal*, **127**, 2545 (1980).
 15. J. Galy, A. Casalot, J. Darriet, and P. Hagenmuller, *Bull. Soc. Chim. Fr.*, 227 (1967).
 16. (a) J. Galy, J. Darriet, A. Casalot, and J. B. Goodenough, *J. Solid State Chem.*, **1**, 339 (1970); (b) J. B. Goodenough, *ibid.*, **1**, 349 (1970).
 17. J. Stringer, *J. Less-Common Metals*, **8**, 1 (1965).
 18. G. Andersson, *Acta. Chem. Scand.*, **8**, 1599 (1954).
 19. C. R. Walk and J. S. Gore, *This Journal*, **122**, 68C (1975).
 20. M. S. Whittingham, *Prog. Solid State Chem.*, **12**, 1 (1978).
 21. K. M. Abraham, Unpublished results.

Insoluble Sulfide Positive Electrodes for Organic Electrolyte Lithium Secondary Batteries

Fred W. Dampier*¹

EIC Corporation, Newton, Massachusetts 02158

ABSTRACT

The behavior of CuS, NiS, SiS₂, MnS₂, and FeS as positive electrodes for rechargeable Li cells was investigated using a 1M LiAsF₆/THF electrolyte. Of these sulfides CuS gave the best performance delivering 1.6 and 0.98 eq/mol of CuS at 1 mA/cm² after 4 and 20 cycles, respectively. These capacities translate into specific energies of 348 and 211 W-hr/lb based on the weight of CuS and actual cell voltages. It was found that both NiS and SiS₂ can be cycled for 40 cycles but the capacities were not adequate for battery applications. Deterioration of the Li electrode due to reaction of the Li with the electrolyte and reduction of the electrolyte on the CuS electrode below ~1.5V appear to be the main factors limiting the cycle life of the Li-CuS cell.

Monosulfides of the transition metals such as CuS and NiS have been extensively studied as positive electrodes for primary Li/organic electrolyte cells (1-7). Primary Li-CuS batteries have been developed by several manufacturers (1, 6) and 112 W-hr/lb has been achieved (1) for D-size cells. The monosulfides previously have been considered of minimal reversibility because of the low solubility of alkali and other metal sulfides in organic electrolytes (9) and their lack of a crystal structure favoring intercalation of Li⁺ similar to TiS₂ (8). However, when exploratory work (10) with a CuS positive electrode revealed that the Li-CuS cell is reversible, it was decided to investigate the behavior of CuS and other insoluble sulfides as positive electrodes.

In this paper results are presented of an investigation of the behavior of CuS, NiS, SiS₂, MnS₂, and FeS positive electrodes in rechargeable Li cells. The selection of these sulfides for investigation was made on the basis of the specific energy calculations presented in Table I, cost, elemental abundance, and previous work reported in the literature (1, 2, 9). The results have been evaluated primarily in terms of the merits of each material for practical application in high energy density rechargeable batteries.

Experimental

Cell construction.—The cells consisted of two Li negative electrodes (3.5 × 3.5 cm) on either side of the sulfide positive electrode, separated by two layers of a 0.025 mm thick polypropylene separator (Celgard 2400). Cells were assembled by wrapping the positive electrode in a "U" fold of two layers of separator, then sandwiching the wrapped electrode between two Li electrodes. The element was then inserted into a rectangular glass cell case (inside L × W × H: 4.5 × 1.5

× 7.0 cm), using polypropylene shims to insure a snug fit.

The Li electrodes (3.5 × 3.5 cm) were prepared by pressing a layer of 0.38 mm thick Li foil (Foote Mineral Company) on both sides of a 0.08 mm thick 3 Ni10-3/0 grid (Exmet Corporation). Either pressed powder or Teflon bonded positive electrodes were used depending on the properties of the sulfide active material and the purpose of the particular test. Pressed powder sulfide positives were prepared following a procedure described earlier (7) by pressing a blend of 50% active material, 45% graphite (No. 1651, Southwestern Graphite Company) and 5% polyethylene powder (Microthene FN-500, U.S. Industrial Chemicals) onto a 3 mil thick Ni15-4/0 grid.

The Teflon bonded positive electrodes (2.54 × 2.54 cm) were prepared by pressing a mixture of 50% sulfide active material, 50% Shawinigan carbon black, and du Pont No. 30 Teflon dispersion on an Exmet 5

Table I. Specific energies of insoluble sulfide positive electrodes

| Compound | Eq. wt.* | No. of electrons | E*** | W-hr/lb |
|--|----------|------------------|------|---------|
| A. Complete reduction | | | | |
| NiS | 52.32 | 2 | 2.02 | 469 |
| CuS | 54.74 | 2 | 2.23 | 495 |
| FeS | 50.89 | 2 | 1.97 | 471 |
| MnS | 50.44 | 2 | 1.36 | 328 |
| MnS ₂ | 66.47 | 4 | 2.00 | 366 |
| Ag ₂ S | 130.84 | 2 | 2.28 | 212 |
| VS | 48.40 | 2 | 1.50 | 376 |
| CoS | 52.44 | 2 | 1.97 | 457 |
| B. Partial Reduction to monosulfide | | | | |
| SiS ₂ | 53.10 | 2 | 2.27 | 520 |
| TiS ₂ | 63.00 | 2 | 1.87 | 361 |
| MnS ₂ | 66.52 | 2 | 2.65 | 484 |
| FeS ₂ | 66.98 | 2 | 2.83 | 514 |

* Electrochemical Society Active Member.

¹ Present address: GTE Laboratories, Incorporated, Waltham, Massachusetts 02254.

Key words: lithium, organic electrolytes, energy storage, tetrahydrofuran.

** Includes weight of required Li.
 *** The cell potentials were computed from the free energies of formation at 25°C tabulated by Gibson and Sudworth (19), except for FeS₂ where the NBS (26) value was used.

Ni5-5/0 grid and sintering the dried (overnight at 105°C) electrodes at ~300°C for 20 min under flowing argon. The procedure was similar to the one described earlier by Holleck and co-workers (11).

Electrolyte preparation.—Tetrahydrofuran (THF) (MC/B, Chromatoquality) was dried by passage through a glass column (height, 38 cm) filled with Linde 4A molecular sieves. The solvent was then passed through a second 38 cm column of fresh sieves, to achieve a water absorption capacity equivalent to a 76 cm column. Lithium hexafluoroarsenate (LiAsF₆, electrochemical grade) was obtained from United States Steel, Agri-Chemical Division, and was used as-received.

The preparation of the electrolyte and the construction of cells were all carried out in an argon-filled glove box with a relative humidity maintained at less than 0.002% (0.5 ppm), as measured by a dew point hygrometer (Alnor Instrument Company, Niles, Illinois).

Positive electrode materials.—The CuS, SiS₂, and FeS used to prepare positive electrodes were obtained commercially from Fisher, Atomergic Chemetals, and Fisher, respectively. However, the NiS and MnS₂ used in the present work were synthesized.

Nickel sulfide (α -NiS) was formed by dissolving 146g of NiSO₄ · 6H₂O (Harshaw) in 600 ml of distilled H₂O to which 100 ml of 14M NH₄OH was added followed by 170 ml of 24% (NH₄)₂S solution (Fisher Certified). The NiS precipitate was filtered and washed until the washwater gave a negative test with dimethylgloxime (0.16 μ g detection limit). The precipitate was then dried at 120°C for 48 hr in a tube furnace flushed with N₂.

Manganous disulfide, MnS₂ (Hauerite) was prepared using the procedure developed by Biltz and Weichmann (12). In brief, 5g of MnSO₄ · H₂O (Fisher, Certified) was dissolved in 20 ml of water then 20 ml of a boiling potassium polysulfide solution was added. The potassium polysulfide solution was prepared by dissolving 25g of anhydrous K₂S (Fisher) in 100 ml of water, bringing the solution to a boil, then adding 25g of sulfur (Ventron Corporation) in small portions over a 20 hr period. The slurry thus obtained was evaporated to dryness under vacuum in a glass tube, sealed, then heated to 170° ± 10°C. After 60 hr at this temperature the tube was broken open and the product was collected, washed first with 1 liter of hot water then with methanol without exposing it to air. Excess S was next removed from the MnS₂ by treatment with CS₂ in a Soxhlet extractor for 24 hr. Finally the compound was vacuum dried for 24 hr over NaOH at 100°C and transferred under vacuum into the glove box.

Results and Discussion

Copper sulfide.—The capacity change as a function of cycle number for Li-CuS cells using a 1M LiAsF₆/THF electrolyte and discharged to 1.5 and 1.45V are shown in Fig. 1 and 2, respectively. Over 300 cycles were obtained for the Li-CuS cell described in Fig. 2 by replacing the Li electrodes and the electrolyte after cycles 41 and 204. Since the capacity was greatly improved for more than 30 cycles each time the cell was refurbished, there is no indication that a cycling limit was reached for the CuS electrode even after 300 cycles. Examination of disassembled cells indicated that the capacity loss on cycling was probably due primarily to deterioration of the Li electrode. However, other factors which will be discussed later such as electrolyte reduction at the CuS electrode toward the end of discharge also appear to be involved.

The CuS electrodes used in cells 1-3 were of the Teflon-bonded type described earlier and contained 49% CuS in cells 1 and 2 and 73% CuS in cell 3. The nominal capacities of the electrodes were calculated

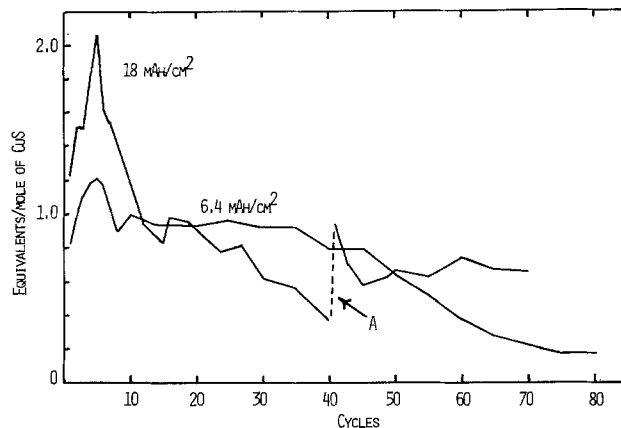


Fig. 1. Capacity changes of Li-CuS cells as a function of cycle number. $i_D = i_C = 1.0$ mA/cm². Voltage limits: 1.5V on D, 2.9V on C. Nominal capacities 6.4 and 18 mA-hr/cm² for cells 1 and 3, respectively. Li electrodes and electrolyte replaced at point A.

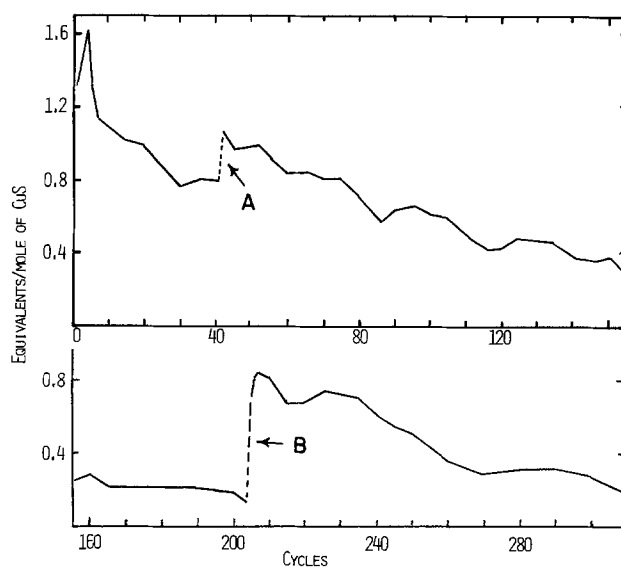


Fig. 2. Capacity changes of an Li-CuS cell as a function of cycle number. $i_D = i_C = 1.0$ mA/cm². Voltage limits: 1.45V on D and 2.90V on C. Nominal capacity cell 2, 8.4 mA-hr/cm². A, B—Li electrodes and electrolyte replaced.

on the basis of a 1.0 eq/mol CuS utilization and 6.45 cm².

The decline in capacity with cycle life observed for the Li-CuS cell as shown in Fig. 1 demonstrates that with LiAsF₆/THF the cell cycles well with little loss in capacity for about 35 cycles, after which the capacity rapidly falls. This same basic trend is seen in Fig. 2 although the voltage limits are slightly different and the Li electrodes were replaced. The voltage limits for cell 1 (Fig. 1) were initially 1.5V on discharge and 3.0V on charge, but near the end of the fifth cycle, the cell potential suddenly became erratic and failed to reach an endpoint, behavior typical of dendrite shorting. The charging voltage limit was then set at 2.90V and no further problems with dendrite shorting were encountered.

Because the Li-CuS cell has a long sloping discharge curve extending below 1.3V at 1 mA/cm² (Fig. 3) it was thought that a 1.50V discharge cut-off might needlessly sacrifice capacity. Thus, for cell 2 the discharge cut-off was extended to 1.45V and as Fig. 2 shows, considerable extra capacity was obtained without any sacrifice in cycle life.

During cycling, the charge time for the Li-CuS cell was approximately 30% shorter than the discharge time for the first four cycles yielding A-hr efficiencies

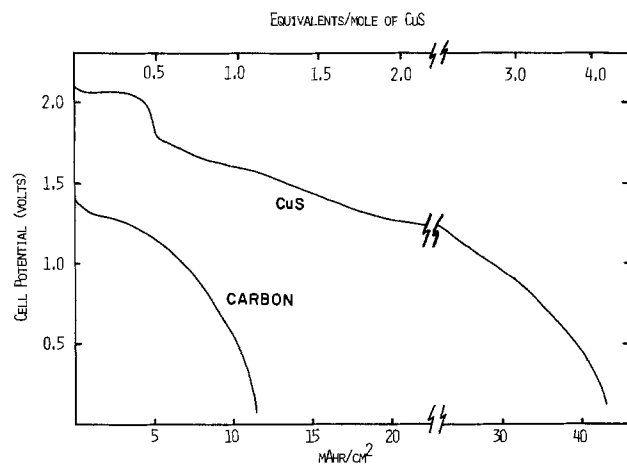


Fig. 3. Electrolyte decomposition compared at Teflon-bonded carbon black and CuS electrodes. $i = 1.0 \text{ mA/cm}^2$; $1\text{M LiAsF}_6/\text{THF}$, CuS electrode capacity 20.4 mA-hr/cm^2 at 1.0 eq/mol CuS .

greater than 100% (see Fig. 4 and Table II). Since it is known from previous voltammetric work (13) that $1\text{M LiAsF}_6/\text{THF}$ resists reduction down to the Li potential on a Ni working electrode, the only explanation remaining to account for the extra discharge capacity is that the electrolyte is either being reduced on the CuS or the carbon black added to the electrode to increase its conductivity.

To determine the extent of electrolyte reduction at CuS and Shawinigan carbon black, Teflon-bonded electrodes made of each of these materials were discharged to 0.10V vs. Li . The results which are presented in Fig. 3 show that below 1.4V much more electrolyte is reduced on CuS than on carbon. Since a greater capacity would be expected at the carbon black electrode with its high surface area and porosity, it seems likely that CuS or one of its reduction products may be a catalyst for the reduction of $\text{LiAsF}_6/\text{THF}$. This conclusion is reinforced by the fact that of the other oxide and sulfide positives which have been investigated in Li cells such as TiS_2 , SiS_2 , and MnO_2 all except NiS give A-hr efficiencies less than 100% as would be expected. Electrolyte decomposition has also been observed by Eichinger (5) at sintered Ni and CuS in $\text{LiClO}_4/\text{DMF}$.

Although electrolyte reduction at the CuS electrode near the end of discharge may lead to some minor deterioration of the CuS electrode, the major factor reducing cycle life of the Li-CuS cell appears to be deterioration of the Li electrode. The Li electrodes removed from Li-CuS, cell No. 2 after 41 cycles

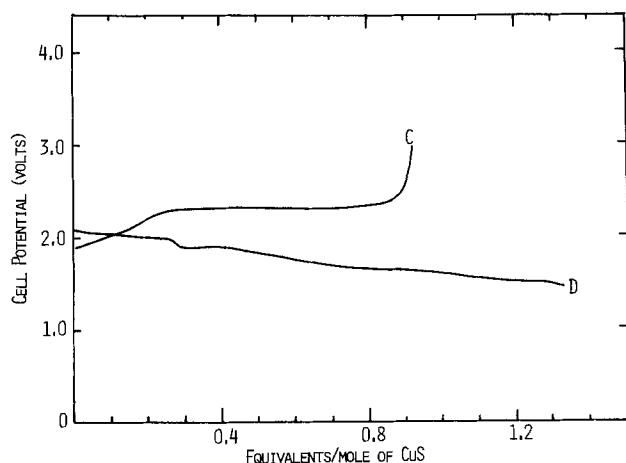


Fig. 4. Charge-discharge curves of the Li-CuS cell for the first cycle. Cell 2, $i_D = i_C = 1.0 \text{ mA/cm}^2$.

Table II. A-hr efficiencies during cycling for Li-CuS and Li-NiS cells*

| Cycle No. | CuS A-hr efficiency (%) | NiS A-hr efficiency (%) |
|-----------|-------------------------|-------------------------|
| 1 | 138 | 123 |
| 2 | — | 110 |
| 3 | 140 | 111 |
| 4 | 119 | 119 |
| 5 | 107 | 114 |
| 6 | 106 | 117 |
| 7 | 103 | 118 |
| 10 | 92 | 113 |
| 20 | 101 | 144 |
| 30 | 90 | 110 |
| 40 | 104 | 142 |

* CuS efficiencies for cell No. 2.

were found to be shiny except for the part opposite the CuS positive which was dark brown. Although the Li in this dark area opposite the CuS electrode was heavily corroded, when the surface film was scratched away it was found that considerable Li remained and the 0.38 mm thick foil was in no place consumed through to the Exmet grid. However, when cell No. 2 was disassembled after 205 cycles the Li electrodes were found to consist of a paste-like mixture of brown precipitate and small Li granules ($<0.5 \text{ mm}$) down to the Exmet grid with no trace of the original Li foil. The interelectrode space and the separator also contained an appreciable quantity ($\sim 0.5\text{g}$) of a brown precipitate which may be similar to the $\text{Li}_{1.2}\text{F}_{1.2}\text{As}_{0.68}\text{O}_{1.1}$ polymer reported by Koch (13, 14). These observations suggest that cell No. 2 was only capable of very shallow cycles by cycle 204 because the Li electrode had deteriorated to such an extent that all the Li foil was consumed and the Li granules which remained were electrically isolated from the current collector by a coating of reaction products. The large increase in the cycling capacity of cell No. 2 after cycle 205 when the cell was reassembled with new Li electrodes further confirms that the cycle life of the cell was limited primarily by failure of the Li electrode.

Knowing the amount of Li originally present on the Li electrodes, Q_0 , the amount of Li plated during the 162 cycles from cycles 42 to 204, Q_p , the coulombic cycling efficiency of the Li electrode, \bar{E} can be computed for cell No. 2 using the relation

$$\bar{E} = 1 + \frac{Q_r - Q_0}{Q_p} \quad [1]$$

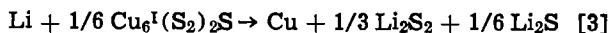
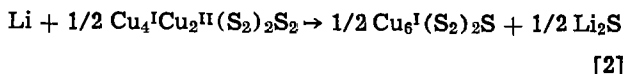
where Q_r is the amount of Li foil remaining on the grid of the Li electrode at the end of the experiment. For cell No. 2, $Q_r = 0$, $Q_0 = 568 \text{ C/cm}^2$, $Q_p = 2480 \text{ C/cm}^2$, therefore from Eq. [1] the average cycling efficiency of the Li electrode, \bar{E} was 77% from cycles 42 to 204. This is comparable with the 88.0% average Li cycling efficiency obtained by Koch and co-workers (15) for the Li electrode in half-cells with $1.5 \text{ LiAsF}_6/\text{THF}$ electrolyte cycled at 5.0 mA/cm^2 to a depth of 1.1 C/cm^2 . It is likely that the somewhat lower average efficiencies observed for the Li/CuS cell were due to the greater cycle depth and the larger number of cycles. Thus the limited cycle life of the Li/CuS cell observed in the present study is due to the failure of the Li electrode and can be accounted for in terms of the known inefficiency of the Li electrode in $\text{LiAsF}_6/\text{THF}$ found in the earlier work in half-cells. Neither failure of the CuS positive electrode nor electrolyte reduction at the positive electrode appear to be factors limiting the cycle life although they may cause the gradual decline in capacity observed with increasing cycle number.

The thick coating of brown precipitate found on the separator of cell No. 1 when it was disassembled was analyzed using the method described by Koch (14). After three washings with distilled H₂O using a centrifuge and drying (2 hr at 110°C), 0.45g of solid was obtained for analysis. Although infrared spectra (KBr pellet) of the material showed a much weaker absorption peak at 795 cm⁻¹ than expected, characteristic octahedral crystals of As₂O₃ were obtained when the brown solid was heated to 400°C in a capillary tube. From these and other analytical tests it was concluded that the brown precipitate found coating the separator from cell No. 1 was similar to the Li_{1.2}F_{1.2}As_{0.66}O_{1.1} polymer described by Koch (14) produced by the reduction of LiAsF₆/THF electrolyte at the Li electrode during cycling.

In principle, analysis of the CuS electrode and the electrolyte for other electrolyte reduction products would lead to an understanding of the effect of electrolyte reduction at the positive electrode on cycle life. However, such studies were not carried out because it was clear that the low cycling efficiency of the Li electrode (*i.e.*, 77%) was the major problem and that future efforts should be directed toward the search for electrolytes with greater anodic stability.

Typical charge-discharge curves for the Li-CuS cell at 1.0 mA/cm² are shown in Fig. 3 and 4. The distinct plateau which occurs at ~0.28 to 0.5 eq/mol suggests a simple stepwise reduction of CuS to Cu₂S as postulated by previous workers (3). However, examinations in our laboratory (16) of the CuS used in the present work (Fisher, ACS reagent) by modal analysis (grain counting with a petrographic microscope) revealed that the CuS contained ~89% CuS as covellite and 10% Cu₂S as chalcocite. Investigations (17, 18, 22) of the structure of covellite using x-ray diffraction techniques have shown that it is not a simple cupric salt but a more complex compound which could be represented as Cu₄^ICu₂^{II}(S₂)₂S₂ in which only one-third of the Cu is present as Cu(II).

The cathodic reduction of covellite is obviously a very complex process and although numerous reactions are possible the following reaction steps are tentatively suggested on the basis of the limited amount of data presently available



The equilibrium potentials of reactions [2] and [3] vs. Li⁺/Li were estimated as 2.40 and 2.04V, respectively, using the potentials calculated from the tabulated values of the free energies of formation (19) for the reduction of CuS and Cu₂S by Li. From voltammetric studies in DMSO (20) it appears that reaction [4] occurs at approximately 1.99V vs. Li⁺/Li. However, the work of Rauh and co-workers (10, 21) in THF indicates that the reduction of disulfide is kinetically difficult and substrate dependent and may proceed at much lower potentials at rates greater than ~0.5 mA/cm².

The discharge curve for CuS given in Fig. 4 shows a first plateau ending at 0.28 eq/mol which corresponds to a utilization efficiency of 93% based on reaction [2] taking into account that the CuS active material was ~89% covellite. On the other hand, for the Li-CuS cell described in Fig. 3 the first discharge plateau ended at 0.5 eq/mol which is higher than the 0.30 eq/mol expected. This increased capacity could be due to uneven distribution of CuS in the paste or changes in the covellite produced during sintering at 300°C but the exact cause of the increase is not known.

Crystallographic studies (17, 22) have indicated that CuS as covellite has an ABAACA type layer structure but the S-S distance between A layers is so short [*i.e.*, 2.09Å (17)] that a strong covalent bond would be assumed rather than van der Waals bonding as in TiS₂ (8). Thus an intercalation type discharge-charge mechanism appears unlikely for covellite. The plateau observed in the discharge curve suggests a heterogeneous discharge mechanism such as postulated in reactions [2]-[4] but it is possible that the reaction mechanism could include both displacement and topochemical steps. To determine the overall reaction mechanism for the covellite electrode it is clear that extensive x-ray studies will be required. Such studies were beyond the scope of the present investigation.

Nickel sulfide.—The capacity change as a function of cycle number for the Li-NiS cell using an LiAsF₆/THF electrolyte is compared in Fig. 5 with results for the Li-CuS cell. The Li-CuS cell is clearly far superior both in terms of cycle life and capacity. The NiS cell described in Fig. 5 used a Teflon-bonded electrode (1.1 mm thick) containing 30% NiS and 70% carbon black with a nominal capacity of 6.1 mA-hr/cm² calculated on the basis of a 1.0 eq/mol utilization. Pressed powder NiS electrodes (41 mA-hr/cm²) were also tested but they cycled poorly, the utilization dropping below 0.2 eq/mol by the eighth discharge.

Similar to TiS₃ (23), NiS gives a high utilization on the first discharge but fails to accept sufficient charge to duplicate the discharge performance during the second and following cycles. Since the discharge curve for the Li-NiS cell shows a single long plateau at ~1.6V at 1 mA/cm² (see Fig. 6), the capacity is highly dependent on the value of the discharge cut-off potential. Thus, when a Li-NiS cell was discharged to a 1.04V cut-off, a capacity of 2.0 eq/mol was obtained, part of which was probably due to reduction of the electrolyte toward the end of discharge. Another indication of electrolyte reduction, as described earlier for CuS, are A-hr efficiencies greater than 100%. A comparison of the A-hr efficiencies for NiS and CuS in Table II shows that the A-hr efficiencies are somewhat smaller for NiS but they remain well above 100% much longer than CuS where they stabilize near 100% after about 10 cycles.

Charge-discharge curves typical for the Li-NiS cell at 1.0 mA/cm² are shown in Fig. 6. The discharge curve for NiS has only a single plateau which would be expected since Ni(I) has no appreciable degree of stability. However, the potential fails to show a sharp

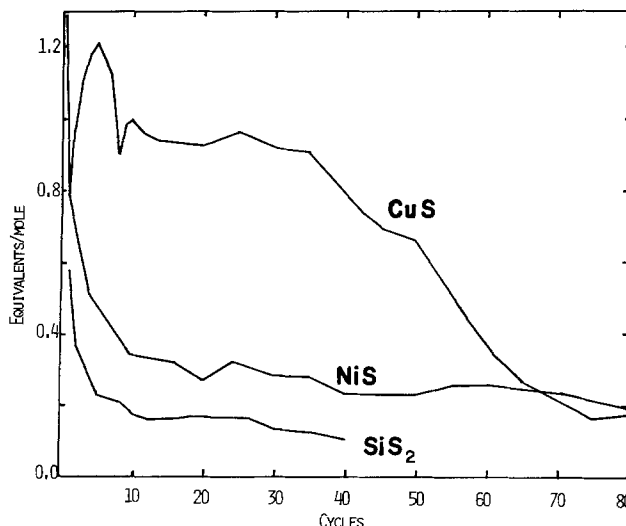


Fig. 5. A comparison of the cycling performance of Li cells with CuS, NiS, and SiS₂ positive electrodes, $i_D = i_C = 1.0 \text{ mA/cm}^2$. CuS results are for cell 1.

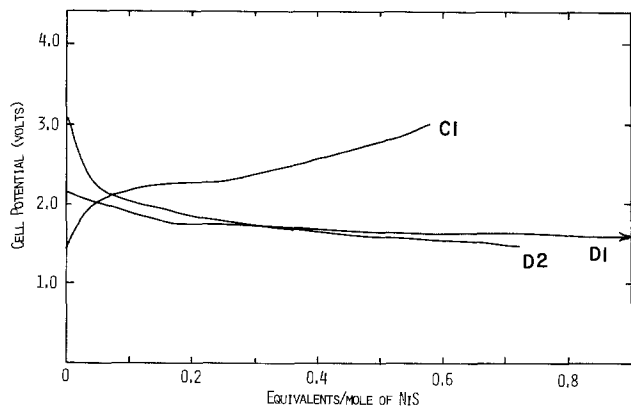


Fig. 6. Charge-discharge curves of the Li-NiS cell. $i_D = i_C = 1.0 \text{ mA/cm}^2$. Voltage limits: 1.50V on D, 3.00V on C.

upturn indicating the end of charge, even for cells charged to 3.80V.

Since the α -NiS used in the present work was synthesized in our laboratory using a procedure similar to the one described by Jasinski and Burrows (2) and later used by Pistoia (25), it is noteworthy that our NiS cells outperformed the earlier cells [e.g., 1.28 compared to 0.88 and 0.49 eq/mol to a 1.5V cut-off for the cells in Ref. (2) and (25), respectively]. The greater capacity of our cells can be attributed in part to the use of LiAsF₆/THF which is much more conductive and less viscous than the LiClO₄/PC and LiClO₄/EC used in the earlier work.

Silicon disulfide.—The cycling performance for the Li-SiS₂ cell using an LiAsF₆/THF electrolyte is shown in Fig. 5. Compared to CuS which gives almost ten times the capacity after ten cycles, the SiS₂ electrode is of marginal interest for practical batteries. The SiS₂ electrodes used in this study were of the pressed powder type (0.9 mm thick) described earlier and were 40% SiS₂, 54% graphite, and 6% polyethylene. Pressed powder SiS₂ electrodes were used because the preparation of Teflon-bonded electrodes involves the use of a water paste and SiS₂ hydrolyzes very rapidly to form H₂S and SiO₂.

The A-hr efficiencies calculated for the Li-SiS₂ cell described in Fig. 5 were all less than 100%. Thus SiS₂ does not appear to act as a catalyst for the reduction of the LiAsF₆/THF electrolyte even down to a 1.0V discharge cut-off. The SiS₂ (rhombic) used to prepare the electrodes is reported (24) to have a layer structure but it is not known if the bonding between the layers is van der Waals favoring Li intercalation or covalent.

Typical charge-discharge curves for the Li-SiS₂ cell are shown in Fig. 7. The peculiar peak in the first charge curve at 0.22 eq/mol remains well defined for the first 15 cycles after which it weakens until it disappears after 30 cycles. From observations of the SiS₂ as it was received from the manufacturer in large lumps, it was evident that it was a heterogeneous mixture about 90% SiS₂ and 10% impurities. Thus the plateaus in the charge-discharge curves are probably due to the heterogeneous nature of the active material.

Manganese disulfide.—The MnS₂ which was synthesized was evaluated using pressed powder electrodes (45.2% MnS₂, 50.1% graphite, 4.6% polyethylene) to avoid the possibility of MnS₂ decomposition if a Teflon-bonded construction was used. The open-circuit potential of the Li-MnS₂ cell was 3.29V immediately after it was assembled which is higher than the 2.65V OCP predicted in Table I. However, when an Li-MnS₂ cell was discharged at 1.0 mA/cm² the potential dropped to 2.35V within 30 sec, and to 1.45V after 5 min. On recharge the potential rose to the 4.00V charge limit

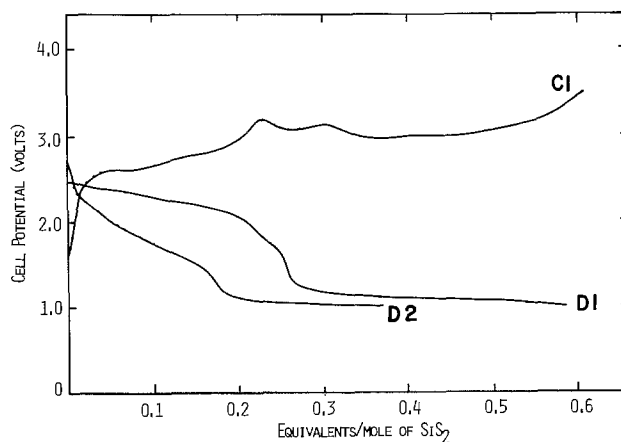


Fig. 7. Charge-discharge curves for an Li-SiS₂ cell, $i_D = 1.0 \text{ mA/cm}^2$, $i_C = 0.75 \text{ mA/cm}^2$. Voltage limits: 1.0V on D, 3.80V on C.

within 4 min at 1 mA/cm². The second discharge was no better than the first, the potential dropping to 1.57V after 3 min. The capacity of the MnS₂ electrode tested was 13 mA-hr/cm² based on a 1.0 eq/mol utilization. Thus, the first discharge amounted to a utilization of only 0.013 eq/mol which indicates that MnS₂ is for all practical purposes electrochemically inert.

Ferrous sulfide.—When an Li-FeS cell with FeS as β -pyrrhotite was discharged at 1.0 mA/cm² the potential fell from the 3.16V OCV to 1.47V in 18 min. On recharge at 1.0 mA/cm² the potential rose to the 2.90V limit within less than 2 min. The capacity of the Teflon-bonded FeS electrode was 3.4 mA-hr/cm² based on a 1.0 eq/mol utilization. Thus the first discharge yielded only 0.18 eq/mol to a 1.45V voltage limit which indicates that β -pyrrhotite is not a practical electrode material for room temperature Li batteries. Even when the current density was lowered to 0.10 mA/cm² after two cycles, the utilization for the third cycle was still only 0.12 eq/mol.

These results for the FeS electrode are of some interest because they demonstrate that at 0.1 mA/cm² negligible reduction of the LiAsF₆/THF electrolyte occurs down to 1.45V on either FeS or carbon since the electrode contained 50% carbon black. Furthermore, because the electrode could not be charged below 2.90V, the results for FeS clearly demonstrate that little capacity can be obtained by cycling just the electrolyte on carbon. These findings, along with others previously discussed, provide further evidence that the CuS electrode is intrinsically reversible during deep cycling.

Conclusions

The specific energies achieved during cycling for the five insoluble sulfides which were investigated are compared in Table III. Out of this group only CuS per-

Table III. Specific energies achieved for various insoluble sulfides as positive electrodes for rechargeable lithium batteries*

| Positive electrode material | $E_{1/2}$ (V) | i (mA/cm ²) | W-hr/lb achieved at cycle number | | | | |
|-----------------------------|---------------|---------------------------|----------------------------------|-----|-----|-----------|------------|
| | | | 1 | 4 | 10 | x | y |
| CuS | 1.70 | 1.0 | 288 | 348 | 235 | 211 (C20) | 164 (C30) |
| NiS | 1.62 | 1.0 | 299 | 110 | 74 | 61 (C20) | 61 (C30) |
| SiS ₂ | 1.12 | 1.0 | 86 | 41 | 27 | 24 (C20) | 21 (C30) |
| MnS ₂ | 1.85 | 1.0 | 2 | — | — | — | — |
| FeS | 1.86 | 1.0 | 46 | — | — | — | — |
| TiS ₂ (27) | 2.0 | 2-10 | 224 | — | — | 206 (C76) | 179 (C121) |
| VO ₂₋₁₈₆ (28) | 2.4 | 0.16 | ~325 | — | — | 285 (C5) | 255 (C35) |

* The specific energies were calculated using actual cell potentials and only the weight of the positive electrode active materials omitting the weight of the Li anode, carbon, grids, and hardware. $E_{1/2}$ is the mid-discharge potential.

formed sufficiently well to merit consideration for use in practical Li secondary batteries. Although $\text{VO}_{2.186}$ clearly outperformed both CuS and TiS_2 in terms of specific energy for the first 35 cycles, the only available data (28) are for small thin $\text{VO}_{2.186}$ electrodes (i.e., 1.3 cm^2 , 1.9 mA-hr/cm^2) discharged at very low rate. The TiS_2 electrode gives excellent cycle life at moderate rate, but recent (28) performance gains compared to earlier work (23, 29) appear to be the result of improved methods of electrode fabrication and the choice of electrolyte. Since the active material loading for the TiS_2 electrode described in Table III was not reported (28), it is somewhat difficult to compare the TiS_2 data with the present results for CuS which were obtained using electrodes with loadings up to 18 mA-hr/cm^2 that were not optimized. However, even with the available information, it is clear that CuS will continue to merit consideration for rechargeable batteries because of its high specific energy, ready availability, and its low cost compared with other positive electrode materials.

The main problem with the CuS positive electrode does not appear to be the intrinsic reversibility of CuS but rather the decline in capacity observed during cycling with electrodes with practical loadings. It has been concluded from chemical analysis and inspection of Li electrodes from failing cells that deterioration of the Li electrode due to reaction of Li with the electrolyte is the major cause of the capacity decline seen during cycling.

Reduction of the $\text{LiAsF}_6/\text{THF}$ electrolyte on the CuS electrode toward the end of discharge also limits the cycle life of the Li-CuS cell but it is a much less serious problem. In principle, electrolyte reduction at the CuS electrode could be greatly reduced and the cycle life improved by raising the discharge cut-off from 1.45 to 1.55V or higher. However, the Li-CuS cell has a discharge curve with a long plateau extending below 1.55V and any gain in cycle life would involve some sacrifice in capacity. A more fundamental solution to the problem of capacity decline would be the selection of an electrolyte more resistant to reduction at the Li electrode than $\text{LiAsF}_6/\text{THF}$.

Acknowledgment

We are pleased to acknowledge that this work was supported by the U.S. Department of Energy under Contract EY-76-C-02-2520.

Manuscript submitted Sept. 17, 1979; revised manuscript received April 20, 1981.

Any discussion of this paper will appear in a Discussion Section to be published in the June 1982 JOURNAL. All discussions for the June 1982 Discussion Section should be submitted by Feb. 1, 1982.

REFERENCES

1. J. P. Gabano, V. Déchenaux, G. Gerbier, and J. Jammot, *This Journal*, **119**, 459 (1972).
2. R. Jasinski and B. Burrows, *ibid.*, **116**, 442 (1969).
3. J. P. Gabano, G. Gerbier, and J. F. Laurent, in "Proc. 23rd Power Sources Symp.," Atlantic City, New Jersey, p. 80, 1969, PSC Publication Committee, Red Bank, NJ.
4. D. Hebert and J. Ulam, U.S. Pat. 3,043,896 (1962).
5. G. Eichinger and H. P. Fritz, *Electrochim. Acta*, **20**, 753 (1975).
6. M. R. Kegelman, U.S. Pat. 3,847,674 (1974).
7. F. W. Dampier, *This Journal*, **121**, 656 (1974).
8. M. S. Whittingham, *ibid.*, **123**, 315 (1976).
9. G. Eichinger and J. O. Besenhard, *J. Electroanal. Chem. Interfacial Electrochem.*, **72**, 1 (1976).
10. R. D. Rauh, K. M. Abraham, S. B. Brummer, F. W. Dampier, G. F. Pearson, and J. K. Surprenant, U.S. Dept. of Energy, Contract No. EY-76-C-02-2520 (1978).
11. J. R. Driscoll, G. L. Holleck, D. E. Toland, and S. B. Brummer, Eleventh Quarterly Report, U.S. Army ECOM-74-0030-11, AD-A031601, Oct. 1976.
12. W. Biltz and F. Wiechmann, *Z. Anorg. Allg. Chem.*, **228**, 268 (1936).
13. S. B. Brummer, F. W. Dampier, V. R. Koch, R. D. Rauh, T. F. Reise, and J. H. Young, Final Report, N.S.F. Grant AER-03779, NTIS No. PB 290 934, Jan. 1978.
14. V. R. Koch, *This Journal*, **126**, 181 (1979).
15. J. L. Goldman, R. M. Mank, J. H. Young, and V. R. Koch, *ibid.*, **127**, 1461 (1980).
16. W. W. Harvey, J. L. Schad, and P. H. Yu, U.S. Energy Research and Development Admin. Interim Status Report No. COO-2730-1, Contract No. E(11-1)-2730, Dec. 1975.
17. L. G. Berry, *Am. Mineral.*, **39**, 504 (1954).
18. R. T. Shuey, "Semiconducting Ore Minerals," Chap. 12, Elsevier, London (1975).
19. J. G. Gibson and J. L. Sudworth, "Specific Energies of Galvanic Reactions," Chapman and Hall Ltd., London (1973).
20. M. V. Merritt and D. T. Sawyer, *Inorg. Chem.*, **9**, 211 (1970).
21. R. D. Rauh, K. M. Abraham, G. F. Pearson, J. K. Surprenant, and S. B. Brummer, *This Journal*, **126**, 523 (1979).
22. I. Otfedal, *Z. Kristallogr.*, **83**, 9 (1932).
23. G. L. Holleck and J. R. Driscoll, *Electrochim. Acta*, **22**, 647 (1977).
24. Gmelins Handbuch, System No. 15, Part B, P. 750, Verlag Chemie, Weinheim (1959).
25. G. Pistoia, *This Journal*, **118**, 153 (1971).
26. Nat. Bureau of Standards, Circular 500, "Selected Values of Chemical Thermodynamic Properties" (1952).
27. M. S. Whittingham, *Prog. Solid State Chem.*, **12**, 41 (1978).
28. D. W. Murphy, P. A. Christian, F. J. DiSalvo, and J. N. Carides, *This Journal*, **126**, 497 (1979).
29. L. H. Gaines, R. W. Francis, G. H. Newman, and B. M. L. Rao, in "Proc. 11th IECEC," State Line, Nevada, p. 418 (1976).

Cathode-Limited Li/SOCl₂ Cells

K. A. Klinedinst*

GTE Laboratories, Incorporated, Power Sources Center, Waltham, Massachusetts 02254

ABSTRACT

The ambient temperature discharge characteristics of cathode-limited Li/SOCl₂ cells have been investigated at discharge rates ranging over five orders of magnitude (from about 2 μ A/cm² to about 0.5 A/cm²). The cell voltages and discharge capacities (per unit cathode volume) are compared as a function of discharge current density. The use of alternative cathode materials which catalyze the electroreduction of SOCl₂ is discussed, as are the dependencies of the average load voltage and the cathode utilization efficiency upon cathode thickness at high discharge rates. The relationship between the interelectrode spacing and the high rate discharge characteristics of cathode-limited Li/SOCl₂ cells has also been investigated.

Various aspects of the ambient temperature discharge characteristics of cathode-limited Li/SOCl₂ cells have previously been reported (1-3). (A cathode-limited cell is one whose discharge terminates due to the exhaustion of the carbon black cathode capacity.) Presented here are the results of an investigation of the discharge characteristics of cathode-limited Li/SOCl₂ cells in which the effects of varying discharge rate, cathode thickness, cathode composition, and interelectrode separation have been explored.

Experimental

Description of the cells and test procedures.—The electrolyte was a 1.5-1.8M solution of LiAlCl₄ in SOCl₂. The anodes were cut from a 0.76 mm thick sheet of lithium metal. Unless otherwise indicated, the cathodes contained 91% Shawinigan acetylene black and 9% PTFE and ranged in thickness between 0.025 and 1.3 mm. The thinnest cathodes (0.025-0.280 mm thick) were supported upon sheets of 0.127 mm thick nickel foil. Expanded nickel screen was used as the current collector for the thicker cathodes. Unless otherwise specified, nonwoven glass fiber paper 0.127 mm thick was used as the separator material. The electrodes and electrolyte have been described in more detail in a preceding paper (1).

Two different cell constructions were employed. For cells discharged at rates above 0.1 mA/cm², the cells were contained within sealed glass envelopes. The details of the construction of these glass envelope cells have been described previously (1). For cells discharged at rates below 0.1 mA/cm², the long discharge times required the use of a different cell construction. At these lower rates, AA-size stainless steel cylindrical cans were used to contain the cells. The lithium anode was first pressed onto the inside wall of the can. Next, a cylinder of porous glass separator paper was placed within the can. Finally, a 13 cm³ sheet of cathode material was shaped into a cylinder and inserted into the center of the can. Nickel metal lead wires were welded to the can and to the cathode substrate, and the can containing the cell was completely immersed within a pool of electrolyte contained within a glass tube. A glass cap was sealed to the tube through which passed two metallic feedthroughs which had been welded to the nickel lead wires. Every cell contained large excesses of both lithium and SOCl₂.

The cells were all discharged to termination across constant loads, the voltages being recorded as a function of time by the use of a datalogger. From two to four cells were discharged at each rate. Reported below are the averaged results obtained from each set

of duplicate tests. All of the cells were discharged at room temperature (between 22° and 25°C).

Scanning electron microscopy.—The spent cathodes were removed from the cells discharged at rates below 0.1 mA/cm². Disassembly of the cells was carried out in an inert atmosphere. Any adhering LiAlCl₄ salt was washed from each cathode by a brief immersion in excess distilled propylene carbonate. After drying, the now brittle cathodes were "flexed" so as to cause them to fracture into a number of pieces. These segments of spent cathode material were mounted and transferred to a JSM-U3 scanning electron microscope without exposure to the air. After the sample chamber had been evacuated, the cathode cross sections were examined microscopically.

Data analysis.—The cell voltage *vs.* time data were first transcribed to graph paper from the datalogger tapes. The average discharge voltages (E_{avg}) were obtained by averaging over each discharge curve to the point at which the voltage began to decline rapidly. The average discharge rate (I_{avg}) was calculated by dividing E_{avg} by the constant load (R). The current density was calculated by dividing I_{avg} by the geometric surface area of cathode (A). The discharge duration (t) was taken to be the time elapsed from the beginning of the discharge to the point at which the cell voltage had reached 90% of E_{avg} . In order to compare cathodes of different thicknesses, the discharge duration was normalized by dividing by the cathode thickness (T). The discharge capacity (C) was obtained by a graphical integration of the discharge curve from the beginning of the discharge to the point at which the cell voltage had reached 90% of E_{avg} . (The capacity is expressed below per unit cathode area and per unit cathode thickness.) The time required for the voltage on load to drop from 90% of E_{avg} to 70% E_{avg} divided by the discharge duration has been taken as a measure of the relative rate of voltage decline at the end of the approximately linear portion of the discharge curve.

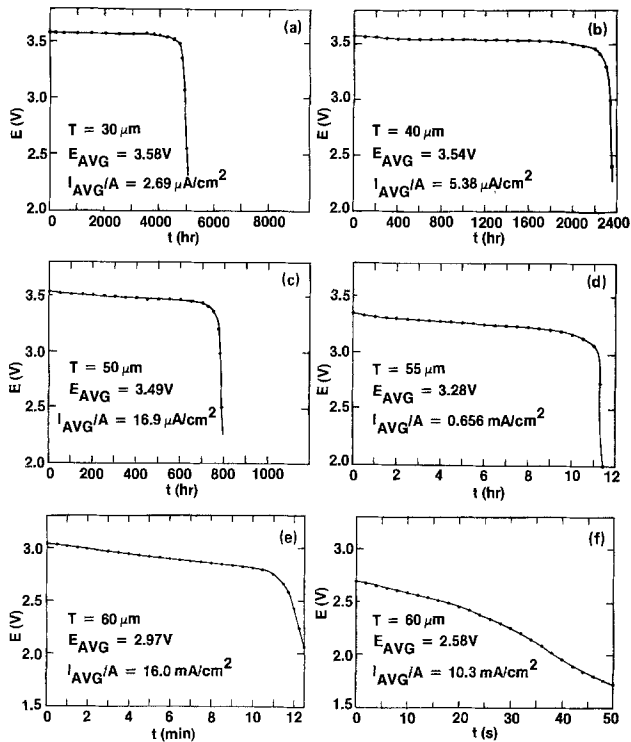
Results and Discussion

The Li/SOCl₂ cell is characterized by a high open-circuit voltage (about 3.650V) and by the fact that, when discharged under constant load or constant current conditions at moderate rates, the voltage on load remains relatively constant until close to the end of the discharge when a relatively rapid voltage decline is observed. However, the higher the discharge rate, the larger is the voltage range spanned during the initial, linear portion of the discharge curve.

This effect is demonstrated in Fig. 1 which contains typical discharge curves for cells discharged with average current densities ranging from a few micro-

* Electrochemical Society Active Member.

Key words: cathode, discharge, polarization, capacity, catalysis.

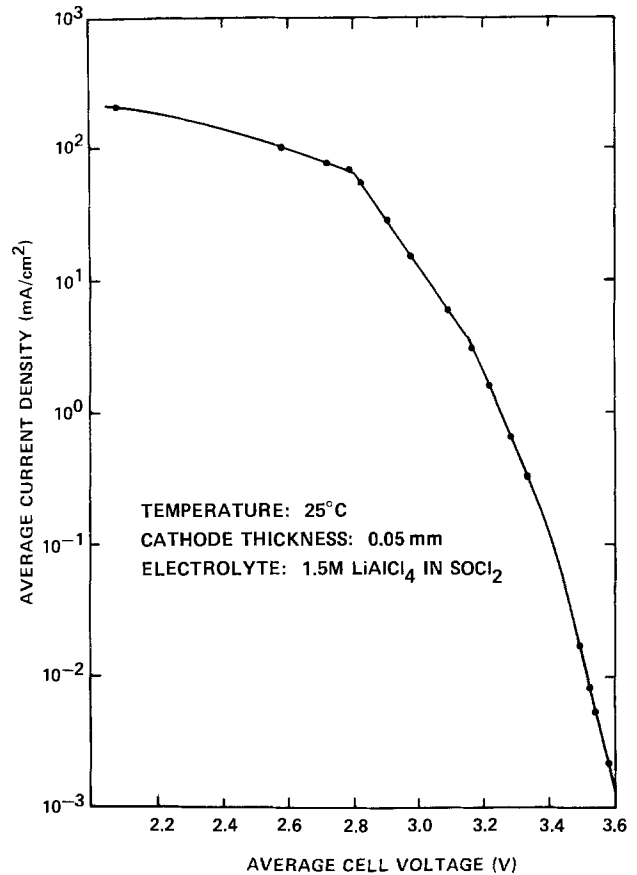
Fig. 1. Li/SOCl₂ cell discharge curves

amps per cm² to more than a tenth of an amp per cm². The data plotted in Fig. 1(a) through 1(f) are summarized in Table I in which are listed the average current densities, the average discharge voltages, and the voltage range spanned during the first 80% of the discharge.

Additionally, as shown in Fig. 1, the increasing discharge rate results not only in an increase in the slope of the approximately linear portion of the discharge curve, but also in a decrease in the relative rate of voltage decline at the end of the approximately linear portion of the curve. The time required for the voltage on load to drop from 90% of E_{avg} to 70% of E_{avg} expressed as a percentage of the discharge duration has been taken as a measure of this characteristic of the Li/SOCl₂ discharge curve. It has been found that, at very low rates (between 2 and 20 $\mu\text{A}/\text{cm}^2$), the time required for E to drop from 0.9 E_{avg} to 0.7 E_{avg} is, on the average, about 4% of the discharge duration. At intermediate rates (between 0.3 and 10 mA/cm^2), the time required for E to decrease from 0.9 E_{avg} to 0.7 E_{avg} is, on average, about 9% of the discharge duration. However, at high discharge rates (between 10 and 200 mA/cm^2), the time required for E to drop from 0.9 E_{avg} to 0.7 E_{avg} is about 30% of the discharge duration.

These observations can be conveniently summarized by noting that, as the average discharge rate increases, the average voltage on load decreases and the approximate shape of the discharge curve changes from that of a step function to that of a downward ramp.

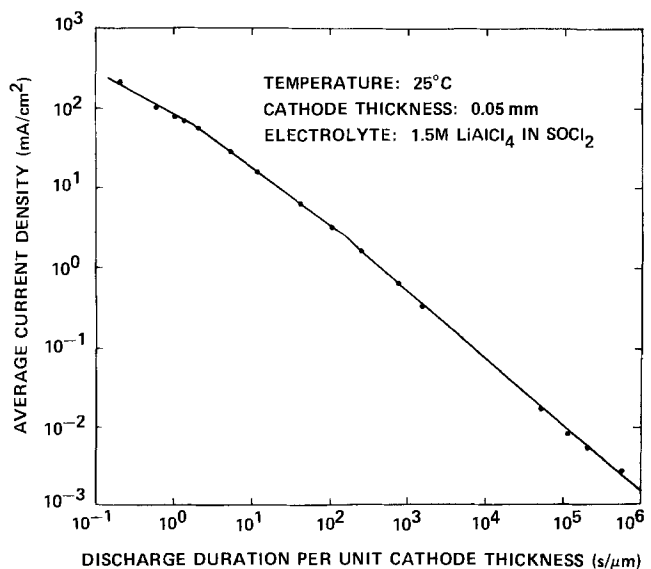
The average voltage on load is plotted as a function of the logarithm of the average current density in Fig. 2 for discharge rates ranging from 2.7 $\mu\text{A}/\text{cm}^2$ to 0.21 A/cm^2 . Over this range of discharge rates, E_{avg}

Fig. 2. Li/SOCl₂ cell polarization curve

varies from 3.58V (close to the open-circuit voltage) to 2.07V. Pronounced changes in slope are observed to occur at current densities of about 3 and 60 mA/cm^2 .

The discharge duration per unit cathode thickness is plotted as a function of the average current density on a log-log scale in Fig. 3. Each point on this graph corresponds to a point in the preceding log current density vs. cell voltage plot (Fig. 2). Again, notice the pronounced changes in slope occurring at current densities of about 3 and 60 mA/cm^2 . The linearity of the log current density vs. log discharge duration plot is an example of a general relationship first expressed by Peukert (4). (In this equation, α and β are constants.)

$$It^\alpha = \beta \quad [1]$$

Fig. 3. Li/SOCl₂ cell discharge duration vs. discharge rateTable I. Li/SOCl₂ cell polarization characteristics

| I_{avg}/A (A/cm^2) | E_{avg} (V) | ΔE (V) |
|--|---------------|----------------|
| 2.69×10^{-6} | 3.58 | 0.02 |
| 5.38×10^{-6} | 3.54 | 0.05 |
| 1.69×10^{-5} | 3.49 | 0.07 |
| 6.56×10^{-4} | 3.28 | 0.14 |
| 1.60×10^{-3} | 2.97 | 0.20 |
| 1.03×10^{-1} | 2.58 | 0.25 |

More recently, it has been observed that the Peukert equation can be used in general to describe the discharge behavior of primary as well as secondary batteries (5). Such batteries characteristically deliver a limiting capacity at low rates. Thus, Peukert-type equations are not generally useful to express the discharge behavior of primary batteries at low discharge rates. However, the cells described here did not display a limiting capacity even at rates in the microamp per cm² range.

The relationship between the current density and the discharge duration (per unit cathode thickness) corresponding to the three segments of the Peukert plot defined by the two above-mentioned changes in slope can be expressed as follows (where the units of I are amperes per cm² and those of t/T are seconds per micrometer of cathode thickness).

For $3 \times 10^{-6} \text{ A/cm}^2 \leq I \leq 3 \times 10^{-3} \text{ A/cm}^2$,

$$I(t/T)^{0.84} = 0.167 \quad [2]$$

For $3 \times 10^{-3} \text{ A/cm}^2 \leq I \leq 6 \times 10^{-2} \text{ A/cm}^2$,

$$I(t/T)^{0.72} = 0.0954 \quad [3]$$

For $6 \times 10^{-2} \text{ A/cm}^2 \leq I \leq 2 \times 10^{-1} \text{ A/cm}^2$,

$$I(t/T)^{0.52} = 0.0846 \quad [4]$$

The data presented in Fig. 3 can be equivalently expressed by plotting the logarithm of the current density vs. the discharge capacity per unit cathode volume. Thus, in Fig. 4 the discharge capacities (in units of mA-hr per cm² of cathode area for a 50 μm cathode thickness) are plotted as a function of the logarithm of the current density for discharge rates between 2 μA/cm² and 0.2 A/cm². When the data are plotted in this fashion, the absence of a limiting capacity at low discharge rates is even more striking. In fact, at very low rates the measured capacities are much larger than would be predicted from an extrapolation of the higher rate data.

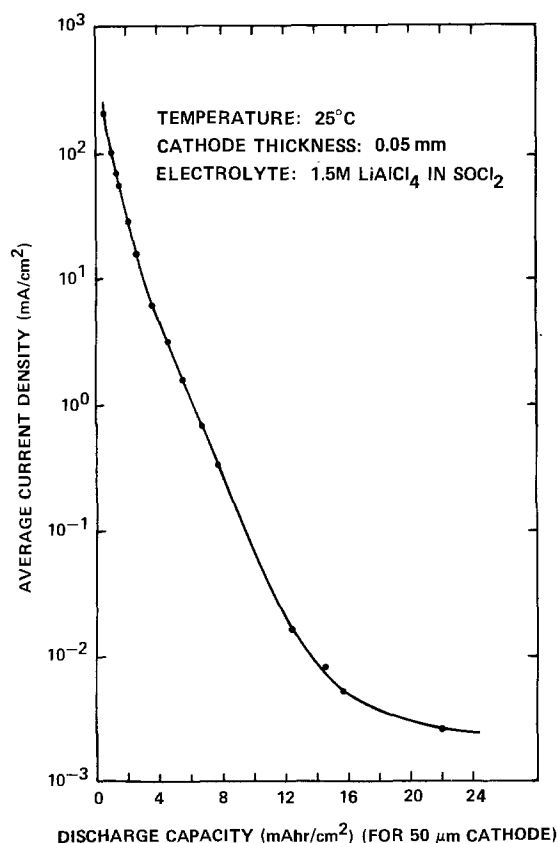
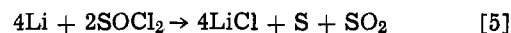


Fig. 4. Li/SOCl₂ cell discharge capacity vs. discharge rate

The generally accepted overall Li/SOCl₂ discharge reaction can be written as (6)



The S and SO₂ are soluble in the excess SOCl₂ electrolyte. However, the negligible solubility of the LiCl causes it to precipitate within the porous carbon black cathode as it is formed therein. Thus, the limiting capacity of a cathode-limited cell should be calculable from the amount of LiCl that can be contained within the cathode pores.

Scanning electron micrographs of the edges of spent cathode material were used to determine the thicknesses of the fully discharged cathodes. The cathodes from the cells discharged at the 2.7 μA/cm² rate were found to have increased in thickness from about 30 μm to about 55 μm during the 9 month discharge period. Assuming the entire pore volume of the expanded cathodes to be filled with crystalline LiCl, a cathode initially 50 μm thick would, after being so expanded, yield a capacity of about 11 mA-hr per cm² of geometric surface area—half the electrical capacity actually obtained. This observation suggests that, at least for discharge rates in the microamp per cm² range, the commonly accepted discharge reaction may not apply and that much less LiCl (or other insoluble discharge product) is formed per mole of oxidized metallic lithium than is formed at higher rates. Alternatively, given enough time, it may be possible for the LiCl reaction product to dissolve and be deposited upon surfaces other than within the porous cathode.

As shown in Fig. 2, cathode-limited Li/SOCl₂ cells with thin PTFE bonded carbon cathodes polarize to a relatively small degree when discharged at current densities no higher than a few milliamps per cm² of geometric surface area. However, much more severe polarization is encountered at higher discharge rates, the more severe the greater the current density. Thus, alternative cathode materials have been sought by the use of which improved performance characteristics might be attained at moderate to high discharge rates (2, 7, 8).

As shown in Fig. 5 and 6, sizable increases in both cell operating voltage and discharge capacity have been realized by enriching the carbon voltage and discharge capacity have been realized by enriching the carbon black cathode with 9 weight percent (w/o) finely divided metallic platinum. In particular, as shown in Fig. 5 for discharge rates between 1 and 150 mA/cm², between 200 and 300 mV improvements in cell operating voltage may be achieved by the use of such cathodes. Moreover, as shown in Fig. 6, sizable increases in discharge capacity (from 50 to 100%) have also been found to result from the use of such platinum-enriched cathode materials.

Even with the use of catalytic cathode materials, however, Li/SOCl₂ cells often exhibit limiting currents considerably below those that would be required to satisfy certain applications. It is true that, as shown in Fig. 7 for the standard cathode material, somewhat higher load voltages may be achieved by increasing the cathode thickness. However, the higher the discharge rate and the greater the cathode thickness, the smaller is the improvement in polarization to be gained by a given increase in thickness. This effect is demonstrated in Table II in which the average load voltage is listed as a function of cathode thickness for Li/SOCl₂ cells discharged at 25°C with the standard 1.8M LiAlCl₄ electrolyte, with standard carbon black cathodes, and at a constant 58 mA/cm² rate. As shown, an increase in cathode thickness beyond about 0.25 mm has no significant effect upon cell polarization at this moderately high discharge rate.

The effect of increasing cathode thickness upon cathode utilization efficiency parallels the relationship be-

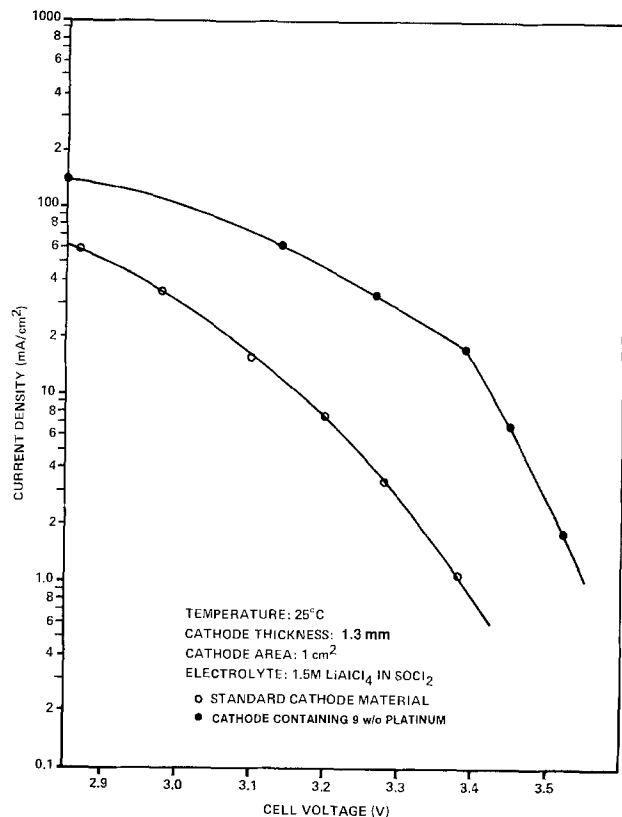


Fig. 5. Li/SOCl₂ polarization curves with standard and platinum-enriched cathode materials.

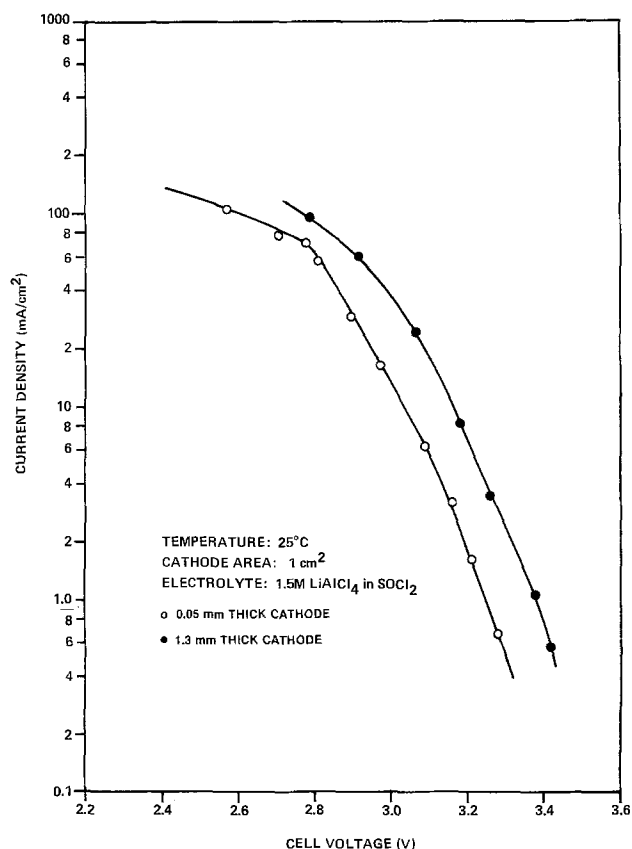


Fig. 7. Li/SOCl₂ polarization curves with 0.05 and 1.3 mm cathode thicknesses.

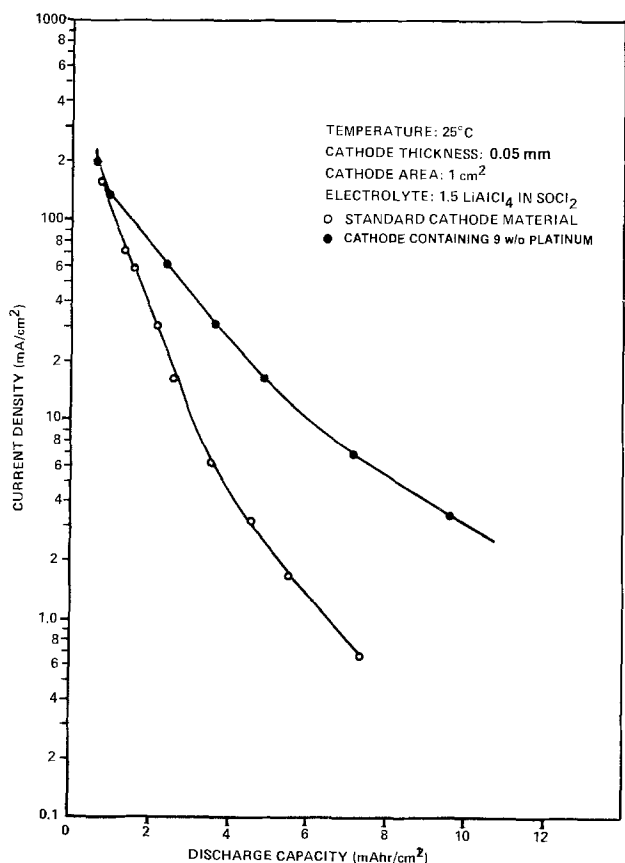


Fig. 6. Li/SOCl₂ discharge capacity vs. discharge rate with standard and platinum-enriched cathode materials.

tween cathode thickness and polarization. The discharge capacity per unit cathode volume (for a 1 cm² geometric cathode surface area) is plotted vs. the cath-

ode thickness in Fig. 8 for Li/SOCl₂ cells discharged at 25°C with the standard electrolyte, with standard carbon black cathodes, and at a 30 mA/cm² discharge rate. As shown, the cathode utilization efficiency decreases steadily with increasing cathode thickness, the most rapid variation in utilization efficiency occurring with thicknesses less than about 0.15 mm. Thus, the thicker the cathode, the less efficiently is the added cathode pore volume utilized in the storage of solid discharge products. [This effect is also demonstrated in the Peukert-type plot contained in Fig. 6 of Ref. (1) for current densities ranging between 3 and 100 mA/cm².] The rapid decrease in utilization efficiency with increasing cathode thickness reflects the fact that the higher the discharge rate, the more the LiCl discharge product tends to be preferentially deposited near to the surface of the cathode which faces the lithium anode (1, 9). Thus, the higher the discharge rate, the more the portion of the cathode nearest the anode is utilized more effectively than are the interior portions of the cathode.

Both of the observed effects, the relative insensitivity of the load voltage to cathode thickness and the reduction in cathode utilization efficiency with increasing thickness, result from the same cause—the relatively poor conductivity of the 1.8M LiAlCl₄ electrolyte solution ($2 \times 10^{-2} \Omega^{-1} \text{cm}^{-1}$ at 25°C). As the cathode is traversed from the side facing the lithium anode to the interior, the *I-R* losses accumulate, effectively

Table II. Li/SOCl₂ average load voltage vs. cathode thickness for $i = 58 \text{ mA/cm}^2$

| Cathode thickness (mils) | Average load voltage (V) |
|--------------------------|--------------------------|
| 2 | 2.82 ± 0.01 |
| 11 | 2.88 ± 0.01 |
| 30 | 2.88 ± 0.01 |
| 40 | 2.88 ± 0.01 |

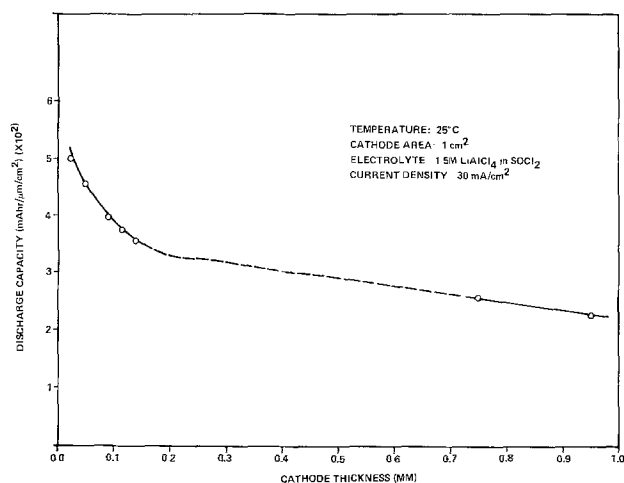


Fig. 8. Li/SOCl₂ cathode utilization vs. cathode thickness

negating the reduction in overvoltage that would otherwise result from a reduction in the specific current density (the discharge rate per unit of real cathode surface area). Moreover, as the precipitating LiCl builds up within the cathode pores, the more severe these I - R losses become. Thus, the higher the current density, the more the discharge reaction tends to concentrate toward the side of the cathode nearest the anode. The resulting preferential buildup of LiCl at the entrances to the cathode pores further magnifies the I - R losses leading to an even less uniform cathode utilization profile. It is this ever worsening mass transport situation which is responsible for the change in shape of the discharge curve with increasing discharge rate and for the steep decline in discharge capacity that accompanies an increase in discharge rate.

In order to demonstrate the magnitude of the effect of solution I - R losses upon the high rate performance characteristics of cathode-limited Li/SOCl₂ cells as well as to determine quantitatively the importance of interelectrode spacing in the determination of these characteristics, the following experiments were performed. Li/SOCl₂ cells with 0.050 mm thick standard carbon black cathodes and with the standard 1.8M LiAlCl₄ electrolyte were discharged at 25°C across 4, 7, and 10Ω loads. Five thicknesses of glass fiber separator paper were used, the approximate thicknesses being 0.068, 0.14, 0.21, 0.34, and 0.45 mm. Glass-coated metal weights were used to ensure good interfacial contact between the cell components. Thus, the interelectrode separation was established by the separator thickness. At least two cells containing each of the five thicknesses of separator paper were discharged to termination across each of the three constant loads. The average load voltages and discharge rates are compared in Fig. 9.

In general, the greater the interelectrode spacing, the lower was the average load voltage at constant current density. Similarly, the apparent limiting current decreased markedly with increasing interelectrode spacing. However, the discharge capacities were found to be independent of the interelectrode separation. Qualitatively similar results were obtained when the entire series of experiments was repeated at 65°C.

Perhaps the most striking result of these measurements is the linearity of the Tafel plot obtained with the 0.068 mm interelectrode spacing, indicating that the intrinsic limiting current determined by the kinetics of the Li/SOCl₂ discharge reaction is well in excess of 500 mA/cm² at room temperature, with a cathode thickness of only 0.05 mm, and in the absence of any catalytic cathode materials.

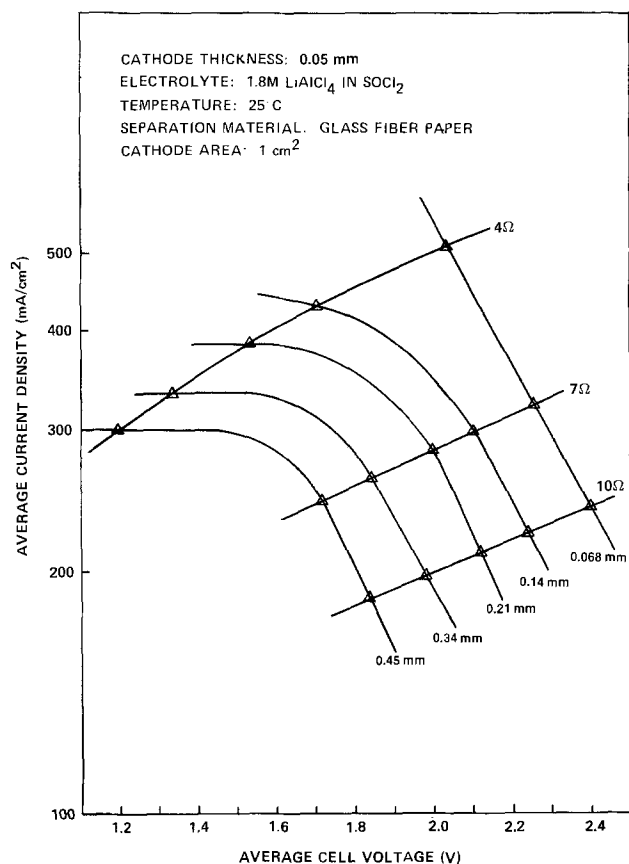


Fig. 9. Li/SOCl₂ polarization curves with varying separator thicknesses.

Summary

The ambient temperature discharge characteristics of cathode-limited Li/SOCl₂ cells have been investigated at discharge rates ranging over five orders of magnitude (from about 2 μA/cm² to about 0.5 A/cm²). The discharge characteristics of these cells have been summarized and compared. As the average discharge rate increases, the average voltage on load decreases and the approximate shape of the discharge curve changes from that of a step function to that of a downward ramp. Contrary to expectations, no limiting capacity was found, even at discharge rates as low as a few microamps per cm². Further, the cells discharged at the lowest current density so far examined (about 2.7 μA/cm²) exhibited capacities twice those expected assuming the validity of the commonly accepted overall discharge reaction.

Sizable increases in both cell operating voltage and discharge capacity have been realized by enriching the carbon black cathode with finely divided metallic platinum which catalyzes the electroreduction of the SOCl₂. Improvements in the high rate discharge characteristics of cathode-limited Li/SOCl₂ cells can also be accomplished by increases in cathode thickness. However, the magnitudes of these improvements are limited by solution I - R losses which become increasingly severe the higher the discharge rate and the greater the discharge duration. These solution resistance effects are also responsible for the rapid decline in average load voltage that results from an increasing interelectrode spacing at high discharge rates. It has been shown that, at room temperature and in the absence of any catalytic cathode materials, the intrinsic limiting current determined by the kinetics of the Li/SOCl₂ discharge reaction is well in excess of 500 mA/cm².

Manuscript submitted Dec. 1, 1980; revised manuscript received April 20, 1981. This was Paper 55 presented at the Hollywood, Florida, Meeting of the Society, Oct. 5-10, 1980.

Any discussion of this paper will appear in a Discussion Section to be published in the June 1982 JOURNAL. All discussions for the June 1982 Discussion Section should be submitted by Feb. 1, 1982.

Publication costs of this article were assisted by GTE Laboratories, Incorporated.

REFERENCES

1. K. A. Klinedinst and M. J. Domeniconi, *This Journal*, **127**, 539 (1980).
2. K. A. Klinedinst, in "Power Sources for Biomedical Implantable Applications and Ambient Temperature Lithium Batteries," B. B. Owens and N. Margalit, Editors, p. 579, The Electrochemical Society Softbound Proceedings Series, Princeton, NJ (1980).
3. K. A. Klinedinst, in "Proceedings of the 29th Power Sources Symposium," Atlantic City, NJ, pp. 118-121 (June 1980).
4. G. W. Vinal, "Storage Batteries," 4th ed., p. 216, John Wiley and Sons, Inc., New York (1955).
5. R. Selim and P. Bro, *This Journal*, **118**, 829 (1971).
6. C. R. Schlaikjer, F. Goebel, and N. Marincic, *ibid.*, **126**, 513 (1979).
7. L. R. Giattino and V. O. Catanzarite, U.S. Pat. 4,167,608 (1979).
8. A. N. Dey, N. Hamilton, W. Bowden, and P. Witalis, ERADCOM Grant No. DAAB07-78-C-0563, Report No. DELET-TR-78-0563-3 (November 1979).
9. A. N. Dey and P. Bro, *This Journal*, **125**, 1574 (1978).

Effects of Deep Cycling on Lead Positive Plates

C. P. Wales* and A. C. Simon*¹

Naval Research Laboratory, Washington, DC 20375

ABSTRACT

Characteristics of the active material in lead positive plates were determined by light and electron microscopy, and by surface area analysis as the plates were cycled. Average size of PbSO₄ in discharged plates gradually decreased with cycling. Some PbO₂ usually remained within the PbSO₄ crystals. Capacity loss was mainly caused by large areas developing where the PbO₂ did not reduce on discharge. The rate of capacity loss decreased from 1.7 to 0.9% per cycle as discharge current density increased from 125 to 2000 A/m² (3 hr to 4 min discharge rates). Capacity loss was only 0.3% per cycle at 18 A/m² (24 hr rate) which suggests a different reaction mechanism. Surface area of the active material increased as discharge current density increased. The values for charged and discharged surface areas tended to approach each other with cycling.

Energy constraints in the USA have caused an increased focus on the use of electric vehicles. This interest has directed our attention to the effects of power demands on the lead-acid battery and to the question of the differences in electrode microstructure that might be produced by different rates of discharge. As the first stage of our investigation, the effect of different rates of discharge on the negative electrode was studied (1). In the present work the investigation has been extended to the positive plate.

Formed positive plates may have various structures depending on paste composition, treatment, and forming conditions. Despite the initial differences, plates cycled the same way are converted to practically the same microstructure after cycling, with the structure being a function of current density and mode of operation (2). Current density has a large effect on positive electrodes of lead-acid batteries because the rate at which reactions take place is governed by diffusion and crystallization processes, with the reaction mainly involving dissolved Pb⁺⁺ ions rather than solid-state reactions (3). Other important factors that affect structure are the temperature and the proportions of α -PbO₂ and β -PbO₂ in the plate (4, 5).

Discharges begin with nucleation of PbSO₄ on PbO₂ surfaces that are in contact with the electrolyte. Further growth of PbSO₄ depends on dissolution of nearby PbO₂ and deposition of PbSO₄ on the surface of the PbSO₄ (6). Particles of inactive PbO₂ that remain within the PbSO₄ at the end of a discharge form a conductive network and serve as nuclei for crystallization of the PbO₂ during charge (6, 7).

Experimental

The positive and negative plates used in this study were commercial plates of the type used in automotive batteries. The active materials had not been formed. Positive plate size was 144 × 122 × 1.75 mm, not including the tabs. The grids were 4% antimony-lead. Before putting a positive plate in use, active material pellets were removed to outline seven equal areas as described earlier (1). Approximately 61.6g of unformed active material remained, which was 64% of the amount originally present.

Experimental cells and procedures were generally the same as in our negative electrode study (1), except that the cells contained one positive plate and two negative plates. The forming charge began within 30 sec after a positive plate was put into 1.150 sp gr acid. A positive plate was formed 18 hr at 50 A/m² followed by 22.5 hr at 20 A/m². Then the acid was adjusted to 1.255 sp gr and maintained at 1.250-1.260 during the cycling. The two negative plates in a cell had a much greater capacity than the one positive plate and were formed separately.

Positive plates were discharged at 18, 125, 500, or 2000 A/m² geometric area. This resulted in discharges lasting, respectively, 24 hr, 3 hr, 0.5 hr, and 4 min during the first six cycles. Final cell potentials were 1.8, 1.75, 1.5, and 1.0V. A particular positive plate was always discharged at the same current density for its entire life. Adjustments to cell current were made after removal of each sample, so that positive plate current density remained constant. Capacity discharges were done at cycles 1-6 and every 10 cycles thereafter. In all other cycles the positive plates were discharged to 80% of the previous capacity discharge. Cycling was done at room temperature (19°-25°C). Charges

* Electrochemical Society Active Member.

¹ International Lead Zinc Research Associate at Naval Research Laboratory.

Key words: particles, electrode, current density, discharge.

were always done at 31.25 A/m^2 , except for the forming charge.

Samples cut from the positive plates were washed 45-60 min in distilled water and then dried at 60°C . Fractured cross sections of the active material were examined using an AMR Model 1000 scanning electron microscope. Other plate portions were impregnated with plastic, cut into cross sections, polished, and examined by optical microscopy. The BET surface area was determined with a Micromeritics Model 2205 surface area analyzer, using about 5g of active material broken into pieces that were 5 mm or smaller. The material was degassed 40 min at 100°C in argon before analysis.

Results and Discussion

Figure 1 shows the change in discharge capacity with cycling. Values for the first 26 cycles are averages of results from two or three positive plates that were cycled independently. Individual measurements deviated by an average of 2.3% from the values in Fig. 1. Values given for cycles 32-76 are individual measurements. When capacity declined rapidly as a plate approached failure the discharge potential sometimes reached the cut-off value and a plate would be 100% discharged before the next regularly scheduled capacity discharge. Capacities are compensated for the removal of samples and are given as if the quantity of active material used at cycle 1 had remained constant. Capacity and structure changed more rapidly with the deep discharges used in the present work than they would have changed if SAE cycles had been used.

During the early cycles the capacity varied inversely with current density, as one would expect (Fig. 1). All three positive plates cycled at 125 A/m^2 showed a much greater rate of capacity loss than did the plates cycled at the other current densities. Plates discharged at 18 A/m^2 maintained their capacity much longer than plates discharged at 125 - 2000 A/m^2 . The difference between the capacity obtained at cycles 30-50 when using 125 - 2000 A/m^2 and the capacity when using 18 A/m^2 suggests that a change in discharge mechanism occurred between 18 and 125 A/m^2 .

Figure 2 gives capacities as a percent of the capacity obtained at cycle 1. If part of the active material becomes inactive after a certain number of cycles, then capacity would be expected to decrease more rapidly when cells were cycled at the lower current densities because a larger proportion of the active material is reduced as current density is decreased. In agreement with this, Fig. 2 shows that the rate of capacity loss did increase as discharge current density decreased from 2000 to 125 A/m^2 . At 18 A/m^2 , however, the trend is reversed and the capacity loss is significantly lower. This suggests strongly that the discharge is

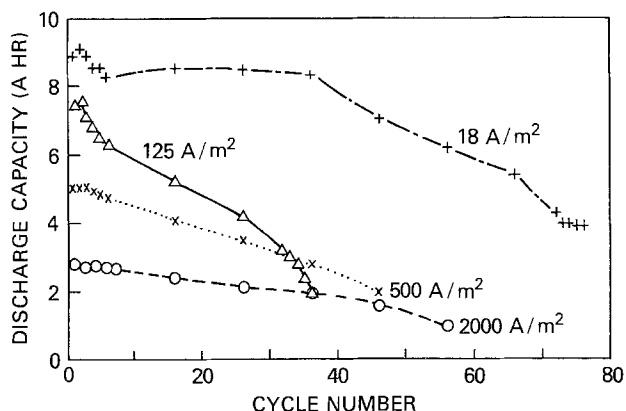


Fig. 1. Capacity discharges of positive plates. Discharge current densities are given on the curves.

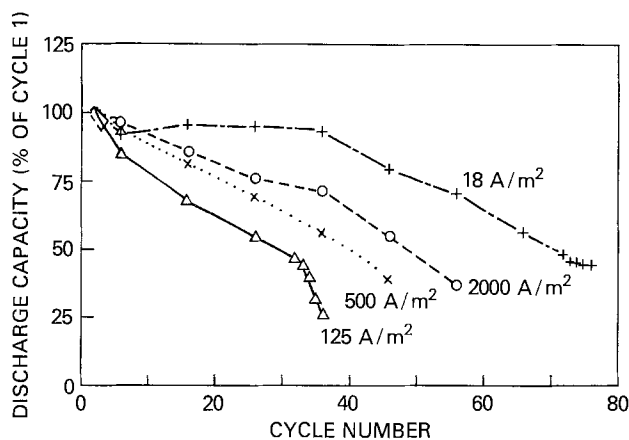


Fig. 2. Positive plate capacity relative to the capacity at cycle 1. For clarity the individual values at cycles 1-5 are omitted.

limited by a different mechanism at 18 A/m^2 than at 125 - 2000 A/m^2 . At the lowest current density used in this work the reaction apparently had sufficient time so that diffusion processes did not limit cell capacity.

The rate of capacity loss was 0.3% per cycle for discharges at 18 A/m^2 . This is the same as the rate of loss when negative plates were cycled at 18 A/m^2 (1). The positive plates lost capacity at about 1.7, 1.2, and 0.9% per cycle when discharged at 125 , 500 , and 2000 A/m^2 (Fig. 2). These values are all higher than the 0.7% per cycle loss obtained when negative plates were cycled at 125 - 2000 A/m^2 (1).

The changes in positive plate potentials during discharge are shown in Fig. 3. Potentials were lower in the first part of a discharge at cycle 1 and in the early cycles than they were at later cycles. The cycles between 1 and 26 gave potentials intermediate between those shown in Fig. 3. Polarization of the active material increased when current density was increased. The increased polarization was indicated in Fig. 3 by the lowered potential during the first half of a discharge, and by a decrease in the amount of discharge that was obtained before the potential began to fall rapidly.

Since the negative plates in the experimental cell had considerably more capacity than the positive plates, the negative plates only varied a few hundredths of a volt during the course of a discharge. Therefore, approximate cell potentials can be obtained by adding 0.96 , 0.96 , 0.95 , and 0.89V , respectively, to the values shown in Fig. 3 for discharges at 18 , 125 , 500 , and 2000 A/m^2 .

Structure of discharged plates.—The effect of discharge current density on PbSO_4 crystal size was im-

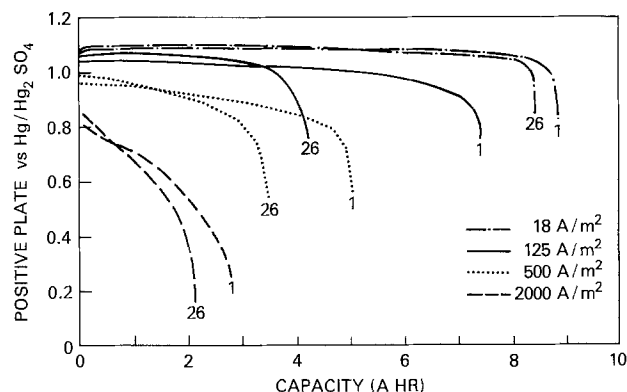


Fig. 3. Discharge potentials between the positive plate and the $\text{Hg}/\text{Hg}_2\text{SO}_4$ reference electrode. Potentials are shown for cycles 1 and 26 at four rates of discharge. The current density used at cycle 1 was repeated in all subsequent discharges.

mediately evident after a single discharge of the positive plates. Scanning electron microscope photographs of fractured cross sections after discharges are shown in Fig. 4 and 5. The PbSO_4 size varied inversely with current density. The major changes in PbSO_4 crystal size with cycling are summarized in Table I for the first 26 cycles. The size ranges were based on measurements of SEM photographs. To help minimize sampling error, the photographs were usually taken from at least three different samples of each electrode, and from two electrodes that were independently given the same cycling treatment. Although most of the active material was in the range of sizes given in Table I, one could also find particles outside these ranges.

The average size of the PbSO_4 gradually decreased with cycling, particularly in the early cycles (Table I). When using the lower discharge rates of 18 and 125 A/m^2 the size decrease occurred over a longer number of cycles. Samples taken later than cycle 26 from positive plates discharged at 125-2000 A/m^2 contained the same size PbSO_4 as was found at cycle 26 (Table I). However, at 18 A/m^2 average PbSO_4 size slowly decreased for about another 20 cycles although remaining in the 5-10 μm range.

Some PbO_2 was always present in the discharged plates, and can be seen in Fig. 4 and 5. The amount of PbO_2 remaining at the end of a discharge increased as discharge current density increased (compare Fig. 4 and 5). The increased PbO_2 reflects the lower discharge capacity obtained at the higher currents. The amount of PbO_2 in discharged electrodes also increased as the number of cycles increased. At the end of cycle 6 discharge at 125-2000 A/m^2 most of the PbSO_4 was obscured by a PbO_2 covering. As the cycling continued fewer and fewer PbSO_4 crystals were visible at the end of a discharge because of the increasing presence of PbO_2 . After discharges at 18 A/m^2 , much



Fig. 4. Positive active material at the end of cycle 1 discharge at 18 A/m^2 , the 24 hr rate. The smallest particles are PbO_2 . Medium size and large crystals are PbSO_4 .

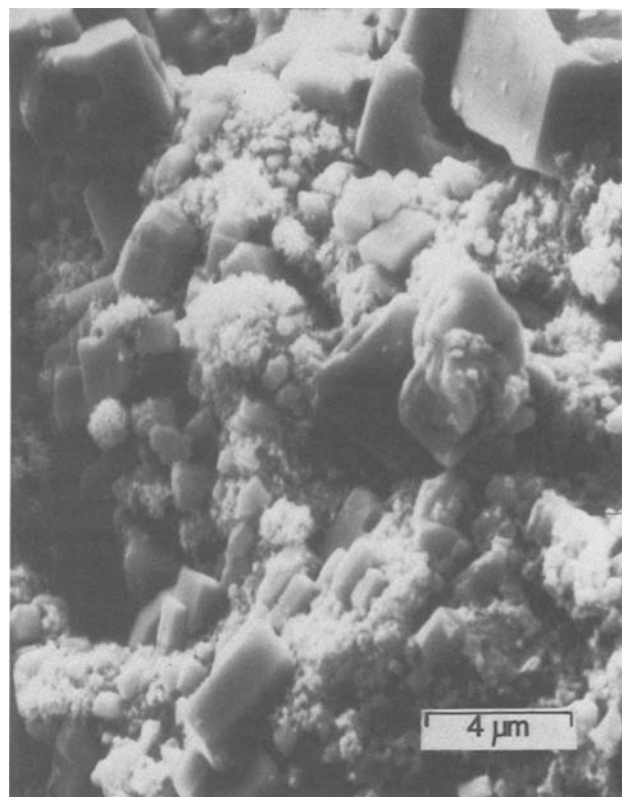


Fig. 5. Positive active material at the end of cycle 1 discharge at 2000 A/m^2 , the 4 min rate. Note the smaller PbSO_4 size and increased amount of PbO_2 compared to Fig. 4.

less PbO_2 was present and the amount of PbO_2 increased more slowly with cycling.

The examination of electrode cross sections by optical microscopy revealed some things not evident from examination by the scanning electron microscope and confirmed others. The first discharge of the positive plates produced closely packed PbSO_4 (Fig. 6). The PbSO_4 crystals often contained PbO_2 , with the amount of PbO_2 within the PbSO_4 increasing as discharge current increased. The SEM examinations gave no hint of the large amount of PbO_2 inside the PbSO_4 crystals. These PbO_2 particles play an important part in the recharge process (6, 7). As the cycling was continued, the active material gradually changed its consistency (Fig. 7).

During discharges at 18 and 125 A/m^2 the PbO_2 was reduced to PbSO_4 at sites throughout the electrode. Although electrodes discharged at 125 A/m^2 had the same structure at the outer layers as in the interior at cycle 1, there was a tendency for large particles to form in the interior of the electrode as cycling at 125 A/m^2 continued. Electrodes discharged at 18 A/m^2 did

Table I. Range of sizes that were common for PbSO_4 crystals in discharged positive plates (μm)

| Cycle | Current density (A/m^2) | | | |
|-------|------------------------------------|-----------------------|------------------------|------------------------|
| | 18 | 125 | 500 | 2000 |
| 1 | Most 10-20 Many 1-10 | Most 2-6 Some 1-10 | Most 0.5-3 Some 3-8 | Most 0.5-3 Some 3-8 |
| 6 | Most 5-10 Some 1-20 | Most 1-5 Some 5-10 | Most 0.5-3 Some 3-5 | Most 0.5-3 Some 3-5 |
| 16 | Most 5-10 Few over 10 | Same as cycle 6 | Most 0.5-3 Few 3-5 | Same as cycle 6 |
| 26 | Most 5-10 Scarce over 10 | Most 1-5 Some 5-8 | Same as cycle 16 | Same as cycle 6 |

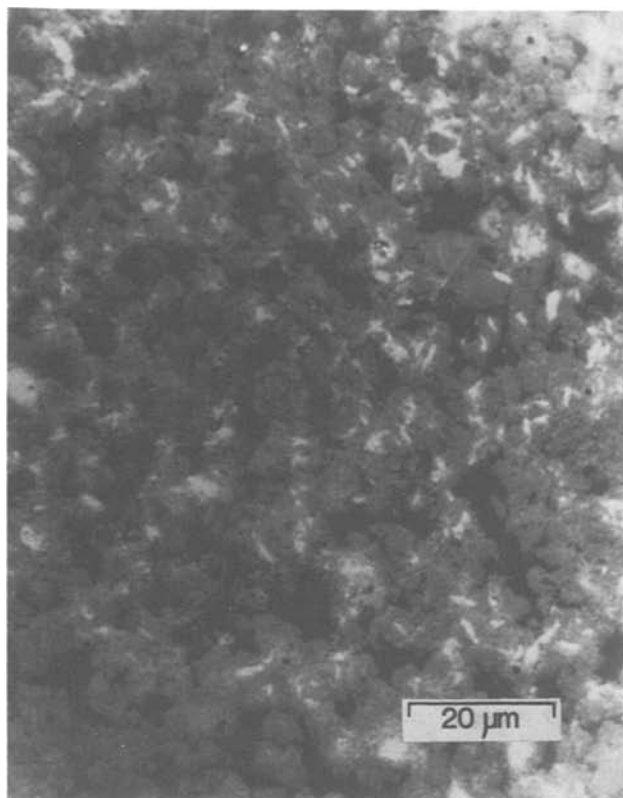


Fig. 6. Cross section through part of the positive plate at the end of cycle 1 discharge at 500 A/m², the 0.5 hr rate. Lightest color is PbO₂, medium gray is PbSO₄, and darkest gray is void space between the active material particles.

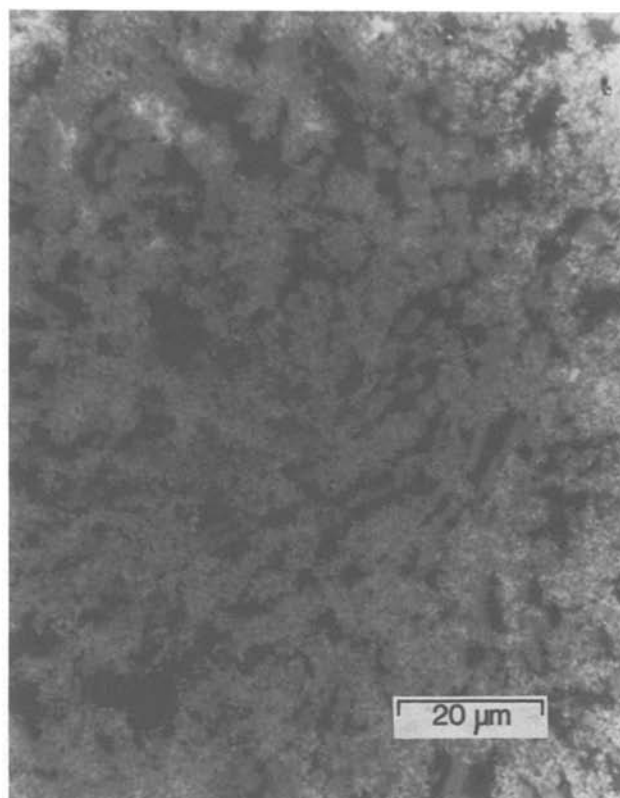


Fig. 7. Cross section through part of the negative plate at the end of cycle 26 discharge at 500 A/m². Compare with Fig. 6.

not develop a difference between the outer layers and the interior. When using discharges at 500 or 2000 A/m², the PbSO₄ formed mainly near the surfaces of the electrode with some areas in the interior showing no reduction of PbO₂. Bode *et al.* reported similar results for the effect of discharge current density on PbSO₄ content (8). The areas shown in Fig. 6 and 7 were in the outer 30% of the plate, the regions where most of the reduction and oxidation took place when discharges were done at 500 A/m². Diffusion became an increasingly limiting factor at the higher current densities. The amount of PbO₂ remaining in the center of a discharged plate was largest for 2000 A/m². Even after 56 cycles using 2000 A/m² as the discharge rate, some of the central areas still had PbO₂ apparently unchanged since the forming charge.

The amount of PbO₂ that remained at the end of a discharge gradually increased with cycling. Large areas developed where the active material consisted entirely of PbO₂ at the end of a discharge. For example, after cycle 26 discharge at 125 A/m², an estimated 30-40% of the active material remained in the form of areas of PbO₂ without PbSO₄. Even at 18 A/m² about 15-25% of the active material consisted of separate PbO₂ areas at the end of cycle 26 discharge. After cycle 1 discharge at 18 or 125 A/m², no large areas consisting only of PbO₂ were found, although much PbO₂ remained within the PbSO₄ crystals.

At the higher discharge current densities, the development of increasing amounts of inactive PbO₂ in the outer layers was partly offset by a gradual attack on the PbO₂ in the interior, the PbO₂ which had taken little part in discharges at the early cycles. As a result, the amount of PbO₂ in the interior gradually decreased with cycling. This active material in the interior must have prevented capacity from falling as rapidly as would have taken place if all of the active material had been used at cycle 1.

The amount of void space in discharged active material increased as discharge current density increased. At any given current density the amount of voids also increased with cycling. The increase in porosity that occurred in 26 cycles can be seen by comparing Fig. 7 with Fig. 6. Because PbO₂ occupies a smaller volume than PbSO₄, the increase in void space is attributed to the larger amount of PbO₂ in discharged electrodes.

The decrease in discharge capacity with cycling appeared to result from failure of PbO₂ to reduce to PbSO₄, rather than from PbSO₄ not oxidizing on charge. Increasingly large amounts of PbO₂ remained at the end of a discharge as capacity decreased, while the amount of PbSO₄ in a charged electrode remained low. Loss of active material from the plates was not a major factor during the first half of the cycling. Shedding of active material became a problem late in the cycle life and may have contributed to the final drop in capacity.

Several differences were evident between the structures in discharged positive plates and the structures in negative plates that had been discharged at the same current densities (1). The PbSO₄ size tended to increase when negative plates were cycled, in contrast to the decrease in size for positive plates. The PbSO₄ concentration was only a little larger near the surfaces of negative plates than in the interior after discharges at 2000 A/m², while strong differences were found in positive plates. Negative plates also differed in showing an increase in the amount of discharged active material remaining at the end of charges. The positive and negative plates were similar in having approximately the same ranges for sizes of PbSO₄, and having increasing amounts of charged active material remaining at the end of discharges as the electrodes were cycled.

Structure of charged plates.—Charged plates that were given an equal number of cycles generally resembled each other when examined by the SEM re-

ardless of which discharge rate was used. Charged active material consisted of clumps of PbO_2 containing small PbO_2 crystals about 0.1-0.3 μm in size. A few of the PbO_2 clumps contained small PbSO_4 crystals. Typical clump size was 1-4 μm after cycle 6 charge, decreased between cycle 6 and 16, and then remained approximately constant. Clump size was smallest in electrodes that had been discharged at 18 A/m^2 .

When cross sections of charged positive plates were viewed by optical microscopy very little PbSO_4 was found. The charged plates that had always been discharged at 18 A/m^2 had a uniform structure throughout the active material with PbO_2 present as small particles. Charged plates given repeated cycles with discharges at 125 A/m^2 gradually developed larger PbO_2 clumps in the interior of the plates while the PbO_2 near the surface remained small. The PbO_2 clumps were randomly distributed at cycle 6 when using 125 A/m^2 but were mainly in the center of a cross section at cycle 16 and later.

The centers of charged plates that had been discharged at 500 or 2000 A/m^2 always had large clumps of PbO_2 which resembled the PbO_2 present at the end of the forming charge. The small change from the appearance after the forming charge probably resulted from the PbO_2 in the plate interior undergoing only a slight reduction during the discharges, followed by oxidation during charges. Charged electrodes given 26 or more cycles using 2000 A/m^2 as the discharge rate had smaller particles in the interior near the grid than elsewhere in the interior, but these particles near the grid were still larger than the PbO_2 in the outer layers.

Particles in the outer layers of a charged electrode always discharged at 500 A/m^2 resembled the small particles found when using 18 or 125 A/m^2 . In charged plates always discharged at 2000 A/m^2 , particles in the outer layers were much larger than those formed at the lower rates at cycle 6. The PbSO_4 developed during a discharge at 2000 A/m^2 was on the surface of large PbO_2 clumps. The centers of the original PbO_2 clumps were not reduced in the early cycles, but in later cycles increasing amounts of small PbO_2 clumps were present in the outer layers of plates always discharged at 2000 A/m^2 .

Active material consistency.—The consistency of the active material was strongly affected by cycling conditions. For the cycle 1 discharges the active material was much harder at 18 A/m^2 than at higher current densities. Charged active material was always a little softer than discharged active material at the same cycle. Although the active material was fastened firmly to the grids initially, it gradually softened with cycling and became quite fragile by the time that over 50% of the original capacity had been lost. The grids became increasingly brittle with cycling.

These changes can be correlated with structural changes observed in the active material. The unusually large PbSO_4 crystals that develop during cycle 1 discharge at 18 A/m^2 (Table I) give the active material a hardness never found under other conditions. Smaller PbSO_4 crystals present more opportunity for movement when a force is applied, and result in softer active material. In addition, PbO_2 particles are much smaller than PbSO_4 and give the active material less strength. The increasing amounts of the PbO_2 that became inactive with cycling perhaps resulted from loss of physical contact with the conducting grids. If so, this lack of contact would contribute to the loss of strength that was observed.

Surface area.—It has been shown that the surface area of formed positive plates increased as the proportion of $\beta\text{-PbO}_2$ to $\alpha\text{-PbO}_2$ increased (5, 9, 10). For formed plates with high $\beta\text{-PbO}_2$ content, the BET spe-

cific surface area decreased as acid concentration decreased, from 7.5 m^2/g in 3.5M H_2SO_4 to 5.2 m^2/g in 1.5M H_2SO_4 (5). Capacity was not proportional to the surface area of formed plates (5). Formed positive plates in the present work averaged 5 m^2/g , which is reasonable for a mixture of $\alpha\text{-}$ and $\beta\text{-PbO}_2$.

Current density had a strong effect on the specific surface area of discharged electrodes (Fig. 8). The values reported in the present work for cycles 1-27 were averages of surface areas measured from two or three electrodes that were cycled independently. A sample consisted of 14 pellets of active material. Surface areas from the individual electrodes had an average variation of 0.43 m^2/g from the values reported here. Repetition of a measurement usually gave less than 1% variation when surface area was 5 m^2/g or greater. Accuracy decreased when surface area was low, with repeated measurements differing by 1-4% for 1-3 m^2/g . These variations were smaller than structural variations within the samples.

The values in Fig. 8 can be compared to results of Voss and Freundlich (5) where $\beta\text{-PbO}_2$ plates would be expected to give BET specific surface areas of about 2.0, 3.0, and 5.2 m^2/g after discharges at 18, 125, and 350 A/m^2 , respectively. Cycle number was not specified. Wiesener and Reinhardt reported surface area of about 3 m^2/g in the early cycles for cells discharged at what was apparently the 2 hr rate, with surface areas slowly rising to about 4.5 m^2/g at cycle 70 (10).

The large PbSO_4 crystals that were produced at a low current density (Fig. 4) cause a low surface area for electrodes discharged slowly. Discharged electrodes had larger surface areas when higher current densities were used because the average size of the PbSO_4 crystals was smaller and also because less PbSO_4 formed before the discharge ended, which resulted in larger amounts of PbO_2 remaining.

Charged active material always had a higher surface area than discharged active material (compare Fig. 8 with Fig. 9); an expected result because PbO_2 particles are much smaller than PbSO_4 crystals. One might expect all of the charged electrodes to give the same surface area, since all used the same charge current density. However, the structures produced during discharge were not entirely destroyed during charge. Consequently, electrodes with the lowest surface area after a discharge tended to have the lowest area after being recharged. The differences in surface area of the charged active material were not nearly as great as the differences in the discharged active material. As cycling progressed the values for charged and discharged surface areas tended to approach each other. This was caused by increasing amounts of PbSO_4 remaining in the charged electrode and increasing amounts of PbO_2 remaining in the discharged electrode as the capacity slowly decreased with cycling.

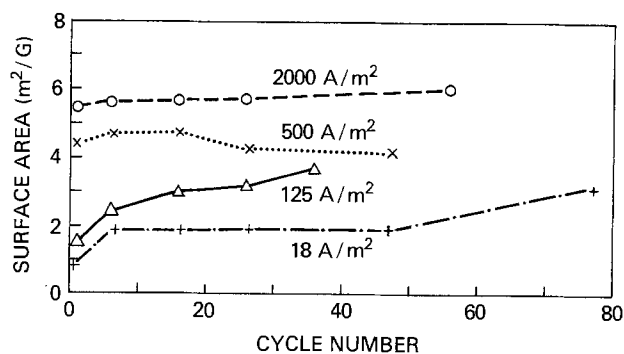


Fig. 8. BET specific surface areas of positive active material at the end of capacity discharges.

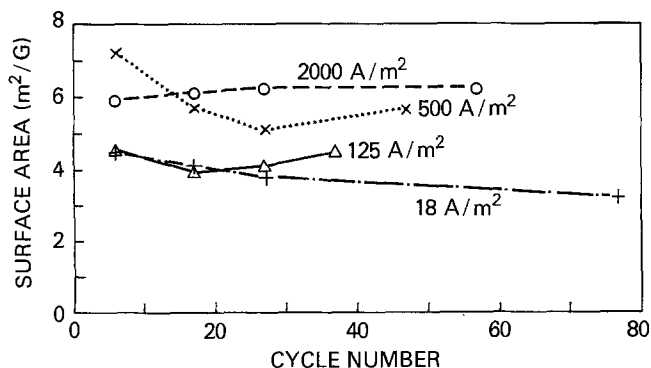


Fig. 9. BET specific surface areas after charges at 31.25 A/m². These positive electrodes were always discharged at the current densities given on this figure.

The specific surface area of unformed positive active material was 0.7 m²/g, probably not significantly different from the 0.8 m²/g for unformed negative active material (1). At the end of the forming charge the specific surface area of the positive active material had increased to about 5 m²/g while the negative active material had decreased to only 0.2 m²/g. Throughout the cycling the charged negative active material had only 3-4% of the surface areas given in Fig. 9 and discharged negative plates had only 4-6% of the values given in Fig. 8. This difference was caused by the high surface area of the PbO₂ particles always present in positive plates and the low surface area of the Pb particles in negative plates. It is surprising that discharged plates had such a great difference in surface area, since the sizes of PbSO₄ in positive and negative plates were comparable. Obviously the PbO₂ and Pb that remained in the discharged plates had a strong effect on specific surface area.

Summary and Conclusions

Positive plate capacity decreased with cycling because of PbO₂ failing to be reduced during discharge, instead of PbSO₄ not being oxidized during charge. An increasing proportion of the active material became inactive as the electrodes were cycled. The rates of capacity loss were 0.9, 1.2, 1.7, and 0.3%, respectively, for discharges at 2000, 500, 125, and 18 A/m². There were indications that the reaction at 18 A/m² was limited by a different mechanism than the diffusion processes which limit discharges at the higher rates.

The PbSO₄ crystal size varied inversely with current density and gradually decreased with cycling, particularly in the early cycles. The PbSO₄ crystals often contained PbO₂ that was not evident until the PbSO₄ crystals were cut open. In addition, as the cycling continued increasingly large areas of PbO₂ remained in discharged electrodes. The amount of void space in

discharged electrodes increased with cycling and when discharge current density increased.

The active material consistency was strongly affected by cycling conditions. The hardest active material was obtained after the initial discharge at 18 A/m², and was caused by the unusually large PbSO₄ crystals that developed. At all discharge current densities the active material gradually softened with cycling as smaller crystals developed. The active material became quite fragile by the time that half of the original capacity was lost, and the grids became increasingly brittle.

Further work should be done to determine the reasons for the apparent change in mechanism when low discharge rates are used. Work should also be done to determine why part of the PbO₂ becomes inactive with repeated cycling. The inactivity may result partly from a change in the PbO₂ structure, and partly from loss of electrical contact.

Acknowledgment

This work was supported by the U.S. Department of Energy's Applied Battery and Electrochemical Research Project under interagency agreement EC-76-A-31-1003. Thanks are extended to the International Lead Zinc Research Organization, Incorporated, for their support of one of the authors and for permission to participate in this investigation.

Manuscript submitted May 11, 1981; revised manuscript received July 7, 1981.

Any discussion of this paper will appear in a Discussion Section to be published in the June 1982 JOURNAL. All discussions for the June 1982 Discussion Section should be submitted by Feb. 1, 1982.

Publication costs of this article were assisted by the Naval Research Laboratory.

REFERENCES

1. C. P. Wales, S. M. Caulder, and A. C. Simon, *This Journal*, **123**, 236 (1981).
2. A. C. Simon and S. M. Caulder, *ibid.*, **118**, 659 (1971).
3. D. Berndt, "Power Sources 2," D. H. Collins, Editor, p. 17, Pergamon Press, Oxford, England (1970).
4. P. Reinhardt, M. Vogt, and K. Wiesener, *J. Power Sources*, **1**, 127 (1976).
5. E. Voss and J. Freundlich, "Batteries 1," D. H. Collins, Editor, p. 73, Pergamon Press, Oxford, England (1963).
6. A. C. Simon, C. P. Wales, and S. M. Caulder, *This Journal*, **117**, 987 (1970).
7. A. C. Simon, S. M. Caulder, and J. T. Stemmler, *ibid.*, **122**, 461 (1975).
8. H. Bode, H. Panesar, and E. Voss, *Chem. Ing. Tech.*, **41**, 878 (1969).
9. D. Kordes, *ibid.*, **38**, 638 (1966).
10. K. Wiesener and P. Reinhardt, *Z. Phys. Chem. Leipzig*, **256**, 285 (1975).

Corrosion of Plated Nickel in Formamide-Water Mixtures

Lal Bahadur, V. B. Singh, and P. K. Tikoo

Department of Chemistry, Banaras Hindu University, Varanasi-221005, India

ABSTRACT

Corrosion behavior of plated nickel in formamide-water mixtures has been studied at 25°C galvanostatically covering the whole range of solvent composition. It has been observed that solvent composition has a pronounced effect on the corrosion behavior of nickel and it has been found that nickel is anodically active in water-rich solvent composition region while it becomes passive in formamide-rich region.

Corrosion studies of metals and alloys in nonaqueous media have been the center of interest during recent years (1-7) because of the wide use of organic solvents in different industries, chemical laboratories, and development of new energy sources. Corrosion in such cases affects the quality of chemical product, leads to failure of chemical units, and reduces the life of batteries, etc. From this view point the corrosion studies in nonaqueous media have attracted the attention of researchers in this field. However, while using nonaqueous solvents, the presence of water is hardly avoidable in many cases. So, studies on the effect of water on the corrosion of metals and alloys in organic solvents are quite essential to prevent corrosion in such media. Although some results have been reported in literature (8-20) on such work, the content of water has been kept very low in these investigations. Therefore it was of interest to make a systematic study on electrochemical behavior of metals in aqueous binary mixtures of organic solvents covering the whole range of solvent composition. Also, such work is of importance in view of growing interest in aqueous binary mixtures of organic solvents in many fields; simply by changing the composition of mixed solvent various physicochemical properties like viscosity, dielectric constant, solvent structure, percentage content of protic and aprotic constituents, etc. can be easily varied. Such variation will certainly affect the solvation ability of the solvent mixture and electrical conductivity of the solution which in turn will influence the structure and consequently the nature of electrical double layer formed at metal/solution interphase which governs the behavior of metals in contact with such solutions.

While choosing a class of aqueous binary mixtures for such work, previous work on amide-water mixtures was kept in view. Studies of different physicochemical properties of aqueous binary mixtures of amide(s) have shown (21) that nonsubstituted amide (e.g., formamide)-water mixtures behave in a quite different manner as compared to mono- and di-substituted amides (e.g., N-methylformamide and N,N-dimethylformamide)-water mixtures. But the main stimulus for the present work was given by our previous work on conductance of various electrolytes in different amide(s)-water mixtures. Very pronounced effect of dehydration of ions by the cosolvent (amide) [i.e., the detachment of some of the water molecules associated with an ion in pure water as a result of the addition of the cosolvent due to stronger solvent-solvent (water-cosolvent) interaction than ion-solvent (water) interaction] was observed in DMF-water mixtures (22) in a water-rich solvent composition region, while the same effect was observed in an amide-rich region in formamide-water mixtures (23). In view of the above, it has been planned to make a sys-

tematic investigation of the electrochemical behavior of various metals in different amide(s)-water mixtures. As a first step in this direction, it was decided to choose formamide-water mixtures for the present work covering the whole range of solvent composition. Further, due to wide use of nickel for protective and decorative purposes, this metal has been chosen for the present investigation.

This paper contains studies on corrosion behavior of plated nickel in formamide-water mixtures at 25°C.

Experimental

Formamide (L.R., B.D.H.) was purified as suggested by Dawson *et al.* (24). Formamide-water mixtures of compositions 2, 15, 25, 40, 50, 60, 75, and 98 mol percent (m/o) formamide were prepared by weight using doubly distilled water.

The galvanostatic method was used for the polarization studies. Constant current was drawn from a power supply ranging between 5 μ A and 100 mA. Nickel was electroplated on a scratch-free mechanically polished copper electrode using Watts' bath (25). The working nickel-plated electrodes had areas of 2 cm² with a 4 cm long tag for electrical connection. The thickness of the nickel coating was sufficient (\sim 0.1 mm) to avoid any interference of base metal (copper) in the corrosion study. The experiments were carried out with 100 ml test solvent mixtures in a Pyrex glass cell and an electronically controlled air thermostat was used to maintain the temperature at 25° \pm 0.5°C. The potential measurements were made by a precision potentiometer (Pye, Catalogue No. 7569 P) with reference to a saturated calomel electrode. The null point was detected with the help of a multiflex galvanometer (Type MG-4). To minimize the IR drop in solution a Luggin capillary was used with a calomel electrode. The tip of the capillary was kept very close (\sim 0.5 mm) to the surface of the test electrode. For each composition of the solvent mixture, the variation of open-circuit potential with time was measured. It was observed that a practically constant potential was attained after 1 hr in almost all the cases. Current-potential measurements were made after the test electrode attained a constant potential in the test solution. Measurements were made in solvent mixtures of different compositions mentioned earlier. Cathodic polarizations were determined first, the open-circuit potential was then re-established, and anodic polarizations were determined.

Results and Discussion

The anodic and cathodic polarization behavior of the plated nickel in galvanostatic mode in different compositions of formamide-water mixtures are shown in Fig. 1 covering the whole range of solvent composition. For clear depiction, the cathodic curves for all the solvent compositions are not shown in the figure because the cathodic pattern in solvent mixtures other

Key words: corrosion, passivity, formamide-water mixtures, galvanostatic, infrared, x-ray, scanning electron microscope.

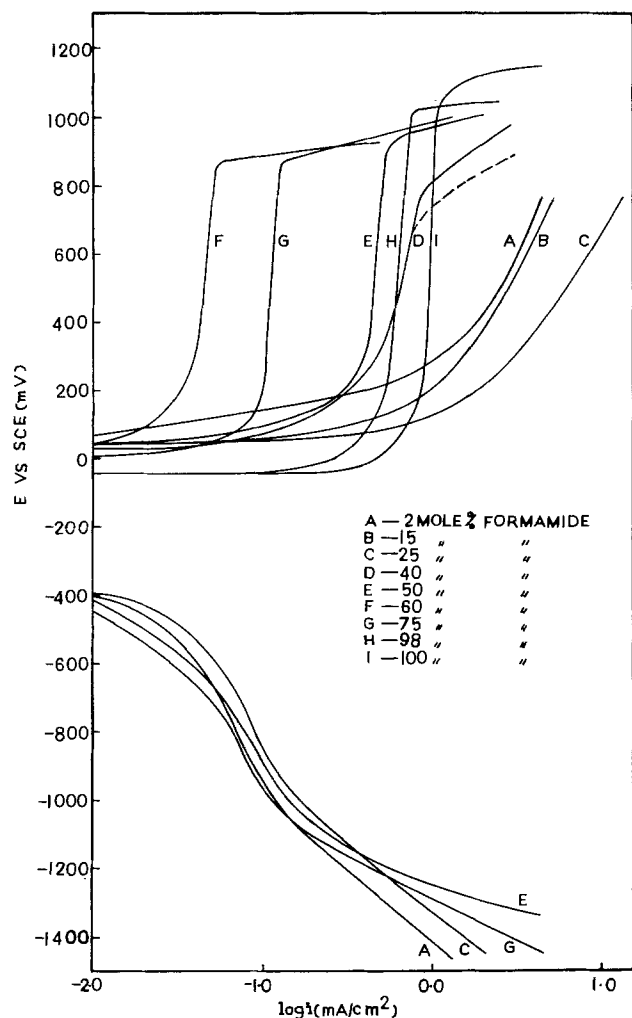


Fig. 1. Polarization behavior of plated nickel in different compositions of formamide-water mixture.

than shown in the figure is almost the same and some of them overlap with each other. As it is clear from the figure, nickel is cathodically more polarized than anodically in each case. However, the change in the solvent composition does not appreciably change the cathodic behavior of the metal indicating similar cathodic reaction irrespective of the solvent composition. But a change in solvent composition has a very pronounced effect on the behavior of anodic dissolution of the metal. As can be seen from the figure, in water-rich (2-25 m/o formamide) and in formamide-rich (60-100 m/o formamide) solvent composition regions, anodic curves shift toward higher current density with the increase of formamide content in the solvent mixture while a reverse trend was observed in intermediate solvent compositions (25-60 m/o formamide). In addition to this, it was interesting to observe the formation of a greenish-white sluggish material in water-rich solvent mixtures (up to 40 m/o formamide). It was formed in the vicinity of the test electrode and settled down in the cell; while in formamide-rich solvent mixtures (beyond 60 m/o formamide) a light green coloration of the test solution was observed which deepened with the increase of formamide content in the solvent mixture.

In order to discuss the role of solvent composition on the behavior of anodic dissolution of nickel, it is preferable to start with an extreme case, say pure water, and to proceed with the effect of addition of formamide in water. As is known and observed in the present investigation also, nickel is almost passive in

pure water. It can be seen from Fig. 1 that addition of even small amounts of formamide (e.g., 2 m/o) activated the surface and started the dissolution of the metal. Further addition of formamide led to a shift of the curve (Fig 1, curves B and C) more and more toward higher current density indicating that metal dissolution is increasingly facilitated in these solvent mixtures. This trend persists up to 25 m/o formamide solvent composition. It can also be seen from the figure (curves A, B, and C) that no clear passivity was observed in these cases. However, beyond 25 m/o formamide content in solvent mixture the reverse trend was observed up to 60 m/o formamide solvent composition. It is interesting to note that in the solvent mixture containing 40 m/o formamide the electrode surface tends toward passivation though clear passivity was not observed. This shows that this particular solvent composition is the transition composition from clear dissolution toward the tendency for passivation. In this particular case beyond a certain current density (~ 1 mA/cm²) fluctuations in the potential during measurements were observed (shown by dotted line in Fig. 1, curve D). It appears from this observation that the film initially formed at the surface either does not adhere properly to the surface or is porous and/or loses its protectiveness. The fluctuations in potential appeared to be associated with rapid passivation and then activation of the electrode possibly caused by spalling. Such spalling has been observed by other researchers (7, 12, 13) also in the case of zinc, cadmium, and beryllium. As formamide content is further increased in the solution mixture, clear passivity was observed and the passive region shifted toward the lower current density region (Fig. 1, curves E and F). The earliest passivity (i.e., at lowest current density) was observed in the solvent mixture containing 60 m/o formamide. Further addition of formamide (i.e., formamide > 60 m/o) resulted in a shift of the passive region again toward the higher current density and this trend persisted right up to the pure formamide. The present results are similar to those of Demo (10) who reported that a low water content in organic solvents led to passivation but in the presence of a high water content the film lost its protectiveness and corrosion was enhanced.

The results obtained in the present investigation can be explained in the light of the following probable phenomena which may be governing factors for the observed active-passive behavior. First, the electrochemical dissolution of nickel; second, its (nickel ion) preferential solvation with formamide and third, the reaction of this solvated ion with water forming some insoluble anodic product in the water-rich region. The diffusion of nickel ions from the phase boundary to the bulk of the solution is also an additional governing factor. In the water-rich region (up to 25 m/o formamide solvent composition) it seems that nickel complex with formamide is not stabilized and the third phenomenon mentioned above is favored giving insoluble sluggish compound. As formamide is further increased in the solvent mixture, the third phenomenon is expected to be less favored due to a decrease in the water content and at the same time an increase in formamide increases appreciably the kinematic viscosity of the solvent mixtures which hinders the diffusion of nickel ions into the bulk of the solvent. Probably for this reason nickel ions are accumulated at the surface and passivity is observed. Thus an increase in formamide content from 40 to 60 m/o leads to an early passivation. In solvent mixtures sufficiently rich in formamide (>60 m/o) formation of nickel complex is probably favored. In this region, it can be likely that the high dielectric constant (~ 110) plays an important role in stabilizing the nickel complex with formamide. Hence, with an increase in formamide

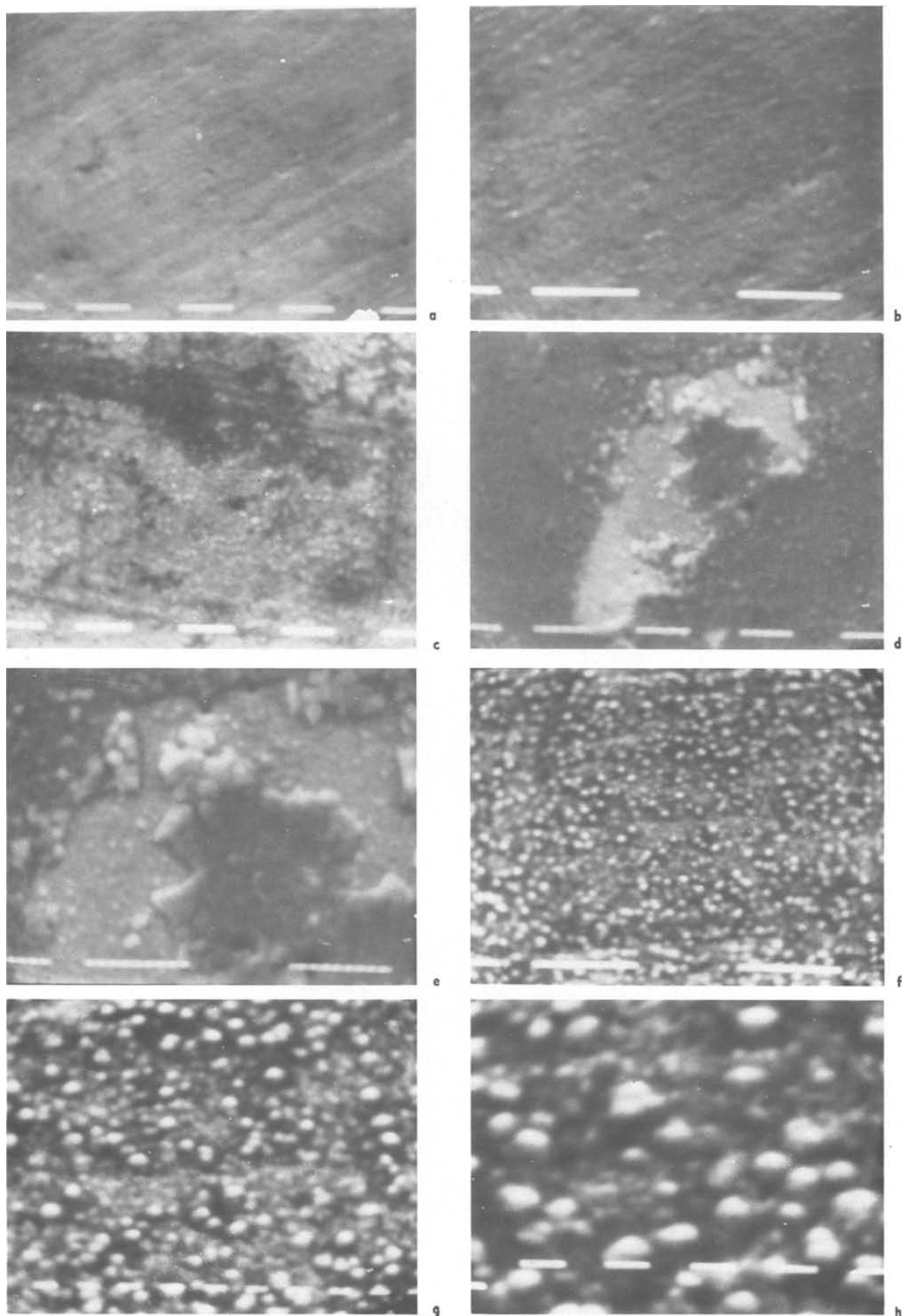


Fig. 2. Scanning electron micrograph of the working electrode after the polarization studies. In 15 m/o F: a, 1250 \times ; b, 2500 \times . In 40 m/o F: c, 1250 \times ; d, 1250 \times ; e, 2500 \times . In 60 m/o F: f, 2500 \times ; g, 5000 \times ; h, 10,000 \times .

content, more and more nickel ions are taken away from the phase boundary because they can be stabilized in the bulk, resulting in the shift of passive region toward the higher current density. This is also evident from an increasingly deeper color of the solution with the increase of formamide content.

As is clear from the above discussion, the effect of water content on the anodic dissolution behavior of metal in nonaqueous medium is very complex, particularly if the whole range of solvent composition is covered. Its net effect depends on the competitive effect of other constituents of the solution. So it seems difficult to assign any particular effect of water, whether it enhances the dissolution or passivation. Such complexity has been realized by others also (10, 17). Farina and co-worker (17) observed that in the presence of an increasing quantity of water the stability of the oxide film becomes greater in case of iron in methanol while the addition of water increases the dissolution rate of iron in DMF. So it requires extensive investigation before coming to any definite conclusion regarding the role of water in corrosion behavior of metals.

The sluggish anodic products obtained in different solvent mixtures rich in water (2, 15, 25, 40 m/o F), were decanted, washed with acetone, and dried in a vacuum desiccator. They were subjected to infrared and x-ray analyses and were found to be the same. The infrared spectrum shows a broad band at 3400 cm^{-1} due to $\nu(\text{OH})$ and a band at 300 cm^{-1} showing nickel-oxygen bonding. This indicates the presence of nickel hydroxide/nickel-oxide. The x-ray powder pattern of the material, subsequently, showed the presence of nickel oxide (NiO) and nickel hydroxide. However, a few additional lines also appeared in the pattern but were not sharp enough to help in the identification of the definite constituent. Formation of such metal hydroxide contaminated with respective metal has been reported by earlier investigators (14-16) for zinc, cadmium, and magnesium during anodic dissolution.

The surface of each working electrode was examined by scanning electron microscope after subjecting these to the electrochemical studies. An inspection of these photomicrographs reveals that they can be classified into three categories depending on the composition of the solvent mixture, viz: (i) 2-25 m/o formamide, (ii) in the vicinity of 40 m/o formamide, (iii) from 50 m/o up to pure formamide. It is remarkable to note that the galvanostatic studies lead to the same conclusion also (Fig. 1). The representative photomicrographs from each group are shown in (Fig. 2a-h). The photomicrographs a and b show no film formation on the surface and the metal surface was in the process of continuous dissolution in the first case. An uneven film formation is observed in the second case (Fig. 2c-e) which appears to be an oxide layer. The spalling of the surface becomes more apparent as different zones of the same surface are scanned (Fig. 2c, d). A uniform compact layer (probably oxide layer) is clearly realized in the third case where complete passivity was observed by polarization studies (Fig. 2f, g, h).

Conclusions

It can be concluded here that for nickel in formamide-water mixtures, a solvent mixture containing 25 m/o formamide is most corrosive while in 60 m/o formamide solvent composition, the earliest passivation is observed.

The explanations given above for the observed anodic dissolution behavior of nickel in solvent mixtures taken for the present work are not too conclusive or sufficient to propose a general mechanism; it requires further investigations of the same and other similar systems covering other parameters also. The work along these lines is in progress and will follow this communication.

Acknowledgments

Thanks are due to Professor B. M. Shukla, Head of the Chemistry Department, for providing necessary facilities and to the Head of the Department of Metallurgical Engineering, Institute of Technology, Banaras Hindu University, for allowing the use of SEM and x-ray.

Manuscript submitted March 11, 1980; revised manuscript received June 5, 1981.

Any discussion of this paper will appear in a Discussion Section to be published in the June 1982 JOURNAL. All discussions for the June 1982 Discussion Section should be submitted by Feb. 1, 1982.

REFERENCES

1. E. Heitz, in "Advances in Corrosion Science and Technology," Vol. 4, M. G. Fontana and R. W. Staehle, Editors, Chap. 3, Plenum Press, New York (1974).
2. S. Baillozor, *Electrochim. Acta*, **23**, 1309 (1978).
3. K. E. Heusler, *Z. Elektrochem.*, **66**, 177 (1962).
4. N. Hackerman, E. S. Snavely, Jr., and L. D. Fiel, *Corros. Sci.*, **7**, 39 (1967).
5. E. Heitz and C. M. V. Meysenbug, *Werkst. Korros.*, **16**, 178 (1965).
6. E. Heitz, *ibid.*, **21**, 360 (1970).
7. T. C. Franklin and C. R. Parsons, *This Journal*, **109**, 641 (1962).
8. H. Scholl and B. Grzelak, *Electrochim. Acta*, **23**, 749 (1978).
9. D. Posadas, A. J. Ariva, and J. J. Podesta, *ibid.*, **16**, 1025, 1041 (1971).
10. J. J. Demo, *Chem. Eng. World*, **7**, 115 (1972).
11. F. Mansfeld, *This Journal*, **118**, 1412 (1971); **120**, 188 (1973).
12. H. Aida, I. Epelboin, and M. Garreau, *ibid.*, **118**, 243 (1971).
13. H. Vaidyanathan, M. E. Straumanis, and W. J. James, *ibid.*, **121**, 7 (1974).
14. M. E. Straumanis and B. K. Bhatia, *ibid.*, **110**, 357 (1963).
15. W. J. James, G. E. Stoner, and M. E. Straumanis, Tech. Rep. No. 4, ONR (1963).
16. D. T. Sorensen, A. W. Davidson, and J. Kleinberg, *J. Inorg. Nucl. Chem.*, **13**, 64 (1960).
17. C. A. Farina, G. Faita, and F. Olivani, *Corros. Sci.*, **18**, 465 (1978).
18. J. W. Johnson, S. C. Chen, J. S. Chang, and W. James, *ibid.*, **17**, 813 (1977).
19. E. Constantinescu and E. Heitz, *ibid.*, **16**, 857 (1976).
20. U. R. Evans, *Electrochim. Acta*, **16**, 1825 (1971).
21. (a) A. Assarson and F. V. Eirich, *J. Phys. Chem.*, **72**, 2710 (1968); (b) P. Rohdewald and M. Moldner, *ibid.*, **77**, 373 (1973); (c) C. de Visser and G. Somsen, *Z. Phys. Chem. (N.F.)*, **92**, 159 (1974); (d) H. Weingartner, M. Holz, and H. G. Hertz, *J. Solution Chem.*, **7**, 689 (1978).
22. D. Singh, Lal Bahadur, and M. V. Ramanamurti, *ibid.*, **6**, 703 (1977).
23. (a) M. V. Ramanamurti and L. Bahadur, *Indian J. Chem.*, **14A**, 1015 (1976); (b) L. Bahadur and M. V. Ramanamurti, *This Journal*, **128**, 339 (1981).
24. L. R. Dawson, T. M. Newell, and W. J. McCreary, *J. Am. Chem. Soc.*, **76**, 6024 (1954).
25. F. A. Lowenheim "Modern Electroplating," 3rd ed., John Wiley & Sons, Inc., New York (1974).

Two-Layer Formation of Passivating Films on Cobalt in Neutral Solution

Toshiaki Ohtsuka and Norio Sato*

Electrochemistry Laboratory, Corrosion Research Group,
Faculty of Engineering, Hokkaido University, Sapporo 060, Japan

ABSTRACT

Layer structure and thickness of passivation oxide films on cobalt have been investigated at stationary and transient states in solution of 0.30 mol dm⁻³ boric acid-0.075 mol dm⁻³ sodium borate mixture of pH 8.4 by means of chemical analysis and *in situ* ellipsometry combined with electrochemical measurements. A two-layer structure composed of an inner CoO and an outer Co_{3-Δ}O₄ is found in a potential range more positive than 0.75V (*vs.* the hydrogen electrode at the same solution). The nonstoichiometry changes from Δ = 0 to 0.33 with increasing anodic potential. The outer Co_{3-Δ}O₄ layer thickness increases linearly with potential, whereas the inner layer thickness is not a simple function of potential, but depends on the film formation procedure. A step-wise potential increase gives an initial rapid growth of the outer Co_{3-Δ}O₄ layer followed by a gradual thickening of the inner CoO layer. The transient film growth behavior is interpreted in terms of a field-assisted ion diffusion mechanism, and the self-diffusion coefficient in the inner CoO layer is estimated to be $D/\text{cm sec}^{-1} = 6.5 \times 10^{-21} \sim 2.6 \times 10^{-20}$.

The previous papers (1-4) have shown that the passive oxide film on cobalt is potential dependent in neutral boric acid-sodium borate solution of pH 8.4. At potentials more negative than 0.86V, referred to the hydrogen electrode in the same solution (HESS), a slightly soluble oxide film of CoO 2 ~ 3 nm thick is formed under stationary potentiostatic conditions (2-3). At more positive potentials a two-layered film is formed, consisting of an inner CoO and an outer Co_{3-Δ}O₄ layer (2-3). The nonstoichiometry Δ of the outer layer depends on the anodic potential, changing from Δ = 0 at 1.15V to Δ = 0.33 at 1.4V. The outer layer thickness increases linearly with the potential, whereas the inner layer thickness is not a simple function of potential. In the present paper the kinetics and mechanism of electrochemical formation of two-layered oxide films on cobalt were studied by using a potential step technique associated with the ellipsometric measurements.

Experimental

The specimens were prepared from cobalt rods of 99.99% purity (Johnson-Matthey Limited) into polycrystalline sheets 0.8 mm thick with the surface area of 5 or 10 cm². The specimen pretreatment was the same as that described in the previous papers (1-4). The electrolytes were prepared from doubly distilled water and analytical grade reagents. Anodic formation of the passive films on cobalt was performed in a mixture of 0.30 mol dm⁻³ boric acid and 0.075 mol dm⁻³ sodium borate solutions at pH 8.4. Cathodic reduction of the passive films was conducted in a mixture of boric acid and sodium borate solutions at pH 6.5. A boric acid solution at pH 5.3 and a mixture of 0.5 mol dm⁻³ NH₄Cl and 0.5 mol dm⁻³ NH₄OH at pH 9.6 were also used for spontaneous dissolution of the passive films. Furthermore, a solution of boric acid-sodium borate mixture at pH 8.4 containing Co(II) ions at concentration of 1.03 mg dm⁻³ was used for anodic deposition of a Co(III) oxide film from Co(II) ions on a Pt electrode with the surface area of 10 cm². All the solutions were deaerated by bubbling purified nitrogen gas for more than 24 hr.

* Electrochemical Society Active Member.

Key words: metals, anode, ellipsometry, passivity.

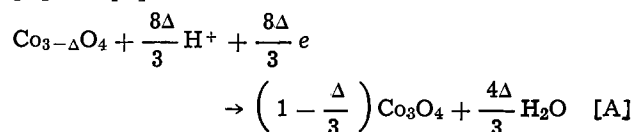
The ellipsometer used was of horizontal type with a quarter-wave plate placed on the side of incident beam. The fast axis of the plate was fixed at a 45° orientation. Measurements were made by the standard null method at a wavelength of λ/nm = 546 and at an incidence angle of φ₁ = 73.303° (3, 5).

All measurements were made at 20.0 ± 0.2°C. The potential of cobalt electrodes was measured in reference to a saturated calomel electrode (SCE) and converted to a scale of the hydrogen electrode in the same solution (HESS).

The amount of cobalt ion dissolved into solutions was analyzed by a colorimetric nitroso-R-salt method.

Result

Two-layer structure of passivation films.—Figure 1 illustrates the results of ellipsometric measurements (Fig. 1a), the amount of dissolved Co(II) ion from the passive film, W_d , and the decay of potential, φ, (Fig. 1b) during a galvanostatic cathodic reduction of a passive film on cobalt. The passive film was formed by 1 hr oxidation at a constant potential in the solution of pH 8.4 and the reduction was performed at a constant current in the solution of pH 6.5. The loci of polarizer azimuth P and analyzer azimuth A are directly plotted in Fig. 1a, where P_0 and A_0 correspond to the oxide-free reference surface of cobalt; $P_0 = 28.68^\circ$ and $A_0 = 4.43^\circ$ determine the complex refractive index of metallic cobalt, $\hat{n}_{Co} = 2.83-3.86i$ (2, 3). The loci δP vs. δA exhibit two breaks at the points marked on Q_c^0 and Q_c^M , which appear to correspond to two breaks observed in W_d vs. Q_c and ϕ vs. Q_c curves. In view of the previous results (3, 4), it is found that Q_c^0 is the cathodic charge required for the nonstoichiometry Δ of the outer Co_{3-Δ}O₄ layer to decrease to Δ = 0, and that Q_c^M is the charge required for the outer layer to be completely reduced to Co²⁺ ions. Thus, the reaction for Q_c^0 and the reaction for $Q_c^M - Q_c^0$ are respectively represented by reactions [A] and [B]



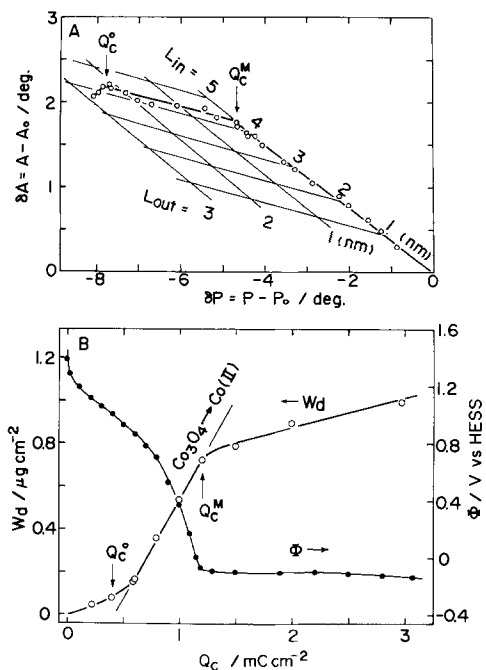


Fig. 1. Cathodic reduction of a passive film at constant C.D., $i_c = 5 \mu\text{A cm}^{-2}$ in borate solution of pH 6.5. The film was formed at constant potential, $\Phi = 1.34\text{V}$, for 1 hr in borate solution of pH 8.4. (a) Change of ellipsometric parameters P and A during the reduction. (b) Amount of dissolved Co(II) from the film W_d and potential decay Φ as a function of cathodic charge Q_c passed during the reduction.



The third stage of film reduction after Q_c^M is the reduction of the inner CoO layer.

To determine the complex refractive indexes of the layers, the best fit approach was made between the theoretical δA vs. δP loci for different complex refractive indexes and the experimental ones by taking into account the approximate film thickness estimated from the film charge in anodic oxidation and in cathodic reduction. The complex refractive indexes thus determined for the outer layer are $\hat{n}_{\text{Co}_2\text{O}_3} = 3.2-0.95i$ and $\hat{n}_{\text{Co}_3\text{O}_4} = 3.2-0.5i$, and for the inner layer $\hat{n}_{\text{CoO}} = 2.3-0.1i$ (2, 3). In Fig. 1 the theoretical lines are also drawn for various thicknesses of the outer and the inner layers.

Figure 2 shows the δA vs. δP loci during the spontaneous dissolution of the passive film in two different solutions of $0.5 \text{ mol dm}^{-3} \text{ NH}_4\text{OH}-0.5 \text{ mol dm}^{-3} \text{ NH}_4\text{Cl}$ mixture at pH 9.6 and of 0.30 mol dm^{-3} boric acid at pH 5.3, where no composition change of the film appears to occur during the dissolution because of the absence of applied cathodic current. The δA vs. δP curves in Fig. 1 and 2 are almost the same.

Transient behavior.—To elucidate the layer growth, ellipsometric transient measurements of the film were carried out in two-step oxidation, in which, after renewal of the solution containing no dissolved cobalt ion, a potential step was applied to a preoxidized cobalt electrode. Figure 3 shows a δA - δP curve observed after a potential step from 1.04 to 1.24V is applied to a passivated cobalt that has been oxidized at $\Phi = 1.04\text{V}$ (V) for 1 hr. The filled circle in Fig. 3 indicates the values of δP and δA observed after direct 1 hr oxidation at 1.24V starting from the oxide-free cobalt surface. It is noted that more than 6 hr of oxidation is required for the δP - δA value of two-step oxidation to reach that of direct one-step oxidation for 1 hr.

By superimposing on the results of Fig. 3 the theoretical δP - δA loci calculated for two-layered films

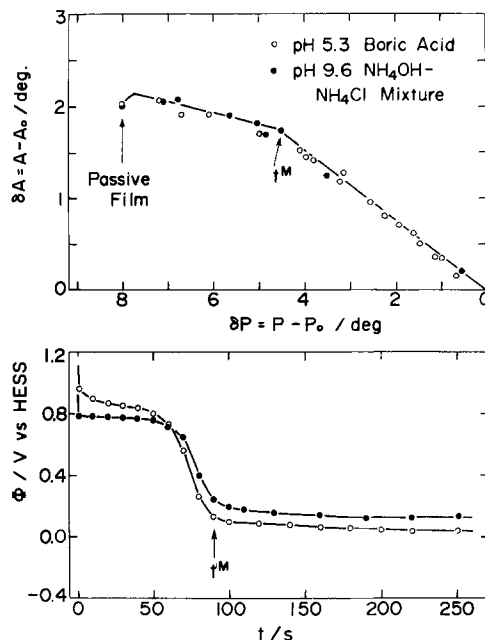


Fig. 2. Change of ellipsometric parameters P and A and potential decay during spontaneous dissolution of a passivation film in solutions of $0.5 \text{ mol dm}^{-3} \text{ NH}_4\text{OH}-0.5 \text{ mol dm}^{-3} \text{ NH}_4\text{Cl}$ mixture (Δ) and of 0.3 mol dm^{-3} boric acid (\circ). The break marked by t^M in the δP - δA loci corresponds to a point where the potential decays from the first to the second wave.

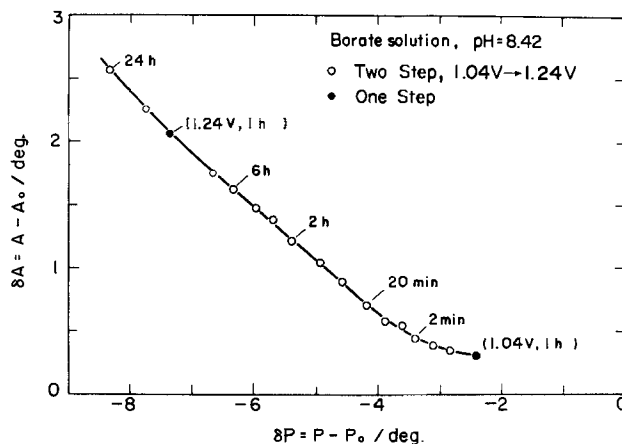


Fig. 3. Change in δA vs. δP loci with time during the second step at $\Phi = 1.24\text{V}$ in two-step oxidation in borate solution of pH 8.4. The electrode was first oxidized at $\Phi = 1.04\text{V}$ for 1 hr (1st step) and after renewal of the solution was oxidized further at $\Phi = 1.24\text{V}$ (2nd step).

with the complex refractive indexes, $\hat{n}_{\text{CoO}} = 2.3-0.1i$ and $\hat{n}_{\text{Co}_3\text{O}_4} = 3.2-0.5i$, as a function of layer thickness, the thickness of the both layers can be evaluated as a function of time during oxidation. In Fig. 4 and 5 the thickness change thus estimated is plotted together with the current density (C.D.) change. In Fig. 4 the thickness for 1.54V oxidation at which gaseous oxygen evolves on the electrode was estimated using the complex refractive index of $\hat{n}_{\text{out}} = 3.2-0.95i$ for the outer Co_2O_3 layer. It is seen that initially the outer layer increases accompanying no appreciable growth of the inner layer and that the inner layer begins to thicken after the outer layer grows to a certain thickness comparable to the thickness formed by direct one-step oxidation. It is noted that the inner layer formed by two-step oxidation is thinner than that formed by direct one-step oxidation. This is due to the anodic deposition of a Co(III) film from Co(II)

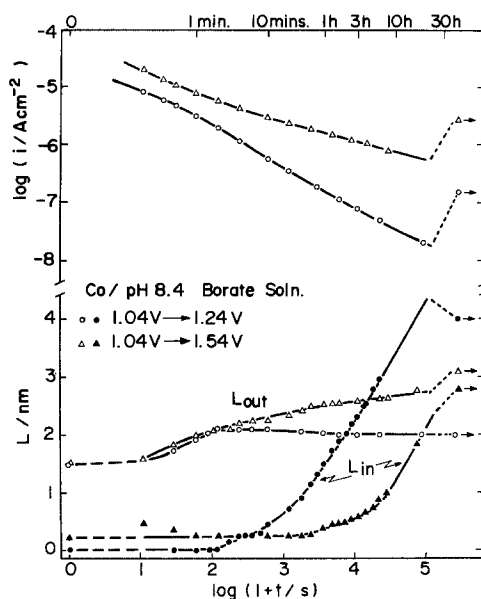


Fig. 4. Anodic C.D. i and thicknesses of two layers L_{in} and L_{out} as a function of time during the second step at $\Phi = 1.24\text{V}$ and 1.54V in two-step oxidation in borate solution of pH 8.4. The electrode was first oxidized at $\Phi = 1.04\text{V}$ for 1 hr. The arrows on the right side indicate C.D.'s and thicknesses in direct one-step oxidation for 1 hr.

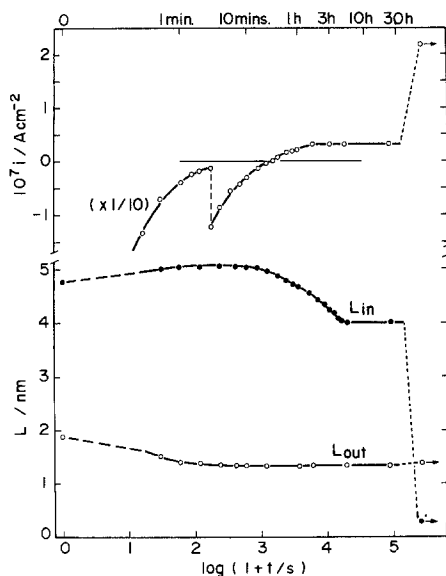


Fig. 5. Anodic C.D. and thicknesses of the two layers as a function of time during the second step at $\Phi = 1.04\text{V}$ in two-step oxidation in borate solution of pH 8.4. The electrode was first oxidized at $\Phi = 1.24\text{V}$ for 1 hr. The arrows on the right side indicate C.D. and thicknesses in direct one-step oxidation.

ions in aqueous solution produced prior to the film formation, as is shown later.

When the potential is stepped down (Fig. 5), an initial cathodic current causes a decrease of the outer layer thickness, producing a slight increase of the inner layer thickness, and then a definite decrease of the inner layer thickness occurs toward a steady-state value of 4.0 nm without yielding any change in the outer layer thickness after the C.D. turns to be anodic.

The preferential growth of the outer layer, which occurs in an initial period of potential step oxidation (Fig. 4), also takes place during galvanostatic oxidation, as shown in Fig. 6. In this case the anodic C.D. of $1 \mu\text{A cm}^{-2}$ was applied to a passivated cobalt electrode that has been oxidized at 1.03V for 1 hr. Before

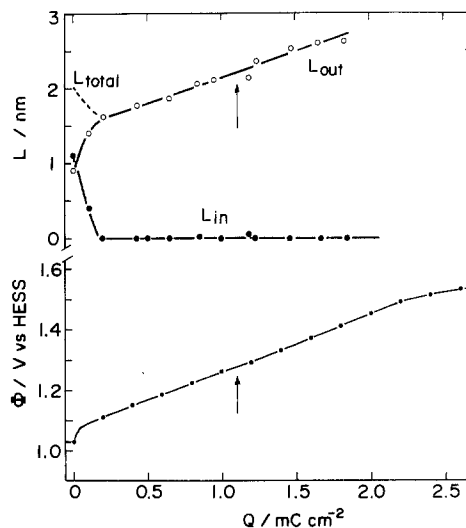


Fig. 6. Change in thickness and potential during galvanostatic oxidation at $i = 1 \mu\text{A cm}^{-2}$ of a film-covered cobalt electrode ($L_{in} = 1.1 \text{ nm}$ and $L_{out} = 0.9 \text{ nm}$) which has been oxidized at $\Phi = 1.03\text{V}$ in borate solution of pH 8.4. The arrow in the figure indicates the amount of charge passed at which the complex refractive index of $\text{Co}_3\text{-O}_4$ layer begins to change.

the galvanostatic oxidation, the film has consisted of the inner layer of 1.1 nm and the outer layer of 0.9 nm. Application of a small anodic current first causes a rapid increase of the outer layer with a decrease of the inner layer and then the film of a single Co_3O_4 layer ($\hat{n} = 3.2-0.5i$) with a linear rise of potential.

Finally, the film transforms to Co_2O_3 ($\hat{n} = 3.2-0.95i$) without producing any increase of the inner layer.

In Fig. 7 the change in the δA vs. δP loci is illustrated for the second step of oxidation at different potentials in the range of two-layer formation, starting from a passivated cobalt electrode that has been oxidized at 1.04V for 1 hr. The δP - δA value corresponding to the film formed by direct one-step oxidation for 1 hr lies on the extrapolated growth line of two-step oxidation. At potentials more positive than 1.34V the locus of the second step oxidation even after 22 hr (\bullet) does not reach the value of the passivated electrode directly oxidized in one step for 1 hr (\circ). The second step oxidation at 1.54V gives rise to transformation of Co_3O_4 to Co_2O_3 in an initial

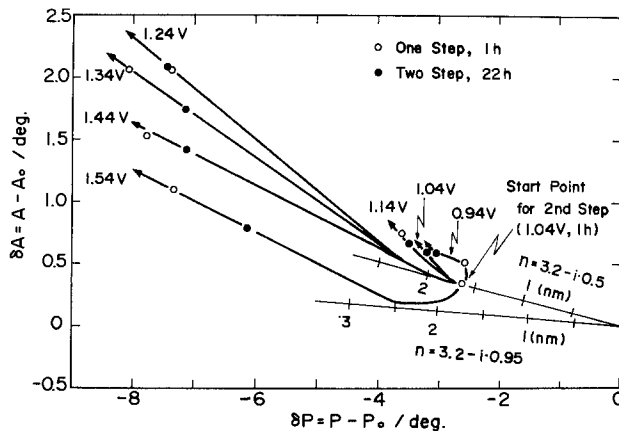


Fig. 7. Change in δA vs. δP loci during the second step at different potentials in two-step oxidation in borate solution of pH 8.4. The electrode was first oxidized at $\Phi = 1.04\text{V}$ for 1 hr. The filled circles indicate the values of δP and δA after 22 hr of the second step in two-step oxidation and the open circles the values after 1 hr in direct oxidation.

period, as suggested by a change in the complex refractive index from $\hat{n} = 3.2-0.5i$ to $3.2-0.95i$.

Comparisons of the thickness and the final C.D. are made in Fig. 8 between direct 1 hr oxidation and two-step 22 hr oxidation. In this figure the thickness and the C.D. in the potential region where the film of a single CoO layer is formed is also plotted. In the potential region for a two-layer film formation the final anodic C.D. in two-step oxidation is one-tenth times as small as that in direct one-step oxidation. Difference in C.D. between the potential regions of Co_3O_4 and Co_2O_3 formation can be seen in two-step oxidation, but becomes indistinct in direct one-step oxidation. The thickness of the outer layer does not depend on whether the film is formed by one-step or two-step oxidation and increases nearly linearly with potential except for the film formed above 1.4V. The inner layer thickness, however, differs in different oxidation procedures. It appears that the inner layer thickness of two-step oxidation is larger at potentials below 1.2V and smaller at potentials above 1.3V than that of direct one-step oxidation. From the above results it follows that the thickness of the outer layer is determined only by the oxidation potential, whereas the thickness of the inner layer is dependent on the oxidation procedure.

Anodic deposition of Co(II) ion in solution.—The previous work (1) has shown that the amount of Co(II) ion dissolved in solution was $0.5 \mu\text{g cm}^{-2}$ in 5 sec oxidation and $0.03 \mu\text{g cm}^{-2}$ in 1 hr oxidation at constant potential 1.34V starting from the film-free surface. This means that the Co(II) ion dissolved in solution in the initial period of anodic passivation is anodically deposited on the passivated cobalt. Another evidence on the anodic deposition is given from an experiment in which Pt electrode is potentiostatically oxidized for 1 hr in the boric acid-sodium borate solution of pH 8.4 containing Co(II) ion of concentration 1.03 mg dm^{-3} . Figure 9 shows the amount of Co(II) ion anodically deposited from the solution to form a cobalt oxide film on Pt, which was estimated from the decrease of Co(II) ion concentration in the solution after potentiostatic 1 hr oxidation at constant

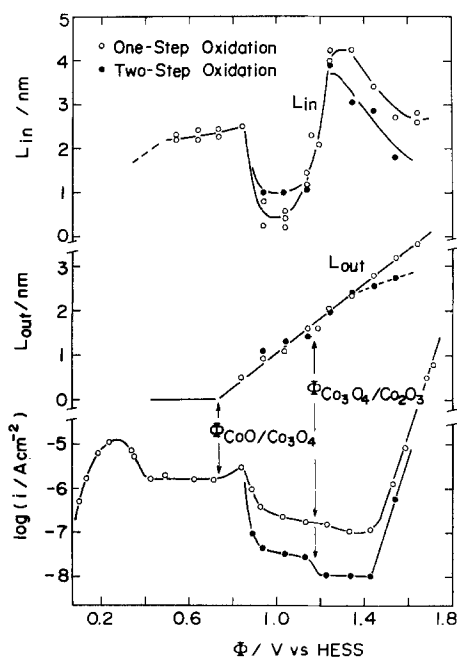


Fig. 8. Comparison of film thickness and anodic C.D. between one-step and two-step oxidations in borate solution of pH 8.4. The film thickness and anodic C.D. were measured after 1 hr for one-step oxidation and after 22 hr for two-step oxidation.

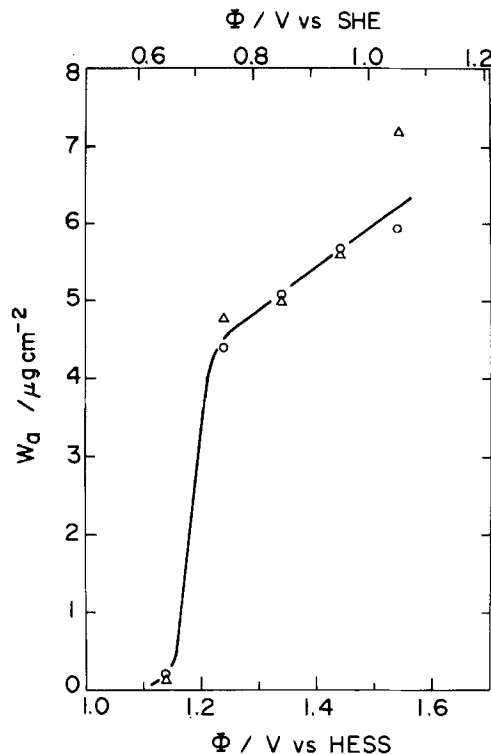


Fig. 9. Amount of cobalt ion anodically deposited on Pt electrode from borate solution containing Co(II) ions. The amount of cobalt ion deposited was estimated from the decrease of Co(II) ion in solution during potentiostatic oxidation (Δ) and the cathodic Co(II) ion dissolution from the film into solution of pH 6.5 during subsequent galvanostatic reduction at $i = 10 \mu\text{A cm}^{-2}$ (\circ).

potential. The amount of Co(II) deposited was also evaluated from the amount of Co(II) ion dissolved from the film on Pt by galvanostatic reduction at $10 \mu\text{A cm}^{-2}$ in the boric acid-sodium borate solution of pH 6.5. The anodic oxidation of Co(II) ion in the solution to form the film takes place at potentials more positive than 1.2V, which is in agreement with the potential at which an abrupt increase of the inner layer thickness as well as the outer layer nonstoichiometry Δ commences.

Discussion

Potential distribution in the passivation film.—We consider the two-layered structure of an inner CoO and an outer $\text{Co}_3-\Delta\text{O}_4$ shown in Fig. 10 and the potential distribution in the film shown in Fig. 11. If the reactions between the phases are in equilibrium at all the interphases, the irreversible potential differences in CoO (II phase) and in $\text{Co}_3-\Delta\text{O}_4$ (III phase) are given by

$$\Delta\Phi_{II} = \Phi_{\text{CoO}/\text{Co}_3\text{O}_4} - \Phi_{\text{Co}/\text{CoO}} \quad [1]$$

$$\Delta\Phi_{III} = \Phi_{\text{CoO}/\text{Co}_3-\Delta\text{O}_4} - \Phi_{\text{CoO}/\text{Co}_3\text{O}_4} \quad [2]$$

where $\Phi_{\text{Co}/\text{CoO}}$, $\Phi_{\text{CoO}/\text{Co}_3\text{O}_4}$, and $\Phi_{\text{CoO}/\text{Co}_3-\Delta\text{O}_4}$ are the potentials of electrode systems consisting of Co/CoO, Co/CoO/Co₃O₄, and Co/CoO/Co₃- Δ O₄, respectively. If we assume the potential of $\Phi_{\text{Co}/\text{CoO}}$ to be $0.14 \pm 0.04\text{V vs. HESS}$, thermodynamically estimated by Göhr (6), and the potential of $\Phi_{\text{CoO}/\text{Co}_3\text{O}_4}$ to be 0.75V, experimentally established by the authors (1, 4, 7), the irreversible potential difference in the CoO phase is

$$\Delta\Phi_{II}/\text{V} = 0.61 \pm 0.06 \quad [3]$$

It is this potential difference which creates the driving force for growth of the CoO layer. It follows from Eq. [2] that the irreversible potential difference in the outer $\text{Co}_3-\Delta\text{O}_4$ phase can not be defined as a con-

stant value, but varies depending on the nonstoichiometry Δ .

Thermodynamically, we can describe the outer layer composition as a function of electrode potential. The layer structure may also be thermodynamically described, but a number of kinetic parameters are required for the determination of the composition profile in depth.

A kinetic model for two-layer formation.—There have been only a few theoretical studies on the two-layer growth on metals. Yurek, Hirth, and Rapp (8) and Shaw and Rolls (9) have derived kinetic equations of two-layer growth for relatively thick oxide scales on metals. We propose here a kinetic mechanism of two-layer growth in anodic oxide films, which explains the observed transient behavior of anodic oxide film on cobalt. For simplification we assume that the diffusing ion through the film toward the solution is Co(II) ion and that the inner and the outer layers are CoO and Co₃O₄, respectively. Further, we assume the reaction scheme shown in Table I, where subscripts I, IIa, IIb, IIIa, IIIb, and IV indicate respectively the locations in the electrode system illustrated in Fig. 10. The reaction rate is expressed in terms of mol flux of cobalt(II) ion $k_x(x=a,b,\dots)$ /mol-Co(II) ion sec⁻¹ cm⁻².

From the mass balance of transferring ions, the following relationship can be obtained among the reaction rates

$$k_a = k_b \quad [4]$$

$$k_b = k_c + k_d \quad [5]$$

$$k_c = k_e \quad [6]$$

and

$$k_e = k_f + k_g \quad [7]$$

We now introduce the following quantities for the reaction rates

$$i_{II}/A\text{-cm}^{-2} = 2Fk_b \quad [8]$$

$$i_{III}/A\text{-cm}^{-2} = 2Fk_e \quad [9]$$

$$i_{diss}/A\text{-cm}^{-2} = 2Fk_f \quad [10]$$

$$i_{depos}/A\text{-cm}^{-2} = 2Fk_h \quad [11]$$

where i_{II} and i_{III} correspond respectively to the ionic C.D. of diffusing Co(II) ion through the inner CoO and the outer Co₃O₄ layers, and i_{diss} and i_{depos} to the dissolution C.D. and the deposition C.D. These ionic C.D.'s can be used to describe the three experimentally measurable quantities, i_a , L_{in} , and L_{out} by taking the mass balance given by Eq. [4], [5], [6], and [7] into account. From reactions [a], [b], [g], and [h], the anodic C.D. that can be measured is given by

$$\begin{aligned} i_a &= F \left(2k_a - 2k_d + \frac{2}{3}k_g + \frac{2}{3}k_h \right) \\ &= \frac{4}{3}i_{III} - \frac{1}{3}i_{diss} + \frac{1}{3}i_{depos} \end{aligned} \quad [12]$$

Table I. Reaction scheme for growth of CoO/Co₃O₄ two-layered film on Co

| Reaction | Rate (mol-Co ion sec ⁻¹ cm ⁻²) |
|--|---|
| [a] $I\text{Co} \rightarrow II_a\text{Co}^{2+} + 2I e^-$ | k_a |
| [b] $II_a\text{Co}^{2+} \rightarrow II_b\text{Co}^{2+}$ | k_b |
| [c] $II_b\text{Co}^{2+} \rightarrow III_a\text{Co}^{2+}$ | k_c |
| [d] $II_b\text{Co}^{2+} + III_a\text{Co}_3\text{O}_4 + 2I e^- \rightarrow 4II_b\text{CoO}$ | k_d |
| [e] $III_a\text{Co}^{2+} \rightarrow III_b\text{Co}^{2+}$ | k_e |
| [f] $III_b\text{Co}^{2+} \rightarrow IV\text{Co}^{2+}$ | k_f |
| [g] $III_b\text{Co}^{2+} + 4/3IV\text{H}_2\text{O} \rightarrow 1/3III_b\text{Co}_3\text{O}_4 + 8/3IV\text{H}^+ + 2/3I e^-$ | k_g |
| [h] $IV\text{Co}^{2+} + 4/3IV\text{H}_2\text{O} \rightarrow 1/3III_b\text{Co}_3\text{O}_4 + 8/3IV\text{H}^+ + 2/3I e^-$ | k_h |

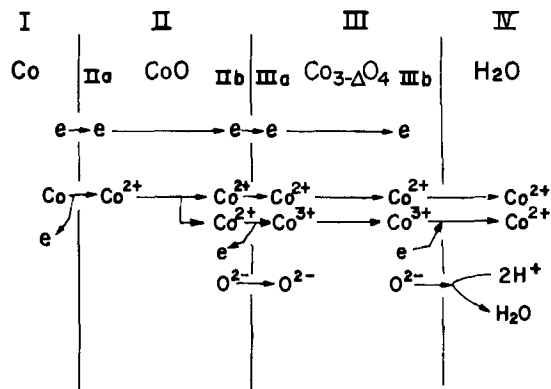


Fig. 10. Illustration of phase arrangement and reactions in two-layered passive films on cobalt.

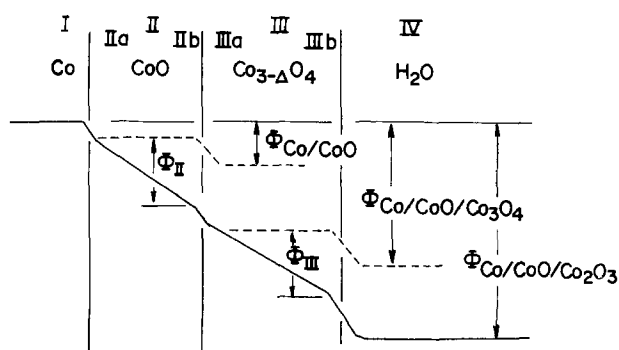


Fig. 11. A model of potential distribution in the two-layered passive film on cobalt. Dotted lines indicate the possible potential distribution at equilibrium for Co/CoO and Co/CoO/Co₃O₄ electrodes.

Since the inner layer increases in thickness by reaction [d], the growth rate can be described from Eq. [6] and [7] in terms of i_{II} and i_{III}

$$\begin{aligned} \frac{dL_{in}}{dt} &= 8Fk_d \tilde{L}_{CoO} \\ &= 4(i_{II} - i_{III}) \tilde{L}_{CoO} \end{aligned} \quad [13]$$

where $\tilde{L}_{CoO}/\text{nm cm}^2 \text{ C}^{-1}$ is the thickness of CoO equivalent to 1 C cm⁻² of Co(II) ion. The outer layer grows by reactions [g] and [h], and its thickness decreases by reaction [d]

$$\begin{aligned} \frac{dL_{out}}{dt} &= 2F(k_g + k_h - 3k_d) \tilde{L}_{Co_3O_4} \\ &= (i_{III} - i_{diss} + i_{depos} - 3(i_{II} - i_{III})) \tilde{L}_{Co_3O_4} \end{aligned} \quad [14]$$

where $\tilde{L}_{Co_3O_4}/\text{nm cm}^2 \text{ C}^{-1}$ is the thickness of Co₃O₄ equivalent to 1 C cm⁻² of Co(II) ion. Values of \tilde{L}_{CoO} and $\tilde{L}_{Co_3O_4}$ were experimentally obtained; $\tilde{L}_{CoO}/\text{nm cm}^2 \text{ C}^{-1} = 9.1 \times 10^2$ and $\tilde{L}_{Co_3O_4}/\text{nm cm}^2 \text{ C}^{-1} = 7.7 \times 10^2$ (2, 3). From Eq. [13] and [14] it is evident that the growth of one layer is strongly dependent on the ionic C.D. of the diffusing Co(II) ion in the other layer.

It is assumed that the ionic flux through the layer is a function of electric field strength $E = \Delta\phi/L$ following the Cabrera-Mott theory (10, 11).

$$i_{II} = i_{II,0} \exp(B_{II} \Delta\phi_{II}/L_{in}) \quad [15]$$

$$i_{III} = i_{III,0} \exp(B_{III} \Delta\phi_{III}/L_{out}) \quad [16]$$

where $i_{II,0}$ and $i_{III,0}$ indicate the ionic self-diffusion C.D. at zero field, and B_{II} and B_{III} are constants given

below

$$B_{II} = Z_{II}a_{II}F/RT \quad [17]$$

$$B_{III} = Z_{III}a_{III}F/RT \quad [18]$$

in which Z_{II} or Z_{III} is the ionic valency of migrating ion, and a_{II} or a_{III} the jumping distance for ion migration.

Equations [12]-[16], which represent the increasing or decreasing thickness of the layers, can be used to understand qualitatively the observed transient behavior and may predict the thickness in some cases.

Film thickness at steady states.—At the stationary state, where $(dL_{in}/dt) = 0$, $(dL_{out}/dt) = 0$, and $(di_a/dt) = 0$, the ionic transfer across every interphase is equal to the ionic diffusion through every layer

$$i_{ss} = i_{II} = i_{III} = i_{diss} \quad [19]$$

where i_{ss} represents the anodic C.D. at the stationary state. Correspondingly, the thicknesses are determined by Eq. [15] and [16]. As $\Delta\Phi_{II}$ remains equal to the irreversible potential difference given by Eq. [1] or [3] irrespective of the anodic potential, the thickness of the inner layer, L_{in} , is determined by the dissolution rate, i_{diss} , of the outer layer. It follows therefore that the inner layer, even if it is soluble, will grow to a certain thickness in the presence of the protective outer layer. Since the outer layer sustains an increasing potential difference $\Delta\Phi_{III}$ with anodic potential $\Delta\Phi_T$, its thickness will increase with anodic potential at the stationary state

$$\Delta\Phi_{III} = \Delta\Phi_T - \Delta\Phi_{II} \quad [20]$$

In our experimental results the thickness of the outer layer satisfies the above prediction for both one-step and two-step oxidation films, as shown in Fig. 8, whereas the thickness of the inner layer behaves differently depending on the formation procedure. It is thus suggested that the outer layer can approach the stationary thickness more quickly than the inner layer.

Anodic deposition of Co(II) in solution.—The difference in the inner layer thickness between one-step oxidation film and two-step oxidation film is caused by the anodic deposition reaction [h] in Table I, which occurs only in the one-step oxidation. As shown in Fig. 8 and 9, the potential at which the anodic deposition from Co(II) ion commences is in agreement with the potential at which an abrupt change of the inner layer thickness is observed. A question is now raised why the inner CoO layer does become thick, when Co(II) ions in the solution are deposited to form the outer layer of higher valence oxide. As the outer layer thickness increases by anodic deposition from Co ion, the rate of Co(II) ion diffusion in the outer layer decreases because of a decreasing electric field intensity in the layer according to Eq. [16] and eventually becomes negligible compared with the ionic diffusion rate in the inner layer

$$i_{II} \gg i_{III} = 0 \quad [21]$$

From Eq. [13] therefore the inner layer growth rate is

$$\frac{dL_{in}}{dt} = 4i_{II}\tilde{L}_{CoO} \quad [22]$$

which means that almost all Co(II) ions flowing through the inner layer to the CoO/Co₃O₄ interphase go into reaction [d] to form a new CoO layer at the expense of the outer Co₃O₄ layer. In this case the inner CoO layer may thicken without any diffusion of Co(II) ion through outer Co₃-O₄ layer which is a barrier against ion flow. By two-step oxidation, because of the absence of dissolved Co(II) ions in the solution, the film growth requires the diffusion of

Co(II) through both the layers and hence the film growth rate is small compared with that in one-step oxidation where the anodic deposition is involved.

Inner layer growth.—As shown in Fig. 4, when an anodic potential step was applied to a passivated cobalt, the outer layer was observed to grow first in an initial period of time until its thickness reached a steady value, where $dL_{out}/dt = 0$. The initial growth of the outer layer was followed by a gradual increase of the inner layer thickness in the later period of time while the outer layer thickness remained constant. Therefore, for the later stage of film growth, we obtain by substituting $dL_{out}/dt = 0$ and $i_{depos} = 0$ into Eq. [13] and Eq. [14] the following equations

$$\frac{dL_{in}}{dt} = (i_{II} - i_{diss})\tilde{L}_{CoO} \quad [23]$$

$$i_a = i_{II} \quad [24]$$

Equation [23] means that the dissolution rate of the outer layer plays a large role in determining whether the inner layer increases or decreases after the outer layer reaches the stationary thickness. From Eq. [18] and the result shown in Fig. 4 and 5, it follows that the potential step from 1.04 to 1.24V causes the inner layer to grow because $i_{II} > i_{diss}$ and that the reverse potential step brings about a decrease of the inner layer because $i_{II} < i_{diss}$.

The growth rate of the inner layer can be described from the results of Fig. 4 and from Eq. [24] by assuming the Cabrera-Mott relation of Eq. [15]. Figure 12 shows the relationship between the logarithm of anodic C.D. i_{II} and the inverse of the inner layer thickness during the second step oxidation at 1.24V after the outer layer reaches the stationary thickness. From the slope and intersect of the curve, $B_{II} \Delta\Phi_{II}/cm = 4.3 \cdot 10^{-7}$ and $i_{II,0}/A \cdot cm^{-2} = 1.2 \cdot 10^{-8}$. If we assume $\Delta\Phi_{II} = 0.61(V)$ from Eq. [3], $B_{II}/cm \cdot V^{-1} = 7.1 \times 10^{-7}$. From the value of B_{II} Eq. [17] gives $a_{II}/cm = 1.8 \times 10^{-8}$ at $Z_{II} = 2$, and $a_{II}/cm = 3.6 \times 10^{-8}$ at $Z = 1$. By comparing the estimated a_{II} values with the distance between the neighboring Co ions in CoO, calculated to be 0.30 nm from the lattice constant of 0.426 nm, it is likely that the migrating species is monovalent cobalt vacancy. The ionic conductivity κ at low fields may be written as

$$\kappa = \left| \frac{\partial I_{II}}{\partial (\Delta\Phi_{II}/L_{in})} \right|_{(\Delta\Phi_{II}/L_{in}) \rightarrow 0} = i_{II,0} B_{II} \quad [25]$$

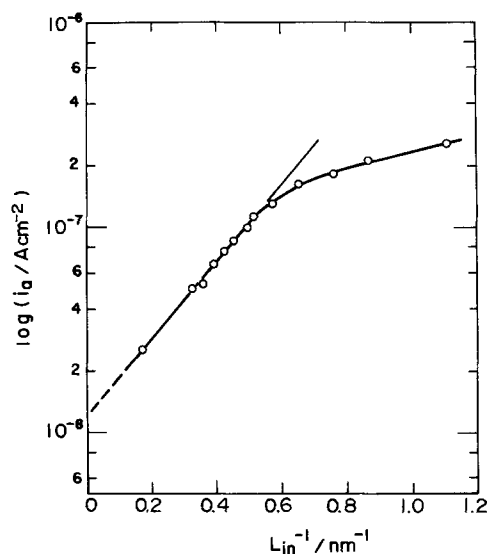


Fig. 12. Relation between inverse of the inner layer thickness and the anodic C.D. in logarithmic scale. Data correspond to the results of $\Phi = 1.24V$ oxidation in Fig. 4.

and is estimated to be $\kappa/S \text{ cm}^{-1} = 8.5 \times 10^{15}$. Furthermore, the self-diffusion constant D of moving species in the inner layer may be estimated using Einstein-Nernst relation (12), as follows

$$D = \frac{i_{IL0} B_{II} RT}{z^2 F^2} \cdot \frac{1}{C_{Co}} \quad [26]$$

where $C_{Co}/\text{mol cm}^{-3}$ is the number of mol of CoO in unit volume and is calculated to be $C_{Co}/\text{mol cm}^{-3} = 0.086$ from the lattice constant. We estimate that $D/\text{cm}^2 \text{ sec}^{-1} = 6.5 \times 10^{-21}$ for $Z = 2$ and $D/\text{cm}^2 \text{ sec}^{-1} = 2.6 \times 10^{-20}$ for $Z = 1$. No comparable self-diffusion constant can be found in the literature and the estimated values in this work are 10^{10} times as large as the value extrapolated from the diffusion data for CoO obtained at high temperature above 1200 K by Richardson *et al.* (13) and by Chen *et al.* (14). The discrepancy may be attributed to a large concentration of lattice defects in the anodic oxide film.

Conclusion

The following conclusions may be drawn;

1. Cobalt is covered with a two-layered oxide film consisting of an inner CoO and an outer Co_3O_4 or Co_2O_3 in the passive potential region more positive than Φ/V vs. HESS = 0.75 in neutral boric acid-sodium borate solution at pH 8.4.

2. A growth model is presented for electrochemical two-layer formation, which explains the observed dependence of film thickness on the potential and on the time of oxidation.

3. The outer layer reaches within 1 hr the stationary thickness which increases nearly linearly with the electrode potential, and the inner CoO layer requires much longer oxidation time before the stationary thickness is reached. The inner layer thickness that grows in a few hours' oxidation depends not only on the potential but also on the oxidation procedure. It is revealed that the growth of the inner CoO layer is influenced by the ionic diffusion in the outer layer.

4. Anodic deposition of a $\text{Co}_{3-\Delta}\text{O}_4$ layer ($0 \leq \Delta \leq 0.33$) from Co(II) ion in solution of pH 8.4 can take place at Co(II) ion concentrations as small as 1.03 mg dm^{-3} in the potential region more positive than 1.2V. Therefore, the anodic oxide film on cobalt becomes thick in the presence of Co(II) ion in solution.

5. The ion migration in the anodic oxide film is likely to be assisted by high electric field and represented by the rate equation $i = i_0 \exp(B\Delta\Phi/L)$ for each individual layer.

6. The self-diffusion coefficient in the inner CoO layer is estimated to be $D/\text{cm}^2 \text{ sec}^{-1} = 6.5 \times 10^{-21} \sim 2.6 \times 10^{-20}$.

Acknowledgment

One of the authors (T.O.) gratefully acknowledges a scholarship from the Sakkokai Foundation.

Manuscript submitted Aug. 27, 1980; revised manuscript received March 5, 1981.

Any discussion of this paper will appear in a Discussion Section to be published in the June 1982 JOURNAL. All discussions for the June 1982 Discussion Section should be submitted by Feb. 1, 1982.

Publication costs of this article were assisted by Hokkaido University.

REFERENCES

1. T. Ohtsuka and N. Sato, *Jpn. Inst. Met.*, **39**, 60 (1975).
2. T. Ohtsuka, K. Kudo, and N. Sato, *ibid.*, **40**, 124 (1976).
3. K. Kudo, N. Sato, and T. Ohtsuka, "Passivity of Metals," R. P. Frankenthal and J. Kruger, Editors, p. 918, The Electrochemical Society Soft-bound Proceedings Series, Princeton, NJ (1978).
4. N. Sato and T. Ohtsuka, *This Journal*, **125**, 1735 (1978).
5. K. Kudo and N. Sato, *Bull. Fac. Eng. Hokkaido Univ.*, No. 61, p. 45 (1971).
6. H. Göhr, *Electrochim. Acta*, **11**, 827 (1966).
7. T. Ohtsuka and N. Sato, *Corros. Eng. (Boshoku Gijutsu)*, **24**, 489 (1975).
8. G. J. Yurek, J. P. Hirth, and R. A. Rapp, *Oxid. Met.*, **8**, 265 (1974).
9. R. D. Shaw and R. Rolls, *Corros. Sci.*, **14**, 343 (1974).
10. N. Sato and T. Noda, *Electrochim. Acta*, **22**, 839 (1977).
11. N. Cabrera and N. Mott, *Rep. Progr. Phys.*, **12**, 163 (1949).
12. P. Kofstad, "Nonstoichiometry, Diffusion, and Electrical Conductivity in Binary Metal Oxides," p. 100, Wiley-Interscience, New York (1972).
13. R. E. Carter and F. D. Richardson, *Trans. AIME*, **200**, 1244 (1954); **203**, 336 (1955).
14. W. K. Chen, N. L. Peterson, and W. T. Reeves, *Phys. Rev.*, **186**, 887 (1969).

Transistor Action Using ZrO₂ Electrochemical Cells

Robert E. Hetrick* and W. C. Vassell

Ford Motor Company, Research Staff, Dearborn, Michigan 48121

ABSTRACT

Transistor action is reported at elevated temperatures in a ceramic structure composed of two ZrO₂ electrochemical cells separated by an enclosed volume. The "emitter" cell pumps O₂ from an ambient atmosphere into the volume (base region) where it is returned to the ambient by the "collector" cell. Electrical operation, analogous to that of semiconductor transistors, can be understood in terms of the limiting currents caused by the Pt cathode of the collector cell. Small-signal voltage and current gain are illustrated in common transistor external circuit arrangements. The results for each arrangement also serve to illustrate various electrochemical aspects of ZrO₂ cells. A simple model is described which accounts for the main steady-state characteristics. The frequency response of the device is determined primarily by the double-layer capacity of the Pt/ZrO₂ interface. This approach to transistor action should be applicable to other electrochemical systems.

In a previous paper (1) it was shown that transistor action could be observed in an electrochemical ceramic structure composed of two ZrO₂ oxygen-concentration cells separated by an enclosed volume. Complementary to a concept by Letaw and Bardeen (2) using liquid electrolytes, the present approach to transistor action is general and should be applicable to a number of electrochemical systems. The purpose of this paper is to elaborate on the operation of the device. In particular, operation is illustrated in a number of common transistor configurations (common base, common emitter, common collector). A simple analytical model is put forward which accounts for the main steady-state characteristics. Those properties of the electrolyte, electrode, or electrode/electrolyte combination which determine or limit the device operation are discussed. In some cases the device proves to be a convenient structure for studying cell properties such as cathodic polarization phenomena.

For the present electrochemical system, the high operating temperature and low frequency response which attend oxygen ion conducting solid electrolytes would undoubtedly limit device usefulness to special applications. One such application is that of O₂ sensing in the automotive exhaust where the O₂ concentration provides a convenient, real-time measure (3) of engine intake air-to-fuel ratio (A/F). The latter quantity is a key parameter influencing many aspects of engine performance. High sensitivity O₂ sensors based on the properties of the present device structure could be useful for engine diagnostics or in the feedback control of A/F especially with regard to engines operating in the fuel-efficient lean A/F region.

Experimental

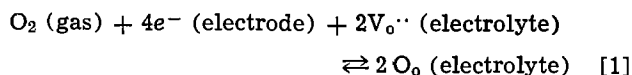
The device is shown in Fig. 1a. The active components are two electrochemical cells whose electrolytes are in the form of disks of ceramic ZrO₂ doped with 8 mol percent Y₂O₃. The disks have a typical diameter of 1.0 cm and a thickness of 0.1-0.2 cm. The material was obtained from the Ceramic Products Division of the Corning Glass Works. Because of the large concentration of oxygen vacancies introduced by the dopant, the material is a strong O⁼ ionic conductor (4) and well suited for use as a solid electrolyte. Sputtered Pt films with thicknesses ranging from 0.5-1.0 μm were used as electrodes. As a result of sintering during high temperature firing (800°-1000°C), the films adopt a porous sponge-like structure (5). Pt paste was also

used for electrodes, but sputtered films gave the most reproducible results. The cells are separated by an enclosed volume defined by a hollow ceramic spacer (0.1 cm in length) joined to each cell with ceramic glue (Aremco 552) or glass frit (General Electric RE-X). As discussed below, some types of operation require the volume to have a small leak to the ambient. This can be accomplished by making the seals somewhat leaky or by drilling a small hole into the spacer or cell face. Similar structures for O₂-sensing applications have been discussed (6).

The device is operated in a furnace at temperatures ranging from 600° to 1000°C. The ambient atmosphere is fixed by the use of calibrated gases containing O₂ at partial pressures ranging from 10⁻² to 10 kPa in N₂. The total pressure is 100 kPa. The typical electrolyte resistance during operation was on the order of 50Ω.

Principles of Transistor Operation

Electrical operation is based on the electrochemical pumping of O₂ from the ambient into the enclosed volume (base region) by one cell (the emitter) while at the same time collecting and returning that O₂ to the ambient with the other cell (the collector). The use of ZrO₂ cells as very efficient O₂ pumps in this partial pressure region is well established (7-9). The overall electrochemical reaction step is given by Eq. [1]



where V_O^{··} represents an oxygen-ion vacancy and *e* is the electronic charge (5, 10-13). Numerous studies of ZrO₂ cells have brought out the complexity of the intermediate steps which combine to produce the overall reaction. When ionic current is drawn, one of these steps can become rate limiting leading to electrode polarization phenomena. For the O₂ partial pressures and electrodes used in this work, these studies indicate minimal polarization associated with the anodic release of oxygen, while under certain conditions, large cathodic polarization can occur on the uptake of oxygen. This polarization is related to the limited ability of the Pt electrodes to deliver O₂ to the electrode/electrolyte interface. The specific intermediate step responsible for this limitation, which plays an important role in the present device operation, has not yet been unambiguously identified. The actual electrochemical step does not appear to be rate limiting for *T* > 700°C, and an equilibrium exchange current density, *i*₀ ~ 1 A/cm², has been determined

* Electrochemical Society Active Member.

Key words: transistor, solid electrolyte, ZrO₂, cathode polarization.

for porous Pt electrodes in this temperature range (14).

If an O_2 partial pressure difference exists at opposing sides of a ZrO_2 cell, an emf is developed whose magnitude is given at equilibrium by the Nernst equation (Eq. [2])

$$\text{emf} = (RT/4F) \ln (P_1/P_2) \quad [2]$$

where R and F are the gas and Faraday constants while P_1 and P_2 represent the effective oxygen pressures or activities at the opposing electrode/electrolyte interfaces. In the analysis given below Eq. [2] is used to represent the cell emf's even though ionic current is drawn. The use of an equilibrium result to describe a nonequilibrium situation is justified when the current densities drawn are considerably less than i_0 .

In the following, device operation is discussed primarily in the context of the common-base (CB) configuration. This will begin with a qualitative discussion of steady-state characteristics and the corresponding a-c amplification functions that can be realized because of these characteristics. Following this is a more detailed discussion of those cell parameters which define steady-state operation. Next a simple model describing steady-state behavior both in the CB and other configurations is put forth and compared with experiment. Small-signal parameters commonly used to compute transistor amplifier gain and impedance coefficients are derived from the steady-state model. With increasing frequency, the deviation in small-signal behavior from that predicted by the steady-state parameters is discussed in terms of several capacitive effects. The curves shown on subsequent figures are experimentally derived unless expressly indicated.

Steady-state operation.—Figure 1b shows the device wired in the CB configuration. In normal operation the emitter cell is "forward biased" by V_E to emit O_2 from the ambient into the base region. At the same time the collector cell is "reverse biased" by V_C through the load resistor R_L to collect the emitted O_2 and return it to the ambient. The emitter and collector currents are labeled by I_E and I_C , respectively. With the base electrodes of each cell connected, one has a three terminal device biased like an n-p-n semiconductor transistor. Because of the particular device structure, electrical operation is also similar. In fact, the device can be used to perform a number of com-

mon transistor functions including a-c or small-signal voltage, current, and power amplification.

To understand device operation qualitatively, imagine that I_E has been fixed at a nominal value to pump O_2 into the enclosed volume. If the collector cell is open circuited, a steady state will occur when the flux ($i_E/4e$) of O_2 molecules entering the volume equals the flux leaving by means of a leak aperture. The steady state will be characterized by an O_2 partial pressure in the base, $P(B)$, as well as an absolute pressure, which are greater than their counterparts in the ambient. These pressure differences "drive" the leakage flux. If there were no leak, only a null emitter current would be possible in steady state (neglecting a number of small effects or processes such as electronic conductivity which would invariably result in a finite value of I_E). In this case V_E would generate a transient emitter current which builds a $P(B)$ value just large enough to produce a Nernst emf at the emitter cell which exactly offsets V_E . If a collector bias of proper polarity is now applied, O_2 molecules will be withdrawn from the base at a rate given by $I_C/4e$. As I_C is increased, $P(B)$ decreases with commensurate changes occurring in O_2 leakage. In particular, as $P(B)$ falls below $P(A)$ (the O_2 partial pressure in the ambient), the direction of leakage changes and O_2 is drawn into the volume. As discussed below, the principal leakage mechanism is one in which O_2 diffuses through its carrier gas (e.g., N_2 or CO_2) in response to differences between $P(B)$ and $P(A)$. Because of the device structure, I_C must eventually saturate. The maximum saturation value would equal the fixed value of I_E plus a leakage contribution equivalent to the maximum flux of O_2 molecules that the leak aperture will pass [occurring for $P(B) \ll P(A)$]. In practice this maximum value is not achieved. As the steady-state value of $P(B)$ decreases, a point is reached where the collector cathode cannot deliver O_2 at a greater rate, and the cathode becomes completely polarized. As a consequence $P(B)$ saturates at some finite value and the maximum leakage current is not quite realized.

With an operating point established in the saturation region, the collector cell presents a high effective a-c impedance since small changes in collector bias, ΔV_C , serve primarily to modulate the degree of cathode polarization. By adjusting V_C , the total impedance of the collector circuit can be further increased by choosing an arbitrarily large value of R_L . At the same time, the impedance of the emitter circuit remains low, consisting primarily of the electrolyte resistance R_E . Accordingly, a modulation in emitter current, ΔI_E , can be achieved with a modest variation in emitter bias, ΔV_E . If ΔI_E is small, the collector-cell current will undergo a nearly identical modulation, ΔI_C , while still remaining in a saturated condition. However, the collector current is drawn through a much higher resistance resulting in a higher voltage modulation ($=\Delta I_C R_L$). As in the case of a semiconductor transistor, the a-c gain or ratio of collector circuit to emitter circuit voltage modulation is given within a certain range by R_L/R_E . Similar considerations hold for gain coefficients in other configurations. In many cases these coefficients or other device parameters serve to isolate various electrochemical aspects of ZrO_2 cells for study.

Results and Discussion

Figure 2 shows a plot of I_C vs. V_{CB} (the collector or output characteristic) for various values of I_E at $T = 800^\circ C$ and $P(A) = 1.0$ kPa. Voltages are measured with respect to the common lead while currents are positive in the directions shown. As discussed, I_C shows saturation behavior with increasing collector bias. Higher saturation currents occur for larger I_E . Each curve in the family is labeled both with I_E , which

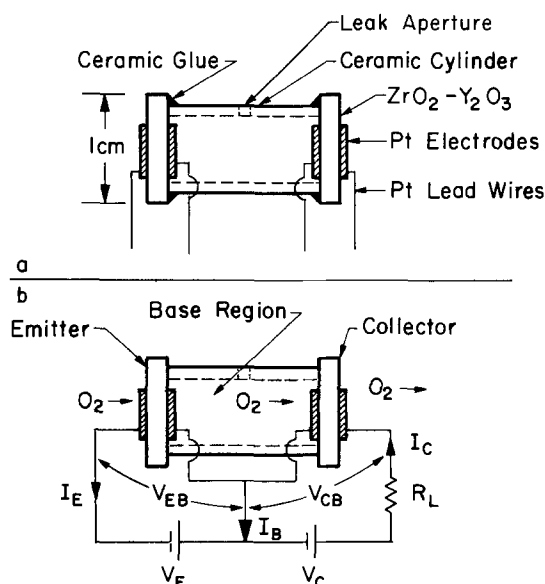


Fig. 1. a, Schematic view of the ZrO_2 transistor. b, Transistor wired in the CB configuration.

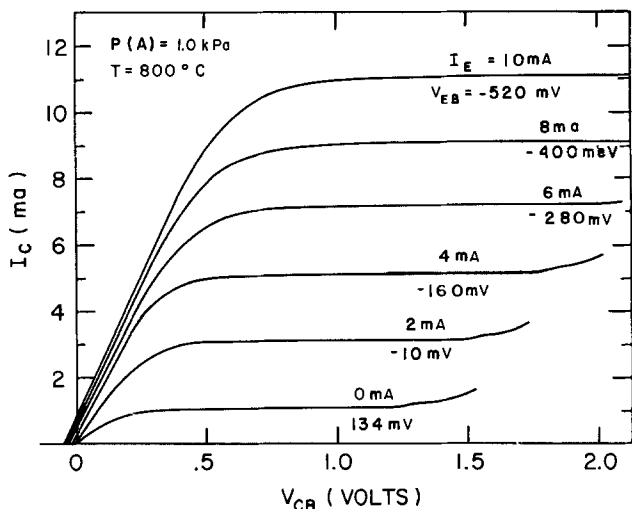


Fig. 2. Collector current vs. collector to base voltage (output characteristic) for the CB configuration.

is held constant, and with the emitter bias at saturation. Figure 3 shows the corresponding input or emitter characteristic in which I_E is plotted against V_{EB} at constant values of V_{CB} . The sign of V_{EB} has been changed in this figure to avoid the appearance of a negative input resistance. Inspection of both curves shows that the emitter resistance remains low ($\sim 60\Omega$) while the dynamic collector resistance is large ($\sim 2 \times 10^4\Omega$) at saturation. Referring to the collector characteristic, as V_C and accordingly V_{CB} are increased, saturation eventually terminates with a "breakdown" in which I_C begins to increase again. As is discussed more fully below, breakdown is accompanied by a large decrease in $P(B)$ which is reflected as a large increase in input resistance in the input characteristic (see the $V_{CB} = 1.5V$ curve in Fig. 3). In Fig. 2, O_2 leakage through leak apertures is evidenced by the fact that $I_C > I_E$. Gas leakage can be identified with the electrical current (leakage current), I_B , flowing in the base lead as expressed in Eq. [3]

$$I_B = I_C - I_E \quad [3]$$

The main factor which determines the essential features of the collector characteristic is the O_2 transfer limitation of the collector cathode mentioned previously. This process, as well as that of leakage, can be investigated by opening the emitter circuit and measuring the leakage curve ($I_E = 0$) of the characteristic

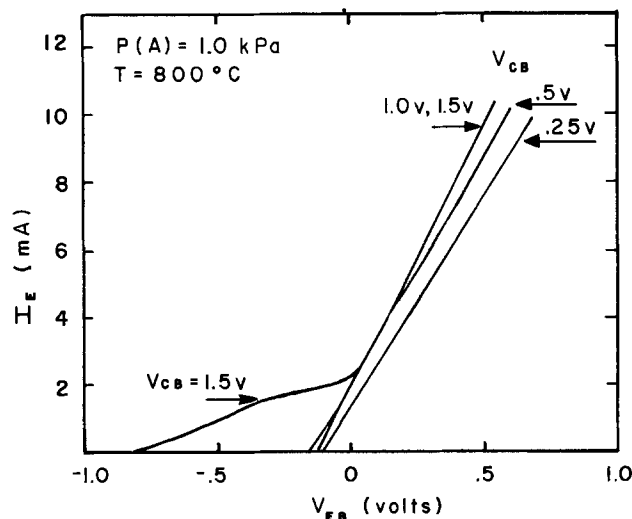


Fig. 3. Emitter current vs. emitter to base voltage (input characteristic) for the CB configuration.

while monitoring the emitter-base voltage V_{EB} . The open emitter cell acts as an O_2 pressure sensor allowing determination of $P(B)$ from the Nernst equation when $P(A)$ is fixed by the use of calibrated gases. Figure 4 shows a plot of I_C and V_{EB} vs. V_{CB} for this case with the same ambient conditions as Fig. 2. The important point is that V_{EB} , and hence $P(B)$, saturates (at the same value of V_{CB} that I_C saturates) indicating that I_C is limited by the polarization of the collector. For the case shown, the O_2 partial pressure at saturation is $P(BO) = 3 \times 10^{-3}$ kPa of (the extra label O identifying conditions where the only electrical current flowing in the base and collector circuits results from O_2 leakage). By varying $P(A)$ one finds that the saturated leakage current, I_{CO} , can be related to $P(BO)$ by Eq. [4]

$$I_{CO} = (1/R_{DC})P^n(BO) \quad [4]$$

Here R_{DC} (on the order of $5.0 \text{ kPa}\cdot\text{A}^{-1}$ for $0.5 \mu\text{m}$ electrodes) represents the "resistance" the cathode presents to the delivery of O_2 while n is a constant having values ranging from $0.5 < n < 1.0$. The DC in the subscript suggests that the resistance is related to a diffusion process in the cathode.

As has been reported by other authors (5, 10, 12), the values of these parameters are strongly dependent on the method of electrode application, thickness, sintering temperature, and heavy current passage ($\sim 1 \text{ A/cm}^2$ in $100 \text{ kPa } O_2$). These factors determine the texture of the electrode which in turn governs the details of the cathodic polarization. When $n = 1$, a limiting process involving molecular O_2 (e.g., pore diffusion) is likely and when $n = 0.5$, a process involving atomic O is limiting. A systematic study of these effects was not performed. In this work consistent and repeatable results were found using sputtered Pt electrodes.

We assume that Eq. [4] is the limiting form of a more general O_2 transfer expression for the cathode which can be approximated by Eq. [5]

$$I_C = (1/R_{DC})(P(B) - P(CB))^n \quad [5]$$

where $P(CB)$ represents the effective O_2 partial pressure at the electrode/electrolyte interface of the cathode. As V_{CB} increases in the saturation region, a large effective O_2 partial pressure difference develops across the cathode ($P(CB) \ll P(B)$) and Eq. [5] approaches the limiting form of Eq. [4]. At low values of V_{CB} , Eq. [5] is the main relationship determining the curvature of the collector characteristic, as is discussed in the steady-state model developed later.

The dependence of leakage current on O_2 pressure can be characterized by a single parameter obtained

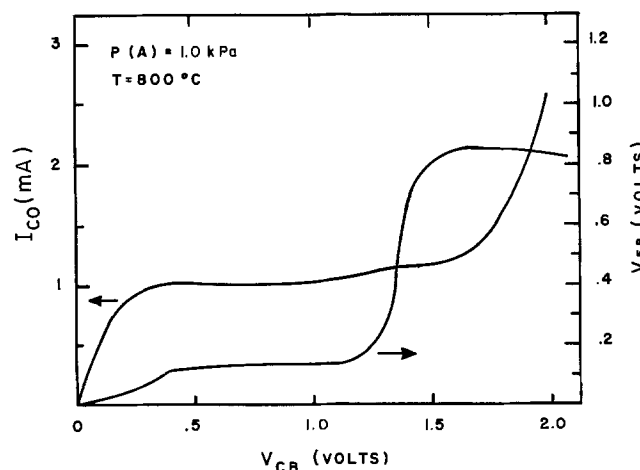


Fig. 4. Collector current and emitter to base voltage vs. collector to base voltage with the emitter cell open circuited.

from the data such as that of Fig. 4 in the presaturation region. The relation shown in Eq. [6] holds over a wide range of $P(B)$ values

$$I_B = (1/R_{DL})(P(A) - P(B)) \quad [6]$$

Similar to the constant in Eq. [4], R_{DL} represents the resistance of the leak to the flux of O_2 . Figure 5 shows a typical plot of I_B vs. $P(B)$ from which the R_{DL} value is obtained.

Breakdown.—When the collector bias is increased, a breakdown region which is characterized by an increasing collector current eventually results, as in the case of semiconductor transistors. Although device operation is precluded in this region, a brief discussion of breakdown properties is useful for illustrating further how the present structure can be used to study interesting aspects of ZrO_2 cells in a variety of gaseous ambients.

The essential features of breakdown are illustrated in Fig. 4. For that case, the open emitter voltage starts to depart from its saturation value (0.134V) at V_{CB} 1.2V and rises sharply to approximately 0.85V, corresponding to $P(B) = 1.1 \times 10^{-14}$ kPa, where it peaks and eventually begins a slight decline. Simultaneously, I_{CO} starts to increase gradually from its saturation value. With increasing V_{CB} , I_{CO} rises more rapidly and for a range of collector voltages the slope of the curve may in some circumstances yield a dynamic resistance which approaches the bulk electrolyte resistance of the collector cell. Operation in this region is sluggish, being attended by long-term drifts in all electrical parameters not fixed by the external circuit. For example, as V_{CB} just reaches the point of breakdown, the drifts are in the direction of increasing values of V_{CB} while I_{CO} slowly decreases to a steady-state value. If V_{CB} is caused to increase beyond 3-4V, however, I_{CO} tends to increase continuously with time. These drifts are probably associated respectively with a reduction and finally decomposition of the collector electrolyte (7) consistent with the low values of $P(B)$ indicated by V_{EB} . The details of breakdown are systematically influenced by the composition of the ambient gas phase both in the amount of O_2 present and in the nature of the carrier gas employed. For example, the onset of breakdown occurs at smaller V_{CB} values as $P(A)$ decreases.

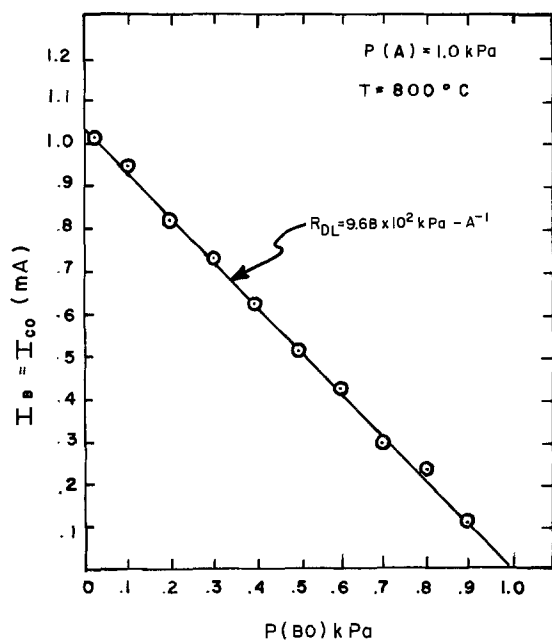


Fig. 5. Collector current vs. O_2 partial pressure in the base with the emitter open circuited.

Employing single ZrO_2 cells in the form of platelets or tubes, numerous authors (9, 15) have observed current breakdown subsequent to a saturation region. Yanagida *et al.* (10) suggested that with increasing applied voltage, the effective O_2 partial pressure at the Pt/electrolyte interface of the cathode, $P(CB)$, has been lowered sufficiently to reduce the electrolyte resulting in an enhanced degree of electronic conductivity. Initially present only at the cathode surface, this conductivity would eventually spread throughout the electrolyte as V_{CB} increases. Such a surface conductivity could render the entire electrolyte surface active for taking up the ambient O_2 , thereby removing a portion of the electrode polarization and allowing additional O_2 to be pumped. We have observed that if V_C is initially applied so that V_{CB} lies in the breakdown region and is then removed, V_{EB} and the open-circuit value of V_{CB} remain at high values ($\sim 0.8V$) for a period of time before each relaxes to 0.0V. The longer that V_C is applied, the longer it takes for the relaxation to occur. Recovery times are even longer if the O_2 content in the ambient is reduced. These observations are consistent with a cumulative reduction of the electrolyte. After V_C has been removed, the reduced ceramic continues to pump O_2 until it eventually equilibrates with $P(A)$. Lower $P(A)$ prolongs the relaxation.

Using open-ended tubular electrolytes, others (9) have found that the very low O_2 pressures (e.g., 10^{-14} kPa) achieved with O_2 pumping are not due to the complete electrochemical removal of O_2 , but are a consequence of the presence of CO_2 , H_2O , or other oxygen-bearing species present as impurities in the feedgas. With sufficient pumping voltage, these species are electrolyzed producing CO or H_2 whose reaction with the remaining O_2 is catalyzed by the Pt electrodes. Since these oxidation reactions are strongly favored, very low O_2 pressures will result if the stoichiometric ratio for the unreacted species can be approached (e.g., if $[P_{CO}(B)/P_{O_2}(B)] \cong 2$). For a given pump voltage this condition will be promoted if the feedgas contains larger CO_2 or H_2O pressures or lower O_2 pressures. Figure 6 shows plots of I_{CO} and V_{EB} vs. V_{CB} for the same device when the ambient gases are nominally 0.25% O_2 in CO_2 and 0.25% O_2 in N_2 . The behavior is nearly identical until breakdown, which occurs much earlier for the ambient containing CO_2 . For the present interpretation, the CO_2 result is explained by a substantial CO_2 electrolysis which quickly produces enough CO to eliminate the remaining O_2 .

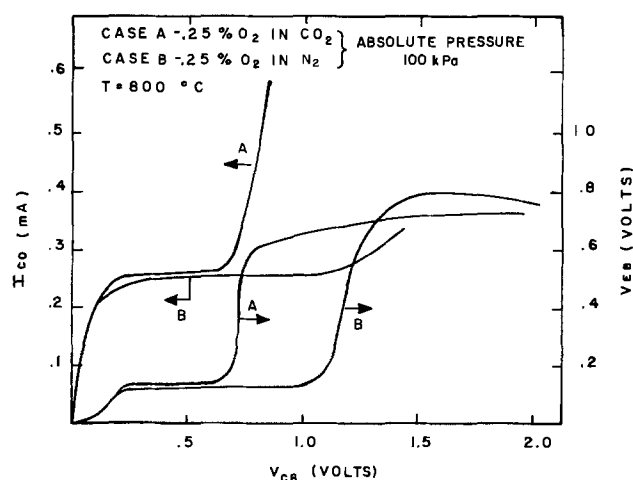


Fig. 6. Collector current and emitter to base voltage vs. collector to base voltage with the emitter open circuited for two different ambients; A, 0.25% O_2 in CO_2 ; and B, 0.25% O_2 in N_2 ; both at 100 kPa total pressure.

The data shown in Fig. 7 are also consistent with these results. When O₂ is injected into the base with a forward-biased emitter cell, the breakdown moves to higher V_{CB} voltages due to the increased value of P(B) at saturation. Besides the progressive negative shift of the characteristic due primarily to the IR drop in the emitter, the main feature is the shift of the breakdown to higher V_{CB} with increasing I_E. This coupling between output (collector) and input (emitter) circuits is a form of internal voltage feedback which, although present in conventional semiconductor transistors, is much larger in the present device.

At low collector voltages, V_{EB} is negative for positive values of I_E. This is due to both the IR drop in the emitter electrolyte and the Nernst emf resulting from the "overpressuring" of the base [P(B) > P(A)] when the injected O₂, instead of being electrochemically collected, is forced out the leak. This is also seen in Fig. 2 where, with increasing I_E, the I_C = 0 intercept shifts to negative V_{CB} values as the base is overpressured.

In summary, the main processes occurring at breakdown appear to be accountable in terms of phenomena previously observed with ZrO₂ cells. As was the case in the prior discussion of cathode polarization, the present device structure allows these processes to be manifested in a manner which is particularly convenient for study.

Steady-state model.—Using the values of R_{DC} and R_{DL} obtained from the leakage curve, the steady-state device behavior can be modeled by assuming that each cell represents a circuit element which shows an IR drop due to electrolyte resistance and a Nernst emf consistent with the O₂ partial pressures at each electrode. For an emitter circuit without an external series resistor, one has

$$V_E = I_E R_E - \frac{RT}{4F} \ln \frac{P(A)}{P(B)} \quad [7]$$

while for the collector circuit

$$V_C = I_C (R_L + R_C) + \frac{RT}{4F} \ln \frac{P(A)}{P(CB)} \quad [8]$$

and

$$V_{CB} = V_C - I_C R_L \quad [9]$$

Equations [3] and [5]-[8] allow computation of the input and output characteristics for any suitable independent variable.

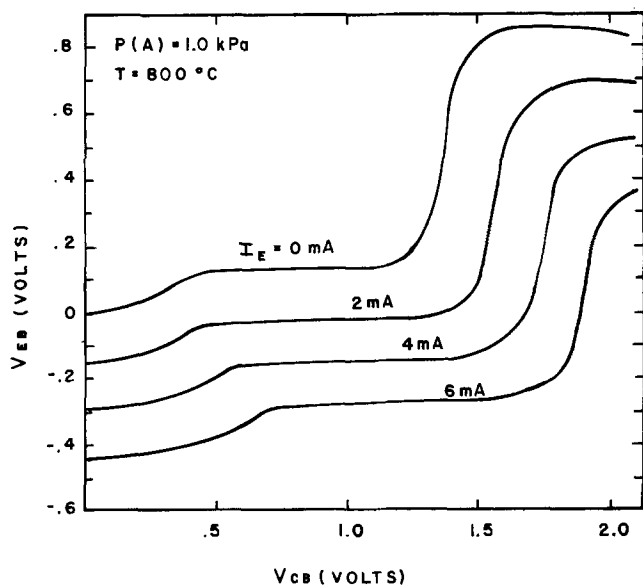


Fig. 7. Emitter to base voltage vs. collector to base voltage for various emitter currents.

A limiting case occurs when leakage is nonexistent (R_{DL} = ∞) and the O₂ transport limitation by the collector cathode is negligible (R_{DC} = 0). In that case

$$P(B) = P(A) \exp \left[\frac{-4F}{RT} (V_C - I_E (R_L + R_C)) \right] \quad [10]$$

and

$$I_B = 0, \quad P(CB) = P(B)$$

$$I_E = I_C = \frac{V_C + V_E}{(R_L + R_C + R_E)}$$

As is reasonable, the external current is determined by the series combination of applied voltages and ohmic resistances, the base electrodes acting as short circuits. The steady-state value of P(B) is exponentially promoted by I_E which injects O₂ and diminished by V_C which withdraws O₂.

Using parameters appropriate for the data of Fig. 2 (R_{DL} = 9.68 × 10² kPa-A⁻¹, R_{DC} = 5.9 kPa-A⁻¹, R_E = 60Ω, R_C = 56Ω, P(A) = 1.0 kPa, T = 1073 K), Fig. 8 shows the collector characteristic obtained from a solution of the above equations. There is reasonable agreement with Fig. 2 if the breakdown phenomenon which is not included in the model is ignored. At low values of V_{CB} the curvature of the measured output characteristic has as much as 30% lower current values than the computed data. This may in part reflect an oversimplified choice of n and R_{DC} to specify the cathode polarization. Although the model, and the latter aspect in particular, is not exact, it proves very useful for determining trends in device behavior with parameter variations.

The extent of the O₂ activity drop that develops across the cathode is shown by the model results of Fig. 9 where P(B) and P(CB) are plotted as a function of V_{CB} for I_E = 0 and 2 mA. At a given V_{CB} both P(B) and P(CB) increase with increasing emitter current.

Finally, unlike a semiconductor transistor, the present device has four external terminals if the base leads of the emitter and collector cells are not connected. This allows a degree of flexibility in biasing as shown by the three alternate arrangements of Fig. 10 which all result in nearly equivalent CB-type performance. The major effect of the different arrangements is to allow the polarity of the biasing for each cell to be varied. Further, for the arrangements of Fig. 10b and 10c, the low-frequency input and output signals will be in phase which is normal for CB mode, while for the arrangements of Fig. 10a and b the signals will be 180° out of phase which is a new feature.

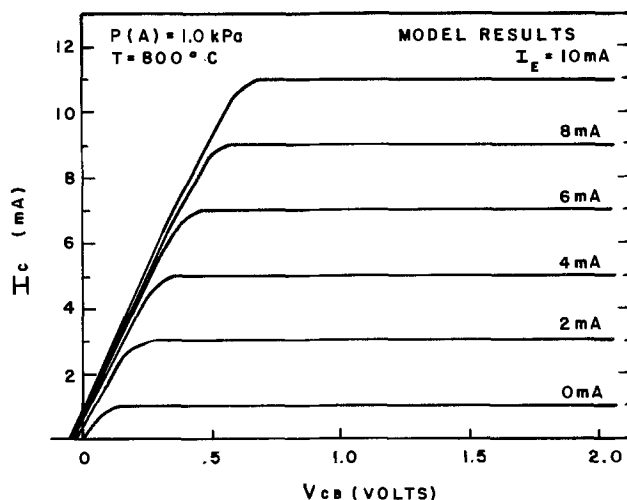


Fig. 8. Model results for the output characteristic in the CB mode.

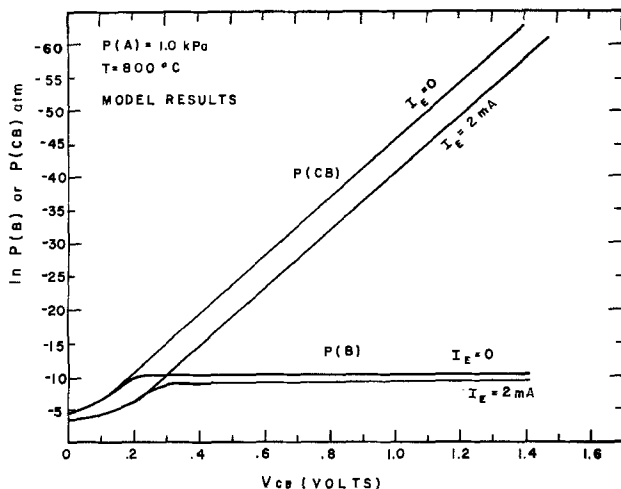


Fig. 9. Model results for the variation of O_2 partial pressure in the base and at the Pt/ ZrO_2 interface of the collector cathode vs. collector to base voltage.

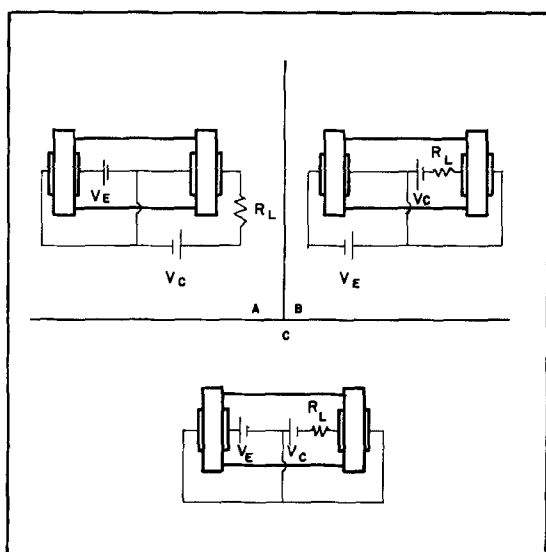


Fig. 10. Alternate arrangements to achieve CB-type characteristics.

Small-signal analysis.—As discussed previously, the device can be used as a small-signal amplifier in a manner analogous to that for npn transistors. In the CB mode V_C and V_E are adjusted to establish an operating point on the output characteristic. The slope of the load line is set by R_L . Inspection of Fig. 2 shows that even with a near vertical load line (low R_L), current gain, $G_I = \Delta I_C / \Delta I_E$ (where Δ signifies small-signal values), will never exceed unity as is typical for the CB mode. For a load line with a much smaller slope, voltage gain, $G_V = \Delta V_{CB} / \Delta V_{EB}$, can be realized. In fact voltage gains of 70 have been measured. Physically, gain results because the input modulation ΔV_{EB} , produces a small variation in $P(B)$, which under saturation conditions and with a large R_L , produces a much larger percentage variation in $P(CB)$. The latter variation, through the Nernst term in Eq. [8], provides the dominant modulation of the collector-cell voltage drop.

Characterization of amplification properties is most conveniently done using the standard small-signal parameterization of the steady-state input and output characteristics for a given mode. These parameters quantify the components of a small-signal equivalent circuit from which the low-frequency a-c response of the device can be computed. Hybrid parameters are used in the present work and their properties are dis-

cussed in Ref. (16). Choosing a typical operating point in the saturation region for the data under discussion, one finds (Fig. 2) that the current amplification factor $\alpha_{fb} = (\Delta I_C / \Delta I_E)_{V_{CB}} = 1.00$ indicating that all of the emitted current is collected. The conductance $h_{ob} = (\Delta I_C / \Delta V_{CB})_{I_E} = 2 \times 10^{-4}$ mhos shows the small slope of the saturated collector characteristic. The emitter input resistance $h_{ib} = (\Delta V_{EB} / \Delta I_E) = 60 \Omega$ is accounted for by the emitter electrolyte resistance. This quantity is most easily obtained from Fig. 3. The reverse amplification factor $\mu_{rb} = (\Delta V_{EB} / \Delta V_{CB})_{I_C} = 10^{-2}$ and can most easily be obtained from Fig. 7. This parameter quantifies the internal feedback property discussed previously. In this case μ_{rb} is larger than for Si transistors ($\sim 10^{-4}$) and reflects the fact that $P(B)$ is changing slightly in the region of collector saturation with the result that the Nernst component of V_{EB} is affected. Using these parameters, well-known formulas (16) exist for computing gain coefficients as well as input and output resistances in the various amplifier operating modes. Useful and instructive approximations to these coefficients can be obtained from the model equations. For example, although a variation ΔV_{EB} will produce a modulation $\Delta P(B)$, a reasonable approximation is that $\Delta \ln(P(B)/P(A))$ is small in Eq. [7] so that the input resistance R_{IN} is given by

$$R_{IN} = \frac{\Delta V_{EB}}{\Delta I_E} \sim R_E \quad [11]$$

Further, in the region of saturation $P(CB) \ll P(B)$ and Eq. [3], [5], and [6] can be used to obtain a current gain G_I given by

$$G_I = \frac{\Delta I_C}{\Delta I_E} \sim \frac{R_{DL}}{R_{DL} + R_{DC}} \quad [12]$$

Using R_{DL} and R_{DC} values for the sample of Fig. 2, $G_I \sim 0.994$ while the measured gain is essentially unity for low values of R_L (the effect of R_L on gains for the actual and model results in discussed more fully below). $G_I < 1.0$ because an increase in I_E produces a corresponding increase in $P(B)$ which serves to reduce the leakage current I_B . Since the collector is drawing both the emitted and leakage currents, $(\Delta I_C / \Delta I_E) < 1$. Finally from Eq. [9] one finds that $\Delta V_{CB} = -\Delta I_C R_L$. Using Eq. [11] and [12] in this relation yields a voltage gain given by

$$G_V = \frac{\Delta V_{CB}}{\Delta V_{EB}} = \frac{R_{DL} R_L}{(R_{DL} + R_{DC}) R_E} = G_I \frac{R_L}{R_E} \sim \frac{R_L}{R_E} \quad [13]$$

For low R_L ($< 10^4 \Omega$) experimental results reasonably approximate this prediction.

The model can also be used to separately calculate all of the small-signal hybrid parameters. The results are only simple under saturation conditions where one finds $\mu_{rb} = h_{ob} = 0$, $h_{ib} = R_E$, and $\alpha_{fb} = R_{DL} / (R_{DL} + R_{DC})$. The null result for the first two parameters is consistent with the neglect of any breakdown processes in the model which results in "hard" saturation behavior. This model deficiency leads to errors when one attempts to calculate limiting amplification parameters [e.g., maximum possible voltage or current gains, maximum (minimum) input (output) resistances]. For example, the model calculation shows voltage gain increasing indefinitely with R_L , whereas experimentally the gain saturates at high R_L . Perusal of the small-signal analyses shows that this saturation is expected due to the nonzero values of μ_{rb} and h_{ob} . Although the model is not accurate in these limiting calculations, it proves useful for identifying device parameters which should be modified to improve amplification features.

Common emitter (CE) and collector (CC) configurations.—As with semiconducting transistors, the present

device can be wired in the CE and CC configurations. Qualitatively all of the steady-state and a-c features normally associated with these configurations are manifested by the present device. These include both a-c current and voltage gain in the CE mode as well as current gain in the CC mode. As with the CB mode, model calculations provide a good qualitative description of steady-state characteristics. Low frequency gain parameters determined by R_{DL} , R_{DC} , and other external circuit parameters are in reasonable agreement with experiment. Since no new device parameters or cell characteristics are revealed by these modes, their detailed properties are not discussed.

Frequency response.—The small-signal frequency response of the device is determined by two capacitive aspects of the structure. The most important is the double layer capacity of the collector cathode which is prominent under conditions of collector saturation. The second is the pseudocapacity associated with changing the value of $P(B)$ within the base volume. Specifically, transient currents in excess or deficit of steady-state values must be drawn in the emitter circuit to modify $P(B)$ which in turn determines the amount of current drawn in the collector circuit. The magnitude of these transients, and correspondingly the pseudocapacity, will be proportional to the magnitude of the base volume. Electrically these effects are manifested by changes in the Nernst emf. In semiconducting transistors the analog is the so-called diffusion pseudocapacity in which the emitter must inject/withdraw an excess of minority carriers from the base in order to support a diffusion current of minority carriers across the base.

Which of the two capacitive effects limit the frequency response depends on the external circuit. R_L is the key parameter. As discussed below, the double layer capacity (C) is on the order of $0.1 \times 10^{-8} \text{F}$ for the present device geometry and operating conditions. When in series with $R_L = 10^3 \Omega$, one has a time constant $\tau = R_L C \sim 0.1$ sec. For the same conditions, the time constant, τ_P , associated with the pseudocapacity, C_P , is approximately 10^{-2} sec (see below). Hence double layer effects are limiting. Large values of R_L (with the attendant loss of frequency response) are appropriate to achieve voltage gain in the CB mode. In the CC and CE modes however, very low values of R_L are appropriate for realizing a-c current gain. Although double layer effects would then be greatly reduced, pseudocapacity emerges as the response limiting factor.

Because the double layer capacity at the Pt/ZrO₂ interface is so large, pseudocapacitive effects are usually of secondary importance and will not be discussed in detail. It is worth noting however that τ_P is not determined solely by the resistance, R_E , of the emitter circuit. This is because the leak and the saturated collector cell act as effective shunt resistances of C_P . This can be understood by considering that both act to moderate or offset the effect of the emitter cell in changing $P(B)$. In practice the effective shunt resistance of the collector is quite small ($\sim 1 \Omega$) and fixes τ_P at approximately 10^{-2} sec for devices used in this work. More detail on this aspect will be given in a future publication (17) concerning use of the device as an O₂ sensor.

The double layer capacity of the Pt/ZrO₂ interface is well illustrated in the CB configuration. Figure 11 shows experimental results for the roll off in small-signal CB voltage gain, $G_V = \Delta V_{CB}/\Delta V_{EB}$, with increasing frequency for several values of R_L . Also shown is the phase angle by which the output lags the input. The drop in response occurs at lower frequencies for larger R_L values indicating that capacity in the collector circuit is the cause of the roll off.

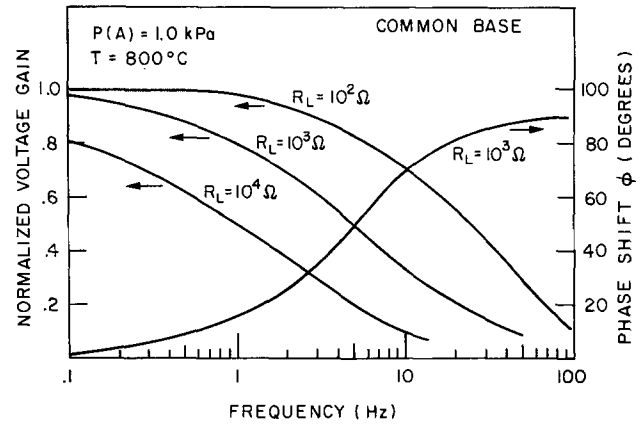


Fig. 11. Experimental results for a combined frequency plot of the normalized small-signal voltage gain and the phase shift of the collector voltage relative to the emitter voltage for various R_L values. The zero frequency gains in each case are $G(R_L = 10^4 \Omega) = 30$, $G(R_L = 10^3 \Omega) = 12$, $G(R_L = 10^2 \Omega) = 3$.

Previous studies (18) have shown that the apparent double layer capacities at the Pt/ZrO₂ interface can be very high, on the order of several hundred $\mu\text{F}/\text{cm}^2$. During operation in the saturation region, the modulation ΔV_{CB} is largely accomplished by changes in the polarization emf which must be supported by the charging/discharging of the cathode double layer capacity through R_L . This capacity was studied by biasing the collector to the saturation region and monitoring the transient response of I_C to superimposed voltage pulses of 0.1V. If no anode polarization is assumed, and since the cathode is blocking for any steady-state increase in current, the cathode is isolated for transient capacity studies. The time integral of the observed changing current, when divided by the voltage increment, yields a capacitance of approximately $250 \mu\text{F}/\text{cm}^2$ at 800°C . For a 0.35cm^2 cathode area and $R_L = 10^3 \Omega$, one finds $\tau = R_L C \sim 0.09$ sec and $(1/2\pi\tau) \sim 2$ Hz, a frequency in the range of most rapid gain decrease (Fig. 11). This capacity was found to be independent of bias voltage in the saturation region.

The capacity measured with the pulse technique increased with temperature as shown in Fig. 12, with an activation energy $\Delta E = 10.5$ kcal/mole. A similar temperature dependence was found by Chu and Seitz

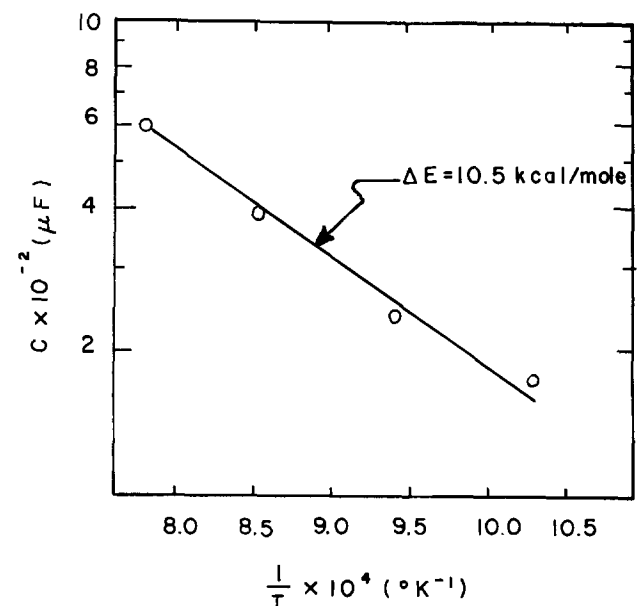


Fig. 12. Collector cathode double layer capacity vs. $1/T$ computed from experimental results.

(19). As far as the authors know, no adequate theory has been advanced to explain these capacitive properties. It seems reasonable to speculate that the large apparent capacities may in part be due to the partial reduction and oxidation of the electrolyte adjacent to the Pt cathode as it attempts to come to equilibrium with changing values of $P(\text{CB})$ during voltage applications. Such an effect would also be promoted by higher temperatures as is observed.

As R_L is reduced, the frequency response of the device improves until the pseudocapacitive effects discussed previously become limiting. As mentioned at the beginning, the low frequency response dictated by these effects coupled with a high operating temperature will undoubtedly limit the usefulness of the present device to special applications.

Summary

In summary, the present device illustrates an approach to transistor action in which a chemical species at a high ambient activity is emitted into a base region from which it is collected and returned to the ambient. Voltage, current, and power gain can be realized by the appropriate choice of external circuits and their parameters. As mentioned previously, this approach appears general and hence applicable to a variety of other electrochemical systems. For a given atomic species chosen as a charge carrier, a reasonable first choice of emitter and collector electrolyte would be dictated by the necessity of high ionic conductivity. The key technical problem would probably be the fabrication of a leak-tight or nearly leak-tight base structure or medium which would support a large variation in the activity of the species. The specialized circumstances attending the use of different electrochemical systems will probably result in equally specialized applications.

Acknowledgment

The author wishes to thank Dr. E. M. Logothetis of the Research Staff for numerous helpful discussions.

Manuscript submitted Oct. 15, 1980; revised manuscript received March 17, 1981.

Any discussion of this paper will appear in a Discussion Section to be published in the June 1982 JOURNAL. All discussions for the June 1982 Discussion Section should be submitted by Feb. 1, 1982.

Publication costs of this article were assisted by the Ford Motor Company.

REFERENCES

1. R. E. Hetrick and W. C. Vassell, *Appl. Phys. Lett.*, **37**, 494 (1980).
2. H. Letaw, Jr., and J. Bardeen, *J. Appl. Phys.*, **25**, 600 (1954).
3. R. E. Hetrick, E. M. Logothetis, and D. K. Hohnke, in "Proceedings of the Topical Conference on Physics in the Automotive Industry," To be published by AIP.
4. T. H. Etsell and S. N. Flengas, *Chem. Rev.*, **70**, 339 (1970).
5. S. Pizzini, M. Bianchi, P. Colombo, and S. Torchi, *J. Appl. Electrochem.*, **4**, 305 (1974).
6. D. M. Haaland, *Anal. Chem.*, **49**, 1813 (1977).
7. D. Yuan and F. A. Kroger, *This Journal*, **116**, 594 (1969).
8. J. Fouletier, G. Vitten, and M. Kleitz, *J. Appl. Electrochem.*, **5**, 111 (1975).
9. C. B. Alcock and S. Zador, *ibid.*, **2**, 289 (1972).
10. H. Yanagida, R. J. Brook, and F. A. Kroger, *This Journal*, **117**, 593 (1970).
11. R. J. Brook, W. L. Pelzmann, and F. A. Kroger, *ibid.*, **118**, 185 (1971).
12. T. H. Etsell and S. N. Flengas, *ibid.*, **118**, 1890 (1971).
13. M. Kleitz, Thesis, University of Grenoble.
14. R. E. Carter, in "EMF Measurements in High Temperature Systems," C. B. Alcock, Editor, p. 103, The Inst. Min. Metall., London (1968).
15. C. M. Mari, S. Pizzini, T. A. Giorgi, L. Rosai, and M. Borghi, *J. Appl. Electrochem.*, **7**, 215 (1977).
16. H. Malmstadt, C. Enke, and E. Toren, "Electronics for Scientists," Chap. 3, W. A. Benjamin, Inc., New York (1962).
17. R. E. Hetrick and W. A. Fate, To be published.
18. J. E. Bauerle, *J. Phys. Chem. Solids*, **30**, 2657 (1969).
19. S. H. Chu and M. A. Seitz, *J. Solid State Chem.*, **23**, 297 (1978).

Reduction of Concentration Overpotential in Pulsed Current Electrolysis

A. A. Bedrossian¹ and H. Y. Cheh*

Department of Chemical Engineering and Applied Chemistry, Columbia University, New York, New York 10027

ABSTRACT

Pulsed current electrolysis reduces irreversibilities from mass transfer limitations. This results in an increase of the reacting species concentration in the diffusion layer and a reduction of the concentration overpotential. Consequently, high values of instantaneous currents have often been applied in practice. In this paper, theoretical calculations are presented for the reduction of concentration overpotential by pulsed current electrolysis. Experimental verification of the theoretical results is given.

Recently, the application of pulsed current to electrochemical systems has gained a great deal of attention. Cheh (1) and Ibl (2) have reported independently mass transfer studies of pulsed current electrolysis by using a Nernst diffusion model. Hale (3, 4) and Vis-

wanathan *et al.* (5) have included convection as well as diffusion in mass transfer calculations. It has also been shown, that for short pulses under reasonable convective conditions, calculations based on the diffusion model yield adequate results (5). In this paper, calculations on the reduction of concentration overpotential by pulsed current electrolysis are reported. Experimental verification of these calculations is presented.

* Electrochemical Society Active Member.

¹ Present address: Halcon Research and Development Corporation, New York NY 10016.

Key words: concentration overpotential, pulsed electrolysis.

Theoretical

Concentration overpotential is defined by

$$\eta_c = \frac{RT}{nF} \ln \frac{c_i}{c_b} \quad [1]$$

where η_c is the concentration overpotential, c_i and c_b are the concentration of the reacting species at the electrode-solution interface and in the bulk solution, respectively, and R , T , n , and F have their usual meanings.

Under d-c electrolysis condition the concentration overpotential, $(\eta_{dc})_i$, is frequently expressed in terms of the limiting current density for the reaction by

$$(\eta_{dc})_i = \frac{RT}{nF} \ln \left(1 - \frac{i_{dc}}{(i_{dc})_1} \right) \quad [2]$$

where

$$(i_{dc})_1 = -nFDc_b/\delta \quad [3]$$

i_{dc} is the applied d-c current density, $(i_{dc})_1$ is the d-c limiting current density for the reaction, D is the diffusion coefficient of the reacting ion, and δ is the thickness of the diffusion layer under direct current conditions.

In accordance with the Nernst diffusion model, c_i under pulsed current and periodic state conditions (1) can be calculated along the lines given in (1):

During periods when the current is on

$$\frac{(c_i - c_b)nFD}{i_p\delta} = 1 - \frac{8}{\Pi^2} \sum_{j=1}^{\infty} \frac{\exp[-(2j-1)^2a\tau]}{(2j-1)^2} \cdot \frac{(\exp[(2j-1)^2a\theta] - \exp[(2j-1)^2a\theta_1])}{(\exp[(2j-1)^2a\theta] - 1)} \quad [4]$$

During periods when the current is off

$$\frac{(c_i - c_b)nFD}{i_p\delta} = \frac{8}{\Pi^2} \sum_{j=1}^{\infty} \frac{\exp[-(2j-1)^2a\tau]}{(2j-1)^2} \cdot \frac{(\exp[(2j-1)^2a\theta] - \exp[(2j-1)^2a\theta_1])}{(\exp[(2j-1)^2a\theta] - 1)} \quad [5]$$

where

$$a = \Pi^2 D / 4\delta^2 \quad [6]$$

$$\tau = t - N\theta \quad [7]$$

i_p is the applied pulsed current density, θ is the cycle time of the pulse, θ_1 and θ_2 are the on and off period of the pulse, respectively, and N is the number of cycles already passed.

By combining Eq. [1] to [5] and by assuming that i_p is equal to i_{dc} , the reduction of concentration overpotential by pulsed current electrolysis when the system has reached a periodic state can be calculated by:

During periods when the current is on

$$\frac{(\eta_p)_c}{(\eta_{dc})_c} = \ln \left[1 - \frac{i_p}{(i_{dc})_1} \left(1 - \frac{8}{\Pi^2} \sum_{j=1}^{\infty} \frac{\exp[-(2j-1)^2a\tau]}{(2j-1)^2} \cdot \frac{(\exp[(2j-1)^2a\theta] - \exp[(2j-1)^2a\theta_1])}{(\exp[(2j-1)^2a\theta] - 1)} \right) \right] / \ln \left(1 - \frac{i_p}{(i_{dc})_1} \right) \quad [8]$$

During periods when the current is off

$$\frac{(\eta_p)_c}{(\eta_{dc})_c} = \ln \left[1 - \frac{i_p}{(i_{dc})_1} \frac{8}{\Pi^2} \sum_{j=1}^{\infty} \frac{\exp[-(2j-1)^2a\tau]}{(2j-1)^2} \cdot \frac{(\exp[(2j-1)^2a\theta] - \exp[(2j-1)^2a\theta_1])}{(\exp[(2j-1)^2a\theta] - 1)} \right] / \ln \left(1 - \frac{i_p}{(i_{dc})_1} \right) \quad [9]$$

where $(\eta_p)_c$ is the concentration overpotential under pulsed and periodic state conditions.

Since $(\eta_p)_c$ is a function of time in a given period, the average reduction for one complete cycle is given by

$$\left[\frac{(\eta_p)_c}{(\eta_{dc})_c} \right]_{\text{avg}} = \frac{1}{\theta_1 + \theta_2} \left[\int_0^{\theta_1} \left[\frac{(\eta_p)_c}{(\eta_{dc})_c} \right]_{\text{Eq. [8]}} d\tau + \int_{\theta_1}^{\theta_2} \left[\frac{(\eta_p)_c}{(\eta_{dc})_c} \right]_{\text{Eq. [9]}} d\tau \right] \quad [10]$$

Equations [8]-[10] provide a complete description of the reduction of concentration overpotential under pulsed conditions. Numerical evaluations of these equations are illustrated at various values of $i_p/(i_{dc})_1$ and $a\theta = 0.5$. Typical results from Eq. [8] and [9] at $\theta_1/\theta = 0.4$ are shown in Fig. 1. In this figure, the region, $0 < a\tau \leq 0.2$, represents the period when the current is on whereas the region, $0.2 < a\tau \leq 0.5$, is the period when the current is off. It is seen that the concentration overpotential increases during the on-period and the concentration overpotential decreases during the off-period. Results from Eq. [10] are presented in Fig. 2 which shows the average value of the concentration overpotential under pulsed conditions as a function of applied pulsed current density and duty cycle. At very low currents, the application of pulsed current has little effect on the mass transfer of the system. This fact is responsible for the result that as $i_p/(i_{dc})_1 \rightarrow 0$, $(\eta_p)_c/(\eta_{dc})_c \rightarrow \theta_1/\theta$. On the other hand, when i_p increases, the value of $(\eta_p)_c/(\eta_{dc})_c$ decreases. This is because as the d-c limiting current density is approached, the value of $(\eta_{dc})_c$ also increases drastically.

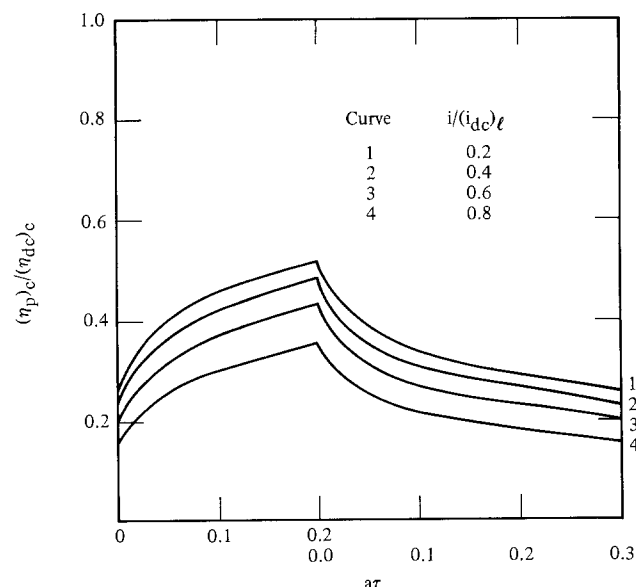


Fig. 1. Instantaneous values of $(\eta_p)_c/(\eta_{dc})_c$. Duty cycle = 0.4, $a\theta = 0.5$.

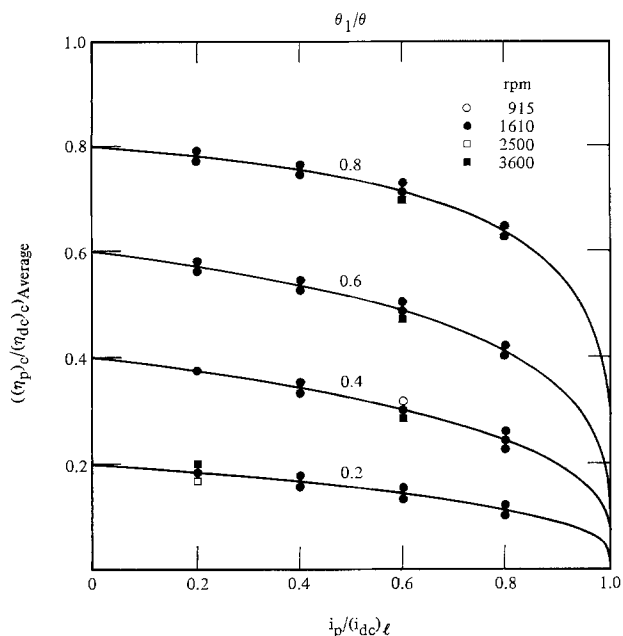


Fig. 2. Theoretical and experimental values of the average reduction of concentration overpotential. ($a\theta = 0.5$).

Experimental

The experimental system consisted of a Pine Instrument rotating Pt disk electrode (area = 0.46 cm²), a Pt counterelectrode, a saturated calomel reference electrode with a Luggin capillary and an electrolyte containing 3 mM K₄Fe(CN)₆ and 3 mM K₃Fe(CN)₆ in 1M KCl. A Tacussel function generator (Model G STP-3C) and a Kepco power supply (Model BOP36-1.5M) were used as current sources for d-c and pulsed current electrolysis. The potential between the rotating disk electrode and the reference electrode was measured and recorded on a Tektronix oscilloscope (Model 5103N). In the present system, it was found that the location of the reference electrode had a negligible effect on the overpotential measurements.

In order to compare experimental results with those predicted by Eq. [8] and [9], overpotentials under both d-c and pulsed conditions were measured. It was also found that the activation overpotential contributed a significant portion of the total overpotential. In the presence of an excess supporting electrolyte, the concentration overpotential is represented by the difference between the total and the activation overpotential (6). Direct current-potential relationship was measured at six rotation speeds in order to determine the d-c limiting current densities, transport properties, kinetic parameters, activation and concentration overpotentials. Experimental current-potential curves are given in Fig. 3 and detailed analyses of the results are presented in the Appendix. Based on the measured values of transport properties, the cycle times for pulses were chosen for different rotating speeds such that $a\theta$ was always 0.5. The applied pulse current densities were 0.2, 0.4, 0.6, and 0.8 of $(i_{dc})_1$. Experimental pulsed current-potential qualitatively similar to those in Fig. 1 were recorded on an oscilloscope at duty cycles of 0.2, 0.4, 0.6, and 0.8. The average potential over an entire cycle was then integrated graphically. After subtracting the activation overpotential from the total overpotential, the experimental concentration overpotential results are included in Fig. 2. There is good agreement between the theoretical and experimental results.

Conclusions

The reduction of concentration overpotential by pulsed current electrolysis was calculated by using a Nernst diffusion model. The results were compared

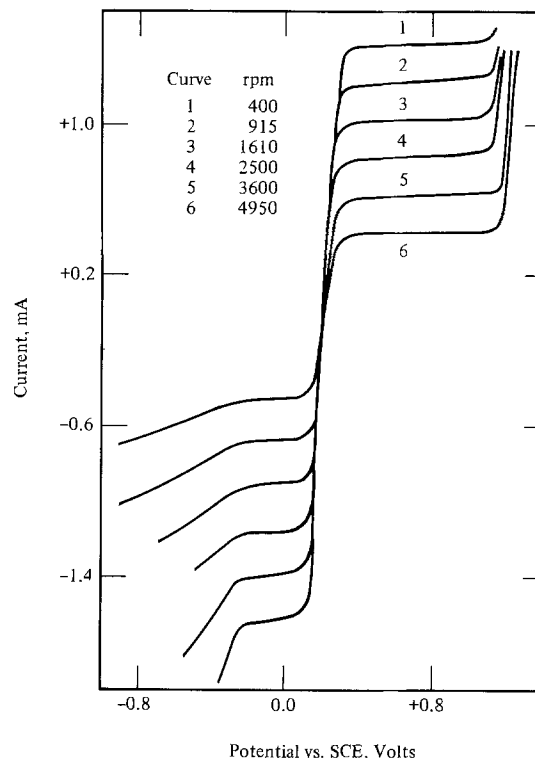


Fig. 3. Current-potential behavior for the ferri-ferrocyanide system.

with experimental measurements which were made in a ferri-ferrocyanide system with an excess of supporting electrolyte. Good agreements were obtained between the theoretical and experimental results.

Acknowledgments

This work was supported by the Jet Propulsion Laboratory, California Institute of Technology under NASA Contract NAS7-100. One of us (A.A.B.) would like to acknowledge partial support in the form of a fellowship from the American Association of University Women. The authors also wish to thank Mr. Harvey Frank of the Jet Propulsion Laboratory for a number of stimulating discussions during the course of this work.

Manuscript submitted March 12, 1981; revised manuscript received June 22, 1981.

Any discussion of this paper will appear in a Discussion Section to be published in the June 1982 JOURNAL. All discussions for the June 1982 Discussion Section should be submitted by Feb. 1, 1982.

APPENDIX

Evaluation of Diffusion Coefficients of $[\text{Fe}(\text{CN})_6]^{-3}$ and $[\text{Fe}(\text{CN})_6]^{-4}$

The d-c limiting current densities for both cathodic and anodic reactions were measured from current-potential curves at six rotation speeds. The kinematic viscosity for the electrolyte was measured by an Ostwald viscometer and was found to be 0.01 cm²/sec. The diffusion coefficient was then calculated by the following equation which was first derived by Newman (7)

$$(i_{dc})_1 = \frac{0.62048nF\nu\text{Sc}^{-2/3}\nu^{1/2}\omega^{1/2}C_b}{1 + 0.298\text{Sc}^{-1/3} + 0.14514\text{Sc}^{-2/3}} \quad [\text{A-1}]$$

where ν is the kinematic viscosity of the electrolyte, ω is the rotation speed, and Sc is the Schmidt number which is ν/D . The diffusion coefficients which fitted best results from the six rotation speeds were found to be 6.9×10^{-6} cm²/sec for $[\text{Fe}(\text{CN})_6]^{-3}$ and 8.4×10^{-6} cm²/sec for $[\text{Fe}(\text{CN})_6]^{-4}$ at $22^\circ \pm 1^\circ\text{C}$. Once the diffusion coefficients are known, the thickness of the Nernst diffusion layer can be calculated readily by Eq. [3].

Evaluation of the Kinetic Parameters

We begin with the Butler-Volmer equation to represent the ferri-ferrocyanide system

$$i = i_0 \left[\left(\frac{i_{l,a} - i}{i_{l,a}} \right) \exp \left[\frac{\alpha n F}{RT} \eta \right] - \left(\frac{i_{l,c} - i}{i_{l,c}} \right) \exp \left[\frac{-(1 - \alpha) n F}{RT} \eta \right] \right] \quad [\text{A-2}]$$

where i_0 is the exchange current density, α is the transfer coefficient, and $i_{l,a}$ and $i_{l,c}$ are the anodic and cathodic limiting current densities. By differentiating i w.r.t. η and evaluating the result at $\eta = 0$, we obtain

$$i_0 = \frac{\left(\frac{di}{d\eta} \right)_{\eta=0}}{\frac{nF}{RT} + \left(\frac{1}{i_{l,c}} - \frac{1}{i_{l,a}} \right) \left(\frac{di}{d\eta} \right)_{\eta=0}} \quad [\text{A-3}]$$

This equation allows one to evaluate i_0 from experimental data at each rotating speed. The average value of i_0 over the six rotation speeds was found to be 5.73 mA/cm². The transfer coefficient α can then be evaluated by applying Eq. [A-1] to the experimental data. The value of α was estimated to be 0.16.

For a system with an excess supporting electrolyte, η is the sum of η_c and η_a where η_a is the activation overpotential which can be determined by

$$i = i_0 \left[\exp \left(\frac{\alpha n F}{RT} \eta_a \right) - \exp \left(\frac{-(1 - \alpha) n F}{RT} \eta_a \right) \right] \quad [\text{A-4}]$$

η_c can now be determined by subtracting η_a from η which has been determined experimentally.

LIST OF SYMBOLS

a a constant defined in Eq. [6]
 c_b, c_i concentration of reacting ion at the electrode surface and in the bulk solution, respectively

D diffusion coefficient of reacting ion
 F Faraday's constant
 i current density
 i_{dc}, i_p d-c current density, and pulsed current density, respectively
 $(i_{dc})_l$ d-c limiting current density
 $i_{l,a}, i_{l,c}$ anodic limiting current density and cathodic limiting current density, respectively
 i_0 exchange current density
 n number of electrons transferred in reaction
 N number of cycles in a pulse train
 R universal gas constant
 Sc Schmidt number
 T temperature
 t time
 α transfer coefficient
 δ thickness of the Nernst diffusion layer
 η overpotential
 η_a, η_c activation overpotential and pulse concentration, respectively
 $(\eta_{dc})_c, (\eta_p)_c$ d-c concentration overpotential and pulse concentration overpotential, respectively
 $\theta_1, \theta_2, \theta$ on-time, off-time, and cycle time of a pulse, respectively
 ν kinematic viscosity of the electrolyte
 τ time defined in Eq. [7]
 ω rotation speed

REFERENCES

- H. Y. Cheh, *This Journal*, **118**, 551 (1971).
- N. Ibl, *Surf. Technol.*, **10**, 81 (1980).
- J. M. Hale, *J. Electroanal. Chem. Interfacial Electrochem.*, **6**, 187 (1963).
- J. M. Hale, *ibid.*, **8**, 332 (1964).
- K. Viswanathan, M. A. F. Epstein, and H. Y. Cheh, *This Journal*, **125**, 1772 (1978).
- J. Newman, "Electrochemical Systems," Prentice-Hall, Englewood Cliffs, NJ (1973).
- J. Newman, in "Advances in Electrochemistry and Electrochemical Engineering," Vol. 5, P. Delahay and C. W. Tobias, Editors, p. 87, Interscience Publishers, New York (1967).

Investigation of Laser-Enhanced Electroplating Mechanisms

J. Cl. Puipe,*¹ R. E. Acosta,* and R. J. von Gutfeld

IBM Thomas J. Watson Research Center, Yorktown Heights, New York 10598

ABSTRACT

The mechanism responsible for the very high plating rates at electrodes illuminated by a laser beam was investigated. Absorption of the laser energy by the electrode results in a localized increase in temperature at the metal-solution interface. This leads to: (i) a shift in the rest potential, (ii) an increase in the charge transfer rate, and (iii) strong microstirring of the solution due to thermal gradients and, at high laser power densities, to strong local boiling. Verification of the first two effects was achieved by measuring the enhancement in plating rates as a function of overpotential, laser power, and substrate thickness and by comparing these results with measurements using solutions at various bulk temperatures. Observation of the cathode through a video monitor, as well as detection of bubble formation using a miniature microphone, verified that a correlation exists between the ejection of bubbles from the cathode and sharp increases in the current. Application of laser-enhanced electroplating for maskless generation of patterns is also briefly discussed.

A large local increase of current density at the point of incidence of a laser beam on a cathode was first reported by von Gutfeld *et al.* (1-3). Plating rates enhanced by as much as a factor of 1000 were reported for nickel, copper, and gold deposition. It has been shown (2-4) that electroless plating and electroetching

rates can also be substantially increased by absorption of laser light.

In this paper a study of the enhancement mechanism is presented. The aim was to investigate whether the laser enhancement is due only to strong microstirring of the solution or whether it is due to a significant increase in the charge transfer rate. In other words, if the reaction were not mass transport limited, would the reaction rate be influenced significantly by the

* Electrochemical Society Active Member.

¹ Present address: Werner Ffuhmann AG, Ringstrasse 9, 8600 Dubendorf, Switzerland.

Key words: battery, boiling, masking, mass transport.

laser light absorption? In order to answer this question the laser-enhanced plating rates were measured as a function of overpotential.

Previous experiments showed that back illumination of a thin cathode led to the same enhancement as that for front illumination (1). Hence a significant contribution of a photocatalytic effect is excluded. We therefore postulate that the phenomena involved are related to a local increase of temperature at the metal-solution interface as a result of laser light absorption. The findings reported in this paper permit us to elaborate on a thermal model for the explanation of the observed plating current enhancements. The influence of the laser power and the substrate thickness (which influences the radial heat flow in the cathode) on the deposition rate and on the plated spot diameter were also investigated.

Fundamental Studies

Experimental conditions.—Experiments were conducted under potentiostatic control in a Pyrex glass cell containing vertical electrodes approximately 1 cm on a side, Fig. 1. The laser light was directed normally onto the cathode through a small hole in the anode. The anode consisted of a copper plate, the cathode of a thin film of gold or copper. Thin films were used to reduce heat dissipation in the cathode. In some experiments a small, well-defined, active area was required. The cathode was then covered by a photoresist layer a few microns thick, except for a hole of the same diameter as the laser beam, measured to $\sim 1/e$ of its maximum intensity. The details of this structure are given in Fig. 2. The laser beam diameter was adjusted by positioning a microscope objective lens (2.5 \times) at a distance from the sample so that 67% of the laser power was incident on the active area of the cathode. The laser wavelength was chosen so that the laser beam was essentially not absorbed in the electrolyte, but was at least partially absorbed at the cathode. The experimental conditions are summarized in Table I.

Enhanced plating rates as a function of overpotential.—Figure 3 shows the polarization curve for the system Cu/CuSO₄ without laser irradiation. In this curve one clearly distinguishes the overpotential region in which the current is mass transport limited from the region where charge transfer is the limiting step of the reaction. Figure 4 shows the polarization curve of the same system with periodic irradiation by the laser. Here the laser beam diameter was equal to

Table I. Experimental conditions

| | |
|-----------|---|
| Solution | CuSO ₄ , 0.05M H ₂ SO ₄ , 1M |
| Electrode | Metallic film: Au or Cu Metallic film thickness: 500-10,000Å |
| Laser | Beam diameter: 100-500 μ m Incident laser power density: 0.1-2 kW/cm ² Wavelength: 5145Å |

that of the active cathode area (*i.e.*, 200 μ m). Periodic pulsing of the laser was used to prevent excessive plating buildup that would result from continuous irradiation. This ensures a more accurate measurement of the plating enhancement, since the cathode is little changed during the short duration of the laser pulses. Figure 5 shows the same polarization curve as Fig. 4, but with a logarithmic current scale. The logarithmic current scale allows a more accurate reading of the current enhancement. The apparent slower current response is due to an artifact of the apparatus. The different overvoltage regions of the comb-shaped curves (Fig. 4 and 5) are analyzed in more detail below.

The mass transport controlled region.—According to the limiting current plateau of the polarization curve of Fig. 3, the mass transport controlled deposition extends from an overpotential of -200 to -650 mV. In

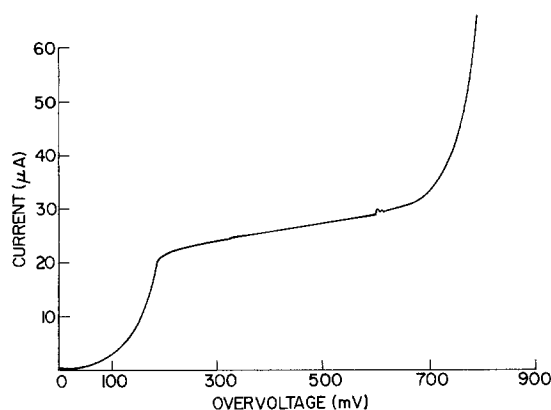


Fig. 3. Polarization curve for copper electrodeposition at room temperature with the cathode of Fig. 2 (current and overvoltage are negative). Electrode diameter, 550 μ m; voltage scanning speed, 4 mV/sec.

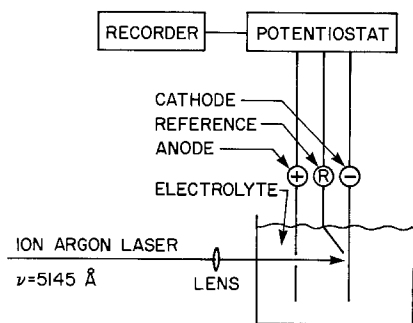


Fig. 1. Schematic of the apparatus

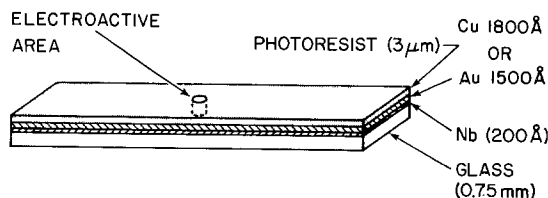


Fig. 2. Structure of the cathode and typical thicknesses of the various layers.

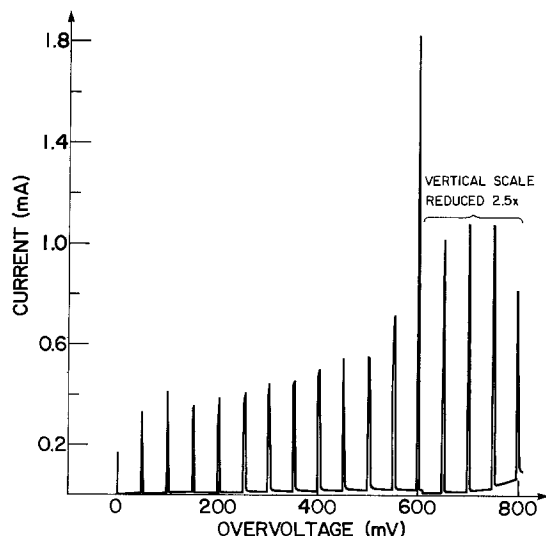


Fig. 4. Polarization curve for copper electrodeposition with periodic laser illumination (cathode of Fig. 2). Laser power, 210 mW; electrode diameter = laser beam diameter = 200 μ m; voltage scanning speed, 5 mV/sec.

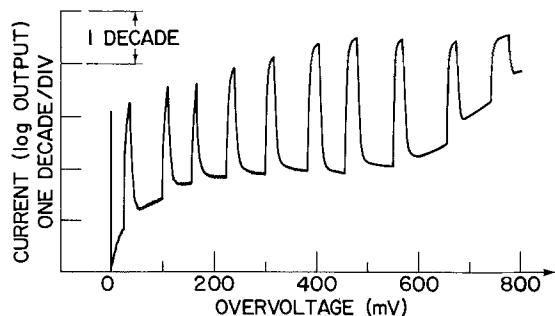


Fig. 5. Polarization curve for copper electrodeposition with periodic laser illumination on cathode of Fig. 2 (log current scale). Incident laser power, 500 mW; electrode diameter, 200 μm ; voltage scanning speed, 5 mV/sec.

this region the maximum enhancement² measured on an electrode of the same size as the laser beam is 400 \times , Fig. 5. A current density of more than 18 A/cm² is reached. This plating rate, which is extremely high for this dilute solution, corresponds to a deposit growth rate of more than 6 $\mu\text{m}/\text{sec}$. Other experiments in the mass transport controlled region, with the electrode not defined by a hole in the photoresist but rather on a plain wafer of 1 cm² area, resulted in enhanced plating rates of more than 1000 \times , like those reported earlier (1). The apparent discrepancy is due to a smaller limiting current density without laser for large area electrodes. A decrease in the electrode size to very small dimensions leads to diffusion which is no longer one dimensional but spherical, and thereby increases the value of the limiting current for these small area cathodes. The influence of the electrode diameter on the limiting current density is shown in Fig. 6. The enhancement ratio for an electrode with an area much larger than the cross section of the laser beam is determined taking into account the small area irradiated by the laser. However, the enhancement is referred to the limiting current density of the large electrode, thus such cathodes show enhancements three times larger than the values shown in Fig. 4 and 5.

We attribute the enhancement of the limiting current to stirring through local convection of the solution due to a strong thermal gradient near the cathode interface (1,2). We have also found that for higher laser power densities local boiling of the solution produces strong additional stirring. Observation of the cathode through a video monitor showed that the bubbles were ejected into the solution normally from the vertical electrode. The effect of this additional stir-

²The enhancement is the ratio of the plating current obtained with and without laser illumination.

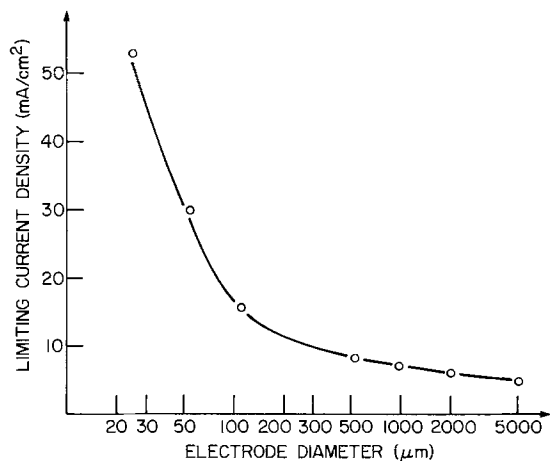


Fig. 6. Influence of the electrode diameter on the limiting current density of copper deposition without laser irradiation.

ring has been measured quantitatively by recording the limiting current density for the copper deposition while the cathode was illuminated by pulsed laser light, the intensity of which produced boiling of the solution at the cathode. The bubble formation generated an acoustic wave which was detected with a miniature microphone attached to the external wall of the cell. Figure 7 shows both the acoustic wave (trace A) and the limiting current (trace B) simultaneously recorded on a dual beam oscilloscope. Six milliseconds after the beginning of the light pulse, trace A showed a sharp increase in the acoustic signal due to boiling of the solution, and at the very same time the limiting current increased by a factor of 4. This increase in the limiting current is due to the stirring generated by the ejection of one or more bubbles in the solution.

The charge transfer controlled region.—The comb-shaped curves of Fig. 4 and 5 also show significant increases in the current for overpotentials well below the region where the reaction is mass transport limited. The increase in the reaction rate is believed to be due to higher temperature produced in the region of laser light absorption. The influence of temperature on the reaction rate has been studied quantitatively in a separate experiment in which the entire volume of the electrolyte was heated. The results are shown in Fig. 8. At a potential of -20 mV an increase of temperature from 25° to 85°C speeds up the reaction by a factor of more than 50.

It is seen from the curves of Fig. 8 that a shift of rest potential toward more positive values occurs with increasing temperature. This shift in rest potential is shown in more detail in Fig. 9. A shift of the equilibrium potential with increasing temperature is expected from thermodynamic considerations (5). The shift of the rest potential has been measured as a function of the laser power (Fig. 10) on an electrode of the same diameter as the laser beam. By comparing the results of Fig. 9 and 10 one obtains a relationship between the incident laser power density and the temperature at the interface, Fig. 11. The domain of extrapolation (B-C) gives approximate values for the interfacial temperature as a function of incident laser power density. A separate experiment showed that for laser power densities between B and C, strong boiling occurred with bubbles ejected normally from the cathode. This is consistent with the temperatures obtained by extrapolation.

Due to the positive shift of the rest potential at the hotter part of the cathode it is possible to plate locally on a large electrode with no background plating. This is achieved by maintaining the cathode at the potential value corresponding to the rest potential of the

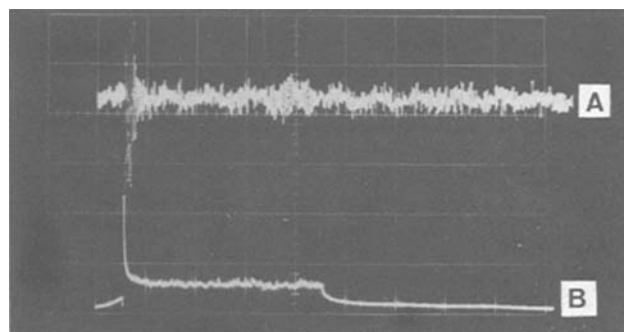


Fig. 7. The influence of boiling on the stirring of the solution. Trace A: acoustic signal; trace B: limiting current density for the system described in Table I. Abscissa, 10 msec/div for A and B; ordinate, 2 mA/div for B. Substrate: see Fig. 2, with Cu 1800Å, no photoresist. Laser pulse length, 45 msec; duty cycle, 1/4; incident laser power during the on time, 320 mW. Laser beam diameter, approximately 200 μm .

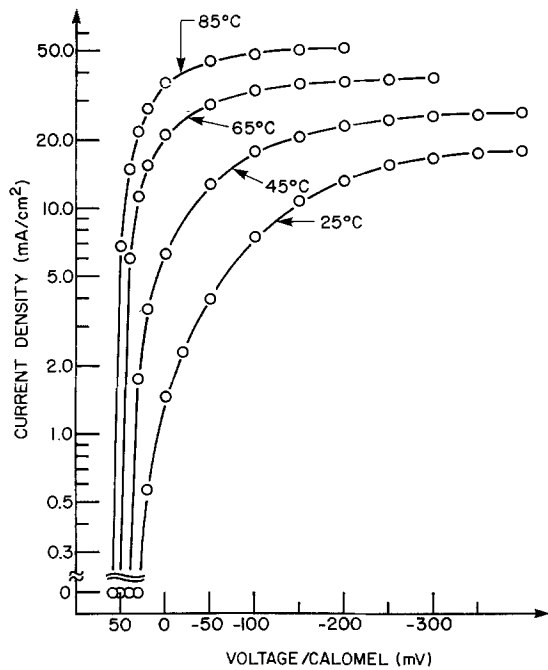


Fig. 8. Influence of temperature on the polarization curves of Cu/CuSO_4 . A rotating disk electrode (200 rpm) with a diameter of 7.6 mm was used.

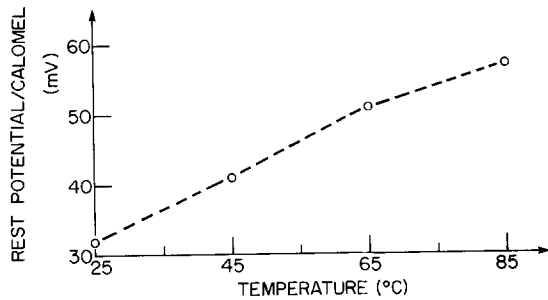


Fig. 9. Rest potential of the system Cu/CuSO_4 as a function of electrolyte temperature.

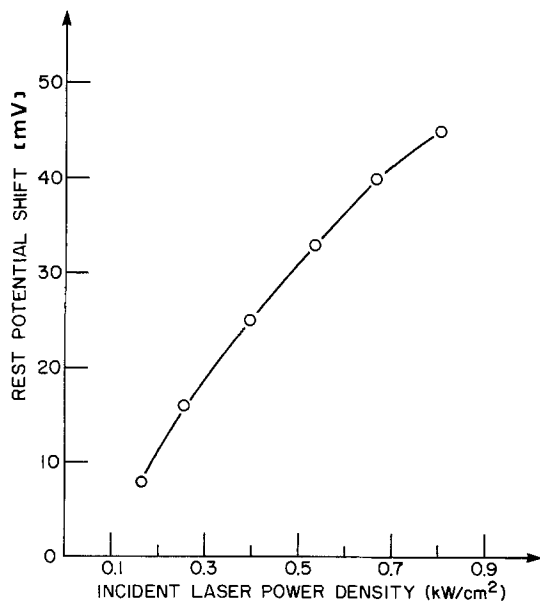


Fig. 10. Rest potential shift for the system Cu/CuSO_4 as a function of laser power density.

system Cu/Cu^{++} at room temperature. Since the illuminated part then has a more positive rest potential than the potential imposed on the rest of the elec-

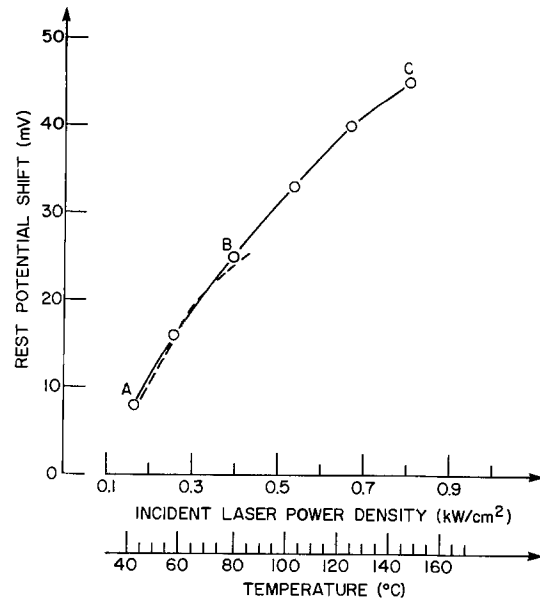


Fig. 11. Rest potential shift as a function of laser power density, indicated by —, and of temperature indicated by - - -. The figure is a superposition of Fig. 9 and 10. A, B, and C are referred to in the text.

trode, plating occurs there and only there. According to the definition of enhancement previously given, the enhancement approaches infinity; however the absolute current increase is found to be one order of magnitude lower than under mass transport controlled conditions. Figure 12 shows the current densities obtained at different overpotentials as a function of the laser power density. The curve at $\eta = 0$ corresponds to the conditions for no background plating; the curve at $\eta = -50$ mV is in the charge transfer controlled region, and the one at $\eta = -600$ mV is in the mass transport controlled region.

The shift of the rest potential has other implications. The situation in which two regions of different rest potentials are electrically connected constitutes a battery. Thus, laser light focused onto a copper electrode immersed in an electrolyte will result in simul-

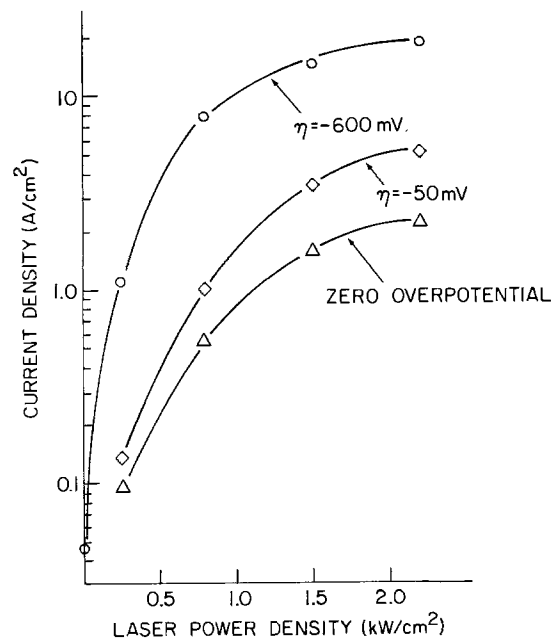


Fig. 12. Laser-enhanced current densities for different overpotentials as a function of the laser power density. Base: Nb, 200 Å/1500 Å evaporated on glass; electrode diameter, 200 μm ; overpotential values referred to room temperature.

taneous plating and etching without the use of an electrical circuit. For the solution in Table I, plating occurs in the region of higher temperature, i.e., the region of laser light absorption, while simultaneous etching occurs in the colder adjacent regions. For a circular beam, this will result in a plated central circular spot surrounded by an etched annulus, Fig. 13. The necessary condition for plating in the hotter region is a positive shift of the rest potential with increasing temperature, which is not a universal behavior for electrochemical systems. The temperature coefficient for the potential shift is determined by the negative of the entropy change for the cell reaction (5). Reference (5) gives the temperature coefficient of the equilibrium potential for several systems, both positive and negative shifts are tabulated. The system nickel/nickel citrate has been studied in our laboratory (6). It has a negative rest potential shift with increasing temperature. According to this, we expect dissolution to occur at the hotter region and plating on the adjacent colder annulus. This is shown in Fig. 14

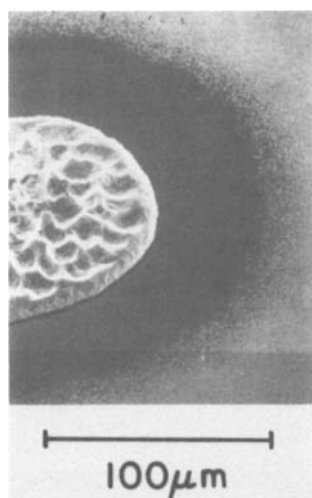


Fig. 13. SEM micrograph of copper deposited with no external electrical circuit. Base Nb, 200 Å/Cu, 1800 Å evaporated on glass; incident laser power, 450 mW.

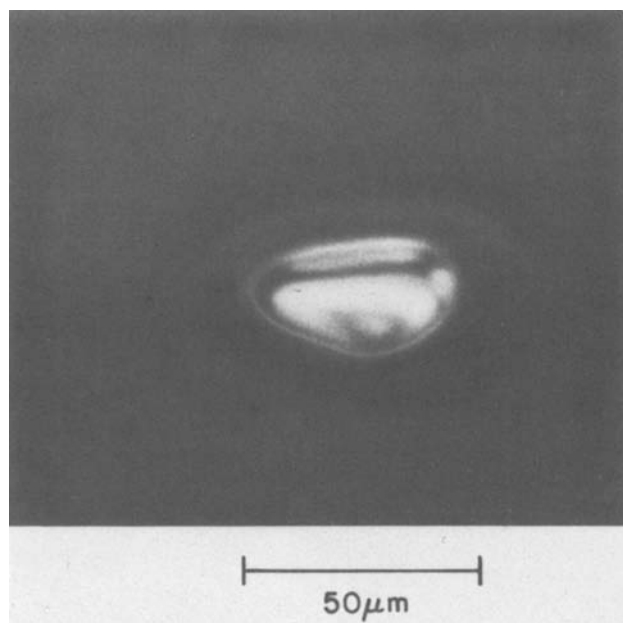


Fig. 14. SEM micrograph of nickel etching and plating with no external electrical circuit. Solution: NiSO_4 , 0.2M; Na_3cit , 0.1M; pH, 6.5. Base: Ni, 5000 Å on glass; incident laser power, 650 mW.

for a nickel cathode immersed in nickel citrate solution in conjunction with a focused laser beam.

Laser-enhanced plating mechanism: thermal model.—From the considerations above we postulate that in the presence of laser light the enhancement of the reaction rate is due to an increase of temperature at the metal-solution interface, which has three separate effects: (i) strong microstirring of the solution due to thermal gradients, with additional stirring at high laser power densities due to strong local boiling of the solution; (ii) an increase in the charge transfer rate with increasing temperature. This effect is more dependent on the nature of the system metal/electrolyte than the microstirring of the solution. For aqueous plating solutions the stirring will not vary substantially from one system to another, but the variation of the reaction rate with temperature at the interface is strongly dependent on the system; and (iii) a shift in the rest potential. The direction and magnitude of the shift depends on the system used.

Since the temperature change at the interface is responsible for the enhancement of the reaction, several experiments were undertaken in which the temperature at the interface could be varied. This was achieved by changing either the thickness of the metallic layer of the cathode or the incident laser power density. For these experiments the electrode was maintained at the rest potential and the resulting plating in the illuminated region occurred well below the limiting current. The total charge, Q , for each deposit was equal to $5 \times 10^{-4}\text{C}$. The laser was applied for sufficiently long time intervals to insure steady-state thermal conditions at the interface. The laser beam diameter was approximately 200 μm ; the thickness of the metallic film of the cathode (on a glass substrate) was varied between 500 and 10,000 Å. The main effect of increasing the metallic layer thickness is a decrease in the maximum temperature attained by the cathode interface due to the increased radial heat flow. The radial heat dissipation occurs mainly in the metallic layer because of its much higher heat conductivity compared to that of the supporting glass substrate. For thick metallic layers we expect a larger plated spot diameter. This trend is observed in Fig. 15. The increase of spot diameter for substrate thicknesses ranging from 500 to 10,000 Å varies by a factor of 2. The temperature along the radial direction decreases rapidly with increasing distance from the center for values greater than the beam radius, so that plating does not extend much beyond the beam circumference even with the thickest layers investigated here. Figure 15 also shows that an increase of the metallic film thickness decreases the laser enhanced current. We attribute this directly to the lower interfacial temperature.

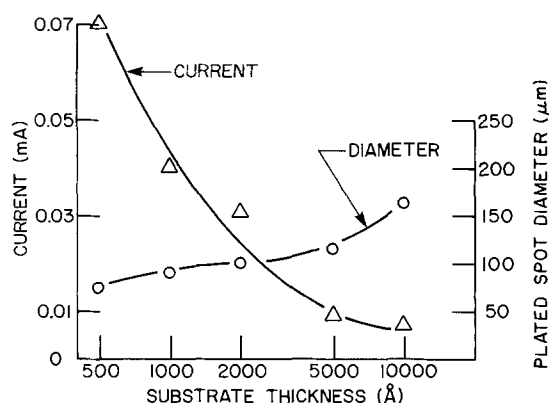


Fig. 15. Influence of the metallic film thickness on deposition rate and resulting deposited spot diameter. $Q = 5 \cdot 10^{-4}\text{C}$ for each deposit; incident laser power, 100 mW.

With increasing laser power (maintaining fixed beam diameter) we observed the expected trends for the enhanced current and plated spot diameter, Fig. 16. For an incident laser power ranging from 100 to 300 mW the laser enhanced current increases by a factor of 13, whereas for the same power range the plated spot diameter increases by a factor of 2. This can again be explained by the strongly nonlinear radial temperature profile in conjunction with a sub-linear plating enhancement that occurs for small temperature increases above ambient (2).

Applications

Copper lines in microcircuits have been connected or bridged using the laser-enhanced electroplating method, Fig. 17. The bridges were made by manual translation of a horizontal cathode under a focused laser beam. A lens with a magnification factor of 20 was used. The bridging work was done at low overpotential conditions which resulted in almost no background plating. The electrical resistance of these laser plated bridges is low. The solution used for this circuit repair experiment was CuSO_4 , 0.5M/ H_2SO_4 , 0.01M.

Improvements in the optics used to focus the beam made it possible to reduce the width of the plated line to 2 μm . Figure 18 shows a line plated on an electrode using a copper fluoborate solution under thermobattery conditions, i.e., without an external power source. This width is consistent with the limitations expected from both diffraction theory and from the aberration produced by the electrolyte layer. However, we believe this width is not the lowest attainable size. One can expect a smaller width with the use of a more elaborate lens design and possibly by decreasing the dwell time of the laser on the cathode.

For practical applications we see at least two important reasons for plating in the low overpotential region: (i) the possibility of avoiding, or minimizing, background plating and (ii) a better quality of deposit than that obtained in the mass transport controlled region.

Besides offering a means for maskless pattern generation through the use of a scannable laser beam, this technique can also result in a major cost saving when precious metals are to be deposited selectively. Clearly the technique is most useful for localized, small area plating.

Acknowledgments

We are grateful for expert technical assistance by D. R. Vigliotti throughout the experimental phase of this work. In addition we thank C. Aliotta for assistance with the SEM's and B. Stoeber, J. D. Olsen, and V.

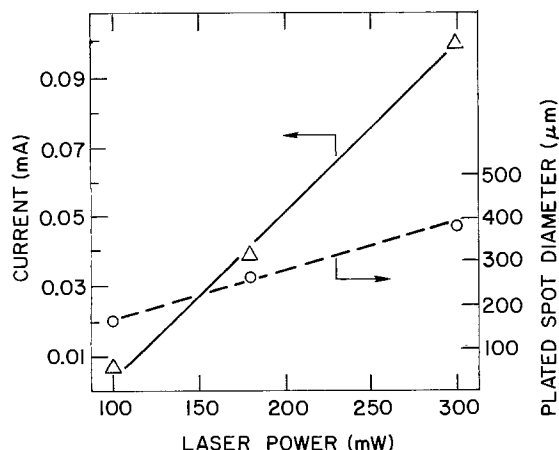


Fig. 16. Influence of the laser power on the deposition rate and deposited spot diameter. $Q = 5 \cdot 10^{-4}\text{C}$ for each deposit; metallic film thickness, 10,000 \AA .

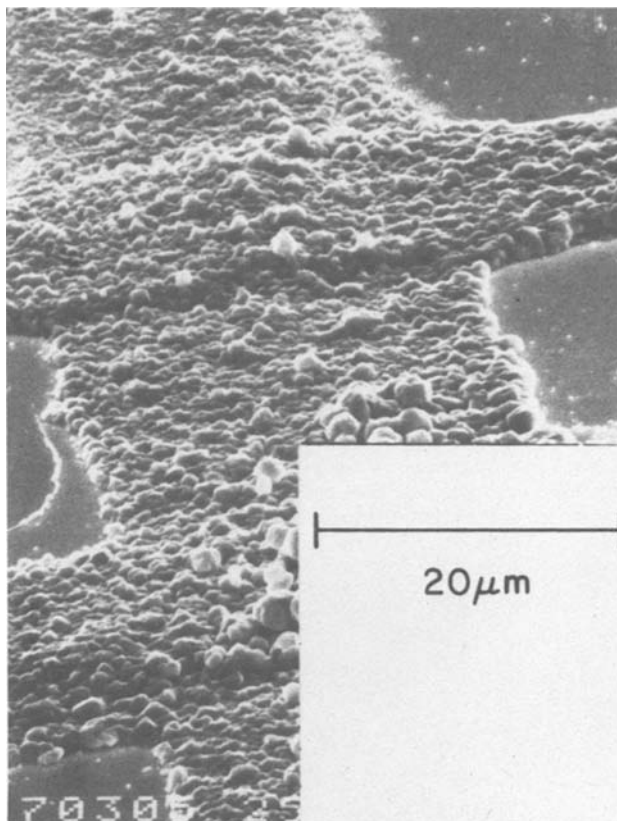


Fig. 17. SEM micrograph of a laser-enhanced plated bridge. Solution: CuSO_4 , 0.5M; H_2SO_4 , 0.01M. Laser power, 360 mW; laser light focused through a lens 20 \times ; base: Nb, 200 \AA /Au, 1500 \AA with electroplated copper lines.

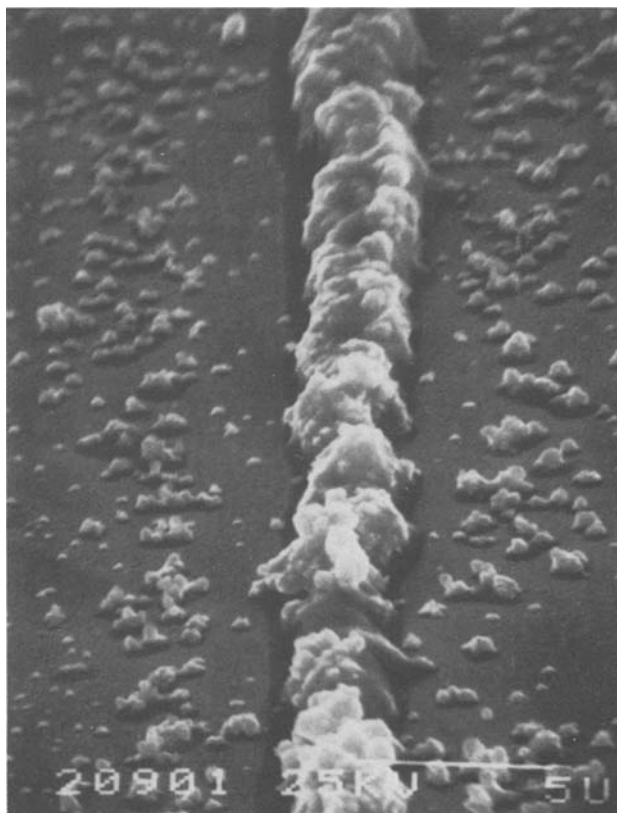


Fig. 18. Laser plated line of copper. Base: Nb, 200 \AA /Cu, 1000 \AA evaporated on glass; laser beam focused through a microscope lens 20 \times ; incident power, 50 mW.

Ranieri for technical contributions during various aspects of the research. We are also grateful to Dr. J. Cl. Chastang for his help in improving the optics of the experiment to obtain smaller plated deposits.

Manuscript received Feb. 24, 1981. This was Paper 373 presented at the Hollywood, Florida, Meeting of the Society, Oct. 5-10, 1980.

Any discussion of this paper will appear in a Discussion Section to be published in the June 1982 JOURNAL. All discussions for the June 1982 Discussion Section should be submitted by Feb. 1, 1982.

Publication costs of this article were assisted by IBM.

REFERENCES

1. R. J. von Gutfeld, E. E. Tynan, R. L. Melcher, and S. E. Blum, *Appl. Phys. Lett.*, **35**, 651 (1979).
2. R. J. von Gutfeld, E. E. Tynan, and L. T. Romankiw, Abstract No. 472, p. 1185, The Electrochemical Society Extended Abstracts, Los Angeles, CA (Oct. 14-19, 1979).
3. R. J. von Gutfeld and J. Cl. Puipe, *Oberfläche-Surface*, **11**, 294 (1981).
4. L. Kulynych, L. Romankiw, and R. J. von Gutfeld, *IBM Technical Disclosure Bulletin*, **23**, 1262 (1980).
5. K. J. Vetter, "Electrochemical Kinetics," p. 15, Academic Press, New York (1967).
6. J. Horkans, Unpublished results.

Ceramic-Coated Positive Current Collectors for Li-Al/LiCl-KCl/FeS₂ Batteries

G. Bandyopadhyay

Argonne National Laboratory, Materials Science Division, Argonne, Illinois 60439

ABSTRACT

Several electronically conducting ceramic and metallic coatings were investigated to determine their potential for use as current collectors in the positive electrodes of Li-Al/molten LiCl-KCl/FeS₂ battery cells. Static and in-cell corrosion tests in laboratory-scale cells were performed; the static tests were considerably more severe than the in-cell tests. Chemical vapor deposited (CVD) TiC and TiN coatings on inexpensive iron-based substrates showed significant promise in both tests. Analysis of the results led to the recommendation that the coating quality and thickness, the substrate type, the coating procedure, the design of the cell components, and the electrochemical conditions be optimized to achieve maximum coating stability in long-term operation of Li-Al/FeS₂ cells.

High performance Li-Al/iron sulfide secondary batteries are being developed by Argonne National Laboratory (ANL) (1) for electric vehicle propulsion and for energy storage in electric utility systems. In the cells of these batteries, negative electrodes of solid lithium-aluminum alloy and positive electrodes of iron sulfide (either FeS or FeS₂) are used. At an operating temperature of 400°-500°C, the electrolyte LiCl-KCl remains in a molten state (the eutectic melting point of the electrolyte is 352°C). The overall reaction that takes place in the Li-Al/FeS_x (x = 1 or 2) cell on discharge can be written as (2)



where the composition of the positive electrode at complete discharge of a stoichiometric cell would be Li₂S and Fe. The reverse of these reactions occurs on recharging the cell.

Since the presence of lithium, lithium-aluminum, and iron sulfides makes the cell environment very reactive at elevated temperatures, the selection of suitable materials for various cell components is extremely critical for successful performance and commercialization of these batteries. The development of one such key component, the positive current collector, is the subject of this study.

Although low carbon or stainless steel performs reasonably well as the negative current collectors in Li-Al/FeS_x cells, extensive static, electrochemical, and in-cell corrosion testing of several commonly available metals and metallic alloys indicated that the selection of a suitable corrosion-resistant, cost-effective

positive current collector poses a much more difficult problem (2-5). This is particularly true for FeS₂-type electrodes, in which the sulfur activity is considerably higher than that in FeS-type electrodes. Since Li-Al/FeS₂-type cells must be developed in order to achieve the long-term commercialization goals, it is important to identify and/or develop suitable positive current-collector materials for such cells. The only metal or metallic alloy that is known to exhibit the required chemical stability in an FeS₂-type electrode environment is molybdenum. However, molybdenum is expensive and difficult to fabricate in the shapes required for current-collector applications. Efforts are therefore underway to identify alternative positive current-collector materials for FeS₂-type cells. Electrically conducting ceramic coatings on inexpensive metallic substrates are being considered for such current-collector applications. The selection of suitable ceramics for coatings and the investigation of the stability of these coatings in static and in-cell corrosion environments is the subject of this paper.

Selection of Materials

The criteria for the selection of ceramic coating materials for current-collector application include (i) sufficient electronic conductivity of the ceramic for adequate current-collection efficiency, (ii) corrosion resistance in the FeS₂ and LiCl-KCl environment at 400°-500°C, (iii) resistance to spalling under mechanical and thermal stresses, and (iv) cost effectiveness. Several metal borides, carbides, nitrides, and doped oxides are known to be good electronic conductors (6-8), and the coating technology of many of these materials is well developed (7, 9). Kuora *et al.* (10, 11) and Claar *et al.* (12) have performed preliminary

Key words: corrosion, chemical vapor deposition, titanium nitride and titanium carbide coatings.

thermodynamic stability calculations on the borides, carbides, and nitrides of iron, niobium, tantalum, titanium, and zirconium with respect to the formation of metal sulfides at $\sim 400^\circ\text{--}500^\circ\text{C}$ in the presence of FeS_2 . The calculations indicate that iron boride, TiB_2 , TiN , TiC , TaC , and niobium carbides should be stable in an FeS_2 environment. The oxidation potentials of TiN , TiC , TaC , FeB , and Nb_2C in LiCl-KCl were calculated and measured by Kuora *et al.* (10, 11). These data indicated that the above-mentioned materials could be suitable for positive current-collector application in the Li-Al/FeS_2 battery cell if the charge voltage was limited to 2.2V. The density, melting point, electrical resistivity, thermal expansion coefficient (which is important for compatibility with the substrates), and oxidation potential of several of the candidate coating materials and Mo and Fe are listed in Table I.

Experimental Procedure

Test specimens.—Most of the coated specimens for static corrosion tests were coupons $\sim 25.4 \times 25.4 \times 0.5$ mm in size. Coated screens (60 mesh) were also tested for their stability, because similar screens may be needed in-cell to prevent movement of electrode particles from their respective positions. For in-cell tests, coated positive components (identified later) were used in laboratory-scale Li-Al/FeS_2 cells.

AISI 1008 steel and ANL-5-0¹ alloy substrates were used. ANL-5-0 alloy was selected because it has exhibited better corrosion resistance than low carbon steel in an FeS environment (14).

Chemical vapor deposition (CVD) and rf-sputtering techniques were used to coat the substrates. The Materials Technology Corporation of Dallas, Texas, prepared most of the CVD coatings (*e.g.*, TiC , TiN ,² TiCN , TiB_2 , and combinations of TiC and TiN), and rf-sputtered coatings (*e.g.*, Cr , Mo , MoS_2 , MoSi_2 , $\text{Cr} + \text{TiN}$, $\text{Mo} + \text{TiN}$, $\text{TiC} + \text{TiN}$, and $\text{TiN} + \text{TiC}$) were prepared by Hohman Plating Company, Dayton, Ohio. The CVD coating thicknesses were varied from 5 to 25 μm ; the total coating thickness in all rf-sputtered samples was $\sim 7 \mu\text{m}$.

Static corrosion tests.—The test specimens were placed in a graphite crucible in an argon-filled glove box and were completely covered with one of the following powders or powder mixtures: (i) equal-volume mixtures of FeS_2 ($-50 +150$ size fractions³) and LiCl-KCl (-50 size fraction) which simulated the fully charged positive-electrode environment in a cell; (ii) FeS_2 ($-50 +150$) to study the effect of sulfide alone on the corrosion behavior; (iii) eutectic LiCl-KCl (-50) to study the corrosion due to salt;

¹ ANL-5-0 is an in-house ANL alloy with the composition [weight percent (w/o)] 95.5Fe-4.5Mo.

² CVD-TiN coatings always included an $\sim 1 \mu\text{m}$ underlayer of TiC for improved adherence.

³ These size fractions are similar to those used in-cell for electrode fabrication.

Table I. Properties of some selected materials*

| Material | Density (g/cm ³) | Melting point (°C) | Electrical resistivity ($\mu\Omega\text{-cm}$) [†] | Linear thermal expansion ($\mu\text{m}/\text{m}\cdot^\circ\text{C}$) [‡] | Oxidation potential (vs. Li) (V) |
|------------------|------------------------------|--------------------|---|---|----------------------------------|
| TiN | 5.43 | 2950 | 21-25 | 9.4 | 3.16 |
| TiC | 4.25 | 3150 | 53-105 | 7.5 | 2.67 |
| TiB ₂ | 4.52 | 2980 | 9-15 | 8.1 | — |
| NbC | 7.82 | 3760 | 51-74 | 6.9 | — |
| FeB | 7.15 | 1540 | — | — | 2.64 |
| Mo | 10.20 | 2620 | 5.2 | 5.6 | 2.70 |
| Fe | 7.87 | 1539 | 9.7 | 14.7 | 2.13 |

* From Ref. (6, 7, 10, and 13).

[†] Room-temperature values.

[‡] Between 0 and 1000°C.

and (iv) equal-volume mixtures of iron sulfide (FeS_2 or FeS in $-50 +150$ size fractions) and LiCl-KCl containing Fe powder (-325) to study the effect of sulfur activity, which varied with S:Fe mol ratio in the corrosion bath, on the corrosion behavior.

The crucibles were then heated to 500°C and were maintained at that temperature for the duration of the static tests. After the tests, the specimens were cleaned in water and alcohol, weighed, and examined macroscopically and microscopically.

The static test conditions were considerably more severe than those in the in-cell tests. The coatings that exhibited superior performance in the static tests were subsequently tested for in-cell stability.

In-cell tests.—In-cell tests were performed in small-scale, unsealed prismatic Li-Al/FeS_2 cells, similar to those that had been used for separator testing (15, 16). A schematic representation of the small-scale cells (7.6×12.7 cm), which were described in detail elsewhere (15, 16), is shown in Fig. 1. The cells were assembled in the semicharged state. The positive and negative electrodes consisted of powder mixtures of FeS , Li_2S , and eutectic electrolyte ($-50 +150$ size fractions), and Li-Al (17.45 w/o Li), Al, and electrolyte ($-50 +150$ size fractions), respectively. The materials were mixed in suitable proportions and amounts⁴ and then hot pressed at 450°C . The stability of coated positive components such as the particle retainer screen, the electrode frame, and the current-collector plate in a cell environment were examined in these tests.

Results and Discussion

Characterization of as-received coatings.—Optical and scanning-electron microscopy indicated that the as-received coatings on AISI 1008 steel and ANL-5-0 alloy were, in general, uniform and dense with good adherence to the substrate. Typical micrographs of CVD-TiN and -TiC coatings are shown in Fig. 2. However, the edges of the coupon specimens sometimes revealed the presence of cracks or spalled coatings, indicating the difficulty of coating sharp edges and corners of specimens. Rf-sputtered coatings appeared to adhere well to the substrate, with porosity often detected on the surface. The sputtered coat-

⁴ The proportions of various active materials determined the level of charge for the cell, whereas the amounts determined the theoretical capacity in (A-hr) of the cells.

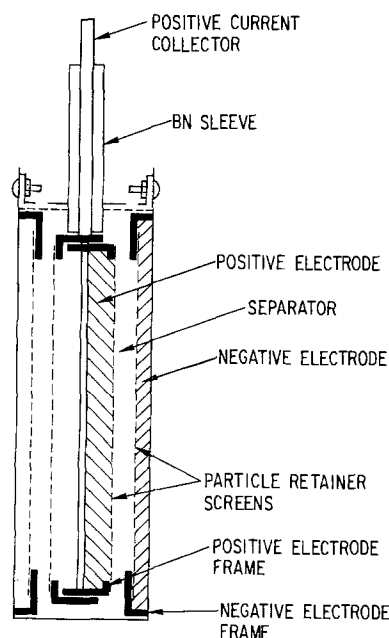


Fig. 1. Schematic of cell for testing coated components

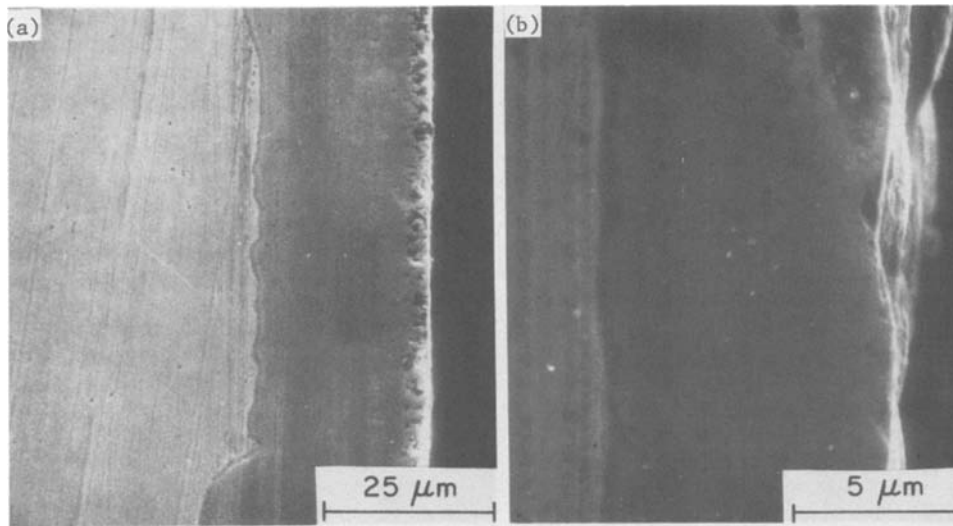


Fig. 2. Scanning electron micrographs of AISI 1008 steel specimens coated with (a) CVD-TiN and (b) CVD-TiC.

ings on sharp edges sometimes showed cracking or local spalling, similar to that observed on CVD-coated samples.

As discussed below, CVD-TiN and -TiC coatings showed the most promise and were therefore examined in more detail. Auger spectroscopy of these coatings indicated the presence of adsorbed oxygen on the surface. The bulk of the coatings, also examined by Auger spectroscopy after removing the surface by sputtering, did not show evidence of any impurities. Residual stresses⁵ (which could influence the coating stability significantly in a corrosion environment) on the CVD-TiN and -TiC coated AISI 1008 coupons (coating thickness $\sim 10 \mu\text{m}$) were determined by x-ray diffraction analysis. Data were obtained only on the square faces, as the edges were too narrow for effective measurements; the surface measurements were made in the x and y direction at several locations on the square faces. The elastic constants used for these calculations and the range of calculated surface residual stresses are shown in Table II. Although the elastic-constant data contain uncertainties that can introduce systematic proportional errors in the stress values, the presence of significant compressive but nearly uniform residual stresses on the coated surfaces is evident.

Static corrosion tests.—The first series of static corrosion tests was performed to identify the coatings that showed enough promise to warrant further investigation and development for future applications. The static test results from several coated AISI 1008 steel coupons and a few selected monolithic ceramics that were tested in equal-volume mixtures of LiCl-KCl and FeS_2 at 500°C are summarized in Table III. Note that hot-pressed TiN and TiC showed no evidence of corrosive attack, indicating the inherent stability of these materials in the environment, whereas TiB_2 showed $\sim 4\%$ weight loss during a 300 hr test.

⁵ Residual stress measurements were done by Lamda Research, Incorporated, Cincinnati, Ohio.

Table II. Elastic constants* and calculated surface residual stresses on CVD-TiN and -TiC coated AISI 1008 steel

| Coating | Elastic modulus (MPa) | Poisson's ratio† | Surface residual stress (MPa)‡ |
|---------|-----------------------|------------------|--------------------------------|
| TiN | 250.3×10^3 | 0.26 | -1310 to -1448 |
| TiC | 310.3×10^3 | 0.18 | -1379 to -1862 |

* From Ref. (6 and 17).

† Poisson's ratio for TiN is assumed here to be similar to that for SiN.

‡ Negative sign indicates compressive stresses.

The CVD-TiC, -TiN, and -TiCN coatings provided significant protection to the low carbon steel substrate, although some attack⁶ was observed from the edges and corners of the specimens. In contrast, CVD-TiB₂ and all the rf-sputtered coatings and coating combinations (including the TiC and TiN coatings) exhibited severe or complete reaction in <300 hr, and therefore were not considered for further investigation.

In their present quality and form, the CVD-TiC and -TiN were still vulnerable to corrosion. Additional tests were therefore performed to identify the cause and location of coating failures in these specimens in the static experiments. Several variables were considered during these tests. Table IV gives results on the percent weight loss of AISI 1008 steel and ANL-5-0 alloy substrates, both uncoated and coated with

⁶ The extent of attack is described later.

Table III. Summary of static corrosion test* results in FeS_2 + LiCl-KCl (1:1 volume) at 500°C

| Materials | Performance |
|---|---|
| Hot pressed: TiN, TiC | No evidence of chemical attack |
| Hot pressed: TiB_2 | Some attack after 300 hr of corrosion |
| CVD coatings: TiC, TiN (with underlayer of TiC), TiCN CVD coating: TiB_2 | Severe attack or complete reaction in <300 hr |
| Rf-sputtered coating: Cr, Mo, MoS_2 , MoSi_2 , (Cr + TiN), (Mo + TiN), (TiC + TiN), (TiN + TiC) | Severe attack or complete reaction in <300 hr |

* Maximum test duration 1000 hr.

Table IV. Data from static corrosion tests performed at 500°C for 300 hr

| Substrate | Coating | | Weight loss as percent of total weight of coated sample after corrosion in | | |
|-----------------|-------------|-----------------------------|--|----------|----------------|
| | Composition | Thickness (μm) | FeS_2 + LiCl-KCl | LiCl-KCl | FeS_2 |
| AISI 1008 steel | None | — | 100.00 | 0.80 | 100.00 |
| | | 10 | 22.30 | 2.50 | 0.22 |
| | | 19 | 32.50 | 2.45 | 4.92 |
| | TiC | 23 | 42.40 | 1.40 | 3.22 |
| | | 10 | 3.91 | 0.22 | 0.28 |
| | | 13 | 37.10 | 0.52 | 2.59 |
| ANL-5-0 alloy | None | — | 100.00 | 0.77 | ~ 100.00 |
| | | 10 | 2.08 | 0.13 | 0.03 |
| | | 16 | 100.00 | 0.41 | 4.02 |
| | TiC | 20 | 100.00 | 0.80 | 3.15 |
| | | 5 | 42.5 | 0.46 | 0.05 |
| | | 10 | 100.0 | 1.18 | 1.41 |
| 13 | 6.8 | +0.03 | 0.04 | | |

various thicknesses of CVD-TiN and -TiC, in three different corrosion environments (FeS_2 , LiCl-KCl, and equal volume mixtures of $\text{FeS}_2 + \text{LiCl-KCl}$). The data show several important features: (i) In general, the coatings provided protection to the substrate; the protection was greatest in an FeS_2 environment. (ii) The $\text{FeS}_2 + \text{LiCl-KCl}$ environment was much more corrosive than either FeS_2 or LiCl-KCl alone. (iii) The corrosion resistance of the specimens was strongly dependent on the coating thickness. (iv) The substrates that were tested in this study did not appear to influence the stability or corrosion resistance of the coatings.

Extensive microstructural examinations were performed to determine the nature of the coating failures in these samples. In all corrosion-tested specimens,

the attack appeared to have initiated at the edges and corners of the specimens. Typical examples of such attack in LiCl-KCl and FeS_2 environments are shown in Fig. 3. Although the weight loss of the coated specimens in these environments was $<5\%$ (Table IV), the vulnerability of the coating at sharp corners and edges is evident. The specimens tested in the $\text{FeS}_2 + \text{LiCl-KCl}$ environment exhibited much more severe corrosion of the substrate in the areas exposed by spalling of the coating. Figure 4 shows an example of exaggerated substrate corrosion initiated from the edge of the sample. Although the LiCl-KCl eutectic did not react with the substrates to any significant degree (Table IV), its presence in the sulfide environment resulted in exaggerated corrosion, probably because the molten salt contributed to early failure of

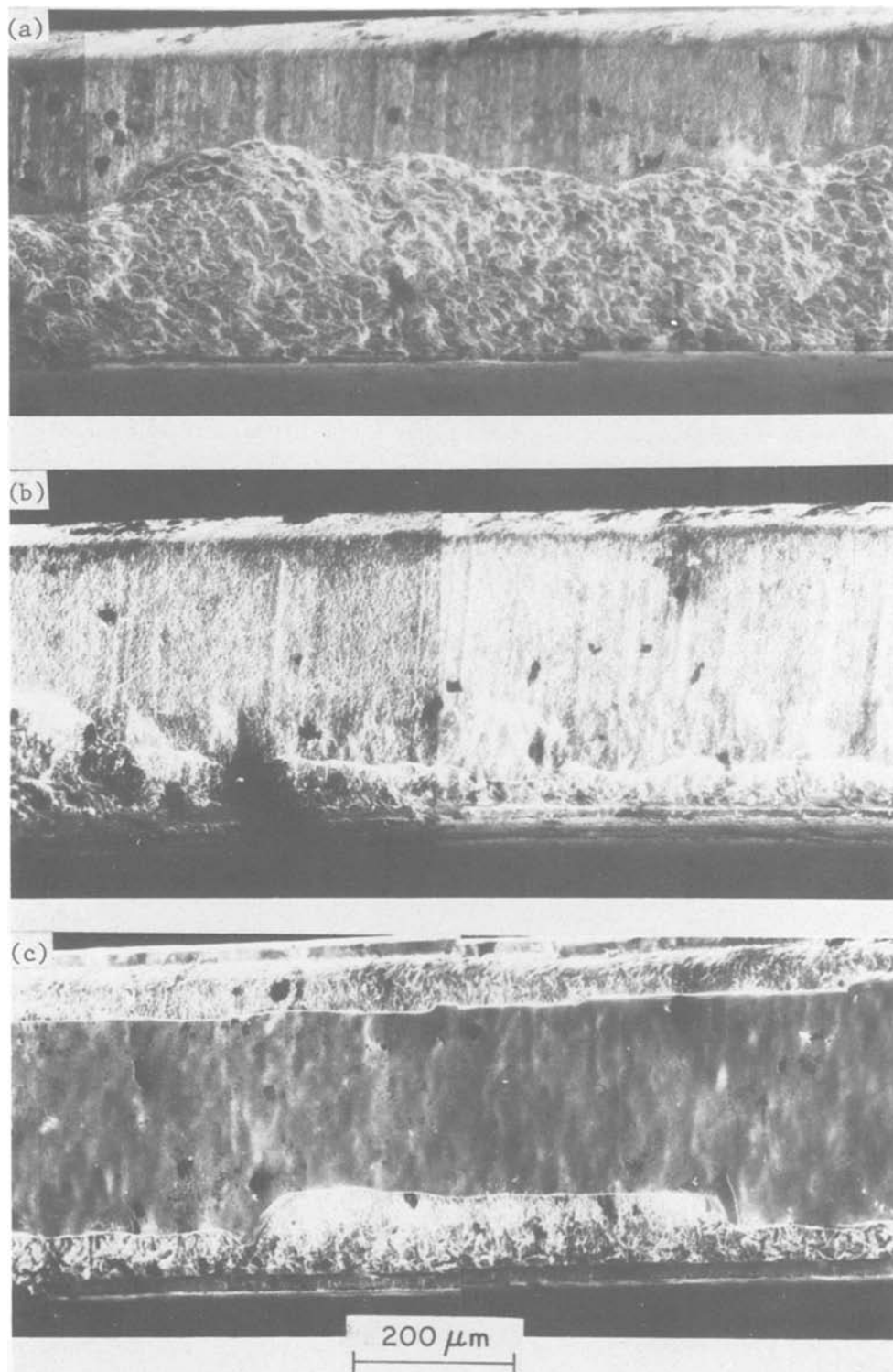


Fig. 3. Composite scanning electron micrographs of the edges of CVD-coated AISI 1008 steel specimens showing coating spalled after corrosion tests for 300 hr at 500°C. (a) 10 μm thick TiN in LiCl-KCl; (b) 10 μm thick TiN in FeS_2 ; (c) 10 μm thick TiC in FeS_2 .

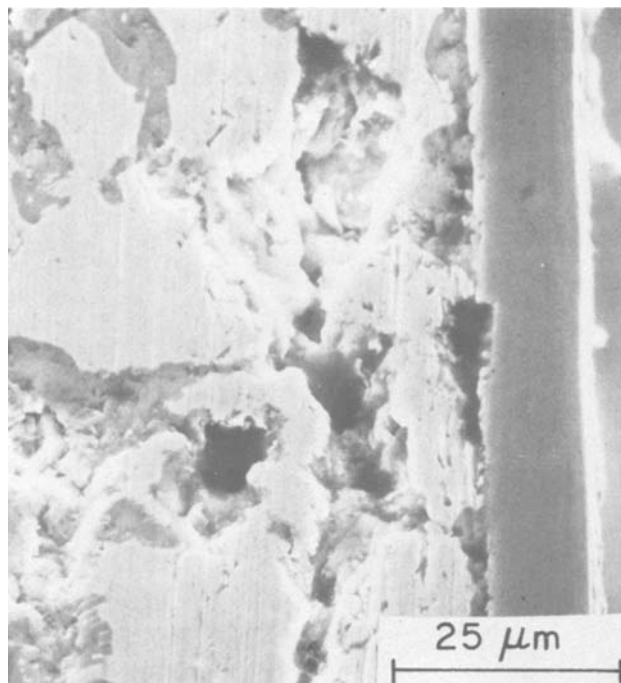


Fig. 4. Scanning electron micrograph of CVD-TiN coated AISI 1008 steel specimen tested in $\text{FeS}_2 + \text{LiCl-KCl}$ (equal volume mixture) at 500°C for 300 hr, showing severe corrosion of the substrate adjacent to relatively unaffected coating. Initiation of attack on the substrate was due to coating failure at the edges.

the coating and/or facilitated transport of sulfide ions to the reaction site.

The vulnerability of the coated samples at the corners and edges is probably related to the difficulty in coating these areas. We noted earlier that a substantial compressive stress exists on the coated surfaces of the sample. Although no information is available about the stresses at the edges and corners, one can speculate that large compressive stresses on the surfaces could generate significant shearing stresses at the corners. Such stresses would tend to spall the coating from these regions. The effect of the residual stresses should be even more significant in the presence of a corrosive environment such as salt or sulfide, which might lead to stress-corrosion cracking of the coatings at the sharp corners of the specimens.

The surface residual stresses in the coatings are expected to depend on the coating thickness, the substrate types, and the coating preparation procedure. A detailed study of these parameters and their relation to the coating stability and corrosion resistance of the specimens is beyond the scope of this investigation. However, the strong dependence of the sample performance on the coating thickness (Table IV) is probably related to the effect of coating thickness on surface residual stresses which, in turn, determines the tendency of the coatings to spall.

To determine the effect of sulfur activity on coatings, static tests were performed on TiN-coated AISI 1008 steel by varying the S:Fe mol ratio in the corrosion bath. In Fig. 5, the activity of sulfur at 500°C and percent sample lost after 300 hr corrosion tests are shown as a function of S:Fe mol ratio. A sharp drop in corrosion rate was observed as the composition shifted slightly to the iron-rich side of FeS_2 . The drop in corrosion rate corresponds to the rapid drop of the sulfur activity. Note that the coating was vulnerable, although to a much smaller extent, even in an $\text{FeS} + \text{LiCl-KCl}$ environment. This is probably because the coating failure was initiated by the high residual stresses and the corrosion environment. Sub-

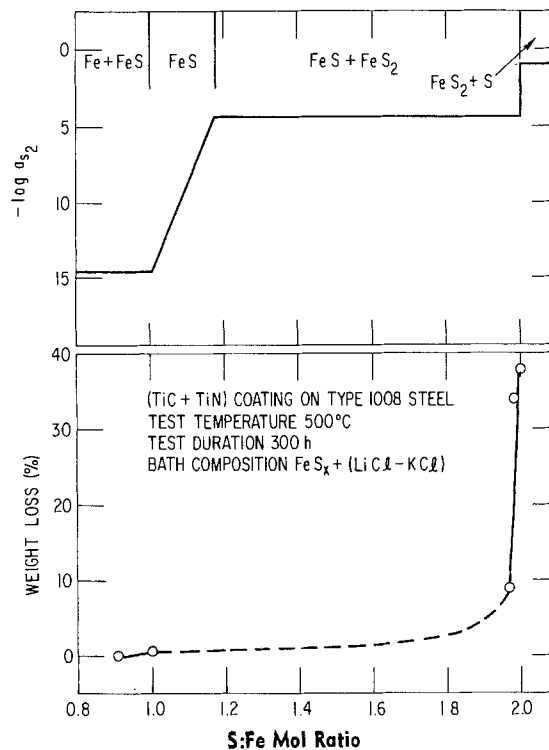


Fig. 5. (Top) sulfur activity and (bottom) corrosion of $5\ \mu\text{m}$ TiC + $10\ \mu\text{m}$ TiN-coated samples as a function of S:Fe mol ratio.

sequently, the sulfur activity essentially determined the corrosion rates of the substrate.

Several static tests in $\text{FeS}_2 + \text{LiCl-KCl}$ at 500°C were performed on 60 mesh AISI 1008 screens coated with CVD-TiC and -TiN (coating thickness varied from 2 to $10\ \mu\text{m}$) to study the possibility of using such screens as positive particle retainers in the cell. The results showed that the coated screens were severely attacked by the corrosion environment in <300 hr, indicating that the coating stability can be strongly influenced by the geometry of the specimens.

The static corrosion test results as reported above indicate that the coatings will probably need further improvement to be stable in long-term applications. Since surface residual stresses are expected to play a key role in coating stability, it will be important to investigate the effect of the type, geometry, and physical and mechanical state of the substrate, the variables of the coating processes, and the coating thicknesses on the residual stress and its distribution, and on the corrosion resistance of the specimens. In addition to optimizing the quality and the thickness of the coating to minimize the residual stresses on the surfaces, one can recommend, based on the currently available static corrosion test data, the following modifications for improved in-cell performance of the coatings: (i) design the current collectors and frames without sharp corners and edges, and (ii) maintain slightly iron-rich FeS_2 in the positive electrodes to take advantage of the precipitous reduction of sulfur activity just below the fully charged state and thereby reduce corrosion on the positive components.

In-cell tests.—Despite the vulnerability of presently available TiN and TiC coatings in static corrosion tests, laboratory-scale in-cell tests were performed using TiN-coated positive components because the in-cell test conditions are considerably milder (lower temperature and lower sulfur activity, as compared to FeS_2 , for a majority of the charge-discharge cycling times) than those of the static tests. No attempts were made to incorporate the above-mentioned recommendations in these preliminary in-cell tests.

Four laboratory-scale Li-Al/FeS₂ cells were assembled with 50 A-hr theoretical capacity using positive components made of monolithic TiN or CVD-TiN coated AISI 304 stainless steel. The cells were operated between charge and discharge cut-off potentials of 2.1 and 1.0V, respectively. Table V lists the cell numbers, the materials used for separators and positive components, the number of days and cycles of operation, the coulombic efficiency and utilization of the cells at a current density of 50 mA/cm², and the cause for termination of the tests. The cell cans, negative frames, and negative particle retainer screens in all these cells were made of AISI 304 stainless steel. The coulombic efficiency and utilization in these cells are comparable to those of similar laboratory-size Li-Al/FeS cells (15, 16).

Note from Table V that cell MS-5 was assembled using a monolithic hot-pressed TiN plate. The plate was placed between the two positive electrodes. Current collection from the positive side was achieved through the TiN plate and also through the positive frames that were in contact with the TiN plate. The current leadout was welded to the frame. During post-test examination, the TiN plate broke into several pieces. However, the thickness of the plate did not change during the cell operation, and no reaction product was detected. This is in agreement with the static corrosion test results, which indicated that TiN is stable in FeS₂/LiCl-KCl at 500°C.

Cell MS-6 was assembled using coated current-collector plates, frames, and screens. During disassembly of this cell, no attempt was made to identify the cause of the internal short that developed during operation; the primary purpose was to examine the positive components without damaging them during disassembly. The current-collector plate and the frames did not show any evidence of corrosion (Fig. 6). However, the screens were extensively corroded. The corrosion of coated screens is in agreement with the static test results.

Since the coated screens performed poorly in-cell, MS-8 was assembled without positive particle retainer screens. To prevent particle movement in this cell, sintered MgO separators (~55% theoretical density), which are characterized by extremely small pores (average diameter <1.0 μm) and a narrow pore size distribution (15), were used. Post-test examination of this cell showed no evidence of corrosion attack on the coated components (Fig. 7). Local coating loss was sometimes detected; however, the substrates did not show any evidence of corrosive attack, thus indicating that coating loss may have occurred during the cutting of the cell and sample preparation. Sintered MgO separators performed satisfactorily in this cell and did not exhibit any evidence of chemical reaction or active material in the separator (Fig. 8).

Cell MS-9 was assembled using coated positive current-collector plate, frames, BN fabric separators, and molybdenum screens for positive particle retention. Again, the post-test examination of this cell

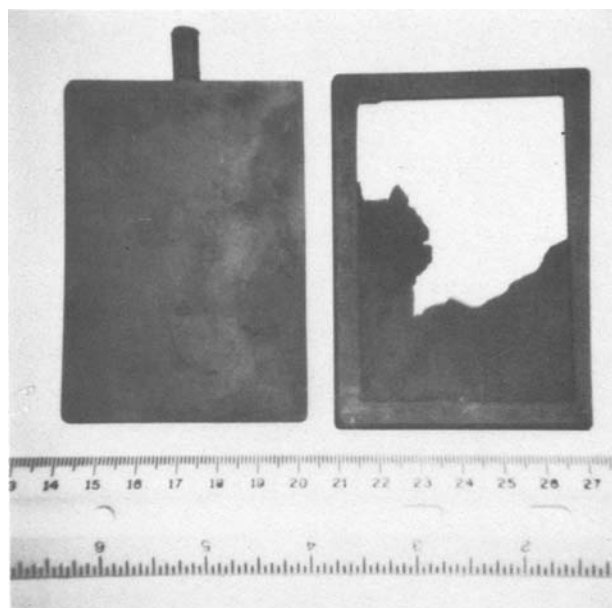


Fig. 6. Photographs of positive current-collector plate, frame, and screen after test in cell MS-6.

showed no evidence of corrosion attack of the coated components.

The in-cell test results, as presented above, indicate that monolithic TiN was chemically stable in the cell environment. Titanium nitride coated AISI 304 stainless steel current-collector plates and frames exhibited no evidence of corrosive attack, indicating that such coatings are indeed attractive candidates for use in an Li-Al/FeS₂ cell. Use of stainless steel instead of low carbon steel as the substrate may have contributed somewhat to the better stability of the in-cell positive components; stainless steel is known to be more corrosion resistant than low carbon steel in the positive-electrode environment (4). However, static tests of uncoated stainless steel in FeS₂/LiCl-KCl resulted in severe corrosion (4). Thus, the coating must have provided significant protection to the substrate. The coated particle retainer screens, however, were unstable in the cell environment; thus, the screens will have to be modified, or different materials used. Alternatively, screens may be eliminated from the cell assembly, as demonstrated in cell MS-8, by using sintered separators.

The stability of TiN-coated current collectors and frames in the laboratory-size Li-Al/FeS₂ cells in short-term tests is very encouraging. The results indicate that a moderate improvement in the coating quality, proper selection of the type and the condition of the substrate, some changes in the design of the current collectors and frames, and an optimized electrochemical condition for cell operations might lead to long-term stability of these coatings in the Li-Al/FeS₂ cell environment.

Table V. Li-Al/FeS₂ cells: component descriptions and performance data

| Cell number | Separator | Positive components | | | Days of operation/ number of cycles | Utilization (%) | Coulombic efficiency (%) | Cause of termination |
|-------------|---|----------------------------------|-------------|---|--|-----------------|--------------------------|---|
| | | Current-collector plate | Frame | Screens | | | | |
| MS-5 | BN fabric | Hot-pressed TiN (1.9 mm thick) | Hastelloy B | Hastelloy B (200 mesh) | 30/48 | 45.0 | 90.0 | Voluntarily terminated |
| MS-6 | BN fabric | 10 μm TiN coating on Type 304 SS | | 10 μm TiN coating on 100 mesh Type 304 SS | 20/15 | 61.0 | 100.0 | Internal short |
| MS-8 | Sintered MgO (~55% theoretical density) | | | None | 25/23 | 61.0 | 80.0 | Break in the welded joint in the positive current-collector plate |
| MS-9 | BN fabric | | | 100 mesh molybdenum | 15/12 | 61.0 | 90.0 | Internal short |

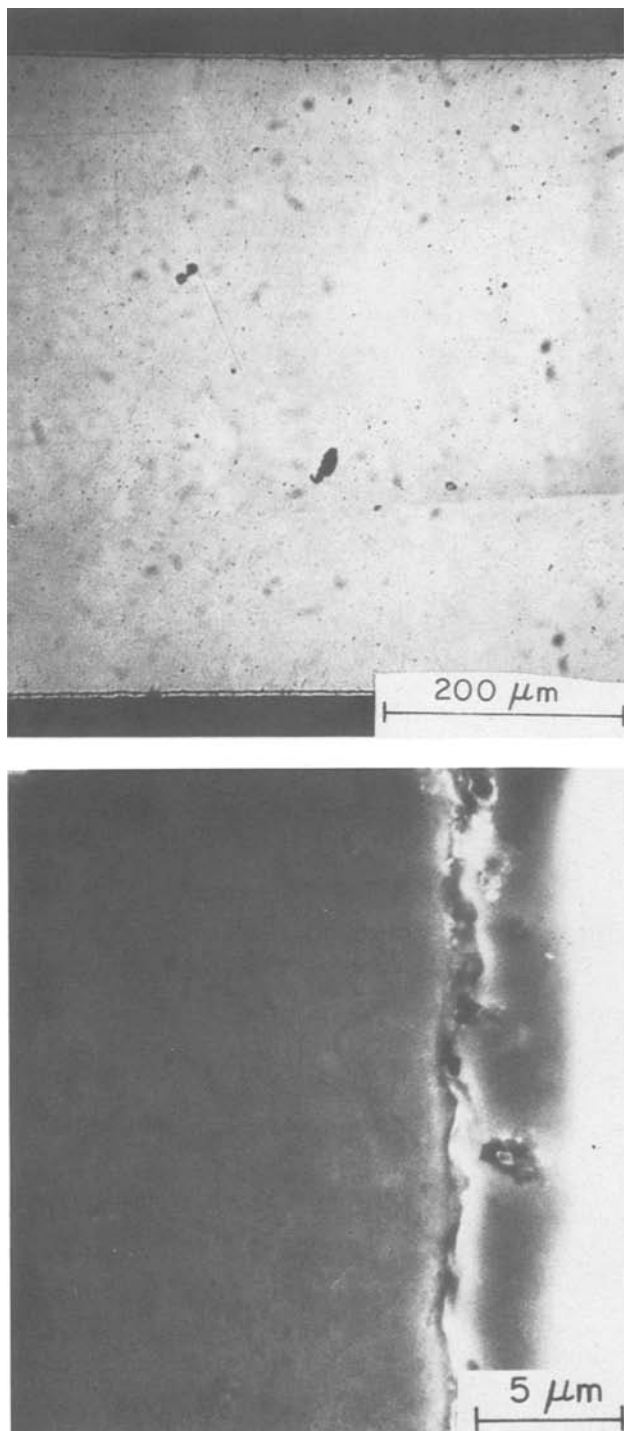


Fig. 7. Micrographs of polished section of coated current collector for cell MS-8. (a, top) Metallographic section and (b, bottom) SEM photograph.

Summary and Conclusions

Several electronically conducting ceramic and metallic candidate coatings and coating materials were investigated to determine their potential for use in positive components of Li-Al/FeS₂ battery cells. Chemical vapor deposited (CVD) and rf-sputtered coatings on inexpensive iron-based alloy substrates were considered. Static corrosion tests, which were considerably more severe than the in-cell tests, indicated that although none of the coatings tested in this investigation were completely satisfactory, CVD-TiC and -TiN coatings showed significant promise. The failure in the CVD-TiC and -TiN coatings in the static tests was initiated from the corners and edges

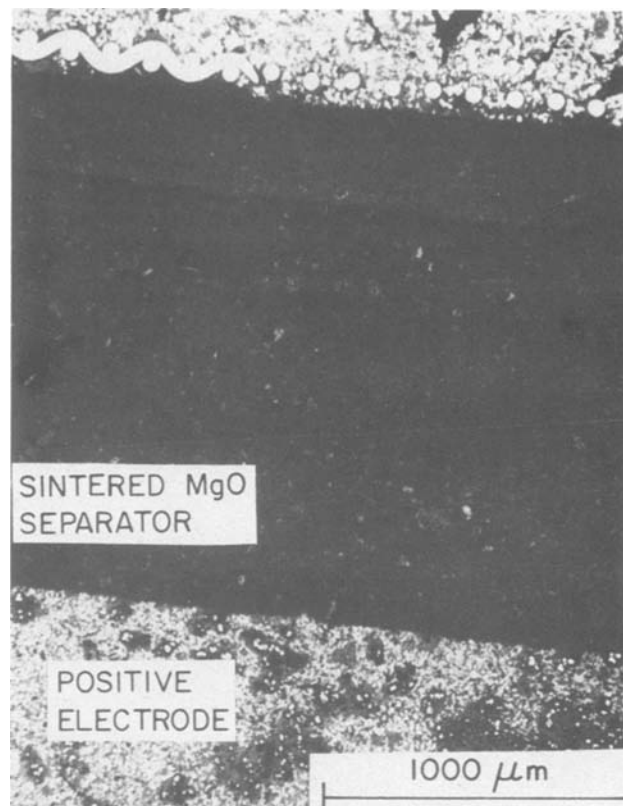


Fig. 8. Composite photograph of a polished section from cell MS-8 showing the sintered MgO separator.

of the specimens. The high compressive surface residual stresses, which were measured on the coated specimens by x-ray diffraction, and the corrosive media probably produced stress-corrosion cracking and spallation of the coatings. The coating stability was strongly dependent on the coating thickness and the geometry of the specimens.

The coatings performed significantly better in the in-cell tests because of the milder (lower temperature and lower sulfur activity) corrosion environment than that in the static tests. Monolithic TiN current-collector plate and TiN-coated AISI 304 stainless steel positive current-collector plates and frames were completely stable in Li-Al/FeS₂ cell after ~30 days of operation. The coated particle retainer screens, however, were unstable; therefore, alternate materials, modification, or elimination of the screens will be required.

Analysis of the static and in-cell test results led to several recommendations for application of the CVD-TiN and -TiC coatings in Li-Al/FeS₂ cells. Since surface residual stresses are expected to play a key role in the coating stability, they must be minimized through optimization of the coating quality and thickness, the substrate type, the coating procedure, and the design of the cell components. Designing positive cell components without sharp corners and edges should significantly improve the coating stability. In addition to optimizing coating quality and the component design, maintaining slightly iron-rich FeS₂ in the fully charged condition is recommended for improved coating performance. Optimized coating quality and electrochemical conditions for cell operation, and an improved cell design, should lead to long-term stability of these coatings in Li-Al/FeS₂ cells.

Acknowledgments

The author wishes to express his appreciation to T. M. Galvin for his assistance at all stages of the experimental work, J. T. Dusek for scanning electron

microscopic examinations, D. F. Busch for Auger spectroscopy, and J. A. Smaga, J. E. Battles, and R. B. Poeppl for critical review of the paper. This work was supported by the U.S. Department of Energy, Division of Energy Storage.

Manuscript submitted March 2, 1981; revised manuscript received June 19, 1981. This was Paper 112 presented at the Hollywood, Florida, Meeting of the Society, Oct. 5-10, 1980.

Any discussion of this paper will appear in a Discussion Section to be published in the June 1982 JOURNAL. All discussions for the June 1982 Discussion Section should be submitted by Feb. 1, 1982.

Publication costs of this article were assisted by Argonne National Laboratory.

REFERENCES

1. P. A. Nelson *et al.*, Progress Report for the Period October 1978-September 1979, Argonne National Laboratory Report ANL-79-94 (1979).
2. J. E. Battles, in "Critical Materials Problems in Energy Production," C. Stein, Editor, pp. 769-804, Academic Press, New York (1976).
3. J. E. Battles, J. A. Smaga, and K. M. Myles, *Metal. Trans. A*, **9**, 183 (1978).
4. J. A. Smaga, F. C. Mrazek, K. M. Myles, and J. E. Battles, in "Materials Considerations in Liquid Metals Systems in Power Generation," N. J. Hoffman and G. A. Whitlow, Editors, pp. 52-64, NACE, Houston, TX (1978).
5. D. O. Raleigh, J. T. White, and C. A. Ogden, *This Journal*, **126**, 1087, 1093 (1979).
6. "Plenum Press Handbook of High-Temperature Materials," No. 1—Materials Index, by T. B. Shaffer; No. 2—Properties Index, by G. V. Samsonov, Plenum Press, New York (1964).
7. J. L. Pentecost, in "High Temperature Inorganic Coatings," John Huminik, Jr., Editor, pp. 10-109, Reinhold Publishing Corp., New York (1963).
8. G. J. May, *J. Mater. Sci.*, **14**, 633 (1979).
9. G. V. Samsonov and A. P. Epik, in "Coatings of High-Temperature Materials," H. H. Hausner, Editor, pp. 7-111, Plenum Press, New York (1966).
10. N. Kuora, N. P. Yao, and J. Kincinus, *J. Electrochem. Soc. Jpn.*, **46**, 395 (1978).
11. N. Kuora, J. E. Kincinus, and N. P. Yao, Argonne National Laboratory Reports ANL-75-1, pp. 56-58, and ANL-75-36, pp. 50-51 (1975).
12. T. D. Claar and J. T. Dusek, Argonne National Laboratory Report ANL-78-21, p. 44 (1978).
13. "Metals Handbook," Eighth Edition, Vol. I. American Society for Metals, Metals Park, OH (1961).
14. J. A. Smaga, Argonne National Laboratory Report ANL-79-39, p. 83 (1979).
15. G. Bandyopadhyay, J. T. Dusek, and T. M. Galvin, *Ceramurgia International*, **5** (3), 95 (1979).
16. R. B. Swaroop, C. W. Boquist, and J. E. Battles, Abstract 52, p. 145, The Electrochemical Society Extended Abstracts, Pittsburgh, Pennsylvania, Oct. 15-20, 1978.
17. E. M. Lenoce, in "Ceramics for High Performance Applications," J. J. Burke, A. E. Gorum, and R. N. Katz, Editors, pp. 123-145, Brook Hill Publishing Co., Chestnut Hill, MA (1974).

Behavior of Some Ions in Mixed Organic Electrolytes of High Energy Density Batteries

Yoshiharu Matsuda,* Hitoshi Nakashima, Masayuki Morita, and Yoshio Takasu

Department of Industrial Chemistry, Faculty of Engineering,
Yamaguchi University, Tokiwadai, Ube, Yamaguchi, Japan

ABSTRACT

Some physicochemical properties of the mixed solvents of propylene carbonate and 1,2-dimethoxyethane dissolving various salts have been measured at 30°C, in order to clarify the mixing effect of the organic electrolytes for high energy density batteries. The vapor pressure and laser Raman spectra of the mixed solvents provided significant information regarding the solvent-solvent interactions. Ionic conductivities under infinite dilution condition were determined by the measured molar conductivities of the salts and transport numbers of the ions; the Stokes' radii of the ions in the mixed solvents were also estimated. A specific solvation of cations with 1,2-dimethoxyethane in the mixed solvents seems to give captured cations like a crown ether does. These solvent-solvent and ion-solvent interactions mainly contribute to the excellent conductance of the electrolyte using the mixed solvents.

In the course of development of high energy density batteries with organic electrolytes, solutions containing mixed solvents have been used as the electrolyte solutions. For instance, mixed solvents of propylene carbonate (PC) with 1,2-dimethoxyethane (DME) (1, 2), γ -butyrolactone with tetrahydrofuran (3), and the like have been employed to obtain good cell performance. Among the properties of the solvents, low viscosity and high dielectric constant are important in obtaining a highly conductive electrolyte, because the former contributes to low resistance for ion transport in the solution and the latter serves to lower the ionic dissociation energy. The excellent mixing effect of the solvents on the conductivity has been reported in previous papers (4-8). Up to the present however, the

reason for the improvement of the conductivity by mixing the solvents has not been appreciably clarified, in spite of the brief discussion connected with the data of dielectric constant and viscosity (7, 8).

In this work, the fundamental properties of the mixed solvents of PC and DME dissolving some salts were investigated in order to explain their synergistic effects. The examined characteristics are vapor pressure, viscosity, laser Raman spectrum, electric conductivity, and transport number of ion. From these data, some of the information concerning the solvent-solvent and ion-solvent interactions was obtainable, and the behavior of the ions in the mixed PC-DME system was discussed in detail.

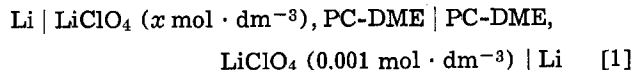
Experimental

PC and DME were purified by the methods described previously (5, 9). Water contents were determined by

* Electrochemical Society Active Member.
Key words: mixed organic solvent, electric conductivity, Stokes' radius, specific solvation.

Karl Fisher titration and were below $80 \text{ mg} \cdot \text{dm}^{-3}$ in PC and $50 \text{ mg} \cdot \text{dm}^{-3}$ in DME. The LiClO_4 was an extra pure reagent by Kanto Kagaku Company Limited. NaClO_4 , KClO_4 , NH_4ClO_4 , $(\text{C}_2\text{H}_5)_4\text{NClO}_4$, LiCl , and LiBr were of the same grade by Wako Pure Chemical Industries, Limited. LiBF_4 and LiPF_6 were obtained from Morita Chemical Industries, Limited. These reagents were used after drying under reduced pressure at the appropriate temperatures (80° - 170°C) for 24 hr.

The vapor pressure of the solvents and solutions was measured by a static method (10). The viscosity, dielectric constant, and electrical conductivity were measured by the same methods as in the previous paper (8). The transport numbers of Li^+ and ClO_4^- ions were determined through measuring the electromotive force of the concentration cell with a liquid junction, Eq. [1], as used by Hoare and Wiese (11)



The transport number of ClO_4^- ion was calculated by using Eq. [2]

$$E = - (2RT t_{\text{ClO}_4^-} / F) \ln (x/0.001) \quad [2]$$

where E and $t_{\text{ClO}_4^-}$ are the electromotive force of the cell, Eq. [1], and the transport number of ClO_4^- ion, respectively, and other symbols have their usual meanings.

Molar conductivity and Stokes' radius of an ion were evaluated in the usual methods by using the experimental values of specific conductivity, transport number, and viscosity. All measurements were carried out at 30°C unless otherwise noted.

Results and Discussion

The vapor pressure of a mixed organic solvent is related to the fundamental properties of thermodynamics. Usually, the vapor pressure of real mixed organic solvent is given by Eq. [3]

$$P = P^{\circ}_A x_A \gamma_A + P^{\circ}_B x_B \gamma_B \quad [3]$$

where P , P°_A , and P°_B are the vapor pressures of the mixed solvent and the pure solvents, A and B, respectively. x_A and x_B are the molar fractions of A and B in the mixed solvent, and γ_A and γ_B are the activity coefficients of A and B. If both γ_A and γ_B are unity, Eq. [3] is identical with Raoult's equation and the mixed solvent is an ideal liquid. The measured vapor pressure of the PC-DME system at various temperatures is shown in Fig. 1. Positive deviations from the straight lines in the figure indicate $\gamma > 1$ and a nonideal condition formed by mixing the two solvents. It is considered that a certain association of the PC molecules

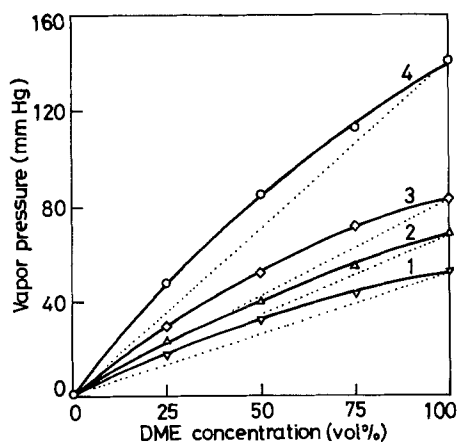


Fig. 1. Correlation between composition and vapor pressure of PC-DME mixed system at various temperatures, curve 1, 20°C ; curve 2, 25°C ; curve 3, 30°C ; curve 4, 40°C .

in the pure solvent is weakened by addition of DME, which is supported by the results of laser Raman spectra discussed in a later section of this paper. This interaction between PC and DME molecules would be one of the causes of the excellent conductance of PC-DME solutions of LiClO_4 and NaClO_4 .

The mixing effect of the solvents on the electric conductance can be better understood under the infinite dilution condition. Table I shows the limiting molar conductivities, Λ^∞ , of some salts consisting of univalent cations and anions in PC-DME mixed system. The values of Λ^∞ were determined by extrapolating the molar conductivities measured, Λ , to zero concentration in the Λ vs. $C^{1/2}$ plots (C represents the concentration of the salt, $10^{-3} \leq C \leq 10^{-2} \text{ mol} \cdot \text{dm}^{-3}$) (7, 8). The Λ^∞ in the solutions composed of a higher percentage of DME (or 100% DME) was not determinable by the above procedure because of nonlinearity of the plots. This is also the case for 75% DME containing LiCl . The molar conductivities of the salts increase with increasing DME concentration in the solvent. It suggests that under such infinite dilution condition ion-ion interactions are fairly weak and then the molar conductivity mainly depends on the degree of facility in ion movement, or the ionic mobility. By Eq. [4], the limiting ionic mobility, u_i^∞ , can be correlated to the limiting molar ionic conductivity, λ_i^∞ , which is further calculated from the limiting molar conductivity and transport numbers, t_i^∞ , by using Eq. [5]

$$u_i^\infty = \lambda_i^\infty / F \quad [4]$$

$$\lambda_i^\infty = t_i^\infty \Lambda^\infty \quad [5]$$

where subscript i denotes the types of the ions.

In order to determine the λ_i^∞ , the limiting transport numbers of Li^+ and ClO_4^- ions were measured in the PC-DME mixed system and the results are listed in Table II. The transport number of Li^+ ion increases with increasing DME concentration in the solvent. In Fig. 2 the limiting molar ionic conductivities or ionic mobilities of Li^+ and ClO_4^- are shown as a function of DME content in the solvent. The molar ionic conductivities increase with DME concentration because of lowering of the solvent viscosity. However, some differences are observed in the variations of molar ionic conductivities of these two kinds of ions, and it implies some different ion-solvent interactions depending on the kind of ions.

For other cations and anions, limiting molar ionic conductivities are shown in Table III, in which measured viscosity of the solvent is included. The values of λ_i^∞ were calculated by substituting the data of the limiting molar conductivities of the salts, Λ^∞ , into Eq. [6]

$$\lambda_{M^+}^\infty = \Lambda_{M\text{ClO}_4}^\infty - \lambda_{\text{ClO}_4^-}^\infty \quad [6-a]$$

$$\lambda_{X^-}^\infty = \Lambda_{\text{LiX}}^\infty - \lambda_{\text{Li}^+}^\infty \quad [6-b]$$

where M^+ and X^- represent the cation and the anion,

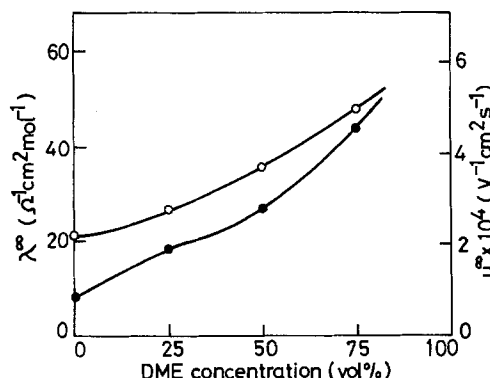


Fig. 2. Limiting molar ionic conductivities (λ^∞) and mobilities (u^∞) of Li^+ (\bullet) and ClO_4^- (\circ) in PC-DME mixed system.

Table I. Limiting molar conductivities of some salts in PC-DME mixed system

| DME conc. (v/o) | Λ^∞ ($\Omega^{-1} \text{ cm}^2 \text{ mol}^{-1}$) | | | | | | | | |
|-----------------|--|--------------------|-------------------|----------------------------------|---|------|------|-------------------|-------------------|
| | LiClO ₄ | NaClO ₄ | KClO ₄ | NH ₄ ClO ₄ | (C ₂ H ₅) ₄ NClO ₄ | LiCl | LiBr | LiBF ₄ | LiPF ₆ |
| 0 | 29.5 | 30.3 | 36.4 | 41.3 | 34.9 | 20.8 | 28.5 | 34.0 | 29.3 |
| 25 | 45.4 | 46.8 | 49.3 | 53.9 | 49.2 | 37.0 | 41.4 | 49.0 | 40.4 |
| 50 | 63.2 | 65.9 | 72.2 | 67.0 | 68.4 | 47.5 | 54.0 | 63.8 | 55.0 |
| 75 | 92.0 | 92.6 | 89.6 | 91.2 | 87.0 | — | 73.0 | 88.6 | 81.5 |

Table II. Limiting transport numbers of Li⁺ and ClO₄⁻ ions

| DME conc. (v/o) | $t_{\text{Li}^+}^\infty$ | $t_{\text{ClO}_4^-}^\infty$ |
|-----------------|--------------------------|-----------------------------|
| 0 | 0.28 | 0.72 |
| 25 | 0.41 | 0.59 |
| 50 | 0.43 | 0.57 |
| 75 | 0.48 | 0.52 |

respectively. It is obvious from Table III that the molar conductivities of all ions tend to increase with increasing DME content in the solvent similarly to those of Li⁺ and ClO₄⁻ ions. Thus, the low viscosity of DME would mainly contribute to the high conductivity of the solution.

Generally, ionic mobility depends on both viscosity of the solvent and size of ion. From the data presented above, Stokes' radius of the ion, R_s , which corresponds to the size of ion in solution, is evaluated by Stokes' equation, Eq. [7]

$$R_s = Z_i F^2 / 6\pi\eta_0 \lambda_i^\infty N_A \quad [7]$$

where Z_i , F , η_0 , and N_A are number of ionic charge, Faraday constant, viscosity of the solvent, and Avogadro constant, respectively. The Stokes' radii of the ions were calibrated by the method using a series of tetraalkylammonium ions (12), and the resulting radii are shown in Table IV. Every anion tends to have increasing Stokes' radius with an increase in DME content. This seems to be due to the replacement of solvating PC molecules by DME added. On the other hand, the radii of the cations, especially Li⁺ and Na⁺ ions, are almost constant in the solutions containing 25-75% DME. In Fig. 3, R_s of the ions in 100% PC solvent and 50% PC-50% DME mixed solvent are plotted against the crystallographic radii of the ions, R_c , cited from the literature (13). R_s of the anions decreases with increasing R_c both in 100% PC solvent and in 50% PC-50% DME mixed solvent, which is the general phenomenon observed in hydration. The cations in 100%

PC solvent behave almost in the same manner. However, R_s of the cations in the mixed solvent are scarcely different from one another. Such unique characteristics with respect to the Stokes' radii of cations may be explicable from the viewpoint of a specific (or selective) solvation.

Another information on the ion-solvent interaction is obtainable from some spectroscopic data. Figure 4 shows typical laser Raman spectra of the PC-DME-LiClO₄ system in the C=O region. With LiClO₄ dissolved in PC, the wave number of the C=O stretching band of PC (1782 cm⁻¹) is shifted to a higher value and the intensity decreases to a certain extent. This means the solvation of Li⁺ ion with PC molecules

through a coordinated bond such as $\text{Li}^+ \cdots \text{O}=\text{C}$.

On the other hand, the shifts of the wave number toward higher values with the addition of DME to PC are due to the weakening of C=O bond by added DME. This suggests that the degree of the intermolecule association of PC is reduced by the addition of DME. Such a phenomenon suggesting a solvent-solvent interaction would relate to the experimental results of vapor pressure of the mixed solvent shown in Fig. 1, and the excellent conductance of PC-DME containing perchlorates. In the case of PC-DME mixed system containing LiClO₄, the influence of LiClO₄ addition on the shift of wave number is rather small in the high DME content region; it might be because of the decreasing solvation of Li⁺ ion with PC in the mixed solvents. Since the variation of the C—O—C stretching band of DME was not remarkable either, the interaction between Li⁺ ion and DME molecules was not discussed from this viewpoint.

As a measure of the ion-solvent interaction, the solvation number of the ion, N_s , was estimated by Eq. [8]

$$N_s = \frac{4}{3} \pi (R_s^3 - R_c^3) / v_s \quad [8]$$

Table III. Viscosity of the solvent and limiting molar ionic conductivities of some ions in PC-DME mixed system

| DME conc. (v/o) | η_0 (cP) | λ^∞ ($\Omega^{-1} \text{ cm}^2 \text{ mol}^{-1}$) | | | | | | | | | |
|-----------------|---------------|--|-----------------|----------------|------------------------------|--|-------------------------------|-----------------|-----------------|------------------------------|------------------------------|
| | | Li ⁺ | Na ⁺ | K ⁺ | NH ₄ ⁺ | (C ₂ H ₅) ₄ N ⁺ | ClO ₄ ⁻ | Cl ⁻ | Br ⁻ | BF ₄ ⁻ | PF ₆ ⁻ |
| 0 | 2.24 | 8.3 | 9.1 | 15.2 | 20.1 | 13.7 | 21.2 | 12.5 | 20.2 | 25.7 | 21.6 |
| 25 | 1.45 | 18.6 | 20.0 | 22.5 | 27.1 | 22.4 | 26.8 | 18.4 | 22.8 | 30.4 | 21.8 |
| 50 | 0.94 | 27.2 | 29.9 | 36.2 | 31.0 | 32.4 | 36.0 | 20.3 | 26.8 | 36.6 | 27.8 |
| 75 | 0.62 | 44.2 | 44.8 | 41.8 | 43.4 | 39.2 | 47.8 | — | 28.8 | 44.4 | 37.8 |

Table IV. Stokes' radii of some ions in PC-DME mixed system

| DME conc. (v/o) | R_s (nm) | | | | | | | | | |
|-----------------|-----------------|-----------------|----------------|------------------------------|--|-------------------------------|-----------------|-----------------|------------------------------|------------------------------|
| | Li ⁺ | Na ⁺ | K ⁺ | NH ₄ ⁺ | (C ₂ H ₅) ₄ N ⁺ | ClO ₄ ⁻ | Cl ⁻ | Br ⁻ | BF ₄ ⁻ | PF ₆ ⁻ |
| 0 | 0.48 | 0.46 | 0.36 | 0.32 | (0.40)** | 0.31 | 0.41 | 0.32 | 0.28 | 0.31 |
| 25 | 0.41 | 0.40 | 0.38 | 0.35 | 0.39 | 0.35 | 0.42 | 0.38 | 0.32 | 0.39 |
| 50 | 0.42 | 0.41 | 0.37 | 0.40 | 0.40 | 0.37 | 0.47 | 0.42 | 0.37 | 0.42 |
| 75 | 0.41 | 0.41 | 0.42 | 0.42 | 0.43 | 0.40 | — | 0.49 | 0.41 | 0.44 |
| R_c (nm)* | 0.060 | 0.095 | 0.133 | 0.148 | 0.400 | 0.200 | 0.181 | 0.195 | — | — |

* Crystallographic ionic radius.
 ** By the assumption in Ref. (12).

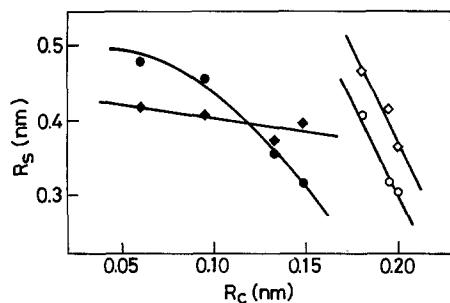


Fig. 3. Correlation between crystallographic ionic radius (R_c) and Stokes' radius (R_s). Open symbols, anion; closed symbols, cation. \circ , \bullet : in PC, \diamond , \blacklozenge : in PC + DME (1:1).

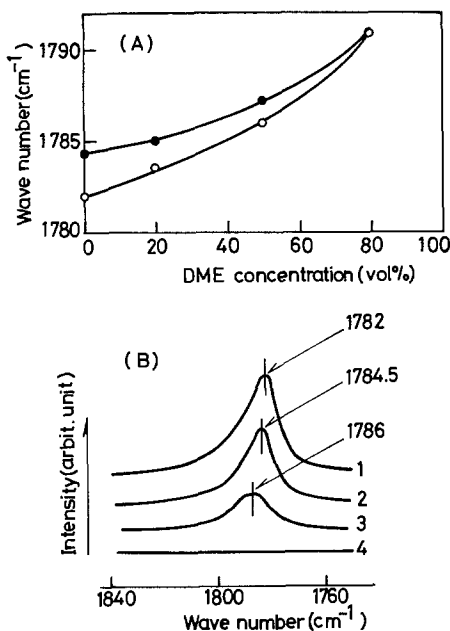


Fig. 4. C = O stretching band in PC-DME-LiClO₄ system. (A) Wave number of the band as a function of the solvent composition, \circ : solvent, \bullet : solution of 1 mol · dm⁻³ LiClO₄. (B) Variation of the band, 1: PC, 2: PC + 1 mol · dm⁻³ LiClO₄, 3: PC + DME (1:1), 4: DME.

where v_s is the molecular volume of the solvent, being considered to be 0.142 nm³ for PC and 0.174 nm³ for DME based on molecular weight and density. It was assumed in the calculation that the cations are solvated preferentially with DME in the mixed solvents owing to the reason explained later, while the anions are solvated with PC and DME in the same ratio as the bulk composition of the solvent. The data of R_s shown in Table IV represent the validity of this assumption. The resulting solvation numbers of the ions are summarized in Table V. The slight increase in N_s of the anions with the DME content may be associated with the decrease in the dielectric constant of the solvent (8). Among the cations, Li⁺ and Na⁺ ions seem to be highly subject to the specific solvation with DME in the mixed solvents. Their solvation numbers greatly

Table V. Solvation number

| DME conc. (v/o) | N_s | | | | | | | |
|-----------------|-----------------|-----------------|----------------|------------------------------|--|-------------------------------|-----------------|-----------------|
| | Li ⁺ | Na ⁺ | K ⁺ | NH ₄ ⁺ | (C ₂ H ₅) ₄ N ⁺ | ClO ₄ ⁻ | Cl ⁻ | Br ⁻ |
| 0 | 3.2 | 2.8 | 1.3 | 0.9 | (0)* | 0.6 | 2.2 | 0.7 |
| 25** | 1.7 | 1.5 | 1.3 | 1.0 | 0.0 | 1.0 | 1.9 | 1.3 |
| 50** | 1.8 | 1.6 | 1.2 | 1.4 | 0.0 | 1.1 | 2.6 | 1.8 |
| 75** | 1.7 | 1.6 | 1.7 | 1.7 | 0.4 | 1.4 | — | 2.8 |

* By the assumption in Ref. (12).

** For the specific solvation of cations with DME.

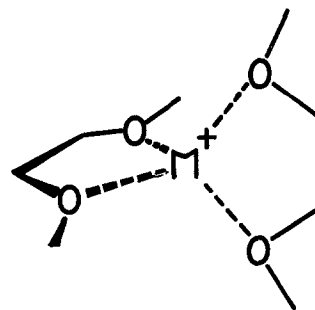


Fig. 5. A model for specifically solvated cation with two molecules of DME.

decrease with mixing DME into PC, and those in the mixed solvents are almost constant in the range of 25-75% DME. The specific solvation of the cations with larger R_c (K⁺ and NH₄⁺) is relatively weak. These phenomena would be caused by not only an electrostatic circumstance but also a spatial relation between the ion and the solvent molecule.

It may not be so general for ions to be solvated selectively with such molecules having lower dielectric constant as DME in the PC-DME mixed solvents ($\epsilon_r = 64.4$ for PC, 7.2 for DME). However, the present case seems to be analogous to that in the specific solvation of Li⁺ ion with THF (14, 15). A scheme presented in Fig. 5 is proposed as a model for the specific solvation with DME, suggesting the stability of alkali metal cations captured by crown ethers in PC solvent (16). The specific solvation with DME would result from the strong coordinate bond by two oxygen atoms whose configuration is spatially significant. In the present work, however, any definitive evidence by the spectroscopic method was not obtained concerning the direct interaction between the cation and the oxygen atoms of DME. According to the stereochemistry of DME, the number of the molecules solvating a cation must be less than two as shown in Table V. For the cations with larger ionic size, K⁺ and NH₄⁺, therefore, the coordination of DME becomes weak to give a poorer specific solvation. Consequently, the specific solvation of cations with DME, decreasing their Stokes' radii, contributes to the improvement in the conductivity of the PC-DME mixed solutions of LiClO₄ and NaClO₄. That is, the ionic mobility, or the ionic conductivity, of Li⁺ and Na⁺ in the PC-DME mixed solvent is increased because of the relatively small radius of the solvated ion, as well as owing to the suitable viscosity and dielectric constant of the solvent.

Acknowledgments

The authors wish to thank Professor K. Yoshihara and Mr. T. Murao of the Institute for Molecular Science for the use of laser Raman spectrometer and useful discussions. Also, they are grateful to the Grants in Aid for Scientific Research by Japan Ministry of Education (No. 505577 and 555313) for partial support of this research.

Manuscript submitted Feb. 17, 1981; revised manuscript received June 19, 1981.

Any discussion of this paper will appear in a Discussion Section to be published in the June 1982 JOURNAL. All discussions for the June 1982 Discussion Section should be submitted by Feb. 1, 1982.

Publication costs of this article were assisted by Yamaguchi University.

REFERENCES

- H. Ikeda, T. Saito, and H. Tamura, *Denki Kagaku*, **45**, 314 (1977).
- H. Ikeda, S. Ueno, T. Saito, S. Nakaido, and H. Tamura, *ibid.*, **45**, 391 (1977).
- K. Nakamura, T. Iijima, and M. Fukuda, Preprint of 16th Battery Symposium, Japan, p. 46 (1975).
- R. Jasinski, *Electrochem. Technol.*, **6**, 28 (1968).

5. T. Saito, H. Ikeda, Y. Matsuda, and H. Tamura, *J. Appl. Electrochem.*, **6**, 85 (1976).
6. Y. Matsuda, Extended Abstract of 3rd Japan-USSR Seminar on Electrochemistry, p. 173 (1978).
7. Y. Matsuda and H. Satake, *Denki Kagaku*, **47**, 743 (1979).
8. Y. Matsuda and H. Satake, *This Journal*, **127**, 877 (1980).
9. Y. Matsuda, Y. Ouchi, and H. Tamura, *J. Appl. Electrochem.*, **4**, 53 (1974).
10. E. Koizumi and S. Ouchi, *Nippon Kagaku Zasshi*, **91**, 510 (1970).
11. J. P. Hoare and C. R. Wiese, *This Journal*, **121**, 83 (1974).
12. R. A. Robinson and R. H. Stokes, "Electrolyte Solutions," p. 124, Butterworths, London (1959).
13. C. M. Criss and M. Salomon, in "Physical Chemistry of Organic Solvent Systems," A. K. Covington and T. Dickinson, Editors, Chap. 2, p. 261, Plenum Press, London (1973).
14. R. Fernández-Prini, in "Physical Chemistry of Organic Solvent Systems," A. K. Covington and T. Dickinson, Editors, Chap. 5, p. 525, Plenum Press, London (1973).
15. C. N. Hammonds and M. C. Day, *J. Phys. Chem.*, **73**, 115 (1969).
16. Y. Takeda, H. Yano, M. Ishibashi, and H. Isozumi, *Bull. Chem. Soc. Jpn.*, **53**, 72 (1980).

Electrochemical Nitration of Aromatic Hydrocarbons in Aprotic Media

J. M. Achord and C. L. Hussey*

Department of Chemistry, The University of Mississippi, University, Mississippi 38677

ABSTRACT

The electrochemical nitration of anthracene, naphthalene, 1-nitronaphthalene, and toluene was examined in aprotic solvents. Controlled potential electrolysis of anthracene in acetonitrile containing tetra-*n*-butylammonium nitrite resulted in low yields of 9-nitroanthracene. Oxidation of naphthalene in acetonitrile containing N_2O_4 at potentials insufficient to oxidize N_2O_4 resulted in high yields of 1-nitronaphthalene, while electrolysis of naphthalene at potentials sufficient to oxidize N_2O_4 resulted in moderate yields of dinitronaphthalenes. Similar experiments involving cooxidation of N_2O_4 and toluene gave moderate yields of 2- and 4-nitrotoluene in both acetonitrile and nitromethane. Nitronium ion was electrogenerated and used to effect nitration of toluene and 1-nitronaphthalene in acetonitrile. The nitrotoluene isomer distributions obtained were similar to those observed during nitration of toluene with nitronium salts. The results obtained during coelectrolysis of either 1-nitronaphthalene or toluene with N_2O_4 were interpreted in terms of electrophilic attack by nitronium ion solvated via electrolytically generated acid. Coelectrolysis of tetra-*n*-butylammonium nitrate and toluene in acetonitrile and nitromethane did not produce nitrated products. However, electrolysis of solutions of $LiNO_3$ and toluene in nitromethane gave low yields of mononitrotoluenes. Rotating disk measurements of the oxidation half-wave potentials of several nitroaromatic hydrocarbons are presented.

Several investigators have demonstrated that it is possible to electrochemically induce the nitration of aromatic hydrocarbons in aprotic media (1-5). Electrochemical nitration experiments have resulted in products which suggest direct nitration of the aromatic ring (1-5) and nitration of the alkyl side chain on alkyl substituted aromatic hydrocarbons (2). A variety of solvents, supporting electrolytes, and nitrating agents have been employed for these studies. However, the general approach used in most electrochemical nitration experiments was similar. The aromatic hydrocarbon to be nitrated was oxidized anodically in aprotic solvents that contained either dissolved nitrite or nitrate salts, or dinitrogen tetroxide.

A number of aromatic hydrocarbons have been successfully nitrated by means of these electrochemical nitration procedures. Oxidation of anthracene at a platinum anode in molten tetra-*n*-butylammonium nitrate resulted in the formation of 9-nitroanthracene, 1,10-dinitroanthracene, and 9,10-dinitroanthracene (1). Electrolytic oxidation of mesitylene at a platinum electrode in nitromethane containing tetra-*n*-butylammonium nitrate gave 2-nitromesitylene and 3,5-dimethylbenzyl nitrate (2). Electrolysis of naphthalene at a carbon anode in this same solvent and supporting

electrolyte resulted in small amounts of 1-nitronaphthalene (2). Electrochemical oxidation of anthracene, anisole, *N,N*-dimethylaniline, naphthalene, trimethoxybenzene, and several dimethoxybenzenes in acetonitrile containing $AgNO_2$ yielded mononitro ring substituted products (3). Both 1- and 2-nitronaphthalene, the latter in small quantities, were obtained when naphthalene was oxidized at platinum electrodes in acetonitrile containing N_2O_4 (4, 5).

Two different mechanisms have been suggested to account for the nitrated products obtained during electrochemical nitration experiments involving oxidation of aromatic hydrocarbons in solutions containing NO_2^- and N_2O_4 . These mechanisms include reaction of the electrogenerated aromatic hydrocarbon radical cation with NO_2 radical (3, 4) and homogeneous acid catalyzed nitration of the aromatic hydrocarbon by anodically generated acid (5). Nitrated products arising from experiments involving NO_3^- ion in aprotic solvents have been attributed to electrophilic attack by electrogenerated NO_2^+ ion or reactions involving NO_3^- radical (2).

The electrochemically induced nitration of several aromatic hydrocarbons was studied in acetonitrile and nitromethane containing either NO_2^- , $NO_2(N_2O_4)$, or NO_3^- . This study was undertaken in order to gain additional insight into the mechanistic aspects and

* Electrochemical Society Active Member.

Key words: organic, free radicals, electrolysis, synthesis.

synthetic utility of electrochemical nitration procedures. The results of this investigation are reported in this paper.

Experimental

Chemicals.—Anthracene and naphthalene (Fisher ACS Certified Reagents) were recrystallized before use. 1-Nitronaphthalene (Aldrich) and toluene (Fisher ACS Certified Reagent) were used without further treatment. Spectrophotometric grade acetonitrile, MeCN, (Burdick and Jackson) was stored over 3A molecular sieve (Linde) and passed through a column containing fresh molecular sieve and activated alumina directly into the electrolysis cell. Further attempts to purify this solvent resulted in degradation of its quality. Spectrophotometric grade nitromethane, MeNO₂, (Aldrich, Gold Label) was stored over molecular sieve prior to use. The supporting electrolyte, tetra-*n*-butylammonium hexafluorophosphate, TBAFP, was synthesized and purified according to standard procedures. Dinitrogen tetroxide, N₂O₄, (Matheson 99.5%) was contaminated with N₂O₃ as received. The green N₂O₃ contaminant was eliminated by passing dry oxygen gas through the chilled, liquified N₂O₄ until a golden brown color was obtained. Appropriate amounts of N₂O₄ were introduced volumetrically into the electrolysis cell. For simplicity the amount of N₂O₄ used in each experiment is denoted by the NO₂ formal concentration. Lithium nitrate, LiNO₃, (J. T. Baker, reagent), tetra-*n*-butylammonium nitrate, TBANO₃, (Fluka, purum), and tetra-*n*-butylammonium nitrite, TBANO₂, (Fluka, purum) were dried at 70°C under vacuum for 24 hr.

Instrumentation.—Voltammetric oxidation half-wave potential measurements were made using an AMEL Model 552 potentiostat programmed by means of an AMEL Model 566 function generator. Current potential curves were recorded on a Houston Model 100 X-Y recorder. Controlled electrode rotation was provided by means of a Pine Instruments Model ASR electrode rotator. The cell and electrodes used for these measurements were very similar to those detailed in a previous publication (6), except that the glassy carbon working electrode was provided with a longer shaft. Potentials are reported with respect to an Ag/Ag⁺ (0.01M) reference electrode isolated from the bulk solution via a Vycor plug. The cell was thermostated to 25.0 ± 0.2°C in a water bath.

Controlled potential electrolysis experiments were coulometrically monitored by coupling the potentiostat to an AMEL Model 731 digital integrator. A three-electrode sealed cell of conventional design with a working volume of approximately 60 ml was used during these experiments. The working electrode was a platinum gauze basket and the counterelectrode was a platinum wire spiral separated from the working electrode compartment via a fine porosity fritted disk. Solutions were prepared and the cell was filled and sealed in a nitrogen atmosphere in a KSE dry box equipped with a 3 CFM inert gas purifier.

Product identification and analysis.—Products arising from electrochemical nitration experiments were analyzed using gas-liquid chromatography (GLC). Gas chromatographic analyses were performed using a Hewlett-Packard Model 5710A gas chromatograph equipped with a flame ionization detector. The chromatograph was furnished with 1m × ¼ in. copper columns packed with 8% OV-3 on Gas Chrom-Z. It was operated over a temperature range of 80°-280°C with helium carrier gas. Products resulting from experiments involving naphthalene were analyzed also using a Waters Associates liquid chromatograph equipped with a u.v. detector operated at 254 nm. The liquid chromatograph contained a Whatman Partisil PXS column and employed a mobile phase of 92% cyclohexane-8% ethyl acetate (v/v). The iden-

tity of all reported products was confirmed by comparison of their mass spectra and chromatographic retention properties with those of authentic samples. A Hewlett-Packard Model 5985 gas chromatograph/mass spectrometer system was used to obtain mass spectra.

Results

Electrolysis of anthracene and TBANO₂ in MeCN.—Solutions of anthracene (0.05M) and TBANO₂ (0.1M) in MeCN containing 0.1M TBAFP were electrolyzed at 1.2V vs. Ag/Ag⁺ following the procedure of Laurent *et al.* (3). The applied potential was sufficient to oxidize both anthracene and TBANO₂ (Table I). Large bubbles of brown NO₂ gas were produced at the cell anode and high currents were observed. The former observation is consistent with data which indicate that NO₂ is a product of the oxidation of NO₂⁻ in aprotic solvents (10, 11). Controlled potential electrolysis was continued until approximately 1.0F of charge per mole of anthracene was passed. The resulting solution was yellow and GLC analysis revealed that some anthracene had been converted to 9-nitroanthracene in low yield, ca. 1.2%. The overall results obtained using anthracene and TBANO₂ were very similar to those reported by Laurent *et al.* (3) for controlled potential electrolysis of anthracene and AgNO₂ in MeCN. The copious quantities of NO₂ gas formed at the anode frequently interrupted electrical contact between the working electrode and the counterelectrode during electrolysis. As a result, this nitration procedure was found difficult to control and was not further investigated.

Electrolysis of naphthalene and N₂O₄ in MeCN.—Controlled potential electrolysis experiments were performed on solutions of naphthalene and N₂O₄ (0.1M) in MeCN containing 0.1M TBAFP. These experiments were conducted as a function of naphthalene concentration, applied potential, and charge passed. The results that were obtained during these studies are most conveniently described in terms of the applied potential employed, since the distribution and composition of products obtained were markedly dependent on the applied potential.

Potentials below approximately 1.75V resulted in the formation of 1-nitronaphthalene in comparatively high yields (Table II). Small amounts of 2-nitronaphthalene could also be detected. The ratio of 1-nitro- to 2-nitronaphthalene was approximately 17 ± 3. The potential used for these experiments, 1.50V, was sufficient to oxidize naphthalene (Table I), but insufficient to oxidize N₂O₄. Figure 1 shows a plot of the percent yield based on the current of 1-nitronaphthalene prod-

Table I. Voltammetric oxidation half-wave potentials^a

| Compound | E _{1/2} ^b (V) | Ref. |
|---|---------------------------------------|-----------|
| Anthracene | 0.84 ^c | (7) |
| Anthracene | 1.12 ± 0.02 | This work |
| 1,5-dinitronaphthalene | 2.07 ± 0.01 | This work |
| 1,8-dinitronaphthalene | 2.05 ± 0.01 | This work |
| LiNO ₃ | 1.77 ^c | (8) |
| Naphthalene | 1.34 ^c , 1.31 ^c | (7) |
| Naphthalene | 1.33 ± 0.01 | This work |
| NO ₂ (N ₂ O ₄) ^d | 1.82 | (4) |
| 1-nitronaphthalene | 1.62 ^c | (9) |
| 1-nitronaphthalene | 1.81 ± 0.02 | This work |
| 2-nitrotoluene | 2.20 ± 0.02 | This work |
| 4-nitrotoluene | 2.22 ± 0.02 | This work |
| TBANO ₂ | 0.58 | This work |
| TBANO ₃ | 1.76 ^c | (8) |
| Toluene | 1.98 ^c , 1.93 ^c | (7) |
| Toluene | 1.85 ± 0.01 | This work |

^a Oxidation half-wave potentials were estimated from current-voltage curves obtained for the compound of interest at a glassy carbon electrode rotating at 3.98 rad sec⁻¹ in MeCN containing 0.1M TBAFP.

^b Unless otherwise noted, potentials are reported vs. the Ag/Ag⁺ (0.01M) reference electrode.

^c vs. Ag/Ag⁺ (0.1M).

^d N₂O₄ is the species oxidized at this potential.

Table II. Results for electrochemical nitration of naphthalenes

| Starting material ^a | Conc. (M) | E (V) | Charge passed ^b (%) | % Yield nitronaphthalenes ^c | | |
|--------------------------------|-----------|-------|--------------------------------|--|------|------|
| | | | | 1- | 1,5- | 1,8- |
| Naphthalene | 0.025 | 1.50 | 100 | 91 | — | — |
| Naphthalene | 0.050 | 1.50 | 100 | 64 | — | — |
| Naphthalene | 0.100 | 1.50 | 100 | 92 | — | — |
| Naphthalene | 0.050 | 1.75 | 100 | 40 | 12 | 10 |
| Naphthalene | 0.025 | 2.00 | 100 | 19 | 15 | 13 |
| Naphthalene | 0.050 | 2.00 | 100 | 32 | 20 | 18 |
| Naphthalene | 0.050 | 2.00 | 200 | — | 28 | 26 |
| Naphthalene | 0.100 | 2.00 | 100 | 79 | 2 | 1 |
| 1-Nitronaphthalene | 0.050 | 2.00 | 100 | — | 20 | 21 |
| Naphthalene | 0.050 | 2.50 | 100 | 13 | 24 | 22 |

^a Experiments were conducted in MeCN containing 0.2M NO₂ and 0.1M TBAFP.

^b 100% of the charge passed is equivalent to 1.0 F/mol of starting material.

^c Based on the amount of starting material.

uct obtained *vs.* the charge passed, where 100% of the charge is equivalent to 1.0F of charge per mol of naphthalene. Data with which to construct this plot were obtained by periodically analyzing small samples of solution by GLC taken from the working electrode compartment of the cell during the course of several electrolysis experiments.

Figure 1 indicates that the production of 1-nitronaphthalene under the conditions employed outruns the percentage of charge passed through the cell, *i.e.*, the formation of 1-nitronaphthalene from naphthalene is essentially complete after only a small fraction of the charge necessary to effect the one-electron oxidation of naphthalene has been provided. The role of adventitious water added to the electrolysis cell was also examined. It is significant from a practical synthetic viewpoint that the quantity of water introduced into the MeCN used in these experiments is not deleterious to the formation of 1-nitronaphthalene, at least within the concentration range studied (Fig. 1).

Formation of dinitronaphthalenes.—Controlled potential electrolysis of solutions of naphthalene and N₂O₄ in MeCN at potentials equal to or exceeding 1.75V resulted in the formation of 1-nitronaphthalene, 1,5-dinitronaphthalene, and 1,8-dinitronaphthalene (Table II). Small amounts of 2,3-dinitronaphthalene were also detected, but the yield of this material was always less than 2%. A significant amount of intractable, tarry

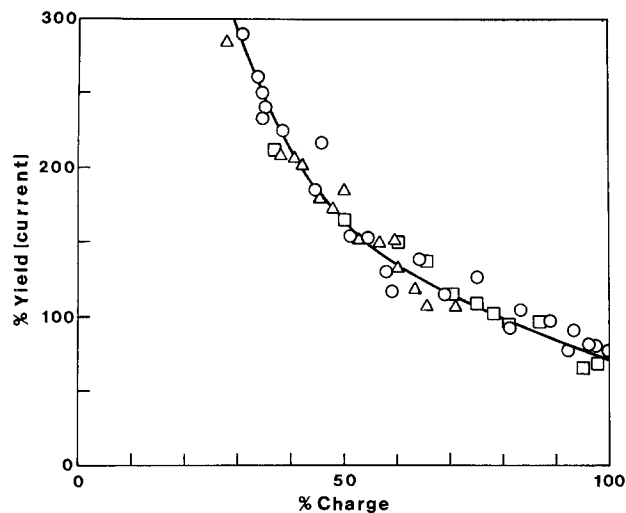


Fig. 1. Variation of the current yield of 1-nitronaphthalene with the charge passed during electrolysis of a solution of N₂O₄ (0.1M) and naphthalene (0.025M) in MeCN + 0.1M TBAFP at 1.50V vs. Ag/Ag⁺ (0.01M). ○, MeCN containing ca. 6 × 10⁻³M H₂O; □, MeCN containing ca. 2 × 10⁻²M H₂O; △, MeCN containing less than 6 × 10⁻³M H₂O.

material could also be isolated during these experiments. However, attempts to identify or further characterize this material were unsuccessful. The yield of dinitronaphthalene products obtained after passage of 1.0F of charge per mol of naphthalene appears optimum when the naphthalene concentration is approximately 25% of the NO₂ formal concentration. Further electrolysis until 2.0F of charge per mol of naphthalene are provided somewhat improves the overall material yield of dinitronaphthalenes. The amount of dinitronaphthalene compounds formed at a fixed ratio of naphthalene to NO₂ increased with the applied potential. The distribution of dinitronaphthalene isomers obtained from the electrochemical nitration of naphthalene, *ca.* 52% 1,5- and 48% 1,8-, is distinctly different than that observed for most chemical nitrations, approximately 33% 1,5- and 67% 1,8- (12). The dinitronaphthalene isomer distribution observed did not change appreciably with the applied potential over the potential range investigated.

The data collected in Table I indicate that potentials equal to or greater than 1.75V are sufficient to oxidize both naphthalene and N₂O₄. Furthermore the dinitronaphthalene products obtained would appear to originate by a mechanism that is at least in part different than that which results in mononitronaphthalenes. Evidence to support a nitration mechanism that is different than the process which produces mononitronaphthalenes can be obtained from Fig. 2. This figure shows plots of the material yield of 1-nitronaphthalene and the combined material yields of 1,5- and 1,8-dinitronaphthalene *vs.* the percent charge passed during a controlled potential electrolysis experiment at 2.25V. Data with which to construct these plots were obtained in the same manner as was the data used to construct Fig. 1.

Examination of Fig. 2 reveals that 1-nitronaphthalene is rapidly formed from naphthalene in the same fashion as was described in the previous section. The formation of dinitronaphthalene products, which appear after approximately 75% of the charge has been passed based on 1.0F of charge per mol of naphthalene, appears closely associated with the cumulative

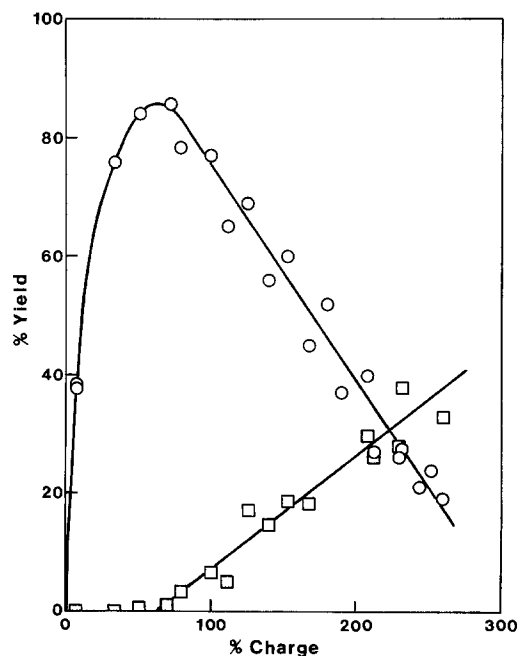


Fig. 2. Dependence of the material yield of 1-nitronaphthalene and dinitronaphthalenes on the charge passed during electrolysis of a solution of N₂O₄ (0.1M) and naphthalene (0.025M) in MeCN + 0.1M TBAFP at 2.25V vs. Ag/Ag⁺ (0.01M). ○, 1-nitronaphthalene; □, dinitronaphthalenes.

electrolysis process. The plots shown in Fig. 2 suggest that the dinitration of naphthalene proceeds through rapid, intermediate formation of 1-nitronaphthalene in high yield. This step is followed by a slower nitration process, which results in the formation of dinitronaphthalenes concurrent with the disappearance of 1-nitronaphthalene. The absolute value of the slope of the descending portion of the plot for the oxidation of 1-nitronaphthalene at 2.25V, 0.33, indicates that a substantial portion of the charge passed involves the oxidation of solute species other than 1-nitronaphthalene, e.g., N_2O_4 . The ascending portion of the plot for formation of dinitronaphthalenes was slightly smaller, 0.20. If it is assumed that the oxidation of 1-nitronaphthalene is essential to the formation of dinitronaphthalenes, then the oxidation of 1-nitronaphthalene does not correspond to the formation of dinitronaphthalenes with 100% efficiency. A parasitic process, most likely oxidation of 1-nitronaphthalene to give high molecular weight materials (5, 13, 14) probably takes place. It was also possible to obtain a ratio and yield of 1,5- and 1,8-dinitronaphthalenes by controlled potential electrolysis of solutions of 1-nitronaphthalene and N_2O_4 in MeCN which were similar, within experimental error, to that obtained from electrolysis of solutions containing naphthalene and N_2O_4 (Table II).

Electrolysis of toluene and N_2O_4 in MeCN and MeNO₂.—Electrolysis experiments were conducted with solutions of toluene and N_2O_4 in MeCN and MeNO₂ to obtain additional information about electrochemical nitration processes utilizing N_2O_4 . Controlled potential electrolysis experiments at potentials equal to or in excess of 1.75V resulted in the formation of 2- and 4-nitrotoluene (Table III) and small amounts of 3-nitrotoluene. The yield of the latter was less than 3%. The yield of 2- and 4-nitrotoluenes obtained varied with the applied potential (Table III). Controlled potential electrolysis experiments were conducted at 2.00V with solutions of toluene and N_2O_4 in MeCN to which a small amount of water had been added. The results obtained (Table III) indicate that water exerts a slight retarding effect on the formation of nitrotoluene products. An electrolysis experiment was conducted with toluene and N_2O_4 dissolved in MeNO₂ at an applied potential of 2.00V. The results of this experiment, shown in Table III, were generally the same as those obtained using MeCN as the solvent, but the combined yields of nitrotoluenes were less than observed with MeCN under the same conditions, e.g., 39% for MeCN vs. 26% for MeNO₂. The isomer distribution for the nitrotoluenes produced during the electrolysis experiments reported in this section, ca. 60% 2- and 40% 4-nitrotoluene, was comparable to that reported for chemical nitration of toluene (15). It did not change within experimental

Table III. Results for electrochemical nitration of toluene

| Electrolysis medium ^a | E (V) | Charge passed ^b (%) | % Yield nitrotoluenes ^c | |
|---|-------|--------------------------------|------------------------------------|----|
| | | | 2- | 4- |
| 0.2M NO ₂ in MeCN | 1.75 | 100 | 23 | 14 |
| 0.2M NO ₂ in MeCN | 2.00 | 100 | 23 | 16 |
| 0.2M NO ₂ in MeCN | 2.00 | 200 | 34 | 22 |
| 0.2M NO ₂ + 0.02M H ₂ O in MeCN | 2.00 | 100 | 20 | 13 |
| 0.2M NO ₂ in MeNO ₂ | 2.00 | 100 | 15 | 11 |
| 0.2M NO ₂ in MeCN | 2.50 | 100 | 27 | 18 |
| 0.2M NO ₂ in MeCN | 2.50 | 200 | 36 | 25 |
| 0.04M LiNO ₃ in MeCN | 2.50 | 100 | — | — |
| 0.04M LiNO ₃ in MeNO ₂ | 2.50 | 100 | 6 | 4 |

^a Solutions were 0.05M in toluene and 0.1M in TBAFP.

^b 100% of the charge passed is equivalent to 1.0 F/mol of starting material.

^c Based on the amount of starting material.

error over the potential region investigated.

Applied potentials of 1.75V or greater were sufficient to oxidize both toluene and N_2O_4 . Furthermore, the $E_{1/2}$ value for toluene oxidation is similar to that for oxidation of 1-nitronaphthalene (Table I). On this basis the electrolysis process by which nitrotoluenes are formed would be expected to be similar to that by which dinitronaphthalenes are produced from 1-nitronaphthalene. Figure 3 shows a plot of the percent yield as a function of the charge passed during controlled potential electrolysis experiments at 2.00V. The formation of nitrotoluenes during these experiments, albeit somewhat inefficient, nevertheless closely follows the cumulative charge passed in a manner similar to that observed during electrolysis experiments in which dinitronaphthalenes are formed (Fig. 2). The slope of this plot, 0.30, was similar to that observed during formation of dinitronaphthalenes.

Electrogenerated NO₂⁺ ion in MeCN.—Cauquis and Serve (16) report that NO₂ undergoes a one-electron oxidation to NO₂⁺ ion in aprotic solvents. Solutions of NO₂⁺ in dry MeCN are known to exhibit considerable stability (17). Controlled potential electrolysis at an applied potential of 2.00V was performed on solutions of N_2O_4 (0.1M) in MeCN that did not contain aromatic hydrocarbons to examine the possibility of effecting nitration with electrochemically generated NO₂⁺ ion. Toluene and 1-nitronaphthalene were added to electrolyzed solutions of N_2O_4 in MeCN in separate experiments after the applied potential was discontinued. Dinitronaphthalenes and mononitrotoluenes formed in these solutions were monitored as a function of time using GLC. A plot of the combined yields of dinitronaphthalenes and mononitrotoluenes vs. elapsed time is shown in Fig. 4. Data used to construct this plot were obtained after passage of 1.0F of charge per mol of 1-nitronaphthalene or toluene added after cessation of the electrolysis. The reaction of both toluene and naphthalene with electrogenerated NO₂⁺ ion appeared rapid during the first few minutes and then slowed

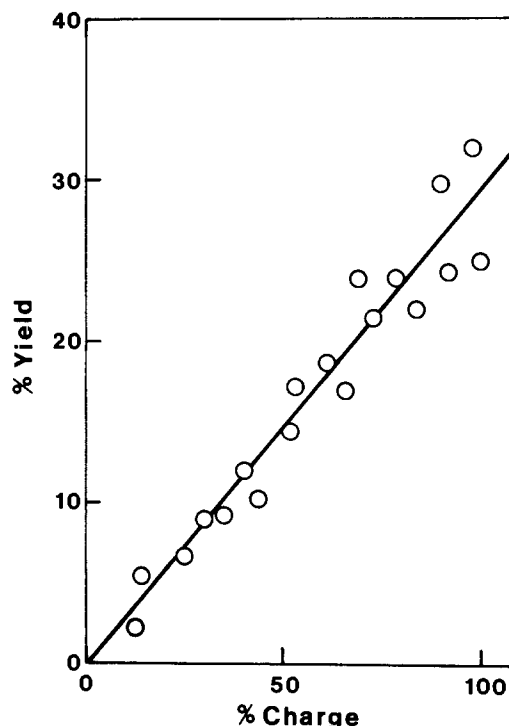


Fig. 3. Material yield of mononitrotoluenes as a function of charge passed during electrolysis of a solution of N_2O_4 (0.1M) and toluene (0.05M) in MeCN + 0.1M TBAFP at 2.00V vs. Ag/Ag⁺ (0.01M).

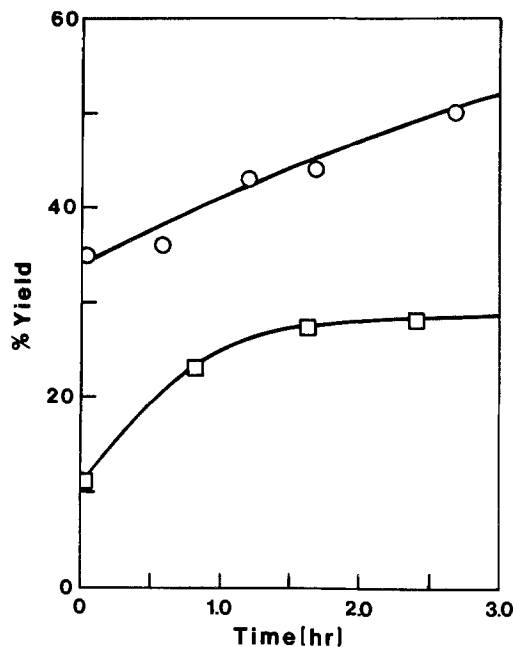


Fig. 4. Variation of the yield of nitrotoluenes and dinitronaphthalenes with time after the addition of toluene and 1-nitronaphthalene to solutions of N_2O_4 (0.1M) in MeCN + 0.1M TBAFP that were electrolyzed at 2.00V vs. Ag/Ag⁺ (0.01M). ○, dinitronaphthalenes; □, nitrotoluenes.

considerably as time progressed. The nitrotoluene isomer distribution obtained from this experiment was 67% 2-nitrotoluene and 33% 4-nitrotoluene. It was in excellent agreement with values reported for nitronium salt nitrations of toluene (15). The quantity of 3-nitrotoluene formed during these experiments was not subjected to detailed examination. However the amount produced appeared to be very small. The nitration of 1-nitronaphthalene by the same procedure resulted in a dinitronaphthalene isomer distribution of approximately 39% 1,5- and 61% 1,8-dinitronaphthalene. Unfortunately there appears to be a paucity of literature data concerning the dinitronaphthalene isomer distribution resulting from nitronium salt nitrations of 1-nitronaphthalene with which to compare this data. The yield of dinitronaphthalene products obtained after 3 hr was slightly greater than observed during cooxidation of naphthalene with N_2O_4 .

Electrolysis of toluene and NO_3^- in MeCN and MeNO₂.—The anodic oxidation of NO_3^- ion in aprotic solvents has been studied by several investigators (8, 18-20). Although there is some argument as to the actual mechanism by which NO_3^- ion is oxidized, most workers suggest that species like NO_2^+ , NO_3^+ , or N_2O_5 may be formed during the oxidation process. Electrochemical nitration experiments were conducted on solutions of toluene and NO_3^- in both MeCN and MeNO₂ at applied potentials of 2.00V to examine the nitration capability of these solutions during oxidation of NO_3^- . The applied potential employed was sufficient to oxidize both NO_3^- and toluene (Table I).

The results of these experiments were highly dependent on the source of NO_3^- and the solvent chosen. For example, the use of TBANO₃ as the source of NO_3^- in electrolysis experiments conducted in both MeCN and MeNO₂ did not result in the formation of nitrotoluenes. When solutions of toluene in MeNO₂ were saturated with LiNO₃ and electrolyzed at 2.00V small amounts of 2- and 4-nitrotoluene could be detected (Table III). The isomer distribution of nitrotoluenes formed was 60% 2- and 40% 4-nitrotoluene. Mononitrotoluenes were not observed when similar solutions of toluene and LiNO₃ in MeCN were electrolyzed at 2.00V. The yield of nitrotoluenes obtained

during these experiments was generally very inferior to that found during experiments with N_2O_4 . Significant quantities of low boiling compounds were observed with GLC after coelectrolysis of NO_3^- ion and toluene in MeCN and MeNO₂. It is quite likely that the NO_3^- oxidation products attack the solvent or supporting electrolyte to produce these species. Similar effects have been reported during oxidation of NO_3^- in MeCN (8).

Discussion

Information obtained during the present study concerning the formation of 1-nitronaphthalene from naphthalene and N_2O_4 during electrolysis supports the acid catalyzed homogeneous nitration mechanism proposed by Ebersson *et al.* (5). It is obvious that 1-nitronaphthalene is formed during electrolysis experiments by a rapid nitration reaction that is independent of the cumulative charge. A similar type of process is probably responsible for the formation of 9-nitroanthracene during the electrolysis of anthracene and TBANO₂ in MeCN, since the experimental conditions are fundamentally the same as those employed during oxidation of aromatic hydrocarbons in solutions containing NO_2 . It is also quite likely that at least some of the products reported by Laurent *et al.* (3) arise through a similar mechanism.

The process or agent responsible for the production of dinitronaphthalenes and nitrotoluenes during electrolysis experiments involving cooxidation of the parent hydrocarbon and N_2O_4 appears different from that proposed by Ebersson *et al.* (5). The formation of these products seems closely associated with the direct electrolytic production of the active nitrating species. If dinitronaphthalenes originated via the same route that produces 1-nitronaphthalene, then formation of dinitronaphthalenes in significant quantities would be expected concurrent with the production of 1-nitronaphthalene during experiments at 1.50V. However, applied potentials of 1.75V and above are requisite to effect nitration of aromatic hydrocarbons less reactive than naphthalene.

It is interesting to speculate about the process which results in the formation of dinitronaphthalenes and nitrotoluenes during coelectrolysis of the parent hydrocarbon and N_2O_4 . It has been demonstrated that nitronium ion can be electrogenerated in MeCN containing N_2O_4 at potentials above 1.75V and used to nitrate toluene and 1-nitronaphthalene. The nitrotoluene isomer distribution obtained during this procedure was almost identical to that reported for nitration of toluene using NO_2PF_6 or NO_2BF_4 in sulfolane (Table IV). Nitronium salt nitration is thought to arise through electrophilic attack by NO_2^+ from an unsolvated ion pair, e.g., $NO_2^+PF_6^-$ (15, 21). The dinitronaphthalene and nitrotoluene isomer distributions that result

Table IV. Isomer distribution for toluene nitration

| Nitration system | Temp (°C) | Isomer distribution (%) | | | Ref. |
|--|-----------|-------------------------|-----|------|-----------|
| | | 2- | 3- | 4- | |
| 75% (v/v) HNO ₃ -H ₂ SO ₄ in sulfolane | 25 | 56.3 | 2.6 | 41.0 | (21) |
| 30% (v/v) HNO ₃ -H ₂ SO ₄ in sulfolane | 25 | 62.0 | 3.4 | 34.6 | (21) |
| NO ₂ BF ₄ in MeNO ₂ | 25 | 65.7 | 3.2 | 31.1 | (15) |
| NO ₂ PF ₆ in sulfolane | 25 | 67.6 | 1.4 | 31.0 | (15) |
| N ₂ O ₅ in sulfolane | 25 | 65.1 | 3.1 | 31.8 | (15) |
| Electrochemical (N ₂ O ₄ in MeCN, 2.00V) | 25 | 58 | ~2 | 40 | This work |
| Electrochemical (N ₂ O ₄ in MeNO ₂ , 2.00V) | 25 | 58 | — | 42 | This work |
| Electrochemical ^a (NO ₂ ⁺ in MeCN) | 25 | 67 | — | 33 | This work |

^a Toluene was added to a solution of electrogenerated NO₂⁺.

from coelectrolysis experiments suggest less positional selectivity for the nitrating species than attack by unsolvated nitronium ion. This could result from steric effects. Although $\text{NO}_2^+ \text{PF}_6^-$ ion pairs are anodically generated above 1.75V, the parent hydrocarbons are also oxidized. It is probable that hydrogen ion is also produced at the anode by one or more of the processes proposed by Ebersson *et al.* (5). Under these conditions the NO_2^+ ion may be solvated in some way by anodically generated acid. This would lead to an increase in size or bulkiness for this nitrating agent and account for steric factors which could decrease the quantity of 2-nitrotoluene and 1,8-dinitronaphthalene obtained during coelectrolysis experiments compared to experiments involving unsolvated nitronium ion. A similar solvation effect is known to decrease the quantity of 2-nitrotoluene obtained during nitration of toluene by NO_2^+ ion solvated in sulfuric acid (15, 21).

Although a direct comparison cannot be made, the yields of nitrated compounds obtained via electrochemical nitration of aromatic hydrocarbons in organic solvents containing N_2O_4 appear comparable to those reported for conventional chemical nitration processes. This is especially true when the quantity of nitrating reagents expended in the latter procedures are considered. Nitration of aromatic hydrocarbons by means of electrogenerated NO_2^+ ion also has interesting possibilities and is the subject of further investigation in this laboratory. The yields obtained in the present study for electrochemical nitration experiments utilizing either NO_2^- or NO_3^- ion were inferior to those obtained using N_2O_4 or electrogenerated NO_2^+ ion. The low yields obtained during experiments with NO_3^- ion preclude definitive information concerning the agent by which nitration occurs during concurrent oxidation of NO_3^- ion and aromatic hydrocarbons. However, the isomer distribution of 2- and 4-nitrotoluene products was identical to that observed during similar experiments with N_2O_4 .

Acknowledgment

The authors acknowledge financial support of this work by the Chemistry and Materials Science Department, Lawrence Livermore National Laboratory through Subcontracts 4288309 and 2207701. Helpful discussions concerning this work were held with Dr. R. R. McGuire and Mr. C. Coon of LLNL, and Dr. J. S.

Wilkes, F. J. Seiler Research Laboratory, USAF Academy.

Manuscript submitted April 13, 1981; revised manuscript received June 1, 1981.

Any discussion of this paper will appear in a Discussion Section to be published in the June 1982 JOURNAL. All discussions for the June 1982 Discussion Section should be submitted by Feb. 1, 1982.

Publication costs of this article were assisted by the University of Mississippi.

REFERENCES

1. G. R. Davies and B. J. Woodhall, *J. Appl. Electrochem.*, **1**, 137 (1971).
2. K. Nyberg, *Acta Chem. Scand.*, **25**, 3246 (1971).
3. A. Laurent, E. Laurent, and P. Locher, *Electrochim. Acta*, **20**, 857 (1975).
4. C. L. Perrin, *J. Am. Chem. Soc.*, **99**, 5516 (1977).
5. L. Ebersson, L. Jonsson, and F. Radner, *Acta Chem. Scand.*, **B32**, 749 (1978).
6. C. L. Hussey, T. M. Laher, and J. M. Achord, *This Journal*, **127**, 1484 (1980).
7. L. Ebersson, in "Organic Electrochemistry," M. M. Baizer, Editor, pp. 447-468, Marcel Dekker, New York (1973).
8. R. S. Rao, S. B. Milliken, S. L. Robinson, and C. K. Mann, *Anal. Chem.*, **42**, 1076 (1970).
9. H. Lund, *Acta Chem. Scand.*, **11**, 1323 (1957).
10. G. Cauquis and D. Serve, *C. R. Acad. Sci. Paris, Ser. C*, **270**, 1773 (1970).
11. C. E. Castellano, J. A. Wargon, and A. J. Arvia, *J. Electroanal. Chem. Interfacial Electrochem.*, **47**, 371 (1973).
12. E. R. Ward, C. D. Johnson, and L. A. Day, *J. Chem. Soc.*, 487 (1959).
13. K. Nyberg, *Acta Chem. Scand.*, **25**, 3770 (1971).
14. K. Nyberg, *ibid.*, **27**, 503 (1973).
15. G. A. Olah, S. J. Kuhn, and S. H. Flood, *J. Am. Chem. Soc.*, **83**, 4571 (1961).
16. G. Cauquis and D. Serve, *C. R. Acad. Sci. Paris, Ser. C*, **267**, 460 (1968).
17. S. J. Kuhn and G. A. Olah, *J. Am. Chem. Soc.*, **83**, 4564 (1961).
18. H. Schmidt and H. Stange, *Z. Anorg. Allg. Chem.*, **293**, 274 (1957).
19. G. Cauquis and D. Serve, *C. R. Acad. Sci. Paris, Ser. C*, **262**, 1516 (1966).
20. M. Colombi, G. Fiori, and L. Formaro, *J. Electroanal. Chem. Interfacial Electrochem.*, **44**, 21 (1973).
21. G. A. Olah, S. J. Kuhn, S. H. Flood, and J. C. Evans, *J. Am. Chem. Soc.*, **84**, 3687 (1962).

Trapping of Anodically Generated Cations with Carbon Monoxide: The Anodic Koch Reaction

James P. Coleman*

Monsanto Company, Corporate Research and Development, St. Louis, Missouri 63166

ABSTRACT

Aliphatic carbenium ions, generated via anodic oxidation of saturated hydrocarbons in strongly acidic solutions, may be trapped efficiently with carbon monoxide, at atmospheric or elevated pressures, to yield carboxylic acids. Product distribution in the case of *n*-pentane oxidation may be explained in terms of kinetic *vs.* thermodynamic control in the carbonylation step.

Although a few investigations have been made (1-5), the use of carbon monoxide in organic electrosynthesis, an area which offers some interesting possibilities, has not been extensively investigated. I report here the

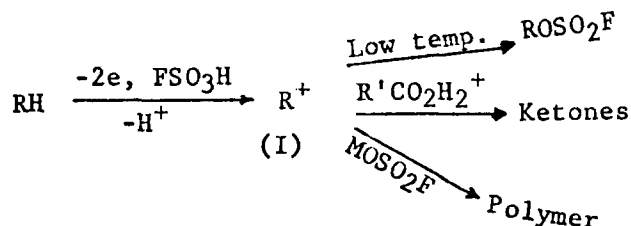
* Electrochemical Society Active Member.

Key words: anodic Koch reaction, alkane carboxylation, carbon monoxide, fluorosulfonic acid.

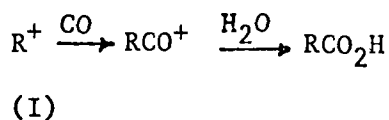
results of some preliminary studies on the anodic oxidation of alkanes in strong acids in the presence of carbon monoxide at both atmospheric and elevated pressures.

The direct anodic oxidation of alkanes in anhydrous fluorosulfonic acid has been demonstrated (6), and,

although the exact details of the oxidation mechanism are still the subject of some discussion (6-10), it has been shown that the overall reaction involves two-electron oxidation to an intermediate carbenium ion which undergoes further reactions dependent on the nature of the acid medium



The object of the present study was to trap the carbenium ion (I), formed under these conditions, with carbon monoxide and, thus, accomplish an anodically assisted Koch reaction (11) leading to a carboxylic acid



The carboxylation of saturated hydrocarbons has been reported previously.

Antimony pentafluoride in fluorosulfonic acid (12) or in liquid hydrogen fluoride (13) has been used to convert, respectively, methane to acetic acid and methylcyclopentane to cyclohexanecarboxylic acid. Saturated hydrocarbons with tertiary C—H bonds may be carboxylated in less acidic media by using protonated olefins as hydride-abstracting agents (14) in stoichiometric quantities.

Anodic oxidation would seem, however, to offer the possibility of a more attractive approach to carboxylation of saturated hydrocarbons without the use of additional reagents and generation of by-products.

Experimental

Reactions were carried out at constant current using a Lambda Model LP-412A-FM power supply. Preliminary voltammetry was carried out using a cell described previously (6), a Wenking 70HVI/90 potentiostat, an Exact Electronics Model 505 function generator, and a Pd-H₂ reference electrode (15).

Three different preparative cells were used during the course of this work. The first, cell [1], was a conventional glass H-cell, 40 ml volume, with sintered-glass divider, Pt gauze anode (4 cm²), and with a sintered-glass gas sparger directly below the anode. The second cell, cell [2], was a similar H-cell without the built-in gas sparger. Instead, the anode was a disk (18 mm diam) of platinum gauze mounted on the bottom of a sintered-glass disk of the same diameter sealed to a tube through which gas was passed into the cell. Cell [3] was a modified pressure reactor, a Parr Model 4521, 1 liter Monel autoclave. The autoclave was equipped with a glass liner, a mechanical stirrer made of Teflon, and two platinum-foil electrodes (10 cm²) mounted on a Teflon holder and situated 6 cm apart on either side of the agitator and close to the bottom of the reactor. Electrical connection was made with a commercially available "Conax" insulated power lead seal, and temperature was monitored with a glass-coated thermocouple (type J) immersed in the cell solution. Working volume was typically 100 ml.

Fluorosulfonic acid (Allied) and trifluoromethanesulfonic acid (3M Company) were distilled prior to use. Solutions of water in fluorosulfonic acid were prepared at -60°C and allowed to warm to room temperature.

Electrolysis at atmospheric pressure was carried out by sparging a hydrocarbon-saturated stream of carbon monoxide over the anode operating at constant current.

The pressure cell was operated remotely from outside a specially designed area, part of a larger high pressure reaction facility. Electrolyte and excess hydrocarbon were charged into the cell which was sealed and pressurized with carbon monoxide, typically to 1000 psig, and electrolysis at constant current was begun.

Products were isolated by carefully quenching the acidic solutions in icewater (vigorous hydrolysis of FSO₃H), extraction with methylene chloride, and back-extraction of carboxylic acid product into sodium carbonate solution. Acidification of the carboxylate solution allowed carboxylic acid and neutral products to be isolated separately.

Analysis of the products was carried out by GC, NMR, and mass spectrometry.

GC analysis utilized two columns—a 10-ft, 10% PEGA-1% H₃PO₄ on Chromosorb W, 55°C, or a 14-ft 5% FFAP on Chromosorb W 80°/12 min to 175° at 10°/min.

Samples were esterified with methanol-HCl prior to analysis. Authentic samples of cyclohexanecarboxylic acid, methylcyclopentanecarboxylic acid, *n*-hexanoic acid, 2-methylpentanoic acid, 2-ethylbutyric acid, and cyclopentanecarboxylic acid were employed as standards.

NMR spectroscopy was performed on a Varian T-60 spectrometer and mass spectra obtained on a Varian MAT CH7A mass spectrometer.

Cautionary note.—Fluorosulfonic acid is prepared by combining anhydrous HF and sulfur trioxide, has some of the safety hazards of both and, thus, should be treated with extreme caution. During the course of this investigation an unopened 5 pint bottle of fluorosulfonic acid exploded for no apparent reason, causing considerable damage but, fortunately, no injuries since the appropriate safety precautions were being taken. The value of such safety precautions in handling this material cannot be overemphasized.

Results

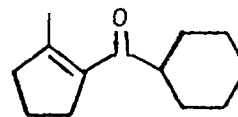
Studies at atmospheric pressure showed that carbon monoxide had no effect on the previously reported (6) voltammetry of cyclohexane in fluorosulfonic acid-potassium fluorosulfonate (*E*_p = 1.12V vs. Pd/H₂). No competing oxidation of carbon monoxide was evident under these conditions. Preparative studies at 1 atm were, therefore, initiated while the high pressure reactor was being constructed.

Cyclohexane was selected as the substrate for initial study because of its relative ease of oxidation and predicted simplicity of product distribution.

Table I shows the results obtained by oxidizing cyclohexane at a platinum anode in fluorosulfonic acid solutions saturated with carbon monoxide at 1 atm.

With KFSO₃ as the electrolyte a modest 18% current efficiency for the formation of cyclohexanecarboxylic acid was observed.

The major product under these conditions was a mixture of hydrocarbon oligomers containing small amounts of the ketone (II) formed in a manner de-



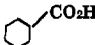
(II)

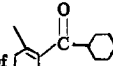
scribed previously (6). By using water as the electrolyte (H₃O⁺ FSO₃⁻), and trapping agent for acylium cations, current efficiency was increased to almost 60%

Table I. Anodic carboxylation of cyclohexane at atmospheric pressure in fluorosulfonic acid^a

| Electrolyte | Charge passed (C) | RCO ₂ H current efficiency ^b (%) | Ratio of carboxylic acid to neutral product ^c |
|---|-------------------|--|--|
| FSO ₃ H-KFSO ₃ (0.1M) | 1260 | 18 | 0.23 |
| FSO ₃ H-H ₂ O (0.5M) | 1170 | 37 | 0.69 |
| FSO ₃ H-H ₂ O (1.5M) | 1170 | 57 | 2.1 |
| FSO ₃ H-H ₂ O (3.0M) | 1170 | 56 | 3.1 |
| FSO ₃ H-H ₂ O (3.0M) | 0 | No products formed (18 hr) | |

^a Cell 1, 50 mA, 25°C, CO = 100 ml/min.

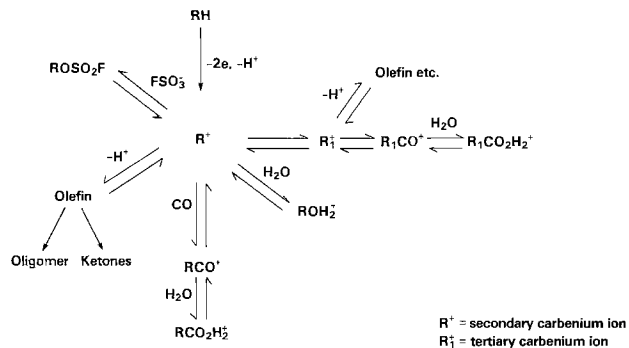
^b Crude product >95% 

^c Oligomeric products, traces of  cf. earlier work.

with a concomitant decrease in the formation of neutral products. Increasing water concentration beyond 1.5M did not give any further increase in current efficiency.

It should be noted that the carboxylic acid formed from cyclohexane in this manner is almost exclusively the unrearranged material, cyclohexanecarboxylic acid. Only trace amounts of methylcyclopentanecarboxylic acid were observed.

n-Pentane was the next system studied, and results are shown in Table II. At ambient temperature current efficiency was lower than for the analogous reaction with cyclohexane and a mixture of three isomeric acids was obtained, the rearranged material predominating. Upon repeating this reaction at -25°C a cleaner, more efficient reaction was observed, yielding, almost exclusively, the rearranged product. In contrast, the first pressure reaction, at 1000 psig, yielded a mixture of products derived mainly from the unrearranged carbon skeleton. Further reactions in the high pressure electrolysis system are summarized in Table III. Cyclohexane was carboxylated more efficiently than at


Scheme I. Reaction pathways in anodic carboxylation of alkanes

atmospheric pressure, again with almost exclusive formation of unrearranged product. The limits of sustainable current density for this reaction were not pursued but increasing from 10 to 20 mA/cm² had no deleterious effect.

An alternative solvent system, the more expensive but more easily handleable trifluoromethanesulfonic acid, was studied briefly. As may be seen from Table III, respectable but slightly lower yields were obtained for the carboxylation of cyclohexane in trifluoromethanesulfonic acid.

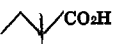
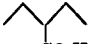
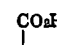
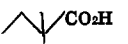

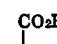
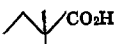
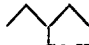
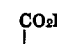
Cyclopentane gave results similar to cyclohexane in fluorosulfonic acid, *n*-pentane was discussed previously and *n*-hexane gave an unresolved mixture of C₇ acids with 69% current efficiency.

Discussion

The direct, anodic oxidation of saturated hydrocarbons to give carbenium ion-derived products in strongly acidic solutions is well established (6-10). The present work has demonstrated that carbon monoxide will function efficiently as a nucleophile in such systems, giving carboxylic acid products without undergoing a competing oxidation process.

The results obtained may be understood by reference to Scheme (I). Electrolytic oxidation provides a simple method of converting the saturated hydrocarbon RH

Table II. Anodic carboxylation of *n*-pentane in fluorosulfonic acid




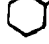
| Electrolyte | T (°C) | CO pressure | Charge passed (C) | Carboxylic acids, current efficiency (%) | Carboxylic acids, distribution (%) | Ratio of carboxylic acid to neutral product ^c |
|---|--------|-------------|-------------------|--|--|--|
| FSO ₃ H-H ₂ O (1.5M) ^a | 25 | 1 atm | 1080 | 40 |  62 | 1.1 |
| | | | | |  29 | |
| | | | | |  9 | |
| FSO ₃ H-H ₂ O (1.5M) ^a | -25 | 1 atm | 1080 | 74 |  95 | 12 |
| | | | | |  4 | |
| | | | | |  1 | |
| FSO ₃ H-H ₂ O (1.5M) ^b | 25 | 1000 psig | 1080 | 57 |  15 | 4.5 |
| | | | | |  54 | |
| | | | | |  31 | |

^a Cell 2, 50 mA, CO = 100 ml/min.

^b Cell 3, 200 mA.

^c Oligomeric products; traces of unsaturated ketones.

Table III. Anodic carboxylation of alkanes at elevated pressure (1000 psig CO)^a

| Substrate | Electrolyte | Current density (mA/cm ²) | Charge passed (C) | Carboxylic acids, current efficiency (%) | Carboxylic acids, distribution |
|-------------------|---|---------------------------------------|-------------------|--|---|
| Cyclohexane | FSO ₃ H-H ₂ O (1.5M) | 10 | 8640 | 83 |  CO ₂ H (99%) |
| Cyclohexane | FSO ₃ H-H ₂ O (1.5M) | 20 | 17,280 | 82 |  CO ₂ H (99%) |
| Cyclohexane | CF ₃ SO ₃ H-H ₂ O (1.5M) | 10 | 17,280 | 60 |  CO ₂ H (99%) |
| Cyclopentane | FSO ₃ H-H ₂ O (1.5M) | 20 | 17,280 | 80 |  CO ₂ H (99%) |
| <i>n</i> -Pentane | FSO ₃ H-H ₂ O (1.5M) | 20 | 17,280 | 57 | See Table II |
| <i>n</i> -Hexane | FSO ₃ H-H ₂ O (1.5M) | 20 | 17,280 | 69 | Mixed C ₇ acids |

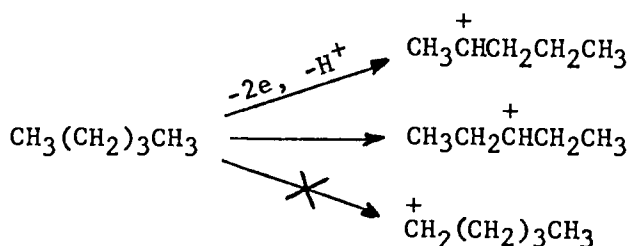
^a Cell 3, 100-150 ml electrolyte, 20g alkane.

into the secondary carbenium ion R⁺. Competition between the various reaction pathways shown then determines the distribution of products obtained.

The first observation made, regarding the beneficial effect of water in this system, may be explained in terms of acylium ion trapping. Carbonylation of the carbenium ion R⁺ is reversible (16) and, at ambient temperature in the absence of a nucleophile such as water (H₃O⁺) to trap the acylium ion, side reactions via deprotonation to form the olefin will be significant. Further, in the absence of an acylating agent, the products of such side reactions will be simply oligomeric hydrocarbons (6). The fluorosulfonate anion is not thought to play a significant role in stabilizing the secondary carbenium ion, R⁺, at ambient temperatures although the formation of secondary fluorosulfonate esters at low temperature has been proposed (9), and methyl and ethyl fluorosulfonates have been generated anodically under similar conditions (17).

The principal factors influencing the product distribution obtained from a given carbenium ion appear to be temperature, CO pressure, and R⁺ structure.

If we consider the results obtained with *n*-pentane vs. cyclohexane, it is apparent that in the latter case, under the conditions employed, kinetic control predominated at all times and the reaction path, as with cyclopentane, is simply the vertical line in Scheme (I). In the case of *n*-pentane we observe a mixture of kinetic and thermodynamic control, the balance of which may be changed by modifying conditions. In agreement with previous work (18) the initially formed carbenium ions are the secondary cations resulting from proton loss at the 2- and 3- positions. No primary products were observed.



With carbon monoxide at elevated pressure this mixture of carbenium ions is trapped efficiently to give a product mixture representative of the carbenium ions initially formed. However, at low temperature and low carbon monoxide pressure, the carbonylation reaction is much slower and almost complete rearrangement to the more stable tertiary carbenium ion occurs prior to carbonylation. At ambient temperature and low pressure, conditions are between the two previous extremes although still in favor of the thermodynamically controlled product.

n-Hexane gives a more complex product mixture and no attempt was made in this case to study its behavior in detail, although one would expect to observe phenomena similar to those observed with *n*-pentane.

No products of further oxidation of initially formed carboxylic acids were observed in these reactions as long as the hydrocarbon substrate was not depleted. This is to be expected since introduction of the electron-withdrawing —CO₂H₂⁺ group has been shown to render the parent hydrocarbon less susceptible to further oxidation (19).

Further oxidation of carboxylic acids can occur at higher potentials, with products derived from oxidation of the hydrocarbon chain, rather than Kolbe-type products, being obtained (19, 20).

Summary and Conclusions

The trapping of anodically generated aliphatic carbenium ions with carbon monoxide has been demonstrated for the first time, allowing the efficient carboxylation of saturated hydrocarbons in strongly acidic solutions. In the present study, electrolytic oxidation has simply been used as a convenient means of generating the carbenium ion from the corresponding hydrocarbon without great attention being paid to the electrode reaction.

The results obtained may be readily interpreted in terms of numerous equilibria set up in such acidic solutions.

The possibility of using this approach for the carboxylation of other, more complex systems suggests itself and will be pursued.

Manuscript submitted March 25, 1981; revised manuscript received June 1, 1981. This was Paper 437 presented at the St. Louis, Missouri, Meeting of the Society, May 11-16, 1980.

Any discussion of this paper will appear in a Discussion Section to be published in the June 1982 JOURNAL. All discussions for the June 1982 Discussion Section should be submitted by Feb. 1, 1982.

Publication costs of this article were assisted by the Monsanto Company.

REFERENCES

1. T. Inoue and S. Tsutsumi, *J. Am. Chem. Soc.*, **87**, 3525 (1965).
2. D. M. Fenton, U.S. Pat. 3,481,845 (1969).
3. B. E. Conway, J. W. Loveland, and W. C. Neikam, U.S. Pat. 3,252,878 (1966).
4. D. Cipris and I. L. Mador, *This Journal*, **125**, 1954 (1978).
5. G. Silvestri, S. Gambino, G. Filardo, M. Guainazzi, and R. Ercoli, *Gaz. Chim. It.*, **102**, 818 (1972).
6. J. Bertram, J. P. Coleman, M. Fleischmann, and D. Fletcher, *J. Chem. Soc. Perkin II*, 374 (1973).
7. S. Pitti, F. Bobilliar, A. Thiebault, and M. Herlem, *Anal. Lett.*, **8**, 241 (1975).

8. S. Pitti, M. Herlem, and J. Jordan, *Tetrahedron. Lett.*, 3221 (1976).
9. J. P. Coleman and D. Pletcher, *J. Electroanal. Chem. Interfacial Electrochem.*, **87**, 111 (1978).
10. J. Devynk, P. L. Fabre, A. Ben-Hadid, and B. Tremillon, *J. Chem. Res. (M)*, 2467 (1979).
11. See for example, J. Falbe, "Carbon Monoxide in Organic Synthesis," Springer-Verlag, Berlin (1970).
12. H. Hogeveen, J. Lukas, and C. F. Roobeek, *Chem. Commun.*, 920 (1969).
13. R. Paatz and G. Weisgerber, *Chem. Ber.*, **100**, 984 (1967).
14. Y. Souma and H. Sano, *Bull. Chem. Soc. Jpn.*, **47**, 1717 (1974).
15. M. Fleischmann and H. Hiddlestone, *J. Instr. Sci.*, **1**, 667 (1968).
16. H. Hogeveen, *Adv. Phys. Org. Chem.*, **10**, 29 (1973).
17. J. P. Coleman and D. Pletcher, *Tetrahedron. Lett.*, 147 (1974).
18. H. P. Fritz and T. Wurminghausen, *J. Chem. Soc. Perkin II*, 610 (1976).
19. D. Pletcher and C. Z. Smith, *J. Chem. Soc. Perkin I*, 948 (1975).
20. C. J. Myall, D. Pletcher, and C. Z. Smith, *J. Chem. Soc. Perkin I*, 2035 (1976).

Oxidation of Alkylbenzenes by Electrogenerated Hydroxyl Radical

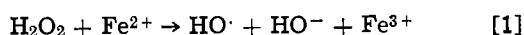
Tomokazu Matsue, Masamichi Fujihira,* and Tetsuo Osa*

Pharmaceutical Institute, Tohoku University, Aobayama, Sendai 980, Japan

ABSTRACT

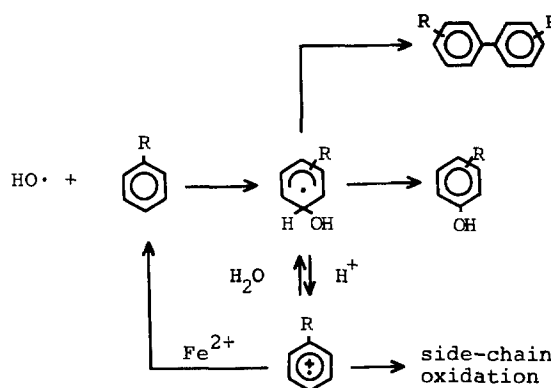
The oxidation of some alkylbenzenes by the hydroxyl radical, which is produced by the reaction of Fe^{2+} with H_2O_2 electrogenerated from O_2 in aqueous solution, was carried out. In the reaction, Fe^{3+} , generated by the above reaction, is also reduced to Fe^{2+} at the potential of reduction of O_2 . The reaction products are hydroxylated products of the aromatic rings and side-chain oxidation products. In the oxidation of toluene at $[\text{H}^+] = 0.2\text{M}$, the yield of the former was higher than that of the latter, whereas the opposite was observed in the oxidations of ethylbenzene and cumene. From the results obtained at $[\text{H}^+] = 0.001\text{M}$, it appears that α -hydrogen abstraction from the side chains by the hydroxyl radical might make a certain contribution to the formation of side-chain oxidation products. The current efficiencies at low concentration of Fe^{2+} were very high, and the yields of the corresponding alcohols were very low, indicating that the carbonyl compounds were produced by the reaction between intermediate radicals and O_2 dissolved in the solution. The relatively high yield of the *meta*-isomer under O_2 saturated in solution can be explained by the fast addition of O_2 to hydroxycyclohexadienyl radical followed by elimination of $\text{HO}_2\cdot$ to yield phenolic products. Although the influence on the addition of α -cyclodextrin to the electrolyte solution on the regio-selectivity of phenol formation was small, it was observed that the *para*-isomer forms are slightly high.

The combination of hydrogen peroxide and a ferrous salt, "Fenton's reagent" (1), is an effective oxidant of various types of organic compounds. The actual oxidant of Fenton's reagent is the hydroxyl radical (2) generated by the reduction of hydrogen peroxide with ferrous ion



Oxidation of aromatics by the hydroxyl radical has been extensively investigated (3-19), and the products have usually been phenols and side-chain oxidation products. From radiation chemistry and spectroscopic results with u.v. and ESR, Walling *et al.* (4) concluded that the oxidation of substituted benzene derivatives by hydroxyl radical proceeded by the mechanism (5) illustrated in Scheme 1. The addition of the hydroxyl radical to an aromatic ring such as toluene is rapid compared with the hydrogen abstraction from the side chain (13, 16). However, in the hydroxyl radical oxidation of some aromatic compounds in which C-H bond energies of the side chain are relatively low, hydrogen abstraction may make a certain contribution to the reaction. This paper describes a study of the reaction of several alkylbenzenes with the hydroxyl radical generated by an electrochemical method which

is apparently very different from the homogeneous conditions investigated by previous researchers. The presence of oxygen dissolved in electrolyte solution affected the product distribution. The effect of α -cyclodextrin (α -CD) on product distribution was also investigated. This molecule has the ability to include various compounds in its cavity in aqueous solution (20).



Scheme 1. The schematic mechanism for oxidation of aromatics by hydroxyl radical.

* Electrochemical Society Active Member.
Key words: Fenton's reagent, hydroxyl radical, α -cyclodextrin, hydroxylation.

Experimental

All electrolyses were carried out using a Yanaco VE-8 controlled potential electrolyzer. The electrolysis cell was a divided H-type with a graphite cathode (30 × 20 × 2 mm) purchased from Tokai Carbon Company (G 2080), a Pt gauze anode, and a saturated calomel electrode (SCE) as the reference electrode inserted near the cathode. The catholyte consisted of 10 μl of substrate and FeSO₄ dissolved in 50 ml of aqueous H₂SO₄ solution and was stirred with a magnetic bar. Oxygen gas (1 atm) was bubbled through the catholyte so that a constant concentration of oxygen in solution was maintained. The electrode potential of the cathode at [H⁺] = 0.2M and at [H⁺] = 0.02M was set at -0.5V vs. SCE, and at [H⁺] = 0.001M was set at -0.6V vs. SCE.

After electrolysis, the catholyte was extracted with ether and this extract was concentrated under a reduced pressure for gas chromatography. Gas chromatographic analyses were carried out using Shimadzu GC-6A and GC-4CM chromatographs equipped with flame ionization detectors; oven temperatures were programmed from 80° to 200°C. Nitrogen was used as the carrier gas. The columns used in the analyses were 2m × 3 mmφ SUS packed with Carbowax 20M, DEGS, denatured lanolin, Silicon OV-1, and Silicon DC-560. Denatured lanolin was particularly suitable for separation of *meta*(*m*)- and *para*(*p*)-isomers of phenolic products. Current efficiencies were determined according to the mechanism proposed by Walling *et al.* (4), *i.e.*, one hydroxyl radical and one aromatic molecule produce the corresponding phenolic product or alcohol, and two hydroxyl radicals are consumed in forming the corresponding carbonyl compound. The current was maintained below 5 mA since the current efficiencies showed a tendency to decrease with higher values.

Cyclic voltammetric experiments were carried out using a conventional electrochemical instrument with a glassy carbon electrode in aqueous 0.1M H₂SO₄ solution. The potentials were referred to an SCE. The cell design used for cyclic voltammetry was similar to that previously described (21).

The dissociation constants of α-CD complexes were determined by spectrophotometric method (22).

Results

The electrochemical generation of hydroxyl radical was carried out by the reduction of oxygen in the presence of Fe²⁺ in aqueous solution. The cyclic voltammograms of oxygen (air saturated) and Fe³⁺ on a Tokai glassy carbon electrode in aqueous 0.1M H₂SO₄ solution are shown in Fig. 1. The peak potential of the reduction of Fe³⁺ was more positive than the onset potential of the reduction of oxygen. Therefore, Fe³⁺ generated by the reaction between Fe²⁺ and H₂O₂ was reduced to regenerate Fe²⁺ in the reduction of oxygen. From the results, the following mechanism

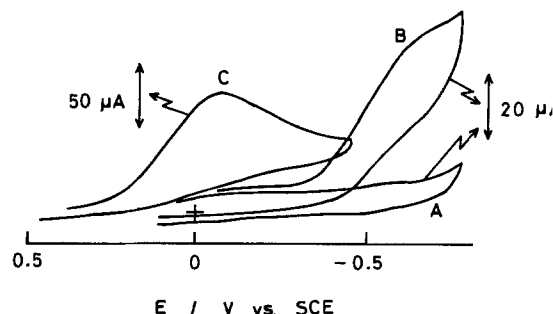
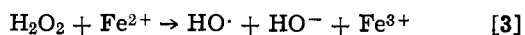
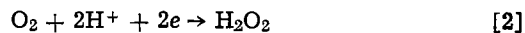


Fig. 1. Cyclic voltammograms at Tokai glassy carbon electrode in aqueous 0.1M H₂SO₄ solution: (A) under N₂ saturated; (B) under air saturated; (C) 1.0 × 10⁻³M Fe₂(SO₄)₃ under N₂ saturated.

was deduced for the generation of hydroxyl radical by the electrochemical method



The reaction products in the oxidations of alkylbenzenes (toluene, ethylbenzene, and cumene) by electrogenerated hydroxyl radical were generally classified into hydroxylated products of aromatic rings and oxygenated ones of side chains. The electrolysis time was restricted to an hour to avoid further oxidations of the reaction products. The results are summarized in Tables I-III.

In the oxidation of toluene by electrogenerated hydroxyl radical at [H⁺] = 0.2M, the hydroxylation of the aromatic ring predominated over the side-chain oxidation, whereas the opposite results were observed in the oxidations of ethylbenzene and cumene. Most of the side-chain oxidation products were carbonyl com-

Table I. Oxidation of toluene by electrogenerated hydroxyl radical at 0°C

| Run | [H ⁺] (M) | [Fe ²⁺] (M) | Yield (%) [*] | | C.E. ^{**} |
|-----|--------------------------|----------------------------|------------------------|--|--------------------|
| | | | PhCHO | Cresol (<i>o</i> : <i>m</i> : <i>p</i>) | |
| 1† | 0.2 | 0.05 | 38 | 38 | |
| 2 | 0.2 | 0.05 | 20 | 67 (40:54:6) | 9 |
| 3‡ | 0.2 | 0.05 | 25 | 64 (40:54:6) | 3 |
| 4 | 0.2 | 0.005 | 61 | 30 (47:45:8) | 24 |
| 5 | 0.02 | 0.05 | 8 | 82 (41:53:6) | 9 |
| 6‡ | 0.02 | 0.05 | 13 | 74 (43:50:7) | 3 |
| 7 | 0.001 | 0.05 | 14 | 79 (44:50:6) | 9 |
| 8 | 0.001 | 0.005 | 16 | 71 (53:36:11) | 10 |
| 9§ | 0.2 | 0.01 | 6 (11) | 6 (53:3:43) | |

^{*} Based on all products detected by gas chromatography.

^{**} Current efficiency.

† At room temperature.

‡ α-CD was added to the electrolyte (concentration of α-CD was 1.0 × 10⁻²M).

§ Result by Walling *et al.*, yield was based on H₂O₂; number in parenthesis is yield of benzyl alcohol.

Table II. Oxidation of ethylbenzene by electrogenerated hydroxyl radical at 0°C

| Run | [H ⁺] (M) | [Fe ²⁺] (M) | Yield (%) | | C.E. |
|-----|--------------------------|----------------------------|---------------------|--|------|
| | | | PhCOCH ₃ | EP (<i>o</i> : <i>m</i> : <i>p</i>) [*] | |
| 1 | 0.2 | 0.05 | 64 | 21 (44:49:5) | 15 |
| 2** | 0.2 | 0.05 | 64 | 20 (59:38:12) | 5 |
| 3 | 0.2 | 0.005 | 83 | 9 (48:41:11) | 63 |
| 4 | 0.02 | 0.05 | 40 | 43 (41:52:7) | |
| 5 | 0.001 | 0.05 | 45 | 43 | 23 |
| 6 | 0.001 | 0.005 | 49 | 39 (43:38:19) | 30 |

^{*} EP = ethylphenol.

^{**} α-CD was added to the electrolyte (concentration of α-CD; 1.0 × 10⁻²M).

Table III. Oxidation of cumene by electrogenerated hydroxyl radical at 0°C

| Run | [H ⁺] (M) | [Fe ²⁺] (M) | Yield (%) | | C.E. |
|-----|--------------------------|----------------------------|---------------------|--|------|
| | | | PhCOCH ₃ | <i>i</i> -PP (<i>o</i> : <i>m</i> : <i>p</i>) [*] | |
| 1 | 0.2 | 0.05 | 40 | 19 (47:43:10) | 11 |
| 2** | 0.2 | 0.05 | 19 | 27 (46:38:16) | 5 |
| 3 | 0.2 | 0.005 | 80 | 7 (39:37:24) | 53 |
| 4 | 0.02 | 0.05 | 24 | 47 (46:48:6) | 9 |
| 5 | 0.001 | 0.05 | 36 | 41 | 8 |
| 6 | 0.001 | 0.005 | 48 | 42 (30:45:25) | 22 |

^{*} *i*-PP = iso-propylphenol.

^{**} α-CD was added to the electrolyte (concentration of α-CD; 1.0 × 10⁻²M).

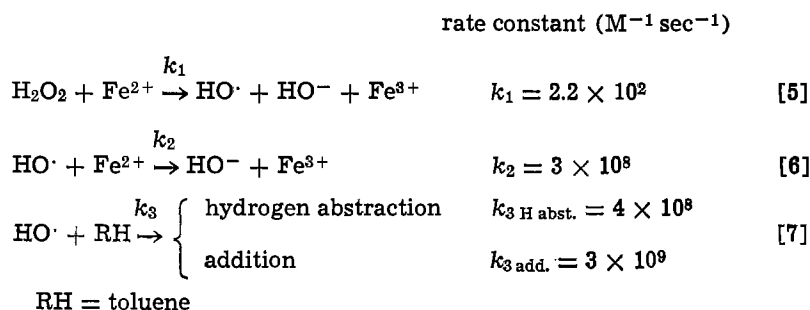
pounds; benzaldehyde was obtained from toluene and acetophenone from ethylbenzene and cumene. Formation of the corresponding alcohols, which may be intermediates in the formation of carbonyl compounds, biphenyl derivatives, and bibenzyl derivatives was very low. In ethylbenzene oxidation, side-chain oxidation occurred only at the α -position. Products of β -position oxidation, such as β -phenethyl alcohol and phenylacetaldehyde, could not be detected. In cumene oxidation, phenol could not be detected although the auto-oxidation of cumene at high acidity results in the formation of phenol as the main product (23).

The pH of the reaction medium had a great influence on the product distribution. The yields of the corresponding phenolic products at $[H^+] = 0.001M$ were higher than those observed at $[H^+] = 0.2M$ since the low proton concentration lessens the conversion from the hydroxycyclohexadienyl radicals (adducts) to the cation radicals of the starting materials (15). The concentration of Fe^{2+} dissolved in the electrolyte solution also affected the yields of the phenolic products. At $[H^+] = 0.2M$, lowering the concentration of Fe^{2+} resulted in a decrease in the yields of phenolic products and an increase in the current efficiencies. Under such a condition ($[H^+] = 0.2M$, $[Fe^{2+}] = 0.005M$), high yields of side-chain oxidation products were also

Discussion

The first reaction in the oxidation by Fenton's reagent is the generation of hydroxyl radical from hydrogen peroxide and Fe^{2+} in the reaction medium. Since the rate constant for this step [$2.2 \times 10^2 M^{-1} sec^{-1}$ (24)] is very low in comparison with those for the subsequent reactions, the generation of hydroxyl radical is the rate-determining step in the oxidation of aromatics by Fenton's reagent. Further reduction by Fe^{2+} converts the initially formed hydroxyl radical to hydroxyl anion and this step acts as a major competitive reaction with the oxidation of aromatics by hydroxyl radical. Accordingly, in order to realize a high efficiency, it is necessary that the rate of reaction between a substrate and the radical be greater than that of the competitive reduction.

The reaction mode of aromatics with hydroxyl radical may be classified into two types. One is hydrogen abstraction from the side chain by hydroxyl radical, and the other is the addition reaction of the radical to the aromatic ring. In the oxidation of toluene by hydroxyl radical, the latter reaction takes precedence over the former (13, 16). However, the contribution of the former reaction to the oxidations of ethylbenzene and cumene becomes larger, since the α -hydrogen in these cases are more easily abstracted

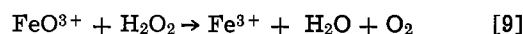


observed as well as high current efficiencies. The lower Fe^{2+} concentration minimizes the reduction of the intermediate cation radicals, formed in the oxidations, back to the starting materials (5). However, the yields of the phenolic products were almost independent of the acidity and of the concentration of Fe^{2+} when the proton concentration was less than 0.02M. The temperature during electrolysis had an influence on the reaction. The oxidation of toluene at low temperature ($0^\circ C$), gave a higher yield of cresol (67%) than that observed at room temperature.

The results obtained for the oxidation of toluene in the present work by the electrochemical method when compared with those obtained for homogeneous oxidation by hydroxyl radical as carried out by Walling *et al.* (4) differed in the following ways: (i) The yield of cresol isomers was higher, (ii) the yield of benzyl alcohol was lower, and (iii) the yield of *m*-isomer of cresols was relatively high and that of *p*-isomer was low (e.g., *o*:*m*:*p* isomer ratio of cresol at $[H^+] = 0.2M$ was 40:54:6). Similar results were observed in the oxidations of ethylbenzene and cumene.

The addition of α -CD to the electrolyte solution had little effect on the product distribution. In toluene oxidation, a slight increase in the yield of side-chain oxidation products was observed. The addition of α -CD for ethylbenzene oxidation resulted in a slight increase in the *p*-isomer ratio of ethylphenol, although it did not affect the overall yield of ethylphenol isomers. In cumene oxidation, a small enhancement of overall yield of *iso*-propylphenol, accompanying an increase of the *p*-isomer was observed. The current efficiencies were decreased by the addition of α -CD.

The pH of the reaction medium is one of the important factors determining efficiencies. The equilibrium in Eq. [8] must lie to the right at low proton concentration (3). $FeOOH^{2+}$ produced in this equilibrium decomposes and this is followed by further reaction as shown below



Consequently, the efficiency of the reaction may be low at low proton concentrations. Indeed, from our results, current efficiencies became low with decreasing acidity.

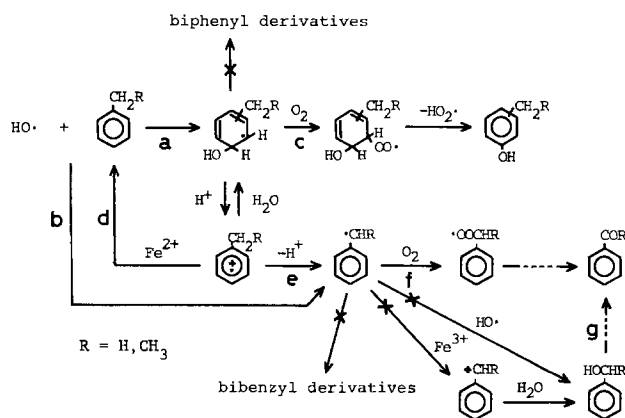
Next, we consider the characteristics of the oxidation by electrogenerated hydroxyl radical in the present work. The half-life of hydrogen peroxide formed by the reduction of oxygen at electrode surface is 6.3×10^{-2} sec under the pseudo-first-order condition; $[Fe^{2+}] = 0.05M$ ($[Fe^{2+}] \gg [H_2O_2]$). According to the Einstein-Smolchowski equation (25), average distance of H_2O_2 transport by diffusion from the electrode surface during 6.3×10^{-2} sec is 1.3×10^{-3} cm, assuming a diffusion coefficient of H_2O_2 of 1.35×10^{-5} $cm^2 sec^{-1}$ (26). The thickness of the reaction layer may extend about 10^{-3} cm from the electrode surface. Most of the oxidation therefore should proceed in the diffusion layer. On the other hand, the concentration of the substrate may be higher due to adsorption than that of the bulk solution. Accordingly, the oxidation by the electrochemical method was expected to be influenced partly by the electrode surface and the solution near the electrode. The results, however, did not differ greatly from the results observed in the

homogeneous oxidation except for the effect of oxygen which is described later.

A reasonable mechanism for the oxidation of toluene and ethylbenzene by electrogenerated hydroxyl radical is illustrated in Scheme 2 and may be compared with the one proposed by Walling *et al.* (4). In the present reactions, the role of oxygen as the oxidant in phenol formation must be large since the relatively high yields of the *m*-isomers and low yields of the *p*-isomers differed from those in the previous work where Fe^{3+} and/or Cu^{2+} was used as oxidant (4, 5). These results are in agreement with the report (4) that the yield of the *p*-isomer was low in the homogeneous oxidation of toluene by hydroxyl radical in the presence of excess oxygen. The isomer distribution of the phenolic products can be regulated by the reactivity of oxidant with adducts and by the equilibrium between the adducts and cation radicals formed by their dehydration. The following path c can be proposed in order to explain the relatively high yield of the *m*-isomer and low yield of the *p*-isomer, observed in solutions saturated with oxygen. The addition of oxygen to the adducts is considered to be very fast as suggested by Dorfman *et al.* (17), and the resulting hydroxycyclohexadienylperoxy radicals are converted easily to yield phenols. The fast reaction of oxygen with the adducts seems to contribute to the relatively high yield of the *m*-isomer, whereas using Fe^{3+} as the oxidant for step c the isomer distribution must be determined by the equilibrium and NIH-type shift as suggested by Walling *et al.* (4). Their results suggest that the rate of the oxidation by Fe^{3+} may be much smaller than that of oxygen addition to the adducts.¹ The fast addition of oxygen also causes the low yield of biphenyl derivatives. However, the exact mechanism for step c is still unclear.

The current efficiency and product distribution were greatly affected by Fe^{2+} concentration because of the reduction of the intermediate cation radical back to the starting material as shown in, Scheme 2, path d. Direct electron transfer from the substrate to hydroxyl radical is prevented (4). The intermediate cation radical undergoes deprotonation and forms the radical (path e) which yields the side-chain oxidation products. According to the mechanism proposed by Snook and Hamilton (6), the alcoholic compounds, formed by the oxidation of the above radical, react again with hydroxyl radical to produce the carbonyl compounds, path g. However, it is deemed that another pathway, *i.e.*, reaction of the above radical with oxygen in so-

¹ The addition rate of oxygen to alkyl radicals is considered to be almost diffusion controlled (28) whereas the oxidation rate of the radical by metal ion seems to be lower (27). Judging from the ratio of the yields of the phenolic products to those of the side-chain oxidation products in toluene oxidation in the presence of Fe^{3+} (4), the rate constant for the adduct oxidation by Fe^{3+} should be $\approx 5 \times 10^6 \text{ M}^{-1} \text{ sec}^{-1}$.



Scheme 2. The schematic mechanism for oxidations of toluene and ethylbenzene by electrogenerated hydroxyl radical in this work.

lution (path f) to form the carbonyl compounds without the formation of alcohols (29), may make a large contribution. This conclusion is derived from the following observation: (i) The yields of alcoholic compounds and bibenzyl derivatives were very low compared with those observed in the homogeneous oxidations in the absence of oxygen (4). (ii) The current efficiencies at low Fe^{2+} and high proton concentration, where relatively high yields of the carbonyl compounds were observed, were very high compared with those at other conditions; these results indicate that one hydroxyl radical was consumed in the formation of one molecule of the carbonyl compounds. Oxygen addition to the radical is considered to be extremely fast and is probably diffusion controlled in many instances (28), so that the yields of bibenzyl derivatives may be low. In cumene oxidation, the methyl group is probably lost in carbonyl formation from the peroxy radical.

Next, we must consider the contribution made by hydrogen abstraction by hydroxyl radical, path b. The acid-catalyzed conversion of the adduct to the intermediate cation radical can occur to a lesser extent when the proton concentration is less than 0.02M, because the yields of the phenolic products were almost independent of proton and Fe^{2+} concentrations under such conditions. In such circumstances, the phenols are formed via addition, path a, and a great deal of the side-chain oxidation products are formed via path b. In toluene oxidation by hydroxyl radical at $[\text{H}^+] = 0.001\text{M}$, most of the products were cresol isomers, which indicates that the addition of the radical to the aromatic ring occurs more easily than the hydrogen abstraction from the side chain by the radical. However, the yields of phenolic products in the oxidations of ethylbenzene and cumene were only 40-50% at $[\text{H}^+] = 0.001\text{M}$. Accordingly, hydrogen abstraction from the α -position may make a certain contribution to the reaction in the oxidations of these compounds.

Finally, the effect of α -CD added to the electrolyte solution must be discussed. By the addition of α -CD, slight increases in the *p*-isomers of the phenolic products were observed in ethylbenzene and cumene oxidations. This fact may be accounted for by the following argument. When these compounds are included in α -CD's cavity, *o*- and *m*-positions of the substrates are not subject to attack of the hydroxyl radical since these positions are blocked by the inner wall of α -CD (30-32). On the other hand, the *p*-position is open to the solution so that the *p*-isomer is formed preferentially (Fig. 2). However, in the case of toluene included in α -CD, the side chain seems to be open to the solution because the toluene oxidation by hydroxyl radical in the presence of α -CD yielded more side-chain oxidation products than phenolic products. Although the included substrate is rapidly replaced by free molecules in solution (22), 60-80% of substrate is included in α -CD at any instance under the present conditions as the dissociation constants of α -CD-alkylbenzene (toluene, ethylbenzene, and cumene) complexes are $2-5 \times 10^{-3}\text{M}$ (no remarkable difference in the values among the three complexes is observed). In spite of the fact that such relatively high inclusion complexes are attained, α -CD had only a small effect on the product distributions. The current efficiencies

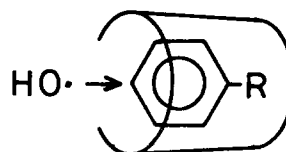


Fig. 2. Selective attack of hydroxyl radical to *p*-position of substrate included in α -CD.

in the presence of α -CD were very low for all cases. These results may be explained in the following two ways: (i) since the substrates can be included in the interior of the α -CD's cavity, the hydroxyl radical can scarcely attack the substrate in α -CD, but can attack free substrate; (ii) the hydroxyl radical reacts with added α -CD in a competitive reaction with the oxidation of substrate by the radical.

Manuscript submitted Dec. 4, 1980; revised manuscript received ca. March 20, 1981.

Any discussion of this paper will appear in a Discussion Section to be published in the June 1982 JOURNAL. All discussions for the June 1982 Discussion Section should be submitted by Feb. 1, 1982.

Publication costs of this article were assisted by Tohoku University.

REFERENCES

- H. J. H. Fenton, *J. Chem. Soc.*, **65**, 8234 (1894).
- F. Haber and J. J. Weiss, *Proy. R. Soc. London, Ser. A*, **147**, 322 (1934).
- C. Walling, *Acc. Chem. Res.*, **8**, 125 (1975).
- C. Walling and R. A. Johnson, *J. Am. Chem. Soc.*, **97**, 363 (1975).
- C. Walling, D. M. Camaioni, and S. S. Kim, *ibid.*, **100**, 4814 (1978).
- M. E. Snook and G. A. Hamilton, *ibid.*, **96**, 860 (1974).
- R. Tomat and E. Vecchi, *J. Appl. Electrochem.*, **1**, 185 (1971).
- T. Wellmann and E. Steckhan, *Chem. Ber.*, **110**, 3561 (1977).
- R. O. C. Norman and R. J. Pritchett, *J. Chem. Soc. B*, **1967**, 926.
- C. R. E. Jefcoate and R. O. C. Norman, *ibid.*, **1968**, 48.
- S. Steenken, P. O'Neill, and D. Schulte-Frohlinde, *J. Phys. Chem.*, **81**, 31 (1977).
- P. O'Neill, S. Steenken, and D. Schulte-Frohlinde, *ibid.*, **81**, 31 (1977).
- K. Sehested, H. Corfitzen, H. C. Christensen, and E. J. Hart, *ibid.*, **79**, 310 (1975).
- J. Holcman and K. Sehested, *ibid.*, **80**, 1642 (1976).
- K. Sehested, J. Holcman, and E. J. Hart, *ibid.*, **81**, 1363 (1977).
- M. Anber and P. Neta, *Int. J. Appl. Radiat. Isot.*, **18**, 493 (1967).
- L. M. Dorfman, I. A. Taub, and R. E. Buhler, *J. Chem. Phys.*, **36**, 3051 (1962).
- M. K. Eberhardt, *J. Phys. Chem.*, **79**, 1913 (1975).
- M. K. Eberhardt and M. I. Martinez, *ibid.*, **79**, 1917 (1975).
- W. Saenger, *Angew. Chem. Int. Ed. Engl.*, **19**, 344 (1980).
- M. Fujihira and T. Kuwana, *Electrochim. Acta*, **20**, 565 (1975).
- F. Cramer, W. Saenger, and H.-Ch. Spatz, *J. Am. Chem. Soc.*, **89**, 14 (1967).
- R. E. Kirk and D. F. Cramer, "Encyclopedia of Chemical Technology," Vol. 10, p. 293, Interscience Publisher, Inc., New York (1953).
- A. Glasel, L. Hsu, and B. L. Funt, *This Journal*, **127**, 315 (1980).
- J. O'M. Bockris and A. K. N. Reddy, "Modern Electrochemistry," Vol. 1, p. 304, Plenum Press, New York (1970).
- O. K. Borggaard, *Acta Chem. Scand.*, **26**, 3393 (1972).
- C. Walling, G. M. El-Taliawi, and R. A. Johnson, *J. Am. Chem. Soc.*, **96**, 133 (1974).
- K. U. Ingold, *Acc. Chem. Res.*, **2**, 1 (1969).
- É. Dauóczy and D. Gál, *J. Chem. Soc. Faraday 1*, **75**, 236 (1979).
- T. Osa, T. Matsue, and M. Fujihira, *Heterocycles*, **6**, 1833 (1977).
- T. Matsue, M. Fujihira, and T. Osa, *This Journal*, **126**, 500 (1979).
- T. Matsue, M. Fujihira, and T. Osa, *Bull. Chem. Soc. Jpn.*, **52**, 3692 (1979).

Anodic Evolution of Oxygen on Sputtered Iridium Oxide Films

S. Hackwood,* L. M. Schiavone,* W. C. Dautremont-Smith,* and G. Beni*

Bell Laboratories, Holmdel, New Jersey 07733

ABSTRACT

We report on the electrocatalytic properties of sputtered iridium oxide films (SIROF's) in acidic electrolytes. Long term stability (240 hr) is demonstrated. Typical steady-state currents are 75 mA/cm² at 1.85V (*vs.* RHE), which is 50% higher than previously reported. In addition, we introduce a new method of determining Tafel slopes based on the short-time decay of the oxygen evolution reaction (OER) current, corrected for the capacitive component. Tafel plots are presented for samples of different thickness and degree of hydration. The high current density and absence of corrosion demonstrate the superior catalytic properties of SIROF's *vs.* iridium over the entire voltage range investigated.

The production of hydrogen is an important commercial process, particularly as hydrogen can be used as a nonpolluting fuel (1). A simple and clean way of producing hydrogen is by electrolysis of water (2). The technology of electrolysis can be substantially improved and many research efforts have been aimed in this direction. At present, electrolysis has a low efficiency due to the high activation overvoltage for oxygen evolution. In addition, for most metals, electrolysis is accompanied by corrosion at high anodic potentials. Thus, much recent research has been focused on finding a better catalyst for the oxygen electrode.

* Electrochemical Society Active Member.
Key words: electrolytes, Tafel slopes, decay.

Commercial electrolyzers using alkaline electrolytes employ anodes such as nickel-plated iron and ferrous nickel alloys (3). More advanced electrolyzers, however, use acid electrolytes, as for example, the solid polymer electrolyte (SPE) electrolyzer developed by General Electric (4). For this acidic electrolyzer a number of anode materials have been proposed, *e.g.*, binary and ternary alloys of Pb, Ir, Ru, Ti, Ta, Nb, Zr, and W. In acidic electrolytes, it has been established that iridium shows the highest catalytic activity for the oxygen evolution reaction (OER).

These findings are based on a purely empirical approach. Few studies have been aimed at establishing the intrinsic factors affecting the OER so that we lack

the information necessary for a theoretical approach for finding better electrocatalysts. Semi-empirically (5), it has become accepted that a good OER catalyst must (i) have a relatively high electronic conductivity; (ii) be capable of existing in a number of valence states; and (iii) have a high affinity for adsorbed OH^- intermediates. Moreover, the electrode must not corrode; hence research has been restricted to the noble metals and their alloys.

Recent studies (6-9) have pointed out that a common factor among different electrodes known to be good electrocatalysts for OER (for example, Ir, Ru, Ni) is the presence of a relatively thick surface oxide film. These thick oxide films have a large ion insertion charge capacity. In many cases (10) reversible ion insertion, with concomitant oxidation reduction, is accompanied by changes in the optical and electrical properties of the films, *i.e.*, the films exhibit electrochromism. An example is the electrochromism of anodic iridium oxide films (AIROF's) (11). AIROF's show good electrocatalytic activity for the OER, producing a higher current density at a given overvoltage than bare iridium (8).

The electrochromic reaction in AIROF's takes place in the region of $\sim 1\text{V}$ *vs.* reversible hydrogen electrode (RHE) in $0.5\text{M H}_2\text{SO}_4$ and is thus a precursor of the OER which occurs with significant rate at $\sim 1.5\text{V}$ (*vs.* RHE). Although the relationship between anodic electrochromism and OER catalysis is not yet understood, it is possible that high electronic conductivity in combination with the increased OH^- content in the colored state favors the OER.

Although AIROF's have higher OER rates than Ir, they dissolve at significant rates at low voltages ($1.4\text{--}1.6\text{V}$ *vs.* RHE), and very rapidly at voltages above 1.6V (*vs.* RHE) in acidic solution (8). Therefore, they are of little use as practical catalysts. In a study of the electrochromic behavior of iridium oxide films, we produced films by reactive sputtering (12). These sputtered iridium oxide films (SIROF's) showed electrochromic behavior similar to that of AIROF's but with significantly higher stability in acidic electrolytes. We expected, therefore, that SIROF's might show superior stability to that of AIROF's under OER conditions. In the sputter deposition of a thin film, highly energetic species in the vapor phase impinge onto a cold substrate. This rapid quenching may produce metastable structures that are thermodynamically unstable at room temperature.

Cyclic voltammograms for sputtered iridium oxide films (SIROF's) are similar to those for AIROF's but differ in detail, *e.g.*, the potential at which the peak in the oxidation-reduction current occurs is $\sim 0.80\text{V}$ (RHE) rather than $\sim 0.95\text{V}$ (RHE). Both voltammograms at quasi-equilibrium rates are nearly symmetric about the voltage axis within the range $+0.25 \rightarrow +1.25$ (*vs.* RHE) resulting in excellent reversibility when operated within this range of potentials where electrochromism is observed. We have previously shown (13) that SIROF's exhibit a high OER electrocatalytic activity (similar to AIROF's) but, in contrast to AIROF's, are stable OER electrocatalysts.

In this paper we report a detailed characterization of the electrocatalytic activity of SIROF's. In the next section we describe the film preparation and describe the general parameters necessary to produce films with high catalytic activity. In the "Results" section we report the effects of hydration, and the long-term stability tests for oxygen evolution. We then report the catalytic activities of films prepared under different sputtering conditions. Finally, we analyze the intrinsic, as opposed to steady-state, activity of SIROF's. For this purpose, we introduce a new method of measuring the intrinsic catalytic activity, based on application of a pulsed voltage. In this way we have obtained Tafel plots over a wide voltage range. In the final section we summarize the main conclusions drawn from these

measurements and discuss the general implications of this work for electrocatalysis research.

Experimental

Film preparation.—SIROF's were deposited on tantalum or on quartz substrates. For depositions on quartz, standard photoresist patterning and lift-off techniques were used to produce a sharp edge in the SIROF, at which a stylus instrument was used to measure film thickness (14). Electrocatalytic activity of SIROF's was investigated using tantalum substrates. The substrates were washed in detergent bath, rinsed in distilled water, ultrasonically cleaned in isopropyl alcohol, and vapor degreased in isopropyl alcohol. SIROF's were deposited from an iridium target in an O_2 plasma using a conventional diode rf sputtering system as described in Ref. (12). The pressure of oxygen in the sputtering chamber was 8 or 20 mTorr. Deposition times ranged between 20 min and 4 hr producing films of thickness 200–320Å.

Electrochemical characterization.—The electrochemical properties of the SIROF's were examined in $0.5\text{M H}_2\text{SO}_4$ electrolyte made up from spectroscopic grade sulfuric acid and deionized water. Using potentiostatic control, the current voltage characteristics of the SIROF's were examined in the potential range -0.25 – $+1.15\text{V}$ *vs.* a saturated calomel reference electrode. The cyclic voltammograms, for both AIROF's and SIROF's, recorded at a sweep rate of 100 mV/sec , are shown in Fig. 1.

SIROF's and AIROF's are ion-insertion materials, and the voltammograms in the range of $0\text{--}1\text{V}$ (*vs.* SCE) show almost complete reversibility.¹ A charge capacity, ΔQ , can be defined as the charge inserted when the potential is stepped between two arbitrarily chosen limits. ΔQ is related to the film thickness and the number of accessible iridium sites (10). For SIROF's over the potential step of $0\text{--}1\text{V}$, the number of accessible sites is ~ 0.7 per Ir atom.

Electrocatalytic activity.—The electrocatalytic activity of SIROF's was examined by measuring the OER current in $0.5\text{M H}_2\text{SO}_4$ in the voltage range $1.50\text{--}2.50\text{V}$ (*vs.* RHE). OER current characteristics were examined

¹ It is interesting that the hydrogen peaks are missing. This absence has been observed also for AIROF's grown on tin oxide [see J. L. Shay, G. Beni, and L. M. Schlavone, *Appl. Phys. Lett.*, **33**, 942 (1978)] and interpreted as due to the nonexposure of the substrate to the solution. On the other hand, the peak absence could be due to the presence of organic impurities in the deionized water. [See B. E. Conway, *Anal. Chem.*, **45**, 1331 (1973).]

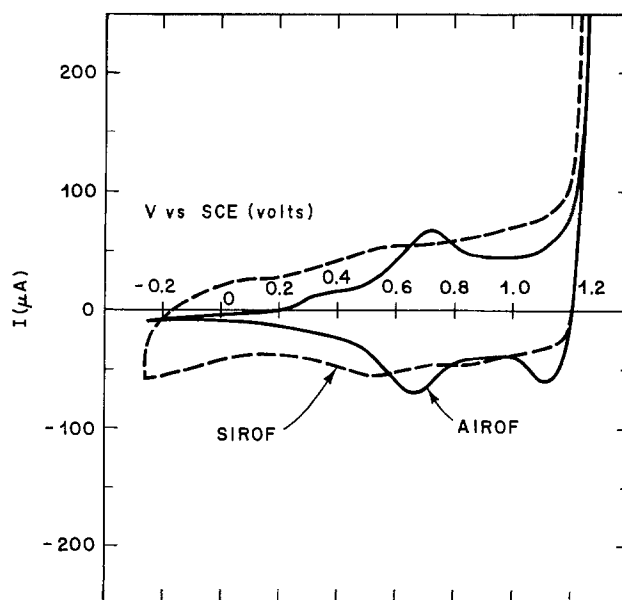


Fig. 1. Cyclic voltammograms for SIROF's and AIROF's recorded at a sweep rate of 100 mV sec^{-1} , in $0.5\text{M H}_2\text{SO}_4$.

for SIROF's as a function of: (i) degree of hydration, (ii) time, and (iii) film thickness. The response of SIROF's to a square wave voltage between the OER voltage, and a lower, more cathodic voltage was also investigated to provide a measure of the intrinsic catalytic activity from which Tafel plots could be constructed. On completion of these experiments, the cyclic voltammogram and charge capacity of the SIROF were remeasured. In addition, the electrolyte was analyzed for iridium content by the stannous iodide method described in Ref. (15), and by atomic emission. The electrolyte solution was stirred throughout the experiments, and all of the data reported are corrected for IR losses in the electrolyte.

Results

In this section we report measurements of (i) the effect of hydration on the catalytic activity of SIROF's, (ii) steady-state oxygen evolution currents, and (iii) Tafel plots for various films.

Hydration.—Figure 2 shows the oxygen evolution current as a function of time at 1.95V (*vs.* RHE) for an as-deposited SIROF (3000Å thick) of total charge capacity $\Delta Q = 70 \text{ mC cm}^{-2}$. The current increases by approximately 20% during the first few minutes of operation, but then decreases. A current decay similar to this occurs for most other materials used as OER anodes. The initial increase in the SIROF OER current is possibly due to an "opening" of the film structure by hydration. Volume changes induced by the electrochromic process in as-deposited SIROF's have been recently reported (14). It has been shown that SIROF's, after a few ion-insertion cycles, expand by incorporation of water, and hydration increases the rate of ion insertion by about an order of magnitude. Similarly, we see from Fig. 2 that hydration also increases the oxygen evolution current.

The effects of hydration are also evident in the cyclic voltammograms shown in Fig. 3. The solid line shows the voltammogram produced on initial cycling of an as-deposited SIROF between 0 and 1V (*vs.* SCE) in 0.5M H_2SO_4 , and the dashed line is that of the same sample after 10 min of OER. The total charge transferred increases on hydration; in this case ΔQ increases from 51 to 57 mC cm^{-2} . This increase could be due to an increase in the number of sites exposed to the electrolyte, which is consistent with the picture of a more "opened" structure of the film. Figures 2 and 3 thus indicate that hydration of the deposited films is important for good OER catalytic activity.²

² An alternative explanation of the OER current maximum is adsorption of impurities from deionized water.

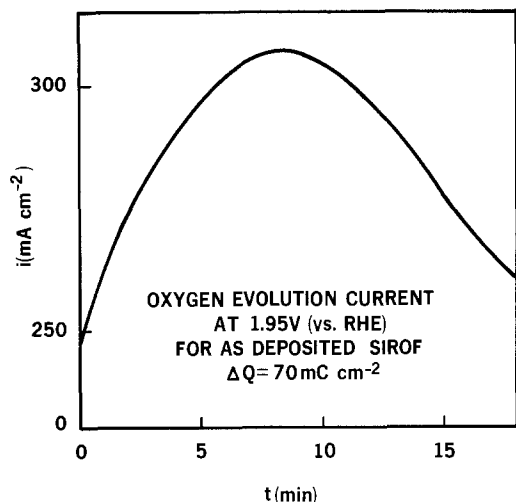


Fig. 2. Oxygen evolution current as a function of time at 1.95V (*vs.* RHE) for an as-deposited SIROF (3000Å thick) of total charge capacity $\Delta Q = 70 \text{ mC cm}^{-2}$.

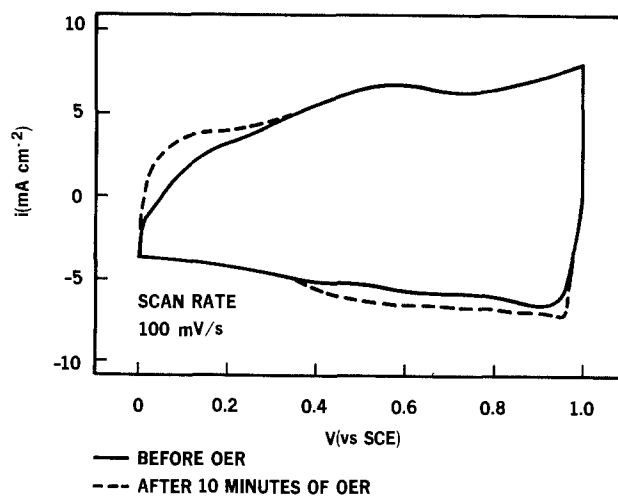


Fig. 3. The solid line shows the voltammogram produced on initial cycling of an as-deposited SIROF between 0 and 1V (*vs.* SCE) in 0.5M H_2SO_4 and the dashed line is that of the same sample after 10 min of OER.

Steady-state current.—Figure 4 shows the oxygen evolution current at 1.95V (*vs.* RHE) for a film of total charge capacity, (measured after hydration) $\Delta Q = 70 \text{ mC cm}^{-2}$ and film thickness as deposited of $\sim 3200\text{\AA}$. The initially high current decreases with time and reaches a steady state after ~ 5 days. This steady-state current remains constant at $\sim 75 \text{ mA cm}^{-2}$ for over 18 days (the time limit of the experiment).

The SIROF did not corrode during OER, and no iridium was detected in the electrolyte. The voltammogram and total ΔQ recorded after 18 days of OER were unchanged from the initial values. In contrast, at 1.95V (RHE), pure iridium corrodes. In Ref. (16) the measured corrosion current is $58 \mu\text{C/cm}^{-2}$ per cycle of potential sweep.³ At this rate an amount of iridium metal equivalent to that contained in the sputtered film would be lost in approximately 20 min.

Figure 5 shows the OER current for SIROF's of three different thicknesses. Thickness (d) and charge capacity (ΔQ) of the SIROF's are shown in the inset in the upper right corner of the figure. The OER current density is seen to be dependent on film thickness, but not linearly as for thickness *vs.* charge density. There is a difference in the OER currents for the two thicker films of only 50%, whereas, the thicknesses of the two films differ by a factor of ~ 7 . It has been postulated (8, 17) for AIROF's that the high catalytic activity is due to a highly porous structure. This, however, does not seem to be true for SIROF's. A highly porous structure implies a high surface to vol-

³ Note that noble metals dissolve faster under alternating currents.

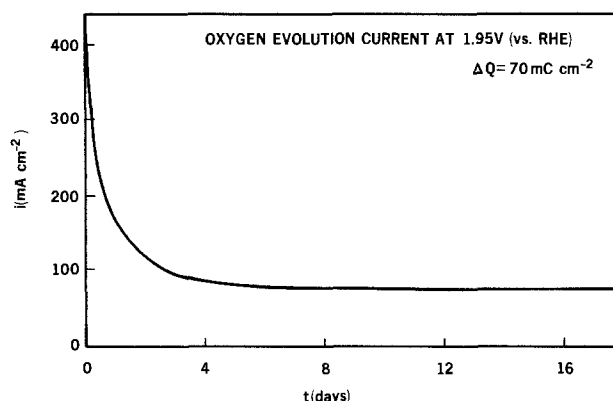


Fig. 4. Oxygen evolution current at 1.95V (*vs.* RHE) for a film of total charge capacity, (measured after hydration) $\Delta Q = 70 \text{ mC cm}^{-2}$ and film thickness (as deposited) of $\sim 3200\text{\AA}$.

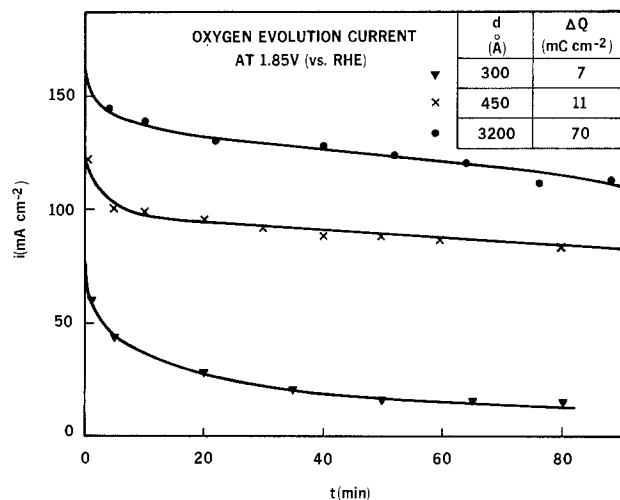


Fig. 5. OER current for SIROF's of three different thicknesses

ume ratio, independent of film thickness increases. If the catalytic activity were due to the number of active surface sites, activity and OER current would be linearly dependent on film thickness. The thinnest film shows substantially lower OER; this is, however, not due to an intrinsic factor, but to poor mechanical stability, as evidenced by loss of portions of the film. (It is possible that a critical thickness of the sputtered film must be reached before a mechanically stable layer is obtained.)

Tafel plots.—There has been uncertainty in how to measure the intrinsic catalytic activity of oxide films (18). The difficulty arises because the OER current decays at a variable rate from its initial value to the steady-state value which may not be achieved for a number of days. The catalytic activity is usually (8) measured by the value of the OER current after an arbitrarily specified time, (e.g., 10 min following the onset of OER). This, however, leads to errors in the interpretation of the Tafel slopes because, in many cases, decay times vary with different voltages plots. A further difficulty with this type of measurement is that the initial value of the OER current is dependent on the history of the anode.

To overcome this problem, we have employed a pulse technique which gives a measure of intrinsic catalytic activity. In Fig. 6(a), we show the current response to an applied 0.5 Hz square wave voltage, pulsed between +1.95 and +0.05V (vs. RHE). The current corresponding to the anodic voltage is plotted as a solid line, whereas the cathodic current is shown as a dashed line. The sharp current spikes are due to the charging and discharging of the overall film capacitance (double layer and ion insertion). The OER current is measured by the slowly decaying current following the initial current spike. By extrapolating these current decays to intersect the current axis at $t = 0$, we obtain a measure of the OER current. Figure 6(b) shows the current obtained under voltage driving conditions identical to those of Fig. 6(a) but following 5 min polarization at +0.05V (vs. RHE). It can be seen that the OER currents are unchanged. This procedure of determining intrinsic catalytic activity is reproducible, and has been repeated on many samples under different conditions.

Using this method we have been able to construct Tafel plots for SIROF's and compare them with Tafel plots obtained for iridium. Figure 7 shows Tafel plots for iridium and an SIROF in the potential range 1.5–2.2V (vs. RHE). The figure shows that at low voltages the Tafel plots of iridium and SIROF differ substantially. At the lowest voltages the current for SIROF is approximately two orders of magnitude higher than that for iridium. At high voltages, the oxygen evolu-

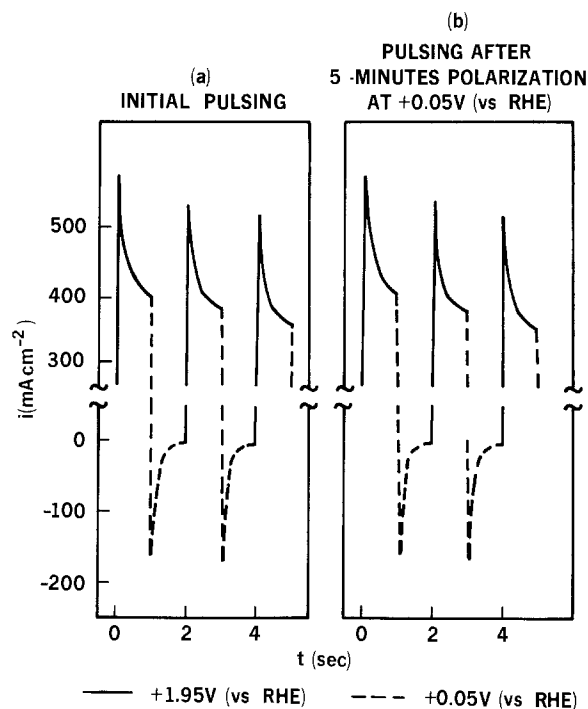


Fig. 6. Pulse technique to measure intrinsic catalytic activity. In (a), we show the current response to an applied 0.5 Hz square wave voltage, pulsed between +1.95 and +0.05V (vs. RHE). The current corresponding to the anodic voltage is plotted as a solid line, whereas the cathodic current is shown as a dashed line. In (b) is shown the current obtained under voltage driving conditions identical to those (a) but following 5 min polarization at +0.05V (vs. RHE). It can be seen that the OER currents are unchanged.

tion currents are similar. The dashed line delineates the voltage region above which Ir corrodes (16) at a rate greater than $200 \mu\text{A cm}^{-2}$.

Finally, Figure 8 compares the Tafel plots of three different samples of SIROF's. The samples were deposited at oxygen pressures of either 20 or 8 mTorr with a total charge capacitance ΔQ of 70 and 35 mC cm^{-2} , respectively, as indicated in the upper left inset. From the figure, it can be seen that the intrinsic catalytic activity of these films is similar.

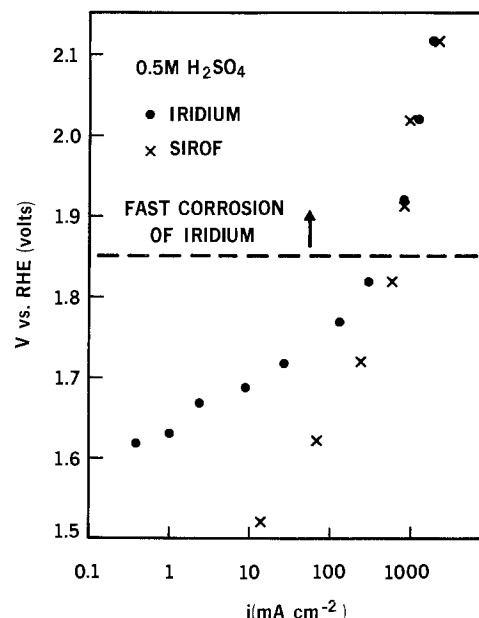


Fig. 7. Tafel plots for iridium and an SIROF in the potential range 1.5–2.2V (vs. RHE).

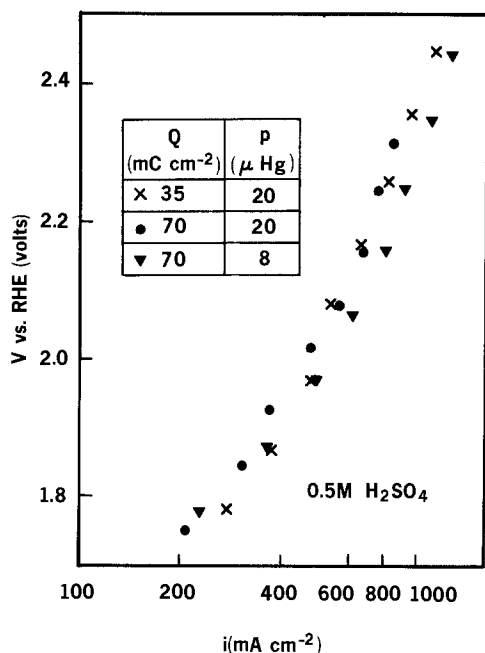


Fig. 8. Tafel plots of three different samples of SIROF's. The samples were deposited at oxygen pressures of either 20 or 8 mTorr with a total charge capacitance ΔQ of 70 and 35 mC cm⁻², respectively, as indicated in the upper left inset.

Conclusions

From these results, we can draw two main conclusions. Firstly, sputtered iridium oxide films show high OER catalytic activity. In the steady state the oxygen evolution reaction current is 75 mA cm⁻² (geometric area) at 1.95V (vs. RHE), which is approximately equal to that for bare iridium. The intrinsic (i.e., measured with the voltage pulsing technique) OER current shows that the catalytic activity of SIROF's is approximately two orders of magnitude larger than that of bare iridium at low overvoltages and approximately equal to bare iridium at high overvoltages.

Secondly, SIROF's show excellent corrosion resistance, even at high overvoltages. We observed no corrosion during 18 days of operation at 1.95V (vs. RHE) in 0.5M H₂SO₄. In addition, no corrosion was observed during the pulsed experiments.

Our results demonstrate, also, that the catalytic activity is not simply due to a large effective surface area because of a macroscopically porous structure. In fact, no significant change of catalytic activity was observed for films differing in thickness by almost an order of magnitude. Thus, the superior activity of iridium oxide is not due to a large number of iridium atoms exposed to the electrolyte, but is a property of the oxide itself.

It is conceivable that by reactively sputtering, we are not simply producing a large surface area catalyst, but a material which could not be formed under thermodynamic equilibrium. Indeed, the free energy of the SIROF is likely to be far higher than the free energy of iridium oxide. We may thus expect the structure to be amorphous or to contain a large number of oxygen vacancies. This structure may be regarded also as a "microscopically porous" structure. This hypothesis should be substantiated by detailed

x-ray structure analysis of the films. Work in this direction is in progress (19, 20). A large number of vacancies favors the OER because hydroxyl anions have easy access (via the vacancies) to the bulk of the film. In this case the "oxide-path" of oxygen evolution (21) would be the rate-determining mechanism of the reaction.

Finally, we speculate that our interpretation of the high catalytic activity and high stability of SIROF's (if correct) is also applicable to other oxides, since the SIROF's catalytic properties are due to the particular structure formed during sputtering, and not to a high number of metal ions exposed to the electrolyte.

Manuscript submitted March 12, 1981; revised manuscript received June 5, 1981.

Any discussion of this paper will appear in a Discussion Section to be published in the June 1982 JOURNAL. All discussions for the June 1982 Discussion Section should be submitted by Feb. 1, 1982.

Publication costs of this article were assisted by Bell Laboratories.

REFERENCES

1. See, e.g., "Hydrogen: Its Technology and Implications," K. E. Cox and K. D. Williamson, Jr., Editors, CRC Press Inc. (1979).
2. See, e.g., T. Takahashi, in "Solar Hydrogen Energy Systems," T. Ohta, Editor, p. 35, Pergamon Press, New York (1979).
3. A. P. Fickett and F. R. Kalhammer, in "Hydrogen: Its Technology and Implications," K. E. Cox and K. D. Williamson, Jr., Editors, p. 4, CRC Press, Inc. (1979).
4. See "Hydrogen: Its Technology and Implications," K. E. Cox and K. D. Williamson, Jr., Editors, p. 22, CRC Press, Inc., (1979).
5. J. P. Hoare, "The Electrochemistry of Oxygen," Interscience, New York (1968).
6. D. A. J. Rand and R. J. Woods, *J. Electroanal. Chem. Interfacial Electrochem.*, **55**, 375 (1974).
7. D. N. Buckley and L. D. Burke, *J. Chem. Soc. Faraday Trans. I*, **71**, 1447 (1975).
8. See, e.g., S. Gottesfeld and S. J. Srinivasan, *J. Electroanal. Chem. Interfacial Electrochem.*, **84**, 117 (1977).
9. J. Mozota, M. Vukovic, and B. E. Conway, *ibid.*, **114**, 153 (1980).
10. G. Beni, 3rd International Meeting on Solid State Ionics, Tokyo, (1980); and *Solid State Ionics*, To be published.
11. G. Beni, C. E. Rice, and J. L. Shay, *This Journal*, **127**, 1342 (1980) and references therein.
12. L. M. Schiavone, W. C. Dautremont-Smith, G. Beni, and J. L. Shay, *Appl. Phys. Lett.*, **35**, 823 (1979).
13. G. Beni, L. M. Schiavone, J. L. Shay, W. C. Dautremont-Smith, and B. S. Schneider, *Nature*, **282**, 281 (1979).
14. S. Hackwood, W. C. Dautremont-Smith, G. Beni, L. M. Schiavone, and J. L. Shay, *This Journal*, **128**, 1212 (1981).
15. E. W. Berg and H. L. Youmas, *Anal. Chem. Acta*, **25**, 470 (1961).
16. D. N. Buckley and L. D. Burke, *J. Chem. Soc. Faraday Trans. I*, **71**, 2431 (1976).
17. E. J. Frazer and R. Woods, *J. Electroanal. Chem. Interfacial Electrochem.*, **102**, 127 (1979).
18. K. J. Vetter, "Electrochemical Kinetics," Academic Press, New York (1967).
19. S. Hackwood, P. K. Gallagher, and G. Beni, *Solid State Ionics*, To be published.
20. S. Hackwood, A. Dayem, and G. Beni, *Phys. Rev. B*, To be published.
21. J. O'M. Bockris and A. K. N. Reddy, "Modern Electrochemistry," Plenum Press, New York (1970).

Moderate Temperature Na Cells

III. Electrochemical and Structural Studies of $\text{Cr}_{0.5}\text{V}_{0.5}\text{S}_2$

and Its Na Intercalates

K. M. Abraham* and L. Pitts

EIC Laboratories, Incorporated, Newton, Massachusetts 02158

ABSTRACT

Cathodic behavior of the layered mixed metal sulfide, $\text{Cr}_{0.5}\text{V}_{0.5}\text{S}_2$, has been studied in a rechargeable Na cell having the configuration

Liquid $\text{Na}/\beta''\text{-Al}_2\text{O}_3/\text{Na}^+$ -containing electrolyte/ $\text{Cr}_{0.5}\text{V}_{0.5}\text{S}_2$

The cell operates at 130°C and utilizes as electrolyte a 1M solution of NaI in 1,2-bis(2-methoxy-ethoxy)ethane, (triglyme). The first discharge of $\text{Cr}_{0.5}\text{V}_{0.5}\text{S}_2$ yielded a capacity of 0.95 e/mole of the sulfide. However, the rechargeable capacity was limited to ~70% of the first discharge. The mechanism of discharge of $\text{Cr}_{0.5}\text{V}_{0.5}\text{S}_2$ involves Na intercalation. More than one crystallographically distinct phase has been identified in the compositional range, $0 < y \leq 1$ in $\text{Na}_y\text{Cr}_{0.5}\text{V}_{0.5}\text{S}_2$.

The layered transition metal disulfides and diselenides have received widespread interest as rechargeable cathodes for electrochemical cells utilizing alkali metal anodes (1, 2). While most of the interest has been in rechargeable Li cells, some recent studies, particularly from this laboratory, have explored the usefulness of several dichalcogenide cathodes for secondary Na cells (3-6). Thus, we have evaluated the cathodic behavior of the disulfides (3), TiS_2 , VS_2 , and $\text{Nb}_{1.1}\text{S}_2$, and the diselenides (4), TiSe_2 and VSe_2 in a moderate temperature Na cell. This cell, which is a modification of the rechargeable Na/soluble S cell we described earlier (7, 8), utilizes a $\beta''\text{-Al}_2\text{O}_3$ solid electrolyte separator and an organic electrolyte comprising NaI in 1,2-bis(2-methoxy-ethoxy)ethane, (triglyme). Our x-ray structural studies (3, 4) of the electrochemically cycled cathodes showed that in all transition metal chalcogenides, the cathode reaction involved Na intercalation during discharge and deintercalation during recharge.

The topochemical reaction of the layered transition metal dichalcogenides with Na is often accompanied by structural changes of the host lattice so that in a given Na_yMX_2 ternary more than one crystallographically distinct phase appears with the degree of intercalation (2, 9-12). These crystallographic changes are often revealed in the electrochemical discharges which show potential plateaus closely correlating the structural changes (3, 4). In the case of the disulfides investigated, these structural changes affected cathode rechargeability. Thus with VS_2 and TiS_2 cathodes, only the Na associated with certain phase regions of the Na_yMS_2 ternary was rechargeable (3, 5).

The mixed metal disulfide, $\text{Cr}_{0.5}\text{V}_{0.5}\text{S}_2$ presents an interesting situation since the structural characteristics of the Na intercalates and consequently its electrochemical properties would be influenced by both Cr and V. In this paper we present our results on the structural and electrochemical properties of $\text{Cr}_{0.5}\text{V}_{0.5}\text{S}_2$ and $\text{Na}_y\text{Cr}_{0.5}\text{V}_{0.5}\text{S}_2$.

Experimental

All the experiments were conducted in the absence of air and moisture under an argon atmosphere in a Vacuum Atmospheres dry box or by using standard procedures employed for the manipulation of air sensi-

tive compounds (13). Elemental analyses were carried out by Galbraith Analytical Services, Knoxville, Tennessee.

Synthesis of the sulfides.— $\text{Cr}_{0.5}\text{V}_{0.5}\text{S}_2$.—The sulfide was synthesized via a two-step process combining the procedures of Van Laar (14) and Murphy (15). Initially $\text{LiCr}_{0.5}\text{V}_{0.5}\text{S}_2$ was synthesized by the reaction of H_2S with an intimate mixture of Li_2CO_3 , V_2O_5 , and Cr_2O_3 present in the mol ratio of 1:0.5:0.5 at 700°C for 16 hr.

The air sensitive $\text{LiCr}_{0.5}\text{V}_{0.5}\text{S}_2$ thus obtained was delithiated by the reaction of an $\text{I}_2/\text{CH}_3\text{CN}$ solution at room temperature. The dark $\text{Cr}_{0.5}\text{V}_{0.5}\text{S}_2$ produced was washed several times with CH_3CN and dried *in vacuo* at ~150°C. The material was characterized by x-ray and elemental analyses. The Debye-Sherrer x-ray data, shown in Table I, is consistent with a layered 1T-CdI₂ type structure with $a = 3.22\text{\AA}$ and $c = 5.71\text{\AA}$.

VS_2 .—The compound was synthesized in the same manner as that of $\text{Cr}_{0.5}\text{V}_{0.5}\text{S}_2$ using Li_2CO_3 and V_2O_5 (3, 16). It exhibited a 1T-CdI₂ structure (16).

Sodium intercalates of $\text{Cr}_{0.5}\text{V}_{0.5}\text{S}_2$.—Sodium intercalates of various compositions were prepared by adding the disulfide to a requisite quantity of Na-naphthalide (0.3M in THF) and stirring the resulting mixture for 3 days at room temperature. In preparing the fully intercalated compounds, $\text{Na}_{1.0}\text{MS}_2$, a 30% excess of the naphthalide solution was initially used. The sodiated compound was separated by filtration and dried *in vacuo* initially at room temperature and then at ~70°C for 12 hr. The filtrate was analyzed for

Table I. X-ray diffraction data of $\text{Cr}_{0.5}\text{V}_{0.5}\text{S}_2$

| d (obs), Å | d (cal), Å | I/I ₀ | hkl |
|------------|------------|------------------|-------|
| 5.71 | 5.71 | 40 | 0 0 1 |
| 2.78 | 2.79 | 5 | 1 0 0 |
| 2.49 | 2.50 | 100 | 1 0 1 |
| 2.01 | 1.99 | 65 | 1 0 2 |
| 1.61 | 1.61 | 30 | 1 1 0 |
| 1.57 | 1.57 | 25 | 1 0 3 |
| 1.55 | 1.55 | 10 | 1 1 1 |
| 1.43 | 1.43 | 10 | 0 0 4 |
| 1.35 | 1.35 | 10 | 2 0 1 |
| 1.27 | 1.25 | 5 | 2 0 2 |

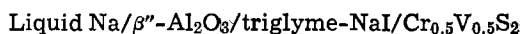
$a = 3.22\text{\AA}$ and $c = 5.71\text{\AA}$.

* Electrochemical Society Active Member.
Key words: cathode, cycling, x-ray, phases.

unreacted Na-naphthalide by titrating an aqueous solution of the filtrate with a standard solution of HCl acid. The composition of the sodium intercalate thus obtained was further checked by elemental analysis and showed good agreement.

X-ray powder patterns of the samples were recorded using $\text{CuK}\alpha$ radiation and a Debye-Sherrér camera.

Electrochemical cell.—The electrochemical cell incorporating a $\beta''\text{-Al}_2\text{O}_3$ tube was of the same type described previously (3, 7). The sulfide cathodes were fabricated in the form of pressed electrodes from a cathode mix consisting of ~50 weight percent (w/o) sulfide, 40 w/o Shawinigan carbon (50% compressed), and 10 w/o Teflon (du Pont 7A), as described previously (3, 4). The electrolyte was a 1M solution of NaI in 1,2-bis(2-methoxy-ethoxy)ethane, triglyme (3). The assembled cell had the configuration



The cells were cycled galvanostatically after thermostating at 130°C (3, 4, 7).

Results and Discussion

Structure of $\text{Cr}_{0.5}\text{V}_{0.5}\text{S}_2$.—The disulfide has a hexagonal layered 1T-CdI₂-type structure similar to that of TiS_2 or VS_2 . The unit cell parameters $a = 3.22\text{\AA}$ and $c = 5.71\text{\AA}$ are comparable to those of VS_2 , $a = 3.22\text{\AA}$ and $c = 5.74\text{\AA}$, and TiS_2 , $a = 3.41\text{\AA}$ and $c = 5.69\text{\AA}$. VS_2 has only recently been characterized (16). The existence of the hexagonally layered mixed metal sulfides, $\text{Cr}_N\text{V}_{1-N}\text{S}_2$ and $\text{Fe}_N\text{V}_{1-N}\text{S}_2$ has been established in the recent studies of Murphy and co-workers (15). Their studies, however, emphasized $\text{Cr}_{0.75}\text{V}_{0.25}\text{S}_2$, focusing on their use as reversible cathodes in non-aqueous solvent Li cells. The structural data on $\text{Cr}_{0.5}\text{V}_{0.5}\text{S}_2$ are reported here for the first time.

Electrochemical behavior of $\text{Cr}_{0.5}\text{V}_{0.5}\text{S}_2$.—An electrochemical cell incorporating a $\text{Cr}_{0.5}\text{V}_{0.5}\text{S}_2$ cathode was discharged at a low rate, i.e., at 0.5 mA/cm², to determine the capacity and the shape of the discharge curve. Typical discharge curves for two different cells are shown in Fig. 1 and 2. The first discharge corresponds to a capacity of 0.95 e⁻/mol of $\text{Cr}_{0.5}\text{V}_{0.5}\text{S}_2$.

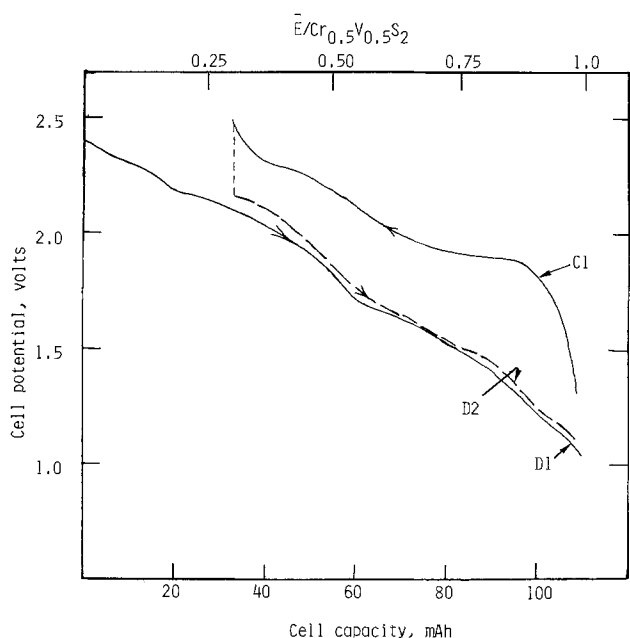


Fig. 1. Galvanostatic discharges and charges of the cell, liquid $\text{Na}/\beta''\text{-Al}_2\text{O}_3/\text{triglyme, NaI}/\text{Cr}_{0.5}\text{V}_{0.5}\text{S}_2$ at 130°C. Curves D1 and D2 are the first and second discharges. Curve C1 is the first charge. Current density = 0.5 mA/cm².

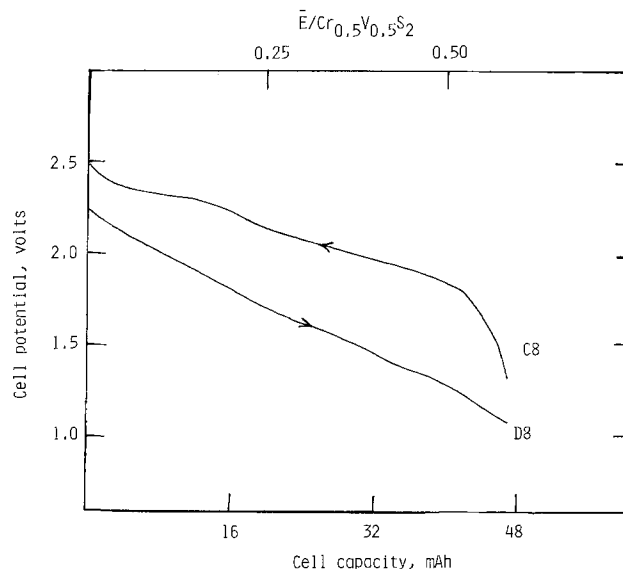


Fig. 2. The eighth cycle of a liquid $\text{Na}/\beta''\text{-Al}_2\text{O}_3/\text{triglyme, NaI}/\text{Cr}_{0.5}\text{V}_{0.5}\text{S}_2$ cell at 130°C. Current density = 0.5 mA/cm².

The discharge shows a somewhat gradual but definite end point to 1.1V. The first discharge is characterized by three potential regions spanning the Na compositional ranges (y) approximately at $0 < y < 0.17$, $0.17 < y \leq 0.55$, and $0.55 < y \leq 0.95$. In the first charge, only 70% of this capacity was recharged to 2.5V. The charge curve shows a definite end point at this stage. The capacity in the second discharge was 0.67 e⁻/ $\text{Cr}_{0.5}\text{V}_{0.5}\text{S}_2$. Capacity losses with further cycling were minor and occurred in a gradual fashion, reflecting, as we found previously (3), electrode structural factors. However, the later cycles, illustrated in Fig. 2 by cycle 8 of a second cell, do not show the multistep characteristics seen in the early cycles; but rather the potential profiles of the later cycles are almost linear.

The Debye-Sherrér x-ray pattern of a $\text{Cr}_{0.5}\text{V}_{0.5}\text{S}_2$ cathode cycled nine times and terminated at the end of the discharge is tabulated in Table II. The pattern, on the basis of the structural data discussed below for $\text{Na}_y\text{Cr}_{0.5}\text{V}_{0.5}\text{S}_2$ ternaries, can be assigned to two different crystallographic phases of the $\text{Na}_y\text{Cr}_{0.5}\text{V}_{0.5}\text{S}_2$ ternary. Evidently Na discharge into and recharge from $\text{Cr}_{0.5}\text{V}_{0.5}\text{S}_2$ involves intercalation and deintercalation, respectively. The processes are, however, accompanied by crystallographic phase changes in the $\text{Na}_y\text{Cr}_{0.5}\text{V}_{0.5}\text{S}_2$ ternaries.

Structural aspects of the $\text{Na}_y\text{Cr}_{0.5}\text{V}_{0.5}\text{S}_2$ ternaries.—Sodium intercalates of $\text{Cr}_{0.5}\text{V}_{0.5}\text{S}_2$ and VS_2 were prepared by reaction of the respective sulfide with Na-naphthalide. The x-ray pattern for $\text{Na}_y\text{Cr}_{0.5}\text{V}_{0.5}\text{S}_2$ where $y = 1$ is shown in Table III. The pattern can be satisfactorily indexed for a 3R rhombohedral structure with space group $R\bar{3}M$, isomorphous with $\text{Na}_{1.0}\text{TiS}_2$ (17) and $\text{Na}_{1.0}\text{CrS}_2$ (18). The lattice parameters are $a = 3.52\text{\AA}$ and $c = 19.65\text{\AA}$. In this structure, which may be designated as the trigonal antiprismatic (TAP) form, sulfur forms a cubic close packing while the

Table II. X-ray diffraction data of cycled* $\text{Cr}_{0.5}\text{V}_{0.5}\text{S}_2$

| d, Å | d (cal), Å | I/I ₀ | hkl |
|------|------------|------------------|-----------------|
| 7.05 | 7.08 | 0.8 | 0 0 3 (TP) |
| 6.53 | 6.55 | 0.8 | 0 0 3 (TAP) |
| 2.60 | 2.59 | 1.0 | 1 0 4 (TAP) |
| 2.40 | 2.34 | 0.4 | 0 1 5 (TP) |
| 2.07 | 2.06 | 0.2 | 1 0 7 (TAP, TP) |

* Many of the expected lines in the x-ray pattern were absent, probably due to interference from the carbon and Teflon present in the electrode.

Table III. X-ray diffraction data of $\text{Na}_{1.0}\text{Cr}_{0.5}\text{V}_{0.5}\text{S}_2$

| d (obs), Å | d (cal), Å | I/I ₀ | hkl |
|------------|------------|------------------|--------|
| 6.55 | 6.55 | 0.7 | 0 0 3 |
| 3.02 | 3.01 | 0.1 | 1 0 1 |
| 2.60 | 2.59 | 1.0 | 1 0 4 |
| 2.06 | 2.06 | 0.3 | 1 0 7 |
| 1.91 | 1.91 | 0.5 | 0 1 8 |
| 1.76 | 1.76 | 0.8 | 1 1 0 |
| 1.70 | 1.70 | 0.1 | 1 1 3 |
| 1.56 | 1.54 | 0.1 | 0 1 11 |
| 1.50 | 1.51 | 0.1 | 2 0 2 |
| 1.45 | 1.46 | 0.4 | 0 2 4 |
| 1.29 | 1.29 | 0.3 | 2 0 8 |
| 1.20 | 1.20 | 0.3 | 0 2 10 |

$a = 3.52\text{Å}$, $c = 19.65\text{Å}$.

transition metal atoms and Na occupy distorted octahedral interstices in alternate layers (14).

We have also prepared Na intercalates of nominal compositions $\text{Na}_{0.2}\text{Cr}_{0.5}\text{V}_{0.5}\text{S}_2$, $\text{Na}_{0.4}\text{Cr}_{0.5}\text{V}_{0.5}\text{S}_2$, $\text{Na}_{0.6}\text{Cr}_{0.5}\text{V}_{0.5}\text{S}_2$, and $\text{Na}_{0.8}\text{Cr}_{0.5}\text{V}_{0.5}\text{S}_2$. The compositions $\text{Na}_{0.2}\text{Cr}_{0.5}\text{V}_{0.5}\text{S}_2$ and $\text{Na}_{0.4}\text{Cr}_{0.5}\text{V}_{0.5}\text{S}_2$ appeared to be homogeneous phases whereas the other materials constituted a mixture of the TAP phase and of the phase corresponding to $\text{Na}_{0.4}\text{Cr}_{0.5}\text{V}_{0.5}\text{S}_2$. The x-ray pattern of the latter material is tabulated in Table IV. The ternary appears to have a phase isostructural with that of Na_yTiS_2 for $0.38 < y < 0.72$, discussed by Rouxel (17). This phase, which may be designated as the trigonal prismatic (TP) phase, (space group R3M) has a rhombohedral structure with Na occupying trigonal prismatic sites and the transition metal atoms octahedral sites. The lattice parameters of $\text{Na}_{0.4}\text{Cr}_{0.5}\text{V}_{0.5}\text{S}_2$ are $a = 3.24\text{Å}$ and $c = 21.24\text{Å}$. An isostructural phase was identified also in the Na_yVS_2 ternaries for $0.3 \leq y \leq 1$ by Wiegiers (11). It is to be noted that these Na_yVS_2 compositions of Wiegiers were prepared by a high temperature route.

For $\text{Na}_{1.0}\text{VS}_2$, Wiegiers identified two other phases, a TAP phase isostructural with NaCrS_2 and a hexagonal form isostructural with Li_yTiS_2 (19) or LiVS_2 (14). For comparison with the low temperature synthetic route employed in the present study for $\text{Na}_y\text{Cr}_{0.5}\text{V}_{0.5}\text{S}_2$, we have prepared $\text{Na}_{0.8}\text{VS}_2$ and $\text{Na}_{1.0}\text{VS}_2$ by the Na-naphthalide reaction. The structural data for $\text{Na}_{1.0}\text{VS}_2$ are listed in Table V. The sample contains a mixture of the hexagonal form, $a = 3.22\text{Å}$, $c = 7.3\text{Å}$ and the TAP form, $a = 3.54\text{Å}$ and $c = 19.74\text{Å}$. The results are in agreement with those of Wiegiers and support his suggestion that the TP form of $\text{Na}_{1.0}\text{VS}_2$ is a high temperature form. Our samples of $\text{Na}_{0.4}\text{VS}_2$ and $\text{Na}_{0.8}\text{VS}_2$ were homogeneous TP phases with $c = 7.08\text{Å}$ and 6.94Å , respectively. A sample of NaVS_2 we obtained electrochemically (3) had the hexagonal structure.

It thus appears that the structural characteristics of $\text{Na}_{1.0}\text{Cr}_{0.5}\text{V}_{0.5}\text{S}_2$ more closely resemble that of $\text{Na}_{1.0}\text{CrS}_2$ in that only the TAP phase is present. Our samples of $\text{Na}_y\text{Cr}_{0.5}\text{V}_{0.5}\text{S}_2$, $y = 0.6$ and 0.8 , were heterogeneous mixtures with the components having lattice parameters identical to those of $\text{Na}_{0.4}\text{Cr}_{0.5}\text{V}_{0.5}\text{S}_2$ and $\text{Na}_{1.0}\text{Cr}_{0.5}\text{V}_{0.5}\text{S}_2$. Only a poorly defined pattern was

Table IV. X-ray diffraction data of $\text{Na}_{0.4}\text{Cr}_{0.5}\text{V}_{0.5}\text{S}_2$

| d (obs), Å | d (cal), Å | I/I ₀ | hkl |
|------------|------------|------------------|--------|
| 7.08 | 7.08 | 1.0 | 0 0 3 |
| 2.78 | 2.75 | 0.1 | 1 0 1 |
| 2.37 | 2.34 | 0.8 | 0 1 5 |
| 2.06 | 2.06 | 0.4 | 1 0 7 |
| 1.94 | 1.93 | 0.4 | 0 1 8 |
| 1.75 | 1.77 | 0.1 | 0 0 12 |
| 1.68 | 1.69 | 0.3 | 1 0 10 |
| 1.62 | 1.62 | 0.2 | 1 1 0 |

$a = 3.24\text{Å}$, $c = 21.24\text{Å}$.

Table V. X-ray diffraction data of $\text{Na}_{1.0}\text{VS}_2$ *

| d (obs), Å | d (cal), Å | I/I ₀ | hkl | |
|------------|------------|------------------|---------|-----------|
| | | | H-phase | TAP phase |
| 7.24 | 7.30 | 0.3 | 0 0 1 | |
| 6.58 | 6.58 | 0.3 | | 0 0 3 |
| 2.80 | 2.79 | 0.3 | 1 0 0 | |
| 2.60 | 2.60 | 1.0 | | 1 0 4 |
| 2.37 | 2.37 | 0.5 | 1 0 1 | |
| 2.20 | 2.20 | 0.2 | 1 0 2 | |
| 2.07 | 2.07 | 0.4 | | 1 0 7 |
| 1.90 | 1.92 | 0.5 | | 0 1 8 |
| 1.82 | 1.82 | 0.1 | 0 0 4 | |
| 1.77 | 1.77 | 0.5 | | 1 1 0 |
| 1.70 | 1.71 | 0.2 | | 1 1 3 |
| 1.61 | 1.61 | 0.2 | 1 1 0 | |
| 1.54 | 1.55 | 0.2 | | 1 1 11 |
| 1.46 | 1.46 | 0.8 | | 0 2 4 |
| 1.37 | 1.38 | 0.1 | 2 0 1 | |
| 1.35 | 1.32 | 0.1 | 2 0 2 | |
| 1.30 | 1.30 | 0.3 | | 2 0 8 |
| 1.20 | 1.20 | 0.3 | | 0 2 10 |
| 1.16 | 1.17 | 0.1 | | 1 1 12 |

* A mixture of trigonal antiprismatic (TAP) ($a = 3.54\text{Å}$, $c = 19.74\text{Å}$) and hexagonal (H) ($a = 3.22\text{Å}$, and $c = 7.30\text{Å}$) phases.

obtained for $\text{Na}_{0.2}\text{Cr}_{0.5}\text{V}_{0.5}\text{S}_2$; but, from the magnitude of the d values apparently corresponding to the (ool) reflections, the phase appears to be a second stage compound, as found in the low Na content intercalates of TiS_2 and VS_2 .

Cell chemistry in relation to phase changes.—The structural data presented above show that probably three crystallographically distinct phases are present in the $\text{Na}_y\text{Cr}_{0.5}\text{V}_{0.5}\text{S}_2$ ternary for $0 < y \leq 1$. But, our x-ray data are insufficient to obtain the exact break-points in the phase-compositional relationships. However, we can attempt at a correlation from the discharge curve shown in Fig. 1. The two potential plateaus observed in the Na compositional (y) ranges, $y < 0.17$ and $0.17 < y \leq 0.55$ may correspond to a second stage phase and a first stage trigonal prismatic phase, respectively. The x-ray data presented in Table II for the cycled cathode, having the nominal composition $\text{Na}_{0.9}\text{Cr}_{0.5}\text{V}_{0.5}\text{S}_2$, show that it contains both TP and TAP phases. Then, the third potential region, spanning the range $0.55 < y \leq 0.95$, may encompass both a biphasic region, comprising the TP and TAP phases and a single phase region, comprising the TAP phase. For a biphasic region, one expects a corresponding plateau in the voltage-composition curve. However, our cell data are a result of both kinetic and thermodynamic factors and a true plateau region is not observed in the discharge curve at the compositional range $0.55 < y \leq 0.95$. For the same reasons, the biphasic regions expected (20) at the beginning of the discharge and at the transition stage from the second stage compound to the first stage TP phase are not clearly seen in the discharge curve. It is to be noted that, previously, we found (3) correlations among the phase-compositional regions and the discharge profiles of TiS_2 and VS_2 cathodes. It is noteworthy that in the first discharge of $\text{Cr}_{0.5}\text{V}_{0.5}\text{S}_2$, Na intercalation is achieved for virtually all values of y , $0 < y \leq 1.0$. In this respect, $\text{Cr}_{0.5}\text{V}_{0.5}\text{S}_2$ resembles VS_2 (3). In TiS_2 on the other hand, the discharge was limited to 0.85 Na/mol of TiS_2 .

The fractional rechargeability (i.e., 70%) of the capacity in the first discharge of $\text{Cr}_{0.5}\text{V}_{0.5}\text{S}_2$, except for the specific capacity involved, resembles the behavior of the other sulfides we previously investigated, namely, TiS_2 , VS_2 , and $\text{Nb}_{1.1}\text{S}_2$. In all cases, a fraction of the capacity in the first discharge is not recharged in the following charge. In general, it appears that at low values of y in the Na_yMX_2 ternaries the crystallographic phase present is a second stage phase and that the Na involved in this phase is not rechargeable, at least at the rates employed in our studies.

Table VI. Specific energies of Na/MS₂ couples based on experimental capacities and voltages

| Metal sulfide | Equivalents/mol of MS ₂ | Mid-discharge voltage (V) | Specific energy (W-hr/kg) |
|---|------------------------------------|---------------------------|---------------------------|
| Cr _{0.5} V _{0.5} S ₂ | 0.70 | 1.9 | 273 |
| VS ₂ * | 0.70 | 1.8 | 258 |
| TiS ₂ * | 0.65 | 1.7 | 215 |
| Nb _{1.1} S ₂ * | 0.50 | 1.5 | 119 |

* Data from Ref. (3).

Our data indicate that the maximum rechargeable capacity of the Cr_{0.5}V_{0.5}S₂ cathode is 0.7 e⁻/mol. With an average cell voltage of 1.9V, the theoretical specific energy of the cathode is 273 W-hr/kg. The specific energies of the Na/MS₂ couples tabulated in Table VI show that Cr_{0.5}V_{0.5}S₂ outperforms TiS₂, VS₂, or Nb_{1.1}S₂.

Acknowledgment

This work was supported by National Aeronautics and Space Administration under Contract No. NAS3-21726.

Manuscript submitted March 27, 1981; revised manuscript received June 23, 1981.

Any discussion of this paper will appear in a Discussion Section to be published in the June 1982 JOURNAL. All discussions for the June 1982 Discussion Section should be submitted by Feb. 1, 1982.

REFERENCES

1. K. M. Abraham, *J. Power Sources*, **7**, 1 (1981).
2. M. S. Whittingham, *Prog. Solid State Chem.*, **12**, 1 (1978).
3. K. M. Abraham, L. Pitts, and R. Schiff, *This Jour-*

- nal, **127**, 2545 (1980).
4. K. M. Abraham and L. Pitts, *ibid.*, **128**, 1060 (1981).
5. G. H. Newman and L. P. Klemann, *ibid.*, **127**, 2097 (1980).
6. D. A. Winn, J. M. Shemilt, and B. C. H. Steele, *Mater. Res. Bull.*, **11**, 59 (1976).
7. K. M. Abraham, R. D. Rauh, and S. B. Brummer, *Electrochim. Acta.*, **23**, 501 (1978).
8. K. M. Abraham, R. D. Rauh, and S. B. Brummer, in "Electrode Materials and Processes for Energy Conversion and Storage," J. D. E. McIntyre, S. Srinivasan, and F. G. Will, Editors, p. 985, The Electrochemical Society Softbound Proceedings Series, Princeton, NJ (1977).
9. B. G. Silbernagel and M. S. Whittingham, *Mater. Res. Bull.*, **10**, 29 (1975).
10. A. Leblanc-Soreau, M. Danob, L. Trichet, and J. Rouxel, *ibid.*, **9**, 191 (1974).
11. G. A. Wieggers, R. Van der Meer, H. Van Heiningen, H. J. Kloostenboer, and A. J. A. Alberink, *ibid.*, **9**, 1261 (1974).
12. J. Rouxel, *J. Solid State Chem.*, **17**, 223 (1976).
13. D. F. Shriver, "The Manipulation of Air Sensitive Compounds," McGraw-Hill Book Co., New York (1969).
14. B. Van Laar and D. J. W. Ijdo, *J. Solid State Chem.*, **3**, 590 (1971).
15. D. W. Murphy, J. N. Carides, F. J. DiSalvo, C. Cros, and J. V. Waszczak, *Mater. Res. Bull.*, **12**, 825 (1977).
16. D. V. Murphy, C. Cros, F. J. DiSalvo, and J. V. Waszczak, *Inorg. Chem.*, **16**, 3027 (1977).
17. J. Rouxel, M. Danot, and J. Bichon, *Bull. Soc. Chem. Fr.*, 3930 (1971).
18. F. M. R. Engelsman, G. A. Wieggers, F. Jellinek, and B. Van Laar, *J. Solid State Chem.*, **6**, 574 (1973).
19. J. Bichon, M. Danot, and J. Rouxel, *C. R. Acad. Sci.*, **276**, 1283 (1973).
20. M. S. Whittingham, *J. Electroanal. Chem. Interfacial Electrochem.*, **118**, 229 (1981).

Solubility Products of Metal Oxides in Molten Salts by Coulometric Titration of Oxide Ion Through Zirconia Electrodes

M. L. Deanhardt*¹ and K. H. Stern*

Naval Research Laboratory, Chemistry Division, Washington, D.C. 20375

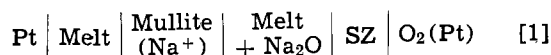
ABSTRACT

Solubility products of nickel and cobalt oxides in molten NaCl (1100 K) and Na₂SO₄ (1200 K) have been measured by coulometric titration of the respective chlorides (NiCl₂, CoCl₂) and sulfates (NiSO₄, CoSO₄) with electrochemically generated oxide ion, using a stabilized zirconia electrode as an oxide pump. The metal oxide equilibria were complicated by competitive paths leading to Na₂O₂, NaNiO₂, and NaCoO₂ formation. Activity coefficients of soluble nickel and cobalt salts were also determined from a comparison of experimental data and thermodynamic calculations.

A knowledge of the behavior of metal oxides in molten salts is important in understanding corrosion processes in marine-operated gas turbines, molten salt fuel cells and batteries, salt processing baths, and solar energy storage by molten salts. Measurement of the solubility of metal oxides used as protective coatings in such systems is needed. This information should aid

in the development of new materials and in the prevention of hot corrosion.

Recent studies (1, 2) have shown that stabilized zirconia (SZ), an oxide-conducting solid electrolyte, can function as an O²⁻ ion pump in molten NaCl at 1100 K and Na₂SO₄ at 1200 K. By applying a voltage to the cell

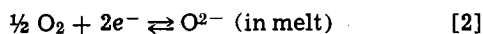


* Electrochemical Society Active Member.

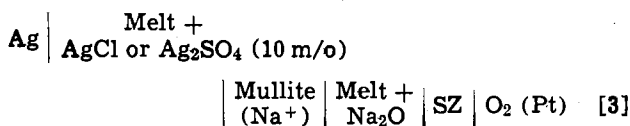
Key words: ceramics, cell, current, emf.

¹ Present address: Chemistry Department, George Mason University, Fairfax, Virginia 22030.

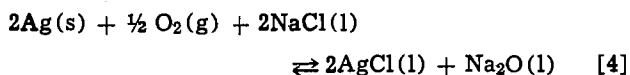
the O^{2-} ion concentration of the melt under study may be increased or decreased by driving the reaction at the O_2 electrode



left or right. The O^{2-} activity in the melt is measured potentiometrically with another SZ electrode using the cell

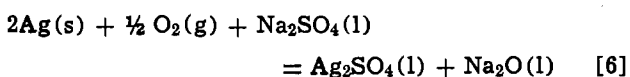


The reaction and emf of cell [3] in molten NaCl are



$$E_{\text{cell}} = E^\circ - \frac{RT}{2F} \ln \left(\frac{a_{\text{AgCl}}^2 a_{\text{Na}_2\text{O}}}{P_{O_2}^{1/2} a_{\text{NaCl}}^2} \right) \quad [5]$$

Similarly, the reaction and emf of cell [3] in molten Na_2SO_4 are



$$E_{\text{cell}} = E^\circ - \frac{RT}{2F} \ln \left(\frac{a_{\text{Ag}_2\text{SO}_4} a_{\text{Na}_2\text{O}}}{P_{O_2}^{1/2} a_{\text{Na}_2\text{SO}_4}} \right) \quad [7]$$

The SZ electrode in cell [1] (referred to as the generating electrode) serves as an O^{2-} ion source, while the SZ electrode in cell [3] (referred to as the indicating electrode) serves as an O^{2-} ion monitor.

It is known (3-5) that in $\text{Na}_2\text{O-NaCl}$ and $\text{Na}_2\text{O-Na}_2\text{SO}_4$ melts, oxide is partially converted to peroxide according to the following reaction



At constant O_2 pressure

$$[\text{Na}_2\text{O}_2]/[\text{Na}_2\text{O}] = K_{e1} P_{O_2}^{1/2} = K'_{e1} \quad [9]$$

where the brackets denote mol fractions. Cell [3] responds only to changes in the activity of Na_2O in the melt. The following relationships between the measured emf in Eq. [5] and [7] and equivalents of charge Q passed through cell [1] have been derived and verified (2):

1. Electrolysis of Na_2O into the melt

$$E_{\text{cell}} = E^\circ - \frac{RT}{2F} \ln \left([\text{Na}_2\text{O}]_o + \frac{Q}{2n(K'_{e1} + 1)} \right) \quad [10]$$

2. Electrolysis of Na_2O out of the melt

$$E_{\text{cell}} = E^\circ - \frac{RT}{2F} \ln \left[\left([\text{Na}_2\text{O}]_a - \frac{Q}{2n} \right) / (K'_{e1} + 1) \right] \quad [11]$$

where

$$E^\circ = E^\circ - \frac{RT}{2F} \ln \left(\frac{\gamma_{\text{Na}_2\text{O}} a_{\text{AgCl}}^2}{P_{O_2}^{1/2} a_{\text{NaCl}}^2} \right) \text{ for NaCl}$$

$$E^\circ = E^\circ - \frac{RT}{2F} \ln \left(\frac{\gamma_{\text{Na}_2\text{O}} a_{\text{Ag}_2\text{SO}_4}}{P_{O_2}^{1/2} a_{\text{Na}_2\text{SO}_4}} \right) \text{ for Na}_2\text{SO}_4$$

where n = total number of moles, $\gamma_{\text{Na}_2\text{O}}$ = activity coefficient of Na_2O , $[\text{Na}_2\text{O}]_o$ = initial (impurity) concentration of Na_2O , and $[\text{Na}_2\text{O}]_a$ = added concentration of Na_2O . It is assumed that the electrolysis is slow enough that the oxide/peroxide equilibrium (Eq. [8]) is maintained at all times.

In the present work, this technique has been applied to the measurement of the solubility products of NiO

and Co_3O_4 in NaCl at 1100 K, and NiO and CoO in Na_2SO_4 at 1200 K. Solubility products were determined from coulometric titration curves, obtained by measuring the charge passed through the generating SZ electrode as a function of the emf of the indicating cell [3]. Oxygen pressure above the melts was ~ 0.2 atm. Activity coefficients of sodium oxide in both NaCl and Na_2SO_4 were needed in order to define the solubility products in terms of mol fractions. Values of $\gamma_{\text{Na}_2\text{O}}$ have been reported in an earlier work (6). It is also possible to calculate values of $\gamma_{\text{Na}_2\text{O}}$ using the data of Ref. (2). These calculations, along with a comparison of the values of $\gamma_{\text{Na}_2\text{O}}$ obtained from the two studies, are given in this work. Gupta and Rapp (7) recently measured the solubility of nickel and cobalt oxide in molten Na_2SO_4 as a function of salt basicity ($\log a_{\text{Na}_2\text{O}}$). Their results, as well as results of thermodynamic calculations, are compared with the results of this study. A preliminary report of this study (8) can be found elsewhere.

Experimental

Experiments were carried out in a helium-oxygen-filled (20% O_2) dry box (Vacuum/Atmospheres Corporation) with a recirculating dry train in which moisture and CO_2 were generally kept below 1 ppm. The electrodes, cell design, and experimental techniques have been described elsewhere (1, 2). High purity (99.8%) alumina crucibles were used in all experiments.

Reagents.—Reagent grade NaCl and Na_2SO_4 were vacuum-dried at 500°C before use. Anhydrous NiCl_2 and CoCl_2 (Alfa Products) were used without pretreatment. Anhydrous NiSO_4 and CoSO_4 were prepared from reagent-grade hydrate salts using a procedure described by Sanderson (9). The prepared salts were analyzed for purity by atomic absorption analysis of Ni and Co. All weighings and transfer operations were carried out in the dry box in which the experiments were done.

Procedures.—The emf of cell [3] was measured with a high impedance electrometer (Keithley Model 616). Cathodic potentials were applied to the generating SZ electrode using a PAR 173 potentiostat/galvanostat. The charge passed through cell [1] was measured with a PAR 179 digital coulometer. Since the coulometric titrations were generally run overnight, charge passed and emf's measured were recorded automatically on a Fluke 2200B data logger.

Least squares fits of the experimental data were calculated using a Hewlett Packard Model 9815S computer and its associated software. The titration curves were plotted with a Hewlett Packard Model 9865A digital plotter interfaced to the 9815S computer.

The melts were analyzed for their Co and Ni content before each titration. Samples were taken by dipping cold ceramic rods (high purity alumina) into the melt. The quenched-melt samples were analyzed using a Perkin Elmer Model 360 atomic absorption spectrophotometer.

Results

Solubility products of nickel and cobalt oxides.—The metal ion was added to the melt as NiCl_2 and CoCl_2 , respectively, in NaCl, and as NiSO_4 and CoSO_4 in Na_2SO_4 . As O^{2-} is coulometrically added to the melt, the insoluble metal oxide precipitates. A plot of emf vs. Q results in a titration curve. An example of such a plot is shown in Fig. 1 for the titration of NiCl_2 in molten NaCl. Similar titration curves were observed for CoCl_2 in a molten NaCl, and NiSO_4 and CoSO_4 in molten Na_2SO_4 .

The reduction of oxygen to oxide could be carried out by either controlled potential electrolysis or controlled current electrolysis. In either case, care was taken not to exceed the electrolysis potential at which zirconia is reduced to substoichiometric ZrO_2 (2). A

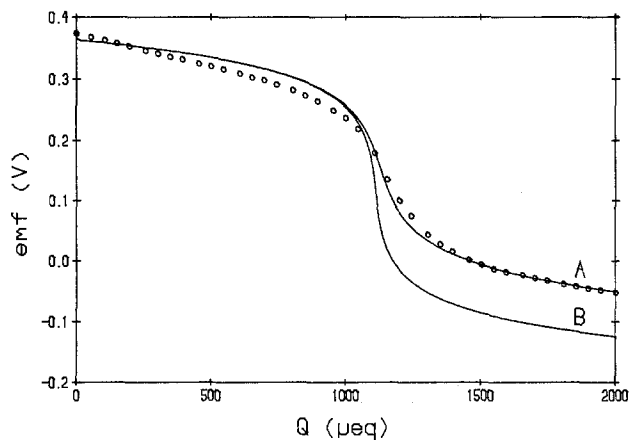
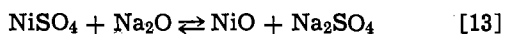
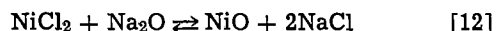


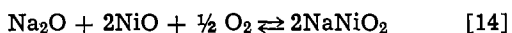
Fig. 1. Titration of NiCl_2 with Na_2O in molten NaCl . $[\text{NiCl}_2]_0 = 3.18 \times 10^{-4}$; $T = 1100 \text{ K}$; $P_{\text{O}_2} = 0.213 \text{ atm}$; (○) experimental points; (—) least squares fit using Eq. [24]; A. $K_{\text{sp}} = 2.8 \times 10^{-12}$, $K_{e1} = 6$, $K_{e2} = 4.4 \times 10^{-4}$; B. $K_{\text{sp}} = 2.8 \times 10^{-12}$, $K_{e1} = K_{e2} = 0$.

typical titration took $\sim 24 \text{ hr}$ at an electrolysis current of $\sim 2.5 \text{ mA}$ and a total Q of $\sim 2000 \mu\text{equiv}$. The 24 hr period was ample time for the generated precipitate to equilibrate with the melt. This was substantiated by obtaining similar titration curves at longer time intervals and lower current densities. Close agreement between the calculated and observed end points of the titration curve also indicates precipitate-melt equilibration.

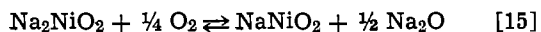
Two stable forms of nickel oxide exist in both molten NaCl and Na_2SO_4 . In acidic melts (low oxide activity) the predominant form of nickel is NiO . Before the end point of each titration, the oxide activity remains low due to the following reactions



After all of the nickel precipitates as NiO , the melt becomes basic (high oxide activity). In basic melts, NiO reacts with Na_2O and O_2 to form NaNiO_2 (7)

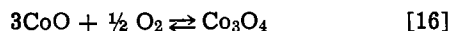


(The presence of Na_2NiO_2 in the melt is unlikely, especially in the presence of oxygen. Using thermodynamic data in Table I, the equilibrium constant for the reaction

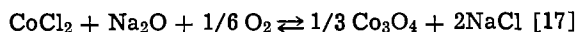


is 4.4×10^2 at 1100 K and 1.6×10^2 at 1200 K . At the oxygen pressures and Na_2O activities encountered during the titrations, the activity ratio of NaNiO_2 to Na_2NiO_2 would be greater than 10^5 .)

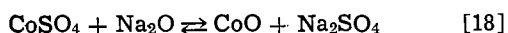
The form of cobalt oxide depends on the temperature and oxygen pressure according to the following equilibrium



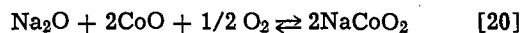
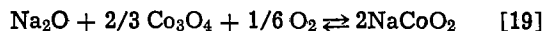
Using thermodynamic data in Table I, the equilibrium pressures of oxygen, P_{O_2} , at 1100 and 1200 K are 0.015 and 0.55 atm , respectively. At 1100 K and 0.2 atm O_2 , the stable form of cobalt oxide, Co_3O_4 , precipitates up to the end point



At 1200 K and 0.2 atm O_2 , the stable form of cobalt oxide, CoO , precipitates



In basic melts (past the end point), cobalt oxide reacts with Na_2O and O_2 to form sodium cobaltate, NaCoO_2 , as indicated in the following equations



As sodium oxide is added coulometrically to each melt, three equilibria are established. For example, in the case of nickel in molten NaCl the equilibria are represented by Eq. [8], [12], and [14]. Each titration curve can be derived theoretically by considering all three equilibria simultaneously. For brevity, theoretical calculations are discussed below only for the case of nickel in molten NaCl .

The K_{sp} is defined in terms of the equilibrium constant for reaction [12], viz.

$$K_{\text{sp}} = 1/K_{12} = [\text{Na}_2\text{O}] [\text{NiCl}_2] \quad [21]$$

and the equilibrium constant for reaction [14] is

$$K'_{e2} = K_{e2} P_{\text{O}_2}^{1/2} = [\text{NaNiO}_2]^2 / [\text{Na}_2\text{O}] \quad [22]$$

The equilibrium constant for reaction [8] is defined in Eq. [9]. Letting Q equal the number of equivalents of charge passed through cell [1], the amount of oxide that reacts to form NiO , Na_2O_2 , and NaNiO_2 at equilibrium is $Q/2n - [\text{Na}_2\text{O}]$. It is assumed that the initial Na_2O concentration in the melt is negligible. The amount of NiO formed is $[\text{NiCl}_2]_0 - [\text{NiCl}_2]$, where $[\text{NiCl}_2]_0$ is the initial concentration of NiCl_2 . Combining these two relationships results in the following equation

$$Q/2n - [\text{Na}_2\text{O}] = [\text{NiCl}_2]_0 - [\text{NiCl}_2] + [\text{Na}_2\text{O}_2] + \frac{1}{2} [\text{NaNiO}_2] \quad [23]$$

Substitution of Eq. [9], [21], and [22] into Eq. [23] yields

$$Q/2n - [\text{NiCl}_2]_0 - K_{\text{sp}}(1/[\text{Na}_2\text{O}]) + K'_{e1} + 1 \left(\frac{[\text{Na}_2\text{O}]}{[\text{Na}_2\text{O}]} + K'_{e2} \frac{([\text{Na}_2\text{O}]^{1/2}/2)}{([\text{Na}_2\text{O}]} \right) \quad [24]$$

The relationship between $[\text{Na}_2\text{O}]$ and the emf of cell [3] can be calculated from Eq. [5]

$$[\text{Na}_2\text{O}] = \exp \left\{ \frac{2F}{RT} (E'' - E_{\text{cell}}) \right\} \quad [25]$$

E'' can be calculated from the standard potential of cell [3] (10, 11), the activity coefficient of Na_2O (see Discussion section), and the activity coefficients of the binary salts used in the reference electrode (10, 12). For molten NaCl at 1100 K and $20\% \text{ O}_2$, $E'' = -0.520 \text{ V}$. For molten Na_2SO_4 at 1200 K and $20\% \text{ O}_2$, $E'' = -1.037 \text{ V}$. Substitution of Eq. [25] into Eq. [24] gives the $E_{\text{cell}} - Q$ relationship for the titration of NiCl_2 with Na_2O in molten NaCl

$$Q/2n - [\text{NiCl}_2]_0 = -K_{\text{sp}} \left[\exp \left\{ \frac{2F}{RT} (E'' - E_{\text{cell}}) \right\} \right]^{-1} + (K'_{e1} + 1) \left[\exp \left\{ \frac{2F}{RT} (E'' - E_{\text{cell}}) \right\} \right] + K'_{e2} \frac{1}{2} \left[\exp \left\{ \frac{2F}{RT} (E'' - E_{\text{cell}}) \right\} \right] \quad [26]$$

The three equilibrium constants in Eq. [26] were calculated for each titration by multiple regression analysis (13) which provided the minimum sum of squares of differences between the observed and calculated values of Q . Results are listed in Table II. Equilibrium constants in Eq. [26] are defined in terms of mol fractions. The numbers in parentheses indicate the range of the data for four titrations. Equilibrium constants calculated in this manner were used to plot the titration curve labeled A in Fig. 1. In addition, multiple regression analyses were used to determine K_{sp} values

Table I. Thermodynamic data

| Compound | ΔG°_f (1100 K) (kJ/mol) | ΔG°_f (1200 K) (kJ/mol) | Reference |
|--------------------------------------|---|---|-----------|
| AgCl(l) | -7.33×10^1 | | (10) |
| Ag ₂ SO ₄ (l) | | -3.33×10^2 | (11) |
| CoCl ₂ (l) | -1.70×10^2 | | (16) |
| CoO(s) | -1.56×10^2 | -1.50×10^2 | (16) |
| Co ₃ O ₄ (s) | -4.89×10^2 | -4.51×10^2 | (16) |
| CoSO ₄ (s) | | -4.45×10^2 | (16) |
| NaCl(l) | -3.11×10^2 | | (16) |
| NaNiO ₂ (s) | -3.19×10^2 | -3.00×10^2 | (17) |
| Na ₂ NiO ₂ (s) | -3.98×10^2 | -3.74×10^2 | (17) |
| Na ₂ O(s) | -2.67×10^2 | -2.50×10^2 | (16) |
| Na ₂ O ₂ (s) | -2.78×10^2 | -2.54×10^2 | (16) |
| Na ₂ SO ₄ (l) | | -3.94×10^2 | (16) |
| NiCl ₂ (s) | -1.43×10^2 | | (18) |
| NiO(s) | -1.41×10^2 | -1.32×10^2 | (18) |
| NiSO ₄ (s) | | -4.05×10^2 | (18) |
| SO ₃ (g) | | -2.61×10^2 | (16) |

assuming no peroxide, nickelate, or cobaltate formation (i.e., $K_{e1} = K_{e2} = 0$). The curve labeled B in Fig. 1 was calculated from these data. Due to a calculation error, the B-labeled curves in the preliminary report of this study (8) were plotted incorrectly.

Also included in Table II are equilibrium constants calculated from thermodynamic data in Table I. There are no data reported in the literature for $(\Delta G^\circ_f)_{\text{NaCoO}_2}$. In order to carry out the calculations, we have assumed that $(\Delta G^\circ_f)_{\text{NaCoO}_2} = (\Delta G^\circ_f)_{\text{NaNiO}_2}$.

Activity coefficients of soluble salts of nickel and cobalt.—The data in Table II were used to calculate the activity coefficients of the soluble salts of nickel and cobalt in the two melts. Each activity coefficient was calculated using the experimental equilibrium constant (defined in terms of mol fractions), the thermodynamic equilibrium constant (defined in terms of activities), and the activity coefficient of Na₂O. The calculated values along with literature values are given in Table III. The standard states for the salts are the pure solids (pure liquid for CoCl₂) and therefore the activity coefficients measure deviations from Raoult's law. The activity coefficient for NaCoO₂ in both NaCl and Na₂SO₄ is based on the assumption that $(\Delta G^\circ_f)_{\text{NaCoO}_2} = (\Delta G^\circ_f)_{\text{NaNiO}_2}$.

Discussion

The total number of mols of Na₂O added to a NaCl or Na₂SO₄ melt was determined by measuring the charge passed through the generating SZ electrode. The indicating SZ electrode, which monitors the unreacted oxide ion in the melt, responds only to the activity of sodium oxide. In order to measure the solubility products of nickel and cobalt oxides in terms of mol fractions, it is necessary to know the activity coefficient of Na₂O in these systems.

In a recent study, Stern (6) reported the activity coefficients of Na₂O in molten NaCl (1100 K) and Na₂SO₄ (1200 K) to be 1.07×10^{-4} and 3.6×10^{-4} , respectively. These data indicated large negative de-

Table III. Activity coefficients of soluble salts of nickel and cobalt

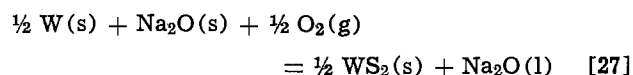
| Melt | Salt | γ (This work)* | γ (Literature) | Reference |
|---|--------------------|-----------------------------|-----------------------|-----------|
| NaCl (1100 K) | NiCl ₂ | $(2.2-5.8) \times 10^{-2}$ | 2.36×10^{-2} | (14) |
| | NaNiO ₂ | $(0.3-1.2) \times 10^2$ | | |
| | CoCl ₂ | $(0.6-2.2) \times 10^{-2}$ | 1.57×10^{-2} | (15) |
| Na ₂ SO ₄ (1200 K) | NaCoO ₂ | $(3.4-5.6) \times 10^{2**}$ | | |
| | NiSO ₄ | $(2.0-9.6) \times 10^{-3}$ | 0.11-0.24 | (7) |
| | NaNiO ₂ | 5.2-6.6 | 2.8-84 | (7) |
| | CoSO ₄ | $(0.7-1.9) \times 10^{-2}$ | 0.60-3.0 | (7) |
| | NaCoO ₂ | 1.3-4.1** | 2.8-84† | (7) |

* Range for four titrations.

** Assuming $(\Delta G^\circ_f)_{\text{NaCoO}_2} = (\Delta G^\circ_f)_{\text{NaNiO}_2}$.

† Assuming $\gamma_{\text{NaCoO}_2} = \gamma_{\text{NaNiO}_2}$.

viations from Raoult's law for the Na₂O-NaCl and Na₂O-Na₂SO₄ melts. The work was based on the cell reaction



The activity of Na₂O in the melt was measured with an SZ electrode. The mol fraction of Na₂O was calculated from the added amount of Na₂O, the known equilibrium constant of Eq. [9], and the assumption that $\gamma_{\text{Na}_2\text{O}} = \gamma_{\text{Na}_2\text{O}}$.

In another recent work (2), we reported on the use of the SZ electrode to transport oxide ion into and out of molten salts. The cell reactions were the same as in this study (reactions [4] and [6]). Oxide ion was added electrochemically to molten NaCl and Na₂SO₄ via the SZ electrode, experimentally verifying the $E_{\text{cell}} - \log Q$ relationship of Eq. [10]. When $Q/2n(K'_{e1} + 1) \gg [\text{Na}_2\text{O}]_0$, experimental plots of E_{cell} vs. $\log Q$ were linear with the expected $-2.303RT/2F$ slopes. The value of $\gamma_{\text{Na}_2\text{O}}$ can be calculated from the intercept of the $E_{\text{cell}} - \log Q$ plot. The intercept is equal to $E^\circ + 2.303RT/2F \log [2n(K'_{e1} + 1)]$, where $\gamma_{\text{Na}_2\text{O}}$ is included in the E° term. Again, if one assumes that $\gamma_{\text{Na}_2\text{O}_2} = \gamma_{\text{Na}_2\text{O}}$, the value of K'_{e1} can be calculated from the thermodynamic data in Table I. From these calculations, the average values of the activity coefficients of Na₂O in molten NaCl (1100 K) and Na₂SO₄ (1200 K) are 1.7×10^{-4} and 4.5×10^{-4} , respectively.

Activity coefficients from the two works are thus in reasonable agreement with one another, well within a factor of two. Since the cell reactions in this work and the work of Ref. (2) are the same, and the electrochemical addition of Na₂O is probably more accurate than the direct addition of Na₂O, we believe that the numbers, 1.7×10^{-4} and 4.5×10^{-4} , are the more reliable values of $\gamma_{\text{Na}_2\text{O}}$ and are therefore used in this study.

The data in Table II indicate that the major reaction of Na₂O in the melts is formation of the insoluble metal

Table II. Equilibrium constants derived from titration and thermodynamic data

| Solvent | Sample titrated | Reaction | Equilibrium constant* (titration data) | Equilibrium constant** (thermodynamic data) |
|---|-------------------|--|---|--|
| NaCl (1100 K) | NiCl ₂ | NiO + 2NaCl \rightleftharpoons NiCl ₂ + Na ₂ O | $(1.9-4.9) \times 10^{-12}$ | 1.82×10^{-17} |
| | | Na ₂ O + 1/2 O ₂ \rightleftharpoons Na ₂ O ₂ | 2.6 | 3.11 |
| | CoCl ₂ | Na ₂ O + 2NiO + 1/2 O ₂ \rightleftharpoons 2NaNiO ₂ | $(0.2-4.4) \times 10^{-3}$ | 1.57×10^4 |
| | | 1/3 Co ₃ O ₄ + 2NaCl \rightleftharpoons CoCl ₂ + Na ₂ O + 1/6 O ₂ | $(0.9-3.3) \times 10^{-11}$ | 3.34×10^{-17} |
| | | Na ₂ O + 1/2 O ₂ \rightleftharpoons Na ₂ O ₂ | 1-17 | 3.11 |
| Na ₂ SO ₄ (1200 K) | NiSO ₄ | Na ₂ O + 2/3 Co ₃ O ₄ + 1/6 O ₂ \rightleftharpoons 2NaCoO ₂ | $(1.8-6.6) \times 10^{-5}$ | 1.25×10^{24} |
| | | NiO + Na ₂ SO ₄ \rightleftharpoons NiSO ₄ + Na ₂ O | $(1.6-8.0) \times 10^{-11}$ | 7.02×10^{-17} |
| | CoSO ₄ | Na ₂ O + 1/2 O ₂ \rightleftharpoons Na ₂ O ₂ | 8-71 | 1.40 |
| | | Na ₂ O + 2NiO + 1/2 O ₂ \rightleftharpoons 2NaNiO ₂ | $(4.9-8.0) \times 10^{-2}$ | 4.79×10^3 |
| | | CoO + Na ₂ SO ₄ \rightleftharpoons CoSO ₄ + Na ₂ O | $(0.8-2.2) \times 10^{-10}$ | 7.30×10^{-18} |
| | | Na ₂ O + 1/2 O ₂ \rightleftharpoons Na ₂ O ₂ | 3-12 | 1.40 |
| | | Na ₂ O + 2CoO + 1/2 O ₂ \rightleftharpoons 2NaCoO ₂ | $(0.43-9) \times 10^{-2}$ | 1.54×10^{24} |

* Defined in terms of mol fractions.

** Defined in terms of activities.

† Assuming $(\Delta G^\circ_f)_{\text{NaCoO}_2} = (\Delta G^\circ_f)_{\text{NaNiO}_2}$.

oxides: NiO, Co₃O₄, and CoO. The competing equilibria (i.e., peroxide, nickelate, or cobaltate formation) are not significant before the end points of the titrations. This is borne out by curves A and B in Fig. 1. Curve A (competing equilibria assumed) and B (competing equilibria ignored) are identical up to the end point of a titration. This also explains the close agreement between the observed and calculated end points as shown in Table IV. The observed end point was determined by taking the second derivative of the titration curve; the calculated end point was based on the initial amount of metal added to the melt.

The titration curves strongly suggest that competing equilibria exist in these systems. The Na₂O activities after the end points are lower than one would expect based only on metal oxide formation. Formation of peroxide and nickelate or cobaltate would indeed lower the activity of Na₂O after the titration end point. Confirmation of Na₂O₂ in NaCl and Na₂SO₄, and NaNiO₂ in Na₂SO₄ has been reported in the literature (3, 4, 7).

The calculated activity coefficients for NiCl₂ and CoCl₂ in molten NaCl (Table III) agree very well with values reported by Hamby and Scott (14, 15). Comparable values of the activity coefficients of NaNiO₂ and NaCoO₂ in molten NaCl were not available in the literature. The calculated activity coefficients of soluble salts of nickel and cobalt in molten Na₂SO₄ were compared with data of Gupta and Rapp (7). In order to compare the activity coefficients for NaNiO₂ with the value obtained by Gupta and Rapp, their value of ΔG°_f was changed to that used in this work. Good agreement occurs for the activity coefficients of NaNiO₂ and NaCoO₂; however, our activity coefficients for NiSO₄ and CoSO₄ were at least a factor of ten lower than those reported by Gupta and Rapp.

Another way of expressing the data in Table II is to report the solubility of nickel and cobalt oxides as a function of salt basicity ($-\log a_{\text{Na}_2\text{O}}$). This type of information should assist in developing better materials to combat molten salt corrosion. Plots of solubility vs. salt basicity are given in Fig. 2 and 3. Solubilities are defined in terms of the soluble metal concentration. For example, in the case of NiO in molten NaCl, the solubility is equal to the sum of [NiCl₂] + [NaNiO₂]. Each of the concentrations can be calculated as a function of sodium oxide activity using the appropriate equilibrium constants reported in Table II. Solid lines in Fig. 2 and 3 indicate the actual range of sodium oxide activities encountered during the titrations; dashed lines are extrapolated values.

The solubility of NiO in molten Na₂SO₄ (curve A) is compared to the data of Gupta and Rapp (7) (curve C) in Fig. 3. The curves agree well in terms of the position of minimum solubility; however, the solubility of NiO determined in this study is about an order of magnitude higher than that reported by Gupta and Rapp. Their data were calculated at an oxygen pressure of 1 atm instead of the 0.2 atm used in this study, but this difference would only slightly shift the solubility at high sodium oxide activities, since [NaNiO₂] is dependent on P_{O₂}.

Conclusions

The results of this study clearly show that the SZ electrode can be used to determine the solubility products of metal oxides in molten salts. Solubility products of NiO and CoO (Co₃O₄ in molten NaCl) have been

Table IV. Typical titration curve end points

| Solvent | Sample titrated | Observed end point ($\mu\text{equiv.}$) | Calculated end point ($\mu\text{equiv.}$) |
|---|-------------------|---|---|
| NaCl (1100 K) | NiCl ₂ | 1130 | 1110 |
| | CoCl ₂ | 1230 | 1230 |
| Na ₂ SO ₄ (1200 K) | NiSO ₄ | 1130 | 1060 |
| | CoSO ₄ | 1130 | 1080 |

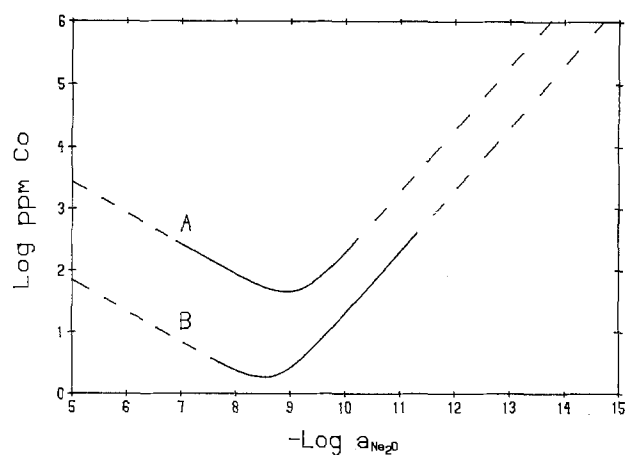


Fig. 2. Solubility of cobalt oxide. (—) Oxide activities encountered during titration, (---) extrapolated values. (A) CoO in molten Na₂SO₄, [CoSO₄]_o = 7.77 × 10⁻⁴, P_{O₂} = 0.200 atm, K_{sp} = 1.0 × 10⁻¹⁰, K_{e2} = 4.2 × 10⁻³. (B) Co₃O₄ in molten NaCl, [CoCl₂]_o = 3.60 × 10⁻⁴, P_{O₂} = 0.200 atm, K_{sp} = 9.0 × 10⁻¹², K_{e2} = 1.8 × 10⁻⁵.

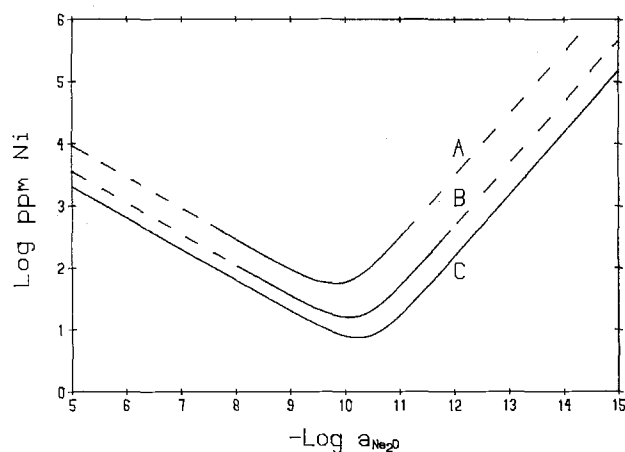


Fig. 3. Solubility of nickel oxide. (—) Oxide activities encountered during titration, (---) extrapolated values. (A) NiO in molten Na₂SO₄, [NiSO₄]_o = 7.67 × 10⁻⁴, P_{O₂} = 0.202 atm, K_{sp} = 1.6 × 10⁻¹¹, K_{e2} = 4.9 × 10⁻². (B) NiO in molten NaCl, [NiCl₂]_o = 3.18 × 10⁻⁴, P_{O₂} = 0.213 atm, K_{sp} = 2.8 × 10⁻¹², K_{e2} = 4.4 × 10⁻⁴. (C) Data of Gupta and Rapp (7).

determined in molten NaCl and Na₂SO₄ as have equilibrium constants of competing equilibria leading to the formation of Na₂O₂, NaNiO₂, and NaCoO₂. Activity coefficients of soluble salts of nickel and cobalt were also calculated and compared with literature values.

Manuscript submitted Feb. 2, 1981; revised manuscript received ca. June 12, 1981.

Any discussion of this paper will appear in a Discussion Section to be published in the June 1982 JOURNAL. All discussions for the June 1982 Discussion Section should be submitted by Feb. 1, 1982.

Publication costs of this article were assisted by the Naval Research Laboratory.

REFERENCES

- K. H. Stern, *This Journal*, **127**, 2375 (1980).
- M. L. Deanhardt and K. H. Stern, *J. Phys. Chem.*, **84**, 2831 (1980).
- K. H. Stern, R. Panayappan, and D. R. Flinn, *This Journal*, **124**, 641 (1977).
- K. H. Stern, M. L. Deanhardt, and R. Panayappan, *J. Phys. Chem.*, **83**, 2848 (1979).
- M. L. Deanhardt and K. H. Stern, *This Journal*, **127**, 2600 (1980).
- K. H. Stern, *Electrochim. Acta*, **24**, 509 (1979).

7. D. K. Gupta and R. A. Rapp, *This Journal*, **127**, 2194 (1980).
8. M. L. Deanhardt and K. H. Stern, in "Third International Symposium on Molten Salts," G. Mamtov, M. Blander, and G. P. Smith, Editors, p. 376, The Electrochemical Society Softbound Proceedings Series, Pennington, NJ (1981).
9. R. T. Sanderson, *J. Chem. Ed.*, **29**, 539 (1952).
10. G. J. Janz and C. G. M. Dijkhuis, *Natl. Stand. Ref. Data Ser.*, *Natl. Bur. Stand.*, No. 28 (1969).
11. K. K. Kelley, Bureau of Mines, Bulletin 406 (1937).
12. D. A. Shores and R. C. John, *J. Appl. Electrochem.*, **10**, 275 (1980).
13. W. J. Dixon and F. J. Massey, Jr., "Introduction to Statistical Analysis," p. 212, McGraw-Hill, New York (1969).
14. D. C. Hamby and A. B. Scott, *This Journal*, **115**, 704 (1968).
15. D. C. Hamby and A. B. Scott, *ibid.*, **117**, 319 (1970).
16. JANAF Thermochemical Tables, *Natl. Stand. Ref. Data Ser.*, *Natl. Bur. Stand.*, No. 37 (1971) and 1974, 1975, 1978 Supplements.
17. B. J. Shau, P. C. S. Wu, and P. Chiotti, *J. Nucl. Mater.*, **67**, 13 (1977).
18. A. D. Mah and L. B. Pankratz, Bureau of Mines, Bulletin 668 (1976).

Adsorption of Benzo-(f)-Quinoline on Gold and the Kinetics of the Quinone-Hydroquinone and the Iron(III)/Iron(II) Systems

G. M. Schmid* and T. A. Holmes¹

Department of Chemistry, University of Florida, Gainesville, Florida 32611

ABSTRACT

The adsorption of benzo-(f)-quinoline on gold electrodes in 1.0M H₂SO₄ was estimated from differential capacity data. Between 0.0 and +0.7V adsorption is nearly independent of potential and can be fitted equally well to the Frumkin isotherm and to the isotherm with virial coefficients, $\Delta G^{\circ}_{ads} \simeq -35 \text{ kJ mol}^{-1}$. Apparent standard rate constants for the quinone-hydroquinone system were obtained from low overpotential ($\pm 20 \text{ mV}$) and those for the Fe(III)-Fe(II) system from impedance (20-800 Hz) measurements. For the quinone-hydroquinone system the rate constant decreases exponentially with benzo-(f)-quinoline coverage from $k_a^{\circ} = 2.0 \times 10^{-3} \text{ cm sec}^{-1}$ at $\theta = 0$ to $k_a^{\circ} = 3.2 \times 10^{-4} \text{ cm sec}^{-1}$ at $\theta = 0.40$. For the Fe(III)-Fe(II) system the decrease is from $k_a^{\circ} = 1.3 \times 10^{-2} \text{ cm sec}^{-1}$ at $\theta = 0$ to $k_a^{\circ} = 4.2 \times 10^{-3} \text{ cm sec}^{-1}$ at $\theta = 0.20$, again exponential in θ . The decrease cannot be explained by changes in the outer Helmholtz plane, $\Delta\phi_2$, caused by benzo-(f)-quinoline, since $\Delta\phi_2$'s calculated for the quinone-hydroquinone system are 3 to 4 times larger than those obtained for Fe(III)-Fe(II). The decreases are ascribed to changes in free energy of activation due to interaction between the adsorbed layer and electroactive species.

The ability of organic and inorganic molecules and ions adsorbed at interfaces to control the rate of an electrochemical reaction has long been of interest. Such a substance may exert this control in several ways: (i) The substance may form a surface film which acts as a physical barrier to restrict the diffusion of ions or molecules to or from the electrode surface. (ii) The interaction of the substance with the surface metal atoms may prevent these metal atoms from participating in the electrochemical reaction. This simple blocking effect decreases the number of surface metal atoms at which reaction can occur, in proportion to the coverage at the electrode surface. (iii) If the electrode reaction involves the formation of adsorbed intermediates, the presence of adsorbed substances may interfere with the formation of these intermediates. Reaction may then proceed by alternate paths through other intermediates containing the adsorbed substances, thus affecting the activation energy of the reaction. (iv) Finally, the adsorption of substances on the electrode may change the structure of the electrical double layer at the electrode solution interface, which will affect the rates of the electrochemical processes (1).

The substances in question frequently act as inhibitors. It is often not possible to assign a simple general mechanism of action to an inhibitor because the mechanism may change with experimental conditions such as inhibitor concentration, the pH of the solution, the nature of the anions in the solution, the nature of the metal, and the extent of reaction to form secondary inhibitors. One approach to a better understanding of the mechanism by which corrosion inhibitors operate is to simplify the electrochemical system. Thus, much work has been done in determining the effect of the adsorption on mercury and solid metals of organic inhibitors on the kinetics of simple charge transfer reactions (2-5).

Weber *et al.* (6) and Kuta and Smoler (7) as well as Müller and Lorenz (8) were among the first to suggest the equation

$$k_{\theta} = (1 - \theta) k_{\theta=0} + \theta k_{\theta=1} \quad [1]$$

for the standard rate constant, k_{θ} , of an electrochemical reaction at a given value of the fractional coverage, θ . Here $k_{\theta=0}$ and $k_{\theta=1}$ are the value of the standard rate constant for $\theta = 0$ and $\theta = 1$, respectively. For $k_{\theta=0} \gg k_{\theta=1}$ and $\theta < 1$, Eq. [1] becomes the "blocking equation"

$$k_{\theta} \simeq (1 - \theta) k_{\theta=0} \quad [2]$$

Sathyanarayana (9) suggested the following relation to describe his experimental results

* Electrochemical Society Active Member.
¹ Present address: IBM Corporation, Essex Junction, Vermont 05432.

Key words: electrochemical kinetics and adsorption, quinone-hydroquinone, Fe(III)-Fe(II), benzo-(f)-quinoline coverage, Au electrodes.

$$k_{\theta} = (1 - \theta)^b k_{\theta=0} \quad [3]$$

where b is a constant ($b > 1$) which accounts for lateral repulsive interaction between adsorbate molecules. Niki and Hackerman (10) have suggested that the electrochemical reaction will proceed only at those sites where at the same time b water molecules are present on the electrode surface and that the surface area occupied by such an aggregate will correspond to the cross section of the activated complex. The probability of finding b water molecules simultaneously in neighboring positions is $(1 - \theta)^b$, so that a relationship of the type of Eq. [3] may be expected. Lipkowski and Galus (11) obtained Eq. [3] by using the Flory-Huggins (12) isotherm in describing the adsorption of the activated complex.

Substantial deviations from these relations are observed (11, 13-16). To account for these deviations Parsons (17) proposed after Frumkin (18) that the change in the potential at the outer Helmholtz plane (OHP), due to surfactant adsorption, be taken into account when interpreting kinetic data. Damaskin and Afanas'ev (4) have suggested that the potential at the plane corresponding to the center of the activated complex may be useful in describing the electrochemical reaction rate as a function of fractional coverage. This potential can differ from that calculated by Parsons' method. Sathyanarayana (19) discusses an elementary electrostatic model where the dipole and its mirror image give rise to a potential at the site where the activated complex is located.

During surfactant adsorption on the electrode surface, one can expect a change in the interaction between the electroactive species and the surface layer as the solvent molecules are replaced by adsorbate molecules. A change in the free energy of activation of the electrochemical reaction following the change in the surface layer structure during adsorption can be taken into account in terms of the activity coefficient of the electroactive species in the transition state of the reaction. This idea has been formalized by Parsons (20), Danilov and Loshkarev (21), Avilova *et al.* (22), and Afanas'ev and Ternovskoi (23) to various degrees of complexity and usefulness.

The effect of the adsorption of benzo-(f)-quinoline on electrochemical reaction rates has been studied by several authors (24-29). However, a correlation between fractional coverage data and rate constants is still not available. The present work is an attempt at such a correlation on gold electrodes for the Fe(II)/Fe(III) and the quinone/hydroquinone system.

Experimental

A four electrode system was used consisting of test electrode, polarizing electrode, auxiliary electrode, and reference electrode.

The test electrode was a gold bead of 0.13 cm² geometric area made by heating a 7.9×10^{-3} cm diam wire of fine gold (Engelhard Industries) in a hydrogen-air flame. The electrode was inserted into a Teflon holder and the assembly slipped into a glass tube which could be mounted in the top of the cell. The electrode was cleaned with warm chromic-sulfuric acid solution and rinsed thoroughly with triply distilled water.

The polarizing electrode was a 1.0 mm diam platinum wire bent into a circle such that the test electrode was in the center and in the same horizontal plane as the polarizing electrode. The auxiliary electrode was a platinum cylindrical gauze (Engelhard Industries) of approximately 500 cm² apparent surface area. Both of these electrodes were plated with gold from a thiosulfate bath prepared according to Zak (30). The reference electrode was a saturated calomel electrode (SCE). All potentials are reported *vs.* the normal hydrogen electrode (NHE).

All solutions were prepared from water distilled from alkaline permanganate and twice more from a quartz still. The supporting electrolyte was 1.0M sulfuric acid made from Mallinckrodt ACS grade 98% sulfuric acid. It was purified by electrolyzing between gold electrodes for 12 hr at 10 mA. Ferric sulfate and ferrous sulfate stock solutions, 0.1M each, were prepared from Fisher Scientific Company certified reagent ferric sulfate and ferrous sulfate, respectively. The test solutions were prepared volumetrically from the standardized stock solutions using deaerated, electrolyzed 1.0M sulfuric acid for dilution. Quinone and hydroquinone test solutions were prepared gravimetrically just prior to each experiment from Fisher Scientific Company purified grade quinone and J. T. Baker purified grade hydroquinone. A 0.1M benzo-(f)-quinoline (R.S.A. Corporation) stock solution was prepared gravimetrically without further purification.

The electrochemical cell was cleaned daily with warm chromic-sulfuric acid and thoroughly rinsed with electrolyzed supporting electrolyte. Prior to making measurements, the electrochemical cell was purged of oxygen with a constant stream of helium (99.99%) for at least 30 min. During measurements helium was passed over the test solution. The test solution was replaced at least three times a day with fresh solution. This procedure produced reproducible results.

Prior to the kinetic measurements, the differential capacity was measured in supporting electrolyte alone or with benzo-(f)-quinoline at 17 different potentials between -0.05 and 1.65V. Polarization of the test electrode was accomplished using a Sensitive Research Instrument Corporation potentiometer/voltmeter. The test solution was potentiostated at -0.05V and deaerated for 30 min. Measurements were taken every 10 min (20 min for high concentrations of benzo-(f)-quinoline) at 100 mV intervals in quiescent solutions and were made in the anodic direction only. At the end of each run, the solution was replaced with fresh solution and the procedure repeated. At each potential, data were taken between 350 and 10,000 Hz (usually at five frequencies) using a General Radio 1608-A bridge with an external oscillator (General Radio 1310-A). The amplitude of the alternating current applied to the electrode was less than 5 mV rms and was monitored with a Hewlett-Packard Model 400 HR vacuum tube voltmeter. An external null detector (General Radio Model 1232-A) was used for bridge balance. The bridge was operated in the floating mode. A 10 Henry choke isolated the d-c from the a-c circuits. Potentials were measured *vs.* SCE using a Keithley 610 BR electrometer ($10^{14}\Omega$ input impedance). To achieve bridge balance, it was sometimes necessary to insert a decade resistor (General Radio 1432-J) in series with the internal resistor of the bridge.

The supporting electrolyte solution was then replaced by the electrochemically active test solution. The test solutions were stirred for 15 min prior to the taking of any measurements. The kinetics of the quinone-hydroquinone system were determined from steady-state low overpotential-current density data. Measurements were made over a range of 20 mV through the equilibrium potential in 2.5 mV steps using a Wenking 61 TRS potentiostat monitored by a Keithley 660 guarded differential voltmeter. Apparent effective exchange currents were obtained from the slopes of the potential-current curves. The Fe(II)/Fe(III) system was studied using the faradaic impedance technique. The total impedance of the cell was measured as a function of the frequency between 20 and 800 Hz. The solution resistance and the differential capacitance were subtracted (31) and the series resistive and capacitive components of the reaction impedance plotted *vs.* $\omega^{-1/2}$.

Results and Discussion

Adsorption of benzo-(f)-quinoline in 1M sulfuric acid solutions.—The base dissociation constant in aqueous solution for benzo-(f)-quinoline is 7.76×10^{-6} (32). Hence in acidic solutions this compound will be protonated to the quinoline cation.

Differential double layer capacitance vs. potential data in 1M H₂SO₄ with various concentrations of benzo-(f)-quinoline are shown in Fig. 1. The double layer capacity was obtained by extrapolation of the straight-line plots of capacity vs. $\omega^{-1/2}$ to infinite frequency. Frequency dispersion in the range measured was < 10%. The 1M H₂SO₄ curve is characterized by an ever increasing capacitance up to +0.8V where a small maximum occurs followed by a slight decrease in capacitance up to +1.2V. At this point a rapid decrease in capacitance occurs indicating the adsorption of water.

Upon the addition of benzo-(f)-quinoline to the sulfuric acid solution, a substantial reduction in the differential capacitance is seen for each concentration until at 0.1M benzo-(f)-quinoline a virtually flat capacitance-potential curve is obtained between +0.4 and +1.4V. At concentrations of benzo-(f)-quinoline greater than 1.0×10^{-5} M it is seen that even at +1.6V the capacitance does not attain the same magnitude as that found in 1M H₂SO₄ indicating that the adsorption of water is hindered by the presence of the benzo-(f)-quinoline.

The fractional coverage for each concentration studied of benzo-(f)-quinoline between 0.0 and +1.2V was calculated according to (33)

$$C_{\theta} = (1 - \theta) C_{\theta=0} + \theta C_{\theta=1} \quad [4]$$

Where C_{θ} is the differential capacity at coverage θ , and $C_{\theta=0}$ and $C_{\theta=1}$ are the corresponding capacities at $\theta = 0$ and $\theta = 1$, respectively. The capacities measured in 0.1M benzo-(f)-quinoline were assumed to represent $C_{\theta=1}$. This is probably a very good assumption since the capacitance data for 0.01 and 0.1M benzo-(f)-quinoline did superimpose for the potentials between 0.8 and 1.2V and were very similar over the remainder of the potential region covered. The results are shown in Fig. 2. Each of the fractional coverage curves shows a small minimum centered at +0.3V. Only the 10^{-5} M benzo-(f)-quinoline curve shows a decreasing fractional coverage with increasing potential. The remaining three higher concentrations increase with increasing potential.

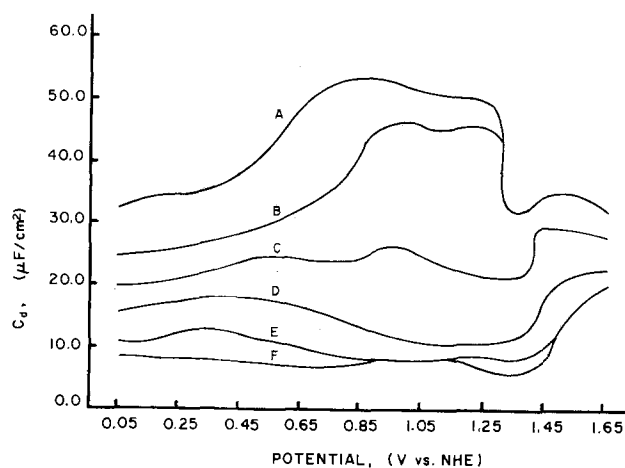


Fig. 1. Differential capacitance vs. potential in 1.0M H₂SO₄ with various concentrations of benzo-(f)-quinoline. Curve A, 1.0M H₂SO₄; curve B, 1.0M H₂SO₄ plus 1.0×10^{-5} M benzo-(f)-quinoline; curve C, 1.0M H₂SO₄ plus 1.0×10^{-4} M benzo-(f)-quinoline; curve D, 1.0M H₂SO₄ plus 1.0×10^{-3} M benzo-(f)-quinoline; curve E, 1.0M H₂SO₄ plus 1.0×10^{-2} M benzo-(f)-quinoline; curve F, 1.0M H₂SO₄ plus 1.0×10^{-1} M benzo-(f)-quinoline.

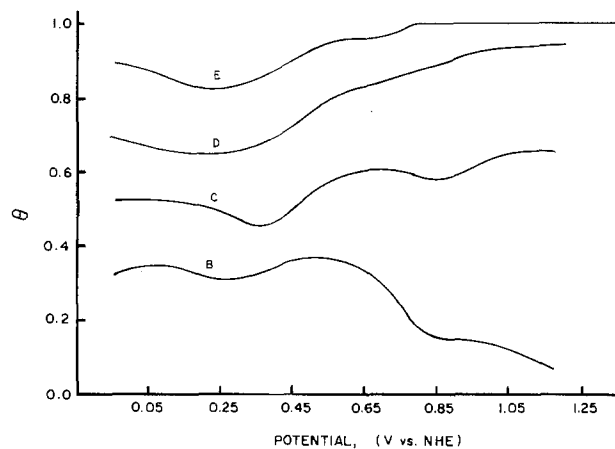


Fig. 2. Fractional coverage, θ vs. potential in 1.0M H₂SO₄ with various concentrations of benzo-(f)-quinoline. Curve B, 1.0M H₂SO₄ plus 1.0×10^{-5} M benzo-(f)-quinoline; curve C, 1.0M H₂SO₄ plus 1.0×10^{-4} M benzo-(f)-quinoline; curve D, 1.0M H₂SO₄ plus 1.0×10^{-3} M benzo-(f)-quinoline; curve E, 1.0M H₂SO₄ plus 1.0×10^{-2} M benzo-(f)-quinoline.

Between 0.0 and +0.7V the fractional coverage-concentration curves can be fitted equally well to the Frumkin isotherm (34) and to the isotherm with virial coefficients (35), two isotherms especially suited to the adsorption of organic molecules. The results are shown in Table I. Both isotherms have an arbitrary constant, a , which represents the two-dimensional interaction between the adsorbed particles. In all cases, the constant is less than zero, indicating a repulsion between adsorbed molecules. Both isotherms show similar variation in the parameters a and B with potential with a being smallest and B largest at +0.3V. This behavior might be expected from a large organic molecule close to the potential of zero charge. The latter has been reported in the vicinity by various authors (36). Adsorption is almost independent of potential as indicated by the almost constant free energy of adsorption, $\Delta G^{\circ}_{\text{ads}}$.

Electrochemical kinetics of the quinone-hydroquinone system.—Typical plots of the current density vs. overpotential are shown in Fig. 3. From the slopes of the least squares straight lines (correlation coefficient 0.9959) the apparent effective exchange current densities were calculated using the low overvoltage approximation (37), assuming a one-step, two-electron reaction. These results are shown in Table II along with the experimentally determined equilibrium potential, E_e .

The charge transfer coefficient, α , and the apparent standard rate constant, k_a° , were determined using the following expressions

Table I. Calculated values of a , B , and $\Delta G^{\circ}_{\text{ads}}$ for the Frumkin isotherm and the isotherm with virial coefficients

| E (V) | Frumkin Isotherm* | | | Isotherm with virial coefficients** | | |
|-------|-------------------|----------------------------|--|-------------------------------------|----------------------------|--|
| | a | $B \times 10^{-5}$ (l/mol) | $\Delta G^{\circ}_{\text{ads}}$ (kJ/mol) | a | $B \times 10^{-5}$ (l/mol) | $\Delta G^{\circ}_{\text{ads}}$ (kJ/mol) |
| 0.05 | -3.51 | 4.08 | -32.0 | -5.12 | 0.927 | -34.0 |
| 0.15 | -3.95 | 6.61 | -33.2 | -5.51 | 1.44 | -35.1 |
| 0.25 | -4.42 | 8.39 | -33.8 | -5.82 | 1.56 | -35.3 |
| 0.35 | -4.58 | 9.03 | -34.0 | -5.97 | 1.67 | -35.5 |
| 0.45 | -3.91 | 4.28 | -32.1 | -5.36 | 0.824 | -33.7 |
| 0.55 | -3.66 | 5.88 | -32.9 | -5.39 | 1.52 | -35.3 |
| 0.65 | -3.19 | 6.22 | -33.1 | -5.02 | 1.82 | -35.7 |
| 0.75 | -2.36 | 2.60 | -30.9 | -4.55 | 1.02 | -34.3 |

* Frumkin isotherm: $Bc = \frac{\theta}{1-\theta} \exp(-2a\theta)$.

** Isotherm with virial coefficients: $Bc = \theta \exp(-2a\theta)$.

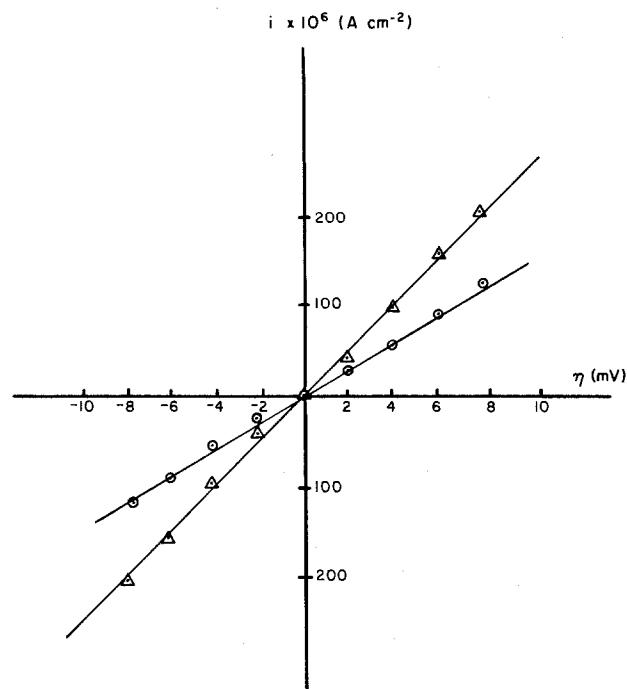


Fig. 3. Typical plots of current density vs. overpotential for the quinone-hydroquinone electrochemical system in 1.0M H_2SO_4 . Δ $7.47 \times 10^{-4}\text{M}$ quinone plus $9.79 \times 10^{-4}\text{M}$ hydroquinone; \odot $7.47 \times 10^{-4}\text{M}$ quinone plus $2.40 \times 10^{-4}\text{M}$ hydroquinone.

$$\ln(i_0/c_Q) = -\alpha nFE_e/RT + \ln(nFk_a^0) \quad [5]$$

$$\ln(i_0/c_{\text{H}_2\text{Q}}) = (1 - \alpha) nFE_e/RT + \ln(nFk_a^0) \quad [6]$$

The plot is shown in Fig. 4. The standard rate constant was found to be $1.98 \times 10^{-3} \text{ cm sec}^{-1}$ at a formal potential of 0.6879V. The cathodic charge transfer coefficient determined from the variation of the quinone concentration was 0.57, and from the variation of the hydroquinone concentration it was 0.38. This discrepancy may indicate that the reaction proceeds as two separate one-electron steps and not as a concerted two-electron transfer. This result is not unexpected and has been observed by other investigators (38-41). In this case, the measured effective exchange current represents $2i_{0,1}i_{0,2}/(i_{0,1} + i_{0,2})$, where $i_{0,1}$ and $i_{0,2}$ are the exchange currents of the two separate steps.

Electrochemical kinetics of the quinone-hydroquinone system in 1.0M H_2SO_4 with benzo-(f)-quinoline.—The results of the kinetic experiments in the presence of benzo-(f)-quinoline are presented in Table III together with the corresponding data for 1.0M H_2SO_4 . It is seen that the charge transfer coefficient increases with increasing benzo-(f)-quinoline concentration, but then decreases again. It is felt that

Table II. Apparent exchange current densities, i_0^a , and equilibrium potentials at various quinone, Q, and hydroquinone, H_2Q , concentrations in 1.0M H_2SO_4

| Solution | $i_0^a \times 10^3$ (A cm^{-2}) | E_e (V vs. NHE) |
|---|---|----------------------|
| $2.81 \times 10^{-4}\text{M Q}$ | 182 | 0.6759 |
| $5.18 \times 10^{-4}\text{M Q}$ | 222 | 0.6893 |
| $1.11 \times 10^{-3}\text{M Q}$ | 309 | 0.6935 |
| $1.68 \times 10^{-3}\text{M Q}$ | 409 | 0.6981 |
| H ₂ Q concentration = constant = $7.55 \times 10^{-4}\text{M}$ | | |
| $2.4 \times 10^{-4}\text{M H}_2\text{Q}$ | 195 | 0.7024 |
| $4.70 \times 10^{-4}\text{M H}_2\text{Q}$ | 266 | 0.6948 |
| $9.79 \times 10^{-4}\text{M H}_2\text{Q}$ | 345 | 0.6854 |
| $2.01 \times 10^{-3}\text{M H}_2\text{Q}$ | 472 | 0.6767 |

Q concentration = constant = $7.47 \times 10^{-4}\text{M}$.

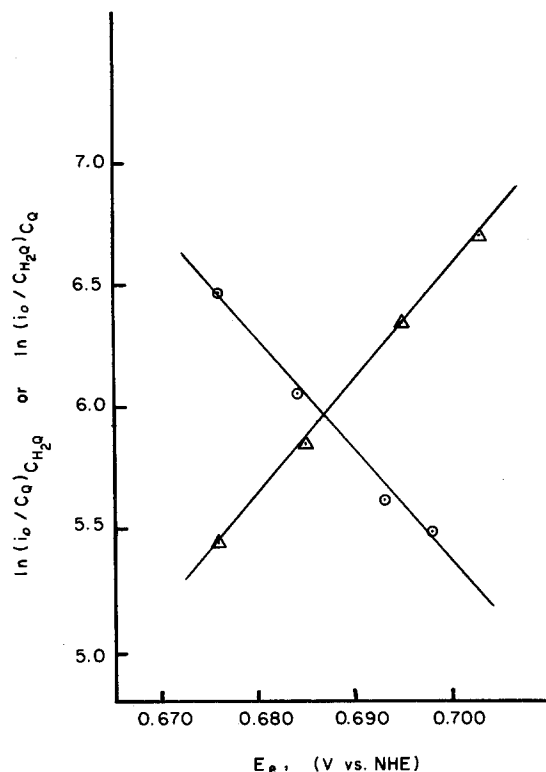


Fig. 4. Plot of $\ln(i_0/c_Q)$ and $\ln(i_0/c_{\text{H}_2\text{Q}})$ vs. E_e for the variation of the concentration of quinone, \odot , with constant hydroquinone concentration, and for the variation of the concentration of hydroquinone, Δ , with constant quinone concentration in 1.0M sulfuric acid.

this behavior does not represent a change in mechanism, but is the result of normal experimental error. The average value of the charge transfer coefficient for the variation of the quinone concentration was found to be 0.54 ± 0.09 , and for the variation of the hydroquinone concentration 0.44 ± 0.05 . The formal potential was found to be $0.6877 \pm 0.0017\text{V}$, independent of the concentration of benzo-(f)-quinoline. The dependence of the standard rate constant on coverage is logarithmic and this is shown in Fig. 5. In $1.0 \times 10^{-2}\text{M}$ benzo-(f)-quinoline ($\theta = 0.75$) and in $1.0 \times 10^{-1}\text{M}$ benzo-(f)-quinoline ($\theta = 1.0$), the experimentally determined values of the current density with applied overvoltage were those of background only and were not different from those determined in 1.0M H_2SO_4 with no electroactive species added.

Everett *et al.* (40) studied the quinone-hydroquinone system on rhodium in 1.0M HClO_4 . The standard rate constant was determined at various coverages of

Table III. Charge transfer coefficient, standard rate constant, and $\Delta\phi_2$ for the quinone-hydroquinone system, in 1.0M H_2SO_4 with and without added benzo-(f)-quinoline

| Concentration of benzo-(f)-quinoline | θ | α_Q | $\alpha_{\text{H}_2\text{Q}}$ | $k_a^0 \times 10^3$ (cm sec^{-1}) | $\Delta\phi_2^*$ (mV) | $\Delta\phi_2^{**}$ (mV) |
|--------------------------------------|----------|------------|-------------------------------|---|--------------------------|-----------------------------|
| 0 | 0.0 | 0.57 | 0.38 | 1.98 | — | — |
| $1.0 \times 10^{-5}\text{M}$ | 0.05 | 0.56 | 0.45 | 1.70 | 9 | 4 |
| $1.0 \times 10^{-4}\text{M}$ | 0.20 | 0.62 | 0.50 | 0.815 | 45 | 22 |
| $1.0 \times 10^{-3}\text{M}$ | 0.40 | 0.42 | 0.42 | 0.316 | 112 | 56 |

$\bar{\alpha}_Q = 0.54 \pm 0.09$

$\bar{\alpha}_{\text{H}_2\text{Q}} = 0.44 \pm 0.05$

* Calculated according to Eq. [7] with $Z = 0$, $\alpha = 0.5$, and $n = 1$ (two one-electron steps, intermediate protonation) (38).

** Calculated according to Eq. [7] with $Z = 0$, $\alpha = 0.5$, and $n = 2$ (one two-electron step).

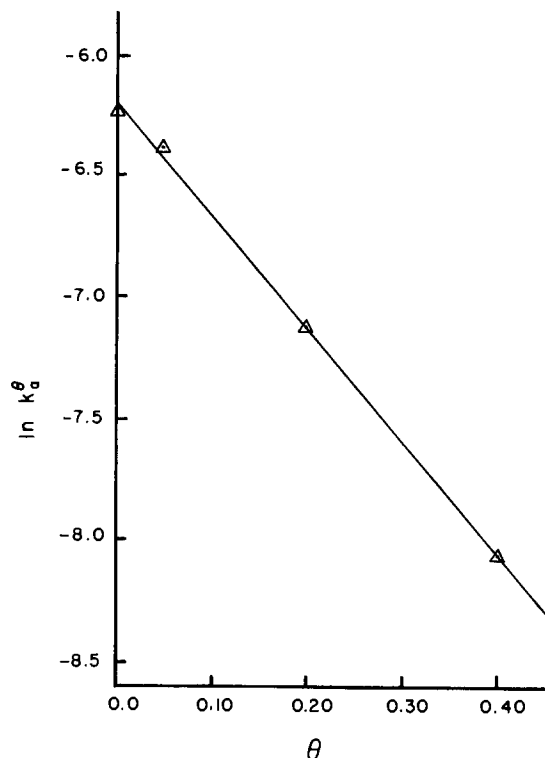


Fig. 5. Variation of the standard rate constant with fractional coverage for the quinone-hydroquinone system.

oxygen and was found to decrease linearly up to $\theta = 0.75$ and remain constant at higher coverages. This behavior was explained as being due to the geometric blocking model showing that the charge transfer reaction is much more rapid at free rhodium than at oxygen-covered rhodium. However, the model cannot explain the logarithmic dependence found here for benzo-(f)-quinoline.

Due to the adsorption of the benzo-(f)-quinoline, the potential at the OHP, ϕ_2 , will change as the concentration is varied. In the absence of a geometric blocking effect, the change in this potential, $\Delta\phi_2$, can be calculated according to (17)

$$\frac{k_a^\theta}{k_a^0} = \exp \left\{ - (Z + n\alpha) \frac{F}{RT} \Delta\phi_2 \right\} \quad [7]$$

where k_a^θ is the standard rate constant at some fractional coverage θ , and Z is the charge of the reduced species. The results of these calculations are included in Table III.

Changes in the surface layer structure resulting from interaction between electroactive species and the surface layer will alter the free energy of activation and this will result in the inhibition or acceleration of the electrochemical reaction. Afanas'ev and Ternovskoi (23) and Avilova *et al.* (22) have suggested that in the presence of adsorbed molecules, the concentration of the electroactive species within the surface layer is determined by an additional free energy term associated with the transfer of electroactive molecules from the bulk of the solution into the structured surface layer. They suggested the equation (23)

$$k_a^\theta = k_a^0 \exp(-2a\gamma\theta)$$

where a is a constant characterizing the interaction between the adsorbate molecules and γ is a constant describing the degree to which the surface layer is disturbed when an electroactive molecule is incorporated into the surface layer. Thus a plot of $\ln(k_a^\theta/k_a^0)$ vs. θ should yield a straight line with a slope of $-2a\gamma$.

This is indeed observed as is evident in Fig. 5. The least squares fit for the line is $\ln(k_a^\theta/k_a^0) = -4.80\theta + 0.09$. The intercept of $+0.09$ is small and can be ascribed to experimental error.

Electrochemical kinetics of the Fe(II)/Fe(III) system.—A typical plot of the resistive and capacitive components of the faradaic impedance is shown in Fig. 6. The plots are linear and are nearly parallel. Thus, R_r is the sum of charge transfer and diffusion impedance and $1/\omega C_r$ is solely the diffusion impedance. The charge transfer resistance can then be determined by extrapolating the reaction resistance to infinite frequency, $1/\omega^{1/2} = 0$, since the diffusion impedance then goes to zero.

From the charge transfer resistance the apparent exchange current densities were calculated and are shown in Table IV, together with the observed equilibrium potentials. From these data the charge transfer coefficient was found to be 0.58 for the variation of the Fe(III) concentration at constant Fe(II) concentration and 0.51 for the variation of the Fe(II) concentration at constant Fe(III) concentration. The standard rate constant is 1.30×10^{-2} cm sec $^{-1}$ at the formal potential of 0.6678V.

The Fe(II)/Fe(III) system is a well-studied reaction due to its simplicity (38). On platinum Gerischer (42) found the charge transfer coefficient to be 0.58 in 1.0M H $_2$ SO $_4$ and the standard rate constant was 3×10^{-3} cm sec $^{-1}$. In 1.0M HClO $_4$ Randles and Somerton (43) found the standard rate constant to be 5×10^{-3} cm sec $^{-1}$. Anson (44) determined the standard rate constant for the iron system in 1.0M H $_2$ SO $_4$, 1.0M NaHSO $_4$, and 1.0M NaHSO $_4$ plus 1.0M Na $_2$ SO $_4$ and found that the rate constant was highest at 5.3×10^{-3} cm sec $^{-1}$ in 1.0M H $_2$ SO $_4$ solution and decreased to 2.7×10^{-3} cm sec $^{-1}$ and 1.4×10^{-3} cm sec $^{-1}$ for the 1.0M NaHSO $_4$ and 1.0M NaHSO $_4$ plus 1.0M Na $_2$ SO $_4$ electrolytes, respectively. Angell and Dickinson (45) found 7×10^{-3} cm sec $^{-1}$ in 0.5M H $_2$ SO $_4$ and Samec and Weber (46) obtained 3.2×10^{-3} cm sec $^{-1}$ in 0.5M H $_2$ SO $_4$ and 8.0×10^{-3} cm sec $^{-1}$ in 0.5M Na $_2$ SO $_4$ of pH of 2.2. On rhodium in 1.0M HClO $_4$ the charge transfer coefficient is 0.59 and the standard rate constant 4.60×10^{-4} cm sec $^{-1}$ (40). This rate constant is generally lower than usually found for the Fe(II)/Fe(III) system, but this is probably due to the electrode material used.

It is seen that the charge transfer coefficient determined in this work on gold is in agreement with those values determined by other investigators. The standard rate constant determined here, 1.30×10^{-2} cm sec $^{-1}$, is in good agreement with the value of 1.0×10^{-2} cm sec $^{-1}$ found in 0.5M H $_2$ SO $_4$ (45). Both are

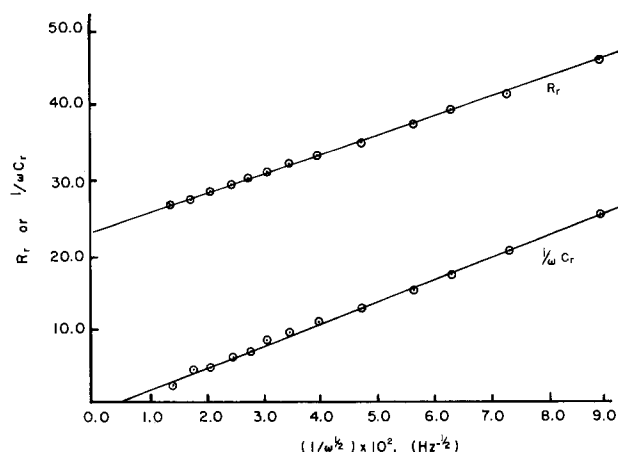


Fig. 6. Resistive and capacitive components of the faradaic impedance for 4.75×10^{-3} M Fe(II) and 1.29×10^{-2} M Fe(III) in 1.0M sulfuric acid.

Table IV. Charge transfer resistance, apparent exchange current density i_0^a , and equilibrium potentials at various Fe(II) and Fe(III) concentrations in 1M H₂SO₄

| Solution | Charge transfer resistance (Ω) | $i_0^a \times 10^6$ (A cm ⁻²) | E_e (V vs. NHE) |
|---|--------------------------------|---|-------------------|
| 1.25 × 10 ⁻³ M Fe(III) | 58.6 | 3.37 | 0.6283 |
| 2.01 × 10 ⁻³ M Fe(III) | 40.7 | 4.86 | 0.6427 |
| 3.57 × 10 ⁻³ M Fe(III) | 33.0 | 5.98 | 0.6605 |
| 6.66 × 10 ⁻³ M Fe(III) | 27.9 | 7.08 | 0.6749 |
| 1.29 × 10 ⁻² M Fe(III) | 24.3 | 8.15 | 0.6740 |
| Fe(II) concentration = constant = 4.75 × 10 ⁻³ M | | | |
| 1.19 × 10 ⁻³ M Fe(II) | 69.5 | 2.84 | 0.6940 |
| 2.38 × 10 ⁻³ M Fe(II) | 52.3 | 3.78 | 0.6785 |
| 4.75 × 10 ⁻³ M Fe(II) | 33.0 | 5.98 | 0.6608 |
| 9.50 × 10 ⁻³ M Fe(II) | 25.6 | 7.72 | 0.6443 |
| 1.90 × 10 ⁻² M Fe(II) | 20.6 | 9.58 | 0.6290 |

Fe(III) concentration = constant = 3.57 × 10⁻³M

higher by a factor of 10² than the one determined by Bockris *et al.* in 1M H₂SO₄ (47).

Electrochemical kinetics of the Fe(II)/Fe(III) system in 1.0M H₂SO₄ with benzo-(f)-quinoline.—The results of the kinetic experiments in the presence of benzo-(f)-quinoline are presented in Table V together with the corresponding data for 1.0M H₂SO₄. Experiments at 1.0 × 10⁻³M benzo-(f)-quinoline ($\theta = 0.40$) were highly irreproducible and are omitted.

The standard rate constant found in 1.0M H₂SO₄, 1.30 × 10⁻² cm sec⁻¹, decreased to 1.01 × 10⁻² cm sec⁻¹ in 1.0 × 10⁻⁵M benzo-(f)-quinoline and to 4.21 × 10⁻³ cm sec⁻¹ in 1.0 × 10⁻⁴M benzo-(f)-quinoline. In 1.0 × 10⁻⁵M benzo-(f)-quinoline, the charge transfer coefficient is 0.48, and 0.51 in 1.0 × 10⁻⁴M benzo-(f)-quinoline. These two values are generally lower than those found in the literature, but agree well with the charge transfer coefficient found in 1.0M H₂SO₄ for the variation of Fe(II) concentration ($\alpha = 0.51$). In the presence of 1.0 × 10⁻⁵M benzo-(f)-quinoline the formal potential was found to be 0.6704V, and for 1.0 × 10⁻⁴M benzo-(f)-quinoline the formal potential was 0.6708V. These values are in good agreement with the formal potential calculated in 1.0M H₂SO₄ ($E^\circ_F = 0.6678V$).

A comparison of the $\Delta\phi_2$ values calculated according to Eq. [7] with those obtained for the quinone-hydroquinone system (Tables III and V) shows the latter to be larger by a factor of 2-4. This would indicate that changes in the ϕ_2 potential are not the principal cause for the reduction in the standard rate constant, although the effective ϕ_2 potential may well be different for the two systems because of differences in the distance of closest approach. Still the decrease in the rate constant with coverage appears to be logarithmic, $\ln(k_a^\theta/k_a^0) = -5.68\theta + 0.01$. This may well indicate that both systems are inhibited by similar mechanisms. Again, the intercept, +0.01, is small and probably due to experimental error.

The explanation that the adsorption of benzo-(f)-quinoline increases the free energy of activation due

Table V. Charge transfer coefficient, standard rate constant, and $\Delta\phi_2$ for the Fe(II)/Fe(III) system in 1.0M H₂SO₄ with and without added benzo-(f)-quinoline

| Concentration of benzo-(f)-quinoline | θ | α^* | $k_a^0 \times 10^3$ (cm sec ⁻¹) | $\Delta\phi_2^{**}$ (mV) |
|--------------------------------------|----------|------------|---|--------------------------|
| 0 | 0.0 | 0.51 | 13.0 | — |
| 1.0 × 10 ⁻⁵ M | 0.05 | 0.48 | 10.1 | 2.6 |
| 1.0 × 10 ⁻⁴ M | 0.20 | 0.51 | 4.2 | 11.5 |

* Obtained from experiments at constant Fe(III) concentration.
** Calculated according to Eq. [7] with $Z = 2$.

to interaction between adsorbed layer and electroactive species is reasonable since the adsorbed layer is expected to increase the positive charge of the electrode surface by elimination of sulfate species during adsorption. This effectively increases the electrostatic repulsion between the more positively charged surface layer and the electroactive species, here positively charged also. Thus, electrostatic repulsion in the Fe(II)/Fe(III) system plays a role similar to the difficulty in penetration of the adsorbed layer in the quinone-hydroquinone system.

Conclusions

The adsorption of benzo-(f)-quinoline on gold electrodes in 1.0M H₂SO₄ between 0.0 and +0.7V can be described by the Frumkin isotherm and the isotherm with virial coefficients. In this potential range, adsorption is almost independent of potential. The apparent standard rate constant for both the quinone-hydroquinone and the Fe(III)/Fe(II) system is an exponential function of coverage at $\theta \leq 0.40$ and $\theta \leq 0.20$, respectively. Such an exponential function would be expected if changes in the ϕ_2 -potential caused by the adsorbed species are the principal cause for the decrease in rate constant. However, the changes calculated for the quinone-hydroquinone system are 2-4 times larger than those for the Fe(III)-Fe(II) system. Alternatively, an exponential decrease in rate constant can be caused by an increase in free energy of activation due to interaction between adsorbed layer and electroactive species.

Manuscript submitted Feb. 18, 1981; revised manuscript received June 12, 1981.

Any discussion of this paper will appear in a Discussion Section to be published in the June 1982 JOURNAL. All discussions for the June 1982 Discussion Section should be submitted by Feb. 1, 1982.

REFERENCES

- C. I. Antropov, *Corros. Sci.*, **7**, 607 (1967).
- C. N. Reilley and W. Stumm, in "Progress in Polarography," Vol. 1, P. Zuman, Editor, Interscience Publishers, New York (1962).
- J. Heyrovsky and J. Kuta, "Principles of Polarography," Academic Press, New York (1966).
- B. B. Damaskin and B. P. Afanas'ev, *Elektrokhimiya*, **13**, 1099 (1977).
- M. A. Loshkarev, F. A. Danilov, G. E. Bol', and L. G. Sechin, *ibid.*, **13**, 593 (1977).
- J. Weber, J. Kouteck'y, and J. Koryta, *Z. Elektrochem.*, **63**, 583 (1959).
- J. Kuta and I. Smoler, *ibid.*, **64**, 285 (1960).
- W. Müller and W. Lorenz, *Z. Phys. Chem. (Frankfurt)*, **27**, 23 (1962).
- S. Sathyanarayana, *J. Electroanal. Chem. Interfacial Electrochem.*, **10**, 119 (1965).
- K. K. Niki and N. Hackerman, *ibid.*, **32**, 257 (1971).
- J. Lipkowski and Z. Galus, *ibid.*, **61**, 11 (1975).
- M. L. Huggins, *J. Phys. Chem.*, **46**, 151 (1942); P. J. Flory, *J. Chem. Phys.*, **10**, 51 (1942).
- N. Tanaka, Ken-Ichi Kanno, and A. Yamada, *J. Electroanal. Chem. Interfacial Electrochem.*, **65**, 703 (1975).
- B. Behr, J. Taraszewska, and J. Stroka, *ibid.*, **58**, 71 (1975).
- A. A. Kazsrov and M. A. Loshkarev, *Elektrokhimiya*, **3**, 681 (1967).
- B. N. Afanas'ev and G. I. Avilova, *ibid.*, **12**, 1190 (1976).
- R. Parsons, in "Advances in Electrochemistry and Electrochemical Engineering," Vol. 1, P. Delahay, Editor, p. 1, Interscience, New York (1961).
- A. N. Frumkin, *Z. Phys. Chem.*, **164**, 121 (1933).
- S. Sathyanarayana, *J. Electroanal. Chem. Interfacial Electrochem.*, **50**, 195 (1974).
- R. Parsons, *ibid.*, **21**, 35 (1969).
- F. I. Danilov and M. A. Loshkarev, *Elektrokhimiya*, **11**, 1536 (1975).
- G. I. Avilova, B. N. Afanas'ev, and L. V. Reznik, *ibid.*, **11**, 1054 (1975).

23. B. N. Afanas'ev and L. A. Ternovskoi, *ibid.*, **10**, 901 (1974).
24. T. P. Hoar, "Pittsburgh International Conference on Surface Reactions," p. 127, Corrosion Publishing Co., Pittsburgh, PA (1948).
25. H. Meissner and E. Haberfellner, *Aluminum (Duesseldorf)*, **52**, 507 (1976).
26. H. Fischer and W. Seiler, *Corros. Sci.*, **6**, 159 (1966).
27. W. Seiler, D. Oeder, and H. Fischer, *Z. Phys. Chem. (Leipzig)*, **243**, 267 (1970).
28. I. C. Radacanu and W. Lorenz, *Electrochim. Acta*, **16**, 995 (1971).
29. I. C. Radacanu and W. Lorenz, *ibid.*, **16**, 1143 (1971).
30. T. Zak, *Gold Bull.*, **8-4**, 126 (1975).
31. B. B. Damaskin, "The Principles of Current Methods for the Study of Electrochemical Reactions," p. 61, McGraw-Hill, Inc., New York (1967).
32. D. D. Perrin, "Dissociation Constants of Organic Bases in Aqueous Solution," Butterworths, London (1965).
33. A. N. Frumkin, *Z. Phys.*, **35**, 792 (1926).
34. A. N. Frumkin, *Z. Phys. Chem.*, **116**, 466 (1925).
35. R. Parsons, *Trans. Faraday Soc.*, **51**, 1518 (1955); **55**, 999 (1959).
36. G. M. Schmid and M. E. Curley-Fiorino, in "Encyclopedia of Electrochemistry of the Elements," A. J. Bard, Editor, Chap. IV-3, Marcel Dekker, Inc., New York (1975).
37. J. O'M. Bockris and A. K. N. Reddy, "Modern Electrochemistry," Vol. 2, Plenum Publishing Corp., New York (1970).
38. K. J. Vetter, "Electrochemical Kinetics, Theoretical and Experimental Aspects," Academic Press, New York (1967).
39. K. J. Vetter, *Z. Elektrochem.*, **56**, 797 (1952).
40. K. G. Everett, L. A. Drew, S. J. Ericson, and G. M. Schmid, *This Journal*, **125**, 389 (1978).
41. J. M. Hale and R. Parsons, *Trans. Faraday Soc.*, **59**, 1429 (1963).
42. H. Gerischer, *Z. Elektrochem.*, **54**, 366 (1950).
43. J. E. B. Randles and K. W. Somerton, *Trans. Faraday Soc.*, **48**, 937 (1952).
44. F. C. Anson, *Anal. Chem.*, **33**, 939 (1961).
45. D. H. Angell and T. Dickinson, *J. Electroanal. Chem. Interfacial Electrochem.*, **35**, 55 (1972).
46. Z. Samec and J. Weber, *ibid.*, **77**, 163 (1977).
47. J. O'M. Bockris, R. J. Mannan, and A. Damjanovic, *J. Chem. Phys.*, **48**, 1898 (1968).

Effect of Sinusoidal A.C. on the Kinetics of Cu/Cu²⁺ Reaction in Acidic Sulfate Solution

Srinivasan Venkatesh*¹ and Der-Tau Chin*

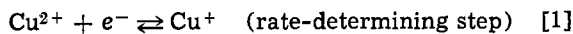
Department of Chemical Engineering, Clarkson College of Technology, Potsdam, New York 13676

ABSTRACT

A study has been made of the effect of high amplitude a.c. on the kinetics of a copper rotating disk electrode in acidic copper sulfate solutions. It was found that the rest potential was shifted toward the negative direction, and the exchange current density and the Tafel slopes increased with the superimposition of a.c. A mathematical model which took into account the periodical change in the surface concentration, the double layer capacity, the surface and the ohmic overpotential, was proposed to explain the observed phenomena.

This work is concerned with the effect of a high amplitude alternating current (a.c.) on the kinetics of copper deposition and dissolution reactions in acidic copper sulfate solutions.

The kinetics of this system without any superimposed a.c. have been extensively investigated. Mattson and Bockris (1) performed galvanostatic measurements of copper electrodes. They concluded that the reaction was controlled by a redox process between cupric and cuprous ions and arrived at the following consecutive reaction steps



Hurlen (2) found that the rate of this reaction was independent of pH in the pH range 0-5. Bockris and Kita (3) performed experiments on different types of copper electrode surfaces, such as electrodeposited copper and He-quenched copper. They found that the kinetic parameters changed with the nature of the copper surfaces. Several other investigators (4-19) confirmed that the Cu/Cu²⁺ electrode reaction in aqueous sulfate and perchlorate solutions involved two consecu-

tive charge transfer steps with Cu⁺ as the intermediate. Hurlen *et al.* (20) studied experimentally the kinetics of the Cu⁺/Cu charge transfer step. Their results conformed with the earlier morphological data on the spiral and pyramidal growth of Cu electrodeposits (21).

Sheshadri (22) has studied the growth of single crystals of Cu on nickel from acidic CuSO₄ solutions and has shown that superimposed a.c. brought about morphological changes in Cu deposits. He observed a gradual truncation of pyramids to smooth and flat deposits in the presence of a.c. The effect of a.c. on the corrosion of copper concentric neutral wires in underground environments has been investigated by Kruger *et al.* (23). They found that a.c. caused accelerated attack with pit formation and that the oxygen availability and the presence of chloride ions in solution favored the attack on the wires.

In the present work, a sinusoidal a-c modulation method has been used to study the kinetics of the copper electrode in sulfuric acid with the rotating disk electrode. In this method, a constant alternating current is passed through the electrode-electrolyte interface, and the resulting time-averaged (or d-c) electrode potential is measured as a function of d-c density at the electrode (24-26). A mathematical model taking into account the double layer capacity, the ohmic drop, and the change in the electrode surface concentration is proposed to predict the effect of a.c.

* Electrochemical Society Active Member.

¹ Present address: Hooker Chemical Company, Niagara Falls, New York 14302.

Key words: electrodeposition, dissolution, polarization, impedance.

Experimental

A copper rotating disk was used as the working electrode. The details of the experimental setup are given in Ref. (27) and are only briefly described here. A Pyrex cell was used to accommodate the working electrode, the counterelectrode, a Luggin capillary, a thermometer, and a gas bubbler. The copper working electrode was modified from a Pine Instrument DT ring electrode, as described by Chin (28). It consisted of a Teflon support rod and a replaceable copper disk electrode of 0.794 cm in diameter. The rotation of the electrode was provided by a Pine Instrument PIR high speed rotator. The counterelectrode was a platinum screen. A saturated calomel electrode was used as the reference electrode and was placed in a separate reference compartment. Both the reference and the working electrode compartments were filled with the same electrolyte under study. The Luggin capillary was placed along the axis of rotation about 2 mm from the electrode surface. The electrolyte was 0.025–0.15M CuSO₄ in 0.5M H₂SO₄ and was deaerated by bubbling N₂ for 2–3 hr prior to the start of experiment. All the measurements were carried out at 22° ± 1°C.

The electrical circuit for a-c modulation is shown in Fig. 1. The current was controlled by connecting a known resistor across the reference and the working electrode terminals of a Wenking LT73 potentiostat and by controlling the voltage drop across them. The sinusoidal signal input to the potentiostat was adjusted by an audio oscillator and power amplifier (General Radio Type 1308-A). The d-c potential developed across the reference and the working electrodes, ϕ_{DC} , was measured with a d-c electrometer (Keithley 602 Solid State). The alternating potential, ϕ_{AC} , was measured with a true rms voltmeter (Hewlett Packard 3466) after filtering the d-c potential through a differential amplifier/filter (Tektronix AM502). The alternating potential waves were observed on an oscilloscope (Tektronix SC503).

The chemical composition² of the copper-disk electrode was determined by a spectrographic analysis. The electrode was initially polished with 400 and 600 grit emery paper and then electropolished in chromic acid. The electrode was further cleaned in 20% nitric acid, rinsed with distilled water, 5% H₂SO₄, again with distilled water, and transferred to the cell.

A sinusoidal a.c. of known magnitude and frequency was applied to the cell, and the new rest potential of the copper electrode was measured by letting d.c. equal zero. The difference between the new rest potential and the equilibrium electrode potential without a.c. was computed as a shift in the rest potential, ϕ_{sh} . Subsequently, by varying the d.c. across the cell, the resultant d-c potential and the alternating potentials were measured to obtain the cathodic and the anodic

² Spectrographic analysis of copper disk electrode (weight percent): Cu, 99.93; Ag, 0.0005; Al, 0.001; Ni, 0.002; Zn, <0.01; Sn, <0.002; Fe, 0.50; Mg, 0.0003; Si, 0.003.

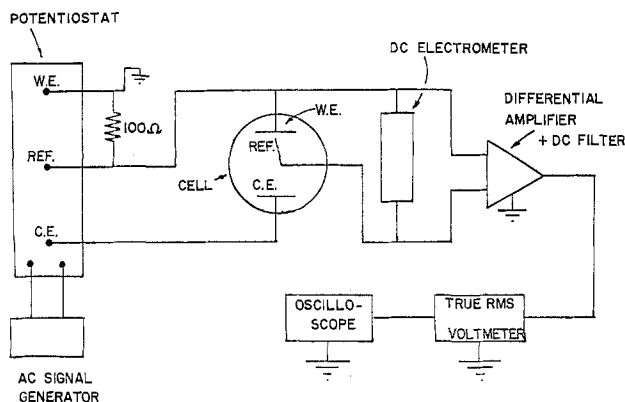


Fig. 1. A-C modulation electrical circuit

polarization curves. The exchange current densities and the Tafel slopes were obtained by the Tafel extrapolation method. The waveforms of the alternating potentials were observed with the oscilloscope and the oscillograms were taken at various applied a-c and d-c values.

A set of faradaic efficiency tests was performed. The electrodes were rinsed with distilled water, dried, and weighed before the start of each experiment. The electrodes were then pretreated by the procedure mentioned earlier and transferred to the cell. The experiments were performed at various d-c values superimposed with 25 mA/cm² rms a.c. After each run, the electrode was rinsed with distilled water, dried, and weighed again to determine the weight loss or gain of the electrode. Assuming a two-electron transfer reaction, the faradaic efficiency was determined. After the faradaic efficiency test, the electrode surface was coated with a thin layer of gold using a gold sputterer (International Scientific Company PS2 coating unit), and was examined under a scanning electron microscope (International Scientific Company Super Mini-SEM).

Results

Polarization curves.—Figure 2 shows a set of polarization curves for the copper rotating disk electrode in 0.05M CuSO₄ + 0.5M H₂SO₄ when 60 Hz sinusoidal a.c. was superimposed across the cell. The values of a-c varied from 0 to 150 mA/cm² rms. The data were obtained at a rotational speed of 2500 rpm; at this speed no appreciable concentration polarization was observed. The polarization curves were plotted after compensating for the ohmic drop. The anodic and the cathodic Tafel slopes for the polarization curve without a.c. were 41.5 and -142.2 mV, respectively, in good agreement with the values of 42 and -128 mV reported by Bockris and Kita (3). It can be seen that there was a shift in the rest potential toward the negative direction until a critical value was reached. Thereafter, the rest potentials were shifted back in the noble direction. The anodic and the cathodic Tafel slopes and the exchange current density were changed by a.c. The change is of an apparent property of a-c rectification, and the values with superimposed a.c. could be regarded as the apparent Tafel slopes and the apparent exchange current density. Furthermore, with superimposed a.c. the anodic and the cathodic Tafel lines no longer intersected at the rest potential; hence, an apparent anodic exchange current density i_{oa} , and an apparent cathodic exchange current density i_{oc} were calculated.

Evaluation of kinetic parameters.—Figures 3 and 4 show the apparent exchange current densities and the Tafel slopes as a function of superimposed a.c. The apparent cathodic exchange current density and the magnitude of the apparent cathodic Tafel slope increased consistently with increasing a.c. At high values of a.c., the apparent cathodic Tafel slopes ($-\beta_c$) were close to infinity. The i_{oa} curve initially increased with a.c., reached a maximum around 50 mA/cm² rms a.c., and then decreased with further increase in a-c densities. The apparent anodic Tafel slope, β_a , also exhibited the same behavior, but it peaked somewhere between 25 and 50 mA/cm² rms a.c. Figure 5 shows the rest potential shift, ϕ_{sh} , which exhibited a minimum around 50 mA/cm² rms a.c. The apparent exchange current densities, the apparent Tafel slopes, and the shift in the rest potentials are tabulated in Table I.

A-C potentials of the copper electrode.—In Fig. 6, the resulting root mean square of the alternating voltage (AV) component of the copper electrode potential due to the passage of a.c. is plotted against the d-c potentials. It is seen that as the d-c potential increased in the noble direction from the rest potential, the resulting AV decreased. This indicates that the impedance to

Fig. 2. Polarization curves for Cu in 0.05M CuSO₄ + 0.5M H₂SO₄ for various superimposed a.c. (60 Hz) at a rotational speed of 2500 rpm.

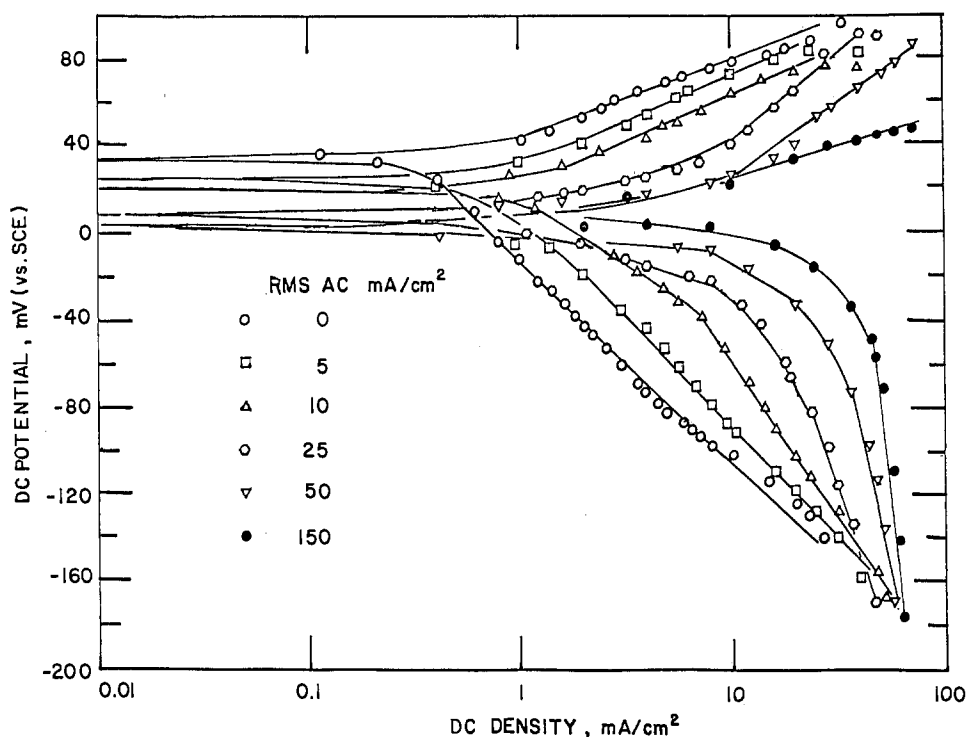
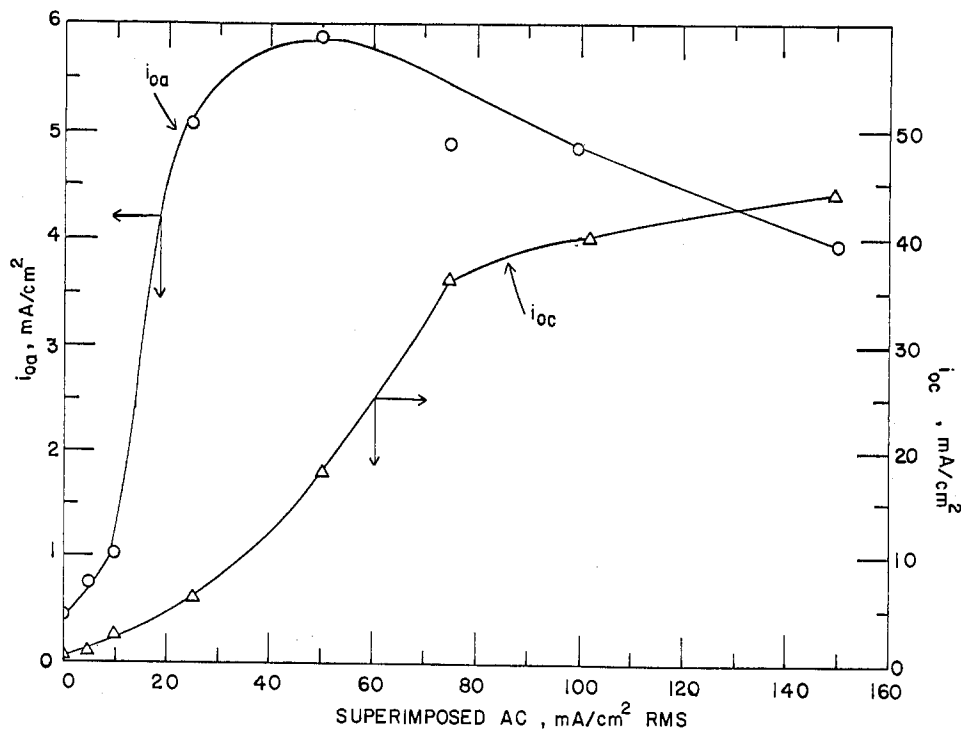


Fig. 3. Anodic and cathodic exchange current densities vs. superimposed a.c. (60 Hz) for Cu in 0.05M CuSO₄ + 0.5M H₂SO₄.



a.c. decreases when the d-c potential was shifted away from the rest potential. Increasing the d-c potential in the active direction (from the rest potential) decreased the resulting AV, until the superimposed a.c.

reached 50 mA/cm² rms. Thereafter at higher AV values, the AV decreased with increasing d-c potential in the active direction. The oscillograms of the resultant AV at various a-c and d-c densities were re-

Table I. Effect of 60 Hz a.c. on the kinetic parameters of the Cu/Cu⁺⁺ reaction in 0.05M CuSO₄ + 0.5M H₂SO₄

| Superimposed a.c. (mA/cm ² rms) | <i>i</i> _{0a} (mA/cm ²) | <i>i</i> _{0c} (mA/cm ²) | β_a (mV) | $-\beta_c$ (mV) | ϕ_{rest} (mV vs. SCE) | ϕ_{sh} (mV) | $\phi_{equil.}$ (mV vs. SCE) |
|--|--|--|----------------|-----------------|----------------------------|------------------|------------------------------|
| 0 | 0.455 | 0.456 | 42.9 | 106 | 30 | 0 | 30 |
| 2 | 0.5 | 0.35 | 42.2 | 104 | 29 | -1 | 30 |
| 5 | 0.759 | 0.818 | 41.1 | 103 | 24 | -9 | 33 |
| 10 | 1.06 | 2.94 | 42.7 | 144 | 20 | -14 | 34 |
| 25 | 5.06 | 6.11 | 99.4 | 157 | 8 | -24 | 33 |
| 50 | 5.88 | 17.6 | 73.7 | 261 | 4 | -29.5 | 33.5 |
| 75 | 4.88 | 35.6 | 40.0 | 556 | 4 | -28 | 32 |
| 100 | 4.86 | 38.3 | 57.7 | 671 | 5 | -28.5 | 33.5 |
| 150 | 3.92 | 43.8 | 31.2 | 1089 | 10 | -24.5 | 34.5 |

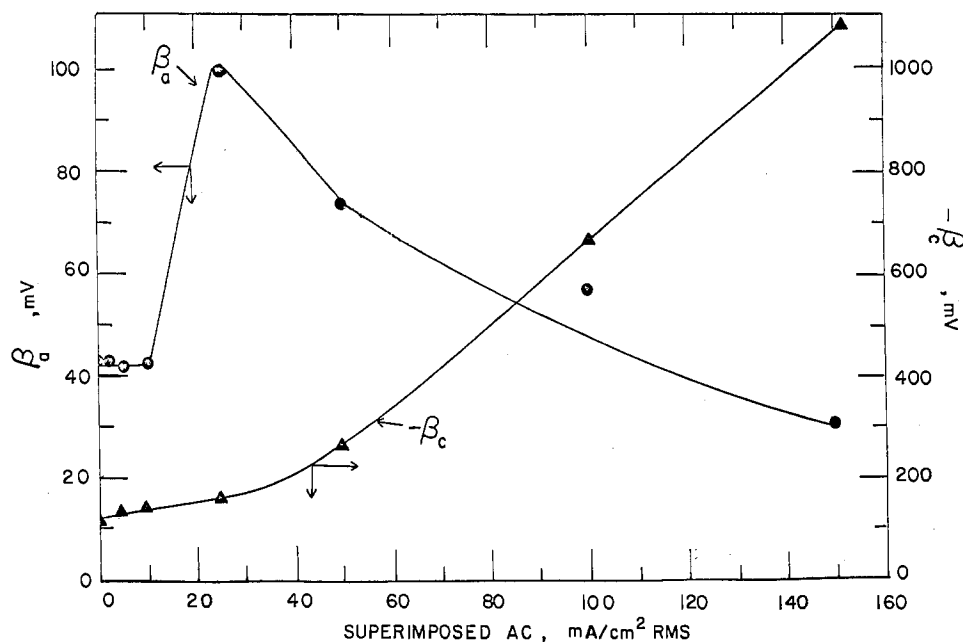


Fig. 4. Anodic and cathodic Tafel slopes at various superimposed a.c. (60 Hz) for Cu in 0.05M CuSO₄ + 0.5M H₂SO₄.

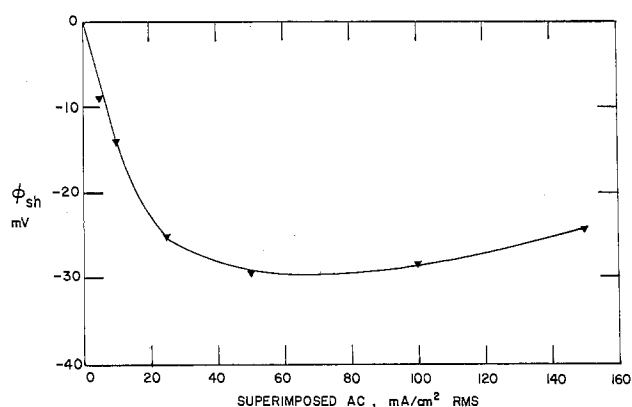


Fig. 5. Rest potential vs. superimposed a.c. (60 Hz) for Cu in 0.05M CuSO₄ + 0.5M H₂SO₄.

corded on a storage oscilloscope. It was found that the AV waveforms were slightly distorted from the sinusoidal shape.

Results of the faradaic efficiency tests.—The results obtained from the faradaic efficiency tests are summarized in Table II. The experiments were performed for both anodic and cathodic reactions. At 25 mA/cm² rms a.c., the efficiency tests were done at three different d-c values; one in the anodic, and two in the cathodic region. The faradaic efficiencies determined in all the tests were close to 100%, assuming that two electrons were transferred in the overall electrode reaction. Assuming the efficiency to be 100%, the number of electrons transferred was found to be two, as shown in the last column of Table III. It can be concluded from these results that the number of electrons transferred did not change during the application of a.c.

At the end of the faradaic efficiency test, the electrode surface was examined under an SEM. Figure 7 shows the effect of 25 mA/cm² rms of a.c. on the morphology of copper deposits obtained with 10C of

charge at a cathodic d-c density of 4 mA/cm². It is seen that a.c. greatly increased the grain size of the copper deposits. In the anodic dissolution region, a.c. was found to increase the size of pits. The results were similar to the application of a.c. on the zinc electrode in zinc chloride solutions (29).

Effect of CuSO₄ concentration of kinetic parameters.

—The a-c modulation experiments were also performed at different concentrations of CuSO₄. The Cu/Cu²⁺ reaction was found to be of a first order without the presence of a.c. When a.c. was superimposed, the apparent Tafel slopes (and hence the apparent transfer coefficients) changed with increasing concentrations of CuSO₄. Since the transfer coefficients have to be constant to determine the reaction order, the reaction order when a.c. was superimposed was not determined. However, the kinetic parameters derived from the polarization curves at different concentrations of CuSO₄ are reported in Table III.

Effect of a-c frequencies.—Figure 8 shows the effect of a-c frequency on the polarization curves at 25 mA/cm² rms a.c. It is seen that the shift in the rest potential decreased with increasing a-c frequency. The a-c frequency seemed to affect the cathodic Tafel region near the rest potential. Otherwise, there was no significant effect on the cathodic Tafel region. On the anodic portion, higher a-c frequencies shifted the polarization curves toward the zero a-c curve.

Discussion

The behavior of the polarization curves obtained by the a-c modulation can be attributed to the faradaic rectification process as explained in Ref. (24). There are other possibilities by which a.c. could influence the kinetics of the Cu-electrode reaction. These include: (i) the effect of a.c. on the rate-determining step and the number of electrons transferred in the overall electrode reaction; (ii) the formation of a copper-sulfate complex under the influence of a.c.; and

Table II. Results of the faradaic efficiency test

| Run number | i_{ac} (mA/cm ² rms) | i_{dc} (mA/ cm ²) | ϕ_{dc} (mV vs. SCE) | ϕ_{ac} (mV rms) | Total charge (C) | Region | Faraday efficiency (η %) | No. electrons trans- ferred (n) |
|------------|---|---------------------------------------|--------------------------------|-------------------------|------------------------|--------|--------------------------------------|--|
| CU267 | 0 | 10 | 50 | 0 | 39.90 | Anod. | 93.0 | 2.15 |
| CU268 | 0 | -4 | -80 | 0 | 10.60 | Cath. | 107.0 | 1.87 |
| CU269 | 25 | 30 | 107 | 130 | 45.32 | Anod. | 100.7 | 1.99 |
| CU271 | 25 | -4 | -40 | 150 | 9.56 | Cath. | 100.3 | 1.99 |
| CU272 | 25 | -35 | -271 | 89 | 43.32 | Cath. | 97.0 | 2.06 |

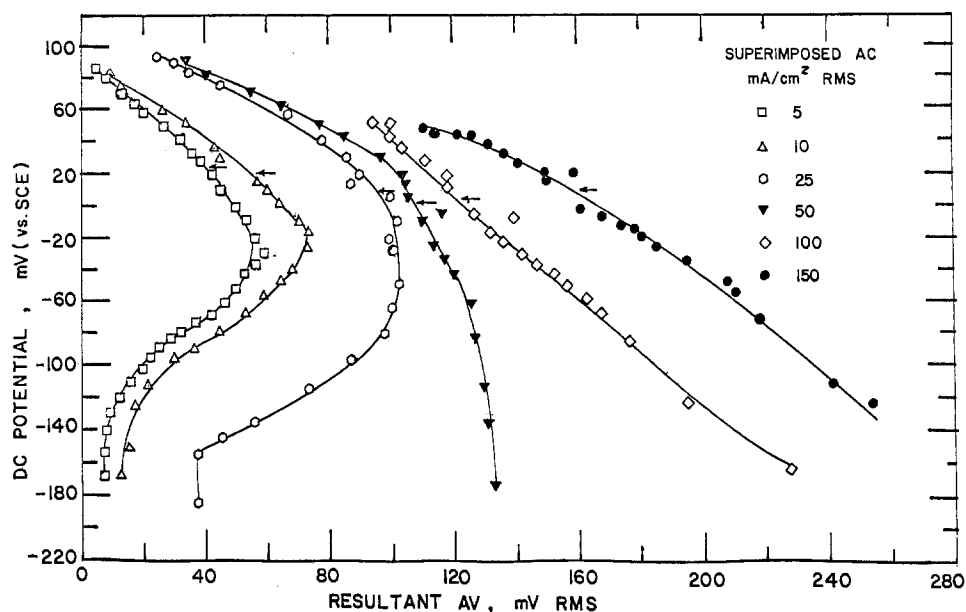


Fig. 6. Resultant a-c potential vs. d-c potential at various superimposed a.c. (60 Hz) for Cu in 0.05M $\text{CuSO}_4 + 0.5\text{M H}_2\text{SO}_4$. The arrows indicate the electrode rest potentials.

(iii) change in the surface characteristics of the copper electrode. The results of the faradaic efficiency test clearly ruled out the first possibility, for the number of electrons transferred in the Cu/Cu^{2+} reaction was two, with and without the application of a.c. To examine the second possibility, an a-c modulation experiment was also carried out using a Cu rotating disk electrode in 0.05M $\text{Cu}(\text{ClO}_4)_2$ and 0.5M HClO_4 . This was done to compare the behavior of Cu in H_2SO_4 to that in HClO_4 electrolyte with superimposed a.c. The polarization curves obtained in HClO_4 solution at zero a.c. and 25 mA/cm^2 rms superimposed a.c. are shown in Fig. 9 after compensating for the ohmic drop in the electrolyte. Perchlorate ion is known to be a noncomplexing agent. Due to the similarity in the behavior of the polarization curves in HClO_4 and H_2SO_4 , it can be concluded that there was no complex formation of Cu with the sulfate ions in H_2SO_4 electrolyte. On the other hand, the SEM photomicrographs exemplify the changes in the surface morphology with a.c. Hence, the observed behavior can be interpreted as a surface phenomenon and the a-c rectification.

The effect of a-c rectification on the behavior of the polarization curves can be explained by a mathematical model of a rotating disk electrode, taking into account the surface concentration change, the double layer capacity, the ohmic resistance, and the concentration overpotential.

The total current density, i , is given by a d-c component, i_{DC} , and an a.c. component

$$i = i_{\text{DC}} + i_p \sin \omega t \quad [4]$$

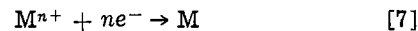
where i_p is the peak-to-peak value of a.c. and ω is the a-c frequency. The d-c portion aids the charge transfer reaction. A part of the a.c., i_{fAC} , also contributes to the charge transfer reaction. The other part, i_c , charges up the double layer and is the capacitance current. Hence, the total current density can be written as

$$i = i_{\text{DC}} + i_p \sin \omega t = i_{\text{DC}} + i_{\text{fAC}}(t) + i_c(t) \quad [5]$$

The total faradaic current density is

$$i_f = i_{\text{DC}} + i_{\text{fAC}} \quad [6]$$

For a metal/metal-ion system of the type



i_f may be given by the Butler-Volmer equation (30)

$$i_f = i_o \left(\frac{c_s}{c_x} \right)^\gamma \exp \left\{ \left(\frac{\alpha n F}{RT} \eta_s \right) - \exp \left(- \frac{\beta n F}{RT} \eta_s \right) \right\} \quad [8]$$

where α and β are the anodic and the cathodic transfer coefficients, η_s is the surface overpotential, i_o is the ex-

Table III. Effect of a.c. (60 Hz) and concentration of CuSO_4 on the kinetic parameters of the Cu/Cu^{++} reaction

| Concentration | i_{oa} (mA/cm^2) | i_{oc} (mA/cm^2) | β_a (mV) | $-\beta_c$ (mV) | ϕ_{rest} (mV vs. SCE) | ϕ_{sh} (mV) | $\phi_{\text{equil.}}$ (mV vs. SCE) |
|---|--|--|----------------|-----------------|--------------------------------------|-------------------------|--|
| Superimposed a.c. = 0 mA/cm^2 rms | | | | | | | |
| 0.025M $\text{CuSO}_4 + 0.5\text{M H}_2\text{SO}_4$ | 0.272 | 0.28 | 26.8 | 138 | 22 | 0 | 22 |
| 0.05M $\text{CuSO}_4 + 0.5\text{M H}_2\text{SO}_4$ | 0.455 | 0.456 | 22.9 | 106 | 28 | 0 | 28 |
| 0.1M $\text{CuSO}_4 + 1\text{M H}_2\text{SO}_4$ | 0.77 | 0.775 | 24.8 | 106 | 39 | 0 | 39 |
| 0.15M $\text{CuSO}_4 + 1.5\text{M H}_2\text{SO}_4$ | 0.878 | 0.878 | 22.7 | 87.1 | 42 | 0 | 42 |
| Superimposed a.c. = 5 mA/cm^2 rms | | | | | | | |
| 0.025M $\text{CuSO}_4 + 0.5\text{M H}_2\text{SO}_4$ | 1.08 | 1.01 | 31.6 | 114 | 10 | -1.3 | 11.3 |
| 0.05M $\text{CuSO}_4 + 0.5\text{M H}_2\text{SO}_4$ | 0.759 | 0.818 | 41.1 | 103 | 24 | -9.0 | 33.0 |
| 0.1M $\text{CuSO}_4 + 1\text{M H}_2\text{SO}_4$ | 0.937 | 1.66 | 36.3 | 131 | 33 | -2.0 | 35.0 |
| 0.15M $\text{CuSO}_4 + 1.5\text{M H}_2\text{SO}_4$ | 0.580 | 1.26 | 39.8 | 100 | 33 | -2.2 | 35.2 |
| Superimposed a.c. = 25 mA/cm^2 rms | | | | | | | |
| 0.025M $\text{CuSO}_4 + 0.5\text{M H}_2\text{SO}_4$ | 2.53 | 11.0 | 54.1 | 362 | 0 | -114 | 11.4 |
| 0.05M $\text{CuSO}_4 + 0.5\text{M H}_2\text{SO}_4$ | 5.06 | 6.10 | 99.4 | 157 | 8 | -25.0 | 33.0 |
| 0.1M $\text{CuSO}_4 + 1\text{M H}_2\text{SO}_4$ | 3.25 | 9.17 | 67.0 | 196 | 10 | -23.3 | 33.3 |
| 0.15M $\text{CuSO}_4 + 1.5\text{M H}_2\text{SO}_4$ | 4.49 | 7.81 | 85.0 | 165 | 18 | -20.0 | 38.0 |
| Superimposed a.c. = 50 mA/cm^2 rms | | | | | | | |
| 0.025M $\text{CuSO}_4 + 0.5\text{M H}_2\text{SO}_4$ | 1.84 | 16.9 | 36.1 | 564 | -8 | -18.0 | 10.0 |
| 0.05M $\text{CuSO}_4 + 0.5\text{M H}_2\text{SO}_4$ | 5.88 | 17.6 | 73.7 | 261 | 4 | -29.5 | 33.5 |
| 0.1M $\text{CuSO}_4 + 1\text{M H}_2\text{SO}_4$ | 6.69 | 16.0 | 77.8 | 209 | -4 | -33.0 | 29.0 |
| 0.15M $\text{CuSO}_4 + 1.5\text{M H}_2\text{SO}_4$ | 12.8 | 24.0 | 135 | 257 | 4 | -34.3 | 36.3 |

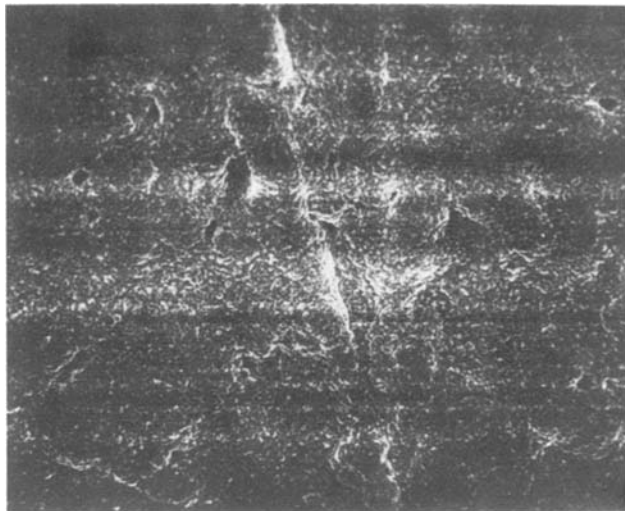


Fig. 7. Scanning electron micrographs of the Cu deposits after experiments at various cathodic d-c densities in 0.05M CuSO₄ + 0.5M H₂SO₄. The d-c and a-c densities (60 Hz) at which the experiments were performed are indicated on each picture. Magnification 280X.

change current density, and γ is a kinetic parameter. The capacitance current may be expressed as

$$i_c = \frac{d}{dt} (C_{dl} i_s) \quad [9]$$

where C_{dl} is the double layer capacity which is a function of η_s . Combining Eq. [8] and [9] and assuming that α , β , and γ do not change with the application of a.c., one has

$$i = i_{DC} + i_p \sin \omega t = i_o \left(\frac{c_s}{c_\infty} \right)^\gamma \left\{ \exp \left(\frac{\alpha n F}{RT} \eta_s \right) - \exp \left(- \frac{\beta n F}{RT} \eta_s \right) \right\} + \frac{d}{dt} (C_{dl} i_s) \quad [10]$$

at

$$t = 0, \quad \eta_s = \eta_{DC} \quad [11]$$

where η_{DC} is the d-c overpotential.

The total overpotential is equal to the sum of the surface overpotential, the concentration overpotential, and the ohmic overpotential

$$\eta = \eta_s + \eta_{conc} + \eta_{ohm} \quad [12]$$

$$\eta_{conc} = \frac{RT}{nF} \ln \frac{c_s}{c_\infty} \quad [13]$$

$$\eta_{ohm} = i \rho l \quad [14]$$

where ρ is the specific resistance of the electrolyte and l is the distance between the reference capillary and the working electrode.

To determine the surface concentration, c_s , one needs the convective diffusion equation for the mass transport of ionic species

$$\frac{\partial c}{\partial t} + v_y \frac{\partial c}{\partial y} = D \frac{\partial^2 c}{\partial y^2} \quad [15]$$

The boundary conditions are

$$c(y, 0) = c_\infty$$

$$c(\infty, t) = c_\infty \quad [16]$$

$$-D \frac{\partial c}{\partial y} (0, t) = \frac{i_f(t)}{nF}$$

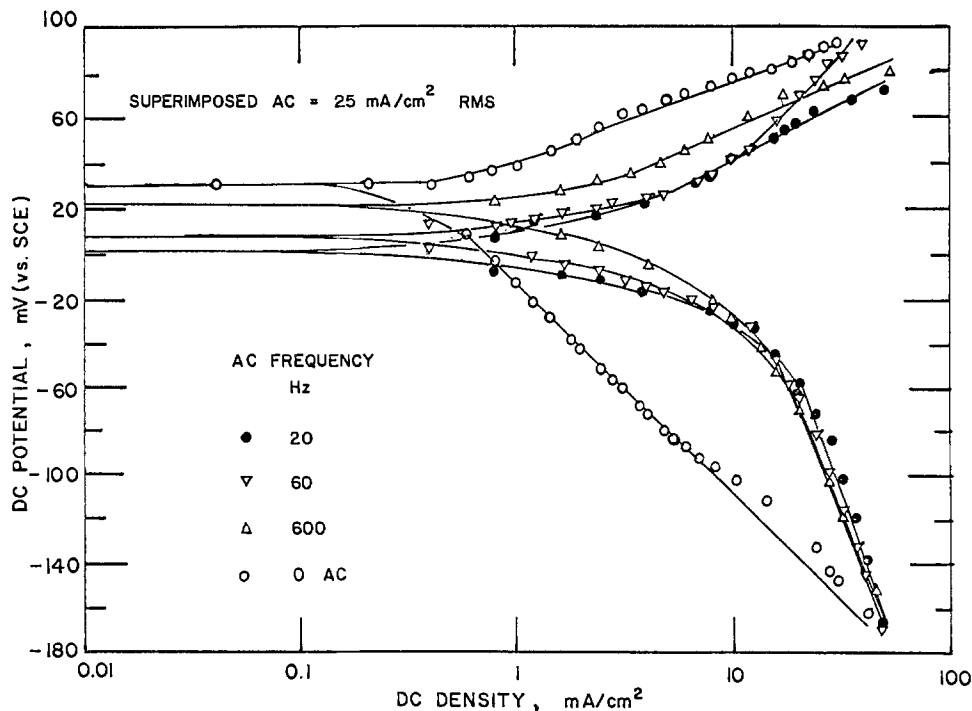
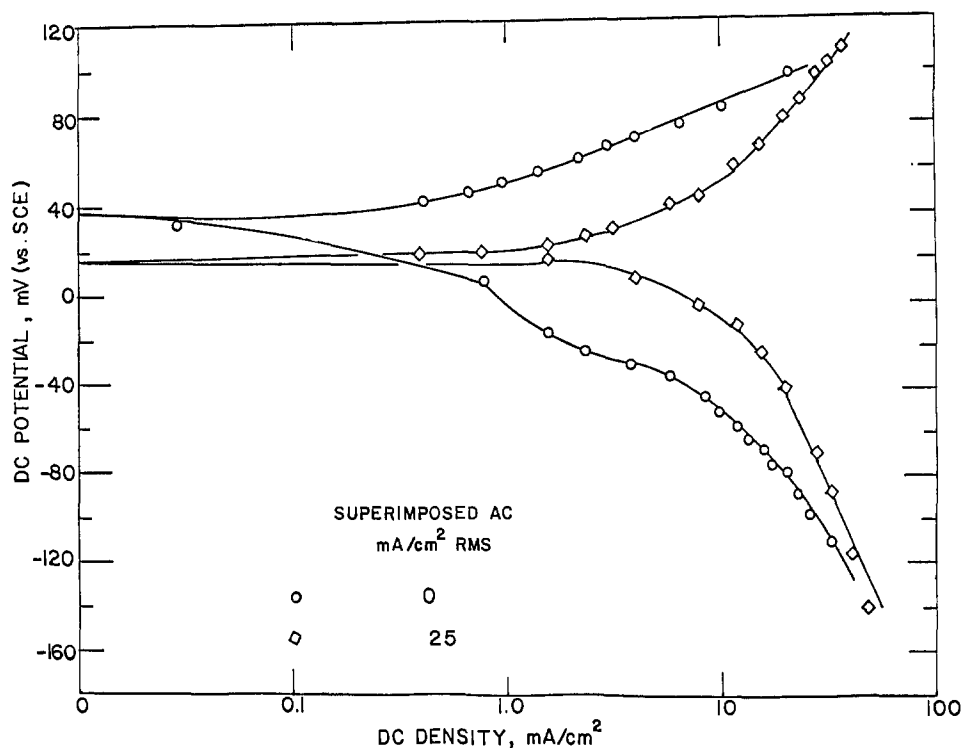


Fig. 8. Effect of a-c frequency on the polarization curves at 25 mA/cm² rms superimposed a.c. for Cu in 0.05M CuSO₄ + 0.5M H₂SO₄.

Fig. 9. Polarization curves for Cu in 0.05M copper perchlorate + 0.5M perchloric acid at 0 and 25 mA/cm² rms superimposed a.c. (60 Hz). Speed of rotation = 2500 rpm.



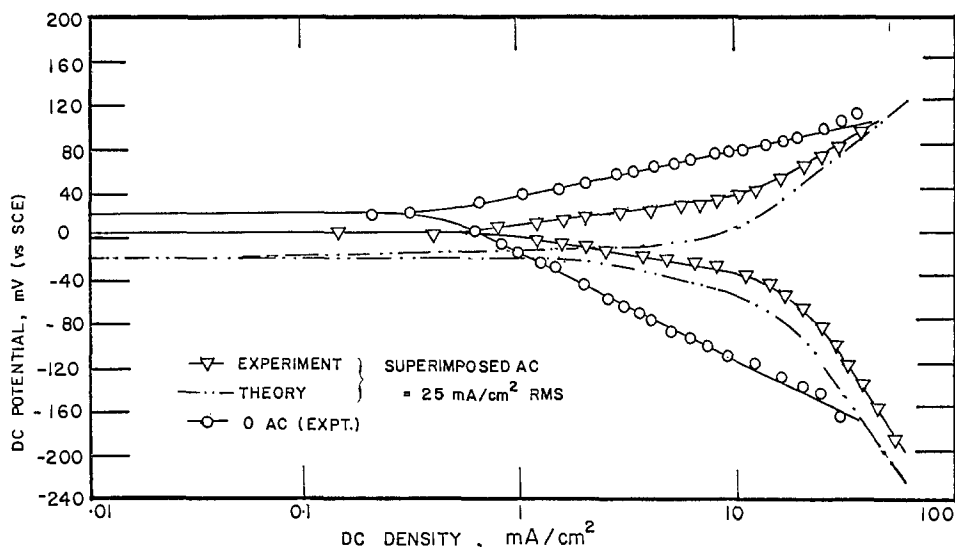
Here c is the concentration of the ionic species and c_0 is the bulk concentration, y is the axial coordinate, D is the diffusion coefficient, v_y is the velocity components in the y direction, i_f is the faradaic current density, n is the number of electrons transferred, and F is the Faraday constant. The major assumptions involved are that there is an excess of supporting electrolyte and uniform current distribution on the electrode surface.

The foregoing model has been solved numerically with a digital computer. The details of the solution procedure are given in Ref. (27). The calculations were performed for the a-c modulation of a copper rotating disk electrode in 0.05M CuSO₄ and 0.5M H₂SO₄. The polarization curve, i.e., d-c current density vs. the d-c potential, was evaluated by feeding the input parameters, i_0 , α , and β obtained from the experimental polarization curve without a-c. A value of 0.4 was chosen for the kinetic parameter, γ , as suggested by Newman (30). An experimental value of the double layer capacity of 56 $\mu\text{F}/\text{cm}^2$ was used for the calculation. This value was obtained by Bockris and co-worker (8, 10) and was independent of the electrode potential for $-200 \text{ mV} < \eta_s < 200 \text{ mV}$.

Figure 10 shows the polarization curves obtained from the theory at a superimposed a.c. of 25 mA/cm² rms (60 Hz). The curves were plotted after the compensation for the ohmic potential drop in the electrolyte. For comparison, the experimental values without any superimposed a.c. and at 25 mA/cm² rms a.c. are also shown in the figure. The theoretical curves clearly demonstrate that the a-c rectification is directly responsible for (i) the shift in rest potential toward the negative direction, (ii) an increase in the exchange current density, and (iii) an increase in both anodic and cathodic Tafel slopes. These results qualitatively agree with the observed phenomena. Since the mathematical model assumes that real kinetic parameters, such as i_0 , β_a , β_c , and γ are not affected by the superimposition of a.c., the new exchange current density and the Tafel slopes can be regarded as an apparent property associated with the high amplitude a-c rectification.

Despite the similarities between the theoretical and the experimental polarization curves, there is a lack of quantitative agreement. The theory seems to overpredict the effect of a.c. The discrepancy can be at-

Fig. 10. Theoretical and experimental polarization curves for Cu RDE in 0.05M CuSO₄ + 0.5M H₂SO₄ at 25 mA/cm² rms superimposed a.c. at 60 Hz. The experimental curve obtained without a.c. is shown by the open circles, —○—.



tributed to various reasons, such as the roughening of the electrode surface during the experimental polarization measurements, the formation of an oxide layer during the anodic dissolution runs, and the nonuniform current distribution on the disk electrode. Further results obtained from the model will be published in a later report.

Conclusions

A study has been made of the effect of high amplitude sinusoidal a.c. on the kinetics of the copper electrode in acidic sulfate solutions using a rotating disk electrode. It was found that the anodic exchange current densities increased with increasing a-c densities until a critical value of 50 mA/cm² rms was reached; thereafter, the anodic exchange current density started decreasing with further increase in a-c densities. The cathodic exchange current densities increased with increasing a.c. The apparent values of the Tafel slopes increased with a-c superimposition. The rest potentials were shifted in the negative direction until the critical a-c density and further increase in a.c. shifted the rest potential back toward the noble direction. A mathematical model has been proposed to predict the phenomena of the high amplitude a-c rectification. The numerical results showed the characteristics similar to those observed in the experimental polarization measurements.

Acknowledgments

This work was supported by the National Science Foundation Grant ENG77-25153. Acknowledgment is also made to the donors of the Petroleum Research Fund, administered by the American Chemical Society, for partial support of this research. Special thanks are due to A. J. Wallace, Jr., and J. L. Griffin, of General Motors Research Laboratories, for their help in the chemical analysis of the copper rotating disk electrode, and to the Institute of Colloid and Surface Science at Clarkson for using the scanning electron microscope.

Manuscript submitted Dec. 16, 1980; revised manuscript received April 28, 1981. This was Paper 408 presented at the Hollywood, Florida, Meeting of the Society, Oct. 5-10, 1980.

Any discussion of this paper will appear in a Discussion Section to be published in the June 1982 JOURNAL. All discussions for the June 1982 Discussion Section should be submitted by Feb. 1, 1982.

Publication costs of this article were assisted by Clarkson College of Technology.

LIST OF SYMBOLS

| | |
|------------------|---|
| c | concentration of the ionic species, mol/m ³ (mol/cm ³) |
| c _s | surface concentration of the ionic species, mol/m ³ (mol/cm ³) |
| c _∞ | bulk concentration of the ionic species, mol/m ³ (mol/cm ³) |
| C _{dl} | double layer capacitance, F/m ² (F/cm ²) |
| D | diffusion coefficient of the ionic species, m ² /sec (cm ² /sec) |
| F | Faraday constant, 9.65 × 10 ⁷ C/kg-equiv. (96500 C/g equiv.) |
| i | current density, A/m ² (A/cm ²) |
| i ₀ | exchange current density, A/m ² (A/cm ²) |
| i _{oa} | anodic exchange current density, A/m ² (A/cm ²) |
| i _{oc} | cathodic exchange current density, A/m ² (A/cm ²) |
| i _{AC} | AC density, A/m ² (A/cm ²) |
| i _c | capacitance current density, A/m ² (A/cm ²) |
| i _{DC} | d-c density, A/m ² (A/cm ²) |
| i _f | total faradaic current density, A/m ² (A/cm ²) |
| i _{fAC} | faradaic portion of i _{AC} , A/m ² (A/cm ²) |
| i _p | amplitude of a-c density, A/m ² (A/cm ²) |
| l | distance between the working electrode and the reference capillary, m (cm) |
| n | number of electrons transferred in the electrode reaction, kg equiv./mol (g equiv./mol) |

| | |
|---|---|
| R | gas constant, 8.314 J/mol K (1.987 cal/mol K) |
| t | time, sec |
| T | absolute temperature, K |
| y | axial coordinate, m (cm) |

Greek symbols

| | |
|---------------------|---|
| α | anodic transfer coefficient, dimensionless |
| β | cathodic transfer coefficient, dimensionless |
| β _a | anodic Tafel slope, V |
| β _c | cathodic Tafel slope, V |
| γ | kinetic parameter in Eq. [8], dimensionless |
| η | overpotential, V |
| η _{conc} | concentration overpotential, V |
| η _{DC} | d-c overpotential, V |
| η _{ohm} | ohmic overpotential, V |
| η _s | surface overpotential, V |
| ν | kinematic viscosity, m ² /sec (cm ² /sec) |
| ρ | specific resistance of the electrolyte, Ω · m (Ω · cm) |
| φ _{AC} | a-c component of the electrode potential, V |
| φ _{DC} | d-c component of the electrode potential, V |
| φ _{equil.} | thermodynamical equilibrium electrode potential, V |
| φ _{rest} | rest electrode potential when i _{DC} is zero, V |
| φ _{sh} | shift in the rest electrode potential, V |
| ω | a-c frequency, Hz (rad/sec) |
| Ω | speed of rotation, rad/sec |

REFERENCES

- E. Mattson and J. O'M. Bockris, *Trans. Faraday Soc.*, **55**, 1586 (1956).
- T. Hurlen, *Acta Chem. Scand.*, **15**, 630 (1961).
- J. O'M. Bockris and H. Kita, *This Journal*, **109**, 928 (1962).
- O. R. Brown and H. R. Thirsk, *Electrochim. Acta*, **10**, 383 (1965).
- T. Hurlen, *ibid.*, **7**, 653 (1962).
- J. O'M. Bockris and M. Enyo, *Trans. Faraday Soc.*, **58**, 1187 (1962).
- A. Damjanovic, T. H. V. Setty, and J. O'M. Bockris, *This Journal*, **113**, 429 (1966).
- G. W. Tindall and S. Bruckenstein, *Anal. Chem.*, **40**, 1042, 1051, 1637 (1968).
- L. H. Jenkins, *This Journal*, **117**, 630 (1970).
- L. H. Jenkins and R. B. Durham, *ibid.*, **117**, 1506 (1970).
- D. Landolt, R. H. Mueller, and C. W. Tobias, *ibid.*, **118**, 40 (1971).
- K. M. Gorbunova and Z. A. Tkachik, *Electrochim. Acta*, **16**, 191 (1971).
- N. A. Hampson and R. J. Latham, *Trans. Faraday Soc.*, **66**, 3131 (1970); **67**, 1440 (1971).
- H. C. Albaya and W. J. Lorenz, *Z. Phys. Chem. N.F.*, **81**, 294 (1972).
- G. Razumney and J. O'M. Bockris, *J. Electroanal. Chem. Interfacial Electrochem.*, **46**, 185 (1973).
- I. R. Burrows, J. A. Harrison, and J. Thompson, *ibid.*, **58**, 241 (1975).
- I. R. Burrows, K. L. Dick, and J. A. Harrison, *Electrochim. Acta*, **21**, 81 (1976).
- O. J. M. Slayman and W. J. Lorenz, *ibid.*, **19**, 791 (1975).
- H. Schweikert, A. A. ElMiligy, A. Melendez, and W. J. Lorenz, *J. Electroanal. Chem. Interfacial Electrochem.*, **68**, 19 (1976).
- T. Hurlen, G. Ottesen, and A. Staurset, *Electrochim. Acta*, **23**, 39 (1978).
- H. Seiter, H. Fischer, and L. Albert, *ibid.*, **2**, 97 (1960).
- B. S. Sheshadri, *Plat. Surf. Finish.*, **65**, 43 (1978).
- J. Kruger, U. Bertocci, F. Escalante, and J. L. Mullen, Report No: NBSIR-77-1232 (ERDA), Nat. Bur. Standards, Washington, DC (1977).
- S. Venkatesh and D-T. Chin, *Isr. J. Chem.*, **18**, 56 (1979).
- D-T. Chin and T. W. Fu, *Corrosion*, **35**, 514 (1979).
- D-T. Chin and S. Venkatesh, *This Journal*, **126**, 1908 (1979).
- S. Venkatesh, Ph.D. Thesis, Clarkson College of Technology, Potsdam, NY (August 1980).
- D-T. Chin, *This Journal*, **120**, 631 (1973).
- D-T. Chin and S. Venkatesh, *ibid.*, **128**, 1439 (1981).
- J. Newman, "Electrochemical Systems," p. 175, Prentice Hall, Englewood Cliffs, NJ (1973).

Protection of Semiconductor Photoanodes with Photoelectrochemically Generated Polypyrrole Films

Rommel Noufi*¹ Dennis Tench,* and Leslie F. Warren*

Rockwell International, Microelectronics Research and Development Center, Thousand Oaks, California 91360

ABSTRACT

Results are presented which show that photoelectrochemically generated polypyrrole films protect semiconductor photoanodes (e.g., Cd chalcogenides, GaAs, and Si), from degradation while permitting electron exchange between the semiconductor and the electrolyte. The performance characteristics and stability of such film-covered photoelectrodes are discussed.

In an earlier brief communication (1), we described the electrochemical generation of conducting polypyrrole films on n-GaAs and the characteristics of the resulting photoanodes. It was demonstrated that such polymer films inhibit photodegradation of the semiconductor, presumably by impeding ion/solvent transport. Good photoanode performance characteristics, from an electrochemical solar cell standpoint, were also observed, as might be expected for films having high electronic conductivity. For polypyrrole electro-deposited on metallic electrodes, conductivities in the 10-100 $\Omega^{-1} \text{ cm}^{-1}$ range have been reported (2).

In the present paper, details of our earlier work and results obtained for other semiconductor materials are presented. Emphasis is on the stabilization provided by polypyrrole films and their effect on the photoanode performance characteristics. The role of redox couples, both in the electrolyte and incorporated within the polymer matrix, is also discussed.

Experimental Details

Unless otherwise noted, polypyrrole films were electrodeposited from mechanically stirred acetonitrile solutions containing 0.5M pyrrole and 0.2M Et_4NBF_4 (supporting electrolyte). Based on a few experiments, comparable results were obtained for films deposited from analogous methylene chloride electrolytes, and from aqueous H_2SO_4 solutions (pH 1.5-1.9) containing 0.2-0.5M pyrrole. The counterelectrode was a 25 cm^2 Pt foil. Deposition on Pt electrodes was performed at a constant potential of +0.85V vs. SCE (saturated calomel electrode). Deposition on n-type semiconductors was performed under tungsten-halogen illumination (100 mW/cm^2) at constant potential (0.45V vs. SCE for n-GaAs, 0.2V for the Cd chalcogenides, and 0.4V for n-Si) such that the current, which remained practically constant except for an initial spike, was in the 2-3 mA/cm^2 range. Based on the charge passed (20 mC/cm^2), the film thickness used in the present work was 50-100 monolayers. All electrode potentials are reported vs. SCE and measurements were made with IR compensation. Illumination for photoresponse studies was also provided by a tungsten-halogen lamp. Additional experimental details are given elsewhere (1).

Semiconductors were single crystals ($\sim 0.2 \text{ cm}^2$) and were polished using aqueous alumina slurries to 1 μm particle size before mounting in RTV silicone rubber (M-Coat C, M-Line Accessories, Romulus, MI). Crystal orientations were perpendicular to the c-axis for CdS and CdSe, $\langle 111 \rangle$ for CdTe, and $\langle 111 \rangle$ or $\langle 110 \rangle$ (comparable results) for GaAs. Ohmic contacts were made by standard techniques. GaAs electrodes were etched in a 1:1 mixture of concentrated H_2SO_4 and

30% H_2O_2 for about 15 sec (until matte black finish was obtained) prior to use. Si electrodes were etched in 49% aqueous HF solution for 10 sec. CdSe, CdTe, and CdS electrodes were etched in 4M HNO_3 , concentrated HNO_3 , and 6M HCl, respectively. CdSe and CdTe were dipped in a polyselenide solution after etching.

Results and Discussion

Electrodeposited polypyrrole films were first prepared (on Pt electrodes) by Diaz *et al.* (2), who also investigated their electrical and electrochemical properties (2-4). They found that films deposited from acetonitrile/tetraethylammonium tetrafluoroborate electrolytes are adherent (on metal electrodes) and consist of polymerized pyrrole units plus BF_4^- anions, typically in the ratio of about 4:1 (2). The films are stable in air to at least 250°C (3) and as electrodes in both aqueous and nonaqueous electrolytes (2-4). Reversible electrochemical oxidation of the film is evident from cyclic voltammetry and is associated with a transition from insulating (reduced form) to highly conducting (oxidized form) behavior (4). This film redox process involves exchange of anions between the film and the electrolyte, as evidenced by the dependence of the redox potential on the nature of the electrolyte (4). Anodic of the transition potential (about -0.2V vs. SCE in both aqueous and acetonitrile solutions), polypyrrole films exhibit electrochemical behavior similar to that observed for Pt electrodes, i.e., solution redox reactions occur reversibly. Data obtained in our laboratory are in general agreement with these results, except that the films appear to slowly decompose with potential cycling in aqueous solutions (containing ferro-ferricyanide) of pH > 13, long-term stability above pH 10 being questionable.

Electroactive species can also be incorporated in the film matrix. For example, polypyrrole films containing $\text{Fe}(\text{CN})_6^{3-}$ are produced from acetonitrile electrolytes containing this anion instead of BF_4^- . Cyclic voltammograms for a polypyrrole- $\text{Fe}(\text{CN})_6^{3-}$ film (on Pt) in an aqueous ferro-ferricyanide solution are shown in Fig. 1. Voltammetry peaks corresponding to the $\text{Fe}(\text{CN})_6^{3-/4-}$ redox reaction are evident at about 0.2V. The linear dependence of the peak heights on sweep rate and the near coincidence of the anodic and cathodic peak potentials are characteristic of a surface-bound redox species. The voltammetric behavior depicted in Fig. 1 was unchanged after more than 50 cycles. Upon transfer of such electrodes to solutions not containing electroactive species, the peaks corresponding to the $\text{Fe}(\text{CN})_6^{3-/4-}$ reaction gradually disappear as the redox species is lost to the solution. Likewise, the ferro-ferricyanide reaction on polypyrrole films deposited from solutions containing only BF_4^- anions initially exhibits the reversibility characteristic of Pt (some peak separation) but the anodic and cathodic peaks become more coincidental with potential cycling in the ferro-ferricyanide solution.

* Electrochemical Society Active Member.

¹ Present address: Solar Energy Research Institute, Golden, Colorado 80401.

Key words: electrochemical solar cells, photoanode stabilization, polymer films.

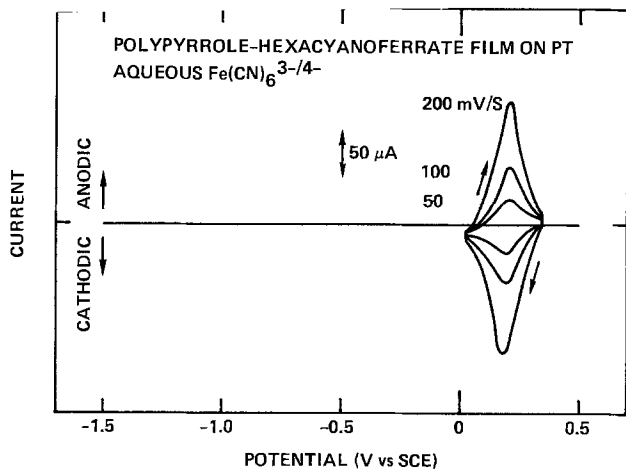


Fig. 1. Cyclic voltammograms at various sweep rates for a polypyrrole- $\text{Fe}(\text{CN})_6^{3-}$ film on Pt ($\sim 0.1 \text{ cm}^2$) in aqueous 0.1M $\text{Fe}(\text{CN})_6^{3-/4-}$ solution ($\text{pH} \sim 10$).

These results show that electroactive species can be incorporated within polypyrrole films and clearly demonstrate the mobility of anions in the polymer matrix.

Photoanode stabilization.—As discussed previously for n-GaAs (1), polypyrrole films stabilize semiconductor photoanodes against degradation while permitting electron exchange with the electrolyte. This is illustrated for n-GaAs in Fig. 2, n-CdSe in Fig. 3, and n-Si in Fig. 4. In all cases, the short-circuit photocurrent for the unprotected (bare) semiconductor decays rapidly (within a few minutes), presumably because of formation of an insoluble blocking surface layer of photodecomposition product, whereas that for the polypyrrole-coated photoanode remains practically constant. Note that polypyrrole films also afford n-GaAs electrodes protection from dissolution in aqueous electrolytes, although in this case stabilization is less obvious since the photodecomposition products are typically soluble (5). At longer times, the film generally peels from the semiconductor surface *in toto* and the photocurrent decays. This is evident in Fig. 4 for coated n-Si after about 3 min. However, in some cases the film remains intact for several days (Fig. 2) and charge equivalent to more than the total weight of the crystal is passed without significant weight loss or degradation of the surface (inspected after film removal). Roughening the semiconductor surface by abrasion prior to film deposition appears to improve the film adhesion.

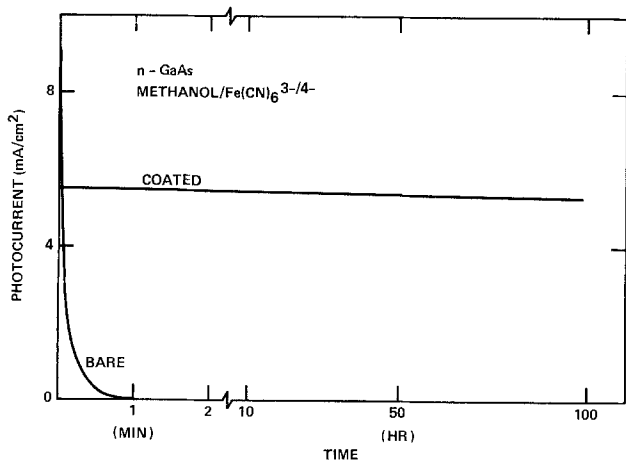


Fig. 2. Short-circuit photocurrent vs. time for bare and polypyrrole-coated n-GaAs electrodes in methanol/ $0.2\text{M Fe}(\text{CN})_6^{3-/4-}$ / $0.1\text{M Et}_4\text{NBF}_4$ solution.

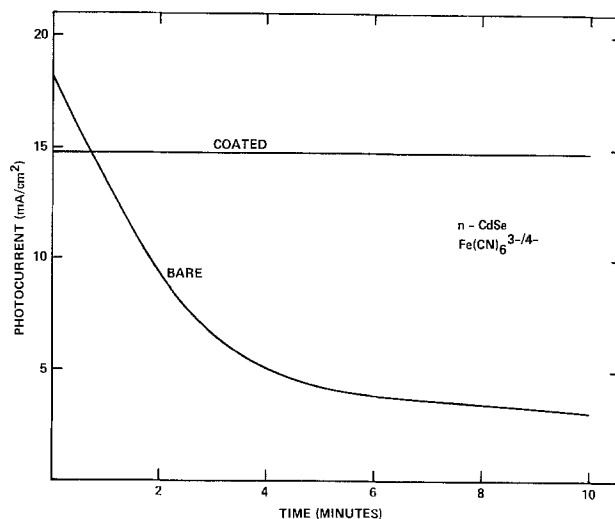


Fig. 3. Short-circuit photocurrent vs. time for bare and polypyrrole-coated n-CdSe electrodes in aqueous $0.2\text{M Fe}(\text{CN})_6^{3-/4-}$ / $0.1\text{M Fe}(\text{CN})_6^{3-}$ solution ($\text{pH} \sim 13$).

Peeling problems may be associated with the permeability of polypyrrole films to solvent/solute species, since film stability appears to depend on the nature of the redox couple and/or pH of the electrolyte and in certain instances semiconductor decomposition underneath polypyrrole films is apparent. For example, polypyrrole-coated n-CdSe photoanodes are stabilized by $\text{Fe}(\text{CN})_6^{3-/4-}$ electrolytes ($\text{pH} = 10-13$), but in $\text{Fe}^{3+/2+}$ perchlorate solutions ($\text{pH} = 1$), a red layer, presumably Se^0 , forms within a few minutes under the polymer film (which appears to be intact). These and related observations with a variety of semiconductor materials suggest that polypyrrole films are permeable to solvent/solute species, and that some photodecomposition may occur at the film-semiconductor interface, eventually causing the film to peel. The anion mobility discussed in the preceding section is in accord with this view. Insoluble decomposition products, e.g., hydroxides, Se^0 , etc., may in some cases collect at the semiconductor-film interface and hinder or slow further degradation.

The apparent permeability of polypyrrole films to solvent/solute species poses a serious question regard-

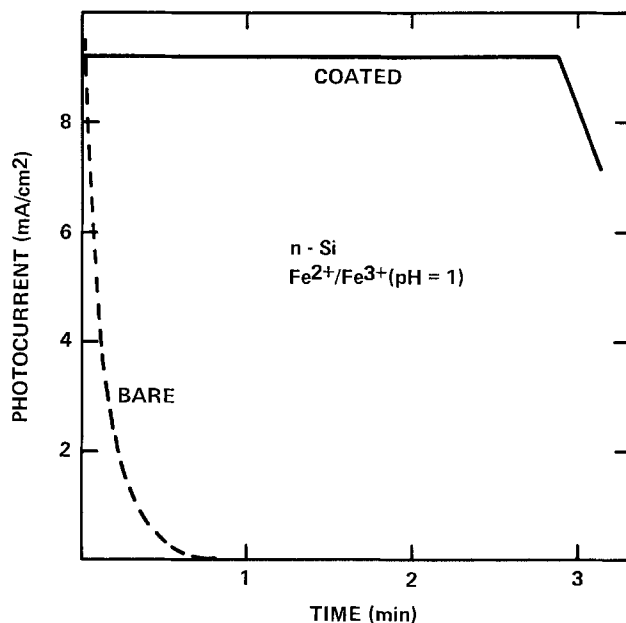


Fig. 4. Short-circuit photocurrent vs. time for bare and polypyrrole-coated n-Si in aqueous $0.2\text{M Fe}(\text{ClO}_4)_2$ / $0.1\text{M Fe}(\text{ClO}_4)_3$ / 0.1M HClO_4 solution.

ing the long-term stability of solar conversion devices employing such films. However, it may be possible to circumvent this problem. For example, sufficiently large immobile anions or redox species included in the film during electrodeposition would be expected to significantly reduce the film permeability. Encouragement for this approach is provided by the observed oxidation/reduction of the $\text{Fe}(\text{CN})_6^{3-/4-}$ within the polypyrrole film matrix (see preceding section). Although the hexacyanoferrate species was found to be mobile in polypyrrole, there are many larger organic redox species for which this should not be the case. For example, we have deposited conducting polypyrrole films on Pt from acetonitrile/0.01M $\text{Cu}(\text{SPc})/0.1\text{M}$ pyrrole, where SPc is the tetrasulfophthalocyanin tetraanion. The photoelectrochemical properties of such films are currently under investigation. Other approaches are, of course, also possible, including the use of other conducting polymer films or a synergistic combination of film and electrolyte redox couple to provide long-term photoanode stability. Along these lines, we have deposited polyaniline films (6) on various semiconductors with results comparable to those obtained for polypyrrole.

Output characteristics of coated photoanodes.—Polypyrrole films apparently do not significantly affect the semiconductor energy levels important in photoelectrochemical processes. Thus, for film-coated electrodes, the flatband potential (V_{FB}) determined by a-c impedance or from the photocurrent onset, is practically unchanged, compared to the bare electrode, and remains dependent on the pH of the electrolyte. Also, except for the Cd chalcogenides and Si in acidic ferrocyanide solutions, where appreciable cathodic dark currents are observed, the measured open-circuit photovoltages (V_{oc}) are generally close to the expected values ($V_{\text{R}} - V_{\text{FB}}$), where V_{R} is the electrolyte redox potential. This is illustrated by the data in Table I, for which V_{FB} values were determined from the photocurrent onset and may not correspond to those measured by a-c impedance in all cases. The V_{R} values, which were measured at a Pt electrode, correspond well with the standard handbook E° values. Note that the V_{oc} values for polymer-coated n-GaAs and n-CdTe in ferro-ferricyanide solution containing excess CN^- are practically equivalent to the bandgap of the respective semiconductors. The increase in V_{oc} produced by excess CN^- can be accounted for by the observed negative shift in V_{FB} , but irreversible photooxidation of adsorbed CN^- (e.g., to CNO^-) may also play a role. Since the cell voltage rapidly goes to zero when the electrode illumination is interrupted, the effect of the latter is probably small.

Table I. Measured and calculated open-circuit voltages (V_{oc}) for various polypyrrole-coated photoanodes in aqueous solutions

| Semiconductor | Electrolyte* | V_{FB} (V vs. SCE) | Calculated V_{oc} ($V_{\text{R}} - V_{\text{FB}}$) | Measured V_{oc} |
|---------------|--------------|-----------------------------|---|--------------------------|
| n-GaAs | A | -0.5 | 1.0 | 0.95 |
| | B | -0.5 | 0.8 | 0.6 |
| | C | -1.1 | 1.3 | 1.2 |
| n-CdTe | D | -1.3 | 1.5 | 1.37 |
| | A | -0.2 | 0.7 | 0.55 |
| | B | -0.2 | 0.55 | 0.2 |
| n-CdSe | C | -1.15 | 1.4 | 1.2 |
| | D | -1.25 | 1.5 | 1.3 |
| | A | -0.1 | 0.6 | 0.5 |
| n-CdS | B | -0.1 | 0.45 | 0.1 |
| | C | -0.8 | 1.0 | 0.9 |
| | D | -1.1 | 1.3 | 1.1 |
| n-Si | A | -0.4 | 0.9 | 0.65 |
| | B | -0.4 | 0.75 | 0.3 |
| | C | -0.8 | 1.0 | 0.9 |
| n-Si | D | -1.3 | 1.5 | 1.25 |
| | A | 0.0 | 0.5 | 0.4 |

* Electrolyte A is 0.2M $\text{Fe}^{2+}/0.1\text{M}$ Fe^{3+} perchlorates (pH = 1, $V_{\text{R}} = 0.51\text{V}$); electrolyte B is 0.2M $\text{Fe}(\text{CN})_6^{4-}/0.1\text{M}$ $\text{Fe}(\text{CN})_6^{3-}$ (pH = 1, $V_{\text{R}} = 0.35$); electrolyte C is 0.2M $\text{Fe}(\text{CN})_6^{4-}/0.1\text{M}$ $\text{Fe}(\text{CN})_6^{3-}$ (pH = 13, $V_{\text{R}} = 0.22$); and electrolyte D is 0.2M $\text{Fe}(\text{CN})_6^{4-}/0.1\text{M}$ $\text{Fe}(\text{CN})_6^{3-}/0.1\text{M}$ CN^- (pH = 13, $V_{\text{R}} = 0.22\text{V}$).

The effect of the polymer film on the photocurrent was difficult to ascertain since results for films produced under ostensibly the same conditions were variable, probably because of the difficulties associated with reproducing the substrate surface and film thickness. The latter was assumed to be directly proportional to the charge passed during deposition which may not be a valid assumption, especially since some semiconductor photodegradation undoubtedly occurs as deposition is initiated. In some cases, the photocurrents for the polymer-coated electrodes approached those for the bare semiconductor but the behavior depicted in Fig. 5 was more typical. In this case, the film is seen to reduce the photocurrent by about 30%. This reduction could be due to light absorption within the film or enhanced charge carrier recombination associated with interface states formed at the semiconductor-film interface. As mentioned previously, the reduction in open-circuit voltage (Fig. 5) is apparently due to cathodic dark current introduced by the film, which suggests that interface states may play a role. However, if such effects are not too pronounced, performance characteristics for polypyrrole-coated electrodes could approach those for the bare semiconductor for sufficiently thin films. Of course, a compromise would be required between photoanode stability and performance.

Summary and Conclusions

The results presented here show that electrodeposited polypyrrole films suppress photodegradation of semiconductor photoanodes while permitting efficient electron exchange with the electrolyte. Performance characteristics attainable with such film-coated photoanodes are typically comparable to those obtained for the bare electrode. Peeling is currently a problem which appears to be associated with permeability of the film to solvent/solute species. One promising approach for future work is to incorporate immobile redox species

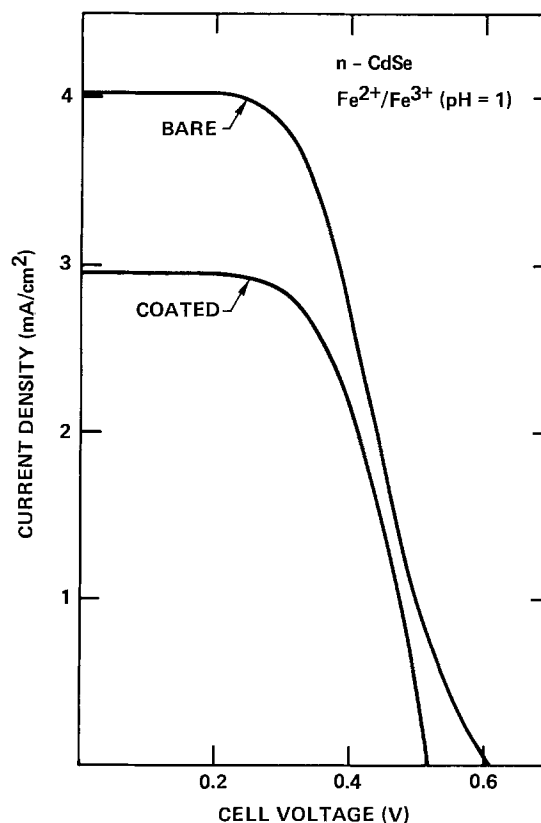


Fig. 5. Photocurrent-voltage curve for bare and polypyrrole-coated n-CdSe in aqueous 0.2M $\text{Fe}(\text{ClO}_4)_2/0.05\text{M}$ $\text{Fe}(\text{ClO}_4)_3/0.1\text{M}$ HClO_4 solution.

in the film to reduce permeability to electrolyte solvent/solute species.

Acknowledgment

The authors gratefully acknowledge support of this work by the Solar Energy Research Institute under Subcontract No. XG-0-9276.

Manuscript submitted March 16, 1981; revised manuscript received June 22, 1981.

Any discussion of this paper will appear in a Discussion Section to be published in the June 1982 JOURNAL. All discussions for the June 1982 Discussion Section should be submitted by Feb. 1, 1982.

Publication costs of this article were assisted by Rockwell International.

REFERENCES

1. R. Noufi, D. Tench, and L. F. Warren, *This Journal*, **127**, 2310 (1980).
2. A. F. Diaz, K. K. Kanazawa, and G. P. Gardini, *J. Chem. Soc. Chem. Commun.*, 635 (1979).
3. K. K. Kanazawa, A. F. Diaz, R. H. Geiss, W. D. Gill, J. F. Kwak, J. A. Logan, J. F. Rabolt, and G. B. Street, *ibid.*, 854 (1979).
4. A. F. Diaz and J. I. Castillo, *ibid.*, 397 (1980).
5. H. Gerischer, *Ber. Bunsenges.*, **69**, 578 (1965).
6. A. F. Diaz and J. A. Logan, *J. Electroanal. Chem. Interfacial Electrochem.*, **111**, 111 (1980).

Technical Notes



Properties of Borosilicate Glass Capillaries Used in Computer-Controlled Electrocapillary Measurements by the Maximum Bubble Pressure Method

Takashi Kakiuchi¹ and David M. Mohilner*

Department of Chemistry, Colorado State University, Fort Collins, Colorado 80523

In our previous studies of organic electrosorption (1, 2) in which the electrocapillary curves were measured by a computer-controlled capillary electrometer (3, 4) the precision of the measurements was $\pm 0.1 \text{ mNm}^{-1}$ and we were of the opinion that a single calibration of the maximum bubble pressure (MBP) capillary would remain valid over a period of many months. Recently, in preparation for a new study on the effect of temperature on organic electrosorption, because of the low temperature coefficient of interfacial tension, we improved the instrument (5) so that the 95% confidence limits of a triplicate measurement are now $\pm 0.02 \text{ mNm}^{-1}$. We decided it would be wise, with this greatly improved precision, to test whether, in fact, the presumption that a capillary calibration remains valid over an extended period of time really is justified. We therefore monitored two MBP capillaries, one over a period of 4½ months, the other over a period of 8½ months, with almost daily calibrations. The surprising result of this study was that, in fact, the radius of both capillaries increased approximately linearly with time and that this increase is significant for accurate electrocapillary measurements. The purposes of this note are to report the results of these measurements and also to give what we have found to be the best method of preparation of reliable MBP capillaries.

Preparation of MBP Capillaries

The method of preparing MBP capillaries which we report here has been developed empirically over a period of several years. It is the method which we

have found yields the most reliable capillaries. The capillaries are drawn from 0.5 mm borosilicate capillary tubing. A 15 cm length of this capillary tubing is first but-sealed to a 15 cm length of ¼-in. OD borosilicate glass tubing. (¼ in. OD tubing is employed because we use Teflon Swagelok unions to connect the capillary to the mercury reservoir.) The glass is then soaked in ethanol saturated with KOH for 5 hr to remove any traces of greasy material. Then it is rinsed in distilled water and soaked for 5 hr in a mixture of concentrated sulfuric and nitric acids, rinsed with distilled water, and dried in the oven at 130°C. After this precleaning the glass is immersed in an aqueous solution of 5% HF and 30% HNO₃ for 5 min. This mixture is similar to the one recommended by Crawley (6) as a universal glass cleaning reagent. The HF etches a thin layer of glass from the capillary wall so that the new surface formed is less dependent on its history. The capillary is then rinsed thoroughly with triple distilled water and dried in the oven at 130°C. Then the capillary is drawn using a fairly cool gas-oxygen flame and examined with a Bausch and Lomb stereozoom microscope at 120× to see if its radius is approximately correct. A correct radius is approximately 7.0 μm. If the radius is correct the capillary is bent into a "U" shape. [For a photograph of an MBP capillary see Fig. 2, Ref. (3).] To be correct the narrowest portion of the capillary must be several millimeters long and be gently tapering. The capillary is then cut where narrowest with a silicon carbide knife and annealed at 550°C for 2 hr to remove strain around the bend.

The capillary bore is next dewetted. This is absolutely necessary because if solution penetrates between the glass wall and the mercury the effective radius will change with electrode potential due to the

* Electrochemical Society Active Member.

¹ Permanent address: Department of Agricultural Chemistry, Kyoto University, Kyoto, Japan.

Key words: capillaries, electrocapillarity, maximum bubble pressure.

interaction of the electrical double layers on the mercury and on the glass. The glass surface is always negatively charged (7) whereas the charge on the mercury varies from negative to positive. The interaction between the two double layers (8) can produce appreciable hydrostatic pressure when the mercury is negatively charged causing a decrease in the effective radius. Water vapor from a beaker of water at room temperature is first drawn through the capillary for 2 hr using an aspirator in order to ensure that the glass surface has a sufficient density of OH groups. The bore of the capillary is then dewetted with freshly distilled liquid trimethylchlorosilane and rinsed with chloroform. We had originally dewetted our MBP capillaries (1) with dimethyldichlorosilane which had been recommended by Payne (9), but careful checking with our improved capillary electrometer has shown that the radius of the capillaries dewetted with this compound exhibit a short-term instability which is probably due to the formation of polymethylsiloxane produced from the excess water which is always inside the capillary. Evidently pieces of this polymer can move to the capillary orifice causing the effective radius to become narrower. There is no possibility of polymer formation with trimethylchlorosilane and the hexamethylsiloxane which does form with the excess water is easily washed out with the chloroform.

After the capillary has been dewetted it is filled with mercury, placed in an electrolyte solution, and its potential adjusted to that of the electrocapillary maximum. Then it is pressurized to determine what pressure will push the mercury to the orifice. If the pressure is correct (about 80 cm mercury) the tip is recut removing only about 1 mm of glass, because the end of the capillary must be wet by the solution in order to get a correct MBP measurement.

MBP Capillary Calibration Over an Extended Period of Time

The calibrations of the MBP capillaries were all based on the sessile drop measurements of mercury in an aqueous 0.05M Na_2SO_4 solution at 25°C reported in 1961 by Smolders and Duyvis (10) which is the most accurate absolute determination of the interfacial tension of a mercury electrode available. Their reported value of the interfacial tension at the electrocapillary maximum is $426.2 \pm 0.2 \text{ mNm}^{-1}$. The reference electrode employed when calibrating in this solution was a glass sodium ion electrode (Orion 94-11A). However we found (5) that actually this reference electrode is not stable enough for use with our new level of precision and the very stable two phase lead amalgam-lead sulfate electrode (11) is inconvenient to use in calibration. Therefore we have adopted a secondary standard, 0.1M NaCl, by calibrating a capillary with 0.05M Na_2SO_4 and determining the interfacial tension at the electrocapillary maximum at 25°C. The value of the interfacial tension at the electrocapillary maximum in 0.1M NaCl at 25°C is $425.78 \pm 0.02 \text{ mNm}^{-1}$. The reference electrode used when calibrating in 0.1M NaCl is the Ag/AgCl electrode of the thermal electrolyte type (12).

Figures 1 and 2 are plots of the measured radius of the two capillaries (A and B, respectively) vs. the date of calibration. In the case of capillary A (Fig. 1), it was calibrated nearly daily vs. 0.05M Na_2SO_4 for a period of 3 months. Then the capillary was stored in triple distilled water for 5½ months. Finally it was calibrated five more times vs. 0.1M NaCl. Note that these last calibrations fall on the least squares straight line established for the calibration vs. 0.05M Na_2SO_4 . Capillary B (Fig. 2) was calibrated only vs. 0.1M NaCl for a period of 4½ months.

The fact that the radius of capillary A continued to increase at a constant rate when it was stored in triple

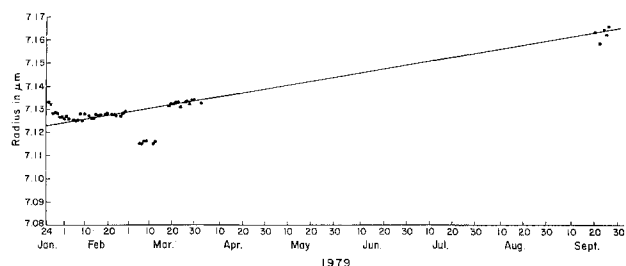


Fig. 1. Calibration of capillary A. Points to left were calibrated with 0.05M Na_2SO_4 . Points to right were calibrated with 0.1M NaCl. During period between the two sets of points the capillary was immersed in triple distilled water.

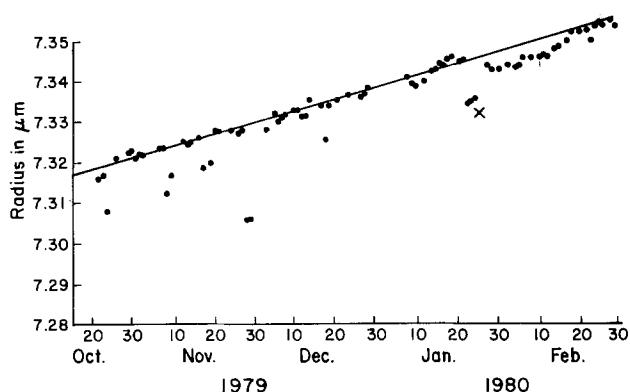


Fig. 2. Calibration of capillary B. Calibration was made using 0.1M NaCl. Points marked with X indicate when capillary was inadvertently dried for 15 min.

distilled water for 5½ months suggests that the glass is swelling by absorption of water molecules at the capillary tip. This phenomenon is similar to the swelling of a piece of macaroni on cooking, and therefore we have decided to refer to the phenomenon as the "macaroni effect."

The fact that the slopes of the least squares calibration lines for the two capillaries are different is probably due to the fact that the wall thicknesses of the two capillaries were different. For capillary A the rate of increase of radius was $0.0016 \mu\text{m day}^{-1}$. For capillary B the rate was $0.0028 \mu\text{m day}^{-1}$. For example, this means that for capillary A, if the true value of the interfacial tension is 425.78 mNm^{-1} , and if the initial radius was $7.13 \mu\text{m}$, the apparent interfacial tension calculated on the assumption of an unchanged capillary radius would be -0.67 mNm^{-1} in error in one week. Since the experimental error in our measurements (5) is only $\pm 0.02 \text{ mNm}^{-1}$ this would constitute an unacceptable error. In the case of capillary B if the initial radius was $7.33 \mu\text{m}$, the error in one week would be -1.1 mNm^{-1} . Thus one sees that assuming the capillary radius remains constant for only a week can result in errors in the interfacial tension which are 30 to 50 times larger than the 95% confidence limits of the measurement. Moreover occasionally for reasons which are not really clear, a calibration can exhibit an excursion which might be as large as the straight line produced in two months (cf. Fig. 2). (It is possible that these excursions might be due to movement of mercuric oxide, which is unavoidable, to the orifice.) The one large excursion in Fig. 2 marked X was due to the fact that the capillary was inadvertently dried for 15 min. Note, however, that after this drying the calibration did eventually return to the straight line. We take this phenomenon as further proof that what is happening is the swelling of the glass.

These measurements make it clear that the only safe procedure is to calibrate the MBP capillary daily. We have adopted daily calibration as our standard

procedure and we strongly recommend this. Actually a calibration only requires about 1½ hr including time for rinsing the cell and deaeration. We calibrate by measuring in triplicate the maximum bubble pressure at only 11 points in the vicinity of the electrocapillary maximum. We determine by digital computer the interfacial tension at the maximum by means of a least squares cubic fit to the average pressures.

Acknowledgment

This work was supported by the National Science Foundation under grant No CHE76-83432. Acknowledgment is also made to the donors of the Petroleum Research Fund administered by the American Chemical Society for partial support of this research. This work constitutes a portion of the research in a collaborative international program on thermodynamic studies of the inner part of the electrical double layer supported in part by the North Atlantic Treaty Organization (NATO). We express our gratitude to the late Professor Patricia R. Mohilner, Department of Computer Science, Colorado State University who wrote the computer program used in this study.

Manuscript submitted April 16, 1981; revised manuscript received June 24, 1981.

Any discussion of this paper will appear in a Discussion Section to be published in the June 1982 JOURNAL. All discussions for the June 1982 Discussion Section should be submitted by Feb. 1, 1982.

REFERENCES

1. H. Nakadomari, D. M. Mohilner, and P. R. Mohilner, *J. Phys. Chem.*, **80**, 1761 (1976).
2. D. M. Mohilner, H. Nakadomari, and P. R. Mohilner, *ibid.*, **81**, 244 (1977).
3. J. Lawrence and D. M. Mohilner, *This Journal*, **118**, 1596 (1971).
4. J. Lawrence and D. M. Mohilner, *ibid.*, **118**, 259 (1971).
5. D. M. Mohilner and T. Kakiuchi, *ibid.*, **128**, 350 (1981).
6. R. H. A. Crawley, *Chem. Ind.*, **45**, 1205 (1953).
7. G. Jones and L. A. Wood, *J. Chem. Phys.*, **13**, 106 (1945).
8. J. T. G. Overbeek, in "Colloid Science," Vol. 1, Chap. 4, H. R. Kruyt, Editor, Elsevier, Amsterdam (1952).
9. R. Payne, *J. Electroanal. Chem.*, **7**, 343 (1964).
10. C. A. Smolders and E. M. Duyvis, *Recl. Trav. Chem.*, **23**, 636 (1961).
11. D. M. Mohilner, T. Kakiuchi, and J. Taraszewska, *Can. J. Chem.*, **59**, 1872 (1981).
12. R. G. Bates, "Determination of pH," 2nd ed., John Wiley and Sons, New York 1973).

Photovoltage Response to Temperature Change at Oxide Semiconductor Electrodes

Benjamin Reichman*¹

Christopher Newport College, Newport News, Virginia 23606

and Charles E. Byvik

NASA Langley Research Center, Hampton, Virginia 23665

One of the most important parameters in determining the energy conversion efficiency of a semiconductor photoelectrode used in a photoelectrochemical cell is its flatband potential (FBP). The more negative the flatband potential with respect to hydrogen for an n-type semiconductor used to photoelectrolyze water, the higher the energy conversion efficiency. The flatband potential of a highly doped n-type semiconductor electrode is determined by the electron affinity (EA) of the electrode material and the voltage drop across the Helmholtz layer (1, 2). The EA is a bulk parameter of the semiconductor material and can be changed only by modifying the bulk composition. The potential drop across the Helmholtz layer is dependent on the state of the electrode surface and on the solution used. The Helmholtz layer potential drop is determined by the point of zero zeta potential (pzpz) (1, 2) of the semiconductor surface. Measurements of the pzpz for some n-type semiconducting materials have been reported by Butler *et al.* (2). These measurements were made mainly on oxide semiconductor materials in powder form and correlation between the pzpz and the electronegativity was suggested. They also discuss the effect of temperature on the flatband potential of oxide electrodes (3).

We wish to report the results of a study of the effect of cell temperature on the onset potential of some n-type oxide semiconductor electrodes. We show that

the change of the onset potential with temperature is due to the potential change across the Helmholtz layer. The amount of this change depends on the pzpz of the semiconductor electrode. The pzpz of some n-type semiconducting oxide electrodes was determined based on these temperature measurements, and was found to be in general agreement with the values given elsewhere (2). This technique can be used to determine the pzpz of semiconductor electrodes.

Experimental

Single crystals of TiO₂ (rutile), SrTiO₃, and α -Fe₂O₃ and polycrystalline WO₃ were used as electrodes. The first two single crystal electrodes were etched in hot 5% phosphoric acid, and the third was etched with 6M HCl. The polycrystalline WO₃ was formed by heating a tungsten disk to 500°C in air. Ohmic contacts to the single crystal electrodes were formed with In-Hg alloy and a wire was attached using silver paste. The wire was inserted through a glass tube, and the unexposed surface covered with epoxy. The onset potential, which is related to the flatband potential, was taken from the photocurrent-voltage recordings using a conventional three-electrode system. The light from a 150W xenon lamp was chopped and the photocurrent recorded using a lock-in amplifier. The cell was held inside a stirred and heated water bath. A reversible hydrogen electrode (RHE) was used as a reference electrode for most of the experiments. In some experiments conducted in basic solutions, an Hg/HgO electrode was used as a reference electrode for comparison. Solutions of NaOH (pH = 13) and H₂SO₄ (pH = 2) were used.

* Electrochemical Society Active Member.

¹ Present address: Energy Conversion Devices, Incorporated, Troy, Michigan 48064.

Key words: cell, potential, photoelectrochemistry.

Results and Discussion

Several changes in the photocurrent-voltage curves were noted on increasing the temperature of a photoelectrochemical cell where TiO_2 , SrTiO_3 , Fe_2O_3 , or WO_3 were used as photoanodes. These changes are demonstrated for the case of SrTiO_3 as an example in Fig. 1. Generally, with increasing cell temperature, (i) the onset potential for the photocurrent (which is related to the FBP) is shifted to more positive potentials, (ii) the initial slope of the current-voltage curve increases, and (iii) the saturation photocurrent increases. These effects, for SrTiO_3 , give rise to an overall increase in the solar-to-chemical energy conversion efficiency up to cell temperatures of about 80°C ; then efficiency decreases. These general trends exist up to 150°C and are discussed elsewhere (4). Here, the change in the onset potential with cell temperature is studied in more detail. In Fig. 2, the change in the onset potential of the photocurrent is shown for several n-type oxide semiconductor electrodes as a function of temperature. A linear change of the onset potential (with respect

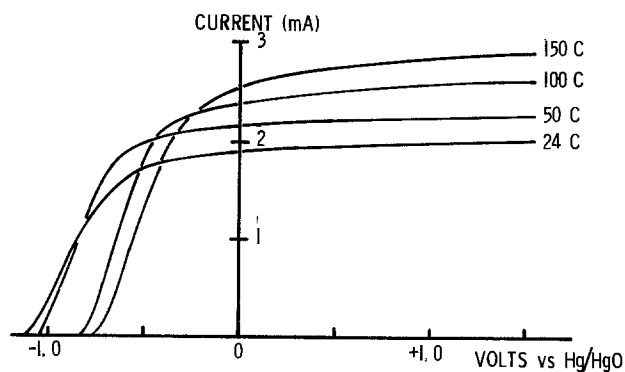


Fig. 1. Typical photocurrent-voltage curves for an SrTiO_3 -based photoelectrolysis cell in 0.1M NaOH for temperatures ranging from room temperature to 150°C .

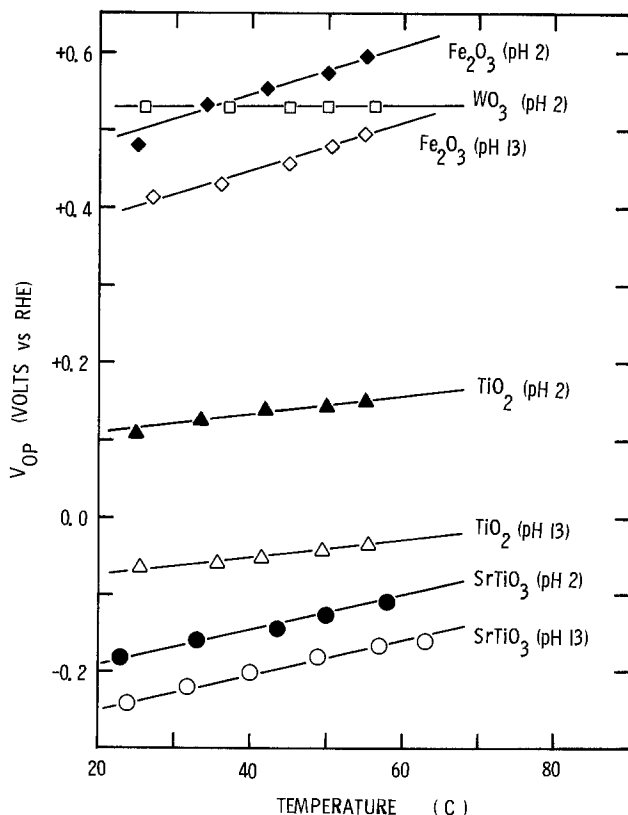


Fig. 2. Temperature dependence of the onset potential for TiO_2 , WO_3 , Fe_2O_3 , and SrTiO_3 .

to the reversible hydrogen electrode RHE) is observed in all the cases. The slope of the change is different from electrode to electrode, the highest slopes observed for Fe_2O_3 and SrTiO_3 , and the lowest for WO_3 . These measurements were repeated with solutions of different pH, and in Fig. 2 it can be seen that the slope of the onset potential vs. temperature is about the same for each electrode with solutions of either $\text{pH} = 13$ or $\text{pH} = 2$.

The FBP of the semiconductor electrode with respect to a reference electrode can be described by Eq. [1]

$$V_{\text{FB}} = EA - \Delta_{\text{FC}} - \Delta_{\text{pH}} - E_0 \quad [1]$$

where EA is the electron affinity of the semiconductor (in volts), Δ_{FC} is the potential difference between the conduction bandedge and the Fermi level of the semiconductor, Δ_{pH} is the voltage drop across the Helmholtz layer, and E_0 is the potential of the reference electrode with respect to vacuum. In principle, the temperature change can affect the FBP (V_{FB}) with respect to a reference electrode by changing Δ_{FC} , the Helmholtz layer (Δ_{pH}), and the potential of the reference electrode with respect to vacuum (E_0). The potential difference between the conduction band and the Fermi level for a nondegenerately doped n-type semiconductor is

$$\Delta_{\text{FC}} = \frac{RT}{F} \ln \frac{n}{N_c} \quad [2]$$

where n is the free carrier density, N_c is the density of states in the conduction band, and F is Faraday's constant.

The voltage drop across the Helmholtz layer at oxide semiconductor surfaces can be written as (2)

$$\Delta_{\text{pH}} = \frac{2.3RT}{F} \log \frac{[\text{H}^+]}{[\text{H}^+]_{\text{pzzp}}} = \frac{2.3RT}{F} (\text{pH} - \text{pH}_{\text{pzzp}}) \quad [3]$$

where pH_{pzzp} is the pH of the solution at which the voltage drop across the Helmholtz layer is zero. When inserted into Eq. [1], one gets

$$V_{\text{FB}} = EA - \frac{RT}{F} \ln \frac{n}{N_c} - \frac{2.3RT}{F} (\text{pH} - \text{pH}_{\text{pzzp}}) - E_0 \quad [4]$$

Equation [4] shows the explicit dependence of the FBP on the potential drop in the Helmholtz layer as well as the well-known dependence of the FBP on the pH of the solution. The dependence of V_{FB} on the temperature is also expressed here. If a reference electrode which is reversible to hydrogen ions is chosen (e.g., H_2/H^+ or Hg/HgO), the FBP with respect to this electrode will in principle be independent of the pH since

$$E_0 = 4.5\text{V} - \frac{2.3RT}{F} \text{pH}$$

Then

$$\frac{\delta V_{\text{FB}}}{\delta T} = \frac{2.3R}{F} \text{pH}_{\text{pzzp}} - \frac{R}{F} \ln \frac{n}{N_c} \quad [5]$$

This resulting equation predicts that the FBP of an oxide semiconductor electrode will shift linearly with increasing temperature to a more positive potential with a slope which is independent of the pH of the solution and which is determined by the magnitude of the pH_{pzzp} . The more basic the electrode surface, the higher the pH_{pzzp} , resulting in a larger change in the FBP with cell temperature. The dependence of the onset potential with temperature for the electrodes studied is shown in Fig. 2. It should be noted that the dependence is linear and the slopes are positive as indicated by Eq. [5]. The pH_{pzzp} for each electrode was determined using Eq. [5] and the slopes of these curves for $\text{pH} = 2$ and $\text{pH} = 13$ solutions, and are given in Table I. Also given in Table I are the carrier concen-

Table I. Comparison of the pH_{pzzp} determined for two-solution pH values with values cited in the literature for the oxide semiconductor electrodes. The semiconductor parameters used in Eq. [5] are also listed. The carrier concentrations were determined from Mott-Schottky plots. The slopes are taken from Fig. 2

| Electrode | pH (25°C) | V_{FB} vs. RHE (25°C) | Slope (mV/deg) | n (cm ⁻³) | N_c (cm ⁻³) | pH_{pzzp} | pH_{pzzp} (average) | pH_{pzzp} (literature) |
|--------------------------------|-----------|-------------------------|----------------|-------------------------|---------------------------|-------------|-----------------------|--------------------------|
| Fe ₂ O ₃ | 2 | +0.5 | 2.9 | 5.1×10^{17} | 2.4×10^{20} | 9.8 | 9.3 | 8.6 |
| | 13 | +0.4 | 2.7 | | | 8.8 | | |
| SrTiO ₃ | 2 | -0.18 | 2.25 | 3.2×10^{17} | 6.8×10^{19} | 8.9 | 9.3 | 8.6 |
| | 13 | -0.24 | 2.4 | | | 9.7 | | |
| TiO ₂ | 2 | +0.11 | 1.15 | 6.2×10^{19} | 3.0×10^{21} | 4.1 | 5.0 | 5.8 |
| | 13 | -0.07 | 1.5 | | | 5.8 | | |
| WO ₃ | 2 | +0.53 | 0.1 | 7.6×10^{19} | 9.8×10^{19} | 0.5 | 0.5 | 0.43 |
| | | | | | | | | |

trations and density of states for each of the semiconductor materials which were used to determine the magnitude of the second term on the right-hand side of Eq. [5]. The average value for the pH_{pzzp} of each electrode is shown in Fig. 3. It should be noted that the tungsten trioxide sample is degenerately doped and therefore the second term on the right-hand side of Eq. [5] is zero. Also shown in Table I and Fig. 3 are pH_{pzzp} values for these semiconductor materials taken from the literature. The curve drawn in Fig. 3 is taken from Ref. (2). Good agreement is observed between the values obtained in this work and the values taken from the literature. Since Eq. [5] properly describes the observed behavior of the onset potential of the oxide semiconductors reported here, the changes in the FBP with temperature are attributed to thermal effects on the potential across the Helmholtz layer. Thermal-induced changes in the pzzp [see Ref. (5)], EA , E_o , and Δ_{FC} [see Ref. (3)] for TiO₂ are of smaller significance than found in this study. The small difference in the pH_{pzzp} measured at different pH values (see Table I) may be due to the deviation from the ideal 59 mV/pH dependence at 298 K of the flatband potential.

It is interesting to note that in terms of the correlation suggested by Butler and Ginley (2) between the electronegativity of the semiconductor and the pH_{pzzp} , the pH_{pzzp} of Fe₂O₃ is expected to be more acidic than found. However, the value obtained by us for this material is closer to that of SrTiO₃ as is observed also by others from measurements with the powder materials. The trend in the slopes (hence the pH_{pzzp}) observed

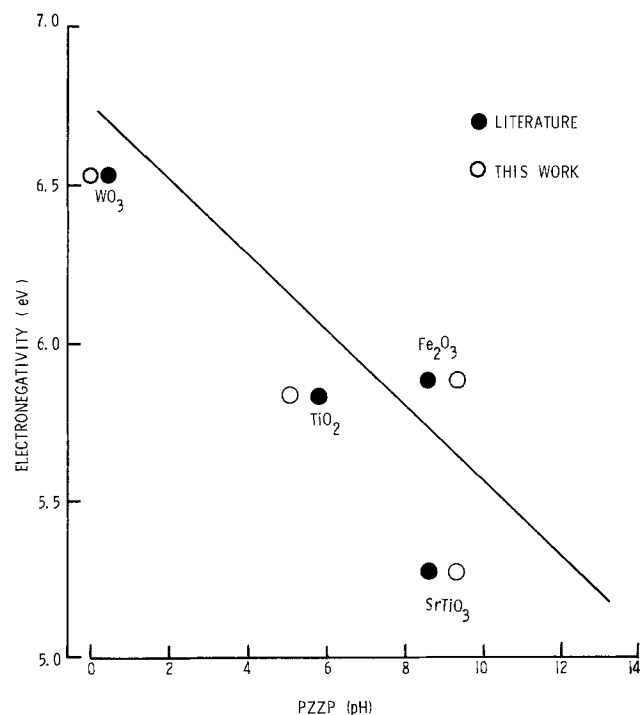


Fig. 3. Comparison of the literature values of the pH_{pzzp} with values determined in this work as a function of electronegativity. The line is taken from Ref. (2).

with the other materials are as predicted from the correlation of the pH_{pzzp} with the electronegativity (2) of the semiconductor: smallest for WO₃ and highest for SrTiO₃.

This conclusion leads to two important considerations for choosing semiconducting materials to be used as photoelectrodes in a photoelectrochemical cell. First, the FBP of the photoelectrode is dependent on the EA of the electrode material and on the potential across the Helmholtz layer. The FBP is more negative the smaller the EA and the more acidic the electrode surface (smaller pH_{pzzp}). While the EA of the electrode material cannot in principle be changed, the pH_{pzzp} can be changed (6). It was suggested (6) that by binding more acidic groups to the surface of TiO₂, for example, the FBP could be shifted to more negative values. The method we describe here can be used to evaluate in a relatively easy way any change in the acidity of the electrode surface following treatment. (The common methods of evaluating the pH_{pzzp} of the materials in the powder form will not be applicable here.)

Second, we discussed the possibility of increasing the solar-to-chemical energy conversion efficiency of a photoelectrochemical cell by increasing the cell temperature (4). For SrTiO₃ and TiO₂, the photocurrent increases by increasing the cell temperature and the overall efficiency begins to increase. At cell temperatures higher than about 80°C, the efficiency begins to decrease because the onset potential for these materials has shifted to more positive values.

Our study suggests that by decreasing the value of the pH_{pzzp} (e.g., by binding acidic groups to the surface), the amount of the thermally induced shift in the onset potential of the photoelectrodes may be reduced, thus improving the efficiency of the photoelectrochemical cell by increasing the temperature.

Acknowledgment

We wish to acknowledge Mr. F. R. Parker for his able assistance in the performance of these experiments.

Manuscript submitted Dec. 4, 1980; revised manuscript received May 26, 1981. This was Paper 594 presented at the Hollywood, Florida, Meeting of the Society, Oct. 5-10, 1980.

Any discussion of this paper will appear in a Discussion Section to be published in the June 1982 JOURNAL. All discussions for the June 1982 Discussion Section should be submitted by Feb. 1, 1982.

Publication costs of this article were assisted by NASA Langley Research Center.

REFERENCES

- M. A. Butler and D. S. Ginley, *Chem. Phys. Lett.*, **47**, 319 (1977).
- M. A. Butler and D. S. Ginley, *This Journal*, **125**, 228 (1978).
- M. A. Butler and D. S. Ginley, *Nature*, **273**, 524 (1978).
- C. E. Byvik, L. F. Koons, and B. Reichman, Paper 356 presented at The Electrochemical Society Meeting, St. Louis, Missouri, May 11-16, 1980.
- Y. G. Berube and P. L. DeBruyn, *J. Coll. Interface Sci.*, **27**, 305 (1968).
- M. Tomkiewicz, *This Journal*, **127**, 1518 (1980).

DISCUSSION SECTION



This Discussion Section includes discussion of papers appearing in the *Journal of The Electrochemical Society*, Vol. 127, No. 12, December 1980, and Vol. 128, No. 1, 2, 3, and 4, January, February, March, and April 1981.

Electrochemical Aspects of the Cadmium Impregnation Process

T. Palanisamy, Y. K. Kao, D. Fritts, and J. T. Maloy
(pp. 2535-2544, Vol. 127, No. 12)

R. Barnard and F. L. Tye:¹ The authors are to be commended on a generally interesting and useful paper. However, their preference for oxidation of hydrogen adsorbed by nickel rather than discharge of nickel cadmium alloy as the more likely cause of the "stepped discharge" profile is surprising.

In an earlier paper Barnard *et al.*² checked whether hydrogen adsorption by the nickel sinter could account for the secondary step. The results showed clearly that hydrogen adsorption was far too small to account for the instances of large stepped-discharge profiles. Concerning the findings by Fritts *et al.* depicted in their Fig. 11, it is agreed that the increased hydrogen adsorption takes place as the cathodic potential is increased, but under equivalent conditions the contribution by Ni₅Cd₂₁ is much greater. The region studied by Fritts *et al.* (-1.1 to -0.7V SCE) is always complicated by the overlap of hydrogen oxidation, nickel cadmium alloy oxidation, as well as nickel hydroxide formation. Studies concerning bulk γ -Ni₅Cd₂₁ confirm the thin film behavior and indicate that the discharge involves the near stoichiometric formation of both Ni(OH)₂ and Cd(OH)₂. Hydrogen adsorption by this alloy also contributes a negligible discharge capacity.

T. Palanisamy,³ **Y. K. Kao,**⁴ **D. Fritts,**⁵ and **J. T. Maloy:**⁶ We appreciate the interest by Barnard and Tye in our paper.

Since our main interests were in the impregnation process and the quality of the cadmium electrodes prepared according to our new suggestions, we have not gone into the details of "stepped discharge" profile. But we have concentrated in bringing out the implications of our results and their relevance to the cadmium electrode in actual use.

The results in Fig. 11 of our paper, as agreed by Barnard *et al.*, translate into stepped discharge behavior in Ni-Cd batteries. We concede, as indicated in our original text, that other factors such as excessive carbonation of the electrolyte and the formation of alloys like Ni₅Cd₂₁ can lead to similar discharge curves. However, conditions that promote one or more of the above contributions can be identified. One would expect Ni₅Cd₂₁ alloy to be formed from rather reactive Ni metal produced by reduction of Ni(OH)₂ either formed by corrosion of the Ni sinter or by deliberate addition as in the reference of Barnard *et al.*² Higher depths of discharge of the negative electrode (compare the potentials for the reaction

$M(OH)_2 + 2e \rightleftharpoons M + 2 OH^-$ where $M = Ni, Cd$) will tend to increase the amount of Ni(OH)₂ and thereby Ni₅Cd₂₁ on subsequent charge/overcharge.

The contribution of the oxidation of absorbed hydrogen to the stepped discharge curve is expected to be predominant in situations favorable for the evolution of hydrogen. When the nickel substrate is not completely covered with active cadmium material (as in the microelectrode work shown in our figure), the accidental formation of Ni₅Cd₂₁ is stoichiometrically limited by the available cadmium and hydrogen evolution on nickel would be the predominant reaction during overcharge. Thus, in those cases when the loading of active cadmium material per void volume is low, the contribution of the oxidation of absorbed hydrogen to the stepped discharge curve is expected to be high.

Clearly the stepped discharge behavior arises from a combination of factors as suggested in our paper and they are all important depending on the cycling regime, loading level, overcharge conditions, and depth of discharge, to mention a few.

Effect of Plating Parameters on Electrodeposition of NiFe

J. Horkans (pp. 45-49, Vol. 128, No. 1)

A. H. Du Rose:⁷ In this paper and in the preceding 1979 paper [Ref. (8) in the paper under discussion], the author presents not only information on NiFe deposition but interesting data on hydrogen evolution.

The author evidently does not believe boric acid acts as a buffer in Ni or NiFe solutions so possibly the word "folklore" should have been used instead of "lore" (p. 45). Actually Table II shows two cases in which boric acid has prevented burned deposits at higher current density by preventing alkalization when i_1 is approached. "As a guide," i_1 values for hydrogen, determined from the 1979 paper, may be used; 2.8 mA cm⁻² for solutions 1 and 2, 0.8 for 3 and 4, 28 for 5 and 6, and 8 mA cm⁻² for solutions 7 and 8. Unfortunately the current densities for solutions at pH 2 in both papers were not carried to the limiting current density.

The author expects (p. 48) a buffer to decrease the efficiency and also lead to less anomalous deposition. However, the effect on efficiency would depend on the effective pK of the buffer and the current density or cathode film pH. Results in Table II are inconsistent and interpretation of the thickness data in the 1979 paper is difficult because of deposit distribution questions and the low current density used for the 1600 rpm rate of agitation.

Boric acid probably lowers the precipitation pH of a basic iron compound as it does for nickel. One might therefore expect more anomalism when boric acid is present at least for the pH 3 solutions. In this connection it would be of interest to know at what pH the basic iron compound forms, and how this corresponds with the Dahms and Croll mechanism at low current density or low pH. Is adsorbed FeOH a factor?

Interpretation of the results in this paper depends much on the interesting results given in the 1979 paper on H₂ evolution in sulfate and chloride solutions. It is surprising that this difference has not been noted

⁷ Retired, Pinellas Park, Florida 33565.

¹ Berc Group Limited, Group Technical Centre, Tottenham, London, England N15 3TJ.

² R. Barnard, K. Edmondson, J. A. Lee, and F. L. Tye, *J. Appl. Electrochem.*, 6, 107 (1976).

³ University of Dayton Research Institute, Dayton, Ohio 45469.

⁴ Department of Chemical and Nuclear Engineering, University of Cincinnati, Cincinnati, Ohio 45221.

⁵ U.S. Air Force Aeropropulsion Laboratory, Wright-Patterson AFB, Ohio 45433.

⁶ Department of Chemistry, Seton Hall University, South Orange, New Jersey 07079.

before, although one would like more assurance that the Cl_2 and O_2 from the insoluble anode had no effect at the cathode.

Assuming the i_1 values to be correct, it would be of interest to try to rationalize the difference between chloride and sulfate solutions in accordance with some version of the Stokes and Robinson "hydration correction" [Ref. (9) in the paper under discussion]. NaCl will increase and Na_2SO_4 decrease the acidity of acid solutions including boric acid. So, e.g., at pH 2, the sulfate solution contains more acid (by some interpretation) than the chloride solution. This may be due not only to different degrees of hydration of Na^+ but also of H^+ .

Calculation will show that two of the citrate (pK 3.08, 4.75, 5.4) protons were involved in H_2 evolution in Fig. 6 of the 1979 paper (after correcting for H^+ diffusion and using $D = 6.65 \times 10^{-6} \text{ cm}^2 \text{ sec}^{-1}$ for citric acid). Possibly the cathode pH did not go high enough to use the last hydrogen. Therefore it would not be expected that boric acid (tetraborate or the trimer) would be effective where the pK in NaCl and Na_2SO_4 solutions are ~ 6.2 and 8, respectively [Table 4, Ref. (9) in the paper under discussion]. In a nickel solution the pK for boric acid is lower and it can act as a buffer at an advantageous pH.

As suggested by the author, the dissociation rate of the buffer is a factor to be considered. Also it should be noted that there is a wide disparity in experimentally determined cathode film pH values. There may not be a marked rise in pH until the H_2O discharge reaction is closely approached producing OH^- .

J. Horkans:⁸ There is no question that boric acid plays an important role in the electrodeposition of Ni and NiFe. Du Rose argues that the effect of boric acid is due to its role as a buffer. The paper under discussion uses the definition that a buffer is a proton reservoir or sink which opposes a pH change. In the case of NiFe deposition, the buffer would provide protons to resist the surface alkalization due to H_2 evolution. Given this definition, neither this nor the earlier paper⁹, also discussed, shows evidence of buffering by boric acid.

Table II does show instances where H_3BO_3 prevents burning of deposits, but this in itself is not evidence that buffering occurs. If H_3BO_3 is buffering according to the above definition, then the increased supply of protons at the electrode surface will result in a decrease in the current efficiency of the alloy plating. On the contrary, Table II shows that H_3BO_3 does not decrease the current efficiency. It is not valid to say that the effect on efficiency depends on the pK of the buffer and the pH at the interface; if the pK of the acid is too high, it is not serving as a buffer. Alternatively, if its dissociation rate is too low, it cannot buffer under the dynamic conditions occurring near the electrode during H_2 evolution. For this latter reason, the equilibrium pH measurements of Du Rose¹⁰ may not be directly applicable to the nonequilibrium conditions during metal deposition.

There may be other mechanisms, such as adsorption, through which H_3BO_3 can influence NiFe deposition. Boric acid is shown to have the largest effect under conditions where iron hydroxide precipitation is most extensive. i.e., near the hydrogen limiting current, at high pH, and in SO_4^{2-} solutions. Perhaps some influence of H_3BO_3 on $\text{Fe}(\text{OH})_2$ precipitation is possible, as Du Rose suggests, but this is speculative as yet. There is no firm experimental evidence which could establish the validity of either of the above mechanisms.

As Du Rose does not specify in what way he finds Table II to be inconsistent, a reply to this comment cannot be given. The fact that the current density in footnote 9 was not near the H_2 limiting current does not invalidate the conclusions concerning the effects of anion and H_3BO_3 on the efficiency of Ni deposition.

The remainder of the discussion contribution concerns footnote 9, not the present paper. The anion dependence of hydrogen limiting current cannot be explained by a "hydration correction," since these solutions are at constant pH and, by definition, have the same acidity. Such a model is also precluded by the fact that the addition of Na_2SO_4 to NaClO_4 solution did not increase the H_2 limiting current. It is also unlikely that reduction of gases evolved at the counter-electrode is contributing to the observed current. The low solubility of O_2 in solution implies that it could contribute only a small fraction of the observed current. Chlorine is more soluble in H_2O than O_2 , yet the H_2 limiting currents in Cl^- -containing solutions are lower than those in Cl^- -free solutions. This shows that Cl_2 reduction currents are insignificant.

In calculating the number of protons which citric acid contributes to the hydrogen evolution current in a pH 3.0 solution 0.75M in NaCl and 0.1M in citric acid, one must consider the concentrations of the various citrate species. Only H_4Cit and H_3Cit^- are present at significant concentrations (0.054M and 0.045M, respectively, as calculated from the pK values). If only the first proton is available, the proton reservoir will have a concentration of 0.054M; if two protons are available, this value becomes 0.15M ($2 \times 0.054 + 0.045$); if three, 0.25M ($3 \times 0.054 + 2 \times 0.045$). The observed limiting current of Fig. 6 in footnote 9 lies between the values predicted from two and three contributed protons, assuming all species have a diffusion coefficient of $6.65 \times 10^{-6} \text{ cm}^2/\text{sec}$. The diffusivities of the ions need not be the same as that of the undissociated acid, however, and thus it is difficult to say how many protons from citric acid participate in the electrode reaction. Whether a given proton does so depends, as stated above, on its pK , the interfacial pH, and the rate of dissociation.

Reaction Model for Iron Dissolution Studied by Electrode Impedance

I. Experimental Results and Reaction Model

M. Keddam, O. R. Mattos, and H. Takenouti
(pp. 257-266, Vol. 128, No. 2)

M. Cid and M. C. Petit:¹¹ M. Keddam, O. R. Mattos, and H. Takenouti have performed an impressive piece of experimental work on iron dissolution. We would like to raise two points.

1. In their paper the authors based to a large extent their interpretation on the assumption that the high frequency arc consists of only one time constant. This is in contradiction with the paper by H. Schweickert, W. J. Lorenz, and H. Friedburg,¹² according to which this arc must be interpreted by two overlapping time constants. Can the authors comment on the possibility of decomposition of an impedance loop in two or several poorly separated time constants?

2. In the model proposed, the frequency dependence of the impedance is accounted for by coverage relaxation effects. Can the authors give additional information on the delimitation between this approach and an alternative way as surface relaxation introduced by Schweickert *et al.*?¹²

⁸ IBM Corporation, Thomas J. Watson Research Center, Yorktown Heights, New York 10598.

⁹ J. Horkans, *This Journal*, 125, 1861 (1979).

¹⁰ A. H. Du Rose, *Plating*, 64, 52 (1977).

¹¹ Laboratoire de Mécanique Physique, Université de Bordeaux I, 33405 Talence, Cedex, France.

¹² H. Schweickert, W. J. Lorenz, and H. Friedburg, *This Journal*, 127, 1693 (1980).

M. Keddam,¹³ O. R. Mattos,¹⁴ and H. Takenouti;¹⁵ Both comments are very central to the discrepancy existing between our approach of the iron anodic dissolution and that adopted by W. J. Lorenz and co-workers. Most of our argumentation was emphasized in the Discussion¹⁵ of their last paper.¹⁶ Unfortunately it seems that our remarks and comments related to the present Discussion were not sufficiently answered.

1. A very large number of impedance data on solid electrodes is now available. With practically no exception, when performed over a wide range of frequencies their loci in the complex plane consist in an association of more or less depressed semi-circles. This holds not only for the high frequencies loop considered in footnote 16, but also for the loops exhibited at lower frequencies by electrodes submitted to dissolution or deposition. When modeling a-c behaviors it turns out that the very basic problem is to estimate whether each depressed semi-circle can be resolved in a few overlapping time constants or represented by a practically infinite number of time constants (transmission line) such as a Warburg impedance. In fact, this is known to be an extremely difficult task. The statement that a distorted impedance loop must be definitely resolved into two time constants rather than into a higher number can be advocated only by fitting high precision experimental data and by producing a complete set of statistical parameters showing that standard and systematic deviations are at their minimum. To our knowledge this was not done in the present case. Moreover, as we have shown,¹⁷ pulse techniques (e.g., galvanostatic double pulse¹⁸) are of no help since they absolutely require the *a priori* assumption that the impedance actually obeys a postulated equivalent circuit. Obviously such an assumption makes the problem under consideration meaningless.

2. This second point deals with the very origin of the time or frequency dependence of the metal/electrolyte interphase. In the present state of knowledge this problem is somewhat of a semantic nature. The so-called "surface relaxation" can be merely regarded as an aphorism since of course we are faced with relaxation phenomena taking place at the electrode surface. On its own, this terminology does not throw any light on what really relaxes. A crude assimilation of the surface to the geometric area (roughness effect) is completely irrelevant since relaxation associated with passivation, e.g., Fig. 6, E_5 in the paper under discussion, should arise from a steadily decreasing electrode area. The observed relaxation processes including the d-c behavior of the electrode as their low frequency limit are most likely related to the ability of the surface to locally allow electron transfer. In that sense the term of "site" may be conveniently used, each time constant being induced by the variation of the surface density of distinct kinds of sites. Now the problem remains of the exact nature of these sites. It seems to us that this aspect can be clarified on the basis of an exhaustive experimental work focused on the influence of composition and structure of both phases on the interphase behavior. In our opinion, our paper brought serious evidence that, in the present case, these sites strongly depend on the electrolyte pH and must involve some kind of chemical bond between surface atoms and electrolyte species.

Therefore, it is quite reasonable to propose a model with partial surface coverages for characterizing these sites. This is not at all harmful to the idea that these sites are also under the dependence of crystallographic or solid-state properties on the metal side but up to now this was not supported by convincing proofs. On the contrary, experiments performed with iron-base amorphous alloys hence free of crystallographic kinks or defects have shown a behavior nearly similar to crystalline iron.¹⁹ This seems to further substantiate our interpretation.

Electron Transfer Reactions at Passive Tin Electrodes

S. Kapusta and N. Hackerman (pp. 327-332, Vol. 128, No. 2)

J. O'M. Bockris and S. U. M. Khan;²⁰ The theoretical interpretation made by the authors of their results in a study of redox reactions at passive tin electrodes evokes some comments because of the (partly admitted) lack of consistency between theory and experiment.

Experimentally, the authors well confirm that the linear Tafel relation is obtained both in the cathodic and anodic region for the redox reaction, $K_3Fe(CN)_6/K_4Fe(CN)_6$, they used. This result also supports the earlier reported Tafel linearity for similar redox reactions on passive iron by Olmedo *et al.*,²¹ and on other metal electrodes by several authors.²²⁻²⁴

The basic model used by the authors (cf., Eq. [20]) to represent current/overpotential relation involves thermal fluctuation as the origin of energy states in the ions in solution to and from which electrons exchange with the metal oxides. If the energy states in ions in solution arise by means of such fluctuations, however, the distribution is Gaussian (cf., Eq. [20]), and hence, a nonlinear Tafel relation is always expected, in contrast to experimental observation. It is evident from the Gaussian distribution of energy state used in Eq. [20] that current/overpotential relation should show maximum at higher overpotential range ($|\eta| \leq 2V$), where a limiting region does not appear and if the proper value of reorganization energy, λ , is used. The value of λ , used by the authors, is that of Hale.²⁵ However, this value is erroneous because the image terms were neglected in the calculation.

The fluctuation concept was introduced by Levich²⁶ to provide a physical interpretation of the continuity of Tafel lines. The thought process is that the outer sphere solvent molecules, due to their vibrational motion, interacts with the redox ion, giving rise to fluctuation in the energy of the central redox ion sufficient for it to be activated. However, this view ends up with the Gaussian distribution of energy states and a nonlinear Tafel line.

We therefore suggest an alternative model. There are sufficient classical modes of motion (e.g., translation) in the solvent to give the redox complex enough interaction to affect the activation of the ion solvent bond. There is spectroscopic evidence²⁷⁻²⁹ of classical motion of solvent molecules in water. In such a model, the energy distribution is Maxwellian, and the quan-

¹³ O. R. Mattos, Doctoral Thesis, University of Paris (1981).

²⁰ Department of Chemistry, Texas A&M University, College Station, Texas 77843.

²¹ A. M. T. Olmedo, R. Pereiro, and D. J. Schiffrin, *J. Electroanal. Chem. Interfacial Electrochem.*, **74**, 19 (1976).

²² F. C. Anson, N. Ruthjen, and R. D. Frisbee, *This Journal*, **117**, 477 (1970).

²³ R. V. Moshtev, *Electrochim. Acta*, **16**, 2039 (1971).

²⁴ K. Niki and H. Mizola, *J. Electroanal. Chem. Interfacial Electrochem.*, **62**, 307 (1976).

²⁵ J. M. Hale, in "Reactions of Molecules at Electrodes," N. S. Hush, Editor, Interscience, London (1971).

²⁶ V. G. Levich, "Physical Chemistry: An Advanced Treatise," Vol. 9B, chap. 12, H. Eyring, D. Henderson, and W. Jost, Editors, Academic Press, New York (1970).

²⁷ D. Eisberg and W. Kaufmann, "The Structural Properties of Water," Oxford University Press, Oxford (1969).

²⁸ J. Schiffer and D. F. Hornig, *J. Chem. Phys.*, **49**, 4150 (1968).

²⁹ R. E. Moore, O. Ferral, F. M. Koeppel, and A. J. Krisge, *J. Am. Chem. Soc.*, **93**, 1 (1971).

¹⁴ Groupe de Recherche No. 4 du C.N.R.S., "Physique des Liquides et Electrochimie," Associé à l'Université Pierre et Marie Curie, 75230 Paris Cedex 05, France.

¹⁵ COPPE/UF RJ, Rio de Janeiro, ZC.00 Brazil.

¹⁶ M. Keddam, O. R. Mattos, and H. Takenouti, *This Journal*, **128**, 1294 (1981).

¹⁷ H. Schweickert, W. J. Lorenz, and H. Friedburg, *ibid.*, **127**, 1693 (1980).

¹⁸ C. Gabrielli, M. Keddam, O. R. Mattos, and H. Takenouti, *J. Electroanal. Chem. Interfacial Electrochem.*, **117**, 147 (1981).

¹⁹ H. Schweickert, A. A. El Miligy, A. Melendez, and W. J. Lorenz, *ibid.*, **68**, 19 (1976).

tum statistics are similar to those considered in the theories of reactivity in gas and liquid phases.^{30,31} Thus, one can have a current/overpotential relation of the following type: For cathodic current, i_c , we get

$$i_c = c \int \rho(E) f(E) P_T(E) D_{ox}(E) dE \quad [1]$$

where c is a constant, $\rho(E)$ is the density electron state in metal, $f(E)$ is the Fermi distribution of electron, $P_T(E)$ is the tunneling probability of electron, and $D_{ox}(E)$ is the distribution of electronic states of oxidized ions in solution, which is expressed in this model as:

Expressing $\rho(E)$, $f(E)$, and $D_{ox}(E)$ in Eq. [1], we get

$$i_c = c^1 \int E^{1/2} \frac{1}{[e^{(E-E_0)/kT} + 1]} P_T(E) \exp[-(E_0 + \beta e_0 \eta_c - E)/kT] dE \quad [2]$$

where c^1 is a constant, E_0 is the ground electronic state energy of oxidized acceptor obtained from Born-Haber cycle for the process $M(e) + A^+ \rightarrow M^{---}A$, β is the symmetry factor around 0.5, and η_c is the cathodic overpotential and negative. After integration, the expression [2] gives

$$i_c = i_0 \exp(-\beta e_0 \eta_c / kT) \quad [3]$$

where i_0 is essentially independent of potential. Thus, one gets a linear Tafel relation from this model for which the distribution is Maxwellian (cf., Schmickler³²).

S. Kapusta and N. Hackerman:³³ We appreciate Dr. Bockris' and Dr. Khan's comments since they raise important questions regarding the present state of understanding of charge transfer at semiconducting and metal electrodes.

Our Eq. [20] can be analytically solved with certain assumptions, e.g., that charge transfer occurs mainly within $1 kT$ at the edge of the conduction band or, in the case of metals, the Fermi level. Taking bare metal electrodes as an example, we obtain for the cathodic current density

$$i_c = i_0 \exp \left[\frac{\lambda}{4kT} \right] \exp \left[- \frac{(\lambda - e\eta)^2}{4kT\lambda} \right] \quad [1]$$

and an equivalent expression for the anodic current. Here i_0 is the exchange current density, basically independent of potential, λ is the reorganization energy of the redox couple in solution, and η is the overpotential. Other symbols have their usual meaning.

As has been shown by Levich,³⁴ no exponential relation between current and potential can be expected from Eq. [1] which is in contradiction with experimental results. Only for the case $\lambda \ll \eta$ can Eq. [1] be approximated by

$$i_c = i_0 \exp \left(\frac{e\eta}{kT} \right) \quad [2]$$

Theoretical and experimental evidence³⁵ indicates that λ values are about 1-2 eV for most redox couples, i.e., within the experimentally accessible overpotential range. In particular, the value of $\lambda = 1.2$ eV for the $Fe(CN)_6^{4/3-}$ couple gives the best agreement with

³⁰ E. A. Moelwyn-Hughes, "Chemical Statistics and Kinetics of Solutions," Academic Press, New York (1971).

³¹ A. M. North, "The Collision Theory of Chemical Reactions in Liquids," Barnes and Noble, New York (1964).

³² W. Schmickler, *J. Electroanal. Chem. Interfacial Electrochem.*, **82**, 65 (1977).

³³ Department of Chemistry, Rice University, Houston, Texas 77001.

³⁴ V. G. Levich, in "Advances in Electrochemistry and Electrochemical Engineering," Vol. 4, P. Delahay, Editor, Interscience, New York (1966).

³⁵ J. M. Hale, in "Reactions of Molecules at Electrodes," N. S. Hush, Editor, Wiley-Interscience, London (1971).

our experimental results. The same value was used by Heusler³⁶ on passive Nb electrodes. Lower values have also been reported: 0.65 eV,³⁴ 0.4 ± 0.2 eV,³⁷ and 0.75 eV.³⁸ It is likely that these discrepancies can be accounted for by uncertainties in the determination of other parameters used in solving Eq. [20], e.g., flatband potential, donor energy, effective mass of the electron, etc.

The use of the "linear approximation," i.e., Boltzmann distribution, to represent the energy levels in solution instead of our Eq. [1] and [2] (Gaussian) results in a solution of Eq. [20] having constant transfer coefficient, i.e., linear Tafel slopes.³⁹⁻⁴¹ It seems, however, that the use of three-dimensional translational modes is inconsistent with the model used for the charge transfer reaction. An alternative explanation of the constancy of the transfer coefficient with potential can be found considering the effect of inner sphere vibration on outer sphere reactions, as proposed by Schmickler.⁴¹ This results in an apparent linear distribution of energy levels in solution arising from the two (i.e., inner and outer sphere) harmonic contributions.

Exothermic Reactions Among Components of Lithium-Sulfur Dioxide and Lithium-Thionyl Chloride Cells

S. Dallek, S. D. James, and W. P. Kilroy
(pp. 508-516, Vol. 128, No. 3)

M. A. Mueller and M. J. Domeniconi:⁴² In this communication, the authors report the results of a very well-structured series of experiments designed to identify components of Li/soluble cathode cells which may react so vigorously to cause batteries to explode. With respect to the Li/SOCl₂ system, we have conducted a similar investigation, and in general our data agree with those reported by the authors. However, with respect to the reactivity of the initial components of the Li/SOCl₂-system, we wish to offer an alternative interpretation of the data.

On the basis of the data shown in Fig. 8(E) of the paper under discussion, the authors concluded that the initially present components of an undischarged battery are quite unreactive even after the lithium had melted. We had observed this same phenomenon, as shown in Fig. 1(B) below, and were initially puz-

³⁶ K. E. Heusler and M. Schulze, *Electrochim. Acta*, **20**, 237 (1975).

³⁷ R. Memming and F. Moellers, *Ber. Bunsenges. Phys. Chem.*, **76**, 475 (1972).

³⁸ R. A. Van den Berghe, F. Cardon, and W. P. Gomes, *Surf. Sci.*, **39**, 368 (1973).

³⁹ W. Schmickler and J. Ulstrup, *Chem. Phys.*, **19**, 217 (1977).

⁴⁰ W. Schmickler, *J. Electroanal. Chem. Interfacial Electrochem.*, **82**, 65 (1977).

⁴¹ W. Schmickler, *Electrochim. Acta*, **20**, 137 (1975); *ibid.*, **21**, 161 (1976); *Ber. Bunsenges. Phys. Chem.*, **77**, 991 (1973).

⁴² Altus Corporation, San Jose, California 95112.

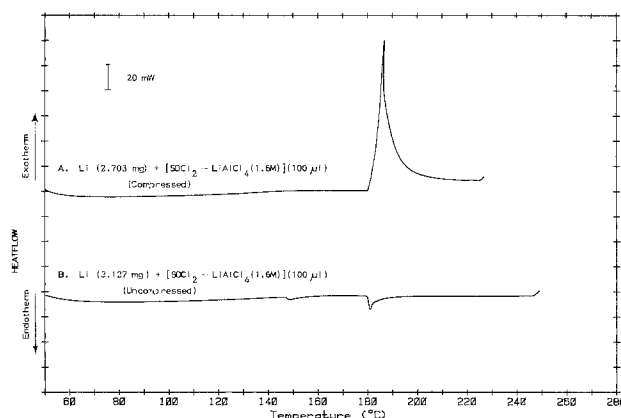


Fig. 1.

zled by the results. The stability of the system below 180°C can be explained by the protective LiCl film on the anode; above 180°C, we were surprised that this film apparently continued to prevent a direct reaction between Li and SOCl₂. On the assumption that these results were dependent on the experimental conditions, we prepared a sample in which the lithium was placed between two stainless steel plates and compressed to and maintained at a pressure representative of that found in Li/SOCl₂ batteries. The reactivity of the components under these conditions is considerably different above the melting point of Li, as shown in Fig. 1(A) above. In this case, a substantial exothermic reaction between the components is observed. It would appear, therefore, that above 180°C, the system is in only a metastable state, and that the thermodynamically favored reaction between molten lithium and thionyl chloride can proceed under conditions in which the LiCl loses its ability to act as a protective barrier. We believe such conditions generally prevail in complete Li/SOCl₂ cells, and are the principal reason for the phenomenon known as "thermal runaway."

We therefore conclude that the initial components of an undischarged Li/SOCl₂ battery must be considered very reactive after the lithium has melted, and that it is only under a limited set of conditions that the components may coexist without exothermic reaction.

S. Dallek, S. D. James, and W. P. Kilroy:⁴³ Mueller and Domeniconi suggest that our failure to observe a reaction between Li and SOCl₂-LiAlCl₄ at the melting point of Li is due to a significant departure of our DSC tests from battery conditions, *viz.*, to our lack of the Li compression that exists in most if not all Li batteries. In their very interesting experiment, Li compressed between stainless steel plates reacted violently as soon as the Li melted.

We may speculate that, in Mueller and Domeniconi's experiment, when Li melted (with its 20% volume increase) the spring pressure extruded a large, virgin, unpassivated Li surface which immediately reacted violently with the hot SOCl₂ giving their exotherm. However, we doubt that this situation holds in the jellyrolled C and D cells where most of the explosions have been reported. Here Li is contained on metal Exmet where on melting, Li flow could occur perpendicular to the plane of the Li without creating a sub-

⁴³ Naval Surface Weapons Center, Electrochemistry Branch, White Oak, Silver Spring, Maryland 20910.

stantial amount of fresh Li surface. The possibility should also be considered that the spring material acted as a catalytic surface (like C black) for the reduction of SOCl₂ and when Li melted, a shorted, high-rate cell was created. This situation also would not normally be present in a real battery. We reiterate that their experiment is very interesting; it certainly requires follow-up tests to elucidate its nature.

The Hydrogen Evolution Reaction on Electrodeposited Gold, Nickel, and Zinc Rotating Disk Electrodes

P. C. Andricacos and H. Y. Cheh (pp. 838-840, Vol. 128, No. 4)

Richard Haynes:⁴⁴ Several points should be questioned regarding this paper:

1. The validity of the kinetic constants derived from the data might be questioned regarding the lack of a: (i) definition of steady state and (ii) statistical treatment of data for such a limited range of potential, current, and rotational speed.

2. The contribution, if any, of deposition of hydrogen from H₂O is not considered especially regarding point (i).

3. Mechanism and rate-determining steps for the hydrogen evolution reaction are not uniquely determined by Tafel slopes and dependencies on proton concentration. These mechanisms and rate-determining steps have been shown to be a function of the metal, solution, and overpotential.⁴⁵ From the data presented here it is not possible to be so conclusive. A number of other possibilities could explain the observed data.

P. C. Andricacos and H. Y. Cheh:⁴⁶ 1. A careful analysis on the accuracy of our data was made during our work. For sake of brevity, we did not include our analysis in the paper. The statements made in our paper concerning our data are correct.

2. The limiting current density for hydrogen evolution is consistent with the Levich equation. We conclude that the deposition of hydrogen from H₂O cannot be a significant reaction in our study.

3. We have stated in our paper that our results are consistent with certain mechanisms. We have not claimed that mechanisms and rate-determining steps are uniquely determined by Tafel slopes and dependencies on proton concentration.

⁴⁴ Western Electric Company, Engineering Research Center, Princeton, New Jersey 08540.

⁴⁵ R. Haynes, *Electrochim. Acta*, 16, 1129 (1971).

⁴⁶ Department of Chemical Engineering and Applied Chemistry, Columbia University, New York, New York 10027.

Erratum

In the paper "Electrochemistry and Reactions of Transition Metal and Oxygen Ions in Dimethyl Sulfoxide" by Fred C. Frederick and Keith E. Johnson, which appeared in the October 1981 issue of the JOURNAL, pp. 2070-2073, Fig. 2 should appear as

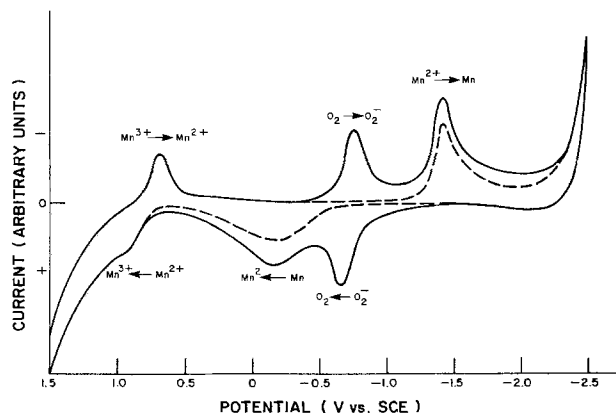


Fig. 2. Cyclic voltammogram of Mn(III) in DMSO solution. Solid line: with O₂ wave included. Broken line: corrected for O₂.

The figure caption is correct as it appears.



Lattice Defects in Semiconducting $\text{Hg}_{1-x}\text{Cd}_x\text{Te}$ Alloys

I. Defect Structure of Undoped and Copper Doped $\text{Hg}_{0.8}\text{Cd}_{0.2}\text{Te}$

H. R. Vydyanath*

Honeywell Electro-Optics Center, Lexington, Massachusetts 02173

ABSTRACT

Undoped $\text{Hg}_{0.8}\text{Cd}_{0.2}\text{Te}$ crystals were subjected to high temperature equilibration at temperatures ranging from 400° to 655°C in various Hg atmospheres. Hall effect and mobility measurements were carried out on the crystals quenched to room temperature subsequent to the high temperature equilibration. The variation of the hole concentration in the cooled crystals at 77 K as a function of the partial pressure of Hg at the equilibration temperatures, together with a comparison of the hole mobility in the undoped samples with that in the copper-doped samples, has yielded a defect model for the undoped $\text{Hg}_{0.8}\text{Cd}_{0.2}\text{Te}$ crystals, according to which, the undoped crystals are essentially intrinsic at the equilibration temperatures and the native acceptor defects are doubly ionized. Native donor defects appear to be negligible in concentration, implying that the p-to-n conversion in these alloys is mainly due to residual foreign donor impurities. The thermodynamic constants for the intrinsic excitation process as well as for the incorporation of the doubly ionized native acceptor defects in the undoped crystals have been arrived at. Copper appears to be incorporated on metal lattice sites acting as a single acceptor with little compensation. Results on the heavily copper-doped samples indicate that the quench from the equilibration temperatures was imperfect resulting in a large fraction of the copper precipitating during the quench. From results of experiments where the cooling rate from the equilibration temperatures was intentionally varied in the undoped samples, a qualitative correlation was established between the quenching efficiency and the presence of macroscopic defects such as voids and inclusions in the samples.

The importance of the pseudobinary semiconducting $\text{Hg}_{1-x}\text{Cd}_x\text{Te}$ alloys as a useful infrared detector material has long been recognized (1, 2). The bandgap of these alloys is variable depending on the proportions of HgTe and CdTe present in them; the variable bandgap makes these alloys suitable for infrared detector applications over a wide spectral range.

Considerable deviations from stoichiometry arise in these alloys prepared at elevated temperatures; these deviations result in electrically active point defects which in turn influence the carrier concentration and the lifetime in the material. Very little information exists on the systematic investigation of the nature of defects and the variation of the concentration of these defects in these alloys as a function of the physico-chemical conditions of preparation. In fact, much disagreement prevails regarding the origin of p-type to n-type conversion in these alloys (2-5).

As part of a program aimed at investigating the defect structure of the undoped $\text{Hg}_{1-x}\text{Cd}_x\text{Te}$ alloys as well as the mode of incorporation of dopants, the present paper reports on the study of the undoped and copper-doped $\text{Hg}_{0.8}\text{Cd}_{0.2}\text{Te}$.

Based on the results of Hall effect and mobility measurements on the undoped and copper-doped crystals quenched to room temperature subsequent to high

temperature equilibration, defect models for the undoped and copper-doped $\text{Hg}_{0.8}\text{Cd}_{0.2}\text{Te}$ have been arrived at. Thermodynamic constants for the intrinsic excitation constant and the incorporation of the native acceptor defects have been evaluated. These constants satisfactorily explain the electrical data in the undoped as well as the copper-doped crystals.

Experimental

Starting material.—The compositional uniformity of the $\text{Hg}_{1-x}\text{Cd}_x\text{Te}$ alloy samples used in the investigation was $x = 0.2 \pm 0.005$. Most of the experiments were carried out with starting material that was free of macroscopic defects such as precipitates, pores, and Hg or Te inclusions; in a few experiments where the intent was to establish the effect of macroscopic defects on the efficiency of quenching the high temperature equilibrium, material with a relatively high density of voids and inclusions was used. In order to assure ourselves that equilibrium was attained at temperatures as low as 400°–460°C within reasonable annealing periods (2-3 weeks), and also to increase the efficiency of quenching the high temperature equilibrium, the thickness of most of the $\text{Hg}_{0.8}\text{Cd}_{0.2}\text{Te}$ samples used in the present investigation was restricted to ≤ 0.04 cm. The residual donor or acceptor concentration in the starting undoped $\text{Hg}_{0.8}\text{Cd}_{0.2}\text{Te}$ material was $\leq 10^{16}$ cm⁻³.

* Electrochemical Society Active Member.

Key words: lattice, defects, copper doping, $\text{Hg}_{1-x}\text{Cd}_x\text{Te}$, hole mobility, semiconductors.

Copper doping.—Doping to different concentrations of copper was obtained by evaporating various amounts of copper on to the surface of the undoped samples and subsequently diffusing in the copper in a known atmosphere of Hg. Copper concentration obtained in the doped samples was determined by atomic absorption analysis carried out by Photometrics, Incorporated, Lexington, Massachusetts.

It is to be noted that the samples used for copper diffusions at temperatures below 400°C had been previously annealed at 250°C for several months in order to reduce the native acceptor defect concentration to less than 10^{15} cm^{-3} . Since copper has a high diffusivity in $\text{Hg}_{1-x}\text{Cd}_x\text{Te}$ alloys (6-7), diffusion times of 6-8 weeks were found adequate for uniform doping of samples (0.04 cm thick) at temperatures below 400°C; uniform doping at these temperatures was confirmed by sequentially lapping away the material from both sides of the samples and making certain that the hole concentrations did not change.

High temperature annealing.—Prior to the anneals, crystals were cleaned in organic solvents followed by a Br-methanol etch and a final rinse in DI water. Annealing experiments in various partial pressures of Hg were carried out in evacuated quartz ampuls containing a small amount of Hg also, to obtain the desired Hg vapor pressure. In those experiments where the desired Hg pressure was high enough, an isothermal setup was used where the free Hg and the $\text{Hg}_{0.8}\text{Cd}_{0.2}\text{Te}$ samples were kept at the same temperature; the vapor pressure of Hg in such a setup depended on the amount of free Hg in the ampul and the volume of the ampul. In experiments where the desired Hg pressure was low a two-temperature zone setup was used; the $\text{Hg}_{0.8}\text{Cd}_{0.2}\text{Te}$ crystals were kept at the higher temperature end of the ampul and the free Hg at the lower temperature end; the vapor pressure of Hg obtained corresponded to the saturation pressure of Hg at the lower temperature and was independent of the amount of Hg in the ampul. The limits of Hg pressure, within which the solid is stable at a given temperature, were obtained from the partial pressure-temperature data for HgTe (8) and $\text{Hg}_{1-x}\text{Cd}_x\text{Te}$ alloys (9-10).

Equilibration periods ranging from 16 to 24 hr were used for annealing at temperatures of 500°C or greater and a two week equilibration was used for annealing temperatures of 460° and 400°C. Subsequent to the anneals, the samples were rapidly quenched in ice water, to freeze in as much of the high temperature equilibrium as possible; in a few cases the samples were air cooled from the equilibration temperatures.

Electrical measurements.—Hall effect and resistivity measurements were made using the van der Pauw method (11). Magnetic field strengths of 400 and 4000G were used for the measurement of the Hall coefficient.

Results

Only those Hall coefficient measurements where the Hall coefficient R_H did not vary with varying magnetic field strength, (400-4000G) were used in evaluating the hole concentrations in the crystals. This ensured that the samples did not show mixed conduction (12) and the carrier concentration was given by

$$\frac{1}{|R_H|q}$$

Figure 1 shows the variation of the Hall coefficient as a function of the temperature of measurement for the undoped samples equilibrated at different temperatures under known partial pressures of Hg and quenched to room temperature. It is evident from the figure that at temperatures exceeding 145 K the contribution from the intrinsic carriers becomes important, whereas at temperatures between 77 and 145 K the Hall coefficient is temperature independent indicating that the native

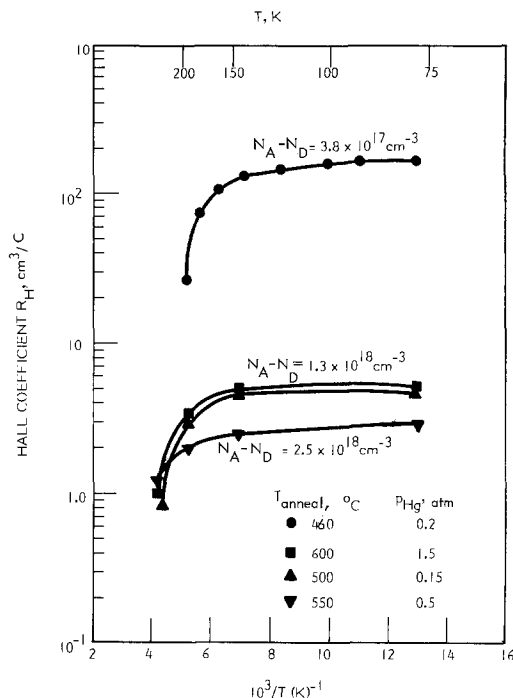


Fig. 1. Hall coefficient as a function of measurement temperature for undoped $\text{Hg}_{0.8}\text{Cd}_{0.2}$ samples equilibrated at the indicated temperatures and partial pressures of Hg and quenched to room temperature.

acceptors are completely ionized at 77 K for concentrations ranging from 10^{17} to 10^{18} cm^{-3} . Based on this inference, all the Hall effect measurements on the undoped samples were carried out at 77 K, and the resulting hole concentration was assumed to give a measure of the native acceptor defect concentration incorporated at the higher equilibration temperatures.

Figure 2 shows the hole concentrations at 77 K as a function of the partial pressure of Hg for the undoped crystals annealed at various temperatures and quenched to room temperature. The samples are invariably p-type for all partial pressures of Hg (throughout the existence region) at temperatures greater than 400°C and the hole concentration is roughly inversely proportional to the partial pressure of Hg, p_{Hg} . Phase boundary limits at each temperature are indicated by arrows in the figure. The solid lines

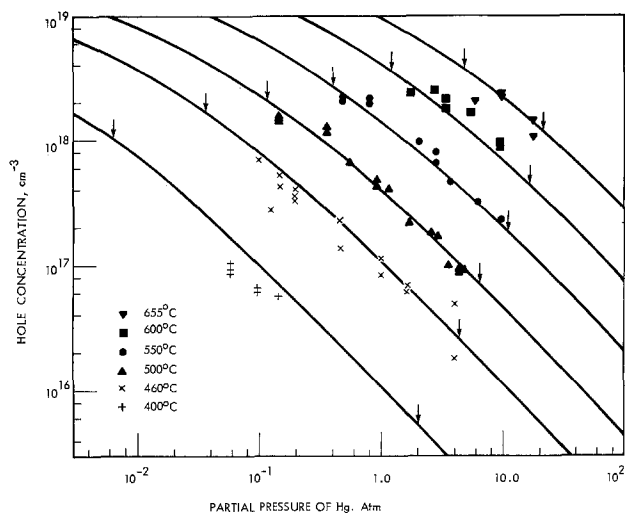


Fig. 2. Hole concentration at 77 K as a function of the partial pressure of Hg for undoped $\text{Hg}_{0.8}\text{Cd}_{0.2}$ crystals annealed at various equilibration temperatures and quenched to room temperature; solid lines correspond to the values calculated on the basis of the defect model discussed in the text.

shown in the figure correspond to the hole concentrations calculated on the basis of the defect model for the undoped crystals, to be discussed later.

Figure 3 shows the variation of the Hall coefficient as a function of the temperature of measurement for crystals doped with different copper concentrations. Just as with the undoped crystals, most of the copper present in the electrically active form appears to be completely ionized between 77 and 145 K, and at temperatures greater than 145 K the contribution from the intrinsic carriers becomes significant. The total amount of the electrically active copper concentration in the samples was inferred from the hole concentrations obtained at 145 K.

Figure 4 shows the hole mobility at 77 K for the undoped crystals as a function of the hole concentration. The data indicate that the hole mobility decreases with increase in hole concentration. Figure 5 shows the hole mobility at 77 K in various copper-doped samples. The temperatures at which the various copper diffusions were done are also indicated in the figure. It is apparent from Fig. 4 and 5 that the copper-doped samples

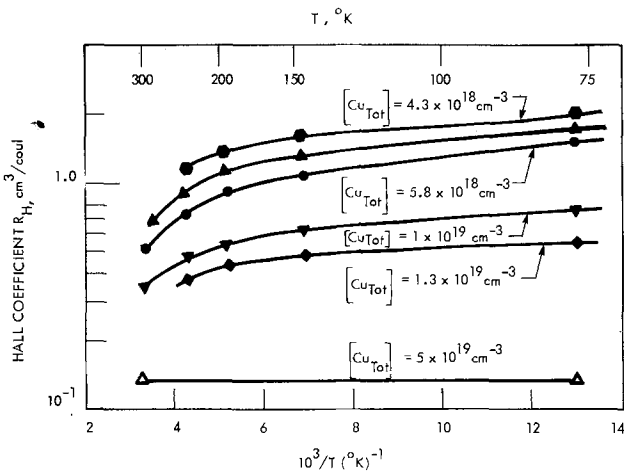


Fig. 3. Hall coefficient as a function of measurement temperature for copper-doped $Hg_{0.8}Cd_{0.2}$ crystals.

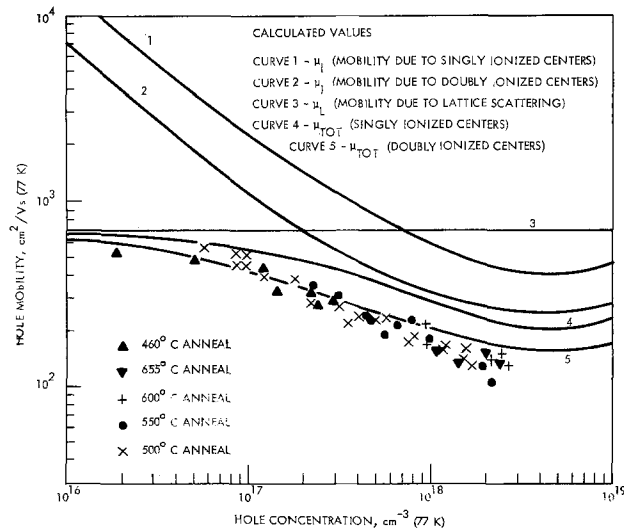


Fig. 4. Experimental and calculated hole mobility at 77 K as a function of the hole concentration for undoped $Hg_{0.8}Cd_{0.2}$ crystals; curves 1 and 2 show the calculated mobility due to impurity scattering (curve 1 for singly ionized centers and curve 2 for doubly ionized centers), line 3 shows the mobility due to lattice scattering, and curves 4 and 5 show the overall mobility calculated by reciprocally combining the impurity scattering mobility and the lattice scattering mobility (curve 4 for singly ionized centers and curve 5 for doubly ionized centers). See Appendix A for details of calculations.

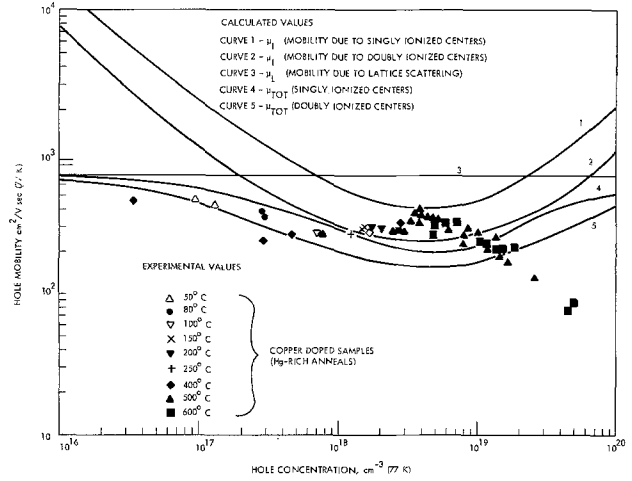


Fig. 5. Experimental and calculated hole mobility at 77 K as a function of the hole concentration for copper-doped $Hg_{0.8}Cd_{0.2}$ crystals; curves 1 and 2 show the calculated mobility due to impurity scattering (curve 1 for singly ionized centers and curve 2 for doubly ionized centers), line 3 shows the mobility due to lattice scattering, and curves 4 and 5 show the overall mobility calculated by reciprocally combining the impurity scattering mobility and lattice scattering are also shown in the figures. See Appendix A for details of calculations.

have higher hole mobilities than the undoped samples containing similar hole concentrations. The mobilities calculated on the basis of the combined ionized impurity and lattice scattering are also shown in the figures.

Figure 6 compares the electrical conductivity at 77 K obtained in the undoped crystals containing a relatively large concentration of voids and inclusions (~ 1000 per cm^2) with those containing a negligible concentration of these (≤ 20 per cm^2) subsequent to anneals at $500^\circ C$ in different partial pressures of Hg and air cooled or quenched to room temperature; the voids and inclusions in the samples were approximately 10-30 μm in diameter, and depending on how the bulk crystals were grown, the inclusions were either Hg rich or Te rich. Figure 7 shows the electrical conductivity at 77 K, obtained in the undoped crystals containing a large concentration of voids and inclusions and which were air cooled to room temperature subsequent to anneals at $500^\circ C$ in different partial pressures of Hg. Figures 6 and 7 clearly show that the electrical conductivity variations as a function of the partial pressure of Hg are similar for undoped crystals with and without voids and inclusions that were quenched to room tem-

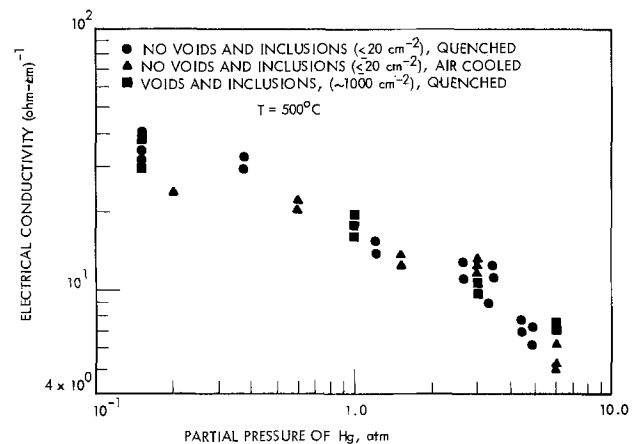


Fig. 6. Electrical conductivity at 77 K for various sets of undoped $Hg_{0.8}Cd_{0.2}Te$ crystals containing different concentrations of voids and inclusions, and quenched or air cooled subsequent to anneals in different Hg pressures at $500^\circ C$.

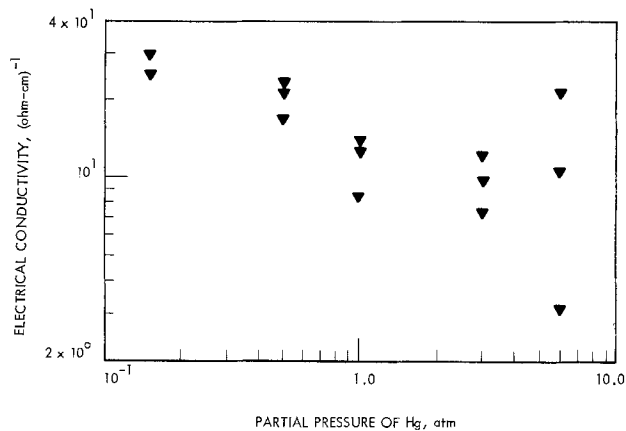


Fig. 7. Electrical conductivity at 77 K for undoped $\text{Hg}_{0.8}\text{Cd}_{0.2}\text{Te}$ crystals containing a large concentration of voids and inclusions and air cooled subsequent to anneals in different Hg pressures at 500°C .

perature subsequent to equilibration at 500°C ; the results are also similar for the undoped crystals containing virtually no voids and inclusions and which were air cooled from 500°C . However, considerable scatter is obtained in the results for the undoped crystals containing a large concentration of voids and inclusions and which were air cooled from 500°C .

Discussion

Defect equilibria.—The way in which the concentrations of defects vary as a function of the physicochemical conditions of preparation (temperature, partial pressure of Hg or partial pressure of Te_2 , and/or the dopant concentration) can be arrived at by utilizing the quasichemical approach developed by Kröger and Vink (13). The quasichemical approach has been used in many binary compounds to establish defect models (14). In such an approach, atomic and electronic defects are considered as chemical species and defect formation reactions along with the corresponding mass action relations are formulated. The concentrations of all the defect species comprising the electroneutrality condition and the dopant balance equation (for the doped crystals) are then expressed in terms of the relevant mass action constants and the concentration of one defect species. This results in equations containing the various mass action constants and the concentrations of one single defect species; numerical solution will then yield the concentration of this defect species for given values of the mass action constants. Once the concentration of one defect species is determined the concentrations of all the other defect species can be evaluated via the mass action relations.

Defect formation reactions and mass action relations for various defect species are listed in Table I. The defect notations are according to the scheme of Kröger and Vink (13), in which the major symbol indicates the

defect, the subscript denotes the type of lattice site occupied, and the superscript indicates the charge. Superscripts prime (') and dot (·) stand for effective negative and positive charges, respectively, while a cross (x) stands for a neutral charge. Thus V''_{Hg} indicates a doubly negatively ionized vacant lattice site of Hg. Square brackets indicate concentrations expressed as site fractions. The native acceptor defect species considered in this paper are the vacancies of Hg instead of the interstitials of Te. Electrical measurements cannot distinguish between the two species and hence the results will be the same if interstitials of Te are considered as the native acceptor defect species instead. Recent work on the defect structure of CdTe (15, 16) determined by Hall effect and tracer self-diffusion data indicates the presence of appreciable concentrations of Te interstitials in addition to the vacancies of Cd. Although the results of the present work showed no evidence of presence of any native donor defects such as Hg_i or V_{Te} , etc. in any appreciable concentration, Table I includes these defects also for purposes of later discussion in the paper.

Defect state in the cooled crystals.—Ideally, *in situ* high temperature physical property measurements and measurements on the crystals quenched from the equilibration temperatures should both be used to arrive at defect states prevailing at the high temperature as well as in the cooled crystals; much information regarding precipitation of atomic defects during quenching can be obtained by correlating the defect state in the cooled crystals with that obtained at the equilibration temperatures. CdTe (15-19) is only one of the few materials that has been studied extensively from such a viewpoint. In the present work, however, the defect state in the cooled crystal shall be used to derive information regarding the defect state prevailing at the equilibration temperatures.

While attempting to deduce the high temperature defect state of the crystals from measurements on the crystals quenched to room temperature from the high temperature physicochemical conditions, a few assumptions are made. The assumptions are (i) that the electrons and the holes recombine during cooling, (ii) that all the atomic defects at the high temperature are frozen in, and (iii) that the intrinsic carrier concentration $n_i = K_i^{1/2}$ at the measurement temperature \ll concentration of the electrically active atomic defects so that the Fermi level is pinned at the defect level and the carrier concentration in the cooled crystals gives the concentration of the atomic defects corresponding to the high temperature equilibrium. The first assumption is always satisfied and the third one is also satisfied as long as the carrier concentration measurement temperature is low enough for n_i to be low. The second assumption requires that the crystals be quenched fast enough that the precipitation of the atomic defects is not given rise to.

Approximation to the electroneutrality condition and dopant balance condition.—When the electroneutrality

Table I. List of the defect formation reactions, mass action constants, electroneutrality condition, and dopant balance equation

| Reaction | Mass action relation |
|---|---|
| 1. $\text{O} \rightarrow \text{e}' + \text{h} \cdot; E_1$ | $K_1 = [\text{e}'] [\text{h} \cdot]$ |
| 2. $\text{Hg}^{\text{Te}}_{\text{Hg}} \rightarrow \text{V}''_{\text{Hg}} + 2\text{h} \cdot + \text{Hg}(\text{g}); \text{H}''_{\text{VHg}}$ | $K''_{\text{VHg}} = [\text{V}''_{\text{Hg}}] [\text{h} \cdot]^2 p_{\text{Hg}}$ |
| 3. $\text{V}''_{\text{Hg}} \rightarrow \text{V}'_{\text{Hg}} + \text{h} \cdot; E_{\text{A}1\text{V}}$ | $K_{\text{A}1\text{V}} = [\text{V}'_{\text{Hg}}] [\text{h} \cdot] / [\text{V}''_{\text{Hg}}]$ |
| 4. $\text{V}'_{\text{Hg}} \rightarrow \text{V}^{\cdot}_{\text{Hg}} + \text{h} \cdot; E_{\text{A}2\text{V}}$ | $K_{\text{A}2\text{V}} = [\text{V}^{\cdot}_{\text{Hg}}] [\text{h} \cdot] / [\text{V}'_{\text{Hg}}]$ |
| 5. $(\text{Hg}_{0.8}\text{Cd}_{0.2})\text{Te}(\text{S}) \rightarrow 0.8 \text{Hg}(\text{g}) + 0.2 \text{Cd}(\text{g}) + 1/2 \text{Te}_2(\text{g});$ $K_{\text{Hg}_{0.8}\text{Cd}_{0.2}\text{Te}}$ | $K_{(\text{Hg}_{0.8}\text{Cd}_{0.2}\text{Te})} = p_{\text{Hg}}^{0.8} p_{\text{Cd}}^{0.2} p_{\text{Te}_2}^{1/2}$ |
| 6. $\text{O} \rightarrow \text{V}''_{\text{Hg}} + \text{V}''_{\text{Te}}; \text{H}''_{\text{S}}$ | $K''_{\text{S}} = [\text{V}''_{\text{Hg}}] [\text{V}''_{\text{Te}}]$ |
| 7. $\text{Hg}^{\text{Te}}_{\text{Hg}} \rightarrow \text{V}''_{\text{Hg}} + \text{Hg}''_{\cdot\cdot}; \text{H}''_{\text{F}}$ | $K''_{\text{F}} = [\text{V}''_{\text{Hg}}] [\text{Hg}''_{\cdot\cdot}]$ |
| 8. $\text{Hg}(\text{l}) \rightarrow \text{Hg}(\text{g}); \text{H}_{\text{Hg}}$ | $K_{\text{Hg}} = p_{\text{Hg}}/a_{\text{Hg}}$ |
| 9. $\text{Te}(\text{l}) \rightarrow 1/2 \text{Te}_2(\text{g}); \text{H}_{\text{Te}}$ | $K_{\text{Te}} = p_{\text{Te}_2}^{1/2}/a_{\text{Te}}$ |
| 10. Electroneutrality condition: $[\text{e}'] + [\text{Cu}'_{\text{Hg}}] + [\text{V}'_{\text{Hg}}] + 2[\text{V}''_{\text{Hg}}] = [\text{h} \cdot] + [\text{Cu}^{\cdot}_{\cdot}] + [\text{Hg}^{\cdot}_{\cdot}] + 2[\text{Hg}''_{\cdot\cdot}] + 2[\text{V}''_{\text{Te}}]$ | |
| 11. Copper balance equation: $[\text{Cu}'_{\text{Hg}}] + [\text{Cu}^{\cdot}_{\cdot}] = [\text{Cu}_{\text{tot}}]$ | |

condition and the dopant balance equation (Table I) are approximated by only the dominant members (20), one can obtain the variation of the defect concentrations as a function of p_{Hg} and the total copper concentration (for copper-doped crystals) in the form

$$\text{Concentration} \propto p_{Hg}^r [Cu_{tot}]^s$$

where r and s are small integers or fractions.

Table II lists the exponents of p_{Hg} and $[Cu_{tot}]$ for the variation of the concentrations of the different defects for various approximations to the electroneutrality condition.

Native acceptor defects.—The fact that the hole concentration in the undoped crystals is proportional to p_{Hg}^{-1} (Fig. 2) indicates that the crystals are essentially intrinsic at the high temperature (Table II, electroneutrality approximation $[e'] = [h']$); however, as can be noted from Table II, for a situation where the crystal is intrinsic, all the native acceptor defects vary as p_{Hg}^{-1} irrespective of the charge state of the defects. In order to establish the charge state of the native acceptor defects dominant in the undoped crystals the electrical characteristics of the undoped and the acceptor doped crystals will be compared. Figure 4 shows that the hole mobilities in the undoped crystals at 77 K decrease with an increase in the hole concentration indicating that the contribution of ionized impurity scattering to the hole mobilities is substantial. If so, the fact that a majority of the copper-doped crystals shown in Fig. 5 have higher mobilities than the undoped crystals indicates that the ionized impurity scattering is less in the copper-doped crystals; the results can be explained if copper is a single acceptor occupying Hg lattice sites and the native acceptor defects in the undoped crystals are doubly ionized. Based on the theory of ionized impurity scattering (21) for comparable hole concentrations, the mobilities due to ionized impurity scattering in the copper-doped crystals containing x number of singly ionized copper centers can be expected to be twice that in the undoped crystals containing $x/2$ number of the doubly ionized native

acceptor defect centers. Also, in those crystals where the electrically active copper concentration exceeds the intrinsic carrier concentration at the annealing temperatures, thus extrinsically doping them, the native acceptor defect concentration decreases with an increase in the copper concentration as a consequence of the mass action effect. As can be seen from Table II, as soon as the crystals become extrinsic with copper doping and the electroneutrality approximation becomes $[Cu'_{Hg}] = [h']$, the doubly ionized native acceptor defects decrease in proportion to the square of the copper concentration in the crystals ($[V''_{Hg}] \propto [Cu_{tot}]^{-2}$). This is shown schematically in Fig. 8. Hence, in samples doped with copper to greater than the intrinsic carrier concentration, the concentration of the doubly ionized native acceptor defects is considerably depressed. If the native acceptor defects were singly ionized, their concentration would decrease in an inverse linear proportion to $[Cu_{tot}]$ as soon as the copper concentration exceeds the intrinsic carrier concentration (Table II and Fig. 8); however, the hole mobility of such samples should be no different from that of the undoped crystals for comparable hole concentrations. It may be argued that the larger hole mobility in the heavily copper-doped samples (Fig. 5) may result from shorting paths due to the high concentrations of copper; however, the fact that the hole mobility in the copper-doped samples decreases for hole concentrations in excess of 10^{19} cm^{-3} (Fig. 5) rules out this explanation. It should also be noted from Fig. 4 and 5 that the hole mobilities are essentially the same for both the copper-doped and the undoped samples when the hole concentration is less than 10^{17} cm^{-3} . This result indicates that ionized impurity scattering is probably less significant for hole concentrations less than 10^{17} cm^{-3} . Hole mobilities calculated by reciprocally combining the mobility due to lattice scattering and the mobility due to ionized impurity scattering (see Appendix A for details) are also shown in Fig. 4 and 5 for the cases of singly ionized and doubly ionized scattering centers; clearly, for the undoped crystals, the agreement between the experimental values and the calculations is better for the case of the doubly ionized scattering centers, whereas for the copper-doped crystals the agreement is better for the case of the singly ionized scattering centers. It should be noted that the

Table II. Variations of the defect concentrations as a function of p_{Hg} and/or copper concentrations for various approximations to the electroneutrality condition

| Type of defect and approximation to the electroneutrality condition | [] $\propto p_{Hg}^r [Cu_{tot}]^s$ | | Hole concentration in the cooled crystals | |
|---|-------------------------------------|----|---|---|
| | r | s | r | s |
| 1. $[e'] = [h'] = \sqrt{K_1}$ | 0 | 0 | | |
| $[V''_{Hg}]$ | -1 | 0 | -1 | 0 |
| $[V'_{Hg}]$ | -1 | 0 | -1 | 0 |
| $[Hg'_{i}]$ | +1 | 0 | +1 | 0 |
| $[Hg''_{i}]$ | +1 | 0 | +1 | 0 |
| $[V''_{Te}]$ | +1 | 0 | +1 | 0 |
| $[Cu'_{Hg}] = [Cu_{tot}]$ | 0 | 1 | 0 | 1 |
| 2. $[Cu'_{Hg}] = [Cu_{tot}] = [h']$ | 0 | 1 | 0 | 1 |
| $[V''_{Hg}]$ | -1 | -2 | | |
| $[V'_{Hg}]$ | -1 | -1 | | |
| $[Hg'_{i}]$ | +1 | +1 | | |
| $[Hg''_{i}]$ | +1 | +2 | | |
| $[V''_{Te}]$ | +1 | +2 | | |
| 3. $[h'] = 2[V''_{Hg}]$ | -1/3 | 0 | -1/3 | 0 |
| $[e']$ | +1/3 | 0 | | |
| $[V'_{Hg}]$ | -2/3 | 0 | | |
| $[Hg'_{i}]$ | +2/3 | 0 | | |
| $[Hg''_{i}]$ | +1/3 | 0 | | |
| $[V''_{Te}]$ | +1/3 | 0 | | |
| $[Cu'_{Hg}] = [Cu_{tot}]$ | 0 | 1 | | |
| 4. $[V''_{Hg}] = [V''_{Te}] = \sqrt{K''_2}$ | 0 | 0 | | |
| $[e']$ | 1/2 | 0 | | |
| $[h']$ | -1/2 | 0 | | |
| $[V'_{Hg}]$ | -1/2 | 0 | | |
| $[Hg'_{i}]$ | +1/2 | 0 | | |
| $[Hg''_{i}]$ | 0 | 0 | | |
| $[Cu'_{Hg}] = [Cu_{tot}]$ | 0 | 1 | | |
| 5. $[V''_{Hg}] = [Hg''_{i}] = \sqrt{K''_3}$ | 0 | 0 | | |
| $[e']$ | 1/2 | 0 | | |
| $[h']$ | -1/2 | 0 | | |
| $[V'_{Hg}]$ | -1/2 | 0 | | |
| $[Hg'_{i}]$ | +1/2 | 0 | | |
| $[Hg''_{i}]$ | 0 | 0 | | |
| $[V''_{Te}]$ | 0 | 0 | | |
| $[Cu'_{Hg}] = [Cu_{tot}]$ | 0 | 1 | | |

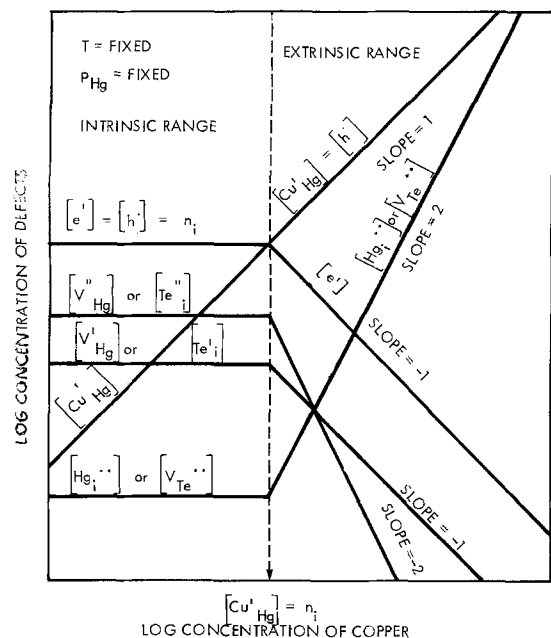


Fig. 8. Schematic variation of $[e']$, $[h']$, $[Cu'_{Hg}]$, $[V''_{Hg}]$ (or $[Te''_{i}]$), $[V'_{Hg}]$ (or $[Te'_{i}]$), and $[Hg''_{i}]$ (or $[V''_{Te}]$) as a function of the electrically active copper concentration in $Hg_{0.8}Cd_{0.2}Te$ at a fixed temperature and partial pressure of Hg.

Brooks-Herring expression (21) used for calculating the mobility due to ionized impurity scattering is applicable only for nondegenerate semiconductors and hence the mobility calculations shown in Fig. 4 and 5 for hole concentrations in excess of 10^{19} cm^{-3} should not be deemed significant; for such large carrier concentrations impurity banding effects also become important.

Absence of compensation in the undoped and copper-doped crystals.—Absence of compensation in the undoped as well as the copper-doped crystals of $\text{Hg}_{0.8}\text{Cd}_{0.2}\text{Te}$ is evidenced by a few inferences. First, the hole mobilities in the undoped crystals are only dependent on the hole concentration and are independent of the temperature of anneal; if there was any compensation by native defects, the concentration of these defects would be expected to be exponentially dependent on temperature and the mobility dependence on the hole concentration would not have been nearly as linear as shown in Fig. 4. Second, if the undoped crystals had a considerable concentration of native donor defects compensating the native acceptor defects the concentration of these native donor defects would have considerably increased via the mass action effect as soon as the copper concentration exceeded the intrinsic carrier concentration and the crystal became extrinsic (Table II and Fig. 8). Since the copper-doped crystals, in fact, have higher mobilities than the undoped crystals for comparable hole concentrations, the undoped and the copper-doped crystals seem to be uncompensated and the native donor defect concentration in $\text{Hg}_{0.8}\text{Cd}_{0.2}\text{Te}$ seems to be negligible. Absence of compensation also has been established in $\text{Hg}_{0.6}\text{Cd}_{0.4}\text{Te}$ (22).

Origin of p-type to n-type conversion.—In the absence of any systematic defect studies in $\text{Hg}_{1-x}\text{Cd}_x\text{Te}$ various reasons for p-type to n-type conversion have been proposed (2-5, 23, 24). Reynolds *et al.* (23) observed that the $\text{Hg}_{0.8}\text{Cd}_{0.2}\text{Te}$ crystals annealed under Hg-saturated conditions converted to n-type below 360°C and the electron concentration was independent of temperature of anneal below 360°C . The temperature independence of the electron concentration under Hg-saturated conditions led them to conclude that the crystals were n-type due to residual donors in the crystals and not due to any native donor defects. Similar inferences and conclusions were reported recently by Bartlett *et al.* (24) for $\text{Hg}_{0.8}\text{Cd}_{0.2}\text{Te}$. Schmit and Stelzer (25) observed that their undoped $\text{Hg}_{0.6}\text{Cd}_{0.4}\text{Te}$ samples also turned n-type at temperatures below 350°C under Hg-saturated conditions. Also the conversion temperatures were different for different samples. Although the temperature independence of the electron concentration in the undoped crystals of $\text{Hg}_{0.8}\text{Cd}_{0.2}\text{Te}$ (23, 24) and $\text{Hg}_{0.6}\text{Cd}_{0.4}\text{Te}$ (25) for Hg-saturated conditions does not, by itself, rule out the n-type conversion to be due to native donor defects (see Appendix B), the fact that the different samples in the experiments of Schmit and Stelzer (25) converted to n-type at different temperatures indicates that the conversion in these samples was due to residual foreign donors in the crystals, the samples with a higher residual foreign donor concentration being able to convert to n-type at a higher temperature. Also it was noticed in the present work that certain of the p-type samples (10^{15} - 10^{16} cm^{-3}) did not convert to n-type even when annealed in Hg-saturated conditions at temperatures below 350°C . If the n-type conversion occurs due to native donor defects the inability to convert some of these samples is difficult to explain. In these samples the residual acceptor impurity concentration exceeded the residual donor impurity concentration and hence p-type to n-type conversion was not possible at any temperature. These arguments support our conclusion in the previous section that the native donor defects in $\text{Hg}_{0.8}\text{Cd}_{0.2}\text{Te}$ are negligible in concentration; (probably

much less than 10^{15} cm^{-3} at 350°C - 400°C). The conversion to n-type in $\text{Hg}_{0.8}\text{Cd}_{0.2}\text{Te}$, as well as $\text{Hg}_{0.6}\text{Cd}_{0.4}\text{Te}$ does not appear to be due to native donor defects. The assumption that the p-type to n-type conversion in $\text{Hg}_{1-x}\text{Cd}_x\text{Te}$ alloys occurs due to native donor defects appears erroneous (2-5), and such a conversion only occurs due to residual donor impurities; also the conversion is only possible for samples with residual donor impurity concentration exceeding the residual acceptor impurity concentration in the crystals.

Correlation of the quenching efficiency with the presence of voids and inclusions.—Results of Fig. 6 and 7 indicate that the electrical conductivity variations in the cooled crystals at 77 K as a function of the partial pressure of Hg at the equilibration temperatures can be a sensitive function of the cooling rate, particularly for samples containing a large concentration of voids and inclusions ($\sim 1000 \text{ per cm}^2$). For samples containing a relatively small concentration of voids and inclusions ($\leq 20 \text{ per cm}^2$) the results are approximately the same except under very low Hg pressures where the air-cooled samples have smaller electrical conductivity than the quenched samples (Fig. 6). Electrical conductivity, rather than hole concentration, has been plotted in Fig. 6 and 7 for ease of comparison of the results of different anneals; for instance, some of the air-cooled samples showed mixed conductivity due to the formation of thin n-type inversion layers formed by a reduction in the hole concentration due to precipitation of native acceptor defects during cooling and/or partial type conversions of the samples. When such layers are thin, the overall conductivity is still dominated by holes ($p\mu_p > n\mu_n$) even if the Hall coefficient is negative ($n\mu_n^2 > p\mu_p^2$), hence electrical conductivity for such samples was assumed to reflect the bulk crystal properties better than the Hall effect results. It can be inferred from Fig. 6 and 7 that the cooling rate obtained from air cooling the samples is not high enough to retain the high temperature equilibrium in the samples containing a large concentration of voids and inclusions, thus resulting in a reduction of the concentration of the native acceptor defects at 500°C . The diffusion distances for equilibration are lower in the presence of a large concentration of voids and inclusions, hence crystals containing a large concentration of these can come to equilibrium at an intermediate temperature between 500°C and room temperature during air cooling, whereas crystals containing fewer of them retain the high temperature equilibrium to a greater degree. It should also be noted from Fig. 7 that quenching in ice water is fast enough for crystals containing a large concentration of voids and inclusions to retain the 500°C equilibrium. Although experiments with varying cooling rates were not undertaken at higher temperatures it is reasonable to assume that the effect of the presence of voids and inclusions on the quenching efficiency is greater at temperatures higher than 500°C and lower at lower temperatures.

Analysis of the carrier concentration in the undoped crystals.—In the detailed analysis of the carrier concentration in the cooled crystals, the complete electroneutrality condition is considered. In order to distinguish the high temperature state of the crystal from the low temperature state of the crystal (cooled crystals) subscripts HT (high temperature) and LT (low temperature) are used.

For the undoped crystals, knowing that the native acceptor defects are doubly ionized and that the native donor defects are negligible in concentration and neglecting the influence of residual donors and acceptors, the complete electroneutrality condition becomes

$$[e']_{\text{HT}} + 2[V''_{\text{Hg}}]_{\text{HT}} = [h]_{\text{HT}} \quad [1]$$

Expressing $[e']$ and $[V''_{\text{Hg}}]$ in terms of the mass action

constants defined in Table I, we obtain

$$(K_i[h\cdot]_{HT} + (2K''_{VHg}|[h\cdot]^2 p_{Hg})_{HT} = [h\cdot]_{HT} \quad [2]$$

or

$$[h\cdot]_{HT}^3 - (K_i[h\cdot]_{HT} = 2(K''_{VHg}|p_{Hg})_{HT}$$

The concentration of holes obtained in the cooled crystals is given by

$$[h\cdot]_{LT} = 2[V''_{Hg}]_{HT} = (2K''_{VHg}|[h\cdot]^2 p_{Hg})_{HT}$$

or

$$[h\cdot]_{HT} = (2K''_{VHg}|p_{Hg})_{HT}^{1/2} [h\cdot]_{LT}^{1/2} \quad [3]$$

Combination of [2] and [3] with some simplification gives

$$[h\cdot]_{LT}^{3/2} (2K''_{VHg}|p_{Hg})_{HT}^{1/2} + (K_i)_{HT} [h\cdot]_{LT} = (2K''_{VHg}|p_{Hg})_{HT} \quad [4]$$

For given values of K_i and K''_{VHg} at various temperatures, the solution of Eq. [4] gives the hole concentration in the cooled crystals as a function of p_{Hg} . By a procedure of trial and error, the values of K_i and K''_{VHg} were optimized at each temperature to give the best fit between the experimentally observed hole concentrations and the calculated values. The calculated values are shown in Fig. 2 as solid lines. The agreement between the experimental values and the calculations appears to be within limits of experimental error.

Mass action constants K_i and K''_{VHg} determined from the present investigation (valid for temperatures between 400° and 655°C) are given by

$$K_i = 5.77 \times 10^{-4} \exp(-0.57 \text{ eV/kT}) (\text{Site Fr})^2 \quad [5]$$

and

$$K''_{VHg} = 7.9 \times 10^2 \exp(-2.24 \text{ eV/kT}) (\text{Site Fr})^3 \text{ atm} \quad [6]$$

Noting that there are 1.26×10^{22} molecules/cm³ in $Hg_{0.8}Cd_{0.2}Te$, we get

$$K_i = 9.16 \times 10^{40} \exp(-0.57 \text{ eV/kT}) \text{ cm}^{-6} \quad [7]$$

and

$$K''_{VHg} = 1.58 \times 10^{69} \exp(-2.24 \text{ eV/kT}) \text{ cm}^{-9} \text{ atm} \quad [8]$$

Both K_i and K''_{VHg} influence the absolute values of the carrier concentration obtained in the cooled crystals and the variation of the carrier concentration as a function of p_{Hg} . From Table II, it can be seen that the hole concentration in the cooled crystals (equal to twice the concentration of the doubly ionized native acceptor defects at the anneal temperature) is expected to be proportional to p_{Hg}^{-1} for crystals which are intrinsic, whereas it is expected to be proportional to $p_{Hg}^{-1/3}$ for crystals which are extrinsic with the situation $[h\cdot] = 2[V''_{Hg}]$ at the high temperature. Thus, for a given value of K''_{VHg} , if the chosen K_i value was such that $[V''_{Hg}]$ was comparable in concentration to $[e']$ and $[h\cdot]$, at the high temperature, the power dependence of the calculated hole concentration in the cooled crystals was between $-1/3$ and -1 . On the other hand, if the chosen K_i values were high compared to the hole concentration in the cooled crystals, the calculated hole concentration varied strictly as p_{Hg}^{-1} . The absolute values of the calculated hole concentrations depended both on K' and K''_{VHg} . In order to show how sensitive the calculated hole concentrations are to the variation in the K_i values at the anneal temperatures, the hole concentrations in the cooled crystals were calculated as a function of p_{Hg} for K_i values 25% higher and 25% lower than given by expression [7] for K_i . The calculated hole concentrations in the cooled crystals for K_i values given by the expression as well as for K_i values $\pm 25\%$ are shown for $T = 500^\circ\text{C}$ in Fig. 9; the K''_{VHg} value in the calculations was kept

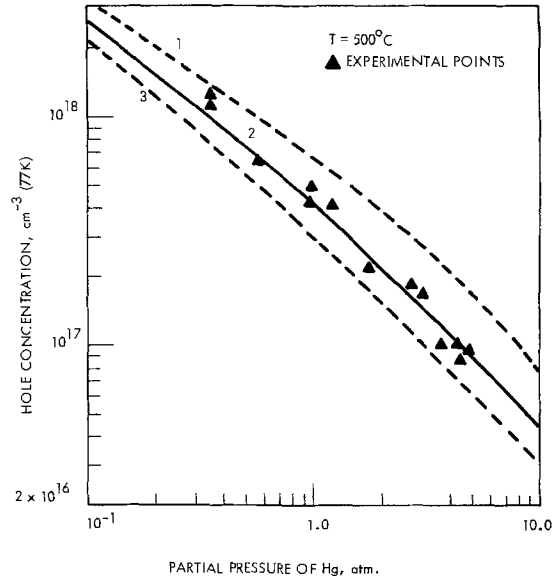


Fig. 9. Defect model calculations of the hole concentrations at 77 K for undoped $Hg_{0.8}Cd_{0.2}Te$ annealed at 500°C in various partial pressures of Hg and quenched to room temperature; solid line 2 represents calculations using K_i values given by expression [7] of the text, whereas the dashed lines 1 and 3 correspond to calculations using K_i values differing from those of expression [7] by $\pm 25\%$; experimental points are also shown for comparison.

constant as given by expression [8]. It appears that $\pm 25\%$ variations in K_i do not affect the calculations adversely.

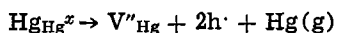
Assuming simple parabolic conduction and valence bands and nondegenerate semiconductor statistics the expression for K_i is written as

$$K_i = 2(m_e m_h)^{3/2} (\pi kT/h^2)^3 \exp(-E_g/kT) \text{ cm}^{-6} \quad [9]$$

where m_e and m_h are the effective masses of electrons and holes, respectively, and E_g is the energy gap. $E_g = E_g(0) + \alpha T$ where $E_g(0)$ corresponds to the energy gap at 0 K. A linear increase of the energy gap with increase in temperature has been verified by various researchers for temperatures up to 400 K (26-30). To the author's knowledge, no measurements on the energy gap or the intrinsic carrier concentration at temperatures much in excess of 400 K exist in the literature. If we assume the linear temperature dependence of the gap to hold good at temperatures greater than 400 K, with $E_g(0) \approx 0.1 \text{ eV}$ (3) and inclusion of the T^3 term in the exponent term (Eq. [9]), we get 0.32 eV for the enthalpy associated with K_i . This value is lower than the value of 0.57 eV found from the present investigation expressions [5] and [7]). The possible nonparabolicity of the bands at the higher temperatures and a nonnegligible temperature dependence of the effective masses of carriers may account for the higher enthalpy associated with K_i given by expression [7].

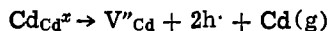
The dependence of the calculated hole concentrations in the cooled crystals on the value of K''_{VHg} can be judged by the inspection of Eq. [4] which indicates that for crystals which are intrinsic at the annealing temperature, the second term on the left-hand side dominates, with the result that the hole concentration in the cooled crystals is proportional to the value of K''_{VHg}/K_i . As a result it is not hard to realize that for given values of K_i the hole concentrations in the cooled crystals depend on K''_{VHg} in just the opposite way as they did with K_i for fixed K''_{VHg} values. Thus, just as $\pm 25\%$ variations in K_i did not adversely affect the calculations (Fig. 9), we believe similar variations can be tolerated in the value of K''_{VHg} .

From the present work the enthalpy for the reaction



has been established to be 2.24 eV.

For comparison with CdTe, the enthalpy associated with the reaction



is evaluated to be 4.72 eV (15). The higher enthalpy associated with a similar defect reaction for CdTe is reasonable in view of the fact that CdTe has a larger melting point and bandgap than $\text{Hg}_{0.8}\text{Cd}_{0.2}\text{Te}$ and, hence, stronger bonding.

Table III summarizes the values of some of the mass action constants defined in Table I. Included in the table are the values of K_i and K''_{VHg} applicable for $T = 400^\circ\text{--}655^\circ\text{C}$ as well as the K_i value applicable for $T = 27^\circ\text{--}400^\circ\text{C}$.

The mass action constants K_i and K''_{VHg} established from the present work can explain the results on indium-doped (31), iodine-doped (32) and phosphorus-doped $\text{Hg}_{0.8}\text{Cd}_{0.2}\text{Te}$ (33) satisfactorily.

Defect isotherms for undoped $\text{Hg}_{0.8}\text{Cd}_{0.2}\text{Te}$.—Once the values of K_i and K''_{VHg} are known, it is possible to calculate the concentrations of various defects as a function of p_{Hg} at any given temperature. Such a defect isotherm for $T = 500^\circ\text{C}$ is shown in Fig. 10. As can be seen from the figure, the crystal is essentially intrinsic except at low Hg pressures at higher temperatures where native acceptor defects begin to become comparable in concentration to intrinsic carriers.

Hole concentration in undoped $\text{Hg}_{0.8}\text{Cd}_{0.2}\text{Te}$ under Hg-saturated and Te-saturated conditions.—The highest and the lowest Hg pressures in the experimental data indicated by arrows in Fig. 2, correspond to the Hg pressure under Hg-saturated conditions and the Hg pressure under Te-saturated conditions, respectively (8-10). Figure 11 shows the hole concentration variation in the cooled crystals as a function of temperature of equilibration for Hg-saturated and Te-saturated conditions. The temperature dependences of the hole concentration are given by

$[h \cdot]$ (Hg saturated)

$$= 1.54 \times 10^{24} \exp(-1.13 \text{ eV}/kT) \text{ cm}^{-3}$$

and

$[h \cdot]$ (Te saturated)

$$= 2.36 \times 10^{20} \exp(-0.314 \text{ eV}/kT) \text{ cm}^{-3}$$

Isohole concentration plot for $\text{Hg}_{0.8}\text{Cd}_{0.2}\text{Te}$.—Knowledge of K_i and K''_{VHg} permits us to calculate hole concentrations in the cooled crystals as a function of the physicochemical conditions of preparation, namely, p_{Hg} and T . Such a plot is shown in Fig. 12. As can be seen from Fig. 12, the undoped material is p-type throughout the existence region for all temperatures as long as the residual foreign acceptor concentration is greater than the residual foreign donor concentration in the crystals. This figure is different from the isocarbrier concentration plot reported in Ref. (2, 4) where

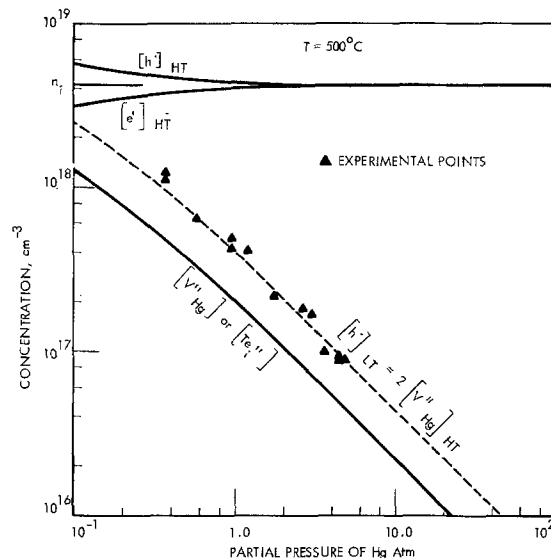


Fig. 10. Calculated defect concentrations as a function of the partial pressure of Hg at the equilibration temperature of 500°C ; dashed line represents the calculated hole concentration in the cooled crystals at 77 K ; experimental points are also shown for comparison.

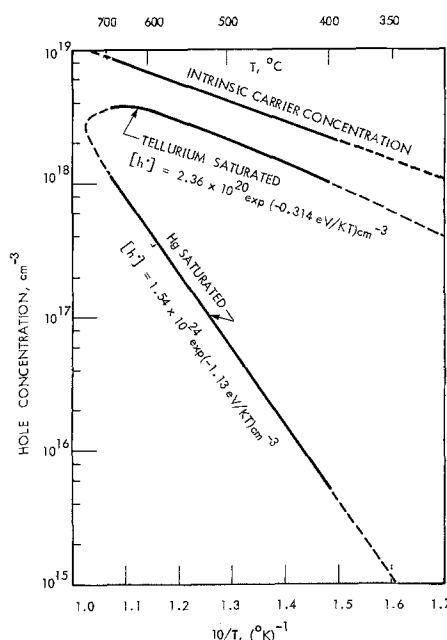


Fig. 11. Calculated hole concentration lines at 77 K as a function of temperature for undoped $\text{Hg}_{0.8}\text{Cd}_{0.2}\text{Te}$ equilibrated in Hg-saturated and Te-saturated conditions and quenched to room temperature. Calculations for temperature ranges outside the experimental work reported in this paper are shown dashed; intrinsic carrier concentration as a function of temperature is also shown.

p-type to n-type conversion was attributed to native donor defects. It can also be seen that the highest deviation from stoichiometry (or the highest hole concentration in the cooled crystals) attainable in undoped $\text{Hg}_{0.8}\text{Cd}_{0.2}\text{Te}$ is $< 3 \times 10^{18} \text{ cm}^{-3}$.

Defect isotherms for copper-doped $\text{Hg}_{0.8}\text{Cd}_{0.2}\text{Te}$.—With the assumption that all of the electrically active copper is present as Cu'_{Hg} , defect concentrations as a function of the electrically active copper concentration and p_{Hg} can be calculated. As before, we define high temperature and low temperature states of the crystal using subscripts HT and LT, respectively. The complete electroneutrality condition and the copper balance equation are

Table III. Values of the parameters for the equilibrium constants $K = K_0 \exp(-H/kT)$ defined in Table I

| Equilibrium constant | K_0 (Site Fr, atm) | H (eV) | Source |
|--|-----------------------|----------|--|
| 1. K_i | 5.77×10^{-4} | 0.57 | This work ($400^\circ\text{--}655^\circ\text{C}$) |
| 2. K''_{VHg} | 7.9×10^2 | 2.24 | |
| 3. K_i | 1.4×10^{-5} | 0.354 | ($27^\circ\text{--}400^\circ\text{C}$) |
| 4. $K_{\text{Hg}_{0.8}\text{Cd}_{0.2}\text{Te}}$ | 2.75×10^9 | 2.06 | Ref. (10) |
| 5. K_{Hg} | 7.84×10^4 | 0.62 | Ref. (8) |
| 6. K_{Te} | 1.82×10^6 | 1.27 | |

There are 1.26×10^{22} molecules/ cm^3 in $\text{Hg}_{0.8}\text{Cd}_{0.2}\text{Te}$.

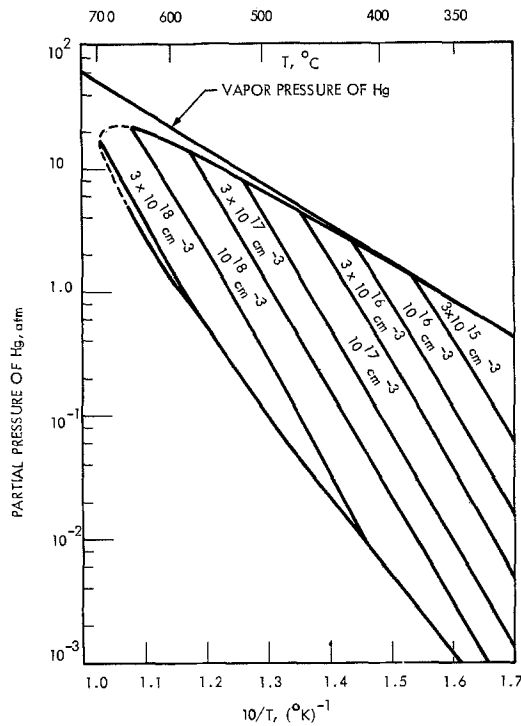


Fig. 12. Calculated isohole concentration lines at 77 K for $\text{Hg}_{0.8}\text{Cd}_{0.2}\text{Te}$ as a function of the partial pressure of Hg and temperature of equilibration.

$$[e']_{\text{HT}} + 2[V''_{\text{Hg}}]_{\text{HT}} + [\text{Cu}'_{\text{Hg}}] = [h']_{\text{HT}} \quad [10]$$

and

$$[\text{Cu}'_{\text{Hg}}]_{\text{HT}} = [\text{Cu}_{\text{tot}}]_{\text{HT}} \quad [11]$$

In terms of the mass action constants K_i and K''_{VHg} , the electroneutrality condition is rewritten as

$$(K_i/[h'])_{\text{HT}} + 2(K''_{\text{VHg}}/[h']^2 p_{\text{Hg}})_{\text{HT}} + [\text{Cu}_{\text{tot}}] = [h']_{\text{HT}} \quad [12]$$

or

$$[h']_{\text{HT}}^3 - [h']_{\text{HT}}^2 [\text{Cu}_{\text{tot}}] - K_i [h']_{\text{HT}} = 2(K''_{\text{VHg}}/p_{\text{Hg}})_{\text{HT}} \quad [13]$$

In the cooled crystals, the hole concentration is given by

$$[h']_{\text{LT}} = 2[V''_{\text{Hg}}]_{\text{HT}} + [\text{Cu}_{\text{Hg}}]_{\text{HT}} = 2[V''_{\text{Hg}}]_{\text{HT}} + [\text{Cu}_{\text{tot}}]_{\text{HT}} \quad [14]$$

or, expressing $[V''_{\text{Hg}}]$ in terms of K''_{VHg} and $[h']$, we get

$$[h']_{\text{LT}} = (2K''_{\text{VHg}}/[h']^2 p_{\text{Hg}})_{\text{HT}} + [\text{Cu}_{\text{tot}}]_{\text{HT}} \quad [15]$$

With the knowledge of the mass action constants K_i and K''_{VHg} established for the undoped crystals, defect concentrations ($[V''_{\text{Hg}}]$, $[h']_{\text{HT}}$, $[h']_{\text{LT}}$, etc.) as a function of copper concentration for a fixed p_{Hg} or as a function of p_{Hg} for fixed copper concentration can be calculated from Eq. [13] and [15]. Figure 13 shows the defect isotherm for $T = 500^\circ\text{C}$ and $p_{\text{Hg}} = 3$ atm as a function of the total copper concentration in the crystal. Similarity between Fig. 8 and 13 is to be noted. While Fig. 8 is drawn with approximation to the neutrality condition, Fig. 13 has been drawn with the consideration of the complete electroneutrality condition.

Imperfect quench for heavily copper-doped samples.—The electrically active copper concentration in various samples as inferred from the Hall effect measurements was found to be lower than the total copper concentration in the samples inferred from atomic absorption analysis (Table IV). From arguments in the previous sections, compensation by native donor de-

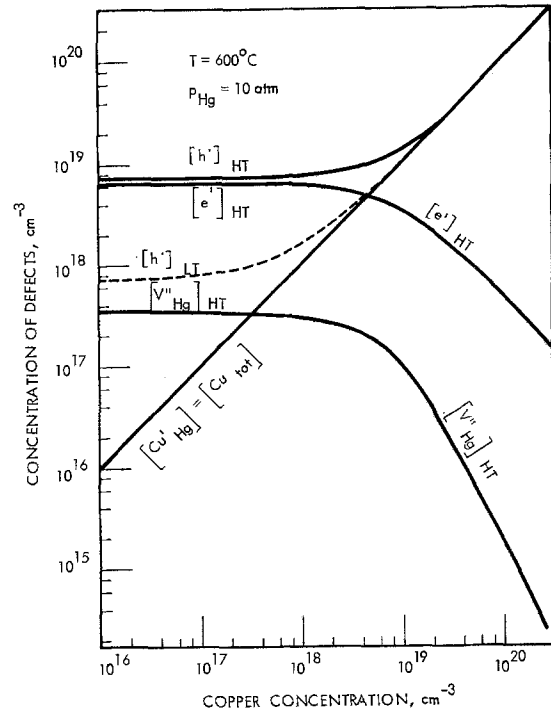


Fig. 13. Calculated defect concentrations as a function of the electrically active copper concentration in the crystals at the equilibration temperature of 500°C and $p_{\text{Hg}} = 3$ atm; dashed line corresponds to the calculated hole concentration in the cooled crystals at 77 K.

fects or by copper interstitials (acting as donors) is ruled out as the explanation. On the other hand, precipitation of copper during quenching or the solubility limit of copper at the equilibration temperatures can explain the discrepancy. If the explanation is one of the solubility limit, it is hard to reason why samples having total copper concentration less than 10^{19} cm^{-3} also show electrically active copper less than the total amount of chemically inferred copper concentrations. Owing to the high diffusivity of Cu in $\text{Hg}_{1-x}\text{Cd}_x\text{Te}$ (6, 7), we are inclined to believe that precipitation of copper as CuTe or Cu_2Te during quenching results in the electrically active copper (as found by Hall effect measurements) to be less than that obtained by chemical analysis. The fact that the fraction of electrically active copper decreases for higher and higher copper concentrations (as determined by chemical analysis) also supports the view that precipitation occurs during quenching since the diffusion distance between copper atoms for precipitation to occur can be expected to decrease as $[\text{Cu}_{\text{tot}}]^{-3}$. Efforts to improve the quenching efficiency by breaking open the ampuls and quenching the samples directly in water did not result in any improvement. It appears that the high diffusivity of copper results in an imperfect quench from the equilibration temperature. If we believe that precipitation occurs during quenching, the solubility of electrically

Table IV. Comparison of the concentrations of electrically active copper and the total amount of copper (as determined from atomic absorption analysis) for samples doped with copper at 500° and 600°C

| Temperature ($^\circ\text{C}$) | Total copper concentration (cm^{-3}) (atomic absorption) | Electrically active copper concentration (cm^{-3}) (Hall effect) |
|----------------------------------|---|---|
| 500 | 3.4×10^{20} | 10^{19} |
| 500 | 1.6×10^{19} | 5×10^{18} |
| 500 | 8.7×10^{18} | 4.3×10^{18} |
| 600 | 2.2×10^{21} | 5×10^{19} |
| 600 | 4.8×10^{20} | 1.3×10^{19} |
| 600 | 3×10^{20} | 10^{19} |
| 600 | 8.6×10^{19} | 4.8×10^{18} |

active copper at $T = 500^\circ\text{--}600^\circ\text{C}$ appears to be in excess of 10^{20} cm^{-3} .

Conclusion

Lattice defect models for undoped and copper-doped $\text{Hg}_{0.8}\text{Cd}_{0.2}\text{Te}$ have been established via Hall effect and mobility measurements on crystals equilibrated under different partial pressures of Hg at high temperatures and quenched to room temperature. According to the models, native donor defects are negligible in concentration, native acceptor defects are doubly ionized, and copper acts as a single acceptor occupying Hg lattice sites. Equilibrium constants for the intrinsic excitation constant, as well as the incorporation of the doubly ionized native acceptor defects, have been established.

Acknowledgments

The author wishes to thank J. A. Carruthers of NASA for his interest in this work. Thanks are due to J. L. Schmit for making variable temperature Hall effect measurements for one of the undoped samples. Technical assistance by J. Donovan and P. Crickard with the experimental portion of the work is greatly appreciated. Thanks are also due to D. A. Nelson for many fruitful discussions on the calculations of hole mobility in these alloys. This work was supported by NASA under Contract NAS8-33245.

Manuscript submitted Nov. 18, 1980; revised manuscript received ca. July 23, 1981. This was Paper 588 presented at the Los Angeles, California, Meeting of the Society, Oct. 14-19, 1979.

Any discussion of this paper will appear in a Discussion Section to be published in the June 1982 JOURNAL. All discussions for the June 1982 Discussion Section should be submitted by Feb. 1, 1982.

Publication costs of this article were assisted by Honeywell Electro-Optics Center.

APPENDIX A

Calculations of Hole Mobility at 77 K in Undoped and Copper-Doped $\text{Hg}_{0.8}\text{Cd}_{0.2}\text{Te}$

The decrease of hole mobility at 77 K with an increase in the hole concentration in the undoped crystals (Fig. 4) indicates that the contribution of ionized impurity scattering to the mobility at 77 K is not negligible.

For a nondegenerate semiconductor with parabolic bands, the mobility due to ionized impurity scattering as given by the Brooks-Herring expression (21) is

$$\mu_i = 27^{1/2} \pi^{-3/2} (kT)^{3/2} (\epsilon_0 \epsilon_s)^2 (m_0)^{-1/2} (m^*/m_0)^{-1/2} \times N_I^{-1} \left\{ \ln(1+b) - \frac{b}{1+b} \right\}^{-1} \quad [\text{A-1}]$$

where

$$b = \frac{24m_0 (m^*/m_0) k^2 (\epsilon_0 \epsilon_s)}{e^2 \hbar^2 p'} \quad [\text{A-2}]$$

and

$$p' = p + (N_A - N_D - p) (p + N_D) / N_A \quad [\text{A-3}]$$

In expressions [A-1], [A-2], and [A-3], k is the Boltzmann's constant, T is the temperature, ϵ_0 is the free space permittivity, ϵ_s is the static dielectric constant, m_0 is the free electron mass, (m^*/m_0) is the effective mass ratio of holes, N_I is the number of scattering centers given by the total number of ionized donors and acceptors, e is the electronic charge, and \hbar is Planck's constant. With $T = 77\text{ K}$, (m^*/m_0) (holes) = 0.7 (34). $\epsilon_s = 17.5$ (3) the expression for the mobility due to ionized impurity scattering becomes

$$\mu_i = 8 \times 10^{20} N_I^{-1} \left\{ \ln(1+b) - \frac{b}{1+b} \right\}^{-1} \quad [\text{A-4}]$$

and

$$b = 9.42 \times 10^{18} / p' \quad [\text{A-5}]$$

In general

$$N_I = ([A'] + [D']) + 4([A''] + [D'']) + 9([A'''] + [D''']) + \dots \quad [\text{A-6}]$$

where $[A']$, $[A'']$, $[A''']$, etc. are the concentrations of the singly charged, doubly charged, and triply charged acceptors; a similar definition holds for the donor concentrations $[D']$, $[D'']$, $[D''']$, etc. The multiplying factors of 4, 9, etc. in Eq. [A-6] arise because the centers are doubly ($z = 2$) and triply ($z = 3$) charged, etc. For the case where the undoped and the copper-doped crystals are not compensated (as discussed in the main text) we have

$$N_I = [A'] + 4[A''] + \dots \quad [\text{A-7}]$$

Since the defects are completely ionized at 77 K in both the undoped and the copper-doped crystals (see main text for details), $p' = p$ (77 K) for the undoped as well as the copper-doped crystals. Using Eq. [A-4] and [A-5], μ_i was calculated as a function of p (77 K) for the case of (i) $N_I = [A'] = p$ (77 K) (dominance of singly charged centers) and (ii) $N_I = 4[A''] = 2p$ (77 K) (dominance of doubly charged centers).

The calculated mobilities due to ionized impurity scattering for the cases of the dominances of the singly charged centers and dominance of the doubly charged centers are shown as dashed lines in Fig. 4 and 5. Extrapolating the hole mobility due to lattice scattering to be $700\text{ cm}^2/\text{Vsec}$ at 77 K the overall hole mobility as a function of the hole concentration at 77 K was calculated by reciprocally combining the mobility due to ionized impurity scattering and that due to lattice scattering

$$1/\mu_{\text{TOT}} = \frac{1}{\mu_{\text{lattice}}} + \frac{1}{\mu_{\text{ionized}}} = \frac{1}{700} + \frac{1}{\mu_{\text{ionized}}} \quad [\text{A-8}]$$

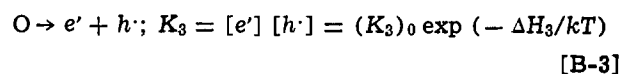
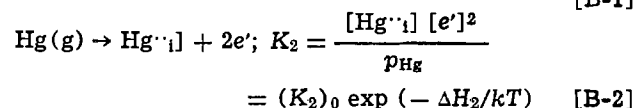
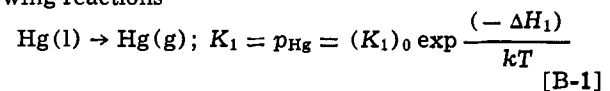
The calculated overall hole mobility as a function of the hole concentration is shown in Fig. 4 and 5 as solid lines.

APPENDIX B

Temperature Independence of the Native Donor Defect Concentration

Results of Reynolds *et al.* (23) on $\text{Hg}_{0.8}\text{Cd}_{0.2}\text{Te}$ and of Schmit and Stelzer (25) on $\text{Hg}_{0.6}\text{Cd}_{0.4}\text{Te}$ indicate that the crystals turn n-type below $300^\circ\text{--}350^\circ\text{C}$ under Hg-saturated conditions and the electron concentration under Hg-saturated conditions remains independent of the anneal temperature.

If the conversion is thought to be due to some sort of native donor defects, it remains to explain under what circumstances the temperature independence could arise. For an explanation of this we consider the following reactions



Two electroneutrality approximations can be considered:

$$\text{Case 1: } [e'] \approx [h'] = \sqrt{K_3}$$

$$\text{Case 2: } [e'] \approx 2[\text{Hg}\cdot\cdot\cdot]$$

Case 1: $[e'] = [h']$. From Eq. [B-2], $[\text{Hg}\cdot\cdot\cdot] = K_2 p_{\text{Hg}} / [e']^2$. Substituting $[e'] = [h'] = \sqrt{K_3}$ from [B-3] and for p_{Hg} from [B-1], we get

$$[\text{Hg}\cdot\cdot\cdot] = \frac{K_1 K_2}{K_3} = \frac{(K_1)_0 (K_2)_0}{(K_3)_0} \exp \left(\frac{-\Delta H_1 - \Delta H_2 + \Delta H_3}{kT} \right)$$

If $\Delta H_3 = \Delta H_1 + \Delta H_2$, $[\text{Hg}\cdot\cdot\cdot]$ will be independent of temperature and the electron concentration under Hg-saturated conditions will be independent of temperature in the cooled crystals.

Case 2: $[e'] \approx 2 [Hg\cdot\cdot_1]$

From [B-2],

$$[Hg\cdot\cdot_1] = K_2 p_{Hg}/[e']^2 \\ = K_2 p_{Hg}/4 [Hg\cdot\cdot_1]^2$$

or

$$[Hg\cdot\cdot_1] = (K_2 p_{Hg}/4)^{1/3} \\ = \left(\frac{(K_2)_0 (K_1)_0}{4} \right)^{1/3} \exp\left(\frac{-\Delta H_1 - \Delta H_2}{3kT} \right)$$

Thus if $\Delta H_1 = -\Delta H_2$, $[Hg\cdot\cdot_1]$ will be independent of temperature and the electron concentration in the cooled crystals under Hg-saturated conditions will also be independent of temperature.

It should be noted that while $Hg\cdot\cdot_1$ are considered for the native donor defects here, the arguments are similar if $V\cdot\cdot_{Te}$ are considered instead.

REFERENCES

- W. D. Lawson, S. Nielson, E. H. Putley, and A. S. Young, *J. Phys. Chem. Solids*, **9** (1959).
- D. Long and J. L. Schmit, "Semiconductors and Semimetals," Vol. 5, R. K. Willardson and A. C. Beer, Editors, p. 234, Academic Press, New York (1970).
- R. Dornhaus and G. Nimtz, "Solid State Physics," Vol. 78, Springer-Verlag, New York (1976).
- R. A. Farrar, G. J. Gillham, R. Bartlett, and M. Quelch, *J. Mater. Sci.*, **12**, 836 (1977).
- R. F. Brebrick and J. P. Schwartz, *J. Electron. Mater.*, **9**, 485 (1980).
- A. I. Andrievskii, A. S. Teodorovich, and A. D. Shneider, *Sov. Phys. Semicond.*, **7**, 1112 (1974).
- E. S. Johnson and J. L. Schmit, *J. Electron. Mater.*, **6**, 25 (1977).
- R. F. Brebrick and A. J. Strauss, *J. Phys. Chem. Solids*, **26**, 989 (1965).
- J. P. Schwartz, T. Tung, and R. F. Brebrick, *This Journal*, **128**, 438 (1981).
- T. Tung, L. Golonka, and R. F. Brebrick, *ibid.*, **128**, 451 (1981).
- L. J. van der Pauw, *Philips Tech. Rev.*, **20**, 220 (1959).
- R. A. Smith, "Semiconductors," Cambridge University Press (1968).
- F. A. Kröger and H. J. Vink, "Solid State Physics III," F. Seitz and D. Turnbull, Editors, p. 307, Academic Press, New York (1956).
- F. A. Kröger, "The Chemistry of Imperfect Crystals," second revised edition, Vol. 2, Chap. 14-16, North Holland (1974).
- S. S. Chern, H. R. Vydyanath, and F. A. Kroger, *J. Solid State Chem.*, **14**, 33 (1975).
- S. S. Chern and F. A. Kröger, *ibid.*, **14**, 44 (1975).
- D. de Nobel, *Philips Res. Rep.*, **14**, 361 (1959).
- F. A. Selim, V. Swaminathan, and F. A. Kröger, *Phys. Status Solidi A*, **29**, 465 (1975).
- V. Swaminathan, F. A. Selim, and F. A. Kröger, *ibid.*, **30**, 721 (1975).
- G. Brouwer, *Philips Res. Rep.*, **9**, 366 (1954).
- H. Brooks, *Phys. Rev.*, **83**, 879 (1952); *Adv. Electron. Electron Phys.*, **7**, 156 (1955).
- H. R. Vydyanath, J. Danovan, and D. A. Nelson, *This Journal*, **128**, 2625 (1981).
- R. A. Reynolds, M. J. Brau, H. Kraus, and R. T. Bate, *J. Phys. Chem. Solids*, **32**, Suppl. 1, 511 (1971).
- B. E. Bartlett, P. Capper, J. E. Harris, and M. J. T. Quelch, *J. Cryst. Growth*, **49**, 600 (1980).
- J. L. Schmit and E. L. Stelzer, *J. Electron. Mater.*, **7**, 65 (1978).
- J. D. Wiley and R. N. Dexter, *Phys. Rev.*, **181**, 1181 (1939).
- M. W. Scott, *J. Appl. Phys.*, **40**, 4077 (1969).
- J. L. Schmit and E. L. Stelzer, *ibid.*, **40**, 4865 (1969).
- Y. Nemrousky and E. Finkman, *ibid.*, **50**, 8107 (1979).
- C. Verie, *Phys. Status Solidi*, **17**, 889 (1966).
- H. R. Vydyanath, *This Journal*, **128**, 2619 (1981).
- H. R. Vydyanath and F. A. Kröger, *J. Electron. Mater.*, **10**, No. 1 (1982).
- H. R. Vydyanath and R. C. Abbott, Submitted to *J. Appl. Phys.*
- M. W. Scott, E. L. Stelzer, and R. J. Hager, *J. Appl. Phys.*, **47**, 1408 (1976).

Lattice Defects in Semiconducting Hg_{1-x}Cd_xTe Alloys

II. Defect Structure of Indium-Doped Hg_{0.8}Cd_{0.2}Te

H. R. Vydyanath*

Honeywell Electro-Optics Center, Lexington, Massachusetts 02173

ABSTRACT

Hall effect measurements were carried out on indium-doped Hg_{0.8}Cd_{0.2}Te crystals quenched to room temperature subsequent to equilibration at 500° and 600°C under various partial pressures of Hg. All the indium-doped crystals were n-type under moderate to high partial pressures of Hg whereas they were p-type at very low Hg pressures. The concentration of electrons obtained in the cooled crystals was lower than the intrinsic carrier concentration at the equilibration temperatures. Also the electron concentration was much lower than the indium concentration in the crystals and was found to increase with increasing Hg pressures at the equilibration temperatures and with increase in the total indium present in the crystals. These inferences have led to a defect model according to which most of the indium is incorporated as In₂Te₃(S) dissolved in Hg_{0.8}Cd_{0.2}Te(S) with only a small fraction of indium acting as single donors occupying Hg lattice sites. Based on such a model, calculated electron concentrations in the cooled crystals as a function of indium concentration and partial pressure of Hg are in agreement with the experimentally observed values.

The role of indium as a donor and its influence on the native defect structure has been investigated in

CdS (1-2) and CdTe (3-4). However, such a systematic investigation into the mode of incorporation of indium and its influence on the native defects has not so far been carried out for Hg_{1-x}Cd_xTe alloys. The defect structure of undoped Hg_{0.8}Cd_{0.2}Te, the thermo-

* Electrochemical Society Active Member.

Key words: defect, indium doping, Hg_{1-x}Cd_xTe, electron mobility, semiconductors.

dynamic constants for the incorporation of the native acceptor defects, and the intrinsic excitation constant in $\text{Hg}_{0.8}\text{Cd}_{0.2}\text{Te}$ have been established in the preceding paper (5) hereafter referred to as part I. The present work was undertaken to study the behavior of indium in $\text{Hg}_{0.8}\text{Cd}_{0.2}\text{Te}$ as a function of the physicochemical conditions of preparation (p_{Hg} , T , indium concentration, etc.) and to explain the properties of the indium-doped crystals with the knowledge of the defect structure of the undoped crystals (5).

Experimental

Indium was evaporated onto the surface of the undoped $\text{Hg}_{0.8}\text{Cd}_{0.2}\text{Te}$ crystals ($x = 0.2 \pm 0.005$) and the indium was diffused in at 600°C and $p_{\text{Hg}} = 10$ atm and at 500°C and $p_{\text{Hg}} = 3$ atm. Diffusion times of 24 hr at 600°C and 7 days at 500°C into samples of thickness ≤ 0.04 cm were found to be adequate for the homogeneous diffusion of indium. The concentration of indium in each sample was determined from atomic absorption analysis carried out by Photometrics, Incorporated, Lexington, Massachusetts. The residual impurity concentration in the starting undoped $\text{Hg}_{0.8}\text{Cd}_{0.2}\text{Te}$ was $\leq 10^{16}$ cm^{-3} . The thicknesses of the samples were minimized as much as possible in order to improve the quenching efficiency from the equilibration temperatures as well as to assure thermodynamic equilibrium within reasonable equilibration times. The equilibration procedure in various Hg atmospheres is similar to that described in part I. Subsequent to the equilibration, the samples were quenched to room temperature; in a few cases the samples were air cooled to room temperature from the equilibration temperatures. The samples were lapped, polished, and etched in Br-methanol solution. Hall effect and electrical resistivity measurements were made using the van der Pauw method (6). Magnetic field strengths of 400 and 4000G were used for the Hall effect measurements.

Results

As mentioned in part I, only those Hall effect results which did not vary with the magnetic field and thus showed no mixed-type conduction were used in evaluating the carrier concentrations in the samples using the expression

$$n = \frac{1}{R_{\text{Hq}}}$$

The Hall effect data on all the samples doped to reasonable concentrations of indium and annealed at medium to high partial pressures of Hg showed n-type conductivity and the electron concentration in the samples at 77 and 300 K did not vary much, indicating that the indium was all ionized at 77 K. Figures 1 and 2 show the electron concentration in the cooled crystals as a function of the total indium present in the samples at $T = 500^\circ$ and 600°C for various partial pressures of Hg. From the figures, it is apparent that the electron concentration in the samples increases with an increase in the total indium concentration in the samples and also increases as the partial pressure of Hg at the equilibration temperatures increases. It is to be noted that although the electron concentration is a function of the total indium present in the crystals, the electron concentration is much lower than the total amount of indium present in the crystals.

Figure 3 shows the electron mobility at 77 K in various indium-doped samples as a function of the electron concentration. These mobilities are lower than values reported for $\text{Hg}_{0.8}\text{Cd}_{0.2}\text{Te}$ samples containing low donor concentrations (7).

Figure 4 shows a comparison of the electron concentration obtained at 77 K as a function of the partial pressure of Hg at 500°C for crystals that were doped with various indium concentrations and were air

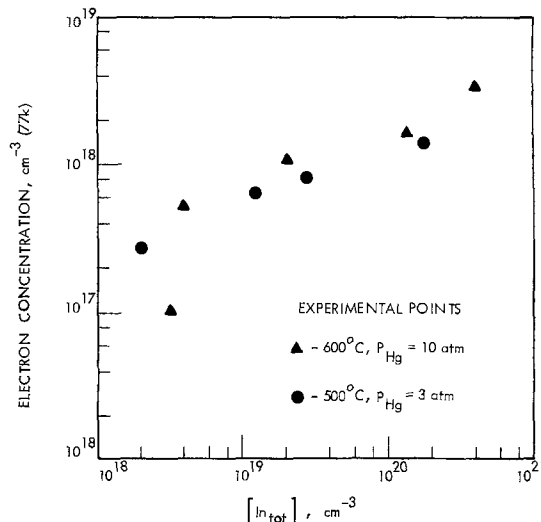


Fig. 1. Electron concentration at 77 K as a function of the total indium concentration for $\text{Hg}_{0.8}\text{Cd}_{0.2}\text{Te}$ crystals annealed at 500° and 600°C under the indicated partial pressures of Hg and quenched to room temperature.

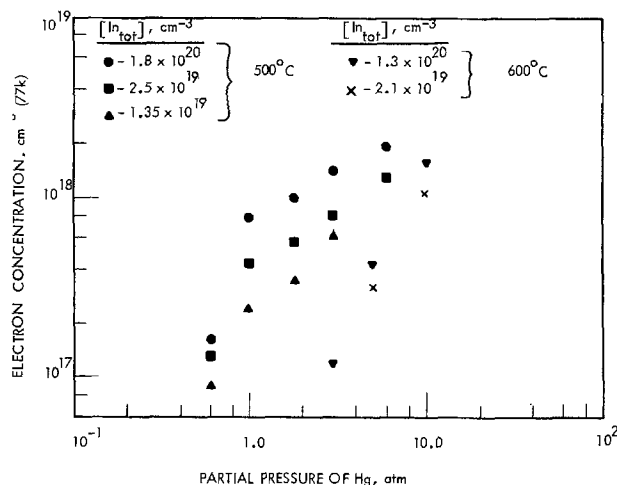


Fig. 2. Electron concentration at 77 K as a function of the partial pressure of Hg for $\text{Hg}_{0.8}\text{Cd}_{0.2}\text{Te}$ crystals doped with various amounts of indium and annealed at 500° and 600°C and quenched to room temperature.

cooled or quenched to room temperature. It appears from the results that higher electron concentrations are obtained in the air-cooled samples than in the quenched samples, the deviations between the two sets of samples being greater at lower Hg pressures.

Discussion

The approach utilized in arriving at a defect model for the indium-doped $\text{Hg}_{0.8}\text{Cd}_{0.2}\text{Te}$ is similar to that used for the undoped and copper-doped $\text{Hg}_{0.8}\text{Cd}_{0.2}\text{Te}$ in part I. Also any defect model that is established to explain the experimental results in the indium-doped crystals should be consistent with the observations in the undoped and the copper-doped crystals of part I.

Choice of a defect model.—Based on the value of the intrinsic excitation constant K_i arrived at for $\text{Hg}_{0.8}\text{Cd}_{0.2}\text{Te}$ (part I) for temperatures between 400° – 655°C , data shown in Fig. 1 and 2 indicate that the electron concentration obtained in the cooled crystals is much less than the intrinsic carrier concentration at the equilibration temperatures.

Three different models can be considered to explain the electron concentration data shown in Fig. 1 and 2.

In the first model considered, a fraction of the indium is assumed to be present as singly positively

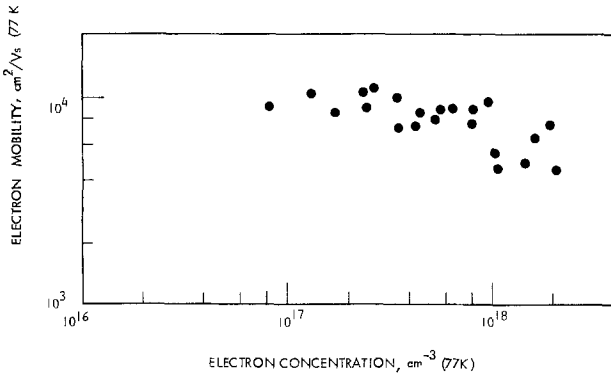
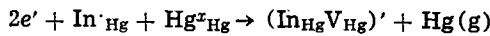


Fig. 3. Electron mobility at 77 K as a function of the electron concentration in indium-doped $Hg_{0.8}Cd_{0.2}Te$ crystals.

charged donors occupying Hg lattice sites while the rest of it is assumed to be present as negatively charged associates of singly positively charged indium on Hg lattice sites and doubly negatively charged native acceptor defects. Most of the indium is assumed to be self-compensated as given by the electro-neutrality approximation

$$[In'_{Hg}] = [(In_{Hg}V_{Hg})'] = [In_{tot}]/2$$

For such a model the dependence of $[e']$ on $[In_{tot}]$ and p_{Hg} is inferred from the reaction



and the mass action constant

$$K_{(In_{Hg}V_{Hg})} = [(In_{Hg}V_{Hg})'] p_{Hg} / [e']^2 [In'_{Hg}] \quad [1]$$

with

$$[(In_{Hg}V_{Hg})'] = [In'_{Hg}] = [In_{tot}]/2$$

$$[e'] \propto [In_{tot}]^0 p_{Hg}^{1/2} \text{ from [1]}$$

Although this model qualitatively explains the weak donor activity of indium it predicts an independence of electron concentration as a function of the total indium present in the samples, contrary to the results shown in Fig. 1 and 2.

In the second model considered, most of the indium is assumed to be present as neutral triplets $(In_{Hg}V_{Hg}In_{Hg})^x$ formed by the association of two singly positively charged indium donor species on Hg lattice

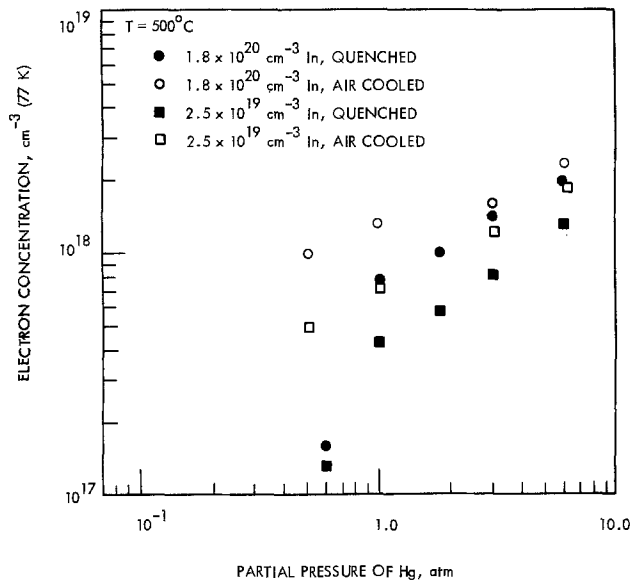
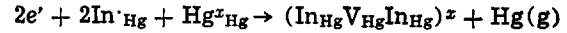


Fig. 4. Electron concentration at 77 K as a function of the partial pressure of Hg for crystals doped with different indium concentrations and quenched or air cooled subsequent to equilibration at 500°C.

sites with a doubly negatively charged native acceptor defect; a small fraction of the indium is assumed to be present unassociated on Hg lattice sites acting as donors.

The reaction of interest is



and the mass action relation is given by

$$K_{(In_{Hg}V_{Hg}In_{Hg})^x} = [(In_{Hg}V_{Hg}In_{Hg})^x] p_{Hg} / [e']^2 [In'_{Hg}]^2 \quad [2]$$

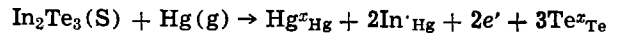
Since we know that the electron concentration obtained in the cooled crystals is less than the intrinsic carrier concentration at the equilibration temperatures, the electroneutrality condition at the equilibration temperatures can be approximated by

$$[e'] = [h'] = \sqrt{K_i}$$

and for $[(In_{Hg}V_{Hg}In_{Hg})^x] = [In_{tot}]/2$ as the approximation to the indium balance equation $[In'_{Hg}] \propto [In_{tot}]^{1/2} p_{Hg}^{1/2}$ at the equilibration temperatures. Although this model qualitatively explains the variation of electron concentration as a function of the indium in the crystals and the partial pressure of Hg at the equilibration temperatures, the calculated electron concentration in the cooled crystals considering the complete neutrality condition shows a much steeper dependence on p_{Hg} than observed experimentally. Also, the model predicts the crystals will turn p-type even at Hg pressures close to saturation pressures, contrary to the results of Fig. 2.

The third model considered is one where most of the indium is assumed to be present as In_2Te_3 dissolved in $Hg_{0.8}Cd_{0.2}Te$, with a small fraction of In on Hg lattice sites acting as donors. The dependence of the electron concentration on the indium in the crystals and p_{Hg} can be inferred from the reaction describing the incorporation of In_{Hg} from the $In_2Te_3(S)$ dissolved in $Hg_{0.2}Cd_{0.2}Te$.

The reaction of interest is



The mass action relation is given by

$$K_{(In_2Te_3-In'_{Hg})} = [In'_{Hg}]^2 [e']^2 / a_{In_2Te_3} p_{Hg} \quad [3]$$

where $a_{In_2Te_3}$ is the activity of $In_2Te_3(S)$.

For

$$[e'] = [h'] = \sqrt{K_i} \gg [In'_{Hg}]$$

from relation [3]

$$[In'_{Hg}] \propto a_{In_2Te_3}^{1/2} p_{Hg}^{1/2} \propto \gamma_{In_2Te_3}^{1/2} X_{In_2Te_3}^{1/2} p_{Hg}^{1/2} \quad [4]$$

where $\gamma_{In_2Te_3}$ and $X_{In_2Te_3}$ stand for the activity coefficient and the mol fraction of $In_2Te_3(S)$ dissolved in $(Hg_{0.8}Cd_{0.2})Te(S)$.

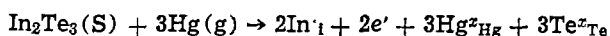
In the cooled crystals at 77 K

$$[e']_{77K} = [In'_{Hg}] - 2[V''_{Hg}] \propto X_{In_2Te_3}^{1/2} p_{Hg}^{1/2} \propto [In_{tot}]^{1/2} p_{Hg}^{1/2} \quad [5]$$

Hence, the dependence of e' in the cooled crystals on the indium concentration in the samples and the partial pressure of Hg at the equilibration temperatures is explainable.

A defect situation where the crystal is saturated with the dopant has been observed for iodine-doped CdS (8) where $CdI_2(S)$ was present as a pure second phase; however, the concentration of the iodine donor species on sulfur lattice sites was independent of the activity of $CdI_2(S)$, a_{CdI_2} since a_{CdI_2} was taken to be unity for pure $CdI_2(S)$. In the present case, if the $In_2Te_3(S)$ does not dissolve in $Hg_{0.8}Cd_{0.2}Te(S)$ but re-

mains as a pure second phase, the activity of $\text{In}_2\text{Te}_3(\text{S})$ becomes unity and the electrically active fraction of indium $[\text{In}'_{\text{Hg}}]$ becomes independent of the activity of In_2Te_3 and in turn becomes independent of the amount of $\text{In}_2\text{Te}_3(\text{S})$ or the total amount of indium present in the crystals (Eq. [3]-[5]) contrary to our experimental observations (Fig. 1 and 2). However, if $\text{In}_2\text{Te}_3(\text{S})$ dissolves in $\text{Hg}_{0.8}\text{Cd}_{0.2}\text{Te}(\text{S})$, the activity of $\text{In}_2\text{Te}_3(\text{S})$, $a_{\text{In}_2\text{Te}_3}$, becomes a variable, increasing with increasing amount of the dissolved $\text{In}_2\text{Te}_3(\text{S})$ and reaching a value of unity when the solubility limit is reached, and $\text{In}_2\text{Te}_3(\text{S})$ becomes a pure second phase. For such a situation, the electrically active fraction of indium $[\text{In}'_{\text{Hg}}]$ becomes a function of the activity of $\text{In}_2\text{Te}_3(\text{S})$ and thereby a function of the amount of $\text{In}_2\text{Te}_3(\text{S})$ or the total amount of indium present in the crystals (Eq. [3]-[5]); the electron concentration in the cooled crystals which is directly proportional to the amount of the electrically active indium becomes a function of the total indium present in the crystals (Eq. [5]). Hence the dissolution of $\text{In}_2\text{Te}_3(\text{S})$ in $\text{Hg}_{0.8}\text{Cd}_{0.2}\text{Te}(\text{S})$ is an essential requirement in explaining the dependence of the electron concentration in the cooled crystals on the total indium present in the crystals. It should also be mentioned at this stage that if indium in interstitial sites is considered to be the donor species instead of indium on Hg lattice sites the incorporation reaction is written as



and the mass action constant

$$K = [\text{In}'_i]^2 [e']^2 / a_{\text{In}_2\text{Te}_3} p_{\text{Hg}}^3$$

for an intrinsic crystal with $[e'] = [h'] = \sqrt{K_i}$

$$[\text{In}'_i] \propto p_{\text{Hg}}^{3/2} a_{\text{In}_2\text{Te}_3}^{1/2}$$

The electron concentration in the cooled crystals for such a situation can be expected to be dependent on p_{Hg} much more than experimentally observed. Also, such a model predicts that the crystals turn p-type at Hg pressures close to saturation pressures contrary to the experimental results (Fig. 1 and 2). Thus, in addition to the requirement that $\text{In}_2\text{Te}_3(\text{S})$ be in solid solution of $\text{Hg}_{0.8}\text{Cd}_{0.2}\text{Te}(\text{S})$ the requirement that the majority of the electrically active indium be present substitutionally on Hg lattice sites rather than in interstitial sites must also be satisfied in order to explain the experimental results.

The fact that the experimental results require that In_2Te_3 be in solution of $\text{Hg}_{0.8}\text{Cd}_{0.2}\text{Te}$ up to about 1-2 mol percent (m/o) is not unreasonable. HgTe, CdTe, and In_2Te_3 all have zinc blende structures with not too largely different lattice parameters (6.43Å for HgTe, 6.47Å for CdTe, and 6.15Å for In_2Te_3) and, in fact, it has been established by Woolley *et al.* (9) and Spencer (10) that amounts of up to 15 m/o In_2Te_3 dissolve in HgTe and the energy gap increases with increasing In_2Te_3 concentration somewhat significantly beyond about 5 m/o. We assume however, that in our experiments for In_2Te_3 concentration less than 1 m/o, the influence on the energy gap of $\text{Hg}_{0.8}\text{Cd}_{0.2}\text{Te}$ is negligible. The assumption appears justified since no drastic variation in the concentration of carriers is encountered with increasing indium concentration in the crystal. Pure In_2Te_3 is known to be p-type with an energy gap of 0.3 eV (10) and in fact one of the samples that was doped to 5×10^{21} atoms/cm³ of indium showed excessive In_2Te_3 formation and the sample was p-type.

Preliminary x-ray and Auger analysis data also seem to support the model of indium being present as $\text{In}_2\text{Te}_3(\text{S})$ dissolved in $\text{Hg}_{0.8}\text{Cd}_{0.2}\text{Te}(\text{S})$. Auger analysis of the surface of a sample containing greater than 10^{21} cm⁻³ of indium indicated the surface to be rich in

indium and tellurium and the composition corresponded to In_2Te_3 . X-ray analyses indicated evidence of lattice parameter changes with an increase in the concentration of indium from 3×10^{19} cm⁻³ to 3×10^{20} cm⁻³ with no evidence of the presence of a second phase, whereas clear evidence of the presence of a second phase was obtained in samples containing greater than 10^{21} cm⁻³ of indium. Although not entirely conclusive, these data seem to support the idea that $\text{In}_2\text{Te}_3(\text{S})$ is soluble in $\text{Hg}_{0.8}\text{Cd}_{0.2}\text{Te}$ from 1 to 5 m/o at 500°-600°C.

Analysis of the carrier concentration in the cooled crystals.—Denoting the high temperature defect state by subscript HT, the complete electroneutrality condition and the indium balance equation can be written as

$$[e']_{\text{HT}} + 2[V''_{\text{Hg}}]_{\text{HT}} = [\text{In}'_{\text{Hg}}]_{\text{HT}} + [h']_{\text{HT}} \quad [6]$$

and

$$[\text{In}'_{\text{Hg}}]_{\text{HT}} + 2[\text{In}_2\text{Te}_3]_{\text{HT}} = [\text{In}_{\text{tot}}] \quad [7]$$

Expressing all the quantities in the electroneutrality condition [6] in terms of the mass action constants defined in part I, we get

$$[e']_{\text{HT}} + 2K''_{\text{VHg}} [e']_{\text{HT}}^2 / K_i^2 p_{\text{Hg}} = [\text{In}'_{\text{Hg}}] + K_i / [e']_{\text{HT}}$$

or

$$2[e']_{\text{HT}}^3 K''_{\text{VHg}} / K_i^2 p_{\text{Hg}} + [e']_{\text{HT}}^2$$

$$- [\text{In}'_{\text{Hg}}] [e']_{\text{HT}} - K_i = 0 \quad [8]$$

Owing to the narrow bandgap of $\text{Hg}_{0.8}\text{Cd}_{0.2}\text{Te}$, the correctness of the assumption of $K_i = [e'] [h'] =$ constant for a fixed temperature for large donor or acceptor concentrations is arguable. Since all our experimental results have shown systematic variations of carrier concentrations as a function of the imposed physicochemical conditions in accordance with the mass action approach, we feel our assumption is a valid one.

In the crystals quenched to room temperature from the equilibration temperatures

$$[e']_{77\text{K}} = [\text{In}'_{\text{Hg}}]_{\text{HT}} - 2[V''_{\text{Hg}}]_{\text{HT}}$$

or

$$[e']_{77\text{K}} = [\text{In}'_{\text{Hg}}] - 2K''_{\text{VHg}} [e']_{\text{HT}}^2 / K_i^2 p_{\text{Hg}} \quad [9]$$

values of the mass action constants K_i and K''_{VHg} are given by (part I)

$$K_i = 9.16 \times 10^{40} \exp(-0.57 \text{ eV/KT}) \text{ cm}^{-6} \quad [10]$$

and

$$K''_{\text{VHg}} = 1.58 \times 10^{69} \exp(-2.24 \text{ eV/KT}) \text{ cm}^{-9} \text{ atm} \quad [11]$$

with the knowledge K''_{VHg} and K_i (Eq. [8]) gives $[e']_{\text{HT}}$ and $[V''_{\text{Hg}}]$ as a function of $[\text{In}'_{\text{Hg}}]$ for various partial pressures of Hg.

The product of the mass action constant defined by Eq. [3] and the activity of $\text{In}_2\text{Te}_3(\text{S})$, $K_{(\text{In}_2\text{Te}_3 - \text{In}'_{\text{Hg}}) a_{\text{In}_2\text{Te}_3}}$ and $[e']_{77\text{K}}$ are also immediately obtained as a function of $[\text{In}'_{\text{Hg}}]$ from Eq. [3] and [9], respectively. Comparison of the calculated $[e']_{77\text{K}}$ as a function of $[\text{In}'_{\text{Hg}}]$ with the experimental values of Fig. 1 gives the concentration of the electrically active fraction of indium as a function of the total indium present in the crystals as shown in Fig. 5. Values of $K_{(\text{In}_2\text{Te}_3 - \text{In}'_{\text{Hg}}) a_{\text{In}_2\text{Te}_3}}$ calculated earlier as a function of $[\text{In}'_{\text{Hg}}]$ can then be related to the total indium concentration in the crystals and in turn to the amount of In_2Te_3 present in the crystals from the indium balance Eq. [6]. Figure 6 shows $K_{(\text{In}_2\text{Te}_3 - \text{In}'_{\text{Hg}}) a_{\text{In}_2\text{Te}_3}}$ as a function of $[\text{In}_2\text{Te}_3]$ present in the crystals. Since the slope of the curves on the log-log scale is different from unity, it appears that the activity coefficient of $\text{In}_2\text{Te}_3(\text{S})$ dissolved in $\text{Hg}_{0.8}\text{Cd}_{0.2}\text{Te}(\text{S})$ is not constant, but varies with the amount of $\text{In}_2\text{Te}_3(\text{S})$. Once the values of $K_{(\text{In}_2\text{Te}_3 - \text{In}'_{\text{Hg}}) a_{\text{In}_2\text{Te}_3}}$ as a function of $\text{In}_2\text{Te}_3(\text{S})$ are

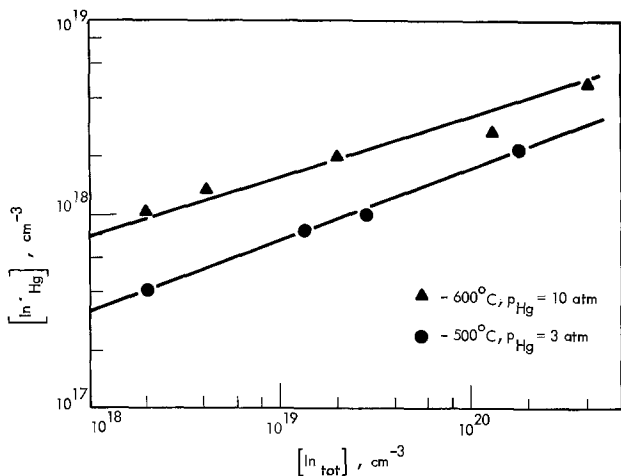


Fig. 5. Concentration of electrically active indium as a function of the total indium present in the crystals subsequent to equilibration at $500^\circ C, p_{Hg} = 3 \text{ atm}$ and at $600^\circ C, p_{Hg} = 10 \text{ atm}$.

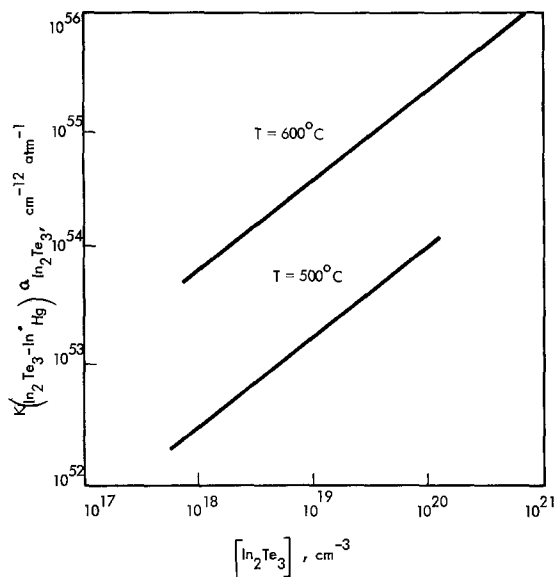


Fig. 6. Calculated value of the product of the mass action constant $K([In_2Te_3 - In \cdot_{Hg}])$ and the activity of $In_2Te_3(S)$ ($= [In \cdot_{Hg}]^2 [e']^2 / p_{Hg}$; expression [3] in the text) as a function of the concentration of In_2Te_3 present in the indium-doped crystals subsequent to equilibration at 500° and $600^\circ C$.

known from Fig. 6, it is possible to calculate $[e']_{77K}$, $[e']_{HT}$, $[V''_{Hg}]_{HT}$, $[In \cdot_{Hg}]$, and $[In_2Te_3]$ as a function of $[In_{tot}]$ and p_{Hg} from Eq. [3], [7], [8], and [9].

Figures 7 and 8 show the calculated defect concentrations at $T = 500^\circ C, p_{Hg} = 3 \text{ atm}$, and $T = 600^\circ C, p_{Hg} = 10 \text{ atm}$ as a function of the indium concentration in the crystals. Calculated values of the carrier concentrations in the cooled crystals are also shown along with the experimental values. The agreement between the calculated values and the experimental ones appears satisfactory. The figures also predict that the crystal is essentially intrinsic with most of the indium being present as In_2Te_3 with only a small fraction present as single donors occupying Hg lattice sites. The concentration of the native acceptor defects is essentially constant in the figures since the partial pressure of Hg is kept constant and the crystals are essentially intrinsic.

Figure 9 shows the calculated defect concentrations at $T = 500^\circ C$ as a function of the partial pressure of Hg for a fixed indium concentration in the crystal. It can be noticed from the figure that although the total indium concentration is fixed in the crystal, the amount of the electrically active indium varies as a function of the partial pressure of Hg as predicted from the in-

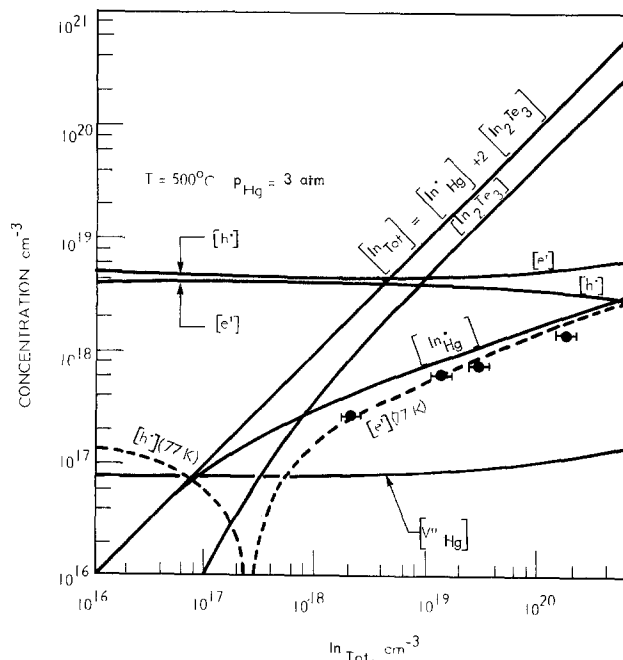


Fig. 7. Calculated defect concentrations ($[e']$, $[h \cdot]$, $[V''_{Hg}]$, $[In \cdot_{Hg}]$, and $[In_2Te_3]$) as a function of the total indium present in the indium-doped $Hg_{0.8}Cd_{0.2}Te$ crystals subsequent to equilibration at $500^\circ C$ and $p_{Hg} = 3 \text{ atm}$; dashed lines show the calculated carrier concentrations obtained in the cooled crystals at $77 K$; experimental points are also shown for comparison.

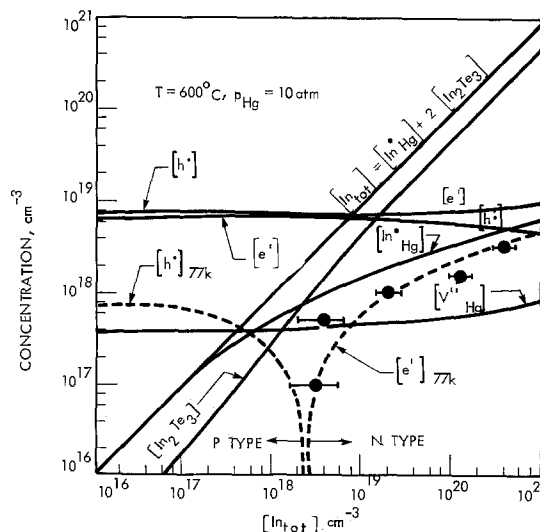


Fig. 8. Calculated defect concentrations ($[e']$, $[h \cdot]$, $[V''_{Hg}]$, $[In \cdot_{Hg}]$, and $[In_2Te_3]$) as a function of the total indium present in the indium-doped $Hg_{0.8}Cd_{0.2}Te$ crystals subsequent to equilibration at $600^\circ C$ and $p_{Hg} = 10 \text{ atm}$; dashed lines show the calculated carrier concentrations obtained in the cooled crystals at $77 K$; experimental points are also shown for comparison.

corporation reaction for In_{Hg} from $In_2Te_3(S)$ (Eq. [3]). The concentration of the native acceptor defects ($[V''_{Hg}]$) also varies in Fig. 9 since the partial pressure of Hg is a variable. The calculated electron concentration values at $77 K$ as a function of p_{Hg} are in agreement with the experimental values shown in the figure. The p to n transition in the cooled crystals (Fig. 7 through 9) occurs when $[In \cdot_{Hg}] = 2[V''_{Hg}]$.

Figures 10 and 11 show the calculated electron concentrations in the crystals at $77 K$ for various indium concentrations in the crystals at $T = 500^\circ$ and $600^\circ C$ as a function of p_{Hg} . Agreement between the calculated values and the experimental ones appears satisfactory.

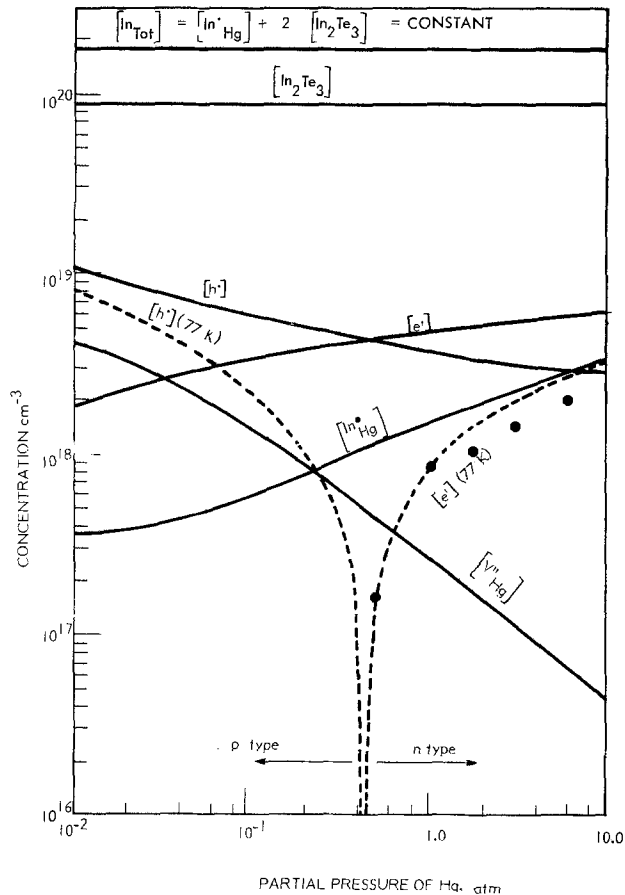


Fig. 9. Calculated defect concentrations ($[\text{e}']$, $[\text{h}']$, $[\text{V}''_{\text{Hg}}]$, $[\text{In}'_{\text{Hg}}]$, and $[\text{In}_2\text{Te}_3]$) as a function of the partial pressure of Hg at the equilibration temperature of 500°C for a fixed indium concentration of $1.8 \times 10^{20} \text{ cm}^{-3}$ in $\text{Hg}_{0.8}\text{Cd}_{0.2}\text{Te}$ crystals; dashed lines show the calculated carrier concentrations obtained in the cooled crystals at 77 K; experimental points are also shown for comparison.

It is interesting to note from Fig. 8 through 11 that even for very high indium concentrations the crystals turn p-type under low Hg pressures thus demonstrating the complexity of dopant incorporation in defect semiconductors.

Effect of cooling rate on the electron concentration.

—The results of Fig. 4 indicate that the electron concentration obtained in the indium-doped samples which are air cooled from 500°C is higher than in the ones quenched from 500°C , the deviation being greater at lower Hg pressures. This implies that the native acceptor defects frozen in the air-cooled samples is lower than in the quenched samples, thereby increasing the electron concentration in the samples air cooled from the equilibration temperatures. It is not presently clear why the native acceptor defects rather than the indium atoms tend to precipitate out during air cooling.

Electron mobility in the indium-doped samples.—

As shown in Fig. 3, the electron mobility at 77 K in the indium-doped samples is on the order of $10^4 \text{ cm}^2/\text{Vsec}$, decreasing to lower values for electron concentrations exceeding 10^{18} cm^{-3} . These values are an order of magnitude lower than reported previously (7) for low donor concentrations ($<10^{15} \text{ cm}^{-3}$). The data shown in Fig. 3 correspond to various indium-doped samples containing indium concentrations varying from approximately $5 \times 10^{18} \text{ cm}^{-3}$ to greater than 10^{20} cm^{-3} ; these samples also contain doubly ionized native acceptor defects varying from 10^{17} cm^{-3} to $5 \times 10^{17} \text{ cm}^{-3}$ in concentrations corresponding to the

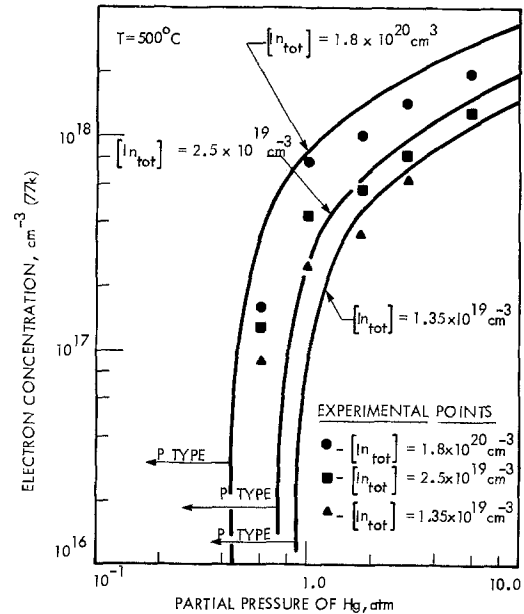


Fig. 10. Calculated electron concentration at 77 K in various indium-doped $\text{Hg}_{0.8}\text{Cd}_{0.2}\text{Te}$ crystals as a function of the partial pressure of Hg after the crystals are annealed at 500°C and quenched to room temperature; experimental points are also shown for comparison.

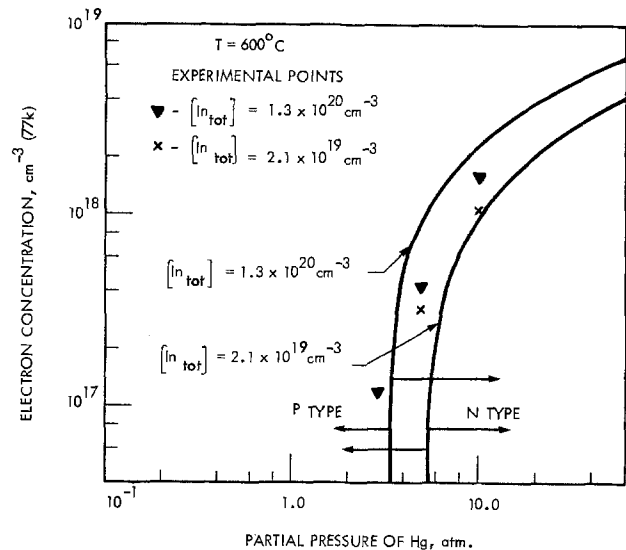


Fig. 11. Calculated electron concentration at 77 K in various indium-doped $\text{Hg}_{0.8}\text{Cd}_{0.2}\text{Te}$ crystals as a function of the partial pressure of Hg after the crystals are annealed at 600°C and quenched to room temperature; experimental points are also shown for comparison.

annealing temperature of $500^\circ\text{--}600^\circ\text{C}$ under various partial pressures of Hg. The large electrically active indium concentrations ($10^{17}\text{--}10^{18} \text{ cm}^{-3}$) and the compensating doubly ionized native defect concentrations probably account for the much lower mobilities.

Conclusion

A defect model for indium-doped $\text{Hg}_{0.8}\text{Cd}_{0.2}\text{Te}$ has been established from Hall effect measurements on indium-doped crystals equilibrated under various partial pressures of Hg and temperatures and quenched to room temperature. According to the model, most of the indium is incorporated into the crystals as $\text{In}_2\text{Te}_3(\text{S})$ dissolved in $\text{Hg}_{0.8}\text{Cd}_{0.2}\text{Te}(\text{S})$ with only a small fraction being present as single donors occupying the Hg lattice.

Acknowledgments

The author wishes to thank J. A. Carruthers of NASA for his interest in the work. Thanks are also due to J. Donovan and P. Crickard for the Hall effect measurements and T. Orent and L. I. Knudson, both of Honeywell, Minneapolis, for Auger and x-ray analyses of the samples. This work was supported by NASA under Contract NAS8-33245.

Manuscript submitted Nov. 18, 1980; revised manuscript received ca. July 23, 1981.

Any discussion of this paper will appear in a Discussion Section to be published in the June 1982 JOURNAL. All discussions for the June 1982 Discussion Section should be submitted by Feb. 1, 1982.

Publication costs of this article were assisted by Honeywell Electro-Optics Center.

REFERENCES

1. V. Kumar and F. A. Kröger, *J. Solid State Chem.*, **3**, 387 (1971).
2. G. H. Hershman, V. P. Zlomanov, and F. A. Kröger, *ibid.*, **3**, 401 (1971).
3. S. S. Chern, H. R. Vydyanath, and F. A. Kröger, *ibid.*, **14**, 33 (1975).
4. S. S. Chern and F. A. Kröger, *ibid.*, **14**, 44 (1975).
5. H. R. Vydyanath, *This Journal*, **128**, 2609 (1981).
6. L. J. van der Pauw, *Philips Tech. Rev.*, **20**, 220 (1959).
7. W. Scott, *J. Appl. Phys.*, **43**, 1055 (1972).
8. H. R. Vydyanath, S. S. Chern, and F. A. Kröger, *J. Phys. Chem. Solids*, **34**, 1317 (1973).
9. J. C. Woolley and B. Ray, *ibid.*, **15**, 27 (1960b).
10. P. M. Spencer, *Br. J. Appl. Phys.*, **15**, 625 (1964).

Lattice Defects in Semiconducting $\text{Hg}_{1-x}\text{Cd}_x\text{Te}$ Alloys

III. Defect Structure of Undoped $\text{Hg}_{0.6}\text{Cd}_{0.4}\text{Te}$

H. R. Vydyanath,* J. C. Donovan, and D. A. Nelson

Honeywell Electro-Optics Center, Lexington, Massachusetts 02173

ABSTRACT

Hall effect measurements were carried out on undoped $\text{Hg}_{0.6}\text{Cd}_{0.4}\text{Te}$ crystals quenched to room temperature subsequent to equilibration at temperatures varying from 450° to 720°C under various partial pressures of Hg. The variation of the hole concentration as a function of the partial pressure of Hg indicates that the native acceptor defects are doubly ionized. Native donor defects are found to be negligible in concentration and the p-type to n-type conversion is shown to be due to residual donors and not due to native donor defects. Thermodynamic constant for the incorporation of the doubly ionized native acceptor defect has been established.

Schmit and Stelzer (1) have reported electrical data on $\text{Hg}_{0.6}\text{Cd}_{0.4}\text{Te}$ crystals annealed at various temperatures under Hg-saturated and Te-saturated conditions. Brebrick and Schwartz (2) have recently analyzed these data on the basis of a defect model that assumes all the p-type crystals to be compensated by native donor defects and predicts the conversion of p-type to n-type in the crystals to be due to native donor defects. Conclusions of recent defect structure investigation in undoped $\text{Hg}_{0.8}\text{Cd}_{0.2}\text{Te}$ (3) are in contradiction to those of Brebrick and Schwartz (2). Since an exact power dependence of the hole concentration on the partial pressure of Hg at the annealing temperatures is not possible to evaluate from the experimental results of Schmit and Stelzer (2), which were done under Hg-saturated and Te-saturated conditions only, the present work was undertaken to obtain additional electrical data at various intermediate partial pressures of Hg in addition to those of Schmit and Stelzer (1). These data have enabled us to establish a more precise power dependence of the hole concentration on the partial pressure of Hg at the annealing temperatures; the hole concentration in the cooled crystals has been found to vary as $p_{\text{Hg}}^{-1/3}$ indicating that the dominant native acceptor defects at the annealing temperatures are doubly ionized. Just as for undoped $\text{Hg}_{0.8}\text{Cd}_{0.2}\text{Te}$ (3) the electrical data in $\text{Hg}_{0.6}\text{Cd}_{0.4}\text{Te}$ have been explained satisfactorily on the basis that the native acceptor defects are doubly ionized, that the native donor defects are negligible in concentration, and that the conversion to n-type in $\text{Hg}_{0.6}\text{Cd}_{0.4}\text{Te}$

crystals is due to residual foreign donors. The dependence of the hole concentration on the partial pressure of Hg and the temperature of equilibration has led to the establishment of the thermodynamic constant for the incorporation of the doubly ionized native acceptor defect.

Experimental

The composition of the crystals used in the present work corresponded to $x = 0.4 \pm 0.005$. The residual impurity concentration was $<10^{16} \text{ cm}^{-3}$. In order to improve the efficiency of quenching the high temperature equilibrium, the thickness of the samples was restricted to $<0.04 \text{ cm}$. Equilibration periods ranged from 24 hr at temperatures $>500^\circ\text{C}$ up to 2-3 weeks at 450°C . The procedure of equilibrating the samples in various Hg pressures and quenching the samples subsequent to equilibration is identical to that of part I (3). It should be mentioned here that while Schmit and Stelzer (1) used Te powder along with the samples for equilibration under Te-saturated conditions, we have used equivalent Hg pressures (4-6). Subsequent to the equilibration, the samples were quenched to room temperature. The samples were lapped, polished, and etched in Br-methanol solution. Hall effect and electrical resistivity measurements were made using the van der Pauw method (7). Magnetic field strengths of 400 and 4000G were used for the Hall effect measurements.

Results

As mentioned in part I (3) only those Hall effect results which did not vary with the magnetic field and, thus, showed no mixed-type conduction, were

* Electrochemical Society Active Member.

Key words: defect, $\text{Hg}_{1-x}\text{Cd}_x\text{Te}$, hole mobility, semiconductors.

used in evaluating the hole concentrations in the samples using the expression

$$p = \frac{1}{R_{HQ}}$$

Hall coefficient as a function of temperature of measurement is shown in Fig. 1 for undoped ($\text{Hg}_{0.6}\text{Cd}_{0.4}\text{Te}$) samples equilibrated at the indicated temperatures and partial pressures of Hg. It can be inferred from the figure that the ionization of the native acceptor defects appears to be complete around 190-200 K and at higher temperatures intrinsic carriers begin to become important. We have used hole concentration measurements at 192 K to infer the concentration of native acceptor defects present at the equilibration temperatures. Figures 2 and 3 show the hole concentration at 192 K as a function of the partial pressure of Hg for various equilibration temperatures ranging from 450° to 720°C. The hole concentration increases with decrease in the partial pressure of Hg, but more weakly than was found for $\text{Hg}_{0.8}\text{Cd}_{0.2}\text{Te}$ (part I) (3). In undoped $\text{Hg}_{0.8}\text{Cd}_{0.2}\text{Te}$ the hole concentration varied as p_{Hg}^{-1} (part I), whereas, results of Fig. 2 and 3 indicate that the hole concentration in undoped $\text{Hg}_{0.6}\text{Cd}_{0.4}\text{Te}$ varies as $p_{\text{Hg}}^{-1/3}$ and increases with increase in temperature.

Figures 4 and 5 show the mobility of holes at 77 and 192 K as a function of the hole concentration. The

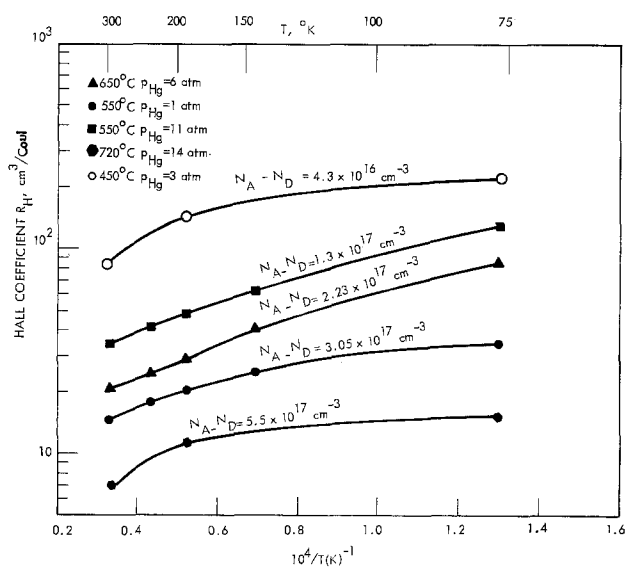


Fig. 1. Hall coefficient as a function of measurement temperature for undoped $\text{Hg}_{0.6}\text{Cd}_{0.4}\text{Te}$ samples annealed at the indicated temperatures and partial pressures of Hg and quenched to room temperature.

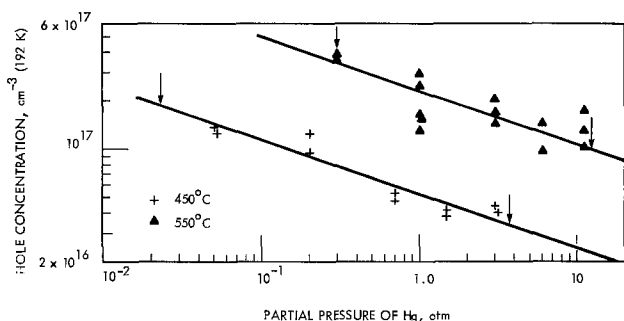


Fig. 2. Hole concentration at 192 K as a function of the partial pressure of Hg for undoped $\text{Hg}_{0.6}\text{Cd}_{0.4}\text{Te}$ crystals annealed at 450° and 550°C and quenched to room temperature; solid lines correspond to the values calculated on the basis of the defect model.

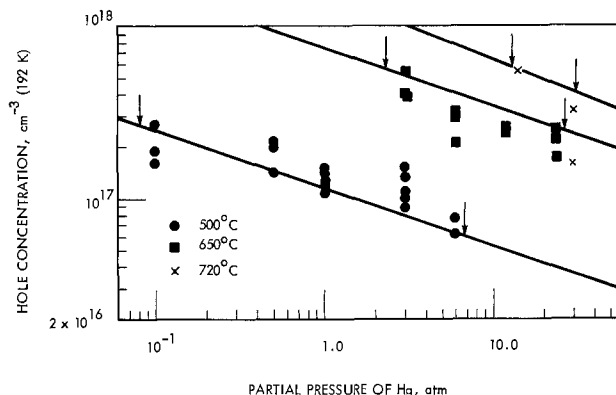


Fig. 3. Hole concentration at 192 K as a function of the partial pressure of Hg for undoped $\text{Hg}_{0.6}\text{Cd}_{0.4}\text{Te}$ crystals annealed at 500°, 650°, and 720°C and quenched to room temperature; solid lines correspond to the values calculated on the basis of the defect model.

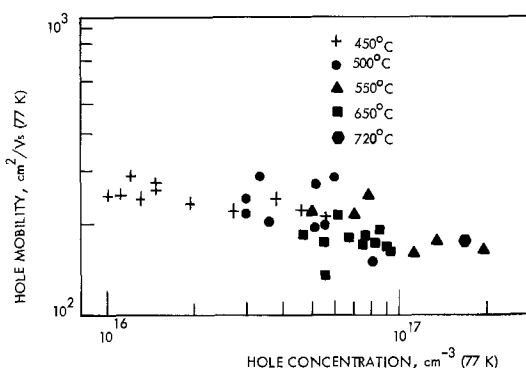


Fig. 4. Hole mobility at 77 K as a function of the hole concentration for undoped $\text{Hg}_{0.6}\text{Cd}_{0.4}\text{Te}$.

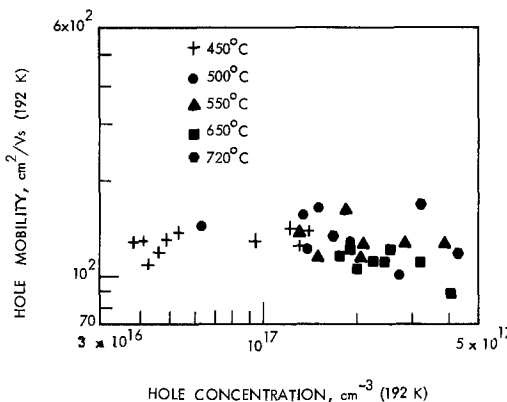


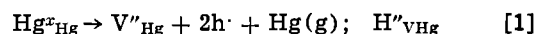
Fig. 5. Hole mobility at 192 K as a function of the hole concentration for undoped $\text{Hg}_{0.6}\text{Cd}_{0.4}\text{Te}$.

hole mobilities at 77 K are lower than those obtained for $\text{Hg}_{0.8}\text{Cd}_{0.2}\text{Te}$ (part I) (3).

Discussion

The quasichemical approach used to arrive at the defect model has already been described in part I (3) and, hence, is not detailed here.

Native acceptor defects.—The fact that the hole concentration in the crystals is proportional to $p_{\text{Hg}}^{-1/3}$ (Fig. 2 and 3) indicates that the native acceptor defects are doubly ionized. The formation and ionization of these defects can be described by the following reaction and mass action relation



$$K''_{\text{VHg}} = [\text{V}''_{\text{Hg}}] [\text{h}^{\cdot}]^2 p_{\text{Hg}} \quad [2]$$

If the electroneutrality condition is dominated by V''_{Hg} and h' then we have

$$[h'] \approx 2[V''_{\text{Hg}}] > [e']$$

From expression [2] we get

$$[h'] = [2K''_{\text{VHg}}]^{1/3} p_{\text{Hg}}^{-1/3}$$

The dominance of V''_{Hg} at the equilibration temperatures implies that the undoped ($\text{Hg}_{0.6}\text{Cd}_{0.4}$)Te crystals are not intrinsic, unlike undoped ($\text{Hg}_{0.8}\text{Cd}_{0.2}$)Te crystals (part I), in $\text{Hg}_{0.6}\text{Cd}_{0.4}\text{Te}$, at the annealing temperatures

$$[h'] = 2[V''_{\text{Hg}}] > \sqrt{K_i} > [e']$$

whereas, in $\text{Hg}_{0.8}\text{Cd}_{0.2}\text{Te}$

$$2[V''_{\text{Hg}}] < [e'] = [h'] \sqrt{K_i} \quad (\text{part I})$$

Thus, although the native acceptor aspects are doubly ionized in both $x = 0.2$ and $x = 0.4$ crystals, the dependence of the hole concentration on the partial pressure of Hg in the cooled crystals is different for the two compositions.

The fact that the intrinsic carrier concentration for the $x = 0.2$ material is higher than that for the $x = 0.4$ is a consequence of the lower bandgap for the $x = 0.2$ material.

Comparison of present experimental results with previous work.—Our experimental results differ from those of Schmit and Stelzer (1) at higher temperatures of equilibration as well as for Te-saturated conditions. We did not observe any decrease in the hole concentration at $T > 600^\circ\text{C}$, as found by Schmit and Stelzer. Also, we obtain higher native acceptor defect concentrations (or higher hole concentrations) under Te-rich conditions than Schmit and Stelzer did. It is to be noted that the electrical data in Ref. (1) were obtained for crystals annealed in Hg vapor and Te_2 vapor, with Hg or Te being at the same temperature as $\text{Hg}_{0.6}\text{Cd}_{0.4}\text{Te}$. It is known that the saturation Hg pressure over $\text{Hg}_{0.6}\text{Cd}_{0.4}\text{Te}$ (4-6) is less than that of pure Hg itself, the difference being higher at temperatures greater than 500°C . Hence, by exposing the $\text{Hg}_{0.6}\text{Cd}_{0.4}\text{Te}$ crystals to saturated-Hg vapor at greater than 500°C , in the experiments of Schmit and Stelzer (1), compositional changes in the samples may have arisen. Also, similar arguments apply for anneals in saturated Te_2 vapor, reported in Ref. (1). In addition, it is also known (4-6) that the partial pressures of Te_2 over $\text{Hg}_{0.6}\text{Cd}_{0.4}\text{Te}$ under Te-saturated conditions are orders of magnitude lower than partial pressures of Hg under Te-saturated conditions. Hence, depending on the kinetics of the different equilibration processes and depending on the fact that during the heat-up of the samples and the tellurium source, the sample may not have stayed within the existence region, compositional changes for anneals under Te-saturated conditions may also have risen in the experiments of Ref. (1). In the present work, however, equilibrations under Te-saturated conditions were done in Hg vapor at equivalent partial pressures of Hg (4-6) rather than in Te_2 vapor. As discussed in part I, macroscopic defects such as voids, Hg or Te inclusions, etc. can affect the quenching efficiency of the crystals. Presence of these may also account for the lower hole concentrations obtained by Schmit and Stelzer (1).

p-type to n-type conversion in undoped ($\text{Hg}_{0.6}\text{Cd}_{0.4}$)Te.—Schmit and Stelzer (1) found the undoped ($\text{Hg}_{0.6}\text{Cd}_{0.4}$)Te samples converted from p-type to n-type under Hg-saturated conditions at temperatures below about 350°C . The conversion temperatures for the two crystals that they experimented with were different and the electron concentration in both samples was independent of the equilibration

temperature at temperatures below the conversion temperatures. If the p-type to n-type conversion is due to native donor defects, a temperature dependence of the electron concentration should be expected just as is observed for the hole concentration (1) unless the enthalpies associated with the vaporization of Hg(1), the intrinsic excitation constant, and the incorporation of the native donor defects are of such a sign and magnitude that the electron concentration in the cooled crystals is independent of the anneal temperature. For details see Appendix B of part I. However, if the conversion is due to native donor defects, the p-type to n-type conversion temperature should be the same for different samples as long as native donor defects are larger in concentration than the foreign donors. Thus, even if the temperature independence of electron concentration under Hg-saturated conditions can be explained on the basis of native donor defects, different conversion temperatures for different samples cannot be explained unless the conversion is due to foreign donor impurities present in the crystals. Hence, the concentration of native donor defects in undoped ($\text{Hg}_{0.6}\text{Cd}_{0.4}$)Te crystals appears to be negligible and, at least, less than 10^{15} cm^{-3} at 300°C .

Absence of compensation.—While attempting to explain the low experimental mobilities of holes in ($\text{Hg}_{0.6}\text{Cd}_{0.4}$)Te, Scott *et al.* (8) assumed that all the undoped p-type samples were heavily compensated. This implied that the compensation mechanism in their crystals was probably a result of the dominance of either Schottky defects ($[V''_{\text{Hg}}] = [V'\cdot_{\text{Te}}]$) or Frenkel defects ($[V''_{\text{Hg}}] = [\text{Hg}\cdot\cdot_i]$) (2). Evidence of any such compensation in our samples is lacking. Figure 4 indicates that the hole mobilities at 77 K vary (although only weakly) as a function of only the hole concentration in the crystals, irrespective of the partial pressure of Hg and the temperature of the anneal. If there was any compensation by native donor defects, the concentration of these defects can be expected to be exponentially dependent on temperature and the mobility dependence on the hole concentration would not have been as linear as shown in Fig. 4.

It should be pointed out that mobility results similar to those of Scott *et al.* (8) mentioned above, have been observed by others (9-14). For instance, electron and hole mobilities less than predicted by the Brooks-Herring expression for the ionized impurity scattering (9) have been reported by Reynolds *et al.* (10) for ($\text{Hg}_{0.8}\text{Cd}_{0.2}$)Te. These authors explain the discrepancy to be due to the inadequacy of the Brooks-Herring formula for doping levels on the order of 10^{16} cm^{-3} in the n-type material and of 10^{18} cm^{-3} in the p-type material, and they choose not to invoke compensation as the reason. Ionized impurity mobility calculations at 77 K in degenerately doped n-type GaAs (11), n-type HgSe (12), and p-type Ge (13) at 77 K where the Brooks-Herring formula has considerably overestimated the mobilities due to ionized impurity scattering have also been reported. Recent calculations of Nishizawa *et al.* (14) for hole mobilities due to ionized impurity scattering in ($\text{Hg}_{0.82}\text{Cd}_{0.18}$)Te yielded values 4.5 times larger than the experimentally measured mobilities. According to these authors, the discrepancy between the theoretical and experimental mobilities of holes due to ionized impurity scattering is a common feature of many semiconductors. In view of these arguments it appears that more thorough calculations of hole mobilities in $\text{Hg}_{1-x}\text{Cd}_x\text{Te}$ alloys are needed.

Mass action constant K''_{VHg} .—Since the power dependence of the hole concentration on the partial pressure of Hg in the cooled crystals does not appear to be greater than 1/3, the only dominant species at the annealing temperatures appear to be the holes and

the native acceptor defects ($[e'] \ll [V''_{\text{Hg}}] = [h\cdot]/2$). Assuming that $[h\cdot] = 2[V''_{\text{Hg}}]$ at the high temperature as well as in the cooled crystals, from Eq. [2] we get

$$K''_{\text{VHg}} = ([h\cdot]^3/2)p_{\text{Hg}} \quad [3]$$

Using a procedure of trial and error, an expression for K''_{VHg} in the form of $Ae^{-Q/kT}$ was arrived at, which best explained the experimental results of Fig. 2 and 3 at various temperatures. Greater emphasis was placed on the results at lower annealing temperatures with the assumption that results from the highest temperature anneals may suffer from a greater quenching inefficiency. The value of K''_{VHg} was evaluated to be

$$K''_{\text{VHg}} = 6.61 \times 10^{65} \exp(-2.29 \text{ eV}/kT) (\text{cm}^{-9} \text{ atm}) \quad [4]$$

or, in terms of site fractions, (there are 1.33×10^{22} molecules/cm³ in $\text{Hg}_{0.6}\text{Cd}_{0.4}\text{Te}$)

$$K''_{\text{VHg}} = 0.279 \exp(-2.29 \text{ eV}/kT) \text{ site Fr}^3 \text{ atm} \quad [5]$$

The hole concentrations calculated based on this value of K''_{VHg} are shown in Fig. 2 and 3 as solid lines. The agreement between the experimental results and the calculated values appears satisfactory.

Since $\text{Hg}_{0.6}\text{Cd}_{0.4}\text{Te}$ melts at a higher temperature than $\text{Hg}_{0.8}\text{Cd}_{0.2}\text{Te}$ and has a greater bandgap, the enthalpy associated with the incorporation of the doubly ionized acceptor defect can be expected to be higher in $x = 0.4$ material than in $x = 0.2$ material. The enthalpy for $x = 0.4$ from Eq. [4] is 2.29 eV, whereas, that for $x = 0.2$ material established in part I is 2.24 eV.

Since the intrinsic carriers do not dominate the electroneutrality condition in $x = 0.4$ material for temperatures between 450°–720°C, evaluation of the intrinsic excitation constant $K_1 = [e'][h\cdot]$ was not possible. However, from the results of Fig. 2 and 3 it appears that the intrinsic carrier concentration is less than $3 \times 10^{16} \text{ cm}^{-3}$ at 450°C and less than $3 \times 10^{17} \text{ cm}^{-3}$ at 720°C. These upper limits of the intrinsic carrier concentrations are lower than those extrapolated from the empirical expressions for n_i for $x = 0.4$ in literature (15).

Hole concentrations for anneals under Hg-saturated and Te-saturated conditions.—With the knowledge of the partial pressures of Hg under Hg-saturated and Te-saturated conditions (4-6) and the value of K''_{VHg} (expressions [4] and [5]) established in the previous section, the hole concentrations in the crystals cooled to room temperature after anneals at different temperatures can be calculated from Eq. [3]. Figure 6 shows the calculated hole concentrations under Hg-saturated and Te-saturated conditions. It is to be noted that the calculations assume the concentrations of the residual donors and acceptors to be negligible in comparison with the native defect concentrations at the anneal temperatures. Figure 6 shows the experimental results of the present work, as well as those of Schmit and Stelzer (1). It is clear from the figure that quenching inefficiencies or the presence of voids and inclusions in the material (part I) can cause scatter in the data, particularly at higher temperatures. Also, the decrease of hole concentration with increase in temperature at $T > 600^\circ\text{C}$ for Hg-saturated conditions observed in Ref. (1) appears to arise from the quenching inefficiencies and is not a real effect since our results show a continuous increase in hole concentration with increase of temperature from 450° to 720°C. Residual impurity concentrations were neglected in the electroneutrality condition used to arrive at the hole concentration calculations detailed in the previous section. At lower temperatures of annealing the presence of residual donor concentrations can considerably affect the hole concentration in the sam-

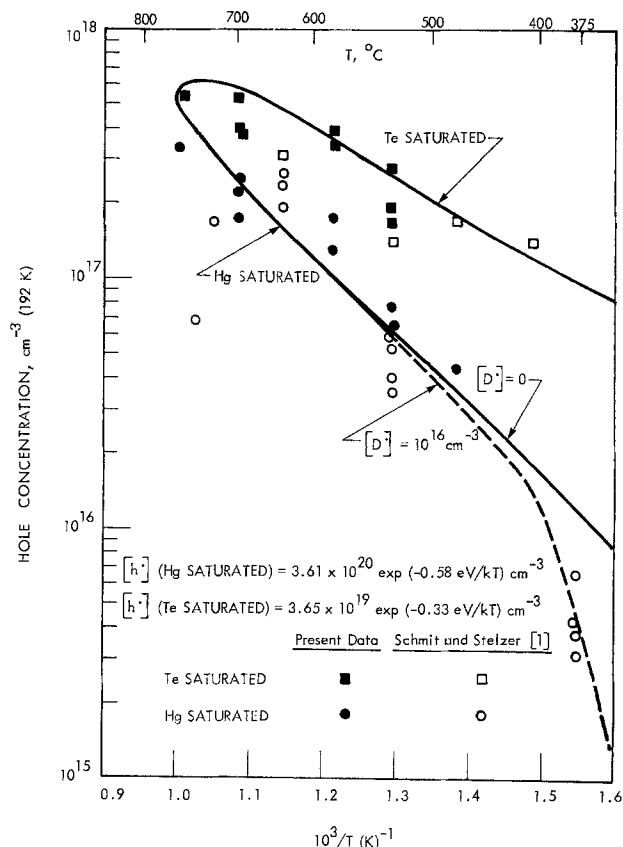


Fig. 6. Calculated hole concentration lines at 192 K as a function of annealing temperature for undoped $\text{Hg}_{0.6}\text{Cd}_{0.4}\text{Te}$ equilibrated in Hg- and Te-saturated conditions.

ples. The Appendix details the calculation of the hole concentration in the crystals in the presence of residual donors. Such a calculation assuming a residual donor concentration of 10^{16} cm^{-3} is shown as a dashed line in Fig. 6. It is clear from the figure that the results of Ref. (1) at 375°C under Hg-saturated conditions can be explained if the crystals are assumed to have approximately 10^{16} cm^{-3} residual donors.

The expressions for the hole concentrations in the cooled crystals as a function of temperature for Hg-saturated and Te-saturated conditions are given by

$$[h\cdot] (\text{Hg-saturated}) = 3.61 \times 10^{20} \exp(-0.58 \text{ eV}/kT) \text{ cm}^{-3} \quad [6]$$

and

$$[h\cdot] (\text{Te saturated}) = 3.65 \times 10^{19} \exp(-0.33 \text{ eV}/kT) \text{ cm}^{-3} \quad [7]$$

Isohole concentration plot.—Hole concentration calculations as a function of the anneal temperature and the partial pressure of Hg as detailed in the two previous sections enable us to draw lines of constant deviation from stoichiometry as a function of temperature and partial pressure of Hg. A plot of such lines of constant hole concentration is shown in Fig. 7. The upper and lower Hg pressures within which the solid is stable at each temperature were obtained from references (4-6). Comparison of this plot with a similar one for $\text{Hg}_{0.8}\text{Cd}_{0.2}\text{Te}$ (part I, Fig. 12) indicates that the concentration of native acceptor defects obtained in $x = 0.4$ material is lower than in $x = 0.2$ material. The temperature dependence of the hole concentration in the cooled crystals is also shallower for $x = 0.4$ than for $x = 0.2$ owing to the fact that the $x = 0.2$ crystals are intrinsic at the anneal temperatures, whereas the $x = 0.4$ crystals are not.

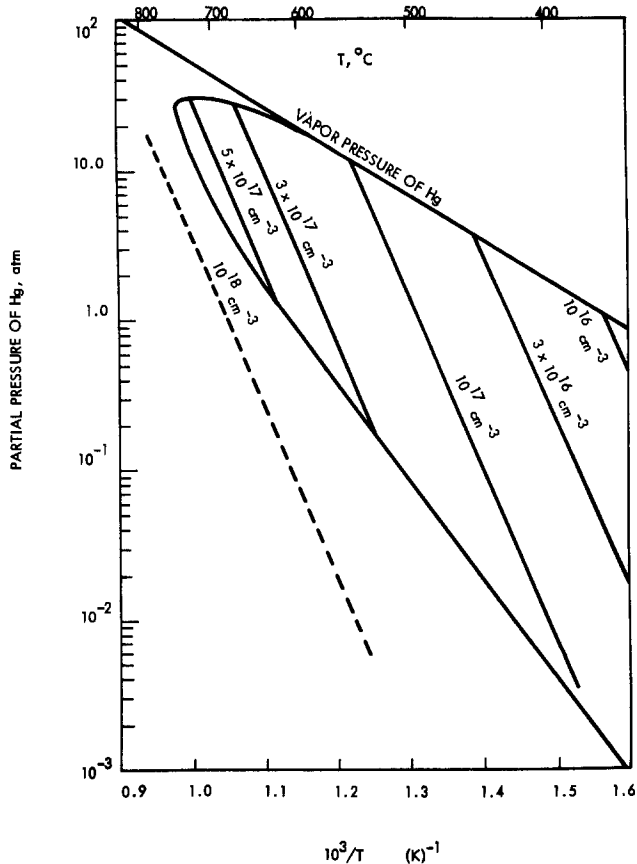


Fig. 7. Calculated isohole concentration lines at 192 K for $\text{Hg}_{0.6}\text{Cd}_{0.4}\text{Te}$ as a function of the partial pressure of Hg and temperature of annealing.

Hole mobility in $\text{Hg}_{0.6}\text{Cd}_{0.4}\text{Te}$.—Figures 4 and 5 show that the hole mobility at 77 K decreases with increase in hole concentration whereas it is relatively independent of the hole concentration at 192 K indicating that the hole mobility at 192 K is almost completely dominated by lattice scattering whereas ionized impurity scattering contributes to the mobility at 77 K. The absolute hole mobility at 77 K as well as its dependence on the hole concentration in $\text{Hg}_{0.6}\text{Cd}_{0.4}\text{Te}$ are less than in $\text{Hg}_{0.8}\text{Cd}_{0.2}\text{Te}$ (part I) (3).

Conclusion

Based on the variation of the hole concentration as a function of the partial pressure of Hg in crystals annealed at various temperatures and quenched to room temperature, the dominant native acceptor defects in undoped $\text{Hg}_{0.6}\text{Cd}_{0.4}\text{Te}$ have been established to be doubly ionized. The mass action constant describing the incorporation of the doubly ionized acceptor defect explains the experimental results satisfactorily.

Acknowledgments

The authors wish to thank J. A. Carruthers for his interest in the work. Special thanks are due to R. A. Lancaster for furnishing the crystals. This work was supported by NASA under Contract NAS8-33245.

Manuscript submitted Nov. 18, 1980; revised manuscript received ca. July 23, 1981.

Any discussion of this paper will appear in a Discussion Section to be published in the June 1982 JOURNAL. All discussions for the June 1982 Discussion Section should be submitted by Feb. 1, 1982.

Publication costs of this article were assisted by Honeywell Electro-Optics Center.

APPENDIX

Hole Concentration Calculations in $\text{Hg}_{0.6}\text{Cd}_{0.4}\text{Te}$ Containing Residual Donors

Electroneutrality condition:

High temperature

$$2[V''_{\text{Hg}}]_{\text{HT}} = [h']_{\text{HT}} + [D'] \quad [\text{A-1}]$$

Cooled crystals

$$[h']_{\text{LT}} = 2[V''_{\text{Hg}}]_{\text{HT}} - [D'] \quad [\text{A-2}]$$

Subscripts HT and LT in Eq. [A-1] and [A-2] refer to the high temperature and low temperature defect states, respectively; $[D']$ refers to concentration of residual donors in the samples, assumed to be always ionized and independent of anneal temperature.

Expressing the species in Eq. [A-1] and [A-2] in terms of the mass action constant K''_{VHG} (Eq. [2] of main text) we get

$$2K''_{\text{VHG}}/([h']^2_{\text{HT}}\rho_{\text{Hg}}) = [h']_{\text{HT}} + [D']$$

or

$$[h']^3_{\text{HT}} + [h']^2_{\text{HT}}[D'] = 2K''_{\text{VHG}}/\rho_{\text{Hg}} \quad [\text{A-3}]$$

In the cooled crystals

$$[h']_{\text{LT}} = 2K''_{\text{VHG}}/([h']^2_{\text{HT}}\rho_{\text{Hg}}) - [D'] \quad [\text{A-4}]$$

with the knowledge of K''_{VHG} (Eq. [2] of the main text) hole concentration in the cooled crystals can be calculated from Eq. [A-3] and [A-4] for various fixed residual donor concentrations in the crystals.

REFERENCES

1. J. L. Schmit and E. L. Stelzer, *J. Electron. Mater.*, **7**, 65 (1978).
2. R. F. Brebrick and J. P. Schwartz, *ibid.*, **9**, 485 (1980).
3. H. R. Vydyanath, *This Journal*, **128**, 2609 (1981).
4. R. F. Brebrick and A. J. Strauss, *J. Phys. Chem. Solids*, **26**, 989 (1965).
5. J. P. Schwartz, T. Tung, and R. F. Brebrick, *This Journal*, **128**, 438 (1981).
6. T. Tung, L. Golonka, and R. F. Brebrick, *ibid.*, **128**, 451 (1981).
7. L. J. van der Pauw, *Philips Tech. Rev.*, **20**, 220 (1959).
8. W. Scott, E. L. Stelzer, and R. J. Hager, *J. Appl. Phys.*, **47**, 1408 (1976).
9. H. Brooks, *Phys. Rev.*, **83**, 879 (1952); *Adv. Electron. Electron Phys.*, **7**, 156 (1955).
10. R. A. Reynolds, M. J. Brau, H. Krause, and R. T. Bate, *J. Phys. Chem. Solids*, **32**, Suppl. 1, 511 (1971).
11. E. J. Moore, *Phys. Rev.*, **160**, 618 (1967).
12. J. G. Broerman, *ibid.*, **183**, 754 (1969).
13. D. M. Brown and R. Bray, *ibid.*, **127**, 1953 (1962).
14. J. Nishizawa, K. Suto, M. Kitanura, M. Sato, Y. Takase, and A. Ito, *J. Phys. Chem. Solids*, **37**, 33 (1976).
15. J. L. Schmit and E. L. Stelzer, *J. Appl. Phys.*, **40**, 4865 (1969).

The Properties of LPCVD SiO₂ Film Deposited by SiH₂Cl₂ and N₂O Mixtures

K. Watanabe,¹ T. Tanigaki, and S. Wakayama

Sony Research Center, Fujitsuka-cho, Hodogaya, Yokohama, Japan

ABSTRACT

The distribution of Cl in LPCVD SiO₂ film deposited by SiH₂Cl₂ and N₂O was measured by IMMA. Cl was distributed broadly near the SiO₂-Si interface even in unannealed film. In thick LPCVD SiO₂ films on Si, surface roughness was observed after thermal oxidation. Cl was markedly piled up near the interface between the thermally grown oxide and the Si substrate. In thin films, surface roughness induced by oxidation was not observed. Cl distribution after oxidation was almost the same as that of unannealed film. The Cl pile-up is not caused by oxidation, but by the existence of the Si-SiO₂ interface. The cause of surface roughness is attributed to a smaller concentration of oxygen than Cl at the interface.

CVD (chemical vapor deposited) SiO₂ film, which is indispensable to Si planar technology, has been formed conventionally by the reaction of SiH₄ and O₂ at about 400°C at atmospheric pressure. LP (low pressure)-CVD SiO₂ film formed by the reaction of SiH₂Cl₂ and N₂O at about 900°C has been examined, because it is denser, its thickness is more uniform, and because samples are easier to produce compared with conventional CVD SiO₂ film (1). Oxidation treatment after deposition of the LPCVD SiO₂ film on Si, however, induces surface roughness. Many bumps on the SiO₂ surface and many etch pits on Si are observed.

Surface roughness may be caused by HCl or Cl₂ produced by the decomposition of SiH₂Cl₂, since similar phenomena have been observed in HCl oxidation (2-4). There may be a high concentration of Cl ions in the LPCVD SiO₂ film. In this paper the Cl distribution in the LPCVD SiO₂ film was investigated by ion microprobe mass analyzer (IMMA). Cl distribution, the relation between surface roughness and Cl distribution, and the mechanism of surface roughness were studied before and after oxidation and before and after N₂ anneal. To investigate the Cl distribution in the LPCVD SiO₂, whose growth mechanism is different from that of thermal SiO₂, we studied the effect of Cl on the SiO₂-Si interface. We are thus able to determine under which conditions useful LPCVD SiO₂ film could be produced.

Experimental

LPCVD SiO₂ films were formed on silicon wafers by the reaction of SiH₂Cl₂ and N₂O at 0.6 Torr at about 900°C. The two reactant gases, controlled by mass flowmeters, were mixed in the reactor. The evacuation system consisted of a mechanical booster pump and rotary pump. The flow rate of SiH₂Cl₂ was varied from 15 to 50 cm³/min. The N₂O flow rate was fixed at 100 cm³/min. The growth rate was from 55 to 70 Å/min. The films were deposited on 2 in. Si wafers set vertically on a quartz boat, perpendicular to the gas flow. Thickness of the film was measured by ellipsometry. The index of refraction of the film, *n*, was from 1.44 to 1.46. Infrared spectrum of the film showed the absorption at 9.4 μm caused by the Si—O bond. The absorption of Si—N bond was not observed at 12 μm.

To investigate the Cl redistribution of the film, the samples were oxidized in dry O₂ ambient or annealed in N₂ ambient. Since the samples were oxidized or annealed in the furnace different from that used in deposition, the possibilities of Cl in these ambients were eliminated.

¹ Present address: DISC Development Division, Sony Corporation, 7-35 Kitashinagawa 6, Shinagawa-ku, Tokyo.
Key words: CVD silicon dioxide low pressure, silicon dioxide chlorine distribution, Si-SiO₂ interface, thermal oxidation.

The different flow rates of SiH₂Cl₂ in our growth condition did not influence the chlorine concentration and distribution.

The depth profile was analyzed as follows. The surface of the sample was coated by Au evaporation to reduce charge accumulation and sputter-etched with a focused primary ion beam (~18.5 keV, O₂⁺, 20 μm^φ). In order to get a uniform sputtering yield the beam was raster-scanned over a small area on the sample surface (400 × 320 μm). The electronic aperture system was used to eliminate the crater-wall effect. Integrated ³⁵Cl⁺ secondary ion intensity was measured during a 40 sec period. At the same time, ²⁸Si⁺ signals in the matrix were counted to normalize the Cl ion intensity. The depth of the crater was measured by Talystep with a mechanical stylus. The sputtering rates were approximately constant i.e., R_s = 4 Å/sec. Although previous researchers have experienced insulator sample charging problems which have caused the redistribution of mobile ions, we did not experience this phenomenon, and we were able to confirm that the Cl ions had not been redistributed by the as-implanted profile of Cl in SiO₂ film about 1000Å thick. The instrument used in this study was an Applied Research Laboratories ion microprobe mass analyzer.

Results

Characteristics of Cl distribution.—Figure 1a shows Cl distribution in an LPCVD SiO₂ film of 2400Å. Figure 1b shows the Cl distribution after the N₂ anneal at 1100°C for 1 hr. The two films were chemically pre-etched to prevent accumulation of an electrical charge on the film. We found that Cl ions are not uniformly distributed at all depths and the peak concentration is about 10¹⁹ ions/cm³.

The maximum Cl ion intensity in the LPCVD SiO₂ film appeared to be at about 500Å from the SiO₂-Si interface. This is subjected to an error of about 100Å, however, because the interface cannot be precisely monitored by Si ion intensity. Si ion intensity gradually changes near the SiO₂-Si interface because of the difference of the sputtering rate and the yield of SiO₂ and Si.

To verify the IMMA measurement, we measured the Cl ion intensity of Cl ion-implanted SiO₂ (implantation conditions: 60 keV, 5 × 10¹⁵ ions/cm²) film deposited by SiH₄ and O₂ at 420°C. The measuring conditions were the same as Fig. 1. Figure 2 shows the resulting Cl distribution. This profile agrees with the Gaussian profile which is based on the LSS theory. Maximum ion intensity is near the theoretically predicted depth of 515Å. This result confirms that the ion intensity of

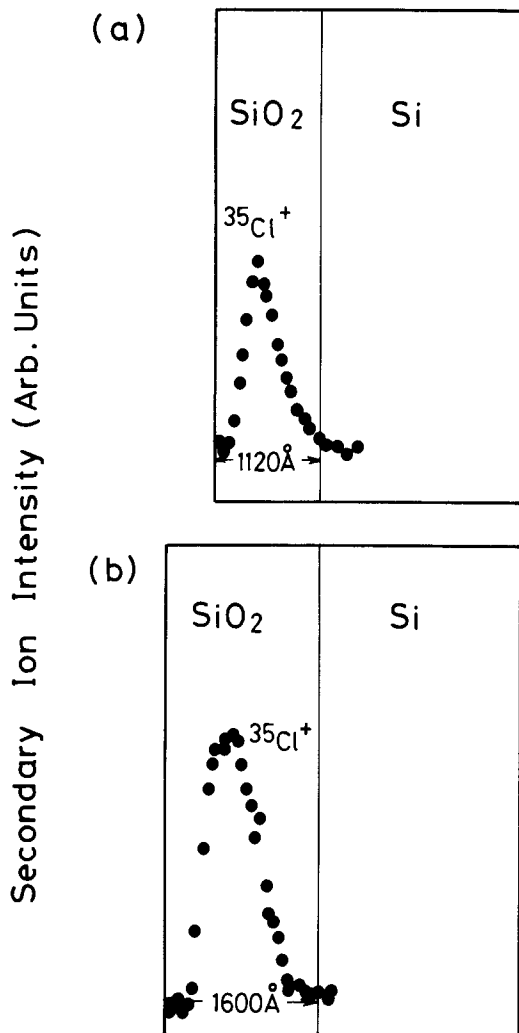


Fig. 1. Cl distribution of a chemically pre-etched LPCVD SiO₂ film (a) as deposited (b) after N₂ anneal at 1100°C for 1 hr.

secondary ion ³⁵Cl⁺ has a linear relation to the Cl concentration.

To verify the accuracy of the Cl³⁵ in-depth profile in thick SiO₂ film, eight points (Q21 to Q28) on the sample surface were analyzed at different depths. The results are shown in Fig. 3a. In this figure, *N* represents the number of sampling times. Figure 3b shows the in-depth profile of the same sample, but the areas analyzed were ion etched prior to depth-profile analysis to determine the influence of ion etching on these points. The resultant profile of Cl distribution is reproducible. Distribution in nonetched sample is the same as that in etched samples. The number of Cl ions escaping from the side walls of craters is negligible and the knock-on Cl ions or electrical fields induced by sputtering do not affect Cl distribution. Figures 3a and b show that Cl has a flat distribution near the SiO₂ surface and piles up near the interface.

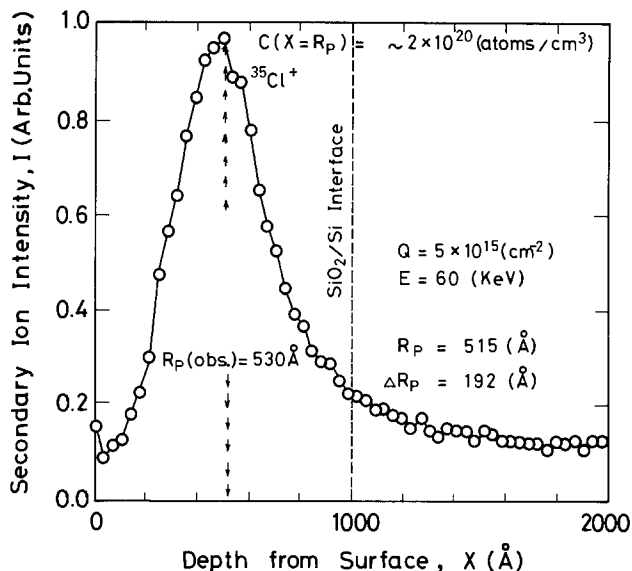


Fig. 2. Cl ion intensity of Cl ion-implanted CVD SiO₂ as deposited.

The Cl distribution in samples of three different thickness, 1500, 2600, and 6000Å, before and after thermal oxidation is shown in Fig. 4. The characteristics of the Cl distribution are as follows: (i) Cl ions are distributed broadly near the interface as the film is deposited. Cl distribution is flat near the surface. (ii) Before annealing the magnitude and profile of Cl distribution near the interface are independent of the film thickness. (iii) Cl ions move toward the newly formed interface as the thermally oxidized layer grows. (iv) In the 6000Å film, Cl concentration near the interface increases and its profile becomes sharp after oxidation. The additional Cl ions come from outside the pile-up region. In the 1500 and 2600Å films, the Cl profile remains unchanged after oxidation, although, of course, distribution shifts to the new interface. (v) Cl distribution remains unchanged after the N₂ anneal at 1100°C for 1 hr.

Surface roughness is observed only in the 6000Å film. This can be attributed to the remarkable piling-up of Cl at the interface. The surface roughness induced by oxidation is accompanied by the redistribution of Cl. (In thin films surface roughness is not observed after a 1 hr oxidation.) Pancake shapes in thick LPCVD SiO₂ films, as shown in Fig. 5a, are observed after oxidation. Their diameter is from 5 to 10 μm, measured by Talystep. The center of the risen area is about 3000Å high. Many etch pits are observed on the silicon surface after removal of SiO₂ by diluted HF, as shown in Fig. 5b. The approximately 300Å deep pits are square or rectangular because of the anisotropic etching to the Si(100) wafer. A schematic drawing of a section of the SiO₂-Si structure is shown in Fig. 6. We can assume that SiO₂ thickness is constant over the convex and concave regions because the oxygen intensity in these regions, measured by EPMA, is constant.

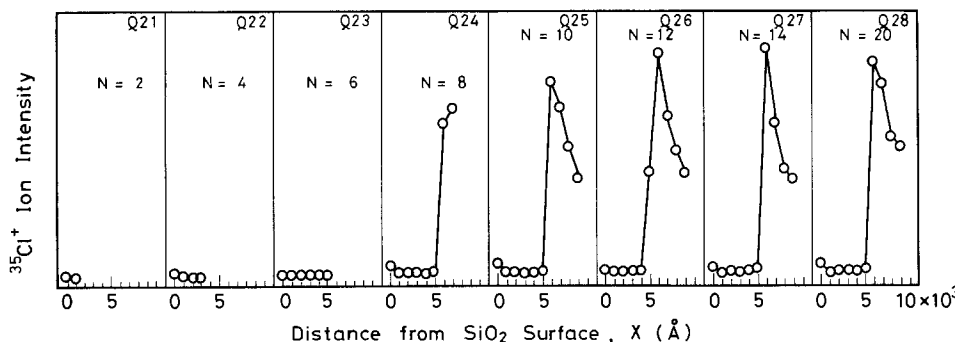


Fig. 3. (a) Cl ion distribution at eight different places (Q21-Q28) on LPCVD SiO₂ surface.

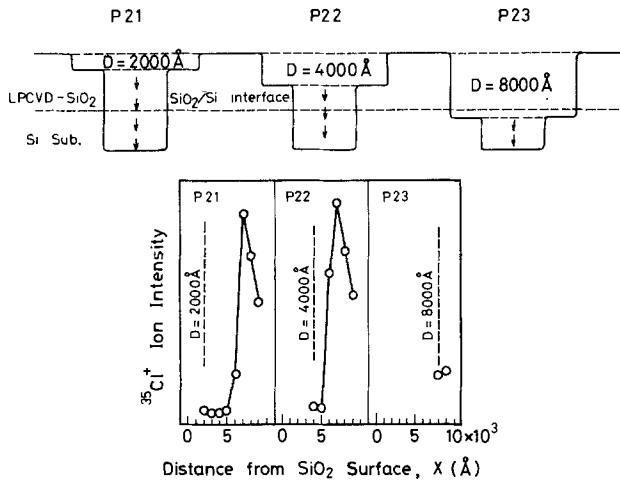


Fig. 3 (b) Cl distribution after ion etching of LPCVD SiO₂ to three different depths, D, Å.

After N₂ annealing of the film surface roughness is not observed. Oxidation following N₂ annealing, however, induces surface roughness. The fact that Cl distribution remains unchanged after N₂ annealing suggests that no surface roughness would be produced after the annealing, but that surface roughness would be induced after oxidation.

The influence of Cl distribution.—The influence of Cl ions in SiO₂ on the etching rate and on flatband voltage V_{FB} was investigated. The rate of etching to LPCVD SiO₂ and to conventional CVD SiO₂ is shown in Fig. 7. The rate of etching to CVD SiO₂ (deposited

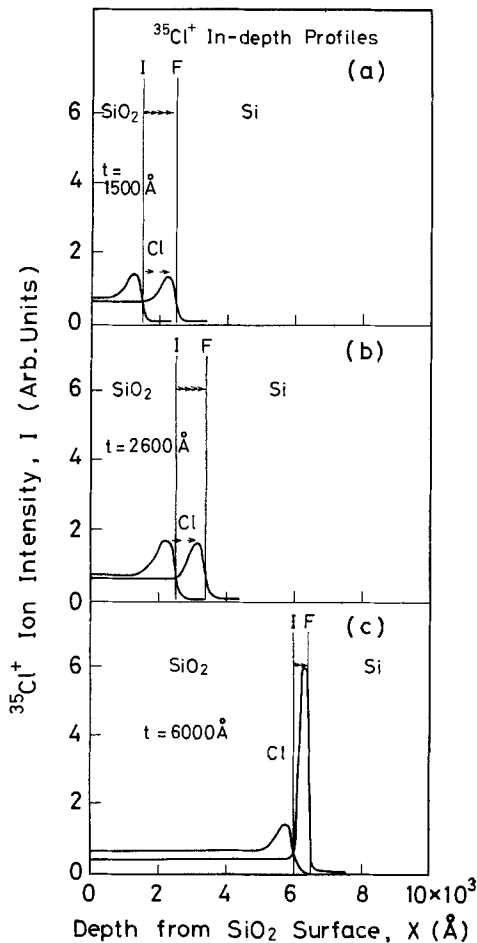


Fig. 4. Cl in-depth profile for three different thickness as deposited. I indicates the interface as deposited. F indicates the interface after oxidation at 1000°C for 1 hr.

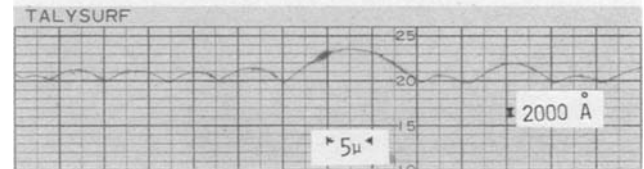
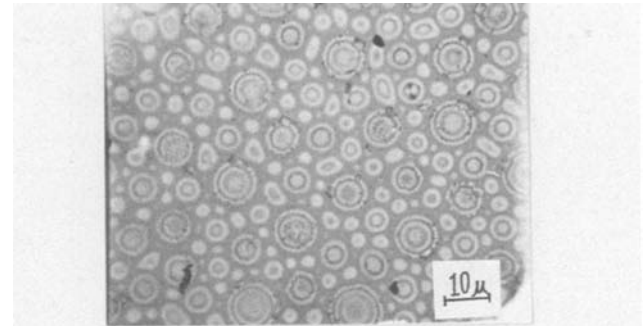


Fig. 5. (a) Surface of a thick LPCVD SiO₂ film after 1000°C anneal.

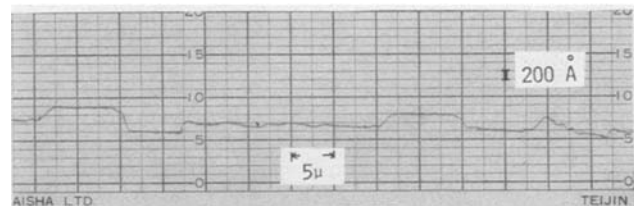
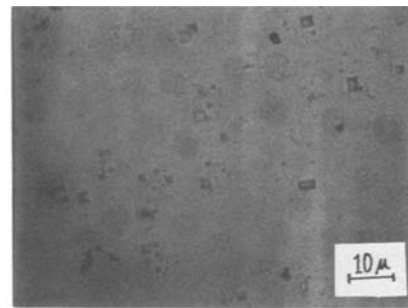


Fig. 5. (b) Surface of Si after removal of SiO₂ layer of the same sample as (a).

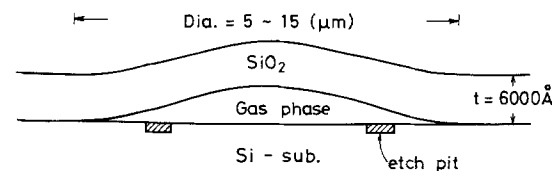


Fig. 6. Schematic illustration of the section of SiO₂-Si when surface roughness is observed.

by SiH₄ and O₂ at 420°C at atmospheric pressure) is constant, since this film does not include Cl ions. The rate of etching to LPCVD SiO₂ film decreases when the film becomes less than 1500 Å thick. This tendency is also observed in another etchant, NH₄F:HF = 60:1. Figure 8 shows the thickness dependence of V_{FB} on MOS structures [n-type (100) 2-3 Ω-cm Si] obtained

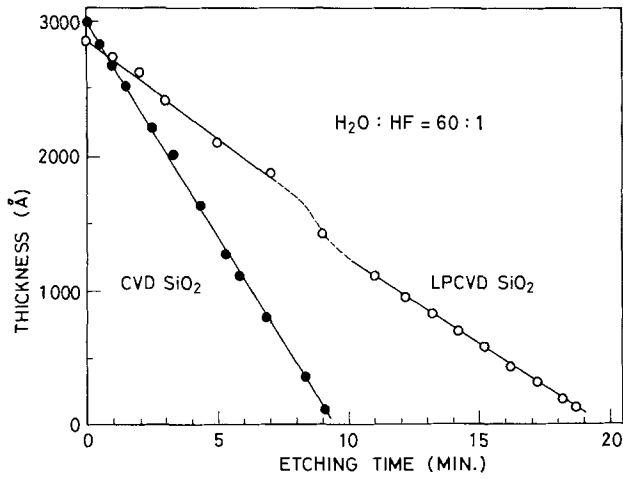


Fig. 7. Etching rates of LPCVD SiO₂ and atmospheric pressure CVD SiO₂.

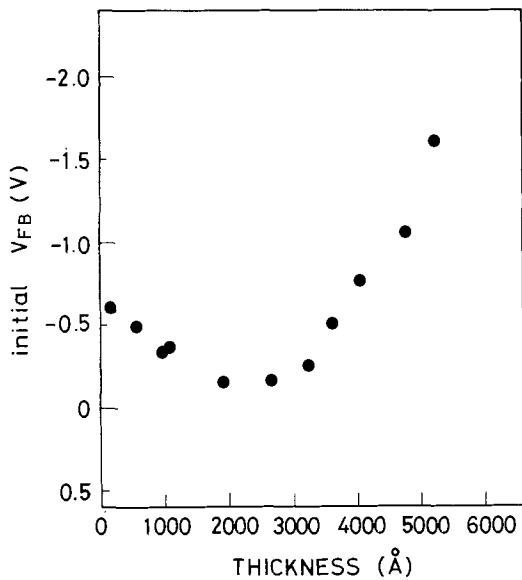


Fig. 8. Flatband voltage of Al-LPCVD SiO₂-Si structures obtained from step-etching of thick film about 6000Å thick.

from the step etching film about 6000Å thick. These data show that negative charges accumulate near the interface. To estimate the magnitude of these charges, we assumed that the charges were distributed as in Fig. 9. The negative charge density ρ is defined as

$$\rho = -b\rho_0 \quad (b > 0) \quad [1]$$

where ρ_0 is the density of uniformly distributed positive charge and b is a constant. The flatband voltage shift, ΔV_{FB} , caused by fixed charges in SiO₂ is given

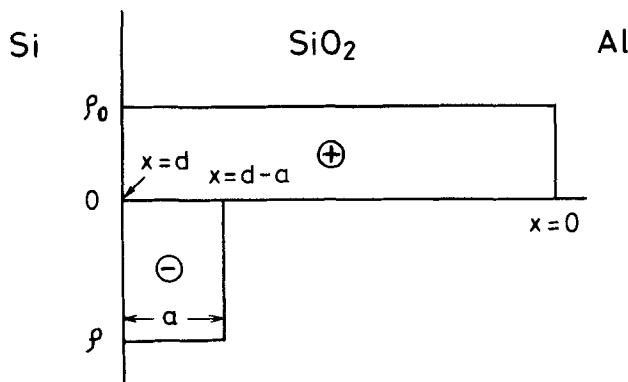


Fig. 9. Assumed charge distribution in LPCVD SiO₂ film

$$\Delta V_{FB} = -\frac{1}{C_0} \int_0^d \frac{x\rho(x)}{d} dx \quad [2]$$

where C_0 is the oxide capacitance and d is the oxide thickness. ΔV_{FB} has a minimum value at $d = ab$. The difference of ΔV_{FB} between $d = 0$ and $d = ab$ is

$$\delta V_{FB} = \frac{\rho_0}{2\epsilon_0} b(1-b)a^2 \quad [3]$$

The results show that $\delta V_{FB} = -0.5V$ and $ab = 2500\text{\AA}$. If $a = 1000\text{\AA}$, then $b = 2.5$, $\rho = 1.4 \times 10^{16} \text{ qcm}^{-3}$ and $\rho_0 = 0.56 \times 10^{16} \text{ qcm}^{-3}$. Since the order of magnitude of Cl concentration is 10^{19} cm^{-3} , the small portion of Cl has a negative charge.

Both the etching result and V_{FB} result do not bear directly on the profile of Cl distribution but do indicate that the film is not uniform.

Discussion

Cl ions are distributed broadly near the SiO₂-Si interface as the LPCVD SiO₂ film is deposited. It is well known that Cl ions distribute at the interface in HCl/O₂ oxidation. In thermal oxidation, SiO₂ films grow by the reaction of Si and O₂ and the growth rates depend on the film thickness. However, since the growth of SiO₂ at the interface by HCl/O₂ oxidation is simultaneous with the piling up of Cl, it is not clear in the case of thermally grown film whether the cause of the Cl pile-up is oxidation or the existence of the interface. On the contrary, CVD films grown by the chemical reaction of gases without consuming Si substrate and the growth rates are constant. The difference between the growth mechanism of thermally grown film and CVD film leads us to conclude that, in the case of CVD film, Cl distribution is determined not by the mechanism of Si oxidation but by the existence of the SiO₂-Si interface. If the cause of the Cl pile-up is existence of the interface, then it is clear that the profile of Cl concentration is independent of the thickness of unannealed LPCVD film. If the cause of Cl pile-up were the oxidation, Cl in LPCVD film would pile up at the SiO₂ surface or distribute uniformly because the oxidation of SiH₂Cl₂ in gas phase occurs at the surface.

The effect of the interface on Cl distribution can also be seen in the redistribution of Cl after the N₂ annealing of Cl-implanted SiO₂ film as is shown in Fig. 10. The distribution of Cl in conventional CVD films before annealing is shown in Fig. 2. Cl redistributes

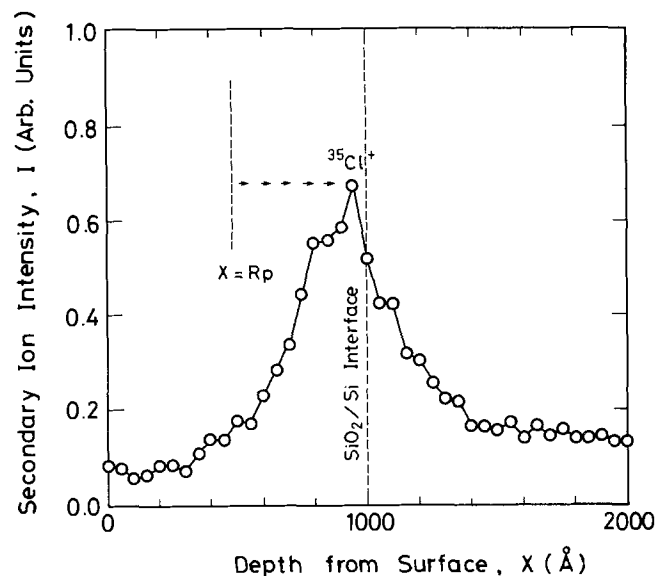


Fig. 10. Cl ion intensity of Cl ion implanted CVD SiO₂ after oxidation at 1000°C N₂ for 1 hr.

at the interface after N_2 annealing, although the extra implanted Cl ions are diffused out. The peak concentration of Cl after N_2 annealing of the Cl-implanted SiO_2 film is 10^{19} ions cm^{-3} . This value is equal to that of Cl in unannealed LPCVD SiO_2 film. Although we cannot explain the mechanism for Cl peak formation near the SiO_2 -Si interface, we believe that Cl ions in SiO_2 are attracted to the interface by the existence of the interface.

Cl profile after heat-treatment.—Because thermal oxidation in some way causes the movement of the SiO_2 -Si interface, Cl ions move toward the interface as the thermally oxidized layer grows. The velocity of Cl ions moving toward the interface is higher than the velocity of the interface movement caused by oxidation, as shown in Fig. 4. In this sense Cl ions are mobile in SiO_2 film.

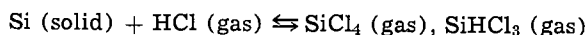
Because the Cl profile is unchanged in thin films and the total number of Cl ions is preserved after oxidation and N_2 annealing, Cl ions do not diffuse out by thermal treatment. Cl ions are stably incorporated in SiO_2 film.

Cause of surface roughness.—After the oxidation of thick LPCVD SiO_2 film, the Cl profile near the interface changes remarkably. This behavior is explained as follows: In thermal oxidation oxygen diffuses through oxide and reacts on silicon. The concentration of diffused oxygen ions at the interface depends on the thickness of the film, but the concentration of Cl ions near the interface is independent of the thickness of unannealed film. Oxygen competes with Cl in reaction on Si. Since the oxygen concentration at the interface is sufficiently large in thin films, the reaction of Si-O is dominant and SiO_2 is formed even though Cl reacts on Si. In a thick film, because of the insufficient supply of oxygen to the interface, the Si-Cl formed by the reaction of Si and Cl cannot be completely transformed into SiO_2 and remains as a gas phase of Si-O-Cl. Pancake shapes are then formed. The gas of Si-O-Cl lifts the SiO_2 layer. Cl induces etch pits on the Si wafer. It is for this reason that surface roughness is observed only in thick films.

The following experiment shows clearly the thickness dependence of surface roughness. After the deposition of LPCVD SiO_2 film 2600Å thick, conventional CVD SiO_2 8000Å thick is deposited by the reaction of SiH_4 and O_2 at 420°C. The Cl distribution of LPCVD SiO_2 is unaffected by the low temperature deposition of CVD SiO_2 . Wafers without the CVD SiO_2 deposition and wafers with the deposition were oxidized in dry O_2 for 1 hr at 1000°C. Though the integrated Cl concentrations are the same in both samples, the surface roughness is observed only in the film with addition of CVD SiO_2 . Thus we can conclude that the surface roughness does not depend on the total amount of Cl, but does depend on the oxygen concentration at the interface.

Though we do not identify the gas at the SiO_2 -Si interface, it seems to be the same as that produced by HCl/O_2 oxidation. Monkowski *et al.* (2) have suggested that the gas formed by HCl/O_2 oxidation is oxygen-rich chlorosiloxane. Lin (5) has discussed this oxygen-rich chlorosiloxane, $Si_nO_{2n-3}Cl_6$ ($n = 2-11$), which is formed in reduced oxygen pressure and appropriate chlorine atmosphere.

Surface roughness is not observed after N_2 annealing in spite of there being no O_2 concentration at the interface. This can be explained in the following manner: Silicon is etched by HCl



This reaction is reversible. Etching by Cl will not cause surface roughness. When oxygen is present, however, the formation of Si-O-Cl continues irreversibly.

Comparison between oxidation rate and etching rate.—Let us now consider the oxidation rate of Si under

LPCVD SiO_2 film x Å thick. Oxygen flow F_1 in SiO_2 can be expressed as

$$F_1 = D \frac{C_o - C_i}{x} \quad [4]$$

where D is the diffusion constant of oxygen, C_o and C_i are the oxygen concentrations at the oxide surface and at the SiO_2 -Si interface, respectively. Oxygen flow at interface F_2 is

$$F_2 = K_s C_i \quad [5]$$

where K_s is the chemical surface-reaction rate constant for oxidation. In a steady state, that is where $F_1 = F_2$

$$C_i = \frac{DC_o}{K_s x + D} \quad [6]$$

The growth rate of SiO_2 is given by

$$\frac{dx}{dt} = \frac{B}{A + 2x} \quad [7]$$

where $A \equiv 2D/K_s$, $B \equiv 2DC_o/N_1$, and N_1 is the O_2 concentration in SiO_2 . We can determine the values of A and B from oxidation. After dry O_2 oxidation for 1 hr at 1000°C of 2630Å thick LPCVD film, oxide thickness increased to 3370Å. Average oxidation rate and average thickness are 12.3 Å/min and 3000Å, respectively. The oxidation rates of films with three different initial thickness are plotted in Fig. 11. We can obtain $A = 3000$ Å and $B = 11.3 \times 10^4$ Å²/min. In HCl/O_2 oxidation of (100) Si, using the data of Deal *et al.* (6, 7) A and B are given as follows: $A = 2530$ Å, $B = 2.6 \times 10^4$ Å²/min at 1% HCl and $A = 4300$ Å, $B = 4.4 \times 10^4$ Å²/min at 4.5% HCl. Linear rate of oxidation $B/A = (C_o/N_1)k_s$ is 10 Å/min in HCl oxidation both at 1% and 4.5%, whereas it is 37 Å/min in LPCVD SiO_2 . If C_o is the same in both these films, the values of k_s and D of LPCVD SiO_2 are large compared with those of HCl/O_2 oxidized SiO_2 .

The rate of Si consumption, R_o , is derived from the oxidation rate

$$R_o = \frac{N_1 B}{N(A + 2x)} = \frac{B}{2(A + 2x)} \quad [8]$$

where N is the density of Si, 5×10^{22} cm^{-3} .

We concluded that the Cl etching rate, R_e , was

$$R_e = 5 \text{ Å/min}$$

because Si was etched to a 300Å depth by Cl at 1000°C for 1 hr. From the above estimation, we can approxi-

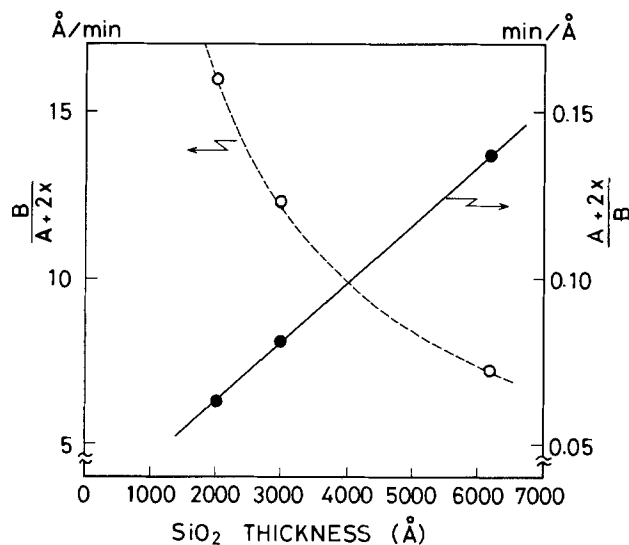


Fig. 11. Oxidation rate $B/A + 2x$ and its reciprocal rate of three different LPCVD SiO_2 thicknesses.

mate the point at which the film becomes too thick to be without surface roughness. The Cl etching rate is smaller than the oxidation rate

$$R_e < \frac{B}{2(A + 2x)} \quad [9]$$

By substituting the experimental values for A , B , and R_e

$$x < 4100\text{\AA} \quad [10]$$

This value agrees with the experimental results. It is reasonable to assume that the existence of surface roughness depends on whether the Cl etching rate or the oxidation rate is higher.

By measuring surface state density, we confirmed that the microstructure of surface roughness does not appear after oxidation in thin LPCVD SiO₂ film on Si. Surface state density of the film as deposited and after N₂ annealing at 1100°C for 1 hr is comparable to that of thermally grown SiO₂.

Comparison of Cl profiles.—The Cl distribution in LPCVD SiO₂ film is broader than that in HCl/O₂ oxidized film. In HCl/O₂ oxidized film, Cl piles up within 200Å from the SiO₂-Si interface (6). In Cl₂/O₂ oxidized film, however, Cl ions distribute broadly within 1000Å (7). The difference between the Cl distribution in HCl/O₂ and Cl₂/O₂ oxidized films may be caused by H₂O produced by HCl/O₂ oxidation (8). In LPCVD SiO₂ films, judging from the reaction of SiH₂Cl₂ and N₂O and from the deposition pressure, H₂O is not produced. The Cl distribution in LPCVD SiO₂ is almost the same as that in Cl₂/O₂ oxidized film.

Summary

Cl distribution in LPCVD SiO₂ film deposited by SiH₂Cl₂ and N₂O was measured by IMMA. We found that Cl ions are distributed approximately 1000Å from the SiO₂-Si interface. The rate of etching to SiO₂ and the flatband voltage are affected by Cl distribution. The Cl distribution is independent of the thickness of unannealed film. After the oxidation Cl ions move toward the newly formed interface. In films thinner than 4000Å, the Cl profile remains unchanged after the oxidation, but in thick films Cl concentration near the interface is increased and surface roughness is observed. Cl distribution remains unchanged after N₂ annealing at 1100°C. From these results, it is appar-

ent that the phenomenon of Cl pile-up is not caused by the mechanism of oxidation but by the existence of the interface itself. Surface roughness after oxidation depends on whether the Cl etching rate of the oxidation rate is higher. In a high oxygen concentration at the interface, the oxidation rate is larger than the Cl etching rate and surface roughness is not observed. In a low oxygen concentration, Si is etched by Cl and Si-O-Cl is formed. The surface of SiO₂ films is lifted by the gases and etching pits are observed. In this case Cl ions markedly pile up at the interface. When there is no O₂ (such as in N₂ annealing), even if Si is etched by Cl, Si-O-Cl is not formed and surface roughness is not observed.

Taking into account our estimation of the Cl etching rate and the oxidation rate, we can conclude that oxidation at 1000°C for 1 hr does not induce surface roughness when LPCVD film is less than 4000Å thick. We believe that LPCVD SiO₂ will be useful as the gate oxide of Si devices.

Acknowledgments

The authors thank K. Kajiwara for the measurements of EPMA and S. Takahashi for her help with sample preparation.

Manuscript submitted Feb. 23, 1981; revised manuscript received June 22, 1981.

Any discussion of this paper will appear in a Discussion Section to be published in the June 1982 JOURNAL. All discussions for the June 1982 Discussion Section should be submitted by Feb. 1, 1982.

Publication costs of this article were assisted by Sony Corporation.

REFERENCES

1. R. S. Rosler, *Solid State Technol.*, 63 (April 1977).
2. J. Monkowski, R. E. Tressler, and J. Stach, *This Journal*, 125, 1867 (1978).
3. A. Rohatgi, S. R. Butler, F. J. Feigl, H. W. Kraner, and K. W. Jones, *ibid.*, 126, 143 (1979).
4. K. Hirabayashi and J. Iwamura, *ibid.*, 120, 1595 (1973).
5. S. S. Lin, *ibid.*, 126, 1081 (1979).
6. B. E. Deal, A. Hurrle, and M. J. Schulz, *ibid.*, 125, 2024 (1978).
7. Y. J. Meulen, C. M. Osburn, and J. F. Ziegler, *ibid.*, 122, 284 (1975).
8. B. R. Singh and P. Balk, *ibid.*, 125, 453 (1978).

Au/Ni/SnNi/n-GaAs Interface: Ohmic Contact Formation

Atilla Aydinli¹

Engineering Physics Department, University of Virginia, Charlottesville, Virginia 22901

and Robert J. Mattauch

Electrical Engineering Department University of Virginia, Charlottesville, Virginia 22901

ABSTRACT

The Au/Ni/SnNi/GaAs interface has been studied in order to understand ohmic contact formation. Depth profiling in conjunction with Auger electron spectroscopy has been used to determine impurity distribution in as-deposited and alloyed films and were correlated to electrical parameters. We find that ohmicity can be achieved without Sn due to Au-induced Ga vacancies and Ni-induced breakup of background Si covalent bonds. However, addition of Sn to the system lowers the specific contact resistances greatly.

Various studies have been conducted on metal-GaAs ohmic contact systems. Most of these are concerned

with electrical and metallurgical properties of the contacts as well as their long-term reliability. The majority of the systems studied include Au-based metal contacts. Among them Ni/Au-Ge/GaAs is favored in many applications and have been exten-

¹ Present address: Department of Physics, Kansas State University, Manhattan, Kansas 66506.

Key words: interfaces, bonding, ohmicity.

sively studied (1-3). A similar system is Au/Ni/SnNi/n-GaAs, which is used quite successively in mm-wave Schottky barrier devices. We report here the results of a study on this system. Auger electron spectroscopy (AES) combined with *in situ* sputter etching was used to obtain chemical profiles which were correlated with electrical measurements. Attention was paid to the role played by each element of the system in the formation of the ohmic contact. This is particularly important since new information is becoming available on the interaction of different impurities with each other in GaAs (4).

Experimental Procedure

In order to identify the role of each element in Au/Ni/SnNi/n-GaAs ohmic contact, we studied SnNi/GaAs, Ni/SnNi/GaAs, and Au/Ni/SnNi/GaAs systems. In each case the GaAs used consisted of a 3.3 μm thick epitaxial layer doped to $2.3 \times 10^{17} \text{ cm}^{-3}$ on a substrate doped with Si to $2.8 \times 10^{18} \text{ cm}^{-3}$. All the metal layers were electroplated through conventionally defined 175 μm diam windows opened in the SiO_2 layer covering the GaAs epitaxial layers. Both SnNi and Ni were pulse plated from stannous-nickelous and nickelous chloride solutions, respectively, while Au was d-c plated from Autronex solution. The unmasked back-sides of the wafers were ohmically contacted with the Au/Ni/SnNi process prior to anode metallization. After sample preparation, individual chips each bearing one anode, were cut with a high speed diamond wheel dicing saw in preparation for heat-treatments. Each chip was soldered at 130°C to a 0.79 mm diam Ni post and the anode was contacted with 50 μm diam Au wire for electrical measurements, which were carried out both before and after heat-treatment. Such treatment was carried out on a Ta strip in a chamber containing constantly replenished forming gas (95% N_2 -5% H_2). For prolonged heat-treatments, a bore furnace was used.

Auger electron spectroscopy (AES) and argon ion sputtering were used for chemical analysis. The AES data were taken in derivative form and peak-to-peak amplitudes of Auger transitions were used to calculate the surface coverages in atomic percentages (5). Optical microscopy was used to determine surface uniformity before and after sputter etching. AES analysis was carried out on each chip with a 5 keV 25 μm diam electron beam having a current of approximately 1 μA . Depth profiling was done with a 1 keV Ar-ion beam at a pressure of 5.0×10^{-5} Torr. The depth profiles are presented in atomic percentages vs. sputter time. Relevant sputter etch rates are given in the text.

Device electrical measurements were taken with a Tektronix 576 curve tracer and a Boonton 75B-S8 capacitance bridge. Structure series resistance, R_s and ideality factor, η were calculated from *I-V* characteristics of the diodes in accordance with the method of Polhamus (6). Built-in voltage values were calculated from $(1/C^2)$ vs. V plots.

Results

SnNi/GaAs interface.—Samples analyzed after SnNi electroplating showed the metal film to be composed of 10% Sn and 90% Ni. Depth profiles indicated that these percentages were maintained throughout the 2800Å film thickness, as shown in Fig. 1. The metal/GaAs interface was found to be sharp. Although Ni is seen to extend further into GaAs than Sn, this effect is thought to be due to differential sputtering during the Auger profile analysis. The depth profile of an SnNi/n-GaAs interface after heat-treatment at 400°C for 20 min is shown in Fig. 2. The surface spectrum showed carbon and oxygen as well as Sn and Ni. Neither Ga nor As was observed on the surface. Figure 2 shows evidence of fast diffusion of Ni into GaAs. The relative stoichiometry of Ga and As in Ni rich region indicates a diffusion process rather than eutectic alloying. Unlike Au/GaAs, SnNi/GaAs junctions do not dissociate the semiconductor. The stationary behavior of Sn is due to an apparently larger diffusion coefficient of Ni

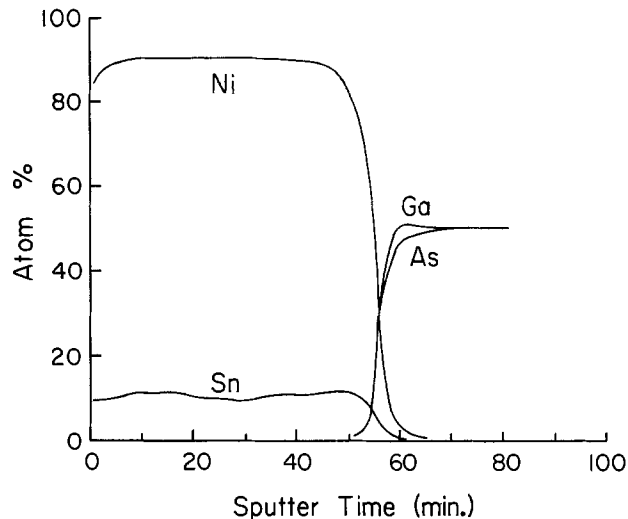


Fig. 1. Depth profile of as-plated SnNi/GaAs junction

than Sn in GaAs and the fact that Sn-Ni binary system has very few compounds (7, 8). *I-V* measurements of nonheat-treated structures exhibited diode behavior with ideality factors, η , ranging from 1.07 to 1.2. Plots of $(1/C^2)$ vs. V gave built-in potentials of 0.750-0.775V. Heat-treatment at 300° and 400°C did not change built-in potential values appreciably. The value of the ideality factors deteriorated slightly due to heat-treatment of 400°C for 20 min. More important, however, the series resistance of diodes increased threefold.

The behavior of SnNi/n-GaAs at high temperatures can be explained as follows: Ni is an acceptor in GaAs while Sn is a donor. At high temperature Ni diffuses farther into GaAs due to its higher diffusion coefficient, compensating the donor concentration and thereby raising the series resistance of the diode. It should be kept in mind that this process may lead to a p-n junction (9) and electrical data then would have to be viewed accordingly.

Ni/SnNi/GaAs interface.—Results similar to those for the SnNi/GaAs interface were obtained when a 3000Å thick layer of Ni was electroplated onto plated SnNi on GaAs. Results of the electrical measurements were the same as SnNi/GaAs. The chemical depth profile of these junctions after heat-treatment at 400°C for 10 min is shown in Fig. 3. Diode behavior with an increase in series resistance R_s as mentioned for the SnNi/GaAs system was observed. We also observe that Sn has remained stationary at the Ni/SnNi interface while Ni diffused into GaAs as in the case of

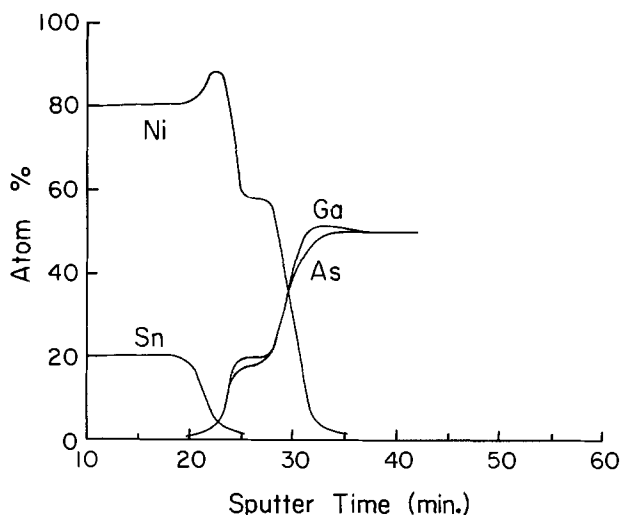


Fig. 2. Depth profile of SnNi/GaAs junction annealed at 400°C/20 min.

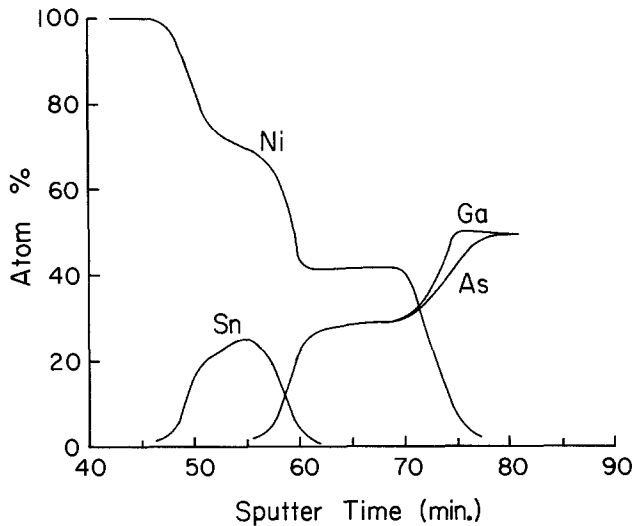


Fig. 3. Depth profile of Ni/SnNi/GaAs junction annealed at 400°C/10 min.

SnNi/GaAs. The difficulty of introducing Sn into GaAs in these systems is in contrast with Au/Ni/SnNi/GaAs system discussed next where a uniform distribution of Sn throughout the alloyed junction is observed.

Au/Ni/SnNi/GaAs interface.—The formation of an ohmic contact to n-type GaAs depends on greatly increasing the majority carrier concentration at the metal-semiconductor interface in order to cause increased tunneling current. In the case of Au/Ni/SnNi/n-GaAs samples both Au and Ni are acceptors in GaAs whereas Sn is a donor. As pointed out above in the cases of SnNi/GaAs and Ni/SnNi/GaAs, neither the concentration nor diffusion kinetics of Sn is suitable to achieve the needed excess carrier concentration to produce an ohmic contact. However, in Au/GaAs junctions both Ga and As are known to diffuse through Au metallizations even at room temperatures. At higher temperatures, Au tends to gather Ga, creating Ga vacancies in GaAs.

In Au/Ni/SnNi/GaAs junctions, Sn is expected to diffuse into Au-induced Ga vacancies thereby producing an excess electron concentration. Ni is expected to provide good wetting so that Sn does not "ball up" during the alloying process. The process is similar to that occurring for Au/Ni-Ge/GaAs contacts with Sn taking the place of Ge. A depth profile for a nonalloyed structure is shown in Fig. 4. As expected, such structures exhibited diode behavior of the nature mentioned above for the SnNi/GaAs samples. Heat-treatment of Au/Ni/SnNi/GaAs samples was carried out at 232°,

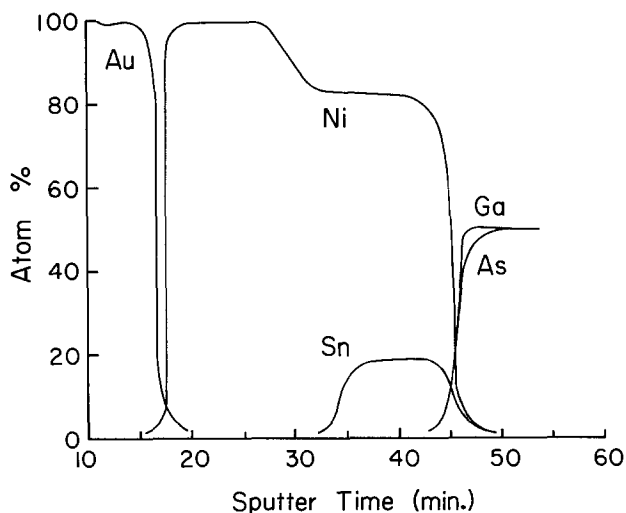


Fig. 4. Depth profile of as-plated Au/Ni/SnNi/GaAs junction

328°, and 420°C. Samples were held at their respective temperatures for 10 sec and the strip heater power supply was turned off to allow cooling. Heating rates were 700°, 560°, and 500°C/min, respectively. The samples alloyed at 232°C were uniform under microscopic observation. Surface analysis showed 18% Sn on Au, suggesting grain boundary diffusion of Sn through the Ni layer. Depth profiling of the samples did not indicate any diffusion of Au into Ni or of Ni or Sn into GaAs. However, samples alloyed at 328° and 420°C were ohmic but had visibly grainy surfaces. Surface analysis of these samples revealed measurable amounts of Au, Sn, Ni, and Ga but not As. Depth profiles of these samples however were not consistent due to lateral inhomogeneity. Samples prepared in the same manner on large area wafers without any SiO₂ mask were homogenous upon alloying when observed by optical microscopy.

A depth profile of a fully alloyed (420°C for 10 sec) Au/Ni/SnNi/n-GaAs contact with Au overlayer plated after alloying is shown in Fig. 5. Region I consists of Au electroplated after the alloying process to ensure good solderability. Region II is Ga rich starting at the Au-alloyed junction interface. Arsenic is observed after sputter etching 5 more minutes. This is consistent with our previous observation of Ga but not of As on the surface of heat-treated Au/Ni/SnNi/GaAs junctions. A slight As richness is apparent in region III but not enough to account for the excess Ga in region II. We suspect that some As may have evaporated from region II during heat-treatment prior to region I Au deposition. Ni reaches its peak at the region II/III interface. It is obvious from region IV that Ni diffuses the furthest into GaAs. It is crucial to note that the Sn concentration throughout the alloyed junction is very low, although it may be high from an electrical doping standpoint. The average depth of the (163 min) ion sputtered region was 3 μm. We refrain from assigning specific thickness intervals due to the existence of a five element alloy. The changing composition of the alloy undoubtedly results in a varying etch rate.

Discussion and Conclusions

The specific contact resistances of various contacts were also measured. After establishing an ohmic contact on both sides of a wafer it was cut into 0.01 × 0.01 in. size chips with a dicing saw. The *I-V* measurement was taken by soldering the chip on two 0.015 in. diam nickel posts on each end and connecting a high input impedance voltmeter (Keithley 610) across the sample next to the chip ohmic contacts. The current was supplied with a precision current source (Keithley 227) to the ends of the nickel posts. The resulting *I-V* curve was linear. Contact resistance was obtained by sub-

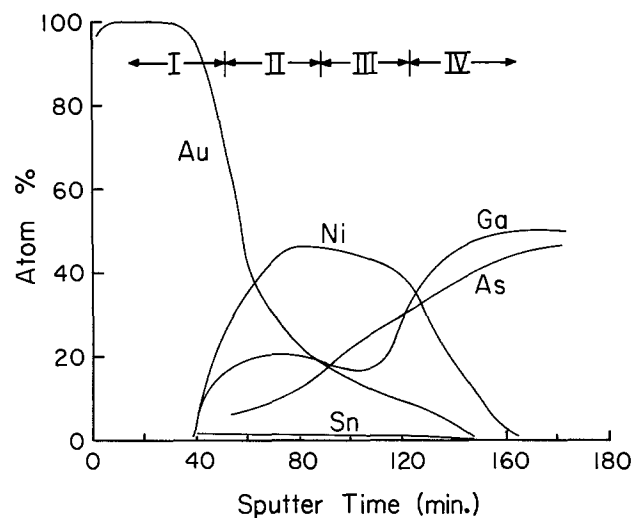


Fig. 5. Depth profile of fully alloyed Au/Ni/SnNi/GaAs ohmic contact (420°C/10 sec) with Au overlayer electroplated.

tracting material bulk resistance from measured resistance and dividing it by two. With this technique contact resistances of $5 \times 10^{-5} \Omega \text{ cm}^2$ or lower was routinely obtained, although low $10^{-4} \Omega \text{ cm}^2$ was also measured. This data is consistent with published contact resistance of $3\text{-}7 \times 10^{-5} \Omega \text{ cm}^2$ of a similar alloy system (10). Thus the Au/Ni/Sn-Ni/GaAs contacting process has been found to give rise to specific contact resistances lower than achieved by the Au/Ni-Ge/GaAs process (1, 2). An investigation of the former contact indicates that while the consideration that the diffusion of Sn into Ga vacancies created by an Au/GaAs reaction as the sole mechanism of ohmic contact formation is interesting, it seems simplified at best. This is felt to be the case not only due to the very low concentration of Sn in alloyed junctions and the diffusion kinetics of Sn in GaAs being not favorable, but also due to the existence of large concentrations in Ni well into the GaAs. One may expect that such high concentrations of electrically active Ni would compensate Sn resulting in the formation of a p-n junction. Experiments prompted by this concern on Au/Ni/n-GaAs showed that contact ohmicity can be obtained without Sn. However in a comparative study, the specific contact resistance of the Au/Ni/SnNi/n-GaAs ohmic contact ($\sim 3.5 \times 10^{-4} \Omega \text{ cm}^{-2}$) was two orders of magnitude lower than that of the Au/Ni/n-GaAs ohmic contact ($\sim 4.4 \times 10^{-2} \Omega \text{ cm}^{-2}$). Since the existence of electrically inactive Si in boat-grown GaAs is known, the formation of an ohmic contact in the Au/Ni/n-GaAs system is attributed to either of two possible processes: (i) Ni diffusion into GaAs and subsequent breaking of inactive Si-Si bonds of background Si in GaAs thereby producing active Si impurities (4); or (ii) Au giving rise to the formation of Ga vacancies into which active Si diffuses. In either case the background concentration of Si in the epitaxial GaAs is relatively low, possibly resulting in high specific contact resistance ($\sim 4.4 \times 10^{-2} \Omega \text{ cm}^2$) of the tested Au/Ni/GaAs contacts. The addition of even low concentrations of electrically active Sn is sufficient to provide a greater concentration of donor impurities thus lowering the contact resistance.

We have refrained from detailed interpretation of the depth profiles since we do not have detailed understanding of ion-induced effects on alloyed junctions during sputter etching. The effects of differential sputtering and ion knock-in should be identified and taken into account before further analysis can be carried out.

We have investigated the Au/Ni/Sn-Ni/GaAs ohmic contact systems at various stages of contact formation by means of Auger analysis coupled with *in situ* sputter etching. As indicated above, our data indicate that despite introduction of high concentrations of p-type impurities it is possible to obtain an ohmic contact in Au/Ni/n-GaAs systems. The formation of an ohmic contact is attributed to activation of background n-type impurities by Ni and occupation by these impurities of Au-induced Ga vacancies. Addition of Sn to Au/Ni/n-GaAs system lowers the specific contact resistance by at least two orders of magnitude.

Acknowledgments

We would like to acknowledge the support of NSF contract, ENG. 78-05356 and Equipment grant ENG. 7746768. We are grateful to M. Yoder for beneficial discussions. One of us (A.A) would like to express his gratitude to Turkish Ministry of Education for financial support.

Manuscript submitted March 30, 1981; revised manuscript received June 9, 1981.

Any discussion of this paper will appear in a Discussion Section to be published in the June 1982 JOURNAL. All discussions for the June 1982 Discussion Section should be submitted by Feb. 1, 1982.

Publication costs of this article were assisted by the University of Virginia.

REFERENCES

1. G. Y. Robinson, *J. Vac. Sci. Technol.*, **13**, 884 (1976).
2. G. Y. Robinson, *Solid State Electron.*, **18**, 331 (1975).
3. M. Wittmer, R. Pretorius, J. Mayer, and M. A. Nicolof, *ibid.*, **20**, 433 (1977).
4. Max Yoder, "Complexes and Their Effects on III-V Compounds," Semi-Insulating III-V Materials Conference, Univ. of Nottingham, April 1980.
5. "Handbook of Auger Electron Spectroscopy," Physical Electronic Industries, Eden Prairie, MN (1976).
6. W. Polhamus, Masters Thesis, University of Virginia (1976).
7. M. Hansen and K. Anderko, "Constitution of Binary Alloys," McGraw-Hill, New York (1958).
8. J. Bennett and H. Tompkins, *This Journal*, **123**, 999 (1976).
9. G. Ottaviani, *J. Vac. Sci. Technol.*, **16**, 1112 (1979).
10. W. M. Kelly and G. T. Wrixon, *Electron. Lett.*, **14**, (1978).

Packaging Improvement of a Liquid Cooled Silicon Chip

M. D. Reeber and R. G. Frieser*

IBM General Technology Division, East Fishkill, Hopewell Junction, New York 12533

ABSTRACT

Because of the increasing density of devices on a chip (to increase the effectiveness of computers) the amount of heat generated per unit area of chip increases as well. This must be removed efficiently to prevent failure of the device. In order to provide reliable nucleation sites for boiling on silicon surfaces, a number of techniques may be used, one of which is the combination of mechanical abrasion coupled with the removal of induced defects by liquid etchants. Consistent nucleation, which does not occur on polished silicon surfaces, is required to assure proper heat transfer of silicon circuit chips. Heat transfer data for treated and untreated surfaces are presented.

Heat generated in operating silicon semiconductor devices must be removed in order to prevent burnout or fatigue failure of the device. To increase the usefulness of computers using these devices, it is necessary to package the devices more densely and to increase their operating speed. Both of these considerations combine to increase the quantity of heat generated per unit volume of computer, and improving packaging efficiency requires the removal of this large heat load. One useful technique for removing this heat is to submerge the device in a bath of perfluorohexane which will be operated at its boiling point of 56°C. Perfluorohexane is an inert dielectric fluid that does not interact with any of the materials used in semiconductor packaging. Boiling is an efficient technique for transferring heat from a solid to a fluid.

Theory

When a heat generating solid is placed in a fluid, the fluid in the vicinity of the solid warms up as heat is transferred by conduction. Most fluids (including perfluorohexane) are poor conductors and the fluid heats up near the solid. Because of the thermal expansion of the fluid, the hot fluid has a lower density than the remaining cooler fluid, and consequently moves away from the heat generating surface. This gives rise to convection currents in the fluid and brings additional cool fluid into contact with the solid. As we increase the quantity of heat generated in the solid, both the convection rate and the fluid temperature increase.

The major impediment to heat flow at this point is the velocity profile of the fluid at the surface of the hot body. The fluid in actual contact with the solid is moving at zero velocity, and some short distance away it increases to its maximum velocity. The nonmoving layer at the surface of the solid is called the stagnant layer and heat must cross it by conduction. Since the fluid is a poor conductor, a large temperature gradient is developed across this layer even though it is quite thin. The solid becomes considerably hotter than the bulk of the fluid, eventually reaching or passing the boiling point of the fluid as we increase the heat flow.

Boiling will improve the efficiency of the heat transfer process by: (i) breaking up the stagnant layer and eliminating the temperature gradient between the bulk of the fluid and the solid and, (ii) contributing the latent heat of boiling to the heat transfer process. However, boiling cannot proceed until a bubble is established. This requires either sufficient excess energy to form the vapor-liquid interface, or a geometry that is particularly favorable for this purpose. Without this geometry, the excess energy is supplied by raising the

temperature of the solid far above the boiling point of the fluid.

To assure proper heat transfer to the fluid, the surface of the semiconductor must contain a large number of sites at which bubbles of vapor can be consistently and easily nucleated. These sites are essentially non-existent in a polished silicon surface and must be built into any surface that we wish to use for this purpose. Among the techniques that may be used to provide nucleation sites for boiling, we have found that a combination of sandblasting followed by a preferential etch provides a consistently high density of active sites. The study of heat transfer on a variety of surfaces, specially prepared, was performed on silicon wafers. Once a satisfactory technique had been obtained, this process was applied to a product chip. A more extensive discussion of techniques to provide nucleation sites is published elsewhere (1).

Experiment

Such a useful active surface is produced by first sandblasting with a water slurry of alumina at about 60 psi. This results in a highly stressed surface, roughened by the action of the oxide. The surface is then etched with a 5N aqueous solution of KOH mixed at 1:1 ratio with methyl alcohol (2). The etching takes place at 80°C for about 1-2 min in a typical example. The heat transfer efficiency of the surface is not particularly sensitive to the etch time. The surface is thoroughly rinsed with distilled water and air dried. The action of the etchant on silicon is anisotropic, accentuated by the presence of locally stressed regions. Thus, the etching further increases the irregularities beyond those generated in the surface by the original sandblasting.

This treatment results in a surface that is largely pitted, as can be seen in Fig. 1. These pits usually have irregular outlines, most edges are sharp, and undercutting is prevalent. Occasionally, long, narrow, very deep pitting can be seen. In Fig. 1, the cross is about 10 μm long, 1 μm wide, and 5 μm deep.

The thermal behavior of treated wafers was established and shown in Fig. 2, in the apparatus (3) designed specifically for this purpose. The silicon wafer, with the treated side in contact with the fluid is cemented to a phenolic mount (D). Heat is supplied by the heater disk (A) which is in thermal contact with the wafer. The heater disk contains a winding (C), and thermocouple (B).

Other thermocouples measure the temperature of the block and the fluid. The construction of the apparatus is such that over 95% of the heat generated in the sample holder by the heater block is transferred to the fluid through the silicon wafer with the treated surface

* Electrochemical Society Active Member.

Key words: nucleation sites, silicon surfaces, heat transfer.

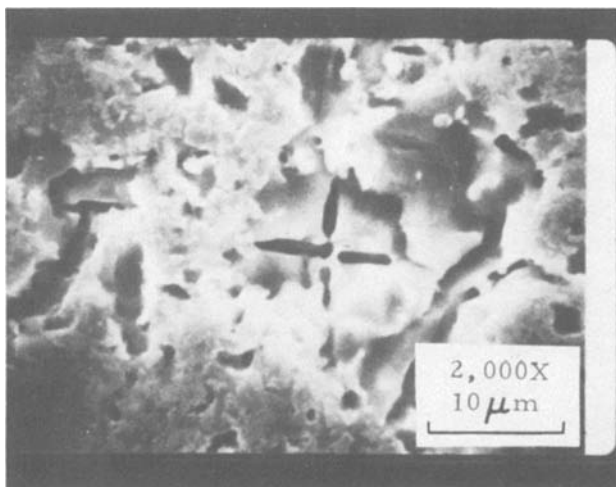


Fig. 1. Treated surface—SEM photograph, normal incidence

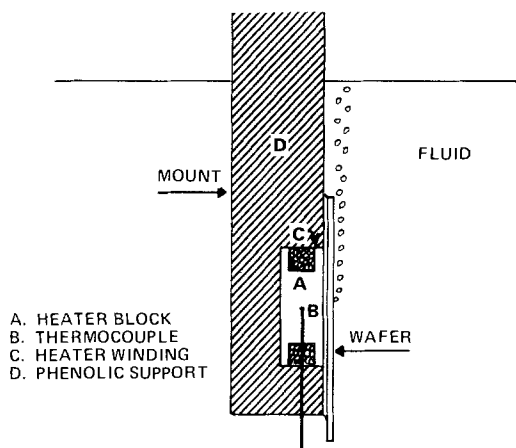


Fig. 2. Heat transfer apparatus

in contact with the fluid. The wafer is considerably larger than the heat source, so that edge effects, which would be disastrous in this investigation, are eliminated.

Results

The curves shown in Fig. 3 summarize the results of our investigation. Heat transfer is shown for three types of surfaces: (i) polished, (ii) sandblasted, and (iii) sandblasted followed by chemical etching.

The polished silicon surface, a standard production wafer, shows no tendency to nucleate. Within the power limitations of the apparatus, approximately 2 W/cm², heat transfer from the untreated silicon surface remained in the convective region of the heat transfer curve. This is shown by the linear relation between power and temperature. When this material is used in a semiconductor device that is submerged in

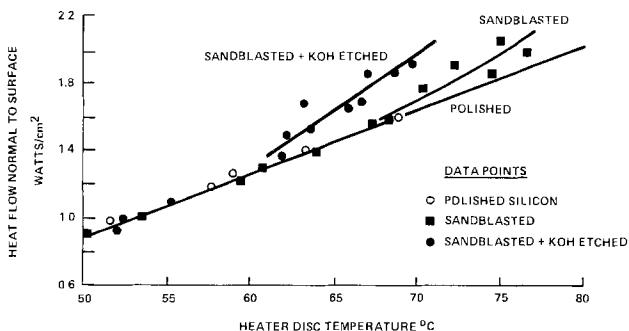


Fig. 3. Heat transfer to C₆F₁₄ for base, sandblasted, and etched surfaces.

the dielectric fluid, boiling only occurs at the cut edges of the chip and is delayed until the chip temperature rises well above the boiling temperature of the fluid. In some cases, boiling does not occur at all and overheating of the chip results.

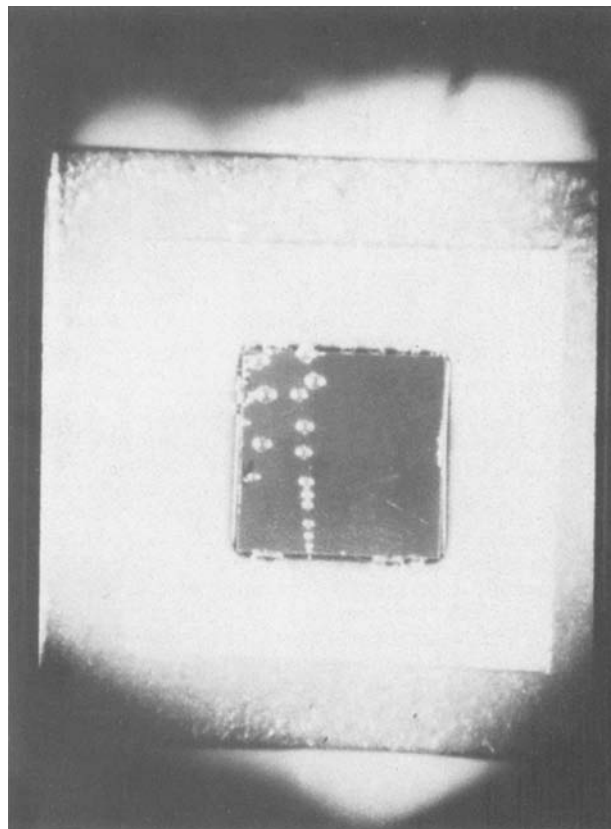


Fig. 4. Boiling from an untreated chip at 4.2W

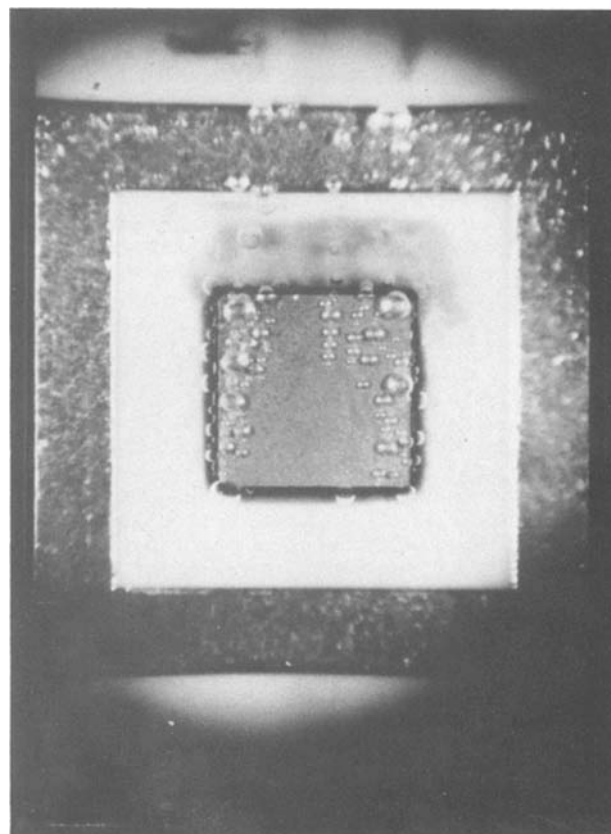


Fig. 5. Boiling from a treated chip at 4.2W

Sandblasting improves the situation somewhat, with boiling starting at about 1.6 W/cm², because only a limited number of nucleation sites have been provided. The sandblasted surface curve separates from the polished surface curve at 12°C above the boiling temperature. In other words, the surface is 12°C above the boiling temperature of the liquid before boiling will start on the sandblasted surface.

The best performing surface, sandblasted plus etched, initiated boiling at only 1.3 W/cm². The separation of the curve from the convection line occurs at only 4°C above the boiling temperature of the fluid.

The important question is: How does the real chip perform in the fluid environment? Figure 4 shows a typical silicon chip mounted on its substrate by means of an array of solder balls. The space between the chip and the substrate is sealed to prevent effects in that narrow space from interfering with our perception of back-side effects. A close look reveals that nucleation occurs at a few isolated locations at the edge of the chip. Nucleation sites can be identified by following the bubble trails back to their origin.

Figure 5 shows a treated chip in the same condition as before, the same power level, fluid temperature, chip size, and mounting. Here multiplicity of nucleation sites extends over the entire back surface of the chip.

Summary

We have demonstrated that untreated silicon is not suitable for heat transfer systems whose efficiency depends on boiling at the back of the chip. We have shown that proper treatment will reduce chip temperature and insure controlled chip temperatures in this kind of environment.

Manuscript submitted Feb. 10, 1981; revised manuscript received June 29, 1981.

Any discussion of this paper will appear in a Discussion Section to be published in the June 1982 JOURNAL. All discussions for the June 1982 Discussion Section should be submitted by Feb. 1, 1982.

Publication costs of this article were assisted by IBM Corporation.

REFERENCES

1. R. G. Frieser and M. D. Reeber, *J. Appl. Electrochem.*, **10**, 449 (1980).
2. J. B. Price, in "Semiconductor Silicon 1973," H. R. Huff and R. R. Burgess, Editors, p. 339, The Electrochemical Society Softbound Proceedings Series, Princeton, NJ (1973).
3. M. D. Reeber and R. G. Frieser, *IEEE-CHMT*, **3**, 387 (1980).

TEM Observations of Defects in Ge-Doped LPE GaAs and Al_{0.4}Ga_{0.6}As

Wilfried R. Wagner*

Bell Laboratories, Murray Hill, New Jersey 07974

ABSTRACT

The formation of structural defects in degenerate Ge-doped LPE GaAs and Al_{0.4}Ga_{0.6}As films was investigated. At growth initiation temperatures of 780°C, Ge doping does not result in structural defects even in films grown from solutions containing ~50 a/o Ge and even after heat-treatment at 720° and 820°C. On the other hand, films grown from heavily Ge-doped solutions below the decomposition temperature of GeAs (737°C) contained defects after a 15 hr heat-treatment at the growth temperature. These defects consisted of dislocation clusters and were only observed in films grown on substrates with elevated dislocation densities. It is concluded that the observed defects did not nucleate from the threading dislocations, but from GeAs or GeAs₂ particles decorating the dislocations.

In the past, the subject of structural defects in GaAs and Al_xGa_{1-x}As has received considerable attention (1, 2), but now interest in this subject has shifted to other III-V compound semiconductor alloy systems such as In-Ga-As-P. Nevertheless, the significant quantities of AlGaAs-GaAs lasers and LED's being manufactured today still require that a major effort in this materials technology be directed toward improving device characteristics and yield. In this direction, attempts to improve device resistances by improving the conductivities of the heteroepitaxial layers comprising the device have been unsuccessful. The reason for this is indicated in the paper of Wolfe and Stillman (3). In GaAs it was found that for Si, Ge, Sn, Se, S, and Te donor doping, at $(N_a + N_d) = 10^{17}$ cm⁻³, N_d equals $3N_a$, while for $(N_a + N_d) = 10^{18}$ /cm³, N_a equals N_d . Essentially, self-compensation negates the conductivity benefits that should have been realized from the increased doping. The nature of the compensating centers is of considerable interest. In their paper (3)

Wolfe and Stillman invoked impurity-vacancy complexes, but dopant-induced structural defects examined by transmission electron microscopy (TEM) have usually been found to be extrinsic, i.e., interstitial in nature (4-7). There exists then a disagreement between the presumed nature of dopant-induced point defects in GaAs that could only be reconciled by complex point defect interactions (8). Further disagreement seems to be indicated by the effects of Sn and Ge in GaAs. Except for these two, the compensation effects described by Wolfe and Stillman (3) have been correlated with dopant-induced structural defects in GaAs (2, 4, 5, 7). Yet it is accepted that Sn and Ge doping of GaAs, however high, does not induce structural defects in epitaxial films, even subsequent to heat-treatment.

In our work on Te-induced defects in GaAs (4) and Al_{0.4}Ga_{0.6}As (2), we proposed that the formation of the observed interstitial defects depends on the existence of nucleation sites consisting of second phase clusters whose principal constituent is the dopant species, i.e., GaTe and Al₂Te₃. In this paper, we re-

* Electrochemical Society Active Member.

Key words: thin films, transmission electron microscopy, liquid phase epitaxy, structural defects, heat-treatment, Ge doping.

examine this model for the case of Ge doping of GaAs and $\text{Al}_{0.4}\text{Ga}_{0.6}\text{As}$ films grown by LPE and subsequently heat-treated. Ge is the principal p-type dopant used in the LPE growth of GaAs and $\text{Al}_x\text{Ga}_{1-x}\text{As}$ films in LED's and heterojunction lasers. Degenerate Ge-doped GaAs layers are frequently used as contact layers in such devices. Structural defects may not be generated in such layers or device reliability will be degraded.

Experimental

The epitaxial films for this study were grown by LPE on {100} GaAs substrates doped with Si or Te. The dislocation densities of one class of substrates used was $3000/\text{cm}^2$; another class contained $1-2 \times 10^4/\text{cm}^2$ dislocations as determined by the application of the A/B etch. All samples consisted of two-layer heterostructures, an $\text{Al}_{0.8}\text{Ga}_{0.2}\text{As}$ film was grown first as an etchant blocking layer, followed by the p^{++} GaAs or p^{++} $\text{Al}_{0.4}\text{Ga}_{0.6}\text{As}$ sample films, 2-4 μm thick. The growth solution of the sample film contained 20-55 atomic percent (a/o) Ge, but most samples were grown from solutions containing 40 a/o Ge. The growth initiation temperature of the sample films was 720° and 780°C with a temperature gradient resulting in growth rates of 4 $\mu\text{m}/\text{hr}$. The Al composition of the $\text{Al}_{0.4}\text{Ga}_{0.6}\text{As}$ films was corrected for the decrease in the Al distribution coefficient arising from the high Ge doping (9) and was confirmed by measuring the lattice mismatch between the GaAs substrate and the sample film by x-ray diffractometry (10, 11).

The sample wafers were first polished to a 125 μm thickness, then diced into 3 mm disks. Samples were evacuated together with a large quantity of GaAs powder (1×10^{-6} Torr) in quartz ampuls then heat-treated at 720°C for 15 or 60 hr, and at 820°C for 15 hr. Self-supporting TEM samples were fabricated by etching a hole into the back-side of the disks using the PA etch. The high Al content of the buffer layer would stop the etching action, subsequently this layer was removed by warm conc. HCl. Final electron transparency was achieved using the 10:1:1, $\text{H}_2\text{SO}_4:\text{H}_2\text{O}:\text{H}_2\text{O}_2$ etchant. A JEOL-JEM 200 kV transmission electron microscope was used to evaluate the defect distribution occurring in the individual samples.

Results

Observations of As-grown samples.—In GaAs and $\text{Al}_{0.4}\text{Ga}_{0.6}\text{As}$ films grown from solutions containing 20-55 a/o Ge and at 720° or 780°C no contrast features were observed initially in the TEM that could be attributed to the high Ge doping. Neither dislocations nor precipitates were observed in films grown on low dislocation density substrates. Simple threading dislocations were observed in GaAs and $\text{Al}_{0.4}\text{Ga}_{0.6}\text{As}$ films grown on highly dislocated substrates (Fig. 1). Other diffraction contrast was not observed in such films (Table I). At a growth temperature of 780°C and a growth solution doping of 54.5 a/o Ge the GaAs-Ge phase boundary was crossed and Ge films resulted. The expected crossed grid of misfit dislocations was observed in such specimens at the substrate-epi interface.

Table I.

| Growth temp. ($^\circ\text{C}$) | Ge doping (a/o) | Substrate defects (cm^{-2}) | Threading dislocations observed (cm^{-2}) | Heat-treatment (hr \times $^\circ\text{C}$) | Dislocation climb observed |
|-----------------------------------|-----------------|--|--|--|----------------------------|
| 780 | 20-55 | 1000 | No | 15 \times 720 | No |
| 780 | 40 | 1000 | No | 60 \times 720 | No |
| 780 | 40 | 1000 | No | 15 \times 820 | No |
| 780 | 40 | 10^4 | 10^4 | 15 \times 720 | No |
| 780 | 40 | 10^4 | 10^4 | 15 \times 820 | No |
| 720 | 40 | 1000 | No | 15 \times 720 | No |
| 720 | 40 | 1000 | No | 60 \times 820 | No |
| 720 | 40 | 1000 | No | 15 \times 820 | No |
| 720 | 40 | 10^4 | 10^4 | 15 \times 720 | Yes |
| 720 | 40 | 10^4 | 10^4 | 60 \times 720 | Yes |
| 720 | 40 | 10^4 | 10^4 | 15 \times 820 | Yes |
| 720 | 0 | 10^4 | 10^4 | 15 \times 720 | No |

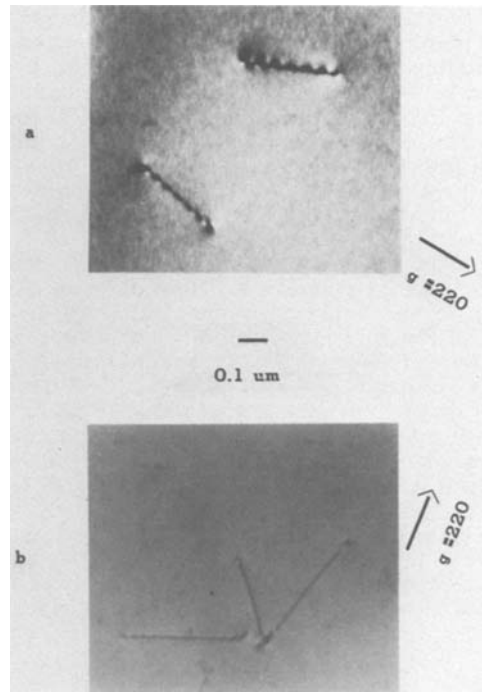


Fig. 1. Largest aggregate of threading dislocations observed in films grown on highly dislocated substrates. (a) Ge-doped GaAs; (b) Ge-doped $\text{Al}_{0.4}\text{Ga}_{0.6}\text{As}$.

The result of heat-treatments.—Dislocation multiplication and climb was observed to have taken place (Fig. 2) in GaAs and $\text{Al}_{0.4}\text{Ga}_{0.6}\text{As}$ films grown at 720°C on high dislocation-density substrates and from solutions containing 40 a/o Ge, after a 15 hr heat-treatment at 720°C . More extensive dislocation networks (Fig. 3) were observed in such films after a longer heat-treatment (60 hr at 720°C) or after a 15 hr heat-treatment at 820°C . Under quasi-kinematical diffraction conditions, contrast effects were observed in GaAs films that appeared to arise from small precipitates along the

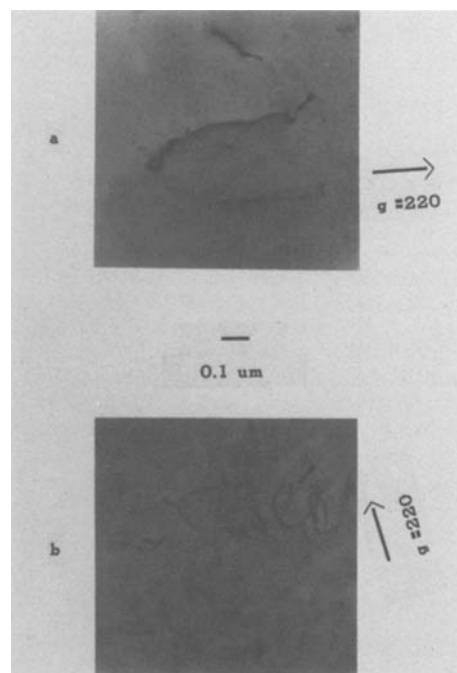


Fig. 2. Dislocation cluster observed in Ge-doped films heat-treated for 15 hr at 720°C . (a) GaAs; (b) $\text{Al}_{0.4}\text{Ga}_{0.6}\text{As}$.

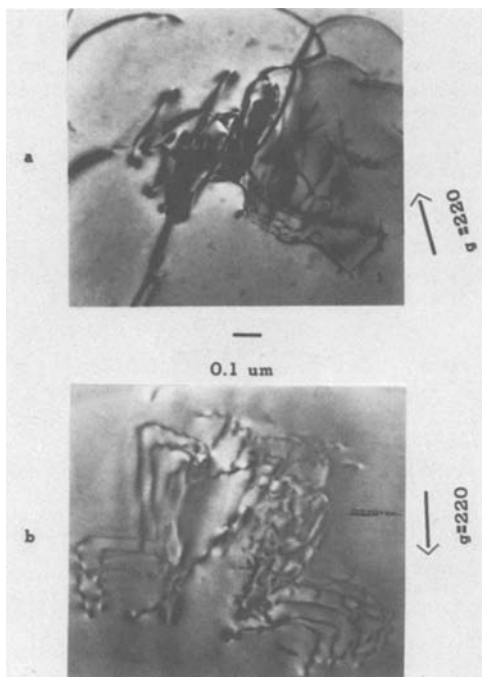


Fig. 3. Dislocation cluster observed in Ge-doped films heat-treated for 15 hr at 820°C. (a) GaAs; (b) $\text{Al}_{0.4}\text{Ga}_{0.6}\text{As}$.

dislocation line segments. Such contrast effects were not observed in $\text{Al}_{0.4}\text{Ga}_{0.6}\text{As}$ films. After a 15 hr heat-treatment at 720°C or at 820°C, structural defects were not observed in GaAs and $\text{Al}_{0.4}\text{Ga}_{0.6}$ films grown on substrates with low ($<3000/\text{cm}^2$) dislocation densities. These films were grown from solutions containing 20-55 a/o Ge and were grown at 720° and at 780°C. GaAs and $\text{Al}_{0.4}\text{Ga}_{0.6}\text{As}$ films grown at 780°C and from solutions of 40 a/o Ge on substrates with high dislocation densities ($1-2 \times 10^4/\text{cm}$) contained only simple threading dislocations even after a 15 hr heat-treatment at 720° or at 820°C. These results are summarized in the table.

Discussion

In epitaxial films, one type of dopant-related structural defect may form during epitaxial growth and usually consists of dislocations or stacking faults originating at precipitates (4). Another class of defects may occur during the heat-treatment of doped films and usually consists of either vacancy or interstitial loops (2). Structural defects formed as a result of the massive Ge-doping of the LPE growth solutions were not expected to occur in the as-grown GaAs and $\text{Al}_{0.4}\text{Ga}_{0.6}\text{As}$ films. Substantial stress centers, such as second phase particles at least large enough to punch out generator dislocation loops (12) to the growth interface, have to exist in such films. Subsequently the dislocation loop is extended by the advancing growth interface forming a large defect. Such second phase particles could consist of Ge, GeAs, or GeAs₂, but the growth conditions used in this experiment locate our films well within the GaAs phase field (13), therefore such second phase particles are not expected. Also, for films grown from 780°C the absence of second phase particles is indicated *a priori* by the curves relating growth solution doping to resultant free carriers (2, 4, 14; 15). Prior studies found that growth solution doping within the limit of a constant distribution coefficient does not result in defects in the as-grown films (2, 4). A constant distribution coefficient for Ge in GaAs ($N_a - N_d < 1 \times 10^{20}/\text{cm}^3$) and $\text{Al}_{0.4}\text{Ga}_{0.6}\text{As}$ ($N_a - N_d < 2 \times 10^{18}$) has been reported (14, 15), indicating that defects do not occur.

The formation of defects such as dislocation loops during heat-treatment depends upon the presence of diffusing point defects as well as strain centers to nucleate the loops (12), while the diameter of such loops depends on the concentration of the nucleation centers, the concentration of the point defects, and the diffusivity of the point defects. It was observed for films grown at 720°C that in both the Ge-doped GaAs and the $\text{Al}_{0.4}\text{Ga}_{0.6}\text{As}$ films the presence of threading dislocations was a precondition for the occurrence of dislocation multiplication and climb during heat-treatment. This is quite evident in Fig. 2b where an existing threading dislocation (arrow) has bowed out into a helix. The threading dislocations, however, do not appear to be the actual nucleating centers for the observed defects. Assuming that the point defects which cause the observed line defects in films grown at 720°C are present also in Ge-doped films grown at 780°C and subsequently heat-treated at 720° or 820°C, then the absence of dislocation multiplication and climb in films grown from 780°C must lie in the absence of suitable nucleation sites. Suitable nucleation sites would not consist of ordinary threading dislocations; they should consist of jogged dislocations or dislocations decorated by precipitates. This was the reason the low growth temperature of 720°C was selected. Both GeAs and GeAs₂ (16) are stable below 730°C. At a growth temperature of 720°C, momentary deviations from equilibrium growth kinetics combined with the enhanced nucleation and the changed thermodynamic potential at the emergence points of the threading dislocations are thought to result in the decoration of the threading dislocations with GeAs or GeAs₂ clusters. This cannot take place above the decomposition temperature (736° and 732°C, respectively) of these phases, therefore the diffusing point defects in films grown at 780°C could not aggregate along the threading dislocations and induce dislocation multiplication and climb.

In experiments with Te-doped GaAs and $\text{Al}_{0.4}\text{Ga}_{0.6}\text{As}$ films it was possible to prevent the formation of defects by decomposing the nucleation sites during heat-treatment above the melting point of the second phase particle (2, 4). But once the generator loop existed, the extrinsic dislocation loops continued to grow larger even during heat-treatment above the decomposition temperature of the nucleation center. The continued defect formation during heat-treatment even above the melting point of the precipitate points out the likely interaction between the threading dislocation and the precipitate. A precipitate becoming attached to a dislocation at the growth interface very likely induces a jog or kink. This means that such particles need not be large enough to punch out generator loops and explains why they were not directly resolved. Heat-treatment above the melting point of the precipitate would decompose the particle, but not the generator loop, and the dislocation could still climb as a result of a point defect flux.

The presence of point defect complexes in heat-treated, Ge-doped $\text{Al}_{0.4}\text{Ga}_{0.6}\text{As}$ films is indicated by a recent photoluminescence study (15). An observed decrease in photoluminescence intensity after heat-treatment was attributed to high concentrations of nonradiative centers that formed during heat-treatment. The present observation of increased defect complexity as a function of heat-treatment time or increased heat-treatment temperature confirms the activity of point defect diffusion. It is likely that a diffusion process enhanced by the stress field of the threading dislocation (18) and assisted by pipe diffusion along the dislocation results in the occurrence of the observed line defects. The formation of these defects may be examined with a model based on a complex point defect consisting of a substitutional impurity associated with at least one vacancy (3, 17). In considering a different point defect, it must be noted that the observed decrease in the PL intensity of heat-treated

$\text{Al}_{0.4}\text{Ga}_{0.6}\text{As}$ (15) must be the result of point defect interactions resulting in nonradiative centers. While Ge interstitials are expected to be fast diffusing and could cause the observed dislocation climb by combining with vacancies at the threading dislocations, resulting in climb (18), this mechanism would result in improved PL efficiencies. In the same vein, an interstitial Ge-vacancy complex is not likely to form as Ge is known to be amphoteric. More substantial interstitial complexes certainly do not form. The Ge-doping of GaAs and $\text{Al}_{0.4}\text{Ga}_{0.6}\text{As}$ is known to result in only very small lattice dilation (19, 20) that appear to be exclusively due to electronic effects.

In this experiment we did not differentiate if the observed dislocation climb was of interstitial or vacancy origin, mechanisms similar to Hurle's (8) could be applied to explain either effect. Frenkel defects formed during heat-treatment supply Ga and As vacancies which are "strongly gettered" (8) by the substitutional Ge impurity thereby increasing the concentration of the point defect complexes. The resulting supersaturation of Ga and As interstitials can then combine at the threading dislocation to form Ga_IAs_I and incorporate as a step into the dislocation line. Alternatively, a simple decomposition reaction of the Ge-vacancy complex at the nucleation site or the existing defect will also result in a germanium decorated, climbing dislocation. Again, more of the diffusing defect complex could be formed during heat-treatment from the interaction of As vacancies and the substitutional impurity to maintain the equilibrium vacancy concentration. More extensive TEM studies, as well as precision lattice parameter measurements need to be utilized to identify the dislocation climb mode and to reveal the nature of the diffusing point defect.

Conclusions

The massive germanium doping of LPE GaAs and $\text{Al}_{0.4}\text{Ga}_{0.6}\text{As}$ films grown at 720°C results in the formation of high concentrations of point defects during heat-treatment at 720° and at 820°C. During heat-treatment at 720° and 820°C the point defects diffuse to nucleation sites and decompose, resulting in the formation of dislocation aggregates. The nucleation sites for the observed defects appear to consist of GeAs or GeAs_2 clusters that form during growth only near threading dislocations in the doped epitaxial films. For films grown above the melting point of the GeAs or GeAs_2 phases the nucleation sites do not exist near the threading dislocations and as a result the dislocation aggregates do not form.

Acknowledgments

The author wishes to thank J. L. Zilko, D. L. Van Haren, K. R. Stiles, and A. E. Milgram for their

assistance in preparing the specimens. Extensive discussions with V. Swaminathan, P. S. Anthony, and N. E. Schumaker have been very rewarding.

Manuscript submitted April 20, 1981; revised manuscript received June 15, 1981. This was Paper 459 presented at the Hollywood, Florida, Meeting of the Society, Oct. 5-10, 1980.

Any discussion of this paper will appear in a Discussion Section to be published in the June 1982 JOURNAL. All discussions for the June 1982 Discussion Section should be submitted by Feb. 1, 1982.

Publication costs of this article were assisted by Bell Laboratories.

REFERENCES

1. P. Petroff, *Inst. Phys. Conf. Ser. No. 23*, 73 (1975).
2. W. R. Wagner, *J. Appl. Phys.*, **49**, 173 (1978).
3. C. M. Wolfe and G. E. Stillman, *Appl. Phys. Lett.*, **27**, 564 (1975).
4. W. R. Wagner, *Inst. Phys. Conf. Ser. No. 33b*, 65 (1977).
5. P. W. Hutchinson and P. S. Dobson, *J. Met. Sci.*, **10**, 1636 (1975).
6. T. Kotani, O. Veda, K. Akita, Y. Nishitani, K. Kusunoki, and O. Ryuzan, *J. Cryst. Growth*, **38**, 85 (1977).
7. M. S. Abrahams, J. Blanc, and C. Buiocchi, *Philos. Mag.*, **23**, 795 (1971).
8. D. T. J. Hurle, *Inst. Phys. Conf. Ser. No. 33a*, 113 (1978).
9. H. T. Minden, R. Premo, and C. V. Collins, *J. Cryst. Growth*, **27**, 316 (1974).
10. W. J. Bartels and W. Nijman, *ibid.*, **44**, 518 (1968).
11. W. R. Wagner, V. Swaminathan, C. C. Chang, R. Dingle, and D. L. Van Haren, *This Journal*, Submitted for publication.
12. T. Y. Tan and W. K. Tice, *Philos. Mag.*, **34**, 615 (1976).
13. M. B. Panish, *J. Less Common Metals*, **10**, 416 (1966).
14. D. R. Ketchow, *This Journal*, **121**, 1237 (1974).
15. V. Swaminathan, N. E. Schumaker, J. L. Zilko, W. R. Wagner, and C. A. Parsons, *J. Appl. Phys.*, **52**, 417 (1981).
16. M. Hansen, in "Constitution of Binary Alloys," p. 165, McGraw-Hill, New York (1958).
17. E. W. Williams and H. B. Bebb, in "Semiconductors and Semimetals," Vol. 8, R. K. Willardson and A. C. Beer, Editors, p. 321, Academic Press, New York (1972).
18. W. C. Dash, *J. Appl. Phys.*, **31**, 2275 (1960).
19. D. L. Rode, R. L. Brown, and M. A. Aframowitz, *J. Cryst. Growth*, **30**, 299 (1975).
20. W. R. Wagner, *This Journal*, To be published.

High Temperature Flow Resistance of Micron Sized Images in AZ Resists

H. Hiraoka and J. Pacansky

IBM Research Laboratory, San Jose, California 95193

ABSTRACT

A simple u.v. curing process is described that renders micron sized images in AZ resists resistant to flow when heated to temperatures as high as 210°C. The u.v. treatment prevents the image flow problems usually encountered in reactive ion etching processes.

The implementation of reactive ion etching (RIE) in lithographic processes has created new demands on resists (1); one of the foremost is the resistance to flow at the high temperatures created by a plasma discharge. It is not uncommon for micron size images to flow when subjected to the temperatures that could be over 200°C in an RIE environment. The well-known and widely used class of lithographic materials labeled the AZ resists consists of a mixture of a diazo-oxide (I) and a phenolic resin (IV) (see Scheme I). Most members of the class of AZ resists, for example, have exhibited image flowing at high temperatures. This report describes a very simple u.v. curing process that renders images in any member of the AZ family of resists stable to flow at temperatures over 200°C.

Experimental

Resist patterns.—AZ-2400 (trademark of the Shipley Company, Newton, Massachusetts) was spin-coated onto silicon wafers, and subsequently prebaked at 83°C for 12 min. The wafers were exposed to a 20 keV electron beam using a vector scan type apparatus at a dose of 2×10^{-5} C/cm². The patterns were developed in (1:3) AZ-2401 developer.

A Hanonia SH(616A) medium pressure mercury lamp with a total u.v. output of 6.3W was used for the u.v. curing; the intensity at 2540Å was 2×10^{-4} W/cm². The lamp was used either without filters or with a Corning No. 054 glass filter (0%T for $\lambda < 3000$). The imaged resists were exposed in air at a distance of 15 cm away from the lamp. Exposures were also conducted with the imaged resist under vacuum.

Heat treatment.—A hot plate or a vacuum oven was used for the heat-treatment. The procedure consistently followed was to set the hot plate or the oven at the specified value; the wafers with the resist patterns were then placed on the heated surfaces so that very rapid heating took place. The temperature was measured with a thermocouple that was firmly attached to the surface of the hot plate.

Procedure.—A direct comparison was made between patterns u.v. cured and not u.v. cured by breaking a resist line pattern into two pieces through the lines. When a comparison was made between the u.v. exposed and the unexposed samples both pieces of the pair were heated side by side at the same time for identical periods in order to avoid inconsistencies in the data. Afterwards, the wafers were coated with aluminum thin films for SEM inspection. The SEM micrographs were obtained with an ISI Super II SEM.

In order to test the effect of wavelength and the atmosphere on the process irradiations were performed with and without filters in the mercury lamp with the sample contained in a vacuum system or in air.

Key words: u.v. treatment, reactive ion etching, lithography.

Results

In Fig. 1(a) and (b) the effect is shown for a postbake at 95°C for 30 min in air. Figure 1(a) displays the resist without a postbake while Fig. 1(b) shows the patterns after a postbake. Clearly a thermal flow of the resist has occurred during the postbake. Figures 1(c) and (d), however, show that u.v. exposure prior to a postbake at 100°C completely eliminated thermal flow of the resist pattern. For example, in Fig. 1(d) the results are shown for patterns with no postbake that were exposed to u.v. light and then heated at 100°C for 30 min in air. For comparison, Fig. 1(c) contains an SEM of original patterns with no postbake.

In essence the results summarized in Fig. 1 demonstrate the detrimental effect of postbake before u.v. curing on flow resistance of resist images. Elimination of the postbake prior to u.v. curing is a paramount consideration for the process to be successful; this is amply demonstrated by the results that follow.

The exposure time required for the u.v. cure is a function of the temperature at which the resist patterns must not flow. In general, the exposure time increases as the temperature at which the resist is heated increases. Figures 2 and 3 demonstrate this for resist patterns heated at 155° and 210°C, respectively. Figure 2(a) contains an SEM micrograph of the resist pattern obtained after development; Fig. 2(b) shows the effect of u.v. exposure for 15 min followed by heating at 155°C for 30 min with no prebake; Fig. 2(c) shows the effect of heating without the u.v. cure. The contrast between Fig. 2(b) and (c) vividly demonstrates the beneficial effect of the u.v. cure, which under the conditions used in the present studies requires an exposure time of 15 min for flow resistance at $\approx 150^\circ\text{C}$. For flow resistance of the resist patterns at 210°C a longer exposure time is required. In Fig. 3(a) the re-

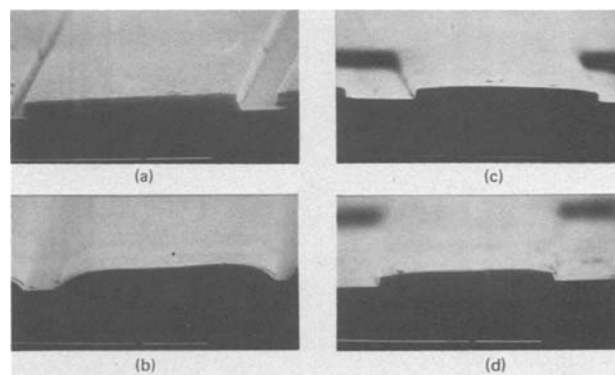


Fig. 1. The effect of postbake on the resist patterns in the AZ-2400; (a) the resist patterns without postbake; (b) the resist patterns after postbake at 95°C for 30 min in air; (c) the resist patterns without postbake; (d) the resist patterns exposed to the u.v. light, then subsequently heated at 100°C for 30 min in air.

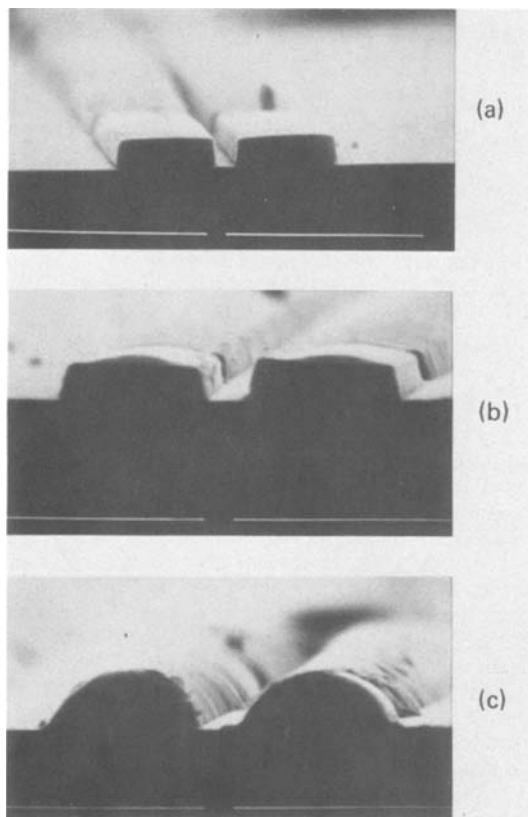


Fig. 2. The effect of a 15 min u.v. exposure on the resist patterns in AZ-2400; (a) the patterns with no postbake; (b) the resist patterns exposed to the u.v. light for 15 min in air, then subsequently heated at 155°C for 30 min; (c) the resist patterns heated at 155°C for 30 min without the u.v. exposures.

sist pattern is shown after development. Figure 3(b) contains an SEM showing the complete loss of the patterns after heating to 210°C for 25 min. Figure 3(c) shows that a 15 min u.v. exposure has dramatically retarded but has not stopped the image flowing at 210°C. Figure 3(d), however, clearly demonstrates that a 30 min exposure has prevented the catastrophic image flow at 210°C.

Discussion

Irradiation of an AZ type resist with u.v. light after images have been developed renders the material resistant to flow at high temperatures. The u.v. exposure, however, will only be effective when done without a postbake. This point must be stressed because it is a common practice to postbake resists in order to enhance the quality of the film.

Another important requirement for the u.v. cure is that longer exposure times are required for flow resistance at higher temperatures. For example, it was shown that an exposure time of about 30 min was needed for flow resistance at 210°C. This exposure time also suffices for temperatures somewhat higher than 210°C (the high temperature limit was not tested because temperatures around 210°C are believed to approximate those found under RIE conditions). The amount of time required for the u.v. cure seems rather excessive but the mercury lamp used in this study has a relatively low output of u.v. light in comparison to other high pressure mercury lamps (2). A conservative estimate that is easily obtained is that lamps are available with >200 times the u.v. output of the Hanonia lamp used in this study; consequently, exposure times of about 10-20 sec are possible. In this respect the implementation of the u.v. curing described

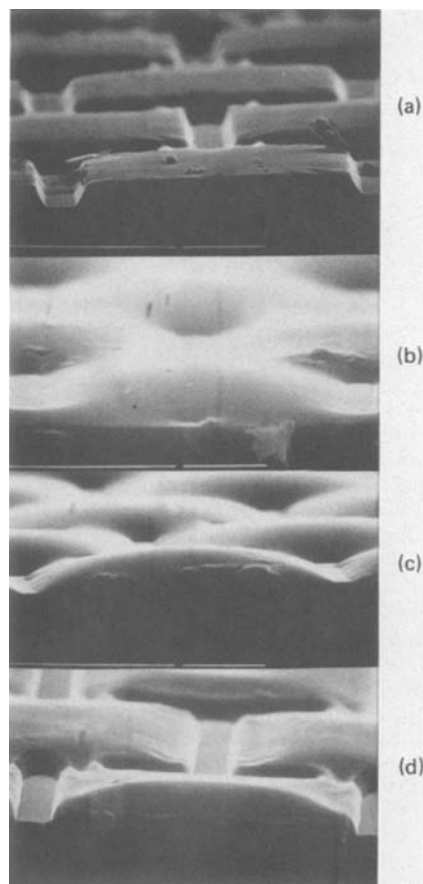
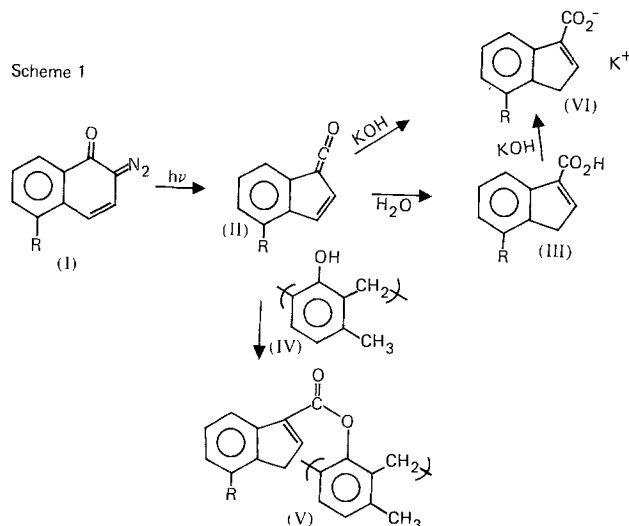


Fig. 3. The effect of increasing u.v. curing time; (a) original patterns; (b) no u.v. hardening but heated at 210°C for 25 min; (c) u.v. exposure for 15 min, then heated at 210°C for 25 min; (d) u.v. exposure for 30 min, then heated at 210°C for 25 min.

in this report into a commercial process becomes quite attractive.

In general, the u.v. cure works for the AZ class of resists. On the basis of the known photochemical mechanism (3) operative in the AZ class of resists an explanation was sought for this phenomenon. The photoactive compound in the resist is a diazo-oxide (I) that is photochemically converted to a ketene (II) as shown in Scheme I. In the presence of moisture (II)



forms the carboxylic acid (III), or, in the absence of moisture (e.g., high vacuum) the ketene (II) reacts with the resin (IV) to form the ester (V). Under the conditions used in the experiments described in this

report the u.v. curing seems to be independent of whether the irradiations are performed in vacuum or in the atmosphere. Furthermore, infrared studies indicate that neither the carboxylic acid (III) or the ester (V) are photochemically produced; instead the salt of the carboxylic acid (VI) is produced. Studies have shown that the origin of the salt formation is due to residual developer (KOH) left in the resist after development. Since the ketene (II) or the acid (III) reacts vigorously with bases then salt formation easily proceeds. The production of the potassium indene carboxylate salt in this manner renders the resist more resistant to flow at high temperature.

Summary

A simple u.v. cure has been described whereby the high temperature flow resistance of the AZ class of resists is dramatically improved. The u.v. cure involves exposure of the imaged resist to light after development and appears to work under a variety of exposure conditions. The salient feature that makes the chem-

istry of the u.v. cure different from that normally found in the resist is that the potassium indene carboxylate salt is photochemically produced instead of the indene carboxylic acid.

Manuscript submitted March 16, 1981; revised manuscript received July 10, 1981.

Any discussion of this paper will appear in a Discussion Section to be published in the June 1982 JOURNAL. All discussions for the June 1982 Discussion Section should be submitted by Feb. 1, 1982.

Publication costs of this article were assisted by IBM Corporation.

REFERENCES

1. G. C. Schwartz and P. M. Schaible, *Solid State Technol.*, 85 (1980).
2. For a comparison of commonly used mercury lamps, see J. G. Calvert and J. N. Pitts, "Photochemistry," p. 691, John Wiley and Sons, New York (1967).
3. J. Pacansky and J. Lyerla, *IBM J. Res. Dev.*, 23, 42 (1979).

High Pressure Plasma (HPP) Deposition of Polycrystalline Silicon Ribbons

K. R. Sarma* and M. J. Rice, Jr.*

Motorola Incorporated, Semiconductor Group, Solar Energy R&D Department, Phoenix, Arizona 85008

ABSTRACT

A high pressure plasma (HPP) deposition process has been characterized for its potential in producing polycrystalline silicon films (ribbons) at low cost. Gas chromatographic (GC) analysis of HPP deposition reactor effluent gases has been used for characterizing the deposition process. Silicon tetrachloride, trichlorosilane, dichlorosilane, and silane have been evaluated as possible silicon source gases for silicon deposition by HPP. Deposition efficiencies have been determined under various experimental conditions such as rf power of HPP, concentration and flow rate of reactant gases, and substrate temperature. These efficiencies were found to be higher than those obtained by a conventional chemical vapor deposition (CVD) process under all conditions of practical interest. The observed improvements in HPP silicon deposition may be explained using thermodynamics, operative kinetic processes, and deposition mechanisms. Economic potential of the HPP deposition process for producing silicon films appears favorable.

Chemical vapor deposition (CVD) of silicon by high temperature (1000°-1200°C) hydrogen reduction of a chlorosilane such as SiHCl_3 is a well-established process used extensively in the semiconductor industry. It is used for producing bulk polycrystalline silicon as well as thin films of silicon in polycrystalline or in single crystal form. In many of these processes, cold-wall deposition systems are used to prevent wall deposition. This CVD process, as it is used, is characterized by low chemical and energy utilization efficiency, low throughput rate, and high cost. Recently, devices for which silicon material cost is a major part of the total cost (e.g., solar cells) have provided an impetus for development of advanced technologies capable of reducing the cost of depositing silicon. We have been investigating a high pressure plasma (HPP) deposition process as a means for depositing polycrystalline silicon ribbons (films) at low cost (1-4). Unlike many low pressure plasma processes used in the semiconductor industry that operate in the pressure range of few Torr, this HPP operates at a pressure near one atmosphere.

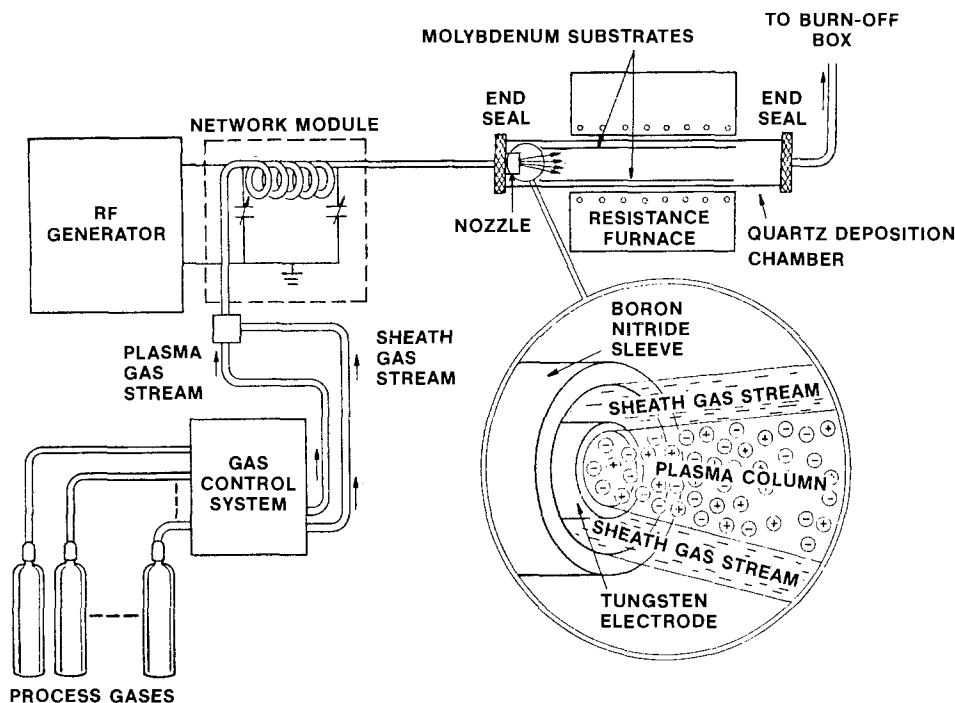
The HPP deposition system, which is schematically shown in Fig. 1, includes a 13.56 MHz rf generator, an impedance matching module, a plasma beam nozzle, and a hot-wall deposition reactor. Silicon films are deposited onto the substrates covering the deposition reactor walls by introducing hydrogen and chlorosilane directly into the rf circuit through a tubular output coil in the impedance matching module. The tubular output coil terminates in a nozzle containing a hollow tungsten electrode. Tuning the impedance matching module for resonance creates, at the tip of the electrode, a high voltage which results in an electrical discharge plasma. Due to macroscopic motion of the reactant gas stream through the electrode, the plasma extends into the space in front of the nozzle as a jet. Emission spectroscopic measurements have indicated localized temperatures in the vicinity of 4000°C in the plasma beam.

Previously, the feasibility of depositing semiconductor grade purity polycrystalline silicon films, at high chemical utilization efficiencies, using SiCl_4 and SiHCl_3 as silicon source gases has been shown (1, 2). In this paper, we will present the results of a more detailed characterization effort. The HPP deposition

* Electrochemical Society Active Member.

Key words: chromatography, thermodynamics, semiconductor, quenching, kinetics.

Fig. 1. Schematic of the high pressure plasma (HPP) deposition system.



process is thoroughly characterized by on-line gas chromatography (GC) as a function of various experimental parameters such as rf power of the HPP, concentrations and flow rates of input reactant gases, and substrate temperature. These results on HPP deposition are compared with results obtained under CVD conditions. The observed results are discussed in terms of thermodynamics and deposition mechanisms and kinetic and transport processes operative in HPP deposition.

Experimental

Experimental work consisted of determining silicon deposition efficiency using an on-line GC. The HPP deposition apparatus used in this investigation is shown schematically in Fig. 1. The fused silica deposition reactor was of $5 \times 5 \text{ cm}^2$ cross section. The walls of this reactor were covered with 1 mm thick molybdenum substrates. The auxiliary resistance furnace employed had a hot zone length of 30 cm and served for controlling the substrate temperature. Molybdenum acts as a temporary substrate (5) for producing self-supporting silicon ribbons; i.e., silicon films deposited on Mo substrates are separated from the substrate, by cooling from deposition temperature, due to differential thermal expansion coefficients of Mo and Si.

The effluent gas stream from the deposition reactor was split into two gas streams as shown in Fig. 2. The large gas stream was sent to a hydrogen and chlorosilane burn-off box and exhaust. The small gas stream was sent to a six port gas sampling valve of a Hewlett Packard 5840A Reporting Gas Chromatograph with a thermal conductivity detector. A 10 ft stainless steel column packed with Chromosorb-W and a 20% loading of SF-96 as the absorbant phase were used. The instrument was calibrated for retention time and detector response by sampling gas with known concentrations of HCl, SiH_2Cl_2 , SiHCl_3 , and SiCl_4 in H_2 , which was passed through the reactor and sampling system at room temperature. Calibrations were made with individual constituents and with mixtures. Column temperature was time programmed to shorten analysis time, starting at 35°C , increased at a rate of $30^\circ\text{C}/\text{min}$ to 80°C , and remained at that temperature until the analysis was complete. Using 30 ml/min hydrogen carrier gas, retention times of 0.92, 1.75, 2.52, and 3.43 min were obtained for HCl, SiH_2Cl_2 , SiHCl_3 ,

and SiCl_4 , respectively, and the GC run was terminated at 4 min. The column cooled to 35°C in 3.5 min allowing a new sample to be taken every 7.5 min. Application of GC for characterization of silicon CVD processes has been described in the literature (6) and detailed theory and practice of GC analysis may be found in many of the standard textbooks, e.g., Ref. (7). Since the sample gas to be analyzed is cooled to the column temperature this technique is not suitable for studying chemical equilibrium in the high temperature environment, but can be used to obtain reactant utilization efficiency.

Figure 3 shows a typical chromatograph. Using the composition of effluent gases from the deposition reactor determined by the GC analysis, the deposition efficiency (reactant utilization efficiency), η , is calculated as follows

$$\eta = \frac{(\text{Si/Cl})_{\text{in}} - (\text{Si/Cl})_{\text{out}}}{(\text{Si/Cl})_{\text{in}}} \cdot 100\%$$

where $(\text{Si/Cl})_{\text{in}}$ and $(\text{Si/Cl})_{\text{out}}$ are the silicon to chlorine ratios in the input and effluent gas streams. For example, when using SiCl_4 as the silicon source gas, $(\text{Si/Cl})_{\text{in}}$ will be 0.25. $(\text{Si/Cl})_{\text{out}}$ is calculated as

EXHAUST PIPE FROM PLASMA DEPOSITION REACTOR

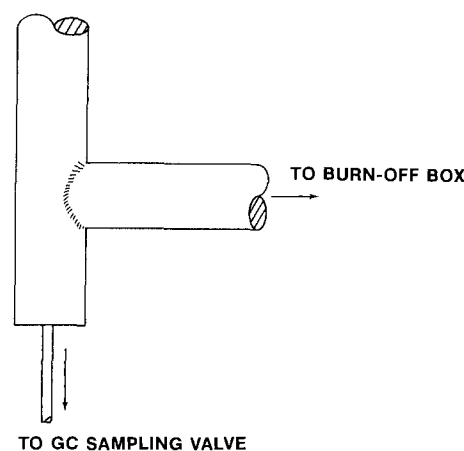


Fig. 2. Gas chromatographic (GC) gas sampling arrangement

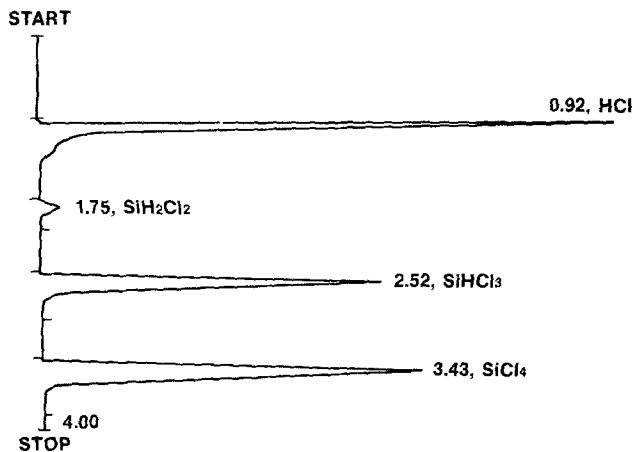


Fig. 3. Example of a typical chromatograph of the HPP reactor effluent gas stream.

follows

$$(\text{Si/Cl})_{\text{out}} = \frac{m_{\text{Si}}}{m_{\text{Cl}}} = \frac{100 - m_{\text{HCl}}}{m_{\text{Cl}}}$$

where

$$m_{\text{Si}} = m_{\text{SiH}_2\text{Cl}_2} + m_{\text{SiHCl}_3} + m_{\text{SiCl}_4} = 100 - m_{\text{HCl}}$$

$$m_{\text{Cl}} = m_{\text{HCl}} + 2m_{\text{SiH}_2\text{Cl}_2} + 3m_{\text{SiHCl}_3} + 4m_{\text{SiCl}_4}$$

and m_{HCl} , $m_{\text{SiH}_2\text{Cl}_2}$, m_{SiHCl_3} , and m_{SiCl_4} are mole percentages of HCl, SiH_2Cl_2 , SiHCl_3 , and SiCl_4 , respectively, in the effluent gas stream, as determined by GC analysis. Deposition efficiencies calculated from GC measurements were found to be repeatable to within $\pm 0.5\%$. Under certain conditions, gas phase nucleation in the deposition reactor was excessive and led to powder growth, instead of dense film growth. Also some of this powder was found to leave the reactor with the effluent gas stream, resulting in a difference between deposition efficiencies determined by GC analysis and weight gain measurements. (Silicon particles in the gas stream were filtered out before going into the GC column.) Deposition efficiencies were found to agree well with the values calculated from weight of silicon deposited when powder growth was absent. For comparative purposes, results were also obtained for the CVD mode of operation (i.e., without HPP beam) under otherwise identical conditions.

Results

RF power required for a stable HPP beam was found to increase with increases in concentration and flow rate of the reactant gas stream. Once a stable HPP beam is established at a particular rf power, a further increase in rf power is not found to have any noticeable effect on silicon deposition efficiency. Hence in all the experiments rf power employed was kept close to the minimum required for a stable operation of the HPP beam.

Silicon tetrachloride.—Table I summarizes results obtained using SiCl_4 as the silicon source gas. Reactant concentration can be seen to have a major effect on deposition efficiency both for CVD and HPP modes of operation. In general, the effect of increased flow rate is to decrease the deposition efficiency as expected. One major exception to this is the case for 1100°C , $\text{Cl/H} = 0.04$ deposition, where increasing the flow rate increased the efficiency. For HPP, flow rate seems to have a similar but smaller effect. Substrate temperature, in the range of $1050^\circ\text{--}1150^\circ\text{C}$, did not seem to have much effect on deposition efficiency either for CVD or HPP except for lower reactant concentrations (e.g., $\text{Cl/H} = 0.04$). Deposition enhancement by HPP was found to occur for low reac-

Table I. Summary of results obtained using SiCl_4 as silicon source gas

| T (°C) | Mode | Flow rate (liters/ min) | Deposition efficiency (%) for reactant concentration | | |
|-----------|------|-------------------------------|---|---------------|---------------|
| | | | Cl/H = 0.04 | Cl/H = 0.8 | Cl/H = 0.1 |
| 1050 | CVD | 15 | 43.6 | 18.8 | 11.9 |
| | HPP | 15 | 41.8 | 19.1 | 10.6 |
| | CVD | 30 | 33.8 | 13.9 | 10.1 |
| 1100 | HPP | 30 | 42.6 | 14.4 | 9.5 |
| | CVD | 15 | 40.9 | 19.2 | 12.9 |
| | HPP | 15 | 43.1 | 19.6 | 11.9 |
| 1150 | CVD | 30 | 46.0 | 17.1 | 12.0 |
| | HPP | 30 | 50.0 | 18.2 | 11.0 |
| | CVD | 15 | 54.0 | 20.3 | 13.0 |
| | HPP | 15 | 54.4 | 20.6 | 11.8 |
| | CVD | 30 | 50.8 | 19.6 | 13.7 |
| | HPP | 30 | 55.1 | 19.9 | 11.5 |

tant concentrations ($\text{Cl/H} = 0.04$). Effect of reactant concentration, Cl/H , is plotted in Fig. 4 both for CVD and HPP for a substrate temperature of 1100°C and reactant flow rate of 30 liters/min. Also, in Fig. 4, the thermodynamic equilibrium efficiency calculated (1, 3) for 1100°C deposition is shown. Both the CVD and HPP efficiencies can be seen to be higher than the equilibrium predictions, particularly at high concentrations. (See section on Transport processes for discussion of reasons for this.)

Trichlorosilane.—Results obtained with SiHCl_3 are summarized in Table II. Similar to the case with SiCl_4 , reactant concentration seems to have a major effect for both CVD and HPP modes of operation. In the case of CVD, in general, the effect of increasing flow rate is to decrease deposition efficiency except for depositions with $\text{Cl/H} = 0.4$ and with substrate temperature in the range of $1100^\circ\text{--}1200^\circ\text{C}$. In the case of HPP, changing the flow rate from 15 to 30 liters/min seemed to improve the deposition efficiency in many cases and in some cases substantially. The effect of substrate temperature is plotted in Fig. 5, for concentrations $\text{Cl/H} = 0.08$ and 0.1 and flow rate = 30 liters/min. A maxima in concentration can be seen at 1100°C both for CVD and HPP. The effect of reactant concentration is plotted in Fig. 6 for a substrate temperature of 1100°C and flow rate of 30 liters/min. For comparison, efficiencies calculated from thermodynamic equilibrium (1, 3) are also plotted. Deposition enhancement by HPP is highest for lower concentrations. Also, while CVD efficiencies are consistently lower than equilibrium efficiencies, HPP efficiencies are found to be higher than equilibrium values for $\text{Cl/H} < 0.12$.

Dichlorosilane.—Table III shows the results obtained with SiH_2Cl_2 . It also shows the calculated equilibrium efficiencies for an 1100°C substrate temperature. The

Table II. Summary of results obtained using SiHCl_3 as silicon source gas

| T (°C) | Mode | Flow rate (liters/ min) | Deposition efficiency (%) for reactant concentration | | |
|-----------|------|-------------------------------|---|----------------|---------------|
| | | | Cl/H = 0.04 | Cl/H = 0.08 | Cl/H = 0.1 |
| 1050 | CVD | 15 | 40.5 | 30.9 | 26.5 |
| | HPP | 15 | 49.3 | 35.6 | 29.8 |
| | CVD | 30 | 39.0 | 25.0 | 21.7 |
| 1100 | HPP | 30 | 53.5 | 35.1 | 32.7 |
| | CVD | 15 | 47.3 | 35.7 | 32.3 |
| | HPP | 15 | 54.3 | 38.5 | 33.5 |
| 1150 | CVD | 30 | 48.5 | 34.0 | 29.3 |
| | HPP | 30 | 55.1 | 37.9 | 34.0 |
| | CVD | 15 | 51.9 | 34.2 | 30.7 |
| 1200 | HPP | 15 | 49.3 | 35.6 | 32.3 |
| | CVD | 30 | 53.9 | 31.7 | 27.8 |
| | HPP | 30 | 55.7 | 35.8 | 31.7 |
| | CVD | 15 | 48.0 | 34.9 | 30.5 |
| | HPP | 15 | 49.8 | 37.3 | 33.2 |
| | CVD | 30 | 51.6 | 31.4 | 29.0 |
| HPP | 30 | 68.4 | 39.0 | 33.5 | |

Fig. 4. Deposition efficiency with SiCl_4 source. (Total reactant flow rate = 30 liters/min, substrate temperature = 1100°C). Note that the concentration range in this figure extends beyond the one given in Table I.

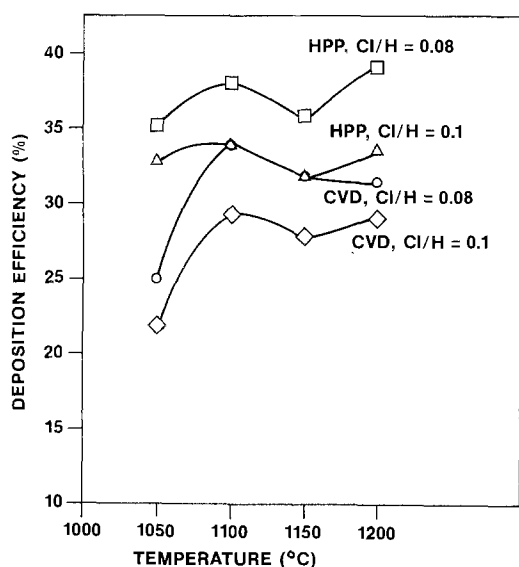
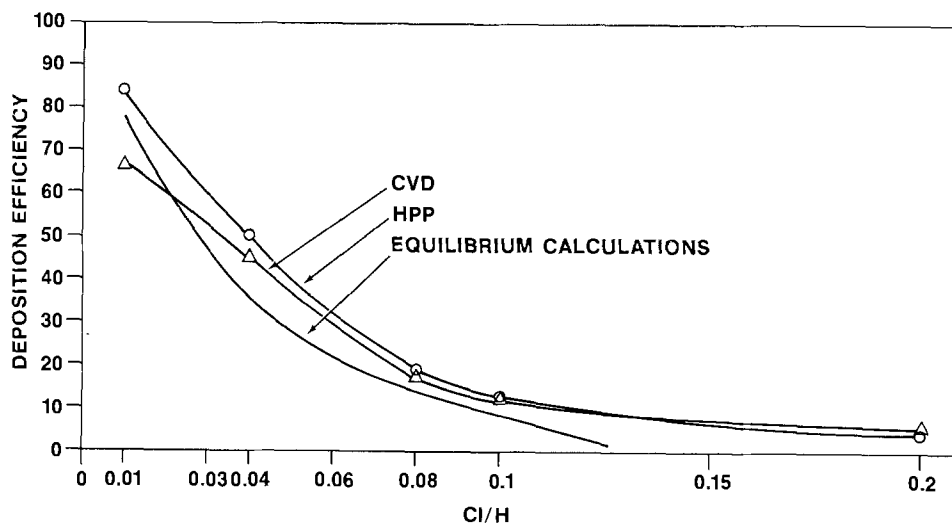


Fig. 5. Deposition efficiency vs. substrate temperature for SiHCl_3 source. (Total reactant flow rate = 30 liters/min).

HPP efficiencies, in general, are found to be higher than CVD values. Deposition enhancement by HPP appears to be higher (compared to CVD) for lower substrate temperatures and lower reactant concentrations. HPP efficiencies can be seen to be quite close to the calculated equilibrium efficiencies for an 1100°C substrate temperature. Gas phase nucleation leading to powder growth was found to be a problem when

using SiH_2Cl_2 both with CVD and HPP modes of operation. This problem was found to become more severe with increases in flow rate, concentration, and substrate temperature.

Silane.—Silane was also investigated as a source gas for silicon deposition. However, powder growth was found to be a problem with both CVD and HPP under all conditions of practical interest that result in reasonable throughput rate. Hence work with SiH_4 was discontinued.

Throughput rate.—Apart from deposition efficiency, throughput rate (in which throughput rate is used as the amount of silicon deposited in unit time) is another important parameter affecting the cost of depositing silicon. Reactor throughput rate determines the number of reactors (capital) required for a given capacity, which in turn determines production floor space requirements. Throughput rate can be calculated knowing reactant concentration and flow rates and deposition efficiency. Figure 7 shows the calculated throughput rates for SiCl_4 and SiHCl_3 source gases under CVD and HPP modes of operation as functions of concentration for a substrate temperature of 1100°C and a total reactant flow rate of 30 liters/min. For SiCl_4 , throughput rate shows a maximum both for CVD and HPP modes of operation. This is in agreement with equilibrium calculations. In the case of SiHCl_3 , throughput rate can be seen to increase with increasing reactant concentration both for CVD and HPP modes of operation, which is again in agreement with equilibrium calculations. However, a practical limit on throughput rate will be set by deposit mor-

Fig. 6. Deposition efficiency with SiHCl_3 source. (Total reactant flow rate = 30 liters/min, substrate temperature = 1100°C). Note that the concentration range in this figure extends beyond the one given in Table II.

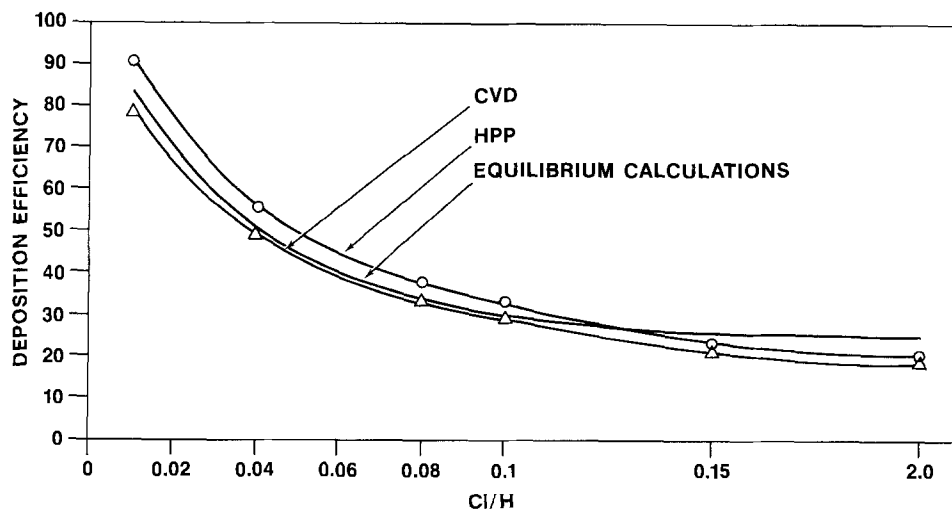


Table III. Summary of results obtained using SiH_2Cl_2 as silicon source gas

| T (°C) | Mode | Flow rate (liters/ min) | Deposition efficiency (%) for reactant concentration | | | |
|-----------|------|-------------------------------|---|----------------|----------------|----------------|
| | | | Cl/H = 0.01 | Cl/H = 0.02 | Cl/H = 0.04 | Cl/H = 0.08 |
| 1000 | CVD | 15 | 76.8 | 66.6 | 57.3 | 50.3 |
| | HPP | 15 | 81.6 | 70.5 | 59.5 | 52.0 |
| 1050 | CVD | 15 | 81.9 | 76.4 | 63.2 | 57.3 |
| | HPP | 15 | 85.4 | 87.6 | 69.1 | 57.5 |
| 1100 | CVD | 15 | 86.8 | 78.6 | 70.0 | 57.5 |
| | HPP | 15 | 87.4 | 80.0 | 71.3 | 56.4 |
| | EQBM | — | 89.0 | 80.0 | 68.0 | 57.0 |

phology considerations and the increasing severity of gas phase nucleation leading to powder growth. Increasing reactant concentrations are found to lead to nodule and whisker growth instead of smooth film growth. These problems are found to limit the maximum usable concentration to about Cl/H = 0.1, when using SiHCl_3 . Thus the practical throughput rate obtainable from SiHCl_3 is about a factor of two higher than that from SiCl_4 . Also, practical throughput rate can be seen to be higher with HPP compared to CVD when using SiCl_4 and SiHCl_3 . For Cl/H = 0.1, throughput rate is over 15% higher with HPP compared to CVD when using SiHCl_3 . Practical throughput rate obtainable from SiH_2Cl_2 is found to be similar to the one with SiHCl_3 in spite of the higher deposition efficiency. This is due to the lower limit on concentration necessary to avoid powder growth.

Discussion

For a low-cost process, both deposition efficiency and throughput rate (silicon production rate) have to be high. While the H_2 and chlorosilanes from the deposition reactor effluent can be separated and recovered from HCl and recycled through the deposition reactor for improved reactant utilization efficiency, there is a cost associated with the recovery process. Hence, the higher the deposition efficiency is, the lower the recovery costs and thus the lower the cost of deposi-

tion. From the experimental results, deposition efficiency can be seen to be higher for the HPP mode of operation than for CVD under cases of practical interest. Furthermore, under several cases of practical interest, HPP deposition efficiency is found to be higher than the equilibrium value calculated by assuming thermodynamic equilibrium in the reactor at the substrate temperature. In the following we discuss this and explain some of the observations using thermodynamic and kinetic considerations and the operative deposition mechanisms and transport processes.

Thermodynamic factors.—Classical thermodynamic discussions assume equilibrium conditions and practical silicon deposition reactors do not generally operate under equilibrium conditions. The authors note that the plasma system used here cannot be characterized as equilibrium with both severe gradients in temperature and compositional profiles. However, thermodynamics can be used as a qualitative tool to evaluate results and the reasonableness of experimental observations. Chemical thermodynamic equilibria of the system Si-H-Cl, relevant to HPP deposition involving temperatures of up to 5000 K have been calculated (1, 3) using Gordon and McBrides's computer program (8). This program is based on a free energy minimization technique. All possible species between Si, H, and Cl for which data existed in JANAF tables (9) were considered in these calculations, namely, Cl, Cl^+ , Cl^- , Cl_2 , e, H, H^+ , H^- , HCl, H_2 , Si(s), Si(l), Si(g), Si^+ , SiCl, SiCl_2 , SiCl_3 , SiCl_4 , SiH, SiH^+ , SiH_4 , SiH_2Cl_2 , SiHCl_3 , Si_2 , and Si_3 . Figure 8 is an example of the results of these calculations showing the relative concentrations of various species at equilibrium as a function of temperature, for a reactor pressure of 1 atm and a reactant input concentration, C/H = 0.1. It should be noted that SiH_2Cl_2 , SiHCl_3 , and SiCl_4 have not been shown in the figure for reasons of clarity and that their mol fractions are less than 10^{-3} above 1700 K and decrease rapidly with increasing temperature. With this information the deposition efficiency can be calculated utilizing the input Si/Cl ratio and the equilibrium Si/Cl ratio. The

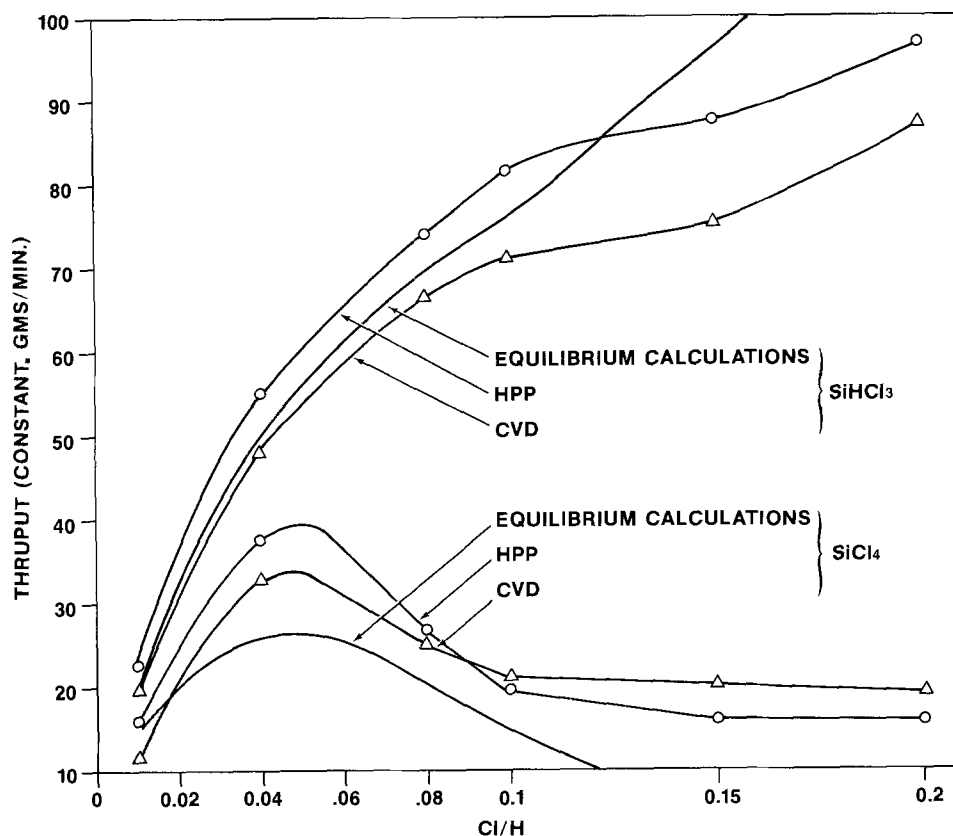


Fig. 7. Reactor throughput as a function of reactant concentration.

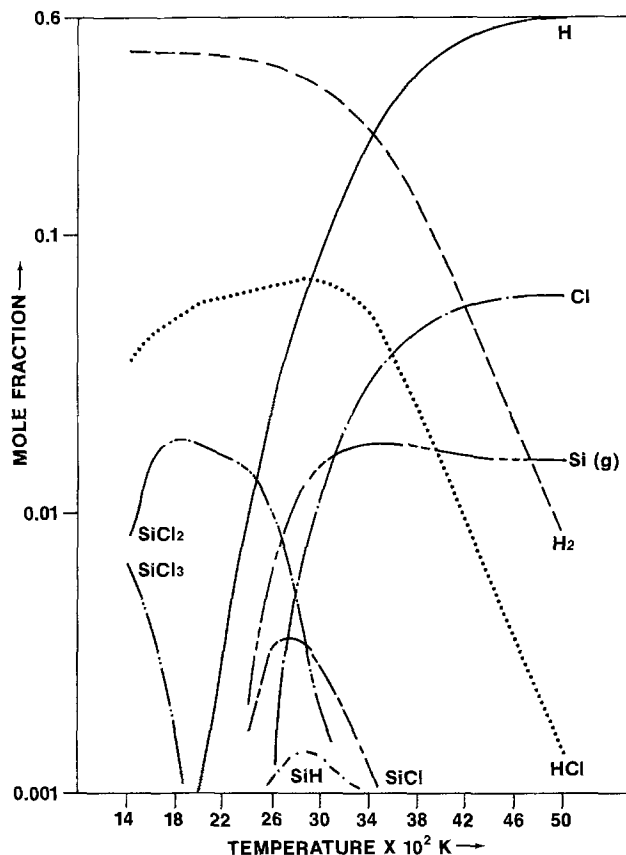


Fig. 8. Relative concentrations of various species in Si-H-Cl system as a function of temperature for $P = 1$ atm, and $Cl/H = 0.1$, obtained from chemical equilibrium calculations [Ref. (1, 3)].

calculated deposition efficiency as a function of temperature is shown in Fig. 9 for $SiHCl_3$ source, 1 atm reactor pressure and $Cl/H = 0.1$. It should be noted that in Fig. 9, for temperatures above the boiling point of silicon, 2950 K, efficiency should be considered as reaction efficiency rather than deposition efficiency. With increasing temperature from 1100°C, the efficiency can be seen initially to decrease slightly

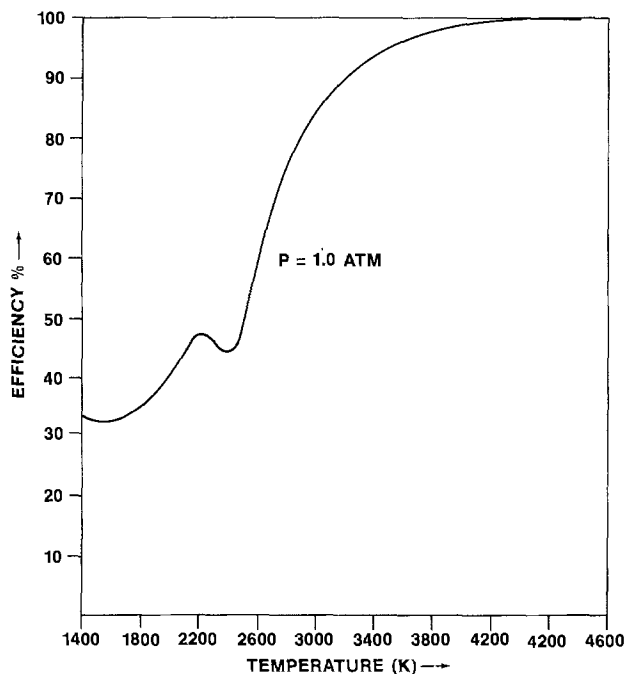


Fig. 9. Equilibrium deposition efficiency with $SiHCl_3$ as a function of temperature (1, 3).

then to increase gradually to around 45% at 1900°C, then to decrease somewhat, and finally increase rapidly and saturate around 4000°C at nearly 100%. The rationale for investigating HPP deposition is that by quenching the equilibrium mixture present at the very high plasma temperature where efficiencies are extremely high it should be possible to obtain higher efficiencies than from the equilibrium mixture present under lower temperature CVD conditions. From experimental results, it can be seen that although improvements in efficiencies are not as much as thought possible, useful improvements in efficiencies were obtained. As a practical matter, with the system geometry used here, the process is neither a pure plasma process nor a pure CVD process, but rather a plasma-enhanced CVD process. High efficiencies can be obtained from the plasma process by proper quenching; however, to form dense, smooth films of silicon the substrates were heated to 1000°C. It is probable that the process gases approach CVD conditions at some point in the reactor. We discuss factors that determine the efficiency improvements obtainable by HPP in the next sections.

The relative performance (deposition efficiency) of $SiCl_4$, $SiHCl_3$, and SiH_2Cl_2 is in agreement with thermodynamic predictions as can be seen from Fig. 10 (1, 3), which shows equilibrium efficiencies as a function of concentration. While equilibrium calculations predict etching (zero deposition) for a Cl/H of 0.125 at 1100°C for $SiCl_4$, it has not been observed, either for CVD or HPP even up to Cl/H of 0.2. In the case of CVD, this has been explained by Van der Putte *et al.* (10) by taking into account species dependent ordinary diffusion coefficients and thermal diffusion. We further discuss this under the section Transport processes.

Silicon deposition mechanisms.—In the case of conventional cold wall CVD reactors, the deposition mechanism generally involves transport of reactants to the substrate surface, chemical reaction on the surface producing silicon atoms, and incorporation of these atoms into the growing silicon film. However, a second deposition mode involves occurrence of chemical reactions in the gas phase producing free silicon atoms, condensation of these atoms into nuclei in the gas phase, transport of these nuclei to the substrate surface, and their incorporation into the growing silicon film. This latter mode of deposition becomes important in CVD reactors with the use of SiH_2Cl_2 and SiH_4 source gases, higher substrate temperatures, and hot wall deposition systems (11-13).

With HPP deposition, however, the gas phase nucleation and deposition mode is found to be important under all conditions regardless of the type of chlorosilane, its concentration, and the reactor (substrate) temperature employed. One of the consequences of gas phase nucleation can be powder growth; i.e., silicon nuclei, instead of reaching the substrate surface and contributing to film growth, grow in the vapor phase to a larger size forming silicon powder. This powder either lands on the substrate surface or exits from the deposition reactor along with the effluent gas stream. Powder formation constitutes a loss process, and furthermore creates problems in the exhaust gas (chlorosilane and hydrogen) recovery system. While it has not been possible to estimate the relative contributions to film deposition rates of these two different mechanisms in the HPP deposition process, powder formation can be at an inconsequential level in operation of the system (2) under practical film growth conditions. The reasons for this are discussed in the section on Transport processes.

Kinetic factors.—Kinetic processes could play a dominant role in deposition processes, and they have

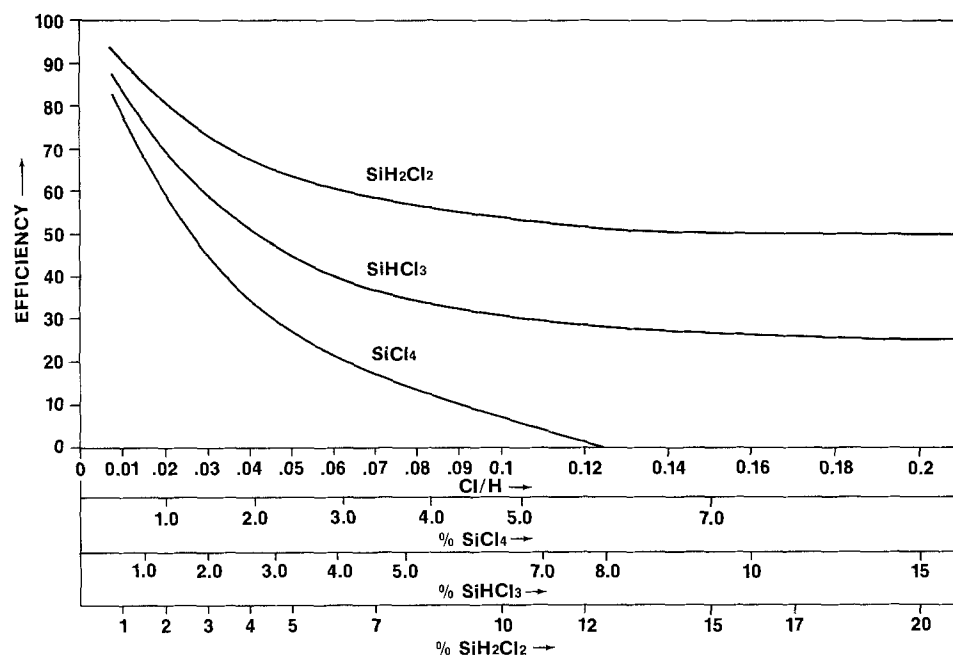


Fig. 10. Calculated equilibrium deposition efficiency a function of concentration with chlorosilanes SiCl_4 , SiHCl_3 , and SiH_2Cl_2 for $T = 1100^\circ\text{C}$ and $P = 1 \text{ atm}$ (1, 3).

been studied extensively by various investigators of silicon CVD. In the following, we discuss the various kinetic processes that we believe could explain the observed results with HPP. In HPP deposition, reactant gases experience temperatures up to 4000°C in the plasma as they are introduced into the deposition reactor. Localized chemical equilibrium can be assumed in the atmospheric pressure plasma. At 4000°C , the predominant species are H , Cl , $\text{Si}(\text{g})$, H_2 , and HCl (see Fig. 8). As this high temperature gas stream flows through the reactor and impinges on the reactor walls, it will be quenched. When the temperature lowers through the boiling point of silicon (2677°C), there will be a driving force for condensation of silicon vapor. Upon further cooling through the silicon melting temperature ($\sim 1410^\circ\text{C}$), there will be a driving force for solidification of silicon. At the same time, as the temperature is lowered, there is a tendency for formation of SiCl_2 and SiCl_3 species. However, silicon condensation could occur before the equilibrium concentrations of SiCl_2 and SiCl_3 species increase. When this happens, reaction between the condensed phase and HCl will be the rate-limiting step in the attainment of equilibrium as the gas mixture is quenched. This sequence of events can qualitatively explain the improvements in deposition efficiencies observed with the HPP deposition process.

Another kinetic factor of importance in HPP deposition is the incorporation of gas phase nucleated silicon into the silicon film growing on the substrate surface. Substrate temperature and gas flow behavior (laminar or turbulent) were found to have a major influence on this step. Higher substrate temperatures and turbulence in the gas stream enhance the incorporation of silicon nuclei into the growing silicon film. Substrate temperature in excess of 1000°C was found to be sufficient for a dense film growth. In the following section we discuss the operative transport processes in the HPP deposition reactor.

Transport processes.—Mass transport processes can profoundly influence a deposition process. There are several excellent papers [e.g., Ref. (14)] dealing with this subject pertaining to CVD silicon using cold-wall reactors. Srivastava *et al.* (15) have modeled hot wall silicon deposition reactors and have given an excellent discussion of silicon particle transport properties and processes, in which they considered the agglomeration of gas phase nucleated particles in the absence of chemical reaction.

A complete understanding of the HPP deposition process requires consideration of the operative mass transport processes along with simultaneous chemical reactions. In the HPP reactor gaseous species as well as gas phase nucleated particles are present. Transport of these species to the substrate surface is due to both convective and diffusive processes. Two important regions of the HPP reactor can be identified to be: entry region, where the plasma beam is introduced into the deposition reactor which is schematically shown in Fig. 11, and the isothermal region where the substrate temperature is controlled at a desired level using the auxiliary furnace. Gas flow in the reactor was found to be in a turbulent regime for the conditions investigated, which is in agreement with Reynold's number calculations based on the reactor dimensions. We believe that, at the entry region, the HPP deposition model can be schematically illustrated as shown in Fig. 11. At the entry region of the reactor, the gas stream from the plasma beam disperses as it moves through the reactor and impinges on the reactor walls. Within a short distance after this region, a turbulent flow is well established through the rest of the deposition zone. There will be a stagnant region near the reactor walls (substrate surfaces) where the mass transport is by diffusion. The axial gas stream at a given position along the reactor length can be assumed to be of uniform composition due to mixing by turbulent eddies.

The driving force for diffusion is due to concentration gradients (Fick) as well as thermal gradients (Soret). While the Fick diffusion coefficient is positive for all species (i.e., diffusion down to concentration gradient), the Soret diffusion coefficient will be negative for some species (i.e., in a temperature gradient, lighter species tend to move toward high temperatures and heavier species toward low temperatures). Steep radial temperature gradients exist at the entry region of the reactor, where the plasma core gases are much hotter than the substrate temperature. In this region thermal diffusion is expected to be important. This situation is fortuitous, since the silicon particles nucleated in the gas phase due to their higher density compared to the gas stream, will be transported to the substrate surfaces by thermophoretic force (Soret effect) and become incorporated into the growing silicon film. While submicron sized particles deposit by a diffusion process, particles larger than about a micron will deposit by turbulence-induced inertial impaction (15).

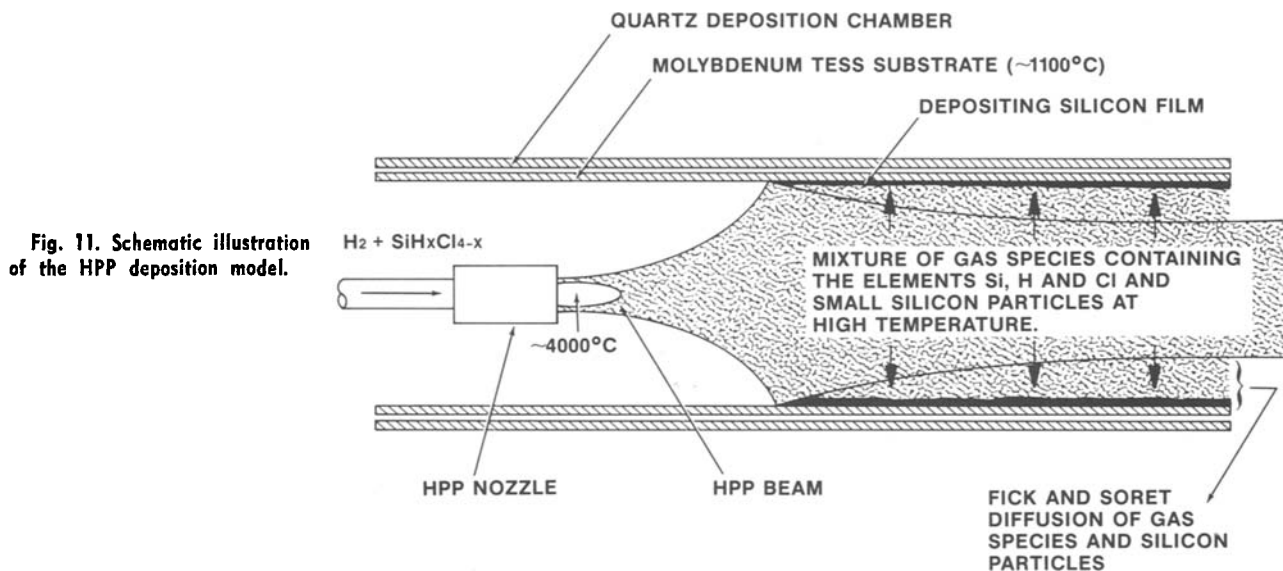


Fig. 11. Schematic illustration of the HPP deposition model.

In the isothermal region of the reactor, mass transport through the stagnant layer is due only to Fick diffusion. Diffusion coefficients of heavier molecules (e.g., SiCl_4 , SiHCl_3 , etc.) are lower than lighter ones (e.g., HCl). This leads to a condition where the concentration (Cl/H) near the substrate surface is lower than in the bulk ambient gas stream (which is related to reactor input concentration). As a result, experimental deposition efficiencies can be higher than the theoretical predictions since the effective Cl/H ratio at the substrate is lower than the input value. This is indeed observed in the case of SiCl_4 input, both for CVD and HPP, at high concentrations (see Fig. 5). A similar phenomenon is observed in the case of cold-wall CVD reactors also (10). At this time we cannot explain, with certainty, why the deposition enhancement by HPP is highest for lower concentrations, which is observed with all silicon sources. It may be due to a concentration-dependent gas phase nucleation phenomenon and/or transport properties.

Economic potential of HPP deposition.—Under conditions of high practical throughput rates, deposition efficiencies are higher for the HPP mode of operation compared to the CVD mode. With the reactor geometry used here an increase in efficiency of 4-5% was realized. This implies that the chlorosilane and hydrogen recovery system for the effluent gases would need a smaller capacity. Also, the amount of silicon deposited per unit time is about 15% higher for the HPP than the CVD mode, requiring fewer reactors for the same output. These savings should be considered along with the added expense for rf generators. Electrical energy requirements are believed to be approximately the same for HPP and CVD, since the energy input for HPP is found to go mostly toward reactant gas heating (1-4) with a corresponding reduction in electrical requirements for the resistance furnace. The type of silicon source could also influence the economics. When using SiH_2Cl_2 , the HPP mode may not offer substantial advantages since the CVD mode has a high deposition efficiency also. Presently SiH_2Cl_2 is very expensive, compared to SiHCl_3 and SiCl_4 , although this may change with new production methods currently being developed. Considering the increased deposition efficiencies and increased silicon deposited per unit time when using SiCl_4 and SiHCl_3 under high throughput conditions, the HPP mode offers economic advantages over CVD when the high effluent gas recovery costs are considered.

Conclusions

A high pressure plasma (HPP) deposition process, operating at a pressure of about 1 atm, has been characterized for its potential for producing polycrystalline silicon ribbons. Silicon tetrachloride, trichlorosilane, dichlorosilane, and silane have been examined as silicon source gases. Use of silane is found to be impractical due to excessive gas phase nucleation and powder growth. Improvements in deposition efficiencies were observed with HPP when using SiCl_4 , SiHCl_3 , or SiH_2Cl_2 , compared to the CVD mode of operation. These improvements were found to be highest at lower reactant gas concentrations. In general, deposition efficiency dependence on reactant flow rate was found to be smaller for HPP compared to CVD. The observed results were discussed in terms of the thermodynamics of the Si-H-Cl system at plasma beam temperatures ($\sim 4000^\circ\text{C}$), operative deposition mechanisms, and the kinetic and transport processes in the reactor. Based on the observed results, it is believed that HPP deposition has economic advantages over CVD deposition for producing silicon ribbons from SiCl_4 and SiHCl_3 sources.

Acknowledgments

This research was supported in part by SERI/DOE under Contract No. XS-9-8277-1. The authors also wish to thank Dr. I. A. Lesk for his critical reading of this manuscript.

Manuscript submitted March 4, 1981; revised manuscript received ca. July 8, 1981.

Any discussion of this paper will appear in a Discussion Section to be published in the June 1982 JOURNAL. All discussions for the June 1982 Discussion Section should be submitted by Feb. 1, 1982.

Publication costs of this article were assisted by Motorola Incorporated.

REFERENCES

1. K. R. Sarma, A. Baghdadi, R. W. Gurtler, and M. Cota, in "Sixth International Conference on Chemical Vapor Deposition," L. F. Donaghey, P. Rai-Choudhury, and R. N. Tauber, Editors, pp. 97-106, The Electrochemical Society Softbound Proceedings Series, Princeton, NJ (1977).
2. K. R. Sarma, R. W. Gurtler, and W. C. Ramsey, in "Proceedings of 7th International Conference on Chemical Vapor Deposition," T. Sedgewick *et al.*, Editors, pp. 176-189, The Electrochemical Society Softbound Proceedings Series, Princeton, NJ (1979).

3. K. R. Sarma, R. W. Gurtler, A. Baghdadi, M. Cota, and W. C. Ramsey, in "Proceedings 13th IEEE Photovoltaic Specialists Conference," pp. 446-447, June 1978.
4. K. R. Sarma, *Solid State Technol.*, **23** (4), 143 (1980).
5. K. R. Sarma and M. J. Rice, Jr., *IEEE Trans. Electron Devices*, ed-27(4), 651 (1980).
6. R. Nuttall, *This Journal*, **113**, 1293 (1966).
7. H. Purnell, "Gas Chromatography," John Wiley & Sons, Inc., New York (1962).
8. Gordon and McBride, "Chemical Equilibrium Computer Program," NASA-Lewis Research Center.
9. D. R. Stull and H. Prophet, "JANAF Thermochemical Tables," National Bureau of Standards, Washington, DC.
10. P. Van Der Putte, L. J. Giling, and J. Bloem, *J. Cryst. Growth*, **31**, 299 (1975).
11. T. U. M. S. Murthy, N. Miyamoto, M. Shimbo, and J. Nishizawa, *J. Cryst. Growth*, **33**, 1 (1976).
12. K. J. Sladek, *This Journal*, **118**, 654 (1971).
13. F. C. Eversteijn, *Philips Res. Rep.*, **26**, 134 (1971).
14. C. W. Monke and L. F. Donaghey, *This Journal*, **124**, 561 (1977).
15. R. Srivastava and R. K. Gould, 7th Quarterly Report, DOE/JPL 954862 (Aug. 1979).

Chemical Characterization of Complex Oxide Products on Titanium-Enriched 310SS

A. S. Nagelberg* and R. W. Bradshaw*

Sandia National Laboratories, Exploratory Chemistry Division I, Livermore, California 94550

ABSTRACT

The phases present in the complex oxide scales formed on titanium-modified 310 stainless steel alloys after exposure to coal gasification atmospheres are described. The significant titanium concentrations in the inner Cr_2O_3 layer have been shown to arise from the substitution of titanium for chromium in the Cr_2O_3 due to the increased stability of Ti^{3+} at low oxygen partial pressures. In the absence of manganese, the external layer after a 100 hr exposure at 1255 K consists of TiO_2 and a cubic spinel phase. When manganese is present in the base alloy, MnTiO_3 is found instead of TiO_2 . The absence of external sulfides on the surface of these alloys has been explained by the preferential formation of mixed oxides containing base metal elements.

The development of alloys that exhibit low corrosion rates is a critical problem in the reliability of coal gasifier internal components. The internal components are exposed to high pressure (0.7-1.0 MPa) and high temperature (1000-1300 K) environments. Typical gasifier atmospheres contain a mixture of hydrogen [15-50 mole percent (m/o)], water (15-40 m/o), carbon dioxide (4-20 m/o), carbon monoxide (5-15 m/o), methane (8-20 m/o), and hydrogen sulfide (0.03-1.0 m/o) (1). In these atmospheres at elevated temperatures, alloys tend to form rapidly growing oxide and sulfide scales.

The Ni-30Cr alloy group and 310 stainless steel alloys are representative of the nickel-base and iron-base alloys considered for use in coal gasifiers (2-4). Bradshaw and co-workers (5-7) have studied the effect of minor alloying additions on the corrosion resistance of these two alloys and have shown that titanium has a marked effect on improving corrosion resistance. Alloys without titanium additions were heavily sulfidized after a 100 hr exposure forming both external sulfides as well as internal sulfides at the scale-metal interface (Fig. 1). Titanium was found to preclude the formation of both external and internal sulfides in 100 hr exposures at 1255 K.

Titanium-containing alloys formed a complex scale after 100 hr (5, 7), as shown in Fig. 2, which contains only oxide phases. The 2-3 μm thick outer scale is titanium-rich and contains large amounts of manganese (when manganese is present in the base alloy). Below this outer scale is a 10-15 μm dense scale of Cr_2O_3 (Fig. 2) containing significant concentrations of titanium. Internal titanium oxides and silicon oxides (when silicon is present in the base alloy) are found within $\sim 10 \mu\text{m}$ layer below the scale-metal interface.

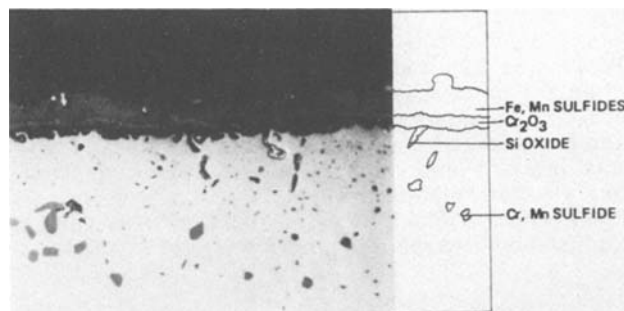


Fig. 1. Corrosion scale structure of 310 SS exposed to high BTU atm for 100 hr at 1255 K.

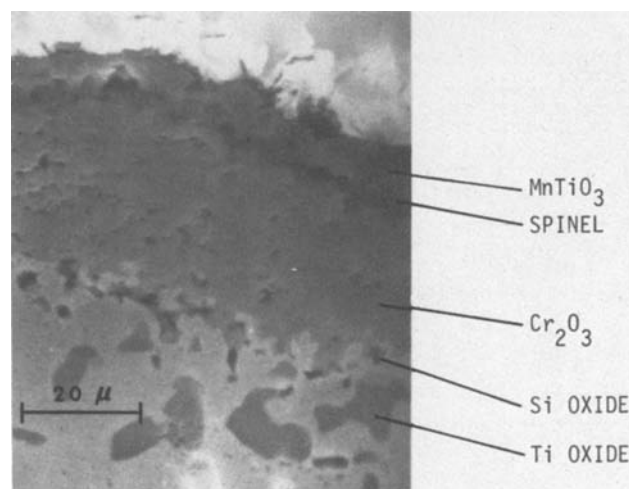


Fig. 2. Corrosion scale structure of Fe-22Cr-23Ni-3Ti-1.5Mn-0.5Si coupon exposed to high BTU atm for 100 hr at 1255 K.

* Electrochemical Society Active Member.

Key words: alloy, coal gasification, corrosion, oxidation.

At longer times (>300 hr), titanium sulfides appeared below the oxide scale and internal oxides.

In-depth investigations of the chemical composition of corrosion scales formed on the 310-base alloys with titanium additions are described in this paper. These investigations suggest possible explanations for the unexpectedly high titanium contents observed in the Cr₂O₃ scale and lack of sulfide formation at the gas-scale interface.

Experimental

Alloys examined in this study were developed by Bradshaw *et al.* (5, 7) for coal gasification applications. The alloys are based on 310 stainless steel (Fe-25Cr-20Ni) and a modified alloy that remains austenitic with the addition of 3 weight percent (w/o) titanium, (Fe-22Cr-23Ni-3Ti). Additions of titanium as well as the major impurities in 310 SS, manganese and silicon, were made to examine the effect of these constituents on corrosion behavior as previously discussed (7). The chemical composition of alloys used in this study is given in Table I. Subsequently, "modified alloy" refers to the composition Fe-22Cr-23Ni-3Ti, and any other additions are referred to in the text.

Alloy coupons were polished to 180 grit finish before exposure to the two different atmospheres given in Table II at 1255 K (1800°F) for up to 139 hr. The first atmosphere, high BTU, is representative of the gaseous species expected in a high BTU coal gasifier with the H₂S level at its expected upper extreme. The second atmosphere, simulated high BTU, reproduces the effective oxygen and sulfur partial pressures of the high BTU coal gasifier atmosphere at 1255 K without carbon-bearing species. Both atmospheres resulted in the formation of similar corrosion scales, and subsequently no distinction is made.

After exposure, oxidized sample surfaces were examined by x-ray diffraction analysis. Metallographic samples were first prepared by vapor depositing a flash of chromium or vanadium followed by gold before being plated with 1-2 mm of nickel. This coating procedure was required to avoid edge rounding and to retain the outer scale which was otherwise easily removed by metallographic polishing. After plating, the samples were sectioned and metallographically polished before examination by optical microscopy, scanning electron microscopy (SEM), and energy dispersive analysis (EDA). Several samples were further examined by electron microprobe analysis.

Table I. Chemical analysis of alloys (w/o)

| Alloys | Fe | Cr | Ni | Ti | Mn | Si | C |
|------------------------------|-----|------|------|------|------|------|-------|
| 310 | Bal | 29.6 | 18.3 | — | 1.0 | 0.9 | — |
| 310 HP (Fe-25Cr-20 Ni) | Bal | 25.3 | 19.9 | 0.23 | — | — | — |
| Fe-22Cr-23Ni-3Ti | Bal | 21.9 | 22.9 | 3.2 | — | — | 0.079 |
| Fe-22Cr-23Ni-3Ti-0.5Si | Bal | 22.1 | 22.7 | 3.3 | — | 0.51 | 0.079 |
| Fe-22Cr-23Ni-3Ti-1.5Mn | Bal | 22.4 | 22.7 | 3.2 | 1.53 | — | 0.089 |
| Fe-22Cr-23Ni-3Ti-1.5Mn-0.5Si | Bal | 22.0 | 22.6 | 3.3 | 1.52 | 0.52 | 0.072 |

Table II. Compositions of atmospheres

| Gas (v/o) | High-BTU | Simulated high BTU |
|--------------------------------|----------|--------------------|
| H ₂ S | 1.0 | 1.0 |
| H ₂ O | 40.0 | 32.0 |
| H ₂ | 24.0 | 16.6 |
| CO | 18.0 | — |
| CO ₂ | 12.0 | — |
| CH ₄ | 5.0 | — |
| Ar | — | 50.4 |
| log P _{O₂} | -14.72 | -14.19 |
| log P _{S₂} | -5.43 | -4.83 |

Temperature = 1255 K.

P_{O₂} and P_{S₂} represent values from equilibrium thermodynamic calculations at a total pressure of 1 atm.

Chromium oxide and titanium oxide powder mixtures were prepared for comparison with the diffraction patterns obtained from the scales formed on the alloys studied. Mixtures of powders containing TiO₂ to Cr₂O₃ mol ratios ranging from 0.075 to 7.0 were compacted in a 1/2 in. diam die and initially fired in air at 1625 K for 12 hr. A second firing was performed at 1300 K in an H₂/H₂O mixture of 1:1 for 30 days.

Results

X-ray diffraction results.—The presence of titanium in the alloys results in complicated x-ray diffraction spectra. The phases identified on the modified alloys are given in Table III. The scales on the modified alloy (Fe-22Cr-23Ni-3Ti) and the modified alloy containing silicon (Fe-22Cr-23Ni-0.5Si) were identified as consisting of Cr₂O₃, TiO₂ (rutile), a cubic spinel phase, and a mixed Cr₂O₃ · nTiO₂ phase (8, 9). The lines observed for the Cr₂O₃ · nTiO₂ phase after long exposures to the corrosion atmosphere are limited, but can be only identified with the shear structures reported by Anderson (8). X-ray diffraction patterns of mixtures of Cr₂O₃ and TiO₂ fired in the low P_{O₂} atmosphere exhibited similar diffraction patterns, indicating the presence of the Cr₂O₃ · nTiO₂ phases where n = 3, 4, and 5.

X-ray diffraction patterns were significantly different for the alloys 1.5 w/o Mn (Fe-22Cr-23Ni-3Ti-1.5Mn and Fe-22Cr-23Ni-3Ti-1.5Mn-0.5Si). The manganese additions eliminated the diffraction lines associated with TiO₂ (rutile) and the Cr₂O₃ · nTiO₂ phase, but lines identified with MnTiO₃ appeared. As observed in the other scales, Cr₂O₃ and a cubic spinel phase were identified.

Electron microprobe results.—Elemental profiles through the corrosion scales were determined by electron microprobe (EM) analysis and the results are shown in Fig. 3 and 4. The titanium content increases from 2 to 10 w/o as the metal-scale interface is approached. These titanium levels are greater than the reported solubilities in Cr₂O₃ (<<1 w/o) in established phase diagrams (8, 9).

An electron microprobe trace of the scale on a manganese-containing alloy, Fig. 4, indicated that the outer oxide scale was MnTiO₃ with the manganese and titanium weight proportions nearly equal (atomic weight of Cr = 52.0, Ti = 47.9). In addition, the concentration profiles showed that manganese tracked titanium exactly in the outer scale. The manganese content in the chromium-containing layer was less than the sensitivity of the microprobe for manganese, ≈0.01 w/o.

Discussion

The x-ray diffraction measurements showed that titanium enhanced the formation of complex oxides such as MnTiO₃ or the cubic spinels. A precise identification of the chemical constituents in the spinel phase is difficult due to the similarity of lattice parameters for mixed oxides of the metallic constit-

Table III. X-ray diffraction results

| Sample | Phases* |
|--|--|
| 310 HP (Fe-25Cr-20 Ni) | Cr ₂ O ₃ Fe _{1-x} S Fe ₃ S ₂ |
| Fe-22Cr-23Ni-3Ti and Fe-22Cr-23Ni-3Ti-0.5Si | Cr ₂ O ₃ TiO ₂ Spinel [(Fe,Ti)O ₄ , FeCr ₂ O ₄] Cr ₂ O ₃ · nTiO ₂ |
| Fe-22Cr-23Ni-3Ti-1.5Mn and Fe-22Cr-23Ni-3Ti-1.5Mn-0.5Si | Cr ₂ O ₃ Spinel [(Fe,Mn) ₂ TiO ₄], (Fe,Mn)Cr ₂ O ₄] MnTiO ₃ |

* Order of listing reflects relative diffraction pattern strengths, i.e., first phase listed exhibited strongest diffraction pattern.

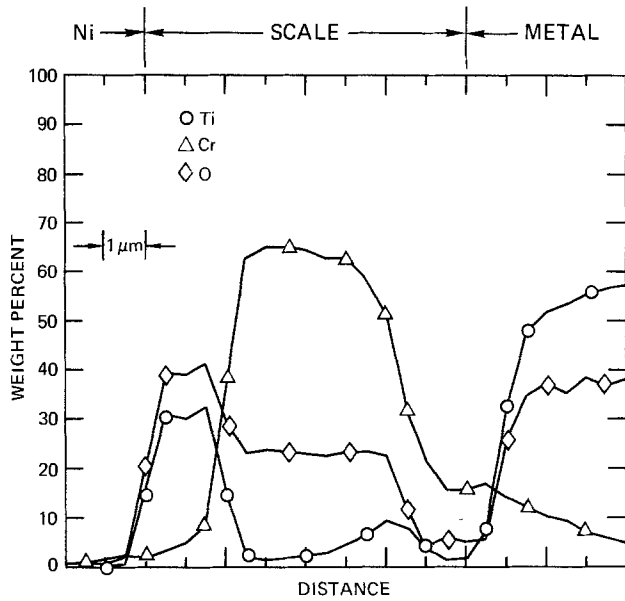


Fig. 3. Electron microprobe trace for titanium, chromium, and oxygen of Fe-22Cr-23Ni-3Ti-1.5Mn-0.5Si coupon exposed to high BTU atm for 100 hr at 1255 K.

uents of the alloy (10). Both iron-chromium oxide (FeCr_2O_4) and iron-titanium oxide (Fe_2TiO_4) have spinel structures and the lattice parameters are similar, 8.377 and 8.535Å, respectively. The lattice parameters observed for the cubic spinel in the oxide scales on the modified alloys that do not contain manganese ranged from 8.45 to 8.49Å, suggesting the formation of a mixed iron-chromium-titanium oxide ($\text{Fe}_{1-x}\text{Cr}_{2(1+x)}\text{Ti}_x\text{O}_4$) with a spinel structure. When manganese was an alloy constituent, the intensities of the spinel diffraction peaks were enhanced. This very rapid diffusion of manganese through Cr_2O_3 scales has been previously observed (11). Manganese easily substitutes for iron forming the spinel structure compounds Mn_2TiO_4 and MnCr_2O_4 with lattice parameters of 8.679 and 8.437Å, respectively. Again, the spinel phase formed

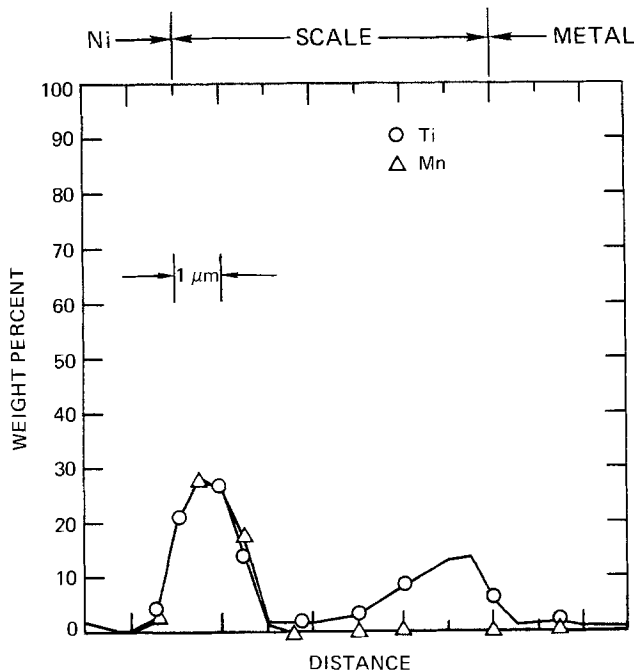


Fig. 4. Electron microprobe trace for titanium and manganese of Fe-22Cr-23Ni-3Ti-1.5Mn-0.5Si coupon exposed to high BTU atm for 100 hr at 1255 K.

can have a variable lattice parameter depending on Cr, Ti, Fe, and Mn contents, ($\text{Mn,Fe}_{1-x}\text{Cr}_{2(1+x)}\text{Ti}_x\text{O}_4$).

The solubility of titanium in Cr_2O_3 has been reported to be very low (8, 9), and such behavior is not unexpected since the substitution of a Ti^{4+} on a Cr^{3+} site requires the formation of one cationic vacancy for every three substituted titanium atoms. In the chromium oxide layers formed in this study, titanium concentrations as high as 10 w/o were observed. A possible explanation of the high titanium levels observed in this study is the formation of a mixed chromium-titanium oxide, $\text{Cr}_2\text{O}_3 \cdot \text{TiO}_2$. The composition of the chromium-rich mixed oxide phase at 1255 K is in dispute, being either $\text{Cr}_2\text{O}_3 \cdot 2\text{TiO}_2$ or $\text{Cr}_2\text{O}_3 \cdot 3\text{TiO}_2$ (8, 9). In any event, the titanium content for either phase is in excess of that observed, and if these phases were responsible for the high titanium levels observed, stronger x-ray diffraction peaks for those phases would be expected.

The reported phase diagrams were all generated at high oxygen partial pressures (8, 9), while the highest oxygen partial pressure experienced by the scale is $\sim 10^{-15}$ atm. It is in this oxygen pressure range between the gas atmosphere ($P_{\text{O}_2} \approx 10^{-15}$ atm) and the scale-metal interface ($P_{\text{O}_2} \approx 10^{-21}$ atm) at 1255 K that TiO_2 decomposes to Ti_3O_5 (12, 13) via a number of shear structures of the chemical formula $\text{Ti}_n\text{O}_{2n-1}$ (14), as shown in Fig. 5. The shear structures are related to TiO_2 and form because additional titanium atoms can be accommodated in the TiO_2 lattice by a slight sliding of crystal planes. Further lowering of the P_{O_2} to $\sim 10^{-25}$ atm results in the formation of Ti_2O_3 at 1255 K. Both Ti_2O_3 and Cr_2O_3 have similar crystal structures. The similarity of the lattice parameters of Ti_2O_3 ($a = 4.94\text{Å}$, $c = 13.659\text{Å}$) and Cr_2O_3 ($a = 4.954\text{Å}$, $c = 13.584\text{Å}$) (13), and the size of Ti^{3+} ($r = 0.76\text{Å}$) and Cr^{3+} ($r = 0.63\text{Å}$) ions (15), suggest the possibility that the high titanium level observed in the Cr_2O_3 scale is the result of an increased titanium solubility in Cr_2O_3 at low oxygen partial pressures. Obviously, an increase in the stability of Ti^{3+} would result at low P_{O_2} .

As a first approximation to estimate the titanium solubility, it was assumed that the substitution of titanium onto chromium sites in Cr_2O_3 is ideal. Applying Temkins rule (16), it is found that the activity of Ti_2O_3 is given by

$$a_{\text{Ti}_2\text{O}_3} = N_{\text{Ti}}^2 \quad [1]$$

where N_{Ti} is the fraction of cationic sites occupied by titanium atoms. A maximum value of $a_{\text{Ti}_2\text{O}_3}$ can be calculated as a function of P_{O_2} by considering the

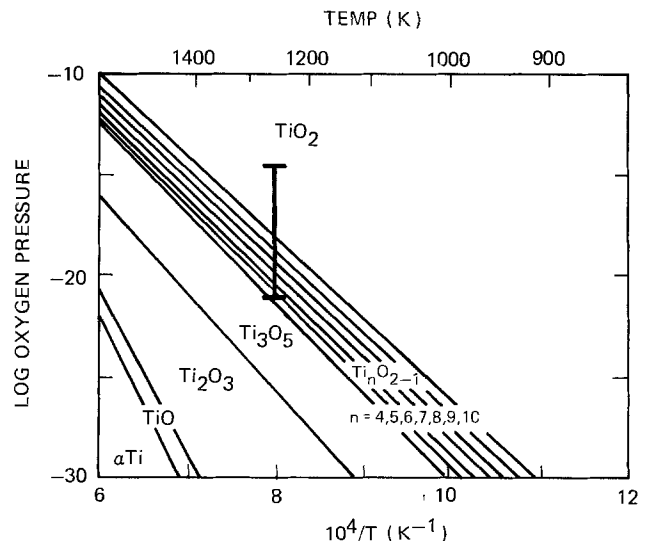
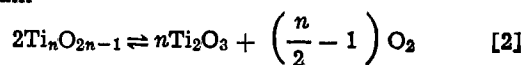


Fig. 5. Stability diagram for titanium oxides (12)

equilibrium



where n is determined by the stable phase at the selected P_{O_2} and temperature. For example, at 1225 K and $P_{\text{O}_2} = 10^{-20}$ atm, the stable titanium oxide is Ti_6O_{11} as can be seen in Fig. 5. At this oxygen pressure, Eq. [2] can be rewritten as



Obtaining the stabilities of the titanium oxides is a sequential process, since the stability of the oxygen-deficient oxide ($\text{Ti}_n\text{O}_{2n-1}$) is related to that of the oxygen-rich oxide ($\text{Ti}_{n+1}\text{O}_{2n+1}$). The stability (free energy of formation) of $\text{Ti}_n\text{O}_{2n-1}$ was obtained by considering the P_{O_2} at which $\text{Ti}_{n+1}\text{O}_{2n+1}$ decomposes to $\text{Ti}_n\text{O}_{2n-1}$ obtained from Fig. 5 and the known stability of TiO_2 . The procedure produces stabilities for $\text{Ti}_n\text{O}_{2n-1}$ in agreement with other sources (12, 13).

A value of the $a_{\text{Ti}_2\text{O}_3}$ in metastable equilibrium with Ti_6O_{11} at 1255 K and a P_{O_2} of 10^{-20} atm can be calculated using Eq. [4] and the calculated stability of Ti_6O_{11} (-4098 kJ/mol), where

$$\ln a_{\text{Ti}_2\text{O}_3} = \frac{\Delta G^\circ_f(\text{Ti}_6\text{O}_{11}) - 3\Delta G^\circ_f(\text{Ti}_2\text{O}_3)}{3RT} - \frac{1}{3} \ln P_{\text{O}_2} \quad [4]$$

A value of $\Delta G^\circ_f(\text{Ti}_2\text{O}_3) = -1177$ kJ/mol was obtained from JANAF (17). This value of $a_{\text{Ti}_2\text{O}_3}$ at $P_{\text{O}_2} = 10^{-20}$ atm is 0.063. From Eq. [1] this is equivalent to a value of $N_{\text{Ti}} = 0.25$ in Cr_2O_3 saturated with titanium at $P_{\text{O}_2} = 10^{-20}$ atm or the chemical composition $\text{Cr}_{1.5}\text{Ti}_{0.5}\text{O}_3$. Values of N_{Ti} calculated by a similar procedure as a function of oxygen pressure are shown in Fig. 6.

An assumption about the spatial variation of oxygen chemical potential in the Cr_2O_3 scale must be made before a comparison of the calculated titanium contents with experimental results can be made. If it is assumed that a linear oxygen potential gradient exists within the Cr_2O_3 layer, the calculated curve of the Cr:Ti metal weight ratio shown in Fig. 7 can be compared to the experimental curve obtained from the EM concentration profiles. The use of the Cr:Ti weight ratio plot gives a sensitive technique to ob-

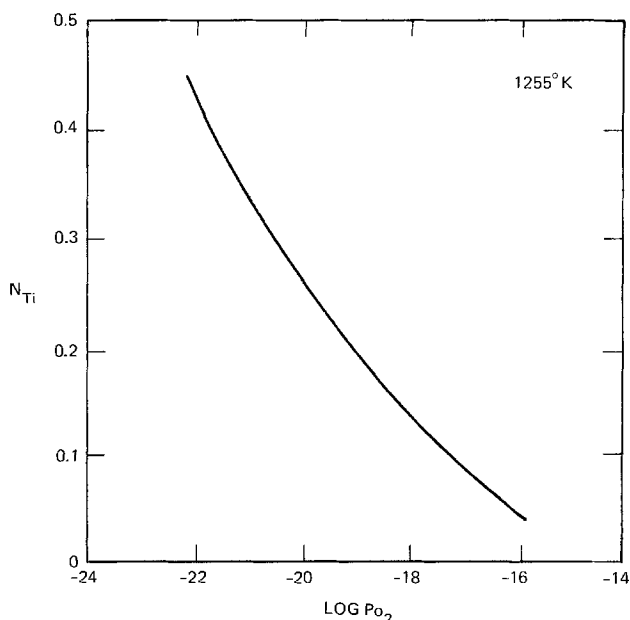


Fig. 6. Calculated variation of titanium cationic fraction (N_{Ti}) with oxygen partial pressure.

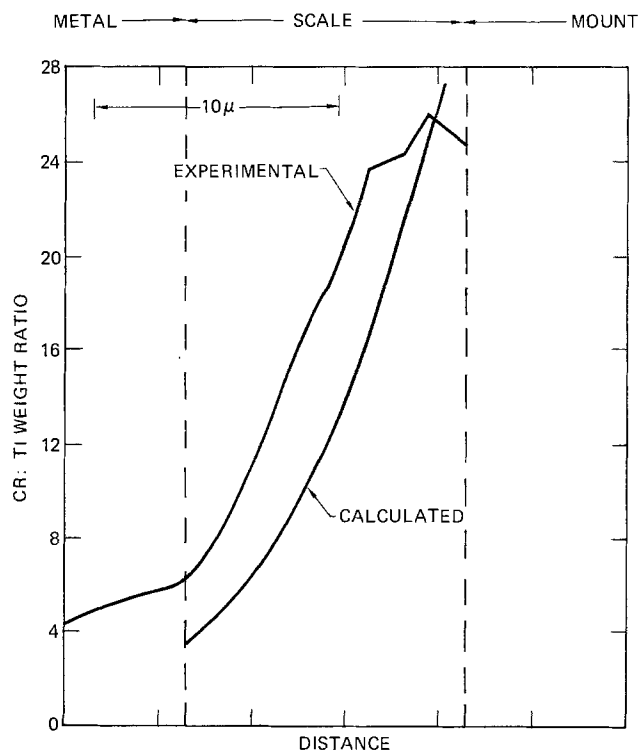


Fig. 7. Spatial variation of chromium to titanium weight ratio in Cr_2O_3 layer of Fe-22Cr-23Ni-3Ti-1.5Mn-0.5Si scale.

serve the oxide composition since the EM results are sensitive to surface irregularities in the cross-sectional polishing. The formalism of the Wagner theory for the oxidation of metals (18) requires that for a linear oxygen potential gradient to exist in the solid solution scale, the mobility of titanium and chromium must be equal. In addition, the requirement of a negligible oxygen partial pressure variation of chromium diffusivity in Cr_2O_3 has been shown (19). It is seen in Fig. 7 that the calculated and experimental curves exhibit similar curvatures and at no point does the experimental titanium concentration exceed the calculated saturation concentration. The close agreement makes it reasonable to assume that the high observed titanium levels are due to the substitution of Ti^{3+} for Cr^{3+} in the Cr_2O_3 lattice.

For chromium oxide forming alloys such as 310 type alloys, sulfide formation is supposed to occur by both the permeation of sulfur through the chromia layer to the base metal and migration of base metals to the external surface. Bradshaw (7) has discussed the possible causes for the apparent reduced permeation of sulfur through oxide scales on titanium-modified 310 alloys. A possible explanation of the role titanium plays in minimizing the formation of sulfides on the external surface is straightforward. The x-ray diffraction results indicated that the presence of titanium enhances the formation of complex oxides containing base metals that migrate to the external surface. The effect of the formation of a complex Fe-Ti oxide on the relative stability fields in an Ellingham diagram is shown in Fig. 8. Instead of the equilibrium of iron and its oxides being defined by the Fe-FeO equilibrium (solid line), it is defined by the Fe-FeTiO₃ equilibrium (11) (dashed line) in the presence of pure TiO₂. The transition moves the equilibrium oxygen partial pressure from 1×10^{-15} to 3×10^{-18} atm. The formation of an FeTiO₃ phase instead of FeO would also shift the line for oxide-sulfide equilibrium as shown by the dashed line in Fig. 8.

As seen in Fig. 8, the region containing the range of oxygen and sulfur partial pressures typical of the coal gasification process straddles the line represent-

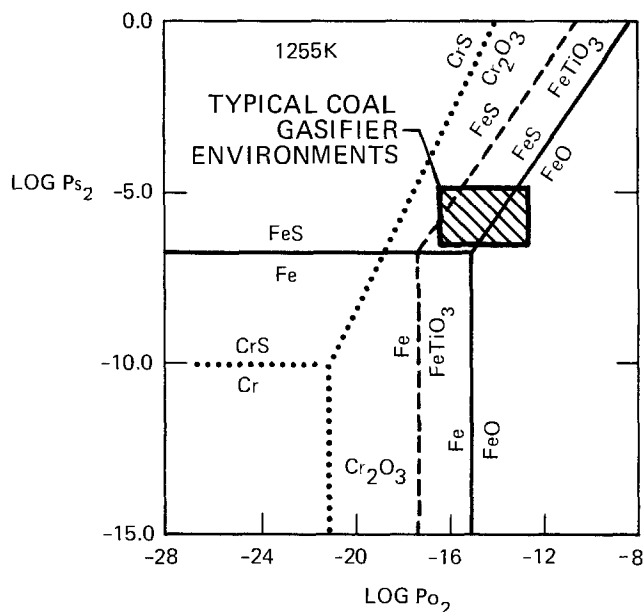


Fig. 8. Ellingham diagram for iron-sulfur-oxygen system at 1255 K. Dashed line indicates the changes that occur in the presence of TiO_2 . The dotted lines represent the chromium-sulfur-oxygen system and are given for comparison.

ing the sulfide-oxide equilibrium when the formation of a complex oxide is not considered. However, all except the most severe atmospheres ($\log P_{S_2} \geq \log P_{O_2} + 10.96$) lie in the stability region for $FeTiO_3$. Thus any base metal that reaches the external surface is converted to a complex oxide instead of being converted to a molten sulfide. An exception is nickel which exists in 310 at an activity insufficient to form a pure nickel sulfide phase (20).

Summary

An explanation of the high titanium levels observed in the Cr_2O_3 scale formed on a titanium-modified 310 stainless steel by Bradshaw *et al.* (2) has been presented. Titanium in the form of Ti^{3+} is believed to substitute for chromium atoms in the Cr_2O_3 lattice. The observed increase in titanium solubility as the scale-metal interface is approached through the Cr_2O_3 layer has been shown to be caused by the increased Ti^{3+} stability as the oxygen partial pressure is decreased. The titanium levels and spatial variation can be explained by the formation of a solid solution of Ti_2O_3 in Cr_2O_3 at the reduced oxygen partial pressures present throughout the layer.

X-ray diffraction studies have indicated that the external layer formed on the titanium-modified alloys without manganese was a mixture of TiO_2 and a cubic spinel phase, $Fe_{1+x}Cr_{2(1-x)}Ti_xO_4$, with x being small. When manganese was present in the modified alloy, the external layer consisted of $MnTiO_3$ and a cubic spinel phase, probably $[(Mn,Fe)_{1+x}Cr_{2(1-x)}Ti_xO_4]$. The formation of complex oxides containing base metals which would otherwise tend to form sulfides in coal gasification atmospheres appears to be enhanced

by the presence of titanium. The formation of complex oxides such as $MnTiO_3$ or $MnCr_2O_4$ effectively shifts the atmosphere, typical of the coal gasification process, from a region in the Fe-S-O Ellingham diagram that straddles the equilibrium between base metal sulfides and oxides to a region that solely allows the formation of oxides.

Acknowledgments

The authors appreciate the assistance of Dale Boehme for the x-ray diffraction identifications, Clarence Karfs for the scanning electron microscopy, and Ron Gorniak for the electron microprobe measurements. This work was supported by the U.S. Department of Energy, DOE, under Contract DE-ACO4-76DP00789.

Manuscript submitted Oct. 3, 1980; revised manuscript received Feb. 5, 1981.

Any discussion of this paper will appear in a Discussion Section to be published in the June 1982 JOURNAL. All discussions for the June 1982 Discussion Section should be submitted by Feb. 1, 1982.

Publication costs of this article were assisted by Sandia National Laboratories.

REFERENCES

1. A. McNab, in "Proceedings of the Workshop on Materials Problems and Research Opportunities in Coal Conversion," pp. 33-48, Ohio State Univ. (NSF, 1974).
2. V. T. Hill and M. A. H. Howes, *Mater. Performance*, **17**, 22 (1978).
3. M. Danielewski and K. Natesan, *Oxid. Met.*, **12**, 227 (1977).
4. K. Natesan, in "Proceedings of the Conference on Erosion/Corrosion of Coal Conversion System Materials, Berkeley, CA," p. 222, NACE, Houston (1979).
5. R. W. Bradshaw, R. E. Stoltz, and D. R. Adolphson, Final Report, SAND78-8277, Sandia National Laboratories, Livermore, CA, March 1979.
6. R. W. Bradshaw and R. E. Stoltz, *J. Mater. Energy Systems*, **2**, 3 (1980).
7. R. W. Bradshaw, To be published *Oxid. Met.*
8. S. Somiya, S. Hirano, and S. Kamiya, *J. Sol. State. Chem.*, **25**, 273 (1978).
9. W. Lee, *Deut. Keram. Gesell. Ber.*, **47**, 169 (1970).
10. Joint Committee on Powder Diffraction Standards, "Power Diffraction File, Search Manual, 1976."
11. R. K. Wild, *Corros. Sci.*, **17**, 87 (1977).
12. K. G. Geraghty and L. F. Ponaghey, *Thin Solid Films*, **40**, 375 (1977).
13. I. A. Vasil'eva *et al.*, *Dokl. Akad. Nauk SSR*, **235**, 839 (1977).
14. S. Andersson and A. Magnelli, *Naturwissenschaften*, **43**, 495 (1956).
15. "Handbook of Chemistry and Physics," 51st ed., pF152, CRC, Cleveland (1970).
16. M. Temkin, *Acta Phys. Chim. URSS*, **20**, 411 (1945).
17. JANAF Thermochemical Tables, Dow Chemical Co., Midland, MI.
18. C. Wagner, "Atom Movements," p. 153, American Society for Metals, Cleveland (1951).
19. P. Kofstad, "Nonstoichiometry, Diffusion, and Electrical Conductivity in Binary Metal Oxides," p. 207, John Wiley & Sons, Inc., New York (1972).
20. K. T. Jacob, D. Bhogeswam Rao, and H. G. Nelson, *Oxid. Met.*, **13**, 25 (1979).

The Deposition of Silicon Films by Pyrolytic Decomposition of SiF₂ Gas

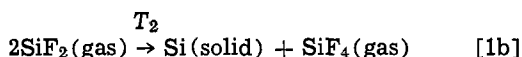
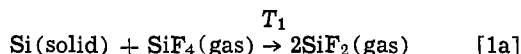
M. Janai, S. Aftergood, R. B. Weil, and B. Pratt

Department of Physics and Solid State Institute, Technion-Israel Institute of Technology, Haifa 32000, Israel

ABSTRACT

Production of silicon films by a silicon fluoride transport reaction is described here. The effect of various deposition parameters including temperature, partial pressure, and gas flow rate on the deposition kinetics was investigated. X-ray analysis, surface electron spectroscopy, optical absorbance and reflectance, and electrical measurements indicate that the films have properties similar to those of silicon films obtained by CVD from silane.

The silicon fluoride transport reaction has been suggested by Wolf *et al.* as a low cost purification process of metallurgical-grade silicon. Combined with a simultaneous on-line CVD process the method can be used for the production of silicon sheets for photovoltaic solar cell arrays (1, 2). The purification capability of this process has been further investigated by Ingle *et al.* (3). The process makes use of the cyclic reaction sequence



T_1 is a temperature above 1100°C and T_2 is in the range of 450°-850°C. In a complete cycle of the process the SiF₄ gas reacts with silicon at temperature T_1 to yield SiF₂, which in turn decomposes on a substrate held at temperature T_2 , resulting in the deposition of a solid silicon film and the release of SiF₄ gas. The SiF₄ is circulated in the system in a closed loop. The purification potential of the process results from the preferential reaction of SiF₄ with the silicon rather than with its impurities at the temperature T_1 , and from the higher condensation temperature of the metalfluoride impurities which may be formed in the high temperature zone (1-3).

We have studied the above transport reaction for its thin film deposition capability, with pure solid silicon as the starting material. This process may be useful in polysilicon deposition for microelectronics purposes since deposition takes place even at the relatively low temperature of 550°C and the films have high specular reflectance, which is desirable for photolithographic processing. Films deposited at 550°C, however, are amorphous and for some applications might have to be annealed at a higher temperature for a short period of time to increase the charge carrier mobility. A further advantage of the CVD process utilizing the silicon fluoride transport reaction is that oxygen leaking into the system may be easily adsorbed on an appropriate getter, as discussed below. In the silicon fluoride transport process the SiF₄ may be cycled again and again through the deposition in cost savings.

We have reported previously (5) on a deposition system where SiF₂ is transported from the high temperature zone to the substrate without going through an intermediate zone with a temperature lower than that of the substrate. In the present work we have studied a deposition system where the gas is quenched down to room temperature at the exit of the high temperature zone (T_1) and is transported at room

temperature to the substrate, which is held at temperature T_2 . The effect of various deposition parameters on the deposition kinetics and the properties of the resultant film are described below.

System Description

The deposition system is schematically depicted in Fig. 1. About 200 silicon cubes 2.5 mm on edge each were cut from a Czochralski grown silicon single crystal. The cubes were held in a vertical quartz tube which was mounted in a resistively heated furnace. The temperature of the silicon (T_1) was monitored by an external thermocouple. The temperature of the silicon cubes was between 0° and 20°C higher than the reading of the external thermocouple, depending on the height level of the silicon in the column. The walls of the tube at the exit of the furnace were cooled, forming a temperature gradient of approximately 200°C/cm between 1000° and 100°C in the gas.

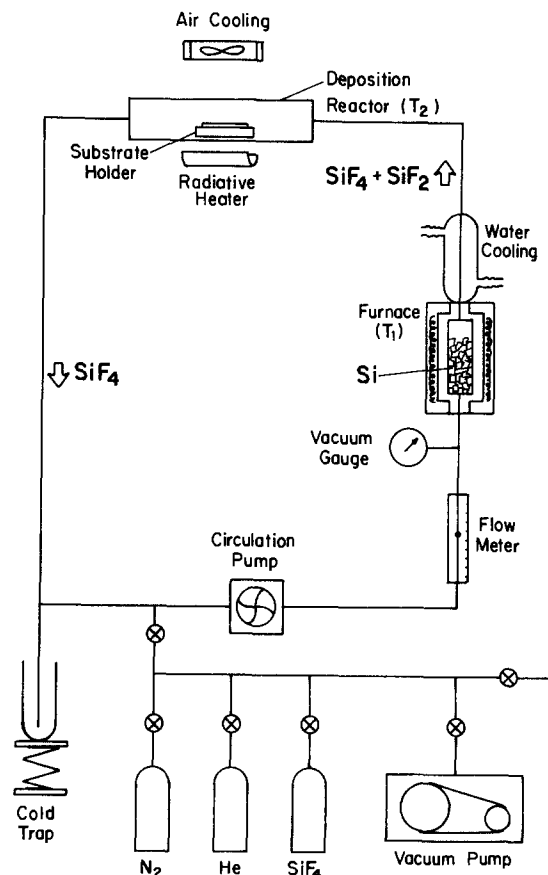


Fig. 1. Schematic illustration of the deposition system

Key words: thin films, amorphous Si:F, polymerization, CVD kinetics.

The gas was transported from the high temperature zone to the deposition zone in a 70 cm long glass tube. The substrates in the deposition zone were supported on a radiatively heated graphite holder, placed in a horizontal quartz tube 45 mm in diameter. The walls of the deposition reactor were air-cooled. The temperature gradient over the deposition region was less than 1°C/cm. A Dia-Vac™ pump was used to circulate the gas in the system. A Matheson Model 603 ball type flowmeter monitored the gas flow rate. The total volume of the system was approximately 1.5 liters.

In a typical deposition cycle the silicon cubes were rinsed in HF acid to remove any oxide layer. The silicon cubes were placed in the quartz tube and the system was pumped, purged with nitrogen and helium, and again pumped down to a vacuum of 0.05 Torr. The pump was turned off and SiF₄ from an external tank was admitted into the system until the desired SiF₄ initial pressure was achieved. The SiF₄ was then solidified in a liquid-air trap inside the system. Once the SiF₄ completely solidified the heaters were turned on and the system was pumped again to remove any volatile species. Once the temperatures T_1 and T_2 had stabilized the vacuum pump was disconnected, the SiF₄ was re-evaporated into the system, and the circulation pump was turned on. The pressure in the hot system was usually 7% higher than the SiF₄ initial pressure of the room temperature system. In a typical deposition cycle (e.g., sample E-14) we used the following deposition parameters: SiF₄ initial pressure = 80 Torr, $T_1 = 1100^\circ\text{C}$, $T_2 = 600^\circ\text{C}$, and flow rate 0.3 mol/hr. No carrier gas was used. Unless otherwise specified, each deposition run lasted 30 min. At the end of each deposition run the SiF₄ gas was returned to the storage tank by refreezing it. The SiF₄ pressure in the system and the silicon weight were determined before and after the deposition.

Fused silica substrates were used in most depositions. The gas source was Matheson 99.7% purity SiF₄ (6). As indicated above, the gas was further purified by freezing it to 77 K and pumping off the volatile species.

Effect of Deposition Parameters on Deposition Kinetics

Experimental.—The thickness of the films was routinely determined from their reflectance traces in an infrared spectrophotometer by the interference fringes method (7). For the calibration of these measurements we determined first the wavelength dependence of the refractive index, $n(\lambda)$, of one of our samples whose thickness was determined with an interference microscope. This refractive index was used in turn to calculate the thickness of all other samples according to

$$d = \frac{N \cdot \lambda_N}{2n(\lambda_N)} \quad (N = 1, 2, \dots)$$

where d is the film thickness, N is the order of the reflectance minima, and λ_N is the wavelength of the minima of order N .

Thickness uniformity.—The uniformity of the film thickness was found to depend mostly on the method of cooling the walls of the deposition reactor, probably due to its effect on convection currents in the gas. Under usual deposition conditions the film thickness uniformity was better than 1%/cm perpendicular to the gas flow direction, and monotonically decreasing at about 4%/cm over an 8 cm long sample parallel to the gas flow direction. The latter effect was probably associated with the depletion of SiF₂ from the gas along the direction of flow. In the experiments reported below we used 1 cm² samples placed repro-

ducibly on the substrate holder about 3 cm from its leading edge.

Time dependence of film thickness.—Figure 2 shows the dependence of the sample thickness on the deposition time for periods between 20 and 60 min. The linear curve which passes through the origin indicates that the deposition rate is constant with time. It implies that any time-dependent variables in the deposition system (such as the SiF₂ and SiF₄ partial pressures) either reach their steady-state values quickly relative to our deposition time scale, or their time-dependent effect on the variation of the deposition rate is negligible.

Reaction temperature (T_1).—The temperature T_1 was varied between 1060° and 1200°C. Figure 3 shows a semilog plot of the film thickness deposited in 30 min vs. the reciprocal of temperature T_1 . For temperatures lower than 1060°C the deposited layer was too thin to be measured by our optical technique. We did not exceed 1200°C because of material limitations imposed by the quartz tube. As shown below, the deposition rate is proportional to the SiF₂ generation rate, so that Fig. 3 indicates a generation rate activation energy of 54 ± 4 kcal/mol (2.3 ± 0.2 eV).

Deposition temperature (T_2).—The temperature T_2 was varied between 475° and 675°C. Figure 4 shows a semilog plot of the 30 min deposition thickness vs. reciprocal substrate temperature. Below 550°C the deposition rate increased with temperature with an ac-

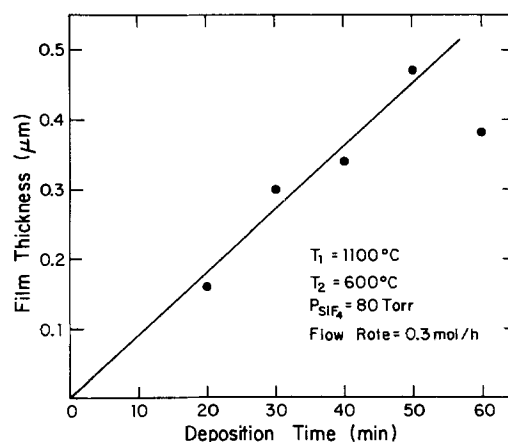


Fig. 2. Dependence of the deposited silicon film thickness on the deposition time.

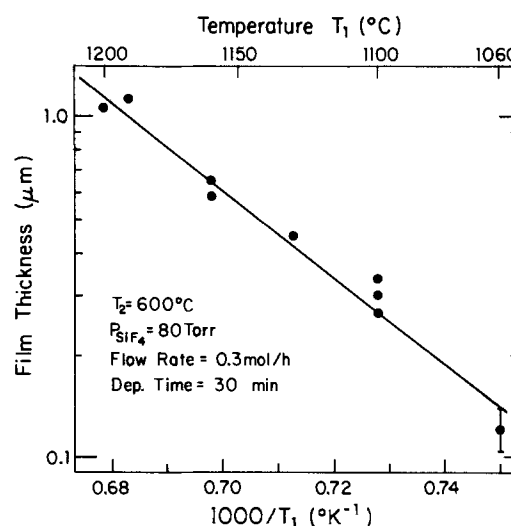


Fig. 3. Dependence of the deposition rate on the temperature of the reactor in which SiF₂ is formed.

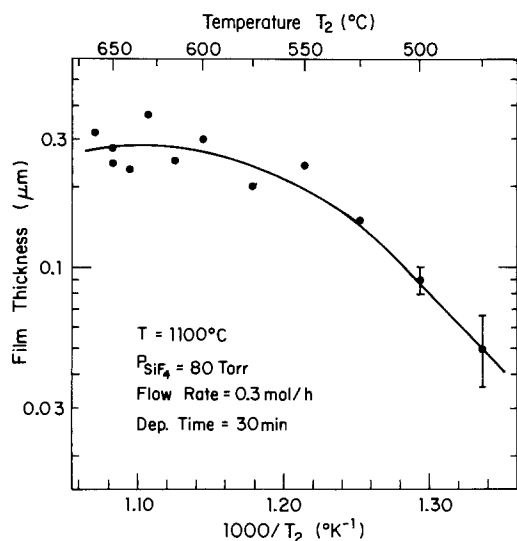


Fig. 4. Dependence of the deposition rate on the substrate temperature.

tivation energy of 29.0 ± 1.5 kcal/mol (1.26 eV). The maximum deposition rate was achieved around a substrate temperature of 620°C , and was almost constant over the temperature range $600^\circ\text{--}675^\circ\text{C}$. Depositions made with a different setup (5) indicated that above 675°C the deposition rate decreases with temperature, and above 900°C no silicon deposition could be detected even after extended deposition periods.

Flow rate.—The gas flow rate (measured in units of moles per unit time) was determined from a calibration curve of the 603 flowmeter for SiF_4 under standard conditions (760 Torr, 21°C) by multiplying the standard flow rate by $(P/760)^{1/2}$ where P is the system pressure in Torr. As shown below, under most deposition conditions the molar fraction of SiF_2 in the system was small, particularly in the section of the system following the deposition reactor. Since the flowmeter was mounted after the deposition reactor the monitored flow was practically that of the SiF_4 alone. Figure 5 shows the dependence of the deposition rate on the gas flow rate for flow values between 0.18 and 0.63 mol/hr. As seen from the figure, in this range the deposition rate increases linearly with flow rate.

Pressure.—Since the molar fraction of SiF_2 in the system was relatively low the total pressure of the system was approximately the partial pressure of the

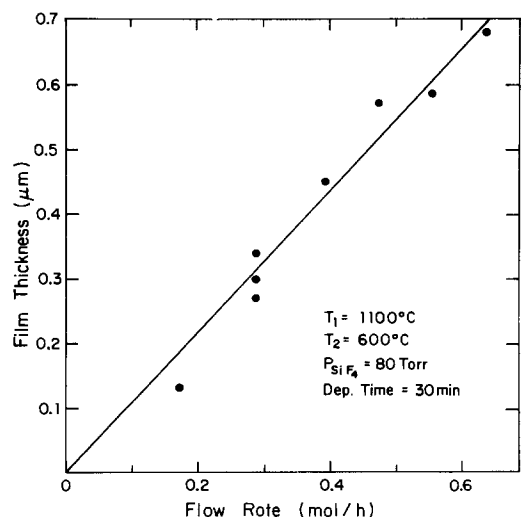


Fig. 5. Dependence of the deposition rate on the SiF_4 gas flow rate for a constant pressure of SiF_4 in the system.

SiF_4 gas. Depositions were made with SiF_4 initial pressures between 70 and 220 Torr. In these experiments we kept the setting of the ball of the flowmeter at a constant height for all pressures. Under these conditions (8)

$$\rho v^2 = \text{constant} \quad [2]$$

where ρ is the density of the gas in the system in units of mass per unit volume (or moles SiF_4 per unit volume) and v is the gas flow velocity in units of volume per unit time. From Eq. [2] we obtain that

$$v = A \cdot \rho^{-1/2} \approx A \cdot 135 \cdot P^{-1/2} \quad [3]$$

and

$$\text{flow rate} = v \cdot \rho \approx A \cdot P^{1/2}/135 \quad [4]$$

where P is the initial pressure in Torr in the room temperature system, ρ, v , and the flow rate are given in units of mol/liter, liters/hr, and mol/hr, respectively, and A is a system constant obtained experimentally by multiplying v by $\rho^{1/2}$, and it depends on the setting of the flowmeter. The constant 135 is the square root of the standard pressure (760 Torr) times the specific volume of SiF_4 at room temperature at 760 Torr (24.08 liter/mol) (6). Under the condition of Eq. [2], we observed no difference in deposition rate for the various SiF_4 initial pressures. For $A^2 = 21$ mol · liter/hr², we obtained a deposition rate of 0.32 ± 0.03 μm per 30 min deposition or 1.8 ± 0.2 Å/sec (see Fig. 6, left scale).

During depositions, which all started with given initial SiF_4 pressures, a pressure drop varying between 5 and 40% was observed. This pressure drop was nearly linear with deposition rate with varying T_1 . The pressure drop ΔP for experiments with various initial SiF_4 pressures, at constant T_1 and ρv^2 , is shown in Fig. 6 (right scale). From the slope in Fig. 6 and the deposition parameters given in the figure one gets a pressure drop $\Delta P/P = 12\%$. It can be seen that the absolute pressure drop was linear with the initial pressure, for a constant ρv^2 value, while under the same conditions the deposited film thickness was independent of the pressure. (The scatter of the experimental results probably reflects the degree of control we had on the parameter $A^2 = \rho v^2$ and on the system temperatures in the various depositions.) From the above considerations we obtain the empirical relation

$$\Delta P/P = B(T) \cdot f(\rho v^2) \cdot \Delta t \quad [5]$$

where B is a constant depending on the system temperatures, Δt is the deposition time, and f is a function of the parameter ρv^2 , determined by the kinetics of the

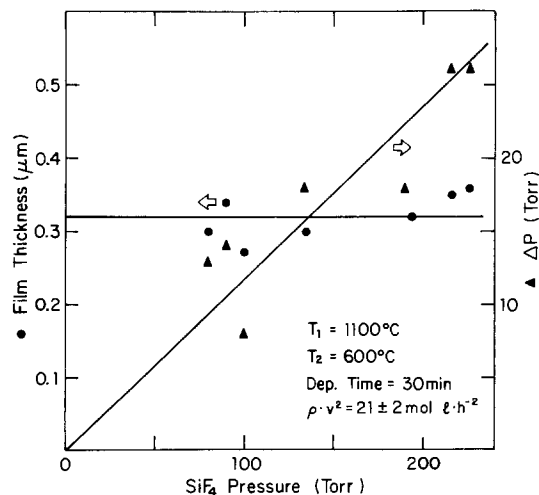


Fig. 6. Dependence of the deposition rate (●, left scale) and the pressure drop in the system during a 30 min deposition (▲, right scale) as a function of the initial pressure in the system.

mechanism causing the pressure drop. From measurements of ΔP under constant initial P and varying flow rates we obtained $\Delta P \propto v^{1.8 \pm 0.3}$ which suggests that in Eq. 5, $f(\rho v^2) = \rho v^2$. The probable reason for the pressure drop has been identified as condensation of SiF_2 molecules in the form of $(\text{SiF}_x)_n$ polymers on the water-cooled walls of the tube following the high temperature zone (9). In Table I the results of two similar deposition runs—one with, and one without water-cooled walls—are given. The original reason for water cooling the walls at the exit of the high temperature zone was to reduce the length of the tube section over which the wall temperature was between 450° and 900°C, thus limiting the back-reaction given by Eq. [1b] in the unwanted sections of the system. The results shown in Table I demonstrate, however, that with no water cooling, where the tube walls were heated to 100°–300°C by the hot gas flow, polymerization was significantly reduced and the deposition rate was increased. As seen from the table, without water cooling the percentage pressure drop was reduced by a factor of 4, and the deposition rate was increased by a factor of 1.8. The pressure drop in depositions E-44 and E-45 implies a loss of 11×10^{-4} and 2.5×10^{-4} mol of SiF_4 from the gas, respectively. Assuming (9) that the majority of the polymerization is of the form $(\text{SiF}_2)_n$, this SiF_4 gas loss is equivalent to the removal of an equal number of mols of silicon transported from the high temperature zone, i.e., 31 and 7.7 mg silicon, respectively. The loss of the transported silicon due to polymerization is significant in view of the fact that the total silicon weight deposited on the substrate and substrate holder in these two depositions was only 6.8 and 12.4 mg, respectively.

Other observations.—A direct correlation between the total silicon mass transport, as measured by the loss of silicon weight in the high temperature reaction zone during a deposition, and the thickness of the deposited film was observed. The weight loss in a typical deposition run (e.g., in deposition E-14) was 120 mg. However, only approximately 3% of the transported silicon coated the substrate and substrate holder in that deposition experiment. From the observed value of ΔP we know that 13% of the transported silicon was lost in condensation of $(\text{SiF}_2)_n$ polymers. The rest of the transported silicon appeared as deposits on the walls of the tube at the exit of the high temperature zone where the temperature was in the range of 450°–900°C. Silicon deposits were observed also on the walls of the deposition reactor. A thin silicon deposit was also observed on the hot wall at the entrance to the high temperature reactor, probably due to SiF_2 which did not decompose in the deposition zone and so completed a full cycle in the system. This happened particularly with low substrate temperature depositions. A full flow cycle in the system at F.R. = 0.3 mol/hr took 1.25 min, which sets a lower limit on the lifetime of the SiF_2 molecule in the gas.

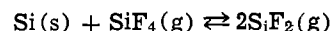
The diffuse part of the reflectance of the films deposited below $T_2 = 700^\circ\text{C}$ was equal to or lower than that of silicon films deposited from silane. During deposition, under intense illumination of the gas

white smoke could be observed, probably arising from $(\text{SiF}_2)_n$ long polymer chains swept along by the gas stream. This smoke was minimized by water cooling the tube between the high temperature reactor and the deposition reactor. However, the presence of this smoke did not affect the smoothness of the deposited silicon films. In fact, the smoothness of the films was so high that it was difficult to focus the beam of a scanning electron microscope on the sample surface because of lack of features.

After some depositions, a thin oxide layer could be observed on the silicon cubes at the bottom of the silicon column in the high temperature reactor. By weighing the silicon at the end of each deposition run before and after rinsing it in HF acid we estimate a typical oxidation rate of 2 mg SiO_2 per deposition cycle, which is equivalent to an oxygen leak of 4.5×10^{-5} mol per deposition cycle. No other effects of this oxygen leak (or outgassing) could be observed in the system and in particular no oxygen was observed in the deposited films. In view of the fact that there was no outlet for this gas during the deposition we conclude that the lower section of the silicon column in the flow system acts as a getter to remove oxygen from the circulating gas.

Discussion of Deposition Kinetics Experimental Results

Our results for depositions at $T_2 > 550^\circ\text{C}$ are consistent with the assumption that the rate-limiting process of the transport reaction is the conversion of SiF_4 into SiF_2 in the high temperature zone (2). In the high temperature reaction zone equilibrium conditions prevail and the reaction there can be written as



$Kp(T)$, the pressure equilibrium constant of the reaction, is given by

$$Kp(T) = P_{\text{SiF}_2}^2 / P_{\text{SiF}_4} \quad [6]$$

where P_{SiF_2} and P_{SiF_4} are the partial pressures of the SiF_2 and SiF_4 gases, respectively. Out of each mol of SiF_4 entering the high temperature reaction zone, a fraction α is converted into pairs of SiF_2 molecules. The partial pressures in the high temperature reactor can be written as

$$P_{\text{SiF}_4} = [(1 - \alpha) / (1 + \alpha)] \cdot P \quad [7a]$$

and

$$P_{\text{SiF}_2} = [2\alpha / (1 + \alpha)] \cdot P \quad [7b]$$

where P is the sum of the partial pressures $P_{\text{SiF}_4} + P_{\text{SiF}_2}$. In terms of α , the pressure equilibrium constant can be written as

$$Kp(T) = 4\alpha^2 P / (1 - \alpha^2) \quad [8]$$

which for small values of α gives

$$\alpha \cong (Kp(T) / 4P)^{1/2} \quad [9]$$

The experimental value of α can be obtained by dividing the total number of transported silicon mols per deposition run by the total number of SiF_4 mols that flowed through the reactor. Equation [9] predicts that under equilibrium conditions in the high temperature reactor α will be proportional to the inverse square root of P , and will be temperature activated with half the activation energy of $Kp(T)$. Fitting the results of our weight-loss measurements to the functional dependence given by Eq. [9] we obtain

$$\alpha = [1.15 \times 10^8 / P^{1/2}] \cdot \exp(-E/RT_1) \quad [10]$$

where $E = 54 \pm 4$ kcal/mol, $R = 1.987 \times 10^{-3}$ kcal/mol · K, T_1 is the temperature in K, and P is given in Torr. The highest value of α in our experimental regime, $\alpha \cong 0.13$, was obtained for $T_1 = 1473$ K and

Table I. Summary of results of two similar depositions, one with water cooling of the walls of the glass tube at the exit of the high temperature reaction zone, and the other without water cooling.

| Deposition results | Deposition parameters | |
|----------------------------|-----------------------|-----------------------|
| | With water cooling | Without water cooling |
| Sample No. | E - 44 | E - 45 |
| Deposited film thickness | 0.58 μm | 1.05 μm |
| Pressure drop | 17% | 4.3% |
| Source silicon weight loss | 293 mg | 335 mg |

$P = 80$ Torr. In most of the depositions α was less than 0.1, which justifies the approximation $\alpha \ll 1$ made in Eq. [9], and the assumptions made above regarding the monitoring of the total pressure and the flow rate. We found the value of α to be independent of the flow rate, which justifies the assumption of equilibrium conditions at the high temperature reactor under our experimental conditions. Equilibrium at the high temperature reactor may be maintained as long as the flow velocity of the gas through the reactor is slow relative to the length of the silicon column divided by the reaction rate.

As indicated above, the rate-limiting process was found to be the reaction in the high temperature (T_1) zone. It is thus consistent to assume that the deposition rate is proportional to the number of SiF_2 molecules arriving at the deposition reactor per unit time, which is proportional to the value of α times the SiF_4 flow rate. Indeed, as can be seen from Fig. 5, it was found that the deposition rate is linear with the flow rate. In the experiments in which we varied the total pressure and kept the value of ρv^2 constant, the flow rate was proportional to $P^{1/2}$ (Eq. [4]) and, since α is proportional to $P^{1/2}$ (Eq. [9]), the deposition rate is expected to be independent of P , as was observed (Fig. 6). From these results we also conclude that under a constant flow velocity (in units of volume per unit time) the deposition rate should increase with the square root of the SiF_4 pressure, and under constant flow rate (in mols per unit time) the deposition rate should vary as the inverse square root of the pressure.

As for the polymerization dynamics, it is recalled that under constant P and v the temperature (T_1) dependence of $\Delta P/\Delta t$ scaled linearly with the deposition rate. This implies a linear dependence of $\Delta P/\Delta t$ on α , that is, on the partial pressure of SiF_2 in the system. This would be consistent with a monomolecular production mechanism for $(\text{SiF}_2)_n$ polymers. On the other hand, from measurements of the dependence of $\Delta P/\Delta t$ on the flow rate and on the total pressure, it was found that $\Delta P/\Delta t$ is proportional to $\rho v^2 \cdot P$, which in turn is proportional to $P^2 \cdot v^2$ (see Fig. 6 and Eq. [5]). This implies that $\Delta P/\Delta t$ is proportional to $P^{3/2} \cdot v^2$ after one takes out the monomolecular reaction dependence on αP . This higher order pressure dependence of $\Delta P/\Delta t$ may imply that the pressure of SiF_4 at the polymerization sites enhances the $(\text{SiF}_2)_n$ polymerization rate. The mechanism for the observed pressure and velocity dependence of the polymerization kinetics still remains to be explained.

Film Properties

The optical transmittance and reflectance of the films were measured with Beckman Models ACTA MVII and IR 4250 spectrophotometers. From these measurements the refractive index and the absorption coefficient were derived. Within experimental accuracy these results are identical to previously published results on CVD silicon deposited below 675°C from silane (10).

The optical properties of all films deposited below 675°C were identical. Debye-Scherrer x-ray diffraction analysis of films deposited in another reactor (5) indicated that films deposited between 700° and 900°C are polycrystalline, while below 700°C the films are amorphous, as indicated by the broad diffraction halos and indistinguishable second and third rings in the diffraction patterns. At deposition temperatures between 850° and 900°C a thin yellow powdery deposition was observed. No deposition could be observed above 900°C. The room temperature electrical resistivity of the films deposited below 700°C was $2 \times 10^5 \Omega \cdot \text{cm}$. From photoconductivity measurements a carrier lifetime of the order of 10^{-10} sec is estimated, assuming a mobility of $1 \text{ cm}^2/\text{V sec}$. The results of the

electrical, optical, and ESR measurements of these films were published elsewhere and they are characteristic of anneal-stable amorphous silicon films (5).

Impurities in the films have been studied by surface electron spectroscopy (Auger and XPS) with a PHI system Model 590A and 555. Depth profiling Auger spectroscopy under Ar^+ sputter etching showed $99.6 \pm 4\%$ purity silicon. Oxygen and carbon signals could not be observed within a detectability limit of 0.2 a/o XPS (x-ray photoelectron spectroscopy) confirmed these results regarding oxygen and carbon, but it showed about 0.6 a/o fluorine in the film. The fluorine in the film. The fluorine concentration in the film has been further studied by the nuclear reaction $^{19}\text{F}(P,\alpha)^{16}\text{O}^*$, as described previously (5). This technique was found to have a resolution of 50 ppm with our counting times. The results showed a concentration between 0.5 and 1.5 a/o fluorine, depending on the substrate temperature during deposition (5). The reason we were not able to detect this fluorine by Auger depth profiling and got smaller values in XPS than with the ion implantation system is probably because the fluorine in the samples is in the form of SiF_4 gaseous molecules which were trapped in the film during deposition. During depth profiling sputter etching these molecules are freed and pumped out of the electron spectrometer, so they could not be detected by the Auger technique which is sensitive only to the composition of the first two or three monolayers of the film. The XPS technique probes at a depth of approximately 20Å, while the nuclear reaction probed the fluorine concentration at a depth of 500Å below the surface, where the SiF_4 molecules can be found. This point has recently been supported by infrared spectroscopy associated with Auger spectroscopy measurements (11). These silicon fluoride molecules were found to be electronically inactive, and there is evidence that when the sample is anneal crystallized at 800°C they leave the film (3, 11).

In summary, we have demonstrated a new deposition method of silicon films from SiF_2 vapor. Deposition temperature can be as low as 550°C with acceptable deposition rates. The properties of the films were found to be similar to the properties of silicon films prepared in the same temperature range by CVD from silane. The transport reaction given by Eq. [1] was studied and the fractional conversion of SiF_4 into SiF_2 at equilibrium at temperatures above 1060°C was deduced. This transport reaction can also be used in conjunction with glow discharge deposition system of fluorinated amorphous silicon (a-Si:F) where the SiF_2 decomposition is assisted by an electric field. This approach is currently being investigated in our laboratory.

Acknowledgments

This research was supported in part by the United States-Israel Binational Science Foundation (BSF), Jerusalem, Israel, and by the Fund for the Promotion of Research at the Technion. The authors acknowledge the efficient technical support of A. Kessel in constructing the deposition system. Our thanks to R. Brenner for XPS and Auger analysis, to Prof. R. Kalish for ion implantation services, and to K. Levin for electrical measurements.

Manuscript submitted Dec. 18, 1980; revised manuscript received July 9, 1981.

Any discussion of this paper will appear in a Discussion Section to be published in the June 1982 JOURNAL. All discussions for the June 1982 Discussion Section should be submitted by Feb. 1, 1982.

REFERENCES

1. M. Wolf, Proc. 11th IEEE Photovoltaic Specialists Conference, Phoenix, Arizona (1975).
2. M. Wolf, A. G. MacDiarmid, G. T. Noel, and K.

- Thallum, in "Proc. 12th IEEE Photovoltaic Specialists Conference" (1976).
3. W. M. Ingle, R. Chaney, and S. Thompson, *Motorola Quarterly Reports* 2257/1-2257/8, ERDA JPL Contract No. 954442 1976-1978.
 4. C. H. Van Dyke, in "The Bond to Halogens and Halogenoids," Part I, A. G. MacDiarmid, Editor, p. 142, Marcel Dekker, Inc., New York (1972).
 5. M. Janai, R. Weil, K. H. Levin, B. Pratt, R. Kalish, G. Braunstein, M. Teicher, and M. Wolf, *J. Appl. Phys.*, To be published.
 6. W. Braker and A. L. Mossman, "Matheson Gas Data Book," 5th ed., p. 509, Matheson, New Jersey (1971).
 7. L. I. Maissel and R. Glang, "Handbook of Thin Film Technology," pp. 11-4 to 11-14, McGraw-Hill Company, New York (1970).
 8. See, e.g., "Variable Area Flowmeter Handbook," Vol. 1 (Fischer & Porter Catalog 10A 1021).
 9. C. C. Pease, U.S. Pat. 2,840,588 (1958).
 10. M. Janai, D. D. Allred, D. C. Booth, and B. O. Seraphin, *Solar Energy Mater.*, **1**, 11 (1979).
 11. C. J. Fang, L. Hey, H. R. Shanks, K. J. Grutz, and M. Cardona, *Phys. Rev. B*, To be published.

Electronic Characterization of Heteroepitaxial Silicon-on-Sapphire by Surface Photovoltage Spectroscopy

J. Lagowski*

Massachusetts Institute of Technology, Cambridge, Massachusetts 02139

and L. Jastrzebski* and G. W. Cullen*

RCA Laboratories, Princeton, New Jersey 08540

ABSTRACT

Surface photovoltage spectroscopy was successfully applied to silicon-on-sapphire and it enables simultaneous determination of band structure, trapping centers, deep levels, the refractive index, and the film thickness. Studies of "as-grown" and ion-implanted films revealed a noticeable degree of amorphization manifested by 1.45 eV energy gap structure clearly resolved in addition to standard 1.1 eV structure of bulk Si. Three deep levels were identified, i.e., electron trap at $E_c - E_t = 0.25$ eV, hole trap at $E_t - E_v = 0.15$ eV, and deep centers at $E_c - E_t = 0.6$ eV. It has been found that the degree of amorphization and concentration of deep centers in the layers depends on the thermal history of the SOS film.

Rapidly growing need for high speed, radiation resistance CMOS memories and microprocessors with large capacity and high packing density puts new demands on SOS technology. One of the factors which can limit circuit performance is the presence of deep levels in the silicon-on-sapphire. Deep levels acting as traps can decrease speed, shift threshold voltage, and/or cause excessive junction leakage of transistors in the circuit. A nonuniform distribution of deep centers across a wafer can result in nonuniform yield and circuit performance on the wafer. These facts emphasize the importance of developing methods to experimentally assess the sources of deep centers in as-grown layers and processed silicon films.

Techniques for the characterization of heteroepitaxial silicon have been reviewed by Ham (1). Most of these methods rely on the measurement of test structures on processed wafers or on resistivity and capacitance measurements on as-grown films. Recently a u.v. reflectance method has been developed which allows quantitative characterization of the crystallinity in SOS films (2). These techniques have been designed as effective and practical tools for establishing screening criteria to inspect the quality of as-grown wafers used for fabrication of device structures. They do not provide direct information about deep levels in SOS films.

Previous studies of polycrystalline and amorphous silicon and of dislocation structures in elemental semiconductors have demonstrated the promising character of photoelectric measurements in assessing the electronic and optical properties of silicon, and in identifying

the mechanisms of phenomena related to defects and disorder (3-5). The photovoltage spectroscopy technique selected for the present study is rather specific among photoelectric effects as it permits the measurement of bulk material as well as the conducting or high resistivity films on insulating or metallic substrates (6-8). Furthermore, this technique does not require ohmic contacts, and if necessary it can be utilized in a nondestructive, contactless, configuration employing capacitive coupling to the sample. Therefore, as-grown wafers and wafers after different processing steps can be analyzed without the fabrication of test structures. Also a light spot can be easily focused to a small area which permits the characterization of defect distribution on a microscale.

This investigation has been undertaken to assess the feasibility of using photovoltage measurements for characterization of defects in SOS. Information concerning the deep states (their energy levels and relaxation time) and the basic parameters of SOS layers (the band structure, the film thickness, and the refractive index) were obtained from the spectral, transient, and temperature dependence of the photovoltage. The measurements performed on layers after different stages of processing (as-grown, ion-implanted, and heat-treated) show that the photovoltage technique is able to detect a variety of defect structures in SOS films.

Experimental

In the present study the photovoltage generated by a monochromatic light (energy range 0.5-3.5 eV) was measured with respect to a semitransparent gold electrode separated from the SOS film by a 10 μ m thick Mylar foil (MIS configuration) or directly evaporated on SOS film (MS configuration).

* Electrochemical Society Active Member.

Key words: defects, amorphous, silicon-on-sapphire, surface photovoltage.

As shown schematically in Fig. 1, the measurements of chopped light a-c photovoltage were performed using lock-in detection, while the photovoltage transient was measured with a signal averager. The SOS wafers were placed on the cold finger of a variable temperature cryostat. This provides the capability to precisely adjust the sample temperature in a range from 10 to 300 K.

The illumination intensity was selected on a level sufficiently low that the generated photovoltage (of the magnitude between 10^{-7} and 5×10^{-3} V) satisfied "low signal" conditions (i.e., $|\Delta V| \ll kT/q$).

In order to separate possible surface state effects, the photovoltage spectra were measured in various ambients (room atmosphere, $N_2 + H_2O$, vacuum 10^{-6} Torr). Furthermore, comparative studies were carried out on the same films utilizing both the MIS and MS configurations. It is concluded, on the basis of these studies, that the surface has a negligible effect on the photovoltage spectra up to the energy of about 2.5 eV. The surface sensitive effects for higher photon energy are most likely related to the enhanced role of surface recombination ($\alpha d > 1$ where α is the absorption coefficient and d is the film thickness).

A typical photovoltage spectrum of an SOS film is schematically represented in Fig. 2. In the subbandgap region ($h\nu < E_g$) the photovoltage is due to photoionization or photothermoionization transitions involving deep levels. Accordingly, it can be used to judge the effect of growth and processing parameters on deep level characteristics. For $h\nu > E_g$ (intrinsic excitation)

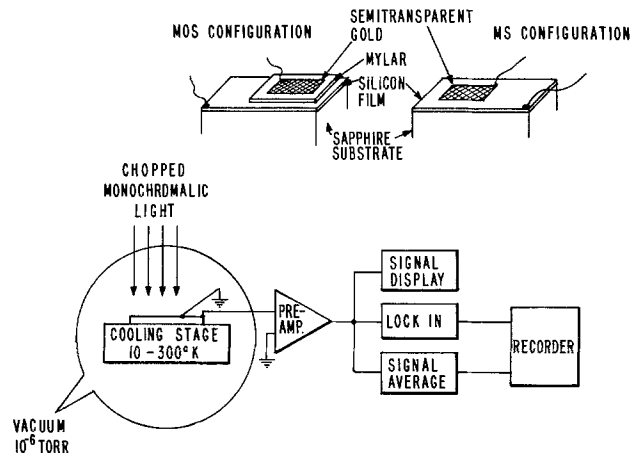


Fig. 1. Experimental arrangement for photovoltage measurement and sample configuration.

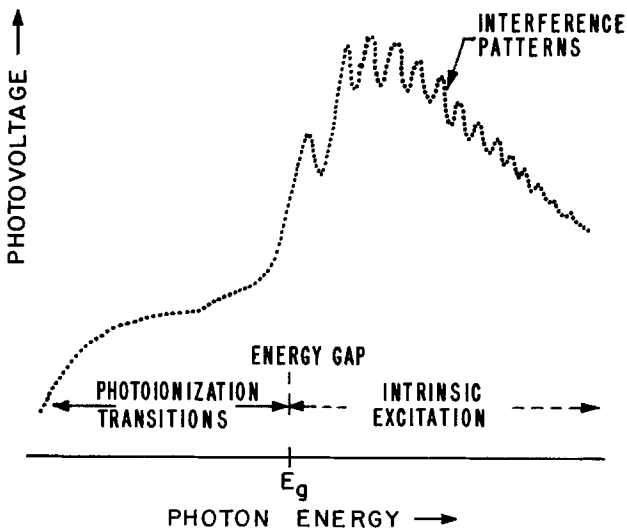


Fig. 2. Schematic representation of photovoltage spectra of silicon-on-sapphire films.

the photovoltage is due to photogenerated electron hole pairs. In comparison with bulk material, thin film photovoltage exhibits a specific feature, i.e., a series of interference maxima occurring at wavelengths $\lambda_k = 2nd/k$; where $k = 1, 2, 3, \dots$; n is the refractive index dependent on energy; and d is the film thickness.

Photovoltage transient measurements were also carried out in order to determine the lifetime of excess carriers and/or trapping characteristics. It has been found that the photovoltage transient of SOS films is dominated by trapping of excess carriers rather than by recombination transitions. This provides the possibility to determine the energy levels of trapping centers from the temperature dependence of photovoltage relaxation time.

The results discussed were obtained with SOS samples listed in Table I.

Results and Discussions

Band structure transitions.—The room temperature photovoltage spectra of silicon-on-sapphire films for photon energy corresponding to intrinsic excitation are presented in Fig. 3. The first and very pronounced increase of photovoltage occurs in the vicinity of the energy gap (E_g) of bulk Si. However, the second photovoltage increase for photon energy $h\nu \approx 1.4$ eV is also clearly observed in all spectra. It should be noted that a rapid rise of photoresponse and of the absorption coefficient for photon energy 1.4-1.8 eV is a specific feature of amorphous silicon (4, 9) and it is attributed to the optical energy gap of a-Si, $E_g \approx 1.45$ -1.5 eV. The photovoltage increase observed for silicon-on-sapphire is significant, as it indicates the presence of partial amorphization of SOS films. It should also be noted that the magnitude of the increase in the photovoltage between 1.4 and 1.8 eV was noticeably different for different samples, which indicates that a degree of amorphization of SOS films depends on growth and processing parameters.

The analysis of interference minima and maxima (intentionally not included in spectra of Fig. 3, which represented average photovoltage) enables the determination of $d \cdot n$, and thus relative changes of the refractive index vs. energy. The results given in Fig. 4 indicate that the energy dependence of the refractive index of silicon-on-sapphire is practically identical with that of bulk Si (dotted line) (10) up to the energy of about 2.8 eV. For $h\nu > 2.8$ eV a slight discrepancy between the bulk Si and epitaxial film is observed, however in this region determination of the refractive index from interference patterns becomes less reliable due to a significant absorption and a rapid decrease of the amplitude of interference patterns. The observed similarity is not surprising since even a-Si films have refractive indexes close to values observed in single crystal Si (9). Accordingly, SOS films characterized by only a slight degree of amorphization should in principle exhibit refractive indexes identical with bulk Si.

Using the bulk Si value of n , the thickness of the measured films was determined as: $d_1 = 0.60 \mu\text{m}$, $d_2 = 0.63 \mu\text{m}$, $d_3 = 0.61 \mu\text{m}$, and $d_4 = 0.61 \mu\text{m}$, for samples S1 to S4, respectively. These values were identical to film thickness determined using commercially available thickness monitor.

Table I. Silicon-on-sapphire samples employed in the photovoltage studies

| Sample | History | Annealing conditions |
|--------|--|---------------------------|
| S.1 | As grown | Not annealed |
| S.2 | Boron implant $1 \times 10^{11} \text{ cm}^{-2}$ | Not annealed |
| S.3 | Phosphor implant $4 \times 10^{11} \text{ cm}^{-2}$ | Not annealed |
| S.4 | Phosphor implant $1 \times 10^{12} \text{ cm}^{-2}$ | 1 hr, 900°C in dry oxygen |

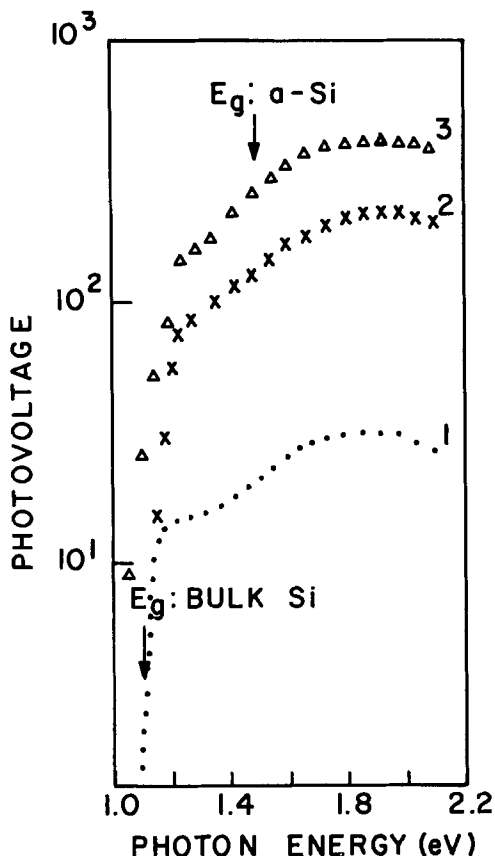


Fig. 3. 300 K photovoltage spectra of silicon-on-sapphire films in a region of intrinsic excitation. Each spectrum was averaged regarding the interference maxima-minima. The spectrum of sample 4 is not shown for clarity, since it was practically identical with sample 2.

Vicinity of energy gap and deep level photoionization transitions.—Figure 5 presents room temperature “open-circuit” photovoltage spectra of SOS films measured using the MS structure. Drastic differences between “as-grown” films and ion-implanted films are clearly visible in the low energy region (deep level transitions) and in the vicinity of the energy gap. The sharp photovoltage increase in sample 1 for $h\nu \approx E_g$ becomes much broader in samples 2 and 4, and it practically cannot be resolved for unannealed sample 3. The same features were found to be characteristics for photovoltage spectra measured in the MOS configuration, which indicates negligible contribution from photoionization of surface states (which in general can affect MOS measurements) and from photoinjection of excess carriers from the metal.

A typical low temperature (230 K) photovoltage spectrum measured in the MOS configuration is given

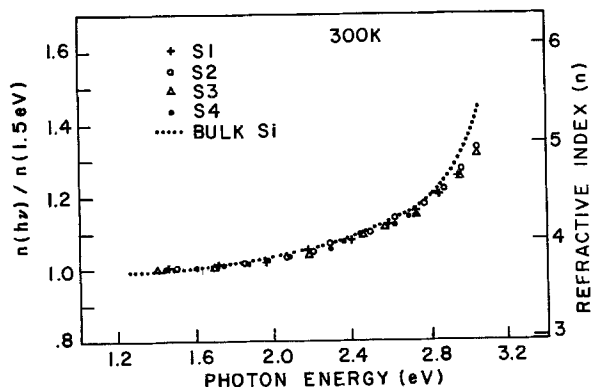


Fig. 4. Refractive index of SOS films vs. photon energy. Bulk Si refractive index was taken after Ref. (10).

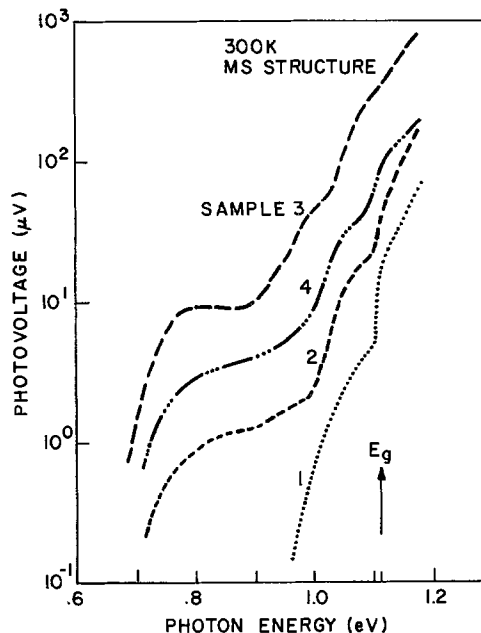


Fig. 5. Open-circuit photovoltage spectra of MS structures prepared on SOS films.

in Fig. 6. The lack of a sharp increase in the photovoltage for sample 3 in the vicinity of $h\nu = E_g$ is also evident at this temperature.

Decreasing the temperature further (see Fig. 7) converts the broad spectrum of sample 3 into a clearly visible edge. Such behavior can be explained by assuming that ion implantation introduces a high density of levels located in the vicinity of valence and conduction bandedges. Transitions between these levels combined with thermal excitation (photothermoionization transitions) effectively mask the band-to-band excitation of free carriers at higher temperatures. At low temperatures photothermoionization transitions are negligible and band-to-band excitation of free carriers become dominant. Thus, a rapid photovoltage increase due to (bulk) band-to-band excitation ($h\nu \approx 1.18$ eV) becomes clearly visible.

As seen in Fig. 5 and 6, ion-implanted samples exhibit a pronounced increase in the photovoltage in the low photon energy range ($h\nu > 0.6$ eV) apparently due

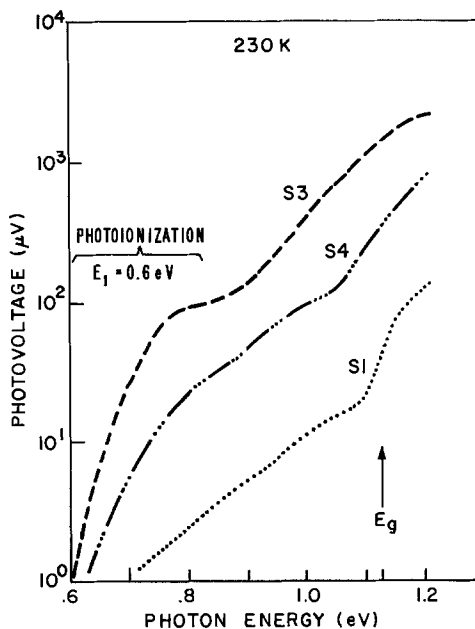


Fig. 6. 230 K photovoltage spectra of SOS films (MOS configuration).

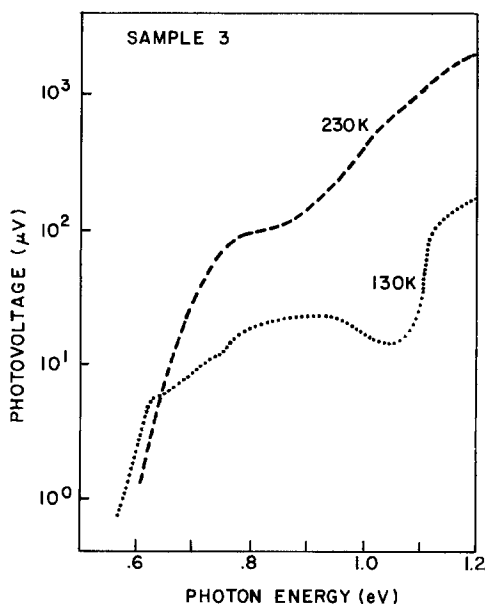


Fig. 7. Photovoltage (MOS configuration) spectra of sample 3 measured at 230 and 130 K, respectively. Note at 130 K the appearance of well-defined photovoltage edge in the vicinity of energy gap.

to photoionization of deep defect levels. Consistent with this interpretation, the low energy photovoltage threshold has been found to satisfy a power dependence on energy $\Delta V \sim |h\nu - E_t|^p$, with $E_t = 0.6$ eV (see Fig. 8).

It may be of interest to note that a similar low energy (about $h\nu \approx 0.6$ eV) threshold is commonly observed in photoelectric response and absorption coefficient of polycrystalline and amorphous Si (4, 8) and also in plastically deformed bulk Si which contains high densities of intentionally introduced dislocations (11).

Temperature dependence of photovoltage.—A typical plot of the temperature dependence of the a-c photovoltage in SOS films is shown in Fig. 9. Two regions are clearly distinguished. In the higher temperature

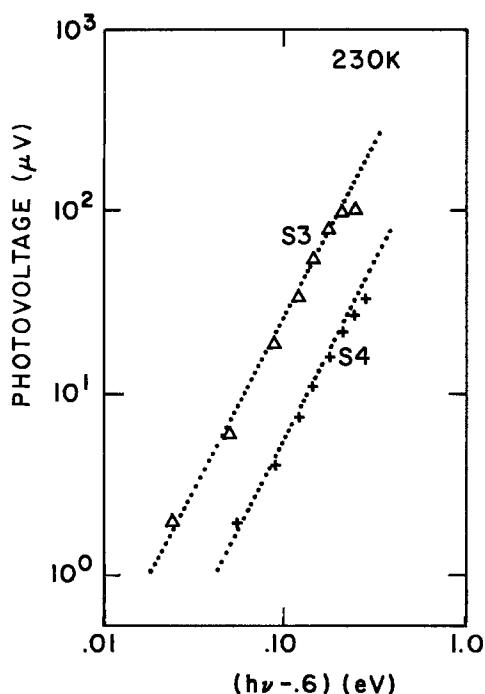


Fig. 8. The analysis of low energy photovoltage threshold (see text).

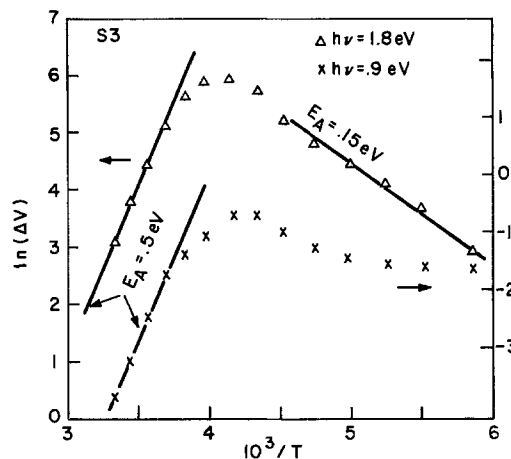


Fig. 9. Temperature dependence of photovoltage of sample S3 (MOS configuration).

region (300–220 K) the subband and intrinsic photovoltage increases exponentially with $1/T$. A corresponding activation energy ($E_A \approx 0.5$ eV) was found to be identical for all samples. Furthermore, the same activation energy governs the photovoltage increase for intrinsic ($h\nu > E_g$) and subbandgap ($h\nu < E_g$) excitation. A similar increase of photovoltage or photoconductivity was previously observed for polycrystalline Si (3) and for plastically deformed Si (12). A suggested interpretation of these findings involve thermal excitation of deep traps located about 0.5–0.6 eV below conduction band associated with defects or dangling bonds due to edge dislocations (3, 12).

In the lower temperature region ($T < 220$ K) the measured photovoltage decreases due to an increase of the photovoltage relaxation time, τ . The amplitude of a-c photovoltage generated by the light chopped at angular frequency, ω , can be expressed as (7)

$$\Delta V_{\text{measured}} = \Delta V (1 + \omega^2 \tau^2)^{-1/2} \quad [1]$$

Accordingly, at higher temperatures where the relaxation time is short enough to satisfy $\omega^2 \tau^2 \ll 1$, $\Delta V_{\text{measured}}$ reflects the amplitude of the steady-state photovoltage ΔV . For lower temperatures the relaxation time becomes very long (see next section). Thus, $\omega^2 \tau^2 \gg 1$ and the measured photovoltage $\Delta V_{\text{measured}} = \Delta V \cdot 1/\omega\tau$. It was found (from direct transient measurements described in the next section) that in low temperature region ($T < 220$ K), ΔV is practically constant, and thus the decrease of photovoltage after passing through the maximum is caused by an increase in relaxation time.

It is also seen in Fig. 9 that the relaxation time increase at low temperatures is different for intrinsic excitations ($h\nu = 1.8$ eV) and subbandgap ($h\nu = 0.9$ eV) excitation. As discussed in the next section, these differences can be explained considering that under intrinsic excitation τ is determined by thermal excitation of minority carriers from trapping levels while for subbandgap illumination the relaxation time is determined by nonradiative recombination transitions to traps, which are weakly dependent on temperature.

Photovoltage transient and trapping of photogenerated carriers.—Typical transients of photovoltage in SOS films for intrinsic illumination are shown in Fig. 10a, b, for samples 3 and 4, respectively, at room temperature. These transients generated by intrinsic excitation were found to be identical for MOS and MS configurations. It is seen that an increase of the illumination intensity (I) results in the appearance of fast nonexponential decay, denoted as region "A." However, the slow exponential tail denoted as region "B" remains unaffected by illumination intensity. It is of interest to note that transients in Fig. 10 constitute almost a "textbook" illustration of the photoelectric

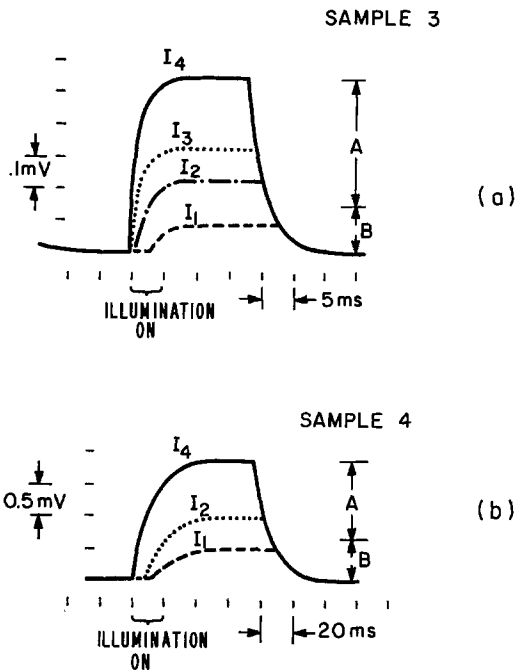


Fig. 10. Room temperature photovoltage transients of samples 3 and 4, respectively. The illumination intensity increases in the sequence $I_4 > I_3 > I_2 > I_1$. Transients measured for $h\nu = 1.8$ eV.

transient in the typical case of pronounced trapping (13). Thus, the exponential tail "B" can be considered as due to the thermal release of trapped minority carriers.

The corresponding exponential time constant is given as

n-type; $\tau^{-1} = \sigma_p v_t N_v e^{-E_A/kT}$ where $E_A = E_t - E_v$ [2a]

p-type; $\tau^{-1} = \sigma_n v_t N_c e^{-E_A/kT}$ where $E_A = E_c - E_t$ [2b]

where [2a] and [2b] describe the time constant of the thermal release of trapped holes and electrons, respectively.

According to [2a], [2b] the trapping relaxation time should increase exponentially with $1/T$, upon decreasing the temperature. As shown in Fig. 11, such behavior was indeed observed experimentally, for both p- and n-type samples (2 and 3, respectively). Determined energies of minority carrier trapping levels are: electron traps (p-type Si) 0.25 eV below the conduc-

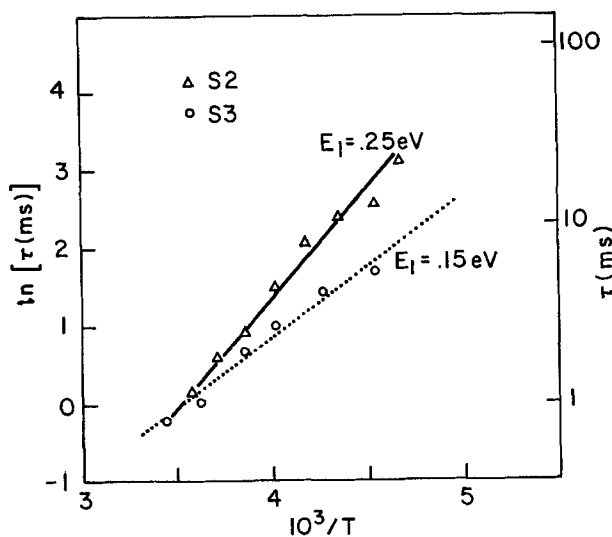


Fig. 11. Temperature dependence of trapping time, τ , for p-type sample S2 and n-type S3. Transients measured for $h\nu = 1.8$ eV.

tion band; and hole traps (n-type Si) 0.15 eV above the valence band. It is evident that the latter value agrees very well with an energy $E_A = 0.15$ determined in the previous section (see Fig. 9) from the temperature dependence of the amplitude of the a-c photovoltage. The estimated (from expressions [2]) values of the effective capture cross sections $K_p = \sigma_p \cdot v_T$ and $K_n = \sigma_n \cdot v_T$ are in order of 10^{-11} cm³ sec⁻¹ and 10^{-13} cm³ sec⁻¹ for hole and electron traps, respectively.

Transient analysis in terms of parameters of trapping centers could not be performed for "as-grown" sample 1, due to the very low magnitude of photovoltage signal caused by a high density of lifetime killing centers.

Summary

It has been shown that photovoltage measurements detect differences in defect density in SOS wafers in different stages of processing. The results obtained from subband and interband photovoltage measured in as-grown and processed SOS wafers can be summarized as follows.

1. Photovoltage measurements established the presence of deep levels located close to the center of the energy gap (0.6 eV) in all SOS films. The density of these levels is a function of processing: increases after ion implantation and is reduced by the heat-treatment.
 2. The photoelectric response of SOS films is dominated by trapping phenomena which are very similar to those encountered in bulk Si containing a high density of dislocations or in polycrystalline Si. It has been established that the characteristics of the trapping process (e.g., time constant, activation energy) depend on film processing. Hole trapping levels located 0.15 eV above the valence band and electron traps located about 0.25 eV below the conduction band have been found in ion-implanted films.
 3. It has been found that ion implantation causes drastic changes in the density of states in the vicinity of bandedges. These changes have been reduced, but not totally eliminated, by annealing.
 4. It has been found that all ion-implanted and "as-grown" films exhibit a slight degree of amorphization. Thus, the structure characteristic of amorphous silicon (energy gap at about 1.45 eV) was clearly resolved for SOS films, in addition to the standard energy gap structure (1.1 eV) bulk Si.
 5. The refractive index (as a function of photon energy) of SOS films was found to be very similar to that of bulk Si.
- A summarizing energy level diagram of silicon-on-sapphire is shown in Fig. 12 together with corresponding photoionization transitions (arrows) in n- and p-type material. We believe that the above results dem-

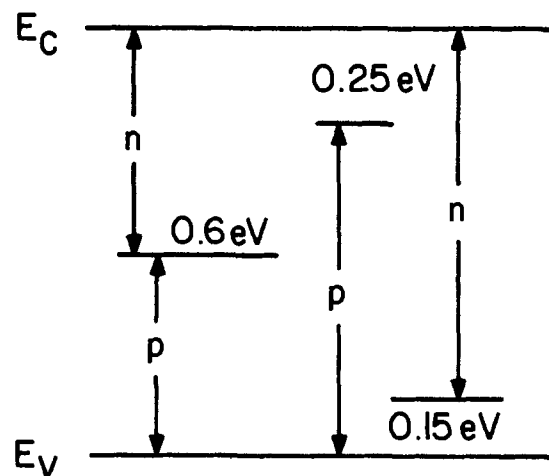


Fig. 12. Energy levels and transition diagrams in n- and p-type SOS films.

onstrate the potential of photovoltage as a unique technique to provide a reliable means for the characterization of deep centers in SOS wafers during different stages of processing. Furthermore, the large magnitude of the photovoltage signal in ion-implanted and annealed wafers confirms the possibility to extend this technique for the characterization of deep levels on a microscale.

Manuscript submitted Oct. 12, 1980; revised manuscript received July 7, 1981.

Any discussion of this paper will appear in a Discussion Section to be published in the June 1982 JOURNAL. All discussions for the June 1982 Discussion Section should be submitted by Feb. 1, 1982.

Publication costs of this article were assisted by RCA Laboratories.

REFERENCES

1. W. E. Ham, in "Heteroepitaxial Semiconductors for Electronic Devices," G. W. Cullen and C. C. Wang, Editors, p. 216, Springer Verlag, New York (1978).
2. P. J. Zanzucchi and M. T. Duffy, *Appl. Opt.*, **17**, 3477 (1978); M. T. Duffy, P. J. Zanzucchi, W. E. Ham,

- J. F. Corboy, and G. W. Cullen, "Method to Determine the Quality of Sapphire," NBS SP 400-63, May 1980.
3. H. W. Brandhorst and A. E. Potter, *J. Appl. Phys.*, **35**, 1997 (1964).
4. W. E. Spear, Proc. 5th Int. Conf. on Amorphous and Liquid Semicond., p. 1, Garmisch-Partenkirchen, Sept. 1973.
5. E. Kamieniecki, *J. Phys. C*, **9**, 1211 (1976) and references quoted therein.
6. J. Lagowski, W. Walukiewicz, M. Slusarczyk, and H. C. Gatos, *J. Appl. Phys.*, **50**, 5059 (1979).
7. L. Jastrzebski and J. Lagowski, *RCA Rev.*, **41**, 181 (1980).
8. B. Goldstein and D. Szostak, *Surf. Sci.*, In press.
9. M. Hirose, M. Taniguchi, and Y. Osaka, in "Proc. 7th Int. Conf. on Amorphous and Liquid Semicond.," p. 352, Edinburgh, June 1977.
10. H. R. Phillips and E. A. Taft, *Phys. Rev.*, **129**, 37 (1960).
11. Level 0.6 in Si (dislocation) e.g., J. R. Patel, L. R. Testardi, and P. E. Freeland, *Phys. Rev. B*, **13**, 3548 (1976).
12. T. Figielski, in "Proc. IVth Int. School on Defects," p. 251, Zakopane, Poland, June 1973, Polish Scientific Publishers, Warsaw (1974).
13. See, for example, R. A. Smith, "Semiconductors," Cambridge University Press, New York (1959).

The Solid Electrolyte System $\text{RbCu}_4\text{Cl}_3(\text{I}_{2-x}\text{Cl}_x)$, $0 \leq x \leq 0.40$

I. Stability

K. Nag¹ and S. Geller

Department of Electrical Engineering, University of Colorado, Boulder, Colorado 80309

ABSTRACT

The stoichiometric solid electrolyte, $\text{RbCu}_3\text{Cl}_3\text{I}_2$, can be converted, by cold-work, to a new low symmetry phase with the probable composition $\text{RbCu}_4\text{Cl}_3(\text{I}_{1.96}\text{Cl}_{0.04})$ (and very small amounts of CuI and probably, $\text{Rb}_2\text{Cu}_3\text{Cl}_5$). The new phase has a crystal structure which appears to be related to that of the cubic phase. It transforms rapidly to the cubic phase with formula $\text{RbCu}_4\text{Cl}_3(\text{I}_{1.96}\text{Cl}_{0.04})$ at temperatures above 75°C . The new phase is stable in a very narrow temperature range, almost surely not wider than $0^\circ\text{--}35^\circ\text{C}$. It has a conductivity of $1.5 \times 10^{-4} \Omega^{-1} \text{cm}^{-1}$ at 298 K. Stoichiometric $\text{RbCu}_4\text{Cl}_3\text{I}_2$ is thermodynamically stable in the narrow temperature range $200^\circ \pm 15^\circ\text{C}$. The solid solution range $\text{RbCu}_4\text{Cl}_3(\text{I}_{2-x}\text{Cl}_x)$ $0.00 \leq x \leq 0.40 \pm 0.01$ has been confirmed. For $0.02 \leq x \leq 0.40$, the materials appear to be stable from at least 78 K to their preparation temperatures which depend on x . None of these can be made to convert to the new phase; that is to say, the only established route to the new phase is through cold-working of the stoichiometric phase.

In an earlier paper (1), it was reported briefly that there exists a solid solution range in $\text{RbCu}_4\text{Cl}_3(\text{I}_{2-x}\text{Cl}_x)$ with $0.00 \leq x \leq 0.40$. In the present work, we have studied the effects of substitution of chloride for iodide ions on the practical stability and on the conductivity. Because of the considerable detail involved in the description of the results, it has been decided to divide the presentation into two parts: part I will be devoted mainly to the stability and part II mainly to the conductivity studies of the materials.

With the passing of time, there are new developments with regard to the nature of the stoichiometric material. A pellet and some powdered material from

the same prepared specimen that had been stored in a capped vial in a desiccator for several months were checked by x-ray powder diffraction. It was found that all the material in the pellet was a new phase related to the solid electrolyte; a slight amount of CuI was present, but no other phases were detected. In the case of the powder, the same new phase was present, but so was cubic solid electrolyte and apparently somewhat more CuI than for the pellet. The solid electrolyte, however, had a smaller lattice constant, indicating that it had the composition given by $\text{RbCu}_4\text{Cl}_3(\text{I}_{1.96}\text{Cu}_{0.04})$. After two years, no further change in either part of this specimen has been found. When the material from the powder or pellet was heated to 200°C , the cubic solid electrolyte was regenerated from the new phase, except that it had a lattice constant of 10.028\AA , 0.004\AA less than that of the

¹ On leave from Indian Association for the Cultivation of Science, Calcutta 700032 India.

Key words: solid electrolyte, cuprous ion conductor, rubidium cuprous chloriodide, transformation, stability.

stoichiometric phase, indicating again a formula $\text{RbCu}_4\text{Cl}_3(\text{I}_{1.96}\text{Cl}_{0.04})$; CuI was also present. After two years, this material did not revert to the new phase.

Remarkably, no other specimen, regardless of composition, has changed on standing this way. Numerous experiments resulted in a method of forcing the change, namely, by cold-work, as will be described later. Although the new phase can be produced by this method, the material is strained as indicated by the appearance of the high angle region of the x-ray powder pattern. In the case of the stored specimen, the high angle lines in the x-ray powder photographs of the new phase are relatively sharp; at present, it is not known how the changes occurred in this specimen. The experiments carried out subsequently lead to the conclusion that they could not have resulted simply from the instability of the compound.

Only the stoichiometric material undergoes the transition by cold-work; even a very small substitution of Cl^- for I^- ions, e.g., $x = 0.02$, inhibits it. A smaller lattice constant for the cubic phase, whether other phases present are detectable or not, means that some Cl^- ions are replacing iodide ions in the material.

The new phase is not isostructural with either β - or γ - RbAg_4I_5 (2). However, it does appear to have a structure related to that of α - RbAg_4I_5 (3) or $\text{RbCu}_4\text{Cl}_3\text{I}_2$ (1).

The materials with $x \neq 0$ appear to be stable over a much wider temperature range than the stoichiometric material. In all cases, care must be taken to prepare the materials in the temperature range appropriate to the particular composition.

Experimental

Materials preparation.— CuCl was prepared by the reduction of an aqueous solution of CuCl_2 (from $\text{CuCl}_2 \cdot 2\text{H}_2\text{O}$) with Na_2SO_3 in accordance with the method of Keller and Wycoff (4). The white crystalline material so obtained may be preserved indefinitely if stored dry. CuI was obtained by reacting CuSO_4 with KI and $\text{Na}_2\text{S}_2\text{O}_3$ in aqueous solution as described by Kauffman and Pinnell (5). The CuI that precipitates in microcrystalline form was separated from the solution with some difficulty. The product was thoroughly washed and then dried *in vacuo*. However, an x-ray powder photograph of this material indicated the presence of occluded $\text{Na}_2\text{S}_2\text{O}_3$.² Therefore, the material was dissolved in aqueous HI (Baker, 47-51%); undissolved material was separated by filtration with a sintered glass crucible (G-4). Water was added slowly to the filtrate while stirring until precipitation of the CuI was complete. The CuI settled readily and was separated by and washed on a glass frit. Washing with water was continued until the filtrate was acid-free. Finally three washings with dry acetone were made; the material was then dried in a vacuum oven at 100°C for 12 hr.

RbCl (Cerac 99.9%) was used after drying *in vacuo* at 100°C for 4 hr.

Sample preparation.—Appropriate amounts of RbCl , CuCl , and CuI (originally ground fine with agate mortar and pestle) to prepare about 3.5g of $\text{RbCu}_4\text{Cl}_3(\text{I}_{2-x}\text{Cl}_x)$ were weighed into a glass vial and thoroughly mixed by shaking. The mixture was then pelletized in a $\frac{1}{2}$ in. tungsten carbide die at 1 kbar pressure with a Carver press. The pellet was then put into a Pyrex test tube which was evacuated, flushed with dry nitrogen, evacuated, and again flushed with dry nitrogen. The pressure was then reduced to $\frac{1}{2}$ atm and the tube sealed off. The material was then melted in a furnace at about 320°C and held at this

² Commercially obtained CuI , probably prepared by the same method (5), contains $\text{Na}_2\text{S}_2\text{O}_3$.

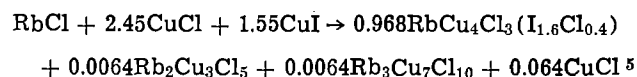
temperature for 10 min, with occasional stirring of the melt. The tube was then removed from the furnace and after cooling to room temperature, broken open inside a nitrogen-recirculating glove box. The pellet was pulverized and ground fine with an agate mortar and pestle. After repelletizing and sealing the material in a Pyrex tube as before, the material was annealed at the "desired" temperature³ for 4 hr. Our experiments led to the conclusion that in all, four regrindings, repelletizings, and annealings of 4 hr, maximized the chance of obtaining a single phase material. X-ray powder diffraction photographs with both $\text{CuK}\alpha$ and $\text{CrK}\alpha$ radiation were taken with 114.6 mm diam Norelco cameras. The $\text{CrK}\alpha$ photographs were used for lattice constant measurement. The lattice constants and annealing temperatures for the various samples prepared are shown in Table I. Lattice constants are plotted vs. x in Fig. 1.

Results and Discussion

Lattice constants and composition.—Our studies have shown that phase-pure stoichiometric $\text{RbCu}_4\text{Cl}_3\text{I}_2$ is obtained when the annealing is done in the narrow range $\pm 5^\circ\text{C}$ about 205°C . The lattice constant of this material is $10.032 \pm 0.001\text{\AA}$. Although it is not possible to detect the presence of very small amounts of other phases in large excess of the solid electrolyte, the determination of the lattice constant is a powerful indicator as to whether impurity phases are present or not. When attempts were made to prepare the stoichiometric compound at temperatures outside the temperature range 200° - 210°C , the materials obtained always had lattice constants lower than 10.032\AA (see Table II and later discussion of stability of the materials).

The existence of a solid solution range $\text{RbCu}_4\text{Cl}_3(\text{I}_{2-x}\text{Cl}_x)$ has been established⁴ prior to the present work, and the earlier reported range, $0.00 \leq x \leq 0.40$ has been confirmed to ± 0.01 . In the stoichiometric compound, only Cl^- ions surround the Rb^+ ions; new experiments corroborate the previous result (8) that small amounts of these Cl^- ions cannot be replaced by I^- ions, accounting for the formulation that we use, i.e., $\text{RbCu}_4\text{Cl}_3(\text{I}_{2-x}\text{Cl}_x)$.

The lowest lattice constant in the series is $10.001 \pm 0.001\text{\AA}$ for $\text{RbCu}_4\text{Cl}_3(\text{I}_{1.6}\text{Cl}_{0.4})$. An attempt to prepare a specimen with formula $\text{RbCu}_4\text{Cl}_3(\text{I}_{1.55}\text{Cl}_{0.45})$ did not give single phase material. It contained the solid electrolyte $\text{RbCu}_4\text{Cl}_3(\text{I}_{1.6}\text{Cl}_{0.4})$, i.e., with lattice constant 10.001\AA (see Fig. 1). Other phases were difficult to detect in the powder photograph. The reaction is



³ It was found that the "desired" temperature was a function of x .

⁴ References (6) and (7) notwithstanding.

⁵ This CuCl is really unreacted material.

Table I. Lattice constants and preparation annealing temperatures for the system $\text{RbCu}_4\text{Cl}_3\text{I}_2$

| x | a_0 (Å) | Annealing temperature ($^\circ\text{C}$) | |
|-------|-----------|--|-------------|
| 0 | 10.032 | 205 \pm 5 | |
| 0.01 | 10.031 | | |
| 0.02 | 10.030 | | |
| 0.03 | 10.029 | | |
| 0.04 | 10.028 | | |
| 0.05 | 10.027 | | |
| 0.10 | 10.021 | | |
| 0.14 | 10.017 | | |
| 0.175 | 10.015 | | 195 \pm 5 |
| 0.20 | 10.013 | | |
| 0.27 | 10.008 | | |
| 0.32 | 10.005 | | |
| 0.40 | 10.001 | 175 \pm 5 | |

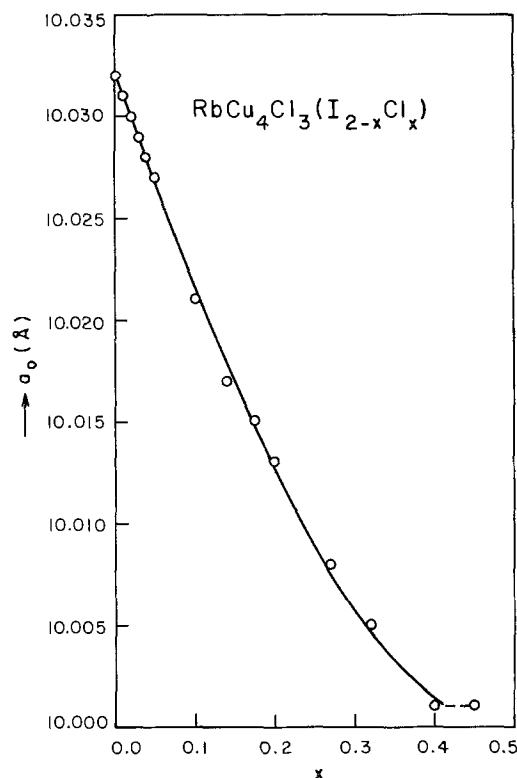


Fig. 1. Lattice constant vs. x in $\text{RbCu}_4\text{Cl}_3(\text{I}_{2-x}\text{Cl}_x)$

This reaction was verified by an attempted preparation of "RbCu₄Cl₃(ICl)," in which case the cubic solid electrolyte with $a_0 = 10.001\text{Å}$, as before, as well as the three other phases were seen in the powder photograph.

The two compounds Rb₂Cu₃Cl₅ and Rb₃Cu₇Cl₁₀ have been mentioned in Ref. (9) [and Rb₂Cu₃Cl₅ in Ref. (10)]; we have confirmed their existence by preparation by solid-state reaction. (Appropriate mixtures of RbCl and CuCl were ground together in an agate mortar, pelletized, inserted in a tube, evacuated, flushed with dry nitrogen, finally sealed off with N₂ pressure of ½ atm, and heated at 140°C for 6 hr. Each was given two additional regrindings, pelletizings, etc., and annealings at 140°C for 6 hr.) The material reported in Ref. (10) as RbCu₄Cl₅ is a mixture of Rb₂Cu₃Cl₅, Rb₃Cu₇Cl₁₀, and CuCl in mol ratio 1:1:10.

In the preparation of a solid electrolyte with specific x , the required annealing temperature must be reduced as x increases (see Table I). For example, attempts to prepare RbCu₄Cl₃(I_{1.6}Cl_{0.4}) at temperatures above 180°C gave cubic materials with lattice constant greater than 10.001Å. This implies that these materials have $x < 0.40$, even though it was often difficult to discern the extra phases in the x-ray powder photographs (see later discussion).

The annealing temperatures given in Table I are those that were found to be optimum. A comparison of results on specimens with $0 \leq x \leq 0.10$ prepared at two different annealing temperatures, 205° ± 5°C and 180°C, is given in Table II. In this range of composition, there is no doubt that the higher temperature annealings are required. It is noteworthy that after the samples were prepared by annealings at 180°C, reannealing⁶ at the higher temperature resulted in increased lattice constant. This implies homogenization either by further reaction of the solid electrolyte with incompletely reacted constituents or possibly

⁶ This should be understood to mean additional cycles including regrinding, repelletizing, etc., as described under Sample preparation.

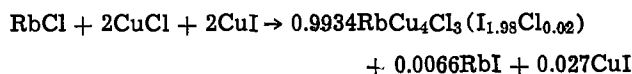
Table II. Lattice constants of specimens in system RbCu₄Cl₃(I_{2-x}Cl_x) prepared at two different temperatures*

| x | 205° ± 5°C | 180°C |
|------|------------|--------|
| 0 | 10.032 | 10.030 |
| 0.01 | 10.031 | 10.028 |
| 0.02 | 10.030 | 10.027 |
| 0.03 | 10.029 | 10.026 |
| 0.05 | 10.027 | 10.025 |
| 0.10 | 10.021 | 10.020 |

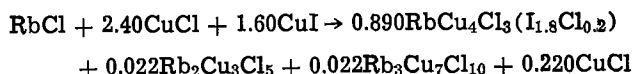
* Higher temperature results are the correct ones: see text.

the further reactions of a continuous mixture of solid solutions, in a narrow range, of course.

When an attempt was made to prepare RbCu₄Cl₃I₂ at 225°C, the lattice constant of the cubic phase was 10.030Å also (see Table II). This may mean that the following reaction occurred



An attempt to prepare RbCu₄Cl₃(I_{1.6}Cl_{0.4}) at 225°C gave a cubic phase with lattice constant 10.013Å, and when tried at 205°C, gave 10.006Å. These results may be explained by reference to Fig. 1; a lattice constant of 10.013Å means $x = 0.20$, and of 10.006Å means $x = 0.29$. The reaction for the first case is very likely



A similar reaction may readily be written for the second case.⁷

Stoichiometric RbCu₄Cl₃I₂.—X-ray powder diffraction photographs and diffractometer patterns were taken of a sample of the stoichiometric RbCu₄Cl₃I₂ that had been stored in a closed vial in a desiccator for several months. Part of the sample was still in pellet form and part was powder. Both were different from stoichiometric RbCu₄Cl₃I₂: The pellet contained a new low symmetry phase plus a very small amount of CuI; the powder contained the low symmetry phase, cubic solid electrolyte with $a_0 = 10.028\text{Å}$ (therefore having $x = 0.04$) and perhaps slightly more CuI. After two years, no further changes have taken place in the two parts of the specimen; therefore it is unlikely that the changes observed resulted from slow decomposition. It is not known why the two parts of the specimen behaved differently. No other specimen, regardless of composition, has converted in either of these ways over much longer periods of time than transpired for the initial observation.

Judging from the x-ray powder pattern, the structure of the new phase seems still to be related to the RbAg₄I₅ structure (3) (with which all members of the RbCu₄Cl₃(I_{2-x}Cl_x) system are isostructural), but it is not isostructural with either β- or γ-RbAg₄I₅ (2). Table III lists powder diffraction data, taken with a diffractometer, for the new phase. For comparison, data are given also for the cubic RbCu₄Cl₃(I_{1.96}Cl_{0.04}) solid electrolyte phase.

Attempts were made to prepare the new phase directly. These included trying to introduce I⁻ vacancies and substitution of various types and amounts of other ions for Rb⁺ and for Cu⁺. These experiments were unsuccessful.

We sought to obtain the new phase in another way, namely, by pressurizing, depressurizing, grinding, and repeating. Applied pressure was 5000 kg cm⁻² for

⁷ In part of the following section, we show that the single phase RbCu₄Cl₃(I_{1.6}Cl_{0.4}) prepared at 180°C decomposes in the same way at higher temperatures.

Table III. Powder diffraction data* for the new phase and for cubic $\text{RbCu}_4\text{Cl}_3(\text{I}_{1.96}\text{Cl}_{0.04})$

| New phase | | Cubic phase | | |
|------------------|------------------|------------------|------------------|----------|
| d _{hkl} | I/I ₀ | d _{hkl} | I/I ₀ | hkl |
| 6.943 | 63 | 7.091 | 34 | 110 |
| 6.259 | 3 | | | |
| 6.176 | 15 | | | |
| 5.821 | 21 | 5.790 | 19 | 111 |
| 5.463 | 7 | | | |
| 4.627 | 16 | | | |
| 4.466 | 16 | 4.485 | 11 | 210 |
| 4.294 | 11 | | | |
| 4.242 | 21 | | | |
| 4.197 | 4 | | | |
| 3.544 | 42 | 4.094 | 4 | 211 |
| 3.347 | 5 | 3.545 | 47 | 220 |
| 3.290 | 68 | 3.343 | 3 | 221 |
| 3.267 | 75 | | | |
| 3.217 | 7 | | | |
| 3.094 | 17 | 3.171 | 3 | 310 |
| 3.028 | 100 | 3.024 | 100 | 311 |
| 2.985 | 88 | | | |
| 2.931 | 64 | 2.895 | 14 | 222 |
| 2.745 | 20 | 2.781 | 2 | 320 |
| 2.729 | 3 | | | |
| 2.687 | 23 | 2.680 | 4 | 321 |
| 2.658 | 5 | | | |
| 2.641 | 6 | | | |
| 2.628 | 7 | | | |
| 2.547 | 6 | | | |
| 2.534 | 5 | 2.507 | 6 | 400 |
| 2.418 | 14 | | | |
| 2.391 | 8 | 2.364 | 2 | 411, 330 |
| 2.285 | 4 | 2.301 | 10 | 331 |
| 2.277 | 6 | | | |
| 2.235 | 7 | | | |
| 2.177 | 10 | | | |
| 2.133 | 14 | | | |
| 2.124 | 12 | | | |
| 2.062 | 4 | 2.047 | 40 | 422 |
| 2.031 | 5 | | | |
| 2.020 | 20 | | | |
| 1.998 | 23 | 2.006 | 5 | 430 |
| 1.986 | 43 | | | |
| 1.965 | 33 | 1.967 | 10 | 510, 431 |
| 1.944 | 40 | | | |
| | | 1.930 | 44 | 511, 333 |
| 1.908 | 31 | | | |
| 1.895 | 3 | | | |
| 1.874 | 3 | | | |
| 1.862 | 28 | 1.862 | 5 | 520, 432 |
| 1.848 | 46 | | | |
| 1.822 | 6 | | | |
| 1.816 | 10 | | | |
| 1.774 | 21 | 1.773 | 28 | 440 |

* The data are arranged to show that the two structures are related. The relative intensities are given for the individual materials. The strongest line of the cubic phase has at least 2.3 times the intensity of the strongest line of the new phase.

½ hr. After seven such treatments, the material was found to be completely converted to the new phase. It was found that grinding continuously for 3 hr or alternately pressurizing and depressurizing alone did not result in conversion. As a consequence of this experiment, a device was built to perform the cold-work automatically. It consists essentially of a hardened steel base to which is attached a stainless steel cylinder with ⅜ in. ID. These parts rotate about a hardened steel piston with ¼ in. diam attached to a variable speed reciprocating motor. About 200 mg of the sample to be cold-worked are put into the cylinder. The motor and piston are adjusted over the specimen so that it is off the center of rotation and rather close to the cylinder wall. When the machine is turned on, the piston pounds the material against the hardened steel base. The powder spreads about inside the cylinder, and unless it clings to the wall receives almost continuous pounding. In effect, the particles are subjected to both normal and shear stresses. Unfortunately, some powder adheres strongly to the cylinder wall. This powder could be removed, the whole sample homogenized, pounding continued, and so on. However, we used this method mainly to determine whether different specimens could be made to transform to the new phase. There is no doubt that the method was useful in this respect. After 24 hr of

pounding, a specimen of stoichiometric $\text{RbCu}_4\text{Cl}_3\text{I}_2$ was converted partially to the new phase; CuI was also detected. The unchanged cubic solid electrolyte still present had $a_0 = 10.032\text{\AA}$.

Nonstoichiometric specimens with compositions $0.02 \leq x \leq 0.40$ were also subjected to this treatment for longer periods, in some cases, as many as eight days. X-ray powder diffraction photographs indicated no change in any of these materials. It is therefore concluded that only the stoichiometric $\text{RbCu}_4\text{Cl}_3\text{I}_2$, with $x < 0.02$, undergoes this change.

Measurements of conductivity⁸ vs. temperature were made on a sample of the completely transformed material prepared by pressurizing, depressurizing, grinding, and repeating (PDGR). The cell used was: Ag| $\text{RbCu}_4\text{Cl}_3\text{I}_2$, Ag|transformed material| $\text{RbCu}_4\text{Cl}_3\text{I}_2$, Ag|Ag. The plot of $\log_{10}(\sigma T)$ vs. $10^3/T$ is shown in Fig. 2. At 298 K, the material has a conductivity of $1.45 \times 10^{-4} \Omega^{-1} \text{cm}^{-1}$. The conductivity increases linearly to $2.87 \times 10^{-3} \Omega^{-1} \text{cm}^{-1}$ at 348 K. [For the linear portion of the curve between 298 and 348 K, the activation enthalpy of motion, h_m , is 0.43 eV, indicating that the material is not a good solid electrolyte (12).] Just at 348 K, the conductivity rises sharply; σT increases by two orders of magnitude in the range 348-365 K. At 378 K, the conductivity reached $0.24 \Omega^{-1} \text{cm}^{-1}$, and at 440 K, $0.47 \Omega^{-1} \text{cm}^{-1}$. An x-ray powder diffraction photograph taken of the material following the measurements shows the presence of cubic $\text{RbCu}_4\text{Cl}_3(\text{I}_{1.96}\text{Cl}_{0.04})$; strangely, no CuI or other phases were detected. However, when some new phase material was heated at 80°C, again the cubic phase with formula $\text{RbCu}_4\text{Cl}_3(\text{I}_{1.96}\text{Cl}_{0.04})$ was regenerated; in this case CuI was detected in the powder photograph.

⁸ These results are included here because they elucidate the relation of the new phase to the cubic phase. For cell preparation and other details of conductivity measurement, see part II (11); it should be noted that the heating cycle was not included in the preparation of the cell.

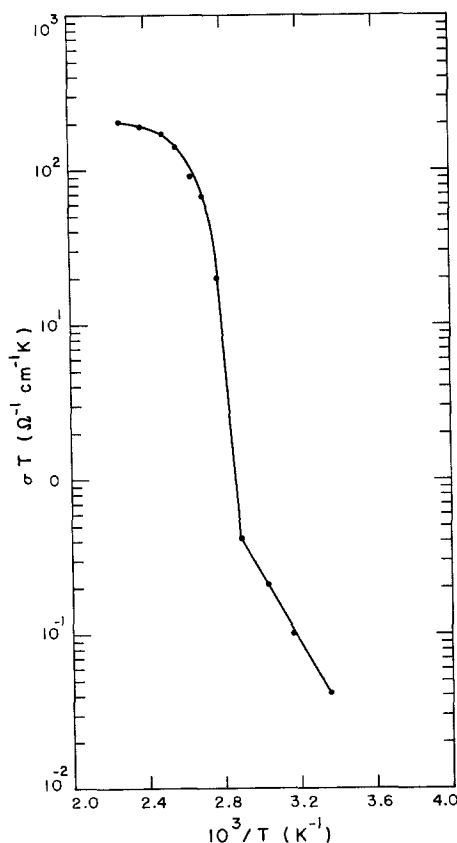
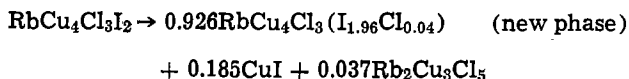


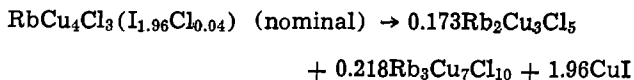
Fig. 2. Conductivity multiplied by temperature vs. reciprocal temperature for the new phase.

The results of the conductivity experiment prove that the new phase converts easily to the cubic solid electrolyte phase, *i.e.*, in a few minutes at the appropriate temperature. This implies that although it must be prepared by a route which must involve some decomposition of the stoichiometric material, it probably has the composition $\text{RbCu}_4\text{Cl}_3(\text{I}_{1.96}\text{Cl}_{0.04})$ or very close to it. It is also very clear that the transition is first order.

Much before the conductivity experiment on the transformed material, portions of it were heated at higher temperatures, 140° and 200°C. In all cases the lattice constant of the cubic solid electrolyte indicated a composition $\text{RbCu}_4\text{Cl}_3(\text{I}_{1.96}\text{Cl}_{0.04})$, within experimental error, $-0.01 \leq \Delta x \leq 0.00$. If the composition of the new phase is actually the same as that of the regenerated cubic phase, the decomposition could be written as follows



The $\text{Rb}_2\text{Cu}_3\text{Cl}_5$ is not detected in either the powder photographs or diffractometer patterns of either the transformed material (*i.e.*, containing the new phase) or the reheated transformed material (*i.e.*, containing the regenerated cubic solid electrolyte phase), very likely because it is only 3 mol percent of the total and its strongest line is apparently much less intense than that of the strongest line of CuI. This conclusion is supported by the results of another experiment. Some of the transformed material, prepared by cold-work (PDGR), was heated at 60°C for 3 days, the new phase decomposed completely according to



Only a few of the low angle lines of the first two phases on the right of the equation were observed in the powder photographs taken with $\text{CuK}\alpha$ radiation.

There is the possibility that the new phase may have iodide vacancies and a deficiency of Cu^+ ions. The formula would then be $\text{RbCu}_{3.92}\text{Cl}_3(\text{I}_{1.92}\text{V}_{0.08})$, that is, if only CuI were exsolved. If the decomposition is as written in the last equation and the structure is ordered, the formula must be close to $\text{Rb}_{51}\text{Cu}_{200}\text{Cl}_{153}\text{I}_{98}$. This would be the minimum unit cell content. The volume of such a cell would be about 13 times larger than that of $\text{RbCu}_4\text{Cl}_3\text{I}_2$. This seems unlikely. We believe that the most likely possibility is that indicated earlier; namely, that the new phase has the composition $\text{RbCu}_4\text{Cl}_3(\text{I}_{1.96}\text{Cl}_{0.04})$ with some disorder among the iodide and small number of chloride ions in sites analogous to those in the crystal structure of the cubic phase. It may be difficult to ascertain the truth in this case, because it does not seem probable that single crystals can be produced; however, further work is planned in this direction.

It was stated above that the material that was prepared by cold-work (PDGR) decomposed completely after being held at 60°C for 3 days. The original transformed material from the pellet showed incomplete, but considerable, decomposition after 5 days at 50°C; also, another sample held at 40°C for 3 days showed substantial decomposition. While an experiment on this material was not done at 60°C, there is an indication that the cold-worked material decomposes more rapidly than the other. The greater rate of decomposition is consistent with the strain in the material indicated by the powder photographs. In any case the experiments indicate that the new phase is not thermodynamically stable at 40°C or higher.

Both materials, *i.e.*, the one prepared by cold-work (PDGR) and the original one from the pellet, decompose partially when kept at liquid nitrogen temperature for 16 hr. Again the rate of decomposition of the former is greater than that of the latter. Decomposition also takes place when the new phase is kept at -5°C for 12 days. Thus the new phase, if it is thermodynamically stable at all, is so in a very narrow temperature range, almost surely not greater than 0° to 35°C .

In the foregoing, we have distinguished between the new phase which was first found in the stored material and the same, but strained, new phase which was prepared by cold-work. It may appear that we mean to imply that the transformation that occurred in the stored material did so simply because of the instability of stoichiometric $\text{RbCuCl}_3\text{I}_2$. However, we must emphasize that this cannot be the case, because, as pointed out, no other specimen of the stoichiometric material has behaved in the same way. We must admit that we do not know how the original changes occurred, but it is probable that they occurred by cold-work. Unfortunately, there is no indication, in the record, that this is or is not the case and too much time has elapsed for the original preparer to recall just what had occurred.

Experiments on the stability of stoichiometric cubic $\text{RbCu}_4\text{Cl}_3\text{I}_2$ indicate that it is thermodynamically stable in only a narrow temperature range about 200°C, perhaps no greater than $\pm 10^\circ$ – 15°C . At temperatures outside this range, it decomposes, but not always in the same way (see Table IV).

The stability relationships of the stoichiometric cubic phase, the cubic $\text{RbCu}_4\text{Cl}_3(\text{I}_{1.96}\text{Cl}_{0.04})$ phase and new phase with respect to each other are summarized in Fig. 3.

$\text{RbCu}_4\text{Cl}_3(\text{I}_{2-x}\text{Cl}_x)$, $0.00 < x \leq 0.40$ compositions.—Exhaustive experiments were not carried out, but those that have been done (Table V) indicate that one may expect that all compositions with $x \neq 0$ should be stable between their optimum preparation temperatures (Table I) and liquid N_2 temperature. This stability cannot be guaranteed to be thermodynamic over the whole temperature ranges.

It should be emphasized, that specimens with $x = 0.02$ and $x = 0.05$ could not be converted to the new phase by 3 days of continuous cold-work.

Table IV. $\text{RbCu}_4\text{Cl}_3\text{I}_2$ stability experiments

| Experiment* | Observations† |
|-------------------------------|---|
| 40°C, 5 days | CuI + S.E.: $x > 0$, but lines too broad to measure a_0 |
| 60°C, 5 days | CuI + S.E.: $a_0 = 10.028\text{Å} \Rightarrow x = 0.04$ |
| 140°C, 3 days | CuI + S.E.: $a_0 = 10.028\text{Å} \Rightarrow x = 0.04$ |
| 175°C, 3 hr | CuI + S.E.: $a_0 = 10.028\text{Å} \Rightarrow x = 0.04$ |
| 225°C, 15 hr | No CuI detected, $a_0 = 10.030\text{Å} \Rightarrow x = 0.02$ |
| -5°C , 2 months | CuI + S.E. (broad lines) + $\text{Rb}_2\text{Cu}_3\text{Cl}_5$ + $\text{Rb}_3\text{Cu}_7\text{Cl}_{10}$ |
| -196°C , 15 hr | $a_0 = 10.032\text{Å}$, much CuI, decomposed stoichiometrically |

* Experiments done at $185^\circ < T < 215^\circ\text{C}$ indicate no change in a_0 or phase purity.

† S.E. = solid electrolyte.

Table V. $\text{RbCu}_4\text{Cl}_3(\text{I}_{2-x}\text{Cl}_x)$ stability experiments

| Experiment | Observations |
|--------------|---|
| $x = 0.40$: | 225°C, 16 hr $a_0 = 10.013\text{Å} \Rightarrow x = 0.20$ |
| | 205°C, 16 hr $a_0 = 10.006\text{Å} \Rightarrow x = 0.29$ |
| | 140°C, 16 hr No change, <i>i.e.</i> , $a_0 = 10.001\text{Å}$ |
| | 60°C, 8 days No change |
| | -196°C , 3 days No change |
| $x = 0.32$: | 210°C, 16 hr $a_0 = 10.008\text{Å} \Rightarrow x = 0.27$ |
| $x = 0.05$: | 60°C, 6 days No change, <i>i.e.</i> , $a_0 = 10.027\text{Å}$ |
| | -196°C , 4 days No change |
| $x = 0.04$: | -196°C , 2 days No change, <i>i.e.</i> , $a_0 = 10.028\text{Å}$ |
| $x = 0.03$: | -196°C , 2 days No change, <i>i.e.</i> , $a_0 = 10.029\text{Å}$ |

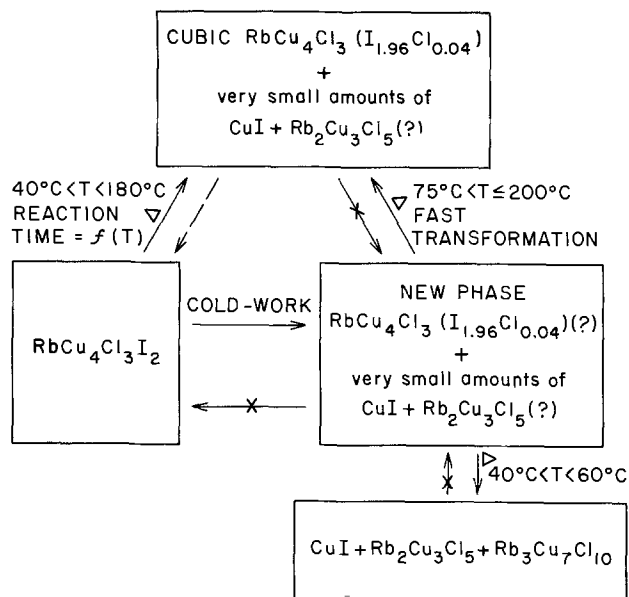


Fig. 3. Summary of stability relationships of stoichiometric $\text{RbCu}_4\text{Cl}_3\text{I}_2$, cubic $\text{RbCu}_4\text{Cl}_3(\text{I}_{1.96}\text{Cl}_{0.04})$, and the new phase.

Note added in proof:

It appears that the new phase produced by the cold-working of stoichiometric $\text{RbCu}_4\text{Cl}_3\text{I}_2$ is isostructural with a thermodynamically stable phase of $\text{CsCu}_4\text{Cl}_3\text{I}_2$ (to be published). The x-ray diffraction data given in Table III have been indexed on an orthorhombic cell with $a = 13.908$, $b = 24.752$, $c = 11.664\text{\AA}$, probably good to $\pm 0.005\text{\AA}$. (This indexing does not account for the very low intensity line with $d_{hkl} = 6.259\text{\AA}$.) The possible space groups are $Cmca$ (D_{2h}^{18}) and $C2ca$ (C_{2v}^{17}).

Acknowledgments

This work was supported by the National Science Foundation under Grant No. DMR-11378-A01. One of us (S.G.) wishes to thank the College of Engineering and Applied Science of the University of Colorado for the award of a Croft Research Professorship for the Fall semester, 1980, during which part of this work was carried out.

Manuscript received March 31, 1981.

Any discussion of this paper will appear in a Discussion Section to be published in the June 1982 JOURNAL. All discussions for the June 1982 Discussion Section should be submitted by Feb. 1, 1982.

Publication costs of this article were assisted by the National Science Foundation.

REFERENCES

1. S. Geller, J. R. Akridge, and S. A. Wilber, *Phys. Rev. B*, **19**, 5396 (1979).
2. S. Geller, *ibid.*, **14**, 4345 (1976).
3. S. Geller, *Science*, **157**, 310 (1967).
4. R. N. Keller and H. D. Wyckoff, *Inorg. Synth.*, **2**, 1 (1946).
5. G. D. Kauffman and R. P. Pinnell, *ibid.*, **6**, 3 (1960).
6. T. Takahashi, O. Yamamoto, Y. Takeda, and R. Kanno, Third International Meeting on Solid Electrolytes, Tokyo, Sept. 15-19, 1980, Extended Abstr. C218, p. 272.
7. M. Tokumoto, N. Ohnishi, Y. Okada, and T. Ishiguro, *ibid.*, C219, p. 275.
8. S. Geller, J. R. Akridge, and S. A. Wilber, *This Journal*, **127**, 251 (1980).
9. T. Takahashi, O. Yamamoto, S. Yamada, and S. Hayashi, *ibid.*, **126**, 1654 (1979).
10. T. Matsui and J. B. Wagner, Jr., *ibid.*, **124**, 937 (1977).
11. S. Geller, K. Nag, and A. K. Ray, *This Journal*, **128**, 2675 (1981).
12. H. Sato, in "Solid Electrolytes," S. Geller, Editor, pp. 3-39, Springer-Verlag, Heidelberg (1977).

The Solid Electrolyte System $\text{RbCu}_4\text{Cl}_3(\text{I}_{2-x}\text{Cl}_x)$,

$$0 \leq x \leq 0.40$$

II. Electrical Conductivity

S. Geller, K. Nag,¹ and A. K. Ray

Department of Electrical Engineering, University of Colorado, Boulder, Colorado 80309

ABSTRACT

Electrical conductivity has been measured as a function of temperature and composition in the system $\text{RbCu}_4\text{Cl}_3(\text{I}_{2-x}\text{Cl}_x)$. Room temperature conductivities, uncorrected for deviation of bulk from x-ray densities, decrease very nearly linearly from $0.39 \Omega^{-1} \text{cm}^{-1}$ for the stoichiometric composition to $0.28 \Omega^{-1} \text{cm}^{-1}$ for $x = 0.40$. Corrections for density could increase these values by about 10%. The enthalpies of activation of motion for the Cu^+ ions range from 0.112 eV for $x = 0.00$ to 0.117 eV for $x = 0.40$, indicating that the decrease in conductivity with increasing x is caused by the disorder introduced by the replacement of iodide by chloride ions.

In this paper, we give the results of measurements of conductivity as a function of temperature and composition in the $\text{RbCu}_4\text{Cl}_3(\text{I}_{2-x}\text{Cl}_x)$ system. The conductivities decrease very nearly linearly with increasing x . This is attributed to a decrease in the mobility of the Cu^+ ions (which is very sensitive to h_m , the activation enthalpy of motion) caused by the disorder introduced by the substitution of Cl^- for I^- ions.

¹ On leave from the Indian Association for the Cultivation of Science, Calcutta 700032 India.

Key words: solid electrolyte, conductivity, solid solution, cuprous ion conductor, rubidium cuprous chloriodide.

The conductivity results obtained on stoichiometric $\text{RbCu}_4\text{Cl}_3\text{I}_2$ in the present work cast doubt on the existence of low temperature transitions reported earlier (1). The "apparent transitions" are very likely caused by development of hairline cracks in the pills.

Experimental

Details on starting materials and on preparation of the solid electrolyte samples are given in part I (2). The preparation of the cells for the conductivity measurements was one of the formidable problems in this investigation. Unlike the case with the conductivity

measurements on $\text{NH}_4\text{Cu}_4\text{Cl}_3(\text{I}_{1.9}\text{Cl}_{0.1})$ (3), we could not find a way to use copper powder as electrode material either in pure form or mixed with various proportions of solid electrolyte.

The procedure which turned out to be best for obtaining 6.35 mm diam pellets of 3 mm length with 0.2 mm electrodes at the ends with densities of the solid electrolyte in the range 94-96% of theoretical is described here. We use a die made of 440-C hardened stainless steel of $\frac{1}{4}$ in. ID with a finely polished inner surface. At the bottom of the die is a small tungsten carbide piston of $\frac{1}{4}$ in. diam and $\frac{1}{4}$ in. long. 35 mg of an intimate mixture of the 1 μm Ag powder² and solid electrolyte (1:1 by weight) are placed in the die on the small piston. This material is smoothed with the help of a longer piston, being careful that no particles adhere to the wall of the die. The material is then subjected to a pressure of 600 kg cm^{-2} for about 1 min. Pressure and piston are removed and 400 mg of the solid electrolyte added. Again this material is compressed at the same pressure. Then 35 mg of electrode material are added, and again pressure is applied. Then another $\frac{1}{4}$ in. diam- $\frac{1}{4}$ in. long tungsten carbide piece is inserted followed by a 2 in. long piston. A heating tape is wound about the die and a Chromel-Alumel thermocouple inserted between the tape and die. The die is heated slowly to a temperature of 50°C and a pressure of 3000 kg cm^{-2} applied. Temperature and pressure are held at these values for 10 min. Pressure is released and temperature slowly raised to 80°C over a period of 1 hr. Then the temperature is slowly decreased to room temperature over a period of 2 hr. The pill is then readily removed from the die, examined under the microscope for small cracks and for measurement of dimensions with an eyepiece micrometer.

Conductivities as a function of temperature were measured with essentially the same equipment as described elsewhere (1,4). A thin layer of the 1 μm Ag powder is spread over the electrode surfaces of the pill to improve contact between the platinum electrodes (formerly silver) of the equipment [see Fig. 1 of Ref. (4)] and the electrode surfaces of the specimen. Dry nitrogen flows continuously around the specimen.

Measurements were also made on carbon resistors with accurately known resistances over the range of resistances of the specimens and over the range of frequencies used in the measurements of the solid electrolyte resistances. (Generally the frequencies were close to 5 kHz.) Appropriate corrections were made.

Checks on conductivity results obtained with the vector impedance measuring device were made with a General Radio 1650B impedance bridge used in conjunction with a GR 1310 oscillator and GR 1232A tuned null detector. Agreement was very good (within 1%) in all cases.

Results and Discussion

In Fig. 1, $\log_{10}(\sigma T)$ vs. $10^3/T$ is plotted for three runs on the same pellet of stoichiometric $\text{RbCu}_4\text{Cl}_3\text{I}_2$ between room temperature (295 K) and 450 K. A separate pellet was used to obtain the low temperature data shown in Fig. 1 and 2.

On the first heating from room temperature, ($10^3/T = 3.35$), there is a slight deviation from the straight line beginning at $10^3/T = 2.50$ ($T = 400$ K). [In Ref. (1) such a deviation was not observed; the measurements were made only to 385 K.] On cooling, the points obtained all fitted a straight line very well. The sample was removed from the apparatus and kept in a desiccator. On the following day, a second heating cycle was performed; the points obtained lie on a

straight line (within experimental error) though not quite as well as for the two prior runs. The slopes for the first two give h_m (the enthalpy of activation of motion) equal to 0.112 eV; the slope of the third

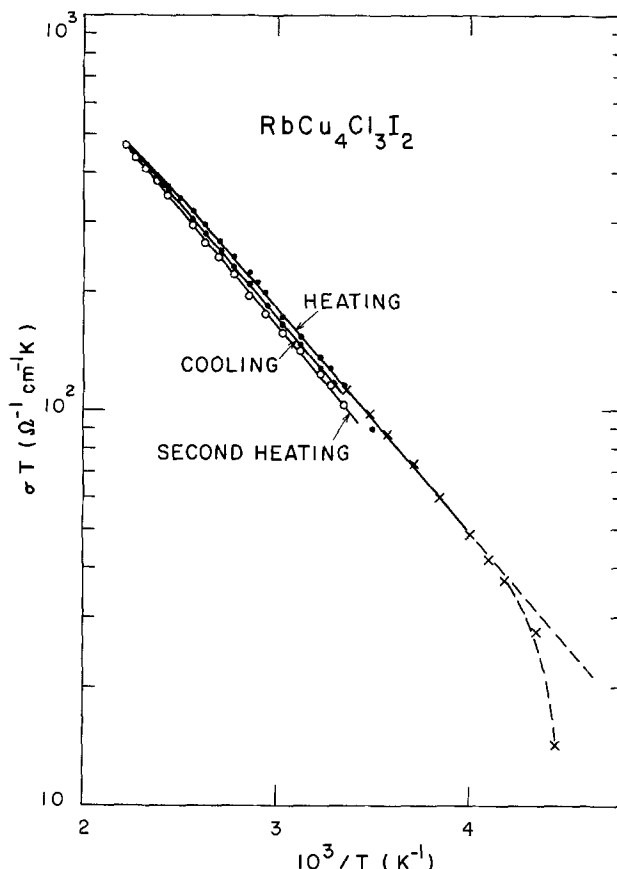


Fig. 1. Conductivity multiplied by temperature vs. reciprocal temperature for stoichiometric $\text{RbCu}_4\text{Cl}_3\text{I}_2$. See text for details.

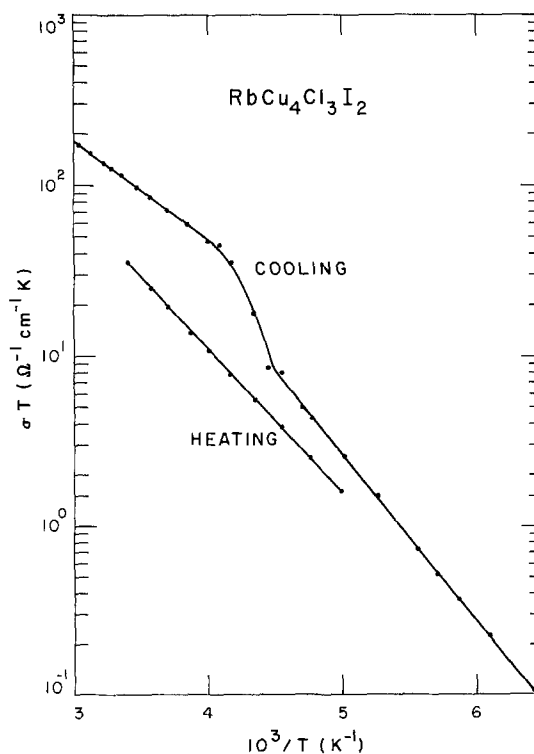


Fig. 2. Conductivity multiplied by temperature vs. reciprocal temperature in the subambient temperature region for a specimen of stoichiometric $\text{RbCu}_4\text{Cl}_3\text{I}_2$.

² 99.99% pure (Cerac).

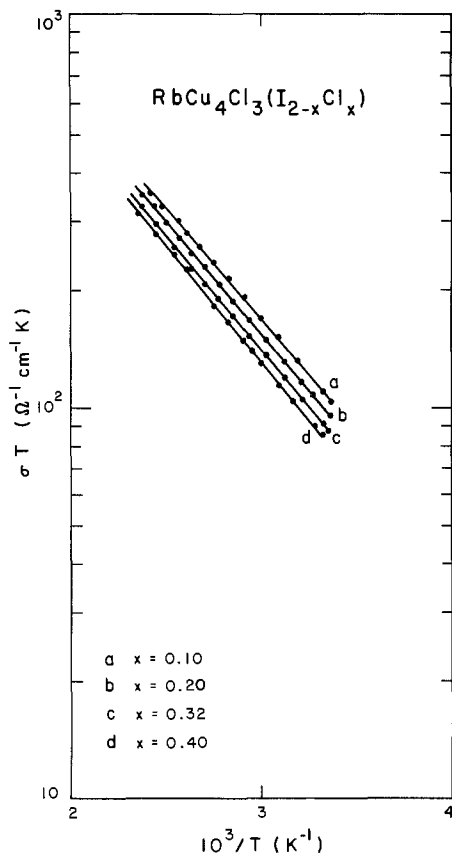


Fig. 3. Conductivity multiplied by temperature vs. reciprocal temperature for representative specimens in the $\text{RbCu}_4\text{Cl}_3(\text{I}_{2-x}\text{Cl}_x)$ system.

gives 0.115 eV. (Note: all straight line fits to the data were performed by linear regression analysis.)

It is to be noted that no deviation from the straight lines occurred at high temperatures for any specimen with $x > 0$ (Fig. 3). Considering the observations that had been made on the stability of the stoichiometric material [see part I (2)], it was at first believed that the deviation from the straight line resulted from some decomposition of the solid electrolyte. (It should be mentioned that this deviation was observed on three separately investigated pellets.) An x-ray powder photograph of the tested material indicated that no decomposition had occurred. We can only speculate that the deviation perhaps resulted from an unfavorable reaction of the stoichiometric $\text{RbCu}_4\text{Cl}_3\text{I}_2$ with the silver in the electrode at the solid electrolyte-electrode interface. Some further reaction might have occurred during the overnight period, because the conductivities dropped slightly; the change of the room temperature conductivity between the two heating cycles was $0.04 \Omega^{-1} \text{cm}^{-1}$, i.e., from 0.39 to $0.35 \Omega^{-1} \text{cm}^{-1}$.

It has been observed that the measured conductivity of a pellet decreases as the pellet ages. This is true for all x . Reaction with Ag is believed to be involved, but it is not yet known what it is. In any case, for best results the pellets for measurement should be freshly prepared as described earlier.

Shown also in Fig. 1 and 2 are the results of measurements made on a fresh pellet at subambient temperatures. Down to 250 K, the points obtained lie on the same straight line as the initial higher temperature data (to 400 K). A deviation from the straight line begins at 235 K and at 225 K looks as though a first order transition were occurring. Figure 2 shows a continuation of the data for $\text{RbCu}_4\text{Cl}_3\text{I}_2$ down to 156 K. Data were then taken on warming the same specimen through the region in which there appeared to be a transition during the cooling cycle. All these data lie on a straight line and therefore do not indicate a transition. The conductivity values were lower in the heating cycle. Also the slope is much steeper than the slope between 250 and 400 K ($m = 840$ vs. 565, see Table I).

After the measurements (to room temperature) the pellet was examined under a microscope; a hairline crack was detected. An x-ray powder pattern of the solid electrolyte showed that no decomposition had occurred. We therefore conclude that the cause of the results shown below room temperature in Fig. 1 and 2 is the hairline crack in the pellet that must have occurred at around 250 K.

Considering the close relationship of the crystal structures of RbAg_4I_5 and $\text{RbCu}_4\text{Cl}_3\text{I}_2$, the results of the earlier (1) conductivity measurements implied transitions in $\text{RbCu}_4\text{Cl}_3\text{I}_2$ similar to those in RbAg_4I_5 (5). However, the present results cast doubt on the existence of these transitions in the $\text{RbCu}_4\text{Cl}_3\text{I}_2$. This is a tentative conclusion awaiting further experiments with an improved low temperature device (now on order) for x-ray diffraction experiments and differential scanning calorimetric measurements by others (for which the required equipment is not directly available here).

In Fig. 3, $\log_{10}(\sigma T)$ vs. $10^3/T$ is plotted for representative members of the $\text{RbCu}_4\text{Cl}_3(\text{I}_{2-x}\text{Cl}_x)$ system in the temperature range 295-425 K. The straight line fits were obtained by linear regression analysis of the data. Various results of the measurements made on all the specimens are given in Table I, including x-ray densities, bulk densities of the pellets, activation enthalpies of motion, h_m , the slopes and intercepts of the straight lines (in the form $\log_{10}(\sigma T) = m(10^3/T) + b$), σ at 298 K, and 419 K (the solid electrolyte transition temperature of AgI).

The attainable densities of the pills listed in Table I are 94-96% of the x-ray densities. An experiment was performed to try to determine the effect on the conductivity of deviation of density from the x-ray density. A pellet of $\text{RbCu}_4\text{Cl}_3\text{I}_2$ with 91% of the x-ray density gave a conductivity of $0.37 \Omega^{-1} \text{cm}^{-1}$;

Table I. Conductivity results for the $\text{RbCu}_4\text{Cl}_3(\text{I}_{2-x}\text{Cl}_x)$ system

| x | X-ray density (g cm^{-3}) | Bulk density of pellet as % of theoret. | Temp range (K) | h_m , obs'd. (eV) | h_m calc* (eV) | m^{**} | b^{**} | $\sigma(298 \text{ K})$ ($\Omega^{-1} \text{cm}^{-1}$) | $\sigma(419 \text{ K})^\dagger$ ($\Omega^{-1} \text{cm}^{-1}$) |
|------|---|--|----------------------|---------------------------|------------------------|----------|----------|---|---|
| 0.00 | 4.604 | 94 | 460-298 | 0.112 | 0.112 | 565 | 3.958 | 0.39 | 0.97 |
| 0.10 | 4.558 | 96 | 415-298 | 0.112 | 0.114 | 565 | 3.925 | 0.36 | 0.90 |
| 0.14 | 4.540 | 94 | 415-298 | 0.112 | 0.116 | 564 | 3.898 | 0.34 | 0.85 |
| 0.20 | 4.509 | 94 | 430-298 | 0.114 | 0.116 | 577 | 3.922 | 0.33 | 0.83 |
| 0.27 | 4.473 | 96 | 298 | | | | | 0.31 | |
| 0.32 | 4.447 | 95 | 420-298 | 0.115 | 0.119 | 579 | 3.887 | 0.30 | 0.76 |
| 0.40 | 4.404 | 96 | 440-300 | 0.117 | 0.121 | 590 | 3.891 | 0.28 | 0.72 |

* See text.

** As in $\log_{10}(\sigma T) = -m/T + b$.

† As obtained from straight line fit.

at 94% the conductivity is $0.39 \Omega^{-1} \text{cm}^{-1}$ (Table I). Thus a difference of 3% in density gives a difference of 5% in conductivity. If the effect were linear one would expect $\text{RbCu}_4\text{Cl}_3\text{I}_2$ crystals to have a conductivity of $0.43 \Omega^{-1} \text{cm}^{-1}$ at 298 K and $1.06 \Omega^{-1} \text{cm}^{-1}$ at 419 K.

These results as well as those for h_m reported here for $\text{RbCu}_4\text{Cl}_3\text{I}_2$ differ from those reported earlier (1). The former results were $0.47 \Omega^{-1} \text{cm}^{-1}$ at 298 K, a predicted $1.53 \Omega^{-1} \text{cm}^{-1}$ at 419 K and $h_m = 0.15 \text{eV}$ for the activation enthalpy of motion. The substantial differences in the second and third values from those given in Table I resulted from a systematic error (which should have been, but was not recognized at that time). Nevertheless, all the conductivities are quite high and it is correct to say that $\text{RbCu}_4\text{Cl}_3\text{I}_2$ has the highest room temperature ionic conductivity of all solid electrolytes. In fact, even the material $\text{RbCu}_4\text{Cl}_3(\text{I}_{1.6}\text{Cl}_{0.4})$ with the largest amount of Cl^- ion has a higher conductivity at 298 K than RbAg_4I_5 . However at 419 K, $\alpha\text{-AgI}$ has the highest ionic conductivity.

In Fig. 4, the room temperature conductivities are plotted as a function of composition, x in $\text{RbCu}_4\text{Cl}_3(\text{I}_{2-x}\text{Cl}_x)$. (These conductivities are uncorrected for density, as are all results in Fig. 1-3.) It is seen that the conductivities decrease almost linearly with increasing x . The conductivity is given simply by $\sigma = nq\mu$, where n is the charge carrier concentration, q is the charge, and μ is the mobility. Because the lattice constant decreases with increasing x , the charge carrier concentration increases with decreasing x , but not very much, i.e., from $1.585 \times 10^{22} \text{cm}^{-3}$ for $x = 0.00$ to $1.600 \times 10^{22} \text{cm}^{-3}$ for $x = 0.40$, a difference of +0.9%. This increase in n should cause a 0.9% increase in σ .

The reason for the decrease in conductivity with increasing x is very likely the decrease in mobility caused by the disorder resulting from substitution of the Cl^- for I^- ions. The mobility is very sensitive to the value of h_m . In Table I, the values of h_m are given to three decimal places. This is required to demonstrate the sensitivity of σ to h_m . If we calculate h_m from

$$h_m = kT \log [ne^2 D_0 / k\sigma T]$$

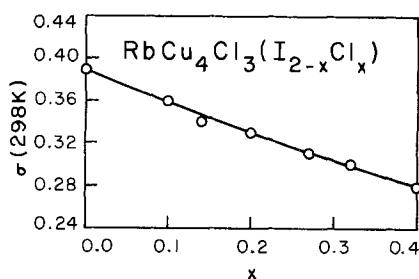


Fig. 4. Conductivity at 298 K vs. x in $\text{RbCu}_4\text{Cl}_3(\text{I}_{2-x}\text{Cl}_x)$

where D_0 is the diffusion preexponential factor, k the Boltzmann constant, and e the charge of the proton, and take D_0 equal to the value for stoichiometric $\text{RbCu}_4\text{Cl}_3\text{I}_2$ (i.e., assuming $h_m = 0.112 \text{eV}$) constant for all x , the values of h_m obtained are those listed next to the experimental ones in Table I. The value of D_0 for $x = 0.00$ is $3.1 \times 10^{-4} \text{cm}^2 \text{sec}^{-1}$. The values for σ are the experimental ones for 298 K and are listed in Table I. It is seen that the largest deviation from the experimental values is less than 4%. It is also seen that a change in h_m of 8% results in a change of 28% in the conductivity.

It is highly probable that the increase in h_m with decreasing x is real. The replacement of I^- by Cl^- ions might be expected to affect adversely the "windows" through which the charge carriers must move; that is to say, the barrier heights are increased on the average, as indicated by increase in h_m , and this in turn decreases the mobility.

Note added in proof:

As a result of continuing work on related materials, we no longer believe that electrode reaction is the cause of decreased conductivity once measurements have been made to high temperature (see left column, p. 2677). There is increasing evidence that the cause is mechanical (rather than chemical), namely increased grain boundary width in the pellet, drastic, as manifested by fine cracks, or, more subtle, localized recrystallization. Further discussion of this matter is included in a publication now in preparation.

Acknowledgments

This work was supported by the National Science Foundation under Grant No. DMR-11378-A01. One of us (S.G.) wishes to thank the College of Engineering and Applied Science for the award of a Croft Research Professorship for the Fall semester, 1980, during which part of this work was carried out.

Manuscript received March 31, 1981.

Any discussion of this paper will appear in a Discussion Section to be published in the June 1982 JOURNAL. All discussions for the June 1982 Discussion Section should be submitted by Feb. 1, 1982.

Publication costs of this article were assisted by the National Science Foundation.

REFERENCES

1. S. Geller, J. R. Akridge, and S. A. Wilber, *Phys. Rev. B*, **19**, 5396 (1979).
2. K. Nag and S. Geller, *This Journal*, **128**, 2670 (1981).
3. S. Geller, J. R. Akridge, and S. A. Wilber, *ibid.*, **127**, 251 (1980).
4. S. Geller, S. A. Wilber, G. F. Ruse, J. R. Akridge, and A. Turkovič, *Phys. Rev. B*, **21**, 2506 (1980).
5. S. Geller, *ibid.*, **14**, 4345 (1976).

On the Tetrachloroaluminate Dissociation in Aluminum Chloride-1-n Butylpyridinium Chloride Mixtures

J. P. Schoebrechts¹ and B. P. Gilbert

Laboratory of Analytical Chemistry and Radiochemistry, University of Liège, B-4000 Sart Tilman-Liège, Belgium

ABSTRACT

The dissociation of tetrachloroaluminate anions in room temperature AlCl_3 -1-n butylpyridinium chloride mixtures has been investigated as far as both reproducibility and reliability are concerned. The determination of the dissociation constants is based on the aluminum electrode potential variation measured around the equimolar composition. Experimental conditions have been determined which avoid the reduction of the pyridinium cation by Al in slightly basic melts and where the potentials of the Al electrode are stable. The average values of the dissociation constants are, respectively, $(1.2 \pm 0.2)10^{-13}$, $(4.5 \pm 0.4)10^{-13}$, and $(7.5 \pm 0.8)10^{-13}$ at 40°, 49°, and 55°C and are systematically lower than previously published values. The corresponding average values of ΔH and ΔS are, respectively, equal to 20.3 kcal mol⁻¹ and 6.5 eu. It has also been shown that the dissociation equilibrium of AlCl_4^- into Al_2Cl_7^- and Cl^- is the only one required even in very acidic melts (up to 66.6 m/o of AlCl_3), provided a correction is made for the junction potential.

For the past few years, several groups of scientists have been interested in aluminum chloride containing melts. Most of these investigations deal with AlCl_3 -alkali halide mixtures because of their particular properties. In particular, the chloroacidity ($p\text{Cl}$) can be varied to a large extent, especially about the equimolar composition range (1-4). It has also been shown that the acidic nature of such melts stabilizes low oxidation state ions and organic radical cations (5-12). However, as pointed out by Koch *et al.*, the use of aluminum chloride-inorganic chloride molten salts for organic reaction investigation is limited, essentially because of temperature problems (13).

Recently, a new molten salt, first reported by Hurley and Wier (14), namely a 67/33 mol percent (m/o) aluminum chloride-ethylpyridinium bromide mixture, has been proposed as solvent for organic studies (15). It is liquid at room temperature, apparently very acidic (in a chloroacidity sense), and exhibits a large electrochemical window. However, although it has been used successfully to investigate different organic or inorganic systems (13, 15, 16), no quantitative data exist, either about the acidic strength of such melt or about the dependence of the acidic properties with respect to the melt composition. The main reason is that the mixture ethylpyridinium bromide- AlCl_3 is liquid at room temperature only in a limited range of composition, close to 2:1 and no investigation has been made outside this range.

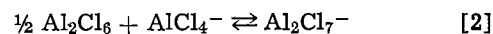
As a consequence, investigations have been directed to mixtures of AlCl_3 with other pyridinium salts, mainly n-methyl and n-butylpyridinium chlorides. The latter appears to be the most interesting; it is liquid at temperatures lower than 40°C across a large composition range (66-43 m/o of AlCl_3) whereas the former mixture is liquid at room temperature only in the range of 2:1 composition. Physical and spectroscopic properties of these melts (pure or mixed with benzene) have been investigated by Osteryoung *et al.* (19, 21, 24) and King *et al.* (18). Electrochemical studies of organic [mainly aromatic (20, 25)] and inorganic solutes [Fe(III)/Fe(II) (22), Cu(II,I) (17), Ni(II,0) (26)] as well as the reduction of the melt in acidic (27) or basic (31) mixtures have also been performed.

One of the main conclusions of these studies is that a better knowledge (qualitative and quantitative) of the equilibria involved is needed (22).

Qualitative information has been obtained from Raman measurements. It was concluded that the same dissociation equilibrium [1] which characterizes the high temperature inorganic chloroaluminate melts, exists in the room temperature melt



The spectrum of AlCl_4^- and Al_2Cl_7^- are well defined and exhibit much sharper lines than for conventional chloroaluminates (24). Furthermore, reaction [2] seems quantitative



and an exactly 2:1 mixture shows essentially the Al_2Cl_7^- spectrum, contrary to the high melting mixtures.

Osteryoung and Gale have tentatively estimated by potentiometric titration the corresponding equilibrium constant (K_1) at various temperatures and the ΔG of reaction [1]. The proposed constant at 30°C is six orders of magnitude lower than for NaCl-AlCl_3 mixtures at 175°C (19). The results indicate, however, a lack of reproducibility in the basic side of the titration curve due to partial spontaneous reduction of the melt by the Al indicator electrode (31). Furthermore, no significant difference in the potential span with temperature was found, unlike the AlCl_3 - NaCl system. The experimental equilibrium constant was then regarded as a maximum value. Titrations of the melt diluted with benzene led to similar conclusions (19, 27).

Another way of obtaining quantitative information about the equilibrium constant (K_1) is to investigate the potential variation of a $p\text{Cl}$ sensitive couple other than aluminum. Osteryoung *et al.* proposed a more precise value of K_1 based on the titration curve of Ni(II) followed by a nickel electrode. The assumptions were, however, that NiCl_4^{2-} is the only complex formed on the basic side and that the equivalence point potential of the Ni(II) titration curve is the potential of the neutral point of the melt (26).

The purpose of this work was then to find out if improving experimental conditions could lead to more precise and reproducible equilibrium constant determinations.

¹ Chercheur à l'Institut Interuniversitaire des Sciences Nucleaires, Brussels, Belgium.

Key words: chloroaluminate melts, butylpyridinium, equilibrium constants, potentiometry.

Experimental

Melts were prepared by mixing sublimed AlCl_3 (Fluka, iron-free) and 1-n-butylpyridinium chloride (BPC) as described by Robinson and Osteryoung (20). Provided careful preparation of 1-n-butylpyridinium chloride (20) was carried out, colorless melts were obtained.

Potentiometric titrations have been performed by accurately weighed (± 0.1 mg) additions of AlCl_3 crystals to a basic melt rather than BPC addition to a slightly acidic melt. The latter procedure was indeed found less satisfactory because BPC dissolves slowly and, with stirring, sticks to the aluminum indicator electrode causing a local increase of basicity. As already mentioned (19, 31), highly basic melts react with aluminum by formation of radicals and the potential measurements become erratic.

The electrochemical cell was made of a Pyrex vessel provided with 5 ground joints. The electrode design is identical to the one described (12) except that the joints have been replaced by ground joints. The indicator electrodes were either an Al wire (Analar m3N) or a glassy carbon disk electrode (Tokai). The reference electrode is an Al wire in a 2:1 AlCl_3 :BPC melt. The reference compartment is separated from the melt by a Pyrex soft glass junction as described by Moe (28).

The melt is thermostated ($\pm 0.5^\circ\text{C}$) by a constant temperature bath (ethylene glycol) circulating in a jacket around the electrochemical cell and an external thermostat.

Potentiometric measurements were performed with an H.P. 3465A digital voltmeter. Before use, the aluminum electrodes (previously cleaned with an H_2SO_4 , HNO_3 , H_3PO_4 mixture and dried) are digested for 1 day in an acidic mixture; the electrode is then removed from the cleaning melt and wiped completely free of melt. Following this procedure, the potential measurements are stable within 1 mV for several hours, even in a 49% melt. In some cases, erratic measurements have been observed in basic melts, together with the appearance of a slightly blue color and the melt and the electrode are then discarded.

The electrochemical measurements other than potentiometry were performed with a Princeton Applied Research polarograph, Model 170.

All handling of the melts and electrochemical experiments were performed inside a dry box with water and oxygen content below 20 ppm.

Results and Discussion

As already mentioned there have been two different ways of evaluating the stability constant of equilibrium [1]: (i) A direct potentiometric titration which is apparently limited on the basic side by the Al reduction of the melt, even if diluted with benzene; and (ii) an indirect determination from a pCl sensitive couple $\text{Ni}(0)/\text{Ni}(\text{II})$. This couple is, however, sensitive to pCl essentially on the basic side because of an NiCl_4^{2-} complex formation. Considering the assumptions made, an $\text{Ni}(\text{II})$ potentiometric titration allows one only to estimate the minimum pCl variation in order to complex quantitatively the nickel, provided that the complex formation constant is known. From this minimum pCl variation, it is then possible to estimate a maximum value of the constant K_1 .

We have tentatively chosen to improve the determination of the equilibrium constant from direct potentiometric titration of the melt with Al electrodes based on the experimental finding that reduction of the melt occurs only at a certain point of basic compositions and an Al electrode could still be used in a narrow range. The extent of this range depends on the cleanliness of the melt and the physical state of the Al surface. With Al electrodes pretreated as de-

scribed above, the experimental cathodic potential limits in the basic side are -1.15 , -1.11 , and -1.02V , respectively, at 40° , 49° , and 55°C . These limits correspond to the most cathodic potentials observed in basic melts where no "apparent" reduction of the melt can be observed, i.e., the Al electrode potential is stable within 0.5 mV for a period of at least 2 hr under constant stirring, no color is developing around the electrode, and the background recorded by cyclic voltammetry at a glassy carbon electrode exhibits no wave in the whole useful electrochemical range. The aluminum reduction of the melt produces a mono-cation radical which can be either oxidized or reduced, respectively, at -0.56 and -0.96V vs. the potential of Al in a 2:1 AlCl_3 -BPC melt (31).

By using melt compositions so that the potential does not exceed the limits and the experimental procedure described above, the titration curve (shown in Fig. 1) could be reproduced in any case.

In some cases, the limits above were exceeded with no apparent reduction of the melt (as defined above). An example of a titration curve obtained under these conditions is shown in Fig. 2. The most basic points are located 0.07V beyond the limiting potential. Despite the fact that for this particular experiment the potentials were very stable, it was found difficult to reproduce the same titration curve, starting with a new melt and a new Al electrode. The problem of reproducibility of very basic points indicates that the kinetics of melt reduction depends primarily, at a given melt composition, on the physical state of the Al electrode.

If the Al electrode exhibits a potential depending essentially on the Al/Al(III) couple, our results are apparently in contradiction with the recent work of Gale and Osteryoung (31). Assuming a very slow reduction of the pyridinium cation in our titration curves, their results indicate that the potential of an Al electrode in a 0.8/1 melt should be around -1.4V whereas Fig. 2 indicates for the same melt a potential of -1.2V . A possible explanation is that the pyridinium cation reduction is not as slow as we think (but it is then difficult to understand the stability of our potential measurements), or that the results of

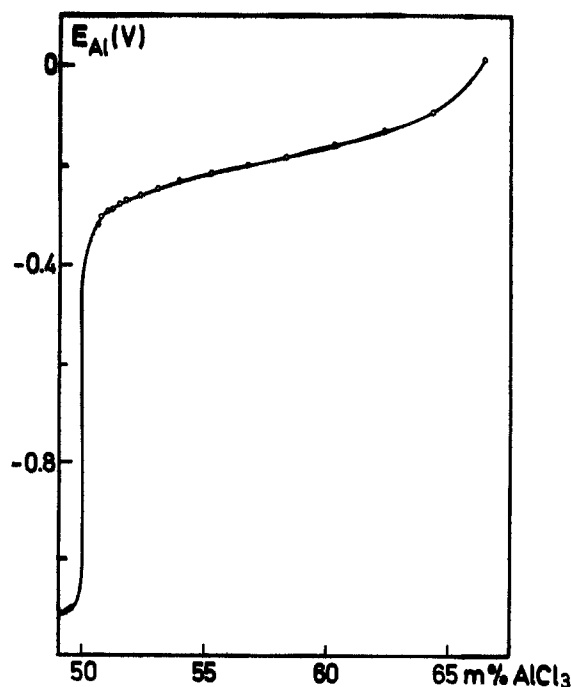


Fig. 1. Complete titration curve of a basic melt at 40°C . E_{Al} : the potential of an Al electrode in the melt vs. an Al electrode in 2:1 reference melt.

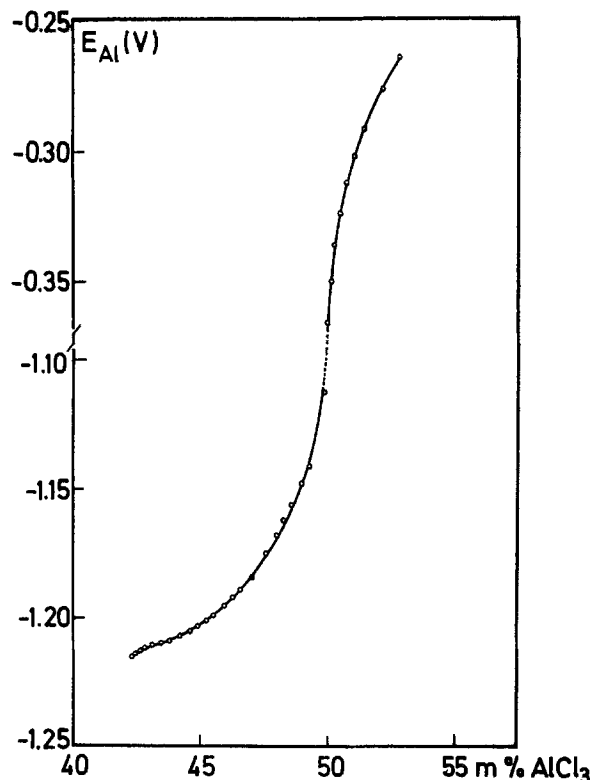


Fig. 2. Titration curve of a very basic melt at 40°C in the equimolar range.

Gale were obtained from dynamic methods on a glassy carbon electrode where a strong nucleation underpotential for the Al deposition may occur as it is the case in acidic mixtures (27).

Besides the problems of precise potentials measurements on the basic side, the determination of the stability constant by comparing the equivalence point and acidic point potentials of the titration curve is probably not very satisfactory because of the large experimental errors on the direct equivalence point potential measurement. The only quantity which can be determined with precision is the amount of AlCl_3 (or BPC) added to reach the equivalence point. Two different methods have then been used in order to evaluate the equilibrium constant without measuring directly the equivalence point potential.

Assuming a constant concentration of AlCl_4^- in the vicinity of the equivalence point and a constant liquid junction potential (19), the simple treatment of Torsi and Mamantov was applied. By using successive potential differences between an acidic and a basic point, the cell voltage can be written as follows

$$E_A - E_B = \frac{4RT}{3F} \ln ((\gamma_{\text{Al}_2\text{Cl}_7^-})_A \cdot [\text{Al}_2\text{Cl}_7^-]_A (\gamma_{\text{Cl}^-})_B [\text{Cl}^-]_B) - \frac{4RT}{3F} \ln (K_1 [\text{AlCl}_4^-]^2 (\gamma_{\text{AlCl}_4^-})^2) \quad [3]$$

where E_A and E_B are the potentials measured, respectively, at an acidic composition A and a basic composition B, $(\gamma_{\text{Al}_2\text{Cl}_7^-})_A$, $(\gamma_{\text{Cl}^-})_B$, and $\gamma_{\text{AlCl}_4^-}$ are the respective activity coefficients, $[\text{Al}_2\text{Cl}_7^-]_A$, $[\text{Cl}^-]_B$, and $[\text{AlCl}_4^-]$ are the corresponding concentrations (expressed in $\text{mol} \cdot \text{kg}^{-1}$), and K_1 is the thermodynamic dissociation constant of equilibrium [1].

As previously discussed (32), the activity coefficients of Al_2Cl_7^- , Cl^- , and AlCl_4^- are not known. However, as the concentrations of Cl^- in the basic region and Al_2Cl_7^- in the acidic side do not vary to

a great extent, it can be assumed that the corresponding $(\gamma_{\text{Cl}^-})_B$ and $(\gamma_{\text{Al}_2\text{Cl}_7^-})_A$ are constant (32). For the same reason, $\gamma_{\text{AlCl}_4^-}$ can also be considered as constant on both acidic and basic sides. The cell voltage can then be rewritten as

$$E_A - E_B = \frac{4RT}{3F} \ln ([\text{Al}_2\text{Cl}_7^-]_A [\text{Cl}^-]_B) - \frac{4RT}{3F} \ln \bar{K}_1 \quad [4]$$

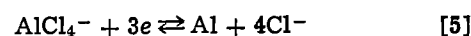
where \bar{K}_1 is a conditional equilibrium constant equal to

$$\frac{K_1 [\text{AlCl}_4^-]^2 (\gamma_{\text{AlCl}_4^-})^2}{(\gamma_{\text{Cl}^-})_B \cdot (\gamma_{\text{Al}_2\text{Cl}_7^-})_A}$$

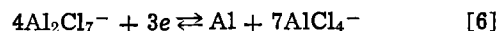
As will be seen below, the good agreement between the experimental titration curve and the theoretical curve calculated on the basis of concentration changes, indicates that the assumption made on the constancy of the activity coefficients is reasonable.

The $[\text{Al}_2\text{Cl}_7^-]_A$ and $[\text{Cl}^-]_B$ are calculated from the added amounts of AlCl_3 . The procedure and the precise determination of the amount of AlCl_3 added at the equivalence point by a linearization method, are explained in Appendix A.

The second method involves the calculation of the standard potentials E_B° and E_A° corresponding to the respective reactions



and



The equivalence point molar composition is adjusted for a minimum standard deviation on E_B° and E_A° ; the equilibrium constant is then simply calculated from

$$E_B^\circ = E_A^\circ + \frac{4RT}{3F} \ln K_1 \quad [7]$$

A more detailed description of the procedure is given in Appendix B.

In Table I, we have summarized some of the results obtained at three different temperatures and the precision on each of the experimental constants. The results obtained from method 1 or 2 were found similar within experimental errors but method 2 is preferred because it involves less assumptions and allows the complete calculation of the titration curve, even in more acidic melts. It can be noticed that at 40°C, the measurements are reproducible within 25%. The temperature variation of the results corresponds to an average value of ΔH and ΔS equal, respectively, to 20,300 $\text{cal} \cdot \text{mol}^{-1}$ and 6.5 eu.

In Table II, we compare our results with the previously published values. Because it is possible that mixed potentials are involved in our titration curves (19, 31), the stability of potential measurements indicates that the kinetics of basic melt reduction must be particularly slow provided that the above-mentioned melt compositions are not exceeded. The resulting equilibrium constants were found systematically lower than the constants obtained by other workers below 120°C and are thus considered as

Table I. Experimental values of K_1 at different temperatures

| T (°C) | Method 1 | | Method 2 | |
|--------|----------------------|-------------------------------|----------------------|-------------------------------|
| | $K_1 \cdot 10^{+18}$ | $\sigma_{K_1} \cdot 10^{+18}$ | $K_1 \cdot 10^{+18}$ | $\sigma_{K_1} \cdot 10^{+18}$ |
| 40 | 0.9 | 0.2 | 1.3 | 0.4 |
| | 1.8 | 0.3 | 3.0 | 0.9 |
| | 1.0 | 0.1 | 1.0 | 0.2 |
| | 1.1 | 0.05 | 1.3 | 0.1 |
| | 3.6 | 0.2 | 4.5 | 0.4 |
| 49 | 6.2 | 0.6 | 7.3 | 1.0 |
| | 6.2 | 0.6 | 7.8 | 0.6 |

Table II. Comparison of K_1 values at different temperatures

| T (°C) | $K_1 \cdot 10^{13}$ | $K_1 \cdot 10^{13a}$ |
|--------|--------------------------------------|------------------------|
| 30 | 3.8 ^c 2.2 ^d | 0.3 ^b |
| 40 | 1.73 ^e | 1.2 ± 0.2 |
| 49 | 11.9 ^{b,c} | 4.5 ± 0.4 |
| 55 | 21.7 ^{b,c} | 7.5 ± 0.8 |
| 60 | <57 ^c | 15 ^b |
| 120 | <3.6 · 10 ^{8c} | 5 · 10 ^{8b} |
| 175 | <1.2 · 10 ^{8c} | 1.7 · 10 ^{8b} |

^a Our results, average values.

^b Extrapolated values.

^c From Ref. (19).

^d From Ref. (27).

^e From Ref. (26).

closer to the true value for which no Al reaction with basic melt would occur.

All previous equilibrium constant determinations were obtained from melts whose composition was in the vicinity of the equimolar BPC- AlCl_3 melt. Titration curves were also extended to more acidic mixtures, up to the 2:1 composition (see the acidic part of Fig. 1). Systematic deviations between experimental and calculated potentials, increasing with the melt acidity for melt compositions higher than 55 m/o were observed. Tentative interpretation of these deviations based on the introduction of a second equilibrium such as [8] were unsuccessful



The necessary equilibrium formation constant K_2 was found much too high (six order of magnitude) with respect to what is expected by extrapolation at room temperature of K_2 constants known for inorganic chloroaluminates (3).

Another explanation involves the fact that the exact formulation of the emf is given by (33)

$$-FE = \int_I^{\text{II}} \left(\frac{1}{3} d\mu_{\text{AlCl}_3} - \frac{t_{\text{Al}}}{3} d\mu_{\text{AlCl}_3} - t_{\text{BP}^+} d\mu_{\text{BPC}} \right) \quad [9]$$

In the preceding calculations, only the first term is taken into account.

For titration curves involving inorganic chloroaluminate, it has been generally accepted that either the last two terms are indeed negligible (2,3) or can be calculated based on the assumption that the cation is the only current carrying species (4). In agreement with the work by King and Øye (33), for room temperature organic chloroaluminate melts, the organic cation cannot be considered with certainty as the only current carrying species because of its much larger size with respect to the inorganic cation. By measuring conductivities of various molten methylpyridinium halides, Newman *et al.* concluded that the principal charge carrier is the anion simply because chloride melts are better conductors than bromide melts. However, such a simple conclusion cannot be made when comparing the conductivities of several alkylpyridinium halides where both the alkyl chain and the halide were changed (29).

In the pyridinium chloroaluminates, it is reasonable to consider that the main current carrying species can be the pyridinium cation, the AlCl_4^- and Cl^- anions (33), since the Al_2Cl_7^- anions have a much lower mobility due to their size. The chloride anions may contribute to the current only on the basic side where their concentration is not negligible with respect to other ions. This can be taken into account by assuming that t_{Cl^-} is proportional to the Cl^- concentration (30).

By integrating the last two terms of Eq. [9] and introducing the equilibrium $\text{AlCl}_3 + \text{Cl}^- \rightleftharpoons \text{AlCl}_4^-$, a correction (E_j) to the initial emf can be calculated

$$E_j = -\frac{RT}{F} \left(\ln \frac{[\text{BP}^+]}{[\text{BP}^+]_{\text{ref}}} \right) \cdot t_{\text{BP}^+} + \frac{RT}{F} \cdot t_{\text{AlCl}_4^-} \cdot \ln \frac{[\text{AlCl}_4^-]}{[\text{AlCl}_4^-]_{\text{ref}}} + \frac{RT}{F} \cdot k \cdot ([\text{Cl}^-]_{\text{ref}} - [\text{Cl}^-]) \quad [10]$$

As already discussed by Von Barner *et al.* (30) the various transport numbers and k are not known but, considering that the mobilities of the ions are roughly inversely proportional to their ionic radii, an appropriate evaluation of the E_j correction term can be made. With this assumption, the maximum chloride ion contribution to E_j is of the order of one mV at 25°C and will therefore be neglected. The approximate t_{BP^+} and $t_{\text{AlCl}_4^-}$ are then, respectively, 0.6 and 0.4. By introducing these values to Eq. [10], the whole corrected theoretical titration curve can then be evaluated.

Two different experiments were performed. The first one involves the titration of a basic melt by successive AlCl_3 additions with a 66 m/o AlCl_3 reference; the second one involves the titration of a very acidic (66.6 m/o AlCl_3) by BPC additions with a 57 m/o AlCl_3 reference. Because of the problems encountered by BPC additions (see the experimental part), only the acidic part of the curve was recorded in this case. In both cases the agreement between the theoretical and experimental potentials was now remarkably good (Table III). The average deviations were, respectively, ±1.4 mV and ±2 mV, for the whole titration curve, *i.e.*, even for the very acidic points (66 m/o). We have also noticed that no agreement was found assuming only one current carrying species, either BP^+ or AlCl_4^- .

Finally, in the acidic part of the titration curve, the derivative of the potential *vs.* the total mol fraction of AlCl_3 exhibits a minimum near the 57 m/o AlCl_3 composition. In this region, the electrode potentials are less sensitive to pCl than in the 1:1 or 2:1 AlCl_3 :BPC melts. A 57 m/o melt would then be the most appropriate in a reference compartment with an Al electrode.

From this study, it can be concluded that: (i) Some experimental conditions can be adjusted to give reproducible values of the equilibrium constant K_1 . Because the titration curve involves mixed potentials, the values may not correspond to the exact K_1 value and are then considered as maximum values as in previous works (19). However, the stability of our potential measurements in the basic side, indicates that the melt reduction by Al is particularly slow and our results must be close to the true K_1 value. (ii) Only one equilibrium is necessary to fit the whole experimental titration curve, provided a complete formulation of the emf is taken into account.

Table III. Comparison in acidic medium of experimental potentials ($E_{\text{Exp.}}$) and theoretical potentials without ($E_{\text{Th.1}}$) and with ($E_{\text{Th.2}}$) corrections for the junction potentials (E_j). Reference: an Al electrode in 66.2 m/o AlCl_3

| m/o AlCl_3 | $E_{\text{Exp.}}$ (V) | $E_{\text{Th.1}}$ (V) | $E_{\text{Th.2}}$ (V) |
|---------------------|-----------------------|-----------------------|-----------------------|
| 50.54 | -0.314 | -0.314 | -0.314 |
| 50.71 | -0.3 | -0.303 | -0.304 |
| 50.95 | -0.291 | -0.292 | -0.292 |
| 51.14 | -0.285 | -0.285 | -0.285 |
| 51.45 | -0.275 | -0.275 | -0.275 |
| 51.86 | -0.265 | -0.264 | -0.265 |
| 52.29 | -0.257 | -0.255 | -0.256 |
| 52.99 | -0.244 | -0.242 | -0.244 |
| 53.92 | -0.231 | -0.228 | -0.230 |
| 55.17 | -0.215 | -0.211 | -0.214 |
| 56.73 | -0.195 | -0.193 | -0.197 |
| 58.23 | -0.180 | -0.176 | -0.180 |
| 60.26 | -0.157 | -0.151 | -0.157 |
| 62.29 | -0.129 | -0.120 | -0.130 |
| 64.27 | -0.090 | -0.077 | -0.093 |
| 66.33 | +0.009 | +0.050 | +0.015 |

Acknowledgments

We thank Professor G. Duyckaerts for fruitful discussions and are indebted to the Institut Interuniversitaire des Sciences Nucléaires (Brussels) for the financial aid given to our laboratory.

Manuscript submitted Feb. 9, 1981; revised manuscript received July 8, 1981.

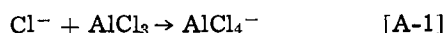
Any discussion of this paper will appear in a Discussion Section to be published in the June 1982 JOURNAL. All discussions for the June 1982 Discussion Section should be submitted by Feb. 1, 1982.

APPENDIX A

The titration involves successive additions of weighed amounts of AlCl_3 to a basic melt of initial weight W_0 (in grams). The amount of added AlCl_3 is calculated so that only the 49-52 m/o composition range is investigated.

Let n be the total number of AlCl_3 mols added from the starting point. The subscript A, B, and Q will be used to describe, respectively, an acidic side, a basic side, or the equivalence point.

Assuming that the following reactions are quantitative



the concentrations $[\text{Al}_2\text{Cl}_7^-]_A$ and $[\text{Cl}^-]_B$ involved in Eq. [4] are easily calculated if n_Q is known

$$[\text{Al}_2\text{Cl}_7^-]_A = \frac{(n_A - n_Q) 10^3}{(W_0 + n_A \times 133.33)} \quad [\text{A-3}]$$

$$[\text{Cl}^-]_B = \frac{(n_Q - n_B) 10^3}{(W_0 + n_B \times 133.33)} \quad [\text{A-4}]$$

In order to evaluate precisely the experimental number of mols of AlCl_3 necessary to reach the equivalence point (n_Q), a linearization method similar to the one described by Gran (23) has been applied to the more precise points, i.e., the acidic side points.

The potential of an Al electrode in an acidic melt is given by the Nernst equation

$$E_A = E_A^\circ + \frac{RT}{3F} \ln \frac{[\text{Al}_2\text{Cl}_7^-]_A^4}{[\text{AlCl}_4^-]_A^7} + E_R + E_A^J \quad [\text{A-5}]$$

where E_R and E_A^J are, respectively, the reference electrode potential (unknown but constant) and the junction potential.

Because the composition range investigated to calculate the equilibrium constant is very narrow, we will assume that the E^J and the $[\text{AlCl}_4^-]$ are constant. The relation [A-5] can then be rewritten as follows

$$E_A^\circ + E_A^J = E_A - E_R - \frac{RT}{3F} \ln \frac{(n_A - n_Q)^4 (W_0 + n_A \times 133.33)^3}{(3.28 \cdot 10^{-3} (W_0 + n_Q \times 133.33) - n_A + n_Q)^7 \times 10^9} \quad [\text{B-2}]$$

$$E_A = E_A^{\circ'} + \frac{4RT}{3F} \ln [\text{Al}_2\text{Cl}_7^-]_A \quad [\text{A-6}]$$

$$(E_B + E_B^J) = E_B - E_R - \frac{RT}{3F} \ln \frac{(3.28 \cdot 10^{-3} (W_0 + n_Q \times 133.33) + n_B - n_Q) (W_0 + n_B \times 133.33)^3}{(n_Q - n_B)^4 \times 10^9}$$

From [A-3], [A-6], and rearranging, one obtains

$$\exp\left(\frac{E_A \times 3F}{4RT}\right) (W_0 + n_A \times 133.33) = k(n_A - n_Q) \quad [\text{A-7}]$$

$$\text{where } k = \frac{10^{+3}}{\exp\left(\frac{-3F \times E_A^{\circ'}}{4RT}\right)}$$

A plot of $\exp(3F \times E_A/4RT) (W_0 + n_A \times 133.33)$ vs. n_A gives a straight line allowing the evaluation of k and n_Q by a least-squares fitting computer program. An

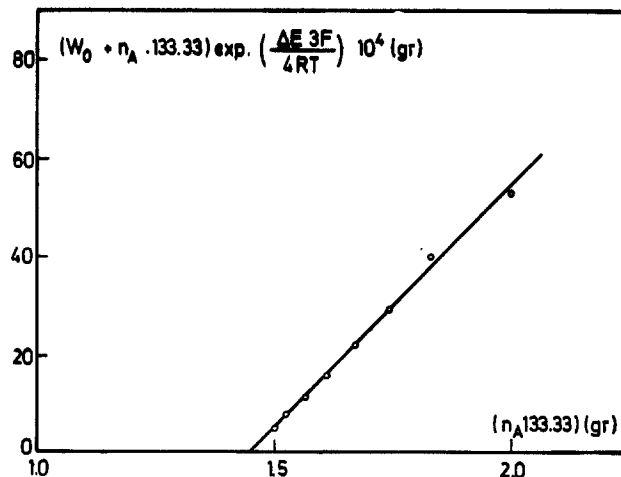


Fig. 3. Determination of the amount of AlCl_3 added to reach the equivalence point following the method of Gran (23).

example of such a plot is given in Fig. 3. Knowing n_Q , the program computes \bar{K}_1 from every successive basic and acidic point and relation [4], then the equivalence point potential and the whole theoretical curve.

APPENDIX B

In order to evaluate the equilibrium constant from the respective $[\text{Al}_2\text{Cl}_7^-]$, $[\text{Cl}^-]$, and $[\text{AlCl}_4^-]$, another method of evaluating precisely n_Q (as defined in Appendix A) is explained below.

1. A first approximate value of n_Q is given to the computer program. Assuming that the reactions [A-1] and [A-2] (see Appendix A) are quantitative, the necessary $[\text{Al}_2\text{Cl}_7^-]$, $[\text{Cl}^-]$, and $[\text{AlCl}_4^-]$ (which is not assumed as constant in this case) can then be evaluated for every point of the titration curve.

For example, in the acidic side, the number of AlCl_4^- mols equals the number of AlCl_4^- mols at the equivalence point less the number of added AlCl_3 mols in excess to the equivalence point. The $[\text{AlCl}_4^-]_A$ is then

$$\frac{(3.28 \cdot 10^{-3} (W_0 + n_Q \times 133.33) - (n_A - n_Q)) \times 10^3}{(W_0 + n_A \times 133.33)} \quad [\text{B-1}]$$

where W_0 , n_A , and n_Q have the same meaning as above. The $[\text{Al}_2\text{Cl}_7^-]_A$ is given by the same relation as in Appendix A (Eq. [A-3]).

2. From [A-5], [A-3], [B-1], and the experimentally measured potentials $(E_A - E_R)$, the $(E_A^\circ + E_A^J)$ can then be calculated for each acidic side point

From a similar development and the Nernst equation applied to reaction [5], the $(E_B^\circ + E_B^J)$ can also be evaluated for each point in basic melts

3. The respective standard deviation (σ) on all the $E_A^\circ + E_A^J$ and $E_B^\circ + E_B^J$ values is then calculated.

4. A new value of n_Q is chosen by the computer; the calculation process restarts from the beginning and leads to a new set of $E_A^\circ + E_A^J$, $E_B^\circ + E_B^J$, and σ values.

The final values of n_Q , $E_A^\circ + E_A^J$, and $E_B^\circ + E_B^J$ are obtained by successive modification of n_Q in order that the standard deviation (σ) is minimum.

Assuming a negligible junction potential between the acidic and basic points ($E_A^J - E_B^J \approx 0$), the equilibrium constant is then evaluated from relation [7] as explained in the text.

REFERENCES

1. B. Tremillon and G. Letisse, *J. Electroanal. Chem. Interfacial Electrochem.*, **17**, 371 (1968).
2. G. Torsi and G. Mamantov, *Inorg. Chem.*, **10**, 1900 (1971).
3. L. G. Boxall, H. L. Jones, and R. A. Osteryoung, *This Journal*, **120**, 223 (1973).
4. A. A. Fannin, L. A. King, and D. W. Seegmiller, *ibid.*, **119**, 801 (1972).
5. T. C. F. Munday and J. D. Corbett, *Inorg. Chem.*, **5**, 1263 (1966).
6. N. J. Bjerrum, C. R. Boston, and G. P. Smith, *ibid.*, **6**, 1162 (1967).
7. N. J. Bjerrum and G. P. Smith, *ibid.*, **6**, 1968 (1967).
8. G. Torsi, K. W. Fung, G. M. Begun, and G. Mamantov, *ibid.*, **10**, 2285 (1971).
9. N. J. Bjerrum, *ibid.*, **9**, 1965 (1970); **10**, 2578 (1971).
10. R. F. Fehrmann, N. J. Bjerrum, and M. A. Andreasen, *ibid.*, **14**, 2259 (1975).
11. G. Ting, K. W. Fung, and G. Mamantov, *This Journal*, **123**, 624 (1976).
12. B. Gilbert, V. Demarteau, and G. Duyckaerts, *J. Electroanal. Chem. Interfacial Electrochem.*, **89**, 123 (1978).
13. V. R. Koch, L. L. Miller, and R. A. Osteryoung, *J. Am. Chem. Soc.*, **98**, 5277 (1976).
14. F. H. Hurley and T. P. Wier, *This Journal*, **98**, 203 (1951).
15. H. L. Chum, V. R. Koch, L. L. Miller, and R. A. Osteryoung, *J. Am. Chem. Soc.*, **97**, 3264 (1975).
16. H. L. Chum, D. Koran, and R. A. Osteryoung, *ibid.*, **100**, 310 (1978).
17. C. L. Hussey, L. A. King, and R. A. Carpio, *This Journal*, **126**, 1029 (1979).
18. R. A. Carpio, L. A. King, R. E. Lindstrom, J. C. Nardi, and C. L. Hussey, *ibid.*, **120**, 1644 (1979).
19. R. J. Gale and R. A. Osteryoung, *Inorg. Chem.*, **18**, 1603 (1979).
20. J. Robinson and R. A. Osteryoung, *J. Am. Chem. Soc.*, **101**, 323 (1979).
21. J. Robinson, R. C. Bugle, H. L. Chum, D. Koran, and R. A. Osteryoung, *ibid.*, **101**, 3776 (1979).
22. C. L. Hussey, L. A. King, and J. S. Wilkes, *J. Electroanal. Chem. Interfacial Electrochem.*, **102**, 321 (1979).
23. G. Gran, "Int. Congress on Analytical Chemistry," Vol. 77, Sect. 3 (1952).
24. R. J. Gale, B. Gilbert, and R. A. Osteryoung, *Inorg. Chem.*, **17**, 2728 (1978).
25. J. Robinson and R. A. Osteryoung, *J. Am. Chem. Soc.*, **102**, 4415 (1980).
26. R. J. Gale, B. Gilbert, and R. A. Osteryoung, *Inorg. Chem.*, **18**, 2723 (1979).
27. J. Robinson and R. A. Osteryoung, *This Journal*, **127**, 122 (1980).
28. N. S. Moe, *Anal. Chem.*, **46**, 968 (1974).
29. D. S. Newman, N. Rohr, and D. Kirklin, *This Journal*, **119**, 797 (1972).
30. J. H. Von Barner and N. J. Bjerrum, *Inorg. Chem.*, **12**, 1891 (1973).
31. R. J. Gale and R. A. Osteryoung, *This Journal*, **127**, 2167 (1980).
32. A. A. Fannin, L. A. King, and D. W. Seegmiller, *ibid.*, **119**, 801 (1972).
33. H. A. Øye and L. A. King, *Inorg. Nucl. Chem. Lett.*, **16**, 547 (1980).

Technical Note



Semiconducting Zinc Oxide Films Prepared by Metal Organic Chemical Vapor Deposition from Diethyl Zinc

A. P. Roth and D. F. Williams

Division of Chemistry, National Research Council of Canada, Ottawa, Ontario, Canada K1A 0R6

Zinc oxide exhibits large piezoelectric and optical coupling coefficients, and is often used in acousto-electric and acousto-optic devices (1). It is also an extrinsic n-type semiconductor with a room temperature bandgap of 3.3 eV and can be used as a transparent semiconducting electrode in opto-electronic devices such as solar cells. Indium tin oxide is generally used as the transparent electrode for many solar cells; it is typically an n-type semiconductor due to oxygen deficiencies. If relatively high conductivity in zinc oxide could also be achieved either by preparing nonstoichiometric films or by doping, this source material would be less expensive than indium tin oxide. Nonstoichiometric films would experimentally be the simplest and most economical to prepare, if a sufficiently high conductivity could be achieved. Zinc oxide films have been prepared by rf sputtering (2) and more recently by magnetron sputtering (3). Short reports have also been published of the metal organic chemical vapor deposition of zinc oxide (4, 5), but the aim of these

authors was to prepare high resistivity stoichiometric films.

We have a particular interest in semiconducting zinc oxide and have recently studied the growth characteristics and related electrical properties of films prepared by the controlled oxidation of diethyl zinc (DEZ). Changes in the substrate temperature were found to significantly alter the film deposition rate and resistivity, two critical factors for any potential zinc oxide electrode applications.

The zinc oxide films were deposited on clean Pyrex glass substrates over an area of $\sim 1.5 \text{ cm} \times 3 \text{ cm}$. The substrates were supported on a graphite susceptor which top surface had been cut at an angle of 15° from the horizontal axis of the reactor tube to provide a grazing incidence gas flow over the substrates. The susceptor/substrate combination was placed in the center of this horizontal square quartz reactor tube, $3.5 \times 3.5 \times 50 \text{ cm}$, and this central area then enclosed in a cylindrical aluminum reflector containing two 500W quartz halogen lamps. These lamps could heat the

Key words: zinc oxide, chemical vapor deposition, diethyl zinc.

substrate to temperatures of up to 900°C. A calibrated thermocouple encased in thin stainless steel monitored the substrate/susceptor temperature throughout the film preparation.

All fittings to the reactor tube were either quartz or stainless steel. Gas flow into the reactor tube was all passed through mass flow controllers. High purity argon (99.999%) was used as an inert gas and also as a carrier gas by bubbling through DEZ contained in a steel bottle in a temperature controlled bath. Homogeneous gas phase reactions between diethyl zinc and oxygen occur even at room temperature and thus, the DEZ was kept separated from the oxygen until it reached the reaction zone. This was achieved by attaching to the oxygen inlet a small diameter quartz tube which extended inside the reactor to ~2 cm in front of the substrate edge. Gas-phase homogeneous reactions which lower the film growth rate and damage film quality were further minimized by reducing the overall pressure of the system below atmospheric. A more extensive description of the apparatus and experiments will be given later in a full-length paper.

The experiments were all performed at a pressure of 76 Torr (10.13 kPa) with a constant argon flow (2 SLM) and partial pressures of DEZ and oxygen of 1.85×10^{-2} Torr (2.46 Pa) and 1.3×10^{-1} Torr (17.3 Pa), respectively. In the substrate temperature range investigated, 280°–480°C, clear homogeneous films of 2 cm² were grown with an average optical transmission of 85–90% for film thicknesses between 4000 and 8000 Å. Room temperature electrical properties of these films were obtained by four probe conductivity and by Hall measurements. Film thickness was measured by a Sloan Dektak profilometer.

The variation of the film deposition rate and electrical properties are presented in Fig. 1 and 2, which show the importance of the substrate temperature on the film characteristics. In the low temperature range (below 370°C), the film growth rate is constant while the resistivity decreases drastically from 30 to 8×10^{-2} Ωcm. In this range, a white ZnO deposit appears on the reactor walls downstream of the reaction area, caused by the homogeneous reaction of O₂ with the metalorganic which is only partly decomposed at these temperatures. The decrease in the resistivity can be related to an improvement of the crystallization of

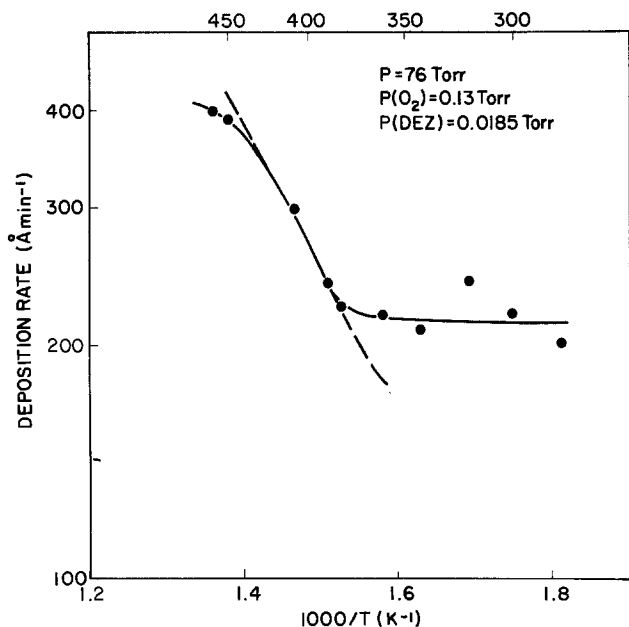


Fig. 1. Variation of the growth rate of zinc oxide films as a function of substrate temperature. Diethyl zinc, pp. 0.0185 Torr, and oxygen, pp. 0.13 Torr were used with argon carrier gas, overall pressure 76 Torr.

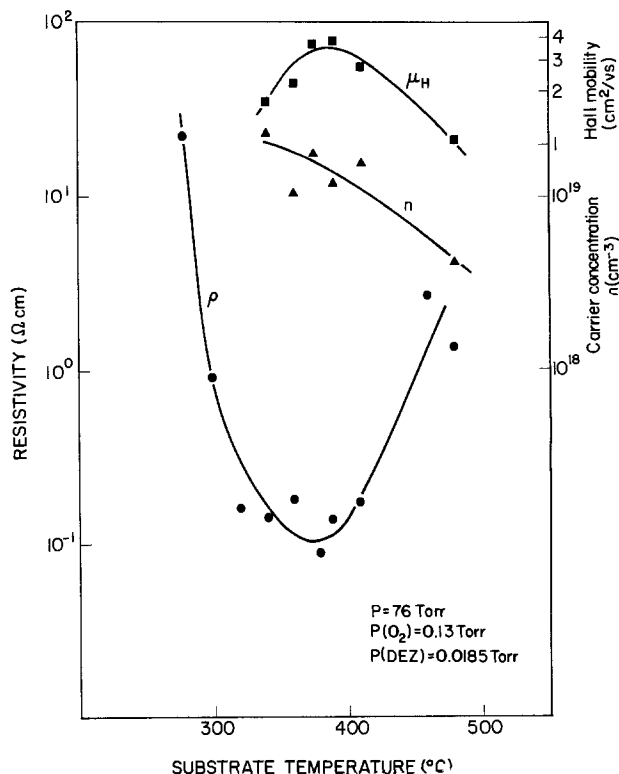


Fig. 2. Variation of the zinc oxide film resistivity, carrier concentration, and carrier mobility with substrate temperature. Deposition conditions were the same as for Fig. 1.

the films as shown by the increase of the Hall mobility μ_H .

When the temperature of the substrate is further increased, the growth process becomes reaction-rate controlled (Fig. 1). The film growth rate (GR) in such a case can be represented by the relation (6)

$$GR = KT \exp(-E/RT)$$

where K depends on the order of the reaction and on the reacting gas flow rates, and R is the gas constant. The dashed line in Fig. 1 corresponds to an activation energy of 30 kJ/mol (0.31 eV/molecule) and $K = 85 \text{ Å min}^{-1} \text{ K}^{-1}$. A saturation in the deposition rate appears around 450°C indicating a mass transport limited regime. In this temperature range (above 370°C) the parasitic deposit on the reactor walls disappears almost completely and the amount of oxygen which is used in the direct film growth increases. Furthermore the ratio of zinc to oxygen included in the films also changes. This can be inferred from the decrease of the carrier concentration (Fig. 2), that is from the decrease of the film nonstoichiometry due to interstitial zinc or oxygen vacancies. The parallel variation of μ_H causes a net increase of the film resistivity.

The variation of the film resistivity with substrate temperature is therefore caused by the competition between crystallization and degree of nonstoichiometry of the films. It has been observed (5) that, in ZnO films deposited by MOCVD at atmospheric pressure on glass substrates using a much higher O₂/Zn mol ratio than in our own experiments, the degree of c-axis orientation of the crystallites increases with temperature up to 400°C and decreases above that temperature. A phenomenon such as this is very likely to have an effect on μ_H as observed.

In summary, thin transparent semiconducting films of zinc oxide can be grown relatively easily by the controlled oxidation of diethyl zinc. The temperatures needed to produce relatively low resistivity films are ~350°–400°C; film electrical properties are strongly dependent upon this decomposition temperature, other

temperatures giving film resistivity increases due to decreasing carrier concentration and decreasing carrier mobility.

Manuscript submitted Feb. 11, 1981; revised manuscript received May 26, 1981.

Any discussion of this paper will appear in a Discussion Section to be published in the June 1982 JOURNAL. All discussions for the June 1982 Discussion Section should be submitted by Feb. 1, 1982.

Publication costs of this article were assisted by the National Research Council of Canada.

Some Problems in Plasma Etching of Al and Al-Si Alloy Films

Kado Hirobe,* Yoshinori Kureishi, and Takashi Tsuchimoto

Computer Development Laboratories, Limited, 1450, Kodaira-Shi, Tokyo 187, Japan

Generally, aluminum and aluminum-silicon alloy films are widely used as the electric interconnection metal in large scale integrated circuits (LSI). The technology by which fine patterns can be precisely defined in Al and Al-Si films has been indispensable to high density and high speed LSI. Among various kinds of etching methods for the films, the plasma etching in the parallel plate electrode reactor is considered one of the most useful methods to delineate high resolution patterns in the films.

This technology has been developed by several workers (1-4), and it has been well known that the etching method has excellent characteristics, such as anisotropy and less undercutting than the conventional plasma etching in a barrel type reactor and wet chemical etching in acid solutions.

However, there are some problems which were encountered when the technology was applied to the metallization processes. These problems come from the characteristics inherent in the etching technology.

One of the purposes of this work is to survey the problems which were introduced when the etching technology was applied to the metallization process of LSI devices.

Another purpose is to find the origins of these problems and to provide effective approaches to solve them.

In this work, plasma etching of Al and Al-Si alloy films was carried out in a parallel plate, anode coupling type of reactor. Wafers were placed on the susceptors which were placed on the lower Al electrode coated with an aluminum oxide film. This electrode was grounded and rotated at the rate of 4 rpm. RF power of 380 kHz was applied to the upper electrode. An optical emission spectrometer was attached to the chamber. The spectrometer was used to measure the intensity of spectra emitted from the plasma during etching. The 396.2 nm peak of Al atomic spectrum was used (5), as well as the AlCl₃ 261.4 nm peak. CCl₄ was used as the etching gas. Etching experiments were carried out using two types of substrates. One of them was a flat substrate coated with Al or Al-Si alloy films of uniform thickness. The other was a substrate with steps about 1 μm in height. Both pure Al and Al-Si alloy films were deposited on the substrates by a planar magnetron sputter system.

* Electrochemical Society Active Member.

Key words: metallization, sputtering, surface oxide film, emission spectroscopy, plasma etching, Al alloy film.

REFERENCES

1. G. S. Kino and R. S. Wagers, *J. Appl. Phys.*, **44**, 1480 (1973).
2. J. C. Yen, *J. Vac. Sci. Technol.*, **12**, 47 (1975).
3. T. Hata, T. Minanukawa, O. Morimoto, and T. Hada, *J. Cryst. Growth*, **47**, 171 (1979).
4. C. K. Lau, S. K. Tikku, and K. M. Lakin, *This Journal*, **127**, 1843 (1980).
5. S. K. Ghandi, R. J. Field, and J. R. Shealy, *Appl. Phys. Lett.*, **37**, 449 (1980).
6. B. J. Baliga and S. K. Ghandi, *This Journal*, **123**, 941 (1976).

In our early experiment, when the etching technology was applied to delineate patterns in the films, the following problems were observed: (i) Surface oxide film caused a delay in the initiation of the etching reaction of Al with CCl₄, and the delay time varied from several tens of seconds to several minutes, as shown in Fig. 1. (ii) The reproducibility of etch rate of the films was poor. The etch rate varied from about 80 to 170 nm/min under the same condition, and so it was difficult to determine the end of etching by time. (iii) Al residues were observed along the steps of the substrate and around the hillocks of annealed Al films. The residues of Al caused low current leakage and in the worst case, electric shorts occurred between the adjacent Al patterns. (iv) After Al-Si alloy film etching, Si remained as residue on the substrate. The residues also led to leakage of electric current between the adjacent Al patterns. (v) Furthermore, severe degradation of photoresist film patterns was found after etching, especially at relatively high rf current or rf power.

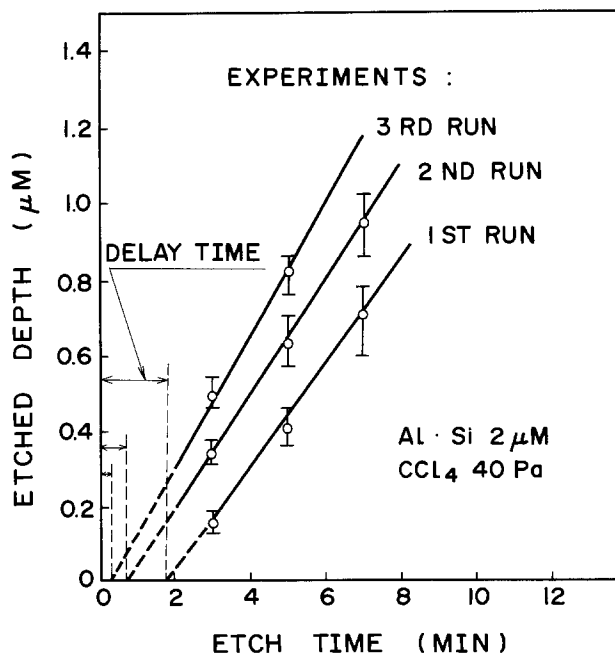


Fig. 1. Etched depth as a function of etch time

It was found that the delay time in etching was decreased with increasing rf current, as shown in Fig. 2. The delay time at higher rf currents was more reproducible than that at lower rf currents. Etching at high rf current for a long time, however, caused the degradation of photoresist films by substrate heating. Etching at high rf current for a short time, such as less than 2 or 3 min at 1A, caused no damage to the photoresist films. Therefore, one of the effective etching procedures was attained by using a two-step etching technique. This etching consisted of the 1st step etching at higher rf current for a short time and then the 2nd step etching at lower rf current to the etch end.

Figure 3 shows typical emission intensity during etching by the two-step technique. The Al etching was started at high rf current, in this case 1A or at rf power density of 0.46 W/cm². The initiation of etching

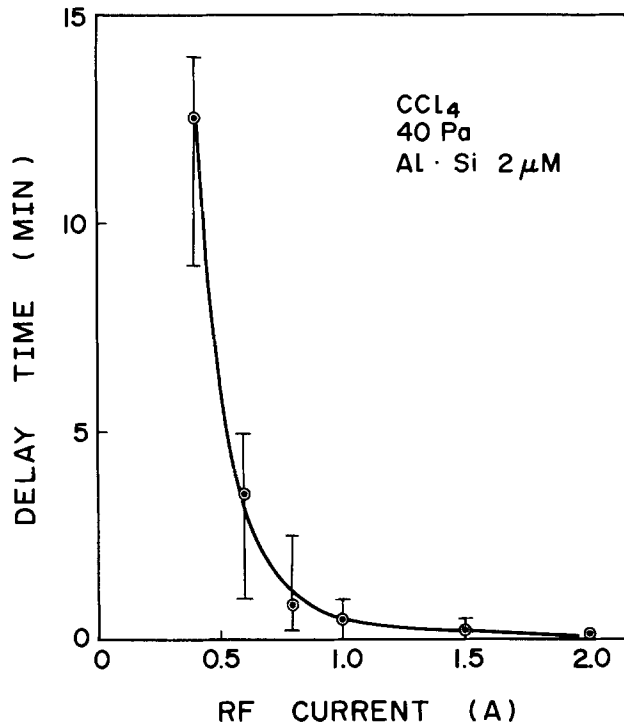


Fig. 2. Dependence of the delay time on the rf current

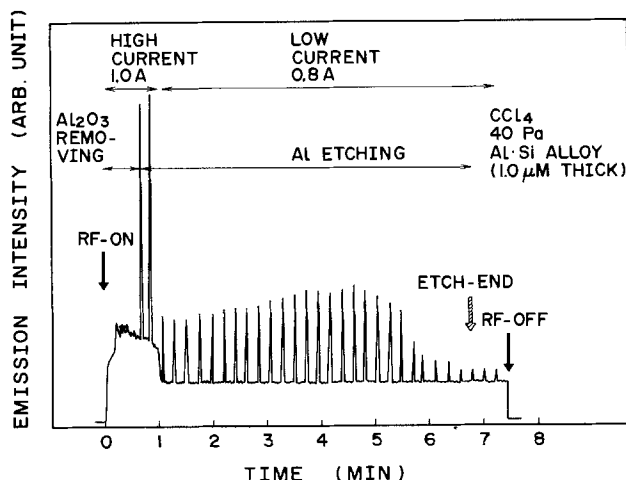


Fig. 3. Typical emission intensity during etching Al-Si alloy film by the two-step etching technique: RF current 1 and 0.8A correspond to 0.46 and 0.31 W/cm² of power density, respectively. Etching was monitored by the Al 396.2 nm line. The lower electrode was rotated at the rate of 4 rpm, and so emission peaks were observed 4 times per minute.

was detected by the strong 396.2 nm peaks on the figure. RF current was decreased to 0.8A or to 0.31 W/cm² of power density after the occurrence of the strong emission peaks. As the end point was approached, the emission intensity leveled off. Thus, the end point could be detected precisely from batch to batch.

Another technique for removing the protective surface oxide easily and reproducibly, was to supply inert gases such as Xe and Kr to the etching gas. Figure 4 represents a dependence of the delay time on etching gas composition for CCl₄ and Xe. It was found that the appropriate addition of Xe to CCl₄ could greatly decrease the delay time even if the rf current was as low as 0.6A. Decrease of the delay time is considered to be due to removing the surface oxide with the aid of bombardment by energetic Xe⁺.

Figure 5 shows typical residues of Al along the steps of the substrate after Al etching. It was found that the steeper the slope of the edge, the more Al remained. One of the reasons for the occurrence of the Al residues was considered to be due to the anisotropic etching of the parallel plate reactor. The etch rate of Al depends on the incidence angle of ions (6), and it is reduced around step edges with incidence angles of about 90 degrees. Another reason was that the Al film at the base of the edge was much thicker than that on the flat area of the substrate. Overetching or ex-

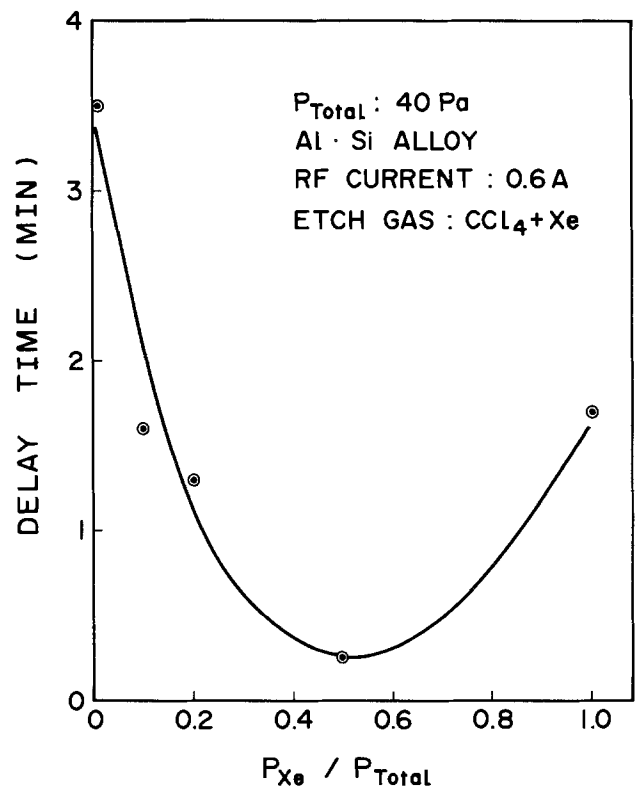


Fig. 4. Dependence of the delay time on the etching gas composition.

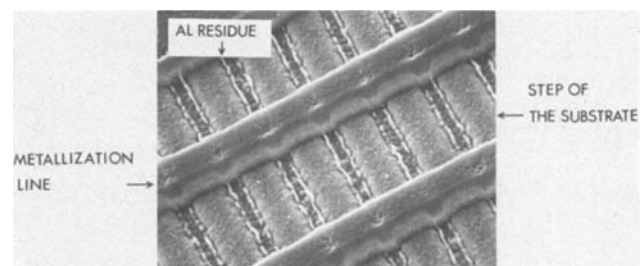


Fig. 5. SEM photograph of Al residues along the steps of the substrate.

cessive etching was one approach to solving the problem. However, a more basic and effective approach was to reduce the steepness of the steps, namely to achieve a smooth surface topography.

Si residues on the substrate after etching the Al-Si alloy film were effectively removed by CF_4 plasma etching.

In summary, some problems which were encountered in plasma etching of Al and Al-Si alloy films were investigated in this work. The protective oxide film caused a delay in the initiation of the etching reaction. The film was effectively and reproducibly removed by a relatively high rf current or by mixed CCl_4 -Xe gas plasma at low rf current. A reproducible Al etching process was developed by using the two-step technique. Al residues along the steps of the substrate were found to be due to the surface topography of the substrate and the characteristics of the etching technology.

Acknowledgment

The authors wish to thank Dr. K. Sugawara and Mr. Y. Nitta for valuable discussions and suggestions about this work.

Manuscript submitted March 28, 1980; revised manuscript received April 10, 1981.

Any discussion of this paper will appear in a Discussion Section to be published in the June 1982 JOURNAL. All discussions for the June 1982 Discussion Section should be submitted by Feb. 1, 1982.

Publication costs of this article were assisted by Hitachi, Limited.

REFERENCES

1. N. Hosokawa, R. Matsuzaki, and T. Asamaki, *Jpn. J. Appl. Phys.* (Suppl. 2, Pt. 1), 435 (1974).
2. R. G. Poulsen, H. Nentwich, and S. Ingrey, Proceedings of the International Electron Devices Meeting, Washington, DC, December 1976, pp. 205-208.
3. T. O. Herndon and R. L. Burke, Interface '77 Kodak Microelectronics Symposium, Monterey, CA, October 1977.
4. P. M. Schaible, W. C. Metzger, and J. P. Anderson, *J. Vac. Sci. Technol.*, 15(2), 334 (1978).
5. A. Iida, T. Mizutani, and H. Komatsu, *Shingaku Giho* (in Japanese), 79(94), 15 (1979).
6. G. D. Boyd et al., The 21st Electronic Materials Conference, Boulder, CO, 1979.

Polishing of CdTe Surfaces by Diamond Milling

J. A. Mroczkowski

Honeywell Electro-Optics Center, Lexington, Massachusetts 02173

The preparation of semiconductor wafers usually involves either mechanical polishing with a wet abrasive slurry, etching, or chemical mechanical polishing. A new dry technique for polishing zincblende structure compounds is described in this article, based on cleaving the top layers of an oriented semiconductor with a single diamond edge. The technique, which is an adaptation of the diamond milling process commonly used for polishing aluminum surfaces to precision flatness for large area infrared optical scanning systems, has been found to be very useful for the preparation of CdTe substrates for LPE $Hg_{1-x}Cd_xTe$ film growth (1).

The principle of the diamond milling process is illustrated in Fig. 1. Figure 2 shows the effect of different milling directions $\langle h'k'l' \rangle$ across low index (111)A, (110), and (100) CdTe surfaces.

For the (111)A surface only milling directions within a few degrees of the set of 3 $[2\bar{1}1]$ directions in the (111)A plane resulted in smooth polishing of the surface, while other directions resulted in rough surfaces. Figure 2 shows the sequence of good and poor polishing directions across 36 cleaved pieces from the same original (111)A surface which were reassembled with the pieces rotated relative to the first by increas-

ing angles in the sequence 5, 15, 30, 45, 55, 60, 65, 75, 90, 105, 120, . . . 355 degrees running from left to right and then down consecutive rows. It should be noted that piece 14 in the sequence was misplaced at the very end, and the seventh piece from the end was positioned at the incorrect angle. When these errors are recognized the contrasts in the polishing results clearly show a threefold symmetry of optimum milling directions across the (111)A surface.

The $[2\bar{1}1]$ polishing directions could be uniquely identified by using a 0.6328 micron helium neon laser beam at normal incidence on the initially rough pol-

Key words: semiconductor surfaces, stress/strain, aluminum.

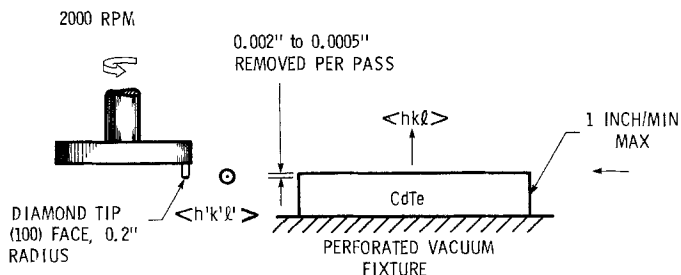


Fig. 1. Schematic of diamond milling process of CdTe (hkl) surfaces along $[h'k'l']$ directions in the (hkl) plane.

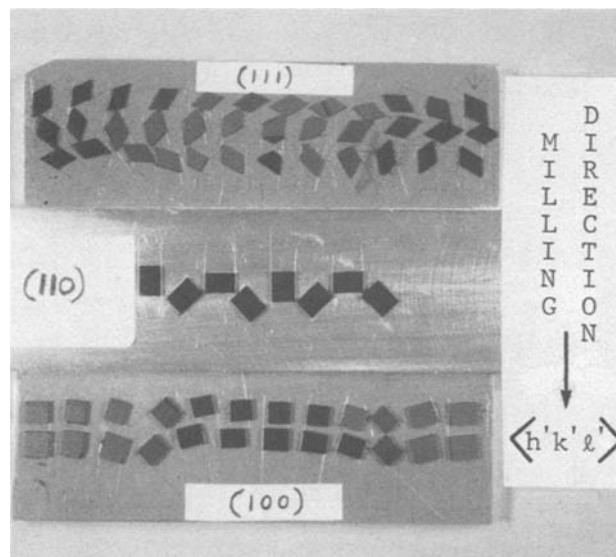


Fig. 2. Demonstration of the effect of different milling directions. After breaking up 3 initial single surfaces into small pieces the pieces were reassembled for milling at consecutively increasing angles.

ished CdTe (111)A surface, and observing the selective reflections from the 3 groups of {110} microfacets. By transmitting the beam through a small aperture in a screen placed in front of the CdTe, three reflected bright spots could be projected on the screen at twice the angle between either of the 3 {110} directions and the $\langle 111 \rangle$ direction, i.e., 70.5° . The same identification and polishing procedures worked for the $(\bar{1}\bar{1}\bar{1})$ B surfaces with $[2\bar{1}1]$ milling directions.

For the (110) surface eight pieces from one initial single (110) surface were rotated in consecutively increasing steps of 45° . The results shown in Fig. 2 suggest that the milling direction is unimportant.

For the (100) surfaces with orthogonal {110} facets 24 pieces were reassembled with increasing angles relative to the first piece in the top left-hand corner in the sequence 5, 15, 45, 75, 85, 90, 95, 105, . . . 355. The results appeared to indicate only 2 permissible $[110]$ milling directions.

The CdTe zincblende crystal structure shows that stereo-hindrance is possible between the 3 $[2\bar{1}\bar{1}]$ directions resulting in smooth surfaces and the 3 $[2\bar{1}1]$ directions resulting in rough surfaces. The unimportance of the milling direction on (110) surfaces is not surprising in view of the fact that the (110) surfaces are the preferential cleavage surfaces. The results on the (100) surfaces exhibiting apparent twofold symmetry instead of the expected fourfold symmetry were surprising; they could only be explained on the basis that the (100) surfaces were insufficiently oriented in the cutting plane of the diamond.

Etching, x-ray, and Nomarski phase contrast analyses of the CdTe samples were used to estimate the extent of surface damage and smoothness. Figures 3a and b show two (111)A samples of CdTe, number 8 and 14 from that shown in Fig. 2, which had been milled across the surface in different directions. These samples had the right third area unetched after diamond milling, the middle third etched in Br methanol solution to a depth of about 5 microns, and the left

third etched for about 20 microns. Figures 4a and b show the boundaries between the 5 micron etched and unetched surfaces. Significant surface gouging was detected in the samples which had not been polished in the optimum direction, while there was virtually no gouging on surfaces which had been polished in the optimum direction. In addition, very little difference was seen in the 5 micron etched and the unetched surfaces. At 20 microns of etching slight "orange peel" features were observed.

Double crystal x-ray spectroscopy using copper $K\alpha$ radiation and etched (111) germanium as the first crystal was used to assess polishing damage. X-ray rocking curves were obtained on both the diamond polished CdTe surfaces and also adjacent surfaces which had 5 microns etched off. An etched (111) silicon reference as the second crystal showed a diffracted x-ray half-width of about 40 sec.

For the (111)A samples 2θ was 23.8 degrees and the unetched surface of the sample polished with the optimum milling direction showed a half-width of 50 sec. No improvement was seen in the adjacent etched areas.

The (110) surfaces were examined using (220) reflections with a 2θ angle of 39.3 degrees. A reference cleaved surface showed a half-width of 60 sec. A milled unetched surface showed a half-width of 170

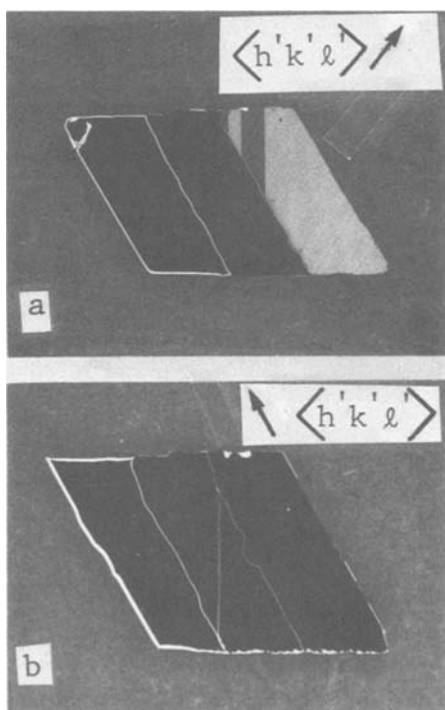


Fig. 3. a, b: Enlarged micrographs of (111)A pieces 8 and 14 shown in Fig. 2 milled at 65° and 0° , respectively, from the optimum direction. Left third and middle third areas had 20 and 5 microns etched off. Right-side areas are unetched. Note twins running through piece 8.

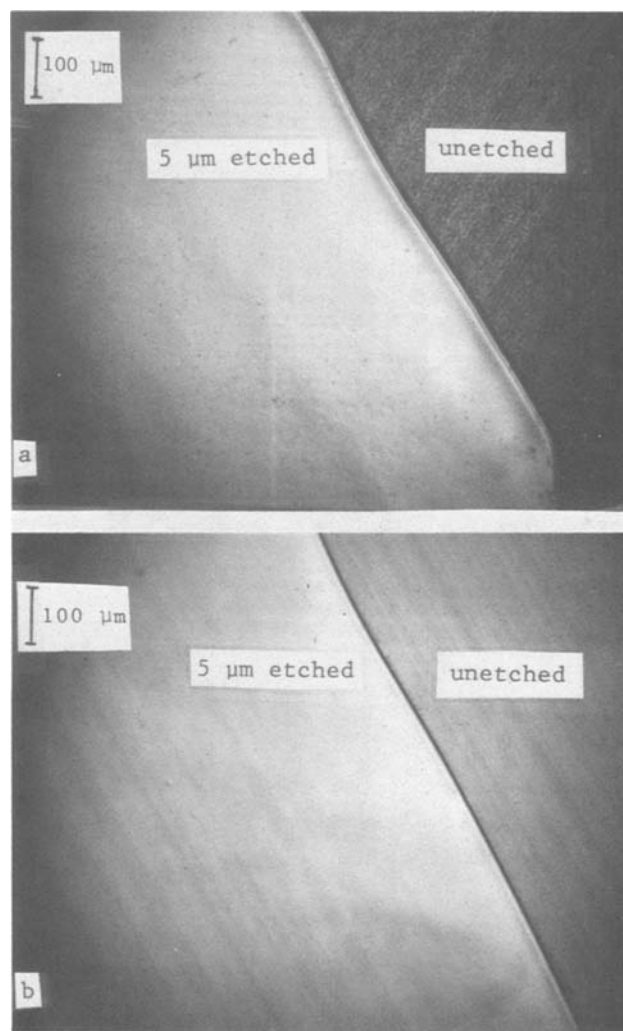


Fig. 4. a, b: Nomarski phase contrast of boundaries between the unetched and 5 micron etched (111)A surfaces shown in Fig. 3a and b. In Fig. 4a extensive surface pitting is revealed by the dark contrast areas on the as-milled unetched surface. In Fig. 4b the parallel regions of slightly varying contrast reveal very small differences in the surface topology due to the finite diamond edge radius and very small imperfections in the diamond edge.

sec, while an adjacent surface which had 5 microns removed by etching showed a half-width of 150 sec.

The (100) surfaces were examined using (400) reflections with a 2θ angle of 56.8 degrees. Half-widths of 100 and 110 sec were obtained on the etched and unetched surfaces, respectively.

The relation between the x-ray line width $\Delta\theta$ and a uniform depth-wise strain distribution $\Delta d/d$ is

$$\frac{\Delta d}{d} = \text{Cot } \theta \Delta\theta$$

From the values of $\Delta d/d$ obtained on the unetched surfaces it appeared that the strains in the (111)A and (100) surfaces were comparable, and much less than on the (110) surface. In addition the (110) surfaces showed a significant number of gouged pits left behind after diamond milling compared to almost none on the (111)A and (100) surfaces.

The half-width data on unetched and 5 micron etched surfaces suggest that most of the polishing damage was confined to within 5 microns of the surfaces. A more quantitative estimate of the upper limit to the damage depths on the unetched (111)A and (100) surfaces was then made by determining the depths x from within which most of the reflected x-rays were diffracted the same fraction, G_x . From Cullity (2)

$$G_x = 1 - \exp - (2\mu x / \sin \theta)$$

where $\mu = 1540 \text{ cm}^{-1}$ was also determined from (2), and θ is the angle of incidence. For the (111)A surface 95% of the diffracted energy came from within 2 microns of the surface, compared to 5 microns for the (100) surface. From these estimates we infer that the smallest damage depth was obtained on the (111)A surface.

To fulfill demands for polished CdTe substrates for LPE $\text{Hg}_{1-x}\text{Cd}_x\text{Te}$ crystal growth with preferred (111)A surfaces, only these surfaces were subsequently routinely polished. Figure 5 shows the mirror smooth quality of a reflection of an infrared CCD photomask from a $5 \times 4 \text{ cm}^2$ diamond polished CdTe substrate. Figures 6a and b show the flatness of a large area 1 mm thick unsupported substrate. The straightness of the fringe pattern is believed to be limited not by the technique, but only by the thinness of the substrate and possibly the intrinsic strain anisotropy of the A and B surfaces.

In summary, a technique of polishing CdTe with a single diamond edge has been described which involves the cleaving off of thin surface layers when the shearing forces produced by the diamond edge are directed along select crystallographic directions. Very smooth mirrorlike surfaces have been obtained with low work damage and no chemical contamination beyond surface interaction with the ambient atmosphere. The technique should be applicable to other semiconductors which have the same crystal structure and are not too hard.

Acknowledgment

The author is indebted to D. Brown, W. Gordon, R. Traflet, and A. Maccullum for assistance in the mechanical engineering, A. Benson, J. Coblert, and L. Newell for their skillful assistance in diamond polishing, and E. Warekois of Mann Labs, Cambridge, Massachusetts for his x-ray analysis. This work was supported, in part, by the Air Force Materials Laboratory under Contract No. F33615-78-C-5156, Wright-Patterson AFB, Ohio 45433.

Manuscript submitted Aug. 4, 1980; revised manuscript received June 15, 1981.

Any discussion of this paper will appear in a Discussion Section to be published in the June 1982 JOURNAL.

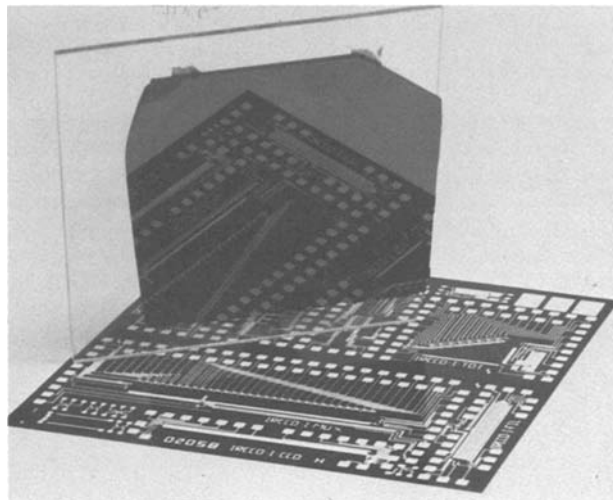


Fig. 5. Reflection of an infrared CCD photomask from a diamond polished (111)A CdTe surface.

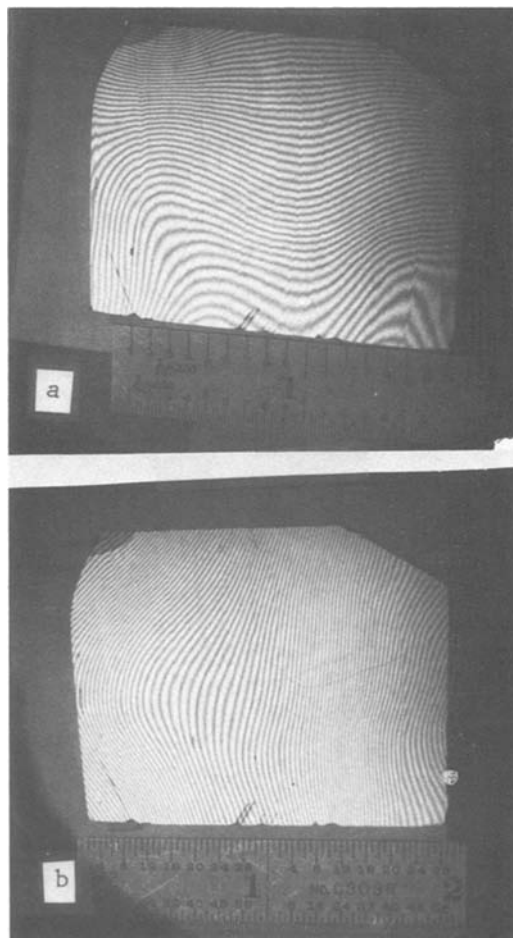


Fig. 6. a, b: Interferograms of a large area 1 mm thick unsupported CdTe (111)A slice under an optical flat.

All discussions for the June 1982 Discussion Section should be submitted by Feb. 1, 1982.

Publication costs of this article were assisted by Honeywell Incorporated.

REFERENCES

1. J. A. Mroczkowski and H. R. Vydyanath, *This Journal*, **128**, 655 (1981).
2. R. D. Cullity, "Element of X-Ray Diffraction," pp. 270, 467, Addison-Wesley Company, Inc., Reading, MA (1956).

DISCUSSION SECTION



This Discussion Section includes discussion of papers appearing in the *Journal of The Electrochemical Society*, Vol. 128, No. 1, 3, and 6, January, March, and June 1981.

Resolution Limits of PMMA Resist for Exposure with 50 kV Electrons

A. N. Broers (pp. 166-170, Vol. 128, No. 1)

G. Langner and W. Stickel:¹ In this paper, Dr. Broers compares light optical and electron beam lithography on the basis of the conventional image contrast defined by

$$C_{pp} = \frac{I_{max} - I_{min}}{I_{max} + I_{min}} \quad [1]$$

I denotes the intensity, C_{pp} indicates peak-to-peak contrast. This definition applies to continuous tone images with a linear transfer characteristic and is commonly used in the analysis of photographic and TV images. In lithography it is important that the boundaries between the areas of undissolved resist and dissolved resist are positioned with a minimum error and show steep walls (even undercut for lift-off process). This requires the exposure of patterns with a steep lateral intensity gradient. A contrast definition of merit in lithography should take into account the edge slope of the exposing spot profile. A suitable definition is the "edge contrast C_E " given by

$$C_E = \frac{2}{\pi} \tan^{-1} \frac{W}{E} C_{pp} \quad [2]$$

C_{pp} is defined by Eq. [1]. Both definitions are depicted in Fig. 1. Broers stated that E-beam lithography is superior to light-optical lithography on grounds of the contrast C_{pp} for linewidth below 0.8 μm . It can be shown² that the edge contrast of an E-beam lithography system as compared to a light optical system is higher already for linewidths below 1.4 μm for the system chosen by Broers.

A. N. Broers:³ I agree with the point made by G. Langner and W. Stickel and believe it is an important point. I also discussed the difference in edge contrast for electron beam and optical exposure qualitatively

¹ IBM Corporation, East Fishkill Facility, Hopewell Junction, New York 12533.

² G. Langer and W. Stickel, *Optik*, To be published.

³ IBM Corporation, East Fishkill Facility, Hopewell Junction, New York 12533.

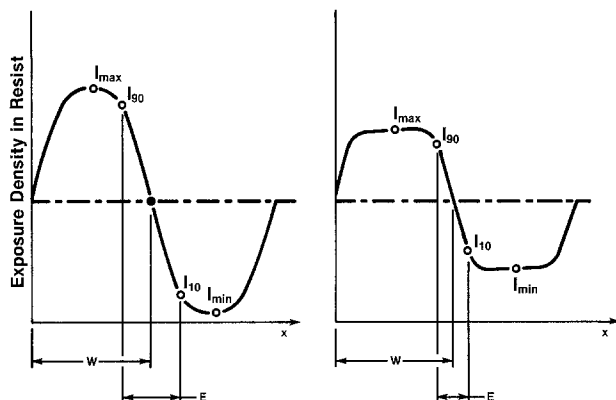


Fig. 1. Typical exposure density profiles and quantities used in the contrast definitions.

when referring to Fig. 1. Langner and Stickel's C_E is a good measure of edge contrast and this is more important in determining the definition of resist patterns than the line/space contrast C_{pp} . In their comparison of optical and electron beam exposure, however, they have assumed that the optical system is incoherently illuminated. In practice partial coherence is usually employed because it improves contrast, particularly edge contrast.⁴ Their conclusion about the turnover point between optics and electron beam may, therefore, be pessimistic with respect to optics.

Transmission Electron Observations of the Early Stage of Epitaxial Growth of Silicon on Sapphire

S. Hamar-Thibault and J. Trilhe (pp. 581-585, Vol. 128, No. 3)

H. F. Mataré:⁵ The authors have carried out a thorough structural analysis of the first stages of nucleation of SOS-films. It is important that partially coherent growth has been proven in contradiction to the theory of complete elastic adaptation, i.e., coherent layer growth.

It is also important that here an apparent discrepancy is resolved, when the authors state: (i) "The distortion of the silicon lattice decreases with growing time" (page 581) and (ii) "There is a progressive increase in the misfit between silicon- and sapphire lattices with increasing deposit time" (page 583).

As is well known, silicon films on sapphire improve in perfection (mobility, lifetime) as they become thicker. Beyond a μm , the interface dislocations and the influence of the interface charge states are much decreased. Distortion decreases away from the interface. However, the lattice parameters are closer near the interface. Here the silicon islands elastically adapt to the sapphire lattice, resulting in the stresses calculated at some 10^{10} dynes/cm². Similar values have been derived from the difference in expansion-coefficients.⁶

Also, the influence on the bandgap was indicated.⁶ The regular appearance of the silicon nuclei in the initial growth stages⁷ cannot hide the fact that the interface lattice misfit requires a certain number of atomic layers to relieve the strain and grow out from the highly defect (Al-doped) mating plane (as shown by TEM; see, e.g., footnote 6, page 253) into a useful layer. An interface state density of some 10^{11} cm⁻² and a dislocation density in this range⁸ requires at least 1000 lattice parameters for a decrease by a factor of 1000, i.e., to get into the range of 10^8 cm⁻².

It is conceivable that laser annealing⁹ will reorder the SOS lattice but also redistribute the aluminum across the entire layer. The interface state density of 10^{11} e/cm² was confirmed recently on SOS layers.¹⁰

It appears that SOS is useful for fast recovery and radiation resistant devices (thicker layers) and less for

⁴ M. C. King, "Principles of Optical Lithography," Chapter in VLSI Electronics Microstructure Science, Vol. 1 & 2, Einsbruch, Editor, Academic Press, New York (1981).

⁵ Los Angeles, California 90049.

⁶ H. F. Mataré, "Defect Electronics in Semiconductors," p. 481, Wiley-Interscience, New York (1971).

⁷ "Heteroepitaxial Semiconductors for Electronic Devices," G. W. Cullen and C. C. Wang, Editors, p. 40, Springer, New York (1978).

⁸ Only 1% difference in lattice constants required. See footnote 6, p. 476 and H. F. Mataré, "Light Emitting Devices," Part I in "Advances in Electronics & Electron Physics," Vol. 42, Academic Press, New York (1976).

⁹ G. A. Sai-Halasz et al., *Appl. Phys. Lett.*, 36, 15 (1980).

¹⁰ P. Krusius et al., *ibid.*, 38, 1 (1981).

submicron, vertical structures (see footnote 7, p. 93) and that seeded, lateral epitaxy may solve the problems of thin monocrystals.¹¹

An Improved Model for Analyzing Hole Mobility and Resistivity in p-Type Silicon Doped with Boron, Gallium, and Indium

L. C. Linares and S. S. Li (pp. 601-608, Vol. 128, No. 3)

F. L. Madarasz,¹² J. E. Lang,¹³ and F. Szmulowicz:¹⁴ In reading the paper by Linares and Li (LL) we have found several errors and misapplications of existing theories for mobility calculations in semiconductors.

Firstly, LL state they use the Barber¹⁵ temperature dependent density of states (TDDOS) effective mass. The inadequacies of the Barber mass model are well known.^{16,17} The model ignores the strong nonparabolicity of the heavy hole band in the <110> directions, and grossly oversimplifies the light hole band's nonparabolicity by a piecing together of two parabolic bands, which results in a discontinuous band.

As a consequence of using the Barber mass the carrier concentration is underestimated, especially the contribution from the heavy hole band. The net result is that any determination of the conductivity mobility from resistivity measurements and a carrier concentration obtained through the use of the Barber model will be overestimated. We therefore feel that any agreement between experimental and theoretical values of mobility, in Fig. 1 of the LL paper, is somewhat fortuitous.

Secondly, we want to show that given the strong nonparabolicity and anisotropy of the valence bands in silicon it is not possible to write the conductivity mobility, μ_i , for the *i*th band in terms of an energy averaged relaxation time $\langle\tau_i\rangle$ as LL did in their Eq. [1] which is

$$\mu_i = \frac{e\langle\tau_i\rangle}{m_{ci}^*} \quad [1]$$

Here *e* is the electronic charge and $\langle\tau_i\rangle$ takes the form

$$\langle\tau_i\rangle = \frac{\int E^{3/2} \tau_i \partial f_0 / \partial E dE}{\int E^{3/2} \partial f_0 / \partial E dE} \quad [2]$$

where f_0 is the equilibrium Fermi-Dirac distribution function. m_{ci}^* is the conductivity effective mass which is canonically defined by the equation for the conductivity

$$\sigma = \frac{pe^2}{m_c^*} \langle\tau\rangle \quad [3]$$

where *p* is the carrier concentration.

It is implicit in the definition of m_{ci}^* , Eq. [3], that τ must be isotropic and at most energy dependent, i.e., $\tau = \tau(E)$. However, because of the nonspherical-nonparabolic nature of the light hole band (LL treat the heavy hole and split-off bands as parabolic) any intra- or interband transition including that band will yield a transition rate which depends on the magnitudes as well as the directions of the incident and scattered wave vectors of the charge carriers with respect to the axes of the Brillouin zone.^{18,19} This re-

sults in an anisotropic relaxation rate which depends on the magnitude and direction of the incident wave vector, precluding the use of Eq. [3] to define m_{ci}^* for the light hole band, and the use of Eq. [1.]

Even if an isotropic relaxation time could be justified, an energy averaged relaxation time as given by Eq. [2] will not arise in the conductivity mobility if the band structure is nonspherical-nonparabolic. This conclusion follows from the fact that in the general Kane band model the relationship between wave vector \vec{k} and the band energy is given by

$$k^2 = \frac{2m_0}{\hbar^2} \gamma(E, \hat{k}) \quad [4]$$

where m_0 is the rest mass of an electron and \hbar is Planck's constant divided by 2π . The factor, $\gamma(E, \hat{k})$, is a complicated function of energy and direction in \mathbf{k} -space which, in general, is not separable into *E* and \hat{k} dependences. With Eq. [4], and the basic integral definitions of conductivity and carrier concentration (for cubic symmetry and in the nondegenerate limit), it can be shown that

$$\sigma = \frac{pe^2}{(2m_0)^2} \frac{\int_{E, \Omega} \left(\frac{\partial \Gamma(k, \hat{k})}{\partial k} \right)^2 f_0 \tau \gamma^{1/2}(E, \hat{k}) \frac{\partial \gamma(E, \hat{k})}{\partial E} dE d\Omega}{\int_{E, \Omega} \gamma^{1/2}(E, \hat{k}) \frac{\partial \gamma(E, \hat{k})}{\partial E} E f_0 dE d\Omega} \quad [5a]$$

$$\equiv \mu_c pe \quad [5b]$$

Here, Ω is a solid angle in \mathbf{k} -space and Γ is a result of the inversion of Eq. [4], i.e.

$$E = \frac{\hbar^2}{2m_0} \Gamma(k, \hat{k}) \quad [6]$$

For the general case of a nonspherical-nonparabolic band, the general case and angular dependences are not separable in the integrands of Eq. [5a]. The implication is that an energy averaged relaxation time, as that in Eq. [2], cannot be factored in Eq. [5a] and thus a conductivity effective mass as defined by Eq. [3] cannot be obtained. We therefore question LL's calculation of the conductivity effective mass for their light-hole band.

Thirdly, consider the expression given by Eq. [3] of the LL paper

$$\tau_i = \frac{1}{\delta} \left(1 + \frac{m_{Di}^*}{m_{Dj}^*} \frac{\tau_{jj}}{\tau_{ij}} \right) \tau_{ii} \quad [7]$$

where

$$\delta = 1 - \frac{\tau_{11}\tau_{22}}{\tau_{12}\tau_{21}} \quad [8]$$

and the $m_{Dj}^*(T)$ are the TDDOS effective masses associated with the *i*th and *j*th bands. From the original work, Bir *et al.*,²⁰ an expression like Eq. [6] may be extracted, but only with the restriction of spherical-parabolic bands, where m^* is a constant. Given this restriction the masses which occur in Eq. [7] are the m^* 's obtained from the curvature of each band.

LL claim that the procedure for going from a parabolic to a nonparabolic band is to simply substitute the TDDOS effective mass for m^* , and cite Radcliffe²¹ and Barrie²² as having shown this. Quite the contrary, both Radcliffe and Barrie attempt to generalize relaxa-

¹¹ J. C. C. Fan *et al.*, *ibid.*, 38, 1 (1981).

¹² Universal Energy Systems, Dayton, Ohio 45432 (Visiting Scientist, Materials Laboratory, AFWAL/MLPO, Wright-Patterson AFB, Ohio 45433).

¹³ Department of Physics, University of Dayton, Dayton, Ohio 45469 (Visiting Scientist, Materials Laboratory, AFWAL/MLPO, Wright-Patterson AFB, Ohio 45433).

¹⁴ University of Dayton Research Institute, Dayton, Ohio 45469.

¹⁵ H. D. Barber, *Solid State Electron.*, 10, 1039 (1967).

¹⁶ F. L. Madarasz, J. Lang, and P. Hemenger, *J. Appl. Phys.*, 52, 4646 (1981).

¹⁷ H. Nakagawa and S. Zukotynski, *Can. J. Phys.*, 55, 1485 (1977).

¹⁸ F. L. Madarasz and F. Szmulowicz, *Phys. Rev. B*, 24, 4611 (1981).

¹⁹ M. Tiersten, *J. Phys. Chem. Solids*, 25, 1151 (1964).

²⁰ G. H. Bir, E. Normantas, and G. E. Pikns, *Sov. Phys. Solid State*, 4, 867 (1962).

²¹ J. R. Radcliffe, *Proc. Phys. Soc. London A*, 68, 675 (1955).

²² R. Barrie, *Proc. Phys. Soc. London B*, 69, 553 (1956).

tion rates for different inband scattering processes when going from a spherical-parabolic band, in which $E = \hbar^2 k^2 / 2m^*$, to a spherical-nonparabolic band, in which $E = f(|\vec{k}|)$. In their generalizations they showed that the substitution of $\hbar^2 k (dE/dk)^{-1}$ for m^* tended to account for variations in the temperature dependences of mobilities, which the spherical-parabolic model could not account for.

Furthermore, LL cite Braggins²³ as having successfully used the substitution of the TDDOS effective mass for m^* . In fact what Braggins writes is $1/m^*(E) = \hbar^2 k (dE/dk)^{-1}$, which is only a matter of notation. This "band effective mass" $m^*(E)$ is not directly related to the (temperature dependent) TDDOS effective mass nor is it the true DOS effective mass.^{16,17}

The substitution of $\hbar^2 k (dE/dk)^{-1}$ for m^* is not a prescription for the substitution of the TDDOS effective mass for m^* when treating nonparabolic bands. The TDDOS effective mass arises in only one place and that is in the calculation of the carrier concentration. If one starts out with a truly nonspherical-nonparabolic band structure like the valence bands of Si, and then derives a relaxation rate for the i th band from its definition

$$\frac{1}{\tau_i(\vec{k})} = - \left. \frac{\partial g_i(\vec{k})}{\partial t} \right|_{\text{coll}} \frac{1}{g_i(\vec{k})} \quad [9]$$

where $g(\vec{k})$ is the deviation from f_0 , one will at most find the rest mass, m_0 , of the charge carrier in the resulting expressions. The rest mass appears only because of normalization (see Eq. [4]). The reason the true DOS effective mass, which is energy dependent in the case of a (non)spherical-nonparabolic band, does not occur is that the collision integral includes the transition rate and $g(\vec{k})$. This means that the DOS never appears as a simple factor. And it is the DOS which is needed for the DOS effective mass.

Fourthly, although LL state at the beginning of their paper that they employ the nonspherical-nonparabolic silicon valence band structure through the use of the Barber model, later they go on to state, "The anisotropy of the energy spectrum is not considered in this model, because from the transport theory of parabolic bands it is known that anisotropy has no influence on the temperature dependence of mobility, but only on its absolute value." We agree with this conclusion for lattice limited mobility,²⁴ and would like to emphasize this point as well since Tiersten¹⁹ has shown that the use of spherical energy surfaces can lead to an error in the lattice limited mobility of ~20%.

Lastly, we focus our attention on the empirical formula γ_{hh}^a which is used to correct acoustic phonon-hole scattering for the influence of hole-hole interactions. This formula as given by LL

$$\gamma_{hh}^a = 1.0004 - 4.013373 \times 10^{-19} N_A \quad [10]$$

depends on the concentration of acceptors, N_A , rather than on the concentration of holes which in itself is quite puzzling. Furthermore, note that this formula produces a value comparable to that obtained from the theoretical expression for γ_{hh} , which they display in their Eq. [12], only at an impurity concentration of 3×10^{17} . Since data in Fig. 1 seem to cover a range greater than that for which the formula applies, some other correction must have been applied below 10^{15} and above 3×10^{17} . The form of this empirical correction is important because it helps to produce the proper shape of the curve in Fig. 1, enhancing the agreement with the data.

Not only have the authors varied τ_0 and W to fit the data, but they have also adjusted the constants in the

empirical formula to produce the proper dependence on carrier concentration shown in Fig. 1. Because the empirical formula is without physical justification, it would seem that the fit shown in Fig. 1 is artificial.

In summary, we feel the oversimplified band model used by LL coupled with the use of an energy averaged relaxation time for nonspherical-nonparabolic bands, and the improper use of Eq. [7] in the text as well as the use of the empirical formula γ_{hh}^a , will seriously affect calculations of mobilities and carrier concentrations. Only a detailed consistent calculation involving an accurate band model and a full solution of the transport equations allowing for anisotropic scattering can provide a complete picture of electronic transport in silicon.

L. C. Linares:²⁵ The primary reason for the publication of this paper was apparently misunderstood by the authors of the discussion. The main intent of this work is to present a more complete and accurate representation of mobility and resistivity in p-type silicon that would be of practical engineering utility. In presenting a work of this type, one is always faced with a choice between extremely intricate and difficult theoretical details and some reasonably simple engineering models of the very complicated physical reality. Unfortunately, what one gains in tractability, one loses in completeness and mathematical sophistication. The usual assumptions made by most workers in the analysis of mobility are: (i) an energy averaged relaxation time, (ii) isotropic mobility, and (iii) spherical parabolic valence bands. While retaining the first two assumptions, we hoped to improve agreement between theoretical calculations and experimental measurements by modeling a temperature dependent effective mass based on Barber's²⁶ work, thus approximating the nonparabolic nature of the valence bands.

Barber's model provides, via simple calculations, values of effective mass that more accurately reflect the experimentally observable variability of effective mass with changes in temperature and dopant density. The model never presumed to be the final answer to everyone's questions concerning the band structure of silicon; however, within its limitations, it accomplishes its intended purpose, to improve the accuracy of mobility calculations by approximating the temperature dependence of the effective mass. It is curious that the authors of the discussion cite the work of Nakagawa and Zukotynski²⁷ as expressing the inadequacies of the Barber model, when Nakagawa and Zukotynski never even mention Barber or his work.

In mobility calculations, most authors have limited their analyses to only scattering by acoustical phonons, or optical phonons, or ionized impurities, or neutral impurities, or combinations of these. Our paper attempts to present a more complete picture by considering all of the above mechanisms as well as interband and hole-hole scattering. The use of a temperature dependent effective mass contributes significantly to the improvement between theoretical calculations and experimental values; but equally important is the more complete treatment of the scattering which includes corrections for hole-hole scattering. The empirical formula used to correct acoustic phonon-hole scattering for the influence of hole-hole interactions resulted from an attempt to neither underestimate nor overestimate the effect. The justifications and rationale behind this empirical expression are well stated in a previous work.²⁸ This empirical formula, derived in footnote 28, has been used in its original form both in our paper and by Thurber *et al.*,²⁹ where excellent agree-

²⁵ Department of the Air Force, USAF Academy, Colorado 80840.

²⁶ H. D. Barber, *Solid State Electron.*, **10**, 1039 (1967).

²⁷ H. Nakagawa and S. Zukotynski, *Can. J. Phys.*, **55**, 1485 (1977).

²⁸ S. S. Li, *Solid State Electron.*, **21**, 1109 (1978).

²⁹ W. R. Thurber, R. L. Mathis, and Y. M. Liu, *Nat. Bur. Stand. Spec. Publ.*, **400-36** (1978).

²³ T. T. Braggins, Thesis, Syracuse University (1975).

²⁴ P. Lawaetz, *Phys. Status Solidi*, **11**, K117 (1965).

ment was reported between theoretical calculations and experimental determinations of mobility in p-type silicon. The constants were not adjusted to fit our particular situation. On the other hand, the adjustment of the acoustic and optical deformation potential constants via τ_0 and W , respectively, has always been a perfectly acceptable procedure. Until a complete theoretical treatment of the true nature of the valence bands is undertaken, no one will know the true value of these constants.

In conclusion, we stress that, although limited by the simple model of the band structure, this work is of significant practical value as a reasonable engineering study of mobility and resistivity in p-type silicon. We agree that it will take a detailed, consistent calculation involving an exact band model and a full solution of the transport equations allowing for isotropic scattering, to provide a complete picture of electronic transport in silicon. We hope that our work will encourage others to develop such a picture and satisfy everyone's needs.

The Quenching of $Y_2O_3:Eu$ Luminescence by Cerium

M. J. Fuller (pp. 1381-1383, Vol. 128, No. 6)

G. Blasse:³⁰ Fuller has nicely shown that the presence of cerium in $Y_2O_3:Eu$ quenches the Eu^{3+} luminescence, because the absorption of the Ce^{4+} ion competes successfully with the charge-transfer absorption of the Eu^{3+} ion.

The cerium-codoped samples fired in air show an absorption band at $<230-300$ nm just extending into the visible. This was ascribed to Ce^{4+} . In view of the pale-yellow color of CeO_2 ³¹ this seems to be correct. It is well known that this is a charge-transfer transition.³² Reduced samples showed an absorption band in the visible region which was ascribed to Ce^{3+} (4f-5d transition). This assignment seems to be unlikely, because (i) Ce_2O_3 is white,³¹ (ii) the 4f-5d transitions of the Ce^{3+} ion in oxides are usually situated in the ultraviolet.³³

³⁰ Rijksuniversiteit Utrecht, Fysisch Laboratorium, 3508 Utrecht, The Netherlands.

³¹ L. Eyring, "Handbook on the Physics and Chemistry of Rare Earths," Chap. 27, Gschneidner and Eyring, Editors, North Holland Publ. Co., New York (1979).

³² H. E. Hoefdraad, *J. Inorg. Nucl. Chem.*, **37**, 1917 (1975).

³³ G. Blasse and A. Brill, *J. Chem. Phys.* **47**, 5139 (1967).

If the visible absorption band is neither due to Ce^{3+} nor to Ce^{4+} , the only alternative is a $Ce^{3+}-Ce^{4+}$ intervalence charge-transfer transition. This would imply that the cerium ions occupy nearest neighbor lattice sites. Compositions in between CeO_2 and Ce_2O_3 are strongly colored due to transitions of this type.³¹

Fuller proposes that three substitutional Ce^{4+} ions introduce one cation vacancy. It seems more probable that two substitutional Ce^{4+} ions introduce one interstitial oxygen ion, because Y_2O_3 has a fluorite lattice with ordered anion vacancies. The latter will be filled up if tetravalent ions are introduced. If these defects form an associate $(2Ce_Y \cdot O_i)_x$ or even clusters (like in the fluorite lattice),³⁴ we have the possibility of $Ce^{3+}-Ce^{4+}$ neighbors in the reduced samples. These may also be responsible for the photochromic properties. This alternative assignment seems to be worthwhile to investigate further using spectroscopical and electrical techniques.

M. J. Fuller:³⁵ Blasse's suggestion that the visible absorption of the thermally reduced $Y_2O_3:Ce$ samples is due to $Ce^{3+}-Ce^{4+}$ intervalence charge transfer is an interesting alternative to my assignment of it to 4f-5d transitions in Ce^{3+} . While the breadth of the absorption band certainly more resembles that for a charge transfer state than for 4f-5d transitions, I dismissed the former alternative on the basis that random cerium substitution at low concentrations would not produce the required nearest neighbor lattice sites. Although, as Blasse mentions, the 4f-5d transitions of Ce^{3+} in Y_2O_3 should be expected to lie in the ultraviolet range, there are examples of oxidic host lattices, and notably $Y_3Al_5O_{12}$ in which the 4f-5d absorptions of Ce^{3+} extend significantly into the visible region (i.e., to ≥ 500 nm).

However, if Blasse's suggestion that Ce^{4+} substitution is not random but occurs as associates is correct, then the possibility of intervalence charge transfer absorption becomes much more likely. In view of this, I agree that further investigations would be worthwhile in an attempt to resolve this matter.

³⁴ See, e.g., K. E. D. Wapenaar and J. Schoonman, *This Journal*, **126**, 667 (1979).

³⁵ Thorn Lighting Limited, Enfield, Middlesex, England EN1 1UL.



A Technique for Profiling a Laser Beam and Its Application to the Recrystallization of Polysilicon Films

B. P. Von Herzen, T. I. Kamins,* and C. I. Drowley**

Hewlett-Packard Laboratories, Palo Alto, California 94304

Abstract: A rapid method of obtaining the intensity distribution of a cw laser beam used for the recrystallization of polysilicon has been demonstrated. Correlation of the structure of the recrystallized polysilicon with the spatial distribution of the laser light shows the importance of controlling the mode structure and, consequently, the intensity distribution of the laser beam.

Introduction: Melting and recrystallization of a fine-grain polysilicon film with a cw laser has been shown to improve its electrical properties so that MOSFETs can be fabricated with their active channels in the resulting layer of large-grain, recrystallized material (1,2). The structure of the polysilicon has been shown to depend on the local temperature and the temperature gradients during recrystallization (3). In particular, the entire thickness of the polysilicon must be melted to obtain the large-grain structure necessary for device fabrication (4). More complex applications, such as "lateral seeded annealing" (5,6), will depend more critically on the detailed power distribution in the laser beam.

In this note we will describe a method of mapping the intensity of the laser beam as a function of position and relate this distribution to the structure of the recrystallized polysilicon. The technique employs a photodiode to measure the light distribution at the position of the wafer surface which is to be recrystallized so that the effect of the optical elements in the light path, as well as the laser itself, can be considered.

Experimental Apparatus: The technique has been used with a Coherent Model 5000 laser annealing system, which includes an 18 W cw argon ion laser. In this system, the laser beam is scanned across the wafer surface by galvano-

meter-controlled mirrors. A variable-focus flat-field lens causes the light to strike the wafer surface at normal incidence for all positions on the wafer surface.

To measure the beam profile, a photodiode is inserted into the annealer in place of the wafer to be processed. The photodiode is attached to a silicon wafer for ease of handling in the system, and this assembly is held by the vacuum chuck which normally holds the wafer to be processed. A 2 μ m diameter pinhole is mounted in front of the photodiode to improve the spatial resolution. A filter is placed in the optical path to attenuate the laser beam by a factor of approximately 10,000 so that the photodiode is not damaged by the laser. The distance from the surface of the backing wafer to the pinhole is accurately known so that the optical system can be offset to measure the intensity distribution at the desired focal position.

A Hewlett-Packard 9845 desktop computer system is used to control the process (Fig. 1). A signal from the HP9845 is sent along an HP

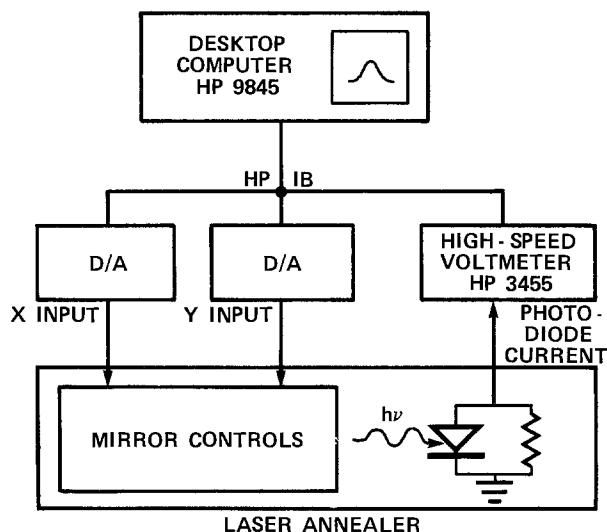


Fig. 1. Block Diagram of Profiling Apparatus

* Electrochemical Society Active Member

** Electrochemical Society Student Member

Keywords: Polycrystalline silicon, laser recrystallization, lasers

interface bus (HP-IB) to control two A/D converters, which provide the signals to raster the galvanometer-controlled, beam-deflection mirrors across the pinhole. The beam is typically moved in $5\mu\text{m}$ steps at a rate of 20 Hz. With these typical parameters, the spatial resolution is approximately $7\mu\text{m}$. The photodiode output current is sampled typically 10 ms after the mirrors are moved, which allows for their 1-10 ms settling time. Only a small voltage of about 50 mV appears across the 100 ohm load resistor in parallel with the photodiode. Thus, the photodiode operates essentially in the short-circuit mode, and the output varies nearly linearly with light intensity. The signal from the photodiode is sampled by an HP3455 voltmeter, and the digital output is sent over the HP-IB to the HP9845, which correlates the beam intensity with position and stores and displays the data.

The data may be displayed in a quasi-three-dimensional format or in two dimensions, with the intensity of the shading representing the intensity of the beam. A representative profile is shown in Fig. 2 in both formats. In this case it is seen that the beam is not Gaussian but shows a combination of modes. The mode structure can be changed by varying the input power to the laser or the elements of the optical system and is more Gaussian at lower input powers.

As an alternate beam-profiling technique, the pinhole can be omitted, and the signal observed as the laser moves across the edge of the photodiode can be differentiated to obtain the beam profile. This alternate technique, however, relies on numerical differentiation of experimental data and tends, therefore, to be noisy. Since smoothing of the data leads to loss of resolution, we prefer the first technique described.

Correlation With Structure of Polysilicon: The shape of the beam has been correlated with the structure of the recrystallized polysilicon. In these experiments a $0.55\mu\text{m}$ thick film of conventional LPCVD polysilicon was deposited at 625°C onto a $1.4\mu\text{m}$ thick layer of thermally grown silicon dioxide on a 3-inch diameter, (100)-oriented silicon wafer. The polysilicon was capped with a layer of LPCVD silicon nitride approximately 6 nm thick to prevent agglomeration of the polysilicon while it was molten (7). The substrate was heated to 500°C during recrystallization, and the laser was scanned across the wafer with a velocity of 25 cm/sec using the internal driving electronics in the annealer.

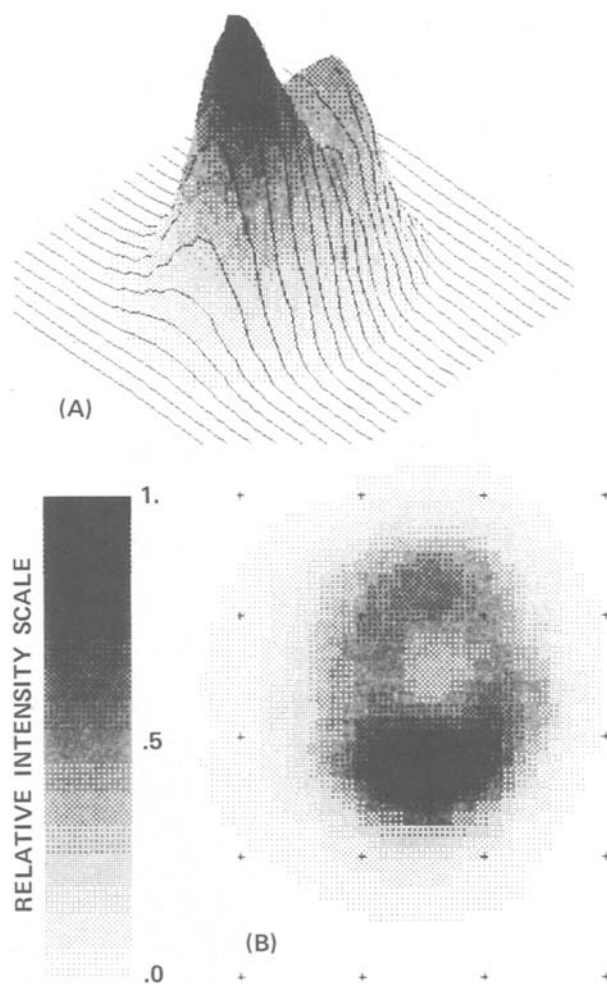


Fig. 2. Laser beam profile: (a) Three-dimensional plot. (b) Two-dimensional plot with darker shading indicating the more-intense portions of the beam.

The width of the recrystallized region varies with laser power, increasing rapidly after the onset of melting, then varying slowly with further increases in laser power. The structure of the polysilicon depends on the distribution of the power in the laser beam. If enough energy is deposited into a region to melt the entire thickness of the polysilicon film, it recrystallizes into a large-grain structure with a relatively smooth surface. If only a portion of the thickness melts, the solidifying material is seeded by the underlying fine-grain polysilicon which did not melt, and a large-grain structure is not obtained.

The grain structure is, therefore, related to the power distribution within the laser beam. A rapid decrease in intensity with

position at the top and bottom edges of the melted region provides an abrupt transition between large-grain polysilicon and unmelted material. A gradual decrease in the intensity results in a wide region which melts only through a portion of its thickness, with the resulting intermediate grain size and rough surface.

Figure 3 shows such a correlation. At the bottom of the beam only a narrow region of partial melting with its roughened surface is seen between the large-grain and unaffected polysilicon (Figs. 3b and 3c). At the top of the beam, the intensity decreases more gradually from the primary peak, with a secondary peak occurring about $90\mu\text{m}$ away from the main peak. The transition between unaffected and large-grain polysilicon is much broader on this side.

When the spacing between adjacent scans is made less than the width of the large-grain region, the gradual decrease in the intensity will cause a portion of the previously recrystallized material to be partially remelted. This remelting, in turn, can leave a roughened surface, which will be more difficult to process, although it may not be degraded crystallographically.

At higher powers with the beam profile shown, the transition from the unmelted to the large-grain region occurs in the steepest parts of the profile, resulting in narrow transitions on both sides.

Summary: We have shown a relatively straightforward method of measuring the intensity distribution of the laser beam used to recrystallize polysilicon. Observation of the structure in the recrystallized material shows the importance of controlling the intensity distribution in the laser beam and, consequently, the modes present. Control is expected to become critical for more sophisticated applications, such as seeded recrystallization.

Acknowledgement: The authors would like to thank Drs. D. Ilic and F. Schwettmann for their encouragement during this investigation.

References:

1. K.F. Lee, J.F. Gibbons, K.C. Saraswat, and T.I. Kamins, *Appl. Phys. Lett.* **35**, 173 (1979).
2. T.I. Kamins, K.F. Lee, J.F. Gibbons, and K.C. Saraswat, *IEEE Trans. Electron Devices* **ED-27**, 290 (1980).
3. D.K. Biegelsen, N.M. Johnson, D.J. Bartelink, and J.D. Moyer, *Appl. Phys. Lett.* **38**, 150

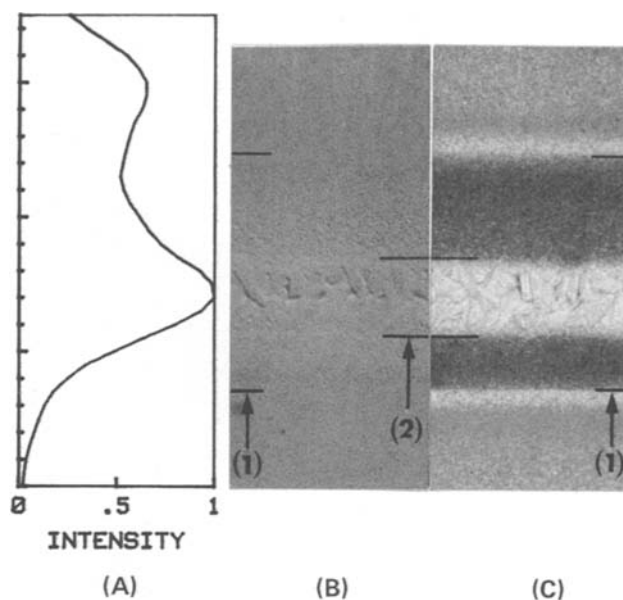


Fig. 3.

Effect of laser intensity distribution: (a) Peak intensity normal to the scanning direction; each mark on the vertical scale represents $10\mu\text{m}$. (b) Structure of polysilicon after laser recrystallization (Nomarski phase contrast). (c) Structure after grain-boundary delineation by Sirtl etching: (1) Melted width; (2) large-grain region.

- (1981).
4. A. Gat, L. Gerzberg, J.F. Gibbons, T.J. Magee, J. Peng, and J.D. Hong, *Appl. Phys. Lett.* **33**, 775 (1978).
5. J. Sakurai, S. Kawamura, H. Mori, and M. Nakano, *Japan. J. Appl. Phys.* **20**, L176 (1981).
6. T.I. Kamins, T.R. Cass, C.J. Dell'Oca, K.F. Lee, R.F.W. Pease, and J.F. Gibbons, *J. Electrochem. Soc.* **128**, 1151 (1981).
7. T.I. Kamins, *J. Electrochem. Soc.* **128**, 1824 (1981).

Manuscript received Sept. 24, 1981.

Publication costs of this article were assisted by Hewlett-Packard Laboratories.

A Semipermeable Anode for Silicon Electrorefining

J. M. Olson and K. L. Carleton

Solar Energy Research Institute, Golden, Colorado 80401

The development of inexpensive silicon solar cells depends critically on the availability of a low cost, high purity silicon. Electrochemical methods offer the potential for producing (1,2) and purifying (3) silicon but these processes usually produce material with a low space-time yield (4) and limited purity. We have recently developed a semipermeable anode that enhances the effectiveness of the silicon electrorefining process and permits the low temperature fabrication of "silicon" anode plates, a prerequisite for the operation of an efficient, multiplate electrorefining process. The anode is solidified from a hypereutectic solution of copper and metallurgical grade silicon (mgSi) to form a two-phase system consisting of a primary silicon phase embedded in a Cu_3Si matrix. At the temperature of operation (750°C), the interdiffusion of Cu and Si in the Cu_3Si phase is fast (5), $D=2.5 \times 10^{-5}\text{cm s}^{-1}$. Hence, this silicide phase can be used under certain conditions as a filter for purifying silicon. When combined with an electrorefining process, this filtering action ostensibly improves the

purity of the electrodeposited silicon as compared to previous work (3) by about two orders of magnitude.

A schematic of the electrorefinement setup is shown in Figure 1. The melt composition is similar to that used in previous work (2), however, the K_2SiF_6 is synthesized in situ by reactively dissolving $\text{SiF}_4(\text{g})$ in a KF rich melt. The electrolyte is purified by a pre-electrolysis step using a reverse bias of 2.0 volts. The cathode is typically a high density, high purity graphite. The silicon-copper anode (30 w/o mgSi) is fused and solidified in situ with the electrolyte serving as a flux.

In Table I, we compare the chemical purity (as measured by spark source mass spectrometry) of the starting material (mgSi in Cu/Si anode) with the purity of the refined, electrodeposited silicon.

From an electrorefining viewpoint, those elements which have an electronegativity

Argon Flow

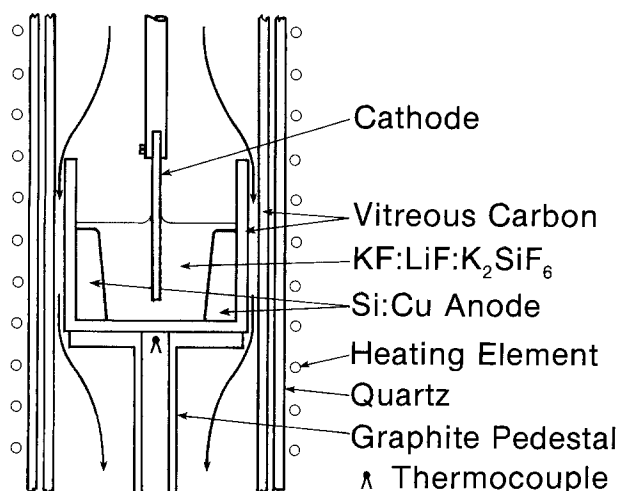


Figure 1. Schematic of electrorefinement cell

*Electrochemical Society Active Member

Keywords: Silicon, semipermeable anode, electro-refining, electrodeposition

TABLE I. Typical metal impurity concentration in the mgSi used to form the anode and in the refined, electrodeposited silicon.

| Metal Impurity | mgSi (ppma) | Refined Si (ppma) |
|----------------|-------------|-------------------|
| Al | 3400.0 | 1.0 |
| B | 17.0 | 0.7 |
| Ba | 9.4 | <0.02 |
| Ca | 290.0 | <0.07 |
| Cu | ---- | 0.2 |
| Cr | 40.0 | <0.2 |
| Fe | >2500.0 | 0.1 |
| Mg | 85.0 | 0.9 |
| Mn | 550.0 | 0.03 |
| Mo | 1.4 | <0.03 |
| Ni | 39.0 | <0.1 |
| P | 14.5 | 3 |
| S | 7.0 | 0.4 |
| Ti | 290.0 | <0.1 |
| V | 250.0 | <0.05 |
| Zr | 13.0 | <0.03 |

greater than that of silicon will remain at the anode (e.g., Cu, B, P, etc). Elements with an electronegativity less than that of Si (e.g., Al, Cr, Ti, V, and Zr) normally would not be segregated in a closed, steady state electrorefining process. From Table I, we find, however, that with the Si:Cu₃Si anode, these impurities are efficiently segregated. The most probable mechanism responsible for this result is the diffusional trapping of these metals in the bulk of the anode. While the interdiffusion coefficient in Cu₃Si is fast, it is expected that other metallic impurities will have typical solid state diffusion coefficients in the Cu₃Si matrix. To be transferred to the cathode, these impurities must be present at the surface of the anode. After the surface has been depleted, the electrotransport of the impurities to the cathode will be limited by diffusion in the bulk of the anode, essentially trapping these impurities.

The final copper concentration illustrates the effectiveness of the electrochemical segregation mechanism for elements with an electronegativity less than that of silicon. The data for copper strongly suggests that the final concentrations of B and P are not intrinsic but may be an artifact of postdeposition contamination and, as such, are subject to further improvement. Efforts to reduce this contamination are in progress.

The interdiffusion coefficient of copper and silicon in Cu₃Si is a function of the intrinsic diffusion coefficients for the species D_{Si} and D_{Cu}. The ratio D_{Cu}/D_{Si} is unknown at this time. From marker experiments, Veer et al (5) claim that Cu is the diffusing species in Cu₃Si (i.e. D_{Cu}/D_{Si} >> 1), but they did not consider the complicating effects of interface drag on the motion of the marker (6). Our preliminary experiments (7) indicate that Cu diffusion may dominate but that the diffusion of silicon is also significant.

Electrocrystallization of coherent, stable films of silicon is a natural result of the electrorefining process if the current density is less than a critical value. This critical current density is strongly affected by electrolyte composition, temperature, and hydrodynamic conditions in the melt. Current densities in excess of 100mA/cm² have yielded dense, coherent, thick films on graphite substrates. For i = 20-30mA/cm², grain sizes of 200μm are typical. Deposits on vitreous carbon have similar characteristics.

Electrical characteristics of the refined polycrystalline silicon have been measured. The conductivity type is generally n-type. The resistivity is 0.3-0.7 ohm-cm. The Hall mobility is 90-110 cm²/Vs with a carrier concentration of ~4x10¹⁷ cm⁻³. The minority carrier lifetime as measured by the V_{OC} decay technique is 10-20μs. The interpretation of these data relative to previous work is the subject of another paper (7). In general, however, this material has a higher minority carrier diffusion length and lifetime than similar polycrystalline silicon produced by other techniques (8).

In summary, polycrystalline silicon can be electrodeposited from metallurgical grade silicon in a molten salt system. The use of a Si:Cu₃Si semipermeable anode as the silicon source enhances the purification process and facilitates the fabrication of anode plates.

REFERENCES

1. G.M. Rao, D. Elwell, and R.S. Feigelson, *This Journal*, 127, 1940 (1980).
2. J.M. Olson in "Photovoltaics Research Branch Semiannual Report", A. Zunger, Editor, Solar Energy Research Institute, Document No. SERI/PR-611-737, July 1980.
3. R. Monnier and J.C. Giacometti, *Helv. Chem. Acta*, 47, 345 (1964).
4. D. Inman and S.H. White, *J. Appl. Electrochem.* 8, 375 (1978).
5. F.A. Veer, B.H. Kolster, and W.G. Burgers, *Trans. Metall. Soc. AIME*, 242, 669 (1968).
6. K.N. Tu and J.W. Mayer, in *Thin Films - Interdiffusion and Reactions*, edited by J.M. Poate, K.N. Tu, and J.W. Mayer, p. 382, Wiley Interscience, New York (1978).
7. J.M. Olson and K. Carleton, to be published.
8. Amal K. Ghosh, Charles Fishman, and Tom Feng, *J. Appl. Phys.* 51, 446 (1980).

Manuscript received Sept. 18, 1981.

Publication costs of this article were assisted by the Solar Energy Research Institute.

Moderate Temperature Na Cells

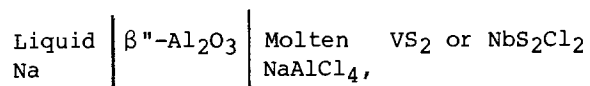
IV. VS_2 and NbS_2Cl_2 as Rechargeable Cathodes in Molten $NaAlCl_4$

K. M. Abraham,* M. W. Rupich, and L. Pitts

EIC Laboratories, Inc., Newton, Massachusetts 02158

Recent work from this laboratory has shown (1-3) that the layered transition metal dichalcogenides which intercalate Na are useful as cathodes for a rechargeable moderate temperature Na cell which operates at 130°C and utilizes 1,2-Bis(2-methoxy-ethoxy)ethane/NaI(1M) as the electrolyte. However, practical uses of those cells are limited by factors such as limited thermal stability of the organic electrolyte, relatively low rate capabilities and fractional irreversibility of the chalcogenide cathodes due to crystallographic phase changes. To circumvent these problems, we have evaluated molten $NaAlCl_4$ as an alternative electrolyte. This study has led to the discovery of novel chemical and electrochemical reactions between molten $NaAlCl_4$ and the metal sulfide cathodes, for example VS_2 . These reactions result in the *in situ* formation of novel, high energy density cathode materials showing high electrochemical reversibility. In this paper we present our preliminary results on the cycling of Na cells utilizing VS_2 or NbS_2Cl_2 as the cathode in molten $NaAlCl_4$.

VS_2 was synthesized as described previously (1). NbS_2Cl_2 was synthesized according to the procedure in ref. 4. The experimental cell, operating at 165°C, has the configuration,



Cell setup and operation have already been described (1,5). Basic $NaAlCl_4$ was prepared by melting a mixture of NaCl and $AlCl_3$, slightly rich in NaCl, at 190°C and purified by preelectrolysis between two Al electrodes. Prior to adding to the cell, the electrolyte was mixed with a slight excess of NaCl to insure its basicity.

*Electrochemical Society Active Member.

Key Words: Transition Metal Chalcogenides, Cycling.

A cell with VS_2 as the cathode exhibits an open-circuit-voltage (OCV) of 3.05V at 165°C. The first discharge of the cell to 1.8V usually yields capacities between 0.90 and 0.70 electrons/vanadium (e^-/V) at current densities between 1 and 5 mA/cm². The discharge occurs at three voltage regions - a downward sloping region between 2.8 and 2.4V, with ~8% of the capacity, another downward sloping region between 2.4 and 2.2V, with ~25% of the capacity, and a plateau at 2.2V with the remaining capacity. The mid-discharge voltage is slightly above 2.2V. The first recharge to 3.5V usually corresponds to 100% of the discharge. The recharge occurs in three major voltage regions - an upward sloping region between 1.8V and 2.2V, with ~20% of the capacity, a second upward sloping region between 2.2 and 3.1V, with ~20% of the capacity, and a plateau at 3.2V, with the remaining capacity. The discharge and recharge curves exhibit considerable hysteresis (Cycle 1 in Fig. 1). Repeated cycling of the Na/ VS_2 cell between 1.8V and 3.5V results in a gradual increase in cathode capacity with

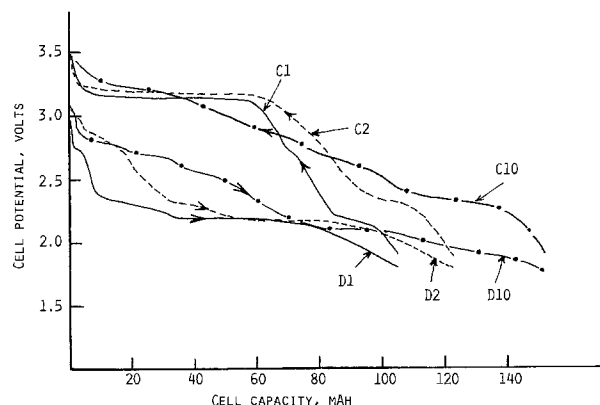


Fig. 1. Galvanostatic cycling curves for a liquid Na/ $\beta\text{-Al}_2\text{O}_3$ / $NaAlCl_4$, VS_2 cell at 165°C. Voltage limits, 1.8 and 3.5V. Curves marked D's are discharges and those marked C's are charges. Current = 16 mA (2 mA/cm²). The VS_2 cathode has a 120 mAh $1e^-$ theoretical capacity.

the mid-discharge voltage moving to higher values and the mid-charge voltage moving to lower values. The capacity increases to values between 1.2 and 1.3e⁻/V in about 10 cycles. These characteristics are illustrated in the three cycles of the cell shown in Fig. 1.

It was found, however, that if after the first discharge to 1.8V the cell is allowed to stand on open circuit at 165°C, instead of being recharged immediately, the OCV increases from 1.9V to a constant value of 2.3V in a period of ~75 hr (Cycle 1 in Fig. 2). This indicates a reaction between the discharged cathode and NaAlCl₄. Moreover, the recharge capacity of the cell after this open circuit stand is about twice that of the previous discharge, i.e., 1.6e⁻/V for the cell in Fig. 2. Most of the recharge occurs at a plateau at ~3.2V. During the next few cycles the discharge capacity to 1.8V increases to even higher values, with the respective recharges to 3.5V showing capacities higher than the discharges. The capacity then reaches a constant value of ~2.6 to 2.8e⁻/V in 5 to 8 cycles. The cycling of the cell then becomes 100% coulombically efficient. The mid-discharge voltage is ~2.5V and the mid-charge voltage is ~2.8V. The discharge proceeds in four major voltage steps (Cycles 6 and 28 in Fig. 2). The cell exhibits excellent rechargeability. One cell has been cycled more than 100 times with very little capacity loss. The average current density was 4.5 mA/cm² of β"-Al₂O₃.

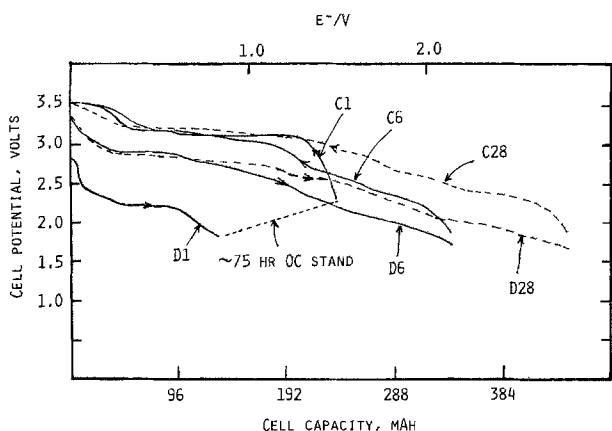


Fig. 2. Galvanostatic cycling curves for a liquid Na/β"-Al₂O₃/NaAlCl₄, VS₂ cell at 165°C prior to and after the open circuit (OC) stand. Curves marked D's are discharges and those marked C's are charges. Voltage limits, 1.8 and 3.5V. Current = 16 mA (2 mA/cm²).

The same behavior is observed in cells which are initially constructed with NaVS₂ as the cathode. Thus, in a cell with NaVS₂ the initial OCV of 1.9V increased to 2.3V in ~16 hr at 165°C. The initial charge to 3.5V corresponded to 1.3e⁻/V and the potential profiles of the charge were identical to those seen in Cycle 1 in Fig. 2. The cell capacity increased to 2.4e⁻/V in the following discharge. The voltage profiles of this discharge and subsequent cycles were identical to those of Cycles 6 and 28 in Fig. 2.

Analysis of solid cathodes from several cycled cells, after removal of NaAlCl₄ by washing with CH₃CN, indicated that the higher capacities result from the cycling of an *in situ* synthesized compound of the apparent composition VS_{2.7}Cl_{1.6}. The latter compound appears to be related to NbS₂Cl₂, which has a pseudo-one-dimensional chain structure (4).

NbS₂Cl₂ was synthesized and its cycling behavior examined. The first discharge of NbS₂Cl₂ to 1.8V yields a capacity equivalent to 2e⁻/NbS₂Cl₂. The following recharge to 3.6V is nearly 100% efficient. The second and subsequent discharges yield an average reversible capacity of 2.8e⁻/NbS₂Cl₂. Typical cycles are shown in Fig. 3. The cycling characteristics of NbS₂Cl₂ are very similar to that of the *in situ* synthesized compound of the Na/VS₂ cell. This is depicted in Fig. 4.

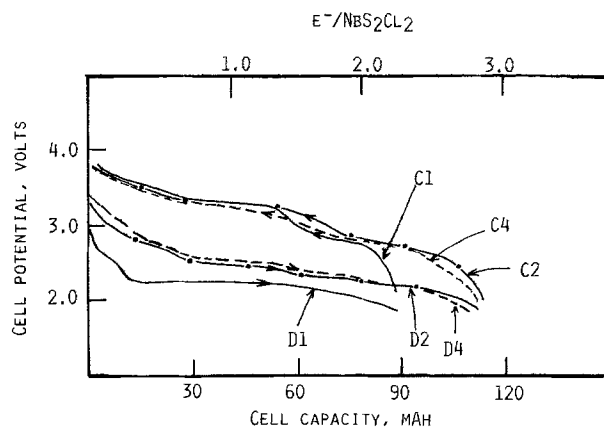


Fig. 3. Galvanostatic cycling curves for a liquid Na/β"-Al₂O₃/NaAlCl₄, NbS₂Cl₂ cell at 165°C. Curves marked D's are discharges and those marked C's are charges. Voltage limits, 1.8 and 3.6V. Current = 10 mA (1 mA/cm²).

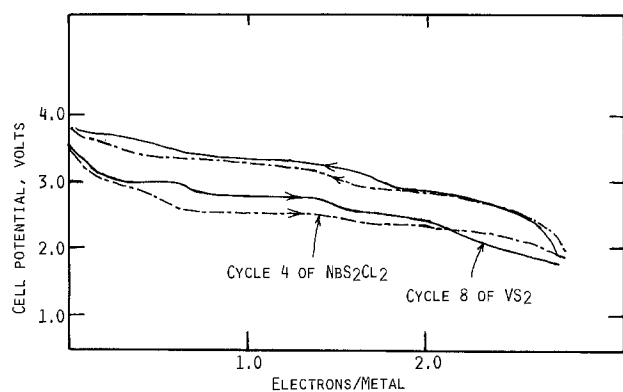


Fig. 4. A comparison of the cycling curves of Na/VS₂ and Na/NbS₂Cl₂ cells.

Cycling behavior similar to that of VS₂ in molten NaAlCl₄ is also exhibited by many other dichalcogenides, including VSe₂ (6). The cycling behavior of NbS₂Cl₂ and related compounds in basic NaAlCl₄ is considerably different from that of S in this melt (7) and the sulfur halides in the acidic NaAlCl₄ melt (8,9).

Our research on this novel chemistry is continuing. In future papers (10) we will discuss the mechanisms of cathode cycling, rate/capacity of the cathodes, and performance characteristics of practical cells.

ACKNOWLEDGEMENTS

This work was supported by the National Aeronautics and Space Administration under Contract No. NAS3-21726. Fruitful discussions with Dr. S. B. Brummer of EIC Laboratories and Dr. Joseph Singer of NASA-Lewis Research Center, Cleveland, OH, are gratefully acknowledged.

REFERENCES

1. K. M. Abraham, L. Pitts and R. Schiff, *J. Electrochem. Soc.*, **127**, 2545 (1980).
2. K. M. Abraham and L. Pitts, *J. Electrochem. Soc.*, **128**, 1060 (1981).
3. K. M. Abraham and L. Pitts, *J. Electrochem. Soc.*, in press.
4. V. H. Shafer and W. Beckman, *Z. Anorg. Allg. Chem.*, **225**, 347 (1966).
5. K. M. Abraham, R. D. Rauh and S. B. Brummer, *Electrochim. Acta*, **23**, 501 (1978).
6. K. M. Abraham and M. W. Rupich, U.S. Patent applied for.
7. K. M. Abraham and M. W. Rupich, to be published.
8. G. Mamantov, R. Morassi, M. Matsunaga, Y. Ogato, J. P. Wiaux and E. J. Frazer, *J. Electrochem. Soc.*, **127**, 2319 (1980).
9. J. J. Auborn and S. M. Granstaff, *Proc. 15th IECEC*, 575 (1980).
10. K. M. Abraham, M. W. Rupich, J. Singer and S. B. Brummer, to be published.

Manuscript submitted July 10, 1981; revised manuscript received Sept. 4, 1981.

Reference Electrode Development for Molten LiCl-KCl Eutectic Electrolyte

Laszlo Redey*

Chemical Engineering Faculty, Technical University of Budapest, Hungary

and Donald R. Vissers*

Argonne National Laboratory, Argonne, Illinois 60439

Molten LiCl-KCl binary salt electrolytes are often used in high-temperature electrochemical studies; the eutectic composition of this electrolyte is frequently used (1,2) because of its relatively low melting point (352°C) and high decomposition voltage (3.62 V). One major use of the LiCl-KCl system is as the electrolyte in lithium alloy/iron sulfide battery cells (3). This article describes the development, calibration, and evaluation of a reference electrode for these cells containing LiCl-KCl eutectic electrolyte.

A reference electrode must have a thermodynamically well-defined, reproducible potential and possess a suitable geometry with adequate mechanical strength. For battery testing, its electrochemical and mechanical stability must be measured in thousands of service hours. The choice of a reference electrode was based on an evaluation of our preliminary experiments (4) and of published findings with the following electrodes: Cl_2/Cl^- (5,6), $\text{Ag}/\text{AgCl}/\text{Cl}^-$ (7,8), Pt/Pt^{2+} (2), $\text{Ni}/\text{NiS}/\text{S}^{2-}$ (9), $\text{Li-Al}/\text{Li}^+$ (10-12). Two systems were selected for further development: (a) the $\text{Ni}/\text{Ni}_3\text{S}_2/\text{S}^{2-}$ electrode of the second kind, which was shown (4) to have excellent long-term stability, and (b) the $\text{Li-Al}/\text{Li}^+$ electrode of the first kind, which has excellent short-term stability and reproducibility making it suitable as an *in-situ* calibration standard for the $\text{Ni}/\text{Ni}_3\text{S}_2/\text{S}^{2-}$ electrode.

Development of the Ni/Ni₃S₂ Reference Electrode

The high lithium and sulfur activities present in the lithium-aluminum/iron sulfide cell system make strict demands on the reference electrode and thus sharply limit the choice of suitable materials. A schematic diagram indicating the electrode design and construction materials is shown in Fig. 1. Beryllia tubing (1/8 in. OD and 1/16 in. ID) has been shown to be an excellent electrode housing. The inner compartment of the

*Electrochemical Society Active Member.

electrode contains a substantial surplus of high-purity Li_2S powder, which maintains a stable, well-defined saturation concentration (748 ppm in LiCl-KCl eutectic at 425°C) for very long periods (\approx year). The diffusion barrier, with a resistance of 10 to 20 k Ω is either constructed of Y_2O_3 fibers or a close fitting solid Al_2O_3 plug. The latter leaves open only a fine capillary pathway to the outer electrolyte. The electrodes are assembled "dry" in a high-purity helium-atmosphere glove box and are activated by letting molten electrolyte penetrate through the diffusion barrier; an anodic treatment (approx. 0.1-2 C charge with 5-20 $\mu\text{A}/\text{cm}^2$ on the Ni wire) is used to form the Ni_3S_2 layer on the metal wire.

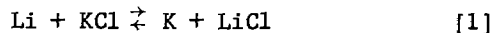
Four identically prepared electrodes were immersed into a pool of Li_2S -saturated LiCl-KCl eutectic contained in a high-purity Al_2O_3 (McDaniel 998) beaker. During a 30-day test period after electrode activation, we found not more than ± 0.3 mV potential variation from the mean value, which was calculated from potential differences between electrode pairs measured four times a day. Slow ($<1^\circ\text{C}/\text{min}$) temperature cycling from 400-460°C did not increase this variation. Fluctuation of the mean values was within 0.5 mV.

Development of the Li-Al/Li⁺ Electrode as a Calibration Standard

Since aging and other effects might cause changes of the $\text{Ni}/\text{Ni}_3\text{S}_2/\text{S}^{2-}$ electrode potential, an *in-situ* calibration technique was developed.

Like the hydrogen electrode in protonic solvents, the Cl_2/Cl^- electrode, from a thermodynamic standpoint, is excellent for use in establishing a reference potential in the LiCl-KCl electrolyte. Use of this electrode, however, is hindered by severe experimental difficulties. The other natural choice, the Li/Li^+ electrode, is ill-defined because of the lack of real equilibrium as a consequence

of the following reaction (13):



A third (theoretically possible) electrode having a common element with the electrolyte, the K/K⁺ electrode is thermodynamically unstable in the system, see equation [1], as it has too high a vapor pressure in the required temperature range.

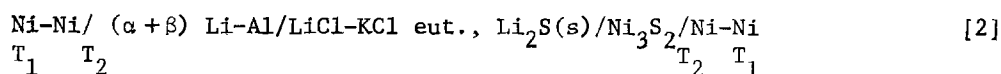
When lithium is alloyed with aluminum, however, its activity is decreased and thus the quantity of potassium formed is small and the system approaches equilibrium. Furthermore, as long as the two-phase ($\alpha + \beta$) Li-Al alloy composition is present (~10-46 at. % Li), the potential is independent of the lithium content of the alloy (9-11). The Li-Al/Li⁺ electrode, therefore, was selected as the calibration standard.

The construction of the Li-Al electrode is similar to that of the Ni/Ni₃S₂ electrode shown in Fig. 1, except that powdered Li-Al alloy is substituted for Li₂S. Another way to prepare the Li-Al electrode is to wind a short piece of aluminum wire around the nickel wire (Fig. 1) and cathodically produce the two-phase alloy.

However, we observed that Li-Al electrodes having only small quantities of the alloy (a few mg) are prone to instability with a potential shift in the positive direction and so the constant value may hold only for days or hours. To overcome the problem of this uncertainty, we have developed an intermittent charging technique to electrochemically generate the electrode *in-situ*. This technique allows us to measure the rest potential of the Li-Al electrode during cathodic treatment of the aluminum wire and observe from these measurements the establishment of an equilibrium condition. In Figure 2, the potential indicated by the apparent consecutive steady-state, open-circuit values reaches a constant level which corresponds to the two-phase ($\alpha + \beta$) equilibrium value. This simple technique is used to prepare the primary calibration standard.

Evaluation of the Ni/Ni₃S₂ Electrode

The calibration cell utilizes the couple:



where T₁ is the temperature of the glove-box and T₂ is the cell temperature. According to the primary-standard concept, the potential of the two-phase ($\alpha + \beta$) Li-al alloy is defined as zero at any temperature in order that this alloy serve as a thermodynamic reference state. Consequently, the emf of the cell described in Eq. 2 is the potential of the Ni/Ni₃S₂ electrode on this "standard" potential scale. Least-squares fitting of the E-T data defines the cell voltage (E in mV) according to the following relationship:

$$E = 1367.5 + 0.097(T-700) \quad [3]$$

where T is the cell temperature in K.

Thermal cycling between 360 and 500°C causes no hysteresis and indicates excellent reproducibility. Other aspects of this measurement will be published elsewhere (14). The electrode potential obeys the Nernst equation, and is controlled by the activity of S²⁻ ions (15). X-ray diffraction analysis of material taken from the nickel sulfide electrode indicates that the anodically formed compound is Ni₃S₂. Studies indicate the Li-Al electrode potential is not measurably affected by the presence of Li₂S.

The cell described by Eq. 2 is almost free of liquid-liquid junction potential. Although the Ni₃S₂ may maintain a concentration step function, in the diffusion barrier region, its solubility is very low. Using the Ni/Ni²⁺ standard potential value (2), the calculated Ni²⁺-ion activity is approximately 10⁻¹² g ion/kg in Li₂S saturated eutectic at 700 K.

The Ni/Ni₃S₂ reference electrode described above possesses a well-defined potential of excellent stability. For example, these electrodes have undergone many thermal cycles from operating temperature to room temperature and back with no observable mechanical or electrochemical effects. Many of our electrodes performed well for longer than one year of continuous service in Li-Al/FeS cell testing, thus proving their chemical stability and compatibility. Although only this example of use is given here, this reference electrode can be utilized successfully in other LiCl-KCl electrolyte systems as well.

ACKNOWLEDGEMENT

This work was performed under the auspices of the U.S. Department of Energy. We thank Dr. D. L. Barney and Dr. R. K. Steunenberg for their encouragement and support of our work.

REFERENCES

1. H. A. Laitinen and H. C. Gaur, *Anal. Chim. Acta*, **18**, 1 (1958).
2. H. A. Laitinen and C. H. Liu, *J. Am. Chem. Soc.*, **80**, 1015 (1958).
3. D. L. Barney, *et al.*, High Performance Batteries for Electric Vehicle Propulsion and Stationary Energy Storage, Progress Report for the Period October 1978-September 1979, ANL-79-94, Argonne National Laboratory (1980).
4. L. Redey and D. R. Vissers, Extended Abstracts of Electrochem. Soc. Meeting, Boston, May 6-11, 1979, Abstr. No. 371.
5. P. J. Drossbach, *This Journal*, **103**, 700 (1956).
6. H. A. Laitinen and J. W. Parkey, *J. Am. Chem. Soc.*, **81**, 1053 (1959).
7. M. Takahashi, *Denki Kagaku*, **25**, 432 (1957).
8. J. O'M. Bockris, G. J. Hills, (*Chem. Abstr.* 1958, 13475 b), D. Inmann and L. Young, *J. Sci. Instr.* **33**, 438 (1956).
9. C. H. Liu, A. J. Zielen and D. M. Gruen, *This Journal*, **120**, 67 (1973).
10. N. P. Yao, L. A. Heredy and R. C. Saunders, *This Journal*, **118**, 1039 (1971).
11. J. R. Selman, D. K. DeNuccio, C. J. Sy and R. K. Steunenberg, *This Journal*, **124**, 1160 (1977).
12. C. John Wen, B. A. Boukamp, R. A. Huggins and W. Weppner, *This Journal*, **126**, 2258 (1979).
13. R. N. Seefurth and R. A. Sharma, *This Journal*, **122**, 1049 (1975).
14. Z. Tomczuk, L. Redey and D. R. Vissers, to be published.
15. L. Redey and D. R. Vissers, to be published.

Manuscript received July 20, 1981.

Publication costs of this article were assisted by Argonne National Laboratory.

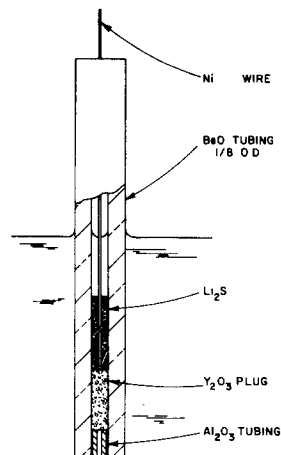


Fig. 1. Construction of Ni/Ni₃S₂/S²⁻ Reference Electrode

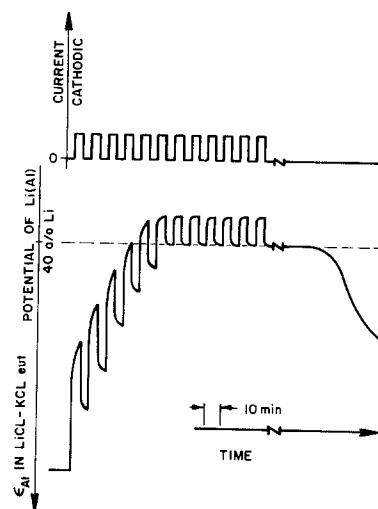


Fig. 2. Typical Diagram Obtained During Intermittent Changing of Al Wire with Li

Influence of Metal Ions on the O₂ Reduction of Noble Metals in Alkaline Solutions

R. Amadelli, J. Molla,* P. Bindra,** and E. Yeager**

Case Laboratories for Electrochemical Studies and Department of Chemistry,
Case Western Reserve University, Cleveland, Ohio 44106

Underpotential deposited layers of Pb (1) and Tl (2,3) have been found to produce substantial increments in the catalytic activity of Au for O₂ reduction in alkaline solutions. In the course of a systematic study of such effects we found these same species to enhance the activity of Pt for O₂ reduction, including high area Pt catalyst on carbon supports in alkaline solutions. The purpose of this note is to call attention to this effect which may be useful to electrochemists concerned with increasing the activity of high area Pt electrocatalysts for O₂ reduction.

EXPERIMENTAL

The O₂ reduction has been examined on smooth Pt, high area Pt on carbon supports and smooth Au with the rotating disk ring electrode in 1 M NaOH (Baker, low in carbonates) which was pre-electrolyzed as described elsewhere (4). For the dispersed supported catalyst the material has been applied to an ordinary pyrolytic graphite (OPG) electrode as a thin Teflon bonded layer similar to the technique of Tarasevich (5).

For the measurements without Tl or Pb present the smooth Au and Pt electrodes were treated in two ways. For one the electrodes were cycled between 0 and -0.70 V (all potentials are given vs. Hg/HgO) at 50 mV/s until steady state behavior was obtained and then the current potential curves (Figs. 3,4) was recorded either point by point or scanning towards more positive potentials. Almost negligible hysteresis was observed with measurements made with increasing and decreasing potentials. The second procedure involved treating the electrode at -0.9 V for 30 s before recording each polarization curve,

otherwise with the same treatment. In the runs with Pb or Tl present, the conditions of the electrode were the same except that the pre-treatment at -0.90 V was not used. The ring was of the same material as the disk and was maintained at +0.125 V for Au and +0.25 V for Pt.

RESULTS AND DISCUSSION

Cyclic voltammetry studies show that thallium forms a UPD layer on Au with a pronounced peak at ~ -0.20 V (Fig. 1).

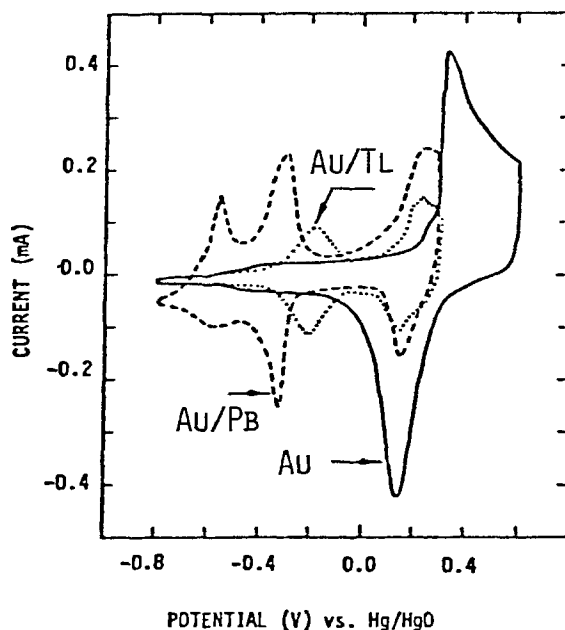


Fig. 1 Cyclic voltammety curves for Au in N₂ saturated 1 M NaOH in the absence (solid line) and in the presence of 5.8x10⁻⁵ M Pb(II) (dashed line) and 2.6x10⁻⁶ M Tl(I) (dotted line). Scan rate: 50 mV/s. Electrode area: 3 cm². T = 25°C.

* Electrochemical Society Student Member.

** Electrochemical Society Active Member.

Key words: catalysis, electrodeposition electrode.

This peak potential is independent of the scan rate but depends markedly on the pH, shifting in the anodic direction by 57 mV/pH unit. Decreasing the pH results in a considerable broadening of the peak. This phenomenon may be due to complexation of Tl(I) with OH^- . Kulba *et al.* (6) reported two possible complexes of Tl in alkaline solutions: inner and outer sphere complexes of the form $[\text{Tl}(\text{OH})_n(\text{H}_2\text{O})_x]^{1-n}$. The relative amount of the two complexes depends on the pH. The anodic region of the Au voltammogram appears to be greatly modified by the presence of Tl. A similar phenomenon has been observed for Pb on Au (1,2). The Tl and Pb adsorption on Pt is considerably more complex (Fig. 2) than on Au due to anodic film formation at less positive potentials on Pt. It is possible that Tl and/or Pb adsorb on the anodic film covered Pt, for example in forms such as Pt-O-PbOH or $\text{Pt-O} \begin{matrix} \nearrow \text{Pb} \\ \searrow \end{matrix}$ where the H

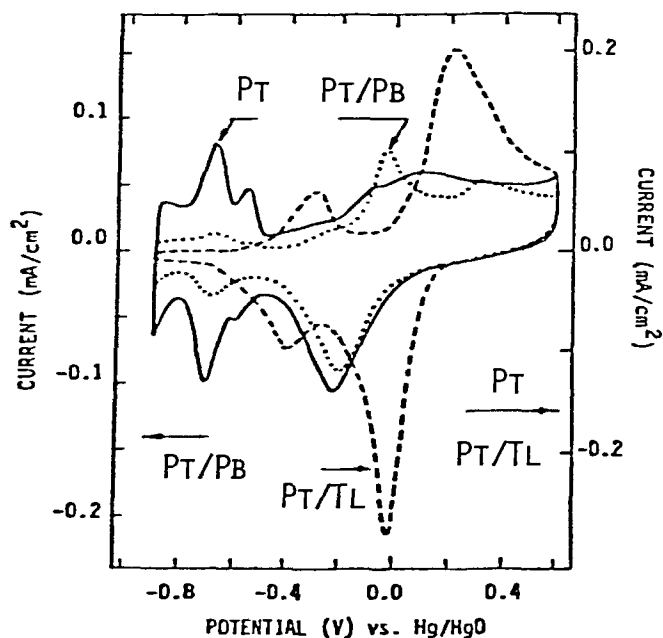
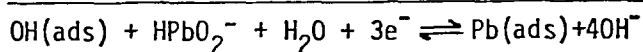
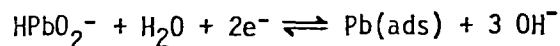
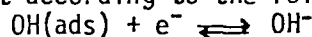


Fig. 2 Cyclic voltammograms for Pt in N_2 saturated 1 M NaOH in the absence (solid line) and in the presence of 2×10^{-5} M Pb(II) (dashed line) and 1×10^{-5} M Tl(I) (dotted line). Scan rate: 50 mV/s. Electrode area: 7.5 cm^2 . $T = 25^\circ\text{C}$.

of the PtOH has been replaced by Pb and water in the inner coordination sphere of Pb is not shown. Alternatively, Pb can underpotential deposit according to the following process:



This implies that the adsorption of the metal ion suppresses the anodic film formation. A similar effect may also occur on Au on which OH adsorption occurs already at $E > 0.45$ V RHE. Hydrogen adsorption is also inhibited when foreign metal ions adsorb or underpotential deposit on Pt.

Figs. 3 and 4 show the polarization curves for O_2 reduction in 1 M NaOH on Au and Pt (the latter both in low and high area form) with and without Tl(I) and Pb(II) added to the electrolyte.

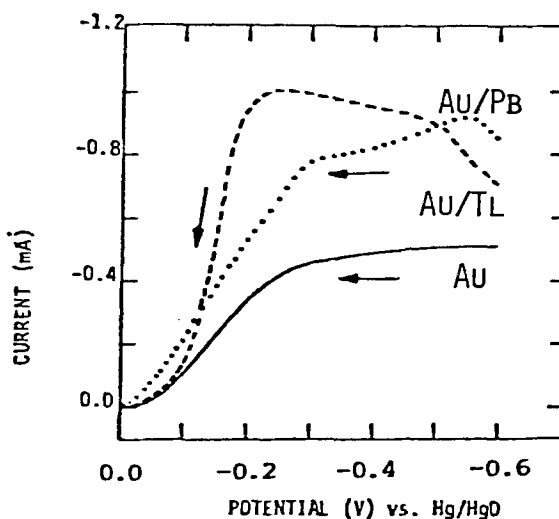


Fig. 3 Polarization curves for O_2 reduction on Au in 1 M NaOH in the absence (solid line) and in the presence of 1.4×10^{-4} M Pb(II) (dotted line) and 6.6×10^{-6} M Tl(I) (dashed line). Scan rate: 10 mV/s. Rotation rate: 3600 rpm. Electrode area: 0.196 cm^2 . $T = 25^\circ\text{C}$.

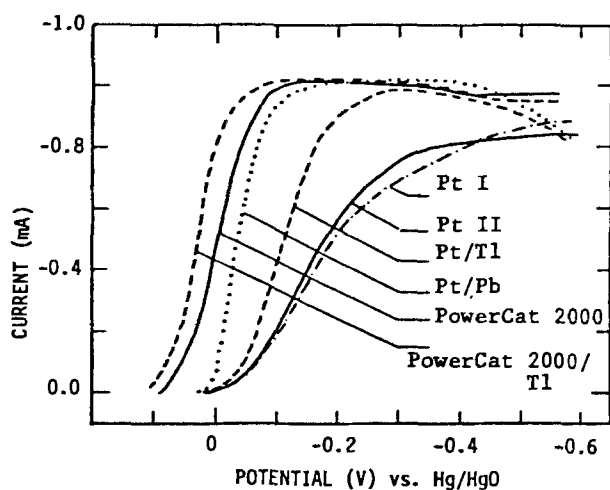


Fig. 4 Polarization curves for O_2 reduction on different substrates in 1 M NaOH. Tl(I) concentration: 6.6×10^{-6} M for Au, 3.2×10^{-6} M for Pt and 1.1×10^{-5} M for Powercat 2000. Pb(II) concentration: 2×10^{-6} M. Scan rate: 10 mV/s except for Powercat obtained point by point). Electrode area: 0.196 cm^2 . Powercat 2000 supported as a thin coating on OPG. Pt I: no cathodic pretreatment, Pt II: cathodic pretreatment.

With Au in pure NaOH solutions, O_2 reduction proceeds by the series mechanism with the further reduction and decomposition of the HO_2^- very slow. This results in $2 e^-$ per O_2 reaching the electrode surface. With the addition of $> 10^{-5}$ M Tl to the electrolyte, the current on Au is very substantially increased although the half wave potential is not changed very markedly. Rotating disk-ring data, analyzed using the method of Wroblowa *et al.* (7), indicate that the process now proceeds by parallel mechanism with close to $4 e^-$ per O_2 reaching the electrode surface. For example, at 25°C in 1 M NaOH + 6.6×10^{-6} M Tl(I), $k_1/k_2 = 0.4$ (k_1 , k_2 are the rate constants for the 4 and $2 e^-$ reductions to OH^- , respectively). While part of the current increase is due to k_1 , a significant portion of the increase produced by the Tl addition also appears to be associable with an increase in the reduction and/or decomposition of the peroxide at the electrode surface. In contrast to the results with Tl, even in solutions containing up to 10^{-4} M Pb(II), the O_2 reduction on Au still proceeds through only the series mechanism

although the peroxide elimination through reduction and/or decomposition is greatly increased.

With the addition of $> 10^{-6}$ M Pb or Tl to 1 M NaOH the O_2 reduction on Pt is very substantially increased and the half wave potentials are shifted to much more anodic values, particularly on smooth Pt. Rotating disk-ring studies indicate the O_2 reduction to proceed by the parallel mechanism both with and without Pb or Tl present but the ratio of k_1/k_2 is substantially increased as is also k_1 .

The high area catalyst Powercat 2000 was obtained from Stonehart Associates (Madison, Connecticut) and consists of dispersed Pt on a carbon support with a Pt area of $\sim 100 \text{ m}^2/\text{g}$. Prior experiments with this catalyst in gas-fed O_2 cathodes in the authors' laboratory have indicated unusually high activity. Even so, the addition of 10^{-6} M Tl results in a substantial increase in the current density in the potential region where kinetic control is involved. Pb produces a similar effect although not quite as large.

The reduction and oxidation of HO_2^- on Au and Pt have also been examined in N_2 saturated 1 M NaOH containing Tl or Pb. The peroxide reduction current is increased by approximately 2 fold on both Pt and Au in the presence of 10^{-6} M Pb or Tl as potentials of 0.0 to -0.4 V. The authors believe that most of the increase in current observed with the Tl and Pb additives is caused by the destabilization of the anodic film on the Pt and Au by the adsorbed metal species. Adzic *et al.* (8) have reached the same conclusions as to the destabilization of the anodic films analogous to the observation of Bruckenstein *et al.* with Hg and Bi on Pt. With the Pb particularly the O_2 reduction proceeds at potentials which are quite anodic compared to those when the UPD peaks are observed (Fig. 1). It is unlikely that a simple UPD layer is found at such anodic potentials and it is more likely that a complex ion species containing Pb is the adsorbed species.

Acknowledgement

The authors are pleased to acknowledge sup-

port for this work by the U.S. Department of Energy.

References

1. R. R. Adzic, A. V. Tripkovic and Markovic, *J. Electroanal. Chem.* 114, 37 (1980).
2. R. Amadelli, P. Bindra and E. Yeager, Extended Abstracts, ECS Fall Meeting 1980, Hollywood, Florida.
3. J. E. E. McIntyre and W. F. Peck. Proceedings of the Third Symposium on Electrode Processes, The Electrochemical Soc. Inc., (1979).
4. R. W. Zurilla, R. K. Sen and E. Yeager, *J. Electrochem. Soc.* 125, 1103 (1978).
5. S. I. Andruseva, M. R. Tarasevich and K. A. Radyushkina, *Electrokhimiya* 13, 253 (1977).
6. F. Ya. Kul'ba, Yu. B. Yakovlev and E. A. Kopylov, *Russian Journal of Inorganic Chemistry* 15(8), 1088 (1970).
7. H.S. Wroblowa, Y.D. Pan, G. Razumney, J. *Electroanal. Chem.* 60, 195 (1976).
8. R.R. Adzic and N.M. Markovic, ISE 31st Meeting, Extended Abstracts, Vol. 2, p. 527, Venice, 1980.

Manuscript submitted March 24, 1981; revised manuscript received Sept. 23, 1981.

Publication costs of this article were assisted by Case Western Reserve University.



An Assessment of the Processes Leading to Pit Nucleation on Iron

M. Janik-Czachor¹

Department of Chemistry, Northwestern University, Evanston, Illinois 60201

ABSTRACT

In this review the controversial issues of the processes leading to the chemical breakdown of passivity are discussed. The following problems are considered: (i) aggressive anion concentration buildup and the effect of potential; (ii) effect of defects and inhomogeneities within the metal phase and/or within the passivating film; (iii) the possibility of incorporation of aggressive ions into the film; (iv) effect of aggressive ions on film thickness and structure; (v) significance of the induction period, and (vi) relevance of the prevention of repassivation.

Pitting is one of the most dangerous forms of localized corrosion of passive metals in solutions containing aggressive ions X^- ($=Cl^-, Br^-, I^-$). The mechanism of processes leading to pit nucleation is still a subject of controversy (1-25).

Some authors distinguish between an initiation and a propagation step in pitting (1-3, 5, 7, 13, 14, 17). For them the crucial questions with the initiation step are: (i) how the aggressive ions change the protective ability of the passivating film locally, so that it no longer prevents high anodic currents from flowing, and (ii) what is the role of the potential of pit nucleation, E_{np} .² Others claim that there is no fundamental difference between the initiation and propagation steps (4, 8, 12), since direct contact between the bare metal and the electrolyte occurs instantaneously upon the immersion of the passive metal. Local weak spots or flaws always exist within the film; the aggressive electrolyte instantaneously penetrates the film at these flaws and reacts with the bare metal, resulting in rapid metal dissolution.

The experimental background for these two approaches has been reviewed by Janik-Czachor, Wood, and Thompson (6).

To decide which of the approaches is likely to be applicable for iron, the present state of understanding of passivity on iron must be taken into account (26-37).

In the stationary state, passive iron is covered by a film, several nanometers in thickness, having low ionic conductivity, and supporting electric fields of the order of 10^6 V/cm. Optical measurements suggest that it is an insulator with a principal energy gap above 5.5 eV (32, 33).

Although local defects always exist within the film, there is experimental evidence that no bare metal surface is exposed to the electrolyte (26, 27). Iron in the

active state dissolves as Fe(II), whereas in the passive state the primary dissolution product is Fe(III). According to Vetter (26), in the passive state the reactions $Fe \rightarrow Fe^{+2} + 2e$ and $Fe^{+2} \rightarrow Fe^{+3} + e^-$ are excluded. So the primary products of iron dissolution in the active and in the passive state are basically different. Only after pitting commences, that is, the initiation step is essentially over, does Fe(II) appear as a corrosion product from the pits, whereas Fe(III) production continues from the remaining passive surface. It is reasonable to assume, therefore, that there is an initiation step for pitting of passive iron. In attempting to rationalize the information available, the following problems are discussed:

1. Aggressive ion concentration buildup and the effect of potential.
 2. Effect of defects and inhomogeneities within the metal phase and/or within the passivating film.
 3. The possibility of incorporation of aggressive ions into the film.
 4. Effect of aggressive ions on film thickness and structure.
 5. Significance of the induction period, τ .
 6. Relevance of the prevention of repassivation.
- The author's point of view is presented.

Aggressive Anion Concentration Buildup and the Effect of Potential

The important questions for initiation are: (i) how sufficient halide becomes available at the initiation sites to stop repassivation effectively; (ii) does this occur at specific sites as a result of local processes on the passive film surface or in the adjacent environment; and (iii) why breakdown of the film only occurs after a certain critical potential is exceeded. Many authors agree that E_{np} is a characteristic parameter for pitting. The existing data show that E_{np} decreases as the concentration of the aggressive ions C_{x^-} increases and depends on their nature (see Fig. 1). It is also influenced by the presence of inhibitors but does not depend on pH (1-3, 6, 7, 13, 14, 24, 25, 39, 41, 44-46). The following relationship is obeyed for E_{np}

$$E_{np} = a - b \ln C_{x^-}/C_{inh} \quad [1]$$

¹ On leave from the Institute of Physical Chemistry, Polish Academy of Sciences, Warsaw, Poland.

Key words: metals, films, corrosion, passivity.

² The situation is more complex. There exists a critical pitting potential E_{cp} sometimes called "the protection potential" (3, 6, 17, 38-43). Usually $E_{cp} < E_{np}$. Below E_{cp} the pits once initiated can be stopped. The existing data infer however that when E_{np} is determined in a way that eliminates the time for breakdown, $E_{np} = E_{cp}$ (13, 14, 24, 42, 44).

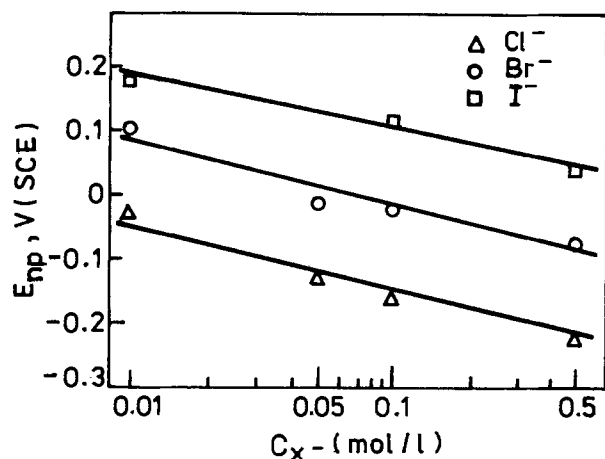


Fig. 1. Critical pitting potential vs. halide concentration (25). (Reprinted with permission of *Werkstoffe und Korrosion*.)

The relatively high values of the slope b (≥ 100 mV/decade C_x) suggests a strong halide effect (1, 3, 7, 13, 14, 24, 25). An increase in inhibitor concentration C_{inh} , shifts E_{np} to more positive values. Some authors (1, 13, 14, 16, 44, 45) have suggested, therefore, that the first step of pit nucleation is halide adsorption and that there is a competitive adsorption process between halide and inhibitors that results in the E_{np} shift.

Coverage with a halide and an inhibitor depends on the electrode potential and the concentration of these species in the bulk electrolyte. Strehblow (48) has considered this dependence in detail and concluded that in the absence of any inhibitor, coverage with X^- increases logarithmically with potential; he assumed that E_{np} corresponds to a critical coverage above which there are sufficient aggressive ions at the surface to break down the film. When an inhibitor is also present, the relations between the critical coverage and E_{np} is given by a formula similar to Eq. [1].

Why do halides tend to adsorb locally?

There are various inhomogeneities and defect sites within the metal phase and/or in the film. It is, therefore, reasonable to expect a preferential adsorption of halide at these sites. The important role of such defects and inhomogeneities in halide agglomeration is considered in more detail in the next section.

It is interesting to recall here the point made long ago by Kolotyrkin (1) that the passive metal surface never dissolves homogeneously. The halides migrate to the sites of accelerated dissolution. Therefore, the critical concentration of halide will first be attained at these sites. Indeed there is direct evidence that chlorides already agglomerate as islands on the passive surface at potentials less than E_{np} (49, 52). Heusler and Fischer (14, 50) considered island formation; they pointed out that the solubility of chloride in the oxide on iron is negligibly small. Under these conditions, chemisorption of chloride is said to yield preferentially chloride islands rather than a statistical distribution, even if the passivated surface were completely homogeneous.

Effect of Defects and Inhomogeneities Within the Metal Phase

Some authors rule out the role of surface inhomogeneities in pit nucleation (13, 14, 51) and assume that it is a stochastic process (54, 55). However these concepts are contrary to the common observation that pits form at grain boundaries (3, 15, 64), nonmetallic inclusions (3, 6, 10, 15, 17, 53-59, 61-63, 65-70), and at some dislocations (60).³ These findings are not surprising,

³ In particular, the important effect of nonmetallic inclusions on pit nucleation has been studied in detail in our laboratory and is discussed elsewhere (57, 70).

since in reality commercial metals and alloys, and indeed the surfaces of materials as pure as those prepared by zone refining, are not "ideal," homogeneous systems. Metals contain nonmetallic inclusions, second-phase particles, and usually some segregation of impurities; the boundaries of such phases with the matrix are likely regions of susceptibility to pit nucleation. The passivating film over these regions is certainly defective, and its structure and composition are different from that over the metal matrix. Studies with the aid of modern surface analytical techniques may provide more detailed information about the composition and the structure of these regions.

Even in the absence of aggressive ions, a somewhat accelerated dissolution of a passivated metal has been observed at certain inhomogeneities, like nonmetallic inclusions (10, 71). More rapid dissolution at these sites in the presence of aggressive ions should certainly lead to their local accumulation there. On the other hand, electron probe microanalysis has given evidence for the formation of chloride salt island at the boundary between sulfide inclusions and the metal matrix for iron and steels prepassivated electrochemically (72) or in air (59), when polarized in chloride solution, even at potentials less than E_{np} .

There is always a "spectrum" of the induction period for pit nucleation, τ , suggesting a "spectrum" of susceptibility for different sites on the surface (73). This behavior is characteristic for commercial alloys and for high purity metals. For the latter one can, therefore, expect that agglomeration of halides will occur at the most susceptible sites, e.g., impurity segregates, certain dislocation configurations, etc. Summarizing the above discussion, it is suggested that various inhomogeneities within the metal phase and/or the surface film help aggressive ions to agglomerate on the passivated metal surface.

Adsorption alone cannot change the protective abilities of the passivating film. Other processes must be operative, simultaneously or subsequently. Two processes are usually discussed and will be considered here: (i) incorporation of halides into the passive film and (ii) film thinning and alteration of its structure due to halide action.

Incorporation of X^- into the Passivating Film

Various models of pit nucleation postulate migration of aggressive ions through the thermal or anodic passivating film lattice by ionic migration under an electric field or by field-independent anion exchange (2, 18, 20, 74-76), processes which are likely to be accompanied by a change in the film conductivity. The available evidence for aluminum is contradictory (6, 7, 12). For iron in a borate buffer solution, it has been found from electrochemical and ellipsometric measurements that the induction period for pit nucleation, τ , increases with an increase in the film thickness (74). It was concluded, therefore, that this resulted from the longer path chloride ions had to traverse to reach the metal surface when the film was thicker. This explanation seems unlikely, however, because no change in the ionic conductivity of the film has been found due to chloride action (14, 50). Furthermore, Auger electron spectroscopic (AES) measurements have not given any evidence for chloride entry into the film (Fig. 2) (6, 17, 77, 78).

Some valid reasons against the concept of migration of aggressive species through the film lattice have been advanced by Vetter and Strehblow (13, 79). Transport of metal ions and chloride ions through the passivating layer occurs under a high electric field 10^8 V/m. For an exchange of oxygen ions by chloride ions, the divalent O^{2-} ions must migrate against this high field, which is unlikely. It also seems unlikely that large ions, such as ClO_4^- and SO_4^{2-} , which can also

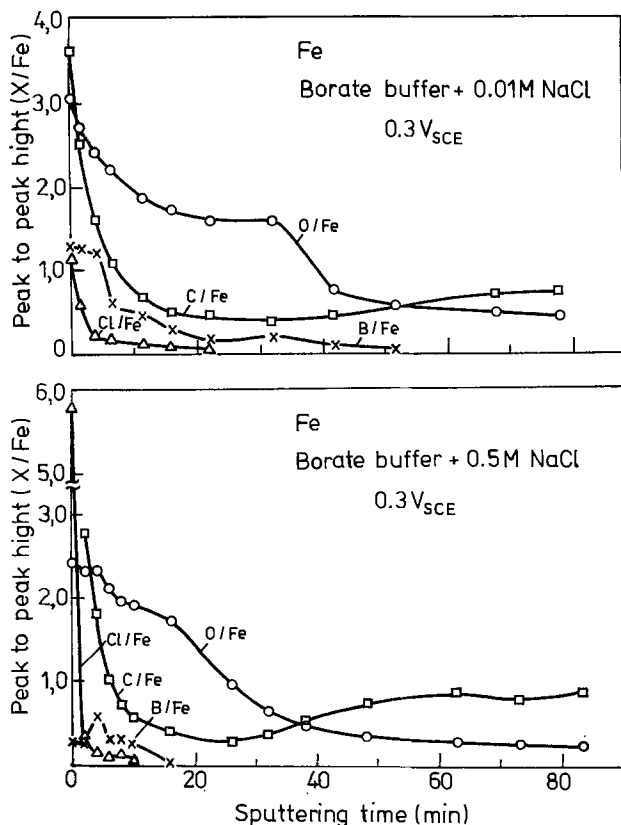


Fig. 2. Depth profiles of the passivating film on iron prepassivated in borate buffer solution and polarized at $E = 300 \text{ mV}_{\text{SCE}}$ in borate buffer solution containing (a) 0.01M NaCl, (b) 0.5M NaCl (77). (Reprinted with permission of *Werkstoffe und Korrosion*.)

provide pitting, should migrate through the passive film lattice.

Effect of Aggressive Ions on the Passivating Film Thickness

Existing data show no agreement on the effect of chloride ions on the thickness or structure of the passivating film on iron.

Ellipsometric measurements indicated that the film thickens due to chloride action (2, 74, 80). For example, McBee and Kruger (74) reported that chloride ions produce changes at all wavelengths in the visible spectrum of the film on iron, formed and held at $E < E_{\text{np}}$; they interpreted this to be caused by film thickening. On the other hand, at $E > E_{\text{np}}$, the visible spectrum is affected at only a few wavelengths when chloride is introduced into the borate buffer solution in which the film is formed. The authors claim, therefore, that subtle changes in the film due to chloride action are affected by the potential at which the film is exposed to chloride, and these changes are related to the tendency for the film to breakdown, when $E > E_{\text{np}}$. The manner in which ellipsometric data, which averages the behavior of the entire surface, are influenced by local action, such as halide island formation, breakdown and repair processes, film undermining, etc. has not been clarified.

As mentioned above, the use of AES with ion milling has enabled in-depth composition profiles of films to be determined (17, 77, 78, 81). It was concluded that the polarization of passive samples at $E > E_{\text{np}}$ and $t < \tau$ in chloride solution makes the film easier to sputter (77), (Fig. 2). However, it is not clear whether the observed effect is due to thinning of the film or to a change in the film structure.

Recent findings with the iron rotating disk ring electrode (14, 50, 51) may have brought valuable insight to the processes under consideration. The ring current,

indicative of Fe(III) production, in borate or phthalate buffers grows linearly with the chloride concentration, but there is no effect on the total disk current density (Fig. 3). The authors assume that this ring current increase must be due to the dissolution of the passivating $\gamma\text{-Fe}_2\text{O}_3$ layer. They claim that the increase in oxide dissolution stops as soon as the new steady state is established, corresponding to a thinner oxide layer from which Fe(III) dissolves faster than in the absence of chloride. The chemisorbed halide may replace oxygen ions or hydroxyl ions on the passivating film. The authors assume that the decrease in film thickness is localized and occurs under chloride islands formed over the film. Local fluctuations in island life, location and development and in passivating film thickness occur and may result in complete local removal of the film at sufficiently high anodic potentials. This is accompanied by a steep increase of Fe(II) production, when pitting commences (Fig. 3). Problems with this concept include its lack of direct evidence that the salt deposits do thin the passivating film and the absence of a detailed theory of how they do it.

This discussion has shown why it is reasonable to expect accumulation of halides at heterogeneities in the passivating film. However, even at these weak spots the removal of the film evidently requires a certain period of time; Fe(II) production, indicative of film breakdown, is clearly detected not immediately, but only after a certain time has elapsed (Fig. 3).

Our coulometric measurements (77, 78) for the iron/borate buffer system have shown that the amount of charge necessary to reduce cathodically the passivating oxide film tends to diminish after the passivated metal has been exposed to chloride or bromide containing borate buffer at $E < E_{\text{np}}$. The effect increases with halide concentration, (Fig. 4). A similar effect of halide has been found for iron in phosphate-borate buffer (22). The suggestion has been made, therefore, that the passivating film on iron should be thinning before pitting commences. Our primary *in situ* measurements by Raman spectroscopy seem to confirm this suggestion. The Raman intensities of the bands corresponding to the passivating film formed on iron in borate buffer diminished after an exposure of the passivated metal to a chloride-containing solution, at $E < E_{\text{np}}$ (82). This infers that there is less of the original passivating oxide film on the metal surface after exposure to chloride. The conclusion is also supported by the re-

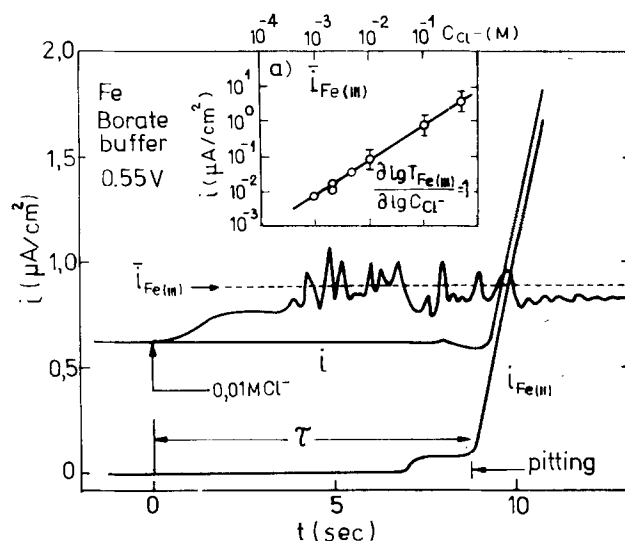


Fig. 3. Effect of time on total current i , and Fe(II) and Fe(III) dissolution of passive iron after addition of chloride into borate buffer solution. Inset—Effect of chloride concentration on mean current of Fe(III) dissolution. Ring disk electrode measurements (14). (Reprinted with permission of *Werkstoffe und Korrosion*.)

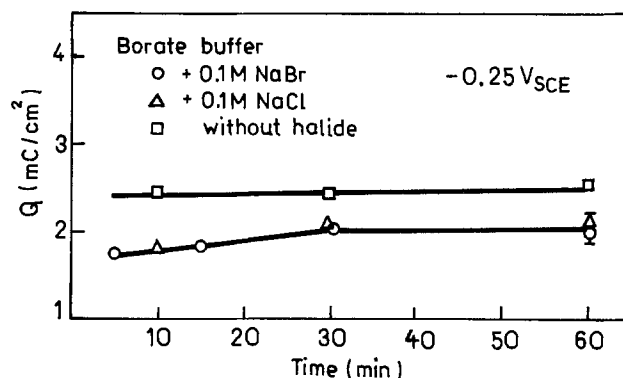
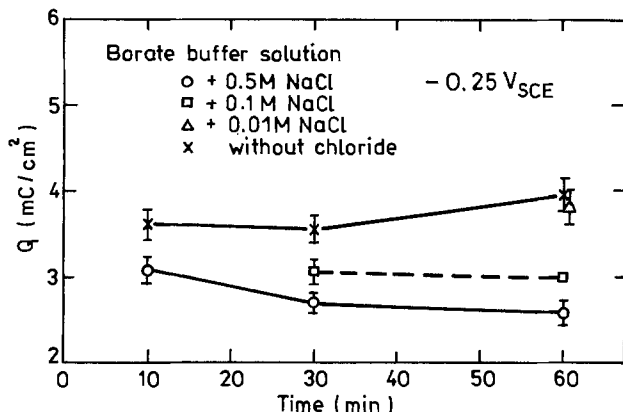


Fig. 4. (a, left) Effect of time of polarization at -250 mV in solutions containing various additions of chloride on the amount of charge, Q , for complete cathodic reduction of an iron surface prepassivated in borate buffer solution. (b, right) Effect of passivation time in borate buffer containing various halides on Q (77). (Reprinted with permission of *Werkstoffe und Korrosion*.)

sults of Valverde and Wagner (91, 92). These authors argue that halide ions enhance release of cations from the surface of transition metal oxides, since these cations form complexes with halide ions. Their experimental results show an increase in the dissolution rate of some iron oxides with an increase in chloride or bromide concentration in acid solution. However a systematic investigation of the chemical characteristics of the relevant iron oxides is lacking, as is a knowledge of the morphology of the dissolving surface.

Significance of the Induction Period, τ

Many authors believe that τ represents a characteristic feature of the pit initiation stage (2, 3, 5, 6, 14, 17, 20, 21, 23, 25, 41, 44, 51, 64, 73, 83, 84). They consider that once conditions for pitting are established, the first pit appears after an induction period, and that within this period, conditions are established which are necessary for the breakdown of passivity.

The previous discussion suggested that the incorporation of X^- into the film is unlikely, and that the aggressive action leading to pitting takes place at the film/solution interface.

For the effect of halide concentration on τ the following relation is obeyed

$$1/\tau = \text{const. } C^{n_x} \quad [2]$$

The constant n is 1 for iron in chloride solution (84), suggesting that the reaction leading to pit nucleation is 1st order with respect to chloride since $1/\tau$ is an estimate of the rate of the breakdown process. It is interesting to note that the mean rate of dissolution of the passivating film $\bar{i}(\text{Fe,III})$ increases linearly with chloride concentration, (Fig. 3), in agreement with $n = 1$. Careful kinetic measurements by Heusler and Fischer (14) and by Janik-Czachor (25) have shown that the effect of potential on τ is given by

$$\ln \tau/\tau_0 = E_0/\Delta E \quad [3]$$

τ_0 is the minimum induction period, for $\Delta E = E - E_{np} \rightarrow \infty$. τ_0 does not depend on halide concentration (Fig. 5) but does depend on its kind and is an order of magnitude higher for I^- than for the other halides (Table I). The slope $E_0 = \partial \ln \tau / \partial (1/\Delta E)$ diminishes with halide concentration (Fig. 5) and strongly depends on the anion (Table I).

Equation [3] is analogous to the relation governing the mean time of formation of two-dimensional nuclei as a function of overvoltage. A suggestion has been made that pit nucleation starts with a formation of two-dimensional nuclei of the chloride salt layer (14), which leads to thinning of the film and eventually to its complete removal locally.

The validity of the model based on Eq. [3] has been confirmed only for iron and Fe-5% Cr alloy (14, 25, 51). There are indications that it may also be applicable to nickel (85), Fe-13% Cr alloy (86), and aluminum (87), but the data cover a too narrow range of τ to enable a decisive conclusion to be reached.

Further experiments are also necessary to test the validity of Eq. [3] for other systems. The effect of the kind of aggressive ions must also be clarified.

The other factor that should be investigated is the effect of bound water in the passivating film. Some authors argue that, e.g., in stainless steels, the bound water may restrain pit formation, that is, increase τ significantly (21, 23). It is not clear how bound water influences halide island and salt formation or how important this effect is. On the other hand, there are

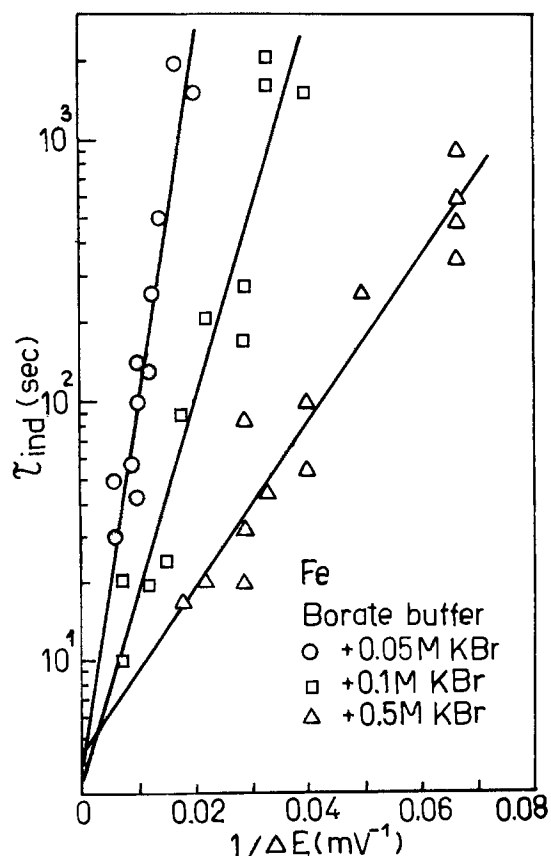


Fig. 5. Effect of potential on the induction period of pit nucleation on iron (25). (Reprinted with permission of *Werkstoffe und Korrosion*.)

Table I. The constants τ_0 and E_0 (Eq. [3]) for iron in borate buffer solution containing various halogen ions

| X ⁻ | 0.01M | | 0.05M | | 0.1M | | 0.5M | | Remarks |
|-----------------|----------------|------------|----------------|------------|----------------|------------|----------------|------------|-----------|
| | τ_0 (sec) | E_0 (mV) | τ_0 (sec) | E_0 (mV) | τ_0 (sec) | E_0 (mV) | τ_0 (sec) | E_0 (mV) | |
| Cl ⁻ | 2.0 | 250 | — | — | 2.0 | 150 | 2.0 | 120 | Ref. (14) |
| Br ⁻ | — | — | 4.0 | 139 | 3.6 | 71 | 4.4 | 32 | Ref. (25) |
| I ⁻ | 43 | 125 | — | — | 45 | 24 | 37 | 17 | Ref. (25) |

opinions that a high anodic electric field will expel water from the metal/film interface, producing an almost dehydrated film (31).

Relevance of the Prevention of Repassivation

There is a strong evidence that X⁻ not only promotes breakdown of passivity but also prevents repassivation of active sites. For example, at moderate concentrations of X⁻, when the potential of the electrode is stepped from the active dissolution range into the pitting range only incomplete passivation occurs (44). Rapid metal dissolution continues at some sites, whereas the rest of the surface passivates. However, the electrode potential governs the aggressive action of X⁻, because stepping the potential from the active into the passive range results in complete passivation (24, 38, 41, 44).

Some authors believe that the role of chloride ions in the breakdown of passivity is largely to prevent repair during a dynamic breakdown/repair process (4, 8, 12, 19, 21, 23). However, careful electrochemical measurements for iron did not give evidence that this process occurs in the stationary passive state (26-28, 88). One may argue that these breakdown/repassivation sites are so small that it is difficult to detect them with electrochemical methods. However, these events should lead to a distinct irreproducibility of the experimental data, which is not the case for iron in the absence of the aggressive ions. Modern techniques of noise analysis may provide an insight into this problem. On the other hand, in a nonstationary state, breakdown of the film occurs (88), and when a bare metal surface is thus exposed to the aggressive electrolyte, prevention of repassivation becomes a decisive factor.

With the aid of a ring disk electrode, Strehblow (88) has claimed to demonstrate that temporary breakdown of passivity occurs in the absence of X⁻, when the nonstationary state is introduced by an abrupt potential change within the passive region. The ring disk electrode sensitively and rapidly detected temporary Fe(II) production, indicative of active metal dissolution, when stepping the potential from, e.g., 1.3-0.7 V_H (Fig. 6). The bared metal surface underwent repassivation within a few seconds.⁴ However, the presence of X⁻ prevented repassivation and produced pitting instantaneously at remarkably high nucleation rates (13, 88). There were certain similarities to findings of MacDougall (4, 89, 90).

When the active centers are generated, pit development may conveniently occur. This process has its own mechanism and rate-determining steps and strongly influences the pitting process (2, 7, 8, 11, 13, 16, 93-102).

Conclusions

Upon contact of passivated iron with a halide-containing solution at a potential higher than the pit nucleation potential, processes occur which, after an induction period, result in pitting.

The possible processes that occur either consecutively or simultaneously and lead to a concentration buildup of the aggressive ions are as follows:

1. Agglomeration of halide in solution near the surface, particularly near various inhomogeneities.

2. Preferential localized adsorption of halide at these inhomogeneities.

Coverage with halide increases with electrode potential. The defects and/or chemical inhomogeneities facilitate the localized agglomeration, so that a critical accumulation can be attained locally at sufficiently high anodic potential.

The way in which the adsorbed halides change the protective ability of the passivating film is most controversial. The present discussion has shown, however, that incorporation of halide into the film is unlikely. Moreover, for the passivating film under steady-state conditions the importance of breakdown/repassivation events has not yet been demonstrated. On the other hand, there exists evidence that the following processes leading to the breakdown of passivity are likely to occur:

1. Thinning of the film and formation of the halide islands, i.e., pit prenuclei.

2. Local removal of the passivating film at sufficiently high anodic potentials and its replacement by halide salt film.

The specificity of the type of halide ion manifests itself in their relative aggressiveness. The potential of pit nucleation and the minimum induction period are higher for I⁻ than for Cl⁻ and Br⁻. Presumably the catalytic effect of film thinning is weakest for iodide.

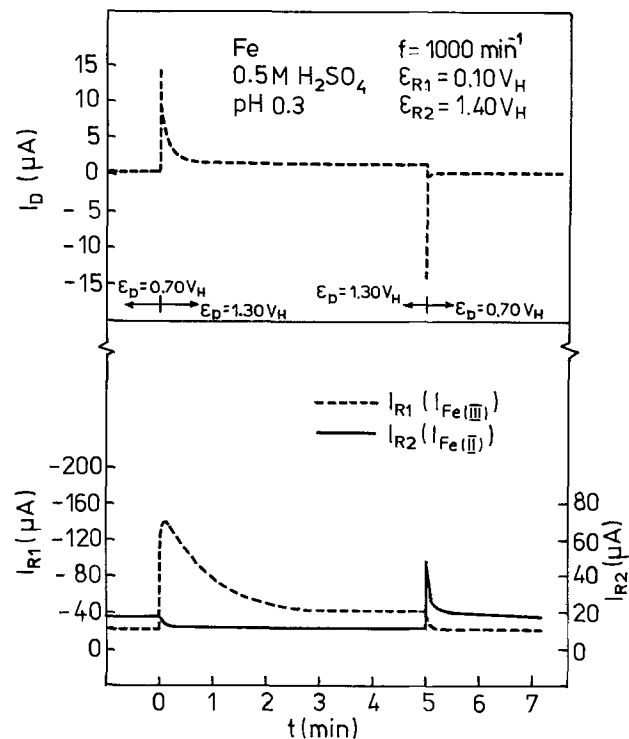


Fig. 6. Effect of time on the total current i_d and Fe(II) and Fe(III) dissolution i_{R1} and i_{R2} , respectively, after stepping potential from 1.3 V_h down to 0.7 V_h, 0.5 M H₂SO₄, ring disk electrode measurements (88). (Reprinted with permission of *Werkstoffe und Korrosion*.)

⁴ The result seems to be quite convincing. In general, however, analysis of the potential step ring disk electrode measurements should be done with caution, since the instrumental artifacts caused by the interaction of the potentiostat with the ring disk electrode system may occur (103).

More detailed information on the effect of various halides and electrode potential on film structure, film thickness, and film thickness fluctuations are necessary. The existence and properties of the breakdown/repassivation events should also be examined further.

Acknowledgment

The author expresses her gratitude to Professor Z. Smailowska for her interest in the pitting experiments. Helpful discussions with Professors J. Kruger, K. E. Heusler, G. C. Wood, and B. R. MacDougall are gratefully acknowledged. Thanks are also due to Professor M. B. Ives and Dr. W. Raczynski for their criticism of the manuscript.

Manuscript submitted June 5, 1981; revised manuscript received June 26, 1981. This was Paper 68 presented at the Minneapolis, Minnesota, Meeting of the Society, May 10-15, 1981.

Any discussion of this paper will appear in a Discussion Section to be published in the June 1982 JOURNAL. All discussions for the June 1982 Discussion Section should be submitted by Feb. 1, 1982.

REFERENCES

- Ya. M. Kolotyrkin, *Corrosion*, **19**, 261 (1963).
- J. Kruger, "Passivity and Its Breakdown on Iron and Iron-Base Alloys," p. 91, NACE (1976).
- Z. Szklarska-Smailowska, "Localized Corrosion," p. 312, NACE (1974).
- B. R. MacDougall, *This Journal*, **126**, 919 (1979).
- H. J. Engell, *Electrochim. Acta*, **22**, 987 (1977).
- M. Janik-Czachor, G. C. Wood, and G. E. Thompson, *Br. Corros. J.*, **15**, 154 (1980).
- H. Kaesche, "Korrosion der Metalle," Chap. 12, Springer Verlag, New York and Heidelberg (1979).
- J. R. Galvele, in "Passivity of Metals," R. P. Frankenthal and J. Kruger, Editors, p. 285, The Electrochemical Society, Princeton, NJ (1978).
- M. Cohen, *ibid.*, p. 521.
- L. I. Freiman and Ya. M. Kolotyrkin, "Korroziia i zashchita ot Korozii," p. 5, Moscow (1979).
- H. W. Pickering and R. P. Frankenthal, "Localized Corrosion," p. 261, NACE-3 (1974).
- G. C. Wood, W. H. Sutton, J. A. Richardson, and T. N. Riley, "Localized Corrosion," p. 526, NACE (1974).
- K. J. Vetter and H. H. Strehblow, "Localized Corrosion," p. 240, NACE (1974).
- K. E. Heusler and L. Fischer, *Werkst. Korros.*, **27**, 551 (1976).
- P. D. Tomashov and G. P. Chernova, "Korroziia i Korroziionnostoikee Splavy," Ed. Metallurgia, Moscow (1973).
- J. L. Rosenfeld, "Korroziia i Zashchita Metallov," Ed. Metallurgia, Moscow (1970).
- M. Janik-Czachor, *Zashch. Met.*, **16**, 256 (1980).
- A. D. Davydov, *Elektrokhimia*, **14**, 979 (1978).
- V. M. Novakovski and V. M. Sorokina, *Zashch. Met.*, **2**, 416 (1966).
- H. H. Strehblow, *Werkst. Korros.*, **27**, 792 (1976).
- G. Okamoto, *Corros. Sci.*, **13**, 471 (1973).
- K. Ogura and N. Takesue, *Corrosion*, **36**, 487 (1980).
- H. Saito, T. Shibata, and G. Okamoto, *Corros. Sci.*, **19**, 693 (1979).
- M. Janik-Czachor, *Br. Corros. J.*, **6**, 57 (1971).
- M. Janik-Czachor, *Werkst. Korros.*, **30**, 255 (1979).
- K. J. Vetter, *Ber. Bunsenges. Phys. Chem.*, **55**, 275 (1971).
- K. J. Vetter, "Electrochemical Kinetics," Academic Press, New York (1967).
- K. E. Heusler, *Ber. Bunsenges. Phys. Chem.*, **72**, 1197 (1968).
- M. Nagayama and M. Cohen, *This Journal*, **109**, 781 (1962).
- M. Nagayama and M. Cohen, *ibid.*, **110**, 678 (1963).
- N. Sato, in "Passivity of Metals," R. P. Frankenthal and J. Kruger, Editors, p. 29, The Electrochemical Society, Princeton, NJ (1978).
- D. J. Wheeler, B. D. Cahan, C. T. Chen, and E. Yeager, *ibid.*, p. 546.
- B. D. Cahan and C. T. Chen, Paper 71 presented at The Electrochemical Society Meeting, Minneapolis, MN, May 10-15, 1981.
- N. Sato, in "Passivity and Its Breakdown on Iron and Iron Base Alloys," p. 2, NACE (1976).
- R. P. Frankenthal, *ibid.*, p. 10.
- J. O'M. Bockris, *Electrochim. Acta*, **16**, 1859 (1971).
- C. Wagner, *Ber. Bunsenges. Phys. Chem.*, **77**, 1090 (1973).
- Z. Szklarska-Smailowska and M. Janik-Czachor, *Br. Corros. J.*, **4**, 138 (1969).
- L. I. Freiman, Lap Le Min, and Ya. M. Kolotyrkin, *Z. Phys. Chem.*, **252**, 76 (1973).
- M. Pourbaix, L. Klimzack-Mathieu, Ch. Martens, J. Meuniers, Ch. Vanlengenhaghe, L. de Munch, J. Laureys, L. Neelmans, and M. Warzee, *Corros. Sci.*, **3**, 217 (1963).
- Z. Szklarska-Smailowska and M. Janik-Czachor, *Corros. Sci.*, **11**, 901 (1971).
- N. Pessal and C. Liu, *Electrochim. Acta*, **16**, 1987 (1971).
- B. E. Wilde and E. Williams, *ibid.*, **16**, 1971 (1971).
- W. Schwenk, *Corrosion*, **20**, 129 (1964).
- P. Leckie and H. H. Uhlig, *This Journal*, **113**, 1261 (1966).
- H. H. Strehblow and B. Titze, *Corros. Sci.*, **17**, 461 (1977).
- J. L. Rozenfeld and I. S. Danilow, *ibid.*, **7**, 129 (1967).
- H. H. Strehblow, Thesis, Berlin 1971.
- M. Janik-Czachor, A. Szummer, and Z. Szklarska-Smailowska, *Corros. Sci.*, **15**, 775 (1975).
- K. E. Heusler and L. Fischer, *Werkst. Korros.*, **27**, 697 (1976).
- K. E. Heusler and L. Fischer, *ibid.*, **27**, 788 (1976).
- J. A. Petit, B. Kondo, and F. Dabosi, *Corrosion*, **36**, 145 (1980).
- R. P. Frankenthal and H. W. Pickering, *This Journal*, **119**, 1304 (1972).
- T. Schibata and T. Takeyama, *Corrosion*, **33**, 243 (1977).
- N. Sato, *This Journal*, **123**, 1197 (1976).
- M. Smailowski, Z. Szklarska-Smailowska, M. Rychcik, and A. Szummer, *Corros. Sci.*, **9**, 123 (1969).
- M. Janik-Czachor, *Bull. Acad. Sci. Polon., Ser. Sci. Chim.*, **25**, 561 (1977).
- M. Janik-Czachor, A. Szummer, and Z. Szklarska-Smailowska, *Br. Corros. J.*, **7**, 90 (1972).
- H. Chojnowska-Loboda, Thesis, Warsaw 1978.
- W. Schatt and H. Worch, *Corros. Sci.*, **9**, 869 (1969).
- J. Degerbeck, *Werkst. Korros.*, **29**, 179 (1978).
- L. J. Freiman, Ya. M. Kolotyrkin, G. S. Raskin, I. I. Reformatskaja, O. I. Lukina, E. A. Ukjanin, and A. E. Volkov, in Proc. of the 1st Soviet-Japanese Seminar on Corrosion, Moscow, 1977, p. 220.
- P. Forchhammer, and H. J. Engell, *Werkst. Korros.*, **20**, 1 (1969).
- Z. Szklarska-Smailowska and M. Janik-Czachor, *Corros. Sci.*, **7**, 65 (1967).
- M. Kesten, *Corrosion*, **32**, 94 (1976).
- P. E. Manning, D. J. Duquette, and W. F. Savage, *Corrosion*, **36**, 313 (1980).
- Z. Szklarska-Smailowska, A. Szummer, and M. Janik-Czachor, *Br. Corros. J.*, **5**, 159 (1970).
- M. Janik-Czachor, E. Lunarska, and Z. Szklarska-Smailowska, *Corrosion*, **31**, 394 (1975).
- A. Desestret, P. Poyet, H. Coriou, and L. Grall, *Mem. Sci. Rev. Metall.*, **2**, 133 (1975).
- Z. Szklarska-Smailowska, *Corrosion*, **28**, 288 (1972).
- Ya. M. Kolotyrkin and L. J. Freiman, *Dokl. Akad. Nauk SSSR*, **220**, 156 (1975).
- A. Szummer and M. Janik-Czachor, *Br. Corros. J.*, **9**, 216 (1974).
- M. Janik-Czachor and M. B. Ives, in "Passivity of Metals," R. P. Frankenthal and J. Kruger, Editors, p. 369, The Electrochemical Society, Inc., Princeton, NJ (1978).
- C. L. McBee and J. Kruger, "Localized Corrosion," p. 252, NACE (1974).
- T. P. Hoar, D. C. Mears, and G. P. Rothwell, *Corros. Sci.*, **5**, 279 (1965).
- T. P. Hoar, *ibid.*, **7**, 341 (1967) and **17**, 219 (1977).
- M. Janik-Czachor and S. Koszczyszyn, In preparation.
- M. Janik-Czachor, Proc. of the 3rd International

- Corrosion Conference, Warsaw, 21-25 April, 1980, p. 245.
79. K. J. Vetter, "Localized Corrosion," NACE-3, p. 9, p. 259 (1974).
 80. W. Kozłowski and Z. Szklarska-Smialowska, In preparation.
 81. Z. Szklarska-Smialowska, M. Janik-Czachor, and H. Viefhaus, *Corros. Sci.*, **16**, 644 (1976).
 82. M. Janik-Czachor and R. P. Van Duyne, Unpublished results.
 83. T. P. Hoar and W. R. Jacob, *Nature*, (London), **216**, 1299 (1967).
 84. H. J. Engell and N. D. Stolica, *Z. Phys. Chem. NF*, **20**, 113 (1959).
 85. K. E. Heusler, in "Passivity of Metals," R. P. Frankenthal and J. Kruger, Editors, p. 77, The Electrochemical Society, Inc., Princeton, NJ (1978).
 86. A. Broli, H. Holtan, and H. Siguerdsson, *Werkst. Korros.*, **26**, 629 (1975).
 87. A. Broli, H. Holtan, and M. Midjo, *Br. Corros. J.*, **8**, 173 (1973).
 88. B. P. Löchel and H. H. Strehblow, *Werkst. Korros.*, **31**, 353 (1980).
 89. B. MacDougall, *This Journal*, **125**, 1883 (1978).
 90. B. MacDougall, *ibid.*, **127**, 789 (1980).
 91. N. Valverde and C. Wagner, *Ber. Bunsenges. Phys. Chem.*, **80**, 330 (1976).
 92. N. Valverde, *ibid.*, **80**, 333 (1976).
 93. L. J. Freiman, Lan Le Min, and G. S. Raskin, *Zashch. Met.*, **9**, 680 (1973).
 94. G. T. Burstein and D. H. Davies, *Corros. Sci.*, **20**, 1143 (1980).
 95. J. Mankowski and Z. Szklarska-Smialowska, *ibid.*, **17**, 725 (1977).
 96. J. Mankowski and Z. Szklarska-Smialowska, *ibid.*, **15**, 493 (1975).
 97. H. W. Pickering and R. P. Frankenthal, *This Journal*, **119**, 1297 (1972).
 98. B. G. Ateya and H. W. Pickering, in "Passivity of Metals," R. P. Frankenthal and J. Kruger, Editors, p. 350, The Electrochemical Society, Inc., Princeton, NJ (1978).
 99. J. Galvele, *This Journal*, **123**, 464 (1976).
 100. M. Janik-Czachor and Z. Szklarska-Smialowska, *Corros. Sci.*, **8**, 215 (1968).
 101. Y. Hisamatsu, T. Yoshi, and Y. Matsumura, "Localized Corrosion," p. 427, NACE (1974).
 102. H. H. Strehblow and J. Weners, *Z. Phys. Chem. NF*, **98**, 199 (1975).
 103. B. D. Cahan, Private communication.